National Research Council Canada
Ottawa, Canada K1A 0R6

Conseil national de recherches Canada
Ottawa, Canada K1A 0R6

Postage paid at Ottawa
Publications mail
Registration No. 1240447

Port payé à Ottawa
Poste-publication
Enregistrement n° 1240447

Canadian Journal of Chemistry

Volume 80, Number 1, January 2002

Revue canadienne de chimie

Volume 80, numéro 1, janvier 2002

2000 John C. Polanyi Award Lecture
Mother Nature and the molecular Big Bang

R.J. Dwayne Miller

1–24

Electron-spin conservation and methyl-substitution effects on bonds in closed- and open-shell systems — A G3 ab initio study of small boron-containing molecules and radicals

Clement Poon and Paul M. Mayer

25–30

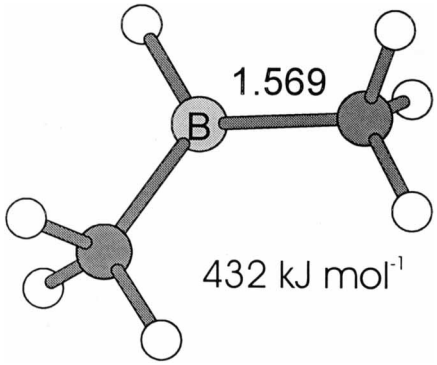

Continued on inside back cover / Suite au verso

Front Cover: (*Concluded*)
Image (A) identifies the heavy atom positions (from the Protein Data Bank, identification code 1BZR) that can be seen at one angle. A second image (B) is visible at different viewing angles that shows the secondary structures outlined as sleeves to depict atom–atom correlations through the protein secondary structure. The computer-generated hologram is constructed from the two single frame images. The physical motion convolved to the iron–oxygen bond-breaking event (as seen in the hologram) is created by several small angle increments in the EF helix according to the structure differences between oxy- and deoxy-tertiary structures and can be observed simply by moving the viewing angle (rotate head or cover). The motion on the cover has been amplified by an order of magnitude to provide clear visibility. See Miller, in this issue, pp. 1–24 on the biomechanics of protein motions and energy transduction of molecular bonds.

To view the hologram properly a directed light is best (e.g., gallery lights, track lighting) or sunlight. Any reasonably collimated light source will provide good visibility as long as it is bright enough.

Page couverture : (*Suite et fin*)
On aperçoit sur l'illustration (A) la position de l'atome lourd (d'après la Protein Data Bank, code d'identification 1BZR), visible sous un angle précis. La deuxième illustration (B), sous un autre angle, révèle les structures secondaires, représentées sous une forme tubulaire et illustrant les corrélations interatomiques dans la structure secondaire de la protéine. L'hologramme généré par ordinateur est élaboré à l'aide de ces deux vues. Le mouvement physique convolutionné de la rupture du lien fer–oxygène (représenté sur l'hologramme) découle de nombreuses petites augmentations d'angle dans l'hélice EF que l'on peut associer aux différences de structure entre les structures tertiaires des formes oxy et déoxy. Il peut être observé par la simple modification de l'ange de vue (rotation du tube ou couvercle). Le mouvement sur le couvercle a été amplifié par facteur décimal afin d'assurer la précision. *Cf.* Miller, dans ce numéro, pp. 1–24, sur la biomécanique du mouvement des protéines et la transduction de l'énergie des liaisons moléculaires.

L'hologramme sera rendu de façon optimale sous faisceau (c.-à-d. projecteurs) ou sous la lumière du soleil. Cela dit, toute source de lumière suffisamment collimatée permettra la visualisation pour autant qu'elle soit assez puissante.

Canada

Printed in Canada by / Imprimé au Canada par
University of Toronto Press Inc.
Typesetting by / Typographie par
NRC Research Press / Presses scientifiques du CNRC

0008-4042 200201 80 1 1-1

Synthesis and reactivity of novel Schiff bases containing boronate esters

David W. Norman, Janet P. Edwards, Christopher M. Vogels, Andreas Decken, and Stephen A. Westcott

31–40

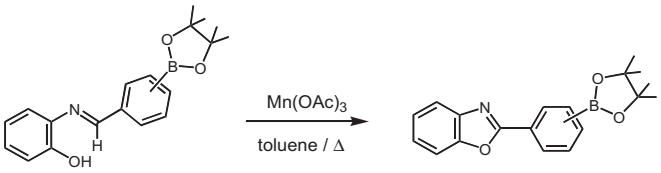

Cationic thiolate and selenolate complexes of platinum(IV)

Michael C. Janzen, Michael C. Jennings, and Richard J. Puddephatt

41–45

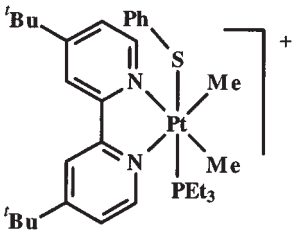

Mechanistic studies of photohydration of *m*-hydroxy-1,1-diaryl alkenes

John G. Cole and Peter Wan

46–54

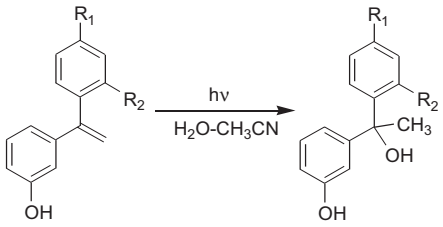

Iron complexes of the dibenzophospholyl ligand: a synthetic and crystallographic study

Andreas Decken, Melanie A. Neil, C. Adam Dyker, and Frank Bottomley

55–61

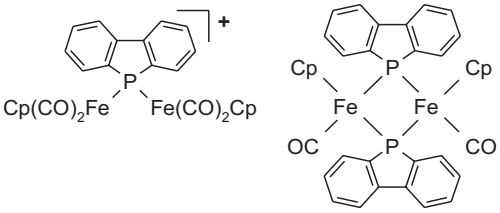

Environmental photodegradation of pyrimidine fungicides — Kinetics of the visible-light-promoted interactions between riboflavin and 2-amino-4-hydroxy-6-methylpyrimidine

E. Haggi, S. Bertolotti, S. Miskoski, F. Amat-Guerri, and N.A. García

62–67

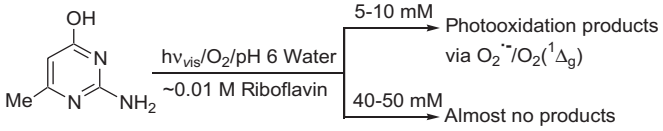

Continued on facing page / Suite à la page précédente

Monte-Carlo calculation of the primary yields of H_2O_2 in the $^1H^+$, $^2H^+$, $^4He^{2+}$, $^7Li^{3+}$, and $^{12}C^{6+}$ radiolysis of liquid water at 25 and 300°C

Jintana Meesungnoen, Jean-Paul Jay-Gerin, Abdelali Filali-Mouhim, and Samlee Mankhetkorn

68–75

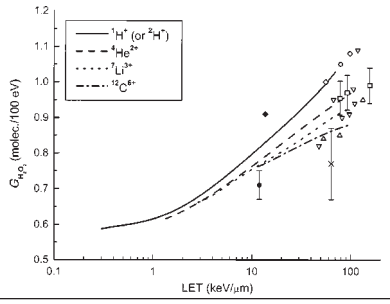

Synthesis of a hexasaccharide fragment of the capsular polysaccharide of *Streptococcus pneumoniae* type 3

Dirk J. Lefeber, Eneko Aldaba Arévalo, Johannis P. Kamerling, and Johannes F.G. Vliegenthart

76–81

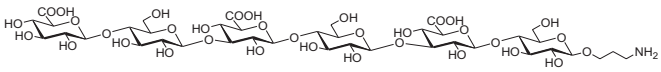

Kinetics and mechanism of hydrolysis of 3-diazobenzofuran-2-one and its hydrolysis product (3-hydroxybenzofuran-2-one)

Y. Chiang, A.J. Kresge, and Q. Meng

82–88

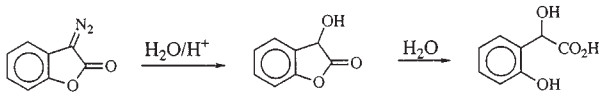

The endothermic nature of the binding of anionic bile salts to a cationic adsorbent

Celia K. Williams, William C. Galley, and G. Ronald Brown

89–93

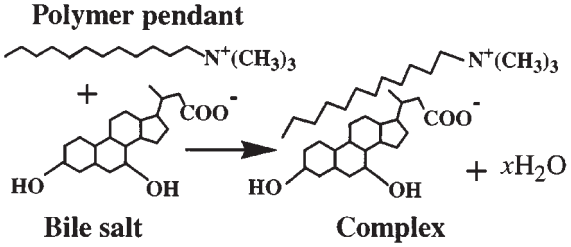

On the generation of oxirene and dimethyloxirene by retro-Diels–Alder reactions, and reactions of dimethyloxirene: a computational study

C. Delamere, C. Jakins, and E. Lewars

94–105

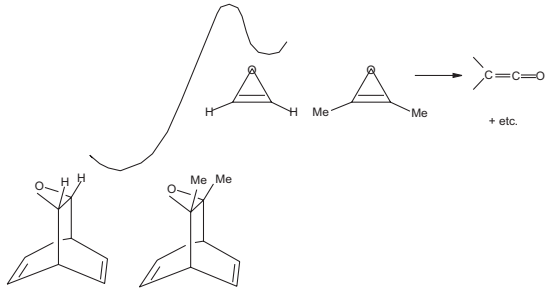

Concluded on previous page / Suite et fin à la page précédente

Inhibition de la corrosion de l'alliage d'aluminium 6063 au moyen de composés inorganiques dans une solution de chlorure de sodium à 3 %

L. Bazzi, R. Salghi, E. Zine, S. El Issami, S. Kertit et B. Hammouti

106–112

1-Propanol hydrate by IR spectroscopy

Jean-Joseph Max, S. Daneault, and Camille Chapados

113–123

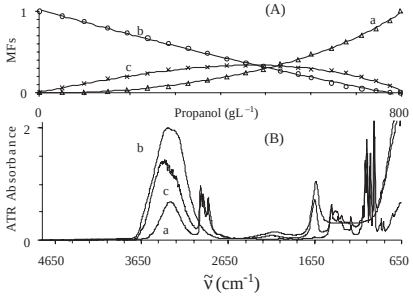

Author Index	**AI-1**	**Index des auteurs**	**AI-1**
Instructions to Authors	**I-1**	**Recommandations aux auteurs**	**R-1**
Notes for Authors of papers presenting the results of X-ray crystal-structure anaylses	**I-5**	**Recommandations aux auteurs d'articles décrivant la determination de structures cristallines par diffraction des rayons X**	**R-6**

The Canadian Journal of Chemistry is affiliated with the Canadian Society for Chemistry and publishes papers in all areas of chemistry.

La Revue canadienne de chimie est affiliée à la Société canadienne de chimie et publie des articles dans tous les domaines de la chemie.

2000 John C. Polanyi Award Lecture
Mother Nature and the molecular Big Bang

R.J. Dwayne Miller

Abstract: Biological molecules are mesoscopic systems that bridge the quantum and classical worlds. At the single molecule level, there are often more than 1×10^4 degrees of freedom that are involved in protein-mediated processes. These molecules are sufficiently large that the bath coordinate convolved to the reaction at an active site is defined by the surrounding protein tertiary structure. In this context, the very interatomic forces that determine the active protein structures create a strongly associated system. Thus, the bath fluctuations leading to reactive crossings involve highly hindered motions within a myriad of local minima that would act to cast the reaction dynamics into the high viscosity limit appropriate to glasses. However, the time scales observed for biological events are orders of magnitude too fast to meet this anticipated categorization. In this context, the apparent deterministic nature of biological processes represents an enormous challenge to our understanding of chemical processes. Somehow Nature has discovered a molecular scaffolding that enables minute amounts of energy to be efficiently channeled to perform biological functions without becoming entrapped in local minima. Clearly, energy derived from chemical processes is highly directed in biological systems. To understand this problem, we must first understand how energy is redistributed among the different degrees of freedom and fully characterize the protein relaxation processes along representative reaction coordinates in relation to these dissipative processes. This paper discusses the development of new nonlinear spectroscopic methods that have enabled interferometric sensitivity to protein motions on femtosecond time scales appropriate to the very fastest motions (i.e., bond breaking or the molecular "Big Bang") out to the slowest relaxation steps. This work has led to the *Collective Mode Coupling Model* as an explanation of the required reduced dimensionality in biological systems. Within this model, the largest coupling coefficients of the reaction coordinate are to the damped inertial collective modes of the protein defined by the strongly correlated secondary structures. These modes act to guide the reaction along the correct seam(s) in an otherwise highly complex potential energy surface. The mechanism by which biological molecules have been able to harness chemical energy over meso-length scales represents the first step towards higher levels of organization. The new insight afforded by the collective mode mechanism may prove important in understanding this larger issue of scaling in biological systems.

Key words: biodynamics, energy transduction, ultrafast spectroscopy, nonlinear spectroscopy, primary processes in biology.

Résumé : Les molécules biologiques sont des systèmes mésoscopiques qui font le pont entre les mondes quantiques et classiques. Au niveau des molécules individuelles, les processus catalysés par les protéines impliquent souvent plus de 1×10^4 degrés de liberté. La taille de ces molécules est suffisamment importante pour que les coordonnées de bain associées à la réaction au niveau d'un site actif soit définies par la structure tertiaire de la protéine avoisinante. Dans ce contexte, les forces interatomiques qui déterminent les structures des protéines active créent un système fortement associé. Il en résulte que les fluctuations du bain qui conduisent à des échanges réactifs impliquent des mouvements fortement empêchés à l'intérieur d'une myriade de minima locaux qui permettrait de fixer la dynamique réactionnelle dans les limites des viscosités élevées apparentées aux états vitreux. Toutefois, les échelles de temps observées pour les ordres d'amplitude des événements biologiques sont beaucoup trop rapides pour être caractérisés de la sorte. Dans ce contexte, la nature apparemment déterministe des processus biologiques représente un défi énorme pour notre compréhension des processus chimiques. La Nature a donc découvert un échafaudage moléculaire qui permet à de faibles quantités d'énergie d'être canalisées de façon efficace afin de pouvoir réaliser des fonctions biologiques sans être piégées dans des minima locaux. Il est clair que, dans les systèmes biologiques, l'énergie provenant des processus chimiques est fortement orientée. Dans le but de comprendre ce problème, on doit avant tout comprendre comment l'énergie est redistribuée entre les divers degrés de liberté et de bien caractériser les processus de relaxation des protéines le long de coordonnées réactionnelles représentatives en relation avec ces processus de dissipation d'énergie. Dans ce travail, on discute du développement de nouvelles méthodes spectroscopiques non linéaires qui ont permis d'associer une sensibilité interférométrique aux mouvements des protéines à des échelles de temps de l'ordre de la femtoseconde appropriées aux mouvements les plus rapides (par exemple, le bris d'une liaison ou du « Big Bang » moléculaire) en présence des mouvements de relaxation les plus lents. Ce travail a conduit au *Modèle de couplage en mode collectif* pour expliquer la dimensionalité réduite requise dans les systèmes biologiques. Dans ce modèle, les coefficients de couplage

Received 10 May 2001. Published on the NRC Research Press Web site at http://canjchem.nrc.ca on 31 January 2002.

R.J.D. Miller. Departments of Chemistry and Physics, 60 St. George Street, University of Toronto, Toronto, ON, M5S 1A7, Canada. (Telephone: (416) 978-1528; fax: (416) 978-2537; e-mail: dmiller@lphys.chem.utoronto.ca).

 DOI: 10.1139/V01-199 © 2002 NRC Canada

les plus grands d'une coordonnée réactionnelle sont introduits pour amoindrir les modes collectifs de la protéine définis par les structures secondaires à forte corrélation. Ces modes agissent pour guider la réaction le long des points de jonction appropriés d'une surface d'énergie potentielle qui est par ailleurs très complexe. Le mécanisme par lequel les molécules biologiques ont pu exploiter l'énergie chimique sur des échelles de longueur méso correspond à la première étape vers des niveaux d'organisation plus élevés. Le mécanisme de mode collectif fournit une approche intuitive qui pourrait s'avérer importante pour la compréhension du sujet plus large qu'est la mise à l'échelle dans les systèmes biologiques.

Mots clés : biodynamique, énergie, transduction, spectroscopie ultrarapide, spectroscopie non linéaire, processus primaires en biologie.

[Traduit par la Rédaction]

Introduction

This paper represents a written account of the John C. Polanyi Award Lecture for research in physical chemistry. As such, it will take on a different flavour from a scientific report or review and will attempt to identify an important new direction of chemical research. In particular, the discussion will focus on transition-state processes to keep within the spirit of Polanyi's own pioneering contributions to our current understanding of transition-state processes — albeit with a new direction identified with respect to understanding biological processes from a chemical dynamics perspective.

To make the discussion as general as possible, to the point of being obvious, let me begin by offering a mission statement. Science is arguably the most important human enterprise with respect to its impact on the human condition. It is a social activity within the confines of objective analysis that leads to model building and empowerment through predictable outcomes. There are no boundaries to scientific investigations. The scientific mission can be understated in a simple fashion as: "The quest to understand the Universe". Thus, Science is an intellectual challenge without endpoint and will hopefully engage humanity for the ages to come.

In this quest, there are many length scales and time scales associated with different phenomena that come under examination. On cosmological length scales, one is concerned with an expanding Universe and the defining moment of the Big Bang — the ultimate $t = 0$ boundary condition. With the recent refinement of the Hubble constant, the Universe is now known to be over 8 billion years old and we are able to describe certain events as early as 1×10^{-20} s after the Big Bang (1, 2). This picture and violence to which all of creation has been born stirs everyone's imagination. I would like to draw attention to a much smaller scale of the Universe; one that nevertheless can be envisaged to hold similar defining moments. Figure 1 shows a constellation of star-like objects. It is a representation of the oxygen binding site in heme proteins and is one of my favourite parts of the Universe. I will loosely refer to this as the Proximal Histidine Constellation of atoms. The stars as drawn are the heavy atom positions as determined from X-ray diffraction studies of single crystals. These positions are inspired points as if we were equipped with special glasses that enable us to defy quantum mechanics and observe the core electrons around each carbon emitting X-rays to reveal their positions. At the centre is a giant red star, the iron atom, to which oxygen binds and is transported throughout our bodies. This figure schematically catches a rare event at the defining moment that a new molecule is born — "The Molecular Big Bang". The iron—oxygen bond has just broken as depicted in analogy to a supernova event and the oxygen molecule moves away from the iron atom along a repulsive surface of the product channel appropriate for generating deoxyheme and oxygen. The forces and energy released are depicted as the bright supernova. Chemically, this energy is stored in terms of changes in the charge distribution at the binding site. As opposed to the great distances between stars where the ramifications of a singularity do not affect other points of light, in this part of the Universe there are weak interactions that couple all adjacent points to varying degrees. The Proximal Histidine Constellation will change its location in this part of the sky. The atoms will move to new positions that are lower in energy with the difference in energy being transmitted to the bath (free space in this analogy).

The marvel of this process is that it occurs in a highly directed fashion. To appreciate how magnificent this molecular machinery is requires some calibration to the enormous complexity of proteins — Nature's building blocks. Only a small section of the total protein is shown in Fig. 1 to focus attention on the oxygen binding site. The reaction saddle point requires that the protein move to a region in nuclear configuration space that accommodates the domed porphyrin ring of the deoxyheme (product state). The total available phase space for distinct nuclear configurations is as astronomical as anything contemplated for the heavens. Consider myoglobin as an example of one of the simplest heme proteins. It is a single protein molecule that is responsible for oxygen storage in muscles. This molecule has a primary sequence of 100 amino acids to yield a distinct structure comprised of over 1200 atoms or 3600 degrees of freedom (3). If one considers only the angular coordinate of the amide linkage responsible for the secondary structure, the H-bond potential is relatively shallow and there are three orientations that are approximately degenerate (within kT at room temperature) with respect to nearest-neighbour orientations (4, 5). The number of possible structural permutations for this molecule are 1×3^{100} or 5×10^{47} different configurations, considering only one angular coordinate. This one coordinate gives some feeling of the enormous complexity imbedded in the very structure of biological systems.

Despite this complexity, topological patterns appear in the potential energy landscape of proteins. Again using heme proteins as a representative example, the structure of the oxygen binding site in heme proteins is highly conserved (3). The proximal histidine and associated EF helical sections of heme proteins has evolved into a topological domain that controls oxygen binding. How are proteins able to find these distinct topologically active domains within all the possible

© 2002 NRC Canada

Fig. 1. The constellation proximal histidine and the molecular Big Bang. Schematic representation of the defining moment of the passage through a reaction saddle point that leads to the breaking of the covalent bond between iron (in red) and oxygen at the oxygen binding site in heme proteins.

structures available to the system? There is a related question with respect to the chemistry that proteins illicit and regulate. Once an active structure is found, how is the system able to sample the reaction pathway on realistic time scales? Both of these questions are related to the observed time scales or dynamics for protein motions along a small subset of the total coordinate space. The first question pertains to the protein folding problem that was first posed by Levinthal (4). This question has taken on great significance with respect to advancing the frontier of biotechnology. Many proteins can now be synthesized but most are found to be inactive when produced in vitro. The laboratory conditions do not include chaperon proteins that play a critical role in "seeding" the folding process. Nevertheless, there are ample examples of proteins that denature under different conditions and refold to their active state in a seemingly pathway independent manner (5, 6). If such processes were to occur through a random sampling process of all available phase space, it would take geological time scales for proteins to execute even simple functions. It would seem that these systems are poised to find the correct global minima in their structures through a greatly constrained search of configuration space. There must be large numbers of degrees of freedom that are strongly correlated to reduce the sampling process to the relevant time frame.

The question reduces to the factors leading to the correlation of events in either protein-folding or -mediating reactions. This problem has often been stated in terms of Levinthal's paradox: How is it possible for a system with so many degrees of freedom to be able to find the correct path (structure) on the relevant time scales to life? (4–6). This paradox needs to be further defined as one could make similar paradoxical observations with respect to any macroscopic object. For example, one could make the same query with

© 2002 NRC Canada

respect to the time scale for the formation of ice. The difference is that crystals of ice have a periodic structure with a well-defined symmetry. The unit cell is based on only five water molecules arranged in a tetrahedral structure about a central water molecule. This structure is considerably lower in energy than other configurations and subsequent water molecules are strongly driven to form a periodic crystal with this unit cell. Once the crystal structure is formed the crystallization process is seeded and subsequent stages of crystallization ensue rapidly. In each phase of growth, there are only a few degrees of freedom sampling a very coarse grain potential energy surface in comparison to proteins. This distinction brings forward a very important concept. One can rationalize the time scale for protein motions within the same context as ice formation if there is a very deep global minimum. However, in this case, other possible configurations would have very large barriers separating them from the lowest energy structure and the object could be *classified as rigid. It would be inanimate, incapable of supporting life functions.* In order for biological molecules to respond to subtle changes in environment and regulate activity accordingly (i.e., function), there must be nearly degenerate minima imbedded in the structural diversification and there cannot be large barriers separating these structures. Otherwise, the system would either not be able to access an important structure or would become statistically trapped in the deepest minima.

In some sense, the chemically active agents (functionally active proteins, enzymes) in biological systems have to be "alive" at the single molecule level. It is in this context that one should view with marvel how these biological molecules operate and direct relatively minute amounts of chemical energy along the correct pathways to sustain even higher levels of organization among the constituent elements.

The fact that a directionality can be imprinted on such systems is intriguing not only from entropic considerations but also from enthalpic considerations of the driving forces with respect to the operating dynamics. Any molecular system that has numerous degenerate minima with shallow barriers separating the minima operates further from linear response than more rigid systems. The displacements involve larger amplitude motions along pathways interconnecting minima and thus sample more significantly anharmonic components in the many body potential than systems with deep minima (more rigid systems). In this case, one might expect the system should undergo rapid energy redistribution among the relevant degrees of freedom. Once again, one is found asking how such systems can possibly direct a process within the above boundary conditions imposed on living systems. The energetics or enthalpic factors should be randomized too rapidly to impose a directionality to the process.

To restate Levinthal's paradox: Within the constraints of degenerate, readily accessed minima, how is it possible for biological molecules to find their correct structures to perform their functions on the relevant time scales? To further drive home the dilemma, Fig. 2*a* shows a single frame of the protein structure used to computer generate the white light hologram of the structure of sperm whale myoglobin shown on the cover. The positions of all the heavy atoms are retrieved from the highest resolution X-ray structure determination to date (7). In viewing the hologram (stereogram) the atoms should appear floating in space with no apparent rhyme or reason for their particular positions; yet there must be some inherent feature in the structure that yields this particular pattern. This image dramatically drives home the notion of Levinthal's paradox. How does the system find the active subset of structures out of the multitude available to it? Further, once the active structure is adopted for myoglobin, how is it able to sample the correct pathway for oxygen binding and release? (One would expect some degree of correlated motion through the secondary structure. A single frame depicting the helical sections is shown in Fig. 2*b*).

The work to be discussed below will focus on the latter issue, i.e., the mapping problem associated with how biological molecules relax along reaction coordinates to perform functions, somehow steering clear of entrapment in the myriad of local minima. First, it should be noted that in a large number of important biological processes, there is often just a single bond made or broken at an active site. The energy of the reaction is transduced into some higher order function. The transduction process invariably involves structural relaxation along a reaction coordinate towards the product state. Work is done both in relaying the chemical energy into another channel and in relaxation to stabilize the product. The atomic motions in response to the bond breaking and (or) making may be subtle but it must be recalled that these motions are occurring on a backdrop of an enormously complex potential energy landscape. To perform a function (do useful work) the motions must be highly directed; otherwise the system would become trapped in the myriad of local minima. The length scale and time scale of these motions is largely the issue. Crudely speaking, there must be a "director" that imposes a high degree of correlation in the sampling process over the length and time variables. To understand how biological molecules work, we are searching for this director, the ordering element.[1]

Throughout this discussion, heme proteins will be used as model systems to examine this problem. The primary motivations for this selection are that their functionally relevant motions can be optically triggered and a great deal of spectroscopic and structural information is available for this class of proteins. In addition, the structural changes associated with oxygen binding in hemoglobin serve as the cornerstone for our current understanding of molecular cooperativity and allosteric regulation (3, 8).

For background information, the oxygen-binding curve for hemoglobin is shown in Fig. 3 (8, 9). The dependence of oxygen binding on the partial pressure of oxygen shows a rather dramatic change about a critical value. This behaviour is in stark contrast to the purely bimolecular kinetics exhib-

[1] The use of the term director has an analogy to the conductor of an orchestra. The conductor dictates the tempo (time correlation on the different instruments) to the ensemble and enables music to prevail over noise. At the risk of being anthropomorphic, the topological element or director to biological functions must dictate temporal and length scale correlations to enable biological molecules to make "music/life" from the surrounding chaos.

© 2002 NRC Canada

Fig. 2. Single-frame images used to construct the computer-generated hologram on the cover. (*a*) Position of heavy atoms only (from the Protein Data Bank, identification code 1BZR). (*b*) Secondary structures outlined as sleeves to depict atom–atom correlations through secondary structure. The physical motion convolved to the bond-breaking event on the cover is created by several small angle increments in the EF helix according to the structure differences between oxy- and deoxy-tertiary structures (7). The motion on the cover was amplified by an order of magnitude so as to be clearly visible.

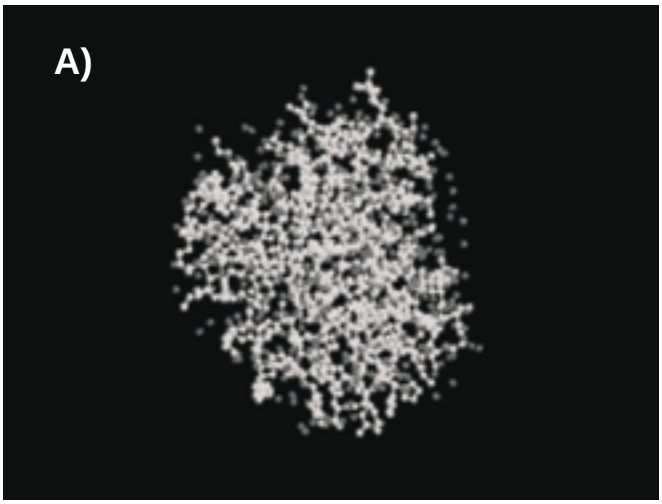

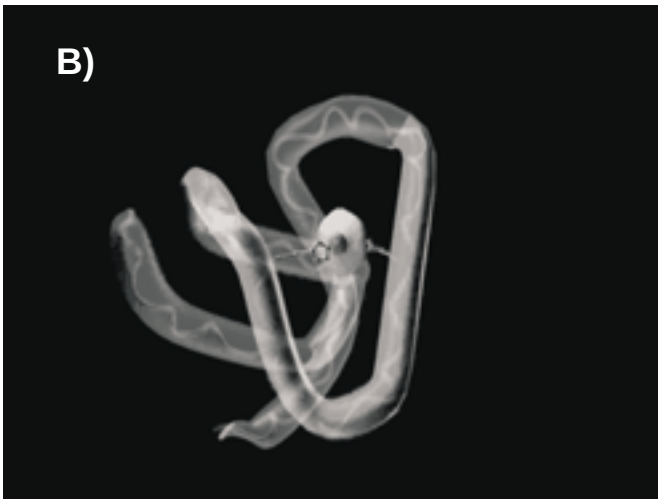

ited by myoglobin that is shown for comparison. Myoglobin is a single heme protein; whereas hemoglobin is comprised of four nearly identical heme proteins (two α- and two β-heme protein subunits) that are very similar to myoglobin. The unusual behaviour of hemoglobin with respect to myoglobin was ascribed to a type of molecular communication between the four subunits with respect to the state of oxygenation that could not be present for the single protein case. Within the Monod model, the oxygen binding curve can be fit assuming there are only two different states for oxygen binding; a high affinity form referred to as the R state and a low affinity form coined the T state (8, 10). This simple two-state description of the oxygen-binding process gained firm footing from the pioneering crystallographic work of Perutz that determined that there were in fact two distinctly different structures for hemoglobin (8). The difference between the fully oxygenated (R) and fully deoxygenated (T) crystal structures depicted a ball-and-socket type motion about the α–β contact region. The motion involves a net 15° rotation and approximately 6 Å translation of the more than 10 000 different degrees of freedom of the protein. Hemoglobin appears to be a "nanomotor", activating a pneumatic switch, that toggles the system between a high- and a low-affinity form through motions dictated along the quaternary coordinate of the protein assembly. Note that the energy powering this nanomotor is simply the four chemical bonds involved in oxygen binding at the heme sites in each protein.

This R to T structural transition is in dynamical equilibrium with its surroundings and becomes most heavily weighted to undergo a transition once the partial pressure of oxygen produces an average loss of more than two oxygens per hemoglobin. The binding affinity for oxygen differs by a factor of 60 for the two structures (11). The system behaves as a nonlinear amplifier with nearly 20 dB gain with respect to changes in the partial changes in oxygen about a critical value. The evolutionary significance of this seemingly simple process should not be under appreciated. The structural transition of hemoglobin acts to hold on to oxygen as long as possible before it delivers the oxygen to deoxygenated areas. In effect, the structural transition increases the diffusion length of oxygen into the tissues while providing a feedback mechanism to provide oxygen to regions undergoing differential metabolic rates. This process was critical to the development of larger more complex organisms. In some sense if it were not for this process, we would have to be more than an order of magnitude smaller (difference in effective diffusion lengths for oxygen transport mediated through myoglobin relative to hemoglobin). To drive this point home further, even clams have evolved a dimeric hemoglobin molecule that exhibits molecular cooperativity of this kind (12). This process is one of the simplest examples of molecular cooperativity; yet was essential to the scaling of multicellular organisms to higher levels of complexity.

The "R-to-T switch" represents an example of coupled reaction coordinates. By some mechanism, the state of ligation at one heme is communicated to neighbouring heme proteins and affects the kinetics of oxygen binding at these remote sites. This process is interesting to contemplate as the distance between heme sites is approximately 30 Å. If this process were to occur in a homogeneous aqueous environment, it would be impossible for a reaction at one site to affect another at these distances. The effective concentration of the hemes is approximately 10 mM. The reaction volume extends only out to the second solvation layer and, at this density, the water rearrangements would completely screen any changes in charge or other forces from affecting an adjacent site. Neither enthalpic nor entropic factors could be modulated at the adjacent site in a purely aqueous environment. The mechanism of communication must involve the surrounding globin to provide a *through space coupling* between reaction sites. The globin has a number of evolutionary features. The primary function is to simply provide a wrapper about each heme porphyrin motif to prevent dimerization. The structure of this globin wrapper has evolved further to pro-

© 2002 NRC Canada

Fig. 3. Oxygen-binding curves comparing myoglobin to hemoglobin (8). The dramatically different dependence on partial pressure of oxygen between myoglobin and hemoglobin is the signature of molecular communication possible in a quaternary protein complex (hemoglobin) that is not possible for a monomeric protein (myoglobin).

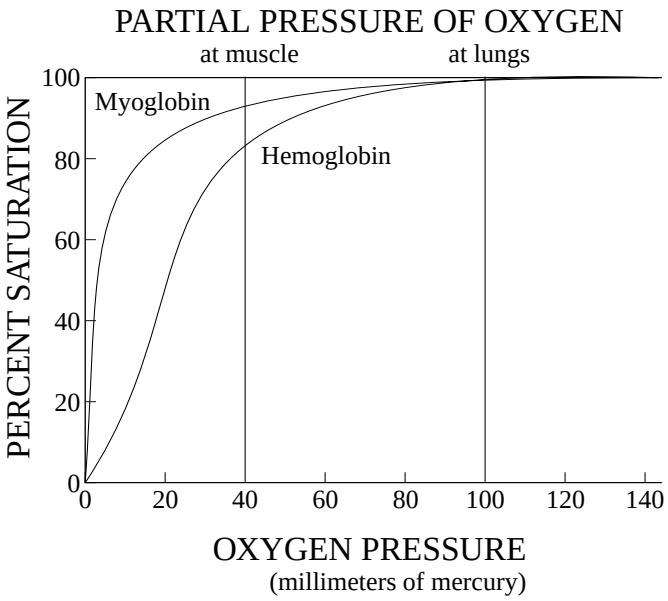

vide pH-sensitive activation barriers to O_2 binding and other environmental responses. Higher organization involved the formation of the tetrameric hemoglobin molecules. Close examination of the structural changes between fully oxygenated and fully deoxygenated hemoglobin shows that the largest structural changes are about the quaternary coordinate. It is for this reason that the system is believed to exhibit such a simplified response as described within the Monod two-state model. However, the driving force for the motion about the quaternary contacts must be convolved to the structural changes at the tertiary level. The forces are ultimately derived from the Fe—O_2 bond and this coordinate is directly connected to the tertiary structural fluctuations. So the problem of understanding the large amplitude motions involved in the allosteric regulation of oxygen binding in hemoglobin can be reduced to understanding the coupling of the reaction forces to deterministic structural changes at the tertiary level. The structural changes at the tertiary level are ultimately responsible for modifying the force balance along the quaternary coordinate.

Myoglobin will be used as the model system to understand the tertiary structural changes along the Fe-ligation coordinate. Myoglobin is nearly identical to the heme protein subunits of hemoglobin with the exception that it does not form dimers in solution and thus enables isolation of tertiary motions. The bond-breaking coordinate at the oxygen-binding site leads to structural changes in the surrounding globin. These changes are depicted in Fig. 4. In the ligated- or oxy-form, the iron is hexavalent and resides in-plane within the porphyrin ring. Upon dissociation of the iron—ligand bond, the iron becomes pentavalent, high-spin, and moves out of the porphyrin ring by 0.5 Å. In the process, the porphyrin ring deforms in a puckering motion. These displacements are referred to as the heme-doming coordinate. This motion is thought to focus the reaction forces normal to the heme plane and preferentially couple to the EF helical section through the closest contact point defined by the proximal histidine-94 (13, 14). Until recently, the picture that had emerged from X-ray crystallographic studies was that the heme doming caused a tilting and rotation of the proximal histidine that ultimately led to a small translational motion of the EF helix. It is this helical section that forms a significant fraction of the protein–protein contact at the α–β interface. More recent high-resolution studies have shown that this picture may need to be revised. The iron out-of-plane motion leads to a more subtle "barrel-roll" motion of the EF helix without significant relaxation of the histidine orientation relative to the heme (7). In either case, the doming of the iron is viewed to be the epicentre for the reaction forces leading to differential motion of the EF helix relative to other points in space, to effectively translate the reaction forces from the heme site to the protein–protein contact points (quaternary coordinate) in hemoglobin.

The schematic shown in Fig. 4 gives a "before" and "after" picture for the structural changes. The dynamic pathway connecting the oxy- and deoxy-tertiary structures is required information for understanding the mechanics of this motion. There are two different possible views for the operating length scales of the motion or force/response function of the protein (15). One view is that the motions are *localized*. First, the heme domes. This creates a potential energy gradient that is more localized at the proximal histidine. Small-scale fluctuations along the helix ultimately lead to displacement of the EF helix along the proper coordinate. The whole process can be likened to a series of falling dominos with the length scale on the order of one amino acid. First, one domino falls (heme doming), this action displaces the force to a new location and causes the next domino (proximal histidine region) to fall and then the next, etc. This dynamical picture will be referred to as the Localized Strain Model, where strain is defined as a change in volume element (localized over one amino acid residue in this case). This localized strain process would be distinguishable from other possible mechanisms by the observed dynamics for the protein relaxation. *Given the highly associated nature of proteins, localized motions of this type would involve a diffusive sampling of the protein relaxation and the relaxation would be expected to show stretched exponential behaviour typical of glass-like systems* (16, 17). For the most part, protein-relaxation processes have been characterized to show stretched exponential behaviour such that this view of the mechanics is consistent with a large body of information related to protein dynamics (18–21).

At the opposite extreme, it is possible that the heme doming is coupled to a much more rigid body on the relevant time scale. In this case, the reaction force would be extensively distributed in space (15). The mass displacements in this limit could be reduced to the displacement of a superposition of collective modes involving the whole protein. The relevant length scale would be the effective radius of the protein. This collective mode description of the ensuing relaxation is similar to concepts introduced to understand the

© 2002 NRC Canada

Fig. 4. Expanded view of tertiary structure changes in the vicinity of the heme pocket. In the oxy-state (solid black), the iron resides in plane. Upon breaking of the iron—ligand bond (O_2, CO, NO, etc.), the iron moves out-of-plane and the porphyrin puckers. This motion is coupled to the adjacent helices. The doming of the iron is the epicentre for the forces that ultimately lead to the motion of the EF helix as modulated through the proximal histidine contact, opposite the ligand binding site (modified from refs. 8 and 25).

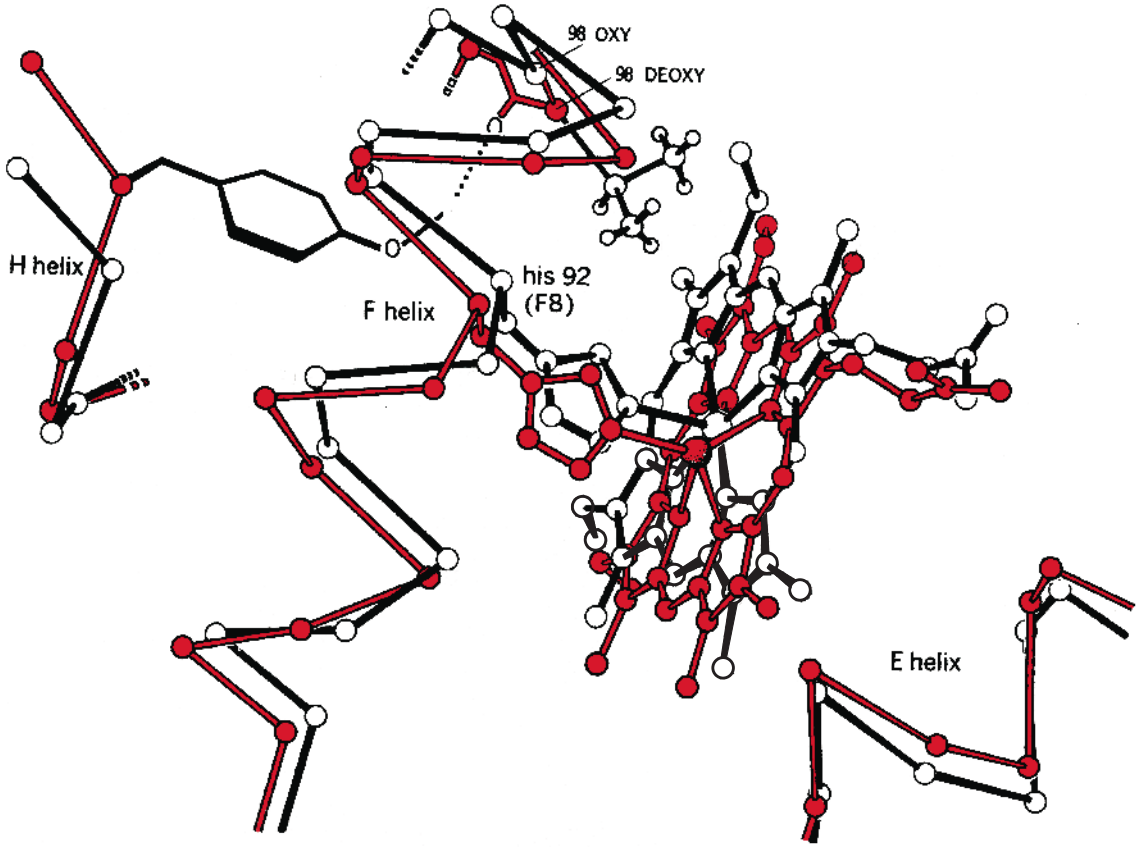

importance of nondiffusive relaxation processes found in liquids (22, 23). In the case of charge transfer, the liquid reaction and (or) relaxation coordinate convolved to the change in charge density about a solute is found to be dominated by the inertial "free-streaming" collective motions of the liquid that occur on time scales much faster than diffusive relaxation. A modal description of the correlated motion of molecules in the liquid state is somewhat tenuous as these motions in liquids can also be described within a localized basis (23). Individual motions are only instantaneously correlated and have random phase factors. Motions of molecules in the liquid state are also highly damped, such that there in no clear demarcation between nondiffusive and diffusive behaviour. However, in proteins, there is a much stronger degree of correlation of atomic displacements imposed on the system by the covalent bonding, corresponding to the primary sequence and the various forces responsible for the secondary and tertiary structure. After all, these are single molecules and a modal description should be more apt for proteins than liquids. This long length scale view will be referred to as the Collective Mode Model. The true picture will involve some intermediate length scale from these two limiting views in that the forces cannot displace all collective modes of the protein uniformly, otherwise there would be no directionality imposed on the system. *The distinguishing feature of the collective mode description is the modal description of the displacements with a degree of mode selective coupling between the bond making and (or) breaking coordinate and the bath modes* as defined by protein scaffolding surround the heme site.

Functionally relevant protein motions

All mechanisms describing the coupling of the reaction forces to functionally relevant protein motions must take into account how the energy is directed along specific coordinates. The energy must be harnessed specifically to perform the function or do work. As such, the structural changes are deterministic. The reaction energy is expected to be highly directed to perform the function without having the bond energy so highly distributed among the different degrees of freedom that the forces involved do not rise above the thermal noise.

In the case of heme proteins, the functionally important or relevant motions necessarily involve a displacement of the exterior atoms relative to the interior to communicate the state of ligation at the heme site. If there is no relative motion of the exterior atoms, the forces at the protein interface remain unchanged. Thus, there must be a volume change or strain (defined as $\Delta V/V$) at the individual protein level. To be clear, there may be other displacements internal to the protein, however, these will be shielded from the other proteins

© 2002 NRC Canada

unless there is a relative displacement of the exterior residues.[2] Thus, molecular communication is established between proteins through material strain. The strain creates stresses at adjacent protein(s), and thereby modifies the activation barrier for the coupled reaction coordinate at a remote site. This through space coupling provides exponential gain to the control parameter (strain) over the coupled reaction coordinate. In the case of hemoglobin, the strain that develops in the R-to-T transition lowers the barrier for adopting the domed heme configuration. The barrier only needs to be modulated by 0.1 eV at room temperature to cause the deoxygenation rate to increase by two orders of magnitude. Relative to the Fe—O_2 bond energy, this amount of energy transduction amounts to a conversion efficiency of approximately 10%. This efficiency may seem fairly modest, however, it must be born in mind that there are 10 000 degrees of freedom in the protein system. Rather than uniformly exciting all the system modes, the bond energy is extremely well focused along a very narrow subset of configurations. In this light, the degree of directionality imposed on the reaction coordinate by the protein active structure is indeed impressive.

The main point is that the molecular communication pathway is defined by the evolution of protein strain. This is the "talking coordinate" between proteins that indicates the state of ligation at the irons. Concepts of strain are the 3-D equivalents of Hooke's Law for a 1-D spring. Strain is a fourth rank tensor that describes displacements that are both longitudinal (compression and (or) dilation) and tranverse (shear) to the applied stress (reaction force field). Two different kinds of functionally relevant protein motions can be defined: (*i*) motions that lead to a net change in volume; and (*ii*) shear displacements. In the first case, motions of this type would be acoustic in nature and involve longitudinal strain elements. In the second case, the transverse components to the functionally relevant protein motions do not necessarily lead to a change in volume element but rather a change in effective shape.

By studying the protein strain dynamics in real time, one should be able to discern between the aforementioned Localized Strain and Collective Mode Coupling Models. The challenge is to come up with experimental methods that are capable of following these different kinds of motions. In particular, it should be noted that the displacement of the helical sections involve net rms motions of less than 0.1 Å. A very sensitive method is needed to follow such motions with the prerequisite time resolution to follow the structural relaxation from the very fastest events (e.g., bond-breaking event or molecular Big Bang) out to full reequilibration. A type of protein seismology is needed; a method that is sensitive to longitudinal displacements and one that can be related to transverse motions or shear. By measuring the strain dynamics, it is possible to determine if the molecular communication pathway is set up predominantly through localized strain; or alternatively, motions involving the displacement of collective modes or segmental motions of the protein. Specifically, Localized Strain would be characterized by stretched exponential processes; whereas the Collective Mode mechanism would be characterized by nondiffusive relaxation processes occurring on time scales comparable to the inverse frequency of these damped motions. In this latter case, the observed dynamics could be associated with a modal frequency and potentially directly connected to the structural element involved. One last point, of the two classes of functionally relevant protein motions, the shear is most important. For a system such as heme proteins where there is no centre of symmetry, a directed process must necessarily involve anisotropic displacements. The development of anisotropy is most strongly correlated to shear and is the *definitive observation of mode selective coupling* in the reaction coordinate.

Energy redistribution processes in biological macromolecules

The quest as outlined above is to understand how relatively minute amounts of energy can be so highly directed in such complex, metastable, systems such as proteins. In this context, the first line of inquiry should focus on how energy becomes dispersed among the different degrees of freedom. This information can be connected through fluctuation and dissipation theorems to the equilibrium fluctuations along the reaction coordinate (24–27). In 1986, we undertook the first direct time-resolved study of vibrational energy relaxation pathways in proteins (24). This work stemmed from the development of a new spectroscopic method that made it possible to follow the time evolution of vibrational energy relaxation into translational degrees of freedom on ps time scales. This time scale is comparable to the typical lifetimes of vibrational modes (frequencies > 1000 cm^{-1}) such that it was possible to follow even the primary relaxation events.

The experimental concept is shown in Fig. 5. By exploiting the extremely short-lived excited-state lifetimes of deoxyheme proteins and Fe(III) oxidation states, it is possible to selectively deposit a photon of energy at the iron porphyrin site. In the visible part of the spectrum, this amount of energy is approximately the same as the ligand bond energy such that it provides an ideal means to monitor selectively the energy redistribution process originating at the heme porphyrin, as it should occur during the bond-breaking event itself. It should be noted that the heme porphyrin ring is generally attached to the protein through only one covalent bond to the iron at the proximal site. This contact point involves nuclear motions that are largely orthogonal to the porphyrin ring and is decoupled from the majority of the vibrational modes that define the porphyrin. The heme porphyrin moiety approximates a molecule in solution in the sense that the dominant relaxation pathways involve van der Waals contacts with the surrounding bath. For a molecule in solution, the bath would be comprised of solvent molecules executing fluctuations appropriate to the liquid state. In the protein case, the bath is the globin surrounding the heme site in which modulation of the van der Waals contacts would necessarily involve more correlated motions via the primary, secondary, and tertiary structural elements of the protein. Originally, it was felt that the

[2] This statement assumes that the forces are dominated by nearest neighbour interactions. In cases, where there is a charge transfer process, the forces may be more long-range electrostatic forces.

© 2002 NRC Canada

Fig. 5. Schematic of optical excitation of heme proteins to selectively deposit a photon of energy at the heme site and the ensuing of the vibrational energy redistribution dynamics in myoglobin.

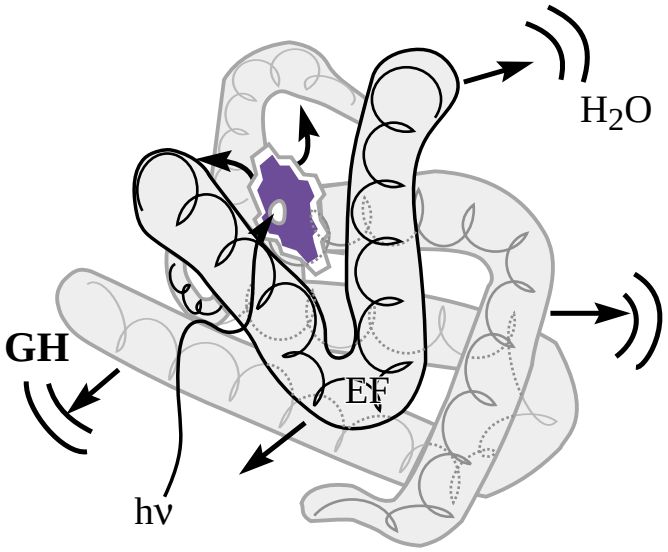

protein could serve as a model system for understanding collisional exchange of energy in disordered systems such as solutions but with the distinct advantage that a more microscopic model could be developed from the structural information available on proteins (24). As opposed to solution, all the relative atomic positions of the interacting system were known from X-ray crystallographic studies of the protein structures.

At the time these studies were conducted, very little was known about the energy relaxation processes in proteins. Proteins were and are still considered to be a special subclass of highly associated systems that can be described within a glass description of the operating dynamics. Within this description, one might expect the transfer of vibrational energy into translational energy in the surrounding water to be very slow, i.e., thermal conductivity is generally slow in glasses due to the many scattering sites (mismatch in local density of states). Alternatively, the energy dissipation process could be modeled within the framework of molecular solids. From the foreknowledge that the initially perturbed site is coupled to adjacent residues of the protein by van der Waals forces, it was thought that the energy flow from the heme porphyrin to the globin could be modelled in analogy to the well-studied dynamics of molecular crystals (eg. napththalene or anthracene). In this scenario, the initially hot heme would undergo very rapid intramolecular vibration energy redistribution within the heme porphyrin at excess energies above the statistical limit to the vibrational density of states (region III in the spectral density — see Fig. 6) (26). For typical anharmonic couplings between a normal mode basis, this process leads to a Boltzmann distribution corresponding to an elevated vibrational temperature at the heme site on a 100 fs time scale (27). The subsequent energy exchange process to the surrounding protein matrix would have to go through the low frequency motions that are responsible for modulation of the van der Waals contacts at the heme site (collisional energy exchange). The so-called doorway modes to the vibrational relaxation process would be

Fig. 6. Vibrational density of states diagram (25). The basis states for describing vibrational energy flow are the modes of the heme porphyrin, the surrounding globin, and water. The coupling that leads to energy redistribution between these different degrees of freedom is treated as a weak perturbation. The highest density of accepting modes in both the globin and water is in the lowest energy range such that the lowest frequency skeletal modes of the porphyrin act as doorway modes for energy flow from the heme to the globin and (or) water reservoirs. Note: there is generally a sparse region in the vibrational density of states (region II) that leads to a bottleneck in the energy redistribution.

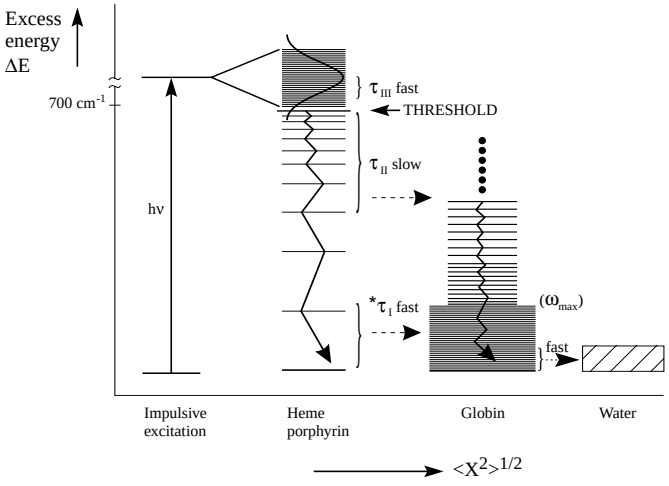

the high density of state region for modes below 200 cm^{-1} (region I of Fig. 6) (25, 26). The relaxation process can be captured analytically through a first-order time-dependent perturbation treatment. Explicitly, the relaxation for any given mode (i) can be written as,

$$[1] \qquad [2\pi c T_1]^{-1} = \frac{18\pi}{\hbar} \sum_{j=1} \sum_{k=1} \{|\langle i|V^{(3)}_{ijk}|jk\rangle|^2 \, \delta(\omega_i - \omega_j - \omega_k)(n_j + n_k + 1)\}$$

where T_1 is the relaxation time, c is the speed of light, n_j, and n_k are the temperature-dependent probabilities for modes j, k, respectively, and $V^{(3)}_{ijk}$ is the cubic term in the anharmonic coupling of the modes. This equation is essentially a Fermi Golden Rule expression describing the energy flow where the sum is over all possible relaxation pathways that conserve energy (δ term) and momentum. In the overall vibrational cascade to lower and lower frequency motions and spreading of the energy over more and more atoms, there is a region in the vibrational density of states (region II) where this conservation condition can not be met. There is not a corresponding set of acceptor modes in this energy range that enable the decay of a high frequency mode into two lower frequency modes and conserve energy. The threshold between rapid IVR (region III) and this bottleneck (region II) is expected to occur around 700 cm^{-1} (26). If the highest frequency cutoff for the accepting modes of the surrounding protein can be modelled in analogy to the solid state, this cutoff should occur at approximately 200 cm^{-1}. In this case, all the vibrational modes within the spectral region defined between 700 and 200 cm^{-1} will not be able to decay by the

© 2002 NRC Canada

Fig. 7. Hydrodynamic model for vibrational energy flow. At high excess energies (region III), there is very rapid energy redistribution (statistical limit; dynamics determined by average anharmonic coupling). The energy flows out to the surroundings primarily via region I modes. This process is modeled as a larger hole (higher density of accepting modes). As the energy pours out of region III through region I, there is a nonstatistical accumulation in region II. The region I and II modal densities are separated by a barrier to depict the two-phonon barrier that separates the two energy regimes in molecular solids.

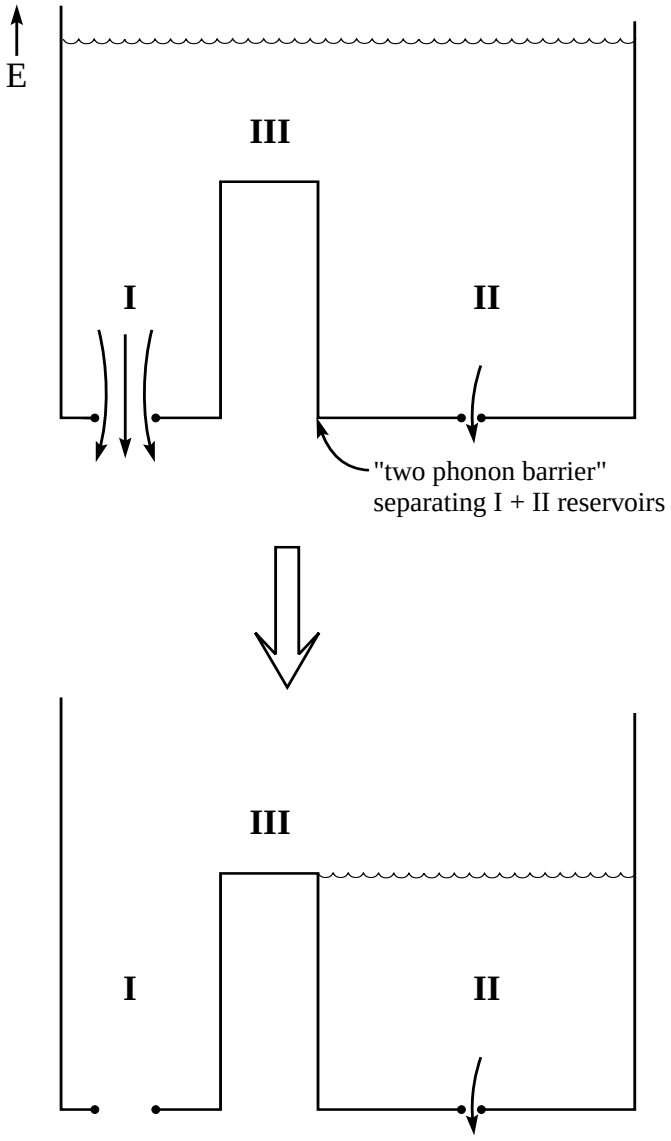

emission of one quanta pathways of excess vibrational energy into the surrounding protein. Instead, the relaxation process would require an emission pathway involving at least two vibrational quanta of one accepting mode or combinations. The relaxation would involve higher order terms in the perturbative expansion of the anharmonic potential than just the cubic term needed to describe one quantum transitions to lower frequencies. The smaller magnitude of this perturbative term would lead to much slower relaxation.

A simple hydrodynamic model is shown in Fig. 7 to get across the main concepts of the energy redistribution process. Based on solid-state relaxation processes, the vibrational energy flow from the heme to the protein matrix would be expected to involve a fast initial relaxation process (ps time scales) followed by a much slower process with approximately half the excess energy dissipated into the protein from region II modes on a 100 ps time scale (26). The key prediction is the slow relaxation component that is ascribed to the expected "two-phonon barrier" between the intermediate vibrational spectral density of states of the heme donor modes and surrounding protein acceptor modes (25, 26).

The above treatment requires either experimental or theoretical input with respect to the spatially distinct spectral density of states to be assigned to the heme porphyrin and protein as a starting basis. Molecular dynamics calculations are generally needed to estimate the protein modal density. The relaxation process can also be simulated in MD calculations of this nature by using initial starting conditions in which the heme porphyrin ring modes have excess kinetic energy, corresponding to the excess photon energy, beyond the equilibrated system. A full-blown MD calculation was carried out explicitly modelling the optical excitation process using this approach (27). This study likewise made the prediction that the initial relaxation step should occur on ps time scales with approximately half the energy relaxing within the 40–60 ps time frame. This simulation also made the important prediction that once the energy was transferred from the hot heme to the surrounding protein matrix, it would be extensively distributed throughout the protein by collisional-like coupling of the heme to collective modes of the protein matrix.

The other model that was prevalent at the time that bears mentioning here is the vibrational *soliton model* of Davydov and Scott et al. (28, 29). This model was developed as a potential explanation for how energy is so efficiently directed in biological systems. This particular model is attractive as it offers a potential explanation for the near ubiquitous occurrence of the α-helix in biological systems. This model viewed the helix as the essential topological feature that provides a conduit for transferring energy from one region in space to another without spreading. The mechanical motions along the helix must be decoupled from the surroundings to prevent the energy from spreading, i.e., to create a nondispersive condition on the energy flow. Waves obeying this condition were first observed as canal waves that tended to not damp or spread spatially in the usual manner. This self-sustaining, stationary, character to the wave properties was identified with nonlinear coupling between different propagation modes and is referred to as a soliton wave. The appeal of this model is that it offers an explanation for the highly directional response of biological systems and identifies this property with a topological feature of the right length scale to permit scaling from atomic to the mesoscopic length scales appropriate to biological functions. The occurrence of solitons can be reduced to solving a nonlinear wave equation; in this case the nonlinear Schrodinger equation accorded to vibrational modes of the protein (28, 29). Solutions to this equation produce deformations that involve propagating nondispersing wavepackets that travel along the helix at velocities significantly slower than the speed of sound. The soliton velocity is related to anharmonic terms that necessarily reduce the effective velocity from harmonic

© 2002 NRC Canada

(more rigid) terms in the interaction potential. Within this model, one would also expect the vibrational energy relaxation to be very slow — by definition of the soliton ansatz. There are conceptual problems with respect to exciting such a mode in a biological system and how the soliton could transfer energy to adjacent sites if it is truly a nondispersive mode. These issues aside, this model provides an interesting starting point for discussing the connection between topological features in the protein structure and correlation to energy transduction mechanisms.

Picosecond thermal grating studies of energy redistribution

With the above background, our first experimental observations were surprising. Briefly, the experiment consisted of exciting preferentially a short-lived heme approximately in the centre of the protein and monitoring the evolution of the short-lived electronic excited state into the final energy reservoir — translational energy of the bath. This study was accomplished by using grating excitation to encode a spatially modulated excitation profile in the sample and monitoring the ensuing relaxation of vibrational energy into translational energy by the diffraction of a time-delayed probe pulse off the corresponding modulated index of refraction. The modulation arises from the thermal expansion that results from the relaxation of vibrational energy into translational degrees of freedom.

The most significant developments of this work were: the analytical solution to the thermal elastic equations to connect the temperature-dependent index of refraction and sound fields to molecular relaxation processes; and the achievement of ps time resolution to an effectively photoacoustic approach (24, 30). The appropriate equations defining the experimental observables are governed by the relations (30):

$$[2] \qquad \frac{\partial^2 u}{\partial x^2} - \frac{1}{v^2}\frac{\partial^2 u}{\partial t^2} = \frac{a(3\lambda' + 2\mu)}{\lambda' + 2\mu}\frac{\partial (T - T_0)}{\partial x}$$

$$[3] \qquad \rho C_v \frac{\partial (T - T_0)}{\partial t} - \alpha_{\text{th}} \frac{\partial^2 (T - T_0)}{\partial x^2} = 2Q[1 + \cos(kx)]\gamma e^{-\gamma t}$$

These relations define the material displacement (u) or acoustic field excited in response to a temperature (T) gradient. This is a 1-D analysis along the grating wavevector (k) where a certain amount of heat (Q) is deposited in the material to give a temperature rise as defined by the constant volume heat capacity (C_v), thermal conductivity (α_{th}), and the density (ρ). The amplitude of the displasement is related to the thermal expansion coefficient (a) and the terms λ', μ are material constants related to elasticity. The source term is the RHS of eq. [2]; where γ defines the microscopic relaxation rate constant (vibration to translation and (or) rotation degrees of freedom).

The analytical solution to these coupled equations is:

$$[4] \qquad u(x,t) = A \sin kx \left\{ \frac{1}{b^2 + \omega^2}\left[\frac{b}{\omega}\sin(\omega t) - \cos(\omega t) + e^{-bt}\right] - \frac{1}{\gamma^2 + \omega^2}\left[\frac{\gamma}{\omega}\sin(\omega t) - \cos(\omega t) + e^{-bt}\right]\right\}$$

where b is a constant related to thermal diffusion (decay of grating image) and ω is the acoustic radial frequency at the grating wavevector.

The results are plotted in Fig. 8 for various values for the thermal relaxation rate normalized to the grating acoustic period. The relaxation of energy into translational degrees of freedom (heat) leads the excitation of a standing acoustic wave (the sound field replica of the optical pattern encoded in the material) that beats in and out of phase as the two counterpropagating acoustic waves move past one another. The first maxima in the signal response occurs at one-half an acoustic period from $t = 0$. The most important feature to note is that the effect of finite relaxation processes cause a shift in the acoustic phase. The shift can be directly connected to the relaxation rate. Within typical signal to noise ratios, relaxation times of less than one-twentieth an acoustic period can be determined. The acoustic phase shift and connection to the underlying dynamics (31) is the same as the phase shift exploited in phase modulation fluorescence spectroscopy to determine excited-state lifetimes. The main distinction with this spectroscopy is that it gives a direct observable of the nonradiative relaxation channel and can be used to monitor photodark states.

The highest time resolution is attained by going to the highest possible acoustic (modulation) frequency. By using counterpropagating 355 nm excitation and probe pulse sequences, it was possible to image acoustic frequencies greater than 10 GHz. The grating fringe spacing was less than 120 nm and the effective time resolution was limited by the speed of sound giving rise to expansion over distances comparable to the protein diameter (24, 25). The first data of its kind is shown in Fig. 9. The rise time of the acoustic sound field is convolved to the excitation pulses used in the experiment. From this initial work, it was determined that the vibrational energy relaxed into translational energy of the surrounding bath on a timescale faster than 22 ps (24, 25). Rather than taking greater than 40 ps for the energy to travel *just from the heme to the globin*, the vibrational energy was essentially completely dissipated into translational energy involving acoustic modes of the protein and water. The energy would have to have been extensively delocalized to undergo rapid collisional exchange with the water on the observed time scale.

The qualitative features of these observations were consistent with the MD calculation, however, the dynamics were much faster than predicted. These calculations were conducted with the protein in vacuo. Inclusion of a water layer, found a significant increase in the relaxation rate that brought the calculated results into good agreement with these experiments (25). This work illustrated that there is no effective two-phonon barrier to relaxation processes in proteins. The two-phonon barrier expectation was based on the highest frequency phonon cutoffs in molecular crystals. In proteins, the atoms are covalently bonded such that the gap

© 2002 NRC Canada

Fig. 8. Calculated thermal grating signals (30). The grating signal is plotted for various nonradiative relaxation times (γ^{-1}) relative to the acoustic period of the grating. Curves 1, 2, 3 correspond to $\gamma^{-1} = 0$, $0.1\tau_{ac}$, τ_{ac}, respectively, where τ_{ac} is the grating acoustic period. The finite relaxation times appear as a phase shift in the acoustic modulation of the signal.

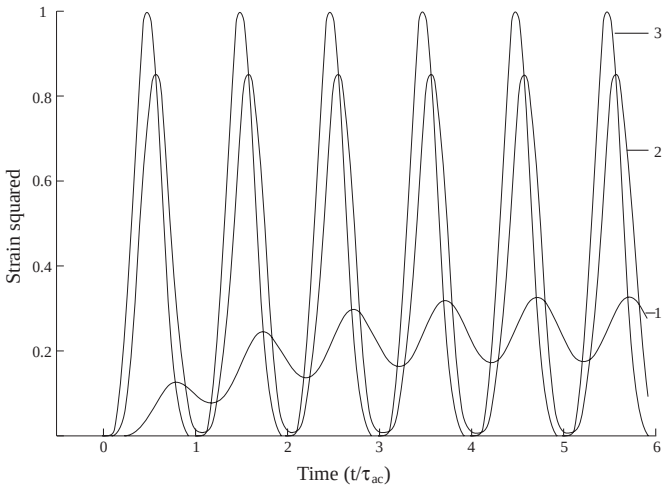

in the spectral density of states is much less pronounced. There may be variations in local density of states for a particular mode but there will also be a pathway enabling a high frequency mode to relax into two lower frequency modes.

Since this initial work, a number of experiments have been conducted using various probes to follow more selectively the relaxation of the excited heme porphyrin modes (32, 33–35). The main body of this work is consistent with the above findings. The only other work that has been able to follow the energy flow to the exterior of the protein used broadening of IR transitions to improve the time resolution (35). This latter work was able to show the expected biphasic relaxation process where half the energy is dissipated into the surrounding water layer within 8 ps and the remaining energy arrives within 15 ps, in good agreement with our earlier studies. Work in this area continues and the most recent picture is consistent with the above description (31, 32, 33–35).

The most important single message that has come from this work is that the energy redistribution processes in proteins are extremely fast. The energy flow all the way from the centre of the protein to the surrounding water layer occurs on time scales comparable or faster than the half period of the lowest frequency breathing mode of the protein. Thus, the collective or spatially extended segmental motions of the protein molecule must be strongly damped. This observation has implications for the vibrational soliton concepts in directing energy in biological systems. Vibration solitons require the nonlinear coupling of all the modes. Based on the rapid damping of the low frequency modes demonstrated by these studies, vibration solitons can not exist in proteins. The effect of water on the coupling has not been included in these theoretical treatments. The collisional exchange with water is too dissipative a process, and the independent collisional events do not lend themselves to the phased excitation required, to support such long-lived states (especially

Fig. 9. Picosecond transient grating studies of vibrational energy relaxation in heme proteins. The upper curve is the instrument response, the middle curve is for met-cyanohemoglobin, and the lower curve is for Malachite Green in ethanol. The rise is instrument response limited by the speed of sound and put an upper limit of 22 ps on the full relaxation process from vibrational energy flow from the heme porphyrin all the way to collisional exchange with the water (25).

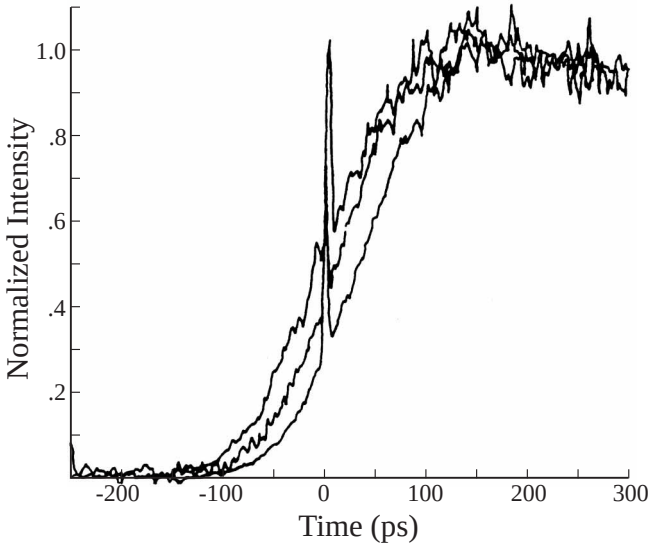

over the required spectrum). The bottom line is that energy exchange processes are exceedingly fast in proteins and complete equilibration of excess vibrational energy (mechanical) into translational degrees of freedom occurs on ps to approximately 10 ps time scales.

Architectured phase space models

The fact that proteins undergo extremely rapid energy redistribution is a further challenge to understanding how chemical energy can be directed in biological systems. It was not until the above revelations that my group became earnestly interested in the "directed energy" problem. Once we found that the energy became randomized so rapidly, it became even more difficult to reconcile the observed dynamical processes in biological systems.

In principle, one could treat the directed energy problem in biological systems classically. There are enough degrees of freedom that quantum effects such as phase of the various modes should cancel to give a good approximation to a classical system. We should, then, be able to define a classical Hamiltonian that describes the protein response to a perturbation. There would be a kinetic energy term and a potential energy term defining how the energy of the perturbation is directed. From the above experiments, it is clear that the energy could not be highly directed through kinetic energy terms. Energy being directed as a traveling mechanical deformation would constitute a vibrational wavepacket and would require a nondispersive condition on the vibrational energy propagation (soliton-like character as discussed above). This mechanism for directing the energy can be ruled out. The above experiments demonstrate that the vibrational energy is too quickly randomized. Thus, the energy is

© 2002 NRC Canada

directed through effects mediated through changes in potential energy of the system. Put in another way, the energy must be directed through steric effects. The potential energy landscape of the protein is constructed such that only a relatively small number of pathways are extensively explored through thermal fluctuations, i.e., there exist coordinates that are more labile than others and undergo larger rms fluctuations. These coordinates provide the map for the protein to move from the reactant surface to the product and vice versa.

In chemistry language, the motions are constrained to follow a certain path by steric hinderance. This concept is used repeatedly in chemistry but should be more precisely defined in this problem. In particular, the length scale and time scales need to be defined or this is not a helpful concept. To drive home this point, the sampling process can be likened to particle motion on a slide. I've often made the analogy of the motions along the reaction coordinate to the motion one would experience in a water slide park. There always appears to be one water slide that is straight down. Motion along this potential energy surface from the top of the slide (reaction saddle point) would constitute the path of steepest decent. However, there are generally a great many different slides with meandering pathways from the top to the bottom. The motion of even complex objects with many degrees of freedom (e.g., you) can be constrained to follow a very directed path in such contexts. There is one important distinction to be made in this analogy. We need to consider the net rms motions involved in the protein's functional response relative to those in relation to the background thermal noise. The net displacement of the helical sections about the heme group is on the order of 0.1 Å or less. This value should be compared to the thermal fluctuations inferred from the Debye–Waller factors of the X-ray diffraction pattern of myoglobin that are on the order of 0.03 Å (36, 37). The net displacement is on the same order of magnitude as the background thermal noise. Within the above analogy, one would have to imagine going down a slide during an earthquake! You may start on one slide then midcourse jump to a different slide many times before arriving at the bottom (product state).

In some sense, to state that the directionality of the problem is imposed by the 3-D structure of the protein or steric hinderence is a nonstatement. With the dynamics for energy redistribution now at least qualitatively understood, it is obvious this is so. The real question is what is the length scale and time scale that the reaction proceeds along a particular coordinate. Within the mechanical slide analogy, what is the length scale and time scale of motion along a particular energy gradient? How high is the slide (energetics)? What structure elements are confining the sampling process?

As discussed above, the mechanics of the motion can be separated into a short length scale limit (Localized Strain) or a spatially distributed description (Collective Mode Coupling). This issue of the length scale of the response function is relevant to the degree of directionality and time scales for the structural encoded functions. A useful toy problem to consider is the response of an elastomer to a time-dependent force. In the limit of slowly varying forces, the polymer will deform slowly almost like a liquid. There is distribution of barrier heights. However, the polymers are able to thermally sample different configurations and those that experience larger displacements in the presence of the applied force will lead to a deformation along the applied stress. Now, consider the case of an impulsive force. The same elastomer will behave more like a rigid elastic body. If the area of the applied force is changed and (or) time scale, one would observe different behaviour between highly viscous fluid behaviour to solid-like behaviour. This gendanken experiment simply serves to remind us that all response functions have both a k (length^{-1}) and ω (time^{-1}) dependence. This statement holds true for dielectric functions, magnetic susceptibilty, mechanical response functions, and related many body effects. At the time of our studies, we simply did not know the relevant functional dependence with respect to these two parameters. For the most part, proteins were believed to be "glassy" states such that relaxation along a reaction coordinate should be best described by stretched exponential relaxation processes (short slide and (or) diffusive sampling). However, this view was based primarily on NMR and flash photolysis studies of protein relaxation on relatively long time scales. What if, on the time scale of the bond breaking, there isn't enough time for the protein to sample localized fluctuations, and the strong atom–atom correlations imposed on the system lead to a more spatially extended, rigid-like, response. We were missing key pieces of information related to how the protein responds during the time interval most relevant to the initial curve crossing process at the reaction saddle point, i.e., the very fastest time scales. To fully understand how energy is directed in biological systems, we need to study the mechanical response of the protein on all relevant time scales — from the chemical Big Bang out to full relaxation (over 10 decades in time).

Put in another context, we don't know the coupling coefficient of the reaction coordinate to the various degrees of freedom of the bath. The pathway from the global minima of the reactant to the reaction saddle point and subsequent relaxation to the product global minima involves nuclear fluctuations with contributions from all possible motions. In transition state theory, the rate of passage across the saddle point is dominated by those motions that are the highest frequency and involve the greatest amount of relaxation energy (38). To understand, how the reaction coordinate can be so highly directed into specific motions, the relaxation energetics need to be correlated to various relaxation phases of the protein to determine the dominant pathway or director to the sampling process.

Functionally relevant protein motions probed by four-wave mixing

The challenge, experimentally, is to come up with methods that are capable of observing the functionally relevant protein motions on all pertinent time scales. The motions at the ligation site can be relatively large, as the forces originate at this point. However, the communication pathway must involve the exterior atoms and as pointed out these motions can be exceedingly small if the force is distributed over a large number of atoms. Further, these structural changes constitute an important class of photodark processes. There is no transition moment tied directly to these motions. To probe these exceedingly small, highly correlated motions, an

© 2002 NRC Canada

Fig. 10. Transient grating setup with diffractive optic element (DOE) (49).

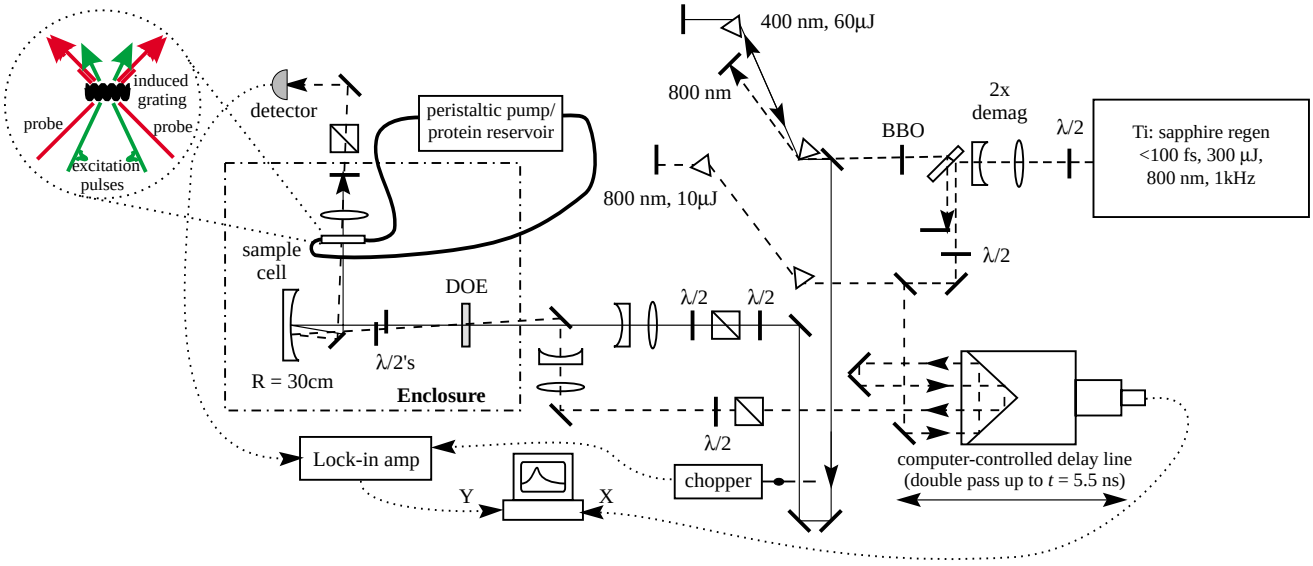

interferometric approach is needed. Transient grating or four-wave mixing approaches offer this possibility.

The transient grating experimental setup and pulse protocol is shown in Fig. 10. Two excitation pulses are used to write an optical interference pattern in the sample. This image is stored as a periodic modulation of the complex index of refraction that can be probed by diffracting off a probe pulse at the Bragg angle. In essence, this is a single period hologram and the protein sample serves as the holographic storage medium. By choosing the excitation and sample conditions, it is possible to selectively study population dynamics, energy redistribution, or functionally important protein motions. The diffracted signal intensity is given by the relation (38):

$$[5] \qquad \eta(\omega) = \exp\left(\frac{-2.3D_{av}(\omega)}{\cos\Theta_0}\right)\left(\frac{\pi d}{\lambda\cos\Theta_0}\right)^2 [\Delta k(\omega)^2 + \Delta n(\omega)^2]$$

where η is the diffraction efficiency, D_{av} is the average optical density at the probe wavelength λ at the Bragg angle (Θ_0) for diffraction and d is the sample thickness. The terms Δk and Δn refer to excitation induced changes in the *Im* and *Re* components to the complex index of refraction at the probe wavelength. The population terms can be selectively monitored by the periodic modulations in Δk (absorption). However, the protein motions and energetics are detected through changes in the real part of the index of refraction (Δn). Specifically, the relaxation energetics can be monitored through temperature-dependent changes in the index of refraction (Δn_{th} re: thermal expansion and increased linewidths through hot band transitions and collisional broadening). The functionally important protein motions will likewise affect the index of refraction through mass displacements and associated index of refraction changes ($\Delta n_{protein}$). These terms of interest are detected in quadrature with population contributions to the dynamics (Δn_{pop}). The population contribution stems from changes in the optical spectrum and attendant changes in the optical dispersion (index of refraction). This effect can be estimated through a Kraemers–Kronig analysis (31). By using probe wavelengths as far away from either excited state or ground state resonances, it is possible to attain a good degree of isolation of the protein strain dynamics and energetics from what could be considered trivial population effects (in so much as conventional methods can determine this property).

Our studies of the energetics used deoxyheme proteins in which there were no photophysical processes other than vibrational energy relaxation. The proteins have extremely short-lived electronic excited states with out a photolabile ligand bonded to the iron. This work has been discussed above. To probe the functionally relevant protein motions, carboxymyoglobin (MbCO) was used. Photodissociation of the CO ligand can be optically triggered with 100% quantum efficiency by exciting into the either the Q band or Soret band of the heme (33, 39). These excited states are thought to be adiabatically mixed with the deoxy electronic surface (40) and the iron ligand bond found to undergo photodissociation in less than 50 fs (33). Thus, it is possible to photoinitiate the oxy- to deoxy-structure transition on a suitably fast time scale to cover all the possible motions, even those connected to crossing the reaction saddle point, i.e., times during the chemical Big Bang. In these studies, carboxyheme proteins were chosen over oxygen-bound species. The simple reason is that oxygen tends to show complex rebinding kinetics with less than 6% quantum yield for ligand escape; whereas photodissociation of CO from the iron gives a 96% quantum yield for ligand escape (41). The carboxy-forms give access to the full relaxation pathway or full range of functionally relevant protein motions — from the very initial event associated with bond breaking out to ligand escape and finally rebinding.

The original intent of our work in this area was to follow the relaxation energetics subsequent to photodissociation of the Fe—ligand bond. The amount of energy involved in the protein relaxation is an important parameter in understanding the biomechanics of the motion. The very first studies

© 2002 NRC Canada

Fig. 11. (*a*) Deoxymyoglobin. The top curve shows the results for 532 nm grating excitation and 1.064 μm probe of deoxymyoglobin. This experiment is the control for a purely thermal process. The lower curve is under identical conditions except the temperature has been reduced to near the thermal expansion point of the medium to illustrate the purely thermal nature of the signal. (*b*) Carboxymyoglobin. The upper curve is at room temperature. The lower curve is under identical conditions except at the zero thermal expansion point. This study illustrates the nonthermal nature of the protein-driven acoustics. The dominant relaxation phase is less than 100 ps (re: Fig. 7 and grating acoustic period) and there does not appear to be significant slower relaxation processes out to 10 ns.

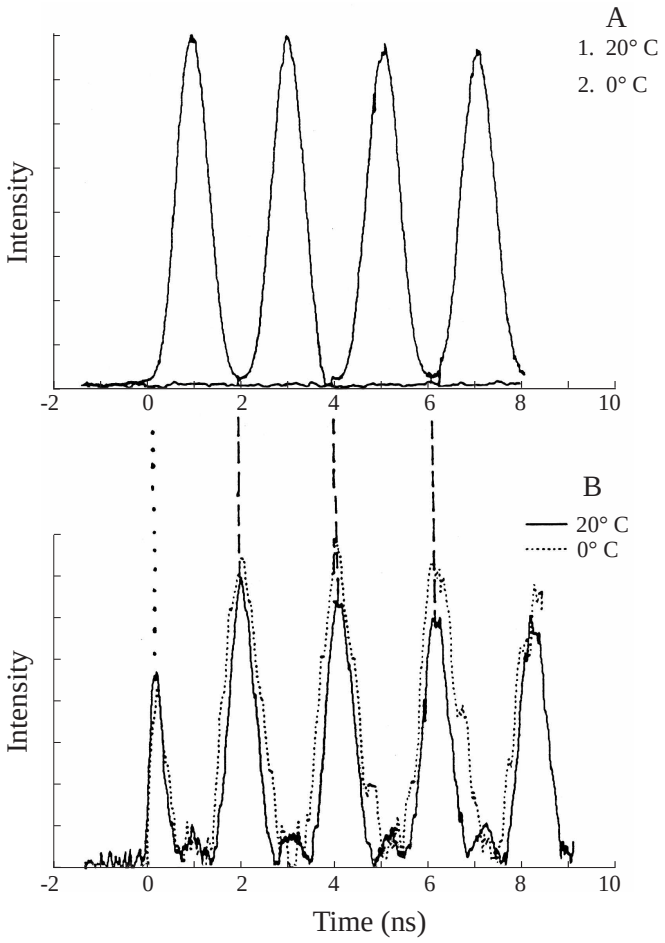

were a major revelation to the process. Rather than observing simple thermally driven sound fields under grating excitation (re: the energetics), we observed large nonthermal sound fields generated by the protein motion in response to the bond dissociation (42). These findings are shown in Fig. 11. The top panel shows the results for deoxymyoglobin (deoxyMb) under the same conditions as carboxymyoglobin (MbCO). The deoxyMb study is the control for a purely thermal process. Note the acoustics are 100% modulated and the first maximum occurs at one-half of an acoustic period from $t = 0$ as expected for thermally excited acoustic grating. Close inspection of the acoustic phase shows that the redistribution of the absorbed photon energy into translational degrees of freedom occurs within 10 ps as discussed above. The thermal nature of the signal is confirmed by going to the zero thermal expansion point of the solution where the signal disappears. In contrast, MbCO shows acoustic modulation that is 180° out-of-phase with the pure thermal response. Most important, the acoustic modulation persists and still dominates the signal near the zero thermal expansion point. This study showed that the protein was undergoing a significant volume change on time scales less than 100 ps. The protein volume changes define the protein strain — one of the key markers of functionally relevant protein motions as defined above. Perhaps the most important observation from this data is that there did not appear to be any significant (<20%) slow component to the protein strain evolution (42, 43). The bond breaking seemed to couple directly the protein strain without any appreciable extended relaxation dynamics (at least out to 10 ns). This observation led initially to the collective mode coupling model for describing the bond energy transduction to protein motions (15).

The above study has some ambiguity with respect to population contributions to the signal and a much more precise determination of the initial dynamics was needed instead of an upper limit. To resolve the dynamics, a counterpropagating grating beam geometry was adopted using 585 nm excitation and probe pulse sequences (31). The larger grating wavevector enabled the coupling of the protein motion to much higher acoustic frequencies and correspondingly higher temporal resolution to the protein strain dynamics. These results are shown in Fig. 12 where the acoustic phase difference between deoxyMb and MbCO are compared directly under identical conditions. This study illustrated that the protein strain was nearly completely developed within 4 ps. In fact, it is apparent from this data that the bond energy is displacing an acoustic mode of the protein faster (by approximately 6 ps) than the energy is becoming randomized into translation energy into the bath (defined by deoxyMb control). This study illustrated that the initial protein strain dynamics involve coupling to collective modes of the protein, i.e., the observed mass displacement corresponds to a strongly damped mode in the 1×10 cm^{-1} range. The significance of these findings should not be lost. The protein is executing functionally relevant motions faster than the energy randomization process discussed in the previous section. The displacement of collective modes in this regard would act to guide the system close to the global minimum of the product distribution before the directionality imposed on the system is lost.

This novel application of grating spectroscopy represents true protein seismology — listening to proteins move by optically monitoring the sound fields produced by the motion. The observed dynamics and connection to the protein strain demonstrates the initial response to be mediated through the coupling of the bond breaking to collective acoustic-like modes of the protein. Other proteins have been studied with nearly identical optical properties and show different amplitudes for the protein-driven acoustic waves. The speed by which all the proteins develop the dominant strain components in the tertiary relaxation is the most interesting observation. There appears to be no evidence for the stretched exponential relaxation processes that might be expected for a more localized strain evolution and glass-like behaviour. It is

© 2002 NRC Canada

Fig. 12. Counterpropagating grating studies of MbCO at 585 nm. The acoustic phase of the protein-driven sound fields are directly compared to those of the purely thermally driven process. The photodissociation of the ligand leads to protein displacements that are shifted by 6 ps relative to the vibrational to translational energy relaxation process, i.e., the dominant phase of the initial protein relaxation along the dissociation coordinate occurs faster than the energy redistribution process.

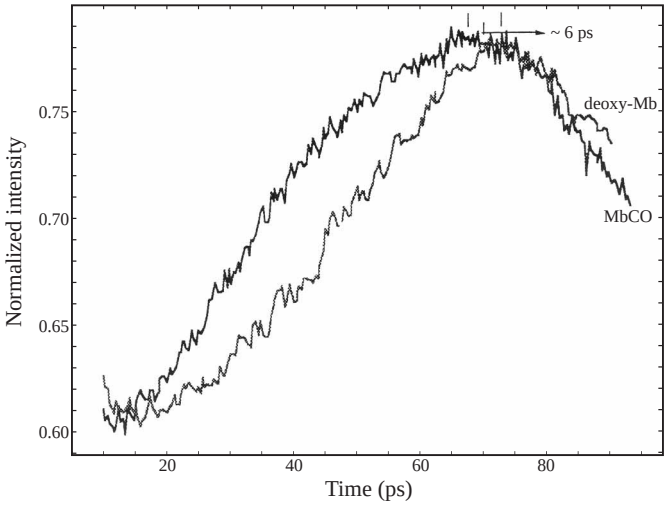

important to point that these observations do not dispute previous observations of stretched exponential relaxation behaviour for proteins but rather emphasize the different k and ω dependence of the mechanical response function. Previous measurements were more sensitive to local motions near the heme (via the selection of probe transitions); whereas the protein driven acoustics probe the global relaxation coordinate. It is this coordinate that is sensed by neighbouring proteins such that the grating experiment directly probes the molecular communication coordinate.

The mechanics for this motion involve the coupling of the heme doming, as the epicentre of the reaction force, to the surrounding helical sections that are displaced in a segmental fashion, i.e., the atom–atom correlation is described as the displacement of a collective mode. Whether or not these motions can be ascribed to an imprinted directionality on the reaction coordinate requires a determination of the anisotropic nature of these motions. Since the protein has no centre of symmetry, the reaction forces should lead to highly anisotropic mass displacements on time scales faster than energy redistribution. To observe this effect on the right time scale requires subpicosecond time resolution and higher sensitivity to the index of refraction changes depicting the protein motion.

Diffractive-optics-based nonlinear spectroscopy — Optical analogue of NMR

It has long been appreciated that the signal-to-noise, in any inherently low signal experiment, can be significantly improved by the use of phase-locked heterodyne detection. In NMR, the radiated magnetic field from the cavity is mixed with a reference rf field and detected in quadrature with the reference field. If it were not for the ability to use phase-locked detection for signal processing, NMR would be orders of magnitude less sensitive and would have made far less impact in chemistry. The same methodology can be used in principle to determine multiple time correlations of optical and IR transitions that would access different time regimes and provide structural and (or) dynamical information on strongly correlated many body processes (dynamic structure of liquids, proteins). This detection modality may seem straightforward with respect to its wide implementation in NMR, however, it should be recognized that this approach requires phase stabilities in excess of $\lambda/100$. In NMR, the phase stability between the reference and the signal field emanated from the cavity is not an issue. The effective wavelength is in the meter range. The prospect of keeping paths and phase stable to better than 1 ppm is fairly routine. In contrast, in the optical domain, the signal wavelength is on the order of 500 nm. To achieve $>\lambda/100$ phase stability in this range, path lengths of the different interacting optical beams must be kept constant to within just a few molecular bond lengths (<5 nm variation). This degree of phase stability may seem out of reach considering that acoustical noise introduces micron pathlength fluctuations. Phase-locked signal detection has, however, been accomplished using feedback loops with interferometrically determined reference points. Unfortunately, this approach is cumbersome and is not robust (drifts and requires finding the set points daily). For this reason, there have only been a few reports of phase-locked heterodyne detection in the optical domain.

The quest for improved signal-to-noise is never ending. There is always some experiment that could be conducted — if only one had better signal-to-noise. The possibility of using phase-locked heterodyne detection for four-wave mixing studies has been a long-standing experimental challenge. Rogers and Nelson (44) published a paper outlining the use of a transmission grating to give automatic alignment of transient grating experiments. Similar approaches have been used in the past with respect to using gratings as beam splitters and phase masks are used on a large scale for imaging periodic structures in fibres for the fabrication of fibre Bragg gratings used in wavelength division multiplexing. The distinction of the work of Rogers and Nelson was that the grating generated a "finder" beam. The phase stability of the various beams was not addressed but merely noted that the spatial alignment could potentially be used for heterodyne detection. At the time, we had spent considerable effort on active feedback approaches and had attained as high as $\lambda/300$ phase stability. This limit was only achieved if the beams passed through the same transfer optics after an interferometric reference. It was obvious to us that as long as a diffractive element could be designed to provide a point of symmetry and all the beams passed through the same optics after this reference point, the system would be as stable as active feedback. It was at that point that we realized the best approach would be to specifically engineer a surface relief diffractive optic to provide all the necessary beams at the proper phase matching angle, along with a reference beam, with as large a bandwidth as possible for applications in multicolour fs experiments. This revelation has led to a number of important innovations involving the use of diffractive optics for implementing nonlinear spectroscopies (45–51), from generating tilted phase fronts for true fs time resolution

© 2002 NRC Canada

in a noncollinear beam geometry (less than 200 as broadening) (51) to complex high-order beam geometries (47).

In the case of four-wave mixing, it is fairly straightforward to design an optimized diffractive optic for proper phase matching and multicolour performance. The optic is a simple square-modulated surface relief pattern of the correct height for optimal performance in the desired wavelength range. We have since designed diffractive optics for six-wave, 2-D Raman, experiments that require at least 20 harmonics to generate the required beam pattern and careful attention to the amplitudes of the different Fourier components to enable two-colour experiments with a reference of a predetermined amplitude (48). This novel approach was essential to the first successful determination of the direct $\chi^{(5)}$ response of a liquid that demonstrated the short coherence times of simple fluids (47, 48).

The power of this approach in amplifying small signals can be seen simply by expanding the relations for the detected signal field in the presence of a reference field. The detected signal intensity (I_{OHD}) can be written as (49):

$$[6] \qquad I_{OHD} = \left|E_{ref}\right|^2 + \left|E_{sig}(t)\right|^2 + 2\left|E_{ref}\right|\left|E_{sig}(t)\right|\cos\left(\phi_{sig} - \phi_{ref}\right)$$

Where E_{ref} is the reference field, E_{sig} is the signal field, the φs give the corresponding phase of these fields. The *Re* and *Im* terms to the nonlinear response can be separated by simply changing the relative phase of the reference to the signal field. The *Im* term is related to absorption. In contrast, the *Re* term is related to the modulations in the index of refraction and constructive interference along the signal direction requires a 90° phase shift. Since the two contributions are 90° phase-shifted in their affect on the signal field, it is possible to unambiguously separate the two effects. This feature is not possible with conventional signal intensity measurements and will be a key point below in the discussion of selectively detecting the protein motions. With respect to amplifying the signal, the important point to note is the cross term between the reference and signal field (second term in eq. [6]). This term serves to amplify the signal by several orders of magnitude.

Increased signal amplitude is one issue but really the objective is to increase the signal-to-noise ratio (SNR). If the process amplifies the signal as well as the noise, there is no gain in the detection sensitivity. The SNR for heterodyne detection depends on many factors; the most important are the phase stability and the laser stability (45, 52). Of these two considerations, the single most important criterion is the phase stability between the reference and signal fields. Since the phase of the signal field is determined by the phases of the excitation and probe fields, the phases of all four beams (two excitation, probe, and reference beams) must be stable to within λ/100 (45, 49). It is this requirement that compounds the difficulty in using active feedback. The diffractive optic automatically provides a phase reference through the diffraction process. Any number of beams can be phase-locked or more correctly phase-stabilized using a diffractive optic. Just how good is this diffractive optic approach? Figure 13 shows a schematic of the experimental setup and a demonstration experiment using the $\chi^{(3)}$ response of liquid CS_2 (45). The optical arrangement is a simple 1:1 image relay system using either slightly off-axis spherical mirrors (slight aberration) or off-axis parabolic mirrors. The open arms in the optical relay permit the introduction of various optical elements for independent adjustment of the phase, polarization, and timing of the different beams. The system is very compact. A single optic replaces a plethora of conventional beamsplitters, optical delays, and interferometers that would otherwise be required. The laser used in this study was unamplified and was attenuated to a few mW of average power to conduct a time domain equivalent of Raman scattering to emphasize the sensitivity of the approach. The relative phase of the reference beam is tuned by the simple tilting of a microscope cover slip to adjust the relative phase delay. As can be readily observed, the signal is phase scanned from the *Re* signal component expected for CS_2 (90° phase shift) to the *Im* signal component. The most impressive detail is the observation of the *Im* term. This signal corresponds to the amount of absorption of the excitation fields by stimulated Raman absorption. The effective optical absorption of this process at the excitation levels used would correspond to a change in transmission of the probe of significantly less than 1×10^{-8} (estimated from diffraction efficiency).

The dramatic improvement in SNR is shown in Fig. 14 where detection of the signal intensity using the conventional approach is compared directly to heterodyne detection using diffractive optics. The improvement is quite dramatic for this small signal case. The phase stability is found to be as high as λ/300 for periods of minutes and λ/100 for periods of hours to days (45, 49). This extraordinary phase stability for all four interacting fields is a consequence of the symmetry of the imaging system and optical paths. The symmetry makes the optical imaging immune to beam-pointing noise such that air currents are the primary limitation. This high stability enables signal averaging with phase-locked detection over extensive integration times. The enhancement in the signal-to-noise is typically greater than 100:1 (45) and can be in excess of 1×10^6:1 if done perfectly (38, 52). Previously, transient grating methods were shown to be on par with some of the most sensitive absorption spectroscopies such as cavity ring down, intracavity photoacoustic, and photoacoustic spectroscopies (53). The enhancement factor now possible with the above simple, single optic, approach makes four-wave mixing approaches one of the most sensitive absorption-based methods developed to date. Only FM modulation (side band) spectroscopy has demonstrated greater sensitivity (re: near single molecule detection) (54) and similar modulation methods could be introduced to a high resolution frequency domain analogue of this approach to further enhance the sensitivity. The primary limitation of the heterodyne-detected grating sensitivity is the effective pathlength. The length is defined by the beam interaction region such that this method is confined to small pathlength samples.

Heterodyne detection of protein motions — Observation of mode selective coupling

The development of diffractive-based nonlinear spectroscopy was a key step forward in this problem. With this approach, it was possible to increase the sensitivity and

© 2002 NRC Canada

Fig. 13. Diffractive-optics-based heterodyne detected transient grating signals — impulsive Raman scattering observed for CS_2 as a function of relative phase delay. The derivative-like signal component at $\Delta\varphi = 0$ is the *Im* term and represents the amount of light absorbed through stimulated anti-Stokes Raman processes. The inset shows an expanded view of the diffractive optic setup (see text).

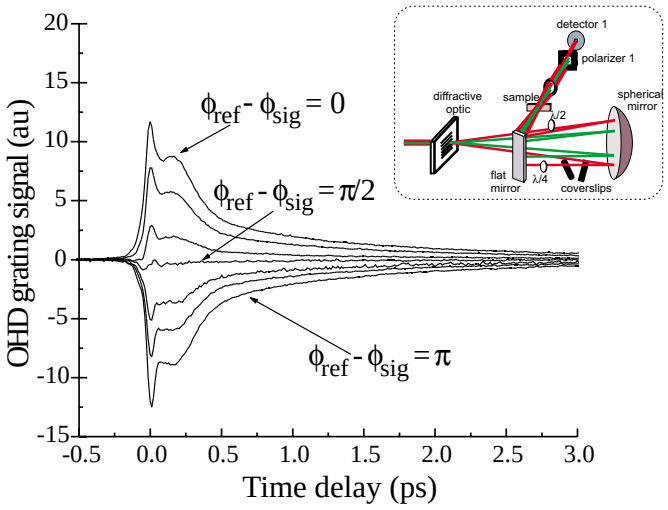

unambiguously separate the phase from the amplitude terms of the grating signal. The stage was set to fully explore highly directed protein motions and (or) reaction coordinates in biological systems.

In this regard, one would ideally like to have an orientated sample to optically probe the induced birefringence that would develop from anisotropic mass displacements. In solution, it isn't feasible to align the proteins but it is possible to take advantage of the polarized nature of optical transitions to photoselect an orientation. For heme proteins, the relevant transition involve those that are *x*,*y*-polarized in the plane of the heme. In essence, using polarized excitation pulses, it is possible to induce an aligned distribution of excited molecules. The photoselection process induces an absorption anisotropy in the sample or dichroism defined as:

$$[7] \qquad r_{\mathrm{Im}}(t) = \frac{Im\,(\chi_{1111}{}^{(3)}(t)) - Im\,(\chi_{1122}{}^{(3)}(t))}{Im\,(\chi_{1111}{}^{(3)}(t)) + 2\,Im\,(\chi_{1122}{}^{(3)}(t))}$$

The subscripts of the $\chi^{(3)}$ tensor refer (left to right) to the polarizations of the two excitation pulses, probe, and signal field. This relation defines the normalized difference in absorption between parallel and perpendicular polarizations of the probe light relative to the excitation used to induce the anisotropy. For an *x*,*y*-polarized transition, the absorption anisotropy can be shown analytically to have a value of 0.1 (49, 50).

The ability to separate the *Re* and *Im* terms of the $\chi^{(3)}$ susceptibility now makes it possible to define the phase anisotropy (birefringence) in analogy to the absorption anisotropy (dichroism), i.e.,

$$[8] \qquad r_{\mathrm{Re}}(t) = \frac{Re(\chi_{1111}{}^{(3)}(t)) - Re(\chi_{1122}{}^{(3)}(t))}{Re(\chi_{1111}{}^{(3)}(t)) + 2\,Re(\chi_{1122}{}^{(3)}(t))}$$

Fig. 14. Demonstration of signal-to-noise improvement using diffractive optics for passive phase stabilization. The noisy curve is for CS_2 using direct detection of the signal. The other curve is for the same sample, under identical conditions, using the *Im* and *Re* parts of the heterodyne detected signal (data shown in Fig. 13).

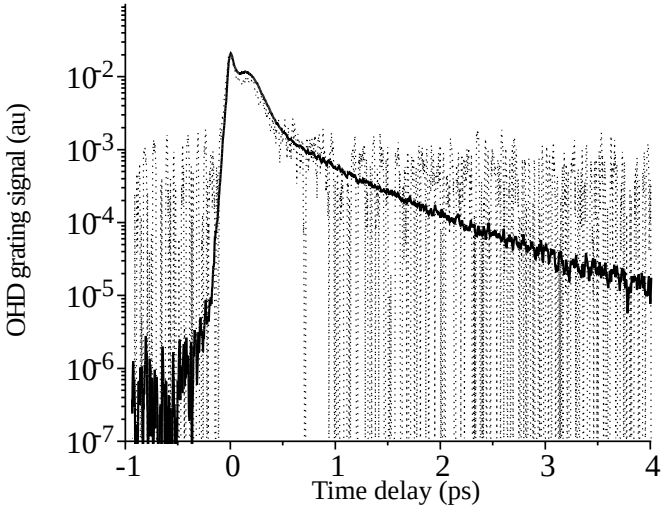

Figure 15 shows the diffractive-optics-based heterodyne detection of both the absorption anisotropy and the phase anisotropy (50). The absorption anisotropy is that predicted for this system at the probe wavelength. The most important feature is the dramatically different behaviour of the phase anisotropy. Rather than a monotonic decay with rotational diffusion, the *Re* part of the signal shows complex behaviour with both rise and decay features that are very distinctive relative to the absorption-based signal. This difference illustrates the significantly different affect the protein motions and relaxation have on the transient absorption relative to the index of refraction changes. The protein relaxation only has a second-order effect on the transient absorption, as manifest in subtle shifts in the spectrum. In contrast, the protein motions directly affect the index of refraction through the differential mass displacements in response to the photoinduced reaction forces. The significantly different dynamics and amplitudes for the observed anisotropy serve as testimony to the affect of the protein motion on the *Re* signal component.

The two most important features of the data shown in Fig. 15 are the amplitude of the phase anisotropy and the dynamics. The amplitude is nearly 0.4 and is far too large for a circular transition to be a simple photoselection effect. The signal components can be transformed to the molecular frame. From this analysis, it was determined that the protein is undergoing differential expansion and compression for directions parallel and orthogonal to the heme plane. In other words, the protein is changing its shape. In this respect, the other interesting feature is that it is doing so within 500 fs. This motion seems to be the dominant relaxation component leading to this unusually large birefringence. There are also ps thermalization components but once this part is separated from the problem by the use of model compounds, it appears the 500 fs component is the primary motion that leads to anisotropic mass displacements.

This motion is the key signature of a directed response for the protein. By going to higher excitation, the strongly

© 2002 NRC Canada

Fig. 15. Diffractive-optics-based heterodyne detection of protein motions. The phase anisotropy is the top curve. The bottom curve gives the absorption anisotropy. Two different time bases are shown to clearly depict the early time protein dynamics. Note: the significantly larger anisotropy in the *Re* part of the signal that develops within 500 fs, distinct from changes in absorption.

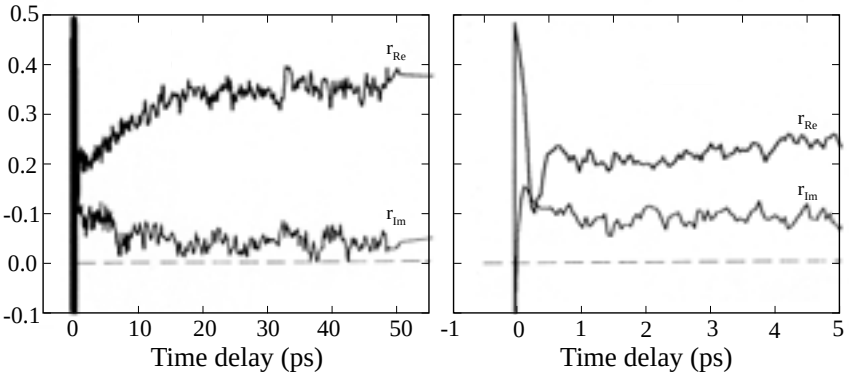

damped features of this singular component are more readily observable (50). This time scale may seem unusually fast for a relaxation process, however, these dynamics should be compared to other relaxation phenomena in the condensed phase. It has now been well-established that solvent relaxation involves the significant involvement of free streaming inertial modes (22, 23). In most cases, more than 50% of the solvent relaxation process occurs through these collective librational-like motions. As discussed above, these motions can be described as collective by the short-range order imposed by the weak intermolecular forces and inertial effects that lead to correlations that persist long enough to be categorized as a mode. These motions are not diffusive and generally involve 100 fs components. In protein systems one would expect the correlation to be even stronger and more persistent in both length scale and time scale. So the observed time scale can be rationalized. The most significant distinction of the present work is the observation of anisotropy in the protein relaxation. It has long been speculated that certain motions in the liquid state would be more important in promoting a reactive crossing. Despite fairly exhaustive investigations, there hasn't been an observation of mode selective coupling to the bath modes of liquids. It would appear that the spectral density of states (number of modes available) is all that matters and the coupling coefficient of the reaction to the different bath modes of the liquid state is not strongly varying (22, 23). Clearly, information is being lost in the liquid studies or the different modes are very similar (all involve the motion of a small number of identical solvent molecules). For biological systems, it is anticipated that the protein structure has been highly refined for the expressed purpose of generating mode selective coupling to direct the chemical energy. The above study made this important connection and is the first example of mode selective coupling of a reaction to the bath (in this case the globin surrounding the active site).

With the identification of this response as an example of mode selective coupling, the observed time scale can be correlated to microscopic processes. From the above treatment, we know that the energy becomes rapidly randomized in biological molecules. Any motions involving frequency components in the 100 to 10 cm^{-1} range should be highly damped. The 500 fs component would correspond to the half period of a highly damped mode of approximately 20 cm^{-1}. From a normal mode analysis of Seno and Go, it was found that the protein structural changes of myoglobin in going from the ligated oxy- to deoxy-tertiary structure can be reconstituted to better than 60% accuracy by the simple displacement of six low-frequency collective modes in the range of 5–20 cm^{-1} (36, 37). The all important mechanical coupling to the EF helical section would involve a mass displacement with a period very close to 20 cm^{-1}. The fact that this topological feature is so strongly conserved, and is the most intimate contact to the largest atomic displacements of the reaction coordinate, projected along the iron motion, support the interpretation of the observed anisotropic mass displacement to the EF helical section. More precisely worded, the largest coupling coefficient of the reaction coordinate is to the collective mode involving segmental motion of the EF helical section. Of course, there will be associated displacements that make up the superposition state defining the motions. Fluctuations of the EF domain would, however, serve to focus the reaction forces and efficiently direct the protein relaxation along the correct seam in a rather complex and tortuous potential energy landscape.

The experimental evidence for the collective mode coupling mechanism of energy transduction illustrates one of the most profound examples of mode selective coupling in chemical reactions. The term profound is not used lightly here as it is meant to convey the importance of these observations with respect to how biological molecules bridge the quantum aspects of chemical reactions to the meso-scale appropriate to biological functions.

The basic features of the collective mode coupling mechanism are shown in Fig. 16. To give this concept a Canadian context, this schematic follows the guiding principle of the famous *Group of Seven* artists who pioneered the portrayal of Canadian landscapes. These artists quickly sketched the scene, then made successive sketches from previous versions, until only the most salient, inspiring, details of the image remained. In some sense, this is what Nature has done to remove complexity, by spatially averaging over various length and time scales to remove fine grain features in the potential energy landscape. To reflect this effect, the individual heavy atoms of myoglobin in Fig. 16 have been replaced by the helical secondary structures that serve to delineate the

© 2002 NRC Canada

Fig. 16. Schematic of the collective mode coupling mechanism. The helical secondary structures are drawn as segments to illustrate the strong atom–atom correlations in these topological regions relative to the larger rms motions at the loop regions that are modeled as hinges for the segmental motion.

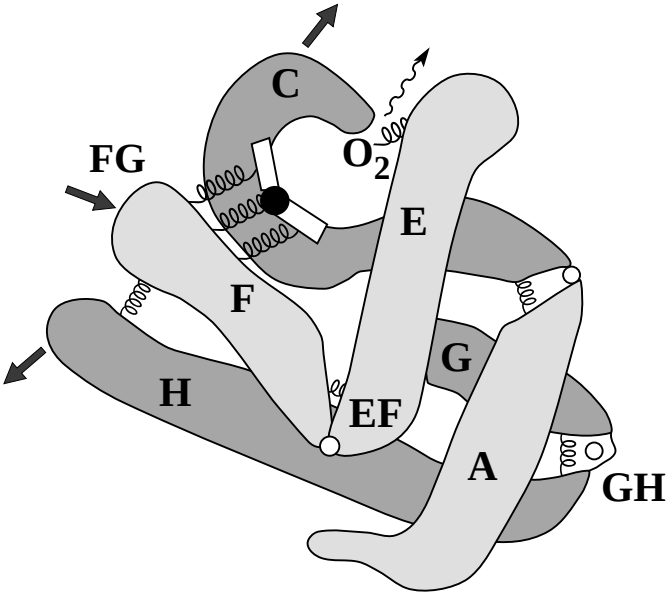

more rigid structure elements in the protein architecture. The rms motions of these regions are much smaller than the loop regions of the globin that serve as hinge points for segmental fluctuations of the helices. The breaking of the Fe—ligand bond creates an epicentre for the reaction forces that lead to the iron motion out of the heme plane and the mechanical coupling to the surrounding helices of the globin. The motions that are energetically favorable with respect to the new charge distribution at the iron will experience a larger displacement than those opposed to the reaction force field. The resultant effect is that the segmental motions of the protein's secondary structure strongly guide the system along the correct seam in the reactive surface with a very coarse grain sampling process. In this manner the system avoids becoming trapped in local minima. Furthermore, the functionally relevant motions become highly directed on a time scale that is competitive with the extremely fast energy redistribution processes discussed above. For example, once the EF helical section samples the low energy path, involving the barrel roll motion, the excess driving force becomes dissipated and the system has been displaced almost completely to the new global energy minimum distribution corresponding to the deoxy tertiary structure. From the energetics of the relaxation process, as discerned from the thermal components to the grating signals, it appears that the system propagates more than 60% of the way towards to this point through the inertial collective mode displacements (15).

Long time dynamics — "It ain't over till it's over"

I have given numerous talks covering the above observations and interpretations of the biomechanics of protein

Fig. 17. Protein response to ligand escape. The dynamics for MbCO are shown out to long time to illustrate the strongly two-tiered nature of the protein response at –1.5°C (to eliminate thermal contributions). The *Re* part of the signal shows the initial collective mode response to ligand dissociation, followed by a quiescent period (small amplitude rise due to motion of the CO through the protein) of approximately 400 ns, and then a rather abrupt expansion of the protein (purely single exponential decay; decrease in the index of refraction with expansion). In contrast, the *Im* component shows a flat baseline offset on this time scale and recovers with the expected kinetics for CO recombination on ms time scales. This difference is highlighted in the inset on a linear scale.

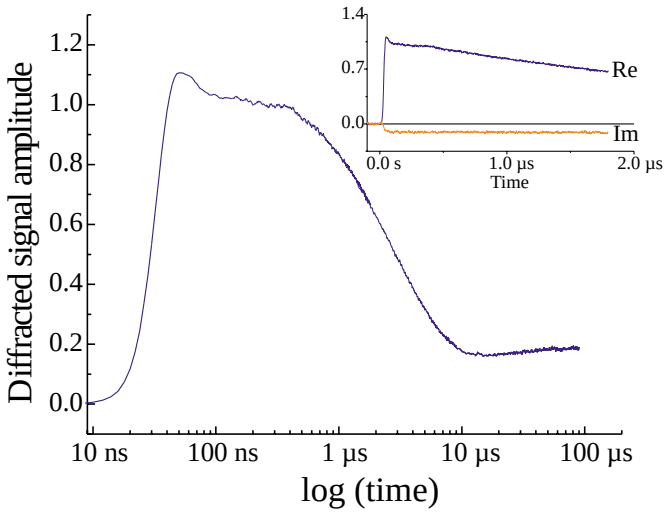

functions. Prior to joining the faculty at the University of Toronto (1995), I gave an overview of our work in this area when Professor Ron Kluger questioned the importance of the fs and (or) ps dynamics in biological functions. (A quite lively and enjoyable discussion ensued in which we each questioned how early events led us to be present in the same lecture room.) Basically, it was argued that processes occurring on µs to ms time scales are more relevant to biological functions as these time scales reflect the thermodynamics and kinetics controlling the process. We found ourselves in agreement here. Our work and the above discussion was aimed at how a biological system samples a reaction saddle point and relaxes to the new product state (executes a function) without getting lost in the myriad of local minima, i.e., transition-state crossings of complex systems. Prior to our work, most studies had found that protein relaxation involved glass-like behaviour as depicted by stretched exponential relaxation dynamics extending over several decades in time (16–21). The above work established that the initial protein relaxation phase is dominated by coupling to collective modes of the protein that would act to avoid entrapment in local minima before the onset of the glass-like response. How important is this directional "kick" that is imposed on the system? My group and I had long contemplated extending the dynamical studies to cover the full spectrum of protein motions. We wanted to determine which relaxation mechanism dominated the process, collective modes or glass-like dynamics. This important point could be established by measuring the relaxation energy associated with

© 2002 NRC Canada

Fig. 18. Proteinquakes. The case for fluid-like dynamics is contrasted to segmental sampling of the conformational distribution. The delayed onset and abrupt change in protein volume of opposite sign can be understood if the protein structure remains relatively rigid as the CO samples a discrete number of interconnected void spaces as the ligand escapes to the aqueous phase.

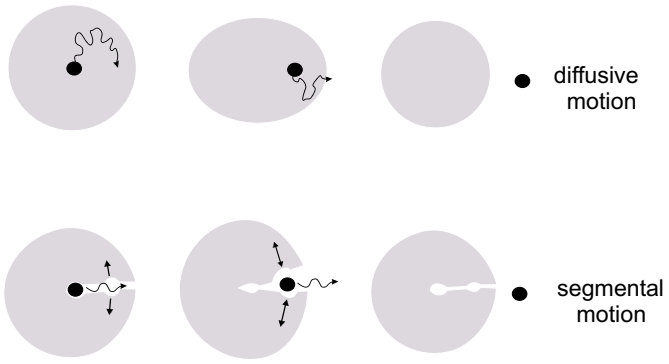

each phase of relaxation (15). This correlation would establish the driving force and response built into the system.

The experimental setup to extend the time base is very similar to the fs setup. A diffractive optic setup was employed with some minor changes. The most significant difference was that a CW laser was used for the probe and reference, with a transient digitizer to provide the time resolution. The diffractive optic was designed to have up to five different fringe spacings so we could measure transport properties and clearly separate thermal contributions to the signal from other contributions. We were originally expecting that we would observe a biphasic response, i.e., the fast collective mode relaxation phase (too fast to be resolved with this setup) followed by a slow stretched exponential relaxation process. Instead, we found, yet again, very different dynamics depicting the long time protein motions. Rather than a stretched exponential component, we observed a dramatic two-step feature to the protein response function (46, 55). These results are shown in Fig. 17 near the zero thermal expansion point to remove the thermal grating components. The two-tier nature of the protein response is most obvious in the log *t* plot where the time scale is compressed. The two most significant features are the initial signal level (collective mode relaxation phase), followed by a quiescent period of several hundred ns, then a large volume change, that is opposite in sign to the original motion, occuring on the μs time scale. By conducting a fringe-spacing dependence, we were able to determine that the solvation of the CO in water creates an index of refraction change (due to the volume excluded to create the cavity in water for the CO) that is 35% of the original signal amplitude. With this information, the μs decay component can be unambiguously assigned to the CO escape from the protein. This feature was then followed by another quiescent period during which the signal decays through bimolecular recombination with the solvated CO to regenerate the ground state and fully reequilibrate the protein system.

Close examination of the dynamics found that the observed protein response actually consisted of a small amplitude exponential rise in the signal followed by a nearly order of magnitude larger exponential component of opposite sign (55). The dynamics could be well-fit to a previous model that used a discrete subset of sites within the protein for the CO and treated the ligand transport as a thermally activated hopping process (56). The observed dynamics are in good agreement with transient IR studies of the shift in the CO vibrational spectrum with escape to the aqueous phase using fixed time delays (57). These comparisons solidify the assignment of the unusual two-tiered dynamical signature to CO transport through the protein. Most important, the rather large change in signal amplitude and most significantly the sign change, demonstrates that the protein relaxation is not a simply monotonic relaxation process along the Fe-ligation coordinate. Stretched exponential relaxation processes are monotonically decaying functions and it is not possible to describe the sign change (reversal) as a glass-like relaxation process. This is an important distinction that merits further consideration.

The CO transport through the protein is not an orthogonal coordinate to the bonding at the active site. This point has been neglected in many treatments and it is obvious from this work that the motion of the CO to the active site must be convolved to the protein relaxation coordinate. In this context, the mechanism of transport of receptor molecules through proteins has been a long debated problem. The protein structure must be rigid enough to maintain functional integrity; yet be fluid enough to permit ready access of receptor molecules to the active site. From phosphorescence quenching studies, it has been inferred that ligands, the size of oxygen, are able to access all possible pathways within protein (58). This statement is based on phosphorescence studies of buried chromophores in which the oxygen concentration dependence is found to be consistent with diffusion limited quenching. In contrast, cryogenic X-ray diffraction studies of myoglobin have found that there are only a few cavities in the protein that can accommodate diatomic ligands (59). All pathways are not accessible. In addition, there is no apparent contiguous pathway that connects the active site to the surface to assist ligand transport in and out of the protein. In fact, if the protein structure was frozen, there would be more than a 100 kcal mol^{-1} barrier to oxygen or CO escape (60). Clearly, protein dynamics are important in creating fluctuating passageways connecting the various void spaces within the protein that act to mediate the transport process. What is the mechanism that enables proteins to conserve structural integrity, yet readily shuttle ligands in and out of buried active sites? To resolve this issue requires real time measurements to fully resolve the dynamics that promote ligand transport. The grating measurements were the first to fully resolve ligand motion through a protein in real time. Based on the above observations, it can be concluded that ligand motion does not involve a completely random, diffusive, walk as inferred from quenching studies. Rather, there appear to be discrete sites within the protein. The essentially single exponential character of the CO final escape step implies that there is either one dominant channel or that the subset of conformations that enable ligand access to the solvent have very similar activation barriers.

The most surprising finding was the much larger volume change of the protein accompanying the final step of CO escape to the aqueous phase. If the protein was sampling a continuous distribution of conformations, akin to a fluid response, there should be a continuous distribution of volumes

© 2002 NRC Canada

Fig. 19. Collective mode coarse grain sampling of reaction coordinate and (or) functional motions. (*a*) Initial inertial collective mode response. The bond breaking displaces preferentially those modes most strongly coupled to the Fe. This motion is most likely the EF topological domain. This motions constitutes the largest fraction of the driving force (≥6 kcal mol^{-1}) and displaces the system very close to the conformational distribution of the fully relaxed deoxy structure (inset). (*b*) Intraprotein transport. Thermal fluctuations with a small amount of strain energy (2 to 3 kcal mol^{-1}) involved in the structural relaxation as the CO samples discrete void sites within the protein. Inset schematically represents a thermally assisted hopping process near the global energy minimum. (*c*) Ligand escape. The protein executes a change in volume that is comparable or larger to the initial relaxation phase. This process is largely entropically driven. All phases of the protein motion can be understood on the basis of a coarse grain sampling process through segmental fluctuations of the secondary structural elements that form topological domains to guide the system through otherwise extremely complex potential energy surfaces.

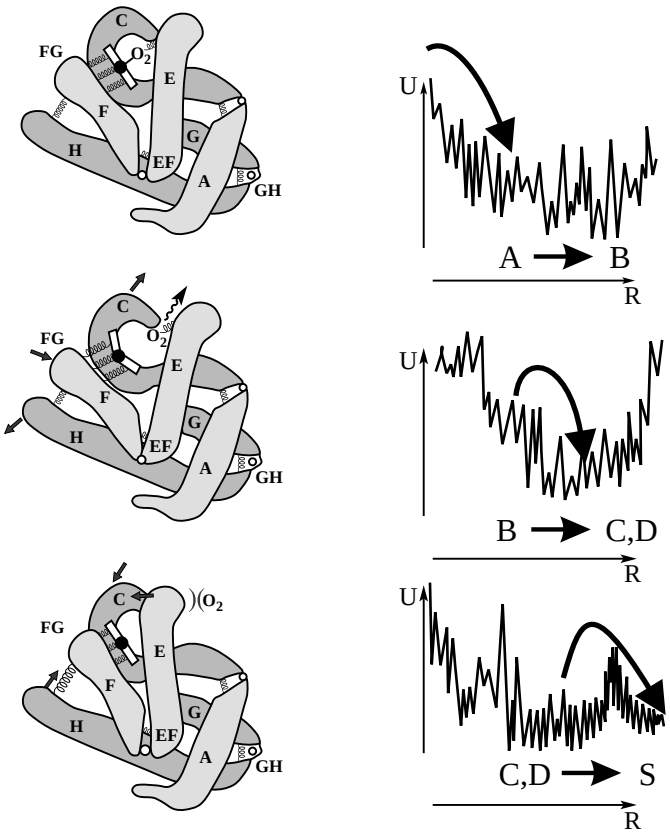

corresponding to the two end points as the protein uniformly deforms about the ligand. There should also be a distribution of arrival times characteristic of a diffusive random walk. The delayed onset to this large volume change indicates that the protein is not uniformly deforming to accommodate the ligand but rather undergoing a discontinuous change in structure commensurate with CO escape. Such a process can be rationalized if the protein retains its structural integrity with CO displacement. This phase of the motion would explain the rather small initial change in protein strain or volume; only when the CO leaves the protein does the system exhibit the differential volumes of solvation for CO in the two media (protein and water). The mechanics of this motion are shown schematically in Fig. 18 in which continuous "fluid-like" deformation of the protein about the ligand is contrasted with segmental fluctuations that would conserve the protein volume until ligand escape. The relatively negligible changes in the protein volume as the ligand moves to discrete voids imbedded in the structure demonstrates that the protein is "rigid" in the conformational sampling process. The much larger change in volume with ligand escape to the aqueous phase could then be likened to a quake, i.e., segmental displacement in response to a stress. The terminology "proteinquake" has been used previously as an analogy for understanding the relaxation processes of proteins (61). The above experiment has demonstrated that this analogy is far more appropriate than could have been envisaged prior to these experimental studies. In so far that quake phenomena involve localized strain and relaxation, there is a length scale that needs to be attributed to the process. The strongly tiered (discrete) nature of the protein response suggests that the segmental motions involve fluctuations over the pathlength that connects the void spaces to the surface. This observation clearly illustrates the remarkable degree of molecular engineering that has enabled biological systems to bridge the diffusive properties of liquids with the structural integrity of solids.

Summary

With the above long time studies, we have interferometrically followed protein motions over 12 decades in time to cover the complete range of relaxation phenomena. The general picture that has emerged is summarized in Fig. 19. The main message is that the long-range correlations of atomic motions mediated through the protein secondary structure (and tertiary contacts) greatly reduces the reaction phase space. On short time scales, the relaxation of the protein through a reaction saddle point (reactant to product state) is propagated by the displacement of the inertial collective modes of the protein matrix. The helices move in relation to the less rigid loops in a manner that strongly guides the system along the correct seam. Using the relaxation energetics as the overriding criteria, this motion along the reaction surface is the dominant mechanism. It should be noted that this is the most efficient mechanism possible. By preferential coupling to collective modes of the protein, the reaction forces map the atoms close to the global energy minima corresponding to the product state — at the speed of sound. The importance of the inertial collective phase of the relaxation process is understandable as the very fast energy redistribution processes in these metastable systems would trap the system in local minima otherwise. This work has lead to the proposal that the secondary structures of macromolecules are the director we have been seeking. These topological structural elements have the correct length scale to enable the system to jump from the atomic level, fine grain features, to the mesoscale appropriate to biological functions. In other words, it is the secondary structures such as helices that effectively coarse grain the sampling process.

In this context, Levinthal's paradox is the same as all paradoxes — a misstatement of the problem. Proteins and other biological macromolecules do not have enormous numbers

© 2002 NRC Canada

of *independent* degrees of freedom. There are significant enthalpic factors that lead to secondary structures (and tertiary contacts) that in turn lead to a high degree of correlated motion. In the case of myoglobin, the degree of correlation seems to be so strong that the displacement of less than five modes, as opposed to 1×10^4, can constitute more than 60% of the structural relaxation connecting the oxy to deoxy-tertiary structures (36, 37).

We can now return to the hologram (cover) provided to visually capture this effect. In viewing from right to left, one should see the individual heavy atoms become dressed by a van der Waals surface, like a sleeve, in which the highly directed correlations through the helical secondary structures are depicted (single frame shown in Fig. 2*b*). In moving one's head further from right to left, it should be possible to view what would appear to be the segmental motion of the EF topological domain in response to the heme doming with ligand dissociation. One has to imagine these fluctuations occurring within the background of random thermal fluctuations. The key point is the degree of correlation with respect to length scale.

In order for the secondary structures to satisfy the conditions of imposing the directionality on biological processes, there needs to be a correlation over both length scale and time scale. The correlation over time scales is imposed as a further condition on the problem as most biological processes involve many different intermediates and exhibit functionally relevant kinetics over many decades in time. As observed for CO transport through the myoglobin, there is evidence for a highly simplified response that implicates segmental fluctuations in the sampling process out at least six decades in time relative to the periods of the modes involved. Rigorously speaking, there will be deformations in these secondary structures that appear more localized and impart some liquid-like components to the motion over this time range. However, these localized deformations are likely short-lived and an average structure element showing strong conservation of the secondary structures is inferred from the highly simplified protein response to ligand escape. The concept of secondary structures imposing strong correlations on the sampling process invites a simple mechanical model of how biological systems become highly constrained with respect to their total available configuration space. It is proposed that this type of segmental motion leads to coarse grain sampling over all relevant time scales and fully satisfies the conditions as the director.

Finally, there is one other important point that should be made and emphasized. A great deal of previous work has likened protein dynamics to glass dynamics. This comparison has some merit as both proteins and glasses are highly associated systems. However, glasses are structurally homogeneous, isotropic, systems. In contrast, proteins are highly heterogeneous, being comprised of significantly more rigid structure elements (helices and (or) secondary structures) in relation to strategically placed liquid-like domains (loops). It is the juxtaposition of liquid domains with structurally more rigid domains that enables the system to exhibit coarse grain sampling. In a glass system, a perturbation relaxes through a continuum of different length scales, and associated barriers, to anneal to the lower energy state. This relaxation process exhibits classic stretched exponential behavior. Proteins will exhibit similar trends over short length scales. However, as the perturbation involves longer and longer length scales of motion, eventually the analogy with glasses has to break down. After all, the protein has a well-defined boundary at the aqueous interface. At some point, the discrete nature of the system has to become manifest in the observed response. The present work points to this distinction and highlights the dramatic departure of protein dynamics from glasses once the length scale approaches that appropriate to the biological functions (mesoscale). Thus, proteins and other biological macromolecules are distinct states of matter. The heterogeneity of the structural elements is the key to their amazing properties to retain structural integrity and (or) functionality with fluid-like dynamics — a true hybrid state of matter. We need to properly recognize the global aspects of the reaction coordinate in this regard. Our current inability to strongly influence biological functions with site-directed mutations (save a few examples of charge-transfer processes) is largely a consequence of not treating the global aspects of the reaction coordinate. Future studies of protein dynamics and structure will likely lead to more refined control over biological processes and may give us our greatest insights into chemistry in general.

Acknowledgements

The work discussed above was funded primarily by the Natural Sciences and Engineering Research Council of Canada (NSERC). Supplemental support for the work on diffractive optics was provided by Photonics Research Ontario. Initial funding was provided by the National Institute of Health (U.S.A.). The author has had the privilege to work with a number of dedicated individuals during the course of these studies. In particular, Hui-Ling Chui, Gami Dadusc, John Deak, Laura Genberg, Greg Goodno, Una Marvet, Jennifer Ogilvie, Lynn Richard, and Peter Schulenberg deserve special recognition for their efforts to reveal the intricacies of transition-state processes in biological processes. Special thanks goes to Ron Kluger for stimulating discussion and being the driving force behind a collaboration to use these concepts and (or) spectroscopies to explore chemically modified hemoglobins.

References

1. E. Hubble. Proc. Natl. Acad. Sci. U.S.A. **15**, 167 (1929).
2. R. Tripp and D. Branch. Astrophys. J. **525**, 209 (1999).
3. M.F. Perutz, J.V. Kilmartin, K. Nagai, A. Szabo, and S.R. Simon. Biochemistry, **15**, 378 (1976).
4. C. Levinthal. Chim. Phys. **65**, 44 (1968).
5. K.A. Dill. Curr. Opin. Struct. Biol. **3**, 99 (1993).
6. A. Gutin, A. Sali, V. Abkevich, M. Karplus, and E.I. Shakhnovich. J. Chem. Phys. **108**, 6466 (1998).
7. H.D. Bartunik, G.A. Kachalova, and A.N. Popov. Science (Washington, D.C.), **284**, 473 (1999).
8. R.E. Dickerson and I. Geis. Hemoglobin: Structure, function, evolution, and pathology. The Benjamin/Cummings Publishing Company, Inc., Menlo Park, California. 1983.
9. J.V. Kilmartin. Br. Med. Bull. **32**, 209 (1976).
10. J. Monod, J. Wyman, and J.-P. Changeux. J. Mol. Biol. **12**, 88 (1965).

© 2002 NRC Canada

11. L.P. Murray, J. Hofrichter, E.R. Henry, and W.A. Eaton. Biophys. Chem. **29**, 63 (1988).
12. S.D. Longa, A. Gambacurta, A. Bertollini, M. Girasole, A.C. Castellano, and F. Ascoli. Eur. Biophys. J. **29**, 559 (2001).
13. B.R. Gelin and M. Karplus. Proc. Natl. Acad. Sci. U.S.A. **74**, 801 (1977).
14. J.M. Friedman, T.W. Scott, G.J. Fisanick, S.R. Simon, E.W. Findsen, M.R. Ondrias, and V.W. MacDonald. Science (Washington, D.C.), **229**, 187 (1985).
15. R.J.D. Miller. Acc. Chem. Res. **27**, 145 (1994).
16. T.A. Jackson, M. Lim, and P.A. Anfinrud. Chem. Phys. **180**, 131 (1994).
17. R.G. Palmer, D.L. Stein, E. Abrahams, and P.W. Anderson. Phys. Rev. Lett. **53**, 958 (1984).
18. D.G. Lambright, S. Balasubramanian, and S.G. Boxer. Chem. Phys. **158**, 249 (1991).
19. F. Post, W. Doster, G. Karvounis, and M. Settles. Biophys. J. **64**, 1833 (1993).
20. S.J. Hagen and W.A. Eaton. J. Chem. Phys. **104**, 3395 (1996).
21. I.E.T. Iben, D. Braunstein, W. Doster, H. Frauenfelder, M.K. Kong, J.B. Johnson, S. Luck, P. Ormos, A. Schutle, P.J. Steinbac, A.H. Xie, and R.D. Youg. Phys. Rev. Lett. **62**, 1916 (1989).
22. R. Jimenez, G. Fleming, and P. Kumar. Nature (London), **369**, 471 (1994).
23. Y. Wang and R.M. Stratt. J. Chem. Phys. **100**, 5123 (1994).
24. L. Genberg, F. Heisel, G. McLendon, and R.J.D. Miller. J. Phys. Chem. **91**, 5521 (1987).
25. R.J.D. Miller. Ann. Rev. Phys. Chem. **42**, 581 (1991).
26. D.D. Dlott. J. Opt. Soc. Am. B, **7**, 1638 (1990).
27. E.R. Henry, W.A. Eaton, and R.M. Hochstrasser. Proc. Natl. Acad. Sci. U.S.A. **83**, 8982 (1986).
28. A.S. Davydov. Usp. Fiz. Nauk. **138**, 603 (1982).
29. A.C. Scott, E. Gratton, E. Shyamsunder, and G. Careri. Phys. Rev. B: Condens. Matter, **32**, 5551 (1985).
30. L. Genberg, Q. Bao, S. Gracewski, and R.J.D. Miller. Chem. Phys. **131**, 81 (1989).
31. J. Deak, H.L. Chiu, C.M. Lewis, and R.J.D. Miller. J. Phys. Chem. B, **102**, 6621 (1998).
32. R. Lingle, Jr., X. Xu, H. Zhu, S.-C. Yu, J.B. Hopkins, and K.D. Straub. J. Am. Chem. Soc. **113**, 3992 (1991).
33. J.W. Petrich, J.L. Martin, D. Houde, C. Poyart, and A. Orzag. Biochemistry, **26**, 7914 (1987).
34. Y. Mizutani and T. Kitagawa. Science (Washington, D.C.), **278**, 443 (1997).
35. T. Lian, B. Locke, Y. Kholodenko, and R.M. Hochstrasser. J. Phys. Chem. **98**, 11 648 (1994).
36. Y. Seno and N. Go. J. Mol. Biol. **216**, 95 (1990).
37. Y. Seno and N. Go. J. Mol. Biol. **216**, 111 (1990).
38. H.J. Eichler, P. Gunter, and D.W. Pohl. Laser-induced dynamic gratings. Springer–Verlag, Berlin. 1986.
39. Q.H. Gibson and S. Ainsworth. Nature (London), **180**, 1416 (1957).
40. A.T.N. Kumar, F. Rosca, A. Widom, and P.M. Champion. J. Chem. Phys. **114**, 701 (2001).
41. E.R. Henry, J.H. Sommer, J. Hofrichter, and W.A. Eaton. J. Mol. Biol. **166**, 443 (1983).
42. L. Genberg, L. Richard, G. McLendon, and R.J.D. Miller. Science (Washington, D.C.), **251**, 1051 (1991).
43. L. Richard, L. Genberg, J. Deak, H.L. Chiu, and R.J.D. Miller. Biochemistry, **31**, 10 703 (1992).
44. J.A. Rogers and K.A. Nelson. Physica B: (Amsterdam), **219–220**, 562 (1996).
45. G.D. Goodno, G. Dadusc, and R.J.D. Miller. J. Opt. Soc. Am. B, **15**, 1791 (1998).
46. G. Dadusc, G.D. Goodno, H.L. Chiu, J.P. Ogilvie, and R.J.D. Miller. Isr. J. Chem. **38**, 191 (1998).
47. V. Astinov, K.J. Kubarych, C.J. Milne, and R.J.D. Miller. Opt. Lett. **25**, 853 (2000).
48. V. Astinov, K.J. Kubarych, C.J. Milne, and R.J.D. Miller. Chem. Phys. Lett. **327**, 334 (2000).
49. G.D. Goodno, V. Astinov, and R.J.D. Miller. J. Phys. Chem. A, **103**, 10 619 (1999).
50. G.D. Goodno, V. Astinov, and R.J.D. Miller. J. Phys. Chem. A, **103**, 10 630 (1999).
51. G.D. Goodno, V. Astinov, and R.J.D. Miller. J. Phys. Chem. B, **103**, 603 (1999).
52. M.D. Levenson and G.L. Eesley. Appl. Phys. (Berlin), **19**, 1 (1979).
53. R.J.D. Miller, R. Casalegno, K. Nelson, and M.D. Fayer. Chem. Phys. **72**, 371 (1982).
54. T.P. Carter, M. Manavi, and W.E. Moerner. J. Chem. Phys. **15**, 1768 (1988).
55. G. Dadusc, J.P. Ogilvie, P. Schulenberg, U. Marvet, and R.J.D. Miller. Proc. Natl. Acad. Sci. U.S.A. In press (2001).
56. D. Beece, L. Eisenstein, H. Frauenfelder, D. Good, M.C. Marden, M.L. Reinisch, A.H. Reynolds, L.B. Sorensen, and K.T. Yue. Biochemistry, **19**, 5147 (1980).
57. T.A. Jackson, M. Lim, and P.A. Anfinrud. Int. Conf. on Time-Resolved Vib. Spectrosc. Proc. Conf. 7th, 1995. 9.
58. M. Brunori. Biophys. Chem. **86**, 221 (2000).
59. V. Srajer, T. Teng, T. Ursby, C. Pradervand, Z. Rev, S. Adachi, W. Schildkamp, D. Bourgeoi, M. Wulff, and K. Moffat. Science (Washington, D.C.), **274**, 1726 (1996).
60. D.A. Case and M. Karplus. J. Mol. Biol. **132**, 343 (1979).
61. A. Ansari, J. Berendzen, S.F. Bowne, H. Frauenfelder, I.E.T. Iben, T.B. Sauke, E. Shyamsunder, and R.D. Young. Proc. Natl. Acad. Sci. U.S.A. **82**, 5000 (1985).

© 2002 NRC Canada

Electron-spin conservation and methyl-substitution effects on bonds in closed- and open-shell systems — A G3 ab initio study of small boron-containing molecules and radicals

Clement Poon and Paul M. Mayer

Abstract: High level ab initio molecular orbital theory calculations have been used to study the geometries and thermochemistry of molecules and free radicals substituted by BH_2, $BHCH_3$, and $B(CH_3)_2$. The heats of formation and RR′B—X bond strengths (RR′ = H, H; H, CH_3; CH_3, CH_3 and X = CH_3, NH_2, OH, F, SiH_3, PH_2, SH, and Cl) together with those for the open-shell systems RR′B—Y· (RR′ = H, H; H, CH_3; CH_3, CH_3 and Y = CH_2, NH, O, SiH_2, PH, and S) have been calculated at the G3 level of theory. The trends observed for the homolytic bond strengths in the closed-shell systems are those expected from electronegativity arguments, i.e., as the difference in electronegativity between the two atoms in the B—X bond increases, the bond strength increases. Methyl substitution on B in the closed- and open-shell species increases the ionic contribution to the bond thereby decreasing the bond strength. The lowest possible homolytic dissociation energy for the free radicals RR′BY· is lower than those of their closed-shell counterparts, yet the B—Y· bonds are shorter. This is due to the demands of spin conservation in the dissociation of the radicals favouring the formation of higher energy products.

Key words: ab initio calculations, bond dissociation energy, organoboron compounds, thermochemistry.

Résumé : Faisant appel à des calculs théoriques d'orbitales moléculaires ab initio à niveau élevé, on a étudié les géométries et la thermochimie de molécules et de radicaux substitués par des groupes BH_2, $BHCH_3$ et $B(CH_3)_2$. On a calculé les chaleurs de formation et les forces des liaisons des composés RR′B—X (RR′ = H, H; H, CH_3; CH_3, CH_3 et X = CH_3, NH_2, OH, F, SiH_3, PH_2, SH et Cl) ainsi que les valeurs correspondantes pour les systèmes à couches ouvertes RR′B–Y· (RR′ = H, H; H, CH_3; CH_3, CH_3 et Y = CH_2, NH, O, SiH_2, PH et S) au niveau G3 de la théorie. Les tendances observées pour les forces homolytiques des liaisons des systèmes à couches ouvertes correspondent à celles auxquelles on pourrait s'attendre sur la base d'arguments d'électronégativité, c'est-à-dire que la force de la liaison augmente avec une l'augmentation dans la différence d'électronégativité entre les deux atomes de B—X. Une substitution du B par un méthyle dans les espèces à couches ouvertes ou fermées provoque une augmentation de la contribution ionique à la liaison accompagnée d'une diminution de la force ionique. L'énergie de dissociation homolytique la plus faible pour les radicaux libres RR′BY· est inférieure à celles de leurs contreparties en couches fermées, mais les liaisons B—Y· sont toutefois plus courtes. Ce fait résulte des demandes de conservation de spin dans la dissociation des radicaux qui favorise la formation de produits d'énergie plus élevée.

Mots clés : calculs ab initio, énergie de dissociation de liaison, composés organiques du bore, thermochimie.

[Traduit par la Rédaction]

Introduction

The strength of a bond between two atoms is one of the most fundamental molecular properties in chemistry. Since few bond strengths (homo- or heterolytic) can be measured directly, estimates are usually derived from molecular and fragment heats of formation (ΔH_f°). Experimental determination of free radical ΔH_f° values (and thus homolytic bond strengths) are inherently difficult and relatively few values are available (1). The two most common methods for deriving free radical ΔH_f° values are by halogen abstraction kinetics and the appearance energy (AE) method (2). A typical approach to the former involves reacting a molecule RH with a halogen atom X· in a very low pressure reactor to form a free radical R· and HX, the halogen concentration being monitored spectroscopically. The enthalpy change of the reaction can be determined by measuring the temperature dependence of the forward and reverse reaction rate constants. If the ΔH_f° values for RH, HX, and X· are known, that of R· can be derived. In the AE technique, molecules RB are chosen so that upon dissociative ionization by photons (for examples see refs. 2 and 3) or monoenergetic electrons (for examples see refs. 4–6) the products R· and B^+ are formed.

Received 21 August 2001. Published on the NRC Research Press Web site at http://canjchem.nrc.ca on 10 January 2002.

C. Poon[1] and P.M. Mayer[2]. Chemistry Department, University of Ottawa, ON K1N 6N5, Canada.

[1]Undergraduate researcher.
[2]Corresponding author (telephone: (613) 562-5800 ext. 6038; fax: (613) 562-5170; email: pmayer@science.uottawa.ca).

 DOI: 10.1139/V01-185 © 2002 NRC Canada

In its simplest form, the AE relates the ΔH_f° values of the two products to that of RB, and if ΔH_f° (B^+) and ΔH_f° (RB) are known, ΔH_f° (R) can be determined. Both techniques suffer from limitations, the most significant being that stable molecules RH and RB must be introduced into an apparatus. This poses a problem when the free radicals under study contain functional groups that make the molecules difficult to synthesize or handle.

In light of these difficulties, the development of reliable ab initio molecular orbital methods for estimating molecular thermochemistry has driven a rebirth in the field. In particular, the development of composite techniques such as the G2 and G3 series of methods by Curtiss and Pople and co-workers (7–13) and the complete basis set approach of Petersson and co-workers (14, 15) have allowed researchers to calculate reliable (±10 kJ mol^{-1}) ΔH_f° values for a wide variety of molecules and free radicals. In addition, since theory is not limited by the availability or the handling of compounds, it is possible to exhaustively cover permutations of molecular structures and study substituent effects for a wide variety of properties such as ΔH_f°, proton affinity, electron affinity, gas-phase acidity, bond strength, etc.

A family of compounds that are not amenable to experimental study are the boranes, organoboron compounds involving boron bound to organic substituents. Over the years, there has been extensive experimental study of carbon-containing molecules and the strengths of bonds in hydrocarbons. Boron has not been as widely studied, likely due to the difficulty in handling the compounds as mentioned above. Interest in boron-containing compounds is more than just academic, however, as boron is found in ceramic materials such as boronitrides. Substitution of the boronitride backbone can be used to obtain different properties of the end material and so reliable bond strength and ΔH_f° data are useful.

The homolytic bond dissociation energy (*BDE*), or homolytic bond strength, of a bond in a molecule is defined as the energy change of the reaction that breaks the bond to form two free radicals. Therefore, the homolytic BDE of the B—X bond in BH_2X is the ΔE for the following reaction:

$$BH_2X \rightarrow BH_2\cdot + X\cdot$$

$$BDE = \Delta E = E\ (BH_2\cdot) + E\ (X\cdot) - E\ (BH_2X)$$

In this paper, we calculate the homolytic B—X bond strengths and the heats of formation of BH_2CH_3, BH_2NH_2, BH_2OH, and BH_2F as well as the methyl-substituted analogues $BH(CH_3)CH_3$, $BH(CH_3)NH_2$, $BH(CH_3)OH$, $BH(CH_3)F$ and $B(CH_3)_3$, $B(CH_3)_2NH_2$, $B(CH_3)_2OH$, and $B(CH_3)_2F$. In addition, the second row analogues of these compounds were included for comparison (BH_2SiH_3, BH_2PH_2, BH_2SH, BH_2Cl, $BH(CH_3)SiH_3$, $BH(CH_3)PH_2$, $BH(CH_3)SH$, $BH(CH_3)Cl$, $B(CH_3)_2SiH_3$, $B(CH_3)_2PH_2$, $B(CH_3)_2SH$, and $B(CH_3)_2Cl$). The impact on the B—X bond of a free radical centre on X is also explored in each of the above systems (except for the halogens).

Computational procedures

Standard ab initio molecular orbital calculations (16) were carried out using the GAUSSIAN 98 (17) suite of programs. The geometries of all species were optimized at the HF/6-31G(d) and MP2/6-31+G(d) levels of theory. Vibrational frequencies were also calculated at these levels. A recent assessment of theoretical procedures for treating free radicals concluded that for those with low-spin contamination in the SCF wavefunction, MP2 provided reasonable geometries for subsequent single-point energy calculations (18). All of the radicals presented in this study fall into this category. The MP2/6-31+G(d) geometries were used to obtain G3 (13) total energies. G3 theory approximates the energy of a species at the QCISD(T)/G3large level of theory by a series of additive corrections to a base MP4/6-31G(d) energy. The G3large basis set is a modified version of the standard 6-311+G(3df,2p) basis set in which more polarization functions are added to first row elements (3*d2f*), fewer on second row elements (2*df*), and core polarization functions are incorporated. Details of the properties of the G3large basis set can be found in the original publication by Curtiss et al. (13). G3 incorporates a scaled (by 0.8929) HF/6-31G(d) zero-point vibrational energy (*ZPE*), spin-orbit corrections for atoms, and the use of the MP2(full)/G3large calculation to take into account core-correlation contributions. Finally, an empirical higher-level correction (HLC) accounts for residual basis set errors. The G3 total energies were converted to heats of formation according to the atomization method outlined by Nicolaides et al. (19). Thermal corrections to 298 K employed the scaled HF/6-31G(d) frequencies and known thermal corrections for the elements. Optimized geometries in the form of Gaussian archive entries, are available as supporting information. Copies of material on deposit may be purchased from the Depository of Unpublished Data, Document Delivery, CISTI, National Research Council Canada, Ottawa, ON K1A 0S2, Canada (http://www.nrc.ca/cisti/irm/unpub_e.shtml for information on ordering electronically). This material has also been deposited with the Cambridge Crystallographic Data Centre. Copies of the data can be obtained, free of charge, on application to the Director, CCDC, 12 Union Road, Cambridge CB2 1EZ, U.K. (Fax: 44-1223-336033 or e-mail: deposit@ccdc.cam.ac.uk).

Results and discussion

Heats of formation

The calculated G3 heats of formation at 0 and 298 K, together with available experimental data at 298 K, are presented in Tables 1 and 2. The only experimental values available for comparison are for the fragmentation products (Table 2), and agreement between theory and experiment is generally good, except for $BH_2\cdot$ which shows a difference of 128 kJ mol^{-1}. The experimental heat of formation for $BH_2\cdot$ (200.83 kJ mol^{-1}) was indirectly derived by Fehlner and Koski (20) from the appearance energy for the formation of BH_2^+ from BH_3 and the ionization energy of $BH_2\cdot$. Both measurements were made with beams of unresolved electrons and are thus, subject to considerable error (6). This example highlights the difficulty of experimentally determining the ΔH_f° values for boron-containing free radicals. Ab initio calculations at a variety of levels of theory result in values ranging from 312 to 322 kJ mol^{-1} (21–25), similar to the present G3 result of 329 kJ mol^{-1}.

© 2002 NRC Canada

Table 1. Calculated heats of formation for closed- and open-shell species.[a]

Closed-shell species	Symmetry	$\Delta H^\circ_{f\,0}$	$\Delta H^\circ_{f\,298}$	Open-shell species	Symmetry	$< S^2 >$	$\Delta H^\circ_{f\,0}$	$\Delta H^\circ_{f\,298}$
BH_2CH_3	C_1	47	37	$BH_2CH_2\cdot$	C_{2v}	0.757	220	213
BH_2NH_2	C_{2v}	–65	–77	$BH_2NH\cdot$	C_s	0.774	186	181
BH_2OH	C_s	–262	–270	$BH_2O\cdot$	C_{2v}	0.766	–58	–61
BH_2F	C_{2v}	–298	–302	$BH_2SiH_2\cdot$	C_s	0.761	289	281
BH_2SiH_3	C_1	184	173	$BH_2PH\cdot$	C_s	0.785	305	297
BH_2SH	C_s	3	–4	$BH_2S\cdot$	C_{2v}	0.762	130	127
BH_2PH_2	C_s	106	95	$(CH_3)HBCH_2\cdot$	C_1	0.757	158	145
BH_2Cl	C_{2v}	–70	–74	$(CH_3)HBNH\cdot$	C_1	0.768	133	122
$(CH_3)HBCH_3$	C_1	–19	–35	$(CH_3)HBO\cdot$	C_s	0.764	–117	–127
$(CH_3)HBNH_2$	C_s	–124	–141	$(CH_3)HBSiH_2\cdot$	C_1	0.763	234	221
$(CH_3)HBOH$	C_s	–329	–343	$(CH_3)HBPH\cdot$	C_s	0.774	251	237
$(CH_3)HBF$	C_s	–371	–380	$(CH_3)HBS\cdot$	C_s	0.761	73	64
$(CH_3)HBSiH_3$	C_1	118	102	$(CH_3)_2BCH_2\cdot$	C_1	0.758	92	74
$(CH_3)HBPH_2$	C_1	44	28	$(CH_3)_2BNH\cdot$	C_1	0.765	74	58
$(CH_3)HBSH$	C_1	–59	–71	$(CH_3)_2BO\cdot$	C_s	0.762	–177	–192
$(CH_3)HBCl$	C_s	–140	–150	$(CH_3)_2BSiH_2\cdot$	C_1	0.764	175	158
$(CH_3)_2BCH_3$	C_1	–88	–109	$(CH_3)_2BPH\cdot$	C_s	0.769	192	173
$(CH_3)_2BNH_2$	C_1	–183	–205	$(CH_3)_2BS\cdot$	C_1	0.760	14	0.31
$(CH_3)_2BOH$	C_1	–392	–411					
$(CH_3)_2BF$	C_2	–440	–455					
$(CH_3)_2BSiH_3$	C_1	52	31					
$(CH_3)_2BPH_2$	C_1	–19	–40					
$(CH_3)_2BSH$	C_1	–121	–139					
$(CH_3)_2BCl$	C_1	–209	–222					

[a]All values in kJ mol^{-1}.

The new theoretical values in Table 1 are useful for deriving additivity parameters for estimating molecular heats of formation for boron-containing compounds. Successive methyl substitution on BH_2CH_3 results in decreases in $\Delta H^\circ_{f\,298}$ of 72 and 74 kJ mol^{-1}. This is quite different from the hydrocarbons where methyl substitution lowers the $\Delta H^\circ_{f\,298}$ by 21 kJ mol^{-1} in going from ethane to propane, and by 29 kJ mol^{-1} in going from propane to isobutane (26). The effects of methyl substitution are largely independent of the other groups present, with all of the RR′BX molecules exhibiting decreases in $\Delta H^\circ_{f\,298}$ upon the addition of successive methyl groups of ~70 kJ mol^{-1}. The smallest effect is observed when X is NH_2 (64 kJ mol^{-1}) and PH_2 (67 kJ mol^{-1}). For open-shell systems, the effect of methyl substitution on $RR'BCH_2\cdot$ is similar to that for the closed-shell analogue (68–71 kJ mol^{-1}), while for other RR′BY· species the effect is slightly smaller (63 ± 3 kJ mol^{-1}).

The RR′B—X bond

The trends in the B—X bond length and strength are evident from Table 3. The B—X bond gets shorter in going from a Group 4 to a Group 7 substituent, while the homolytic *BDE* shows an increase across the periodic table (Table 3). This is the same as the trend observed for CH_3—X bonds which has been explained by electronegativity arguments (27–30). As the difference in electronegativity of the two bonded atoms increases, the homolytic bond strength increases. Electronic interactions in these systems will be dominated by the vacant *p*-orbital on boron. The π-donor substituents NH_2, OH, and F all donate electron density from a lone pair to the vacant *p*-orbital on B, resulting in a stabilizing two-electron interaction. The degree of π donation decreases across the first row from NH_2 to F while the inductive effect due to the difference in electronegativity of the atoms increases in the same order. Apparent from the observed trend in bond strengths is that the electronegativity effects outweigh stabilization due to π donation. The pseudo-π orbital on the methyl group in BH_2CH_3 is involved in a weaker hyperconjugation interaction with the vacant *p*-orbital on B. All of these interactions are present (to a lesser extent) with the analogous second row substituents. This is highlighted by the geometries of BH_2NH_2 and BH_2PH_2. The former molecule is a planar C_{2v} structure which maximizes the overlap of the *n*(N) and *p*(B) orbitals, while the latter has a puckered phosphorous centre.

The effect of methyl substitution on the BH_2 group generally (but not universally, see below) decreases the homolytic bond strength, lengthening the B—X bond (Table 3). The effects of methyl substitution in the RR′B—CH_3 and RR′B—SiH_3 series are small, the bond strength decreasing only 2 and 3 kJ mol^{-1} (for CH_3) and 3 and 1 kJ mol^{-1} (for SiH_3) upon the successive addition of two methyl groups on B. When X is a π-donor group the changes in bond strength are more significant. One rationale for the behaviour can be obtained by examining the molecular orbitals in these systems. Of the π-donor substituents NH_2 and OH, the $n(X) \rightarrow p(B)$ molecular orbital is the HOMO only for NH_2. For OH, the HOMO is an antibonding (with respect to the B—O bond) orbital incorporating a B—H (or B—CH_3) group and the O—H bond. The observed trend suggests that methyl substitution enhances the antibonding character of the HOMO, thus weakening the bond. The largest effect is for BH_2NH_2 where successive methyl substitution lowers the B—N bond strength by 10 and 8 kJ mol^{-1}. Another way of rationalizing

© 2002 NRC Canada

Table 2. Comparison of calculated and experimental heats of formation for dissociation products.[a]

Species	Symmetry	$\Delta H^\circ_{f\,0}$ G3	$\Delta H^\circ_{f\,298}$ G3	NIST[b]	LBLHLM[c]
$BH_2\cdot$	C_{2v}	329	329	200.832	201 ± 63
BH_2^+	C_{2v}	1120	1120	1145.5[d]	1146
$\cdot BHCH_3$	C_1	261	255		
$^+BHCH_3$	C_1	941	943		
$\cdot B(CH_3)_2$	C_1	195	183		
$^+B(CH_3)_2$	C_1	784	761		
$^3CH_2\cdot\cdot$	C_{2v}	396	397	386.4	390
$^1CH_2\cdot\cdot$	C_{2v}	426	426		
$CH_3\cdot$	D_{3h}	145	142	147 ± 1145.6873	145.8 ± 1149.0
CH_3^-	C_{3v}	144	140	135.8 ± 3.8	139 ± 8
$^3NH\cdot\cdot$	$C_{\infty v}$	363	364	376.5	376.6 ± 16.7, 376.5 ± 16.7
$^1NH\cdot\cdot$	$C_{\infty v}$	527	529		
$NH_2\cdot$	C_{2v}	189	186	190.372	188.7 ± 1.3, 191.6 ± 1.3
NH_2^-	C_{2v}	121	118	112.5 ± 3.8, 49.4 ± 19.2	113 ± 4, 49 ± 19
$^3O\cdot\cdot$		247	249	249.18	249.2 ± 0.1, 246.8 ± 0.1
$^1O\cdot\cdot$		446	448		
$OH\cdot$	$C_{\infty v}$	35	35	38.98706	39.0 ± 1.2, 38.4 ± 1.2
OH^-	$C_{\infty v}$	–137	–137	–137.2 ± 0.84	–137
$F\cdot$		77	79	79.38 ± 0.30, 79.39014	79.4 ± 0.30, 77.4 ± 0.30
F^-		–252	–251	–248.6 ± 1.1	–249
$^3SiH_2\cdot\cdot$	C_{2v}	374	372		
$^1SiH_2\cdot\cdot$	C_{2v}	272	270		289 ± 8
$SiH_3\cdot$	D_{3h}	208	202		202.9 ± 6.3
SiH_3^-	C_{3v}	70	65	62.3 ± 9.2, 486 ± 9.6	63 ± 10, 486 ± 10
$^3PH\cdot\cdot$	$C_{\infty v}$	246	246	253.55	236 ± 8, 237 ± 8
$^1PH\cdot\cdot$	$C_{\infty v}$	341	341		
$PH_2\cdot$	C_{2v}	140	137	125.938	139.5, 142.2 ± 2.5
PH_2^-	C_{2v}	18	14	27 ± 9.2, <9.2 ± 19.7	27 ± 10
$^3S\cdot\cdot$		275	276	277.17 ± 0.15	277.0 ± 0.3, 274.7 ± 0.3
$^1S\cdot\cdot$		391	392		
$SH\cdot$	$C_{\infty v}$	141	141	139.3272	139.3 ± 5.0, 136.5 ± 5.0
SH^-	$C_{\infty v}$	–83	–83	–81.2 ± 9.2, –68.62	–69
$Cl\cdot$		120	121	121.301 ± 0.008, 121.3021	121.3, 119.6
Cl^-		–234	–232	–227.4, –227.4 ± 0.84	–227 ± 1

[a]All values in kJ mol^{-1}.
[b]Values found in the NIST Webbook (26).
[c]Values found in LBLHLM (1).
[d]Based on the reported *IE* of 9.8 eV and $\Delta H_f^\circ(BH_2\cdot)$ of 200.832 kJ mol^{-1}.

the observed trend is from the view point of competing covalent and ionic contributions to the B—X bond:

$$RR'B—X \text{ vs. } RR'B^+X^-$$
$$a \qquad b$$

Methyl substitution lowers the heterolytic bond strength (Table 4), thus increasing the ionic (nonbonding) contribution to the bond. This is most clearly seen in the case of X = F and Cl (Tables 3 and 4). Methyl substitution makes the B—F and B—Cl bonds longer, though the homolytic bond strength increases. The heterolytic bond strengths for the dimethyl-substituted molecules are now closer to the homolytic bond strengths (966 vs. 717 kJ mol^{-1} for X = F and 751 vs. 526 kJ mol^{-1} for X = Cl) indicating that these bonds are influenced to a greater degree by the nonbonding ionic structure *b*.

The RR′B—Y· bond

When the BH_2 moiety is substituted by a free radical group, there is a general decrease in the B—Y· bond length from the closed-shell counterpart (Table 3). There are two possible sets of dissociation products for these RR′BY· radicals:

$$RR'B—Y\cdot \rightarrow {}^2RR'B\cdot + {}^1Y\cdot\cdot$$

$$RR'B—Y\cdot \rightarrow {}^2RR'B\cdot + {}^3Y\cdot\cdot$$

The lowest energy states of CH_2, NH, O, PH, and S are their triplet states. However, Wigner spin-conservation demands that spin be maintained in the unimolecular dissociation (31–33). The shorter B—Y· bonds in the $RR'BCH_2\cdot$, RR′BNH·, RR′BO·, RR′BPH·, and RR′BS· radicals (relative to the corresponding B—X bonds) are consistent with their greater homolytic bond strengths when the products involving the singlet-state Y· groups are formed. While the dissociation to form the lower energy products (incorporating the

© 2002 NRC Canada

Table 3. Bond lengths and bond strengths in closed- and open-shell organoboron compounds.[a]

	Bond length[a]			Homolytic bond strength[b]		
X or Y·	BH_2—	$B(CH_3)H$—	$B(CH_3)_2$—	BH_2—	$B(CH_3)H$—	$B(CH_3)_2$—
—CH_3	1.563	1.569	1.577	434	432	429
—CH_2·	1.535	1.540	1.547	513[c]	506[c]	501[c]
				542[d]	536[d]	531[d]
—NH_2	1.400	1.405	1.410	592	582	574
—NH·	1.352	1.381	1.405	512[c]	498[c]	489[c]
				677[d]	662[d]	654[d]
—OH	1.365	1.373	1.379	634	633	629
—O·	1.316	1.325	1.336	639[c]	630[c]	623[c]
				838[d]	830[d]	822[d]
—F	1.342	1.351	1.361	710	715	717
—SiH_3	2.022	2.030	2.040	358	355	354
—SiH_2·	1.933	1.949	1.964	420[c]	406[c]	397[c]
				318[d]	305[d]	295[d]
—PH_2	1.861	1.882	1.902	370	364	359
—PH·	1.790	1.807	1.821	278[c]	264[c]	256[c]
				373[d]	359[d]	351[d]
—SH	1.772	1.783	1.797	474	468	462
—S·	1.739	1.754	1.769	462[c]	468[c]	459[c]
				595[d]	584[d]	575[d]
—Cl	1.737	1.750	1.768	524	526	526

[a]Bond lengths (Å) optimized at the MP2/6-31+G(d) level of theory.
[b]G3 values in kJ mol^{-1} at 298 K.
[c]Triplet Y product.
[d]Singlet Y product.

Table 4. Heterolytic bond strengths in closed-shell organoboron compounds.[a,b]

	Heterolytic bond strength[b]		
X	BH_2—	$B(CH_3)H$—	$B(CH_3)_2$—
—CH_3	1224	1109	1006
—NH_2	1315	1193	1085
—OH	1253	1063	1035
—F	1172	1139	966
—SiH_3	1011	896	796
—PH_2	1039	919	815
—SH	1041	922	817
—Cl	962	851	751

[a]Values in kJ mol^{-1} at 298 K.
[b]Heterolytic bond strengths defined as $E(RR'B^+) + E(X^-) - E(RR'BX)$.

triplet state Y· groups) will not strictly be forbidden, the dissociating radicals have equilibrium geometries that are adiabatically connected to the higher energy products. While these homolytic bond strengths are unlikely to be realized in experiment due to avoided crossings with states leading to the lower energy products, they provide a rationale for the observed shorter RR′B—Y· bonds as compared to the corresponding RR′B—X bonds. The BH_2CH_2· radical has a planar structure, allowing a stabilizing one-electron interaction between the occupied *p*-orbital on C and the unoccupied *p*-orbital on B. This interaction is larger than the hyperconjugation that takes place in the closed-shell analogue, resulting in a shorter and stronger bond regardless of the products formed (Table 3). For $RR'BSiH_2$·, the lowest energy products are $^2RR'B\cdot + {}^1SiH_2\cdot\cdot$. In this case, the shortening of the B—Si bond in going from the closed- to open-shell systems is consistent with the formation of the higher energy product pair $^2RR'B\cdot + {}^3SiH_2\cdot\cdot$ (Table 3). Methyl substitution in the RR′B—Y· radicals has a similar effect as observed for the closed-shell molecules, i.e., it lowers the strength of the B—Y· bond by increasing the nonbonding ionic $RR'B^+Y^-\cdot$ contribution.

Summary

The G3 computational method was employed to estimate the heats of formation and bond strengths in a series of organoboron compounds RR′BX and free radicals, RR′BY·. The trends observed for the relative lengths and strengths of the B—X and B—Y· bonds can be understood on the basis of electronegativity arguments and spin-conservation rules. There is a universal decrease in the B—Y· bond length compared to their closed-shell counterparts which corresponds to a tendency to favour higher energy dissociation products rather than the lower energy product pairs. Successive methyl substitution on the boron atom increases the ionic contribution to the B—X and B—Y· bonds thereby increasing the bond lengths.

Acknowledgments

PMM thanks the Natural Sciences and Engineering Research Council of Canada (NSERC) for continued financial support and the HPCVL consortium for cpu time on the IBM SP2 at Queen's University. CP thanks the Natural Sciences and Engineering Research Council of Canada

© 2002 NRC Canada

(NSERC) for an Undergraduate Summer Research Award during the tenure of which this work was completed.

References

1. S.G. Lias, J.E. Bartmess, J.F. Liebman, J.L. Holmes, R.D. Levin, and W.G. Mallard. J. Phys. Chem. Ref. Data, **17**, (Suppl. 1) (1988).
2. J. Berkowitz, G.B. Ellison, and D. Gutman. J. Phys. Chem. **98**, 2744 (1994).
3. J.C. Traeger and R.G. McLoughlin. J. Am. Chem. Soc. **103**, 3647 (1981).
4. J.L. Holmes and F.P. Lossing. Int. J. Mass Spectrom. Ion Processes, **58**, 113 (1984).
5. J.L. Holmes, F.P. Lossing, and A. Maccoll. J. Am. Chem. Soc. **110**, 7339 (1988).
6. J.L. Holmes, F.P. Lossing, and P.M. Mayer. J. Am. Chem. Soc. **113**, 9723 (1991).
7. L.A. Curtiss, K. Raghavachari, G.W. Trucks, and J.A. Pople. J. Chem. Phys. **94**, 7221 (1991).
8. L.A. Curtiss, J.E. Carpenter, K. Raghavachari, and J.A. Pople. J. Chem. Phys. **96**, 9030 (1992).
9. L.A. Curtiss, K. Raghavachari, and J.A. Pople. J. Chem. Phys. **98**, 1293 (1993).
10. L.A. Curtiss, K. Raghavachari, and J.A. Pople. J. Chem. Phys. **103**, 4192 (1995).
11. L.A. Curtiss, M.P. McGrath, J.-P. Blaudeau, N.E. Davis, R.C. Binning, and L. Radom. J. Chem. Phys. **103**, 6104 (1995).
12. L.A. Curtiss, P.C. Redfern, B.J. Smith, and L. Radom. J. Chem. Phys. **104**, 5148 (1996).
13. L.A. Curtiss, K. Raghavachari, P.C. Refern, V. Rassolov, and J.A. Pople. J. Chem. Phys. **109**, 7764 (1998).
14. J.A. Montgomery, M.J. Frisch, J.W. Ochterski, and G.A. Petersson. J. Chem. Phys. **110**, 2822 (1999).
15. J.W. Ochterski, G.A. Petersson, and J.A. Montgomery. J. Chem. Phys. **104**, 2598 (1996).
16. W.J. Hehre, L. Radom, P.v.R. Schleyer, and J.A. Pople. Ab initio Molecular Orbital Theory. Wiley, New York. 1986.
17. M.J. Frisch, G.W. Trucks, H.B. Schlegel, G.E. Scuseria, M.A. Robb, J.R. Cheeseman, V.G. Zakrzewski, J.A. Montgomery, R.E. Stratmann, J.C. Burant, S. Dapprich, J.M. Millam, A.D. Daniels, K.N. Kudin, M.C. Strain, O. Farkas, J. Tomasi, V. Barone, M. Cossi, R. Cammi, B. Mennucci, C. Pomelli, C. Adamo, S. Clifford, J. Ochterski, G.A. Petersson, P.Y. Ayala, Q. Cui, K. Morokuma, D.K. Malick, A.D. Rabuck, K. Raghavachari, J.0B. Foresman, J. Cioslowski, J.V. Ortiz, A.G. Baboul, B.B. Stefanov, G. Liu, A. Liashenko, P. Piskorz, I. Komaromi, R. Gomperts, R.L. Martin, D.J. Fox, T. Keith, M.A. Al-Laham, C.Y. Peng, A. Nanayakkara, C. Gonzalez, M. Challacombe, P.M.W. Gill, B. Johnson, W. Chen, M.W. Wong, J.L. Andres, C. Gonzalez, M. Head-Gordon, E.S. Replogle, and J.A. Pople. Gaussian 98 Rev. A.7. Gaussian, Inc., Pittsburgh, Pennsylvania. 1998.
18. P.M. Mayer, C.J. Parkinson, D.M. Smith, and L. Radom. J. Chem. Phys. **108**, 604 (1998).
19. A. Nicolaides, A. Rauk, M.N. Glukhovtsev, and L. Radom. J. Phys. Chem. **100**, 17 460 (1996).
20. T.P. Fehler and W.S. Koski. J. Am. Chem. Soc. **86**, 2733 (1964).
21. J.A. Pople, B.T. Luke, M.J. Frisch, and J.S. Binkley. J. Phys. Chem. **89**, 2198 (1985).
22. J.M.L. Martin, J.P. Francois, and R. Gijbels. Chem. Phys. Lett. **163**, 387 (1989).
23. J.M.L. Martin. Chem. Phys. Lett. **273**, 98 (1997).
24. L.A. Curtiss and J.A. Pople. J. Chem. Phys. **89**, 614 (1988).
25. M.D. Allendorf and C.F. Melius. J. Chem. Phys. **101**, 2670 (1997).
26. National Institute of Standards and Technology, Gaithersburg, Maryland. 2000. NIST Chemistry WebBook. NIST Standard Reference Database Number 69. H.Y. Afeefy, J.F. Liebman, and S.E. Stein. Neutral thermochemical data; S.G. Lias and J.F. Liebman. Ion energetics data. *Edited by* P.J. Linstrom and W.G. Mallard. <http://webbook.nist.gov> (Accessed August 2001).
27. R.J. Boyd, J.N.M. Glover, and J.A. Pincock. J. Am. Chem. Soc. **111**, 5152 (1989).
28. S.L. Boyd, R.J. Boyd, P.W. Bessonette, D.I. Kerdraon, and N.T. Aucoin. J. Am. Chem. Soc. **117**, 8816 (1995).
29. S.L. Boyd and R.J. Boyd. J. Am. Chem. Soc. **119**, 4214 (1997).
30. P.M. Mayer, M. Glukhovtsev, J.W. Gauld, and L. Radom. J. Am. Chem. Soc. **119**, 12 889 (1997).
31. E.P. Wigner. Gott. Nachr. **4,** 375 (1927).
32. G. Herzberg. Molecular spectra and molecular structure III: Electronic spectra and electronic structure of polyatomic molecules. Van Nostrand Reinhold Co., New York. 1966.
33. J.H. Beynon and J.R. Gilbert. Application of transition state theory to unimolecular reactions: An introduction. Wiley–Interscience, New York. 1984.

© 2002 NRC Canada

Synthesis and reactivity of novel Schiff bases containing boronate esters

David W. Norman, Janet P. Edwards, Christopher M. Vogels, Andreas Decken, and Stephen A. Westcott

Abstract: Condensation of 2-aminophenol with boronate ester derivatives of benzaldehyde afforded the corresponding boron-containing Schiff bases, 2-$HOC_6H_4N{=}C(H)C_6H_4R$ (**1a**: R = 2-Bpin; **1b**: R = 3-Bpin; **1c**: R = 4-Bpin; pin = 1,2-$O_2C_2Me_4$). Crystals of **1b** were triclinic, space group $P\bar{1}$, a = 11.9420(6), b = 13.0871(7), and c = 13.2720(7) Å, α = 70.983(1), β = 67.793(1), and γ = 78.380(1)°, Z = 2. Reaction of 2-aminophenol with 2-$HC(O)C_6H_4B(OH)_2$ in EtOH, however, gave a macrocyclic dimer **2** with a OBOBO structural unit. The molecular structure of this dimer has been confirmed by an X-ray diffraction study. Crystals of **2** were monoclinic, space group $P2_1/c$, a = 10.0447(8), b = 21.0894(15), and c = 12.6214(9) Å, β = 105.301(2)°, Z = 4. Further reaction of these Schiff bases with manganese triacetate in toluene afforded 2-arylbenzoxazoles **3a**–**c** via an oxidative cyclization pathway. The molecular structure of the 4-Bpin derivative (**3c**) was characterized by an X-ray diffraction study. Crystals of **3c** were monoclinic, space group $P2_1/n$, a = 6.5392(3), b = 16.3330(8), and c = 16.1942(8) Å, β = 97.9620(10)°, Z = 4.

Key words: boron heterocycles, Schiff bases, arylbenzoxazoles.

Résumé : La condensation du 2-aminophénol avec des dérivés boronates de benzaldéhyde conduit à la formation des bases de Schiff correspondantes contenant du bore, 2-$HOC_6H_4N{=}C(H)C_6H_4R$ (**1a**: R = 2-Bpin; **1b**: R = 3-Bpin; **1c**: R = 4-Bpin; pin = 1,2-$O_2C_2Me_4$). Les cristaux du composé **1b** sont tricliniques, groupe d'espace $P\bar{1}$, avec a = 11,9420(6), b = 13,0871(7) et c = 13,2720(7) Å, α = 70,983(1), β = 67,793(1) et γ = 78,380(1)° et Z = 2. La réaction du 2-aminophénol avec le 2-$HC(O)C_6H_4B(OH)_2$ dans l'éthanol conduit toutefois à la formation du dimère macrocyclique **2** qui comporte une unité structurale OBOBO. La structure moléculaire de ce dimère a été confirmée par diffraction des rayons X. Les cristaux du composé **2** sont monocliniques, groupe d'espace $P2_1/c$, avec a = 10,0447(8), b = 21,0894(15) et c = 12,6214(9) Å, β = 105,301(2)° et Z = 4. Des réactions subséquentes de ces bases de Schiff avec du triacétate de manganèse dans le toluène conduisent à la formation des 2-arylbenzoxaoles (**3a**–**c**) par le biais d'une voie réactionnelle de cyclisation oxydante. La structure moléculaire du dérivé 4-Bpin (**3c**) a été caractérisée par diffraction des rayons X. Les cristaux du composé **3c** sont monocliniques, groupe d'espace $P2_1/n$, avec a = 6,5392(3), b = 16,3330(8) et c = 16,1942(8) Å, β = 97,9620(10)° et Z = 4.

Mots clés : hétérocycles du bore, bases de Schiff, arylbenzoxazoles.

[Traduit par la Rédaction]

Introduction

Compounds containing boronic acids [$RB(OH)_2$] or boronate esters [$RB(OR')_2$] have been used extensively as synthons in the Suzuki–Miyaura cross-coupling reaction for a variety of applications (1–11). Interest in these compounds also arises from their potent biological activities (12–21). For instance, aminoboronic acids are among the most potent inhibitors of serine proteases, a diverse group of proteolytic enzymes responsible for the generation of most disease processes (13–18). The synthesis of aminoboronic acid-containing compounds, however, is often a complicated procedure requiring several complex organic transformations (1, 7). As a result, the range of compounds containing boronic acids is surprisingly small. As part of our investigation into generating novel aminoboron compounds (22–24), we decided to examine the synthesis and reactivity of Schiff bases derived from 2-aminophenol and benzaldehydes containing boronate esters. Results of our study are presented herein.

Results and discussion

Schiff bases are important intermediates in organic chemistry and have been used to prepare a number of pharmaco-

Received 24 August 2001. Published on the NRC Research Press Web site at http://canjchem.nrc.ca on 10 January 2002.

D.W. Norman, J.P. Edwards, C.M. Vogels, and S.A. Westcott.[1] Department of Chemistry, Mount Allison University, Sackville, NB E4L 1G8, Canada.
A. Decken.[2] Department of Chemistry, University of New Brunswick, Fredericton, NB E3B 5A3, Canada.

[1]Corresponding author (telephone: (506) 364-2351; fax: (506) 364-2313; e-mail: swestcott@mta.ca).

[2]Author to whom correspondence about crystallography may be addressed (telephone: (506) 453-4875; fax: (506) 453-4981; e-mail: adecken@unb.ca).

 DOI: 10.1139/V01-188 © 2002 NRC Canada

Table 1. Crystallographic data collection parameters for **1b**, **2**, and **3c**.

	1b	**2**	**3c**
Formula	$C_{38}H_{44}B_2N_2O_6$	$C_{26}H_{18}B_2N_2O_3 \cdot 1.5CH_2Cl_2$	$C_{19}H_{20}BNO_3$
FW	646.37	555.43	321.17
Crystal system	Triclinic	Monoclinic	Monoclinic
Space group	$P\bar{1}$	$P2_1/c$	$P2_1/n$
a (Å)	11.9420(6)	10.0447(8)	6.5392(3)
b (Å)	13.0871(7)	21.0894(15)	16.3330(8)
c (Å)	13.2720(7)	12.6214(9)	16.1942(8)
α (°)	70.983(1)	90	90
β (°)	67.793(1)	105.301(2)	97.9620(10)
γ (°)	78.380(1)	90	90
V (Å^3)	1808.29(16)	2578.9(3)	1712.94(14)
Z	2	4	4
ρ_{calcd} (g cm^{-3})	1.187	1.431	1.245
Crystal size (mm^3)	0.40 × 0.35 × 0.20	0.30 × 0.30 × 0.35	0.18 × 0.23 × 0.55
T (K)	173(1)	173(1)	173(1)
Radiation	Mo Kα (λ = 0.71073)	Mo Kα (λ = 0.71073)	Mo Kα (λ = 0.71073)
μ (mm^{-1})	0.079	0.390	0.083
Total reflections[a]	19912	28199	18770
Total unique relections	12584	9224	6156
$I > 4\sigma(F)$	8560	7072	4173
No. of variables	521	432	302
R_{int}	0.0152	0.0211	0.0304
Theta range (°)	1.65–32.50	1.93–32.50	1.78–32.50
Largest difference peak/hole (e Å^{-3})	0.451/–0.281	0.715/–0.646	0.346/–0.137
S (GoF) on F^2 [a]	1.038	1.132	0.966
R_1 ($I > 2\sigma(I)$)[b]	0.0573	0.0.527	0.0488
wR_2 (all data)[c]	0.1736	0.1725	0.1379

[a] $S = (\Sigma[w(F_o^2 - F_c^2)^2/(n-p))^{1/2}$.
[b] $R_1 = \Sigma||(F_o| - |F_c||/\Sigma|F_o|$.
[c] $wR_2 = (\Sigma w(F_o^2 - F_c^2)^2/\Sigma wF_o^4)^{1/2}$, where $w^{-1} = \sigma^2(F_o^2) + (aP)^2 + bP$, where $P = (\max(F_o^2, 0) + 2F_c^2)/3$. For **1b**, a = 0.1068, b = 0; for **2**, a = 0.1088, b = 0.0676; for **3c**, a = 0.0859, b = 0.

Scheme 1.

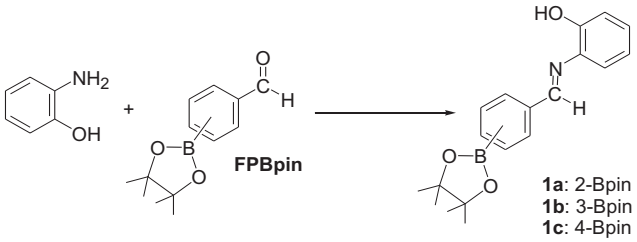

logically important compounds (29–34). For instance, Whiting and co-workers (29) have recently used imines containing boronate esters to make enantio-enriched γ-phenyl-γ-amino alcohols. In this study, we found that pinacol-protected derivatives of formylphenylboronic acid [(4,4,5,5-tetramethyl-1,3,2-dioxaborolan-2-yl)benzaldehyde (FPBpin)] add to 2-aminophenol in organic solvents to give crystalline compounds having spectroscopic data consistent with the Schiff bases **1a**–**c** (Scheme 1). As expected, a shift for the methine proton from 10 to 9 ppm is observed in the ^{1}H NMR spectra and a resonance at ca. 160 ppm in the ^{13}C NMR spectra corresponds to the N=CH carbon (25). Likewise, formation of these compounds can be monitored by the diagnostic C=N stretching band in the IR spectra at ca. 1620 cm^{-1} (31). Interestingly, a broad peak at around

Fig. 1. Molecular structure of **1b** with ellipsoids drawn at the 30% probability level. Hydrogen atoms were omitted for clarity.

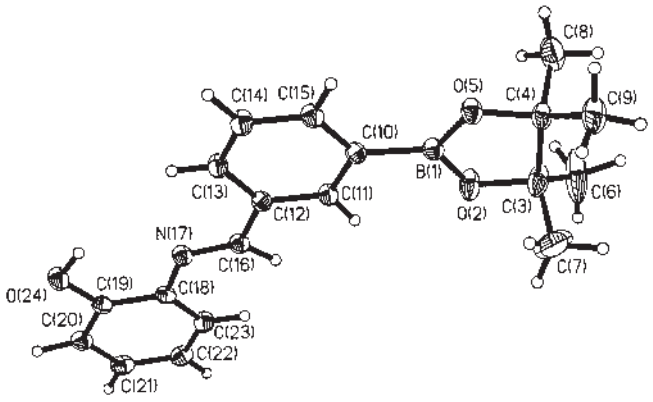

30 ppm in the ^{11}B NMR spectra indicates that the boron atom lies in a three-coordinate environment (35), even for the 2-Bpin derivative **1a**. This result is somewhat surprising in light of boron's propensity to form coordinative N→B bonds (36).

Although attempts to grow crystals of **1a** suitable for X-ray diffraction studies proved unsuccessful, the molecular structure of the 3-Bpin derivative **1b** (Fig. 1) confirms that no appreciable intermolecular interactions exist between the

© 2002 NRC Canada

Table 2. Selected bond lengths (Å) and angles (°) for **1b** and **2**.

Bond lengths (Å)		Bond angles (°)	
Compound 1b			
Molecule A		*Molecule A*	
B(1)—O(2)	1.3614(15)	O(2)-B(1)-O(5)	113.52(10)
B(1)—O(5)	1.3653(14)	O(2)-B(1)-C(10)	121.12(10)
B(1)—C(10)	1.5600(16)	O(5)-B(1)-C(10)	125.33(10)
C(12)—C(16)	1.4734(14)	N(17)-C(16)-C(12)	122.93(10)
C(16)—N(17)	1.2723(14)	C(16)-N(17)-C(18)	121.36(9)
N(17)—C(18)	1.4221(13)	O(24)-C(19)-C(20)	118.27(10)
C(19)—O(24)	1.3648(13)	O(24)-C(19)-C(18)	121.22(9)
Molecule B		C(21)-B(2)-N(8)	107.04(9)
B(31)—O(32)	1.3697(14)	B(2)-O(1)-B(1)	117.78(9)
B(31)—O(35)	1.3739(13)	C(10)-O(2)-B(2)	110.89(9)
B(31)—C(40)	1.5644(15)	C(30)-O(3)-B(1)	110.62(9)
C(42)—C(46)	1.4728(14)	C(9)-N(8)-B(2)	107.27(9)
C(46)—N(47)	1.2791(13)	C(29)-N(28)-B(1)	107.14(9)
N(47)—C(48)	1.4203(13)	*Molecule B*	
C(49)—O(54)	1.3675(14)	O(32)-B(31)-O(35)	113.35(9)
O(24)···H(39)	2.564	O(32)-B(31)-C(40)	120.54(9)
O(35)···H(24)	2.330	O(35)-B(31)-C(40)	126.10(9)
O(32)···H(21)	2.542	N(47)-C(46)-C(42)	123.45(10)
		C(46)-N(47)-C(48)	121.25(9)
Compound 2			
B(1)—O(1)	1.4194(16)	O(1)-B(1)-O(3)	110.67(9)
B(1)—O(3)	1.5075(15)	O(1)-B(1)-C(1)	120.21(10)
B(1)—C(1)	1.6493(18)	O(3)-B(1)-C(1)	108.79(10)
B(1)—N(28)	1.6544(15)	O(1)-B(1)-N(28)	108.44(9)
B(2)—O(1)	1.4154(16)	O(3)-B(1)-N(28)	99.42(8)
B(2)—O(2)	1.5162(15)	C(1)-B(1)-N(28)	107.24(9)
B(2)—C(21)	1.6476(17)	O(1)-B(2)-O(2)	111.14(9)
B(2)—N(8)	1.6581(16)	O(1)-B(2)-C(21)	119.63(10)
C(7)—N(8)	1.2958(15)	O(2)-B(2)-C(21)	109.36(9)
C(27)—N(28)	1.2976(15)	O(1)-B(2)-N(8)	108.67(9)
N(8)—C(9)	1.4196(15)	O(2)-B(2)-N(8)	98.89(8)
N(28)—C(29)	1.4226(15)		
C(7)—N(8)	1.2958(15)		

Scheme 2.

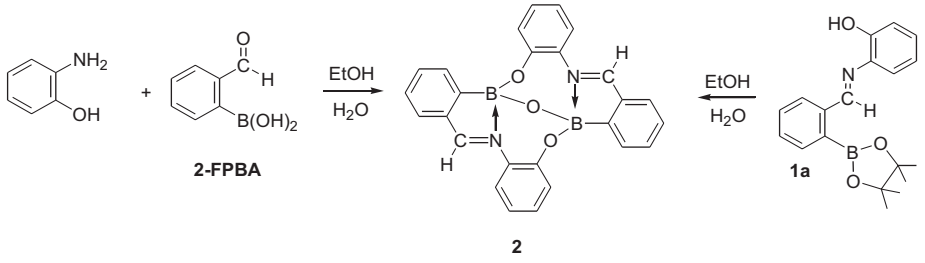

Lewis acidic boron atom and the imine nitrogen. Crystallographic data are given in Table 1[3], selected bond distances and angles shown in Table 2, and atomic coordinates are provided in Table 3. The imine C(16)—N(17) bond distances of 1.272(1) (molecule A) and 1.279(1) Å (molecule B) are comparable to azomethine compounds derived from salicylaldehyde and phenylboronic acid (31, 36). The B—O bond distances (av = 1.368(1) Å) are also typical for three-coordinate Bpin groups (25) and significantly shorter than those observed in chelate complexes with diphenylborinic

[3] Supplementary material may be purchased from the Depository of Unpublished Data, Document Delivery, CISTI, National Research Council Canada, Ottawa, ON K1A 0S2, Canada. For information on obtaining material electronically go to http://www.nrc.ca/cisti/irm/unpub_e.shtml. Crystallographic information has also been deposited with the Cambridge Crystallographic Data Centre. Copies of the data can be obtained free of charge via www.ccdc.cam.ac.uk/conts/retrieving.html (or from the Cambridge Crystallographic Data Centre, 12, Union Road, Cambridge CB2 1EZ, UK; fax: +44 1223 336033; or deposit@ccdc.cam.ac.uk).

© 2002 NRC Canada

Table 3. Atomic coordinates (1×10^4) and equivalent isotropic displacement parameters (Å^2, 1×10^3) for **1b**.

	x	*y*	*z*	U_{eq}
B(1)	7513(1)	8388(1)	1906(1)	33(1)
O(2)	6389(1)	8904(1)	1967(1)	54(1)
C(3)	6550(1)	10035(1)	1315(2)	59(1)
C(4)	7814(1)	10186(1)	1285(1)	38(1)
O(5)	8412(1)	9075(1)	1419(1)	38(1)
C(6)	5508(2)	10737(1)	1944(3)	121(1)
C(7)	6545(3)	10104(2)	142(2)	128(1)
C(8)	7787(2)	10526(1)	2297(2)	68(1)
C(9)	8574(1)	10934(1)	204(1)	58(1)
C(10)	7705(1)	7127(1)	2332(1)	31(1)
C(11)	6690(1)	6527(1)	2767(1)	32(1)
C(12)	6794(1)	5395(1)	3145(1)	30(1)
C(13)	7940(1)	4841(1)	3092(1)	38(1)
C(14)	8955(1)	5420(1)	2673(1)	43(1)
C(15)	8842(1)	6552(1)	2296(1)	36(1)
C(16)	5695(1)	4819(1)	3570(1)	32(1)
N(17)	5721(1)	3790(1)	3847(1)	33(1)
C(18)	4645(1)	3262(1)	4232(1)	30(1)
C(19)	4829(1)	2127(1)	4464(1)	31(1)
C(20)	3846(1)	1505(1)	4844(1)	37(1)
C(21)	2680(1)	2019(1)	5001(1)	40(1)
C(22)	2486(1)	3141(1)	4774(1)	41(1)
C(23)	3460(1)	3764(1)	4387(1)	38(1)
O(24)	5964(1)	1599(1)	4323(1)	41(1)
B(31)	–536(1)	2119(1)	4135(1)	30(1)
O(32)	–66(1)	1931(1)	4981(1)	46(1)
C(33)	–1100(1)	1903(2)	6028(1)	58(1)
C(34)	–2127(1)	1576(1)	5771(1)	38(1)
O(35)	–1764(1)	2027(1)	4528(1)	31(1)
C(36)	–748(2)	1077(3)	7001(1)	120(1)
C(37)	–1337(2)	3050(2)	6157(2)	97(1)
C(38)	–2138(1)	355(1)	6003(1)	61(1)
C(39)	–3395(1)	2074(1)	6330(1)	49(1)
C(40)	299(1)	2426(1)	2865(1)	29(1)
C(41)	1498(1)	2642(1)	2605(1)	31(1)
C(42)	2304(1)	2928(1)	1492(1)	30(1)
C(43)	1900(1)	2997(1)	605(1)	41(1)
C(44)	718(1)	2790(1)	842(1)	48(1)
C(45)	–82(1)	2512(1)	1960(1)	38(1)
C(46)	3528(1)	3174(1)	1310(1)	32(1)
N(47)	4348(1)	3417(1)	333(1)	32(1)
C(48)	5509(1)	3665(1)	201(1)	29(1)
C(49)	6313(1)	3879(1)	–927(1)	34(1)
C(50)	7492(1)	4142(1)	–1203(1)	40(1)
C(51)	7872(1)	4189(1)	–351(1)	41(1)
C(52)	7085(1)	3992(1)	763(1)	41(1)
C(53)	5909(1)	3732(1)	1039(1)	36(1)
O(54)	5925(1)	3833(1)	–1756(1)	51(1)

Note: U_{eq} is defined as one third of the trace of the orthogonalized U_{ij} tensor.

acid (ca. 1.5 Å), where the boron atom is four coordinate (37).

Compounds **1b** and **1c** could also be prepared in ethanol using a catalytic amount of formic acid. However, we found that reactions of 2-FPBpin with 2-aminophenol in ethanol containing adventitious water gave the novel Schiff base dimer **2** as the only new boron-containing product. It is possible that the formation of **2** proceeds via initial cleavage of the pinacol groups in 2-FBpin to give 2-formylphenylboronic acid. We found that the reaction of this aldehyde with 2-aminophenol in wet ethanol does indeed give condensation product **2** (Scheme 2). Another possible route to this

© 2002 NRC Canada

Table 4. Atomic coordinates (1×10^4) and equivalent isotropic displacement parameters (Å^2, 1×10^3) for **2**.

	x	*y*	*z*	U_{eq}
B(1)	9593(1)	1517(1)	9052(1)	19(1)
B(2)	7404(1)	1500(1)	9527(1)	19(1)
O(1)	8796(1)	1702(1)	9776(1)	20(1)
O(2)	6647(1)	1812(1)	10282(1)	22(1)
O(3)	11096(1)	1669(1)	9538(1)	24(1)
C(1)	9466(1)	790(1)	8550(1)	20(1)
C(2)	10229(2)	666(1)	7778(1)	27(1)
C(3)	10353(2)	61(1)	7355(1)	32(1)
C(4)	9737(2)	–461(1)	7723(1)	31(1)
C(5)	8986(1)	–364(1)	8486(1)	25(1)
C(6)	8809(1)	255(1)	8879(1)	20(1)
C(7)	7956(1)	263(1)	9655(1)	21(1)
N(8)	7362(1)	756(1)	9939(1)	19(1)
C(9)	6546(1)	744(1)	10702(1)	20(1)
C(10)	6152(1)	1370(1)	10859(1)	21(1)
C(11)	5304(1)	1491(1)	11555(1)	25(1)
C(12)	4868(2)	975(1)	12076(1)	30(1)
C(13)	5265(2)	351(1)	11916(1)	31(1)
C(14)	6122(1)	229(1)	11230(1)	26(1)
C(21)	6440(1)	1536(1)	8251(1)	19(1)
C(22)	5095(1)	1294(1)	8075(1)	24(1)
C(23)	4121(1)	1301(1)	7049(1)	29(1)
C(24)	4456(1)	1570(1)	6145(1)	29(1)
C(25)	5761(1)	1835(1)	6284(1)	25(1)
C(26)	6761(1)	1818(1)	7318(1)	20(1)
C(27)	8068(1)	2119(1)	7308(1)	20(1)
N(28)	9256(1)	2010(1)	7995(1)	19(1)
C(29)	10526(1)	2302(1)	7973(1)	20(1)
C(30)	11552(1)	2078(1)	8887(1)	21(1)
C(31)	12920(1)	2278(1)	9048(1)	25(1)
C(32)	13221(1)	2692(1)	8273(1)	28(1)
C(33)	12192(1)	2907(1)	7359(1)	27(1)
C(34)	10815(1)	2717(1)	7200(1)	23(1)
C(35)	9221(2)	1628(1)	5013(2)	53(1)
Cl(1)	7883(1)	1469(1)	3830(1)	59(1)
Cl(2)	10769(1)	1232(1)	4970(1)	70(1)
C(36)	5563(7)	236(3)	4741(4)	68(1)
Cl(3)	6687(2)	6(1)	5931(1)	86(1)
Cl(4)	3872(2)	–2(1)	4638(2)	112(1)

Note: U_{eq} is defined as one third of the trace of the orthogonalized U_{ij} tensor.

Fig. 2. Molecular structure of **2** with ellipsoids drawn at the 30% probability level. Hydrogen atoms were omitted for clarity.

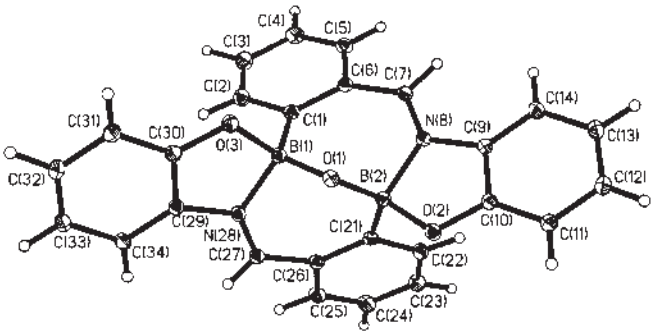

Fig. 3. Molecular structure of **3c** with ellipsoids drawn at the 30% probability level. Hydrogen atoms were omitted for clarity.

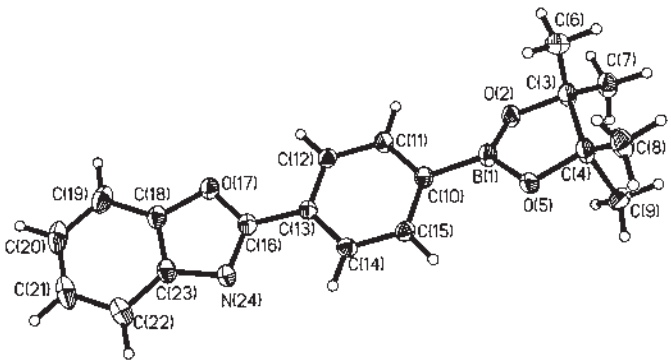

© 2002 NRC Canada

Scheme 3.

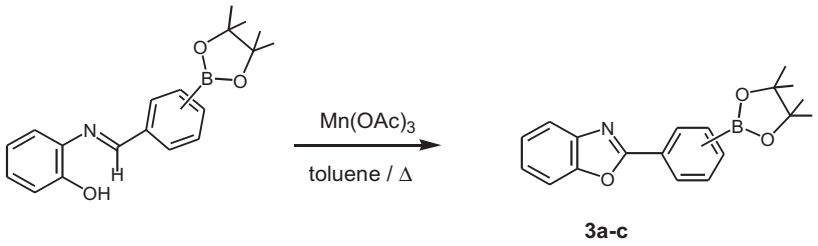

Scheme 4.

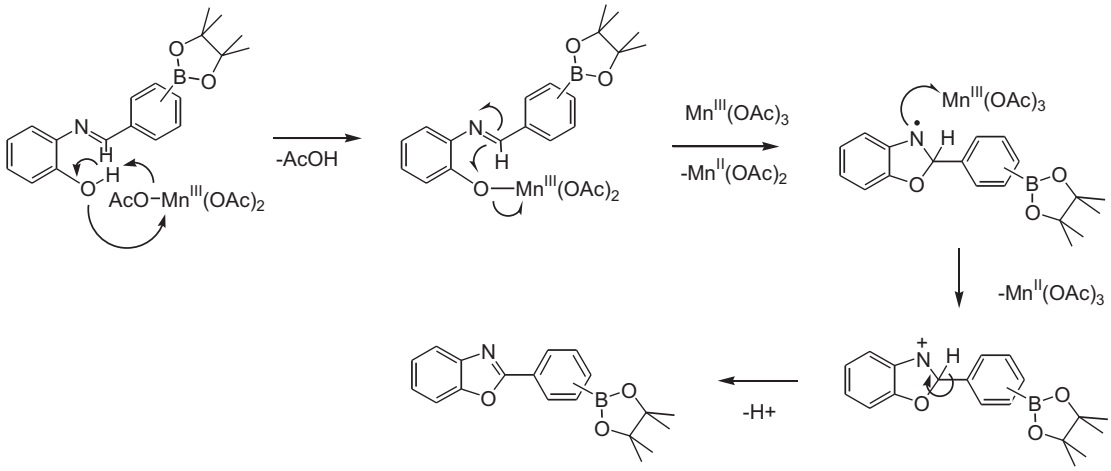

Table 5. Selected bond lengths (Å) and angles (°) for **3c**.

Bond lengths (Å)	
B(1)—O(2)	1.3366(15)
B(1)—O(5)	1.3430(12)
B(1)—O(2A)	1.4681(19)
B(1)—C(10)	1.5635(13)
C(16)—O(17)	1.3229(12)
C(16)—N(24)	1.3407(12)
O(17)—C(18)	1.4015(12)
C(23)—N(24)	1.3927(11)
Bond angles (°)	
O(2)-B(1)-O(5)	112.08(9)
O(2)-B(1)-O(2A)	33.74(8)
O(5)-B(1)-O(2A)	111.56(10)
O(2)-B(1)-C(10)	122.89(10)
O(5)-B(1)-C(10)	123.52(8)
O(2A)-B(1)-C(10)	120.81(10)
O(17)-C(16)-N(24)	115.88(8)
O(17)-C(16)-C(13)	122.50(8)
N(24)-C(16)-C(13)	121.45(8)

dimer involves initial formation of **1a** with subsequent cleavage of the pinacol group to give a boronic acid Schiff base. This transient imine could rapidly dehydrate to form **2**. Indeed, we observed that addition of ethanol to preformed **1a** gave bright yellow crystals of dimer **2**.

The molecular structure of **2** is shown in Fig. 2 and crystallographic data are given in Table 1. Selected bond distances and angles shown in Table 2, and atomic coordinates are provided in Table 4. The two fragments form seven-membered rings and are connected via a BOB bridge (B(1)-O(1)-B(2) = 117.8°) with average B—O bond distances of 1.417(2) Å. Interestingly, the two phenolic B—O distances are slightly longer (1.508(2) and 1.516(2) Å) than the bridged BOB bonds. Similar distances and angles have been reported for other BOB ring systems (38–47). The aldimine functionality in **2** is stabilized by N→B interactions with average B—N bonds of 1.651(2) Å. Similar bond distances have been reported in related oxime (48) and salen derivatives (49–51). The ^{11}B NMR spectra of **2** show a peak at 7 ppm, which also suggests that the boron atom remains four coordinate in solution (52). Although blue electroluminescence has been observed in similar organoboron compounds (40–42), this behavior is not observed for **2**.

As Schiff bases are ubiquitous in transition metal chemistry, we decided to investigate the use of these compounds as ligands for biologically active metals (such as Fe, Mo, Cu). Although initial attempts failed in this regard, we found that reaction of these Schiff bases gave the corresponding boron-containing benzoxazoles in varying yields (Scheme 3). Benzoxazoles are an important family of compounds that are found in a variety of natural products with potent biological activities (53–62). As a result, these compounds have attracted a considerable amount of attention for their medicinal and agrochemical uses.

Although the synthesis of benzoxazoles can be accomplished via a number of different methods, oxidative intramolecular cyclization of readily prepared phenolic Schiff bases provides a general route to these important organic compounds (62–67). Indeed, recent work by Varma et al. (61, 62) has shown that manganese triacetate can be used as a relatively benign oxidizing agent for reactions involving

© 2002 NRC Canada

Table 6. Atomic coordinates (1×10^4) and equivalent isotropic displacement parameters (Å^2, 1×10^3) for **3c**.

	x	*y*	*z*	U_{eq}
B(1)	4684(2)	7560(1)	5615(1)	39(1)
O(2)	2796(2)	7448(1)	5823(1)	41(1)
O(2A)	2680(2)	7151(1)	5408(1)	42(1)
C(3)	2719(2)	6560(1)	6103(1)	45(1)
C(4)	5067(2)	6415(1)	6430(1)	48(1)
O(5)	6087(1)	7064(1)	6043(1)	48(1)
C(6)	1977(4)	6059(2)	5430(2)	59(1)
C(6A)	1449(5)	5775(2)	5614(2)	55(1)
C(7)	1355(8)	6587(2)	6820(3)	51(1)
C(7A)	1484(10)	6850(3)	6717(4)	50(1)
C(8)	5904(4)	5605(1)	6373(2)	56(1)
C(8A)	5905(5)	5666(2)	5859(3)	64(1)
C(9)	5722(3)	6742(2)	7397(1)	52(1)
C(9A)	5542(5)	6212(2)	7268(2)	64(1)
C(10)	5264(1)	8316(1)	5102(1)	34(1)
C(11)	3740(1)	8722(1)	4557(1)	38(1)
C(12)	4243(1)	9349(1)	4039(1)	36(1)
C(13)	6303(1)	9574(1)	4053(1)	31(1)
C(14)	7843(1)	9195(1)	4612(1)	35(1)
C(15)	7320(2)	8572(1)	5129(1)	36(1)
C(16)	6870(2)	10180(1)	3454(1)	37(1)
N(17)	5523(1)	10475(1)	2841(1)	44(1)
O(17)	5523(1)	10475(1)	2841(1)	44(1)
C(18)	6730(2)	10960(1)	2383(1)	43(1)
C(19)	6175(3)	11395(1)	1648(1)	63(1)
C(20)	7762(3)	11795(1)	1327(1)	70(1)
C(21)	9782(3)	11766(1)	1716(1)	67(1)
C(22)	10355(2)	11333(1)	2450(1)	57(1)
C(23)	8756(2)	10932(1)	2769(1)	41(1)
N(24)	8831(1)	10424(1)	3463(1)	39(1)
O(24)	8831(1)	10424(1)	3463(1)	39(1)

Note: U_{eq} is defined as one third of the trace of the orthogonalized U_{ij} tensor.

sensitive functional groups. We found that $Mn(OAc)_3$ can also be used with **1a**–**c** to give the corresponding boron-containing benzoxazoles **3a**–**c** in low to moderate yield. A proposed mechanism for the manganese promoted intramolecular cyclization of Schiff bases **1a**–**c** is shown in Scheme 4 (61, 62). An alternate mechanism exists whereby initial coordination of the Schiff base to the metal centre occurs via the imine nitrogen atom followed by nucleophilic attack of the oxygen atom to the imine carbon. The formation of these heterocycles can be monitored by the disappearance of the aldimine N=CH functionality in the ^{1}H NMR spectra. The ^{11}B NMR spectra show a broad peak at 31 ppm for the three-coordinate boron atom. The molecular structure of **3c** is shown in Fig. 3 and crystallographic data provided in Table 1. Selected bond distances and angles are shown in Table 5, and atomic coordinates provided in Table 6. Bond distances are similar to those observed for **1b** and **2** and once again no considerable intermolecular interaction is observed between the imine nitrogen and the boron atom. As expected, the imine C(16)=N(24) bond distance (1.341(1) Å) is somewhat shorter than the C(23)—N(24) distance (1.393(1) Å). Unfortunately, attempts to generate the 2-Bpin derivative **3a** using either **1a** or **2** gave only minor amounts of the desired product (by ^{1}H NMR spectroscopy) along with a number of unidentified products.

Experimental

General

All reagents and solvents used were obtained from Aldrich. NMR spectra were recorded on a JEOL JNM-GSX270 FT NMR spectrometer. ^{1}H NMR chemical shifts are reported in ppm and referenced to residual protons in deuterated solvent at 270.1 MHz. ^{11}B{^{1}H} NMR chemical shifts are referenced to external $F_3B{\cdot}OEt_2$ at 86.6 MHz. ^{13}C{^{1}H} NMR chemical shifts are referenced to solvent carbon resonances as internal standards at 67.8 MHz. Multiplicities are reported as singlet (s), doublet (d), triplet (t), quartet (q), multiplet (m), broad (br), and overlapping (ov). Infrared spectra were obtained using a Mattson Genesis II FT-IR spectrometer and reported in cm^{-1}. Melting points were measured uncorrected with a Mel-Temp apparatus. Microanalyses for C, H, and N were carried out at Desert Analytics (Tucson, AZ). The synthesis of pinacolated derivatives of formylphenylboronic acids has been described elsewhere

© 2002 NRC Canada

(25). All reactions were carried out in the air and products are stable indefinitely under such conditions.

*Synthesis of **1a***

2-(4,4,5,5-Tetramethyl-1,3,2-dioxaborolan-2-yl)benzaldehyde (2-FPBpin) (524 mg, 2.27 mmol) was added to a solution of 2-aminophenol (248 mg, 2.27 mmol) in THF (15 mL) and magnesium sulfate (10.0 g). After four days at room temperature the yellow solution was concentrated to 5 mL and stored at 0°C for three days. A brown precipitate was filtered, washed with diethyl ether (3 × 10 mL), and dried under vacuum to give **1a**. Yield: 429 mg (59%) of a brown solid; mp 120–122°C. IR (Nujol) (cm^{-1}): 3413, 3049, 2918, 2858, 1699, 1620, 1587, 1562, 1481, 1462, 1375, 1346, 1317. ^{1}H NMR ($CDCl_3$) δ: 9.04 (s, 1H, C*H*=N), 7.95 (d, *J* = 8 Hz, 1H, Ar), 7.78 (d, *J* = 8 Hz, 1H, Ar), 7.46 (m, 2H, Ar), 7.18 (m, 2H, Ar), 7.02 (d, *J* = 8 Hz, 1H, Ar), 6.92 (ov d of d, *J* = 8 Hz, 1H, Ar), 1.34 (s, 12H, pin). ^{11}B NMR δ: 30 (br). ^{13}C NMR δ: 161.2 (*C*=N), 152.0, 140.1, 136.0, 134.4, 133 (br, *C*-B), 131.0, 130.2, 128.7, 127.9, 120.1, 117.5, 115.4, 83.7 (BO*C*), 24.9 (BOC*C*H_3).

*Synthesis of **1b***

3-(4,4,5,5-Tetramethyl-1,3,2-dioxaborolan-2-yl)benzaldehyde (3-FPBpin) (508 mg, 2.16 mmol) was added to a solution of 2-aminophenol (238 mg, 2.16 mmol) in anhydrous ethanol (10 mL). The clear yellow solution was heated at reflux for 1 h, after which the reaction mixture was stored at 5°C for 2 days. The resultant precipitate was filtered, washed with hexane (2 × 10 mL), and dried under vacuum to give **1b**. Yield: 609 mg (87%) of a pale yellow solid; mp 116–117°C. IR (Nujol) (cm^{-1}): 3408, 2924, 2856, 1626, 1462, 1365, 1252, 1140. ^{1}H NMR ($CDCl_3$) δ: 8.70 (s, 1H, C*H*=N), 8.30 (s, 1H, Ar), 8.05 (d, *J* = 8 Hz, 1H, Ar), 7.95 (d, *J* = 8 Hz, 1H, Ar), 7.51 (ov d of d, *J* = 8 Hz, 1H, Ar), 7.29 (d, *J* = 8 Hz, 1H, Ar), 7.22 (ov d of d, *J* = 8 Hz, 1H, Ar), 7.03 (d, *J* = 8 Hz, 1H, Ar), 6.93 (ov d of d, *J* = 8 Hz, 1H, Ar), 1.37 (s, 12H, pin). ^{11}B NMR δ: 32 (br). ^{13}C NMR δ: 157.2 (*C*=N), 152.3, 138.0, 135.7, 135.5, 135.1, 131.0, 130 (br, *C*-B), 128.8, 128.3, 120.1, 115.8, 115.0, 84.1 (BO*C*), 24.8 (BOC*C*H_3).

*Synthesis of **1c***

4-(4,4,5,5-Tetramethyl-1,3,2-dioxaborolan-2-yl)benzaldehyde (4-FPBpin) (1.01 g, 4.33 mmol) was added to a solution of 2-aminophenol (477 mg, 4.33 mmol) in anhydrous ethanol (25 mL) whereupon the solution was heated at reflux for 2 h. After 12 h at room temperature a bright yellow solid formed from the reaction mixture. The precipitate was filtered, washed with hexane (2 × 10 mL), and dried under vacuum to give **1c**. Yield: 1.27 g (91%) of a bright yellow solid; mp 114–115°C. IR (Nujol) (cm^{-1}): 3371, 2927, 2858, 1622, 1585, 1510, 1462, 1360, 1288, 1234, 1167, 1144, 1086. ^{1}H NMR ($CDCl_3$) δ: 8.64 (s, 1H, C*H*=N), 7.93 (ov m, 4H, Ar), 7.28 (d, *J* = 8 Hz, 1H, Ar), 7.20 (ov d of d, *J* = 8 Hz, 1H, Ar), 7.02 (d, *J* = 8 Hz, 1H, Ar), 6.90 (t, *J* = 8 Hz, 1H, Ar), 1.35 (s, 12H, pin). ^{11}B NMR δ: 31 (br). ^{13}C NMR δ: 156.9 (*C*=N), 152.4, 137.9, 135.3, 135.0, 133 (br, *C*-B), 129.0, 127.8, 120.0, 115.8, 115.0, 84.0 (BO*C*), 24.8 (BOC*C*H_3).

*Synthesis of **2***

2-Formylphenylboronic acid (253 mg, 1.69 mmol) was added to a solution of 2-aminophenol (184 mg, 1.69 mmol) in anhydrous ethanol (15 mL). The clear yellow solution was heated at reflux for 3 h whereupon the solution was allowed to cool to room temperature. After 12 h a bright yellow precipitate formed, which was filtered, washed with hexane (3 × 5 mL), and dried under vacuum to give **2**. Yield: 226 mg (62%) of a bright yellow solid; mp 180°C (dec). IR (Nujol) (cm^{-1}): 2912, 2857, 1628, 1460, 1375, 1270, 1164. ^{1}H NMR ($CDCl_3$) δ: 8.71 (s, 2H, C*H*=N), 7.54 (d, *J* = 8 Hz, 2H, Ar), 7.43 (m, 2H, Ar), 7.25 (ov m, 8H, Ar), 6.95 (m, 4H, Ar). ^{11}B NMR δ: 7 (br). ^{13}C NMR δ: 160.1 (*C*=N), 158.4, 135.9, 134.5, 133.4, 133.0, 132.7, 132.1, 130 (br, *C*-B), 128.0, 118.7, 115.7, 114.4. Anal. calcd. for $C_{26}H_{18}B_2N_2O_3$: C 72.95, H 4.24, N 6.54; found: C 72.49, H 4.20, N 6.37.

*Reaction of **1a** with Mn(OAc)$_3$*

Manganese triacetate (934 mg, 3.48 mmol) was added to a solution of **1a** (563 mg, 1.74 mmol) in toluene (20 mL) and the dark brown solution was heated at reflux for 2 h. The precipitated manganese salts were removed by suction filtration and the toluene was removed under vacuum to afford a dark brown solid. The mixture was analyzed by ^{1}H NMR spectroscopy and showed the presence of minor amounts of **3a** along with a number of unidentified products. Attempts to isolate **3a** proved unsuccessful.

*Synthesis of **3b***

Manganese triacetate (1.36 g, 5.07 mmol) was added to a solution of **1b** (819 mg, 2.54 mmol) in toluene (20 mL) and the dark brown solution was heated at reflux for 2 h. The precipitated manganese salts were removed by suction filtration and the toluene was removed under vacuum to afford a dark red solid. The solid was dissolved in hexane (25 mL), filtered through alumina, and allowed to crystallize at 5°C over 72 h. The resultant solid was filtered, washed with cold hexane (3 × 5 mL), and dried to give **3b**. Yield: 314 mg (39%) of a red-brown solid; mp 131–132°C. IR (Nujol) (cm^{-1}): 2933, 2914, 2856, 2360, 1734, 1587, 1456, 1409, 1367, 1323. ^{1}H NMR ($CDCl_3$) δ: 8.70 (s, 1H, Ar), 8.34 (d, *J* = 8 Hz, 1H, Ar), 7.95 (d, *J* = 8 Hz, 1H, Ar), 7.76 (ov m, 1H, Ar), 7.57–7.53 (ov m, 2H, Ar), 7.35 (ov m, 2H, Ar), 1.37 (s, 12H, pin). ^{11}B NMR δ: 31 (br). ^{13}C NMR δ: 163.2 (*C*=N), 150.9, 142.2, 137.8, 134.0, 133 (br, *C*-B), 130.3, 128.4, 126.6, 125.1, 124.6, 120.1, 110.7, 84.2 (BO*C*), 25.0 (BOC*C*H_3). Anal. calcd. for $C_{19}H_{20}BNO_3$: C 71.04, H 6.29, N 4.36; found: C 71.24, H 6.18, N 4.59.

*Synthesis of **3c***

Manganese triacetate (934 mg, 3.48 mmol) was added to a solution of **1c** (563 mg, 1.74 mmol) in toluene (20 mL) and the dark brown solution was heated at reflux for 2 h. The precipitated manganese salts were removed by suction filtration and the toluene was removed under vacuum to afford a dark brown solid. The solid was dissolved in hexane (25 mL), filtered through alumina, and allowed to crystallize at 5°C over 72 h. The resultant solid was filtered, washed with cold hexane (3 × 5 mL), and dried to give **3c**. Yield: 157 mg (28%) of a pale brown solid; mp 186–188°C. IR

© 2002 NRC Canada

(Nujol) (cm^{-1}): 2964, 2891, 1732, 1709, 1604, 1570, 1545, 1454, 1362, 1268, 1244, 1140, 1092. ^{1}H NMR ($CDCl_3$) δ: 8.28 (d, *J* = 8 Hz, 2H, Ar), 7.98 (d, *J* = 8 Hz, 2H, Ar), 7.79 (ov m, 1H, Ar), 7.60 (ov m, 1H, Ar), 7.37 (ov m, 2H, Ar), 1.38 (s, 12H, pin). ^{11}B NMR δ: 31 (br). ^{13}C NMR δ: 163.1 (*C*=N), 150.9, 142.2, 135.3, 132 (br, *C*-B), 129.4, 126.8, 125.4, 124.7, 120.2, 110.7, 84.2 (BO*C*), 25.0 (BOC*C*H_3). Anal. calcd. for $C_{19}H_{20}BNO_3$: C 71.04, H 6.29, N 4.36; found: C 71.38, H 6.39, N 4.54.

X-ray crystallography

Crystals of **1b**, **2**, and **3c** were grown from methylene chloride solutions at 5°C. Single crystals were mounted using a glass fibre and Paratone-N oil and frozen in the cold stream of the goniometer. Data were collected on a Bruker AXS P4/SMART 1000 diffractometer using ω and φ scans with a scan width of 0.3° and 30 s exposure times. The detector distance was 4 cm. The data were reduced (SAINT) (26) and corrected for absorption (SADABS) (27). The structures were solved by direct methods and refined by full-matrix least-squares on F^2 (SHELXTL) (28). All nonhydrogen atoms were refined anisotropically. Hydrogen atoms were located in Fourier difference maps and refined isotropically. For **2**, one molecule of CH_2Cl_2 was disordered over two positions, generated by an inversion center. For **3c**, a disorder in the oxazole ring (N/O(17) and N/O(24)) was refined by determining the occupancy using an isotropic model and fixed at 50% for consecutive cycles. A disorder in the Bpin fragment was refined by determination of the occupancy using an isotropic model and subsequently fixed at 55% for O(2), C(6), C(7), C(8), and C(9) and 45% for O(2a), C(6a), C(7a), C(8a), and C(9a).

Conclusion

We have prepared new Schiff bases containing boronate ester groups via condensation reactions with pinacolated formylphenylboronic acids (FPBpin) and 2-aminophenol. Reactions of the 2-FPBpin derivative gave a novel dimer containing a seven-membered ring with a BOB bridge. The aldimine functionality in this dimer is stabilized by an intramolecular N→B interaction. Addition of metals to the 3- and 4-Bpin Schiff-bases lead to the formation of boron-containing benzoxazoles which could be isolated in moderate yield. The use of $Mn(OAc)_3$ for these reactions provides a gentle and efficient route to making benzoxazoles that have the potential to be readily functionalized using Suzuki–Miyaura cross-coupling reactions.

Acknowledgments

Thanks are gratefully extended to the Heart and Stroke Foundation of New Brunswick, the Research Corporation (Cottrell College Science Award), the University of New Brunswick, and Mount Allison University for financial support. We also wish to thank Dan Durant for his expert technical assistance and anonymous reviewers for helpful comments.

References

1. N. Miyaura and A. Suzuki. Chem. Rev. **95**, 2457 (1995).
2. B.M. Trost and M.D. Spagnol. J. Chem. Soc. Perkin Trans 1, 2083 (1995).
3. D.M.T. Chan, K.L. Monaco, R.P. Wang, and M.P. Winters. Tetrahedron Lett. **39**, 2933 (1998).
4. B. Carboni, C. Pourbaix, F. Carreaux, H. Deleuze, and B. Maillard. Tetrahedron Lett. **40**, 7979 (1999).
5. N. Fárfan, H. Höpfl, V. Barba, M.E. Ochoa, R. Santillan, E. Gomez, and A. Gutierrez. J. Organomet. Chem. **581**, 70 (1999).
6. F. Minutoloand and J.A. Katzenellenbogen. Organometallics, **18**, 2519 (1999).
7. D.S. Matteson. Tetrahedron, **45**, 1859 (1989).
8. N.A. Petasis and I.A. Zavialov. J. Am. Chem. Soc. **120**, 11798 (1998).
9. R.A. Batey, D.B. MacKay, and V. Santhakumar. J. Am. Chem. Soc. **121**, 5075 (1999).
10. M. Yamamoto, M. Takeuchi, and S. Shinkai. Tetrahedron, **54**, 3125 (1998).
11. H. Eggert, J. Frederiksen, C. Morin, and J. Chr. Norrild. J. Org. Chem. **64**, 3846 (1999).
12. C. Morin. Tetrahedron, **50**, 12521 (1994).
13. G.S. Weston, J. Blázquez, F. Baquero, and B.K. Shoichet. J. Med. Chem. **41**, 4577 (1998).
14. V.S. Stoll, B.T. Eger, R.C. Hynes, V. Martichonok, J.B. Jones, and E.F. Pai. Biochemistry, **37**, 451 (1998).
15. J. Adams, M. Behnke, S. Chen, A.A. Cruickshank, L.R. Dick, L. Grenier, J.M. Klunder, Y. Ma, L. Plamondon, and R.L. Stein. Bioinorg. Med. Chem. Lett. **8**, 333 (1998).
16. C. Gao, B.J. Lavey, C.L. Lo, A. Datta, P. Wentworth Jr., and K.D. Janda. J. Am. Chem. Soc. **120**, 2211 (1998).
17. W. Han, J.C. Pelletier, L.J. Mersinger, C.A. Kettner, and C.N. Hodge. Org. Lett. **1**, 1875 (1999).
18. J.D. Cox, N.N. Kim, A.M. Traish, and D.W. Christianson. Nat. Struct. Biol. **6**, 1043 (1999).
19. T. Pandey and R.V. Singh. Main Group Met. Chem. **23**, 345 (2000).
20. T. Pandey and R.V. Singh. Synth. React. Inorg. Met.-Org. Chem. **30**, 855 (2000), and refs. therein.
21. T. Pandey and R.V. Singh. Met.-Based Drugs, **7**, 7 (2000).
22. C.M. Vogels, H.L. Wellwood, T.L. Hennigar, K. Biradha, M.J. Zaworotko, and S.A. Westcott. Can. J. Chem. **77**, 1196 (1999).
23. R.T. Baker, T.M. Cameron, and S.A. Westcott. Chem. Commun. 2395 (1998).
24. A. Appel, T.M. Cameron, C.A.G. Carter, M.K.J. Gagnon, G. Mann, R.T. Baker, D.J. Harrison, C.M. Vogels, and S.A. Westcott. Current topics in the chemistry of boron. *Edited by* T.B. Marder and A.D. Hughes. Royal Society of Chemistry, Cambridge. 2000. p. 407.
25. C.M. Vogels, L.G. Nikolcheva, D.W. Norman, H.A. Spinney, A. Decken, M.O. Baerlocher, F.J. Baerlocher, and S.A. Westcott. Can. J. Chem. **79**, 1115 (2001).
26. SAINT 6.02. Bruker AXS, Inc. Madison, Wisconsin, U.S.A. 1997–99.
27. G.M. Sheldrick. SADABS. Bruker AXS, Inc. Madison, Wisconsin, U.S.A. 1999.
28. G.M. Sheldrick. SHELXTL 5.1. Bruker AXS, Inc. Madison, Wisconsin, U.S.A. 1997.
29. H.E. Sailes, J.P. Watts, and A. Whiting. Tetrahedron Lett. **41**, 2457 (2000).
30. F. Firooznia, C. Gude, K. Chan, N. Marcopulos, and Y. Satoh. Tetrahedron Lett. **40**, 213 (1999).

© 2002 NRC Canada

31. H. Höpfl, M. Sánchez, N. Farfán, and V. Barba. Can. J. Chem. **76**, 1352 (1998).
32. M.P. Hughes and B.D. Smith. J. Org. Chem. **62**, 4492 (1997).
33. M.P. Groziak, A.D. Ganguly, and P.D. Robinson. J. Am. Chem. Soc. **116**, 7597 (1994).
34. I.B. Sivaev, A.B. Bruskin, V.V. Nesterov, M. Yu. Antipin, V.I. Bregadze, and S. Sjöberg. Inorg. Chem. **38**, 5887 (1999).
35. H. Nöth and B. Wrackmeyer. *In* Nuclear magnetic resonance spectroscopy of boron compounds. Springer-Verlag, Berlin. 1978.
36. H. Höpfl, M. Sánchez, V. Barba, N. Farfán, S. Rojas, and R. Santillan. Inorg. Chem. **37**, 1679 (1998).
37. J. Grünefeld, W. Kliegel, S.J. Rettig, and J. Trotter. Can. J. Chem. **77**, 439 (1999).
38. W. Maringgele, M. Noltemeyer, and A. Meller. Organometallics, **16**, 2276 (1997).
39. Q.G. Wu, G. Wu, L. Brancaleon, and S. Wang. Organometallics, **18**, 2553 (1999).
40. Q.G. Wu, M. Esteghamatian, N.X. Hu, Z. Popovic, G. Enright, S.R. Breeze, and S. Wang. Angew. Chem. Int. Ed. Engl. **38**, 985 (1999).
41. S-F. Liu, C. Seward, H. Aziz, N-X. Hu, Z. Popović, and S. Wang. Organometallics, **19**, 5709 (2000).
42. Q. Wu, M. Esteghamatian, N-X. Hu, Z. Popović, G. Enright, S. Wang, Y. Tao, and M. D'lorio. Chem. Mater. **12**, 79 (2000).
43. A. Lang, H. Nöth, and M. Schmidt. Chem. Ber. **128**, 751 (1995).
44. U. Bossek, H. Hummel, T. Weyhermüller, K. Wieghardt, S. Russell, L. van der Wolf, and U. Kolb. Angew. Chem. Int. Ed. Engl. **35**, 1552 (1996).
45. V.C. Gibson, C. Redshaw, W. Clegg, and M.R.J. Elsegood. Polyhedron, **16**, 2637 (1997).
46. R. Anulewicz-Ostrowska, S. Luliński, J. Serwatowski, and K. Suwińska. Inorg. Chem. **39**, 5763 (2000).
47. V. Barba, D. Chucutle, R. Santillan, and N. Farfán. Can. J. Chem. **79**, 1229 (2001).
48. W. Kliegel, S.J. Rettig, and J. Trotter. Can. J. Chem. **62**, 1363 (1984).
49. P. Wei and D.A. Atwood. Inorg. Chem. **37**, 4934 (1998).
50. P. Wei, T.S. Keizer, and D.A. Atwood. Inorg. Chem. **38**, 3914 (1999).
51. B.N. Ghose. Synth. React. Inorg. Met.-Org. Chem. **16**, 1383 (1986).
52. H. Höpfl. J. Organomet. Chem. **581**, 129 (1999).
53. F.F. Stephens and J.D. Bower. J. Chem. Soc. 2971 (1949).
54. K. Nakagawa, H. Onoue, and J. Sugita. Chem. Pharm. Bull. **12**, 1135 (1964).
55. E. Tauer and K.H. Grellmann. J. Org. Chem. **46**, 4252 (1981).
56. G. Speier. J. Mol. Catal. **41**, 253 (1987).
57. R.G. Srivastava and P.S. Venkataramani. Syn. Commun. **18**, 1537 (1988).
58. K.H. Park, K. Jun, S.R. Shin, and S.W. Oh. Tetrahedron. Lett. **37**, 8869 (1996).
59. Y. Sato, M. Yamada, S. Yoshida, T. Soneda, M. Ishikawa, T. Nizato, K. Suzuki, and F. Konno. J. Med. Chem. **41**, 3015 (1998).
60. A.D. Rodríguez, C. Ramírez, I.I. Rodríguez, and E. González. Org. Lett. **1**, 527 (1999).
61. R.S. Varma, R.K. Saini, and O. Prakash. Tetrahedron Lett. **38**, 2621 (1997).
62. R.S. Varma and D. Kumar. J. Heterocyclic Chem. **35**, 1539 (1998).
63. M.H. Jung, J.-G. Park, B.-S. Ryu, and K.-W. Cho. J. Heterocyclic Chem. **36**, 429 (1999), and refs. therein.
64. R.J. Perry, B.D. Wilson, and R.J. Miller. J. Org. Chem. **57**, 2883 (1992).
65. T. Kondo, S. Yang, K.-T. Huh, M. Kobayashi, S. Kotachi, and Y. Watanabe. Chem. Lett. 1275 (1991).
66. M.R. DeLuca and S.M. Kerwin. Tetrahedron Lett. **38**, 199 (1997).
67. M.I. E-Sheikh, A. Marks, and E.R. Biehl. J. Org. Chem. **46**, 3256 (1981).

© 2002 NRC Canada

Cationic thiolate and selenolate complexes of platinum(IV)

Michael C. Janzen, Michael C. Jennings, and Richard J. Puddephatt

Abstract: The reaction of the adamantanoid compounds $[Hg_4(EPh)_6(L)_4][ClO_4]_2$ (E = S or Se, L = PEt_3 or PPh_3) with $[PtMe_2(bu_2bpy)]$ (bu_2bpy = 4,4′-di-*tert*-butyl-2,2′-bipyridine) occurs easily to give the first examples of cationic thiolate or selenolate derivatives of platinum(IV), $[PtMe_2(EPh)L(bu_2bpy)][ClO_4]$, and the addition is shown to occur with *trans* stereochemistry. The new complexes are characterized by NMR spectroscopy and when L = PEt_3 by X-ray structure determinations. When L = PPh_3, a competitive reaction leads to methyl group transfer from platinum to mercury to give MeHgEPh (E = S or Se).

Key words: oxidative-addition, platinum, thiolate, selenolate, mercury.

Résumé : La réaction de composés adamantanoïdes $[Hg_4(EPh)_6(L)_4][ClO_4]_2$ (E= S ou Se, L = PEt_3 ou PPh_3) avec $[PtMe_2(bu_2bpy)]$ (bu_2bpy = 4,4′-di-*tert*-butyl-2,2′-bipyridine) se produit facilement pour fournier les premiers exemples de dérivés thiolates ou sélénolates cationiques du platine(IV), $[PtMe_2(EPh)L(bu_2bpy)][ClO_4]$ et on a observé que l'addition se produit avec une stéréochimie *trans*. Les nouveaux complexes ont été caractérisés par spectroscopie RMN et, lorsque L = PEt_3, par diffraction des rayons X. Lorsque L = PPh_3, une réaction parallèle conduit à un transfert de groupe méthyle à partir du platine vers le mercure pour donner le MeHgEPh (E = S ou Se).

Mots clés : addition oxydante, platine, thiolate, sélénolate, mercure.

[Traduit par la Rédaction]

Introduction

There is a rich chemistry resulting from reactions of Hg—X bonds from mercury(II) compounds to the organoplatinum(II) centres in complexes $[PtMe_2L_2]$ and related compounds (1, 2). For example, oxidative addition of HgX_2 to $[PtMe_2(bu_2bpy)]$ (bu_2bpy = 4,4′-di-*tert*-butyl-2,2′-bipyridine) (**1**) gives $[PtMe_2(HgX)(X)(bu_2bpy)]$ (X = Cl, Br, O_2CCF_3) (1). However, if the platinum(II) centre is less electron rich or the mercury centre is less electrophilic, the reaction may occur to give a platinum–mercury donor–acceptor bond. This form of reactivity is observed with $[Pt\{CH_2C_6H_4P(o\text{-tolyl})_2\}(S_2CNMe_2)]$ and HgX_2 (X = Br, I) and for the reaction of **1** with $[PtMe_2(HgX)(X)(bu_2bpy)]$ (X = Cl, Br, O_2CCF_3) (2). Further reactions of these products can occur to give overall alkyl–halide exchange reactions, with the formation of $[PtXMeL_2]$ and MeHgX (1*g*). No reactions involving Hg(II)—E (E = S, Se) bonds with organoplatinum(II) complexes have yet been reported. It is known that oxidative addition of the Sn(IV)—E bonds in the ring compounds $[(R_2SnE)_3]$ (R = Me, Ph) to complex **1** occurs easily, giving interesting platinum(IV) complexes containing PtESnESn rings (3). By analogy, it was considered possible that oxidative addition of the Hg(II)—E bonds of the adamantanoid compounds $[Hg_4(EPh)_6(L)_4][ClO_4]_2$ (**2a**–**d**) (Chart 1), might give novel cage complexes containing platinum(IV) centres (4, 5).

It was found that the reactions of **1** with compounds **2a**–**d** occurred easily but with fragmentation of the adamantanoid units to give the first cationic thiolato or selenelato complexes of platinum(IV), as described below. The SE^- ligand (E = S or Se) is reducing in nature and tends to form stable complexes with platinum(II) rather than platinum(IV) (6). Since cationic platinum(IV) complexes are more easily reduced than neutral ones, it is not surprising that the known thiolate or selenolate derivatives of platinum(IV) are all neutral (7). However, it will be seen that cationic REPt(IV) complexes can be prepared and that they may have good thermal stability.

Results

The reaction of complex **1** with $[Hg_4(EPh)_6(L)_4][ClO_4]_2$ (**2**) appeared to occur mostly according to eq. [1].

[1] $$[PtMe_2(bu_2bpy)]\ (\mathbf{1}) + 0.5[Hg_4(EPh)_6L_4][ClO_4]_2\ (\mathbf{2}) \rightarrow [PtMe_2(EPh)L(bu_2bpy)][ClO_4]\ (\mathbf{3}) + Hg(EPh)_2L + Hg(0)$$

For example, when L = PEt_3, a mixture of products was formed from which the corresponding complex $[PtMe_2(EPh)(PEt_3)(bu_2bpy)][ClO_4]$ (E = S (**3a**) or Se (**3b**)) could be crystallized as an air-stable yellow solid. The other products from the reaction were not isolated in pure form and the identity of the proposed product $Hg(EPh)_2L$ (eq. [1]) remains uncertain, as discussed below.

Received 10 August 2001. Published on the NRC Research Press Web site at http://canjchem.nrc.ca on 10 January 2002.

M.C. Janzen, M.C. Jennings, and R.J. Puddephatt.[1] Department of Chemistry, University of Western Ontario, London, ON N6A 5B7, Canada.

[1]Corresponding author (telephone: (519) 661-2111, ext. 86336; fax: (519) 661-3022; e-mail: pudd@uwo.ca).

 DOI: 10.1139/V01-187 © 2002 NRC Canada

Fig. 1. A view of the molecular structure of complex **3a** roughly down the S—Pt bond, showing the orientation of the phenyl group with respect to the bu_2bpy ligand. Only one component of each of the disordered ethylphosphorus groups is shown for clarity.

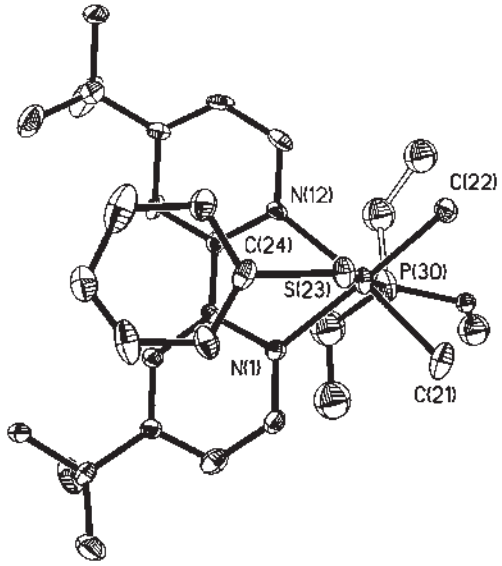

Chart 1. NN = bu_2bpy.

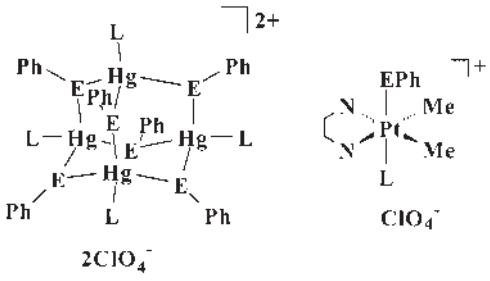

2a, E=S, L=PEt_3 **3a**, E=S, L=PEt_3
2b, E=Se, L=PEt_3 **3b**, E=Se, L=PEt_3
2c, E=S, L=PPh_3 **3c**, E=S, L=PPh_3
2d, E=Se, L=PPh_3 **3d**, E=Se, L=PPh_3

Complexes **3a** and **3b** were characterized spectroscopically and crystallographically. The ^{1}H NMR spectrum of **3a** contained a single methylplatinum resonance, with the coupling constant ($^2J_{Pt,Me}$ = 66 Hz) in the range expected for methylplatinum(IV) complexes with methyl *trans* to nitrogen (8). The presence of a single methylplatinum resonance indicates that the product is formed by *trans* oxidative addition and so supports the structure shown in Chart 1. The mirror symmetry (C_s) of **3a** is also shown by the presence of only three aromatic bu_2bpy peaks and one *tert*-butyl peak in the ^{1}H NMR spectrum. The presence of the triethylphosphine ligand is shown in the ^{31}P NMR spectrum of **3a** by the presence of a singlet resonance at δ = 0.29, with satellites due to the coupling ($^1J_{Pt,P}$ = 1895 Hz) and in the ^{1}H NMR spectrum by the observation of coupling to the methylplatinum protons with $^3J_{P,Pt,Me}$ = 5 Hz. The magnitude of the coupling constant ($^1J_{Pt,P}$ = 1895 Hz) is consistent with the phosphine being *trans* to EPh, but is too high for a phosphine *trans* to a methyl group (9, 10). The resonances in the

Fig. 2. A view of the molecular structure of complex **3b**. Only one component of each of the disordered ethyl and phenyl groups is shown for clarity.

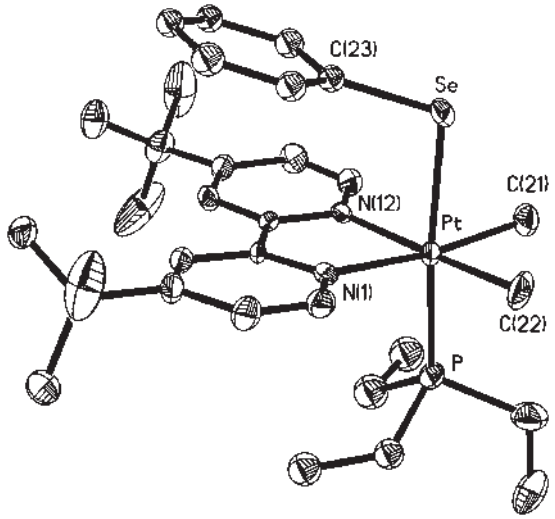

^{1}H NMR spectrum due to the EPh protons appear over the range δ = 6.25–6.52 and are lower in chemical shift than is normal for aryl protons, probably because they lie in the shielding region of the aromatic bu_2bipy ligand (7). The NMR data has thus defined a structure with the phosphine ligand *trans* to the EPh group at platinum(IV). The spectra for complex **3b** are similar and are listed in the *Experimental* section.

The structures of **3a** and **3b** were determined crystallographically and are shown in Figs. 1 and 2, respectively, with relevant bond parameters listed in Table 1. The two compounds are isomorphous and have similar structures, with the EPh and PEt_3 ligands mutually *trans* at platinum(IV). In each complex, the phenyl substituent of the EPh ligand is oriented above the bipyridyl ligand. This leads to π-stacking (11) with intercentroid distances between the phenyl and N(1) pyridyl ring of 3.81 Å for **3a** and 3.64 Å for **3b** and between the phenyl and N(12) pyridyl ring of 4.04 Å for **3a** and 4.45 Å for **3b**. The Pt—P bond lengths are 2.315(5) and 2.291(4) Å for complexes **3a** and **3b**, respectively; comparison with other phosphine complexes of platinum(IV) (12) suggests that these distances are relatively short and, therefore, the EPh ligand has only a moderate *trans* influence. The slightly longer Pt—P bond in **3a** as compared to **3b** may indicate that the SPh ligand has a marginally higher *trans*-influence than SePh. In **3a**, the Pt—S bond distance of 2.398(5) Å and the Pt-S-C angle of 108.9(8)° are unexceptional. The only other structurally characterized arylthiolate complex of platinum(IV) with a two-coordinate sulfur atom is [(η^5-C_5Me_5)$PtMe_2$(S-*p*-C_6H_4Me)], which has Pt—S = 2.344(1) Å and Pt-S-C = 108.4(2)° (13), very similar to the corresponding values in **3a**. The cubane complex [{$PtMe_3$(μ_3-SPh)}$_4$], which contains four-coordinate sulfur atoms with sulfur *trans* to methyl, has a longer Pt—S = 2.506(5) Å and a more open angle Pt-S-C = 118.1(7)° (14). Several arylthiolate complexes of platinum(II) with two-coordinate sulfur atoms have been structurally characterized, and the bond parameters for the Pt-S-C units are similar to those for complex **3a** (15). In complex

© 2002 NRC Canada

Table 1. Selected bond distances (Å) and angles (°) for complexes **3a** and **3b**.

	3a (E = S)	**3b** (E = Se)
Bond distances (Å)		
Pt—P	2.315(5)	2.291(4)
Pt—E	2.398(5)	2.512(2)
Pt—N(1)	2.14(1)	2.13(1)
Pt—N(12)	2.16(1)	2.12(1)
Pt—C(21)	2.13(2)	2.10(2)
Pt—C(22)	2.05(2)	2.10(1)
Bond angles (°)		
P-Pt-E	176.7(2)	174.9(1)
C-E-Pt	108.9(8)	106.1(8)

Scheme 1. NN = bu_2bpy.

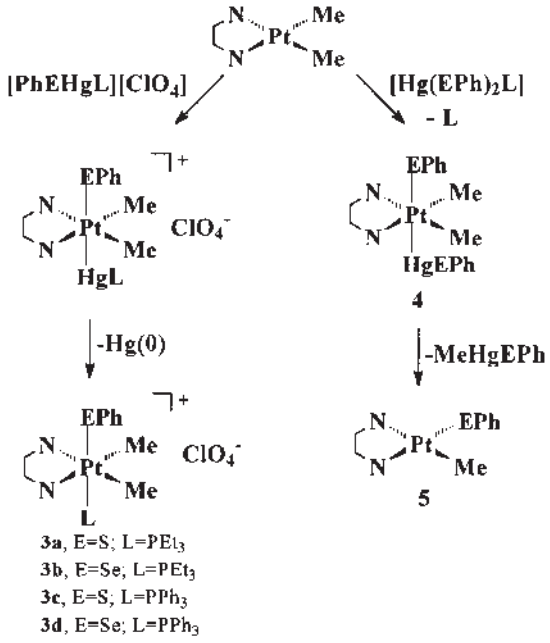

3b, the distance Pt—Se = 2.512(2) Å and angle Pt-Se-C = 106.1(9)° are similar to those in the known neutral Pt(IV)–SePh complexes. For example, corresponding parameters are $[PtMe_2(SePh)_2(phen)]$ (2.4896(9) Å, 103.7(2)°) (7) and $[PtMe_2(SePh)_2(bpy)]$ (2.478(1) Å, 2.498(1) Å, 103.4(4)°, 103.1(3)°) (7).

The reaction of complex **1** with $[Hg_4(SPh)_6(PEt_3)_4][ClO_4]_2$ (**2a**) was monitored by ^1H and ^{31}P NMR spectroscopy in an attempt to identify the other products of eq. [1]. Complex **3a** was readily identified as a major product (ca. 75% based on **1**), and it was shown that one equivalent of **2a** consumed at least 2 equivalents of **1** as required by eq. [1]. A second major product was identified by a resonance in the ^{31}P NMR spectrum at δ = 16.7, with satellites due to the coupling ($^1J_{P,Hg}$ = 2817 Hz). It is tentatively suggested that this complex is $Hg(SPh)_2(PEt_3)$ (eq. [1]), but it was not possible to isolate it in pure form to carry out further characterization. If the formulation is correct, it is likely to form a dimer or oligomer by forming $Hg_2(\mu\text{-SR})$ bridges (4, 16). The formation of trace amounts of metallic mercury was visually evident. In a similar reaction of **1** with **2b**, complex **3b** was identified as the major product, but several mercury(II) phosphine complexes appeared to be formed as indicated by several singlet resonances in the range δ = 5–24 in the ^{31}P NMR spectrum.

Table 2. Crystal data and experimental details.

Complex	**3a**·CH_2Cl_2	**3b**·CH_2Cl_2
Empirical formula	$C_{33}H_{52}Cl_3N_2O_4PSPt$	$C_{33}H_{52}Cl_3N_2O_4SePt$
FW	890.12	952.14
T (K)	200	200
λ (Å)	0.71073	0.71073
Space group	$P2_1$	$P2_1$
a (Å)	13.4447(6)	13.3754(4)
b (Å)	8.0461(4)	8.1982(3)
c (Å)	18.9052(9)	18.9704(6)
β (°)	109.443(3)	109.970(1)
V (Å^3)	1928.5(2)	1955.1(1)
Z	2	2
$D_{calcd.}$ (g cm^{-3})	1.533	1.617
μ (mm^{-1})	3.977	4.801
$F(000)$	882	948
R_1 [$I > 2\sigma(I)$][a]	0.1054	0.0442
wR_2 [$I > 2\sigma(I)$][a]	0.2691	0.1125

[a] $R_1 = \Sigma||F_o| - |F_c||/\Sigma|F_o|$; $wR_2 = [\Sigma w(F_o^2 - F_o^2)^2/\Sigma wF_o 4]^{1/2}$.

The reaction of **1** and the triphenylphosphine derivatives $[Hg_4(EPh)_6L_4][ClO_4]_2$ (L = PPh_3; E = S (**2c**) or Se (**2d**)) were somewhat more complex. Again, the complexes $[PtMe_2(EPh)L(bu_2bpy)][ClO_4]$ (E = S (**3c**) or Se (**3d**)) were isolated as yellow solids. They were readily characterized by comparison of their ^1H and ^{31}P NMR spectra with those of the structurally characterized complexes **3a** and **3b**. When the reaction of **1** with **2c** was monitored by NMR spectroscopy, complex **3c** was identified as one major product. In addition, the ^{31}P spectrum contained a resonance at δ = 26.2 ($^1J_{P,Hg}$ = 3215 Hz) tentatively assigned to $Hg(SPh)_2(PPh_3)$. In the ^1H NMR spectrum, the known methylmercury(II) compound MeHgSPh was readily identified (17), present at about half the concentration of **3c**. A similar reaction of **1** with **2d** gave complex **3d** and a compound having $\delta(^{31}P)$ = 29.2 ($^1J_{P,Hg}$ = 3177 Hz), tentatively identified as $Hg(SePh)_2(PPh_3)$, while MeHgSePh was identified by its ^1H NMR spectrum (18).

The stoichiometry of these reactions can be understood by considering that the adamantanoid mercury(II) complexes (**2**) react as if they were comprised of two components: $[Hg_4(EPh)_6L_4][ClO_4]_2$ = 2[PhEHgL][ClO_4] + 2[$Hg(EPh)_2$L] (Scheme 1). The major product **3** is formed by oxidative addition of the fragment [PhEHgL][ClO_4] to **1** with loss of mercury metal. It is not known at which stage the mercury atom is extruded, or even at what stage the adamantane derivative fragments, but Scheme 1 shows one possible route. The oxidative addition probably occurs by a polar mechanism initiated by nucleophilic attack of the electron-rich platinum(II) centre of complex **1** to the electrophilic mercury(II), leading to the observed *trans* addition in the product complex **3**. There are several precedent-setting examples for the loss of mercury(0) from Pt–Hg bonded compounds, such as the reaction of *trans*-$[(2\text{-}Me_2NCH_2C_6H_4)_2Pt]$ with $Hg(O_2CMe)_2$ to yield $[(2\text{-}Me_2NCH_2C_6H_4)_2Pt(O_2CMe)_2]$ and Hg(0) (19).

© 2002 NRC Canada

The minor product MeHgEPh formed in the reactions of **1** with **2c** and **2d** is likely to be formed by the competing oxidative-addition reaction of complex **1** with the fragment $[Hg(EPh)_2L]$ to give intermediate **4** (Scheme 1), which can undergo reductive elimination to yield MeHgEPh and [PtMe(EPh)(bu_2bpy)] (**5**). Complex **5** would then react with more **2** to give additional MeHgEPh. The formed complexes (**3**) are thermally stable, and therefore, cannot be the source of formation of MeHgEPh.

Clearly these reactions are more complex than was envisaged and they did not yield the anticipated platinum–mercury-bonded cage complexes. Nevertheless, they do give a simple route to the first cationic thiolate and selenolate complexes of platinum(IV), and it is shown that these compounds are both air-stable and thermally stable.

Experimental

General

NMR spectra were recorded by using a Varian 300 MHz spectrometer. Chemical shifts are reported with respect to TMS (^{1}H) or external H_3PO_4 (^{31}P) references. Solvents were dried and freshly distilled prior to use. Complexes **2** (4) and [$PtMe_2$(bu_2bpy)] (20) were prepared according to the literature procedures. CAUTION: toxic methylmercury compounds are formed in some reactions; appropriate precautions should be taken.

[($PtMe_2$(SPh)(PEt_3)(bu_2bpy)][ClO_4] (3a)

A mixture of [$PtMe_2$(bu_2bpy)] (80 mg, 0.162 mmol) and **2a** (133 mg, 0.162 mmol) was dissolved in CH_2Cl_2 (5 mL) and the mixture was stirred for 10 min. The yellow solution was filtered through dry Celite, and pentane (40 mL) was added to the filtrate to precipitate the product as a yellow microcrystalline solid, which was isolated by filtration, washed with pentane, and dried in vacuo. Yield: 58%. ^{1}H NMR (CD_2Cl_2) δ: 8.56 (d, $^3J_{6,5}$ = 6 Hz, $^3J_{Pt,H6}$ = 14 Hz, 2H, H6), 7.95 (d, $^4J_{3,5}$ = 2 Hz, 2H, H3), 7.70 (dd, $^3J_{5,6}$ = 6 Hz, $^3J_{5,3}$ = 2 Hz, 2H, H5), 6.52–6.25 (m, 5H, C_6H_5), 1.42 (d, $^3J_{P,Me}$ = 5 Hz, $^2J_{Pt,H}$ = 66 Hz, 6H, Pt-Me), 1.46 (s, 18H, *t*-Bu), 1.38 (m, $J_{H,H}$ = 8 Hz, $J_{P,H}$ = 8 Hz, 6H, CH_2), 0.81 (m, $J_{H,H}$ = 8 Hz, $J_{P,H}$ = 8 Hz, 9H, CH_3). ^{31}P NMR δ: –2.7 (s, $^1J_{Pt,P}$ = 1976 Hz, P-Pt). Anal. calcd. for $C_{32}H_{50}ClN_2O_4PSPt\cdot CH_2Cl_2$: C 43.78, H 5.79, N 3.09; found: C 43.88, H 5.83, N 2.99. Crystals suitable for X-ray crystallographic study were grown over a period of several days by slow diffusion of pentane into a CH_2Cl_2 solution at 22°C.

[($PtMe_2$(SePh)(PEt_3)(bu_2bpy)][ClO_4] (3b)

This complex was prepared similarly, except that **2b** was used instead of **2a**. Yield: 52%. ^{1}H NMR (CD_2Cl_2) δ: 8.52 (d, $^3J_{6,5}$ = 6 Hz, $^3J_{Pt,H6}$ = 14 Hz, 2H, H6), 8.05 (d, $^4J_{3,5}$ = 2 Hz, 2H, H3), 7.59 (dd, $^3J_{5,6}$ = 6 Hz, $^3J_{5,3}$ = 2 Hz, 2H, H5), 6.85–6.42 (m, 5H, C_6H_5), 1.52 (d, $^3J_{P,Me}$ = 5 Hz, $^2J_{Pt,H}$ = 65 Hz, 6H, Pt-Me), 1.46 (s, 18H, *t*-Bu), 1.38 (m, $J_{H,H}$ = 7 Hz, $J_{P,H}$ = 7 Hz, 6H, -CH_2), 0.81 (m, $J_{H,H}$ = 7 Hz, $J_{P,H}$ = 8 Hz, 9H, -CH_3). ^{31}P NMR δ: –5.83 (s, $^1J_{Pt,P}$ = 1966 Hz, P-Pt). Anal. calcd. for $C_{32}H_{50}ClN_2O_4PSePt\cdot CH_2Cl_2$: C 41.68, H 5.50, N 2.94; found: C 41.55, H 5.41, N 2.84. Crystals were grown as described for **3a**.

[($PtMe_2$(SPh)(PPh_3)(bu_2bpy)][ClO_4] (3c)

This was prepared similarly except that **2c** was used instead of **2a**. Yield: 43%. ^{1}H NMR (CD_2Cl_2) δ: 7.88 (d, $^4J_{3,5}$ = 2 Hz, 2H, H3), 7.85 (d, $^3J_{6,5}$ = 6 Hz, $^3J_{Pt,H6}$ = 15 Hz, 2H, H6), 7.46–7.00 (m, 15H, C_6H_5), 6.61–6.30 (m, 5H, SC_6H_5), 1.71 (d, $^3J_{P,Me}$ = 5 Hz, $^2J_{Pt,H}$ = 65 Hz, 6H, Pt-Me), 1.43 (s, 18H, *t*-Bu). ^{31}P NMR δ: –0.2 (s, $^1J_{Pt,P}$ = 1802 Hz, P-Pt). Anal. calcd. for $C_{44}H_{50}ClN_2O_4PSPt$: C 54.80, H 5.23, N 2.90; found: C 54.71, H 5.19, N 2.80.

[($PtMe_2$(SePh)(PPh_3)(bu_2bpy)][ClO_4] (3d)

This was prepared similarly except that **2d** was used instead of **2a**. Yield: 39%. ^{1}H NMR (CD_2Cl_2) δ: 7.93 (d, $^4J_{3,5}$ = 2 Hz, 2H, H3), 7.81 (d, $^3J_{6,5}$ = 6 Hz, $^3J_{Pt,H6}$ = 14 Hz, 2H, H6), 7.50–6.95 (m, 15H, C_6H_5), 6.53–6.20 (m, 5H, SeC_6H_5), 1.75 (d, $^3J_{P,Me}$ = 5 Hz, $^2J_{Pt,H}$ = 66 Hz, 6H, Pt-Me), 1.44 (s, 18H, *t*-Bu). ^{31}P NMR δ: –3.6 (s, $^1J_{Pt,P}$ = 1860 Hz, P-Pt). Anal. calcd. for $C_{44}H_{50}ClN_2O_4PSePt$: C 52.25, H 4.98, N 2.77; found: C 52.07, H 4.79, N 2.69.

X-ray structure determinations

Crystals of **3a** and **3b**, as perchlorate salts, were mounted on glass fibres. Data were collected using a Nonius Kappa-CCD diffractometer using COLLECT software (21*a*). Crystal cell refinement and data reduction were carried out using the Nonius DENZO package (21*a*). The data were scaled using SCALEPACK (21*a*) and no other absorption corrections were applied. The SHEXTL 5.1 program was used to solve the structure by direct methods, followed by successive difference Fouriers (21*b*). Crystallographic details are listed in Table 2.[2] The two compounds are isomorphous, each crystallizing in space group $P2_1$ with one molecule of CH_2Cl_2 of solvation. For complex **3a**, two of the ethyl groups on the phosphorus atom were modeled as isotropic, half occupancy moieties. Only one of each disordered ethyl group is shown in Fig. 1 for clarity. The third ethyl group was also kept isotropic. For complex **3b**, the phenyl ring attached to the selenium atom was modeled as two half-occupancy rings with isotropic carbon atoms. Two of the ethyl groups on the phosphorus atom were also modeled as isotropic, half-occupancy moieties. In Fig. 2 only one of each disordered group is shown for clarity. In both compounds, there was disorder of the CH_2Cl_2 molecule and of the ClO_4^- anion, and they were modeled with geometrical constraints.

Acknowledgments

We thank the NSERC (Canada) for financial support and for a scholarship to MCJ. RJP thanks the Government of Canada for a Canada Research Chair. Thanks are given to

[2] Supplementary material may be purchased from the Depository of Unpublished Data, Document Delivery, CISTI, National Research Council Canada, Ottawa, ON K1A 0S2, Canada. For information on obtaining material electronically go to http://www.nrc.ca/cisti/irm/unpub_e.shtml. Crystallographic information has also been deposited with the Cambridge Crystallographic Data Centre (CCDC Nos. 168359–168360). Copies of the data can be obtained free of charge via www.ccdc.cam.ac.uk/conts/retrieving.html (or from the Cambridge Crystallographic Data Centre, 12, Union Road, Cambridge CB2 1EZ, UK; fax: +44 1223 336033; or deposit@ccdc.cam.ac.uk)

© 2002 NRC Canada

Prof. P.A.W. Dean for a generous gift of samples of complexes **2** and for helpful discussions.

References

1. (*a*) M.C. Janzen, M.C. Jennings, and R.J. Puddephatt. Inorg. Chem. **40**, 1728 (2001); (*b*) J. Fornies, A. Martin, V. Sicilia, and P. Villarroya. Organometallics, **19**, 1107 (2000); (*c*) A.J. Canty and G. van Koten. Acc. Chem. Res. **28**, 406 (1995); (*d*) A.F.M.J. van der Ploeg, G. van Koten, K. Vrieze, and A.L. Spek. Inorg. Chem. **21**, 2014 (1982); (*e*) A.F.M.J. van der Ploeg, G. van Koten, K. Vrieze, A.L. Spek, and A.J.M. Duisenberg. J. Chem. Soc. Chem. Commun. 469 (1980); (*f*) J.K. Jawad and R.J. Puddephatt. Inorg. Chim. Acta, **31**, L391 (1978); (*g*) J. Kuyper. Inorg. Chem. **17**, 1458 (1978).
2. (*a*) I. Ara, L.R. Falvello, J. Fornies, V. Sicilia, and P. Villarroya. Organometallics, **19**, 3091 (2000); (*b*) L.R. Falvello, J. Fornies, A. Martin, R. Navarro, V. Sicilia, and P. Villarroya. Inorg. Chem. **36**, 6166 (1997); (*c*) M. Krumm, E. Zangrando, L. Randaccio, S. Menzer, A. Danzmann, D. Holthenrich, and B. Lippert. Inorg. Chem. **32**, 2183 (1993); (*d*) A.F.M.J. van der Ploeg, G. van Koten, K. Vrieze, A.L. Spek, and A.J.M. Duisenberg. Organometallics, **1**, 1066 (1982); (*e*) A.F.M.J. van der Ploeg, G. van Koten, and K. Vrieze. J. Organomet. Chem. **226**, 93 (1982).
3. (*a*) M.C. Janzen, H.A. Jenkins, L.M. Rendina, J.J. Vittal, and R.J. Puddephatt. Inorg. Chem. **38**, 2123 (1999); (*b*) M.C. Janzen, H.A. Jenkins, M.C. Jennings, L.M. Rendina, and R.J. Puddephatt. J. Chem. Soc. Dalton Trans. 1713 (1999).
4. P.A.W. Dean, J.J. Vittal, and M.H. Trattner. Inorg. Chem. **26**, 4245 (1987).
5. J.J. Vittal. Polyhedron, **15**, 1585 (1996).
6. (*a*) M.S. Hannu, R. Oilunkaniemi, R.S. Laitinen, and M. Ahlgen. Inorg. Chem. Comm. **3**, 397 (2000); (*b*) S. Ford, M.R. Lewtas, C.P. Morley, and M. Di Vaira. Eur. J. Inorg. Chem. 933 (2000); (*c*) E. Martin, B. Toledo, H. Torrens, F.J. Lahoz, and P. Terreros. Polyhedron, **17**, 4091 (1998); (*d*) N. Feeder, R.J. Less, J.M. Rawson, and J.N.B. Smith. J. Chem. Soc. Dalton Trans. 4091 (2000); (*e*) S.A. Batten, J.C. Jeffery, L.H. Rees, M.D. Rudd, and F.G.A. Stone. J. Chem. Soc. Dalton Trans. 2839 (1998); (*f*) S. Yamazaki and A.J. Deeming. Polyhedron, **15**, 1847 (1996); (*g*) P.K. Khanna, C.P. Morley, M.B. Hursthouse, K.M.A. Malik, and O.W. Howarth. Heteroat. Chem. **6**, 519 (1995); (*h*) V.G. Albano, M. Monari, I. Orabona, A. Panunzi, and F. Ruffo. J. Am. Chem. Soc. **123**, 4352 (2001).
7. (*a*) K.-T. Aye, J.J. Vittal, and R.J. Puddephatt. J. Chem. Soc. Dalton Trans. 1835 (1993); (*b*) A.J. Canty, H. Jin, B.W. Skelton, and A.H. White. Inorg. Chem. **37**, 3975 (1998); (*c*) A.J. Canty and H. Jin. J. Organomet. Chem. **565**, 135 (1998); (*d*) J.E. Hux and R.J. Puddephatt. J. Organomet. Chem. **437**, 251 (1992); (*e*) J.R. Hall, D.A. Hirons, and G.A. Swile. J. Organomet. Chem. **174**, 355 (1979).
8. C.J. Levy and R.J. Puddephatt. J. Am. Chem. Soc. **119**, 10 127 (1997).
9. (*a*) A. Bayler, A.J. Canty, B.W. Skelton, and A.H. White. J. Organomet. Chem. **595**, 296 (2000); (*b*) A. Bayler, A.J. Canty, P.G. Edwards, B.W. Skelton, and A.H. White. J. Chem. Soc. Dalton Trans. **19**, 3325 (2000).
10. D.M. Crumpton and K.I. Goldberg. J. Am. Chem. Soc. **122**, 962 (2000).
11. I. Dance and M. Scudder. J. Chem. Soc. Dalton Trans. 1579 (2000).
12. (*a*) B.L. Edelbach, R.J. Lachicotte, and W.D. Jones. J. Am. Chem. Soc. **120**, 2843 (1998); (*b*) S. Al-Jibori, C. Crocker, W.S. McDonald, and B.L. Shaw. J. Chem. Soc. Dalton Trans. 2589 (1981); (*c*) J.F. Hoover and J.M. Stryker. Organometallics, **8**, 2973 (1989); (*d*) A.R. Middleton, G. Wilkinson, M.B. Hursthouse, and N.P. Walker. J. Chem. Soc. Dalton Trans. 663 (1982).
13. W.A. Howard and R.G. Bergman. Polyhedron, **17**, 803 (1998).
14. D.C. Craig and I.G. Dance. Polyhedron, **6**, 1157 (1987).
15. (*a*) J.C. Jeffrey, R. Navarro, H. Razay, and F.G.A. Stone. J. Chem. Soc. Dalton Trans. 2471 (1981); (*b*) M.K. Cooper, N.J. Hair, and D.W. Yaniuk. J. Organomet. Chem. **150**, 157 (1978).
16. Y.Y. Kim, H.J. Lee, H.J. Nam, and D.Y. Noh. Bull. Korean Chem. Soc. **22**, 17 (2000).
17. R.D. Bach and A.T. Weibel. J. Am. Chem. Soc. **98**, 6241 (1976).
18. A.J. Canty, A.J. Carty, and S.F. Malone. Inorg. Chem. **19**, 133 (1983).
19. A.F.M.J. van der Ploeg, G. van Koten, K. Vrieze, and A.L. Spek. Inorg. Chem. **21**, 2014 (1982).
20. (*a*) G.S. Hill, M.J. Irwin, C.J. Levy, L.M. Rendina, and R.J. Puddephatt. Inorg. Synth. **32**, 149 (1998); (*b*) J.D. Scott and R.J. Puddephatt. Organometallics, **2**, 1643 (1983).
21. (*a*) Nonius. Delft. 1998; (*b*) G.M. Sheldrick. SHEXTL 5.1. Program for crystal structure refinement. Madison, WI. 2000.

© 2002 NRC Canada

Mechanistic studies of photohydration of *m*-hydroxy-1,1-diaryl alkenes

John G. Cole and Peter Wan

Abstract: The photohydration of a variety of *m*-hydroxy-1,1-diaryl alkenes (**8**–**10**) and related systems (**11** and **12**) has been studied in aqueous CH_3CN solution. All of these alkenes photohydrate efficiently in 1:1 H_2O–CH_3CN, to give the corresponding 1,1-diarylethanol (Markovnikov addition) products with high chemical and quantum yields. The aim of this study was to further probe the mechanism of photohydration reported for the parent *m*-hydroxy-α-phenylstyrene (**5**), which has been proposed as consisting of a water trimer-mediated excited state (formal) intramolecular proton transfer (ESIPT) from the phenolic proton to the β-carbon of the alkene moiety to give an observable (by laser flash photolysis (LFP)) *m*-quinone methide intermediate **6**. For this purpose, derivatives of **5** with substituents (methyl or methoxy) on the α-phenyl ring as well as related model compounds were explored. Product studies, quantum yields, fluorescence, and nanosecond laser flash data are reported that are consistent with two distinct mechanisms for photohydration of these compounds: one involving water-mediated ESIPT (**8**, **9**), as observed for the parent compound **5**, and one involving direct protonation of the β-carbon by solvent water (**11** and **12**), with compound **10** possibly operating via both mechanisms.

Key words: photohydration, solvent-assisted excited state intramolecular proton transfer (ESIPT), *m*-quinone methide, diarylmethyl carbocation.

Résumé : Opérant en solution aqueuse de CH_3CN, on a étudié la photohydratation d'une variété de *m*-hydroxy-1,1-diarylalcènes (**8**–**10**) et de systèmes apparentés (**11** et **12**). Tous ces alcènes se photohydratent facilement dans un mélange 1:1 de H_2O–CH_3CN et ils conduisent à la formation des 1,1-diaryléthanols correspondants (addition de Markovnikov) avec des rendements chimiques et quantiques élevés. Le but de cette étude était d'examiner plus à fond le mécanisme de photohydratation proposé pour le *m*-hydroxy-α-phénylstyrène fondamental (**5**) soit une réaction catalysée par un trimère d'eau et caractérisée par un transfert intramoléculaire de proton dans l'état excité (TIPEE) (formel) à partir du proton phénolique vers le carbone β de la partie alcène avec la formation d'un intermédiaire *m*-quinonemétide (**6**) qui peut être observé par photolyse éclair au laser (PEL). À cette fin, on a étudié des dérivés de **5** portants des substituants (méthyle ou méthoxy) sur le noyau α-phényle ainsi que des composés modèles apparentés. Les résultats d'études faites sur la nature des produits et les rendements quantiques ainsi que les données relatives à la photolyse éclair au laser au niveau de la nanoseconde peuvent s'accommoder de deux mécanismes distincts pour la photohydratation de ces composés: l'un implique un TIPEE catalysé par l'eau (**8**, **9**) semblable à celui observé avec le composé fondamental (**5**) et l'autre implique une protonation directe du carbone β par une molécule d'eau du solvant (**11**, **12**); le composé **10** pourrait réagir par une combinaison de ces deux mécanismes.

Mots clés : photohydratation, transfert intramoléculaire de proton dans l'état excité (TIPEE), *m*-quinonemétide, carbocation diarylméthyle.

[Traduit par la Rédaction]

Introduction

Excited state intramolecular proton transfer (ESIPT), a process of wide interest in chemistry, occurs most readily for those molecules whose acidity and basicity of both the proton donor and proton acceptor groups, respectively, are enhanced upon electronic excitation. ESIPT naturally leads to the formation of tautomers that are generally difficult to form via thermal chemistry (1). In almost all cases, the above mentioned proton transfers occur between heteroatoms, and the process is generally reversible. The first cited example of an ESIPT between a phenol and a carbon (alkene) was reported by Kalanderopoulos and Yates (2) in the efficient photohydration of *o*-hydroxystyrene (**1**) (eq. [1]). Photolysis of **1** in aqueous CH_3CN gave the *o*-quinone methide **2**, via

[1] 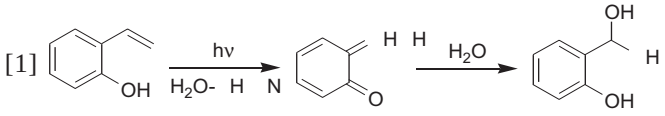

1

ESIPT from the phenol to the β-carbon. Nucleophilic attack by water at the α-carbon of **2** gives the overall hydration

Received 16 September 2001. Published on the NRC Research Press Web site at http://canjchem.nrc.ca on 15 January 2002.

J.G. Cole and P. Wan.[1] Department of Chemistry, Box 3065, University of Victoria, BC V8W 3V6, Canada.

[1]Corresponding author (telephone: (250) 721-8976; fax: (250) 721-7147; e-mail: pwan@uvic.ca).

 DOI: 10.1139/V01-196 © 2002 NRC Canada

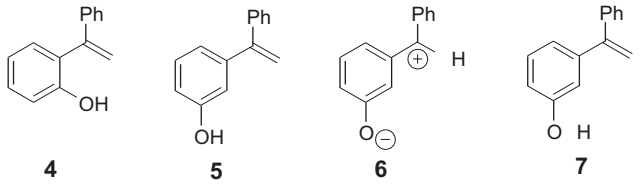

product **3**. Available evidence suggests that **2** does not return to **1** under the conditions employed, this being an example of an irreversible ESIPT. Recent work from our group (3) on the related compound **4** confirms the formation of an *o*-quinone methide (by laser flash photolysis (LFP) experiments) from these compounds, which is generated within the laser pulse (≈10 ns). Moreover, we have also recently shown that the *meta* isomer (**5**) also photohydrates efficiently, but via a water trimer-mediated ESIPT, to give *m*-quinone methide **6** as the initially formed intermediate (4), as deduced from LFP experiments and the much lower reactivity of **7**, as well as other data (4). The crucial *m*-quinone methide intermediate **6** is formed within the laser pulse. In addition, there is efficient quenching of fluorescence of **5** by added water, concomitant with increased efficiency for the formation of **6**. These data support a mechanism of water-mediated ESIPT from the phenol to β-carbon that is probably concerted (or two very fast steps: deprotonation from the phenol OH followed by protonation of the β-carbon via a proton "relay" mechanism mediated by water). A similar mechanism may also be operative for the *para* isomer, although its intrinsically weak fluorescence emission made detailed mechanistic studies problematic.

The mechanism of the water trimer-mediated ESIPT from phenol to the β-carbon (of the alkene) of *m*-hydroxystyrenes warrants further investigation. In this work, the photohydrations of *m*-hydroxy-α-phenylstyrenes with electron donating substituents (methyl and methoxy) **8**–**10** are investigated. The related dimethoxystyrenes **11** and **12** without an *m*-hydroxy substituent were also studied for additional mechanistic insights.

Results and discussion

Materials

1,1,-Diarylalkenes **8**–**12** were made via dehydration of the corresponding 1,1-diarylethanols **13**–**17**, which in turn were made by the reaction of the corresponding Grignard reagent with 3′-hydroxyacetophenone (for **8**–**10**), 3′-methoxyacetophenone (for **11**), or acetophenone (for **12**). The Grignard reagents were made by standard reaction of the corresponding arylbromides with Mg metal. The isolated yields of the alkenes were generally >60%.

Product studies and quantum yields

Preparatory photolyses of **8**–**12** (argon purged, ~10^{-3} M, 1:1 (v/v) H_2O–CH_3CN, Rayonet RPR-100 photochemical reactor, 254 nm, ~15°C, <5 min) gave the corresponding alcohols (photohydration products) **13**–**17** in essentially quantitative yields (eqs. [2] and [3]). Control experiments showed no reaction in the absence of irradiation. Quantum yields for photohydration (Φ_P, alcohol formation) in 1:1 H_2O–CH_3CN for **8**–**12** were determined relative

[2]

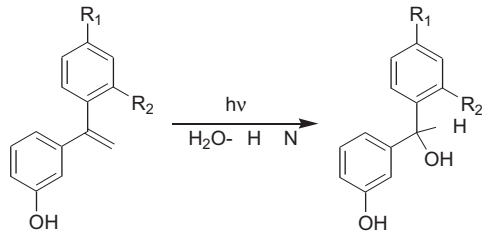

8 R_1 = H , R_2 = H
9 R_1 = O H , R_2 = H
10 R_1 = R_2 = O H

1 R_1 = H , R_2 = H
14 R_1 = O H , R_2 = H
15 R_1 = R_2 = O H

[3]

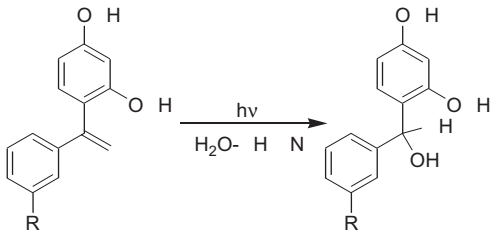

11 R = O H
1 R = H

16 R = O H
17 R = H

to that reported for parent **5** (4) using ^{1}H NMR (Table 1). *m*-Hydroxystyrenes **8**–**10** have Φ_P's significantly higher than **5** (Φ_P = 0.22), whereas styrenes **11** and **12** have comparable values to **5**. The significantly higher quantum yields observed for the *m*-hydroxy-substituted compounds (**8**–**10**) compared to **11** and **12** are suggestive of a different mechanism for photohydration, perhaps similar to that reported for **5**; whereas **11** and **12** can only react via a simple photoprotonatiom pathway.

The photohydrations of **8**–**12** can be monitored readily by UV–vis spectrophotometry, since the alcohol products have much lower extinction coefficients over most of the spectrum (Fig. 1). The change in absorption spectra vs. irradiation time shows a linear relationship until at least 60% conversion, at which point the product may compete for light. Using this method for following the photohydration efficiency of these compounds, the dependence of Φ_P vs. water content (in CH_3CN) are shown in Fig. 2. The quantum yields for **8** and **9** increase rapidly with small additions of water, reaching a plateau at about 7–15 M H_2O. This behaviour is similar to that observed for **5**. However, unlike compounds **5**, **8**, and **9**, the Φ_P's of **10**–**12** have an apparent linear dependence on water concentration in CH_3CN; that is, the Φ_P's increase in a much more gradual fashion. This implies that bulk solvent water is required to accomplish efficient photohydration via photoprotonation for **10**–**12**, whereas a different mechanism requiring much less water content operates for the photohydration of **8** and **9**.

Solvent isotope effects for the photohydration quantum yield ($\Phi_P(H_2O)/\Phi_P(D_2O)$) were determined by comparing the Φ_P in H_2O–CH_3CN and D_2O–CH_3CN solutions (Table 1) using the above UV–vis method. Primary solvent isotope effects for **8** and **9** were evident at low water concentrations ($\Phi_P(H_2O)/\Phi_P(D_2O)$ ~2 at 0.9 M H_2O–D_2O in CH_3CN). At higher water concentrations, no isotope effect was observed ($\Phi_P(H_2O)/\Phi_P(D_2O)$ ~1 at 7.4 M H_2O–D_2O in CH_3CN). This

© 2002 NRC Canada

Table 1. Summary of quantum yield data and photophysical properties of compounds studied.

Compound	Φ_p [a]	$\Phi_P(H_2O)/\Phi_P(D_2O)$ [b]	Φ_f [c]	τ_f (ns) [d]	τ_{INT} (μs) [e]
5[f]	0.22	>1	0.20	5.6 ± 0.3	0.047
8	0.40	1.8	0.12	4.4 ± 0.4	0.25
9	0.41	2.3	0.011	<1	3.0
10	0.31	3.0	0.008	<1	70
11	0.24	5.0	0.006	<1	4.4, 55
12	0.17	4.0	0.004	<1	3.5, 50

[a]Quantum yield for photohydration in 1:1 H_2O–CH_3CN, as measured using the reaction of **5** as secondary standard (estimated error, ±10%).
[b]Solvent isotope effect for photohydration (in 0.9 M $H_2O(D_2O)$ in CH_3CN for **8** and **9**; in 7.4 M $H_2O(D_2O)$ in CH_3CN for **10**–**12**).
[c]Fluorescence quantum yield in neat CH_3CN (λ_{ex} = 285 nm; 2-aminopyridine as standard; estimated error, ±10%).
[d]Fluorescence lifetime in neat CH_3CN, as measured by single photon counting. Only lifetimes >1 ns are measurable using the system available.
[e]Lifetime(s) of observed *m*-QM or carbocation in 1:1 H_2O–CH_3CN, as detected by LFP. Biphasic decays observed where two lifetimes are quoted.
[f]Data from ref. 4.

Fig. 1. UV–vis traces for photohydration of **10** in 1:1 H_2O–CH_3CN. Each trace was taken after 20 s photolysis at 254 nm. The final trace is that of the photohydration product **15**.

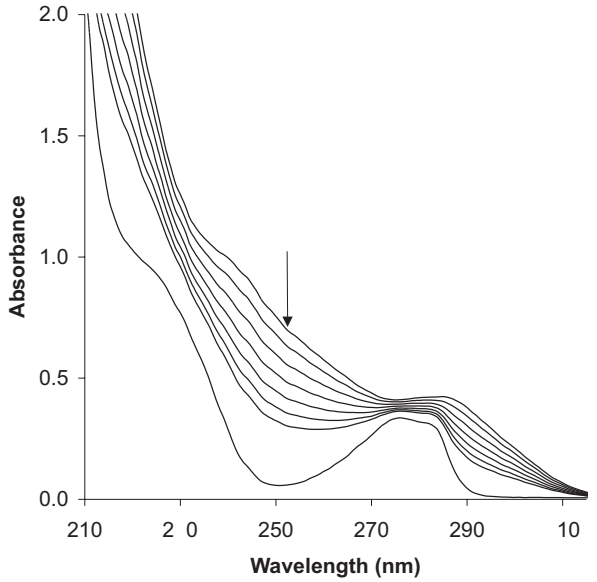

Fig. 2. Plots of quantum yields of photohydration for **8**–**12** vs. water concentration (in CH_3CN).

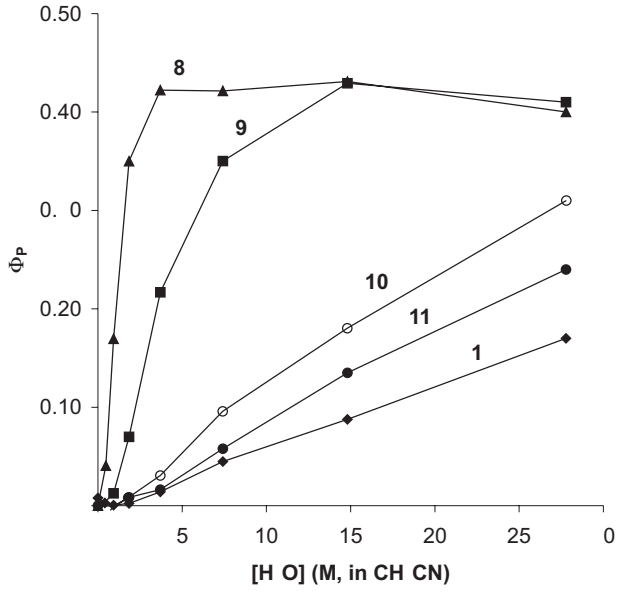

suggests a change in mechanism on going to solutions of high water content, where Φ_P values reach a plateau region (Fig. 2). The solvent isotope effects on the photohydration of **10**–**12** are quite large, with $\Phi_P(H_2O)/\Phi_P(D_2O)$ in the range 3–5. Unlike **8** and **9**, the isotope effects are independent of the concentration of water used (7–15 M H_2O–D_2O).

Steady-state and time-resolved fluorescence studies

Quantum yields of fluorescence (Φ_f) of **8**–**12** in dry CH_3CN were measured relative to 2-aminopyridine (5) (Table 1). The lack of large Stokes shifts in the fluorescence emission spectra indicates that the normal form (i.e., not the phenolate or a tautomeric form) of each compound is responsible for the emission. The addition of methoxy substituents (**9**–**12**) significantly reduces Φ_f, presumably through enhancement of non-radiative decay pathways.

To probe the mechanisms of photohydration further, steady-state fluorescence spectra were taken as a function of water content in CH_3CN. The fluorescence emission of **8** is quenched efficiently with small additions of water, and is essentially quenched by 3.7 M water (Fig. 3). Less efficient quenching was observed when D_2O was used (approximately half as efficient, up to 1.9 M $H_2O(D_2O)$). It is significant to note that at this same water concentration, Φ_P for **8** has essentially reached its maximal value (Fig. 2). Both **9** and **10** exhibit an initial *increase* in fluorescence emission intensity with small additions of water (up to 1.9 M) (Fig. 4*a*), followed by slower quenching by water (relative to **8**), requiring about 50% water to completely quench the emission (Fig. 4*b*). The weaker fluorescence emissions of both **11** and **12** prevented reliable studies of their water-quenching phenomena. However, neither compound exhibited a growth in fluorescence emission on the addition of water. Although the photophysical details are beyond the scope of this study, one possible reason for the observed growths in fluorescence emission intensity with added water (at low water concentrations) for **9** and **10** is associated with hydrogen bonding by added water to the phenol moiety, with the associated changes in structure and intrinsic emission efficiency. Since their Φ_f (in neat CH_3CN) are already low, slight changes to its emission quantum yield would be readily noticeable.

© 2002 NRC Canada

Fig. 3. Fluorescence quenching of **8** by H_2O in CH_3CN.

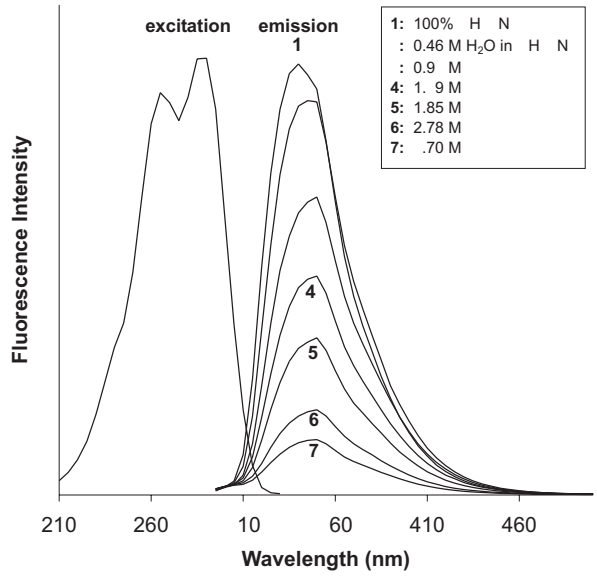

Fig. 4. (*a*) Effect on fluorescence intensity of **9** by added H_2O (in CH_3CN) up to 1.85 M; (*b*) above 1.85 M.

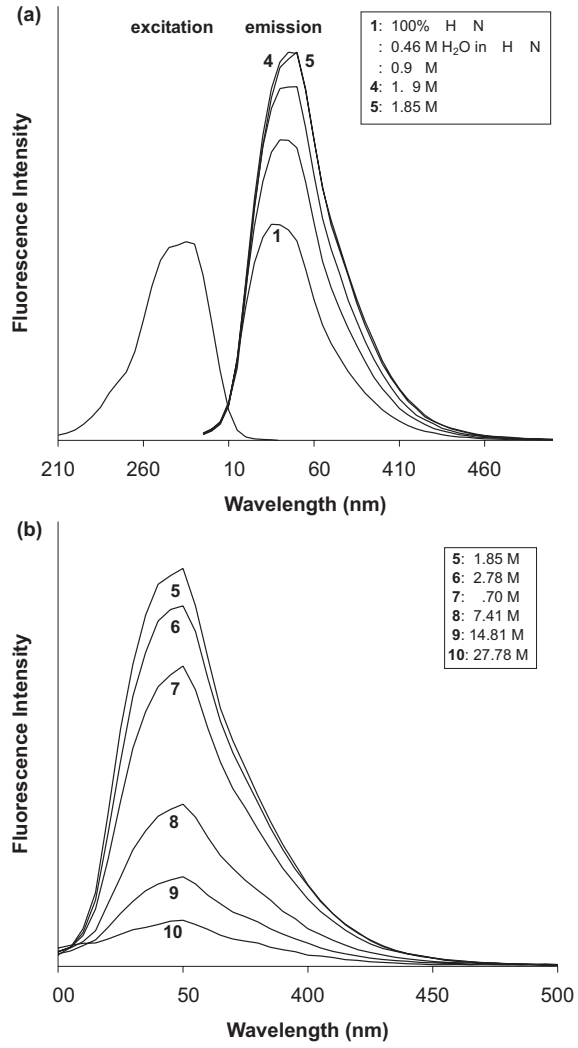

Fig. 5. Stern–Volmer plots of fluorescence quenching of **8** by H_2O (in CH_3CN) using steady-state fluorescence data (H_2O: ■; D_2O: □) and using fluorescence lifetime data (H_2O only: ▲). The solid lines are fits to the square of the water concentration ($[H_2O]^2$).

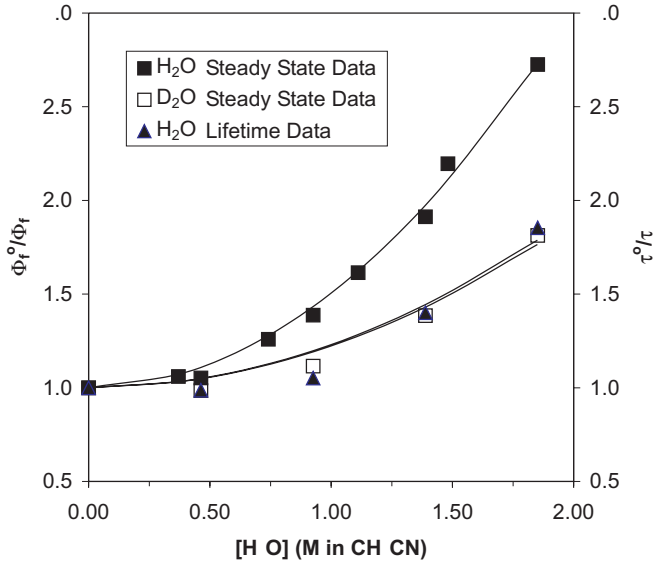

Fig. 6. LFP transients of **8**–**10** in 1:1 H_2O–CH_3CN oxygen-purged solution, 10 ns after laser excitation (266 nm).

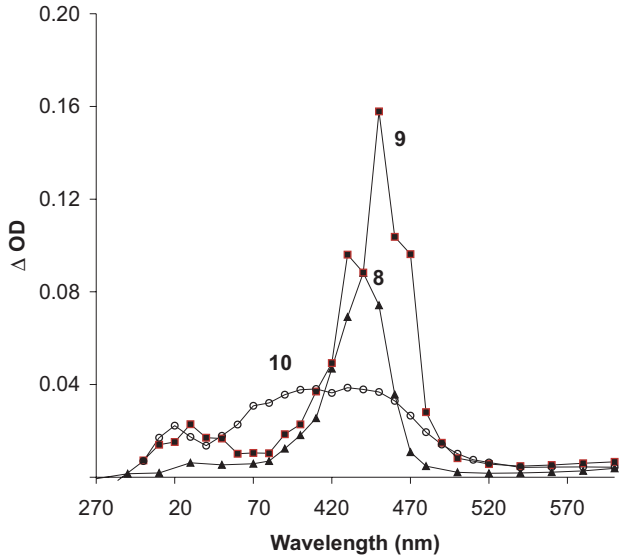

Fluorescence lifetimes (τ_f) were measurable only for **8** (4.4 ± 0.4 ns, neat CH_3CN) (Table 1). Addition of small amounts of water (<2 M) decreased its lifetime as anticipated (4.4, 4.1, 3.1, 2.3 in 0.5, 0.9, 1.4, 1.9 M H_2O, respectively). Stern–Volmer plots of fluorescence quenching by $H_2O(D_2O)$ using steady-state and lifetime data are shown for **8** in Fig. 5. Comparison of the steady-state and lifetime plots show that both static (pre-excitation) and dynamic (post-excitation) quenching of **8** are occurring. The non-linear nature of the plots also suggest that, on average, more than one water molecule is involved with each excited singlet state of

© 2002 NRC Canada

Fig. 7. LFP transients of **11** and **12** in 1:1 H_2O–CH_3CN oxygen-purged solution, 10 ns after laser excitation (266 nm).

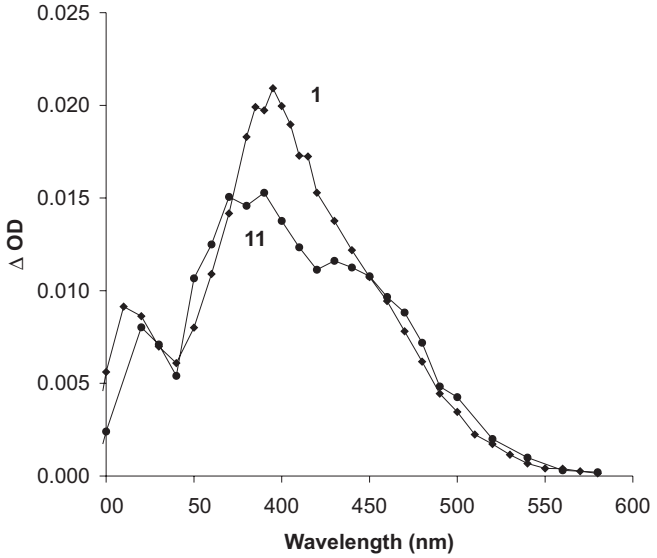

8. Modifying the Stern–Volmer plot so that the concentration of water is squared ($[H_2O]^2$) provides the best fit of the data (Fig. 5). Thus, at low water concentrations in CH_3CN, an average of two water molecules are required to quench the fluorescence, via both the static and dynamic mechanisms.

Laser flash photolysis (LFP)

Nanosecond LFP of **8** and **9** (266 nm; YAG laser; <20 mJ; 20°C) in 1:1 H_2O–CH_3CN resulted in sharp, strongly absorbing transients similar to those previously reported as *m*-QMs (4). LFP of **10** under the same conditions led to a broader transient signal. All three transients appear immediately after the laser pulse (≈10 ns) and are shown in Fig. 6. Purging with oxygen or nitrogen had no significant effect on the profile or lifetime of the transients. The signals decay to baseline in a mono-exponential fashion. Excitation in dry CH_3CN gave no transient signal, thus indicating that water is necessary for the formation of the reactive intermediate. The lifetime of these transients increase with electron-donating substituents on the α-phenyl ring, consistent with an electron deficient species (Table 1).

LFP of the **11** and **12** (lacking a *m*-hydroxy group) in 1:1 H_2O–CH_3CN gave broad transients observed immediately after the laser pulse (Fig. 7) that are insensitive to the presence of oxygen. Excitation of these compounds in the absence of water (dry CH_3CN) did not lead to any transient. Since these compounds lack an *m*-hydroxy group, they cannot form *m*-QMs. Based on their similarity to published data on arylmethyl carbocations (6), they are assigned to diarylmethyl carbocations **18** and **19**, obtained via Markovnikov photoprotonation by water at the β-carbon. Interestingly, both of these diaryl carbocations show a biphasic decay (two pseudo-first-order decays) to baseline across the transient profile (Fig. 8). This suggests the presence of two absorbing species with essentially identical absorption spectra but different reactivity (resulting in two decay rates). A similar biphasic decay was reported for the photo-generated 9-*p*-methoxyphenyl-9-xanthenylium cation (**20**) in aqueous ethanol (7). The short-lived species (≈ 0.1 ms) was assigned to the ion pair (geminate) recombination of the cation and hydroxide ion, while the longer lived species (≈10 ms) was assigned to the reaction of the cation with water. The ratio of the two observed quenching rates of **20** is similar to those obtained for the LFP intermediates **18** and **19**.

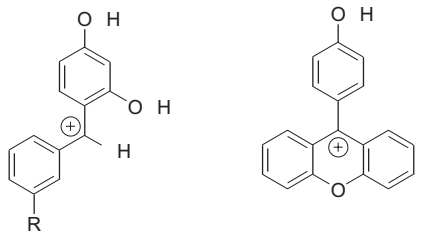

18 R = O H
19 R = H
0

The effect of water content (in CH_3CN) on the strength of the LFP transients observed for **8** and **11** are shown in Fig. 9. In dry CH_3CN (as previously mentioned), no signals were observed. However, with small additions of water (<3.7 M in CH_3CN), the transient generated from **8** rapidly grows in, reaching a plateau region at ≈3.7 M H_2O. The carbocation signal of **18** appears only weakly at this water concentration. At much higher water concentrations (5–20 M H_2O), the signal increased in an apparent linear fashion with water concentration. The transient lifetimes observed for both **8** and **11** are shorter at higher water content, consistent with them being carbocation-like species. For **8**, at low water concentrations in CH_3CN the lifetime of the transient is relatively long (14 μs with 0.5 M H_2O). As more water is added, the intermediate lifetime steadily decreases (750 ns in 3.7 M H_2O), reaching 250 ns in 1:1 H_2O–CH_3CN.

It is interesting to note that the two plots observed in Fig. 9 for **8** and **11** are essentially identical to their plots of Φ_P vs. water content (Fig. 2).

Mechanisms of photohydration

Although molecules **8**–**12** photohydrate efficiently in aqueous solution, as shown by the high quantum yields for 1,1-diarylalcohol formation measured in 1:1 H_2O–CH_3CN, it is clear that substantial differences exist with respect to their mechanisms of photosolvolysis. The Φ_P's of **8** and **9** have a water concentration effect that is essentially identical to that observed for **5**. The lifetimes of the transients generated by LFP of **5**, **8**, and **9** are consistent with the increase in the electron donating capability of the *para* substituents on the α-phenyl ring. Most notably, the single-exponential decay of those transients, rather than a biphasic decay, distinguish these intermediates from simple arylmethyl carbocations such as **18**–**20**, indicating that the transients generated from **8** and **9** are most probably *m*-QMs **21** and **22**. It was initially anticipated that the mechanism of photosolvolysis for **8** and **9** would be similar to that reported for **5** involving an excited state (formal) intramolecular proton transfer mediated by a cluster of three water molecules, as shown in **23**. This mechanism was proposed for **5** when it was noted that three water molecules were required to fit the fluorescence quenching data (static and dynamic components). Three water mole-

© 2002 NRC Canada

Fig. 8. Biphasic pseudo-first-order decays of the LFP intermediate of **11** monitored at 475 nm in a 1:1 H_2O–CH_3CN oxygen purged solution. Inset: decay at shorter time scales (lifetimes are 4.4 and 55 μs).

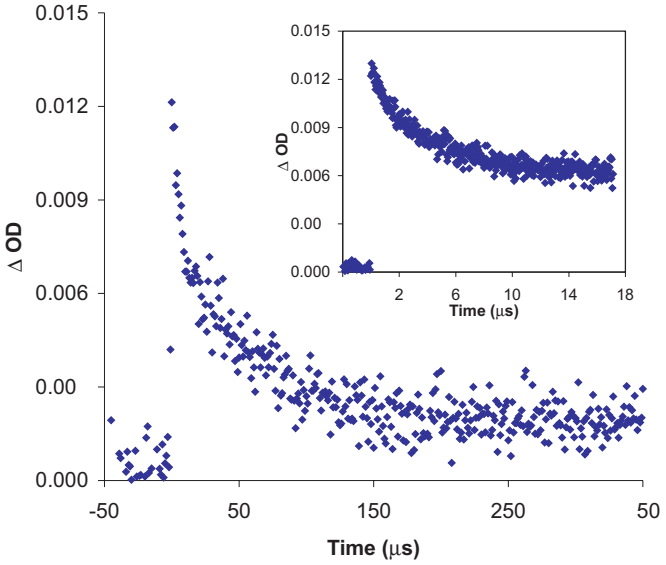

cules hydrogen bonded in a chain could span the distance between the phenol and β-carbon in **23**. However, due to the rapid formation (within the laser pulse) of *m*-QM **6**, it was not possible by LFP to discern whether the proton transfers were concerted or in sequence. The fluorescence quenching data of **8** show that only two water molecules are involved in its proton transfer mechanism. This is insufficient to bridge the distance between the phenol and β-carbon on the alkene. Thus, the intramolecular proton transfer is more likely two excited-state proton transfers with only one water molecule required at each of the acidic and basic sites, as shown in **24**. This would still generate a *m*-QM, although without being a formal intramolecular proton transfer. It appears that the electron donating ability of the *p*-methyl group on the α-phenyl ring of **8** (relative to a hydrogen on **5**) is sufficient in reducing the water requirement of QM formation. Unfortunately, the peculiar fluorescence growth of **9** upon addition of water does not allow for proper Stern–Volmer analysis to determine (on average) how many water molecules are required for quenching of its excited state.

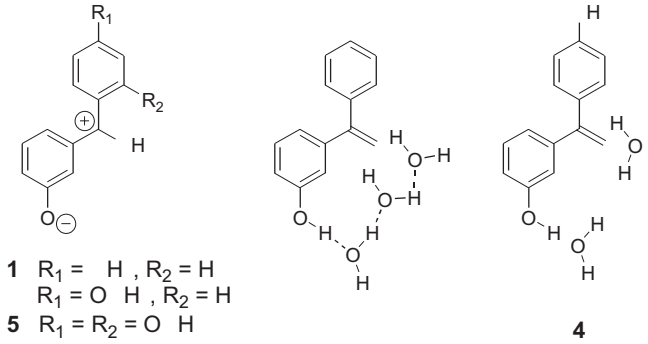

Both **11** and **12** photohydrate to give the corresponding Markovnikov alcohol. Considering the lack of a phenol functionality on these compounds, the reactions must proceed via a diarylmethyl carbocation intermediate. The efficiency of these reactions depend on bulk water concentration, and they have a large primary isotope effect implying that the excited state proton transfers in these cases is not as "early" as for **8** and **9**. The LFP transients show an interesting biphasic decay pattern, similar to that reported for xanthylium cation **20** (7), which was photogenerated by photodehydroxylation of the corresponding alcohol (which generates an initial cation–hydroxide ion pair). In analogy to the assignments made for the kinetic data for **20** (7), the biphasic decay is interpreted as arising from two forms of the carbocation: one being an ion pair with hydroxide ion, and the other the solvent-separated (solvated) carbocation. The shorter-lived species is assigned to the ion pair and the longer-lived species to the solvated carbocation.

Fig. 9. Δ OD vs. water concentration for the transients observed for **8** and **11** (in CH_3CN) immediately after (≈10 ns) excitation by LFP.

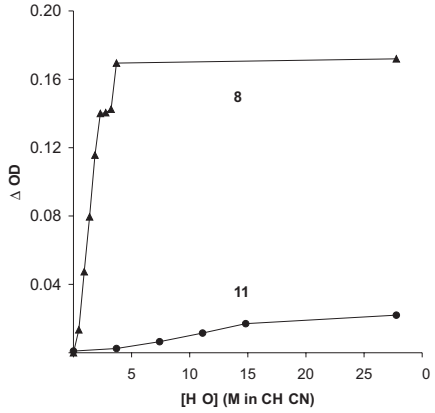

The photohydration of **10** shows characteristics of mechanisms involving a *m*-QM as well as those of a simple carbocation intermediate. The dependence of Φ_P on water concentration and solvent isotope effect support the idea that **10** reacts via a carbocation, similar to the mechanism for **11** and **12**. However, evidence that **10** generates a *m*-QM is in the observed decay profile of the intermediate: it lacks a biphasic decay, implying that an ion pair is not formed. Indeed, the intermediate observed for **10** is sufficiently long-lived that a shorter-lived component would have been observable. Since it is clearly mono-exponential, intermediate quenching via ion-pair combination is not occurring, and the species is best assigned to a *m*-QM **25**.

Summary

New insights into the mechanisms of photohydration of 1,1-diarylalkenes have been made. *m*-Hydroxystyrenes **8** and **9** undergo ESIPT to form *m*-QM, followed by reaction with water to form the corresponding 1,1-diarylalcohol. The reaction requires only small volumes of water to be present to reach maximum quantum efficiency. *o*,*p*-Dimethoxystyrenes **11** and **12** undergo ESPT from solvent water to form carbocations **18** and **19**, which then react with either a hydroxide ion or water to yield the alcohol product. The reactions require bulk solvent water to be observable, and do not react in CH_3CN solutions with small amounts of water.

© 2002 NRC Canada

Compound **10**, which is both a *m*-hydroxystyrene and a *o,p*-dimethoxystyrene, shows characteristics of both mechanisms. However, the lifetime of the LFP intermediate shows evidence of a *m*-QM rather than a carbocation intermediate.

Experimental

General

^{1}H NMR spectra were recorded on a Bruker AC–300 (300 MHz) instrument. UV–vis spectra were obtained using Cary 5 UV/Vis, Cary 1E UV/Vis, and Cary 50 Bio scanning spectrophotometers in conjunction with fluorescence, LFP, and Φ_P measurements, respectively. The fluorescence spectra were taken on a Photon Technology International A-1010 (PTI) Quanta Master™ Luminescence Spectrometer. High resolution mass spectra were obtained on a Kratos Concept H (EI) instrument and the uncorrected melting points in a Gallencamp melting point apparatus. IR spectra were recorded on a PerkinElmer Spectrum One FTIR spectrophotometer either as KBr pellets (for solid compounds), or on NaCl plates (as a neat oil). Photolyses were carried out in 100-mL quartz tubes using a Rayonet RPR 100 photochemical reactor with 254 nm lamps (up to 16). The solvents THF, CH_3CN, and CH_2Cl_2 were distilled before use with THF and CH_3CN pre-drying over K and CaH_2, respectively. 3-Hydroxyacetophenone, 3-methoxyacetophenone, acetophenone, 4-bromotoluene, 4-bromoanisole, and 1-bromo-2,4-dimethoxybezene were purchased from Aldrich.

3′-Hydroxy-4″-methyl-1,1-diphenylethene (8)

The Grignard reagent was prepared by adding a solution of 4-bromotoluene (5.5 mL, 45 mmol) in anhydrous THF (25 mL) dropwise to Mg (0.87 g, 35.8 mmol) in anhydrous THF (100 mL) under nitrogen. The resulting mixture was heated at reflux for 2 h, then 3-hydroxyacetophenone (1.82 g, 13.4 mmol) was added dropwise, and then the mixture kept at reflux for more 2 h. Saturated aqueous NH_4Cl was added and the solution was subjected to standard workup (extraction with CH_2Cl_2, washing of the organic with saturated brine solution, drying ($MgSO_4$), filtration, and evaporation to dryness in vacuo), to afford the crude product alcohol 3′-hydroxy-4″-methyl-1,1-diphenylethanol (**13**) (≈70%). Molecule **13** was refluxed in CH_3CN with a catalytic amount of dilute H_2SO_4, to yield the crude oil **8**. Purification by column chromatography in 9:1 CH_2Cl_2–EtOAc yielded pure material (oil). ^{1}H NMR ($CDCl_3$) δ: 2.35 (s, 3H, CH_3), 4.87 (s, 1H, OH), 5.39 (s, 2H, $=CH_2$), 6.78 (m, 2H, Ar), 6.90 (d, J = 8.0 Hz, 1H, Ar), 7.10–7.24 (m, 5H, Ar). HRMS calcd. for $C_{15}H_{14}O$: 210.1045; found: 210.1047.

3′-Hydroxy-4″-methoxy-1,1-diphenylethene (9)

The Grignard reagent was prepared as above using 4-bromoanisole (5.8 mL, 46 mmol), Mg (0.87 g, 35.8 mmol), and 3-hydroxyacetophenone (3.02 g, 22 mmol) to yield the crude product alcohol 3′-hydroxy-4″-methoxy-1,1-diphenylethanol (**14**). Molecule **14** was refluxed in CH_3CN with a catalytic amount of H_2SO_4 (aq) to yield the crude oil **9**. Purification by column chromatography in 4:1 hexanes–EtOAc yielded clean product, which was recrystallized from CH_3Cl and hexanes with an overall yield of 25% (1.35 g, 5 mmol): mp 66–68°C. ^{1}H NMR ($CDCl_3$) δ: 3.81 (s, 3H, OCH_3), 4.73 (s, 1H, OH), 5.35 (d, J = 6.6 Hz, 2H, $=CH_2$), 6.78–6.92 (m, 5H, Ar), 7.16–7.26 (m, 3H, Ar). HRMS calcd. for $C_{15}H_{14}O_2$: 226.0994; found: 226.0994.

3′-Hydroxy-2″,4″-dimethoxy-1,1-diphenylethanol (15)

The appropriate Grignard reagent was prepared from 1-bromo-2,4-dimethoxybenzene (9.0 mL, 62 mmol), Mg (2.12 g, 87 mmol), and 3-hydroxyacetophenone (3.62 g, 27 mmol). The resulting crude oil was washed with benzene to remove the byproduct dimethoxybenzene, resulting in **15** in a 60% yield. Recrystallization from ethanol and hexanes gave pale green cubic crystals in 40% yield): mp 144–146°C. IR (cm^{-1}): 3457 (s), 3310 (s). ^{1}H NMR ($CDCl_3$) δ: 1.77 (s, 3H, CH_3), 3.58 (s, 3H, OCH_3), 3.80 (s, 3H, OCH_3), 4.48 (s, 1H, OH), 4.69 (s, 1H, OH), 6.45 (d, J = 2.9 Hz, 1H, Ar), 6.50 (dd, J = 8.5, 2.5 Hz, 1H, Ar), 6.63 (dd, J = 8.1, 2.6 Hz, 1H, Ar), 6.79 (m, 2H, Ar), 7.09 (t, J = 8.1 Hz, 1H, Ar), 7.30 (d, J = 8.8 Hz, 1H, Ar). HRMS calcd. for $C_{16}H_{18}O_4$: 274.1205; found: 274.1205.

3′-Hydroxy-2″,4″-dimethoxy-1,1-diphenylethene (10)

Molecule **15** (0.40 g, 1.4 mmol) was dissolved in THF (120 mL) and a catalytic amount (one drop) of 10 N H_2SO_4 was added. The solution was heated at reflux for 2 h. Quenching of the reaction with distilled water (100 mL), neutralization with Na_2CO_3 (aq), and general workup (extraction into CH_2Cl_2, drying with anhydrous $MgSO_4$) yielded **10** as on oil. Recrystallization from $CHCl_3$ and hexanes gave light brown cubic crystals with an overall yield of 64%: mp 79–81°C. IR (cm^{-1}): 3445 (s), 3097 (m). ^{1}H NMR ($CDCl_3$) δ: 3.62 (s, 3H, OCH_3), 3.82 (s, 3H, OCH_3), 4.59 (s, 1H, OH), 5.27 (d, J = 1.5 Hz, 1H), 5.63 (d, J = 1.5 Hz, 1H), 6.46–6.51 (m, 2H, Ar), 6.69–6.72 (m, 2H, Ar), 6.88 (d, J = 7.4 Hz, 1H, Ar), 7.11–7.15 (m, 2H, Ar). HRMS calcd. for $C_{16}H_{16}O_3$: 256.1099; found: 256.1101.

2′,3″,4′-Trimethoxy-1,1-diphenylethanol (16)

The appropriate Grignard reagent was prepared from 1-bromo-2,4-dimethoxybenzene (2.4 mL, 17 mmol), Mg (0.41 g, 17 mmol), and 3′-methoxyacetophenone (2 mL, 14 mmol) to afford the crude product alcohol. Purification by column chromatography starting with CH_2Cl_2 and increasing polarity with ethyl acetate yielded the clean product oil **16** (~60%). ^{1}H NMR ($CDCl_3$) δ: 1.79 (s, 3H, CH_3), 3.58 (s, 3H, OCH_3), 3.76 (s, 3H, OCH_3), 3.80 (s, 3H, OCH_3), 4.49 (s, 1H, OH), 6.44 (d, J = 2.2 Hz, 1H, Ar), 6.50 (dd, J = 8.8, 2.2 Hz, 1H, Ar), 6.70 (d, J = 8.1 Hz, 1H, Ar), 6.79 (d, J = 7.4 Hz, 1H, Ar), 6.92 (s, 1H, Ar), 7.13 (t, J = 8.0 Hz, 1H, Ar), 7.30 (d, J = 8.8 Hz, 1H, Ar). HRMS calcd. for $C_{17}H_{20}O_4$: 288.1362; found: 288.1362.

2′,3″,4′-Trimethoxy-1,1-diphenylethene (11)

Molecule **16** (2.21 g, 7.6 mmol) was heated at reflux in a solution of CH_3CN and dilute H_2SO_4. Quenching and workup as for **10** yielded clean **11** in >80% yield. ^{1}H NMR ($CDCl_3$) δ: 3.62 (s, 3H, OCH_3), 3.76 (s, 3H, OCH_3), 3.83 (s, 3H, OCH_3), 5.29 (d, J = 1.5 Hz, 1H, =CH), 5.65 (d, J = 1.5 Hz, 1H, =CH), 6.48–6.52 (m, 2H, Ar), 6.79 (dd, J = 8.1, 1.5 Hz, 1H, Ar), 6.80–6.86 (m, 2H, Ar), 7.12–7.20 (m, 2H,

© 2002 NRC Canada

Ar). HRMS calcd. for $C_{17}H_{18}O_3$: 270.1256; found: 270.1256.

2′,4′-Dimethoxy-1,1-diphenylethanol (17)

The Grignard reaction involving 1-bromo-2,4-dimethoxybenzene (2 mL, 14 mmol), Mg (0.56 g, 23 mmol), and acetophenone (2 mL, 17 mmol) gave the crude product alcohol. Purification by column chromatography in CH_2Cl_2 gave the clean product **17** in 45% yield: mp 84–86°C. IR (cm^{-1}): 3550 (s). ^1H NMR ($CDCl_3$) δ: 1.79 (s, 3H, CH_3), 3.55 (s, 3H, OCH_3), 3.82 (s, 3H, OCH_3), 4.46 (s, 1H, OH), 6.44 (d, *J* = 2.2 Hz, 1H, Ar), 6.50 (dd, *J* = 8.1, 2.2 Hz, 1H, Ar), 7.15–7.29 (m, 6H, Ar). HRMS calcd. for $C_{16}H_{18}O_3$: 258.1256; found: 258.1260.

2′,4′-Dimethoxy-1,1-diphenylethene (12)

Molecule **17** (1.40 g, 5.4 mmol) was heated at reflux in CH_3CN and dilute H_2SO_4. Quenching of the reaction and general workup yielded the clean oil **12** in 90% yield. IR (cm^{-1}): 3081 (m). ^1H NMR ($CDCl_3$) δ: 3.62 (s, 3H, OCH_3), 3.84 (s, 3H, OCH_3), 5.31 (d, *J* = 1.5 Hz, 1H, =CH), 5.68 (d, *J* = 1.5 Hz, 1H, =CH), 6.50–6.54 (m, 2H, Ar), 7.14–7.34 (m, 6H, Ar). HRMS calcd. for $C_{16}H_{16}O_2$: 240.1150; found: 240.1148.

Product studies

In a typical photolysis, 20 mg of substrate in 1:1 (v/v) H_2O–CH_3CN (100 mL) was purged with argon for 10 min before and during irradiation at 254 nm in a Rayonet RPR-100 photochemical reactor equipped with a cooling finger (≈15°C). Representative preparatory photolyses are described below.

Photolysis of 8

Photolysis of **8** in 1:1 H_2O–CH_3CN (~10^{-3} M, 5 min, 16 lamps) followed by standard workup led to the alcohol product **13** (100%). ^1H NMR ($CDCl_3$) δ: 1.89 (s, 3H, CH_3), 2.20 (s, 1H, OH), 2.31 (s, 3H, CH_3), 5.05 (s, 1H, OH), 6.68 (m, 1H, Ar), 6.89–6.93 (m, 2H, Ar), 7.09–7.18 (m, 3H, Ar), 7.25–7.30 (m, 2H, Ar). HRMS calcd. for $C_{15}H_{16}O_2$: 228.1150; found: 228.1149.

Photolysis of 9

Photolysis of **9** in 1:1 H_2O–CH_3CN (as above) gave the alcohol product **14** (100%). ^1H NMR ($CDCl_3$) δ: 1.88 (s, 3H, CH_3), 2.23 (s, 1H, OH), 3.77 (s, 3H, CH_3), 5.26 (s, 1H, OH), 6.68 (m, 1H, Ar), 6.78–6.84 (m, 2H, Ar), 6.89 (m, 2H, Ar), 7.14 (t, *J* = 8.0 Hz, 1H, arom), 7.27–7.32 (m, 2H, Ar). HRMS calcd. for $C_{15}H_{16}O_3$: 244.1099; found: 226.1102.

Quantum yield measurements

Fluorescence quantum yields (Φ_f) for **8**–**12** in neat CH_3CN were measured relative to 2-aminopyridine in 0.1 N H_2SO_4 (Φ_f = 0.60 ± 0.05) (5). Solutions were studied at three concentrations (absorbance ≈ 0.10, 0.07, and 0.04 at λ_{ex} = 285 nm, argon purged) to rule out aggregation effects. Yields were calculated by integrating the emission bands and correcting for the solvent refractive indexes. Weak fluorescence from the solvent was corrected for (by subtraction) by measuring blank samples. Errors are estimated at 10%.

Quantum yields of photohydration (Φ_P) were determined relative to **5** (Φ_P = 0.22) in 100 mL 1:1 H_2O–CH_3CN. Samples (20 mg) of **8**–**12** and **5** were alternately irradiated in a Rayonet photochemical reactor (8 lamps, 2 min, 254 nm). The solutions were then worked up by addition of brine, extraction with CH_2Cl_2 (3 times), washing with distilled H_2O, drying over anhydrous $MgSO_4$, and removal of solvent under vacuum. Samples were analysed by ^1H NMR, with conversion to product being calculated by the relative integration of distinct starting material and product peaks, namely the alkene β-carbon becoming a methyl group. The ratio of known and unknown conversion to product is assumed to be equal to the ratio of their Φ_P. Total conversion to product was kept below 35%. Errors are estimated at ±0.05.

Φ_P at concentrations of water in CH_3CN other than 1:1 H_2O–CH_3CN were determined via UV–vis spectroscopy. A typical experiment involved preparing 8 cuvettes with solutions ranging from neat CH_3CN to 1:1 H_2O–CH_3CN. An equal aliquot (>10 μL) of a stock solution (10–15 mg in 3 mL CH_3CN) was added to each cuvette, and the samples were checked by absorption to be of equal concentration. Shifts in the absorption profile due to added water were not seen. The samples were simultaneously irradiated in a carousel in a photochemical reactor at 254 nm with 4 lamps. Irradiation occurred in 20 s intervals with absorption spectra taken between irradiation periods. The change in absorption at a given wavelength (250 nm) is proportional to the Φ_P for that solution, thus Φ_P for a variety of water concentrations were determined relative to that observed in 1:1 H_2O–CH_3CN. Even though the 1,1-diarylalcohols (**13**–**17**) have ϵ that are much lower than the conjugated 1,1-diarylalkenes at the monitored wavelength, light scavenging by the photoproduct was limited by determining the relative Φ_P at low conversion (~20%). Errors estimated to be ±10%.

Laser flash photolysis (LFP)

All transient spectra and lifetimes were obtained using a Nd:YAG laser (Spectra Physics Quanta-Ray GCR-3 or GCR-11, <20 mJ) with pulse width of ≈10 ns and excitation wavelength of 266 nm. Signals were digitized with a Tektronix TDS 520 recorder. Samples were prepared with OD ≈ 0.3 at 266 nm. Flow cells were used for all spectra obtained. The solutions were purged with nitrogen or oxygen for ≈10 min before excitation. Static cells were used for relative Δ OD experiments, and were purged with oxygen for 5 min prior to analysis. Each static sample was not flashed more than 10 times to limit photodegradation of the sample.

Fluorescence measurements

Steady-state fluorescence was conducted on a Photon Technology Internation A-1010 (PTI) Quanta-Master luminescence spectrometer. All solutions (absorbance ≈ 0.1 at λ_{ex} = 285 nm, except 290 nm for **8**) were purged for 5 min with argon prior to excitation. It was found that the photohydration product was far more fluorescent than the starting material, and prolonged exposure to the excitation lamp would lead to small amounts of product. To minimize this, solutions were allowed to equilibrate to 20°C in the absence of light, and the emission was measured every 5 nm. This method gave reproducible emission bands even after 3 scans,

© 2002 NRC Canada

indicating that no photoproduct was interfering with the fluorescence emission. Fluorescence lifetimes of **8** were measured on a PTI LS-1 instrument using time-correlated single-photon-counting techniques (10 000 counts, λ_{ex} = 290 nm, λ_{em} = 340 nm).

Acknowledgments

We thank the Natural Sciences and Engineering Research Council of Canada (NSERC) for supporting this research in the form of research grants (to PW) and the University of Victoria for a post-graduate fellowship (to JGC).

References

1. (*a*) M. Kasha. J. Chem. Soc. Faraday Trans. 2, **82**, 2379 (1986); (*b*) S.J. Formosinho and L.G. Arnaut. J. Photochem. Photobiol. A, **75**, 21 (1993); (*c*) D. Le Gourrierec, S.M. Ormson, and R.G. Brown. Prog. React. Kinet. **19**, 211 (1994).
2. P. Kalanderopoulos and K. Yates. J. Am. Chem. Soc. **108**, 6290 (1986).
3. K.L. Foster, S. Baker, D.W. Brousmiche, and P. Wan. J. Photochem. Photobiol. A, **129**, 157 (1999).
4. M. Fischer and P. Wan. J. Am. Chem. Soc. **121**, 4555 (1999).
5. D.E. Eaton. Pure Appl. Chem. **60**, 1107 (1988).
6. R.A. McClelland. Tetrahedron, **52**, 6823 (1996).
7. T. Okuyama, K. Ueno, Y. Morishima, M. Kamachi, and T. Osaka. Chem. Lett. 1129 (1990).

© 2002 NRC Canada

Iron complexes of the dibenzophospholyl ligand: a synthetic and crystallographic study

Andreas Decken, Melanie A. Neil, C. Adam Dyker, and Frank Bottomley

Abstract: Iron complexes bearing the dibenzophospholyl (DBP) ligand have been prepared. Reaction of DBP-Li with $CpFe(CO)_2Br$ gave $[(\mu_2\text{-DBP})Fe_2Cp_2(CO)_4]Br$ and reaction of DBP-Li with $CpFe(CO)_2I$ gave $[(\mu_2\text{-DBP})Fe_2Cp_2(CO)_4]I$. Reaction of bis(1,1′-dibenzophospholyl) and $[CpFe(CO)_2]_2$ yielded a mixture of *cis*- and *trans*-$(\mu_2\text{-DBP})_2Fe_2Cp_2(CO)_2$. The mixture was also obtained on heating of $[(\mu_2\text{-DBP})Fe_2Cp_2(CO)_4]X$ (X = Br, I). The ligands are σ-bonded through the phosphorus atom in all complexes. The compounds were characterized by ^1H, ^{13}C, and ^{31}P NMR and IR spectroscopies, mass spectrometry, micro analysis, and X-ray diffraction.

Key words: dibenzophospholyl, iron, heterocycle.

Résumé : On a préparé des complexes du fer portant le ligand dibenzophospholyle (DBP). La réaction du DBP-Li avec le $CpFe(CO)_2Br$ conduit à la formation du $[(\mu_2\text{-DBP})Fe_2Cp_2(CO)_4)]Br$ alors que la réaction du DBP-Li avec le $CpFe(CO)_2I$ conduit à la formation du $[(\mu_2\text{-DBP})Fe_2Cp_2(CO)_4)]I$. La réaction du bis(1,1′-dibenzophospholyle) avec le $[CpFe(CO)_2]_2$ conduit à un mélange des isomères *cis*- et *trans*- du $(\mu_2\text{-DBP})Fe_2Cp_2(CO)_4]X$ (X = Br, I). Dans chacun de ces complexes, les ligands sont liés aux atomes de phosphore par des liaisons σ. Les composés ont été caractérisés par RMN du ^1H, du ^{13}C et du ^{31}P, spectroscopie IR, spectrométrie de masse, microanalyses et diffractions des rayons X.

Mots clés : dibenzophospholyle, fer, hétérocycle.

[Traduit par la Rédaction]

Introduction

Benzannelated phospholyl ligands such as **1**–**3** have recently emerged as interesting ligands in organometallic chemistry (1). Their hydrocarbon analogues bind primarily through the π-electron system, but **1**–**3** can also ligate metals

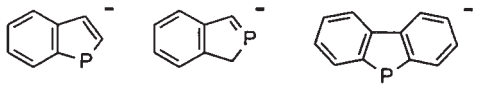

1 **2** **3**

through the phosphorus lone pair, resulting in complexes containing ligands with σ-, π-, and mixed-bonding modes. We recently reported the synthesis and characterization of manganese complexes of dibenzophospholyl (DBP, **3**) (2). The ligands were σ-bonded, bridging two metal atoms in the complexes $(\mu_2\text{-DBP})(\mu_2\text{-Br})Mn_2(CO)_8$ (**4**) and $(\mu_2\text{-DBP})_2Mn_2(CO)_8$ (**5**), which is unusual for metal complexes of phospholyl ligands and in contrast to the bonding observed for their hydrocarbon analogues.

We are exploring the chemistry of DBP with emphasis on the differences between its modes of coordination and those

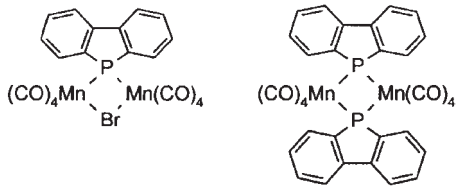

4 **5**

of the fluorenyl analogue and of ligands **1** and **2**. In light of the diverse and controversial chemistry of the fluorenyl complexes $[(\eta^6\text{-}C_{13}H_9)FeCp$ and $(\eta^5\text{-}C_{13}H_9)FeCp]$ (3), we prepared iron complexes of the dibenzophospholyl anion, **3**. The characterization, structures, and properties of the products are reported here.

Results

Synthesis and properties

Compounds **6** and **7** were synthesized from DBP-Li and $CpFe(CO)_2X$ (X = Br, I) in THF at room temperature in high yields (93 and 87%, respectively) (Scheme 1). Heating of **6** or **7** in refluxing xylenes resulted in the formation of trace amounts of **8** with Cp_2Fe as the major product, as well as large amounts of intractable green solids (Scheme 2). Compound **8** was also obtained by reaction of bis(1,1′-dibenzophospholyl) (**9**) and $Cp_2Fe_2(CO)_4$ in refluxing xylenes as a mixture of *cis*- and *trans*-isomers (ratio 1:15) in 75% yield (Scheme 3).

The products were characterized by elemental analysis, IR and NMR spectroscopies, mass spectrometry, and X-ray dif-

Received 4 September 2001. Published on the NRC Research Press Web site at http://canjchem.nrc.ca on 11 January 2002.

A. Decken,[1] M.A. Neil, C.A. Dyker, and F. Bottomley. Department of Chemistry, University of New Brunswick, P.O. Box 45222, Fredericton, NB E3B 6E2, Canada.

[1]Corresponding author (telephone: (506) 453-4875; fax: (506) 453-4981; e-mail: adecken@unb.ca).

 DOI: 10.1139/V01-193 © 2002 NRC Canada

Scheme 1.

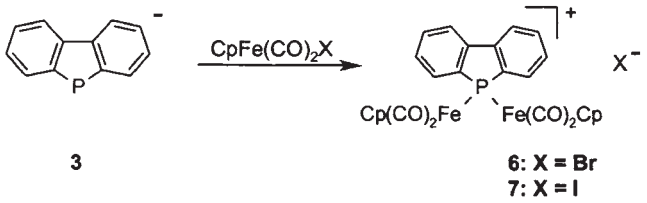

3 **6: X = Br** **7: X = I**

Scheme 2.

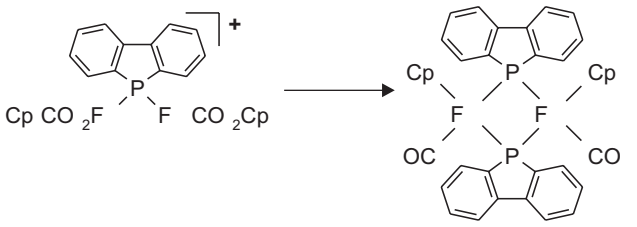

Fig. 1. View of the cation of **6**, thermal ellipsoids at the 30% probability level. Hydrogen atoms have been omitted for clarity.

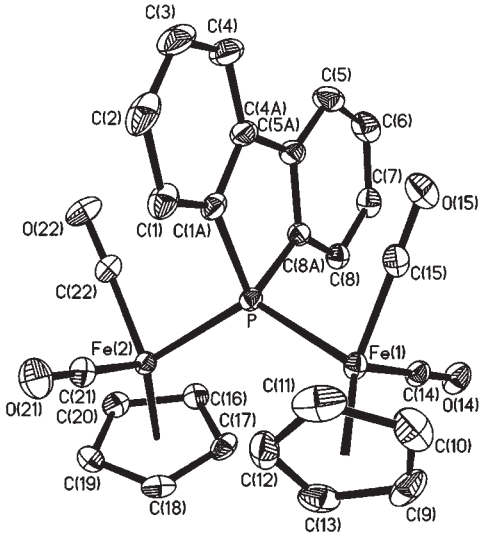

Scheme 3.

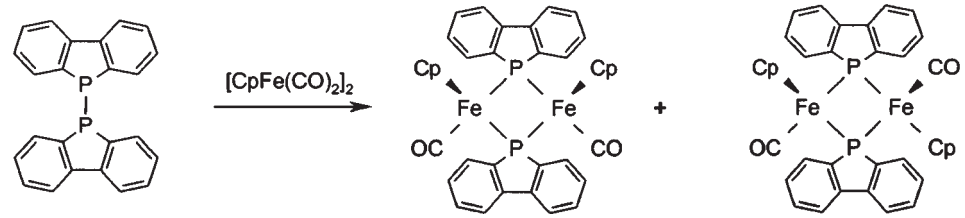

9 ***cis*-8** ***trans*-8**

fraction. The complexes were either yellow (**6**, **7**) or green (**8**), diamagnetic, crystalline solids. They were mildly air and moisture sensitive; compounds **6** and **7** decompose slowly, especially in the presence of light, while **8** was indefinitely stable under an inert atmosphere, both in solution and in the solid state. Compounds **6**, **7**, and *cis*-**8** were insoluble in nonpolar hydrocarbons and only sparingly soluble in polar organic solvents, while *trans*-**8** was virtually insoluble in all organic solvents. Compound **8** decomposed slowly in $CHCl_3$.

Discussion

Reaction of DBP-Li with either $CpFe(CO)_2Br$ or $CpFe(CO)_2I$ yielded the $[(\mu_2\text{-DBP})Fe_2Cp_2(CO)_4]^+$ cation as the halide salts **6** and **7**, respectively. Crystallographic and spectroscopic data revealed that the structure of the cations in **6** and **7** were identical, both in the solid state and in solution. Formation of the ionic complex was in contrast to the analogous reaction between DBP-Li and $Mn(CO)_5Br$, which yielded the neutral complex **4** (2). The corresponding cation $[(\mu_2\text{-DBP})Mn_2(CO)_{10}]^+$ was not observed. Ring closure of $[(\mu_2\text{-DBP})Fe_2Cp_2(CO)_4][X]$ to give $(\mu_2\text{-DBP})(\mu_2\text{-X})Fe_2Cp_2(CO)_2$ requires the loss of two molecules of CO from the cation and incorporation of the halide atom into the four membered ring. Bond dissociation energies (BDE's) for metal carbonyl bonds have recently been investigated for manganese and iron carbonyl complexes (13). DFT calculations showed that BDE's were significantly higher for Fe—CO bonds in $Cp_2Fe_2(CO)_4$ compared to Mn—CO bonds in $Mn_2(CO)_{10}$ and the Fe—CO bonds in $Fe_2(CO)_9$. If the same trend holds for $CpFe(CO)_2$ and $Mn(CO)_5$ complexes of DBP, loss of carbonyl ligands and ring formation is expected to be more difficult in cyclopentadienyl iron carbonyls compared to manganese carbonyls. This rationale is substantiated by the fact that several complexes of general formula $(\mu_2\text{-PR}_2)(\mu_2\text{-X})Mn_2(CO)_8$ (14) and $(\mu_2\text{-PR}_2)(\mu_2\text{-X})Fe_2(CO)_6$ (15) have been structurally authenticated, while there are no examples of $(\mu_2\text{-PR}_2)(\mu_2\text{-X})Fe_2Cp_2(CO)_2$. Heating of **6** or **7** in refluxing xylenes resulted in the formation of trace amounts of **8** with Cp_2Fe as the major product, as well as large amounts of intractable green solids. There was no evidence for the intermediacy of $(\mu_2\text{-DBP})(\mu_2\text{-X})Fe_2Cp_2(CO)_2$. Compound **8** can be prepared in 75% yield directly from $Cp_2Fe_2(CO)_4$ and **9**. A mixture of *cis*- and *trans*-**8**, was obtained in a 1:15 ratio. No reaction was observed at temperatures below 80°C and the *cis*/*trans* ratio did not change in the 80–144°C temperature range. There was no *cis* → *trans* or *trans* → *cis* conversion in xylenes as determined by ^1H and ^{31}P NMR of the pure isomers as well as mixtures. The *trans* isomer of **8** was highly symmetric in solution as evident by ^1H and ^{13}C NMR spectroscopy which showed 4 peaks in the aromatic C-H region. In contrast, the *cis*-isomer of **8** showed 8 signals in the ^1H and ^{13}C NMR in the aromatic C-H region. The loss

© 2002 NRC Canada

Table 1. Crystal data and structure refinement for **6**, **7**, and *cis*-**8**.

	6·$CH_3C(O)CH_3$	**7**·$CH_3C(O)CH_3$	*cis*-**8**·1/2$C_6H_{14}O_3$
Empirical formula	$C_{29}H_{24}BrFe_2O_5P$	$C_{29}H_{24}Fe_2IO_5P$	$C_{39}H_{33}Fe_2O_{3.50}P_2$
FW	675.06	722.05	731.29
Crystal size (mm)	0.20 × 0.30 × 0.40	0.30 × 0.20 × 0.20	0.20 × 0.20 × 0.225
Color/habit	Orange/irregular	Orange/parallelepiped	Orange/parallelepiped
T (K)	173(1)	173(1)	173(1)
Wavelength (Å)	0.71073	0.71073	0.71073
Crystal system	Monoclinic	Monoclinic	Tetragonal
Space group	$P2_1/c$	$P2_1/c$	$P\text{-}42_1m$
a (Å)	17.0403(8)	17.1235(13)	19.0245(14)
b (Å)	9.1669(4)	9.3829(7)	19.0245(14)
c (Å)	18.6136(8)	19.0714(14)	9.2713(11)
α (°)	90	90	90
β (°)	111.745(1)	112.720(2)	90
γ (°)	90	90	90
Volume (Å^3)	2700.7(2)	2826.4(4)	3355.6(5)
Z	4	4	4
Abs. coeff,(mm^{-1})	2.651	2.212	0.999
Theta range (°)	1.29–32.50	1.29–32.50	1.51–32.50
No. of reflns. collected	28 764	30 244	37 833
No. of indep. reflns. / *R*(int)	9651/0.0219	10097/0.0283	6286/0.0246
Max./min. transm.	0.721/0.608	0.826/0.682	0.908/0.853
No. of data/restr./params.	9651/0/415	10097/2/415	6286/0/288
S (GoF) on F^2 [a]	0.945	1.119	1.013
R_1 ($I > 2\sigma(I)$)[b]	0.0368	0.0475	0.0310
wR_2 (all data)[c]	0.0974	0.138	0.0760
Largest diff. peak/hole (e Å^{-3})	0.972/–0.728	3.102/–0.909	0.608/–0.225

[a] $S = (\sum w(F_o^2 - F_c^2)^2/(n-p))^{1/2}$.

[b] $R_1 = \sum ||(F_o| - |F_c||/\sum |F_o|$.

[c] $wR_2 = (\sum w(F_o^2 - F_c^2)^2/\sum wF_o^4)^{1/2}$, where $w^{-1} = \sigma^2(F_o^2) + (aP)^2 + bP$, where $P = (\max(F_o^2, 0) + 2F_c^2)/3$. For **6**, $a = 0.0538$, $b = 0$; for **7**, $a = 0.0648$, $b = 4.62$; for *cis*-**8**, $a = 0.0473$, $b = 0$.

of symmetry is a result of repulsive interactions between the DBP ring systems and the carbonyl ligands (see molecular structure section below) causing the Fe_2P_2 ring to fold. There was no mixing of the hydrogen atom positions as evident by NOESY spectroscopy, which shows no signals due to exchange (0.5 s mixing time).

In complexes **6**–**8** the metal was σ-coordinated by the phosphorus atom of the ligand. There was no involvement of the ligands' π-electrons. This is consistent with the structures of the manganese carbonyl complexes **4** and **5** and in contrast to iron complexes of the fluorenyl ligand ($C_{13}H_9$), where η^6-coordination to the six-membered ring is observed (3*b*, 16). The existence of (η^5-$C_{13}H_9$)FeCp is still controversial and a crystallographic study has not been reported in the literature (3). Compounds **6**–**8** are the first iron complexes of benzannelated phospholyls and to the best of our knowledge the only previous attempt was by Mathey and co-workers (17), who found that reaction between **1** and $FeCl_2$ gave only intractable products.

Molecular structures

A thermal ellipsoid plot of **6** is shown in Fig. 1 (a thermal ellipsoid plot for the cation in **7** has been omitted because it is identical to the cation in **6**). Crystal data and selected interatomic distances and angles of the cations of both compounds are compared in Tables 1 and 2, respectively.

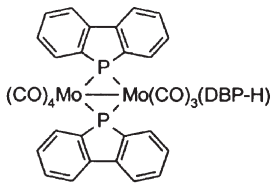

10

The structures are isomorphous and the metric parameters of the cations are almost identical. In each structure, the phosphorus atom is tetrahedrally coordinated with almost equivalent P—Fe interatomic distances (av 2.2904(6) Å for **6** and 2.2955(9) Å for **7**) and P—C (av 1.835(2) Å for **6** and 1.835(3) Å for **7**). The P—Fe distances compare well with those reported for the two known crystal structures of $[(\mu_2\text{-}R_2P)Fe_2Cp_2(CO)_4]^+$ complexes (18, 19). The P—C distances are slightly longer than in the related complexes **4** (av 1.818 (6) Å) (2), **5** (av 1.824(2) Å), and **10** (av 1.79(2) Å) (20). The DBP skeleton is planar and nearly orthogonal to the Fe_2P plane (torsion angle, 88.6°). The cations are skewed with dihedral angles of 76.92(2)° (**6**) and 77.42(2)° (**7**) for the Cp(1)-Fe(1)-Fe(2)-Cp(2) vectors. The Fe(1)-P-Fe(2) angle (124.93(3)° for **6** and 125.41(4)° for **7**) is large in comparison to the M-P-M angles in **4** (102.20(7)°), **5** (102.12(2)°), and **10** (av 76.1(2)°) and is a result of the open

© 2002 NRC Canada

Table 2. Selected bond distances (Å) and angles (°) for **6** and **7**.

	6	**7**
Bond distances (Å)		
Fe(1)—P	2.2908(6)	2.2957(9)
Fe(2)—P	2.2900(6)	2.2954(9)
Fe(1)—Cp(1)	1.7305(3)	1.7325(5)
Fe(2)—Cp(2)	1.7314(3)	1.7320(4)
Fe(1)—C(14)	1.791(2)	1.794(4)
Fe(1)—C(15)	1.776(3)	1.784(3)
Fe(2)—C(21)	1.781(2)	1.788(3)
Fe(2)—C(22)	1.782(2)	1.791(4)
P —C(1A)	1.835(2)	1.836(3)
P —C(8A)	1.835(2)	1.834(3)
C(1A)—C(4A)	1.407(3)	1.415(5)
C(4A)—C(5A)	1.478(3)	1.470(5)
C(5A)—C(8A)	1.405(3)	1.422(5)
Bond angles (°)		
C(1A)-P-C(8A)	89.76(10)	90.06(16)
C(1A)-P-Fe(1)	107.51(7)	108.70(11)
C(8A)-P-Fe(1)	108.91(7)	111.04(11)
C(1A)-P-Fe(2)	110.71(7)	109.18(10)
C(8A)-P-Fe(2)	109.34(7)	106.73(11)
Fe(1)-P-Fe(2)	124.93(3)	125.41(4)
P-Fe(1)-Cp(1)	127.15 (2)	124.78 (3)
P-Fe(1)-C(14)	93.24(7)	92.09(12)
P-Fe(1)-C(15)	87.65(8)	88.05(12)
Cp(1)-Fe(1)-C(14)	121.80(7)	123.92(12)
Cp(1)-Fe(1)-C(15)	123.16(8)	124.63(12)
C(14)-Fe(1)-C(15)	94.32(11)	93.25(16)
P-Fe(2)-Cp(2)	125.09(2)	126.22 (3)
P-Fe(2)-C(21)	91.87(8)	93.01(10)
P-Fe(2)-C(22)	88.36(8)	88.19(11)
Cp(2)-Fe(2)-C(21)	123.00(8)	123.19(10)
Cp(2)-Fe(2)-C(22)	125.07(7)	122.81 (12)
C(21)-Fe(2)-C(22)	93.48(11)	93.74(16)
C(4A)-C(1A)-P	111.84(17)	111.6(2)
C(1A)-C(4A)-C(5A)	113.17(19)	113.5(3)
C(8A)-C(5A)-C(4A)	113.4(2)	113.3(3)
C(5A)-C(8A)-P	111.74(16)	111.5(3)

Fig. 2. View of *cis*-**8**, thermal ellipsoids at the 30% probability level. Hydrogen atoms have been omitted for clarity.

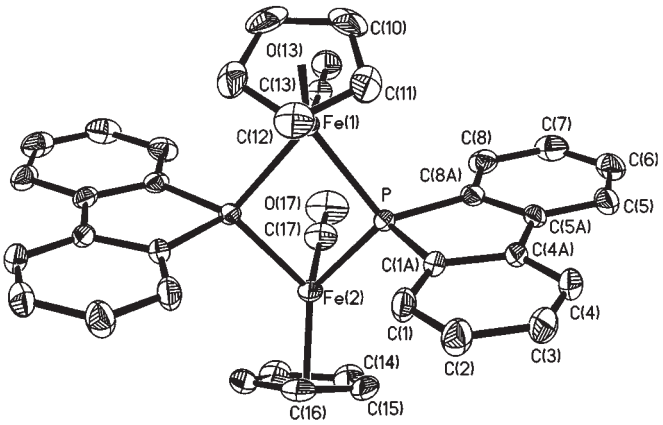

Table 3. Selected bond distances (Å) and angles (°) for *cis*-**8.**

Bond distances (Å)	
Fe(1)—P	2.2345(4)
Fe(2)—P	2.2434(4)
Fe(1)—Cp(1)	1.7060(3)
Fe(2)—Cp(2)	1.7245(3)
Fe(1)—C(13)	1.739(3)
Fe(2)—C(17)	1.731(3)
P—C(1A)	1.8264(16)
P—C(8A)	1.8253(15)
C(1A)—C(4A)	1.4081(19)
C(4A)—C(5A)	1.458(3)
C(5A)—C(8A)	1.404(2)
C(13)—O(13)	1.147(3)
C(17)—O(17)	1.146(4)
Bond angles (°)	
C(1A)-P-C(8A)	89.50(7)
C(1A)-P-Fe(1)	115.73(5)
C(8A)-P-Fe(1)	115.40(5)
C(1A)-P-Fe(2)	117.01(5)
C(8A)-P-Fe(2)	119.73(5)
Fe(1)-P-Fe(2)	100.576(15)
Cp(1)-Fe(1)-P	128.158(15)
Cp(1)-Fe(1)-C(13)	122.20(7)
P#1-Fe(1)-P	77.73(2)
C(13)-Fe(1)-P	93.12(6)
P-Fe(2)-P#1	77.360(19)
Cp(2)-Fe(2)-P	129.081(16)
Cp(2)-Fe(2)-C(17)	123.72(8)
C(17)-Fe(2)-P	91.89(7)
C(4A)-C(1A)-P	112.19(12)
C(1A)-C(4A)-C(5A)	112.65(15)
C(8A)-C(5A)-C(4A)	113.98(13)
C(5A)-C(8A)-P	111.64(12)

Fig. 3. View of *cis*-**8** showing the folding of the Fe_2P_2 plane. Hydrogen atoms and the cyclopentadienyl rings have been omitted for clarity. Cp(1) and Cp(2) are the centroids of the cyclopentadienyl rings.

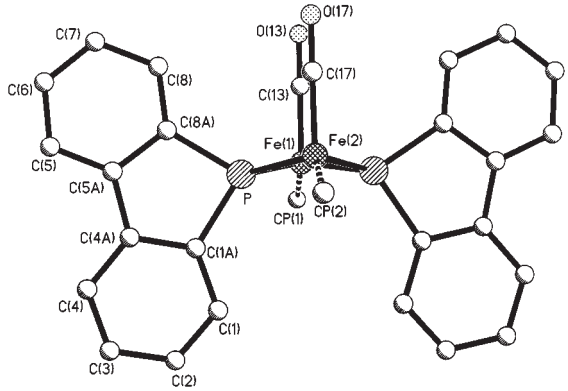

M_2P framework. Complexes **4** and **5** consist of M_2PX (X = Br, P) four-membered rings and **9** contains an additional M–M bond; both of these features are missing in **6** and **7**. The Fe···Fe distances are 4.062 Å (**6**) and 4.080 Å (**7**) and there-

© 2002 NRC Canada

fore no direct Fe–Fe interactions are present. The halide anions stack along the *y* axis forming hydrogen bonds, the shortest being 2.912 Å (Br···H(20)) and 2.944 Å (I···H(10)) and there are no additional interionic contacts. Compounds **6** and **7** crystallize as acetone solvates and the solvent molecules are located in channels along the *y* axis. The acetone molecules are hydrogen bonded via the carbonyl oxygen atom (O(26)···H(1) = 2.327 Å for **6** and O(26)···H(8) = 2.456 Å for **7**).

A thermal ellipsoid plot of *cis*-**8** is shown in Fig. 2 and selected interatomic distances and angles are given in Table 3.

Molecules of *cis*-**8** crystallize in the space group $P\text{-}42_1m$ and the $Fe_2(CO)_2$ moiety as well as the centroids of the cyclopentadienyl rings lie on a mirror plane. The phosphorus atom is tetrahedrally coordinated with almost equivalent P—Fe (2.2345(4) Å and 2.2434(4) Å) and P—C (1.8264(16) Å and 1.8253(15) Å) interatomic distances. The P—C distances are shorter than those in complexes **6** and **7**, and are comparable to those in **4** (av 1.818(6) Å) (2), **5** (av 1.824(2) Å) (2), and **10** (av 1.79(2) Å) (20). The four-membered Fe_2P_2 ring displays obtuse angles at the phosphorus atoms (100.576(15)°), which are similar to those in **4** and **5**, and acute angles at the iron centers (77.360(19)°). The Fe···Fe distance is 3.445 Å and therefore no direct Fe–Fe interaction is present. The most intriguing feature of the structure of *cis*-**8** is the orientation of the planar DBP skeleton. Repulsive interactions between the DBP ring system and the carbonyl groups cause a folding of the Fe_2P_2 ring, resulting in a 22.9° angle between the two PFe_2 planes (Fig. 3). The only related structure to *cis*-**8** is that of $(\mu_2\text{-}P(OR)_2)_2Fe_2Cp_2(CO)_2$ ($(OR)_2$ = $OCH_2CMe_2CH_2O$) where a folding of the Fe_2P_2 ring by 18.3° was observed (21). In comparison, the four-membered Mn_2PBr ring in **4** and Mn_2P_2 ring in **5** are planar. The DBP skeleton in *cis*-**8** is almost orthogonal to the Fe_2P planes (torsion angle, 89.6°), which is consistent with the conformation in **4** and **5**. *cis*-**8** crystallizes as a diglyme solvate and the solvent molecules are located in channels along the *z* axis. The diglyme molecules are hydrogen bonded via the peripheral oxygen atoms (O(22)···H(10) = 2.547 Å), each oxygen atom coordinating two molecules of *cis*-**8**. This results in aggregates containing two molecules of *cis*-**8** and one solvent molecule.

Experimental

General

All reactions were carried out under an atmosphere of argon utilizing standard Schlenk techniques. Solvents were dried and distilled according to standard procedures (4). Melting points were measured in open glass capillaries using a Gallenkamp melting point apparatus and were uncorrected. ^1H, ^{13}C, and ^{31}P NMR spectra were recorded on a Varian Unity 400 spectrometer operating at 399.99, 100.6, and 161.31 MHz, respectively. ^1H and ^{13}C spectra were referenced relative to tetramethylsilane and ^{31}P spectra were referenced relative to external triphenylphosphine (δ = –6.0). Electron impact (EI) and fast atom bombardment (FAB) mass spectrometry experiments were performed on a Kratos MS-50 mass spectrometer, with 3-nitrobenzyl alcohol as the FAB matrix and helium as the bombarding gas. Infrared spectra were obtained on a Bruker IFS 25 instrument. Unless otherwise stated, all reagents were obtained from commercial suppliers and used without further purification. $CpFe(CO)_2Br$ (5), $CpFe(CO)_2I$ (6), and bis(1,1′-dibenzophospholyl) (7) were prepared according to literature procedures.

Lithium shavings were obtained from lithium rods (99% under mineral oil). Flash chromatography was carried out using Merck silica gel (330–400 mesh). Elemental analyses were preformed by Galbraith Laboratories, Knoxville, TN.

Preparation of [(μ_2-DBP)$Fe_2Cp_2(CO)_4$]Br (6)

To a solution of 1-phenyldibenzophosphole (0.50 g, 1.9 mmol) in THF (5 cm^3) was added lithium shavings (10-fold excess) and the mixture stirred overnight. The solution was decanted and aluminum trichloride (0.085 g, 0.64 mmol) was added, resulting in a dark brown-red solution (7, 8). The mixture was added dropwise to a solution of $CpFe(CO)_2Br$ (0.99 g, 3.86 mmol) in THF (5 cm^3), producing a dark red solution. Within ten minutes, the solution became yellow-brown and a yellow precipitate formed. The solid was isolated by filtration, washed with hexane, and dried under vacuum to give **6** as a bright yellow solid. Yield: 1.10 g, 1.79 mmol, 93%, mp 184°C (dec.). IR (KBr disk) (cm^{-1}) ν_{CO}: 1978 (m-s), 1988 (m-s), 2026 (m-s), 2040 (m-s). ^1H NMR (acetone-d_6) δ: 8.24 (d, J = 7.6 Hz, 2H), 8.07 (dd, J = 7.6, 7.6 Hz, 2H), 7.65 (m, 2H), 7.60 (m, 2H), 5.30 (s, 10H). ^{13}C NMR (acetone-d_6) δ: 212.33 (*C*O), 212.14 (*C*O), 150.70 (d, $J_{P,C}$ = 27 Hz), 138.84 (d, $J_{P,C}$ = 6 Hz), 131.22, 130.10 (d, $J_{P,C}$ = 14 Hz), 129.64 (d, $J_{P,C}$ = 10 Hz), 123.14 (d, $J_{P,C}$ = 5 Hz). $^{31}P\{^1H\}$NMR ($CDCl_3$) δ: 30. MS-FAB *m*/*z* (%): 608 (0.33) $[C_{34}H_{26}Fe_2P_2]^+$ $[(C_{12}H_8P)_2Fe_2Cp_2]^+$, 366 (12) $[C_{24}H_{16}P_2]^+$ $[(C_{12}H_8P)_2]^+$, 360 (2) $[C_{19}H_{13}FeO_2P]^+$ $[(C_{12}H_8P)FeCp(CO)_2]^+$, 332 (6) $[C_{18}H_{13}FeOP]^+$ $[(C_{12}H_8P)FeCp(CO)]^+$, 304 (43) $[C_{17}H_{13}FeP]^+$ $[(C_{12}H_8P)FeCp]^+$, 248 (8) $[C_{17}H_{13}P]^+$ $[C_{12}H_8PCp]^+$, 183 (45) $[C_{12}H_8P]^+$, 177 (2) $[C_7H_5FeO_2]^+$ $[CpFe(CO)_2]^+$, 128 (4) $[C_{10}H_8]^+$, 121 (42) $[C_5H_5Fe]^+$ $[CpFe]^+$, 65 (18) $[C_5H_5]^+$, 56 (23) $[Fe]^+$.

Preparation of [(μ_2-DBP)$Fe_2Cp_2(CO)_4$]I (7)

In analogy to the preparation of **6**, 1-phenyldibenzophosphole (0.50 g, 1.9 mmol), lithium shavings (10-fold excess), aluminum trichloride (0.085 g, 0.64 mmol), and $Fe(Cp)(CO)_2I$ (1.17 g, 3.85 mmol) gave **7** as a bright yellow solid. Yield: 1.12 g, 1.69 mmol, 87%, mp 208°C (dec.). MS-FAB *m*/*z* (%): 537 (2.5) $[C_{26}H_{18}Fe_2O_4P]^+$ $[(C_{12}H_8P)Fe_2(CO)_4Cp_2]^+$, 481 (1.1) $[C_{24}H_{18}Fe_2O_2P]^+$ $[(C_{12}H_8P)Fe_2(CO)_2Cp_2]^+$, 425 (3) $[C_{22}H_{18}Fe_2P]^+$ $[(C_{12}H_8P)Fe_2Cp_2]^+$, 360 (1.5) $[C_{19}H_{13}FeO_2P]^+$ $[(C_{12}H_8P)FeCp(CO)_2]^+$, 304 (2) $[C_{17}H_{13}FeP]^+$ $[(C_{12}H_8P)FeCp]^+$, 183 (4) $[C_{12}H_8P]^+$, 177 (7) $[C_7H_5FeO_2]^+$ $[CpFe(CO)_2]^+$, 132 (40) $[C_{10}H_{12}]^+$, 128 (12) $[C_{10}H_8]^+$, 121 (7) $[C_5H_5Fe]^+$ $[CpFe]^+$, 85 (47) $[CFeO]^+$ $[Fe(CO)]^+$, 56 (100) $[Fe]^+$. Anal. calcd. for $C_{12}H_8IO_4PFe_2$: C 47.03, H 2.73; found: C 46.85, H 2.88. ^1H, ^{13}C, and ^{31}P NMR and IR data were identical to those reported above for **6**.

Preparation of (μ_2-DBP)$_2Fe_2Cp_2(CO)_2$ (8)

A solution of $Cp_2Fe_2(CO)_4$ (0.29 g, 0.819 mmol) in xylenes (6 cm^3) was added dropwise to a suspension of bis(1,1′-dibenzophospholyl) (0.30 g, 0.819 mmol) in xylenes (7 cm^3) to give a dark red mixture. This was heated to reflux

© 2002 NRC Canada

and within ten minutes the colour of the solution changed to green and a green precipitate formed. After 70 min the dark green mixture was slowly cooled to room temperature. The green precipitate was collected on a sintered funnel, washed with pentane, and dried under reduced pressure to give *trans*-**8** as a green solid. The mother liquor was concentrated to dryness to give a mixture of *trans*- and *cis*-**8**. Flash column chromatography of the mixture using a 2:3 mixture of benzene–pentane gave *cis*-**8** as a green solid. Yield of *trans*-**8**: 0.39 g, 0.581 mmol, 71%, mp 307°C (dec.). IR (KBr disk) (cm^{-1}) ν_{CO}: 1912 (s), 1917 (s). ^1H NMR ($CDCl_3$) δ: 8.72 (d, *J* = 7.6 Hz, 4H), 7.96 (d, *J* = 7.2 Hz, 4H), 7.64 (dd, *J* = 7.8, 7.8 Hz, 4H), 7.52 (dd, *J* = 7.8, 7.8 Hz, 4H), 3.83 (s, 10H). ^{13}C NMR ($CDCl_3$, HMQC) δ: 131, 122, 127, 128, 80. ^{31}P NMR (C_6D_6) δ: –49. MS-EI$^+$ *m*/*z* (%): 664 (46) $[C_{36}H_{26}Fe_2O_2P_2]^+$ $[(C_{12}H_8P)_2Fe_2(CO)_2(C_5H_5)_2]^+$, 636 (13) $[C_{35}H_{26}Fe_2OP_2]^+$ $[(C_{12}H_8P)_2Fe_2(CO)(C_5H_5)_2]^+$, 608 (78) $[C_{34}H_{26}P_2Fe_2]^+$ $[(C_{12}H_8P)_2Fe_2(C_5H_5)_2]^+$, 425 (58) $[C_{22}H_{18}PFe_2]^+$ $[(C_{12}H_8P)Fe_2(C_5H_5)_2]^+$, 366 (73) $[C_{24}H_{16}P_2]^+$ $[(C_{12}H_8P)_2]^+$, 360 (60) $[C_{19}H_{13}FeO_2P]^+$ $[(C_{12}H_8P)Fe(CO)_2Cp]^+$, 304 (72) $[C_{17}H_{13}PFe]^+$ $[(C_{12}H_8P)Fe(C_5H_5)]^+$, 248 (58) $[C_{17}H_{13}P]^+$ $[C_{12}H_8PCp]^+$, 183 (80) $[C_{12}H_8P]^+$, 121 (59) $[C_5H_5Fe]^+$ $[FeCp]^+$, 65 (27) $[C_5H_5]^+$ $[Cp]^+$, 56 (30) $[Fe]^+$, 28 (100) $[CO]^+$. Yield of *cis*-**8**: 0.023 g, 0.034 mmol, 4%, mp 242°C (dec.). IR (KBr disk) (cm^{-1}) ν_{CO}: 1937 (s), 1942 (s). ^1H NMR ($CDCl_3$) δ: 8.90 (d, *J* = 7.6 Hz, 2H), 8.68 (d, *J* = 7.6 Hz, 2H), 8.04 (d, *J* = 8.0 Hz, 2H), 7.91 (d, *J* = 6.4 Hz, 2H), 7.74 (dd, *J* = 7.6, 7.2 Hz, 2H), 7.58 (dd, *J* = 7.6, 7.2 Hz, 2H), 7.50 (m, 4H), 3.69 (s, 10H). ^{13}C NMR ($CDCl_3$, HMQC) δ: 130, 130, 128, 128, 127, 122, 121, 80. ^{31}P NMR (C_6D_6) δ: –40. Anal. calcd. for $C_{36}H_{28}O_3P_2Fe_2$ (*cis*-**8**·H_2O): C 61.74, H 4.32; found: C 61.09, H 4.55.

X-ray diffraction experiments

Crystals suitable for diffraction studies were grown from acetone (**6**, **7**) (9) or by vapour diffusion using diglyme–pentane (*cis*-**8**) at –23°C. Single crystals of **6**, **7**, and *cis*-**8** were mounted on thin glass fibers using Paratone-N oil and frozen in the cold nitrogen stream of the goniometer. Data were collected on a Bruker AXS P4/SMART 1000 diffractometer using ω and φ scans with a scan width of 0.3° at 10 s (**6**) and 30 s (**7**, *cis*-**8**) exposure times. A hemisphere of data was collected at a detector distance of 4 cm. Crystal decay was not observed. The data were reduced (SAINT) (10) and corrected for absorption (SADABS) (11). The structures were solved by direct methods and refined by full-matrix least-squares on F^2 (SHELXTL) (12). All non-hydrogen atoms were refined anisotropically. Hydrogen atoms were located and refined isotropically where possible. Hydrogen atoms of the solvent molecule for *cis*-**8** were included in calculated positions and refined using a riding model, while those of the acetone molecules in **6** and **7** were omitted. Crystallographic data are summarized in Table 1 and selected interatomic distances and angles are presented in Tables 2 and 3.[2]

Acknowledgments

Dr. Larry Calhoun (UNB) is thanked for assistance with the NMR experiments and Mr. Gilles Vautour (UNB) for mass spectrometry. We are grateful to the Natural Sciences and Engineering Research Council of Canada (NSERC) and the University of New Brunswick for financial support of this work.

References

1. (*a*) F. Mathey. Coord. Chem. Rev. **137**, 1 (1994); (*b*) F. Mathey. Chem. Rev. **88**, 429 (1988); (*c*) F. Mathey and P.L. Floch. Coord. Chem. Rev. **179**–**180**, 771 (1998); (*d*) F. Mathey. New J. Chem. **11**, 585 (1987); (*e*) D. Gudat, S. Häp, L. Szarvas, and M. Nieger. J. Chem. Soc. Chem. Commun. 1637 (2000); (*f*) D. Gudat, M. Nieger, and M. Schrott. Chem. Ber. **128**, 259 (1995); (*g*) D. Gudat, M. Schrott, and M. Nieger. J. Chem. Soc. Chem. Commun. 1541 (1995); (*h*) D. Gudat, M. Schrott, V. Bajorat, M. Nieger, S. Kotila, R. Fleischer, and D. Stalke. Chem. Ber. **129**, 337 (1996); (*i*) D. Gudat, A.W. Holderberg, N. Korber, M. Nieger, and M. Schrott. Z. Naturforsch. B, **54**, 1244 (1999); (*j*) D. Gudat, M. Schrott, V. Bajorat, M. Nieger, S. Kotila, R. Fleischer, and D. Stalke. Chem. Ber. **129**, 337 (1996); (*k*) D. Gudat. Coord. Chem. Rev. **163**, 71 (1997).
2. A. Decken, M.A. Neil, and F. Bottomley. Can. J. Chem, **79**, 1321 (2001).
3. (*a*) P.M. Treichel and J.W. Johnson. Chem. Soc. Chem. Commun. 688 (1976); (*b*) J.W. Johnson and P.M. Treichel. J. Am. Chem. Soc. **99**, 1427 (1977); (*c*) N.A. Ustynyuk, N.A. Pomazanova, L.N. Novikova, D.N. Kravtsov, and Y.A. Ustynyuk. Izv. Akad. Nauk SSSR, Ser. Khim. **7**, 1688 (1986); (*d*) T.A. Albright, P. Hofmann, R. Hoffmann, C.P. Lillya, and P.A. Dobosh. J. Am. Chem. Soc. **105**, 3396 (1983).
4. D.D. Perrin, W.L.F. Armarego, and D.R. Perrin. Purification of laboratory chemicals. Pergamon Press, New York. 1980.
5. B.F. Hallam and P.L. Pauson. J. Chem. Soc. 3030 (1956).
6. R.B. King and G.A. Stone. Inorg. Synth. **7**, 110 (1963).
7. F. Nief and L. Ricard. J. Organomet. Chem. **464**, 149 (1994).
8. E.H. Braye, I. Caplier, and R. Saussez. Tetrahedron, **27**, 5523 (1971).
9. Crystals were also grown by vapor diffusion using CH_2Cl_2/hexanes at –23°C. The CH_2Cl_2 molecules are disordered over several positions which could not be modeled properly. Metric parameters of the cation were identical to those of the acetone solvates.
10. SAINT 6.02. Bruker AXS Inc. Madison, Wisconsin. 1997–99.
11. G.M. Sheldrick. SADABS. Bruker AXS Inc., Madison,Wisconsin. 1999.
12. G.M. Sheldrick. SHELXTL 5.1. Bruker AXS Inc., Madison,Wisconsin. 1997.
13. (*a*) T.A. Barckholtz and B.E. Bursten. J. Organomet. Chem. **596**, 212 (2000); (*b*) M.L. Drummond and B.E. Bursten. Manuscript in preparation.
14. (*a*) U. Flörke. Z. Kristallogr. **211**, 908 (1996); (*b*) U. Flörke, and H.-J. Haupt. Acta Cryst. C, **53**, 876 (1997); (*c*) U. Flörke and H.-J. Haupt. Acta Cryst. C, **53**, 1799 (1997).

[2] Supplementary material may be purchased from the Depository of Unpublished Data, Document Delivery, CISTI, National Research Council Canada, Ottawa, ON K1A 0S2, Canada. For information on obtaining material electronically go to http://www.nrc.ca/cisti/irm/unpub_e.shtml. Crystallographic information has also been deposited with the Cambridge Crystallographic Data Centre (CCDC Nos. 168659 (**6**), 168660 (**7**), and 168661 (*cis*-**8**)). Copies of the data can be obtained free of charge via www.ccdc.cam.ac.uk/conts/retrieving.html (or from the Cambridge Crystallographic Data Centre, 12, Union Road, Cambridge CB2 1EZ, UK; fax: +44 1223 336033; or deposit@ccdc.cam.ac.uk).

© 2002 NRC Canada

15. (*a*) R.L. De. J. Organomet. Chem. **243**, 331 (1983); (*b*) N.J. Taylor, G.N. Mott, and A.J. Carty. Inorg. Chem. **19**, 560 (1980); (*c*) K. Evertz and G. Huttner. Chem. Ber. **120**, 937 (1987). (*d*) F. Bitterer, D.J. Brauer, F. Dorrenbach, F. Gol, P.C. Knuppel, O. Stelzer, C. Kruger, and Y.-H. Tsay. Z. Naturforsch. B, **46**, 1131 (1991); (*e*) K. Fischer and H. Vahrenkamp. Z. Anorg. Allg. Chem. **475**, 109 (1981).
16. (*a*) J.T. Spencer and R.N. Grimes. Organometallics, **6**, 323 (1987); (*b*) F. Pierre, A. Stricker, C. Moinet, S. Sinbandhit, and L. Toupet. J. Organomet. Chem. **553**, 253 (1998).
17. F. Nief, C. Charrier, F. Mathey, and M. Simalty. Phosphorus Sulfur, **13**, 259 (1982).
18. G. Effinger, W. Hiller, and I.-P. Lorenz. Z. Naturforsch. B, **42**, 1315 (1987).
19. I.-P. Lorenz, W. Pohl, H. Nöth, and M. Schmidt. J. Organomet. Chem. **475**, 211 (1994).
20. K. Maitra, V.J. Catalano, and J.H. Nelson. Bull. Soc. Chim. Fr. **134**, 471 (1997).
21. J.T. Spencer, J.A. Spencer, R.A. Jacobson, and J.G. Verkade. New J. Chem. **13**, 275 (1989).

© 2002 NRC Canada

Environmental photodegradation of pyrimidine fungicides — Kinetics of the visible-light-promoted interactions between riboflavin and 2-amino-4-hydroxy-6-methylpyrimidine

E. Haggi, S. Bertolotti, S. Miskoski, F. Amat-Guerri, and N.A. García

Abstract: To clarify the evolution of pyrimidine fungicides under natural aquatic environmental conditions, the visible-light-promoted degradation of the model fungicide 2-amino-4-hydroxy-6-methylpyrimidine (AHMPD) has been studied in air-equilibrated pH 6 aqueous solutions in the presence of riboflavin (Rf), employing time-resolved and stationary kinetic–spectroscopic methods. AHMPD, a compound practically inert towards the attack of singlet molecular oxygen ($O_2(^1\Delta_g)$), quenches excited singlet and triplet states of Rf with rate constants of 2.7×10^9 M^{-1} s^{-1} and 2.7×10^7 M^{-1} s^{-1}, respectively. In the presence of AHMPD, the photodecomposition of Rf, which occurs from the excited triplet state of the pigment, depends on the concentration of the fungicide: at ≥40–50 mM a limited photochemistry occurs due to the quenching of excited singlet Rf, while at ca. 5–10 mM triplet Rf is largely photogenerated and subsequently quenched either by oxygen, giving rise to $O_2(^1\Delta_g)$, or by AHMPD, yielding semireduced Rf through an electron transfer process. Flash photolysis experiments and indirect auxiliary tests confirm the presence of superoxide anion generated by the reaction of Rf anion radical with the dissolved oxygen. The neat result of this intricate scheme of competitive reactions is the photodegradation of both AHMPD and Rf, mainly through a superoxide anion-mediated oxidation, although some contribution of $O_2(^1\Delta_g)$-mediated photooxidations cannot be disregarded.

Key words: photooxidation, pyrimidine derivatives, riboflavin, singlet molecular oxygen, superoxide anion.

Résumé : Dans le but de clarifier l'évolution des fongicides à base de pyrimidine dans les conditions environnementales aquatiques naturelles, on a étudié la dégradation du fongicide modèle 2-amino-4-hydroxy-6-méthylpyrimidine (AHMPD), sous l'influence de la lumière UV–vis, en solutions aqueuses à pH de 6 équilibrées avec l'air, en présence de riboflavine (Rf) et faisant appel à des méthodes spectroscopie résolues dans le temps et de cinétique stationnaire. L'AHMPD, un composé pratiquement inerte vis-à-vis des attaques par l'oxygène moléculaire singulet ($O_2(^1\Delta_g)$), piège les états singulets et triplets excités de la Rf avec des constantes de vitesse de $2{,}7 \times 10^9$ M^{-1} s^{-1} et de $2{,}7 \times 10^7$ M^{-1} s^{-1} respectivement. En présence d'AHMPD, la photodécomposition de la Rf se produit à partir de l'état triplet excité et elle dépend de la concentration du fongicide: à des concentrations ≥ 40–50 mM, la photochimie est limitée en raison du piégeage du singulet excité de la Rf alors que, aux environs de 5–10 mM, la Rf et pratiquement toute photogénérée avant d'être piégée ou par l'oxygène avec formation de $O_2(^1\Delta_g)$ ou par l'AHMPD avec formation de Rf semiréduite par un processus de transfert d'électron. Des expériences de photolyse éclair et des tests auxiliaires indirects confirment la présence de l'anion superoxyde généré par la réaction du radical anion Rf avec l'oxygène dissous. Le résultat net de ce schéma complexe de réactions compétitives est une photogénération à la fois dAHMPD et de Rf, principalement par une oxydation par le superoxyde catalysée par l'anion, même si l'on ne peut pas éliminer complètement des photooxydations catalysées par le $O_2(^1\Delta_g)$.

Mots clés : photooxydation, dérivés de la pyrimidine, riboflavine, oxygène moléculaire singulet, anion superoxyde.

[Traduit par la Rédaction]

Introduction

Many agricultural chemicals widely present in nature as water and soil contaminants are nitrogen-containing aromatic heterocycles (1), and their thermal and photochemical degradations in water have been topics of growing interest in the last decades (2). Purification of contaminated waters, including the elimination of pathogens, can be cheaply and efficiently carried out by the *lagooning* method, i.e., by the combined action of spontaneous physical, chemical, and bio-

Received 25 June 2001. Published on the NRC Research Press Web site at http://canjchem.nrc.ca on 14 January 2002.

E. Haggi. UARG. Universidad Nacional de la Patagonia Austral. 9400 Río Gallegos, Argentina.
S. Bertolotti, S. Miskoski, and N.A. García.[1] Departamento de Química y Física, Universidad Nacional de Río Cuarto, 5800 Río Cuarto, Argentina.
F. Amat-Guerri. Instituto de Química Orgánica, CSIC, Juan de la Cierva 3, 28006 Madrid, Spain.

[1]Corresponding author (e-mail: ngarcia@exa.unrc.edu.ar).

 DOI: 10.1139/V01-192 © 2002 NRC Canada

logical processes taken place in lagoons in the presence of oxygen and sunlight (3). In particular, in many cases the photo-induced elimination from the aqueous environment of said *N*-heterocycles has shown to be a potentially applicable procedure, and in some cases the reactions involved have been studied (4). Following this line, in recent papers (5, 6) we have reported the kinetics of the dye-sensitized photooxygenation of several hydroxypyridines, hydroxypyrimidines, and hydroxyquinolines with the basic molecular structures of known *N*-heteroaromatic pesticides (1). The kinetics of the photosensitized oxidation, in aqueous or chloroform solution, of the pyrimidine fungicides ethirimol (5-*n*-butyl-2-diethylamino-4-hydroxy-6-methylpyrimidine), dimethirimol (5-*n*-butyl-2-dimethylamino-4-hydroxy-6-methylpyrimidine), and four analogous pyrimidines, all with structures closely related to that of the model compound 2-amino-4-hydroxy-6-methylpyrimidine (AHMPD), has been previously studied (7, 8).

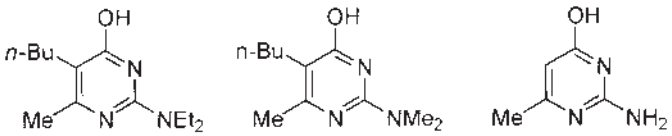

Ethirimol Dimethirimol AHMPD

In a recent paper (9), we have demonstrated that in the photooxidation of AHMPD in the presence of Rose Bengal — the synthetic xanthene dye most frequently used as a sensitizer (10) — a singlet molecular oxygen-mediated mechanism exclusively operates, with photooxygenation quantum efficiencies ranging from 0.005 in acetonitrile–water (4:1 v/v), to 0.41 in pH 11 water. The reaction sequence, which has been already sufficiently described (4, 11), is depicted in processes [1]–[6], where S is a dye sensitizer responsible for the visible light absorption (RB in the case of ref. (9)), $^1S^*$ and $^3S^*$ are the respective singlet and triplet excited states of S, $O_2(^3\Sigma_g^-)$ is the ground-state molecular oxygen, and $O_2(^1\Delta_g)$ is the singlet molecular oxygen generated by energy transfer from $^3S^*$ to $O_2(^3\Sigma_g^-)$. $O_2(^1\Delta_g)$ can be physically deactivated by collision with solvent molecules (process [4]), or with AHMPD and (or) the sensitizer (process [5]), or can react with the latter compounds giving rise to oxidation products (process [6]). Our results indicated

[1]–[3]

$$S \xrightarrow[[1]]{h\nu} {}^1S^* \xrightarrow[[2]]{} {}^3S^* \xrightarrow[k_{ET}\ [3]]{O_2(^3\Sigma_g^-)} S + O_2(^1\Delta_g)$$

[4] $$O_2(^1\Delta_g) \xrightarrow[k_d]{} O_2(^3\Sigma_g^-)$$

[5] $$O_2(^1\Delta_g) \xrightarrow[k_q]{\text{AHMPD and (or) S}} O_2(^3\Sigma_g^-)$$

[6] $$O_2(^1\Delta_g) \xrightarrow[k_r]{\text{AHMPD and (or) S}} \text{products}-6$$

that the degradation of AHMPD by sensitized photooxidation is efficient only in highly alkaline solutions — a very improbable case in natural waters — and that this procedure could be exclusively applicable in programmed experiments under controlled conditions.

Another more natural alternative route for the photodegradation of water contaminants takes advantage of the presence of some natural dyes in surface waters. In particular, riboflavin (Rf), a well-known natural pigment present in waters of rivers, lakes, and seas (12), has been postulated as a possible sensitizer for the natural photooxidative degradation of some herbicides and related compounds (13–15).

Nevertheless, the role of Rf in the visible-light-promoted decomposition of hydroxy-*N*-heteroaromatic pesticides has been scantily investigated, and only with reference to pyridine derivatives (16, 17), although this information is particularly important for the prediction of the photolysis rates of these contaminants in natural waters. For this reason, the main aim of the present work was to study the behavior of Rf as a sensitizer for the photodecomposition of the model fungicide AHMPD, as well as to gain information on the physical and chemical interactions taking place in this and similar systems.

Experimental

Materials

2-Amino-4-hydroxy-6-methylpyrimidine (AHMPD), 2-aminopyrimidine, 4-hydroxypyrimidine, 6-methylpyrimidine, superoxide dismutase (SOD) from bovine erithrocytes, riboflavin (Rf), Rose Bengal (RB) (all from Sigma), and sodium azide (Aldrich) were employed as received. All irradiated solutions were buffered at pH 6 (NaH_2PO_4–NaOH (18)).

Methods

Static aerobic photolysis of pH 6 aqueous solutions containing AHMPD (either 0.4 to 0.5 mM for the observation of changes in UV spectra or 5 mM for oxygen uptake measurements) and Rf (0.01 to 0.03 mM) or RB (Abs_{560} = 0.4) were carried out in a PTI unit provided with a high pass monochromator and 150 W Xe lamp, irradiating with 440 ± 10 nm (Rf solutions) or 560 ± 10 nm (RB solutions), or in a home-made photolyzer for nonmonochromatic irradiation (150 W quartz halogen lamp). The last photolyzer was only employed in the comparable runs of Rf-sensitized oxygen uptake. In the latter case, a cut-off filter (400 nm) ensured that the light was only absorbed by the sensitizer. The relative rates of oxygen consumption by the system AHMPD–Rf with or without SOD or sodium azide (NaN_3) were obtained from the respective initial slopes of the plots of oxygen consumption vs. irradiation time, under comparable experimental conditions. A specific oxygen electrode (Orion 97–08) was employed. The rates of Rf photodecomposition in nitrogen-saturated solutions, either in the presence or in the absence of AHMPD, were roughly evaluated by the absorbance decrease at 445 nm for a given irradiation time. The stationary quenching of the Rf fluorescence (absorbance at 440 nm = 0.1) was studied with a RF 5301-PC Shimadzu spectrofluorimeter at 25 ± 1°C in air-equilibrated solutions. Fluorescence lifetimes were measured with a time-correlated single photon counting technique on an Edinburgh FL-

© 2002 NRC Canada

9000CD instrument. In both cases, excitation and emission wavelengths were 445 and 515 nm, respectively. Ground-state absorption spectra were registered in a Hewlett-Packard 8452A diode array spectrophotometer.

Nitrogen-saturated aqueous solutions of Rf (0.01 mM) were photolyzed using a flash photolysis apparatus. A ns Nd:YAG laser system (Spectron) at 355 nm was the excitation source, employing a 150 W xenon lamp as analyzing light. The detection system comprised a PTI monochromator and a red-extended photomultiplier (Hamamatsu R666). The signal, acquired and averaged by a digital osciloscope (Hewlett-Packard 54504A), was transferred to a PC via a HPIB parallel interface, where it was analysed and stored.

Results

Rf-sensitized photooxygenation of AHMPD

The irradiation of the system AHMPD – Rf – oxygen (air) – pH 6 water with light of wavelength higher than 400 nm — a spectral region in which AHMPD is transparent — produced changes in the UV–vis absorption spectrum of the mixture (Fig. 1, lower inset) that indicate chemical changes in both the pyrimidine and the dye, with simultaneous oxygen consumption. Although the existence of photodegradation pathways that do not consume oxygen cannot be excluded, these processes must not be important, because the irradiation, under comparable conditions, of deoxygenated solutions of AHMPD and Rf produces practically undetectable spectral changes in the 200–300 nm range, where AHMPD absorbs. The same is true for air-saturated solutions of the related compounds 2-aminopyrimidine, 4-hidroxypyrimidine, and 6-methylpyrimidine.

For comparative purposes, 1 mM AHMPD water solutions were irradiated in parallel experiments employing Rf or RB as sensitizers, and the respective rates of oxygen uptake were measured. It is known that with RB as sensitizer an exclusive $O_2(^1\Delta g)$-mediated mechanism operates, with a quantum efficiency of 0.01 in water (9), and, as expected, the first-order plot for oxygen uptake is linear (Fig. 1, main). To the contrary, a similar graphical representation for the experiment with Rf showed a neat curvature (Fig. 1, main), indicating that the Rf-sensitized photooxidation of AHMPD cannot be interpreted through an exclusive $O_2(^1\Delta_g)$-mediated pathway, as with RB, and that other interactions between ground-state AHMPD and ground- and (or) excited (singlet or triplet)-state Rf could also be operative. In addition, the Rf photodegradation rate observed in the irradiation of a nitrogen-saturated water solution of Rf (0.02 mM) in the absence of AHMPD was higher than that found in the presence of 1 mM AHMPD (Fig. 1, upper inset).

Oxygen consumption was observed in the irradiation of the system AHMPD (5 mM) – Rf (absorbance at 445 nm: 0.5) – oxygen – water (relative rate = 1). Under comparable conditions, the rate of oxygen uptake in the former system was greatly reduced in the following cases (Fig. 2): (*i*) irradiating in the presence of 10 μg mL^{-1} of SOD, an enzyme that behaves as a quencher of superoxide anion ($O_2^{\cdot-}$)-mediated photooxidations when used in similar concentrations (19–22) (relative rate = 0.78); (*ii*) irradiating in the presence of 1 mM sodium azide, a well known selective physical quencher of $O_2(^1\Delta g)$ (4) (relative rate = 0.41); and (*iii*) irradiating the system AHMPD–Rf but with a concentration of AHMPD of 40 mM or higher (relative rate for 40 mM AHMPD = 0.61). No oxygen uptake was detected when 5 mM AHMPD was replaced by similar concentrations of 2-aminopyrimidine, 4-hydroxypyrimidine, or 6-methylpyrimidine.

Fig. 1. First-order plots for oxygen uptake upon visible-light irradiation of pH 6 aqueous solutions containing: (●) RB (Abs. at 560 nm = 0.47) plus AHMPD 5 mM, and (○) Rf (Abs. at 445 nm = 0.52) plus AHMPD 0.5 mM. Lower inset: spectral changes upon Rf-sensitized photoirradiation of the mixture Rf (0.02 mM) – AHMPD (0.5 mM) in pH 6 water; numbers on the spectra represent irradiation times in min. Upper inset: absorption spectra of Rf (0.02 mM) in nitrogen-saturated solutions: (*a*) non-photolyzed; (*b*) photolyzed 7 min in the presence of 1 mM AHMPD; (*c*) photolized 7 min (for details see *Experimental section*).

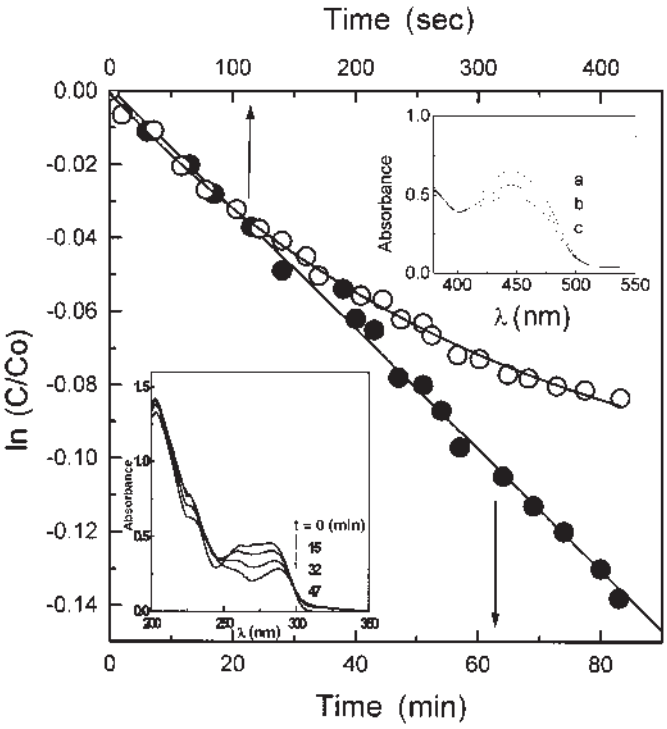

Ground-state association between AHMPD and Rf was not observed by absorption spectroscopy. The difference spectra in the 380–600 nm range, obtained by subtraction of the spectrum of 0.02 mM Rf from those of mixtures 0.02 mM Rf + up to 10 mM AHMPD, were identical to those of the corresponding AHMPD solutions.

Results indicate the operation of a complex mechanism that possibly includes specific interactions of AHMPD with singlet (^{1}Rf*) and triplet (^{3}Rf*) excited states of Rf, represented by processes [7] and [8].

[7] $^1Rf^* + AHMPD \xrightarrow{^1k_q} Rf + AHMPD$ (or products−7)

[8] $^3Rf^* + AHMPD \xrightarrow{^3k_q} Rf + AHMPD$ (or products−8)

Quenching of ^{1}Rf*

The fluorescence properties of Rf in water are well known. Rf exhibits an intense emission band at 515 nm with a fluorescence quantum yield of 0.25 (23). The presence of

© 2002 NRC Canada

Fig. 2. Rates of oxygen uptake upon irradiation of air-equilibrated pH 6 aqueous solutions containing Rf (0.02 mM) and: (*a*) AHMPD (5 mM); (*b*) AHMPD (5 mM) and SOD (10 μg mL^{-1}); (*c*) AHMPD (40 mM); and (*d*) AHMPD (5 mM) and NaN_3 (1 mM). Each set of points represents the mean value of four runs.

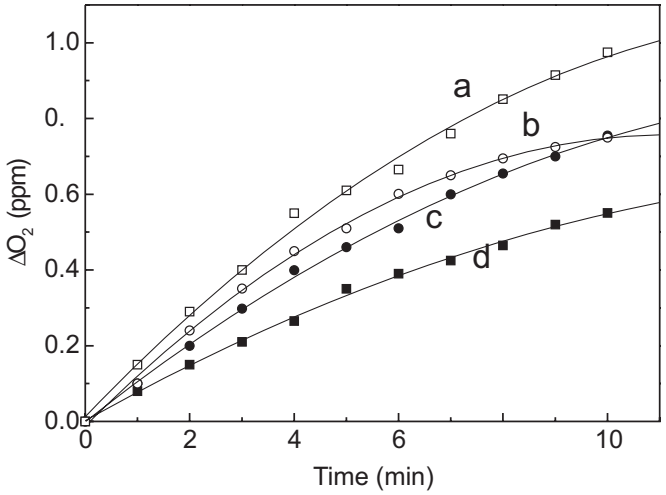

Fig. 3. Transient absorption spectra of Rf (0.01 mM) in argon-saturated aqueous solution, in the absence (●) and in the presence (□) of AHMPD (8 mM) taken at 1 and 20 μs after the laser pulse, respectively. Inset: Stern–Volmer plots for the quenching of ^{3}Rf* (argon-saturated solution) (○) and ^{1}Rf* (air-equilibrated solution) (●) by AHMPD.

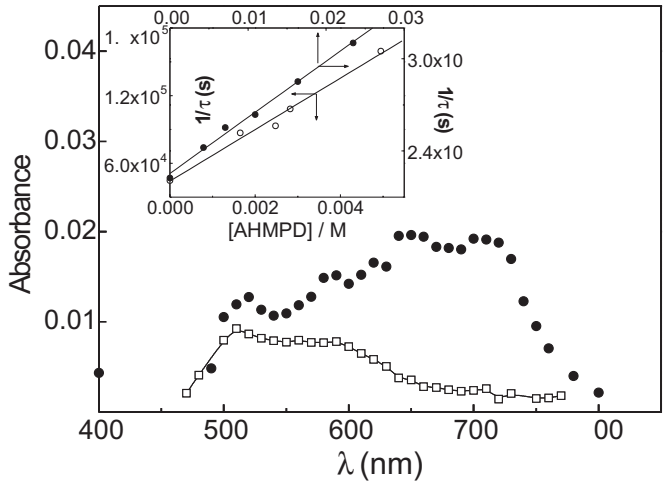

AHMPD ≥ 10 mM produces a detectable quenching of the Rf fluorescence, as determined by either static- or time-resolved fluorescence measurements. Monitoring the fluorescence intensity of Rf in the absence (I_o) and in the presence (I) of different AHMPD concentrations, the classical Stern–Volmer treatment ($I_o/I = 1 + {}^1K_{SV}$ [AHMPD]) allows the determination of the Stern–Volmer constant ($^1K_{SV}$ = 12.5 M^{-1}), which is equal to the ratio $^1k_q/^1k_d$, where ^1k_d is the rate constant for thermal deactivation of ^{1}Rf* (process [9]). Time-resolved experiments yielded a ^1k_d value of 1.9 × 10^8 s^{-1}, corresponding to a Rf fluorescence lifetime in water ($^1\tau_o$) of 5.2 ns, in excellent agreement with reported values (24). Consequently, a ^1k_q value of 2.4 × 10^9 M^{-1} s^{-1} is deduced.

[9] $$^1Rf^* \xrightarrow{^1k_d} Rf$$

On the other hand, ^1k_q values (process [7]) can also be graphically calculated through Stern–Volmer treatment ($1/^1\tau = 1/^1\tau_o + {}^1k_q$ [AHMPD]) by evaluation of the respective $^1\tau$ values in the presence of different concentrations of AHMPD (Fig. 3, inset). The value so-determined (^1k_q = 2.7 × 10^9 M^{-1} s^{-1}) is practically the same, within an estimated error of ±10%, as that obtained by the static fluorescence measurements.

Quenching of ^{3}Rf*

The photodegradation of Rf in water, in the absence of oxygen and under visible light irradiation, predominantly proceeds through the triplet state (25). In our case, ^{3}Rf* was generated by a 355-nm laser pulse, and the ^{3}Rf* disappearance was monitored from the first-order decay of the absorbance at 670 nm, a zone where the interference from other possible species is negligible. ^{3}Rf* lifetime was neatly reduced by the presence of AHMPD. The triplet decay was measured at low Rf concentration (typical 0.02 mM) and at low enough laser energy, to avoid self-quenching and triplet–triplet annihilation effects, respectively. Employing the expression $1/^3\tau = (1/^3\tau_o) + {}^3k_q$ [AHMPD] (where $^3\tau_o$ and $^3\tau$ are the experimentally determined lifetimes of ^{3}Rf* in the absence and in the presence of AHMPD, respectively), a value for the bimolecular rate constant ^3k_q of 2.7 × 10^7 M^{-1} s^{-1} was obtained (process [8], Fig. 3, inset).

The transient absorption spectrum of the Rf solution 1 μs after the laser pulse (Fig. 3, main, upper trace) has been already reported for ^{3}Rf* (17, 26–29). The shape of the spectrum obtained in the presence of 8 mM AHMPD (Fig. 3, main, lower trace) was similar to that already reported (17, 30) to account for electron transfer processes to ^{3}Rf* from different electron-donor substrates of environmental and biological relevance (5, 17, 28, 29, 31), with the concomitant generation of the well-known anion radical $Rf^{\cdot -}$ (28, 29, 32, 33) (process [10]). The radical cation $AHMPD^{\cdot +}$ that simultaneously appears was not detected, likely due to its absorption in a different wavelength range than the observed one, or to its very short lifetime.

[10] $$^3Rf^* + AHMPD \xrightarrow{k_{10}} Rf^{\cdot -} + AHMPD^{\cdot +}$$

Discussion

It is known that many aromatic compounds form relatively stable dark complexes with Rf (34–36). In the case of the system AHMPD–Rf, no ground-state interactions could be detected by absorption spectroscopy. Besides, the excellent concordance between the values of the rate constant ^1k_q obtained for AHMPD by both static-nd time-resolved experiments on the quenching of the fluorescence of Rf (2.4 × 10^9 M^{-1} s^{-1} and 2.7 × 10^9 M^{-1} s^{-1}, respectively) corroborates the absence of said interactions.

The spectral changes in Fig. 1 reveal that the Rf-sensitized aerobic irradiation of 0.4 mM AHMPD produces chemical transformations. Additionally, oxygen uptake experiments (Fig. 2) indicate the participation in the photoprocesses of

© 2002 NRC Canada

reactive oxygen species generated directly or indirectly by ^{1}Rf* and (or) ^{3}Rf*. In spite of the high value of the rate constant for the interaction ^{1}Rf*–AHMPD (^1k_q, process [7]) — close to the diffusion limit — relatively high concentrations of AHMPD are necessary to prevent triplet state population (75 mM, to quench 50% ^{1}Rf*, process [7]).

The competitive pathways represented by processes [3] (and, subsequently, [5] and [6]) and [8] are generated from ^{3}Rf* (37, 38). While processes [5] and [8] can be merely physical events, process [6] can involve the consumption of both Rf and AHMPD. The predominance of a given process will depend on the competition between O_2 and AHMPD for the quenching of ^{3}Rf*. It is known that the quenching of ^{3}Rf* by O_2 occurs with a rate constant $k_{(11)}$ of 9×10^8 M^{-1} s^{-1} (39). Nevertheless, in kinetic terms, and taking into account that the reported quantum yield values for the generation from ^{3}Rf* of $O_2(^1\Delta_g)$ (process [3], with S = Rf) and $O_2^{\cdot-}$ (process [11]) are 0.49 and 0.009, respectively (40), the direct generation of $O_2^{\cdot-}$ by electron transfer from ^{3}Rf* to O_2 can be considered negligible.

$$[11] \quad {}^3\mathrm{Rf}^* + \mathrm{O}_2 \xrightarrow[k_{(11)}]{} \mathrm{Rf}^{\cdot+} + \mathrm{O}_2^{\cdot-}$$

^{3}Rf* is quenched by AHMPD with a global ^3k_q value of 2.7×10^7 M^{-1} s^{-1} (process [8]). As suggested by laser flash photolysis experiments, process [10] would yield the radical anion $Rf^{\cdot-}$. Process [10] does not occur when AHMPD is replaced by 2-aminopyrimidine, 4-hydroxypyrimidine, or 6-methylpyrimidine, as judged by the absence of spectral (UV) perturbations and oxygen consumption in the respective runs. This fact could be a consequence of the enhanced electron donating ability of AHMPD due to the simultaneous presence of amino, hydroxy, and methyl groups in the aromatic ring. Under aerobic conditions, process [10], with [AHMPD] = 5–10 mM, could compete with the generation of $O_2(^1\Delta_g)$ (process [3]). Consequently, under air-saturated conditions, i.e., with a concentration of dissolved oxygen approximately equals to 0.26 mM (41), $O_2^{\cdot-}$ could be formed by electron transfer from $Rf^{\cdot-}$ to O_2 (process [12]). Indirect evidence in support of the participation of $O_2^{\cdot-}$ in the photooxidation of AHMPD was provided by the SOD inhibition of the oxygen uptake (Fig. 2, line b), as well as by the already commented results from flash photolysis experiments.

$$[12] \quad \mathrm{Rf}^{\cdot-} + \mathrm{O}_2 \xrightarrow[k_{(12)}]{} \mathrm{Rf} + \mathrm{O}_2^{\cdot-}$$

$$[13] \quad \mathrm{O}_2^{\cdot-} + \mathrm{AHMPD} \xrightarrow[k_{(13)}]{} \mathrm{products}\text{–}13$$

A rate constant value of 1.4×10^8 M^{-1} s^{-1} has been recently reported (29) for the generation of $O_2^{\cdot-}$ from $Rf^{\cdot-}$ (process [12]), a reaction that at the same time regenerates ground-state Rf. It is well known that $O_2^{\cdot-}$ is a key intermediate in the oxygen redox chemistry of a number of biological and organic substrates (42). Taken into account the former discussion, the oxygen consumption in the Rf-sensitized photooxidation of AHMPD can be explained through an $O_2^{\cdot-}$-mediated mechanism.

As we have demonstrated before (9), AHMPD hardly reacts with $O_2(^1\Delta_g)$ generated with RB as a sensitizer. Hence, the inhibitory effect on the oxygen uptake observed in the irradiation of the system AHMPD–Rf–O_2–NaN_3 (Fig. 2, line d) possibly obeys the known quenching of ^{3}Rf* by the azide anion (29), and (or) the quenching of the photooxidation of Rf via $O_2(^1\Delta_g)$ (process [6], with S = Rf), for which a rate constant k_{rRf} of 6×10^7 M^{-1} s^{-1} has been reported (4).

The species $Rf^{\cdot-}$ could also be generated from ^{1}Rf, especially under relatively high concentrations of AHMPD. The semireduction of Rf from its singlet state has been previously proposed to explain the Rf-photoinitiated vinyl polymerization (28), and the interaction of Rf chromophore radical (from flavin mononucleotide) with ascorbic acid (43). In our case, the lack of photoproducts from this possible pathway, and the decrease of oxygen consumption at high AHMPD concentrations (Fig. 2, line c), could be explained by the existence of a fast back electron transfer reaction in the pair of radical ions so-generated, especially in water, as already suggested by other authors (28, 30).

Concluding remarks

Rf-sensitized irradiation of water solutions of AHMPD produces chemical transformations in both Rf and AHMPD. In air-saturated solution a nonsimple scheme of competitive processes operates, involving triplet Rf. Under sensitizing conditions, i.e., with Rf concentration in the range of 0.02 mM, the photodegradation of the dye and (or) AHMPD depends on the concentration of AHMPD. At AHMPD concentrations ≥ 40 mM, the massive quenching of excited singlet Rf dominates, preventing in practice the whole photoprocess. At AHMPD concentrations ≤ 5–10 mM, excited triplet Rf is formed and, then, is quenched by either oxygen or AHMPD, yielding $O_2(^1\Delta_g)$ and semireduced Rf ($Rf^{\cdot-}$), respectively. Subsequently, $O_2^{\cdot-}$ can be produced from the reaction of $Rf^{\cdot-}$ with dissolved oxygen and, as a result, both AHMPD and Rf are photodegraded. AHMPD disappears mainly by oxygenation. In the absence of oxygen, Rf photodegradation is favored because its regeneration via $O_2^{\cdot-}$ production is precluded.

Finally, it can be said that, in the context of the Rf-sensitized fate of water-soluble contaminants under natural environmental conditions, AHMPD-type compounds are degradable through a photooxidative event.

Acknowledgements

Thanks are given to CONICET, CONICOR, SECyT UNRC, and SECyT UNPA, of Argentina, and to CSIC and the Ministerio de Educación y Cultura of Spain, for financial support.

References

1. C. Tomlin (*Editor*). The pesticide manual. British Crop Protection Council and The Royal Society of Chemistry, London, U.K. 1994.
2. N.A. García. J. Photochem. Photobiol. B. **22**, 185 (1994).
3. K.D. White and J.G. Joel. Water Environ. Res. **71**, 676 (1999).
4. F. Wilkinson, W. Helman, and A.B. Ross. J. Phys. Chem. Ref. Data, **24**, 663 (1995).
5. A. Pajares, J. Gianotti, E. Haggi, G. Stettler, F. Amat-Guerri, S. Criado, and N.A. García. J. Photochem. Photobiol. A. **119**, 9 (1998).

© 2002 NRC Canada

6. F. Amat-Guerri, A. Pajares, J. Gianotti, G. Stettler, S. Bertolotti, S. Miskoski, and N.A. García. J. Photochem. Photobiol. A. **126**, 59 (1999).
7. G.J. Harkness and C.H.J. Wells. Pestic. Sci. **12**, 215 (1981).
8. S.R. Dixon and C.H.J. Wells. Pestic. Sci. **14**, 444 (1983).
9. A. Pajares, J. Gianotti, G. Stettler, E. Haggi, S. Miskoski, S. Criado, F. Amat-Guerri, and N.A. García. J. Photochem. Photobiol. A. **135**, 207 (2000).
10. D.C. Neckers. J. Photochem. Photobiol. A. **47**, 1 (1989).
11. C. Tanielian, R. Mechin, R. Seghrouchni, and C. Schweitzer. Photochem. Photobiol. **71**, 12 (2000).
12. A. Momzikoff, R. Santus, and D.R. Kearns. Mar. Chem. **12**, 12 (1983).
13. D.R. Ross and D.G. Crosby. J. Agric. Food Chem. **21**, 335 (1976).
14. J. Silber, N. Silbera, and C.M. Previtali. J. Agric. Food Chem. **24**, 697 (1976).
15. A. de la Rochette, E. Silva, I. Bilourez-Aragón, A. Mancini, A.-M. Edwards, and P. Moliére. Photochem. Photobiol. **72**, 815 (2000).
16. A. Pajares, J. Gainotti, E. Haggi, G. Stettler, F. Amat-Guerri, S. Bertolotti, S. Criado, and N.A. García. Dyes Pigm. **41**, 233 (1999).
17. A. Pajares, J. Gianotti, G. Stettler, S. Bertolotti, S. Criado, A. Posadaz, F. Amat-Guerri, and N.A. García. J. Photochem. Photobiol. A. **139**, 199 (2001).
18. R.C. Weast and M. Astle (*Editors*). Handbook of Chemistry and Physics. CRC Press, Boca Ratón, Florida. 1981.
19. R.M. Baxter and J.H. Carey. Nature (London), **306**, 575 (1983).
20. L.-Y. Zang and H.P. Misra. J. Biol. Chem. **267**, 17 547 (1992).
21. P.G. Tratniek and J. Hoignè. Environ. Sci. Technol. **25**, 1596 (1991).
22. S. Criado, S. Bertolotti, and N.A. García. J. Photochem. Photobiol. B. **34**, 79 (1996).
23. G. Weber and F.W. Teale. Trans. Faraday Soc. **53**, 646 (1958).
24. A.W. Varnes, R.B. Dodson, and E.L. Eehry. J. Am. Chem. Soc. **94**, 946 (1972).
25. B.J. Fritz, S. Kasal, and K. Matsui. Photochem. Photobiol. **45**, 113 (1987).
26. W.M. Moore and R.C. Ireton. Photochem. Photobiol. **25**, 347 (1977).
27. J.P. Fouassier and E. Chesneau. Makromol. Chem. **192**, 245 (1991).
28. S.G. Bertolotti, C.M. Previtali, A.M. Rufs, and M.V. Encinas. Macromolecules, **32**, 2920 (1999).
29. C. Lu, W. Lin, W. Wang, Z. Han, S. Yao, and N. Lin. Phys. Chem. Chem. Phys. **2**, 329 (2000).
30. B. Orellana, A.M. Rufs, M.V. Encinas, C.M. Previtali, and S. Bertolotti. Macromolecules, **32**, 6570 (1999).
31. P.F. Heelis. Chem. Soc. Rev. **11**, 15 (1982).
32. J.N. Chacón, J. McLearie, and R.S. Sinclair. Photochem. Photobiol. **47**, 64 (1988).
34. S. Miskoski and N.A. García. Coll. Czech. Chem. Commun. **56**, 1838 (1991).
35. J.F. Pereira and G. Tollin. Biochim. Biophys. Acta, **143**, 79 (1967).
36. E.J. Wilson. Biochemistry, **5**, 1351 (1966).
37. C.S. Foote. Photochem. Photobiol. **54,** 659 (1991).
38. P.F. Heelis. *In* Chemistry and biochemistry of flavoenzym. Vol. 1. *Edited by* F. Muller. Boca Ratón, Florida. 1991.
39. C.Y. Lu, Z.H. Han, J.X. Pan, W.Z. Lin, W.F. Wang, and S.D. Yao. J. Radiat. Res. Radiat. Process. **18**, 12 (2000).
40. C.M. Krishna, S. Uppuluri, P. Riesz, J.S. Zigler, and D. Balasubramanian. Photochem. Photobiol. **54**, 51 (1991).
41. S.L. Murov. Handbook of Photochemistry. Marcel Dekker, New York, 1973.
42. J.R. Kanofsky. Free Radical Res. Commun. **87**, 12 (1991).
43. P.F. Heelis, B. Parsons, G.O. Phillips, and J.F. McKellar. Photochem. Photobiol. **33**, 7 (1981).

© 2002 NRC Canada

Monte-Carlo calculation of the primary yields of H_2O_2 in the $^1H^+$, $^2H^+$, $^4He^{2+}$, $^7Li^{3+}$, and $^{12}C^{6+}$ radiolysis of liquid water at 25 and 300°C

Jintana Meesungnoen, Jean-Paul Jay-Gerin, Abdelali Filali-Mouhim, and Samlee Mankhetkorn

Abstract: Monte-Carlo simulations are used to calculate the primary yield of hydrogen peroxide ($G_{H_2O_2}$) of the radiolysis of pure, deaerated liquid water as a function of linear energy transfer (LET) of the incident radiation over the range ~0.3–100 keV μm^{-1}, at 25 and 300°C. The radiations include $^1H^+$, $^2H^+$, $^4He^{2+}$, $^7Li^{3+}$, and $^{12}C^{6+}$ ions with energies from 0.17 MeV to 3.6 GeV. At 25°C, it is found that our $G_{H_2O_2}$ values, calculated with protons of different initial energies, show a monotonic increase as a function of LET, in agreement with the commonly assumed expectation of an increase in molecular yields with increasing LET. Our calculated H_2O_2 yields at 300°C increase significantly faster with LET than do their corresponding 25°C values, showing that the temperature dependence of $G_{H_2O_2}$ at higher LET is less than for low-LET radiation. We also report our results on the temporal variations of the H_2O_2 yields, in the interval ~$1 \times 10^{-13} - 1 \times 10^{-6}$ s, at 25 and 300°C and for the different types of radiation considered. Finally, we find that for incident ions of equal LET > 10 keV μm^{-1}, $G_{H_2O_2}$ decreases as the ion velocity increases, from protons (or deuterons) to carbon ions. These differences produced in $G_{H_2O_2}$ by changing the type of radiation are explained by the greater mean energy of secondary electrons from the higher velocity ions, which penetrate to a greater average distance from the actual particle track, with a corresponding decrease in molecular yields. Our calculated $G_{H_2O_2}$ values compare generally well with the experimental data available from the literature and are also in good accord with the predictions of deterministic diffusion-kinetic model calculations reported earlier.

Key words: liquid water, radiolysis, primary yields, hydrogen peroxide (H_2O_2), linear energy transfer (LET), accelerated protons and heavy ions, temperature, Monte-Carlo simulations.

Résumé : À l'aide des méthodes de simulation Monte-Carlo, nous calculons le rendement primaire de peroxyde d'hydrogène ($G_{H_2O_2}$) produit lors de la radiolyse de l'eau pure désaérée en fonction du transfert d'énergie linéique (TEL) du rayonnement incident, dans la gamme ~0,3–100 keV μm^{-1}, à 25 et 300°C. Les rayonnements ici utilisés sont les ions $^1H^+$, $^2H^+$, $^4He^{2+}$, $^7Li^{3+}$ et $^{12}C^{6+}$ accélérés à des énergies allant de 0,17 MeV à 3,6 GeV. À 25°C, nous trouvons que les valeurs de $G_{H_2O_2}$, calculées pour des protons incidents de différentes énergies initiales, croissent de façon monotone en fonction du TEL, en accord avec ce que l'on attend en général, à savoir que les rendements des produits moléculaires augmentent avec le TEL. Les rendements calculés en H_2O_2 à 300°C augmentent notablement plus vite avec le TEL que leurs valeurs correspondantes à 25°C, montrant qu'à TEL plus élevé la dépendance en température de $G_{H_2O_2}$ est moindre que pour des rayonnements à faible TEL. Nous rapportons aussi les résultats concernant les variations temporelles des rendements de H_2O_2, dans l'intervalle ~$1 \times 10^{-13} - 1 \times 10^{-6}$ s, à 25 et 300°C et pour les divers types de rayonnements étudiés. Nous trouvons enfin que, pour des ions incidents d'égal TEL > 10 keV μm^{-1}, $G_{H_2O_2}$ décroît lorsque la vitesse de l'ion augmente, en passant des protons (ou deutérons) aux ions carbone. Ces différences produites dans $G_{H_2O_2}$ en changeant le type de rayonnement sont expliquées par la plus grande énergie moyenne des électrons secondaires éjectés par les ions de plus haute vitesse, qui pénétrent ainsi, en moyenne, à une plus grande distance de la trajectoire de la particule incidente, entraînant une diminution concomitante des rendements moléculaires. Nos valeurs calculées de $G_{H_2O_2}$ se comparent en général bien avec les données expérimentales disponibles dans la littérature et sont également en bon accord avec les prédictions de calculs modèles diffusionnels déterministes présentés antérieurement.

Mots clés : eau liquide, radiolyse, rendements primaires, peroxyde d'hydrogène (H_2O_2), transfert d'énergie linéique (TEL), protons et ions lourds accélérés, température, simulations Monte-Carlo.

Received 6 June 2001. Published on the NRC Research Press Web site at http://canjchem.nrc.ca on 11 January 2002.

J. Meesungnoen,[1] J.-P. Jay-Gerin,[2] and A. Filali-Mouhim. Département de médecine nucléaire et de radiobiologie, Faculté de médecine, Université de Sherbrooke, Sherbrooke QC J1H 5N4, Canada.
S. Mankhetkorn. Laboratory of Physical Chemistry, Molecular and Cellular Biology, Faculty of Science, Burapha University, Bangsaen, Chonburi 20131, Thailand.

[1]Also at: Laboratory of Physical Chemistry, Molecular and Cellular Biology, Faculty of Science, Burapha University, Bangsaen, Chonburi 20131, Thailand.
[2]Corresponding author (telephone: (819) 346-1110, ext. 14682/14773; fax: (819) 564-5442; e-mail: jaygerin@courrier.usherb.ca).

 DOI: 10.1139/V01-195 © 2002 NRC Canada

Introduction

The radiolysis of pure deaerated liquid water by low-LET (linear energy transfer, or energy loss per unit track length) radiation (such as ^{60}Co γ-rays, high-energy X-rays, or accelerated electrons) leads principally to the formation of the free radicals and molecular products e^-_{aq}, H·, ·OH, H_2, H_2O_2, and H_3O^+ (for reviews, see refs. 1 and 2). Under usual irradiation conditions, these species are generated nonhomogeneously in widely separated regions of high ionization and excitation densities, commonly referred to as "spurs," along the radiation's path. The so-called "primary" radical and molecular yields (or "escape" yields) $G_{e^-_{aq}}$, $G_{H\cdot}$, $G_{\cdot OH}$, G_{H_2}, and $G_{H_2O_2}$ represent the numbers of species of each kind formed per 100 eV of absorbed energy that remain after spur expansion owing to diffusion. At room temperature, this spur expansion is essentially complete on the time scale of ~1×10^{-6} s after the initial energy deposition. At this time, the species that have escaped from spur reactions are distributed homogeneously throughout the bulk of the solution and available to react with added solutes at moderate concentrations.

For ^{60}Co γ radiation at neutral pH and 25°C (average LET ~0.3 keV μm^{-1}), the normally accepted values of the primary yields (expressed in units of molec./100 eV, molec. = molecules)[3] are the following (1–5):

$$G_{e^-_{aq}} = 2.65 \quad G_{H\cdot} = 0.60 \quad G_{H_2} = 0.45$$

$$G_{\cdot OH} = 2.80 \quad G_{H_2O_2} = 0.68 \quad G_{-H_2O} = 4.15,$$

where G_{-H_2O} denotes, at this stage, the corresponding yield of water molecules decomposed.

A key phenomenon in the radiolysis of water and aqueous solutions is the variation of these primary yields with the type (or LET) of the incident radiation (for example, see refs. 1, 2, and 6–14). With increasing LET, the isolated "spherical" (on the average) spurs of low-LET radiation are formed increasingly closer together and eventually coalesce to form continuous columns of species consisting of a cylindrical track "core" surrounded by a "penumbra" (15, 16). Under those conditions, more free radicals are formed in close proximity with a correspondingly increased probability of reacting with one another to produce the molecular products or to reform water. The radical yields are therefore expected to diminish as the LET increases, whereas the molecular yields increase and the net water decomposition yield decreases. As an exception to this rule, hydroperoxyl ($HO_2\cdot$, or its deprotonated form $O_2^{\cdot-}$, pK_a = 4.8) radicals are produced as primary species, under high-LET irradiation, in yields substantially higher (increasing, typically, from ~0.06 to 0.2 molec./100 eV over an LET range of ~100–650 keV μm^{-1}) (9, 13, 17–21) than the tiny yield observed in low-LET radiolysis (~0.02 molec./100 eV at ~0.3 keV μm^{-1}) (22). Let us also mention the peculiar behavior of $G_{H\cdot}$, which first increases with increasing LET, going from 0.6 molec./ 100 eV at ~0.3 keV μm^{-1} to a maximum of ~0.68 molec./100 eV near 6.5 keV μm^{-1}, and then decreases steeply at higher LET (23).

Hydrogen peroxide is the main oxidizing molecular product in water radiolysis. Because of its high escape yields and its reactivity, H_2O_2 is of great importance in fields such as nuclear engineering (13) and radiation biology (5, 24). Measurements of $G_{H_2O_2}$ by different investigators in water at neutral pH and ambient temperature as a function of LET have been compiled recently by McCracken et al. (13), Meesungnoen et al. (25),[4] and Pastina and LaVerne (26). These latter authors (26) also determined radiation chemical yields of hydrogen peroxide in water at pH 6.5 using protons, helium ions, and carbon ions at energies of a few to 30 MeV. There is a large amount of scatter in the H_2O_2 yields for all LET values above ~5 keV μm^{-1} (13, 25, 26). This uncertainty becomes even greater when temperature effects are considered because H_2O_2 is unstable at elevated temperature, and there is only a relatively small amount of experimental data available for high-LET radiation (12, 13, 27–29). Up to now, the influence of both the LET and temperature on the radiation chemistry of water has been modeled by deterministic (30) and Monte-Carlo (23, 31) calculations over the temperature range 25–300°C. To gain further insights into the effects of varying LET and temperature on the H_2O_2 yield, we performed in the present study Monte-Carlo simulations of the radiolysis of neat, deaerated liquid water to calculate the variations of $G_{H_2O_2}$ with LET, using different types of radiation ($^1H^+$, $^2H^+$, $^4He^{2+}$, $^7Li^{3+}$, and $^{12}C^{6+}$ ions) up to ~100 keV μm^{-1}, at 25 and 300°C. The results were tested against the available experimental data and compared with deterministic diffusion-kinetic modeling calculations reported earlier.

Monte-Carlo simulations

A full description of our Monte-Carlo modeling of the radiolysis of liquid water at ambient temperature has been given elsewhere (32–35). In brief, the energy deposition by the incident radiation (accelerated protons or heavier ions) and by all the secondary electrons that it generates occurs through the slowing down of those particles via a variety of inelastic scattering processes, including ionization, electronic and (or) vibrational excitation of single water molecules, and excitation of plasmon-type collective modes ("physical stage"). The species created during the physical stage reorganize rapidly and produce the "initial" radical and molecular products of the radiolysis, distributed in a highly nonhomogeneous track structure ("physicochemical stage"). The computer codes that we used to cover these two stages are TRACPRO and TRACELE (33). The complex spatial distribution of reactants at ~1×10^{-13} s, which is provided as an output of the program TRACELE, is then used directly as the starting point for the so-called "stage of nonhomogeneous chemistry." This third and final stage, during which the various radiolytic species diffuse and react with one another until all spur and (or) track reactions are complete, was covered by our TRACIRT simulation code (32, 34, 35), using the "independent reaction times" (IRT) method (36) to model the nonhomogeneous reaction kinet-

[3]These units for the radiation chemical yields are used throughout in this paper. For conversion into SI units: 1 molec./100 eV ≈ 1.0364 × 10^{-7} mol J^{-1}.

[4]In the LET range ~0.3–6.5 keV μm^{-1}.

© 2002 NRC Canada

ics.[5] The calculations were performed by simulating short (~5–100 μm) particle track segments, over which the LET remains essentially constant. Typically, ~5000 to 140 000 reactive chemical species are generated in those simulated track segments (depending on the LET), thus ensuring only small statistical fluctuations in the determination of average yields.

As for the calculation of $G_{H_2O_2}$ at 300°C, we used an extended version of our Monte-Carlo computer code, which had recently been developed to include the effects of high temperature on water radiolysis (31, 38). In this version, the thermalization distances (r_{th}) of subexcitation electrons[6] (42, 43) are assumed to decrease linearly with increasing temperature by a factor of 2 between 25 and 300°C (38). This choice was shown to offer the best agreement of the calculated yields $G_{e^-_{aq}}$ and G_{H_2} with experimental data at elevated temperature in the case of low-LET radiation (38). Physically, such a decrease in r_{th} as the temperature increases could be linked to an increase in the scattering cross sections of subexcitation electrons that would account for the corresponding loss of structural order in liquid water owing to the increasing breaking of hydrogen bonds with temperature. Moreover, in accordance with our previous Monte-Carlo calculations (23, 31, 38), $G_{H_2O_2}$ at 300°C was computed at 1×10^{-7} s (rather than 1×10^{-6} s at 25°C) after irradiation, which is the time at which conventional homogeneous chemistry takes over at this temperature.

For incident protons, the influence of the LET on $G_{H_2O_2}$ was investigated at 25 and 300°C over the ranges ~0.3–70 and ~0.25–50 keV μm^{-1}, respectively, by varying the proton energy between ~300 and 0.17 MeV (25). To reproduce the effects of ^{60}Co γ-radiolysis, we used ~300-MeV protons whose average LET value obtained in the simulations was ~0.3 keV μm^{-1}. The effect of LET on $G_{H_2O_2}$ at 25°C was determined for the different radiation types considered by varying the incident particle energy from ~300 to 0.17 MeV/nucleon (~0.3–70 keV μm^{-1}) for $^2H^+$, ~300 to 1.10 MeV/nucleon (~1.3–99 keV μm^{-1}) for $^4He^{2+}$, ~300 to 3.22 MeV/nucleon (~2.9–100 keV μm^{-1}) for $^7Li^{3+}$, and ~300 to 19 MeV/nucleon (~11.6–99 keV μm^{-1}) for $^{12}C^{6+}$. The corresponding average LET values of these various particles over the energy ranges covered were in good agreement with the data reported by Watt (44) and the recommendations of ICRU 49 (45) for liquid water (of density 1 g cm^{-3}).

Results and discussion

Figures 1 and 2 display our calculated values of $G_{H_2O_2}$ as a function of LET for pure, deaerated liquid water, using incident protons as the primary particles, at 25 and 300°C, obtained at homogeneity at 1×10^{-6} and 1×10^{-7} s, respectively. Available experimental data at both temperatures (3, 13, 17, 26, 29, 46–52) are also included in the figures for the sake of comparison. At ~300°C, it should be noted that the only literature data with which a direct comparison can be made are those of Elliot et al. (3) and of Kent and Sims (50) for ^{60}Co γ-rays, and of Sims and co-workers (29) for proton energies in the range 1.2–5.9 MeV. At ambient temperature, our computed $G_{H_2O_2}$ values increase continuously by about 0.44 molec./100 eV from ~0.3 to 70 keV μm^{-1} (Fig. 1; see also Fig. 2*d* of ref. 25).[7] As can be seen from Fig. 2, at 300°C, $G_{H_2O_2}$ is first nearly invariant (at ~0.35 molec./100 eV) with increasing LET from ~0.25 to 2 keV μm^{-1}, and then increases significantly faster than do its corresponding 25°C values (up to ~1.11 molec./100 eV at 50 keV μm^{-1}), showing that the temperature dependence of $G_{H_2O_2}$ is less at higher LET than for low-LET radiation. This result is expected considering the overlapping of the individual spurs along the main particle track as the LET increases, with a resultant increase in the combination of the intervening radical species and hence, in the H_2O_2 yields. Owing to the cylindrical nature of the track structure at high LET, a relatively high portion of these radicals will not escape because as they diffuse along the axis of the track their decay reactions, which are not diffusion controlled for the most part, will be less inhibited by an increase in temperature than those for the isolated spherical spurs of low-LET radiation (12, 27, 30, 31). Despite the relatively large scatter associated with the high-LET $G_{H_2O_2}$ data, the results of our proton track simulations compare well with experiment over the whole LET range studied. In particular, the experimental values of $G_{H_2O_2}$ for ^{60}Co γ-irradiated water at 25 and 300°C (3, 17, 26, 46–49) are well reproduced by our calculated H_2O_2 escape yields for ~300 MeV incident protons; a result that follows from the fact that high-energy protons produce tracks of (on average) isolated spurs, which are very much like those produced by fast electrons in γ radiolysis (14, 25, 26, 33, 34). From Figs. 1 and 2, it should also be noted that our computed $G_{H_2O_2}$ values are quantitatively consistent with the predictions of the deterministic diffusion-kinetic model calculations of Swiatla-Wojcik and Buxton (30) for both 25 and 300°C. Our $G_{H_2O_2}$ results at 25°C are equally close to those calculated by Burns and Sims (17) using the Schwarz diffusion model (47, 53), but they show a monotonic increase in the LET range studied contrary to these authors who found a slight maximum in $G_{H_2O_2}$ around 55–80 keV μm^{-1} (Fig. 1).

These variations of $G_{H_2O_2}$ with LET at 25 and 300°C do not arise from changes in the initial (at ~1×10^{-13} s) yields of hydrogen peroxide, which are essentially constant over the whole LET range covered (see Fig. 3), but rather from the reactions that contribute to the formation or decay of this species in the nonhomogeneous chemical stage. To gain further insights into the origin of the LET dependence of $G_{H_2O_2}$, it is thus of interest to examine the unfolding of the various reactions involving H_2O_2 in the radiation spurs and (or) tracks as they expand by diffusion. This can readily be done with our Monte-Carlo simulations, which enable us to determine quantitatively the LET dependence of each reac-

[5]The IRT simulation methodology has the advantage over deterministic modeling calculations in that, instead of using the "typical, average spur" concept, it correctly incorporates reactants from the same ionization in their actual nonhomogeneous spatial distribution (30, 37).

[6]Subexcitation electrons are those that have kinetic energies less than the first electronic excitation threshold of the medium (~7.3 eV in liquid water) (2, 39–41).

[7]With increasing temperature from 25 to 300°C, it is known that $G_{H_2O_2}$ decreases almost linearly at low LET (see, for example, refs. 3, 27, and 38).

© 2002 NRC Canada

Fig. 1. Variation of the primary hydrogen peroxide yield ($G_{H_2O_2}$) (in molec./100 eV) of the radiolysis of liquid water at 25°C as a function of LET over the range ~0.3–70 keV μm^{-1}. The solid curve represents the results of our Monte-Carlo simulations, using protons as incident particles, obtained at homogeneity at 1 × 10^{-6} s (see text). Experiment: ^{60}Co γ-rays ((+) refs. 3 and 46, (▼) ref. 17, (□) ref. 26, (Δ) ref. 47, (▲) refs. 48 and 49, (●) ref. 50); protons ((★) ref. 17, (■) ref. 26, (▹) ref. 29, (◆) ref. 47, (○) ref. 51, (◇) ref. 52). Absorbed dose-average LET values used for protons are taken from refs. 13, 17, 26, and 44. The dotted line is a least-squares fit to the bulk of H_2O_2 yield data for different investigators at room temperature obtained by McCracken et al. (13) and taken by these authors as being representative of "track-escape" yields for H_2O_2. Comparison is also made with the predictions of the deterministic diffusion-kinetic model calculations of Swiatla-Wojcik and Buxton (30) at 25°C (–◂–) and with the values calculated by Burns and Sims (17) using the Schwarz diffusion model (–•–). Note that a comparison of the results of our proton track simulations at 25°C with the available experimental H_2O_2 yields over the LET range ~0.3–6.5 keV μm^{-1} has been presented previously in Fig. 2*d* of ref. 25.

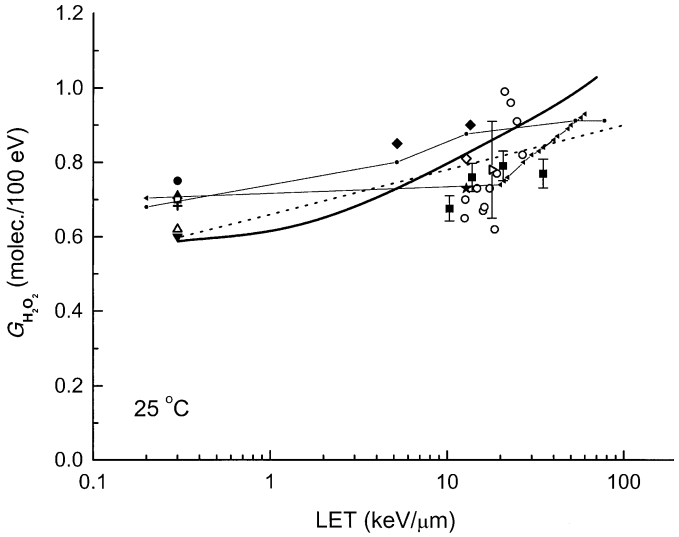

Fig. 2. Variation of the primary hydrogen peroxide yield ($G_{H_2O_2}$) (in molec./100 eV) of the radiolysis of liquid water at 300°C as a function of LET over the range ~0.25–50 keV μm^{-1}. The solid curve represents the results of our Monte-Carlo simulations, using protons as incident particles, obtained at homogeneity at 1 × 10^{-7} s (see text). Experimental data are from Elliot et al. (3) (×) and Kent and Sims (at 270°C) (50) (●) for ^{60}Co γ-rays, and from Sims and co-workers (29) for protons of energies 5.9 MeV (~14.3 keV μm^{-1}) (at 250°C), 2.6 MeV (~23.3 keV μm^{-1}) (at 250°C), and 1 MeV (~34.5 keV μm^{-1}) (at 280°C, extrapolated yield) (▹). Absorbed dose-average LET values used here for protons are taken from refs. 44 and 45. Comparison is also made with the H_2O_2 yield values predicted from the deterministic diffusion-kinetic model calculations of Swiatla-Wojcik and Buxton (ref. 30) at 300°C (–▸–).

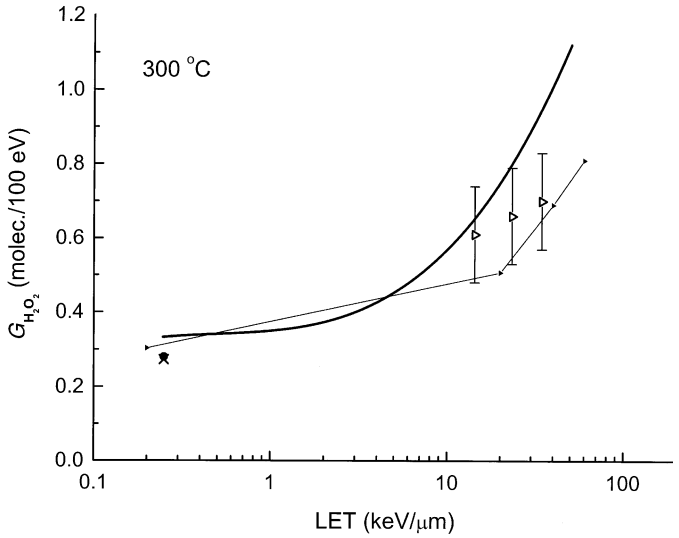

tion. At both 25 and 300°C, the four most important reactions (denoted [R1]–[R4]) that are involved in the primary yield of H_2O_2 in irradiated, deaerated liquid water over the LET range studied, are the following:[8]

[8]For a detailed description of the full reaction scheme considered in our simulations, see refs. 31, 34, and 38.

© 2002 NRC Canada

Fig. 3. Time dependences of the H_2O_2 yields (in molec./100 eV) calculated from our Monte-Carlo simulations of the radiolysis of liquid water by protons of various LET in the time interval $1 \times 10^{-13} - 1 \times 10^{-6}$ s (see text): (*a*) at 25°C, for LET values ~0.3, 4.52, 10.2, 35, and 63.7 keV μm^{-1}; and (*b*) at 300°C, for LET values ~0.25, 5, 14.6, 20.7, and 45.5 keV μm^{-1}. The initial H_2O_2 yields at 25 and 300°C obtained from the simulations at ~1×10^{-13} s, after "contact" reactions have been allowed to take place (refs. 33 and 34), are essentially constant over the whole LET range covered. The thin solid line marked (–■–) in Fig. 3*a* shows the time-dependent yields of H_2O_2 in the electron radiolysis of liquid water as obtained by Pimblott and LaVerne (54) from the inverse Laplace transform of best fit to experimental ·OH scavenger data at room temperature and pH 7. Symbols, representing experimental data for ^{60}Co γ-rays at 25°C, 1×10^{-6} s, and ~0.3 keV μm^{-1}, and at 300°C, 1×10^{-7} s, and ~0.25 keV μm^{-1}, are the same as in Figs. 1 and 2, respectively.

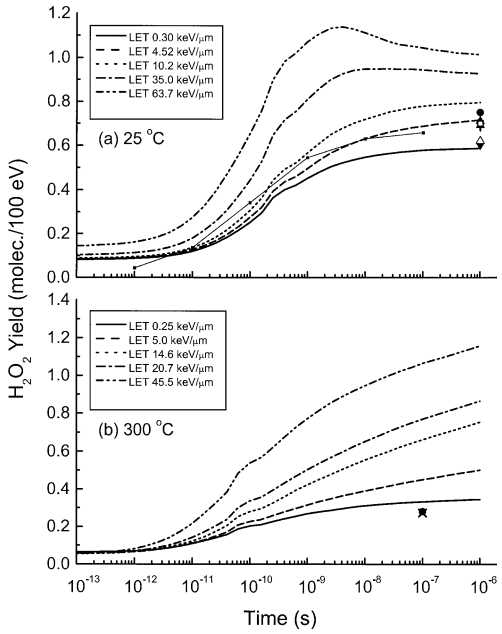

[R1] $\cdot OH + \cdot OH \rightarrow H_2O_2$

[R2] $H_2O_2 + e^-_{aq} \rightarrow \cdot OH + OH^-$

[R3] $H^+ + HO_2^- \rightarrow H_2O_2$

[R4] $H_2O_2 + OH^- \rightarrow HO_2^- + H_2O$

$HO_2^- + H_2O \rightarrow H_2O_2 + OH^-$

Figure 4 compares, at the two temperatures considered, the effect of increasing LET on the extent (expressed as a cumulative $\Delta G_{H_2O_2}$ value) of each of these reactions over the time interval of nonhomogeneous spur chemistry, using protons of different initial energies as incident particles. As one can see in the figure, in the whole LET range covered, hydrogen peroxide is formed mainly by the rxn. [R1] of the ·OH radical with itself, whereas its decay is dominated by rxn. [R2]. At 25°C (Fig. 4*a*), the extent of rxn. [R1] slightly increases as a function of LET in the range ~0.3–2 keV μm^{-1}, and rises much more steeply at higher LET. Rather similarly, the contribution of rxn. [R2] to the removal of H_2O_2 is nearly constant below ~2 keV μm^{-1}, and shows a marked increase,

Fig. 4. Influence of the LET on the extents $\Delta G_{H_2O_2}$ (in molec./100 eV) of the main intra-spur and (or) track rxns. [R1]–[R4] that contribute to the formation and decay of H_2O_2 (see text) in our Monte-Carlo simulations of the radiolysis of liquid water by protons of different initial energies between ~300 and 0.17 MeV: (*a*) at 25°C, over the LET range ~0.3–70 keV μm^{-1} and in the time interval $1 \times 10^{-13} - 1 \times 10^{-6}$ s; and (*b*) at 300°C, over the LET range ~0.25–50 keV μm^{-1} and in the time interval $1 \times 10^{-13} - 1 \times 10^{-7}$ s.

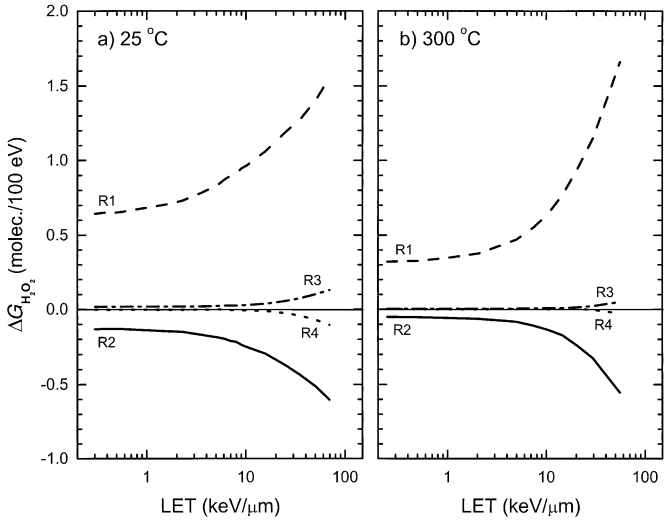

in magnitude, at higher LET, though this increase remains less than about half the corresponding yield variation $\Delta G_{H_2O_2}$ due to rxn. [R1]. As for rxns. [R3] and [R4], our simulation results show that their extents are very small, except at LET values above ~20 keV μm^{-1} where they start to increase somewhat. The overall effect at 25°C is an increase in the hydrogen peroxide yields with increasing LET as shown in Fig. 1. Upon increasing temperature from 25 to 300°C (Fig. 4*b*), the fractions of H_2O_2 either formed by rxn. [R1] or removed by the back rxn. [R2] are decreased by about 50% in the low-LET range (~0.25–2 keV μm^{-1}) (31, 38, 55). Such a decrease can be explained by the fact that these reactions are partially diffusion controlled with rate constants that vary less with temperature than the diffusion in water of the individual species involved (27, 38). At high LET, however, the extents of rxns. [R1] and [R2] show little changes compared to their corresponding values at 25°C, a result attributed to the cylindrical nature of the track structure geometry for which both of these reactions are less inhibited by an increase in temperature (see above). As for the contributions of rxns. [R3] and [R4], they can be regarded at 300°C as negligible over the entire LET range studied ($\Delta G_{H_2O_2}$ = 0.05 and –0.03 molec./100 eV at ~50 keV μm^{-1}, respectively) (Fig. 4*b*). The net effect of LET on $G_{H_2O_2}$ at 300°C is shown in Fig. 2.

Figure 3 shows the influence of LET on the time-dependent H_2O_2 yields at 25 and 300°C, over the range $1 \times 10^{-13} - 1 \times 10^{-6}$ s, obtained from our simulations with protons of various initial energies in the range ~300–0.17 MeV. At 25°C, for LET below approximately 30 keV μm^{-1}, the H_2O_2 yield increases gradually with time to a nearly constant value at ~1×10^{-6} s (Fig. 3*a*). In contrast, above ~30 keV μm^{-1}, the yield of H_2O_2 begins to rise steeply with

© 2002 NRC Canada

Fig. 5. Variations of the primary H_2O_2 yield ($G_{H_2O_2}$) (in molec./100 eV), at 1×10^{-6} s, of the radiolysis of liquid water at 25°C as a function of LET for different types of radiation up to ~100 keV μm^{-1} (see text). The different simulated results are shown as the following lines: (—) protons (or $^2H^+$), (– –) $^4He^{2+}$, (- -) $^7Li^{3+}$, (– - –) $^{12}C^{6+}$. Experiment: $^2H^+$ ((◆) ref. 9, (●) ref. 12), $^4He^{2+}$ ((◇) ref. 9, (Δ) ref. 17, (□) ref. 26, (○) ref. 47, (▽) ref. 51), $^7Li^{3+}$ ((×) ref. 12). Absorbed dose-average LET values used for the various radiations considered are taken from refs. 13, 26, 44, and 47.

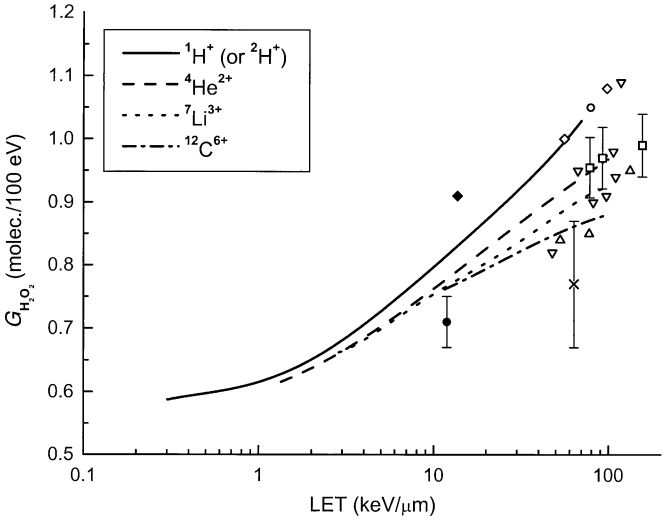

Fig. 6. Time dependences of the H_2O_2 yields (in molec./100 eV) calculated from our Monte-Carlo simulations of the radiolysis of liquid water at 25°C, in the time scale of $1 \times 10^{-13} - 1 \times 10^{-6}$ s, for different types of incident radiation, including $^1H^+$, $^2H^+$, $^4He^{2+}$, $^7Li^{3+}$, and $^{12}C^{6+}$ ions, at the same LET (~30 keV μm^{-1}).

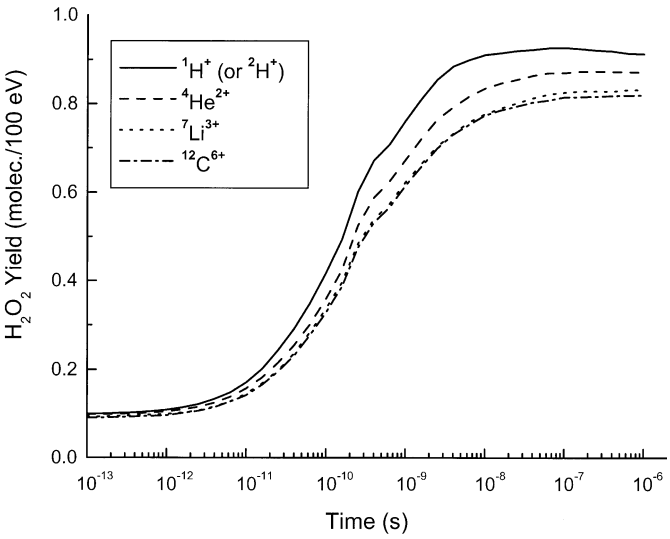

time, then passes through a maximum around 1–10 ns and falls slightly to a plateau region at longer time. These variations in the temporal dependences of the hydrogen peroxide yield mainly reflect, in the LET range studied, the interplay intervening between the time- and LET-dependent spur rxns. [R1] and [R2], which respectively generate and remove H_2O_2. As can also be seen in Fig. 3*a*, our simulation results are in good agreement with the H_2O_2 yields calculated previously by Pimblott and LaVerne (54) using the inverse Laplace transform of best fit to experimental ·OH scavenger data at neutral pH. At 300°C, the calculated time dependence of the H_2O_2 yield at low LET qualitatively resembles that obtained at 25°C (Fig. 3*b*). However, with increasing LET, the maximum observed at 25°C in the 1–10 ns time domain is no longer present at 300°C. In fact, at this latter temperature, the yield of H_2O_2 increases monotonically as a function of time and seems to continue to increase above ~1×10^{-6} s. At present, unfortunately, there are no systematic literature data with which to compare our results on the temporal variation of the H_2O_2 yield at elevated temperatures.

The variations of $G_{H_2O_2}$ as a function of LET for different radiation types up to ~100 keV μm^{-1}, at 25°C, are shown in Fig. 5. These radiations include protons, $^2H^+$, $^4He^{2+}$, $^7Li^{3+}$, and $^{12}C^{6+}$ ions, and their corresponding incident energy and LET ranges are given above. Our calculated $G_{H_2O_2}$ values using protons are identical to those using deuterons of the same LET (or the same velocity), which is in agreement with the experimental observation that protons of energy E and deuterons of energy $2E$ give similar radiation chemical yields (14, 51, 56). Below ~10 keV μm^{-1}, the behavior of $G_{H_2O_2}$ depends very little on the type of radiation. This is expected, since in this region of low LET the track of a charged particle consists, as seen above, of a random succession of spatially isolated spurs, and the observed chemistry of such a particle should therefore be much like that of a fast proton (11, 14). As can be seen in Fig. 5, for incident ions of equal LET > 10 keV μm^{-1}, $G_{H_2O_2}$ decreases as the ion velocity increases, from protons (or deuterons) to carbon ions.[9] This irradiating-ion dependence of the yields of hydrogen peroxide at a given LET is also shown in Fig. 6, which compares the temporal variations of the H_2O_2 yields at 25°C, over the range $1 \times 10^{-13} - 1 \times 10^{-6}$ s, obtained from our simulations using the different incident ions studied here with an equal LET of ~30 keV μm^{-1}. Such results indicate, as it has been frequently noted (for example, see refs. 2, 7, 11, 14, and 59), that LET does not uniquely determine the correct radiation chemical effects of particle track structures. This is explained by the greater mean energy of secondary electrons (the so-called low-LET "short" and "branch" tracks in the terminology of Mozumder and Magee (60), or

[9]For kinetic energies of ions small compared to their rest-mass energy, the nonrelativistic Bethe stopping power equation (57) is well approximated by (in SI units):

$$-\frac{dE}{dx} = \left(\frac{1}{4\pi\varepsilon_0}\right)^2 \frac{4\pi z^2 e^4}{m_0 V^2} NZ \ln\left(\frac{2m_0 V^2}{I}\right)$$

where ze is the charge on the incident ion, V is the ion velocity, m_0 is the rest mass of an electron, NZ is the number of electrons per m^3 of the absorbing medium, and I is the mean excitation and ionization potential of the bound electrons in the absorber (for liquid water, I = 79.7 ± 0.5 eV, see ref. 58). It follows from this equation that for two different ions of equal LET, the one with the higher charge will have the higher velocity (11, 14).

© 2002 NRC Canada

"δ-rays") from the higher velocity ion, which will penetrate to a greater average distance from the main particle track, and lead to a greater dispersion of the initial radical positions around the track (61). In other words, the actual mean initial volume density of free radicals formed in the track will be lower. Under these conditions, a greater fraction of those radicals will be allowed to escape recombination as they subsequently diffuse with consequent tendency for increase in the radical yields measured after track expansion along with decreased molecular product yields (11, 23, 61). As can be seen from Fig. 5, the results of our simulated H_2O_2 escape yields compare generally well with available experimental data. The agreement is remarkably good with the recent experimental $G_{H_2O_2}$ values of Pastina and LaVerne (26) for 5-, 15- and 20-MeV $^4He^{2+}$ ions. As for the temporal variations in the H_2O_2 yields shown in Fig. 6 for protons, $^2H^+$, $^4He^{2+}$, $^7Li^{3+}$, and $^{12}C^{6+}$ ions of the same LET (~30 keV μm^{-1}), there are no literature data with which a direct comparison of our results can be made.

Conclusion

In this paper, we have presented Monte-Carlo simulations of the radiolysis of pure, deaerated liquid water at neutral pH to calculate the variations of the primary yield of hydrogen peroxide with the LET of incident protons over the ranges ~0.3–70 keV μm^{-1} and ~0.25–50 keV μm^{-1} at 25 and 300°C, respectively, and of different radiation types, including $^2H^+$, $^4He^{2+}$, $^7Li^{3+}$, and $^{12}C^{6+}$ ions, up to ~100 keV μm^{-1} at 25°C. The results show that, at both temperatures, $G_{H_2O_2}$ increases monotonically as a function of LET. This increase, which is mainly due to a greater combination of the ·OH radicals formed by the decomposition of water molecules, is significantly faster at 300°C, showing that the effect of temperature at higher LET is less than for low-LET radiation. We also find that, above ~10 keV μm^{-1}, the H_2O_2 yields depend on the type of the irradiating ions. At a given LET, $G_{H_2O_2}$ decreases as the ion velocity increases, from protons to carbon ions, clearly indicating that LET does not uniquely determine the correct radiation chemical effects of particle track structures. Our calculated $G_{H_2O_2}$ values compare generally well with the available experimental data and are also in good accord with the predictions of deterministic diffusion model calculations reported previously.

Acknowledgment

We thank Professor Jay A. LaVerne (University of Notre Dame) for sending us the experimental hydrogen peroxide yield values for protons, helium ions, and carbon ions reported in ref. 26. We also thank Dr. Howard E. Sims (AEA Technology, Harwell, U.K.) for making refs. 29 and 52 available to us. Financial support from the Canadian Institutes of Health Research (Grant No. MT-14617) is gratefully acknowledged.

References

1. J.W.T. Spinks and R.J. Woods. An introduction to radiation chemistry. 3rd ed. Wiley, New York. 1990. p. 243. See also R.J. Woods and A.K. Pikaev. Applied radiation chemistry: radiation processing. Wiley, New York. 1994. p. 166.
2. C. Ferradini and J.-P. Jay-Gerin. Can. J. Chem. **77**, 1542 (1999).
3. A.J. Elliot, M.P. Chenier, and D.C. Ouellette. J. Chem. Soc. Faraday Trans. **89**, 1193 (1993).
4. H.A. Schwarz. J. Phys. Chem. **96**, 8937 (1992).
5. C. Ferradini and J. Pucheault. Biologie de l'action des rayonnements ionisants. Masson, Paris. 1983. p. 25.
6. N.F. Barr and R.H. Schuler. Radiat. Res. **7**, 302 (1957).
7. A.O. Allen. The radiation chemistry of water and aqueous solutions. D. Van Nostrand Co., Princeton, New Jersey. 1961. p. 49.
8. J. Pucheault. *In* Actions chimiques et biologiques des radiations. 5ème Sér. *Edited by* M. Haïssinsky. Masson, Paris. 1961. p. 31.
9. A. Appleby and H.A. Schwarz. J. Phys. Chem. **73**, 1937 (1969).
10. I.G. Draganić and Z.D. Draganić. The radiation chemistry of water. Academic Press, New York. 1971. p. 123.
11. A. Appleby. Radiat. Phys. Chem. **34**, 121 (1989).
12. A.J. Elliot, M.P. Chenier, D.C. Ouellette, and V.T. Koslowsky. J. Phys. Chem. **100**, 9014 (1996).
13. D.R. McCracken, K.T. Tsang, and P.J. Laughton. Aspects of the physics and chemistry of water radiolysis by fast neutrons and fast electrons in nuclear reactors. Report AECL-11895. Atomic Energy of Canada Ltd., Chalk River, Ontario. 1998.
14. J.A. LaVerne. Radiat. Res. **153**, 487 (2000); J.A. LaVerne. *In* Radiation research. Vol. 2. *Edited by* M. Moriarty, C. Mothersill, C. Seymour, M. Edington, J.F. Ward, and R.J.M. Fry. Allen Press, Lawrence, Kansas. 2000. p. 46.
15. J.L. Magee and A. Chatterjee. *In* Kinetics of nonhomogeneous processes. *Edited by* G.R. Freeman. Wiley, New York. 1987. p. 171.
16. A. Mozumder. Fundamentals of radiation chemistry. Academic Press, San Diego, California. 1999. p. 41.
17. K.F. Baverstock and W.G. Burns. Nature (London), **260**, 316 (1976); W.G. Burns and H.E. Sims. J. Chem. Soc. Faraday Trans. 1, **77**, 2803 (1981).
18. J.A. LaVerne and R.H. Schuler. J. Phys. Chem. **91**, 6560 (1987); J. Phys. Chem. **96**, 7376 (1992).
19. J.A. LaVerne. Radiat. Phys. Chem. **34**, 135 (1989).
20. C. Ferradini and J.-P. Jay-Gerin. Radiat. Phys. Chem. **51**, 263 (1998).
21. G. Baldacchino, D. Le Parc, B. Hickel, M. Gardès-Albert, Z. Abedinzadeh, D. Jore, S. Deycard, S. Bouffard, V. Mouton, and E. Balanzat. Radiat. Res. **149**, 128 (1998); G. Baldacchino, V. Trupin-Wasselin, S. Bouffard, E. Balanzat, M. Gardès-Albert, Z. Abedinzadeh, D. Jore, S. Deycard, and B. Hickel. Can. J. Physiol. Pharmacol. **79**, 180 (2001).
22. E. Bjergbakke and E.J. Hart. Radiat. Res. **45**, 261 (1971).
23. J. Meesungnoen, J.-P. Jay-Gerin, A. Filali-Mouhim, and S. Mankhetkorn. Chem. Phys. Lett. **335**, 458 (2001).
24. C. von Sonntag. The chemical basis of radiation biology. Taylor and Francis, London. 1987. See also R.V. Bensasson, E.J. Land, and T.G. Truscott. Excited states and free radicals in biology and medicine: contributions from flash photolysis and pulse radiolysis. Oxford University, Oxford. 1993.
25. J. Meesungnoen, M. Benrahmoune, A. Filali-Mouhim, S. Mankhetkorn, and J.-P. Jay-Gerin. Radiat. Res. **155**, 269 (2001) (published erratum appears in Radiat. Res. **155**, 873 (2001)).
26. B. Pastina and J.A. LaVerne. J. Phys. Chem. A, **103**, 1592 (1999).
27. A.J. Elliot. Rate constants and *G*-values for the simulation of the radiolysis of light water over the range 0–300°C. Report AECL-11073. Atomic Energy of Canada Ltd., Chalk River, Ontario. 1994.
28. G.R. Sunaryo, Y. Katsumura, D. Hiroishi, and K. Ishigure. Radiat. Phys. Chem. **45**, 131 (1995); K. Ishigure, Y. Katsumura, G.R. Sunaryo, and D. Hiroishi. Radiat. Phys. Chem. **46**, 557

© 2002 NRC Canada

(1995); Y. Katsumura, G. Sunaryo, D. Hiroishi, and K. Ishigure. Prog. Nucl. Energy, **32**, 113 (1998).
29. H.E. Sims, C.B. Ashmore, P.K. Tait, and W.S. Walters. *In* Proceedings of JAIF international conference on water chemistry in nuclear power plants, Kashiwazaki, Japan, October 13–16, 1998. p. 894; C.B. Ashmore, H.E. Sims, P.K. Tait, and W.S. Walters. The measurement of water radiolysis product yields at high temperature and pressure. Final report. Report AEAT-2223. U.K. Atomic Energy Authority. 1997–98.
30. D. Swiatla-Wojcik and G.V. Buxton. J. Chem. Soc. Faraday Trans. **94**, 2135 (1998).
31. M.-A. Hervé du Penhoat, J. Meesungnoen, T. Goulet, A. Filali-Mouhim, S. Mankhetkorn, and J.-P. Jay-Gerin. Chem. Phys. Lett. **341**, 135 (2001).
32. Y. Frongillo, M.-J. Fraser, V. Cobut, T. Goulet, J.-P. Jay-Gerin, and J.P. Patau. J. Chim. Phys. **93**, 93 (1996). See also V. Cobut, Y. Frongillo, J.-P. Jay-Gerin, and J.P. Patau. J. Chim. Phys. **91**, 1018 (1994).
33. V. Cobut, Y. Frongillo, J.P. Patau, T. Goulet, M.-J. Fraser, and J.-P. Jay-Gerin. Radiat. Phys. Chem. **51**, 229 (1998).
34. Y. Frongillo, T. Goulet, M.-J. Fraser, V. Cobut, J.P. Patau, and J.-P. Jay-Gerin. Radiat. Phys. Chem. **51**, 245 (1998).
35. T. Goulet, M.-J. Fraser, Y. Frongillo, and J.-P. Jay-Gerin. Radiat. Phys. Chem. **51**, 85 (1998).
36. P. Clifford, N.J.B. Green, M.J. Pilling, and S.M. Pimblott. J. Phys. Chem. **91**, 4417 (1987); N.J.B. Green, M.J. Pilling, S.M. Pimblott, and P. Clifford. J. Phys. Chem. **94**, 251 (1990); S.M. Pimblott, M.J. Pilling, and N.J.B. Green. Radiat. Phys. Chem. **37**, 377 (1991).
37. S.M. Pimblott and J.A. LaVerne. Radiat. Res. **122**, 12 (1990). See also S.M. Pimblott and N.J.B. Green. Res. Chem. Kinet. **3**, 117 (1995).
38. M.-A. Hervé du Penhoat, T. Goulet, Y. Frongillo, M.-J. Fraser, Ph. Bernat, and J.-P. Jay-Gerin. J. Phys. Chem. A, **104**, 11757 (2000).
39. R.L. Platzman. Radiat. Res. **1**, 558 (1954); Radiat. Res. **2**, 1 (1955).
40. J. Weiss. Nature (London), **174**, 78 (1954); J. Chim. Phys. **52**, 539 (1955).
41. M. Michaud, P. Cloutier, and L. Sanche. Phys. Rev. A: At. Mol. Opt. Phys. **44**, 5624 (1991).
42. T. Goulet and J.-P. Jay-Gerin. J. Phys. Chem. **92**, 6871 (1988); Radiat. Res. **118**, 46 (1989); T. Goulet, J.P. Patau, and J.-P. Jay-Gerin. J. Phys. Chem. **94**, 7312 (1990).
43. T. Goulet, J.-P. Jay-Gerin, Y. Frongillo, V. Cobut, and M.-J. Fraser. J. Chim. Phys. **93**, 111 (1996).
44. D.E. Watt. Quantities for dosimetry of ionizing radiations in liquid water. Taylor and Francis, London. 1996.
45. ICRU Report 49. Stopping powers and ranges for protons and alpha particles. International Commission on Radiation Units and Measurements, Bethesda, Maryland. 1993.
46. I.G. Draganić, M.T. Nenadović, and Z.D. Draganić. J. Phys. Chem. **73**, 2564 (1969).
47. R.H. Bisby, R.B. Cundall, H.E. Sims, and W.G. Burns. Faraday Discuss. Chem. Soc. **63**, 237 (1977).
48. A.O. Allen and R.A. Holroyd. J. Am. Chem. Soc. **77**, 5852 (1955).
49. A.O. Allen and H.A. Schwarz. *In* Proceedings of the 2nd United Nations International Conference on the Peaceful Uses of Atomic Energy, Geneva, 1–13 September 1958. Vol. 29. P/1403. United Nations, Geneva. 1958. p. 30.
50. M.C. Kent and H.E. Sims. *In* Proceedings of the 6th international conference on water chemistry of nuclear reactor systems. British Nuclear Energy Society, London. 1992. p. 153.
51. A.R. Anderson and E.J. Hart. Radiat. Res. **14**, 689 (1961).
52. H.E. Sims. Ph.D. Thesis, University of Salford, Salford, U.K. 1978. (Quoted in ref. 29).
53. H.A. Schwarz. J. Phys. Chem. **73**, 1928 (1969). See also W.G. Burns and A.R. Curtis. J. Phys. Chem. **76**, 3008 (1972); W.G. Burns, H.E. Sims, and J.A.B. Goodall. Radiat. Phys. Chem. **23**, 143 (1984).
54. S.M. Pimblott and J.A. LaVerne. J. Phys. Chem. A, **101**, 5828 (1997).
55. D. Swiatla-Wojcik and G.V. Buxton. J. Phys. Chem. **99**, 11 464 (1995).
56. H. Bichsel and M. Inokuti. Nucl. Instrum. Methods Phys. Res. B, **134**, 161 (1998).
57. H.A. Bethe and J. Ashkin. *In* Experimental nuclear physics. Vol. 1. *Edited by* E. Segrè. Wiley, New York. 1953. p. 166. See also U. Fano. Ann. Rev. Nucl. Sci. **13**, 1 (1963).
58. H. Bichsel and T. Hiraoka. Nucl. Instrum. Methods Phys. Res. B, **66**, 345 (1992). See also M. Dingfelder, D. Hantke, M. Inokuti, and H.G. Paretzke. Radiat. Phys. Chem. **53**, 1 (1998); H. Paul and M.J. Berger. *In* Atomic and molecular data for radiotherapy and radiation research. Report IAEA-TECDOC-799. International Atomic Energy Agency, Vienna. 1995. p. 415.
59. C. Ferradini. *In* Actions biologique et chimique des radiations ionisantes. Vol. 1. *Edited by* B. Tilquin. Éditions Ciaco, Bruxelles. 1990. p. 52.
60. A. Mozumder and J.L. Magee. Radiat. Res. **28**, 203 (1966); J. Chem. Phys. **45**, 3332 (1966).
61. R.H. Schuler and A.O. Allen. J. Am. Chem. Soc. **79**, 1565 (1957).

© 2002 NRC Canada

Synthesis of a hexasaccharide fragment of the capsular polysaccharide of *Streptococcus pneumoniae* type 3

Dirk J. Lefeber, Eneko Aldaba Arévalo, Johannis P. Kamerling, and Johannes F.G. Vliegenthart

Abstract: In the framework of the development of a new generation of neoglycoconjugate vaccines against *Streptococcus pneumoniae*, the synthesis is described of a spacer-containing hexasaccharide fragment related to the capsular polysaccharide of *S. pneumoniae* type 3. Hexasaccharide β-D-Glc*p*A-(1→4)-β-D-Glc*p*-(1→3)-β-D-Glc*p*A-(1→4)-β-D-Glc*p*-(1→3)-β-D-Glc*p*A-(1→4)-β-D-Glc*p*-(1→O-$(CH_2)_3NH_2$) (**1**), comprised of three repeating units, was synthesized via a blockwise strategy employing suitably protected disaccharide building blocks. Carboxylic groups were introduced by selective oxidation with TEMPO (2,2,6,6-tetramethyl-1-piperidinyloxy) in the last reaction steps. Deprotection afforded target hexasaccharide **1**.

Key words: oligosaccharide synthesis, *Streptococcus pneumoniae* type 3, TEMPO oxidation.

Résumé : Dans le cadre du développement d'une nouvelle génération de vaccins néoglycoconjugués actifs contre le *Streptococcus pneumoniae* et faisant appel à une stratégie de synthèse par blocs à l'aide de disaccharides protégés de façon appropriée, on a réalisé la synthèse d'un fragment hexasaccharidique apparenté au polysaccharide capsulaire du *S. pneumoniae* de type 3 et contenant un espaceur, soit le β-D-Glc*p*A-(1→4)-β-D-Glc*p*-(1→3)-β-D-Glc*p*A-(1→4)-β-D-Glc*p*-(1→3)-β-D-Glc*p*A-(1→4)-β-D-Glc*p*-(1→O-$(CH_2)_3NH_2$) (**1**) qui trois motifs. Les groupes carboxyliques ont été introduits en procédant à une oxydation sélective à l'aide de TEMPO (2,2,6,6-tétraméthyl-1-pipéridinyloxy) dans les dernières étapes réactionnelles. La déprotection fournit l'hexasaccharide recherché, **1**.

Mots clés : synthèse d'oligosaccharide, *Streptococcus pneumoniae* de type 3, oxydation par TEMPO.

[Traduit par la Rédaction]

Introduction

Diseases caused by encapsulated bacteria can be prevented by vaccination with neoglycoconjugate vaccines as proven for *Haemophilus influenzae* type b (1), *Neisseria meningitidis* type C (2), and *Streptococcus pneumoniae* serotypes (3). These vaccines are prepared by conjugation of an isolated polysaccharide or a mixture of polysaccharide-derived oligosaccharides to a protein carrier. For a detailed investigation of the immune response to these types of vaccines, neoglycoproteins with a well-defined carbohydrate structure need to be available.

Neoglycoconjugates related to *S. pneumoniae* type 3 have been prepared by coupling di-, tri-, or tetrasaccharide fragments in several carbohydrate–protein ratios to a nontoxic mutant of diphtheria toxin (CRM_{197}) (4). While immunization experiments with these conjugates in mice showed that increasing IgG antibody titres were found with increasing oligosaccharide chain length, no difference was found with respect to the oligosaccharide loading (5).

The use of conjugates that contain larger oligosaccharide fragments than in the study described above might lead to an improved immunogenicity. Furthermore, human antibodies can better recognize larger epitopes on the polysaccharide than do animal antibodies, as shown for neoglycoproteins consisting of synthetic oligosaccharides related to the capsular polysaccharide of *S. pneumoniae* type 23F (6). For these reasons, a program was started for the synthesis of a *S. pneumoniae* type 3 related hexasaccharide fragment (**1**), comprised of three cellobiuronic acid repeating units (Fig. 1).

Received 13 July 2001. Published on the NRC Research Press Web site at http://canjchem.nrc.ca on 21 January 2002.

Dedicated to the memory of Ray Lemieux, one of the most inspiring glycoscientists.

D.J. Lefeber, E. Aldaba Arévalo, J.P. Kamerling, and J.F.G. Vliegenthart.[1] Bijvoet Center, Department of Bio-Organic Chemistry, Utrecht University, P.O. Box 80.075, NL-3508 TB Utrecht, The Netherlands.

[1]Corresponding author (fax: (+31) 30 2 540 980; e-mail: j.f.g.vliegenthart@chem.uu.nl).

Results and discussion

The synthesis for tetrasaccharide acceptor **11** was previously described (4). Two disaccharide donors (**6** and **10**, Scheme 1) were tested for the ability to couple with **11** to afford protected hexasaccharide **12** (Scheme 2).

For the synthesis of disaccharide thioethyl donor **6**, first monosaccharide acceptor **4** was prepared by debenzylidenation of **2** (7) using trifluoroacetic acid (→**3**, 88%) and subsequent selective benzoylation using benzoyl chloride

 DOI: 10.1139/V01-190 © 2002 NRC Canada

Fig. 1. Target hexasaccharide **1** comprising three repeating units of the capsular polysaccharide of *S. pneumoniae* type 3.

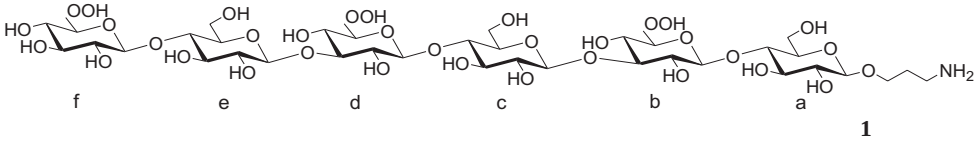

Scheme 1. Synthesis of disaccharide donors **6** and **10**. Reagents and conditions: (*a*) CF_3COOH, H_2O, CH_2Cl_2, 88%; (*b*) PhCOCl, Et_3N, CH_2Cl_2, 50%; (*c*) 10% TMSOTf, CH_2Cl_2, 75%; (*d*) 11% TMSOTf, CH_2Cl_2, 83%; (*e*) (*i*) $(PPh_3)_3Rh(I)Cl$, DABCO, $CH_3C_6H_5$–EtOH–CH_2Cl_2 (10:5:1), (*ii*) NIS, H_2O, THF, 68%; (*f*) Cl_3CCN, DBU, CH_2Cl_2, 86%.

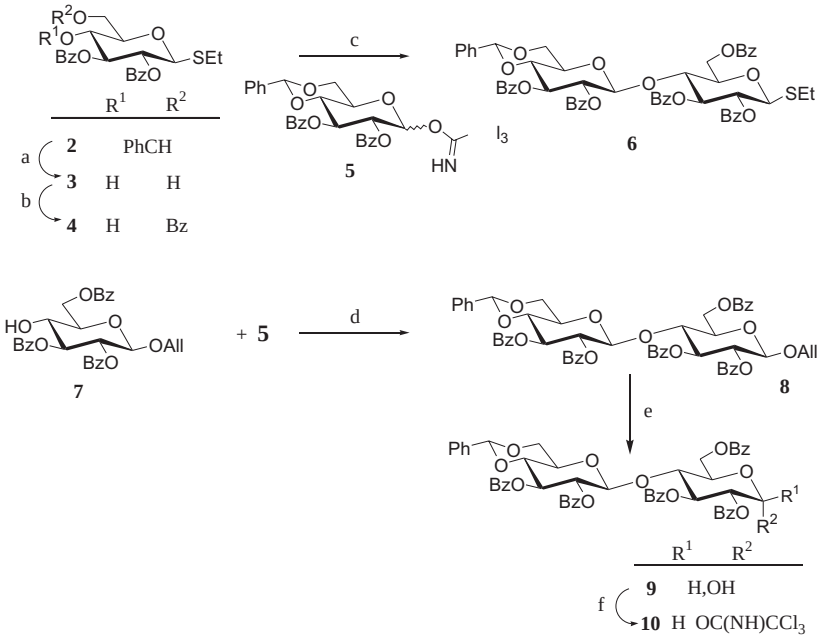

Scheme 2. Synthesis of hexasaccharide **1**. Reagents and conditions: (*a*) 10% TMSOTf, CH_2Cl_2, 63%; (*b*) CF_3COOH, H_2O, CH_2Cl_2, 75%; (*c*) TEMPO, aqueous NaOCl, KBr, Bu_4NBr, aqueous NaCl, aqueous $NaHCO_3$, CH_2Cl_2, 70%; (*d*) (*i*) NaOMe, MeOH (pH 10), (*ii*) $NaBH_4$, 10% Pd/C, 0.05 M NaOH, 61%.

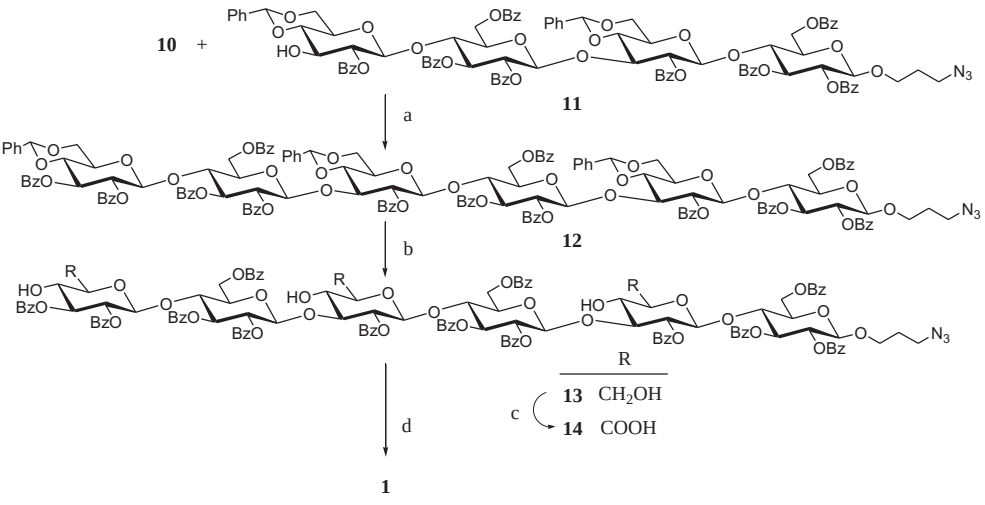

(→**4**, 50%). Coupling of **4** with imidate donor **5** (4) using 10% TMSOTf as a promoter gave **6** in a yield of 75%. For the synthesis of disaccharide imidate donor **10**, first **8** was prepared in 83% yield by coupling of acceptor **7** (4) and donor **5** with 11% TMSOTf as a promoter. Then, deallylation of **8** using tris(triphenylphosphine)rhodium(I) chloride and *N*-iodosuccinimide (→**9**, 68%) and subsequent trichloroacetimidation gave **10** (86%).

For the preparation of protected hexasaccharide **12** (Scheme 2), tetrasaccharide acceptor **11** (4) was coupled

© 2002 NRC Canada

Table 1. 500 MHz ^{1}H NMR data of **1** at 305 K (in ppm).

	H-1	H-2	H-3	H-4	H-5	H-6a	H-6b
Glc[a]	4.50 (7.8)	3.33	3.64	3.61	n.d.[a]	3.98	3.80
GlcA[b]	4.53 (8.1)	3.56	3.79	n.d.	n.d.		
Glc[c]	4.82 (8.0)	3.38	3.65	3.62	n.d.	3.98	3.80
GlcA[d]	4.53 (8.0)	3.56	3.79	n.d.	n.d.		
Glc[e]	4.82 (8.0)	3.38	3.65	3.62	n.d.	3.98	3.80
GlcA[f]	4.50 (8.2)	3.36	3.51	3.51	3.75		

Note: The signals for the 3-aminopropyl spacer are: δ = 4.05 and 3.83 ($OCH_2CH_2CH_2NH_2$), 3.16 ($OCH_2CH_2CH_2NH_2$), 2.01 ($OCH_2CH_2CH_2NH_2$). $J_{1,2}$ couplings are presented in parentheses.

[a]n.d. = not determined.

with donor **6** using *N*-iodosuccinimide and triflic acid as a promoter system. Low yields of product (<8%) were obtained when the reaction was performed at 0°C or lower temperatures. Hexasaccharide **12** could, however, be obtained in a yield of 63% by coupling **11** with disaccharide imidate donor **10** using 10% TMSOTf as a promoter at room temperature. After debenzylidenation of **12** using trifluoroacetic acid (→**13**, 75%), the free primary hydroxyl functions were oxidized. Treatment of **13** with TEMPO and sodium hypochlorite (8) was found to be efficient for the oxidation of the three primary hydroxyl groups in the presence of secondary functions, and **14** was obtained in 70% yield. ^{1}H NMR analysis after methylation with diazomethane showed three singlets at δ = 3.39, 3.30, and 3.23 ($COOCH_3$). Debenzoylation of **14** with sodium methoxide and reduction of the azide using sodium borohydride and 10% Pd/C afforded target hexasaccharide **1** in 61% yield. The identity of the compound was established by ^{1}H NMR spectroscopy (Table 1) and mass spectrometry.

In conclusion, a versatile synthetic route was developed using a block wise strategy for the preparation of hexasaccharide fragment **1**, representing three repeating units of the capsular polysaccharide of *S. pneumoniae* type 3. The carboxylic acids were efficiently introduced by selective oxidation using TEMPO.

Experimental section

General

All chemicals were of reagent grade and were used without any further purification. Reactions were monitored by TLC on Silica gel 60 F254 (Merck); compounds were visualized, after examination under UV light, by heating with 10% (v/v) ethanolic H_2SO_4, orcinol (2 mg mL^{-1}) in 20% (v/v) methanolic H_2SO_4, or ninhydrin (1.5 mg mL^{-1}) in BuOH–H_2O–HOAc (38:1.75:0.25). In the work-up procedures of the reaction mixtures, the organic solutions were washed with appropriate amounts of the indicated aqueous solutions, then dried ($MgSO_4$), and concentrated under reduced pressure at 20–40°C on a water bath. Column chromatography was performed on Silica gel 60 (Merck, 0.063–0.200 mm). Optical rotations were measured in $CHCl_3$, unless stated otherwise, with a PerkinElmer 241 polarimeter, using a 10 cm, l mL cell. ^{1}H NMR spectra in $CDCl_3$ were recorded at 27°C with a Bruker AC 300 spectrometer; the δ values are given in ppm relative to the signal for internal Me_4Si (δ = 0). ^{13}C (APT, 75 MHz) NMR spectra in $CDCl_3$ were recorded at 27°C with a Bruker AC 300 spectrometer; indicated ppm values for δ are relative to the signal of $CDCl_3$ (δ = 76.9). The ^{1}H NMR spectrum of **1** was recorded in D_2O at 32°C with a Bruker AMX 500 spectrometer, and the δ values are given in ppm relative to the signal for internal acetone (δ = 2.225). Two-dimensional TOCSY and ROESY spectra were recorded using a Bruker AMX 500 apparatus (500 MHz) to assign the spectra of compounds **1**, **12**, **13**, and **14**. Residues *a–f* (Fig. 1) were assigned on the basis of interglycosidic ROESY cross-peaks. Matrix-assisted laser desorption ionization time-of-flight (MALDI-TOF) spectra were obtained on a Voyager-DE™ mass spectrometer using 2,4-dihydroxybenzoic acid (DHB) in H_2O as a matrix. Elemental analyses were carried out by H. Kolbe Mikroanalytisches Laboratorium (Mülheim an der Ruhr, Germany).

*Ethyl 2,3-di-*O*-benzoyl-1-thio*-β-D-*glucopyranoside (3)*

To a solution of ethyl 2,3-di-*O*-benzoyl-4,6-*O*-benzylidene-1-thio-β-D-glucopyranoside (**2**) (7) (1.37 g, 2.63 mmol) in CH_2Cl_2 (36 mL) were added CF_3COOH (1.5 mL) and H_2O (0.2 mL). The mixture was stirred for 16 h, diluted with CH_2Cl_2, washed with 10% (w/v) aqueous $NaHCO_3$ until neutral pH and 10% (w/v) aqueous NaCl, and the organic layer was dried, filtered, and concentrated. The residue was purified by column chromatography (CH_2Cl_2–MeOH, 98:2) to obtain **3** (1.0 g, 88%). $[\alpha]_D^{20}$ +76 (*c* = 1). R_f = 0.05 (CH_2Cl_2–EtOAc, 9:1). ^{1}H NMR ($CDCl_3$) δ: 7.97–7.93 and 7.53–7.34 (2m, 10H, 2*Ph*CO), 4.74 (d, $J_{1,2}$ = 9.8 Hz, 1H, H-1), 2.76–2.73 (m, 2H, SCH_2CH_3), 1.26 (t, 3H, SCH_2CH_3). ^{13}C NMR ($CDCl_3$) δ: 167.4 and 165.2 (2Ph*C*O); 129.1 and 128.7 (2*Ph*CO, quaternary C); 83.6 (C-1); 79.9, 78.2, 70.1, and 69.9 (C-2–C-5); 62.3 (C-6); 24.3 (SCH_2CH_3); 14.8 (SCH_2CH_3). Anal. calcd. for $C_{22}H_{24}O_7S$ (432.4): C 61.11, H 5.59; found C 60.99, H 5.74.

*Ethyl 2,3,6-tri-*O*-benzoyl-1-thio*-β-D-*glucopyranoside (4)*

To a solution of **3** (0.95 g, 2.2 mmol) in CH_2Cl_2 (50 mL) and Et_3N (0.37 mL) at 0°C was added dropwise a solution of benzoyl chloride (0.27 mL, 2.3 mmol) in CH_2Cl_2 (10 mL). After stirring for 24 h, the mixture was diluted with CH_2Cl_2, washed with 10% (w/v) aqueous NaCl, and the organic layer was dried, filtered, and concentrated. The crude residue was purified by column chromatography (CH_2Cl_2–EtOAc, 95:5) to give **4** (0.6 g, 50%). $[\alpha]_D^{20}$ +60 (*c* = 1). R_f = 0.51 (CH_2Cl_2–EtOAc, 9:1). ^{1}H NMR ($CDCl_3$) δ: 8.05–7.91 and 7.46–7.28 (2m, 15H, 3*Ph*CO), 5.60 and 5.47 (2t, each 1H, H-2,3), 4.82 (d, $J_{1,2}$ = 9.9 Hz, 1H, H-1), 2.82–2.64 (m, 2H, SCH_2CH_3), 1.24 (t, 3H, SCH_2CH_3). ^{13}C NMR ($CDCl_3$) δ: 166.8, 166.7, and 165.2 (3Ph*C*O); 83.4 (C-1); 78.2, 77.2, 70.2, and 69.3 (C-2–C-5); 63.6 (C-6); 24.1 (SCH_2CH_3); 14.8 (SCH_2CH_3). Anal. calcd. for $C_{29}H_{28}O_8S$ (536.5): C 64.92, H 5.26; found C 65.05, H 5.31.

*Ethyl (2,3-di-*O*-benzoyl-4,6-*O*-benzylidene-*β-D-*glucopyranosyl)-(1→4)-2,3,6-tri-*O*-benzoyl-1-thio*-β-D-*glucopyranoside (6)*

A solution of **4** (50 mg, 0.09 mmol) and 2,3-di-*O*-benzoyl-4,6-*O*-benzylidene-D-glucopyranosyl trichloroacetimidate **5** (4) (87 mg, 0.14 mmol) in dry CH_2Cl_2 (2 mL), containing 4 Å molecular sieves, was stirred under Ar for 1 h. Then, TMSOTf (2.5 μL, 14 μmol) was added. After 30 min, the

© 2002 NRC Canada

mixture was neutralized with dry pyridine, filtered over cotton, diluted with CH_2Cl_2, and washed with 10% (w/v) aqueous NaCl. The organic layer was dried, filtered, and concentrated. The residue was purified by column chromatography (toluene–EtOAc, 95:5) to obtain **6** (67 mg, 75%). $[\alpha]_D^{20}$ +41 (*c* = 1). R_f = 0.76 (CH_2Cl_2–EtOAc, 9:1). ^{1}H NMR ($CDCl_3$) δ: 8.05–7.85 and 7.49–7.31 (2m, 30H, *Ph*CH, 5*Ph*CO), 5.74 and 5.61 (2t, $J_{1,2}$ = 9.9 Hz, each 1H, H-2,3), 5.44 (dd, $J_{1',2'}$ = 7.7, $J_{2',3'}$ = 9.5 Hz, 1H, H-2′), 5.42 (t, 1H, H-3′), 5.20 (s, 1H, PhC*H*), 4.83 (d, 1H, H-1′), 4.68 (d, 1H, H-1), 4.49 (dd, $J_{5',6a'}$ = 2.1, $J_{6a',6b'}$ = 12.2 Hz, 1H, H-6a), 4.40 (dd, $J_{5',6b'}$ = 4.8 Hz, 1H, H-6b), 2.70-2.56 (m, 2H, SCH_2CH$_3$), 1.16 (t, 3H, SCH$_2$CH_3). ^{13}C NMR ($CDCl_3$) δ: 136.4 (*Ph*CH, quaternary C); 101.7 and 101.1 (PhCH, C-1′); 83.3 (C-1); 67.5 (C-6′); 62.5 (C-6); 24.2 (SCH_2CH$_3$); 14.8 (SCH$_2$CH_3). Anal. calcd. for $C_{56}H_{50}O_{15}S$ (995.0): C 67.59, H 5.06; found C 67.56, H 5.01.

*Allyl (2,3-di-*O*-benzoyl-4,6-*O*-benzylidene-*β*-*D*-glucopyranosyl)-(1→4)-2,3,6-tri-*O*-benzoyl-*β*-*D*-glucopyranoside (8)*

A solution of allyl 2,3,6-tri-*O*-benzoyl-β-D-glucopyranoside **7** (4) (0.48 g, 0.93 mmol) and 2,3-di-*O*-benzoyl-4,6-*O*-benzylidene-D-glucopyranosyl trichloroacetimidate **5** (4) (1.02 g, 1.64 mmol) in dry CH_2Cl_2 (15 mL), containing 4 Å molecular sieves, was stirred under Ar for 1 h. Then, TMSOTf (35 μL, 0.19 mmol) was added. After 45 min, the mixture was neutralized with dry pyridine, filtered over cotton, diluted with CH_2Cl_2, and washed with 10% (w/v) aqueous NaCl. The organic layer was dried, filtered, and concentrated. The residue was purified by column chromatography (toluene–EtOAc, 95:5) to obtain **8** (0.76 g, 83%). $[\alpha]_D^{20}$ +27 (*c* = 1). R_f = 0.37 (toluene–EtOAc, 9:1). ^{1}H NMR ($CDCl_3$) δ: 8.05–7.85 and 7.50–7.25 (2m, 30H, *Ph*CH, 5*Ph*CO), 5.78–5.65 (m, 1H, OCH$_2$C*H*=CH$_2$), 5.72 and 5.60 (2t, $J_{2,3}$ = 9.6, $J_{2',3'}$ = 9.6 Hz, each 1H, H-3,3′), 5.43 and 5.40 (2dd, $J_{1,2}$ = 7.7, $J_{1',2'}$ = 7.8 Hz, each 1H, H-2,2′), 5.21 (s, 1H, PhC*H*), 5.17–5.10 and 5.08–5.03 (2m, each 1H, OCH$_2$CH=CH_2), 4.83 and 4.72 (2d, each 1H, H-1,1′), 4.49 (dd, $J_{5,6a}$ = 2.1, $J_{6a,6b}$ = 12.1 Hz, 1H, H-6a), 4.39 (dd, $J_{5,6b}$ = 4.5 Hz, 1H, H-6b), 4.27–4.20 and 4.07–3.99 (2m, each 1H, OCH_2CH=CH$_2$), 4.11 and 3.63 (2t, each 1H, H-4,4′), 3.76 (ddd, 1H, H-5), 3.61 (dd, $J_{5',6a'}$ = 4.6, $J_{6a',6b'}$ = 10.6 Hz, 1H, H-6a′), 3.31 (ddd, 1H, H-5′), 2.83 (t, $J_{5',6b'}$ = 10.6 Hz, 1H, H-6b′). ^{13}C NMR ($CDCl_3$) δ: 165.4, 165.2, 165.0, 164.9, and 164.7 (5Ph*C*O); 136.4 (P*h*CH, quaternary C); 117.5 (OCH$_2$CH=*C*H$_2$); 101.7, 101.0, and 99.2 (PhCH, C-1,1′); 69.7 (O*C*H$_2$CH=CH$_2$); 67.4 (C-6′); 62.2 (C-6). Anal. calcd. for $C_{57}H_{50}O_{16}$ (991.0): C 69.08, H 5.08; found C 69.16, H 5.05.

*(2,3-Di-*O*-benzoyl-4,6-*O*-benzylidene-*β*-*D*-glucopyranosyl)-(1→4)-2,3,6-tri-*O*-benzoyl-*D*-glucopyranose (9)*

To a solution of **8** (1.5 g, 1.5 mmol) in absolute EtOH (40 mL), toluene (80 mL), and CH_2Cl_2 (8 mL) were added a catalytic amount of diazabicyclo[2.2.2]octane (DABCO) and tris(triphenylphosphine)rhodium(I) chloride (0.4 g). After stirring at reflux for 4 h, the mixture was concentrated. The residue was dissolved in THF (75 mL), and water (10 mL) and NIS (0.6 g) were added. After 20 min, the mixture was concentrated, diluted with CH_2Cl_2, washed with 10% (w/v) aqueous $NaHSO_3$ (2×) and 10% (w/v) aqueous NaCl, and the organic layer was dried, filtered, and concentrated. The crude residue was purified by column chromatography. Impurities were eluted with toluene–EtOAc (95:5), and **9** was obtained as a light brown syrup by elution with toluene–EtOAc (9:1) (0.99 g, 68%). R_f = 0.17$^{\alpha}$/0.08$^{\beta}$ (toluene–EtOAc, 8:2). ^{1}H NMR ($CDCl_3$) δ: 8.08–7.85 and 7.49–7.23 (2m, 30H, *Ph*CH, 5*Ph*CO), 5.63 (t, 1H, H-3′), 5.46 (dd, $J_{1',2'}$ = 7.7, $J_{2',3'}$ = 9.5 Hz, 1H, H-2′), 5.23 (s, 1H, PhC*H*), 4.89 (d, 1H, H-1′), 4.49 (dd, $J_{5,6a}$ = 2.0, $J_{6a,6b}$ = 12.3 Hz, 1H, H-6a), 4.40 (dd, $J_{5,6b}$ = 3.8 Hz, 1H, H-6b), 3.63 (dd, $J_{5',6a'}$ = 4.9, $J_{6a',6b'}$ = 10.6 Hz, 1H, H-6a′), 3.32 (dt, $J_{5',6b'}$ = 10.4 Hz, 1H, H-5′), 2.94 (t, 1H, H-6b′). ^{13}C NMR ($CDCl_3$) δ: 165.8, 165.4, 165.0 (2C), and 164.9 (5Ph*C*O); 136.5 (*Ph*CH, quaternary C); 101.9 and 101.1 (Ph*C*H, C-1′); 95.5 and 90.1 (C-1$^{\alpha}$,1$^{\beta}$); 67.7 (C-6′); 62.0 (C-6). Anal. calcd. for $C_{54}H_{46}O_{16}$ (951.0): C 68.21, H 4.87; found C 68.16, H 5.02.

*(2,3-Di-*O*-benzoyl-4,6-*O*-benzylidene-*β*-*D*-glucopyranosyl)-(1→4)-2,3,6-tri-*O*-benzoyl-α-*D*-glucopyranosyl trichloroacetimidate (10)*

To a solution of **9** (1.0 g, 1.1 mmol) in dry CH_2Cl_2 (14 mL) were added Cl_3CCN (1.2 mL) and DBU (40 μL). After stirring for 16 h, the mixture was concentrated and the residue was purified by column chromatography (toluene–EtOAc, 88:12) to yield **10** (0.99 g, 86%). $[\alpha]_D^{20}$ +83 (*c* = 1). R_f = 0.32 (toluene–EtOAc, 9:1). ^{1}H NMR ($CDCl_3$) δ: 8.55 (s, 1H, N*H*), 8.08–7.85 and 7.47–7.16 (2m, 30H, *Ph*CH, 5*Ph*CO), 6.68 (d, $J_{1,2}$ = 3.7 Hz, 1H, H-1), 6.12 (dd, $J_{2,3}$ = 10.2, $J_{3,4}$ = 8.6 Hz, 1H, H-3), 5.66 (t, $J_{2',3'}$ = $J_{3',4'}$ = 9.6 Hz, 1H, H-3′), 5.49 (dd, 1H, H-2), 5.48 (dd, $J_{1',2'}$ = 7.7 Hz, 1H, H-2′), 5.25 (s, 1H, PhC*H*), 4.95 (d, 1H, H-1′), 4.54 (dd, $J_{5,6a}$ = 2.0, $J_{6a,6b}$ = 12.2 Hz, 1H, H-6a), 4.44 (dd, $J_{5,6b}$ = 3.8 Hz, 1H, H-6b), 4.30 (ddd, $J_{4,5}$ = 10.0 Hz, 1H, H-5), 4.22 (dd, 1H, H-4), 3.69 (t, $J_{4',5'}$ = 9.5 Hz, 1H, H-4′), 3.64 (dd, $J_{5',6a'}$ = 4.8, $J_{6a',6b'}$ = 10.5 Hz, 1H, H-6a′), 3.34 (dt, $J_{5',6b'}$ = 10.3 Hz, 1H, H-5′), 2.99 (t, 1H, H-6b′). ^{13}C NMR ($CDCl_3$) δ: 165.4, 165.3 (2C), and 164.8 (2C) (5Ph*C*O); 160.3 (O*C*(NH)CCl$_3$); 136.4 (*Ph*CH, quaternary C); 101.8 and 101.1 (Ph*C*H, C-1′); 92.8 (C-1), 67.6 (C-6′); 61.6 (C-6).

*3-Azidopropyl (2,3-di-*O*-benzoyl-4,6-*O*-benzylidene-*β*-*D*-glucopyranosyl)-(1→4)-(2,3,6-tri-*O*-benzoyl-*β*-*D*-glucopyranosyl)-(1→3)-(2-*O*-benzoyl-4,6-*O*-benzylidene-*β*-*D*-glucopyranosyl)-(1→4)-(2,3,6-tri-*O*-benzoyl-*β*-*D*-glucopyranosyl)-(1→3)-(2-*O*-benzoyl-4,6-*O*-benzylidene-*β*-*D*-glucopyranosyl)-(1→4)-2,3,6-tri-*O*-benzoyl-*β*-*D*-glucopyranoside (12)*

A solution of **10** (70 mg, 63 μmol) and **11** (4) (65 mg, 35 μmol) in dry CH_2Cl_2 (1 mL), containing 4 Å molecular sieves, was stirred under Ar for 1 h. Then, TMSOTf (1.1 μL, 6 μmol) was added. After 30 min, the mixture was neutralized with dry pyridine, filtered over cotton, diluted with CH_2Cl_2, and washed with 10% (w/v) aqueous NaCl. The organic layer was dried, filtered, and concentrated. The residue was purified by column chromatography (toluene–EtOAc, 95:5) to obtain **12** (59 mg, 63%). $[\alpha]_D^{20}$ +59 (*c* = 1). R_f = 0.46 (toluene–EtOAc, 9:1). ^{1}H NMR ($CDCl_3$) δ: 5.56 (t, 1H, H-3^a), 5.45 (t, 1H, H-3^f), 5.38 (t, 1H, H-3^e), 5.29 (t, 1H, H-3^c), 5.26 (2H, H-2^a,2^f), 5.16 (1H, H-2^e), 5.15 (1H, H-2^b), 5.14 (1H, H-2^c), 5.12 (2H) and 5.09 (2s, 3PhC*H*), 5.06

© 2002 NRC Canada

(1H, H-2^d), 4.67 (d, $J_{1,2}$ = 7.8 Hz, 1H, H-1^e), 4.64 (d, $J_{1,2}$ = 7.8 Hz, 1H, H-1^c), 4.59 (d, $J_{1,2}$ = 7.8 Hz, 1H, H-1^f), 4.54 (d, $J_{1,2}$ = 7.8 Hz, 1H, H-1^a), 4.50 (d, $J_{1,2}$ = 7.8 Hz, 1H, H-1^b), 4.34 (d, $J_{1,2}$ = 7.8 Hz, 1H, H-1^d), 3.97 (t, 1H, H-4^e), 3.90 (t, 2H, H-4^a,3^b), 3.85 (t, 1H, H-3^d), 3.84 (t, 1H, H-4^c), 3.77 and 3.45 (OCH_2CH$_2$CH$_2$N$_3$), 3.55 (H-5^a), 3.25 (H-5^e), 3.21 (H-5^c), 3.12 (OCH$_2$CH$_2$CH_2N$_3$), 3.05 (H-5^b), 2.93 (H-5^d), 2.66 (H-6^f), 2.65 (H-6^b), 2.53 (H-6^d), 1.72-1.57 (m, 2H, OCH$_2$CH_2CH$_2$N$_3$). ^{13}C NMR (CDCl$_3$) δ: 136.4 (*Ph*CH, quaternary C); 101.4, 101.3 (2C), 101.1, 100.9 (2C), 100.6, 99.8, and 99.7 (3Ph*C*H, C-1^a,1^b,1^c,1^d,1^e,1^f); 66.2 (O*C*H$_2$CH$_2$CH$_2$N$_3$); 47.6 (OCH$_2$CH$_2$*C*H$_2$N$_3$); 28.7 (OCH$_2$*C*H$_2$CH$_2$N$_3$). MALDI-TOF-MS *m*/*z*: 2713 [M + Na]$^+$.

3-Azidopropyl (2,3-di-O-benzoyl-β-D-glucopyranosyl)-(1→4)-(2,3,6-tri-O-benzoyl-β-D-glucopyranosyl)-(1→3)-(2-O-benzoyl-β-D-glucopyranosyl)-(1→4)-(2,3,6-tri-O-benzoyl-β-D-glucopyranosyl)-(1→3)-(2-O-benzoyl-β-D-glucopyranosyl)-(1→4)-2,3,6-tri-O-benzoyl-β-D-glucopyranoside (13)

To a solution of **12** (84 mg, 31 μmol) in CH_2Cl_2 (0.85 mL) were added CF_3COOH (75 μL) and H_2O (75 μL). The mixture was stirred for 4 h, diluted with CH_2Cl_2, washed with 10% (w/v) aqueous $NaHCO_3$ until neutral pH and 10% (w/v) aqueous NaCl, and the organic layer was dried, filtered, and concentrated. The residue was purified by column chromatography (toluene–EtOAc, 6:4→4:6) to obtain **13** (55 mg, 75%). $[\alpha]_D^{20}$ +45 (*c* = 1). R_f = 0.21 (toluene–EtOAc, 1:1). ^{1}H NMR (CDCl$_3$) δ: 5.57 (t, 1H, H-3^e), 5.50 (t, 1H, H-3^a), 5.39 (t, 1H, H-3^c), 5.33 (dd, 1H, H-2^f), 5.31 (dd, 1H, H-2^a), 5.30 (dd, 1H, H-2^e), 5.25 (t, 1H, H-3^f), 5.23 (dd, 1H, H-2^c), 5.03 (br t, 2H, H-2^b,2^d), 4.76 (d, $J_{1,2}$ = 7.7 Hz, 1H, H-1^f), 4.63 (2H, H-1^e,6^e), 4.53 (d, 1H, H-1^a), 4.52 (d, 1H, H-1^c), 4.43 (d, $J_{1,2}$ = 8.0 Hz, 1H, H-1^b), 4.42 (d, $J_{1,2}$ = 8.0 Hz, 1H, H-1^d), 4.31 (3H, H-6^a,6a^c,6a^e), 4.18 (dd, 1H, H-6b^a), 4.14 (dd, 1H, H-6b^c), 3.99 (t, 1H, H-4^e), 3.98 (t, 1H, H-4^a), 3.83 (t, 1H, H-4^c), 3.82 (H-5^e), 3.78 and 3.45 (OCH_2CH$_2$CH$_2$N$_3$), 3.73 (H-4^f), 3.58 (t, 1H, H-3^d), 3.56 (H-5^c), 3.54 (H-5^a), 3.51 (t, 1H, H-3^b), 3.36 (H-4^d), 3.32 (H-4^b), 3.23 (H-5^f), 3.15–3.09 (m, 2H, OCH$_2$CH$_2$CH_2N$_3$), 3.00 (H-5^d), 2.96 (H-5^b), 1.72–1.55 (m, 2H, OCH$_2$CH_2CH$_2$N$_3$). ^{13}C NMR (CDCl$_3$) δ: 101.1 (2C), 100.6 (3C), and 100.5 (C-1^a,1^b,1^c,1^d,1^e,1^f); 66.2 (O*C*H$_2$CH$_2$CH$_2$N$_3$); 62.2, 62.1, 62.0 (2C), 61.8, and 61.3 (C-6^a,6^b,6^c,6^d,6^e,6^f); 47.6 (OCH$_2$CH$_2$*C*H$_2$N$_3$); 28.7 (OCH$_2$*C*H$_2$ CH$_2$N$_3$). MALDI-TOF-MS *m*/*z*: 2440 [M + Na]$^+$.

3-Azidopropyl (2,3-di-O-benzoyl-β-D-glucopyranosyluronic acid)-(1→4)-(2,3,6-tri-O-benzoyl-β-D-glucopyranosyl)-(1→3)-(2-O-benzoyl-β-D-glucopyranosyluronic acid)-(1→4)-(2,3,6-tri-O-benzoyl-β-D-glucopyranosyl)-(1→3)-(2-O-benzoyl-β-D-glucopyranosyluronic acid)-(1→4)-2,3,6-tri-O-benzoyl-β-D-glucopyranoside (14)

To a solution of **13** (50 mg, 21 μmol) in CH_2Cl_2 (0.22 mL) were added TEMPO (catalytic amount), and 40 μL of a solution of KBr (2.4 mg) and Bu_4NBr (3.2 mg) in saturated aqueous $NaHCO_3$ (0.4 mL). The mixture was stirred vigorously at 0°C, when 122 μL (total) of a solution of saturated aqueous NaCl (0.44 mL), saturated aqueous $NaHCO_3$ (0.22 mL), and aqueous NaOCl (13% Cl active, 0.56 mL) was added dropwise. After 45 min, the mixture was acidified with 4 M HCl (pH 4), diluted with CH_2Cl_2, and the organic layer was washed with 10% (w/v) aqueous NaCl, dried, filtered, and concentrated. The residue was purified by column chromatography. Impurities were eluted with CH_2Cl_2–acetone (8:2), and **14** (35 mg, 70%) was eluted with CH_2Cl_2–acetone–HOAc, (8:2:0.5). R_f = 0.05 (CH_2Cl_2–acetone–HOAc, 8:2:1). MALDI-TOF-MS *m*/*z*: 2490 [M + Na]$^+$, 2512 [M – H + 2Na]$^+$, 2534 [M – 2H + 3Na]$^+$, 2556 [M – 3H + 4Na]$^+$.

A small amount was methylated with diazomethane in methanol for analysis. ^{1}H NMR (CDCl$_3$) δ: 5.55 (t, 1H, H-3^e), 5.54 (t, 1H, H-3^a), 5.39 (t, 1H, H-3^c), 5.36 (2H, H-2^f,3^f), 5.26 (dd, $J_{1,2}$ = 7.8, $J_{2,3}$ = 9.6 Hz, 1H, H-2^e), 5.20 (dd, $J_{1,2}$ = 7.8, $J_{2,3}$ = 9.5 Hz, 1H, H-2^a), 5.15 (dd, $J_{2,3}$ = 9.7 Hz, 1H, H-2^c), 5.08 (2t, each 1H, H-2^b,2^d), 4.83 (d, $J_{1,2}$ = 7.6 Hz, 1H, H-1^f), 4.65 (d, 1H, H-1^e), 4.61 (dd, 1H, H-6^e), 4.53 (d, $J_{1,2}$ = 8.0 Hz, 2H, H-1^b,1^c), 4.52 (d, 1H, H-1^a), 4.48 (d, $J_{1,2}$ = 7.9 Hz, 1H, H-1^d), 4.38 (dd, 1H, H-6a^a), 4.33 (dd, 1H, H-6a^c), 4.28 (dd, 1H, H-6b^e), 4.17 (dd, 1H, H-6b^a), 4.13 (dd, 1H, H-6b^c), 4.10 (t, 1H, H-4^e), 4.04 (t, 1H, H-4^a), 3.91 (H-4^f), 3.90 (t, 1H, H-4^c), 3.81 (H-5^e), 3.78 and 3.44 (OCH_2 CH$_2$CH$_2$N$_3$), 3.76 (H-4^d), 3.74 (H-4^b), 3.69 (H-5^f), 3.63 (t, 1H, H-3^d), 3.57 (t, 1H, H-3^b), 3.56 (H-5^c), 3.55 (H-5^a), 3.51 (d, $J_{4,5}$ = 9.6 Hz, 1H, H-5^d), 3.49 (d, $J_{4,5}$ = 9.6 Hz, 1H, H-5^b), 3.39, 3.30, and 3.23 (3s, each 3H, COOCH_3), 3.09 (OCH$_2$CH$_2$CH_2N$_3$), 1.70–1.59 (m, 2H, OCH$_2$CH_2CH$_2$N$_3$).

3-Aminopropyl (β-D-glucopyranosyluronic acid)-(1→4)-(β-D-glucopyranosyl)-(1→3)-(β-D-glucopyranosyluronic acid)-(1→4)-(β-D-glucopyranosyl)-(1→3)-(β-D-glucopyranosyluronic acid)-(1→4)-β-D-glucopyranoside (1)

To a solution of **14** (20 mg, 8 μmol) in MeOH (3 mL) was added NaOMe until pH 10, and after 5 h, water (1 mL) was added. After stirring for 16 h, TLC (EtOAc–MeOH–H_2O, 12:5:3) showed the formation of a new spot (R_f = 0.1), and the mixture was neutralized with Dowex H$^+$, filtered, and concentrated. A solution of the residue in water was washed with CH_2Cl_2 (3×), and the aqueous layer was concentrated. Then, a solution of the residue in 0.1 M NaOH (0.4 mL) was added dropwise to a suspension of 10% Pd/C (0.8 mg) and $NaBH_4$ (3.5 mg) in doubly distilled water (0.3 mL). After 2 h, when TLC (EtOAc–MeOH–H_2O, 12:5:3) showed the formation of a ninhydrin-positive spot on the baseline, the mixture was acidified with Dowex H$^+$ (pH 4), then loaded on a short column of Dowex 50 W × 2 (H$^+$, 200–400 mesh). After elution of contaminants with water, elution with 1% NH_4OH afforded **1** after concentration and lyophilization from water (2×) (5.4 mg, 61%). $[\alpha]_D^{20}$ = –17 (*c* = 0.4, H_2O). MALDI-TOF-MS *m*/*z*: 1091 [M + H]$^+$, 1112 [M + Na]$^+$, 1134 [M – H + 2Na]$^+$, 1156 [M – 2H + 3Na]$^+$. For ^{1}H NMR data, see Table 1.

Acknowledgments

This work was supported by the European Union program VACNET (grant ERB BIO 4CT960158).

References

1. R.W. Ellis and D.M. Granoff. Development and clinical uses of *Haemophilus* b conjugate vaccines. M. Dekker, New York. 1994.

© 2002 NRC Canada

2. P. Richmond, R. Borrow, E. Miller, S. Clark, F. Sadler, A. Fox, N. Begg, R. Morris, and K. Cartwright. J. Infect. Dis. **179**, 1569 (1999).
3. M.B. Rennels, K.M. Edwards, H.L. Keyserling, K.S. Reisinger, D.A. Hogerman, D.V. Madore, I. Chang, P.R. Paradiso, F.J. Malinoski, and A. Kimura. Pediatrics, **101**, 604 (1998).
4. D.J. Lefeber, J.P. Kamerling, and J.F.G. Vliegenthart. Chem. Eur. J. **7**, 4411 (2001).
5. B. Benaissa-Trouw, D.J. Lefeber, J.P. Kamerling, J.F.G. Vliegenthart, K. Kraaijeveld, and H. Snippe. Infect. Immun. **69**, 4968 (2001).
6. E. Alonso de Velasco, A.F.M. Verheul, A.M.P. van Steijn, H.A.T. Dekker, R.G. Feldman, I.M. Fernández, J.P. Kamerling, J.F.G. Vliegenthart, J. Verhoef, and H. Snippe. Infect. Immun. **62**, 799 (1994).
7. P.J. Garegg, I. Kvarnström, A. Niklasson, G. Niklasson, and S.C.T. Svensson. J. Carbohydr. Chem. **12**, 933 (1993).
8. A.E.J. de Nooy, A.C. Bezemer, and H. van Bekkum. Synthesis, 1153 (1996).

© 2002 NRC Canada

Kinetics and mechanism of hydrolysis of 3-diazobenzofuran-2-one and its hydrolysis product (3-hydroxybenzofuran-2-one)

Y. Chiang, A.J. Kresge, and Q. Meng

Abstract: Rates of acid-catalyzed hydrolysis of 3-diazobenzofuran-2-one, measured in concentrated aqueous perchloric acid and hydrochloric acid solutions, were found to correlate well with the Cox–Yates X_o excess acidity function, giving $k_{H^+} = 1.66 \times 10^{-4}$ M^{-1} s^{-1}, $m^{\ddagger} = 0.86$ and $k_{H^+}/k_{D^+} = 2.04$. The normal direction ($k_H/k_D > 1$) of this isotope effect indicates that hydrolysis occurs by rate-determining protonation of the substrate on its diazo-carbon atom. It was found previously that the next higher homolog of the present substrate, 4-diazoisochroman-3-one, also undergoes hydrolysis by this reaction mechanism but with a rate constant 15 times greater than that for the present substrate; this difference in reactivity can be understood in terms of the various resonance forms that contribute to the structures of these substrates. The product of the present hydrolysis reaction is 3-hydroxybenzofuran-2-one, which itself quickly undergoes subsequent acid-catalyzed hydrolysis to 2-hydroxymandelic acid. The acidity dependence of this subsequent hydrolysis is much shallower than that of the diazo compound precursor, and rates of reaction correlate as well with $[H^+]$ as with X_o. This is due in part to incursion of a nonproductive protonation on the hydroxy group of 3-hydroxybenzofuran-2-one that impedes hydrolysis and produces saturation of acid catalysis. Rates of hydrolysis of the hydroxy compound were also measured in dilute $HClO_4$ and NaOH solutions as well as in CH_3CO_2H, $H_2PO_4^-$, $(CH_2OH)_3CNH_3^+$, and NH_4^+ buffers, and the rate profile constructed from these data showed the presence of uncatalyzed and hydroxide ion-catalyzed reactions. This hydroxide-ion catalysis became saturated at [NaOH] ≅ 0.05 M, implying occurrence of yet another nonproductive substrate ionization.

Key words: diazo compound hydrolysis, lactone hydrolysis, Cox–Yates excess acidity, acid catalysis, alcohol protonation.

Résumé : On a observé que les vitesses de réactions d'hydrolyse acidocatalysées de la 3-diazobenzofuran-2-one en solutions aqueuses des acides perchlorique et chlorhydrique donnent une bonne corrélation avec la fonction d'acidité en excès de Cox–Yates, X_o, qui conduit à $k_{H^+} = 1{,}66 \times 10^{-4}$ M^{-1} s^{-1}, $m^{\ddagger} = 0{,}86$ et $k_{H^+}/k_{D^+} = 2{,}04$. La direction normale ($k_H/k_D > 1$) de cet effet isotopique indique que l'hydrolyse se produit par une étape de protonation du substrat cinétiquement déterminante sur l'atome de carbone du diazo. On avait observé antérieurement que l'homologue directement supérieur au substrat étudié, la 4-diazoisochroman-4-one, subit aussi une hydrolyse par ce mécanisme réactionnel, mais que la constante de vitesse de sa réaction est 15 fois supérieure à celle observée avec le substrat étudié ici; cette différence de réactivité peut s'expliquer en termes de diverses formes de résonance qui contribuent aux structures de ces substrats. Le produit d'hydrolyse du produit considéré ici est la 3-hydroxybenzofuran-2-one qui subit rapidement une hydrolyse acidocatalysée subséquente conduisant à l'acide 2-hydroxymandélique. La dépendance de cette hydrolyse subséquente sur l'acidité est beaucoup plus faible que celle sur le diazo précurseur et les constantes de vitesse donnent aussi une bonne corrélation avec $[H^+]$ ainsi qu'avec X_o. Ce résultat est dû en partie à l'incursion d'une protonation non productive sur le groupe hydroxyle de la 3-hydroxybenzofuran-3-one qui inhibe l'hydrolyse et qui produit une saturation de la catalyse acide. Les constantes de vitesse du composé hydroxylé ont aussi été mesurées dans des solutions diluées de $HClO_4$ et de NaOH ainsi que dans des tampons de CH_3CO_2H, $H_2PO_4^-$, $(CH_2OH)_3CNH_3^+$ et NH_4^+ et les profils de vitesses construits à partir de ces données mettent en évidence l'existence de réactions non catalysées et d'autres catalysées par l'ion hydroxyde. Cette catalyse par l'ion hydroxyde devient saturée à [NaOH] ≅ 0,05 M, ce qui implique l'existence d'une autre ionisation non productive du substrat.

Mots clés : hydrolyse de composés diazo, hydrolyse de lactones, acidité en excès de Cox–Yates, catalyse acide, protonation d'alcool.

[Traduit par la Rédaction]

Received 30 July 2001. Published on the NRC Research Press Web site at http://canjchem.nrc.ca on 17 January 2002.

Y. Chiang, A.J. Kresge,[1] and Q. Meng. Department of Chemistry, University of Toronto, Toronto, ON M5S 3H6, Canada.

[1]Corresponding author (telephone and fax: (416) 978-7259; e-mail: akresge@chem.utoronto.ca).

 DOI: 10.1139/V01-191 © 2002 NRC Canada

Fig. 1. Comparison of rates of hydrolysis of 3-diazobenzofuran-2-one in concentrated perchloric (O) and hydrochloric (Δ) acids with rates of hydrolysis of 3-hydroxybenzofuranone in concentrated hydrochloric acid (◇).

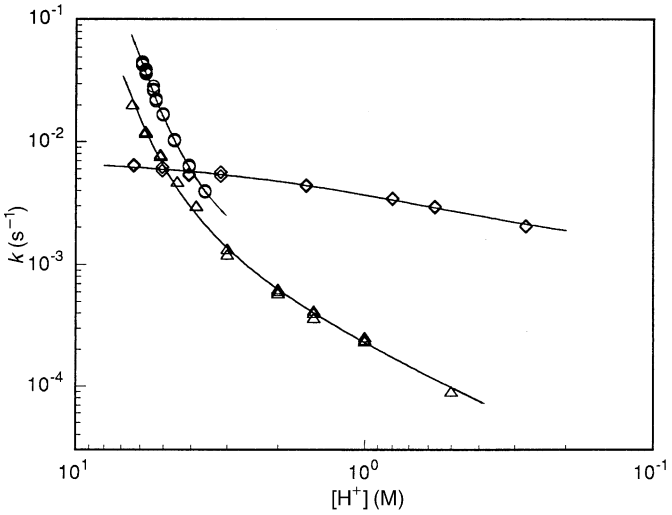

Introduction

It has been reported that irradiation of 3-diazobenzofuran-2-one (**1**) in low-temperature matrices produces the ketene **2** and the oxocumulene **3** (eq. [1]) (1). To learn whether these interesting molecules are also formed upon irradiation of 3-diazobenzofuran-2-one in aqueous solution at ambient temperature, and, if so, how they react with water, we have undertaken a study of the photolysis of this substance in aqueous media.

[1] 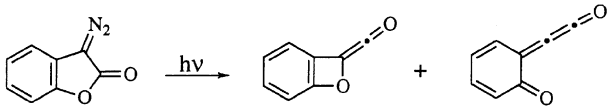

1 **2** **3**

Diazo compounds such as **1** also undergo acid-catalyzed hydrolysis in aqueous solution, and such hydrolysis could interfere with our photolysis study. To determine whether this would be so, we also examined the hydrolysis reaction. The results proved to be interesting in their own right, and we therefore report them separately here.

The acid-catalyzed hydrolysis of diazo compounds usually produces the corresponding hydroxy derivative, which in the present system would be the hydroxy lactone, 3-hydroxybenzofuran-2-one (**4**) (eq. [2]). We have found that this is indeed the case, but that this product is then quickly hydrolyzed itself, giving 2-hydroxymandelic acid (**5**) (eq. [3]) as the ultimate reaction product. We have measured rates of this second hydrolysis reaction as well.

[2] 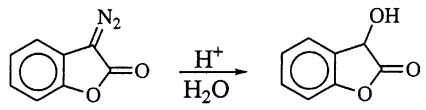

1 **4**

[3] 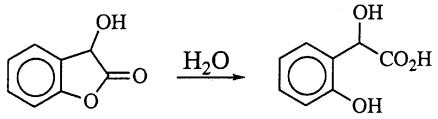

4 **5**

Experimental section

Materials

2-Hydroxymandelic acid (2) (**5**) was made by sodium borohydride reduction of 2-hydroxyphenylglyoxylic acid, itself prepared by selenium dioxide oxidation of 2-hydroxyacetophenone (2*a*). As reported (2), 2-hydroxymandelic acid could not be obtained completely free of solvent, and it was consequently used as an ethyl acetate solvate. 3-Hydroxybenzofuran-2-one (2*a*) (**4**) was synthesized by treating 2-hydroxymandelic acid with dicyclohexylcarbodiimide. 3-Diazobenzofuran-2-one (3) (**1**) was prepared by converting 2-hydroxyphenylglyoxylic acid into benzofuran-2,3-dione, using refluxing acetic anhydride to effect ring closure, and then making the tosyl hydrazone and cleaving that with sodium hydroxide (3). The spectral and physical properties of these substances agreed with literature values.

All other materials were best available commercial grades.

Kinetics

Rates of reaction were measured spectrophotometrically, using a Cary 220 spectrometer whose cell compartment was thermostatted at 25.0 ± 0.05°C. Rates of hydrolysis of 3-diazobenzofuran-2-one were monitored by following the decrease of its absorbance at λ = 310 nm, where neither 3-hydroxybenzofuran-2-one nor 2-hydroxymandelic acid absorb to any significant extent, and rates of hydrolysis of 3-hydroxybenzofuran-2-one were monitored by following the increase of 2-hydroxymandelic acid absorbance at λ = 278 nm. The data for both reactions conformed to the first-order rate law well, and observed first-order rate constants were determined by least-squares fitting of a single exponential function.

Product analysis

Product compositions were determined by HPLC using a Varian Vista 5500 instrument with a NovaPak C18 reverse-phase column and methanol–water (60/40 = v/v) as the eluent. Products were identified by comparing retention times and UV spectra with those of authentic samples.

Results and discussion

Product analysis

Rate constants for the hydrolysis of 3-diazobenzofuran-2-one and 3-hydroxybenzofuran-2-one, determined in concentrated acid solutions as described below, are displayed in Fig. 1. It may be seen that both reactions are acid-catalyzed but that the acidity dependences of the two processes are quite different. Because the rates cross one another and have the same value in the vicinity of [H^+] = 4 M, this medium was chosen for product analysis. The reactions are also quite fast at this concentration, with half-lives of the order of 2 min. Samples of reaction mixtures were, therefore, taken

© 2002 NRC Canada

Fig. 2. Rates of hydrolysis of 3-diazobenzofuran-2-one in concentrated perchloric acid (O) and hydrochloric acid (Δ) solutions plotted according to eq. [4].

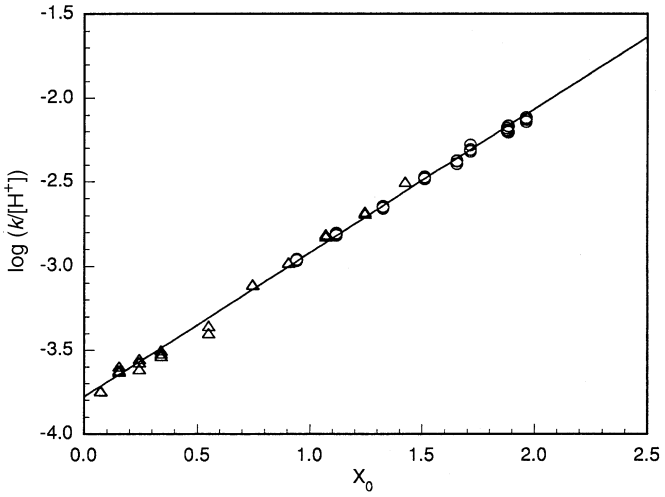

at short time intervals, were quenched into sufficient sodium acetate solution to give a buffer of pH ≅ 5, and were then immediately analyzed by HPLC.

The reaction mixture formed upon a 1.0 min exposure of 3-diazobenzofuran-2-one to 4 M perchloric acid consisted of, in addition to unreacted substrate, both 3-hydroxybenzofuran-2-one and 2-hydroxymandelic acid in a roughly 2:1 ratio. Another sample taken after 2.0 min exposure showed the same two products but now in approximately comparable amounts. Successive samples taken at later times gave progressively smaller amounts of 3-hydroxybenzofuran-2-one at the expense of increasing amounts of 2-hydroxymandelic acid, until after 15 min only the hydroxymandelic acid was left. This is the behavior expected of two successive reactions and it confirms that 3-hydroxybenzofuran-2-one is first formed by the hydrolysis of 3-diazobenzofuran-2-one and that it then quickly hydrolyzes further to 2-hydroxymandelic acid.

Product analyses were also conducted for the hydrolysis of 3-hydroxybenzofuran-2-one itself. This was done in 0.1 M perchloric acid solution, in an acetic acid buffer of $[H^+] = 3 \times 10^{-5}$ M, in a tris-(hydroxymethyl)methylammonium ion buffer of $[H^+] = 8 \times 10^{-9}$ M, in an ammonium ion buffer of $[H^+] = 5 \times 10^{-10}$ M, and in 0.01 M sodium hydroxide solution. 2-Hydroxymandelic acid was the only product found in the perchloric acid and sodium hydroxide solutions and in the acetic acid buffer as well. 2-Hydroxymandelic acid was also the principle product formed in the tris-(hydroxymethyl)methylammonium ion and the ammonium ion buffers, but a minor amount of a second, unidentified product was also formed in each of these buffers. These minor products could be the corresponding 2-hydroxymandelic acid amides formed by aminolysis of the lactone starting material by the amine buffer components.

3-Diazobenzofuran-2-one

Rates of hydrolysis of 3-diazobenzofuran-2-one were measured in perchloric acid solutions over the concentration range $[HClO_4] = 3.6–5.8$ M and in hydrochloric acid solutions over the range [HCl] = 0.5–6.4 M; the data obtained are summarized in Table S1.[2] Some rate measurements were also made in D_2O solutions of hydrochloric acid-*d* over the range [DCl] = 0.5–6.2 M, and these data are listed in Table S1[2] as well.

The observed first-order rate constants determined in these concentrated acid solutions increased with increasing solution acidity more steeply than in direct proportion to acid concentration. This is commonly the case for reaction rates measured in concentrated acids, and the data in such situations are generally analyzed using an acidity function rather than acid concentration as a measure of acid strength. The X_o scale applied as shown in eq. [4] appears to be the best function available for this purpose (4),

$$[4] \qquad \log (k_{obs}/[H^+]) = \log (k_{H^+}) + m^{\ddagger}X_o$$

and the present data were therefore analyzed using this expression with X_0 values for HCl and $HClO_4$ solutions taken from the literature (5). Figure 2 shows that the data conformed to this relationship well, and that a single correlation sufficed to represent measurements made in the two acids. Least-squares analysis gave the hydrogen ion catalytic coefficient $k_{H^+} = (1.66 \pm 0.03) \times 10^{-4}$ M^{-1} s^{-1} and the slope parameter $m^{\ddagger} = 0.857 \pm 0.007$.

The X_o scale has not been determined for DCl solutions in D_2O, but several other acidity functions have been shown to have the same value in D_2O as in H_2O when the comparison is made at the same molar acid concentration (6). It seems likely that this would be so for the X_o scale as well, and the rate constants determined here for hydrolysis of 3-diazobenzofuran-2-one in DCl were therefore correlated using X_o values obtained on this basis. These data also conformed to the expression of eq. [4] well, and least-squares analysis gave $k_{D^+} = (8.15 \pm 0.12) \times 10^{-5}$ M^{-1} s^{-1} and $m^{\ddagger} = 0.837 \pm 0.008$. Combination of the results obtained in H_2O and D_2O provides the isotope effect $k_{H^+}/k_{D^+} = 2.04 \pm 0.05$.

The normal direction of this isotope effect ($k_H/k_D > 1$) indicates that proton transfer is rate-determining in this reaction (7) and that the process occurs by the standard mechanism for diazo compound hydrolysis in which rate-determining protonation of the diazo-carbon atom is followed by rapid displacement of nitrogen by a molecule of water (eq. [5]) (8). Another mechanism that is sometimes found for diazo compound hydrolysis consists of rapid and reversible carbon protonation followed by rate-determining loss of nitrogen, but such a scheme would give an inverse isotope effect, $k_{H^+}/k_{D^+} < 1$ (7), contrary to the present result.

[5] 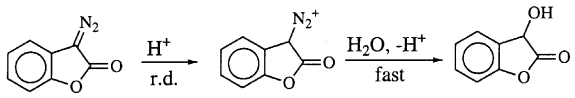

The next higher homolog of the presently examined substrate, 4-diazoisochroman-3-one (**6**), also undergoes

[2] Tables of rate data (Tables S1–S5) have been deposited and may be purchased from the Depository of Unpublished Data, Document Delivery, CISTI, National Research Council Canada, Ottawa, ON K1A OS2, Canada (http://www.nrc.ca/cisti/irm/unpub_e.shtml for information on ordering electronically).

© 2002 NRC Canada

Fig. 3. Rates of hydrolysis of 3-hydroxybenzofuran-2-one in concentrated perchloric acid solutions.

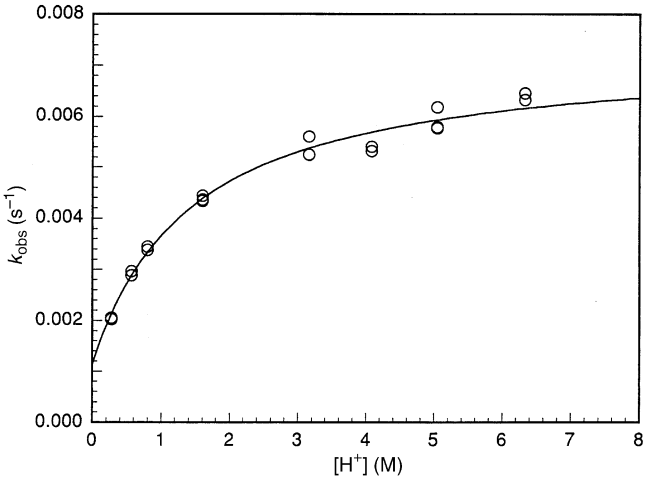

Fig. 4. Rate profile for the hydrolysis of 3-hydroxybenzofuran-2-one in aqueous solution at 25°C.

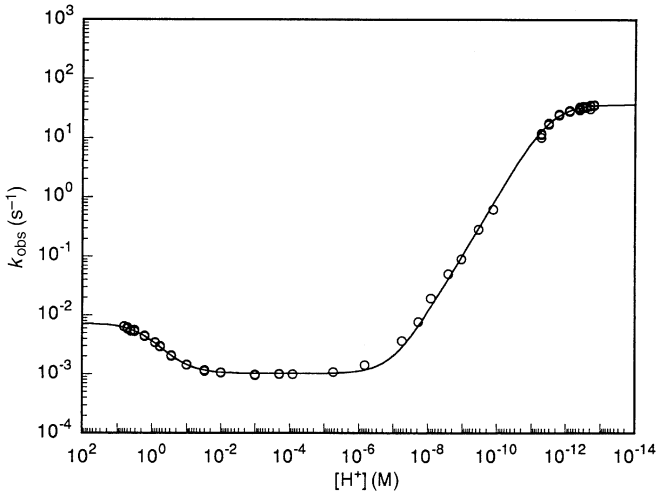

acid-catalyzed hydrolysis by a rate-determining proton transfer mechanism (9); its hydrogen-ion catalytic coefficient, however, is 15 times greater than that for the presently examined substrate. This difference in reactivity can be understood in terms of the various resonance forms that contribute to the structure of these diazo lactones. One of the principle resonance forms of the diazo group puts negative charge on the adjacent carbon atom, as in **7**, and, since this is the site to which the positively charged proton is transferred, the rate of reaction will increase with increasing contribution of this form. This negative charge can also be shifted onto the oxygen atom of the lactone carbonyl group, as in **8**, and, since this removes negative charge from the reactive position, the rate of reaction will decrease with increasing contribution of this form. The lactone carbonyl group, however, is also conjugated with the lactone ether oxygen atom, giving rise to resonance form **9**, which opposes conjugation of the carbonyl with the diazo group, thus raising the contribution of form **7** and increasing the rate of reaction. This opposing conjugation will be stronger in the case of 4-diazoisochroman-3-one than in the case of 3-diazobenzofuran-2-one, because the latter is a phenolic lactone whose ether oxygen atom is also conjugated with its benzene ring. In the isochromanone system, therefore, as compared to the benzofuranone system, the contribution of form **9** will be greater, that of form **8** less, and that of form **7** greater, leading to a greater rate of reaction.

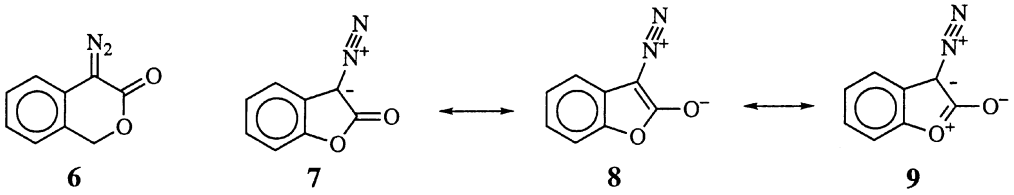

6 **7** **8** **9**

This argument is supported by the fact that *N*,*N*-dimethylphenyldiazoacetamide (**10**) is considerably more reactive toward acid-catalyzed hydrolysis than is the corresponding ester, methylphenyldiazoacetate (**11**) (10). This is in keeping with the greater electron-donating ability of NMe_2 over OMe and the consequent greater contribution to the structure of the amide made by the resonance form corresponding to **9**.

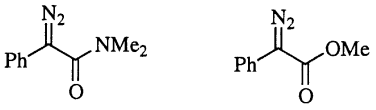

10 **11**

3-Hydroxybenzofuran-2-one (concentrated acids)

Rates of hydrolysis of 3-hydroxybenzofuran-2-one were measured in concentrated perchloric acid solutions over the concentration range $[HClO_4]$ = 0.28–6.3 M. The data obtained are summarized in Table S2.[2]

Figure 1 shows that observed first-order rate constants for this hydrolysis reaction in these concentrated acid solutions increase with acidity much less steeply than do those for the hydrolysis of 3-diazobenzofuran-2-one, and Fig. 3, where the data are plotted on a nonlogarithmic scale, reveals that this is because acid catalysis of the hydroxy substrate becomes saturated at the high concentration end of the range investigated. This saturation of acid catalysis suggests that a nonproductive protonation of 3-hydroxybenzofuran-2-one is taking place, in addition to the productive protonation that

© 2002 NRC Canada

results in lactone hydrolysis; the molecule does, of course, have such a nonproductive protonation site in its hydroxyl group, as shown by the reaction scheme of eq. [6].

[6] 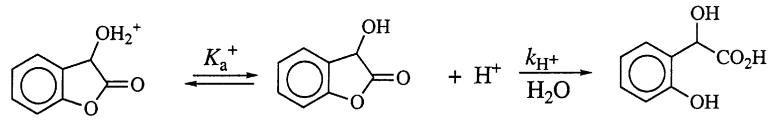

The presence of this nonproductive protonation requires modification of the simple X_o correlation function of eq. [4]; a term must be added to take this additional reaction into account. A further modification of eq. [4] is required, moreover, by the occurrence of an uncatalyzed lactone hydrolysis reaction (eq. [7]) in addition to the acid-catalyzed process. The presence of such an uncatalyzed reaction is evidenced by the significant rate intercept at zero acid concentration shown by Fig. 3 and, perhaps more convincingly, by the long central horizontal plateau shown by the rate profile for this reaction (Fig. 4), constructed as detailed below. In addition, it seems likely that the acid-catalyzed reaction occurs by a simple A2 mechanism in which water is an active reactant (11). It has been shown in simpler systems that the reaction order in water activity for such a process is two (11) and a term taking this into account should also be added to eq. [4].

The final correlating function incorporating all of these

[7] 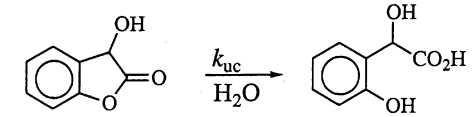

additional features is shown as eq. [8], in which the rate and equilibrium constants are defined by eqs. [6] and [7],

$$[8] \quad \log \{(k_{obs} - k_{uc})/[H^+]\} = \log k_{H^+} + m^{\ddagger}X_o + \log \{K_a^+/(K_a^+ + [H^+]10^{mX_o}\} + 2\log a_{H_2O}$$

a_{H_2O} is the activity of water, supplied here on the mol fraction scale, and $m^{\ddagger}$ and m are the X_o slope parameters for the rate and equilibrium processes, respectively. This expression contains five dependent parameters to be determined by the fit of experimental data (k_{H^+}, k_{uc}, K_a^+, $m^{\ddagger}$, and m), which, unfortunately, proved to be too many: least-squares analysis failed to produce a sensible result. The number of parameters could be reduced to four, however, by supplying a value of k_{uc} (= 0.001 s^{-1}) based on the intercept at zero acid concentration of Fig. 3 and the central plateau of Fig. 4, and this modification of eq. [8] did produce a sensible result. Least-squares analysis gave k_{H^+} = (4.49 ± 0.17) × 10^{-3} M^{-1} s^{-1}, K_a^+ = 1.48 ± 0.17 M, pK_a^+ = –0.17 ± 0.05, $m^{\ddagger}$ = 0.68 ± 0.11, and m = 0.04 ± 0.12.

Very shallow acidity function dependences, similar to the m value obtained here, have been found for the equilibrium protonation of simple alcohols, whereas somewhat steeper dependences, consistent with the present value of $m^{\ddagger}$, occur in the hydrolysis of simple esters (12). The result pK_a^+ = –0.17, on the other hand, makes the conjugate acid of 3-hydroxybenzofuran-2-one somewhat less strongly acidic than oxygen-protonated simple alcohols, for which pK_a ≅ –2.0 (12). This, however, is again as might be expected, inasmuch as hydrogen bonding between the positively charged hydroxyl group and the adjacent carboxyl oxygen atom in the present system will stabilize the undissociated acid and thus, reduce its acid strength.

It is interesting that results similar to those produced by the analysis described above may be obtained by treating the data in a much simpler way, without recourse to an acidity function, using the expression of eq. [9] as the correlating equation.

$$[9] \quad k_{obs} = (k_{H^+}[H^+] + k_{uc})K_a^+/(K_a^+ + [H^+])$$

Least-squares fitting of this expression gives the results k_{H^+} = (5.07 ± 0.84) × 10^{-3} M^{-1} s^{-1}, K_a^+ = 1.44 ± 0.29 M, pK_a^+ = –0.16 ± 0.09, and k_{uc} = (1.12 ± 0.27) × 10^{-3} s^{-1}, which are not significantly different from values obtained by the X_o analysis. This simple treatment is successful in this case because the dependence of K_a^+ and k_{H^+} on X_o are both quite shallow and approximate quite well a simple dependence on [H^+].

3-Hydroxybenzofuran-2-one (dilute solutions)

Rates of hydrolysis of 3-hydroxybenzofuran-2-one were also measured in dilute aqueous perchloric acid solutions over the concentration range [$HClO_4$] = 0.0002–0.1 M, in dilute aqueous sodium hydroxide solutions over the concentration range [NaOH] = 0.003–0.1 M, and in acetic acid, biphosphate ion, tris-(hydroxymethyl)methylammonium ion, and ammonium ion buffers. The ionic strength of these solutions was maintained at 0.10 M by the addition of sodium perchlorate as required. These data are summarized in Tables S3–S5.[2]

The rate measurements in buffers were performed using a series of solutions of varying buffer concentration but constant buffer ratio and, since the ionic strength was constant, also constant hydrogen ion concentration. Observed first-order rate constants determined in each solution series increased linearly with increasing buffer concentration, and the data were, therefore, analyzed using the buffer dilution expression shown in eq. [10]. Least-squares fitting produced zero-buffer-concentration intercepts (k_{int}) which,

$$[10] \quad k_{obs} = k_{int} + k_{cat}[buffer]$$

together with the observed first-order rate constants determined in perchloric acid and sodium hydroxide solutions, were used to construct the rate profile shown in Fig. 4. Hydrogen ion concentrations of the buffer solutions needed for this purpose were obtained by calculation, using thermodynamic acidity constants for the buffer acids from the literature and activity coefficients recommended by Bates (13).

© 2002 NRC Canada

This rate profile shows the hydrogen-ion-catalyzed and uncatalyzed reactions plus saturation of hydrogen-ion catalysis noted above, and it also shows a hydroxide-ion-catalyzed process with saturation of hydroxide-ion catalysis as well. This saturation of hydroxide-ion catalysis implies incursion of yet another nonproductive ionization of the substrate, and a complete rate law formulated by adding this feature to the rate expression of eq. [9] is shown as eq. [11]; Q_a^o is the equilibrium constant for this nonproductive ionization and Q_w is the ionization constant of water.

[11] $$k_{obs} = (k_{H^+}[H^+] + k_{uc})K_a^+/(K_a^+ + [H^+]) + k_{HO^-}\ Q_w/(Q_a^o + [H^+])$$

Least-squares analysis using this expression gave the results $k_{H^+} = (5.42 \pm 0.43) \times 10^{-3}$ M^{-1} s^{-1}, $k_{uc} = (1.01 \pm 0.02) \times 10^{-3}$ s^{-1}, $K_a^+ = 1.33 \pm 0.15$ M, $pK_a^+ = -0.12 \pm 0.05$, $k_{HO^-} = (6.37 \pm 0.17) \times 10^3$ M^{-1} s^{-1}, and $Q_a^o = (2.75 \pm 0.10) \times 10^{-12}$ M, $pQ_a^o = 11.56 \pm 0.02$.[3] These values of k_{H^+}, k_{uc}, and K_a^+ agree well with determinations of these quantities obtained by the other treatments of the experimental data described above; the weighted averages of all results are $k_{H^+} = (4.63 \pm 0.16) \times 10^{-3}$ M^{-1} s^{-1}, $k_{uc} = (1.01 \pm 0.02) \times 10^{-3}$ s^{-1}, and $K_a^+ = 1.40 \pm 0.11$ M, $pK_a^+ = -0.15 \pm 0.03$.

There are two candidates for the nonproductive ionization of 3-hydroxybenzofuran-2-one that could be responsible for saturation of hydroxide-ion catalysis of the hydrolysis of its lactone functional group: (*i*) ionization of the hydroxyl group to give an alcoholate anion (eq. [12]); and (*ii*) ionization of the carbon—hydrogen bond next to the lactone function to give an enolate ion (eq. [13]). Both of these reactions put negative charge near the lactone group and thus, hinder reaction of this group with a negatively charged hydroxide ion.

[12] 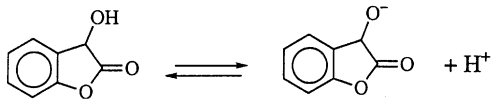

[13] 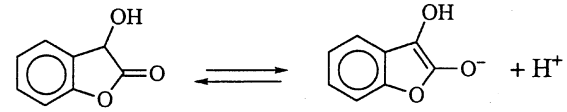

It is difficult to choose between these two alternatives. A Hammett–Taft relation correlating acidity constants of secondary alcohols (14) leads to the estimate $pK_a = 12.0$ for the hydroxyl group ionization of eq. [12], which is consistent with the experimentally determined value $pQ_a^o = 11.6$. On the other hand, $pK_a = 12.3$ has been reported for the carbon acid ionization of benzofuran-2-one itself (15) (**12**) (eq. [14]), which again is not inconsistent with the presently determined value.

[14] 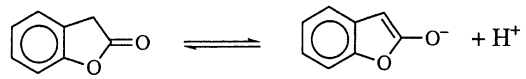

12

The carbon acid ionization reaction of eq. [13] raises the possibility of an alternative lactone hydrolysis route, replacing the traditional attack of hydroxide ion on the lactone carbonyl carbon atom leading to a tetrahedral intermediate. This alternative route (eq. [15]) has the enolate ion (**13**) breaking down to give a ketene (**14**), which then rapidly hydrates to a carboxylic acid enolate ion (**15**), and that ketonizes to the final 2-hydroxymandelic acid product (**16**).

[15] 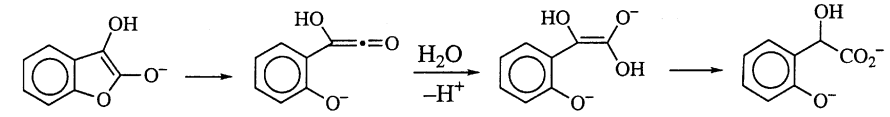

13 **14** **15** **16**

The generation of ketenes from ester enolates like this is a well-known reaction (16), and the hydration and ketonization of analogs of **14** and **15** without the *ortho*-phenoxide group are known to be very fast reactions (17). On the other hand, although 3-phenylbenzofuran-2-one (**17**) readily ionizes to its enolate ion (**18**) (eq. [16]), hydrolysis of this lactone is believed to occur by the traditional tetrahedral intermediate route and not through the corresponding ketene (15).

[16] 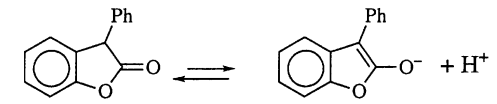

17 **18**

[3] This is a *concentration* dissociation constant applicable at the ionic strength (0.10 M) at which it was determined.

© 2002 NRC Canada

Acknowledgement

We are grateful to the Natural Sciences and Engineering Research Council of Canada (NSERC) and the United States National Institutes of Health for financial support of this work.

References

1. O.L. Chapman, C.-C. Chang, J. Kolc, N.R. Rosenquist, and H. Tomioka. J. Am. Chem. Soc. **97**, 6586 (1975).
2. (*a*) R. Howe, B.S. Rao, and H. Heyneker. J. Chem. Soc. (C), 2510 (1967); (*b*) A.J. Hoefnagel, J.A. Peters, and H. van Bekkum. Rec. Trav. Chim. Pays–Bas, **115**, 353 (1996).
3. W.M. Horspool and G.D. Khandelwal. J. Chem. Soc. (C), 3328 (1971).
4. A.J. Kresge, H.J. Chen, G.L. Capen, and M.F. Powell. Can. J. Chem. **61**, 249 (1983).
5. R.A. Cox and K. Yates. Can. J. Chem. **59**, 2116 (1981).
6. (*a*) E. Högfeldt and J. Bigeleisen. J. Am. Chem. Soc. **82**, 15 (1960); (*b*) J. Sierra, M. Ojeda, and P.A.H. Wyatt. J. Chem. Soc. (B), 1570 (1970); (*c*) R.A. Cox, S.-O. Lam, R.A. McClelland, and T.T. Tidwell. J. Chem. Soc. Perkin Trans. 2, 272 (1979).
7. J.R. Keefe and A.J. Kresge. Investigation of rates and mechanisms of reactions. *In* Techniques of chemistry. Vol. VI. *Edited by* C.F. Bernasconi. Wiley–Interscience, New York. 1986. Chap. XI.
8. (*a*) R.P. Bell. The proton in chemistry. Cornell Univ. Press, Ithaca, New York. 1973. pp. 164–171; (*b*) M. Regitz and G. Maas. Diazo compounds, properties and synthesis. Academic Press, New York. 1986. pp. 122–134.
9. E.A. Jefferson, A.J. Kresge, and S.W. Paine. Can. J. Chem. **74**, 1369 (1996).
10. M.-H. Bui-Nguyen, H. Dahn, and J.F. McGarrity. Helv. Chim. Acta, **63**, 63 (1980).
11. R.A. Cox. Adv. Phys. Org. Chem. **35**, 1 (2000).
12. A. Bagno, G. Scorrano, and R.A. More O'Ferrall. Rev. Chem. Intermed. **7**, 313 (1987).
13. R.G. Bates. Determination of pH theory and practice. Wiley–Interscience, New York. 1973. p. 49.
14. D.D. Perrin, B. Dempsey, and E.P. Serjeant. pK_a Prediction for organic acids and bases. Chapman and Hall, New York. 1981. p. 127.
15. D.M. Heathcote, G.A. DeBoose, J.H. Atherton, and M.I. Page. J. Chem. Soc. Perkin Trans. 2, 535 (1998).
16. T.T. Tidwell. Ketenes. Wiley, New York. 1995. p. 67.
17. Y. Chiang, A.J. Kresge, V.V. Popik, and N.P. Schepp. J. Am. Chem. Soc. **119**, 10 203 (1997).

© 2002 NRC Canada

The endothermic nature of the binding of anionic bile salts to a cationic adsorbent

Celia K. Williams, William C. Galley, and G. Ronald Brown

Abstract: The binding of a hydrophobic bile salt, sodium chenodeoxycholate, by a polyacrylamide with *N*,*N*,*N*-trimethylammonium dodecyl chloride (QPDA12) pendant groups was studied to evaluate the thermodynamic parameters associated with the binding. The Langmuir equation was used in interpreting the data obtained from HPLC measurements. An increase in binding affinity was observed with increasing temperature indicating that the driving force for binding is derived from an increase in entropy ($\Delta S°$ = 253 J mol^{-1} K^{-1}) despite the positive, or unfavourable, enthalpy change ($\Delta H°$ = 53 kJ mol^{-1}). The positive thermodynamic parameters associated with the binding suggest that the disruption of hydrophobic and (or) ionic hydration associated with the bile salts and cationic polymer is the driving force for the binding.

Key words: bile salts, endothermic binding, polymer sorbents, solvent randomization.

Résumé : La liaison d'un sel biliaire hydrophobe, le chenodeoxycholate de sodium par un polyacrylamide portant des substituants chlorure de *N*,*N*,*N*-trimethydodecylammonium (QPDA12) a été étudiée pour évaluer les paramètres thermodynamiques associés à la liaison. L'équation de Langmuir a été utilisée pour interpréter les données obtenues par HPLC. Une augmentation de l'affinité de liaison a été observée lors de l'augmentation de la température. Ceci indique que la formation de la liaison provient principalement de l'augmentation de l'entropie ($\Delta S°$ = 253 J mol^{-1} K^{-1}) en dépit d'un changement non favourable d'enthalpie positive ($\Delta H°$ = 53 kJ mol^{-1}). Les valeurs positives des paramètres thermodynamiques du processus de l'association suggèrent que la dissolution de la cage d'hydratation associée aux régions hydrophobes et ioniques des sels biliaires et du polymère cationique est le moteur de l'association.

Mots clés : sels biliaires, liaison endothermique, les sorbents polymères, désorganisation de la cage d'hydratation.

Introduction

The ingestion of insoluble cationic polymer resins has been effective as one of the weapons employed in lowering blood cholesterol, hence cardiovascular diseases (1–3). Bile acids are synthesized from cholesterol in the liver, stored in the gallbladder in the conjugated form, and secreted into the duodenum at ingestion of a meal. After the emulsification of the fats in the jejunum by the formation of micellar aggregates (4, 5), more than 99% of the bile salts are reabsorbed and recirculated back to the liver by the enterohepatic circulation. Bile salt binding resins in the gastrointestinal tract can compete with the reabsorption, thereby inducing the liver to consume cholesterol. This leads to a reduction of plasma cholesterol due to the conversion to bile acids as the primary route of the consumption of plasma cholesterol.

Received 16 July 2001. Published on the NRC Research Press Web site at http://canjchem.nrc.ca on 16 January 2002.

C.K. Williams and W.C. Galley.[1] Department of Chemistry, McGill University, 801 Sherbrooke Street West, Montreal, QC H3A 2K6, Canada.
G.R. Brown.[2] Faculty of Arts and Science, Brock University, St. Catharines, ON L2S 3A1, Canada.

[1]Corresponding author (fax: (514) 398-3797; e-mail: william.galley@mcgill.ca).
[2]Deceased.

Cholestyramine (Questran), a styrene-divinylbenzene copolymer developed in 1959 (6), and colestipol (Colestid), a copolymer of tetraethylene-pentamine and epichlorohydrin (7) are the bile salt sequestering resins currently in wide clinical use. However, they have low efficiency in vivo due to the nonspecific nature of the binding (8–10). To realize significant reduction in cholesterol levels, patients must consume large amounts (up to 24 g/day for cholestyramine).

The development of a clearer understanding of the molecular basis of the binding process is central to the creation of resins that would prove effective in the sequestering of bile salts. The empirical determination of the relative enthalpic and entropic contributions to the binding would prove invaluable in the evaluation of molecular models that can provide direction in the search and creation of more effective resins in the sequestering of bile acids.

The binding of the negatively charged bile salts with cationic resins has most often been considered as a process dominated by the attraction between the oppositely charged ions (11–13). A contribution to the binding due to hydrophobic interactions has been proposed (11–16) based largely on differences observed in binding that were dependent on the hydrophobicity of either the polymer or the bile salt. However, despite the fact that the binding can involve the association of species with large nonpolar moieties, the decomposition of these non-ionic contributions into a van der Waals attraction between the interacting partners and a

 DOI: 10.1139/V01-197 © 2002 NRC Canada

Fig. 1. The chemical structure of *N*,*N*,*N*-trimethylammonium dodecyl chloride (QPDA12) resin.

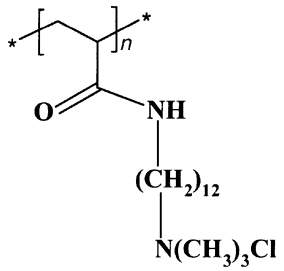

true hydrophobic association derived from solvent randomization has been lacking.

In the present work, the temperature dependence of the binding affinities for bile salts with a lightly cross-linked polyacrylamide resin functionalized with *N*,*N*,*N*-trimethylammonium dodecyl chloride (QPDA12) (Fig. 1) was studied. The specific goal was to evaluate the relative thermodynamic contributions to the binding process. The somewhat surprising observation that association of the anionic bile salt with the cationic resin is endothermic and entropy driven is discussed in terms of the dominant role played by the changes in solvation that occur in the binding process.

Experimental

Materials

Sodium cholate (NaC) and sodium chenodeoxycholate (NaCDC) were purchased from Sigma and were used as received. Sodium cacodylate ($(CH_3)_2AsO_2Na$) was from Baker. The QPDA12 resin with chloride as counter-ions was a previously synthesized and quaternized sample (17). The functionality (*f*) was determined to be 2.00 ± 0.07 mmol of trimethylammonium pendant groups per g of dry resin, performed by gravimetric analysis. The chloride counter-ions were precipitated in the form of silver chloride by the addition of 1:1 of 16 M nitric acid and 0.103 M silver nitrate. The precipitate was filtered, washed, dried, and weighed to constant weight.

Adsorption studies

The procedures used for the sorption studies were as described previously (16). The bile salt solutions were prepared in an aqueous 5.0 mM sodium cacodylate buffer, pH range between 7.2 and 7.5. Sodium cacodylate buffer was used in this study to maintain a low ionic strength, which was 5 mM at the concentration employed. A stock bile salt solution (7 mM) was normally diluted with buffer to generate concentrations as low as 0.23 mM. The polymer resin (10 mg) was added to 20 mL of buffer solution containing varying bile salt concentrations. The mixtures were agitated with a mechanical shaker in a constant temperature bath at 120 oscillations per min for more than 18 h at the desired temperature (24–60°C). Reverse-phased high-performance liquid chromatography (HPLC) was used to follow the binding, according to procedures described previously (18).

Fig. 2. Binding isotherms of chenodeoxycholate by QPDA12 at different temperatures.

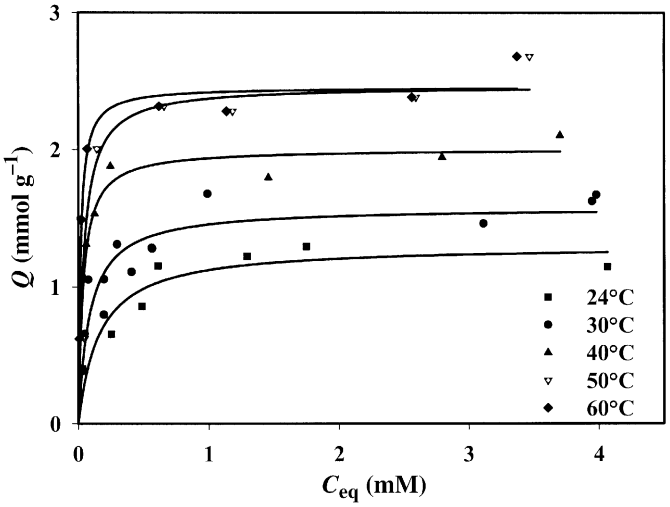

The bile salt concentrations in the solutions at equilibrium (C_{eq}) and the amount of bile salt bound per g of resin Q (mmol g^{-1}) were calculated, and the binding isotherms were plotted from these results. The isotherms were then analyzed in terms of a Langmuir equation

$$[1] \qquad Q = \frac{Q_m K C_{eq}}{1 + K C_{eq}}$$

with the use of SigmaPlot Software Version 5.00 that yielded the "best-fit" values for *K* and Q_m, the site binding constant, and max *Q* or binding capacity, respectively.

Results

The binding isotherms for sodium chenodeoxycholate with QPDA12 in 5.0 mM sodium cacodylate buffer at pH 7.2 at several temperatures ranging from 24–60°C appear in Fig. 2. The lines through the data points represent the isotherms calculated using the values obtained for Q_m and *K* from the nonlinear fit to eq. [1] and represent the best-fit.

There are two features in the binding isotherms that manifest themselves with an increase in temperature, Q_m and *K*. The value of Q_m at a particular temperature represents the saturation level of the binding, or the binding capacity of the resin. It displays an increase with temperature, and plateaus at 50°C. The values of Q_m divided by the functionality of the resin (*f*), yields the max number (*n*) of bile salt anions bound per functional sites on the resin. Values of *n* are seen in Table 1 to increase with temperature to a limit somewhat in excess of 1:1. This apparent increase in available binding sites on the resin is not accompanied within experimental error, with any indication of either a cooperative form of binding or the presence of more than one binding constant. The resin preparations employed in this work were in the form of aggregated beads. The twofold increase in the available binding sites occurring primarily at lower temperatures appears to arise from a decrease in aggregation with temperature. This influence of temperature on the binding behavior is

© 2002 NRC Canada

Table 1. Thermodynamic parameters for the binding of chenodeoxycholate by QPDA12 over the temperature range studied.

Temperature (K)	$K \times 10^{-3}$ (M^{-1})	$\Delta G° = -RT \ln K$ (kJ mol^{-1})	Q_m	$n = Q_m/f$
297	7.62	–22.1	1.18	0.59
303	11.8	–23.6	1.58	0.79
313	28.0	–26.6	2.01	1.01
323	24.6	–27.2	2.47	1.24
333	103	–32.0	2.47	1.24

Fig. 3. Normalized binding isotherms illustrating the enhancement in binding affinity.

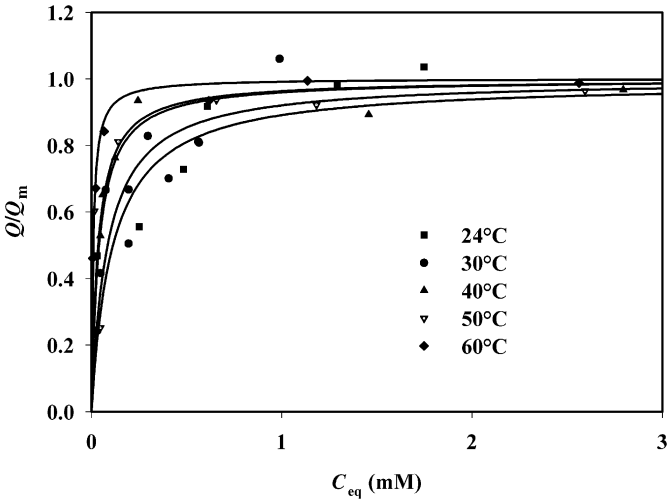

overshadowed by the much larger enhancement in the binding constant over the temperature range of the experiment.

An increase in the strength of the binding, as indicated by increase in K, with rising temperature is also obtained from the analysis of the isotherms in Fig. 2. This enhancement is more apparent in Fig. 3 where the isotherms are represented as Q/Q_m, or have been normalized to the saturation level. The value of C_{eq} required to produce half-saturation clearly is lower as the temperature rises reflecting an increase in K. In accordance with le Chatelier's principle, this increase in K with temperature is indicative of an endothermic process that must therefore, be entropy-driven. The binding capacity of the resin and the site binding constant K, obtained at each temperature appear in Table 1 along with the standard Gibbs free energy of binding which was computed from K.

The increasingly negative $\Delta G°$ as the temperature increased resulted in the linear plot appearing in Fig. 4. The slope based on the fundamental thermodynamic relation

$$[2] \qquad \Delta G_T^o = \Delta H^o - T\Delta S^o$$

represents the standard entropy change ($\Delta S°$) for the binding of sodium chenodeoxycholate with QPDA12 and the y-intercept represents the standard enthalpy change ($\Delta H°$). A linear regression analysis of the relation in Fig. 4 results in a $\Delta S°$ of positive 253 ± 35 J mol^{-1} K^{-1} and a positive $\Delta H°$ of 53 ± 11 kJ mol^{-1}. Alternatively, the data from Table 1 are displayed in the form of a van't Hoff plot (ln K vs. $1/T$) in Fig. 5. The increasing K with temperature manifests itself as

Fig. 4. The standard Gibbs free energy of binding against temperature for chenodeoxycholate by QPDA12.

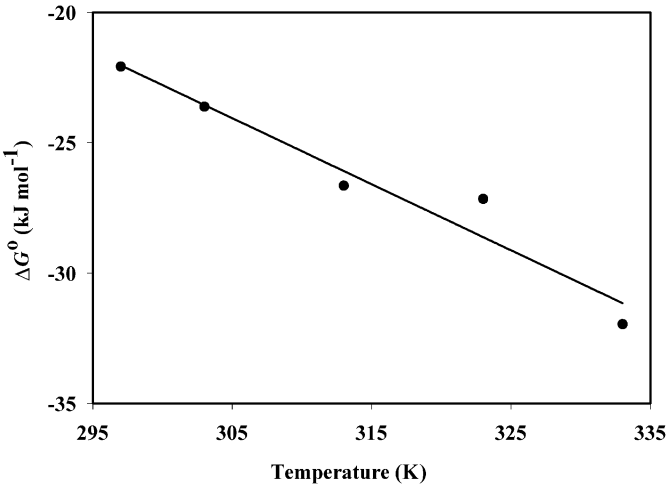

a slope ($-\Delta H°/R$) that is clearly negative, emphasizing the positive nature of the $\Delta H°$ for the process. The linear regression analysis on this plot results in positive values for $\Delta H°$ and $\Delta S°$ of 53 ± 11 kJ mol^{-1} and 252 ± 34 J mol^{-1} K^{-1}, respectively. As expected, the thermodynamic parameters derived from the two plots are in agreement, albeit with uncertainties weighted somewhat differently.

It can be noted from Table 2 that at 313 K, for example, the value of the change in $\Delta G°$ of –27 kJ mol^{-1} derives from a balance of larger positive $\Delta H°$ and $T\Delta S°$ values. At all given temperatures, the entropic driving force not only contributes to the binding but also is sufficiently large to overcome the endothermic nature of the process resulting in significantly negative standard free energy changes.

Discussion

Binding processes in which favourable charge–charge or charge – polar interactions appear to provide the molecular basis for the spontaneity of the event, can be particularly deceptive. The association of the anionic bile salt with the cationic resin represents an example in which the Coulombic attraction between the charged moieties should appear as a negative enthalpy change that provides the driving force for the process. The observation of an enhancement in the binding affinity of bile acids for the QPDA12 cationic resin with increasing temperature, the signature of an endothermic process, calls for an expansion of the molecular picture in which attraction between two oppositely charged species dominates. Randomization within the system, or a positive $\Delta S°$, is responsible for the binding and is sufficiently large to overcome the positive $\Delta H°$, or unfavourable overall endothermic nature of the binding process that is occurring within the system.

Binding events that are endothermic, and therefore entropy driven, are frequently observed and associated with processes in which changes in solvation, particularly with water as the solvent, are a dominant factor. The binding of Ca^{2+} ion in aqueous solution to thermolysin (19), a calcium-binding protein, represents an elegant example. While favourable charge–charge and ion–dipole interactions appear

© 2002 NRC Canada

Fig. 5. The van't Hoff plot for the binding of chenodeoxycholate by QPDA12.

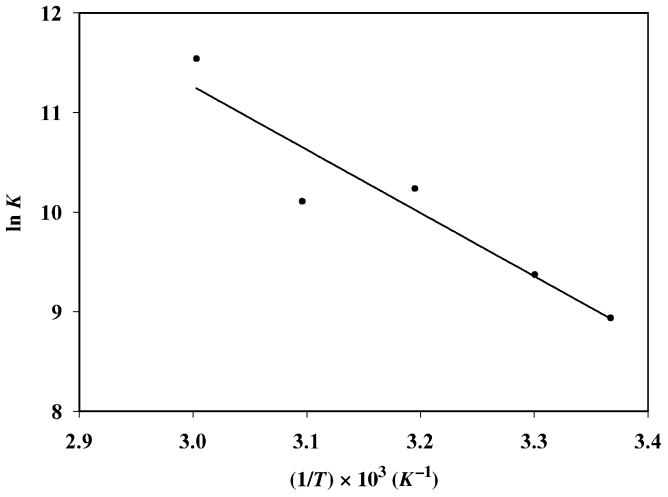

in the X-ray structure (20, 21) of the calcium-bound protein, the strongly endothermic nature of the binding points to the stripping off, or liberation, of the water of ionic hydration as the dominant feature of the process. The condensation of the Ca^{2+} ion and the protein into a single entity, is not only accompanied by, but is actually driven by, the disorder produced in the overall solution.

The significant role played by the solvent in self-assembly processes, as well as binding, has appeared in recent years from the evaluation of the thermodynamic parameters associated with the stability of globular proteins. Based on DSC data the spontaneous refolding of "random-coil" polypeptide chains into their native globular structures, at least in the lower temperatures range, is endothermic and entropy driven (22). This is again in contrast with the simple picture that ignores the solvent. This latter example represents a case in which randomization of the hydrophobic hydration associated with nonpolar side chains, rather than ionic hydration, appears to provide the driving force. The binding of bile salts with human serum albumin followed by flow calorimetry is also another example that has been documented to be endothermic and entropy driven (23).

The observation of $\Delta G°$ values arising as a balance between much larger positive $\Delta H°$ and positive $\Delta S°$ values, is frequently encountered with processes occurring in aqueous solution. This is referred to as enthalpy–entropy compensation and can be noted in the binding of the chenodeoxycholate to QPDA12 in this study. The individual positive $\Delta H°$ and positive $\Delta S°$ values that are observed for the binding appear too large in magnitude to be associated with binding as a bimolecular event. They again draw attention to the role that solvent reorganization must be playing in determining the strength of the binding between these ionic components. It should be emphasized, however, that as a consequence of this compensation between the large positive $\Delta H°$ and $\Delta S°$ parameters, smaller exothermic contributions might well be playing a pivotal role in converting the overall $\Delta G°$ from positive to that of a spontaneous process (negative) while retaining the overall endothermic nature of the binding. These essential contributions could exist in the form of direct charge–charge and van der Waals interactions between the binding partners.

Table 2. Thermodynamic parameters calculated from $\Delta S°$ of 253 J mol^{-1} K^{-1} and $\Delta H°$ of 53 kJ mol^{-1} for the binding of chenodeoxycholate by QPDA12.

Temperature (K)	$T\Delta S°$ (kJ mol^{-1})	$\Delta G° = \Delta H° - T\Delta S°$ (kJ mol^{-1})
297	75.5	–22.3
303	77.1	–23.8
313	79.6	–26.4
323	82.1	–28.9
333	84.7	–31.4

Preliminary results of the binding of sodium cholate to the QPDA12 adsorbent in cacodylate buffer also display positive entropy and enthalpy changes, albeit of smaller magnitudes.

In the present work, both the bile salts and the pendants on the resin share the characteristic of being hydrophobic as well as ionic. Irrespective of whether the solvation changes that occur involve ionic or hydrophobic hydration, or both, it is evident that the disruption of ordered water molecules plays an important role in the binding of bile salts with the cationic resin.

Conclusions

The binding of chenodeoxycholate to QPDA12 displayed an endothermic nature in the form of measured binding constants that increased with a rise in temperature. The overall driving force for the binding occurs despite the large unfavourable enthalpy change and is due to an even larger increase in the entropy of binding. The enthalpy–entropy compensation favouring entropy as the net driving force for the binding suggests that the randomization of ordered solvent surrounding the interacting moieties dominates the process. These solvation changes may involve ionic, hydrophobic hydration, or both. Ongoing work centers on the comparison of binding data in the presence of competing anions and solvent perturbations with models that include the solvent as a significant player in the binding process.

Acknowledgements

Financial support from the Natural Sciences and Engineering Research Council of Canada (NSERC) is gratefully acknowledged. Dr. G. Ronald Brown passed away during the preparation of this manuscript. I dedicate this article in his memory with fond memories.

References

1. D.H. Blankenhorn. Can. J. Cardiol. **5**, 206 (1989).
2. G. Brown, J.J. Albers, L.D. Fisher, S.M. Schaefer, J.-T. Lin, C. Kaplan, X.-Q. Zhao, B.D. Bisson, V.F. Fitzpatrick, and H.T. Dodge. New Engl. J. Med. **323**, 1289 (1990).
3. J. Loscalzo. New Engl. J. Med. **323**, 1337 (1990).
4. A.F. Hofmann. Biochem. J. **89**, 57, (1963).
5. D.R. Holt. Arch. Intern. Med. **130**, 574, (1972)
6. S.S Bergen, T.B. VanItallie, D.M. Tennet, and W.H. Sebrell. Proc. Soc. Exp. Biol. Med. **102**, 676 (1959).

© 2002 NRC Canada

7. N.A. Nelson and G.E. Vanderberg. U.S. Patent 3 692 895, 1972.
8. K.A. Schulman, B. Kinosian, T.A. Jacobson, H. Glick, M.K. William, H. Koffer, and J.M. Eisenberg. J. Am. Med. Assoc. **254**, 3025 (1990)
9. C.M. Benson, C. Haynes, S. Blanchard, and D. Ellis. J. Pharm. Sci. **82**, 80, (1993).
10. E.R. Stedronsky. Biochim. Biophys. Acta, **1210**, 255 (1994).
11. G. Wu, G.R. Brown, and L.E. St-Pierre. Langmuir, **12**, 466 (1996).
12. X.X. Zhu, G.R. Brown, and L.E. St-Pierre. J. Pharm. Sci. **81**, 65 (1992).
13. W.E. Baille, W.Q. Huang, M. Nichifor, and X.X. Zhu. J. Macromol. Sci. Pure Appl. Chem. **A37**, 677 (2000).
14. W.H. Johns and T.R. Bates. J. Pharm. Sci. **59**, 329 (1970).
15. S. Lindenbaum and T. Higuchi. J. Pharm. Sci. **64**, 1889 (1975).
16. X.X. Zhu, G.R. Brown, and L.E. St-Pierre. J. Macromol. Sci. Pure Appl. Chem. **A29**, 711 (1992).
17. G. Wu and G.R. Brown. React. Polym. **14**, 49 (1991).
18. X.X. Zhu and G.R. Brown. Anal. Lett. **23**, 2011 (1990).
19. J.D. Buchanan, R.J.T. Corbett, and R. Roche. Biophys. Chem. **23**, 183 (1986).
20. B.W. Matthews, L.H. Weaver, and W.R. Kester. J. Biol. Chem. **24**, 8030 (1974).
21. P.M. Colman, J.N. Jansonius, and B.W. Matthews. J. Mol. Biol. **70**, 701 (1972).
22. P.L. Privalov. Crit. Rev. Biochem. Mol. Biol. **25**, 281 (1990).
23. F. Scagnolari, A. Roda, A. Fini, and B. Grigolo. Biochim. Biophys. Acta, **791**, 274 (1984).

© 2002 NRC Canada

On the generation of oxirene and dimethyloxirene by retro-Diels–Alder reactions, and reactions of dimethyloxirene: a computational study

C. Delamere, C. Jakins, and E. Lewars

Abstract: The isomerization of oxirene (oxacyclopropene) (**1**) to ketene, dimethyloxirene (**7**) to dimethylketene via the oxo carbene ("ketocarbene"), and the retro-Diels–Alder extrusion of oxirene and dimethyloxirene from their formal adducts (**9** and **24**, respectively) with benzene were studied computationally. All species were optimized at the MP2(fc)/6–31G(df,p) level; the species involving **1** were also subjected to MP2(fc)/6–31G(df,p) frequency and single-point CCSD(T)/6–31G(df,p) calculations. At the CCSD(T)/6–31G(df,p)//MP2(fc)/6–31G(df,p) level **1** isomerized to ketene in one step with a barrier of 2.8 kJ mol^{-1} and a reaction energy of –320.6 kJ mol^{-1}. The extrusion of **1** from **9** had a late transition state and activation and reaction energies of 264.2 and 214.2 kJ mol^{-1}, respectively, cf. cyclopropene extrusion from its adduct (192.3 and 95.9 kJ mol^{-1}), indicating an antiaromatic destabilization energy of 214.2 – 95.9 = 118 kJ mol^{-1} for **1**. The carbene **8** from ring-opening of **7** lay 10.9 kJ mol^{-1} above **7** (CCSD(T)/6–31G(df,p)//MP2(fc)/6–31G(df,p)), but the transition state could not be found; **8** isomerized to dimethylketene (252.7 kJ mol^{-1} below **7**) with a barrier of 16.4 kJ mol^{-1}, and to *s*-(*Z*)- and *s*-(*E*)-butenone with barriers of 28.5 and 35.4 kJ mol^{-1}, respectively. The UV (TDDFT, B3P86/6–311++G**//MP2(fc)/6–31G(df,p)) spectra of **1** and **7** were calculated. Discrepancies were seen between the calculated IR spectra of **7** (bis(trifluoromethyl)oxirene) and perfluoroethylmethyloxirene, and those attributed to these species in earlier matrix-isolation work.

Key words: oxirene, dimethyloxirene, ab initio, retro-Diels–Alder, Diels–Alder.

Résumé : Faisant appel à des calculs théoriques, on a étudié les réactions d'isomérisation de l'oxirène (oxacyclopropène) (**1**) en cétène et du diméthyloxirène (**7**) en diméthylcétène par le biais de l'oxocarbène (cétocarbène) ainsi que la réaction d'extrusion de rétro-Diels–Alder de l'oxirène et du diméthyloxirène à partir de leurs adduits formels (respectivement **9** et **24**) dans le benzène. Toutes les espèces ont été optimisées au niveau MP2(fc)/6-31G(df,p); les espèces impliquant le composé **1** ont aussi été soumises à des calculs de fréquence MP2(fc)/6-31G(df,p) et ponctuels CCSD(T)/6-31G(df,p). Au niveau CCSD(T)/6-31G(df,p)//MP2(fc)/6-31G(df,p), le composé **1** s'isomérise en cétène en une étape avec une barrière de 2,8 kJ mol^{-1} et une énergie de réaction de –320,6 kJ mol^{-1}. L'extrusion de **1** à partir de **9** implique un état de transition tardif et des énergies d'activation et de réaction de 264,2 et 214,2 kJ mol^{-1}, cf. pour l'extrusion du cyclopropène de son adduit (192,3 et 95,9 kJ mol^{-1}) ce qui implique une énergie de déstabilisation antiaromatique de 214,2 – 95,9 = 118 kJ mol^{-1} pour **1**. L'énergie du carbène **8** provenant de l'ouverture de cycle de **7** est supérieure (CCSD(T)/6–31G(df,p)//MP2(fc)/6–31G(df,p)) de 10,9 kJ mol^{-1} à celle de **7**, mais on n'a pas pu déterminer son état de transition. Le produit **8** s'isomérise en diméthylcétène (énergie de 252,7 kJ mol^{-1} inférieure à celle de **7**) avec une barrière de 16,4 kJ mol^{-1} et en *s*-(*Z*)- et *s*-(*E*)-buténone avec des barrières respectivement de 28,5 et 35,4 kJ mol^{-1}. On a calculé les spectres UV (TDDFT; B3P86/6–311++G**//MP2(fc)/6–31G(df,p)) des composés **1** et **7**. On a observé des divergences entre les spectres IR calculés des composés **7** (bis(trifluorométhyl)oxirène) et perfluoroéthylméthyoxirène et ceux attribués à ces espèces dans un travail antérieur au cours duquel ils auraient été isolés dans des matrices.

Mots clés : oxirène, diméthyloxirène, ab initio, rétro-Diels–Alder, Diels–Alder.

[Traduit par la Rédaction]

Introduction

The C_2H_2O potential energy surface continues to be one of the most intensively scrutinized surfaces, almost 30 years after the first computational studies (1). The realistic synthetic objectives (other structures can be drawn) on this surface are molecules **1** (oxirene), **2** (oxo carbene or "ketocarbene" methanoylcarbene or formylcarbene), **3** (ketene), **4** (oxiranylidene or carbenaoxirane), **5** (hydroxyethenylidene or hydroxyvinylidene), and **6** (ethynol or

Received 6 July 2001. Published on the NRC Research Press Web site at http://canjchem.nrc.ca on 21 January 2002.

C. Delamere, C. Jakins, and E. Lewars.[1,2] Department of Chemistry, Trent University, Peterborough, ON K9J 7B8, Canada.

[1]Adjunct Professor: Department of Chemistry, Queen's University, Kingston, ON K7L 3N6, Canada.
[2]Corresponding author (fax: (705) 748-1625; e-mail: elewars@trentu.ca).

 DOI: 10.1139/V01-194 © 2002 NRC Canada

Fig. 1. The more realistic synthetic objects on the C_2H_2O potential energy surface (other species can be drawn) and the dimethyl analogues of **1** and **2** (**7** and **8**).

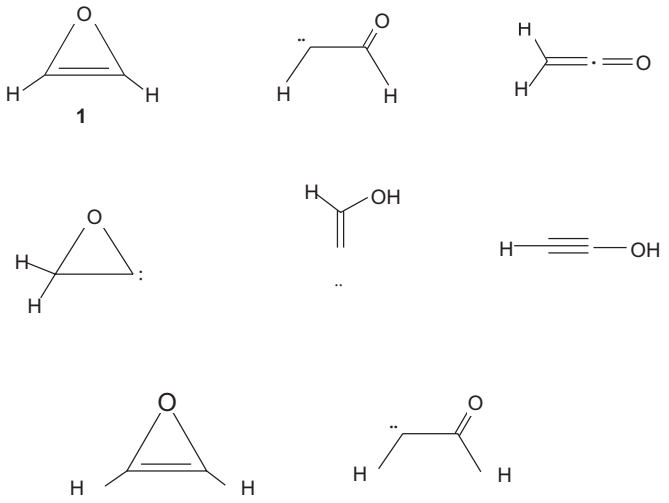

hydroxyacetylene) (Fig. 1). In this paper our calculations on the reactions of **1** and **7** and on the possibility of generating them by retro-Diels–Alder reactions are presented. Molecules **4** (2), **5** (3), and **6** (4), which are outside the scope of this paper, have been discussed in the literature. Oxirene (**1**) is perhaps, next to the industrially important ketene, the most intensively studied of the species **1**–**6**; the oxirene literature has been reviewed to 1983 (5). Notable subsequent developments have been the reports that: (*i*) monomethyl oxirene (6) but not oxirene (7) can be generated by neutralization of the radical cation in a mass spectrometer. (*ii*) Bachmann et al. (8) observed in a cryogenic matrix an IR absorption that they ascribed to the C—C double bond stretch of dimethyloxirene. This and earlier matrix-isolation work by Torres et al. (9), in which the detection of perfluoroalkyloxirenes was claimed, are apparently the only reports of the isolation of oxirenes. (*iii*) If oxirene is indeed a true intermediate, i.e., a relative minimum on the potential energy surface, its existence is borderline (10, 11), and the barrier to its isomerization to the carbene **2** by ring-opening with C—O bond cleavage is extremely low (12). The existence of **2** is also uncertain (5, 12), and **1** may isomerize directly to ketene **3** without going through **2**. The best computed potential energy surface so far (12) gives **1** → **2** and **2** → **3** barriers heights of 1.3 and 20.2 kJ mol^{-1}, respectively. (*iv*) Disubstitution with groups of widely different electronic natures (from a "periodic scan" of H, BH_2, CH_3, NH_2, OH, and F) destabilizes the putative minimum, except for CH_3 and perhaps F (13). (*v*) Benzoannelation stabilizes the oxirene system (14), but push–pull substitution, effective for other antiaromatic (15) molecules like cyclobutadiene (16), does not seem to work here (17).

The recent assertion (2) that of all of the C_2H_2O species only **3**, **4**, and **6** are likely to be accessible by thermal retro [4+2] reactions (18); the demonstration that, at least among simple "first-row" substituents, only CH_3 appears to distinctly stabilize oxirene (13); and the report (8) of the generation of **7** via the carbene **8**, where experiment was augmented by semiempirical calculations of reaction profiles, prompted us to explore the retro-Diels–Alder extrusion of **1** and **7** and the reactivity of **7**, at reasonably high ab initio levels.

Computational methods

Ab initio (19, 20) geometries and frequencies were calculated with Gaussian 98W[3] on 1 GHz Pentium 3 and 1.5 GHz Pentium 4 computers, with the Windows NT operating system. Geometry optimizations were followed by frequency calculations (21) at the same level to verify that the structure was the desired relative minimum (no imaginary frequencies) or transition state (one imaginary frequency), and to obtain zero-point energies (ZPEs) to correct for the frozen-nuclei energy. Animation of the imaginary frequency of transition states usually served to confirm the nature of the reaction coordinate, i.e., to identify the reactant and product (for the transition state linking **1** and ketene an intrinsic reaction coordinate (IRC) calculation (22) was also done). The correction factor to MP2(fc)/6–31G(df,p) ZPEs is estimated to be in the range 0.96–0.97 (23), and a correction was not used, as its effect on energy differences is negligible (see below). For molecules too large for MP2(fc)/6–31G(df,p) frequency calculations the use of HF/3–21G ZPEs (multiplied by 0.9207 (23)) is shown to be reasonable. The choice of MP2(fc)/6–31G(df,p) geometry optimizations and coupled-cluster (24) CCSD(T)/6–31G(df,p)//MP2(fc)/6–31G(df,p) single-point calculations is discussed below. Absolute total energies, ZPEs, and ZPE-corrected energies are available in the supplementary material tables.[4] Löwdin bond orders (25) were from single-point HF/3–21G calculations with Spartan[5] on Gaussian 98W MP2(fc)/6–31G(df,p) geometries.

Results and discussion

Reliability of the computational methods

The very extensive study of Vacek et al. (11) showed that the curvature of the potential energy surface (i.e., where stationary points exist and whether particular stationary points are minima or saddle points) for C_2H_2O at the geometry of the parent oxirene is quite sensitive to correlation levels and basis sets: the C_{2v} oxirene structure is always a stationary point, but its response to the computational level is some-

[3] R.E. Stratman, J.C. Burant, S. Dapprich, J.M. Millam, A.D. Daniels, K.N. Kudin, M.C. Strain, O. Farkas, J. Tomasi, V. Barone, M. Cossi, R. Cammi, B. Mennucci, C. Pomelli, C. Adamo, S. Clifford, J. Ochterski, G.A. Petersson, P.Y. Ayala, Q. Cui, K. Morokuma, D.K. Malick, A.D. Rabuck, K. Raghavachari, J.B. Foresman, J. Cioslowski, J.V. Ortiz, A.G. Baboul, B.B. Stefanov, G.Liu, A. Liashenko, P. Piskorz, I. Komaromi, R. Gomperts, R.L. Martin, D.J. Fox, T. Keith, M.A. Al-Laham, B. Johnson, W. Chen, M.W. Wong, J.L. Andres, C. Gonzalez, M. Head-Gordon, E.S. Replogle, and J.A. Pople. Gaussian 98, Revision A.9. Gaussian, Inc. Pittsburgh, PA. 1998.

[4] Supplementary material may be purchased from: The Depository of Unpublished Data, Document Delivery, CISTI, National Research Council Canada, Ottawa, Canada, K1A 0S2.

[5] PC Spartan Pro, Version 1.0.3. Wavefunction Inc. 18401 Von Karman, Suite 370, Irvine, California. January 2000.

© 2002 NRC Canada

Table 1. Calculated relative energies of the species (Fig. 2) on the MP2(fc)/6–31G(df,p) oxirene potential energy surface.

	MP2(fc)/6–31G(df,p)		CCSD(T)/6–31G(df,p)//MP2(fc)/6–31G(df,p)	
Species	With MP2 etc. ZPE	With HF/3–21G ZPE	With MP2 etc. ZPE	With HF/3–21G ZPE
1, Oxirene	0	0	0	0
1t, Transition state	47.8	44.3	2.8	–0.74
3, Ketene	–329.0	–330.5	–320.6	–322.1

Note: MP2 ZPEs are uncorrected (see text), HF/3–21G ZPEs have been multiplied by 0.9207 (23).

what fickle. Hartree–Fock calculations always yield a relative minimum and DFT a transition state, but the result of MP2, quadratic CI (QCISD and QCISD(T)), and coupled cluster (CCSD and CCSD(T)) calculations is basis set dependent. We sought the highest level that would be practical, with our facilities, for the somewhat large molecules (up to 11 heavy atoms) we wished to examine, and which would also give the same potential energy surface curvature for **1** as did the highest levels used by Vacek et al., namely CCSD(T) with triple-ζ basis sets containing several *d* shells and an *f* shell on C and O and several *p* shells and a *d* shell on H. At these very high levels, **1** was a relative minimum with ring-opening vibrational modes of 139–163 cm^{-1}. The lowest correlated level used by Vacek et al. (11), which predicted **1** still is a minimum, was MP2(fc)/6–311G(df,p) with ring-opening mode of 129 cm^{-1}. We find that at the MP2(fc)/6–31G(df,p) level (doubly split rather than triply split valence shell) **1** is still a minimum, with ring-opening mode of 153 cm^{-1}. This is almost the lowest standard ab initio correlated level where **1** is a minimum (omitting the *p* functions on H, **1** still has a minimum, with ring-opening frequency of 148 cm^{-1}) and, therefore, we chose this for all geometry optimizations, and also calculated frequencies at this level for formal adducts of **1** and benzene, and smaller species. To improve relative energies, single-point CCSD(T)/6–31G(df,p)//MP2(fc)/6–31G(df,p) calculations were also done on these smaller MP2(fc)/6–31G(df,p) geometries (our longest calculation, numerical frequencies on a $C_8H_{10}O$ C_1 symmetry species, took 11 days on a 1.5 GHz Pentium 4). We could not use DFT — this always makes oxirene and dimethyloxirene transition states. It should be noted that it has not yet been settled whether oxirene is a relative minimum or a transition state: there is no direct experimental evidence for the parent molecule, and even at the highest levels used so far (11) the results are somewhat quirky as some CCSD(T) calculations with large basis sets gave an imaginary ring-opening frequency. These results should settle the question of the feasibility of generating **1** (assuming it is a minimum) and **7** (which is very likely a minimum (13)) by thermal retro-Diels–Alder reactions, and delineate the intramolecular reactions of **7.**

Oxirene (1), ring-opening

On the MP2(fc)/6–31G(df,p) potential energy surface **1** is a relative minimum that passes through transition state **1t** with a barrier of 2.8 kJ mol^{-1} to form ketene **3**, which lies 320.6 kJ mol^{-1} below **1** (CCSD(T)/6–31G(df,p) single point energies, Table 1 and Fig. 2). The highest-level calculations reported so far for this reaction sequence, CCSD(T)/6–311G(df,p) by Scott et al. (12), are also shown in Fig. 2. They too assign oxirene a low barrier to ring opening, but predict the carbene (**2**) to be a minimum slightly below **1** with a barrier (20.2 kJ mol^{-1}) to the hydrogen migration that transforms it into ketene, whereas at our level carbene **2** is not a stationary point. Scott et al. also find that at the MP2/6–311G(df,p) (triply split) level **2** is not a stationary point and **1** goes to **3** with a barrier of 43.8 kJ mol^{-1}. Our MP2(fc)/6–31G(df,p) barrier is 47.8 kJ mol^{-1}, but this is markedly lowered by a single point CCSD(T)/6–311G(df,p) calculation to 2.8 kJ mol^{-1} (Table 1).

All levels place ketene **3** far below **1**. The MP2(fc)/6–31G(df,p) level, used for all the geometry optimizations in this work, thus concurs with the CCSD(T)/6–311G(df,p) optimizations (12) in finding **1** to be a minimum with a small barrier to ring opening. The activation energy of –0.74 kJ mol^{-1} from the HF/3–21G ZPE correction is probably an artifact of applying a ZPE from one level of calculation to a very small raw energy difference obtained at another level. The use of HF/3–21G ZPEs, where MP2 ZPEs were not routinely feasible, is justified below in the discussion of the data in Table 2; they were calculated in all cases for consistency. Our MP2(fc)/6–31G(df,p) oxirene structure (see below) is similar to the CCSD(T)/6–311G(df,p) structure of Scott et al. (12), and our oxirene-to-ketene transition state **1t** (Fig. 2) resembles their carbene-to-ketene transition state.

Oxirene (1), retro-Diels–Alder extrusion

Four retro-Diels–Alder reactions were examined (Fig. 3; this also shows bond lengths and orders, discussed below). For the formation of **1**, the formal oxirene–benzene adduct **9**, the transition state **10**, and the products **1** and **11**, were optimized at the MP2(fc)/6–31G(df,p) level; the vibrational frequencies were calculated at this level; and single-point CCSD(T)/6–31G(df,p) calculations were performed on the MP2 geometries (MP2(fc)/6–31G(df,p) as well as HF/3–21G ZPE corrections were applied to the MP2 and CCSD(T) energies). For the formation of cyclopropene, **12**–**14** and **11** were optimized at the MP2(fc)/6–31G(df,p) level and single-point CCSD(T)/6–31G(df,p) calculations were performed on the MP2 geometries, but only HF/3–21G ZPE corrections were applied to the MP2 and the CCSD(T) energies. For the extrusion of ethene from the formal adduct with benzene, and for the prototypical retro-Diels–Alder reaction, the conversion of cyclohexene to ethene and 1,3-butadiene analogous calculations were done on **11**, and **15**–**17**, and on **17**–**20**. Benzene was chosen as the "diene" because its stability seems to offer the best chance of obtaining the dienophiles **1** and **7** from a retro-Diels–Alder reaction.

The relative energies for these extrusion reactions are shown in Table 2. The use of ZPEs from HF/3–21G frequencies rather than MP2(fc)/6–31G(df,p) frequencies, a practi-

© 2002 NRC Canada

Fig. 2. Reaction profiles for ring opening of oxirene. CCSD(T)/6–31G(df,p)//MP2(fc)/6–31G(df,p) with MP2(fc)/6–31G(df,p) ZPE (see Table 1); the CCSD(T)/6–311(df,p) calculation is from ref. 12. For clarity, the ketene minimum is shown separately for the two routes leading to it.

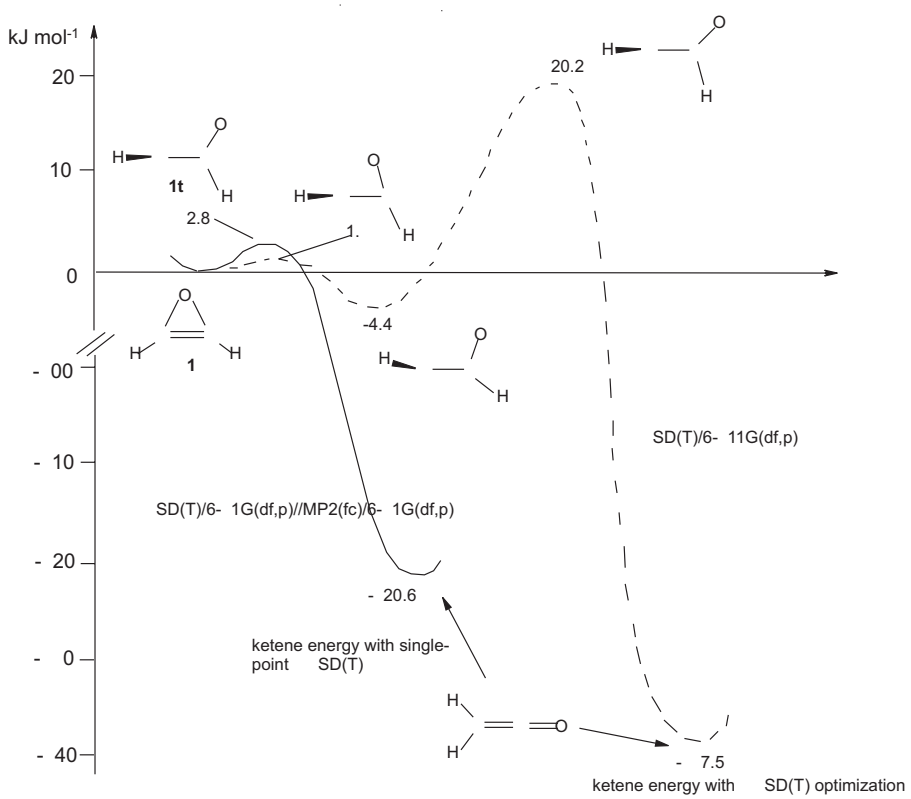

cal necessity since several formal benzene adducts were examined, makes little difference to the relative energies. In Table 2, where both were calculated for two systems (**10** and **1** + **11**), the HF ZPE gives a relative energy ca. 3 kJ mol^{-1} higher for the transition state (**10**), and ca. 7 kJ mol^{-1} higher for the products (**1** + **11**). In Table 1, where both were calculated for **1t** and for **3**, the maximum discrepancy is 3.5 kJ mol^{-1}. For a comparison of the eight systems, which show a maximum discrepancy of 3.7 kJ mol^{-1} (for **8ta** and **8tb**), see below. Correcting the MP2 ZPEs by 0.96 (the correction factor is estimated to be 0.96–0.97) (23), has practically no effect on the relative energies: 241.7 becomes 242.5, 261.3 becomes 262.1, 216.2 becomes 217.4, and 207.5 becomes 208.7 (cf. Table 2). Because MP2(fc)/6–31G(df,p) frequency calculations on all the benzene adducts were scarcely practical (particularly in the dimethyloxirene series, where we estimate the time for each calculation to vary from a minimum of 22 to up to 44 days), we chose to consistently use HF/3–21G ZPEs. Where MP2 optimizations were not followed by frequency calculations we have assigned the structure the status of a minimum or a transition state by analogy with **9** and **10**. Figure 4 depicts the reaction profiles for the CCSD(T)/6–31G(df,p)//MP2(fc)/6–31G(df,p) (with HF/3–21G ZPE) calculations in Table 2.

For the extrusion of ethene from cyclohexene, the experimental activation and reaction energies have been reported to be 266 and 161 kJ mol^{-1}, respectively (26). Our calculated corresponding energies are 267.7 and 200.7 kJ mol^{-1} for the MP2(fc)/6–31G(df,p), and 273.3 and 176.5 kJ mol^{-1} for the CCSD(T)/6–31G(df,p)//MP2(fc)/6–31G(df,p) levels (Table 2). Bearing in mind that the calculated energy differences are 0 K enthalpy differences, the agreement is good and gives us confidence in the other calculated relative energies. The activation energy for oxirene extrusion is, as expected, much higher than that for oxirene ring-opening (below), and confirms that detecting **1** from a thermal retro-Diels–Alder reaction is probably impossible. Our best value (CCSD(T) single-point with MP2 ZPE) for this retro-Diels–Alder activation energy is 261.3 kJ mol^{-1}.

The main value of these calculations is not so much the demonstration that thermal extrusion of oxirene from **9** is not a feasible route to **1** (which was not in serious doubt), but rather the light they shed on the relative energies and the structures of the species involved. Concerning the energetics of these reactions (Fig. 4), consider the changes seen on going from the prototypical retro-Diels—Alder reaction, the fragmentation of cyclohexene (**18**) to ethene and 1,3-butadiene, to the conversion of dihydrobarrelene (**15**) to ethene and benzene: the increased strain imposed by the etheno bridge, and the formation of the resonance-stabilized benzene, should raise the energy of the reactants relative to that of the products. This will decrease the reaction energy and, considering the transition state on a reaction coordinate diagram as the intersection of reactant and product curves (the Bell–Evans–Polanyi concept (27)), should also decrease the activation energy, and in fact these calculated energies go from ca. 177 to 6 (*sic*) and 273 to 159 kJ mol^{-1}, respectively. Comparing the reaction profile of **12** with that of **15**, there is

© 2002 NRC Canada

Fig. 3. Retro-Diels–Alder extrusions of oxirene, cyclopropene, and ethene from formal adducts with benzene, and fragmentation of cyclohexene to ethene and 1,3-butadiene. Key bond lengths are shown in Å for MP2(fc)/6–31G(df,p) geometries, and Löwdin bond orders in parentheses for HF/3–21G calculations on the MP2(fc)/6–31G(df,p) geometries.

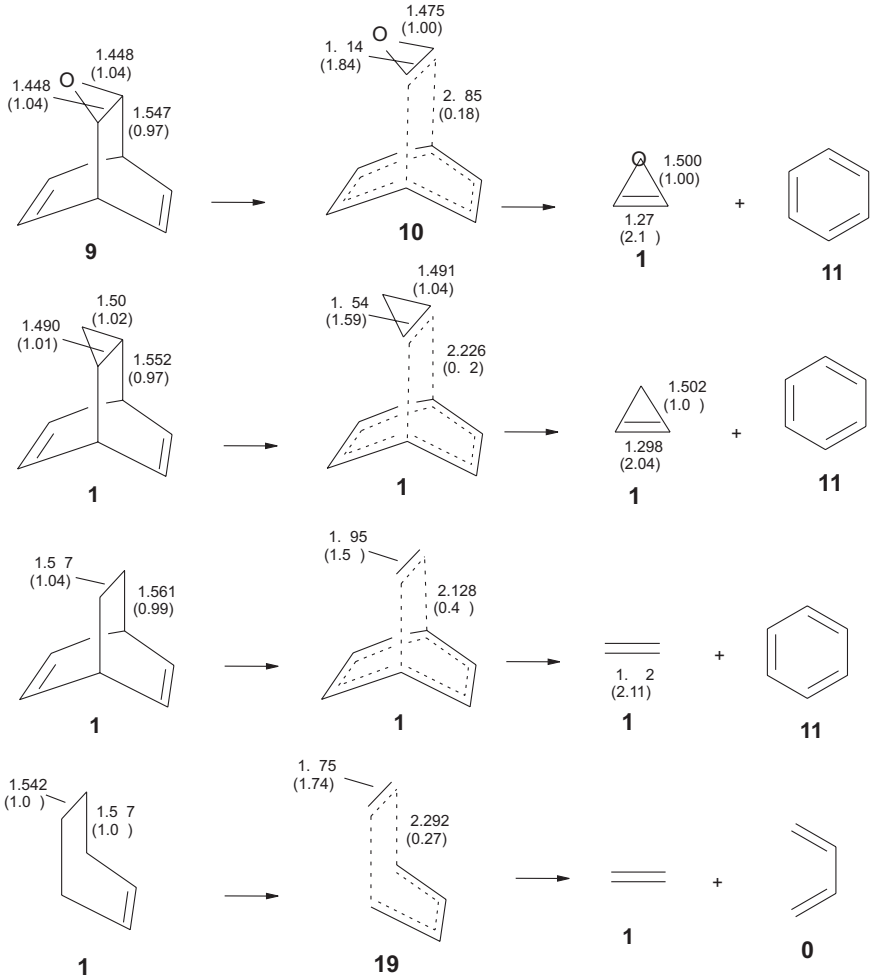

Scheme 1. Isodesmic reactions for formation of cyclopropane and cyclopropene.

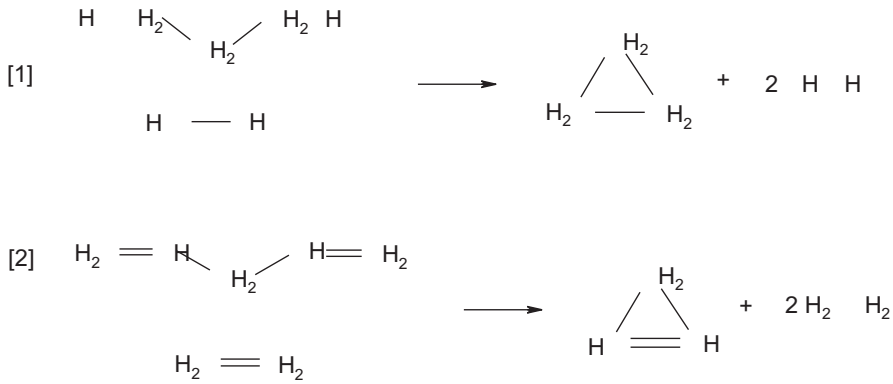

increased strain in both reactant and products caused by the introduction of three-membered rings (benzene is common to both reactions). However, in the reactants an ethano bridge becomes a cyclopropane unit (**15** cf. **12**), while in the products ethene becomes cyclopropene. From the simplest view-point the effect of this depends on the increase in strain on going from ethane to cyclopropane compared to that in going from ethene to cyclopropene, or more precisely, on the isodesmic reaction energies (28) for rxn. [1] compared to rxn. [2] (Scheme 1; these reactions are written to illustrate the concept, and can obviously be simplified by removing a CH_3CH_3 or a CH_2CH_2 from each side). This amounts to the strain energy of cyclopropane vs. cyclopropene (115 vs. 218 kJ mol^{-1} (29)). Our calculations on rxns. [1] and [2] by

© 2002 NRC Canada

Table 2. Calculated relative energies (kJ mol^{-1}) of the species in the extrusion reactions of oxirene, cyclopropene, and ethene from formal adducts with benzene, and in the retro Diels–Alder reaction of cyclohexene.

	MP2(fc)/6–31G(df,p)		CCSD(T)/6–31G(df,p)//MP2(fc)/6–31G(df,p)	
Species	With MP2 etc. ZPE	With HF/3–21G ZPE	With MP2 etc. ZPE	With HF/3–21G ZPE
9, Oxirene–benzene adduct	0	0	0	0
10, Transition state	241.7	244.5	261.3	264.2
1 + **11**, Products	216.2	222.9	207.5	214.2
12, Cyclopropene–benzene adduct	n.a.[a]	0	n.a.	0
13, Transition state	n.a.	166.5	n.a.	192.3
14 + **11**, Products	n.a.	104.3	n.a.	95.9
15, Ethene-benzene adduct	n.a.	0	n.a.	0
16, Transition state	n.a.	136.4	n.a.	158.7
17 + **11**, Products	n.a.	14.2	n.a.	5.7
18, Cyclohexene	n.a.	0	n.a.	0
19, Transition state	n.a.	267.7	n.a.	273.3
17 + **20**, Products	n.a.	200.7	n.a.	176.5

Note: Relative energies are given only for isomeric species – collections of species, e.g. **9**, **10**, and **1** + **11.** MP2 ZPEs were uncorrected (see text), HF/3–21 ZPEs were multiplied by 0.9207 (23). See Fig. 4.

[a]n.a. = MP2 ZPE not calcd.

Fig. 4. Reaction profiles for the retro-Diels–Alder extrusions of oxirene, cyclopropene, and ethene from formal adducts with benzene, and fragmentation of cyclohexene to ethene and 1,3-butadiene, calculated at the CCSD(T)/6–31G(df,p)//MP2(fc)/6–31G(df,p) level with HF/3–21G ZPE corrections. Based on the data in Table 2.

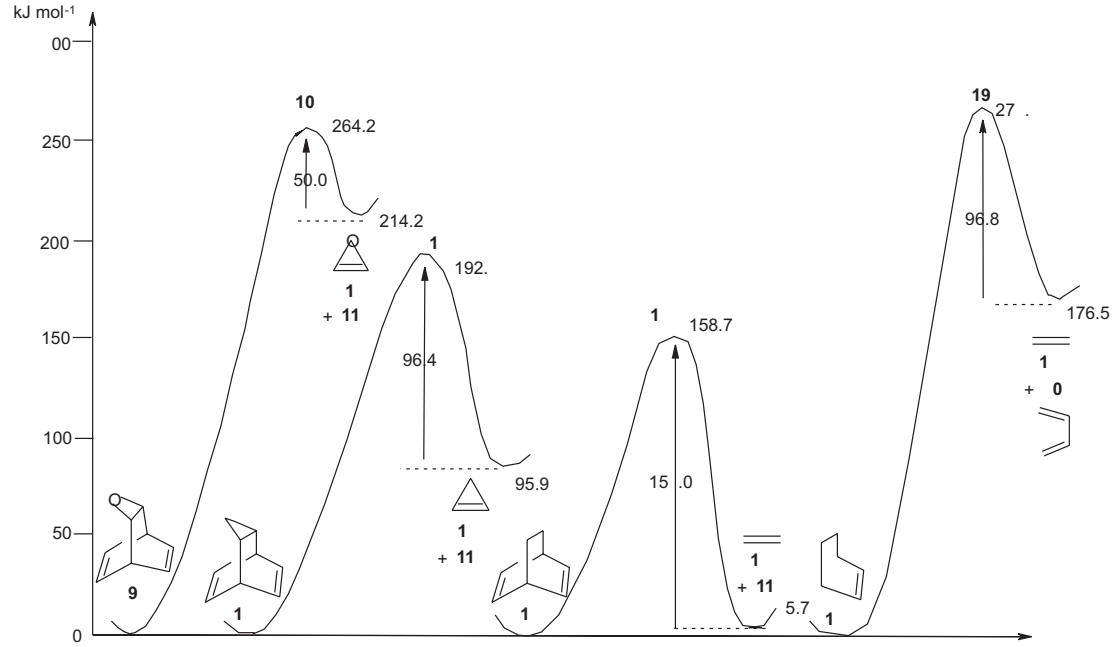

the fast but accurate (30) pBP/DN* DFT method (31), as implemented in Spartan, gave 103 vs. 210 kJ mol^{-1} for ΔE. Naively, one would expect the reaction energy to rise by about 100 kJ mol^{-1} and the activation energy by somewhat less: the former is calculated to increase from 5.7 to 95.9 kJ mol^{-1} and the latter from 158.7 to 192.3 kJ mol^{-1} (Fig. 4).

The energetics of the retro Diels–Alder reaction of **12** compared to **9** are particularly interesting. If we assume that replacing a CH_2 group in a three-membered ring by an O has only a small effect on strain energy (and indeed the strain in cyclopropane and oxacyclopropane (oxirane) is similar, 118 cf. 105 kJ mol^{-1}, respectively (32)), then the difference in the reaction energies of these two extrusions directly reflects the antiaromatic (15) destabilization of oxirene. The value for this difference (214.2 – 95.9 = 118 kJ mol^{-1}) compares well with our independent estimate[6] of ca. 124 kJ mol^{-1} for this antiaromatic destabilization (this may be compared with the partly experimental estimate (33) of 201–230 kJ mol^{-1} for the notoriously reactive cyclobutadiene). As expected, the change in activation energy, which only partly reflects the antiaromaticity of oxirene, is smaller

[6]C. Jakins and E. Lewars. Unpublished results.

© 2002 NRC Canada

Table 3. Bond order and energetics measures of the lateness of the retro-Diels–Alder transition states **19**, **16**, **13**, and **10**.

Transition state	Bond order measure	Energetics measure
19	1/2(0.74 + 1 – 0.27) = 0.74	273.3/(273.3 + 96.8) = 0.74
16	1/2(0.53 + 1 – 0.43) = 0.55	158.7/(158.7 + 153.0) = 0.51
13	1/2(0.59 + 1 – 0.32) = 0.64	192.3/(192.3 + 96.4) = 0.67
10	1/2(0.84 + 1 – 0.18) = 0.83	264.2/(264.2 + 50.0) = 0.84

Note: See Figs. 3 and 4.

(264.2 – 192.3 = 72 kJ mol^{-1}); nevertheless, this is a large fraction of the increase in reaction energy, and indicates that an oxirene moiety is substantially formed in the transition state. This conclusion is reinforced by examination of the structures of the species in these reactions.

The information from the structures (Fig. 3) in these retro-Diels–Alder reactions complements that from the relative energies, and we will refer to changes in bond order (BO) as these are most readily apprehended (they correlate reasonably with bond length changes). The C-C double bond BOs in the dienophiles (**1**, **14**, **17**) and in the corresponding bond of the pro-dienophile moieties of the reactants are, as expected, close to 2 and 1, respectively. This makes it easy to gauge the lateness of a transition state by comparing the C-C BO of the incipient C-C double bond with the BOs of the corresponding bond in the reactant and product; the case for using BOs in this way has been made by Lendvay (34). These BO changes correspond complementarily with those of the two equivalent bonds (all the reactants are of C_s or C_{2v} symmetry) tethering the diene and dienophile moieties. The sum of the dienophile and tether BOs is always close to 2, varying from 1.91 in **13** to 2.02 in **10**. Consider the prototypical retro-Diels–Alder reaction, **18** → **19** → **17** + **20** (Fig. 3): in **19** the BO of the incipient C-C double bond is 1.74, and comparing this with the corresponding BOs in **18** and **17**, close to 1 and 2, respectively, shows that this reaction has a late transition state, with ethene largely extruded; in agreement with this view, the tether bonds BOs have gone from 1.03 in **18** to only 0.27. For simplicity we can use the extent of C-C double bond formation as the criterion of the lateness of the transition states in these reactions, and thus say that **19** lies 74% of the way along the reaction coordinate. Complementing the structural evidence, the energy profile for this reaction (Fig. 4) shows a transition state much closer in energy to the products than to the reactant, which in accordance with the Hammond postulate (35) likely resembles the products. By the above criteria, the extrusion reaction of ethene from dihydrobarrelene (**15** → **16** → **17** + **11**) has a transition state midway between reactants and products (53% along the reaction coordinate) that is in almost perfect accord with its reaction profile, which places **16** slightly closer to the products than to the reactants. The extrusion reaction of cyclopropene from cyclopropanodihydrobarrelene (**12** → **13** → **14** + **11**) has a transition state slightly more advanced than that of the ethene extrusion (59% along the reaction coordinate), and again this agrees with the reaction profile.

Of special interest is the extrusion of oxirene from barrelene oxide (**9** → **10** → **1** + **11**), which may be profitably compared with the cyclopropene extrusion. The transition state here is considerably later than that for the cyclopropene case (84 vs. 59% along the reaction coordinate), although strain factors should be similar in both cases. This is in essentially perfect accord with the energetics, where the reaction profile shows a transition state far closer in energy to the products than the reactants. Such a late transition state is of course expected from a reaction that requires the formation of an antiaromatic, high-energy molecule.

The quantitative relationship between the lateness of these transition states as measured by bond orders and by energetics is interesting. We choose here as the BO measure the mean of the increase in BO from unity of the incipient C-C double bond and the decrease in BO from unity of the tether bond (Table 3 makes this clear). As the energetics measure we use the activation energy of the forward reaction divided by the sum of the activation energies of the forward and reverse reactions (thus for a degenerate reaction this gives an energetics measure of 0.5 or 50%). The results of these calculations are shown in Table 3. The agreement between the two measures is striking.

We note that lower-energy, possibly ionic, pathways are likely to effectively compete with these pericyclic processes, and indeed although flash thermolysis of a (bis)methoxycarbonyl derivative of **9** intriguingly gave some ketene, the main pathway was isomerization to cycloheptatrienecarboxaldehydes (36).

Dimethyloxirene (7), ring-opening and subsequent reactions

Dimethyloxirene (**7**) is interesting because it is the only substituted oxirene, which high-level calculations have clearly indicated it to be a relative minimum rather than a transition state (13), and in a careful and comprehensive study its infrared spectroscopic detection has been claimed (8). The energetics of our calculations on the ring-opening of **7** to oxo carbene ("ketocarbene") **8** and the reactions of **8** are summarized in Table 4 and Fig. 5.

Carbene **8** is calculated to lie above the oxirene. As is the case with the carbene-like transition state **1t** (Table 1 and Fig. 2) in the ring-opening of the parent oxirene (the parent carbene is not a stationary point at the MP2(fc)/6–31G(df,p) level), the relative energy of **8** decreases significantly on going from the MP2 to the (single-point) CCSD(T) level, i.e., from 33.2 to 10.9 kJ mol^{-1} (Table 4 and Fig. 5). Despite much effort we were unable to locate a properly characterized transition state connecting the oxirene and the carbene. The structure **7t** in Figs. 5 and 6 was obtained by coordinate driving (closing the C-C-O carbene angle in steps of 5° to approach the angle of oxirene) and optimizing each structure, subject to this angle restraint, at the MP2(fc)/6–31G(df,p) level. The highest-energy structure along this path (C-C-O = 110°) was subjected to a single-point CCSD(T)/6–31G(df,p) calculation. Coordinate driving is not guaranteed to find a transition state (37), and the relatively large C-C-O

© 2002 NRC Canada

Table 4. Calculated energies (kJ mol^{-1}) of the species in the ring-opening and subsequent reactions of dimethyloxirene (**7**).

	MP2(fc)/6–31G(df,p)		CCSD(T)/6–31G(df,p) single point	
Species	MP2 etc. ZPE	HF/3–21G ZPE	MP2 etc. ZPE	HF/3–21G ZPE
7, Dimethyloxirene	0	0	0	0
7t, Transition state for **7** to oxo carbene **8**[a]	37.6[b]	37.6[b]	10.3[b]	10.3[b]
8, Oxo carbene	33.2 (35.4 cf. **7** with no ZPE)	32.1 (35.4 cf. **7** with no ZPE)	10.9 (13.1 cf. **7** with no ZPE)	9.8 (13.1 cf. **7** with no ZPE)
8ta, Transition state for oxo carbene to *s*-(*Z*) enone (**8a**)	38.9	35.3	28.5	24.8
8tb, Transition state for oxo carbene to *s*-(*E*) enone (**8b**)	48.4	44.7	35.4	31.7
8tc, Transition state for oxo carbene to dimethylketene (**8c**)	35.4	34.4	16.4	15.3
8a, *s*-(*Z*)-Enone	–264.3	–264.0	–273.8	–273.5
8b, *s*-(*E*)-Enone	–265.6	–265.0	–275.1	–277.4
8c, Dimethylketene	–255.9	–257.4	–252.7	–254.2

Note: MP2 ZPEs are uncorrected (see text), HF/3–21G ZPEs have been multiplied by 0.9207 (23). The CCSD(T) calculations are at the MP2(fc)/6–31G(df,p) geometry.

[a]Non-optimized structure – see text.

[b]cf. **7** with no ZPE.

Fig. 5. Reaction profiles for ring opening of dimethyloxirene to the oxo carbene and for reactions of the oxo carbene using CCSD(T)/6–31G(df,p)//MP2(fc)/6–31G(df,p) with MP2(fc)/6–31G(df,p) ZPE, except for **7t**, which is from coordinate driving and is not fully optimized. Based on the data in Table 4.

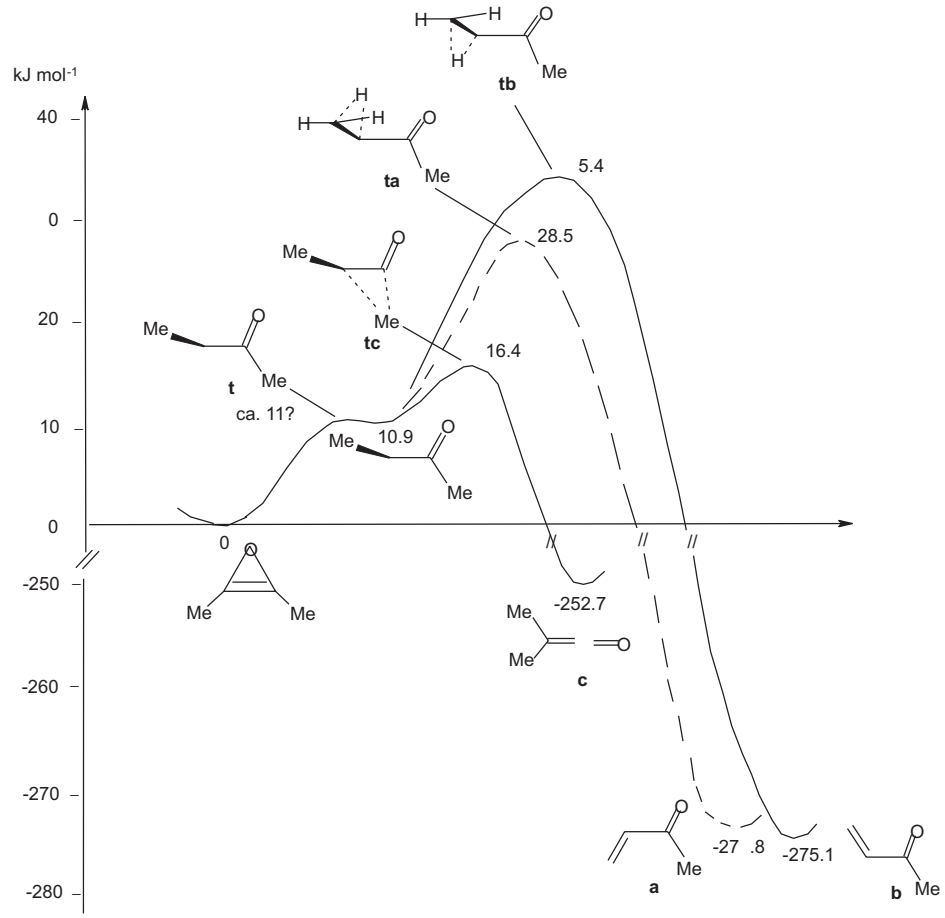

angle of 110° for **7t**, cf. 64.9° and 121.0° for the oxirene and carbene, respectively, suggests that the geometry of this structure may differ significantly from that of the correct transition state; although in accordance with the Hammond postulate (35), the transition state probably does lie closer to the carbene than to the oxirene. Since **7t** was not a properly

© 2002 NRC Canada

Fig. 6. Geometries of oxirene (**1**), dimethyloxirene (**7**), the oxo carbene (**8**), and the approximate (from coordinate driving) transition state structure **7t** calculated at the MP2(fc)/6–31G(df,p) level. Bond lengths are in Å and angles are in degrees.

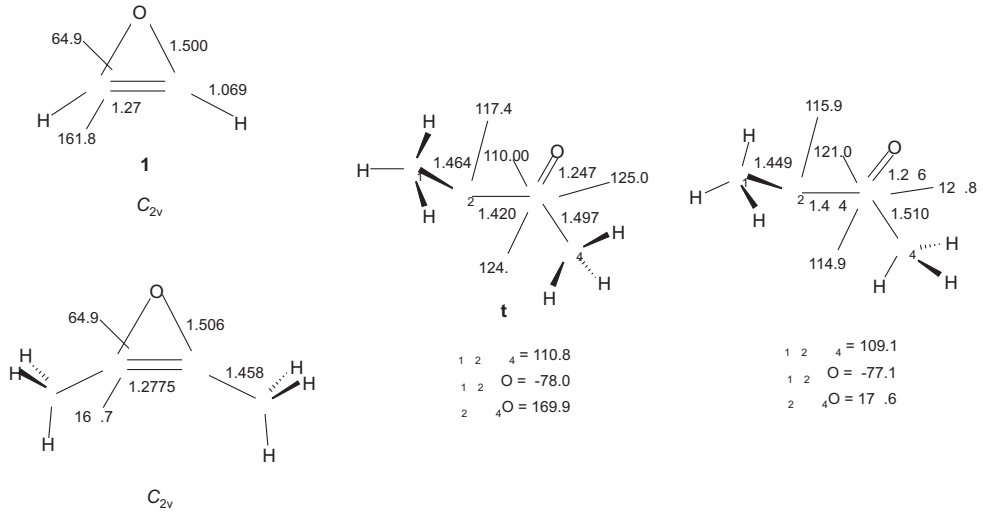

optimized, stationary point ZPEs were not calculated for it (38) and the relative energies given for it in Table 4 represent the differences between the raw ab initio energies of **7** and **7t**. If we uniformly compare the energies of **7**, **7t**, and **8** without ZPE corrections, then at the MP2 level **7t** is ca. 2 kJ mol^{-1} *above* **8** but at the single-point CCSD(T) level it is 3 kJ mol^{-1} *lower*, implying that although the coordinate driving structure approximates the true transition state connecting **7** and **8**, this transition state lies only slightly above **8** (Fig. 5). The CCSD(T) dimethyloxirene–carbene energy difference is probably reliable, and places a lower limit on the barrier to ring-opening of this oxirene at about 11 kJ mol^{-1}, compared to 2.8 kJ mol^{-1} (1.3 kJ mol^{-1} for the CCSD(T)-optimized PES (12)) for the opening of the parent oxirene. Our geometries for oxirene **1**, dimethyloxirene **7**, oxo carbene **8**, and the approximate transition state for **7t** are shown in Fig. 6.

The oxo carbene **8** was calculated to readily undergo the standard carbene reactions of hydrogen and alkyl migration to give the butenones **8a** and **8b** (conformers),and dimethylketene (**8c**), with barriers of 35.4 – 10.9 = 17.6, 28.5 – 10.9 = 24.5, and 16.4 – 10.9 = 5.5 kJ mol^{-1}, respectively, (Fig. 5 and Table 4). In thermal processes, dimethyloxirene should drain away via the oxo carbene to give mainly dimethylketene. Our finding of a lower activation energy for the formation of dimethylketene than for butenone is consistent with the observation that in the gas phase collisional deactivation of vibrationally excited carbene **8** increases the ratio of dimethylketene to butenone, suggesting that the latter comes from higher vibrational levels of **8** (39).

We briefly comment on the (primarily experimental) work of Bachmann et al. (8) on dimethyloxirene and on the report by Torres et al. (9) on the preparation of perfluoroalkyloxirenes. Bachmann et al. photolyzed 3-diazo-2-butanone and confirmed by trapping with CO the formation of carbene **8**. Irradiation of **8** in a xenon matrix gave a species, stable below 25 K, that was assigned the structure of dimethyloxirene. An IR band at 2127.6 cm^{-1} from the perdeuterio diazoketone was attributed to the C=C stretch of **7**-d_6, and a band at 2137 cm^{-1} from the nondeuterated precursor was attributed to the C=C stretch of dimethyloxirene. HF/3–21G calculations on **1** and **7** and HF/6–31G** calculations on **1** supported these assignments. Table 5 contains our calculated vibrational spectra of oxirene, dimethyloxirene, and dimethyloxirene-d_6, at the MP2(fc)/6–31G(df,p) level. The correction factor for MP2(fc)/6–31G(df,p) frequencies should be close to 0.94 (23); using this value, the C=C stretch of dimethyloxirene-d_6 is calculated to come at 1969 cm^{-1} and the C=C stretch of dimethyloxirene at 1974 cm^{-1}. Both bands should be very weak or undetectable. On the other hand, the second-strongest band (49%, C—D stretch) in the calculated dimethyloxirene-d_6 spectrum should appear at about 2108 cm^{-1}, quite close to the observed 2127.6 cm^{-1} band. Although the band that was attributed to the C=C stretch of dimethyloxirene-d_6 could have been due to C—D stretch in that molecule, the IR results for undeuterated dimethyloxirene cast doubt on the claim that these two species were observed in the Bachmann et al. work. The only band in the IR spectrum of undeuterated dimethyloxirene that could conceivably appear at 2137 cm^{-1} is the C=C stretch, but our calculations place it distinctly (163 cm^{-1}) lower, and in any case it should be at best very weak. We question the strength of the IR evidence for the observation of dimethyloxirene, although (Fig. 5) this compound is indeed likely to be the proximate product from the carbene **8** in a thermal rearrangement.

Irradiation of the putative dimethyloxirene with broadband light of $\lambda > 230$ nm, but not with monochromatic 457.9 nm light, was reported (8) to lead to dimethylketene. This is consonant with the predicted UV spectrum of **7**, which we calculated on the MP2 geometry by the usually reliable TDDFT method (40) as implemented (41) in Gaussian 98, at the recommended (40) B3P86/6–311++G** level; Table 6 gives the calculated UV spectra of **1** and **7**. The dimethyl compound is predicted to lack absorption above ca. 290 nm (the zero-intensity absorptions are only formally forbidden, e.g., acetone is calculated to have an oscillator strength = 0 band at 290 nm, but in fact shows a very weak ϵ 13 band at 279 nm, a band that initiates a plethora of photo-

© 2002 NRC Canada

Table 5. Calculated vibrational spectra of oxirene, dimethyloxirene, and dimethyloxirene-d_6, at the MP2(fc)/6–31G(df,p) level.

Oxirene	Dimethyloxirene	Dimethyloxirene-d_6
153 (1) Ring-opening	128 (8) C—Me rotation	104 (8) C—Me rotation
	195 (0) Ring-opening	185 (9) C-C-C-C bend
502 (100) C—H out-of-plane bend	213 (11) C-C-C-C bend	192 (0) Ring-opening
907 (50) C—O stretch coupled to C—H bend	930 (32) C—O stretch coupled to C—H bend	790 (10) C—O stretch coupled to C—H bend
986 (8) C—H in-plane bend	1071 (11) C—H bend	876 (7) C—H bend coupled to C-C-C-C bend
1801 (2) C=C stretch	1080 (6) C—H bend	1079 (100) C—O stretch coupled to C—H bend
3414 (60) C—H stretch	1177 (100) C—O stretch coupled to C—H bend	1084 (20) C—H bend
	1504 (42) C—H bend	1154 (24) C—O stretch coupled to C—H bend
	1528 (26) C—H bend	2095 (0) C=C stretch
	2100 (0) C=C stretch	2243 (49) C—D stretch
	3122 (94) C—H stretch	2375 (16) C—D stretch
	3206 (29) C—H stretch	2398 (11) C—D stretch
	3234 (25) C—H stretch	

Note: Band positions are in cm^{-1} and relative intensities are given in parentheses. All bands of relative intensity ≥ 5% and the ring-opening and C=C stretch bands are listed. None of the spectra have imaginary frequencies. A correction factor has not been applied to the band positions.

Table 6. UV spectra of oxirene (**1**) and dimethyloxirene (**7**), calculated by TDDFT (singlet → singlet), at the B3P86/6–311++G** level, using MP2(fc)/6–31G(df,p) geometries.

Oxirene	Dimethyloxirene
316 (0.0035, 49)	290 (0.0000, 0)
257 (0.0009, 13)	284 (0.0137, 100)
231 (0.0022, 31)	257 (0.0000, 0)
227 (0.0000, 0)	238 (0.0012, 9)
200 (0.0000, 0)	224 (0.0011, 8)
184 (0.0071, 100)	223 (0.0017, 12)

Note: Band positions are in nm and intensities (in parentheses) are given as oscillator strengths and relative intensities, respectively.

chemical reactions). The TDDFT UV of **7** is, thus, at least consistent with the reported (8) photochemical behavior.

The first credible report of the detection of an oxirene was that by Torres et al. (9). They tentatively assigned the bis(trifluoromethyl)oxirene structure (**21**) to one species, and concluded that another species was perfluoroethylmethyloxirene (**22**) by virtue of its formation from isomeric α-diazoketones **23a** and **23b**. We calculated the IR spectrum of **21** at the relatively fast MP2(fc)/6–31G* level after confirming that the calculated IR spectra of **1** and **7** had changed little on going from the 6–31G(df,p) to the 6–31G* basis set: **1** acquires an imaginary ring-opening mode (153 → 39*i* cm^{-1}) and the other bands move ca. 20–50 cm^{-1} to smaller wavenumber (except for C=C stretch, 1801 → 1799 cm^{-1}), whereas the bands of **7** shift (up and down) by up to 33 cm^{-1} (ring-opening mode, 128 → 132 and C=C stretch 2100 → 2090 cm^{-1}). If we realize that **21** may be a potential energy surface relative minimum, rather than the transition state implied by the imaginary frequency, the calculated and (tentative) experimental spectra of **21** may be compared (Table 7). It is not simple to draw a definite conclusion from this comparison, because the experimental intensities were characterized only qualitatively, the calculated intensities are only semiquantitative (42), and matrix effects (43) can cause observed frequencies to deviate somewhat from calculated gas-phase values. If we consider just those bands reported to be medium and strong, and bear in mind that a deviation of about 50 cm^{-1} is quite reasonable, we might correlate (calcd./exp.; Table 7) the 625 (3)/660 m, 1185 (62)/1160 m, and 1228 (100)/1275 s cm^{-1} bands, but the 1325 m cm^{-1} band has no calculated counterpart. For **22**, band positions but not intensities were reported; these might be compatible with other perfluoro-C_5 molecules, although obtaining the same spectrum from **23a** and **23b** clearly supports the assigned structure. It must be noted, however, that in their ma-

Table 7. Calculated vibrational spectrum of bis(trifluoromethyl)oxirene (**21**) at the MP2(fc)/6–31G* level, and the experimental spectrum tentatively assigned to **21** (9).

Calculated	Experimental
92*i* (10) Ring-opening	560 w
438 (1) C-C-C-C bend/C—F bend coupled	660 m
558 (1) C-C-C-C bend/C—F bend coupled	730 w
578 (1) C-C-C-C bend/C—F bend coupled	875 w
625 (3) C-C-C-C bend/C—F bend coupled	1160 m
856 (1) C-C-C-C stretch/C—F stretch coupled	1275 s
1010 (5) C—O stretch	1325 m
1185 (62) C—F stretch	
1190 (4) C—F stretch	
1192 (19) C—C bend/C—F stretch coupled	
1212 (32) C—C stretch/C—F stretch coupled	
1238 (100) CF_3—C stretch	
1966 (2) C=C stretch	

Note: The calculated spectrum band positions (in cm^{-1}) have been multiplied by the recommended (23) correction factor of 0.9434, and relative intensities are given in parentheses. All calculated bands of relative intensity >0% are given.

© 2002 NRC Canada

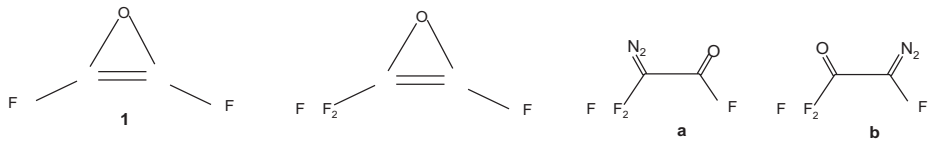

Fig. 7. Retro-Diels–Alder extrusion of dimethyloxirene from its adduct with benzene. Key bond lengths are shown in Å for MP2(fc)/6–31G(df,p) geometries, and Löwdin bond orders in parentheses for HF/3–21G calculations on the MP2(fc)/6–31G(df,p) geometries. The relative energies of reactant, transition state, and products, at the MP2(fc)/6–31G(df,p) level with HF/3–21G ZPE corrections, are given.

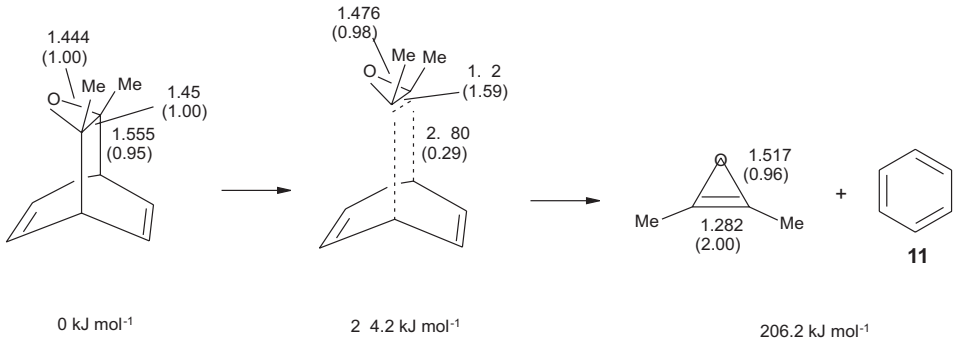

trix isolation study of perfluoro-3-diazo-2-butanone, Laganis et al. (44) were unable to obtain the IR spectrum ascribed (9) to **21**. We conclude that it is doubtful that any oxirene has yet been observed under matrix isolation conditions.

Dimethyloxirene (7), retro-Diels–Alder extrusion

Finally, we briefly summarize our results for the extrusion of **7** from its formal benzene adduct **24** (Fig. 7). Because of the size of **24**, it was studied only by optimization at the MP2(fc)/6–31G(df,p) level with HF/3–21G ZPE corrections; the structural and energetic similarities of **10** and **25** make us confident that **25** is indeed a transition state, and the results with the parent systems (Table 2) indicate that only small changes in relative energies should occur on going to the CCSD(T) level with MP2 ZPEs. Comparison with Fig. 3 shows, concentrating on bond orders, that the dimethyloxirene extrusion transition state **25** is significantly earlier than that for oxirene extrusion. If we say that **10** (Fig. 3) is about 80% (bond orders: 1.84–1 and 1–0.18) along the reaction coordinate, then **25** is only about 60–70% (1.59–1 and 1–0.29) along the way to completion. This is expected if dimethyloxirene is in fact stabilized by the methyl groups, i.e., it should be easier to extrude it. Oddly, this is scarcely reflected in the calculated energetics of the reaction; if we compare at the MP2(fc)/6–31G(df,p) level with HF/3–21G ZPE corrections the dimethyl case (Fig. 7) and the parent system (Table 2), we see that extrusion of **7** has calculated activation and reaction energies of 234.2 and 206.2 kJ mol^{-1}, respectively, while extrusion of **1** has 244.5 and 222.9 kJ mol^{-1} as the corresponding values.

Conclusions

Oxirene was calculated to isomerize directly to ketene with a barrier of 2.8 kJ mol^{-1}; that the carbene was not an intermediate may be an artifact of the CCSD(T)/6–31G(df,p)//MP2(fc)/6–31G(df,p) computational level. At this level the formal oxirene–benzene adduct is calculated to undergo a retro-Diels–Alder reaction with a barrier of 264 kJ mol^{-1}, and so the oxirene, even if a genuine potential surface relative minimum, is likely to be undetectable. Comparison of the extrusion reactions for oxirene and cyclopropene indicated an antiaromatic destabilization energy for oxirene of 118 kJ mol^{-1}. There are discrepancies between our calculations and IR bands reported for dimethyloxirene and for bis(trifluoromethyl)oxirene.

The dimethyloxirene → oxo carbene transition state could not be characterized, but the carbene was a relative minimum 10.9 kJ mol^{-1} above the oxirene (CCSD(T)/6–31G(df,p)//MP2(fc)/6–31G(df,p)). The carbene was predicted to isomerize to dimethylketene with a barrier of 16.4 kJ mol^{-1}, while the two conformers of butenone were calculated to be formed with barriers of about 30 kJ mol^{-1}. Comparing the oxirene and dimethyloxirene extrusions (at the MP2(fc)/6–31G(df,p) level with HF/3–21G ZPEs and bond orders), the dimethyloxirene extrusion involves an earlier transition state as judged by bond orders, yet has only a slightly lower activation energy.

Acknowledgment

We thank the Natural Sciences and Engineering Research Council of Canada (NSERC) for financial support.

References

1. (*a*) M.J.S. Dewar and C.A. Ramsden. J. Chem. Soc. Chem. Commun. 688 (1973); (*b*) A.C. Hopkinson. J. Chem. Soc. Perkin Trans. 2, 794 (1973).
2. G. Maier, H.P. Reisenauer, and M. Cibulka. Angew. Chem. Int. Ed. Engl. **38**, 105 (1999).
3. (*a*) J.M. Anglada and J.M. Bofill. Int. J. Quantum Chem. **62**, 153 (1997); (*b*) W.J. Bouma, R.H. Nobes, L. Radom, and C. Woodward. J. Org. Chem. **47**, 1869 (1982); (*c*) Y. Apeloig and R. Schreiber. Tetrahedron Lett. 4555 (1978).
4. E. Lewars and I. Bonnycastle. J. Mol. Struct. (Theochem). **418**, 17 (1997), and refs. therein.

© 2002 NRC Canada

5. E. Lewars. Chem. Rev. **83**, 519 (1983).
6. F. Turecek, D.E. Drinkwater, and F.W. McLafferty. J. Am. Chem. Soc. **113**, 5958 (1991).
7. C.E.A. Hop, J.L. Holmes, and J.K. Terlouw. J. Am. Chem. Soc. **111**, 441 (1989).
8. C. Bachmann, Y. N'Guessan, F. Debû, M. Monnier, J. Pourcin, J.-P. Aycard, and H. Bodot. J. Am. Chem. Soc. **112**, 7488 (1990).
9. M. Torres, J.L. Bourdelande, and O.P. Strausz. J. Am. Chem. Soc. **105**, 1698 (1983).
10. G. Vacek, B.T. Colegrove, and H.F. Schaefer. Chem. Phys. Lett. **177**, 468 (1991).
11. G. Vacek, J.M. Galbraith, Y. Yamaguchi, H.F. Schaefer, R.H. Nobes, A.P. Scott, and L. Radom. J. Phys. Chem. **98**, 8660 (1994).
12. A.P. Scott, R.H. Nobes, H.F. Schaefer, and L. Radom. J. Am. Chem. Soc. **116**, 10 159 (1994).
13. J.E. Fowler, J.M. Galbraith, G. Vacek, and H.F. Schaefer. J. Am. Chem. Soc. **116**, 9311 (1994).
14. (*a*) E. Lewars. Can. J. Chem. **78**, 297 (2000); (*b*) E. Lewars. J. Mol. Struct. (Theochem), **360**, 67 (1996).
15. (*a*) S. Zilberg and Y. Haas. J. Phys. Chem. A, **102**, 10 843 (1998); (*b*) N.L. Bauld, T.L. Welsher, J. Cessac, and R.L. Holloway. J. Am. Chem. Soc. **100**, 6920 (1978).
16. (*a*) H.J. Lindner and B. von Gross. Chem. Ber. **107**, 598 (1974); (*b*) R. Gompper, F. Hoisboer, W. Schmidt, and G. Seybold. J. Am. Chem. Soc. **95**, 8479 (1973).
17. E. Lewars. J. Mol. Struct. (Theochem), **391**, 39 (1997).
18. (*a*) R.F.C. Brown. Pyrolytic methods in organic chemistry. Academic Press, New York. 1980. p. 259; (*b*) H. Kwart and K. King. Chem. Rev. **68**, 415 (1968).
19. W.J. Hehre, L. Radom, P.v.R. Schleyer and J.A. Pople. Ab initio molecular orbital theory. Wiley-Interscience, New York. 1986.
20. J.B. Foresman and A. Frisch. Exploring chemistry with electronic structure methods. 2nd ed. Gaussian Inc., Pittsburgh. 1996.
21. (*a*) W.J. Hehre, L. Radom, P.v.R. Schleyer and J.A. Pople. Ab initio molecular orbital theory. Wiley-Interscience, New York. 1986. Section 6.3; (*b*) J.B. Foresman and A. Frisch. Exploring chemistry with electronic structure methods. 2nd ed. Gaussian Inc., Pittsburgh. 1996. Chap. 4.
22. J.B. Foresman and A. Frisch. Exploring chemistry with electronic structure methods. 2nd ed. Gaussian Inc., Pittsburgh. 1996. Chap. 8.
23. A.P. Scott and L. Radom. J. Phys. Chem. **100**, 16 502 (1996).
24. I.N. Levine. Quantum Chemistry. 5th ed. Prentice Hall, Upper Saddle River, New Jersey. 2000. pp. 568–573 and refs. therein.
25. M.A. Natiello and J.A. Medrano. Chem Phys. Let. **105**, 180 (1984); **110**, 445 (1984).
26. K.N. Houk, Y. Li, and J.D. Evanseck. Angew. Chem. Int. Ed. Engl. **31**, 682 (1992).
27. S.S. Shaik, H.B. Schlegel, and S. Wolfe. Theoretical aspects of physical organic chemistry. Wiley, New York. 1992. Chap. 1.
28. D.A. Ponomarev and V.V. Takhistov. J. Chem. Educ. **74**, 201 (1997).
29. E.L. Eliel and S.H. Wilen. Stereochemistry of organic compounds. Wiley, New York. 1994. pp. 677, 755.
30. W. Hehre and L. Lou. A guide to density functional calculations in Spartan. Wavefunction Inc., Irvine, CA. 1997.
31. (*a*) A.D. Becke. Phys. Rev. A, **38**, 3089 (1988); (*b*) A.D. Becke. Phys. Rev. A, **33**, 2786 (1986); (*c*) J.P. Perdew. Phys. Rev. B, **33**, 8822 (1988); (*d*) B. Delley and D.E. Ellis. J. Chem. Phys. **76**, 1949 (1982).
32. A. Skancke, D. Van Vechte, J.F. Liebman, and P.N. Skancke. J. Mol. Struct. **376**, 461 (1996), and refs. therein.
33. A.A. Deniz, K.S. Peters, and G.J. Snyder. Science (Washington, D.C.), **286**, 1119 (1999).
34. G. Lendvay. J. Phys. Chem. **98**, 6098 (1994).
35. (*a*) G.S. Hammond. J. Am. Chem. Soc. **77**, 334 (1955); (*b*) M. Solà and A. Toro-Labbé. J. Phys. Chem. A, 103, 8847 (1999), and refs. 2–8 therein.
36. E.G. Lewars and G. Morrison. Can. J. Chem. **55**, 966 (1977).
37. S.S. Shaik, H.B. Schlegel, and S. Wolfe. Theoretical aspects of physical organic chemistry. Wiley, New York. 1992. pp. 73–75.
38. J.B. Foresman and A. Frisch. Exploring chemistry with electronic structure methods. 2nd ed. Gaussian Inc., Pittsburgh. 1996. p. 62.
39. C. Marfisi, P. Verlaque, G. Davidovics, J. Pourcin, L. Pizzala, J.P. Aycard, and H. Bodot. J. Org. Chem. **48**, 533 (1983).
40. K.B. Wiberg, R.E. Stratman, and M.J. Frisch. Chem. Phys. Lett. **297**, 60, (1998).
41. R.E. Stratman, G.E. Scuseria, and M.J. Frisch. J. Chem. Phys. **109**, 8218 (1998).
42. (*a*) M.D. Halls and H.B. Schlegel. J. Phys. Chem. **109**, 10 587 (1998); (*b*) H. Lampert, W. Mikenda, and A. Karpfen. J. Phys. Chem. A, **101**, 2254 (1997); (*c*) D.H. Magers, E.A. Salter, R.J. Bartlett, C. Salter, B.A. Hess, and L.J. Schaad. J. Am. Chem. Soc. **110**, 3435 (1988).
43. I.R. Dunkin. Matrix-isolation techniques. A practical spproach. Oxford University Press, New York. 1998.
44. E.D. Laganis, D.S. Janik, T.J. Curphey, and D.M. Lemal. J. Am. Chem. Soc. **105**, 7457 (1983).

© 2002 NRC Canada

Inhibition de la corrosion de l'alliage d'aluminium 6063 au moyen de composés inorganiques dans une solution de chlorure de sodium à 3 %

L. Bazzi, R. Salghi, E. Zine, S. El Issami, S. Kertit et B. Hammouti

Résumé : L'effet de l'addition de certains composés inorganiques sur le comportement à la corrosion d'un alliage d'aluminium 6063, dans une solution de chlorure de sodium à 3 % est étudié à l'aide des méthodes électrochimique et métallographique. Les composés testés sont les oxo-anions MoO_4^{2-}, CrO_4^{2-}, NO_2^- et les cations métalliques Li^+ et Mg^{2+}. Les résultats obtenus montrent que les composés testés inhibent le processus de corrosion de l'alliage 6063. Le caractère inhibiteur le plus marqué est obtenu en présence des ions Li^+. L'augmentation de la concentration de ces ions a pour effet d'accroître la différence entre le potentiel de piqûration et le potentiel de corrosion. L'efficacité maximale de l'ordre de 85 % est atteinte dès une concentration de 5×10^{-3} M. L'élévation de la température de 25 à 55°C a pour effet d'améliorer la résistance à la corrosion de l'alliage 6063 dans le milieu témoin. Cependant, en présence des ions Li^+, l'efficacité inhibitrice subit une décroissance lorsque la température augmente.

Mots clés : corrosion, inhibition, composés inorganiques, alliage d'aluminium 6063, NaCl 3 %.

Abstract: Some inorganic compounds have been tested as corrosion inhibitors for 6063 aluminium alloy in 3% NaCl by electrochemical and metalographic methods. The compounds were MoO_4^{2-}, CrO_4^{2-}, NO_2^- oxo-anions and Li^+ and Mg^{2+} metallic cations. Results obtained show that these compounds inhibited corrosion of 6063 aluminium alloy, and that the Li^+ cations were the best inhibitors. The difference between pitting potential and corrosion potential increase by increasing the concentration of Li^+. The maximum inhibition efficiency (E% = 85%) was attained at 5×10^{-3} M. Increasing temperature from 25 to 55°C improve corrosion resistance of 6063 aluminium alloy in the absence of Li^+. However, in the presence of these cations, E% decreased at elevated temperature.

Key words: corrosion, inhibition, inorganic compounds, 6063 aluminium alloy, 3% NaCl.

Introduction

L'aluminium et ses alliages acquièrent leur stabilité à travers le film d'oxyde-hydroxyde formé à la surface. Bockris et Minevski (1) ont examiné le mécanisme de passivation de l'aluminium et de ses alliages. Ils ont conclu que pour des valeurs de pH allant de 8 à 11, il y a formation d'une couche poreuse constituée par $Al(OH)_3$ de structure amorphe et par Al_2O_3 cristallisé. Cependant, les ions chlorures sont caractérisés par leur facilité à pénétrer dans ce film et par la formation de complexes solubles. L'inhibition de la corrosion des alliages d'aluminium a fait l'objet de travaux antérieurs. Parmi les inhibiteurs classiques les plus utilisés nous citons les chromates, les silicates et les molybdates (2–6). Des techniques expérimentales telles que les méthodes électrochimiques et les méthodes d'analyse de surface ont pu contribuer à mieux connaître le mécanisme d'inhibition de ces ions. Treverton et al. (7) ont suggéré que les ions chromates pénètrent à travers les défauts et les inclusions du film d'oxyde. Ils réagissent avec les ions métalliques pour former un oxyde mixte Cr_2O_3–Al_2O_3 et par suite empêcher la formation de complexes d'aluminium solubles. Konno et al. (8) ont montré que les ions chromates s'adsorbent à la surface du film d'oxyde. Ils forment une monocouche qui limite l'hydratation du film passif et par suite sa détérioration. Brett et al. (9) ont reporté que l'action des ions chromates dépend du potentiel d'électrode et qu'ils sont fortement adsorbés au voisinage du potentiel de piqûration. Selon d'autres auteurs (10) l'adsorption des ions chromates a pour effet de neutraliser les charges positives à la surface. Ils réduisent de ce fait la pénétration des ions chlorures dans le film d'oxyde et contribuent à la stabilité de la phase oxyde amorphe. Dans des travaux antérieurs (2, 3), nous avons illustré le rôle que peuvent jouer les ions chromates dans

Reçu le 4 mai 2001. Publié au site Web des Presses scientifiques du CNRC, http://revcanch.cnrc.ca le 22 janvier 2002.

L. Bazzi[1] et S. El Issami. Laboratoire de chimie – physique, Faculté des sciences d'Agadir, B. P. 28/S, Agadir, Maroc.
R. Salghi et E. Zine. Laboratoire de l'établissement autonome de contrôle et de coordination des exportations, B. P. 1710, Ancien port, Agadir, Maroc.
S. Kertit. Laboratoire de Physico-chimie des matériaux, associé à l'AUPELF-UREF (LAF502); École normale supérieure de Takaddoum, B. P. 5118, Rabat, Maroc.
B. Hammouti. Laboratoire de corrosion et chimie des eaux, Faculté des sciences d'Oujda, Oujda, Maroc.

[1]Auteur correspondant (courriel : lbazzi@caramail.com).

 DOI: 10.1139/V01-189 © 2002 CNRC Canada

Tableau 1. Composition chimique en poids de l'alliage d'aluminium 6063.

Elément	Al	Mg	Si	Mn	Fe	Zn	Cu	Ti	Ni	Cr
Poids (%)	Balance	0,53	0,44	0,04	0,19	< 0,002	< 0,030	< 0,002	< 0,003	< 0,002

l'inhibition de la corrosion de l'alliage d'aluminium 6063 en milieu neutre non pollué par les ions cuivriques. Le mécanisme de leur action a été expliqué par leur adsorption sur des sites privilégiés pour empêcher le processus de déposition du cuivre à la surface métallique.

Shalaby et al. (11) ont étudié le comportement électrochimique de l'aluminium dans une solution de chlorure de sodium en présence des ions silicates. Ils ont constaté qu'à faibles concentrations (1×10^{-4} M), les ions aluminium réagissent avec le silicate de sodium pour former un film très mince moins soluble et plus compact que la bayérite. Selon ces auteurs, il s'agit de composés cristallins de type $Na_2O{\cdot}Al_2O_3{\cdot}Si_2O{\cdot}H_2O$. Néanmoins, pour des concentrations supérieures, le film passif peut perdre son pouvoir protecteur.

Shaw et al. (12) ont réalisé un prétraitement électrochimique du film passif de l'aluminium dans une solution décimolaire de molybdate de sodium. Ce prétraitement améliore de manière significative la résistance à la corrosion de l'aluminium dans une solution de chlorure de sodium. L'analyse par XPS de ce film indique une prédominance des espèces hydratées de Mo(VI) et Mo(IV) par rapport aux ions chlorures. Cependant, Breslin et al. (13) ont suggéré que la réduction de Mo(VI) en Mo(IV) n'est pas suffisante pour expliquer la performance de l'aluminium en milieu NaCl 0,5 M en présence d'ions molybdates et que ces derniers interviennent par leur pouvoir oxydant dans la croissance de la couche passive. Bazzi et al. (5) ont suggéré que les ions molybdates agissent sur le processus anodique en minimisant la sensibilité à la piqûration de l'alliage d'aluminium 6063.

Fernandes et al. (14, 15) ont examiné l'effet des ions lithium sur le comportement de l'aluminium dans des solutions carbonates. Les résultats obtenus par ces auteurs indiquent la prédominance des ions Li^+ dans le film passif. Rangel et Travassos (16) ont montré qu'en présence des ions chlorures le film riche en ions lithium manifeste une certaine résistance à l'attaque localisée caractérisée par le déplacement du potentiel de piqûration vers des valeurs plus positives. La stabilité de ce film a été mise en évidence par emploi de la voltampérométrie cyclique (16).

Malgré le nombre relativement élevé de travaux consacrés à l'inhibition de la corrosion des alliages d'aluminium, il reste tout de même un certain nombre d'aspects sujets à controverse. Les auteurs ont essentiellement axé leurs recherches sur le comportement anodique, le mécanisme d'action de la plupart des inhibiteurs testés à débattre. D'autant plus que l'action inhibitrice d'un tel inhibiteur peut varier d'un alliage à un autre. Nous nous sommes aperçus également de la rareté des travaux entrepris sur l'inhibition de la corrosion des alliages d'aluminium par les cations métalliques. Nous citons en particulier les ions lithium et magnésium. L'effet inhibiteur des ions lithium est peu étudié dans les milieux chlorurés. La plupart des études ont été réalisées en milieux bicarbonates (14–16).

L'objectif de ce travail est l'étude de l'inhibition de la corrosion de l'alliage d'aluminium 6063 au moyen de composés

Fig. 1. Courbes de polarisation de l'alliage d'aluminium 6063 sans et avec addition d'inhibiteur à 25°C.

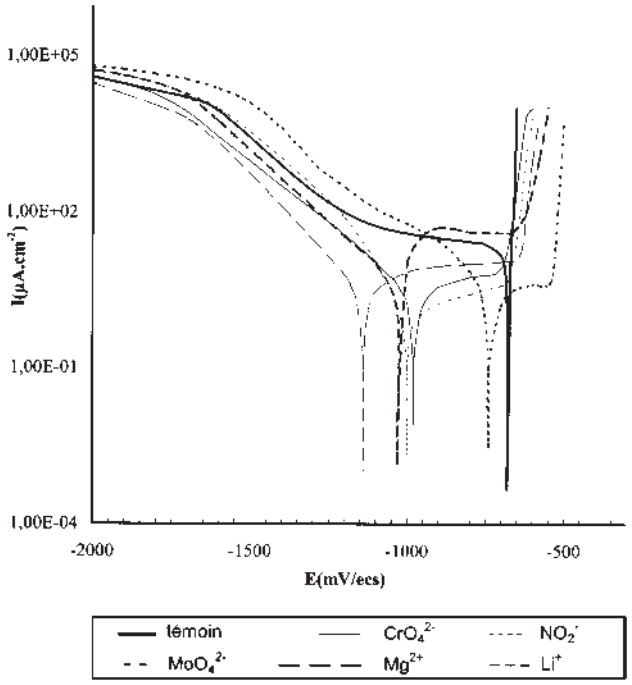

suivants : $Na_2CrO_4{\cdot}2H_2O$; $Na_2MoO_4{\cdot}2H_2O$; Li_2SO_4; $MgSO_4$ anhydre et $NaNO_2$.

Partie expérimentale

Nous avons retenu dans cette étude l'alliage d'aluminium 6063 de la classification de l'Association d'aluminium américain. Il est couramment utilisé dans l'industrie agricole et agro-alimentaire. La composition exacte de cet alliage est donnée dans le tableau 1.

La solution corrosive est une solution à 3 % de chlorure de sodium. Le milieu électrolytique est préalablement désaéré pendant 0,5 h par barbotage d'azote. L'homogénéisation de l'électrolyte est assurée par une agitation magnétique. Le pH du milieu est ajusté à la valeur 7,5 par ajout de l'acide chlorhydrique ou de la soude.

Les solutions contenant les composés inorganiques sont préparées, par dissolution dans le milieu témoin, des composés suivants : $Na_2CrO_4{\cdot}2H_2O$; $Na_2MoO_4{\cdot}2H_2O$; Li_2SO_4; $MgSO_4$ anhydre et $NaNO_2$ de marque Merck et de pureté supérieure à 99 %.

L'électrode de travail est un disque de 0,5 cm^2 de surface enrobé dans une résine afin d'avoir une surface d'attaque uniforme. La préparation de l'état de surface de l'électrode de travail comporte une abrasion mécanique successivement à l'aide de papier au carbure de silicium de granulométrie décroissante, suivie d'un rinçage à l'eau bidistillée, puis d'un séchage à l'air comprimé.

© 2002 CNRC Canada

Tableau 2. Paramètres électrochimiques relatifs au comportement de l'alliage d'aluminium 6063 dans le milieu témoin sans et avec addition d'inhibiteur.

Milieu	E_{cor} (mV s^{-1})	E_{piq} (mV s^{-1})	I_{cor} (μA cm^{-2})	$E_{piq} - E_{cor}$ (mV)	E (%)
Témoin	–680	–680	21	—	—
Mg^{2+} (5×10^{-2})	–1030	–620	7	410	67
Li^{+} (5×10^{-2})	–1140	–620	4	520	81
CrO_4^{2-} (5×10^{-3})	–980	–660	6	320	71
MoO_4^{2-} (5×10^{-2})	–740	–510	9	230	57
NO_2^{-} (5×10^{-2})	–1000	–640	14	360	35

Fig. 2. Courbes de polarisation de l'alliage d'aluminium 6063 sans et avec addition d'ions Li^{+} à différentes concentrations.

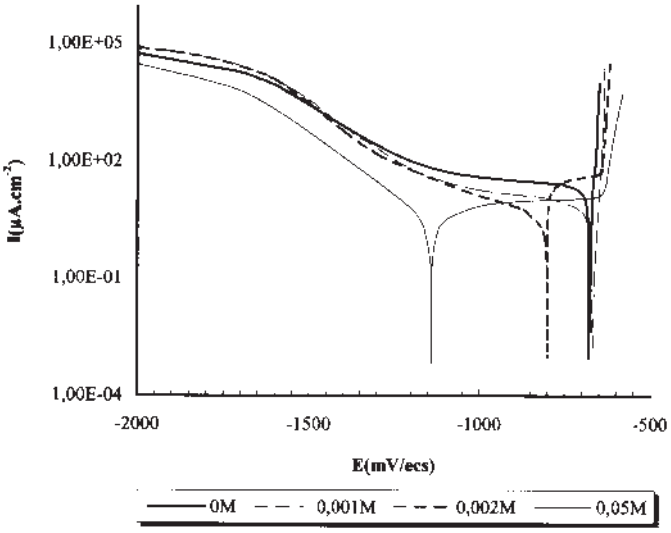

Avant le tracé des courbes de polarisation, l'électrode de travail est polarisée à –2 V s^{-1} pendant 2 min pour réduire les espèces électroactives pouvant exister à la surface métallique (17, 18). On fait ensuite évoluer le potentiel appliqué vers des valeurs croissantes, passant du domaine cathodique au domaine anodique.

Pour tous les essais potentiodynamiques, nous avons adopté une vitesse de balayage de potentiel de 1 mV s^{-1}. Celle-ci nous permet d'obtenir une bonne reproductibilité des résultats et en même temps de nous placer dans des conditions quasi-stationnaires (19–21).

Les échantillons destinés à l'examen métallographique sont découpés sous forme de plaquettes rectangulaires de 1,5 cm × 1 cm de surface et de 1 mm d'épaisseur. Avant chaque essai, les échantillons subissent un polissage mécanique à l'aide de papier abrasif de granulométrie décroissante, suivi d'un polissage chimique dans une solution de composition : H_3PO_4 65 % – H_2SO_4 25 % – HNO_3 10 % pendant 5 min (22), puis un dégraissage à l'acétone, un rinçage à l'eau bidistillée et enfin un séchage à l'air comprimé.

Le montage expérimental utilisé dans l'étude électrochimique est l'ensemble AMEL constitué par un générateur pilote (Amel 568) qui délivre un signal électrique au potentiostat pour faire varier le potentiel avec le temps suivant des vitesses de balayage réglables, un potentiostat (Amel 2049) qui impose un potentiel à l'électrode de travail modulable suivant une vitesse de balayage, une interface (Amel 560/A), qui permet la lecture du courant et sa transformation en potentiel à travers une résistance et un enregistreur (Kipp and Zonen) permettant le tracé automatique des courbes intensité–potentiel.

Les essais de corrosion sont effectués dans une cellule électrochimique à double paroi en verre Pyrex. La cellule est munie d'orifices permettant l'introduction du gaz (azote), de l'électrode de travail, de l'électrode de référence et de l'électrode auxiliaire. L'électrode de référence est une électrode au calomel saturé, positionnée à l'extérieur de la cellule. Le contact avec l'électrolyte est assuré à l'aide d'un capillaire et d'un pont en verre rempli d'une solution de chlorure de potassium saturée. Le rôle du pont est de minimiser la diffusion des ions chlorures de l'électrode de référence vers la solution électrolytique et de maintenir l'électrode de référence à température ambiante lorsqu'on fait varier la température de l'électrolyte. La contre-électrode est un disque en platine placé en face de l'électrode de travail. La cellule électrochimique est reliée à un thermostat à circulation d'eau permettant de maintenir l'électrolyte à la température de traitement (entre 25 et 55°C dans notre travail).

Résultats

Étude comparative

La fig. 1 représente les courbes de polarisation relevées dans une solution à 3 % de chlorure de sodium sans et avec addition de composés inorganiques. Les paramètres électrochimiques sont donnés dans le tableau 2.

Nous remarquons que l'addition des ions Li^{+} (5×10^{-2} M), Mg^{2+} (5×10^{-2} M), CrO_4^{2-} (5×10^{-3} M) et NO_2^{-} (5×10^{-2} M) a pour effet un déplacement remarquable du potentiel de corrosion (E_{cor}) vers des valeurs plus négatives. Le déplacement le plus important est obtenu avec l'addition des ions lithium. L'allure des courbes anodiques montre que l'alliage d'aluminium 6063 présente un phénomène de passivation avec rupture de passivité par attaque localisée. Le potentiel de piqûration reste peu affecté par la présence de ces ions. L'addition des ions molybdates à 5×10^{-2} M au milieu électrolytique conduit à un déplacement du potentiel de piqûration (E_{piq}) vers des valeurs plus nobles.

L'étude comparative de l'effet inhibiteur des ions testés montre que les ions lithium présentent la meilleure action inhibitrice aussi bien dans le domaine anodique que dans le domaine cathodique. En effet l'estimation de la vitesse de corrosion par extrapolation de la pente de Tafel indique que la valeur minimale est obtenue par addition des ions Li^{+}. De plus, la différence entre le potentiel de corrosion et le poten-

© 2002 CNRC Canada

Tableau 3. Paramètres électrochimiques de l'alliage d'aluminium 6063 dans le milieu témoin sans et avec addition des ions lithium à différentes concentrations.

Milieu	E_{cor} (mV s^{-1})	E_{piq} (mV s^{-1})	I_{cor} (μA cm^{-2})	$E_{piq} - E_{cor}$ (mV)	E (%)
Témoin	–680	–680	21	—	—
1×10^{-3}	–700	–680	16	20	26
2×10^{-3}	–800	–650	7	150	68
5×10^{-3}	–966	–660	3,5	306	84
1×10^{-2}	–1062	–644	3,9	418	82
5×10^{-2}	–1140	–620	4,1	520	81

Fig. 3. État de surface de l'alliage d'aluminium 6063 après essai d'immersion de longue durée.

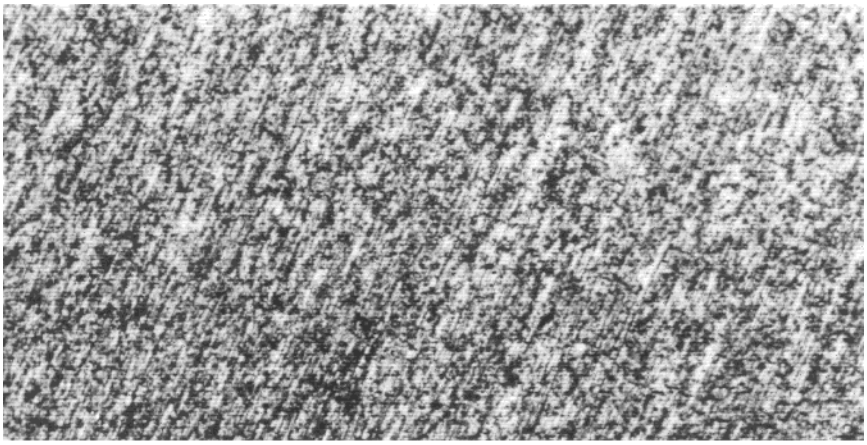

(a) après 15 jours d'immersion dans NaCl 3% (T=25°C) (× 100)

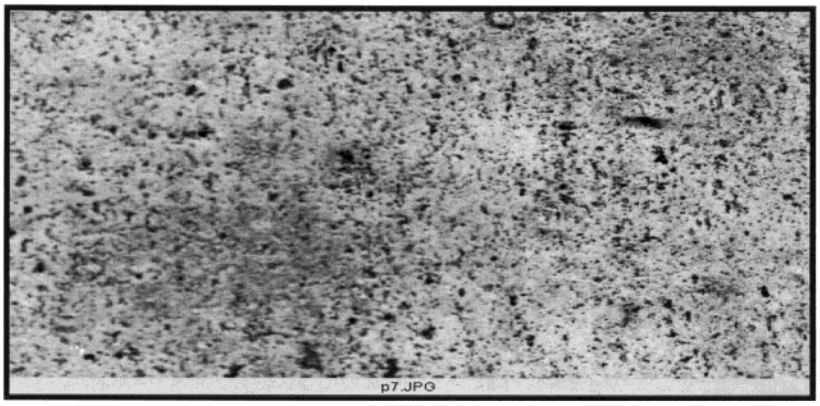

(b) après 15 jours d'immersion dans NaCl 3% contenant les ions Li^+ à 5 10^{-2} M (T=25°C) (× 100)

tiel de piqûration est très élevée en présence des ions Li^+ comparativement aux valeurs déterminées par addition des autres ions étudiés (tableau 2). Compte tenu de ces résultats, nous avons jugé opportun d'effectuer une étude détaillée de l'action inhibitrice des ions lithium sur la corrosion de l'alliage 6063.

Étude détaillée de l'influence des ions lithium

La fig. 2 illustre les courbes de polarisation de l'alliage 6063 dans une solution de NaCl 3 % sans et avec addition des ions lithium à différentes concentrations comprises entre 0 et 5×10^{-2} M. Le tracé de ces courbes est effectué à 25°C. Les différents paramètres électrochimiques déduits de ces courbes sont rassemblés dans le tableau 3.

Au terme des résultats obtenus, les remarques suivantes peuvent être annoncées : (*i*) l'addition des ions Li^+ favorise la passivation de l'alliage 6063. L'étendue du domaine de passivation est d'autant plus marquée que la concentration en ions Li^+ est importante. (*ii*) Les densités de courant cathodique subissent une nette diminution à partir d'une concentration de 1×10^{-2} M en ions Li^+. (*iii*) La densité de courant de corrosion diminue avec l'accroissement de la teneur en ions Li^+ et devient constante lorsque la concentration de ces ions dépasse 5×10^{-3} M. (*iv*) L'addition des ions

© 2002 CNRC Canada

Fig. 4. Courbes de polarisation de l'alliage d'aluminium 6063 dans le milieu témoin à différentes températures.

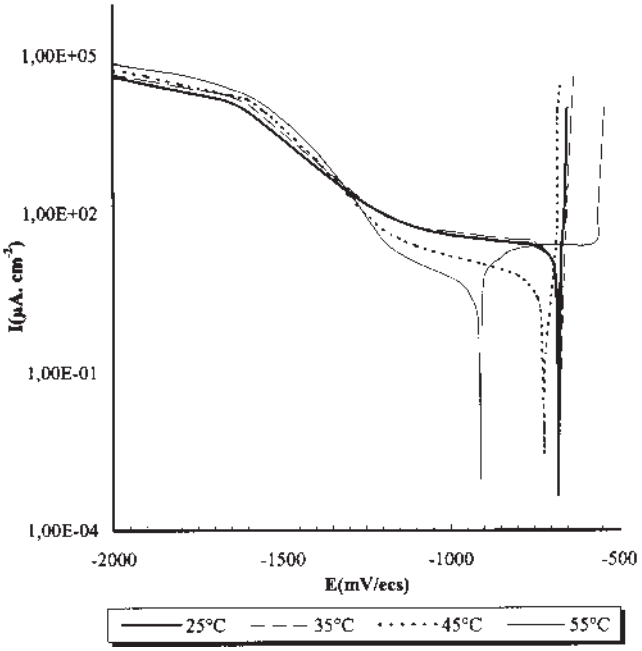

Fig. 5. Courbes de polarisation de l'alliage d'aluminium 6063 dans le milieu contenant 5×10^{-2} M en ions Li^+ à différentes températures.

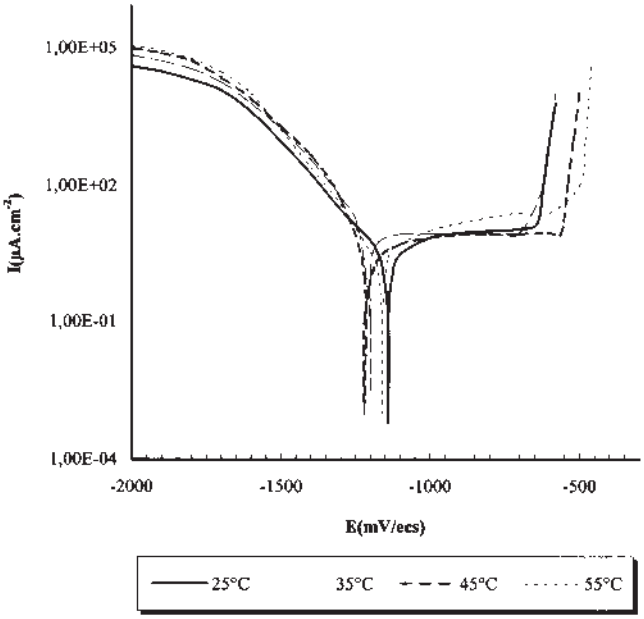

Li^+ au milieu corrosif s'accompagne d'un déplacement du potentiel de corrosion vers des valeurs négatives. Ce déplacement est d'autant plus marqué que la teneur en ces ions est élevée.

L'efficacité inhibitrice des ions Li^+ est définie par l'expression suivante :

$$[1] \qquad E\% = \frac{I^{\circ}_{cor} - I_{cor}}{I^{\circ}_{cor}} \times 100$$

où I_{cor} et I°_{cor} représentent respectivement les densités de courant de corrosion dans le milieu avec et sans inhibiteur. Notons que l'efficacité inhibitrice augmente avec la teneur des ions lithium en solution et atteint une valeur maximale de l'ordre de 84 % à 5×10^{-3} M. Pour des concentrations supérieures, cette efficacité inhibitrice demeure sensiblement constante.

Essais de longue durée

Afin de corréler les résultats des tests électrochimiques accélérés aux phénomènes réels de la corrosion de l'alliage 6063 et de son inhibition, nous avons réalisé des essais d'immersion de longue durée dans une solution de NaCl 3 % sans et avec addition des ions lithium. L'état de la surface après 15 jours d'immersion est illustré par la fig. 3. En absence des ions lithium, on signale une destruction locale du film qui se traduit par l'apparition de piqûres à la surface (fig. 3*a*). En présence des ions Li^+, la surface de l'alliage 6063 reste pratiquement intacte après 15 jours d'immersion (fig. 3*b*); ce qui témoigne de la bonne action de ces ions.

Étude de l'influence de la température

Compte tenu de l'importance du facteur température, une étude électrochimique sur le comportement de l'alliage 6063 dans une solution de NaCl 3 % sans et avec addition d'ions lithium à 5×10^{-2} M pour des températures comprises entre 25 et 55°C a été réalisée. Les courbes de polarisation correspondantes obtenues sont représentées sur les figs. 4 et 5. Les paramètres électrochimiques sont donnés dans le tableau 4.

L'examen de ces résultats permet de faire les constatations suivantes.

En absence des ions Li^+, l'augmentation de la température de 25 à 55°C s'accompagne d'une nette diminution de la densité de courant de corrosion (I_{cor}). Le potentiel de corrosion subit quand à lui un déplacement vers des valeurs plus négatives. Cependant, la différence $\Delta E = E_{piq} - E_{cor}$ n'est significative qu'à la température 55°C. Ces résultats montrent que l'élévation de la température de 25 à 55°C améliore la résistance à la corrosion uniforme et par piqûre de l'alliage 6063 dans NaCl 3 %.

En présence des ions Li^+, la densité de courant de corrosion est très inférieure à celle du témoin pour toutes les températures d'essai. La faible efficacité inhibitrice obtenue à 45 et 55°C est due à la faible vitesse de corrosion enregistrée dans le milieu témoin à ces températures. La différence $\Delta E = E_{piq} - E_{cor}$ est nettement supérieure à celle déterminée dans le milieu témoin et ce pour toutes les températures d'essai. Ce résultat montre la bonne performance de l'alliage 6063 en présence des ions Li^+.

Discussion

L'étude comparative de l'action d'une série de composés inorganiques sur la résistance à la corrosion de l'alliage d'aluminium 6063 a été réalisée en milieu NaCl 3 %. Les résultats obtenus montrent que l'addition des ions Li^+, Mg^{2+}, CrO_4^{2-} et NO_2^- améliorent la résistance à la corrosion de l'alliage d'aluminium 6063. On assiste en effet à une diminution de la densité de courant de corrosion et à un accrois-

© 2002 CNRC Canada

Tableau 4. Paramètres électrochimiques de l'alliage d'aluminium 6063 dans le milieu sans et avec addition des ions Li^+ à 5×10^{-2} M.

Milieux	T (°C)	E_{cor} (mV s^{-1})	E_{piq} (mV s^{-1})	I_{cor} (μA cm^{-2})	$E_{piq} - E_{cor}$ (mV)	E (%)
Témoin	25	–680	–680	21	0	—
	35	–680	–680	23	0	
	45	–720	–680	11	40	
	55	–800	–560	5	240	
Li^+	25	–1140	–620	4	520	81
	35	–1220	–620	5	600	78
	45	–1200	–540	6	660	45
	55	–1160	–500	4	660	20

sement de l'écart entre le potentiel de corrosion et le potentiel de piquration en présence de ces ions.

L'étude comparative de l'action inhibitrice des ions testés permet de distinguer les ions Li^+ comme meilleur inhibiteur de toute la série examinée; ce qui nous a incité à réaliser une étude détaillée de l'influence de ces ions. Les résultats obtenus dans ce cadre montrent que l'augmentation de la concentration des ions Li^+ en solution provoque un déplacement de E_{cor} vers des valeurs plus négatives. Ce déplacement s'accompagne d'une diminution des densités de courant cathodiques d'autant plus marquée que la concentration des ions Li^+ est élevée. Ces ions ont donc une action cathodique. L'efficacité inhibitrice atteint une valeur maximale de l'ordre de 84 % dès une concentration égale à 5×10^{-3} M et l'écart $\Delta E = E_{piq} - E_{cor}$ s'élargit lorsque la teneur en ions Li^+ croît. Les travaux de Morans et al. (23) sur l'action des ions Li^+ envers la corrosion des alliages d'aluminium 8090 et 2091 corroborent les résultats présentés dans ce manuscrit. Ces auteurs ont montré que la dissolution des alliages 8090 et 2091 décroît avec l'élévation de la teneur en ions Li^+ en solution, ce qui a été expliqué par la participation de ces ions à la formation de la couche de passivation à la surface métallique. Gui et Devine (24) ont mis en évidence la présence du lithium à la surface métallique de l'alliage d'aluminium 6061 par analyse au SIMS du film d'oxyde. Par ailleurs Graig et al. (25) ont attribué l'effet inhibiteur des ions Li^+ à la formation du méta-aluminate de lithium ($LiAlO_2$) à l'interface métal–électrolyte. Ce composé, étant moins soluble, se précipite à la surface métallique et conduit à la stabilité du film d'oxyde.

L'augmentation de la température de la solution corrosive provoque un changement du comportement de l'alliage 6063. La densité de courant de corrosion (I_{cor}) décroît avec l'élévation de la température pour atteindre la valeur minimale à 55°C. Ce phénomène pourrait être attribué à la nature du film d'oxyde-hydroxyde formé à la surface métallique. Selon Vedder et Vermilya (26), le développement du film d'oxyde-hydroxyde se fait en trois étapes : d'abord la formation de l'hydroxyde d'aluminium amorphe ($Al(OH)_3$) suivie par la formation de la boehmite cristallisée (AlOOH). Ces deux étapes sont rapides et engendrent une couche poreuse, identique aux membranes bipolaires. La dernière étape est souvent lente, durant laquelle il y a germination de la bayérite ($Al_2O_3 \cdot 3H_2O$) sous forme d'une couche compacte. L'élévation de la température augmente la cinétique de germination de la bayerite et par suite affaiblit les propriétés électrocatalytiques du film passif. La variation de la température de 25 à 55°C a aussi pour effet de minimiser la sensibilité à la piqûration de l'alliage 6063. Les ions lithium catalysent probablement la croissance du film d'oxyde dans les zones d'adsorption des ions Cl^-. Ils réagissent avec les ions chlorures pour former le chlorure de lithium plutôt que le chlorure d'aluminium (14, 15). Ce dernier est reconnu comme précurseur de la corrosion localisée des alliages d'aluminium (1).

Conclusion

Sur la base des résultats et discussions ci-dessus, les conclusions suivantes peuvent être annoncées : (*i*) Tous les ions testés présentent un caractère inhibiteur plus ou moins marqué vis-à-vis de la corrosion de l'alliage d'aluminium 6063 en milieu NaCl 3 %. (*ii*) L'étude comparative de l'action de ces composés inorganiques montre que les ions lithium sont ceux qui ont la meilleure action. Ils présentent un caractère d'inhibition cathodique et réduisent la sensibilité à la piqûration de l'alliage 6063. Ils améliorent donc les propriétés protectrices du film d'oxyde formé à la surface. (*iii*) L'étude de l'influence de la température révèle que l'alliage d'aluminium devient de plus en plus résistant lorsque la température de la solution témoin croît de 25 à 55°C. (*iv*) En présence des ions Li^+, l'augmentation de la température provoque une décroissance de l'efficacité inhibitrice, mais améliore de manière effective la résistance à la corrosion par piqûre de l'alliage d'aluminium 6063.

Remerciements

Nous tenons à remercier le Centre International de la Physique Théorique Trieste (Italie) pour son soutien dans le cadre du programme de recherche n° 96–447 RG/CHE/AF/AC.

Bibliographie

1. J.O.M. Bockris et L.J.V. Minevski. J. Electroanal. Chem. **349**, 375 (1993).
2. L. Bazzi, S. Kertit et M. Hamdani. Rev Metall. **92**, 690 (1995).
3. L. Bazzi, S. Kertit et M. Hamdani. J. Chem. Phys. **94**, 93 (1997).
4. R. Salghi, L. Bazzi, B. Hammouti, S. Kertit, A. Bouchtart et Z. El Alami. Ann. Chim.-Sci. Mat. **25**, 593 (2000).
5. L. Bazzi, S. Kertit et M. Hamdani. J. Chem. Phys. **92**, 1612 (1995).
6. B.A. Shaw, G.D. Davis, T.L. Fritz et K.A. Olver. J. Electrochem. Soc. **137**, 350 (1990).

© 2002 CNRC Canada

7. T.A. Treverton, M.P. Amor et A. Bosland. Corros. Sci. **33**, 1411 (1992).
8. H.B. Konno, S. Kobayashi, H. Takahashi et M. Nagayama. Corros. Sci. **22**, 913 (1982).
9. C.M.A. Brett, I.A.R. Gomes et P.S. Marttins. Corros. Sci. **36**, 915 (1994).
10. J.S. Wainright, O.J. Murphy et M.R. Antonio. Corros. Sci. **33**, 281 (1992).
11. L.A. Shalaby, K.M. Elsobhi et A.A. Abdul azim. Corros. Sci. **14**, 637 (1974).
12. B.A. Shaw, G.D. Davis, T.L. Fritz et K.A. Olver. J. Electrochem. Soc. **137**, 350 (1990).
13. C.B. Breslin, G. Treceacy et W.M. Carrol. Corros. Sci. **36,** 1143 (1994).
14. J.C.S. Fernandes, M.G.S. Ferreira et C.M. Rangel. J. Appl. Electrochem. **20**, 874 (1990).
15. J.C.S. Fernandes et M.G.S. Ferreira. Electrochim. Acta, **37**, 2659 (1992).
16. C.M. Rangel et M.A. Travassos. Corros. Sci. **33**, 327 (1992).
17. C.B. Breslin et L.P. Friery. Corros. Sci. **36**, 231 (1994).
18. S. Berrada, M. Elboujdaini et E. Ghali. J. Appl. Electrochem. **22**, 1065 (1992).
19. W. Neil et C. Garrard. Corros. Sci. **36**, 837 (1994).
20. W.M. Carrol et C.B. Breslin. Corros. Sci. **33**, 1161 (1992).
21. C.B. Breslin, L.P. Friery et W.M. Carroll. Corros. Sci. **36**, 85 (1994).
22. J. Benard, A. Michel, J. Philibert et J. Talbot. Métallurgie générale. Masson, Paris. 1984.
23. J.P. Morans, E.A. Tarke, G.E. Stoner et G.L. Cahen. NACE, Paper No. 203. Houston, Texas. 1986.
24. J. Gui et T.M. Devine. Scripta Metall. **21**, 853 (1987).
25. J.G. Craig, R.C. Newman, M.R. Jarrett et N.J.H. Holroyd. J. Physique, Colloque C3, No. 9 (suppl.). **48**, 825 (1987).
26. W. Vedder et D.A.Vermilyea. Trans. Faraday. Soc. **65**, 561 (1969).

© 2002 CNRC Canada

1-Propanol hydrate by IR spectroscopy

Jean-Joseph Max, Stéphane Daneault, and Camille Chapados

Abstract: The mid-IR attenuated total reflectance (mid-IR–ATR) spectra of a series of 1-propanol and water mixtures were obtained. Factor analysis (FA) applied to spectra gave the spectra of three principal species and their abundance: pure water, pure propanol, and a 1-propanol hydrate (1:1). When compared to the pure solvents, the hydrate propanol bands were modified which indicated that the valence bonds were perturbed. The assignment of the hydrate IR bands was made by comparing them with those of pure 1-propanol and pure water. No monomer was observed which indicated that all species were associated. The simplest representation of the different associations is by groups of two on which an intermolecular bond (H-bond) can be placed. The exchange between the molecules can be represented by the following equation: $(H_2O\cdots H_2O) + (CH_3CH_2CH_2OH\cdots OHCH_2CH_2CH_3) \rightleftharpoons 2(CH_3CH_2CH_2OH\cdots OH_2)$. The hydrate's formation constant (K_f) is 1.2 (±0.2). This value is less than the one expected from the association of freely moving molecules, indicating that the hydrophobic interactions of the 1-propanol aliphatic chains decrease the strength of the hydrogen bond between water and alcohol in the hydrate.

Key words: IR spectroscopy, ATR spectroscopy, 1-propanol, liquid, aqueous solutions, eigenspectra, hydrate, factor analysis.

Résumé : Nous avons obtenu une série de spectres infrarouges par réflectance totale atténuée de solutions aqueuses de 1-propanol. L'analyse par facteurs des spectres nous a révélé le spectre de trois espèces principales en donnant leur abondance en fonction de la concentration: l'eau pure; le propanol pur et un hydrate de 1-propanol (1:1). En comparant le spectre de l'hydrate avec celui du solvant pur, nous notons que les bandes sont légèrement modifiées ce qui indique que les liaisons de valence du propanol sont perturbées. L'attribution des bandes ir de l'hydrate a été faite en les comparant avec celles du 1-propanol pur et de l'eau pure. Nous n'observons aucune bande que nous puissions attribuer au monomère ce qui indique que toutes les espèces sont associées. Le modèle le plus simple qui représente cette association est par groupe de deux avec liaison hydrogène entre eux. L'échange entre les deux espèces est représenté par l'équation suivante: $(H_2O\cdots H_2O)+(CH_3CH_2CH_2OH\cdots OHCH_2CH_2CH_3) \rightleftharpoons 2(CH_3CH_2CH_2OH\cdots OH_2)$. La constante de formation de l'hydrate, K_f, est 1.2 (±0.2). Cette valeur est plus petite que ce à quoi nous pouvons nous attendre de molécules qui seraient entièrement libres de se déplacer dans la solution. Nous interprétons cette diminution par l'interaction hydrophobique entre l'eau et le 1-propanol dont les chaînes aliphatiques feraient diminuer la force des liaisons hydrogène entre l'eau et l'alcool.

Mots clés : spectroscopie infrarouge, spectroscopie ATR, 1-propanol, liquide, solutions aqueuses, eigenspectra, hydrate, analyse par facteurs.

Introduction

Based on molar volume, refractive index, and density measurements, it was determined that water and methanol mixtures behave as a ternary system and not as an ideal binary one (1, 2). Similar data (3) for the system 1-propanol–water ($PrOH–H_2O$) indicate that this system is not an ideal mixture, although a thorough analysis of it has not been made. IR spectroscopy is a technique capable of identifying the different species that exist in the mixtures and determining their abundance (4–17). Both transmission and attenuated total reflectance (ATR) methods can be used to obtain IR spectra of liquids. Because the OH stretch vibrations are strong absorbers, IR transmission measurements of aqueous solutions are difficult to perform (18). Nevertheless, Zhao and Malinowski (16) used this technique to study methanol–water mixtures in the 1850–2700 cm^{-1} range, where only a combination band is observed. Unfortunately, the CaF_2 cell used superposed strong interference fringes on the spectrum. With a thickness of 104 μm, the other principal bands in the mid-IR region saturated and could not be used for the analysis. However, the ATR configuration can be used to obtain the complete mid-IR spectrum of aqueous systems with high reproducibility and without fringes. Librovich, Maiorov, and co-workers (4), among the earliest users of ATR, showed that aqueous solutions could be studied quantitatively by IR–ATR. However, they did not study the alcohol–water system that is the object of the present study.

We developed an adequate quantitative IR–ATR method that provides consistently reliable results as long as the following basic requirements are met: (*i*) a proper crystal whose refractive index is far from that of the solution (5);

Received 6 April 2001. Published on the NRC Research Press Web site at http://canjchem.nrc.ca on 25 January 2002.

J.-J. Max,[1] S. Daneault, and C. Chapados.[2] Département de chimie-biologie, Université du Québec à Trois-Rivières, Trois-Rivières, QC G9A 5H7, Canada.

[1]Present address: Scientech R&D, 247 Thibeau, Cap-de-la-Madeleine, QC G8Y 6X9, Canada.

[2]Corresponding author (telephone: (819) 376-5052; fax: (819) 376-5084; e-mail: Camille_Chapados@uqtr.uquebec.ca).

 DOI: 10.1139/V01-198 © 2002 NRC Canada

Table 1. Parameters of the experimental mixtures.

Sample composition						MF		
	PrOH		Water		Molar ratio	PrOH	Water	PrOH–H_2O
Sample number	g L^{-1}	*M*	g L^{-1}	*M*				
1	0.0	0.00	997.0	55.34	0:55.34	0.000	1.000	0.000
2	49.8	0.83	944.9	52.44	1:63.29	0.002	0.938	0.058
3	98.6	1.64	884.6	49.09	1:29.93	0.009	0.873	0.110
4	151.0	2.51	817.9	45.39	1:18.07	0.019	0.797	0.167
5	193.8	3.22	777.6	43.15	1:13.38	0.038	0.740	0.198
6	239.8	3.99	715.3	39.69	1:9.95	0.059	0.671	0.238
7	285.1	4.74	664.5	36.88	1:7.77	0.079	0.603	0.277
8	328.7	5.47	607.1	33.69	1:6.16	0.110	0.540	0.302
9	371.3	6.18	556.1	30.86	1:5.00	0.150	0.481	0.316
10	414.0	6.89	500.6	27.78	1:4.03	0.195	0.418	0.329
11	455.3	7.57	453.0	25.14	1:3.32	0.242	0.364	0.334
12	494.0	8.22	404.2	22.43	1:2.73	0.291	0.321	0.325
13	532.4	8.86	344.5	19.12	1:2.16	0.359	0.259	0.321
14	570.6	9.49	308.7	17.13	1:1.80	0.411	0.225	0.303
15	600.5	9.99	265.0	14.71	1:1.47	0.471	0.185	0.285
16	645.3	10.74	206.1	11.44	1:1.07	0.543	0.121	0.275
17	677.2	11.27	162.9	9.04	1.25:1	0.624	0.078	0.245
18	711.5	11.84	121.0	6.71	1.76:1	0.700	0.051	0.199
19	743.6	12.37	82.1	4.56	2.72:1	0.785	0.029	0.147
20	774.5	12.88	40.6	2.25	5.72:1	0.884	0.008	0.086
21	797.6	13.27	0.0	0.00	13.27:0	1.000	0.000	0.000

(*ii*) an adequate angle of incidence of the IR beam; and (*iii*) a suitable crystal length. When these conditions are satisfied, the IR–ATR spectra reflect the system's chemical changes (5). We have previously used this technique to study alkali halide aqueous solutions and made several acid–base titrations by IR (6–15, 17). It was found that water combines with ions to form stable clusters when a binary salt (NaCl, KCl, CsCl), a strong acid (HCl), or a strong base (NaOH) is dissolved in it (6–9, 13, 15, 17). We also detected the formation of complexes in aqueous sulfuric and phosphoric acids using this technique (11, 12, 14). Some of these complexes had previously been deduced only from thermodynamic and electrochemical measurements.

In our previous studies, principal factor analysis (FA) was applied to a series of IR spectra, to determine the abundance of the species. This type of analysis is suitable in those cases where some of the species can easily be obtained from the set of experimental spectra. Other methods of applying FA can be used (19), but are more demanding (16, 20). Zhao and Malinowski (16) applied windows factor analysis to a series of spectra obtained from mixtures of water and methanol in the 1850–2700 cm^{-1} range. They determined that a complex made of two water molecules and one methanol molecule is formed.

The purpose of the present study was to analyze the complete mid-IR spectra of mixtures of PrOH and water: (*i*) to determine the number of species present in the mixtures; (*ii*) to determine the abundance of each species; (*iii*) to determine the composition of the species; (*iv*) to obtain the complete mid-IR spectra of any complexes formed; and (*v*) to compare the spectrum of these complexes with that of pure PrOH and pure water.

Experimental and data treatment

Chemicals and solutions

1-Propanol (Omega, HPLC grade, purity > 99.5%, water content < 0.08%) was used without further purification. Deionized water was used to prepare the aqueous solutions. Each sample was prepared by weighing PrOH and water in a 10-mL volumetric flask to the desired concentration. A series of 21 samples ranging from 0 to 797.6 g L^{-1} of PrOH were prepared whose compositions are given in Table 1. Pure D_2O (Aldrich Chemical Co., purity 99.9 atom% D) was used to prepare a mixture of 381.8 g L^{-1} of PrOH and 592.3 g L^{-1} of heavy water.

IR measurements

The IR measurements were obtained using a model 510P Nicolet FT IR spectrometer equipped with a TGS detector. Two KBr windows isolated the measurement chamber from the outside. The samples were contained in a Circle cell (SpectraTech, Inc.) equipped with a ZnSe crystal rod (8 cm long) in an ATR configuration (making 11 internal reflections, the incident beam is at an angle of 45° with respect to the rod's axis). The window region of the ZnSe rod is between 4800 and 650 cm^{-1}. The spectra were taken under nitrogen flow to ensure low CO_2 and water vapor residues in the spectrometer. An accumulation of 200 scans with a resolution of 4 cm^{-1} were obtained for each spectrum. All measurements were made at 26.5°C ± 0.3°C. The cell was carefully washed and dried before each measurement. Since model 510P is a single-beam spectrometer, a background

© 2002 NRC Canada

was taken with the empty cell before the measurement of each sample.

The IR measurements consisted of obtaining the ATR background intensity (R_0) and the ATR sample intensity (R). The ratio of R/R_0 produced intensity I for the spectral range being studied. The 2153 data points ($I(\tilde{\nu})$ vs. $\tilde{\nu}$ (in cm^{-1})) of each spectrum were then transferred to a Microsoft Excel spreadsheet program on a personal computer for numerical treatment. Next, intensity (I) was transformed into ATR absorbance (log (1/I)). A small baseline shift (less than 0.01 ATR Abs) was made to obtain a null mean absorbance in the 4600–4450 cm^{-1} region.

Factor analysis

Considering the set of experimental data, we know that the spectra of water and PrOH are those of pure species (eigenspectra). Therefore, FA can be performed using the following iterative procedure on a personal computer (11, 12): (*i*) water and PrOH are used as principal factors in FA. These are multiplied by the principal spectra and added (Σ (MF × eigenspectra)). Their combined spectra are compared to the experimental spectra to give residual factors that are minimized subject to the restriction that there be no negative band. A least-squares fit procedure is used to monitor best fit; (*ii*) the residues serve to identify another principal factor; (*iii*) the latter is added to the principal factors and step 1 is repeated with the added factor. The iteration is stopped when the residues are at the minimum values; (*iv*) when the final MF values are multiplied by the sample principal spectra concentrations, the species concentrations are obtained.

Results and discussion

Experimental ATR spectra

The 21 IR–ATR spectra of the water–PrOH mixtures are presented in Fig. 1. This series of spectra presents evolving characteristics with a regular pattern. The water spectrum (bottom spectrum, no. 1) shows the broad intense ν_{OH} (ν_1 and ν_3) band of water from 3600 to 3000 cm^{-1}, the ν_2 band at 1638 cm^{-1}, and the weak broad combination band at 2115 cm^{-1}. The strong libration band, whose max is situated below 650 cm^{-1}, produces a far wing that starts near 1000 cm^{-1}. The spectrum of PrOH is presented at the top of Fig. 1 (trace 21): the C-H stretching bands are situated in the 3000 to 2700 cm^{-1} range; the C-H and O-H deformation bands near 1400 cm^{-1}; and the C-O and C-C stretch bands near 1000 cm^{-1}. Table 2 shows the complete assignment of the bands. Dilution results in a decrease in the intensity of the PrOH bands and in an increase in those of water. Some bands are split or displaced and new bands are observed indicating the presence of other species. These are sorted out by the FA procedure.

Subtraction of the water spectrum

We have previously reported quantitative subtraction of the water spectrum in aqueous systems using the water bands as indicators providing that no negative bands emerge from the process (6–9, 11–15). However, because of the overlapping of the ν_{OH} bands of water and PrOH (Figs. 1 and 2B) the water spectrum subtraction is more difficult than in previous cases. To aid in the water spectral subtraction, we used all of the following indicators: (*i*) the combination band $\nu_2 + \nu_L$ near 2115 cm^{-1} (but being broad and weak this indicator had a large error); (*ii*) the deformation band of water (ν_2) near 1638 cm^{-1} could be used but only in a limited way because it overlapped with the neighboring absorption; (*iii*) the second derivative technique could be used only as a supplementary technique because it was is not very effective in reducing the bandwidth of the water bands because they were too broad (17); (*iv*) the spectrum of a mixture of PrOH and heavy water (1:4.66 molar ratio) was obtained since the D_2O ν_{OD} band was far away from the PrOH ν_{OH} band, with no overlap between the two. For item (*iv*), the heavy water spectrum could be subtracted easily and the information transported to the PrOH water system. The use of all these techniques permitted us to subtract adequately the spectrum of water from those of the mixtures.

Fig. 1. Experimental IR–ATR spectra of 21 mixtures of PrOH and water. The bottom spectrum (no. 1) is that of pure water and is situated on the zero level; the others are successively displaced by 1 au. The top spectrum is that of pure PrOH (no. 21). The composition of the others is given in Table 1. The vertical lines are situated at 3343 and 1638 cm^{-1}.

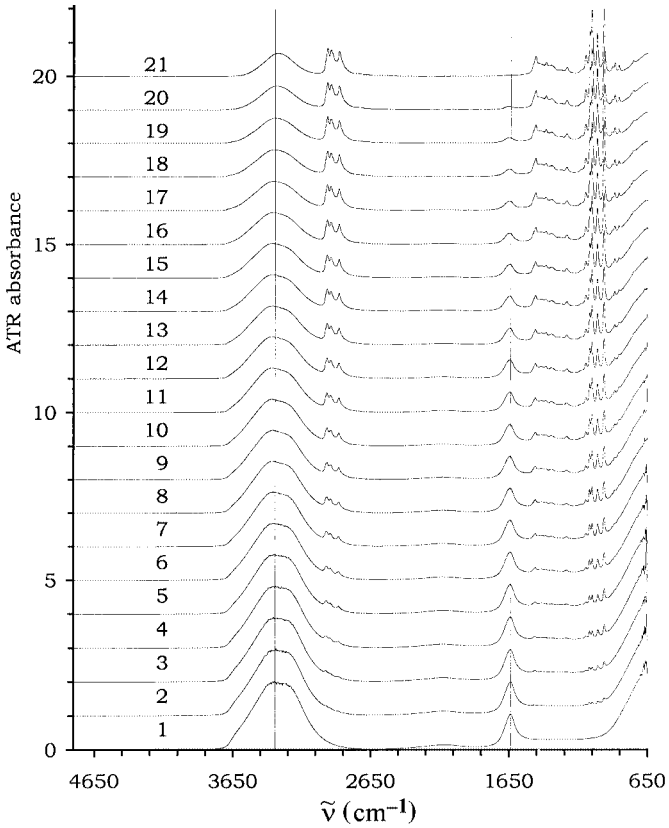

Factor analysis using two principal factors

The pure PrOH and pure water spectra that are principal and orthogonal spectra (eigenspectra) in the FA procedure are presented in Figs. 2B*a* and 2B*b*, respectively. At the end of step one of the procedure, the MFs are determined (Fig. 2A): that of pure water decreases linearly with increas-

© 2002 NRC Canada

Table 2. Position (in cm^{-1}) of the IR bands of liquid PrOH, PrOH–H_2O, PrOH–D_2O, and H_2O.

Approximate movement of fundamental modes	Mode (C_s)	PrOH (g) Fukushima and Zwolinski (22)	PrOH	PrOH This work	PrOH *I*	PrOH–H_2O This work	PrOH–H_2O *I*	H_2O[a]
H_2O OH s + ν_{ext}						3660	sh, w	3620
H_2O OH s + ν_{ext}						3540	sh	3528
PrOH OH s	ν_1 (A′)	3687	3356	3320	L, m	~3428	hidden	
H_2O OH s						~3400	L, S	3389
H_2O OH s						~3270	sh	3222
CH_3 as	ν_2 (A″)	2978	2967	2963	m	2969	m	
CH_3 as	ν_3 (A′), $2\nu_9$	2978	2967	2963	m	2969	m	
CH_2 as	ν_4 (A″), $\nu_{10} + \nu_{12}$, $2\nu_{10}$	2946	2933	2937	m	2942	m	
CH_2 as	ν_5 (A″), $2\nu_{12}$	2929		2905[b]		?		
CH_2 as	ν_6 (A′)	2892	2874	2878	m	2883	m	
CH_3 s, CH_2 s	ν_7 (A′)	2892	2874	2878	m	2883	m	
CH_2 s	ν_8 (A′)	2892	2874	2878	m	2883	m	
	$\nu_{10} + \nu_{14}$			2853[b]	sh, vw	?		
	$\nu_{10} + \nu_{16}$			2739	vvw	2735	vvw	
	$2\delta_{OH}$?			2720, 2676	vvw	2680	vvw	
Comb.	$\nu_{OH} + \nu_{18}$, $\nu_{15} + \nu_{18}$			2577, 2535	vvw	2540	vvw	
H_2O: comb.	$\delta_{OH} + \delta_{ext}$					2140	L, vw	2115
Comb.	$\nu_{19} + \nu_{21}$			2062	vvw			
Comb.	$2\nu_{21}$			2033	vvw			
Comb.	$\nu_{21} + \nu_{22}$							
$2\nu_{22}$			1936	vvw	1922	vvw		
Comb.	$\nu_{22} + \nu_{23}$			1850	vvw			
H_2O:OH def	δ_{OH}			1655	vvw	1652	m	1638
Comb.	$\nu_{23} + \nu_{25}$							
CH_2 bend	ν_9 (A′)			1480 sh	sh, w	1480	sh, w	
		1464	1464	1466 db	w	1467	db, m	
				1457 db	w	1460	db, m	
CH_3 a def, CH_2 bend	ν_{10} (A′)							
CH_2 bend	ν_{11} (A′)							
CH_3 a def	ν_{12} (A″)							
				1439[b]	sh, vvw	1442	vvw	
Comb.	$\nu_{21} + \nu_{26}$			1420	w			
Comb.	Far-IR (hydrate) + mid-IR					1416	w	
CH_2 wag	ν_{13} (A′)	1393	1381	1382	vw	1387	w	
CH_3 s def	ν_{14} (A′)	1393	1381	1382	w	1387	w	
OH def	?		1340	1345	w	1348	w	
CH_2 wag	ν_{15} (A′)	1300	1300	1293	vvw	1295	vw	
CH_2 twist	ν_{16} (A″)	1276		1272	vvw	1270	vw	
CH_3 rock, CH_2 twist	ν_{17} (A″)	1237						
COH bend	ν_{18} (A′)	1218	1232	1235	w	1235	w	
Comb.	$\nu_{23} + \nu_{28}$			1185	vvw			
Comb.	$\nu_{23} + \nu_{29}$			1132	sh, vw	1127	sh, vw	
CH_3 rock			1099	1099	m	1096	w	
CH_3 rock, CH_2-CH_2 s	ν_{19} (A′)	1066	1068	1067	S	1069	S	
CH_3 rock, CH_2-CH_2 s	ν_{19} (A′)	1047	1056	1054	vS	1050	S	
CH_2 twist	ν_{20} (A″)	1044						
CH_3-CH_2 s, CH_2-CH_2 s	ν_{21} (A′)	1013	1018	1016	S	1010	S	
CH_2-O s	ν_{22} (A′)	971	969	968	vS	963	vS	
Comb.	$2\nu_{26}$			903	vw	910	sh	
CH_3 rock, CH_2-CH_2 s, CH_2-O s	ν_{23} (A′)	898	887	887	w	890	w	
CH_3 rock, CH_2 rock	ν_{24} (A″)	858	858	858	w	858	sh	
Comb.	ν_{25} ν_{30}			832 sh				

© 2002 NRC Canada

Table 2 (*concluded*).

Approximate movement of fundamental modes	Mode (C_s)	PrOH (g) Fukushima and Zwolinski (22)	PrOH	PrOH This work	PrOH *I*	PrOH–H_2O This work	PrOH–H_2O *I*	H_2O[a]
Comb.	$\nu_{26}+\nu_{27}$			810				
Comb.	$\nu_{26}+\nu_{28}$			768 sh	vvw			
CH_2 rock	ν_{25} (A′′)	758	756	754	vw			
Comb.	$\nu_{26}+\nu_{29}$			687 sh	vvw			
				662	vvw			
H_20_{lib}						~490	L, S	613
CH_2-CH_2-O bend, CH_3-CH_2-CH_2 bend	ν_{26} (A′)	463		~460		~460		
D_20_{lib}								
H_20_{lib}								395
CH_3-CH_2-CH_2 bend, CH_2-CH_2-O bend	ν_{27} (A′)	332		~330				
CH_2-O int. rot.	ν_{28} (A′′)	286		~286				
CH_3-CH_2 int. rot.	ν_{29} (A′′)	240		~240		~240		
H_20_{lib}								183
CH_2-CH_2 int. rot.	ν_{30} (A′′)	131 (calc.)		~130				
H_20_{lib}								50

[a]From analysis with Gaussian (17).
[b]Obtained with second derivatives.

ing PrOH concentration (trace b) while that of PrOH increases regularly but not linearly (trace a). The residues (Fig. 2C) are not null: a pattern emerges with added water that reaches its max at solution 9 whereupon it decreases. This is indicative of at least another species in the solutions. The spectrum of this species, a propanol hydrate, was normalized to 13.27 mol L^{-1} (the concentration of pure PrOH) to allow comparison on an equimolar basis (Fig. 3B).

Factor analysis using three principal spectra

The three principal spectra used in FA procedure are shown in Fig. 3B: **a** (PrOH), **b** (H_2O), **c** (propanol hydrate). The MFs retrieved are given in Fig. 3A and listed in Table 1. The residues from the differences between experimental and calculated spectra are given in Fig. 3C. The strongest residue feature was found to be less than 2% of the strongest band in Fig. 3B situated in the 1000 cm^{-1} region. The other residues' features are much less than 0.5% where bands absorb. Attempts to use more than three species in FA were unsuccessful because the residues could not then be significantly decreased. We found similar results with aqueous NaI solutions (15). From these results, we concluded that three species were sufficient to describe the entire series of 21 mixtures of PrOH and water.

The MFs given in Fig. 3A were converted into total water and PrOH concentration, and the results presented as a function of gravimetry in Fig. 4. The correlation between the experimental results (symbols O and Δ) and the theoretical predictions (full line) is excellent and indicates that the procedure is adequate and that the results are reliable. These results confirm that only pure PrOH, pure H_2O, and one PrOH hydrate are present in the solutions. Consequently, one and only one hydrate is formed over the entire solubility range of the PrOH and water mixtures. The equilibrium existing between the three species in the mixtures is studied in the following section.

1-Propanol hydrate equilibrium formation

Molar ratio of the 1-propanol hydrate

The spectrum of the PrOH hydrate was calculated in the following way. Sample 9 contains 371.34 g L^{-1} of PrOH and 556.10 g L^{-1} of water (Table 1). The spectrum of pure PrOH and that of pure H_2O were subtracted from the spectrum of the sample no. 9 using the MFs 0.150 and 0.481 for pure PrOH and H_2O spectra, respectively. Pure liquid PrOH is 797.6 g L^{-1} and pure H_2O is 997.0 g L^{-1}. Therefore, the PrOH hydrate remaining was composed of 371.34 – 0.150 × 797.6 = 251.70 g L^{-1} (4.188 mol L^{-1}) of PrOH with 556.10 – 0.481 × 997.0 = 76.54 g L^{-1} (4.249 mol L^{-1}) of water giving a molar ratio of 1.000:1.015. According to the IR analysis, the PrOH hydrate is therefore made of one molecule of alcohol and one molecule of water: PrOH–H_2O. This representation of the hydrate is used to indicate the H-bonding between one PrOH molecule and one water molecule. It does not refer to an isolated entity.

The case of ideal mixture

To evaluate the chemical signification of the PrOH hydrate formation, we compare, in this section, the results predicted for an ideal mixture of PrOH and water with the results obtained by FA of the IR–ATR measurements.

Alcohol and water are known to be strongly associated in a polymeric organization through hydrogen bonding in liquid and solid states (21, 22). The resulting molecules have some intermolecular modes that the monomeric molecules do not have (22). Monomeric molecules are rare in liquid water and liquid PrOH. Given the difficulty in dealing with a polymeric organization, a reasonable simplification is to as-

© 2002 NRC Canada

Fig. 2. FA results with two eigenspectra. (A) MFs retrieved: (*a*) PrOH (Δ); and (*b*) pure water (O); (B) IR–ATR spectra: (*a*) PrOH and (*b*) water; (C) residues of the difference between experimental and calculated (Σ MF × eigenspectrum). Spectra are in the same order as in Fig. 1.

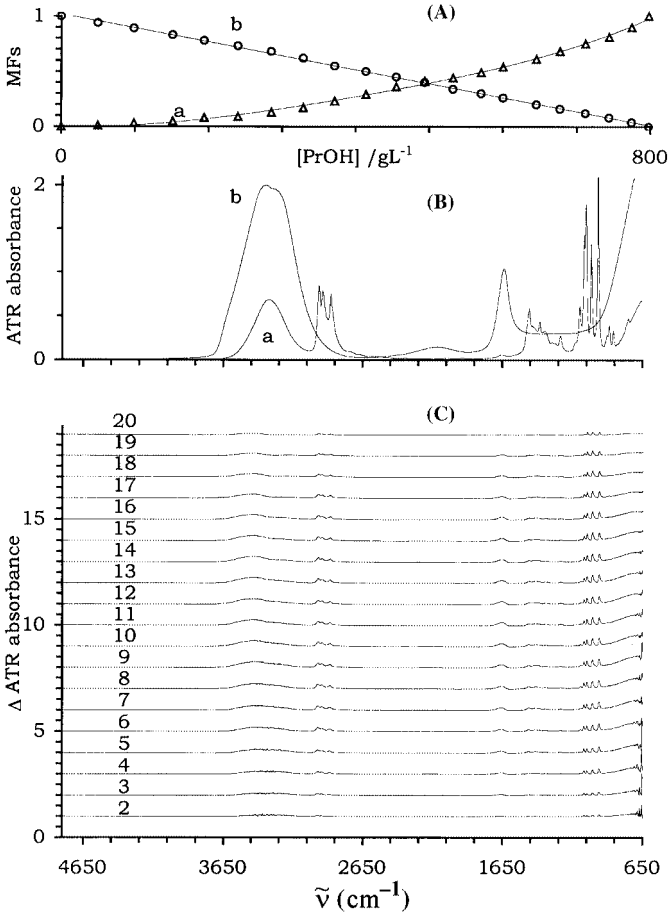

Fig. 3. FA results with three eigenspectra. (A) MFs retrieved for the mixtures: (*a*) PrOH (Δ); (*b*) H_2O (O); and (*c*) PrOH–H_2O (×); (B) IR–ATR spectra of the three eigenspectra; (C) residues in the same order and spacing as in Fig. 1.

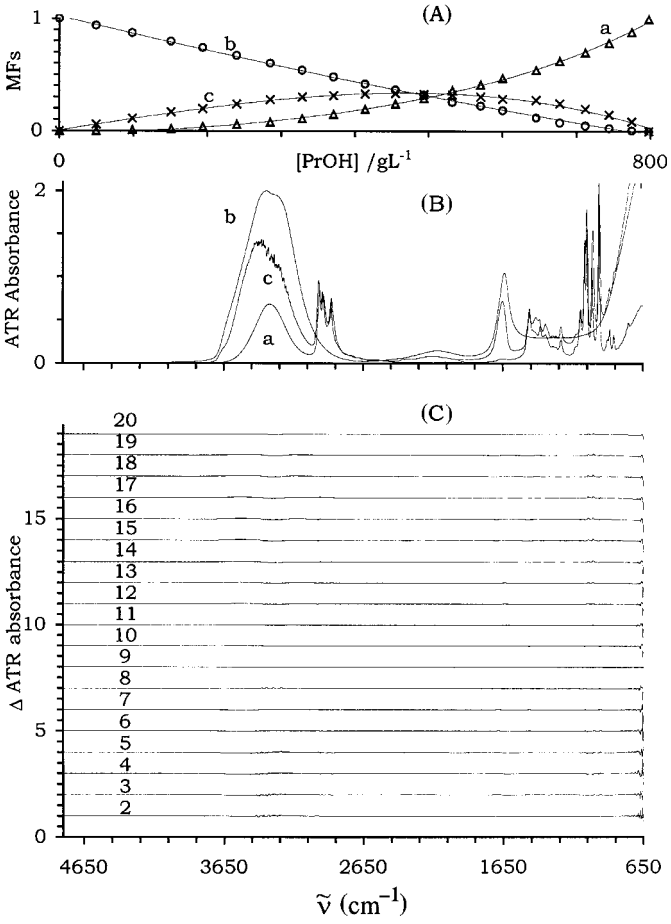

sume that both are made up of dimers. Such a dimer model directly follows the intermolecular interactions observed by IR spectroscopy. Hence, $(PrOH)_2$ and $(H_2O)_2$ indicate a particular strong interaction (hydrogen bond) between two identical molecules. Each molecule in these pairs can also have strong interactions with other molecules. In the following calculations, we will evaluate the transfer of a hydrogen bond between two identical molecules to a hydrogen bond between two different molecules.

In an ideal mixture of these dimers, each molecule of either $(H_2O)_2$ or $(PrOH)_2$ will associate with either H_2O or PrOH with equal probability. An $(H_2O)_2$ dimer may become $(H_2O)_2$ or PrOH–H_2O and a $(PrOH)_2$ dimer may transform into $(PrOH)_2$ or PrOH–H_2O if the hydrogen bonds are assumed to be equivalent in the three situations. Therefore, the probability for a dimer to be $(H_2O)_2$ or $(PrOH)_2$ in an equimolar mixture is 0.25 and that to be a hydrate PrOH–H_2O is $2 \times 0.25 = 0.5$. For a nonequimolar mixture containing *n* mol of water and *m* mol of PrOH, the probability for a particular molecule to be water or PrOH is $n/(m + n)$ and is $m/(m + n)$, respectively. The probability $p_{(H_2O)_2}$ for a particular dimer to be $(H_2O)_2$ is therefore:

$$[1] \qquad p_{(H_2O)_2} = \frac{n}{n+m} \times \frac{n-1}{n+m-1}$$

Because the number of mol is high, eq. [1] can be approximated by:

$$[2] \qquad p_{(H_2O)_2} \approx \left(\frac{n}{n+m}\right)^2 = \left(\frac{1}{1+a}\right)^2$$

where $a = m/n$ is the mol ratio between PrOH and H_2O.

In the same way, the probabilities $p_{(PrOH)_2}$ and $p_{H_2O\cdot PrOH}$ for a dimer to be $(PrOH)_2$ or PrOH–H_2O are given by:

$$[3] \qquad p_{(PrOH)_2} \approx \left(\frac{m}{n+m}\right)^2 = \left(\frac{a}{1+a}\right)^2$$

and

$$[4] \qquad p_{H_2O\cdot PrOH} \approx \frac{2nm}{(n+m)^2} = \frac{2a}{(1+a)^2}$$

The values calculated with eqs. [2]–[4] are plotted in Fig. 5A: **a** ($(PrOH)_2$), **b** ($(H_2O)_2$), **c** (PrOH–H_2O). These results were transformed into concentrations by multiplying

© 2002 NRC Canada

Fig. 4. Correlation plot between the concentration retrieved from the IR spectra with that obtained by gravimetry: water (O) and PrOH (Δ).

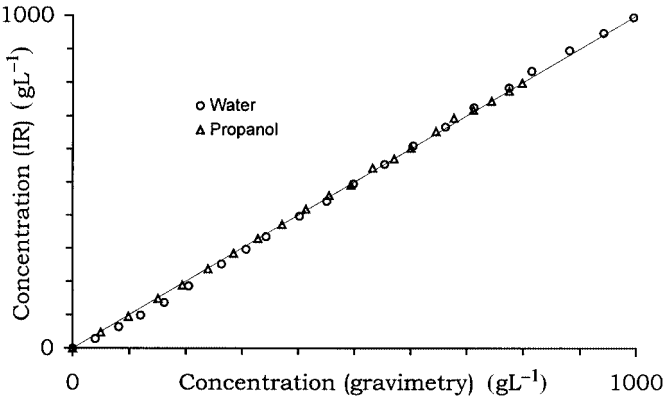

the above probabilities by the total concentration (in mol L^{-1}), giving the concentrations of water and PrOH in equivalent monomeric species. To follow its PrOH concentration, the values obtained for the PrOH hydrate are divided by 2 because it contains only one PrOH molecule. The results are represented by full lines in Fig. 5B. These results depict an ideal situation where the associated species have the same probabilities: PrOH–PrOH, PrOH–H_2O, and H_2O–H_2O.

Comparison with the concentrations obtained by FA

The concentrations of the three principal species present in the mixtures of PrOH and water retrieved by FA from the IR measurements are given as symbols in Fig. 5B. The PrOH hydrate concentration is counted in PrOH equivalent. Experimental values for pure PrOH and for pure H_2O are greater than the theoretical values (full lines in Fig. 5B). The H_2O values show an apparent smaller deviation than that of PrOH because it is related to a scale four times higher ([H_2O] (left ordinate), [PrOH] (right ordinate)). Experimental values for PrOH–H_2O are smaller than the theoretical values (Fig. 5B*c*). From this we concluded that mixtures of water and PrOH do not behave like ideal solutions. Only part of the polymeric water on the one hand and polymeric PrOH on the other hand break up to produce PrOH hydrate.

The PrOH hydrate formation is governed by the following equilibrium:

$$[5] \quad (H_2O)_2 + (CH_3CH_2CH_2CH)_2 \rightleftharpoons 2(CH_3CH_2CH_2OH{\cdot}H_2O)$$

with the PrOH hydrate formation constant given by:

$$[6] \quad K_f = \frac{[CH_3CH_2CH_2OH \cdot H_2O]^2}{[(CH_3CH_2CH_2OH)_2][(H_2O)_2]}$$

The value of K_f in the ideal mixture situation depicted by eqs. [2]–[4] is 4 (the reciprocal of the squared probability) whereas it is 1.2 ± 0.2 when it is obtained from the concentrations retrieved by FA (Fig. 5C). Large error bars are found at both ends of this figure because the concentration of one type of dimer is very weak there. A K_f value of 1.2 is almost three times less than the ideal mixture value of 4.

Stronger dimer association in liquid PrOH results from van der Waals interactions between the aliphatic groups. Excess PrOH dimers are present because they are not easily broken up by the weaker hydrogen bonding between water and the OH group of PrOH. Hydrogen bonding between water and PrOH being weaker does not easily break the PrOH dimers giving an excess of PrOH dimers. Note that PrOH is soluble in water, while 1-butanol is much less soluble and 1-pentanol is almost insoluble. With linear aliphatic alcohol, with more than four carbons, the hydrophobic interactions are stronger than hydrophilic interactions and cannot be broken by the hydrogen bonding between the OH of the alcohol and water molecules.

These results indicate that the composition of PrOH–water solutions consists of mixtures of only three species: pure PrOH, pure water, and PrOH hydrate (1:1). Except at the extremities where only the pure solvent exist, the molar fraction of the three species varies continuously with the PrOH concentration. From thermodynamic studies on excess partial molar enthalpies, it was found that different mixing schemes exist depending on the molar fraction of PrOH in the sample (23). The authors of these studies discussed the liquid structure changes on the basis of indirect structural information obtained from overall measurements. The IR results of the present study differ from the previous study because they are obtained from the H-bonding variations observed on vibrational modes. Since both methods are related to very different situations, it is not possible at present to make a comparison between the two results. Many IR measurements (around 10) at small PrOH molar fractions (lower than 0.1) would be needed to confirm the existence of a fourth species postulated by the thermodynamic measurements (23).

FA applied to a series of 21 whole spectra (4700–650 cm^{-1}) of aqueous propanol gave better and more complete information than that obtained by considering only the position of individual absorption bands as was done with a recent Raman study of aqueous methanol (24).

The findings of the present study suggest that each molecule tends to associate with like molecules rather than with unlike molecules. Therefore, clusters of water and PrOH coexist in the same solutions producing microheterogeneities. These microheterogeneities were postulated for an acetonitrile–water system studied by IR (25) and by X-ray diffraction and IR (26).

Spectral features of the 1-propanol hydrate

Comparison between PrOH–H_2O and pure PrOH

To compare it adequately with the other spectra, the PrOH hydrate spectrum (Fig. 3B*c*) is presented in Fig. 6 along with that of pure PrOH.

The band positions and assignments are given in Table 2. Looking first at the C-H stretching bands (Fig. 6B), we note that the integrated intensities between 3010 and 2800 cm^{-1} for the two systems are very similar, although the PrOH hydrate C-H bands are blue-shifted by comparison with those of PrOH, and their intensities are slightly modified. Secondly, in the deformation region of PrOH situated between 1500 and 1120 cm^{-1} (Fig. 6C), the increased intensity observed for PrOH hydrate is mostly due to the absorption of

© 2002 NRC Canada

Fig. 5. (A) Probability for molecule pairs as a function of PrOH concentration calculated under equiprobability condition: (*a*) PrOH dimers; (*b*) H_2O dimers; (*c*) PrOH–H_2O; (B) Species concentration: calculated following equiprobability (lines) and retrieved by IR: (*a*) pure PrOH (Δ); (*b*) pure water (O); and (*c*) PrOH–H_2O (×); (C) formation constant (K_f) of PrOH–H_2O — the average value is at the 1.20 level (horizontal line).

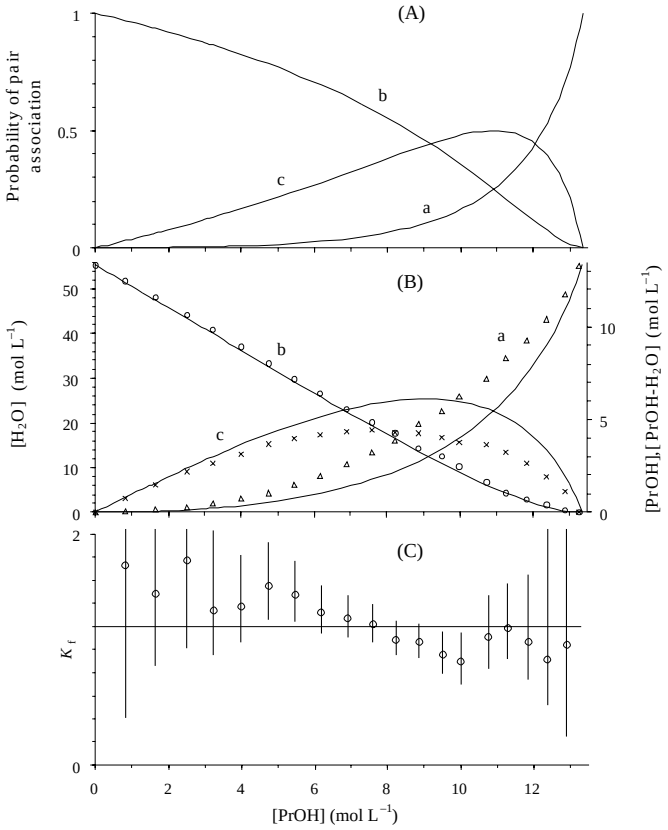

Fig. 6. IR–ATR spectra of pure PrOH (*a*) and PrOH–H_2O (*b*): (A) Complete spectrum; (B) CH stretch region; (C) 1800–1100 cm^{-1} region; (D) 1200–800 cm^{-1} region.

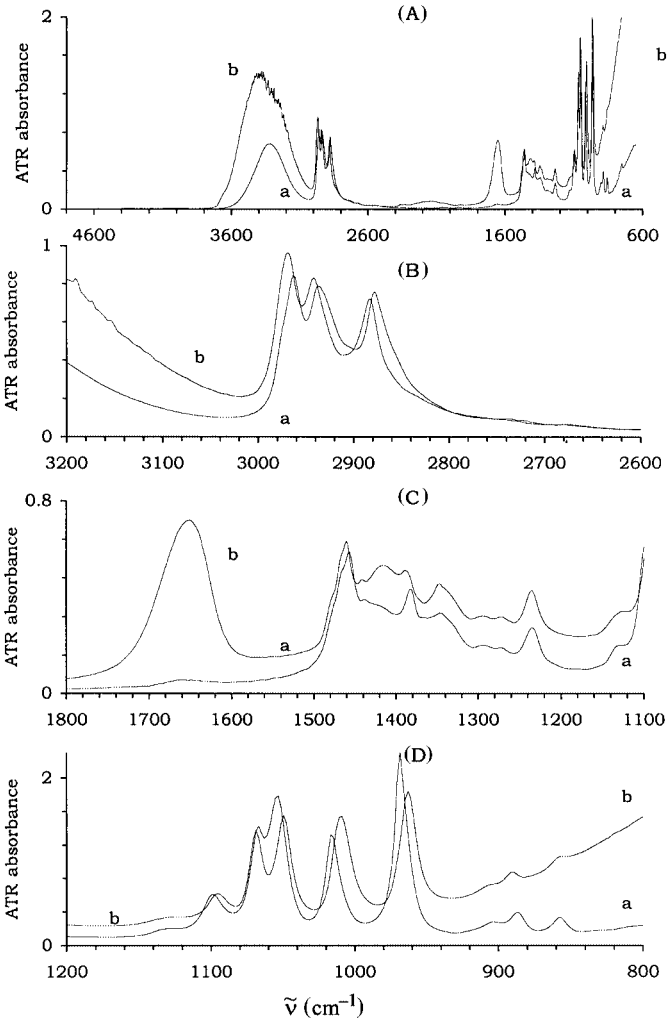

water, although some modifications are observed in the individual components, some of which are blue-shifted, and a new band emerged at 1416 cm^{-1}. Thirdly, the intensity of the PrOH hydrate components in the 1200–800 cm^{-1} region (Fig. 6D) is modified compared to that of PrOH, and the bands are red-shifted. These results indicate that the particular organization of the molecules in the complex PrOH–H_2O perturbs the vibrational modes of PrOH and H_2O.

Assignment of the bands

The position and approximate relative band intensities are given in Table 2. The band assignment listed in the table is based on the normal coordinate analysis work of Fukushima and Zwolinski (27) of PrOH (gas and liquid) and its deuterated analog. Comparing the band positions as given by these authors with that of ours we note that within a few wavenumbers the positions of the pure liquid PrOH are similar. This is acceptable given that the liquid spectra used by Fukushima and Zwolinski come from a data bank (28) and were obtained by transmission measurements, whereas our spectra were obtained by ATR. However, some differences do exist between the two sets of data. The ν_{OH} of liquid PrOH is situated at 3356 cm^{-1} by Fukushima and Zwolinski, whereas we find ν_{OH} at 3320 cm^{-1}. This difference can be explained by the broadness of this band. We have also identified several harmonic and combination bands, some of which are modified in the hydrates.

The 1232 cm^{-1} PrOH band (at 1235 cm^{-1} in Fig. 6C*a*) was assigned by Fukushima and Zwolinski (27) to the COH deformation mode (ν_{18}, Table 2). In the hydrate, a similar band having about the same intensity and shape is situated at the same place (Fig. 6C*b*). However, the presence of water in the hydrate should displace the COH deformation mode. Furthermore, a position of 1232 cm^{-1} for a COH alcohol deformation mode is low. It should, according to Colthup et al. (29), be situated near 1400 cm^{-1}. This is an indication that the assignment of PrOH should be reevaluated.

Fukushima and Zwolinski (27) assigned the 1464 cm^{-1} band of gas and liquid PrOH to ν_9, ν_{10}, ν_{11}, and ν_{12} (Table 2). We observed five components in that region, one of which could be a combination band. The normal coordinate analysis of Fukushima and Zwolinski does not permit greater precision, although these modes are involved in the combination bands in the 2940 cm^{-1} region where they could perturb the C-H absorption bands.

© 2002 NRC Canada

The 1416 cm^{-1} band observed in the hydrate's spectrum is not present in the pure propanol spectrum (Fig. 6C). Since water does not absorb in that region, we tentatively assigned this band to a combination band implying a far-IR band of the hydrate.

Besides verifying the difference band assignment, a new normal coordinate analysis could also verify the assignment of the COH deformation band of PrOH and the other assignment problems mentioned above. Work is in progress on that matter.

Integrated intensity of the O-H stretching vibration in PrOH and water mixtures

The spectrum of the PrOH hydrate was normalized to the concentration of pure liquid PrOH (13.27 mol L^{-1}) to allow comparison on an equimolar basis (Fig. 3B). Since the hydrate is a one-to-one association, the water concentration represented by the spectrum of the hydrate in Fig. 3B is also 13.27 mol L^{-1}. The $\nu_{O\text{-}H}$ intensity of the hydrate has to be compared to that of pure water: 55.35 mol L^{-1}. The pure water spectrum (Fig. 3B*b*) shows an integrated intensity of the O-H stretching band of around 1.6 times higher than that of the PrOH hydrate (Fig. 3B*c*), but with an OH concentration (55.35 × 2/[13.27 × 3]) = 2.8 higher. This indicates that the integrated intensity of the O-H stretching vibration of the PrOH hydrate is greater than that of pure water. As a crude evaluation to sort out the water contribution to the molar integrated intensity of the O-H stretching, we considered the contribution of the $\nu_{O\text{-}H}$ band of the PrOH molecule in the hydrate to be identical to that in pure PrOH and subtracted this contribution from the total integrated intensity in the 3000–3700 cm^{-1} range. The result was estimated to be the contribution of the water molecules to the $\nu_{O\text{-}H}$ band of the hydrate's spectrum. The ratio of the OH stretching integrated intensity of water in PrOH hydrate to that in pure water was found to be 1.6. This indicates that the $\nu_{O\text{-}H}$ integrated intensity of water molecules does not remain constant when the water molecules are in strong interaction with PrOH. To further confirm this result, we evaluated the variation in the integrated intensity of the O-H stretching vibration — in the 3000–3700 cm^{-1} range to avoid any contribution from the C-H vibrations — for each sample. The results are plotted as a function of the sample's water concentration in Fig. 7A (Δ symbols, left ordinate).

Figure 7A also shows that the PrOH concentration in a sample (O symbols, right ordinate) is proportional to the solution water concentration. Therefore, denoting the water and PrOH concentrations by c_w and c_{PrOH}, respectively, we have:

$$[7] \qquad c_{PrOH} = c_0 - ac_w$$

where c_0 is the concentration of pure liquid PrOH and a is the slope observed (= 0.241).

In each sample, the integrated intensity of the O-H stretch band contains the contribution of both water and PrOH, that is:

$$[8] \qquad \int_{\nu_{OH}}^{\text{sample}} I(\nu)d\nu = c_w \int_{\nu_{OH}}^{H_2O} I(\nu)d\nu + c_{PrOH} \int_{\nu_{OH}}^{PrOH} I(\nu)d\nu$$

where the superscript indicates the corresponding contribution. Substituting eq. [7] into eq. [8], one obtains:

Fig. 7. Different parameters of the PrOH–H_2O mixtures are presented as a function of water concentration. (A) PrOH concentration (O, right ordinate) and ν_{OH} integrated intensity (3700–3000 cm^{-1}) (Δ (experimental), (——) calculated: left ordinate); (B) δ_{HOH} integrated intensity (1750–1500 cm^{-1}) (O); (C) ν_{OH} and δ_{HOH} position.

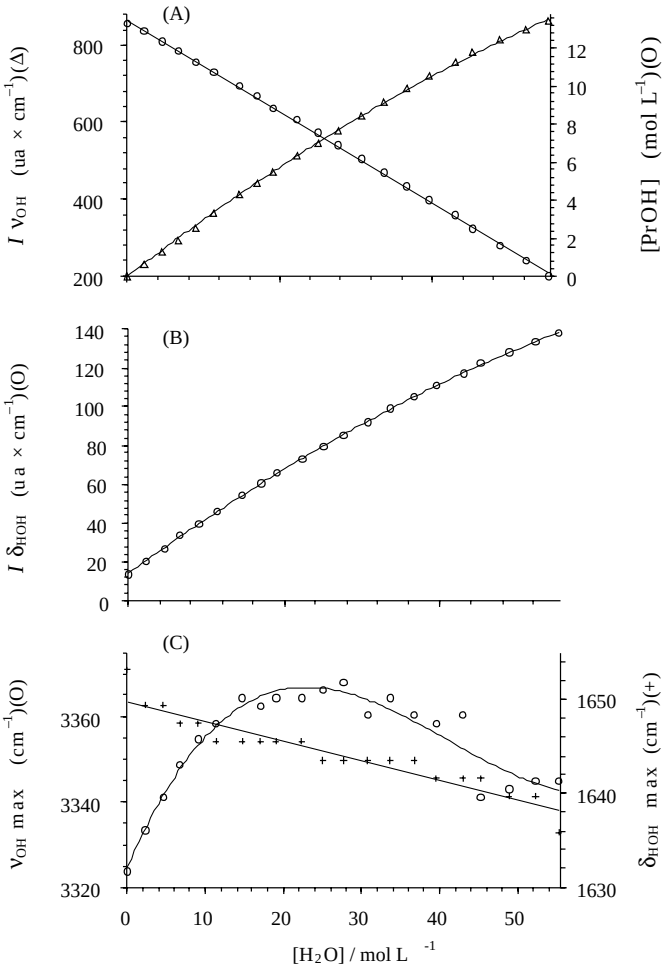

$$[9] \qquad \int_{\nu_{OH}}^{\text{sample}} I(\nu)d\nu = c_w \left\{ \int_{\nu_{OH}}^{H_2O} I(\nu)d\nu - a \int_{\nu_{OH}}^{PrOH} I(\nu)d\nu \right\} + c_0 \int_{\nu_{OH}}^{PrOH} I(\nu)d\nu$$

If the molecular contributions of both water and PrOH to the integrated intensity of the absorption band were unchanged in the hydrate formed, the rightmost term and the term in braces in eq. [9] would be constant. Equation [9] would then represent a linear function of the water concentration c_w, that is, the total $\nu_{O\text{-}H}$ integrated intensity would be proportional to the water concentration. However, Fig. 7A (Δ symbols, left ordinate) clearly shows that such is not the case. Therefore, we must conclude that the molecular contributions of both water and PrOH to the $\nu_{O\text{-}H}$ integrated intensity are changed in the hydrate formed. Furthermore, the slopes observed in Fig. 7A for the total integrated intensity of the O-H stretch band are 14.5 and 8.4 (ATR Abs × cm^2 mol^{-1}) at 0 and 55.35 mol L^{-1} of water, respectively. This indicates that the slope at 0 mol L^{-1} of water (pure PrOH) is nearly twice that at 55.35 mol L^{-1} (pure water). This suggests that

© 2002 NRC Canada

the absorptivity of the O-H stretching vibration of water is multiplied by 2 when the molecule is complexed to one PrOH molecule. This is a new result. It should be noted that the absorptivity of the OH stretching of liquid water is 17 to 19 times stronger than that of water vapor and about half that of ice (21, 30). Therefore, it is not unreasonable that the PrOH–water complex OH stretch absorptivity is twice that of pure liquid water. The above arguments indicate that it is not possible to use the integrated intensities of OH stretching to determine the number of water molecules in the hydrate.

In each sample, the integrated intensity of the O-H stretch band contains the contribution of both water and PrOH and that of PrOH hydrate, that is:

$$[10]\quad \int_{\nu_{OH}}^{\text{sample}} I(\nu)d\nu = c_w \int_{\nu_{OH}}^{H_2O} I(\nu)d\nu + c_{PrOH} \int_{\nu_{OH}}^{PrOH} I(\nu)d\nu + c_{PrOH\ hydrate} \int_{\nu_{OH}}^{PrOH\ hydrate} I(\nu)d\nu$$

where $c_{PrOH\ hydrate}$ represents the PrOH hydrate concentration retrieved by FA. The contributions of both pure water and PrOH are easily obtained using the respective spectra (at the extremity of the curve in Fig. 7A). The results were 15.60 (= 863.1/55.34) and 15.16 (= 201.2/13.27) ATR Abs cm^2 mol^{-1} for water and PrOH, respectively. Note that the former possesses two OH while PrOH possesses only one. This indicates that the integrated intensity of each OH stretching vibration in liquid PrOH is nearly twice that of each of the OH stretching vibrations in liquid H_2O. The integrated intensity due to the PrOH hydrate was obtained by least-squares fitting the experimental values with the right member of eq. [10] calculated using the concentrations retrieved by FA. The molar integrated intensity of the OH stretching in the PrOH hydrate was found to be equal to 41.20 ATR Abs cm^2 mol^{-1}. Therefore, the mean intensity for each of the three OH of the hydrate was estimated to be 13.73 ATR Abs cm^2 mol^{-1}. The latter value is slightly beyond that in pure PrOH while it is near 1.8 times that of pure water. Such a result is fully consistent with the spectrum retrieved for pure PrOH hydrate (Fig. 3B*c*).

Integrated intensity of H_2O deformation vibration in water mixtures

We further evaluated the total integrated intensity of the water deformation band situated near 1638 cm^{-1}. Since PrOH does not have an absorption band in this region, the only contribution to this intensity is due to water. The integrated intensity of each sample was evaluated in the 1750–1500 cm^{-1} range. The results (shown in Fig. 7B), exhibit a nonlinear behavior indicating that the intensity of this vibration of the water molecules is modified when water is associated to PrOH. Therefore, both vibrations (OH stretch and HOH deformation) are enhanced in the PrOH hydrate.

The band position of both the OH stretching and HOH deformation were determined as functions of the sample's water concentration. The results are shown in Fig. 7C. The water deformation (+, right scale) regularly shifts from 1638 to 1650 cm^{-1} as the water concentration decreases. This is consistent with the intensity variation of this absorption band. The variation of the OH stretching position is not monotonic: for pure water it is situated near 3340 cm^{-1}; as the water concentration decreases it slowly shifts to near 3365 cm^{-1} at 25 M H_2O, thereafter it decreases rapidly to 3324 cm^{-1} for pure PrOH. In the mixtures at high water concentration ν_1 and ν_3 of water can be observed (by Gaussian fit) at 3222 and 3389 cm^{-1}, respectively. Below 10 M H_2O, the PrOH OH stretch band is more intense than that of water.

Conclusion

The formation of a PrOH hydrate (PrOH–H_2O) was found by applying FA to the mid-IR–ATR spectra of 21 PrOH–water mixtures. Only one type of hydrate was found over the whole solubility range of the mixtures. This indicates that three species are present in the mixtures: pure H_2O, pure PrOH, and pure PrOH–H_2O hydrate (1:1). The hydrate is formed as soon as PrOH is added to water and reached its peak abundance at 7.57 M PrOH in 25.14 M H_2O. From the IR abundance, the hydrate's formation constant was found to be K_f = 1.2. This is more than three times less than what ideal mixtures would produce and indicates that the hydrophobic interactions of the aliphatic chains in PrOH decrease the association between PrOH and water through hydrogen bonding. This type of interaction would explain the solubility decrease of the alcohols with increasing aliphatic chain length. IR spectroscopy has been used for the first time to evaluate such a decrease quantitatively. The spectrum of the "pure" PrOH hydrate was obtained and the assignment of the bands made. Apart from the water absorption, the spectrum of PrOH–H_2O is similar to that of PrOH with some slight position and intensity changes. Only a small new band appeared in the 1400 cm^{-1} region that we tentatively assigned to a combination of a fundamental mode with an external mode.

References

1. E.D. Katz, K. Organ, and R.P.W. Scott. J. Chromatogr. **352**, 67 (1986).
2. E.D. Katz, C.H. Lochmüller, and R.P.W. Scott. Anal. Chem. **61**, 349 (1989).
3. C. Weast. Handbook of chemistry and physics. 57th ed. CRC Press, Cleveland. 1977. p. D218; p. D252.
4. I.S. Kislina, V.D. Maiorov, N.B. Librovich, and M.I. Vinnik. Russ. J. Phys. Chem. Transl. Zh. Fiz. Khim. **50**, 1676 (1976).
5. J.-J. Max and C. Chapados. Appl. Spectrosc. **53**, 1045 (1999).
6. J.-J. Max, M. Trudel, and C. Chapados. Appl. Spectrosc. **52**, 234 (1998).
7. J.-J. Max and C. Chapados. Appl. Spectrosc. **53**, 1601 (1999).
8. J.-J. Max and C. Chapados. Appl. Spectrosc. **52**, 963 (1998).
9. J.-J. Max and C. Chapados. Can. J. Chem. **78**, 64 (2000).
10. J.-J. Max, M. Trudel, and C. Chapados. Appl. Spectrosc. **52**, 226 (1998).
11. J. Baril, J.-J. Max, and C. Chapados. Can. J. Chem. **78**, 490 (2000).
12. J.-J. Max, C. Ménichelli, and C. Chapados. J. Phys. Chem. A, **104**, 8465 (2000).
13. J.-J. Max and C. Chapados. J. Chem. Phys. **113**, 6803 (2000).
14. C. Ménichelli, J.-J. Max, and C. Chapados. Can. J. Chem. **78**, 1128 (2000).

© 2002 NRC Canada

15. J.J. Max, S. de Blois, A. Veilleux, and C. Chapados. Can. J. Chem. **79**, 13 (2001).
16. Z. Zhao and E.R. Malinowski. Anal. Chem. **71**, 602 (1999).
17. J.-J. Max and C. Chapados. J. Chem. Phys. **115**, 2664 (2001).
18. D.A. Wieliczka, S. Weng, and M.R. Querry. Appl. Opt. **28**, 1714 (1989).
19. E.R. Malinowski and D.G. Howery. Factor analysis in chemistry. Robert E. Krieger, Malabar, Florida. 1989.
20. C. Chapados and M. Trudel. Biophys. Chem. **47**, 267 (1993).
21. H. Ahlborn, X. Ji, B. Space, and P.B. Moore. J. Chem. Phys. **111**, 10 622 (1999).
22. S.M. Craven and F.F. Bentley. Appl. Spectrosc. **26**, 242 (1972).
23. S.H. Tanaka, H.I. Yosihara, A.W.-C. Ho, F.W. Lau, P. Westh, and Y. Koga. Can. J. Chem. **74**, 713 (1996).
24. S. Dixit, W.C.K. Poon, and J. Crain. J. Phys.: Condens. Matter, **12**, L323 (2000).
25. J.E. Bertie and Z. Lan. J. Phys. Chem. B, **101**, 4111 (1997), and refs. therein.
26. T. Takamuku, M. Tabata, A. Yamaguchi, J. Nishimoto, M. Kumamoto, H. Wakita, and T. Yamaguchi. J. Phys. Chem. B, **102,** 8880 (1998).
27. K. Fukushima and B.J. Zwolinski. J. Mol. Spectrosc. **26**, 368 (1968).
28. American Institute of Petroleum. Research project 44. Catalog of selected infrared spectral data. Loose-leaf data sheets, extant: serial nos. 427, 747, and 1604. Thermodynamics Research Center, Texas A&M University, College Station, Texas. 1966.
29. N.B Colthup, L.H. Daly, and S.E. Wiberley. Introduction to infrared and Raman spectroscopy. Academic Press, Inc., Boston. 1990.
30. J.E. Bertie, A.M. Khalique, and H.H. Eysel. J. Phys. Chem. **93**, 2210 (1989), and refs. therein.

© 2002 NRC Canada

Canadian Journal of Chemistry

Author Index
Volume 80, 2002

Revue canadienne de chimie

Index des auteurs
Volume 80, 2002

Amat-Guerri, F., 62
Arévalo, E.A., 76
Bazzi, L., 106
Bertolotti, S., 62
Bottomley, F., 55
Brown, G.R., 89
Chapados, C., 113
Chiang, Y., 82
Cole, J.G., 46
Daneault, S., 113
Decken, A., 31, 55
Delamere, C., 94
Dyker, C.A., 55
Edwards, J.P., 31
El Issami, S., 106
Filali-Mouhim, A., 68
Galley, W.C., 89
García, N.A., 62
Haggi, E., 62
Hammouti, B., 106
Jakins, C., 94
Janzen, M.C., 41
Jay-Gerin, J.-P., 68
Jennings, M.C., 41
Kamerling, J.P., 76
Kertit, S., 106
Kresge, A.J., 82
Lefeber, D.J., 76
Lewars, E., 94
Mankhetkorn, S., 68
Max, J.-J., 113
Mayer, P.M., 25
Meesungnoen, J., 68
Meng, Q., 82
Miller, R.J.D., 1
Miskoski, S., 62
Neil, M.A., 55
Norman, D.W., 31
Poon, C., 25
Puddephatt, R.J., 41
Salghi, R., 106
Vliegenthart, J.F.G., 76
Vogels, C.M., 31
Wan, P., 46
Westcott, S.A., 31
Williams, C.K., 89
Zine, E., 106

© 2002 NRC Canada

Can. J. Chem. Downloaded from www.nrcresearchpress.com by China University of Science and Technology on 09/08/12
For personal use only.

Recommandations aux auteurs

Revue canadienne de chimie

La *Revue canadienne de chimie* (Can. J. Chem.) publie, en français ou en anglais, les résultats de travaux originaux, sous forme d'articles ou de communications, dans les divers domaines de la chimie. Un **article** contient les résultats d'une étude définitive terminée. Une **communication** cherche à diffuser rapidement un travail particulièrement important et opportun. Le texte d'une communication ne devrait normalement pas dépasser huit pages dactylographiées à double interligne, y compris les figures et les tableaux, tout en fournissant suffisamment de détails pour que les experts dans le domaine puissent reproduire l'expérience. Un bref énoncé indiquant l'importance des travaux doit figurer dans le paragraphe d'introduction du manuscrit ou accompagner celui-ci sous forme de lettre de couverture. Cet énoncé doit être préparé avec soin, car il peut influer sur la décision des examinateurs. La soumission de **synthèses critiques** est également encouragée. Les manuscrits soumis pour publication dans la *Revue canadienne de chimie* ne doivent pas être soumis en même temps, ni publiés, ailleurs.

Liste de vérification pour les auteurs

Afin d'éviter des délais de publication, les auteurs devraient s'assurer que

1. toutes les sections du manuscrit sont dactylographiées à double interligne, d'un seul côté de feuilles de papier de format standard, avec marges de 1 po (2,5 cm);
2. un original et trois copies claires du texte et les dessins au trait originaux ou des photographies au fini glacé sont soumises;
3. toutes les pages sont numérotées, en commençant par celle du titre, au haut de la page;
4. la page du titre comporte le titre, les noms des auteurs et l'adresse de l'établissement où les recherches ont été effectuées;
5. l'auteur correspondant est identifié et que ses numéros de téléphone et de télécopieur ainsi que son adresse de courrier électronique, si disponibles, sont donnés;
6. la deuxième page comporte le résumé et les mots clés;
7. le format et le style du manuscrit sont conformes à ceux d'articles récents de la Revue;
8. la lettre de couverture indique les noms d'examinateurs potentiels; et
9. un résumé graphique est fourni sur une page distincte.

Il est possible d'éviter les délais de publication en se conformant aux règles décrites ci-dessous.

Manuscrit

Toutes les parties du manuscrit, y compris les notes infrapaginales, les tableaux, les légendes des illustrations et la bibliographie, doivent être dactylographiées à double interligne, d'un seul côté de feuilles de papier de 8,5 sur 11 po (ou ISO A4) avec marges de 1 po (2,5 cm). La première page ne doit comporter que le titre de l'article, les noms des auteurs, le nom ainsi que l'adresse de l'établissement où les recherches ont été effectuées, le nom de l'auteur correspondant, ses numéros de téléphone et de télécopieur ainsi que son adresse de courrier électronique, si disponibles, et toute note infrapaginale qui s'impose. Le manuscrit comprend les résumés (p. 2), le texte principal, puis, dans l'ordre, les remerciements, la bibliographie, les annexes, les tableaux et les légendes des figures. Les textes des légendes doivent être regroupés sur une ou plusieurs feuilles et présentés par ordre numérique. **Chaque page** du manuscrit doit être numérotée, en commençant par celle du titre, au haut de la page. Il importe de rédiger chaque section avec toute la concision qui assurera une clarté adéquate. **Les auteurs devront soumettre l'original et trois copies nettes du texte.** Les titres ainsi que les résumés fournissent l'information utilisée par les **services de repérage de l'information** dans l'élaboration de leurs bases de données. Ceux-ci doivent par conséquent être brefs et informatifs. À la demande du Chemical Abstracts Service, les directeurs scientifiques encouragent tous les auteurs à indiquer leurs prénoms au complet au lieu d'inscrire leurs initiales.

L'**orthographe** doit suivre *Le Grand Robert*. Les auteurs sont responsables de l'uniformité de l'orthographe dans l'ensemble du texte. Les accents doivent être insérés sur les majuscules.

La **nomenclature**, les **abréviations** et les **symboles des unités de mesure** doivent être conformes aux recommandations internationales, entre autres celles de l'Union internationale de chimie pure et appliquée et de l'Union internationale de physique pure et appliquée. Il est recommandé de se servir du **Système international d'unités** ou, tout au moins, de fournir les équivalences en unités SI. Ce système est décrit dans le *Guide de familiarisation au système métrique*, publié en 1989 par l'Association canadienne de normalisation (178, boulevard Rexdale, Etobicoke, ON M6N 3T3, Canada). Pour des raisons pratiques, on permet certaines exceptions à l'utilisation du Système international d'unités. On pourra continuer d'utiliser la molarité, la kilocalorie, le centimètre réciproque (nombre d'ondes) et l'atmosphère. On trouvera dans *Anal. Chem.* **54**, 155 (1982) une liste provisoire des unités de mesure n'appartenant pas au SI mais qui sont acceptables pour les articles de la Revue. Lorsqu'une formule ou le nom d'un composé chimique est signalé par un chiffre, il convient d'utiliser un chiffre arabe gras.

Les abréviations des noms de substances, de procédés, d'organisations, etc., doivent être définis la première fois qu'ils sont utilisés. Les symboles et les caractères grecs ou d'usage peu répandu doivent être identifiés clairement; les indices supérieurs et inférieurs doivent être lisibles et correctement placés ou indiqués.

Les références suivantes pourront être utiles en nomenclature : chimie organique : *Règles de nomenclature pour la chimie organique — Sections A, B et C* (1965), *Compléments à l'édition française des règles de nomenclature pour la chimie organique (Sections A, B et C)* (1974) et *Règles de nomenclature pour la chimie organique — Sections D et E* (1976) (Société chimique de France, 250, rue Saint-Jacques, 75005 Paris, France); *La nomenclature en chimie organique* (Masson et C^{ie}, Paris, 1967); *Chimie organique — Mode d'écriture des noms systématiques*

Also available in English

Can. J. Chem. Downloaded from www.nrcresearchpress.com by China University of Science and Technology on 09/08/12
For personal use only.

(AFNOR, NF T 01-101, 1969); chimie inorganique : *Nomenclature de chimie inorganique* (Bull. Soc. Chim. Fr., numéro spécial, 1975); *Nomenclature de chimie minérale* (AFNOR, NF T 01-003, 1965). Lorsque la nomenclature n'est pas normalisée par accord international, il convient d'adopter celle de la Société chimique de France (voir, entre autres, Bull. Soc. Chim. Fr.). Il n'est pas nécessaire de suivre rigoureusement les règles de nomenclature chaque fois qu'un composé est mentionné dans le manuscrit, mais le nom reconnu doit y figurer au moins une fois, de préférence vers le début du manuscrit.

Tout manuscrit doit être accompagné d'un **résumé**. Les auteurs doivent indiquer entre trois et cinq mots clés directement sous le résumé; ceux-ci seront utilisés par les services de repérage de l'information. Le résumé doit être précédé du titre et des noms des auteurs (une copie, en page détachée, est destinée au traducteur). Il ne doit pas excéder une page et doit être moins long s'il s'agit d'une communication. **Il ne doit comporter aucune abréviation ou référence.** Les auteurs qui peuvent soumettre des résumés dans les deux langues officielles du Canada, c'est-à-dire en anglais et en français courants, sont encouragés à le faire.

La **partie expérimentale** ou les **calculs** doivent être assez détaillés pour permettre une répétition exacte du travail, mais rester concis et éviter les longues descriptions de méthodes déjà connues; ces dernières devraient être signalées par des références appropriées. **Il convient d'attirer l'attention du lecteur sur tout risque nouveau ou particulier du travail expérimental.**

Analyses et spectres — L'apport d'une preuve pleinement convaincante de l'homogénéité et de l'identité de tous les composés présentés comme nouveaux par les auteurs relève de leur responsabilité. La preuve tant de la pureté que de l'identité inclut normalement de bonnes données analytiques relatives aux éléments. Une mesure précise de la masse d'un ion moléculaire est acceptée comme preuve de la composition chimique à la condition d'être accompagnée d'une preuve établissant de façon indépendante la pureté de l'échantillon. En l'absence de ces données, les spectres de RMN ^{13}C et (ou) ^{1}H de certains composés ou d'autres preuves pourront être acceptés sous réserve de l'approbation d'un spécialiste en la matière et de celle du directeur scientifique.

Constantes de vitesse et d'équilibre — Les résultats expérimentaux primaires devraient être mis à la disposition des lecteurs sous forme de tableaux; ils peuvent être intégrés à l'article ou, plus couramment, à la documentation complémentaire. Dans ce dernier cas, quelques exemples de données expérimentales primaires (par exemple, les absorbances) devraient être insérés dans l'article, plus particulièrement si le traitement des données est nouveau ou déroge aux règles établies. En ce qui concerne les expériences de cinétique, les constantes fondamentales de vitesse devraient être présentées, alors que pour la détermination des fonctions d'acidité, les logarithmes *I*, en tant que fonctions des concentrations d'acides, devraient être fournis. À noter que la seconde est la seule unité de temps acceptable pour les constantes de vitesse.

Les **références bibliographiques** doivent être vérifiées auprès des publications originales. Dans la **bibliographie,** qui suit les remerciements, elles doivent être classées par ordre numérique de mention dans le texte. **Chaque référence bibliographique doit être inscrite dans le texte et être signalée par son numéro clé spécifique inscrit sur la ligne entre parenthèses.** Une référence bibliographique de périodique doit respecter la structure suivante : initiales du prénom de l'auteur, nom de famille de l'auteur, titre du périodique (abrégé conformément à *CASSI*, Chemical Abstracts Service, P.O. Box 3012, Columbus, OH 43210, É.-U.), numéro de volume, page initiale de l'article, année de parution entre parenthèses. Une référence bibliographique de livre, de compte rendu de conférence, de thèse, etc. doit indiquer le nom et les initiales de l'auteur (ou des auteurs), le titre de la publication, le chapitre, le nom et les initiales du rédacteur en chef (ou des rédacteurs en chef) le cas échéant, le nom de la maison d'édition, la ville et l'année de publication et la page ou le chapitre d'où est tirée la citation. Voir un numéro récent de la Revue pour des exemples de présentation.

Les **rapports qui ne sont pas encore approuvés pour publication et les communications personnelles** ne font pas partie de la bibliographie et ne doivent être mentionnés qu'en notes infrapaginales ou entre parenthèses dans le texte, en spécifiant les noms de tous les auteurs et leurs initiales. Lorsqu'un document cité dans un article n'a pas encore été publié ou a paru sous une forme qui le rend difficilement accessible dans une bibliothèque scientifique, l'auteur doit faire parvenir deux copies de ce document au directeur scientifique (une copie seulement, dans le cas d'un article sous presse).

Les **notes infrapaginales** ne devraient figurer dans le texte que lorsqu'elles sont inévitables, mais leur utilisation dans les tableaux est encouragée. Lorsque les notes infrapaginales figurent dans le texte, leurs appels devraient être désignés par des chiffres arabes en exposant (sauf dans le cas des tableaux, voir ci-dessous) et numérotés consécutivement à partir de la première note infrapaginale, y compris toute note apparaissant en page titre. Chaque note doit figurer au bas de la page où elle est signalée, **pas dans la bibliographie**.

Les **équations** doivent être dactylographiées clairement, à triple interligne si elles incluent des exposants ou des indices. Les exposants et les indices doivent être lisibles et correctement placés. Il convient de faire une distinction entre la lettre *l* et le chiffre *un*, et entre la lettre majuscule *O* et le chiffre *zéro*. Une lettre ou un symbole ne devrait représenter qu'une seule entité et devrait être utilisé de façon uniforme dans l'article. Chaque variable doit être définie dans le texte ou dans une **liste des symboles** devant apparaître après la bibliographie. Les variables représentant des vecteurs, des matrices, des matrices vectorielles et des tenseurs doivent être clairement définies. Les numéros d'équation doivent être identifiés par des chiffres arabes placés entre crochets et alignés avec la **marge de gauche**. Aucune distinction n'est faite entre la numérotation des formules mathématiques et celle des formules chimiques.

Les **tableaux** doivent être numérotés de façon continue en chiffres arabes, comporter un titre bref et être mentionnés dans le texte. Toute information contenue dans les tableaux doit être dactylographiée à double interligne, sauf les équations mathématiques ou chimiques, les structures chimiques ou les entrées complexes, lesquelles doivent être dactylographiées à triple interligne. Chaque tableau doit être dactylographié sur une page distincte. Les descripteurs et les notes descriptives infrapaginales doivent être brefs. Les tableaux ne doivent pas contenir de lignes horizontales superflues, ni de lignes verticales. Les notes infrapaginales doivent être signalées par des lettres minuscules supérieures en italique. Une note descriptive qui n'est pas introduite par un appel de note peut être inscrite au bas du tableau à titre de **Nota**.

Annexes — Les illustrations et les tableaux en annexe doivent être numérotés différemment des illustrations et tableaux du corps de l'article, p. ex. fig. A1, tableau A1, etc.

Documentation complémentaire—Le Conseil national

Can. J. Chem. Downloaded from www.nrcresearchpress.com by China University of Science and Technology on 09/08/12
For personal use only.

de recherches administre un Dépôt des données non publiées dans lequel la documentation complémentaire peut être versée, à la demande des auteurs ou du directeur scientifique. La documentation complémentaire peut comprendre de grands tableaux, des calculs complexes et des cartes détaillées qui ne sont pas essentiels à la compréhension ou à l'évaluation du document. Les auteurs qui désirent utiliser ce service doivent clairement indiquer les parties dont ils demandent le dépôt dès la soumission de leur article. Les tableaux et les figures doivent être numérotés de façon consécutive, distinctement de ceux destinés à la publication (p. ex. : fig. D1, tableau D1). Toute donnée déposée doit faire l'objet d'une note infrapaginale à la section appropriée du document.

Les auteurs d'articles décrivant la **structure de macromolécules biologiques selon la diffraction des rayons X par un cristal unique** doivent soumettre à la Protein Data Bank (Brookhaven National Laboratory) toutes les données requises pour valider la discussion, y compris les amplitudes et les phases de rayons X et les coordonnées atomiques dérivées. Si les auteurs le désirent, les directeurs scientifiques demanderont à la Protein Data Bank de ne pas diffuser les données jusqu'à une date convenue. Dans le cas des listes de coordonnées, ce délai ne peut pas dépasser une année après la date d'acceptation du manuscrit. Dans le cas des données complètes sur l'amplitude et les phases des structures, la période précédant la diffusion des données ne peut être supérieure à 4 ans. La date de diffusion spécifiée par l'auteur ainsi que l'envoi des données à la Protein Data Bank seront indiqués par une note infrapaginale dans l'article. Si aucune date de diffusion n'est mentionnée, on présumera que les données sont disponibles dès la parution de la Revue.

Dans le cas de la détermination aux rayons X de la structure de cristaux uniques d'autres molécules, des données suffisantes pour une révision adéquate devraient accompagner le manuscrit. Ces données devraient être soumises en format apte à être placé au Dépôt des données non publiées du Conseil national de recherches du Canada. Des recommandations pour la présentation de données cristallographiques ont paru dans le Can. J. Chem. **80** (1), R-6 (2002). Des directives pour la présentation de données d'analyses thermiques ont paru dans *Analyse thermique — Vocabulaire — Présentation de résultats* (AFNOR, NF T 01-021, 1974) et dans *Normes fondamentales — Grandeurs, unités et symboles de thermique* (AFNOR, NF X 02-204, 1985).

Les **instructions supplémentaires à l'usage des auteurs**, dont il est possible de se procurer des exemplaires auprès du directeur scientifique, contiennent de plus amples détails sur la plupart des sujets discutés ci-dessus. Le format de présentation des données physiques, analytiques et spectroscopiques y est également décrit.

Illustrations

Chaque figure ou groupe de figures doit être préparé de manière à occuper, après une réduction appropriée, l'espace d'une ou deux colonnes du texte. Les dimensions finies maximales d'une illustration sur une colonne sont de 8,6 sur 23,7 cm (3,4 sur 9,3 po) et celles d'une illustration sur deux colonnes de 18,2 sur 23,7 cm (7,2 sur 9,3 po). Les figures (y compris les similigravures) sont numérotées en chiffres arabes selon leur ordre séquentiel et doivent être annoncées dans le texte bien que tous leurs éléments doivent être intelligibles en eux-mêmes. Tous les termes, les abréviations et les symboles qui se trouvent dans les figures doivent être les mêmes que ceux apparaissant dans le texte. Seuls les détails essentiels devraient être identifiés; l'information plus détaillée devrait paraître dans la légende. Chaque illustration doit être identifiée, de préférence au bas, à gauche, par le numéro de la figure et les noms des auteurs, suffisamment éloignés de l'espace réservé à l'illustration.

Les **dessins au trait** originaux doivent être en encre noire ou produits par ordinateur en encre noire sur du papier blanc de première qualité ou un matériau comparable. Quant aux graphiques produits par ordinateur, il faut fournir un imprimé au laser de la meilleure résolution disponible. **Les photocopies ne sont pas acceptables.**

L'épaisseur des lignes doit être suffisante (au moins 0,5 point) pour que la reproduction soit nette; tous les symboles, les indices supérieurs ou inférieurs et les signes décimaux doivent être en bonne proportion avec le reste du dessin et suffisamment marqués pour permettre la réduction nécessaire sans perte de détail. Ne pas utiliser de petits symboles ouverts qui ont tendance à se refermer lorsqu'ils sont reproduits. **Le lettrage produit par imprimante à matrice de point ou par machine à écrire, ou à la main, ne sont pas acceptables.** Le même style de police et la même dimension de lettrage doivent servir dans toutes les figures de dimensions semblables d'un article. Toutes les lignes de coordonnées doivent être tracées à la règle. Les enregistrements originaux de **spectres RMN, IR, RPE,** etc., ne peuvent être reproduits et doivent être redessinés.

Dessins de structures — Les structures et schémas à reproduire doivent être soumis sur des pages distinctes (et non pas insérés dans le texte). Il est fortement recommandé d'exploiter un logiciel de dessin tel que ChemDraw ou ChemWindows. La représentation stéréochimique doit préférablement être illustrée par des lignes en gras de largeur simple et des lignes brisées plutôt que par des coins. La police des désignations d'atomes doit être l'Helvetica de 12 points.

La table des matières est ponctuée de **graphiques synoptiques**. Ces graphiques sont un diagramme, une équation ou tout autre petit dessin qui illustre l'objet de l'article. Le graphique doit être un dessin ou un imprimé laser **original**, soumis sur une page distincte, d'une hauteur maximale de 40 mm et d'une largeur maximale de 85 mm, **sans texte** (si ce n'est des annotations essentielles).

Les **photographies** doivent être en *demi-teintes* sur papier glacé. Il faut préparer ces figures dans leurs dimensions de tirage final.

Les **illustrations en couleurs** sont aux frais de l'auteur. On peut obtenir de plus amples renseignements sur les prix auprès de l'agent de publication, Lea Libiseja, aux Presses scientifiques du CNRC (613-990-6965; télécopieur : 613-952-7656; courriel : lea.libiseja@nrc.ca).

Les Presses scientifiques du CNRC préfèrent recevoir la version électronique des graphiques des manuscrits acceptés et l'utiliseront dans la mesure du possible. Quatre copies de la version papier des illustrations doivent être soumises au Bureau de la rédaction, même s'il faut soumettre la version électronique pour la production.

Si les fichiers électroniques ne sont pas disponibles, la version papier des graphiques sera balayée. Toutefois, le lecteur optique reproduit facilement les défauts (p. ex., le liquide correcteur, les maculations). Il est recommandé de ne pas soumettre de photographies tramées, ni des illustrations balayées imprimées au laser, à cause des moirures qui se forment; une moirure est un motif perceptible et non désiré produit par le rebalayage ou le retramage d'une illustration qui contient déjà un motif de points.

Préparation des fichiers de graphiques électroniques

Les auteurs doivent fournir des copies des fichiers

Can. J. Chem. Downloaded from www.nrcresearchpress.com by China University of Science and Technology on 09/08/12
For personal use only.

électroniques originaux (c.-à-d. les fichiers tirés directement du logiciel sur lequel ils ont été créés) et des **épreuves au laser de haute qualité** des images. **Les fichiers électroniques (c.-à-d. le numéro et le contenu de la figure) doivent correspondre aux épreuves au laser.** Sur l'étiquette de la disquette, il faut indiquer (*i*) l'application et la version du logiciel; (*ii*) le(s) noms(s), la dimension et le suffixe du fichier; et (*iii*) si les fichiers ont été importés d'un autre logiciel. Si les fichiers ont été comprimés, il faut indiquer le format de compression. Les versions PC ou Macintosh des polices True Type ou Type 1 doivent être utilisées. **On ne doit pas se servir des polices de caractères en mode points ou non standard.** Les illustrations électroniques sont acceptés sur les disquettes de 3 1/2 po, cartouches Zip de 100 Mo et CD-ROM.

Toutes les illustrations doivent être soumises dans leurs dimensions de tirage final. Quant aux figures comportant plusieurs parties (p. ex., *a*, *b*, *c*, *d*, etc.) créées sur le même logiciel, elles doivent être assemblées dans un seul fichier plutôt que d'être transmises en plusieurs fichiers.

Il faut **garder** les illustrations le plus simple possible afin d'éviter les embûches. Éviter les textures et les fonds grisés compliqués, particulièrement dans les programmes d'illustration vectorielle.

Fichier en mode points — Les fichiers d'images en mode points sont produits sur une grille dans laquelle chaque carré (ou pixel) correspond à une nuance de noir, de couleur ou de gris. Un fichier en mode point est défini par le nombre de pixels ou d'éléments par pouce. Comme le pixel est défini comme un point, on parle aussi de « points par pouce » ou « ppp ». Plus la résolution de l'image est grande, plus le nombre de points sur une surface donnée est élevé.

Les illustrations soumises en mode points doivent être de définition adéquate. Les exigences minimales de définition sont les suivantes : 600 ppp pour les dessins au trait et les lignes fines (les dessins au trait comportant des lignes fines ou un fond grisé), 300 ppp pour les demi-teintes et les couleurs et 600 ppp pour les combinaisons (demi-teintes avec lettrage à l'extérieur de l'espace réservé à la photo).

Tous les fichiers en *couleurs* soumis doivent suivre la base CMJK (cyan, magenta, jaune et noir). Ces couleurs sont utilisées dans l'impression commerciale tout en couleur. Les graphiques RVB (le rouge, le vert et le bleu sont les couleurs utilisées particulièrement pour produire les images sur un écran) ne s'impriment pas correctement.

Fichiers vectoriels — Les fichiers vectoriels sont des fichiers d'images composées d'éléments comme les lignes et les formes. Ce type de fichier convient habituellement aux dessins au trait.

Fichiers vectoriels en mode points — Le mode points peut être importé dans un logiciel vectoriel ou de dessins aux seules fins d'ajouter et de superposer de l'information, des lignes, du texte, etc. Le mode points ne doit pas être redimensionné, recadré, tourné ou manipulé de toute autre façon après avoir été importé.

Les Presses scientifiques du CNRC préfèrent le logiciel CorelDraw! pour créer des images vectorielles. Pour les autres applications possibles, reportez-vous à la liste des programmes graphiques électroniques à http://www.nrc.ca/cisti/journals/elegrapf.html.

Processus de publication

Soumission — Les textes peuvent être remis au directeur scientifique ou à un membre approprié du Comité de rédaction (voir la p. ii de la Revue). Les auteurs doivent confirmer que leurs recherches sont originales et ne sont pas soumises à l'approbation ailleurs, en totalité ou en partie. L'auteur correspondant doit affirmer que tous les auteurs ont lu et approuvé le manuscrit.

Évaluation — Le directeur scientifique sollicite l'avis d'au moins deux lecteurs indépendants choisis en fonction de leur compétence dans le domaine en question; il garde toutefois l'entière responsabilité des décisions relatives au manuscrit. Les auteurs peuvent proposer des lecteurs mais le directeur scientifique n'est pas limité à ces propositions. On s'attend à ce que les lecteurs soient conscients du caractère privilégié du document dont ils évaluent le contenu scientifique et qu'ils fournissent des arguments raisonnables à l'appui de leur évaluation. Leur identité ne sera pas révélée à l'auteur sans autorisation écrite.

Révision — Lorsqu'un manuscrit qui a été renvoyé à l'auteur pour révision n'a pas été retourné dans les 3 mois qui suivent, la rédaction estime que l'auteur a retiré ce manuscrit; toute révision présentée ultérieurement sera traitée comme un nouvel article. Sauf indication contraire, **il faut présenter le texte dactylographié et trois copies lisibles du manuscrit révisé**. Les révisions et les modifications doivent être ajoutées à la machine à écrire; dans la plupart des cas, il convient de retaper la ou les pages corrigées. La version finale de tout article doit être accompagnée du formulaire de **transfer des droits d'auteur** dûment rempli et signé. On obtiendra ce formulaire auprès du directeur scientifique, dans tout récent numéro de la Revue ou sur le site Web des Presses scientifiques du CNRC.

Une fois le text accepté, toute correspondance doit être adressée aux Presses scientifiques du CNRC, Conseil national de recherches du Canada, Ottawa, ON K1A 0R6, Canada.

Soumission du texte en format électronique — Les auteurs sont priés de soumettre **une copie imprimée ainsi qu'une copie sur disquette de la version approuvée de l'article seulement**. Les fichiers de texte et les fichiers d'illustrations devront être soumis sur des disquettes distinctes. Le nom des auteurs doit être indiqué clairement sur chaque disquette soumise. Le **texte** (y compris les tableaux) devrait être soumis en format de traitement de texte (WordPerfect, Microsoft Word ou TeX est préférable, compatible à IBM ou Macintosh). Les macros en TeX et la documentation pour la préparation des soumissions sont maintenant disponibles à ftp://ftp.tex.ac.uk/tex-archive/macros/latex/contrib/supported/nrc/, ftp://ftp.dante.de/tex-archive/macros/latex/contrib/supported/nrc et ftp://ctan.tug.org/tex-archive/macros/latex/contrib/supported/nrc. Il importe d'indiquer le logiciel de traitement de texte utilisé, la version, de même que le type d'ordinateur (IBM ou Macintosh). En ce qui a trait aux **illustrations**, il convient de se reporter à la section « Préparation des fichiers électroniques des illustrations ». Tout article devra être accompagné d'une lettre faisant foi du fait que la version du texte sur disquette reflète exactement la version imprimée soumise.

Droits de reproduction — L'auteur d'un article qui utilise de la documentation (tableaux, figures, schémas, etc.) protégée par les droits d'auteur doit **obtenir une permission écrite du titulaire de ces droits d'auteur** pour permettre la reproduction de l'information **en format imprimé et électronique.** La lettre d'autorisation doit accompagner le manuscrit soumis.

Épreuves en placards — Une épreuve en placard, des épreuves des illustrations, une copie du manuscrit corrigé et un bon de commande de tirés à part sont envoyés à l'auteur. Afin d'en hâter la publication, les épreuves des communications rapides ne seront pas toujours soumises à l'approbation des auteurs. **Les épreuves en placard doivent être relues attentivement, car elles ne sont pas corrigées par les Presses scientifiques du CNRC.** Elles

doivent en outre être retournées dans les 48 heures suivant leur réception. Au stade des épreuves, il n'est plus temps d'apporter des modifications importantes ni de faire des ajouts ou des suppressions. Toutes questions quant aux épreuves en placard devront être adressées à Lea Libiseja (613-990-6965; télécopieur : 613-952-7656; courriel : lea.libiseja@nrc.ca).

Tirés à part — Pour obtenir des tirés à part, il est nécessaire de remplir le bon de commande et de le retourner avec le paiement (chèque, numéro de carte de crédit, numéro du bon d'achat ou pièce de journal interne) en même temps que les épreuves corrigées et le manuscrit ou, dans le cas de communications rapides, dès que possible. Le tarif des tirés à part qui sont commandés après la parution du numéro de la Revue est fortement majoré. **Les tirés à part ne sont pas fournis gratuitement; ils seront envoyés après réception d'un numéro du bon d'achat ou du paiement.**

Transfert des droits d'auteur — Les auteurs doivent compléter un formulaire de transfert des droits d'auteur au CNRC. Toute permission de republication partielle ou intégrale d'un article doit être obtenue auprès des Presses scientifiques du CNRC.

Can. J. Chem. Downloaded from www.nrcresearchpress.com by China University of Science and Technology on 09/08/12
For personal use only.

Presses scientifiques du CNRC
Conseil national de recherches du Canada
Ottawa, ON K1A 0R6
Canada

Télécopier : 613-952-7656
Courriel : research.journals@nrc.ca
URL: http://revcanchim.cnrc.ca

Révisé en janvier 2002

Can. J. Chem. Downloaded from www.nrcresearchpress.com by China University of Science and Technology on 09/08/12
For personal use only.

Recommandations aux auteurs d'articles décrivant la détermination de structures cristallines par diffraction de rayons X

Bien que nous demandions aux auteurs d'utiliser un programme checkcif élaboré par l'Union internationale de cristallographie, nous n'appliquons pas à la lettre les normes d'Acta Crystallographica C. Nous croyons en effet que toute structure cristalline doit être évaluée en tenant compte de son importance d'ordre chimique. Nous sommes aussi d'avis que les lecteurs doivent disposer de suffisamment d'information sur la structure pour pouvoir juger d'eux-mêmes de la qualité de la structure. Selon nous, les données sollicitées ci-dessous sont nécessaires à cette fin.

Les données cristallographiques suivantes doivent être fournies. (Toutes les quantités mesurées doivent être accompagnées de l'exactitude de mesure.) : formule chimique; poids formulaire (M_r); couleur; forme; dimensions; système cristallin; symbole de groupe spatial (si les définitions diffèrent des définitions conventionnelles, indiquez les positions équivalentes); dimension de la maille; Z; volume de la maille; densité observée (D_m); densité calculée (D_x); température de travail; paramètre de Flack (le cas échéant); rayonnement utilisé et valeur présumée de la longueur d'onde; solvant de cristallisation.

Il faudra soumettre l'information ci-dessous liée à la mesure des données : diffractomètre utilisé

méthode d'enregistrement et de mesure; région de l'espace réciproque explorée; nombre de réflexions mesurées et nombre de relations indépendantes; nombre de réflexions indépendantes mesurées et critère d'observation; R_{int}; détails touchant toute correction particulière, telle que l'absorption ou l'extinction.

La description de l'affinement doit être suffisamment détaillée pour permettre au lecteur d'évaluer sa qualité et son exhaustivité. La source des facteurs de diffusion doit être spécifiée, de même que toute correction apportée pour la dispersion anormale. En outre, un facteur d'accord final ($R = \sum ||F_o| - |F_c||/\sum |F_o|$) défini à la lumière du traitement des réflexions non observées et un R dûment pondéré ($wR(F)$ ou $wR(F^2)$) doivent être soumis avec la fonction de pondération utilisée. En ce qui a trait à l'affinement par moindres carrés, toute approximation (p. ex. blocs diagonaux) doit être spécifiée tout comme la fonction minimisée. La méthode de pondération doit être décrite et doit inclure les critères qui ont guidé l'attribution d'un poids nul à certaines réflexions. L'exactitude de la structure rapportée devrait être confirmée par une méthode différente de celle utilisée pour l'affinement (p. ex. par une synthèse de Fourier différence) et le résultat de cette vérification doit être brièvement décrit.

L'information exigeant des explications ou des renvois doit être présentée en un court paragraphe expérimental. Ce paragraphe doit comprendre de l'information telle que : facteurs de diffusion tirés de *International Tables for Crystallography* (Vol. C); solution de structure : Xtal3.5 (Hall et al. 1997); programme d'affinement : SHELXL97 (Sheldrick 1997); correction d'absorption : ψ-scans (North et al. 1968); correction d'extinction : SHELXL97 (Sheldrick 1997); fonction de pondération, $w = 1/[\sigma^2(c) + (0.0491P)^2 + 0.6387P]$, où $P = (F_o^2 + 2F_c^2)/3$.

Nous préférons que le reste de l'information ci-dessus soit présentée sous forme de tableau, comme suit :

Données sur le cristal	
$C_{22}H_{20}O_2$	V = 1628,3(2) Å^3
MW = 316,399	Z = 4
Bloc incolore	D_m = non mesuré
0,41 × 0,25 × 0,20 mm	D_x = 1,2907 Mg m^{-3}
Monoclinique	T = 123(2) K
$P2_1/c$	μ = 0,081 mm^{-1}
a = 8,0204(5) Å	Rayonnement Mo Kα
b = 9,0398(10) Å	λ = 0,71073 Å
c = 22,5974(15) Å	Solvant de cristallisation : éther diéthylique/méthanol
β = 96,362(6)°	
Cueillette de données	
Enraf-Nonius CAD-4	θ_{max} = 26.28
ω-2θ scans	$h = -9 \rightarrow 9$
3762 réflexions mesurées	$k = 0 \rightarrow 11$
3286 réflexions indépendantes	$l = 0 \rightarrow 28$
2825 réflexions dont $I > 2\ \sigma(I)$	3 réflexions standards à chaque 200 réflexions
Corr. abs. : T_{min} = 0,96, T_{max} = 1,00	Décroissance d'intensité : aucune
R_{int} = 0,025	
Affinement	
Affinement sur F^2	H atomes contraints
$R[F^2 > 2\sigma(F^2)]$ = 0,038	$(\Delta/\sigma)_{max}$ = 0,001
$R[F^2$, toutes les données] – 0.73	$\Delta\rho_{max}$ = 0,315 e Å^{-3}
$wR(F^2)$ = 0,199	$\Delta\rho_{min}$ = -0,197 e Å^{-3}
218 paramètres	Coefficient d'extinction : 0,0072(13)

© 2002 CNRC Canada

Pour les structures de détecteur de surface, certains des paramètres de cueillette de données doivent être modifiés comme il se doit pour décrire la cueillette de données du détecteur de surface. Lorsqu'il s'agit de structures cristallines multiples, toutes les entrées peuvent être indiquées en une seule colonne pour chaque structure.

Nous publierons normalement un tableau des données cristallines. On pourra soumettre un tableau des distances et angles de liaison choisis si ceux-ci sont nécessaires pour expliquer la chimie. Les autres données, telles que les angles de torsion essentiels, les angles entre les plans et les distances intermoléculaires, seront intégrées au texte seulement si elles sont cruciales du point de vue scientifique. Les tableaux des distances de liaison complètes, des coordonnées atomiques, des paramètres thermiques et des positions des atomes H doivent être inclus dans le CIF. Le CIF sera annexé à la version électronique de la Revue. L'auteur devra soumettre une version électronique ainsi qu'une version imprimée du CIF avec son article. On trouvera ci-dessous des instructions sur le dépôt auprès du CCDC.

En ce qui a trait aux structures ayant des atomes affinés de façon anisotropique, un diagramme ORTEP (ou l'équivalent) rendant compte des ellipsoïdes thermiques doit être soumis.

L'existence d'information déposée est indiquée dans les articles par une note en bas de page respectant le format suivant : « Les données complémentaires de cet article sont consignées dans CCDC XXXXXX. Vous pouvez les commander gratuitement à www.ccdc.cam.ac.uk/conts/retrieving.html (ou auprès du Cambridge Crystallographic Data Centre, 12 Union Road, Cambridge CB2 1EZ, R.-U. (Télécopier : 44-1223-336033; courriel : deposit@ccdc.cam.ac.uk). »

Pour se conformer à ces recommandations, les auteurs devront réunir une quantité imposante d'information, mais il est essentiel que la représentation en soit concise et directe. Il ne doit pas s'agir d'un rapport de progression d'analyse narratif ou d'une discussion de la méthode, à moins que ces éléments n'influent directement les conclusions d'ordre chimique.

Instruction pour le dépôt de données cristallographiques

Ces notes portent sur les données cristallographiques associées aux structures organiques et organo-métalliques.

1. Avant de soumettre son article à la Revue canadienne de chimie, l'auteur déposera auprès du Cambridge Crystallographic Data Centre (CCDC) le CIF visé par la publication (courriel : deposit@ccdc.cam.ac.uk).
2. Avant de soumettre le CIF au CCDC, on en vérifiera l'exactitude à l'aide du programme checkcif de CJC/IUCr (adresse Web : http://www.iucr.org/cjc/checkcif.html) ou à l'aide du programme checkcif IUCr (adresse Web : http://www.iucr.org/iucr-top/journals/acta/c/services/checkcif.html). Lorsqu'on vérifie un CIF aux sites Web ci-dessus, la deuxième ligne du CIF doit être : _publ_suggested_journal 'test'
   Ces programmes checkcif produiront une liste de problèmes à examiner ainsi qu'un formulaire de réponse. Vous devriez corriger le CIF afin de résoudre autant de problèmes que possible et soumettre de nouveau le CIF. Il faudra soumettre avec l'article destiné à la Revue une copie des derniers résultats produits par le programme checkcif accompagnée d'un formulaire de réponse rempli (produit par le programme checkcif). Le formulaire de réponse devra contenir les explications nécessaires.
3. Le CCDC fournit en retour un numéro de dépôt pour chaque structure cristalline signalée dans l'article. Il s'agit d'un numéro de 6 chiffres, p. ex. 100345. L'auteur soumettra à la Revue son article ainsi que tous les numéros de dépôt pertinents.
4. Lorsque l'article sera publié, les notes en bas de page voulues apparaîtront, telles que « Les données complémentaires de cet article sont consignées dans CCDC XXXXXX. Vous pouvez les commander gratuitement à www.ccdc.cam.ac.uk/conts/retrieving.html (ou auprès du Cambridge Crystallographic Data Centre, 12 Union Road, Cambridge CB2 1EZ, R.-U. (Télécopier : 44-1223-336033; courriel : deposit@ccdc.cam.ac.uk)»
5. Les données déposées ne seront pas archivées dans la Cambridge Structural Database avant que l'article ne soit publié. Si, après 15 à 18 mois, l'article n'a toujours pas été publié, le CCDC communiquera avec l'auteur pour déterminer la marche à suivre.

Notes à l'intention des auteurs

On peut obtenir une liste de contrôle du dépôt de données sur la page d'accueil Web du CCDC, à http://www.ccdc.cam.ac.uk/, ou par courriel (à fileserv@ccdc.cam.ac.uk). (Votre message ne devra alors contenir que les mots suivants sendme checklist). Cette liste n'est PAS suffisante pour assurer qu'un CIF soit complet en vue de sa vérification par un programme checkcif.

Pour effectuer une vérification à l'aide d'un programme checkcif, la plupart des champs du CIF doivent être remplis. Les résultats vous permettront de déterminer les champs qui doivent être remplis. Veuillez soumettre au CCDC un CIF complet et non pas un qui ne contient que les paramètres exigés par le CCDC. Le CIF sera annexé à la version électronique de tout article publié par la Revue canadienne de chimie.

Can. J. Chem. Downloaded from www.nrcresearchpress.com by China University of Science and Technology on 09/08/12
For personal use only.

© 2002 CNRC Canada

Instructions to Authors

Canadian Journal of Chemistry

Can. J. Chem. Downloaded from www.nrcresearchpress.com by China University of Science and Technology on 09/08/12
For personal use only.

The *Canadian Journal of Chemistry* (Can. J. Chem.) publishes reports of original chemical research, in the form of articles or communications, in either English or French. An **article** reports the results of a completed definitive study. A **communication** is intended for the rapid publication of timely and significant work. The manuscript for a communication should not normally exceed eight double-spaced typewritten pages, including any figures and tables, but should contain sufficient experimental detail to allow repetition of the work by those knowledgeable in the field. A brief statement indicating the significance of the work should appear in the introductory paragraph of the manuscript or be indicated in a covering letter. An author should recognize that timeliness and significance are highly subjective qualities; this statement should, therefore, be prepared with some care. The publication of **critical reviews** is also encouraged. Manuscripts submitted to the *Canadian Journal of Chemistry* must not be published or under consideration elsewhere.

Checklist for Authors

To avoid delays in editorial processing, authors should ensure that

1. all sections of the manuscript are typewritten, double-spaced, on one side of standard size paper with 1-in. (2.5 cm) margins;
2. an original plus three clear copies of the text, and original drawings or glossy prints, are submitted;
3. all pages are numbered at top, beginning with title page;
4. the title page includes the title, authors' names, and the names and addresses of the institution at which work was done;
5. the corresponding author is indicated, with telephone number and, where available, facsimile number and e-mail address;
6. page 2 contains the abstract and key words;
7. the format and style conform to that of current articles in the Journal;
8. the cover letter includes the names of possible reviewers; and
9. a graphical abstract is provided on a separate page.

Delays in publication can be avoided by adherence to the instructions below

The Manuscript

All sections of the manuscript, including footnotes, tables, figure captions, and references, should be typewritten, double-spaced, on one side of good quality paper 8.5 × 11 in. (or ISO A4) with 1-in. (2.5 cm) margins. The first page should contain only the title; the authors' names; the names and addresses of the institution at which the work was done; the name and telephone number and, where available, the facsimile number and e-mail address of the corresponding author; and any relevant footnotes. The manuscript will include the abstract(s) (p. 2) and the main body of the text, followed by, in order, acknowledgements, references, any appendices, tables, and figure captions. Figure captions should be typed on a separate sheet in numerical order. **Each page** of the manuscript should be numbered at the top of the page, beginning with the title page. Writing should be as concise as is commensurate with adequate clarity. **The original and three clear copies of the manuscript and supplementary material to be deposited are required.** Both titles and abstracts provide information for contemporary **alerting and information retrieval services**, and should therefore be informative but brief. In compliance with a request from the Chemical Abstracts Service, the Editors urge all authors to use full forenames rather than initials and (or) one forename.

Spelling should follow that of *Webster's Third New International Dictionary* or the *Oxford English Dictionary*. Authors are responsible for consistency in spelling.

Symbols, units, and **nomenclature** should conform to international recommendations such as those of the International Union of Pure and Applied Chemistry and the International Union of Pure and Applied Physics. **SI units** (Système international d'unités) should be used or SI equivalents should be given. This system is explained and other useful information is given in the *Canadian Metric Practice Guide* (1989) published by the Canadian Standards Association (178 Rexdale Blvd., Etobicoke, ON M6N 3T3, Canada). For practical reasons, some exceptions to SI units are allowed. Units such as molarity, kilocalorie, reciprocal centimetre (wave number), and atmosphere may be used for the foreseeable future. An interim list of acceptable non-SI units is reported in Anal. Chem. **54**, 155 (1982). If a formula or name of a chemical compound is referred to by a number, a boldface Arabic number should be used.

Abbreviations for names of substances, procedures, organizations, etc., must be defined the first time they are used. Symbols and Greek letters or little-used characters should be clearly identified; superscripts and subscripts should be legible and correctly placed.

The following references are pertinent in nomenclature: *Nomenclature of Organic Chemistry, Sections A, B, C, D, E, F, and H*, Pergamon Press, London, 1979; *Nomenclature of Inorganic Chemistry*, Butterworth, London, 1971; *Quantities, Units and Symbols in Physical Chemistry*, Blackwell, London, 1987. Tentative recommendations exist for organometallic nomenclature, *IUPAC Information Bulletin* No. 31, 1973; for stereochemical designations, J. Org. Chem. **35**, 2849 (1970); and for steroids, J. Org. Chem. **34**, 1517 (1969). Although tentative IUPAC rules have been published for carbohydrate nomenclature (Biochemistry, **10**, 3983 (1971)), the Editors recommend the use of the British–American nomenclature (J. Org. Chem. **28**, 281 (1963)), until the IUPAC rules become definitive. For nomenclature not covered by international convention, the usage of the American Chemical Society should be followed, e.g., *The Naming and Indexing of Chemical Compounds* (Introduction to Chemical Abstracts Subject Index **56**, IN (1962)). Rigid adherence to nomenclature rules is not expected each time a compound is mentioned in a manuscript, but the approved names should be given at least once, preferably in an early part of the manuscript.

Each manuscript must be accompanied by an **abstract**. Authors should provide three to five key words directly below the abstract for use by the indexing services. The abstract should

Aussi disponible en français

Can. J. Chem. Downloaded from www.nrcresearchpress.com by China University of Science and Technology on 09/08/12
For personal use only.

be preceded by the title and authors' names so that one copy, on a separate page, can be sent to the translator. The abstract should not exceed one page for articles (shorter for communications) and **should not include abbreviations or references**. Authors who can submit abstracts in both English and French are encouraged to do so.

The **experimental**, or **computational**, material must be sufficiently detailed to permit reproduction of the work, but must be concise and avoid lengthy descriptions of known procedures; the latter should be specified by appropriate references. **A reader's attention should be drawn to any new or unusual hazards encountered in the experimental work**.

Analyses and spectra — It is the responsibility of authors to provide fully convincing evidence for the homogeneity and identity of all compounds they claim as new. Evidence of both purity and identity normally includes good elemental analytical data. An accurate mass measurement of a molecular ion is acceptable as evidence for chemical composition provided that independent evidence for sample purity is given. Where such data are not available, the ^{13}C NMR and (or) ^{1}H NMR spectra of certain compounds, or other evidence, may be acceptable provided that these alternatives are convincing both to an expert in the area and to the Editor.

Rate and equilibrium constants — Primary experimental results should be available to readers in the form of tables, which may be included with the published manuscript or may be treated as supplementary material. In general, examples of the primary experimental data should be included, especially if an innovative or nonstandard data treatment is employed. In papers reporting kinetics experiments, the primary rate constants must be presented, while in papers describing the determination of acidity functions, tables of log *I* as a function of acid concentration should be given. The only acceptable unit of time for a rate constant is the second.

References should be verified by checking the original publications. In the **bibliography**, which follows the acknowledgements, references are numbered and listed in the order in which they are first cited in the text. **Each reference must be cited in the text and designated therein by its unique key number typed on the line in parentheses.** In a reference to the periodical literature, initials precede the surnames of the authors, followed by the name of the periodical (abbreviated in the form used in *CASSI*, Chemical Abstracts Service, P.O. Box 3012, Columbus, OH 43210, U.S.A.), the volume number, initial page number, and year in parentheses. References to books, conference proceedings, theses, etc., should include the name(s) and initials of the author(s), the title of the publication, the name(s) and initials of the editor(s), if any, the name of the publisher, the city and year of publication, and the page or chapter cited. For examples of the appropriate format see a recent issue of the Journal.

Reports not yet accepted for publication and private communications are not acceptable references, and should be included in the text in parentheses or given as a footnote. When citing material that has appeared in a format not readily available in a scientific library, the author must provide the Editor with two copies of the document; for a manuscript "in press," one copy is sufficient.

Footnotes to material in the text should not be used unless they are unavoidable, but their use is encouraged in tables. Where used in the text, footnotes should be cited in the manuscript by superscript Arabic numbers (except in the tables, see below) and should be numbered serially beginning with any that appear on the title page. Each footnote should be typed on the manuscript page on which the reference to it is made; **footnotes should not be included in the list of references.**

Equations should be clearly typed; triple-spacing should be used if superscripts and (or) subscripts are involved. Superscripts and subscripts should be legible and carefully placed. Distinguish between lowercase *l* and the numeral *one*, and between capital *O* and the numeral *zero*. A letter or symbol should represent only one entity and be used consistently throughout the paper. Each variable must be defined in the text, or in a **List of symbols** to appear after the reference list. Variables representing vectors, matrices, vector matrices, and tensors must be clearly identified. Numbers identifying equations must be in square brackets and placed flush with the **left margin**. In numbering, no distinction is made between mathematical and chemical equations.

Tables should be numbered in Arabic numerals in the order cited in the text and each should have a brief title. All information in the tables should be typewritten, double-spaced, except for mathematical or chemical equations, chemical structures, or complicated entries, which should be triple-spaced. Type each table on a separate sheet. Abbreviations may be used in the brief column headings with explanatory footnotes where necessary. Tables should not contain vertical rules or superfluous horizontal rules. Footnotes are indicated by lowercase italic superscript letters. Other descriptive notes may be placed below the table, designated by **Note**.

Appendices — Figures and tables used in an appendix should be numbered sequentially but separately from those used in the main body of the paper, for example, Fig. A1, Table A1, etc.

Supplemental material—The National Research Council of Canada maintains a depository in which supplementary material may be placed, either at the request of the author or suggestion of the Editor. Such material may include extensive tables of data, detailed calculations, and maps not essential for understanding and evaluating the paper. Such material must be clearly marked when the manuscript is submitted. Tables and figures should be numbered in sequence separate from those published with the paper (e.g., Fig. D1, Table D1). The supplemental material should be referred to by footnotes.

Authors of papers describing new **single crystal X-ray diffraction structure determinations** on biological macromolecules must submit to the Protein Data Bank, Brookhaven National Laboratory, all structural data required to validate the discussion, including both X-ray amplitudes and phases and the derived atomic coordinates. If requested by the authors, the Editors will ask the Data Bank not to distribute the information until a specified date. For coordinate lists, this date may not be more than 1 year beyond the acceptance date of the manuscript. For the full structure amplitude and phase data the time interval before distribution may not exceed 4 years. The release date specified by the author will appear in a footnote to the paper along with the statement that the information has been submitted to the Protein Data Bank. In the absence of a specified release date, it will be assumed that the information is available immediately on appearance of the publication.

For single crystal X-ray structure determination of other molecules, sufficient data should be included with the manuscript to allow adequate review. These data should be in a form suitable for deposition in the National Research Council of Canada depository. Recommendations for the presentation of crystallographic data appear in Can. J. Chem. **80** (1), I-5 (2002). Guidelines for the presentation of data from thermal analyses appear in Anal. Chem. **39**, 543 (1967) and **44**, 640 (1972).

Further details on most of these topics are included in the **Supplementary instructions to authors**, copies of which are available from any Editor on request. The format for the presentation of physical, analytical, and spectroscopic data is also described.

Can. J. Chem. Downloaded from www.nrcresearchpress.com by China University of Science and Technology on 09/08/12
For personal use only.

Illustrations

Each figure or group of figures should be planned to fit, after appropriate reduction, into the area of either one or two columns of text. The maximum finished size of a one-column illustration is 8.6 × 23.7 cm (3.4 × 9.3 in.) and that of a two-column illustration is 18.2 × 23.7 cm (7.2 × 9.3 in.). The figures (including halftones) must be numbered consecutively in Arabic numerals, and each one must be referred to in the text and must be self-explanatory. All terms, abbreviations, and symbols must correspond with those in the text. Only essential labelling should be used, with detailed information given in the caption. Each illustration must be identified by the figure number and the authors' names on the back of the page or in the left-hand corner, well away from the illustration area.

Line drawings should be made with black ink or computer-generated in black on high-quality white paper or other comparable material. For computer-generated graphics, supply a laser print at the highest resolution available. **Photocopies are not acceptable.**

All lines must be sufficiently thick (0.5 points minimum) to reproduce well, and all symbols, superscripts, subscripts, and decimal points must be in good proportion to the rest of the drawing and large enough to allow for any necessary reduction without loss of detail. Avoid small open symbols; these tend to fill in upon reproduction. **Lettering produced by dot matrix printers or typewriters, or by hand, is not acceptable.** The same font style and lettering sizes should be used for all figures of similar size in any one paper. Any coordinate lines to appear should be ruled in. Original **NMR, IR, and EPR spectra** are often not reproducible and should be redrawn.

Structural drawings — Structures and schemes should be placed on separate pages (not within the text). Use of a computer drawing program such as ChemDraw or ChemWindows is highly recommended. Single-width bold and broken lines are preferred to wedges for stereochemical notation; 12-pt Helvetica font should be used for atom labels.

Graphical abstracts are published as part of the Table of Contents. The graphical abstract may consist of a small structural diagram, equation, or other informative drawing that serves to illustrate the subject of the article. This must be an **original** laser print or drawing, provided on a separate page, of a maximum size of 40 mm high × 85 mm wide, **without text** (except necessary labels).

Photographs should be *continuous tone* on glossy paper. These figures should be prepared in the final published size.

Colour illustrations will be at the author's expense. Further details on prices are available from Lea Libiseja, Managing Editor, NRC Research Press (613-990-6965; fax: 613-952-7656; e-mail: lea.libiseja@nrc.ca).

NRC Research Press prefers the submission of electronic graphic files for accepted manuscripts and will use these electronic files whenever possible. **Four sets of paper versions of figures must be submitted to the Editorial Office** for the review process, even if electronic versions are to be submitted for use in production.

If electronic files are not available, paper versions of the figures will be scanned. Note that the scanner will easily reproduce flaws (e.g., correction fluid, smudges). Submission of noncontinuous (screened) photographs and scanned illustrations printed out on laser printers is not recommended as moirés develop; a moiré is a noticeable, unwanted pattern generated by rescanning or rescreening an illustration that already contains a dot pattern.

Preparation of Electronic Illustration Files

Authors must supply copies of the original electronic files (i.e., the files directly from the software application that they were created in) and **high-quality laser proofs** of the images. **Electronic files (i.e., fig. number and fig. content) should match the laser proofs**. On the disk label, identify (*i*) the software application and version; (*ii*) file name(s), size, and extension; and (*iii*) if the files have been imported from another software. If you have compressed your files, indicate what compression format was used. PC or Macintosh versions of True Type or Type 1 fonts should be used. **Do not use bitmap or nonstandard fonts.** Electronic graphics can be accepted on the following disks: 3 1/2" disks, 100 MB Zip cartridge, and CD-ROM.

All figures should be submitted at their final published size. For figures with several parts (e.g., *a*, *b*, *c*, *d*, etc.) created using the same software application, assemble them into one file rather than sending several files.

Remember that the more complex your artwork becomes, the greater the possibility for problems at output time. Avoid complicated textures and shadings, especially in vector illustration programs; this increases the chance for a poor-quality final product.

Bitmap (raster) files — Bitmaps are image files produced using a grid format in which each square (or pixel) is set to one level of black, colour, or grey. A bitmap (rasterized) file is broken down into the number of pixels or picture elements per inch (ppi). Pixels per inch is sometimes referred to as dots per inch (dpi). The higher the resolution of an image, the larger the number of pixels contained within the rectangular grid.

The proper resolution should be used when submitting bitmap artwork. The minimum requirements for resolution are 600 dpi for line art and finelines (line art with fine lines or shading), 300 dpi for halftones and colour, and 600 dpi for combinations (halftones with lettering outside the photo area).

All *colour* files submitted must be as CMYK (cyan, magenta, yellow, and black). These colours are used in full-colour commercial printing. RGB graphics (red, green, and blue; colours specifically used to produce an image on a monitor) will not print correctly.

Vector files — Vector files are image files produced using elements such as lines and shapes. Typically these files are used for *line drawings*.

Bitmaps inside vector files — Bitmaps can be imported into vector/draw applications only for the purpose of adding and overlaying information, lines, text, etc. Bitmaps should not be resized, cropped, rotated, or otherwise manipulated after importing.

The preferred software application of NRC Research Press for creating vector images is CorelDraw! For other applications that can be used, see electronics graphics list at http://www.nrc.ca/cisti/journals/elegraph.html.

The Publication Process

Submission — A manuscript should be submitted to the appropriate Editor (see p. ii of each issue). The corresponding author must affirm that all of the authors have read and approved the manuscript and that the manuscript represents original work that is not being considered for publication, in whole or in part, elsewhere.

Evaluation — The Editor will seek advice from two or more independent reviewers who are selected for their knowledge of, and their experience in, the subject treated in the manuscript. The Editor retains full responsibility, however, for all decisions regarding the manuscript. Authors are invited to suggest reviewers who are competent to examine their manuscript, but the Editor is not limited to such suggestions. Reviewers are informed that they have received privileged documents for as-

sessment of scientific merit and are expected to provide reasonable arguments to support their evaluations. Identities of reviewers will not be released to authors without the written consent of the reviewer.

Revision — If a manuscript that was sent to an author for revision is not returned within 3 months, the Editors will consider the manuscript withdrawn by the author; any revised version submitted subsequently will be considered as a new contribution. **The typescript and three clear copies of a revised manuscript should be submitted**, unless the Editors specify otherwise. Handwritten revisions and amendments are not acceptable; in most instances the page(s) involved should be retyped. A completed and signed **Assignment of Copyright** form (available from the Editors, in any current issue of the Journal, or on the web site of NRC Research Press) must accompany the final revision of a manuscript.

Once the paper has been accepted, all correspondence should be with NRC Research Press, National Research Council of Canada, Ottawa, ON K1A 0R6, Canada.

Submission of electronic copy — Authors are requested to submit the **final accepted manuscript only, both in hard copy format and on disk**. Text files and figure files should be submitted on separate disks. All disks must be labeled clearly with the authors' names. **Text** (including tables) should be provided in a word-processing format (any form of WordPerfect, Microsoft Word, or TeX is preferable, IBM compatible or Macintosh). TeX macros for preparing papers for submissions are available at ftp://ftp.tex.ac.uk/tex-archive/macros/latex/contrib/supported/nrc/, ftp://ftp.dante.de/tex-archive/macros/latex/contrib/supported/nrc, and ftp://ctan.tug.org/tex-archive/macros/latex/contrib/supported/nrc. Identify the word-processing software, version number, and type of computer used (IBM or Macintosh). For **figures**, see the section "Preparation of Electronic Illustration Files." Include a statement in the letter accompanying the manuscript that the version on the disk **exactly** matches the final hard copy version.

Copyright material — If a manuscript contains material (figures, tables, etc.) that is protected by copyright, the author must submit to the Editor, before publication, **written permission from the copyright holder** to reproduce the material **for both the print and electronic formats**.

Galley proofs — A galley proof, illustration proofs, the copy-edited manuscript, and a reprint order form are sent to the corresponding author. **Galley proofs must be checked very carefully, as they are not proofread by NRC Research Press**, and must be returned within 48 hours of receipt. To expedite publication, proofs of communications are not always sent to the author. The proof stage is not the time to make extensive corrections, additions, or deletions, and the cost of changes introduced by the author and deemed to be excessive will be charged to the author. Questions concerning galley proofs should be addressed to Lea Libiseja, Managing Editor, NRC Research Press (613-990-6965; fax: 613-952-7656; e-mail: lea.libiseja@nrc.ca).

Reprints — If reprints are desired, the reprint order form must be filled out completely and returned with payment (cheque, credit card number, purchase order number, or journal voucher) at the same time the corrected proofs and manuscript are returned or, in the case of a communication, as soon as possible. Orders submitted after the issue has been printed are subject to considerably higher prices. **The Journal does not provide free reprints and reprints are not mailed until a purchase order number or payment is received.**

Copyright transfer — Authors are required to complete a copyright transfer form assigning all rights to NRC. Requests for permission to republish the paper, in whole or in part, should be sent to NRC Research Press.

Can. J. Chem. Downloaded from www.nrcresearchpress.com by China University of Science and Technology on 09/08/12
For personal use only.

NRC Research Press
National Research Council of Canada
Ottawa, ON K1A 0R6
Canada

Fax: 613-952-7656
E-mail: research.journals@nrc.ca
URL: http://canjchem.nrc.ca

Revised January 2002

Can. J. Chem. Downloaded from www.nrcresearchpress.com by China University of Science and Technology on 09/08/12
For personal use only.

Notes for Authors of papers presenting the results of X-ray crystal-structure analyses

Although authors are asked to use a checkcif program developed by the International Union of Crystallography (IUCr), the standards of Acta Crystallographica C may not be rigorously applied. Every crystal structure should be evaluated taking into account its chemical significance. Sufficient information about a structure should be available so that readers can make their own judgements about the quality of the structure. The quantities requested in the section below are necessary for this purpose.

The following crystallographic data should be given in the manuscript (all measured quantities should be accompanied by a measure of accuracy): chemical formula; formula weight (M_r); colour; crystal form; crystal dimensions; crystal system; space group symbol (if non-standard setting, give related standard setting); unit cell dimensions; Z; unit cell volume; observed density (D_m); calculated density (D_x); working temperature; Flack parameter (if applicable); radiation used and the assumed value for the wavelength; and the solvent for crystallization.

The following information pertaining to the measurement of data should be given: diffractometer used; method of recording and measurement; the region of reciprocal space explored; the number of reflections measured and number of independent reflections; the number of observed independent reflections and observation criterion; R_{int}; and the details of any special corrections such as absorption or extinction.

The final refinement should be reported in sufficient detail to enable the reader to assess its reliability and completeness. The origin of the scattering factors used should be specified, together with any corrections for anomalous scattering. A final agreement index ($R = \sum||F_o| - |F_c||/\sum|F_o|$) defined with respect to the treatment of unobserved reflections and an appropriate weighted R ($wR(F)$ or $wR(F^2)$) should be given with the weighting function used. For least-squares refinement, any approximation (e.g., block-diagonal) should be specified, as should the quantity minimized. The weighting scheme should be given and should include a statement of any reflections assigned zero weight. The correctness of the reported structure should be checked by a method independent of that used for refinement (e.g., by a difference-Fourier synthesis), and the result of this procedure should be briefly reported.

Information requiring explanations or references should be put into a short experimental paragraph. This paragraph would include information such as the following: scattering factors from *International Tables for Crystallography* (Vol. C); structure solution: Xtal3.5 (Hall et al. 1997); refinement program: SHELXL97 (Sheldrick 1997); absorption correction: ψ-scans (North et al. 1968); extinction correction: SHELXL97 (Sheldrick 1997); weighting function, $w = 1/[\sigma^2(c) + (0.0491P)^2 + 0.6387P]$, where $P = (F_o^2 + 2F_c^2)/3$.

The remainder of the above information should be given in a table, such as:

Crystal data	
$C_{22}H_{20}O_2$	V = 1628.3(2) Å^3
MW = 316.399	Z = 4
Colourless block	D_m = not measured
0.41 × 0.25 × 0.20 mm	D_x = 1.2907 Mg m^{-3}
Monoclinic	T = 123(2) K
$P2_1/c$	μ = 0.081 mm^{-1}
a = 8.0204(5) Å	Mo Kα radiation
b = 9.0398(10) Å	λ = 0.71073 Å
c = 22.5974(15) Å	Crystallization solvent: diethyl ether/methanol
β = 96.362(6)°	
Data collection	
Enraf-Nonius CAD-4	θ_{max} = 26.28
ω-2θ scans	h = –9 → 9
3762 measured reflections	k = 0 → 11
3286 independent reflections	l = 0 → 28
2825 reflections with $I > 2\ \sigma(I)$	3 standard reflections every 200 reflections
Abs. Corr.: T_{min} = 0.96, T_{max} = 1.00	Intensity decay: none
R_{int} = 0.025	
Refinement	
Refinement on F^2	H atoms constrained
$R[F^2 > 2\sigma(F^2)]$ = 0.038	$(\Delta/\sigma)_{max}$ = 0.001
$R[F^2$, all data] – 0.73	$\Delta\rho_{max}$ = 0.315 e Å^{-3}
$wR(F^2)$ = 0.199	$\Delta\rho_{min}$ = –0.197 e Å^{-3}
218 parameters	Extinction coefficient: 0.0072(13)

© 2002 NRC Canada

For area detector structures, some of the data collection parameters should be appropriately modified to describe the area detector data collection. For multiple crystal structures, all entries might be put into a single column for each structure.

The journal will normally publish a Table of Crystal Data. A Table of Selected Bond Distances and Angles may be included if required to explain the chemistry. Publication of other data, such as essential torsion angles, angles between planes, and intermolecular distances can be included in the text if scientifically justified. Tables of complete bond distances, atomic coordinates, thermal parameters, and H-atom positions should be included in the deposited CIF. The CIF will be appended to the electronic version of the journal. Both an electronic and hard copy of the CIF should be submitted with the manuscript. Instructions for deposition with the Cambridge Crystallographic Data Centre (CCDC) are given below.

For structures with anisotropically refined atoms, an ORTEP diagram (or equivalent) displaying the thermal ellipsoids should be presented.

The existence of deposited material is indicated in the printed article by a footnote in the following format: "CCDC XXXXXX contains the supplementary crystallographic data for this paper. These data can be obtained, free of charge, via www.ccdc.cam.ac.uk/conts/retrieving.html (or from the Cambridge Crystallographic Data Centre, 12 Union Road, Cambridge CB2 1EZ, U.K. (Fax: 44-1223-336033 or e-mail: deposit@ccdc.cam.ac.uk)."

The volume of information required for compliance with these notes is formidable, and it is essential that the presentation be concise and relevant. It should not be a narrative account of the progress of the analysis or a discussion of method unless these elements have a direct bearing on the chemical conclusions.

Instruction for deposition of crystallographic data

These notes concern the crystallographic data associated with organic and metal-organic structures.

1. Prior to submitting a manuscript to the *Canadian Journal of Chemistry* (CJC), the author must deposit the corresponding CIF with the Cambridge Crystallographic Data Centre (CCDC). The e-mail address to send a CIF to the CCDC is: deposit@ccdc.cam.ac.uk
2. Before submitting the CIF to the CCDC, it should be tested for errors by using the CJC/IUCr checkcif program (Web site address: http://www.iucr.org/cjc/checkcif.html) or the IUCr checkcif program (Web site address: http://www.iucr.org/iucr-top/journals/acta/c/services/checkcif.html). When checking a CIF at the above Web sites, the second line in the CIF should be: _publ_suggested_journal 'test'
   These checkcif programs will give a list of concerns and a response form. You should correct the CIF to eliminate as many problems as possible and resubmit the CIF. When the manuscript is submitted to CJC a copy of the last output from the checkcif program with a completed response form (from the checkcif program) should accompany the manuscript. Adequate explanations should be given on the response form.
3. The CCDC will provide the author with a deposition number for each crystal structure reported in the manuscript. Each number is a 6-digit integer, e.g., 100345. This deposition number should be included with the manuscript when submitting to the journal.
4. When the paper is published an appropriate footnote will be printed, for example: "CCDC XXXXXX contains the supplementary crystallographic data for this paper. These data can be obtained, free of charge, via www.ccdc.cam.ac.uk/conts/retrieving.html (or from the Cambridge Crystallographic Data Centre, 12 Union Road, Cambridge CB2 1EZ, U.K. (Fax: 44-1223-336033 or e-mail: deposit@ccdc.cam.ac.uk)."
5. The deposited data will not be archived to the Cambridge Structural Database until the paper has been published. If, after 15–18 months, the paper has not been published, the CCDC will contact the depositor to determine what should be done with the data.

Notes for Authors

A checklist of data items for deposition can be obtained from the CCDC Home Page on the World Wide Web (http://www.ccdc.cam.ac.uk/) or by e-mail (to fileserv@ccdc.cam.ac.uk with the one-line message sendme checklist). This list is NOT sufficient to complete a CIF for a checkcif program.

To run a checkcif program, most of the fields on the CIF must be filled. The response will tell you about any fields that require completion. Please submit a complete CIF to the CCDC and not one containing only the parameters listed as required by the CCDC. This CIF will be appended to the electronic version of any paper published by the *Canadian Journal of Chemistry.*

Can. J. Chem. Downloaded from www.nrcresearchpress.com by China University of Science and Technology on 09/08/12
For personal use only.

© 2002 NRC Canada

Forthcoming special issues / Numéros spécials à paraître

June 2002	In honour of Professor J. Bryan Jones
August 2002	In honour of Professor Ray Lemieux
November 2002	In honour of Professor Tris Chivers
June 2003	In honour of Professor Don Arnold

Forthcoming articles / Articles à paraître

2001 Alcan Award Lecture From academic research to industrial applications and back again	D.W. Stephan
Magnetic and structural studies on 1,3-diazolate complexes of cobalt(II) — The characterization of three new cobalt(II) molecule-based magnets	V. Sánchez, A. Storr, and R.C. Thompson
The first observed complex of 11-crown-3 ether. X-ray crystal structure and NMR study of (benzo-11-crown-3)$_2$·LiNCS	G.W. Buchanan, M. Azad, and G.P.A. Yap
The hydrolysis of an activated ester by a tris(4,5-di-*n*-propyl-2-imidazolyl)phosphine:Zn^{2+} complex in neutral micellar medium as a model for carbonic anhydrase	T.B. Koerner and R.S. Brown
The syntheses and NMR studies of hexadeca- and octaneopentoxyphthalocyanines	N. Bhardwaj, J. Andraos, and C.C. Leznoff
Substitution reactions at the Ni(III) cation in macrobicyclic complexes — Reaction of metal ion complexes prepared from ligands L^1 (17-oxa-1,4,8,11-tetraazabicyclo[6.5.6]nonadecane) and L^2 (17-oxa-1,4,8,11-tetraazanicyclo[10.5.2]nonadecane) with chloride ion	A.M. Ingham, C. Xu, T.W. Whitcombe, C. Xu, J.N. Bridson, and A. McAuley
Complexation of the La(III) cation by *p*-sulfonatocalix[4]arene — A ^{139}La NMR study	Y. Israeli, C. Bonal, C. Detellier, J.-P. Morel, and N. Morel-Desrosiers
Medium-sized cyclophanes part 59: Nitration of [3.3]- and [3.3.3]metacyclophanes — Through-space electronic interactions between two or three benzene rings	T. Yamato, K. Tsuchihashi, N. Nakamura, M. Hirahara, and H. Tsuzuki
Synthesis of new fluorophores derived from monoazacrown ethers and the coumarin nucleus	E. Brunet, P. García-Losada, J.-C. Rodríguez-Ubis, and O. Juanes
Isentropic compressibility and viscosity of aqueous and methanolic lithium chloride solutions	A. Wahab and S. Mahiuddin
Electrocatalytic dechlorination of atrazine	N.L Stock and N.J. Bunce
Studies on the rearrangement of *ortho*-nitrobenzylidenemalonates and their analogues to 2-aminobenzoate derivatives	E. Lewandowska, S. Kinastowski, and S.F. Wnuk

© 2002 NRC Canada

2001 Alcan Award Lecture
From academic research to industrial applications and back again

Douglas W. Stephan

Abstract: This paper reviews our recent research efforts that have taken us from fundamental studies of the reactivity of Ti and Zr complexes to the development of new olefin polymerization catalysts of significant industrial potential. In furthering our understanding of these systems we have probed the unique chemical pathways by which early metal phosphinimide catalysts undergo activation and deactivation.

Key words: titanium, zirconium, dehydrocoupling, polyphosphines, olefin polymerization, catalysis, deactivation.

Résumé : Ce travail présente une revue de nos récents efforts de recherches qui nous ont permis de passer d'études fondamentales sur la réactivité des complexes du Ti et du Zr au développement de nouveaux catalyseurs pour la polymérisation des oléfines qui présentent un potentiel industriel important. En augmentant notre compréhension de ces systèmes, nous avons été amenés à examiner les voies réactionnelles chimiques uniques par lesquelles les catalyseurs métalliques du phosphinimide originaux subissent des activations et des désactivations.

Mots clés : titanium, zirconium, déhydrocouplage, polyphosphines, polymérisation des oléfines, catalyseur, désactivation.

[Traduit par la Rédaction]

Introduction

The public perceives a linear route from fundamental science to commercial application mediated by research funding. However, this is not quite typical. Research funding certainly is essential to garner a deeper understanding of a particular aspect of fundamental science. However, commercial applications often spring from the combination of probing experiments and a broad perspective on the potential implications of the work. This overview succinctly summarizes our efforts.

We have had a continuing interest in the chemistry of the early transition metals. Early work focused on early–late heterobimetallics (1) while more recent efforts have dealt with the chemistry of Ti-sulfur and -thiolate (2) and Zr–phosphorus chemistry (3). Each of these areas has been reviewed. Much of that work centred on the synthesis, structure, and reactivity of these systems. In more recent efforts, we have focused attention on the application of some of these systems in catalytic processes. In this manuscript, we describe the development of novel Zr-hydride based systems, which are capable of catalyzing the oligomerization of primary phosphines. In a strategy designed to improve these catalysts, we discovered a new class of compounds, which are particularly effective, single-site olefin polymerization catalysts. Subsequent collaborative efforts have taken these systems toward commercial-scale applications, while studies of the chemistry of these catalysts have revealed a number of insights regarding catalyst activation, the role of co-catalysts and deactivation pathways.

Received 17 August 2001. Published on the NRC Research Press Web site at http://canjchem.nrc.ca on 23 January 2002.

D.W. Stephan. School of Physical Sciences, Chemistry and Biochemistry, University of Windsor, Windsor, ON N9B 3P4, Canada. (Fax: (519) 973-7098; e-mail: stephan@uwindsor.ca).

Zr-hydrides in catalytic dehydrocoupling of P—H bonds

In 1995, we reported the synthesis of the novel potassium salt of the zirconocene trihydride anion (4). Subsequently in 1997, we described the related sequence of reactions involving $Cp^*_2ZrCl_2$ with $LiAlH_4$ followed by treatment with BuLi (Scheme 1) (5). This synthetic route proceeds through the isolable intermediate $[(Cp^*_2ZrH(AlH_4)]_2$, ultimately giving the threefold symmetric species $[(Cp^*_2ZrH_3)Li]_3$ in all but quantitative yield (Fig. 1).

The presence of 1% of this compound effects the catalytic dehydrocoupling of primary phosphines such as $PPhH_2$ to P_5R_5 upon heating to 80–100°C for 24 h. Stoichiometric reactions with phosphines afford the isolation of the complexes $[Cp^*_2ZrH(PPh)_2)Li]$ and $[Cp^*_2ZrH(PPh)_3)Li]$, while transient spectroscopic data support the intermediacy of a phosphinidene-hydride $[Cp^*_2ZrH(PPh))Li]$ (4). These data suggest the partial catalytic cycle for dehydrocoupling as depicted in Scheme 2. What remains unclear are the steps between the triphosphanato anion and the products. Further insertions or alternatively, thermal degradation of $[Cp^*_2ZrH(PPh)_3)Li]$ to $(PR)_3$ and thermal reorganization have been proposed as subsequent steps in the formation of P_5Ph_5.

This chemistry was also applied to the catalytic oligomerization of 1,2-diphosphinobenzene. Quenching of the catalysis after only 30 min revealed the formation of the dimerized species $(C_6H_4P(PH))_2$ (Scheme 3). Allowing the catalysis to continue for 12 h affords complete dehydro-

 DOI: 10.1139/V01-203 © 2002 NRC Canada

Scheme 1.

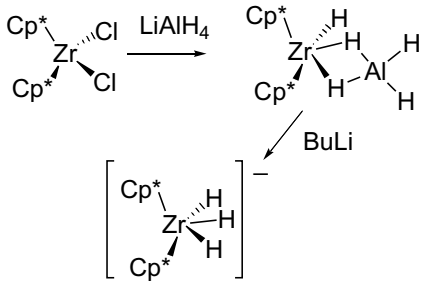

Fig. 1. (*a*) X-ray structure of $[(Cp^*_2ZrH(AlH_4)]_2$. (*b*) X-ray structure of $[(Cp^*_2ZrH_3)Li]_3$.

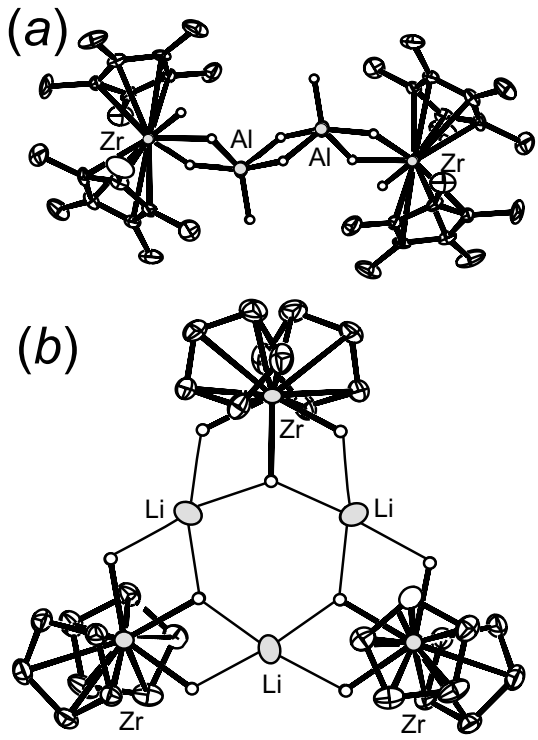

coupling and the formation of the macrocyclic species $(C_6H_4P_2)_8$ (Fig. 2) (6). This species contains 16 contiguous phosphorus atoms in a ring. Although the development of the chemistry of this novel macrocycle is plagued by the insolubility of this species, related work has shown that diphosphinoethane undergoes dehydrocoupling to give the species $(HPCH_2CH_2P)_2$. This species reacts with $AlMe_3$ to give the macrocyclic species $[(PCH_2CH_2PAlMe_2)_2)_4]\cdot 4[AlMe_3]$ (Scheme 4, Fig. 3) (7). This centrosymmetric macrocyclic compound is comprised of four dimeric units that are bridged by two $AlMe_2$ units giving five-membered P_3Al_2 rings. Four additional $AlMe_3$ groups are coordinated to phosphorus, exocyclic to the macrocycle.

A different approach and a transition point

One of the problems faced in extending the chemistry above is the relatively low activity of the catalysts. Thus in developing an approach, we considered sterically less encumbered catalysts, specifically we sought to develop new

Scheme 2.

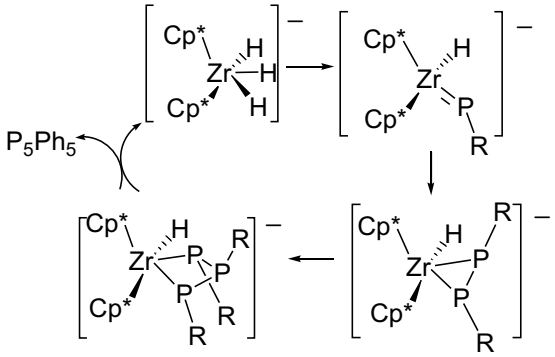

Scheme 3.

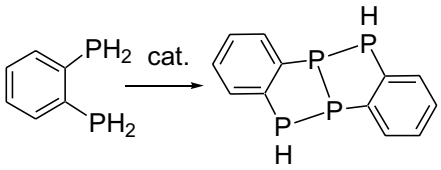

catalyst systems based on non-metallocene complexes. This approach brought to mind the efforts of Wolczanski and coworkers (8) who described the steric analogy between the tri-*tert*-butylmethoxide and cyclopentadienyl ligands (Fig. 4). Applying a related steric analogy, we focused attention on titanium complexes of bulky phosphinimide ligands. This approach offers several potential advantages. Firstly, the conical nature of phosphinimides approximates the cone occupied by cyclopentadienyl ligands. However, the bulk is more removed from the metal center offering potentially enhanced reactivity. Secondly, the ease of synthesis of phosphinimide ligands from the readily available phosphine precursors provides the flexibility to tune the steric and electronic properties of the ligands. Finally, the inclusion of phosphorus-based ligands permits use of ^{31}P NMR spectroscopy as a convenient spectroscopic handle for monitoring reaction progress.

We recognized that while such species may lead to effective dehydrocoupling catalysts for the oligomerization of phosphines, this strategy has not as yet been probed. Instead, we recognized that this logic may also be effective for the major industrial application of olefin polymerization catalysts. It was at this point that we targeted these species and planned to probe their catalytic utility.

Synthesis of catalyst precursors

The syntheses of phosphinimide ligands of the form $R_3PNSiMe_3$ are well-established processes involving the Staudinger reaction of phosphine with N_3SiMe_3. Subsequent reaction with $CpTiCl_3$ readily affords access to a wide variety of complexes of the form $CpTiCl_2(NPR_3)$ (Scheme 5) (9, 10). Similarly, this synthetic route tolerates considerable flexibility in the range of substituents on either the phosphinimide or the cyclopentadienyl rings. In a similar manner the species $(t\text{-}Bu_3PN)TiCl_3$, $(t\text{-}Bu_3PN)_2TiCl_2$, and $(t\text{-}Bu_3PN)_3TiCl$ (11) are prepared via stoichiometric reac-

© 2002 NRC Canada

Fig. 2. X-ray structure of $(C_6H_4P_2)_8$.

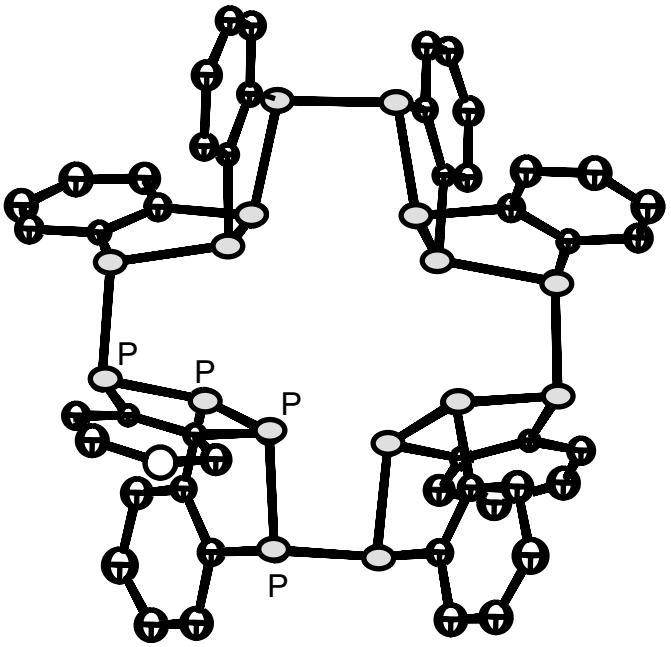

Scheme 4.

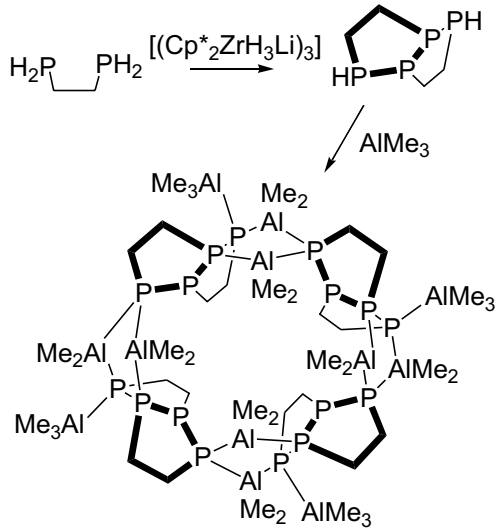

tions of the lithium phosphinimide (t-Bu_3PNLi) and $TiCl_4$ (Scheme 5). Subsequent alkylation of both the cyclopentadienyl-titanium halides as well as the cyclopentadienyl-free complexes is achieved in a straightforward manner employing alkyl-lithium or Grignard reagents, providing a large range of derivatives. In a manner analogous to that reported for several metallocenes, the zwitterionic complexes $CpTiMe(NPR_3)(\mu\text{-}MeB(C_6F_5)_3)$ (Fig. 5) (9) and $(t\text{-}Bu_3PN)_2TiMe(\mu\text{-}MeB(C_6F_5)_3)$ were obtained upon reaction of the $CpTiMe_2(NPR_3)$ or $(t\text{-}Bu_3PN)_2TiMe_2$ with $B(C_6F_5)_3$ (Scheme 6).

Ethylene polymerization

The readily available titanium-phosphinimide compounds, described above in the presence of 500 equiv of methyl-

Fig. 3. X-ray structure of $[(PCH_2CH_2PAlMe_2)_2)_4]\cdot 4[AlMe_3]$.

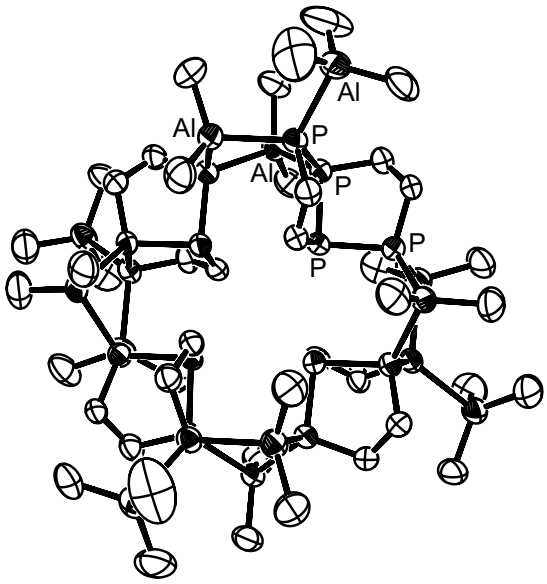

Fig. 4. Steric analogy of Cp_2MCl_2, $CpM(OCR_3)Cl_2$, and $CpM(NPR_3)Cl_2$.

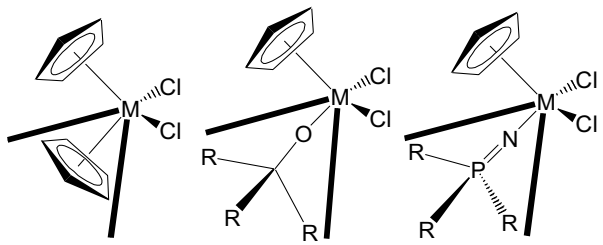

Scheme 5.

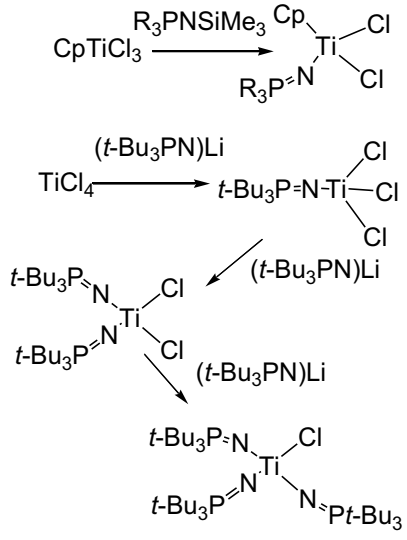

alumoxane (MAO), effect the catalytic polymerization of ethylene at 1 atm and 25°C (Table 1) (9, 10). The level of activity varies with the substituents on the phosphorus center as the catalysts derived from $CpTiCl_2(NPCy_3)$ and $CpTiCl_2(NP\text{-}i\text{-}Pr_3)$ and MAO exhibit relatively low activity

© 2002 NRC Canada

Fig. 5. X-ray structure of the zwitterionic complex CpTiMe(NP-*t*-Bu_3)(μ-MeB(C_6F_5)$_3$).

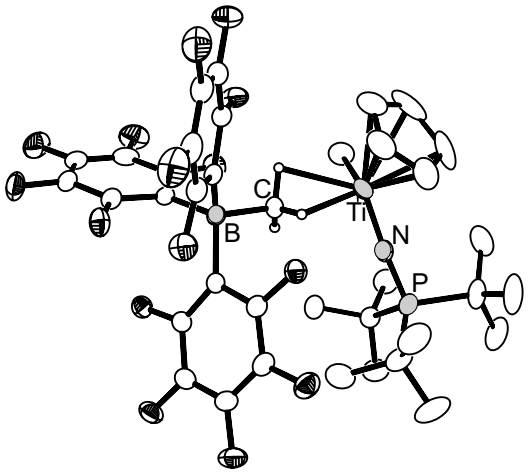

compared to that derived from $CpTiCl_2$(NP-*t*-Bu_3). This latter species with an activity of 652 g PE/mmol/h, approaches that observed from Cp_2ZrCl_2 under the same conditions (895 g PE/mmol/h). It is also noteworthy that the phosphinimide catalyst gives polyethylene of molecular weight 89 000 with a polydispersity of 1.6 consistent with single-site catalysis.

Activation of the analogous dimethyl derivatives of the catalyst precursors with $[Ph_3C][B(C_6F_5)_4]$ results in much higher activity and polyethylene of higher molecular weight (9, 10). While the catalysts derived from $CpTiMe_2(NPCy_3)$ and $CpTiMe_2$(NP-*i*-Pr_3) show a substantial increase in activity giving 231 and 225 g PE/mmol/h, respectively, systems with additional steric crowding such as *t*-$BuCpTiMe_2(NPR_3)$ (R = Cy, *i*-Pr_3, *t*-Bu_3) show significantly higher activity. In these cases, the high activity together with the observation of polydispersities in the range of 7–12 suggest that these screening polymerizations rapidly become diffusion-controlled reactions.

While these results are encouraging, it is clear that for a true commercial potential the catalyst must operate effectively under more demanding conditions of higher temperatures and pressures of ethylene. Such conditions often lead to the degradation of catalysts that are active under the mild conditions of initial laboratory screenings. In collaborative development with researchers at NOVA Chemicals Corporation, the viability of the bis-phosphinimide-based catalyst was demonstrated under commercially relevant solution production conditions (160°C) with the optimization of reagent flows. Under these conditions, Cp_2ZrMe_2 and ($C_5Me_4SiMe_2$N-*t*-Bu)$TiMe_2$ were also tested for comparison. The results demonstrate that the catalyst derived from (*t*-$Bu_3PN)_2TiMe_2$ continues to act as a single-site ethylene polymerization catalyst under these harsh conditions. Polydispersity of 1.9 and good molecular weight of the polymer are achieved with the titanium-phosphinimide catalyst at a remarkably high activity. Our system proved to be almost four times as active as the constrained geometry catalyst under similar conditions (Table 2) (10).

The promising results for the phosphinimide-based catalyst described above clearly warrant further study. This new

Scheme 6.

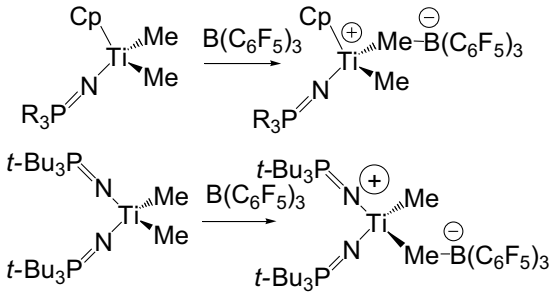

class of early metal catalysts exhibits unique levels of activity and yet appears to operate in a manner similar to that known for related metallocenes. Thus, from our academic perspective we chose to probe the mechanisms by which these systems were deactivated, in the hopes of garnering a deeper understanding of these catalysts. Such information will also assist in the design of new catalysts and applications.

Catalyst deactivation pathways

Ligand degradation

Some of the data above suggest that sterically demanding ligands are worthy of investigation. In this regard we noted the work of Pringle and co-workers (12) who reported a new class of bulky bidentate phosphine ligands where the P atoms are incorporated in a sterically demanding adamantane-like cage. Molecular modeling suggests titanium complexes of phospha-adamantyl-phosphinimides will exhibit a ligand cone angle significantly larger than that of *tert*-butylphosphinimide and thus offer greater steric protection of the metal center. The "cage-phosphines" $PR(C_6H_4O_3Me_4)$ were conveniently prepared from the reaction of RPH_2 with 2,4-pentanedione and subsequent oxidation gave the corresponding phosphinimine. Complexation by titanium followed the methodologies established above (Scheme 7) (13). These complexes were screened for catalytic activity in ethylene polymerizations in the presence of 500 equiv of MAO or combined with $[Ph_3C][B(C_6F_5)_4]$ and showed surprisingly low activities (<10 g PE/mmol/h). In an effort to understand the poor performance of these titanium complexes the interactions with aluminum reagents were investigated. Reaction of $CpTiMe_2(NPR(C_6H_4O_3Me_3))$ as catalysts, with $AlMe_3$ revealed the generation of a number of products. This suggests that Lewis acid activators attack the titanium complexes. This view was supported by the crystallographic characterization of one of the several products, namely $CpTiMe_2(NPCy(C_6H_4O_3Me_5)(\mu\text{-}AlMe_2)(AlMe_3))$ (Scheme 7) (13). In this species, the aluminum reagent has effected ligand rupture and leads to catalyst deactivation.

Increased Lewis acidity

Another class of sterically demanding phosphinimide complexes have been prepared in which one of the substituents on phosphorus is also a phosphinimide group. These ligands are readily prepared by reaction of lithium-phosphinimide salts with chlorophosphines followed by subsequent oxidation of the P(III) centre (14). In the standard

© 2002 NRC Canada

Table 1. Screening for ethylene polymerization (1 atm, 25°C).

Catalyst precursor	Activator	Productivity (g PE/mmol/h)	MW (Da) (pdi)
$CpTiCl_2(N{=}PCy_3)$	MAO	42	3 590 (1.8)
			336 000 (2.2)
$CpTiCl_2(N{=}P\text{-}t\text{-}Bu_3)$	MAO	652	89 900 (1.6)
Cp_2ZrCl_2	MAO	895	116 353 (2.8)
$CpTiMe_2(N{=}P\text{-}i\text{-}Pr_3)$	$Ph_3C[B(C_6F_5)_4]$	225	163 800 (3.9)
$CpTiMe_2(N{=}P\text{-}t\text{-}Bu_3)$	$Ph_3C[B(C_6F_5)_4]$	401	165 800 (3.4)
$t\text{-}BuCpTiMe_2(N{=}PCy_3)$	$Ph_3C[B(C_6F_5)_4]$	1807	310 200 (7.5[a])

[a]This broader pdi was attributable to the high activity of the catalyst. Narrower pdis were obtained under more dilute conditions.

Table 2. Ethylene polymerization under industrially relevant conditions (160°C).

Precursor	Co-catalyst	Productivity (g PE/mmol/h)	MW (Da) (pdi)
$(t\text{-}Bu_3PN)_2TiMe_2$	$[Ph_3C]B(C_6F_5)_4$	62 310	77 500 (1.9)
$(C_5Me_4SiMe_2$ N-*t*-Bu)$TiMe_2$	$[Ph_3C]B(C_6F_5)_4$	16 130	134 500 (2.5)
Cp_2ZrMe_2	$[Ph_3C]B(C_6F_5)_4$	8 850	12 300 (3.8)

manner the corresponding titanium complexes were prepared. The species $CpTi(NPPh_2(NP\text{-}t\text{-}Bu_3))Cl_2$ proved to be a reasonable catalyst precursor yielding a catalyst by activation with MAO which polymerized ethylene with an activity of 300 g/mmol/h. In marked contrast, tests at 1 atm ethylene employing the methyl derivatives and $[Ph_3C][B(C_6F_5)_4]$ showed minimal polymerization activity. Attempts to characterize the cationic species involved the reaction of $CpTi(NPPh_2(NP\text{-}t\text{-}Bu_3))Me_2$ with $B(C_6F_5)_3$. Crystallographic characterization of the product from CH_2Cl_2 confirmed the formulation as $[CpTi(\mu\text{-}Cl)(NPPh_2(NP\text{-}t\text{-}Bu_3))]_2[BC_6F_5)_4]_2$ (Fig. 6) (14). While the mechanism of formation is the subject of speculation, the formation of this species does permit some inferences to be made. While initial interaction of the titanium complex with $B(C_6F_5)_3$ is assumed to involve methyl abstraction, apparently the resulting zwitterion is highly reactive. Clearly the isolation of the chloro-bridged di-cation imply both solvent activation and borate-substituent redistribution. This observation suggests that the electron-withdrawing phosphinimide substituent on the metal-bound phosphinimide ligand results in a highly Lewis acidic Ti species. It is presumably this acidity that prompts deactivation of the catalyst. The activity of the MAO-based catalyst suggests ion-pairing or cation–anion interactions are critical for catalyst stability.

$B(C_6F_5)_3$ as a catalyst poison

While the species $(t\text{-}Bu_3PN)_2TiMe(\mu\text{-}MeB(C_6F_5)_3)$ has been shown above to be an active catalyst for ethylene polymerization, preliminary screening studies showed that the order of addition of the reagents had a dramatic effect on the activity (Table 3) (10). Addition of $(t\text{-}Bu_3PN)_2TiMe_2$ to a solution of $B(C_6F_5)_3$ at 25°C under an ethylene atmosphere gave only a small amount of polyethylene. On the other hand, addition of $B(C_6F_5)_3$ to a solution of $(t\text{-}Bu_3PN)_2TiMe_2$ gave significantly increased activity. These observations prompted NMR studies of the stoichiometric reaction of $(t\text{-}Bu_3PN)_2TiMe_2$ with excess

Scheme 7.

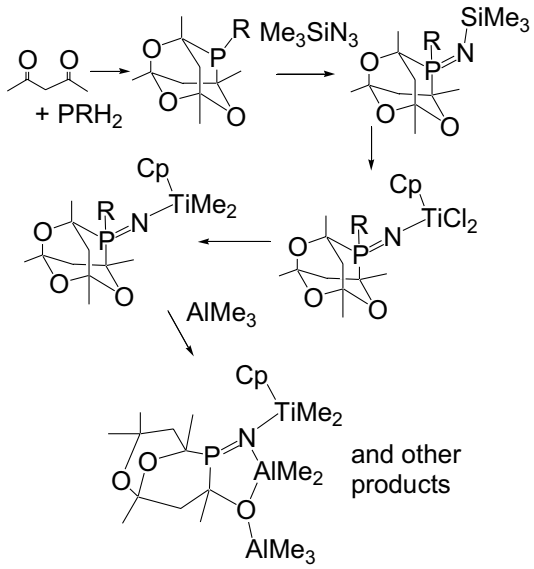

$B(C_6F_5)_3$. In the presence of excess borane, the di-zwitterionic species $(t\text{-}Bu_3PN)_2Ti(\mu\text{-}MeB(C_6F_5)_3)_2$ (Scheme 8, Fig. 7) was obtained (15). This species exhibits negligible polymerization activity, presumably because no formal Ti—C bond remains available for insertion. This observation demonstrates for the first time a dual role for the $B(C_6F_5)_3$ as it acts both as a catalyst activator and a catalyst poison. It is presumably the remote nature of the steric bulk of the phosphinimide ligands that allows access to the metal center by 2 equiv of the borane.

C—H bond activation

The titanium-phosphinimide complexes under discussion are generally active catalysts for polymerization of olefins. However, they also generally show lower activity when activated by MAO. This observation is particularly true for complexes containing sterically less demanding phosphinimide ligands. To probe the root of this observation, reactions of the titanium-phosphinimide complexes with excess $AlMe_3$ were undertaken, in an effort to model the interaction with MAO. In the reaction of $CpTi(NPR_3)Me_2$ with $AlMe_3$, gas evolution was apparent and the resulting product was confirmed crystallographically to be $[CpTi(\mu^2\text{-}Me)(\mu^2\text{-}NPR_3)(\mu^4\text{-}C)(AlMe_2)_3]$ (16, 17). This information confirmed that triple C—H bond activation and the quantitative formation of an unprecedented Ti–Al-carbide cluster occurred (Fig. 8). The Lewis acidity of this complex is evident in the reaction

© 2002 NRC Canada

Fig. 6. X-ray structure of $[CpTi(\mu\text{-}Cl)(NPPh_2(NP\text{-}t\text{-}Bu_3))]_2\text{-}[BC_6F_5)_4]_2$.

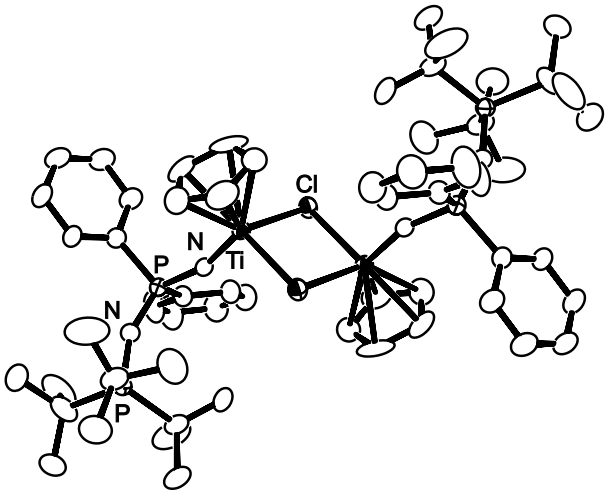

Table 3. Ethylene polymerization and order of addition.

Catalyst precursor	Co-catalyst[a]	Productivity	Order of addition
$(t\text{-}Bu_3PN)_2TiMe_2$	BCF	<50	Precursor to BCF
$(t\text{-}Bu_3PN)_2TiMe_2$	BCF	265	BCF to precursor

[a]BCF = tris(pentfluorophenyl)borane.

Scheme 8.

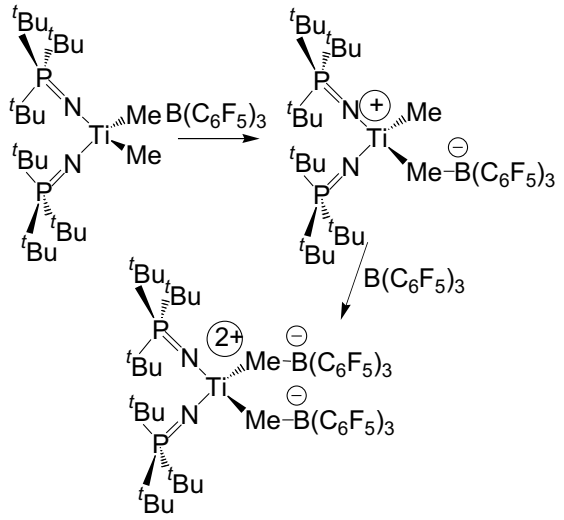

of this species with donors forming alane-donor adducts. In addition, the Lewis basicity of the central carbide carbon is evidenced by reaction with additional $AlMe_3$ that yields a five-coordinate carbide $[CpTi(\mu^2\text{-}Me)(\mu^2\text{-}NPR_3)(\mu^5\text{-}C)\text{-}(AlMe_2)_3\cdot(AlMe_3)]$ (Scheme 9, Fig. 9) (16). The isolation of these C—H bond activation products, particularly the four- and five-coordinate nature of the central carbon is interesting from an academic perspective. However, the isolation of these species has some implications for the catalyst activity.

Fig. 7. (*a*) X-ray structure of $(t\text{-}Bu_3PN)_2Ti(\mu\text{-}MeB(C_6F_5)_3)_2$. (*b*) Coordination sphere of Ti.

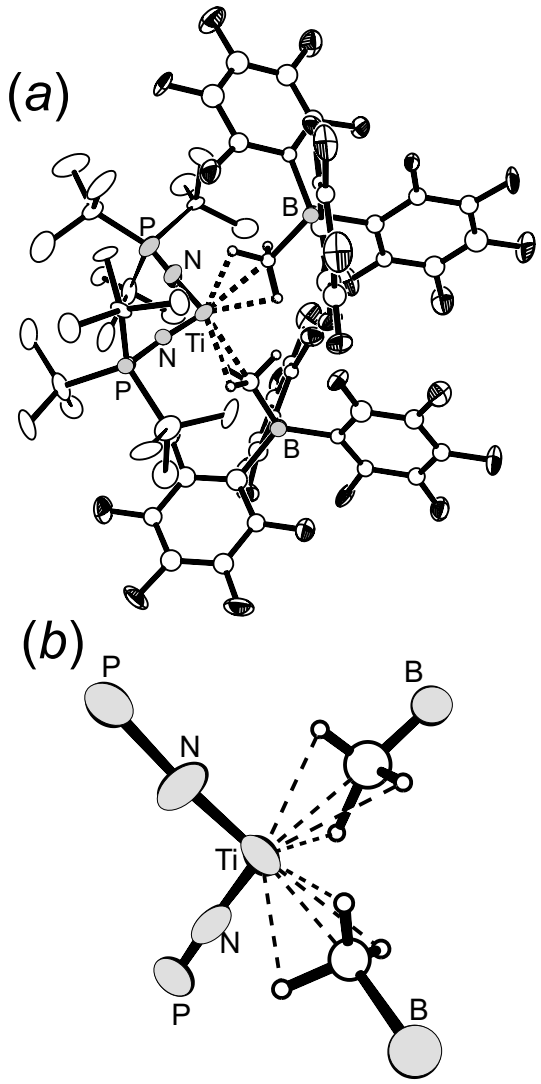

Fig. 8. X-ray structure of $[CpTi(\mu^2\text{-}Me)(\mu^2\text{-}NP\text{-}i\text{-}Pr_3)(\mu^4\text{-}C)(AlMe_2)_3]$.

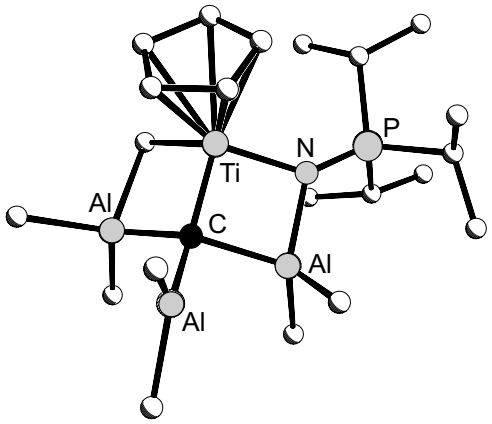

If indeed $AlMe_3$ reacts in a similar manner to MAO, then these observations suggest that C—H bond activation processes may suppress catalytic activity. However, this could

© 2002 NRC Canada

Scheme 9.

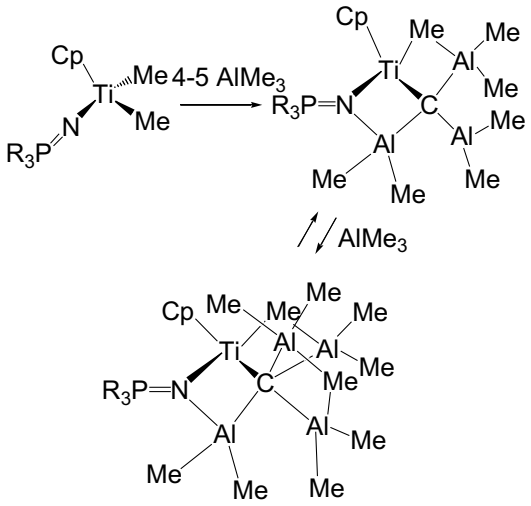

Fig. 9. X-ray structure of $[CpTi(\mu^2\text{-}Me)(\mu^2\text{-}NPPh_3)(\mu^5\text{-}C)(AlMe_2)_3{\cdot}(AlMe_3)]$.

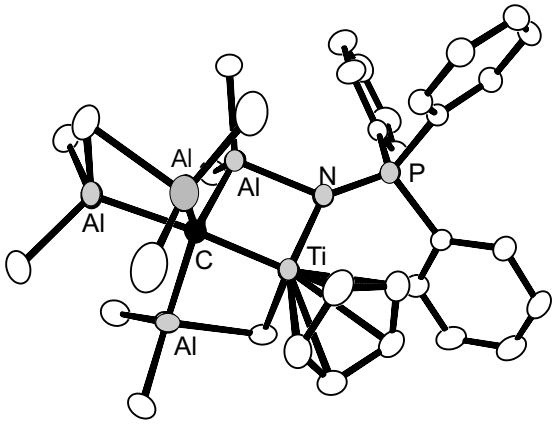

Scheme 10.

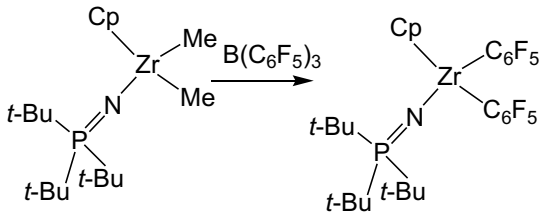

be overstated and thus it may be that interaction of the phosphinimide nitrogen atom with an aluminum center of MAO is sufficient to diminish catalyst activity.

C_6F_5 transfer

Zirconium-phosphinimide complexes of the form $Cp'Zr(NPR_3)X_2$ (Cp′ = Cp*, Cp; X = halide, alkyl or aryl) are readily prepared using synthetic methods very similar to that used to obtain the analogous titanium species (18). In general, regardless of the protocol used for activation, the Zr complexes showed uniformly poor catalyst activity for ethylene polymerization. Probing the cause of the poor activity,

Fig. 10. X-ray structure of $(Cp^*Zr)_4(\mu\text{-}Cl)_5(Cl)(\mu\text{-}CH)_2$.

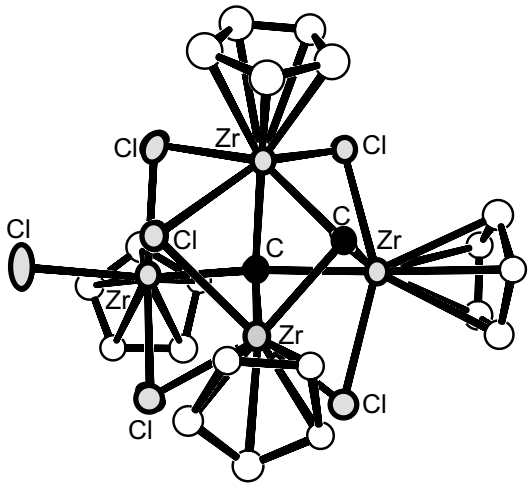

Fig. 11. X-ray structure of $(Cp^*Zr)_5(\mu\text{-}Cl)_6(\mu\text{-}CH)_3$.

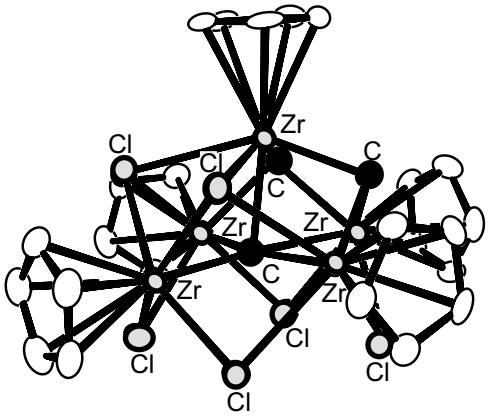

the reaction of complexes of the form $Cp'Zr(NPR_3)Me_2$ (Cp′ = Cp*, Cp) with $B(C_6F_5)_3$ were investigated. Under very mild conditions this reaction was shown by spectroscopic methods to give the species $Cp'Zr(NPR_3)(C_6F_5)_2$ in quantitative yield (Scheme 10) (18). Clearly, this reactivity provides a highly efficient route for the destruction of catalyst activity.

Ligand abstraction and C—H bond activation

Further exploration of the low activity of the Zr analogs prompted reaction of $Cp^*Zr(NP\text{-}t\text{-}Bu_3)Cl_2$ with $AlMe_3$ as a model for the interaction with MAO. While the resulting reaction results in several products as evidenced by ^{31}P NMR spectroscopy, two products were crystallized and structurally characterized. One of the products is the Zr_4 cluster $(Cp^*Zr)_4(\mu\text{-}Cl)_5(Cl)(\mu\text{-}CH)_2$ (Fig. 10) (18). This species is comprised of four Zr atoms bound to a central methine carbon with each Zr atom bonded to a pentamethylcyclopentadienyl ligand and two bridging chloride atoms. One of the Zr atoms also has an additional terminal chloride, while the remaining three Zr atoms are bridged by an additional methine carbon. A second product was identified as $(Cp^*Zr)_5(\mu\text{-}Cl)_6(\mu\text{-}CH)_3$ (Fig. 11) (18). This species, like the previous, is a Zr-cluster comprised of five Cp*Zr fragments about a central methine carbon atom. The Zr atoms form a square-based pyramid

© 2002 NRC Canada

about the central carbon with the basal plane of Zr atoms being bridged by four chloride atoms below the plane. Two chlorine atoms and two pseudotetrahedral methine carbons above the plane bridge the axial Zr center. These two products were obtained in poor yield, nonetheless, these compounds do suggest avenues by which catalyst–co-catalyst interactions can lead to deactivation. Firstly, phosphinimide ligand abstraction clearly occurs which stands in contrast to the related Ti complexes. Secondly, methyl transfer from Al to Zr followed by C—H bond activation is clearly indicated suggesting that C—H bond activation is again involved in catalyst deactivation.

Summary

In summary, our work began addressing very fundamental questions about the reactivity of Ti and Zr complexes. The work on P—H bond activation and catalytic dehydrocoupling of phosphines evolved to a quest for alternative catalyst precursors. In this effort, phosphinimide-based complexes were prepared and it was discovered that these systems provide catalyst precursors that are highly active in ethylene polymerization. In fact, these catalysts rival and in some cases surpass commercial catalysts. While the potential commercialization of these systems is in on-going development in collaboration with researchers at NOVA Chemicals Corporation, our efforts have once again turned to fundamental questions, in this case, deactivation pathways. The study of the unique reactivity exhibited by these systems not only provides a better understanding of these catalysts but also provides insight which could lead to new applications and the design of new catalyst systems.

Acknowledgements

First and foremost, I am grateful for the love and support of Dianne, David, and Katie. I cannot thank them enough. I also wish to acknowledge the administration at the University of Windsor for the provision of a highly supportive environment. My colleagues, in particular Drs. Tuck, Drake, McGarvey, and (the late) Rutherford are acknowledged for establishing a precedent for success. Dr. Steve Loeb is thanked for almost 25 years of friendship and creative discussion. I am indebted to a large group of hard working and talented young scientists that it has been my pleasure to work with over the past 19 years. While a number of these people worked on earlier chemistry not discussed herein, their contributions are very much appreciated. These include the postdoctoral fellows: Yujin Huang, Eva Witt, Peggy McKarns, Nola Etkin, Chris Fermin, Rick Heyn, Zhaomin Hou, Charles Carraz, Luc LePichon, Fred Guerin, Pingrong Wei, and Jim Kickham, as well as the graduate students: Evelyn Kinsch, Graham White, Lucio Gelmini, Hilde Berends, Teresa Wark, Dave Dick, Jianwei Ho, Tim Nadasdi, Tricia Breen, Andrea Firth, Jeffrey Stewart, Chris Ong, Nancy Yue, Silke Courtenay, Aaron Hoskin, Sarah Smith, Emily Hollink, Katie Chan, Chad Beddie, Liam Spencer, Steve Clemens, Ramadan Altwer, and Lourissa Cabrera. In addition, financial support from the University of Windsor, the Natural Sciences and Engineering Research Council of Canada (NSERC), Imperial Oil, Janssen-Ortho, the Petroleum Research Fund, and NOVA Chemicals Corporation is gratefully acknowledged.

References

1. D.W. Stephan. Coord. Chem. Rev. **95**, 41 (1989).
2. D.W. Stephan and T.T. Nadasdi. Coord. Chem. Rev. **147**, 147 (1996).
3. D.W. Stephan. Angew. Chem. Int. Ed. **39**, 315 (2000).
4. M.C. Fermin and D.W. Stephan. J. Am. Chem. Soc. **117**, 12 645 (1995).
5. N. Etkin, A.J. Hoskin, and D.W. Stephan. J. Am. Chem. Soc. **119**, 11 420 (1997).
6. N. Etkin, M.C. Fermin, and D.W. Stephan. J. Am. Chem. Soc. **119**, 2954 (1997).
7. A.J. Hoskin and D.W. Stephan. Angew. Chem. Int. Ed. **40**, 1865 (2001).
8. T.V. Lubben, P.T. Wolczanski, and G.D. Van Duyne. Organometallics, **3**, 977 (1984).
9. D.W. Stephan, J.C. Stewart, F. Guerin, R.E.v.H. Spence, W. Xu, and D.G. Harrison. Organometallics, **18**, 1116 (1999).
10. D.W. Stephan, F. Guerin, R.E.v.H. Spence, L. Koch, X. Gao, S.J. Brown, J.W. Swabey, Q. Wang, W. Xu, P. Zoricak, and D.G. Harrison. Organometallics, **18**, 2046 (1999).
11. F. Guérin, C.L. Beddie, D.W. Stephan, R.E.v.H. Spence, and R. Wurz. Organometallics, **20**, 3466 (2001).
12. V. Gee, A.G. Orpen, H. Phetmung, P.G. Pringle, and R.I. Pugh. Chem. Commun. 901 (1999).
13. C.A. Carraz and D.W. Stephan. Organometallics, **19**, 3791 (2000).
14. N.L.S. Yue and D.W. Stephan. Organometallics, **20**, 2303 (2001).
15. F. Guerin and D.W. Stephan. Angew. Chem. Int. Ed. **39**, 1298 (2000).
16. J.E. Kickham, F. Guerin, J.C. Stewart, and D.W. Stephan. Angew. Chem. Int. Ed. **39**, 3263 (2000).
17. J.E. Kickham, F. Guerin, J.C. Stewart, E. Urbanska, and D.W. Stephan. Organometallics, **20**, 1175 (2001).
18. N.L.S. Yue, E. Hollink, F. Guérin, and D.W. Stephan. Organometallics, **20**, 4424 (2001).

© 2002 NRC Canada

Magnetic and structural studies on 1,3-diazolate complexes of cobalt(II) — The characterization of three new cobalt(II) molecule-based magnets

Victor Sánchez, Alan Storr, and Robert C. Thompson

Abstract: The cobalt(II) compounds ($[Co(imid)_2]_x$ (**1**), $[Co(2\text{-}meimid)_2]_x$ (**2**), $[Co(4\text{-}meimid)_2]_x$ (**3**), $[Co(benzimid)_2]_x$ (**4**), and $[Co_3(imid)_6(imidH)_2]_x$ (**5**) (imid = imidazolate, 2-meimid = 2-methylimidazolate, 4-meimid = 4-methylimidazolate, benzimid = benzimidazolate)), have been synthesized and structurally and magnetically characterized. Electronic and vibrational spectroscopy and thermogravimetric studies on all five compounds support structures involving tetrahedrally coordinated cobalt centers with single-bridging 1,3-diazolate ligands forming extended polymeric lattices. Moreover, X-ray powder diffraction studies on **1** and **5** established, through isomorphism with published structures, that the molecular connectivity in these materials is 3-D. Variable temperature and applied field magnetization studies revealed antiferromagnetism as the primary magnetic exchange process in all five compounds. In addition, **1**, **4**, and **5** show magnetic phase transitions to ferromagnetically ordered states below critical temperatures of 16, 13, and 15 K, respectively. Magnetization measurements at 4.8 K as the applied field was cycled between +55 000 and –55 000 G revealed typical hysteresis behavior and gave remnant magnetizations of 334, 257, and 175 cm^3 G mol^{-1} and coersive fields of 6620, 5280, and 4140 G for **1**, **4**, and **5**, respectively. No evidence for long-range magnetic order was obtained for either **2** or **3**. A comparison of the magnetic properties of three pairs of isostructural iron(II) and cobalt(II) molecule-based magnets shows that while the coersive fields are in general larger for cobalt over iron, the magnitude of the difference varies significantly suggesting that one cannot conclude that cobalt analogues will always be harder magnets.

Key words: cobalt(II), 1,3-diazolates, canted spins, molecule-based magnets.

Résumé : On a synthétisé les composés du cobalt(III) suivants, $[Co(imid)_2]_x$ (**1**), $[Co(2\text{-}meimid)_2]_x$ (**2**), $[Co(4\text{-}meimid)_2]_x$ (**3**), $[Co(benzimid)_2]_x$ (**4**) et $[Co_3(imid)_6(imidH)_2]_x$ (**5**) (imid = imidazoles, 2-meimid = 2-méthylimidazolate, 4-meimid = 4-méthylimidazolate et benzimid = benzimidazolate) et on en a fait la caractérisation structurale et magnétique. Les spectroscopies électronique et vibrationnelle ainsi que des études de thermogravimétrie sur ces composés sont en accord avec des structures impliquant des centres de cobalt à coordination tétraédrique et des ligands 1,3-diazolate servant de pont unique pour former des réseaux étendus de polymères. De plus, en se basant sur les structures des composés **1** et **5** déterminées par diffraction des rayons X et l'isomorphisme avec des structures déjà publiées, on peut en déduire que la connectivité moléculaire dans ces matériaux est 3-D. Des études à températures variables et de magnétisation du champ appliqué révèlent que, pour chacun de ces composés, le processus d'échange magnétique primaire résulte d'antiferromagnétisme. De plus, les composés **1**, **4** et **5** donnent lieu à des transitions de phase magnétique conduisant à des états ferromagnétiquement ordonnés à des températures critiques respectivement de 16, 13 et 15 K. Des mesures de magnétisation à 4,8 K alors que l'on faisait varier le champ appliqué de +55 000 à –55 000 G révèlent l'existence d'un comportement d'hystérèse typique qui conduisent à des magnétisations résiduelles de 334, 257 et 175 cm^3 G mol^{-1} et des champs coersifs de 6620, 5280 et 4140 G respectivement pour les composés **1**, **4** et **5**. Pour les composés **2** et **3**, on n'a pas pu observer d'ordre magnétique à longue portée. Une comparaison des propriétés magnétiques des trois paires d'aimants isostructuraux à base de fer(II) et de cobalt(II) montrent que, alors que les champs coersifs sont généralement plus importants pour le cobalt par rapport au fer, l'amplitude de la différence varie de façon significative; ce qui suggère que l'on ne peut pas conclure que les analogues à base de cobalt sont toujours des aimants plus durs.

Mots clés : cobalt(II), 1,3-diazolates, spins penchés, aimants à base de molécules.

[Traduit par la Rédaction]

Received 21 September 2001. Published on the NRC Research Press Web site at http://canjchem.nrc.ca on 23 January 2002.

V. Sánchez, A. Storr,[1] and R.C. Thompson.[1] Department of Chemistry, The University of British Columbia, Vancouver, BC V6T 1Z1, Canada.

[1]Corresponding authors ((RCT): telephone: (604) 822-4979; fax: (604) 822-2847; e-mail: thompson@chem.ubc.ca; (AS): telephone: (604) 822-3962; fax: (604) 822-2847; e-mail: storr@chem.ubc.ca).

 DOI: 10.1139/V01-202 © 2002 NRC Canada

Introduction

Recent reviews have documented the ability of diazolate ligands to function as bridging bidentate ligands and to act as relatively efficient mediators of magnetic exchange interactions where paramagnetic metal centers are involved (1–3). Studies on binary pyrazolates of copper(II), cobalt(II), iron(II), nickel(II), and manganese(II) show that the 1,2-positioning of the nitrogen atoms in the ligands leads to 1-D linear chain structures with double azolate bridges and short-range antiferromagnetic coupling between metal centers (4–10). In contrast, as has been discussed (11), in related imidazolate systems, the 1,3-positioning of the donor nitrogens in the ligands results in steric constraints which are likely to prevent the formation of double azolate bridges. These ligands may then be expected to singly bridge metals and form higher dimensional 2-D or 3-D structures with the potential for long-range magnetic interactions. As reported previously, these structural (11, 12) and magnetic (11) characteristics are exhibited by $[Fe_3(imid)_6(imidH)_2]_x$ (where imidH = imidazole), a compound in which iron(II) ions are singly bridged by imidazolate ligands in an extended 3-D lattice. Magnetic studies on this compound revealed antiferromagnetic coupling as the primary exchange interaction. Due, it was concluded, to a canting of the spins, residual spin density remained on the metal centers at low temperatures and this led to long-range order and weak ferromagnetism. We later reported (13, 14) the structure and magnetic characterization of iron(II) complexes of 2-methylimidazolate ($[Fe(2\text{-meimid})_2 \cdot 0.13Cp_2Fe]_x$ (2-meimid = 2-methylimidazolate and Cp = cyclopentadienyl) and 4-azabenzimidazolate ($[Fe(4\text{-abimid})_2]_x$ (4-abimid = 4-azabenzimidazolate). Stoichiometrically and structurally these compounds are distinct from the imidazolate analogue ($[Fe_3(imid)_6(imidH)_2]_x$; nonetheless, they too have single-azolate-bridged 3-D structures and show long-range ferromagnetic order at low temperatures. The magnetic properties exhibited by these three iron(II) systems serve to classify them as molecule-based magnets (15). There is considerable interest in materials such as these from the joint perspectives of understanding factors that generate them and of their potential applications (16).

The noncentrosymmetric M-L-M exchange pathway provided by single-bridging 1,3-diazolate ligands appears to be a key factor in generating spin canting and weak ferromagnetism (14). The phenomenon should not be restricted to iron(II). This fact coupled with the observation that the iron centers involved in the primary exchange pathways in the previously investigated systems are tetrahedrally coordinated (a common geometry for cobalt(II)), prompted us to investigate related cobalt systems. Our studies on $[Co(4\text{-abimid})_2]_x$, a compound which exhibits low-temperature ferromagnetism, have already been described (14). Here, we describe work on five additional cobalt systems: $[Co(imid)_2]_x$ (**1**), $[Co(2\text{-meimid})_2]_x$ (**2**), $[Co(4\text{-meimid})_2]_x$ (**3**), $[Co(benzimid)_2]_x$ (benzimid = benzimidazolate) (**4**), and $[Co_3(imid)_6(imidH)_2]_x$ (**5**).

Some studies on **1**–**4** were reported earlier (17–20) while compound **5** is studied here for the first time. We chose to further examine **1**, in particular, because its structure, as determined by single crystal X-ray diffraction studies (17), involves a 3-D extended lattice, suggesting the possibility of ferromagnetic ordering at low temperatures. Polymeric structures also seemed likely for **2**–**4** and an initial objective of the present study was to establish this through single crystal X-ray diffraction work. Unfortunately, we were unable to obtain crystals of these materials suitable for such studies. Although definitive structures of **2**–**4** remain elusive, we report here spectroscopic and thermal analysis data that attest to their polymeric nature. In addition, **5** is shown here to be isomorphous, and presumably isostructural, with the iron analogue, a compound known to have an extended 3-D lattice structure (11, 12). Previous reports on magnetic properties of these systems are limited to some high-temperature studies on **1** (17, 18*c*) and **4** (19). Variable-temperature and variable-field magnetization studies in the current work reveal that **1**, **4**, and **5** are low-temperature molecule-based magnets. No evidence for long-range ferromagnetic order was obtained for either **2** or **3**.

Experimental

Syntheses

Cobaltocene (from Strem), hexaaquacobalt(II) nitrate and hexaaquacobalt(II) chloride (from Mallinkrodt), imidazole (imidH), 2-methylimidazole (2-meimidH), 4-methyimidazole (4-meimidH), and benzimidazole (from Aldrich) were used as supplied. Acetonitrile and xylenes (from Aldrich) were reagent grade and were dried and distilled under an atmosphere of dry dinitrogen before use.

$[Co(imid)_2]_x$ (1)

Hexaaquacobalt(II) nitrate (7.5 g, 33 mmol) was dissolved in 10 mL of hot water and added dropwise to a solution of imidazole (3.4 g, 50 mmol) in 40 mL of hot water. The mixture was brought to boil and the precipitate was immediately filtered and washed with hot water first, then with acetone. The product was isolated as a microcrystalline purple powder and was dried in vacuo at 100°C. Anal. calcd. for $C_6H_6N_4Co$: C 37.3, H 3.1, N 29.0; found: C 37.6, H 3.0, N 28.7. Samples prepared by this route were examined by X-ray powder diffraction and were employed in the magnetic studies. A small quantity of material of the same composition as **1** was obtained by the removal, via thermolysis, of neutral imidazole from $[Co_3(imid)_6(imidH)_2]_x$ (**5**). This thermal treatment of compound **5** was carried out under a flux of dinitrogen utilizing a TA Instruments TGA 51 unit. A 30 min isotherm at 325°C was programmed into the instrument to completely remove the neutral imidazole. Anal. found: C 37.1, H 3.0, N 28.8.

$[Co(2\text{-meimid})_2]_x$ (2)

Hexaaquacobalt(II) nitrate (1.0 g, 3.7 mmol) was dissolved in 10 mL of ethanol and added dropwise to a solution of 2-methylimidazole (3.0 g, 37 mmol) in 40 mL of ethanol. The purple precipitate which formed immediately was filtered off, washed with ethanol, and dried for 1 h at 115°C. Anal. calcd. for $C_8H_{10}N_4Co$: C 43.4, H 4.6, N 25.3; found: C 43.0, H 4.3, N 24.9.

© 2002 NRC Canada

[Co(4-meimid)$_2$]$_x$ (3)

Hexaaquacobalt(II) chloride (1.0 g, 4.2 mmol) was dissolved in 15 mL of water and added dropwise to a solution of 4-methylimidazole (3.0 g, 37 mmol) in 30 mL of water. NaOH (1.48 g, 37 mmol) was dissolved in 5 mL of water and added dropwise to the mixture to complete the precipitation of a fine purple powder. The precipitate was filtered off, washed with water and then ethanol, and air-dried at room temperature. Anal. calcd. for $C_8H_{10}N_4Co$: C 43.4, H 4.6, N 25.3; found: C 43.6, H 4.5, N 25.0.

[Co(benzimid)$_2$]$_x$ (4)

This compound was prepared as previously reported (19). Anal. calcd. for $C_{14}H_{10}N_4Co$: C 57.3, H 3.4, N 19.1; found: C 57.5, H 3.3, N 19.2.

[Co$_3$(imid)$_6$(imidH)$_2$]$_x$ (5)

This compound was obtained as a purple microcrystalline powder by heating a mixture of excess imidazole (2.0 g, 26 mmol) with cobaltocene (0.2 g, 1.06 mmol) in a sealed and evacuated Carius tube at 150°C for 5 days. Dry xylenes and acetonitrile were used to isolate the product from residual ligand. Anal. calcd. for $C_{24}H_{26}N_{16}Co_3$: C 40.3, H 3.6, N 31.3; found: C 40.8, H 3.6, N 31.2.

Physical characterization

Thermal gravimetric analysis (TGA, 35–800°C) measurements were made using a TA Instruments TGA 51 unit. A Varian Cary 5 UV–vis–near-IR spectrophotometer was used to measure electronic spectra (200–3000 nm) at room temperature on Nujol mulls pressed between quartz plates. Infrared spectra (4000–400 cm^{-1}) were recorded at room temperature using KBr disc samples on a Bomen FT IR spectrophotometer. Magnetic properties were examined using a Quantum Design (MPMS) SQUID magnetometer. Magnetic susceptibilities were measured on finely ground powders at 500 and 10 000 G over the temperature range 2–300 K. Magnetization studies as a function of field strength (0–55 000 G) were made on powders at several temperatures and hysteresis magnetization data were obtained on Nujol mull samples by oscillating the applied magnetic field between +55 000 G and –55 000 G at 4.8 K. A specially designed sample holder, as described previously (5*d*), was used to minimize the background signal. Magnetic susceptibilities were corrected for background and for the diamagnetism of all atoms; corrections of 84×10^{-6} (compound **1**), 110×10^{-6} (compounds **2**, **3**, and **5**), and 140×10^{-6} cm^3 mol^{-1} (compound **4**), were employed. Data reported here are on a per mol of metal ion basis. Powder diffractograms for compound **5** were recorded on a Rigaku Rotaflex RU-200BH rotating anode powder X-ray diffractometer (graphite monochromated Cu Kα radiation). Samples were prepared by applying a hexanes slurry of the compound onto a glass plate and allowing the solvent to evaporate.

Results and discussion

Syntheses and structures

Compounds **1**–**4** were obtained as simple binary azolates, by employing modifications of methods reported in the literature for **1**–**3** (18*a*, 20) or, in the case of **4**, by the method of Goodgame and Cotton (19). The methods used produced the materials in powder form, unsuitable for single crystal X-ray diffraction studies. Previously, we reported that the synthetic pathway in which metallocenes are reacted directly with molten azoles can afford a clean and effective method for preparing divalent metal azolate polymers (9–11, 13). The method has been employed by us in the past to obtain single crystals of iron(II) azolate polymers, suitable for single crystal X-ray studies (11, 13, 21). Unfortunately, attempts to prepare compounds **1**–**4** employing this methodology failed to yield suitable crystals of the desired materials.

The structure of [Co(imid)$_2$]$_x$ (**1**) was determined previously by X-ray crystallography (17). It is a 3-D polymer consisting of fused puckered rings of four tetrahedrally coordinated cobalt(II) ions linked by single-bridging imidazolates. The X-ray powder diffractogram of a sample of **1**, synthesized in this work, agrees well with that calculated (22) from single crystal data reported for the compound (17). Indexing the powder diffractogram (23) of the material prepared here gave calculated lattice parameters of $a = b =$ 22.834 and c = 12.983 Å compared to $a = b$ = 22.872 and c = 12.981 Å, previously reported (17). We conclude that the structure of **1** prepared here is that reported earlier for [Co(imid)$_2$]$_x$ (17).

Although the exact structure of compounds **2**–**4** remain unknown, the polymeric nature of the materials is indicated by their physical properties, which to some extent resemble those determined here for compound **1**. The four cobalt(II) compounds are stable both in air and in contact with moisture. They are insoluble in water and common organic solvents, nonvolatile, and thermally robust. They dissolve with decomposition in concentrated mineral acids. Thermal gravimetric analyses show no mass loss due to thermal decomposition or sublimation below 200°C and at higher temperatures the compounds present similar thermal decomposition behavior with no significant weight loss till temperatures above 400°C are reached (Fig. 1). Compound **4** is the most thermally robust of the four compounds in that there is no indication of thermal decomposition below 600°C.

The electronic spectra we obtained on mulls of compounds **1**–**4** are very similar and are consistent with the spectra previously reported for these materials (18*c*, 19, 20). We observed two broad *d*–*d* transition bands, the first one centered (determined visually) around 1110–1130 (broad and structured), and the second one between 570–590 nm, the latter with a shoulder at about 520–540 nm. These can be tentatively assigned to the $^4A_2 \rightarrow {}^4T_1(F)$ and $^4A_2 \rightarrow {}^4T_1(P)$ transitions, respectively, of (distorted) tetrahedral cobalt(II) (6*b*). Very weak and broad bands, likely due to the $^4A_2 \rightarrow {}^4T_2$ transition, were also detected in the 1500–2200 nm region for **1**, **3**, and **4**. Hence, in agreement with the earlier studies, we conclude that these compounds have structures incorporating tetrahedrally coordinated cobalt(II) centers. That there are no neutral imidazole ligands incorporated in the structures is shown by the microanalytical data as well as the absence of a $\nu_{N\text{-}H}$ stretching vibration (24) in both the electronic spectra as well as the IR spectra of these complexes (see the discussion below concerning the observation of this band in compound **5**).

In summary, concerning structures, the similarities in stoichiometry and physical and spectroscopic properties of

© 2002 NRC Canada

Fig. 1. Thermal gravimetric analysis plots.

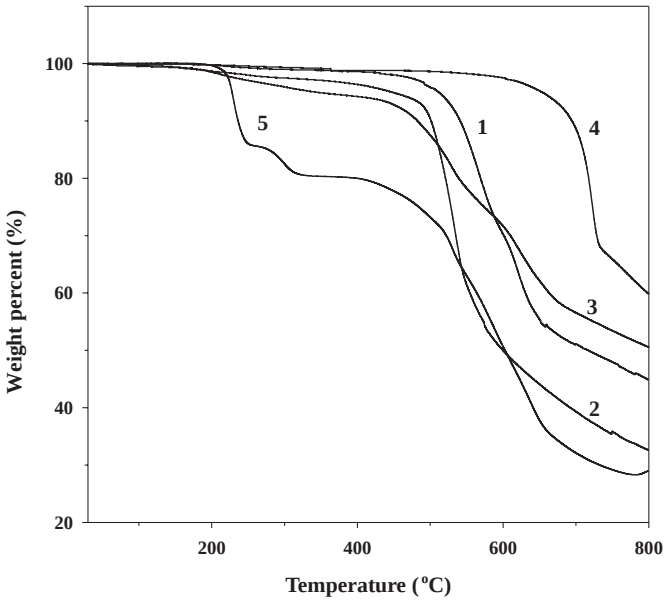

the binary 1,3-diazolates **1**–**4** strongly support the conclusion that, as known definitively for **1**, compounds **2**–**4** also have extended structures with tetrahedrally coordinated metal centers. Moreover, since steric constraints make double-bridging 1,3-diazolates unlikely (11), single azolate bridges and 2-D or 3-D extended structures are more probable structures for these materials than 1-D chains or rings.

The molecule-based magnet ($[Fe_3(imid)_6(imidH)_2]_x$) was prepared earlier in macroscopic crystalline form by the reaction of ferrocene with excess molten imidazole (11). Here, we report that the same reaction employing cobaltocene yields the analogous cobalt compound, $[Co_3(imid)_6(imidH)_2]_x$ (**5**), as a microcrystalline powder. The X-ray powder diffractogram of **5** coincides well with that calculated for $[Fe_3(imid)_6(imidH)_2]_x$ from single crystal X-ray diffraction data (11). Indexing the X-ray powder diffractogram of **5** (23) yields calculated lattice parameters of a = 10.568, b = 12.964, and c = 10.634 Å. These are very similar to those of $[Fe_3(imid)_6(imidH)_2]_x$ (a = 10.591, b = 12.958, c = 10.617 Å) (11). Additional evidence supporting the conclusion that the iron and cobalt compounds are isostructural in addition to being isomorphous comes from spectroscopic studies on **5**. The X-ray determined structure of the iron compound shows the presence of both tetrahedral and octahedral metal centers, the additional coordination sites on the latter being filled by neutral imidazole molecules. The electronic spectrum of compound **5** shows the absorption bands assignable to the $^4A_2 \rightarrow {}^4T_1(F)$ and $^4A_2 \rightarrow {}^4T_1(P)$ transitions of tetrahedrally coordinated Co ions (see previous discussion). Transitions assignable to octahedral cobalt(II) centers are not observable; however, this is not too surprising in view of the fact they would be expected to be an order of magnitude or more weaker than the bands arising from the tetrahedral centers (25). Evidence for the octahedral cobalt centers in **5** comes from the observation of a sharp peak at 2950 nm in the electronic spectrum corresponding to the $\nu_{N\text{-}H}$ stretching vibration of neutral imidazole ligands bound at the octahedral site (11). Finally, we note that the infrared spectrum of **5** and the iron analogue are virtually identical, exhibiting the same vibrational bands at almost the same frequencies. We conclude that **5** has the same structure as the iron analogue (11, 12). In this structure, tetrahedrally coordinated metal ions are connected in chains by singly bridging imidazolate ions. The chains are cross-linked by octahedrally coordinated metal ions. Each tetrahedral center is linked to two others in the same chain and via octahedral centers to two additional chains. Each chain is linked to four different chains via the octahedral centers. A stereoview of a portion of this structure is given as Fig. 3 in ref. 11.

Compound **5** is nonvolatile and does not melt up to the temperature at which its thermal decomposition begins (208°C). Thermal gravimetric analysis of the compound shows that it decomposes in several steps (Fig. 1). Approximately 15% of the initial weight is lost between 208 and 255°C. The next 4% is lost between 255 and 320°C. This total weight loss of 19% corresponds to that expected for the loss of the neutral imidazole ligands. The remaining material has the same composition as compound **1** ($Co(imid)_2$). This is shown by the thermogravimetric data and by the experiment described in the experimental section in which a sample was retrieved from the TA instrument, after heating for 30 min at 325°C, and subjected to elemental analysis. The rest of the thermolysis curve of **5** above 320°C closely parallels that of the authentic sample of **1**.

Magnetic properties

Magnetic susceptibility (χ) and magnetic moment (μ_{eff}) vs. T data over the temperature range 2–150 K in an applied field of 10 000 G are shown in Figs. 2 and 3. Each of the five compounds exhibits a maximum in its χ vs. T plot and a magnetic moment which decreases with decreasing temperature, suggesting the presence of antiferromagnetic exchange. The χ plots for **1**, **4**, and **5**, however, are distinguished from those of **2** and **3** by the presence of a relatively sharp increase in χ as the maximum is reached on cooling. In addition, whereas the magnetic moment plots for **2** and **3** decrease smoothly on decreasing the temperature, the plots for **1**, **4**, and **5** give clear evidence for magnetic anomalies below 20 K. These observations suggested the presence of short-range antiferromagnetic coupling in **2** and **3** and more complex behavior involving the possibility of low-temperature long-range ferromagnetic ordering in **1**, **4**, and **5**. Since saturation effects caused by large applied fields can mask such behavior (14), we examined the magnetic properties of all five compounds at the lower applied field of 500 G. Magnetic susceptibility and moment data at 500 G over the low-temperature region (2–50 K) are shown in Figs. 4 and 5, respectively. While the magnetic properties of **2** and **3** are virtually unchanged at this lower applied field, as expected where only short-range antiferromagnetic interactions are involved, the susceptibility and moment data of **1**, **4**, and **5** are dramatically altered at the lower field below the temperature of the anomaly. Below a critical temperature (T_c = 16, 13, and 15 K for **1**, **4**, and **5**, respectively), the value of the moment increases abruptly to a maximum value (μ_{eff} = 9.4 μ_B at 13 K for **1**, 5.6 μ_B at 10 K for **4,** and 6.0 μ_B at 13 K for **5**) before decreasing again as the temperature decreases to 2 K (Fig. 5). The magnetic transition at T_c is

© 2002 NRC Canada

Fig. 2. Magnetic susceptibility vs. temperature plots at 10 000 G.

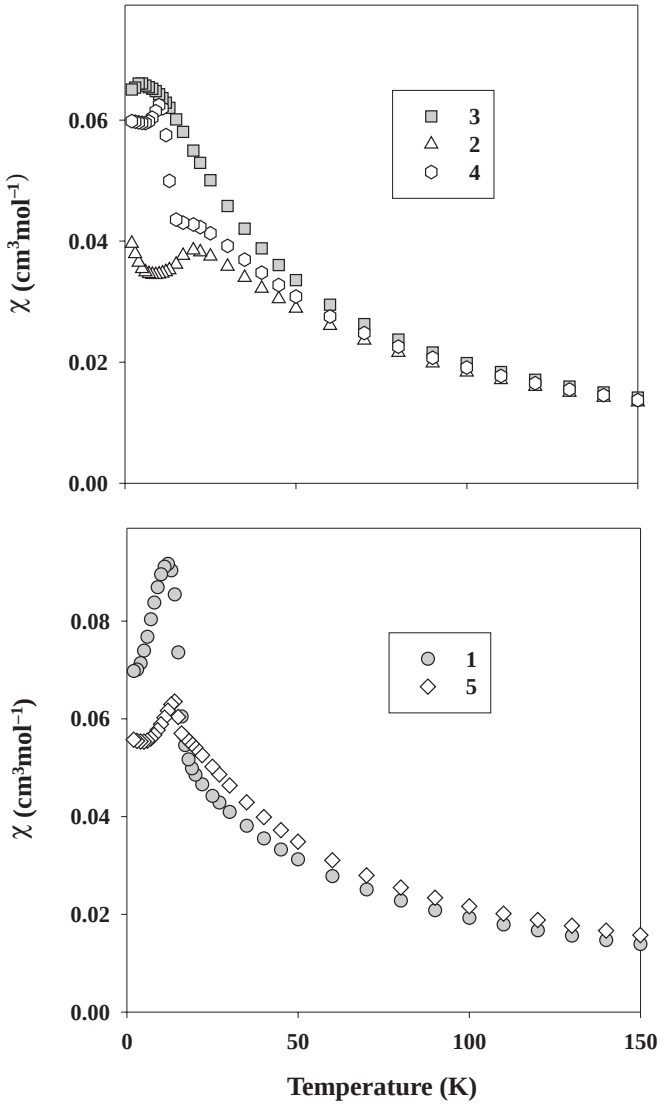

Fig. 3. Magnetic moment vs. temperature plots at 10 000 G.

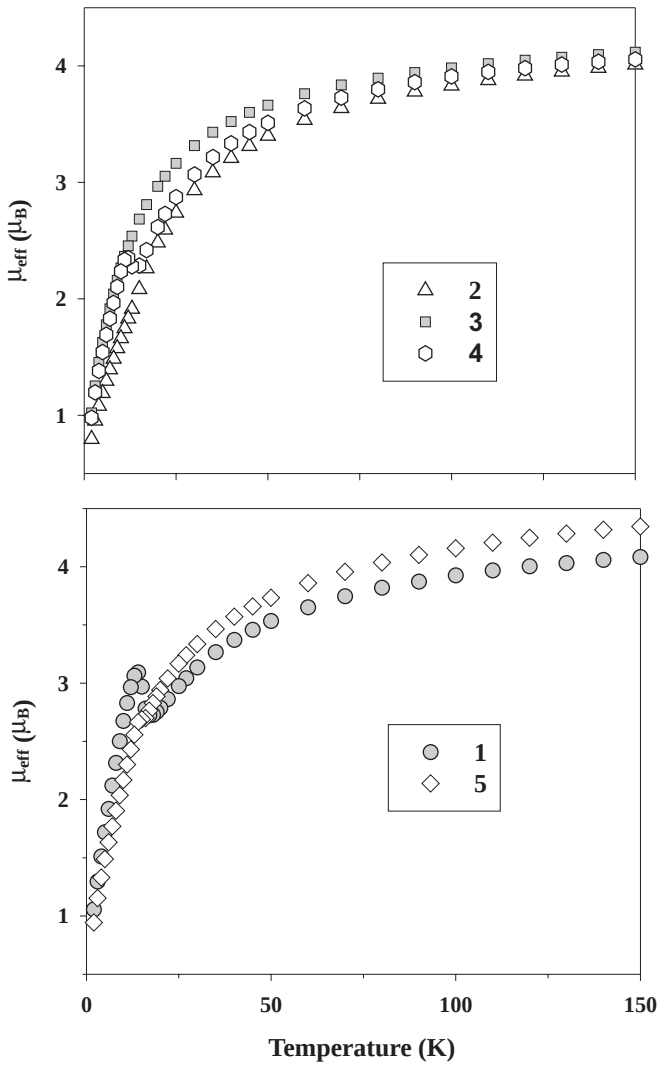

Fig. 4. Magnetic susceptibility vs. temperature plots at 500 G.

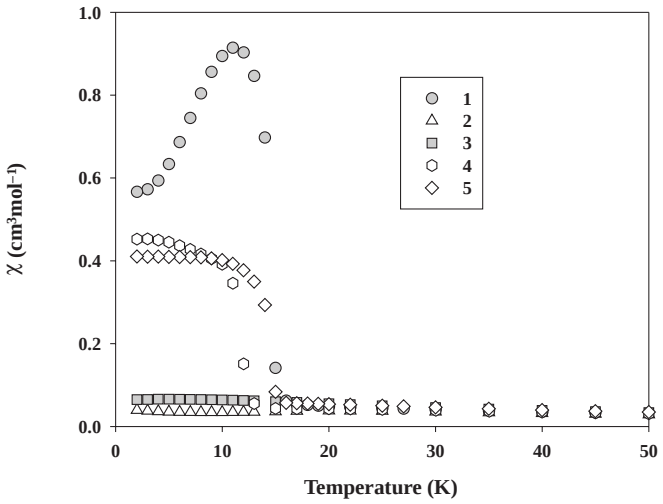

Fig. 5. Magnetic moment vs. temperature plots at 500 G.

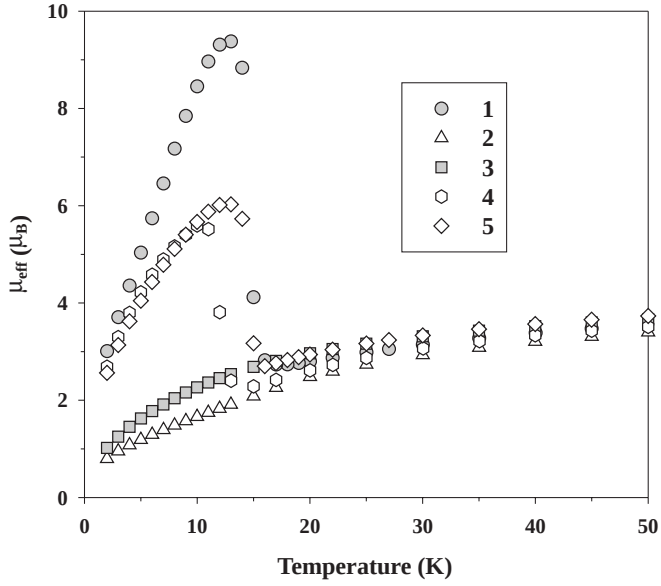

© 2002 NRC Canada

Fig. 6. Magnetization vs. applied field plots at different temperatures.

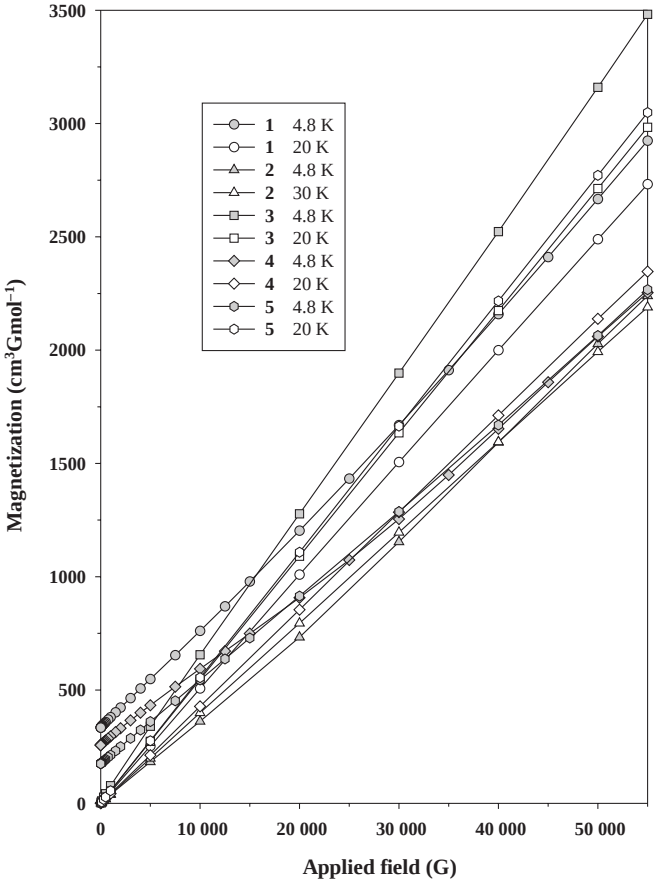

Fig. 7. Field cycled magnetization plots at 4.8 K for **1**, **4**, and **5**.

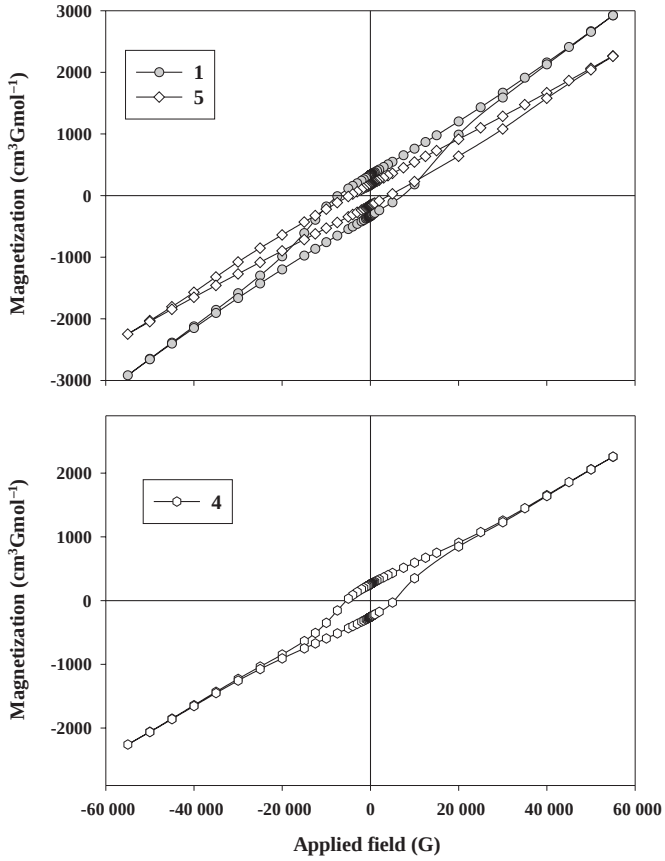

also seen clearly in the χ vs. T plots (Fig. 4) where the abrupt increase in χ below T_c is clearly seen for **1**, **4**, and **5**.

The presence of weak ferromagnetism in **1**, **4**, and **5** is also evident in plots of magnetization vs. applied field (Fig. 6). For these compounds, the plots are linear above T_c and extrapolate to zero magnetization at zero applied field, while below T_c they show extrapolated net magnetization at zero field. That compounds **1**, **4**, and **5** are exhibiting long-range ferromagnetic order and spontaneous magnetization below T_c is further illustrated by hysteresis studies. In these studies, the magnetization was measured at 4.8 K as the applied field was cycled between +55 000 G and –55 000 G. The resulting hysteresis curves are shown in Fig. 7. These plots give remnant magnetizations of 334, 257, and 175 cm^3 G mol^{-1} and coercive fields of 6620, 5280, and 4140 G for **1**, **4**, and **5**, respectively.

The magnetic properties of **1**, **4**, and **5** classify them as molecule-based magnets. In all three compounds, the primary exchange mechanism involves antiferromagnetic coupling between paramagnetic centers and this is combined with a magnetic phase transition to a ferromagnetically ordered state at low temperatures. This behavior is similar to that reported for $[Fe_3(imid)_6(imidH)_2]_x$ (11), $[Fe(2\text{-meimid})_2 \cdot 0.13(FeCp_2)]_x$ (13), and $[Fe(4\text{-abimid})_2]_x$ (14) where, as described in the introduction, it is likely a consequence of spin canting resulting from the noncentrosymmetric M-L-M exchange pathway provided by the single bridging 1,3-diazolate ligands. A spin-canted structure for compounds **1**, **4**, and **5** is supported by the fact that the highest magnetizations measured for these materials were 2924, 2253, and 2267 cm^3 G mol^{-1}, respectively, at 4.8 K and 55 000 G. These values are considerably lower than the theoretical saturation magnetization value of 16 766 cm^3 G mol^{-1} for an $S = 3/2$ system (26).

In contrast to what is observed for **1**, **4**, and **5**, we obtained no evidence for low-temperature ferromagnetic ordering in **2** or **3**. Plots of magnetization vs. applied field extrapolate to zero at zero applied field (Fig. 6) and, moreover, magnetization studies at 4.8 K in which the applied field is cycled between +55 000 and –55 000 G, reveal no evidence of significant hysteresis behavior. Plots of μ_{eff} vs. T decrease smoothly with decreasing temperature (Fig. 3) and χ vs. T plots show only broad maxima at approximately 21 K for **2** and 4 K for **3** (Fig. 2). Paramagnetic impurity in **2** might be the cause of the small increase in magnetic susceptibility at the lowest temperatures studied in the case of this compound (Fig. 2). Unfortunately, we are unable to quantify the magnitude of the antiferromagnetic coupling in **2** and **3** due to the lack of a suitable model for $S = 3/2$ extended 2-D or 3-D lattice systems.

Extensive magnetic data have now been collected on five binary imidazolates of cobalt(II). These are $Co(4\text{-abimid})_2$ (14), and four compounds studied here: $Co(imid)_2$ (**1**), $Co(2\text{-meimid})_2$ (**2**), $Co(4\text{-meimid})_2$ (**3**), and $Co(benzimid)_2$ (**4**). The 4-azabenzimidazolate compound ($Co(4\text{-abimid})_2$) and **1** have similar structures involving single bridging 1,3-

© 2002 NRC Canada

Table 1. Magnetic parameters for some cobalt(II) and iron(II) molecule-based magnets.

Compound[a]	Critical temperature (K)	Coersive field (G)[b]	Remnant magnetization[b] (cm^3 G mol^{-1})	Reference
$Co(4\text{-abimid})_2$	11	100	6	13
$Fe(4\text{-abimid})_2$	21	80	2100	13
$Co(imid)_2$ (**1**)	16	6620	334	This work
$Co(benzimid)_2$ (**4**)	13	5280	257	This work
$Co_3(imid)_6(imidH)_2$ (**5**)	15	4140	175	This work
$Fe_3(imid)_6(imidH)_2$	17	200	2500	11
$Co_2(imid)_4(bipy)$	13	125	1900	10
$Fe_2(imid)_4(bipy)$	11	15	200	10

[a]Abbreviations: imid = imidazolate, benzimid = benzimidazolate, 4-abimid = 4-azabenzimidazolate, bipy = 2,2′-bipyridine.
[b]From hysteresis studies at 4.8 K.

diazolate ligands and extended 3-D connectivities and both exhibit weak ferromagnetism at low temperatures. Although the critical temperatures (T_c) are similar for these two compounds, both the coersive fields and remnant magnetizations differ significantly (Table 1). There is no obvious explanation why $Co(4\text{-abimid})_2$ is such a weak (small remnant magnetization) and soft (small coersive field) magnet compared to **1**, although as suggested previously (14), single-ion effects such as zero-field splitting, which could differ significantly between the two compounds, could be a cause. Interestingly, although evidence suggests the structures of the other three binary imidazolates studied here also involve extended structures, only **4** exhibits low-temperature ferromagnetism with a strength and hardness comparable to that of **1** (Table 1), while **2** and **3** give no evidence for ferromagnetic ordering at low temperatures. It is tempting to suggest that **4** has an extended 3-D molecular network like that of **1** while **2** and **3** have structures of lower dimensionality, perhaps 2-D, in which there is less efficient propagation of the 3-D magnetic ordering. X-ray determined structures of **2**, **3**, and **4,** which would clearly help here, remain an elusive goal of this work.

In summary, regarding binary 1,3-diazolates of cobalt(II), this work shows such materials have extended structures with single bridging diazolate ligands. As in related iron(II) compounds, this bridging arrangement can be expected to lead to canted spin antiferromagnetism; however, whether this translates to long-range ferromagnetic order at low temperatures as seen in $Co(4\text{-abimid})_2$ (**1**) and **4** or only short-range antiferromagnetism as in **2** and **3**, depends on factors not yet fully understood.

With the completion, here, of structural and magnetic studies on compound **5** we now have three pairs of magnetically characterized isostructural iron(II) and cobalt(II) molecule-based magnets: $M(4\text{-abimid})_2$, $M_3(imid)_6(imidH)_2$, and $M_2(imid)_4(bipy)$. Comparison of the magnetic parameters (Table 1) of each of these pairs permits an evaluation of the effect of changing the spin state (S = 3/2 for Co(II) and S = 2 for Fe(II)) on the magnet properties. In general, the coersive fields are larger for cobalt over iron; however, the magnitude of the difference varies significantly from pair to pair and clearly one cannot conclude from this that cobalt analogues will always be harder magnets. Regarding remnant magnetizations, these are significantly smaller for cobalt in the case of the $M(4\text{-abimid})_2$ and $M_3(imid)_6(imidH)_2$ pairs and significantly larger for cobalt in the case of the $M_2(imid)_4(bipy)$ pair. Since, as discussed below, the mechanism by which residual spin arises in the case of the $M_2(imid)_4(bipy)$ pair is likely different from that involved with the other two pairs, this suggests such mechanisms have a significant influence on the magnitude of the remnant magnetization in these systems. It was suggested in the earlier work (11) that the primary exchange pathway in $Fe_3(imid)_6(imidH)_2$ occurs via the chains of tetrahedral metal centers and that spin-canted antiferromagnetism produces the residual spin. The same mechanism is possible for the cobalt analogue **5** studied here. Moreover, spin-canted antiferromagnetism has also been proposed as the only likely source of residual spin for the $M(4\text{-abimid})_2$ pair (14). In contrast, as described previously, in addition to spin-canted antiferromagnetism, a form of ferrimagnetism is likely to contribute significantly to the residual spin in the $M_2(imid)_4(bipy)$ complexes (10). This is a consequence of the fact that the structures of these systems involve alternating octahedral and tetrahedral metal centers. As a consequence of the difference in magnitudes of the moments associated with the different chromophores, antiferromagnetic coupling between neighbors gives rise to a net moment on the lattice. It will be interesting to study more examples of isostructural cobalt and iron pairs to further test these ideas.

Acknowledgements

Funding for the project was provided by the Natural Sciences and Engineering Research Council of Canada (NSERC). P. Borda of this department is thanked for the C, H, N analyses.

References

1. (*a*) S. Trofimenko. Chem. Rev. **72**, 497 (1972); (*b*) S. Trofimenko. Prog. Inorg. Chem. **34**, 115 (1986).
2. P.J. Steele. Coord. Chem. Rev. **106**, 227 (1990).
3. G. La-Monica and G.A. Ardizzoia. Prog. Inorg. Chem. **46**, 151 (1997).
4. M.K. Ehlert, A. Storr, D.A. Summers, and R.C. Thompson. Can. J. Chem. **75**, 491 (1997).
5. (*a*) M.K. Ehlert, S.J. Rettig, A. Storr, R.C. Thompson, and J. Trotter. Can. J. Chem. **67**, 1970 (1989); (*b*) Can. J. Chem. **68**, 1444 (1990); (*c*) Can. J. Chem. **68**, 1494 (1990); (*d*) Can. J. Chem. **69**, 432 (1991); (*e*) Can. J. Chem. **70**, 2161 (1992); (*f*) Can. J. Chem. **71**, 1425 (1993).

© 2002 NRC Canada

6. (*a*) M.K. Ehlert, A. Storr, and R.C. Thompson. Can. J. Chem. **70**, 1121 (1992); (*b*) Can. J. Chem. **71**, 1412 (1993).
7. M.K. Ehlert, S.J. Rettig, A. Storr, R.C. Thompson, F.W.B. Einstein, and R.J. Batchelor. Can. J. Chem. **71**, 331 (1993).
8. M.K. Ehlert, S.J. Rettig, A. Storr, R.C. Thompson, and J. Trotter. Acta. Crystallogr. Sect. C: Cryst. Struct. Commun. **C50**, 1023 (1994).
9. A. Storr, D.A. Summers, and R.C. Thompson. Can. J. Chem. **76**, 1130 (1998).
10. B.O. Patrick, W.M. Reiff, V. Sanchez, A. Storr, and R.C. Thompson. Polyhedron, **20**, 1577 (2001).
11. S.J. Rettig, A. Storr, D.A. Summers, R.C. Thompson, and J. Trotter. J. Am. Chem. Soc. **119**, 8675 (1997).
12. R. Lehnert and F. Seel. Z. Anorg. Allg. Chem. **444**, 91 (1978).
13. S.J. Rettig, A. Storr, D.A. Summers, R.C. Thompson, and J. Trotter. Can. J. Chem. **77**, 425 (1999).
14. S.J. Rettig, V. Sanchez, A. Storr, R.C. Thompson, and J. Trotter. J. Chem. Soc. Dalton Trans. 3931 (2000).
15. O. Kahn. Molecular magnetism. VCH, New York. 1993.
16. O. Kahn. Adv. Inorg. Chem. **9**, 11 (1995).
17. V.M. Sturm, F. Brandl, D. Engel, and W. Hoppe. Acta Crystallogr. Sect. B: Struct. Crystallogr. Cryst. Chem. **B31**, 2369 (1975).
18. (*a*) G.P. Brown and S. Aftergut. J. Polym. Sci. **A2**, 1839 (1964); (*b*) F. Seel and J. Rodrian. J. Organomet. Chem. **16**, 479 (1969); (*c*) A.M. Vecchio-Sadus. Transition Met. Chem. (Dordrecht, Neth.), **20**, 46 (1995).
19. M. Goodgame and F.A. Cotton. J. Am. Chem. Soc. **84**, 1543 (1962).
20. W.J. Eilbeck, F. Holmes, C.E. Taylor, and A.E. Underhill. J. Chem. Soc. A, 128 (1968).
21. S.J. Rettig, V. Sánchez, A. Storr, R.C. Thompson, and J. Trotter. Inorg. Chem. **38**, 5920 (1999).
22. W. Krauss and G. Nolze. PowderCell, version 2.3. Federal Institute for Materials Research and Testing (BAM), Berlin. 1997.
23. J. Laugiert and B. Bochu. MGP-Suite of programs for interpretation of X-Ray experiments. ENSP/Laboratoire des Matériaux et du Génie Physique, BP 46. 38042 Saint Martin d'Hères, France. <http://www.inpg.fr/LMGP and htpp://www.ccp14.ac.uk/tutorial/lmgp/>
24. M.M. Cordes and J.L. Walter. Spectrochim. Acta Part A, **24A**, 1421 (1968).
25. F.A. Cotton and G. Wilkinson. Advanced inorganic chemistry. 4th ed. John Wiley and Sons, New York. 1980. pp. 770–771.
26. R.L. Carlin. Magnetochemistry. Springer–Verlag, Berlin. 1986. pp. 7–9.

© 2002 NRC Canada

The syntheses and NMR studies of hexadeca- and octaneopentoxyphthalocyanines

Namrta Bhardwaj, John Andraos, and Clifford C. Leznoff

Abstract: The syntheses of 3,6-dineopentoxyphthalonitrile and 3,4,5,6-tetraneopentoxyphthalonitrile are described. Condensation of these phthalonitriles with nickel chloride in *N*,*N*-dimethylaminoethanol yielded 1,4,8,11,15,18,22,25-octaneopentoxyphthalocyaninato nickel(II) (**3**) and 1,2,3,4,8,9,10,11,15,16,17,18,22,23,24,25-hexadecaneopentoxyphthalocyaninato nickel(II) (**7**). The ^{1}H NMR spectra of these phthalocyanines and the related 2,3,9,10,16,17,23,24-octaneopentoxyphthalocyaninato nickel(II) (**8**) at temperatures from 205 to 330 K in toluene-d_8 exhibited various degrees of restriction of rotation of the neopentoxy groups. Compound **7** exhibited a single atropisomer at 235 K.

Key words: neopentoxy substituted phthalocyanines, variable temperature NMR, restricted rotation.

Résumé : On décrit les synthèses des 3,6-dinéopentoxy- et 3,4,5,6-tétranéopentoxyphtalonitriles. La condensation de ces phtalonitriles avec du chlorure de nickel dans du *N*,*N*-diméthylaminoéthanol conduit à la formation des 1,4,8,11,15,18,22,25-octanéopentoxyphtalocyaninato nickel(II) (**3**) et 1,2,3,4,8,9,10,11,15,16,17,18,22,23,24,25-hexadécanéopentoxyphtalocyaninato nickel(II) (**7**). Les spectres RMN du ^{1}H de ces phtalocyanines et du 2,3,9,10,16,17,23,24-octanéopentoxyphtalocyaninato nickel(II) (**8**), à des températures de 205 à 330 K, dans le toluène-d_8, mettent en évidence des degrés de restriction à la rotation divers pour les groupes néopentoxy. Le composé **7** se présente sous la forme d'un seul atropisomère, à 235 K.

Mots clés : phtalocyanines substituées par des groupes néopentoxy, RMN à température variable, rotation restreinte.

[Traduit par la Rédaction]

Introduction

Phthalocyanines have attracted a great deal of interest due to their unique properties that include extremely high thermal stability and chemical resistivity (1, 2). Traditionally, phthalocyanines have been used as dyes (1, 2) but recently they have found wide applications (3) in fields including liquid crystals (4, 5), chemical sensors (3, 6, 7), photodynamic therapy of cancer (3, 8), and nonlinear optics (9–11). Applications of peripherally unsubstituted phthalocyanines are limited due their insolubility in common organic solvents and water (10, 11). Phthalocyanines possess an extended π-conjugated electron system which permits π stacking (aggregation) between planar macrocycles, provided the distance between the macrocycles is small (10). Adding substituents to the periphery of the macrocycles increases their solubility since these substituents increase the distance between the stacked phthalocyanines and enable their solvation (10, 12). For many years the neopentoxy group has been used as a bulky substituent to enhance solubility (13–15).

Both 3-neopentoxy- (16) and 4-neopentoxy phthalonitriles (13) were available, but these mononeopentoxy phthalonitriles gave phthalocyanines as mixtures of regioisomers (13, 16). Unfortunately, for many applications, it is preferable to have both soluble and symmetric phthalocyanines. With this idea in mind, we set out to synthesize symmetrical polyneopentoxyphthaloniriles, for condensation to very soluble symmetrical multineopentoxy-substituted phthalocyanines. In the course of this work we noticed considerable restricted rotations of the neopentoxy substitutuents on the phthalocyanines as shown by NMR spectroscopy in temperature coalescence experiments.

Received 5 June 2001. Published on the NRC Research Press Web site at http://canjchem.nrc.ca on 7 February 2002.

N. Bhardwaj, J. Andraos, and C.C. Leznoff.[1] Department of Chemistry, York University, Toronto, ON M3J 1P3, Canada.

[1]Corresponding author (telephone: (416) 736-2100 ext. 33 838; fax: (416) 736-5936; e-mail: leznoff@yorku.ca).

Results and discussions

Synthesis

Treatment of 2,3-dicyano-1,4-hydroquinone (**1**) with sodium methoxide in methanol at room temperature provided the disodium salt of **1**. This salt reacted with neopentyl tosylate in hexamethylphosphoramide (HMPA) at 110°C for 4 days to give 3,6-dineopentoxyphthalonitrile (**2**) in 62% yield. Condensation (17) of **2** with $NiCl_2$ in 2-*N*,*N*-dimethylaminoethanol (DMAE) at reflux (134°C) gave the symmetrical 1,4,8,11,15,18,22,25-octaneopentoxyphthalocyaninato nickel(II) (**3**) in 22% yield (Scheme 1).

Using a different strategy (11) for the preparation of substituted phthalonitriles, commercially available 3,4,5,6-tetrafluorophthalonitrile (**4**) reacted with excess neopentyl alcohol in *N*,*N*-dimethylformamide (DMF) at 100°C in the presence of potassium carbonate to give 3,4,5,6-tetraneopentoxyphthalonitrile (**5**) in 65% yield. We recently described the preparation of the only other symmetrical neopentoxy-substituted phthalonitrile, namely, 4,5-dineopentoxyphthalonitrile (**6**) (18). Condensation of **5** and **6** as

 DOI: 10.1139/V02-002 © 2002 NRC Canada

Scheme 1.

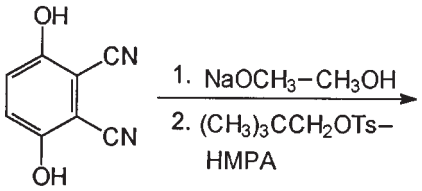

1

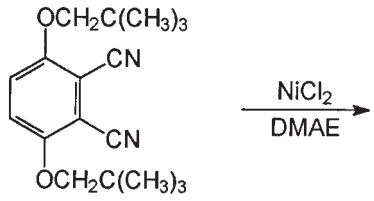

2

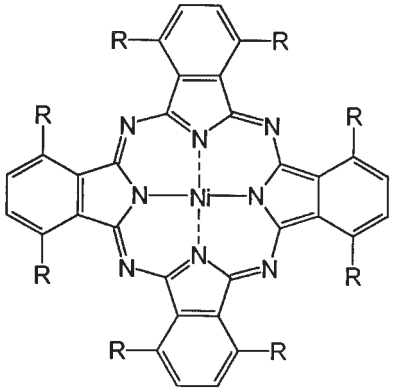

3 R = $OCH_2C(CH_3)_3$

above gave, respectively, the new 1,2,3,4,8,9,10,11,15,16,-17,18,22,23,24,25-hexadecaneopentoxyphthalocyaninato nickel(II) (**7**) in 15% yield and the previously reported (18) 2,3,9,10,16,17,23,24-octaneopentoxyphthalocyaninato nickel(II) (**8**) (Scheme 2). Phthalocyanines **3**, **7**, and **8** were highly soluble in cyclohexane, benzene, toluene, tetrahydrofuran, and chloroform. The FAB and Maldi mass spectra of **3**, **7**, and **8** (18) all gave parent ion clusters. Comparison of the UV–vis spectra of **3**, **7**, and **8** (18) show the expected red-shifts in **3** and **7** due to the alkoxy substituents at the 1,4-positions. Thus, the λ_{max} of the Q (0.0) band of **3** at 748 nm, **7** at 758 nm, and **8** at 672 nm is consistent with other studies, except that the λ_{max} of **7** at 758 nm is over 13 nm red-shifted compared to another less-hindered, branched hexadecahexyloxy- and hexadeca(2-ethyl)hexyloxy-substituted phthalocyaninato nickel (11). Highly hindered substituents at the 1,4 positions of **3** and even more so of **7** obviously enhances the red-shift of the Q band with the phthalocyanine (Pc) nickel **7** representing one of the most red-shifted alkoxy-substituted Pc nickel known. Although

Scheme 2.

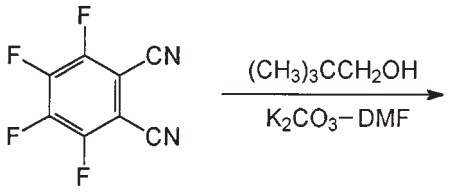

4

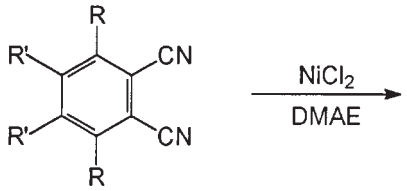

5 R = R' = $OCH_2C(CH_3)_3$

6 R = H, R' = $OCH_2C(CH_3)_3$

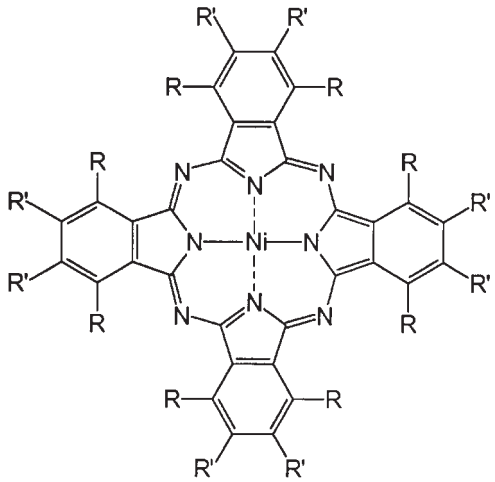

7 R = R' = $OCH_2C(CH_3)_3$

8 R = H, R' = $OCH_2C(CH_3)_3$

metal-free **8** had been made (18), some attempts to make metal-free **3** and **7** were unsuccessful.

NMR studies

Examination of the NMR spectra of the two octaneopentoxyphthalocyanines **3** and **8** at room temperature in benzene-d_6 exhibited the expected three singlets for each compound: 7.40, 4.39, and 1.17 ppm for **3** representing the aromatic, alkoxy, and *tert*-butyl protons, and similarly, absorptions at 8.93, 3.88, and 1.26 ppm for **8**. In the NMR spectrum at room temperature (293 K) of the hexadecaneopentoxyphthalocyanine **7**, however, no aromatic protons were present and one would expect two different alkoxy and

© 2002 NRC Canada

tert-butyl absorptions representing the two different positions of the neopentoxy groups. In fact, two different peaks at 1.39 (9 H) and 1.22 ppm (9 H) for the two kinds of methyl signals were apparent but only a single peak at 4.55 ppm (2 H) corresponding to one kind of OCH_2 group could be accounted for. Though one alkoxy group was missing, a faint bulge in the baseline at ~4 to 5 ppm suggested that restricted rotation of the neopentoxy groups was the likely reason for its absence. Thus, **3**, **7**, and **8** were all subjected to temperature-dependent NMR studies to examine this phenomenon, well-known in other related systems including porphyrins (19), neopentylbenzenes (20–22), neopentylnaphthalenes (23), but to the best of our knowledge not phthalocyanines. Table 1 summarizes the relevant thermokinetic parameters obtained from standard lineshape analyses (24–26) for the three phthalocyanines reported in this work.

Pc7

Figure 1 shows the spectral changes observed in the OCH_2 region from 235 to 355 K in toluene-d_8 solvent (27). The spectrum of **7** at room temperature (293 K) exhibited two different *tert*-butyl signals at 1.37 and 1.22 ppm as expected, but only a single OCH_2 peak at 4.57 ppm. Increasing the temperature of the sample during the NMR experiment resulted in the appearance of a new singlet at 4.82 ppm which was still not as sharp as the other OCH_2 peak, now at 4.49 ppm, even at 355 K. In attempts to freeze out rotations of **7**, NMR spectra were recorded at lower temperatures. At 235 K, one OCH_2 signal showed a typical AB splitting pattern giving a unique chemical shift centered at 4.61 ppm, presumably for the 2,3,9,10,16,17,23,24-neopentoxy-OCH_2 group of **7**. The 1,4,8,11,15,18,22,25-neopentoxy-OCH_2 groups showed what at first may be regarded as two widely separated doublets at 6.05 and 3.88 ppm, respectively. Actually, this is a second AB quartet centered at 5.03 ppm. Lineshape analyses of both OCH_2 signals according to a two-site equal population coupled exchange model (24–26) corresponding to two pairs of diastereotopic protons confirms the steric demands imposed by the neopentoxy groups. Nearly identical results were obtained for each OCH_2 group: an enthalpy of activation of about 10 kcal mol^{-1} and a negative valued entropy of activation of about –10 cal K^{-1} mol^{-1} that contribute to a free energy of activation of about 13 kcal mol^{-1} at 298 K. These findings give support for correlated motions in the neopentoxy groups and suggest that all of them are relatively fixed on the NMR time scale at 235 K and **7** occurs as a single atropisomer at 235 K probably with the 16 neopentoxy groups in an alternating configuration as shown in Fig. 2. Another hexadeca substituted Pc was shown to exhibit a non-planar saddle shape in the solid state (28).

Pc3

Figure 3 shows the spectral changes observed in the OCH_2 region from 225 to 300 K in toluene-d_8 solvent. Superimposed on these spectral changes in this region is a curious phenomenon involving the sudden appearance of an anomalous peak at 5.77 ppm at 265 K which becomes prominent at 255 K and disappears by 235 K. We believe this to be water as the total integration of all water peaks remains constant and a temperature-dependent NMR study of the blank pure toluene-d_8 solvent also produced this peak over the same temperature range. A temperature-dependence study of the HOD peak in toluene-d_8 and other solvents has appeared but no mention was made of the sudden appearance of a new HOD absorption in a narrow temperature range (27). A sharp singlet for the OCH_2 peak at 4.38 ppm at a temperature of 310 K remained sharp until 225 K when significant broadening occurred. By 205 K the singlet split into two separate peaks, but at this temperature the two protons still did not split each other as would be expected for diastereotopic protons. The series of spectra in this region were subjected to lineshape analyses according to an equal population uncoupled two-site exchange model (24–26). The resulting thermokinetic parameters were as follows: $\Delta H^{\ddagger}$ = 15.6 ± 0.7 kcal mol^{-1}, $\Delta S^{\ddagger}$ = 25.6 ± 3.5 cal K^{-1} mol^{-1}, and $\Delta G^{\ddagger}_{298}$ = 8.0 ± 0.3 kcal mol^{-1}. By contrast no formal coalescence behaviour was observed in the aromatic and *tert*-butyl regions of the spectrum over the same temperature range. The aromatic peak shifts slightly from 7.37 to 7.17 ppm while the *tert*-butyl protons shift negligibly from 1.21 to 1.23 ppm. However, concomitant with the splitting of the OCH_2 signal as the temperature was lowered, line broadening was also observed in the *tert*-butyl signal suggesting that coalescence phenomena may be observable in this region at much lower temperatures than examined here.

Results for this phthalocyanine indicate that different molecular motions are occurring for **3** than for the sterically congested **7**. The estimated free energy barrier in **3** is about 5 kcal mol^{-1} lower than for **7** (see Table 1). The large enthalpy of activation is offset by a large positive entropy of activation and is consistent with higher degrees of freedom for motion of the neopentoxy groups in **3** than in **7**. In **7** it is unlikely that rotation about the C(Ar)—O or O—CH_2 bonds is facilitated since this will cause the *tert*-butyl groups to interfere with one another. It is known from previous dynamic NMR studies of neopentylaromatics that energy barriers for rotation about C(Ar)—CH_2 bonds are generally at least 5 kcal mol^{-1} higher than about CH_2—$C(CH_3)_3$ bonds (20–23). As noted above it is expected that the hydrogens of the OCH_2 should be diastereotopic as in each of the corresponding groups in **7**. However, resolution was not possible since an estimate of T_2^{-1} for both peaks in **3** at 225 K was nine times larger than the expected value of the coupling constant (J) of 10 Hz as observed in **7**. Reevaluation of the lineshapes for the OCH_2 region including a coupling constant contribution of 10 Hz gave identical thermokinetic parameters.

Pc8

The ^{1}H NMR spectrum of **8** shows the most complicated pattern of the three phthalocyanines examined. Figs. 4*a*–*c* show the spectral changes in the aromatic, OCH_2, and *tert*-butyl regions from 225 to 300 K in toluene-d_8 solvent. At room temperature, three singlets at 8.95, 3.85, and 1.28 ppm for the aromatic, OCH_2, and *tert*-butyl groups, respectively, are observed. At 260 K significant broadening occurs in all peaks to the point where they almost disappear into the baseline. At 225 K two distinct aromatic peaks of unequal intensity are apparent at 9.31 and 8.62 ppm; similarly, two distinct *tert*-butyl peaks are observed at 1.39 and 1.25 ppm.

© 2002 NRC Canada

Table 1. Summary of thermokinetic parameters obtained from lineshape analyses performed on various regions of ^{1}H NMR spectra for **3**, **7**, and **8**.

Pc	$\Delta H^{\ddagger}$ (kcal mol^{-1})	$\Delta S^{\ddagger}$ (cal K^{-1} mol^{-1})	$\Delta G^{\ddagger}_{298}$ (kcal mol^{-1})	k_c (S^{-1})	T_c (K)
OCH_2 region					
3[a]	15.6 ± 0.7	25.6 ± 3.5	8.0 ± 1.3	418	219
7[b] (5.03 ppm)	10.1 ± 0.4	–9.5 ± 1.5	12.9 ± 0.6	1790	288
7[b] (4.61 ppm)	10.0 ± 0.4	–11.1 ± 1.4	13.3 ± 0.6	146	263
8[c]	13.8 ± 0.5 (A)	6.8 ± 2.1 (A)	11.8 ± 0.5 (A)	151 (A)	251
	13.8 ± 0.5 (B)	7.3 ± 2.1 (B)	11.6 ± 0.5 (B)	192 (B)	
Aromatic region					
8[c]	11.3 ± 0.4 (A)	–2.8 ± 1.6 (A)	12.1 ± 0.4 (A)	384 (A)	259
	11.3 ± 0.4 (B)	–2.3 ± 1.6 (B)	12.0 ± 0.4 (B)	489 (B)	
***tert*-Butyl region**					
8[c]	13.4 ± 0.4 (A)	6.2 ± 1.6 (A)	11.6 ± 0.4 (A)	93 (A)	242
	13.4 ± 0.4 (B)	5.9 ± 1.6 (B)	11.6 ± 0.4 (B)	73 (B)	

[a]Equal populations, J = 0 Hz.
[b]Equal populations, J = 10 Hz.
[c]Unequal populations (p_A = 0.56, p_B = 0.44), J = 0 Hz.

Fig. 1. ^{1}H NMR spectrum of **7** in toluene-d_8 showing spectral changes in the OCH_2 region from 235 to 355 K.

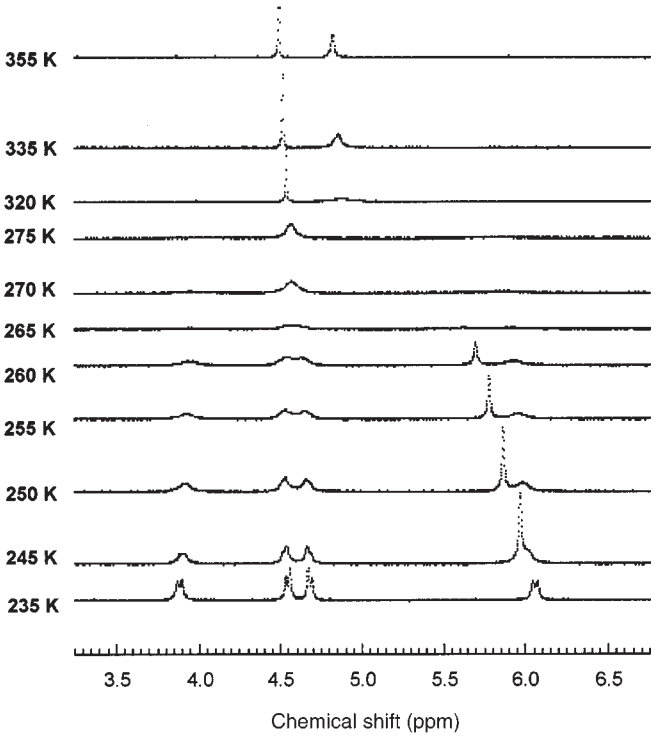

Fig. 2. The suggested atropisomer for **7**.

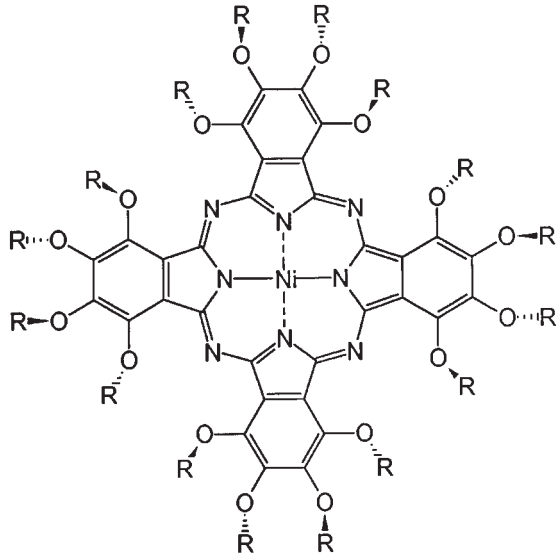

In the OCH_2 region, the singlet at 3.85 ppm becomes an asymmetric triplet as the temperature is lowered. Lineshape analyses according to an unequal population two-site exchange model (26) resulted in a population distribution of p_A = 0.56 and p_B = 0.44 and estimates of free energy barriers of about 12 kcal mol^{-1} for both aromatic and *tert*-butyl regions of the spectrum. These barriers are consistent with those found for **7** as would be expected for interaction between neopentoxy groups ortho to one another. Simulation of the asymmetric triplet for the OCH_2 region is more complex and involves the superposition of *two* unequal population two-site exchange lineshapes. Again, the same population distribution was found as for the aromatic and *tert*-butyl regions with an estimated free energy barrier of about 12 kcal mol^{-1} in each case. The implication of this simulation is that each atropisomer is composed of two different OCH_2 groups: at 230 K a minor conformer has clearly resolvable signals at 3.51 and 4.05 ppm while a major conformer has two very closely spaced signals centered at 3.73 ppm which are not resolvable due to pronounced line broadening. It is expected that the absence of neighbouring neopentoxy groups in the 1, 4, 8, 11, 15, 18, 22, and 25 positions would make these groups more mobile and thus lead to increased broadening of all signals and particularly to complex lineshapes in the OCH_2 region of the spectrum. This is clearly evident when the spectra for **8** are compared with those for **7**. Alternatively, the two distinct aromatic peaks could be due to monomer–dimer equilibria of aggregating phthalocyanines, which is more plausible for the less-hindered **8** than for **3** and **7**. This hypothesis, however, was

© 2002 NRC Canada

Fig. 3. ^{1}H NMR spectrum of **3** in toluene-d_8 showing spectral changes in the OCH_2 region from 200 to 235 K.

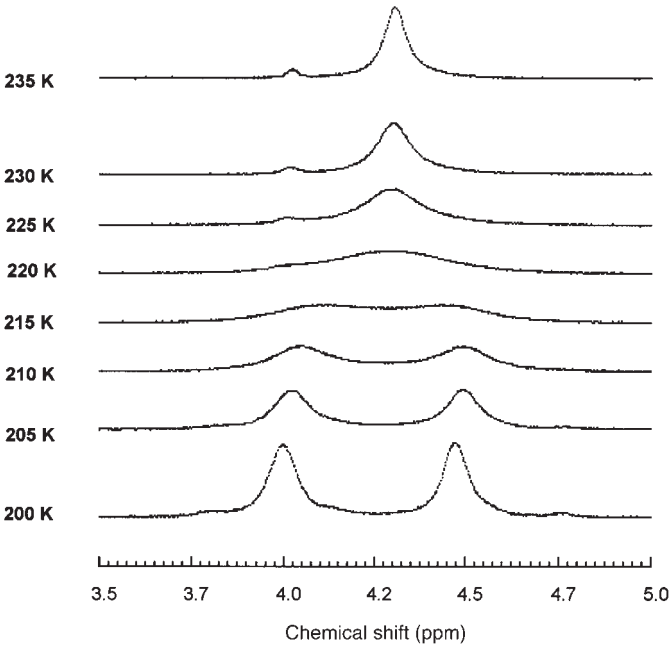

ruled out as ^{1}H NMR spectra of **8** run at 235 K at two different sample concentrations resulted in negligible effects on the absorption of the aromatic protons.

Experimental section

General methods

Inert atmosphere conditions were maintained using Matheson high purity argon. Magnetic stirring methods were utilized during reaction processes. Flash chromatography was performed using silica gel of particle size 40–63 μm. Melting points (mp) were determined using a Kofler hot stage or a Fisher Johns melting point apparatus and are uncorrected.

Nuclear magnetic resonance (NMR) spectroscopy for proton and carbon was performed using a Bruker ARX 400 high-field Fourier transform instrument at room temperature, unless noted otherwise. Chemical shifts are reported in parts per million (δ). The splitting patterns of proton resonances are described as singlets (s), doublets (d), or triplets (t). Coupling constants are reported in Hz for signals that are doublets. Proton-decoupled chemical shifts are reported for the ^{13}C NMR resonances.

Infrared (IR) spectra were recorded on a Unicam Matheson 3000 FT IR spectrometer using KBr discs for solid samples and NaCl discs for liquid samples. Ultraviolet–visible spectra (UV–vis) were recorded on a Hewlett-Packard HP8451A diode array spectrophotometer. Mass spectra (MS) were recorded at 70 eV on a Kratos Profile mass spectrometer in the EI mode for lower molecular weight molecules and in the FAB or MALDI mode for higher molecular weight molecules. Microanalyses were performed by Guelph Chemical Laboratory Ltd., Guelph, Ontario.

Fig. 4. ^{1}H NMR spectrum of **8** in toluene-d_8 showing spectral changes in (*a*) the aromatic region; (*b*) the OCH_2 region; (*c*) the *tert*-butyl region all from 225 to 300 K.

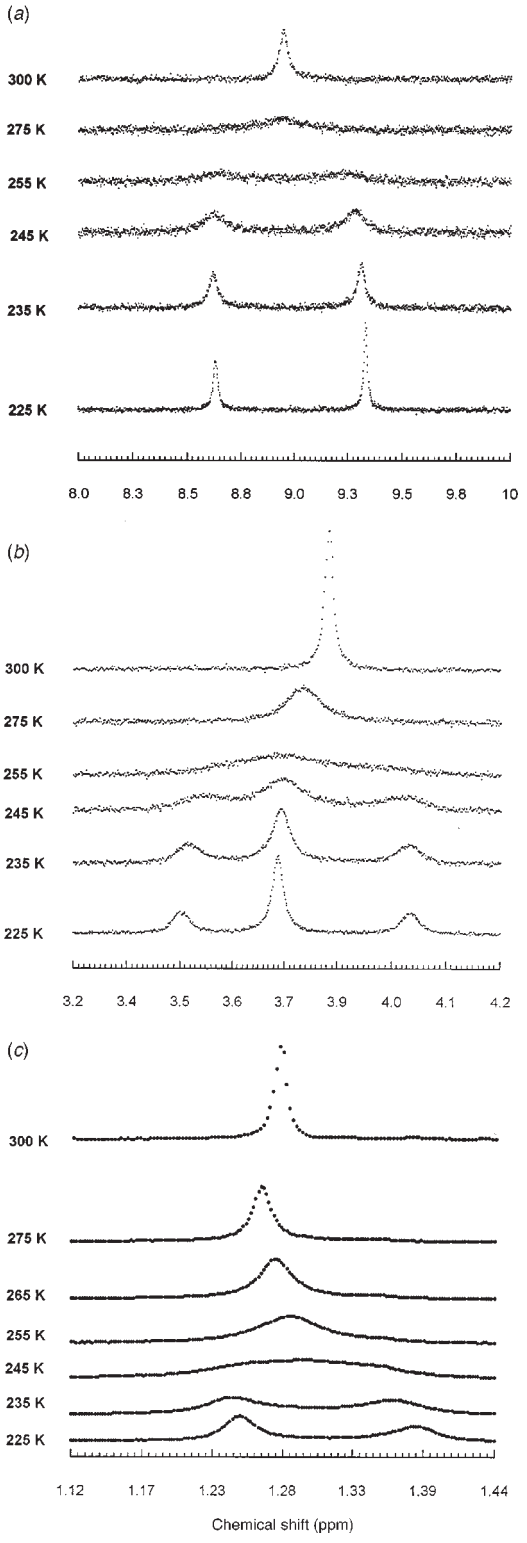

Lineshape analyses: data acquisition

All temperature studies were performed on a Bruker ARX 400 spectrometer using samples prepared in toluene-d_8 solvent. ^{1}H NMR spectra were first recorded at room tempera-

© 2002 NRC Canada

ture and then reacquired at lower or higher temperatures in increments of 5°. Temperatures were read directly from a thermocouple surrounding the probe and are estimated to be within 2 to 3° of the actual temperature of the samples. At each temperature the probe was allowed to equilibrate for about a minute before acquiring data. Test runs at longer equilibration periods (about 10 min) gave spectra identical to those recorded at the above conditions.

Lineshape analyses: data analysis

Digitized spectra were first converted into readable format using [Spec Viewer Free Version] (Advance Chemistry Development). Relevant regions of the spectra were then subjected to lineshape analyses according to expressions given by Sandström (24), Sutherland (25), and Gutowsky and Holm (26) using KaleidaGraph 3.5 (Synergy) software. To account for spectral drift at different temperatures, spectra obtained at higher temperatures were referenced against those recorded at the lowest temperature. Simulated spectra were consistent with two-site exchange systems of either equal or unequal populations. Corresponding estimates of thermokinetic parameters and coalescence temperatures were obtained using standard Eyring expressions given previously (24–26).

3,6-Dineopentoxyphthalonitrile (2)

To 0.151 g (6.56 mmol) of sodium metal dissolved in 5 mL of methanol was added 500 mg (3.13 mmol) of 2,3-dicyanohydroquinone (**1**). This mixture was stirred at room temperature for 2 h. After this time, the methanol was removed under vacuum and to the resulting residue was added 10 mL of HMPA (caution: carcinogen) and 2.27 g (9.38 mmol) of neopentyl tosylate. This mixture was stirred at 110°C for 4 days, cooled to room temperature, and poured into 50 mL of water. The product was extracted using 3 × 50 mL of ether. The combined organic layers were washed with 100 mL of water, followed by 100 mL of brine, and then dried over $MgSO_4$. The ether was removed under vacuum and the crude product was purified by flash silica gel column chromatography using 20% ethyl acetate and 80% hexane as the eluting solvents. The desired product was obtained as a white solid in 62% yield (0.58 g); mp 179–181°C. IR (KBr) (cm^{-1}): 2961, 2229. ^1H NMR ($CDCl_3$) δ: 7.14 (s, 2H), 3.69 (s, 4H), 1.10 (s, 18H). ^{13}C NMR ($CDCl_3$) δ: 155.6, 118.7, 113.0, 105.1, 80.0, 32.2, 26.4. MS *m*/*z* (rel intensity): 300 (M^+, 20), 71 (100). Anal. calcd. for $C_{18}H_{24}N_2O_2$: C 71.97, H 8.05, N 9.33; found: C 72.00, H 8.17, N 9.36.

1,4,8,11,15,18,22,25-Octaneopentoxyphthalocyaninato nickel (3)

A mixture containing 0.300 g (1 mmol) of 1,4-dineopentoxyphthalonitrile (**2**) and 0.0912 g (0.333 mmol) of $NiCl_2$ in 9.9 mL of DMAE was heated to reflux for 48 h. After cooling at room temperature, the reaction mixture was transferred to test tubes. Precipitation of the nickel phthalocyanine was carried out by adding a 90% methanol and 10% water solution. The precipitate was collected by centrifugation and washed twice with methanol. Further purification of the phthalocyanine was carried out by flash silica gel column chromatography using 50% hexane and 50% toluene as the eluting solvents. Final purification involved reprecipitation from toluene–ethanol to give the NiPc as a green solid in 22% yield (69 mg); mp > 300°C. UV–vis λ_{max} (toluene) (log e) (nm): 748 (5.18), 674 (4.58), 444 (4.30), 330 (4.61), 308 (4.66). ^1H NMR (benzene-d_6) δ: 7.40 (s, 1H), 4.39 (s, 2H), 1.17 (s, 9H). FAB-MS *m*/*z*: 1260 (M + 1). Anal. calcd. for $C_{72}H_{96}N_8O_8Ni$: C 68.62, H 7.68, N 8.89; found: C 68.63, H 8.00, N 8.48.

3,4,5,6-Tetraneopentoxyphthalonitrile (5)

To a stirred solution containing 0.50 g (2.5 mmol) of tetrafluorophthalonitrile (**4**) in 15 mL of DMF was added 5.5 g (62.5 mmol) of neopentyl alcohol and 8.6 g (62.5 mmol) of K_2CO_3. The mixture was allowed to stir at 100°C under an argon atmosphere for a period of 24 h. After cooling to room temperature, the reaction mixture was poured onto 50 mL of H_2O and extracted using 3 × 50 mL of ether. The combined organic layers were washed with 100 mL of H_2O followed by 100 mL of brine and then dried over $MgSO_4$. The solvent was removed under vacuum and the crude mixture was purified by flash silica gel column chromatography using toluene as the eluting solvent to give the product in 65% yield (0.76 g); mp 131–133°C. IR (KBr) (cm^{-1}): 2957, 2232. ^1H NMR ($CDCl_3$) δ: 3.81 (s, 2H), 1.10 (s, 4.5H), 1.05 (s, 4.5H). ^{13}C NMR ($CDCl_3$) δ: 153.0, 151.9, 113.3, 104.4, 85.6, 85.2, 32.8, 32.6, 26.7, 26.6. MS *m*/*z* (rel intensity): 472 (M^+, 5), 332 (45), 262 (100). Anal. calcd. for $C_{28}H_{44}N_2O_4$: C 71.15, H 9.38, N 5.93; found: C 71.15, H 9.36, N 6.02.

1,2,3,4,8,9,10,11,15,16,17,18,22,23,24,25-Hexadecaneopentoxyphthalocyaninato nickel (7)

A mixture containing 0.2 g (0.42 mmol) of tetraneopentoxyphthalonitrile (**5**) and 33.5 mg (0.14 mmol) of $NiCl_2$ in 4.2 mL of DMAE was heated to reflux for 48 h. After cooling to room temperature, the reaction mixture was transferred to test tubes. Precipitation of the nickel phthalocyanine was achieved by the addition of water. The precipitate was collected by centrifugation and washed twice with water and once with methanol. The crude phthalocyanine was further purified by flash silica gel column chromatography using 75% hexane and 25% toluene as the eluting solvents. Final purification involved reprecipitation from toluene–ethanol to give the desired NiPc as a green solid in 15% yield (30 mg); mp > 300°C. UV–vis λ_{max} (toluene) (log e) (nm): 758 (5.19), 676 (4.51), 440 (4.25), 386 (4.44), 342 (4.46), 314 (4.69). ^1H NMR (benzene-d_6) δ: 4.55 (s, 2H), 1.39 (s, 9H), 1.22 (s, 9H). FAB-MS *m*/*z*: 1948 (M + 1). Anal. calcd. for $C_{112}H_{176}N_8O_{16}Ni$: C 69.01, H 9.10, N 5.75; found: C 69.02, H 9.29, N 5.51.

2,3,9,10,16,17,23,24-Octaneopentoxyphthalocyaninato nickel (8)

A mixture containing 0.200 g (0.667 mmol) of 1,4-dineopentoxyphthalonitrile and 0.053 g (0.111 mmol) of $NiCl_2$ in

© 2002 NRC Canada

6.6 mL of DMAE was heated to reflux for 48 h. After cooling to room temperature, the reaction mixture was transferred to test tubes. Precipitation of the nickel phthalocyanine was carried out by adding a 90% methanol and 10% water solution. The precipitate was collected by centrifugation and washed twice with methanol. Further purification of the phthalocyanine was carried out by flash silica gel column chromatography using 20% hexane and 80% toluene as the eluting solvents. Final purification of the NiPc involved precipitation using toluene–hexane. The desired NiPc was obtained as a green solid in 28% yield (59 mg): mp > 300°C. UV–vis λ_{max} (toluene) (log e) (nm): 672 (5.17), 640 (4.52), 604 (4.46), 416 (4.37), 336 (4.59), 314 (4.73), 288 (4.78). ^{1}H NMR (benzene-d_6) &: 8.93 (s, 1H), 3.88 (s, 2H), 1.26 (s, 9H). FAB-MS *m*/*z*: 1260 (M + 1). Anal. calcd. for $C_{72}H_{96}N_8O_8Ni$: C 68.62, H 7.68, N 8.89; found: C 69.09, H 8.08, N 8.56.

Conclusion

Two different symmetrical octaneopentoxyphthalocyanines and a hexadecaneopentyoxyphthalocyanine were synthesized by three different routes. All of these neopentoxy-substituted phthalocyanines were highly soluble in organic solvents. The highly hindered hexadecaneopentoxyphthalocyanine (**7**) exhibited a highly red-shifted Q-band at 758 nm. Variable-temperature NMR spectroscopy on an octaneopentoxyphthalocyanine (**3**) and particularly, the hexadecanopentoxyphthalocyanine, demonstrated restricted motion of the neopentoxy groups.

Acknowledgement

We thank the Natural Sciences and Engineering Research Council of Canada (NSERC) for grants in support of this research.

References

1. B.D. Berezin. *In* Coordination compounds of porphyrins and phthalocyanines. John Wiley and Sons, New York. 1981.
2. F.H. Moser and A.L. Thomas. *In* The phthalocyanines. Vols. 1 and 2. CRC, Boca Raton, Florida. 1983.
3. Phthalocyanines: Properties and applications. Vols. 1–4. *Edited by* C.C. Leznoff and A.B.P. Lever. VCH, New York. 1989, 1992, 1993, 1996.
4. C. Piechocki, J. Simon, A. Skoulious, D. Guillon, and P. Weber. J. Am. Chem. Soc. **104**, 5254 (1982).
5. C. Piechocki and J. Simon. Nouv. J. Chim. **9**, 159 (1985).
6. A.W. Snow, W.R. Barger, M. Klusty, H. Wohltjen, and N.L. Jarvis. Langmuir, **2**, 513 (1986).
7. D. Wohrle and M. Kaneko. Yuki Gosei Kagaku Kyokaishi, **45**, 837 (1987).
8. B. Paquette and J.E. van Lier. *In* Photodynamic therapy: Basic principles and clinical aspects. *Edited by* B.W. Henderson and T.J. Dougherty. Marcel Dekker, New York. 1992. p. 145.
9. J.S. Shirk, R.G.S. Pong, S.R. Flom, H. Heckmann, and M. Hanack. J. Phys. Chem. A, **104**, 1438 (2000).
10. M. Hanack and M. Lang. Adv. Mater. (Weinheim, Ger.), **6**, 819 (1994).
11. W. Eberhardt and M. Hanack. Synthesis, 95 (1997).
12. M. Hanack and P. Haisch. Synthesis, 1251 (1995).
13. C.C. Leznoff, S.M. Marcuccio, S. Greenberg, A.B.P. Lever, and K.B. Tomer. Can. J. Chem. **63**, 623 (1985).
14. C.C. Leznoff, P.I. Svirskaya, B. Khouw, R.L. Cerny, P. Seymour, and A.B.P. Lever. J. Org. Chem. **56**, 82 (1991).
15. M. Hu, N. Brasseur, S.Z. Yildiz, J.E. Van Lier, and C.C. Leznoff. J. Med. Chem. **41**, 1789 (1998).
16. C.C. Leznoff and D.M. Drew. Can. J. Chem. **74**, 307 (1996).
17. G. Winter, H. Heckmann, P. Haisch, W. Eberhardt, M. Hanack, L. Luer, H.-J. Egelhaaf, and D. Oelkrug. J. Am. Chem. Soc. **120**, 11 663 (1998).
18. A.Kh. Khanamiryan, N. Bhardwaj, and C.C. Leznoff. J. Porphyr. Phthalocy. **4**, 484 (2000).
19. M. Cornia, C. Valenti, S. Cappacchi, and P. Cozzini. Tetrahedron, **54**, 8091 (1998).
20. J.E. Anderson, H. Pearson, and D.I. Rawson. J. Chem. Soc. Chem. Commun. 95 (1973).
21. B. Nilsson, P. Martinson, K. Olsson, and R.E. Carter. J. Am. Chem. Soc. **96**, 3190 (1974).
22. J.E. Anderson, D.J.D. Barkel, and F.S. Jorgensen. J. Chem. Soc. Perkin. Trans. 2, 199 (1988).
23. J.E. Anderson and D.J.D. Barkel. J. Chem. Soc. Perkin. Trans. 2, 1053 (1984).
24. J. Sandström. Dynamic NMR spectroscopy. Academic Press, London. 1982.
25. I.O. Sutherland. Annu. Rep. NMR Spectrosc. **4**, 71 (1971).
26. H.S. Gutowsky and C.H. Holm. J. Chem. Phys. **25**, 1228 (1956).
27. H.E. Gottlieb, V. Kotlyar, and A. Nudelman. J. Org. Chem. **62**, 7512 (1997).
28. I. Chambrier, M.J. Cook, and P.T. Wood. Chem. Commun. 2133 (2000).

© 2002 NRC Canada

The first observed complex of 11-crown-3 ether. X-ray crystal structure and NMR study of (benzo-11-crown-3)$_2$·LiNCS

G.W. Buchanan, M. Azad, and G.P.A. Yap

Abstract: The title complex crystallizes in the monoclinic $P2_1/c$ space group, with a = 7.7397(8), b = 18.287(2), c = 17.4726(19) Å, β = 94.008(2)°, and Z = 4. The coordination geometry around the lithium cation is pseudooctahedral. The effects of lithium complexation on the ^{1}H and ^{13}C solution NMR spectra are discussed. In the solid-state ^{13}C NMR spectrum at 300 K, very long aliphatic proton spin lattice relaxation times are observed along with broadening of the aliphatic carbon resonances. These results are attributed to the dipolar washout phenomenon, where the presence of a low amplitude motion of the same frequency as the ^{1}H decoupler, leads to less effective removal of the ^{1}H–^{13}C dipolar coupling. At 330 K, there is some sharpening of the aliphatic resonances since there is less interference between the motion and the decoupling frequency.

Key words: crown ether analog, lithium complex.

Résumé : Le complexe mentionné dans le titre cristallise dans le groupe d'espace $P2_1/c$ avec a = 7,7397(8), b = 18,287(2) et c = 17,4726(19) Å, β = 94,008(2)° et Z = 4. La géométrie de coordination autour du cation lithium est pseudooctaédrique. On discute des effets de la complexation avec le lithium sur les spectres RMN du ^{1}H et du ^{13}C. En RMN du ^{13}C à l'état solide à 300 K, on observe que les temps de relaxation spin réseau des protons aliphatiques sont très longs et que les résonances des carbones aliphatiques sont élargies. Ces résultats sont attribués au phénomène d'épuration dipolaire dans lequel la présence d'un mouvement de faible amplitude de fréquence égale à celle du découpleur ^{1}H conduit à une élimination moins efficace du couplage dipolaire ^{1}H–^{13}C. À 330 K, les résonances aliphatiques deviennent plus précises parce qu'il y a moins d'interférence entre le mouvement et la fréquence de découplage.

Mots clés : analogue d'éther couronne, complexe de lithium.

[Traduit par la Rédaction]

Introduction

Crown ethers are important and useful compounds, since they complex the salts of the alkali and alkaline earth metals, thereby profoundly altering their properties (1, 2). The Li^+ ion is of immense physiological importance, since lithium carbonate is an effective treatment for the symptoms of bipolar affected disorder (BAD). Although the cavity size of 14-crown-4 ether is ideal for Li^+ complexation, a number of smaller macrocyclic crown systems have also been found to form stable 1:1 complexes with this cation (3–7).

In these laboratories we have embarked on an extensive program to examine the structures and complexation features of novel crown ether anologs. To date, instances of unusual ligand geometries have been found for dibenzo-20-crown-6 ether (8) and bis(*p*-phenylene)-31-crown-9 (9) while a unique complexation mode has been elucidated for the 2:2 sodium iodide complex of dibenzo-15-crown-4 (10).

Recently, we found that Li^+ can be complexed by a 10-crown-3 ether via a 2:1 sandwich-type system (11) and the X-ray crystal structure of this (benzo-10-crown-3)$_2$·$LiClO_4$ complex indicates an interesting quasioctahedral geometry at lithium.

With respect to 11-crown-3 ethers, one would expect that the increased flexibility in the macrocycle might lead to different complexation features than are present in 10-crown-3. There is, however, no information in the literature, other than our recent determination of the X-ray crystal structure of tris(11-crown-3)triphenylene (12). Since benzo-11-crown-3 ether (**1**) is an oil, no X-ray crystallographic studies have been performed. In the present work, we present the results of an X-ray crystallographic study of (benzo-11-crown-3)$_2$·LiNCS (**2**). The complementarity of the X-ray crystallographic method with solid-state ^{13}C NMR spectroscopy is illustrated and the effects of Li^+ ion complexation on the solution ^{1}H and ^{13}C NMR properties are discussed.

Received 7 June 2001. Published on the NRC Research Press Web site at http://canjchem.nrc.ca on 7 February 2002.

G.W. Buchanan,[1] M. Azad, and G.P.A. Yap. Ottawa-Carleton Chemistry Institute, Department of Chemistry, Carleton University, 1125 Colonel By Drive, Ottawa, ON K1S 5B6, Canada.

[1]Corresponding author (telephone: (613) 520-3841; fax: (613) 520-3749; e-mail: gerald_buchanan@carleton.ca).

 DOI: 10.1139/V01-204 © 2002 NRC Canada

Fig. 1. ORTEP for **2a.**

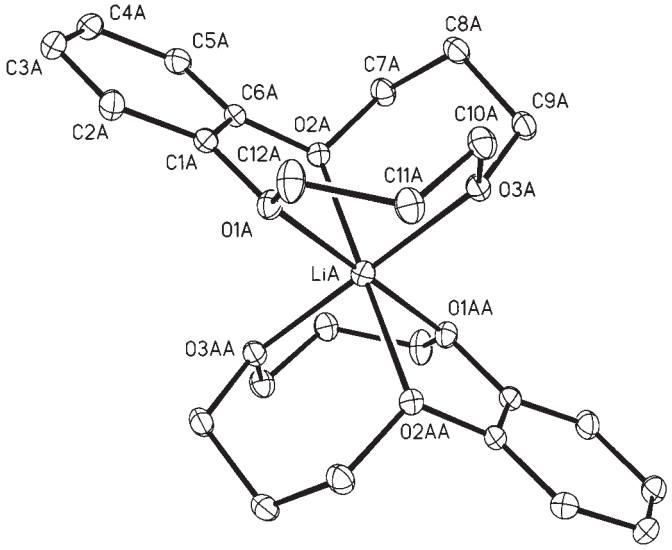

Fig. 2. ORTEP for **2b**.

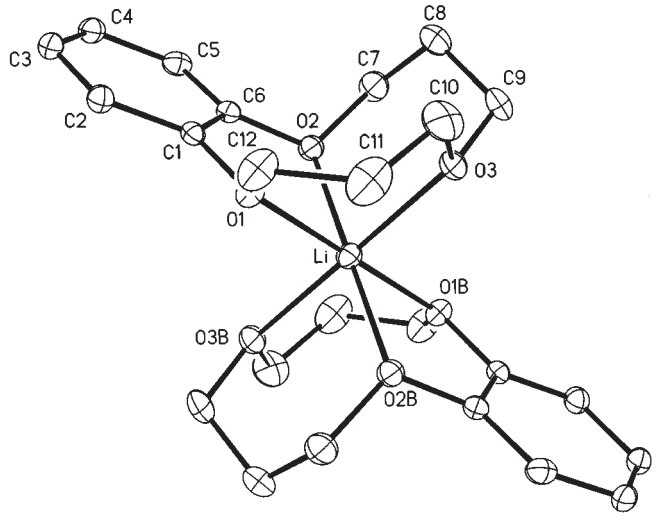

A comparison of the 11-membered ring conformation in the complex is made with that of the free benzo-11-crown-3 in the gas phase as determined via the HyperChem program.

Results and discussion

The ORTEP diagrams for the two crystallographically inequivalent complexes **2** are illustrated in Figs. 1 and 2. The ^{13}C CPMAS NMR spectra recorded at 300 and 330 K are in Fig. 3 and Fig. 4, respectively. Atomic bond lengths are in Table 1, with bond angles collected in Table 2. Torsion angle data are in Table 3 and crystallographic data are in Table 4. Table 5 contains the ^{13}C chemical shifts in solution and in the solid phase. Solution ^{1}H NMR data for **1** and **2** are presented in Table 6.

X-ray crystal structure

The average O-Li-O bond angle involving the six ethereal oxygens is 84.56° with a standard deviation from this mean of 3.97°. This geometry is thus close to the ideal geometry expected for octahedral coordination. The avg Li—O bond length (for the ethereal oxygens) of 2.07 Å is slightly (0.03 Å) shorter than that found in the (benzo-10-crown-3)$_2$·$LiClO_4$ complex (11).

Examination of the torsion angles for the two 11-membered rings of the complex (i.e., **2a** involving O1A, O2A, and O3A vs. **2b**, involving O1, O2, and O3) indicates that the geometries of the two rings are identical. However, the coordination geometry and bond distances from the lithium cation to the ethereal oxygens differs slightly, leading to the two "inequivalent" complexes **2a** and **2b** in the X-ray crystal structure. These differences are small, but larger than the experimental uncertainty and probably arise from crystal packing. For example the LiA—O1A, LiA—O2A, and LiA—O3A bond lengths are 2.059(2), 2.084(2), and 2.091(2) Å, respectively, while the Li—O1, Li—O2, and Li—O3 distances are 2.043(2), 2.039(2), and 2.132(2) Å, respectively.

The two complexes have nearly equivalent ^{13}C solid-state NMR spectra (Figs. 3 and 4), however, there is one additional resonance in the aromatic region of the spectrum between 121 and 127 ppm over that expected from two identical complexes at 300 K and two extra peaks at 330 K.

With respect to the geometry of the 11-membered rings, since 11-crown-3 ether is an oil, there is no X-ray crystal structure available. It is however, of interest to examine the preferred (calculated via HyperChem) gas-phase geometry of benzo-11-crown-3, **1** and compare it with the geometry in the LiNCS complex. These data are presented below. Arbitrarily data for **2b** are used.

Network	Torsion angle in **1** (°)[a]	Torsion angle in **2b** (°)
C1-O1-C12-C11	–148.7	–138.4
C10-C11-C12-O1	98.7	54.7
O3-C10-C11-C12	–78.4	–74.7
C9-O3-C10-C11	161.1	167.6
C10-O3-C9-C8	–74.3	–85.6
C7-C8-C9-O3	–70.6	–70.5
O2-C7-C8-C9	100.6	62.7
C6-O2-C7-C8	–166.6	88.3
C7-O2-C6-C1	109.5	–130.5
O2-C6-C1-O1	–10.9	0.3
C12-O1-C1-C6	61.4	139.3

[a]For gas phase molecules, using the HyperChem program.

From examination of molecular models, it is clear that the conformational changes which occur upon complexation accompany the reorientation of the oxygen lone pairs on O1, O2, and O3 so that one pair of electrons on each oxygen becomes available for pseudooctahedral coordination to the lithium cation.

NMR studies

The signal assignments in the solution ^{1}H NMR spectrum were made using a combination of COSY and NOSY experiments. For example, for **1**, there is a NOESY correlation between the aromatic protons and the aliphatic peak at 4.119.

© 2002 NRC Canada

Fig. 3. (*a*) 50.3 MHz ^{13}C CP MAS NMR spectrum of **2** at 300 K. (*b*) Dipolar dephased 50.3 MHz ^{13}C CP MAS NMR spectrum of **2** at 300 K.

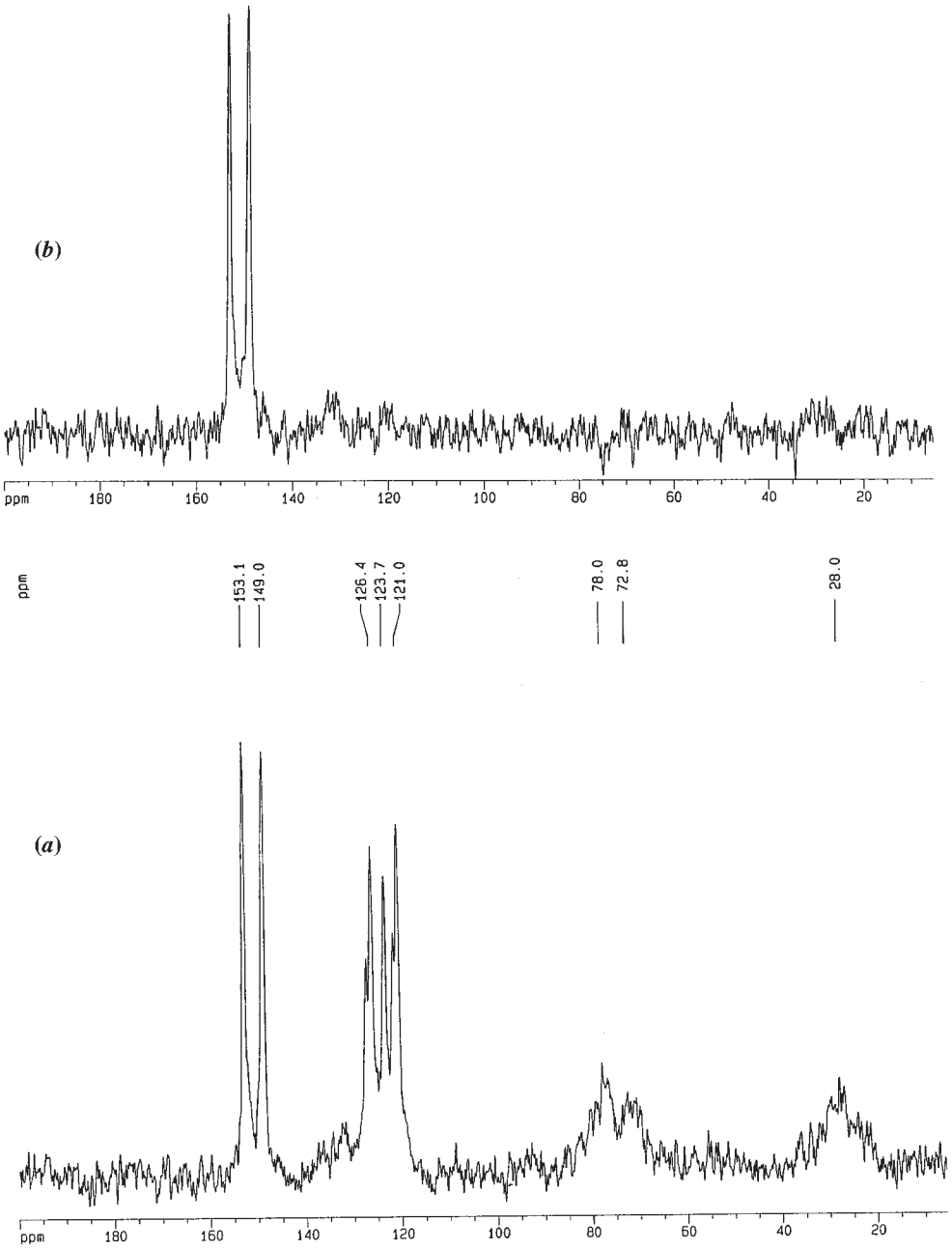

Hence, the later resonance is assigned to the C7,C12 protons since these are more spatially proximate to the aromatic ring. With these assignments in hand, the carbons directly bonded to protons were identified by the HMQC experiment. Similar methods were employed to assign the solution spectra of **2**.

With respect to the effects of Li cation complexation on the ^{1}H and ^{13}C NMR chemical shifts, there is a general trend of deshielding in both spectra. This is consistent with a loss of electron density around the ethereal oxygens due to complexation.

The solid-state ^{13}C CP MAS spectrum of **2** shows additional multiplicity over that obtained in solution in accord with expectations based on the X-ray crystal structure. As mentioned above, there are seven aromatic carbons observed in the spectrum at 300 K, vs. six expected if there were a single symmetrical complex present in the solid state. Distinction between the quaternary carbon resonances for C1 and C6 was made on the basis of the respective C—O bond lengths. Since the C1—O1 bond is shorter (1.372(3) Å) than the C6—O2 bond (1.381(3) Å), one can conclude that there is more double bond character in the C1—O1 bond, which would be expected to lead to a deshielding effect (13). Hence, the resonance at 153.1 ppm is tentatively assigned to C1, while the C2 resonance is deemed to be at 149.0 ppm.

The appearance of the aliphatic carbon resonances as broad lines at 300 K appears to be due to the "dipolar wash-

© 2002 NRC Canada

Fig. 4. 50.3 MHz ^{13}C CP MAS NMR spectrum of **2** at 330 K.

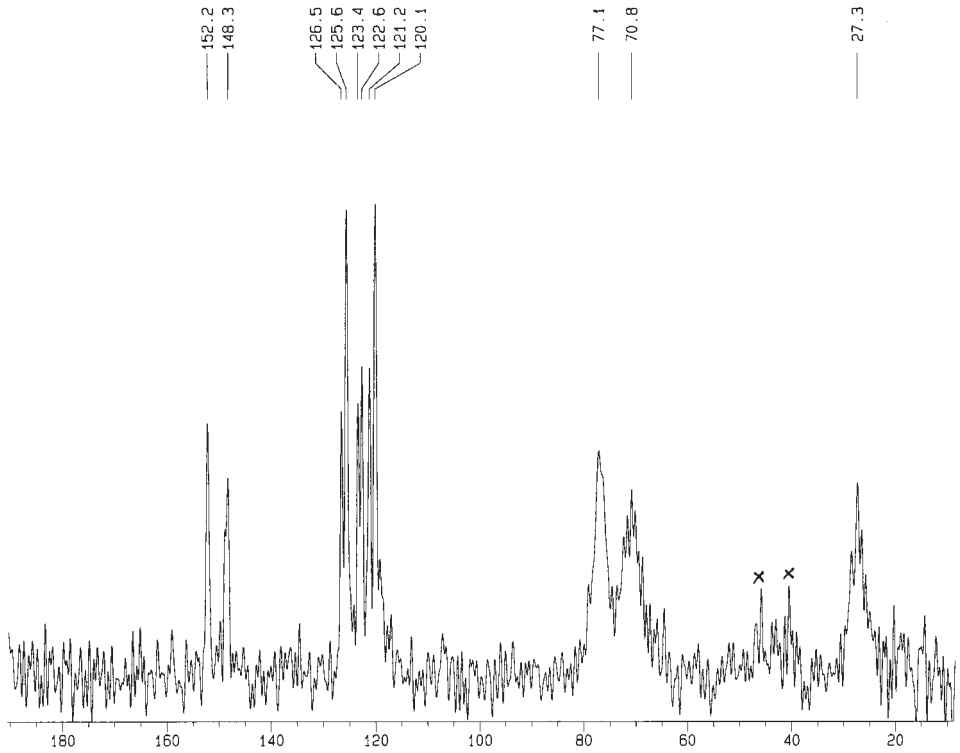

Table 1. Selected atomic bond lengths (Å).

Complex **2a**				Complex **2b**	
O1A—LiA	2.059(2)			O1—Li	2.043(2)
O2A—LiA	2.084(2)			O2—Li	2.039(2)
O3A—LiA	2.091(2)			O3—Li	2.132(2)
O1A—C1A	1.378(3)			O1—C1	1.372(3)
O1A—C12A	1.454(3)			O1—C12	1.449(3)
O2A—C6A	1.385(3)			O2—C6	1.381(3)
O2A—C7A	1.451(3)			O2—C7	1.453(3)
O3A—C9A	1.440(3)			O3—C9	1.428(4)
O3A—C10A	1.427(3)			O3—C10	1.437(4)
C1A—C6A	1.386(3)			C1—C6	1.399(3)
C7A—C8A	1.520(3)			C7—C8	1.513(4)
C8A—C9A	1.525(3)			C8—C9	1.490(5)
C10A—C11A	1.507(3)			C10—C11	1.489(5)
C11A—C12A	1.503(3)			C11—C12	1.484(5)
		S1—C13	1.670(4)		
		N1—C13	1.060(6)		

out" phenomenon first described about 20 years ago (14) and more recently observed in several 18-crown-6 complexes (15, 16). Apparently, the motion of the C-H vectors of the aliphatic carbons in the solid state is occuring on approximately the same timescale (200 MHz) as the ^1H decoupling rf field. Hence, interference is set up between the motionally generated rf field and the ^1H decoupler. This renders the decoupler less effective resulting in a dipolar-broadened ^{13}C spectrum. When the temperature is increased to 330 K (Fig. 4) the increased motional frequency leads to a situation in which there is less interference with the decoupling field and sharper resonances are observed. Coincident with this phenomenon is the observation of very long ^1H spin lattice relaxation times at these sites, with values of ca. 60 s at 300 K and 120 s at 330 K. These long T_1s dramatically increase the time required to obtain spectra for the attached carbons with reasonable signal-to-noise ratios.

In conclusion, we have found the first complex of 11-crown-3 to be a 2:1 complex of benzo-11-crown-3 with LiNCS. X-ray data show that the complex is rigid, but solid-

© 2002 NRC Canada

Table 2. Selected atomic bond angles (°).

Complex **2a**				Complex **2b**	
C1A-O1A-C12A	116.8(2)			C1-O1-C12	116.4(2)
C1A-O1A-LiA	111.3(1)			C1-O1-Li	111.3(1)
C12A-O1A-LiA	126.4(1)			C12-O1-Li	126.8(2)
C6A-O2A-C7A	117.1(2)			C6-O2-C7	116.2(2)
C6A-O2A-LiA	110.8(1)			C6-O2-Li	110.8(1)
C7A-O2A-LiA	122.2(1)			C7-O2-Li	122.8(2)
C9A-O3A-C10A	112.4(2)			C9-O3-C10	113.4(2)
C9A-O3A-LiA	115.6(1)			C9-O3-Li	115.6(2)
C10A-O3A-LiA	123.4(1)			C10-O3-Li	121.6(2)
O1A-C1A-C2A	122.8(2)			O1-C1-C2	124.0(2)
O1A-C1A-C6A	117.1(2)			O1-C1-C6	116.1(2)
O2A-C6A-C1A	116.4(2)			O2-C6-C1	116.7(2)
O2A-C6A-C5A	122.8(2)			O2-C6-C5	123.5(2)
O2A-C7A-C8A	112.0(2)			O2-C7-C8	111.8(2)
C7A-C8A-C9A	114.0(2)			C7-C8-C9	114.8(3)
O3A-C9A-C8A	113.0(2)			O3-C9-C8	114.3(3)
O3A-C10A-C11A	110.8(2)			O3-C10-C11	112.6(3)
C10A-C11A-C12A	113.8(2)			C10-C11-C12	115.6(3)
O1A-C12A-C11A	109.3(2)			O1-C12-C11	110.4(2)
O1A-LiA-O2A	78.7(6)			O1-Li-O2	80.0(6)
O1A-LiA-O3A	85.5(6)			O1-Li-O3	85.4(7)
		S-C13-N	177.7(3)		

Table 3. Selected torsion angles (°).

Complex **2a**		Complex **2b**	
C12A-O1A-C1A-C2A	–44.6(3)	C12-O1-C1-C2	–42.1(3)
C12A-O1A-C1A-C6A	137.1(2)	C12-O1-C1-C6	139.3(2)
C1A-O1A-C12A-C11A	–142.4(2)	C1-O1-C12-C11	–138.4(2)
C6A-O2A-C7A-C8A	89.9(2)	C6-O2-C7-C8	88.3(3)
C7A-O2A-C6A-C1A	–130.2(2)	C7-O2-C6-C1	–130.5(2)
C7A-O2A-C6A-C5A	54.1(3)	C7-O2-C6-C5	54.2(3)
C10A-O3A-C9A-C8A	–84.6(2)	C10-O3-C9-C8	–85.6(3)
C9A-O3A-C10A-C11A	169.1(2)	C9-O3-C10-C11	167.6(3)
O2A-C7A-C8A-C9A	62.7(3)	O2-C7-C8-C9	62.7(4)
C7A-C8A-C9A-O3A	–72.0(3)	C7-C8-C9-O3	–70.5(4)
O3A-C10A-C11A-C12A	–77.1(3)	O3-C10-C11-C12	–74.7(4)
C10A-C11A-C12A-O1A	58.7(3)	C10-C11-C12-O1	54.7(4)

state ^{13}C NMR indicates C–H vector motion in the 11-membered rings with a frequency of ca. 200 MHz.

Experimental

Spectra

All solution NMR spectra were recorded using a Bruker AMX-400 spectrometer equipped with a 5 mm inverse probe and an Aspect X32 computer. An Aspect 3000 process controller was employed and all standard microprograms used are in the Bruker Software Library.

For the NOESY experiment, the mixing time used was selected to be consistent with the $1/T_1$ criterion (17) and in the present case it was set to 0.3 s. For the ^{1}H–^{13}C HMQC experiment, the free induction decays were acquired over 1024 data points for each of the 512 values of the evolution time, with a digital resolution of ca. 8 Hz/point in F1 and 4 Hz/point in F2. The raw data were zero filled in F1 prior to transformation using the qsine window function for both F1 and F2. The proton relaxation delays were set to 1 s. Delays were chosen to emphasize J values of 135–140 Hz.

The ^{1}H–^{1}H COSY experiments were run using *N*-type phase cycling with a 45° mixing pulse. The free induction decays were acquired over 1024 data points for each of the 256 values of the evolution time, with a digital resolution of 5 Hz/point. The raw data were zero filled in F1 prior to transformation using the qsine window function for both F1 and F2. The data were symmetrized about the diagonal.

The solid-phase ^{13}C CP MAS spectra were recorded at 50.3 MHz using a Bruker ASX-200 solid-state NMR spectrometer equipped with a Bruker 7 mm triple resonance MAS probe. The magic angle was set accurately (18) using the ^{79}Br resonance of KBr and maximizing the number of rotational echos in the FID. Magic angle spinning rates were ca. 4 kHz. ^{1}H 90° pulses were 3.5 to 3.8 μs with contact times of 2 ms. Chemical shifts were referenced to the ^{13}C

© 2002 NRC Canada

Table 4. Crystallographic data.

Formula	$C_{25}H_{32}LiNO_6S$
Formula mass	481.52
Crystal system	Monoclinic
Space group	$P2_1/c$
a (Å)	7.7397(8)
b (Å)	18.287(2)
c (Å)	17.4726(19)
β (°)	94.008(2)
V (Å^3)	2466.9(5)
Z (molecules per unit cell)	4
D_c (g cm^{-3})	1.296
Crystal dimensions (mm)	0.20 × 0.20 × 0.20
Radiation (λ, Å)	Mo Kα, 0.70930
Octants measured	h (–10 to 10), k (0–24), l (0–23)
Max 2Θ (°)	28.72
Temperature (K)	203(2)
No. of unique reflections	5897
No. of reflections measured	19 277
No. of reflections with $I_{net} > 2\sigma(I_{net})$	5438
R_1 ($I > 2\sigma(I)$)	0.0610
R_1 (all data)	0.0875
wR_2 ($I > 2\sigma$(I))	0.1880
wR_2 (all data)	0.1987
GoF	1.036
Largest diff. peak and hole (e Å^{-3})	0.848 and –0.642

Table 5. ^{13}C NMR chemical shifts (δ_c from TMS ± 0.1) for benzo-11-crown-3 (**1**) and the (benzo-11-crown-3)$_2$·LiNCS complex **2**.

	1 (0.1 M $CDCl_3$ solution)	**2** (0.1 M $CDCl_3$ solution)	**2** (Solid)
C1	151.3	149.6	153.1
C2	118.8	118.2	(121.5)[a]
C3	123.0	123.8	(126.4)[b]
C4	123.0	123.8	(127.0)[b]
C5	118.8	118.2	(121.0)[a]
C6	151.3	149.6	149.0
C7	69.9	74.1	78.0
C8	29.8	28.3	28.0
C9	66.8	70.3	72.8
C10	66.8	70.3	72.8
C11	29.8	28.3	28.0
C12	69.9	74.1	78.0

[a]Indicates possible interchange of assignments.
[b]Indicates possible interchange of assignments.

resonance of tetrakistrimethylsilyl silane, $Si(Si(CH_3)_3)_4$, which has a chemical shift of 3.7 ppm relative to TMS.

Table 6. Solution (0.1 M in $CDCl_3$) ^{1}H NMR data for **1** and **2**.

	1		**2**	
	δ_H from TMS ± 0.001	J (Hz) ± 0.1	δ_H from TMS ± 0.001	J (Hz) ± 0.1
H2,5	6.942	[a]	7.026	n.o.[b]
H3,4	6.964	[a]	7.026	n.o.[b]
H7,12	4.119	5.2	4.348	5.0
H8,11	1.971	5.2	2.027	5.0
H9,10	3.835	5.2	3.825	5.0

[a]Complex AA′BB′ spin system.
[b]n.o. (non-observable).

X-ray crystallographic measurement and structure solution

A summary of the crystallographic data is given in Table 4.[2] Diffraction intensities were collected on a Bruker AX SMART 1k CCD diffractometer using Mo Kα radiation at 203 K. 0.3° scans were used at 0, 90, and 180°.

Unit cell parameters were determined from 60 data frames collected at different sections of the Ewald sphere. Semiempirical absorption corrections based on equivalent reflections were applied (19). No crystal decay was noted during the data collection. Unit cell parameters and systematic absences are consistent with the $P2_1/c$ space group. The structure was solved by direct methods, completed with difference Fourier syntheses and refined with full-matrix least-squares procedures based on F^2. All non-hydrogen atoms were refined with anisotropic displacement parameters and hydrogen atoms were treated as idealized contributions. All scattering factors and anomalous dispersion factors are contained in the SHEXTL 5.1 program library.

Materials

The synthesis of **1** has been reported earlier (12). Preparation of **2** was accomplished via mixing **1** (0.400 g, 1.92 mmol) with $LiNCS·2H_2O$ (0.100 g, 0.99 mmol) in hot (340 K) ethyl acetate (10 mL). The solvent volume was then reduced by boiling to ca. 7 mL. After standing overnight, the solution yielded yellow opaque crystals which were collected by suction filtration. Subsequent recrystallization from 1:1 ethyl acetate:acetone yielded 0.72 g (89%) of X-ray grade crystals of **2**; mp 110–113°C.

Acknowledgements

G.W.B. thanks the Natural Sciences and Engineering Research Council of Canada (NSERC) and Carleton University for continuing financial support.

References

1. C.J. Pedersen. J. Am. Chem. Soc. **89**, 2495 (1967).

[2] Supplementary material may be purchased from the Depository of Unpublished Data, Document Delivery, CISTI, National Research Council Canada, Ottawa, ON K1A 0S2, Canada (http://www.nrc.ca/cisti/irm/unpub_e.shtml for information on ordering electronically). CCDC No. 174 128 contains the supplementary crystallographic data for this paper. These data can be obtained, free of charge, via www.ccdc.cam.ac.uk/conts/retrieving.html (or from the Cambridge Crystallographic Data Centre, 12 Union Road, Cambridge CB2 1EZ, U.K. (Fax: 44-1223-336033 or e-mail: deposit@ccdc.cam.ac.uk).

© 2002 NRC Canada

2. C.J. Pedersen. *In* Synthetic multidentate macrocyclic complexes. *Edited by* R.M. Izatt and J.J. Christesen. Academic Press, New York. 1978. pp. 1–51.
3. J. Dale and J. Krane. J. Chem. Soc. Chem. Commun. 1012 (1972).
4. F.A.L. Anet, J. Krane, J. Dale, K. Daasvatn, and P.O. Kristiansen. Acta Chem. Scand. **27**, 3395 (1973).
5. C.J. Pedersen and H.K. Frensdorff. Angew. Chem. Int. Ed. Engl. **11**, 16 (1972).
6. G. Shoham, W.N. Lipscomb, and U. Olsher. J. Chem. Soc. Chem. Commun. **105**, 208 (1983).
7. G. Shoham, W.N. Lipscomb, and U. Olsher. J. Am. Chem. Soc. **105**, 1247 (1983).
8. G.W. Buchanan, A. Moghimi, and C. Bensimon. Can. J. Chem. **73**, 100 (1995).
9. G.W. Buchanan, V.M. Reynolds, K. Bourque, and C. Bensimon. J. Chem. Soc. Perkin Trans. 2, 707 (1995).
10. G.W. Buchanan, V.M. Reynolds, and C. Bensimon. J. Mol. Struct. **382**, 69 (1996).
11. G.W. Buchanan, M. Gerzain, G.A. Facey, and C. Bensimon. J. Mol. Struct. **471**, 95 (1998).
12. G.W. Buchanan, M. Azad, and G.P.A. Yap. J. Mol. Struct. (in press).
13. J.B. Stothers. Carbon-13 NMR spectroscopy. Academic Press, New York. 1972.
14. W.P. Rothwell and J.S. Waugh. J. Chem. Phys. **74**, 2721 (1981).
15. G.W. Buchanan, C. Morat, J.P. Charland, C.I. Ratcliffe, and J.A. Ripmeester. Can. J. Chem. **67**, 1212 (1989).
16. K.A. Watson, S. Fortier, M.P. Murchie, J.W. Bovenkamp, A. Rodrigue, G.W. Buchanan, and C.I. Ratcliffe. Can. J. Chem. **68**, 1201 (1990).
17. A.E. Derome. Modern NMR techniques for chemistry research. Pergamon Press, Oxford. 1987.
18. J.S. Frye and G.E. Maciel. J. Magn. Reson. **48**, 125 (1982).
19. R. Blessing. Acta Crystallogr. Sect. A: Fundam. Crystallogr. **A51**, 33 (1995).

© 2002 NRC Canada

Substitution reactions at the Ni(III) cation in macrobicyclic complexes — Reaction of metal ion complexes prepared from ligands L^1 (17-oxa-1,4,8,11-tetraazabicyclo[6.5.6]nonadecane) and L^2 (17-oxa-1,4,8,11-tetraazabicyclo[10.5.2]nonadecane) with chloride ion

Alison M. Ingham, Chao Xu, T.W. Whitcombe, Chengtian Xu, J.N. Bridson, and Alexander McAuley

Abstract: The potentially penta-coordinating ligand L^1 has been synthesized by reaction of the bridge bis-(2-(methylsulfonyl)oxyethyl)ether with the tetraazamacrocycle cyclam (cyclam = 1,4,8,11-tetraazatetradecane). The copper(II) complex was characterized initially and subsequent demetallation provided pure L^1. Electrochemical and chemical oxidation of the nickel(II) species yields a Ni(III) ion (low-spin d^7, rhombic, g_{xx} 2.195, g_{yy} 2.189, g_{zz} 2.027) of sufficient stability in acidic solutions for kinetic measurements to be undertaken of substitution reactions at the sixth site. The isomeric ligand L^2, has been synthesized previously, and reactions of the $[Ni(L^1)(solv)]^{3+}$ and $[Ni(L^2)(solv)]^{3+}$ ions with chloride have also been investigated. In both reactions, an unusually high acid dissociation constant is observed, associated with the proposed replacement of the apical ether oxygen by a water molecule that is bound both to the metal centre and hydrogen bonded to the ether. The structure $[Ni(L^2)](PF_6)_2$ (monoclinic, $P2_1/c$, a = 10.699(2), b = 13.244(4), c = 16.603(2) Å, β = 92.10(1)°) converged at R = 0.055 (R' = 0.057) for 325 parameters using 3293 reflections with $I > 2\sigma(I)$. In this complex, the detachment of the ether O donor to yield a square-planar complex is confirmed. Comparisons are made with substitution rates at other Ni(III) macrocyclic ions.

Key words: nickel(III), substitution, macrobicyclic ligand, synthesis, kinetics.

Résumé : On a synthétisé le ligand potentiellement pentacoordinant L^1 par réaction de l'éther ponté bis-(2-(méthylsulfonyl)oxyéthyl)éther avec le cyclame tétraazamacrocyclique (cyclame = 1,4,8,11-tétraazatétradécane). Initialement, on a caractérisé le complexe au cuivre(II) et sa démétallation subséquente a permis d'obtenir L^1 à l'état pur. Les oxydations électrochimiques et chimiques de complexes de nickel(II) conduisent à la formation d'un ion Ni(III) (d^7 de faible spin, rhombique, g_{xx} 2,195, g_{yy} 2,189, g_{zz} 2,077) qui, en solutions acides, sont suffisamment stables pour permettre d'effectuer des mesures cinétiques sur les réactions de substitution au niveau du sixième site. Le ligand isomère L^2 a été synthétisé antérieurement; on a aussi étudié les réactions des ions $[Ni(L^1)(solv)]^{3+}$ et $[Ni(L^2)(solv)]^{3+}$ avec le chlorure. Dans les deux réactions, on a observé une constante de dissociation acide anormalement élevée qui est associée au remplacement de l'atome d'oxygène de l'éther apical par une molécule d'eau qui est reliée par une liaison hydrogène à l'éther et qui est aussi liée au centre métallique. La structure $[Ni(L^2]](PF_6)_2$ (monoclinique, $P2_1/c$, a = 10,699(2), b = 13,244(4) et c = 16,603(2) Å, β = 92,10(1)°) converge à R = 0,055 (R' = 0,057) pour 325 paramètres en utilisant 3293 réflexions avec $I > 2\sigma(I)$. Dans ce complexe, on a pu confirmer le détachement de l'oxygène de l'éther donneur qui conduit à la formation du complexe plan carré. On a fait une comparaison des vitesses de substitution au niveau d'autres ions macrocycliques du Ni(III).

Mots clés : nickel(III), substitution, ligand macrobicyclique, synthèse, cinétique.

[Traduit par la Rédaction]

Received 16 May 2001. Published on the NRC Research Press Web site at http://canjchem.nrc.ca on 21 February 2002.

A.M. Ingham. Health Canada, Ottawa, ON K1A 0K9, Canada.
C. Xu. Andritz Inc., 3200 Upper Valley Pike, Springfield, Ohio 45504.
T.W. Whitcombe. University of Northern BC, Department of Chemistry, 3333 University Way, Prince George, BC V2N 4Z9, Canada.
C. Xu. East China Normal University, Chemistry Department, Shanghai, China.
J.N. Bridson. Memorial University of Newfoundland, Chemistry Department, 283 Prince Philip Drive, St. John's, NF A1B 3X7, Canada.
A. McAuley.[1] University of Victoria, Department of Chemistry, Victoria, BC V8W 3V6, Canada.

[1]Corresponding author (e-mail: amcauley@uvic.ca).

 DOI: 10.1139/V02-003 © 2002 NRC Canada

Introduction

Although nickel(III) has been an accessible oxidation state for 30 years (1–6), there have been relatively few studies made of substitution processes at this metal centre. Whilst there are some exceptions, in part, this is owing to a generally strongly oxidizing nature and relatively rapid decomposition of the complex ions. It has been estimated that the nickel(III)-hexaaquo ion would have a redox potential in excess of 2 V (7) and, even when ligated as macrocyclic complexes, E^0 values are close to or exceed 1 V (8–12). In the latter systems, use has been made of strongly acidic media to reduce the rate of (aqueous) solvent decomposition. Only in the cases where deprotonated peptides (13, 14) or cyclic amides (15) surround the metal ion are redox potentials lower. However, in these cases, the rate of axial substitution is substantially greater than that for [Ni(III) cyclam$(H_2O)_2$]$^{3+}$ (cyclam = 1,4,8,11-tetraazacyclotetradecane) (16, 17). Recently, in this laboratory, we described the synthesis of bicyclic ligands in which a cyclam ring is fused to a nine- (18) or 10-membered (19) ring containing an ether donor (L^2 and L^3, respectively), to provide a N_4O donor set with only a single site available for substitution in an octahedral complex ion. Spectroscopic observations are consistent with the formation of nickel(III) species of sufficient lifetimes to permit kinetic measurements. The third isomer (L^1) of the N_4O series is one in which the bridge is made between the 1,8-*trans*-nitrogens of cyclam. Complexes formed by this ligand would have a "hemicryptate" structure. This ligand has been prepared recently (20), using essentially the synthetic route described herein, but the process required selective separation of L^1 from the variety of organic products formed. An alternative route is described where individual components of the product ligand mixture form copper(II) complexes that can be separated chromatographically, and subsequent demetallation permits isolation of the free ligands. In this way, yields of about 50% of L^1 and <10% of L^3 were identified together with amounts of dinuclear copper ions that were not characterized further. Nickel(II) complexes have been prepared and oxidation to Ni(III) achieved both electrochemically and by reaction with oxidants such as $Co(III)^{3+}$(aq). In the spectrophotometric titration of the [Ni(III)(L^2)(solv)]$^{3+}$ ion with acid, a pK_a has been identified consistent with a hydrogen ion dependence observed in substitution reactions with chloride ion.

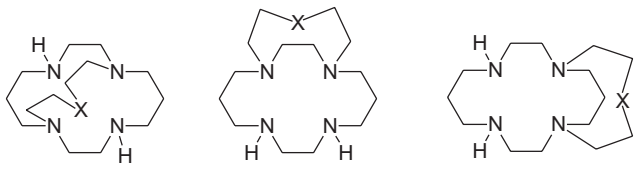

Results

The crystallographic parameters for each of the complexes are contained in Table 1, with selected bond lengths and angles provided in Table 2. An ORTEP diagram of the cation, [Ni(L^2)]$^{2+}$ is shown in Fig. 1. The ion has a square-planar structure, in a *trans*-I geometry, in marked contrast with the corresponding octahedral ion [Ni$(L^2)(ClO_4)$]$^+$ (22) prepared from perchlorate media and where the ether O donor is coordinated in the solid state. In the present system, the Ni—N bond distances are 2.006, 1.998, 1.976, and 1.981 Å, with the longer two bonds to the tertiary nitrogens of the fused nine-membered ring as observed previously (18, 22). The latter distances are completely consistent with the secondary amine bonds observed for Ni(cyclam)$^{2+}$ (1.975 Å), although they are slightly longer than average Ni(II)—N bond found in a variety of macrocyclic complexes (1.945 Å) (28). In the present system, the apical ether atom (Ni—O = 2.306 Å) indicates that the ether is not bound. Furthermore, the closest fluorine of the PF_6^- counter ion is 2.76 Å from the nickel centre. Curiously, the angle subtended by the ether oxygen to the perpendicular from the N_4 plane is 9.1° suggesting that while the Ni—O distance is stretched to a nonbonding value, the structure-fused ring and apical position of the ether is not altered. This contrasts, for example, with the apical nitrogen observed in Pd([9]ane$N_3)_2^{2+}$ (29) where the ring is observed to undergo inversion removing the nitrogen from the coordination environment entirely. In the present complex, the ether could almost be viewed as representing a nascent interaction with the nickel centre. Presumably, the energy barrier between the four- and six-coordinate species must be very small.

In the ligand synthesis, under the experimental conditions employed, there was predominant formation of L^1, although small amounts of L^3 also formed through reaction across the propylene bridge.

There are three isomeric forms of the N_4O ligand, formed either in the present case, or by bridge formation across the ethylene-(9-N_4O) (L^2) or propylene-(10-N_4O) (L^3) elements of the cyclam. Despite growing well-formed crystals from perchlorate and tetrachlorozincate media for both the copper(II) and nickel(II) complexes of ligand L^1, in each case the material was observed not to diffract. This may be the result of significant fluxionality in the ligand leading to random disorder, even at –90°C. Although there is as yet no crystal structure for a complex of L^1, comparison of the NMR data (supplementary Table S5)[2] shows the bicyclic ligand to differ from the other two that have been synthesized previously (18, 19) and for which structural data have been presented.

Electronic spectra

The UV–vis spectrum of [Cu(L^1)]$^{2+}$ in water shows two broad bands with maxima at 537 nm (ε = 185 M^{-1} cm^{-1}) and 280 nm (ε = 4860 M^{-1} cm^{-1}). The more intense band is assigned to charge transfer, while the lower energy band envel-

[2] Supplementary material may be purchased from the Depository of Unpublished Data, Document Delivery, CISTI, National Research Council Canada, Ottawa, ON K1A 0S2, Canada (http://www.nrc.ca/cisti/irm/unpub_e.shtml for information on ordering electronically). CCDC No. 176765 contains the supplementary crystallographic data for this paper. These data can be obtained, free of charge, via www.ccdc.cam.ac.uk/conts.retrieving.html (or from the Cambridge Crystallographic Data Centre, 12 Union Road, Cambridge CB2 1EZ, U.K. (fax: 44-1223-336033 or e-mail: deposit@ccdc.cam.ac.uk).

© 2002 NRC Canada

Table 1. Experimental crystallographic parameters for cation $Ni([9]aneN_4O)^{2+}$.

Formula	$C_{14}H_{28}F_{12}N_4OP_2Ni$
MW	617.03
Crystal system	Monoclinic
Space group	$P2_1/c$ (No. 14)
a (Å)	10.669(2)
b (Å)	13.224(4)
c (Å)	16.403(2)
β (°)	92.10(1)
Z	4
U (Å^3)	2312.5
D_c (g cm^{-3})	1.772
Crystal size (mm)	0.400 × 0.300 × 0.200
Radiation Mo Kα (Å)	0.71069
2θ Range (°)	0.1–50.1
Total reflections	4534
Unique reflections	4294
Observed reflections	3293 [$I > 2\sigma(I)$]
No. of parameters	325
Res e density (e Å^{-3})	0.67, –0.61
GoF	3.08
Max fin shift (esd)	0.00
R, R_w	0.055, 0.057

Note: $R = \Sigma||F_o| - |F_c||/\Sigma|F_o|$; $R_w = [(\Sigma w(|F_o| - |F_c|)^2/\Sigma wF_o^2]^{1/2}$

Table 2. Selected bond lengths, interatomic distances (Å) and angles (°).

$Ni([9]aneN_4O)^{2+}$	
Bond lengths (Å)	
Ni—N1	1.998(4)
Ni—N2	2.006(4)
Ni···O1	2.306
Ni—N3	1.981(4)
Ni—N4	1.976(4)
Ni···F7	2.757
Bond angles (°)	
N2-Ni-N1	86.8(2)
N3-Ni-N1	177.9(2)
N3-Ni-N2	91.1(2)
N4-Ni-N1	95.8(2)
N4-Ni-N2	176.9(2)
N4-Ni-N3	86.3(2)

ops the *d–d* transitions. The spectra obtained for $[Ni(L^1)](ClO_4)_2$ in water and acetonitrile are typical of Ni(II) (d^8) complexes in an octahedral environment. A weak transition seen in acetonitrile at 722 nm is believed to be the spin forbidden transition $^1E_g \leftarrow {}^3A_{2g}$. Like other bicyclic species prepared previously, there is a strong field, and the $^3A_{2g} \leftarrow {}^3T_{1g}(F)$ transition (505 nm) is at a fairly high energy for a high-spin Ni(II) system. Comparative values for $[Ni(II)(L^5)]^{2+}$ are 504 nm (30) and $[Ni(II)(L^2)]^{2+}$ 515 nm (22). The spectrum of $[Ni(L^1)]^{3+}$ shows two strong transitions below 400 nm, ascribed to charge transfer transitions.

EPR spectra

The Ni(III) ion complexes are EPR active, yielding spectra characteristic of a low-spin d^7 ion with rhombic symmetry. Details of several complexes, prepared under identical conditions of 0.5 to 1.0 M [H^+], are provided in Table 3 and the spectrum of the sulfato-complex is presented in Supplementary Fig. S4.[2] It is known that tertiary amine – metal ion bond lengths in Ni(II) complexes are longer than those involving secondary amines (31), which may in part explain the origin of the quasi-rhombic structure since the diagonally opposed bonds may differ in the Ni(III) system. However, there may also be distortion induced by the ligand that could lead to the behaviour differing from the comparable spectra for the other isomeric complexes. In an attempt to prepare a disubstituted complex, fluoride ion was added to the perchlorate solution. No evidence is observed that more than one fluoride ion is attached, even at high concentrations of F^-, although as has been pointed out previously (13), the binding of the second ion may be less thermodynamically favoured at the very low temperatures prevailing during measurement.

Fig. 1. ORTEP diagram of the square-planar $[Ni(L^2)]^{2+}$ ion.

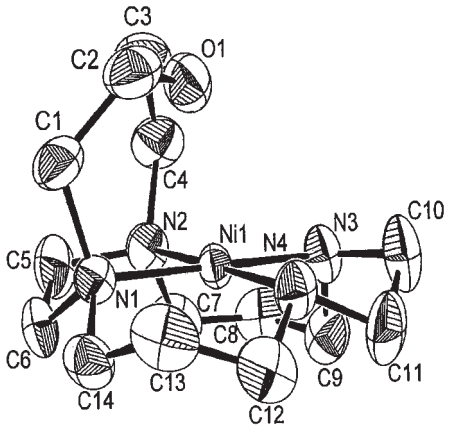

Cyclic voltammetry

Two irreversible redox waves are observed for the $[Cu(L^1)](ClO_4)_2$ complex in acetonitrile. The first, corresponding to the Cu(III)/Cu(II) couple, is seen at 1.25 V, approximately the same potential as the complexes $[Cu(II)([L^n)]^{2+}$ (n = 2, 3). Similarly, the Cu(II)/Cu(I) couple of $[Cu(L^1)]^{2+/+}$ at –1.06 V is quite close to that of $[Cu(L^2)]^{2+/+}$ (–1.04 V), but significantly different from $[Cu(L^5)]^{2+/+}$ (–0.85 V) (30) and $[Cu(L^4)]^{2+/+}$ (–1.16 V) (32).

The redox data obtained for $[Ni(L^1)](ClO_4)_2$ in acetonitrile are summarized in Table 4. The Ni(III) macrobicyclic species are strong oxidants and potentials for the Ni(III)/(II) couple are similar to those obtained for the two isomeric N_4O bicyclic species. An additional irreversible redox process was observed at 1.3 V for $[Ni(III)(L^1)]^{3+}$, which may tentatively be assigned to oxidation to produce a ligand radical. As observed previously, the Ni(I) ions are very powerful reductants.

Stability of $[NiL^1)]^{2+}$ and $[Ni(L^1)]^{3+}$ in aqueous acidic solution

The complex $[NiL^1)]^{2+}$ was stable in 1 M $HClO_4$ (T = 25°C) based upon no measurable change in the spectrum at 520 nm over a 12 h period. In the case of $[Ni(L^1)]^{3+}$, studies were made at 395 nm where the rate of decomposition to the

© 2002 NRC Canada

Table 3. EPR parameters for Ni(III) complexes (T = 77 K), [Ni(III)] ~ 3×10^5 M.

Complex ion	g_{xx}, g_{yy}	g_{zz}	A_{zz} (G)	$A_{xx,yy}$ (G)
$[Ni(L^1)(OH_2)]^{3+}$ [a]	2.195, 2.189	2.027		
$[Ni(L^1)(SO_4)]^{+}$ [b]	2.236, 2.212	2.029		
$[Ni(L^1)(Cl)]^{2+}$ [c]	2.187, 2.165	2.029	28	
$[Ni(L^1)(F)]^{2+}$ [d]	2.217, 2.206	2.024	199	67

[a]Concentration used = 0.5 M $HClO_4$.
[b]Concentration used = 0.3 M H_2SO_4.
[c]Concentration used = 0.5 M HCl.
[d]Concentration used = 0.05 M NaF – 0.5 M $HClO_4$.

Table 4. Redox data for $[Ni(L^1)](ClO_4)_2$ and related complexes.

Complex	Couple	$E_{1/2}$ (V) (vs. Ag^+/Ag)
$[Ni(L^1)]^{2+}$	3+/2+	0.85 (Quasireversible)
	2+/1+	–1.79 (Irreversible)
$[Ni(L^2)]^{2+}$	3+/2+	0.86 (Quasireversible)[a]
	2+/1+	–1.66 (Quasireversible)[a]

[a]See ref. 22.

corresponding Ni(II) complex was found to be independent of $[H^+]$ over the range 0.2 to 1 M (I = 1 M). The rate at 20°C was found to be 7.5 (±0.2) × 10^{-4} s^{-1}, and at 10°C, 2.4 (±0.2) × 10^{-4} s^{-1}. At the latter temperature, the half-life of Ni(III) is approximately 50 min, sufficiently long for monitoring of substitution kinetics without significant interference from decomposition. The presence of acid in the solution appreciably reduces the rate of decomposition of the $[Ni(L^1)(H_2O)]^{3+}$ ion, presumably by preventing decomposition via base-catalyzed pathways (33). In the case of $[Ni(L^2)(H_2O)]^{3+}$, the corresponding decomposition rate was found to be 2.2 (±0.1) × 10^{-4} s^{-1} at 25°C, again independent of hydrogen ion concentration. Interestingly, this behaviour differs significantly from that of Ni(III) cyclam, where decomposition increases as $[H^+]$ decreases over the same range used here.

Chloride substitution at $[Ni(L^n)(solv)]^{3+}$

Substitution reactions at Ni(III) centres have been studied previously, with four-coordinate cyclam-based ligands, (15, 16) and peptides (14). Dissociative interchange mechanisms have been suggested for these processes. The rates of substitution at both $[Ni(L^1)(OH_2)]^{3+}$ and $[Ni(L^2)(OH_2)]^{3+}$ were found to be dependent on the concentration of both chloride and hydrogen ion. For $[Ni(L^1)(OH_2)]^{3+}$, an initial spectroscopic investigation identified an equilibrium confirmed by an isosbestic point at 268 nm. The equilibrium constant was determined spectrophotometrically (T = 10°C) at 317 nm at $[H^+]$ = 0.5 M, I = 1 M. For the reaction $[NiL^{3+}] + Cl^- \rightleftharpoons [NiLCl]^{2+}$, (neglecting charges) the equilibrium constant (K = [NiLCl]/[NiL][Cl]) may be determined using the equation:

$$[NiL]_0[Cl]_0/\Delta OD = ([NiL]_0 + [Cl]_0)/(\Delta\varepsilon)l + 1/K(\Delta\varepsilon)l$$

where ΔOD is the observed optical density change, $\Delta\varepsilon$ is the change in extinction coefficient between the reactant and the product, l is the path length in cm, and $[NiL]_0$ (= 2.2×10^{-4} M) and $[Cl]_0$ are the initial concentrations of $[Ni(L^1)(H_2O)]^{3+}$ and Cl^-, respectively. A plot of $[NiL]_0[Cl]_0/\Delta OD$ vs. ($[NiL]_0$ + $[Cl]_0$) displayed good linearity over the range $[Cl^-] = 7 \times 10^{-3} - 8 \times 10^{-2}$ M, from which a value of K = 170 ± 10 M^{-1} was calculated. This value is similar to the values obtained for the reaction of chloride with $[Ni(cyclam)]^{3+}$ (16).

Fig. 2. Spectrophotometric titration of the $[Ni(L^2)(solv)]^{3+}$ ion with hydrogen ions (λ = 390 nm).

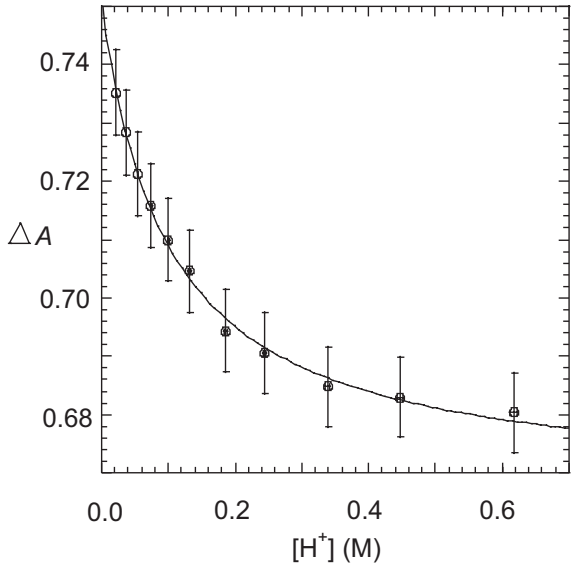

Spectroscopic studies with $[Ni(L^2)(H_2O)]^{3+}$ exhibited small differences in absorbance when $[H^+]$ was varied from 0.5 to 0.002 M. Use was made of this feature in determining a pK_a within this acidity range. Absorbance changes (ΔA) were monitored over the range 200–450 nm when μL aliquots of perchloric acid (4.0 M) were added sequentially to a $[Ni(L^2)]^{3+}$ solution starting at $[H^+]$ = 0.002 M. Corrections were made for dilution and also for any decomposition of the Ni(III) species during the periods of measurement. From ΔA_{390} (Fig. 2), K_a = 0.09 ± 0.04. Similar data values were derived at other wavelengths in the 300–359 nm range. Results of an identical experiment on $[Ni(cyclam)]^{3+}$ showed no similar behaviour.

Substitution reaction kinetics for both systems were investigated with chloride concentrations of approximately 10–40 times in excess of that of the [Ni(III)]. Higher concentrations of chloride appeared to show a second reaction, but absorbance changes were too small to permit significant comment. In both instances, the chloride species formed are considerably more stable than the aquo ion, persisting at

© 2002 NRC Canada

room temperature for several hours. Increased kinetic stability of macrocyclic Ni(III) species has been observed for other Ni(III) macrocyclic complexes with chloride in the axial position (16), and is probably associated with the lower redox potential of these ions. The rate data for the $[Ni(L^1)(H_2O)]^{3+}$ reaction, obtained at λ = 430 nm, are tabulated in Table S6[2] and for the $[Ni(L^2)(H_2O)]^{3+}$ system in Table S7.[2] In general, the scatter of individual values for k_{obs} was in the order of ±5%. For the $[Ni(L^2)(H_2O)]^{3+}$ reaction, measurements were made at λ = 400nm. The observed first-order rate constants (k_{obs}) vary linearly with chloride concentration and plots are provided in Supplementary Figs. S5 and S6,[2] where it is seen that intercepts and slopes vary inversely with $[H^+]$.

Origin of the protonation equilibria for the substitution reaction

There is a significant difference between the present findings and those for the corresponding $[Ni(cyclam)(H_2O)_2]^{3+}$ species (16), although rate data for Cl^- substitution were collected over approximately the same $[H^+]$ range (0.04 to 0.30 M). In the latter case, there is no evidence of any proton dependence in this range, in keeping with a relatively high (>3) pK_a value for proton dissociation of the first aquo group (12). In the present investigation, an initial acid–base reaction occurs at a much higher acid concentration, consistent with an additional process at the metal centre. If the aquo ion in the sixth site was deprotonated, it is unlikely that the chloride ion would readily replace the resultant hydroxo ion in the inner coordination sphere (the reaction rate increases as the pH rises). The weakness of binding between transition-metal ions and ether oxygen donors is confirmed in the O-donor detachment seen in the structure of the planar $[Ni(II)L^2]^{2+}$ ion. A possible mechanism involves the detachment of the axial O donor and its replacement by a water molecule. The enhanced acidity of coordinated water is well-known, and, at lower acid concentrations, the presence of a lone pair on the ether provides a template for formation of a hydrogen bond with the incoming water molecule as shown. This interaction has the effect of increasing the ability of the coordinated water to donate electrons to the nickel(III) thus labilizing the complex. At higher hydrogen ion levels, the ether group preferentially H-bonds to the H_3O^+ present in solution leaving the isolated water bound to the Ni(III), which in turn, becomes more inert towards substitution.

A mechanistic scheme consistent with the observed acid dependence is described below, where (neglecting charges) $NiHL^n$ and NiL^n represent the complex ions as shown (n = 1 or 2) and $NiH(L^n)Cl$ and $Ni(L^n)Cl$, the corresponding chloro complexes:

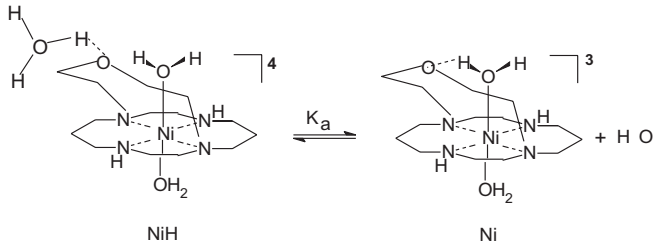

Scheme 1.

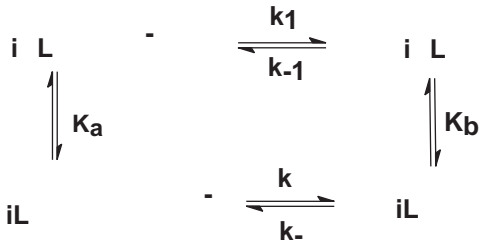

The rate law derived from this equilibrium set may be represented as:

$$[1] \qquad k_{obs} = (k_1[H^+] + k_2K_a)[Cl^-]/(K_a + [H^+]) + (k_{-1}[H^+] + k_{-2}K_b)/(K_b + [H^+])$$

As can be seen, inverse proton dependences are predicted for both the intercepts and slopes of linear plots of k_{obs} vs. $[Cl^-]$. The uncertainties in the data probably reflect the relative instability of the nickel(III) species, especially at lower proton concentrations and higher temperatures.

For the reaction of $[Ni(L^1)(solv)]^{3+}$, a nonlinear least-squares regression of the data showed large errors particularly for K_b which was seen to be several orders of magnitude lower than K_a. A similar regression was therefore carried out using the equation

$$[2] \qquad k_{obs} = (k_1[H^+] + k_2K_a)[Cl^-]/(K_a + [H^+]) + k_{-1}$$

where $K_b << [H^+]$ and the $k_{-2}K_b$ term is negligible. This resulted in a correlation R^2 = 0.98 with k_1 = 273 ± 16 M^{-1} s^{-1}, k_{-1} = 2.76 ± 0.09 s^{-1}, K_1 = 99 ± 12 M^{-1}, k_2 = 1293 ± 690 M^{-1} s^{-1}, and K_a = 0.022 ± 0.02 M. This value of K_1 agrees reasonably with the equilibrium constant determined spectrophotometrically (170 M^{-1}), although the latter result was obtained at only one hydrogen ion concentration, and within the range where the protonated complex might be expected to persist.

For the reaction of $[Ni(L^2)(solv)]^{3+}$, maintaining K_a = 0.09 M and using eq. [2], a nonlinear least-squares regression of the data yielded (R^2 = 0.98) k_1 = 295 ± 54 M^{-1} s^{-1}, k_{-1} = 4.15 ± 0.77 s^{-1}, K_1 = 71 ± 32 M^{-1}, and k_2 = 705 ± 703 M^{-1} s^{-1}. Details of the rates, parameters, and residuals of correlations of observed and calculated rates are provided in Supplementary Tables S6 and S7.[2] The rate constants may be compared with those of the cyclam complex (16) and $[Ni(L^3)(solv)]^{3+}$. The latter system has been studied previously (19). By use of a treatment of the data similar to that herein, values of k_1 = 17 ± 5 M^{-1} s^{-1}, k_{-1} = 0.083 ± 0.012 s^{-1} (K_1 = 205 ± 70 M), and k_2 = 210 ± 121 M^{-1} s^{-1} with K_a = 0.035 ± 0.03 M, similar to the values published. The most noticeable difference is that although the equilibrium constant for the L^3 complex is similar to that for the other two isomeric species, the individual rate constants are substantially smaller. In all three cases, the acidity profile observed is significantly different from that in $[Ni(III)cyclam(H_2O)_2]^{3+}$, where no hydrogen ion dependence is seen with rates at 6.6° for chloride substitution, k_1 = 168 ± 5 M^{-1} s^{-1} and k_{-1} = 1.15 ± 0.10 s^{-1}. These values may be compared with k_1 = 273, 295, and 17 ± 5 M^{-1} s^{-1} for $[NiHL^n(OH_2)_2]^{3+}$ (n = 1, 2, 3), respectively. The rate constants are quite similar, suggesting a common reaction pathway. The value for L^3

© 2002 NRC Canada

is surprising, since of the three bicyclic ligands, only in the case of complexes of this ligand is the nickel ion known to be coplanar with the macrocyclic donor set, and in this regard, the geometry is closest to the cyclam ion. As predicted, there is an increased lability of the hydrogen-bonded ions. For the isomeric species, there is apparently a greater spread of rates, k_2 = 1293 (L^1), 705 (L^2), and 210 (L^3) M^{-1} s^{-1}, although the errors involved are substantially greater.

Unpublished observations (34) in this laboratory on the much more kinetically stable cobalt(III) ion ($[Co(L^3)(H_2O)]^{3+}$) have identified two pK_a values at 2.2 and 3.8 consistent with H^+ dissociations at both *trans*-disposed sites. In the present study, the first pK_a in each case (≈1.05 for L^1, 1.23 for L^2, 1.45 for L^3) is somewhat lower, possibly associated with the d^7 nickel(III) centre. In comparing the macrobicyclic [Ni(III)(9-ane N_4X)] complexes, where X = S, NH, the equilibrium constants for chloride complex formation are substantially smaller (22), and there is no evidence for behaviour similar to that outlined above where the replacement of the coordinated water by the halide is likely to take place in a manner suggestive of dissociative interchange. Further work on other systems is required to confirm this suggestion.

Conclusions

The rates of chloride substitution at three isomeric nickel(III) complexes containing ether bridges, (L^1–L^3) with a macrocyclic N_4 ring similar to cyclam are compared, and show an unusually high proton equilibrium not observed in the reactions of cyclam. This is related to a H-bonded water molecule displacing the ether in the primary coordination sphere of the complex. In this work, the pK involving $[NiL^2(solv)]^{3+}$ has been determined spectrophotometrically. This detachment is confirmed by a crystal structure of the $[Ni(II)L^2]^{2+}$ ion which is square-planar. In all three cases, the rates of reduction to the corresponding Ni(II) complexes by oxidation of water is invariant of $[H^+]$ in contrast to the Ni(III) cyclam complex which reacts more rapidly at lower acidities.

Experimental

Capping of cyclam was achieved by use of bis-(2-(methylsulfonyl)oxyethyl)ether as the bridging molecule.

Bis-(2-(methylsulfonyl)oxyethyl)ether

Triethylamine (104 mL, 0.8 mol) and bis-(2-hydroxyethyl)ether (23.7 mL, 0.25 mol) were dissolved in 1.5 L dichloromethane under a nitrogen atmosphere. The mixture was cooled to –10°C on an ice and salt bath. Methanesulfonylchloride (46.5 mL, 0.6 mol) in 250 mL dichloromethane was added dropwise over a period of 2 h. The mixture was stirred overnight at room temperature. The organic fraction was washed successively with 100 mL 1 M HCl, 3 × 100 mL water, and 100 mL saturated aqueous sodium carbonate, dried with anhydrous sodium sulfate, and the solvent removed under vacuum. The residue was recrystallized from hot methanol to give white crystals. Yield: 53.8 g (82%). ^{1}H NMR (360 MHz) ($CDCl_3$) δ: 3.05 (s, 3H, CH_3), 3.79, 4.37 (t, 2+2H, CH_2-O). ^{13}C NMR (90.6 MHz) ($CDCl_3$) δ: 37.6 (CH_3), 68.6 (CH_2-OMs), 68.9 (CH_2-O). CI-MS (*m*/*z*): 263 (M + 1).

17-Oxa-1,4,8,11-tetraazabicyclo[6.6.5]tetradecane (L^1)

Sodium carbonate (10 g) in a small volume of THF, dried over molecular sieves, was placed under an atmosphere of nitrogen. To this slurry was added cyclam (21) (1 g, 5 mmol) and bis-(2-(methylsulfonyl)oxyethyl)ether (1.3 g, 5 mmol). The mixture was refluxed for 10 days then filtered. The solvent was removed under reduced pressure to yield a crude ligand mixture. The complexes were prepared by addition of $Cu(ClO_4)_2 \cdot 6H_2O$ (1.85 g, 5 mmol) in acetonitrile to a solution of the ligands and refluxing for 1 h. Following removal of the solvent under reduced pressure, the residue was dissolved in water, and filtered. The copper(II) complexes were purified using a Sephadex CM-C25 column (3 × 30 cm), eluting with 0.1 M $NaClO_4$. The major purple band isolated was identified as $[Cu(L^1)](ClO_4)_2$. Yield: 1.37 g (52%). UV–vis (water) (M^{-1} cm^{-1}): ε_{280} = 4860, ε_{537} = 185. FAB-MS calcd. (found) (*m*/*z*): 333.1 (332.8) ($[Cu^{II}(L^1\text{-}H^+)]^+$ and $[Cu(L1)]^+$), 432.1 (432.2) ($[Cu^{II}L^1(ClO_4)]^+$). ES-MS calcd. (found) (*m*/*z*): 166.6 (166.8) ($[Cu^{II}L^1]^{2+}$), 271.2 (271.2) (L^1H^+), 332.1 (332.3) ($[Cu^{II}(L^1\text{-}H^+)]^+$), 432.1 (432.7) ($[Cu^{II}L^1(ClO_4)]^+$). Isotopic distributions are provided as supplementary material Fig S1.[2] Anal. calcd. for $Cu(L^1)(ClO_4)_2 \cdot H_2O$ (%): C 30.5, H 5.9, N 10.2; found: C 30.5, H 5.4, N 10.7.

A minor bluish-purple band was also eluted that was shown to be identical to the copper(II) complex of L^3 prepared by an independent route (19). FAB-MS (mNBA): 432 = $[Cu(L^3)(ClO_4)]^+$, 332 = $[Cu(H_{-1}L^3)]^+$. Anal. calcd. for $[Cu(C_{14}H_{30}N_4O)](ClO_4)_2$: C 31.56, H 5.67, N 10.51; found: C 31.50, H 5.66, N 10.42. Interestingly, there is no evidence for bridge formation across the ethylene carbons that would lead to L^2. The folding required of the bridging molecule makes this process very unlikely.

Following reaction of $[Cu(L^1)]^{2+}$ with excess Na_2S, the solution was allowed to stand for 30 min, whereupon decolourization and CuS precipitation were complete. After filtration and addition of 2 g NaOH, the free ligand was extracted using dichloromethane and, after drying of the organic layer, and solvent removal, a yellow oil was obtained. Yield: 0.61 g (45%) (based on cyclam). ^{1}H NMR (300 MHz) ($CDCl_3$) δ: 1.38, 1.51 (m, 2+2H, CH_2-C), 2.35 (m, 20H, CH_2-N), 3.20, 3.36 (m, 2+2H, CH_2-O). ^{13}C NMR (75.5 MHz) ($CDCl_3$) δ: 25.5 (CH_2-C), 47.9, 51.0, 53.3, 53.6, 57.6 (CH_2-N), 67.5 (CH_2-O). CI-MS (*m*/*z*): 270 (M^+), 271 (M + 1), 299 (M + 29), 311 (M + 41).

$[Ni(L^1)](ClO_4)_2$

To a solution of the ligand (0.61 g, 0.2 mmol) in 25 mL acetonitrile, was added $Ni(ClO_4)_2 \cdot 6H_2O$ (0.73 g, 0.2 mmol) in 10 mL acetonitrile. The solution was refluxed for 24 h, and evaporated to dryness. The residue was dissolved in water, filtered, and the complex purified by elution with 0.1 M $NaClO_4$ on a Sephadex CM-C25 column. The pale purple complex was recrystallized from sodium perchlorate solution. Yield: 0.44 g (42%). UV–vis (water) (M^{-1} cm^{-1}): ε_{339} = 7, ε_{520} = 4.9, ε_{1077} = 2.5; (acetonitrile) (M^{-1} cm^{-1}): ε_{326} = 17, ε_{498} = 8, ε_{722} = 3, ε_{953} = 4. FAB-MS (*m*/*z*) calcd. (found) for ($[Ni^{II}(L^1\text{-}H^+)]^+$): 327.19 (327.1); ($[Ni^{II}(L^1)(ClO_4)]^+$): 427.1

© 2002 NRC Canada

(427.1). Anal. calcd. for $Ni(L^1)(ClO_4)_2$ (%): C 31.8, H 5.7, N 10.6; found (avg of two independent investigations): C 33.1, H 5.9, N 10.9. We are unable to account for the anomalous C analysis. Mass spectra of the product are shown in Supplementary Figs. S2 and S3[2] including a simulated and experimental segment for the isotopic distribution of the $[Ni(L^1)(ClO_4)]^+$ ion.

The complex $[Ni(L^2)(ClO_4)](ClO_4)$ has been characterized crystallographically (22) and details of the oxidation to Ni(III) provided previously.

$[Ni(L^2)](PF_6)_2$

The exchange of the counter ion was achieved by dissolving ca. 50 mg of the crystallized nickel(II) perchlorate, in a saturated solution of $NaPF_6$, followed by slow evaporation to yield, almost quantitatively, brownish-yellow crystals of X-ray quality.

Solutions of $[Ni(III)(L^1)(OH_2)]^{3+}$ were prepared by oxidation of the nickel(II) ion with Co(III)(aq) in perchloric acid. In the kinetic studies, account was taken of the hydrogen ion content of the cobalt stock solution in preparing solutions for investigation. Titration of a sample of Ni(II) complex with 1 equiv of Co(III) showed an isosbestic point at 340 nm. UV–vis data for the resulting Ni(III) ion (M^{-1} cm^{-1}): $\varepsilon_{317} = 2157$, $\varepsilon_{394} = 1440$.

All high-field ^1H and ^{13}C NMR spectra were recorded on either a Bruker AC300 or AMX360 spectrometer. Chemical shifts are reported relative to tetramethylsilane (TMS). UV–vis spectra were obtained on a dual beam Cary 5 UV–vis–near-IR spectrometer, with the solvent as a background reference. Mass spectra were recorded on either a Finnegan GC330 using standard chemical ionization methods or, for salts, using a Kratos Concept double focusing magnetic instrument (liquid secondary ion mass spectra) with either fast atom bombardment (FAB) (*meta*-nitrobenzylalcohol matrix) or by electrospray (ES) techniques. All spectra were run in the positive ion mode unless otherwise shown. For electrospray, ionization was achieved by volatilizing a 1×10^{-4} M solution of the compound in a $CH_3CN–H_2O$ (1:1) solution.

Electron paramagnetic resonance spectra were recorded at 77 K on either a Varian E6 EPR spectrometer or a Bruker EMX300 instrument, with DPPH ($g = 2.0037$) used as an external standard. Elemental analyses were performed by Canadian Microanalytical Services, Vancouver, BC. A Princeton Applied Research Model 273 potentiostat–galvanostat interfaced to an IBM PC computer was used for electrochemical measurements. Cyclic voltammograms were obtained using the Headstart program (Princeton). A standard three-electrode electrochemical cell was employed, with a Pt microelectrode as the working electrode, a Pt bead as the counter electrode, and a Ag^+/Ag reference electrode, linked to the cell via a salt bridge. All electrochemistry was performed in dry acetonitrile solutions containing supporting electrolyte (0.1 M) (usually 0.1 M *t*-Bu_4NClO_4). Solutions were degassed with argon prior to electrochemical measurement. The ferrocinium/ferrocene (Fc^+/Fc) couple was used as an external standard. $E_{1/2}$ values are reported relative to the Ag^+/Ag couple ($E_{1/2}$ (Fc^+/Fc) = 0.1 V vs. (Ag^+/Ag)).

Kinetic measurements were made using an Applied Photophysics DX-17MV stopped-flow and data acquisition system. The nickel(III) solutions were prepared in situ by oxidation of the nickel(II) species in acidic media using a stoichiometric deficiency of Co^{3+}(aq) in 4.5 M $HClO_4$. Ionic strength was maintained with appropriate concentrations of $Li^+–H^+$-ClO_4. Adjustments were made to account for the effect of the acid added to the solution from the $[Co(H_2O)_6]^{3+}$ solution. Reactions were monitored under conditions where pseudo-first-order kinetics prevailed.

Crystallography

The hexafluorophosphate salt ($[Ni(L^2)](PF_6)_2$) was obtained as irregular brown crystals and mounted on a glass fiber using epoxy resin. All measurements were obtained using a Rigaku AFC6S diffractometer, with graphite monochromated Mo Kα radiation. Cell constants and an orientation matrix for data collection were obtained directly, using a least-squares refinement of 21 centred reflections in the range $34.04° < 2\theta < 39.51°$. The data were collected using the θ–2θ scan technique to a max 2θ value of 50.1°. ω scans of several intense reflections, made prior to data collection, had an average width at half-height of 0.31° with a take-off angle of 6.0°. Scans of $(0.94 + 0.35 \tan\theta)°$ were made at a speed of 8.0°/min (in ω). The weak reflections ($I < 10.0\sigma(I)$) were rescanned (maximum of four rescans) and the counts were accumulated to assure good counting statistics. Stationary background counts were recorded on each side of the reflection. The ratio of peak counting time to background counting time was 2:1. Standards were measured prior to every 150 reflections with no noticeable decay in intensity. Of the 4534 reflections collected, 4294 were unique. The data were corrected for Lorentz and polarization effects. The structure was solved by direct methods, using MITHRIL and DIRDIF (23). The non-hydrogen atoms were refined anisotropically, using a full-matrix least-squares approach. Neutral atom scattering factors were taken from Cromer and Weber (24). Anomolous dispersion effects were included in F_{calc} (25); the values for $\Delta f'$ and $\Delta f''$ were those of Cromer (26). All calculations were performed using the teXsan (27) crystallographic software package of Molecular Structure Corporation. Full details of the structure determination, including bond angles and distances, torsion angles, and intensity data are provided in supplementary Tables S1–S4.[2]

Acknowledgements

A.M.I. thanks the Government of South Africa for a Research Studentship, and the University of Victoria for an E. and M. Von Rudloff Scholarship. Chengtian Xu thanks the East China Normal University for a travel award. The support of the Natural Sciences and Engineering Research Council of Canada (NSERC) and the University of Victoria is gratefully acknowledged.

References

1. N.F. Curtis. J. Chem. Soc. 4409 (1960); Coord. Chem. Rev. **3**, 3 (1968).
2. D.C. Olson and J. Vasilevskis. Inorg. Chem. **8**, 1611 (1969); **10**, 463 (1971).
3. G.A. Melson. Coordination chemistry of macrocyclic compounds. Plenum Press, New York. 1979.
4. R.I. Haines and A. McAuley. Coord. Chem. Rev. **33**, 77 (1981).

© 2002 NRC Canada

5. K. Nag and A. Chakravorty. Coord. Chem. Rev. **32**, 77 (1980).
6. E.S. Gore and D.H. Busch. Inorg. Chem. **12**, 1 (1973).
7. S. Bhattacharya, S.R. Mukherjee, and A. Chakravorty. Inorg. Chem. **25**, 3448 (1986).
8. I.J. Clark, I.I. Creaser, L.M. Engelhardt, J.M. Harrowfield, E.R. Krausz, A.M. Moran, A.M. Sargeson, and A.H. White. Aust. J. Chem. **46**, 111 (1993).
9. (*a*) K. Wieghardt, W. Schmidt, W. Herrmann, and H. Kuppers. Inorg. Chem. **22**, 2953 (1983); (*b*) K. Wieghardt, W. Walz, B. Nuber, J. Weiss, A. Ozarowski, H. Stratemeier, and D. Reinen. Inorg. Chem. **25**, 1650 (1986).
10. D.H. Busch. Acc. Chem. Res. **11**, 3 (1978).
11. L. Fabbrizzi and D.M. Proserpio. J. Chem. Soc. Dalton Trans. 229 (1989).
12. E. Zeigerson, G. Ginsburg, N. Schwartz, Z. Luz, and D. Meyerstein. J. Chem. Soc. Chem. Commun. 241 (1979).
13. F.P. Bossu and D.W. Margerum. J. Am. Chem. Soc. **98**, 4003 (1976); Inorg. Chem. **16**, 210 (1977).
14. A.G. Lappin, C.K. Murray, and D.W. Margerum. Inorg. Chem. **17**, 1630 (1978).
15. (*a*) R. Machida, E. Kimura, and Y. Kushi. Inorg. Chem. **25**, 3461 (1986); (*b*) E. Kimura, H. Anan, T. Koike, and M. Shiro. J. Org. Chem. **54**, 3998 (1989).
16. R.I. Haines and A. McAuley. Inorg. Chem. **19**, 719 (1980).
17. M.G. Fairbank and A. McAuley. Inorg. Chem. **24**, 1233 (1985).
18. K.A. Beveridge, A. McAuley, and C. Xu. Inorg. Chem. **30**, 2074 (1991).
19. M. Rodopoulos, T. Rodopoulos, J.N. Bridson, L.I. Elding, S.J. Rettig, and A. McAuley. Inorg. Chem. **40**, 2737 (2001).
20. S. Brandes, S. Lacour, F. Denat, P. Pullumbi, and R. Guilard. J. Chem. Soc. Perkin Trans. 1, 639 (1998).
21. E.K. Barefield, F. Wagner, A.W. Herlinger, and A.R. Dahl. Inorg. Synth. **16**, 222 (1976).
22. A. McAuley, D.G. Fortier, D.H. Macartney, T.W. Whitcombe, and C. Xu. J. Chem. Soc. Dalton Trans. 2071 (1994).
23. (*a*) MITHRIL: C.J. Gilmore. J. Appl. Crystallogr. **17**, 42 (1984); (*b*) DIRDIF94: P.T. Beurskens, G. Admiral, G. Beurskens, W.P. Bosman, R. de Gelder, R. Israel, and J.M.M. Smits. The DIRDIF-94 program system. Technical Report of the Crystallography Laboratory, University of Nijmegen, The Netherlands. 1994.
24. D.T. Cromer and J.T. Weber. International tables for X-ray crystallography. Vol. IV. The Kynoch Press, Birmingham, U.K. 1974. Table 2.2A.
25. J.A. Ibers and W.C. Hamilton. Acta Crystallogr. **17**, 781 (1964).
26. D.T. Cromer. International tables for crystallography. Vol. IV The Kynoch Press, Birmingham, U.K. 1974. Table 2.3.1.
27. teXsan: Crystal structure analysis package. Molecular Structure Corporation, The Woodlands, Texas. 1992.
28. A. McAuley, K. Beveridge, S. Subramanian, and T.W. Whitcombe. J. Chem. Soc. Dalton Trans. 1821 (1991).
29. G. Hunter, A. McAuley, and T.W. Whitcombe. Inorg. Chem. **27**, 2634 (1988).
30. D.G. Fortier and A. McAuley. Inorg. Chem. **28**, 655 (1989).
31. M.J. D'Aniello, Jr., M.T. Mocella, F. Wagner, E.K. Barefield, and I.C. Paul. J. Am. Chem. Soc. **97**, 192 (1975).
32. D.G. Fortier and A. McAuley. J. Am. Chem Soc. **112**, 2640 (1990).
33. (*a*) B. Sonnberger, P. Huhn, A. Wasserburger, and F. Wasgestian. Inorg. Chim. Acta, **196**, 65 (1992); (*b*) E.K. Barefield and M.T. Mocella. J. Am. Chem. Soc. **97**, 4238 (1975).
34. K. Ishihara and A. McAuley. Unpublished observations. 1997.

© 2002 NRC Canada

Complexation of the La(III) cation by *p*-sulfonatocalix[4]arene — A ^{139}La NMR study

Yaël Israëli, Christine Bonal, Christian Detellier, Jean-Pierre Morel, and Nicole Morel-Desrosiers

Abstract: The complexation of La(III) by the water-soluble *p*-sulfonatocalix[4]arene was thermodynamically characterized by ^{139}La NMR. The ^{139}La NMR data are consistent with the formation of a 1:1 complex resulting from electrostatic interactions between the sulfonato groups and La(III). The complexation is entropy-driven and is characterized by a positive standard enthalpy ($\Delta_r H° = 11.0 \pm 0.5$ kJ mol^{-1}) and a positive standard entropy ($\Delta_r S° = 108 \pm 2$ J K^{-1} mol^{-1}), which are in very good agreement with the ones determined previously by microcalorimetry. The linear relationship between the ^{139}La NMR linewidth of the free and of the complexed cation, obtained at temperatures ranging from 290 to 340 K, excludes the formation of complexes or aggregates other than the 1:1 complex. It shows also that upon complexation, the effective radius of La(III) undergoes an increase of 50%, related to the replacement of water molecules of the hydrated cation by sulfonato groups of the ligand.

Key words: complexation, water-soluble calixarene, *p*-sulfonatocalix[4]arene, ^{139}La NMR, lanthanum.

Résumé : La complexation du cation lanthane(III) par le calix[4]arène *para* sulfonaté, soluble dans l'eau a été caractérisée thermodynamiquement par RMN du ^{139}La. Les données de RMN ont mis en évidence la formation d'un complexe 1 : 1 résultant de l'établissement de liaisons électrostatiques entre les groupements sulfonate et le cation La(III). La complexation est contrôlée par l'entropie et est caracterisée par une enthalpie standard positive ($\Delta_r H° = 11.0 \pm 0.5$ kJ mol^{-1}) et une entropie standard positive ($\Delta_r S° = 108 \pm 2$ J K^{-1} mol^{-1}). La relation linéaire entre la largeur à mi hauteur du ^{139}La sous sa forme non complexée et celle du ^{139}La sous sa forme complexée, obtenues à des températures variant de 290 à 340 K, exclut la formation de complexes et d'agrégats autre que le complexe 1 : 1. Cette linéarité montre aussi qu'au cours du processus de complexation, le rayon effectif du La(III) subit une augmentation de 50 %, liée à la substitution de molécules d'eau de la couche d'hydratation du cation par les groupements sulfonate du ligand.

Mots clés : complexation, calixarène soluble dans l'eau, calix[4]arène *para* sulfonaté, RMN du ^{139}La, lanthane.

Introduction

Calixarenes are macrocyclic compounds formed by phenolic units bridged by methylenic groups. They are widely studied since they are easily synthesized, functionalized, and present a hydrophobic cavity suitable for guest species (1, 2). Contrary to most of the calixarenes, the *p*-sulfonatocalixarenes are soluble in water. They provide hydrophobic and hydrophilic binding sites.

The extraction of lanthanides and actinides by calixarenes has received considerable attention. The extraction is enhanced in the case of calixarene-bearing phosphate ester groups (3). When the calixarene is substituted by 1,3-acid diethyl amide, the ligand shows a selectivity preference for larger lanthanides (4). This selectivity is interpreted by the formation of dimeric species while for Lu(III), a heavy lanthanide, a monomeric complex is formed. Formation of polymeric species is also mentioned when four (carbamoylmethyl)diphenylphosphine oxide groups substitute the calixarene. But, in this latter case, the presence of water and nitrate ions labilizes the complexes formed with heavy lanthanides (5). On the contrary, water molecules and nitrate ions have no influence on the geometry of the 1:1 complex formed between lanthanide cations, Ln(III), and the calix[4]arenes functionalized by four amide or phosphine oxide groups, as underlined by an NMR study performed in acetonitrile (5). It is reported in the literature that the extraction of heavy lanthanide cations with small ionic radii by calixarene carboxylate derivatives was favoured in the presence of sodium cations. The encapsulation of the sodium cation increases the rigidity of the extractant and consequently the Na-calix[4]arene species act as a preorganised extractant toward Ln(III) ions (6). The (*N*,*N*-diisobutylcarbamoylmethyl)octylphenylphosphine oxide (CMPO) is gener-

Received 16 August 2001. Published on the NRC Research Press Web site at http://canjchem.nrc.ca on 19 February 2002.

Y. Israëli,[1] C. Bonal, J.-P. Morel, and N. Morel-Desrosiers. Laboratoire de Thermodynamique des Solutions et des Polymères, UMR CNRS 6003, Université Blaise Pascal (Clermont-Ferrand II), 24 avenue des Landais, 63177 Aubière Cedex, France.
Y. Israëli[1] and C. Detellier. Ottawa-Carleton Chemistry Institute, University of Ottawa, Ottawa, ON K1N 6N5, Canada.

[1]Corresponding author (e-mail: yael.israeli@univ-bpclermont.fr).

 DOI: 10.1139/V02-005 © 2002 NRC Canada

ally used as extractant for the actinides. The fixation of CMPO groups to a calixarene increases considerably the extraction efficiency, showing the role played by the calixarene structure toward the selectivity (7, 8).

The *p*-sulfonatocalix[5]arene, *p*-sulfonatocalix[6]arene, and their carboxymethoxy derivatives have a pseudo-planar architecture suitable for uranyl complexation. An X-ray study performed on *p*-sulfonatocalix[5]arene shows that the complexation between the calixarene and the uranyl cation involves the phenolic oxygen atoms, while the complexation with the lanthanide cations occurs through the sulfonato groups (9). It was shown recently by X-ray crystallography that the complex formed between the water-soluble *p*-sulfonatocalix[4]arene and La(III) in the solid state results in discrete units with eight La(III) and six calixarene molecules also involving the sulfonato groups (10). Whereas in basic aqueous solution, Shinkai and co-workers (11) underline the formation of a 1:2 complex, the complexation study of lanthanide cations by the *p*-sulfonatocalix[4]arene in acidic medium undertaken by microcalorimetry leads to the determination of the thermodynamic values associated to the formation of a 1:1 complex (12).

In this paper, the complexation of La(III) by the water-soluble *p*-sulfonatocalix[4]arene is thermodynamically characterized by ^{139}La NMR. This technique also leads to information about the structure of the complex.

Experimental

Chemicals

The 25,26,27,28-tetrahydroxy-5,11,17,23-tetrasulfonic calix[4]arene hexahydrate (**1**) and lanthanum(III) chloride heptahydrate (purity 99%) were purchased from Acros Organics and Aldrich, respectively. The lanthanum chloride was used without further purification. The calixarene was purified by recrystallization from an aqueous solution and dried 24 h in an oven at 80–90°C. An amount of 11 ± 1 molecules of co-crystallized water was quantified by ^{1}H NMR using a 1.77 × 10^{-2} mol dm^{-3} solution of dioxane as internal reference.

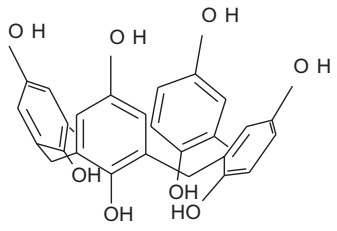

1

NMR measurements

^{139}La NMR spectra were recorded on a Bruker AMX-500 spectrometer at 70.65 MHz. NMR tubes (5 mm) sealed with parafilm were used. The solvent was a mixture of a 1 × 10^{-2} mol dm^{-3} solution of HCl (pH = 2.0), to avoid hydrolysis of La(III), and D_2O (w/w% D_2O = 5.0). All chemical shifts were referenced against the 1.01 mM stock solution of $LaCl_3$ in 10 mM HCl solution, used throughout this study at 300 K. The chemical shift of the stock solution is –0.22 ppm referenced to a 7.1 mM solution of $LaCl_3$ in 5% D_2O (0 ppm at 300 K). A 90° pulse of 16 μs and a spectral width of 14.3 kHz were used. The acquisition time and the relaxation delay ranged from 15 to 35 ms and 35 to 15 ms, respectively; 10 000 – 87 000 scans were accumulated per spectrum. The temperature was estimated to be reliable at ±0.5 K. The linewidths and chemical shifts were determined by fitting each peak with a Lorentzian line shape.

Results

The evolution of the ^{139}La NMR spectra of 1.01 mM solutions of $LaCl_3$, in 10 mM HCl (pH = 2.0), at 300 K in the absence and in the presence of an increasing amount of *p*-sulfonatocalix[4]arene defined by the ratio ρ (ρ = $[calixarene]_{total}/[La(III)]_{total}$), is shown in Fig. 1. Initially, La(III) was characterized by a peak at –0.22 ppm and a linewidth at half-height of 102 Hz. Upon addition of calixarene, only one peak was observed indicating a fast exchange on the ^{139}La NMR time scale between the free La(III) and the complexed cation. The peak shifted to lower frequency and broadened for ρ values varying from 0 to 3.21. For example, for a ρ value of 3.21, the peak shifted from –0.22 to –6.75 ppm and an increase in the linewidth of 213 Hz was observed. The same experiments were performed at various temperatures, ranging from 290 to 340 K, and similar evolution was observed.

Figure 2 shows the evolution of the chemical shifts of La(III) as a function of ρ at various temperatures. The same trend was observed for each temperature: the chemical shift increased strongly for values of the ratio lower than 1 and reached a plateau at higher values, suggesting the formation of a 1:1 complex between La(III) and the calix[4]arene. In acidic aqueous solution (pH 2.0), the *p*-sulfonatocalix[4]arene (C^{4-}) is a tetra-anion, since the four sulfonic groups are totally dissociated (13). On the basis of a 1:1 stoichiometry, the complexation can be described by eq. [1].

$$[1] \quad La(III) + (p\text{-sulfonatocalix[4]arene})^{4-} = (La\text{–}p\text{-sulfonatocalix[4]arene})^{-} \quad (La, C)^{-}$$

Under fast chemical exchange conditions, the observed chemical shift is the population average of the chemical shift of the free cation (δ_A) and of the complexed cation $(La,C)^-$ (δ_B). It is given by eq. [2].

$$[2] \quad \delta_{observed} = \delta_A \times ([La^{3+}]/[La^{3+}]_{total}) + \delta_B \times ([(La,C)^-]/[La^{3+}]_{total})$$

Since $[La(III)] = [La(III)]_0 - [(La,C)^-]$ and $[C^{4-}] = \rho[La(III)]_0 - [(La,C)^-]$ ($[La(III)]_0$ designates the initial concentration of the cation) and assuming that the solutions are dilute enough to neglect the activity coefficients, the concentration of the 1:1 complex deduced from the expression of the stability constant (K) is given by eq. [3]

$$[3] \quad [(La,C)^-] = 0.5C - (0.25C^2 - \rho D)^{1/2}$$

where $C = [La(III)]_0 + \rho[La(III)]_0 + K^{-1}$ and $D = [La(III)]_0^2$.

Equation [3] combined with eq. [2] led to a non-linear regression (14), which was applied on the observed chemical

© 2002 NRC Canada

Fig. 1. ^{139}La NMR spectra of $LaCl_3$ (1.01 mM in 10 mM HCl) in the presence of various amounts of *p*-sulfonatocalix[4]arene at 300 K (ρ = $[calixarene]_{total}/[La^{3+}]_{total}$).

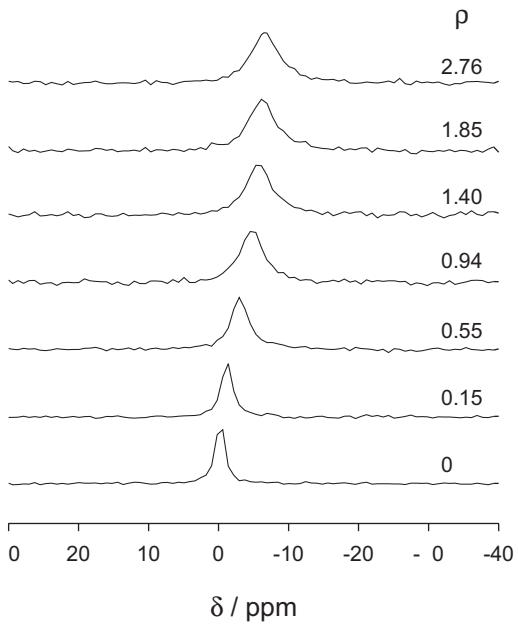

Fig. 2. Variation of ^{139}La chemical shifts of $LaCl_3$ (1.01 mM in 10 mM HCl) as a function of ρ at various temperatures. The points are experimental data and the solid lines are calculated.

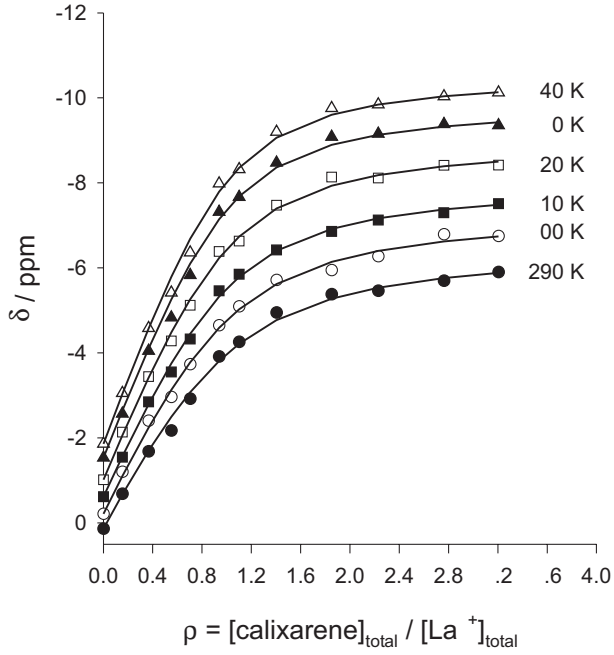

shifts to determine the stability constant of formation of the complex (*K*) and δ_B. The data are reported in Table 1. For example at 300 K, the value of *K* and δ_B obtained are (4.9 ± 0.7) × 10^3 and –7.3 ± 0.2 ppm, respectively. From the van't Hoff plot, a standard enthalpy ($\Delta_r H°$) of 11.0 ± 0.5 kJ mol^{-1} and a standard entropy ($\Delta_r S°$) of 108 ± 2 J K^{-1} mol^{-1} were obtained for the formation of the complex.

The ^{139}La NMR linewidths increased with an increase of the calixarene concentration. For values of ρ higher than 1, it tended to reach a plateau, as shown in Fig. 3. For example, at 290 K, the linewidth varied from 122 Hz (at ρ = 0) to 385 Hz (at ρ = 3.21). Similar to the chemical shift, the observed linewidths are the population average of the linewidth of the two sites, free and complexed La(III) of eq. [1]. They are described by eq. [4].

$$[4] \quad (\Delta\nu_{1/2})_{observed} = (\Delta\nu_{1/2})_A \times ([La^{3+}]/[La^{3+}]_{total}) + (\Delta\nu_{1/2})_B \times ([(La,C)^-]/[La^{3+}]_{total})$$

A non-linear regression, based on a 1:1 stoichiometry model mentioned above, was applied to the observed linewidths. The linewidth of the complex $(\Delta\nu_{1/2})_B$ and the equilibrium constant of formation (*K*) were determined (Table 1). At 300 K, the value of *K* was (11 ± 3) × 10^3, compared to (4.9 ± 0.7) × 10^3 obtained from the evolution of the chemical shift with ρ. This difference can be attributed to the errors characterizing the linewidth, due to the low concentrations of the solutions of La(III) (1 mM), and to the large broadening of the peak. The standard enthalpy and entropy of formation were 10 ± 2 kJ mol^{-1} and 110 ± 5 J K^{-1} mol^{-1}, respectively. These values were similar to those obtained from the chemical shift analysis. The data were also analysed by using the values of *K* obtained from the chemical shift analysis. A good fit was then observed, as shown in Fig. 3, and the linewidths of the complex were in the same order of magnitude as the ones obtained when *K* was varied (Table 1).

Discussion

The ^{139}La NMR data are consistent with the formation of a 1:1 complex between La(III) and *p*-sulfonatocalix[4]arene in acidic medium (pH 2.0). The method leads to the determination of the stability constant *(K)*, the standard enthalpy $\Delta_r H°$), and the standard entropy ($\Delta_r S°$) of complexation. It was reported previously (12) that the counter anion does not actively participate in the complexation process, since the thermodynamic parameters do not depend on the nature of the counter anion (Table 2). Table 2 shows also that the standard enthalpy ($\Delta_r H°$ = 11.0 ± 0.5 kJ mol^{-1}) and entropy ($\Delta_r S°$ = 108 ± 2 J K^{-1} mol^{-1}), obtained by NMR, are in good agreement with the ones measured by calorimetry, 9.2 ± 0.1 kJ mol^{-1} and 112 ± 1 J K^{-1} mol^{-1}, respectively (12).

The complexation of lanthanide cations by *p*-sulfonatocalix[4]arene was studied by Shinkai and co-workers (11) in alkaline media (pH 11.7). It was shown that 1:2 Ln(III)–calixarene complexes are formed. Stability constants were determined from pH-titration methods, giving at 25°C a log *K* value of 19.26 in a 0.1 M ionic strength in the case of La(III). In basic medium (pH 11.7), the complex is formed from covalent bonding between the oxygen atoms of the phenolic groups and La(III), resulting in a high stability constant, while in this study, in acidic medium (pH 2.0), the driving forces are primarily electrostatic between the sulfonato groups and La(III) (12).

The stability constants obtained in this study are in the same order of magnitude as those reported for the complexation of *p*-sulfonatocalix[4]arene with choline derivatives and quaternary ammonium cations, in which case

© 2002 NRC Canada

Table 1. Stability constant (K) of formation of the complex and NMR parameters characteristic of the uncomplexed La(III) and of the complex $(La,C)^{-}$ at various temperatures.

T (K)	K (1×10^{-3})	δ_A (ppm)	δ_B (ppm)	$(\Delta\nu_{1/2})_B$ (Hz)[a]	$(\Delta\nu_{1/2})_B$ (Hz)[b]
290	4.2 ± 0.7	0.13	–6.5 ± 0.2	382 ± 10	413 ± 19
300	4.9 ± 0.7	–0.22	–7.3 ± 0.2	314 ± 6	335 ± 11
310	5.8 ± 0.6	–0.62	–8.0 ± 0.1	297 ± 6	283 ± 7
320	6.5 ± 0.9	–1.02	–9.0 ± 0.2	207 ± 7	218 ± 11
330	8 ± 1	–1.53	–9.9 ± 0.2	189 ± 5	189 ± 5
340	8 ± 1	–1.86	–10.6 ± 0.2	157 ± 2	165 ± 4

[a]In the non-linear regression, K and $(\Delta\nu_{1/2})_B$ are the parameters.
[b]In the non-linear regression, the values of K are the ones determined from the observed chemical shifts.

Fig. 3. ^{139}La NMR linewidths of $LaCl_3$ (1.01 mM in 10 mM HCl) in the presence of various quantities of *p*-sulfonatocalix-[4]arene at various temperatures. The points are experimental data and the solid lines are calculated. To fit the data, the values of the stability constants have been fixed to the ones obtained from the observed ^{139}La chemical shifts.

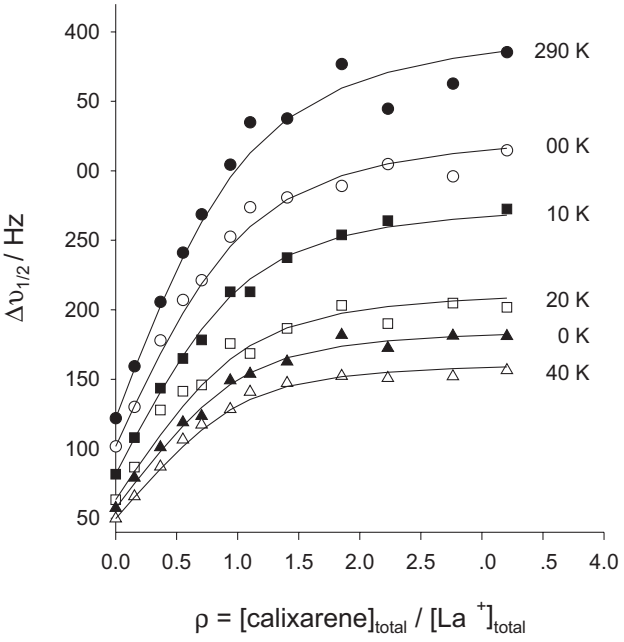

log K ranges from 4.0 to 5.6 at pH 7.3 (15) at 296 K. A value of 1.24×10^4 was obtained for the 1:1 complex formation of the *p*-sulfonatocalix[6]arene with the Auramine O dye at pH 7.0 (16).

The values of $\Delta_r H°$ and $\Delta_r S°$ indicate that the complexation is entropy driven. Moreover, the process is endothermic and so it is energetically unfavourable, while the complexation process is exothermic and enthalpy driven with a series of tetraalkyl ammonium cations (12) and with the trimethylanilinium cation and the *N*,*N*-dimethylindoaniline. The corresponding enthalpies are –26 ± 1 kJ mol^{-1} (17) and –29.3 ± 0.8 kJ mol^{-1} (18), respectively. It was reported that these two cations are inserted into the calixarene cavity. In the case of the trimethylanilinium cation, in acidic medium (pH 0.4), the complexation is driven by hydrophobic forces (19*a*), while in neutral medium (pH 7.3) the driving forces are both hydrophobic and electrostatic (19) and both the phenyl and the ammonium moiety can be inserted into the cavity of the calixarene. The complexation with *N*,*N*-dimethylindoaniline (Phenol Blue) involves electrostatic interactions with the sulfonato groups and hydrogen bonding with the OH groups which stabilize the charge separated excited state of the Phenol Blue (20). The complexation of La(III) by ribose (21) and glucitol (14*b*) have been studied also by ^{139}La NMR and negative enthalpy values of –12 and –10 ± 1 kJ mol^{-1} have been found, respectively. With these ligands, the complex results from interaction of the lone pairs of the hydroxyl oxygen atom with the positive charge of the lanthanum cation. In the case of this study, the complex results from electrostatic interactions between La(III) and the sulfonato groups. These interactions are characterized by positive values both of the enthalpy and the entropy. These positive values are mainly related to the partial desolvation of the cation and the sulfonato groups of the ligand, occurring upon complexation and leading to the release of water molecules (12).

The evolution of the ^{139}La NMR linewidth with the concentration of calixarene is similar to the variation of the chemical shifts, indicating also the formation of a 1:1 complex. The linewidth of the complex ($(\Delta\nu_{1/2})_B$) varies linearly with the inverse of the temperature (Fig. 4*a*) indicating the absence of a chemical exchange contribution to the transverse relaxation rate. Since a fast exchange is observed on the ^{139}La NMR time scale, this linear relationship confirms that the observed linewidths are the population average of the linewidths of the two sites, free and complexed La(III), of eq. [1]. A Lorentzian shape, showing that the extreme narrowing conditions are fulfilled, characterized all the observed ^{139}La NMR signals. The relaxation of ^{139}La is purely quadrupolar and the transverse relaxation time is given by eq. [5] (22, 23).

$$[5] \qquad T_2^{-1} = \pi\,(\Delta\nu)_{1/2} = 2\pi^2/49\chi^2\tau_c$$

where χ is the quadrupolar coupling constant and τ_c is the correlation time.

According to the Debye–Stokes–Einstein relationship (24), τ_c is proportional to the volume of the reorienting entity. In aqueous solution, the La(III) cation is coordinated by nine water molecules (25). The molecular volume of $La(H_2O)_9^{3+}$ is 2.68×10^{-28} m^3 (26), which corresponds to an effective radius estimated to be 4 Å. The plot of $(\Delta\nu_{1/2})_B$ as a function of the linewidth of the uncomplexed cation obtained at different temperatures is a linear plot with a slope of 3.37 ± 0.03 (Fig. 4*b*). It is reasonable to assume that the viscosity of the solution in the presence and in the absence of calixarene is in the same order of magnitude, since the initial concentration of La(III) is weak. The χ values are supposed

© 2002 NRC Canada

Table 2. Thermodynamic parameters of the complexation of La^{3+} with the *p*-sulfonatocalix[4]arene from NMR and microcalorimetric studies (12) at 300 K.

Compound	Method	log *K*	$\Delta_r H°$ (kJ mol^{-1})	$\Delta_r S°$ (J K^{-1} mol^{-1})
$LaCl_3$	Microcalorimetry[a]	4.23 ± 0.05	9.2 ± 0.1	112 ± 1
$La(NO_3)_3$	Microcalorimetry[a]	4.23 ± 0.09	8.5 ± 0.2	109 ± 2
$LaCl_3$	^{139}La NMR	3.7 ± 0.1[b]	11.0 ± 0.5[b]	108 ± 2[b]

[a]Reference 12.
[b]Obtained from the evolution of the chemical shifts.

Fig. 4. (*a*) ^{139}La NMR linewidths of the uncomplexed (A) and complexed (B) La(III) as a function of 1/*T*. (*b*) ^{139}La NMR linewidths of the complexed La(III) as a function of the ^{139}La NMR linewidths of the uncomplexed La(III) obtained at various temperatures: 290 K (●), 300 K (○), 310 K (■), 320 K (□), 330 K (▲), 340 K (△).

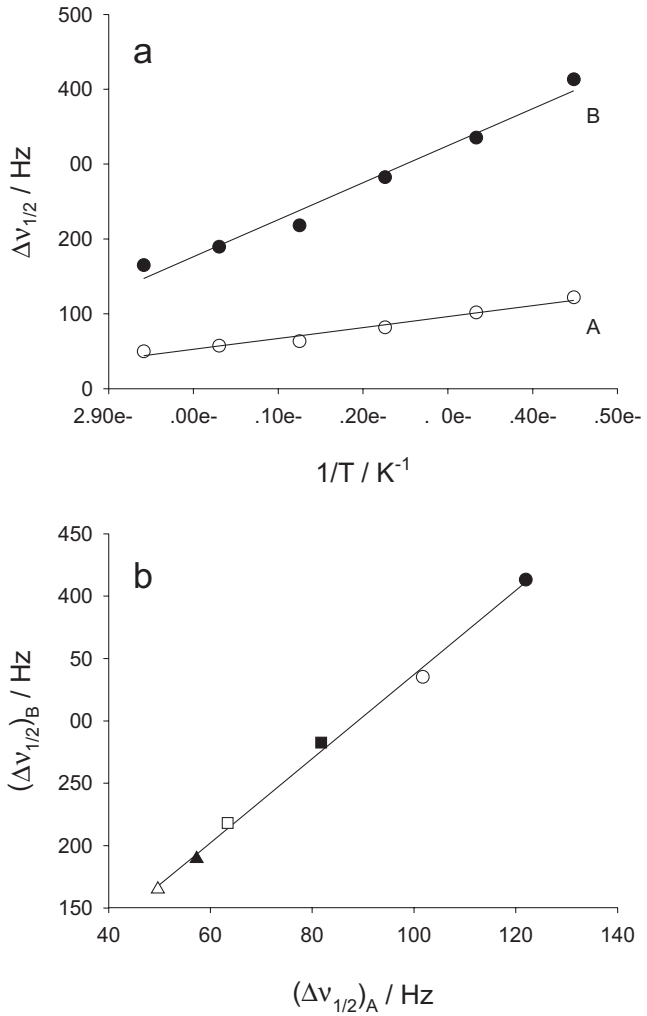

to be similar in the case of the complex and solvated cations. Under these two assumptions, eq. [6] gives the slope of the plot given in Fig. 4*b*.

$$[6] \quad \text{Slope} = ((\Delta\nu)_{1/2})_B / ((\Delta\nu)_{1/2})_A \approx (\tau_c)_B/(\tau_c)_A \approx (a^3)_B/(a^3)_A$$

On the basis of eq. [6], the effective radius of the complex is estimated to be approximately 6 Å, which is in good agreement with the formation of a 1:1 complex and consequently the formation of a 8:6 complex (or of other aggregates) as observed in the solid state (10) can be excluded. The size of the effective radius of La(III) undergoes an increase of 50% upon complexation. The complexation of trivalent lanthanides by CMPO-like calixarenes was studied by ^{1}H NMR in $CDCl_3$ (27). The radii of the uncomplexed calixarene and of the calixarene complexed by La(III) were calculated to be 9.5 and 13.2 Å, respectively, showing an increase of 40%. It is worthwhile to note that the reasonable increase of the radius of La(III) upon complexation confirms the assumption about the similarity between the quadrupolar coupling constant (χ) of the solvated and the complexed cations.

A crystal was obtained from $LaCl_3$ and *p*-sulfonatocalix[4]arene solutions and was analysed by X-ray crystallography (10). Assimilating the calix[4]arene to a sphere, its radius was estimated to be 5.9 Å. This value is similar to that of the radius of the La(III)–*p*-sulfonatocalix[4]arene complex (6 Å) obtained by ^{139}La NMR. This result indicates that the ligand belongs to the inner sphere of coordination of the La(III) cation and that, upon complexation, some molecules of water are replaced by some sulfonato groups.

In conclusion, in acidic aqueous solution, the complex formed between La(III) and *p*-sulfonatocalix[4]arene is a 1:1 complex as shown by ^{139}La NMR and previously by microcalorimetry. The complexation process is characterized by positive enthalpy and entropy values; it is entropy driven. This results from the replacement of water molecules of the hydrated cation by sulfonato groups of the ligand, engaged into electrostatic interactions with La(III). The 1:1 complex formed in aqueous solution can be considered as the first step in the formation of higher stoichiometry complexes leading to the structure observed in the solid state (10).

Acknowledgment

The Natural Sciences and Engineering Research Council of Canada (NSERC) is gratefully acknowledged for a research grant. Dr Glenn Facey is thanked for his help in recording the NMR spectra.

References

1. A. Pocchini and R. Ungaro. Calixarenes and related hosts. *In* Comprehensive supramolecular chemistry. *Edited by* F. Vögtle. Elsevier Science Ltd., Oxford. 1996. p. 103.
2. R. Perrin and S. Harris. *In* Calixarenes: A versatile class of macrocyclic compounds. *Edited by* J. Vicens and V. Böhmer. Kluwer Academic Publishers, London. 1991. p. 235.
3. J.M. Harrowfield, M. Mocerino, B.J. Peachey, B.W. Skelton, and A.H. White. J. Chem. Soc. Dalton Trans. 1687 (1996).

© 2002 NRC Canada

4. P.D. Beer, M.G.B. Drew, A. Grieve, M. Kan, P.B. Leeson, G. Nicholson, M.I. Ogden, and G. Williams. Chem. Commun. 1117 (1996).
5. B. Lambert, V. Jacques, A. Shivanyuk, S.E. Matthews, A. Tunayar, M. Baaden, G. Wipff, V. Böhmer, and J.F. Desreux. Inorg. Chem. **39**, 2033 (2000).
6. K. Ohto, M. Yano, K. Inoue, T. Nagasaki, M. Goto, F. Nakashio, and S. Shinkai. Polyhedron, **16**, 1655 (1997).
7. F. Arnaud-Neu, V. Böhmer, J.-F. Dozol, C. Grüttner, R.A. Jakobi, D. Kraft, O. Mauprivez, H. Rouquette, M.-J. Schwing-Weill, N. Simon, and W. Vogt. J. Chem. Soc. Perkin Trans. 2, 1175 (1996).
8. L.H. Delmau, N. Simon, M.-J. Schwing-Weill, F. Arnaud-Neu, J.-F. Dozol, S. Eymard, B. Tournois, C. Grüttner, C. Musigmann, A. Tunayar, and V. Böhmer. Sep. Sci. Technol. **34**, 863 (1999).
9. J.W. Steed, C.P. Johnson, C.L. Barnes, R.K. Juneja, J.L. Atwood, S. Reilly, R.L. Hollis, P.H. Smith, and D.L. Clark. J. Am. Chem. Soc. **117**, 11 426 (1995).
10. Y. Israëli, G.P.A. Yap, and C. Detellier. Supramol. Chem. **12**, 457 (2001).
11. I. Yoshida, N. Yamamoto, F. Sagara, K. Ueno, D. Ishii, and S. Shinkai. Chem. Lett. 2105 (1991).
12. C. Bonal, Y. Israëli, J.-P. Morel, and N. Morel-Desrosiers. J. Chem. Soc. Perkin Trans. 2, 1075 (2001).
13. (*a*) J.-P. Scharff and M. Mahjoubi. New. J. Chem. **15**, 883 (1991); (*b*) G. Arena, R. Cali, G.G. Lombardo, E. Rizzarelli, D. Sciotto, R. Ungaro, and A. Casnati. Supramol. Chem. **1**, 19 (1992); (*c*) I. Yoshida, N. Yamamoto, F. Sagara, D. Ishii, K. Ueno, and S. Shinkai. Bull. Chem. Soc. Jpn. **65**, 1012 (1992).
14. (*a*) Z. Chen and C. Detellier. J. Solution Chem. **21**, 941 (1992); (*b*) Y. Israëli and C. Detellier. Carbohydr. Res. **297**, 201 (1997).
15. J.-M. Lehn, R. Meric, J.-P. Vigneron, M. Cesario, J. Guilhem, C. Pascard, Z. Asfari, and J. Vicens. Supramol. Chem. **5**, 97 (1995).
16. Y. Zhang, R.A. Agbaria, and I.M. Warner. Supramol. Chem. **8**, 309 (1997).
17. S. Shinkai, K. Araki, and O. Manabe. J. Am. Chem. Soc. **110**, 7214 (1988).
18. W. Tao and M. Barra. J. Chem. Soc. Perkin Trans. 2, 1957 (1988).
19. (*a*) S. Shinkai, K. Araki, T. Matsuda, N. Nishiyama, H. Ikeda, I. Takasu, and M. Iwamoto. J. Am. Chem. Soc. **112**, 9053 (1990); (*b*) S. Shinkai. Tetrahedron, **49**, 8933 (1993).
20. S. Shinkai. Pure Appl. Chem. **58**, 1523 (1986).
21. Z. Chen, N. Morel-Desrosiers, J.-P. Morel, and C. Detellier. Can. J. Chem. **72**, 1753 (1994).
22. C. Detellier. *In* NMR of newly accessible nuclei. Vol. 2. (Chemically and biochemically important elements). *Edited by* P. Laszlo. Academic Press, New York. 1983. p. 105.
23. C. Detellier, H.P. Graves, and K.M. Brière. Alkali metal NMR studies of synthetic and natural ionophore complexes. *In* Isotopes in the physical and biomedical science. Vol. 2. *Edited by* E. Buncel and J.R. Jones. Elsevier, Amsterdam. 1991. Chap. 4. p. 159.
24. M. Bisnaire, C. Detellier, and D. Nadon. Can. J. Chem. **60**, 3071 (1982).
25. (*a*) A. Habenschuss and F.H. Spedding. J. Chem. Phys. **70**, 3758 (1979); (*b*) A. Habenschuss and F.H. Spedding. J. Chem. Phys. **73**, 442 (1980); (*c*) H. Kanno. J. Phys. Chem. **92**, 4232 (1988); (*d*) C. Cossy and A.E. Merbach. Pure Appl. Chem. **60**, 1785 (1988); (*e*) S. Galera, J.M. Lluch, A. Oliva, J. Bertrán, F. Foglia, L. Helm, and A.E. Merbach. New. J. Chem. **17**, 773 (1993).
26. T. Yaita, D. Ito, and S. Tachimori. J. Phys. Chem. B, **102**, 3886 (1998).
27. L.H. Delmau. Extraction de lanthanides et d'actinides trivalents par des calixarènes fonctionnalisés. Etude de la structure des complexes en solution par résonance magnétique nucléaire. Ph.D thèse de l'Université Louis Pasteur de Strasbourg, France, 19 septembre 1997.

© 2002 NRC Canada

Synthesis of new fluorophores derived from monoazacrown ethers and coumarin nucleus

Ernesto Brunet, Pablo García-Losada, Juan-Carlos Rodríguez-Ubis, and Olga Juanes

Abstract: New ionophores derived from azacrown ethers attached to coumarins have been synthesized and characterized. The alkaline-earth complexes of these new ligands were studied from their UV–vis, NMR, and fluorescence data. Some systems displayed bathochromic shifts and fluorescence decreases upon complexation with Ca^{2+} that may make them useful signaling devices of this metal.

Key words: alkaline earth, emission, molecular modeling.

Résumé : On a synthétisé et caractérisé des nouveaux ionophores dérivés d'éthers aza-couronnes attachés à des coumarines. On a étudié les données de spectroscopie UV–vis, de RMN et de fluorescence des complexes de ces nouveaux ligands avec des métaux alcalinoterreux. Dans quelques systèmes, on observe des déplacements bathochromes et une diminution de la fluorescence lors de la complexation avec du Ca^{2+}; cette propriété peut les rendre utiles dans les appareils de détection de ce métal.

Mots clés : alcalinoterreux, émission, modelage moléculaire.

[Traduit par la Rédaction]

Introduction

The coumarin nucleus has been the focus of our recent research concerning the design of photoactive and luminescence probes (1). Coumarins are interesting heterocycles because of their photochemical and photophysical properties (2), leading to numerous industrial and laser dye applications (3). It is well known that coumarins increase their dipolar moment when excited. Albeit the change can be as large as 6 D in some cases, it has been argued that this is too low a variation to support true internal charge transfer (ICT) species in the excited state. Semi-empirical calculations (4) support that it is more likely that the charge separated resonance forms depicted in Fig. 1 have simply a superior contribution in the excited state. Whatever the reason, excitation of coumarin chromophore increases the electron density of its carbonyl groups, this increase being higher when X (Fig. 1) is an effective electron donor as R_2N. Therefore, the interaction of the carbonyl groups of an excited 3-acylcoumarin with metal cations coupled with the presence of an additional cationic receptor might constitute a good signaling device, provided significant selectivity is attained.

In previous work (5), we investigated the behaviour of 3-aroylcoumarins **1** (Fig. 2) towards alkaline earth cations. While compound **1b** (15-crown-5 derivative) displayed small, similar bathochromic shifts in its UV–vis spectra for the studied cations and, therefore, no selectivity, **1c** (18-crown-6 derivative) and especially **1a** (ethylenedioxa derivative) (6) suffered quite a large red shift (+48 nm) only when complexed to Mg^{2+}.

The conduct of **1a** suggested that the carbonyl groups were paramount for the chelation of the metal, the charge–radius ratio of Mg^{2+} being the best fitted within alkaline earth metals, and that only the 15-crown-5 was able to interfere with them. We thus planned the relocation of crowns relative to the 3-acylcoumarin chromophore for them to cooperate, not compete, to obtain different selectivity in cation recognition (7). In this work we report the synthesis of the ligands **2**–**4** (Fig. 2), in which crown ethers are attached to the 3-position of coumarins through a flexible alkoxycarbonyl spacer. The alkaline-earth complexes of these new ligands were studied from their UV–vis (Table 1), ^{1}H NMR (Table 2), and fluorescence data (Table 3).

Results and discussion

Synthesis precious

Preparation of **2**–**4** were performed in four or five steps from the corresponding 4-substituted salicylaldehyde by means of Knoevenagel condensation with malonic acid as the key step (Scheme 1). This reaction took place with moderate yields except in the case of R = NEt_2, in which it was necessary to use diethyl malonate and hence the additional hydrolysis of the resulting ethyl ester. Subsequent treatment with oxalyl chloride led us to the acyl chloride that then re-

Received 13 September 2001. Published on the NRC Research Press Web site at http://canjchem.nrc.ca on 21 February 2002.

E. Brunet, P. García-Losada, J.-C. Rodríguez-Ubis, and O. Juanes.[1] Departamento de Química Orgánica C-1, Facultad de Ciencias, Universidad Autónoma de Madrid, 28049 Madrid, Spain.

[1]Corresponding author (e-mail: olga.juanes@uam.es).

 DOI: 10.1139/V02-006 © 2002 NRC Canada

Fig. 1. Charge-separated resonance forms of 3-acylcoumarins.

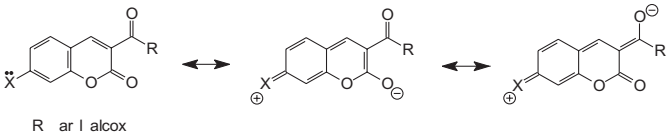

Fig. 2. Studied compounds in this and previous work (see text).

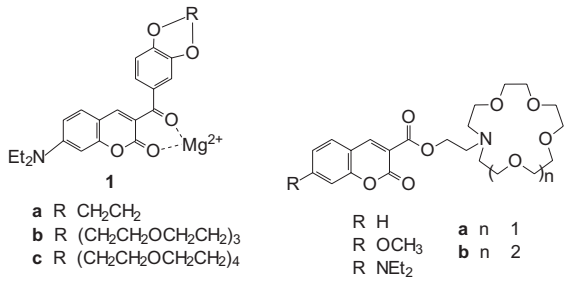

acted with the hydroxyethyl azacrown to afford the final compounds in 45–50% yield.

UV–vis and ^{1}H NMR data

Ligands **2**, **3a**, and **3b** formed complexes of 1:1 stoichiometry with alkaline earth salts as determined by UV–vis and ^{1}H NMR (CD_3CN) titrations. No spectral variations were observed after addition of 1 equiv of metal.

Table 1 and Fig. 3 show that the larger bathochromic shifts occurred for the Et_2N derivatives **4** as expected (vide supra, Fig. 1) but, interestingly, with Ca^{2+} (to a lower extent with Ba^{2+}) and not with Mg^{2+}, in contrast to compounds **1** and other related compounds reported in the literature (8). This sizable red shift indicates that the metal cation closely interacts with the chromophore.

The relatively large deshielding of crown ether NMR proton signals (cf. Table 2) displayed by **4a** when titrated with Ca^{2+}, demonstrates the cation–crown interaction. Besides, the protons of the coumarin ring of **4a** also bear a similar deshielding with Ca^{2+} to that suffered by **1** with Mg^{2+}, where the latter can only interact with the carbonyl groups of the 3-aroylcoumarin. This fact and UV–vis data strongly suggest the carbonyl–crown cooperation in Ca^{2+} binding. Molecular modeling at the ZINDO/1 semi-empirical level predicts relatively stable structures where both the chromen carbonyl and ester groups may participate in the chelation to Ca^{2+} (Fig. 4).

Emission spectra

Only compounds **3** and **4** (**a**, **b**) were fluorescent. Table 3 summarizes the emission parameters of the studied compounds. Compounds **3a** and **3b** showed a slight or moderated increase of fluorescence. The case of complexes **4a** and **4b** with calcium is noteworthy, as they displayed extinction of fluorescence (up to 54%). In general, the presence of the metals should provide new pathways for collisional or static quenching of emission, which might be enhanced if the chromophore and the crown are close and **4b** gives the best host–guest fit.

Table 1. Wavelength of the absorption maxima (nm) of ligands and alkaline earth complexes.

		Complexes		
Compound	Ligand	Mg^{2+}	Ca^{2+}	Ba^{2+}
2a	291	+2	+5	+8
3a	349	+1	+4	+4
4a	418	+4	+15	+11
2b	288	+1	+7	+6
3b	345	+2	+9	+6
4b	418	+4	+20	+15

Scheme 1. Reaction pathway.

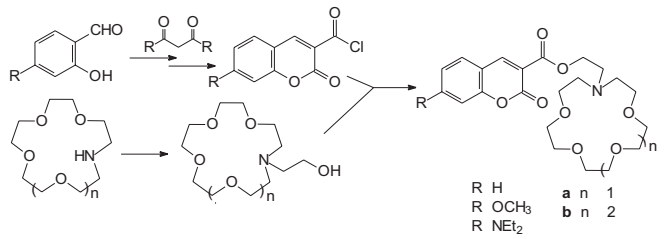

The variation of Stokes' shifts (SS) upon complexation is even more interesting. This is a manifold phenomenon that has been largely discussed in related compounds (9). After excitation, the molecule relaxes in a lapse of ps to the lowest vibrational level of the first excited electronic state (S_1). This relaxation is so fast that it usually occurs before measurements can be made on the system. (10) The lowest S_1 state generally has a longer lifetime that allows changes in the local environment, which may even involve ample conformational movements. Therefore, if excitation increases the molecular dipole moment, as largely occurs in coumarins (11), both reorganization of the solvent and a conformational change may be involved to stabilize the excited state, hence making SS larger (12). These facts are summarized in Fig. 5.

Ligands **3** displayed larger SS as compared to **4**. Excitation should lead to less stable S_1 species in the case of **3** because the charge-separated resonance forms of Fig. 1 must be less stable when the positive charge develops on an OMe group rather than on a NEt_2 group. This increases the need of solvent relaxation by excited **3**, which thus suffers larger SS. On the other hand, the smallest SS were observed in all cases for the Ca^{2+} complexes, indicating that their excited states have the lowest requirement of extra stabilization either by solvation or conformational changes. This is compatible with the proposed cooperation between the crown and the coumarin, in which the metal plays part of the stabilization role to be performed by the solvent, interacting with the negative end of the charge-separated species. The cooperation between the crown and the coumarin imposes a certain rigidity impeding large conformational changes. The stronger the crown-mediated interaction between the coumarin and the metal, the higher the stabilization of the excited state, and hence, the smaller SS. This occurs for the **4b**·Ca^{2+} complex whose spectroscopic data and molecular modeling suggested the strongest coumarin–metal interaction of the studied compounds.

© 2002 NRC Canada

Table 2. ^{1}H NMR chemical shifts (δ, ppm) of compounds **1** and **4a** and Δδ induced by Mg^{2+} and Ca^{2+}.

Compound	H-4	H-5	H-6	H-8	CH_2OCO	CH_2N	CH_2O crown	CH_2N crown
1	8.10	7.55	6.82	6.65	—	—	—	—
1·Mg^{2+}	+0.50	+0.15	+0.23	+0.17				
1·Ca^{2+}	0.00	0.00	0.00	0.00				
4a	8.56	7.58	6.82	6.60	4.38	2.92	3.65	2.85
4a·Ca^{2+}	+0.34	+0.17	+0.12	+0.10	+0.32	+0.22	+0.30	+0.15

Table 3. Wavelengths of the excitation and of the emission maxima (nm).

		Complexes		
Compound	Ligand	Mg^{2+}	Ca^{2+}	Ba^{2+}
3a				
$\lambda_{absorption}$	349	350	353	353
$\lambda_{emission}$	404	403	403	405
ΔInt (%)[a]		+20	+14	+13
Stokes' shift (1×10^3, cm^{-1})	3.9	3.8	3.5	3.6
3b				
$\lambda_{absorption}$	345	347	354	351
$\lambda_{emission}$	404	403	403	404
ΔInt (%)[a]		0	4	+29
Stokes' shift (1×10^3, cm^{-1})	4.2	4.0	3.4	3.7
4a				
$\lambda_{absorption}$	418	422	433	429
$\lambda_{emission}$	464	464	467	466
ΔInt (%)[a]		–9	–50	–33
Stokes' shift (1×10^3, cm^{-1})	2.4	2.1	1.6	1.9
4b				
$\lambda_{absorption}$	418	422	438	433
$\lambda_{emission}$	460	463	468	467
ΔInt (%)[a]		–20	–54	–42
Stokes' shift (1×10^3, cm^{-1})	2.2	2.1	1.4	1.7

[a] $\Delta Int = 100 \times (Int_{comp} - Int_{lig})/Int_{lig}$ (Int = intensity of emission band).

Fig. 3. Spectrophotometric titrations of **4b** with Ca^{2+} and Ba^{2+}.

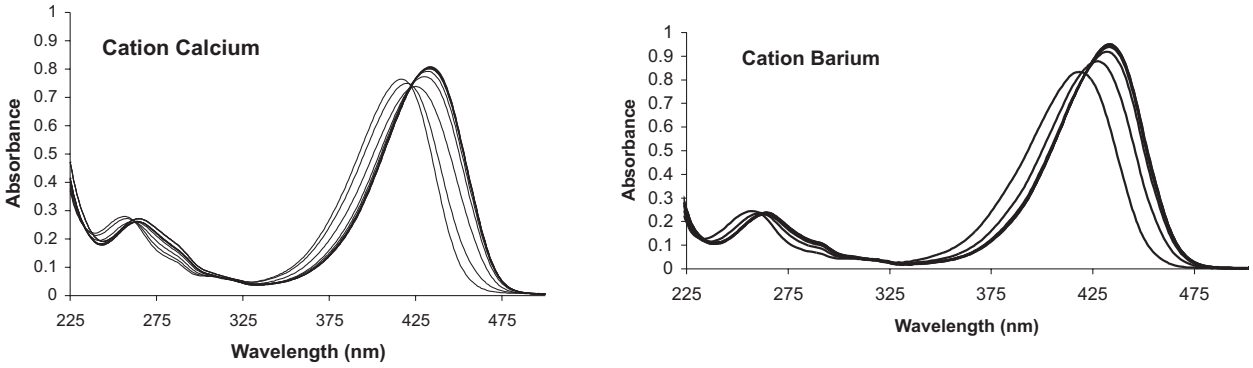

Experimental

General

^{1}H NMR and ^{13}C NMR: Bruker AC-200 (Departamento de Química Orgánica, DCO) and AMX-300 (Servicio Interdepartamental de Invesigación, SIdI). Mass spectra: VG Autospec spectrometer (SIdI) in FAB mode (L-SIMS$^+$) or EI$^+$. Absorption spectra: Lambda 6 PerkinElmer spectrophotometer (DCO). Excitation and emission spectra: LS50 PerkinElmer spectrofluorometer (DCO). The excitation spectra were automatically corrected, and the emission spectra were corrected according to the instrument guidebook. Elemental analyses (C, H) of compounds **2**–**4** (Perkin-Elmer CHN 2400 automatic analyzers, SIdI) were correct within

© 2002 NRC Canada

Fig. 4. Most stable conformations predicted by semiempirical calculations (ZINDO/1) of the indicated complexes showing cooperation or lack thereof between carbonyls.

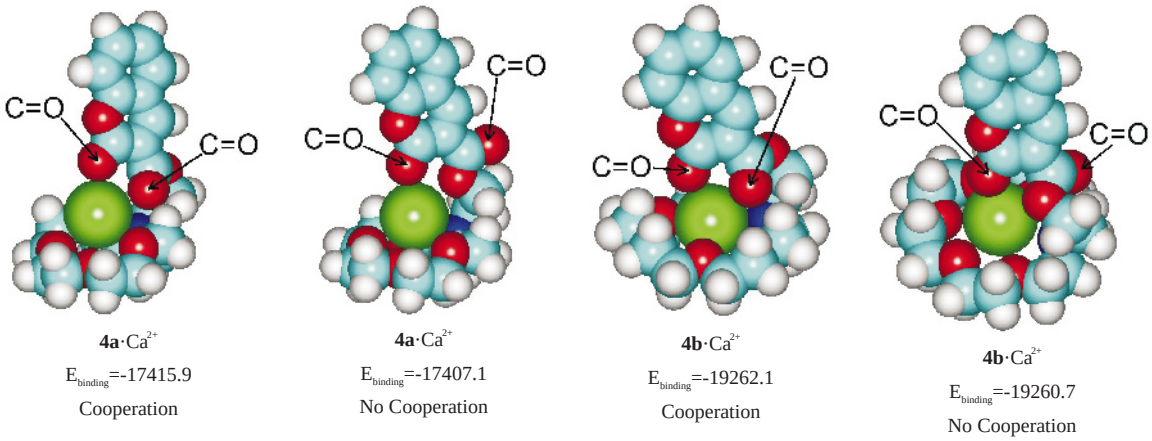

4a·Ca^{2+}
$E_{binding}$=-17415.9
Cooperation

4a·Ca^{2+}
$E_{binding}$=-17407.1
No Cooperation

4b·Ca^{2+}
$E_{binding}$=-19262.1
Cooperation

4b·Ca^{2+}
$E_{binding}$=-19260.7
No Cooperation

Fig. 5. Qualitative absorption–emission diagram.

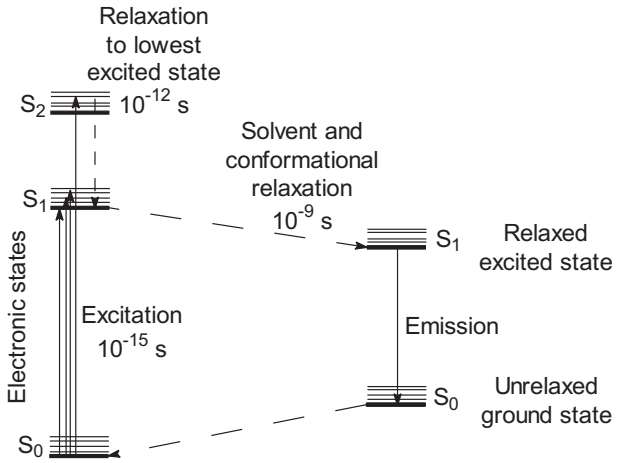

experimental error. All solvents were purified prior to their use. Alkaline earth perchlorates were purchased from Aldrich and used as received. IUPAC names were obtained from ChemWeb: http://cwgen.chemweb.com/autonom/autonomsearch.html.

Synthesis of alkakine earth complexes and absorption and emission measurements

The complexes were formed by addition of equimolecular amounts of the corresponding alkaline earth perchlorate salt in acetonitrile (1×10^{-2} M) to the coumarin solutions (3.2×10^{-5} M for absorption and 3.2×10^{-7} M for emission). Absorption–emission parameters were analyzed from the same spectroscopic grade solvent.

General methods

Synthesis of the 3-carboxycoumarin derivatives

The corresponding commercial salicylaldehyde (0.25 mmol) and malonic acid (0.25 mmol) were dissolved in 3 mL of ethanol. Aniline (3 drops) was added, and the mixture was stirred at room temperature (r.t.) for 48 h. Filtration of the cooled mixture yielded a solid which was triturated with water and then refluxed in 6 N HCl (5 mL) for 30 min. After cooling, a white solid formed which was filtered and washed with water yielding the 3-carboxycoumarin as analytically pure crystals. 3-Carboxycoumarines, precursors of **1** and **2**, were previously reported (13).

Synthesis of the 3-carbonyl chloride coumarin derivatives

To a mixture of the corresponding 3-carboxycoumarin derivative (1 mmol) and two drops of pyridine in dry toluene under argon was added oxalyl chloride (6 mmol). The reaction compounds were stirred for 48–72 h. The solvent was vacuum evaporated and the residue was triturated with diethyl ether to eliminate the oxalic acid. The solid was filtered off and the filtrate evaporated to yield the 3-carbonyl chloride derivative which was used immediately.

Synthesis of azacrown ethanol derivatives

A solution of 500 mg of the commercial azacrown (15/5 or 18/6) in 25 mL of ethanol, was cooled in an ice bath and 2 equiv of ethylene oxide were bubbled through. The resulting solution was heated to 80°C in an autoclave for 8 h. After vacuum solvent evaporation, the final product was obtained as an analytically pure oil.

Synthesis of the azacrown esters 2–4

To a solution of the azacrown derivative (1 mmol) in dry THF (25 mL) heated under reflux, was added dropwise a solution of the 3-carbonyl chloride (1.5 mmol) during a period of 5 h. The mixture was stirred at r.t. for 1 h. After vacuum solvent evaporation, the final product was isolated in the way indicated in each case.

Synthesis of precursors of compounds 2–4

2-(1,4,7,10-Tetraoxa-13-aza-cyclopentadec-13-yl)-ethanol

It was synthesized following the general method starting from commercial aza-15-crown-5 (2.28 mmol) and ethylene oxide (4.56 mmol). Yield: >98%. It was obtained as an analytically pure yellow oil. ^{1}H NMR ($CDCl_3$) δ: 3.6–3.7 (m, 12H, OCH_2CH_2 O), 3.55 (t, 4H, J = 7.2 Hz, OCH_2CH_2N), 3.50 (t, 2H, J = 7.2 Hz, CH_2OH), 2.75 (t, 4H, J = 7.2 Hz, OCH_2CH_2N), 2.65 (t, 2H, J = 7.2 Hz, NCH_2CH_2OH). ^{13}C NMR ($CDCl_3$) δ: 70.6, 70.3, 70.1, 69.9, 69.7 (OCH_2CH_2O),

© 2002 NRC Canada

59.3 (CH_2OH), 57.9 (NCH_2CH_2OH), 55.5 (OCH_2CH_2N). MS (L-SIMS+): 308.2 ($[M + H]^+$, 52%).

2-(1,4,7,10,13-Pentaoxa-16-aza-cyclooctadec-16-yl)-ethanol

It was synthesized following the general method starting from commercial aza-18-crown-6 (2.28 mmol) and ethylene oxide (4.56 mmol). Yield: >98%. It was obtained as an analytically pure light brown oil. ^{1}H NMR ($CDCl_3$) δ: 3.6–3.7 (m, 16H, OCH_2CH_2 O), 3.55 (t, 4H, J = 7.2 Hz, OCH_2CH_2N), 3.50 (t, 2H, J = 7.2 Hz, CH_2OH), 2.75 (t, 4H, J = 7.2 Hz, OCH_2CH_2N), 2.65 (t, 2H, J = 7.2 Hz, NCH_2CH_2OH).^{13}C NMR ($CDCl_3$) δ: 70.5, 70.2, 70.0, 69.7 (OCH_2CH_2O), 59.0 (CH_2OH), 57.8 (NCH_2CH_2OH), 55.1 (OCH_2CH_2N). MS (L-SIMS+): 264.2 ($[M + H]^+$, 47%).

*7-Diethylamino-2-oxo-2*H*-chromene-3-carboxylic acid ethyl ester*

7-Diethylamine salicylaldehyde (0.52 mmol) and diethylmalonate (0.52 mmol) were dissolved in 20 mL of ethanol. Piperidine (3 drops) was added, and the mixture was refluxed for 24 h. After cooling the mixture, the solvent was evaporated and the residue was purified by column chromatography (hexane–ethyl acetate, 4:1), yielding a yellow oil. Yield: 80%. ^{1}H NMR ($CDCl_3$) δ: 8.45 (s, 1H, H-4), 7.30 (d, 2H, J = 8.9 Hz, H-5), 6.55 (dd, 1H, J = 2.5, 8.9 Hz, H-6), 6.40 (d, 1H, J = 2.5 Hz, H-8), 4.30 (q, 2H, J = 7.0 Hz, $CO_2CH_2CH_3$), 3.40 (q, 4H, J = 7.1 Hz, NCH_2CH_3), 1.30 (t, 3H, J = 7.0 Hz, $CO_2CH_2CH_3$), 1.15 (t, 6H, J = 7.1 Hz, NCH_2CH_3). ^{13}C NMR ($CDCl_3$) δ: 164.2 (C-7), 158.4 (C-2), 158.2 (CO), 152.8 (C-9), 149.1 (C-4), 130.9 (C-5), 109.4 (C-6), 108.9 (C-3), 107.6 (C-10), 96.6 (C-8), 61.1 ($CO_2CH_2CH_3$), 45.0 (NCH_2CH_3), 14.3 ($CO_2CH_2CH_3$), 12.3 (NCH_2CH_3). MS (L-SIMS+): 290.2 ($[M + H]^+$, 24%).

*7-Diethylamino-2-oxo-2*H*-chromene-3-carboxylic acid*

The previous compound (0.23 mmol) was dissolved in water and 0.23 mL of 1 M KOH solution was added. The resulting mixture was stirred for 20 h. After addition of 10% HCl until pH = 2, the solid was filtered and washed with water, yielding the analytically pure carboxycoumarine derivative. Yield: 65%; mp 214 to 215°C. ^{1}H NMR ($CDCl_3$) δ: 8.60 (s, 1H, H-4), 7.45 (d, 2H, J = 8.9 Hz, H-5), 6.70 (dd, 1H, J = 2.3, 8.9 Hz, H-6), 6.50 (d, 1H, J = 2.3 Hz, H-8), 3.50 (q, 4H, J = 7.0 Hz, NCH_2CH_3, 1.25 (t, 6H, J = 7.0 Hz, NCH_2CH_3). ^{13}C NMR ($CDCl_3$) δ: 165.2 (C-7), 164.6 (CO), 157.8 (C-2), 153.7 (C-9), 150.0 (C-4), 131.7 (C-5), 110.7 (C-6), 108.2 (C-3), 104.3 (C-10), 96.2 (C-8), 44.9 (NCH_2CH_3), 12.3 (NCH_2CH_3). MS (L-SIMS+): 261.2 ($[M + H]^+$, 31%). Anal. calcd. for $C_{14}H_{15}NO_4$: C 64.36, H 5.79, N 5.36; found: C 64.32, H 5.78, N 5.40.

*2-Oxo-2*H*-chromene-3-carboxylic acid 2-(1,4,7,10-tetraoxa-13-aza-cyclopentadec-13-yl)-ethyl ester (**2a**)*

It was synthesized following the esterification general method starting from the 15-crown-5 derivative (0.325 mmol) and the corresponding 3-carbonyl chloride coumarin (0.48 mmol). The reaction mixture was dissolved in water and extracted with CH_2Cl_2. The aqueous phase was adjusted to pH 7 with a saturated solution of $NaHCO_3$ and extracted with ethyl acetate. Solvent evaporation of the organic layers yielded **2a** as a light brown oil. Yield: 66%. ^{1}H NMR ($CDCl_3$) δ: 8.55 (s, 1H, H-4), 7.75–7.65 (m, 2H, H-5, H-7), 7.35–7.25 (m, 2H, H-8, H-6), 4.42 (t, 2H, J = 7.2 Hz, CO_2CH_2), 3.65–3.45 (m, 16H, OCH_2CH_2O), 2.95 (t, 2H, J = 7.2 Hz, $CO_2CH_2CH_2N$), 2.85 (t, 4H, J = 7.2 Hz, OCH_2CH_2N). ^{13}C NMR ($CDCl_3$) δ: 162.5 (C-2), 155.1 (C-9), 153.9 (CO), 148.7 (C-7), 129.4 (C-5), 128.6 (C-10), 124.7 (C-6), 122.2 (C-3), 116.8 (C-8), 70.9–70.1 (CH_2O), 64.1 (CH_2CO_2), 54.9 (NCH_2CH_2), 54.0 (OCH_2CH_2N). MS (L-SIMS+): 436.2 ($[M + H]^+$, 21%), 458.2 ($[M + Na]^+$, 4%).

*2-Oxo-2*H*-chromene-3-carboxylic acid 2-(1,4,7,10,13-pentaoxa-16-aza-cyclooctadec-16-yl)-ethyl ester (**2b**)*

It was synthesized following the esterification general method starting from the 18-crown-6 derivative (0.325 mmol) and the corresponding 3-carbonyl chloride coumarin (0.48 mmol). The reaction mixture was dissolved in water and extracted with CH_2Cl_2. The aqueous phase was adjusted to pH 7 with a saturated solution of $NaHCO_3$ and extracted with ethyl acetate. Solvent evaporation of the organic layers yielded **2b** as a brown oil. Yield: 73%. ^{1}H NMR ($CDCl_3$) δ: 8.50 (s, 1H, H-4), 7.65–7.55 (m, 2H, H-5, H-7), 7.35–7.25 (m, 2H, H-8, H-6), 4.40 (t, 2H, J = 7.2 Hz, CO_2CH_2), 3.65–3.45 (m, 20H, OCH_2CH_2O), 2.95 (t, 2H, J = 7.2 Hz, $CO_2CH_2CH_2N$), 2.85 (t, 4H, J = 7.2 Hz, OCH_2CH_2N). ^{13}C NMR ($CDCl_3$) δ: 162.7 (C-2), 156.4 (C-9), 155.0 (CO), 148.7 (C-7), 129.4 (C-5), 128.7 (C-10), 124.7 (C-6), 124.3 (C-3), 116.5 (C-8), 70.6–70.1 (CH_2O), 63.6 (CH_2CO_2), 54.1 (NCH_2CH_2), 53.3 (OCH_2CH_2N). MS (L-SIMS+): 480.2 ($[M + H]^+$, 28%), 502.2 ($[M + Na]^+$, 8%).

*7-Methoxy-2-oxo-2*H*-chromene-3-carboxylic acid 2-(1,4,7,10-tetraoxa-13-aza-cyclopentadec-13-yl)-ethyl ester (**3a**)*

It was synthesized following the esterification general method starting from the 15-crown-5 derivative (0.28 mmol) and the corresponding 3-carbonyl chloride coumarin (0.42 mmol). The reaction mixture was dissolved in water and extracted with CH_2Cl_2. The aqueous phase was adjusted to pH 7 with a saturated solution of $NaHCO_3$ and extracted with ethyl acetate. Solvent evaporation of the organic layers yielded a solid which was triturated with diethyl ether to give **3a** as a light brown oil. Yield: 54%. ^{1}H NMR ($CDCl_3$) δ: 8.50 (s, 1H, H-4), 7.50 (d, 2H, J = 8.6 Hz, H-5), 6.85 (dd, 1H, J = 2.5, 8.6 Hz, H-6), 6.75 (d, 1H, J = 2.5 Hz, H-8), 4.40 (t, 2H, J = 7.2 Hz, $CO_2CH_2CH_2N$), 3.95 (s, 3H, OCH_3), 3.70–3.50 (m, 16H, OCH_2CH_2O), 3.00 (t, 2H, J = 7.2 Hz, $COOCH_2CH_2N$), 2.85 (t, 4H, J = 7.2 Hz, OCH_2CH_2N). ^{13}C NMR ($CDCl_3$) δ: 165.2 (C-2), 163.3 (C-9), 157.5 (CO), 149.7 (C-4), 149.7 (C-7), 128.4 (C-5), 127.6 (C-10), 124.7 (C-6), 122.2 (C-3), 116.5 (C-8), 70.9–70.2 (CH_2O), 64.5 (CH_2CO_2), 55.9 (CH_3O), 54.8 (NCH_2CH_2), 54.2 (OCH_2CH_2N). MS (L-SIMS+): 466.3 ($[M + H]^+$, 26%), 488.3 ($[M + Na]^+$, 4%), 504.3 ($[M + K]^+$, 3%).

*7-Methoxy-2-oxo-2*H*-chromene-3-carboxylic acid 2-(1,4,7,-10,13-pentaoxa-16-aza-cyclooctadec-16-yl)-ethyl ester (**3b**)*

It was synthesized following the esterification general method starting from the 18-crown-6 derivative (0.28 mmol) and the corresponding 3-carbonyl chloride coumarin (0.42 mmol). The reaction mixture was dissolved in water and extracted with CH_2Cl_2. The aqueous phase was adjusted to pH 7 with a saturated solution of $NaHCO_3$ and extracted with ethyl acetate. Solvent evaporation of the organic layers yields a solid which was triturated with diethyl ether to give

© 2002 NRC Canada

3b as a light brown oil. Yield: 52%. ^{1}H NMR ($CDCl_3$) δ: 8.50 (s, 1H, H-4), 7.50 (d, 2H, *J* = 8.6 Hz, H-5), 6.85 (dd, 1H, *J* = 2.5, 8.6 Hz, H-6), 6.75 (d, 1H, *J* = 2.5 Hz, H-8), 4.40 (t, 2H, *J* = 7.2 Hz, $CO_2CH_2CH_2N$), 3.85 (s, 3H, OCH_3), 3.70–3.50 (m, 20H, OCH_2CH_2O), 2.95 (t, 2H, *J* = 7.2 Hz, $COOCH_2CH_2N$), 2.85 (t, 4H, *J* = 7.2 Hz, OCH_2CH_2N). ^{13}C NMR ($CDCl_3$) δ: 165.2 (C-2), 155.8 (C-9), 155.0 (CO), 148.7 (C-4), 134.2 (C-7), 129.4 (C-5), 128.6 (C-10), 124.7 (C-6), 122.2 (C-3), 116.8 (C-8), 70.9–70.1 (CH_2O), 63.5 (CH_2CO_2), 56.0 (CH_3O), 54.9 (NCH_2CH_2), 54.0 (OCH_2CH_2N). MS (L-SIMS+): 510.4 ($[M + H]^+$, 30%), 532.4 ($[M + Na]^+$, 6%), 548.3 ($[M + K]^+$, 8%).

*7-Diethylamino-2-oxo-2*H*-chromene-3-carboxylic acid 2-(1,4,7,10-tetraoxa-13-aza-cyclopentadec-13-yl)-ethyl ester (**4a**)*

It was synthesized following the esterification general method starting from the 15-crown-5 derivative (0.32 mmol) and the corresponding 3-carbonyl chloride coumarin (0.49 mmol). The reaction mixture was dissolved in water and extracted with CH_2Cl_2. The aqueous phase was adjusted to pH 7 with a saturated solution of $NaHCO_3$ and extracted with ethyl acetate. The organic layer was washed with 10% HCl, 20% $NaHCO_3$, and water. Solvent evaporation gave **4a** as a dark brown oil. Yield: 45%. ^{1}H NMR ($CDCl_3$) δ: 8.40 (s, 1H, H-4), 7.30 (d, 2H, *J* = 8.9 Hz, H-5), 6.55 (dd, 1H, *J* = 2.5, 8.9 Hz, H-6), 6.40 (d, 1H, *J* = 2.5 Hz, H-8), 4.40 (t, 2H, *J* = 7.2 Hz, $CO_2CH_2CH_2N$), 3.74–3.51 (m, 16H, OCH_2CH_2O), 3.40 (q, 4H, *J* = 7.1 Hz, NCH_2CH_3), 2.92 (t, 2H, *J* = 7.2 Hz, $COOCH_2CH_2N$), 2.85 (t, 4H, *J* = 7.2 Hz, OCH_2CH_2N), 1.30 (t, 6H, *J* = 7.1 Hz, NCH_2CH_3). ^{13}C NMR ($CDCl_3$) δ: 164.0 (C-7), 158.4 (C-2), 158.1 (CO), 152.8 (C-9), 149.3 (C-4), 131.1 (C-5), 111.6 (C-6), 109.4 (C-3), 104.3 (C-10), 96.8 (C-8), 70.3–70.0 (CH_2O), 63.5 (CH_2CO_2), 55.3 (NCH_2CH_2), 54.1 (OCH_2CH_2N), 44.9 (NCH_2CH_3), 12.3 (NCH_2CH_3). MS (L-SIMS+): 507.1 ($[M + H]^+$, 20%), 529.1 ($[M + Na]^+$, 8%).

*7-Diethylamino-2-oxo-2H-chromene-3-carboxylic acid 2-(1,4,7,10,13-pentaoxa-16-aza-cyclooctadec-16-yl)-ethyl ester (**4b**)*

It was synthesized following the esterification general method starting from the 18-crown-6 derivative (0.32 mmol) and the corresponding 3-carbonyl chloride coumarin (0.49 mmol). The reaction mixture was dissolved in water and extracted with CH_2Cl_2. The aqueous phase was adjusted to pH 7 with a saturated solution of $NaHCO_3$ and extracted with ethyl acetate. The organic layer was washed with 10% HCl, 20% $NaHCO_3$, and water. Solvent evaporation gives **4b** as a dark brown oil. Yield: 51%. ^{1}H NMR ($CDCl_3$) δ: 8.40 (s, 1H, H-4), 7.30 (d, 2H, *J* = 8.9 Hz, H-5), 6.55 (dd, 1H, *J* = 2.3, 8.9 Hz, H-6), 6.40 (d, 1H, *J* = 2.3 Hz, H-8), 4.40 (t, 2H, *J* = 7.2 Hz, $CO_2CH_2CH_2N$), 3.74–3.51 (m, 20H, OCH_2CH_2O), 3.40 (q, 4H, *J* = 7.1 Hz, NCH_2CH_3), 3.05 (t, 2H, *J* = 7.2 Hz, $COOCH_2CH_2N$), 2.95 (t, 4H, *J* = 7.2 Hz, OCH_2CH_2N), 1.30 (t, 6H, *J* = 7.1 Hz, NCH_2CH_3). ^{13}C NMR ($CDCl_3$) δ: 164.0 (C-7), 158.4 (C-2), 158.1 (CO), 152.8 (C-9), 149.3 (C-4), 131.1 (C-5), 111.2 (C-6), 109.4 (C-3), 104.3 (C-10), 96.8 (C-8), 70.3–70.0 (CH_2O), 63.5 (CH_2CO_2), 55.3 (NCH_2CH_2), 54.1 (OCH_2CH_2N), 44.9 (NCH_2CH_3), 12.3 (NCH_2CH_3). MS (L-SIMS+): 551.4 ($[M + H]^+$, 25%), 573.3 ($[M + Na]^+$, 9%).

Conclusion

Several new ionophores derived from coumarins bearing aza-crown ethers attached to the 3-position by means of an ethylenoxycarbonyl spacer have been synthesized. We observed that the systems with strong electron donors at the 7-position displayed the largest bathochromic shifts upon complexation with Ca^{2+} but they were irresponsive to Mg^{2+}. NMR data, molecular modeling, and SS of emission strongly suggest cooperation between the chromen nucleus and the crowns in their binding to Ca^{2+} that was accompanied with a relatively large extinction of fluorescence. These facts may make the **4** compounds as leads for useful signaling devices of Ca^{2+} without interference from Mg^{2+}.

Acknowledgements

Financial support from Comisión Interministerial de Ciencia y Tecnología of Spain (CICYT; grants PB90-0176, PB93-0264, PB95-0172, PB98-0103) and indirect funding from FYSE-ERCROS are gratefully acknowledged.

References

1. (*a*) M.T. Alonso, E. Brunet, C. Hernández, and J.C. Rodríguez-Ubis. Tetrahedron Lett. **34**, 7465 (1993); (*b*) J.C. Rodríguez-Ubis, M.T. Alonso, O. Juanes, and E. Brunet. Luminescence, **15**, 331 (2000); (*c*) E. Brunet, M.T. Alonso, O. Juanes, and O. Velasco. Tetrahedron, **57**, 3105 (2001).
2. Ç. Erk, A. Göçmen, and M. Bulut. Supramol. Chem. **11**, 49 (2000).
3. B. Raju and T.S. Vadarajan. J. Phys. Chem. **98**, 8903 (1994).
4. A. Samanta and R.W. Fessenden. J. Phys. Chem. A, **104**, 8577 (2000).
5. E. Brunet, M.T. Alonso, O. Juanes, and J.C. Rodríguez-Ubis. Unpublished results.
6. E. Brunet, M.T. Alonso, O. Juanes, R. Sedano, and J.C. Rodríguez-Ubis. Tetrahedron Lett. **38**, 4459 (1997).
7. B. Valeur and I. Leray. Coord. Chem. Rev. **205**, 3 (2000).
8. I. Leray, J.L. HabibJiwan, C. Branger, J.P. Soumillion, and B. Valeur. J. Photochem. Photobiol. A. **135**, 163 (2000), and refs. cited therein.
9. (*a*) Y. Kimura and N. Hirota. J. Chem. Phys. **111**, 5474 (1999); (*b*) L. Reynolds, J.A. Gardecki, S.J. Frankland, M.L. Horng, and M. Maroncelli. J. Phys. Chem. **100**, 10 337 (1996).
10. J.R. Lakowick. Principles of fluorescence spectroscopy. Plenum Press, New York. 1983. p. 188.
11. (*a*) T. López Arbeloa, F. López Arbeloa, M.J. Tapia, and I. López Arbeloa. J. Phys. Chem. **97**, 4704 (1993); (*b*) K. Rechthale and G. Köhler. Chem. Phys. **189**, 99 (1994).
12. (*a*) J.L. Retsek, S. Gentemann, C.J. Medforth, K.M. Smith, V.S. Chirvony, J. Fajer, and D. Holten. J. Phys. Chem. B, **104**, 6690 (2000); (*b*) H.R. Park, H.C. Lee, T.H. Kim, K. Yang, and K.M. Bark. J. Photochem. Photobiol. **71**, 281 (2000).
13. (*a*) M. Murayama, E. Soto, T. Okubo, I. Morita, M. Dobashi, and M. Maehara. Chem. Pharm. Bull. **20**, 741 (1972); (*b*) J.C. Rodríguez-Ubis. Ph.D Thesis, Universidad Autónoma de Madrid, Spain. 1983.

© 2002 NRC Canada

Isentropic compressibility and viscosity of aqueous and methanolic lithium chloride solutions

Abdul Wahab and Sekh Mahiuddin

Abstract: Densities, speeds of sound, and viscosities of aqueous and methanolic lithium chloride solutions were measured as functions of concentration, m (mol kg^{-1}) ($0.3911 \leq m \leq 19.47$) and temperature ($273.15 \leq T \leq 323.15$ K). Measured values of the density, speeds of sound, and viscosity agree well with previously reported data. The isentropic compressibility isotherms for the aqueous solutions converge at a particular concentration, in the temperature range of the study, providing crucial information regarding the solvation behaviour of the ions. However, for the methanol solutions, the isentropic compressibility isotherms decrease smoothly with concentration and converge on extrapolation. Anion solvation controls the viscosity processes at low temperatures whereas cation solvation controls the same at high temperatures. Total primary solvation numbers of lithium chloride in water and methanol were estimated to be 6.0 and 1.9, respectively.

Key words: lithium chloride, speeds of sound, viscosity, isentropic compressibility, solvation number.

Résumé : On a mesuré les densités, vitesses du son et viscosités de solutions aqueuses et méthanoliques de chlorure de lithium en fonction de la concentration, m (mol kg^{-1}) ($0{,}3911 \leq m \leq 19{,}47$) et de la température ($273{,}15 \leq T \leq 323{,}15$ K). Les valeurs mesurées pour les densités, les vitesses du son et les viscosités sont en bon accord avec les données rapportées antérieurement. Dans le domaine des températures étudiées, les isothermes de compressibilité isentrope pour les solutions aqueuses convergent à une concentration particulière, fournissant de l'information cruciale concernant le comportement des ions vis-à-vis de la solvatation. Toutefois, pour les solutions dans le méthanol, les isothermes de compressibilité isentrope diminue de façon régulière avec la concentration et elles convergent par extrapolation. La solvatation de l'anion contrôle les processus de viscosité à basses températures alors que la solvatation de l'anion la contrôle à températures élevées. Les nombres totaux de solvatation primaire du chlorure de lithium dans l'eau et dans le méthanol sont évalués respectivement à 6,0 et 1,9.

Mots clés : chlorure de lithium, vitesses du son, viscosité, compressibilité isentrope, nombre de solvatation.

[Traduit par la Rédaction]

Introduction

The acoustic and transport behaviour of electrolytes in aqueous and nonaqueous media provide crucial information on the ion solvation in different concentration regions, which are of immense importance to the technologist and theoretician. The structure and existence of free ions, solvated ions, and ion pairs depend on the concentration regions (1).

A number of experimental techniques and theoretical approaches (2, 3) have been employed to study the solvation structure and dynamics of ions in aqueous and nonaqueous media. But the experimental data, obtained by using different techniques, have led to results with large variations regarding solvation number of a particular ion. The reported primary hydration number of lithium ion (2) has a wide distribution between three and seven. Howell and Neilson (4) showed a concentration dependence of hydration numbers, for example, 3.2 at 14 mol kg^{-1} and ~6.5 at 1 mol kg^{-1}, for Li^+ by using the neutron diffraction method. However, the most frequently proposed hydration number of the lithium ion is either 4 obtained from ab initio calculations (3, 5), MD simulations (6), Raman spectra (7, 8), and neutron (9) and X-ray (10) diffraction, or 6 obtained from simulations (11, 12) and X-ray (13) and neutron scattering (4) studies. Recently, Zavitsas (14) made use of freezing point depression to estimate the hydration number of ions and for the Li^+ it is found to be 6.6 ± 0.6. Furthermore, in the system $LiCl{\cdot}nH_2O$, a complete hydration and a direct anion–cation interaction are reported when $n = 6$ and $n = 4$, respectively (15). Tao and Lindsay (16) investigated Brillouin and depolarized Rayleigh scattering of aqueous LiCl solutions and suggested a structural transition at ~9.4 mol kg^{-1}.

X-ray (17, 18) and neutron (19, 20) diffraction techniques showed essentially a hydration number of 6 for Cl^-. But computer simulation (2, 6, 12) results exhibit a wide distribution of primary hydration numbers of Cl^- from 4.9 to 8.5. Cummings et al. (19) observed that the hydration of Cl^- is essentially independent of counter ion by using the neutron diffraction technique. From MD simulations, Tanaka et al. (21) reported comparatively, a rigid geometrical arrangement of hydrated water molecules around Li^+ in contrast to a random distribution of water molecules around Cl^- in an almost saturated solution of LiCl. Yamanaka et al. (17) performed

Received 18 October 2001. Published on the NRC Research Press Web site at http://canjchem.nrc.ca on 19 February 2002.

A. Wahab and S. Mahiuddin.[1] Material Science Division, Regional Research Laboratory, Jorhat-785 006, Assam, India.

[1]Corresponding author (e-mail: mahirrljt@yahoo.com).

 DOI: 10.1139/V02-007 © 2002 NRC Canada

X-ray diffraction studies and showed that the primary hydration shell of Li^+ becomes ordered at high temperatures whereas Cl^- tends to form a rigid hydration shell at low temperatures. Very recently, femtosecond mid-IR non-linear spectroscopic studies (22) have led to a firm conclusion that the hydration shell of Cl^- is rigid relative to that of the cation. From the above discussion it seems that the temperature and concentration are the decisive parameters for the flexible nature of the primary hydration shells of Li^+ and Cl^-.

From NMR measurements, Vogrin and Malinowski (23) reported a consistent solvation phenomena of LiCl in methanol and water media and found total solvation numbers of 4.5 ± 0.2 and 2.8 ± 0.4, in the respective solvents. Recent theoretical (24, 25) as well as experimental (26) studies suggest strikingly different solvation dynamics in methanol relative to water.

In earlier papers (27, 28), it was reported that the isentropic compressibility isotherms converge at a particular concentration because of the saturation of the primary solvation shell of an electrolyte resulting in a rigid structure. On the other hand, the ion–solvent and ion–ion interactions and equilibria in different concentration regions have an influence on transport properties. Therefore, in this paper, we report speeds of sound and viscosities of aqueous and methanolic lithium chloride solutions as functions of concentration and temperature.

Experimental

Lithium chloride (>99%, E. Merck, Darmstad, Germany) was recrystallized twice from double-distilled water and was kept in a vacuum desiccator over P_2O_5. Finally, lithium chloride was dried by heating at 120°C under vacuum before preparing solutions. Anhydrous methanol was prepared from A.R. grade methanol (>99.5%, Qualigens Fine Chemicals, Mumbai, India) as described elsewhere (29). All solutions were prepared by mass with ±0.2% accuracy. The lithium chloride concentrations were checked by gravimetric analysis using $AgNO_3$.

Densities (ρ) of all solutions were measured with an accuracy of ±0.01% by using a single-stem graduated pycnometer of ~9 cm^3 capacity. The pycnometer was calibrated by using double-distilled water. Speeds of sound (u) in aqueous and methanolic lithium chloride solutions were measured with an accuracy of ±0.1 m s^{-1} by using a variable path interferometer (multifrequency ultrasonic interferometer, M-83, Mittal Enterprises, New Delhi, India) at 2 MHz as described previously (27).

Viscosities (η) were measured with a Schott–Geräte AVS 310 unit equipped with micro Ubbelohde viscometers. Viscometers of different constants of 0.009595, 0.03004, 0.1126, and 0.3099 mm^2 s^{-2} were used to measure the efflux time in different concentration and temperature ranges. An average of five efflux times was used for viscosity calculations at each temperature. The experimental uncertainties in the viscosities were within ±0.5%.

All the measurements were performed as functions of concentration, m (mol kg^{-1}) ($0.3911 \leq m \leq 19.47$ and $0.6812 \leq m \leq 9.684$ for aqueous and methanolic lithium chloride solutions, respectively) and temperature ($273.15 \leq T \leq 323.15$ K). Thermostat types Schott–Geräte CT 1450, Lauda RLS 6D, or Julabo F32 HP was used to control the temperature of all the solutions within ±0.02 K.

Results and discussion

The experimental densities of aqueous and methanolic lithium chloride solutions were found to be linear functions of the temperature at a particular concentration. The values of the parameters of the density equation are given in Table 1. Figure 1 shows the isotherms of ρ vs. m at 298.15 K along with the literature data. The measured densities of aqueous lithium chloride solutions are in good agreement with the literature data (30–32) within ±0.4% at 298.15 K. The density values of methanolic solutions are comparable within ±0.5% with the reported data (33) at 287.65 K.

The measured values of speeds of sound in aqueous and methanolic lithium chloride solutions are collected in Table 1S (*Supplementary materials*).[2] The present values of the speeds of sound in aqueous lithium chloride solutions are comparable within ±0.5% with the reported values (34) at 298.15 K. We could not compare the speeds of sound values for the methanolic lithium chloride solutions because of a lack of literature data. However, the present isentropic compressibilities of methanolic lithium chloride solutions are ~2.6% higher than the reported values (35) at 298.15 K.

The isentropic compressibility (κ_s) values for aqueous and methanolic solutions were calculated by using the relationship

$$[1] \qquad \kappa_s = 1/u^2\rho$$

The isentropic compressibilities against concentration of aqueous and methanolic lithium chloride solutions are plotted in Figs. 2 and 3, respectively, at three temperatures. As earlier, an isothermal equation of the following form (27, 28)

$$[2] \qquad \kappa_s = a_1 + b_1 m + c_1 m^d$$

was used to fit the isentropic compressibilities over the entire concentration range. In eq. [2], a_1, b_1, and c_1 are the temperature-dependent parameters, d is a constant parameter, and m is the concentration in mol kg^{-1}. The least-squares fitted values of the parameters of eq. [2] are listed in Table 2. From Table 2 and Figs. 2 and 3, it is apparent that eq. [2] can reproduce the isentropic compressibilities within ±1.1% for aqueous lithium chloride; for methanolic lithium chloride solutions, it was within ±2.2%. It has been observed that the isentropic compressibility isotherms of aqueous lithium chloride solutions converge in the concentration range of 9.25–13.5 mol kg^{-1} in the temperature range of the study (Fig. 2).

Previous studies (15–17, 21) reveal contradictory views about the nature of the hydration sphere of Li^+ and Cl^-. Tanaka et al. (21) suggested a rigid geometrical arrangement of water molecules around the Li^+ against randomly arranged water molecules around the Cl^-. On the other hand, Yamanaka et al. (17) observed a flexible primary hydration sphere for Li^+ at low temperatures and an ordered arrange-

[2] Supplementary material may be purchased from the Depository of Unpublished Data, Document Delivery, CISTI, National Research Council Canada, Ottawa, ON K1A 0S2, Canada (http://www.nrc.ca/cisti/irm/unpub_e.shtml for information on ordering electronically).

© 2002 NRC Canada

Table 1. Least-squares fitted values of the constant parameters of the density equation $\rho = a - b(T - 273.15)$ (T is in K) for aqueous and methanolic lithium chloride solutions.

m (mol kg^{-1})	a (kg m^{-3})	b (kg m^{-3} K^{-1})	Standard deviation in ρ
Aqueous lithium chloride			
0.3911	1016.5 ± 0.4	0.3627 ± 0.0092	0.22
1.156	1036.6 ± 0.5	0.3930 ± 0.0109	0.16
1.357	1039.0 ± 0.3	0.3609 ± 0.0090	0.18
2.129	1054.9 ± 0.3	0.3622 ± 0.0085	0.22
2.472	1063.3 ± 0.3	0.3361 ± 0.0086	0.22
3.771	1086.1 ± 0.3	0.3440 ± 0.0069	0.16
5.055	1106.4 ± 0.2	0.3323 ± 0.0047	0.11
6.229	1128.5 ± 0.4	0.3559 ± 0.0096	0.23
6.473	1129.4 ± 0.2	0.3319 ± 0.0039	0.09
7.544	1146.0 ± 0.1	0.3277 ± 0.0038	0.09
8.613	1160.6 ± 0.1	0.3290 ± 0.0033	0.06
9.211	1173.7 ± 0.2	0.3262 ± 0.0057	0.14
9.325	1176.1 ± 0.2	0.3418 ± 0.0040	0.08
10.33	1190.7 ± 0.1	0.3340 ± 0.0028	0.07
10.58	1194.6 ± 0.1	0.3414 ± 0.0036	0.09
11.42	1206.8 ± 0.2	0.3445 ± 0.0042	0.09
12.44	1216.8 ± 0.1	0.3446 ± 0.0025	0.05
13.44	1234.4 ± 0.2	0.3597 ± 0.0038	0.07
13.61	1235.3 ± 0.1	0.3541 ± 0.0022	0.05
15.07	1253.1 ± 0.1	0.3648 ± 0.0025	0.06
15.59	1258.7 ± 0.1	0.3643 ± 0.0015	0.04
16.20	1266.8 ± 0.1	0.3712 ± 0.0037	0.07
17.13	1277.4 ± 0.1	0.3805 ± 0.0031	0.07
18.09	1287.8 ± 0.1	0.3848 ± 0.0029	0.06
19.47	1301.6 ± 0.1	0.3886 ± 0.0019	0.05
Methanolic lithium chloride			
0.6812	831.73 ± 0.14	0.9114 ± 0.0036	0.05
1.257	848.31 ± 0.22	0.8539 ± 0.0055	0.09
1.881	866.47 ± 0.15	0.8291 ± 0.0037	0.06
2.450	878.86 ± 0.18	0.7810 ± 0.0046	0.08
2.900	890.57 ± 0.14	0.7605 ± 0.0038	0.07
3.801	913.39 ± 0.17	0.7275 ± 0.0044	0.09
4.450	931.14 ± 0.23	0.6927 ± 0.0058	0.12
5.242	949.00 ± 0.06	0.7050 ± 0.0016	0.03
5.985	964.49 ± 0.19	0.6727 ± 0.0047	0.11
6.810	980.83 ± 0.19	0.6704 ± 0.0048	0.11
8.167	1008.8 ± 0.2	0.6682 ± 0.0050	0.11
8.883	1020.2 ± 0.3	0.6710 ± 0.0064	0.13
9.684	1031.7 ± 0.1	0.6496 ± 0.0030	0.07

ment for Cl^- at supercooled and glassy states; they also showed that the hydration number of Li^+ decreases with the decrease in temperature (5.7 at 373 K and 3.5 at 138 K), whereas the hydration number for Cl^- increases with the lowering of temperature. The hydration numbers of Li^+ and Cl^- reported in the literature by several researchers using different techniques, for easy comparison, are summarized in Table 3.

It is evident from Fig. 2 that the lowest concentration of convergence of the isentropic compressibility isotherms is 9.25 mol kg^{-1}, at which the primary hydration shell of the solute is just saturated with $\kappa_{s,h} = 2.548 \times 10^{-10}$ Pa^{-1} (where $\kappa_{s,h}$ is the isentropic compressibility of the hydrated sphere). For the $LiCl{\cdot}nH_2O$ system, a full hydration of Li^+ and Cl^- has been reported (15) at $n = 6$ (9.25 mol kg^{-1}) from the neutron diffraction study. Tao and Lindsay (16) reported a possible structural transition in aqueous LiCl solution at around 9.4 mol kg^{-1} (Fig. 11 of ref. 16) and suggested that the charged ions cause polarization of water molecules in the primary hydration shell. Furthermore, a transition was also observed by Millero et al. (36) at 10.7 ± 0.7 mol kg^{-1} in the plot of $(u - u_0)/m$ vs. $m^{1/2}$, where u_0 is the speeds of sound of pure water and correlated the transition with the hydration structure of the cation. However, we found a transition at 8.8 ± 0.2 mol kg^{-1} in the $(u - u_0)/m$ vs. $m^{1/2}$ plot for the present system.

At 9.25 mol kg^{-1}, over the specified temperature range, all the water molecules were incorporated in the primary hydration shell of lithium chloride resulting in a rigid structure due to the strong and predominant ion–solvent interac-

© 2002 NRC Canada

Fig. 1. Plots of density (ρ) against molality (*m*) at 298.15 K for aqueous and methanolic lithium chloride solutions.

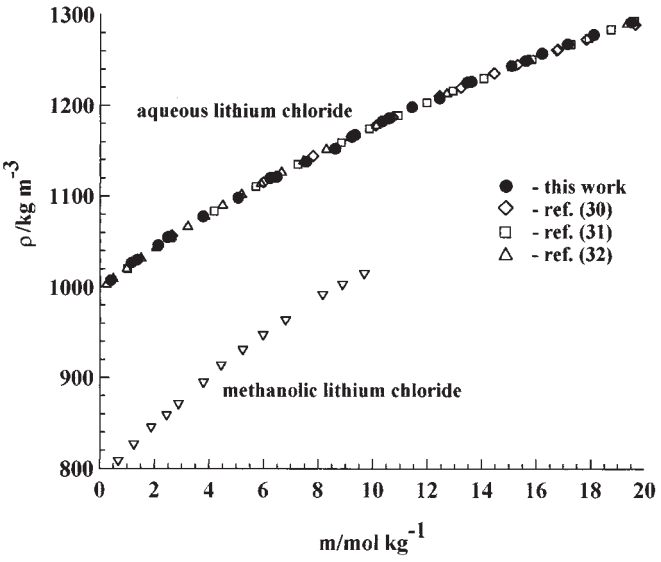

Fig. 2. Variation of isentropic compressibility (κ_s) with molality (*m*) at 273.15 K (○), 298.15 K (□), and 323.15 K (Δ) for aqueous lithium chloride solutions (symbols and solid curves represent experimental and calculated (from eq. [2]) values, respectively).

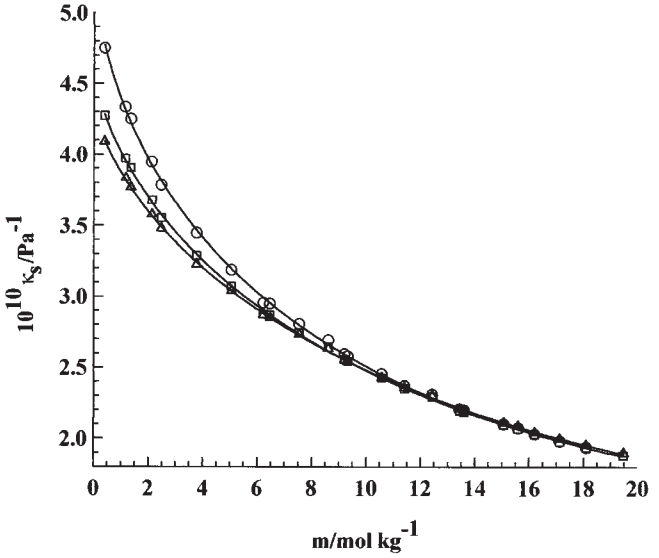

tions. At this critical concentration, the inherent structure and hydrogen bonding of the bulk water are collapsed. The isentropic compressibility value ($\kappa_{s,h} = 2.548 \times 10^{-10}$ Pa^{-1}) at the critical concentration is much lower than that of free water ($\kappa_s = 4.477 \times 10^{-10}$ Pa^{-1}). This indicates that the water molecules are rigidly held in the primary hydration shells of Li^+ and Cl^-. A minimum has been reported at ~9.4 mol kg^{-1} in the dielectric relaxation times (37), which characterize the rotational correlation time of the molecules. This concentration is in good agreement with the critical concentration (9.25 mol kg^{-1}) and indicates a probable correlation with the

Fig. 3. Variation of isentropic compressibility (κ_s) with molality (*m*) at 273.15 K (○), 298.15 K (□), and 323.15 K (Δ) for methanolic lithium chloride solutions (symbols and solid curves represent experimental and calculated (from eq. [2]) values, respectively, and broken curves represent the extrapolated values).

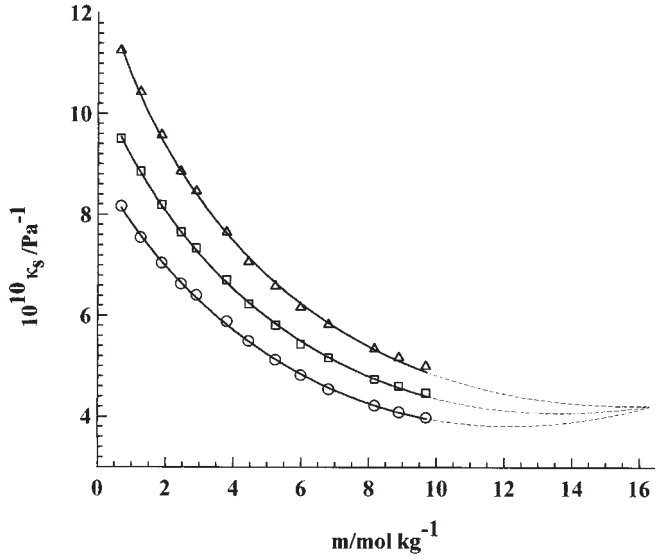

saturation of the primary hydration shell of lithium chloride in water medium.

Beyond 9.25 mol kg^{-1}, the hydration spheres of cations and anions overlap leading to a gradual formation of ion pairs (1) (solvent-shared, solvent-separated, and contact) because of a lesser number of available water molecules around Li^+ and Cl^-. In the entire temperature range of this study, the isentropic compressibility isotherms also converge at 13.5 mol kg^{-1} (Fig. 2). It can be argued that from 9.25 to 13.5 mol kg^{-1}, solvent-separated and (or) solvent-shared ion pairs predominantly exist in the solution; beyond 13.5 mol kg^{-1}, transition to contact-ion pairs is envisaged.

In methanolic lithium chloride solutions, the isentropic compressibility isotherms decrease smoothly with increasing concentration, but do not converge within the experimental concentration and temperature ranges (Fig. 3). On extrapolation, the isotherms converge at 16.30 mol kg^{-1} with $\kappa_{s,h} = 4.20 \times 10^{-10}$ Pa^{-1}. From Figs. 2 and 3, it is clear that the methanolic solution is more compressible in comparison to that of aqueous solution at a particular concentration and temperature. For example, at 0.1 mol fraction of lithium chloride, i.e., at 6.17 mol kg^{-1} aqueous lithium chloride and 3.47 mol kg^{-1} methanolic lithium chloride solutions, the isentropic compressibilities are ~2.9×10^{-10} Pa^{-1} and ~6.9×10^{-10} Pa^{-1}, respectively. This reflects a different solvation behaviour of lithium chloride in methanol than that in water. This difference may be attributed to weak ion–solvent interactions in methanol because of its characteristic structure and as a poor hydrogen bond producer.

The hydration and (or) solvation numbers (n_h) were calculated by using the previously reported empirical equation (27, 28)

$$[3] \qquad n_h = (\kappa_{s,\phi} - \kappa_{s,h} V_\phi)/[V_1(\kappa_{s,h} - \kappa_{s,1})]$$

© 2002 NRC Canada

Table 2. Least-squares fitted values of the parameters of eq. [2] for aqueous and methanolic lithium chloride solutions.

T (K)	a_1 (1×10^{10}) (Pa^{-1})	b_1 (1×10^{10}) (Pa^{-1} kg mol^{-1})	c_1 (1×10^{10}) (Pa^{-1} kg^d mol^{-d})	d	Standard deviation in κ_s (1×10^{12})
Aqueous lithium chloride					
273.15	5.341 ± 0.074	0.1834 ± 0.0419	–1.136 ± 0.035	0.6137 ± 0.0440	1.75
298.15	4.626 ± 0.039	0.2018 ± 0.0480	–0.8167 ± 0.0157	0.7079 ± 0.0404	1.25
323.15	4.350 ± 0.024	0.2541 ± 0.0623	–0.7361 ± 0.0404	0.7777 ± 0.0357	0.890
Methanolic lithium chloride					
273.15	8.918 ± 0.065	–1.507 ± 0.175	0.4132 ± 0.1256	1.387 ± 0.059	3.10
298.15	10.70 ± 0.09	−4.295 ± 1.441	2.723 ± 1.369	1.128 ± 0.048	3.80
323.15	13.32 ± 0.28	3.331 ± 1.963	–5.889 ± 1.719	0.8513 ± 0.0748	6.77

Table 3. Hydration numbers of ions or salt estimated from molecular dynamics (MD), Monte Carlo (MC), ab initio simulation, Raman spectra (R), NMR spectra (NMR), X-ray (X) and neutron (N) diffraction, and adiabatic compressibility (AC) methods.

Solute	Concentration[a]	Hydration number	Method	Reference
Li^+(aq)	13.9–0.258 *m*	3–7	MD, MC	2
	14.0, 3.6, 1.0 *m*	3.2, 6.0, 6.5	N	4
		4	Ab initio	3
		4	Ab initio	5
		4.1	MD	6
	2.64 M, 7.48 M	4	R	7
	5.38 *m*	4	R	8
	2 M	4	N	9
		4	X	10
		6	MD	11
		5.9	Ab initio	12
		6	X	13
		6.6	Freezing point depression	14
	11.1 *m*	5.7 (373 K)	X	17
		3.5 (138 K)		
		4	Ab initio	39
		4	Ab initio	40
Cl^-(aq)	11.1 *m*	6.07	X	17
	4.6 *m*, 10.6 *m*	6.1	X	18
	3.57 *m*, 9.95 *m*	5.9, 5.3	N	19
		6	N	20
	18.5–0.258 *m*	4.9, 8.5	MD, MC	2
		7.2	MD	6
		7	Ab initio	12
LiCl(aq)		2.8	NMR	23
		6.0	AC	35
LiCl (methanol)		4.5	NMR	23
		4.2	AC	35

[a] *m* = mol kg^{-1}, M = mol dm^{-3}.

where $\kappa_{s,\phi}$ is the conventional apparent molal isentropic compressibility (38) of the solution, V_ϕ is the apparent molal volume of the solute, and $\kappa_{s,1}$ and V_1 are the isentropic compressibility and the molar volume of the solvent, respectively. The estimated hydration and (or) solvation numbers of lithium chloride in water and methanol are illustrated in Fig. 4. The primary hydration number for lithium chloride in water was found to be 6.0 at 9.25 mol kg^{-1} and is in excellent agreement with the number of available water molecules per mol of the solute (6.0) at that concentration. The total primary solvation number of lithium chloride in methanol at 16.30 mol kg^{-1} was estimated to be 1.9, which is much smaller than that in water.

To bifurcate the total hydration number of lithium chloride into its individual ionic values, we need the reliable primary hydration number of either Li^+ or Cl^-. Recently, ab initio (39) and quasichemical (3) approaches have established that tetra-coordinated Li^+(aq) is energetically most favored (40). Most attempts (41, 42) to incorporate more than four water molecules in the primary hydration sphere lead invariably to the migration of extra water molecules into the secondary hydration sphere. Hence, by selecting the primary hydration number of Li^+ as 4.0, the primary hydration number of Cl^- is estimated to be 2.0, which is lower than the frequently reported values (2, 17–20) but more or less in agreement with the findings of Yamanaka et al. (17). We could not

© 2002 NRC Canada

Fig. 4. Hydration/solvation number (n_h) vs. molality (m) for (○) aqueous lithium chloride and (□, Δ) methanolic lithium chloride solutions (circles and squares are experimental values and triangles are extrapolated values) at 298.15 K.

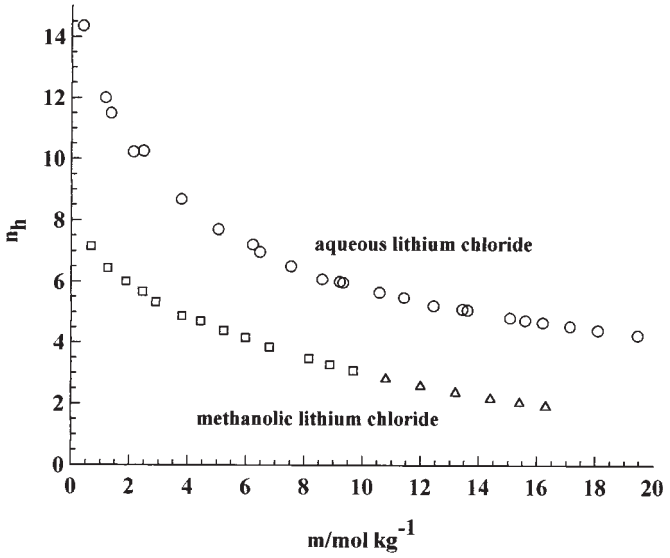

Fig. 5. Variation of viscosities (η) with molality (m) at 273.15 K (●), 298.15 K (■), and 323.15 K (▲) for aqueous lithium chloride solutions.

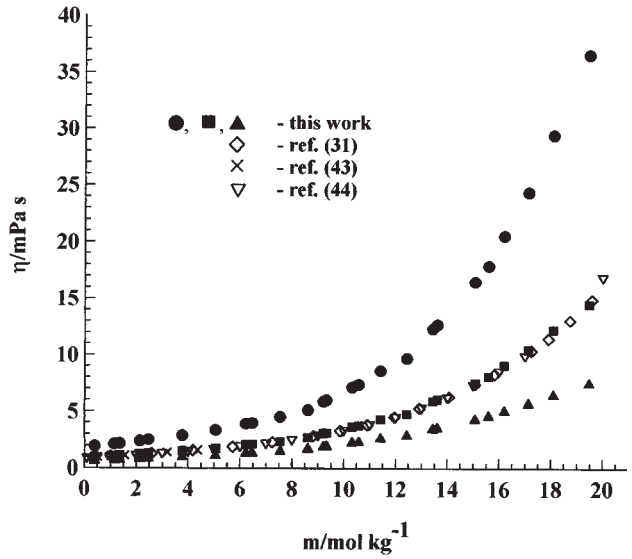

split the total primary solvation number of lithium chloride in methanol because of the lack of reliable literature data.

The experimental viscosities as functions of concentration and temperature for aqueous and methanolic lithium chloride solutions are presented in Table 2S (Supplementary materials).[2] Our viscosity values in water are comparable within ±3.4% of the reported values (31, 43, 44). We could not compare the viscosities of methanolic lithium chloride solutions because of the lack of literature data. Figures 5 and 6 illustrate the η vs. m plots for aqueous lithium chloride along with the literature values and methanolic lithium chloride solutions, respectively.

Fig. 6. Variation of viscosities (η) with molality (m) at 273.15 K (○), 298.15 K (□), and 323.15 K (Δ) for methanolic lithium chloride solutions.

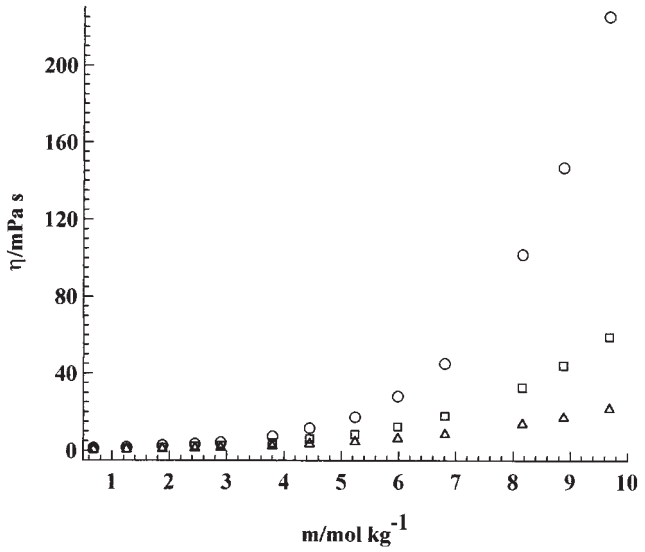

Fig. 7. Dependence of shear relaxation time (τ) with molality (m) at 273.15 K (○), 298.15 K (□), and 323.15 K (Δ) for aqueous lithium chloride solutions.

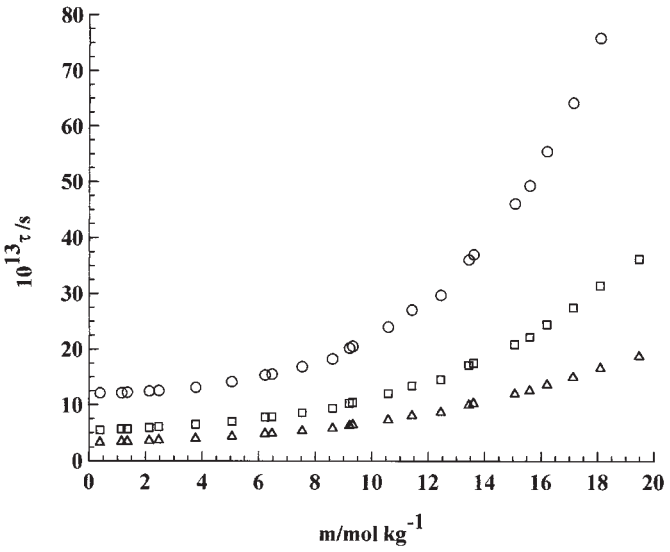

To understand the structure of solutions in different concentration regions, the shear relaxation times (τ) for all the solutions of lithium chloride were determined using the relationship (45)

$$[4] \qquad \tau = 4\kappa_s\eta/3$$

The plots of τ vs. m at different temperatures are shown in Figs. 7 and 8 for aqueous and methanolic solutions, respectively. It is apparent from Fig. 7 that the τ vs. m plots are less exponential at higher temperature. As the temperature decreases the curves become more and more exponential. A similar variation has also been observed for η vs. m plots (Figs. 5 and 6). These trends in τ and η at different tempera-

© 2002 NRC Canada

Fig. 8. Dependence of shear relaxation time (τ) with molality (*m*) at 273.15 K (○), 298.15 K (□), and 323.15 K (Δ) for methanolic lithium chloride solutions.

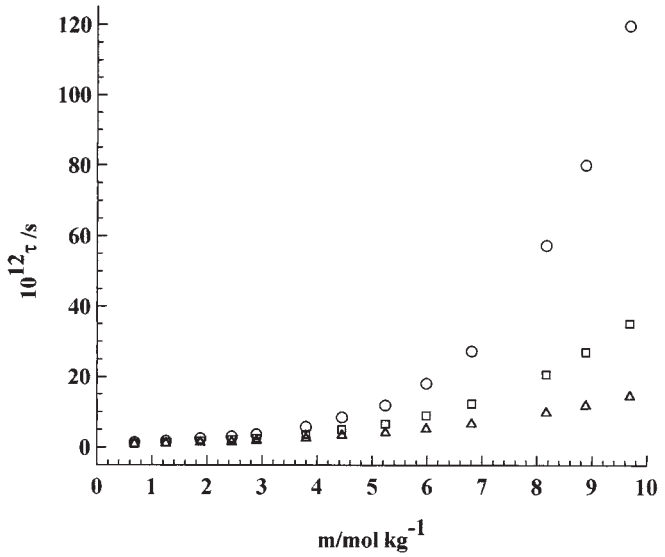

tures (Figs. 5–8) prevail because of the fact that both the normal hydrogen bonds of water (O-H···O) around the cation (46) and the directional hydrogen bonds (47, 48) with anion (O-H···Cl) are reinforced (15, 17) at low temperatures. At room temperature and above, the strong electric field of Li^+ affects the freely moving water molecules to form a rigid hydration shell. Thus, it can be concluded that anion hydration controls the viscosity processes (shear effect) at low temperatures, whereas at high temperatures it is the cation hydration. The same explanation may also hold for the methanolic solutions.

Acknowledgments

Financial assistance from the Department of Science and Technology, New Delhi, is gratefully acknowledged. The authors express their gratitude to the Director of the laboratory for the facilities and interest in this work.

References

1. Y. Marcus. Ion solvation. John Wiley and Sons, Chichester, U.K. 1986. Chap. 4.
2. H. Ohtaki and T. Radnai. Chem. Rev. **93**, 1157 (1993).
3. S.B. Rempe, L.R. Pratt, G. Hummer, J.D. Kress, R.L. Martin, and A. Redondo. J. Am. Chem. Soc. **122**, 966 (2000).
4. I. Howell and G.W. Neilson. J. Phys.: Condens. Matter, **8**, 4455 (1996).
5. C.C. Pye, W. Rudolph, and R.A. Poirier. J. Phys. Chem. **100**, 601 (1996).
6. S. Koneshan, J.C. Rasaiah, R.M. Lynden-Bell, and S.H. Lee. J. Phys. Chem. B, **102**, 4193 (1998).
7. K.H. Michaelian and M. Moskovits. Nature (London), **273**, 135 (1978).
8. W. Rudolph, M.H. Brooker, and C.C. Pye. J. Phys. Chem. **99**, 3793 (1995).
9. A.G. Novikov, M.N. Rodnikova, V.V. Savostin, and O.V. Sobolev. Physica B (Amsterdam), **234–236**, 340 (1997).
10. G. Pálinkás, T. Radnai, and H. Hajdu. Z. Naturforsch. A: Astrophys. Phys. Phys. Chem. **A35**, 107 (1980).
11. S.H. Lee and J.C. Rasaiah. J. Chem. Phys. **101**, 6964 (1994).
12. G. Toth. J. Chem. Phys. **105**, 5518 (1996).
13. T. Radnai, G. Pálinkás, G.I. Szasz, and K. Heinzinger. Z. Naturforsch. A: Astrophys. Phys. Phys. Chem. **A36**, 1076 (1981).
14. A.A. Zavitsas. J. Phys. Chem. B, **105**, 7805 (2001).
15. J.F. Jal, A.K. Soper, P. Carmona, and J. Dupuy. J. Phys.: Condens. Matter, **3**, 551 (1991).
16. N.J. Tao and S.M. Lindsay. J. Phys.: Condens. Matter, **1**, 8709 (1989).
17. K. Yamanaka, M. Yamagami, T. Takamuku, T. Yamaguchi, and H. Wakita. J. Phys. Chem. **97**, 10 835 (1993).
18. T. Yamaguchi, M. Yamagami, H. Wakita, and A.K. Soper. J. Mol. Liq. **65/66**, 91 (1995).
19. S. Cummings, J.E. Enderby, G.W. Neilson, J.R. Newsome, R.A. Howe, W.S. Howells, and A.K. Soper. Nature (London), **287**, 714 (1980).
20. A.H. Narten, F. Vaslow, and H.A. Levy. J. Chem. Phys. **58**, 5017 (1973).
21. K. Tanaka, N. Ogita, Y. Tamura, I. Okada, H. Ohtaki, G. Palinkas, E. Spohr, and K. Heinzinger. Z. Naturforsch. A: Phys. Sci. **A42**, 29 (1987).
22. M.F. Kropman and H.J. Bakker. Science (Washington, D.C.), **291**, 2118 (2001).
23. F.J. Vogrin and E.R. Malinowski. J. Am. Chem. Soc. **97**, 4876 (1975).
24. D.K. Phelps, M.J. Weaver, and B.M. Ladanyi. Chem. Phys. **176**, 575 (1993).
25. S. Roy and B. Bagchi. J. Chem. Phys. **101**, 4150 (1994).
26. M.A. Kahlow, W. Jarzeba, T.J. Kang, and P.F. Barbara. J. Chem. Phys. **90**, 151 (1989).
27. N. Rohman, N.N. Dass, and S. Mahiuddin. J. Chem. Eng. Data, **44**, 465 (1999).
28. N. Rohman, N.N. Dass, and S. Mahiuddin. Aust. J. Chem. **53**, 463 (2000).
29. A.I. Vogel. A textbook of practical organic chemistry. 3rd ed. ELBS, Longman, U.K. 1975. p. 268.
30. J.M. Wimby and T.S. Berntsson. J. Chem. Eng. Data, **39**, 68 (1994).
31. S. Lengyel, J. Tamas, J. Giber, and J. Holdrith. Acta Chim. Acad. Sci. Hung. **40**, 125 (1964).
32. E.W. Washburn (Editor). International critical tables of numerical data, physics, chemistry, and technology. Vol. III. McGraw–Hill, New York. 1928. p. 77.
33. E.W. Washburn (Editor). International critical tables of numerical data, physics, chemistry, and technology. Vol. III. McGraw–Hill, New York. 1928. p. 140.
34. F.T. Gucker, D. Stubley, and D.J. Hill. J. Chem. Thermodyn. **9**, 987 (1977).
35. D.S. Allam and W.H. Lee. J. Chem. Soc. A, 5 (1966).
36. F.J. Millero, M. Fernandez, and F. Vinokurova. J. Phys. Chem. **89**, 1062 (1985).
37. R. Pottel. In Water: A comprehensive treatise. Vol. 3. Edited by F. Erank. Plenum, New York. 1973.
38. M.J. Blandamer. J. Chem. Soc. Faraday Trans. **94**, 1057 (1998).
39. K. Hashimoto and T. Kamimoto. J. Am. Chem. Soc. **120**, 3560 (1998).
40. C.C. Pye. Int. J. Quantum Chem. **76**, 62 (2000).
41. E.D. Glendening and D. Feller. J. Phys. Chem. **99**, 3060 (1995).
42. D. Feller, E.D. Glendening, D.E. Woon, and M.W. Feyereisen. J. Chem. Phys. **103**, 3526 (1995).

© 2002 NRC Canada

43. P.C. Carman. J. Phys. Chem. **73**, 1095 (1969).
44. E.W. Washburn (Editor). International critical tables of numerical data, physics, chemistry, and technology. Vol. V. McGraw–Hill, New York. 1929. p.15.
45. L.E. Kinsler and A.R. Frey. Fundamentals of acoustics. Wiley Eastern Ltd., New Delhi. 1978. p. 224.
46. L.M. Ramaniah, M. Bernasconi, and M. Parrinello. J. Chem. Phys. **109**, 6839 (1998).
47. S.-B. Zhu and G.W. Robinson. J. Chem. Phys. **97**, 4336 (1992).
48. G. Peslherbe, B.M. Ladanyi, and J.T. Hynes. Chem. Phys. **258**, 201 (2000).

© 2002 NRC Canada

The hydrolysis of an activated ester by a tris(4,5-di-*n*-propyl-2-imidazolyl)phosphine–Zn^{2+} complex in neutral micellar medium as a model for carbonic anhydrase

Terry B. Koerner and R.S. Brown

Abstract: The properties of tris(4,5-di-*n*-propyl-2-imidazolyl)phosphine–M^{2+} complexes (**3**–M^{2+}, M = Zn, Co) in neutral micellar media of Brij-35 and Triton X-100 have been studied in water with respect to their quantitative potentiometric titration, Co^{2+}-visible absorption spectra, and ability of the **3**–Zn^{2+} complex to promote the hydrolysis of the activated ester, *p*-nitrophenyl acetate (PNPA). Potentiometric titration of the **3**–$M^{2+}(ClO_4^-)_2$ complexes in 20 mM Brij-35 media yields a steep titration curve indicative of the cooperative consumption of two hydroxides, with computed pK_1 and pK_2 values of 8.75 and 6.25, respectively, and the midpoint of the titration curve (pK_{app}) being 7.50. A similar titration of the Co^{2+} complex also indicates cooperative consumption of two HO^-, and this is tied to the formation of a 4- or 5-coordinate complex, pK_{app} ~ 7.3–7.4. The cooperativity is explained in terms of sequential replacement of the two ClO_4^- ions associated with the **3**–M^{2+} to eventually yield **3**–M^{2+}–HO^-/($HO^-(H_2O)_n$) having the first hydroxide ligated to the metal ion and the second associated as an ion pair. The **3**–Zn^{2+} complex catalyzes the hydrolysis of PNPA in 20 mM Brij-35 and 40 mM Triton X-100. Plots of the observed second order rate constant (k_2) vs. pH in Brij-35 increase linearly with pH and plateau to a value of k_2^{max} = 0.86 M^{-1} s^{-1}, with a kinetic pK_a of 8.7. These data are analyzed by a process wherein the **3**–Zn^{2+}–HO^- is kinetically active in the rate-limiting step of the reaction, while the ion-paired ($HO^-(H_2O)_n$) exists as a spectator to the slow step, possibly promoting rapid breakdown of a tetrahedral intermediate. Analysis of the kinetic data in terms of a model that accounts for the partitioning of PNPA between water and hydrophobic micellar pseudophase indicates that the second-order rate constant of the micelle-bound ester is augmented by 45-fold due to loading of the PNPA substrate into the micelle.

Key words: Brij-35, TritonX-100, neutral micelle, carbonic anhydrase model, kinetics, potentiometric titrations, catalysis, *p*-nitrophenyl acetate hydrolysis.

Résumé : Opérant dans l'eau, dans un milieu micellaire neutre de Brij-35 et de Triton X-100, on a étudié les propriétés des complexes tris(4,5-di-propyl-2-imidazolyl)phosphine–M^{2+} (**3**–M^{2+}, M = Zn, Co) en relation à leurs titrages potentiométriques quantitatifs, à leurs spectres d'absorption visible du Co^{2+} et l'habilité du complexe **3**–Zn^{2+} à faciliter l'hydrolyse de l'ester activé, acétate de *p*-nitrophényle (PNPA). Le titrage potentiométrique des complexes **3**–$M^{2+}(ClO_4^-)_2$ dans un milieu contenant 20 mM de Brij-35 donne lieu à une courbe de titrage à forte pente qui est une indication de la consommation coopérative de deux ions hydroxydes pour lesquelles on a calculé des valeurs de pK_1 et de pK_2 de 8,75 et 6,25 et un point médian de la courbe de titrage (pK_{app}) de 7,50. Un titrage semblable du complexe de Co^{2+} suggère aussi l'existence d'une consommation coopérative de deux HO^- et ceci est lié à la formation d'un complexe 4- ou 5-coordiné avec un pK_{app} ~ 7,3–7,4. On explique ces coopérations en termes d'un remplacement en séquence des deux ions ClO_4^- associés au **3**–M^{2+} qui conduit éventuellement à **3**–M^{2+}–HO^-/($HO^-(H_2O)_n$) dans lequel le premier hydroxyde est lié à l'ion métallique et le second est associé sous la forme d'une paire d'ions. Le complexe **3**–Zn^{2+} catalyse l'hydrolyse du PNPA dans des milieux contenant 20 mM de Brij-35 ou 40 mM de Triton X-100. Dans un milieu contenant du Brig-35, les courbes de la constante de vitesse du deuxième ordre observé (k_2) en fonction de pH augmentent de façon linéaire avec le pH pour atteindre un plateau à une valeur maximale k_2^{max} = 0,86 M^{-1} s^{-1} et un pK_a cinétique de 8,7. On a analysé ces données par un processus dans lequel le complexe **3**–Zn^{2+}–HO^- est cinétiquement actif dans l'étape cinétiquement limitante de la réaction alors que le complexe sous la forme de paire d'ions ($HO^-(H_2O)_n$) existe sous la forme de spectateur dans l'étape la plus lente et favorisant peut-être une dissociation rapide d'un intermédiaire tétraédrique. L'analyse des données cinétiques en fonction d'un modèle qui tient compte du coefficient de partition du PNPA entre l'eau et la pseudophase micellaire hydrophobe indique que la constante du deuxième ordre de l'ester lié à la micelle est augmentée par un facteur de 45 en raison du chargement du substrat PNPA dans la micelle.

Mots clés : Brij-35, Triton X-100, micelle neutre, modèle de l'anhydrase carbonique, cinétique, titrages, catalyse, hydrolyse de l'acétate de *p*-nitrophényle.

[Traduit par la Rédaction]

Received 14 August 2001. Published on the NRC Research Press Web site at http://canjchem.nrc.ca on 22 February 2002.

T.B. Koerner and R.S. Brown.[1] Department of Chemistry, Queen's University, Kingston, ON K7L 3N6, Canada.

[1]Corresponding author (e-mail: rsbrown@chem.queensu.ca).

 DOI: 10.1139/V02-001 © 2002 NRC Canada

Introduction

Carbonic anhydrases (CA) are ubiquitous metalloenzymes, the active site of which contain an essential Zn^{2+} ion bound by three histidine imidazoles (1). The only known physiological role for the various forms of CA is to facilitate the interconversion of carbon dioxide and bicarbonate in the equilibrium $CO_2 + H_2O \rightleftharpoons HCO_3^- + H^+$, and in doing so these enzymes play important roles in respiration, photosynthesis, calcification, and the control of extracellular pH. Although not its physiological role, the enzyme has also shown catalytic activity toward hydration of aldehydes, hydrolysis of carboxylic esters, phosphoric esters, cyanide, cyanate, and thiocyanate (2, 3). The mechanism of action of CA is among the most completely understood for all enzymes and involves ionization of the active site Zn^{2+}–OH_2 (pK_a~7) to form a nucleophilic Zn^{2+}–OH^-, which subsequently attacks the carbonyl group of the substrate.

Numerous small molecule complexes of Zn^{2+} and other transition metal ions have been offered as models for one or more of the catalytic or spectroscopic features of the enzyme (4–8). Despite the prevalence of such models, none of these shows a catalytic activity toward CO_2 hydration that rivals that of the enzyme where the k_{cat} and k_{cat}/K_m terms are 1.4×10^6 s^{-1} and 1.5×10^8 M^{-1} s^{-1} respectively (1*e*). Rather, the available models shown to react with CO_2 (8) do so with second-order rate constants that are somewhat lower than that for $HO^- + CO_2$ (6000 M^{-1} s^{-1} (9)). CA also catalyzes the easily monitored hydrolysis of *p*-nitrophenyl acetate (PNPA, **1**) with a $k_{cat}/K_m = 2500$ M^{-1} s^{-1} (10). This substrate has been used extensively to test the catalytic ability of some model systems toward ester hydrolysis (7*d*, 11), but again none of these reacts faster than direct nucleophilic attack of hydroxide ion (15 M^{-1} s^{-1} (12)).

It is clear from the above rate data that CA employs some features to enhance the activity of a Zn^{2+}-coordinated HO^- relative to HO^- in aqueous solution. One of the often-invoked ways involves a mechanism having a dual role for the metal ion as in **2**, acting to deliver the nucleophile with simultaneous stabilization of the developing (–) charge on the substrate C=O.

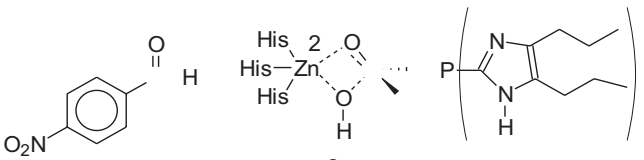

1 **2** **3**

Another factor might involve a medium effect where the hydrophobic environment surrounding the Zn^{2+}–HO^- substantially enhances the nucleophilicity by removing much of the solvation of the hydroxide. The latter possibility has spurred some studies involving encapsulation of Zn^{2+} model complexes into micellar phases, and subsequent investigation of their reactivities toward PNPA and other substrates such as tris *p*-nitrophenyl phosphate and *p*-nitrophenyl-diphenyl phosphate (7*b*, 11*a*, 13).

In the following, we describe our studies of the hydrolysis of PNPA promoted by two neutral micellar systems (14) incorporating the Zn^{2+} complex of tris(4,5-di-*n*-propyl-2-imidazolyl)phosphine (**3**), a complex that we prepared previously (8*b*) as a model for CA. The previous study demonstrated that the complex facilitates the interconversion of CO_2 and HCO_3^- in 80% ethanol–water, the second-order rate constant for attaining equilibrium being 2800 M^{-1} s^{-1}. The study also revealed complications, wherein the complex formed aggregates and also associated with the indicators used for determining the kinetics, suggesting that it might be readily incorporated into a hydrophobic micellar medium. Herein we report that **3**–$Zn^{2+}(ClO_4^-)_2$ can be incorporated into the neutral micellar systems, Brij-35 ($C_{12}H_{25}(OCH_2CH_2)_{23}OH$) and Triton X-100 (*p*-(1,1,3,3-tetramethylbutyl)-phenyl$(OCH_2CH_2)_xOH$, $x = 9.5$, average). Both systems promote the hydrolysis of PNPA as basic forms generated by the formation of what is probably **3**–Zn^{2+}–HO^- having kinetic pK_a values of 8.74 and 8.81, respectively. In addition, we have performed quantitative potentiometric titrations of the Brij-35–**3**–$Zn^{2+}(OH_2)_x$–$(ClO_4^-)_2$ system that reveal a cooperative consumption of two equivalents of OH^- per complex.

Results

There are three observations worth mentioning because they limit the range of study using **3** and Zn^{2+} in the aqueous micellar system. Heterogeneous solutions were observed if the [M^{2+}] was varied above or below the [**3**], suggesting the formation of a micelle-soluble 1:1 ligand–metal complex. The cloudy solutions arise from the free ligand or $M^{2+}(OH^-)_x$, both of which are insoluble in the pH range of this study. Second, at the maximum [**3**–M^{2+}] under which the kinetics were determined, cloudy solutions were observed if the $[surfactant]_t$ was lower than 40 mM for Triton X-100 and 20 mM for Brij-35. This suggests that at high [**3**–M^{2+}] the properties of the micelle are disrupted enough to limit complex solubility, which is known to be a common occurrence in micelle solutions (15). Finally, attempts to control the ionic strength of the Triton X-100 solutions also resulted in cloudy solutions. It has been shown that the aggregation number, the degree of hydration, and the radius of Triton X-100 micelles are all sensitive to the ionic strength and in general these all increase with increasing ionic strength producing micelles that are more diffuse (15*b*). A micelle that is more diffuse and hydrated probably diminishes the solubility of hydrophobic ligands and so limits our studies with Triton X-100 to media in which the ionic strength was not controlled, other than by the presence of the 0.1 M buffers, the upper limit for the ionic strength thus being approximately 0.07 M.

Potentiometric and spectroscopic titrations

At concentrations sufficient for potentiometric pH titration, **3** is not soluble in water, therefore, 20 mM Brij-35 was added to obtain a homogeneous solution. This concentration was much greater than the reported critical micelle concentration (0.04–1.67 mM (15*a*)). In the absence of M^{2+}, **3** in Brij-35 is soluble at low pH (< 4.5) and at high pH (>9.0), but between these values the solutions were cloudy, indicating the fully protonated species **3**–$3H^+$ is soluble in water and is probably not associated with the surfactant to any great extent, while fully deprotonated **3** is soluble in the mi-

© 2002 NRC Canada

celle. However, in the presence of metal ions the solutions are homogeneous at all pH values between 4 and 10.

Shown in Fig. 1 is the potentiometric titration profile for a 1.5 mM solution of **3** and $Zn^{2+}(ClO_4^-)_2$ in the presence of 20 mM Brij-35 at 25°C, I = 0.10 M ($NaClO_4$). A similar curve with $Co^{2+}(ClO_4^-)_2$ (not shown) exhibits the same characteristics. Both profiles indicate complete ligand deprotonation, and thus M^{2+} complexation, by pH 7.0, followed by the consumption of two additional equivalents of hydroxide between 7.0 < pH < 9.0. Attainment of equilibrium was very slow for these titrations, requiring about half an hour between each titration point. A slow attainment of equilibrium for titration of a macrocyclic tetraamine – Zn^{2+} complex in a Triton X-100 micellar system was previously observed by Kimura et al. (13*a*).

The notable aspect of Fig. 1, and the corresponding Co^{2+} titration profile, is the unusually steep consumption of two equivalents of HO^- per **3**–M^{2+} complex exhibited in both the titration curves from 7 < pH < 9. This cannot be explained by a stepwise addition of OH^- or deprotonation of $M^{2+}(OH_2)$, but it can be rationalized by sequential dissociation in a cooperative fashion as represented in eq. [1] for a dibasic acid where $K_2 > K_1$ (16). Given in Fig. 2 are the expanded titration data for the pH 7–9 region of Fig. 1, showing the consumption of 2 equiv. of ^-OH per **3**–Zn^{2+} complex. The line through the data is generated from a NLLSQ fit of the titration data to eq. [2], which was derived for the cooperative dissociation process in eq. [1] with K_1 and K_2 being the first- and second-dissociation constants and K_w being the autoprotolysis constant of H_2O (taken to be 1×10^{-14} M^2). The fit yields computed values are 8.75 and 6.25 for pK_1 and pK_2, respectively (pK_{app} for the midpoint of the titration is 7.50). Similar treatment of the **3**–Co^{2+} potentiometric data gives values for pK_1 and pK_2 of 8.75 and 6.00, respectively (pK_{app}= 7.37).

[1] 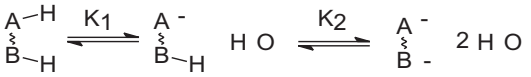

[2] $$\#\,\text{equiv}\,[OH^-] = \frac{K_1[H^+] + 2K_1K_2}{[H^2]^2 + K_1[H^+] + K_1K_2} + \frac{K_w}{[H^+]} - H^+$$

The visible absorption spectra measured between 490–670 nm of a 20 mM Brij-35 solution containing 3.0 mM each of **3** and $Co^{2+}(ClO_4^-)_2$ as a function of pH is given in Fig. 3, along with the pH dependence of the λ_{max} = 575 nm indicating that the pK_{app}, determined by potentiometric titration of the **3**–Co^{2+} complex, is also tied to the formation of an intense purple solution. However, the steepness of the Abs_{575} titration profile from 6.5 < pH < 8.5 is not typical of a single ionization event. The data for the spectroscopic titration best fit to eq. [3][2] with two cooperative ionizations per metal ion, where pK_1 = 8.75, pK_2 = 5.90 (pK_{app} = 7.33), M_a = ([**3**–Co^{2+}][ε_{max}])/2, and K_w is the autoprotolysis constant of water.

[3] $$Abs_{575} = \frac{M_a(K_1[H^+] + 2K_1K_2)}{[H^+]^2 + K_1[H^+] + K_1K_2} + \frac{K_W}{[H^+]} - [H^+] + 0.221\left(\frac{[H^+]}{[H^+] + K_1}\right)$$

Kinetic studies of 3–Zn^{2+} in Brij-35 and Triton X-100 micelle media

The **3**–Zn^{2+} complex catalyzes the hydrolysis of PNPA (0.035 mM) in buffered solutions (0.10 M) in the presence of both Brij-35 (20 mM) and Triton X-100 (40 mM) at 25°C. At each pH the k_{obs} for the hydrolysis of PNPA vs. [**3**–Zn^{2+}] at four concentrations from 0.8 to 4.0 mM gave linear plots with no observable saturation. Second-order rate constants (k_2) for the hydrolysis of PNPA catalyzed by **3**–Zn^{2+} in both Brij-35 and Triton X-100 surfactant were calculated from the slopes of the k_{obs} vs. [**3**–Zn^{2+}] plots at each pH and are given in Tables 1 and 2, respectively. The pH vs. log k_2 profiles for surfactant Brij-35 (Fig. 4) and Triton X-100 (Fig. 5) increase linearly with unit slope as a function of pH and then plateau. Shown in eq. [4] is a mechanism that accounts for the pH dependency of the second-order rate constant, from which can be derived the expression given in eq. [5], where K_a is the kinetic acid-dissociation constant generating the presumed Zn^{2+}–OH^- active species, k_2^{max} is the maximal second-order rate constant for its reaction with PNPA, and (P) indicates the products of the reaction (*p*-nitrophenol(ate) and acetate). NLLSQ fits of the data to eq. [5] generates k_2^{max} (pK_a given in parentheses) values of 0.860 ± 0.099 M^{-1} s^{-1} (8.74 ± 0.06) and 0.023 M^{-1} s^{-1} (8.81 ± 0.11) for Brij-35 and Triton X-100, respectively.

[4] $$\mathbf{3}\text{–}Zn^{2+}(H_2O) \overset{K_a}{\rightleftharpoons} \mathbf{3}\text{–}Zn^{2+}(OH^-) \xrightarrow[k_2\,max]{\text{PNPA}} P$$

[5] $$k_2 = \frac{k_2^{max}K_a}{K_a + [H^+]}$$

Discussion

The system involved in this study comprises M^{2+} complexes of **3**, which are solubilized in neutral micellar media of Brij-35 or Triton X-100. As noted above, homogeneity of the system requires that all components are present: omission of any of M^{2+}, **3**, or micelle agent leads to formation of precipitates. The critical micelle concentration (CMC) for Brij-35 is reported (15*a*) to be between 0.04 and 0.17 mM with an aggregation number (*N*, the average number of surfactant molecules per micelle) of 35–65, while those values for Triton X-100 are 0.08 mM (13*a*) and 79–135 (15*b*). Given a [surfactant]$_t$ of 20 mM for Brij-35 and 40 mM for Triton X-100, one calculates[3] that the actual concentration of micelles is 0.31–0.6 mM and 0.30–0.50 mM, respectively. For the potentiometric titrations in 20 mM Brij-35, we have employed a [**3**] = [Zn^{2+}] = 1.5 mM, while for the spectroscopic titrations the [**3**] = [Co^{2+}] = 3 mM, requiring that each Brij-35 micelle has on average ~2.5–5 **3**–Zn^{2+} com-

[2] This equation is essentially the same as eq. [1], given in ref. 16, with a term to correct the mass balance for an absorbance of the fully protonated species, 0.221([H^+]/([H^+] + K_1)). To undertake the fit, we have the K_1 as the constant ($1 \times 10^{-8.75}$) and K_2 as the variable.

[3] The actual concentration of micelles is given as [micelle] = ([surfactant]$_t$ – CMC)/*N*, where *N* is the aggregation number (see ref. 14, p. 88).

© 2002 NRC Canada

Fig. 1. A titration curve for 1.5×10^{-3} M **3**–$3H^+$ in the presence of equimolar $Zn(ClO_4)_2$ in a 20 mM Brij-35 solution at 25°C, I = 0.10 M ($NaClO_4$).

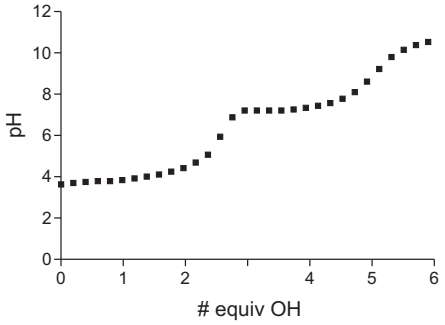

Fig. 2. Potentiometric titration data for the expanded pH 7–9 region of Fig. 1 for **3** in the presence of one equivalent of Zn^{2+}. The line going through the data was calculated from eq. [2] and yields pK_1 = 8.75 and pK_2 = 6.25.

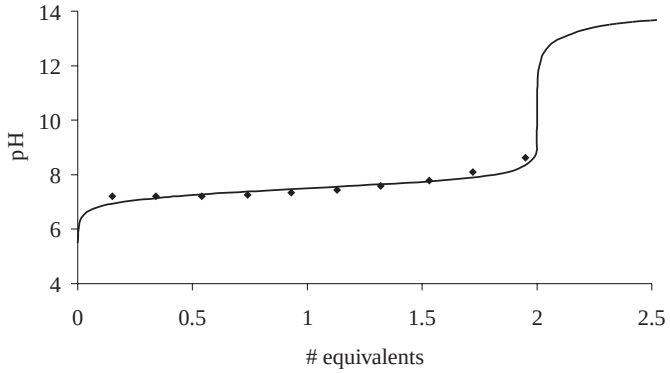

Fig. 3. Visible absorption spectrum of 3 mM **3** in the presence of one equivalent of Co^{2+} in a 20 mM Brij-35 solution as a function of pH (ionic strength not controlled), along with a plot of the absorbance data at λ_{max} = 575 nm vs. pH. The line through the data was calculated using eq. [3]. The dashed line was calculated for a single ionization event with a pK_a = 7.25, ref. 16.

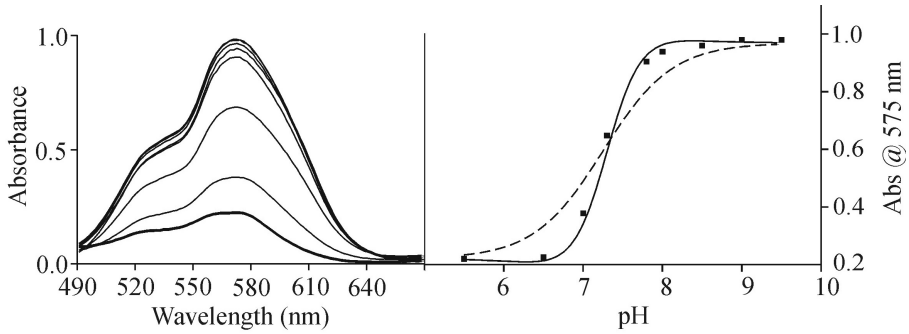

plexes and 5–10 **3**–Co^{2+} complexes. In the case of the kinetic experiments where the [**3**–Zn^{2+}] was varied from 0.8–4.0 mM, the average number of complexes per micelle varies from 1.3–2.6 to 6.4–13 for Brij-35, and 1.5–2.3 to 8–13 for Triton X-100.

Micelles of Brij-35 are described (15*a*) in terms of a spherical model having a central core of radius ~44 Å containing anhydrous and hydrated zones that block solvent flow, and a 7–13 Å thick outer corona, compared to the spines of a sea-urchin, of hydrated poly(oxyethylenes) that permits solvent flow but obstructs the approach of other micelles. That same description suggests that the number of water molecules associated with the poly(oxyethylene) chain ends is about 8 at temperatures from 10–25°C, falling to about 4 at 70°C.

Potentiometric and spectroscopic titrations

The major feature in the potentimetric titration of **3**–$3H^+$ + $Zn^{2+}(ClO_4^-)_2$ or $Co^{2+}(ClO_4^-)_2$ in the Brij-35 medium is the quantitative consumption of five equivalents of hydroxide per **3**–M^{2+} complex, three below pH 7 to form the complex **3**–M^{2+}, and two more between pH 7 and 9 that display a steepness in the titration curve requiring some cooperative process. Accepting the above description of Brij-35 as being largely correct for the conditions employed in our study, and that the inclusion of **3**–M^{2+} does not disrupt the micelle's integrity to any major extent, then under the potentiometric titration conditions each micelle contains on average 2.5–5 **3**–Zn^{2+} complexes or 5–10 **3**–Co^{2+} complexes. Molecular models indicate that when complexed to the three imidazoles, the metal ion is encapsulated by the *n*-propyl groups of the ligand as in **4**, X^- = counterion or H_2O. The exact location and orientation of the complex(es) in the micelle is unknown, but it is likely that they reside in the micellar pseudophase allowing communication between the metal ion core and the various components of the aqueous solvent.

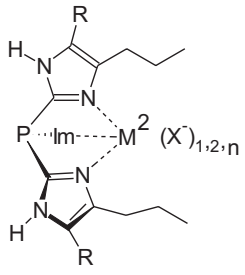

4 Im = (4,5-di-*n*-PrIm)
R = *n*-Pr

It has been suggested that the local dielectric constants (ε_{eff}) of Triton X-100 (17) and Brij-35 (18) micelles are 32 and 38, respectively. The reported dielectric constants are

© 2002 NRC Canada

Table 1. Second-order rate constants for **3**–Zn^{2+} promoted hydrolysis of PNPA (3.0×10^{-5} M) in 0.1 M buffered aqueous Brij-35 (20 mM), I = 0.1 M ($NaClO_4$) at 25 ± 0.1°C, obtained from the slopes of k_{obs} vs. [**3**–Zn^{2+}] plots ($0.8–4.0 \times 10^{-3}$ M) at each pH.

pH	k_2 (M^{-1} s^{-1})[a]
7.0	0.0189 ± 0.0018
7.4	0.0289 ± 0.0012
7.9	0.113 ± 0.007
8.3	0.213 ± 0.017
8.7	0.491 ± 0.026
9.1	0.633 ± 0.021
9.5	0.647 ± 0.024
10.1	0.842 ± 0.031

[a]Errors determined from the fits of the plots of k_{obs} vs. [**3**–Zn^{2+}].

Table 2. Second-order rate constants for **3**–Zn^{2+} promoted hydrolysis of PNPA (3.0×10^{-5} M) in 0.1 M buffered aqueous Triton X-100 (40 mM) at 25 ± 0.1°C, obtained from the slopes of k_{obs} vs. [**3**–Zn^{2+}] plots ($0.8–4.0 \times 10^{-3}$ M).

pH	k_2 (M^{-1} s^{-1})[a]
7.57	0.0057 ± 0.0002
7.80	0.0139 ± 0.0007
8.00	0.0148 ± 0.0008
8.24	0.028 ± 0.002
8.50	0.046 ± 0.001
8.90	0.071 ± 0.002
9.15	0.0807 ± 0.002

Note: Ionic strength not controlled.
[a]Errors determined from the fits of the plots of k_{obs} vs. [**3**–Zn^{2+}].

Fig. 4. Plot of log k_2 vs. pH for the **3**–Zn^{2+} promoted hydrolysis of PNPA in 20 mM $Brij_{35}$ at 25°C. The line through the data points was calculated using eq. [5].

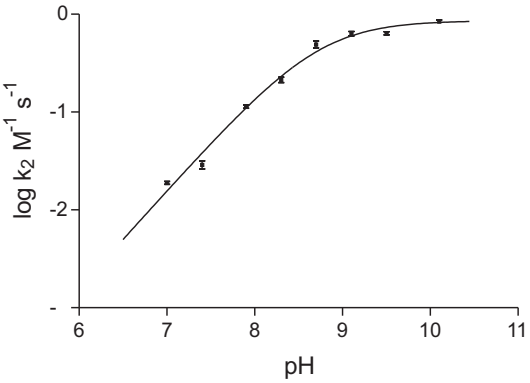

Fig. 5. Plot of log k_2 vs. pH for the **3**–Zn^{2+} promoted hydrolysis of PNPA in 40 mM Triton X-100 at 25°C. The line though the data was calculated using eq. [5].

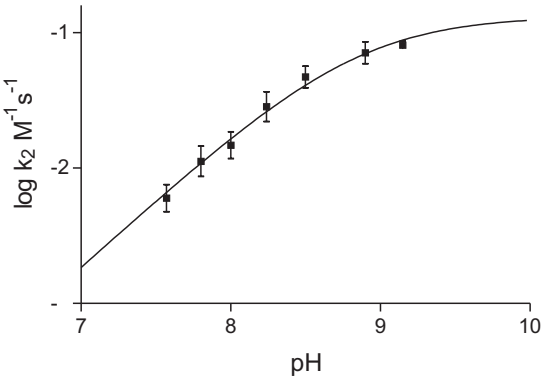

very similar to that of methanol (ε = 31.5) and much lower than that of water (ε = 78.5) (19), which certainly plays an important part in the potentiometric titrations in micellar media which can be understood as M^{2+}–X^- associations.

A highly simplified analysis of the potentiometric titration data considers each micelle to contain a dibasic acid as presented in eq. [1] with $K_2 > K_1$. The mathematical description for this given in eq. [2] nicely fits the pH 7–9 titration data given in Fig. 2, with computed values of pK_1 and pK_2 of 8.75 and 6.25, respectively; the midpoint of the titration (pK_{app}) being 7.5. Because the micelles on average are likely to contain at least two, and up to five, **3**–Zn^{2+} complexes it is probably better to consider the system as a polyprotic acid wherein each dissociation has some influence on the next. Indeed, if the micelle were considered a tetraprotic acid (two complexes, each with two ionizations), one can derive the expression given in eq. [6], to which NLLSQ fitting of the Fig. 2 potentiometric data yields values of pK_1 = 8.75, pK_2 = 6.50, pK_3 = 7.00, and pK_4 = 7.75, argueably giving a better fit to the titration data than does eq. [2]. While expanded fits can be constructed for all possible combinations of ionizations, these do not add to the understanding of the process, so we limit further discussion to the dibasic acid model of eqs. [1] and [2].

[6] $$\#\text{equiv of base} = \frac{K_1[H^+]^3 + 2K_1K_2[H^+]^2 + 3K_1K_2K_3[H^+] + 4K_1K_2K_3K_4}{[H^+]^4 + K_1[H^+]^3 + K_1K_2[H^+]^2 + K_1K_2K_3[H^+] + K_1K_2K_3K_4} + \frac{K_W}{[H^+]} - [H^+]$$

More information about how the association of HO^- affects the metal ion's local environment can be obtained from the spectroscopic titrations of 3 mM **3**–Co^{2+} in 20 mM Brij-35, which also shows the cooperative phenomenon (see Fig. 3). A point of note for the spectroscopic titration is that the consumption of HO^- is tied to the formation of a blue 4- or 5-coordinate Co^{2+} complex (1*f*, 2) and the plot the Abs_{575} vs. pH data given in Fig. 3 can be analyzed in terms of the cooperative consumption of two HO^- by the dibasic acid model (eq. [3]), which yields values for pK_1 and pK_2 of 8.75 and 5.90, respectively (midpoint of titration, pK_{app} = 7.33), values completely consistent with the potentiometric data. The color change promoted by the two hydroxides requires either that they both bind directly to the metal ion, or one does while the other is sufficiently close to perturb the UV-vis spectroscopic properties.

© 2002 NRC Canada

Scheme 1.

$$\underset{\mathbf{a}}{\mathbf{3}-M^{2+}/(ClO_4^-)_2} + 2OH^- \rightleftharpoons \underbrace{\mathbf{3}-M^{2+}-OH^-/(ClO_4^-)+ClO_4^-+OH^-}_{\mathbf{b}}$$

$$\mathbf{3}-M^{2+}-OH^-/(HO^-)+2ClO_4^- \quad (\mathbf{c})$$

Given in Scheme 1 is a process explaining the above data. For neutrality the complex **3**–M^{2+} must initially occupy the reduced polarity micellar pseudophase associated with two ClO_4^- counterions, probably as an ion triplet as in ***a***. In Scheme 1 we have omitted the water molecules associated with the counterions and the metal, but note that these must be present since at pH < 7, prior to the cooperative consumption of HO^-, the Co^{2+} complex is pink, and therefore, octahedral. Although there has been extensive work on ion pairing in cationic micelles, there appears to be relatively little work done with neutral micelle media (14). However, a study by Beltrán et al. (20) shows that the fluorescence of chlorquinaldol (**5**) in a Brij-35 micellar medium under basic conditions correlates with the mole fraction of the Na^+–phenolate ion pair within the micelle microenvironment. Chlorquinaldol does not fluoresce in aqueous solution suggesting the fluorescence is due to ion-pairing within the micelle that is not observed in aqueous solution.

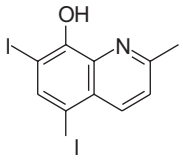

5

Above pH 7, **3**–M^{2+} first consumes a HO^-, probably ligated to the metal, thereby releasing one ClO_4^- to yeild ***b***, which, we suggest, immediately replaces the second ClO_4^- with hydroxide to generate ***c***. The association of the HO^- reduces the coordination of the Co^{2+}, making it 4- or 5-coordinate, which accounts for the color change.

Although cooperative consumption of HO^- by a metal ion seems at first puzzling, there is precedence from the titration of both $Zn(ClO_4)_2$ and $Co(ClO_4)_2$ in methanol (21) that show consumption of two CH_3O^- per metal ion with a steep titration curve suggesting a cooperative process (pK_{app} = 9.75 and 11.35, respectively). Zn^{2+} and Co^{2+} also prefer tetrahedral thiocyanato complexes $[M^{2+}(NCS)_4]$ in the presence of Triton X-100 (22), an interesting observation since a tetrahedral complex is not observed in aqueous solutions. Additionally, Zn^{2+} forms a bis-chloride species in DMSO and methanol with the second halide association constant being larger than the first (23). The driving force for these processes is attributed (23) to reduced charge density at the metal center after binding the first anion, changing the coordination number from six to four or five, and also to an entropy effect resulting from release of coordinating solvent molecules after association of the anion. By analogy the consumption of the first HO^- in the present micellar system to form **3**–M^{2+}–OH^- can reduce both the coordination geometry and the electrostatic attraction of the metal centre for the remaining ClO_4^- in the ion pair so that immediate consumption of the second HO^- ensues. Of course the equilibria shown in Scheme 1 are controlled by a complex balance of enthalpy and entropy effects associated with exchange of ClO_4^- and HO^- between the aqueous and micellar phases, their solvation by associated water molecules in each phase, and their eventual association with the metal ion.

Kinetics of hydrolysis of PNPA promoted by 3–Zn^{2+} in micellar media

The kinetic profiles in Figs. 4 and 5 for the **3**–Zn^{2+} promoted hydrolysis of PNPA in Brij-35 and Triton X-100 suggest a common process where the catalytically active species is generated by consumption of a single HO^- with apparent kinetic pK_a values of 8.74 and 8.81, respectively. The kinetic data must be reconciled with the potentiometric titration data for **3**–Zn^{2+} in Brij-35 that indicates cooperative consumption of two HO^- with pK_1 and pK_2 values of 8.75 and 6.25, respectively, ultimately generating the species **3**–Zn^{2+}–HO^-/(HO^-) proposed in Scheme 1. The kinetic data require a transition state where only one hydroxide is involved in the rate limiting step for the hydrolysis, this probably being the **3**–Zn^{2+}–OH^-. That the kinetic pK_a and first potentiometric pK_1 are identical suggests that the first consumed HO^- generates the active species.

Given in Scheme 2 is a proposed mechanism that accommodates both the kinetic and potentiometric data. Species **A**, **B**, and **C** represent the first association of OH^- with **3**–Zn^{2+}, followed by exchange of ClO_4^- for OH^- accounting for the consumption of 2 equivalents of OH^-. Attack of **3**–Zn^{2+}–OH^- on PNPA might occur in either a concerted fashion to form products directly (24), or in the customary (25) two-step $B_{AC}2$ process via a tetrahedral intermediate (**TI**). In either case we propose that only the **3**–Zn^{2+}–OH^- is kinetically active in the rate-determining step of the reaction with the second OH^- residing in the local environment of the **3**–Zn^{2+}–OH^- as a spectator ion (26). The expulsion of the leaving group could occur spontaneously after the slow step of the reaction, or possibly with trapping of the **TI** by the spectator HO^- as proposed in Scheme 2. Jencks (26*a*, *b*) has termed this "enforced catalysis", which is expected when a proton is transferred to or from an unstable intermediate in order to trap it and limit its return to reactants.

Role of the micelle in catalysis of PNPA hydrolysis by 3–Zn^{2+}

Micelles have been studied for decades as "microreactors", which can compartmentalize and concen-

© 2002 NRC Canada

Scheme 2.

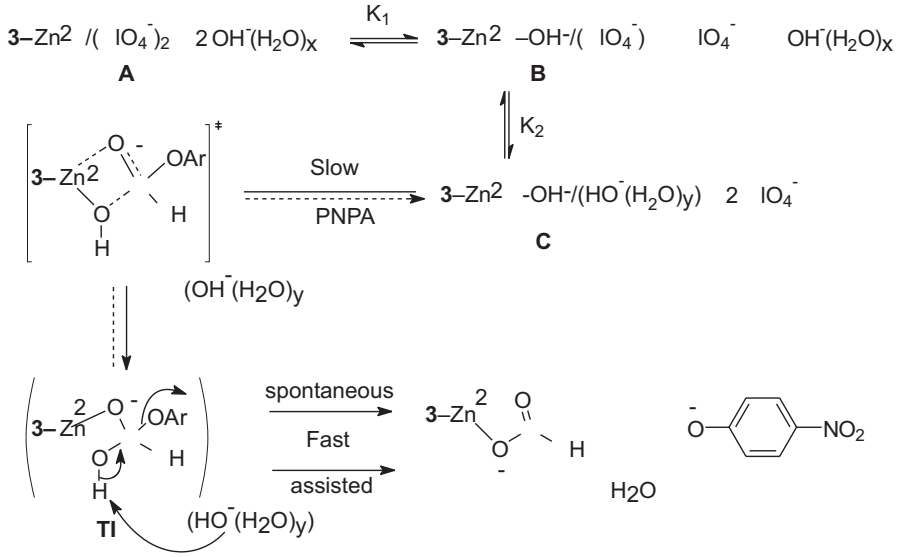

trate substrates and reactants thereby altering the rates of chemical reactions (14, 27). The promotion of reactions by cationic or anionic micelles has been discussed in terms of electrostatic and hydrophobic interactions between the surfactant aggregate and substrate, preferential binding of the transition state relative to the ground state reactants (28), and, in some cases, to alterations of the structure of the surrounding water. Less information is available on the methods by which neutral surfactants enhance reactions, but the same general consideration likely apply. In the present case, the neutral surfactant serves first to solubilize the **3**–M^{2+} complex throughout the entire pH region where hydroxide ions associate with the complex, thus preventing the precipitation of **3** or $M^{2+}(HO^{-})_x$, which was seen in our earlier study that did not utilize micelles (8*b*). The maximal reactivity exhibited by **3**–Zn^{2+}–HO^{-}–Brij-35 toward PNPA hydrolysis (k_2 = 0.86 M^{-1} s^{-1}) appears to be the second highest reported for a metal complex, the highest of which we are aware being Kimura's (13*a*) Zn^{2+}–hexadecyltetraazacyclododecane complex (k_2 = 5.0 $M^{-1}s^{-1}$ at pH 10 in 10 mM Triton X-100 and 10% CH_3CN), but both of these are less reactive than free hydroxide in water (k_{HO^-} = 15 M^{-1} s^{-1} (12)). Nevertheless, the present reactivity may be encouraging given the reduced pK_a of the **3**–$Zn^{2+}(H_2O)_x$ complex relative to that of water, (8.75 vs. 15.5) and the usual Brønsted considerations that indicate **3**–Zn^{2+}–HO^{-} should be a poorer nucleophile than hydroxide. Perhaps this suggests the mechanism involves an electrophilic–nucleophilic role for **3**–Zn^{2+}–HO^{-} (illustrated in Scheme 2) as proposed previously (7*b*, 25, 29).

Simple k_2 reactivity data of PNPA hydrolysis promoted by metal complexes in neutral micellar media, as usually presented, (8*b*, 13, 11) generally ignore the important aspect of the micelle increasing the local concentration of substrate in its interior (15, 27, 30). The omission of this renders mechanistic interpretation and rate comparisons incomplete because the real activity is markedly less (31). Given in Scheme 3 is a schematic representation of the partitioning of the PNPA substrate and the nucleophile between the aqueous

Scheme 3.

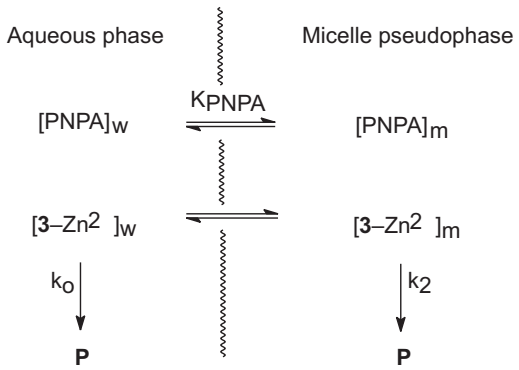

phase and the micellar pseudophase. The value for the partitioning constant (K_{PNPA}) into Brij-35 was determined in a separate experiment by determining the rate of PNPA hydrolysis at constant pH without **3**–Zn^{2+} complex as a function of Brij-35 surfactant concentration (four values between 3 and 20 mM). The data were fit to eq. [7] (32) where k_o is the pseudo-first-order rate constant in the absence of surfactant, k_2 is the pseudo-first-order rate constant within the micellar pseudophase, and [S] = [total surfactant – CMC]. The determined value at pH = 10.1 is K_{PNPA} = 43 ± 5 M^{-1}.

$$[7] \qquad 1/(k_0 - k_{obs}) = (1/(k_0 - k_2))(1 + K_{PNPA}[S])$$

$$[8] \qquad k_{cat} = \frac{k_2^m K_{PNPA}[\mathbf{3}\text{–}Zn^{2+}]}{V_m(1 + K_{PNPA}[S])}$$

The expression shown in eq. [8], derived on the basis of the process shown in Scheme 3, can be used to determine the second-order rate constant within the micelle where k_{cat} is the observed pseudo-first-order rate constant for catalyzed PNPA hydrolysis (over the background reaction at pH 10.1), V_m is the molar volume of reactive region for Brij-35 given in L mol^{-1} (0.5 M^{-1} for the 20 mM concentration of surfactant used in this study) (31), and k_2^m is the computed second-order rate constant for the reaction promoted by **3**–

© 2002 NRC Canada

Zn^{2+} in the micelle taking account of the loading of PNPA into the latter. In deriving eq. [8], we have ignored the potential **3**–Zn^{2+} catalyzed reaction in water since the complex is insoluble without the micelle. At a complex concentration of 2.5 mM, the computed k_2^m value for the complex in Brij-35 is 0.0186 M^{-1} s^{-1}, far less than the observed value of 0.86 M^{-1} s^{-1}, indicating that a factor of 45 is attributed to the loading of PNPA into the micelle. Interestingly, Scrimin et al. (31) previously applied this analysis to the data of Kimura et al. (13*a*) for hexadecyltetraazacyclododecane–Zn^{2+} catalysis of PNPA hydrolysis in Triton X-100, and have found that the micellar effects are almost wholly attributable to the increasing concentrations of reactants in the small volume of the micellar pseudophase. They conclude that when due attention is paid to the concentration loading, the reactivities of micellized metal complexes do not differ significantly from those of the analogous monomeric complexes in water. In our case, such comparison with the aqueous catalysis of PNPA hydrolysis exhibited by **3**–Zn^{2+} is impossible due to its insolubility.

Experimental

Materials

Unless otherwise stated, all reagents and solvents used were purchased as the highest commercial quality and used without further purification. Tris(4,5-di-*n*-propyl-2-imidazolyl) phosphine (**3**) was prepared according to the procedure previously reported (8*b*). The following buffers were purchased from Sigma–Aldrich: HEPES [4-(2-hydroxymethyl)-1-piperazineethanesulfonic acid, pK_a = 7.4], TAPS [3-{[tris(hydroxymethyl)methyl]amino}-1-propanesulfonic acid, pK_a = 8.4], CAPS [3-cyclohexylamino-1-propanesulfonic acid, pK_a = 10.4]. Neutral surfactants (Triton X-100 and Brij-35) were purchased from Sigma–Aldrich. 4-Nitrophenyl acetate (PNPA) was recrystallized three times from ethyl acetate. All aqueous solutions were prepared from deionized water that was distilled and boiled to remove CO_2.

Potentiometric and spectroscopic titrations

Potentiometric titrations of (**3**) (1.5 mM) in the presence and absence of equimolar amounts of $Zn^{2+}(ClO_4^-)_2$ and $Co^{2+}(ClO_4^-)_2$ were performed using a Radiometer Vit 90 Autotitrator under anaerobic conditions (Ar) at ambient temperature in the presence of 20 mM Brij-35 surfactant. The pH was monitored using a Radiometer GK2322 combination (glass/calomel) electrode calibrated with Fisher certified standard aqueous buffers (pH = 4.00 and 10.00) and recorded as a function of added standardized NaOH solution. The NaOH solutions were made by dilution of an 18 M NaOH stock solution and standardized using potassium hydrogen phthalate. Ionic strength was maintained at 0.10 M ($NaClO_4$).

Spectroscopic titrations were performed by monitoring the absorbance change between 490 and 670 nm of a solution of (**3**) (3.0 mM) as a function of pH in the presence of one equivalent of $Co^{2+}(ClO_4^-)_2$ using an OLIS® modified Cary 17 UV-vis spectrophotometer. Solutions were made similarly to those for the potentiometric titrations except for the exclusion of buffer.

Kinetic measurements

The rate of appearance of the hydrolysis product of PNPA (*p*-nitrophenolate ion) was followed by monitoring the increase in absorbance at 380 nm OLIS® modified Cary 17 UV-vis spectrophotometer at 25.0 ± 0.1°C. Reactions were monitored under pseudo-first-order conditions of excess, but equimolar, **3** and $Zn(ClO_4)_2$ in the range of 0.3–4.0 mM. Reactions were followed to at least four half-lives and displayed good first-order behaviour. The pseudo-first-order rate constants (k_{obs}) were determined by NLLSQ fitting of the absorbance vs. time traces to a standard exponential model. All observed rate constants were determined at least in duplicate and second-order rate constants were determined from slopes of k_{obs} vs. concentration of $[Zn^{2+}]_t$ plots.

In a typical experiment approximately 11 mg (2.3×10^{-5} mol) of **3** was placed in a vial fitted with a rubber septum and flushed with argon. Because of the insolubility of the ligand in water, 0.30 mL of acetonitrile was added along with approximately 0.23 mL (2.3×10^{-5} mol) of a $Zn^{2+}(ClO_4^-)_2$ stock solution (0.10 M). This mixture was sonicated until a homogeneous solution was obtained and then used as the **3**–Zn^{2+} stock solution for the day's experiments. Stock solutions were made up daily because of the instability of the ligand in solution over time. Solutions for the kinetic experiments were made in vials by adding enough **3**–Zn^{2+} stock solution so that after dilution, the concentration was between 0.8–4.0 mM. To this stock solution was added 1.5 mL of a stock surfactant solution (40.0 mM Brij-35 or 80.0 mM Triton X-100) and 1.5 mL of a stock buffer solution (0.20 M, I = 0.20, $NaClO_4$). After dilution this gave solutions containing a ligand–metal concentration ranging from 0.8–4.0 mM, a surfactant concentration of 20.0 mM $Brij_{35}$ or 40.0 mM Triton X-100, a buffer concentration of 0.10 M, and ionic strength of 0.10 M. (The Triton X-100 surfactant solutions were not adjusted for ionic strength because precipitates formed if the ionic strength was adjusted to 0.10 M.) The solutions were then pH-adjusted, put into cuvettes and temperature equilibrated in the spectrophotometer before the start of the reaction. The reaction was initiated by the injection of 10.0 μL of a PNPA stock solution (9 mM).

Acknowledgments

The authors gratefully acknowledge the Natural Sciences and Engineering Research Council of Canada (NSERC) and Queen's University for financial support.

References

1. (*a*) D.W. Christianson and C.A. Fierke. Acc. Chem. Res. **29**, 331 (1996); (*b*) W.N. Lipscomb and N. Strater. Chem. Rev. **96**, 2375 (1996); (*c*) Y. Pocker. *In* Enzymatic and model carboxylation and reduction reactions for carbon dioxide utilization. *Edited by* M. Aresta and J.V. Schloss. Kluwer Academic Publishers, Boston. 1990. p. 129; (*d*) L. Banci, I. Bertini, C. Luchinat, and J.M. Moratal. *In* Enzymatic and model carboxylation and reduction reactions for carbon dioxide utilization. *Edited by* M. Aresta and J.V. Schloss. Kluwer Academic Publishers, Boston. 1990. p. 181; (*e*) D.N. Silverman and S. Lindskog. Acc. Chem. Res. **21**, 30 (1988); (*f*) I. Bertini, C. Luchinat, and R. Monnanni. *In* Carbon diox-

© 2002 NRC Canada

ide as a source of carbon. *Edited by* M. Aresta and G. Forti. D. Reidel Publishing Company, Boston. 1987. p. 139.
2. R.S. Brown. *In* Enzymatic and model carboxylation and reduction reactions for carbon dioxide utilization. *Edited by* M. Aresta and J.V. Schloss. Kluwer Academic Publishers, Boston. 1990. pp. 145–180.
3. C.T. Supuran, C.W. Conroy, and T.H. Maren. Proteins, **27**, 272 (1997).
4. (*a*) R.S. Brown and J. Huguet. Can. J. Chem. **58**, 889 (1980); (*b*) C.C. Tang, D. Davalian, P. Huang, and R. Breslow. J. Am. Chem. Soc. **100**, 3918 (1978); (*c*) R. Breslow, J.R. Hunt, R. Smiley, and T. Tarnowski. J. Am. Chem. Soc. **105**, 5337 (1983); (*d*) R. Gegorzik, J. Wirbser, and H. Vahrenkamp. Chem. Ber. **125**, 1575 (1992); (*e*) R. Gregorzik, U. Hartmann, and H. Vahrenkamp. Chem. Ber. **127**, 2123 (1994); (*f*) C. Titze, J. Hermann, and H. Vahrenkamp. Chem. Ber. **128**, 1095 (1995); (*g*) W. Brandt, J. Wirbster, A.K. Powell, and H. Vahrenkamp. Z. Naturforsch. Teil B. **46**, 440 (1991); (*h*) N.N. Murthy and K.D. Karlin. J. Chem. Soc. Chem. Commun. 1236 (1993); (*i*) B. Greener, M.H. Moore, and P.H. Walton. Chem. Commun. 27 (1996); (*j*) J. Wirbser and H. Vahrenkamp. Z. Naturforsch. Teil B. **47**, 962 (1992).
5. (*a*) J. Huguet and R.S. Brown. J. Am. Chem. Soc. **102**, 7572 (1980); (*b*) R.S. Brown, N.J. Curtis, and J. Huguet. J. Am. Chem. Soc. **103**, 6953 (1981); (*c*) R.S. Brown, D. Salmon, N.J. Curtis, and S. Kusuma. J. Am. Chem. Soc. **104**, 3188 (1982); (*d*) R.S. Brown, M. Zamkanei, and J.L. Cocho. J. Am. Chem. Soc. **106**, 5222 (1984).
6. (*a*) M. Brauer, E. Anders, S. Sinnecker, W. Koch, M. Rombach, H. Brombacher, and H. Vahrenkamp. Chem. Commun. 647 (2000); (*b*) C. Kimblin, V.J. Murphy, T. Hascall, B.M. Bridgewater, J.B. Bonanno, and G. Parkin. Inorg. Chem. **39**, 967 (2000); (*c*) Z. Mao, L. Gunter, and R. Eldik. J. Am. Chem. Soc. **122**, 4839 (2000); (*d*) C. Bergquist and G. Parkin. J. Am. Chem. Soc. **121**, 6322 (1999); (*e*) K. Weis and H. Vahrenkamp. Inorg. Chem. **36**, 5592 (1997); (*f*) K.-W. Yang, Y.-Z. Wang, Z.-X. Huang, and J. Suh. Polyhedron, **16**, 109 (1997); (*g*) C. Kimblin and G. Parkin. Inorg. Chem. **35**, 6912 (1996); (*h*) B. Greener, M.H. Moore, and P.H. Walton. Chem. Commun. 27 (1996); (*i*) C. Dowling, V.J. Murphy, and G. Parkin. Inorg. Chem. **35**, 2415 (1996); (*j*) M. Ruf, K. Weis, and H. Vahrenkamp. J. Chem. Soc. Chem. Commun. 135 (1994); (*k*) A. Looney and G. Parkin. Inorg. Chem. **33**, 1234 (1994); (*l*) A. Looney, R. Han, K. McNeill, and G. Parkin. J. Am. Chem. Soc. **115**, 4690 (1993); (*m*) R. Alsfasser, S. Trofimenko, A. Looney, G. Parkin, and H. Vahrenkamp. Inorg. Chem. **30**, 4098 (1991); (*n*) R. Han and G. Parkin. J. Am. Chem. Soc. **113**, 9707 (1991); (*o*) A. Looney, G. Parkin, and A. Rheingold. Inorg. Chem. **30**, 3099 (1991).
7. (*a*) P. Wooley. Nature, **258**, 677 (1975); (*b*) S. Gellman, r. Petter, and R. Breslow. J. Am. Chem. Soc. **108**, 2388 (1986); (*c*) R. Breslow and S. Singh. Bioorg. Chem. **16**, 498 (1988); (*d*) E.I. Kimura, T. Shiota, T. Koike, M. Shiro, and M. Kodama. J. Am. Chem. Soc. **112**, 5805 (1990); (*e*) E.I. Kimura. Prog. Inorg. Chem. **41**, 443 (1994).
8. (*a*) X. Zhang, R. van Eldik, T. Koike, and E. Kimura. Inorg. Chem. **32**, 5749 (1993); (*b*) H. Slebocka-Tilk, J.L. Cocho, Z. Frakman, and R.S. Brown. J. Am. Chem. Soc. **106**, 2421 (1984); (*c*) X. Zhang and R. van Eldik. Inorg. Chem. **34**, 5606 (1995).
9. Y. Pocker and D.W. Bjorkquist. J. Am. Chem. Soc. **99**, 6537 (1977).
10. L.L. Kiefer, J.A. Ippolito, C.A. Fierke, and D.W. Christianson. J. Am. Chem. Soc. **115**, 12581 (1993).
11. (*a*) R. Jairam, P.G. Potvin, and S. Balsky. J. Chem. Soc. Perkin 2, 363 (1999); (*b*) S. Zhu, W. Chen, H. Lin, X. Yin, F. Kou, M. Lin, and Y. Chen. Polyhedron, **16**, 3285 (1997); (*c*) C. Bazzicalupi, A. Bencini, A. Bianchi, F. Corana, V. Fusi, C. Giorgi, P. Paoli, P. Paoletti, B. Valtancoli, and C. Zanchini. Inorg. Chem. **35**, 5540 (1996); (*d*) J. Chin and X. Zou. J. Am. Chem. Soc. **106**, 3687 (1984).
12. W.P. Jencks and J. Carriuolo. J. Am. Chem. Soc. **82**, 1778 (1960).
13. (*a*) E. Kimura, H. Hashimoto, and T. Koike. J. Am. Chem. Soc. **118**, 10963 (1996); (*b*) F.M. Menger, L.H. Gan, E. Johnson, and D.H. Durst. J. Am. Chem. Soc. **109**, 2800 (1987).
14. J.H. Fendler and E.J. Fendler. Catalysis in micellar and macromolecular systems. Academic Press, New York. 1975. pp. 104–193.
15. (*a*) G.D.J. Phillies, R.H. Hunt, K. Strang, and N. Sushkin. Langmuir, **11**, 3408 (1995); (*b*) G.D.J. Phillies and J.E. Yambert. Langmuir, **12**, 3431 (1996).
16. C.J. Willis. J. Chem. Educ. **58**, 659 (1981).
17. M.S. Fernandez and P. Franherz. J. Phys. Chem. **81**, 1755 (1977).
18. C.J. Drummond, F. Grieser, and W.H. Thomas. J. Chem. Soc. Faraday Trans. 1, **85**, 521 (1989).
19. CRC handbook of chemistry and physics. 50th ed. The Chemical Rubber Co., Cleveland, Ohio. 1962.
20. J.L. Beltrán, R. Codony, M. Granados, A. Izquierdo, and M.D. Prat. Talanta, **40**, 157 (1993).
21. A.A. Neverov, P.J. Montoya-Pelaez, and R.S. Brown. J. Am. Chem. Soc. **123**, 210 (2001).
22. Y. Umebayashi, Y. Nagahama, and S. Ishiguro. J. Chem. Soc. Faraday Trans. **93**, 1377 (1997).
23. (*a*) H. Doe and T. Kitagawa. Inorg. Chem. **21**, 2272 (1982); (*b*) H. Doe, A. Shibagaki, and T. Kitagawa. Inorg. Chem. **22**, 1639 (1993).
24. (*a*) S. Ba-Saif, A.K. Luthra, and A. Williams. J. Am. Chem. Soc. **109**, 6362 (1987); (*b*) S. Ba-Saif, A.K. Luthra, and A. Williams. J. Am. Chem. Soc. **111**, 2647 (1989); (*c*) R.A. Hess, A.C. Hengge, and W. Cleland. J. Am. Chem. Soc. **120**, 2703 (1998); (*d*) A.C. Hengge and R.A. Hess. J. Am. Chem. Soc. **119**, 11256 (1997).
25. A.J. Bennet and R.S. Brown. *In* Comprehensive biological catalysis. Vol. 1. *Edited By* M.I. Sinnott. Academic Press Limited, New York. 1998. p. 293.
26. (*a*) W.P. Jencks. Acc. Chem. Res. **13**, 161 (1980); (*b*) W.P. Jencks. Acc. Chem. Res. **9**, 425 (1976); (*b*) I.M. Kovach, M. Belz, M. Larson, S. Rousy, and R.L. Schowen. J. Am. Chem. Soc. **107**, 7360 (1985); (*c*) K.S. Venkatasubban and R.L. Schowen. J. Org. Chem. **49**, 653 (1984).
27. C.A. Bunton, F. Nome, F.H. Quina, and L.R. Romstead. Acc. Chem. Res. **24**, 357 (1991), and refs. therein.
28. O.S. Tee. Adv. Phys. Org. Chem. **29**, 1 (1994).
29. R.S. Brown, J. Huguet, and N.J. Curtis. Met. Ions Biol. Syst. **15**, 55 (1983), and refs. therein.
30. (*a*) N. Pirinccioglu, F. Zaman, and A. Williams. J. Org. Chem. **65**, 2537 (2000); (*b*) O.S. Tee and A.A. Fedortchenko. Can. J. Chem. **75**, 1434 (1997).
31. P.Scrimin, P.Tecilla, U. Tonellato, and C.A. Bunton. Colloids Surf. **144**, 71 (1998).
32. F.M. Menger and C.E. Portnoy. J. Am. Chem. Soc. **89**, 4698 (1967).

© 2002 NRC Canada

Studies on the rearrangement of *ortho*-nitrobenzylidenemalonates and their analogues to 2-aminobenzoate derivatives

Elzbieta Lewandowska, Stefan Kinastowski, and Stanislaw F. Wnuk

Abstract: Reaction of the diethyl 2-nitro-4-(trifluoromethyl)benzylidenemalonate with diethylamine in alcohols resulted in the reduction of the nitro group and the oxidation of the vinylic carbon attached to the phenyl ring. Simultaneous migration of the malonic fragment gave the appropriate 2-amino-4-(trifluoromethyl)benzoate esters. The presence of at least two nitro groups, or one nitro group and trifluoromethyl group on the phenyl ring, attached to the α-carbon and strongly electron withdrawing substituents at the β-carbon (CO_2Et, CN) in *ortho*-nitrobenzylidene systems is necessary for this reductive–oxidative rearrangement to proceed. Reaction of nitrocinnamates with thiols in the presence of triethylamine in tetrahydrofuran gave Michael addition products with different regioselectivity of addition. Ethyl 2-nitrocinnamate undergoes standard β-addition of thiols to a carbon–carbon double bond. However, 2,4-dinitro- and 2,4,6-trinitrocinnamates undergo α-addition of thiols, indicating that the presence of two nitro groups on the phenyl ring can reverse polarity of the carbon–carbon double bond in cinnamate acceptors.

Key words: abnormal Michael reactions, aromatic nitro compounds, benzylidene compounds, rearrangements.

Résumé : La réaction du 2-nitro-4-(trifluorométhyl)benzylidènemalonate d'éthyle avec la diéthylamine dans des alcools conduit à la réduction du groupe nitro et à l'oxydation du carbone vinylique attaché au noyau phényle. La migration simultanée du fragment malonique fournit les esters 2-amino-4-(trifluorométhyl)benzoates appropriés. Pour que ce réarrangement d'oxydoréduction se produise, il est requis d'être en présence d'un système *ortho*-nitrobenzylidène comportant au moins deux groupes nitro ou d'un groupe nitro et d'un groupe trifluorométhyle sur le noyau phényle attaché sur le carbone-α et des substituants fortement électroattracteurs sur le carbone-β (CO_2Et, CN). La réaction des nitrocinnamates avec les thiols en présence de triéthylamine, dans le tétrahydrofurane, conduit à la formation des produits d'addition de Michael avec une régiosélectivité d'addition différente. L'addition de thiols au 2-nitrocinnamate d'éthyle conduit à l'addition β normale sur la double liaison. Toutefois, l'addition de thiols sur les 2,4-dinitro- ou 2,4,6-trinitrocinnamates conduisent à des additions α, ce qui indique que la présence de deux groupes nitro sur le noyau phényle peut inverser la polarité de doubles liaisons carbone–carbone des accepteurs cinnamates.

Mots clés : réactions de Michael anormales, composés nitro aromatiques, composés benzylidènes, réarrangements.

[Traduit par la Rédaction]

Introduction

In previous work, we found that treatment of diethyl 2,4-dinitrobenzylidenemalonate (**1a**) with diethylamine (DEA) in MeOH did not lead to the expected Michael addition of DEA to the carbon–carbon double bond. Instead it gave the 2-amino-4-nitrobenzoic acid derivative **2a** (1) (Scheme 1). Such an unusual reductive–oxidative rearrangement selectively yields a variety of 2-aminobenzoic acid derivatives of type **2** when different primary or secondary alcohols (1, 2), thiols (3), or amines (1, 2) were used in place of MeOH. The new ester, thioester, or amide bond is formed at position 1, and a new ether, thioether, or amine bond is formed at the *C*-malonate carbon.

Such a skeletal rearrangement was also effective for heterocyclic π-deficient analogues in which the electron-withdrawing role of the second nitro group on the phenyl ring was replaced by a sp^2-hybridized nitrogen atom in the ring. Thus, nitropyridylidenemalonate 1-oxides bearing nitro and alkenyl substituents in the *ortho* position to each other (e.g., **3**; Scheme 2) underwent rearrangement to the amino-substituted pyridinecarboxylate derivatives (e.g., **4**) (4).

Synthetic methods involving neighboring group interaction in *ortho*-substituted nitrobenzene derivatives have been reviewed (5, 6), and new examples continue to attract interest (7). Such redox processes, which usually involve an intramolecular aldol condensation of the *ortho* substituent with the nitro group acting as the electrophilic center, have been used to synthesize a variety of heterocyclic compounds. These reactions typically occur under basic conditions with or without external reductive reagents and frequently involve thermal transformations (5).

Photochemically induced transfer of oxygen from a nitro group to an *ortho* substituent of nitrobenzene derivatives is

Received 13 August 2001. Published on the NRC Research Press Web site at http://canjchem.nrc.ca on 22 February 2002.

E. Lewandowska and S. Kinastowski. Department of Chemistry, University of Agriculture, ul. Wojska Polskiego 75, 60-625 Poznan, Poland.
S.F. Wnuk.[1] Department of Chemistry, Florida International University, Miami, FL 33199, U.S.A.

[1]Corresponding author (e-mail: wnuk@fiu.edu).

 DOI: 10.1139/V02-010 © 2002 NRC Canada

Scheme 1.

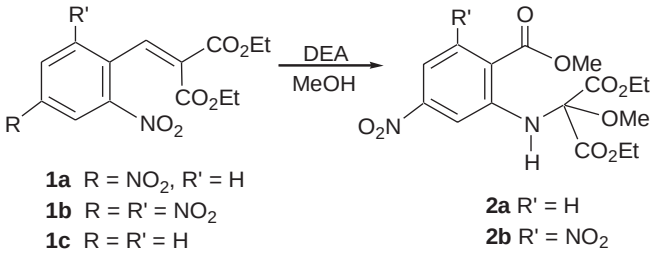

1a R = NO_2, R' = H
1b R = R' = NO_2
1c R = R' = H

2a R' = H
2b R' = NO_2

Scheme 2.

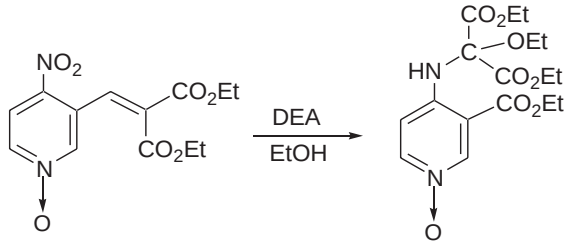

3 **4**

also well known and generates uncyclized nitroso products (5). The latter transformations have been elaborated to employ the *ortho*-nitrophenyl group as a photoremovable protective group for aldehydes and ketones (8) as well as phosphate esters of adenine nucleotides (9). The recent theoretical analysis for the isomerization of 2-nitrotoluene to 2-nitrosobenzyl alcohol is in good qualitative agreement with the available experimental results for the thermal and photoinduced rearrangement of *ortho*-nitrobenzyl compounds (9*c*).

To the best of our knowledge, the transformation of α-phenyl-2-nitrocinnamonitrile to *N*-benzoylanthranilic acid in aqueous–ethanolic alkali (10) is the only analogous example to our rearrangement that exists in the literature. Loudon and Tennant (11) suggested that the possible intermediates in this transformation involved addition of hydroxide ions to the carbon–carbon double bond, followed by an intramolecular aldol-type condensation in which the nitro group provides electrophilic center. We now report selected experiments on the one-step rearrangement of *ortho*-nitrobenzylidenemalonates and their analogues to various 2-aminobenzoic acid derivatives. The scope, limitation, and tentative mechanism of the rearrangement are also presented.

Results and discussion

Effect of the substituted aromatic ring

For the series of nitrobenzylidenemalonates **1a**–**c** reactivity toward rearrangement increased with increasing number of nitro groups on the aromatic ring. Thus, diethyl 2,4-dinitrobenzylidenemalonate (**1a**) undergoes the rearrangement in most cases (1), whereas the 2,4,6-trinitro analogue **1b** rearranges in all cases under the mildest conditions (2, 3). In contrast, diethyl 2-nitrobenzylidenemalonate (**1c**) does not rearrange and forms the stable β-carbonyl Michael adducts of type **9** (R, R′ = H) with amines (1), alkoxides (1), or thiolates (3).

The electron-withdrawing groups influence the rearrangement by (*i*) increasing the acidicity of an α-carbon attached to the aromatic ring, and (*ii*) controlling the oxidative potential of the *ortho*-nitro group. The relative acidities, rates of proton abstraction, and carbanion protonation of 4-nitro-, 2,4-dinitro-, and 2,4,6-trinitrotoluenes in methanolic DMSO have been examined (12). The kinetic ratio for proton abstraction from 2,4-dinitro- and 4-nitrotoluene is 230:1 in DMSO–MeOH (98:2), whereas the ratio for 2,4,6-trinitro- and 2,4-dinitrotoluene is about 100:1 in DMSO–MeOH (60:40). Thus, an increase in kinetic acidity resulting from the introduction of two *ortho*-nitro groups into 4-nitrotoluene is of the order of 2.3×10^4. The corresponding thermodynamic acidities expressed as pK_a values were found to depend strongly on DMSO concentration and are 12.1, 16.6, and 25.7 for 2,4,6-trinitro-, 2,4-dinitro-, and 4-nitrotoluene, respectively (12).

The number of nitro groups also effects the oxidative-reductive properties of these compounds. Bock and Lechner-Knoblauch (13) showed that 1,3,5-trinitrobenzene has the smallest potential for the reduction of the first nitro group (−0.51 V) whereas the reduction potentials of 1,3-dinitrobenzene and nitrobenzene are −0.82 and –1.10 V, respectively. Thus, increasing the number of the nitro groups on the phenyl ring facilitates both formation of the carbanion at the α-carbon (and its subsequent oxidation) and the reduction of first nitro group.

To further study effect of phenyl ring substituents on the rearrangement, 2,6-dinitro- (**6a**), 2-nitro-4-(trifluoromethyl)- (**6b**), and 2-chloro-6-nitrobenzylidenemalonates (**6c**) were prepared in a Knoevenagel condensation ($TiCl_4$–pyridine) (14) between the corresponding aldehydes (**5**) and diethyl malonate (Scheme 3). Reduction of commercially available 2-nitro-4-(trifluoromethyl)benzonitrile with diisobutylaluminum hydride (DIBALH) afforded aldehyde **5b** in 56% yield. This is a substantial improvement on a previously reported synthesis of **5b** when different synthetic approach was used (15). Compound **6a** rearranged under the influence of DEA in ethanol to give **7a** (86%) after 5 days (the rearrangement of **1a** took only a few hours to afford **2a** in 84% yield (1)). It seems that a second nitro group in the *ortho* position in **6a** has some steric influence on the rate of rearrangement.

The 2-nitro-4-trifluoromethyl analog (**6b**) produced under the typical conditions (DEA–EtOH, 24 h at ambient temperature) a stable adduct via ethanol addition to a double bond (**9b**, 51%), plus other by-products including unchanged **6b** and rearranged **7b**. However, prolonged reaction time and elevated temperature (~60°C) led to the expected rearranged product **7b** in 39% yield. Analogous treatment of **6b** with DEA in MeOH gave the rearranged product **8b** (58%) with concomitant transesterification of the malonic moiety. Replacement of the one nitro group by a chloro substituent prevent the rearrangement. Thus, reaction of 2-chloro-6-nitrobenzylidene (**6c**) with DEA–EtOH or amines (DEA, piperidine, or pyrrolidine) under typical conditions resulted in the recovery of **6c**. These results indicate that two strongly electron-withdrawing groups (EWG) must be present in the benzene ring. The data are supported by examination of the Hammett σ values (16) ($\sigma_{NO_2} > \sigma_{CF_3} > \sigma_{Cl}$),

© 2002 NRC Canada

Scheme 3. Reagents and conditions: (*a*) $TiCl_4$/pyridine/THF; (*b*) DEA/EtOH/~25°C; (*c*) DEA/EtOH or MeOH/~55°C.

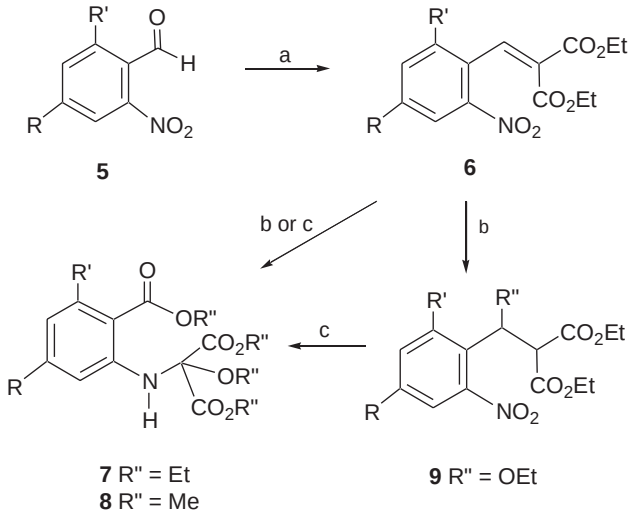

Series: **a** R = H, R' = NO_2
b R = CF_3, R' = H
c R = H, R' = Cl

which reflect the interaction of the substituents with the reaction site by a combination of resonance and field effects.

Effect of the substituents on the vinylic carbons

Substituents with strong electron-acceptor properties (CO_2Et, CN) at the β-carbon in *ortho*-nitrobenzylidene substrates also facilitate this rearrangement. Thus, reaction of ethyl α-cyano-2,4,6-trinitrocinnamate (**10**) (17) with DEA–EtOH gave the rearranged product **12** in 66% yield (Scheme 4). 2,4-Dinitrobenzylidenemalononitrile (**11**) rearranges in DEA–EtOH to yield ethyl 2-[*N*-(dicyano)(ethoxy)-methyl]amino-4-nitrobenzoate (**13a**) (56%) in addition to ethyl 2-amino-4-nitrobenzoate (21%). Treatment of **11** with DEA–MeOH gave the methyl ester **13b**.

Ethyl 2,4-dinitrocinnamate (**15a**), which bears only one EWG at the β-carbon, does not undergo this rearrangement (1). The rearrangement also failed with ethyl 2,4,6-trinitrocinnamate (**14**), despite the fact that the aromatic fragment is identical to the most reactive analogue **1b**. This indicated that the number of nitro groups on the phenyl ring, although a significant factor, is not the only force driving this rearrangement.

Interestingly, nitrocinnamates **14** and **15a**,**b** react with ethanethiol in THF in the presence of a catalytic amount of triethylamine (TEA) to give products **16** and **17a**,**b**. Mass spectra of **16** and **17a**,**b**, in addition to the molecular ions, showed peaks for the ions at *m*/*z* (%) 147 (45), 147 (61), and 133 (100) for **16**, **17a**, and **17b**, respectively. Their elemental compositions $C_6H_{11}O_2S$ $[(C_2H_5SCHCO_2C_2H_5)^+]$ for **16** and **17a** and $C_5H_9O_2S$ $[(C_2H_5SCHCO_2CH_3)^+]$ for **17b** were determined by HR-MS. These compounds are formed by the α-addition of the thiol to the α,β-unsaturated carbonyl compounds, a process that is in contrast to the usually observed

Scheme 4.

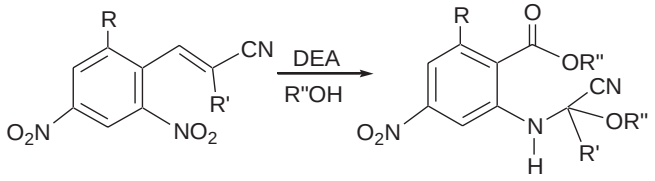

10 R = NO_2, R' = CO_2Et
11 R = H, R' = CN
12 R = NO_2, R' = CO_2Et, R" = Et
13a R = H, R' = CN, R" = Et
13b R = H, R' = CN, R" = Me

β-addition to the carbonyl activated double bond (Michael addition) (18) including cinnamates (19) (Scheme 5). Reaction of **15a** with propanethiol also gave α-addition product **17c** whose structure was confirmed with 2D-NMR experiments. Thus, the heteronuclear multiple bond coherence (HMBC) spectrum showed that aromatic carbons (C6 (135.4) and C1 (140.5)) had a strong coupling to the diastereotopic CH_2 protons at 3.58 and 3.41, whereas no correlation to CH proton at 3.63 was observed. Conversely, the carbonyl carbon at 171.9 shows correlation to the CH proton at 3.63 and only to the one diastereotopic proton at 3.41.

Ethyl 2-nitrocinnamate does not react with propanethiol under similar conditions (TEA–THF). However, treatment of ethyl 2-nitrocinnamate with sodium propanethiolate in EtOH gave the standard β-addition product **18** (Scheme 6). These results indicate that two nitro groups on the phenyl ring reverse polarity of the carbon–carbon double bond in cinnamate acceptors and redirect the regioselectivity of nucleophile addition from the classical β-addition to an abnormal α-addition. Such regioselectivity is controlled by the resonance effect of the nitro groups on the phenyl ring, as opposed to the carboxylate function. Recently, Trost and Dake (20*a*) reported that phosphine-catalyzed reaction of nitrogen nucleophiles with 2-alkynoates also gave α-addition product. Other examples (18*a*) include α-addition of dimethylamine or methanol to methyl 3,3-di(trifluoromethyl)acrylate (20*b*).

Spectral support for the assumption that Michael addition may occur at either the α or β carbon depending on the carbon–carbon double bond polarization was found by comparing the absorption band of the stretching vibration of the double bond in IR spectra of **1a**–**c** (3) and nitrocinnamates. Thus, 2-nitro derivative **1c** displays a medium absorption band at 1641 cm^{-1} (and shows β-addition), whereas the 2,4-dinitro analogue **1a** has only a very weak band at 1642 cm^{-1}. On the other hand, the latter compound shows an active band at 1637 cm^{-1} in Raman spectrum, which points to a symmetrical distribution of π-electron charge density in the carbon–carbon double bond (21). The introduction of the third nitro group resulted in the appearance of a weak absorption band at 1635 cm^{-1} in IR spectrum of **1b**. Analogously, in the cinnamate series 2,4,6-trinitro **14** [1630 cm^{-1} (weak)] and 2,4-dinitro **15a** [1628 cm^{-1} (very weak)] show α-addition, whereas ethyl 2-nitrocinnamate [1634 cm^{-1} (weak to medium)] and ethyl cinnamate [1634 cm^{-1} (medium to strong)] show the β-addition.

The free rotation of the substituents at β-carbon and steric factors seems also to be a factor in rearrangement. Thus,

© 2002 NRC Canada

Scheme 5.

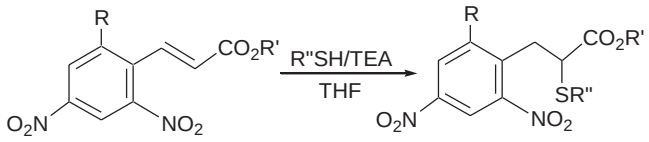

14 R = NO_2, R' = Et
15a R = H, R' = Et
15b R' = H, R' = Me

16 R = NO_2, R' = Et, R" = Et
17a R = H, R' = Et, R" = Et
17b R = H, R' = Me, R" = Et
17c R = H, R' = Et, R" = Pr

Scheme 6.

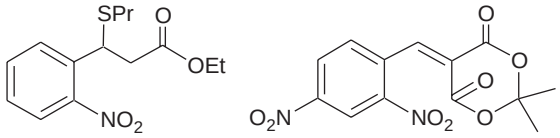

18 **19**

Scheme 7.

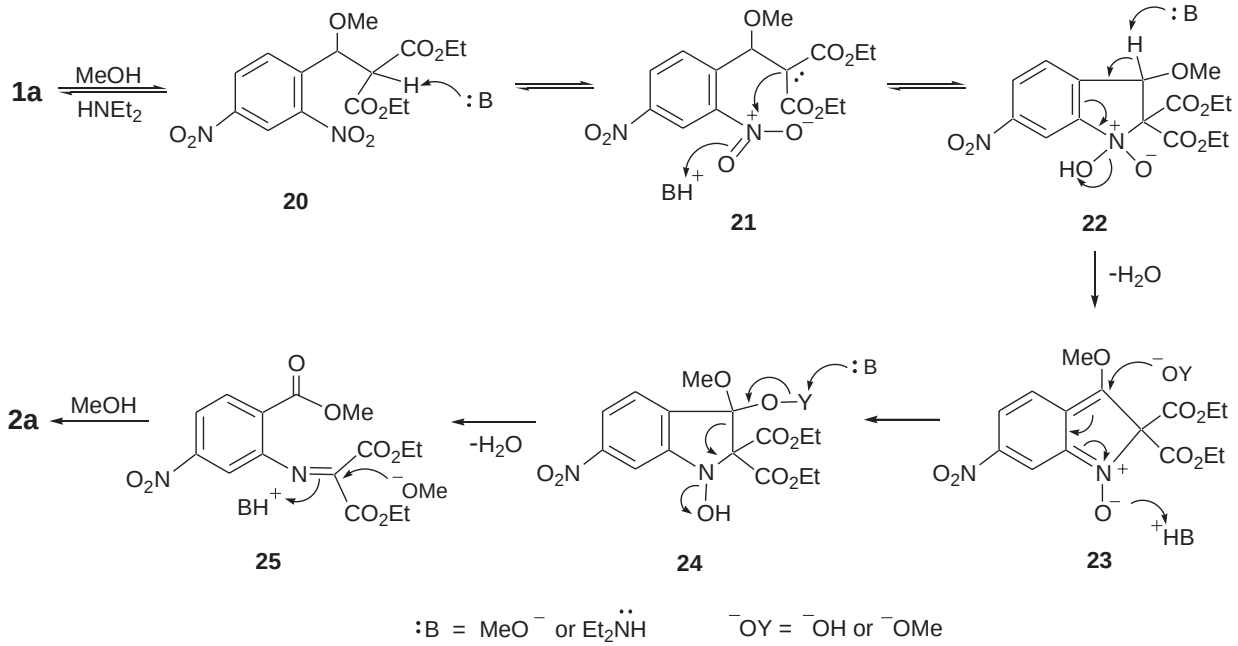

$:B = MeO^-$ or $Et_2\ddot{N}H$ $\quad$ $^-OY = {}^-OH$ or ^-OMe

2,4-dinitrobenzylidene derivative of Meldrum's acid **19** did not yield the rearranged product under standard condition (DEA–EtOH).

Tentative mechanism

The intramolecular nature of this rearrangement was previously proven in experiments using isotopically labelled dimethyl-d_6 malonate and dimethyl-d_6 2,4-dinitrobenzylidenemalonate (1). The possible mechanism might involve the following sequence of steps: (*i*) a classical Michael addition of the alcohol molecule to a π-electron deficient carbon–carbon double bond in **1a** to give **20**; (*ii*) an aldol condensation between carbanion **21** and nitro group to yield the cyclic intermediate **22**; (*iii*) redox processes involving the quinonoid intermediate **23** followed by addition of a second alcohol (or water) molecule that results in regeneration of aromaticity; (*iv*) nucleophilic ring opening of **24** and simultaneous migration of the malonic fragment, which leads directly to the formation of the highly conjugated ester at position 1 and Schiff base at position 2; and (*v*) addition of alcohol to the resulting electron-deficient ketimin of mesoxalic ester **25** at position 2 gives the rearranged product **2a** (Scheme 7). Ketimin **25** would be expected to undergo addition quite readily owing the presence of two EWG at the *C*-malonate carbon in addition to the regular polarization of carbon–nitrogen double bond. A similar mechanism for the conversion of α-phenyl-2-nitrocinnamonitrile to *N*-benzoylanthranilic acid has been suggested (11) (vide supra). In our previous mechanism direct transfer of oxygen from a nitro group to an *ortho*-benzylic position was proposed (1). However, such direct transfers are normally induced photochemically rather than thermally (e.g. in the 2-nitrobenzaldehyde into 2-nitrosobenzoic acid and related rearrangements) (**5b**).

In conclusion, an unusual rearrangement of *ortho*-nitrobenzylidenemalonates (e.g., **1a**,**b** or **6**) and their analogues (e.g., **10** or **11**) in the presence of diethylamine in alcohols produces a variety of 2-aminobenzoate ester derivatives (e.g., **2**, **7**, **8**, **12**, or **13**). The presence of at least two nitro groups, or one nitro group and trifluoromethyl group, on the phenyl ring together with strongly electron-withdrawing substituents at the β-carbon (CO_2Et, CN) in *ortho*-nitrobenzylidene systems, appears to be necessary for this reductive–oxidative rearrangement to proceed. Reaction of nitrocinnamates with thiols in the presence of TEA in THF gave Michael addition products with different regioselectivity of addition. Ethyl 2-nitrocinnamate undergoes the standard β-addition of thiols to the carbon–carbon double bond. However 2,4-dinitro- (**15**) and 2,4,6-trinitrocinnamates

© 2002 NRC Canada

(**14**) undergo abnormal Michael-type α-addition of thiols indicating that the presence of two nitro groups on the phenyl ring can reverse polarity of the carbon–carbon double bond in cinnamate acceptors.

Experimental

Uncorrected melting points were determined with a capillary apparatus. UV spectra were measured with solutions in MeOH. ^{1}H (200 or 400 MHz), ^{13}C (50 or 100 MHz), and ^{19}F (376.5 MHz ($CFCl_3$)) NMR spectra were determined with solutions in $CDCl_3$ unless otherwise specified. Mass spectra (MS and HR-MS) were obtained with electron impact (EI, 20 eV) or atmospheric pressure chemical ionization (APCI) techniques. Merck kieselgel 60-F_{254} sheets were used for TLC and products were detected with 254 nm light. Merck kieselgel 60 (230–400 mesh) was used for column chromatography. Elemental analyses were determined at microanalytical laboratories at Adam Mickiewicz University, Poznan, Poland or Galbraith Laboratories, Knoxville, TN. Reagent grade chemicals were used, and solvents were dried by reflux over and distillation from CaH_2 (except THF–potassium) under argon.

2-Nitro-4-(trifluoromethyl)benzaldehyde (5b)

DIBALH (0.9 mL, 0.71 g, 5 mmol) was added dropwise via syringe to a stirred solution of 2-nitro-4-(trifluoromethyl)benzonitrile (1.08 g, 5 mmol) in dried benzene (20 mL) under N_2 at ambient temperature. After 2 h, reaction mixture was cooled down (ice bath) and 1 M H_2SO_4 (~5 mL) was slowly added. The organic layer was washed ($NaHCO_3$–H_2O, brine), dried ($MgSO_4$) and volatiles were evaporated. Column chromatography (5 → 15% EtOAc–hexane) gave **5b** (0.61 g, 56%); mp 42°C (lit. (15) mp 35°C) with data as reported (15).

Diethyl 2,6-dinitrobenzylidenemalonate (6a)

Procedure A

Titanium(IV) chloride (1.1 mL, 10 mmol) in carbon tetrachloride (2.5 mL) was added dropwise to THF (40 mL) and the mixture was cooled to ~5°C. After 15 min 2,6-dinitrobenzaldehyde (0.98 g, 5 mmol) in THF (5 mL) and diethyl malonate (0.76 mL, 0.80 g, 5 mmol) were added dropwise with stirring. Pyridine (1.6 mL, 20 mmol) in THF (5 mL) was then added dropwise over 20 min. After 24 h, water (8 mL) and diethyl ether (8 mL) were added, the organic layer was separated, and the aqueous layer extracted with ether. The combined ether solution was washed with brine, $NaHCO_3$–H_2O and brine, dried ($MgSO_4$), and concentrated. The precipitate formed on cooling was filtered and recrystallized (EtOH) to give **6a** (1.2 g, 71%); mp 56–57°C. IR ($CHCl_3$) (cm^{-1}): 1720 (C=O). ^{1}H NMR δ: 1.02 and 1.37 (2t, J = 7.4 Hz, 6H, $2CH_3$), 3.98 and 4.34 (2q, J = 7.4 Hz, 4H, $2CH_2$), 7.75 (t, J = 8.3 Hz, 1H, H_{Ar}), 8.10–8.37 (m, 3H, H_{Ar}, CH). EI-MS *m/z*: 338 (5, M^+). Anal. calcd. for $C_{14}H_{14}N_2O_8$: C 49.71, H 4.17, N 8.28; found: C 49.74, H 3.83, N 8.29.

Diethyl 2-nitro-4-(trifluoromethyl)benzylidenemalonate (6b)

Treatment of 2-nitro-4-(trifluoromethyl)benzaldehyde (**5b**; 0.9 g, 4.1 mmol) with diethyl malonate by procedure A gave **6b** (1.2 g, 81%); mp 72°C (EtOH). IR ($CHCl_3$) (cm^{-1}): 1733 (C=O), 1628 (C=C). ^{1}H NMR δ: 1.08 (t, J = 7.1 Hz, 3H, CH_3), 1.38 (t, J = 7.1 Hz, 3H, CH_3), 4.12 (q, J = 7.1 Hz, 2H, CH_2), 4.37 (q, J = 7.1 Hz, 2H, CH_2), 7.61 (d, J = 8.0 Hz, 1H, H_{Ar}), 7.92 (d, J = 7.1 Hz, 1H, H_{Ar}), 8.19 (s, 1H, H_{Ar}), 8.50 (s, 1H, CH). ^{13}C NMR δ: 14.1, 14.5, 62.2, 62.7, 122.7 (q, ^3J = 3.7 Hz), 122.9 (q, ^1J = 273.1 Hz), 130.6 (q, ^3J = 3.3 Hz), 130.8, 131.6, 133.0 (q, ^2J = 34.6 Hz), 134.5, 163.4, 164.6. ^{19}F NMR δ: −63.49 (s). APCI-MS *m/z*: 362 (100, $[M + H]^+$). Anal. calcd. for $C_{15}H_{14}F_3NO_6$: C 49.87, H 3.91, N 3.88; found: C 49.84, H 3.95, N 3.78.

Diethyl 2-chloro-6-nitrobenzylidenemalonate (6c)

The 2-chloro-6-nitrobenzaldehyde (0.93 g, 5 mmol) was treated with diethyl malonate by procedure A to give **6c** (1.3 g, 79%); mp 53°C (EtOH). IR ($CHCl_3$) (cm^{-1}): 1720 (C=O). ^{1}H NMR δ: 1.01 and 1.37 (2t, J = 7.2 Hz, 6H, $2CH_3$), 4.02 and 4.35 (2q, J = 7.2 Hz, 4H, $2CH_2$), 7.43–8.15 (m, 4H, H_{Ar}, CH). EI-MS *m/z*: 329 (1, $M^+(^{37}Cl)$), 327 (3, $M^+(^{35}Cl)$), 292 (100, $[M - Cl]^+$). Anal. calcd. for $C_{14}H_{14}ClNO_6$: C 51.31, H 4.31, N 4.27; found: C 51.30, H 4.28, N 4.27.

Ethyl 2-(*N*-(ethoxy)(diethoxycarbonyl)methyl)amino-6-nitrobenzoate (7a)

Procedure B

DEA (0.2mL, 2.0 mmol) was added to a solution of diethyl 2,6-dinitrobenzylidenemalonate (**6a**; 338 mg, 1 mmol) in EtOH (8 mL) and stirring was continued at ambient temperature for 5 days. The resulting mixture was evaporated and the residue was partitioned (EtOAc, diluted with HCl–H_2O). The organic layer was washed ($NaHCO_3$–H_2O, brine), dried ($MgSO_4$), and evaporated to dryness. Column chromatography (CH_3Cl–CCl_4–EtOAc, 10:5:1) gave **7a** (354 mg, 86%); mp 85°C (EtOH). IR ($CHCl_3$) (cm^{-1}): 3300 (NH), 1720 (C=O). ^{1}H NMR δ: 1.18–1.27 (m, 9H, $3CH_3$), 1.34 (t, J = 7.1 Hz, 3H, CH_3), 3.48 (q, J = 7.1 Hz, 2H, CH_2), 4.22–4.44 (m, 6H, $3CH_2$), 7.14 (dd, J = 7.0, 1.8 Hz, 1H, H_{Ar}), 7.30–7.42 (m, 2H, H_{Ar}), 8.27 (br s, 1H, NH). EI-MS *m/z*: 412 (3, M^+), 265 (100). Anal. calcd. for $C_{18}H_{24}N_2O_9$: C 52.42, H 5.87, N 6.86; found: C 52.38, H 5.82, N 6.86.

Ethyl 2-(*N*-(ethoxy)(diethoxycarbonyl)methyl)amino-4-(trifluoromethyl)benzoate (7b)

Treatment of **6b** (180 mg, 0.5 mmol) by procedure B (~60°C, 24 h) and column chromatography (4 → 15% EtOAc–hexane) gave crude **7b** (~115 mg; purity ~75% (^{1}H NMR) contaminated by **6b** and **9b**). This material was column chromatographed again to give **7b** (85mg, 39%) as a solidified oil. IR ($CHCl_3$) (cm^{-1}): 3300 (NH), 1752, 1739, 1697 (C=O). ^{1}H NMR δ: 1.23 (t, J = 7.2 Hz, 3H, CH_3), 1.25 (t, J = 7.1 Hz, 6H, $2CH_3$), 1.44 (t, J = 7.1 Hz, 3H, CH_3), 3.50 (q, J = 7.1 Hz, 2H, CH_2), 4.27–4.35 (m, 4H, $2CH_2$), 4.43 (q, J = 7.1 Hz, 2H, CH_2), 7.01 (d, J = 8.3 Hz, 1H, H_{Ar}), 7.49 (s, 1H, H_{Ar}), 8.09 (d, J = 8.3 Hz, 1H, H_{Ar}), 9.68 (s, 1H, NH). ^{13}C NMR δ: 14.3 (2C), 14.7, 15.3, 59.7, 61.8, 63.5 (2C), 87.9, 111.9, 114.3, 115.8, 123.9 (q, ^1J = 273.0 Hz),

© 2002 NRC Canada

132.8, 135.9 (q, ^2J = 32.3 Hz), 146.8, 167.6 (2C), 167.6. ^{19}F NMR δ: −64.25 (s). APCI-MS *m/z*: 390 (100, [M + H – EtOH]$^+$). Anal. calcd. for $C_{19}H_{24}F_3NO_7$: C 52.41, H 5.56, N 3.22; found: C 52.62, H 5.41, N 3.33.

Methyl 2-(*N*-(methoxy)(dimethoxycarbonyl)methyl)-amino-4-(trifluoromethyl)benzoate (8b)

Treatment of **6b** (180 mg, 0.5 mmol) by procedure B (~50°C, 24 h; MeOH was used instead of EtOH) and column chromatography (4 → 20% EtOAc–hexane) gave **8b** (110 mg, 58%); mp 128–130°C (MeOH). IR ($CHCl_3$) (cm^{-1}): 3300 (NH), 1740, 1698 (C=O). ^{1}H NMR δ: 3.29 (s, 3H, CH_3), 3.86 (s, 6H, $2CH_3$), 3.98 (s, 3H, CH_3), 7.04 (d, J = 8.1 Hz, 1H, H_{Ar}), 7.34 (s, 1H, H_{Ar}), 8.10 (d, J = 8.2 Hz, 1H, H_{Ar}), 9.68 (s, 1H, NH). ^{13}C NMR δ: 51.5, 52.9, 54.3 (2C), 88.5, 111.4, 114.8, 115.7, 123.8 (q, ^1J = 273.2 Hz), 132.8, 136.3 (q, ^2J = 32.5 Hz), 146.6, 167.2 (2C), 168.1. ^{19}F NMR δ: −64.17 (s). APCI-MS *m/z*: 348 (100, [M + H – MeOH]$^+$). Anal. calcd. for $C_{15}H_{16}F_3NO_7$: C 47.50, H 4.25, N 3.69; found: C 47.63, H 4.32, N 3.62.

Diethyl 2-ethoxy-2-(2-nitro-4-(trifluoromethyl)phenyl)-ethane-1,1-dicarboxylate (9b)

DEA (0.06 mL, 0.6 mmol) was added to a solution **6b** (108 mg, 0.3 mmol) in EtOH (3 mL) and stirring was continued for 24 h at ambient temperature and then at ~35°C for 6 h. Evaporation, work-up (as described in procedure B), and column chromatography (5 → 15% EtOAc–hexane) gave **9b** (62 mg, 51%) as a first eluting product followed by recovered **6b** and **7b**. Compound **9b**: IR ($CHCl_3$) (cm^{-1}): 1751, 1733 (C=O). ^{1}H NMR δ: 1.15, 1.16, 1.30 (3t, J = 7.1 Hz, 9H, $3CH_3$), 3.38–3.59 (m, 2H, CH_2), 3.81 (d, J = 8.3 Hz, 1H, CH), 4.08 (q, J = 7.2 Hz, 2H, CH_2), 4.23–4.31 (m, 2H, CH_2), 5.68 (d, J = 8.3 Hz, 1H, CH), 7.90 (d, J = 8.2 Hz, 1H, H_{Ar}), 7.97 (d, J = 8.2 Hz, 1H, H_{Ar}), 8.17 (s, 1H, H_{Ar}). ^{13}C NMR δ: 14.2, 14.5, 15.4, 59.7, 62.1, 62.3, 66.4, 74.3, 122.0 (q, ^3J = 3.6 Hz), 123.0 (q, ^1J = 272.8 Hz), 129.9 (q, ^3J = 3.2 Hz), 131.1, 131.9 (q, ^2J = 34.3 Hz), 139.7, 149.8, 166.7, 166.8. ^{19}F NMR δ: −63.41 (s). APCI-MS *m/z*: 408 (100, [M + H]$^+$). Anal. calcd. for $C_{17}H_{20}F_3NO_7$: C 50.13, H 4.95, N 3.44; found: C 50.19, H 5.18, N 3.46.

Analogous treatment (8 h, ambient temperature) of **6b** (108 mg, 0.3 mmol) with piperidine (0.06 mL, 0.6 mmol) in EtOH (3 mL) also gave **9b** (83 mg, 68%).

Similar treatment (18 h, ambient temperature) of **6b** (0.25 mmol) with DEA (0.5 mmol) or TEA (0.5 mmol) in MeOH (3 mL) gave analogous adduct of MeOH addition to a carbon–carbon double bond (e.g. **9b**, R″ = OMe, 52%; ^{1}H NMR δ: 3.33 (s, 3H, OCH_3), 3.82 (d, J = 7.8 Hz, 1H, CH), 5.59 (d, J = 7.8 Hz, 1H, CH)) in addition to unchanged **6b** and transmethylation by-products.

Treatment (24h, 50°C) of **9b** (41 mg, 0.1 mmol) with DEA (0.02 mL, 0.2 mmol) in EtOH (2 mL) produced **7b** (17 mg, 40%).

Ethyl 2-(*N*-(cyano)(ethoxy)(ethoxycarbonyl)methyl)-amino-4,6-dinitrobenzoate (12)

Procedure C

Ethyl α-cyano-2,4,6-trinitrocinnamate (17) (**10**; 0.168 g, 0.5 mmol) was dissolved in EtOH (4 mL) and DEA (0.1 mL, 1 mmol) was added at ambient temperature. The mixture was allowed to stand for 6 h and then evaporated to dryness under vacum. The residue was chromatographed (CCl_4–$CHCl_3$–Me_2CO, 10:5:1) and crystallized (EtOH) to give **12** (0.135 g, 66%) as a yellow crystals; mp 120–121°C. UV–vis (MeOH) λ (nm) (ε (M^{-1} cm^{-1})): 367 (3500). IR (KBr) (cm^{-1}): 3100 (NH), 2240 (CN), 1730, 1690 (C=O). ^{1}H NMR δ: 1.20–1.65 (m, 9H, $3CH_3$), 4.00–4.60 (m, 6H, $3CH_2$), 8.45 (d, J = 2.1 Hz, 1H, H_{Ar}), 9.61 (d, J = 2.1 Hz, 1H, H_{Ar}), 10.20 (s, 1H, NH). ^{13}C NMR δ: 13.4, 13.9, 62.9, 64.5, 83.2, 113.4, 114.5, 119.5, 124.5, 138.5, 154.7, 159.6, 163.2. EI-MS *m/z*: 410 (1, M$^+$), 383 (5), 236 (100). Anal. calcd. for $C_{16}H_{18}N_4O_9$: C 46.83, H 4.42, N 13.65; found: C 46.76, H 4.40, N 13.71.

Ethyl 2-(*N*-(dicyano)(ethoxy)methyl))amino-4-nitro-benzoate (13a)

Treatment (18 h) of 2,4-dinitrobenzylidenemalononitrile (17) (**11**; 0.122 g, 0.5 mmol) by procedure C (column chromatography: CCl_4–$CHCl_3$–Me_2CO, 60:10:1) gave ethyl 2-amino-4-nitrobenzoate (22 mg, 21%; mp 90–91°C (lit. (22) mp 89–91°C)) and **13a** (89 mg, 56%) as a second eluting compound; mp 63°C (EtOH). UV–vis (MeOH) λ (nm) (ε (M^{-1} cm^{-1})): 327 nm (2750). IR ($CHCl_3$) (cm^{-1}): 3270 (NH), 2270 (CN), 1720 (C=O). ^{1}H NMR δ: 1.31–1.56 (m, 6H, $2CH_3$), 4.25–4.54 (m, 4H, $2CH_2$), 7.75–8.15 (m, 3H, H_{Ar}), 9.33 (s, 1H, NH). EI-MS *m/z*: 291 (16, [M – HCN]$^+$), 263 (21), 218 (100). Anal. calcd. for $C_{14}H_{14}N_4O_5$: C 52.83, H 4.40, N 17.65; found: C 52.78, H 4.43, N 17.60.

Methyl 2-(*N*-(dicyano)(methoxy)methyl)amino-4-nitro-benzoate (13b)

Treatment of **11** (17) (0.122 mg, 0.5 mmol) by procedure C (18 h, MeOH was used instead of EtOH) and purification (as described for **13a**) gave methyl 2-amino-4-nitrobenzoate (22 mg, 23%; mp 158°C (lit. (23) 154–156°C)) and **13b** (86 mg, 59%; mp 82°C (MeOH)). IR ($CHCl_3$) (cm^{-1}): 3270 (NH), 2270 (CN), 1720 (C=O). ^{1}H NMR δ: 3.92 (s, 3H, CH_3), 4.08 (s, 3H, CH_3), 7.76–8.25 (m, 3H, H_{Ar}), 9.35 (s, 1H, NH). EI-MS *m/z*: 263 (12, [M – HCN]$^+$), 232 (100). Anal. calcd. for $C_{12}H_{10}N_4O_5$: C 49.66, H 3.47, N 19.31; found: C 49.58, H 3.42, N 19.35.

Ethyl (*E*)-2,4,6-trinitrocinnamate (14)

Procedure D

To a stirred solution of 2,4,6-trinitrobenzaldehyde (24) (0.24g, 1 mmol) in anhydrous acetonitrile (15 mL) (carbethoxymethylene)triphenylphosphorane (0.37g, 1.1 mmol) was added in one portion. The resulting cherry reaction mixture was stirred overnight at ambient temperature and then evaporated. The oily residue was chromatographed on silica gel (MeOH–$CHCl_3$, 1:99) and crystallized from MeOH to give **14** (0.202 g, 65%, two crops); mp 52–53°C. UV–vis (MeOH) λ (nm) (ε (M^{-1} cm^{-1})): 234 (21 800). IR (KBr) (cm^{-1}): 1710 (C=O), 1630w (C=C). ^{1}H NMR δ: 1.35 (t, J = 7.0 Hz, 3H, CH_3), 4.29 (q, J = 7.0 Hz, 2H, CH_2), 6.01 (d, J = 16.5 Hz, 1H, CH), 7.99 (d, J = 16.5 Hz, 1H, CH), 9.00 (s, 2H, H_{Ar}). EI-MS *m/z*: 266 (100, [M – OEt]$^+$). Anal. calcd. for $C_{11}H_9N_3O_8$: C 42.45, H 2.91, N 13.50; found: C 42.51, H 2.88, N 13.42.

© 2002 NRC Canada

Reaction of **14** with DEA in ethanol by procedure C did not afford rearranged product and only unchanged **14** was recovered (~81%).

Ethyl (*E*)-2,4-dinitrocinnamate (15a)

Treatment of 2,4-dinitrobenzaldehyde (0.196 g, 1 mmol) with $Ph_3P{=}CHCO_2Et$ by procedure D gave **15a** (181 mg, 68%); mp 91–92°C (lit. (25) mp 94°C). IR ($CHCl_3$) (cm^{-1}): 1705 (C=O), 1628w (C=C). ^1H NMR δ: 1.27 (t, *J* = 7.0 Hz, 3H, CH_3), 4.31 (q, *J* = 7.0 Hz, 1H, CH_2), 6.46 (d, *J* = 16.8 Hz, 1H, CH), 7.84 (d, *J* = 8.5 Hz, 1H, H_{Ar}), 8.11 (d, *J* = 16.8 Hz, 1H, CH), 8.48 (dd, *J* = 8.5, 2.3 Hz, 1H, H_{Ar}), 8.89 (d, *J* = 2.3 Hz, 1H, H_{Ar}).

As a less polar product *Z*-isomer of **15a** (40 mg, 15%) was eluted from the column (^1H NMR δ: 6.24 (dd, *J* = 11.9, 1.8 Hz, 1H, CH), 7.43 (d, *J* = 11.9 Hz, 1H, CH)).

Ethyl 2-ethylthio-3-(2,4,6-trinitrophenyl)propionate (16)

Procedure E

Ethanethiol (0.15 mL, 0.124 g, 2 mmol) and then triethylamine (0.03 mL, 0.022 g, 0.22 mmol) were added to a stirred solution of **14** (0.155 g, 0.5 mmol) in anhydrous THF (5 mL) at ambient temperature. TLC (CCl_4–$CHCl_3$–Me_2CO, 15:5:1) taken after 18 h indicated complete consumption of **14** (R_f = 0.52) with formation of less polar product (R_f = 0.58). After evaporation, the yellowish oily residue was chromatographed ($CHCl_3$) to give **16** (0.159 g, 85%) as a slightly yellow spectroscopically pure oil. IR ($CHCl_3$) (cm^{-1}): 1720 (C=O). ^1H NMR δ: 1.17 (t, *J* = 7.5 Hz, 3H, CH_3), 1.26 (t, *J* = 7.0 Hz, 3H, CH_3), 2.56 (q, *J* = 7.5 Hz, 2H, SCH_2), 3.41–3.85 (m, 3H, CH_2-CH), 4.19 (q, *J* = 7.0 Hz, 2H, CH_2), 8.80 (s, 2H, H_{Ar}). EI-HRMS *m*/*z*: 373.0586 (20, M^+ ($C_{13}H_{15}N_3O_8S$) = 373.0579), 147.0474 (45, ($C_6H_{11}O_2S$) = 147.0479, CH(SEt)CO_2Et).

Compound **16** (as well as **17a**,**b**) was stable when kept at ~5°C for a week. However, significant decomposition (~20%, ^1H NMR) was observed after 3 months.

Ethyl 2-ethylthio-3-(2,4-dinitrophenyl)propionate (17a)

Treatment of **15a** (0.133 g, 0.5 mmol) by procedure E gave **17a** (0.15 g, 91%) as a slightly yellow oil. IR ($CHCl_3$) (cm^{-1}): 1720 (C=O). ^1H NMR δ: 1.22 (t, *J* = 7.4 Hz, 3H, CH_3), 1.29 (t, *J* = 7.0 Hz, 3H, CH_3), 2.68 (q, *J* = 7.4 Hz, 2H, SCH_2), 3.39–3.77 (m, 3H, CH_2-CH), 4.26 (q, *J* = 7.0 Hz, 2H, CH_2), 7.69 (d, *J* = 8.6 Hz, 1H, H_{Ar}), 8.37 (dd, *J* = 8.6, 2.3 Hz, 1H, H_{Ar}), 8.83 (d, *J* = 2.3 Hz, 1H, H_{Ar}). EI-HRMS *m*/*z*: 328.0731 (18, M^+ ($C_{13}H_{16}N_2O_6S$) = 328.0728), 147.0476 (61, ($C_6H_{11}O_2S$) = 147.0479, CH(SEt)CO_2Et).

Methyl 2-ethylthio-3-(2,4-dinitrophenyl)propionate (17b)

Treatment of methyl 2,4-dinitrocinnamate (26) (**15b**; 0.129 g, 0.5 mmol) by procedure E gave **17b** (0.15 g, 93%) as a slightly yellow oil. IR ($CHCl_3$) (cm^{-1}): 1705 (C=O). ^1H NMR δ: 1.23 (t, *J* = 7.4 Hz, 3H, CH_3), 2.75 (q, *J* = 7.4 Hz, 2H, SCH_2), 3.41–3.78 (m, 3H, CH_2-CH), 3.72 (s, 3H, CH_3), 7.68 (d, *J* = 8.4 Hz, 1H, H_{Ar}), 8.39 (dd, *J* = 8.4, 2.3 Hz, 1H, H_{Ar}), 8.82 (d, *J* = 2.3 Hz, 1H, H_{Ar}). EI-HRMS *m*/*z*: 314.0566 (14, M^+ ($C_{12}H_{14}N_2O_6S$) = 314.0572), 133.0328 (100, ($C_5H_9O_2S$) = 133.0323, CH(SEt)CO_2Me).

Ethyl 2-propylthio-3-(2,4-dinitrophenyl)propionate (17c)

Treatment of **15a** (133 mg, 0.5 mmol) with propanethiol (2.0 mmol) by procedure E (column chromatography: $CHCl_3$) gave **17c** (150 g, 88%) as a slightly yellow oil. IR (neat) (cm^{-1}): 1734 (C=O). ^1H NMR δ: 0.97 (t, *J* = 7.3 Hz, 3H, CH_3), 1.26 (t, *J* = 7.1 Hz, 3H, CH_3), 1.59 (septet, *J* = 7.3 Hz, 2H, CH_2), 2.58–2.70 (m, 2H, SCH_2), 3.41 (dd, *J* = 13.3, 6.8 Hz, $1H_A$, from 3-CH_2), 3.58 (dd, *J* = 13.3, 8.1 Hz, $1H_{A'}$, from 3-CH_2), 3.63 (t, *J* = 7.3 Hz, 1H, CH), 4.11–4.25 (m, 2H, CH_2), 7.70 (d, *J* = 8.5 Hz, 1H, H_{Ar}), 8.40 (dd, *J* = 8.4, 2.3 Hz, 1H, H_{Ar}), 8.85 (d, *J* = 2.3 Hz, 1H, H_{Ar}). ^{13}C NMR δ: 13.7 (CH_3), 14.5 (CH_3), 22.9 (CH_2), 34.4 (SCH_2), 35.5 ($3CH_2$), 46.6 (CH), 62.1 (CH_2), 121.0 (C6), 127.3 (C5), 135.4 (C6), 140.5 (C1), 147.4 and 149.6 (C2/4), 171.9 (C=O) (assignments based on DEPT and HETCOR experiments). APCI-MS *m*/*z*: 343 (100, $[M + H]^+$). Anal. calcd. for $C_{14}H_{18}N_2O_6S$: C 49.11, H 5.30, N 8.18; found: C 49.25, H 5.39, N 8.18.

Ethyl 3-propylthio-3-(2-nitrophenyl)propionate (18)

Propanethiol (0.21 mL, 179 mg, 2.35 mmol) was added to a stirred solution of EtONa in EtOH (prepared from Na (50 mg, 2.1 mmol) and EtOH (2.0 mL)) at ambient temperature. After 15 min, ethyl (*E*)-2-nitrocinnamate (27) (130 mg, 0.59 mmol; prepared from 2-nitrobenzaldehyde by procedure D (93%)) dissolved in ethanol (4.0 mL) was added dropwise and the stirring was continued for 2 h. The resulting mixture was evaporated and the residue was partitioned ($CHCl_3$–H_2O). The organic layer was dried ($MgSO_4$), evaporated, and column chromatographed ($CHCl_3$) to give **18** (97 mg, 56%) as an oil. IR (neat) (cm^{-1}): 1740 (C=O). ^1H NMR δ: 0.92 (t, *J* = 7.3 Hz, 3H, CH_3), 1.17 (t, *J* = 7.1 Hz, 3H, CH_3), 1.50–1.57 (m, 2H, CH_2), 2.39 (dt, *J* = 12.6, 7.3 Hz, $1H_A$, SCH_2), 2.50 (ddd, *J* = 12.6, 7.8, 6.6 Hz, $1H_{A'}$, SCH_2), 2.88 (dd, *J* = 15.4, 8.2 Hz, $1H_A$, CH_2), 2.94 (dd, *J* = 15.4, 7.2 Hz, $1H_{A'}$, CH_2), 4.07 (q, *J* = 7.1 Hz, 2H, CH_2), 4.99 (t, *J* = 7.8 Hz, 1H, CH), 7.38 (t, *J* = 7.7 Hz, 1H, H_{Ar}), 7.60 (t, *J* = 7.6 Hz, 1H, H_{Ar}), 7.78 (dd, *J* = 8.0, 1.0 Hz, 2H, H_{Ar}). ^{13}C NMR δ: 13.7 (CH_3), 13.8 (CH_3), 23.0 (CH_2), 34.3 (SCH_2), 39.4 (CH), 42.3 ($2CH_2$), 61.4 (CH_2), 124.5 (C3), 128.4 (C4), 130.1 (C6), 133.4 (C5), 137.4 (C1), 150.1 (C2), 170.3 (C=O) (assignments based on DEPT and HETCOR experiments). APCI-MS *m*/*z*: 298 (100, $[M + H]^+$). Anal. calcd. for $C_{14}H_{19}NO_4S$: C 56.55, H 6.44, N 4.71; found: C 56.46, H, 6.66, N 4.79.

Treatment of ethyl 2-nitrocinnamate (27) (0.5 mmol) with propanethiol (2.0 mmol) by procedure E gave unchanged ethyl 2-nitrocinnamte (91%).

2,2-Dimethyl-5-(2,4-dinitrobenzylidene)-1,3-dioxan-4,6-dione (19)

2,4-Dinitrobenzaldehyde (0.98 g, 5 mmol) was treated with 2,2-dimethyl-1,3-dioxane-4,6-dione (Meldrum's acid) (0.72 g, 5 mmol) by procedure A to give **19** (0.69 g, 43%); mp 138–139°C (EtOH). IR ($CHCl_3$) (cm^{-1}): 1720 (C=O). ^1H NMR δ: 1.82 (s, 6H, $2CH_3$), 7.68 (dd, *J* = 8.4, 0.6 Hz, 1H, H_{Ar}), 8.58 (dd, *J* = 8.4, 2.1 Hz, 1H, H_{Ar}), 8.76 (d, *J* = 0.6 Hz, 1H, CH), 9.12 (d, *J* = 2.1 Hz, 1H, H_{Ar}). EI-MS *m*/*z*: 322 (3, M^+). Anal. calcd. for $C_{13}H_{10}N_2O_8$: C 48.46, H 3.13, N 8.69; found: C 48.38, H 2.86, N 8.56.

© 2002 NRC Canada

Reaction of **19** with DEA in ethanol by procedure C did not afford rearranged product and only unchanged **19** was recovered (~92%).

Acknowledgments

We thank Alberto J. Sabucedo at Advanced Mass Spectroscopy Facility at FIU for his contribution and the Florida International University Foundation for support. We also thank Professor P. N. Preston (Heriot-Watt University) for suggestions concerning mechamism.

References

1. S. Kinastowski and S. Wnuk. Synthesis, 654 (1983).
2. S. Kinastowski, S. Wnuk, and E. Kaczmarek. Synthesis, 111 (1988).
3. S. Kinastowski, E. Kaczmarek, and S. Wnuk. Pol. J. Chem. **64**, 595 (1990).
4. S.F. Wnuk, E. Lewandowska, C.A. Valdez, and S. Kinastowski. Tetrahedron, **56**, 7667 (2000).
5. (*a*) J.D. Loudon and G. Tennant. Quart. Rev. **18**, 389 (1964); (*b*) P.N. Preston and G. Tennant. Chem. Rev. **72**, 627 (1972).
6. R. Behnisch. Aromatische Nitro-Verbindungen. *In* Houben-Weyl. Methoden der Organischen Chemie, 4. Vol. E16d. *Edited by* D. Klamann. Thieme, Stuttgart. 1992. pp. 389–405 (part 1).
7. (*a*) G. Tennant, C.J. Wallis, and G.W. Weaver. J. Chem. Soc. Perkin Trans. 1, 817 (1999); (*b*) J.E.T. Corrie, M.J. Gradwell, and G. Papageorgiou. J. Chem. Soc. Perkin Trans. 1, 2977 (1999).
8. (*a*) V.N.R. Pillai. Synthesis, 1 (1980); (*b*) D. Gravel, J. Hebert, and D. Thoraval. Can. J. Chem. **61**, 400 (1983).
9. (*a*) J.W. Walker, G.P. Reid, J.A. McCray, and D.R. Trentham. J. Am. Chem. Soc. **110**, 7170 (1988); (*b*) J.E.T. Corrie, B.C. Gilbert, V.R.N. Munasinghe, and A.C. Whitwood. J. Chem. Soc. Perkin Trans. 2, 2483 (2000); (*c*) Y.V. Il'ichev and J. Wirz. J. Chem. Phys. A, **104**, 7856 (2000).
10. R. Pschorr and O. Wolfes. Ber. Dtsch. Chem. Ges. **32**, 3399 (1899).
11. J.D. Loudon and G. Tennant. J. Chem. Soc. 3466 (1960).
12. J.P. Lelievre, P.G. Farrell, and F. Terrier. J. Chem. Soc. Perkin Trans. 2, 333 (1986).
13. H. Bock and U.Z. Lechner-Knoblauch. Naturforsch. Teil B, **40B**, 1463 (1985).
14. W. Lehnert. Tetrahedron, **29**, 635 (1973).
15. M.C. Wani, A.W. Nicholas, G. Manikumar, and M.E. Wall. J. Med. Chem. **30**, 1774 (1987).
16. L.P. Hammett. Physical organic chemistry. Reaction rates, equilibria, and mechanism. 2nd ed. McGraw–Hill, New York. 1970. pp. 347–390.
17. S. Kinastowski, S. Wnuk, and E. Kaczmarek. Pol. J. Chem. **63**, 495 (1989).
18. (*a*) E.D. Bergmann, D. Ginsburg, and R. Pappo. Org. React. **10**, 179 (1959); (*b*) R.D. Little, M.R. Masjedizadeh, O. Wallquist, and J.I. McLoughlin. Org. React. **47**, 315 (1995).
19. (*a*) P. Bravo, G. Gaudiano, and T. Salvatori. Gazz. Chim. Ital. **98**, 1046 (1968); (*b*) G. Faust, M. Verny, and R. Vessiere. Bull. Soc. Chim. Fr. 2707 (1975); (*c*) D.W. Lee, J. Choi, and N.M. Yoon. Synth. Commun. **26**, 2189 (1996).
20. (*a*) B.M. Trost and G.R. Dake. J. Am. Chem. Soc. **119**, 7595 (1997); (*b*) I.V. Solodin, A.V. Eremeev, I.I. Chervin, and R.G. Kostyanovskii. Khim. Geterotsikl. Soedin. 1359 (1985).
21. S. Kinastowski and S. Wnuk. Pol. J. Chem. **57**, 625 (1983).
22. H. Seidel and J.C. Bittner. Monatsh. Chem. **23**, 430 (1902).
23. M.P. Hay, B.M. Sykes, W.A. Denny, and C.J. O'Connor. J. Chem. Soc. Perkin Trans. 1, 2759 (1999).
24. F. Sachs and R. Kempf. Ber. Dtsch. Chem. Ges. **35**, 1224 (1902).
25. P. Friedlander and R. Fritsch. Monatsh. Chem. **23**, 534 (1902).
26. P. Pfeiffer. Liebigs Ann. Chem. **411**, 153 (1916).
27. J.V. Sinisterra, Z. Mouloungui, M. Delmas, and A. Gaset. Synthesis, 1097 (1985).

© 2002 NRC Canada

Electrocatalytic dechlorination of atrazine

Naomi L. Stock and Nigel J. Bunce

Abstract: Atrazine (2-chloro-4-ethylamino-6-isopropylamino-*s*-triazine), a photosynthetic inhibitor that is used in large quantities for weed control in corn and sorghum, is dechlorinated in aqueous solution upon electrolysis at a reticulated vitreous carbon cathode in the presence of noble-metal catalysts. Electrocatalytic hydrogenolysis to 2-ethylamino-4-isopropylamino-*s*-triazine occurs in quantitative yield, and is most efficient with palladium-based catalysts. Current efficiency increases with atrazine and catalyst concentration, and decreasing current density. A previously unobserved phenomenon with Pd catalysts is that current must be passed for a certain time before dechlorination commences. This lag time is explained in terms of the palladium lattice absorbing a finite amount of hydrogen before catalytically active hydrogen atoms appear on the catalyst surface.

Key words: electrocatalytic hydrogenoloysis, dechlorination, atrazine, palladium catalysts.

Résumé : Soumise à une électrolyse en solution aqueuse, au niveau d'une cathode de carbone vitreuse et réticulée et en présence de catalyseurs de métaux nobles, l'atrazine (la 2-chloro-4-éthylamino-6-isopropylamino-*s*-triazine), un inhibiteur de la photosynthèse utilisé en grandes quantités pour contrôler les mauvaises herbes dans le maïs et dans le shorgo, subit une déchloration. L'hydrogénolyse électrocatalytique en 2-éthylamino-4-isopropylamino-*s*-triazine se produit avec un rendement quantitatif et les catalyseurs à base de palladium sont les plus efficaces. L'efficacité de courant augmente avec les concentrations d'atrazine et de catalyseur et elle diminue avec la densité du courant. Avec les catalyseurs de Pd, il se produit un phénomène qui n'a pas été observé antérieurement; on doit faire passer le courant pour un certain temps avant que la déchloration ne débute. On explique ce décalage dans le temps en fonction d'une absorption dans un premier temps d'une quantité finie d'hydrogène par le réseau du palladium qui précéderait l'apparition d'atomes d'hydrogène catalytiquement actifs à la surface du catalyseur.

Mots clés : hydrogénolyse électrocatalytique; déchloration; atrazine; catalyseurs de palladium.

[Traduit par la Rédaction]

Introduction

Reactions involving electrochemically generated hydrogen adsorbed to a metal catalyst surface (M) have been known since the beginning of the twentieth century (1, 2). Two classes of these reactions are known: electrocatalytic hydrogenation and electrocatalytic hydrogenolysis (both abbreviated ECH). The former involves the addition of hydrogen to π bonds (3–6), whereas the latter involves the reductive cleavage of σ bonds, as in dechlorination reactions (7–11). Both types of ECH reactions involve the electrochemical reduction of a protic solvent to produce adsorbed hydrogen atoms (H_{ads}, eq. [1]) that react chemically with an adsorbed organic substrate $(R\text{-}X)_{ads}$, eq. [3]): see below, which is adapted from ref. 6.

[1] $2H_2O(\text{or } H_3O^+) + 2e^- + M \rightarrow 2H_{ads}M + 2OH^- \text{ (or } H_2O)$

[2] $R\text{-}X + M \rightarrow (R\text{-}X)_{ads}M$

[3] $(R\text{-}X)_{ads}M + 2H_{ads}M \rightarrow (R\text{-}H)_{ads}M + HX$

[4] $(R\text{-}H)_{ads}M \rightarrow R\text{-}H + M$

ECH always competes with the hydrogen evolution reaction (HER), which proceeds via the Volmer-Heyrovsky-Tafel mechanism (6).

[5] $H_2O + e^- + M \rightarrow H_{ads}M + OH^-$ (Volmer reaction)

[6] $H_{ads}M + H_2O + e^- \rightarrow H_2 + M + OH^-$ (Heyrovsky reaction)

[7] $H_{ads}M + H_{ads}M \rightarrow H_2 + 2M$ (Tafel reaction)

The use of ECH for the remediation of chloroaromatic compounds is potentially advantageous compared with traditional techniques such as adsorption on granular activated carbon (GAC) or incineration. As with other electrochemical technologies, ECH is useful as a "front-end" technology for dechlorinating toxic organic compounds prior to biological treatment (12). Comparing ECH with GAC adsorption, the chloro compounds are dechlorinated rather than simply transferred to a different phase; while in comparison with incineration, ECH avoids the possible formation of toxic byproducts such as chlorinated dibenzodioxins and dibenzofurans. As an

Received 16 September 2001. Published on the NRC Research Press Web site at http://canjchem.nrc.ca on 21 February 2002.

N.L. Stock and N.J. Bunce.[1] Electrochemical Technology Centre, Department of Chemistry and Biochemistry, University of Guelph, Guelph, ON N1G 2W1, Canada.

[1]Corresponding author (e-mail: bunce@chembio.uoguelph.ca).

 DOI: 10.1139/V02-008 © 2002 NRC Canada

electrochemical process, ECH is a "green" technology, which employs ambient temperatures, aqueous media, and electrons rather than chemical additives to promote chemical change. Provided that high current efficiencies can be achieved, ECH is also cost and energy efficient, technically flexible, and readily allows for the selective dechlorination of many different organic compounds (7).

Atrazine (2-chloro-4-ethylamino-6-isopropylamino-*s*-triazine) is used in large quantities in North America to control broadleaf and grassy weeds, primarily in corn and sorghum, and as a result has become a common contaminant in ground and surface water (13). This is of particular concern, since this herbicide has been identified as a possible carcinogen (14) and endocrine disruptor (15).

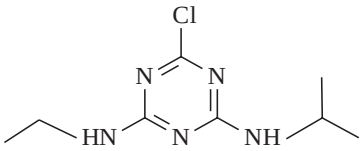

In this work we studied electrocatalytic hydrogenolysis (ECH) as a possible remediation method for the dechlorination of atrazine, using various noble-metal catalysts at a reticulated vitreous carbon (RVC) electrode in aqueous solutions. In particular, we examined the influence of substrate concentration, catalyst concentration and reusability, and current density on dechlorination efficiency.

Experimental

Materials

Analytical grade atrazine (99% pure) was purchased from Supelco (Oakville, Ontario). Technical grade atrazine (Aatrex-Nine-O, 90% pure) was generously donated by Peter Smith (Plant Agriculture Department, University of Guelph), and was purified by hot filtration and recrystallization from methanol. An analytical standard of dechlorinated atrazine (DCA) was generously donated by Dr. Nelson Johnson (Novartis, Jonesboro, North Carolina). All catalyst powders were 5% by weight and were obtained from Aldrich (Oakville, Ontario). Sulphuric acid (H_2SO_4), lithium perchlorate ($LiClO_4$), sodium sulphate (Na_2SO_4), and HPLC grade acetonitrile and methanol were obtained from Fisher Scientific (Toronto, Ontario). Nafion-417 membranes and RVC (80 ppi) were obtained from the Electrosynthesis Company (Lancaster, New York). Platinum foil (99.95% pure), platinum wire (99.95% pure, 0.368 mm diameter), and copper wire (99.9% pure, 1.0 mm diameter) were purchased from Alfa Aesar (Ward Hill, Massachusetts). Water used in all experiments was purified using a Millipore Milli-Q Reagent Water System and had a resistivity of not less than 10 MΩ cm.

Apparatus and procedures

Cyclic voltammetry was conducted on unstirred atrazine–acetonitrile solutions (200 ppm) in a 20 mL open-top glass cell. Both the working and counter electrodes were platinum (0.94 and 1.26 cm^2, respectively). In all experiments, 0.15 M lithium chloride was used as the supporting electrolyte and a sweep rate of 200 mV s^{-1} was employed. All CV experiments were conducted on a computer-controlled EG&G Princeton Applied Research Potentiostat (Model 273). Data were acquired using Model 270/250 Research Electrochemistry Software (version 4.10), converted to ASCII-text format and plotted in Microsoft Excel 2000 (version 9.0.2720). A saturated silver–silver chloride electrode, which was calibrated to 200 mV, was used as a reference electrode. Reference potentials were calculated against a standard hydrogen electrode (SHE).

All electrocatalytic hydrogenations were carried out in a flow-through batch cell (Fig. 1) designed by Patrick Dubé (University of Sherbrooke) and fabricated by Yves Savoret (University of Guelph). In this cell, the anode and cathode compartments were separated with a Nafion 417 membrane. In all experiments the cathode was RVC (80 ppi, 5 mm thick and 36 mm in diameter) with a copper wire lead (enclosed in glass tubing for stability) and the anode was platinum foil (16 mm × 12 mm and 0.1 mm thick) with a platinum wire lead. The anolyte solution was 20 mL of sulphuric acid (1 M) and the catholyte solution was water–methanol (75:5 mL), and contained sodium sulphate as supporting electrolyte to a concentration of 0.15 M. Atrazine was dissolved in the methanol aliquot and catalyst powder was added to the cathode compartment. A cross-shaped stir bar was placed in the cathode compartment and upon stirring, the catholyte solution and catalyst powder were forced through the RVC cathode, resulting in the impregnation of catalyst powder in the cathode. The catalyst remained impregnated in the RVC cathode throughout the experiment. When the charge was removed and the magnetic stirrer turned off, the catalyst powder returned to solution. An Amel Instrument General Purpose Potentiostat/Galvanostat (Model 2049) was used for experiments carried out at constant current. A computer controlled EG&G Princeton Applied Research Potentiostat (Model 273), equipped with Model 270/250 Research Electrochemistry Software (version 4.10) was used for experiments carried out at constant potential. A saturated silver – silver chloride electrode, which was calibrated to 200 mV, was used as a reference electrode. All potentials were calculated against a standard hydrogen electrode (SHE). Samples of the pesticide solutions were removed for HPLC analysis at appropriate time intervals during all experiments.

Degradation of the atrazine solutions was monitored using a Waters Model 600 HPLC unit, equipped with a Waters Model 486 variable UV–vis detector, a reverse phase Genesis C_{18} column (4.6 × 250 mm) and a Waters silica precolumn guard. For all analyses, the detector was set at λ = 220 nm and a methanol–water (80:20) mobile phase (1 mL min^{-1} flow rate) was used. Prior to use, solvents were filtered using Supelco Nylon 66 membranes (0.2 μm × 47 mm) to remove microparticles. All injections were done manually using a Rheodyne syringe (Waters), which injected 25 μL of sample into a 5 μL sample loop. Chromatogram generation and peak integration was carried out with Waters Millennium software (version 1.10).

Identification of the dechlorinated product was determined by Perry Martos (University of Guelph) via LC–MS–MS analyses on a VG Quattro II equipped with a quadrapole MS detector and MassLynx software (version 3.5). The samples were ionized using Atmospheric Pressure Chemical Ioniza-

© 2002 NRC Canada

Fig. 1. Schematic of cell used for ECH.

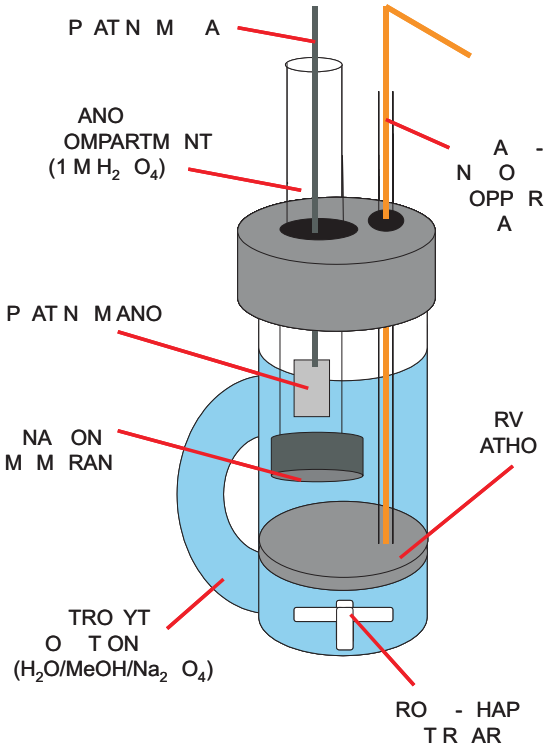

tion (APCI). APCI probe temperatures ranged from 200 to 300°C and cone voltages ranged from 25 to 50 V. Since the samples analyzed by LC–MS contained only single compounds, a column was not required. The mobile phase employed was acetronitrile–water (75:25) (0.6 mL min^{-1} flow rate). The water portion of the mobile phase was spiked with 0.1% formic acid to facilitate ionization of the sample. Prior to use, solvents were filtered to remove microparticles.

Calculations

The apparent current efficiencies for the dechlorination of atrazine were calculated from the number of moles of substrate reacted and the charge passed assuming that two electrons were required for the removal of one chlorine. Changes in volume were taken into consideration due to the removal of samples for analysis.

Results and discussion

The ECH of a 25 ppm solution of atrazine at 50 mA, using as catalyst 50 mg Pd/Al_2O_3, resulted in the rapid production of dechlorinated atrazine (DCA) (2-ethylamino-4-isopropylamino-1,3,5-triazine). The identity of the product was established as DCA by showing that it had the same HPLC retention time and mass spectral properties as authentic material. Following 30 min of ECH treatment, greater than 95% of the atrazine was dechlorinated, and a complete mass balance was obtained (Fig. 2).

Is it really ECH?

Cyclic voltammetry was employed to determine whether the dechlorination of atrazine proceeded via ECH or by direct electroreduction followed by protonation. Ideally the $E_{1/2}$ value for atrazine would have been obtained in the water–methanol solution used for electrolyses, but the reduction of the solvent masked the reduction of atrazine, and so the aprotic solvent acetonitrile was employed instead. In acetonitrile at a platinum cathode, a cyclic voltammogram of 200 ppm atrazine indicated an irreversible reduction process with $E_{1/2}$ = –1.3 V vs. SHE. Upon electrolysis in water–methanol, no reduction was observed at $E = -0.5$ V, and the rate of atrazine reduction was essentially independent of potential at $E \leq -0.8$ V (Fig. 3). Since these potentials are much less negative than $E_{1/2}$ for reduction of atrazine (albeit in acetonitrile) and in the same range as for the reduction of water (–0.83 V (16)), the observed dechlorination of atrazine cannot be as a result of direct electroreduction.

Dechlorination efficiency (Table 1)

The influences of current density, catalyst concentration, variation of the noble-metal catalyst, and initial substrate concentration on the dechlorination efficiency of atrazine were examined. In order to study the effect of current density, a series of 25 ppm atrazine solutions were electrolyzed in the presence of 50 mg Pd/Al_2O_3 at 5, 10, 20, 50, 100, and 200 mA. Applied currents ≥20 mA led to ≥93% loss of the initial atrazine within 30 min (Table 1, entries 1–6). At 10 mA, ECH treatment led to ~65% dechlorination, but at 5 mA dechlorination was negligible. Except for the case of the 5 mA electrolysis, the current efficiency decreased as the applied current increased, and was greatest (16%) at 10 mA (Table 1, entry 2). A decrease in current efficiency with increasing current density was also observed by Yusem and Pintauro (4) upon ECH of soybean oil. The explanation of this effect is that eq. [3], namely electrocatalytic hydrogenation or hydrogenolysis, is in competition with hydrogen evolution, eq. [6]. At high-current densities, the rate of the electrochemical generation of adsorbed hydrogen becomes faster than the rate at which the substrate can migrate to the surface and become adsorbed, eq. [2]. Consequently, a greater proportion of H_{ads} is lost to the unproductive reaction of hydrogen gas evolution, eq. [6].

The influence of catalyst concentration on the dechlorination of atrazine was investigated by employing 0, 25, 50, 100, 200, 400, and 600 mg of Pd/Al_2O_3 catalyst powder in the ECH treatment of 80 mL of a 25 ppm atrazine solution at 50 mA (Table 1, entries 4, 7–13). Catalyst concentrations of 50 mg resulted in the dechlorination of ≥96% of the initial atrazine within 30 min. The control experiment (atrazine without Pd/Al_2O_3) gave negligible reaction, further supporting ECH over the electronation–protonation mechanism. Current efficiency increased with catalyst concentration, with the exception of 600 mg, the maximum catalyst concentration investigated, and the best efficiency (7%) was obtained with a catalyst concentration of 400 mg. We suggest that increasing the amount of catalyst increases the production of *adsorbed* hydrogen (note that at constant current the overall production of hydrogen is independent of the amount of catalyst), thereby promoting hydrogenolysis. At some point, we would expect a further increase in the amount of catalyst to be unproductive, due to clogging the pores of the RVC cathode; this is presumably the explanation for the lower current efficiency observed with 600 mg of catalyst.

© 2002 NRC Canada

Fig. 2. Kinetic curves for the ECH (50 mA, 50 mg Pd/Al_2O_3) of atrazine (25 ppm).

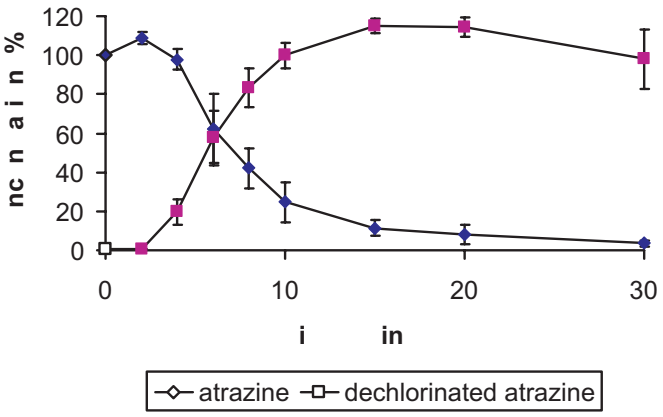

Fig. 3. Influence of constant potential on the degradation of atrazine (25 ppm) using ECH (50 mg Pd/Al_2O_3).

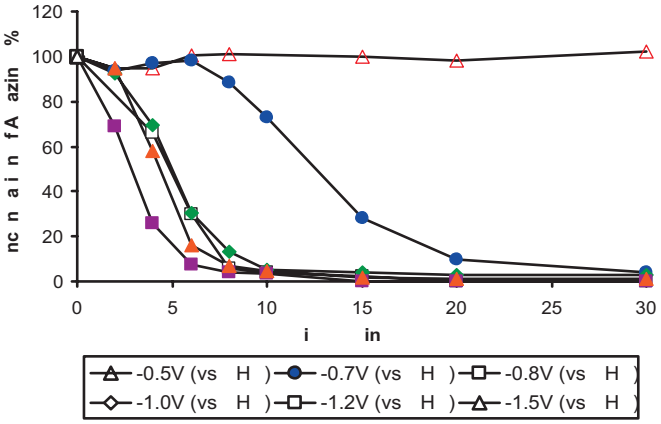

Table 1. Influence of current density, catalyst concentration, various noble-metal catalysts, and initial substrate concentration on the ECH of atrazine.

Entry	Current (mA)	Catalyst	Catalyst concentration (mg)	Initial atrazine concentration (ppm)	Current efficiency (%)[a]	Atrazine dechlorinated (%)[b]
1	5	Pd/Al_2O_3	50	25	5	7
2	10	Pd/Al_2O_3	50	25	16	64
3	20	Pd/Al_2O_3	50	25	6	93
4	50	Pd/Al_2O_3	50	25	4	97
5	100	Pd/Al_2O_3	50	25	4	98
6	200	Pd/Al_2O_3	50	25	4	100
7	50	Pd/Al_2O_3	0	25	0	0
8	50	Pd/Al_2O_3	25	25	1	62
9	50	Pd/Al_2O_3	50	25	3	97
10	50	Pd/Al_2O_3	100	25	4	96
11	50	Pd/Al_2O_3	200	25	5	100
12	50	Pd/Al_2O_3	400	25	7	100
13	50	Pd/Al_2O_3	600	25	6	100
14	20	Rh/Al_2O_3	400	25	2	28
15	20	Pt/Al_2O_3	400	25	4	31
16	20	Raney Ni	400	25	2	31
17	20	Ru/Al_2O_3	400	25	2	35
18	20	Pd/Al_2O_3	400	25	6	97
19	20	$Pd/CaCO_3$	400	25	11	97
20	20	Pd/Al_2O_3	400	4	1	98
21	20	Pd/Al_2O_3	400	83	14	85

[a]Representative experiments were run in triplicate. In these experiments, the average standard deviation was ±0.4%.
[b]Representative experiments were run in triplicate. In these experiments, the average standard deviation was ±6.3%.

The electrocatalytic properties of various noble-metal catalysts — Raney nickel; palladium, platinum, ruthenium, and rhodium on aluminia; and palladium on calcium carbonate — were investigated (Table 1, entries 14–19). Catalysts on carbon powder supports were not included in the study because atrazine rapidly and strongly adsorbed to carbon powder resulting in its removal from solution without a chemical change. Palladium was the most active ECH catalyst (Fig. 4), and current efficiencies of 11 and 6% were achieved with palladium on calcium carbonate and alumina, respectively. This result can be attributed to palladium's ability to both adsorb and absorb hydrogen (17). Similarly, Dabo et al. (18) observed that palladium catalysts offered maximum current efficiencies in the ECH of 4-phenoxyphenol. Palladized carbon felt was found to be an efficient catalyst for the dechlorination of 4-chlorophenol (19) and 2,4-dichlorophenoxyacetic acid (7–9); in the latter studies, current efficiencies for dechlorination reaction followed the sequence Pd > Rh > Ru catalysts.

The influence of the initial substrate concentration on the dechlorination of atrazine was examined using initial atrazine concentrations of 4, 25, and 83 ppm; 50 mA; and 400 mg Pd/Al_2O_3 (Table 1, entries 18, 20, 21). Within 30 min, >80% of the initial atrazine was dechlorinated. Current efficiency increased with increasing initial substrate concentration, a result that can be explained in terms of in-

© 2002 NRC Canada

Fig. 4. Influence of various noble-metal catalysts on the ECH of atrazine (400 mg of catalyst, 20 mA).

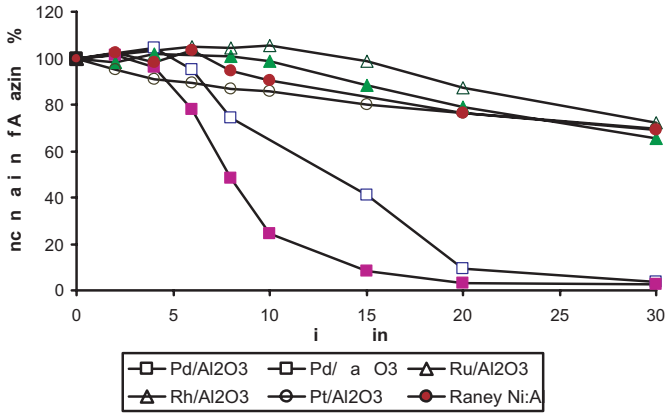

Fig. 5. Concentration of atrazine (A) and dechlorinated atrazine (B) during long-term ECH treatment (20 mA, 50 mg Pd/Al_2O_3) periodically spiked with concentrated atrazine solution.

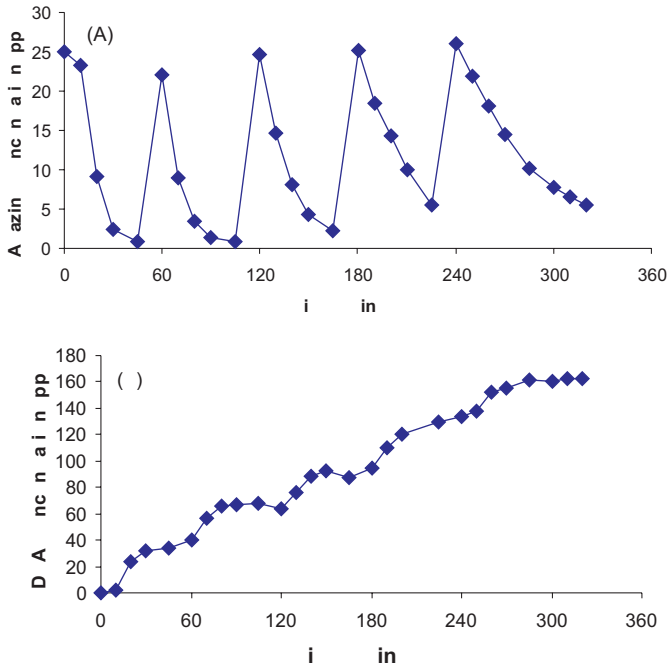

creased adsorption of the substrate on the catalyst (eq. [2]), allowing dechlorination (eq. [3]) to compete more effectively with hydrogen evolution. Previously, Mahdavi et al. (20) found that the current efficiency for the electrocatalytic hydrogenation of cyclohexenone increased with increasing substrate concentration.

Catalyst reusability

Longevity of the catalyst is a critical parameter in any catalytic process. We investigated the reusability of Pd/A_2O_3 for the ECH of atrazine in two different experiments. In the first of these, the Pd/A_2O_3 catalyst (200 mg) was removed by filtration using glass fiber paper after an ECH experiment with 25 ppm of atrazine at 50 mA (catalyst recovery 98 ± 3%). After drying at 80°C, the recycled Pd/A_2O_3 catalyst was used for a second similar ECH experiment; 30 min of electrolysis at 50 mA gave almost complete dechlorination of the starting material, with very similar current efficiency (10% in run 2 compared with 8% in run 1).

Table 2. Current efficiencies and first-order rate constants for the loss of atrazine during long-term ECH treatments (50 mg Pd/Al_2O_3, 20 mA) periodically spiked with concentrated atrazine solution.

Hour	Maximum current efficiency (%)	Rate constant (k) (s^{-1})
1st	5	—
2nd	8	1.23
3rd	6	0.87
4th	4	0.53
5th	3	0.30

In the second experiment, involving Pd/Al_2O_3 catalyst (50 mg), the atrazine solution was electrolyzed continuously at 20 mA, but every 60 min sufficient atrazine was added to restore its concentration to the original value of 25 ppm. The small amount of catalyst for this experiment was chosen so that all of it was trapped in the pores of the RVC and none was inadvertently removed when sampling the solution for analysis. As illustrated in Fig. 5A, the concentration of atrazine rapidly decreased after each addition, although gradual loss of catalyst activity was evident. Figure 5B shows that DCA continuously accumulated in solution during the experiment, eventually reaching a concentration > 160 ppm. Maximum current efficiencies and apparent first-order rate constants for loss of atrazine are listed in Table 2. A first-order plot is illustrated in Fig. 6.

Lag time in dechlorination

The ECH reaction of atrazine, catalyzed by Pd/Al_2O_3, was characterized by a lag time that decreased with an increase of both current density and catalyst concentration (Fig. 7). The lag time (t) was inversely proportional to current density (i) for a fixed catalyst concentration, suggesting that a fixed amount of charge (Q) must pass through the solution before dechlorination of atrazine begins, i.e., $Q = it$. In support of this hypothesis, when atrazine (50 mA, 50 mg Pd/Al_2O_3) was electrolyzed with preactivation of the cathode for 5 min (the lag time observed in Fig. 7A under these conditions) before the introduction of atrazine, the lag time disappeared and the degradation of atrazine was immediate. Furthermore, the maximum current efficiency increased from 4 to 26%. Likewise, in the experiment on long-term catalyst use (Fig. 5A), a lag time was observed only with the initial solution; subsequent additions of atrazine were followed by immediate dechlorination.

We interpret the decreased lag time with higher catalyst concentration in terms of the proportion of the RVC surface that is in contact with catalyst. Since current was constant in the experiments shown in Fig. 7B, the total rate of hydrogen production was the same, but only that produced at Pd was catalytically useful. As noted already, the behaviour of Pd catalysts was unique: no lag time was observed with the other noble metals studied (although it was difficult to determine whether or not a lag time occured with Rh or Ru, because dechlorination was so slow). We therefore hypothesize

© 2002 NRC Canada

Fig. 6. Superimposed first-order kinetic curves for the degradation of atrazine each hour during long-term ECH treatment (20 mg, 50 mg Pd/Al_2O_3) periodically spiked with concentrated atrazine solution.

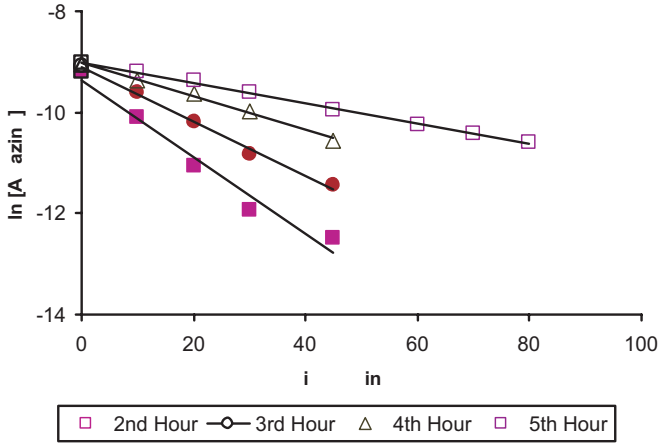

Fig. 7. Occurrence of lag time in the degradation of atrazine. Influence of current density (50 mg Pd/Al_2O_3) (A) and catalyst concentration (50 mA) (B).

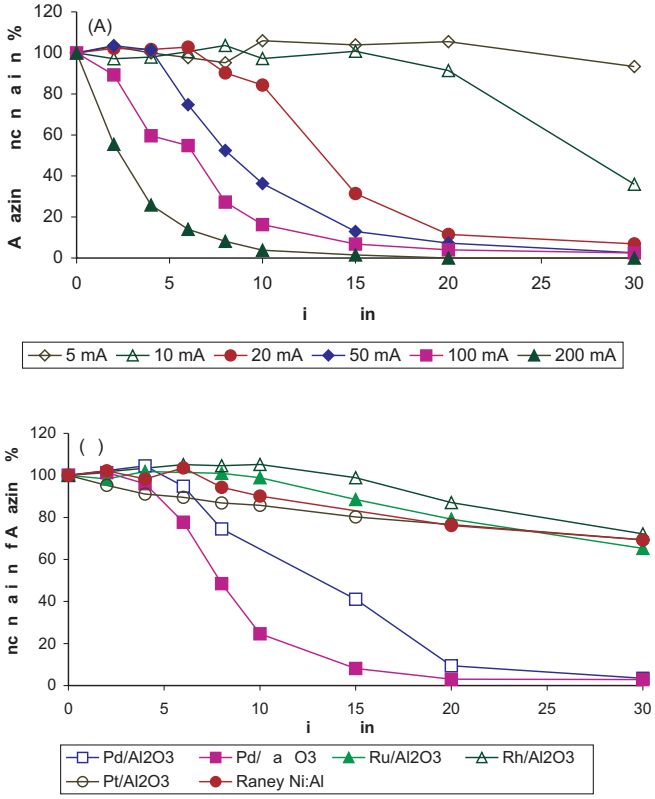

that the unique ability of palladium to both adsorb and adsorb hydrogen (17) accounts for both its superior electrocatalytic properties and the observed lag time. By analogy to a bucket filling with water and then overflowing, we propose that the palladium must first absorb the electrochemically produced hydrogen; once the palladium lattice is "full," hydrogen can be adsorbed at the palladium surface, allowing dechlorination to begin. The following calculation supports the foregoing concept. Consider the experiments in Fig. 7B involving 400 mg of catalyst. We assume that under these conditions the RVC pores are filled with catalyst and hence all the electrolytic hydrogen is formed at a Pd surface. The lag time is 3 min, which at 50 mA corresponds to $Q = 9$ C, or 9×10^{-5} mol H. The mass of Pd (5% on alumina) is 20 mg = 2×10^{-4} mol, i.e., mol H ~ mol Pd. This is consistent with H occupying the interstices of the Pd lattice, but not with Pd merely covering the surface of Pd particles.

In considering why the lag phenomenon had not previously been reported, we noted that most ECH reactions are characterized by reaction times on the order of several hours with samples taken every hour (8) or only at the beginning and end of the experiment (4). In our experiments, complete dechlorination was observed in 30 min and samples were taken every 2 min, making the lag effect easy to observe. Related observations have been reported by Tsyganok et al. (7), in whose dechlorination of 2,4-dichlorophenoxyacetic acid (2,4-D), the electrocatalytic activity of carbon-supported palladium was dramatically enhanced 2 h into the ECH treatment. These authors, who had also noted that preactivation of the cathode resulted in accelerated dechlorination, suggested that preactivation led to the formation of a hydrogen-saturated palladium phase and a change in spatial distribution of the supported Pd-clusters.

Conclusion

We found that electrocatalytic hydrogenolysis is an effective method of dechlorinating atrazine solutions at ppm concentrations. The method may have application to remediation, particularly of waste water streams, though it is not clear whether it has sufficient efficiency to be useful for contaminated ground water. The reaction product, DCA, is formed in quantitative yield. The DCA molecule still retains the *s*-triazine moiety, and it is not clear whether this reaction product will be a photosynthesis inhibitor like the parent molecule. Plant bioassays on the electrolyzed solutions of atrazine are in progress and will be reported separately.

Acknowledgments

We thank Dr. H. Menard, Francois LaPlante, and Patrick Dubé from the University of Sherbrooke for sharing their design of the electrochemical cell, and the Natural Sciences and Engineering Research Council of Canada (NSERC) for financial assistance.

References

1. S. Fokin. Z. Elektrochem. **12**, 749 (1906).
2. M.P. Breteau. Bull. Soc. Chim. Fr. Ser. **4**, 764 (1911).
3. L.L. Miller and L. Christensen. J. Org. Chem. **43**, 2059 (1978).
4. G.J. Yusem and P.N. Pintauro. J. Am. Oil Chemists Soc. **69**, 399 (1992).
5. V. Anaatharaman and P.N. Pintauro. J. Electrochem. Soc. **141,** 2729 (1994).
6. J.M. Chapuzet, A. Lasia, and J. Lessard. *In* Frontiers of electrochemistry. *Edited by* J. Lipkowski and P.N. Ross. VCH Publishers Inc., New York. 1998. pp. 155–196.
7. A.I. Tsyganok, I. Yamanaka, and K. Otsuka. J. Electrochem. Soc. **145**, 3844 (1998).

© 2002 NRC Canada

8. A.I. Tsyganok and K. Otsuka. Appl. Catalysis B: Environ. **22**, 15 (1999).
9. A.I. Tsyganok, I. Yamanaka, and K. Otsuka. Chemosphere, **39**, 1819 (1999).
10. A. Cyr, P. Huot, G. Belot, and J. Lessard. Electrochim. Acta, **35**, 147 (1990).
11. P. Dabo, A. Cyr, F. Laplante, F. Jean, H. Menard, and J. Lessard. Environ. Sci. Technol. **34**, 1256 (2000).
12. J.D. Rodgers, W. Jedral, and N.J. Bunce. Environ. Sci Technol. **33**, 1453 (1999).
13. K.R. Solomon, D.B. Baker, R.P. Richards, K.R. Dixon, S.J. Klaine, T.W. La Point, R.J. Kendall, C.P. Weisskopf, J.M. Giddings, J.P. Giesy, L.W. Hall, and W.M. Williams. Environ. Tox. Chem. **15**, 31 (1996).
14. United States Environmental Protection Agency (USA EPA). The triazine pesticides: atrazine, cyanazine, simazine, and propazine. Government Printing Office, Washington DC. 1999. pp. 1–4.
15. J.C. Eldrige. Biol Reprod. **44**, 133 (1991).
16. D. Dobos. Electrochemical data. Elsevier Scientific Publishing Company, New York. 1975. p. 252.
17. F.A. Lewis. The palladium hydrogen system. Academic Press, New York. 1967. pp. 1–11.
18. P. Dabo, A. Cyr, J. Lessard, L. Brossard, and H.Menard. Can. J. Chem. **77**, 1225 (1999).
19. I.F. Cheng, Q. Fernando, and N. Korte. Environ. Sci. Technol. **31**, 1074 (1997).
20. B. Mahdavi, P. Chambrion, J. Binette, E. Martel, and J. Lessard. Can. J. Chem. **73**, 846 (1995).

© 2002 NRC Canada

Medium-sized cyclophanes, part 59:[1] Nitration of [3.3]- and [3.3.3]metacyclophanes — Through-space electronic interactions between two or three benzene rings

Takehiko Yamato, Koji Tsuchihashi, Noriko Nakamura, Mai Hirahara, and Hirohisa Tsuzuki

Abstract: The the two *tert*-butyl groups of *anti*-6,15-di-*tert*-butyl-9,18-dimethoxy[3.3]metacyclophane (*anti*-**4**) are both ipso-nitrated even under mild reaction conditions such as copper(II) nitrate in an acetic anhydride solution because of the decreased deactivation of the second aromatic ring by the introduced nitro group. On the other hand, *anti*-5,13-di-*tert*-butyl-8,16-dimethoxy[2.2]metacyclophane (*anti*-**1**) undergoes replacement of only one *tert*-butyl group under the same reaction conditions. The higher yields of the twofold ipso-nitration product *anti*-**7** were obtained in nitration of *anti*-**4** with fuming nitric acid or mixed acid (HNO_3–H_2SO_4). Thus, the number of ipso-nitrations at the *tert*-butyl groups of *anti*-**4** was strongly affected by the reactivity of the nitration reagent. Nitration of the corresponding syn-conformer *syn*-**4** with copper(II) nitrate in an acetic anhydride solution, however, led only to the recovery of the starting compound. The presently developed procedure was further applied to the direct removal of the *tert*-butyl group by electrophilic substitution of the larger-sized ring macrocyclic metacyclophanes, *cone*- and *partial-cone*-tri-*tert*-butyl[3.3.3]metacyclophanes **11**.

Key words: [3_n]metacyclophanes, conformation, ipso-nitration, through-space electronic interaction, crystal structure.

Résumé : En raison de la désactivation plus faible du deuxième noyau aromatique par le groupe nitro introduit en premier, les deux groupes *tert*-butyles de l'*anti*-6,15-di-*tert*-butyl-9,18-diméthoxy[3.3]métacyclophane (*anti*-**4**) sont tous les deux nitrés en position ipso, même dans des conditions aussi douces que le nitrate de cuivre(II) en solution dans l'anhydride acétique. Toutefois, dans les mêmes conditions, la nitration du *anti*-5,13-di-*tert*-butyl-6,18-diméthoxy[2.2]-métacyclophane (*anti*-**1**) ne donne lieu qu'au remplacement d'un seul groupe *tert*-butyle. Les rendements élevés du produit de double nitration ipso, le produit *anti*-**7**, sont obtenus par nitration du produit *anti*-**4** à l'aide d'acide nitrique fumant ou par un mélange d'acide (HNO_3–H_2SO_4). Le nombre de nitration ipso au niveau des groupes *tert*-butyles d'*anti*-**4** sont fortement affectées par la réactivité de l'agent de nitration. La nitration du conformère syn correspondant, *syn*-**4** avec du nitrate de cuivre(II) en solution dans l'anhydride acétique ne conduit toutefois qu'à la récupération du produit de départ. On a aussi appliqué la méthode développée ici pour procéder à l'enlèvement direct du groupe *tert*-butyle par substitution électrophile de métacyclophanes macrocycliques à cycles plus grands, les tri-*tert*-butyl[3.3.3]métacyclophanes (**11**) à *cône*- et à *cône-partiel*-.

Mots clés : [3_n]métacyclophanes, conformation, nitration ipso, interaction électronique à travers l'espace, structure cristalline.

[Traduit par la Rédaction]

Introduction

Although the replacement of a *tert*-butyl group by a nitro group in electrophilic aromatic substitution has frequently been described in the literature (2, 3), the yields have generally been modest because of the accompanying side reactions (4, 5). Only in activated compounds are better yields obtained. However, there have been only a few investigations on the ipso-electrophilic aromatic substitution of *tert*-butylarenes having more than two benzene rings (6). Recently, we have reported that ipso-acylation (7) and ipso-nitration (8, 9) of internally methyl-substituted di-*tert*-

Received 22 June 2001. Published on the NRC Research Press Web site at http://canjchem.nrc.ca on 27 February 2002.

T. Yamato,[2] K. Tsuchihashi, N. Nakamura, and M. Hirahara. Department of Applied Chemistry, Faculty of Science and Engineering, Saga University, Honjo-machi 1, Saga-shi, Saga 840-8502, Japan.
H. Tsuzuki. Center of Environmental Analysis, Tohwa Institute for Science, Tohwa University, 1-1-1 Chikushigaoka, Minami-ku, Fukuoka-shi, Fukuoka 815-8510, Japan.

[1]Part 58. See ref. 1.
[2]Corresponding author (e-mail: yamatot@cc.saga-u.ac.jp).

 DOI: 10.1139/V02-009 © 2002 NRC Canada

Scheme 1.

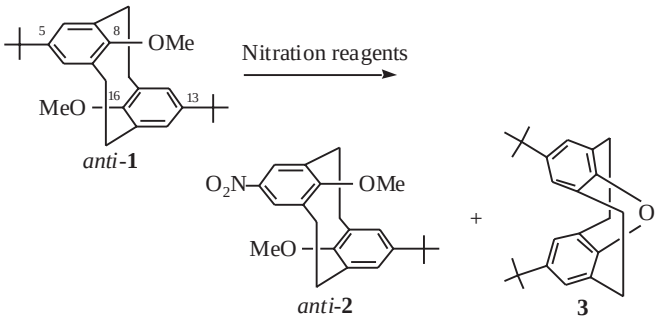

Fig. 1. Two possible through-space electronic interactions of [3.3]MCPs.

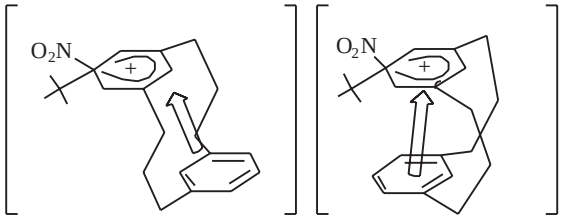

butyl[2.2]- and[3.2]-MCPs (MCP = metacyclophane) leads to the direct introduction of one acyl and one nitro group. However, only one *tert*-butyl group undergoes ipso-acylation under the mild reaction conditions such as acyl chloride in the presence of titanium tetrachloride because of deactivation of the second aromatic ring by the introduced acyl group. Subsequently, we reported (9*b*) that nitration of 5,13-di-*tert*-butyl-8,16-dimethoxy[2.2]MCP (*anti*-**1**) with various nitrating reagents led to mono-ipso-nitration at the *tert*-butyl group to give 5-*tert*-butyl-8,16-dimethoxy-13-nitro[2.2]MCP (*anti*-**2**) as well as the corresponding 17-oxa-[2.2.1](1,3,2)cyclophane **3** arising from intramolecular condensation reaction via *anti–syn*-ring inversion of the nitration intermediate. The latter novel product was obtained owing to the release of the strain in these systems (Scheme 1).

Although the parent [2.2]MCP was first reported as early as 1899 by Pelligrin (10), the synthesis of *syn*-[2.2]MCP was not realized until 85 years later. Mitchell et al. (11) have successfully prepared *syn*-[2.2]MCP at low temperature by using (arene)chromiumcarbonyl complexation to control the stereochemistry. However, *syn*-[2.2]MCP isomerizes readily to the *anti*-isomer above 0°C. Itô and co-workers (12) have also isolated and characterized *syn*-[2.2]MCP without complexation. On the other hand, Mitchell and Boekelheide (13) and Staab et al. (14) succeeded in synthesizing intraannularly substituted *syn*-[2.2]MCPs. However, the internally substituted *anti*- and *syn*-[3.3]MCPs can be easily synthesized and well characterized (15). Thus, the through-space electronic interaction could be achieved through the intraannular positions as in the σ-complex intermediate **A** in the former conformer, but through face-to-face overlapping among the two benzene rings as in the σ-complex intermediate **B** in the latter conformer. Therefore, it is possible to investigate the different behaviour in the nitration of *anti*- and *syn*-[3.3]MCPs and to determine which conformer contributes more strongly to the through-space electronic interaction (Fig. 1).

Scheme 2.

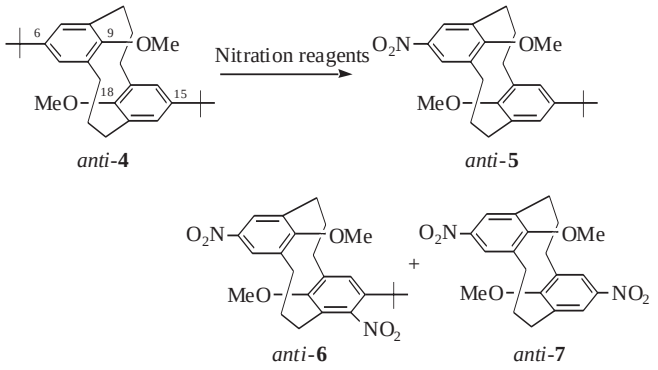

Thus, there is substantial interest in systematically investigating the relationship between neighbouring benzene rings in the ipso aromatic nitrations of larger-sized ring *tert*-butyl-[3.3]MCPs having *anti*- and *syn*-conformations than *tert*-butyl[2.2]MCPs, which might only afford the ipso-nitration product at the *tert*-butyl group because of the formation of the intramolecular condensation product via *anti–syn*-ring inversion of the nitration intermediate (9*b*) being impossible. In this paper we describe the selective introduction of one or two nitro groups by direct replacement of *tert*-butyl groups via the ipso-aromatic nitration of the *meta*-propane-bridged aromatic compounds, *tert*-butyl[3_n]MCPs having more than two arene rings to investigate the through-space electronic interactions occurring among other benzene rings.

Results and discussion

Recently, Vögtle and co-workers (16) reported the preparation of carbocyclic [3_n]metacyclophanes using (*p*-tolylsulfonyl)methyl isocyanide (TosMIC) (17) as the cyclization reagent, which was applied in a new cyclization procedure without phase-transfer conditions (18). However, it has been very difficult to obtain sufficient amounts of the above compounds to investigate their chemical behaviour. Quite recently we described the convenient preparation and conformational properties of [3.3]MCPs as well as the propane-bridged calix[3]arene-analogous macrocyclic MCPs ([3.3.3]MCPs) synthesized by an improved TosMIC method (19) (Scheme 2 and Table 1).

Attempted nitration of *anti*-6,15-di-*tert*-butyl-9,18-dimethoxy[3.3]MCP (*anti*-**4**) (19*a*) with copper(II) nitrate at room temperature for 24 h gave dinitration products *anti*-6-*tert*-butyl-9,18-dimethoxy-5,15-dinitro[3.3]MCP (*anti*-**6**) and *anti*-9,18-dimethoxy-6,15-dinitro[3.3]MCP (*anti*-**7**) in 92% yield as a major product along with mono-ipso-nitrated product *anti*-6-*tert*-butyl-9,18-dimethoxy-15-nitro[3.3]MCP (*anti*-**5**) in 8% yield. Interestingly, both benzene rings are nitrated even in mild reaction conditions such as copper(II) nitrate in an acetic anhydride solution. This result is quite different from the result achieved when only one benzene ring of *anti*-di-*tert*-butyl[2.2]MCP **1** is nitrated under the same reaction conditions because of deactivation of the second aromatic ring by the introduction of the nitro group (9*b*). In

© 2002 NRC Canada

Table 1. Nitration of *anti*-6,15-di-*tert*-butyl-9,18-dimethoxy[3.3]MCP (*anti*-**4**).

Run	Reagent	Time (h)	Products yield (%)[a]		
			anti-**5**	*anti*-**6**	*anti*-**7**
1	$Cu(NO_3)_2$–Ac_2O	24	8 (5)[b]	53 (43)[b]	39 (33)[b]
2	Fuming HNO_3	0.5	0	45 (30)[b]	55 (34)[b]
3	HNO_3–H_2SO_4	0.5	0	0	85 (79)[b]

[a]Yields were determined by GLC analyses.
[b]Isolated yields are shown in parentheses.

Scheme 3.

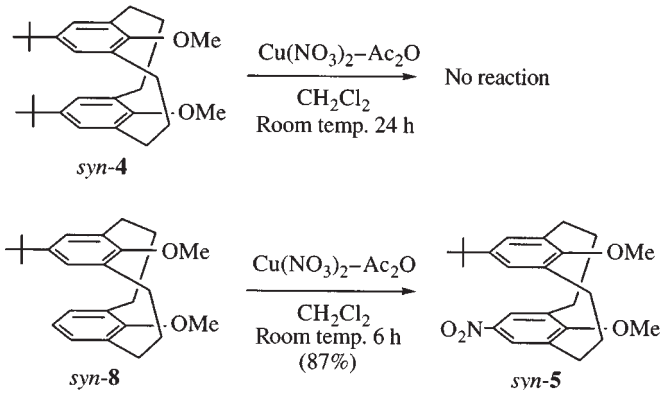

contrast, in the case of [3.3]MCP *anti*-**4**, the second nitration occurred because of the decreased deactivation of the second aromatic ring by the introduction of the nitro group.

Interestingly, the higher yields of the twofold ipso-nitration product *anti*-**7** were obtained in the nitration of *anti*-**4** with fuming nitric acid or mixed acid (HNO_3–H_2SO_4). When the nitration reagent was changed from fuming HNO_3 to the more reactive mixed acid (HNO_3–H_2SO_4), the yield of di-ipso-nitrated product *anti*-**7** increased from 55 to 85% yield. Thus, the extent of ipso-nitration at the *tert*-butyl groups of *anti*-**4** was strongly affected by the reactivity of the nitration reagent. By varying the reactivity of the nitrating reagents the ratio of the dinitration products arising from the second nitration at 5-position *ortho* to the *tert*-butyl group or 6-position at the *tert*-butyl group of *anti*-**5** changed. On the other hand, nitration of *anti*-**6** with fuming HNO_3 or copper(II) nitrate resulted only in the recovery of the starting compound. Formation of a twofold ipso-nitration product *anti*-**7** was not observed under the reaction conditions. These results suggest that *anti*-**6** is not the intermediate for the formation of twofold ipso-nitration product *anti*-**7**. Furthermore, nitration of mono-ipso-nitrated product *anti*-**5** with fuming HNO_3 carried out under the same conditions afforded almost the same ratio of dinitrated products *anti*-**6** and *anti*-**7**. This result strongly suggests that in the first step the ipso-nitration at the *tert*-butyl group must occur to afford *anti*-**5**. In the second step, the different regioselectivity was then observed exclusively to compete with the normal nitration at the 5-position *ortho* to the *tert*-butyl group or ipso-nitration at the *tert*-butyl group on the 6-position because of deactivation of the second aromatic ring by the nitro group. Thus, the positional selectivity for the nitration of *anti*-**4** was strongly affected by the reactivity of the nitration reagent, as has been reported for nitration in normal aromatic systems (20).

Fig. 2. Possible conformation of [3.3.3]MCPs.

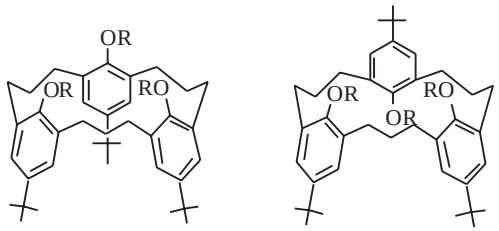

cone Conformation *partial cone* Conformation

The structures of *anti*-**6** and *anti*-**7** were assigned on the basis of elemental analyses and spectral data. Especially, the mass spectral data for *anti*-**6** (M^+ = 442) strongly supports the dinitration product. The ^1H NMR spectrum of *anti*-**6** in $CDCl_3$ shows three singlets at δ 1.40 for *tert*-butyl protons, at δ 3.14 and 3.33 for methoxy protons, and a set of doublets (J = 2.9 Hz) at δ 7.89 and 7.93 for aromatic protons in a strongly deshielded region due to the nitro group. As a result, *anti*-**6** has been assigned to *anti*-6-*tert*-butyl-9,18-dimethoxy-5,15-dinitro[3.3]MCP.

Attempted nitration of *syn*-6,15-di-*tert*-butyl-9,18-dimethoxy[3.3]MCP (*syn*-**4**) (19*a*) with copper(II) nitrate at room temperature for 24 h failed. Only the starting compound was recovered in quantitative yield. In contrast, as mentioned previously, in the case of *anti*-**4**, ipso-nitration products were obtained. It seems that the *anti*-conformer might be much more reactive than *syn*-conformer in the present ipso nitration. Therefore, the intraannular interaction is much more favourable to stabilize the first σ-complex intermediate than the face-to-face overlapping in [3.3]MCP systems. When the nitration reagent was changed from copper(II) nitrate to the more reactive fuming HNO_3 or HNO_3–H_2SO_4, only a complex mixture of nonvolatile materials was produced. But formation of the desired nitro compound *syn*-**7** was not detected (Scheme 3).

In contrast, nitration of *syn*-6-*tert*-butyl-9,18-dimethoxy-[3.3]MCP (*syn*-**8**) with copper(II) nitrate at room temperature for 6 h afforded only the mononitration product *syn*-**5** in 87% yield. No formation of dinitration products were observed. This result is comparable to the same nitration of *anti*-**8**, which predominantly afforded dinitration products *anti*-**6** and *anti*-**7**. Therefore, the deactivation of the second nitration of *syn*-conformer caused by the other aromatic ring substituted by the nitro group may be larger than that of *anti*-conformer.

It was also found that *anti*-6,15-di-*tert*-butyl-9,18-dimethyl[3.3]MCP (*anti*-**9**) (18*b*) with excess copper(II) nitrate in an acetic anhydride solution at room temperature for 24 h failed. Only the starting compound was recovered in

© 2002 NRC Canada

Table 2. Nitration of *cone*-tri-*tert*-butyl-tris[(ethoxycarbonyl)methoxy][3.3.3]MCP (*cone*-**11c**).

			Products (%, yield)[a]		
Run	Nitration reagents	Reaction time (h)	*cone*-**12c**	*cone*-**13c**	*cone*-**14c**
1	$Cu(NO_3)_2$–Ac_2O	24	0	86	14
2	Fuming HNO_3–HOAc	0.5	0	75	25
3	Fuming HNO_3–HOAc	1	0	52	48
4	Fuming HNO_3–HOAc	2	0	0	100

Note: The reaction was carried out at room temperature.
[a]Yields were determined by ^{1}H NMR spectroscopy.

Table 3. Nitration of tri-*tert*-butyl[3.3.3]MCPs **11**.

Substrate	*O*-Substituent	Conformation	Reaction time (h)	Yield (%)[a]
11a	Me	Mobile	0.5	**14a** 100 (95)[b]
11b	Bu	Partial-cone	0.5	**14b** 100 (90)
11c	CH_2COOEt	Cone	2.0	**14c** 100 (90)
11c	CH_2COOEt	Partial-cone	0.5	**14c** 100 (89)
11d	CH_2CONEt_2	Cone	0.5	**14d** 0[c]
11d	CH_2CONEt_2	Partial-cone	0.5	**14d** 0[c]

[a]Yields were determined by ^{1}H NMR spectroscopy.
[b]Isolated yields are shown in parentheses.
[c]Intractable mixture was obtained.

Scheme 4.

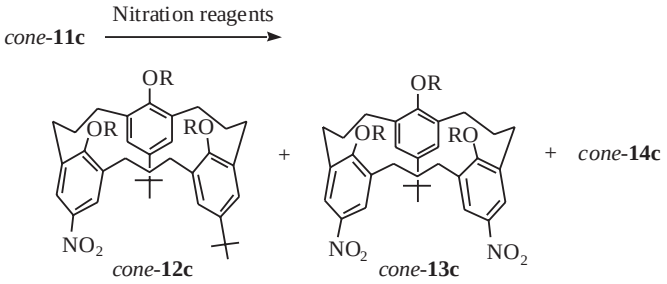

Scheme 5.

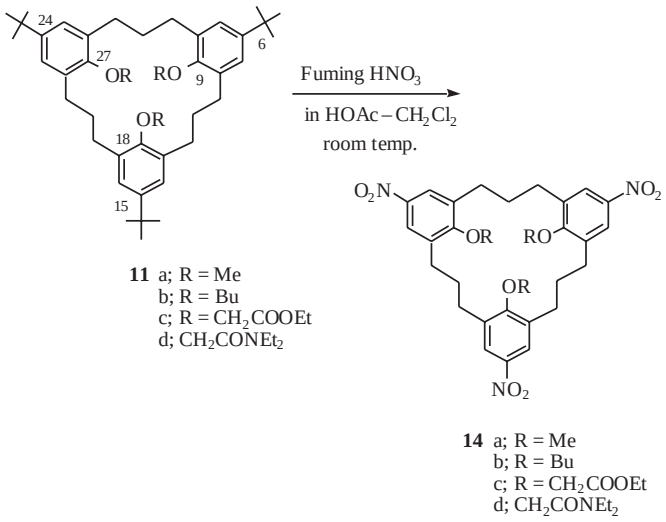

11 a; R = Me
b; R = Bu
c; R = CH_2COOEt
d; CH_2CONEt_2

14 a; R = Me
b; R = Bu
c; R = CH_2COOEt
d; CH_2CONEt_2

quantitative yield. When a similar nitration was carried out with fuming HNO_3, it did not afford the desired *anti*-dinitro[3.3]MCP *anti*-**10**, instead only an intractable mixture was obtained. This result seems to indicate that the methoxy group in *anti*-**4** plays an important role in the present ipso-nitration reaction. The ipso-nitration of *anti*-**4** is attributed to the highly activated character of the aryl ring and the increased stabilization of the σ-complex intermediate arising from a dienone-type σ-complex intermediate which is possible in the case of a methoxy substituent.

As mentioned previously, nitration of [3.3]MCP *anti*-**4** with excess copper(II) nitrate in an acetic anhydride solution led to twofold ipso-nitration at the *tert*-butyl groups to give *anti*-**7** in moderate yield along with dinitrated product *anti*-**6**, thus differing from the nitration of 4-*tert*-butyl-2,6-dimethylanisole under the same conditions which afforded only the starting compound. Recently, Cacace et al. (21) reported an intramolecular proton shift, namely, a ring-to-ring proton migration, in (β-phenylethyl)arenium ions during the cationic alkylation of 1,2-diphenylethanes which occurs at a faster rate than the same reaction conducted with toluene in the gas phase. In the present system, an initial σ-complex intermediate would be stabilized by a through-space electronic interaction with the opposing benzene ring, therefore accelerating the reaction, as in the formylation of *tert*-butyl-[*n*.2]MCPs (7).

To study this ipso-nitration reaction in more detail, we investigated the nitration of MCPs having three benzene rings. Recently, we reported in detail on the influence of *O*-substituents on the conformational isomerism of [3.3.3]MCPs (19*a*) having three benzene rings. We established that interconversion between conformers, which occurs by oxygen-through-the-annulus rotation, can be sterically allowed for methyl and ethyl, but inhibited by *O*-substituents bulkier than the propyl group. Furthermore, there are only two possible conformations, "cone" and "partial-cone" in *O*-alkylation products in contrast to four possible conformations in calix[4]arenes (22). Thus, the conformational isomerism is much simpler than that of *O*-alkylated calix[4]arenes. In comparison with the structural characteris-

© 2002 NRC Canada

Fig. 3. X-ray crystal structure of *cone*-**14c**. Thermal ellipsoids are drawn at 50% probability. Hydrogen atoms have been omitted for clarity.

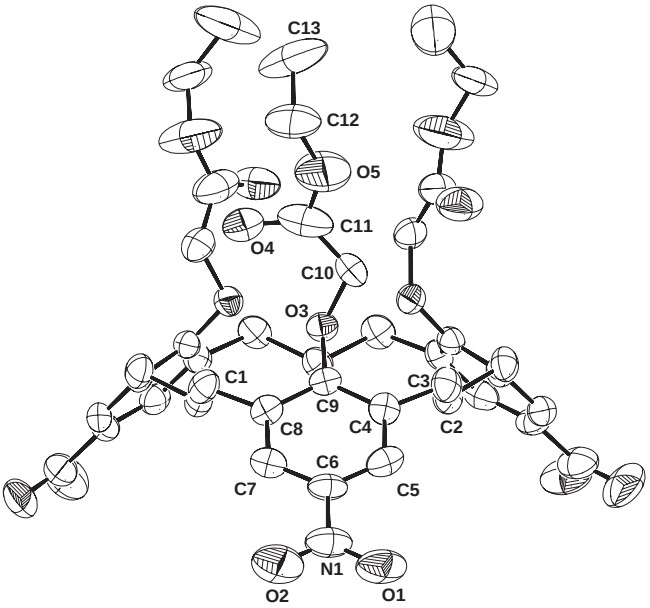

Table 4. Crystallographic data for *cone*-9,18,27-tris[(ethoxycarbonyl)methoxyl-6,15,24-trinitro[3.3.3]MCP (*cone*-**14c**) and *partial-cone*-9,18,27-tris[(ethoxycarbonyl)methoxyl-6,15,24-trinitro[3.3.3]MCP (*partial-cone*-**14b**).

	cone-**14c**	*partial-cone*-**14b**
Formula	$C_{39}H_{45}N_3O_{15}$	$C_{39}H_{45}N_3O_{15}$
FW	795.80	705.86
Crystal size (mm)	0.30 × 0.20 × 0.20	0.35 × 0.25 × 0.20
Space group	Cubic *Ia*-3 (No. 206)	Triclinic $P\bar{1}$ (No. 2)
a (Å)	2528.8 (4)	1158.8 (1)
b (Å)		1923.2 (1)
c (Å)		938.1 (1)
α (°)		95.16 (1)
β (°)		107.13 (1)
γ (°)		85.296 (9)
U (Å^3)	16 171.2 (44)	1986.4 (4)
Z	16	2
$\rho_{calcd.}$ (g cm^{-3})	1.31	1.18
T (K)	293	292
Radiation	Cu Kα	Cu Kα
λ (Å)	1.54184	1.54184
μ (cm^{-1})	8.5	6.5
No. of reflections	6883	7194
Unique reflections	2305	6278
R	0.092	0.073
R_w	0.223	0.102
S	1.07	3.54

tics of calix[4]arenes, whose cyclophane ring is composed of a 16-membered ring, [3.3.3]MCPs have a cavity composed of an 18-membered ring identical to the corresponding *tert*-butylhexahomotrioxacalix[3]arene (23, 24) (Fig. 2).

In fact, treatment of *cone*-6,15,24-tri-*tert*-butyl-9,18,27-tris[(ethoxycarbonyl)methoxy]-[3.3.3]MCP (*cone*-**11c**) with

Fig. 4. X-ray crystal structure of *partial-cone*-**14b**. Thermal ellipsoids are drawn at 50% probability. Hydrogen atoms have been omitted for clarity.

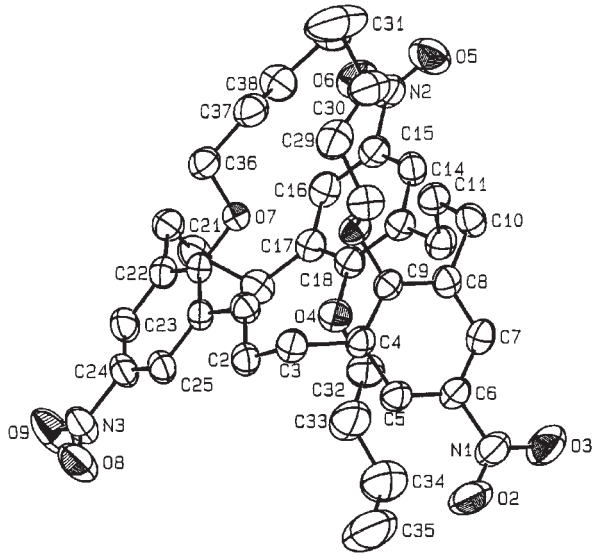

excess copper(II) nitrate in an acetic anhydride solution for 24 h gave a mixture of the dinitration product *cone*-**13c** and trinitration product *cone*-**14c** in 86 and 14% yields, respectively (Table 2). Interestingly, no mononitration product (*cone*-**12c**) was obtained even under the mild conditions such as those used in the nitration of [3.3]MCP *anti*-**4**. When nitration of *cone*-**11c** with fuming HNO_3 in an acetic acid solution was carried out at room temperature for 30 min, a similar result was obtained. Prolonging the reaction time for 2 h resulted in the increase of the yield of *cone*-**14c** from 25% to quantitative yield. These results strongly suggest that the through-space electronic interaction with the other benzene ring does exist in the [3.3.3]MCPs in spite of a larger ring size than that of the [3.3]MCPs (Scheme 4).

Similarly, introduction of three nitro groups by direct replacement of *tert*-butyl groups by ipso-aromatic nitration of 6,15,24-tri-*tert*-butyl-9,18,27-trimethoxy[3.3.3]MCP (**11a**) (19*a*) with fuming HNO_3 under the conditions of 0.5 h and room temperature has been shown to afford 9,18,27-trimethoxy-6,15,24-trinitro[3.3.3]MCP (**14a**) in 95% yield (Scheme 5 and Table 3).

Similar results are obtained in the case of *O*-butoxy derivative *partial-cone*-**11b**, *O*-(ethoxycarbonyl)methoxy derivatives *cone*-**11c** and *partial-cone*-**11c** to furnish complete threefold ipso-nitration under the reaction conditions used to afford the desired trinitro compounds **14b** and **14c** in almost quantitative yields, respectively. However, an attempted nitration of *O*-(*N*,*N*-diethylacetamide) derivative **11d** failed. Only an intractable mixture was obtained. These results might suggest that the cleavage reaction of more reactive *N*,*N*-diethylacetamide groups has occurred under the reaction conditions used. Interestingly, threefold ipso-nitration of partial-cone conformers was completed within 0.5 h, but it took at least 2 h to complete the reaction in the case of the cone conformer. It seems that partial-cone conformers might be much more reactive than cone conformers in the present ipso-nitration.

© 2002 NRC Canada

Single crystal X-ray diffraction analysis was performed on *cone*-**14c** recrystallized from chloroform and methanol and the ORTEP drawing with the atom numbering system is shown in Fig. 3. The structure was solved by direct methods (SIR 92) (25) and refined using the full-matrix least-squares method and Fourier synthesis. Compound *cone*-**14c** crystallized in the centrosymmetric cubic space group *Ia*-3 (No. 206). This compound is located at the special position (Z = 16) and contains a crystallographic C_3 axis of symmetry, showing that the crystallographically independent moiety is one-third of the full molecule (Table 4). It is clear that the three benzene rings are located on the same side (cone conformer) and thus the through-space electronic interaction among the three benzene rings through overlapping could be possible as discussed above. The dihedral angle of the flattened three aromatic rings is about 43.0°, which is much smaller than that of *p*-*tert*-butylhexahomotrioxacalix[3]arene (65.8°) (26). It is also clear that in the solid state, the carbonyl groups are located sideways, not toward the π cavity, probably to avoid the electronic repulsion with each other.

The X-ray molecular structure of *partial*-*cone*-**14b** recrystallized from chloroform and methanol is shown in Fig. 4 with the atom numbering system. The structure was solved by direct methods (SIR 88) (27) and refined using the full-matrix least-squares method and Fourier synthesis. Compound *partial*-*cone*-**14b** crystallized in the centrosymmetric triclinic space group $P\bar{1}$ (No. 2) and located at the general position (Z = 2). The ORTEP drawing clearly shows that two butoxy groups in the compound point upwards with one of them folded into the π cavity formed by two benzene rings. The dihedral angles of the plane defined by the bridge-chain carbons, C(1)-C(2)-C(3)-C(10)-C(11)-C(12)-C(19)-C(20)-C(21) between three aromatic rings, C(4)-C(5)-C(6)-C(7)-C(8)-C(9) and C(13)-C(14)-C(15)-C(16)-C(17)-C(19), and C(22)-C(23)-C(24)-C(25)-C(26)-C(27) are different values, 77.3°, 33.6°, and 35.0°, respectively.

In the partial-cone conformer, one through-space electronic interaction through face-to-face overlapping with the opposing benzene ring similar to that of *syn*-[3.3]MCP and two through-space electronic interactions through the intraannular interaction like that of *anti*-[3.3]MCP are possible. Thus, in the *partial*-*cone*-[3.3.3]MCP both *anti*-conformation and *syn*-conformation are contained in the molecule. Therefore, both initial and second σ-complex intermediates could also be stabilized by a through-space electronic interaction with other benzene rings not only through the face-to-face overlapping but also through the intraannular interaction like σ-complex intermediates **A** and **B** in [3.3]MCPs, as shown in Fig. 1. Furthermore, the deactivation of the third ipso-nitration caused by the two aromatic rings substituted by nitro groups may be smaller than that of the cone conformer, and thus it could be much faster to complete threefold ipso-nitration than the cone conformer. The stability of multimembered carbon skeletons was found to be an advantage, permiting the interconversion of functional groups without ring-opening side reactions, as opposed to the homotrioxacalix[3]arenes with the ethereal linkages (23).

Experimental

All melting points (Yanagimoto MP-S1) were uncorrected. Proton nuclear magnetic resonance (^{1}H NMR) spectra were recorded on a Nippon Denshi JEOL FT-270 spectrometer. Chemical shifts are reported as δ values (ppm) relative to internal Me_4Si. Mass spectra were obtained on a Nippon Denshi JMS-01SG-2 mass spectrometer at an ionization energy of 70 eV using a direct-inlet system through GLC; *m*/*z* values reported include the parent ion peak. Infrared (IR) spectra were obtained on a Nippon Denshi JIR-AQ2OM spectrophotometer as KBr disks. Elemental analyses were performed by Yanaco MT-5. Gas–liquid chromatograph (GLC) analyses were performed using a Shimadzu gas chromatograph (GC-14A); silicone OV-1, 2 m; programmed temperature rise, 12°C min^{-1}; carrier gas nitrogen, 25 mL min^{-1}.

Materials

The preparation of *anti*-dimethoxy[3.3]MCP *anti*-**4** and *syn*-dimethoxy[3.3]MCP *syn*-**4** was previously described (19*a*). *cone*- and *partial*-*cone*-6,15,24-Tri-*tert*-butyl-9,18,27-trialkoxy[3.3.3]MCPs **11a**–**d** were prepared according to the reported procedure (19*a*).

Nitration of *anti*-4 with copper(II) nitrate in acetic anhydride

To a solution of *anti*-6,15-di-*tert*-butyl-9,18-dimethoxy-[3.3]metacyclophane (*anti*-**4**) (117 mg, 0.289 mmol) in a mixture of CH_2Cl_2 (2.5 mL) and acetic anhydride (50 mL) was added $Cu(NO_3)_2 \cdot 3H_2O$ (150 mg, 0.62 mmol) at 0°C. After the mixture had been stirred at room temperature for 24 h, the reaction mixture was poured into ice water and then extracted with CH_2Cl_2, washed with water and 10% aqueous sodium hydrogencarbonate. The extract was dried over anhydrous sodium sulfate and concentrated. The residue was subjected to silica gel (Wako, C-300, 100 g) column chromatography using as eluents hexane–benzene (1:1) and benzene to give *anti*-**5** (6 mg, 5%), *anti*-**6** (55 mg, 43%), and *anti*-**7** (37 mg, 33%), respectively.

anti-*6*-tert-*Butyl-9,18-dimethoxy-15-nitro[3.3]metacyclophane (*anti-*5)*

Pale yellow oil. ^{1}H NMR ($CDCl_3$) δ: 1.33 (s, 9H), 2.12–2.19 (m, 4H), 2.36–2.48 (m, 4H), 2.56–2.66 (m, 4H), 3.12 (s, 3H), 3.20 (s, 3H), 6.97 (s, 2H), 7.90 (s, 2H). MS *m*/*z*: 397 (M^+). Anal. calcd. for $C_{24}H_{31}NO_4$ (397.52): C 72.52, H 7.86, N 3.52; found: C 72.43, H 7.78, N 3.48.

anti-*6*-tert-*Butyl-9,18-dimethoxy-5,15-dinitro[3.3]metacyclophane (*anti-*6)*

Pale yellow prisms (hexane), mp 169–171°C. ^{1}H NMR ($CDCl_3$) δ: 1.40 (s, 9H), 2.01–2.21 (m, 4H), 2.32–2.76 (m, 8H), 3.14 (s, 3H), 3.33 (s, 3H), 7.19 (s, 1H), 7.89 (d, J = 2.9 Hz, 1H), 7.93 (d, J = 2.9 Hz, 1H). MS *m*/*z*: 442 (M^+). Anal. calcd. for $C_{24}H_{30}N_2O_6$ (442.52): C 65.14, H 6.83, N 6.33; found: C 65.25, H 6.84, N 6.48.

anti-*9,18-Dimethoxy-6,15-dinitro[3.3]metacyclophane (*anti-*7)*

Pale yellow prisms (hexane), mp > 300°C. ^{1}H NMR ($CDCl_3$) δ: 2.15–2.25 (m, 4H), 2.47–2.70 (m, 8H), 3.22 (s, 6H), 7.93 (s, 4H). MS *m*/*z*: 386 (M^+). Anal. calcd. for

© 2002 NRC Canada

$C_{20}H_{22}N_2O_6$ (386.41): C 62.17, H 5.74, N 7.25; found: C 62.05, H 5.65, N 7.15.

Nitration of *anti*-4 with fuming nitric acid

To a solution of *anti*-**4** (102 mg, 0.25 mmol) in a mixture of CH_2Cl_2 (2.5 mL) and glacial acetic acid (2.5 mL), fuming HNO_3 (0.83 mL) at 0°C was added. The mixture was stirred at room temperture. After 30 min, the mixture was poured into ice water, extracted with CH_2Cl_2, and washed with water and 10% aqueous sodium bicarbonate. The extract was dried with Na_2SO_4 and concentrated to afford a mixture of *anti*-**6** and *anti*-**7** as a pale yellow solid in a ratio of 45:55 (GLC). The residue was subjected to silica gel (Wako, C-300, 100 g) column chromatography using as eluents hexane–benzene (1:1) and benzene to give *anti*-**6** (33 mg, 30%) and *anti*-**7** (33 mg, 34%).

Nitration of *anti*-4 with mixed acid

To a solution of *anti*-**4** (102 mg, 0.25 mmol) in a mixture of CH_2Cl_2 (2.5 mL) and glacial acetic acid (2.5 mL), mixed acid (a mixture of fuming HNO_3 (1.1 mL) and concentrated sulfuric acid (0.5 mL)) at 0°C was added. The mixture was stirred at room temperture. After 30 min, the mixture was poured into ice water, extracted with CH_2Cl_2, and washed with water and 10% aqueous sodium bicarbonate. The extract was dried with Na_2SO_4 and concentrated. The residue was subjected to silica gel (Wako, C-300, 100 g) column chromatography using as eluents hexane–benzene (1:1) and benzene to give *anti*-**7** (76 mg, 79%).

Nitration of *syn*-8 with copper(II) nitrate in acetic anhydride

To a solution of *syn*-6-*tert*-butyl-9,18-dimethoxy[3.3]-metacyclophane (*syn*-**8**) (88 mg, 0.25 mmol) in a mixture of CH_2Cl_2 (2.5 mL) and acetic anhydride (50 mL) was added $Cu(NO_3)_2 \cdot 3H_2O$ (150 mg, 0.62 mmol) at 0°C. After the mixture had been stirred at room temperature for 24 h, the reaction mixture was poured into ice water and then extracted with CH_2Cl_2, washed with water and 10% aqueous sodium hydrogencarbonate. The extract was dried over anhydrous sodium sulfate and concentrated. The residue was subjected to silica gel (Wako, C-300, 100 g) column chromatography using benzene as the eluent to give *syn*-6-*tert*-butyl-9,18-dimethoxy-15-nitro[3.3]metacyclophane (*syn*-**5**) (87 mg, 87%) as pale yellow prisms (hexane), mp 143–145°C. ^{1}H NMR ($CDCl_3$) δ: 1.06 (s, 9H), 1.83–1.89 (m, 2H), 2.47–2.60 (m, 6H), 3.02–3.18 (m, 4H), 3.50 (s, 3H), 3.57 (s, 3H), 6.57 (s, 2H), 7.48 (s, 2H). MS *m*/*z*: 397 (M^+). Anal. calcd. for $C_{24}H_{31}NO_4$ (397.52): C 72.52, H 7.86, N 3.52; found: C 72.35, H 7.76, N 3.40.

Nitration of 11a with fuming nitric acid

To a solution of 6,15,24-tri-*tert*-butyl-9,18,27-trimethoxy-[3.3.3]metacyclophane (**11a**) (19*a*) (75.0 mg, 0.123 mmol) in a mixture of CH_2Cl_2 (2.0 mL) and glacial acetic acid (2.0 mL), fuming HNO_3 (0.62 mL) at 0°C was added. The mixture was stirred at room temperture. After 30 min, the mixture was poured into ice water, extracted with CH_2Cl_2, and washed with water and 10% aqueous sodium bicarbonate. The extract was dried with Na_2SO_4 and concentrated in vacuo to give a yellow solid (72 mg, 100%). Recrystallization from benzene afforded 9,18,27-trimethoxy-6,15,24-trinitro[3.3.3]metacyclophane (**14a**) (64.0 mg, 89%) as pale yellow prisms, mp 241–243°C. ^{1}H NMR ($CDCl_3$) δ: 1.89–2.00 (m, 6H), 2.58–2.63 (m, 12H), 3.37 (s, 9H), 7.95 (s, 6H). MS *m*/*z*: 579 (M^+). Anal. calcd. for $C_{30}H_{33}N_3O_9$ (579.61): C 62.17, H 5.74, N 7.25; found: C 62.10, H 5.71, N 7.15.

Reaction of *partial-cone*-**11b**, *cone*-**11c**, and *partial-cone*-**11c** with fuming HNO_3 was carried out using the same procedure as described above and details of the products and yields are compiled in Table 3.

partial-cone-*9,18,27-Tributoxy-6,15,24-trinitro[3.3.3]-metacyclophane* (partial-cone-*14b*)

Pale yellow prisms, mp 143–145°C. IR (KBr) υ_{max}: 2958, 2930, 2870, 1585, 1517, 1454, 1379, 1337, 1315, 1263, 1209, 1094, 1063, 1045, 1021, 990, 957. ^{1}H NMR ($CDCl_3$) δ: 0.54–0.62 (m, 3H), 0.83–0.91 (m, 6H), 1.16–2.36 (m, 18H), 2.41–2.52 (m, 4H), 2.65–2.94 (m, 8H), 2.93–3.00 (m, 2H), 3.48–3.58 (m, 2H), 3.65–3.75 (m, 2H), 7.94 (d, *J* = 2.4 Hz, 2H), 7.95 (d, *J* = 2.4 Hz, 2H), 7.96 (s, 2H). MS *m*/*z*: 705 (M^+). Anal. calcd. for $C_{39}H_{51}N_3O_9$ (705.86): C 66.36, H 7.28, N 5.95; found: C 66.18, H 7.48, N 5.93.

cone-*9,18,27-Tris[(ethoxycarbonyl)methoxy]-6,15,24-trinitro[3.3.3]metacyclophane* (cone-*14c*)

Pale yellow prisms ($CHCl_3$–MeOH (1:1)), mp 247–249°C. IR (KBr) υ_{max}: 2923, 2853, 1762 (C=O), 1636, 1587, 1516, 1458, 1432, 1380, 1344, 1288, 1195, 1102, 1164, 909, 894. ^{1}H NMR ($CDCl_3$) δ: 0.81–0.92 (m, 6H), 1.28–1.35 (m, 9H), 2.49–2.62 (m, 6H), 3.06–3.18 (m, 6H), 4.21–4.31 (m, 6H), 4.65 (s, 6H), 7.65 (s, 6H). MS *m*/*z*: 795 (M^+). Anal. calcd. for $C_{39}H_{45}N_3O_{15}$ (795.8): C 58.86, H 5.7, N 5.28; found: C 58.69, H 5.48, N 5.13.

partial-cone-*9,18,27-Tris[(ethoxycarbonyl)methoxy]-6,15,24-trinitro[3.3.3]metacyclophane* (partial-cone-*14c*)

Pale yellow oil. ^{1}H NMR ($CDCl_3$) δ: 1.09 (t, *J* = 7.3 Hz, 3H), 1.24 (t, *J* = 7.3 Hz, 6H), 1.82–3.04 (m, 18H), 3.49 (s, 2H), 3.87 (q, *J* = 7.3 Hz, 2H), 4.07–4.21 (m, 4H), 4.30 (d, *J* = 15.6 Hz, 2H), 4.50 (d, *J* = 15.6 Hz, 2H), 7.94 (s, 2H), 7.96 (s, 4H). MS *m*/*z*: 795 (M^+). Anal. calcd. for $C_{39}H_{45}N_3O_{15}$ (795.8): C 58.86, H 5.7, N 5.28; found: C 58.53, H 5.54, N 5.35.

Attempted nitration of *cone*- (*cone*-**11d**) and *partial-cone*-6,15,24-tri-*tert*-butyl-9,18,27-tris[(*N*,*N*-diethylamino-carbonyl)methoxy][3.3.3]metacyclophane (*partial-cone*-**11d**) with fuming HNO_3 failed. Only an intractable mixture was obtained.

Crystal data for *cone*-14c and *partial-cone*-14b

As a typical procedure, a single crystal was mounted on a quartz fiber and the unit cell constants for *cone*-**14c** were derived from least-squares analysis of the settings of a CAD4 FR590 diffractometer for 25 reflections, in the range of $21.0° < \theta < 22.0°$, $\omega/2\theta$ mode with ω scan width = 0.3 + 0.400 tan θ, scan speed 1.0–20.0 deg min^{-1}, graphite-monochromated Cu Kα radiation; 7402 reflections were measured ($3.50 \leq \theta \leq 65.01°$, $-h$, $-k$, $-l$). Since the maximum values of *h*, *k*, *l* are too large for the program SHELXL-93 (29), only 6883 of reflections whose $(\sin\theta/\lambda)^2 < 0.30$ were used to reduce the maximum values of *h*, *k*, *l*. 2305 unique (merg-

© 2002 NRC Canada

ing R = 0.1502 after absorption correction (max, min transmission factor = 0.9993, 0.7091)), linear and approx. isotopic crystal decay, ca. –5.9% (corrected during the procedure).

The structure was solved by direct methods (SIR 92) (25). Full-matrix least-squares refinement on F^2 with all non-hydrogen atoms, anisotropic and hydrogens in calculated positions with U_{iso} = 1.3 × $U_{(bonded\ atoms)}$ were done. The disorder on C10 and O4 was found and the occupational proportion of C10:C10′ or O4:O4′ was 0.728:0.272. The disorder of C12 and C10 was modeled with isotopic thermal motion and with bond length restraints (C12—C13: 1.52 Å, C12—O5: 1.42 Å), and then refined anisotropically. The occupational proportion of C12:C12′ or C13:C13′ was 0.517:0.483. The weighting scheme is $\omega = 1/(\sigma^2(F_o^2) + (0.1687P)^2 + 26.0206P)$ where $P = (F_o^2 + 2F_c^2)/3$. Final R and R_w values were 0.0921, 0.2228 (refined on F^2). All calculations were performed on a MicroVAX3100 and an IBM RISC System/6000 3100 using MolEN (28) and SHELXL-93 (29).

Similarly, a single crystal was mounted on a quartz fiber and the unit cell constants for *partial-cone*-**14b** were derived from least-squares analysis of the settings of a CAD4 FR 590 diffractometer for 25 reflections, in the range of 24.4° < θ < 26.9°, Enraf-Nonius CAD4 FR586 diffractometer, ω/2θ mode with ω scan width = 0.8 + 0.140 tan θ, scan speed 1.0–7.0 deg min^{-1}, graphite-monochromated Cu Kα radiation; 7194 reflections were measured ($2.31 \le \theta \le 64.92$, $-h$, k, l). 6278 unique (merging R = 0.014, no absorption correction), linear and approx. isotopic crystal decay, ca. –3.8% (corrected during the procedure).

The structure was solved by direct methods (SIR88) (28). Full-matrix least-squares refinement on F with all non-hydrogen atoms, anisotropic and hydrogens isotropic fixed at B_{eq} 4.0 $Å^2$. The weighting scheme was $\omega = 4F_o^2/((\sigma I_o)^2 + 0.0016F_{osup}4)$. Final R and R_w values were 0.073, 0.102 (refined on F). All calculations were performed on a MicroVAX3100 using MolEN (28). Crystallographic data for *cone*-**14c** and *partial-cone*-**14b** are given in Table 4.[3]

Conclusions

We conclude that the selective ipso-nitration of *anti*-di-*tert*-buty[3.3]MCP (*anti*-**4**) led to the direct introduction of one or two nitro group(s) due to a through-space electronic interaction with the opposing benzene ring, similar to the electrophilic aromatic substitution of MCPs. The number of ipso-nitrations of **4** was controlled by the reactivity of the nitration reagent. The current procedure was further applied to the direct removal of a *tert*-butyl group by electrophilic substitution of the larger ring sized macrocyclic metacyclophanes, *cone*- and *partial-cone*-tri-*tert*-butyl[3.3.3]MCPs **11**. Further studies on ipso-nitration are currently in progress in our laboratory.

References

1. T. Yamato, K. Fujita, and H. Tsuzuki. J. Chem. Soc. Perkin Trans. 1, 2089 (2001).
2. R.B. Moodie and K. Schofield. Acc. Chem. Res. **9**, 287 (1976).
3. (*a*) A. Fischer and R. Röderer. Can. J. Chem. **54**, 3978 (1976); (*b*) A. Fischer and K.C. Teo. Can. J. Chem. **56**, 258 (1978); (*c*) A. Fischer and K.C. Teo. Can. J. Chem. **56**, 1758 (1978).
4. (*a*) H. Suzuki. Synthesis, 217 (1977); (*b*) P.C. Myhre and M. Beug. J. Am. Chem. Soc. **88**, 1568 (1966); (*c*) P.C. Myhre, M. Beug, and L.L. James. J. Am. Chem. Soc. **90**, 2105 (1968); (*d*) P.C. Myhre, M. Beug, K.S. Brown, and B. Östman. J. Am. Chem. Soc. **93**, 3452 (1971).
5. (*a*) A. Fischer and R. Röderer. J. Chem. Soc. Chem. Commun. 798 (1975); (*b*) G.A. Olah and S.J. Kuhn. J. Am. Chem. Soc. **86**, 1067 (1964).
6. (*a*) W. Verboom, A. Durie, R.J.M. Egberink, Z. Asfari, and D.N. Reinhoudt. J. Org. Chem. **57**, 1313 (1992); (*b*) E. Kelderman, L. Derhaeg, G.J.T. Heesink, W. Verboom, J.F.J. Engbersen, N.F. van Hulst, A. Persoons, and D.N. Reinhoudt. Angew. Chem. Int. Ed. Engl. **31**, 1075 (1992).
7. (*a*) T. Yamato, J. Matsumoto, K. Tokuhisa, Y. Takezaki, and M. Tashiro. Chem. Express. **6**, 663 (1991); (*b*) T. Yamato, J. Matsumoto, M. Shigekuni, and M. Tashiro. J. Chem. Res. Synop. 198 (1993); (*c*) T. Yamato, J. Matsumoto, S. Kabu, Y. Takezaki, and M. Tashiro. J. Chem. Res. Synop. 44 (1993); (*d*) T. Yamato, K. Maeda, H. Kamimura, K. Noda, and M. Tashiro. J. Chem. Res. Synop. 310 (1995); J. Chem. Res. Miniprint 1865 (1995).
8. M. Tashiro, S. Mataka, Y. Takezaki, M. Takeshita, T. Arimura, A. Tsuge, and T. Yamato. J. Org. Chem. **54**, 451 (1989).
9. (*a*) T. Yamato, H. Kamimura, K. Noda, and M. Tashiro. J. Chem. Res. Synop. 210 (1994); J. Chem. Res. Miniprint 1152 (1994); (*b*) T. Yamato, H. Kamimura, and T. Furukawa. J. Org. Chem. **62**, 7560 (1997).
10. M. Pelligrin. Recl. Trav. Chim. Pays–Bas Belg. **18**, 458 (1889).
11. R.H. Mitchell, T.K. Vinod, and G.W. Bushnell. J. Am. Chem. Soc. **107**, 3340 (1985).
12. Y. Fujise, Y. Nakasato, and S. Itô. Tetrahedron Lett. **27**, 2907 (1986).
13. (*a*) R.H. Mitchell and V. Boekelheide. J. Am. Chem. Soc. **96**, 1547 (1974); (*b*) Y.-H. Lai and H.-L. Eu. J. Chem. Soc. Perkin Trans. 1, 233 (1993).
14. H.A. Staab, W.R.K. Riebel, and C. Krieger. Chem. Ber. **118**, 1230 (1985).
15. (*a*) P.M. Keehn and S.M. Rosenfield. Cyclophanes. Vol. 1. Academic Press, New York. 1983; (*b*) F. Vögtle. Cyclophane chemistry. John Wiley and Sons Ltd., New York. 1993; (*c*) L. Ernst. Prog. Nucl. Magn. Reson. Spectrosc. **37**, 47 (2000).
16. (*a*) J. Breitenbach and F. Vögtle. Synthesis, 41 (1992); (*b*) J. Breitenbach, F. Ott, and F. Vögtle. Angew. Chem. **104**, 360 (1992); Angew. Chem. Int. Ed. Engl. **31**, 307 (1992); (*c*) F. Ott, J. Breitenbach, M. Nieger, and F. Vögtle. Chem. Ber. **126**, 97 (1993).
17. (*a*) O. Possel and A.M. van Leusen. Tetrahedron Lett. 4229

[3] Hydrogen coordinates, temperature factors (anisotropic for carbon atoms), scale factors, and secondary estimation coefficients have been deposited as supplementary material and may be purchased from the Depository of Unpublished Data, Document Delivery, CISTI, National Research Council Canada, Ottawa, ON K1A 0S2, Canada (http://www.nrc.ca/cisti/irm/unpub_e.shtml for information on ordering electronically). CCDC Nos. 177269 and 177270 contain the supplementary crystallographic data for this paper. These data can be obtained, free of charge, via www.ccdc.cam.ac.uk/conts.retrieving/html (or from the Cambridge Crystallographic Data Centre, 12 Union Road, Cambridge, CB2 1EZ, U.K. (Fax: 44-1223-336033 or e-mail: deposit@ccdc.cam.ac.uk).

© 2002 NRC Canada

(1977); (*b*) D. van Leusen and A.M. van Leusen. Tetrahedron Lett. 4233 (1977).
18. (*a*) K. Kobiro, M. Takashi, N. Nishikawa, K. Kikuchi, Y. Tobe, and Y. Odaira. Tetrahedron Lett. **28**, 3825 (1987); (*b*) K. Kurosawa, M. Suenaga, T. Inazu, and T. Yoshino. Tetrahedron Lett. **23**, 5335 (1982); (*c*) T. Shinmyozu, Y. Hirai, and T. Inazu. J. Org. Chem. **51**, 1551 (1986); (*d*) K. Sako, T. Hirakawa, N. Fujimoto, T. Shinmyozu, T. Inazu, and H. Horimoto. Tetrahedron Lett. **29**, 6275 (1988); (*e*) T. Meno, K. Sako, M. Suenaga, M. Mouri, T. Shinmyozu, T. Inazu, and H. Takemura. Can. J. Chem. **68**, 440 (1990); (*f*) T. Meno, K. Sako, M. Suenaga, M. Mouri, T. Shinmyozu, T. Inazu, and H. Takemura. Can. J. Chem. **68**, 440 (1990); (*g*) K. Sako, T. Meno, H. Takemura, T. Shinmyozu, and T. Inazu. Chem. Ber. **123**, 630 (1990); (*h*) K. Sako, T. Shinmyozu, H. Takemura, M. Suenaga, and T. Inazu. J. Org. Chem. **57**, 6536 (1992).
19. (*a*) T. Yamato, L.K. Doamekpor, K. Koizumi, K. Kishi, M. Haraguchi, and M. Tashiro. Liebigs Ann. 1259 (1995); (*b*) T. Yamato, M. Haraguchi, J. Nishikawa, and S. Ide. J. Chem. Soc. Perkin Trans. 1, 609 (1998); (*c*) T. Yamato. J. Inclusion Phenom. **32**, 195 (1998).
20. G.A. Olah. Acc. Chem. Res. **4**, 240 (1971).
21. F. Cacace, M.E. Crestoni, S. Fornarini, and D. Kuck. J. Am. Chem. Soc. **115**, 1024 (1993).
22. (*a*) C.D. Gutsche. Calixarenes. Royal Society of Chemistry, Cambridge, U.K. 1989; (*b*) J. Vicens and V. Böhmer. Calixarenes: A versatile class of macrocyclic compounds. Kluwer Academic Publishers, Cambridge, U.K. 1990; (*c*) C.D. Gutsche, B. Dhawan, K.H. No, and R. Muthukrishnan. J. Am. Chem. Soc. **103**, 3782 (1981); (*d*) C.D. Gutsche. Acc. Chem. Res. **16**, 161 (1983); (*e*) C.D. Gutsche. Calixarenes revisited. Royal Society of Chemistry, Cambridge, U.K. 1998.
23. (*a*) H. Ninagawa and H. Matsuda. Makromol. Chem. Rapid Commun. **3**, 65 (1982); (*b*) C.D. Gutsche and L.J. Bauer. J. Am. Chem. Soc. **107**, 6052 (1985); (*c*) P. Zerr, M. Mussrabi, and J. Vicens. Tetrahedron Lett. **32**, 1879 (1991); (*d*) K. Araki, N. Hashimoto, H. Otsuka, and S. Shinkai. J. Org. Chem. **58**, 5958 (1993); (*e*) P.D. Hampton, Z. Bencze, W. Tong, and C.E. Daitch. J. Org. Chem. **59**, 4838 (1994); (*f*) M. Takeshita and S. Shinkai. Chem. Lett. 125 (1994); (*g*) H. Matsumoto, S. Nishio, M. Takeshita, and S. Shinkai. Tetrahedron, **51**, 4647 (1995).
24. (*a*) T. Yamato. J. Inclusion Phenom. **32**, 195 (1998); (*b*) T. Yamato, M. Haraguchi, J. Nishikawa, and S. Ide. J. Chem. Soc. Perkin Trans. 1, 609 (1998); (*c*) T. Yamato, M. Haraguchi, J. Nishikawa, S. Ide, and H. Tsuzuki. Can. J. Chem. **76**, 989 (1998); (*d*) T. Yamato, F. Zhang, T. Sato, and S. Ide. J. Chem. Res. Synop. 10 (2000); J. Chem. Res. Miniprint 0159 (2000); (*e*) T. Yamato and F. Zhang. J. Chem. Res. Synop. 33 (1999); T. Yamato and F. Zhang. J. Inclusion Phenom. **39**, 55 (2001).
25. A. Altomare, G. Cascarano, C. Giacovazzo, A. Guagliardi, M.C. Burla, G. Polidori, and M. Camalli. J. Appl. Crystallogr. **27**, 435 (1994).
26. K. Suzuki, H. Minami, Y. Yamagata, S. Fujii, and K. Tomita. Acta Crystallogr. Sect C: Cryst. Struct. Commun. **C48**, 350 (1992).
27. M.C. Burla, M. Camalli, G. Cascarano, C. Giacovazzo, G. Polidori, R. Spagna, and D. Viterbo. J. Appl. Crystallogr. **22**, 389 (1989).
28. MolEN. An interactive structure solution procedure. Enraf-Nonius, Delft, The Netherlands. 1990.
29. G.M. Sheldrick. SHELXL-93. Program for crystal structure determinations. University of Göttingen, Göttingen, Germany. 1993.

© 2002 NRC Canada

National Research Council Canada
Ottawa, Canada K1A 0R6

Conseil national de recherches Canada
Ottawa, Canada K1A 0R6

Postage paid at Ottawa
Publications mail
Registration No. 40062591

Port payé à Ottawa
Poste-publication
Enregistrement n° 40062591

Canadian Journal of Chemistry

Revue canadienne de chimie

Volume 80, Number 3, March 2002

Volume 80, numéro 3, mars 2002

2001 Lemieux Award Lecture

Organic chemistry and hemoglobin: Benefits from controlled alteration

Ronald Kluger

217–221

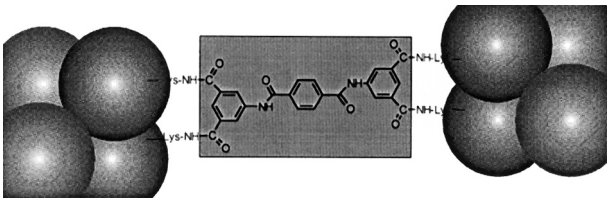

Electron momentum spectroscopy of the frontier electrons of DABCO does not support an sp^3 hybrid lone-pair description

Saul Wolfe, Zheng Shi, C.E. Brion, James Rolke, Yenyou Zheng, Glyn Cooper, Delano P. Chong, and C.Y. Hu

222–227

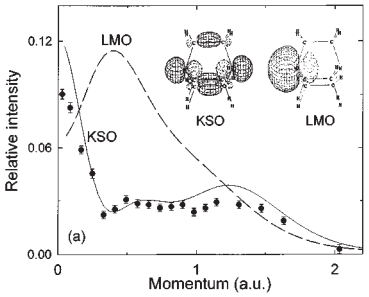

***Ortho* substituent effects on transfer of aryl groups from oxygen to carbon in adducts from diaryloxycarbenes and DMAD**

Xiaosong Lu and John Warkentin

228–234

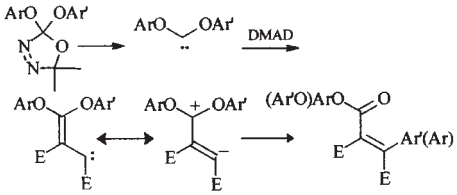

(Ar= C_6H_5, Ar'= *p*-$C_6H_4CH_3$; Ar= C_6H_5, Ar'= *o*-$C_6H_4CH_3$; Ar= *p*-C_6H_4Cl, Ar'= *o*-C_6H_4I; Ar= *p*-C_6H_4Cl, Ar'= *o*-C_6H_4Br; Ar= C_6H_5, Ar'= *o*-C_6H_4I)

Direct-space analysis of the electronic structure of the $YBa_2Cu_3O_6$ and $YBa_2Cu_3O_7$ crystals

Fausto Cargnoni and Marco Scavini

235–244

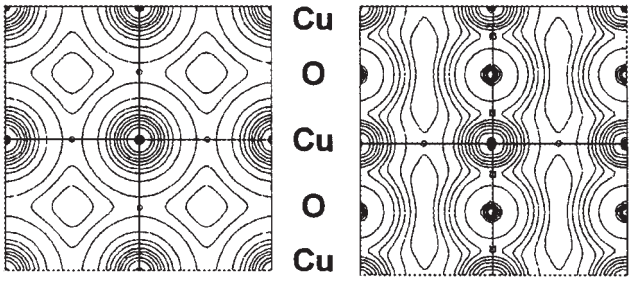

Continued on inside back cover / Suite au verso

Canada

Printed in Canada by / Imprimé au Canada par
University of Toronto Press Inc.
Typesetting by / Typographie par
NRC Research Press / Presses scientifiques du CNRC

0008-4042 200203 80 3 1-

Conformational analysis of the bicyclo[4.4.1]undecan-11-one ring system

Masood Parvez, Ted S. Sorensen, and Fang Sun

245–249

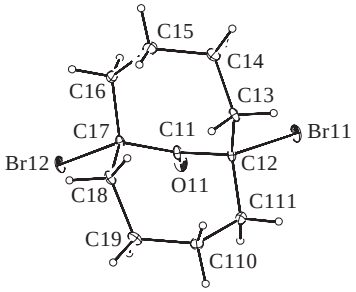

The redox properties of ferrocenyl-substituted aryl azines

Vittorio A. Sauro and Mark S. Workentin

250–262

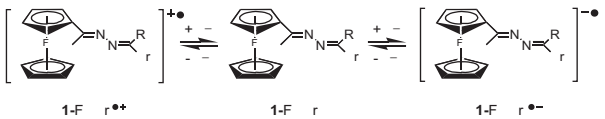

Low temperature interface-mineralizing route to hollow CuS, CdS, and NiS spheres

Xuchuan Jiang, Yi Xie, Jun Lu, Liying Zhu, Wei He, and Xianming Liu

263–268

Reaction of the tamoxifen cation and the bis-(4-methoxyphenyl)methyl cation in aqueous solutions containing 2′-deoxyguanosine

Robert A. McClelland, Cristina Sanchez, Effiette Sauer, and Sinisa Vukovic

269–280

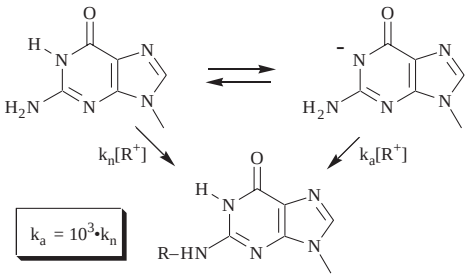

A novel metal-chain extension reaction: synthesis of (X)[Os(CO)$_3$(CN-*t*-Bu)]$_n$Mn(CO)$_5$ (X = Cl, Br, I; *n* = 1, 2, 3)

Faming Jiang, Hilary A. Jenkins, David F. Green, Glenn P.A. Yap, and Roland K. Pomeroy

281–291

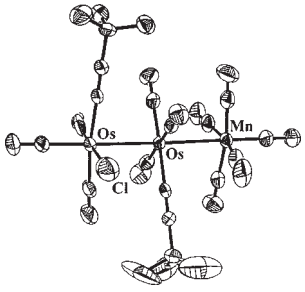

Concluded on facing page / Suite et fin à la page précédente

Molar excess enthalpies for some systems containing the OH and (or) O groups in the same or in different molecules

Jose Carlos Cobos, Isaias Garcia de la Fuente, and Juan Antonio Gonzalez

292–301

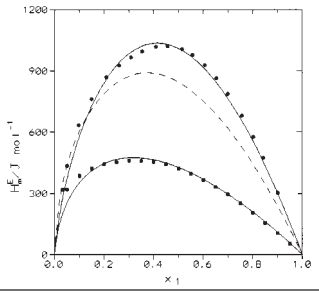

A theoretical study of the mechanism of 1,2-migrations in methoxysiloxycarbene

Paul G. Loncke, Timothy A. Gadosy, and Gilles H. Peslherbe

302–314

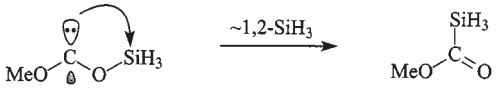

Biocapteurs ampérométriques à cholinestérases pour la détermination des pesticides organophosphorés

Graziella Turdean, Ionel Catalin Popescu et Liviu Oniciu

315–331

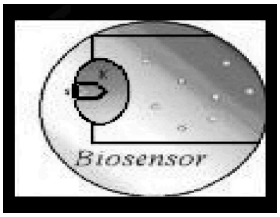

The Canadian Journal of Chemistry is affiliated with the Canadian Society for Chemistry and publishes papers in all areas of chemistry.

La Revue canadienne de chimie est affiliée à la Société canadienne de chimie et publie des articles dans tous les domaines de la chemie.

2001 Lemieux Award Lecture

Organic chemistry and hemoglobin: Benefits from controlled alteration

Ronald Kluger

Abstract: Hemoglobin carries oxygen in circulation within red cells but does not function outside the cells because it fails not only to release oxygen but also dissociates into dimers that make up the tetrameric protein. Bifunctional anionic acylating agents that contain a structurally rigid bridge introduce cross-links that stabilize hemoglobin and alter its oxygen affinity so that it could be used to carry oxygen outside cells. Nitric oxide binds to hemoglobin and in circulation this causes undesirable increases in blood pressure. It had been reported that higher weight collections of hemoglobin do not cause vasoconstriction. Reagents with two pairs of reaction sites joined by a rigid link connect and cross-link two hemoglobins. The resulting bis-tetramers lack the cooperativity of the native protein and bind oxygen too tightly to be useful; occupation by oxygen blocks the sites from nitric oxide. Nitric oxide may be delivered from thionitrosyl groups, which occur in hemoglobin in the red cell. Cross-linked hemoglobin can be specifically nitrosylated. These species can then serve as circulating sources of nitric oxide resulting from an internal electron transfer.

Key words: proteins, hemoglobin, cross-link, red cells, cooperativity, connecting.

Résumé : Dans la circulation sanguine, l'hémoglobine transporte l'oxygène à l'intérieur des cellules rouges, mais à l'extérieur elle ne fonctionne pas parce qu'elle n'est pas en mesure de libérer l'oxygène et, de plus, elle se dissocie en dimères qui forment la protéine tétramère. Les agents acylants anioniques bifonctionnels qui contiennent un pont structuralement rigide permettent d'introduire des liens de réticulation qui stabilisent l'hémoglobine et qui altèrent son affinité pour l'oxygène de façon à la rendre utilisable pour le transport d'oxygène à l'extérieur des cellules. L'oxyde nitrique se lie à l'hémoglobine et dans la circulation ce qui provoque des augmentations indésirables de la pression sanguine. Il a été rapporté que des collections d'hémoglobines de masses moléculaires plus élevées ne provoquent pas de vasoconstriction. Des réactifs avec deux paires de sites réactionnels liés par une jonction rigide permettent de raccorder et de réticuler deux hémoglobines. Les bis-tétramères qui en résultent ne donnent pas lieu à la coopération qui existe dans la protéine naturelle et ils se lient trop fortement à l'oxygène pour être utiles, mais ils ne peuvent donc pas se lier à l'oxyde nitrique. Une extension des raccordements pourrait permettre de résoudre ces problèmes. L'oxyde nitrique peut être obtenu à partir de groupes thionitrosyles que l'on retrouve dans l'hémoglobine des cellules rouges. Il est possible d'effectuer une nitrosilylation spécifique de l'hémoglobine réticulée. Ces espèces servent de sources circulantes d'oxyde nitrique et elles résultent d'un transfert d'électron interne.

Mots clés : protéines, hémoglobine, réticulation, cellules rouges, possibilité de coopération, raccordement.

[Traduit par la Rédaction]

Introduction

Hemoglobin is a protein that is specifically adapted for carrying oxygen in circulation within red blood cells. This enables oxygen-consuming organisms to overcome the low solubility of oxygen in water. Hemoglobin is contained in high concentrations in the red cells where it is protected from destructive oxygen-derived reactive species by detoxifying enzymes. The hemoglobin molecule is a very large tetramer (64 kDa), consisting of two identical α–β heterodimers (1). Each subunit contains a ferrous heme that reversibly binds one equivalent of oxygen. If hemoglobin escapes from the red cell, it ceases to be functional (effectors in the red blood cell lower the affinity of hemoglobin for oxygen) (2). Hemoglobin can also dissociate into dimers, which are excreted through the kidney (3, 4).

Since hemoglobin is a specific chemical entity, it is amenable to alteration through organic chemistry (5). Can hemoglobin be chemically altered so that it can effectively deliver oxygen and remain in circulation outside the red cell? While many chemical approaches have been applied to this prob-

Received 7 September 2001. Published on the NRC Research Press Web site at http://canjchem.nrc.ca on 22 March 2002.

R. Kluger. Davenport Building, Department of Chemistry, University of Toronto, Toronto, ON M5S 3H6, Canada. (e-mail: rkluger@chem.utoronto.ca).

 DOI: 10.1139/V01-200 © 2002 NRC Canada

lem (6), this article will focus on those most closely associated with my research.

Designing cross-linkers

Based on studies of chemical modification of hemoglobin, my research group developed reagents that covalently join the subunits in different dimers while reducing the oxygen affinity to match what we believed would be that of an ideal oxygen carrier (7). Acyl methyl phosphates are water-stable anionic acylating reagents, which convert amino groups to amides (7). They selectively react with amino groups of proteins that are in cationic environments of the proteins. In one homologous set of products, the reaction involves an amino group in each of the two β subunits of the protein: the α-amino group of the N-terminal valine of one β subunit and the ε-amino group of Lys-82. These form cross-links that prevent dissociation of the tetramers into dimers (the dimers do not spontaneously dissociate into monomers, see Scheme 1).

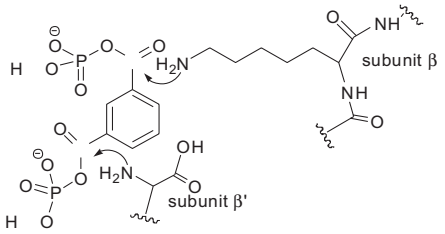

These specifically cross-linked tetramers are stable. They acquire and release oxygen readily and are too large to pass through the kidney in circulation (8). A critical feature of the properties of the altered hemoglobins is that they bind oxygen cooperatively (9) (the successive binding of oxygen to each subunit facilitates binding to another). We introduced cross-links between the β subunits of human hemoglobin with spans of predictable dimensions based on their structures containing unsaturated and aromatic acyl bridge components (9). Examples of these linkages are shown below.

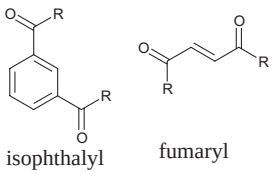
isophthalyl

fumaryl

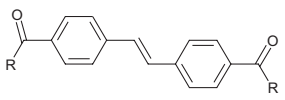
stilbenedicarbonyl

We were able to make a diverse collection of cross-linked hemoglobin tetramers and correlate their properties to their structures. The altered proteins had oxygen affinities that correlated (inversely) with the length of the cross-link. We were able to show that this arose because the cross-link limited the relative relaxation motions of the protein subunit dimers that occur when oxygen is bound (10). Preliminary in vivo testing revealed that the compounds deliver oxygen efficiently in place of red cells (8).

Cross-linked hemoglobin in circulation

Soon after cross-linked hemoglobins became available, commercial exploitation of some of the materials as red cell substitutes in transfusions began. A number of cross-linked hemoglobins of varying structure began their evaluation in biopharmaceutical and academic laboratories, with a few representative citations given here (11–22). Unfortunately, it was widely noted that unlike red cells, cross-linked hemoglobins in general caused a significant increase in blood pressure of the subject (23–26). This appeared to be the most significant drawback to the use of cross-linked hemoglobin as a red cell substitute. Blood pressure is at least partially controlled by levels of nitric oxide along the inner membranes (endothelia) of blood vessels (27). Nitric oxide signals endothelia to induce contraction of the smooth muscle that surrounds the vessel (28). Since the hemes of native hemoglobin bind nitric oxide more strongly than they do oxygen (29, 30), hemoglobin outside the red cell could cause an increase in blood pressure by binding nitric oxide in place of oxygen at vacant ligation sites (31, 32). If this is the case, then the red cell must be able to exclude or replace nitric oxide.

The effects of specific cross-links within hemoglobin, binding of nitric oxide, and induction of hypertension has previously not been explored, which might have been seen as critical information for rational development of a clinical product. Abdul Alayash, head of the United States Food and Drug Administration section that deals with these products is quoted in TheStreet.com (33):

> In general, attempts over the past 50 years to develop viable blood substitutes have failed because the products have never proven to be as safe as blood. One of the biggest problems: Blood substitutes seem to cause a patient's blood pressure to rise suddenly as capillaries that carry oxygen to various parts of the body constrict. Kidneys are especially susceptible to this so-called vasoconstriction, which starves the organ of oxygen and can lead to failure.
>
> This is a major issue and an obvious concern because we know so little about how these products work. We are going to look extra hard at these products because of their safety profile. We're continuously finding surprises after surprises and discovering new issues.

There is little information available that can be used to correlate specific chemical properties to the unwanted effects. The impression from reports of clinical trials from commercial sources is that cross-linked hemoglobin tetramers in general cause hypertension (34). In cases where nonspecific reagents are used to cross-link hemoglobin, reactions between tetramers occur, creating species with masses beyond 64 kDa. These are multimers of tetramers and are common in materials being developed commercially (35). Some of these are implied to have reduced hypertensive properties.

An important physiological study by Winslow et al. (34) showed that the situation is more complex. They found that some cross-linked hemoglobins (and interconnected mix-

© 2002 NRC Canada

tures) induce more hypertension than others. Some cause a persistent effect, while the effect is transient from others. However, the cross-linked species in those studies included many where the chemical modifications were highly heterogeneous and structurally uncharacterized. The similarity of the binding of the NO and O_2 molecules to hemoglobin suggests that oxygen affinity and nitric oxide affinity would be related to each other in modified hemoglobins. Winslow noted, however, that some examples, which contained hemoglobins connected to one another, as well as internal cross-links, appeared to have a lesser hypertensive effect than the specifically cross-linked tetramers that he studied. Can connecting two hemoglobin tetramers affect the inherent hypertensive properties of the molecule? A trivial source for such a change might be that such a species binds oxygen so tightly that NO is not acquired, or it binds oxygen so weakly, that NO is also not held.

We had already developed a set of cross-linked hemoglobins in which oxygen affinity varies with the length of the cross-link (9). All of these maintain cooperative oxygen binding with a Hill coefficient nearly equal to that of native hemoglobin. So while they were candidates as oxygen carriers, they were also likely to be hypertensive. With these materials, Baines et al. (8) began studies that examine the relationship between vasoactivity and oxygen affinity.

Synthesizing bis-tetramers

An intriguing question is thus raised by reports that administering cross-linked hemoglobins that are also connected to one another minimizes hypertensive effects (35, 36). No individually characterized species or specific structures were available. All such materials were produced with nonspecific reagents and were used in mixtures after fractionation to remove low and high molecular weight species. There was no reagent known that could not only cross-link proteins with site selectivity but also create a link with a second protein, which it also cross-links. Creating such a reagent is a novel chemical challenge with potential medicinal significance. We considered various strategies that might create the desired entity. We decided that a single reagent with at least four reaction sites would be the most efficient route to connect and cross-link two tetramers. Since we had found that isophthaloyl reagents were efficient cross-linking reagents, we sought the general structure shown below.

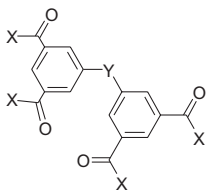

Our first attempt used 3,5-dibromosalicylates as leaving groups (X) and triethylene glycol as a linker (Y) (37). The leaving groups are anionic, although the charge is remote from the site of reaction. The use of modified salicylates was pioneered by Klotz and co-workers (38). My research group made such derivatives for a different purpose (39) and they became popular in the laboratory as skills improved for preparing this class of molecule.

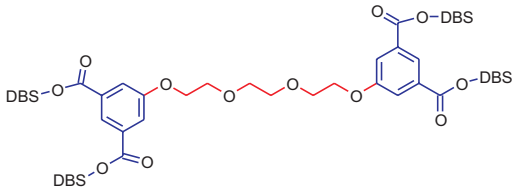

This reagent, however, reacts primarily within one tetramer, probably because it folds onto itself as it reacts (37).

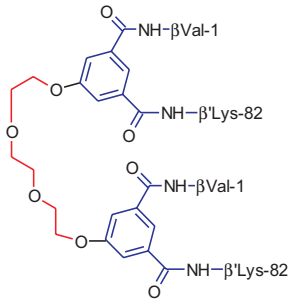

We, therefore, needed a reagent with the same ends but with a different middle, one that keeps the ends apart. A simple synthetic solution for the core of the reagent is

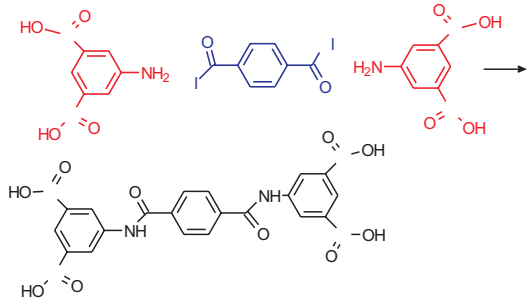

and the resulting tetrakis(3,5-dibromosalicylate) is shown below.

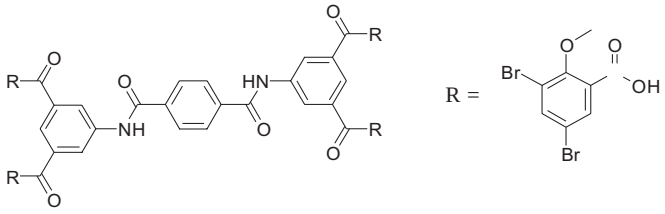

Combining the reagent with hemoglobin gave material that had a molecular weight of about 128 kDa (by size exclusion chromatography based on standards from hemoglobin oligomers) (40). Polyacrylamide gel electrophoresis under nondenaturing conditions also gives the major peak at the same retention time as a 128 kDa standard. SDS capillary electrophoretic analysis (denaturing conditions that separate all subunits) shows that 50% of the material corresponds to a weight of 15 kDa (which would be the unmodified α subunits) and about 33% corresponds to 64 kDa

© 2002 NRC Canada

(which would be four linked β subunits). Peptide mapping revealed that the cross-links occur at β-Lys 82. A schematic structure of the proposed cross-linked bis-tetramer is thus:

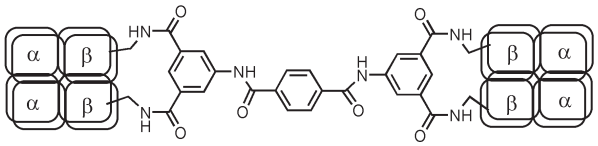

This material has a very high affinity for oxygen (so high that it probably would not dissociate significantly in circulation), and furthermore, the binding of oxygen is not cooperative (n_{50} = 1.2). Therefore, this material probably would not be able to pick up NO since oxygen occupies all sites. This qualifies as the first structurally defined cross-linked bis-tetramer. However, since its binding of oxygen is not cooperative, we made a major change to the environments of both tetramers by placing them in close proximity of each other. Because the tetramer does not release oxygen readily, it would not function well as a red cell substitute. Its low cooperativity would make it even more difficult for oxygen to be released in circulation. One conclusion we reached is that joining hemoglobins can produce a material that may not be vasoconstrictive because it has little capacity for binding nitric oxide once it is oxygenated.

Can the lack of cooperativity and high oxygen affinity in a bis-tetramer be overcome with structural alterations? At the extreme limit, if the link were very long, we would essentially have two independent cross-linked tetramers. Such a product would probably have no functional advantage over the individual cross-linked species. As a result, we next designed reagents with longer connecting spans. Since these have increased hydrocarbon content between reactive ends, lack of solubility in water became a problem with the dibromosalicylates. Fortunately, methyl acyl phosphates are superior activating groups for this purpose and they are readily prepared.

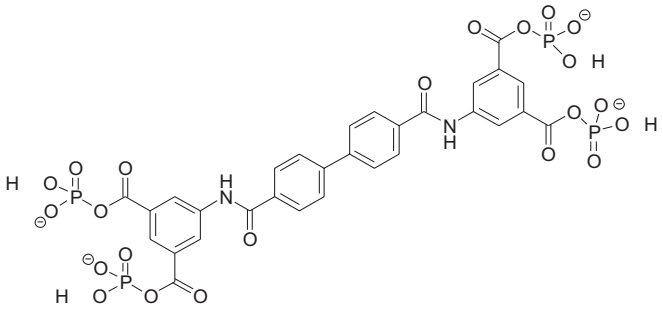

The resulting cross-linked bis-tetrameric product from its reaction with hemoglobin is structurally similar to the product from the smaller reagent in the previous section.

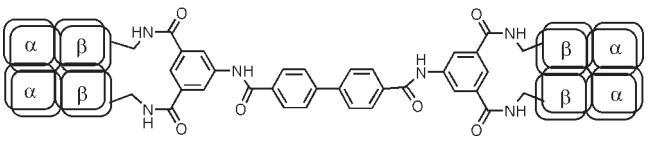

The oxygen-binding properties of this tetramer also showed a very high oxygen affinity and a low degree of cooperativity (n_{50} = 1.2). Based on these results we have created additional reagents that increase the span and also decrease the amount of hydrocarbon in the linker. Preliminary results indicate that these may bind oxygen cooperatively. It appears that these compounds may serve as a basis for investigating the basis of cooperativity in hemoglobin in a general way.

Scheme 1.

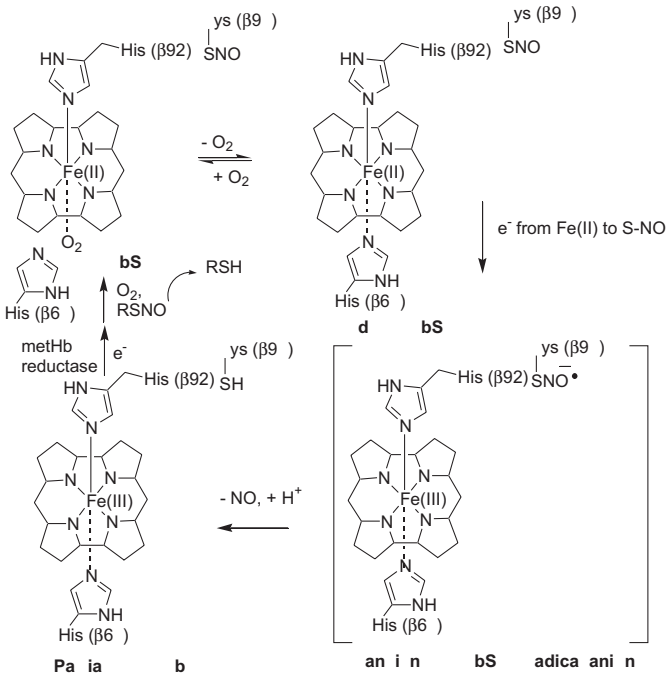

Nitric oxide from Cys-NO

To date, there is no obvious structural solution to avoid binding endogenous NO to modified hemoglobins that are effective as oxygen carriers. As an alternative approach, therefore, we considered ways to have a modified cross-linked hemoglobin serve as a source of NO. Gow and Stamler (30) reported that small amounts of hemoglobin within the red cell have the cysteine thiol at position β-93 in a nitrosylated form (RS-NO), which can transfer the NO group. There is some controversy about the physiological significance of this material, since the functional group does not spontaneously release nitric oxide (but it will transfer the nitrosyl group to a Lewis base acceptor). We used nitrosylating reagents to convert a specifically cross-linked hemoglobin into a species where both β-Cys-93 thiol groups are nitrosylated (41).

In measuring the oxygen affinity of this species, we shuttled in through cycles of oxygenation and deoxygenation while recording its spectrum. We noted that upon deoxygenation, NO was released as the ferrous heme oxidized to the ferric state (the fully Fe(III) material, methemoglobin, has a clearly distinct spectrum). We found that the spectral change was such that two of the hemes were converted to the Fe(III) state while two remained in the Fe(II) state. The two β subunits were nitrosylated so we concluded that an

© 2002 NRC Canada

electron transfer reaction occurred. We proposed the following cycle to account for our observations (Scheme 1) (42).

In the red cell, such a process can occur but the resulting metHb is converted to native hemoglobin by an endogenous reductase. Structural models indicate that the β-Cys93 sulfur atom is 12.9 Å from the closest ferrous heme in deoxyHb, permitting an internal electron transfer (42). Furthermore, coordination of oxygen, an electron withdrawing ligand, increases the heme Fe^{III}/Fe^{II} potential, making it a poorer electron donor. Thus, loss of oxygen would permit the internal electron transfer to occur.

The work described shows that the limits of organic chemistry are not exceeded when the target has a molecular weight of over 128 kDa. Of course, by choosing two equivalents of one starting material with a molecular weight of 64 kDa, it does not take many steps to produce novel materials of interest. Our research has led us to the fascinating problem of determining the sources of cooperativity that are lost in coupled hemoglobins. The next steps should be even more interesting.

Acknowledgments

I thank the Canadian Society for Chemistry for selecting me to give the Lemieux Award Lecture, and I am honored to be associated with the memory of Ray Lemieux and his science. My research has been supported by the Natural Sciences and Engineering Research Council of Canada (NSERC). The most recent work reported here has been in active collaboration with my co-workers, in particular John Pezacki and Noam Ship. I thank all my co-workers in this project and especially Professor Richard T. Jones who generously shared his knowledge and joy in the subject of altered hemoglobins.

References

1. R.E. Dickerson and I. Geis. Hemoglobin: Structure, function, evolution, and pathology. The Benjamin/Cummings Publishing Co., Menlo Park, CA. 1983.
2. R. Benesch and R.E. Benesch. Biochem. Biophys. Res. Commun. **26**, 162 (1967).
3. L.R. Manning, W.T. Jenkins, J.R. Hess, K. Vandegriff, R.M. Winslow, and J.M. Manning. Protein Sci. **5**, 775 (1996).
4. W.K. Bleeker, J. Van Der Plas, R.I.J. Feitsma, J. Agterberg, G. Rigter, E.K.J. Pauwels, and J.C. Bakker. Nucl. Med. Biol. **16**, 365 (1989).
5. R. Kluger. Can. J. Chem. **72**, 2193 (1994).
6. R.M. Winslow. Hemoglobin-based red cell substitutes. Johns Hopkins University Press, Baltimore. 1995.
7. R. Kluger. Synlett, 1708 (2000).
8. A.D. Baines, G. Adamson, P. Wojciechowski, D. Pliura, P. Ho, and R. Kluger. Am. J. Physiol. **274**, F744 (1998).
9. R.T. Jones, C.G. Head, T.S. Fujita, D.T. Shih, J. Wodzinska, and R. Kluger. Biochemistry, **32**, 215 (1993).
10. M.A. Schumacher, M.M. Dixon, R. Kluger, R.T. Jones, and R.G. Brennan. Nature (London), **375**, 84 (1995).
11. D. Su, R.I. Roth, M. Yoshida, and J. Levin. Infect. Immun. **65**, 1258 (1997).
12. A. Barve, A.P. Sen, P.R. Saxena, and A. Gulati. Artif. Cells Blood Sub. **25**, 75 (1997).
13. J.A. Langermans, M.E. Van Vuren-Van Der Hulst, and W.K. Bleeker. J. Lab. Clin. Med. **127**, 428 (1996).
14. W.K. Bleeker, L.M. Zappeij, P.J. Den Boer, J.A. Agterberg, G.M. Rigter, and J.C. Bakker. Artif. Cells Blood Sub. **23**, 461 (1995).
15. P.E. Keipert, C.L. Gomez, A. Gonzales, V.W. Macdonald, and R.M. Winslow. Biomat. Artif. Cells Im. **20**, 737 (1992).
16. T.M. Chang. Transfus. Med. Rev. **3**, 213 (1989).
17. P.E. Keipert and T.M. Chang. Vox Sang. **53**, 7 (1987).
18. E. Bucci, A. Razynska, H. Kwansa, B. Matheson-Urbaitis, M. O'hearne, J.A. Ulatowski, and R.C. Koehler. J. Lab. Clin. Med. **128**, 146 (1996).
19. Z. Abassi, S. Kotob, F. Pieruzzi, M. Abouassali, H.R. Keiser, J.C. Fratantoni, and A.I. Alayash. J. Lab. Clin. Med. **129**, 603 (1997).
20. R. Bolin and F. Devenuto. Prog. Clin. Biol. Res. **122**, 1 (1983).
21. J.P. Savitsky, J. Doczi, J. Black, and J.D. Arnold. Clin Pharmacol Ther. **23**, 73 (1978).
22. R.M. Winslow. Br. J. Haematol. **111**, 387 (2000).
23. R.J. Rohlfs, E. Bruner, A. Chiu, A. Gonzales, M.L. Gonzales, D. Magde, M.D. Magde, Jr., K.D. Vandegriff, and R.M. Winslow. J. Biol. Chem. **273**, 12128 (1998).
24. M. Jing, F.G. Panico, J.L. Panico, M.A. Ledvina, S. Bina, and S.M. Muldoon. Artif. Cells Blood Sub. **24**, 621 (1996).
25. J. Simoni, G. Simoni, G. Newman, and M. Feola. Asaio J. **42**, M773 (1996).
26. R.M. Winslow. Nat. Biotechnol. **16**, 621 (1998).
27. R.F. Furchgott, M.H. Carvalho, M.T. Khan, and K. Matsunaga. Blood Vessels, **24**, 145 (1987).
28. L.J. Ignarro. Faseb J. **3**, 31 (1989).
29. R.F. Furchgott. Circulation, **87**, V3, Suppl.(1993).
30. A.J. Gow and J.S. Stamler. Nature (London), **391**, 169 (1998).
31. T.F. Zuck and J.G. Riess. Crit. Rev. Clin. Lab. Sci. **31**, 295 (1994).
32. R. Motterlini, K.D. Vandegriff, and R.M. Winslow. Transfus. Med. Rev. **10**, 77 (1996).
33. A. Feuerstein. A year and counting, and hemopure's safety still unknown. *In* TheStreet. com. (2001).
34. R.M. Winslow, A. Gonzales, M.L. Gonzales, M. Magde, M. Mccarthy, R.J. Rohlfs, and K.D. Vandegriff. J. Appl. Physiol. **85**, 993 (1998).
35. S.A. Gould, E.E. Moore, F.A. Moore, J.B. Haenel, J.M. Burch, H. Sehgal, L. Sehgal, R. Dewoskin, and G.S. Moss. J. Trauma, **43**, 325 (1997).
36. J. Simoni, G. Simoni, A. Hartsell, and M. Feola. Asaio J. **43**, M714 (1997).
37. R. Kluger, K. Paal, and J.G. Adamson. Can. J. Chem. **77**, 271 (1999).
38. J.A. Walder, R.H. Zaugg, R.Y. Walder, J.M. Steele, and I.M. Klotz. Biochemistry, **18**, 4265 (1979).
39. R. Kluger, Y. Song, J. Wodzinska, C. Head, T.S. Fujita, and R.T. Jones. J. Am. Chem. Soc. **114**, 9275 (1992).
40. R. Kluger, J. Lock-O'brien, and A. Teytelboym. J. Am. Chem. Soc. **121**, 6780 (1999).
41. J.P. Pezacki, A. Pelling, and R. Kluger. J. Am. Chem. Soc. **122**, 10734 (2000).
42. J.P. Pezacki, N.J. Ship, and R. Kluger. J. Am. Chem. Soc. **123**, 4615 (2001).

© 2002 NRC Canada

Electron momentum spectroscopy of the frontier electrons of DABCO does not support an sp^3 hybrid lone-pair description

Saul Wolfe, Zheng Shi, C.E. Brion, James Rolke, Yenyou Zheng, Glyn Cooper, Delano P. Chong, and C.Y. Hu

Abstract: The highest occupied molecular orbital (HOMO) and next-highest occupied molecular orbital (NHOMO) valence orbital electron density distributions of 1,4-diazabicyclo[2.2.2]octane (DABCO) have been investigated by electron momentum spectroscopy, a technique that probes the orbital-like nature of valence (frontier) electron transfer out of a molecule. The experimental results are compared to a range of 6-311++G** calculations to assess the relative merits of three different orbital models that have commonly been used in chemistry. The delocalized (correlated) canonical Kohn–Sham orbitals calculated using the B3LYP or B3PW91 functionals and density functional theory provide near quantitative agreement with the observed valence electron momentum density distributions, and the delocalized canonical molecular orbitals of Hartree–Fock (independent particle) theory are in semiquantitative agreement. In contrast, Pauling's widely used and taught valence bond (hybridization) model, which is equivalent to a localized molecular orbital description, does not correspond at all to the experimental measurements. It follows that, for considerations of electron transfer, the "lone pairs" of DABCO are not localized or hybridized, but rather exist as nondegenerate orbitals that are delocalized differently over the molecular framework. The existence of two different experimental valence orbital electron densities of DABCO provides direct confirmation of the frontier orbital HOMO–NHOMO energy splitting and reordering predicted many years ago by Hoffmann et al. using extended Hückel theory, and interpreted in terms of "through bond" and "through space" interactions.

Key words: orbitals, lone pairs, orbital interaction, hybridization.

Résumé : Faisant appel à la spectroscopie des moments électroniques, une technique qui étudie la nature de type orbitalaire de la valence (frontière) du transfert d'électron à partir d'une molécule, on a déterminé les distributions des orbitales moléculaires haute occupée (« HOMO ») et pratiquement haute occupée (« NHOMO ») de la densité des électrons orbitalaires de valence du 1,4-diazabicyclo[2.2.2]octane (DABCO). On a comparé les résultats expérimentaux à une série de calculs au niveau 6-311++G** afin d'évaluer les mérites relatifs de trois modèles orbitalaires différents qui ont été couramment utilisés en chimie. Les orbitales canoniques délocalisées (avec corrélation) de Kohn–Sham, calculées à l'aide de fonctions B3LYP ou B3PW91 et la théorie de la densité fonctionnelle, correspondent pratiquement de façon quantitative avec les distributions observées pour la densité du moment de l'électron de valence; par ailleurs, les orbitales moléculaires canoniques délocalisées de Hartree–Fock (particule indépendante) présentent un accord semi-quantitatif. Par opposition, le modèle de la liaison de valence (hybridation) de Pauling qui est couramment utilisé et enseigné et qui est équivalent à une description d'orbitales moléculaires localisées ne présente aucune corrélation avec les mesures expérimentales. Il en découle que, pour des considérations de transferts d'électrons, les « paires libres » du DABCO ne sont pas localisées ou hybridées, mais qu'elles existent plutôt sous la forme d'orbitales non dégénérées qui sont délocalisées de façon différente sur le squelette moléculaire. L'existence, dans le cas du DABCO, de deux ensembles expérimentaux différents pour les densités des orbitales électroniques de valence fournit une confirmation directe du dédoublement d'énergie HOMO–NHOMO de l'orbitale frontière et de la réorganisation qui a été prédite il y a plusieurs années par Hoffmann et al. à l'aide de la théorie élargie de Hückel et interprété en fonction d'interactions « par les liaisons » et « à travers l'espace ».

Mots clés : orbitales, paires libres, interaction d'orbitales, hybridation.

[Traduit par la Rédaction]

Received 12 September 2001. Published on the NRC Research Press Web site at http://canjchem.nrc.ca on 20 February 2002.

S. Wolfe[1] and Z. Shi. Department of Chemistry, Simon Fraser University, Burnaby, BC V5A 1S6, Canada.
C.E. Brion,[1] J. Rolke, Y. Zheng, G. Cooper, D.P. Chong and C.Y. Hu.[2] Department of Chemistry, University of British Columbia, Vancouver, BC V6T 1Z1, Canada.

[1]Corresponding authors (e-mail: swolfe@sfu.ca and brion@chem.ubc.ca).
[2]Present address: Department of Chemistry, National Tsinghua University, Taiwan.

 DOI: 10.1139/V01-201 © 2002 NRC Canada

Introduction and background

In the commonly used hybridized valence bond (VB) model of Pauling (1), the electron pairs on the nitrogen atoms of 1,4-diazabicyclo[2.2.2]octane (DABCO) are represented as equivalent, degenerate, localized "lone pairs," as shown in Fig. 1. This corresponds to a localized molecular orbital (LMO) treatment in which the degenerate lone-pair orbitals would exhibit a single-valence ionization energy (i.e., one peak in the valence shell photoelectron spectrum). However, it has been known for many years (2, 3) that extended Hückel (i.e., simple delocalized molecular orbital) theory predicts the two highest occupied (frontier) valence orbitals of DABCO to be nondegenerate with a HOMO/NHOMO[3] splitting of 1.63 eV. Hoffmann et al. (2, 3) interpreted this result in terms of "through-space" and "through-bond" interactions, by means of which the nonbonding electrons on the nitrogen atoms communicate with each other. A first-order through-space treatment (2, 3) would predict that the antisymmetric (AS) antibonding combination of 2*p* functions on the nitrogen atoms (in a simple LCAO-MO description) will comprise the HOMO, while the symmetric (S) bonding combination will comprise the NHOMO. However, when the through-bond interaction is turned on, the frontier orbital energy ordering is predicted to be reversed, i.e., the HOMO is bonding (S), and the NHOMO is antibonding (AS). Experimental studies of the binding energy spectrum of DABCO by Heilbronner and coworkers (4) using high-resolution-photoelectron spectroscopy (PES) later confirmed that the HOMO and the NHOMO of DABCO are indeed nondegenerate, with an observed vertical ionization energy splitting of 2.13 eV.

While the ordering of the frontier orbitals of DABCO could not unequivocally be established from the PES measurements (4), a subsequent detailed vibrational analysis of the two PES bands and extended Hückel calculations of overlap populations by Heilbronner and Muszkat (5) supported the orbital ordering predicted by Hoffmann et al. (2, 3).

In the years since Hoffmann's theoretical examination of DABCO, considerable advances have been made in computational chemistry. In particular, the use of Kohn–Sham density functional theory (DFT) has made highly accurate calculations, including the treatment of electron correlation, possible for larger molecules (6). Concurrently, a new experimental technique, electron momentum spectroscopy (EMS) (7–13), has been found to provide effective imaging of the electron momentum density distributions ($|\psi_j(\mathbf{p})|^2$) of individual valence orbitals (j) of target molecules. A recent detailed consideration of what EMS measures, together with related computational studies, has demonstrated (12) that there is an orbital-like nature to electron transfer as it applies to ionization processes and, by extension, to chemical reactivity. In particular, valence electrons are found to be donated (transferred) in a manner that is very well described by the appropriate Dyson orbital density which, in turn, is well approximated by the delocalized Kohn–Sham or canonical molecular orbital density of the initial state molecule.

EMS is a Fourier transform coincidence electron impact spectroscopy that supplies both binding energy and electron momentum information (7, 12, 13). It should be noted that the momentum space orbital wavefunction ($\psi_j(\mathbf{p})$) is the Fourier transform of the much more familiar position space orbital wavefunction $\psi_j(\mathbf{r})$. Using the plane wave impulse approximation, where $\int d\Omega$ implies the spherical average for the randomly oriented gas-phase target molecules, the observed EMS cross section (σ_{EMS}) (i.e., the measured signal) can be well modeled (7, 8, 13, 14) by an expression of the form

$$[1] \qquad \sigma_{EMS} \propto \int d\Omega |\psi_j(p)|^2$$

Thus, EMS provides momentum space "orbital imaging," corresponding to electron donation from an initial state orbital (12). Consequently, the EMS technique can yield definitive information regarding the nature of the valence electrons transferred out of a target molecule. In particular, it should be possible to determine the nature of the electron density distribution and the symmetric and (or) antisymmetric nature of the frontier orbitals of DABCO. Since the measured signal is directly related to the momentum space orbital electron density distribution (eq. [1]), the experimental results for valence electron transfer out of DABCO should provide a straightforward test of the different orbital models commonly used in chemistry. In particular, EMS can be used to evaluate basis sets (wavefunctions) and different quantum mechanical methods such as Hartree–Fock (HF) theory in either the localized molecular orbital model (LMO), corresponding to simple hybridized VB theory (1) or the delocalized canonical molecular orbital (CMO) models (15, 16), as well as the delocalized canonical Kohn–Sham orbital (KSO) model of density functional theory (6, 17).

It should be noted that the KSOs of DFT intrinsically include electron correlation, but the CMOs and LMOs of HF theory are based on the independent particle (noncorrelated) model. Accurate post-Hartree–Fock calculations, such as configuration interaction (CI) methods, which include electron correlation, are restricted to species containing at most two heavy atoms (8, 12, 18, 19). In addition, CI calculations are much more computationally intensive than DFT treatments, so that accurate CI calculations (or other many-body treatments) are not currently feasible for a molecule as large as DABCO.

Although the ability to probe orbital densities or, indeed, even the notion of orbitals as experimental observables has often been questioned (see, e.g., refs. 20–22), in 1977 Fukui (23) wrote:

> In the present status of experimental techniques, no one has been able to observe the orbital pattern experimentally. However, to date, no one can assert that this is totally impossible. If we could only experimentally obtain any knowledge of HOMO and LUMO patterns, chemistry would be profoundly affected. In that event the orbital pattern concept, which is at present of a somewhat unreal nature, will be provided with a certain empirical nature.

Similarly, while Kohn–Sham orbitals have often been described as fictitious mathematical concepts without any correspondence to reality (see, e.g., refs. 6, 14), in a recent commentary on DFT, Stowasser and Hoffmann (24) wrote:

[3] The HOMO is the highest occupied molecular orbital. The NHOMO is the next-highest occupied molecular orbital.

© 2002 NRC Canada

Fig. 1. Simple VB hybridized lone-pair representation of 1,4-diazabicyclo[2.2.2]octane (DABCO).

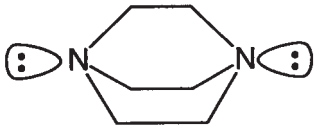

> …chemists know that orbitals are useful, but the physicists and chemists who use density functional theory so fruitfully have by and large shied away from attributing to Kohn–Sham orbitals the reality that (we think) they deserve.

Recent EMS measurements and computational investigations of electron transfer out of the frontier orbitals of methane (8, 12, 25, 26), ammonia (8, 12, 25, 27), water (8, 12, 19, 25), and methanol (9) have been found to be extremely informative for the evaluation of the different orbital models and the nature of the lone pairs in these molecules. This work has now been extended to a study of the orbital electron (momentum) density distributions and the nature of the lone pairs of DABCO.

Experimental and computational details

Binding energy spectra for the outer valence region of DABCO were obtained at a series of azimuthal (ϕ) angles using an energy-dispersive multichannel EMS spectrometer. The design and operational details of this instrument, as well as the data reduction procedures, have been described in some detail (28). The impact energy for these measurements was 1200 eV plus the binding energy. The binding energy spectra for DABCO were deconvoluted using peak positions and widths from the high resolution PES data (4, 5), taking into account the EMS coincidence energy resolution of 1.4 eV full width at half maximum (fwhm). This procedure minimizes any cross-contributions from adjacent peaks. The resulting peak areas for the HOMO and NHOMO of DABCO were each plotted as a function of momentum (related to the ϕ angle; see refs. 7, 13, 28) to give the orbital momentum distributions on a common intensity scale. The DABCO sample (purity > 99%) was obtained from Aldrich and used without further purification other than freeze–thaw cycles to remove dissolved air.

A series of HF and DFT calculations was carried out for DABCO using Gaussian 98 (29) and the 6-311++G** basis set, which is sufficiently saturated and contains an adequate number of diffuse functions to provide good modeling at low momenta (large *r*). The B3PW91 (30, 31) and B3LYP (30) gradient corrected functionals were used in the DFT calculations. The theoretical results refer to optimized geometries. The resulting HF CMO and DFT KSO position space wavefunctions of HF and DFT theory, respectively, were transformed into momentum space using the MOMAP software package (32).

The resulting theoretical momentum distributions were then resolution folded using the experimental angular (momentum) resolution parameters and the RESFOLD (32, 33) program. These procedures allow a direct comparison between a theoretical momentum profile (TMP) and an experimental momentum profile (XMP) for each orbital. Localized molecular orbitals (LMOs) were computed by a repartitioning of the total HF wavefunction, using the Boys localization method (34) implemented in MONSTERGAUSS (35).

Fig. 2. Experimental and theoretical electron momentum density distributions for the HOMO and NHOMO orbitals of DABCO. All are at the 6-311++G** level. The dashed curve is the LMO. See text and legend on the figure for details.

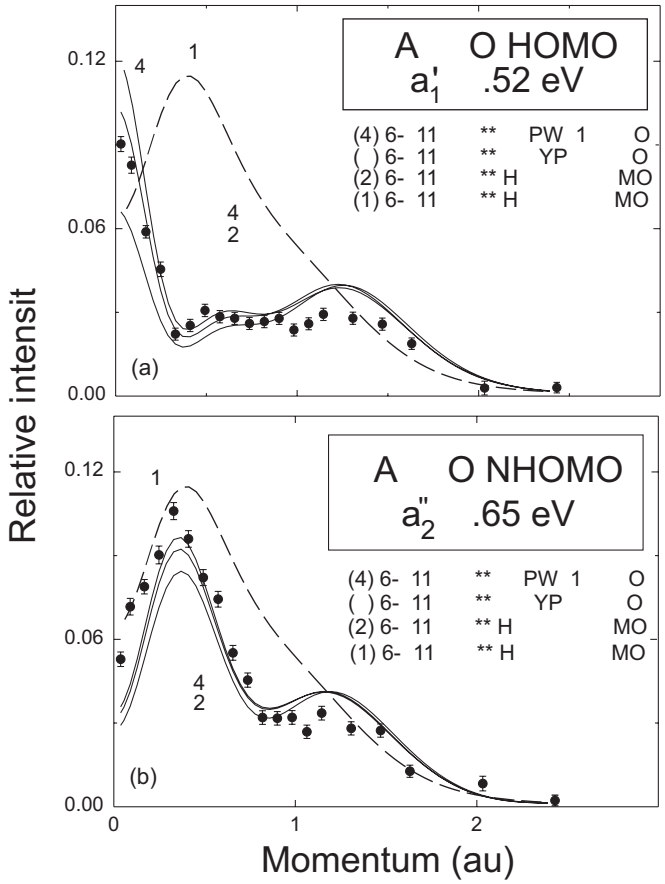

Results and discussion

The EMS binding energy spectrum confirms the earlier PES observations (4, 5) that there are two outer valence IPs (7.52 and 9.6 eV, respectively), and not one corresponding to the presence of degenerate nitrogen lone pairs in DABCO. Figure 2 shows the experimental and calculated electron momentum distributions of the electrons transferred out of the two highest occupied orbitals of DABCO. From a comparison of the measured and calculated momentum distributions at these two binding energies, it is immediately apparent that the degenerate 6-311++G** LMO, i.e., the hybrid lone pair (Fig. 2, curve 1) is *incompatible* with the experimental observations at 7.52 and 9.65 eV. In contrast, the 6-311++G** HF delocalized CMO calculation provides a reasonably good semiquantitative description of the measured orbital momentum density distributions. It is noteworthy that significantly better quantitative agreement with the experimental results is provided by the delocalized KSO DFT models. The two DFT functionals give very similar results, with a marginally

© 2002 NRC Canada

Fig. 3. Different orbital models of the position space electron densities of the HOMO and NHOMO orbitals of DABCO. All calculations are at the 6-311++G** level. The B3LYP DFT method has been employed for the KSOs.

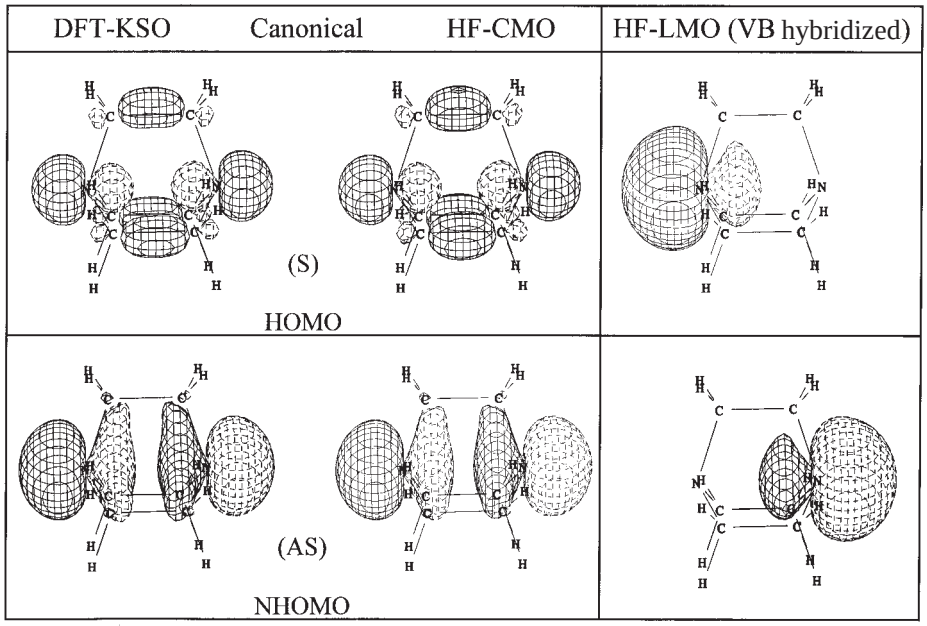

better overall description provided by B3LYP. With the DFT theory and experiment normalized on the HOMO, good agreement is obtained in both shape and intensity for the NHOMO of DABCO.

It is also evident from Fig. 2 that the experimental electron momentum density distribution for the HOMO is predominantly "*s*-type" in character (see, e.g., ref. 36 and Fig. 3 of ref. 37), corresponding to a symmetric (S) orbital, whereas the NHOMO is mainly of "*p*-type" character (see, e.g., ref. 36 and Fig. 4 of ref. 37), i.e., antisymmetric (AS). These experimental findings unequivocally confirm the orbital reordering predicted by Hoffmann et al. (2, 3) for DABCO using a through-space and through-bond rationalization.

The above conclusions regarding the nature of the frontier orbitals of DABCO are entirely consistent with the three-dimensional *position space* representations of the general topographical features of the wavefunction plots of the HOMO and NHOMO shown in Fig. 3, whose KSO (and CMO) plots correspond to the EMS experiments (Fig. 2). At the contour-envelope value shown in Fig. 3 (0.10, i.e., 99% enclosed), the KSO and CMO pictures are very similar, and the S and AS nature of the KSO and CMO HOMO and NHOMO, respectively, predicted by Hoffmann et al. (2, 3) are readily apparent. In contrast, the LMO (hybridized) pictures at the right of Fig. 3, which correspond to equivalent, degenerate, hybridized lone pairs localized on the nitrogens, which do not correspond to experiment, are very different in nature from the KSOs and CMOs.

Preliminary accounts of the present work on DABCO were reported earlier at conferences in Vancouver (38) and Japan (39), and in lectures by one of us (SW) in Japan, Mexico, Israel, and Canada. After our experimental and theoretical work was complete, and as this manuscript was being prepared, another EMS study of DABCO was reported by Takahashi et al. (40). This more limited study compares HOMO and NHOMO measurements for DABCO with several different basis set calculations up to the 6-311++G** level at the delocalized molecular orbital Hartree–Fock level only, with no consideration of Kohn–Sham or localized molecular orbitals. While the experimental results of ref. 40 are qualitatively similar to those reported here, the statistics are not as good, there are fewer data points, and the experimental momentum distributions show significant differences in both shape and intensity from those reported here. These differences probably result from the procedures used by Takahashi et al. (40) to determine the experimental momentum profiles. This was done (40) by setting the spectrometer at two different fixed values of the binding energies and measuring the intensities as a function of ϕ. This type of experimental procedure will almost certainly lead to erroneous cross-contributions from the NHOMO to the HOMO, and vice versa, because of the close energy spacing, and will cause the resulting HOMO and NHOMO intensities to be on different relative intensity scales. As a result, the orbital momentum distributions of ref. 40 will require separate height normalizations to theory. As explained above, these difficulties are avoided in the present work by recording the complete binding energy spectrum in the frontier orbital region at each ϕ angle, with deconvolution of the two peaks. The experimental approach used in the present work therefore minimizes any cross-contributions and also has the advantage of placing the HOMO and NHOMO momentum profiles on a common intensity scale. This permits a more stringent comparison with theory. Although Takahashi et al. (40) show good agreement with their experimental shapes at the 6-311++G** (delocalized) HF level, this finding is likely fortuitous for the reasons stated above (i.e., because of the separate height normalization for each orbital). In this respect their results are at variance with the present work

© 2002 NRC Canada

(Fig. 2) which shows significant quantitative disagreement at the HF level. In fact, reasonable quantitative agreement between theory and experiment is achieved only when electron correlation is included, as seen in the 6-311++G**/B3LYP and B3PW91 DFT calculations of Fig. 2.

In conclusion, the present work for DABCO, in addition to parallel studies of methane, ammonia, water, and methanol (9, 25, 38, 39) all show that (intrinsically correlated) delocalized canonical Kohn–Sham orbitals (KSOs) provide very good quantitative descriptions of the experimentally observed frontier-orbital electron-momentum density distributions. These findings lend strong support to the ideas of Stowasser and Hoffmann (24) regarding the "reality" of Kohn–Sham orbitals. Delocalized HF canonical molecular orbitals (CMOs) provide a good semiquantitative model in which the distribution and location of the valence orbital electron densities are qualitatively correct. In contrast, the still overwhelmingly popular localized (hybrid) VB orbital description *incorrectly distributes and incorrectly locates* the valence orbital electron densities. We believe that the present findings and conclusions regarding the ability of the delocalized KSO and CMO orbital models to describe electron transfer, and the failure of the hybrid orbital model, have profound implications because proper frontier orbital modeling is essential to the understanding of chemistry at the level of valence electron behaviour. These results are likely to be important in areas such as the teaching and practice of chemistry and accurate molecular modeling, as well as for informed input to computer-aided molecular design and reactivity studies where electron transfer is involved.

Acknowledgments

The authors thank the Operating, Equipment, and Collaborative Project Grant programmes of the Natural Sciences and Engineering Research Council of Canada (NSERC), and The Peter Wall Institute for Advanced Studies at UBC for financial support. We thank Pauline Brion for assistance in preparing this manuscript. We are indebted to Professor Imre Csizmadia of the University of Toronto for access to MONSTERGAUSS and its source code.

References

1. (*a*) L. Pauling. The nature of the chemical bond. Cornell University Press, New York. 1960; (*b*) L. Pauling. J. Am. Chem. Soc. **53**, 1367 (1931); (*c*) L. Pauling. J. Chem. Edu. **69**, 519 (1992).
2. R. Hoffmann, A. Imamura, and W.J. Hehre. J. Am. Chem. Soc. **90**, 1499 (1968).
3. R. Hoffmann. Acc. Chem. Res. **4**, 1 (1971).
4. P. Bischof, A. Hashmall, E. Heilbronner, and V. Hornung. Tetrahedron Lett. 4025 (1969).
5. E. Heilbronner and A. Muszkat. J. Am. Chem. Soc. **92**, 3818 (1970).
6. W. Kohn, A.D. Becke, and R.G. Parr. J. Phys. Chem. **100**, 12 974 (1996).
7. C.E. Brion. Int. J. Quantum Chem. **19**, 1397 (1986).
8. C.E. Brion. *In* The physics of electronic and atomic collisions. *Edited by* T. Anderson, B. Fastrap, F. Folkmann, H. Knudsen, and N. Andersen. American Institute of Physics Press, New York. 1993. p. 350, and refs. therein.
9. J. Rolke, Y. Zheng, C.E. Brion, Z Shi, and S. Wolfe. Chem. Phys. **244**, 1 (1999).
10. Y. Zheng, J.J. Neville, and C.E. Brion. Science (Washington, D.C.), **270**, 5237 (1995).
11. J.J. Neville, Y. Zheng, and C.E. Brion. J. Am. Chem. Soc. **118**, 10 533 (1996).
12. C.E. Brion, G. Cooper, Y. Zheng, I.V. Litvinyuk, and I.E. McCarthy. Chem. Phys. **270**, 13 (2001).
13. I.E. McCarthy and E. Weigold. Rep. Prog. Phys. **54**, 789 (1991).
14. P. Duffy, D.P. Chong, M.E. Casida, and D.R. Salahub. Phys. Rev. A: At. Mol. Opt. Phys. **50**, 4704 (1994).
15. R.S. Mulliken. Phys. Rev. **40**, 55 (1932).
16. R.S. Mulliken. Phys. Rev. **41**, 49 (1932).
17. W. Kohn and L.J. Sham. Phys. Rev. **140**, 1133 (1965).
18. D. Feller, C.M. Boyle, and E.R. Davidson. J. Chem. Phys. **86**, 3424 (1987).
19. A.O. Bawagan, C.E. Brion, E.R. Davidson, and D. Feller. Chem. Phys. **113**, 19 (1987).
20. J.F. Ogilvie. J. Chem. Ed. **67**, 280 (1990).
21. F. Pennotti, J. Gerratt, D.L. Cooper and M. Raimondi. J. Mol. Struct: THEOCHEM, **169**, 421 (1988).
22. S.S. Zumdahl. Chemical principles. 3rd ed. Houghton Mifflin Company, Boston. 1998. pp. 658–660.
23. K. Fukui. Int. J. Quantum Chem. **12**, Supp. 1, 277 (1977).
24. R. Stowasser and R. Hoffmann. J. Am. Chem. Soc. **121**, 3414 (1999).
25. S. Wolfe, C.E. Brion, G. Cooper, Y. Zheng, and Z. Shi. Submitted for publication.
26. S.A.C. Clark, T.J. Reddish, C.E. Brion, E.R. Davidson, and R. Frey. Chem. Phys. **143**, 1 (1990).
27. A.O. Bawagan, R. Muller-Fiedler, C.E. Brion, E.R. Davidson, and C. Boyle. Chem. Phys. **120**, 335 (1988).
28. Y. Zheng, J.J. Neville, C.E. Brion, Y. Wang, and E.R. Davidson. Chem. Phys. **188**, 109 (1994), and refs. therein.
29. M.J. Frisch, G.W. Trucks, H.B. Schlegel, G.E. Scuseria, M.A. Robb, J.R. Cheeseman, V.G. Zakrzewski, J.A. Montgomery, Jr., R.E. Stratmann, J.C. Burant, S. Dapprich, J.M. Millam, A.D. Daniels, K.N. Kudin, M.C. Strain, O. Farkas, J. Tomasi, V. Barone, M. Cossi, R. Cammi, B. Mennucci, C. Pomelli, C. Adamo, S. Clifford, J. Ochterski, G.A. Petersson, P.Y. Ayala, Q. Cui, K. Morokuma, D.K. Malick, A.D. Rabuck, K. Raghavachari, J.B. Foresman, J. Cioslowski, J.V. Ortiz, B.B. Stefanov, G. Liu, A. Liashenko, P. Piskorz, I. Komaromi, R. Gomperts, R.L. Martin, D.J. Fox, T. Keith, M.A. Al-Laham, C.Y. Peng, A. Nanayakkara, C. Gonzalez, M. Challacombe, P.M.W. Gill, B. Johnson, W. Chen, M.W. Wong, J.L. Andres, M. Head-Gordon, E.S. Replogle and J.A. Pople. Gaussian 98, Revision A.6. Gaussian, Inc. Pittsburgh, Pennsylvania. 1998.
30. P.J. Stephens, F. Devlin, C.F. Chabalowski, and M.J. Frisch. J. Phys. Chem. **98**, 11 623 (1994).
31. A.D. Becke. J. Chem. Phys. **98**, 5648 (1993).
32. See various contributions to the original HEMS program as recorded by A.O. Bawagan, Ph.D. Thesis, University of Bristish Columbia, Vancouver, British Columbia, 1987. The HEMS program, now known as MOMAP, and also the RESFOLD program, have been recently extensively revised and extended at the University of British Columbia by N.M. Cann and G. Cooper.
33. P. Duffy, M.E. Casida, C.E. Brion, and D.P. Chong. Chem. Phys. **159**, 347 (1992).
34. J.M. Foster and S.F. Boys. Rev. Mod. Phys. **32**, 300 (1960).
35. M.R. Peterson and R. Poirier. MONSTERGAUSS, Version Aug. 1991. Department of Chemistry, University of Toronto,

© 2002 NRC Canada

80 St. George Street, Toronto, Ontario, Canada; R. Poirier. Department of Chemistry, Memorial University of Newfoundland, St. John's, Newfoundland, Canada.
36. K.T. Leung and C.E. Brion. Chem. Phys. **82**, 87 (1983).
37. S. Wolfe and Z. Shi. Isr. J. Chem. **40**, 343 (2000).
38. C.E. Brion, Y. Zheng, G. Cooper, J. Rolke, E.R. Davidson, Z. Shi, and S. Wolfe. *In* Proceedings of the First Annual Conference and Workshop on Electron Motion in Matter. The Peter Wall Institute for Advanced Studies, The University of British Columbia, Vancouver, British Columbia. October 1998.
39. Y. Zheng, C.E. Brion, G. Cooper, J. Rolke, Z. Shi, S. Wolfe, and E.R. Davidson. *In* Abstr. Int. Conf. Phys. Electron. At. Collisions, 22nd, 1999. Vol. 1. *Edited by* Y. Itikawa, K. Okuno, H. Tanaka, A. Yagashita, and M. Matsuzawa. Department of applied physics and chemistry, University of Electrocommunications, Chofu-shi, Tokyo. p. 314.
40. M. Takahashi, M. Matsuo, and Y. Udagawa. Chem. Phys. Lett. **308**, 195 (1999).

© 2002 NRC Canada

Ortho substituent effects on transfer of aryl groups from oxygen to carbon in adducts from diaryloxycarbenes and DMAD

Xiaosong Lu and John Warkentin

Abstract: Diaryloxycarbenes, generated by thermolysis of 2,2-diaryloxy-5,5-dimethyl-Δ^3-1,3,4-oxadiazolines in benzene, reacted with dimethyl acetylenedicarboxylate (DMAD) to afford triesters. The triesters arose by aryl-group transfer from oxygen to carbon (ipso substitution). A cyano group in the *para* position had been shown earlier to favour the ipso substitution whereas a *para*-methoxy group disfavoured it. Surprisingly, the *ortho*-methoxy substituent also favoured ipso substitution. As a tentative rationale, we had proposed that a vinylogous diaryloxycarbene intermediate, with dipolar properties, is formed when a diaryloxycarbene attacks at the *sp*-carbon of DMAD and that an *ortho* substituent, with one or more unshared electron pairs, can stabilize the intermediate by donating electron density to the positive site. In the present work, support for that interpretation and for the importance of a steric effect, was provided by examining the competition between (*i*) *p*-tolyl and phenyl; (*ii*) *o*-tolyl and phenyl; (*iii*) *o*-iodophenyl and phenyl; (*iv*) *o*-iodophenyl and *p*-chlorophenyl; and (*v*) *o*-bromophenyl and *p*-chlorophenyl as potential migrating groups.

Key words: aromatic substitution, carbene, ipso, diaryloxycarbene, oxadiazoline.

Résumé : Les diaryloxycarbènes, générés par thermolyse de 2,2-diaryloxy-5,5-diméthyl-Δ^3-1,3,4-oxadiazolines dans le benzène, réagissent avec l'acétylènedicarboxylate de diméthyle («DMAD») pour conduire à la formation de triesters. Les triesters se forment par un transfert de groupe acyle de l'oxygène au carbone (substitution ipso). Il a été démontré antérieurement que la présence d'un groupe cyano en position *para* favorise la substitution ipso alors qu'un groupe méthoxy la défavorise. De façon surprenante, un substituant méthoxy en *ortho* favorise aussi la substitution ipso. Comme explication de ce résultat, on a suggéré que lorsqu'un diaryloxycarbène attaque au niveau d'un carbone sp du DMAD, il y formation d'un intermédiaire diaryloxycarbène vinylogue ayant des propriétés dipolaires et qu'un substituant *ortho* possédant au moins une paire d'électrons non partagée peut stabiliser l'intermédiaire en donnant de la densité électronique au site positif. Dans le présent travail, en examinant la compétition entre divers groupes migrants potentiels ((*i*) *p*-tolyle et phényle; (*ii*) *o*-tolyle et phényle; (*iii*) *o*-iodophényle et phényle; (*iv*) *o*-iodophényle et *p*-chlorophényle; (*v*) *o*-bromophényle et *p*-chlorophényle), on a obtenu des résultats qui appuient cette interprétation et qui mettent en évidence l'importance d'un effet stérique.

Mots clés : substitution aromatique, carbène, ipso, diaryloxycarbène, oxadiazoline.

[Traduit par la Rédaction]

Introduction

Reactions of neutral nucleophiles with Michael acceptors will generally involve dipolar intermediates, as illustrated in Scheme 1 for the attack of an amine on dimethyl acetylenedicarboxylate (DMAD). If the nucleophile is a carbene, such as a dialkoxycarbene, the attack can produce either a dipole or a cyclopropene, depending on whether the reaction is stepwise or concerted. It is not always easy to distinguish between the stepwise addition with subsequent ring-closing and the concerted cyclopropene formation with subsequent ring-opening, but it is fairly clear that, with a few exceptions (1), reactions subsequent to the initial attack often involve the acyclic dipole. The dipolar species may be in equilibrium with the cyclopropenes, many of which are not stable enough at higher temperatures to accumulate to detectable concentrations (2).

We became interested in reactions of methoxyaryloxy- and diaryloxycarbenes with DMAD as a result of the discovery of aryl group transfer, from oxygen to carbon, to produce triester products (Scheme 2) (3, 4).

There was only one prior example of a similar transfer, from the reaction of an aminothiocarbene with DMAD, Scheme 3 (5). The results in Schemes 2 and 3 could be rationalized in terms of a dipolar carbenic intermediate that accomplishes ipso-aromatic substitution, either by nucleophilic attack at the ipso carbon or via cyclopropanation and subsequent reorganization (Scheme 4) as suggested by Capretta (6) for similar reactions of carbenoids. The mechanism involving nucleophilic attack was favoured when it was found that an electron withdrawing group in the *para* position favoured aryl-group transfer whereas an electron donor group disfavoured the transfer (4). For example, *p*-cyanophenyl mi-

Received 16 September 2001. Published on the NRC Research Press Web site at http://canjchem.nrc.ca on 6 March 2002.

X. Lu and J. Warkentin.[1] Department of Chemistry, McMaster University, Hamilton, ON L8S 4M1, Canada.

[1]Corresponding author (e-mail: warkent@mcmaster.ca).

 DOI: 10.1139/V02-012 © 2002 NRC Canada

Scheme 1.

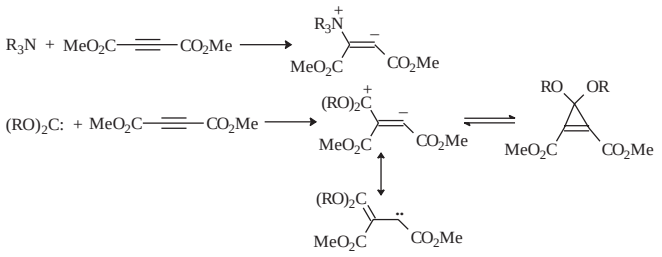

Scheme 2.

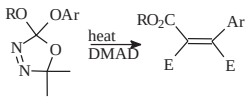

(R= Me or aryl; DMAD= dimethyl acetylenedicarboxylate; E= CO_2Me)

grated exclusively when competing with phenyl, *p*-tolyl, or *p*-methoxyphenyl, and phenyl migrated exclusively when in competition with *p*-methoxyphenyl (4). Surprisingly, *o*-methoxyphenyl had a migratory aptitude comparable to that of phenyl (4), suggesting that the *o*-methoxy substituent exerts opposing effects, an electronic effect presumably analogous to that of the *p*-methoxy substituent, disfavouring substitution, and at least one other effect favouring it.

We now report that the *o*-tolyl group has a higher migratory aptitude than the *p*-tolyl group, although both have a lower migratory aptitude than the phenyl group, and that the *ortho* effect is enhanced with the *o*-iodo- and *o*-bromophenyl groups, both of which migrated in preference to the *p*-chlorophenyl group.

Methods, results, and discussion

Oxadiazolines **4** were prepared from appropriate bis(aryl) carbonates (**1**). Diphenyl carbonate is commercially available and di(*p*-chlorophenyl) carbonate was prepared from 1,1′-carbonyl diimidazole by the sequence of reactions shown in Scheme 5 (7).

Diaryloxyoxadiazolines **5** were prepared by exchange reactions of oxadiazolines **4** with the appropriate substituted phenols (7, 8). Thermolysis of **5** in benzene generated carbonates **6** and carbonyl ylides **7** by competing 1,3-dipolar cycloreversions (see Scheme 6). Evidence for the intermediacy of **7** came from the thermolysis-rate constants (7). Although the effects of the substituents on the thermolysis-rate constants are small, the fact that the *p*-cyano substituted oxadiazoline lost N_2 about twice as fast as the parent is consistent with a transition state in which C2 has become more negative, as it would in the carbonyl ylide. In a concerted mechanism, on the other hand, in which N_2 and acetone are extruded simultaneously, as proposed by Smith (9), carbene character would develop at C2. A cyano group, which would destabilize the carbene, should have a rate-retarding effect and not the observed rate-accelerating effect, if carbene formation were part of the rate-determining step.

Diaryloxycarbenes **8**, which presumably arose from fragmentation of carbonyl ylides **7** (10), reacted with DMAD to

Scheme 3.

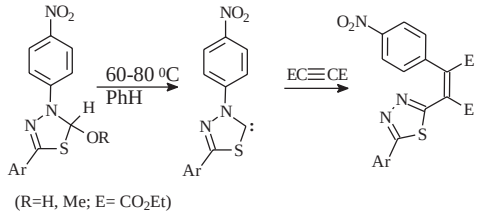

(R=H, Me; E= CO_2Et)

Scheme 4.

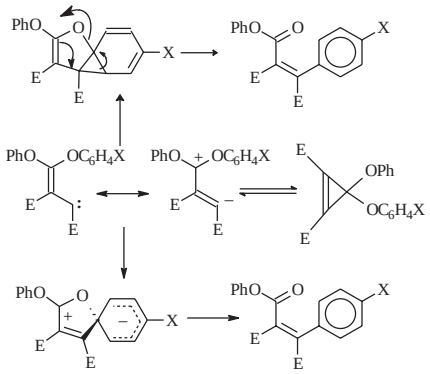

form triesters **10** and **11** through migration of an aryl group from oxygen to carbon. In the case of **8a** (Ar = *p*-C_6H_4Me), **10a** was the minor and **11a** the major triester formed (**10a**:**11a** = 1:4.5). Similarly, in the case of **8b**, the yield of **11b** exceeded that of **10b** (**11b**:**10b** = 1.1:1). Thus, the *para*-methyl group retards migration between 4- and 5-fold, whereas the *ortho*-methyl group retards migration by about 10%, both relative to H. However, *o*-iodophenoxy-(phenoxy)carbene (not shown) reacted with DMAD to afford exclusively the triester from migration of the *o*-iodophenyl group. Similarly, the *o*-iodophenyl and the *o*-bromophenyl groups migrated exclusively when in competition with the *p*-chlorophenyl group of **8c** and **8d**. These results are in Table 1, together with some results published earlier.

Identification of the triester formed by ipso-aromatic substitution by means of mass spectrometry was straightforward. For example, esters **10a** and **10b** gave rise to a base peak from loss of the C_6H_5O fragment of the ester; the aryl group that had migrated to carbon was not lost. On the other hand, **11b** lost the fragment $CH_3C_6H_4O$. Esters **10** and **11** were assigned the *E*-configuration on the basis of analogy to a similar compound, the structure of which was secured by means of X-ray diffraction (4).

In each case, the oxadiazoline source fragmented not only to N_2, the carbene, and acetone, but also to 2-diazopropane and the appropriate diaryl carbonate (Scheme 6). The diazopropane was trapped by 1,3-dipolar cycloaddition to DMAD to form known pyrazole **12** (11).

These results can be interpreted as follows: attack on DMAD by the carbenes **8** leads to isomeric dipolar intermediates (**9**), which can also be represented as vinylogous dioxycarbenes (not shown) that are equilibrated by reversible closure to the appropriate cyclopropene. Such equilibration occurs at 80°C in the case of analogous vinylogous dioxycarbenes (2*c*). If equilibration via the corresponding

© 2002 NRC Canada

Scheme 5.

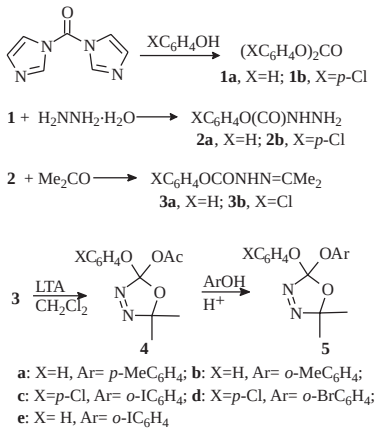

Table 1. Yields and yield ratios of ipso substitution products **10**, **11** in Scheme 6.

Major migrating group (%)	Minor migrating group (%)	Ratio[a]
C_6H_5 (34)	*p*-C_6H_4Me (8)	4.5
C_6H_5 (25)	*o*-C_6H_4Me (22)	1.1
C_6H_5 (38)	*p*-$MeOC_6H_4$ (nd)[b]	Large[c]
o-$MeOC_6H_4$ (25)	C_6H_5 (11)	2.3[c]
p-NCC_6H_4 (37)	*p*-$MeOC_6H_4$ (nd)	Large[c]
p-NCC_6H_4 (26)	*p*-MeC_6H_4 (nd)	Large[c]
p-NCC_6H_4 (37)	C_6H_5 (nd)	Large[c]
o-IC_6H_4 (45)	C_6H_5 (nd)	Large
o-IC_6H_4 (38)	*p*-ClC_6H_4 (nd)	Large
o-BrC_6H_4 (38)	*p*-ClC_6H_4 (nd)	Large

[a]From the actual yields and not the rounded figures in the first two columns.
[b]Not detected.
[c]Reference 4.

cyclopropenes is rapid compared to aryl group transfer, then the Curtin–Hammett principle (12) applies and the group that is transferred by ipso substitution is selected on the basis of the relative stabilities of the transition states and not the ground states. Given that the principle does apply, it is clear from Table 1 that the *p*-tolyl group is transferred more slowly than the phenyl group, whereas the *o*-tolyl group, although it is also transferred more slowly than the phenyl group, is transferred more rapidly than the *p*-tolyl group. Thus, methyl retards nucleophilic aromatic substitution, as befits its electronic effect, but the retardation is diminished when the methyl group is situated *ortho*. Presumably the *o*-methyl group acts to prevent coplanarity of the aryloxy group with the dipolar fragment tethered to it (see Scheme 7) and that geometry provides an improved orientation of the aryloxy group for attack on the ring. Whether that attack involves formation of one bond, at the ipso position only, or two bonds to the aromatic ring to afford a cyclopropane intermediate (6) is not established.

Both *o*-iodophenyl and *o*-bromophenyl are transferred more rapidly than *p*-chlorophenyl, to the extent that the products of migration of *p*-chlorophenyl were not found. From previous work (4), we know that the *p*-cyano group is

Scheme 6.

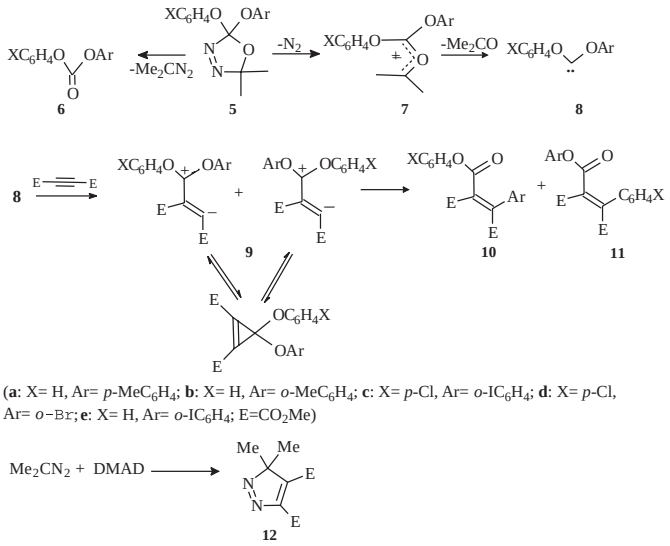

Scheme 7.

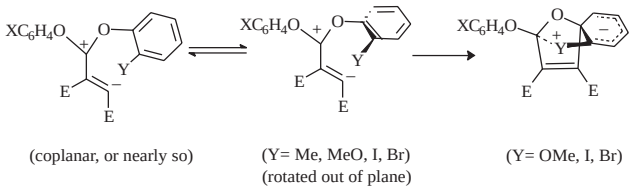

a strong facilitator of migration whereas a *para*-methoxy group stops aryl migration, both relative to H. Although it was not possible to construct a Hammett plot and to determine the value of ρ, an approximate value can be estimated as follows: if we assume that no more than 2% of a minor product might have been missed, then the migration rate ratios were *p*-CNC_6H_4/C_6H_5 > 37/2 and *p*-$MeOC_6H_4/C_6H_5$ < 2/38 (4). Consequently $k_{p\text{-CN}}/k_H \geq 18.5$ or $\log (k_{p\text{-CN}}/k_H) \geq 1.27$ and $k_{p\text{-OMe}}/k_H \leq 1/19$ or $\log (k_{p\text{-OMe}}/k_H) \leq -1.28$. With $\sigma_{p\text{-Cl}} = 0.63$ and $\sigma_{p\text{-OMe}} = -0.27$, the predicted value of ρ is ca. +3.3. The value of $\sigma_{p\text{-Cl}}$ is 0.23, which, together with the estimated value of ρ, leads to the prediction that the *p*-chlorophenyl group should migrate 5 to 6 times faster than phenyl. Since *o*-iodophenyl and *o*-bromophenyl migrated exclusively when in competition with *p*-chlorophenyl, it is clear that both the *ortho*-iodo and *ortho*-bromo substituents enhance migration, relative to H, even more strongly. The large rate-enhancing effects of *o*-iodo and *o*-bromo, relative to H and to *p*-chloro, cannot be a consequence of relative electron withdrawing abilities, which are very similar ($\sigma_{p\text{-I}} = 0.28$, $\sigma_{p\text{-Br}} = 0.23$, $\sigma_{p\text{-Cl}} = 0.23$).

A likely explanation for the observed effects (*o*-MeO >> H, *p*-MeO < H; *o*-I > *p*-Cl > H; *o*-Br > *p*-Cl > H; *o*-Me < H, *p*-Me < H; and *o*-Me > *p*-Me) focuses on the following factors: (*i*) in a nucleophilic ipso substitution, electron donor groups should raise the transition state energy; (*ii*) *p*-methoxy and *p*-methyl groups are donor groups relative to H and both retard the ipso substitution; (*iii*) methyl retards moderately and methoxy retards more strongly, as expected on the basis of their substituent constants ($\sigma_{p\text{-Me}} = -0.14$, $\sigma_{p\text{-OMe}} = -0.28$);

© 2002 NRC Canada

and (*iv*) *p*-cyano and *p*-chloro are inductively electron withdrawing and cyano also withdraws conjugatively. One therefore expects them to favour ipso substitution on rings bearing those groups, as observed for *p*-cyano. *Ortho* groups, on the other hand, must exert three effects. First, they donate or withdraw electrons, qualitatively like their *para* counterparts. Second, they exert a steric effect that *favours* attack at the neighbouring carbon (ipso attack), as indicated by the effect of *o*-methyl. The fact that *p*-methyl is retarding and *o*-methyl is retarding but less so must mean that the steric effect promotes attack by the dipole–carbene on the aromatic ring. Presumably it does this by increasing the populations of conformers in which the aromatic ring to be attacked is not coplanar with the dipolar–carbenic nucleophile (Scheme 7). Third, the *ortho* substituents bearing unshared electrons (MeO, I, Br) must exert a further effect that reinforces the steric effect; these substituents can donate electron density toward the developing positive site to stabilize the transition state for the formation of the intermediate for nucleophilic-aromatic ipso substitution, illustrated in Scheme 7. A cyclopropanation step would also be facilitated by rotating the aromatic ring as a result of steric hindrance. However, cyclopropanation by a nucleophilic carbene is unlikely to be enhanced strongly by an *o*-OMe substituent.

Thus, the tentative explanation advanced earlier (4), for the electronic effect of the *o*-methoxy substituent, is supported by the findings that the *o*-Br and *o*-I substituents are strongly rate enhancing. That explanation is amplified, on the basis of the results with *o*- and *p*-Me, to include a pure steric effect.

Experimental

NMR spectra were recorded on a Bruker AC-200 or AC-300 NMR spectrometer. Infrared spectra were recorded with a Biorad FTS-40 spectrophotometer, with the sample either in CCl_4 or in a KBr pellet. The IR bands are labeled qualitatively with the symbols br, s, and m for broad, strong, and medium intensities, respectively. Bands from C—H stretching vibrations between 3100 and 2850 cm^{-1} are omitted, as are other weak bands. Melting points were recorded on a Thomas Hoover capillary melting point apparatus; they are uncorrected. Mass spectra of compounds containing Cl, Br, or both list all of the observed molecular ion masses, not only the signals for the most abundant isotope(s). Mass spectra for the oxadiazolines are not reported. 2,2-Dioxy-5,5-dimethyl oxadiazolines do not, in general, afford molecular ion signals and their mass spectra have little diagnostic value. They can be recognized from their ^1H and ^{13}C NMR spectra. The latter typically show C2 between δ 136 and 138 and C5 between δ 118 and 120, if the C2 substituents are alkoxy groups and the C5 substituents are methyl groups (13). Some of the ^{13}C NMR spectra of the products showed fewer signals than were expected and coincidence of some signals in diaryl compounds is suspected. Moreover, some maleate-like methyl esters (**10**, **11**) gave only one ^{13}C OMe signal where two methoxy groups were indicated by ^1H NMR spectroscopy.

General thermolysis method

All thermolyses were carried out by immersing the sealed and vacuum-degassed thermolysis tubes containing the samples in a constant-temperature oil bath at 110.0 ± 0.2°C for 24 h. In a typical procedure a solution containing the oxadiazoline (0.6 mmol) and DMAD (0.8 mmol) in benzene (20 mL) was degassed by means of three freeze-pump-thaw cycles before it was heated in a sealed tube at 110°C for 24 h. A small amount of the solution was used for direct GC–MS analysis. Benzene was evaporated from the rest of the solution and the residue was subjected to flash chromatography with 5% ethyl acetate in hexane as the eluting solvent. The spectroscopic data came from products isolated by means of radial or column chromatography from larger-scale experiments with up to 2.2 mmol of oxadiazoline.

bis-*p*-Chlorophenyl carbonate (1b) (14)

A solution of 1,1′-carbonyldiimidazole (9.7 g, 0.060 mol), *p*-chlorophenol (15.2 g, 0.12 mol), silver nitrate (20.4 g, 0.12 mol), and triethylamine (12.1 g, 0.12 mol) in acetonitrile (100 mL) was heated at reflux for 16 h before it was filtered and cooled to room temperature. Hexane was added until no more precipitate was formed. The colourless needle-shaped crystals (9.6 g, 57%) were removed from the slightly dark solution by vacuum filtration; mp 146–147°C. IR (CCl_4) (cm^{-1}): 1781 (s), 1488 (s), 1278 (m), 1224 (br), 1187 (s), 1163 (m), 1104 (m), 1085 (s), 1013 (s). ^1H NMR (200 MHz, $CDCl_3$) δ: 7.19–7.40. ^{13}C NMR (75 MHz, $CDCl_3$) δ: 122.3, 129.8, 132.0, 149.4, 151.7. EI-MS *m*/*z* (%): 286 (M^+, 10), 284 (M^+, 54), 282 (M^+, 90), 238 (52), 168 (25), 128 (42), 111 (100), 99 (59), 75 (68), 63 (46). CI-MS (NH_3) *m*/*z* (%): 304 ($[M + 18]^+$, 1), 302 ($[M + 18]^+$, 7), 300 ($[M + 18]^+$, 10), 282 (M^+, 27).

***p*-Chlorophenyl hydrazinecarboxylate (2b) (14)**

A stirred solution of bis-*p*-chlorophenyl carbonate (4.0 g, 0.014 mol) in CH_2Cl_2 (30 mL) was cooled with a dry ice bath for 15 min before hydrazine monohydrate (0.71 g, 0.014 mol) was added in one portion. The dry ice was removed to let the solution warm gradually to room temperature and stirring was continued for 20 min. Addition of hexane caused colourless needles to precipitate. Vacuum filtration furnished pure **2b** (1.06 g, 40%); mp 144–145°C. IR (CCl_4) (cm^{-1}): 3458 (m), 3304 (m), 1757 (s), 1549 (s), 1462 (m), 1215 (s), 1010 (m), 978 (m). ^1H NMR (200 MHz, $CDCl_3$) δ: 3.87 (s, 2H, NH_2), 6.35 (s, 1H, NH), 7.07–7.31 (m, 4H, Ar). ^{13}C NMR (50 MHz, $CDCl_3$) δ: 122.9, 129.6, 131.2, 149.3, 156.7.

***p*-Chlorophenoxycarbonyl hydrazone of acetone (3b)**

p-Chlorophenyl hydrazinecarboxylate (3.73 g, 0.020 mol) and anhydrous magnesium sulfate (ca. 6 g) were added to acetone (60 mL). Stirring for 24 h followed by filtration and evaporation of the excess acetone produced pure **3b** as colourless crystals (92% yield); mp 98–102°C. IR (CH_2Cl_2) (cm^{-1}): 3383 (m), 1761 (s), 1482 (m), 1356 (m), 1262 (s), 1201 (m), 1090 (m), 1012 (m). ^1H NMR (200 MHz, $CDCl_3$) δ: 1.88 (s, 3H, CH_3), 2.08 (s, 3H, CH_3), 7.10–7.36 (m, 4H, Ar), 7.97 (s, 1H, NH). ^{13}C NMR (75 MHz, $CDCl_3$) δ: 16.4, 25.5, 123.0, 129.5, 131.1, 149.3, 153.1. EI-MS *m*/*z* (%): 229 ($[M + 1]^+$, 5), 227 ($[M + 1]^+$, 15), 128 (74), 99 (100), 56

© 2002 NRC Canada

(37). CI-MS (NH_3) *m*/*z* (%): 229 ([M + 1]$^+$, 32), 227 ([M + 1]$^+$, 100). EI-HRMS *m*/*z* calcd. for $C_{10}H_{11}{}^{35}ClN_2O_2$: 227.0587; found: 227.0575.

2-Acetoxy-2-(*p*-chlorophenoxy)-5,5-dimethyl-Δ^3-1,3,4-oxadiazoline (4c)

A solution of lead tetraacetate (LTA, 11.4 g, 2.57 mmol) in CH_2Cl_2 (60 mL) was cooled with dry ice in isopropyl alcohol. Acetone *p*-chlorophenoxycarbonyl hydrazone (4.84 g, 2.14 mmol) in CH_2Cl_2 (20 mL) was added dropwise to the LTA solution, which was then gradually warmed to room temperature and stirred overnight. After three washings with 5% $NaHCO_3$, drying over anhydrous $MgSO_4$, and evaporation of the solvent, flash column chromatography (5% EtOH–hex) gave **4c** in 36% yield as a yellow oil. IR (CCl_4) (cm^{-1}): 2995 (s), 2930 (s), 2873 (m), 1797 (br), 1735 (s), 1588 (m), 1490 (s), 1462 (m), 1434 (m), 1371 (m), 1278 (m), 1231 (br), 1013 (m), 985 (m). ^{1}H NMR (200 MHz, $CDCl_3$) δ: 1.40 (s, 3H, Me), 1.67 (s, 3H, Me), 2.08 (s, 3H, COMe), 7.14–7.30 (m, 4H, Ph). ^{13}C NMR (75 MHz, $CDCl_3$) δ: 21.3, 22.7, 24.2, 123.0, 123.8, 129.3, 130.4, 133.0, 150.1, 165.9.

2-(*p*-Chlorophenoxy)-2-(*o*-iodophenoxy)-5,5-dimethyl-Δ^3-1,3,4-oxadiazoline (5c)

A solution of **4c** (1.81g, 6.36 mmol) and 2-iodophenol (1.54 g, 7.00 mmol) in CH_2Cl_2 (60 mL) containing catalytic trifluoroacetic acid was heated at reflux for 24 h. Pure **5c** was obtained by means of flash column chromatography (5% EtOH–hex) as a yellow oil, in 43% yield: IR (CCl_4) (cm^{-1}): 1584 (m), 1550 (m), 1486 (s), 1469 (m), 1209 (s), 1155 (s), 1105 (m), 1087 (s), 1014 (m). ^{1}H NMR (200 MHz, $CDCl_3$) δ: 1.34 (s, 3H, Me), 1.37 (s, 3H, Me), 6.80–7.78 (m, 8H, Ar). ^{13}C NMR (75 MHz, $CDCl_3$) δ: 23.5, 23.7, 90.4, 121.4, 122.3, 123.2, 123.8, 126.2, 129.2, 130.5, 135.7, 139.6, 149.9, 151.5.

Thermolysis of 5c in the presence of DMAD

Thermolysis of **5c** (0.28 g, 0.63 mmol) in the presence of DMAD (0.11 g, 0.77 mmol) as described in the general procedure gave carbonate **6c**, aromatic substitution product **10c**, and pyrazole **12**.

***p*-Chlorophenyl *o*-iodophenyl carbonate (6c)**

This compound was obtained in 30% yield as a colourless solid; mp 81–82°C. IR (CCl_4) (cm^{-1}): 1782 (s), 1549 (m), 1488 (m), 1469 (m), 1225 (br), 1190 (s), 1090 (m), 1016 (m), . ^{1}H NMR (200 MHz, $CDCl_3$) δ: 6.99–7.88 (m). ^{13}C NMR (75 MHz, $CDCl_3$) δ: 89.7, 122.3, 128.3, 129.7, 131.9, 139.7, 149.4, 150.8, 151.0. EI-MS *m*/*z* (%): 376 (M$^+$, 5), 374 (M$^+$, 14), 247 (13), 203 (26), 168 (100), 139 (20), 111 (52), 82 (26), 76 (74), 63 (60). EI-HRMS *m*/*z* calcd. for $C_{13}H_8{}^{35}ClIO_3$: 373.9207; found: 373.9213.

(*E*)-*o*-Iodophenylethenetricarboxylic acid 1,2-dimethyl *p*-chlorophenyl ester (10c)

This compound was obtained in 38% yield as a yellow oil. IR (CCl_4) (cm^{-1}): 1738 (br), 1487 (m), 1435 (m), 1278 (m), 1257 (m), 1229 (s), 1197 (s), 1092 (m), 1074 (m), 1013 (s). ^{1}H NMR (200 MHz, $CDCl_3$) δ: 3.82 (s, 3H, OMe), 3.96 (s, 3H, OMe), 6.70–7.90 (m, 8H, Ar). ^{13}C NMR (75 MHz, $CDCl_3$) δ: 53.3, 96.4, 122.2, 128.1, 129.3, 129.4, 130.4, 131.7, 132.9, 139.0, 139.1, 146.6, 148.2, 160.9, 163.8, 164.8. EI-MS *m*/*z* (%): 373 ([M – OC_6H_4Cl]$^+$, 100), 255 (38), 246 (53), 215 (57), 187 (48), 173 (39), 128 (100), 115 (53), 99 (67), 64 (67), 59 (86). CI-MS (NH_3) *m*/*z* (%): 520 ([M + 18]$^+$, 35), 518 ([M + 18]$^+$, 100), 503 ([M + 1]$^+$, 14), 501 ([M + 1]$^+$, 43).

Pyrazole **12**: The spectra of this compound matched those reported previously (10).

2-(*o*-Bromophenoxy)-2-(*p*-chlorophenoxy)-5,5-dimethyl-Δ^3-1,3,4-oxadiazoline (5d)

This compound was obtained in 30% yield as a yellow oil. IR (CCl_4) (cm^{-1}): 2996 (m), 1584 (m), 1550 (m), 1488 (s), 1476 (s), 1443 (m), 1209 (br), 1155 (br), 1108 (s), 1086 (s), 1031 (m), 1014 (m). ^{1}H NMR (200 MHz, $CDCl_3$) δ: 1.33 (s, 6H), 6.99–7.55 (m, 8H). ^{13}C NMR (75 MHz, $CDCl_3$) δ: 22.5, 23.7, 116.4, 122.4, 122.8, 123.6, 126.0, 128.0, 129.2, 130.5, 133.5, 135.7, 148.8, 149.9.

Thermolysis of 5d

The general procedure afforded *o*-bromophenyl *p*-chlorophenyl carbonate **6d** (23%), triester **10d** (38%), and pyrazole **12** (23%).

***o*-Bromophenyl *p*-chlorophenyl carbonate (6d)**

This compound was obtained in in 23% yield as a colourless solid; mp 98.5–99.5°C. IR (CCl_4) (cm^{-1}): 1784 (s), 1488 (m), 1476 (m), 1229 (br), 1194 (s), 1091 (m). ^{1}H NMR (200 MHz, $CDCl_3$) δ: 7.18–7.65 (m). ^{13}C NMR (75 MHz, $CDCl_3$) δ: 116.0, 122.4, 123.3, 128.2, 128.9, 129.8, 132.1, 133.8, 148.3, 149.6, 150.9. EI-MS *m*/*z* (%): 330 (M$^+$, 10), 328 (M$^+$, 40), 326 (M$^+$, 28), 247 (14), 168 (100), 155 (37), 143 (20), 111 (63), 75 (66), 63 (66). CI-MS (NH_3) *m*/*z* (%): 348 ([M + 18]$^+$, 25), 346 ([M + 18]$^+$, 100), 344 ([M + 18]$^+$, 75). EI-HRMS *m*/*z* calcd. for $C_{13}H_8{}^{79}Br^{35}ClO_3$: 325.9345; found: 325.9347.

(*E*)-*o*-Bromophenylethenetricarboxylic acid 1,2-dimethyl *p*-chlorophenyl ester (10d)

This compound was obtained in 38% yield as a yellow oil. IR (CCl_4) (cm^{-1}): 1740 (br), 1487 (m), 1436 (m), 1258 (m), 1230 (s), 1197 (s), 1092 (m), 1072 (m), 1013 (m). ^{1}H NMR (200 MHz, $CDCl_3$) δ: 3.82 (s, 3H, OMe), 3.95 (s, 3H, OMe), 6.73–7.61 (m, 8H, Ar). ^{13}C NMR (75 MHz, $CDCl_3$) δ: 53.5 (coincident OMe signals), 116.8, 122.4, 127.6, 129.6, 130.2, 130.9, 131.9, 133.0, 135.1, 148.3, 161.3, 164.0, 165.1. EI-MS *m*/*z* (%): 423 ([M – OMe]$^+$, 4), 421 ([M – OMe]$^+$, 4), 375 ([M – Br]$^+$, 4), 373 ([M – Br]$^+$, 12), 327 ([M – OC_6H_4Cl]$^+$, 98), 325 ([M – OC_6H_4Cl]$^+$, 100), 299 (58), 297 (58), 246 (31), 209 (92), 207 (92), 128 (62), 99 (90), 59 (77). CI-MS (NH_3) *m*/*z* (%): 474 ([M + 18]$^+$, 25), 472 ([M + 18]$^+$, 100), 470 ([M + 18]$^+$, 75).

2-(*o*-Iodophenoxy)-2-phenoxy-5,5-dimethyl-Δ^3-1,3,4-oxadiazoline (5e)

A solution of 2-acetoxy-2-phenoxy-5,5-dimethyl-Δ^3-1,3,4-oxadiazoline (**4a**) (2.69 g, 0.0108 mol) and *o*-iodophenol (2.84 g, 0.0129 mol) in CH_2Cl_2 (60 mL) containing catalytic trifluoroacetic acid was heated at reflux for 24 h. 2-(*o*-Iodophenoxy)-2-phenoxy-5,5-dimethyl-Δ^3-1,3,4-oxadiazoline (**5e**)

© 2002 NRC Canada

was obtained by means of flash column chromatography (5% EtOH–hex) as a yellow oil, in 38% yield. IR (CCl_4) (cm^{-1}): 3070 (m), 2995 (m), 1769 (m), 1593 (m), 1492 (s), 1469 (s), 1440 (m), 1383 (w), 1369 (m), 1203 (br), 1156 (br), 1105 (br), 1021 (m), 969 (m). ^1H NMR (200 MHz, $CDCl_3$) δ: 1.25 (s, 3H, Me), 1.38 (s, 3H, Me), 6.83–7.78 (m, 9H, Ar). ^{13}C NMR (75 MHz, $CDCl_3$) δ: 23.6, 23.8, 90.6, 121.5, 122.2, 122.8, 125.1, 125.4, 126.2, 129.2, 136.1, 139.6, 151.3, 151.9.

Thermolysis of 2-(*o*-iodophenoxy)-5,5-dimethyl-2-phenoxy-Δ^3-1,3,4-oxadiazoline (5e) with DMAD

The general procedure gave *o*-iodophenyl phenyl carbonate (**6e**), the ester from migration of the *o*-iodophenyl group (**10e**), and pyrazole **12** (16%).

***o*-Iodophenyl phenyl carbonate (6e)**

The carbonate was a clear oil obtained in 20% yield. IR (CCl_4) (cm^{-1}): 3071 (m), 1788 (br), 1594 (m), 1494 (s), 1469 (s), 1441 (m), 1238 (br), 1220 (br), 1186 (br), 1163 (m), 1044 (m), 1022 (m), 1007 (m). ^1H NMR (200 MHz, $CDCl_3$) δ: 7.02–7.43 (m). ^{13}C NMR (75 MHz, $CDCl_3$) δ: 89.9, 121.0, 122.6, 126.6, 128.3, 129.8, 129.9, 139.8, 151.2, 151.3. EI-MS *m*/*z* (%): 340 (M^+, 16), 220 (15), 213 (17), 169 (46), 141 (47), 84 (68), 77 (100), 51 (43). HRMS calcd. for $C_{13}H_9IO_3$: 339.9596; found: 339.9602.

(*E*)-*o*-Iodophenylethenetricarboxylic acid 1,2-dimethyl phenyl ester (10e)

This compound was obtained as a yellow oil in 45% yield. IR (CCl_4) (cm^{-1}): 2958 (s), 2929 (m), 2660 (m), 1739 (br), 1550 (m), 1463 (m), 1435 (m), 1256 (m), 1231 (s), 1192 (s), 1012 (m). ^1H NMR (200 MHz, $CDCl_3$) δ: 3.81 (s, 3H, OMe), 3.96 (s, 3H, OMe), 6.74–7.90 (m, 9H, Ar). ^{13}C NMR (75 MHz, $CDCl_3$) δ: 53.5, 96.7, 121.1, 126.5, 128.3, 129.6, 130.6, 133.7, 139.3, 146.4, 149.9, 161.3, 164.2, 164.9. EI-MS *m*/*z* (%): 435 ($[M - OMe]^+$, 2), 373 ($[M - I]^+$, 67), 339 (93), 255 (60), 246 ($[M - OPh]^+$, 100), 215 (80), 173 (40), 128 (100), 65 (100), 59 (78). CI-MS (NH_3) *m*/*z* (%): 484 ($[M + 18]^+$, 100), 467 ($[M + 1]^+$, 30).

5,5-Dimethyl-2-(*o*-methylphenoxy)-2-phenoxy Δ^3-1,3,4-oxadiazoline (5b)

A solution of the 2-acetoxy-2-phenoxy oxadiazoline **4a** (0.88 g, 3.52 mmol) and *o*-methylphenol (1.14 g, 10.7 mmol) in CH_2Cl_2 (60 mL) containing catalytic trifluoroacetic acid was heated at reflux for 24 h. 2-(*o*-Methylphenoxy)-2-phenoxy oxadiazoline (**5b**) was separated by flash column chromatography (5% EtOH–hex) as a yellow oil in 53% yield. IR (CCl_4) (cm^{-1}): 3067 (m), 2994 (m), 2939 (m), 1592 (m), 1492 (s), 1460 (m), 1383 (m), 1369 (m), 1207 (br), 1156 (br), 1121 (br), 989 (m). ^1H NMR (200 MHz, $CDCl_3$) δ: 1.13 (s, 3H, Me), 1.23 (s, 3H, Me), 2.21 (s, 3H, *o*-$C_6H_4CH_3$), 7.00–7.28 (m, 9H, ArH). ^{13}C NMR (50.3 MHz, C_6D_6) δ: 16.8, 23.4, 24.8, 121.3, 122.4, 122.9, 125.1, 125.3, 126.4, 129.2, 131.1, 131.8, 136.8, 150.1, 151.8.

Thermolysis of 5,5-dimethyl-2-(*o*-methylphenoxy)-2-phenoxy-Δ^3-1,3,4-oxadiazoline (5b) in the presence of DMAD

The general procedure gave products of aromatic substitution that could not be separated. They were identified together and the ratio was calculated from integration of the ^1H NMR signals.

(*E*)-*o*-Methylphenylethenetricarboxylic acid 1,2-dimethyl phenyl ester (10b) and (*E*)-phenylethenetricarboxylic acid 1,2-dimethyl *o*-methylphenyl ester (11b)

These were obtained as a yellow liquid (47% combined yield) in the ratio 1:0.9 by ^1H NMR. IR (CCl_4) (cm^{-1}): 1742 (s), 1265 (m), 1231 (s), 1191 (m). ^1H NMR (200 MHz, $CDCl_3$) (composite spectrum) δ: 1.97 (s, 2.6H, *o*-$C_6H_4CH_3$), 2.39 (s, 3H, *o*-$C_6H_4CH_3$), 3.85 (s, 3H, OMe), 3.90 (s, 5.6H, OMe), 3.92 (s, 2.6H, OMe), 6.54–7.51 (m, 16.8H, ArH). ^{13}C NMR (50.3 MHz, C_6D_6) (composite spectrum) δ: 15.7, 19.8, 53.2, 121.1, 126.0, 126.4, 126.5, 126.9, 128.0, 128.4, 129.1, 129.5, 129.7, 130.3, 130.6, 131.3, 132.8, 136.5, 148.2, 148.7, 149.9, 162.5, 163.0, 166.6, 167.2. EI-MS *m*/*z* (%): 356 ($[M + 2]^+$, 6), 323 ($[M - OMe]^+$, 10), 261 ($[M - OPh]^+$, 67), 247 ($[M - OC_6H_4Me]^+$, 100), 233 (73), 219 (53), 189 (30), 175 (20), 143 (43), 129 (87), 115 (70), 91 (22), 65 (35). CI-MS (NH_3) *m*/*z* (%): 372 ($[M + 18]^+$, 65), 354 (M^+, 100).

***o*-Methylphenyl phenyl carbonate (6b)**

This compound was isolated as a yellow liquid in 31% yield. IR (CCl_4) (cm^{-1}): 1781 (s), 1493 (m), 1232 (br), 1172 (s), 1113 (m). ^1H NMR (200 MHz, $CDCl_3$) δ: 2.32 (s, 3H, Me), 7.19–7.45 (m, 9H, ArH). ^{13}C NMR (50.3 MHz, C_6D_6) δ: 16.1, 121.0, 121.4, 126.4, 126.7, 127.2, 129.7, 130.1, 131.5, 149.7, 151.2, 152.0, 159.3. EI-MS *m*/*z* (%): 229 ($[M + 1]^+$, 10), 228 (M^+, 27), 183 (13), 107 (35), 91 (100), 77 (95), 65 (73). CI-MS (NH_3) *m*/*z* (%): 246 ($[M + 18]^+$, 100).

5,5-Dimethyl-2-(*p*-methylphenoxy)-2-phenoxy-Δ^3-1,3,4-oxadiazoline (5a)

This compound was isolated as a clear oil. IR (CCl_4) (cm^{-1}): 3039 (m), 2994 (s), 2939 (m), 1780 (m), 1593 (s), 1507 (s), 1494 (s), 1458 (m), 1383 (m), 1288 (m), 1087 (br), 989 (m). ^1H NMR (200 MHz, $CDCl_3$) δ: 1.21 (s, 6H), 2.27 (s, 3H), 7.07–7.29 (m, 9H). ^{13}C NMR (75 MHz, $CDCl_3$) δ: 20.6, 23.5, 121.3, 122.1, 124.8, 129.1, 129.5, 134.5, 136.1, 149.4, 151.8.

Thermolysis of 5a in the presence of DMAD

Thermolysis of **5a** (0.8 g, 2.28 mmol) in the presence of DMAD (0.388 g, 2.73 mmol) in 20 mL of dried benzene, removal of the solvent by rotary evaporation, and flash column chromatography followed by radial chromatography gave the following products:

***p*-Methylphenyl phenyl carbonate (6a) (15)**

This compound was isolated in 30% yield. ^1H NMR (200 MHz, $CDCl_3$) δ: 2.33 (s, 3H, *p*-$C_6H_4CH_3$), 7.11–7.43 (m, 9H, ArH). ^{13}C NMR (50.3 MHz, C_6D_6) δ: 20.9, 120.7, 121.0, 126.3, 129.6, 130.1, 136.1, 148.9, 151.1, 152.4. EI-MS *m*/*z* (%): 228 (M^+, 90), 184 (40), 107 (17), 91 (92), 77 (100), 65 (64). CI-MS (NH_3) *m*/*z* (%): 246 ($[M + 18]^+$, 100), 228 (M^+, 27).

(*E*)-*p*-Methylphenylethenetricarboxylic acid 1,2-dimethyl phenyl ester (10a) and (*E*)-phenylethenetricarboxylic acid 1,2-dimethyl *p*-methylphenyl ester (11a)

These products were obtained as a mixture of isomers, in

© 2002 NRC Canada

the ratio 4.5:1 (by ^{1}H NMR) as a yellow oil, in 42% yield. ^{1}H NMR (200 MHz, $CDCl_3$) δ: 2.29 and 2.38 (2s, overall 3H, *p*-$C_6H_4CH_3$), 3.90 (s, 6H, OMe), 6.62–7.53 (m, 9H, ArH). ^{13}C NMR (50.3 MHz, C_6D_6) δ: 21.0, 53.2, 117.3, 120.8, 121.2, 127.9, 129.1, 129.6, 129.8, 130.1, 130.6, 132.9, 136.2, 147.9, 148.2, 162.9, 163.4, 167.2. EI-MS *m*/*z* (%): 356 ($[M + 2]^+$, 3), 323 ($[M – OMe]^+$, 3), 261 ($[M – OC_6H_5]^+$, 67), 247 ($[M – OC_6H_4Me]^+$, 100), 233 (73), 129 (36), 107 (9), 93 (2), 77 (32), 59 (28). CI-MS (NH_3) *m*/*z* (%): 374 ($[M + 20]^+$, 25), 373 ($[M + 19]^+$, 100), 372 ($[M + 18]^+$, 31), 355 ($[M + 1]^+$, 28), 354 (27).

Acknowledgments

The authors gratefully acknowledge the financial support of the Natural Sciences and Engineering Research Council of Canada (NSERC) and the assistance of Mr. Brian Sayer and Dr. Kirk Green with NMR spectroscopy and mass spectrometry.

References

1. For a recent example of a further reaction of a cyclopropene intermediate, see (*a*) X. Lu and J. Warkentin. Org. Lett. **2**, 3501 (2000); (*b*) X. Lu and J. Warkentin. Org. Lett. **3**, 143 (2001).
2. For example, see: (*a*) M.S. Baird, S.R. Buxton, and J.S. Whitley. Tetrahedron Lett. **25**, 1509 (1984); (*b*) J. Al Dulayymi, M.S. Baird, and W. Clegg. Tetrahedron Lett. **29**, 6149 (1988); (*c*) D.L. Boger and C.E. Brotherton-Pleiss. *In* Advances in cycloaddition. Vol. 2. *Edited by* D.P. Curran. JAI Press, Greenwich, CT. 1990. p. 147; (*d*) M.S. Baird, H.L. Fitton, and L. Rajaram. J. Chem. Soc. Perkin Trans.1, 1633 (1994); (*e*) J.R. Al Dulayymi, M.S. Baird, L. Rajaram, and W. Clegg. J. Chem. Res. (*S*), 344 (1994).
3. X. Lu and J. Warkentin. Tetrahedron Lett. **40**, 1483 (1999).
4. X. Lu and J. Warkentin. Can. J. Chem. **79**, 364 (2001).
5. G. Scherowsky, K. Dünnbier, and G. Höfle. Tetrahedron Lett. **24**, 2095 (1977).
6. (*a*) M. Salim and A. Capretta. Tetrahedron, **56**, 8064 (2000); (*b*) G.K. Trammer and A. Capretta. Tetrahedron, **54**, 15499 (1998); (*c*) K. Yong, M. Salim, and A. Capretta. J. Org. Chem. **63**, 9828 (1998).
7. X. Lu, D.L. Reid, and J. Warkentin. Can. J. Chem. **79**, 319 (2001).
8. K. Kassam, D.L. Pole, M. El-Saidi, and J. Warkentin. J. Am. Chem. Soc. **116**, 1161 (1994).
9. W.B. Smith. J. Org. Chem. **60**, 7456 (1995).
10. P. Couture, M. El-Saidi, and J. Warkentin. Can. J. Chem. **75**, 326 (1997).
11. M.W. Majchrzak, M. Békhazi, I. Tse-Sheepy, and J. Warkentin. J. Org. Chem. **54**, 1842 (1989).
12. (*a*) D.Y. Curtin. Rec. Chem. Progr. **15**, 111 (1954); (*b*) J.I. Seeman. Chem. Rev. **83**, 83 (1983).
13. M. El-Saidi, K. Kassam, D.L. Pole, T. Tadey, and J. Warkentin. J. Am. Chem. Soc. **114**, 8751 (1992).
14. P. Vlasak, P. Parik, J. Klicnar, and J. Mindl. Collect. Czech. Chem. Commun. **63**, 793 (1998).
15. D.A. Jaeger, K.B. Tomer, P.D. Woodgate, T. Gebreyesus, C. Djerassi, and R.H. Shapiro. Org. Mass Spectrom. **9**, 551 (1974).

© 2002 NRC Canada

Direct-space analysis of the electronic structure of the $YBa_2Cu_3O_6$ and $YBa_2Cu_3O_7$ crystals

Fausto Cargnoni and Marco Scavini

Abstract: The electronic structure of the $YBa_2Cu_3O_6$ and $YBa_2Cu_3O_7$ crystals is investigated by means of fully periodic-restricted Hartree–Fock LCAO (linear combination of atomic orbitals) pseudopotential calculations. To give a detailed description of the bonding and atomic properties of the materials studied we selected the quantum theory of atoms in molecules approach, and complementary information is obtained from the analysis of the electron localization function in specific cell regions. The main features of the $YBa_2Cu_3O_6$ and $YBa_2Cu_3O_7$ crystals' electron densities are detailed and compared with available experimental data. Since the superconducting transition requires oxidation of the $YBa_2Cu_3O_6$ crystal, we focused on the electronic rearrangements related to the inclusion of oxygen. Cu–O planes, probably responsible for the superconducting transition, exhibit peculiar electronic properties.

Key words: superconducting cuprates, electron density, ab initio calculations.

Résumé : On a étudié la structure électronique de cristaux de $YBa_2Cu_3O_6$ et de $YBa_2Cu_3O_7$ en se basant sur des calculs de pseudopotentiel « LCAO » de Hartree–Fock restreints et totalement périodiques. Afin de pouvoir donner une description détaillée du type de liaison et des propriétés atomiques des matériaux étudiés, on a choisi l'approche de la théorie quantique des atomes dans les molécules et on a obtenu des informations supplémentaires à l'aide de l'analyse de la fonction de localisation de l'électron dans régions spécifiques des cellules. Les détails des caractéristiques principales des densités électroniques dans les cristaux de $YBa_2Cu_3O_6$ et de $YBa_2Cu_3O_7$ sont rapportés et on les compare aux données expérimentales disponibles. Comme la transition de superconduction nécessite une oxydation du cristal de cristaux de $YBa_2Cu_3O_6$, on a porté notre attention sur les réarrangements électroniques apparentés à l'inclusion d'oxygène. Les plans Cu–O, probablement responsables de la transition de superconduction, présentent des propriétés électroniques particulières.

Mots clés : cuprates superconducteurs, densité électronique, calculs ab initio.

[Traduit par la Rédaction]

Introduction

As extensively documented in the literature, one of the common features of cuprates is the dramatic dependence of their electronic structure and transport properties upon oxygen and cation stoichiometry (1, 2).

In particular, $YBa_2Cu_3O_x$ is a nonstoichiometric compound, since the oxygen stoichiometry x can vary from 6 to 7 as a function of the annealing route. $YBa_2Cu_3O_6$ is an insulator; adding oxygen to the structure it becomes metallic, and at low temperatures, it undergoes a transition to superconductor. At the optimal oxygen stoichiometry/concentration ($x = 7$), $T_C = 90$ K (3).

The structure of $YBa_2Cu_3O_x$ (YBCO) also changes as the oxygen concentration changes: $YBa_2Cu_3O_6$ (YBCO6) belongs to the *P4*/*mmm* space group, whereas $YBa_2Cu_3O_7$ (YBCO7) belongs to the *Pmmm* space group.

Received 22 June 2001. Published on the NRC Research Press Web site at http://canjchem.nrc.ca on 15 March 2002.

F. Cargnoni and M. Scavini.[1] Istituto CNR-ISTM and Dipartimento di Chimica Fisica ed Elettrochimica, Via Golgi 19, 20133 Milano-I, Italy.

[1]Corresponding author (e-mail: marco.scavini@unimi.it).

YBCO6 contains six nonequivalent atoms in the asymmetric unit: Y at (1/2, 1/2, 1/2), Ba at (1/2, 1/2, *z*), Cu1 at (0, 0, 0), Cu2 at (0, 0, *z*), O1 at (0, 0, *z*), and O3 at (0, 1/2, *z*) sites. Concerning YBCO7, eight nonequivalent atoms are present in the asymmetric unit: Y at (1/2, 1/2, 1/2), Ba at (1/2, 1/2, *z*), Cu1 at (0, 0, 0), Cu2 at (0, 0, *z*), O1 at (0, 0, *z*), O2 at (1/2, 0, *z*), O3 at (0, 1/2, *z*), and O4 at (0, 1/2, 0) sites. Passing from YBCO6 to YBCO7, the main structural change is the orthorhombic distortion, which is due to the insertion and ordering of O4 along the *b* axis. Figure 1 shows a stick-and-ball representation of structures YBCO6 and YBCO7; the bonding network represented in the panels will be discussed in the *Results and discussion* section.

Oxidation, coupled with the change in the crystal structure, affects the electronic structure of YBCO giving rise to the dramatic change of its transport properties in the normal state and to the superconducting transition.

Theoretical calculations widely investigated the dependence of the YBCO electronic band structure on the oxygen content (4–10). Minor attention was devoted to the electron density rearrangements induced by oxidation (11). Concerning theoretical electron density studies on superconducting cuprates, Acrivos and Stradella (12) topologically investigated the electron density in CuO_2 lamellas embedded in a point-charge lattice simulating the Nd_2CuO_4 crystal. To the best of our knowledge, no similar investigations on the

 DOI: 10.1139/V02-014 © 2002 NRC Canada

Fig. 1. Stick-and-ball representation of the YBCO6 (top) and YBCO7 (bottom panel) crystals' unit cells and atoms. The bonding network represented in the panels reports all interatomic linkages obtained through the topological analysis of the electron density. Qualitatively different bonds are represented with different colours: black (cation–cation), grey (cation–anion), and white (anion–anion).

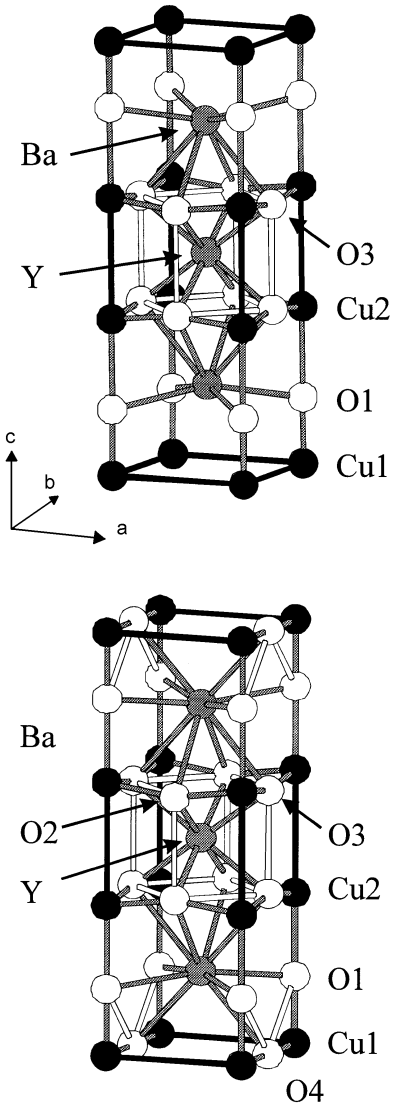

YBCO system are available in the literature. The charges of copper atoms at various oxidation states have been calculated by Brown (13) using an empirical approach.

Relatively few experimental electron-density measurements concerning YBCO crystals are available (14–17). All works deal with single crystal X-ray diffraction experiments at room temperature and examine Fourier difference density maps.

Sasaki et al. (14) studied a crystal with $YBa_2Cu_{2.898}Al_{0.102}O_{6.38}$ composition, ascribing the presence of Al to the contamination from the alumina crucible used in the synthesis. At this oxygen concentration, the crystal was found to belong to the *P*4/*mmm* tetragonal space group. Around the Y and Cu1 positions no significant electron density residuals (edr) appear, i.e., electrons are spherically distributed. Cu2 exhibits two positive edr along the *c* axis, directed along the Cu2–O1 and Cu2–Cu2 vectors. These residuals have been ascribed by the authors to the Cu(3*d*) electron configuration, more precisely to the lack of electrons in the $3d_{x^2-y^2}$ orbital. An asymmetrical electronic distribution was found also near the Ba position, and interpreted as a consequence of the anharmonic thermal vibration of barium.

Buttner et al. (15) studied an orthorhombic crystal (space group *Pmmm*). These authors found strong positive residuals along the Cu2–Cu2 vectors. The residual density around Cu1 ions was interpreted as an electron transfer from Cu(3*d*) to Cu(4*s*) states.

Jang et al. (16, 17) studied both oxidized and reduced samples, to make a direct comparison between the different crystals. In the oxidized sample, the authors noted residual electron density around the Cu1 position, and interpreted it as evidence for Cu1—O1 and Cu1—Cu1 bonding. With regard to Cu2, two positive peaks were observed along the *c* axis, while an electron density depletion appeared between Cu2 and O2. Barium was found to be polarized along *c*. In the reduced sample, the authors found a positive edr along the Cu2–Cu2 vector and a negative edr along Cu2–O1. The authors concluded that the introduction of oxygen in the O4 site significantly changed the electron distribution in the whole unit cell.

In this paper, we present fully periodic ab initio restricted Hartree–Fock (RHF) calculations on the YBCO6 and YBCO7 crystals within a pseudopotential LCAO (linear combination of atomic orbitals) scheme, as implemented in the CRYSTAL-98 (18) computational code. The RHF method is much less common in solid-state chemistry and physics than the density functional approach. Actually, apart from the large overestimation of the electronic band gap, wavefunctions of solids obtained from RHF calculations are generally as accurate as density functional calculations (19). Moreover, it was shown that the electron densities obtained from RHF computations in covalent crystals align with the experimental results (20).

The main purpose of the present investigation is the characterization of the bonding and the atomic properties of YBCO6 and YBCO7 as a function of the oxygen content. Whenever possible, the results obtained are compared with available experimental information on the electron density distribution in the crystal unit cell and its rearrangements due to oxidation (14–17). Particular attention is devoted to the Cu–O superconducting planes, since they are presumed to be responsible for the superconducting behaviour of cuprates at low temperatures (21, 22).

To obtain a quantitative and unambiguous insight into the direct-space description of YBCO6 and YBCO7, we adopted the Quantum Theory of Atoms in Molecules (QTAM) (23) approach. Additional information is recovered through the study of the electron localization function (ELF) (24).

Computational details

The wavefunctions of YBCO6 and YBCO7 were obtained by means of fully periodic pseudopotential restricted Hartree–Fock–Roothaan LCAO calculations, as implemented in the CRYSTAL-98 (18) package. The crystallo-

© 2002 NRC Canada

graphic parameters of the crystals studied were taken from the experimental investigations of Jang et al. (16, 17).

In the case of Y, Ba, and Cu atoms we adopted the small-core pseudopotentials developed by Hay and Wadt (25) in conjunction with the Gaussian basis sets suggested by the authors. Small-core pseudopotential for an atom of the *n*th period includes all the electrons up to the $(n - 2)$th row noble gas, that is [Ne] for Cu, [Ar] for Y, and [Kr] for Ba atoms. Oxygen atoms are described within an all-electron formalism.

With regard to the basis set, Gaussian functions with an exponent lower than 0.1 were cut from the corresponding shells, since they lead to linear dependence in periodic Hartree–Fock calculations. This procedure is largely adopted in computational material science (18). Our choice does not reduce the number of atomic orbitals with respect to the original proposal by Hay and Wadt (25). Moreover, the presence of the crystal symmetry and periodicity should balance the approximation due to the cutting of diffuse Gaussian functions, whose contribution is definitely larger in molecules than in periodic calculations (18, 19). In the case of oxygen, we adopted a standard 6–21G plus *d* polarization function basis set (26), giving this atom a comparable number of atomic orbitals with respect to the metallic atoms. We are confident that the approach described is able to reproduce correctly the changes induced in the total electron density of YBCO6 upon oxidation to YBCO7.

The electronic structure of YBCO6 and YBCO7 is carefully investigated within the QTAM approach (23). Although QTAM applications to condensed-matter systems are quite recent (27), they proved to be a very useful tool to characterize the bonding and atomic properties of the studied systems. QTAM is firmly rooted in quantum mechanics, defines subsystems whose properties are determined by physics (28), and, contrary to more conventional methods of analysis, makes no use of any Hilbert space partitioning to extract information from a wavefunction (23). With respect to this study, QTAM represents the ideal candidate to compare calculated and experimental electron density data. A brief introduction to QTAM and to the notation adopted by the authors can be found elsewhere (29). The main concepts adopted in the discussion will be introduced here when necessary.

To obtain a further insight into the direct-space description of YBCO6 and YBCO7, and particularly into the electronic properties of superconducting Cu-O planes, we recovered additional information from the study of the electron localization function (ELF) (24) in specific regions of the crystal cell. ELF analysis is efficient to discriminate the nature of chemical bonding in ionic, covalent, and metallic materials, as pointed out by Savin et al. (30) in a review article and by Silvi and Gatti (31) in a recent ELF investigation on metals, including copper.

The topological analysis of the electron density was carried out with the TOPOND package (32), developed by Carlo Gatti. This program is interfaced with CRYSTAL and implements QTAM for molecules, polymers, slabs, and crystals. The TOPOND code is also able to recover information about the ELF.

The use of QTAM in the case of pseudopotential calculations requires explanation. Since the theory is based on the analysis of the total electron density of a given system $\rho(\mathbf{r})$, the exclusion of core electrons from the calculated wavefunctions leads to an unphysical behaviour of $\rho(\mathbf{r})$ in the core regions. We, therefore, have to (*i*) ignore the topological behaviour of $\rho(\mathbf{r})$ near the nuclei of metals; and (*ii*) assume that the features of $\rho(\mathbf{r})$ in valence regions are reproduced correctly by our approach, since the core electrons are negligibly affected by the chemical surrounding. The use of small-core instead of large-core pseudopotentials is therefore significant, though increases considerably the computational effort required (about one order of magnitude in CPU time), as demonstrated by Vyboishchikov et al. (33). These authors performed an extensive investigation on several molecules containing transition-metal atoms, and compared electron densities obtained through different approaches, namely large core, small core, and all electron computations. They concluded that the use of small core pseudopotentials gives the electron density the correct topological and quantitative behaviour in valence regions, while adoption of large core pseudopotentials is strongly inadequate (33).

Results and discussion

Bonding network and properties

As a first insight into the properties of YBCO6 and YBCO7 crystals, we discuss the bonding network obtained and its changes upon oxidation, as shown in Fig. 1. Within the framework of QTAM, two atoms are linked to each other if their nuclei are connected by a line (*bond path*) where the electron density $\rho(\mathbf{r})$ is a maximum with respect to any lateral displacement from the line. The point $\mathbf{r}_{bcp}$ where $\rho(\mathbf{r})$ attains its minimum value along the bond path is called a *bond critical point* (bcp). It has been shown (34) that the local properties of the electron density at the bcps sum up very concisely the nature of the interaction occurring between the two linked atoms. In the following, the term "X–Y" bond indicates that atoms X and Y are linked by a bond path.

In YBCO6, Y and Ba atoms are eightfold coordinated, and they are linked to oxygen atoms only. O1 atoms present two oxygen–copper bonds (O1—Cu1 and O1—Cu2, both along the *c* axis) and four O1—Ba bonds, approximately laying onto *ab* planes. O3 atoms behave differently with respect to O1, since they have two bonds with Ba, Y, and Cu2 atoms, and five anion–anion bonds along the *c* axis, thus becoming overall eleven-coordinated. Cu1 is linked to the four first neighbouring copper atoms in the *ab* plane, and forms two Cu1—O1 bonds along the *c* axis. Conversely, Cu2 atoms are bonded to the first four neighbouring O3 atoms laying in the *ab* plane, and two bonds along the *c* axis are formed with O1 and Cu2 atoms. As a result, all copper atoms are six-coordinated.

If we consider the oxidation of the material (YBCO7 crystal), significant variations in the atomic coordination of Ba, Cu1, and O1 atoms are observed. Ba atoms raise their coordination from eight to ten, since two Ba—O4 bonds are formed. Cu1 atoms remain sixfold coordinated, since two copper–copper bonds are replaced with Cu1—O4 bonds. O1 atoms increase their coordination number from six to eight, since two O1—O4 bonds are introduced. O4 atoms are ten-coordinated, and they exhibit four O4—Ba and O4—O1 bonds, along with two O4—Cu1 bonds.

© 2002 NRC Canada

The overall crystal network can be summarized as follows. In the YBCO6 crystal, the two-layered Cu2–O3 atoms build up a caged structure consisting of copper–copper, copper–oxygen, and oxygen–oxygen bonds. The cage extends indefinitely along the *ab* plane, and it includes Y atoms and Y—O bonds. The bonding network of Ba, O1, and Cu1 reflects the alternating cation–anion layered structure.

Oxidation of YBCO6 to YBCO7 does not affect the Cu2–O3 caged structure, while changes are found for Ba (which increases its coordination), Cu1 (which reverts two copper–copper bends into copper–oxygen bonds) and O1 (which forms two anion–anion bonds with O4).

The presence of oxygen–oxygen bonds in YBCO6 and YBCO7 could appear questionable and, in particular, they could be ascribed to the cutting of diffuse basis-set functions from metal atoms. However, both theoretical and experimental studies on ionic crystals revealed the presence of bond paths linking anions (35–37), and analogous cases were found in molecules (38–41). While in molecular systems these bonds are interpreted as evidence of the steric crowding between atoms (38–41), in crystals they can be related to the traditional picture of anions building up a lattice whose interstitial cavities are occupied by cations.

A quantitative picture of the bonding properties of YBCO is obtained through the analysis of the electron density at the crystal's bond critical points. The main features of $\rho(\mathbf{r})$ are reported in Table 1 and discussed in the following. Electron density plots in selected crystal planes are reported in Figs. 2–4, along with the corresponding bonding network.

All bonds (except for Cu—Cu) show a strong closed-shell character. In the case of Ba—O (YBCO6 crystal), the electron density $\rho(\mathbf{r})$ at the bcp is significantly depleted, since the two negative eigenvalues of the Hessian of $\rho(\mathbf{r})$ (λ_1 and λ_2) are comparable to each other and much smaller than the positive one (λ_3). This indicates that bonding between Ba and O is assisted by an electronic charge separation in the internuclear region, as typical of ionic bonds (23). Ba—O bond properties do not depend on the oxidation degree of the crystal, suggesting that Ba cations are negligibly affected by this process despite their increase in coordination due to oxygen insertion.

Y—O bond properties are largely similar to the Ba—O case. The only remarkable feature is that the electron density at the Y—O bcps significantly deviates from cylindrical symmetry, as indicated by nonzero ellipticity values (ε). The eigenvectors associated with λ_1 and λ_2 indicate that $\rho(\mathbf{r})$ is preferentially accumulated away from *ab* planes. This effect slightly strengthens as oxidation takes place, and suggests that Y—O bonds are more sensitive to the crystallographic environment with respect to Ba—O. The ionic nature of Ba—O and Y—O bonds is qualitatively shown in Fig. 4, since the electron density appears spherically distributed around the nuclei of Ba, Y, and O atoms.

The features of Y—O and Ba—O bonds are transferable to O—O, notwithstanding the difference due to atomic charges (Ba—O and Y—O bonds link atoms with opposite charges, at variance with O—O). This result is not contradictory but, on the contrary, grants a large degree of universality to the properties of $\rho(\mathbf{r})$ at the bcp in the case of ionic closed-shell interactions. At variance with respect to the Ba—O case, in YBCO6, O—O bonds exhibit negligible ellipticity values. Analogous with the Y—O case, these linkages are therefore sensitive to the crystal structural and chemical anisotropy. The O3—O3 linkages directed along the *c* axis preferentially distribute charge away from Cu2 first neighbours ($\varepsilon = 0.18$), while an opposite and more marked behaviour is observed in the case of O3—O3 bonds placed onto *ab* planes ($\varepsilon = 0.33$). The picture is substantially maintained when the oxidation of YBCO6 to YBCO7 is considered. In YBCO7, O1—O4 bonds preferentially distribute $\rho(\mathbf{r})$ along *bc* planes (i.e., towards first neighbouring Cu1 atoms).

Copper–copper and copper–oxygen bonds require much more attention, due to their presumed role in the control of the superconductivity properties (21, 22). Cu—O bonds have a strong ionic character, whatever the degree of oxidation of the material and the atoms considered. In fact, similarly to the case of Ba—O, Y—O, and O—O bonds, λ_1 and λ_2 are much smaller (in absolute value) with respect to λ_3, giving $\nabla^2\rho(\mathbf{r})$ a large and positive value.

Despite the similarities between all metal–oxygen bonds, copper atoms present a fundamental difference with respect to the other cations of the crystal. While barium and yttrium assume a nearly spherical valence shell electron density distribution upon bonding with oxygen, copper atoms exhibit a large polarization of their valence shell. More precisely, $\rho(\mathbf{r})$ is depleted along the Cu—O bonding directions and locally concentrated in nonbonding regions, as typical of atoms forming bonds with partial ionic character (29). The above is true for all copper–oxygen bonds (Cu1—O1 and Cu2—O3, see Fig. 3 and 4; Cu1—O4, see Fig. 2) except for Cu2—O1. In fact, no charge depletion in the valence shell of copper is observed along the Cu2—O1 bond path (see Fig. 3), suggesting that this bond is weaker with respect to the other Cu—O bonds. This observation will be quantitatively confirmed below.

Concerning bond ellipticities, in the case of Cu2–O3, a preferential charge accumulation in the *ab* planes is observed, whereas no significant deviation from cylindrical symmetry is observed for Cu2–O1 and Cu1–O1. CuO_2 *ab* layers represent planes of preferential electron density accumulation for Cu—O and O—O bonds. Cu1—O4 bonds (YBCO7) preferentially place electron density onto the two-dimensional copper–oxygen *bc* arrays.

The main structural effects due to oxidation onto Cu—O bonds are: (*i*) the Cu1—O4 bond formation; and (*ii*) the shortening of the Cu2—O1 internuclear distance. As Cu2—O1 changes from 2.47 Å (YBCO6) to 2.31 Å (YBCO7), the electron density and its laplacian significantly increase at the bcp ($\rho(\mathbf{r})$: 0.028 au in YBCO6, 0.041 au in YBCO7; $\nabla^2\rho(\mathbf{r})$: 0.23 au in YBCO6, 0.36 au in YBCO7). These bonds thus approach, without reaching, the values observed at the Cu2—O2 and Cu2—O3 bond critical points ($\rho(\mathbf{r})$ is about 0.1 au and $\nabla^2\rho(\mathbf{r})$ 0.65 au). In conclusion, Cu2—O1 strengthens upon oxidation, but remains weaker than Cu2—O2 and Cu2—O3 bonds. Finally, Cu1—O1 bonds are not significantly affected by oxidation.

Both YBCO6 and YBCO7 exhibit Cu1—Cu1 and Cu2—Cu2 bonds. The analysis of their properties in YBCO6 clearly indicates that they completely differ with respect to all the others present in the crystal. In fact, both in the case of Cu1—Cu1 and Cu2—Cu2, the negative curvatures of the

© 2002 NRC Canada

Table 1. Bonding properties of the YBCO6 and YBCO7 crystals.

Bond	*R*	ρ_{bcp} (1×10^2)	$\nabla^2\rho_{bcp}$ (1×10^2)	λ_1 (1×10^2)	λ_2 (1×10^2)	λ_3 (1×10^2)	ε
YBCO6							
Y—O2	2.402	6.04	33.22	–7.21	–6.04	46.47	0.19
Ba—O1	2.777	3.28	19.28	–3.32	–3.30	25.90	0.01
Ba—O3	2.911	2.34	14.62	–2.31	–2.20	19.13	0.05
Cu1—O1	1.803	13.73	111.00	–8.49	–8.49	128.00	0.00
Cu2—O1	2.473	2.89	23.00	–3.47	–3.47	29.94	0.00
Cu2—O3	1.942	9.88	67.58	–13.04	–9.87	90.49	0.32
Cu1—Cu1	3.860	0.59	0.92	–0.25	–0.25	1.42	0.01
Cu2—Cu2	3.292	0.96	0.41	–0.29	–0.29	0.99	0.00
O3—O3	2.729	3.48	18.71	–3.45	–2.60	24.76	0.33
O3—O3	2.861	2.40	15.64	–2.32	–1.97	19.94	0.18
YBCO7							
Y—O2	2.408	6.05	32.43	–7.76	–5.92	46.11	0.31
Y—O3	2.387	6.39	33.35	–8.43	–6.38	48.16	0.32
Ba—O1	2.749	3.50	20.34	–3.59	–3.57	27.50	0.01
Ba—O2	2.996	1.90	12.18	–1.83	–1.73	15.74	0.06
Ba—O3	2.966	2.05	12.98	–1.98	–1.89	16.85	0.05
Ba—O4	2.888	2.51	15.48	–2.52	–2.49	20.49	0.01
Cu1—O1	1.848	13.11	82.32	–16.25	–12.67	111.25	0.28
Cu1—O4	1.948	9.74	64.10	–12.34	–10.43	86.87	0.18
Cu2—O1	2.313	4.11	36.49	–5.80	–5.78	48.08	0.03
Cu2—O2	1.934	9.95	69.93	–13.91	–10.08	93.91	0.38
Cu2—O3	1.966	9.26	65.22	–12.93	–10.00	88.14	0.29
Cu1—Cu1	3.828	0.42	0.42	–0.15	–0.15	0.73	0.03
Cu2—Cu2	3.390	0.74	0.36	–0.20	–0.17	0.73	0.16
O2—O2	2.832	2.62	16.58	–2.82	–1.76	21.15	0.60
O3—O3	2.852	2.53	15.84	–2.66	–1.79	20.30	0.49
O2—O3	2.731	3.40	18.67	–3.54	–2.82	25.02	0.25
O1—O4	2.685	3.87	20.32	–4.00	–3.17	27.49	0.26

Note: For each bond, we report the internuclear distance (*R*), the electron density value at the bcp (ρ_{bcp}), its laplacian ($\nabla^2\rho_{bcp}$), and the Hessian eigenvalues (λ_i). Apart from *R* (expressed in Å), all other values are in atomic units. The ellipticity (ε) is dimensionless and is defined as $\varepsilon = \lambda_1/\lambda_2 - 1$. In the case of the YBCO6 system, O3—O3 bonds lying onto the *ab* plane are reported in the upper line, while the bonds directed along the *c* axis are in the lower line.

Hessian of $\rho(\mathbf{r})$ at the bcp are smaller but comparable to the positive one. Consistently with the larger internuclear distance (3.860 Å, compared with 3.292 Å), the electron density at the Cu1—Cu1 bcp is about 40% smaller than for Cu2—Cu2. $\rho(\mathbf{r})$ is slightly less concentrated onto the internuclear axis (Cu1—Cu1: $\lambda_1 \cong \lambda_2 \cong -2.5 \times 10^{-3}$ au; Cu2—Cu2: $\lambda_1 \cong \lambda_2 \cong -2.9 \times 10^{-3}$ au), and λ_3 is larger for Cu1—Cu1 than for Cu2—Cu2, despite the larger $\rho(\mathbf{r})$ value of the latter. $\nabla^2\rho(\mathbf{r})$ at these bcps is always positive, but at least one order of magnitude smaller with respect to the other bonds present in YBCO6 and YBCO7. The features of Cu—Cu bonds substantially agree with analogous results obtained in the case of bonding between transition-metal atoms in the oxidized state (see, for example, experimental and theoretical investigations concerning Co–Co in coordination complexes (42, 43)). Cu1—Cu1 appears definitely weaker than Cu2—Cu2, since the electron density at the bcp is smaller and less efficiently concentrated. As our analysis of the ELF will show, there is a definite difference between the nature of Cu1—Cu1 and Cu2—Cu2.

Oxidation of YBCO6 to YBCO7 induces a significant decrease in $\rho(\mathbf{r})$ at all copper–copper bcps (Cu1—Cu1: from 7.4×10^{-3} to 4.2×10^{-3} au; Cu2—Cu2: from 9.6×10^{-3} to 5.9×10^{-3} au), suggesting that insertion of O4 gives rise to the depletion in the valence electron density distribution of all copper atoms, though no Cu2—O4 bonds are formed.

The investigation of the ELF confirms the bonding analysis reported above; a qualitative picture of the ELF is reported in Figs. 2 and 3. The ELF is a local measure of the Pauli repulsion; in the analytical definition given by Becke and Edgecombe (24), it assumes values close to 1.0 in the regions dominated by an antiparallel electron coupling (as happens for covalent interactions or nonbonding electron pairs), while it has near 0.0 values where small coupling between antiparallel electrons occurs (such as the case of closed-shell interactions).

Ba—O and O—O show very low ELF values at the bcps (about 0.02 and 0.03, respectively) confirming their complete ionic character. Slightly greater ELF values are found at Y—O and Cu—O bcps (0.09 for Y—O and 0.08 for Cu—O), indicating a slightly increased shared nature with respect to Ba—O and O—O. Definitely larger ELF values are found only at Cu2—Cu2 bcps, confirming their significant shared character as inferred from the electron density analysis. In YBCO6, the ELF at Cu2—Cu2 bcps assumes a value (0.32) close to the case of metallic copper (0.38) (31) while at

© 2002 NRC Canada

Fig. 2. Isovalue contours of $\rho(\mathbf{r})$ (top), $\nabla^2\rho(\mathbf{r})$ (middle), and ELF($\mathbf{r}$) (bottom panels) for the YBCO6 (left) and YBCO7 (right panels) crystals. Plots represent *ab* planes containing Cu1 atoms. $\rho(\mathbf{r})$: the molecular graph is superimposed to the electron density isovalues lines. Bond paths are traced as heavy lines; bcps are marked with dots. $\nabla^2\rho(\mathbf{r})$: negative (positive) contour values are traced with full (dashed) lines. ELF($\mathbf{r}$): contour values greater (smaller) than 0.5 are traced with full (dashed) lines.

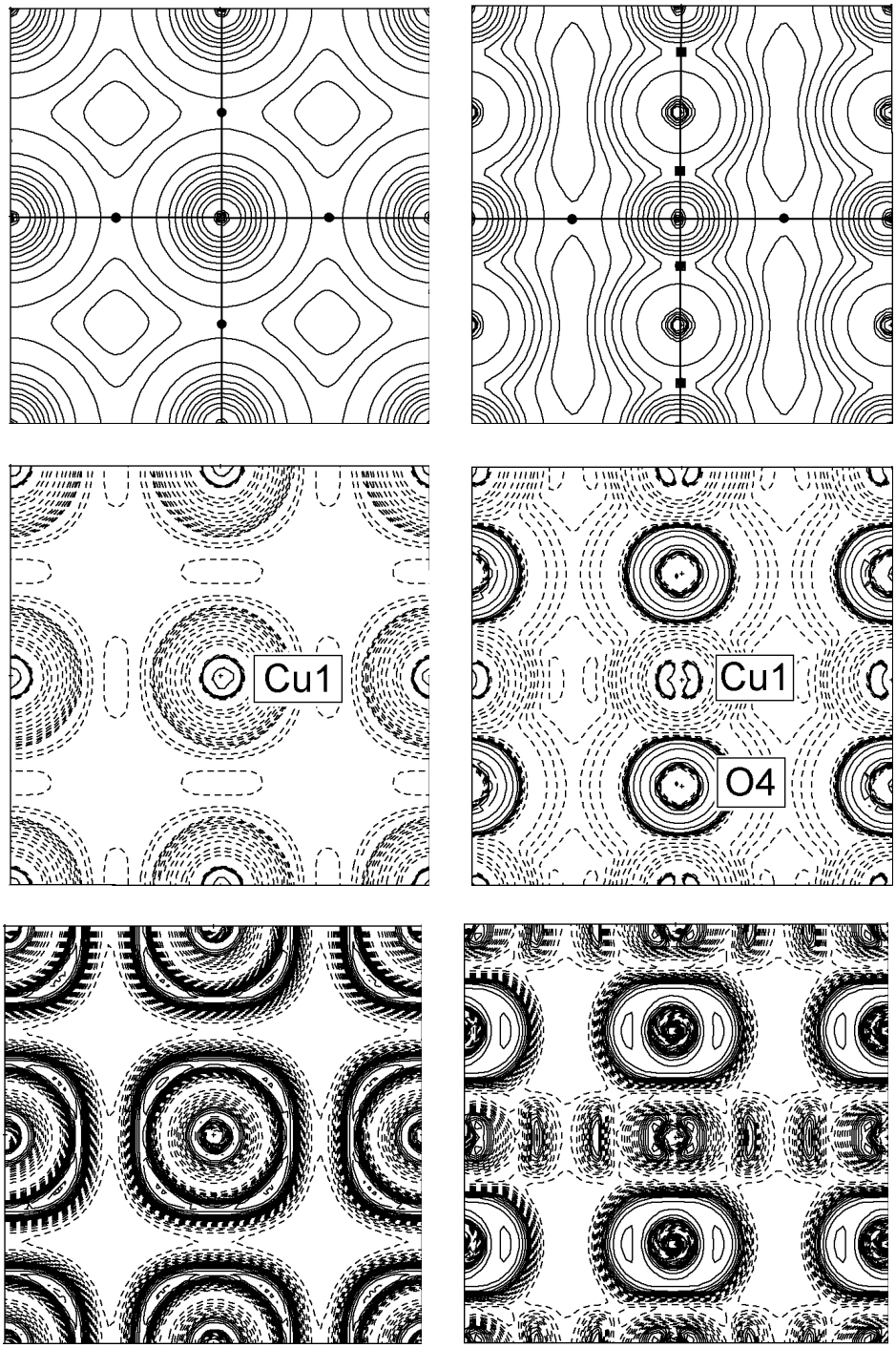

Cu1—Cu1 bcps, it is significantly smaller (0.06), and indicates that a weak coupling between bonding electrons occurs. In the oxidized material (YBCO7) minor changes are observed. The ELF increases to 0.09 at Cu1—Cu1 bcps (see bottom panels of Fig. 2), while in the case of Cu2—Cu2 it undergoes a minor decrease (ELF = 0.30) in spite of the observed large lowering of the electron density (see Fig. 3).

In conclusion, the ELF analysis indicates that the properties of Cu1—Cu1 bonds have a nearly closed-shell character. On the contrary, Cu2—Cu2 bonds are similar to the limiting case of metallic copper (31), notwithstanding the net and large positive charge assumed by Cu2 in YBCO (see next section).

In cuprate superconductors, the superconducting transition temperature usually increases with the number *n* of neighbour-

© 2002 NRC Canada

Fig. 3. Isovalue contour plot of $\rho(\mathbf{r})$ (top), $\nabla^2\rho(\mathbf{r})$ (middle), and ELF($\mathbf{r}$) (bottom panels) for the YBCO6 (left) and YBCO7 (right panels) crystals. Plots represent *ac* planes. See the caption to Fig. 2 for notation.

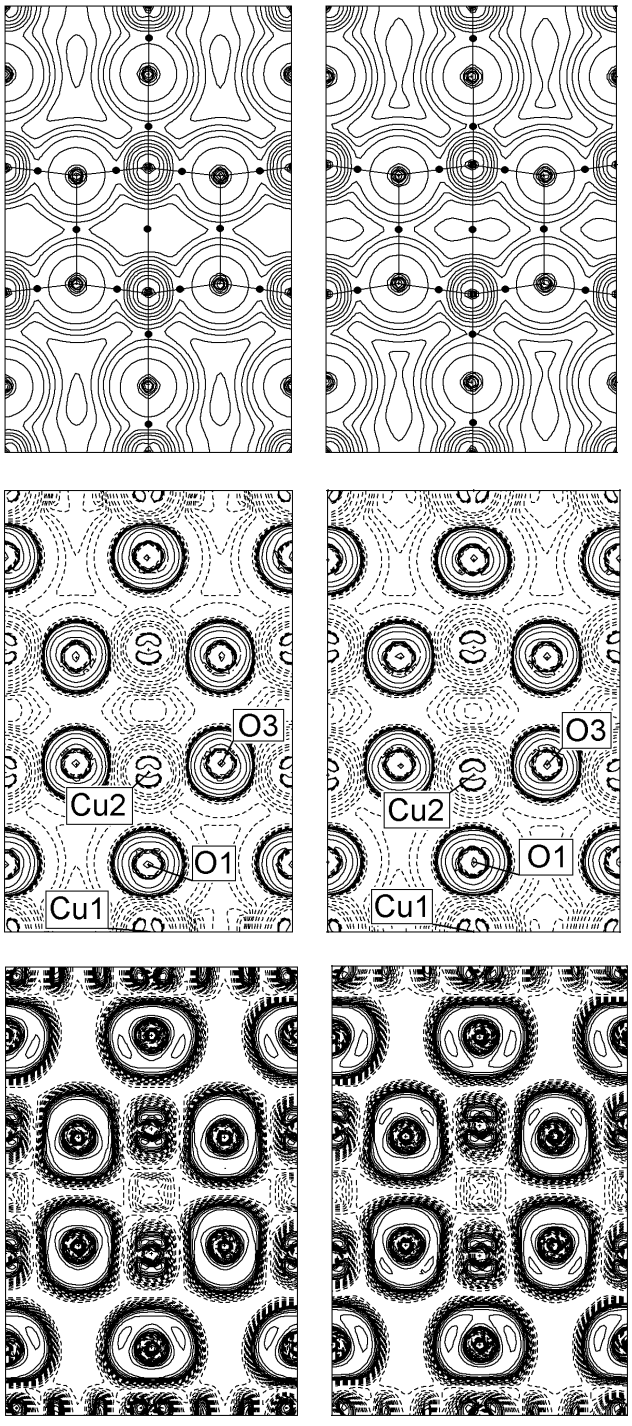

ing CuO_2 *ab* planes. As an example, in $Bi_2Sr_2Ca_{n-1}Cu_nO_y$ the critical temperature T_C is 10, 90, and 110 K for n = 1, 2, and 3, respectively (44). The copper–copper covalent bonds along *c* could support the delocalization of charge carriers in neighbouring superconducting planes, and play a role in the mechanism of charge transport both in the normal and superconducting states.

Atomic properties

QTAM performs an unambiguous partitioning of the physical space in disjointed regions (usually including just one nucleus) termed *atomic basins* and indicated with Ω (23). An important consequence is that many observables can be partitioned in *atomic* contributions that sum up to the system expectation value. In the present investigation, we will focus on: (*i*) the electron population of each atom; and (*ii*) the polarization of their basin electron density. The atomic polarization is rationalized and quantified through the analysis of the first- and the second-electronic moments of each basin, that is, the dipole vector μ (45) and the quadrupole tensor $\mathbf{Q}$ (46, 47), whose components are defined (in Cartesian coordinates) by the following equations:

$$[1] \qquad \mu_i = -\int_{\Omega} \rho(\mathbf{r}) x_i \mathrm{d}\tau$$

$$[2] \qquad Q_{ij} = -\int \rho(\mathbf{r})(3x_i x_j - \delta_{ij} r^2)\mathrm{d}\tau$$

where x_i stands for x, y, and z or, equivalently in the case of the systems studied here, coordinates expressed in the crystals unit cell vectors a, b, and c, respectively. Electron density distributions with spherical symmetry have zero Q_{ii} terms; negative Q_{ii} values indicate an accumulation of charge in the x_i direction at the expense of the directions associated with positive Q_{jj} components.

In YBCO6 and YBCO7, the only significant components of the atomic dipoles are directed along the *c* axis, while generally only the diagonal terms (Q_{aa}, Q_{bb}, and Q_{cc}) of the quadrupole tensors have nonzero values. This means that in this study the eigenvectors of $\mathbf{Q}$ are rigorously (YBCO6) or nearly (YBCO7) placed along the three cell axes *a*, *b*, and *c*. The relevant data of the atomic charge (q) and the atomic first- and second-electronic moments are reported in Table 2. Atomic first-moment values refer to atoms lying in the lower part of the cell represented in Fig. 1.

To get a qualitative picture of the present analysis, in Figs. 2–4 we report plots of the electron density $\rho(\mathbf{r})$ and its laplacian $\nabla^2\rho(\mathbf{r})$ in selected crystal planes. The $\nabla^2\rho(\mathbf{r})$ scalar field is related to the atomic electron density polarization, as it assumes negative values in regions where $\rho(\mathbf{r})$ is locally concentrated and vice versa (23).

We first examined the atomic electronic populations (see Table 2). In YBCO6, the largest positive charge is observed for Cu2 (+2.36e); similar values are found for Y (+2.11e) and Ba (+2.04e), whereas Cu1 atoms exhibit a definitely smaller oxidation degree (+1.17e). The average charge of oxygen atoms is –2.01e, O1 and O2 atoms being respectively "overcharged" and "undercharged" of about 0.1e with respect to the ideal ionic value of –2e. Taking into account the oxidation of the material, all cations increase their positive charge. This additional charge transfer from metallic atoms to oxygen is strongly selective with respect to the different cations. Cu1 loses 1.12e, whereas Y, Cu2, and Ba only lose small amounts (0.13, 0.09, and 0.04e, respectivey); the average oxygen charge decreases to –1.95e. It is worth noting that yttrium atoms are more sensitive than barium atoms with respect to the crystal oxygen content, although Ba is much closer than Y to O4 sites, and no Y—O4 bond is formed. This agrees with the observed dependence of the

© 2002 NRC Canada

Fig. 4. Isovalue contour plot of $\rho(\mathbf{r})$ (left) and $\nabla^2\rho(\mathbf{r})$ (right) for the YBCO6 crystal. Plots refer to *ab* (top) and *ac* (bottom) planes. Top left panel: the Cu2—O2 molecular graph is projected on the plot plane. Left panels: bcps are marked with dots. Right panels: see the caption to Fig. 2 for notation.

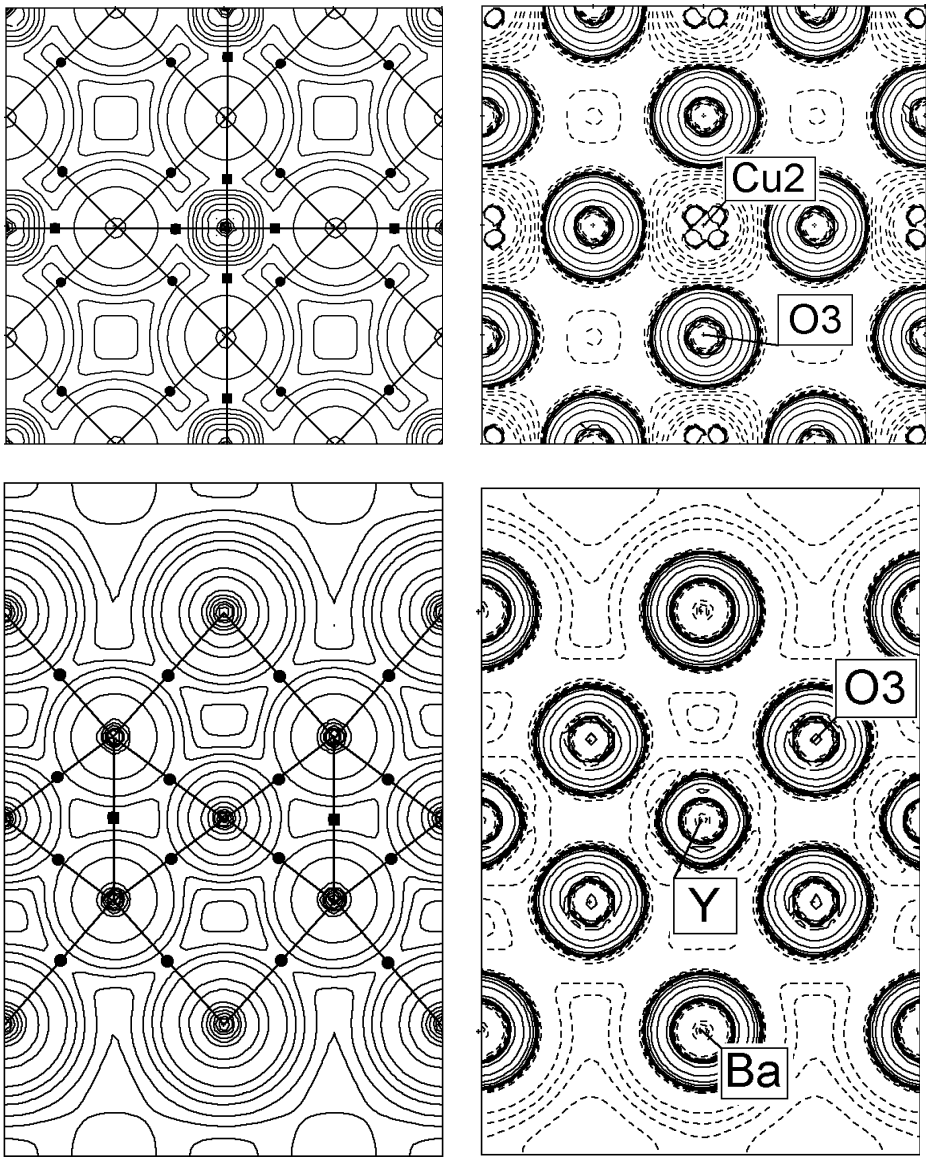

cuprates electronic properties on the rare earth metal placed at the Y site (2).

Focusing on CuO_2 *ab* planes, upon oxidation the overall electron population of Cu2, O2, and O3 undergoes a decrease of 0.16e/plane. This finding is in accordance with the increase of electronic holes in CuO_2 *ab* planes observed upon oxidation.

Comparing the atomic charges of copper atoms with the empirical estimates given by Brown (13), we obtain a good quantitative agreement (i.e., within 0.1e) in the case of Cu1, whatever the oxidation degree of the material considered. In the case of Cu2, QTAM and empirical values are similar in YBCO7, but significantly differ in YBCO6 (QTAM, +2.36e; empirical, +1.9). Both approaches predict that oxidation of YBCO6 increases the positive charge of Cu1 and Cu2. Brown (13) found that Cu2 is more charged than Cu1 in YBCO6 (Cu1, +1.2e; Cu2, +1.9e), the picture being reversed in YBCO7 (Cu1, +2.4e; Cu2, +2.3e); conversely, QTAM data indicate that Cu2 is more charged than Cu1 whatever the oxygen content considered.

The picture given by QTAM agrees with the experimental estimates of copper atom charges given by Akase et al. (48). These authors studied a crystal of $YBa_2Cu_3O_{6.90}$ composition by means of convergent-beam electron diffraction, and assigned to Cu1 and Cu2 a charge of +2.0 and +2.2e, respectively.

The analysis of the first and second electrostatic moments of cations agrees with the rank of ionic behaviour suggested from the previous analysis, and confirms the qualitative observations on the polarization of the valence shell electron density distribution reported in the previous chapter. Ba has the smallest dipole and quadrupole moment components: in the YBCO6 crystal its electronic population is accumulated preferentially along the *c* axis ($Q_{cc} = -0.88$ au), while the *ab*

© 2002 NRC Canada

Table 2. Atomic properties of the YBCO6 and YBCO7 crystals.

Atom	q	μ_c	Q_{aa}	Q_{bb}	Q_{cc}
YBCO6					
Y	+2.11	0.00	–0.73	–0.73	+1.46
Ba	+2.04	+0.21	+0.44	+0.44	–0.88
Cu1	+1.17	0.00	–3.45	–3.45	+6.90
Cu2	+2.36	–0.11	+1.02	+1.02	–2.04
O1	–2.16	+0.02	–0.53	–0.53	+1.06
O3	–1.93	+0.03	+0.10	+1.14	–1.24
YBCO7					
Y	+2.24	0.00	+0.49	+0.17	–0.66
Ba	+2.08	+0.03	+0.61	–0.10	–0.52
Cu1	+2.29	0.00	–3.41	+1.56	+1.84
Cu2	+2.45	–0.10	+0.90	+0.81	–1.71
O1	–2.03	–0.02	–1.06	+0.07	+0.99
O2	–1.89	–0.02	+1.27	–0.04	–1.23
O3	–1.90	–0.02	+0.03	+1.07	–1.10
O4	–1.96	0.00	–1.74	+1.68	+0.06

Note: For each atom we report the atomic charge (q), the c axis component of the atomic first moment (μ), and the three relevant components of the atomic quadrupole moment tensor (Q_{aa}, Q_{bb}, and Q_{cc}). All values are in atomic units. Dipole moments: 1 au = 2.542 D. Quadruple moments: 1 au = 1.345 B.

plane depletion is isotropic ($Q_{aa} = Q_{bb}$). Barium μ_c is positive (+0.21 au), as the Ba atoms' electron density is preferentially distributed towards Cu1. In YBCO7, the c axis electron density accumulation is less intense ($Q_{cc} = -0.52$ au) and nearly symmetric with respect to the Ba nucleus ($\mu_c = +0.03$ au). The anisotropy of the barium electron density along the c axis is consistent with previous experimental findings (14, 16), and should, therefore, not be entirely attributed to its anharmonic thermal motion.

Y atoms have a zero c component of the atomic dipole due to crystal symmetry. The analysis of **Q** indicates that in the YBCO6 crystal Y places electron density preferentially onto *ab* planes ($Q_{aa} = Q_{bb} = -0.74$ au; $Q_{cc} = +1.46$ au). Surprisingly, the picture is completely reversed in YBCO7, where the *ab* planes appear to be slightly depleted ($Q_{aa} = +0.49$ au; $Q_{bb} = +0.17$ au) in favour of a c axis accumulation ($Q_{cc} = -0.66$ au).

The large atomic polarization of copper atoms confirms their lower ionic behaviour with respect to Y and Ba atoms. In YBCO6 the valence shell of Cu1 is deprived along the c axis ($Q_{cc} = +6.91$ au, see Fig. 3) and accumulated onto *ab* planes ($Q_{aa} = Q_{bb} = -3.46$ au, see Fig. 2). As O4 is introduced, nearly equivalent $\rho(\mathbf{r})$ depletions along c and b are observed ($Q_{bb} = +1.56$ au; $Q_{cc} = +1.84$ au), the Cu1 electron density is preferentially accumulated along the a direction and points towards nearest neighbouring Cu1 atoms. Contrary to our findings, and to the investigation of Buttner et al. (15), which indicate a charge depletion along the Cu1–O1 vectors, Sasaki et al. (14) obtained a spherical electron density distribution for Cu1 atoms.

Concerning Cu2, in YBCO6 its valence shell electron density is depleted along the first neighbour Cu2—O3 directions ($Q_{aa} = Q_{bb} = +1.02$ au), while Cu2—O1 bonds are not strong enough to induce an electron density depletion along the c axis (see Figs. 3 and 4). The c axis electron density accumulation is more marked in the Cu2—Cu2 internuclear region ($\mu_c = -0.11$ au), in agreement with the shared nature of this bond. In an atomic orbital picture, we could state that Cu2–O interactions preferentially deprive of electronic population the orbitals with a and b components such as the $3d_{x^2-y^2}$ one, as suggested by Sasaki et al. (14) and by Jang et al. (17). Concerning oxidation to YBCO7, no qualitative changes in the valence shell arrangement of Cu2 are observed. Quantitatively, oxidation induces minor changes in the atomic polarization of copper (μ_c decreases from +0.11 to +0.10 au; Q_{aa} and Q_{bb} change from +1.02 to +0.90 and +0.81 au, respectively; Q_{cc} varies from –2.04 to –1.71 au). Finally, the preferential c axis electron density accumulation of Cu2 is consistent with X-ray experimental investigations (14–17).

The behaviour of oxygen can be summarized as follows. First, O atoms present atomic polarization terms comparable with respect to Y and Ba atoms (μ values close to 0.01 au and **Q** components close to 1.00 au). Second, the polarization of O atoms is dominated by the surrounding Y and Ba atoms, since the electron density is preferentially polarized along Ba—O and Y—O directions. Oxidation does not induce significant changes in O2 and O3, and in YBCO7 these atoms remain thus similar to each other, in agreement with other theoretical investigations (10). Conversely, insertion of O4 induces a significant change in the polarization of O1. While in YBCO6 these atoms equally accumulate electron density along the a and b directions, in YBCO7 the proximity of O4 induces a preferential polarization along a, away from O1—O4 vectors.

Conclusions

We calculated the wavefunctions of YBCO6 and YBCO7 by means of ab initio fully periodic restricted Hartree–Fock pseudopotential LCAO calculations. The electronic structure of the crystals were then investigated by means of a density based (i.e., direct space) approach, namely the quantum theory of atoms in molecules (23).

The analysis of the bonding properties reveals the presence of an extended O2-O3-Cu2 caged structure that includes Y cations. The structure presents O—O bonds with strong closed-shell character, as found for Y—O and Ba—O, while a larger shared nature is found for Cu—O. Cu1—Cu1 bonds are weak, and their properties suggest a nearly closed-shell nature. Contrary to all the other bonds present in the crystals, Cu2—Cu2 bonds have a marked shared (i.e., covalent) character, confirmed by the proximity of the ELF value at the bcp to the case of metallic copper. Since Cu2—Cu2 bonds bridge neighbouring superconducting planes, it is likely that they play an important role in the delocalization of charge carriers in superconducting cuprates.

The analysis of atomic properties indicates that both in the YBCO6 and YBCO7 crystals Ba cations have a nearly +2e charge, while the other cations' electronic populations significantly depend on the oxidation degree considered. Inclusion of O4 in the structure induces a large oxidation of Cu1, but also Y and Cu2 atoms undergo an electron population decrease. Contrary to Ba, Y is sensitive to the crystal structure and oxygen content, in agreement with the dependence of the superconducting properties of cuprates on the rare earth element inserted.

© 2002 NRC Canada

The study of atomic polarization indicates a small anisotropy of the electron density around Ba cations, insofar that there is a preferential accumulation along the *c* axis. Analogous experimental findings suggest that this is a proper electronic effect, and not (only) the result of the anharmonic thermal motion of barium (14, 16).

Concerning copper, in YBCO6 the Cu1 valence charge density is depleted along the Cu1–O1 directions, while in YBCO7 the same is true for the Cu1–O4 vectors also. The valence shell polarization of Cu1 largely depends on the oxygen content.

Cu2 is significantly polarized along the *c* axis, in accordance with experimental data (14, 15, 17). O1 does not deplete the valence shell of Cu2 in both YBCO6 and YBCO7, since Cu2—O1 bonds are weaker than Cu2—O2 and Cu2—O3 bonds. Copper atoms share a significant amount of electron density along the Cu2–Cu2 internuclear region.

Oxygen atoms are weakly polarized, and preferentially place electron density towards Ba and Y atoms.

Acknowledgment

The authors gratefully acknowledge Carlo Gatti for helpful discussions.

References

1. M. Marezio. Acta Crystallogr. Sect. A: Fundam. Crystallogr. **A47**, 640 (1991).
2. M.S. Skakle. Mater. Sci. Eng. **R23**, 1 (1998), and refs. therein.
3. G. Chiodelli, G. Campari Viganò, and G. Flor. Z. Naturforsch. A: Phys. Sci. **44A**, 1167 (1989).
4. P.A. Korzhavy, C. Ambrosch-Draxl, and B. Johansson. J. Low Temp. Phys. **117**, 395 (1999).
5. S.L. Drechsler, J. Malek, and H. Eschrig. Phys. Rev. B: Condens. Matter, **55**, 606 (1997).
6. G.L. Zhao and D. Bagayoko. Int. J. Mod. Phys. B, **13**, 3579 (1999).
7. H. Kamimura and A. Sano. J. Superconduct. **10**, 279 (1997).
8. A.N. Timoshevskii, V.S. Melnikov, and A.E. Krasovskii. Czech. J. Phys. **46**, 929 (1996).
9. K.H. Lee, S.S. Park, C.G. Jo, W.R. Lee, H.M. Lee, and U.S. Choi. Solid State Commun. **100**, 365 (1996).
10. W.E. Pickett. Rev. Mod. Phys. **61**, 433 (1989), and refs. therein.
11. J.K. Burdett. J. Phys. Chem. **100**, 13 263 (1996).
12. J.V. Acrivos and O. Stradella. Int. J. Quantum Chem. **46**, 55 (1993).
13. I.D. Brown. J. Solid State Chem. **90**, 155 (1991).
14. S. Sasaki, Z. Inoue, N. Iyi, and S. Takekawa. Acta Crystallogr. Sect. B: Struct. Sci. **48**, 393 (1992).
15. R.H. Buttner, E.N. Malsen, and N. Spadaccini. Acta Crystallogr. Sect. B: Struct. Sci. **48**, 21 (1992).
16. W.-J. Jang, H. Mori, M. Watahiki, S. Tajima, N. Koshizuka, and S. Tanaka. J. Solid State Chem. **122**, 371 (1996).
17. W.-J. Jang, H. Mori, M. Watahiki, S. Tajima, N. Koshizuka, and S. Tanaka. J. Solid State Chem. **130**, 42 (1997).
18. V.R. Saunders, R. Dovesi, C. Roetti, M. Causà, N.M. Harrison, R. Orlando, and C.M. Zicovich-Wilson. CRYSTAL-98, User's Manual. University of Torino, Torino, Italy. 1999.
19. C. Pisani, R. Dovesi, and C. Roetti. Hartree–Fock ab initio treatment of crystalline materials. *In* Lecture notes in chemistry. Vol. 48. Springer, Berlin. 1988.
20. C. Pisani, R. Dovesi, and R. Orlando. Int. J. Quantum Chem. **42**, 5 (1992).
21. A.W. Sleight. Science (Washington, D.C.), **242**, 1519 (1988).
22. R.J. Cava. Science, **247**, 656 (1990).
23. R.F.W. Bader. Atoms in molecules: A quantum theory. *In* Int. series of monographs on chemistry. Vol. 22. Oxford University Press, Oxford. 1990.
24. A.D. Becke and K.E. Egdecombe. J. Chem. Phys. **92**, 5397 (1990).
25. P.J. Hay and W.R. Wadt. J. Chem. Phys. **82**, 299 (1985).
26. W.J. Hehre, L. Radom, P.V.R. Schleyer, and J.A. Pople. Ab initio molecular orbital theory. Wiley–Interscience, New York. 1986.
27. F. Cargnoni and C. Gatti. Theor. Chem. Acc. **105**, 309 (2001), and refs. therein.
28. R.F.W. Bader. Phys. Rev. B: Condens. Matter, **49**, 13 348 (1994).
29. F. Cargnoni, C. Gatti, E. May, and D. Narducci. J. Chem. Phys. **112**, 887 (2000).
30. A. Savin, R. Nesper, S. Wengert, and T.F. Fässler. Angew. Chem. Int. Ed. Engl. **36**, 1808 (1997).
31. B. Silvi and C. Gatti. J. Phys. Chem. A, **104**, 947 (2000).
32. C. Gatti. TOPOND98, User's Manual. CNR-CSRSRC, Milano, Italy. 1999.
33. S.F. Vyboishchikov, A. Sierraalta, and G. Frenking. J. Comput. Chem. **18**, 416 (1997).
34. R.F.W. Bader and H. Essen. J. Chem. Phys. **80**, 1943 (1984).
35. A. Martin Pendas, A. Costales, and V. Luana. Phys. Rev. B: Condens. Matter, **55**, 4275 (1997).
36. V. Luana, A. Costales, and A. Martin Pendas. Phys. Rev. B: Condens. Matter, **55**, 4285 (1997).
37. Y.A. Abramov. J. Phys. Chem. A, **101**, 5725 (1997).
38. J. Cioslowski and E.D. Fleischmann. J. Chem. Phys. **94**, 3730 (1991).
39. J. Cioslowski. Chem. Phys. Lett. **181**, 68 (1991).
40. J. Cioslowski and S.T. Mixton. Can. J. Chem. **70**, 443 (1992).
41. J. Cioslowski and S.T. Mixton. J. Am. Chem. Soc. **114**, 4382 (1992).
42. A.A. Low, K.L. Kunze, P.J. MacDougall, and M.B. Hall. Inorg. Chem. **30**, 1079 (1991).
43. R. Bianchi, G. Gervasio, and D. Marabello. Helv. Chim. Acta, **84**, 722 (2001).
44. J.M. Tarascon, W.R. McKinnon, P. Barboux, D.M. Hwang, B.G. Bagley, L.H. Green, B.W. Hull, and Y. LePage. Phys. Rev. B: Condens. Matter, **38**, 8885 (1988).
45. R.F.W. Bader, A. Larouche, C. Gatti, M.T. Carrol, P.J. MacDougall, and K.B. Wiberg. J. Chem. Phys. **87**, 1142 (1987).
46. R.F.W. Bader and C. Chang. J. Phys. Chem. **93**, 2946 (1989); 5095 (1989).
47. C. Gatti, A. Ponti, A. Gamba, and G. Pagani. J. Am. Chem. Soc. **114**, 8634 (1992).
48. Z. Akase, Y. Tomokiyo, Y. Tanaka, and M. Watanabe. Physica C: (Amsterdam), **C338**, 137 (2000).

© 2002 NRC Canada

Conformational analysis of the bicyclo-[4.4.1]undecan-11-one ring system

Masood Parvez, Ted S. Sorensen, and Fang Sun

Abstract: The first conformational analysis of a bicyclo[4.4.1]undecan-11-one system (**1**) is presented. Based on low-temperature ^{13}C NMR line-broadening measurements and an X-ray structure of the 1,6-dibromo derivative (**2**), this ketone adopts a chiral conformation with approximate C_2 symmetry about an axis containing the >C=O bond. The observed NMR line-broadening results are consistent with a dynamic interchange of *M* and *P* enantiomeric C_2 conformations, or expressed another way, the "effective" development of an additional C_s symmetry plane bisecting the molecule at right angles to the plane containing the one carbon bridge (overall average C_{2v} symmetry). This process has a $\Delta H^{\ddagger}$ barrier of 42 kJ mol^{-1} for ketone **1** (43 kJ mol^{-1} for **2**).

Key words: bicyclo[4.4.1]undecan-11-one, conformational analysis, NMR line broadening, X-ray structure, enantiomers.

Résumé : On présente la première analyse conformationnelle d'un système bicyclo[4.4.1]undécan-11-one (**1**). Sur la base de mesures à basse température de l'élargissement des raies de RMN du ^{13}C ainsi que sur la structure de son dérivé 1,6-dibromé (**2**) telle que déterminée par diffraction des rayons X, cette cétone adopte une conformation chirale de symétrie approximative C_2 autour d'un axe qui comprend la liaison >C=O. Les résultats observés pour l'élargissement des raies en RMN sont en accord avec un échange dynamique des conformations C_2 énantiomères *M* et *P* ou, exprimé d'une autre façon, avec le développement "effectif" d'un plan de symétrie C_s additionnel qui divise la molécule à angles droits par rapport au plan contenant le carbone du pont (symétrie globale moyenne C_{2v}). Dans la cétone **1**, la barrière d'énergie, $\Delta H^{\ddagger}$, est de 42 kJ mol^{-1} (43 kJ mol^{-1} dans **2**).

Mots clés : bicyclo[4.4.1]undécan-11-one, analyse conformationnelle, élargissement de raies en RMN, diffraction des rayons X, énantiomères.

[Traduit par la Rédaction]

Introduction

Out-out-bicyclo[4.4.1]undecan-11-one (**1**) was synthesized in the expectation that ring-expansion reactions of the one-carbon bridge might yield efficient routes to larger ring systems. For example, such approaches have been used to prepare the bicyclo[3.3.3]undecane ring system from bicyclononan-9-one (1), but unfortunately ketone **1** proved to be resistant to nucleophilic addition reactions, e.g., dimsyl anion.

In characterizing **1**, however, we became interested in the

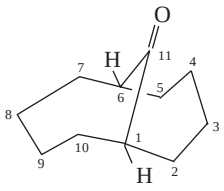

1

conformational behavior of this simple ketone, since the room temperature ^{13}C NMR spectrum clearly showed one broadened peak, which is indicative of a relatively high barrier for a conformational interchange process. Unlike the well-studied bicyclo[3.3.1]nonane ring system (2), there have been no studies of the larger [4.4.1] skeleton. There was also a possibility that the nonreactivity of **1** might be related in some way to its conformation, although this turns out not to be the case.

This paper reports a variable temperature NMR conformational study of **1** and of the 1,6-dibromo derivative (**2**). We also obtained a single crystal X-ray structure of the latter.

Results and discussion

Ketone **1** was prepared by hydrogenation of the known [6+4] cycloadduct of tropone and butadiene (3, 4). Alternative approaches from 2-carboethoxycycloheptanone and 1,4-dialkylating agents (single pot or two-step) were unsuccessful as preparative-scale reactions (low yields, complex mixtures). The room temperature 400 MHz NMR spectrum of **1** shows four complex multiplets, a symmetrical multiplet (2H) at δ 2.78 (H1 and H6), and multiplets at ca. 1.8 (8H), 1.62 (4H), and 1.45 (4H). The 100 MHz ^{13}C NMR spectrum shows four peaks at δ 219.8 (C=O), 55.0 (CH), 28.7 (CH_2), and 26.8 (CH_2). The peak at δ 28.7 (25°C) was noticeably broader than the other three. The ^{13}C NMR peaks at δ 26.8

Received 16 September 2001. Published on the NRC Research Press Web site at http://canjchem.nrc.ca on 15 March 2002.

M. Parvez, T.S. Sorensen,[1] and F. Sun. The Department of Chemistry, University of Calgary, Calgary, AB T2N 1N4, Canada.

[1]Corresponding author (e-mail: sorensen@ucalgary.ca).

 DOI: 10.1139/V02-022 © 2002 NRC Canada

Fig. 1. Schematic representations of the possible symmetry elements present in bicyclo[4.4.1]undecan-11-one (**1**). A, B, etc. represent nonequivalent sites. The view is looking down through the >C=O bond.

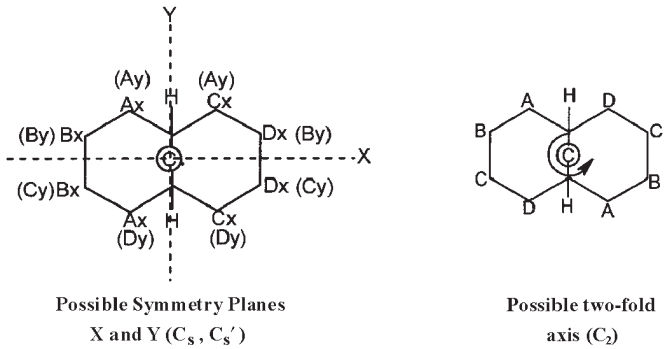

and 28.7 can be assigned to the 3,4,8,9 and 2,5,7,10 carbons, respectively, based on low-temperature ^{1}H–^{13}C HETCOR and ^{1}H COSY spectra, together with coupling constant data. The presence of only four ^{13}C NMR peaks for **1** at 25°C (from a total of eleven carbons) requires at least two separate elements of molecular symmetry (or conformationally averaged symmetry).

Variable temperature NMR spectra of 1

A series of low-temperature ^{1}H (400 MHz) and ^{13}C (100 MHz) NMR spectra were run at 10°C intervals from 25 to –115°C in CD_2Cl_2. In the ^{1}H NMR spectrum, the peak at δ 2.78 is unchanged except for loss of resolution. Changes in the high-field peaks, however, are readily apparent, the most notable being the extreme broadening of the 4H δ 1.45 multiplet, and eventual decoalescence into a 2H quartet at ca. δ 1.1 (J = 12.8 Hz). The other half of this system is buried in a complex series of peaks from δ 1.4 to 2.0.

In the ^{13}C NMR spectrum, the 2C peak at ca. 55 ppm and the >C=O peak are unchanged, but both high-field carbon peaks broaden and eventually devolve into two peaks: δ 28.7 into 24.2 and 30.7; δ 26.8 into 25.1 and 26.4 (the chemical shifts are somewhat temperature dependent).

These low-temperature NMR results (six ^{13}C peaks present, 1:2:2:2:2:2 relative area) are consistent with **1** having essentially a single conformation in which pairs of carbons *remain equivalent even at –115°C*. A structure in which this symmetry is generated by either of two symmetry planes (*X* or *Y*) or a two-fold rotation axis, could be consistent with the low-temperature NMR results, as shown in Fig. 1.

Since, however, the 2C bridgehead carbon peak remains unbroadened, a structure in which the symmetry is generated by either the symmetry plane *X* or the two-fold rotation axis would be more consistent with the low-temperature NMR results. The third possibility involving the *Y* symmetry plane would require concomitant accidental equivalence of the bridgehead-carbon chemical shifts, which in the case of ^{13}C NMR spectroscopy in particular is obviously a less-likely scenario.

The symmetry plane (*X*) model requires different conformations in the two rings, whereas the rotational axis model implies that both rings have the same conformation.

The dynamic NMR line-broadening results noted in this study were quantified by modeling the observed ^{13}C NMR spectra with calculated lineshapes (two-site exchanges). Useable data were obtained from +5 to –75°C (10°C intervals), employing either or both of the averaged ^{13}C peaks. The lower field averaged peak was used from +5 to –35°C, the higher field averaged peak from –35°C to –55°C. At –55°C, broadened decoalesced peaks from the original "δ 28.7 averaged peak" were evident, and at –65°C both sets of broadened decoalesced peaks were present. A plot of the measured rate constants vs. $1/T$ gave a good linear plot: $\Delta H^{\ddagger} = E_a - RT = 42 \pm 1$ kJ mol^{-1} and $\Delta S^{\ddagger} = -2 \pm 2$ J mol^{-1} K^{-1}.

The dynamic conformational process responsible for these line-broadening results can be accommodated by assuming that either of the previously discussed conformations for **1** represent the "frozen-out" structure, and that the dynamic NMR line broadening is caused by a conformational interchange process that generates an additional element of symmetry, i.e. C_2 (ground state) $\overset{C_s}{\rightarrow}$ effective C_{2v} symmetry or C_s (ground state) $\overset{C_2}{\rightarrow}$ effective C_{2v} symmetry. For example, the latter possibility could be envisaged as shown below:

[1] 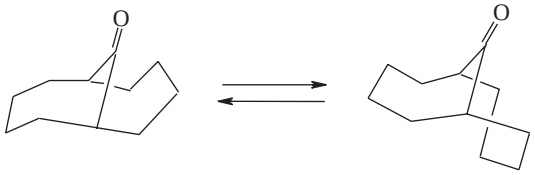

Since either of the above processes seemed possible, we felt that an X-ray structure of the **1** system might provide a more definitive answer to this ambiguity. Ketone **1** is a liquid, but the 1,6-dibromo structure **2**, prepared from **1** using free radical bromination conditions, is a white crystalline solid. Since the bromine presence in **2** could conceivably influence the conformational behavior of the [4.4.1] system, we first carried out ^{1}H and ^{13}C NMR studies on **2**.

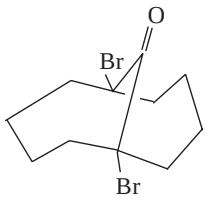

2

As for **1**, both the ^{1}H and ^{13}C NMR spectra of **2** showed dynamic NMR line broadening. At ambient temperature four ^{1}H multiplets were observed at δ 2.55, 2.4, 1.9, and 1.7 (all 4H). The more deshielded pair were both dddd patterns, but the more shielded pair were more complex. On cooling to –77°C, five multiplets were produced at ca. δ 2.45 (6H), 2.1 (2H), 1.9 (2H), 1.72 (4H), and 1.35 (2H). Except for the peak at δ 1.35 (q, J = 12.2 Hz) these multiplets were complex. The presence of the high field quartet in the decoalesced spectrum is a similar result to that observed for **1**.

The ambient ^{13}C NMR spectrum of **2** was also similar to that of **1**, δ 200.7 (CO), 82.0 (Cq), 41.1 (CH_2, C2,5,7,10), and 25.8 (CH_2, C3,4,8,9). The peak at δ 41.1 decoalesces into peaks at δ 43.8 and 36.6, the peak at δ 25.8 into peaks at δ 26.4 and 23.8; the two less-shielded ^{13}C peaks remain

© 2002 NRC Canada

Table 1. Experimental details for structure **2**.

Empirical formula	$C_{11}H_{16}Br_2O$
Formula weight	324.06
Temperature (*K*)	173(2)
Wavelength	0.71069
Crystal system (Å)	Monoclinic
Space Group	$P2_1/n$
Unit cell dimensions (Å)	a = 17.1806(3)
	b = 12.1181(2)[a]
	c = 24.5352(4)
Volume (Å^3)	4808.44(14)
Z	16
$D_{calcd.}$ (Mg m^{-3})	1.791
Absorption coefficient (mm^{-1})	6.7
F(000)	2560
Crystal size (mm^3)	0.30 × 0.15 × 0.05
Independent reflections	11658 [R(int)] = 0.035]
Final R indices [$I > 2\alpha(I)$]	R_1 = 0.087, wR_2 = 0.212
R indices (all data)	R_1 = 0.137, wR_2 = 0.248
(Δ/θ)	0.001
Largest diff. peak and hole (e Å^{-3})	3.79 and –1/19

[a]β = 109.7240(10)°.

unchanged. Although the individual ^{13}C NMR chemical shifts in **2** are quite different from **1**, due to the bromine influence, the dynamic NMR behavior is very similar to **1**. Useable line-broadened ^{13}C NMR spectra were obtained at 5°C intervals over the temperature range of +35 to –55°C. As in the case of **1**, one or the other (or both) of the two high field peaks in **2** could be used for the modeling, giving $\Delta H^{\ddagger}$ = 43 ± 1 kJ mol^{-1}, $\Delta S^{\ddagger}$ = 1 ± 2 J mol^{-1} K^{-1}.

The similar transition-state barrier size for the conformational interchange in **2** compared to **1**, together with the similar high field ^{1}H NMR quartet in the decoalesced spectra of both **1** and **2** strongly argues for conformational correspondence in both structures.

X-ray structure determination of 2

After considerable experimentation, suitable crystals of **2** were obtained for the single crystal X-ray studies (Table 1).

All four of the unique molecules of **2** have a quite similar conformation, and one of these is shown in Fig. 2. In this structure *both rings* have nearly identical conformations, and the molecule as a whole has near C_2 symmetry about an axis through the >C=O bond. This is most clearly shown by a comparison of the C18-C19-C110-C111 (–69.2°) and the C13-C14-C15-C16 (–71.7°) dihedral angles.

There is also evidence that this crystal structure is in agreement with the solution NMR results. For example, one can now assign the highly shielded quartet ($J \approx$ 12–13 Hz) seen in the low-temperature ^{1}H NMR spectrum of both **1** and **2** to the "axial" hydrogens on carbons C15 and C110 in Fig. 2 (labeled X). These hydrogens are unique in having two vicinal hydrogen neighbors (Y) with dihedral angles approaching 180° (hence large J values). A sizeable geminal coupling is also assumed here (Z). Analysis of the low-temperature COSY and HETCOR spectra (see *Experimental*) is fully consistent with this assignment.

Fig. 2. ORTEP plot of 1,6-dibromobicyclo[4.4.1]undecan-11-one (**2**), showing one of the *M* configuration conformational enantiomers.

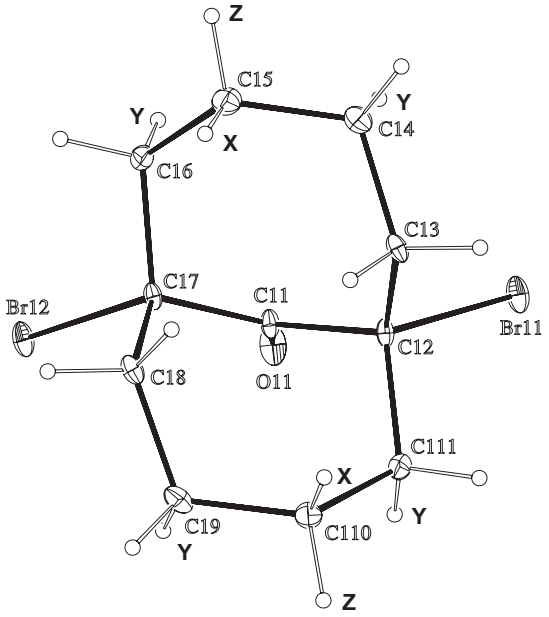

CP MAS ^{13}C NMR spectrum of ketone 2

Another possible correlation between the single crystal X-ray results and the solution-phase NMR data would involve a comparison of the solid state ^{13}C NMR shifts with the respective solution-phase values. In the crystal we expect to see the frozen-out conformation even at 20°C.

There are 16 molecules in the unit cell of **2**, corresponding to eight *M* and eight *P* enantiomers (5), of which four of each are unique. Each of the unique molecules has a similar conformation, but in no case do they have a perfect C_2 axis; therefore, the ^{13}C NMR equivalences seen in the low-temperature solution spectrum of **2** are not totally operative.

^{13}C NMR peaks were observed at δ 202.0, 84.1, 45.1, 36.7 and 26.2, with area ratios ca. 1:2:2:2:4. Linewidths at half height were 160, 470, 234, 215, and 265 Hz, respectively (±10 Hz). The peak at δ 26.2 shows some line-shape evidence for being an overlap of two fairly closely spaced peaks ca. δ 26.5 and 25. The corresponding solution chemical shifts (–77°C) are δ 200.7, 82.0, 43.4, 36.2, 26.1, and 23.5; an agreement of ±2 ppm with the solid-state data and further evidence, therefore, that solid and solution conformations of **2** are similar.

Conclusion

The symmetrization process described in the NMR part of this study ($\Delta H^{\ddagger}$ = 42 and 43 kJ mol^{-1} for **1** and **2**, respectively) can now be rationalized as the interchange of *M* and *P* (C_2) enantiomers of **1** and **2** via an intermediate or transition state of average C_{2v} symmetry. This interconversion can be most easily pictured as a concerted motion of the molecule as a whole, and this process resembles that found in *cis*-decalin interconversions (see eq. [2]). The $\Delta H^{\ddagger}$ conformational barrier in the latter is about 52 kJ mol^{-1} (6), about 25% higher than in our [4.4.1] systems.

© 2002 NRC Canada

[2] 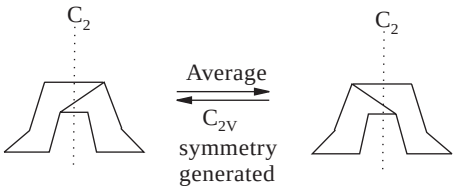

Experimental

The [6+4] adduct of tropone and butadiene was prepared as described (3) and partially purified (ca. 92%) by flash chromatography (SiO_2, hexane). This material (3.6 g, 0.022 mol) and 10% Pd/C (0.8 g) in absolute ethanol (80 mL) was hydrogenated (2) (60 psi H_2, 4.5 h) (1 psi = 6.894 kPa). The mixture was filtered twice through a celite bed and the solvent evaporated under pressure (0.1 mm Hg) to give 3.72 g of an oily liquid. GC–MS analysis showed three impurity peaks with slightly shorter retention times than for **1** (total <10%). For **1**: MS *m/z* (%): 166 (M^+, 95), 111 (68), 98 (72), 96 (76), 95 (78), 82 (78), 81 (93), 55 (80), 67(100). HRMS calcd. for $C_{11}H_{18}O$: 166.1347; found: 166.1358.

1,6-Dibromobicyclo[4.4.1]undecan-11-one (2)

Ketone **1** (1.0 g, 6.0 mmol) and Br_2 (3 equiv) in CCl_4 (200 mL) were irradiated with a 275-watt sunlamp (30 cm) for 5 h. The resulting solution was washed with a Na_2SO_3 solution, $NaHCO_3$ solution, brine, and dried over $MgSO_4$. The residue was crystallized from CH_2Cl_2–hexane (1:10), yielding 1.12 g (58%) fo the product. The NMR data for **2** are described in the *Results and discussion* section. Ketone **2** was recrystallized from various solvent systems, mp 183–184°C. HRMS calcd. for $[M - Br]^+$: 245.03641 (^{81}Br); found: 245.03693.

NMR spectroscopy

Variable-temperature ^1H and ^{13}C NMR spectra were obtained on a Bruker AM-400 spectrometer, using dichloromethane-d_2 solvent. Although the freezing point of CH_2Cl_2 is –97°C, our solutions did not freeze down to –115°C. Temperatures were calibrated using a methanol standard. Line-broadening peaks in the ^{13}C NMR spectrum were modeled using a standard two-site exchange mechanism as applied to two sets of exchanging ^{13}C peaks (modified DNMR-5 program (7)).

NMR analysis of the high field "quartet" in 2

This 2H area feature appears in the frozen-out low-temperature ^1H NMR spectra of **2** (and **1**). The coupling constant is ca. 12–13 Hz, but the individual lines are broadened, suggesting that each of the three *J* values is slightly different. A low-temperature COSY and HETCOR spectrum were obtained, and as identified from the ORTEP drawing in Fig. 2, the quartet for **2** is assigned to the H_X hydrogen on C15 and C110. The COSY spectrum shows this quartet strongly coupled to hydrogens at ca. δ 1.7, 1.9, and 2.45. In each case, these ^1H peaks are featureless or overlapped in the 1D spectrum. In the HETCOR spectrum, each of these "other" ^1H peaks is connected to different carbons; δ 1.9 is the geminal partner of the ^1H assigned as the quartet peak, δ 1.7 is connected to C14 (C19), and δ 2.45 is connected to either C13 (C18) or C16 (C111) (see Fig. 2). In Fig. 2, the vicinal hydrogens having dihedral angles of ca. 160–180° are shown as H_Y and the geminal hydrogen as H_Z. The assumption in this analysis is that the high field quartet can be uniquely assigned to H_X on the basis of three large coupling constants. In this analysis, we show that the COSY and HETCOR information is fully consistent with this assumption. In the case of ketone **1**, the quartet (–100°C) at δ 1.11 ($J \approx 13$ Hz) is well-separated from an overlapped series of peaks from δ 1.5–2. The low-temperature HETCOR spectrum shows that the high field ^1H quartet peak is correctly connected to one of the β-carbon peaks, but the COSY spectrum shows only two correlations, likely because of peak overlaps.

CP MAS spectrum

A CP MAS ^{13}C NMR spectra (140 000 scans) was obtained on a Bruker AMX-300 at 75.48 MHz, spinning rate 8 KHz, 4mm rotor, at 27°C. Peaks were referenced relative to glycine carbonyl (δ 176.3).

X-ray crystal structure determination

Pertinent experimental parameters concerning this determination are given in Table 1. Details of bond lengths, angles, and dihedral angles are provided as *Supplementary material*.[2]

Data collection and structure solution

A colorless plate crystal of $C_{11}H_{16}Br_2O$ was mounted on a glass fiber. All measurements were made on a Nonius Kappa CCD diffractometer with graphite monochromated Mo Kα radiation. Cell constants obtained from the refinement (8) of 11 218 reflections in the range $1.0 < \theta < 28.3°$ corresponded to a primitive monoclinic cell; details of crystal data and structure refinement have been provided in Table 1. The space group was uniquely determined from the systematic absences. The data were collected (9) at a temperature of 173(2) K using the ω–φ scans to a maximum θ value of 28.3°. The data were corrected for Lorentz and polarization effects and for absorption using a multiscan method (8). Since the crystal did not show any sign of decay during data collection a decay correction was deemed unnecessary.

The structure was solved by the direct methods (10) and expanded using Fourier techniques (11). The nonhydrogen atoms were refined anistropically. Hydrogen atoms were included at geometrically idealized positions and were not refined. The final cycle of full-matrix least-squares refinement using SHELXL97 (12) converged (largest parameter shift was <0.001 times its esd) with unweighted and weighted agreement factors, $R = 0.087$ and $wR = 0.248$ (all data), re-

[2] Supplementary material may be purchased from the Depository of Unpublished Data, Document Delivery, CISTI, National Research Council Canada, Ottawa, ON K1A 0S2, Canada. For information on obtaining material electronically go to http://www.nrc.ca/cisti/irm/unpub_e.shtml. Crystallographic information has also been deposited with the Cambridge Crystallographic Data Centre (CCDC No. 176838). Copies of the data can be obtained free of charge via www.ccdc.cam.ac.uk/conts/retrieving.html (or from the Cambridge Crystallographic Data Centre, 12, Union Road, Cambridge CB2 1EZ, UK; fax: +44 1223 336033; or deposit@ccdc.cam.ac.uk).

© 2002 NRC Canada

spectively, and goodness of fit (S = 1.06). The weighting scheme was based on counting statistics and the final-difference Fourier map was essentially featureless. The figures were plotted with the aid of ORTEPII (13).

Acknowledgment

We thank the Natural Sciences and Engineering Research Council of Canada (NSERC) for generous financial support.

References

1. (*a*) J.C. Coll, D.R. Crist, M. del Carmen, G. Barrio, and N.J. Leonard. J. Am. Chem. Soc. **94**, 7092 (1972); (*b*) G.S. Wayne and G.J. Snyder. Synth. Comm. **25**, 3267 (1995).
2. (*a*) N.S. Zefirov and V. Palyulin Top. Stereochem. **20**, 171 (1991); (*b*) J.F. Richardson and T.S. Sorensen. Can. J. Chem. **63**, 1166 (1985).
3. S. Itô, H. Ohtani, S. Narita, and H. Honma. Tet. Letters, 2223 (1972).
4. J.D. Winkler, K.E. Henegar, B.-C.-Hong, and P.G. Williard. J. Am. Chem. Soc. **116**, 4183 (1994), see footnote 20.
5. E.L. Eliel and S.H. Wilen. Stereochemistry of organic compounds. Wiley-Interscience, New York. 1994. p. 1200.
6. B.E. Mann. J. Mag. Reson. **21**, 17 (1976).
7. DNMR 5. D.S. Stephenson and G. Binsch. QCPE II, 365. 1978.
8. Z. Otwinowski and W. Minor. Methods Enzymol. **276**, 307 (1997).
9. R. Hooft. COLLECT. Nonium BV, Delft, The Netherlands. 1998.
10. SIR92. A. Altomare, M. Cascarano, C. Giacovazzo, and A. Guagliardi. H. Appl. Cryst. **26**, 343 (1993)
11. P.T. Beurskens, G. Admiraal, G. Beurskens, W.O. Bosman, R. de Gelder, R. Israel, and J.M.M. Smits. 1994. DIRDIF94. Technical report of the crystallography laboratory. University of Nijmegen, The Netherlands.
12. G.M. Sheldrick. SHELXL 97. University of Göttingen, Germany. 1997.
13. C.K. Johnson. ORTEPII. Report ORNL-5138. Oak Ridge National Laboratory, Tennessee. 1976.

© 2002 NRC Canada

The redox properties of ferrocenyl-substituted aryl azines

Vittorio A. Sauro and Mark S. Workentin

Abstract: A series of ferrocenyl substituted azines (**1**-Fc/Ar, where Ar = 4-$NO_2C_6H_4$, 4-CNC_6H_4, 4-$OCH_3C_6H_4$, C_5H_4N, ferrocene, anthracene, and pyrene) were investigated by electrochemical and photochemical techniques. All the **1**-Fc/Ar exhibited oxidation waves within 60 mV of each other, consistent with the expected oxidation of the ferrocene moiety. The reduction properties of **1**-Fc/Ar is governed by the nature of the Ar substituent. The standard reduction potentials suggest that ferrocene has comparable electron donating abilities as a 4-methoxyphenyl and 4-dimethylaminophenyl group. The anthracenyl azines exhibit one-electron reversible reduction followed by dimerization of the radical anion resulting in dimerization rate constants (k_d) between 5.1×10^4 and 1.5×10^5 M^{-1} s^{-1}. **1**-Fc/Anth and related azines undergo photochemical *E*/*Z* isomerization of the C=N bonds to produce *E*/*Z* and *Z*/*Z* isomers from the thermodynamically most stable *E*/*E* form. Fluorescence at 77 K, was observed for these compounds only after long-wavelength irradiation to produce a mixture of *E*/*E*, *E*/*Z*, and *Z*/*Z* isomers. Fluorescence quantum yields of 0.042, 0.090, and 0.176 were determined for **2**-Anth/H, **2**-Anth/Anth, and **1**-Fc/Anth, respectively. The electrochemical, photochemical, and X-ray data suggest that the azine unit is a conjugation "limiter" and may be a general characteristic of azine molecules.

Key words: azines, electrochemistry, cyclic voltammetry, reduction, electron transfer.

Résumé : Faisant appel à des techniques électrochimiques ainsi que photochimiques, on a étudié une série d'azines de ferrocényles substitués (**1**-Fc/Ar dans lesquels Ar = 4-$NO_2C_6H_4$, 4-CNC_6H_4, 4-$OCH_3C_6H_4$, C_5H_4N, ferrocène, anthracène et pyrène). Tous les **1**-Fc/Ar présentent des vagues d'oxydation à moins de 60 mV les uns des autres, ce à quoi on peut s'attendre pour l'oxydation de la partie ferrocène. Les propriétés de réduction des **1**-Fc/Ar sont définies par la nature du substituant Ar. Les potentiels de réduction standards suggèrent que les propriétés du ferrocène en ce qui a trait à ses possibilités de donner des électrons sont semblables à celles des groupes 4-méthoxyphényle et 4-diméthylaminophényle. Les azines dérivés de l'anthracène donnent lieu à une réduction réversible à un électron suivie d'une dimérisation de l'anion radical avec des constantes de vitesse de dimérisation (k_d) qui vont de $5{,}1 \times 10^4$ à $1{,}5 \times 10^5$ M^{-1} s^{-1}. La **1**-Fc/Anth et les azines apparentées subissent des isomérisations photochimiques *E*/*Z* des liaisons C=N qui conduisent à des mélanges d'isomères *E*/*Z* et *Z*/*Z* à partir de la forme *E*/*E*, thermodynamiquement la plus stable. Ces composés ne donnent lieu à de la fluorescence à 77 K qu'après avoir été soumis à une irradiation à grande longueur d'onde qui permet de produire un mélange des isomères *E*/*E*, *E*/*Z* et *Z*/*Z*. On a déterminé des rendements quantiques de fluorescence de 0,042, 0,090 et 0,176 respectivement pour les **2**-Anth/H, **2**-Anth/Anth et **1**-Fc/Anth. Les données électrochimiques, photochimiques ainsi que celles relatives à la diffraction des rayons X suggèrent que l'unité azine « limite » la conjugaison et que cette propriété est peut-être une caractéristique générale pour les molécules d'azine.

Mots clés : azines, électrochimie, voltampérométrie cyclique, réduction, transfert d'électron.

[Traduit par la Rédaction]

Introduction

Ferrocene and its derivatives have been investigated for their use in a variety of applications, including in organic synthesis (1), in applications tied to their electrochemical properties (1–5), in biological systems (6), as molecular wires and in other nanoelectronic devices (7), and in anion recognition applications (8). Due to the special chemical, stereochemical, and electrochemical properties (1) of ferrocene, there is great interest in ferrocene based ligands for the production of multi-metal containing organometallic complexes that can be used for a variety of applications (9, 10). Ferrocene-containing compounds have also been investigated for their second-order non-linear optical (NLO) properties (3, 11–13).

Ferrocene and its derivatives have been studied extensively using electrochemical techniques (1) and generally show a single one-electron reversible oxidation whose potential varies depending on the substituent attached to the cyclopentadienyl ring (3, 5, 10, 13, 14). The redox properties of the ferrocene group have been exploited to produce molecules that may have potential applications as molecular switches and molecular sensors (15, 16).

Received 30 July 2001. Published on the NRC Research Press Web site at http://canjchem.nrc.ca on 19 March 2002.

V.A. Sauro and M.S. Workentin.[1] Department of Chemistry, The University of Western Ontario, London, ON N6A 5B7 Canada.

[1]Corresponding author (e-mail: mworkent@uwo.ca).

 DOI: 10.1139/V02-019 © 2002 NRC Canada

Azines (>C=N-N=C<) appear to have the structural elements necessary to allow for complete conjugation between the substituents used to make up its structure, although there is now general agreement that the azine unit stops, or at the very least limits, conjugation. The question of conjugation through the azine unit has been investigated both theoretically and experimentally (17–29). Glaser and co-workers (20–29) examined the solid-state structures of a large number of structurally related aryl azines, paying particular attention to the structural consequences of conjugative interactions that manifest themselves in the solid-state structures. As a result of their extensive X-ray analyses, including the conformational properties about the N–N and Ar–C bonds, bond length analysis, and theoretical studies, Glaser and co-workers (25, 27) conclude that the azine unit is a "conjugation stopper," at least in the solid state.

Early and recent electrochemical investigations (2, 30–38) of azines have suggested that they do not exhibit extensive electronic communication through the azine unit. In a more recent study, we reported (39) the redox behavior of an extensive series of substituted acetophenone azines with emphasis on their extent of conjugation. The standard reduction potentials ($E°$) were found to vary as a function of substituent, with electron donating substituents causing the molecules to reduce at more negative potentials than those containing electron withdrawing groups. The azines were found to preferentially reduce at the C=N bond closest to the aryl group substituted with the most electron withdrawing substituent. Based on our extensive substituent-effect study, in this investigation (39) the azine unit was found to impede conjugation, and the limited electronic effects measured could have been purley inductive, supporting the notion of Glaser (20–29).

The electrochemical behavior of ferrocenyl azines has been previously investigated in a few cases (2, 4). Xu-Bing et al. (4) report the redox behavior of ferrocene coupled to bipyridine by an azine linkage, and the cyclic voltammetry (CV) plot shows the expected one-electron reversible oxidation typical of ferrocene-containing molecules. In addition, two-reduction processes were reported by the authors and attributed to the reduction of the -CHNNC($C_{10}H_6N_2$) group, which is consistent with the reduction of other types of azines (30, 35–39). Osborne et al. (2) report the electrochemistry of several azines and related compounds that contain one or two ferrocene groups. The single ferrocene compounds exhibit the expected one-electron reversible oxidation with standard oxidation potentials in the range of +0.38 to +0.67 V vs. SCE in 0.2 M tetrabutylammonium perchlorate – CH_2Cl_2. For compounds containing two ferrocenyl groups, including the azine **1**-Fc/Fc in Scheme 1, the CV show two almost overlapping reversible one-electron oxidations. This indicates that the electronic communication between the two ferrocene subunits through the azine moiety is small. No reduction processes were observed up to –0.5 V vs. SCE in 0.2 M tetrabutylammonium perchlorate – CH_2Cl_2 solution.

To extend our study into the electronic nature of azines, a series of azines containing a ferrocene group were investigated by cyclic voltammetry (CV). Ferrocene was chosen as a substituent because it is an excellent electron donor (1) and when coupled to a substituted aryl azine containing an electron acceptor, the resultant compound could potentially exhibit the NLO response seen in other azines (24, 25) and ferrocene-containing molecules (11–13). Each ferrocene containing molecule investigated for the various applications listed above took advantage of the same general strategy, mainly, to produce molecules where electronic communication between ferrocene and a second group was realized usually by the use of a conjugated bridge. For this reason, the azine unit is synthetically simple to incorporate and could serve as an ideal linkage to allow for the electronic communication between ferrocene and an aryl group; results with other azines, however, show that the azine unit will not allow for conjugative interaction. In the absence of any conjugative effects, the versatility of the azine unit as a linker and the ease in which azines can be synthesized makes them ideal synthons for coupling electron donating and acceptor groups for many applications. An important aspect of any application is an understanding of their electronic properties and that is what we describe here. The various compounds examined are illustrated in Scheme 1, along with a shorter notation used within the text to quickly identify each molecule. The terms Fc, Ar, Anth, Py, and Pyrd refer to ferrocene, aryl, anthracene, pyrene, and pyridine, respectively. In addition, nitro, cyano, and methoxy substituted phenyl rings will be denoted by 4-NO_2, 4-CN, and 4-OCH_3, respectively, where the number four refers to *para* substitution of the phenyl rings. An unsubstituted phenyl ring will be denoted by H (e.g., **2**-Anth/H).

Scheme 1.

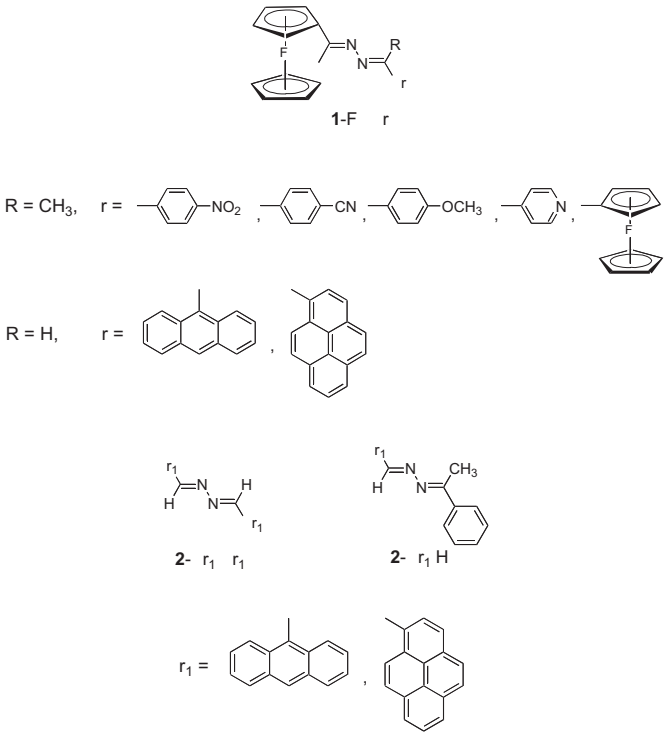

Results and discussion

The electrochemical behavior of the series of ferrocenyl azines (**1**-Fc/Ar) was studied in *N*,*N*-dimethylformamide (DMF), using cyclic voltammetry (CV). The electrochemical characteristics depend on the structure of the aryl

© 2002 NRC Canada

Scheme 2.

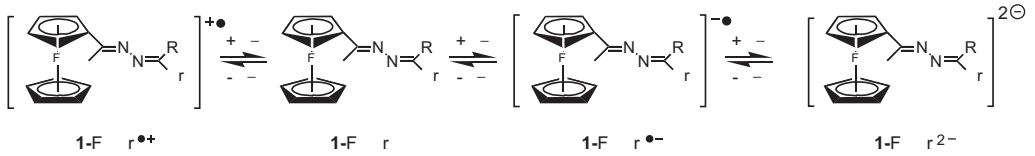

Scheme 3.

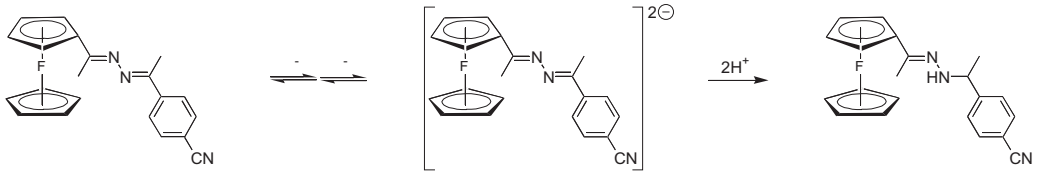

substituent. Ferrocenyl azines that contain a *para*-substituted aryl group exhibit electrochemical behavior similar to that observed for the acetophenone azines (39). Figures 1*a–e* shows a series of cyclic voltammograms for acetylferrocene-4-cyanoacetophenone azine (**1**-Fc/4-CN) in 0.1 M TEAP–DMF using various scan directions and switching potentials. A characteristic voltammetric feature is a single electron anodic wave at positive potentials that is reversible at all scan rates investigated (the wave labeled A in Fig. 1*e*) and is common to all of the **1**-Fc/Ar investigated. The anodic waves are due to formation of the azine radical cation (**1**-$Fc^{\bullet+}$/Ar) and the position of the oxidation is typical for ferrocene-containing molecules, representing the oxidation of the iron core from the Fe^{II} to the Fe^{III} state and vice versa (2). Other voltammetric features include a cathodic wave at negative potentials that is reversible at all scan rates investigated (wave B in Fig. 1*e*), followed at more negative potentials by a second single electron cathodic wave (wave C in Fig. 1*e*). The two reduction waves represent the successive reduction of the corresponding azine to its radical anion (**1**-Fc/$Ar^{\bullet-}$) and then its dianion (**1**-Fc/Ar^{2-}), respectively. This series of events is shown schematically in Scheme 2.

When the CV is scanned in the negative potential direction and goes through the formation of dianion, minor oxidation waves are observed on the reverse scan. These processes are evident only when the scan goes through the formation of **1**-Fc/Ar^{2-} and result from the protonation or some other reaction of **1**-Fc/Ar^{2-}. The dianion is sufficiently basic to be protonated by solvent molecules or, more likely, residual H_2O. Reduction and protonation most likely occur at the C=N moiety adjacent to the substituted aryl group to give a hydrazone (Scheme 3) similar to that observed in the reactions of acetophenone azine radical anions and dianions with trifluoroethanol (TFE) (39). Reduction of the azomethine bond adjacent to the ferrocenyl group occurs at much more negative potential as evidenced by the irreversible reduction at –2.303 V vs. SCE for **1**-Fc/Fc (see below). The identity of the minor products were not determined.

Azines **1**-Fc/Pyrd, **1**-Fc/4-OCH_3, and **1**-Fc/4-NO_2 showed similar voltammetric features as **1**-Fc/4-CN described above. In the cases of **1**-Fc/4-CN, **1**-Fc/Pyrd, **1**-Fc/4-OCH_3, and **1**-Fc/4-NO_2 (Figs. 1*e–h*) the formation of **1**-Fc/$Ar^{\bullet-}$ is completely chemically reversible (dashed line). For this series, standard reduction potentials ($E^{\circ}_{0/\bullet-}$) vary as a function of the electronic properties of the substituent and are summarized in Table 1. The reduction potentials of **1**-Fc/Ar exhibit a significant substituent effect with values differing by more than 1.2 V between **1**-Fc/4-NO_2 and **1**-Fc/4-OCH_3. The more electron withdrawing the substituent the easier the azine is to reduce and the more positive the $E°$ value. The $E^{\circ}_{0/\bullet-}$ are comparable to the $E°$ of the similarly substituted acetophenone azines but with a 4-methoxyphenyl or 4-dimethylaminophenyl group in place of the ferrocene unit (39). This illustrates that ferrocene has similar electron donating characteristics as the two aryl groups, as has been previously suggested by other researchers (10, 12). The reductions of **1**-Fc/Ar are single electron based on the $i_p/\sqrt{\nu}$ values in comparison with the Fe^{II}/Fe^{III} couple.

The dianions of **1**-Fc/4-CN, **1**-Fc/Pyrd, **1**-Fc/4-OCH_3, and **1**-Fc/4-NO_2 are not reversible on the CV timescale up to 50 V s^{-1} in DMF. Typical CVs at low scan rates are also illustrated in Figs. 1*e–h*. The potentials ($E_{p\bullet-/2-}$) for the second reduction follow the same trend with substituent donating and withdrawing ability (see Table 1) and become easier to reduce when electron withdrawing substituents act to reduce the electron density from the radical anion. The substituent effect is slightly smaller for the second wave with potentials differing by 0.8 V through the series **1**-Fc/4-NO_2 to **1**-Fc/4-OCH_3. Once again, the $E_{p\bullet-/2-}$ values indicate that ferrocene has comparable electron donor capabilities as 4-methoxyphenyl and (or) 4-dimethylaminophenyl in comparison to the appropriate acetophenone azines (39). The second reduction wave observed for **1**-Fc/4-OCH_3, however, may not be due to dianion formation but may result from reduction of the azomethine bond adjacent to the ferrocenyl group since the $E_{p\bullet-/2-}$ is comparable to that observed for the first reduction of **1**-Fc/Fc to **1**-$Fc/Fc^{\bullet-}$. The exact nature of this reduction process could not be investigated because it occurs at very negative potentials and into the solvent discharge.

The reduction of the nitro containing ferrocenyl azine warrants further discussion. We previously reported (39) that the reduction of all the nitro containing acetophenone azines occurs at almost identical potentials (~ –1 V vs. SCE). This was attributed to the fact that the reduction appears to be that of azine substituted nitrobenzene molecules and not an aryl-nitro substituted azine. Similarly, reduction of **1**-Fc/4-NO_2 occurs at –0.956 V vs. SCE and supports our earlier suggestion that reduction is occurring at the Ar-NO_2 group and not at one of the azine C=N imine bonds. The reduction

© 2002 NRC Canada

Fig. 1. Cyclic voltammograms of selected azines measured in 0.1 M TEAP–DMF at 0.2 V s^{-1}. Arrows indicate the scan direction. Parts *a–e* are of **1**-Fc/4-CN; (*a*) CV starting at 0 potential and switching after the appearance of wave B. (*b*) CV starting at 0 potential and switching after the appearance of wave C. (*c*) CV starting at 0 potential and switching after the appearance of wave A. (*d*) CV starting at 0 potential and switching after the appearance of wave B and continuing into the positive potential region and switching again after the appearance of wave A. (*e*) CV starting at 0 potential and switching after the appearance of wave C and continuing into the positive potential region and switching again after the appearance of wave A. Parts *f–h* are the CVs of **1**-Fc/Pyrd, **1**-Fc/4-OCH_3, and **1**-Fc/4-NO_2, respectively. Solid lines are the CV going through radical anion and dianion formation and continuing into positive potentials where the radical cation is formed. Dashed lines are the CV when the potential is reversed after formation of the radical anion and continuing into positive potentials where the radical cation is formed.

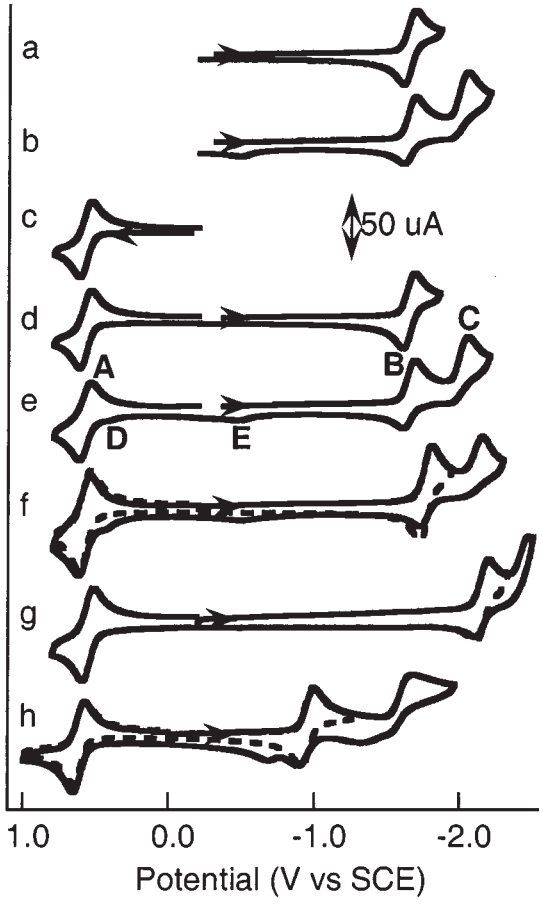

potentials of the nitro containing azines all occur within 44 mV of each other and their values are all approximately equal to –1 V vs. SCE, roughly the same potential as nitrobenzene in the same solvent (–1.1 V vs. SCE). **1**-Fc/4-NO_2 also shows a second less well-defined cathodic wave (Fig. 1*h*) that is due to further reduction of the aryl nitro group, presumably to form hydroxylamines, which are known to result from reduction of aryl-NO_2 compounds (40). The second cathodic wave is not completely reversible and includes other electrochemical processes that make it appear oddly shaped in comparison with other waves due to dianion formation in Fig. 1. Scanning to even more negative potentials (past the formation of dianion) produces two multi-electron waves that are due to further reduction of the protonated **1**-Fc/4-NO_2 dianion to ultimately form amines.

1-Fc/Py shows a one-electron reversible oxidation due to formation of a radical cation, similar to the other ferrocenyl azines discussed thus far (A in Fig. 2*a*). However, **1**-Fc/Py was the only ferrocenyl azine that exhibits a reversible cathodic reduction for the formation of the both the radical anion and dianion and provides values for $E^{\circ}_{0/\bullet-}$ = –1.549 V vs. SCE and $E^{\circ}_{\bullet-/2-}$ = –1.995 V vs. SCE, respectively. This is typical for pyrene-containing molecules (41). Reversing the potential after the formation of the radical anion (B) results in a completely reversible wave. Continuing into the positive potential region results in the CV showing two one-electron reversible waves for the reduction and oxidation of **1**-Fc/Py (dashed line in Fig. 2*a*). No oxidation waves were observed for **2**-Py/H or 1-pyrenecarboxaldehyde up to +1 V whose electrochemical behavior were examined for comparison to **1**-Fc/Py. Formation of the azine (i.e., **1**-Fc/Py and **2**-Py/H) results in a negative potential shift for the formation of the pyrene radical anion in comparison to 1-pyrenecarboxaldehyde. It must be noted that in the case of the azines, it is the C=N bond that is reduced, but the C=O bond is reduced in 1-pyrenecarboxaldehyde. In general, the azomethine group is more easily reduced than the carbonyl group from which it is derived (40). Thus a shift to more positive reduction potentials is expected by replacing the oxygen of a C=O bond with a nitrogen. In the case of the azines, the observed shifts relative to the parent carbonyl compounds is to more negative potentials, suggesting that the effects of replacing the C=O with C=N are offset by the conjugative or inductive effects of the azine unit and its second substituent. For **1**-Fc/Py, the negative shift in reduction potential indicates that there is some electronic communication through the azine moiety with the electron donating ferrocenyl group of **1**-Fc/Py having a larger effect (shift of –0.2 V) than the phenyl ring of **2**-Py/H (shift of –0.12 V). Reduction to the dianion shows only a small effect due to azine formation.

An additional process is also observed in the CVs of the pyrene-containing molecules. The wave for the formation of the dianion is followed very closely by a third reversible reduction wave that can be clearly identified in the CV of **2**-Py/H (Fig. 2*b*). In the cases of **1**-Fc/Py and 1-pyrenecarboxaldehyde, the formation of dianion is coincidental with the third reduction process. This results in a wave that appears as a single reversible reduction wave (at approximately –1.9 V), but it is not completely reversible since the cathodic and anodic peak-current ratios are greater than unity. At faster scan rates, the peak-current ratio does approach unity, indicating that the rate of the third reduction process is slow enough to be outrun by the scan rate. It was noticed that the appearance of the third reduction process was dependant on the quality of the solvent used for the experiment (i.e., [H_2O]). In meticulously dried solvent, the third reduction process for **2**-Py/H was almost not observable. As well, addition of an acid (TFE) to the electrochemical solution of **2**-Py/H, caused an increase in the current for the third reduction. This third reduction process is due to the reduction of the product derived from protonation of the dianion by solvent molecules or any residual water present. The formation of this

© 2002 NRC Canada

Table 1. Electrochemical data for the oxidation and reduction of ferrocenyl and related azines in 0.1 M TEAP–DMF solution.

Azine				
X	Y	$E^{o}_{\bullet+/0}$ (V)[a,b]	$E^{o}_{0/\bullet-}$ (V)[a]	$E^{o}_{\bullet-/2-}$ (V)[a]
Fc	4-NO_2	0.612	–0.956	–1.642[d]
Fc	Anth	0.583	–1.437[c]	—[f]
Anth	H	—[e]	–1.403[c]	—[f]
Anth	Anth	—[e]	–1.232[c]	–1.822
9-Anthraldehyde		—[e]	–1.207[c]	—[f]
Fc	Py	0.576	–1.549	–1.995
Py	H	—[e]	–1.462	–1.859
1-Pyrenecarboxaldehyde		—[e]	–1.338	–1.929
Fc	4-CN	0.577	–1.645	–2.029[d]
Fc	Pyrd	0.579	–1.767	–2.115[d]
Fc	4-OCH_3	0.553	–2.158	–2.439[d]
Fc	Fc	0.572	–2.303[g]	—[f]
Acetylferrocene		0.691	–2.262	—[f]

[a]Reported in V vs SCE.
[b]Oxidation potential of the Fe^{II}/Fe^{III} couple.
[c]Reversible only at faster scan rates.
[d]Peak potential ($E_{p,\bullet-/2-}$) at 0.1 V s^{-1} scan rate.
[e]No oxidation process was observed up to +1 V.
[f]No further reduction processes were observed.
[g]Peak potential at 0.1 V s^{-1}; see text.

Fig. 2. Cyclic voltammograms of selected compounds measured in 0.1 M TEAP–DMF at 0.2 V s^{-1}: (*a*) **1**-Fc/Py; (*b*) **2**-Py/H; and (*c*) 1-pyrenecarboxaldehyde. Arrows indicate scan direction. Dashed lines are the CV when the potential is reversed after radical anion formation.

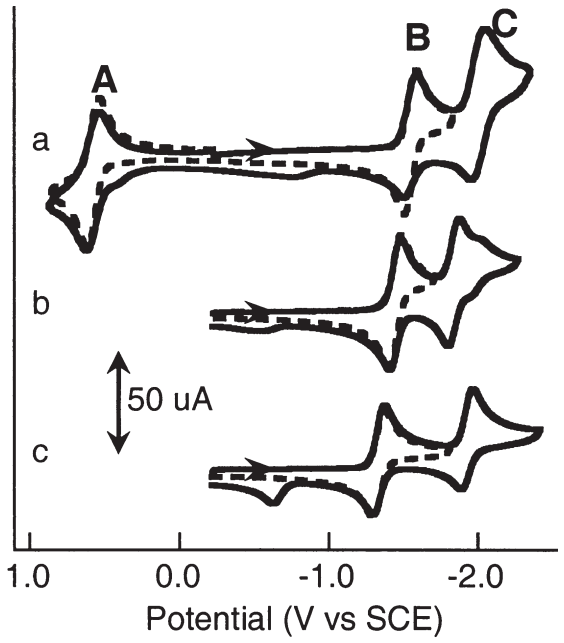

Fig. 3. Cyclic voltammograms of selected compounds measured in 0.1 M TEAP–DMF at 0.2 V s^{-1}. Arrows indicate scan direction: (*a*) **1**-Fc/Anth; (*b*) **2**-Anth/H; (*c*) **2**-Anth/Anth; and (*d*) 9-anthraldehyde.

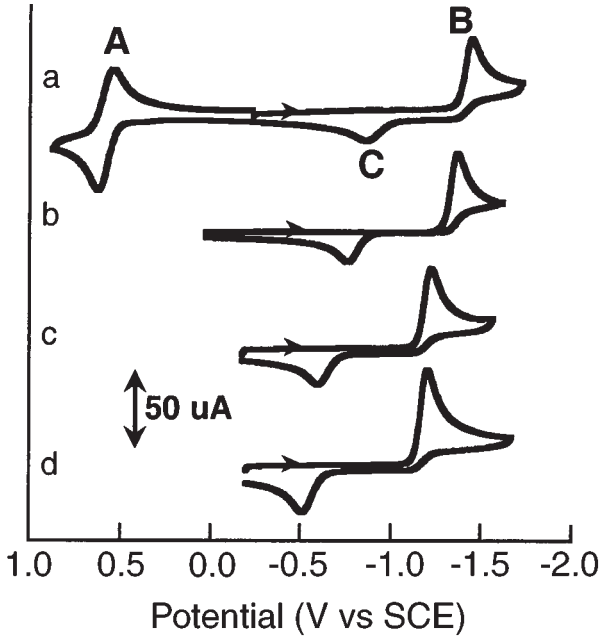

protonated product is also responsible for the minor anodic peaks on the return scan (between –0.5 and –0.8 V, depending on scan rate) due to oxidation of the formed conjugate base for each of the pyrene containing azines. As well, the protonated product is also responsible for the minor peak preceding wave A for **1**-Fc/Py (Fig. 2*a*), which is not observed unless the scan goes through the formation of a dianion. Protonation would interrupt any conjugation that may exist and result in a minor ferrocenyl-containing product that is easier to oxidize than the original azine.

The anthracenyl-containing molecules exhibit different electrochemical behavior compared with the others. Fig. 3*a* shows the CV of **1**-Fc/Anth, which features a completely reversible one-electron wave (A) at positive potentials, as well as an irreversible one-electron cathodic wave (B) at slow

© 2002 NRC Canada

Scheme 4.

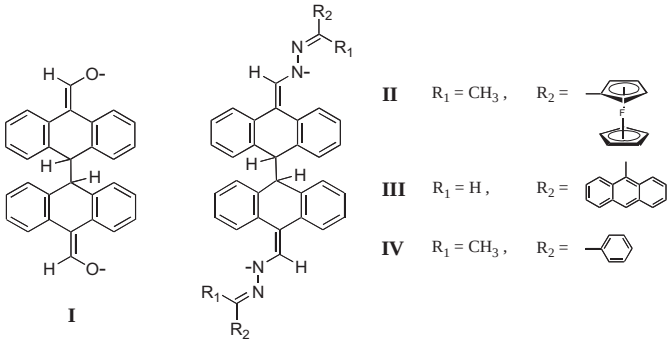

scan rates (i.e., 0.1–0.5 V s^{-1}) that becomes quasi-reversible at faster scan rates (i.e., 15–65 V s^{-1}). The E_p shifts to more negative potentials with increasing scan rate and does not vary linearly with the logarithm of the scan rate (log ν). Also present in the CV for **1**-Fc/Anth is an anodic wave (C) with an E_p at approximately –0.9 V whose intensity decreases relative to the peak current of the irreversible wave as the scan rate is increased. The E_p of wave C shifts towards more positive values with increasing scan rate. This suggests that the anodic wave C is due to a product formed during the reduction process at wave B. The decrease of relative intensity of wave C compared with wave B with increasing scan rate indicates that the formation of the new species is outrun at faster scan rates. Reversing the scan direction towards more negative potentials after the appearance of oxidation wave C results in a CV that is identical to the one obtained on the initial scan, indicating that the product formed upon azine reduction is oxidized back to the original azine. This electrochemical behavior of **1**-Fc/Anth is consistent with electrochemically reversible reduction followed by rapid dimerization. The formed dimer can then be oxidized back to starting azine. Digital simulation of the CV of a reversible reduction followed by dimerization produces similar features (i.e., E_p shifts to more negative values and non-linear E_p vs. log ν) as are observed for the experimental data. Similar voltammetric features are observed in the CVs for other anthracenyl-containing model compounds (Figs. 3*b*–*d*) **2**-Anth/H, **2**-Anth/Anth, and 9-anthraldehyde, which do not show any oxidation processes up to +1 V.

The reduction of 9-anthraldehyde (used as a model compound to examine substituted anthracene reduction, Fig. 3*d*) was examined in 0.1 M TEAP–DMF solution by Lasia and Rami (42). It exhibits similar voltammetric features upon reduction as **1**-Fc/Anth and the other anthracenyl azines. The one-electron cathodic wave results from the formation of the 9-anthraldehyde radical anion that quickly couples (k_d = 1 × 10^5 M^{-1} s^{-1}) (42) with a second radical anion to form a dianionic dimer (I in Scheme 4) and results in the observed one-electron irreversible reduction wave. The anodic wave at ~ –0.5 V on the reverse scan results from the oxidation of the dimer back to 9-anthraldehyde (42) and is not reversible upon switching the scan direction once again. In the case of **1**-Fc/Anth, **2**-Anth/Anth, and **2**-Anth/H, the corresponding dimers II, III, and IV (Scheme 4) are proposed to account for the oxidation waves observed at –0.927, –0.614, and –0.772 V vs. SCE at 0.1 V s^{-1}, respectively. Rate constants for dimerization (k_d) can be calculated using known procedures (43) and appear in Table 2. The k_d value for **1**-Fc/Anth suggests that the electron donating abilities of the ferrocenyl group act to hinder dimer formation. The rates are approximately equal for the remaining anthracenyl azines.

Table 2. Electrochemical data and dimerization rate constants for anthracene containing azines.

Compound	E_p (at 0.2 V s^{-1})[a]	E^{o} [a]	k_d (M^{-1} s^{-1})
1-Fc/Anth	–1.445	–1.437	5.1 × 10^4
2-Anth/H	–1.397	–1.403	1.5 × 10^5
2-Anth/Anth	–1.224	–1.232	3.3 × 10^5
9-Anthraldehyde	–1.203	–1.207	1.8 × 10^5

[a]In V vs. SCE.

For **1**-Fc/Anth, the electrochemical behavior is governed by two independent moieties, namely the ferrocene and the anthracene groups. The ferrocene moiety has the effect of making the anthracenyl unit more difficult to reduce as evidenced by a shift of 0.24 V to more negative potentials relative to 9-anthraldehyde. This indicates that some electronic communication must be occurring through the azine unit. A similar situation is observed for **2**-Anth/H. The reduction of **2**-Anth/Anth also shows evidence for electronic communication. Although the reduction potential of **2**-Anth/Anth occurs at the roughly same potential as 9-anthraldehyde, only one electron is involved in the process. One might expect a two-electron wave for **2**-Anth/Anth if the azine moiety prevented any communication between the two anthracene units (i.e., reduction of both anthracene units simultaneously, similar to the situation previously observed for 4,4′-dinitroacetophenone azine (39)).

The electrochemical behavior of acetylferrocene and acetylferrocene azine (**1**-Fc/Fc) was also examined for comparison with the results obtained for the other **1**-Fc/Ar. **1**-Fc/Fc shows an anodic wave that consists of two one-electron reversible oxidations that have slightly different oxidation potentials (Fig. 4*b*). This results in an oxidation wave that is approximately twice the magnitude of the other one-electron oxidations (Fig. 5) and appears to have a shoulder on the leading edges of the waves. This is consistent with the electrochemistry observed for **1**-Fc/Fc by Osborne et al. (2) who estimates the oxidation potentials of the two ferrocene units to be +0.47 V and +0.56 V vs. SCE in 0.2 M TBAP–CH_2Cl_2. **1**-Fc/Fc also shows a reduction wave at very negative potential caused by the reduction of the C=N bond of the azine unit. This reduction occurs into the solvent discharge, which makes determining the standard potential difficult. Reduction of a C=N bond at such negative potentials results in the formation of minor electroactive species, which are oxidized on the reverse scan and have similar structure to the parent azine. These products most likely result from reaction of the azine radical anion with H_2O or electrolyte or some reduced form of the electrolyte. Figure 4 illustrates the CVs of **1**-Fc/Fc as well as the reference compound, acetylferrocene. The reduction that occurs in the CV of acetylferrocene is the one-electron reduction of the carbonyl group. All electrochemical data is summarized in Table 1.

The Fe^{II}/Fe^{III} couple in the **1**-Fc/Y is subject to a substituent effect as indicated by the oxidation potentials of the two model compounds, ferrocene and acetylferrocene (+0.470 V and +0.691 V vs. SCE in DMF, respectively). The

© 2002 NRC Canada

Fig. 4. Cyclic voltammograms of (*a*) acetylferrocene and (*b*) **1**-Fc/Fc measured in 0.1 M TEAP–DMF at 0.2 V s^{-1}. Arrows indicate scan direction. Dashed line is the CV in the positive potential region only.

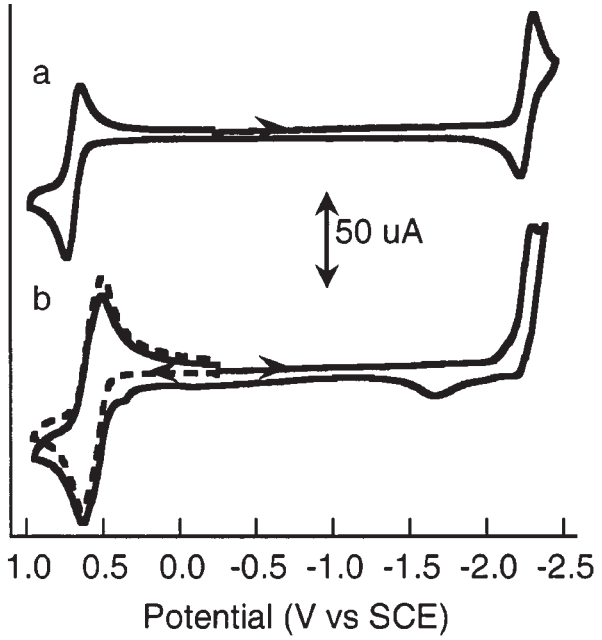

Fig. 5. Cyclic voltammograms of the reversible oxidation waves for the ferrocenyl azines measured in 0.1 M TEAP–DMF at 0.2 V s^{-1} scan rate: (*a*) **1**-Fc/Fc; (*b*) **1**-Fc/4-NO_2; (*c*) **1**-Fc/Anth; (*d*) **1**-Fc/Py; (*e*) **1**-Fc/4-CN; (*f*) **1**-Fc/Pyrd; and (*g*) **1**-Fc/4-OCH_3.

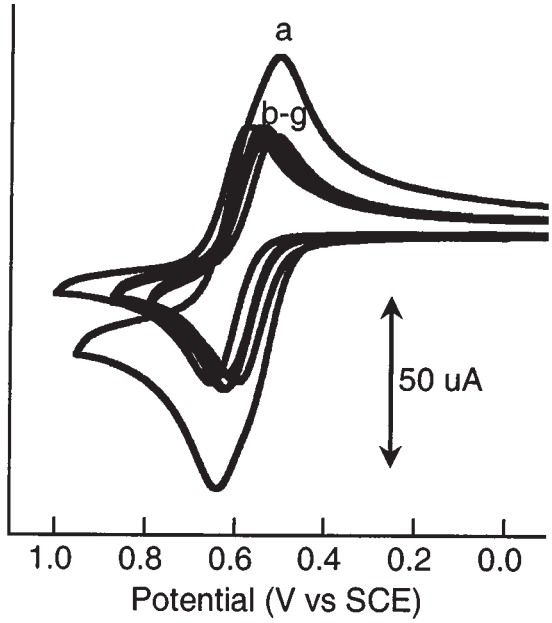

oxidation potentials of the ferrocene unit can be used to probe the effects of adding an azine unit and any possible contribution from the aryl group to the electrochemical behavior of the iron core. The CVs showing the reversible oxidation of **1**-Fc/Ar to **1**-Fc/$Ar^{\bullet+}$ at 0.2 V s^{-1} are shown in Fig. 5. As expected, the ferrocenyl unit becomes easier to oxidize (less positive potentials) with more electron donating substituents and vice versa. All $E^{\circ}_{\bullet+/0}$ are within 59 mV of each other, indicating only a modest substituent effect on the oxidation. This reinforces the notion of little to no conjugation through the azine unit, producing only small substituent effects, particularly on the Fe core. A more illustrative example of the extent of communication through the azine unit is the oxidation of **1**-Fc/Fc that shows two oxidation processes that occur at slightly different potentials. If there was no conjugation through the azine unit, we would expect that the oxidation potentials would be coincidental and that the observed wave would appear as if it were a completely reversible two-electron reduction process. That is, both ferrocene units would be oxidized simultaneously. Thus the oxidation of **1**-Fc/Fc would be similar to the simultaneous double one-electron reduction of 4,4′-dinitroacetophenone azine (39). Since the oxidation of **1**-Fc/Fc appears as two processes at slightly different potentials, there must be some electronic communication through the azine moiety that results in the second oxidation being slightly harder to accomplish (i.e., occurs at more positive potential) than the first.

The heterogeneous rate constants (k_{het}) for electron transfer can be calculated (43, 44) for the compounds investigated and are listed in Table 3. The calculated k_{het} are within the expected range (10–10^{-3} cm s^{-1}) for reversible or quasi-reversible electrode kinetics. Rate constants for compounds **1**-Fc/Fc, **2**-Anth/Anth, **2**-Anth/H, and 9-anthraldehyde could not be determined in this way because they do not exhibit suitable reversible waves, a requirement for the calculation.

The **1**-Fc/Ar compounds offer the opportunity to calculate the HOMO–LUMO energy gap (listed in Table 3). The energy difference between oxidation and reduction potentials is the HOMO–LUMO energy gap and is an indication of the electron donor–acceptor properties of the compound. The variation of $\Delta E_{HOMO-LUMO}$ as a function of the substituent (values differ by more than 30 kcal mol^{-1}) illustrates the "fine tuning" possible for azine electronic properties simply by changing the substituent(s) attached to the azine unit.

To further our examination of the electronic nature of azines, the photochemical behavior of a series of azines containing a chromophoric group (specifically anthracene) was investigated. This allowed for the evaluation of the effect of the ferrocene group on the photochemical characteristics of these azines. Azine photochemistry is governed by *E*/*Z* isomerization of the azomethine bonds (45–51), which has been shown to be a general property of the 2,3-diaza-1,3-butadienes. The photochemistry and photophysics of **2**-Anth/Anth has been thoroughly investigated by Appenroth et al. (48–51). **2**-Anth/Anth can exist as three isomers, *E*/*E*, *E*/*Z*, and *Z*/*Z*, where the *E*/*Z* and *Z*/*Z* isomers can be selectively produced, starting from the thermodynamically stable *E*/*E* form, by irradiation with wavelengths λ = 488 and 436 nm, respectively. It was found that neither of the three isomers fluoresce at room temperature and only the *Z*/*Z* isomer fluoresced at 77 K (51). The fluorescence spectrum of (*Z*/*Z*)-**2**-Anth/Anth contained the same structural features as anthracene and its quantum yield of fluorescence in ethanol was determined to be Φ_f = 0.090 using an excitation wavelength of 350 nm at 77 K.

To investigate the luminescent properties, the fluorescence spectra of the anthracenyl-containing azines were recorded

© 2002 NRC Canada

Table 3. Heterogeneous rate constants and HOMO–LUMO energy gap for ferrocenyl and related azines.

Compound	$E^{\circ}_{\cdot+/0}$ (V)[a]	$E^{\circ}_{0/\cdot-}$ (V)[a]	k_{het} (cm s^{-1})[b]	$\Delta E_{HOMO-LUMO}$ (kcal mol^{-1})[c]
1-Fc/4-NO_2	0.612	–0.956	4.9×10^{-2} [d]	36.2
			5.0×10^{-2} [e]	
1-Fc/Anth	0.583	–1.437	3.1×10^{-2} [e]	46.6
1-Fc/Py	0.576	–1.549	1.9×10^{-2} [d]	49.0
			2.5×10^{-2} [e]	
2-Py/H	—	–1.462	2.4×10^{-2} [d]	—
1-Pyrenecarboxaldehyde	—	–1.338	2.7×10^{-2} [d]	—
1-Fc/4-CN	0.577	–1.645	1.9×10^{-2} [d]	51.2
			3.1×10^{-2} [e]	
1-Fc/Pyrd	0.579	–1.767	1.4×10^{-2} [d]	54.1
			1.6×10^{-2} [e]	
1-Fc/4-OCH_3	0.553	–2.158	1.1×10^{-2} [d]	62.5
			2.0×10^{-2} [e]	
1-Fc/Fc	0.572	–2.303	—	66.3
Acetylferrocene	0.691	–2.262	2.4×10^{-2} [d]	68.1
			1.3×10^{-2} [e]	

[a]Reported in V vs SCE.
[b]Average value for scan rates between 0.05 and 0.5 V s^{-1}.
[c]Energy difference between the HOMO and LUMO energy levels determined from electrochemical data.
[d]Value calculated for a reduction process.
[e]Value calculated for an oxidation process.

Fig. 6. The emission spectra of **1**-Fc/Anth, **2**-Anth/H, and **2**-Anth/Anth in EPA at 77 K using a 350 nm excitation wavelength: (*a*) **2**-Anth/H; (*b*) (dashed line) **2**-Anth/Anth; (*c*) **1**-Fc/Anth.

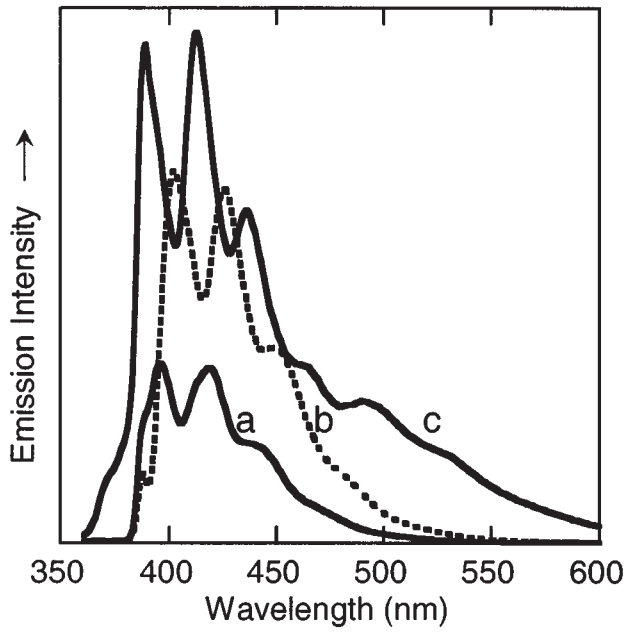

in EPA both at room and low temperature (77 K). Figure 6 shows the fluorescence spectra of **1**-Fc/Anth, **2**-Anth/H, and **2**-Anth/Anth at 77 K. None of the azines showed fluorescence at room temperature, and only weak fluorescence at low temperature when an excitation wavelength of 350 nm was used. Such behavior was observed previously for several different azines including **2**-Anth/Anth (48, 51), where the *E*/*E* isomer was shown to be non-fluorescent. The samples were then exposed to radiation of wavelength 410–490 nm to induce isomerization to the *Z*/*Z* isomer and the fluorescence was reexamined. Once again, little to no emission was observed at room temperature. In contrast, the emission intensity at 77 K was dramatically increased, approximately 12–70 times relative to the samples before irradiation. The low-emission intensity at room temperature can be attributed to efficient energy dissipation in the excited state via *E*/*Z* isomerization of the azomethine bonds. This isomerization process becomes less important at 77 K with a concomitant enhancement of fluorescence since the azine molecules are now contained in the solid glass of the frozen EPA solution. The emission observed for **1**-Fc/Anth, **2**-Anth/H, and **2**-Anth/Anth contains similar structural features as that of anthracene (52).

Appenroth et al. (51), attributed the observed emission of (*Z*/*Z*)-**2**-Anth/Anth to the anthracene chromophore that is twisted out of the molecular plane of the azine moiety in the *Z*/*Z* isomer (53, 54). The twisting results from steric interactions between the azine nitrogen and the anthracene unit. This results in an interruption of any conjugation that may be occurring. The *E*/*Z* isomer of **2**-Anth/Anth did not show any emission at either temperature despite twisting of one of the anthracene units. The situation is very similar for **1**-Fc/Anth and **2**-Anth/H. The need for irradiation at 410–490 nm prior to the observation of any emission suggests that the *E*/*E* isomers of **1**-Fc/Anth and **2**-Anth/H, the thermodynamically most stable and initial structures, do not fluoresce and any fluorescence must come from one of the other two isomers. Similar to **2**-Anth/Anth, long-wavelength irradiation induces isomerization of the C=N bonds and results in fluorescence not observed for the *E*/*E* isomers. Emission from the *E*/*Z* or *Z*/*Z* isomers of **1**-Fc/Anth and **2**-

© 2002 NRC Canada

Table 4. Quantum yields (Φ_f) and total normalized fluorescence intensities of **1**-Fc/Anth, **2**-Anth/H and **2**-Anth/Anth in EPA at room temperature and 77 K.

		Before irradiation		After irradiation	
Azine	Φ_f [a]	r.t.	77 K	r.t.	77 K
1-Fc/Anth	0.176	0.3	3.4	20	242.1
2-Anth/H	0.042	0.08	5.1	1	58.4
2-Anth/Anth	0.090	0.14	7.2	1.7	123.7

Note: Fluorescence intensities are normalized relative to the area under the room temperature emission curve of **2**-Anth/H after irradiation at 410–490 nm.

[a]Quantum yields in EPA at 77 K using 350 nm excitation wavelength relative to that of **2**-Anth/Anth (51). The concentrations of the fluorescence samples were adjusted so that absorption at 350 nm was equivalent.

Anth/H cannot, however, be distinguished since it is unclear whether both C=N bonds need to be in the *Z* configuration or only the C=N bond nearest the anthracenyl group.

The fluorescence quantum yields (Φ_f) of **1**-Fc/Anth and **2**-Anth/H were determined by comparison to the Φ_f previously determined for **2**-Anth/Anth (51) under similar experimental conditions. The determined quantum yields at 77 K are listed in Table 4 along with the normalized fluorescence intensities. Table 4 shows that, in frozen solution where the isomerization is prevented, the fluorescence of **1**-Fc/Anth is twice that of **2**-Anth/Anth and four times that of **2**-Anth/H. The emission intensity of **2**-Anth/Anth is approximately twice that of **2**-Anth/H under all conditions owing to the two anthracenyl groups in **2**-Anth/Anth compared with one in **2**-Anth/H. The fluorescence intensity of **1**-Fc/Anth at room temperature after irradiation was significantly higher than the other two azines. This suggests that radiationless deactivation processes are less favoured for **1**-Fc/Anth than for **2**-Anth/H and **2**-Anth/Anth in fluid solution, and that the ferrocene group may in fact hinder the *E*/*Z* isomerization that is the main deactivation mechanism at room temperature. In addition, fluorescence quenching by ferrocene does not appear to dominate, either at room temperature or 77 K, in comparison to the observed fluorescence of **2**-Anth/H and **2**-Anth/Anth. This suggests that (*Z*/*Z*)-**1**-Fc/Anth (or (*E*/*Z*)-**1**-Fc/Anth) does not exhibit significant electronic communication between the two azine substituents either by through-bond or through-space interactions since ferrocene is known to be a good fluorescence quencher (15, 55). Any fluorescence observed before irradiation presumably results from minor amounts of *E*/*Z* or *Z*/*Z* isomers that may be present in the initial solution, formed by thermal processes.

To extend the solid-state analysis of azines, crystals of **1**-Fc/4-NO_2, **1**-Fc/4-CN, **1**-Fc/Pyrd, and **1**-Fc/Anth suitable for X-ray analysis were grown by slow evaporation of a solution of the azine in an appropriate solvent. All C=N bonds are in their *E* configurations as expected. The average Fe—C bond distances of the ferrocene moiety are all similar (2.030–2.040 Å) and fall within the range commonly found for ferrocene compounds (2, 4, 56) but are shorter than those found in ferrocene itself (2.045 Å) (57). This may be due to any of the conjugative effects of the attached azine, which pulls electron density from the cyclopentadienyl ring and results in the shortening of the average Fe—C bond lengths. All the cyclopentadienyl rings are planar (mean deviation of 0.0002–0.0025 Å) and parallel to each other (angle between rings of 0.9–3.5°). The C—C of the cyclopentadienyl rings, N—N, and C=N bond lengths are similar to those determined for other ferrocenyl azines (2, 4, 12).

Scheme 5.

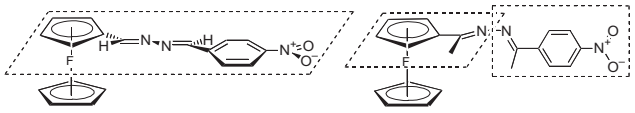

1-Fc/4-NO_2

One striking feature of the determined **1**-Fc/Ar structures is the twisting of the molecules through the azine moiety as indicated by >C=N-N=C< dihedral angles of 99.1–160.9° (see *Supplementary material*). This is in complete contrast with the structure of ferrocenealdehyde-4-nitrobenzaldehyde azine, reported by Houlton and co-workers (12), illustrated in Scheme 5, whose X-ray structure shows an almost complete planarity of the $C_5H_4CHNNCHC_6H_4NO_2$ fragment to produce an extended π system. The similar azine **1**-Fc/4-NO_2 (Scheme 5), which differs only by the addition of two methyl groups, produces a significantly different orientation. This suggests that **1**-Fc/Ar should not exhibit any conjugation through the azine unit. The electrochemical results suggest, however, that there is significant conjugative interactions in the **1**-Fc/Ar in solution. The twisting of the molecules observed in the solid state, therefore, may not be a good reflection of their orientation in solution and may be caused by packing effects in the solid. The same argument was proposed by Glaser and co-workers (22, 25) to explain the nonplanarity of the acetophenone azines in the solid state.

Conclusions

The electrochemical behavior of the **1**-Fc/Ar is governed by the ferrocenyl and aryl group attached to the azine moiety. All the **1**-Fc/Ar showed a reversible oxidation between +0.62 and +0.55 V vs. SCE as a function of the aryl substituent. Electron withdrawing groups resulted in more positive oxidation potentials with only a slight substituent effect on the Fe^{II}/Fe^{III} oxidation, as evidenced by the small variation (59 mV) in potentials. The reduction potentials of **1**-Fc/Ar were determined and electron donating groups showed more negative reduction potentials, whereas less negative potentials were observed for electron withdrawing substituents. For **1**-Fc/Ar, where the aryl group was a substituted benzene ring, the effect of introducing an electron donating ferrocenyl group on azine reduction results in the ferrocene having similar electron donating characteristics as a methoxyphenyl or dimethylaminophenyl group compared with the reduction potentials determined for similar systems (39). The reduction and oxidation potentials determined for **1**-Fc/Ar suggest that there is some electronic communication between the two substituents of the azine moiety in comparison with model compounds. Therefore, we suggest that the azine unit does allow for limited conjugation in the **1**-Fc/Ar as it did for the acetophenone azines (39). The nonplanarity of the **1**-Fc/Ar observed in the solid-state structures, suggest-

© 2002 NRC Canada

ing no conjugation, may not be an accurate reflection of their orientation in solution.

The photochemistry of **1**-Fc/Anth, **2**-Anth/Anth, and **2**-Anth/H is governed by *E*/*Z* isomerization processes and no emission is observed for these compounds either at room temperature or at 77 K. Fluorescence at 77 K is observed after long wavelength irradiation where the thermodynamically most stable *E*/*E* isomer is converted to the *E*/*Z* and *Z*/*Z* isomers from which emission occurs. Any conjugative interactions in the *E*/*E* isomer is interrupted upon formation of the *E*/*Z* or *Z*/*Z* isomer, allowing for fluorescence of the anthracenyl group. The ferrocenyl group in **1**-Fc/Anth has only a slight effect on the anthracenyl fluorescence, enhancing it relative to **2**-Anth/Anth and **2**-Anth/H, and no evidence for intramolecular or inductive quenching by ferrocene was observed under the experimental conditions. The donor–acceptor properties of ferrocenyl azines, however, can be easily manipulated by altering the aryl substituent on the azine unit, making them good candidates for materials applications.

Experimental

Materials

All chemicals used were purchased from Aldrich and used as received unless otherwise stated. For electrochemical experiments only, acetylferrocene, 9-anthraldehyde, and 1-pyrenecarboxaldehyde were recrystallized from suitable solvents prior to use. *N*,*N*-dimethylformamide(DMF) was distilled under reduced pressure over calcium hydride prior to use. Argon was flushed over the DMF during the transfers into the electrochemical cells. Tetraethyl ammonium perchlorate (Kodak) was recrystallized three times and dried under vacuum at 60°C prior to use and stored in a vacuum dessicator. Ferrocene was sublimed once before use. NMR spectra, recorded on a Varian Gemini 300 MHz (300.075 MHz for ^{1}H and 75.462 MHz for ^{13}C) or Varian Mercury 400 MHz instrument (400.0854801 MHz for ^{1}H and 100.6015500 MHz for ^{13}C), are herein referred to as 300 or 400 MHz for ^{1}H and 75 or 100 MHz for ^{13}C. All chemical shifts are reported in parts per million downfield from tetramethylsilane. Melting points were recorded using a Gallenkamp melting point apparatus and are uncorrected. IR data was recorded on a PerkinElmer System 2000 FT-IR. Mass spectra analysis was performed with a Finnigan MAT 8200 mass-data system. Gas chromatography analysis was performed on a Hewlett–Packard 5890 Series II gas chromatograph equipped with a 10 m HP5 column and an FID detector. UV–vis data were collected on a Varian Cary 100 spectrometer. Fluorescence spectra were recorded using an ISA Spex 3 Fluorimeter.

Electrochemistry — cyclic voltammetry

Experiments were performed using either a Princeton Applied Research (PAR) 283 or 263 potentiostat interfaced to a personal computer. PAR M270 software was used to conduct the experiments as well as analyze the derived data. Measurements were conducted in an all-glass cell kept at 25°C. All glassware was predried in an oven and assembled, hot while flushing with argon. The working electrode was glassy carbon (Tokai) and the counter electrode was a platinum flag. The reference electrode was a silver wire housed in a glass tube sealed with a porous ceramic tip and filled with a 0.1 M solution of tetraethylammonium perchlorate (TEAP). The same reference electrode was used in all experiments. Concentrations of 2 mM of azine in 0.1 M TEAP in DMF were used. Ferrocene, tetracyanoethylene, or 4-nitroacetophenone azine (39) were used in all experiments as internal references to a saturated calomel electrode ($E°$ = 0.470, –0.319, and –0.973 V vs. SCE in DMF, respectively). Positive feedback IR compensation was used in all experiments to minimize the effects of uncompensated solution resistance.

Fluorescence

Fluorescence spectra were recorded on an ISA Spex 3 Fluorimeter interfaced to a personal computer. EPA (2:5:5 mixture of ethanol – diethyl ether – isopentane) was prepared from spectroscopic grade solvents and stored in a tightly sealed bottle. Azine solutions were prepared by dissolving the appropriate amount of azine in EPA so that the UV–vis absorbance at 350 nm was the same for all samples and kept below 0.07. Samples were kept in the dark as much as possible during preparation, transport, and storage. Azine solutions were then placed in quartz tubes, purged with argon gas to remove oxygen and sealed with a rubber septa. The samples were placed in the fluorimeter inside a low-temperature sample holder filled with liquid nitrogen (the same samples and apparatus was used for room temperature spectra but without the liquid nitrogen). The samples were checked for any cracks in the frozen solvent and the fluorescence or excitation spectra were recorded. Samples were removed from the liquid nitrogen and allowed to warm to room temperature between runs. Any condensation that accumulated on the tubes during the warming process was removed before immersing into the liquid nitrogen again. The liquid nitrogen was frequently changed in the sample holder to remove interference from ice particles which form at the nitrogen-air interface. Photolysis with light of wavelength 410–490 nm was performed using the setup described below for the long wavelength photolysis. The fluorescence samples were irradiated in the same quartz tubes used for recording the spectra and placed back in the fluorimeter. The samples were irradiated until no increase in the cold emission intensity was observed, approximately 4 h.

Long wavelength photolysis

Photolysis with light of wavelength 410–490 nm was performed using a high-pressure mercury lamp surrounded by a filter solution of $CuSO_4 \cdot 5H_2O$ (2.7 M NH_3) and $NaNO_2$ (58) in a quartz reaction chamber. Photolysis was performed on the fluorescence samples whose preparation is described above.

Synthesis of acetylferrocene azines (1-Fc/Ar)

The symmetric azines **1**-Fc/Fc and **2**-Anth/Anth were synthesized according to a prescribed procedure and the spectral characterization and other physical data matched that previously reported (2, 59). The asymmetrical azines were synthesized by adding the appropriate substituted ketone or aldehyde (1 equiv) to the corresponding acetylferrocene (diethoxyphosphinyl) hydrazone (1 equiv) in benzene–NaH (1.3 equiv). Both the preparation of the acetylferrocene

© 2002 NRC Canada

(diethoxyphosphinyl) hydrazone and azine were prepared according to the published procedures (22, 39).

Preparation of diethyl phosphorohydrazidate

Hydrazine hydrate (20 equiv) was added dropwise to a stirred solution of anhydrous K_2CO_3 (15 equiv) and triethylbenzyl ammonium chloride (0.1 equiv) in CCl_4–CH_2Cl_2 (4:7) at 20–25°C. A solution of diethylphosphite (1 equiv) in CH_2Cl_2 was then added at 20–30°C. The stirring was continued for 6 h after which the K_2CO_3 crystals were filtered off and rinsed with CH_2Cl_2. The solvents were removed and the residue was kept under high vacuum for several hours. The resultant pale yellow liquid was used without further purification.

Preparation of acetylferrocene(diethoxyphosphinyl)-hydrazone

Diethyl phosphorohydrazidate (1 equiv) and acetylferrocene were dissolved in benzene and heated at reflux for 5 h. The benzene was removed by rotary evaporation to yield a crystalline sample. The solid was then purified by recystallization from hexanes–benzene (2:1). The purity of the sample was verified by GC and NMR.

***Acetylferrocene azine (1-Fc/Fc)* (2)**

mp 234–235°C. ^{1}H NMR (300 MHz, $CDCl_3$) δ: 2.16 (s, 6H), 4.17 (s, 10H), 4.34 (t, 4H), 4.71 (t, 4H). Anal. calcd. for xxxx: 452.0637; found: 452.0632.

***9-Anthraldehyde azine (2-Anth/Anth)* (60)**

mp 273–275°C. ^{1}H NMR (300 MHz, $CDCl_3$) δ: 7.60 (m, 4H), 8.09 (d, 2H), 8.60 (s, 1H), 8.80 (br d, 2H), 10.15 (br s, 1H). Anal. calcd. for $C_{30}H_{20}N_2$: 408.1626; found: 408.1621.

The following are, to the best of our knowledge new compounds or the complete spectral data has not yet been reported. X-ray crystallographic data is also available for some **1**-Fc/Ar.

Acetylferrocene(diethylphosphinyl)hydrazone

^{1}H NMR (300 MHz, $CDCl_3$) δ: 1.36 (dt, 6H), 2.05 (s, 3H), 4.18 (m, 11H), 4.55 (m, 2H), 6.35 (br d, 1H).

Acetylferrocene-4-nitroacetophenone azine (1-Fc/4-NO_2)

mp 178–180°C. UV–vis (DMF) λ_{max} (nm) (ε, M^{-1} cm^{-1}): 323 (21 170). FT-IR (CCl_4, cm^{-1}): 3105, 3080, 2920, 1592, 1512, 1342, 855, 821. ^{1}H NMR (300 MHz, $CDCl_3$) δ: 2.23 (s, 3H), 2.38 (s, 3H), 4.23 (s, 5H), 4.45 (t, 2H), 4.81 (t, 2H), 8.05 (d, 2H), 8.27 (d, 2H). ^{13}C NMR (75 MHz, $CDCl_3$) δ: 161.75, 155.95, 148.15, 144.58, 127.26, 123.54, 82.56, 70.55, 70.45, 69.55, 69.25, 67.75, 67.65, 15.95, 14.95. MS *m*/*z* (%): 389 (M^+, 100), 324 (9), 270 (18), 185 (31), 121 (31). Anal. calcd. for $C_{20}H_{19}N_3O_2Fe$: 389.0826; found: 389.0827.

Acetylferrocene-4-cyanoacetophenone azine (1-Fc/4-CN)

mp 156–157°C. UV–vis (DMF) λ_{max} (nm) (ε, M^{-1} cm^{-1}): 296 (25 050). FT-IR (CCl_4, cm^{-1}): 3100, 2960, 2924, 1603, 1573, 1563, 1476, 1364, 1292, 1131, 1106, 1017. ^{1}H NMR (300 MHz, $CDCl_3$) δ: 2.20 (s, 3H), 2.31 (s, 3H), 4.19 (s, 5H), 4.40 (t, 2H), 4.74 (t, 2H), 7.68 (d, 2H), 7.97 (d, 2H). ^{13}C NMR (75 MHz, $CDCl_3$) δ: 161.50, 156.15, 142.82, 132.09, 121.04, 118.81, 112.60, 82.89, 70.57, 69.62, 67.88, 15.99, 14.81. MS *m*/*z* (%): 369 (M^+, 100), 304 (15), 185 (57), 129 (29), 121 (37). Anal. calcd. for $C_{21}H_{19}N_3Fe$: 369.0928; found: 369.0825.

Acetylferrocene-4-methoxyacetophenone azine (1-Fc/4-OCH_3)

This compound was prepared by adding acetylferrocene (1 equiv) to the corresponding *p*-methoxyacetophenone (diethoxyphosphinyl)hydrazone (1 equiv) (22, 39) in refluxing benzene containing NaH (1.3 equiv). A small amount of product was then isolated by preparative HPLC. ^{1}H NMR (300 MHz, $CDCl_3$) δ: 2.18 (s, 3H), 2.27 (s, 3H), 3.84 (s, 3H), 4.22 (s, 5H), 4.40 (br s, 2H), 4.77 (br s, 2H), 6.92 (d, 2H), 7.83 (d, 2H). MS *m*/*z* (%): 379 (M^+, 100), 309 (28), 185 (11), 121 (18). Anal. calcd. for $C_{21}H_{22}N_2OFe$: 347.1081; found: 347.1084.

Acetylferrocene-9-anthraldehyde azine (1-Fc/Anth)

mp 169–170°C. UV–vis (DMF) λ_{max} (nm) (ε, M^{-1} cm^{-1}): 266 (59 070). FT-IR (CCl_4, cm^{-1}): 3087, 3054, 2926, 2854, 1606, 1474, 1384, 1362, 1292, 1107, 1003, 909. ^{1}H NMR (300 MHz, $CDCl_3$) δ: 2.54 (s, 3H), 4.46 (s, 5H), 4.47 (t, 2H), 4.84 (t, 2H), 7.53 (m, 4H), 8.03 (d, 2H), 8.52 (s, 1H), 8.79 (d, 2H), 9.66 (s, 1H). ^{13}C NMR (75 MHz, $CDCl_3$) δ: 156.63, 131.44, 130.64, 130.08, 128.93, 126.86, 125.43, 125.32, 70.80, 70.63, 69.56, 68.11, 16.76. MS *m*/*z* (%): 430 (M^+, 100), 365 (66), 324 (20), 203 (31), 185 (29), 121 (64). Anal. calcd. for $C_{27}H_{22}N_2Fe$: 430.1132; found: 430.1137.

Acetylferrocene-1-pyrenecarboxaldehyde azine (1-Fc/Py)

mp 178–179°C. UV–vis (DMF) λ_{max} (nm) (ε, M^{-1} cm^{-1}): 380 (34 460). FT-IR (CCl_4, cm^{-1}): 3099, 3049, 2984, 2962, 2927, 1742, 1607, 1475, 1361, 1291, 1242, 1107. ^{1}H NMR (300 MHz, $CDCl_3$) δ: 2.58 (s, 3H), 4.30 (s, 5H), 4.47 (br s, 2H), 4.84 (br s, 2H), 8.15 (m, 7H), 8.71 (d, 1H), 8.93 (d, 1H), 9.49 (br s, 1H). ^{13}C NMR (75 MHz, $CDCl_3$) δ: 156.48, 148.01, 132.86, 131.30, 130.66, 130.07, 128.69, 128.56, 127.63, 127.48, 126.22, 126.16, 125.88, 125.68, 125.00, 124.62, 123.06, 70.84, 69.58, 68.06, 16.55. MS *m*/*z* (%): 454 (M^+, 100), 389 (31), 348 (12), 227 (27), 201 (18), 185 (18), 129 (21), 121 (40). Anal. calcd. for $C_{29}H_{22}N_2Fe$: 454.1132; found: 454.1139.

Acetylferrocene-4-acetylpyridine azine (1-Fc/Pyrd)

mp 123–124°C. UV–vis (DMF) λ_{max} (nm) (ε, M^{-1} cm^{-1}): 285 (21 700). FT-IR (CCl_4, cm^{-1}): 3100, 3089, 3038, 2959, 2923, 1608, 1475, 1409, 1364, 1291, 1122, 1107, 1065, 1019, 1002, 889. ^{1}H NMR (300 MHz, $CDCl_3$) δ: 2.19 (s, 3H), 2.38 (s, 3H), 4.19 (s, 5H), 4.40 (br s, 2H), 4.74 (br s, 2H), 7.72 (br s, 2H), 8.66 (br s, 2H). ^{13}C NMR (75 MHz, $CDCl_3$) δ: 161.26, 155.75, 150.08, 145.67, 120.63, 71.04, 70.44, 69.39, 67.67, 15.98, 14.44. MS *m*/*z* (%): 345 (M^+, 100), 280 (18), 185 (38), 121 (20). Anal. calcd. for $C_{19}H_{19}N_3Fe$: 345.0928; found: 345.0932.

Acetophenone-9-anthraldehyde azine (2-Anth/H)

This compound was prepared by adding 9-anthraldehyde (1 equiv) to acetophenone (diethoxyphosphinyl)hydrazone (1 equiv) (39) in refluxing benzene containing NaH (1.3 equiv). mp 95–97°C. UV–vis (EPA) λ_{max} (nm) (ε, M^{-1} cm^{-1}): 257 (105 700). FT-IR (CCl_4, cm^{-1}): 3086, 3055, 3031, 1624, 1611, 1519, 1453, 1444, 1364, 1294, 1021, 889. ^{1}H NMR

© 2002 NRC Canada

(400 MHz, $CDCl_3$) δ: 2.65 (s, 3H), 7.52 (m, 7H), 8.03 (m, 4H), 8.54 (s, 1H), 8.79 (d, 2H), 9.71 (s, 1H). ^{13}C NMR (100 MHz, $CDCl_3$) δ: 165.47, 157.86, 138.27, 131.37, 130.65, 130.37, 130.26, 128.99, 128.51, 127.05, 127.00, 125.77, 125.36, 125.27, 15.95. MS *m*/*z* (%): M^+, 322 (76), 204 (100), 177 (56), 118 (18), 77 (66). Anal. calcd. for $C_{23}H_{18}N_2$: 322.1472; found: 322.1470.

Acetophenone-1-pyrenecarboxaldehyde azine (2-Py/H)

This compound was prepared by adding 9-anthraldehyde (1 equiv) to acetophenone (diethoxyphosphinyl)hydrazone (1 equiv) (39) in refluxing benzene containing NaH (1.3 equiv). mp 115–117°C. UV–vis (DMF) λ_{max} (nm) (ε, M^{-1} cm^{-1}): 380 (41 500). FT-IR (CCl_4, cm^{-1}): 3084, 3050, 1610, 1580, 1496, 1444, 1364, 1294, 1235, 1185, 850. ^1H NMR (400 MHz, $CDCl_3$) δ: 2.68 (s, 3H), 7.47 (m, 3H), 8.08 (m, 5H), 8.22 (m, 4H), 8.72 (d, 1H), 8.94 (d, 1H), 9.52 (br s, 1H). ^{13}C NMR (100 MHz, $CDCl_3$) δ: 165.30, 157.61, 138.39, 133.11, 131.25, 130.61, 130.22, 130.18, 128.86, 128.78, 128.49, 127.44, 127.19, 126.99, 126.42, 126.21, 126.03, 125.81, 124.99, 124.96, 124.59, 122.90, 15.77. MS *m*/*z* (%): 346 (M^+, 100), 227 (47), 201 (80), 145 (20), 119 (9), 77 (30). Anal. calcd. for $C_{25}H_{18}N_2$: 346.1470; found: 346.1465.

X-ray crystallography

Single crystals of **1**-Fc/4-NO_2, **1**-Fc/4-CN, **1**-Fc/Pyrd, and **1**-Fc/Anth were grown by slow evaporation of a concentrated solution of the azine in an appropriate solvent. Crystals were mounted on a glass fibre. Data were collected on a Nonius Kappa-CCD diffractometer using COLLECT (Nonius, 1998) software. The unit cell parameters were calculated and refined from the full data sets. Crystal cell refinement and data reduction was carried out using the Nonius DENZO package. The data were scaled using SCALEPACK (Nonius, 1998) and no other adsorption corrections were applied. The SHELXTL 5.1 (Sheldrick, G.M., Madison, WI) program package was used to solve the structures by direct methods, followed by successive difference Fouriers. All non-hydrogen atoms were refined with anisotropic thermal parameters. The hydrogen atoms were calculated geometrically and were riding on their respective carbon atoms. The crystal data for the structures determined in this report are reported in the *Supplementary material*.[2]

Acknowledgments

The financial support of the Natural Sciences and Engineering Research Council of Canada (NSERC), Canadian Foundation for Innovation, ORDCF, and the University of Western Ontario (ADF) is appreciated. V.A.S. thanks the OGS program for a scholarship. Thanks to Dr. M.C. Jennings and Dr. J.F. Corrigan for crystal structure analyses and structural determinations.

References

1. Ferrocenes: Homogeneous catalysis, organic synthesis, materials science. *Edited by* A. Togni and T. Hayashi. VCH Publishers, New York. 1995.
2. A.G. Osborne, M.W d. Silva, M.B. Hursthouse, K.M.A. Malik, G. Opromolla, and P. Zanello. J. Organomet. Chem. **516**, 167 (1996).
3. K.N. Jayaprakash, P.C. Ray, I. Matsuoka, M.M. Bhadbhade, V.G. Puranike, P.K. Das, H. Nishihara, and A. Sarkar. Organometallics, **18**, 3851 (1999).
4. X. Xu-Bing, D. Chun-Ying, Z. Long-Gen, Y. Xiao-Zeng, Y. Yao, and W. Hua-Qin. Polyhedron, **11**, 1917 (1992).
5. P. Zanello, G. Opromolla, F.F.d. Biani, A. Ceccanti, and G. Giorgi. Inorg. Chim. Acta, **255**, 47 (1997).
6. D. Osella, M. Farrali, P. Zanello, F. Laschi, M. Fontani, C. Nervi, and G. Cavigiolio. Inorg. Chim. Acta, **306**, 42 (2000).
7. B. Bildstein, M. Schweiger, H. Angleitner, H. Kopacka, K. Wurst, K.H. Ongania, M. Fontani, and P. Zanello. Organometallics, **18**, 4286 (1999).
8. R. Altmann, O. Gausset, D. Horn, K. Jurkschat, M. Schürmann, M. Fontani, and P. Zanello. Organometallics, **19**, 430 (2000).
9. B. Neumann, U. Siemeling, H.-G. Stammler, U. Vorfeld, J.G.P. Delis, P.W.N.M. van Leeuwen, K. Vrieze, J. Fraanje, K. Goubitz, F.F.d. Biani, and P. Zanello. J. Chem. Soc. Dalton Trans. 4705 (1997).
10. B. Bildstein, M. Malaun, H. Kopacka, M. Fontani, and P. Zanello. Inorg. Chim. Acta, **300**–**302**, 16 (2000).
11. S. Barlow, H.E. Bunting, C. Ringham, J.C. Green, G.U. Bublitz, S.G. Boxer, J.W. Perry, and S.R. Marder. J. Am. Chem. Soc. **121**, 3715 (1999).
12. A. Houlton, N. Jasim, R.M.G. Roberts, J. Silver, D. Cunningham, P. McArdle, and T. Higgins. J. Chem. Soc. Dalton Trans. 2235 (1992).
13. H.K. Sharma, K.H. Pannell, I. Ledoux, J. Zyss, A. Ceccanti, and P. Zanello. Organometallics, **19**, 770 (2000).
14. M. Prato, M. Maggini, C. Giacometti, G. Scorrano, G. Sandona, and G. Farnia. Tetrahedron, **52**, 5221 (1996).
15. Z. Wang, K. Chen, and H. Tian. Chem. Lett. 423 (1999).
16. Z. Wang, J. Zhu, K. Chen, and H. Tian. J. Chem. Res. **S**, 438 (1999).
17. R. Centore and C. Garzillo. J. Chem. Soc. Perkin Trans. 2, 79 (1997).
18. E.C. Kesslen, W.B. Euler, and B.M. Foxman. Chem. Mater. **11**, 336 (1999).
19. R. Centore, B. Panunzi, and A. Tuzi. Z. Kristallog. **211**, 31 (1996).
20. G.S. Chen, M. Anthamatten, C.L. Barnes, and R. Glaser. Angew. Chem. Int. Ed. Engl. **34**, 1081 (1994).
21. G.S. Chen, M. Anthamatten, C.L. Barnes, and R. Glaser. J. Org. Chem. **59**, 4336 (1994).
22. G.S. Chen, J.K. Wilbur, C.L. Barnes, and R. Glaser. J. Chem. Soc. Perkin Trans. 2, 2311 (1995).
23. R. Glaser, G.S. Chen, and C.L. Barnes. J. Org. Chem. **58**, 7446 (1993).
24. R. Glaser, G.S. Chen, M. Anthamatten, and C.L. Barnes. J. Chem. Perkin Trans. 2, 1449 (1995).
25. R. Glaser and G.S. Chen. J. Comp. Chem. **19**, 1130 (1998).

[2] Supplementary material may be purchased from the Depository of Unpublished Data, Document Delivery, CISTI, National Research Council Canada, Ottawa, ON K1A 0S2, Canada. For information on obtaining material electronically go to http://www.nrc.ca/cisti/irm/unpub_e.shtml. Crystallographic information has also been deposited with the Cambridge Crystallographic Data Centre (CCDC Nos. 178709, 178710, 178711, 178712). Copies of the data can be obtained free of charge via www.ccdc.cam.ac.uk/conts/retrieving.html (or from the Cambridge Crystallographic Data Centre, 12, Union Road, Cambridge CB2 1EZ, UK; fax: +44 1223 336033; or deposit@ccdc.cam.ac.uk).

© 2002 NRC Canada

26. R. Glaser, M. Lewis, and Z. Wu. J. Mol. Model **6**, 86 (2000).
27. M. Lewis, C.L. Barnes, and R. Glaser. Can. J. Chem. **76**, 1371 (1998); (*b*) M. Lewis and R. Glaser. J. Org. Chem. **67**, 1441 (2002).
28. M. Lewis, C.L. Barnes, B.A. Hathaway, and R. Glaser. Acta. Cryst. **C55**, 975 (1999).
29. M. Lewis, C.L. Barnes, and R. Glaser. Acta Cryst. **C56**, 393 (2000).
30. H. Lund. Acta Chem. Scand. **13**, 249 (1959).
31. K.B. Wiberg and T.P. Lewis. J. Am. Chem. Soc. **92**, 7154 (1970).
32. M.A.G. Nieto, M.D.L.d. Castro, and M. Valcarcel. Electrochim. Acta **28**, 1725 (1983).
33. J.H. Barnes, F.M. Triebe, and M.D. Hawley. J. Electroanal. Chem. **139**, 395 (1982).
34. K.L. Handoo and S.K. Handoo. Ind. J. Chem. **19B**, 684 (1980).
35. J. Ludvík, F. Riedl, F. Liska, and P. Zuman. J. Electroanal. Chem **457**, 177 (1998).
36. F. Riedl, J. Ludvík, F. Liska, and P. Zuman. J. Heterocyclic Chem. **33**, 2063 (1996).
37. M. Privman and P. Zuman. J. Electroanal. Chem. **455**, 235 (1998).
38. P. Zuman. Tetrahedron Lett. **41**, 7851 (2000).
39. V.A. Sauro and M.S. Workentin. J. Org. Chem. **66**, 831 (2001).
40. Organic electrochemistry. *Edited by* H. Lund and M.M. Baizer. Marcel Dekker Inc., New York. 1991.
41. T. Gareis, O. Kothe, and J. Daub. Eur. J. Org. Chem. 1549 (1998).
42. A. Lasia and A. Rami. Can. J. Chem. **65**, 744 (1987).
43. A.J. Bard and L.R. Faulkner. Electrochemical methods. Fundamentals and applications. John Wiley & Sons, New York. 1980.
44. R. Nicholson. Anal. Chem. **37**, 1351 (1965).
45. U.W. Grummt. J. Photochem. **31**, 131 (1985).
46. S. Vettermann, K. Gustav, and J. Jungel. J. Mol. Struct. Theochem **10**4 259 (1983).
47. K. Gustav, S. Vettermann, and P. Birner. J. Mol. Struct. Theochem. **88**, 249 (1982).
48. K. Appenroth, M. Reichenbacher, and R. Paetzold. J. Photochem. **14**, 39 (1980).
49. K. Appenroth, M. Reichenbacher, and R. Paetzold. J. Photochem. **14**, 51 (1980).
50. K. Appenroth, M. Reichenbacher, and R. Paetzold. Tetrahedron, **37**, 569 (1981).
51. K. Appenroth, E. Birckner, and M. Reichenbacher. J. Photochem. **37**, 117 (1987).
52. J.D. Coyle. Introduction to organic photochemistry. John Wiley & Sons, New York. 1986.
53. R. Paetzold, M. Reichenbacher, and K. Appenroth. Z. Chem. **21**, 421 (1981).
54. K. Gustav and S. Vettermann. Z. Chem. **18**, 456 (1978).
55. R.E. Bozak. Photochemistry in the metallocenes. *In* Advances in photochemistry. Vol. 8. *Edited by* N. Pitts, G.S. Hammond, and W.A. Noyes. John Wiley & Sons Inc. New York. 1971.
56. R.M.G. Roberts, J. Silver, B.M. Yamin, M.G.B. Drew, and U. Ebergardt. J. Chem. Soc. Dalton Trans. 1549 (1988).
57. J.D. Dunitz, L.E. Orgel, and A. Rich. Acta Cryst. 9 373 (1956).
58. Handbook of photochemistry. 2nd ed. *Edited by* S.L. Murov, I. Carmichael, and G.L. Hug. Marcel Dekker Inc., New York. 1993.
59. S.G. Cohen, S.J. Groszos, and D.B. Sparrow. J. Am. Chem. Soc. **72**, 3947 (1950).
60. K. Appenroth, M. Reichenbacher and R. Paetzold. Z. Chem. **23**, 414 (1983).

© 2002 NRC Canada

Low temperature interface-mineralizing route to hollow CuS, CdS, and NiS spheres

Xuchuan Jiang, Yi Xie, Jun Lu, Liying Zhu, Wei He, and Xianming Liu

Abstract: Submicrometer hollow CuS, CdS, and NiS spheres with diameters between 400 and 1300 nm were successfully prepared through an interface-mineralizing reaction in a $NH_3 \cdot H_2O$–CS_2 solution at low temperature. Several techniques were applied to characterize the interesting self-assembled structures. The compositions of the prepared CuS, CdS, and NiS materials were confirmed by X-ray powder diffraction (XRD), the surface atomic ratios and the valence state of ions were examined by X-ray photoelectron energy spectroscopy (XPS), and the morphologies of products by transmission electron microscope (TEM). The optical properties, including absorption and emission, were recorded by UV–vis absorption and fluorescence spectroscopy, respectively. In this approach, ethylenediamine (en) was substituted by aqueous ammonia ($NH_3 \cdot H_2O$) to avoid violent reactions with carbon disulfide (CS_2). The main advantage to this approach is that both ammonia and CS_2 played multi-functional roles in the assembly of hollow-sphere structures. The reaction sources themselves (CS_2) served as the reaction template and required no other templates to support it. The proposed interface-mineralizing mechanism is discussed, and the hollow-sphere structures obtained are envisioned to have applications in area of materials science.

Key words: hollow-sphere structure, $NH_3 \cdot H_2O$–CS_2, metal sulfides

Résumé : Faisant appel à une réaction de minéralisation à l'interface, dans une solution de $NH_3 \cdot H_2O$–CS_2, à basse température, on a préparé avec succès des sphères creuses de CuS, CdS et de NiS de dimensions sous micrométriques, ayant des diamètres allant de 400 à 1300 nm. On a appliqué plusieurs techniques pour caractériser ces structures intéressantes qui donnent lieu à de l'autoassemblage. Les compositions des produits CuS, CdS et NiS qui ont été préparés ont été confirmées par diffraction de rayons X par des poudres; les rapports de surface atomique et l'état de valence des ions ont été évalués par spectroscopie de l'énergie photoélectronique des rayons X et les morphologies des produits ont été étudiées par microscopie de transmission électronique. Les propriétés optiques, y compris l'absorption et l'émission, ont été enregistrées respectivement par le biais des spectres d'absorption UV–visible et de fluorescence. Dans cette approche, on a substitué l'éthylènediamine (en) par de l'ammoniac aqueux ($NH_3 \cdot H_2O$) afin d'éviter les réactions violentes avec le disulfure de carbone (CS_2); les principaux avantages de cette substitution sont que l'ammoniac et le CS_2 jouent tous les deux plusieurs rôles dans l'assemblage des structures sphériques creuses. De plus, les sources de réaction servent aussi de gabarit pour la réaction, éliminant la nécessité d'avoir d'autre support. On discute du mécanisme proposé pour la réaction de minéralisation à l'interface. On croit que les structures sphériques creuses obtenues ici auront des applications dans le domaine des sciences des matériaux.

Mots clés : structure sphérique creuse, $NH_3 \cdot H_2O$–CS_2, sulfures métalliques.

[Traduit par la Rédaction]

Introduction

Nanomaterials with different morphologies exhibit dissimilar properties (1). Metal chalcogenides have gained much more attention in the field of material science (2) because of their unusual electronic properties and interesting chemical behaviors (3). Nanoparticles, intermediate in size between bulk solids and molecular entities, have been the subject of numerous investigations (4–7), and such nanoparticles can undergo self-assembly into superlattices or special nanostructures (7–11). The future design of functional nanodevices will most likely rely on the principles of molecular self-organization. Many of examples of such compounds with interesting morphologies or special structures have been reported in the literature, including nanostructural rods, wires, cables, or spheres (12–15). Recently, Stupp and Braun (11) constructed semiconductor CdS nanomaterials with three different morphologies: hexagon-pore arrays, layers, and hollow spheres. These nanomaterials were prepared by the reaction of H_2S and Cd^{2+} ions in a lyotropic liquid-crystal template, and were the first reported examples of inorganic non-oxide semiconductor materials. Caruso et al. (16) reported the nanoengineering of silica and silica-polymer spheres by colloid-templated electrostatic layer-by-layer self-assembly. Volkmer et al. (17*a*) reported the spontaneous self-assembly and the resulting superstructures of discrete nanoporous surfactant-encapsulated clusters, mono-

Received 15 August 2001. Published on the NRC Research Press Web site at http://canjchem.nrc.ca on 19 March 2002.

X. Jiang, Y. Xie,[1] J. Lu, L. Zhu, W. He, and X. Liu. Structure Research Laboratory and Laboratory of Nanochemistry & Nanomaterials, University of Science & Technology of China, Hefei, Anhui 230026, P.R. China.

[1]Corresponding author (e-mail: yxielab@ustc.edu.cn).

 DOI: 10.1139/V02-020 © 2002 NRC Canada

layers, and LB films of $(DODA)_{40}(NH_4)_2[(H_2O)_n \subset Mo_{132}O_{372}(CH_3CO_2)_{30}(H_2O)_{72}]$ ($n \approx 50$). Xie and co-workers (18) fabricated submicrometer hollow CdS spheres through self-assembly in the ethylenediamine (en) – carbon disulfide (CS_2) – water system, as well as self-organized peanut-like CdS and ZnS nanostructures in the interface region of organic and inorganic phases. Imhof and co-workers (19) discuss an emulsion templating scheme that employs monodisperse liquid droplets instead of solid particles as the colloidal template,which can be used to produce porous rutile titanium dioxide. The above-mentioned self-organized micro- and nanoparticles have different surface chemical compositions, increased stability, higher surface areas, and different magnetic and optical properties (20), thus making them attractive from both a scientific and a technological viewpoint. The self-organized hollow spheres including composite materials and coatings have diverse applications, such as capsule agents for drug delivery, catalysis, and protecting sensitive agents. To understand the mechanism of self-organization, we report here on the self-organization of the en–CS_2 system to form transitional-metal hollow-sphere structures.

It is known that the properties of aqueous ammonia (the NH_3 content is ~28%) are similar to those of en ($H_2NCH_2CH_2NH_2$). Aqueous ammonia, however, has more advantages than en such as lower price, lower toxicity, and the avoidance of violent reactions with CS_2. More importantly, $NH_3 \cdot H_2O$ reacts softly with CS_2 without any buffers and can lead to self-assembled sulfide nanomaterials with interesting or unique structures. In this paper, we report the self-assembly of hollow CuS, CdS, and NiS spheres with diameters of 400~1300 nm via the interface-mineralizing reaction in a $NH_3 \cdot H_2O$–CS_2 system at low temperature. One obvious advantage of this strategy is that both $NH_3 \cdot H_2O$ and CS_2 play various roles in the formation of the hollow spheres. $NH_3 \cdot H_2O$ acts as the ligand, nucleophile agent, and reaction buffer between NH_3 and CS_2. Meanwhile, in the oil phase, CS_2 serves as the sulfur source and architecture template. This may offer more evidence to support the reaction mechanism proposed in our previous work.

Experimental

Procedure

Based on our strategy, the following one-pot reaction route was designed to prepare hollow metal-sulfides spheres. Carbon disulfide (CS_2) (2.0 mL, ~0.034 mol) was added into aqueous ammonia solution (20.0 mL, the content of NH_3 is 28 wt%), followed by dropwise addition (ca. 30 min) of Cu^{2+}, Cd^{2+}, or Ni^{2+} ions in solution (0.1 mol dm^{-3}, 10.0 mL). The mixture was stirred slowly at room temperature. After the addition of M^{2+} ions, the reaction systems were heated for 1 h at 50°C under vigorous stirring until brown-black precipitates formed. The mixtures were then cooled to room temperature, and the precipitates were filtered, washed with dilute hydrochloric acid solution (0.1 mol dm^{-3}), distilled water, and ethanol for three or more times. The final products were dried in vacuum at 40°C for 4 h, and stored for further investigation.

Fig. 1. The XRD patterns of the prepared samples. (*a*) Hexagonal CuS phase; (*b*) cubic β-CdS phase; (*c*) hexagonal NiS phase.

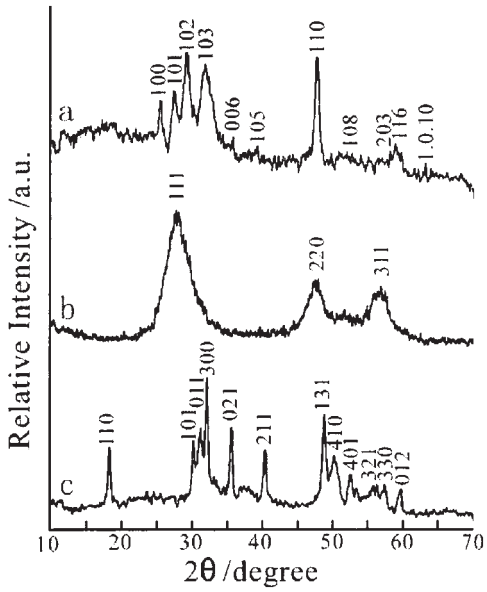

Characterization

Three samples were characterized as follows. The constituents of the final products were confirmed by X-ray powder diffraction (XRD) analysis, carried out with a Japan Rigaku D/max-γ rotation anode X-ray diffractometer, using Ni-filtered Cu Kα radiation at 25°C. A scanning rate of 0.05° s^{-1} was applied to record the patterns in the 2θ range of 10~70°. The morphologies of products were observed with a Hitachi H-800 transmission electron microscope (TEM) at the acceleration voltage of 200 kV, and the high-resolution transmission electron microscopy (HRTEM) images of the products were obtained on a JEOL-2010 transmission electron microscope. A small amount of CuS, CdS, or NiS powder was ultrasonically dispersed in ethanol, followed by adsorption of one droplet of its suspension onto a copper grid for measurement. The electronic binding energy was examined on an X-ray photoelectron spectroscope (XPS), model VGESCALAB Mg Kα ($h\upsilon$ = 1253.6 eV), with a pressure of 1.0×10^{-4} Pa and a revolution of 1.0 eV. Their optical properties were recorded by a UV–vis absorption and fluorescence spectrophotometer. The UV–vis spectra of samples were recorded on a UV–vis Spectrophotometer Specord 200 (Analytik Jena AG) absorption diode array spectrometer using 1-cm quartz curettes. The photoluminescence (PL) spectra of products were performed on a Hitachi 850-fluorescence spectrometer with a Xe lamp at room temperature with an excitation wavelength of 320 nm.

Results and discussion

Figure 1 displays the XRD patterns of products, and the narrow Bragg reflection peaks of the crystalline metal sulfides are all indexed. All of the relative information on the hollow CuS, CdS, and NiS sphere structures are listed in Table 1. Each of the XRD patterns shows a pure-phase compound. From the broaden peaks, the size of the small crystalline particles, estimated roughly by Scherrer's for-

© 2002 NRC Canada

Table 1. The parameters of hollow CuS, CdS, and NiS spheres.

Samples	Lattice parameters (Å) Calcd.	Ref.	Symmetric	Space group	JCPDS files	Particle size (nm)
CuS	a = 3.820 ±0.058 c = 16.502 ±0.067	c = 3.792 c = 16.344	Hexagonal	$P6_3/mmc$	6–464 10–454	10
CdS	a = 5.921 ±0.043	a = 5.818	Cubic	$F\bar{4}3m$		15
NiS	a = 9.843 ±0.028 c = 3.150 ±0.042	a = 9.620 c = 3.149	Hexagonal	$R3m$	12–41	12

Fig. 2. (*a*, *b*) TEM images of hollow CuS spheres; (*c*) a broken hollow CuS sphere; (*d*) the electron diffraction (ED) pattern for hollow CuS spheres; (*e*) HRTEM images for spherical walls composed of many small nanocrystals.

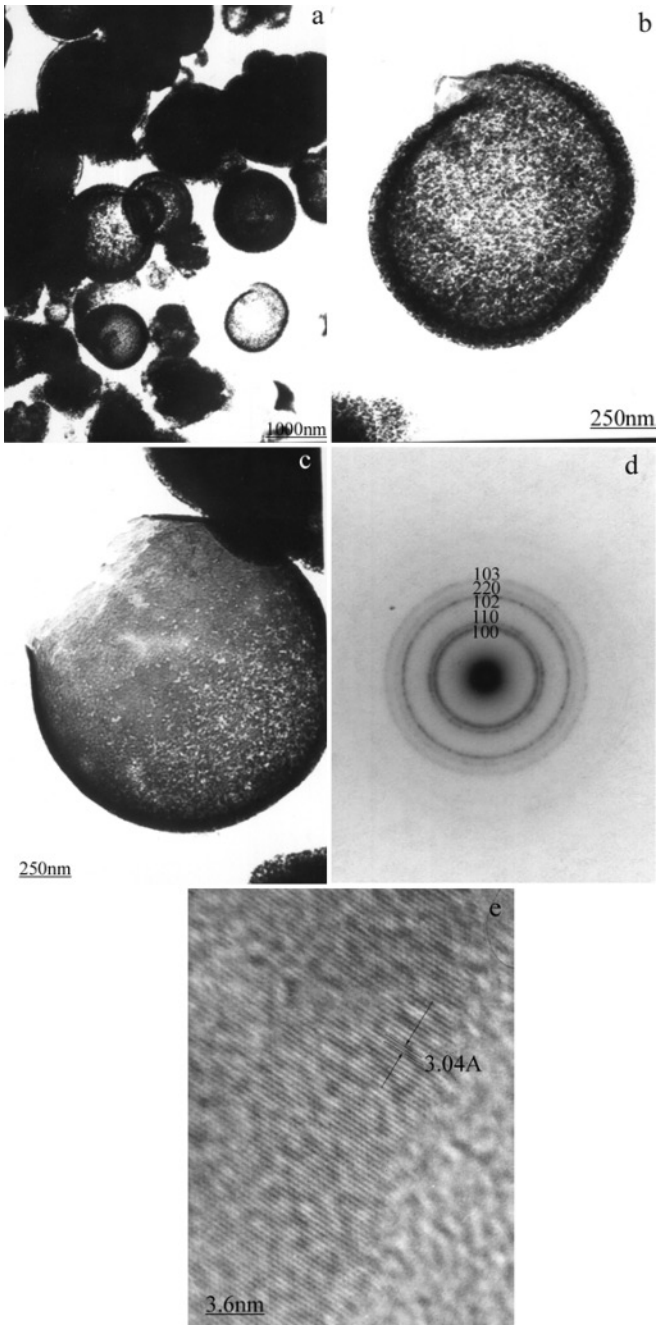

mula (21), is less than 15 nm, which is also confirmed by transmission electron microscope images.

The electronic binding energy values of products were authenticated by XPS spectra. The general scan spectra show the presence of the principle C(1*s*), S(2*p*), and metallic core levels, with no evidence of impurities for all three samples. The binding values, 933.1 eV for Cu(2*p*), 917.8 eV for Cu (LMM), and 162.3 eV for S(2*p*), were identical to the hexagonal CuS phase (405.2 eV for Cd($3d_{5/2}$), 381.0 eV for Cd(MNN), and 161.8 eV for S(2*p*)). The values of 855.3 eV for Ni($2p_{3/2}$) and 162.5 eV for S(2*p*) are also in good agreement with NiS. All the results are in accordance with the published values (22).

The TEM images of hollow metal-sulfides spheres are shown in Figs. 2–4. Figure 2 displays the TEM images of hollow CuS spheres. Figures 2*a* and 2*b* display the hollow spheres with diameters of 400~1300 nm, and the spherical walls are comprised of many small particles with diameters of ca. 10 nm. The strong contrast between the dark edge and pale center of some mineralized hollow CuS spheres is evidence for its hollow nature. In Fig. 2*a*, about 40% of the hollow spheres are filled with small particles. A broken hollow CuS sphere with a diameter of 1000 nm is shown in Fig. 2*c*, in which the open section can be clearly observed. The thickness of sphere walls is about 13~40 nm (Figs. 2*b* and 2*c*). Figure 2*d* shows the electron diffraction (ED) pattern of the CuS particles with Bragg diffraction rings indexed at the 100, 101, 102, 220, and 103 planes, which is in agreement with the XRD pattern (Fig. 1*a*). Meanwhile, the HRTEM image of the hollow CuS sphere is shown in Fig. 2*e*; the lattice spacing distance is ca. 3.05 Å, which is consistent with the 102 plane in the XRD pattern (Fig. 1*a*).

Figure 3 displays the morphology (Fig. 3*a*), ED pattern (Fig. 3*b*), and HRTEM image (Fig. 3*c*) of the hollow CdS spheres. The sphere wall is composed of many nanocrystals with average diameters of 15 nm. About 60% of the structures are hollow spheres, 20% of hollow spheres are filled with small particles, and the others are in an agglomerated disorganized state, which can also be seen from a histogram (Fig. 3*d*). The thickness of hollow CdS spheres is about 50 nm. Three strong ED rings are indexed at the 111, 220, and 311 planes, whereas the two other weaker ED rings are indexed at the 400 and 420 planes for the cubic β-CdS phase. From the HRTEM image, the lattice spacing distance of CdS nanocrystals is ca. 3.35 Å (Fig. 3*c*), which corresponds to the 111 plane in the XRD pattern of CdS (Fig. 1*b*). Similarly, the morphology of the hollow NiS spheres is shown in Fig. 4*a*. The dispersion of the spheres are well separated, showing just a small amount of aggrega-

© 2002 NRC Canada

Fig. 3. The (*a*) TEM image; (*b*) ED pattern; and (*c*) HRTEM image of hollow CdS spheres; and (*d*) a histogram of the data.

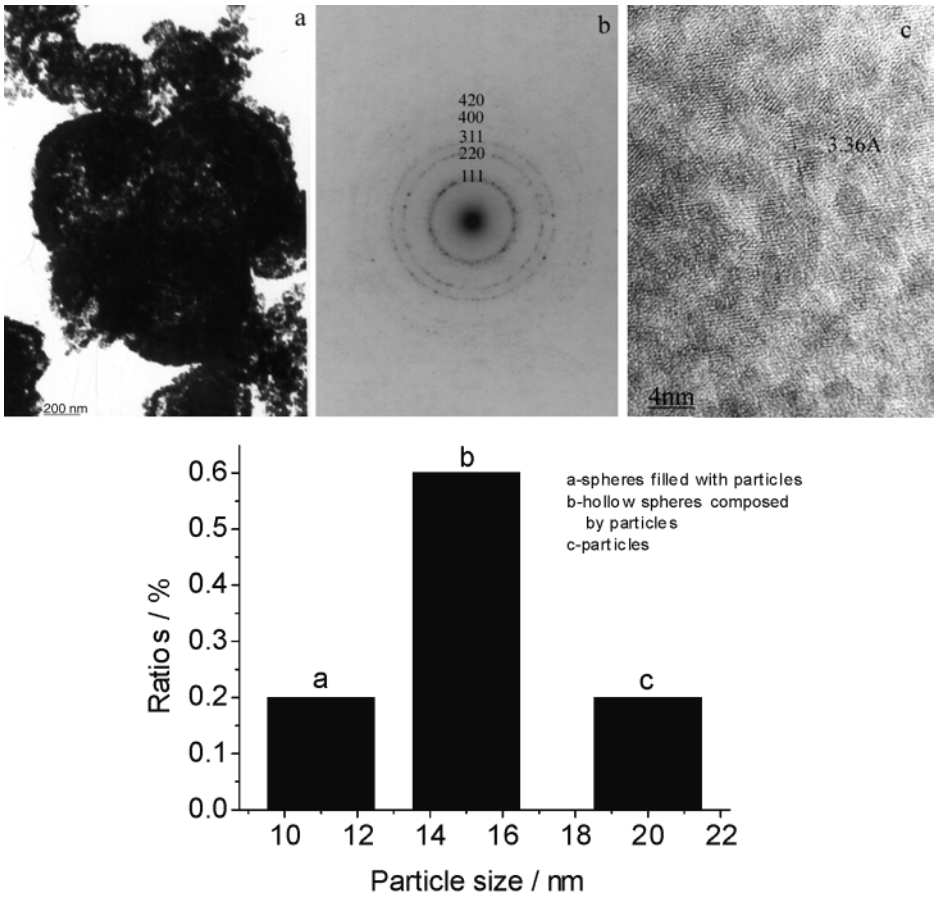

Fig. 4. The (*a*) TEM image; (*b*) ED pattern; and (*c*) HRTEM image of hollow NiS spheres.

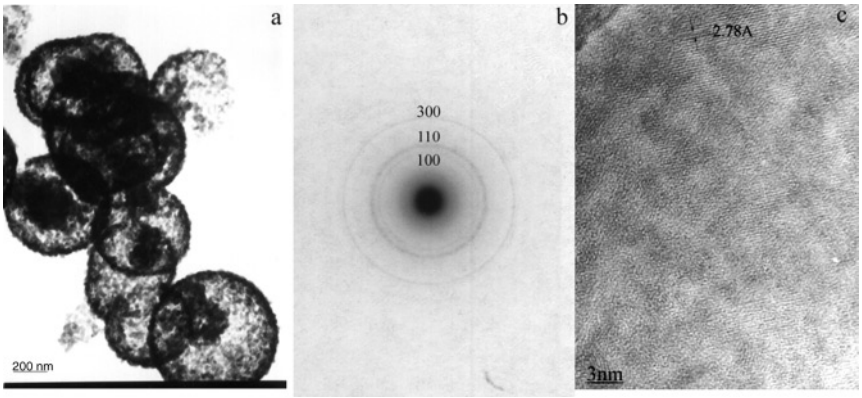

tion. The spherical walls consist of a large amount of particles with average diameters of 12 nm that self-assemble and mineralize on the surface of CS_2 droplets. The ED rings (Fig. 4*b*) are indexed at the 110, 021, and 300 planes for the hexagonal NiS phase, which corresponds to the reflection peaks in the XRD pattern (Fig. 1*c*). Here most parts of NiS are hollow spheres and the thickness of walls are between 13~30 nm. The lattice spacing distance of NiS nanocrystals that comprise the spherical walls is ca. 2.76 Å, corresponding to the 300 plane in the XRD pattern (Fig. 1*c*). All of the above-prepared hollow-sphere structures were heated at 50°C for 12 h, and apart from a little condensation, the hollow spherical structures remained stable. When heated at higher than 120°C for 3 h, the hollow spherical structures were broken and condensed into solid bulk-like materials.

The proposed formation processes of the hollow CuS, CdS, and NiS spheres can be described diagrammatically (Scheme 1).

From Scheme 1, liquid CS_2 added into aqueous ammonia formed small oil droplets due to its sparing solubility (23); they dispersed into a homogeneous solution under a stirring. This was supported by the observations that when stirred, the liquid–liquid heterogeneous $NH_3{\cdot}H_2O$–CS_2 system became opalescent and finally clear, followed by the Tyndall

© 2002 NRC Canada

Scheme 1. Illustration of the interface-mineralizing reaction used to prepare hollow CuS, CdS, and NiS spheres. (*a*) CS_3^{2-} and SCN^- ions formed at the interface of CS_2 oil droplets and the electrostatic attraction with NH_4^+; (*b*) M^{2+} ions were added to $NH_3{\cdot}H_2O$–CS_2 system and $M(NH_3)_n^{2+}$ aggregating around the CS_2 droplets; (*c*) $M(NH_3)_n^{2+}$ ions decomposed, and MS (M = Cu, Cd, or Ni) precipitates simultaneously form at the surface of CS_2 droplets via rxn. [2]; (*d*) the metal sulfides mineralized to form stable MS sphere walls after unreacted CS_2 was evaporated upon heating at 50°C for 1 h.

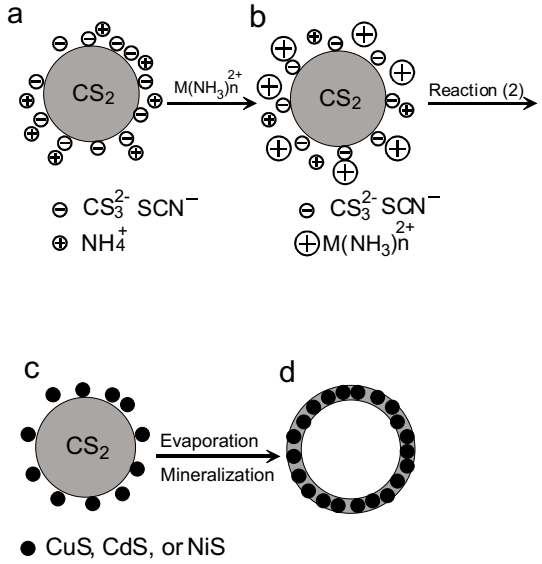

effect observed using a He–Ne laser beam. After about 5 min, the color of the mixed solution turned red. Some freshly formed S^{2-} ions (eq. [1]) aggregated around the unreacted CS_2 droplets, and hence the ammonia complex $M(NH_3)_n^{2+}$ (n = 4 for Cu^{2+} or Cd^{2+} and n = 6 for Ni^{2+}) ions gradually gathered around the surface of droplets of CS_2 because of both electrostatic attractions and additional chemical reactions (eq. [2]). The decomposition of $M(NH_3)_n^{2+}$ ions and the nucleation of nanocrystallites occurred simultaneously on the interface of CS_2 oil droplets with aqueous ammonia (eqs.[2] or [4]). Heating accomplished various roles for the formation of the hollow CuS, CdS, and NiS sphere structures, such as the promotion of the reactions (eqs. [1]~[4]), the evaporation of the unreacted CS_2 oil droplets (the boiling point of CS_2 is 45°C (24)), and the mineralizing of nanoparticles on the surface of droplets. The diffusion of CS_2 may lead to many small holes on the sphere walls, which can be observed by TEM. In addition, if the diffusion of the surrounded CS_2 molecules is homogeneous in all directions, the closed spheres have small holes on the sphere wall (Fig. 2*b*); broken wall or unclosed spheres (Fig. 2*c*) may also be obtained from heterogeneous diffusion of the CS_2 molecules.

The above-mentioned formation mechanism of the hollow-sphere structures may be supported by the following reactions:

[1] $4NH_3 + CS_2 \rightarrow NH_4SCN + (NH_4)_2S$

[2] $M^{2+} + (NH_4)_2S \rightarrow MS\downarrow + 2NH_4^+$

Fig. 5. The UV–vis absorption (solid line) and photoluminescence (dotted line) spectra of the products. They are (*a*) NiS; (*b*) CuS; and (*c*) CdS.

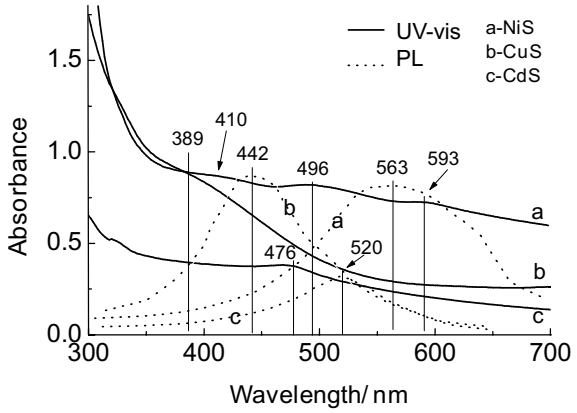

[3] $M^{2+} + 7NH_3 + 2CS_2 \rightarrow M(NH_3)_3(CS_3) + NH_4SCN + 2NH_4^+$

[4] $M(NH_3)_3(CS_3) \rightarrow MS\downarrow + 3NH_3\uparrow + CS_2\uparrow$

where the reaction of CS_2 with a nucleophile in the presence of base (eq. [1]) is a very general one (18*a*). Fackler et al. (25*a*, *b*) have investigated in detail the reactions between NH_3 and CS_2. In these reactions the N atom of NH_3 is nucleophilic, and in basic solutions (pH = ~9.2) is prone to attack CS_2. In our work, the formation of SCN^- ions or $M(MH_3)_3(CS_3)$ was identified by IR spectroscopy. The M^{2+} ions initially formed $M(NH_3)_n^{2+}$ ions or $M(NH_3)_3(CS_3)$ complexes, which are favorable for the slow nucleation and self-assembly of MS nanocrystals around the unreacted CS_2 droplets. With respect to the formation mechanism of the hollow spheres, Imhof and co-workers (19) have stated that the emulsion template formed by surfactant molecules with long chains is favorable for the formation of materials with holes after the surfactants have been removed. Here we prepared hollow MS spheres without the use of any pre-existing templates.

In contrast to the above procedure, when Cu^{2+}, Cd^{2+}, or Ni^{2+} ions were added to the pre-reacted (30 min) mixture of aqueous ammonia with CS_2 at 50°C, the reaction rate of precipitation increased under the similar conditions. Most of the final products were spherical nanoparticles rather than the desired hollow spheres, probably caused by the rapid nucleation of the nanocrystals and the tiny crystals having not enough time to self-assemble. This is because the CS_2 molecules had completely reacted within 30 min. The above-mentioned results indicate that the competitive reactions between the decomposition of $M(NH_3)_n^{2+}$ and the formation of MS nanoparticles were favorable for the formation of hollow-sphere structures.

To examine the importance of the sulfur source (CS_2) in the formation of hollow metal-sulfides spheres, other sulfur sources (Na_2S and $Na_2S_2O_3$) were tested. Unfortunately, only solid particles were prepared from these alternative sulfur sources, because of random release of S^{2-} ions and rapid precipitation, neither of which are suitable for the orderly self-assembly of nanoparticles. Moreover, no stable architectures provided by CS_2 droplets were suitable for the self-

© 2002 NRC Canada

organization of nanocrystals. This indicates that the existence of CS_2 oil droplets is important for the formation of hollow spheres.

To understand the effects of quantum-size "bricks" (which are formed on the sphere walls) on the optical properties, the UV–vis absorption (solid line) and photoluminescence (PL) (dotted line) properties of the hollow-sphere structural sulfides were measured; the results are shown in Fig. 5. Three absorption peaks for hollow NiS spherical materials are seen at 410, 496, and 593 nm (Fig. 5*a*). We speculate that these may be caused by the various structures of NiS bricks that form the NiS sphere walls but the essential causes are unclear and require further investigation. The maximum absorption at 389 nm for CuS nanocrystals (Fig. 5*b*) may be assigned to the optical-band edge–edge transition. Similarly, the maximum absorption at 476 nm for CdS (Fig. 5*c*) is attributed to the optical-band edge–edge transition, although a splitting of the energy bands into discrete, quantized levels occurs (26). The obvious blue shift of the absorption peak may be attributed to the small dimensional bricks that make up the hollow CdS sphere walls, similar to the data reported in ref. 18*a*. In addition, the particles' sizes are calculated and estimated by the absorption edge in the UV–vis spectra; they are calculated to be around 12 nm for CuS, 16 nm for CdS, and 10~35 nm for NiS, (27), which are in agreement with the TEM observations.

The PL excitation spectra (dotted line) of the samples (λ_{ex}= 320 nm) were recorded as follows. The hollow NiS spheres photoluminesce at ca. 563 nm (Fig. 5*a*), while the hollow CuS spheres emit at 442 nm (Fig. 5*b*), and the hollow CdS spheres emit at the maximum of 520 nm (Fig. 5*c*). The differences in emitting wavelengths for metal sulfides maybe caused by the quantum-size bricks that compose the sphere walls. The highly structured shape of the emission suggests that the interaction is not of an excimer (28), but rather a consequence of intermolecular exciton interactions (29).

Conclusion

Hollow CuS, CdS, and NiS spheres with diameters of 400~1300 nm were successfully self-assembled through the interface-mineralizing reaction route in $NH_3{\cdot}H_2O$–CS_2 at 50°C. In this approach, it was worth noting that both ammonia and CS_2 played important multi-functional roles in the formation of hollow-sphere structures. The CS_2 source itself served as the self-organization template for nanoparticles and required no pre-existing templates. This method could be expanded to the self-assembly of hollow spherical structures in material fields.

Acknowledgments

Financial support from the Chinese National Foundation of Natural Science Research and Chinese Ministry of Education are gratefully acknowledged.

References

1. J. Hulliger. Angew. Chem. Int. Ed. Engl. **33**, 143 (1994).
2. (*a*) W.S. Sheldrich and M. Wachhold. Angew. Chem. Int. Ed. Engl. **36**, 206 (1997); (*b*) W. Tremel, H. Kleinke, C. Derstroff, and V. Reisner. J. Alloys Compd. **219**, 73 (1995).
3. B.O. Dabbousi, M.G. Bawendi, O. Onitsuka, and M.F. Rubner. Appl. Phys. Lett. **66**, 1317 (1995).
4. A. Henglein. Chem. Rev. **89**, 1861 (1989).
5. P.E. Lippens and M. Lannoo. Phys. Rev. B, **41**, 6079 (1990).
6. C.B. Murray, D.J. Norris, and M.G. Bawendi. J. Am. Chem. Soc. **115**, 8706 (1993).
7. R.S. Kane, R.E. Cohen, and R. Silbey. J. Phys. Chem. **100**, 7928 (1996).
8. J.E. Bowen Katari, V.L. Colvin, and A.P. Alivisatos. J. Phys. Chem. **98**, 4109 (1994).
9. P.V. Braun, P. Osenar, and S.I. Stupp. Nature (London), **380**, 325 (1996).
10. P.V. Braun, P. Osenar, V. Tohver, S.B. Kennedy, and S.I. Stupp. J. Am. Chem. Soc. **121**, 7302 (1999).
11. P.V. Braun and S.I. Stupp. Mater. Res. Bull. **34**, 463 (1999).
12. P. Yang and C.M. Lieber. Science (Washington, D.C.), **273**, 1836 (1996).
13. R.N. Barnett and U. Landman. Nature (London), **387**, 788 (1997).
14. Y. Xie, Z.P. Qiao, M. Chen, X.M. Liu, and Y.T. Qian. Adv. Mater. **11**, 512 (1999).
15. J.F. Xu, W. Ji, J.Y. Lin, S.H. Tang, and Y.W. Du. Appl. Phys. A: Mater. Sci. Proc. **66**, 639 (1998).
16. F. Caruso, R.A. Caruso, and H. Möhwald. Science (Washington, D.C.), **282**, 1111 (1998).
17. (*a*) D. Volkmer, A.D. Chesne, D.G. Kurth, H. Schnablegger, P. Lehmann, M.J. Koop, and A. Müller. J. Am. Chem. Soc. **122**, 1995 (2000); (*b*) D.G. Kurth, P. Lehmann, A. Müller, and D. Schwahn. J. Chem. Soc. Dalton Trans. **21**, 3989 (2000).
18. (*a*) J.X. Huang, Y. Xie, B. Li, Y. Liu, Y.T. Qian, and S.Y. Zhang. Adv. Mater. **12**, 808 (2000); (*b*) Y. Xie, J.X. Huang, B. Li, Y. Liu, and Y.T. Qian. Adv. Mater. **12**, 1523 (2000).
19. V.N. Manoharan, A. Imhof, J.D. Thorne, and D.J. Pine. Adv. Mater. **13**, 447 (2001).
20. (*a*) D. Walsh and S. Mann. Nature (London), **377**, 320 (1995); (*b*) M. Giersig, T. Ung, L.M. Liz-Marzan, and P. Mulvaney. Adv. Mater. **9**, 570 (1997).
21. J.W. Jeffrey. Methods in crystallography. Academic Press, New York. 1971.
22. C.D. Wagner, W.W. Riggs, L.E. Davis, J.F. Moulder, and G.E. Muilenberg. Handbook of X-ray photoelectron spectroscopy. PerkinElmer Corporation. Physical Electronics Division. Eden Prairie, Minnesota. 1979.
23. The solubility of CS_2 is 20.4 mmol dm^{-3} at 30°C; see: Gmelin handbook of inorganic chemistry. 8th ed. Vol. D4. Springer, Berlin. 1977. p. 193.
24. CRC handbook of chemistry and physics. 45th ed. Chemical Rubber Co., Boca Raton, FL. 1964. p. C-243.
25. (*a*) J.P. Fackler, Jr. and D. Coucouvanis. J. Am. Chem. Soc. **88**, 3913 (1966); (*b*) J.M. Burke and J.P. Fackler. Inorg. Chem. **11**, 2744 (1972). (*c*) B. Krebs and A. Müller. *Z.* Naturforsch. A. **20**, 1664 (1965).
26. H. Weller. Angew. Chem. Int. Ed. Engl. **32**, 41 (1993).
27. (*a*) L.E. Brus. J. Phys. Chem. **90**, 2555 (1986); (*b*) L. Spanhel, M. Haase, H. Weller, and A. Henglein. J. Am. Chem. Soc. **109**, 5649 (1987).
28. B. Broklehurst, D.C. Bull, M. Evans, P.M. Scott, and G. Stanney. J. Am. Chem. Soc. **97**, 2977 (1975).
29. R.M. Hochstrasser and M. Kasha. Photochem. Photobiol. **3**, 317 (1964).

© 2002 NRC Canada

Reaction of the tamoxifen cation and the bis-(4-methoxyphenyl)methyl cation in aqueous solutions containing 2′-deoxyguanosine

Robert A. McClelland, Cristina Sanchez, Effiette Sauer, and Sinisa Vukovic

Abstract: The competition between 2′-deoxyguanosine (**dG**) and water has been quantitatively evaluated for the allylic carbocation derived from tamoxifen and for the stabilized diarylmethyl cation (bis-(4-methoxyphenyl)methyl). Both systems were examined by the competition kinetics method, in which the products were quantitatively analyzed after the S_N1 solvolysis of the corresponding acetate esters in aqueous solutions containing the nucleoside. The principal product of the reaction of both cations with **dG** is the adduct at the NH_2 group, a characteristic of delocalized carbocations. The tamoxifen cation was also examined by laser flash photolysis, with absolute rate constants for the reaction with **dG** and water being obtained and converted into rate constant ratios. The principal result of this study is that there is a three orders of magnitude difference in the reactivity of these cations towards the neutral form of **dG** and its conjugate base. Under acidic conditions where the reaction occurs with neutral **dG**, the guanine–water selectivity is low. Even at relatively high concentrations of **dG**, the majority of the product is alcohol derived from the water reaction. At pH 10 to 11, in contrast, **dG** is present as the anion and this is highly competitive. Yields of adduct as high as 90% can be attained. A consequence of the large difference in reactivities is that at neutral pH the majority of the reaction of the cation with **dG** is actually occurring via the small amount of conjugate base present. A further feature of the results is that the NH_2 adduct is the predominant stable product from the anion. To explain the high rate constant for the reaction forming this product, a mechanism is proposed whereby one of the protons of the NH_2 group is transferred to N1 as the N2–cation bond is forming.

Key words: guanine, DNA adduct, carbocation, tamoxifen.

Résumé : On a évalué de façon quantitative la compétition entre la 2′-désoxyguanosine (**dG**) et l'eau pour le carbocation allylique dérivé du tamoxifène et pour le cation diarylméthyle stabilisé, bis-(4-méthoxyphényl)méthyle. On a examiné les deux systèmes par la méthode des cinétiques en compétition dans laquelle les produits sont analysés de façon quantitative après une solvolyse S_N1 des esters acétiques correspondants en solutions aqueuses contenant le nucléoside. Le produit principal de chacune des réactions des deux cations avec la **dG** est un adduit au niveau du groupe NH_2, une caractéristique des carbocations délocalisés. On a aussi étudié le cation du tamoxifène par photolyses éclairs au laser à partir desquelles on a obtenu des constantes absolues de vitesse pour la réaction avec la **dG** et l'eau, celles-ci étant transformées en rapports de constantes de vitesses. Le principal résultat de cette étude est qu'il y a trois ordres de grandeur de différence dans la réactivité de ces cations vis-à-vis de la forme neutre de la **dG** et de sa forme conjuguée. Dans les conditions acides où la réaction se produit avec la **dG** neutre, la sélectivité guanine–eau est faible. Même à des concentrations élevées de **dG**, la plus grande partie du produit est l'alcool qui provient de la réaction avec l'eau. Par ailleurs, à des pH de 10 à 11, la **dG** est présente sous la forme d'anion qui est fortement compétitif. On peut alors obtenir des rendements d'adduit pouvant atteindre 90%. Une conséquence de la grande différence dans les réactivités est que, au pH neutre, la plus grande partie de la réaction du cation avec la **dG** se produit par le biais de la faible quantité de la base conjuguée qui est présente. Une caractéristique additionnelle des résultats est que l'adduit avec le NH_2 est le produit stable prédominant à partir de l'anion. Pour expliquer la constante de vitesse élevée pour la réaction conduisant à la formation de ce produit, on propose un mécanisme dans lequel un des protons du groupe NH_2 est transféré vers N1 alors que la liaison N2–cation se forme.

Mots clés : guanine, adduit avec l'ADN, carbocation, tamoxifène.

[Traduit par la Rédaction]

Received 30 July 2001. Published on the NRC Research Press Web site at http://canjchem.nrc.ca on 22 March 2002.

R.A. McClelland,[1] C. Sanchez, E. Sauer, and S. Vukovic. Department of Chemistry, University of Toronto, Toronto, ON M5S 3H6, Canada.

[1]Corresponding author (e-mail: rmcclell@alchemy.chem.utoronto.ca).

 DOI: 10.1139/V02-011 © 2002 NRC Canada

Introduction

A common property of chemical carcinogens is the formation of DNA adducts (1). These adducts arise from chemical reactions in which DNA reacts with an electrophile, often an electrophile resulting from metabolism of the parent compound. Tamoxifen **1** (Scheme 1), an antiestrogen used in the treatment and control of breast cancer, is a hepatocarcinogen in the rat (2–4) and causes a small number of endometrial cancers in women (5–7). DNA adducts have been observed in both the animal models (8, 9) and in women treated with the drug (10–14). These are explained by the pathway of Scheme 1 (15–22), whereby an allylic carbocation **3** forms in an S_N1 ionization of a sulfate ester **2b**. The latter is derived from metabolic α-hydroxylation of the parent drug to α-hydroxytamoxifen **2a** followed by sulfate transfer. The principle DNA adducts **4** are isomers (see below) where the the α-carbon of the tamoxifen is attached to the NH_2 group of guanine residues (20–22). This position of attachment to guanine is characteristic of delocalized carbocations (1).

We have described experiments where the cation **3**, the "tamoxifen carbocation," was observed with laser flash photolysis (LFP) (23). The LFP approach has now been employed to study a number of carbocations (24). These are ground-state cations, identical to ones formed in S_N1 solvolyses. The significant advantage of the LFP method is that it is capable of providing direct information on reactivity, both towards the solvent (i.e., water) and to added nucleophiles. A nucleophile of interest because of the relation to carcinogenicity discussed above is guanine or a guanine derivative such as 2′-deoxyguanosine (**dG**). Our previous study (23) showed that the tamoxifen cation is quenched by **dG** in an aqueous solution. However, the selectivity over the reaction with solvent is poor, so that even at the highest concentrations of **dG**, the majority of the cation reacts with solvent. This behavior is typical of carbocations in water (25), but it contrasts dramatically with arylnitrenium ions, the DNA-binding electrophiles derived from carcinogenic amines. Both LFP studies (25, 26) and product analyses (27, 28) show that guanine derivatives are excellent nucleophiles for arylnitrenium ions, even in water.

We have now performed a detailed study of the reaction of the tamoxifen cation with **dG**, employing LFP to measure absolute rate constants and product analyses (competition kinetics) for relative rate constants. Competition kinetic experiments have also been carried out with a diarylmethyl cation, the bis-(4-methoxyphenyl)methyl cation, which has a similar lifetime in water to the tamoxifen cation (29). These studies show that there is very pronounced effect of pH on the **dG** reaction. The neutral form of **dG** is quite unreactive as previously found (25). Its conjugate base, however, is far more reactive, so much so that at pH 7 the principal species that is reacting with the cations is the anion. The difference between the two forms of guanine has been recognized (30), but we are not aware of a detailed kinetic study demonstrating the magnitude of the effect, especially for short-lived carbocations.

Results and kinetic analysis

Rate pH-profiles in 100% aqueous solutions

In our original paper, the sulfate ester **2b** was employed as the precursor in the LFP experiments (23). A transient with

Scheme 1. Ar = C_6H_4-4-$OCH_2CH_2N(CH_3)_2$.

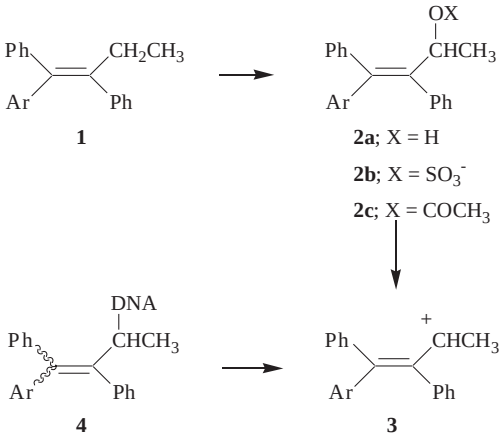

λ_{max} at 460 nm was identified as the tamoxifen cation on the basis of several criteria employed to assign carbocation intermediates (24). A key observation was the quenching by azide ion, in particular, the identity of the azide:water rate constant ratio with one obtained by competition kinetics (product analysis) for the ground-state solvolysis of the sulfate in aqueous solutions containing azide ion.

The sulfate ester has a high reactivity towards solvolysis in the ground state. This limits LFP experiments to solutions with considerable organic component (i.e., 40% acetonitrile) where the lower ionizing power slows the S_N1 reaction. Since acetate esters have been successfully employed as precursors of carbocations in LFP experiments (24), we investigated the appropriate tamoxifen derivative **2c**. This also produces the tamoxifen cation upon irradiation in aqueous solutions. This was established by comparing LFP results with the acetate and the sulfate in 40% acetonitrile. The two gave the same transient with the same decay kinetics.

The acetate is much more stable towards ground-state solvolysis, with a half-life in 100% water of 2 h. We therefore started by carrying out a detailed kinetic study of the decay of the tamoxifen cation in 100% aqueous solutions. Since the buffers accelerated the decay, experiments were performed with serial buffer dilutions at constant buffer ratio (and constant pH), and the rate constant obtained as the intercept of the plot of k vs. buffer concentration. These rate constants, along with ones obtained in solutions of perchloric acid and sodium hydroxide, are plotted as log k_o vs. pH in Fig. 1. Also plotted in this figure are rate constants obtained in a similar manner for the other cation of this study, the bis-(4-methoxyphenyl)methyl cation.

The profile for the latter cation is straightforward. There is a pH-independent region from acidic pH to a pH of about 11 that corresponds to the reaction of the cation with solvent water molecules. The rate constant is 1.0×10^5 s^{-1}. (Table 1 provides a summary of all rate and equilibrium constants measured in this work, along with their errors provided as one standard deviation.) At pH 11, there is a break to a reaction that is first order in hydroxide ion. This obviously represents the cation–hydroxide combination; the second-order rate constant is 3.8×10^6 M^{-1} s^{-1}. One noteworthy feature is the relatively little difference (a factor of 13) between k_w and k_{OH}, typical of short-lived cations in aqueous solutions (31–33).

© 2002 NRC Canada

Fig. 1. pH dependence of the logarithm of the rate constants for the decay of the tamoxifen cation (squares) and the bis-(4-methoxyphenyl)methyl cation (circles) in aqueous solutions. Temperature is 20°C and k_o has units of s^{-1}. The data for the tamoxifen cation have been obtained at a constant ionic strength of 0.10 M maintained with $NaClO_4$. The data for the bis-(4-methoxyphenyl)methyl cation were obtained in solutions with ionic strength less than 0.01 M. The cations were generated by LFP of acetate precursors with irradiation at 248 nm and detection at 460 nm (tamoxifen cation) and 500 nm (bis-(4-methoxyphenyl)-methyl cation). Rate constants in the region pH 3–11 were obtained in buffer solutions, and are based upon extrapolation to zero buffer concentration. The points are experimental. The line for the tamoxifen cation has been drawn on the basis of eq. [2] and the parameters given in the text.

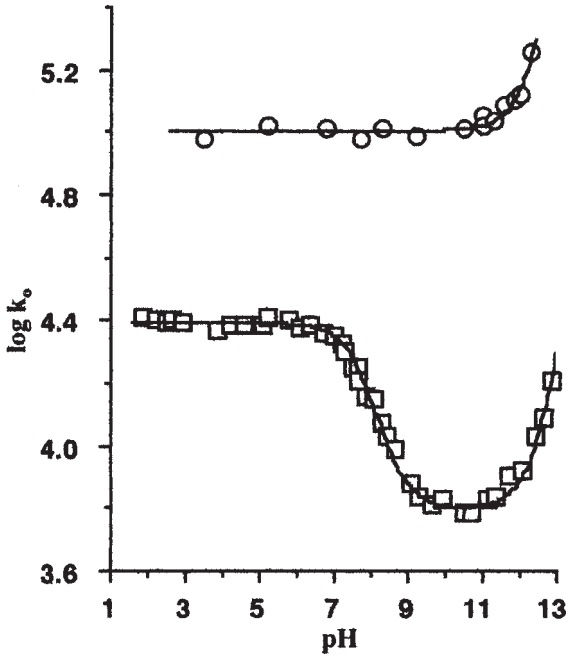

The profile for the tamoxifen cation can be explained by recognizing that there is a side-chain amine. This means that there are two carbocations, a dication $\mathbf{T}^{2+}$ where the amine is protonated and a monocation $\mathbf{T}^{+}$ where the amine is neutral (Scheme 2). Both, in principle, can react with water and hydroxide, giving rise to eq. [1], where K_w is the autoprotolysis constant of water.

$$[1] \qquad k_o = \frac{k_w^{2+}[H^+] + k_{OH}^{2+}K_w + k_w^{+}K_a(\mathbf{T}) + \dfrac{k_{OH}^{+}K_wK_a(\mathbf{T})}{[H^+]}}{[H^+] + K_a(\mathbf{T})}$$

This takes the form of a four-parameter equation (eq. [2]) where $y = k_o$ and $x = [H^+]$.

$$[2] \qquad y = \frac{ax + b + c/x}{x + d}$$

The experimental data were fit to eq. [2] to provide the four parameters. Parameter d (1.34×10^{-8}) is the acidity constant, corresponding to a pK_a of 7.87. This means that the ammonium group in $\mathbf{T}^{2+}$ is one log unit more acidic than in the parent drug. This reflects the electron withdrawing influence of the delocalized positive charge associated with the allylic cation. Parameter a (2.5×10^4 s^{-1}), is equal to k_w^{2+}, the rate constant for water addition to the dication. In terms of the pH profile, this reaction dominates from acidic pH to a pH just before 9; the downward break between pH 7 and 8 is a reflection of the changing acid–base equilibrium. Parameter c ($k_{OH}^{2+}K_wK_a(\mathbf{T}) = 2.2 \times 10^{-17}$) explains the increase in base. This must be due to a reaction of the monocation $\mathbf{T}^{+}$ with hydroxide ion. With $K_a(\mathbf{T})$ known, the rate constant k_{OH}^{+} can be calculated; the value is 1.6×10^5 M^{-1} s^{-1}.

Parameter b (8.4×10^{-5}) accounts for the pH-independent region between pH 9 and pH 11. There are two kinetically equivalent processes that could be responsible, the reaction of hydroxide ion with the dication $\mathbf{T}^{2+}$ and the reaction of water with the monocation $\mathbf{T}^{+}$. The former can be ruled out, since it requires a value of k_{OH}^{2+} of 8.4×10^9 M^{-1} s^1, several orders of magnitude greater than expected. As noted above, hydroxide would not react with a cation of the aqueous lifetime of $\mathbf{T}^{2+}$ at anywhere near this rate. Our conclusion, therefore, is that the pH-independent region in weakly basic solution represents water reacting with the monocation $\mathbf{T}^{+}$. The rate constant for this process (k_w^{+}) is 6.3×10^3 s^{-1}, fourfold smaller than the rate constant k_w^{2+} for the reaction of water with $\mathbf{T}^{2+}$. This greater reactivity of the dication is not surprising. There is undoubtedly a significant stabilization in both cations by the π-interaction with the oxygen of the dimethylaminoethoxy group. This interaction will be stronger when that group is neutral as opposed to where the amine is protonated. In other words, the $(CH_3)_2NCH_2CH_2O$- group must be a better π donor than the $(CH_3)_2HN^+CH_2CH_2O$- group.

Analysis of the rate constants associated with the buffer revealed that the rate accelerations were due to the basic component of the buffer, the terms in (B) that appear in Scheme 2. As with water and hydroxide, reaction in principle could occur with both $\mathbf{T}^{2+}$ and $\mathbf{T}^{+}$, although of the four buffers employed, only tris resulted in rate constants for both the dication and cation that were statistically significant (Table 1). The actual reaction occurring with the buffer is not known. The most likely scenario is a cation–nucleophile combination. However, a reaction where the buffer base acts as a general base to assist the addition of water to the cation is also possible. Arguments have been made that the water reaction itself is generally base-catalyzed, with a second water molecule acting as the base (29).

Decay of the tamoxifen cation in the presence of 2′-deoxyguanosine

These experiments were carried out in 20% acetonitrile for solubility reasons. LFP experiments with **dG** as the trapping nucleophile require irradiation, at 308 nm, with our equipment where the **dG** does not absorb. While **2c** does have absorbance at this wavelength, it is weak. Thus, more concentrated solutions of the precursor were required. These concentrations could not be achieved in 100% aqueous solutions, especially solutions of higher pH where the side-chain amine of **2c** is not protonated. The use of 20% acetonitrile also meant that the solubility of **dG** was increased. Solutions with a **dG** concentration of 20 mM were possible, in contrast to 100% aqueous where 8 mM is about the maximum concentration.

Figure 2 provides the results. The rate constants for the solvent reaction were obtained as described in the previous

© 2002 NRC Canada

Table 1. Summary of rate and equilibrium constants for the reactions of tamoxifen dication $\mathbf{T}^{2+}$, tamoxifen monocation $\mathbf{T}^{+}$, and bis-(4-methoxyphenyl)methyl cation (Ar_2CH^+).

Parameter	$\mathbf{T}^{2+}$	$\mathbf{T}^{+}$	Ar_2CH^+
k_w (s^{-1}) (water)	$(2.5 \pm 0.1) \times 10^4$[a]	$(6.3 \pm 0.2) \times 10^3$[a]	$(1.01 \pm 0.05) \times 10^5$[b]
k_w (s^{-1}) (20% AN)	$(3.2 \pm 0.1) \times 10^4$[a]	$(8.2 \pm 0.3) \times 10^3$[a]	(1.3×10^5)[c]
k_{OH} (M^{-1} s^{-1}) (water)	—[d]	$(1.6 \pm 0.2) \times 10^5$[a]	$(3.8 \pm 0.8) \times 10^6$[b]
pK_a(**T**) (water)	7.87 ± 0.05[a]		
pK_a(**T**) (20% AN)	7.26 ± 0.08[a]		
k_n (M^{-1} s^{-1}) (20% AN)	$(1.0 \pm 0.2) \times 10^5$	~$(1.5–3) \times 10^4$[e]	
k_a (M^{-1} s^{-1}) (20% AN)	$(6.4 \pm 0.8) \times 10^7$	$(1.2 \pm 0.1) \times 10^7$	
pK_a(**G**) (20% AN)	9.27 ± 0.11 (Kinetics)		9.44 ± 0.08 (Fig. 6)
pK_a(**G**) (20% AN)	9.37 ± 0.05 (Spect.)		
k_n:k_w (20% AN) (LFP)	(3.1 ± 0.6)		
k_n:k_w (20% AN) (Pdts.)	(2.7 ± 0.3)	—[d]	(1.21 ± 0.07)[f]
k_a:k_w (20% AN) (LFP)	$(2.0 \pm 0.3) \times 10^3$	$(1.5 \pm 0.1) \times 10^3$	
k_a:k_w (20% AN) (Pdts.)	$(7 \pm 1) \times 10^2$	$(5.7 \pm 0.6) \times 10^2$	$(1.52 \pm 0.13) \times 10^3$[f]
k_{AcO} (M^{-1} s^{-1}) (water)	$(3.4 \pm 0.4) \times 10^5$[a]	—[d]	
$k^{2-}_{HPO_4}$ (M^{-1} s^{-1}) (water)	$(5.5 \pm 0.5) \times 10^5$[a]	—[d]	
k_{tris} (M^{-1} s^{-1}) (water)	$(8 \pm 1) \times 10^4$	$(2 \pm 0.5) \times 10^4$	
$k^{2-}_{CO_3}$ (M^{-1} s^{-1}) (water)	—[d]	$(2.1 \pm 0.4) \times 10^5$	

[a]Ionic strength = 0.1.
[b]Ionic strength < 0.01.
[c]From ref. 29.
[d]Cannot be measured since not significant in competition with other processes.
[e]Estimated.
[f]Ratio calculated for **DdGa**.

Scheme 2.

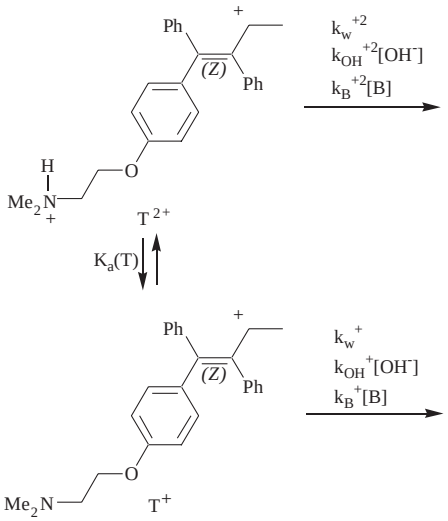

section, with (where appropriate) serial buffer dilutions providing the rate constants at zero buffer concentration. The rate constants for the reaction with **dG** were obtained using dilute buffers, with 5 to 6 concentrations of **dG** ranging from [**dG**] ~ 0.02 M to [**dG**] = 0 at each pH. The rate constants increased in the presence of **dG**. This acceleration was modest in the solutions with pH 4–6, with only about a 15% increase from the solution with no **dG** to the solution with the highest concentration. As the pH increased, however, the effect of **dG** became much more pronounced, and by pH 9 it was possible to triple the rate constant over that in the absence of **dG**. The observed rate constants were plotted against the concentration of added **dG**. These plots were linear. Their slopes, defined as k_{dG}, are plotted as the circles in Fig. 2.

The solvent reaction was analyzed as in the previous section. Values of the parameters so obtained were $K_a(\mathbf{T}) = 5.5 \times 10^{-8}$ (p$K_a(\mathbf{T}) = 7.27$), $k_w^{2+} = 3.2 \times 10^4$ s^{-1}, and $k_w^{+} = 8.2 \times 10^3$ s^{-1}. The two rate constants are slightly larger than the ones obtained in the study in 100% aqueous solutions. This is a typical observation for carbocation–water reactions as acetonitrile is added (29). There is also a difference in the pK_a(**T**) value. This is likely also a solvent effect. Our previous study in 40% acetonitrile resulted in an even lower value of pK_a(**T**) (6.6) (23).

An interesting feature of the reaction with **dG** is that at about the point where the curve for the solvent reaction breaks downward, the profile for the **dG** reaction breaks upward. The reasons for this must be different. The downward break in the solvent profile occurs because of the conversion of $\mathbf{T}^{2+}$ to $\mathbf{T}^{+}$. The upward break in the **dG** profile must represent the onset of a new reaction, the reaction of the cation with the conjugate base of **dG**. This leads to the kinetic model of Scheme 3, which shows the nucleoside reaction occurring in four ways. Both the neutral form of **dG** (**dG-H**) and its conjugate base ($\mathbf{dG}^-$) are nucleophiles, and each, in principle, reacts with $\mathbf{T}^{2+}$ and $\mathbf{T}^{+}$.

The kinetic system of Scheme 3 gives rise to eq. [3] for k_{dG}.

$$[3] \qquad k_{dG} = \frac{(k_n^{2+}[H^+]^2 + \{k_a^{2+}K_a(\mathbf{G}) + k_n^{+}K_a(\mathbf{T})\}[H^+] + k_a^{+}K_a(\mathbf{G})K_a(\mathbf{T}))}{([H^+] + K_a(\mathbf{T}))([H^+] + K_a(\mathbf{G}))}$$

© 2002 NRC Canada

Fig. 2. pH dependence of the logarithm of the rate constants for the decay of the tamoxifen cation in solvent (squares) and the quenching by 2′-deoxyguanosine (**dG**) (circles). Temperature is 20°C, and the solvent is 20:80 (v:v) acetonitrile–water with ionic strength maintained at 0.10 M with sodium perchlorate. Units of k are s^{-1} (solvent reaction) and M^{-1} s^{-1} (**dG** reaction). The cation was generated by excitation of **2c** at 248 nm (solvent data) and 308 nm (**dG** data). The points are experimental. The lines have been drawn on the basis of eq. [2] (solvent reaction) and eq. [4] (**dG** reaction).

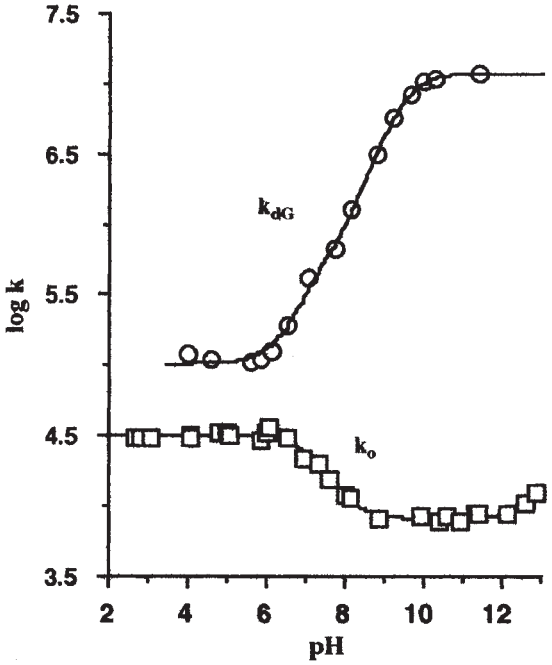

This equation contains two acid acidity constants (K_a(**T**) and K_a(**G**)) referring, respectively, to the ammonium group of the tamoxifen cation and the N1-H proton of **dG**. The rate constants are identified with superscripts "2+" and "+" to differentiate reactions with $\mathbf{T}^{2+}$ and $\mathbf{T}^{+}$ and with subscripts "n" and "a" to differentiate reactions with the neutral and anionic forms of the nucleoside. This equation takes the form of eq. [4], with five adjustable parameters.

$$[4] \qquad y = \frac{ax^2 + bx + c}{(x + d)(x + e)}$$

The experimental data were fit to this equation with the parameter $d = K_a$(**T**) fixed at the value of 5.5×10^{-8} obtained from the analysis of the water reaction. The other four were allowed to vary to values providing the best fit.

The parameter e (5.3×10^{-9}) is the acidity constant for **dG**, and corresponds to a pK_a value of 9.27. We also measured this value spectroscopically under the same solvent conditions, and obtained a value of 9.37. Within the experimental error (Table 1), the value obtained from the kinetic fit is identical. The parameter $a = k_n^{2+} = 1.0 \times 10^5$ M^{-1} s^{-1} is the rate constant for the reaction of the neutral form of **dG** with the dication $\mathbf{T}^{2+}$. The parameter c (3.4×10^{-10}) is equal to $k_a^+ K_a$(**T**)K_a(**G**) and represents the reaction of the conjugate base of **dG** with $\mathbf{T}^{+}$. With values of the acidity constants known, k_a^+ is calculated as 1.2×10^7 M^{-1} s^{-1}. The parameter b (3.4×10^{-2}) represents two kinetically equivalent processes, neutral **dG** reacting with $\mathbf{T}^{+}$ (the k_n^+ process) and anionic **dG** reacting with $\mathbf{T}^{2+}$ (the k_a^{2+} process). The latter must be the major contributor. If the former is responsible, $b = k_n^+ K_a$(**T**), which requires k_n^+ to be 6.2×10^5 M^{-1} s^{-1}. This is a sixfold greater than k_n^{2+}, the rate constant for the reaction of neutral **dG** with the dication. This makes no sense since the dication is the more reactive species. Based upon results for other nucleophiles, k_n^+ will lie in the range $1.5–3 \times 10^4$ M^{-1} s^{-1}, a factor of three to six times smaller than k_n^{2+}. We therefore conclude that the k_n^+ process could contribute about 3% to the term in b. However, 97% of this term must be due to the process in k_a^{2+}. Using this 97% factor, k_a^{2+} is calculated as 6.4×10^7 M^{-1} s^{-1}. It can be seen that this is consistent with the greater reactivity of the dication — k_a^{2+} is fivefold larger than k_a^+.

Scheme 3.

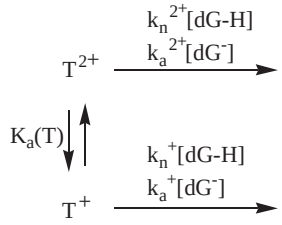

Figure 3 shows how the observed rate constants for the reaction of the tamoxifen cation and **dG** are broken down into the contributions from the four reactions. The curves in this figure were calculated using the rate constants provided in the previous paragraph (with an estimate for k_n^+ of 2×10^4). It can be seen that under acidic conditions the reaction that occurs involves $\mathbf{T}^{2+}$ and the neutral form of **dG**, while under basic conditions, $\mathbf{T}^{+}$ reacts with the anion of **dG**. The principle contributor at pH 7 is the reaction of $\mathbf{T}^{2+}$ with the conjugate base.

Tamoxifen cation and deoxyguanosine — competition kinetics

The experiments described in this section were performed to determine if the pH effect is also observed in the products. The principle adduct of the tamoxifen cation and **dG** has been isolated and characterized previously as compound **TdG** of Scheme 4 (22). This is formed as four diastereomers, arising from the combinations of the (*R*) and (*S*) forms at the α stereocenter and (*E*) and (*Z*) forms about the C=C. The latter arise because the cation undergoes rapid rotation about this bond before capture by nucleophiles. HPLC analysis of this mixture then provided retention times for the four isomers under our HPLC conditions.

Experiments were then performed in which the acetate **2c** was added to solutions of 20% acetonitrile containing 2′-deoxyguanosine, and the ground-state solvolysis reaction allowed to proceed to completion overnight. The products were analyzed by HPLC. With appropriate correction for relative HPLC sensitivities, this provided the ratio of the sum of the concentrations of the four adducts [**TdG**] to the sum of the concentrations of the (*E*) and (*Z*) alcohols [**TOH**]. This ratio was then converted to a competition-kinetic ratio according to eq. [5], where [**dG**] was the concentration of the nucleoside in the solution.

© 2002 NRC Canada

Fig. 3. Breakdown of the reaction of 2′-deoxyguanosine and the tamoxifen cation into components.

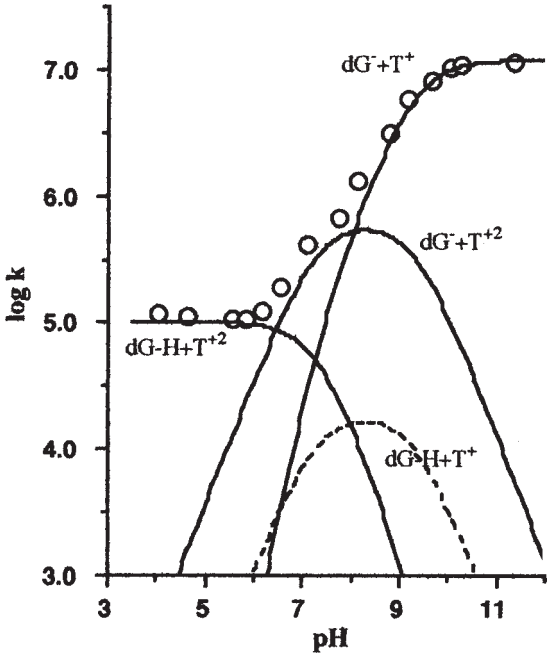

[5] $k_{\mathbf{dG}}/k_o = (1/[\mathbf{dG}])([\mathbf{TdG}]/[\mathbf{TOH}])$

The results are plotted in Fig. 4, and show the same trend as observed in the absolute rate constants, with a significant increase in the selectivity ratio at higher pH. In terms of the analysis of the previous sections, this ratio is given by eq. [6] (see below), obtained by dividing eq. [3] by eq. [1].

The line drawn through the experimental points in Fig. 4 is based on a fit to this equation. Because of the number of parameters involved, the fitting was performed by fixing the values of $K_a(\mathbf{T})$, $K_a(\mathbf{G})$, and $k_w^+:k_w^{2+}$ at the values obtained previously, 5.5×10^{-8}, 5×10^{-10}, and 0.256, respectively. This left the three rate constant ratios as variables; values are provided in Table 1. Also given in this table are values of the same ratios calculated from the absolute rate constants measured with LFP. The values of $k_n^{2+}:k_w^{2+}$ obtained by the two methods are not outside of experimental error. The two values of $k_a:k_w$ are, however, statistically different, with the LFP ratio greater than the product ratio in both cases. A possible explanation is provided in the *Discussion*.

Bis-(4-methoxyphenyl)methyl cation and deoxyguanosine — Competition kinetics

These experiments were performed following the same procedure described in the previous section, with the cation (designated as $\mathbf{D}^+$) being obtained by solvolysis of the acetate ester in solutions of 20% acetonitrile containing **dG**. The HPLC traces showed the peak for the alcohol product **DOH** and three peaks associated with a reaction with **dG**. Since this cation does not generate a new stereocenter (or C=C isomers), each of these peaks must represent a product derived from a different position of attachment to the **dG**.

Scheme 4.

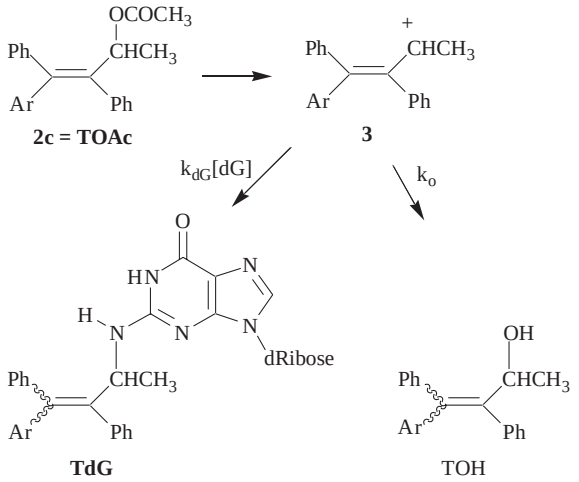

This means that there are four reactions occurring in parallel, one forming alcohol and three forming different **dG** adducts (Scheme 5). These adducts are designated as **DdG1**, **DdG2**, and **DdG3** in order of increasing HPLC retention times.

Figure 5 shows how the areas of the peaks for the four products vary with pH for experiments performed with constant concentrations of **dG** and acetate ester. Under acidic conditions (pH 3–5) the areas are constant. The alcohol is the major product, with only small peaks for the three adducts (note the scale in Fig. 5 is logarithmic). As the pH increases, the alcohol peak decreases significantly, the peaks for **DdG1** and **DdG2** grow, and the peak for **DdG3** disappears. Under basic conditions there is another constant region, with the major peak corresponding to **DdG1**.

A sample of **DdG1** was isolated from a scaled-up reaction at high pH. The NMR spectra in DMSO-d_6 clearly established that this is the N2-adduct. Features of the NMR leading to this assignment were the down-field proton (10.4 ppm) integrating as 1H characteristic of N1H of guanine derivatives, the proton at C8 in its characteristic position near 7.8 ppm, and a proton at 7.4 ppm integrating only as 1H for N2H. The attachment N2H was most clearly seen by the coupling of this proton and the methine proton of the diarylmethyl group (6.0 ppm). This coupling was verified by a 2D COSY experiment.

With a sample of **DdG1** available, the HPLC area ratio for this peak relative to the alcohol was converted to a concentration ratio, and then, with eq. [7], into a ratio of rate constants.

[7] $k_{\mathbf{dG1}}/k_o = (1/[\mathbf{dG}])([\mathbf{DdG1}]/[\mathbf{DOH}])$

The pH dependence of this ratio is shown in Fig. 6. As with the tamoxifen cation the selectivity is modest in acidic solutions, but becomes much more significant at higher pH.

Figure 6 can be explained by a kinetic model where the cation reacts with water in a pH-independent manner to form

[6] $$k_{dG}/k_o = \frac{(k_n^{2+}/k_w^{2+})[H]^{2+} + (k_a^{2+}/k_w^{2+})K_a(\mathbf{G})[H^+] + (k_a^+/k_w^+)(k_w^+/k_w^{2+})K_a(\mathbf{G})K_a(\mathbf{T})}{([H^+] + (k_w^+/k_w^{2+})K_a(\mathbf{T}))([H^+] + K_a(\mathbf{G}))}$$

© 2002 NRC Canada

Fig. 4. pH dependence of the logarithm of the ratio of rate constants k_{dG}:k_w for the competition for the tamoxifen cation between 2′-deoxyguanosine and water. Temperature is 20°C, and the solvent is 20:80 (v:v) acetonitrile–water with ionic strength maintained at 0.10 M with sodium perchlorate. The circles are the experimental data obtained by analysis of the products of the ground-state solvolysis of the acetate **2c**. The solid line was obtained by fitting the data to eq. [6] as described in the text. The dashed line is the ratio of the absolute rate constants measured by LFP; this line was calculated as the difference between the two lines drawn in Fig. 2.

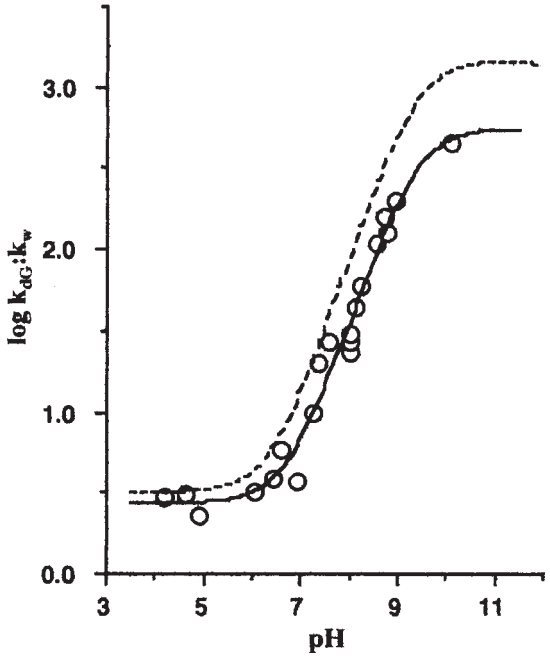

Scheme 5.

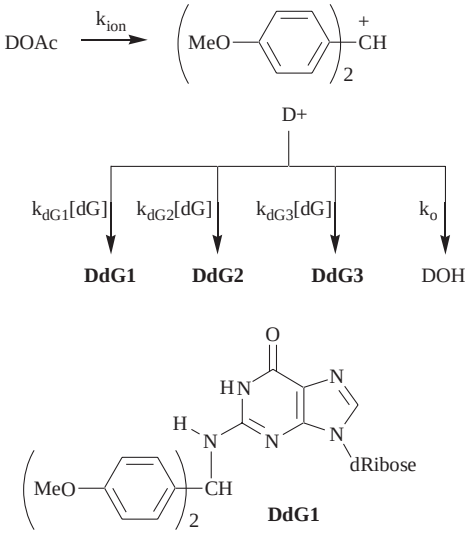

the alcohol, while adduct **DgD1** is formed from both neutral **dG** and its anionic conjugate base. This leads to eq. [8],

$$[8] \qquad k_{\mathbf{dG1}} / k_o = \frac{(k_n^1/k_w)[H^+] + (k_a^1/k_w)K_a(\mathbf{G})}{[H^+] + K_a(\mathbf{G})}$$

Fig. 5. pH dependence of the logarithm of the HPLC areas for the four products observed in the reaction of the bis-(4-methoxyphenyl)methyl cation in 20% acetonitrile in the presence of 2′-deoxyguanosine. The cation was obtained from the solvolysis of bis-(4-methoxyphenyl)methyl acetate. The experiments were performed with a constant concentration of **dG** (0.0096 M) and a constant concentration of the acetate (100 μM).

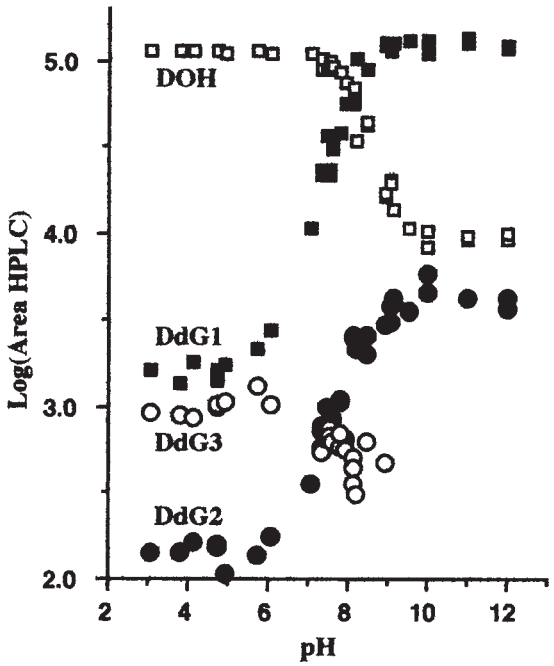

where $K_a(\mathbf{G})$ is the acidity constant of **dG**, k_w is the rate constant for the reaction with water, and k_n^1 and k_a^1 are the rate constants for reactions forming adduct **DgD1**. As above, the subscripts "n" and "a" represent reactions of the neutral and conjugate base forms of **dG**. The superscript "1" indicates that these are reactions forming **DdG1**. Equation [8] contains three variables, two rate constant ratios, and the acidity constant. The experimental data were fit to this equation with all three parameters as adjustable parameters. The results are provided in Table 1. It can be seen that the value of the acidity constant is within experimental error the same as values obtained by a spectroscopic analysis and a kinetic analysis of the tamoxifen system.

The other two **dG** adducts have not been identified. Under acidic conditions where the neutral form of **dG** is reacting, the area of the peak for **DdG3** is 60% of that for **DdG1**. However, both are minor components of the reaction mixture. With the assumption that the HPLC sensitivity for **DdG3** is the same as that of **DdG1**, the ratio k_n^3:k_w is only 0.7 M^{-1}. This means that even at the highest concentrations of **dG** attainable (~20 mM), the yield of **DdG3** is only around 1%. The peak for this adduct is not observed in the basic solutions where the anion of **dG** is reacting. Either this adduct is not formed by the reaction with the anion, or its yield is very small in comparison with the other products.

DdG2 follows the pattern of the major adduct with a significant increase relative to alcohol when the **dG** reacts as the anion. The assumption of the same HPLC sensitivity results in ratios k_n^2:k_w = 0.1 M^{-1} and k_a^2:k_w = 45 M^{-1}. While the latter shows relatively good selectivity over the alcohol,

© 2002 NRC Canada

Fig. 6. pH dependence of the logarithm of the ratio of rate constants k_{dG}:k_w for the competition for the bis-(4-methoxyphenyl)-methyl cation between 2′-deoxyguanosine and water. Temperature is 20°C, and the solvent is 20:80 (v:v) acetonitrile:water. The circles are the experimental data obtained by analysis of the products of the ground-state solvolysis of the bis-(4-methoxyphenyl)methyl acetate. The line was obtained by fitting the data to eq. [8].

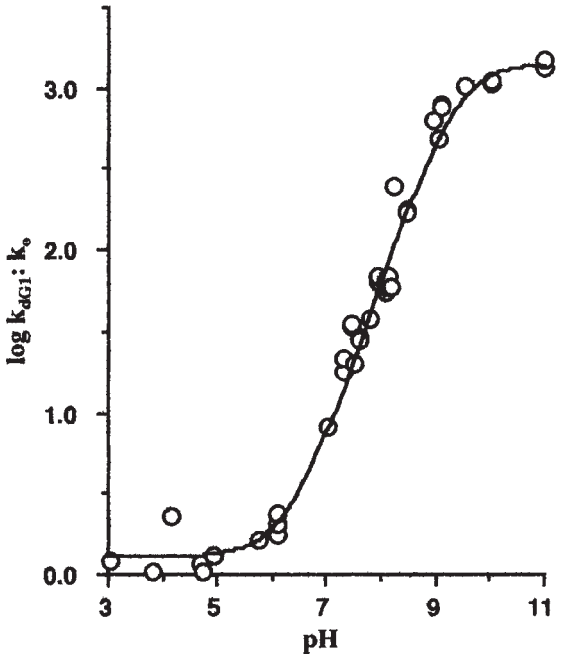

k_a^2:k_a^1 is only 0.03. Thus the yield of **DdG2** is never greater than 3%.

Finally, we note the evidence that the reaction has proceeded via S_N1 solvolyses. This takes the form of experiments where the first-order rate constant for the disappearance of **DOAc** was measured by HPLC. In 20% acetonitrile with the pH at 9.5, rate constants of 0.0018 s^{-1} and 0.0017 s^{-1} were measured for solutions with [**dG**] = 0 and [**dG**] = 0.0096, respectively. The products in the latter are around 90% adducts. The observation that the rate constant is unchanged, within experimental error, shows that the product-determining step has occurred after the rate-determining step; i.e., the reaction is S_N1. A similar experiment was not necessary with the tamoxifen system. The observation of C=C isomers in the products shows that there must have been a cationic intermediate.

Discussion

An attractive approach to model DNA–electrophile interactions is to investigate the reaction with a monomer such as 2′-deoxyguanosine. In this study electrophiles were two delocalized carbocations, the allylic cation derived from the carcinogen tamoxifen, and the bis-(4-methoxyphenyl)methyl cation. Lifetimes of these electrophiles in aqueous solution are 10–200 ms. By carbocation standards, these are relatively long-lived (24). Some relevant comparisons are the benzylic cations derived from ring opening of the diol epoxides of the carcinogen benzo[*a*]pyrene — lifetimes of the order of 50 ns in water (34, 35) — the *p*-methoxybenzyl cation, a benzylic system that has been studied with guanine in the past (36–38) — lifetime of 5 ns (39) — and the diphenylmethyl cation — lifetime of 800 ps (40). The parent benzyl cation is too short-lived to exist in water (41).

The cations of this study clearly show significant differences in reactivity towards the neutral form of 2′-deoxyguanosine and its conjugate base. This difference is seen in the guanine:water selectivities obtained by analyzing products of solvolysis reactions. It is also seen in the absolute rate constants measured with LFP. A greater reactivity of the conjugate base form of a nucleophile is hardly surprising. Previous studies of guanine–electrophile interactions have commented on this in qualitative terms (30, 36–38). We are not aware of a quantitative study, particularly one where rate constants and rate constant ratios were obtained for intermediate carbocations.

For the cations of this study, the difference between the rate constants for the neutral form of **dG** and the conjugate base is about three orders of magnitude. This results in very different selectivities over the solvent reaction. Under acidic conditions where it is the neutral form of **dG** that reacts, the cations preferentially react with water even at the highest concentrations of **dG**. Arylnitrenium ions, the reactive electrophiles derived from arylamine carcinogens, provide an interesting contrast here. These cations react very efficiently with **dG**, with a high selectivity over the water reaction (25–28). This reaction involves the neutral form of **dG**, since the rate constant is unchanged over the pH range 3.5–8.0 (25). (Studies of arylnitrenium ions with anionic **dG** are currently in progress). The following comparison shows how dramatic the difference is. When the tamoxifen cation (as the $\mathbf{T}^{2+}$ form) reacts in acidic solutions containing 1 mM **dG**, only 0.3% of the products are derived from the nucleoside, 99.7% being the alcohol obtained from capture by solvent. The percentage of adducts is even lower for the bis-(4-methoxyphenyl)methyl cation under the same conditions. The 2-fluorenylnitrenium ion has an aqueous lifetime that is identical to that of $\mathbf{T}^{2+}$. When this cation reacts in 1 mM **dG**, 96% of the products are derived from the nucleoside and only 4% from the solvent (24).

Changing to basic conditions where the **dG** has been converted to its conjugate base results in much higher selectivities towards the nucleoside. For example, the bis-(4-methoxyphenyl)methyl cation reacting at pH 11 in the presence of 1 mM **dG** will form 60% **dG** adduct. This is obviously an attractive method for the preparation of adducts for the purpose of structural characterization. The difference between the two forms of **dG** is such that by pH 7 to 7.5, the majority of the reaction that does occur with the nucleoside is the reaction with the small fraction of anion that is present. This is also reflected in an improved selectivity over the solvent reaction. As one example, the **dG**:water selectivity for the bis-(4-methoxyphenyl)methyl cation at pH 7.3 has increased to 13 from its acidic value of 1.2. This increase occurs since 91% of the reaction with **dG** at pH 7.3 is occurring via the conjugate base.

In the tamoxifen system, a comparison was made between ratios of rate constants for the **dG** and water reactions obtained by product analysis and ratios calculated from the absolute rate constants measured with LFP. The two ratios for

© 2002 NRC Canada

Scheme 6.

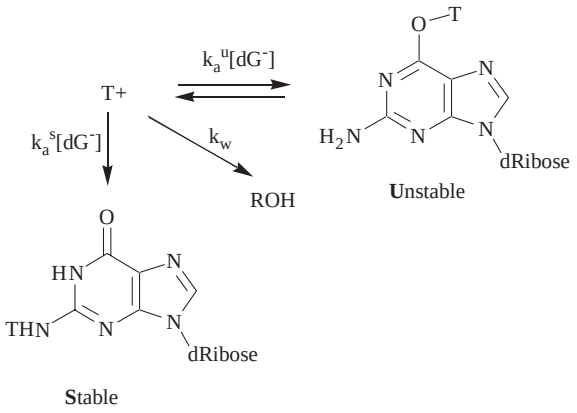

the competition involving the neutral form of **dG** and water were not outside of experimental error (although this error was quite large). On the other hand, the ratios for the anion of **dG** vs. water were statistically different, with a greater ratio being obtained by the LFP experiments. The difference is almost a factor of three. There is a very large difference in the time scales of the two experiments. The LFP measurements occurred on the microsecond time scale. The product analyses, on the other hand, were carried out after 16–24 h, the time required for complete solvolysis of the acetate. This leads to an explanation whereby the reaction of the cation with **dG** anion proceeds reversibly to an unstable adduct in addition to its irreversible reaction forming the stable product, the N2 adducts (Scheme 6). The quenching by the **dG** anion measured as the second-order rate constant in the LFP experiment would then correspond to the sum of the rate constants for the formation of the unstable and stable products ($k_a^u + k_a^s$). The rate constant in the competition experiment would only refer to the latter (k_a^s). Thus, the ratio for the latter would be smaller.

This scenario requires that the unstable adduct be "stable" on the time scale of the LFP experiment, i.e., that it last at least half a millisecond. On the other hand, it must have completely reacted before the products were analyzed. A structure that would satisfy these requirements is the adduct at O6 shown in Scheme 6. Such an adduct is an obvious product of the reaction of a carbocation and the anion of guanine, since it is at O6 that the majority of the negative charge will reside. O6-(*p*-methoxybenzyl)guanosine, the analog derived from the *p*-methoxybenzyl cation, has been shown to be unstable in aqueous solution (36). Its decomposition was pH independent at high pH, and the reaction was proposed to involve ionization to the *p*-methoxybenzyl cation and the guanosine anion. The half-life for this ionization was about 0.5 h. Both the tamoxifen cation and the bis-(4-methoxyphenyl)methyl cation are more stable than *p*-methoxybenzyl, and thus ionizations that result in these cations will be considerably faster. This can be seen in the observation that the acetate esters derived from the two solvolyze at a reasonable rate in water, while *p*-methoxybenzyl acetate is very stable under these conditions. Thus, an O6 adduct formed with the tamoxifen cation (or the bis-(4-methoxyphenyl)methyl cation) is expected to be quite short-lived. It could well survive the time scale of the LFP experiment, but it would not be around after several hours.

Scheme 7.

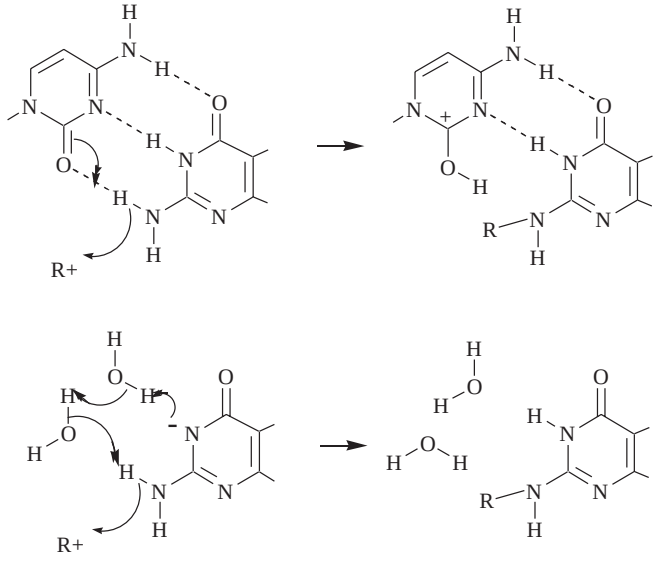

Despite the fact that the negative charge in the **dG** anion is at O6 (and N1), there is still a remarkably large rate constant for the reaction that forms the N2 adduct. This effect is best seen in the competition kinetic experiments with the bis-(4-methoxyphenyl)methyl cation where a single carbocation was involved and the N2 adduct:water product ratio was measured and converted to a rate-constant ratio. The latter changes from 1.2 (k_n^1:k_w) for neutral **dG** to 1500 (k_a^1: k_w) for the anion. The rate constant k_w is the same in the two ratios, with a value of 1.3×10^5 s^{-1} in this solvent (29). Thus, the rate constant k_n^1 for the formation of the N2 adduct with neutral **dG** is 1.6×10^5 M^{-1} s^{-1}, and k_a^1 for the anion is 2.2×10^8 M^{-1} s^{-1}, over three orders of magnitude greater.

Observations of enhanced formation of N2 adducts in the anion of guanine have been made previously (36–38), although it is not clear if free carbocations were involved in all cases. The N2 adduct is also the principle product of the reaction of DNA with the tamoxifen carbocation (20–22), as well as a number of other electrophiles (1). In DNA one of the NH_2 protons is involved in hydrogen bonding to the complementary cytosine. This has led to the recent proposal (42) of a mechanism whereby the proton in the hydrogen bond transfers to the neighboring cytosine as the nitrogen–electrophile bond is forming (top reaction of Scheme 7). In other words, the neighboring cytosine acts as a base to assist the reaction of the NH_2 group by removing one of its protons as the reaction proceeds.

A similar mechanism would explain the high reactivity of the NH_2 group in the guanine anion. Here the base would be the adjacent partially negatively charged nitrogen at N1. The proton at NH_2 could be transferred directly to N1 through a four-center transition state or, perhaps, through the intervention of surrounding water molecules, as shown in the bottom mechanism in Scheme 7. In any case the reaction would lead directly to the product, and there with little or no build-up of positive charge at N2.

© 2002 NRC Canada

Experimental section

α-Hydroxytamoxifen and α-acetoxytamoxifen ((*E*)-1-[4-[2-(dimethylamino)ethoxy]phenyl]-1,2-diphenyl-1-buten-3-ol and its acetate ester) were available from a previous study (43) as were bis-(4-methoxyphenyl)methanol and bis-(4-methoxyphenyl)methyl acetate (44).

*N*2-Bis-(4-methoxyphenyl)methyl-2′-deoxyguanosine was isolated from a scaled-up reaction. 2′-Deoxyguanosine (286 mg, 1 mmol) was added to a mixture of 20 mL acetonitrile and 30 mL of water, and 0.9 mL (0.9 mmol) of sodium hydroxide was added. A solution of bis-(4-methoxyphenyl)methyl acetate (200 mg, 0.7 mmol) in 5 mL of acetonitrile was then slowly added over 8 h, and the mixture left to stand at room temperature, with periodic monitoring by HPLC. When, after 3 days, this indicated that there was no ester remaining, the pH was adjusted to about 5 by the addition of a small amount of 1 M HCl, and the mixture concentrated with a rotary evaporator until only water remained. At this point, a precipitate had formed, which was isolated by filtration. This solid was purified by column chromatography on silica gel with 100% ethyl acetate as the eluting solvent. Fractions were analyzed by HPLC and the fractions containing the adduct were combined and the solvent removed. The solid obtained was purified by dissolving it in a small amount of methanol and then induction of precipitaton by the addition of water. The solid showed only a single peak on HPLC corresponding to the adduct identified as **DdG1**. This was characterized as *N*2-bis-(4-methoxyphenyl)methyl-2′-deoxyguanosine by ^{1}H NMR, with coupled protons being identified by gCOSY experiments. ^{1}H NMR (500 MHz, DMSO-d_6) δ: 2.05–2.10 (m, 1H, H2$_a$′), 2.55–2.6 (m, 1H, H2$_b$′), 3.40–3.45 (m, 1H, H5$_a$′), 3.55–3.60 (m, 1H, H5$_b$′), 3.70 (s, 6H, OCH_3), 3.80 (m, 1H, H4′), 4.30 (m, H3′), 4.83 (t, 1H, C5′-OH), 5.22 (d, 1H, C3′-OH), 6.02 (d, 1H, C_α-H), 6.08 (t, 1H, H1′), 6.94 (d, 4H, Ar-H), 7.21 (d, 4H, Ar-H), 7.36 (d, 1H, N2-H), 7.84 (s, 1H, H8), 10.35 (s, 1H, N1-H). Mass spectra of this material, even with soft ionization techniques, showed only a very small peak for the molecular ion (m/z = 492).

LFP experiments involved ca. 20 ns pulses at 248 or 308 nm (60–120 mJ per pulse) from a Lumonics excimer laser. A pulsed xenon lamp provided the monitoring light. After passing through a monochromator, the signal from the photomultiplier tube was digitized and sent to a computer for analysis. Stock solutions of the acetates (α-acetoxytamoxifen and bis-(4-methoxyphenyl)methyl acetate) of concentration 20–50 mM were prepared in acetonitrile. Immediately before irradiation a small volume was added to the solution of interest (usually in a 25 mL volumetric flask). Final concentrations of the acetates were 50 μM (α-acetoxytamoxifen in water) and 200–300 μM (α-acetoxytamoxifen in 20% acetonitrile and bis-(4-methoxyphenyl)methyl acetate). The solutions were irradiated with laser light at 248 nm (when studying the reaction with the solvent) and at 308 nm (α-acetoxytamoxifen in the presence of 2′-deoxyguanosine). The signals of the transient carbocations were monitored at 460 nm (tamoxifen cation) and 500 nm (bis-(4-methoxyphenyl)methyl cation). These showed excellent first-order decays. Observed first-order rate constants were obtained by fitting the experimental data of absorbance vs. time to the exponential equation. Rate constants for the solvent reaction were obtained as the average of five to eight kinetic runs. For the decay of the tamoxifen cation in the presence of 2′-deoxyguanosine, 12–16 kinetic runs were averaged. The pH of the solutions was established by the use of perchloric acid (pH < 3), sodium hydroxide (pH > 11) with acetate, phosphate, tris, and carbonate buffers in between. When a buffer was employed, serial dilutions were performed to provide four to five solutions of the same pH (as verified by recording the pH with a pH meter). The observed rate constants were linear in the buffer concentration, and the value of k_o, the rate constant in the absence of the buffer, was obtained as the intercept at zero buffer concentration. The experiments with **dG** present were performed with dilute solutions of the buffers (total concentration less than 0.01 M) with four to five concentrations of **dG** ranging up to 20 mM. The rate constants $k_{\mathbf{dG}}$ were obtained by linear regression of the plot of the observed rate constants against the added concentrations of **dG**.

The value of the acid dissociation constant of 2′-deoxyguanosine was measured in 20% acetonitrile, ionic strength = 0.1 M, 20°C by preparing a series of buffer solutions to which had been accurately added the same constant concentration (100 μM) of the nucleoside. Spectra were recorded with a HewlettPackard diode array spectrometer, and titration curves of absorbance vs. pH constructed at several wavelengths. These were fit to the equation $A = (A_{acid}[H^+] + A_{base}K_a)/([H^+] + K_a)$, A_{acid} and A_{base} are the plateau absorbances at low pH and high pH, respectively.

HPLC experiments were performed with a Waters HPLC system comprising a Waters 600E system controller, a Waters 486 tunable absorbance detector set at 238 nm, a Waters 746 data module, and a Waters U6K injector. The column employed was a Waters Symmetry C18 column of 5 μm particle size and dimensions 4.6 mm × 150 mm; the eluting solvent was first passed through a guard column of the same packing material and 4.6 × 25 mm dimensions. Solvents were sparged with helium.

Solutions of α-acetoxytamoxifen and bis-(4-methoxyphenyl)methyl acetate were prepared as described above, by adding the concentrated stock solution in acetonitrile to a solution of 20% acetonitrile. The entire set of experiments with each acetate were performed with the same stock solution to ensure that the final solutions were all of the same concentration, around 100 μM. The solutions were allowed to stand at room temperature for a period of 16–24 h, sufficient time that the signal of the acetate in the HPLC had disappeared.

The products from the α-acetoxytamoxifen were analyzed at 260 nm. Elution at 1 mL min^{-1} involved: (*i*) an initial 0.5 min isocratic run at 25% acetonitrile – 75% acetate buffer (pH 4.5, 0.05 M); (*ii*) a linear gradient to 85% acetonitrile – 15% acetate buffer over 13.5 min; (*iii*) a 3 min isocratic run at 85% acetonitrile – 15% acetate buffer. Peaks were observed at 1 to 2 min (**dG**), 10.5, 10.6 (overlapping (*E*)-**TdG** isomers), 11.8, 11.9 (overlapping (*Z*)-**TdG** isomers), 12.8 ((*E*)-**TOH**)), and 13.5 ((*Z*)-**TOH**). The areas for these peaks were converted into concentration ratios as follows:

$$[9] \qquad [\mathbf{TdG}]/[\mathbf{TOH}] = (1/RF)(\text{Area}(\mathbf{TdG})/\text{Area}(\mathbf{TOH}))$$

© 2002 NRC Canada

where [**TdG**], [**TOH**], Area(**TdG**), and Area(**TOH**) are the sums of the concentrations and HPLC areas of the four **dG** adducts and the two alcohols, respectively, and *RF* is the relative HPLC response factor. The latter was obtained as follows. For a series of solutions of the same total concentration of products, eq. [10] applies:

$$[10] \quad [\mathbf{TdG}] + [\mathbf{TOH}] = \text{Area}(\mathbf{TdG})/F(\mathbf{TdG}) + \text{Area}(\mathbf{TOH})/F(\mathbf{TOH}) = [\mathbf{TOAc}]_o$$

where F(**TdG**) and F(**TOH**) are the HPLC sensitivities of the adducts and alcohols, respectively, and $[\mathbf{TOAc}]_o$ is the constant total concentration of products determined by the initial concentration of acetate ester. Rearrangement gives eq. [11]:

$$[11] \quad \text{Area}(\mathbf{TdG}) = -(F(\mathbf{TdG})/F(\mathbf{TOH}))\text{Area}(\mathbf{TOH}) + F(\mathbf{TdG})[\mathbf{TOAc}]_o$$

where F(**TdG**):F(**TOH**) is equal to *RF*. A plot of the total area of the adducts was indeed linear in the sum of the area of the two alcohols. The slope (–2.2) was the negative of *RF*. It should be noted that there are two assumptions in this treatment: **TdG** and **TOH** account for the products and the HPLC sensitivities of the four forms of **TdG** are equivalent, as is also the case for the two forms of **TOH**. The former is true to at least 95%. There were other small peaks in the HPLC chromatogram (including the cyclic indenes (43)) but these never amounted to more than 5% in total. The identical sensitivities of the two alcohols was seen in the previous study. Further confirmation that this *RF* is reasonable is evident from the observation that the sum of the extinction coefficients measured at 260 nm for 2′-deoxyguanosine and α-hydroxytamoxifen divided by the extinction coefficient for α-hydroxytamoxifen is 2.3. The latter is a relative response factor calculated with the assumption that the two chromophores in the adducts are independent and can be modeled by the chromophores in **dG** and the alcohol.

The products from bis-(4-methoxyphenyl)methyl acetate were analyzed at 230 nm. Elution at 2 mL min^{-1} involved: (*i*) an initial 2.0 min isocratic run at 25% acetonitrile – 75% phosphate buffer (pH 7, 0.02 M); (*ii*) a linear gradient to 50% acetonitrile – 50% phosphate buffer over 8 min; (*iii*) a 5 min isocratic run at 50% acetonitrile – 50% acetate buffer. Peaks were observed at 1 min (**dG**), 5.3 min (**DdG1**), 6.2 min (**DdG2**), 6.4 min (**DdG3**), and 9.0 min (DOH). The ratio of the concentration of the NH_2 adduct **DdG1** to alcohol was obtained with eq. [12] using a relative response factor of 1.25 obtained by coinjecting authentic samples of the two products.

$$[12] \quad [\mathbf{DdG1}]/[\mathbf{DOH}] = (1/RF)(\text{Area}(\mathbf{DdG1})/\text{Area}(\mathbf{DOH}))$$

First-order rate constants for the solvolysis of bis-(4-methoxyphenyl)methyl acetate were obtained by repeat injections starting immediately after preparation of the solution. The area of the peak for the acetate vs. time was fit to the exponential equation.

Acknowledgment

Financial support from the Natural Sciences and Engineering Research Council of Canada (NSERC) is gratefully acknowledged.

References

1. A. Dipple. Carcinogensis, **16**, 437 (1995).
2. G.M. Williams, M.J. Iatropoulos, M.V. Djordjevic, and O.P. Kaltenberg. Carcinogenesis, **14**, 315 (1993).
3. P. Greaves, R. Groonetilleke, G. Nunn, J. Topham, and T. Orton. Cancer Res. **53**, 3919 (1993).
4. G.C. Hard, M.J. Iatropoulos, K. Jordan, L. Radi, O.P. Kaltenberg, A.R. Imondi, and T. Orton. Cancer Res. **53**, 4534 (1993).
5. M.A.-F. Seoud, J. Johnson, and J.C. Weed. Obstet. Gynecol. **82**, 165 (1993).
6. B. Fischer, J.P. Costantino, C.K. Redmond, E.R. Fisher, D.L. Wickerham, and W.M. Cronin. J. Natl. Cancer Inst. **86**, 527 (1994).
7. F.E. van Leeuwen, J. Benraadt, J.W.W. Coebergh, L.A.L. Kiemeney, F.W. Diepenhorst, A.W. van den Belt-Dusebout, and H. van Tinteren. Lancet, **343**, 448 (1994).
8. X. Han and J.G. Liehr. Cancer Res. **52**, 1360 (1992).
9. I.N.H. White, F. de Matteis, A. Davies, L.L. Smith, C. Crofton-Sleigh, S. Venitt, A. Hewer, and D.H. Phillips. Carcinogenesis, **13**, 2197 (1992).
10. K. Hemminki, H. Rajaniemi, B. Lindahl, and B. Moberger. Cancer Res. **56**, 4374 (1996).
11. K. Hemminki, H. Rajaniemi, M. Koskinen, and J. Hansson. Carcinogenesis, **18**, 9 (1997).
12. S. Shibutani, L. Dasaradhi, S. Sugarman, A.P. Grollman, and M. Pearl. Proc. Am. Assoc. Cancer Res. **39**, 636 (1998).
13. S. Shibutani. Environ. Mutagen Res. **20**, 201 (1998).
14. S. Shibutani, N. Suzuki, I. Terashima, S.M. Sugarman, A.P. Grollman, and M.L. Pear. Chem. Res. Toxicol. **12**, 646 (1999).
15. G.A. Potter, R. McCague, and M. Jarman. Carcinogenesis, **15**, 439 (1994).
16. D.H. Phillips, G.A. Potter, M.N. Horton, A. Hewer, C. Crofton-Sleigh, M. Jarman, and S. Venitt. S. Carcinogenesis, **15**, 1487 (1994).
17. D.H. Phillips, P.L. Carmichael, A. Hewer, K.J. Cole, and G.K. Poon. Cancer Res. **54**, 5518 (1994).
18. D.H. Phillips, P.L. Carmichael, A. Hewer, K.J. Cole, I.R. Hardcastle, G.K. Poon, A. Keogh, and A.J. Strain. Carcinogenesis, **17**, 89 (1994).
19. G.K. Poon, B. Walter, P.E. Lonning, M.N. Horton, and R. McCague. Drug. Metab. Dispos. **23**, 377 (1995).
20. M.R. Osborne, A. Hewer, I.R. Hardcastle, P.L. Carmichael, and D.H. Phillips. Cancer. Res. 56, 66 (1996).
21. M.R. Osborne, I.R. Hardcastle, and D.H. Phillips. Carcinogenesis, **18**, 539 (1997).
22. L. Dasaradhi and S. Shibutani. Chem. Res. Toxicol. **10**, 189 (1997).
23. C. Sanchez, S. Shibutani, L. Dasaradhi, J.L. Bolton, P.W. Fan, and R.A. McClelland. J. Am. Chem. Soc. **120**, 13 513 (1999).
24. R.A. McClelland. Tetrahedron, **52**, 6823 (1996).
25. R.A. McClelland, T.A. Gadosy, and D. Ren. Can. J. Chem. **76**, 1327 (1998).
26. R.A. McClelland, A.R. Ahmad, A.P. Dicks, and V.E. Licence. J. Am. Chem. Soc. **121**, 3303 (1999).
27. M. Novak and S.A. Kennedy. J. Am. Chem. Soc. **117**, 574 (1995).

© 2002 NRC Canada

28. S.A. Kennedy, M. Novak, and B.A. Kolb. J. Am. Chem. Soc. **119**, 7654 (1997).
29. R.A. McClelland, V.M. Kanagasabapathy, N. Banait, and S. Steenken. J. Am. Chem. Soc. **111**, 3966 (1989).
30. K.-Y. Moon, and R.C. Moschel. Chem. Res. Toxicol. **11**, 696 (1998), and refs. therein.
31. S. Steenken, J. Buschek, and R.A. McClelland. J. Am. Chem. Soc. **108**, 2808 (1986).
32. R.A. McClelland, N. Banait, and S. Steenken. J. Am. Chem. Soc. **108**, 7023 (1986).
33. R.A. McClelland, M.J. Kahley, P.A. Davidse, and G. Hadzialic. J. Am. Chem. Soc. **118**, 4794 (1996).
34. H.B. Islam, S.C. Gupta, H. Yagi, D.M. Jerina, and D.L. Whalen. J. Am. Chem. Soc. **112**, 6363 (1990).
35. B. Lin, N. Islam, S. Friedman, H. Yagi, D.M. Jerina, and D.L. Whalen. J. Am. Chem. Soc. **120**, 4327 (1998).
36. R.C. Moschel, W.R. Hudgins, and A. Dipple. J. Am. Chem. Soc. **103**, 5489 (1981).
37. R.C. Moschel, W.R. Hudgins, and A. Dipple. J. Org. Chem. **49**, 363 (1984).
38. R.C. Moschel, W.R. Hudgins, and A. Dipple. J. Org. Chem. **51**, 4180 (1986).
39. J.P. Richard, T.L. Amyes, L. Bei, and V. Stubblefield. J. Am. Chem. Soc. **112**, 9513 (1990).
40. J. Chateauneuf. J. Chem. Soc. Chem. Commun. 1437 (1991).
41. F.L. Cozens, V.M. Kanagasabapathy, R.A. McClelland, and S. Steenken. Can. J. Chem. **77**, 2069 (1999).
42. J.J. Dannenberg and M. Tomasz. J. Am. Chem. Soc. **122**, 2062 (2000).
43. C. Sanchez and R.A. McClelland. Can. J. Chem. **78**, 1186 (2000).
44. T.V. Pham. Can. J. Chem. submitted for publication.

© 2002 NRC Canada

A novel metal-chain extension reaction: synthesis of $(X)[Os(CO)_3(CN\text{-}t\text{-}Bu)]_nMn(CO)_5$ (X = Cl, Br, I; *n* = 1, 2, 3)

Faming Jiang, Hilary A. Jenkins, David F. Green, Glenn P.A. Yap, and Roland K. Pomeroy

Abstract: Complexes of formula $(X)[Os(CO)_3(CN\text{-}t\text{-}Bu)]_nMn(CO)_5$ (X = Cl, Br, I; *n* = 1, 2, 3) have been prepared by the reaction of $Os(CO)_4(CN\text{-}t\text{-}Bu)$ with $Mn(CO)_5(X)$ in hexane at room temperature. The characterization of the complexes included the crystal structures of compounds with X = I, *n* = 1, 3 and X = Cl, Br, *n* = 2 (**2ClA** and **2BrB**). The trinuclear products were isolated as two isomers. The major isomer (**2XA**) has an isocyanide ligand attached to each osmium atom, whereas the minor isomer (**2XB**) has both of these ligands bound to the terminal Os atom. The structures contain Os_nMn chains with unbridged Os—Mn bonds (range of lengths are 2.870(1)–2.9245(8) Å) and for compounds with *n* = 2 or 3 Os—Os bonds (range of lengths are 2.8812(4)–2.8928(5) Å). The mechanism of formation is believed to involve replacement of a CO ligand with the $18e^-$ ligand $Os(CO)_4(CN\text{-}t\text{-}Bu)$ at the metal with the coordinated halide, followed by a rearrangement in which the halide ligand migrates to the donor Os atom with concomitant migration in the reverse direction of a carbonyl ligand. The preparation of $(OC)_4(t\text{-}BuNC)OsMn(CO)_4(Cl)$ with an Os–Mn dative bond is also reported along with the $(OC)_4(t\text{-}BuNC)OsRe(CO)_4(X)$ analogues.

Key words: manganese–osmium, rhenium–osmium, dinuclear, metal chain, dative metal–metal bond.

Résumé : On a préparé des complexes de formule $(X)[Os(CO)_3(CN\text{-}t\text{-}Bu)]_nMn(CO)_5$ (X = Cl, Br, I; *n* = 1, 2, 3) par réaction du $Os(CO)_4(CNB\text{-}t\text{-}Bu)$ avec du $Mn(CO)_5(X)$, dans l'hexane, à la température ambiante. La caractérisation des complexes a impliqué la détermination des structures cristallines des composés pour lesquels X = I avec *n* = 1 ou 3 et X = Cl ou Br et *n* = 2 (**2ClA** et **2BrB**). On a isolé deux formes isomères des produits trinucléaires. L'isomère principal (**2XA**) comprend un ligand isocyanure attaché à chaque atome d'osmium alors que, dans l'isomère minoritaire (**2XB**), chacun de ces deux ligands est attaché à l'atome d'osmium terminal. Les structures comportent des chaînes Os_nMn dans lesquelles on retrouve des liaisons Os—Mn qui ne sont pas pontées (longueurs des liaisons allant de 2,870(1) à 2,9245(8) Å) et, dans les cas où n est égal à 2 ou 3, on rencontre aussi des liaisons Os—Os (longueurs des liaisons allant de 2,8812(4) à 2,8928(5) Å). On croit que le mécanisme de formation implique premièrement le remplacement, au niveau du métal coordiné à l'halogène, d'un ligand CO par le ligand à $18e^-$ $Os(CO)_4(CN\text{-}t\text{-}Bu)$, suivi d'un réarrangement dans lequel le ligand halogène migre vers l'atome d'osmium donneur avec une migration concomitante d'un ligand carbonyle dans la direction inverse. On rapporte aussi la préparation du $(OC)_4(t\text{-}BuNC)OsMn(CO)_4(Cl)$ comportant une Os–Mn liaison dative ainsi que celles de ses analogues $(OC)_4(t\text{-}BuNC)OsRe(CO)_4(X)$.

Mots clés : manganèse–osmium, rhénium–osmium, dinucléaire, chaîne de métaux, liaison dative métal–métal.

[Traduit par la Rédaction]

Introduction

Much of the past work from this laboratory has described complexes in which an 18-electron organometallic compound acts as a 2-electron donor ligand to a 16-electron organometallic fragment in much the same way as a conventional ligand such as PPh_3 (1–7). Typical examples of molecules of this type are $(OC)_5OsOs(CO)_3(GeCl_3)(Cl)$ (1), $(L)(OC)_4OsM(CO)_5$ (M = Cr, Mo, W; L = PR_3 (2), CN-*t*-Bu (3)), and $(R_3P)(OC)_4M'Ru(CO)_3(SiCl_3)_2$ (M′ = Ru, Os, but not Fe) (4). These complexes contain an unbridged dative bond between two transition metal atoms and are rare (8); complexes with dative metal–metal bonds supported by bridging ligands are, however, more common (9). There has also been renewed interest in complexes with unbridged dative bonds between a transition metal and a main-group metal (10).

In some of our earliest studies, it was observed that isomerization often occurred for complexes with unbridged dative metal–metal bonds that also contained a halide or (especially) a hydride ligand coordinated to the acceptor metal atom (11, 12). The isomerization involved migration of the halide (or hydride) ligand to the donor atom with

Received 16 October 2001. Published on the NRC Research Press Web site at http://canjchem.nrc.ca on 20 March 2002.

F. Jiang, D.F. Green, and R.K. Pomeroy.[1] Department of Chemistry, Simon Fraser University, Burnaby, BC V5A 1S6, Canada.
H.A. Jenkins. Department of Chemistry, Saint Mary's University, Halifax, NS B3H 3C3, Canada.
G.P.A. Yap. Department of Chemistry, University of Ottawa, Ottawa, ON K1N 6N5, Canada.

[1]Corresponding author (e-mail: pomeroy@sfu.ca).

 DOI: 10.1139/V02-016 © 2002 NRC Canada

concomitant migration of a carbonyl ligand to the acceptor atom (Scheme 1; in this and other schemes presented here the carbonyl ligands not involved in the isomerization have been omitted.) If the halogen ligand is considered a one-electron donor ligand, then the isomerization process results in the conversion of the dative metal–metal bond to a nondative bond.

It is well-known that the presence of a halide ligand in a metal-carbonyl complex often labilizes the carbonyls to ligand substitution (13, 14). The possibility, therefore, exists for further substitution–isomerization reactions on the binuclear compound to yield complexes with extended metal chains. Several previous attempts to exploit this strategy to the synthesis of polynuclear compounds were unsuccessful. Here we report the partial realization of the method in the synthesis of $(X)[Os(CO)_3(CN\text{-}t\text{-}Bu)]_nMn(CO)_5$ (X = Cl, Br, I; n = 1, 2, 3) complexes that contain chains of up to four metal atoms. The tetranuclear complex has been the subject of a communication (15).

Experimental

Unless otherwise stated, manipulations of starting materials and products were carried out under a nitrogen atmosphere with the use of standard Schlenk techniques. Hydrocarbon solvents were heated to reflux over potassium, distilled, and stored over molecular sieves before use. Dichloromethane was dried in a similar manner except that P_2O_5 was employed as the drying agent. The precursory compounds $Mn(CO)_5(X)$ (X = Cl, Br, I) (16), $[Re(\mu\text{-}X)(CO)_4]_2$ (17), and $Os(CO)_4(CN\text{-}t\text{-}Bu)$ (3) were prepared by literature procedures. The reaction vessels were Carius tubes of volumes between 25–50 mL and each were fitted with a Teflon valve. NMR spectra were recorded on a Bruker AMX 400 spectrometer at the appropriate operating frequencies for the ^1H, $^{13}C\{^1H\}$, and $^{31}P\{^1H\}$ NMR spectra. Samples of the complexes used for $^{13}C\{^1H\}$ NMR spectra were enriched to ~30% ^{13}CO. The samples were prepared from more highly ^{13}CO-enriched $M(CO)_5(X)$ (M = Mn, Re), which in turn was prepared by stirring the $M(CO)_5(X)$ in hexane (or toluene) under ^{13}CO (99%; 2 atm) at room temperature for 24 h (13). It was found that the ^{13}CO was scrambled equally over all CO sites in the products. Analytical and spectroscopic data for the new compounds are given in Tables 1–3.

Preparation of $(OC)_4(t\text{-}BuNC)OsMn(CO)_4(Cl)$ (1)

A solution of $Os(CO)_4(CN\text{-}t\text{-}Bu)$ (30 mg, 0.078 mmol) and $Mn(CO)_5(Cl)$ (17 mg, 0.074 mmol) in hexanes (15 mL) was cooled to –196°C and the solution was degassed with three cycles of freeze-pump-thaw; the vessel was covered with aluminum foil. The mixture was stirred under vacuum at room temperature for 20 h. A bright yellow precipitate resulted. The solvent was removed from the precipitate, which was washed with hexane (3 × 2 mL) and then dried on the vacuum line. The product was analytically pure; further purification was prevented by its instability in solution at room temperature. Reaction of $Mn(CO)_5(X)$ (X = Br, I) under similar conditions gave the isomerized products (**1X**; see below).

Scheme 1.

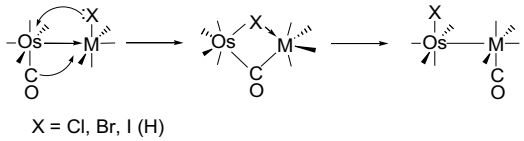

Preparation of $(OC)_3(t\text{-}BuNC)(I)OsMn(CO)_5$ (1I)

To a Carius tube was added $Os(CO)_4(CN\text{-}t\text{-}Bu)$ (39 mg, 0.10 mmol), $Mn(CO)_5(I)$ (32 mg, 0.10 mmol), and hexanes (10 mL); the solution was degassed as before and the reaction tube covered with aluminum foil. The mixture was stirred under vacuum at room temperature. An IR spectrum after 2 days indicated the starting compounds were still present. The vessel was resealed and the solution degassed as before. After a further 5 days of stirring an IR spectrum indicated that only $(OC)_3(t\text{-}BuNC)(I)OsMn(CO)_5$ (**1I**) was present. The resulting yellow solution was transferred into a Schlenk tube, concentrated, and stored at –27°C to give **1I** as yellow crystals (49 mg, 73%). A second preparation under ambient light resulted in the same product plus traces of **2IA** that were separated by chromatography as described below. The chloro and bromo analogues (**1Cl** and **1Br**) were prepared in a similar manner, that is, under ambient light with a reaction period of 5 days.

Preparation of $(OC)_6(t\text{-}BuNC)_2(I)Os_2Mn(CO)_5$ (2IA and 2IB)

A solution of $Os(CO)_4(CN\text{-}t\text{-}Bu)$ (60 mg, 0.15 mmol) and $Mn(CO)_5(I)$ (24 mg, 0.075 mmol) in hexanes (10 mL) was degassed as described above and the reaction vessel sealed under vacuum. The mixture was stirred at room temperature. Compounds $Os(CO)_4(CN\text{-}t\text{-}Bu)$ **1I** and **2I** were present after 2 days as indicated by IR spectroscopy. An IR spectrum of the reaction solution after 7 days indicated the presence of the desired product plus traces of **1I.** The resulting yellow solution was concentrated and subjected to chromatography on a silica gel column (12 × 1 cm). Elution of the column with hexanes–CH_2Cl_2 (8:1) gave two yellow bands; the first contained **1I**, the second **2IA.** The second fraction was collected, concentrated, and stored at –27°C to give **2IA** (41 mg, 53%) as yellow crystals. Further elution of the column with hexanes–CH_2Cl_2 (4:1) yielded a third yellow band from which **2IB** (5 mg, 6%) as yellow crystals was isolated in a manner similar to that for **2IA**. The chloro (**2ClA** and **2ClB**) and bromo (**2BrA** and **2BrB)** analogues were synthesized in an analogous fashion; yields are given in Table 1. It was verified on a small scale that the trinuclear complexes could be also prepared from similar reactions of $Os(CO)_4(CN\text{-}t\text{-}Bu)$ and **1X** in a 1:1 molar ratio.

Preparation of $(OC)_9(t\text{-}BuNC)_3(Br)Os_3Mn(CO)_5$ (3Br)

A degassed solution of $Os(CO)_4(CN\text{-}t\text{-}Bu)$ (58 mg, 0.15 mmol) and $Mn(CO)_5(Br)$ (14 mg, 0.05 mmol) in hexanes (8 mL) was stirred under vacuum at room temperature for ~40 h, during which time a yellow precipitate formed. The IR spectra revealed the solution contained small amounts of **2Br**, whereas the solid was mainly **3Br**. The solution was removed from the solid, which was then recrystallized from toluene–hexanes to furnish **3Br** (28 mg,

© 2002 NRC Canada

Table 1. Analytical ^{1}H NMR data and yields for complexes **1–3X**.

Compound	Yield (%)	%C (calcd.)	%H (calcd.)	%N (calcd.)	^{1}H NMR (δ)[a]
1	65	26.31 (26.56)	1.46 (1.54)	2.14 (2.38)	1.52[b]
1Cl	67	26.62 (26.56)	1.60 (1.54)	2.33 (2.38)	1.64
1Br	41	24.85 (24.69)	1.30 (1.43)	2.11 (2.22)	1.62
1I	73	23.08 (22.99)	1.35 (1.34)	2.09 (2.06)	1.60
2ClA	71	26.97 (26.68)	2.06 (1.92)	2.89 (2.92)	1.61, 1.50
2BrA	32	25.68 (25.48)	1.94 (1.83)	2.75 (2.83)	1.59, 1.50
2IA	53	24.62 (24.33)	1.80 (1.75)	2.63 (2.70)	1.57, 1.51
2ClB	15	26.90 (26.68)	2.07 (1.92)	2.81 (2.96)	1.58
2BrB	11	25.59 (25.48)	1.93 (1.83)	2.81 (2.83)	1.57
2IB	6	24.45 (24.33)	1.74 (1.75)	2.63 (2.70)	1.55
3Cl	41	26.96 (26.74)	2.21 (2.09)	3.02 (3.23)	1.62, 1.47
3Br	41	25.91 (25.86)	1.97 (2.02)	3.02 (3.12)	1.61, 1.47
3I	26	25.07 (24.99)	2.08 (1.95)	2.98 (3.01)	1.58, 1.48
1ReCl	39	21.80 (21.71)	1.23 (1.26)	1.95 (1.95)	1.52[b]
1ReBr	27	20.91 (20.45)	1.33 (1.19)	1.87 (1.83)	1.52[b]
1ReI	44	19.39 (19.26)	1.05 (1.12)	1.66 (1.73)	1.53[b]

[a]Unless otherwise stated, NMR spectra were recorded in $CDCl_3$ at room temperature.
[b]Recorded in CD_2Cl_2 at – 40°C.

Table 2. IR spectra (in hexane) of the new complexes.

Compound	ν(CO) (cm^{-1})	ν(CN) (cm^{-1})
1[a]	2118(m), 2053(s), 2043(sh), 2013(w), 1977(s), 1924(m)	2217(m)
1Cl	2099(m), 2063(s), 2037(s), 2021(m), 2004(s), 1986(sh), 1983(s), 1970(m)	2211(m)
1Br	2098(m), 2063(s), 2036(s), 2021(w-m), 2004(s), 1984(s), 1971(m-s)	2209(w-m)
1I	2096(m-s), 2063(s), 2034(s), 2020(w), 2004(s), 1985(s), 1972(m)	2205(m)
2ClA	2088(m), 2064(s), 2034(m), 2022(s), 2002(s), 1989(s), 1983(m), 1966(m)	2207(w), 2188(m)
2ClB	2101(w), 2064(w), 2047(w), 2036(m), 2002(s), 1996(s), 1969(m), 1963(w)	2204(vw), 2178(m)
2BrA	2087(m), 2064(s), 2034(w), 2022(s), 2002(s), 1989(s), 1983(w), 1966(m)	2205(w), 2187(m)
2BrB	2102(w), 2064(w), 2040(w, sh), 2036(m), 2002(s), 1996(s), 1971(m), 1963(w)	2206(vw), 2176(m)
2IA	2086(m), 2062(s), 2034(m), 2019(s), 2002(s), 1990(s), 1984(w), 1967(m)	2202(w), 2185(m)
2IB	2101(m), 2062(w), 2040(m), 2034(s), 2002(s), 1997(s), 1972(m), 1964(w)	2206(vw), 2176(m)
3Cl	2079(vw), 2064(m), 2041(w), 2020(w), 2015(m), 1994(s), 1987(w, sh), 1961(m)	2202(w), 2183(w), 2171(w)
	2080(w), 2065(s), 2039(w), 2019(w, sh), 2013(m), 1991(vs), 1956(m)	2205(w), 2171(m)
3Br	2079(w), 2064(m-s), 2041(w), 2021(w), 2015(m), 1994(s), 1987(w, sh), 1961(m)	2201(w), 2184(w), 2171(w)
	2080(w), 2064(s), 2039(m), 2020(w, sh), 2013(m), 1991(vs), 1956(m)	2204(w), 2171(m)
3I	2079(w), 2061(m), 2040(w), 2021(w), 2013(m), 1994(s), 1987(w, sh), 1962(m)	2198(w), 2181(w), 2168(w)
	2079(w), 2062(m), 2039(w), 2019(w, sh), 2010(m), 1991(vs), 1956(m)	2201(w), 2171(m)
1ReCl[a]	2119(m), 2074(s), 2039(vs), 1978(s), 1914(s)	2217(w)
1ReBr[a]	2118(m), 2073(s), 2040(vs), 1980(s), 1915(s)	2219(w)
1ReI[a]	2118(m), 2070(s), 2040(vs), 1978(s), 1917(s)	2218(w)

[a]In CH_2Cl_2.

41%) as a yellow crystalline solid. The chloro (**3Cl**) and iodo (**3I**) congeners were synthesized similarly. It was also verified that the **2X** complexes react with excess $Os(CO)_4$(CN-*t*-Bu) under the same conditions to give the corresponding **3X** compounds.

Preparation of $(OC)_4$(*t*-BuNC)$OsRe(CO)_4$(Cl)

A degassed solution of $Os(CO)_4$(CN-*t*-Bu) (44 mg, 0.11 mmol) and $[Re(\mu\text{-}Cl)(CO)_4]_2$ (36 mg, 0.054 mmol) in toluene (15 mL) was stirred under nitrogen at 45°C for ~20 h, during which time a yellow precipitate formed. The mother solution was removed and the precipitate washed with hexanes; the precipitate was then recrystallized from toluene–hexanes at –40°C to afford yellow crystals of (*t*-BuNC)$(OC)_4OsRe(CO)_4$(Cl) (30 mg, 39% yield). The bromo and iodo analogues were prepared in a similar manner.

X-ray structural determination of 1I, 2ClA, 2BrB, and 3I

The structures of **1I**, **2ClA**, and **2BrB** were determined at St. Mary's University, whereas that of **3I** was carried out at the University of Ottawa. The determinations followed the same general procedure. A single (yellow) crystal of suitable size was grown from hexane or hexane–CH_2Cl_2, and mounted on a glass fiber. Data were collected at –50°C for **1I**, **2ClA**, and **2BrB**, and at –70°C for **3I**; a Bruker (Siemens) SMART/CCD diffractometer was used in each case. Crystal data refinement parameters are summarized in Table 4, and selected interatomic distances and angles are

© 2002 NRC Canada

Table 3. ^{13}C NMR data for selected derivatives.

Compound	M–CO	Os–CO	*t*-Bu–C
1[a]	221.2 (1C), 220.8 (2C), 219.2 (1C)	182.4 (2C), 177.3 (1C), 163.0 (1C)	60.8, 29.5
1I	219.8 (4C), 215.6 (1C)	177.4 (1C), 171.8 (1C), 162.4 (1C)	59.8, 30.1
2ClA[b]	222.9 (4C), 218.3 (1C)	193.4 (1C),[c] 191.9 (1C),[c] 189.7 (1C), 183.3 (1C), 174.4 (1C), 164.1 (1C)	59.7, 58.6, 30.0
2ClB[b]	223.8 (4C), 217.8 (1C)	191.9 (4C), 175.1 (1C), 166.3 (1C)	59.1, 30.2
3Cl[b]	223.8 (4C), 218.9 (1C)	194.8 (2C),[d] 194.3 (1C),[e] 192.3 (1C),[e] 191.1 (1C), 191.0 (1C), 185.6 (1C), 176.3 (1C), 166.0 (1C)	59.1, 58.2, 58.0, 29.8, 29.7 (2Me)
1ReCl[a]	194.0 (2C), 188.8 (1C), 186.0 (1C)	180.2 (2C), 175.7 (1C), 164.2 (1C)	29.5
1ReBr[a]	192.7 (2C), 188.5 (1C), 185.3 (1C)	180.3 (2C), 176.0 (1C), 163.6 (1C)	29.5
1ReI[a]	190.4 (2C), 188.1 (1C), 184.2 (1C)	180.7 (2C), 176.4 (1C), 162.7 (1C)	29.5

[a]In CD_2Cl_2 at – 40°C.
[b]In $CDCl_3$ at – 40°C.
[c]*Trans*, $^2J_{C,C}$ = 31.3 Hz.
[d]Degenerate singlets.
[e]*Trans*, $^2J_{C,C}$ = 31.6 Hz.

Table 4. Details of the crystal structure determinations of **1I**, **2ClA**, **2BrB**, and **3I**.

	1I	**2ClA**	**2BrB**	**3I**
Compound	$C_{13}H_9IMnNO_8Os$	$C_{21}H_{18}ClMnN_2O_{11}Os_2$	$C_{21}H_{18}BrMnN_2O_{11}Os_2$	$C_{29}H_{27}IMnN_2O_4Os_3$
Formula weight	679.25	945.16	989.62	1393.98
Crystal system	Monoclinic	Monoclinic	Triclinic	Monoclinic
T (°C)	–50	–50	–50	–70
Space group	$P2_1/c$	$P2_1/n$	$P\bar{1}$	$P2_1/c$
a (Å)	15.0686(8)	12.2794(8)	9.0783(5)	11.503(1)
b (Å)	11.2590(6)	16.5412(11	9.8272(6)	12.394(1)
c (Å)	12.0421(7)	14.3631(10)	17.621(1)	29.959(3)
α (deg)			102.530(1)	
β (deg)	108.245(1)	91.870(1)	100.984(1)	99.894(2)
γ (deg)			95.273(1)	
Cell volume (Å^3)	1940.3(2)	2915.8(3)	1491.9(2)	4207.6(7)
Z	4	4	2	4
$D_{calcd.}$ (mg m^{-3})	2.325	2.153	2.203	2.201
Abs. coeff (mm^{-1})	8.820	9.266	10.305	10.116
Unique data ($I > 2\sigma$)	3428	5134	5198	7166
R[a]	0.0313	0.0315	0.0342	0.0329
wR[b]	0.0817	0.0723	0.0822	0.0478

[a]$R = \Sigma|(|F_o| - |F_c|)|/\Sigma|F_o|$.
[b]$wR = [\Sigma\,(w(|F_o| - |F_c|)^2)/\Sigma(wF_o^2)]^{1/2}$. $w = [\sigma^2(F_o)^2 + kF_o^2]^{-1}$.

given in Tables 5–7.[2] Unit-cell parameters were calculated from reflections obtained from 60 data frames collected at different sections of the Ewald sphere. A statistical measurement of intensity data indicated the space group, and this was borne out by successful refinement of the structure. Semiempirical absorption corrections were applied using redundant data. Full-matrix least-squares refinement on F^2 was performed after solving using Patterson methods and the solution package SHELXTL v. 5.10 (18). Anisotropic thermal parameters were applied to all non-hydrogen atoms; hydrogen atoms were generated at ideal positions and their positions were updated with each refinement cycle. The following disorders in the structures were encountered: (*i*) for **1I**: O(2), O(11), and O(13) were each disordered over two positions; all were refined satisfactorily with 0.5 occupancy factors. (*ii*) For **2ClA**: CO(15) and Cl were disordered and modeled with occupancy factors of 53:47. (*iii*) For **2BrB**: CO(22) and Br were disordered with an occupancy factor of 88:12. Rotational disorder (50%) was also observed for the methyl groups within the *t*-BuNC ligands of **2BrB**.

[2] Supplementary material may be purchased from the Depository of Unpublished Data, Document Delivery, CISTI, National Research Council Canada, Ottawa, ON K1A 0S2, Canada. For information on obtaining material electronically go to http://www.nrc.ca/cisti/irm/unpub_e.shtml. Crystallographic information has also been deposited with the Cambridge Crystallographic Data Centre. Copies of the data can be obtained free of charge via www.ccdc.cam.ac.uk/conts/retrieving.html (or from the Cambridge Crystallographic Data Centre, 12, Union Road, Cambridge CB2 1EZ, UK; fax: +44 1223 336033; or deposit@ccdc.cam.ac.uk).

© 2002 NRC Canada

Table 5. Selected bond lengths (Å) and angles (deg) of **1I**.

Bond lengths (Å)			
Os—Mn	2.9245(8)	Mn—C(11)	1.818(7)
Os—I	2.7734(4)	Mn—C(radial)	1.840(7)–1.857(6)
Os—C(1)	1.895(6)	O—C(Os)	1.06(3)–1.23(3)
Os—C(2)	1.940(7)	O—C(Mn)	1.09(4)–1.22(4)
Os—C(3)	1.924(6)	N—C(4)	1.160(7)
Os—C(4)	2.029(5)	N—C(5)	1.448(7)
Bond angles (deg)			
I-Os-Mn	95.38(2)	C(11)-Mn-Os	179.9(2)
C(4)-Os-Mn	89.14(15)	C(3)-Os-Mn	174.98(18)
C(2)-Os-C(4)	170.1(2)	C(4)-Os-I	85.6(2)
N-C(4)-Os	172.6(5)		
C(11)-Mn-C	92.8(3)–93.9(3)	Os-Mn-C(radial)	86.0(2)–87.30(18)
cis-C-Mn-C(radial)	87.9(3)–93.4(3)	Mn-Os-C(radial)	81.2(2)–89.1(2)
cis-C-Os-C	91.3(2)–94.2(2)		

Table 6. Selected bond lengths (Å) and angles (deg) for **2ClA** and **2BrB**.

	2ClA	**2BrB**		**2ClA**	**2BrB**
Bond lengths (Å)					
Os(1)—Mn	2.900(1)	2.884(1)	Os(1)—C(9)	2.012(7)	
Os(1)—Os(2)	2.8812(4)	2.8895(4)	Os(2)—C(17)	2.033(7)	
Os(2)—X	2.58(1) (2.51(1))[a]	2.568(2) (2.44(2))[a]	Os(2)—C(23)		2.005(7)
Mn—C(1)	1.798(7)	1.808(8)	Os(2)—C(24)		2.003(7)
Mn—C(radial)	1.820(8)–1.847(9)	1.83(1)–1.85 (1)	Os —C(O)	1.921(8)–1.950(8)	1.877(7)–1.95 (1)[b]
Bond angles (deg)					
Os(2)-Os(1)-Mn	176.87(2)	177.54(3)	Os-Mn-C(radial)	83.3(3)–85.0(2)	83.1(3)–86.0(3)
Os(1)-Mn-C(1)	179.2(3)	177.9(2)	Mn-Os(1)-C	90.1(2)–92.4(2)	91.1(3)–91.9(3)
C(ax)-Os(2)-Os(1)	178.1(2)	176.8(2)	Os(1)-Os(2)-C(radial)	86.1(2)–87.6(5) (89.9(7))[a]	87.9(2)–88.6(2) (92(2))[a]
Os(1)-Os(2)-X	87.6 (3) (88.6 (3))[a]	91.15 (2) (89.1 (6))[a]			

[a]Disorder present.
[b]Os(2)—C(21).

Results and discussion

Binuclear OsMn complexes

A bright yellow precipitate resulted when $Os(CO)_4$(CN-*t*-Bu) and $Mn(CO)_5$(Cl) in a 1:1 molar ratio in hexanes was stirred in the dark overnight. From its ^{13}C NMR spectrum at –40°C in CD_2Cl_2 and its IR spectrum it is formulated as $(OC)_4$(*t*-BuNC)OsMn$(CO)_4$(Cl) (**1**) with a donor–acceptor OsMn bond and with both noncarbonyl ligands *cis* to the metal–metal bond (eq. [1]).

[1] $Os(CO)_4(L) + Mn(CO)_5(Cl) \xrightarrow[\text{hexane}]{25°C} -Os(L)-Mn(Cl)- + CO$

L = $CNBu^t$ **1**

In **1** the 18e⁻ compound $Os(CO)_4$(CN-*t*-Bu) acts as a two-electron donor ligand towards the 16e⁻ $Mn(CO)_4$(Cl) moiety. The ^{13}C NMR spectrum of **1** has a 1:2:1 pattern in the Mn–CO region around δ 220, and a 2:1:1 pattern in the Os–CO region (δ 160–185). The latter pattern is typical of complexes such as $(OC)_4$(*t*-BuNC)OsCr$(CO)_5$ in which the 18e⁻ $Os(CO)_4$(CN-*t*-Bu) compound acts as a ligand (3). In particular, the high field resonance in the spectrum of **1** at δ 163.0 is characteristic of this type of complex and is assigned to the carbonyl *trans* to the dative metal–metal bond (1–3, 7). The chemical shift of this resonance in $(OC)_4$(*t*-BuNC)Os[Acc] (Acc = 16e⁻ acceptor fragment) complexes may be a measure of the acceptor strength of the 16e⁻ fragment (19). The shift of this resonance in **1** may be compared with δ 165.1 and 159.3, the shifts found in $(OC)_4$(*t*-BuNC)OsCr$(CO)_5$ and $(OC)_4$(*t*-BuNC)OsOs$(CO)_3(GeCl_3)$(Cl), respectively (3, 19).

Scheme 2.

$Os(CO)_4(L) + Mn(CO)_5(X) \xrightarrow[\text{hexane}]{25°C,\ 7\ d} (OC)_3(X)(L)OsMn(CO)_5 + CO$

L = $CNBu^t$, X = Cl, Br, I → **1** → **1X**

Compound **1** was insoluble in hexane at room temperature; warming **1** in hexane caused it to decompose. Although **1** was stable in CD_2Cl_2 at –40°C, it decomposed in CH_2Cl_2 at room temperature over ~90 min. Two decomposition

© 2002 NRC Canada

Table 7. Selected bond lengths (Å) and angles (deg) of **3I**.

Bond lengths (Å)			
Os(1)—Mn	2.870(1)	Mn—C(11)	1.80(1)
Os(1)—Os(2)	2.8894(5)	Mn—C(radial)	1.81(1)–1.87(1)
Os(2)—Os(3)	2.8928(5)	Os—C(CO)	1.89(1)–1.96(1)
Os(3)—I	2.7768(7)	Os—C(CNBu)	2.01(1)–2.026(9)
Bond angles (deg)			
Os(1)-Os(2)-Os(3)	177.60(2)	Os-Mn-C(radial)	82.7(3)–84.9(3)
Mn-Os(1)-Os(2)	177.04(3)	Mn-Os(1)-C	90.0(2)–93.5(3)
Os(1)-Mn-C(1)	179.5(4)	Os(1)-Os(2)-C	88.1(2)–91.5(3)
Os(2)-Os(3)-C(14)	178.5(3)	Os(2)-Os(3)-C(radial)	83.2(2)–87.8(2)
Os(2)-Os(3)-I	92.63(2)		

Fig. 1. Molecular structure of $(OC)_3(I)(t\text{-BuNC})OsMn(CO)_5$ (**1I**).

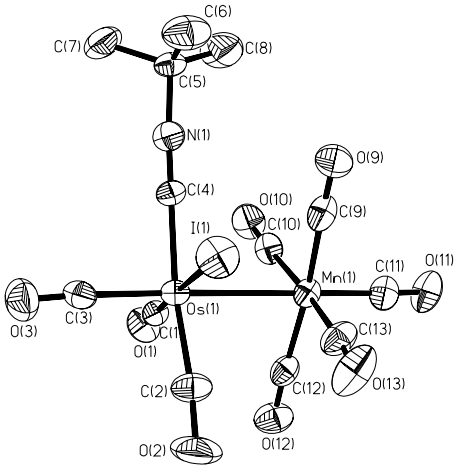

Fig. 2. Molecular structure of $(OC)_3(CI)(CN\text{-}t\text{-Bu})OsOs(CO)_3(CN\text{-}t\text{-Bu})OsMn(CO)_5$ (**2C1A**).

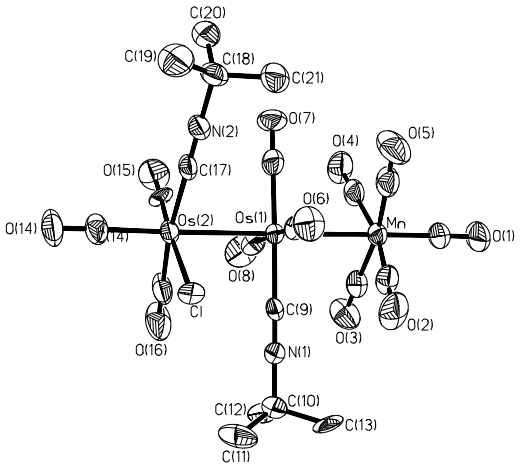

products were identified as $Os(CO)_4(CN\text{-}t\text{-Bu})$ and $Mn(CO)_5(Cl)$ by IR spectroscopy. Dissociation in solution of complexes with weak dative metal–metal bonds has been observed previously (6, 11). Furthermore, in some cases these complexes react with CH_2Cl_2 (20).

When the reaction of $Os(CO)_4(CN\text{-}t\text{-Bu})$ and $Mn(CO)_5(Cl)$ in hexanes was carried out for 7 days in ambient light under vacuum, a second product, which was also analyzed as $MnOs(CO)_8(CN\text{-}t\text{-Bu})(Cl)$ (**1Cl**), was obtained. The reaction with $Mn(CO)_5(X)$ (X = Br, I) and $Os(CO)_4(CN\text{-}t\text{-Bu})$ gave the corresponding $MnOs(CO)_8(CN\text{-}t\text{-Bu})(X)$ (**1Br**, **1I**) derivatives; there was no evidence in the latter reactions for a complex analogous to that of **1**. The crystal structure of **1I** (reported below) revealed that these compounds should be formulated as $(OC)_3(t\text{-BuNC})(X)OsMn(CO)_5$ (X = Cl, Br, I) (Scheme 2). Since the $Mn(CO)_5$ and $Os(CO)_3(CN\text{-}t\text{-Bu})(X)$ fragments are $17e^-$ species, the Mn–Os bonds in these molecules are considered nondative metal–metal bonds.

A view of **1I** is shown in Fig. 1; selected bond lengths and angles for the molecule are listed in Table 5. As can be seen from the figure, the Mn–Os bond is unbridged. There do not appear to be any structures of complexes with unbridged Mn–Os bonds with which to compare the Mn—Os length in **1I** of 2.9245(8) Å. In $CpMnOs_3(\mu_2\text{-CHCHPh})(\mu\text{-H})(\mu\text{-CO})(CO)_{11}$ the Os—Mn length is 2.765(4) Å (21); in the $MnOs_3(\mu_4\text{-C})(CO)_{13}$ the Os—Mn lengths range from 2.7797(9) to 2.8271(7) Å (22). From the (unbridged) metal–metal bond lengths reported for $Mn_2(CO)_{10}$ (2.9038(6) Å) (23) and $Os_3(CO)_{12}$ (average = 2.887 Å) (24) one can estimate the length of an unbridged Mn—Os bond to be ~2.895 Å. The Os–Mn distance in **1I** is, therefore, somewhat longer than expected; it is also significantly longer than the three other Os–Mn lengths reported below.

The formation of complexes of type **1X** involves an isomerization in which the halide X migrates from the Mn to the Os atom in $(OC)_4(t\text{-BuNC})OsMn(CO)_4(X)$ with concomitant migration of a carbonyl ligand from Os to Mn as shown in Scheme 2. As mentioned in the *Introduction*, we have previously observed this type of migration in $(Me_3P)(OC)_4OsRu(CO)_3(SiCl_3)(Br)$ (11). A similar migration is presumably also involved in the formation of $(Me_3P)(OC)_3(H)OsRe(CO)_5$ from $Re(CO)_5(H)$ and $Os(CO)_4(PMe_3)$, although the intermediate with a dative Os–Re bond is not observed (12).

Because of the donor–acceptor character of the metal–metal bond in molecules such as **1** there is expected to be a greater charge separation in these molecules compared with the isomerized derivatives (e.g., **1Cl**). Consistent with this view is that the C—O stretches in **1** (with a dative Os—Mn bond) span the range 1924–2118 cm^{-1}, whereas in **1Cl** the range is 1970–2099 cm^{-1}. It may be the relief of this charge separation that is the driving force for the isomerization. The nondative Os–Re bond in $(Me_3P)(OC)_3(Br)OsRe(CO)_5$ is slightly shorter than the dative Os–Re bond in the closely related $(Me_3P)(OC)_4OsRe(Br)(CO)_4$, an observation consistent

© 2002 NRC Canada

Fig. 3. The ^{13}C NMR spectrum (CO region) of **2C1A** (^{13}CO enriched) in CH_2Cl_2–CD_2Cl_2 (4:1) at – 40°C. The assignment of the signals is given in the inset.

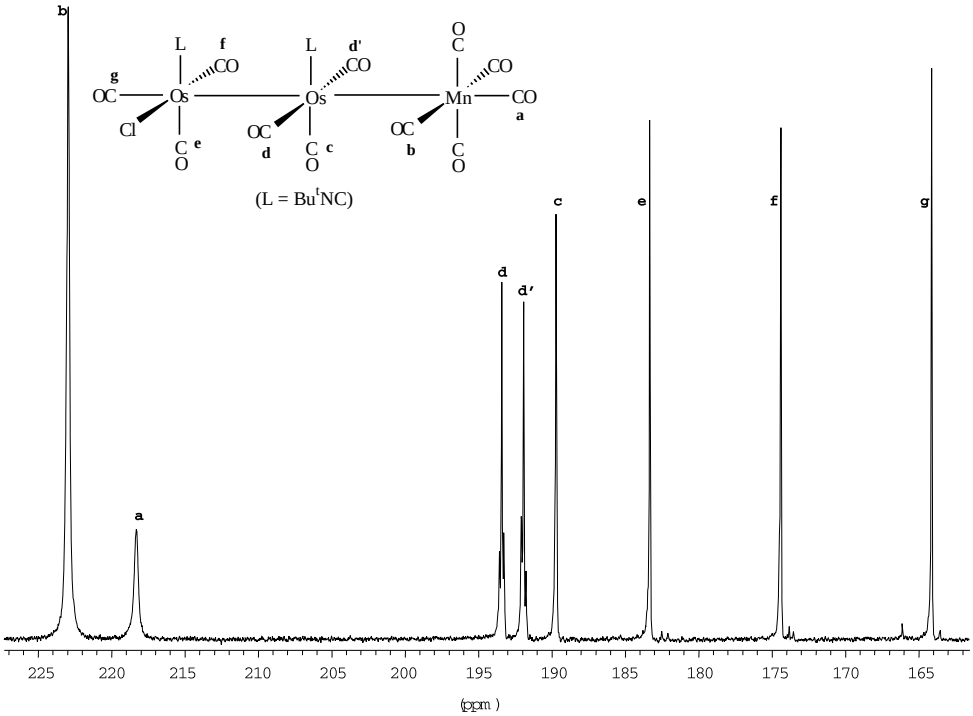

with the view that nondative metal–metal bonds are somewhat stronger than similar dative metal–metal bonds (4, 12, 25).

Trinuclear OsMn complexes

Halide ligands in metal carbonyl complexes such as $M(CO)_{6-n}(X)_n$ (M = Mn (26), Re (27), n = 1; M = Fe (28), Ru, Os (29), n = 2; X = Cl, Br, I) usually activate the complex to carbonyl substitution. It was, therefore, reasoned that the **1X** complexes might undergo further carbonyl substitution by $Os(CO)_4$(CN-*t*-Bu) at the osmium atom and this possibility was found to be correct.

Reaction of **1X** with $Os(CO)_4$(CN-*t*-Bu) in a 1:1 ratio, or the reaction of $Mn(CO)_5(X)$ and $Os(CO)_4$(CN-*t*-Bu) in a 1:2 ratio, readily affords complexes of formula $MnOs_2(CO)_{12}$-(CN-*t*-Bu)$_2$(X) (**2X**) according to Scheme 3. Two isomers of this formula were isolated by column chromatography. The major isomer in each case (**2XA)** is formulated with an $MnOs_2$ backbone with an isocyanide ligand coordinated to each osmium atom. The halide ligand is placed on the terminal Os atom at a site that is both *cis* to the Os–Os bond and the *t*-BuNC ligand (Scheme 3). This is based on the crystal structure and the ^1H and ^{13}C NMR data of **2ClA.** The bromo and iodo analogues have similar ^1H NMR and IR spectra to **2ClA.**

A view of **2ClA** is shown in Fig. 2; selected bond lengths and angles are given in Table 6. The Os—Mn length in **2ClA** of 2.900(1) Å is significantly shorter than the Os—Mn length in **1I** (2.9245(8) Å). This is unexpected because in **1I** the ligands *trans* to the Os–Mn bond are π-acceptor carbonyl ligands, whereas in **2ClA** one of the *trans* ligands is $Os(CO)_3(L)(Cl)$, which is probably a π-donor ligand (7). The latter property would be expected to increase the *d*π–*d*π interactions across the metal–metal bond and hence weaken the Os–Mn bond (see below). The apparent strengthening of the Os–Mn bond in **2ClA** compared with that in **1I** is tentatively assigned to more extensive delocalization and hence stabilization of the metal–metal bonding electrons in **2ClA**.

The Os—Os distance in **2ClA** of 2.8812(4) Å, may be compared with the average Os—Os length (2.887(3) Å) in $Os_3(CO)_{12}$ (24). The Os–Os distances in linear Os_3 chains are, however, somewhat longer than the distance in the triangular cluster. For example, the Os—Os lengths in $Os_3(CO)_{12}(I)_2$ (30), $Os_3(CO)_{12}(SiCl_3)_2$ (31), and $Os_3(CO)_{10}$-$[P(OMe)_3]_2(Br)_2$ (32) are 2.935(2), 2.912(1), and 2.916(2) Å, respectively. In $(OC)_3[MeC(CH_2O)_3P]_2OsOs(CO)_4W(CO)_5$ (33), $(OC)_4$(CN-*t*-Bu)$OsOs(CO)_3$(CN-*t*-Bu)$W(CO)_5$ (34), and $(Ph_3Sb)(OC)_4OsOs(CO)_4Os(CO)_3(Br)_2$ (35), the Os—Os (dative) bond lengths are 2.940(1), 2.907(2), 2.8882(5), and 2.9308 Å, respectively. The Os–Os length in **2ClA**, therefore, appears to be significantly shorter than most comparable unbridged Os–Os distances in noncluster complexes reported in the literature.

The ^{13}C NMR spectrum of **2ClA** in the CO region (Fig. 3) has the expected 1:4 pattern in the Mn–CO region due to the axial and radial carbonyls of the $Mn(CO)_5$ unit; these signals are broadened due to the quadrupole moment of 5/2 of ^{55}Mn. There are six resonances each of intensity 1 in the δ 160–195 region (the region where the resonances of Os–CO groupings normally appear (2, 3, 7, 36)). Such a spectrum is consistent with the solid-state structure when it is realized that the terminal Os atom is chiral because it has four different ligands with three unique ligands occupying a face of the octahedron. The *trans*-carbonyl ligands attached to the central Os atom (labeled d/d′ in Fig. 3) are, therefore, chemically distinct. This is similar to the AB pattern exhibited by protons of a CH_2 unit adjacent to a chiral center in organic

© 2002 NRC Canada

Scheme 3.

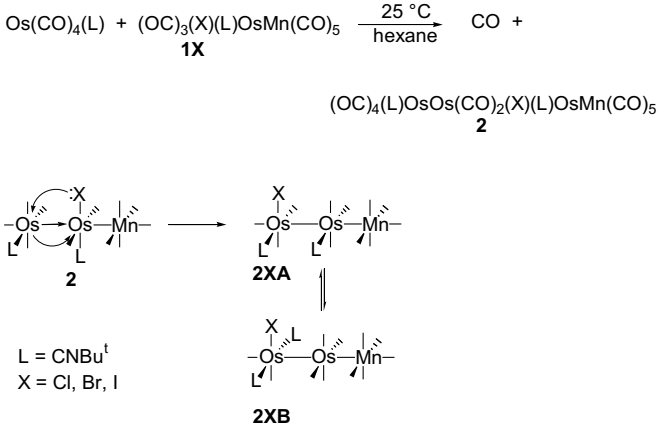

molecules (37). The signals due to these carbonyls also exhibit ^{13}C–^{13}C coupling as expected for chemically different carbonyls that are mutually *trans* to each other (38) and the level of ^{13}C enrichment of the sample (~30%).

From their spectroscopic properties, the minor isomers (**2XB**) are formulated with a similar structure to **2XA**, but with both isocyanide ligands on the terminal osmium atom in a mutually *trans* orientation (Scheme 3). In each case, the ^1H NMR spectrum consists of a singlet that indicates, in the absence of chemical exchange, that both isocyanide ligands are chemically equivalent. The IR spectrum has one very weak and one strong C–N stretch consistent with the view that these ligands are in mutually *trans* sites on the same osmium atom. The ^{13}C NMR spectrum of **2ClB** in CH_2Cl_2–CD_2Cl_2 exhibits two signals in a ratio of 4:1 in the Mn–CO region and three signals in a 4:1:1 ratio in the Os–CO region, as expected.

The structure of **2BrB** was confirmed by X-ray crystallography. A view of the molecule is given in Fig. 4; selected bond lengths and angles are presented in Table 6. The Os—Mn and Os—Os lengths are 2.884(1) and 2.8895(4) Å, respectively, and may be compared with the other Os–Mn and Os–Os lengths discussed above. That the Os–Mn length in **2BrB** is somewhat shorter than that in **2ClA** may reflect fewer steric interactions between the radial ligands on the Mn and Os(1) atoms in **2BrB**.

A solution of pure **2IA** in hexane was stirred under vacuum at room temperature for 90 h. An IR spectrum of the solution at this stage indicated the presence of **2IA**, along with significant amounts of $Mn_2(CO)_{10}$ and trace amounts of **2IB**. Likewise, a solution of **2BrB** in hexane was stirred under vacuum at room temperature for 90 h and an IR spectrum then taken of the solution. The spectrum indicated the presence of **2BrA**, significant amounts of $Mn_2(CO)_{10}$, but little or no starting complex (**2BrB**). In each case there were C–O stretching bands due to unidentified products. These preliminary results indicate that the **A** and **B** forms of **2X** are present in equilibrium in hexane at room temperature. They also show that the complexes are unstable under these conditions and decompose to $Mn_2(CO)_{10}$ and other unidentified products. It may be that decomposition proceeds mainly via form **B**.

There is ample evidence that migration of carbonyl ligands across dative metal–metal is facile (2, 3, 5, 6). For example, the sample used for the spectrum shown in Fig. 3 was prepared from ^{13}CO-enriched $Mn(CO)_5(Cl)$ and unenriched $Os(CO)_4(CN\text{-}t\text{-}Bu)$. It is evident from the spectrum that the label is scrambled over all carbonyl sites in the molecule. Similar isomers to **2A** and **2B** are found for $Os_2(CO)_7(CN\text{-}t\text{-}Bu)_2W(CO)_5$, but in this case the isomers are not in equilibrium in solution at room temperature (34). The migration of the noncarbonyl ligand to the terminal osmium atom in **2BrB** is also reminiscent of the migration observed in the formation of $(OC)_3[MeC(CH_2O)_3P]_2OsOs(CO)_4OsW(CO)_5$ from the addition of $Os(CO)_4[P(OCH_2)_3CMe]$ to $[MeC(CH_2O)_3P](OC)_4OsW(CO)_5$ at 90°C (33). The trinuclear complex in this case contains two dative metal–metal bonds in tandem and has both P ligands coordinated to the terminal Os atom, in a *trans* configuration. This type of migration results in the more bulky noncarbonyl ligand moving to a less sterically hindered site, although the radial site on the terminal Os atom is even less sterically hindered. The *trans* arrangement of the noncarbonyl ligands, which are poorer π-acceptor ligands than CO, would not be expected to be the electronically preferred structure. It is usually found that poor π-acceptor ligands prefer sites *trans* to carbonyl ligands. We have recently argued that there is an electronic preference to have a strong π-acceptor ligand (e.g., CO) *trans* to the metal–metal bond in binuclear complexes. This is because it will reduce the repulsive $d\pi$–$d\pi$ interactions across the metal–metal bond (7).

Fig. 4. Molecular structure of $(OC)_2(Br)(CN\text{-}t\text{-}Bu)OsOs(CO)_4OsMn(CO)_5$ (**2BrB**).

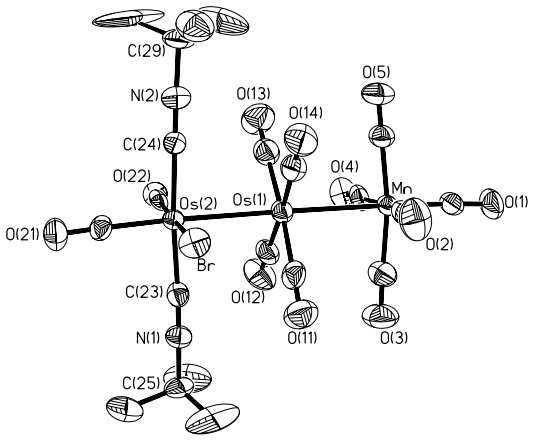

Tetranuclear OsMn complexes

Reaction of $Mn(CO)_5(X)$ and $Os(CO)_4(CN\text{-}t\text{-}Bu)$ in a 1:3 ratio in solution at room temperature readily gave products that analyzed as $MnOs_3(CO)_{14}(CN\text{-}t\text{-}Bu)_3(X)$ (**3X**; eq. [2]); it was also established on a small scale that the same products could be formed from **2X** and with an excess of $Os(CO)_4(CN\text{-}t\text{-}Bu)$ under the same conditions. The X-ray crystal structure of **3I** was determined at –70°C and a view of the molecule is given in Fig. 5; structural parameters are listed in Table 7. The structure consists of an essentially linear Os_3Mn chain with an isocyanide ligand attached to each Os atom. The halide is coordinated, once again, to the terminal Os atom in a site that is *cis* to both the Os–Os bond and a *t*-BuNC ligand.

© 2002 NRC Canada

Fig. 5. Molecular stucture of $(OC)_3(I)(CN\text{-}t\text{-}Bu)OsOs(CO)_3(CN\text{-}t\text{-}Bu)Os(CO)_3(CN\text{-}t\text{-}Bu)OsMn(CO)_5$ (**31**).

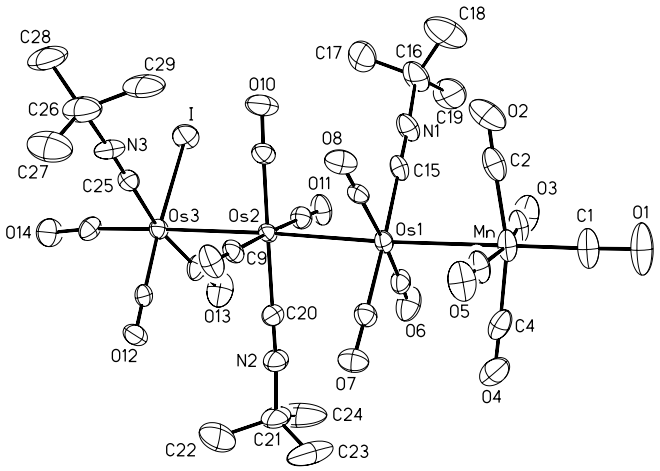

Fig. 6. The ^{13}C NMR spectrum (CO region) of $(OC)_4(t\text{-BuNC})OsRe(CO)_4$ (Br) (^{13}CO enriched) in CH_2Cl_2–CD_2Cl_2 (4:1) at −40°C. The assignment of the signals is given in the inset (L = *t*-BuNC).

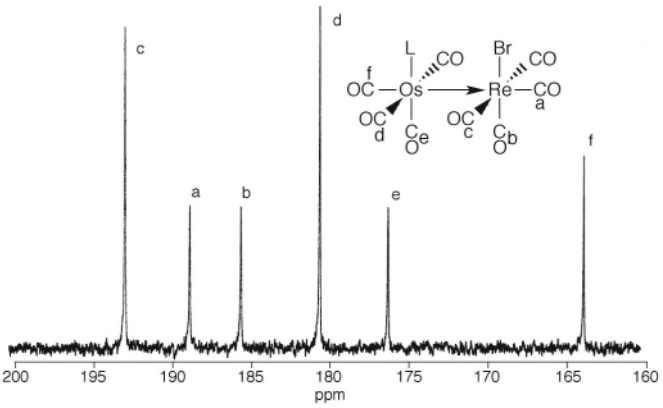

[2] $3Os(CO)_4(L) + Mn(CO)_5(X) \xrightarrow[\text{hexane}]{25\ °C} \underset{\mathbf{3X}}{X\text{–}Os(L)\text{–}Os(L)\text{–}Os(L)\text{–}Mn\text{–}} + CO$

(or **2X**)

$L = CNBu^t$

X = Cl, Br, I

The Os—Mn distance in **3I** at 2.870 (1) Å is the shortest of the four Os—Mn lengths determined in this study and some 0.05 Å shorter than that in **1I**. The Os—Os lengths 2.8894(5) and 2.8928(5) Å in **3I** are not significantly different from the Os—Os lengths in **2ClA** and **2BrB**, and comparable to the Os—Os lengths in $Os_3(CO)_{12}$. From a ground state point of view, therefore, the metal–metal bonds in **3I** appear strong.

The ^{13}C NMR spectrum of ^{13}CO-enriched **3Cl** (Table 3) has two signals in a 4:1 ratio to low field of δ 215 assigned to the carbonyls on manganese, and eight signals to high field of δ 195 assigned to the carbonyls attached to the osmium atoms. The latter signals are of intensity 1 except that at δ 194.8, which is of intensity 2. The spectrum is consistent with the view that **3Cl** has the same structure as found for **3I** in the solid state if two of the resonances are degenerate. As in the spectrum of **2ClA**, because the terminal osmium atom is chiral each carbonyl attached to an osmium atom is chemically different. The methyl resonances in both the ^1H NMR spectra of **3X** (and in ^{13}C NMR spectrum of **3Cl**) show two resonances in the ratio of 2:1. It is probable that the signals due to the methyl groups of the CN-*t*-Bu groups coordinated to the two internal osmium atoms are degenerate.

Only one isomer of **3X** was isolated and it can be assumed to be the result of addition of $Os(CO)_4(CN\text{-}t\text{-}Bu)$ to the major isomer of **2X** (i.e., **2XA**). The substitution of a carbonyl ligand of the $Os(CN\text{-}t\text{-}Bu)_2(X)(CO)_2$ unit in **2XB** would be expected to be slower than in **2XA** for both steric and electronic reasons. The presence of an additional CN-*t*-Bu ligand on the terminal Os atom would block the substitution and increase the strength of the remaining Os–CO bonds.

Attempts to prepare complexes with still longer metal chains have so far been unsuccessful. Stirring $Mn(CO)_5(X)$ in solution with a large excess of $Os(CO)_4(CN\text{-}t\text{-}Bu)$ resulted in only **3X** being formed. Carrying out the same reactions at elevated temperatures resulted in decomposition.

Binuclear OsRe complexes

Complexes of formula $(OC)_4(t\text{-BuNC})OsRe(CO)_4(X)$ (i.e., with dative Os–Re bonds) were synthesized according to eq. [3] as air-stable, yellow crystals. (It was found that the dimeric rhenium precursor gave purer products than the

[3] $2Os(CO)_4(L) + [Re(\mu\text{-}X)(CO)_4]_2$

X = Cl, Br, I

$\xrightarrow[\text{toluene}]{45°\ C} 2(OC)_4(L)OsRe(CO)_4(X)$

1ReX

corresponding $Re(CO)_5(X)$ complexes.) The formulation of the products with a dative metal–metal bond is clearly indicated by ^{13}C NMR spectroscopy (e.g., Fig. 6). In particular, the complexes exhibit three resonances in a 2:1:1 ratio in the region δ 184–194 attributed to the carbonyls of the $Re(CO)_4(X)$ moiety (Table 2). These signals show little quadrupolar broadening presumably because of the large field gradient through the molecule arising from the polar nature of the dative Os–Re bond causing rapid quadrupolar relaxation.

Attempts to isomerize the $(OC)_4(t\text{-BuNC})OsRe(CO)_4(X)$ complexes by heating them in solution at 60°C only resulted in decomposition. It has previously been found that, like nondative metal–metal bonds, dative metal–metal bonds appear strongest when both metals are third-row transition elements (2, 4, 25). The increased strength of the Os–Re bond would contribute to the barrier to the isomerization of the **1ReX** complexes compared with that of the Mn analogues. We point out here that although $(Me_3P)(OC)_4(Br)OsRe(CO)_5$ is known it was not prepared by isomerizarion of

© 2002 NRC Canada

Scheme 4.

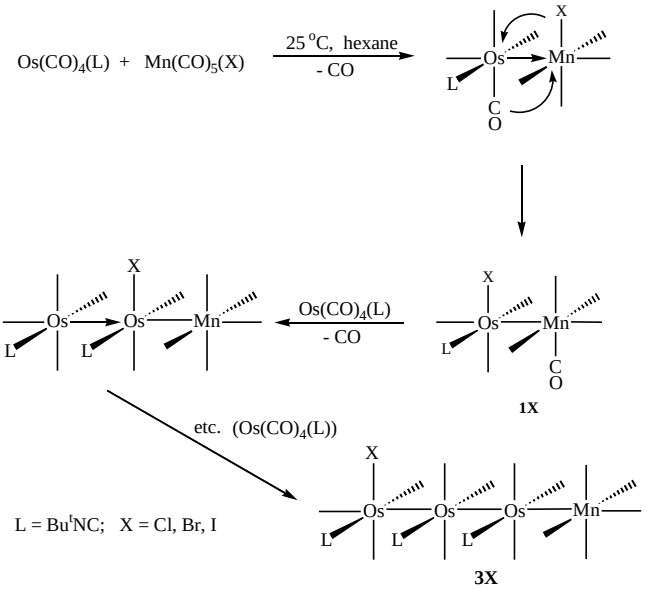

$(Me_3P)(OC)_4OsRe(Br)(CO)_4$, but rather by reaction of $(Me_3P)(OC)_4(H)OsRe(CO)_5$ with CBr_4 (12).

Conclusions

We have previously observed the isomerization of $(Me_3P)(OC)_4OsRu(CO)_3(SiCl_3)(Br)$ with a dative Os–Ru bond to $(Me_3P)(OC)_4(Br)OsRu(CO)_3(SiCl_3)$ with a nondative Os–Ru bond (11). This type of migration has been exploited for the synthesis of $(X)[Os(CO)_3(CN\text{-}t\text{-}Bu)Os]_nMn(CO)_5$ complexes with n = 1, 2, 3. It is believed that there is initial replacement of CO in the $Mn(CO)_5(X)$ or $Os(CO)_3(CN\text{-}t\text{-}Bu)(X)$ unit by the $18e^-$ ligand $Os(CO)_4(CN\text{-}t\text{-}Bu)$. This is followed by rearrangement to the isomer with a nondative metal–metal bond by migration of the halogen ligand to the donor Os atom with concomitant migration in the reverse direction of a carbonyl ligand. This is summarized in Scheme 4.

There are a number of factors involved in the successful synthesis of the Os_nMn complexes. The $18e^-$ $Os(CO)_4(L)$ must be sufficiently basic to form the initial donor–acceptor complex ($Os(CO)_5$ does not undergo these reactions). The noncarbonyl ligand (L) must be sterically undemanding so that it does not block entry of an additional $Os(CO)_4(L)$ ligand. With one exception, this reaction stops at the binuclear derivative for $Os(CO)_4(PR_3)$ ligands (2, 33). Furthermore, in complexes such as $(Me_3P)(OC)_4OsW(CO)_5$ and $(Me_3P)(OC)_4OsRu(CO)_3(SiCl_3)(Br)$ the major isomer has the P ligand *trans* to the dative metal–metal bond (2, 12).

An additional requirement for the formation of the tri- and tetranuclear species is that the dative bond in the intermediates should not be too strong. For example, the $(OC)_4(t\text{-}BuNC)OsRe(CO)_4(X)$ complexes do not isomerize. In addition, the $1e^-$ ligand on the acceptor atom should readily allow the formation of the bridged intermediate. In previous work, we have shown that for $(Me_3P)(OC)_4OsRu(CO)_3(SiCl_3)(X)$ compounds isomerization occurs immediately for X = H and slowly for X = halide. On the other hand, $(Me_3P)(OC)_4OsRu(CO)_3(SiCl_3)_2$ does not undergo this rearrangement (11). Attempts to further exploit this reaction for the preparation of complexes with still longer metal chains are planned.

Acknowledgments

We thank the Natural Sciences and Engineering Research Council of Canada (NSERC) and St. Mary's University for financial support.

References

1. F.W.B Einstein, R.K Pomeroy, P. Rushman, and A.C. Willis. J. Chem. Soc. Chem. Commun. 854 (1983).
2. H.B. Davis, F.W.B. Einstein, P.G. Glavina, T. Jones, R.K. Pomeroy, and P. Rushman. Organometallics, **8**, 1030 (1989).
3. J.A. Shipley, R.J. Batchelor, F.W.B. Einstein, and R.K. Pomeroy. Organometallics, **10**, 3620 (1991).
4. F. Jiang, J.L. Male, K. Biradha, W.K. Leong, R.K. Pomeroy, and M.J. Zaworotko. Organometallics, **17**, 5810 (1998).
5. F.W.B. Einstein, R.K. Pomeroy, P. Rushman, and A.C. Willis. Organometallics, **4**, 250 (1985).
6. F. Jiang, J.L. Male, K. Biradha, W.K. Leong, R.K. Pomeroy, and M.J. Zaworotko. Can. J. Chem. **77**, 1327 (1999).
7. F. Jiang, H.A. Jenkins, K. Biradha, H.B. Davis, R.K. Pomeroy, and M.J. Zaworotko Organometallics, **19**, 5049 (2000).
8. (*a*) A.A. Del Paggio, E.L. Muetterties, D.M. Heinekey, V.W. Day, and C.S. Day. Organometallics, **5**, 575 (1986); (*b*) L.W. Arndt, M.Y. Darensbourg, T. Delord, and B.T. Bancroft. J. Am. Chem. Soc. **108**, 2617 (1986); (*c*) D.A. Roberts, W.C. Mercer, G.L. Geoffroy, and C.G. Pierpont. Inorg. Chem. **25**, 1439 (1986); (*d*) R. Usón, J. Forniés, P. Espinet, C. Fortuño, M. Tomas, and A.J. Welch. J. Chem. Soc. Dalton Trans. 3005 (1988).
9. (*a*) F.H. Antwi-Nsiah, O. Oke, and M. Cowie. Organometallics, **15**, 1042 (1996); (*b*) T. Tanase, H. Toda, K. Kobayashi, and Y. Yamamoto. Organometallics, **15**, 5272 (1996); (*c*) M. Knorr, P. Braunstein, A. Tiripicchio, and F. Ugozzoli. J. Organomet. Chem. **526**, 105 (1996); (*d*) S. Takemoto, S. Kuwata, Y. Nishibayashi, and M. Hidai. Inorg. Chem. **37**, 6428 (1998); (*e*) K. Mashima, A. Fukumoto, H. Nakano, Y. Kaneda, K. Tani, and A. Nakamura. J. Am. Chem. Soc. **120**, 12151 (1998); (*f*) E.M. Lopez, D. Miguel, J. Perez, V. Riera, C. Bois, and Y. Jeannin. Organometallics, **18**, 490 (1999); (*g*) S. Kabashima, S. Kuwata, and M. Hidai. J. Am. Chem. Soc. **121**, 7837 (1999). (*h*) T. Tanase, R.A. Begum, H. Toda, and Y. Yamamoto. Organometallics, **20**, 968 (2001).
10. (*a*) W.-H. Chan, Z.-Z. Zhang, T.C.W. Mak, and C.-M. Che. J. Chem. Soc. Dalton Trans. 803 (1998); (*b*) T. Yamaguchi, F. Yamazaki, and T. Ito. J. Am. Chem. Soc. **121**, 7405 (1999).
11. M.M. Fleming, R.K. Pomeroy, and P. Rushman. J. Organomet. Chem. **278**, C33 (1984).
12. F.W.B. Einstein, M.C. Jennings, R. Krentz, R.K. Pomeroy, P. Rushman, and A.C Willis. Inorg. Chem. **26**, 1341 (1987).
13. J.D. Atwood and T.L. Brown. J. Am. Chem. Soc. **97**, 3380 (1975).
14. D.J. Darensbourg. Adv. Organomet. Chem. **21**, 113 (1982).
15. F. Jiang, H.A. Jenkins, G.P.A. Yap, and R.K. Pomeroy. Inorg. Chem. Commun. **3**, 685 (2000).
16. K. Reimer, A. Shaver, M.L. Quick, and R.J. Angelici. Inorg. Synth. **28**, 154 (1990).
17. G. Dolcetti and J.R. Norton. Inorg. Synth. **16**, 35 (1976).
18. G.M. Sheldrick. SHELXTL v. 5.10; Bruker AXS, Madison, WI, 1997.

© 2002 NRC Canada

19. J.L. Male. Ph.D. thesis. Simon Fraser University, Vancouver, British Columbia. 1996.
20. F.W.B. Einstein, P.G. Glavina, R.K. Pomeroy, P. Rushman, and A.C. Willis J. Organomet. Chem. **317**, 255 (1986).
21. A.B. Antonova, S.V. Kovalenko, E.D. Korniyets, A.A. Johansoson, Yu.T. Struchov, and A.I. Yanovsky. J. Organomet. Chem. **267,** 299 (1984).
22. M.P. Jensen, W. Henerson, D.H. Johnston, and M. Sabat. J. Organomet. Chem. **394**, 121 (1990).
23. M.R. Churchill, K.N. Amoh, and H.J. Wasserman. Inorg. Chem. **20**, 1609 (1981).
24. M.R. Churchill and B.G. DeBoer. Inorg. Chem. **16**, 878 (1977).
25. H. Nakatsji, M. Hada, and A. Kawashima. Inorg. Chem. **31**, 1740 (1992).
26. P.M. Treichel. Comprehensive organometallic chemistry. Vol. 4. *Edited by* G. Wilkinson, F.G.A. Stone, and E. Abel. Pergamon Press, Oxford. 1982. Chap. 29.
27. N.M. Boag and H.D. Kaesz. Comprehensive organometallic chemistry. Vol. 4. *Edited by* G. Wilkinson, F.G.A. Stone, and E. Abel. Pergamon Press, Oxford. 1982. Chap. 30.
28. D.F. Shriver and K.H. Whitmire. Comprehensive organometallic chemistry. Vol. 4. *Edited by* G. Wilkinson, F.G.A. Stone, and E. Abel. Pergamon Press, Oxford. 1982. Chap. 31.1.
29. (*a*) M. A. Bennet, M. I. Bruce, and T.W. Matheson. Comprehensive organometallic chemistry. Vol. 4. *Edited by* G. Wilkinson, F.G.A. Stone, and E. Abel. Pergamon Press, Oxford. 1982. Chap. 32.3; (*b*) 1982. Chap. 33; (*c*) A. F. Hill. Comprehensive organometallic chemistry II. Vol. 7. *Edited by* G. Wilkinson, F.G.A. Stone, and E. Abel. Pergamon Press, Oxford. 1995. Chap. 6.
30. N. Cook, L. Smart, and P. Woodward. J. Chem. Soc. Dalton Trans. 1744 (1977).
31. A.C. Willis, G.N. van Buuren, R. K. Pomeroy, and F.W.B. Einstein. Inorg. Chem. **22**, 1162 (1983).
32. Y.-S. Chen, S.-L. Wang, R.A. Jacobson, and R.J. Angeleci. Inorg. Chem. **25**, 1118 (1986).
33. R.J. Batchelor, H.B. Davis, F.W.B. Einstein, and R.K. Pomeroy. J. Am. Chem. Soc. **112**, 2036 (1990).
34. R.J. Batchelor, F.W.B. Einstein, R.K. Pomeroy, and J.A. Shipley. Inorg. Chem. **31**, 3155 (1992).
35. Y. Liu, W.K. Leong, and R.K. Pomeroy. Organometallics, **17**, 3387 (1998).
36. (*a*) B.E. Mann and B.F. Taylor. ^{13}C NMR data for organometallic compounds. Academic Press. New York. 1981. (*b*) R.F. Alex and R.K. Pomeroy. Organometallics, **6**, 2437 (1987).
37. H. Günther. NMR spectroscopy. Wiley, New York. 1980. p. 197.
38. (*a*) M. Tachikawa, S.I. Richter, and J.R. Shapley J. Organomet. Chem. **128**, C9 (1977); (*b*) S. Aime and D. Osella. J. Chem. Soc. Chem. Commun. 300 (1981); (*c*) A.K. Ma, F.W.B. Einstein, V.J. Johnston, and R. K. Pomeroy. Organometallics, **9**, 45 (1990).

© 2002 NRC Canada

Molar excess enthalpies for some systems containing the OH and (or) O groups in the same or in different molecules

Jose Carlos Cobos, Isaias Garcia de la Fuente, and Juan Antonio Gonzalez

Abstract: In this work, H_m^E data at 298.15 K for the systems 1-nonanol + *n*-C_{12}; 1-nonanol + *n*-C_{14}; 1-hexanol + 3,6,9-trioxaundecane; and 2-(2-butoxyethoxyethanol) + *n*-C_7 are reported. Measurements were carried out with a standard Calvet-type microcalorimeter. Molar excess functions, including enthalpies and entropies, are carefully examined to report on the main features of the studied solutions. Dipole–dipole interactions between ether molecules are, therefore, of great importance in both 1-alkanols + polyoxaalkanes mixtures and between hydroxyether molecules in alkoxyethanols + *n*-alkanes systems. In the second case, it has been attributed to the existence of intramolecular H-bonds in alkoxyethanols as well as to their higher effective-dipole moment in comparison to that of homologous 1-alkanols. DISQUAC is the only model that can be used to accurately represent thermodynamic functions (except molar excess volumes, V_m^E) of all of the solutions under study. UNIFAC underestimates dipole–dipole interactions in 1-alkanols + polyoxaalkanes and alkoxyethanols + *n*-alkanes systems. In exchange, the self-association of the alcohol is overestimated in mixtures of 1-nonanol with *n*-alkanes. Currently, the ERAS model can only be used to examine these solutions. The variation of the V_m^E with the size of the *n*-alkanes is well described.

Key words: excess functions, OH group, O group, interactions, models.

Résumé : Dans ce travail, on rapporte des données de H_m^E, à 298,15 K, pour les systèmes 1-nonanol + *n*-C_{12}; 1-nonanol + *n*-C_{14}; 1-hexanol + 3,6,9-trioxaundécane et 2-(2-butoxyéthoxyéthanol) + *n*-C_7. On a effectué les mesures à l'aide du microcalorimètre de type Calvet standard. Dans le but de bien redélimiter les caractéristiques principales des solutions étudiées, on a examiné en détail les fonctions d'excès, tant les entropies que les enthalpies. Ainsi, les interactions dipôle–dipôle entre les molécules d'éther sont de la plus grande importance dans les mélanges 1-alkanols + polyoxaalcanes et c'est aussi le cas entre les molécules d'hydroxyéthers dans les systèmes alkoxyéthanols + *n*-alcanes. Dans ce cas, on l'attribue à l'existence de liaisons hydrogènes intramoléculaires dans les alkoxyéthanols ainsi qu'à leur moment dipolaire effectif plus élevé par comparaison avec les 1-alkanols homologues. Le modèle DISQUAC est le seul qui peut être utilisé pour représenter de façon adéquate les fonctions thermodynamiques (à l'exception des volumes molaires en excès, V_m^E) de toutes les solutions étudiées. Le modèle UNIFAC sous-estime les interactions dipôle–dipôle dans les systèmes 1-alcanols + polyoxaalcanes et alkoxyéthanols + *n*-alcanes. Par ailleurs, l'autoassociation de l'alcool est surestimé dans les mélanges de 1-nonanol avec les *n*-alcanes. Actuellement, le modèle ERAS ne peut être utilisé que pour traiter ces solutions. On décrit aussi les variations dans les valeurs de V_m^E avec la taille des *n*-alcanes.

Mots clés : fonctions d'excès, groupe OH, groupe O, interactions, modèles.

[Traduit par la Rédaction]

Introduction

Mixtures containing oxygenated compounds, such as ethers (-O- group) and alkanols (-OH group) are of great importance from a practical point of view because they are increasingly used as additives to gasoline owing to their octane-enhancing and pollution-reducing properties (1, 2). Both groups may belong to the same molecule used to build hydroxyethers, which are nonionic amphiphile molecules, and consequently are very effective surfactants with a large number of applications (3–6). From this point of view, it is remarkable that they are considered as priority compounds by the Canadian Enviromental Protection Act in 1999 (www.ec.gc.ca).

Theoretically, solutions involving oxaalkanes are of high interest because of the possibility of studying of a number of effects (e.g., steric or proximity effects, cyclization) on the interactions present in the mixture. Binary systems of oxaalkanes and 1-alkanols are particularly interesting due to their complexity, resulting from the partial destruction of the self-associating alcohols by the active molecules of ethers, and of the new OH—O bonds created. The treatment of this class of systems is, therefore, is a strong test for any theoretical model. Moreover, it is a necessary step to study mixtures containing hydroxyethers, where the intramolecular effects between their -OH and -O- groups is of great importance (7–9).

The OHO project is part of a general program, the "TOM project" (thermodynamics of organic mixtures) (10, 11), in

Received 12 July 2001. Published on the NRC Research Press Web site at http://canjchem.nrc.ca on 20 March 2002.

J.C. Cobos,[1] I.G. de la Fuente, and J.A. Gonzalez. G.E.T.E.F. Dpto. de Termodinámica y Física Aplicada, Facultad de Ciencias, Universidad de Valladolid, 47071 Valladolid, Spain.

[1]Corresponding author (e-mail: jagl@termo.uva.es).

 DOI: 10.1139/V02-018 © 2002 NRC Canada

which mixtures containing the -O- and (or) -OH groups are investigated to determine and characterize the interactions where these groups participate.

We have contributed largely to the OHO project, reporting a large quantity of measurements on the vapor–liquid equilibria (VLE), liquid–liquid equilibria (LLE), solid–liquid equilibria (SLE), molar excess enthalpies (H_m^E), molar excess heat capacities at constant pressure (C_{pm}^E), and molar excess volumes (V_m^E) (see refs. 12–28).

Moreover, in terms of DISQUAC (10,11), a purely physical model based on the rigid lattice theory of Guggenheim (29), we have developed a detailed theoretical study of interactions, where some of the mentioned groups are involved. One of the most important conclusions from these studies is that DISQUAC can be applied to any type of mixtures assuming structure-dependent interaction parameters. DISQUAC, therefore, can be applied to systems where intermolecular H-bonds are present between the same class of molecules (homocoordination in, e.g., 1-alkanols + *n*-alkanes mixtures (30)) or between different molecules (heterocoordination, as in 1-alkanols + amines (31, 32); 1-alkanols + propanal (33); or oxaalkanes + $CHCl_3$ (34)). We have recently shown that DISQUAC is very useful in analyzing those systems where intramolecular H-bonds are also of great relevance (i.e. alkoxyethanols + alkanes mixtures (9)).

The Dortmund version of UNIFAC (35, 36), which ignores proximity or steric effects, fails to describe properties such as H_m^E or C_{pm}^E, which are very sensitive to the molecular structure for the complex mixtures mentioned above (for examples, see refs. 31, 37). Unfortunately, both the DISQUAC and UNIFAC models are based on rigid-lattice theories and $V_m^E = 0$.

The model more widely applied to simultaneously represent H_m^E and V_m^E is the so-called ERAS model (38), which combines the real-association solution model (39–42) (chemical contribution) with the physical contribution, expressed by the Flory equation of state (43). ERAS has been sucessfully applied to solutions such as 1-alkanols + alkanes (44); 1-alkanols + amines (31, 32,45); 1-alkanols + monooxalkanes (46, 47); or amines + *n*-alkanes (45). The lack of a systematic treatment in the framework of this model of 1-alkanols + polyoxaalkanes mixtures underlines the difficulty in studying such solutions. Indeed, only mixtures of 1-propanol with 2,5,8,-trioxanonane or 2,5,8,11-tetraoxadodecane have been studied, assuming that the polyethers are self-associated (48). On the other hand, ERAS can only be applied to those systems where association is expected and is not useful in treating, e.g., monooxalkanes + alkanes mixtures.

The purpose of this paper is to report H_m^E measurements at 298.15 K for the following mixtures: 1-nonanol + *n*-dodecane; 1-nonanol + *n*-tetradecane; 1-hexanol + 3,6,9-trioxaundecane; and 2-(2-butoxyethoxyethanol) + *n*-heptane. These systems will be also analyzed, when possible, in terms of DISQUAC, UNIFAC, and ERAS models.

Experimental

Materials

All the chemicals were from Fluka. Dodecane, 3,6,9-trioxaundecane, and 1-nonanol (purum > 98 mol%); and heptane, tetradecane, and 1-hexanol (puriss p.a., with purity > 99 mol%) were used without further purification. 2-(2-Butoxyethoxy)ethanol (stated purity > 98 mol%) was fractionally distilled many times in a glass 100-theoretical plates column, at a reflux ratio of approximately 25:1 at 1.6 kPa of reduced pressure, until no measurable impurities were observed in a vapor-phase chromatography trace analysis. The final purity was estimated to be 99.9%. Prior to the experimental measurements, all liquids were carefully dried over molecular sieve beads (Union Carbide type 4Å) from Fluka.

Densities of pure compounds at 298.15 K are in good agreement with literature values (49–51) and are equal to those found in previous works (see refs. 16, 18, 19).

Apparatus and procedure

A standard Calvet-type microcalorimeter, equipped with a batch mixing cell with a small (<2%) gas phase, and the experimental technique of Paz Andrade et al. (52) were used to determine H_m^E over the entire mol fraction range. Details of the experimental technique and of the accuracy attained have been described elsewhere (53–55). The calorimeter was thermostated to ±0.005 K and measurements were carried out at 298.15 K.

Binary mixtures were prepared by mass. All weighings were corrected for buoyancy effects, and the error on the final mol fraction is estimated to be less than 0.0001. Conversion to molar quantities is based on the relative atomic mass table issued by IUPAC (56).

Experimental results

The experimental results are listed in Tables 1–4. There are no data in literature for comparison. H_m^E (J mol^{-1}) measurements were fitted using equations of the type represented below.

$$[1] \qquad H_m^E = x_1(1-x_1)\sum_{i=0}^{k} A_i x_1^{i/2}$$

$$[2] \qquad H_m^E = x_1(1-x_1)\sum_{i=0}^{k} A_i (2x_1-1)^i$$

Coefficients in eqs. [1] and [2] were determined by least-squares regression with all points weighted equally. They are given in Table 5, together with the corresponding standard deviations (σ).

Theories

DISQUAC

Assessment of geometrical parameters

The total relative molecular volumes (r_i), surfaces (q_i), and the molecular surface fractions (α_{si}) of the compounds present in the mixture are usually calculated additively on the basis of the group volumes (V_G) and surfaces (A_G), as recommended by Bondi (57) and Kehiaian et al. (58). The geometrical parameters of the groups referred to in this work are given elsewhere (30, 58, 59).

© 2002 NRC Canada

Table 1. Molar excess enthalpies (H_m^E) at 298.15 K for the 1-nonanol (1) + *n*-dodecane (2) system.

x_1	H_m^E (J mol^{-1})	x_1	H_m^E (J mol^{-1})
0.0414	377	0.3726	661
0.0526	430	0.3983	657
0.0605	456	0.4499	654
0.0982	525	0.4973	635
0.1246	553	0.5443	608
0.1410	586	0.5961	574
0.1592	594	0.6446	524
0.1838	616	0.6955	466
0.1942	621	0.7373	416
0.2289	641	0.7959	341
0.2451	637	0.8402	259
0.2969	657	0.8982	169
0.3434	669	0.9342	100

Table 2. Molar excess enthalpies (H_m^E) at 298.15 K for the 1-nonanol (1) + *n*-tetradecane (2) system.

x_1	H_m^E (J mol^{-1})
0.0953	424
0.1504	562
0.3817	707
0.4363	708
0.4708	699
0.5270	676
0.5855	644
0.6318	603
0.6790	553
0.7905	391
0.8929	216

Table 3. Molar excess enthalpies (H_m^E) at 298.15 K for the 1-hexanol (1) + 3,6,9-trioxaundecane (2) system.

x_1	H_m^E (J mol^{-1})	x_1	H_m^E (J mol^{-1})
0.1195	566	0.6183	1345
0.1691	751	0.6574	1297
0.2148	916	0.7089	1204
0.2509	1020	0.7423	1119
0.3118	1185	0.7583	1086
0.3725	1291	0.8052	937
0.4172	1359	0.8575	742
0.4439	1381	0.8968	567
0.5206	1399	0.9518	284
0.5766	1392		

Table 4. Molar excess enthalpies (H_m^E) at 298.15 K for the 2-(2-butoxyethoxy)ethanol (1) + *n*-heptane (2) system.

x_1	H_m^E (J mol^{-1})	x_1	H_m^E (J mol^{-1})
0.0323	320	0.5143	1006
0.0504	435	0.5568	977
0.0979	634	0.6071	928
0.1493	762	0.6532	864
0.2085	869	0.6992	788
0.2599	927	0.7563	681
0.3085	966	0.8019	575
0.3533	995	0.8422	473
0.4091	1017	0.9000	303
0.4563	1020		

Equations

The equations used to calculate G_m^E and H_m^E are the same as in other applications (30). The interactional terms in the excess thermodynamic properties G_m^E and H_m^E contain a DIS (dispersive) and a QUAC (quasichemical) contribution, which are calculated independently by the classical formulas and then simply added. The degree of nonrandomness is thus expressed by the relative amounts of dispersive and quasichemical terms.

$$[3] \qquad G_m^E = G_m^{E,COMB} + G_m^{E,DIS} + G_m^{E,QUAC}$$

$$[4] \qquad H_m^E = H_m^{E,DIS} + H_m^{E,QUAC}$$

where $G_m^{E,COMB}$ is the Flory–Huggins combinatorial term (58, 60).

For the QUAC term, as coordination number the reference value was chosen, i.e. $z = 4$.

The temperature dependence of the interaction parameters g_{st}, h_{st}, and c_{pst} has been expressed in terms of the DIS and (or) QUAC interchange coefficients (30) $C_{st,1}^{DIS}$ and $C_{st,1}^{QUAC}$, where s and t are two functional groups present in the mixture (e.g., OH and O); and l = 1 (Gibbs energy: $C_{st,l}^{DIS/QUAC} = g_{st}^{DIS/QUAC}(T_0)/RT_0$); l = 2 (enthalpy: $C_{st,2}^{DIS/QUAC} = h_{st}^{DIS/QUAC}(T_0)/RT_0$) and l = 3 (heat capacity: $C_{st,3}^{DIS/QUAC} = c_{pst}^{DIS/QUAC}(T_0)/R$). $T_0 = 298.15$ K is the scaling temperature.

Modified UNIFAC (Dortmund version)

Modified UNIFAC (35) differs from the original UNIFAC (61) by the combinatorial term and the temperature dependence of the group interaction parameters (a_{nm}, b_{nm}, c_{nm}).

The equations used to calculate G_m^E and H_m^E are obtained from the fundamental equation for the activity coefficient γ_i of component,

$$[5] \qquad \ln \gamma_i = \ln \gamma_i^{COMB} + \ln \gamma_i^{RES}$$

where $\ln \gamma_i^{COMB}$ is the combinatorial term and $\ln \gamma_i^{RES}$ is the residual term.

Assessment of geometrical and interaction parameters

In modified UNIFAC, main groups are defined to improve correlations. Generally, they are divided in several subgroups, which have different geometrical parameters. The subgroups within the same main group, however, are assumed to have identical group energy-interaction parameters. The geometrical parameters, the relative van der Waals volumes, and the relative van der Waals surfaces of the different subgroups are not calculated from molecular parameters (as in the original UNIFAC) but fitted together with (a_{nm}, b_{nm}, c_{nm}) to the experimental values of the thermodynamic properties considered. The geometrical and interaction parameters are taken from literature (35, 36) and used without modification.

© 2002 NRC Canada

Table 5. Coefficients (A_i) and standard deviations (σ) for least-squares representation of H_m^E by eqs. [1] or [2].

System	A_0	A_1	A_2	A_3	A_4	A_5	σ (J mol^{-1})
1-Nonanol + *n*-C_{12} (eq. [1])	27 203	–141 155	353 036	–474 117	333 801	–97 333	5
1-Nonanol + *n*-C_{14} (eq. [1])	1 033	–2 447	2 721	–1 094			8
1-Hexanol + 3,6,9-trioxaundecane (eq. [2])	5 623	366	172	248			5
2-(2-Butoxyethoxyethanol) + *n*-C_7 (eq. [1])	17 129	–48 357	61 168	–26 836			3

The ERAS model

This model combines the real association solution model (39–42) with Flory's equation of state (43). The excess functions are written as

$$[6] \qquad X_m^E = X_{m,phys}^E + X_{m,chem}^E$$

where X = G (Gibbs energy), H (enthalpy), V (volume). In eq. [6], $X_{m,chem}^E$ is the chemical contribution, mainly due to association reactions, and $X_{m,phys}^E$ represents the physical contribution, resulting from the physical interactions between molecules.

The chemical contribution to the excess properties arises from the chemical interactions between the molecules, in particular hydrogen bonding. Thus, alcohol molecules (A) build linear chains of associated multimers

$$[7] \qquad A_n + A \overset{K_A}{\leftrightarrow} A_{n+1}$$

where n is the degree of self association, ranging from 1 to ∞.

The association constants are assumed to be independent from the chain length. Their temperature dependence is given by

$$[8] \qquad K_A = K_0 \exp[-(\Delta h_A^*/R)(1/T - 1/T_0)]$$

where K_0 is the equilibrium constant at the standard temperature T_0, and Δh_A^* is the enthalpy variation for eq. [7], which corresponds to the hydrogen bonds energy. Reaction [7] is also characterized by the volume change (Δv_A^*) related to the formation of the linear chains.

$X_{m,phys}^E$ is derived from Flory's equation of state (43), which is assumed to be valid not only for the pure components but also for the mixture

$$[9] \qquad \tilde{P}_i\tilde{V}_i / \tilde{T}_i = [\tilde{V}_i^{1/3} / (\tilde{V}_i^{4/3} - 1)] - 1 / (\tilde{V}_i\tilde{T}_i)$$

where i = A, B (second compound), or M (mixture). In eq. [9], $\tilde{V}_i = V_i/V_i^*$, $\tilde{P}_i = P_i/P_i^*$, and $\tilde{T}_i = T_i/T_i^*$ are the reduced parameters for volume, pressure, and temperature, respectively. The reduction parameters for the pure components V_i^*, P_i^*, T_i^* are calculated previous determination of density, thermal expansion coefficient, and compressibility, which can be obtained from experimental *P-V-T* data; they also depend on K_i, Δh_i^*, Δv_i^* (62, 63). The reduction parameters for the mixture P_M^* and T_M^* are calculated via certain mixing rules (44, 62, 63), where X_{AB}, the energetic interaction parameter characterizing the difference of dispersive intermolecular interactions between molecules A and B in the solution and in the pure components, is introduced. It is the only adjustable parameter of the physical part of H_m^E and V_m^E.

As in DISQUAC, the surface and volume of molecules are calculated using Bondi's method (57).

Discussion

1-Nonanol + *n*-alkanes mixtures

DISQUAC properly represents the H_m^E of these systems (Figs. 1–3) using the interaction parameters available in the literature (Table 6, refs. 30 and 79). The results are independent of the size of the of *n*-alkane. In exchange, discrepancies are observed for solutions of the shorter 1-alkanols with long chain *n*-alkanes. This has been attributed to a supplementary endothermic contribution to H_m^E resulting from the breaking of the orientational order of the longer *n*-alkanes (64, 65), which must be added to the main contributions of H_m^E including (*i*) that from the breaking of the H-bonds between alkanol molecules upon mixing; and (*ii*) dipole–dipole interactions between alkanol molecules. The effect of this supplementary contribution is to decrease the number of broken H-bonds in comparison to the case of a shorter *n*-alkane. The experimental H_m^E is, therefore, not as high as one could expect and consequently DISQUAC overestimates, e.g., H_m^E of the 1-propanol + *n*-pentadecane system (30). For longer 1-alkanols, however, the mentioned supplementary contribution vanishes, and DISQUAC correctly predicts the variation of H_m^E with the size of *n*-alkane.

ERAS parameters for these solutions and for pure compounds are listed in Table 7. Results of H_m^E are similar to those obtained using DISQUAC (Figs. 1–3). We must remark that the applied values of Δh_A^* (–25.1 kJ mol) and Δv_A^* (–5.6 cm^3 mol^{-1}) are common for all the 1-alkanols and widely used (44–47, 62, 63).

ERAS represents, rather accurately, V_m^E (Figs. 4 and 5). It is well-known that this magnitude in 1-alkanols + *n*-alkanes systems is the result of several opposing effects: changes in self-association and in physical interactions (dipole–dipole) between alkanol multimers and monomers leads to an increase in volume; a decrease in volume is due to changes in free volume and interstitial accomodation (66). The sign and magnitude of these contributions are sensitive to the lengths of the component molecules (67). For the 1-nonanol + *n*-heptane system, $V_m^E < 0$, except at very low mol fraction of the alcohol, since the fitting of the alkane into the alkanol multimer structure predominates. In constrast, in the 1-nonanol + tetradecane system $V_m^E > 0$, this negative contribution to V_m^E vanishes and the interactional contribution to V_m^E is more relevant.

This complex behaviour is well-described by ERAS decreasing the X_{AB} parameter with the size of the *n*-alkane (Table 7). The same behaviour is observed, for example, in ethanol + *n*-alkanes mixtures (44).

In UNIFAC, alkanols are characterized by the two main groups: OH and CH_3OH (35). The former is subdivided in

© 2002 NRC Canada

Fig. 1. H_m^E at 298.15 K for the 1-nonanol + *n*-heptane system. Points, experimental results (86); solid line, DISQUAC calculations; dashed lines, UNIFAC (UNIF) and ERAS calculations.

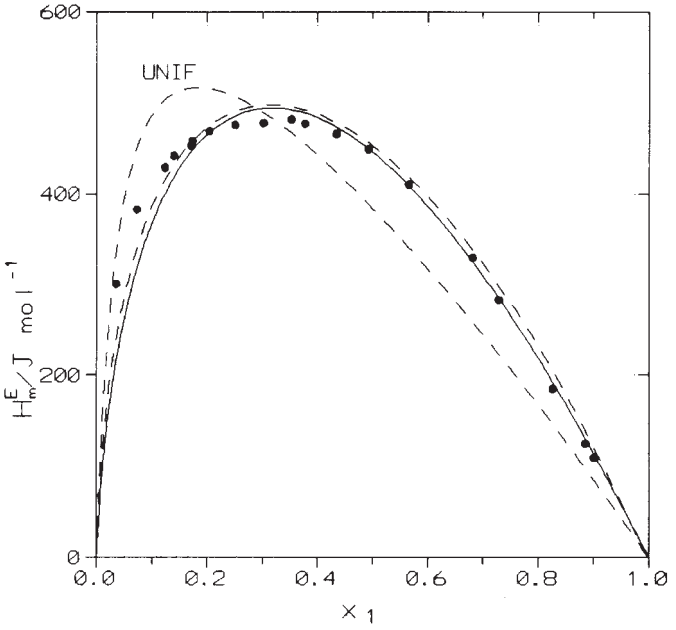

Fig. 2. H_m^E at 298.15 K for the 1-nonanol + *n*-dodecane system. Points, experimental results (this work); solid line, DISQUAC calculations; dashed lines, UNIFAC (UNIF) and ERAS calculations.

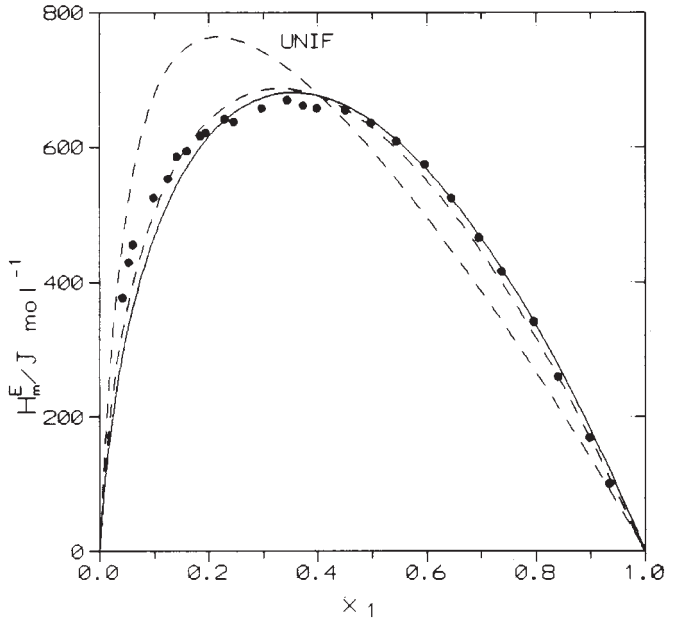

three subgroups: OH(p), OH(s), and OH(t), which represent the hydroxyl group in primary, secondary, and tertiary alkanols. CH_3OH is a group by itself that characterizes methanol. In this framework, UNIFAC provides H_m^E curves that are much more asymmetric than the experimental ones (Figs. 1–3). UNIFAC, therefore, overestimates the self-association of the alkanol.

Fig. 3. H_m^E at 298.15 K for the 1-nonanol + *n*-tetradecane system. Points, experimental results (this work); solid line, DISQUAC calculations; dashed lines, UNIFAC (UNIF) and ERAS calculations.

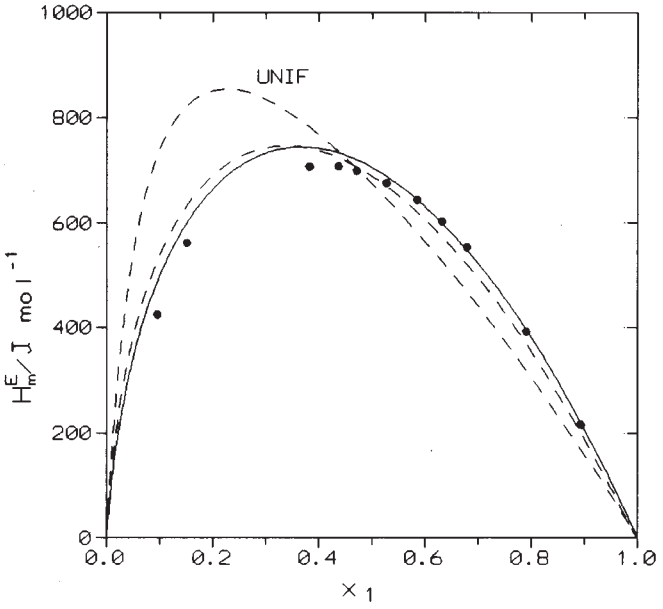

Fig. 4. V_m^E at 298.15 K for the 1-nonanol + *n*-heptane system. Points, experimental results (19); lines, ERAS calculations.

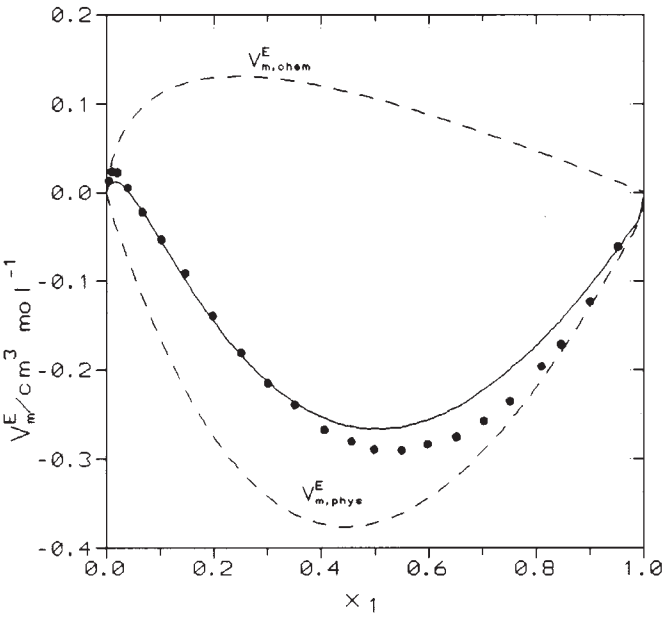

1-Hexanol + 3,6,9-trioxaundecane

We have previously reported H_m^E of systems containing 1-propanol, 1-butanol, 1-pentanol, 1-heptanol, or 1-decanol and the same triether (16). H_m^E (x_1 = 0.5) increases with the size of the alkanol (Fig. 6). The H_m^E variation is parallel to that in diethers or triethers + *n*-alkanes mixtures when the length of the alkane increases (Fig. 6, ref. 59). The H_m^E dependence with respect to mol fraction is nearly symmetrical (Fig. 7). Moreover, $G_m^E < H_m^E$ and TS_m^E is mainly positive (Ta-

© 2002 NRC Canada

Table 6. DISQUAC interchange coefficients for several contacts considered in this work.

Mixture	$C_{st,1}^{DIS}$	$C_{st,2}^{DIS}$	$C_{st,3}^{DIS}$	$C_{st,1}^{QUAC}$	$C_{st,2}^{QUAC}$	$C_{st,3}^{QUAC}$
OH–aliphatic contacts[a]						
1-Hexanol + *n*-alkanes	3.50	1.10	–21.50	12.20	14.40	71.10
1-Nonanol + *n*-alkanes	10.40	3.95	–33.50	12.20	12.60	71.10
1-Decanol + *n*-alkanes	12.80	5.00	–33.50	12.20	12.00	71.10
O–aliphatic contacts[b]						
3,6,9-Trioxaundecane + *n*-alkanes	10.6	18.2	0	2.9	3.7	0
OH–O contacts						
1-Hexanol + 3,6,9-trioxaundecane[c]	3.9	15.0	20.0	0.2	3.9	–5.5
2-(2-Butoxyethoxyethanol) + *n*-alkanes[d]	24.5	15.6	–100.	10.0	20.0	–10.0

[a]References 30 and 79.
[b]Reference 59.
[c]Reference 37.
[d]Reference 9.

Fig. 5. V_m^E at 298.15 K for the 1-nonanol + *n*-tetradecane system. Points, experimental results (18); lines, ERAS calculations.

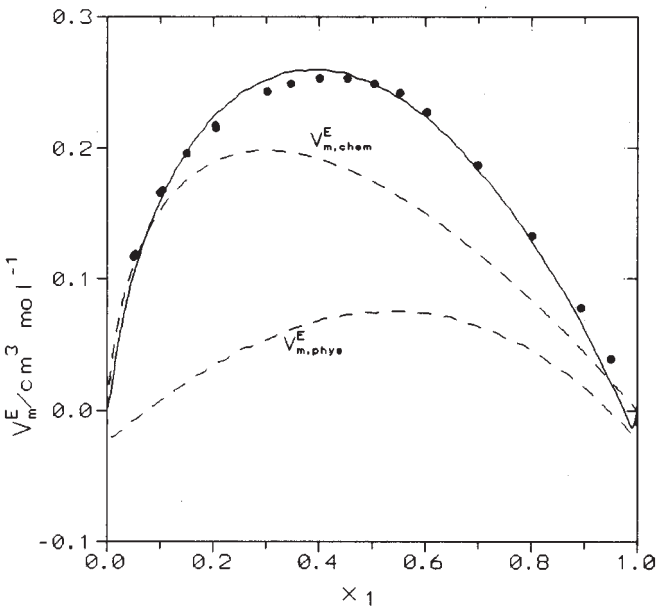

ble 8). All this contrasts with the behaviour of 1-alkanol + monoether systems, where, from 1-propanol, H_m^E varies very little with the chain length of the alkanol (Fig. 6, refs. 20 and 37) and is skewed towards low mol fractions of 1-alkanols. In addition $G_m^E \approx H_m^E$ and TS_m^E is s-shaped or slightly positive (Table 8). These features suggest that in mixtures containing polyoxaalkanes, dipole–dipole interactions between ether molecules play a major role.

In terms of group contributions, there are three different groups in 1-alkanols + oxaalkanes systems (OH, O, and CH_2 (aliphatic)) and three different contacts (OH–CH_2 (30, 79), O–CH_2 (59), and O–OH (37)). DISQUAC accurately represents the H_m^E of these solutions using structure-dependent interaction parameters. It is noteworthy that the OH–O contacts in mixtures of 1-alkanols with 3,6,9-trioxaundecane or other higher oxaalkanes are characterized by interchange coefficients (Table 6), which are derived, following simple rules, from those for the OH–O contacts in systems containing 2,5-dioxahexane or 3,6-dioxaoctane (37).

Table 7. ERAS parameters at 298.15 K for pure compounds in 1-nonanol + *n*-alkanes mixtures.

Compound	V_m (cm^3 mol^{-1})	V^* (cm^3 mol^{-1})	P^* (J cm^{-3})	T^* (K)
1-Nonanol[a]	174.92	146.78	424.4	6258
n-Heptane[b]	147.51	113.70	429.2	4652
n-Dodecane[b]	228.58	184.30	455.0	5339
n-Tetradecane[c]	261.09	213.33	453.7	5603

Note: The physical parameters for the studied mixtures are in J cm^{-3}: 1-nonanol + *n*-heptane, X_{AB} = 4.0; 1-nonanol + *n*-dodecane, X_{AB} = 3.0; 1-nonanol + *n*-tetradecane, X_{AB} = 2.5. For 1-nonanol, K_A = 92, Δh_A^* = –25.1 kJ mol^{-1}, Δv_A^* = –5.6 cm^3 mol^{-1}.
[a]This work.
[b]Reference 80.
[c]Reference 81.

UNIFAC predicts lower H_m^E than DISQUAC. To some extent, it may be due to UNIFAC failing when representing proximity effects in polyoxalkanes + solvents mixtures (68, 69).

At present, there is no treatment in terms of ERAS for these types of solutions.

2-(2-Butoxyethoxyethanol) + *n*-heptane

The H_m^E term arises from: (*i*) the breakening of inter- and intramolecular H-bonds and; (*ii*) the dipole–dipole interactions between alkoxyethanol molecules.

At equimolar composition, the studied systems show $G_m^E > H_m^E$ and large values of C_{pm}^E (9). This is typical behaviour for solutions including a self-associated compound, and thus it occurs in 1-alkanols + *n*-alkanes mixtures. As already mentioned, this self-association is produced via both inter- and intramolecular H-bonds (7–9).

The effective polarity of a molecule with a given dipole moment (μ) can be defined through the effective dipole moment ($\bar{\mu}$) an useful magnitude to examine the impact of polarity on bulk properties (9, 31, 32, 68, 70, 71). It is known that increasing the polarity of molecules leads to miscibility gaps when they are mixed with *n*-alkanes. For example, for the acetonitrile (μ = 3.5 D (49); $\bar{\mu}$ = 1.86) + *n*-C_6 system, the upper critical solution temperature (UCST) is 350.15 K (72), while for the 2-propanone (μ = 2.8 D (49), $\bar{\mu}$ = 1.2) + *n*-C_6 it is 238.15 K (73).

© 2002 NRC Canada

Fig. 6. H_m^E at 298.15 K and equimolar composition vs. *m*, the number of C atoms of 1-alkanols (in mixture with dibutylether or 3,6,9-trioxaundecane) or of *n*-alkanes (in systems with 3,6,9-trioxaundecane). For references of experimental data see ref. 37.

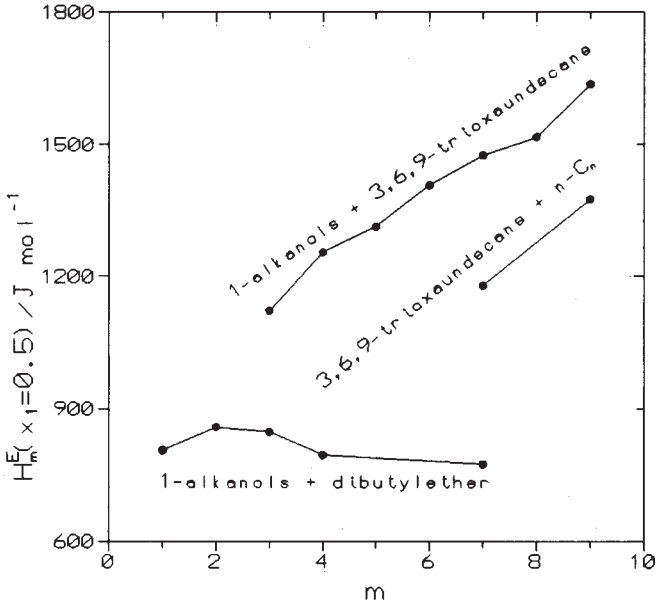

Fig. 7. H_m^E at 298.15 K for the 1-hexanol + 3,6,9-trioxaundecane system. Points, experimental results (this work); solid line, DISQUAC calculations; dashed line, UNIFAC calculations.

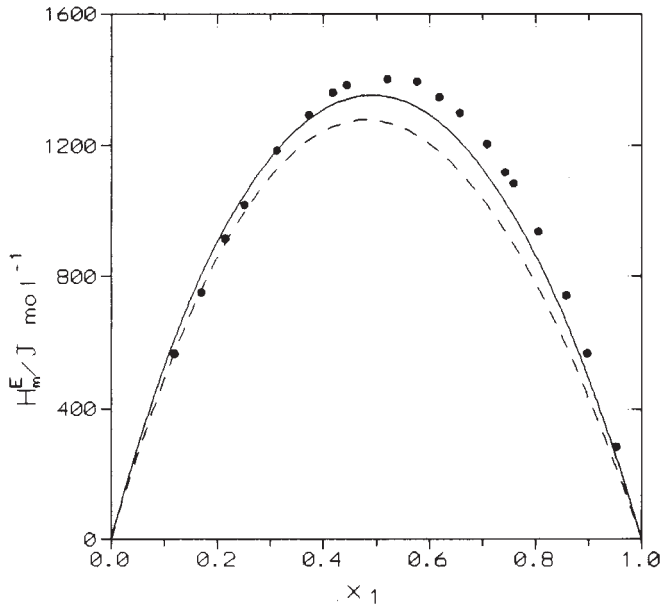

Table 8. Molar excess functions, Gibbs energies (G_m^E), enthalpies (H_m^E), and $TS_m^E = H_m^E - G_m^E$ at 298.15 K and at different mol fractions of the first component for several mixtures.

	G_m^E (J mol^{-1})			H_m^E (J mol^{-1})			TS_m^E (J mol^{-1})		
	x_1 = 0.1	x_1 = 0.5	x_1 = 0.9	x_1 = 0.1	x_1 = 0.5	x_1 = 0.9	x_1 = 0.1	x_1 = 0.5	x_1 = 0.9
1-Decanol + *n*-hexane	454[a]	723[a]	205[a]	354[b]	386[b]	95[b]	–100	–337	–110
1-Decanol + *n*-heptane	500[c]	836[c]	232[c]	386[b]	421[b]	105[b]	–114	–415	–127
1-Hexanol + dipropylether	289[d]	615[d]	187[d]	477[e]	710[e]	171[e]	188	95	–16
1-Hexanol + 3,5,9-trioxaundecane	134[c]	356[c]	130[c]	478[f]	1406[f]	554[f]	344	1050	424
2-(2-Butoxyethoxyethanol) + *n*-heptane	660[c]	1242[c]	367[c]	640[f]	1008[f]	305[f]	–20	–234	–62

[a]Reference 82.
[b]Reference 83.
[c]DISQUAC results.
[d]Reference 84.
[e]Reference 85.
[f]This work.

Alkoxyethanols (1) + *n*-alkanes (2) systems show higher UCSTs than the corresponding mixtures with homologous 1-alkanols[2] (25, 26). Because $\bar{\mu}$(alkoxyethanol) > $\bar{\mu}$(homomorphic 1-alkanol) (9), it implies that initial dipole–dipole interactions are more important in systems with alkoxyethanols than in alcoholic solutions.

For a given *n*-alkane, H_m^E (alkoxyethanol) > H_m^E (homologous 1-alkanol) (Table 8), indicating that intermolecular H-bonds are now less important. This may be due to (*i*) the presence of intramolecular H-bonds, which reduces the number of possible intermolecular H-bonds; and (*ii*) the major relative weight of the mentioned dipole–dipole interactions. Moreover, it should be noted that $H_m^{E,\infty}$ (alkoxyethanol (1) + *n*-alkane (2)) < $H_m^{E,\infty}$ (1-alkanol (1) + *n*-alkane (2)), as this magnitude, independent of the *n*-alkane (30, 74), is 23.4 kJ mol^{-1} at 303.15 K for 1-hexanol (75) and 21.8 kJ mol^{-1} for 1-octanol (76). In mixtures with *n*-heptane at 298.15 K, $H_m^{E,\infty}$ = 15.5 and 14.4 kJ mol^{-1} for 2-propoxyethanol and 2-butoxyethanol, respectively (9, 77). The lower $H_m^{E,\infty}$ values in alkoxyethanols mixtures have been interpreted assuming that the hydroxyether molecules become free through the destruction of the intermolecular H-bonds by the addition of the solvent molecules, and that each alkoxyethanol molecule forms an intramolecular H-bond between the -O- and OH- groups of the same molecule and thus stabilizes itself (77). For such reasons, the H_m^E curves are more symmetrical than those for alcoholic solutions, which are strongly shifted towards lower concentrations of the self-associated compound (Fig. 8).

The decreased importance of intermolecular H-bonds in alkoxyethanol mixtures is also supported by their higher TS_m^E values when they are compared with those of systems involving 1-alkanols (Fig. 9, Table 8).

[2]For example, other homologous molecules considered are 2-ethoxyethanol, 1-pentanol, 2-(2-butoxyethoxyethanol), and 1-decanol.

© 2002 NRC Canada

Fig. 8. H_m^E at 298.15 K for the systems 1-decanol + *n*-hexane (■, 83); and 2-(2-butoxyethoxyethanol) + *n*-heptane (●, this work). Solid lines, DISQUAC calculations; dashed line, UNIFAC results for the mixture including 2-(2-butoxyethoxyethanol).

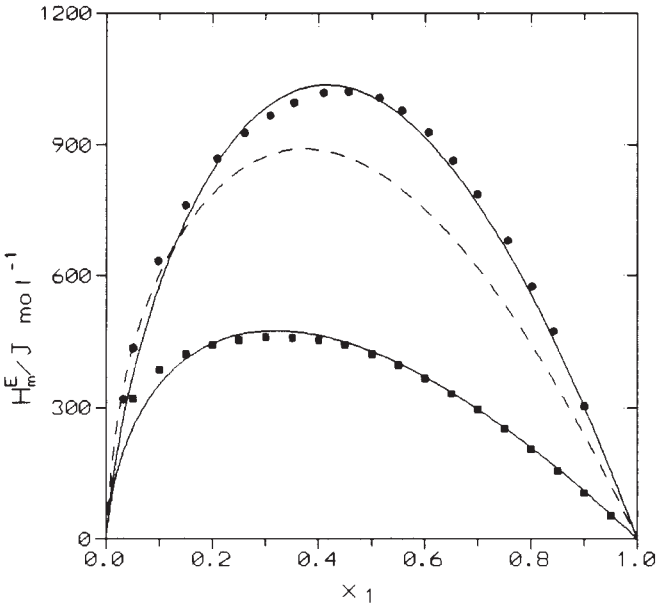

Fig. 9. TS_m^E at 298.15 K for the systems 1-decanol + *n*-hexane (●) and 2-(2-butoxyethoxyethanol) + *n*-heptane (—) (for references, see Table 8).

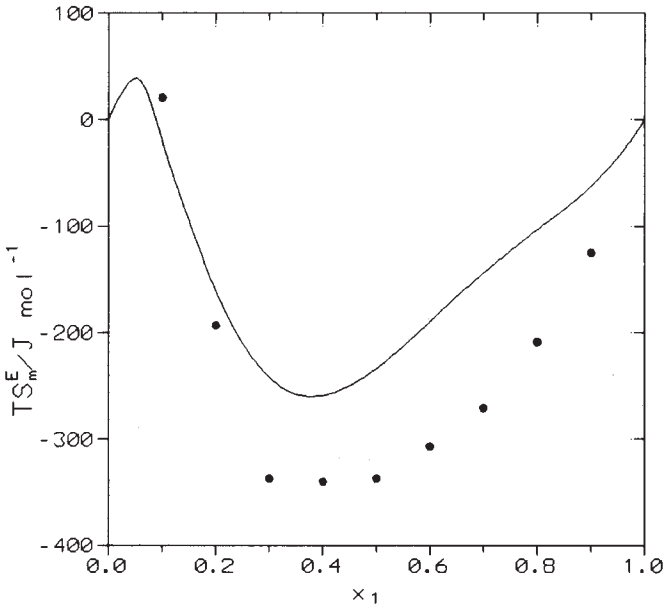

All these features underline the decreased importance of intermolecular H-bonds in alkoxyethanol solutions. DISQUAC accurately represents H_m^E of alkoxyethanols + alkanes mixtures (Fig. 8, ref. 9). The interaction parameters for the OH–O contacts in $CH_3(CH_2)_mOCH_2$ $CH_2OCH_2CH_2OH$ + *n*-C_n systems are practically independent of the hydroxyether (9). Only the first dispersive parameter is different for 2-(2-methoxyethoxyethanol) (9), due to the very high UCSTs of solutions formed by this alkoxyethanol and alkanes (25).

UNIFAC H_m^E results are lower than those from DISQUAC (Fig. 8), implying that dipole–dipole interactions are underestimated, since the UNIFAC interaction parameters used are derived from data on 1-alkanols + oxaalkanes mixtures. The same result occurs in terms of DISQUAC when intramolecular effects are neglected (i.e., when using interaction parameters for the OH–O contacts determined as in UNIFAC) (78). Note that dipole–dipole interactions are actually more important in alkoxyethanols + alkanes mixtures than in 1-alkanols + ethers mixtures. For example, 2-methoxyethanol + *n*-C_7 at equimolar composition (9) is not miscible at room temperature, whereas this is not the case for the 1-butanol (1-alkanol homologous to 2-methoxyethanol) + methylpropylether (oxaalkane homologous to 2-methoxyethanol) system.

Conclusions

Measurements of H_m^E at 298.15 K for 1-nonanol + *n*-C_{12}, 1-nonanol + *n*-C_{14}, 1-hexanol + 3,6,9-trioxaundecane, and 2-(2-butoxyethoxyethanol) + *n*-C_7 have been reported.

Dipole–dipole interactions between ether molecules are of great importance in 1-alkanols + polyoxaalkanes mixtures and between hydroxyether molecules in alkoxyethanols + *n*-alkanes systems. In the second case, the importance of dipole–dipole interactions are due to not only the existence of intramolecular H-bonds in alkoxyethanols but also the higher effective dipole moment compared with that of homologous 1-alkanols.

DISQUAC is the only model that can be used to accurately represent the thermodynamic functions (except V_m^E) of the solutions examined. UNIFAC underestimates the dipole–dipole interactions in 1-alkanols + polyoxaalkanes and alkoxyethanols + *n*-alkanes systems. In exchange, the self-association of the alcohol is overestimated in mixtures of 1-nonanol with *n*-alkanes. The ERAS model only can be used, at present, to treat these solutions. The variation of the V_m^E with the size of the *n*-alkane is well described.

Acknowledgments

This work was supported by the "Consejería de Educación y Cultura de la Junta de Castilla y León y de la Unión Europea, F.S.E.," under the Project VA039/01 and by the "Programa National de I+D+I del MCyT (Spain)" under the Project PPQ2001–1664.

References

1. R.W. Reynolds, J.S. Smith, and T. Steinmetz. Prepr. -Am. Chem. Soc., Div. Pet. Chem. **20**, 255 (1975).
2. R. Csikos, J. Pallay, J. Laky, E.D. Radchenko, B.A. Englin, and J.A. Robert. Hydrocarbon Process. Int. Ed. **55**, 21 (1976).
3. A.V. Deo, N.R. Sanjana, S.B. Kulkarri, M.K. Ghrapurey, and A.B. Biswas. Nature (London), **187**, 870 (1960).
4. K. Kusano, J. Suurkuusk, and I. Wadso. J. Chem. Thermodyn. **5**, 757 (1973).
5. G. Roux, G. Perron, and J.E. Desnoyers. J. Solution Chem. **7**, 639 (1978).
6. M.I. Davis. Chem. Soc. Rev. **22**, 127 (1993).
7. L.S. Prabhumirashi. J. Chem. Soc. Faraday Trans 2, **74**, 1567 (1978).

© 2002 NRC Canada

8. R.L.Brinkley and R. Gupta. Ind. Eng. Chem. Res. **37**, 4823 (1998).
9. J.A. González, J.C. Cobos, F.J. Carmona, I. García de la Fuente, V.R. Bhethanabotla, and S.W. Campbell. Phys. Chem. Chem. Phys. **3**, 2856 (2001).
10. H.V. Kehiaian. Fluid Phase Equilib. **13**, 243 (1983).
11. H.V. Kehiaian. Pure Appl. Chem. **57**, 15 (1985).
12. J.C. Cobos, C. Casanova, G. Roux-Desgranges, and J.-P.E. Grolier. Thermochim. Acta, **137**, 241 (1989).
13. J.C. Cobos, C. Casanova, G. Roux-Desgranges, and J.-P.E. Grolier. J. Chem. Thermodyn. **19**, 791 (1987).
14. J.C. Cobos, I. García, C. Casanova, G. Roux-Desgranges, and J.-P.E. Grolier. Thermochim. Acta, **131**, 73 (1988).
15. J.C. Cobos, I. García, and C. Casanova. Can. J. Chem. **66**, 2618 (1988).
16. J.C. Cobos, I. García, J.A. González, and C. Casanova. J. Chem. Thermodyn. **22**, 383 (1990).
17. J.C. Cobos, I. García, C. Casanova, A.H. Roux, G. Roux-Desgranges, and J.-P.E. Grolier. Fluid Phase Equilib. **69**, 223 (1991).
18. I. García de la Fuente, J.F. Rodríguez, J.A. González, J.C. Cobos, and C. Casanova. J. Chem. Thermodyn. **24**, 23 (1992).
19. I. García de la Fuente, J.F. Rodríguez, J.A. González, J.C. Cobos, and C. Casanova. J. Solution Chem. **21**, 425 (1992).
20. A. Serna, I. García de la Fuente, J.A. González, J.C. Cobos, and C. Casanova. Fluid Phase Equilib. **110**, 361 (1995).
21. U. Domanska, and González. Fluid Phase Equilib. **129**, 139 (1997).
22. U. Domanska, and J.A. González. Fluid Phase Equilib. **147**, 251 (1998).
23. F.J. Carmona, F.J. Arroyo, I. García de la Fuente, J.A. González, and J.C. Cobos Can. J. Chem. **77**, 1608 (1999).
24. F.J. Arroyo, F.J. Carmona, I. García de la Fuente, J.A. González, and J.C. Cobos. J. Solution Chem. **29**, 743 (2000).
25. F.J. Carmona, J.A. González, I. García de la Fuente, and J.C. Cobos. J. Chem. Eng. Data, **44**, 892 (1999).
26. R. Martínez, J.A. González, I. García de la Fuente, and J.C. Cobos. J. Chem. Eng. Data, **45**, 1036 (2000).
27. F.J. Carmona, J.A. González, I. García de la Fuente, J.C. Cobos, V.R. Bhethanabotla, and S.W. Campbell. J. Chem. Eng. Data. **45**, 699 (2000).
28. F.J. Carmona, V.R. Bhethanabotla, S.W. Campbell, J.A. González, I. García de la Fuente, and J.C. Cobos. J. Chem. Thermodyn. **33**, 47 (2001).
29. E.A. Guggenheim. Mixtures. Oxford University Press, Great Britian. 1952.
30. J.A. González, I. García de la Fuente, J.C. Cobos, and C. Casanova. Ber. Bunsen-Ges. Phys. Chem. **95**, 1658 (1991).
31. J.A. González, I. García de la Fuente, and J.C. Cobos. Fluid Phase Equilib. **168**, 31 (2000).
32. J.A. González, I. García de la Fuente, and J.C. Cobos. Can. J. Chem. **78**, 1272 (2000).
33. J.A. González, I. García de la Fuente, and J.C. Cobos. J. Chem. Soc. Faraday Trans. **93**, 3773 (1997).
34. J.A. González, I. García de la Fuente, and J.C. Cobos. Phys. Chem. Chem. Phys. **1**, 275 (1999).
35. J. Gmehling, J. Li, and M. Schiller. Ind. Eng. Chem. Res. **32**, 178 (1993).
36. J. Gmehling, J. Lohmann, A. Jakob, J. Li, and R. Joh. Ind. Eng. Chem. Res. **37**, 4876 (1998).
37. S. Delcros, J.R. Quint, J.-P.E. Grolier, and H.V. Kehiaian. Fluid Phase Equilib. **113**, 1 (1995).
38. A. Heintz. Ber. Bunsen-Ges. Phys. Chem. **89**, 172 (1985).
39. C.B. Kretschmer and R. Wiebe. J. Chem. Phys. **22**, 1697 (1954).
40. H. Renon and J.M. Prausnitz. Chem. Eng. Sci. **22**, 299 (1967).
41. H.V. Kehiaian. Bull. Acad. Pol. Sci. **16**, 165 (1968).
42. H.V. Kehiaian and A.J. Treszczanowicz. Bull. Acad. Pol. Sci. **16**, 171 (1968).
43. P.J. Flory. J. Am. Chem. Soc. **87**, 1833 (1965).
44. M. Bender and A. Heintz. Fluid Phase Equilib. **89**, 197 (1993).
45. H. Funke, M. Wetzel, and A. Heintz. Pure Appl. Chem. **61**, 1429 (1989).
46. T.M. Letcher and P.U. Govender. Fluid Phase Equilib. **140**, 207 (1997).
47. E.R. Rezanova, K. Kammerer, and R.N. Lichtenthaler. J. Chem. Eng. Data, **45**, 124 (2000).
48. S. Mohren and A. Heintz. Fluid Phase Equilib. **133**, 247 (1997).
49. J.A. Riddick, W.B. Bunger, and T.K. Sakano. Organic solvents. *In* Techniques of chemistry. Vol. II. *Edited by* A. Weissberger. Wiley-Interscience, New York. 1986.
50. TRC thermodynamic tables. Hydrocarbons. Thermodynamics research center, Texas A&M University, College Station, Texas. 1986.
51. TRC thermodynamic tables. Non-hydrocarbons. Thermodynamics research center, Texas A&M University, College Station, Texas. 1987.
52. M.I. Paz Andrade, E. Jiménez, and C. Hernández. Anal. Real Soc. Esp. Fis. Y Quim. Ser. B. **68**, 33 (1972).
53. J.C. Cobos, M.A. Villamañán, and C. Casanova. J. Chem. Thermodyn. **16**, 861 (1984).
54. J.C. Cobos and C. Casanova. Fluid Phase Equilib. **20**, 155 (1985).
55. J.C. Cobos and C. Casanova. J. Chem. Thermodyn. *19*, 751 (1987).
56. IUPAC commission on atomic weights and isotopic abundances 1985. Pure Appl. Chem. **58**, 1677 (1986).
57. A. Bondi. Physical properties of molecular crystals. Liquids and glasses. Wiley, New York. 1968.
58. H.V. Kehiaian, J.-P.E. Grolier, and G.C. Benson. J. Chim. Phys. **75**, 1031 (1978).
59. H.V. Kehiaian, M.R. Tiné, L. Lepori, E. Matteoli, and B. Marongiu. Fluid Phase Equilib. **46**, 131 (1989).
60. J.A. González, I. García de la Fuente, J.C. Cobos, C. Casanova, and A. Ait-Kaci. Fluid Phase Equilib. **112**, 63 (1995).
61. A. Fredenslund, R.L. Jones, and J.M. Prausnitz. AIChE J. **21**, 1086 (1975).
62. A. Heintz, and D. Papaioannou. Thermochim. Acta, **310**, 69 (1998).
63. A. Heintz, P.K. Naicker, S.P. Verevkin, and R. Pfestorf. Ber. Bunsenges Phys. Chem. **102**, 953 (1998).
64. M. Costas and D. Patterson. Thermochim. Acta, **120**, 161 (1987).
65. D. Patterson. J. Solution Chem. **23**, 105 (1994).
66. A.J. Treszczanowicz, O. Kiyohara, and G.C. Benson. Bull. Acad. Pol. Sci. Ser. Sci. Chim. 103, (1981).
67. A.J. Treszczanowicz and G.C. Benson. J. Chem. Thermodyn. **10**, 967 (1978).
68. J.A. González, I. García de la Fuente, and J.C. Cobos. Fluid Phase Equilib. **154**, 11 (1999).
69. H.S. Wu and S.I. Sandler. AIChE J. **35**, 168 (1989).
70. J.S. Rowlinson and F.L. Swinton. Liquid and liquid mixtures. 3rd ed. Butterworths, Great Britain. 1982.
71. E. Wilhelm, W. Egger, M. Vencour, A.H. Roux, M. Polednicek, and J.-P.E. Grolier. J. Chem. Thermodyn. **30**, 1509 (1998).
72. I.A. McLure, A. Trejo, and A.P. Ingham. Fluid Phase Equilib. **8**, 271 (1982).

© 2002 NRC Canada

73. G. Spinolo and R. Riccardi. Int. Data. Ser. Selec. Data Mixtures, Ser. A, 77 (1991).
74. R.H. Stokes and C. Burfitt. J. Chem. Thermodyn. **5**, 623 (1973).
75. M.K. Woycicka and W.M. Recko. Bull. Acad. Pol. Sci. Ser. Sci. Chem. **20**, 783 (1972).
76. C.G. Savini, D.R. Winterhalter, and H.C. Van Ness. J. Chem. Eng. Data, **10**, 168 (1965).
77. F. Kimura, S. Murakami, R. Fujishiro, and Y. Toshiyasu. Bull. Chem. Soc. Jpn. **50**, 791 (1977).
78. K. Tamura, A. Osaki, S. Murakami, H. Ohji, H. Ogawa, B. Laurent, and J.-P.E. Grolier. Fluid Phase Equilib. **156**, 137 (1999).
79. U. Domanska and J.A. González. Fluid Phase Equilib. **119**, 131 (1996).
80. J.M. Prausnitz, R.N. Lichtenthaler, and E. Gomes de Azevedo. Molecular thermodynamics of fluid-phase equilibria. 3rd ed. Prentice-Hall, New Jersey. 1987.
81. S. Zhu, S. Shen, G.C. Benson, and B.C.-Y. Lu. J. Chem. Thermodyn. **26**, 35 (1994).
82. S.A. Wieczorek. J. Chem. Thermodyn. **11**, 239 (1979).
83. M.K. Kumaran and G.C. Benson. J. Chem. Thermodyn. **16**, 175 (1984).
84. R. Garriga, S. Martínez, P. Pérez, and M. Gracia. Fluid Phase Equilib. **147**, 195 (1998).
85. D. Iñarrea, J. Valero, P. Pérez, M. Gracia, and C. Gutierrez Losa. J. Chem. Thermodyn. **20**, 193 (1988).
86. A. Amigo, J.L. Legido, R. Bravo, and M.I. Paz-Andrade. J. Chem. Thermodyn. **22**, 1059 (1990).

© 2002 NRC Canada

A theoretical study of the mechanism of 1,2-migrations in methoxysiloxycarbene

Paul G. Loncke, Timothy A. Gadosy, and Gilles H. Peslherbe

Abstract: Intramolecular rearrangements of methoxysiloxycarbene ($CH_3OCOSiH_3$) have been investigated by means of ab initio molecular orbital theory and hybrid density functional theory calculations. Particular attention was paid to 1,2-silyl migration from oxygen to the carbene carbon, and to the analogous 1,2-methyl migration for comparison. A combination of frontier molecular orbital (FMO) theory, natural bond orbital (NBO) analysis, and the theory of atoms in molecules (AIM) were used to shed light on the mechanistic details of these rearrangements. The present analyses clearly indicate that 1,2-silyl migration involves nucleophilic attack by the carbene lone pair at silicon, whereas 1,2-methyl migration seems to involve an anion-like shift of the methyl group from oxygen to the "vacant" carbene *p*-orbital. Finally, based on the computed relative Gibbs free energy barriers, it is apparent that 1,2-silyl migration is much more favorable than 1,2-methyl migration, in keeping with experimental observations.

Key words: carbenes, oxycarbenes, intramolecular rearrangements, 1,2-migrations, quantum chemistry, theory of atoms in molecules, natural bond orbital analysis

Résumé : On a étudié les réarrangements moléculaires du méthoxysiloxycarbène ($CH_3OCOSiH_3$) en faisant appel à des calculs ab initio basés sur la théorie des orbitales moléculaires et sur la théorie de la densité fonctionnelle hybride. On s'est intéressé particulièrement à la migration 1,2 du silyle de l'oxygène vers le carbone du carbène et, pour fins de comparaison, à celle de la migration analogue 1,2 du méthyle. On a utilisé une combinaison de la théorie de l'orbitale moléculaire frontière (OMF), à une analyse de l'orbitale de liaison naturelle (OLN) et à la théorie des atomes dans les molécules (ADM) pour comprendre les détails mécanistiques de ces réarrangements. Les analyses présentées indiquent clairement que la migration 1,2 du silyle implique une attaque nucléophile de la paire libre du carbène sur le silicium alors que la migration 1,2 du méthyle semble impliquer un déplacement semblable à celui d'un anion du groupe méthyle de l'oxygène vers l'orbitale p vacante du carbène. Enfin, sur la base des barrières relatives d'énergie libre de Gibbs, il est apparent que la migration 1,2 du silyle est beaucoup plus favorable que celle de la migration 1,2 du méthyle; ce qui est en accord avec les observations expérimentales.

Mots clés : carbènes, réarrangements intramoléculaires, migrations 1,2, chimie quantique, théorie des atomes dans les molécules, analyse de l'orbitale de liaison naturelle.

[Traduit par la Rédaction]

Introduction

Intramolecular 1,2-migrations from carbon atoms to the carbene centre in alkylcarbenes are fairly well understood (1–3). Extensive experimental and theoretical studies indicate that these rearrangements involve species migrating with anion-like character to the "vacant" carbene *p*-orbital. La Villa and Goodman (4), Bonneau et al. (5), and Moss et al. (6) have shown that alkyl substitution at the migration origin enhances 1,2-H migration rates in alkylhalocarbenes. Liu and Bonneau (7) have also reported that electron donating *p*-substituents accelerate 1,2-H migrations in *p*-substituted benzylchlorocarbenes. Moreover, density functional theory calculations by Keating et al. (8) indicate that electron donating substituents attached to the migration origin of singlet alkylchlorocarbenes lower the activation barriers for 1,2-H and 1,2-Ph migrations. These findings are all consistent with a mechanism involving anion-like migrating species, where the positive charge developing at the migration origin is stabilized by electron donating groups. On the contrary, electron donating substituents attached to the carbene carbon tend to decelerate 1,2-shifts from the migration origin. For instance, Moss et al. (6) have shown that 1,2-H and 1,2-C migrations in alkylfluorocarbenes are slower than those in the corresponding alkylchlorocarbenes. Similarly, La Villa and Goodman (9) found that the 1,2-H shift in methylchlorocarbene is slower than that in methylbromocarbene. Furthermore, ab initio calculations by Evanseck and Houk (10) suggest that 1,2-H migration barriers in alkylcarbenes are raised by electron donating substituents attached to the carbene carbon. These observations seem to suggest that the increased negative-charge density at the carbene carbon due to the presence of electron donating substituents has a net stabilizing effect, which results in decreased reactivity. Furthermore, the transition states for 1,2-

Received 1 August 2001. Published on the NRC Research Press Web site at http://canjchem.nrc.ca on 22 March 2002.

P.G. Loncke, T.A. Gadosy, and G.H. Peslherbe.[1] Centre for Research in Molecular Modeling, and Department of Chemistry & Biochemistry, Concordia University, Montréal, QC H3G 1M8, Canada.

[1]Corresponding author (e-mail: ghp@alcor.concordia.ca).

 DOI: 10.1139/V02-013 © 2002 NRC Canada

Scheme 1.

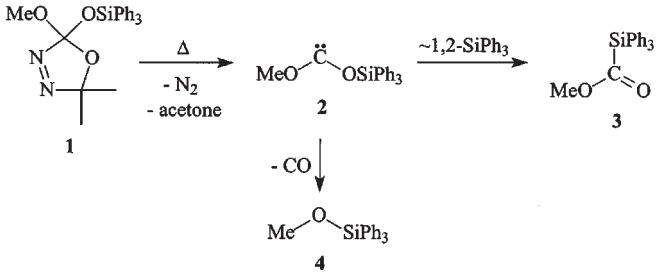

migrations may be destabilized as a result of the increased negative-charge density at the carbene carbon.

In contrast to 1,2-migrations from carbon atoms to the carbene centre, 1,2-migrations from oxygen atoms to the carbene carbon in oxy- and dioxycarbenes are relatively rare and more convoluted. Moss et al. (11) have shown that 1,2-acyl migrations in phenylacyloxycarbenes involve nucleophilic attack by the carbene lone pair at the acyl carbon, whereas Suh et al. (12) have found evidence for a mechanism involving anion-like migrating species in gas-phase 1,2-alkyl migrations in dialkoxycarbenes. On the other hand, Venneri and Warkentin (13) have reported experimental evidence indicating that methoxyallyloxycarbene rearrangements, including 1,2-allyl migrations, occur by a fragmentation–recombination mechanism involving methoxycarbonyl and allylic radicals. Investigations of intramolecular rearrangements in *p*-substituted benzyloxymethoxycarbenes (14) and benzyloxy(benzyloxy)carbenes (15) also support a fragmentation–recombination mechanism involving radicals. In addition, ab initio and density functional theory calculations by Reid and Warkentin (16) suggest that a fragmentation–recombination mechanism involving radicals is energetically feasible for rearrangements of ground-state singlet allyloxyhydroxycarbene.

Methoxytriphenylsiloxycarbene (**2**), generated by thermolysis of 2-methoxy-2-triphenylsiloxy-5,5-dimethyl-Δ^3–1,3,4-oxadiazoline (**1**), was recently reported to undergo 1,2-triphenylsilyl migration from oxygen to the carbene carbon and decarbonylation, affording the methyl triphenylsilylformate (**3**) and methyl triphenylsilyl ether (**4**), respectively, as illustrated in Scheme 1 (17). The reaction was carried out in benzene at 110°C, and the product ratio of ester **3** to ether **4** was found to be 1:3. Moreover, when oxadiazoline **1** was heated in toluene and in the presence of TEMPO, no evidence for products of radical trapping was found. This latter observation suggests that unlike the other dioxycarbene rearrangements (13–15) discussed in the previous paragraph, the rearrangements of carbene **2** do not occur via a pathway involving radicals. Thus, in the case of 1,2-triphenylsilyl migration, there could be two possible mechanisms. The triphenylsilyl group could migrate with anion-like character from oxygen to the vacant carbene *p*-orbital, as illustrated in Scheme 2*a*. Alternatively, the rearrangement could proceed via nucleophilic attack by the carbene lone pair at silicon, as shown in Scheme 2*b*.

To gain insight into the actual mechanisms for the intramolecular rearrangements of methoxytriphenylsiloxycarbene

Scheme 2.

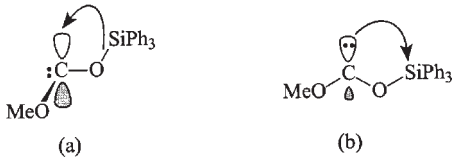

(**2**), we have performed ab initio molecular orbital theory and hybrid density functional theory calculations on methoxysiloxycarbene ($CH_3OCOSiH_3$) as a model system. A preliminary account of our calculations has been recently reported (17). In this article, we report a thorough investigation of 1,2-silyl migration in methoxysiloxycarbene, while we defer the study of other possible carbene rearrangements such as the decarbonylation pathway to a future publication (18). We pay particular attention to the actual mechanism of 1,2-silyl migration, which we shall contrast to that of 1,2-methyl migration.

Computational methods

Standard ab initio molecular-orbital calculations at the Hartree–Fock (HF) and second-order Møller–Plesset (MP2) levels of theory (19) and hybrid density functional theory calculations at the Becke3 Lee–Yang–Parr (B3LYP) level (20), together with 6–31+G* and 6–311+G(2d,p) basis sets (19) were carried out with the Gaussian 98 suite of programs (21). Ground-state minimum-energy structures were optimized with the Berny algorithm (22), while transition-state optimizations were performed using the eigenvector-following method (23–25). Frequency calculations were performed for stationary-point characterization and thermochemical data was obtained within the rigid rotor-harmonic-oscillator approximation using standard statistical mechanical methods implemented in Gaussian 98 (26). Natural bond-orbital (NBO) analysis (27) was also carried out using the NBO program, Version 3.1 (28) available in the Gaussian 98 suite.

A topological analysis of the gradient field of the electron density ($\rho(r)$) was carried out with the AIMPAC series of programs (29, 30), which is based on the theory of atoms in molecules (AIM). AIM provides a simple but rigorous means of partitioning the molecular electronic density into sub regions called basins, each belonging to a given nucleus (31). Each basin can be integrated affording properties usually ascribed to atoms.[2] A maximum, minimum, or saddle point in the topology of $\rho(r)$ is associated with critical points, where the first derivative $\nabla\rho(r)$ is zero. Critical points are classified according to their rank (ω) and signature (σ) as (ω, σ). ω refers to the number of nonzero curvatures of $\rho(r)$ at the critical point, and σ is the sum of the signs of the curvature at the critical point. For example, at a (3, –3) critical point or *attractor,* all three curvatures are negative and at a (3, –1) point or *bond critical point* two curvatures are negative and one is positive. The bond ellipticity ($\varepsilon = \lambda_1/\lambda_2 - 1$), where λ_1 and λ_2 are the two associated (negative) curvatures

[2] The numerical integration parameters used for integration over the atomic basins were 64 ϕ-planes, 48 θ-planes, and 96 radial points per integration within the β-sphere around the nucleus.

© 2002 NRC Canada

Fig. 1. Computed geometries for *trans-trans* **A**, *cis-trans* **B**, and *trans-cis* **C** conformers of methoxysiloxycarbene and rotational transition states, $\mathbf{TS_{AB}}$, and $\mathbf{TS_{AC}}$. Bond lengths are in angstroms and bond angles in degrees. HF, B3LYP (parentheses), and MP2 [brackets], parameters obtained with the 6–311+G(2d,p) basis set are listed.

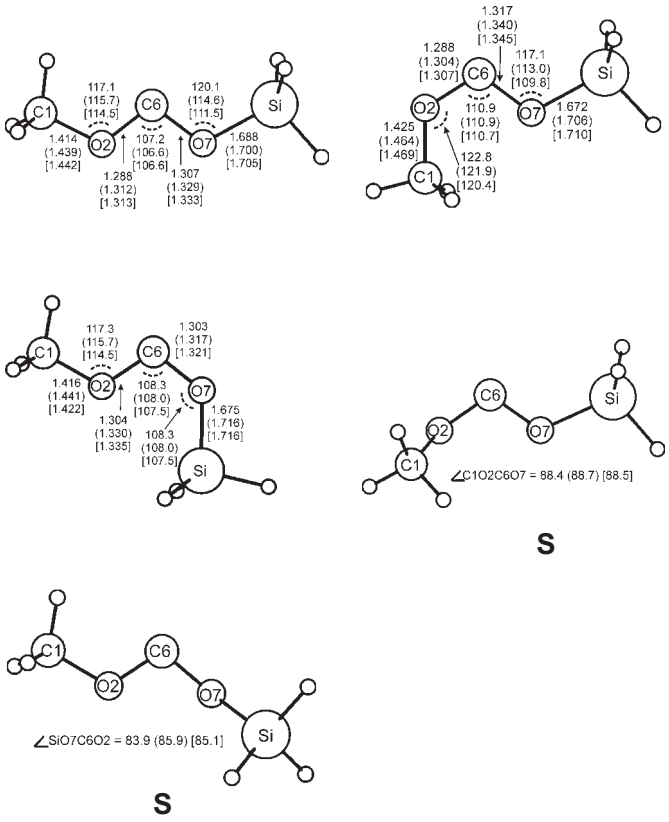

of ρ at a bond critical point directed along axes perpendicular to the bond path, defines a measure of the extent to which charge is preferentially accumulated in a given plane (31). Thus, in a bond with cylindrical symmetry, the ratio λ_1/λ_2 is one and ε is zero. On the other hand, when charge preferentially accumulates in a given plane, as one would expect for a π bond, the associated curvature λ_1 is larger than the curvature λ_2 in the perpendicular direction and thus ε is greater than zero.

Results and discussion

Methoxysiloxycarbene conformers

Geometric conformers computed for methoxysiloxycarbene are shown in Fig. 1. They include a *trans-trans* conformer (**A**), a *cis-trans* conformer (**B**) and a *trans-cis* conformer (**C**). Also shown, are transition-state geometries for *trans-trans* to *cis-trans* isomerization ($\mathbf{TS_{AB}}$), and *trans-trans* to *trans-cis* isomerization ($\mathbf{TS_{AC}}$). Selected geometric parameters are listed in Fig. 1, along with atom labels for identification in this discussion. From the relative Gibbs free energies given in Table 1,[3] it is apparent that **A** is the most stable carbene conformer. It should be mentioned that all calculations were carried out on the closed-shell singlet (S_0) state of the carbene since oxy- and dioxycarbenes are known to have large $S_0 \rightarrow T_1$ and $S_0 \rightarrow S_1$ energy gaps (32–34). For instance, Moss et al. (34) reported that the lowest triplet states of *trans-trans* and *cis-trans* dimethoxycarbene are 76.3 and 76.7 kcal mol^{-1}, respectively, above their corresponding singlet ground-state conformers, based on MP2/6–31G*//HF/6–31G* calculations. Furthermore, the open-shell singlet (S_1) states of these carbenes are reported to lie 104 and 109 kcal mol^{-1}, respectively, above their corresponding singlet S_0 states, according to CIS/INDO/S//HF/6–31G* calculations (34). Feller et al. (32) calculated vertical $S_0 \rightarrow T_1$ gaps for dihydroxycarbene at various levels of theory and found values ranging from 43.4 to 66.3 kcal mol^{-1}, while the lowest energy triplet carbene was found to be 26.4 to 50.0 kcal mol^{-1} above the lowest energy singlet carbene. In the case of methoxysiloxycarbene, the vertical $S_0 \rightarrow T_1$ gaps for **A**, **B**, and **C** computed at the CIS/6–31+G*//MP2/6–31+G* level are 57.8, 56.8, and 55.1 kcal mol^{-1}, respectively, while the $S_0 \rightarrow S_1$ gaps are 116.0, 118.1, and 118.4 kcal mol^{-1}. Moreover, optimization of triplet methoxysiloxycarbene at the MP2/6–31+G* level afforded two conformers that were 55.2 and 55.8 kcal mol^{-1} above the lowest singlet (S_0) state carbene conformer **A**.

Interestingly, the barrier for *trans-trans* **A** to *cis-trans* **B** isomerization (via $\mathbf{TS_{AB}}$) is considerably higher than that for *trans-trans* **A** to *trans-cis* **C** isomerization (via $\mathbf{TS_{AC}}$), as can be seen from the relative Gibbs free energies given in Table 1. This suggests that in conformer **A**, the methoxy oxygen O2, is a better π-electron donor than the siloxy oxygen O7, and consequently O2–C6 has more double-bond character than C6–O7. NBO perturbation-theory energy analysis (27) reveals that the stabilization energy due to $n_{O2} \rightarrow p_{C6}$ delocalization is generally greater than that for $n_{O7} \rightarrow p_{C6}$ interaction (Table 2), while AIM analysis (28–30) indicates that the electron density at the bond critical point ($\rho(r_c)$) between O2 and C6 is greater than that between C6 and O7 (Table 3). These findings are clearly in keeping with the greater double-bond character of the O2–C6 bond. In addition, both NBO and AIM atomic charges show that there is less negative charge on O2 than there is on O7, further supporting the idea that the methoxy oxygen O2 is a better π-electron donor than the siloxy oxygen O7. Moreover, the O2–C6 bond is found to be slightly shorter than the C6–O7 bond (Fig. 1), again supporting the greater double-bond character of O2–C6. Indeed, both the O2–C6 and C6–O7 bonds are expected to have π-type character, which is verified by the fact that the bond ellipticity (ε) is noticeably larger than zero for the two bond paths (Table 3). Notice that the O7–Si bond is virtually aligned with the vacant carbene *p*-orbital in $\mathbf{TS_{AC}}$, whereas the C1–O2 bond is better aligned with the same *p*-orbital in $\mathbf{TS_{AB}}$ (Fig. 1). These features may lead one to believe that stabilization due to $\sigma_{O7-Si} \rightarrow p_{C6}$ cation-like hyperconjugation in $\mathbf{TS_{AC}}$ is greater than that due to $\sigma_{C1-O2} \rightarrow p_{C6}$ hyperconjugation in $\mathbf{TS_{AB}}$, consequently resulting in a lower isomerization barrier via $\mathbf{TS_{AC}}$. According to our NBO perturbation-theory energy analysis, the stabiliza-

[3] Supplementary material may be purchased from the Depository of Unpublished Data, Document Delivery, CISTI, National Research Council Canada, Ottawa, ON K1A 0S2, Canada. For information on obtaining material electronically go to http://www.nrc.ca/cisti/irm/unpub_e.shtml.

© 2002 NRC Canada

Table 1. Relative Gibbs free energies (in kcal mol^{-1}) at 383.15 K and 1.0 atm.

Species	HF 6–31+G*	HF 6–311+G(2d,p)	B3LYP 6–31+G*	B3LYP 6–311+G(2d,p)	MP2 6–31+G*	MP2 6–311+G(2d,p)
A	0.0	0.0	0.0	0.0	0.0	0.0
B	3.3	3.7	2.0	2.3	1.9	2.0
C	2.1	2.8	1.7	2.3	1.8	2.6
$\mathbf{TS}_{AB}$	17.2	17.4	17.7	17.9	18.8	18.8
$\mathbf{TS}_{AC}$	7.1	7.5	7.4	7.7	8.6	8.6
D	–7.6	–7.2	–16.2	–15.8	–16.5	–17.4
E	–16.0	–15.5	–24.6	–24.8	–25.6	–26.4
$\mathbf{TS}_{AD}$	21.3	20.3	10.8	10.8	10.4	9.2
$\mathbf{TS}_{BE}$	21.1	20.5	9.5	9.6	9.3	8.3
F	–48.7	–50.3	–51.8	–53.1	–56.1	–57.6
G	–55.3	–56.6	–57.6	–58.8	–62.5	–63.6
$\mathbf{TS}_{AF}$	62.9	61.2	46.3	45.3	46.8	45.5
$\mathbf{TS}_{CG}$	63.9	62.3	46.8	46.0	47.4	46.3

Note: Gibbs free energies reported in this table are all relative to those for carbene conformer **A**, which are –517.804140, –517.899305, –519.696541, –519.879452, –518.492161, and –518.721227 hartrees at the HF/6–31+G*, HF/6–311+G(2d,p), B3LYP/6–31+G*, B3LYP/6–311+G(2d,p), MP2/6–31+G*, and MP2/6–311+G(2d,p) levels, respectively.

Table 2. Stabilization energies (in kcal mol^{-1}) computed from NBO perturbation-theory energy analysis for the methoxysiloxycarbene conformers.

	RHF		B3LYP	
	6–31+G*	6–311+G(2d,p)	6–31+G*	6–311+G(2d,p)
A				
$n_{O2}\rightarrow p_{C6}$	114.7	116.1	87.5	86.6
$n_{O7}\rightarrow p_{C6}$	95.8	95.8	76.9	77.0
$n_{C6}\rightarrow\sigma^{*}_{O7-Si}$	5.7	5.5	5.0	4.6
$n_{C6}\rightarrow RY^{*}_{Si}$. (total)	—	1.4	—	1.0
B				
$n_{O2}\rightarrow p_{C6}$	115.6	116.1	90.4	90.3
$n_{O7}\rightarrow p_{C6}$	89.7	90.9	70.1	70.8
$n_{C6}\rightarrow\sigma^{*}_{O7-Si}$	5.8	5.5	4.9	4.6
$n_{C6}\rightarrow RY^{*}_{Si}$. (total)	0.7	1.5	—	1.1
C				
$n_{O2}\rightarrow p_{C6}$	100.6	102.5	75.4	75.5
$n_{O7}\rightarrow p_{C6}$	97.3	96.1	79.0	78.1
$n_{C6}\rightarrow\sigma^{*}_{O7-Si}$	14.2	12.5	12.5	11.1
$n_{C6}\rightarrow RY^{*}_{Si}$. (total)	—	—	—	—
Transition state TS_{AD}				
$n_{O2}\rightarrow p_{C6}$	107.1	109.9	89.7	88.9
$n_{O7}\rightarrow p_{C6}$	223.5	220.2	154.5	152.8
$n_{C6}\rightarrow\sigma^{*}_{O7-Si}$	75.9	80.9	54.1	55.8
$n_{C6}\rightarrow RY^{*}_{Si}$. (total)	29.7	26.7	14.9	14.1
Transition state TS_{BE}				
$n_{O2}\rightarrow p_{C6}$	114.1	113.5	94.9	94.2
$n_{O7}\rightarrow p_{C6}$	202.0	203.3	137.8	137.5
$n_{C6}\rightarrow\sigma^{*}_{O7-Si}$	72.9	78.5	49.2	51.6
$n_{C6}\rightarrow RY^{*}_{Si}$. (total)	28.3	27.7	14.1	14.6

Note: The energetic importance of interactions between filled (donor) Lewis-type NBOs and empty (acceptor) non-Lewis NBOs are estimated via second-order perturbation theory analysis of the Fock matrix in the NBO basis, as discussed in ref. 27. The $n_{C6}\rightarrow RY^{*}_{Si}$ (total) denotes the stabilization energies resulting from interaction of n_{C6} with all RY^{*}_{Si} NBOs. The polarization coefficient on Si of the σ^{*}_{O7-Si} NBO about 85% for **A**, **B**, and **C**, and between 90 and 95% in $\mathbf{TS}_{AD}$ and $\mathbf{TS}_{BE}$.

© 2002 NRC Canada

Table 3. Properties of electron density at bond critical points for conformers **A**, **B**, and **C** of methoxysiloxycarbene obtained from AIM analysis.

	C1–O2	O2–C6	C6–O7	O7–Si
A				
HF/6–311+G(2d,p)				
$\rho(r_c)$ (e Å^{-3})	1.68	2.30	2.19	0.89
$\nabla^2\rho(r_c)$ (e Å^{-5})	–4.5	–5.4	–7.7	18.9
ε	0.01	0.21	0.28	0.05
B3LYP/6–311+G(2d,p)				
$\rho(r_c)$ (e Å^{-3})	1.62	2.19	2.11	0.84
$\nabla^2\rho(r_c)$ (e Å^{-5})	–12.3	–13.2	–15.5	14.6
ε	0.01	0.13	0.17	0.05
MP2/6–311+G(2d,p)				
$\rho(r_c)$ (e Å^{-3})	1.69	2.15	2.07	0.81
$\nabla^2\rho(r_c)$ (e Å^{-5})	–11.7	–10.7	–13.7	15.1
ε	0.00	0.13	0.17	0.05
B				
HF/6–311+G(2d,p)				
$\rho(r_c)$ (e Å^{-3})	1.64	2.28	2.13	0.87
$\nabla^2\rho(r_c)$ (e Å^{-5})	–6.6	–5.6	–6.7	18.5
ε	0.01	0.20	0.32	0.05
B3LYP/6–311+G(2d,p)				
$\rho(r_c)$ (e Å^{-3})	1.55	2.22	2.05	0.83
$\nabla^2\rho(r_c)$ (e Å^{-5})	–11.9	–12.5	–15.0	14.3
ε	0.00	0.11	0.20	0.05
MP2/6–311+G(2d,p)				
$\rho(r_c)$ (e Å^{-3})	1.55	2.16	2.00	0.80
$\nabla^2\rho(r_c)$ (e Å^{-5})	–12.3	–10.2	–13.3	14.7
ε	0.06	0.11	0.21	0.05
C				
HF/6–311+G(2d,p)				
$\rho(r_c)$ (e Å^{-3})	1.66	2.19	2.19	0.86
$\nabla^2\rho(r_c)$ (e Å^{-5})	–3.9	–5.0	–7.0	17.8
ε	0.01	0.26	0.27	0.03
B3LYP/6–311+G(2d,p)				
$\rho(r_c)$ (e Å^{-3})	1.61	2.09	2.14	0.80
$\nabla^2\rho(r_c)$ (e Å^{-5})	–12.0	–13.3	–13.9	13.2
ε	0.00	0.16	0.16	0.02
MP2/6–311+G(2d,p)				
$\rho(r_c)$ (e Å^{-3})	1.59	2.04	2.09	0.78
$\nabla^2\rho(r_c)$ (e Å^{-5})	–11.4	–11.4	–12.3	14.0
ε	0.00	0.17	0.16	0.02

Note: $\rho(r_c)$, $\nabla^2\rho(r_c)$, and ε represent the electronic charge density, the Laplacian of the charge density, and bond ellipticity, respectively.

tion energy resulting from $\sigma_{O7-Si} \rightarrow p_{C6}$ hyperconjugation in $\mathbf{TS_{AC}}$ appears to be negligible. We found, however, that $\sigma_{C1-O2} \rightarrow p_{C6}$ hyperconjugation in $\mathbf{TS_{AB}}$ yields a stabilization energy of 6.51 and 7.08 kcal mol^{-1} at the RHF level of theory with 6–31+G* and 6–311+G(2d,p) basis sets, respectively, and 2.23 and 2.05 kcal mol^{-1}, respectively, at the B3LYP level of theory with the same basis sets. Thus, it appears that cation-like hyperconjugation only plays a minor role, if any, in the determination of barrier heights for isomerization.

Silyl migration

We now focus on the mechanism for 1,2-silyl migration in methoxysiloxycarbene. Since no evidence was found for radical-based mechanisms in the rearrangements of methoxytriphenylsiloxycarbene (17), we considered two mechanistic possibilities for 1,2-silyl migration in methoxysiloxycarbene, as proposed earlier for 1,2-triphenylsilyl migration in methoxytriphenylsiloxycarbene (Scheme 2). One of the possibilities involves the silyl group migrating with anion-like character from oxygen to the vacant carbene *p*-orbital located essentially perpendicular to the carbene valence plane, similar to that illustrated in Scheme 2*a*. The other possibility involves nucleophilic attack by the carbene lone pair at silicon in the carbene valence plane, analogous to that shown in Scheme 2*b*.

In terms of frontier molecular orbital (FMO) theory, nucleophilic attack by the carbene lone pair at silicon ap-

© 2002 NRC Canada

Fig. 2. Plots of the highest occupied molecular orbital (HOMO) and the lowest unoccupied molecular orbital (LUMO) for conformer **A** of methoxysiloxycarbene obtained at the HF/6–311+G(2d,p) level.

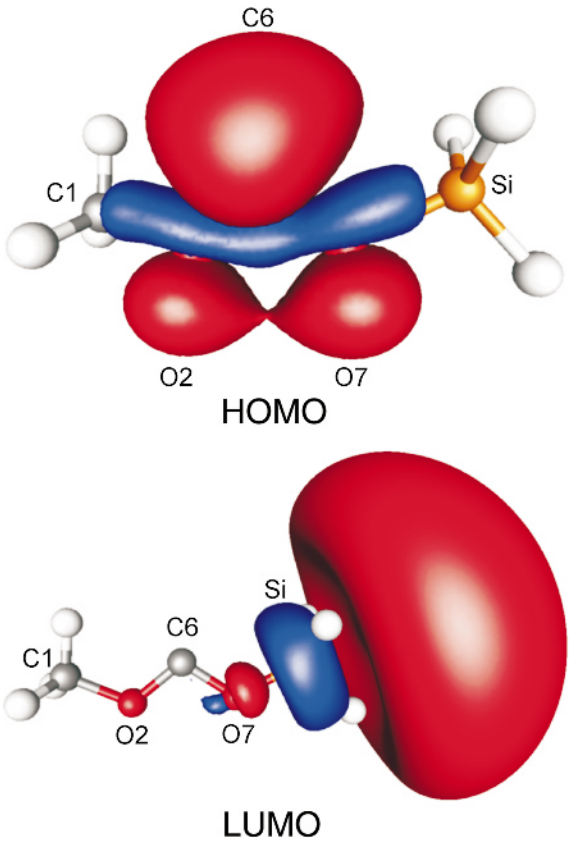

pears to be favored. The HF/6–31+G* orbital energies for conformer **A** are –10.2 eV (HOMO) and 1.82 eV (LUMO). Similar values were obtained for conformers **B** and **C**. For comparison, HF/6–31G* orbital energies reported for *trans-trans* dimethoxycarbene (34) are –10.6 eV (HOMO) and 4.34 eV (LUMO), while those computed at the HF/4–31G level for *trans-trans* methoxyphenoxycarbene (35) are –10.8 eV (HOMO) and 3.33 eV (LUMO). In these two dioxycarbenes, the HOMO is primarily made up of lone pairs on the carbene carbon and its two flanking oxygen atoms, while the LUMO is essentially the vacant carbene *p*-orbital. These dioxycarbenes are not particularly known for their intramolecular reactivity, and this may be due to the large HOMO–LUMO gaps they possess, as well as geometric constraints, which make the interaction between high-lying molecular orbitals (MO) such as the σ_{CO} orbital of the methoxy group and the vacant carbene *p*-orbital difficult. The LUMO energy of conformer **A**, **B**, and **C**, however, is considerably lower than those reported for dimethoxycarbene and methoxyphenoxycarbene, which should facilitate intramolecular rearrangement. Moreover, the orbital energies obtained for **A**, **B**, and **C** are comparable to those reported for phenylacyloxycarbenes, which are known to undergo 1,2-acyl migration (11). For example, the HF/4–31G orbital energies of phenylacetoxycarbene are –10.1 eV (HOMO) and 1.61 eV (LUMO). In this latter carbene, the LUMO is essentially the carbonyl π^*-orbital. Further analysis of the FMOs for conformers **A**, **B**, and **C** reveals that the largest MO coefficient for the LUMO is on Si instead of the carbene carbon C6. For the HOMO, sizeable MO coefficients are found on the methoxy oxygen O2, the carbene carbon C6, and the siloxy oxygen O7. Moreover, it is evident from the FMOs plots shown in Fig. 2 that the LUMO is primarily the σ^*_{O7-Si} orbital, while the n_{O2}, n_{C6}, and n_{O7} nonbonding orbitals almost exclusively make up the HOMO. Thus, in conformers **A** and **B** where the n_{C6} orbital (HOMO) is aligned with the σ^*_{O7-Si} orbital (LUMO), interaction between these two orbitals and hence nucleophilic attack by the carbene lone pair at silicon appear to be favorable.

Fig. 3. Geometries of the transition states for 1,2-silyl migration, $\mathbf{TS_{AD}}$ and $\mathbf{TS_{BE}}$, and the corresponding products *anti*-methyl silylformate **D** and *syn*-methyl silylformate **E**. Bond lengths are in angstroms and angles in degrees. HF, B3LYP (parentheses), and MP2 [brackets] parameters obtained with the 6–311+G(2d,p) basis set are given.

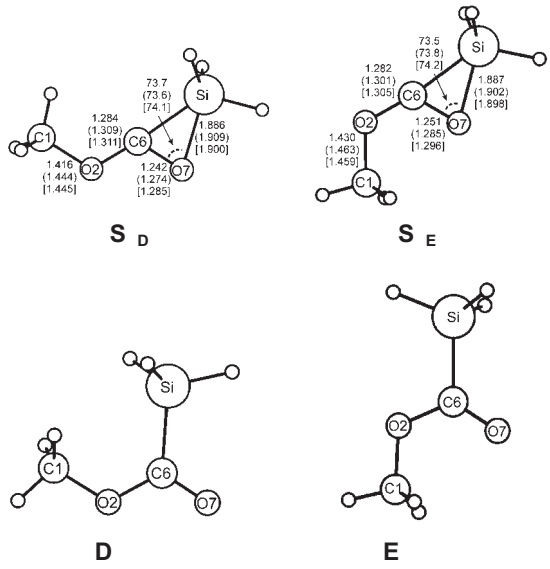

The computed transition-state geometries for 1,2-silyl migration from oxygen to the carbene centre in **A** and **B** are shown in Fig. 3, along with the corresponding products, *anti*-methyl silylformate **D** and *syn*-methyl silylformate **E** (the transition states are simply labeled $\mathbf{TS_{AD}}$ and $\mathbf{TS_{BE}}$, respectively). Relative to the parent carbene conformers (Fig. 1), the dissociating O7–Si bond lengthens considerably, the developing C6–O7 double bond shortens significantly, and there is substantial shrinkage of the C6-O7-Si angle in

Turning our attention to the computed atomic charges, we note that both NBO and AIM atomic charges for the methoxysiloxycarbene conformers listed in Table 4 indicate that the largest positive charge is on Si, which means that this site is most susceptible to nucleophilic attack. In addition, the carbene carbon C6 has a fairly sizeable positive charge, and this may lead one to believe that the carbene carbon is a poor nucleophile. The nucleophilicity of the carbene carbon, however, may actually arise from back donation by lone pairs on the two flanking oxygen atoms that are capable of stabilizing the developing transition state, and this is not necessarily reflected in the atomic charge of the carbene carbon.

© 2002 NRC Canada

Table 4. NBO and AIM atomic charges computed for the methoxysiloxycarbene conformers.

	C1	O2	C6	O7	Si
NBO charges					
A					
HF/6–311+G(2d,p)	−0.09	−0.64	0.55	−0.96	1.40
B3LYP/6–311+G(2d,p)	−0.20	−0.54	0.41	−0.85	1.18
MP2/6–311+G(2d,p)	−0.18	−0.53	0.40	−0.84	1.25
B					
HF/6–311+G(2d,p)	−0.12	−0.63	0.59	−0.99	1.40
B3LYP/6–31+G(2d,p)	−0.24	−0.54	0.46	−0.88	1.18
MP2/6–311+G(2d,p)	−0.18	−0.53	0.40	−0.84	1.25
C					
HF/6–311+G(2d,p)	−0.09	−0.67	0.60	−0.96	1.37
B3LYP/6–311+G(2d,p)	−0.19	−0.58	0.48	−0.84	1.13
MP2/6–311+G(2d,p)	−0.17	−0.58	0.46	−0.84	1.22
AIM Charges					
A					
HF/6–311+G(2d,p)	0.60	–1.35	1.35	–1.55	3.06
B3LYP/6–311+G(2d,p)	0.40	–1.09	1.05	–1.35	2.80
MP2/6–311+G(2d,p)	0.38	–1.12	1.09	–1.38	2.95
B					
HF/6–311+G(2d,p)	0.58	–1.33	1.36	–1.56	3.07
B3LYP/6–31+G(2d,p)	0.36	–1.05	1.06	–1.36	2.79
MP2/6–311+G(2d,p)	0.34	–1.09	1.09	–1.39	2.95
C					
HF/6–311+G(2d,p)	0.59	–1.37	1.37	–1.55	3.06
B3LYP/6–311+G(2d,p)	0.40	–1.10	1.09	–1.35	2.76
MP2/6–311+G(2d,p)	0.38	–1.14	1.13	–1.39	2.94

Table 5. Difference in atomic charges between 1,2-silyl migration transition-states and their respective parent-carbene conformers.

	C1	O2	C6	O7	Si
NBO charges					
TS_{AD}–A					
HF/6–311+G(2d,p)	0.00	0.03	0.01	0.18	−0.22
B3LYP/6–311+G(2d,p)	0.00	0.03	0.02	0.16	−0.21
MP2/6–311+G(2d,p)	0.00	0.02	−0.01	0.18	−0.19
TS_{BE}–B					
HF/6–311+G(2d,p)	0.00	0.03	−0.01	0.17	−0.20
B3LYP/6–311+G(2d,p)	0.01	0.03	0.00	0.15	−0.19
MP2/6–311+G(2d,p)	0.00	0.02	−0.02	0.17	−0.18
AIM charges					
TS_{AD}–A					
HF/6–311+G(2d,p)	−0.01	0.01	−0.09	0.10	−0.03
B3LYP/6–311+G(2d,p)	0.00	0.01	−0.09	0.13	−0.05
MP2/6–311+G(2d,p)	0.00	0.02	−0.12	0.15	−0.03
TS_{BE}–B					
HF/6–311+G(2d,p)	−0.02	0.01	−0.09	0.10	−0.03
B3LYP/6–311+G(2d,p)	0.00	0.00	−0.09	0.12	−0.03
MP2/6–311+G(2d,p)	0.00	0.00	−0.11	0.14	−0.03

the two transition states (Fig. 3). Moreover, the geometries of the transition states are planar, indicating that the silyl group migrates in the plane of the carbene lone pair. These geometric features are consistent with nucleophilic attack by the carbene lone pair at silicon, together with C6–O7 double-bond formation, and are reminiscent of the mechanism proposed by Moss et al. (11) for 1,2-acyl migrations in phenyl(acyloxy)carbenes.

In an effort to monitor the electronic structure changes in going from **A** and **B** to $\mathbf{TS_{AD}}$ and $\mathbf{TS_{BE}}$, respectively, NBO and AIM analyses were also performed on the transition states. NBO perturbation-energy analysis indicates that the

© 2002 NRC Canada

Table 6. Properties of electron density at bond critical points for the 1,2-silyl migration transition-states ($\mathbf{TS_{AD}}$ and $\mathbf{TS_{BE}}$) obtained from AIM analysis.

	O2–C6	C6–O7	C6–Si	O7–Si
Transition state $\mathbf{TS_{AD}}$				
HF/6–311+G(2d,p)				
$\rho(r_c)$ (e Å^{-3})	2.33	2.66	0.51	0.49
$\nabla^2\rho(r_c)$ (e Å^{-5})	–5.8	–9.2	6.1	9.7
ε	0.16	0.07	0.61	1.48
B3LYP/6–311+G(2d,p)				
$\rho(r_c)$ (e Å^{-3})	2.21	2.48	0.52	0.52
$\nabla^2\rho(r_c)$ (e Å^{-5})	–13.2	–17.3	4.1	6.8
ε	0.08	0.03	0.85	1.34
MP2/6–311+G(2d,p)				
$\rho(r_c)$ (e Å^{-3})	2.16	2.38	0.50	0.51
$\nabla^2\rho(r_c)$ (e Å^{-5})	–10.8	–15.0	4.9	7.4
ε	0.08	0.03	2.03	1.05
Transition state $\mathbf{TS_{BE}}$				
HF/6–311+G(2d,p)				
$\rho(r_c)$ (e Å^{-3})	2.34	2.59	0.51	0.49
$\nabla^2\rho(r_c)$ (e Å^{-5})	–6.2	–8.6	6.2	9.4
ε	0.15	0.10	0.50	1.57
B3LYP/6–311+G(2d,p)				
$\rho(r_c)$ (e Å^{-3})	2.25	2.41	0.52	0.52
$\nabla^2\rho(r_c)$ (e Å^{-5})	–13.0	–16.8	4.2	6.9
ε	0.08	0.06	0.85	1.08
MP2/6–311+G(2d,p)				
$\rho(r_c)$ (e Å^{-3})	2.19	2.31	0.49	0.51
$\nabla^2\rho(r_c)$ (e Å^{-5})	–10.7	–14.6	4.9	7.5
ε	0.07	0.06	1.85	0.96

Note: $\rho(r_c)$, $\nabla^2\rho(r_c)$, and ε represent the electronic charge density, the Laplacian of the charge density, and bond ellipticity, respectively.

negative hyperconjugative $n_{C6}\rightarrow\sigma^*_{O7-Si}$ and $n_{C6}\rightarrow RY^*_{Si}$ interactions in **A** and **B** increase tremendously in $\mathbf{TS_{AD}}$ and $\mathbf{TS_{BE}}$, as can be seen from the stabilization energies in Table 2. It is important to note that the σ^*_{O7-Si} orbital is heavily polarized towards Si (the NBO polarization coefficient is about 85–95% on Si). In addition, there is considerable strengthening of the $n_{O7}\rightarrow p_{C6}$ interaction in $\mathbf{TS_{AD}}$ and $\mathbf{TS_{BE}}$ relative to **A** and **B**. Moreover, the NBO charge differences given in Table 5 reveal that there is significant positive charge build-up on Si, considerable positive charge build-up on O7, while the change in charge on C6 appears to be insignificant. These observations are in keeping with nucleophilic attack by the carbene lone pair at silicon, together with simultaneous C6–O7 double bond formation. In addition, there generally appears to be a small build-up of positive charge on O2, which may be a reflection of π-electron stabilization of the two transition states. This is further supported by a small increase in the strength of the $n_{O2}\rightarrow p_{C6}$ interaction at the B3LYP level of theory, but not at the HF level of theory where the reverse is observed (Table 2).

AIM analysis reveals that the electron density at the bond critical point ($\rho(r_c)$) along the O7–Si bond path decreases, while it increases along the C6–O7 bond path in going from **A** and **B** (Table 3) to $\mathbf{TS_{AD}}$ and $\mathbf{TS_{BE}}$ (Table 6). Meanwhile, a new C6–Si bond path with low $\rho(r_c)$ appears in the two transition states. According to the AIM charges, there is sizeable positive charge build-up at the carbene carbon C6, significant positive charge development at O7, and modest positive charge build-up at Si, in the two transition states as indicated in Table 5. These findings are in agreement with nucleophilic attack by the carbene lone pair at silicon, along with simultaneous C6–O7 double-bond formation and O7–Si bond dissociation. There is generally a small build-up of positive charge on O2, which is accompanied by a meagre increase in $\rho(r_c)$ between O2 and C6 in the transition states (Table 6). These latter observations are consistent with modest stabilization of the two transition states by back donation from the O2 lone pairs. The bond ellipticities (ε) of the C6–Si and O7–Si bond paths are fairly large for reasons which may not be immediately obvious, but such occurrences are usually associated with the apparition of three-membered ring structures (31).

The Laplacian of the electron density ($\nabla^2\rho(r)$) allows identification of regions of local charge concentration ($\nabla^2\rho(r) < 0$) and local charge depletion ($\nabla^2\rho(r) > 0$) in the topology of the electron density of a molecule (31). Regions of charge concentration can be mapped to localized electron pairs of the Lewis and VSEPR models. Contour plots of $\nabla^2\rho(r)$ for **A** and $\mathbf{TS_{AD}}$, generated from MP2/6–311+G(2d,p) wavefunctions are shown in Fig. 4. These plots clearly show that the charge concentration corresponding to the carbene lone pair in **A** becomes distorted toward silicon in $\mathbf{TS_{AD}}$, consistent with a mechanism involving nucleophilic attack by the carbene lone pair at silicon. At the same time, the

© 2002 NRC Canada

Fig. 4. Contour maps of the Laplacian of the electron density in the O2-C6-O7 plane for **A** and $\mathbf{TS_{AD}}$ generated from the MP2/6–311+G(2d,p) wavefunction. Solid contour lines correspond to $\nabla^2\rho < 0$ and broken lines are for $\nabla^2\rho > 0$. The dots along the bond paths denote the bond critical points.

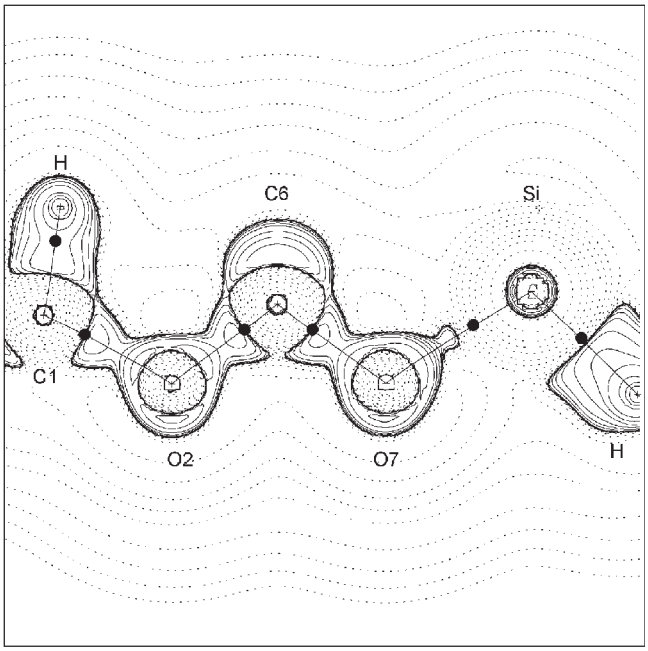

A

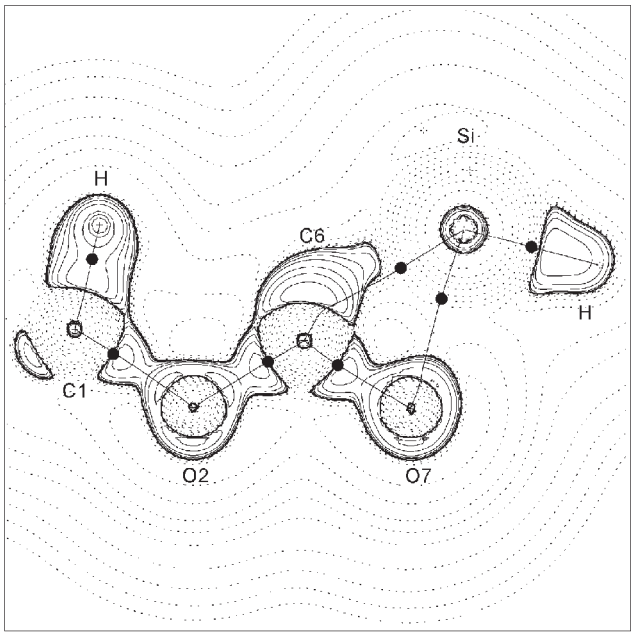

$\mathbf{TS_{AD}}$

charge concentration that appears as a small projection along the O7–Si bond path in **A** disappears in $\mathbf{TS_{AD}}$, reflecting the weakening of the bond during silyl migration.

The relative Gibbs free energy barriers computed for 1,2-silyl migration (via $\mathbf{TS_{AD}}$ and $\mathbf{TS_{BE}}$) at the HF level of theory appear to be overestimated when compared to experimentally determined barriers reported for similar rearrangements (Table 1), as is commonly the case (36–38). However, the B3LYP and MP2 computed barriers seem to be quite reasonable. Relative Gibbs free energy barriers computed at the HF level of theory are between 20.0 and 22.0 kcal mol^{-1}, whereas at the B3LYP and MP2 levels of theory, they are around 8.0 to 11.0 kcal mol^{-1} (Table 1). The latter numbers are consistent with barriers measured for similar rearrangements. For example, the experimentally determined Gibbs free energy barrier for 1,2-acyl migration in phenylbenzoyloxycarbene is 9.9 kcal mol^{-1} (11). For other rearrangements, the barriers are generally lower. Barriers determined experimentally for 1,2-H shifts in *p*-trifluorobenzylchloro-, *p*-chlorobenzylchloro-, and cyclobutylchlorocarbenes are 4.9, 4.5, and 2.3 kcal mol^{-1}, respectively (6,7). For 1,2-C migration in cyclobutylchloro-, cyclopropylchloro-, cyclopropylfluorocarbenes the barriers are 3.8, 3.0, and 4.2 kcal mol^{-1}, respectively (6).

Fig. 5. Geometries of the transition states for 1,2-methyl migration, $\mathbf{TS_{AF}}$ and $\mathbf{TS_{CG}}$, and the corresponding products, *anti*-silyl acetate **F** and *syn*-silyl acetate **G**. Bond lengths are in angstroms and angles in degrees. HF, B3LYP (parentheses), and MP2 [brackets] geometric parameters obtained with the 6–311+G(2d,p) basis set are given.

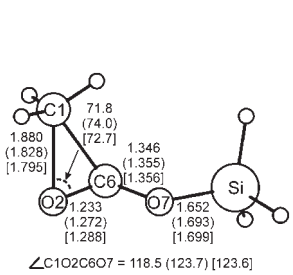

$\mathbf{S_F}$

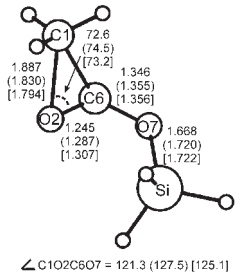

$\mathbf{S_G}$

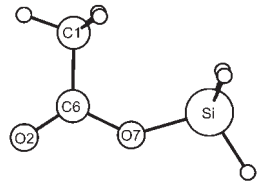

F

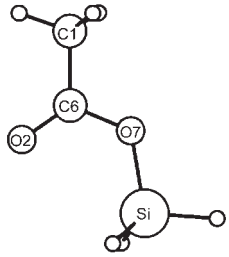

G

Comparison with methyl migration

For comparison and further mechanistic insight, we now focus on the mechanism of 1,2-methyl migration from oxygen to the carbene carbon in methoxysiloxycarbene. Initially, we will examine the possible rearrangement mechanisms in terms of FMO theory. First, let us consider the requirements that would favor nucleophilic attack by the carbene C6 lone pair at the methyl carbon C1. For this mechanism to be favored, sizeable coefficients for the HOMO and LUMO must be located on the C6 and C1 atoms, respectively. Indeed, there is a sizeable coefficient for the HOMO on the C6 atom, but the coefficient for the LUMO on the C1 atom appears to be negligible (Fig. 2).

© 2002 NRC Canada

Table 7. Difference in atomic charges between transition-states for 1,2-methyl migration and their respective parent carbene conformers.

	C1	O2	C6	O7	Si
NBO charges					
TS_{AF}–A					
HF/6–311+G(2d,p)	−0.09	0.03	0.00	−0.03	0.00
B3LYP/6–311+G(2d,p)	−0.13	−0.01	0.10	−0.02	−0.01
MP2/6–311+G(2d,p)	−0.01	−0.08	0.14	−0.13	0.13
TS_{CG}–C					
HF/6–311+G(2d,p)	−0.04	−0.03	0.01	0.01	−0.03
B3LYP/6–311+G(2d,p)	−0.07	−0.06	0.10	0.03	−0.07
MP2/6–311+G(2d,p)	0.05	−0.15	0.15	−0.09	0.09
AIM charges					
TS_{AF}–A					
HF/6–311+G(2d,p)	−0.39	0.01	0.52	0.01	0.00
B3LYP/6–311+G(2d,p)	−0.28	0.08	0.08	0.01	0.00
MP2/6–311+G(2d,p)	−0.27	0.14	0.02	0.01	−0.01
TS_{CG}–C					
HF/6–311+G(2d,p)	0.00	0.03	−0.01	0.00	−0.01
B3LYP/6–311+G(2d,p)	−0.27	0.07	0.08	0.01	0.01
MP2/6–311+G(2d,p)	−0.26	0.13	−0.02	0.02	−0.01

Table 8. Properties of bond critical points for the 1,2-methyl migration transition-states, **TS_{AF}** and **TS_{CG}**, obtained from AIM analysis.

	C1–O2	O2–C6	C6–O7	O7–Si
TS_{AF}				
HF/6–311+G(2d,p)				
$\rho(r_c)$ (e Å^{-3})	1.83	3.12	2.03	0.88
$\nabla^2\rho(r_c)$ (e Å^{-5})	18.0	−4.9	−11.2	20.6
ε	0.07	0.17	0.11	0.05
B3LYP/6–311+G(2d,p)				
$\rho(r_c)$ (e Å^{-3})	0.68	2.49	1.98	0.85
$\nabla^2\rho(r_c)$ (e Å^{-5})	3.2	−17.9	−15.8	15.0
ε	0.84	0.11	0.19	0.05
MP2/6–311+G(2d,p)				
$\rho(r_c)$ (e Å^{-3})	0.72	2.38	1.96	0.82
$\nabla^2\rho(r_c)$ (e Å^{-5})	3.0	−16.7	−15.0	15.5
ε	0.90	0.11	0.19	0.05
TS_{CG}				
HF/6–311+G(2d,p)				
$\rho(r_c)$ (e Å^{-3})	1.61	2.12	2.23	0.85
$\nabla^2\rho(r_c)$ (e Å^{-5})	−5.9	−14.2	−5.5	18.2
ε	0.01	0.39	0.28	0.02
B3LYP/6–311+G(2d,p)				
$\rho(r_c)$ (e Å^{-3})	0.67	2.40	2.08	0.79
$\nabla^2\rho(r_c)$ (e Å^{-5})	3.2	−18.0	−14.6	12.9
ε	0.67	0.11	0.18	0.03
MP2/6–311+G(2d,p)				
$\rho(r_c)$ (e Å^{-3})	0.72	2.27	2.04	0.77
$\nabla^2\rho(r_c)$ (e Å^{-5})	2.9	−16.7	−13.6	−13.6
ε	0.73	0.12	0.18	0.03

Note: $\rho(r_c)$, $\nabla^2\rho(r_c)$, and ε represent the electronic charge density, the Laplacian of the charge density, and bond ellipticity, respectively.

Thus, even though the n_{C6} orbital may be well aligned with the σ^*_{C1-O2} orbital in conformers **A** and **C**, nucleophilic attack by the carbene lone pair at the methyl carbon is expected to be unfavorable. In the case of an anion-like shift of

© 2002 NRC Canada

Fig. 6. Contour maps showing two views of the Laplacian of the electron density for $\mathbf{TS_{AF}}$ in the C1-O2-C6 and O2-C6-O7 planes generated from the MP2/6–311+G(2d,p) wavefunction. Solid contour lines correspond to $\nabla^2\rho < 0$ and broken lines are for $\nabla^2\rho > 0$. The dots along the bond paths denote the bond critical points.

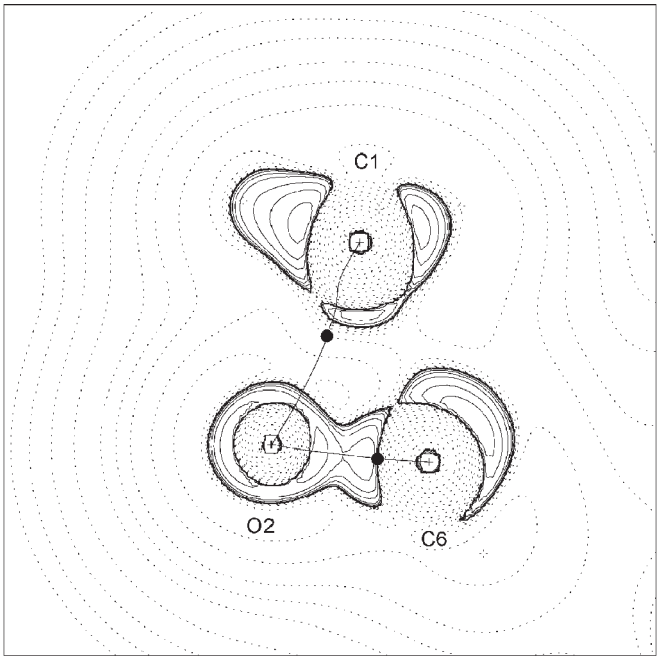

$\mathbf{TS_{AF}}$

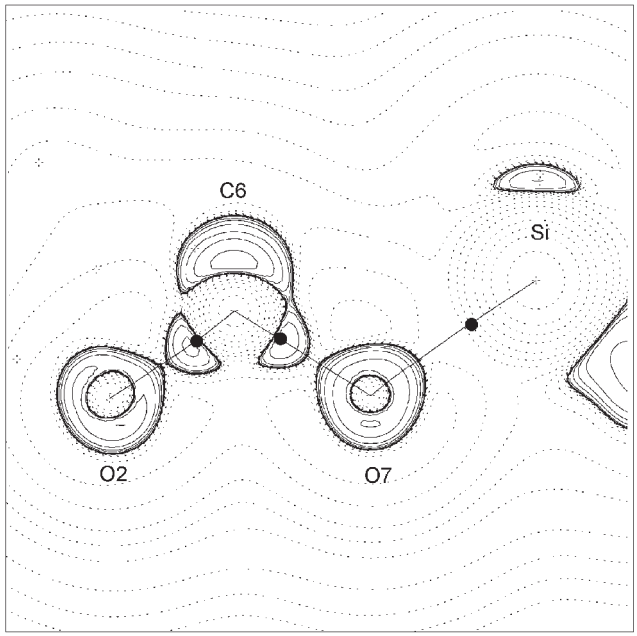

$\mathbf{TS_{AF}}$

the methyl group from oxygen to the carbene carbon, one would expect the σ_{C1-O2} orbital to be a major contributor to the HOMO and a large coefficient for the LUMO on C6. But it is apparent from the FMO plots in Fig. 2 that these conditions are not met, and hence, this latter mechanism may be ruled unfavorable. Furthermore, since the C1–O2 bond is locked in the symmetry plane of the carbene as indicated by the high isomerization barriers via $\mathbf{TS_{AB}}$ (Table 1), alignment of the σ_{C1-O2} orbital with the vacant out-of-plane carbene *p*-orbital would not occur readily.

The transition-state geometries computed for 1,2-methyl migration from oxygen to the carbene centre are shown in Fig. 5, along with the corresponding products, *anti*-silyl acetate **F** and *syn*-silyl acetate **G** (the transition states are labeled $\mathbf{TS_{AF}}$ and $\mathbf{TS_{CG}}$, respectively). In contrast to 1,2-silyl migration, the geometric features of these transition states are more consistent with an anion-like shift of the methyl group from oxygen to the carbene carbon. Compared with ground-state carbene conformers (Fig. 1), the breaking C1–O2 bond becomes elongated, the developing O2–C6 double bond shortens, and the C1-O2-C6 angle shrinks considerably in the two transition states. Most importantly, the methyl group is out-of-plane in the two transition states suggesting that the C1–O2 bond rotates for better alignment with the vacant carbene *p*-orbital.

As done earlier for 1,2-silyl migration, NBO and AIM analyses were used to monitor changes in electronic structure during 1,2-methyl migration. NBO-computed atomic charges seem to suggest that there is generally modest positive charge build-up at the C1 and O2 atoms, while there is positive charge depletion on C6 (Table 7). These observations are somewhat indicative of an anion-like shift of the methyl group from oxygen to the carbene *p*-orbital, accompanied by simultaneous formation of the O2–C6 double bond. In fact, the analysis indicates that formation of both the O2–C6 double bond and the new C1–C6 single bond is essentially complete in the two transition states.

AIM analyses at the B3LYP and MP2 levels of theory indicate that there is a tremendous decrease in $\rho(r_c)$ along the C1–O2 bond path, whereas $\rho(r_c)$ increases slightly along the O2–C6 bond path in going from **A** and **C** (Table 3) to $\mathbf{TS_{AF}}$ and $\mathbf{TS_{CG}}$, respectively (Table 8). There is also significant positive charge development at the C1 atom and sizeable positive charge depletion at the O2 atom, while the charge development at the C6 atom appears to be negligible. There is some deviation, however, from these general trends at the HF level. Nevertheless, the observations at the B3LYP and MP2 levels may be indicative of an anion-like shift of the methyl group from oxygen to the carbene carbon, in concert with the formation of the O2–C6 double bond. Surprisingly, AIM analysis seems to indicate that the C1–C6 bond is not yet fully developed in the transition state, in contrast to the prediction of NBO analysis.

To gain further insight into the electronic structure changes in going from **A** and **C** to $\mathbf{TS_{AF}}$ and $\mathbf{TS_{CG}}$, respectively, we have also compared contour plots of the Laplacian of the electron density $\nabla^2\rho$. Two views of such plots for $\mathbf{TS_{AF}}$ are shown in Fig. 6. The first contour plot is in the C1-O2-C6 plane and the second is in the O2-C6-O7 plane. In the first plot, there appears to be a slight build-up of charge concentration on C1, roughly along the dissociating C1–O2 bond path. This may be associated with an anion-like shift of the methyl group C1 from oxygen to the carbene carbon C6. Furthermore, both plots clearly show that the charge concentration corresponding to the carbene lone pair in **A** (Fig. 4) remains unchanged in $\mathbf{TS_{AF}}$, which is contrary to what was seen earlier for 1,2-silyl migration. This latter ob-

© 2002 NRC Canada

servation rules out the possibility of a mechanism involving nucleophilic attack by the carbene lone pair C6 at the methyl carbon C1.

Finally, the relative Gibbs free energy barriers computed for 1,2-methyl migration (via $\mathbf{TS_{AF}}$ and $\mathbf{TS_{CG}}$) are considerably higher than those computed for 1,2-silyl migration (via $\mathbf{TS_{AD}}$ and $\mathbf{TS_{BE}}$), as can be seen from Table 1. They are more than 40 kcal mol^{-1} higher at the HF level of theory, while they are more than 30 kcal mol^{-1} higher at the B3LYP and MP2 levels of theory. The very high barriers for 1,2-methyl migration are most likely due to the fact that the methyl group must rotate out-of-plane before migration can occur, and this means that the O2–C6 bond that, as discussed earlier, has strong double-bond character, must be broken in the process. This explains why 1,2-methyl migration from oxygen to the carbene centre is energetically unfavorable, a finding that is consistent with the predictions of FMO theory. In contrast, 1,2-silyl migration occurs in the valence plane of the carbene, the C6–O7 double-bond character can be maintained during the process, and the resulting barrier to migration is fairly low. This may explain why only 1,2-silyl migration is observed experimentally (17).

Conclusion

Ab initio molecular orbital theory and hybrid density functional theory calculations were carried out to investigate the mechanisms of intramolecular 1,2-migrations from oxygen to the carbene carbon in methoxysiloxycarbene as a model system for methoxytriphenylsiloxycarbenes. FMO theory, NBO analysis, and AIM theory were also used to shed light on the mechanistic details of 1,2 migrations in these carbenes. Our combined analyses clearly indicate that the mechanism for 1,2-silyl migration from oxygen to the carbene carbon in methoxysiloxycarbene involves nucleophilic attack by the carbene lone pair at silicon. In contrast, 1,2-methyl migration from oxygen to the carbene carbon appears to involve an anion-like shift of the methyl group from oxygen to the carbene *p*-orbital. In addition, the computed relative Gibbs free energy barriers are relatively low for 1,2-silyl migration, but significantly high for 1,2-methyl migration because the latter mechanism involves breaking a bond with considerable double-bond character. These findings are consistent with the fact that thermally generated methoxytriphenylsiloxycarbene rearranges to form the product via 1,2-triphenylsilyl migration not via 1,2-methyl migration (17).

Acknowledgments

This work was funded by research grants from the Natural Science and Engineering Research Council (NSERC) of Canada, the Fonds pour la Formation des Chercheurs et l'Aide à la Recherche (FCAR, Québec), and the Faculty Research and Development Program (FRDP) of Concordia University. Calculations were performed at the Centre for Research in Molecular Modeling (CERMM), which was established with the financial support of the Concordia University Faculty of Arts & Science, the Ministère de l'Éducation du Québec (MEQ), and the Canada Foundation for Innovation (CFI). The authors would like to thank Heidi Muchall for helpful discussions.

References

1. H.F. Schaefer. Acc. Chem. Res. **12**, 288 (1979).
2. R.A. Moss. *In* Advances in carbene chemistry. JAI Press Inc., Greenwich, CT. 1994.
3. M.T.H. Liu. Acc. Chem. Res. **21**, 287 (1994).
4. J.A. LaVilla and J.L. Goodman. J. Am. Chem. Soc. **111**, 6877 (1989).
5. R. Bonneau, M.T.H. Liu, and M.T. Rayez. J. Am. Chem. Soc. **111**, 5973 (1989).
6. R.A. Moss, G.-J. Ho, and W. Liu. J. Am. Chem. Soc. **114**, 959 (1992).
7. M.T.H. Liu and R. Bonneau. J. Am. Chem. Soc. **114**, 3604 (1992).
8. A.E. Keating, M.A. Garcia-Garibay, and K.N. Houk. J. Phys. Chem. A, **102**, 8467 (1998).
9. J.A. LaVilla and J.L. Goodman. Tetrahedron Lett. **31**, 5109 (1990).
10. J.D. Evanseck and K.N. Houk. J. Phys. Chem. **94**, 5518 (1990).
11. R.A. Moss, S. Xue, W. Liu, and K. Krogh-Jespersen. J. Am. Chem. Soc. **118**, 12588 (1996).
12. D. Suh, D.L. Pole, J. Warkentin, and J.K. Terlouw. Can. J. Chem. **74**, 546 (1996).
13. P.C. Venneri and J. Warkentin. J. Am. Chem. Soc. **120**, 11182 (1998).
14. N. Merkley, M. El-Saidi, and J. Warkentin. Can. J. Chem. **78**, 356 (2000).
15. N. Merkley and J. Warkentin. Can. J. Chem. **78**, 942 (2000).
16. D.L. Reid and J. Warkentin. J. Chem. Soc. Perkin Trans. 2, 1980 (2000).
17. J.P. Pezacki, P.G. Loncke, J.P. Ross, J. Warkentin, and T.A. Gadosy. Org. Lett. **2**, 2733 (2000).
18. P.G. Loncke and G.H. Peslherbe. Submitted.
19. W.J. Hehre, L. Radom, P.v.R. Schleyer, and J.A. Pople. Ab initio molecular orbital theory. John Wiley & Sons, New York. 1986.
20. A.D. Becke. J. Chem. Phys. **98**, 5648 (1993).
21. M.J. Frisch, G.W. Trucks, H.B. Schlegel, G.E. Scuseria, M.A. Robb, J.R. Cheeseman, V.G. Zakrzewski, J.J.A. Montgomery, R.E. Stratmann, J.C. Burant, S. Dapprich, J.M. Millam, A.D. Daniels, K.N. Kudin, M.C. Strain, O. Farkas, J. Tomasi, V. Barone, M. Cossi, R. Cammi, B. Mennucci, C. Pomelli, C. Adamo, S. Clifford, J. Ochterski, G.A. Petersson, P.Y. Ayala, Q. Cui, K. Morokuma, D.K. Malick, A.D. Rabuck, K. Raghavachari, J.B. Foresman, J. Cioslowski, J.V. Ortiz, A.G. Baboul, B.B. Stefanov, G. Liu, A. Liashenko, P. Piskorz, I. Komaromi, R. Gomperts, R.L. Martin, D.J. Fox, T. Keith, M.A. Al-Laham, C.Y. Peng, A. Nanayakkara, C. Gonzalez, M. Challacombe, P.M.W. Gill, B. Johnson, W. Chen, M.W. Wong, J. L. Andres, C. Gonzalez, M. Head-Gordon, E.S. Replogle, and J.A. Pople. Gaussian 98. Revision A.7 ed. Gaussian, Inc., Pittsburgh. 1998.
22. H.B. Schlegel. J. Comp. Chem. **3**, 214 (1982).
23. A. Bannerjee, N. Adams, J. Simons, and R. Shepard. J. Phys. Chem. **89**, 52 (1985).
24. J. Simons, P. Jorgensen, H. Taylor, and J. Ozment. J. Phys. Chem. **87**, 2745 (1983).
25. C.J. Cerjan and W.H. Miller. J. Chem. Phys. **75**, 2800 (1981).
26. J.W. Ochterski. Thermochemistry in Gaussian. Gaussian Inc., Pittsburgh, PA. 2000.
27. A.E. Reed, L.A. Curtiss, and F. Weinhold. Chem. Rev. **88**, 899 (1988).
28. E.D. Glendening, A.E. Reed, J.E. Carpenter, and F. Weinhold. NBO 3.0 program manual. 3.1 ed. Theoretical chemistry insti-

© 2002 NRC Canada

tute and department of chemistry, University of Wisconsin, Madison, Wisconsin. 1996.
29. F.W. Biegler-Konig, R.F.W. Bader, and T. Tang. J. Comp. Chem. **3**, 317 (1982).
30. The AIMPAC suite of programs is available from Professor R.F.W. Bader, McMaster University, Canada, and from the AIMPAC website (www.chemistry.mcmaster.ca/aimpac).
31. R.F.W. Bader. Atoms in molecules. A quantum theory. Clarendon Press, Oxford. 1990.
32. D. Feller, W.T. Borden, and E.R. Davidson. J. Chem. Phys. **71**, 4987 (1979).
33. R.S. Sheridan, R.A. Moss, B.K. Wilk, S. Shen, M. Wlostowski, M.A. Kesselmayer, R. Subramanian, G. Kmiecik-Lawrynowicz, and K. Krogh-Jespersen. J. Am. Chem. Soc. **110**, 7563 (1988).
34. R.A. Moss, M. Wlostowski, S. Shen, K. Krogh-Jespersen, and A. Matro. J. Am. Chem. Soc. **110**, 4443 (1988).
35. R.A. Moss, M. Wlostowski, J. Terpinski, and K. Krogh-Jespersen. J. Am. Chem. Soc. **109**, 3811 (1987).
36. J.D. Evanseck, J. Mareda, and K.N. Houk, J. Am. Chem. Soc. **112**, 73 (1990).
37. J.D. Evanseck and K.N. Houk. J. Am. Chem. Soc. **112**, 9148 (1990).
38. R.H. Nobes, L. Radom, and W.R. Rodwell. Chem. Phys. Lett. **74**, 269 (1980).

© 2002 NRC Canada

Biocapteurs ampérométriques à cholinestérases pour la détermination des pesticides organophosphorés

Graziella Turdean, Ionel Catalin Popescu et Liviu Oniciu

Résumé : Le but de cette étude est une présentation comparative des différents types de biocapteurs ampérométriques à cholinestérase pour la détermination des pesticides organophosphorés basée sur l'information bibliographique des 20 dernières années. L'étude contient la présentation de la structure et les propriétés des cholinestérases, les principales réactions impliquées dans le fonctionnement du biocapteur ampérométrique, leurs applications et les facteurs influençant le procès de la détection ou (et) de l'inhibition. Les valeurs de la limite de détection obtenues à l'aide des biocapteurs mono- ou bi-enzymatiques sont relativement plus élevées par rapport à celles obtenues par les méthodes immunologiques ou par chromatographie en phase gazeuse et liquide, qui demeurent les méthodes de référence. Comme il a été montré aussi pour d'autres biocapteurs ampérométriques, l'application du traitement cinétique de Michaelis–Menten, utilisé pour les réactions catalysées par l'enzyme libre, peut être extrapolée pour examiner la réponse des biocapteurs ampérométriques à l'enzyme immobilisée. Le compromis positif entre les avantages et les inconvénients, ainsi que les conditions expérimentales « douces », font du biocapteur ampérométrique monoenzymatique, un outil analytique intéressant pour la détection des pesticides organophosphorés.

Mots clés : biocapteurs ampérométriques, acetylcholinestérase, pesticides organophosphorés, cinétique, inhibition.

Abstract: The purpose of this study is a comparative presentation of the different types of the amperometric biosensors based on cholinesterases for the determination of organophosphorous pesticides using the bibliographical information of the last 20 years. The study contains the presentation of the structure and properties of the cholinesterases, the main reactions implied in the functioning of the amperometric biosensors, their applications and factors influencing the detection or (and) the inhibition process. The detection limit of the mono- or bi-enzymatic amperometric biosensors are relatively higher than those corresponding with the immunobiosensors or with gas and liquid chromatography, which are still considered as the reference methods. As shown, for many other amperometric biosensors, the Michaelis–Menten's kinetic treatment used for reactions catalyzed by free enzymes can be extended to describe the response of amperometric biosensors based on immobilized cholinesterases. The positive compromise between advantages and drawbacks, as well as the "soft" experimental conditions, point to the amperometric monoenzymatic bioelectrode, as an attractive analytical tool for the detection of organophosphorous pesticides.

Key words: amperometric biosensor, acetylcholinesterase, organophosphorous pesticides, kinetic, inhibition.

Introduction

Pendant les dernières années, l'utilisation des pesticides (insecticides, herbicides, fongicides) en quantités de plus en plus importantes — afin de surmonter les nécessités de nourriture réclamées par l'explosion démographique — a entraîné l'augmentation de la pollution de l'environnement, notamment avec des insecticides organophosphorés. Ces substances toxiques possèdent un effet nocif contre les insectes et les mammifères, mais aussi présentent un danger important pour l'être humain, puisqu'elles agissent au niveau du système nerveux.

Dû à leur persistance dans le sol et dans l'eau de la nappe phréatique, les normes nationales et internationales imposent des concentrations maximales admissibles des pesticides de plus en plus faibles. Les méthodes analytiques acceptées pour leur dosage utilisent des techniques très complexes pour l'identification et la détermination. Parmi ces techniques, les plus utilisées sont la chromatographie en phase liquide et en phase gazeuse, souvent couplées à la spectrométrie de masse, techniques très performantes mais aussi laborieuses, coûteuses et qui nécessitent un personnel hautement qualifié.

Étant très spécifique, le mécanisme d'inhibition des cholinestérases induit par les pesticides organophosphorés a conduit au développement de nombreuses techniques d'analyse rapide. Ainsi, une solution moderne aux méthodes déjà classiques est offerte par les méthodes électroanalytiques, qui utilisent des outils simples, capables de délivrer une information rapide dans différents domaines d'application :

Reçu le 27 mars 2000. Publié au site Web des Presses scientifiques du CNRC à http://canjchem.cnrc.ca, le 22 mars 2002.

G. Turdean,[1] I.C. Popescu et L. Oniciu.[2] Département de Chimie Physique, Université Babes-Bolyai, 3400 Cluj-Napoca, Roumanie.

[1]Auteur correspondant (courriel : gturdean@chem.ubbcluj.ro).
[2]Décédé.

 DOI: 10.1139/V02-021 © 2002 CNRC Canada

Fig. 1. Formule générale des pesticides organophosphorés.

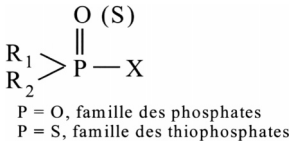

agro-alimentaire (1), biomédical (2, 3) et environnement (4). Parmi ceux-ci, les biocapteurs électrochimiques sont de plus en plus utilisés. Ils consistent dans le couplage d'un récepteur de nature biologique à un transducteur électrochimique. Grâce à l'excellente spécificité des enzymes et à la très bonne sensibilité des transducteurs ampérométriques, la plupart des recherches récentes a été orientée vers la réalisation de biocapteurs ampérométriques enzymatiques. Ceux-ci mettent en valeur, à la fois, la grande variété des éléments de reconnaissance biologiques et les avantages de la technique ampérométrique, comme par exemple : la haute sensibilité et la bonne sélectivité pour l'espèce électroactive; le domaine de linéarité étendu; la fabrication facile d'un appareillage peu coûteux; l'utilisation des matériaux d'électrodes compatibles dans différents milieux.

Depuis la construction du premier biocapteur ampérométrique pour glucose (5) et malgré une activité de recherche intense, les applications des biocapteurs introduites dans la vie courante sont encore rares. L'obstacle majeur au développement et à la commercialisation de ces outils est l'instabilité de l'enzyme immobilisée. À la fois, l'existence de certaines substances susceptibles d'interférer au niveau du transducteur, souvent présentes dans les échantillons à analyser, constitue encore un problème à résoudre.

Les pesticides organophosphorés

Définition

Conformément aux normes du Food and Agricultural Organization (FAO) (6) un pesticide est défini comme « toute substance ou mélange de substances : (*i*) utilisée pour la prévention, la destruction ou le contrôle de tout animal, espèces de plantes, qui cause préjudice pendant, ou interfère avec, la production, le traitement, le stockage, le transport ou la commercialisation des aliments, des produits agricoles, du bois ou des produits en bois, du fourrage pour animaux; (*ii*) administrée aux animaux pour le contrôle des insectes; comme régulateur de croissance des plantes, défoliant, ou agent conservant les fruits pour prévenir leur chute prématurée; (*iii*) appliquée à la récolte (soit avant, soit après) en vue de protéger les produits de la détérioration pendant le stockage et le transport » (6).

Structure

Le grand développement des pesticides organophosphorés a commencé en 1944, quand Schrader a synthétisé le parathion. Les pesticides organophosphorés, dont la formule générale est présentée dans la figure 1, sont des esters, des amines ou des dérivés thiols de l'acide phosphorique ou phosphonique. Les groupements R_1 et R_2 peuvent être des alkyls ou des aryles et X est un groupe hydrolysable aliphatique, aromatique ou hétérocyclique. En général, ils sont des composés solubles dans l'eau. En milieu alcalin, ils sont rapidement hydrolysés et oxydés en acide (thio)phosphorique ou (thio)phosphonique (mono- ou di-substitué).

Modalités d'action des pesticides

L'action des pesticides organophosphorés sur les insectes et les mammifères se situe au niveau du système nerveux. Ces substances toxiques inhibent l'acétylcholinestérase (AChE), entraînant une accumulation d'acétylcholine dans les tissus nerveux. Au niveau des synapses cholinergiques, cette inhibition est due au blocage du site estérique de l'enzyme (phosphorylation ou carbamylation du OH de la sérine du site actif) (7–9) par les composés organophosphorés, qui agissent en compétition avec le substrat spécifique de l'enzyme (10). Cette fixation conduit à la formation de complexes intermédiaires de type phosphoryl- ou carbamyl-AChE, qui s'hydrolysent très lentement (11). L'accumulation de l'acétylcholine due à l'inhibition de l'AChE peut avoir des suites graves : maladies ou même la mort (12).

Sources de pollution par les pesticides

De grandes quantités de ces pesticides peuvent être apportées au milieu aquatique, soit directement (par dispersion), soit indirectement (par lavage des terrains agricoles), ou même accidentellement. La nature, la concentration, la solubilité dans l'eau et la capacité de dégradation des pesticides sont des facteurs qui influencent leur transport dans le milieu aquatique (13).

La contamination humaine par ces différentes substances toxiques se fait principalement par l'intermédiaire de l'eau, des plantes ou des animaux qui ont ingéré des plantes contaminées. Mais elle peut se faire également par ingestion, inhalation ou contact direct (14, 15).

Grâce à leur stabilité, les pesticides peuvent persister dans le sol pendant des mois ou des années. Une proportion importante de ces substances n'atteint pas leur cible et se dépose ou dérive dans différents écosystèmes. Une fraction se sublime dans l'air et fait l'objet d'un transport vers les zones océaniques les plus reculées. En milieu continental, on observe aussi une incorporation à la biomasse terrestre ou limnique.

Normes de qualité pour l'eau potable

Plusieurs normes réglementent l'utilisation et la commercialisation des pesticides. Les précautions concernant la protection des animaux (gibier, poisson) et du personnel, pendant la fabrication ou l'utilisation de ces pesticides, doivent être strictement respectées, certains de ces produits ayant un temps de demi-vie d'environ 3 mois.

Un des problèmes majeurs liés à l'utilisation de ces pesticides est la persistance des métabolites dans les eaux et dans les plantes, que l'on retrouve ultérieurement dans les aliments.

La législation concernant l'utilisation des pesticides est devenue de plus en plus stricte, recommandant des tests nombreux et sensibles. Ainsi la norme fixée pour la production de l'eau potable, par la Communauté Économique Européenne (CEE) (16), limite la teneur maximale en pesticides à 0,1 $\mu g\ L^{-1}$ pour chaque substance de ce groupe et à 0,5 $\mu g\ L^{-1}$ pour l'ensemble des pesticides et de leurs composés de dégradation, pendant que la U.S. Environmental

© 2002 CNRC Canada

Protection Agency établit des niveaux maximums pour chaque pesticide qui doit être mesuré (3).

Méthodes de détection des pesticides dans l'eau, l'air et le sol

Le développement des méthodes de « monitoring » est essentiellement centré sur trois niveaux : (*i*) outil rapide, très sensible et spécifique; (*ii*) technologie sophistiquée et durable ou solide; (*iii*) outil capable de combiner la sensibilité, la flexibilité et la solidité des techniques mentionnées (p. ex. biocapteur). Parmi les nombreuses méthodes de détection des pesticides organophosphorés rapportés dans la littérature — chromatographiques, spectophotométriques, électrochimiques, immunologiques et enzymatiques — nous n'allons détailler ici que les méthodes ampérométriques basées sur l'utilisation des cholinestérases.

Biocapteurs ampérométriques

Définition

Un biocapteur est un dispositif intégré, indépendant, capable de fournir des informations analytiques quantitatives ou demi-quantitatives, utilisant un élément de reconnaissance biologique (récepteur biologique) qui est en contact direct avec un transducteur (17–25). Cette définition est en conformité avec les normes émises par la Commission de l'IUPAC.

Caractéristiques de la détection ampérométrique

Suivant la définition déjà donnée, un biocapteur ampérométrique (BA) est constitué par deux unités opérationnelles de base : le récepteur et le transducteur. Dans le cas de BA, le transducteur est de type ampérométrique. Celui-ci est constitué notamment d'une électrode conventionnelle ou modifiée qui fournit à un potentiel contrôlé, comme signal de réponse, un courant électrique, entretenu par la réaction électrochimique d'une espèce chimique, résultante naturelle de la réaction biochimique ou d'un intermédiaire (médiateur redox), délibérément introduit dans la structure du BA (fig. 2).

Le récepteur peut être de type catalytique (enzyme, organite, cellule, tissu) ou de type non catalytique (anticorps, antigène).

La quantité du substrat impliquée dans la réaction électrochimique, qui est à la base du fonctionnement du transducteur ampérométrique (TA), est donnée par la loi de Faraday. L'intensité (densité) du courant obtenu au niveau de l'interface électrochimique active dépend de la concentration de l'espèce électroactive, du type de transport de masse de l'espèce électroactive et de la valeur du potentiel de l'électrode (par l'intermédiaire d'une relation de type Butler–Volmer).

La construction, les performances et les possibilités d'utilisation des BA dépendent exclusivement de la nature du signal d'excitation et des conditions de transport de masse de l'espèce électroactive vers l'électrode. Selon la forme du signal d'excitation du TA, on peut avoir des mesures ampérométriques (à potentiel contrôlé) ou voltamétriques (balayage de potentiel d'électrode) (25, 26).

Les techniques ampérométriques nécessitant un appareillage simple sont, par conséquent, très utilisées pour la caractérisation des BA. D'autre part, elles ont l'avantage de

Fig. 2. Types de détection ampérométrique directe et indirecte. Enz_{ox}–Enz_{red}, l'enzyme; Med_{ox}–Med_{red}, le médiateur; S, le substrat, P, le produit; X, le reactant ou produit électroactif.

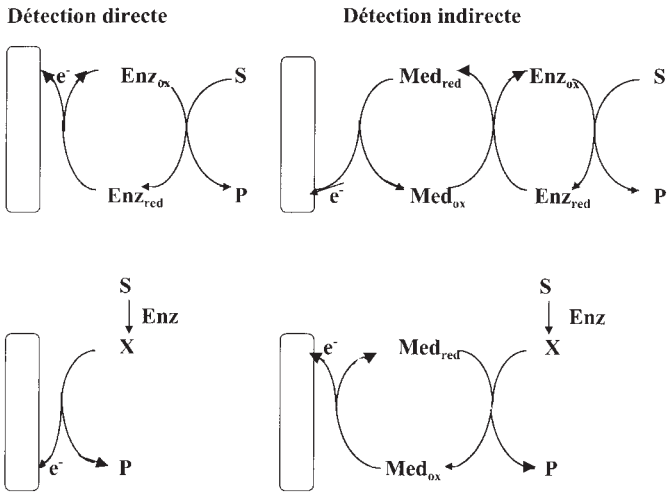

mesurer le courant à des valeurs fixes de potentiel d'électrode (généralement, dans la zone contrôlée par la diffusion), ce qui élimine la contribution du courant capacitif (limite de détection plus basse). Si la solution voisine du TA n'est pas agitée, le signal mesuré varie avec le temps (équation Cotrell), ce qui rend difficile les mesures. Différentes solutions ont été proposées : (*i*) utilisation des TA en régime hydrodynamique (électrode à disque tournant, électrode « wall-jet », etc.); (*ii*) insertion entre le BA et l'échantillon d'une barrière (membrane) qui limite l'augmentation en temps de l'épaisseur de la couche de diffusion; (*iii*) pulsation du potentiel d'électrode d'une valeur initiale correspondant à la zone d'inactivité électrochimique à une valeur finale située dans la zone d'activité électrochimique contrôlée par la diffusion; (*iv*) utilisation de microélectrodes (électrodes ayant une dimension caractéristique d'environ 1×10^{-6} m), avec leurs particularités remarcables (3), notamment : (*a*) le transport de l'espèce électroactive par diffusion sphérique, qui améliore l'accès de celle-ci vers la surface de l'électrode, et (*b*) le courant capacitif réduit, qui augmente le rapport signal/bruit.

Les techniques voltampérométriques (comme la voltampérométrie cyclique) ont d'excellentes capacités de diagnostic. Elles sont utilisées dans le processus d'élaboration et d'insertion du BA dans différentes techniques d'analyses. Les difficultés liées aux appareillages utilisés et à la contribution relativement importante du courant capacitif ($i_c \sim$ vitesse de balayage) limitent l'utilisation de ces techniques pour la détection ampérométrique.

Il est intéressant de remarquer que la sélectivité du BA, déterminée principalement par l'enzyme, peut être aussi modulée par le contrôle adéquat des étapes qui interviennent dans le fonctionnement du TA associé : le transfert de charge à l'interface du TA (contrôle électrochimique) et le transfert de matière vers l'électrode (contrôle hydrodynamique).

Techniques d'immobilisation de l'élément biologique

Les caractéristiques des capteurs à enzyme dépendent des propriétés de l'enzyme immobilisée (27). Dans le cas de l'immobilisation, l'enzyme soluble dans un milieu aqueux se

© 2002 CNRC Canada

Tableau 1. Avantages et inconvénients de l'enzyme immobilisée (31–34).

Avantages	Inconvénients
Augmentation de la stabilité de l'enzyme vis-à-vis de la modification du pH ou de la température;	Augmentation de la complexité du système étudié;
Diminution du coût de l'analyse due à la réutilisation de l'enzyme;	Nécessité pour le substrat de diffuser vers l'enzyme et pour le co-substrat ou le produit de diffuser vers le transducteur;
Fonctionnement sur de longues périodes;	
Utilisation directe de l'enzyme dans le milieu réactionnel qu'il catalyse;	Modifications des propriétés de l'enzyme dues aux interactions support – site actif de l'enzyme et aux différences entre la phase aqueuse et le microenvironnement de l'enzyme
Séparation rapide du milieu réactionnel;	
Utilisation dans des solvants organiques ou à haute température, conditions dans lesquelles normalement l'enzyme perd son activité;	
Facilité de mise en oeuvre des réacteurs en continu; Limitation des interférences	

Fig. 3. Techniques d'immobilisation de l'enzyme.

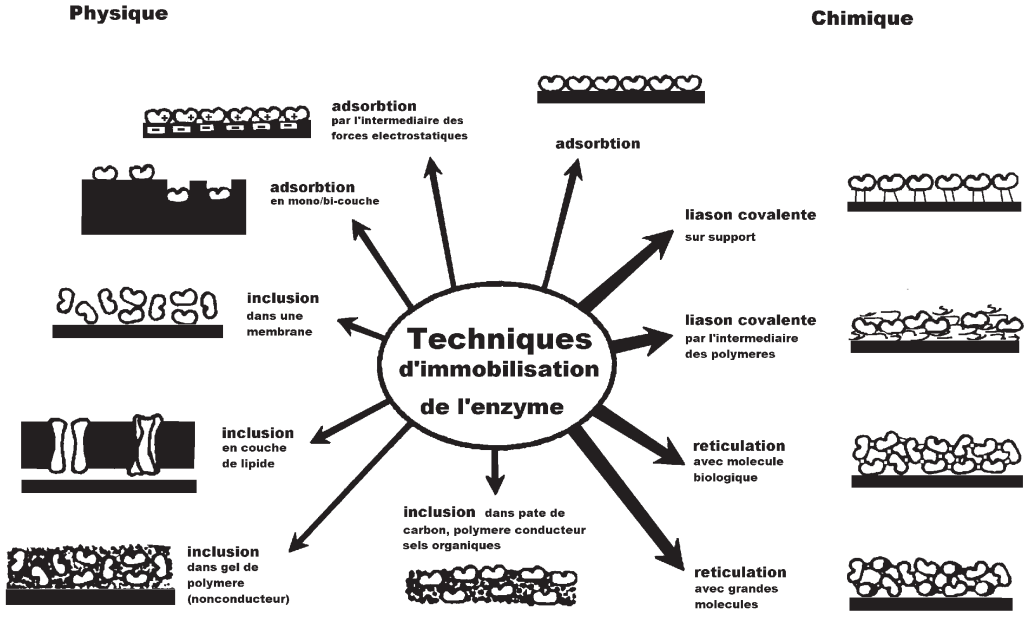

fixe dans une matrice insoluble dans l'eau. Ainsi, on observe une décroissance artificielle de la mobilité de l'enzyme, associée à une transformation de la catalyse homogène en une catalyse hétérogène (28).

Les principales techniques d'immobilisation de l'enzyme sont présentées dans la figure 3.

Les méthodes d'immobilisation doivent garantir (28–30) : (*i*) le maintien de l'intégrité de la conformation tertiaire de l'enzyme, en particulier au niveau du site actif; (*ii*) l'accès du substrat au site actif de la biomolécule; (*iii*) le transport du substrat et du produit à travers la couche biologique immobilisée.

Après immobilisation, les propriétés de l'enzyme peuvent être modifiées par suite des effets conformationnels, des effets stériques et des effets de transfert de matière. Il est évident que les modifications observées sur les propriétés enzymatiques après immobilisation sont la résultante des différents facteurs cités, l'effet de chaque facteur isolé étant à déterminer.

Les avantages et les inconvénients de l'immobilisation de l'enzyme sont présentés dans le tableau 1.

Biocapteurs ampérométriques à cholinestérases

Les cholinestérases

Classification

Les cholinestérases sont divisées en acétylcholinestérase (E.C. 3.1.1.7.) (AChE) et en pseudocholinestérase (E.C. 3.1.1.8.) (p. ex. butyrylcholinestérase) (BuChE) (35–38).

© 2002 CNRC Canada

Historique

L'acétylcholinestérase a été découverte en 1938 par David Nachmanson. Il a isolé et purifié cette enzyme à partir des membranes excitables provenant des nerfs de différents mammifères, oiseaux, reptiles et insectes (39). La plupart des recherches, dirigées vers l'étude de sa structure, ont été réalisées avec de l'enzyme isolée et purifiée de la plaque électrique de l'anguille *Electrophorus electricus* (37, 40, 41).

Structure

L'enzyme est une protéine complexe qui possède un centre anionique, un centre estérique, une multitude de centres périphériques et de nombreux domaines hydrophobes (39). Le site actif de l'enzyme contient le centre anionique, qui fixe les groupements cationiques du substrat (p. ex. sels d'ammonium quaternaire) et le centre estérique (qui possède une sérine), dont le OH est acylé pendant la réaction d'hydrolyse (42, 43) (fig. 4).

Le centre anionique contient des charges négatives, qui proviennent du groupement COO^- des chaînes latérales des acides aminés aspartique ou glutamique. Ce centre anionique permet la fixation des charges positives (p. ex. choline) provenant du substrat (35).

Les principales caractéristiques des cholinestérases sont présentées dans le tableau 2. D'autre part, il faut mentionner que de nombreuses études ont été élaborées sur le comportement des cholinestérases, dans des situations spécifiques, comme par exemple : le viellisement (37, 40, 42–49), l'inhibition des cholinestérases et l'inactivation thermique (50).

Techniques d'immobilisation des cholinestérases

Dans la plupart des applications, l'enzyme doit être immobilisée sous sa forme active (54). L'immobilisation diminue l'action des inhibiteurs irréversibles sur l'activité enzymatique (27). Dans le tableau 3 sont présentées les différentes modalités d'immobilisation de l'AChE et la BuChE (éventuellement couplées avec la choline oxydase, ChO) en fonction du type de détection utilisée. Le pH optimum d'immobilisation est situé entre 7,2 à 7,8 (54).

L'immobilisation de l'enzyme par « liaisons covalentes » met en jeu une réaction chimique, qui réalise une liaison irréversible entre la molécule d'enzyme et les groupements réactifs du support. À ce type de liaison s'ajoutent toujours des phénomènes d'électrosorption, qui consolident la liaison support–enzyme. La formation de la liaison covalente peut conduire à la modification de la structure tridimensionnelle de l'enzyme, altérant son activité enzymatique (28). Pour l'immobilisation de l'AChE par liaison covalente sur une surface de platine, on peut utiliser avec succès différentes méthodes de modification chimique du groupement OH présent sur la surface du support : (*i*) activation des groupements OH par le carbodiimide ou le chlorure de trésil, pour produire des groupements capables de réagir directement avec l'enzyme; (*ii*) modification basée sur la formation de pontages entre les groupements aminés d'un support et de l'enzyme par l'intermédiaire d'un ligand bi- ou multi-fonctionnel, ce qui permet d'écarter le biocatalyseur de son support solide et d'améliorer l'accessibilité du substrat au site actif de l'enzyme (29). De même, l'utilisation du glutaraldéhyde (GA), qui se lie sur les groupements aminés du silane, est également possible. D'autres réactifs hétérofonctionnels (ester

Fig. 4. La structure de l'acétylcholinestérase (A) et comparaison entre la structure de l'enzyme inhibée (B) et de l'enzyme non inhibée (C) (133).

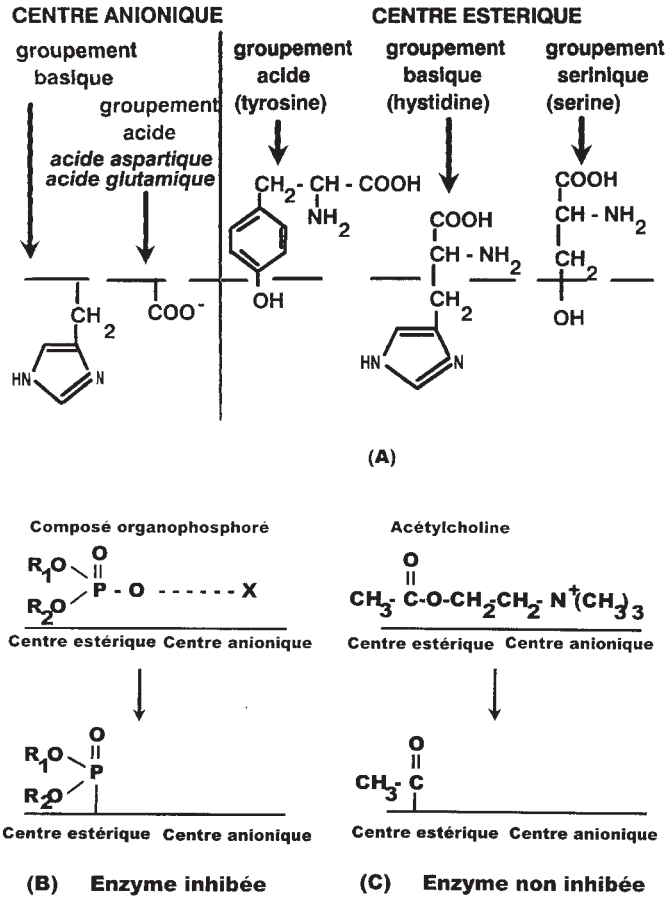

n-γ-maleimidobutyriloxisuccinamidique) sont utilisés et peuvent former des liaisons avec les fonctions thiols de silane (54).

Dans la technique de « co-réticulation », les molécules d'enzyme sont liées entre elles par pontages intermoléculaires, faisant intervenir des agents bi- ou multi-fonctionnels. On obtient ainsi des structures de très haut poids moléculaire. La co-réticulation avec GA fournit des films reproductibles, dans lesquels, la densité enzymatique, l'épaisseur et la nature de la protéine inactive peuvent être contrôlées (28).

Réactions utilisées dans le fonctionnement des biocapteurs ampérométriques à cholinestérases

Les deux principales étapes impliquées dans le fonctionnement des biocapteurs ampérométriques à cholinestérases sont : la réaction biochimique d'hydrolyse catalysée par l'enzyme et la détection électrochimique de l'espèce électroactive formée pendant la réaction biochimique. Les réactions possibles sont synthétisées dans le tableau 4.

Le mécanisme de l'hydrolyse — du plus simple substrat — l'acétylthiocholine (ASCh), catalysé par l'AChE, suit trois étapes (39) décrites dans les schémas suivants (fig. 5).

L'ASCh se fixe sur le site actif de l'enzyme par des liaisons électrostatiques, qui se forment entre la charge positive

© 2002 CNRC Canada

Tableau 2. Les propriétés des cholinestérases.

Caractéristiques	Acétylcholinestérase (E.C. 3.1.1.7.) (estérase spécifique, « vraie » cholinestérase)	Butyrylcholinestérase (E.C. 3.1.1.8.) (estérase non spécifique, pseudo– cholinestérase)
Masse moléculaire (Mét. d'équilibre de sédimentation)	260 000 ± 10 000 Da (40), dont 23,9 % sont dus aux carbohydrates (35)	340 000 Da (35)
Localisation	Tissus nerveux, musculaires, organe électrique, érythrocyte (prédominante) (37, 47), organe (thymus) (51)	Sérum (prédominante) (37), pancréas, foie, certaine glande salivaire (51); existe sous forme soluble dans l'eau (39)
Activateurs	$MgCl_2$, $CaCl_2$, Mn^{2+} et NaCl (51), KCl, $BaCl_2$ (48)	Métaux divalents, aminoacides et alcools (49)
Inhibiteurs	Uréthanes (fisostigmine, neostigmine), sels d'ammonium quaternaires (bleu de méthylène, choline, prostigmine), métaux lourds (30), amine, amide, composés hétérocycliques avec azote (alcaloïdes), alkyl-fluorophosphates, alkyl-polyphosphates, (barbituriques), nicotine, Pb^{2+}, F^- (51, 52)	
Inhibition par l'excès de substrat	Acétylcoline et d'autres substrats (53) en grande concentration (47, 49)	Non observé (47)
pH optimal	7,5–8 (47)	8,5 (47)
Points isoélectriques	4,65–4,7 (47)	4,0 (47)
Stabilité aux variations de pH	Faible (47)	Plus élevée (47)
Substrats possibles :		
Acétylcholine	+ (44)	+ (37, 44)
Propionylcholine	+ (44)	+ (44)
Butyrylcholine	+ (44)	+ (44, 47)
Tributyrylcholine	– (47)	+ (47)
Acétyl-β-méthylcholine	+ (37, 47)	– (37, 47)
Benzoylcholine	– (47)	+ (44, 47)
Phénilacetylcholine	– (47)	+ (47)
Atrolacétylcholine	– (47)	+ (36)
Succinylcholine	–	+ (53)
Butyrylcholine	–	+ (37)

de l'atome d'azote d'ASCh et la charge négative du site anionique de l'enzyme, formant un complexe enzyme–substrat (ES) (étape I). En même temps, la réaction d'acétylation de l'OH de la sérine du site estérique est catalysée par la présence du groupement imidazole basique de l'histidine et par le groupement acide AH (l'hydroxyl de tyrosine). Il y a alors formation de l'enzyme acétylée EA (étape I). La désacétylation (étapes II, III) est une réaction rapide, qui permet la libération de l'enzyme libre (E) en quelques millisecondes.

L'hydrolyse de l'ASCh catalysée par l'AChE, en considérant les deux étapes d'acétylation et de désacétylation, a un mécanisme identique à celui d'une réaction acide–base (39).

La détection électrochimique est réalisée par l'oxydation de la thiocholine – produit électroactif de la réaction biochimique – dans le cas du système monoenzymatique ou par l'oxydation–réduction (en fonction de transducteur) de l'eau oxygénée, dans le cas du système bienzymatique. L'oxydation peut avoir lieu directement sur l'électrode ou par l'intermédiaire des médiateurs redox. Ces différentes modalités de détection possibles seront détaillées et exemplifiées par la suite.

Application des biocapteurs ampérométriques à cholinestérases pour la détection des pesticides organophosphorés

L'utilisation des biocapteurs ampérométriques à cholinestérase est largement répandue pour la détection de la concentration globale en pesticides. Le principe de détection d'un biocapteur est fondé sur l'effet inhibiteur exercé par les pesticides sur l'enzyme immobilisée. La différence entre l'activité enzymatique initiale et celle enregistrée après une incubation dans un échantillon contaminé, fournit des informations d'un côté sur la présence des pesticides et de l'autre côté sur le potentiel toxique et la concentration de l'échantillon (80, 92–94).

Les différents types de biocapteurs ampérométriques utilisés pour la détection des pesticides présentés par la suite sont classifiés selon le type de cholinestérase immobilisée acétylcholinestérase (AChE) ou butyrylcholinestérase (BuChE) et selon le nombre d'enzymes immobilisées (mono-, bi- ou tri-enzymatique).

© 2002 CNRC Canada

Tableau 3. Modalités d'immobilisation de l'AChE et de la BuChE.

Enzyme	Techniques d'immobilisation	Membrane – support – agent d'immobilisation	Electrode de travail	Références bibliographiques
AChE	Inclusion	PVA-SbQ	Pt	55–57
	Liaison covalente	Nylon	Type Clark	58
		Polyéthylénimine 50 % + GA	CV	59
		GA + BSA – nylon	CV	10
		Couplage avec les sels de diazonium, condensation avec diimide – verre silanisé		60
		Nylon	CV	61
	Réticulation	GA	CoPC-SPE	62
		TCNQ – GE – BSA + GA	EG	63
AChE + ChO	Adsorption	Nylon modifié avec le diméthylsulfate + lysine + GA	Type Clark	64
		Pall immunodyne	Pt	65
		TTF-TCNQ – Pt	Pt	66
	Inclusion	PVA-SbQ	Type Clark	67, 68
	Réticulation	ChO + polyasetidine – dialyse AChE + BSA + GA	Pt	58
	ChO réticulation + AChE adsorption	ChO – nylon + GA + AChE – nylon	Type Clark	69
	Réticulation	GA – acétate de cellulose	Pt	70
	Réticulation	GA – nylon	Type Clark	71
	Liaison covalente	Polymère rédox (poly(4-vinylpyridine)Os(2,2′-bipyridine)$_2$Cl par l'intermédiaire de l'avidin	CV	72
			Pt	73
BuChE	Réticulation	GA – TCNQ-graphite	Grafite	74
BuChE + ChO	Inclusion	Membrane de dyalise	Type Clark	75
	Liaison covalente	Nylon Pall Biodyne modifié + carbodiimide	Type Clark	4
AChE ou BuChE	Réticulation	GA + nylon – immobilon Affinity	EPC	76
		GA + BSA	CoPC-EPC	77
AChE + ChO + HRP	Liaison électrostatique	Dialdehyde glutarique	Au	78
BuChE + ChO + HRP	Réticulation	GA	SPE	79

Nota : GA, glutaraldéhyde; CV, carbone vitreux; EPC, électrode à pâte de carbone; PVA-SbQ, alcool polyvinylique; TTF-TCNQ, tétrathiafulvalène-tétracianoquinodiméthane; EG, électrode en graphite; SPE, « screen printed electrode ».

Système monoenzymatique

L'utilisation de la technique ampérométrique monocholinestérique (AChE ou BuChE) nécessite l'utilisation comme substrat de l'acétylthiocholine ou de la butyrylthiocholine. Dans ce cas, la détection électrochimique est réalisée par l'oxydation de la thiocholine, conformément aux réactions 1 (tableau 4) (12, 55–57, 62, 63, 76, 77, 81–86, 95) ou réactions 2 (tableau 4) (57, 80–82, 87, 88).

Les conditions expérimentales de détection des pesticides et les limites de détection correspondantes sont présentées dans le tableau 5.

Du fait que la surtension d'oxydation du substrat (thiocomposé) sur le platine est relativement grande, on préfère utiliser des électrodes en carbone non- ou (et) modifiées. D'autre part l'oxydation de la thiocholine est un procès irréversible et suivant les conditions expérimentales (présence ou absence de l'oxygène, présence ou absence d'un médiateur) (62–63, 77, 96–100) la valeur du potentiel appliqué à l'électrode se situe dans l'intervalle entre –0,2 et –0,85 V/Ag/AgCl. Le mécanisme d'oxydation de la thiocholine (RSH) est analogue à celui de l'oxydation de la cystéine. La détermination du nombre d'électrons impliqués dans ce processus confirme que deux ions de Co (I) s'oxydent en même temps par interaction avec la liaison disulfurée du produit d'oxydation (RSSR) (99, 100).

L'immobilisation de l'AChE est possible par liaison covalente sur graphite modifié avec *N*-cyclo-hexyl-*N′* (2-*N*-méthylmorpholino) éthylcarbodiimide-4-toluènesulphonate (62, 101) ou par inclusion dans un mélange biocomposite, préparé de poudre de graphite, d'une résine époxydique (Epo-Tek H77) et de l'enzyme (12, 102). Dans ces cas, la détection de l'ASChI a lieu à +0,8 V/ESC (97) et de l'ASChCl à +0,7 V/Ag/AgCl. (12, 102) La réalisation d'une électrode biocomposite, dont la construction est simple et rigide, correspond à un biocapteur à usage unique très adéquat pour l'usage dans le domaine médical (102).

© 2002 CNRC Canada

Tableau 4. Réactions impliquées dans le fonctionnement des biocapteurs à cholinestérases.

	Schéma de réaction
	Système monoenzymatique
[1]	$\text{Acétylthiocholine} + H_2O \xrightarrow{AChE_{immobilisée}} \text{thiocholine} + \text{acide acétique}$
	$\text{Thiocholine} \xrightarrow{+0.41\ V/AgAgCl} \text{composé disulfure} + 2H^+ + 2e^-$
[2]	$\text{Butyrylthiocholine} + H_2O \xrightarrow{BuChE_{immobilisée}} \text{thiocholine} + \text{acide butyrique}$
	$\text{Thiocholine} \xrightarrow{+0.41\ V\ /\ AgAgCl} \text{composé disulfure} + 2H^+ + 2e^-$
	Système bienzymatique avec deux enzyme immobilisées
[3]	$\text{Acétylcholine} + H_2O \xrightarrow{AChE_{immobilisée}} \text{choline} + \text{acide acétique}$
	$\text{Choline} + 2O_2 + H_2O \xrightarrow{ChO_{immobilisée}} \text{bétaine} + 2H_2O_2$
	$H_2O_2 \xrightarrow{+0.6\ V\ /\ AgAgCl} O_2 + 2H^+ + 2e^-$
[4]	$\text{Butyrylcholine} + H_2O \xrightarrow{BuChE_{immobilisée}} \text{choline} + \text{acide butyrique}$
	$\text{Choline} + 2O_2 + H_2O \xrightarrow{ChO_{immobilisée}} \text{bétaine} + 2H_2O_2$
	$H_2O_2 \xrightarrow{+0.6\ V\ /\ AgAgCl} O_2 + 2H^+ + 2e^-$
[5]	$\text{Acétylcholine} + H_2O \xrightarrow{ChO_{immobilisée}} \text{choline} + \text{acide acétique}$
	$\text{Choline}[H_2] + \text{ChO}[\text{FAD}]_{\text{immobilisée}} \rightarrow \text{bétaine} + \text{ChO}[FADH_2]$
	$\text{ChO}[FADH_2] \xrightarrow{\text{eld TTF} - \text{TCNQ}} \text{ChO}[\text{FAD}] + 2H^+ + 2e^-$
	Système bienzymatique avec une enzyme libre
[6]	$\text{Acétylcholine} + H_2O \xrightarrow{AChE_{libre}} \text{choline} + \text{acide acétique}$
	$\text{Choline} + 20_2 + H_2O \xrightarrow{ChO_{immobilisée}} \text{bétaine} + 2H_2O_2$
	$H_2O_2 \xrightarrow{+0.6\ V\ /\ AgAgCl} O_2 + 2H^+ + 2e^-$
[7]	$\text{Butyrylcholine} + H_2O \xrightarrow{BuCHE_{libre}} \text{choline} + \text{acide butyrique}$
	$\text{Choline} + 2O_2 + H_2O \xrightarrow{ChO_{immobilisée}} \text{bétaine} + 2H_2O_2$
	$H_2O_2 \xrightarrow{+0.6\ V\ /\ AgAgCl} O_2 + 2H^+ + 2e^-$
	Système trienzymatique avec les enzymes immobilisées
[8]	$\text{Acétylcholine} + H_2O \xrightarrow{AChE_{immobilisée}} \text{choline} + \text{acide acétique}$
	$\text{Choline} + 2O_2 + H_2O \xrightarrow{ChO_{immobilisée}} \text{bétaine} + 2H_2O_2$
	$H_2O_2 + 2H^+ + 2\text{Med(red)} \xrightarrow{HRP} 2H_2O + \text{Med(ox)}$
	$\text{Med(ox)} + e^- \rightarrow \text{Med(red)}$

Nota : Med, médiateur redox.

Afin d'augmenter la stabilité de la biomolécule en vue de son immobilisation, sans que l'immobilisation ait un effet d'inactivation de l'enzyme, ceci a été possible grâce à la modification chimique de l'enzyme à l'aide des polymères synthétiques (p. ex. copolymère acrylamide – acide acrylique) et un agent de condensation comme le réactif Woodward (*N*-éthyl-5-phényloxazolium-3-sulphonate) (103). Une augmentation de la concentration du réactif Woodward réduit le nombre des liaisons hélicoïdales polymère–protéine, tout en maintenant l'activité enzymatique de l'AChE immobilisée.

Le matériel le plus utilisé pour la construction de l'électrode est le platine (55). On peut utiliser aussi une électrode d'argent recouverte d'un film de mercure. Le thiol formé pendant l'hydrolyse de l'iodure de butyrylthiocholine (BuSChI), en présence de BuChE immobilisée par réticulation avec GA sur une membrane de nitrocellulose, forme avec le mercure un composé électroactif, qui se réduit à un potentiel de –0,55 V/ECS. On obtient une limite de détection de 3×10^{-11} M de chlorophos (40). Un autre matériel souvent utilisé est la pâte de carbone, qui permet l'oxydation de la thiocholine à +0,61 V/Ag/AgCl (voltampérométrie hydrodynamique) (57).

Système bienzymatique à enzymes immobilisées

Lorsque l'on utilise l'acétylcholine comme substrat, le système cholinestérique doit être couplé avec une autre enzyme : la choline oxydase (ChO). La détection électrochimique est obtenue par l'oxydation de H_2O_2 produite dans la réaction biochimique sur une anode de platine (68, 71, 73, 96) ou par la mesure de la consommation de l'O_2 impliqué dans la réaction biochimique en utilisant une électrode Clark, conformément aux réactions 3 (tableau 4) (58, 71, 73, 75). Les différentes conditions expérimentales proposés pour la réalisation des biocapteur bienzymatique sont présentées dans le tableau 5.

L'inconvénient de la méthode bienzymatique est que l'étape d'oxydation de la choline peut être fortement influencée par les fluctuations de la teneur en O_2 dans le voisinage de l'électrode. Dans le cas où serait utilisée la détection ampérométrique d'H_2O_2, le fait que celle-ci a lieu à un potentiel relativement élevé, où certains composés peuvent être facilement oxydés, rend la méthode sensible aux interférences (104, 105).

Le plus simple modèle de biocapteur bienzymatique consiste à associer une anode de platine et une cathode de Ag/AgCl (électrode Clark) et à les recouvrir ensuite d'une matrice enzymatique à base d'une membrane d'acétate de cellulose protégée par une membrane Immobilon™. La membrane d'acétate de cellulose protège l'anode de platine contre les éventuels interférents électrochimiques chargés négativement (p. ex. : phénols), très répandus dans l'eau (91).

Les études par voltampérométrie cyclique, avec une électrode d'or recouverte d'une membrane AChE + ChO, soulignent l'importance du transport de masse à l'intérieur de la matrice bienzymatique (tableau 4, équation [3]). L'hydrolyse, au niveau de la couche enzymatique, de l'acétylcholine (ACh) libre en choline (Ch), en présence d'AChE immobilisée, est réalisée avec un bon rendement. La concentration du produit (Ch) dans la matrice enzymatique est proportionnelle avec la concentration de l'ACh en phase aqueuse. Il est possible qu'il existe une lente libération de la Ch du réseau enzymatique, mais la choline oxydase fixe ce produit d'hydrolyse (Ch) avec une sensibilité qui dépend de la concentration d'ACh libre (ou de Ch dans la couche enzymatique) (106).

La voltampérométrie cyclique d'un médiateur (l'hexacyanoferrate (III)) sur une électrode de carbone vitreux avec l'AChE immobilisée indique un comportement irréversible du médiateur, contrairement au cas où l'électrode serait couverte de choline oxydase (ChO) quand le comportement du médiateur est réversible. Une relation non linéaire entre le

© 2002 CNRC Canada

Fig. 5. Mécanisme d'hydrolyse de l'acétylcholine catalysée par l'acétycholinésterase.

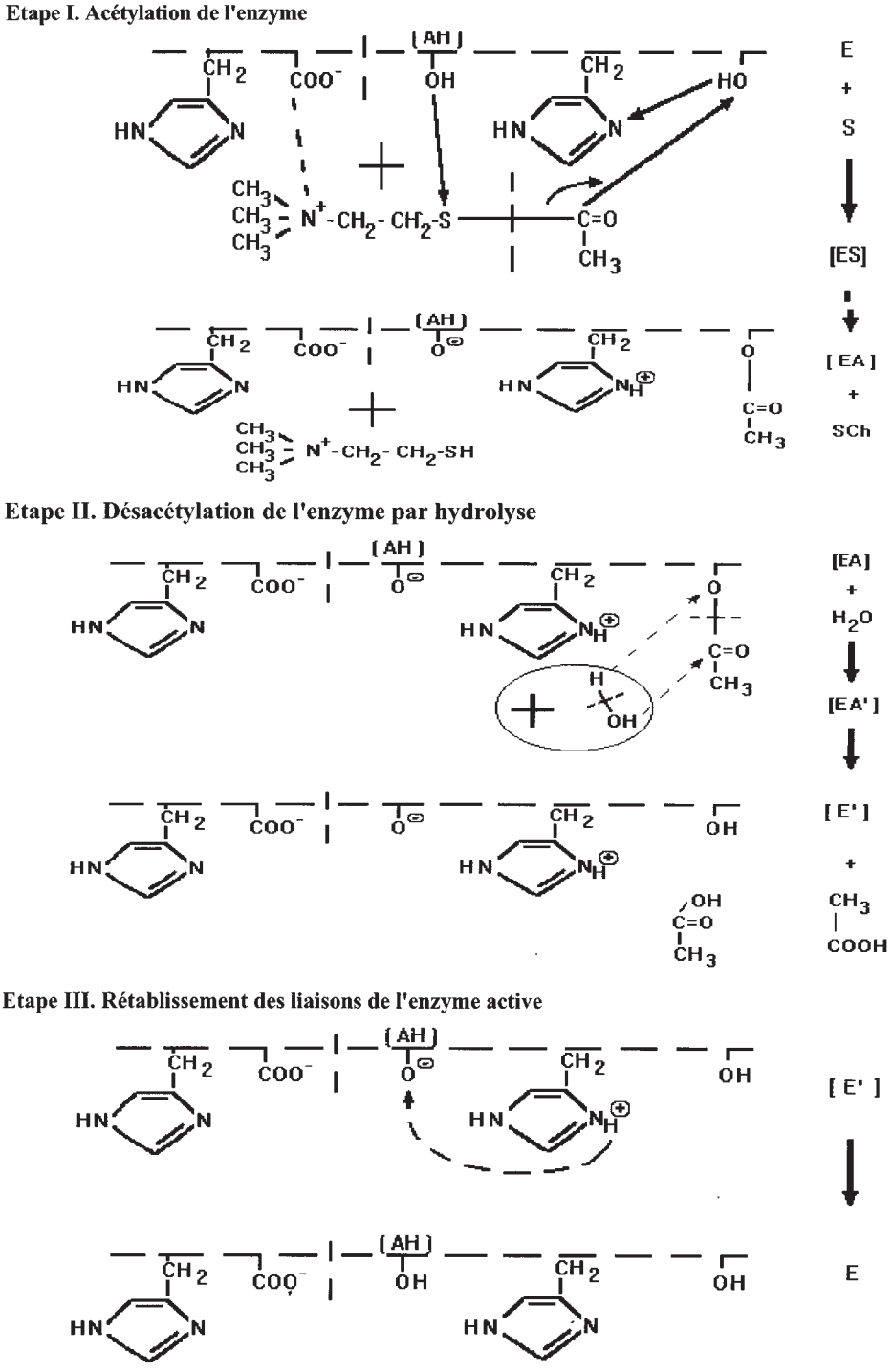

courant de pic (i_p) et la racine carrée de la vitesse de balayage des potentiels ($v^{1/2}$) est observée pour chaque électrode modifiée de ChO, AChE et AChE + ChO, indiquant un transfert de masse lent, dû à la complexité du film. Ainsi, les courbes i_p vs. $v^{1/2}$ révèlent, dans le cas des faibles vitesses de balayage des potentiels, un contrôle diffusif, suivi d'une limitation du courant dû au transfert des électrons observée aux grandes vitesses de balayage du potentiel. Ce phénomène de non linéarité est beaucoup plus prononcé quand l'électrode est modifiée avec un film bienzymatique (AChE + ChO). De même la différence de potentiel entre le pic anodique et le pic cathodique ($\varepsilon_a - \varepsilon_c$) augmente, si la complexité du film augmente (105).

Sur le même principe (réaction 3, tableau 4) a été imaginé un bioréacteur qui contient un complexe AChE–chitine immobilisée sur une colonne à l'aide du glutharaldéhyde (GA). La choline formée dans le réacteur passe dans un récipient contenant un biocapteur à ChO immobilisée sur une membrane de nylon (Pall Immunodyne Affinity) à l'aide de la polyazetidine. Avec ce système (en tampon phosphate, pH 7,5

© 2002 CNRC Canada

Tableau 5. Conditions expérimentales de détection des pesticides en solutions aqueuses à l'aide des biocapteurs ampérométriques.

Enzyme	Substrat	*pH** Température (°C)	*Potentiel appliqué* ET	Inhibiteur	Limite de détection	Références bibliographiques
AChE	ASCh	*7* 20	*0,7 V/Ag/AgCl* Graphite	Paraoxon Dichlorvos	27 μg L^{-1} 22 μg L^{-1}	12
		— 30	*0,410 V/Ag/AgCl* Pt	Différents pesticides	3,9–10,3 μg L^{-1}	55
		7,3 37	*0,3 V/Ag/AgCl* CoPC-EPC	Paraoxon Heptenophos	12 μg L^{-1} 1800 μg L^{-1}	96
		8 30	*0,410 V/Ag/AgCl* Pt	Paraoxon Trichlorfon	110 μg L^{-1} 5 μM	95
		7 20	*0 V/Ag/AgCl* SPE	Paraoxon	0,011–0,019 μg L^{-1}	62
		8 20	*0,41 V/ECS* Pt	Paraoxon	0,3–1 μg L^{-1}	56
		7,2 —	*0,1 V/ECS* Graphite	Paraoxon	49,5 μg L^{-1}	63
BuChE	BuSChCl	*7,3* 37	*0,3 V/Ag/AgCl* CoPC-EPC	Paraoxon Heptenophos	1,5 μg L^{-1} 8,4 μg L^{-1}	96
		7,4 20	*0,1 V/Ag/AgCl* Graphite-TCNQ	DIFP PMSF	0,06 ppm 8 ppm	74
	BuSChI	— 20	*0,61 V/Ag/AgCl* EPC	Diazinon	1,5–4 × 10^{-9} M	57
AChE + ChO	AChCl	*7* —	*0,6 V/Ag/AgCl* Pt	Paraoxon	0,14 ppb	58
		Glycine, 8,5 25	*0,65 V/Ag/AgCl* Pt	Paraoxon	10–100 ppb	71

Nota : CoPC-EPC, électrodes à pâte de carbone modifiée avec la phtalocyanine de cobalt (CoPC); CV, carbone vitreux; ET, électrode de travail; SPE, « screen printed electrode »; ECS, électrode de calomel saturée; TCNQ, 7,7,8,8-tetracyanoquinodiméthane; DIFP, diizopropylfluorophosphate; PMSF, fluorure de phénylmétylsulphonyl; *, tampon phosphate.

à 37°C) on obtient des limites de détection de 1 ppb de malathion et 10 ppb de paraoxon (107).

Le principe de fonctionnement d'un biocapteur avec BuChE + ChO immobilisées est décrit par les réactions 4 (tableau 4) (4, 75).

L'oxydation de l'H_2O_2 dans une solution de tampon glycine 0,1 M, pH 8 à 25°C permet d'obtenir un seuil de détection de 6 μg L^{-1} pour le malathion et de 2 μg L^{-1} pour le paraoxon. Les interférents du paraoxon sont : Pb^{2+}, Hg^{2+}, Cd^{2+}, F^-, PO_4^{3-}, $[Fe(CN)_6]^{3-}$, salicilate, arséniate, acétate, nicotine, nicotinate, nicotinamide, tyrosine, alanine, hexaméthylène tétramine, hydroxyéthylamine (4). La même électrode peut être utilisée en milieu organique — chloroforme–hexan (50 %, v/v) — pour la détection de 4,5 μg L^{-1} paraoxon (75).

Système bienzymatique avec l'acétylcholinestérase en solution et la choline oxydase immobilisée

Le principe de fonctionnement de ce type de biocapteur est présenté dans la réaction 6 (tableau 4) (58, 84). Dans ce cas il faut remarquer, d'une part, qu'on observe une adsorption de l'AChE sur la membrane du biocapteur, ce qui modifie la précision des mesures de l'activité de l'enzyme inhibée. D'autre part, en raison de l'hydrolyse spontanée du paraoxon à pH > 8, dans le cas de l'AChE libre ou immobilisée la stabilité du pesticide impose que l'incubation soit faite à pH 7, de façon à assurer une sensibilité maximale du biocapteur bi-enzymatique. Dans ces conditions, avec une électrode de platine polarisée à +0,6 V/Ag/AgCl (détection de l'oxydation de H_2O_2), on obtient une limite de détection de 2,6 ppb de paraoxon (58).

Système trienzymatique

La possibilité de la réalisation d'un biocapteur trienzymatique a été investiguée en utilisant la séquence des réactions 8 (tableau 4) (72, 73, 78, 79).

Les trois enzymes, l'AChE, la ChO et la peroxydase (HRP), ont été immobilisées en présence d'un polymère redox PVP-Os(bpy)$_2$Cl (chlorure de poly(4-vinylpyridine-Os-2,2′-bypyridine) et d'un agent réticulant, le polyéthylène glycol (PEG), sur une électrode en carbone vitreux (72). D'autres manières d'immobilisation utilisent la réticulation du mélange des trois enzymes avec glutharaldéhyde (GA) sur « screen-printed electrode » (79) ou à l'aide des liaisons

© 2002 CNRC Canada

Fig. 6. Profils de concentration du substrat et du produit de la réaction dans une membrane ayant une concentration enzymatique faible (A), et élevée (B); 1, zone de réaction; 2, zone morte (114).

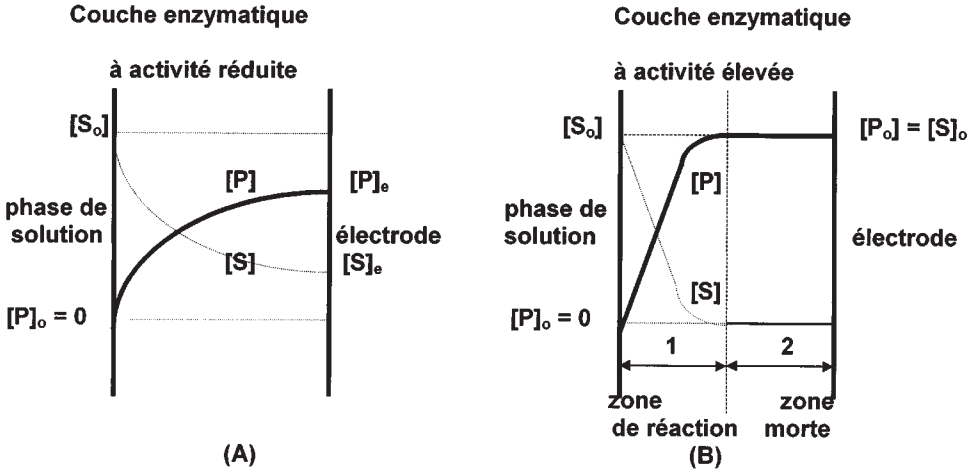

électrostatiques (« self-assembled ») par l'intermédiaire du dialdehyde glutharique sur une électrode en or (78), qui permet la détection de 1 ppb trichlorfon. Pendant l'utilisation du système trienzymatique il est important de contrôler l'hydrolyse spontanée du substrat l'ACh en Ch, qui a lieu quelques minutes après la préparation de la solution d'ACh. La réponse du biocapteur n'est pas satisfaisante, car la choline formée diffuse lentement vers la ChO et, de plus, l'AChE est inhibée par la suite de l'immobilisation dans le polymère redox qui contient de la pyridine, connue comme ayant une action inhibitrice (72).

Influence des conditions expérimentales sur le fonctionnement du biocapteurs ampérométriques à cholinestérases pour la détection des inhibiteurs

Tenant compte de la particularité de la détermination des pesticides à l'aide des biocapteurs enzymatiques, l'influence des conditions expérimentales sur leur fonctionnement doit être examinée séparément sur la réaction enzymatique (enzyme–substrat) et sur celle d'inhibition (enzyme–substrat–inhibiteur).

Influence des conditions expérimentales sur la réaction enzymatique

Nature du milieu tampon

Différents types de solutions tampon (phosphate, glycine, citrate ou acide 4-(2-hydroxyethyl)-piperazine-1-éthane sulfonique (HEPES)) ont été utilisés pour la détection des pesticides. On peut remarquer que certaines de ces solutions tampon contiennent des additifs (comme NaCl, $MgCl_2$, KCl, gélatine) ayant le rôle d'augmenter la stabilité de l'AchE (11, 12, 28, 40, 56, 59, 63, 74, 79, 108).

pH

La dépendance de la réponse du biocapteur du pH du milieu réactionnel repose sur son influence sur l'activité enzymatique de l'AChE (71, 108). Les paramètres cinétiques intrinsèques de l'enzyme immobilisée ne sont pas les mêmes que pour l'enzyme libre, à cause des contraintes conformationnelles, diffusionnelles ou stériques (65). Ainsi, une valeur de pH optimal pour l'activité de l'AChE de 8 a été observée en travaillant dans une solution de tampon phosphate pour l'enzyme immobilisée, alors que pour l'enzyme libre, dans les mêmes conditions, le pH optimal est 9. Le changement du pH optimum pour l'activité enzymatique provoqué par l'immobilisation de l'enzyme est un phénomène connu, fréquemment observé (109). Dans la littérature sont rapportées aussi d'autres valeurs du pH optimal : 7,2 à 8 (phosphate, borate) (62, 63, 76, 77, 8) (phosphate) (56, 109), (HEPES 2,5 mM) (108, 110) et 8,5 (glycine) (71).

Une relation entre la concentration du tampon et le courant généré par le BA a été observée. Généralement, le courant mesuré par le capteur diminue avec l'augmentation de la concentration du tampon. Néanmoins, à une valeur très faible de celle-ci, le courant de fond est très stable. Une solution tampon HEPES, ayant une force ionique de 2,5 mM, maintient une ligne de base stable, avec un minimum de dérive (108, 110).

L'utilisation de certains matériaux pour la réalisation des électrodes composites impose parfois le pH de travail. Par exemple, aux valeurs du pH plus élevées que 7, on a constaté une faible dégradation de l'électrode du graphite–epoxi(Epo-Tek H77)–AChE (12).

Température

La réponse du biocapteur est caractérisée par des valeurs maximales si la température du substrat est de 30°C (67) ou 40°C (110). Néanmoins, généralement les mesures sont effectuées dans l'intervalle de température entre 20 et 30°C, car à partir de 50°C l'enzyme est rapidement dénaturée. Pour améliorer la précision des mesures, la température de travail doit être maintenue à une valeur constante, pour éviter toute fluctuation de la réponse du biocapteur qui pourrait être interprétée comme une inhibition (76).

Nature de la matrice

Les caractéristiques de la matrice utilisée comme support pour l'immobilisation de l'enzyme ont un impact important

© 2002 CNRC Canada

sur les performances du biocapteur : le domaine de réponse linéaire, la sensibilité, le temps de réponse, la stabilité opérationnelle et au stockage pendant la conservation (111).

Dans le cas de l'utilisation d'un système de détection bienzymatique et d'un transducteur de type Clark en milieu biologique, il est recommandé de protéger la matrice enzymatique par une membrane de type Nafion, dont le rôle est d'empêcher l'interférence de l'acide ascorbique — électroactif au potentiel de travail de l'électrode — avec le signal de la choline ou de l'acétylcholine (112). D'autres membranes qui améliorent les propriétés mécaniques de la matrice enzymatique peuvent être l'acétate de cellulose (69) ou le nitrate de cellulose (113). Il faut souligner que la membrane de protection agit comme une barrière de diffusion de l'H_2O_2, produite dans la couche enzymatique, vers l'électrode, en réduisant de 40 % l'amplitude du signal (69). Ainsi, la membrane, en limitant la diffusion du substrat, de l'inhibiteur et de l'H_2O_2, diminue aussi le pourcentage d'inhibition, en réduisant à la fois la concentration d'inhibiteur décelable.

Concentration optimale de l'enzyme immobilisée

Le degré d'inhibition est une expression dépendante de la concentration d'enzyme immobilisée. Quand cette concentration est suffisamment élevée, le biocapteur n'est plus influencé par la présence des inhibiteurs en faible concentration. Ceci s'explique par l'évolution de la concentration du substrat ou du produit dans la couche enzymatique qui est fonction de la quantité d'enzyme immobilisée. Pour une faible concentration d'enzyme immobilisée, la concentration du substrat décroisse lentement dans la couche d'enzyme jusqu'à une valeur stationnaire [S_e], qui se trouve à la surface de l'électrode. Quand la concentration d'enzyme immobilisée est élevée, la consommation du substrat a lieu très vite, dans une région de la couche enzymatique dénommée « de réaction », pendant que la région « morte » est limitée par une « interface », dont la position dépend de la concentration d'enzyme immobilisée (114).

Le signal fourni par le biocapteur dépend de la quantité d'enzyme immobilisée suivant une fonction hyperbolique : (*i*) dans la zone de faible concentration d'enzyme immobilisée, le système est contrôlé par la cinétique enzymatique, le signal étant fortement dépendant de la quantité d'enzyme et de la présence des inhibiteurs ou activateurs; (*ii*) dans la zone de grande concentration d'enzyme immobilisée (palier), le système est contrôlé par la diffusion du substrat, l'enzyme étant en excès vis-à-vis des possibilités d'accès du substrat et, par conséquent, peu dépendant de la présence des inhibiteurs.

Pour une concentration donnée de pesticide, le degré d'inhibition augmente avec la diminution de la quantité de l'enzyme fixée. Ainsi, il est important de fixer de faibles quantités d'enzyme, pour pouvoir déceler des concentrations faibles de pesticides (71).

Influence des solvants organiques

Le remplacement de l'eau par des solvants organiques a parfois comme résultat le changement de la sélectivité de l'inhibiteur enzymatique (p. ex. les inhibiteurs forts de l'enzyme dans l'eau deviennent faibles en milieu organique et vice versa) (115, 116).

La corrélation entre l'activité enzymatique et le degré d'inhibition dû à certains inhibiteurs de type pesticides ou métaux a été étudiée jusqu'à présent essentiellement en milieu aqueux. Le remplacement de l'eau par d'autres solvants non aqueux et l'étude de l'inhibition de l'activité enzymatique dans ces milieux sont justifiés par le fait que certains inhibiteurs ne sont pas solubles ou peu solubles dans l'eau (116, 117).

L'utilisation des biocapteurs enzymatiques pour la détection de l'inhibition de l'activité enzymatique représente un grand intérêt pour l'évaluation et le suivi de la pollution de l'environnement (118). Il est connu que l'AChE, la tyrosinase et la peroxydase, libres ou immobilisées, peuvent être utilisées pour la détection des pesticides (119). Les résidus des pesticides, présents dans l'eau ou dans les aliments en concentrations réduites, peuvent être concentrés facilement en solvants organiques et, après, déterminés à l'aide des biocapteurs (45, 120).

Les études réalisées en milieu non aqueux avec l'AChE immobilisée ont permis de classer les solvants en trois groupes (45) : (*i*) solvants organiques fortement hydrophobes, non miscibles à l'eau, qui n'influencent pas l'activité enzymatique; (*ii*) solvants organiques hydrophobes, partiellement miscibles à l'eau, qui influencent partiellement l'activité enzymatique, la présence de l'eau dans la solution maintient une partie de l'activité enzymatique; (*iii*) solvants organiques hydrophiles (alcools), totalement miscibles à l'eau, qui inactivent totalement l'enzyme par la destruction de la monocouche d'eau nécessaire à son fonctionnement.

En même temps l'activité de l'AChE immobilisée peut être classifiée selon le paramètre de hydrophobicité (log *P*) du solvant, où *P* représente le coefficient de répartition du solvant entre 1-octanol et l'eau (30, 45) : (*i*) non décelable en solvants hydrophiles avec $\log P < 0$; (*ii*) variable en solvants avec $0 < \log P < 2$; (*iii*) forte en solvants hydrophobes avec $\log P > 2$.

Pour les inhibiteurs irréversibles, l'influence des solvants organiques sur l'effet inhibiteur est considérée moins forte que pour les inhibiteurs réversibles (30).

Facteurs influençant l'inhibition de l'enzyme

L'activité de l'enzyme immobilisée utilisée pour la détection des inhibiteurs peut être altérée par la présence des inhibiteurs irréversibles, lorsque leur concentration est élevée ou en cas d'utilisation dans des conditions « dures » (température élevée, pH acide), qui conduisent à la dénaturation de la protéine. Les principaux facteurs qui influencent l'inhibition de l'AChE sont présentés ci-dessous :

Concentration du substrat

L'action des inhibiteurs sur les cholinestérases immobilisées dépend non seulement de la nature de l'enzyme et de l'inhibiteur, mais aussi de la concentration du substrat (27). En comparant la cinétique de réaction en présence du substrat et en présence de l'inhibiteur, il resulte que dans la présence simultanée du substrat et de l'inhibiteur, le processus d'inhibition est une compétition entre le substrat et l'inhibiteur qui se rattachent au même site actif de la cholinestérase. Pour la détection des pesticides à l'aide des biocapteurs on peut utiliser soit l'inhibition en présence du substrat, soit mesurer l'activité enzymatique restante après

© 2002 CNRC Canada

l'incubation du biocapteur en présence de l'inhibiteur (10). La seconde méthode est plus souvent utilisée, car elle élimine la compétition substrat–inhibiteur pour l'enzyme immobilisée.

Temps d'incubation

Le temps d'incubation est déterminé par le degré d'inhibition de l'enzyme. À une concentration donnée de pesticide, le degré d'inhibition augmente jusqu'à une valeur limite avec l'augmentation du temps d'incubation (10, 71). Les systèmes d'analyse en flux (FIA) présentent l'avantage d'être reproductibles et éliminent la nécessité d'atteindre un signal stationnaire (56, 57, 110).

pH

La littérature mentionne que l'inhibition de l'AChE par les composés organophosphorés est maximale au pH physiologique, pH 7,4 pour systèmes bienzymatiques (optimum pour ChO) (114) ou pH entre 8 et 9 pour systèmes monoenzymatiques (30).

Température

Des températures élevées d'incubation entraînent la dénaturation de l'enzyme et l'hydrolyse spontanée du pesticide analysé (71). La température optimale d'incubation est généralement de 30°C, pour un temps d'incubation qui ne doit pas dépasser 30 min.

Nature du pesticide

L'AChE immobilisée est plus rapidement inhibée par les pesticides organophosphorés (paraoxon), que par les pesticides de type carbamates (carbaryl) (10). L'AChE immobilisée à l'aide du glutaraldéhyde (GA) et de l'albumine de sérum bovin (BSA) sur la surface d'une électrode à pH est inactivée irréversiblement en présence des pesticides organophosphorés (dichlorvos) (121, 122).

Régénération

En présence des pesticides organophosphorés, on constate que l'inhibition de l'activité des cholinestérases est irréversible. Mais, dans certaines conditions, l'activité enzymatique peut être totalement récupérée après un certain temps de lavage de l'électrode avec des solutions tamponnées ou, le plus souvent, après une incubation dans des réactifs nucléophiles (9).

La phosphorylation de l'oxime permet la régénération de l'enzyme inhibée et le rétablissement de l'activité enzymatique conformément les équations [9] :

$$[9] \qquad \text{EInh} + \text{R–H} \xrightarrow{K_r} \text{EInh–R–H} \xrightarrow{k_r} \text{E–H} + \text{RInh}$$

Le pourcentage de régénération se calcule en utilisant l'équation [10] (123) :

$$[10] \qquad \%\ \text{réactivation} = \frac{a_{EIA} - a_{EI}}{a_E - a_{EI}} \times 100$$

où : a_E = activité de l'enzyme native; a_{EI} = activité de l'enzyme inhibée; a_{EIA} = activité de l'enzyme réactivée avec régénérateur.

Le degré de régénération spontanée de l'AChE dépend du pH, de la température et de la structure chimique du radical fixé sur l'atome de phosphore.

Lorsque l'activité de l'AChE présente dans une membrane a été fortement inhibée, la régénération de l'activité enzymatique n'est plus totale. Ceci peut être dû au fait que le complexe oxime phosphorylé, formé à l'intérieur de la membrane, diffuse difficilement (124). La faible régénération est due à un processus d'hydrolyse d'un groupement alkyl d'une liaison O–P, lié à la génération simultanée d'une charge négative de l'oxygène du groupement O–P, qui empêche la régénération avec des réactifs nucléophiles (125). La constante de régénération de premier ordre ($k_{r,obs}$) est donnée par l'équation [11] :

$$[11] \qquad \ln\,(A_o - A_r) = -(k_{r,obs}t) + \ln\,(A_o - A_i)$$

où : A_o = activité avant inhibition; A_i = activité après inhibition; A_r = activité après régénération.

Dans la plupart des cas, la régénération de l'AChE se réalise avec la iodure de *N*-méthyl-2-pyridaldoxime (2-PAM) (8, 9, 37, 56, 59, 108, 109, 124–128), conformément à l'équation [12] (129).

Le mécanisme de régénération de l'AChE consiste dans l'attaque nucléophile de l'oxygène du 2-PAM sur l'atome de phosphore, attaque favorisée par l'alcalinité du reste d'histidine (fig. 7).

D'autres oximes peuvent servir à la régénération des cholinestérases : bromure de 1,1′,triméthylène-bis(4-formylpyridinium) dioxime; 4-PAM, 3-PAM (121); mononitrosoacetone (MINA) (110, 130); obidoxime (111, 125); hydroxylamine (9) imidazopyridinium 4-oxime (8) 1-benzyl 2-carbaldoxime pyridinium (8); bromure de 1,1′,triméthylène-bis-(4-hydroxi iminométhyl)pyridinium (TMB-4) (27, 57, 127, 130, 131); isonitrosoacétofenone (NAP) (127); diacétylmonoxime (DAM) (131); chlorure de (1–1,2-diméthyl-2-nitropropyloximéthyl)-2-(hydroxi imométhyl)-3-méthyl imidazolium (ICD467) (126); chlorure de (1,1,méthylène bis(4-(hydroxi iminométhyl)pyridinium) (MMB-4) (126); chlorure de (1-(((4-(aminocarbonyl)pyridinio)métoxi)méthyl)-2-((hydroxi imino)méthyl)pyridinium) (HI-6) (126); chlorure de (oxi-bis-(4-hydroxi iminoéthyl pyridinium-1-méthyl) (toxigonin) (60), sulphosuccinimidyl-6-(biotinamide)hexanoate de sodium (73).

L'efficacité de la régénération dépend de la structure du groupement organophosphoré lié à l'enzyme (8) et, donc, du type d'inhibition (124, 130). Les difficultés de régénération de l'activité enzymatique imposent de réétalonner les biocapteurs après l'inhibition et la régénération (109).

Aspects cinétiques des réactions enzymatiques

Étant donné que le fonctionnement du biocapteur ampérométrique à cholinestérase est basé sur une réaction catalysée par l'enzyme (réactions dans le tableau 4), il faut brièvement examiner les modalités connues pour aborder cette réaction, du point de vue cinétique, dans le cas de l'enzyme immobilisée.

Cinétique enzymatique en phase hétérogène

De nombreux chercheurs ont essayé de modeler la réaction enzymatique quand l'enzyme est immobilisée. La ciné-

© 2002 CNRC Canada

[12]

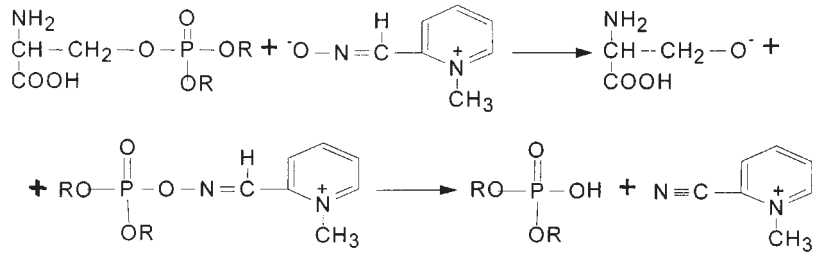

Fig. 7. Mécanisme de régénération de l'AChE inhibée le 2-PAM.

tique des réactions à enzyme immobilisée est complètement différente de celle à enzyme immobilisée parce que (30) : (*i*) l'immobilisation modifie la conformation de l'enzyme; (*ii*) l'interaction enzyme–substrat a lieu dans un milieu différent de celui de l'enzyme en solution; (*iii*) il existe une répartition du substrat entre la matrice contenant l'enzyme immobilisée et la solution; (*iv*) la réaction enzymatique peut être contrôlée par la diffusion.

Pour les enzymes immobilisées, en appliquant le traitement de Michaelis–Menten utilisé pour l'enzyme en solution, on peut déterminer une constante K_M apparente ($K_{M,app}$), qui n'est plus une caractéristique intrinsèque de l'enzyme, mais de la protéine immobilisée et de son environnement (donc du processus électroenzymatique). Cette constante cinétique dépend des phénomènes de diffusion, qui peuvent induire souvent des non linéarités sur les linéarisations utilisées pour calculer sa valeur.

Le processus global régissant le fonctionnement du capteur tient compte de la cinétique enzymatique, des phénomènes de diffusion à l'intérieur du matériau support de l'enzyme et aussi des étapes de transfert de charge avec l'électrode. Ces deux dernières ne sont pas déterminantes de vitesse (c'est-à-dire qu'elles n'interviennent pas dans la cinétique), si le potentiel de détection de l'espèce électroactive est correctement choisi et l'accès du substrat dans la matrice enzymatique est facile. Dans ce cas, la cinétique réactionnelle sera limitée par le processus biochimique. Ainsi, la cinétique peut être régie par la réaction enzymatique, si l'apport en substrat est suffisamment important. L'utilisation d'une convection forcée a été envisagée à l'aide d'une électrode tournante ou d'une agitation magnétique.

La réponse en courant du biocapteur constitue, en fait, une mesure de la vitesse du processus global (que l'on pourrait qualifier d'électroenzymatique), qui se déroule à l'électrode modifiée par le biomatériau. Du fait de la similitude des courbes *v* vs. [S] et *I* vs. [S], obtenues en phase homogène et avec une électrode à enzyme, il est possible d'utiliser le modèle de Michaelis–Menten pour modéliser le fonctionnement de l'électrode à enzyme (catalyse hétérogène). Ce procédé permet d'extraire des mesures expérimentales la constante Michaelis apparente ($K_{M,app}$) et le courant maximum ($I_{max,app}$). Bien que peu rigoureuses (puisqu'elles sont fortement dépendantes des conditions expérimentales), ces grandeurs sont très utiles pour caractériser globalement le comportement du biomatériel immobilisé.

Cinétique de la réaction d'inhibition de l'enzyme

Les inhibiteurs sont des substances capables d'interagir avec l'enzyme et, par conséquent, de réduire la vitesse de la réaction catalysée par l'enzyme. Il existe deux types d'inhibition de l'enzyme : réversible et irréversible. Dans l'inhibition réversible il existe un équilibre entre l'enzyme et l'inhibiteur. L'inhibition irréversible augmente avec le temps de contact enzyme–inhibiteur. Une inhibition totalement irréversible s'obtient quand la concentration de l'inhibiteur irréversible dépasse celle de l'enzyme.

Le mécanisme d'inhibition de l'AChE induit par les organophosphorés est analogue au mécanisme d'hydrolyse du substrat (l'équation 13) (132) et suit deux étapes (conformément les équations 14) :

[13] $$E + S \underset{k_{-1}}{\overset{k_1}{\rightleftharpoons}} ES \xrightarrow{k_2} E + P$$

[14] $$E\text{–}OH + InhX \underset{k_{-1}}{\overset{k_{+1}}{\rightleftharpoons}} E\text{–}OH\text{–}InhX \quad (E) + (P) \quad (EInH) \xrightarrow{k_2} E\text{–}OH\text{–}Inh + X \quad (EP)$$

où : k_1 et k_{-1} sont les constantes de vitesse en sens direct et inverse de la formation de l'intermédiaire (ES); k_2 constante de vitesse de la formation du produit (P). (*i*) La formation réversible, avec la constante k_{+1}, du complexe de Michaelis enzyme–inhibiteur (EInh) très stable; l'attaque de l'inhibiteur (InhX) ayant lieu au niveau du groupement OH de la sérine du site actif de l'enzyme. La stabilité du complexe EInh dépend de la nature du radical X (133); (*ii*) la phosphorylation de l'enzyme, avec la constante k_2, (la liaison de l'inhibiteur par l'intermédiaire de son atome de

© 2002 CNRC Canada

phosphore au site actif de l'enzyme) avec le déplacement du groupement X (15, 113, 134).

La cinétique de détection des pesticides organophosphorés s'étudie par l'incubation de l'enzyme (AChE) libre ou immobilisée en présence de l'inhibiteur suivie par la mesure de l'activité restante (9, 10, 96). Cette approche est basée sur l'équation d'Aldrige [15] (8, 10, 30, 59, 91, 96) :

$$[15] \qquad \ln \frac{I}{I_O} = k_a [\mathrm{Inh}] t$$

où : I_o = signal avant inhibition; I = signal après inhibition (10, 71, 96, 110, 135); k_a = constante bimoléculaire, calculée à l'aide de la relation $k_a = k_2/K_d$ (96, 135), K_d = constante de dissociation du complexe EInh, calculée comme $K_d = k_{-1}/k_{+1}$; [Inh] = concentration d'inhibiteur; t = temps d'incubation.

Conclusions

Étant donnée l'ample utilisation dans le domaine agricole des pesticides organophosphorés, très toxiques, les normes de qualité de l'environnement sont devenues de plus en plus sévères et impératives à appliquer. Dans ce contexte, les propriétés analytiques de biocapteurs doivent être similaires avec les méthodes analytiques utilisées couramment. Les caractéristiques spécifiques des détecteurs demandés pour le contrôle de l'environnement sont : (*i*) spécificité pour un seul substrat (utile dans l'analyse qualitative); (*ii*) mesure de l'effet toxique global pour les systèmes d'alarme; (*iii*) spécificité de groupe pour l'identification rapide d'une classe de substances (utile dans les mesures sélectives).

Le principe de détection des pesticides à l'aide d'un biocapteur ampérométrique est fondé sur leur effet inhibiteur exercé par ceux-ci sur différentes cholinestérases. La différence entre l'activité enzymatique initiale et celle enregistrée après une incubation dans un échantillon contaminé, fournit des informations, d'un côté, sur la présence des pesticides et, de l'autre côté, sur le potentiel toxique de l'échantillon.

La fragilité et la complexité de l'outil biologique le rendent difficile à maîtriser complètement et en même temps constituent le frein le plus important au développement des biocapteurs. Les techniques d'immobilisation, les caractéristiques du transducteur, la technologie associée à la conception du prototype sont les autres facteurs d'ordre scientifique influençant le développement des biocapteurs. Du point de vue commercial, la difficulté réside dans la définition des besoins et la taille encore réduite du marché de l'instrumentation pour l'environnement — fortement conditionnés par la réglementation — malgré que l'effort financier, soit de la recherche, soit des industries, est important.

Différents types d'application ont été classifiés selon le type de cholinestérase et du système enzymatique utilisé. Les meilleures limites de détection citées pour le paraoxon (le plus étudié organophosphoré) sont : 0,3 à 1 μg L^{-1} (AChE) (56) et 1,5 μg L^{-1} (BuChE) (96) ou 0,14 μg L^{-1} = ppb (AChE + ChO) (58) et 2 μg L^{-1} (BuChE + ChO) (4). Le niveau de concentration détecté par le biocapteur se situe au niveau d'alarme, donc il peut être utilisé dans les échantillons d'eau de rivière ou estuaire, quelques jours après l'application des pesticides (136). Ces valeurs sont relativement grandes en comparaison avec celles rapportées pour la technique immunologique (4 ng parathion) (137), ou bien pour la chromatographie en phase gazeuse (0,1 μg L^{-1} metsulfuron-methyl) (138) ou liquide (0,08 μg L^{-1} paraoxon) (139), qui reste comme méthode de référence. La comparaison entre les résultats obtenus à l'aide des biocapteurs et par d'autres méthodes démontre que le biocapteur à cholinestérase peut être employé pour développer une méthode de mesure en continu, applicable dans l'eau de rivière (140). Malgré certains avantages, le biocapteur n'est pas implementé totalement dans le monitoring de l'environnement parce qu'il doit accomplir encore des nécessités demandés pour les techniques robustes comme (*i*) la reproductibilité de longue et courte durée; (*ii*) l'absence des réponses interférentes et (*iii*) la solidité suffisante pendant l'utilisation dans différents matrices de l'environnement.

Bien que ce domaine de recherche ait été étudié depuis un peu plus d'une vingtaine d'années, la recherche active de collaborations pluridisciplinaires (biochimie, toxicologie, écotoxicologie, chimie, électrochimie, physique, électronique et informatique) est laborieuse, et plusieurs programmes nationaux des Ministères de la Recherche ou programmes internationaux coordonnés par la Communauté européenne sont en déroulement présentement.

L'intérêt scientifique pour l'étude et le développement de l'instrumentation analytique est matérialisé par la publication des livres (voir références bibliographiques), d'une revue spécialisée (Biosensors & Bioelectronics) et par l'organisation périodique des congrès spécialement dédiés à ce sujet (p. ex. : BIOSENSORS'98 – Berlin, le 5ème; ou Biosensors'2000 – San Diego le 6ème).

Bibliographie

1. B.J. Schaerter et R. Firstenberg-Eden. J. Food Prot. **51**, 811 (1988).
2. L. Campanella, R. Cocco et M. Tomassetti. J. Pharm. Biomed. Anal. **10**, 741 (1992).
3. E. Tamiya, Y. Sugiura, T. Takeuchi, M. Suzuki, I. Karube et A. Akiyama. Sens. Actuators B, **10**, 179 (1993).
4. L. Campanella, R. Cocco, M.P. Sammartino et M. Tomassetti. Sci. Total Environ. **123/124**, 1 (1992).
5. S.J. Updike et G.P. Hicks. Nature (London), **214**, 986 (1967).
6. J.Kang, V.H. Zettel et N.I. Ward. J. Nutr. Environ. Med. **5**, 325 (1995).
7. W.N. Dahl, A.M.R. Holm et K.H. Schroder. Anal. Chim. Acta, **93**, 91 (1977).
8. D. Kiffer et P. Minard. Biochem. Pharmacol. **35**, 2527 (1986).
9. A.M.N. Hendji, N. Jaffrezic-Renault, C. Martelet, P. Clechet, A.A. Shul'ga, V.I. Strikha, L.I. Netchiporuk, A.P. Soldatkin et W.B. Wlodarski. Anal. Chim. Acta, **281**, 3 (1993).
10. C. La Rosa, F. Pariente, L. Hernandez et E. Lorenzo. Anal. Chim. Acta, **308,** 129 (1995).
11. S. Kumaran et C. Tran-Minh. Electroanalysis, **4**, 949 (1992).
12. D. Martorell, F. Céspedes, E. Martinez-Fabregas et S. Alegret. Anal. Chim. Acta, **290**, 343 (1994).
13. J. Sherma. Anal. Chem. **67,** 1R (1995).
14. A. Bermond. Analusis Magazine, **22**, 8 (1994).
15. D. Heinrich et M. Hergt. Atlas de l'écologie. Librairie Générale de France, Paris. 1993. p. 200.
16. ***. Council Directive 80/778/CEE of 15 july 1980 relating to the quality of water intended for human consumption. Journal Officiel nº L229 du 30.08.1980. p. 8.

© 2002 CNRC Canada

17. D.R. Thevenot, K. Toth, R.A. Durst et G.S. Wilson. Sens. Actuators B, **30**, 81 (1996).
18. L. Blum et P. Coulet. Biosensors. Principles and applications. Marcel Dekker, New York. 1991.
19. A.P.F. Turner, I. Karube et G.S. Wilson. Biosensors. Fundamentals and application. Oxford University Press, New York. 1987.
20. R. Buck. Electrochim. Acta, **36**, 243 (1991).
21. C.-Y. Chen et I. Karube. Curr. Opin. Biotechnol. **3**, 31 (1992).
22. P.G. Edelman et J. Wang. ACS Symp. Ser. **487**, 3 (1992).
23. M.P. Byfield et R.A. Abuknesha. Biosens. Bioelecton. **9**, 373 (1994).
24. A. Sharma et K.R. Rogers. Meas. Sci. Technol. **5**, 461 (1994).
25. L. Oniciu, P. Ilea et I.C. Popescu. Electrochimie tehnologică. Casa cartii de stiinta, Cluj-Napoca. 1995. pp. 323–350.
26. I.C. Popescu. Senzori electrochimici. Lito Universitatea Babes-Bolyai, Cluj-Napoca, 1996.
27. L.P. Kuznetsova, L.I. Kugusheva, E.B. Nikol'skaya et O.V. Yagodina. Zh. Anal. Khim. **45**, 1426 (1990).
28. K. Stein et G. Schwedt. Anal. Chim. Acta, **272**, 73 (1993).
29. R. Scriban. Biotechnologie. 2e éd. Technique and documentation. Lavoisier, Paris. 1984.
30. G.A. Evtugyn, H.C. Budnikov et E.B. Nikolskaya. Talanta, **46**, 465 (1998).
31. A.M. Klibanov. Anal. Biochem. **93**, 1 (1979).
32. ***. Encyclopedia of chemical technology. *Éditeur* : Kirk-Otmer, vol. 9, 3e éd. John Wiley & Sons, New York. 1980. pp. 148–172.
33. L.D. Bowers. Anal. Chem. **58**, 513A (1986).
34. J.L. Boitieux et D. Thomas. Évolution des capteurs biologiques en biotechnologie. 4e Conférence annuelle sur les récepteurs et les biocapteurs, 22 et 23 septembre 1988, pp. 191–209. Paris : Press Universitaire, Paris.
35. O. Lockridge. Bioessays, **9**, 125 (1988).
36. A. Chatonnet et O. Lockridge. Biochem. J. **260**, 625 (1989).
37. P. Mineau. Cholinesterase inhibiting insecticides. Their impact on wildlife and the environment, vol. 2. Elsevier, Amsterdam. 1991. pp. 3–123.
38. J. Massoulie, J. Sussman, S. Bon et I. Silman. Structure and functions of AChE and BuChE. *Dans* Progress in brain research. vol. 98. *Éditeur* : A.C. Cuello. Elsevier, Amsterdam. 1993. pp. 139–146.
39. R.T. Fukuto. Environ. Health Perspect. **87**, 245 (1990).
40. W. Leuzinger, M. Goldberg et E. Cauvin. J. Mol. Biol. **40**, 217 (1969).
41. F. Villatte, V. Marcel, S. Estrada-Mondaca et D. Fournier. Biosens. Bioelecton. **13**, 157 (1998).
42. F.B. Hasan, S.G. Cohen et J.B. Cohen. J. Biol. Chem. **255**, 3898 (1980).
43. B.S. Zhorov, N.N. Shestakova et E.V. Rozengart. Quant. Struct. Act. Relat. **10,** 205 (1991).
44. Z. Radic, N.A. Pickering, D.C. Vellom, S. Camp et P. Taylor. Biochemistry, **32**, 12 074 (1993).
45. N. Mionetto, J.-L. Marty et I. Karube. Biosens. Bioelecton. **9**, 463 (1994).
46. I. Silman et A.H. Futerman. Eur. J. Biochem. **170,** 11 (1987).
47. W. Pilz. Acetylcholinesterase. *Dans* Methods of enzymatic analysis. *Éditeur* : H.-U. Bergmeyer. Verlag Chemie GmBH, Academic Press, New York. 1963.
48. P.J. Garry. Clin. Chem. **17**, 183 (1971).
49. N. Mionetto. Biocapteur ampérométrique pour la détection d'insecticides à action anticholinestérasique. Étude en milieu organique et applications. Thèse de doctorat, Université de Perpignan (France). 1993.
50. S.K. Burgess et S.L. Oxendine. J. Protein Chem. **12**, 651 (1993).
51. K.B. Augustinsson. Acetylcholine esterase and cholinesterase. *Dans* The enzymes. *Éditeurs* : J. Sumner et K. Myrback. Vol. 1, partie 1. Academic Press, New York. 1950. pp. 441–472.
52. J. Leyden Webb (*Éditeur*). Enzyme and metabolic inhibitors. Academic Press, New York. 1963. pp. 146–285.
53. S.G. Cohen, S. Bano Chishti, D.A. Bell, S.I. Howard, E. Salih et J.B. Cohen. Biochim. Biophys. Acta, **1076**, 112 (1991).
54. S.K. Bhatia, M.J. Cooney, L.C. Shriver-Lake, T.L. Fare et F.S. Ligler. Sens. Actuators B, **3**, 311 (1991).
55. J.-L. Marty, N. Mionetto, S. Lacorte et D. Barcelo. Anal. Chim. Acta, **311**, 265 (1995).
56. G. Jeanty et J.-L. Marty. Biosens. Bioelectron. **13**, 213 (1998).
57. G.A. Evtugyn, A.N. Ivanov, E.V. Gogol, J.-L. Marty et H.C. Budnikov. Anal. Chim. Acta, **385**, 13 (1999).
58. C. Cremisini, S. Di Sario, J. Mela, R. Pilloton et G. Palleschi. Anal. Chim. Acta, **311**, 273 (1995).
59. D.M. Ivnitskii et J. Rishpon. Biosens. Bioelectron. **9,** 569 (1994).
60. G. Baum, F.B. Ward et H.H. Weetall. Biochim. Biophys. Acta, **268**, 411 (1972).
61. F. Pariente, L. Hernandez et E. Lorenzo. Anal. Chim. Acta, **273**, 399 (1993).
62. J.J. Rippeth, T.D. Gibson, J.P. Hart, I.C. Hartley et G. Nelson. Analyst, **122**, 1425 (1997).
63. Y.-G. Li, Y.-X. Zhou, J.-L. Feng, Z.-H. Jiang et L.-R. Ma. Anal. Chim. Acta, **382**, 277 (1999).
64. M. Mascini et D. Moscone. Anal. Chim. Acta, **179**, 439 (1986).
65. R.M. Morelis et P.R. Coulet. Anal. Chim. Acta, **231**, 27 (1990).
66. P.C. Pandey, C. Tran-Minh et F. Lantreibecq. Appl. Biochem. Biotechnol. **31**, 145 (1991).
67. E.N. Navera, K. Sode, E. Tamiya et I. Karube. Biosens. Bioelectron. **6**, 675 (1991).
68. J.-L. Marty, K. Sode et I. Karube. Anal. Chim. Acta, **228**, 49 (1989).
69. T.N. Nwosu, G. Palleschi, et M. Mascini. Anal. Lett. **25**, 821 (1992).
70. Z. Huang, R. Villarta-Snow, G.J. Lubrano et G.G. Guilbault. Anal. Biochem. **215**, 31 (1993).
71. M. Bernabei, C. Cremisini, M. Mascini, et G. Palleschi. Anal. Lett. **24**, 1317 (1991).
72. M.G. Garguilo, N. Huynh, A. Proctor et A.C. Michael. Anal. Chem. **65**, 523 (1993).
73. Q. Chen, Y. Kobayashi, H. Takeshita, T. Hoshi et J.-I. Anzai. Electroanalysis, **10**, 94 (1998).
74. J. Kulys et E.J. D'Costa. Biosens. Bioelectron. **6**, 109 (1991).
75. L. Campanella, S. de Luca, M.P. Sammartino et M. Tomassetti. Anal. Chim. Acta, **385**, 59 (1999).
76. P. Skladal. Anal. Chim. Acta, **269**, 281 (1992).
77. G.S. Nunes, P. Skladal, H. Yamanaka et D. Barcelo. Anal. Chim. Acta, **362**, 59 (1998).
78. L. Alfonta, E. Katz et I. Willner. Anal. Chem. **72,** 927 (2000).
79. M. Espinosa, P. Atanasov et E. Wilkins. Electroanalysis, **11**, 1055 (1999).
80. P. Skladal. Bioelectrochem. Bioenerg. **32**, 145 (1993).
81. A.L. Hart, W.A. Collier, et D. Janssen. Biosens. Bioelectron. **12**, 645 (1997).
82. G.S. Nunes, D. Barcelo, B.S. Grabaric, J.M. Diaz-Cruz et M.L. Ribeiro. Anal. Chim. Acta, **399**, 37 (1999).
83. F. Pariente, C. La Rosa, F. Galan, L. Hernandez et E. Lorenzo. Biosens. Bioelectron. **11**, 1115 (1996).
84. M. Khayyami, M.T. Perez Pita, N.P. Garcia, G. Johansson, B. Danielsson et P.-O. Larsson. Talanta, **45**, 557 (1998).

© 2002 CNRC Canada

85. M. Stoytcheva, V. Sharkova et J.-P. Magnin. Electroanalysis, **10**, 994 (1998).
86. M. Stoytcheva, V. Sharkova et M. Panayotova. Anal. Chim. Acta, **364**, 195 (1998).
87. R. Gruss, F. Scheller, M.J. Shao et C.C. Liu. Anal. Lett. **22**, 1159 (1989).
88. U. Wollenberger, U. Loffler, R. Gruss, W. Gopel et F.W. Scheller. Biosensors for choline, choline esters and inhibitors of choline esterase. *Dans* Biosensors: Fundamentals, technologies and applications. *Éditeurs* : F. Scheller et R.D. Schmid. GBF Monographs, vol. 17, VCH-Weinheim, 1992. pp. 35–41.
89. P.D. Hale et R.M. Wightman. Mol. Cryst. Liq. Cryst. **160**, 269 (1988).
90. L. Campanella, M.P. Sammartino et M. Tomassetti. Anal. Lett. **22**, 1389 (1989).
91. M. Bernabei, S. Chiavarini, C. Cremisini et G. Palleschi. Biosens. Bioelectron. **8**, 265 (1993).
92. M.-P. Marco et D. Barcelo. Meas. Sci. Technol. **7,** 1547 (1996).
93. P. Pandard et P. Vasseur. Rev. Sci. Eau, **5**, 445 (1992).
94. P. Gueneau et A.L. Etienne. Les capteurs environnementaux en France, Programme ECOTECH-CNRS, Meudon Bellevue. 1994.
95. G. Turdean, I. Peter, I.C. Popescu et L. Oniciu. Rev. Roum. Chim. **46**, 836 (1997).
96. P. Skladal et M. Mascini. Biosens. Bioelectron. **7,** 335 (1992).
97. M.K. Halbert et R.P. Baldwin. Anal. Chem. **57**, 591 (1985).
98. P. Skladal. Anal. Chim. Acta, **252**, 11 (1991).
99. J.P. Hart et C. Hartley. Analyst, **119,** 259 (1994).
100. S.A. Wring, J.P. Hart et B.J. Birch. Analyst, **116,** 123 (1991).
101. M. Stoytcheva. Anal. Lett. **27**, 3065 (1994).
102. S. Alegret, F. Céspedes, E. Martinez-Fàbregas, D. Martorell, A. Morales, E. Centelles et J. Munoz. Biosens. Bioelectron. **11**, 35 (1996).
103. Y.A. Osinkin, S.N. Popovich, V.V. Chupov et N.A. Plate. Polymer Sci. Ser. B, **36**, 858 (1994).
104. H.C. Budnikov, E.P. Medyantseva et S.S. Babkina. J. Electroanal. Chem. **310,** 49 (1991).
105. B. Lopez Ruiz, E. Dempsey, C. Hua et J. Wang. Anal. Chim. Acta, **173**, 425 (1993).
106. A. Riklin et I. Willner. Anal. Chem. **67**, 4118 (1995).
107. F. Botré, G. Lorenti, F. Mazzei, G. Simonetti, F. Porcelli, C. Botre et G. Scibona. Sens. Actuators B, **18–19**, 689 (1994).
108. C. Tran-Minh, P.C. Pandey et S. Kumaran. Biosens. Bioelectron. **5**, 461 (1990).
109. J.-L. Marty, N. Mionetto, T. Noguer, F. Ortega et C. Roux. Biosens. Bioelectron. **8**, 273 (1993).
110. S. Kumaran et C. Tran-Minh. Anal. Biochem. **200**, 187 (1992).
111. J.-L. Marty, N. Mionetto et R. Rouillon. Anal. Lett. **25**, 1389 (1992).
112. E.N. Navera, M. Suzuki, K. Yokoyama, E. Tamiya, T. Takeuchi et I. Karuba. Anal. Chim. Acta, **281**, 673 (1993).
113. N. Mionetto, R. Rouillon, J.-L. Marty. Z. Wasser-Abwasser-Forsch. **25**, 171 (1992).
114. C. Tran-Minh. Ion-Selective Electrode Rev. **7**, 41 (1985).
115. A. Zaks et A.M. Klibanov. J. Biol. Chem. **263**, 3194 (1988).
116. O. Adeyoju, E.I. Iwuoha et M.R. Smyth. Anal. Lett. **27**, 2071 (1994).
117. G. Turdean et L. Oniciu. Rev. Chim. **49**, 604 (1998).
118. N. Ronzani. Analusis, **22**, 249 (1994).
119. P.J. Gray et R.G. Duggleby. Biochem. J. **257**, 419 (1989).
120. P. Durand, J.M. Nicaud et J. Mallevialle. J. Anal. Toxicol. **8,** 112 (1984).
121. A. Zurn et H. Muller. Fresenius J. Anal. Chem. **346**, 589 (1993).
122. G. Schwedt et M. Hauck. Fresenius Z. Anal. Chem. **331**, 316 (1988).
123. S. Uehara, T. Hiromori, T. Suzuki, T. Kato, et J. Miyamoto. J. Toxicol. Sci. **18**, 179 (1993).
124. H. El Yamani, C. Tran-Minh, M.A. Abdul et D. Chavanne. Sens. Actuators, **15**, 193 (1988).
125. A.N. Ivanov, G.A. Evtugyn, R.E. Gyurcsanyi, K. Toth et H.C.; J.-L. Marty et T. Noguer. Analusis, **21**, 231 (1993). Budnikov. Anal. Chim. Acta, **404**, 55 (2000).
126. T.-M. Shih. Arch. Toxicol. **67**, 637 (1993).
127. I. Cheng-Wang et P.E. Braid. Biochim. Biophys. Acta, **481**, 515 (1977).
128. T. Ghous et A. Townshend. Anal. Chim. Acta, **372**, 379 (1998).
129. R.T. Fukuto. Environ. Health Perspect. **87**, 245 (1990).
130. A.M. Trammel, J.E. Simmons et R.T. Borchardt. Pharm. Res. 115 (1984).
131. T.E. Shellenberger. J. Environ. Sci. Health Part B Pestic. Food Contam. Agric. Wastes, **B15**, 795 (1980).
132. A.R. Main. Can. Med. Assoc. J. **100**, 161 (1969).
133. D. Fournier et A. Mutero. Comp. Biochem. Physiol. **108C**, 19 (1994); D. Fournier et A. Mutero. Comp. Biochem. Physiol. **108C**, 19 (1994).
134. S. Kumaran et M. Morita. Talanta, **42**, 649 (1995).
135. M.C. Quintero, M. Silva et D. Perez-Bendito. Talanta, **38**, 1273 (1991).
136. K.Y. Zhu et W.A. Brindley. Comp. Biochem. Physiol. **103B**, 147 (1992).
137. C.D. Ercegovici, R.P. Vallejo, R.R. Gettig, L. Woods, E.R. Bogus et R.O. Mumma. J. Agric. Food Chem. **29**, 559 (1981).
138. P. Klaffenbach et P.T. Holland. J. Agric. Food Chem. **41**, 396 (1993).
139. C.G. Pinto, J.L.P. Pavon et B.M. Cordero. Anal. Chem. **67**, 2606 (1995).
140. D.M. Ivnitskii et J. Rishpon. Anal. Chim. Acta, **282**, 517 (1993).

© 2002 CNRC Canada

Canadian Journal of Chemistry

Author Index
Volume 80, 2002

Revue canadienne de chimie

Index des auteurs
Volume 80, 2002

Amat-Guerri, F., 62
Andraos, J., 141
Arévalo, E.A., 76
Azad, M., 148
Bazzi, L., 106
Bertolotti, S., 62
Bhardwaj, N., 141
Bonal, C., 163
Bottomley, F., 55
Bridson, J.N., 155
Brion, C.E., 222
Brown, G.R., 89
Brown, R.S., 183
Brunet, E., 169
Buchanan, G.W., 148
Bunce, N.J., 200
Cargnoni, F., 235
Chapados, C., 113
Chiang, Y., 82
Chong, D.P., 222
Cobos, J.C., 292
Cole, J.G., 46
Cooper, G., 222
Daneault, S., 113
Decken, A., 31, 55
Delamere, C., 94
Detellier, C., 163
Dyker, C.A., 55
Edwards, J.P., 31
El Issami, S., 106
Filali-Mouhim, A., 68
Gadosy, T.A., 302
Galley, W.C., 89
García, N.A., 62
Garcia de la Fuente I., 292
García-Losada, P., 169
Gonzalez, J.A., 292
Green, D.F., 281
Haggi, E., 62
Hammouti, B., 106
He, W., 263
Hirahara, M., 207
Hu, C.Y., 222
Ingham, A.M., 155
Israëli, Y., 163
Jakins, C., 94
Janzen, M.C., 41
Jay-Gerin, J.-P., 68
Jenkins, H.A., 281
Jennings, M.C., 41
Jiang, F., 281
Jiang, X., 263
Juanes, O., 169
Kamerling, J.P., 76
Kertit, S., 106
Kinastowski, S., 192
Kluger, R., 217
Koerner, T.B., 183
Kresge, A.J., 82
Lefeber, D.J., 76
Lewandowska, E., 192
Lewars, E., 94
Leznoff, C.C., 141
Liu, X., 263
Loncke, P.G., 302
Lu, J., 263
Lu X., 228
Mahiuddin, S., 175
Mankhetkorn, S., 68
Max, J.-J., 113
Mayer, P.M., 25
McAuley, A., 155
McClelland, R.A., 269
Meesungnoen, J., 68
Meng, Q., 82
Miller, R.J.D., 1
Miskoski, S., 62
Morel, J.-P., 163
Morel-Desrosiers, N., 163
Nakamura, N., 207
Neil, M.A., 55
Norman, D.W., 31
Oniciu, L., 315
Parvez, M., 245
Peslherbe, G.H., 302
Pomeroy, R.K., 281
Poon, C., 25
Popescu, I.C., 315
Puddephatt, R.J., 41
Rodríguez-Ubis, J.-C., 169
Rolke, J., 222
Salghi, R., 106
Sanchez, C., 269
Sánchez, V., 133
Sauer, E., 269
Sauro, V.A., 250
Scavini, M., 235
Shi, Z., 222
Sorensen, T.S., 245
Stephan, W., 125
Stock, N.L., 200
Storr, A., 133
Sun, F., 245
Thompson, R.C., 133
Tsuchihashi, K., 207
Tsuzuki, H., 207
Turdean, G., 315
Vliegenthart, J.F.G., 76
Vogels, C.M., 31
Vukovic, S., 269
Wahab, A., 175
Wan, P., 46
Warkentin, J., 228
Westcott, S.A., 31
Whitcombe, T.W., 155
Williams, C.K., 89
Wnuk, S.F., 192
Wolfe, S., 222
Workentin, M.S., 250
Xie, Y., 263
Xu, C., 155
Xu, C., 155
Yamato, T., 207
Yap, G.P.A., 148, 281
Zheng, Y., 222
Zhu, L., 263
Zine, E., 106

© 2002 NRC Canada

PREVIEW / APERÇU

Forthcoming special issues / Numéros spécials à paraître

June 2002	In honour of Professor J. Bryan Jones
August 2002	In honour of Professor Ray Lemieux
November 2002	In honour of Professor Tris Chivers
June 2003	In honour of Professor Don Arnold

Forthcoming articles / Articles à paraître

Asymmetric total synthesis of (+)-*exo*-brevicomin based on enantioconvergent biocatalytic hydrolysis of an alkene-functionalized 2,3-disubstituted epoxide	S.F. Mayer, H. Mang, A. Steinreiber, R. Saf, and K. Faber
Multinuclear magnetic resonance studies of the aqueous products of the complexes *cis*- and *trans*-$Pt(Ypy)_2(NO_3)_2$ where Ypy = pyridine derivative	F.D. Rochon and C. Tessier
Size and temperature dependence of hydrocarbon solubility in concentrated aqueous solutions of urea and guanidine hydrochloride	G. Graziano
Size dependence of the solubility of nonpolar compounds in different solvents	G. Graziano
Sampling variance as a function of single-increment size for estimation of bitumen in an oil-sand core	Z. Gao and B. Kratochvil
Experimental and theoretical study of the photochemical and thermal decomposition of maleic and dichloromaleic anhydrides	A. Ionescu, N. Piétri, M. Hillebrand, M. Monnier, and J.P. Aycard
Effect of protein binding on charge transfer in DNA: a simple model based on the superexchange mechanism	A. Filali-Mouhim, M. Benrahmoune, and J.-P. Jay-Gerin
Hydrogénation électrocatalytique sur des catalyseurs composites de nickel et hydroxyde d'aluminium en cellule dynamique	P. Dubé, L. Brossard, et H. Ménard
Comparative study of the thermodynamic behaviour of the binary mixtures dimethyl carbonate + (benzene, *n*-heptane, cyclohexane, or toluene)	J.M. Pardo, D. González-Salgado, C.A. Tovar, C.A. Cerdeiriña, E. Carballo, and L. Romaní
Utilisation de vecteurs tournants pour l'optimisation de la formulation de mélanges de solvants	S. Alex
Assigning structures to diastereomeric aliphatic α,α'-dibromo ketones	M. Parvez, S.M.H. Kabir, T.S. Sorensen, F. Sun, and B. Watson

© 2002 NRC Canada

Effect of protein binding on charge transfer in DNA: A simple model based on the superexchange mechanism

Abdelali Filali-Mouhim, Mustapha Benrahmoune, and Jean-Paul Jay-Gerin

Abstract: The effect of protein binding on the electronic coupling between distant redox centers in DNA is investigated in DNA–protein complex systems using the superexchange formalism. The systems (bridges) studied are described by a tight-binding electronic Hamiltonian in which site orbitals interact with one another through an exponentially decaying function of distance. Based on the "continuous-medium approximation," previously developed for large homogeneous three-dimensional systems (J.-M. Lopez-Castillo et al. J. Phys. Chem. **99**, 6864 (1995)), the intervening bridge is defined by a unique dimensionless parameter Γ/E that controls the distance dependence of the electronic coupling. Here, E is the energy separation between the orbitals of the bridging medium and the redox sites (tunneling energy), and Γ is the electronic bandwidth of the bridge taken as a continuous medium. It was found that, for a given value of $(\Gamma/E)_{DNA}$ far from the DNA's resonance conditions and for $(\Gamma/E)_{protein}$ values near the protein's resonance conditions, the electronic coupling is independent of the donor–acceptor distance when the acceptor lies within the "recognition region" of DNA. Moreover, when the redox centers are located on both sides of this region, the electronic coupling is many orders of magnitude larger than it should be, far from the protein's resonance conditions.

Key words: DNA, DNA–protein complexes, long-range electron and hole transfers, electronic coupling, superexchange mechanism, energetic control, continuous-medium approximation.

Résumé : Nous avons étudié, dans le cadre du mécanisme de superéchange, l'effet de la présence d'une protéine sur le couplage électronique entre sites rédox distants dans des complexes ADN–protéines. Les systèmes étudiés sont décrits par un Hamiltonien électronique modèle, basé sur l'approximation des liaisons fortes, dans lequel les divers sites possèdent tous la même énergie et interagissent entre eux selon une fonction exponentielle de la distance. En s'appuyant sur la théorie de l' « approximation du milieu continu », développée précédemment pour le cas de larges systèmes homogènes tridimensionnels (J.-M. Lopez-Castillo et al. J. Phys. Chem. **99**, 6864 (1995)), le milieu intermédiaire entre le donneur et l'accepteur est défini par un paramètre unique, sans dimension, Γ/E, qui contrôle la dépendance en distance du couplage électronique. E est ici l'énergie séparant les orbitales de ce milieu de celles des sites rédox et Γ la largeur de bande électronique du milieu intermédiaire considéré comme milieu continu. Nous avons trouvé que, pour une valeur donnée du rapport $(\Gamma/E)_{ADN}$ loin des conditions de résonance de l'ADN et pour des valeurs de $(\Gamma/E)_{protéine}$ proches des conditions de résonance de la protéine, le couplage électronique est indépendant de la distance donneur-accepteur lorsque l'accepteur est situé dans la région de l'ADN dite de « reconnaissance ». De plus, lorsque les sites rédox sont situés de part et d'autre de cette région, le couplage électronique est de plusieurs ordres de grandeur supérieur à ce qu'il devrait être loin des conditions de résonance de la protéine.

Mots clés : ADN, complexes ADN–protéines, transferts d'électron et de trou à longue distance, couplage électronique, mécanisme de superéchange, contrôle énergétique, approximation du milieu continu.

Introduction

DNA–protein interactions are ubiquitous in nature. Nearly all of the main cellular functions where DNA is involved are carried out in conjunction with proteins. This variety of interactions can be divided into three major categories: regulatory, enzymatic, and structural (1, 2). Regulatory interactions are associated with DNA replication (DNA synthesis) and gene expression, while enzymatic interactions include transcription (RNA synthesis), replication, and DNA repair. Structural interactions involve small, globular proteins, called histones, which play a key role in packaging nuclear DNA into chromosomes. (The entire DNA–histone complex is known as chromatin.) Protein binding to a DNA molecule

Received 24 October 2001. Published on the NRC Research Press Web site at http://canjchem.nrc.ca on 9 April 2002.

A. Filali-Mouhim, M. Benrahmoune, and J.-P. Jay-Gerin.[1] Département de médecine nucléaire et de radiobiologie, Faculté de médecine, Université de Sherbrooke, Sherbrooke QC J1H 5N4, Canada.

[1]Corresponding author (e-mail: jaygerin@courrier.usherb.ca).

 DOI: 10.1139/V02-027 © 2002 NRC Canada

can be stabilized by electrostatic, hydrogen bonding, and (or) hydrophobic interactions, and usually occurs in a sequence-specific DNA region, termed "recognition region," which is selectively recognized by the protein through a discrete DNA-binding domain within its polypeptide chain (1–3).

Charge transfer (CT) through DNA and from proteins to DNA seems to play a crucial role in some of the above biological functions involving DNA–protein complexes (4). In particular, CT is the elementary step that triggers a repair mechanism following oxidative damage to the DNA (4–6). Most studies have hitherto focused on CT processes in a DNA environment alone (for reviews, see ref. 7), but recently CT in DNA–protein assemblies has been examined experimentally in the DNA–methyltransferase *Hha*I (M.*Hha*I) complex (8), where the wild-type enzyme bound to DNA significantly disrupts the base-pair stack and profoundly reduces the ability of DNA to mediate CT. In contrast, by use of a tryptophan mutant of native M.*Hha*I, which leaves the overall structure of the DNA without significant distortions, long-range oxidation damage to DNA is restored, demonstrating that bound proteins can modulate charge migration through the DNA (8). It was also reported that CT could be observed from histones to DNA in γ-irradiated chromatin at 77 K (9), as well as from DNA-bound tripeptides (Lys-Trp-Lys and Lys-Tyr-Lys) to DNA (10). At the theoretical level, recent studies (11) have provided evidence that electron transfer between the catalytic cofactor $FADH^-$ in DNA photolyase (an enzyme that catalyzes photorepair of thymine dimers in UV-damaged DNA by an electron-transfer reaction) and a thymine dimer bound in its active site is not direct, but indirect, with the adenine moiety acting as an intermediate. So far, however, complete three-dimensional structures of DNA–protein complexes have never been incorporated into computations, and many open questions still remain as to how DNA-binding proteins modulate CT reactions through DNA.

It is now clear that the DNA double helix, with its bridge system of four bases stacked upon each other, can act as a promoting medium for efficient one-dimensional CT over long distances (up to ~40–200 Å from the point of origin) (6, 7). Particularly in the last decade, the question of how excess electrons or holes migrate through DNA has attracted considerable interest and generated a great deal of controversy (12–14). During the past three years, however, aided by theoretical breakthroughs and more sophisticated experimental techniques, significant progress has been made toward elucidation of the mechanistic origin of CT processes in DNA (for recent reviews, see refs. 15 and 16). Among the various models that have been advanced, two principal mechanisms of CT in DNA are now considered to explain the wealth of existing experimental data (5–7, 13, 15–33). These are:

(*i*) A coherent, unistep charge tunneling between the localized donor and acceptor sites involving intervening bases as superexchange mediators (superexchange mechanism) (20–22, 34–38). This mechanism is characterized by the absence of any population physically residing on the DNA bridge during the CT process. The dependence of the CT rate constant on the donor–acceptor distance (R_{DA}) is of the form (39)

$$[1] \qquad k_{CT} \propto \exp(-\beta_{eff} R_{DA})$$

where the effective distance–decay coefficient β_{eff} is a characteristic of the bridge ($\beta_{eff} \approx 0.6$–1.8 $Å^{-1}$ for DNA bridges) (35). This single-step superexchange mechanism exhibits a strong dependence on distance, allowing only for short-range transfer.

(*ii*) An incoherent, multistep charge hopping between the bases of the bridge, with the charge wavefunction fully localized on each subsequent base (charge-hopping mechanism) (24, 25, 36, 37, 40–44). Here, the charge transfers by discrete jumps among the intervening bases (usually guanine (G) bases and multiple G units, in the case of hole transfer) in a random walk fashion until it reaches a trap site. The distance dependence of the CT rate constant is described by Ohm's law:

$$[2] \qquad k_{CT} \propto 1/N^{\eta}$$

where N is the number of DNA bases participating in the charge transport (or the number of hopping steps) and the exponent η has a value between 1 and 2 (36). This multistep charge-hopping mechanism depends only weakly on distance, allowing for long-range charge transport. A "transition" from superexchange to charge hopping when increasing the bridge length is found to occur at a "critical" bridge size N_x, which is determined by the energetics of the bridge, the donor–bridge energy gap, and the temperature (37).[2,3]

In comparison to DNA, CT reactions in proteins have been studied extensively at both the experimental and theoretical levels (see, for example, refs. 39, 51, and 52). It is now well established that native and "engineered" proteins can mediate long-range CT over lengths of several tens of angströms (up to ~10–30 Å) between distant redox centers (51, 52). The electronic coupling between these redox centers is a key parameter that controls CT rates in the molecules. Most theoretical approaches used to analyze experimental data were based on the superexchange mechanism (39).

[2] It is interesting to recall here the provocative data by Barton and co-workers (17, 45) in the early 1990s, suggesting a "molecular wire" mechanism in DNA, in which the charge can travel almost coherently through an electronic "π-way" of well-stacked DNA bases, according to a band-like motion (41, 46–48). This possibility that a DNA molecule might act as a conduction-band pathway for conducting electrical charge was first advanced by Eley and Spivey (49) nearly 40 years ago. The question of whether DNA behaves like a wire or like an insulator stimulated much debate (see, for example, ref. 12). Recent studies (12, 15, 20, 28), however, have highlighted that "DNA is by no means a wire," and that the mechanism underlying CT in DNA now appears to be a "sort of hybrid of two well-known CT processes," namely, superexchange and diffusive charge hopping, as mentioned above.

[3] While it now seems that charge carriers are indeed able to shuttle along a single DNA molecule over distances of at least a few tens of angströms, the situation of the electronic transport across long DNA ensembles (>400 Å) is much less clear. Various contradictory findings have been reported, ranging from well-insulating behavior to the support of superconducting currents through DNA (15, 50).

© 2002 NRC Canada

Fig. 1. Schematic representation of the conduction and valence energy bands (shaded areas) of the bridging medium in the framework of the CMA for $V_0 < 0$. In this case, $\Gamma < 0$ and the broadening of the electronic bands takes place on one side only (downwards in this case) of the initial orbital site energy E. $|\Gamma|$ is the electronic bandwidth and E_0 is the energy of redox sites taken as the zero of energy ($E_0 = 0$).

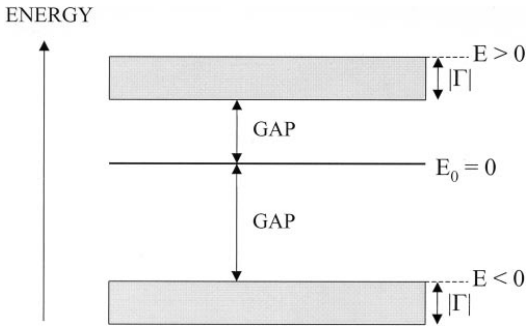

The present endeavor is devoted to the study of the effect of protein binding on the distance dependence of the electronic coupling between donor and acceptor in DNA using the superexchange formalism.[4] For this purpose, instead of focusing on a specific experimental system, here we investigate two DNA–protein model systems, whose energetic parameters are allowed to vary at will. The systematic variation of these parameters will provide us with information on how protein binding influences DNA-mediated CT characteristics.

Model

Formally, in the weak coupling or non-adiabatic limit, the CT reaction rate constant (k) is given by a generalized version of Fermi's Golden Rule (53):

$$[3] \qquad k = \frac{2\pi}{\hbar}\left|T_{DA}\right|^2 (FC)$$

where $\hbar$ is Planck's constant divided by 2π, T_{DA} is the bridge-mediated effective electronic coupling between the donor (D) and acceptor (A) site wavefunctions, and FC is the Franck–Condon factor, a measure of the nuclear motion coupled to the CT process. T_{DA} is given by the sum of the direct through-space interaction (V_{DA}) between the two redox sites and of the superexchange coupling (V_S) that con-

Fig. 2. Molecular structures of 1BBX and 4GAT from the Protein Data Bank (http://www.rcsb.org/pdb). The following DNA sequences are for (*i*) 1BBX: 5′-($C_1T_2A_3G_4C_5G_6C_7G_8C_9T_{10}A_{11}G_{12}$)-3′ and 5′-($C_{13}T_{14}A_{15}G_{16}C_{17}G_{18}C_{19}G_{20}C_{21}T_{22}A_{23}G_{24}$)-3′; (*ii*) 4GAT: 5′-($C_1A_2G_3C_4G_5A_6T_7A_8G_9A_{10}G_{11}A_{12}C_{13}$)-3′ and 5′-($G_{14}T_{15}C_{16}T_{17}C_{18}T_{19}A_{20}T_{21}C_{22}G_{23}C_{24}T_{25}G_{26}$)-3′. The DNA bases are individually indexed from 1 to 24 (1BBX) and from 1 to 26 (4GAT) sequentially from one 5′ end to the 3′ end of the opposite strand. 1BBX has 758 and 2077 atoms for the DNA and protein subsystems, respectively. 4GAT has 823 and 1032 atoms for the DNA and protein subsystems, respectively.

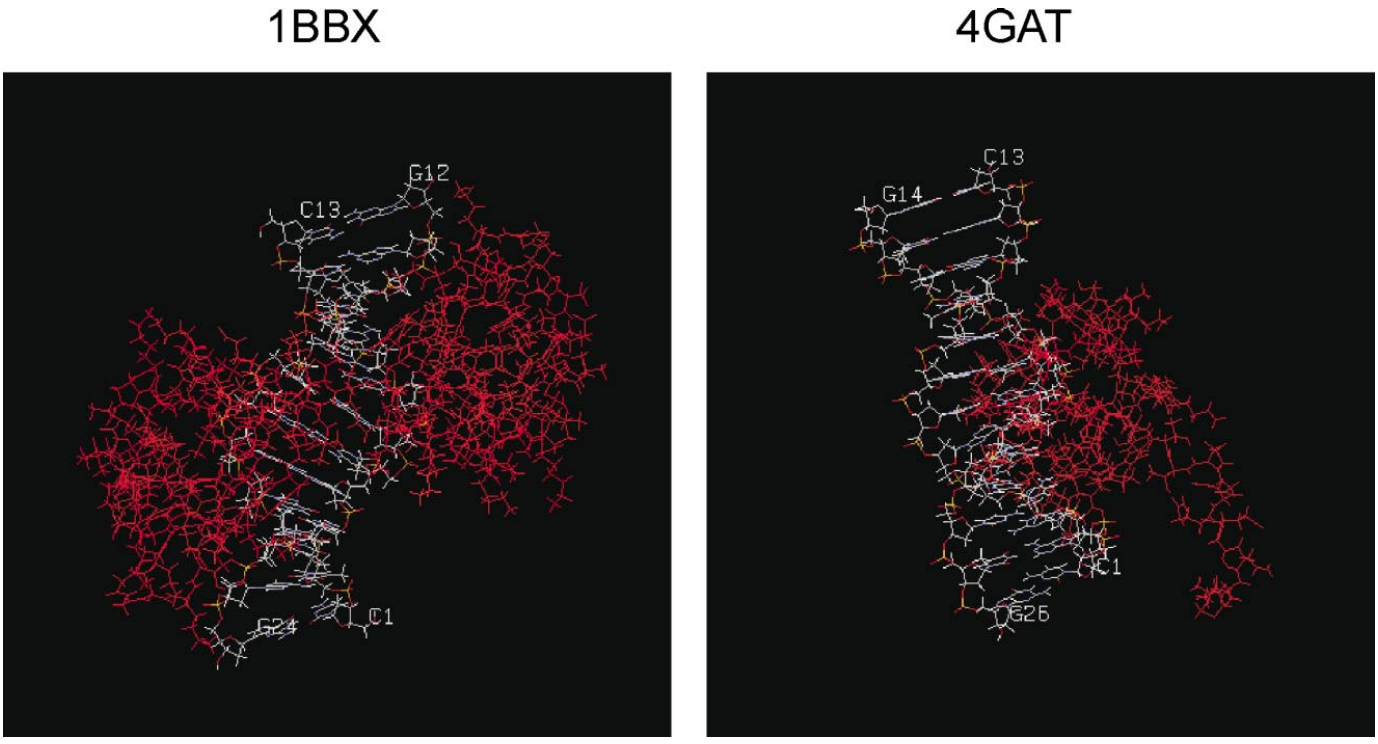

[4] As indicated above, most recent advances are leading to a growing consensus that, at ambient temperature, both superexchange and hopping mechanisms for CT are active in DNA, although in most systems their relative contribution is not known (30). At low temperatures (77 K or below), however, superexchange becomes free from competing phonon-like thermally activated hopping and will thus prevail as the principal mode of CT processes (see, for example, refs. 30, 31, and 36).

© 2002 NRC Canada

Fig. 3. Typical variations of $V_S/V_{DI}V_{FA}$ as a function of d_{IF} in the case of 1BBX for a fixed value of $(\Gamma/E)_{DNA} = -0.6$ (E_{DNA} = 3.58 eV) and various $(\Gamma/E)_{protein}$ values: (*a*) −0.2 ($E_{protein}$ = 7.65 eV); (*b*) −0.4 ($E_{protein}$ = 3.82 eV); (*c*) −0.6 ($E_{protein}$ = 2.55 eV); and (*d*) −0.8 ($E_{protein}$ = 1.91 eV). Here, the initial I site is located on atom C6 of the base 1 and we consider each of the other bases' C6 atoms as a possible final F site. The numbers in Fig. 3*c* refer to the bases' indexes of the 1BBX system, whose sequence is given in Fig. 2.

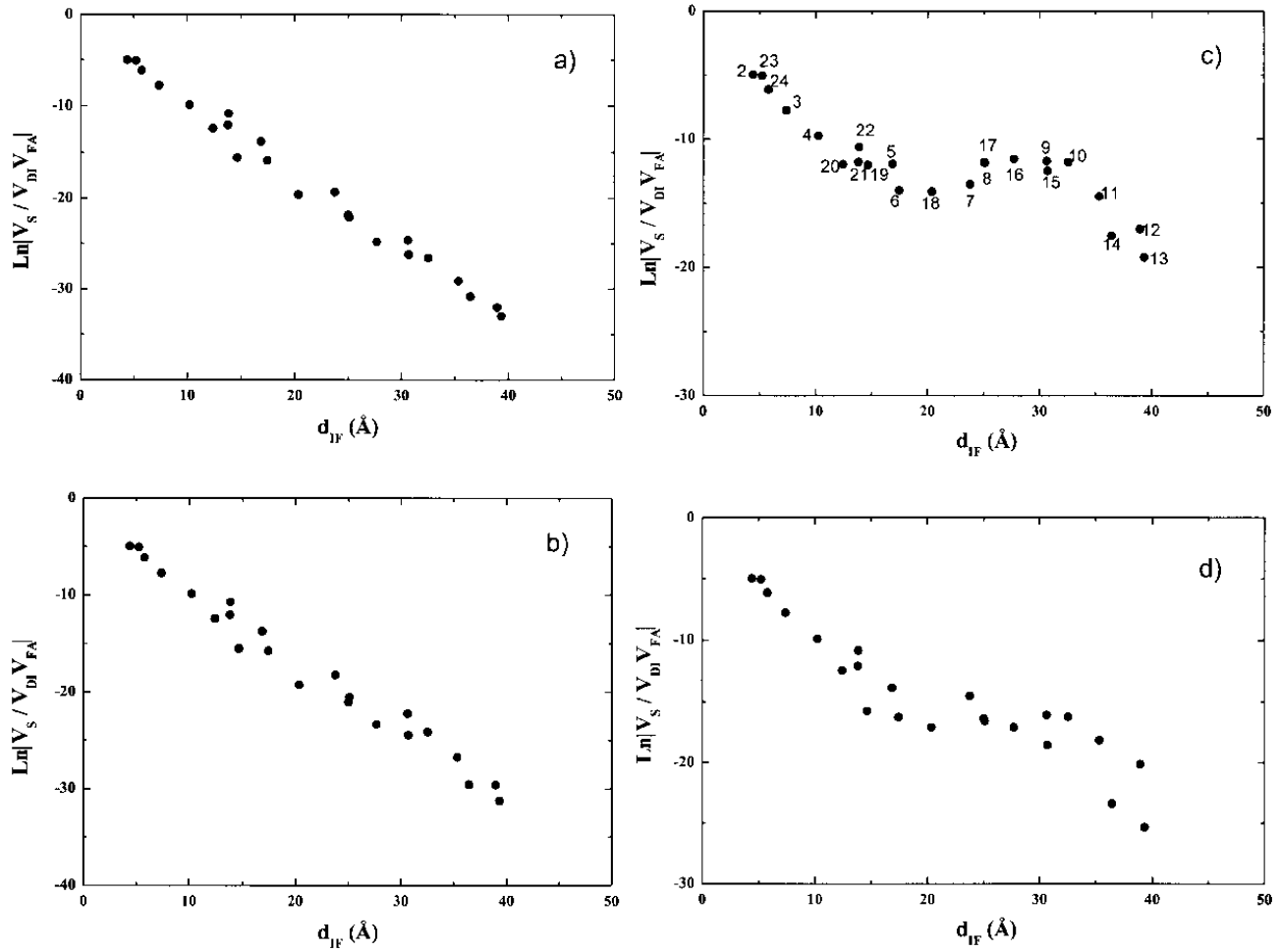

tains the information about the electronic properties (orbital energies and their couplings) of the DNA bridge (39, 53). The direct term V_{DA} is assumed to be negligible for long-range charge transfers and the superexchange term V_S is given by (39, 53–55)

$$[4] \qquad V_S = V_A^T \, G(E_0) V_D$$

where $G(E_0)$ is the Green function (56) for the bridge Hamiltonian, E_0 is the tunneling energy of the transferring charge between the degenerate redox-site orbitals (that is, the D and A orbitals have the same energy), and V_D and V_A are the vectors of interaction of the donor and acceptor with the intervening medium, respectively.[5] If we assume that the D and A sites are each coupled to a single site, respectively, at the entrance (called "initial" site, noted *I*) and at the exit (called "final" site, noted *F*) of the bridge, then V_S can be expressed as

$$[5] \qquad V_S = V_{DI} V_{FA} G_{IF}(E_0)$$

where the matrix element $G_{IF}(E_0)$ is related to the bridge Hamiltonian *H* by

$$[6] \qquad G_{IF}(E_0) = \langle I \,|(E_0 J - H)^{-1}|F\rangle$$

and *J* is the identity matrix.

The present model system is described by the tight-binding Hamiltonian

$$[7] \qquad H = \sum_{i=1}^{N} E \left|i\right\rangle\!\left\langle i\right| + \sum_{i \neq j} V(\boldsymbol{r}_i, \boldsymbol{r}_j) \left|i\right\rangle\!\left\langle j\right|$$

in which bridging sites have only one single *s*-type orbital of the same energy *E* (relative to E_0, taken as the origin of energy) and interact with one another via a pure "through-space" (TS) coupling law (35, 52)

$$[8] \qquad V(\boldsymbol{r}_i, \boldsymbol{r}_j) = V_0 \, e^{-\beta \left| \boldsymbol{r}_i - \boldsymbol{r}_j \right|}$$

where β represents the decay factor of the interaction, $\boldsymbol{r}_i$ and $\boldsymbol{r}_j$ are the coordinates of the interacting sites *i* and *j*, respec-

[5] V_A^T denotes the transpose of V_A.

© 2002 NRC Canada

Fig. 4. Typical variations of $V_S/V_{DI}V_{FA}$ as a function of d_{IF} in the case of 4GAT for a fixed value of $(\Gamma/E)_{DNA} = -0.6$ and various $(\Gamma/E)_{protein}$ values: (*a*) −0.2; (*b*) −0.4; (*c*) −0.6; and (*d*) −0.8. Here, the initial I site is located on atom C6 of the base 1 and we consider each of the other bases' C6 atoms as a possible final F site. The numbers in Fig. 4*c* refer to the bases' indexes of the 4GAT system whose sequence is given in Fig. 2.

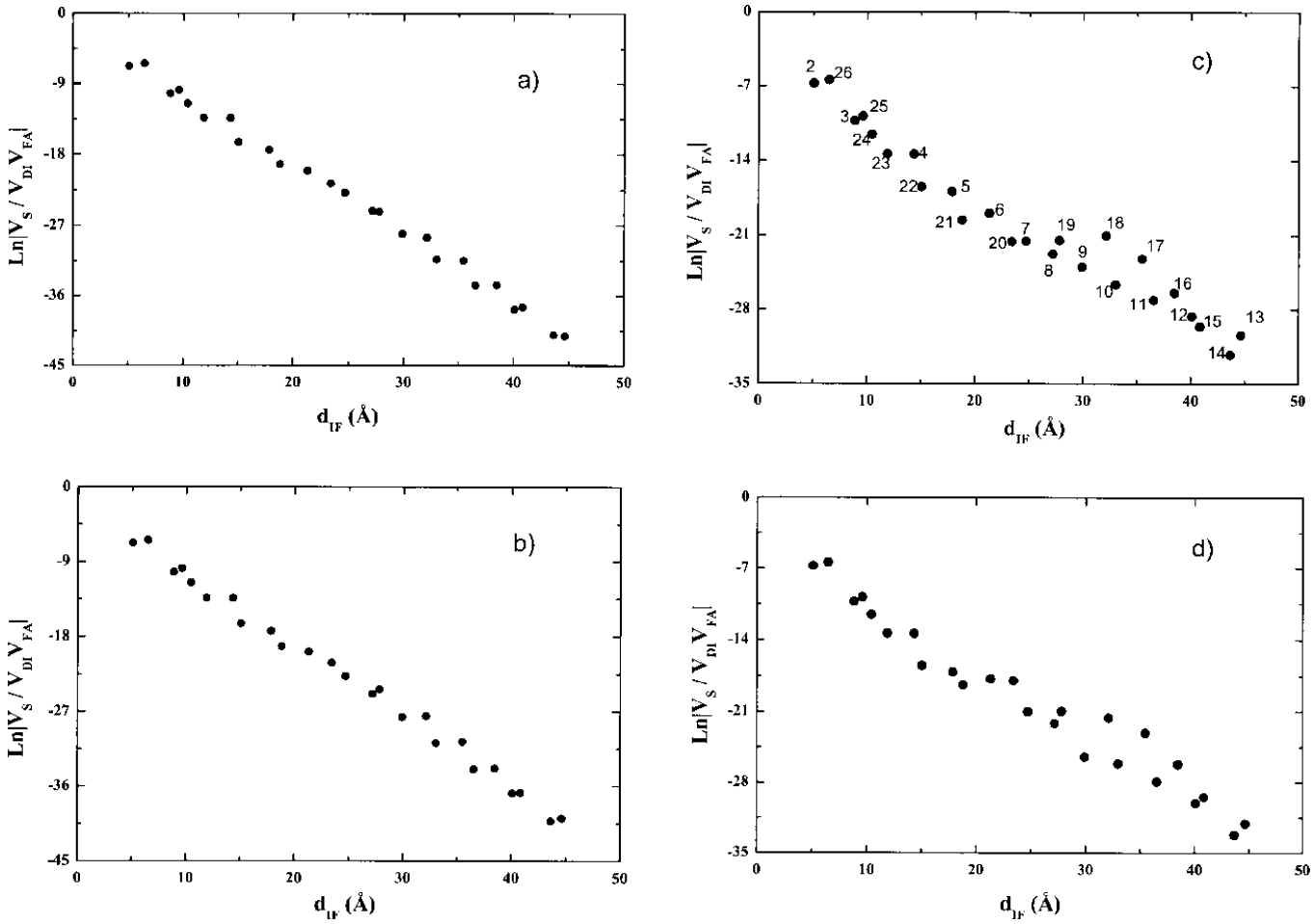

tively, and V_0 is an intersite coupling prefactor.[6] Using what we call the "continuous-medium approximation" (CMA) (54), we have shown in previous studies that this coupling law defines a unique dimensionless parameter Γ/E that controls the distance dependence of V_S in large three-dimensional disordered homogeneous media (54, 57, 58) as well as in proteins (52) and DNA (35). Here, $|\Gamma| = 8\pi\rho|V_0|\beta^{-3}$ is the electronic bandwidth of an associated continuous medium having the same orbital-site density (ρ) as the actual medium. $|\Gamma|$ is an approximate value of the exact half-bandwidth of the discrete medium (54). Noteworthily, for the case of DNA alone in the narrow-band limit ($|\Gamma/E| << 1$), we have shown that the CMA predicts β_{eff} values (~1.6–1.8 Å^{-1}) (35) that are in good order of magnitude agreement with those calculated by Priyadarshy et al. (34) using the same tunneling energies (E = 4–5 eV) and more realistic electronic Hamiltonian modelings of DNA.

A peculiar behavior of our CT model is that the bridging medium is represented by a single *s*-type band, so that the position of the donor–acceptor level with respect to that band determines which mediation mechanism (electron or hole type) prevails (54). This situation is different from that generally encountered in bridged systems such as proteins and DNA, where two bands are simultaneously taken into consideration: the so-called valence and conduction bands. In the latter case, the position of the donor–acceptor level within the existing gap allows the distinction between an electron- or hole-type dominant superexchange mechanism (54, 57, 59). Our CT model would then be suitable when a single band dominates the donor–acceptor electronic coupling.

For the present work, we assume that each of the DNA–protein complexes studied is characterized by two control parameters: $(\Gamma/E)_{DNA}$ and $(\Gamma/E)_{protein}$ for the DNA and the protein, respectively. Of course, this is an approximation when

[6] This *s*-orbital model is a rather simplified modeling of the electronic bridge Hamiltonian. However, this simplification may not be so crude, since the *p*-orbitals of the DNA bases in van der Waals contact along the helix weakly overlap (their interaction is only about 1/3 as large as the π-interaction between *p*-orbitals on neighboring atoms within the bases in the perpendicular plane; see, for example, refs. 12–14, 17, and 34). Based on this simplification, our model offers several important advantages: (*i*) under certain energetic conditions, it is an analytically solvable model; (*ii*) it incorporates in a simple manner the full three-dimensional atomic structure of the DNA–protein bridged system; and (*iii*) calculations based on it are much less consuming in computer time than those required by more refined quantum-chemical modelings.

© 2002 NRC Canada

Fig. 5. Density of states (number of states per unit energy range, in arbitrary units) of the 1BBX DNA–protein complex as a function of energy. Initial orbital energies are the same as in Figs. 3*a–d* and are indicated here by vertical arrows: E_{DNA} = 3.58 eV; $E_{protein}$ = 7.65 eV (*a*); 3.82 eV (*b*); 2.55 eV (*c*); and 1.91 eV (*d*) (E_0 = 0).

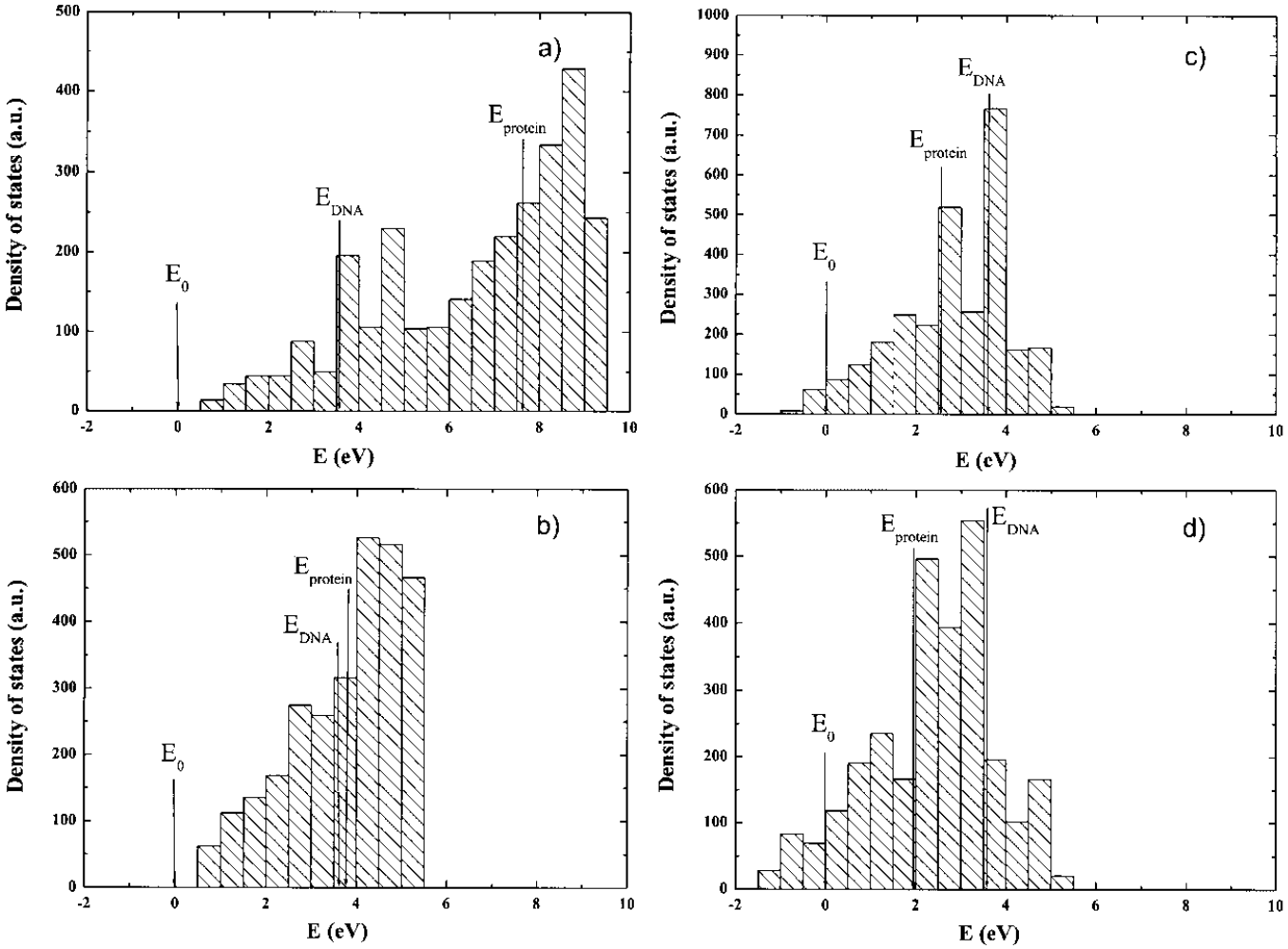

the two electronic bands of the DNA and the protein overlap. Γ is calculated by adopting the parameter values V_0 = –6 eV, β = 1.7 Å^{-1}, and ρ = 0.07 and 0.05 Å^{-3} for the DNA and the protein, respectively. The chosen numerical values of V_0 and β are generally used in the modeling of electronic Hamiltonians for biological charge transfer systems (35, 39, 52, 54, 60), and ρ is taken from our previous studies (35, 52). Under these conditions (Γ < 0), the cases Γ/*E* < 0 and Γ/*E* > 0 correspond to the transfer of electrons (*E* > 0) through unoccupied orbitals and of holes (*E* < 0) through occupied orbitals, respectively. This terminology should, in fact, be reversed for V_0 > 0. A schematic representation of the continuous-medium electronic bands of the bridge is given in Fig. 1. Once Γ is determined, the control parameter is systematically varied, *E* is then deduced, and the Green's function matrix element (G_{IF}) in eq. [5] is computed numerically. From a qualitative point of view, our results are independent of the numerical values given to V_0, β, and ρ because of the universal character of Γ/*E* (35, 52, 54). The coupling prefactors V_{DI} and V_{FA} in eq. [5] are arbitrarily taken since they do not influence the distance decay rate of the electronic coupling.

The atomic coordinates of the two DNA–protein model systems considered in the present study (including hydrogen atoms) (Fig. 2) were obtained from the Protein Data Bank (files: 1BBX.pdb and 4GAT.pdb). Figure 2 shows that 1BBX's protein is a dimeric protein, which is bound to both strands of the DNA double helix, whereas 4GAT's protein is a monomeric protein, which is bound to only one DNA strand. For each system, we assume that the initial I site is located on the C6 atom of the first base and consider each of the other C6 atoms of the DNA bases as possible final F sites. (The phenomena observed are qualitatively independent of the nature and location of initial and final sites, which are arbitrarily chosen.)

Results and discussion

Figures 3*a–d* and 4*a–d* show, for 1BBX and 4GAT, respectively, typical numerical calculations of $V_S/V_{DI}V_{FA}$ as a function of d_{IF} (the distance between the I and F sites) for $(\Gamma/E)_{DNA}$ fixed at –0.6 (E_{DNA} = 3.58 eV) and $(\Gamma/E)_{protein}$ values equal to –0.2, –0.4, –0.6, and –0.8 ($E_{protein}$ = 7.65, 3.82, 2.55, and 1.91 eV, respectively). In most cases, we observe an exponential decay of the electronic coupling with distance (Figs. 3*a*, 3*b* and 4*a*, 4*b*). When $|\Gamma/E|_{protein}$ becomes large enough, however, the coupling decays exponentially as d_{IF} in-

© 2002 NRC Canada

Fig. 6. Typical variations of $V_S/V_{DI}V_{FA}$ as a function of d_{IF} in the case of the 1BBX's protein, for various values of $(\Gamma/E)_{protein}$: (*a*) −0.2; (*b*) −0.4; (*c*) −0.6; and (*d*) −0.8. Note that the initial I site is located on the atom C_α (ALA1) and each of the other protein's atoms is considered as a possible final F site.

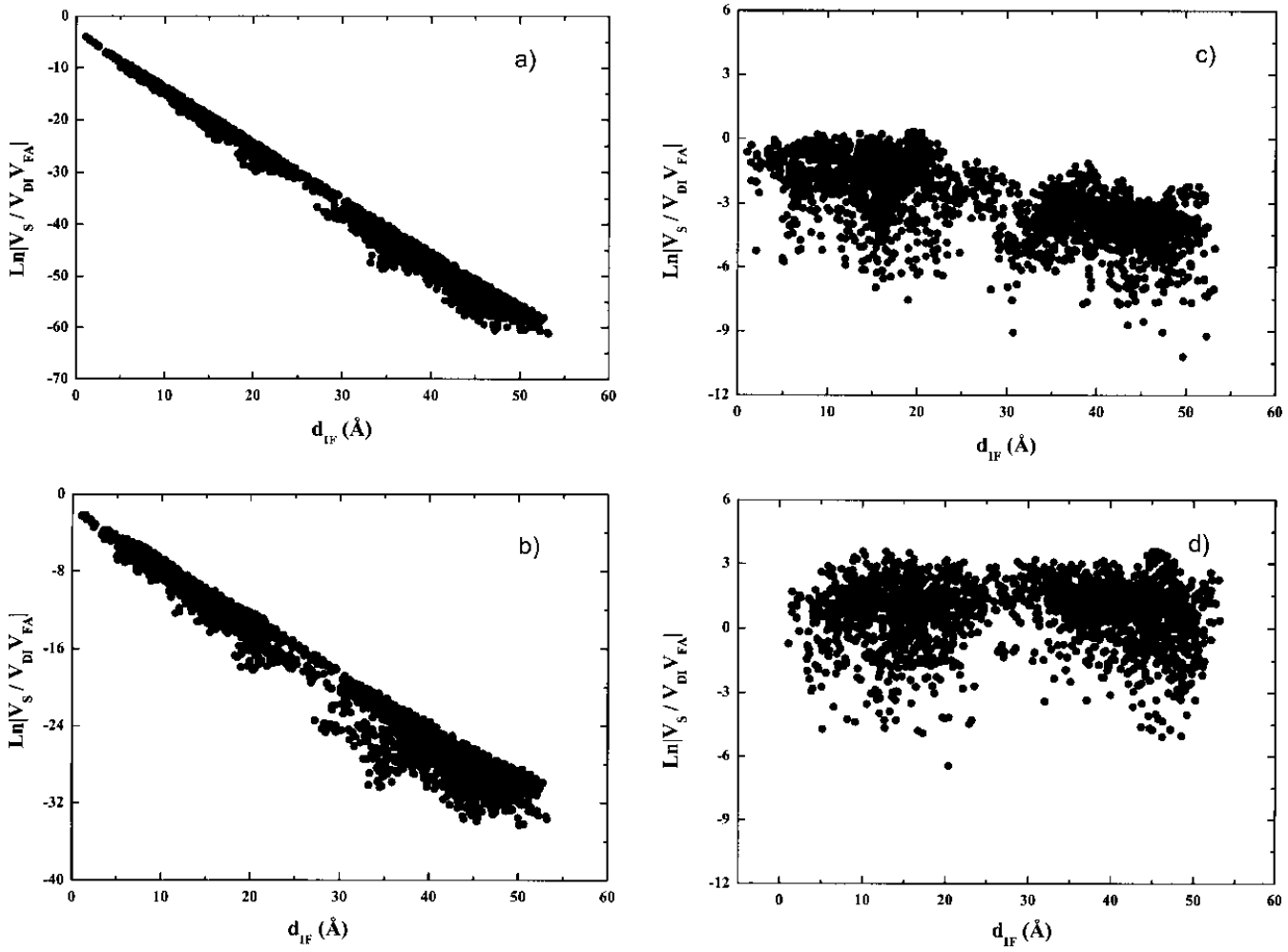

creases, except when the final F site is located within the "recognition region" of the DNA, which lies from bases 5 to 10, bases 15 to 20 for 1BBX (Figs. 2, 3*c*, and 3*d*), and bases 18 to 21 for 4GAT (Figs. 2, 4*c*, and 4*d*). Under those latter conditions, V_S is found to be independent of d_{IF}, similar to a metallic-type CT behavior. Interestingly, we observe that when the F site is located on the other side of this region (with respect to the initial I site), the electronic coupling is many orders of magnitude larger than it should be, far from the protein's resonance conditions. In this situation, the effect of the binding protein on the DNA–protein complex-mediated CT is apparent by only a slight modification of the effective-electronic coupling-decay coefficient β_{eff}, as we have observed (results not shown) by comparing β_{eff} in the DNA alone and in the DNA–protein complexes. We note that these results are independent of the location of the final F site, since the same phenomenon is observed when considering each of the other atoms as a possible location of this site.

Our results can be better understood if we focus on the energy levels of the DNA–protein system. In the case of 1BBX, for example, Figs. 5*a–d* show that the broadening of the electronic energy band mostly takes place on one side below the initial orbital-site energies, as predicted by the CMA. The phenomenon depicted in Figs. 3*c* and 3*d* is then due to the penetration of the donor–acceptor site energy ($E_0 = 0$) into the electronic conduction band of the system (Figs. 5*c* and 5*d*). This originates from effects that occur close to 1BBX's protein resonance conditions.[7] This point is clearly illustrated in Fig. 6, where the electronic coupling through the 1BBX's protein alone is plotted as a function of distance for $(\Gamma/E)_{protein}$ values equal to −0.2, −0.4, −0.6, and −0.8. Here, the initial I site is located on the atom C_α (ALA1), and we consider each of the other protein's atoms as a possible final F site. (Note that the phenomena observed are qualitatively independent of the nature and location of the initial site.) We observed an increase of the dispersion as $|\Gamma/E|_{protein}$ increases (Figs. 6*c* and 6*d*), which is a consequence of the approaching protein's resonance conditions as we have shown in previous studies (52), demonstrating that structural and geometrical effects become important near

[7] Recall that resonance is achieved whenever some energy level of the intervening bridge turns out to coincide with that of the donor–acceptor sites.

© 2002 NRC Canada

Fig. 7. Typical variations of $V_S/V_{DI}V_{FA}$ as a function of d_{IF} in the case of 1BBX for a fixed value of $(\Gamma/E)_{DNA} = 0.6$ ($E_{DNA} = -3.58$ eV) and various $(\Gamma/E)_{protein}$ values: (*a*) 0.6 ($E_{protein} = -2.55$ eV); (*b*) 0.8 ($E_{protein} = -1.91$ eV); (*c*) 2 ($E_{protein} = -0.76$ eV); and (*d*) 4 ($E_{protein} = -0.38$ eV). Here, the initial I site is located on the atom C6 of the base 1 and we consider each of the other bases' C6 atoms as a possible final F site. The numbers in Fig. 7*c* refer to the bases' indexes of the 1BBX system, whose sequence is given in Fig. 2.

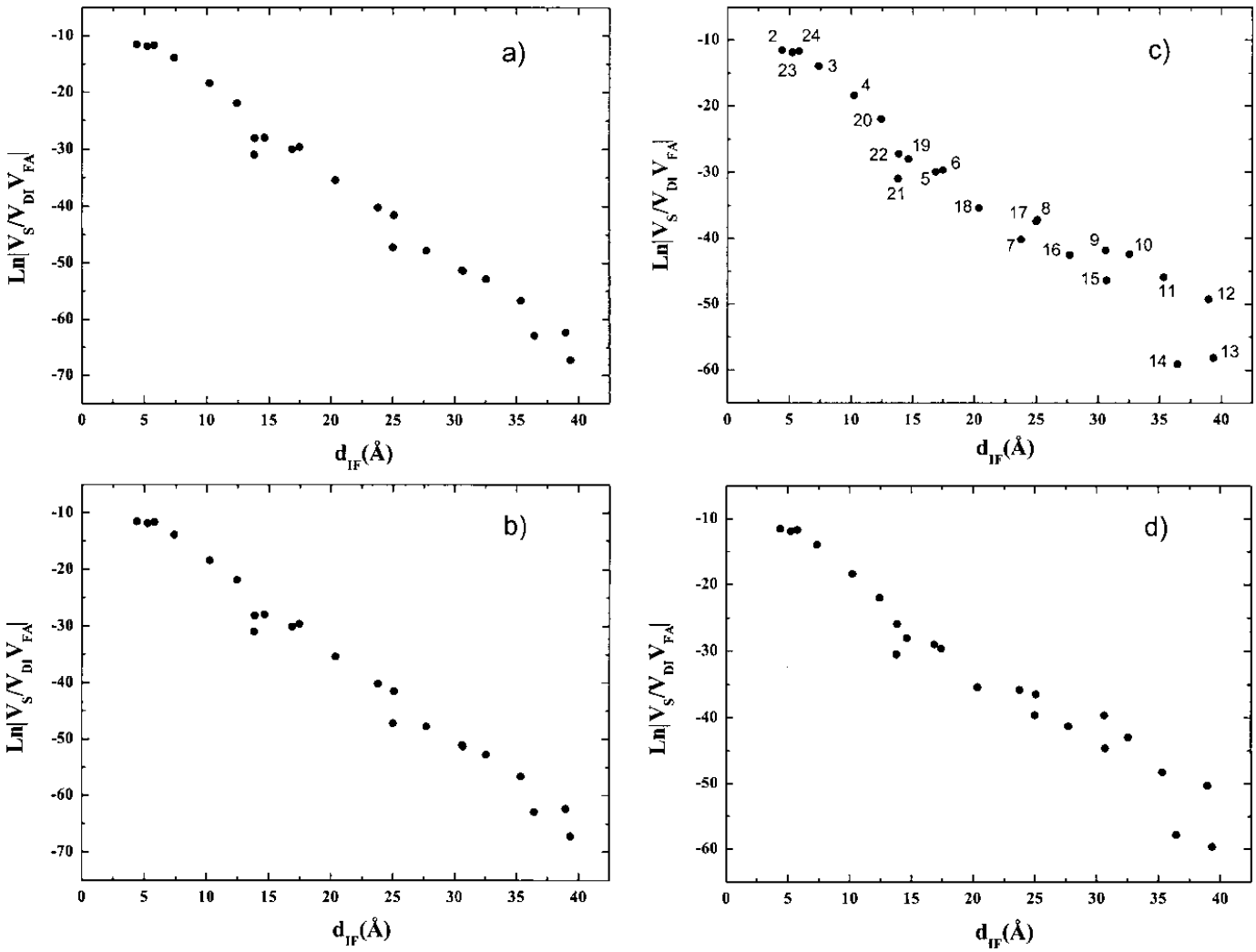

resonance. This result clearly shows that in the DNA–protein bridged system, and for a given $(\Gamma/E)_{DNA}$, the CT pathways involving sites within the protein become important when $|\Gamma/E|_{protein}$ becomes large. The charge particle can thus easily "explore" regions of the protein far from the more direct pathways within DNA, connecting the initial and final sites. These latter conclusions are not valid near DNA's resonance conditions (that is, for $|\Gamma/E|_{DNA} \sim 1$), in which case the charge pathways in the protein are no longer dominant compared with those in DNA, and consequently the phenomena described in Figs. 3 and 4 are not observed.

In the case where $(\Gamma/E)_{protein}$ and $(\Gamma/E)_{DNA}$ are positive, the influence of the protein is observed for large $(\Gamma/E)_{protein}$ values (>1). Figures 7*a–d* show, in the case of 1BBX, typical numerical calculations of $V_S/V_{DI}V_{FA}$ as a function of d_{IF} for $(\Gamma/E)_{DNA}$ fixed at 0.6 ($E_{DNA} = -3.58$ eV) and $(\Gamma/E)_{protein}$ values equal to 0.6, 0.8, 2, and 4 ($E_{protein} = -2.55$, -1.91, -0.76, and -0.38 eV, respectively). The exponential decay of the electronic coupling with distance is still observed for $(\Gamma/E)_{protein}$ equal to 0.6 (Fig. 7*a*) and 0.8 (Fig. 7*b*), whereas no such decay was observed for $(\Gamma/E)_{protein}$ equal to -0.6 (Fig. 3*c*) and -0.8 (Fig. 3*d*). Effects similar to those shown in Figs. 3*c*, 3*d* and 4*c*, 4*d* are also observed for $(\Gamma/E)_{protein} > 1$, but they are not as pronounced when compared, for example, with what is observed in Fig. 3*c*. Moreover, the order of magnitude of the electronic coupling remains much lower in this case than in the case of negative control parameters. As before, these results can be understood from the electronic-band structure formalism: the DNA–protein system is brought to resonance conditions later in the case of $\Gamma/E > 0$ than in the case of $\Gamma/E < 0$, as can be seen from a comparison of the densities of states corresponding to negative (Fig. 5) and positive (Fig. 8) control parameters. This behavior can qualitatively be explained within the CMA (54): the broadening of the energy levels takes place exclusively on only one side (see Fig. 1) of the initial orbital-site energy, making the energy gap

© 2002 NRC Canada

Fig. 8. Density of states (number of states per unit energy range, in arbitrary units) of the 1BBX DNA–protein complex as a function of energy. Initial orbital energies are the same as in Figs. 7*a–d* and are indicated here by vertical arrows: E_{DNA} = –3.58 eV; $E_{protein}$ = –2.55 eV (*a*); –1.91 eV (*b*); –0.76 eV (*c*); and –0.38 eV (*d*) (E_0 = 0).

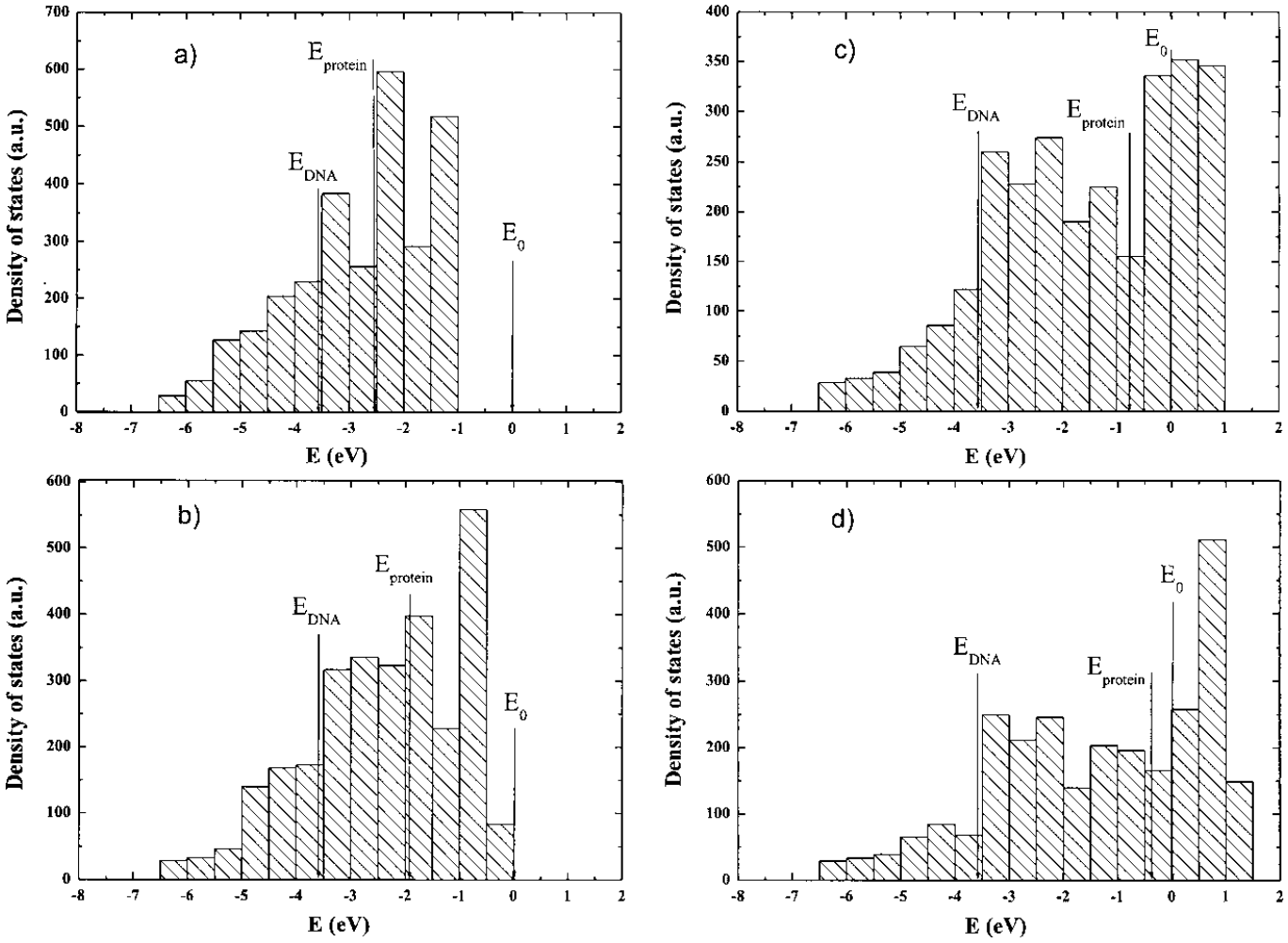

larger for $\Gamma/E > 0$ than for $\Gamma/E < 0$, which explains why superexchange is easier in the latter case. A detailed discussion concerning the sign effects of the control parameters on the electronic coupling is given elsewhere (54).

The importance of the DNA–protein complex's three-dimensional structure is qualitatively captured by the present pure "through-space" coupling model. The effect of the electronic band generated by these TS interactions is expected to remain important under certain energetic conditions even if we consider the presence of other types of bonds, as it has been previously shown in the case of a folded random-chain system where "through-space" and "through-bond" interactions were simultaneously taken into account (61). In particular, the peculiar effect of protein binding on CT in DNA may be expected under relatively large values of the energetic gap between the redox centers and the bridging medium (i.e., $|E_{DNA}| > 3–4$ eV). Nevertheless, our results do not consider any dynamic effect caused by the flexibility and motions of the bridge, which depend on the actual base-pair sequence as well as the water content surrounding the molecule (41, 43, 44, 62–64). These factors could modulate the energetic gap and thus have an effect on the CT reaction rate. To provide an improved quantitative description of the present CT model, further calculations should account for thermal fluctuations of the medium in which CT occurs, combined with a more realistic quantum-chemical modeling of the electronic bridge Hamiltonian (11, 34, 65).

Despite its obvious simplicity, the CT model used here provides information about mechanistic issues that are rather difficult to probe experimentally or that generally require important computing resources. Our results show that in certain cases long-range CT reactions through DNA can be modulated by the presence of binding proteins, in accordance with experiment. These findings could hold important implications with respect to CT in chromosomal DNA, certain functions of DNA in biological systems, and also DNA damage–protection in vivo. In particular, they indicate that, under certain energetic conditions, the presence of a protein could promote CT over very long molecular distances. Experimental investigation is needed to further test such results.

© 2002 NRC Canada

Acknowledgments

We thank Professor Patrick Bertrand (Laboratoire de Bioénergétique et Ingénierie des Protéines, Université Aix-Marseille 1, France) for valuable comments on the manuscript and the "Réseau québécois de calcul de haute performance" (RQCHP) for a generous allocation of computer time. Financial support from the Canadian Institutes of Health Research (Grant No. MT-14617) is gratefully acknowledged.

References

1. B. Alberts, D. Bray, J. Lewis, M. Raff, K. Roberts, and J.D. Watson. Molecular biology of the cell. 3rd ed. Garland Publishing, New York. 1994.
2. V.A. Bloomfield, D.M. Crothers, and I. Tinoco, Jr. Nucleic acids: structures, properties, and functions. University Science Books, Sausalito, CA. 2000.
3. C. Branden and J. Tooze. Introduction to protein structure. Garland Publishing, New York. 1991.
4. B. Demple and L. Harrison. Annu. Rev. Biochem. **63**, 915 (1994).
5. P. O'Neill and E.M. Fielden. Adv. Radiat. Biol. **17**, 53 (1993).
6. S.R. Rajski, B.A. Jackson, and J.K. Barton. Mutat. Res. **447**, 49 (2000); M.E. Núñez, D.B. Hall, and J.K. Barton. Chem. Biol. **6**, 85 (1999); M.E. Núñez, S.R. Rajski, and J.K. Barton. Methods Enzymol. **319**, 165 (2000); D.A. Vicic, D.T. Odom, M.E. Núñez, D.A. Gianolio, L.W. McLaughlin, and J.K. Barton. J. Am. Chem. Soc. **122**, 8603 (2000). See also A. Heller. Faraday Discuss. **116**, 1 (2000); M.E. Núñez, G.P. Holmquist, and J.K. Barton. Biochemistry, **40**, 12465 (2001).
7. P.F. Barbara and E.J.C. Olson. Adv. Chem. Phys. **107**, 647 (1999); M. Faraggi, C. Ferradini, and J.-P. Jay-Gerin. New J. Chem. **19**, 1203 (1995); J. Chim. Phys. **93**, 78 (1996).
8. S.R. Rajski, S. Kumar, R.J. Roberts, and J.K. Barton. J. Am. Chem. Soc. **121**, 5615 (1999); S.R. Rajski and J.K. Barton. J. Biomol. Struct. Dyn. **11** (Special Issue S2), 285 (2000); Biochemistry, **40**, 5556 (2001); H.-A. Wagenknecht, S.R. Rajski, M. Pascaly, E.D.A. Stemp, and J.K. Barton. J. Am. Chem. Soc. **123**, 4400 (2001).
9. P.M. Cullis, G.D.D. Jones, M.C.R. Symons, and J.S. Lea. Nature (London), **330**, 773 (1987).
10. H.-A. Wagenknecht, E.D.A. Stemp, and J.K. Barton. J. Am. Chem. Soc. **122**, 1 (2000); Biochemistry, **39**, 5483 (2000).
11. J. Antony, D.M. Medvedev, and A.A. Stuchebrukhov. J. Am. Chem. Soc. **122**, 1057 (2000); D. Medvedev and A.A. Stuchebrukhov. J. Theor. Biol. **210**, 237 (2001).
12. E.K. Wilson. Chem. Eng. News **79**, 29 (2001); **77**, 43 (1999); **76**, 51 (1998); M.W. Grinstaff. Angew. Chem. Int. Ed. Engl. **38**, 3629 (1999); G. Taubes. Science, **275**, 1420 (1997); U. Diederichsen. Angew. Chem. Int. Ed. Engl. **36**, 2317 (1997); D.N. Beratan, S. Priyadarshy, and S.M. Risser. Chem. Biol. **4**, 3 (1997).
13. T.L. Netzel. J. Chem. Educ. **74**, 646 (1997); *In* Organic and inorganic photochemistry. *Edited by* V. Ramamurthy and K.S. Schanze. Marcel Dekker, New York. 1998. p. 1.
14. M. Ratner, Nature (London), **397**, 480 (1999).
15. C. Dekker and M.A. Ratner. Phys. World, **14**, 29 (2001).
16. F.D. Lewis. *In* Electron transfer in chemistry. Vol. 3. *Edited by* V. Balzani, H.B. Gray, and J.R. Winkler. Wiley-VCH, Weinheim, Germany. 2001. p. 105.
17. R.E. Holmlin, P.J. Dandliker, and J.K. Barton. Angew. Chem. Int. Ed. Engl. **36**, 2714 (1997); S.O. Kelley and J.K. Barton. Chem. Biol. **5**, 413 (1998); *In* Metal ions in biological systems. Vol. 36. *Edited by* A. Sigel and H. Sigel. Marcel Dekker, New York. 1999. p. 211; Science, **283**, 375 (1999); S.O. Kelley, N.M. Jackson, M.G. Hill, and J.K. Barton. Angew. Chem. Int. Ed. Engl. **38**, 941 (1999); M.E. Núñez and J.K. Barton. Curr. Opin. Chem. Biol. **4**, 199 (2000); T.T. Williams, D.T. Odom, and J.K. Barton. J. Am. Chem. Soc. **122**, 9048 (2000); D.T. Odom and J.K. Barton. Biochemistry, **40**, 8727 (2001).
18. T.J. Meade and J.F. Kayyem. Angew. Chem. Int. Ed. Engl. **34**, 352 (1995); E.S. Krider and T.J. Meade. J. Biol. Inorg. Chem. **3**, 222 (1998).
19. J.M. Warman, M.P. de Haas, and A. Rupprecht. Chem. Phys. Lett. **249**, 319 (1996); J.M. Warman, M.P. de Haas, L.D.A. Siebbeles, A. Hummel, R.J.O.M. Hoofman, and G.P. van der Laan. Radiat. Phys. Chem. **60**, 423 (2001).
20. F.D. Lewis, T. Wu, Y. Zhang, R.L. Letsinger, S.R. Greenfield, and M.R. Wasielewski. Science, **277**, 673 (1997); F.D. Lewis, X. Liu, J. Liu, S.E. Miller, R.T. Hayes, and M.R. Wasielewski. Nature (London), **406**, 51 (2000); F.D. Lewis, X. Liu, J. Liu, R.T. Hayes, and M.R. Wasielewski. J. Am. Chem. Soc. **122**, 12037 (2000); F.D. Lewis, R.S. Kalgutkar, Y. Wu, X. Liu, J. Liu, R.T. Hayes, S.E. Miller, and M.R. Wasielewski. J. Am. Chem. Soc. **122**, 12346 (2000); F.D. Lewis, R.L. Letsinger, and M.R. Wasielewski. Acc. Chem. Res. **34**, 159 (2001); F.D. Lewis and Y. Wu. J. Photochem. Photobiol. C: Photochem. Rev. **2**, 1 (2001).
21. K. Fukui and K. Tanaka. Angew. Chem. Int. Ed. Engl. **37**, 158 (1998); K. Fukui, K. Tanaka, M. Fujitsuka, A. Watanabe, and O. Ito. J. Photochem. Photobiol. B: Biol. **50**, 18 (1999).
22. A. Harriman. Angew. Chem. Int. Ed. Engl. **38**, 945 (1999).
23. T. Melvin, S.M.T. Cunniffe, P. O'Neill, A.W. Parker, and T. Roldan-Arjona. Nucleic Acids Res. **26**, 4935 (1998); P. O'Neill and A.W. Parker. *In* Radiation research. Vol. 2. *Edited by* M. Moriarty, C. Mothersill, C. Seymour, M. Edington, J.F. Ward, and R.J.M. Fry. Allen Press, Lawrence, Kansas. 2000. p. 325; P. O'Neill, A.W. Parker, M.A. Plumb, and L.D.A. Siebbeles. J. Phys. Chem. B, **105**, 5283 (2001).
24. E. Meggers, M.E. Michel-Beyerle, and B. Giese. J. Am. Chem. Soc. **120**, 12950 (1998); B. Giese, S. Wessely, M. Spormann, U. Lindemann, E. Meggers, and M.E. Michel-Beyerle. Angew. Chem. Int. Ed. Engl. **38**, 996 (1999); B. Giese and S. Wessely. Angew. Chem. Int. Ed. Engl. **39**, 3490 (2000); B. Giese. Acc. Chem. Res. **33**, 631 (2000); S. Wessely and B. Giese. J. Biomol. Struct. Dyn. **11** (Special Issue S2), 293 (2000); B. Giese, M. Spichty, and S. Wessely. Pure Appl. Chem. **73**, 449 (2001); B. Giese, J. Amaudrut, A.-K. Köhler, M. Spormann, and S. Wessely. Nature (London), **412**, 318 (2001). B. Giese and S. Wessely. Chem. Commun. 2108 (2001).
25. D. Ly, Y. Kan, B. Armitage, and G.B. Schuster. J. Am. Chem. Soc. **118**, 8747 (1996); S.M. Gasper and G.B. Schuster. J. Am. Chem. Soc. **119**, 12762 (1997); D. Ly, L. Sanii, and G.B. Schuster. J. Am. Chem. Soc. **121**, 9400 (1999); P.T. Henderson, D. Jones, G. Hampikian, Y. Kan, and G.B. Schuster. Proc. Natl. Acad. Sci. U.S.A. **96**, 8353 (1999); G.B. Schuster. Acc. Chem. Res. **33**, 253 (2000); L. Sanii and G.B. Schuster. J. Am. Chem. Soc. **122**, 11545 (2000); I.M. Abdou, V. Sartor, H. Cao, and G.B. Schuster. J. Am. Chem. Soc. **123**, 6696 (2001); V. Sartor, E. Boone, and G.B. Schuster. J. Phys. Chem. B, **105**, 11057 (2001).
26. R.F. Anderson and G.A. Wright. Phys. Chem. Chem. Phys. **1**, 4827 (1999). See also R.F. Martin and R.F. Anderson. Int. J. Radiat. Oncol. Biol. Phys. **42**, 827 (1998).

© 2002 NRC Canada

27. I. Saito, T. Nakamura, K. Nakatani, Y. Yoshioka, K. Yamaguchi, and H. Sugiyama. J. Am. Chem. Soc. **120**, 12686 (1998); K. Nakatani, C. Dohno, and I. Saito. J. Am. Chem. Soc. **121**, 10854 (1999); **122**, 5893 (2000); Tetrahedron Lett. **41**, 10041 (2000).
28. M.R. Arkin, E.D.A. Stemp, R.E. Holmlin, J.K. Barton, A. Hörmann, E.J.C. Olson, and P.F. Barbara. Science, **273**, 475 (1996); C. Wan, T. Fiebig, S.O. Kelley, C.R. Treadway, J.K. Barton, and A.H. Zewail. Proc. Natl. Acad. Sci. U.S.A. **96**, 6014 (1999); C. Wan, T. Fiebig, O. Schiemann, J.K. Barton, and A.H. Zewail. Proc. Natl. Acad. Sci. U.S.A. **97**, 14052 (2000).
29. A. Pezeshk, M.C.R. Symons, and J.D. McClymont. J. Phys. Chem. **100**, 18562 (1996). See also M.C.R. Symons. Radiat. Phys. Chem. **45**, 837 (1995).
30. Y. Razskazovskii, S.G. Swarts, J.M. Falcone, C. Taylor, and M.D. Sevilla. J. Phys. Chem. B, **101**, 1460 (1997); A. Messer, K. Carpenter, K. Forzley, J. Buchanan, S. Yang, Y. Razskazovskii, Z. Cai, and M.D. Sevilla. J. Phys. Chem. B, **104**, 1128 (2000); **104**, 6942 (2000); Z. Cai, Z. Gu, and M.D. Sevilla. J. Phys. Chem. B, **104**, 10406 (2000); **105**, 6031 (2001).
31. M.G. Debije, M.T. Milano, and W.A. Bernhard. Angew. Chem. Int. Ed. Engl. **38**, 2752 (1999); W.A. Bernhard, M.G. Debije, M.T. Milano, and Y. Razskazovskiy. *In* Radiation research. Vol. 2. *Edited by* M. Moriarty, C. Mothersill, C. Seymour, M. Edington, J.F. Ward, and R.J.M. Fry. Allen Press, Lawrence, Kansas. 2000. p. 321; M.G. Debije and W.A. Bernhard. J. Phys. Chem. B, **104**, 7845 (2000).
32. V.Ya. Shafirovich, A. Dourandin, N.P. Luneva, and N.E. Geacintov. J. Phys. Chem. B, **101**, 5863 (1997); V. Shafirovich, A. Dourandin, W. Huang, N.P. Luneva, and N.E. Geacintov. Phys. Chem. Chem. Phys. **2**, 4399 (2000); V. Shafirovich, J. Cadet, D. Gasparutto, A. Dourandin, W. Huang, and N.E. Geacintov. J. Phys. Chem. B, **105**, 586 (2001); V. Shafirovich, A. Dourandin, and N.E. Geacintov. J. Phys. Chem. B, **105**, 8431 (2001).
33. K. Kawai, T. Takada, S. Tojo, N. Ichinose, and T. Majima. J. Am. Chem. Soc. **123**, 12688 (2001).
34. S. Priyadarshy, D.N. Beratan, and S.M. Risser. Int. J. Quantum Chem. Quantum Biol. Symp. **23**, 65 (1996); S. Priyadarshy, S.M. Risser, and D.N. Beratan. J. Phys. Chem. **100**, 17678 (1996); J. Biol. Inorg. Chem. **3**, 196 (1998).
35. M. Benrahmoune, A. Filali-Mouhim, and J.-P. Jay-Gerin. Can. J. Physiol. Pharmacol. **79**, 122 (2001).
36. J. Jortner, M. Bixon, T. Langenbacher, and M.E. Michel-Beyerle. Proc. Natl. Acad. Sci. U.S.A. **95**, 12759 (1998). See also: M. Bixon and J. Jortner. Adv. Chem. Phys. **106**, 35 (1999); J. Phys. Chem. B, **104**, 3906 (2000); **105**, 10322 (2001); A.A. Voityuk, N. Rösch, M. Bixon, and J. Jortner. J. Phys. Chem. B, **104**, 9740 (2000); A.A. Voityuk, J. Jortner, M. Bixon, and N. Rösch. J. Chem. Phys. **114**, 5614 (2001); A.A. Voityuk and N. Rösch. J. Phys. Chem. B, **106**, 3013 (2002).
37. M. Bixon and J. Jortner. J. Am. Chem. Soc. **123**, 12556 (2001).
38. A. Troisi and G. Orlandi. Chem. Phys. Lett. **344**, 509 (2001).
39. S.S. Skourtis and D.N. Beratan. Adv. Chem. Phys. **106**, 377 (1999).
40. M. Bixon, B. Giese, S. Wessely, T. Langenbacher, M.E. Michel-Beyerle, and J. Jortner. Proc. Natl. Acad. Sci. U.S.A. **96**, 11713 (1999).
41. F.C. Grozema, Yu.A. Berlin, and L.D.A. Siebbeles. J. Am. Chem. Soc. **122**, 10903 (2000).
42. Yu.A. Berlin, A.L. Burin, and M.A. Ratner. J. Phys. Chem. A, **104**, 443 (2000); J. Am. Chem. Soc. **123**, 260 (2001).
43. D.M.A. Smith and L. Adamowicz. J. Phys. Chem. B, **105**, 9345 (2001).
44. S.V. Rakhmanova and E.M. Conwell. J. Phys. Chem. B, **105**, 2056 (2001). See also E.M. Conwell and S.V. Rakhmanova. Proc. Natl. Acad. Sci. U.S.A. **97**, 4556 (2000).
45. J.K. Barton. Proceedings of the "Robert A. Welch foundation 37th conference on chemical research: 40 years of the DNA double helix." Houston, TX. October 25–26, 1993. p. 171; N.J. Turro and J.K. Barton. J. Biol. Inorg. Chem. **3**, 201 (1998).
46. V. Mujica, A. Nitzan, Y. Mao, W. Davis, M. Kemp, A. Roitberg, and M.A. Ratner. Adv. Chem. Phys. **107**, 403 (1999).
47. Yu.A. Berlin, A.L. Burin, and M.A. Ratner. Superlattices Microstruct. **28**, 241 (2000).
48. A.K. Felts, W.T. Pollard, and R.A. Friesner. J. Phys. Chem. **99**, 2929 (1995).
49. D.D. Eley and D.I. Spivey. Trans. Faraday Soc. **58**, 411 (1962).
50. Y. Okahata, T. Kobayashi, K. Tanaka, and M. Shimomura. J. Am. Chem. Soc. **120**, 6165 (1998); E. Braun, Y. Eichen, U. Sivan, and G. Ben-Yoseph. Nature (London), **391**, 775 (1998); H.-W. Fink and C. Schönenberger. Nature (London), **398**, 407 (1999); P.J. de Pablo, F. Moreno-Herrero, J. Colchero, J. Gómez Herrero, P. Herrero, A.M. Baró, P. Ordejón, J.M. Soler, and E. Artacho. Phys. Rev. Lett. **85**, 4992 (2000); L. Cai, H. Tabata, and T. Kawai. Appl. Phys. Lett. **77**, 3105 (2000); D. Porath, A. Bezryadin, S. de Vries, and C. Dekker. Nature (London), **403**, 635 (2000); A.Yu. Kasumov, M. Kociak, S. Guéron, B. Reulet, V.T. Volkov, D.V. Klinov, and H. Bouchiat. Science, **291**, 280 (2001); A. Rakitin, P. Aich, C. Papadopoulos, Yu. Kobzar, A.S. Vedeneev, J.S. Lee, and J.M. Xu. Phys. Rev. Lett. **86**, 3670 (2001); A.J. Storm, J. van Noort, S. de Vries, and C. Dekker. Appl. Phys. Lett. **79**, 3881 (2001).
51. J.M. Nocek, J.S. Zhou, S. De Forest, S. Priyadarshy, D.N. Beratan, J.N. Onuchic, and B.M. Hoffman. Chem. Rev. **96**, 2459 (1996); D.S. Bendall (Ed.). Protein electron transfer. BIOS Scientific Publishers, Oxford. 1996; H.B. Gray and J.R. Winkler. Annu. Rev. Biochem. **65**, 537 (1996); *In* Electron transfer in chemistry. Vol. 3. *Edited by* V. Balzani, H.B. Gray, and J.R. Winkler. Wiley-VCH, Weinheim, Germany. 2001. p. 3; J.R. Winkler and H.B. Gray. J. Biol. Inorg. Chem. **2**, 399 (1997); R.J.P. Williams. J. Biol. Inorg. Chem. **2**, 373 (1997); C.C. Moser, C.C. Page, X. Chen, and P.L. Dutton. J. Biol. Inorg. Chem. **2**, 393 (1997); C.C. Page, C.C. Moser, X. Chen, and P.L. Dutton. Nature (London), **402**, 47 (1999); C.C. Moser, C.C. Page, and P.L. Dutton. *In* Electron transfer in chemistry. Vol. 3. *Edited by* V. Balzani, H.B. Gray, and J.R. Winkler. Wiley-VCH, Weinheim, Germany. 2001. p. 24; D.N. Beratan and S.S. Skourtis. *In* Biological electron transfer chains: Genetics, composition and mode of operation. *Edited by* G.W. Canters and E. Vijgenboom. Kluwer Academic Publishers, Dordrecht. 1998. p. 9; S.S. Skourtis, G. Archontis, and Q. Xie. J. Chem. Phys. **115**, 9444 (2001); T. Kawatsu, T. Kakitani, and T. Yamato. J. Phys. Chem. B, **105**, 4424 (2001); A.A. Stuchebrukhov. Adv. Chem. Phys. **118**, 1 (2001).
52. J.-M. Lopez-Castillo, A. Filali-Mouhim, É. Nguyen Van Binh-Otten, and J.-P. Jay-Gerin. J. Am. Chem. Soc. **119**, 1978 (1997).
53. A. Kuki. *In* Long-range electron transfer in biology. Structure and bonding. Vol. 75. *Edited by* G.A. Palmer. Springer-Verlag, Berlin. 1991. p. 49.
54. J.-M. Lopez-Castillo, A. Filali-Mouhim, I.L. Plante, and J.-P. Jay-Gerin. J. Phys. Chem. **99**, 6864 (1995).
55. J. Ulstrup. Charge transfer processes in condensed media. Lecture notes in chemistry. Vol. 10. Springer-Verlag, Berlin. 1979.

© 2002 NRC Canada

56. E.N. Economou. Green's functions in quantum physics. 2nd ed. Springer-Verlag, Berlin. 1990.
57. J.-M. Lopez-Castillo, A. Filali-Mouhim, I.L. Plante, and J.-P. Jay-Gerin. Chem. Phys. Lett. **239**, 223 (1995).
58. A. Filali-Mouhim, J.-M. Lopez-Castillo, I.L. Plante, and J.-P. Jay-Gerin. J. Phys. Chem. **100**, 12311 (1996).
59. J.N. Onuchic and D.N. Beratan. J. Chem. Phys. **92**, 722 (1990).
60. J.W. Evenson and M. Karplus. Science, **262**, 1247 (1993).
61. J.-M. Lopez-Castillo and J.-P. Jay-Gerin. J. Phys. Chem. **100**, 14289 (1996).
62. I. Daizadeh, E.S. Medvedev, and A.A. Stuchebrukhov. Proc. Natl. Acad. Sci. U.S.A. **94**, 3703 (1997).
63. R.N. Barnett, C.L. Cleveland, A. Joy, U. Landman, and G.B. Schuster. Science, **294**, 567 (2001).
64. P.K. Bhattacharya and J.K. Barton. J. Am. Chem. Soc. **123**, 8649 (2001).
65. J.M. Gruschus and A. Kuki. J. Phys. Chem. **97**, 5581 (1993).

© 2002 NRC Canada

Hydrogénation électrocatalytique sur des catalyseurs composites de nickel et hydroxyde d'aluminium en cellule dynamique

Patrick Dubé, Louis Brossard et Hugues Ménard

Résumé : L'hydrogénation électrocatalytique (HEC) du cyclohexanone en cyclohexanol a été étudié en milieu aqueux en mettant à profit des électrocatalyseurs à base de poudres composites. Les poudres sont constituées de nanoagrégats de nickel obtenus par déposition physique sous vide, sur des particules de $Al(OH)_3$, AlO(OH) et de γ-Al_2O_3. L'HEC a été réalisée dans une cellule de type dynamique. Le rendement en HEC dépend étroitement de la nature des particules non métalliques laquelle nature influence de façon déterminante l'adsorption–désorption des composés organiques impliqués dans la réaction.

Mots clés : électrocatalyse, oxyde d'aluminium, hydroxyde d'aluminium, hydrogénation, cellule dynamique.

Abstract: The electrocatalytic hydrogenation (ECH) of cyclohexanone into cyclohexanol has been studied in aqueous media with electrocatalysts on composites powders. These powders are formed of nanoaggregates of nickel obtained through a physical deposition under vacuum on particles of $Al(OH)_3$, AlO(OH), and γ-Al_2O_3. The ECH reaction was done in a dynamic cell. Its yield is closely dependent on the nature of the non-metallic particles whose nature greatly influences the adsorption–desorption of the organic compounds involved in the reaction.

Key words: electrocatalysis, aluminum oxide, aluminum hydroxide, hydrogenation, dynamic cell.

[Traduit par la Rédaction]

Introduction

L'hydrogénation électrocatalytique est une technique qui consiste à hydrogéner une molécule organique en utilisant l'hydrogène atomique, adsorbé sur une électrode (1), produit par électrolyse de l'eau. Dans une large mesure, la cinétique de l'hydrogénation électrocatalytique (HEC) est tributaire des matériaux d'électrodes utilisés. Ainsi, les premières électrodes, massives, ont fait place à des électrodes à grandes surfaces spécifiques en utilisant des matériaux ou des alliages métalliques de plus en plus complexes. Les matériaux électrocatalytiques les plus employés sont de la famille du nickel de Raney; ils ont une grande surface active, sont peu coûteux, le dégagement d'hydrogène y est facile et ils ont une bonne stabilité (2). Dès les années 1980, le nickel de Raney a permis d'hydrogéner une grande gamme de molécules organiques (3). Par ailleurs, le nickel de Raney subit une activation au préalable par la lixiviation de l'aluminium en milieu basique, et les phases résiduelles formées ont été déterminées (4, 5), ce qui a permis de confirmer la présence d'hydroxyde d'aluminium ($Al(OH)_3$), d'hydroxyde-oxyde d'aluminium (AlO(OH)) et d'alumine hydratée ($Al_2O_3 \cdot 3H_2O$) résiduel après lixiviation.

Par ailleurs, l'hydrogénation catalytique et l'HEC comprennent une étape d'adsorption de la molécule à hydrogéner (6, 7). Pour le nickel de Raney, des auteurs (8–10) indiquent que l'adsorption de la molécule à hydrogéner est aidée par la présence d'aluminium résiduelle et de ses oxydes, alors que d'autres (11) sont d'avis que l'adsorption de la molécule à hydrogéner a lieu sur les oxydes d'aluminium. Pour appuyer ces hypothèses, des études sur les propriétés d'adsorption de l'hydroxyde d'aluminium et de ses dérivés thermiques (AlO(OH) et Al_2O_3) démontrent que les molécules organiques avec un noyau aromatique comme les hydrocarbures aromatiques polycycliques (HAP) (12), peuvent être adsorbés plus ou moins facilement selon la nature du composé d'aluminium. La coexistence de sites d'adsorption non métalliques, très actifs, et de sites métalliques peu actifs pour l'adsorption des molécules organiques est potentiellement bénéfique pour l'HEC lorsque l'étape la plus lente de la réaction est l'adsorption de la molécule à hydrogéner ou la désorption de la molécule après hydrogénation (13). Le présent article s'intéresse à l'hydrogénation électrocatalytique du cyclohexanone en cyclohexanol en milieu aqueux sur des électrocatalyseurs composites (EC). Les EC sont constitués de très petits agglomérats de nickel déposés sur des particu-

Reçu le 14 août 2001. Publié au site Web des Presses scientifiques du CNRC à http://revcanchimie.cnrc.ca le 28 mars 2002.

P. Dubé et H. Ménard. Université de Sherbrooke, Département de chimie, 2500 boul. Université, Sherbrooke, QC J1K 2R1, Canada.
L. Brossard.[1] Institut de recherche d'hydro-Québec (IREQ), 1800 boul. Lionel-Boulet, Varenne, QC J3X 1S1, Canada.

[1]Auteur correspondant (courriel : brossard.louis@ireq.ca).

 DOI: 10.1139/V02-024 © 2002 CNRC Canada

Fig. 1. Équations de l'hydrogénation électrocatalytique.

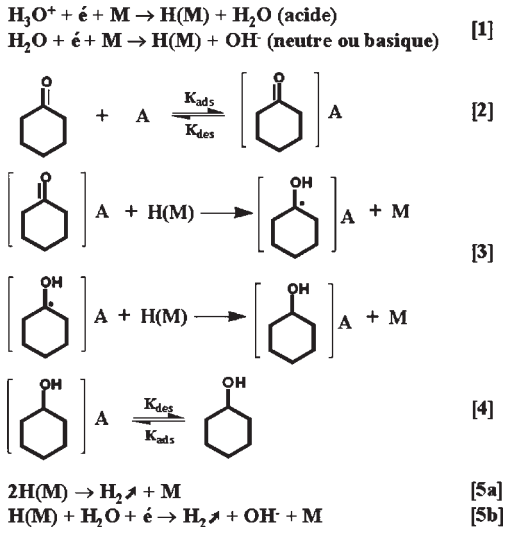

Fig. 2. Cellule électrochimique dynamique.

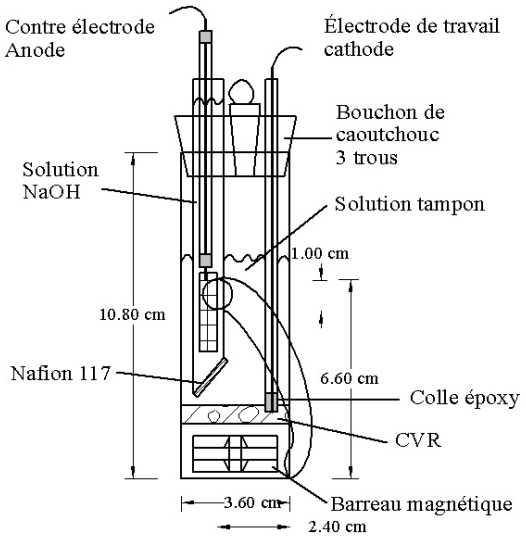

les de $Al(OH)_3$, AlO(OH) ou γ-Al_2O_3. Cette étude s'insère dans le contexte plus global de l'hydrogénation du phénol en cyclohexanol où la formation du cyclohexanone comme intermédiaire est observé.

Réactions d'HEC

L'HEC est un processus qui diffère légèrement de l'hydrogénation catalytique et dont les étapes sont représentées par les équations [1] à [5*b*] (fig. 1). Dans le cas de l'HEC réalisé avec une électrode en matériaux composites, où il y a coexistence de sites métalliques peu adsorbants et de sites non métalliques fortement adsorbants pour les molécules organiques, l'hydrogène atomique est produit in situ par électrolyse de l'eau sur les sites métalliques, eq. [1]. L'adsorption de la molécule à hydrogéner a lieu préférentiellement sur les sites non métalliques (substrat), eq. [2] et l'hydrogène atomique, H(M), réagit avec la molécule organique adsorbée, eq. [3]. La seconde étape de ce processus est plus rapide que la première due à la présence d'un radical (14). La dernière étape est la désorption de la molécule organique hydrogénée pour libérer le site d'adsorption non métallique, eq. [4].

La quantité d'hydrogène adsorbé non utilisée pour l'HEC proprement dite va être perdue sous forme d'hydrogène gazeux, soit par désorption chimique (Tafel), eq. [5*a*] ou électrochimique (Heyrovski), eq. [5*b*].

Détails expérimentaux

Cellule électrochimique

Les essais ont été effectués dans une cellule dynamique en verre (fig. 2) déjà décrite en détail (15, 16). Cette cellule permet la circulation de la solution et de l'électrocatalyseur, ce dernier sous forme de particules qui entrent en contact avec le disque de carbone vitreux réticulé (CVR) poreux (Electrosynthesis Co.). Le CVR agit comme conducteur électrique et permet ainsi la formation d'hydrogène adsorbé sur les particules, M(H), eq. [1]. La contre-électrode est isolée du compartiment cathodique par une membrane de Nafion 117 (DuPont). L'électrolyte du compartiment cathodique (60 mL) est une solution tampon 1 M de phosphate de potassium à pH 7 (KH_2PO_4–NaOH). Un courant de 5 mA est imposé à l'électrode de CVR après avoir ajouté 200 mg de matériaux électrocatalytiques et 0,25 mmol de cyclohexanone à l'électrolyte. L'extraction des molécules organiques se fait dans l'acétate d'éthyle et l'analyse par chromatographie gazeuse se fait avec un standard externe. L'erreur sur ces mesures est estimée à 5 %.

Fabrication des électrocatalyseurs

Les trois poudres de départ utilisées étaient des hydroxydes d'aluminium (Anachemia et Alcan International) ayant des surfaces spécifiques mesurées par BET, de 0,23; 10 et 35 $m^2\ g^{-1}$. Les produits de calcination, le AlO(OH) et le Al_2O_3, ont été obtenus en chauffant la poudre d'hydroxyde d'aluminium ayant une surface BET de 0,23 $m^2\ g^{-1}$, pendant 24 h dans un four à la température appropriée, la poudre était en contact avec l'air ambiant. Le nickel métallique fut ensuite déposé sur les particules de poudre par déposition physique sous vide (*physical vapour deposition*, PVD) (17). Le dépôt obtenu est constitué d'agglomérats de nickel de quelques nanomètres de diamètre visible sur les bords des particules en microscopie électronique à transmission (fig. 3), ce dépôt se retrouve exclusivement à la surface des poudres et le nickel pénètre peu dans les pores (observé en MEB avec un mapping du nickel sur des images non montrées).

Caractérisation des catalyseurs

Les particules d'hydroxyde d'aluminium non chauffé de diverses surfaces spécifiques BET présentent une gamme de taille allant de 5 à 25 μm ainsi qu'une morphologie différente telle que montrée par les images de MEB (fig. 4–6). De plus, la taille des particules est mesurée à l'aide d'un analyseur de taille de type Analysette 22 Compact (Fritsch) en solution aqueuse.

Après calcination des poudres d'hydroxyde d'aluminium de 0,23 $m^2\ g^{-1}$, la surface spécifique est largement tributaire de la température de calcination (18). Cet effet est expliqué par la formation de pores lors de la déshydratation avant

© 2002 CNRC Canada

Fig. 3. Hydroxyde d'aluminium avec des agglomérats de nickel (microscope électronique à transmission).

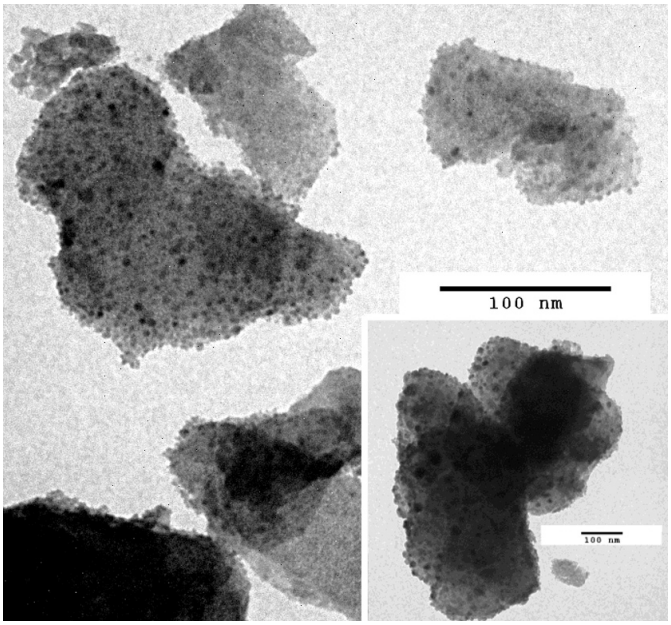

Fig. 4. MEB de particules d'hydroxydes d'aluminium 0,23 m^2 g^{-1} (sans calcination).

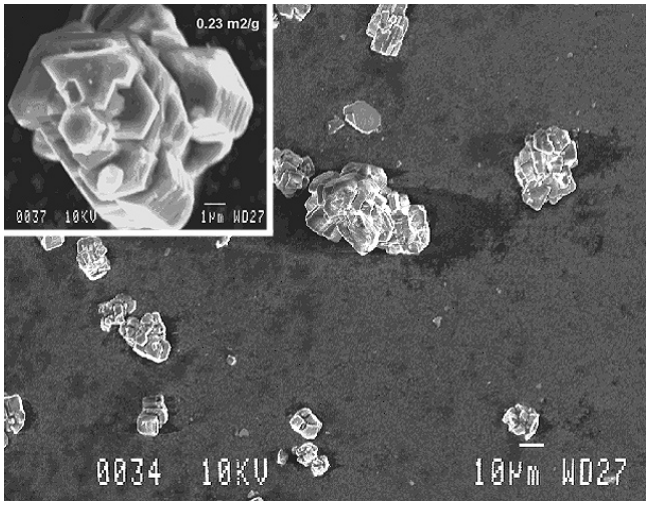

250°C et par la restructuration cristalline après 250°C. La perte en eau permet de modifier la structure chimique de la poudre sans un effet marquant sur la taille des particules (tableau 1).

Résultats et discussion

Adsorption du phénanthrène sur l'hydroxyde d'aluminium

C'est à partir des isothermes d'adsorption du phénanthrène sur l'hydroxyde d'aluminium thermiquement modifié (8) (HATM) que la quantité de phénanthrène adsorbée est donnée en fonction de la masse d'HATM et de la surface spécifique d'HATM pour une concentration (C_e) en phénanthrène de 1,6 mmol L^{-1} (fig. 7). Pour une même masse de

Fig. 5. MEB de particules d'hydroxydes d'aluminium 10 m^2 g^{-1} (sans calcination).

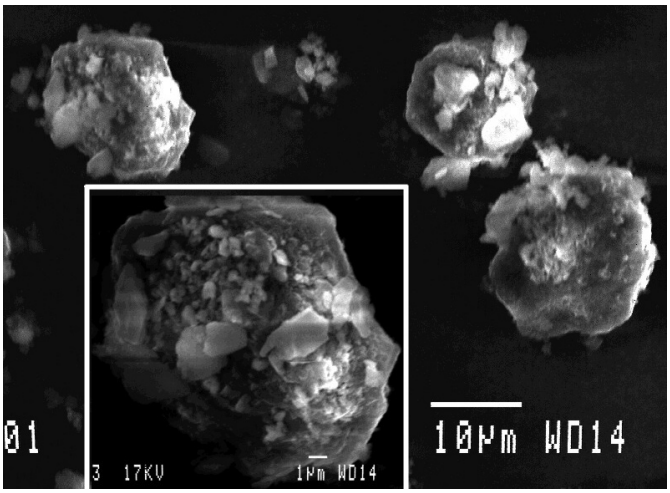

Fig. 6. MEB de particules d'hydroxyde d'aluminium 35 m^2 g^{-1} (sans calcination).

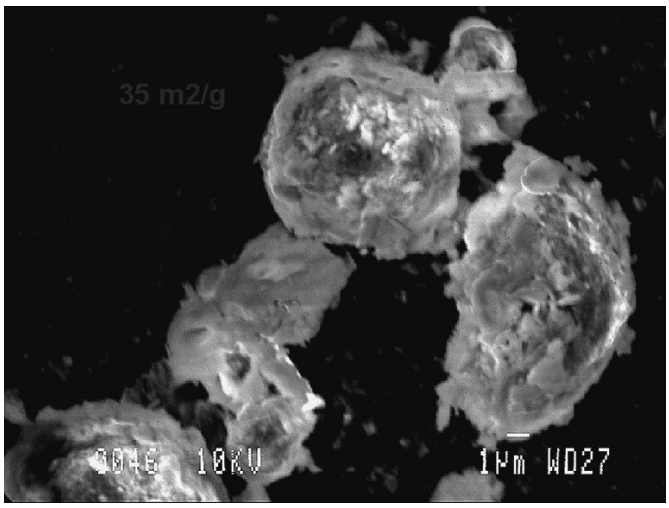

Tableau 1. Caractéristique des poudres d'hydroxyde d'aluminium employés selon la température de calcination.

T ° (°C ±1)	S_{sp} (m^2 g^{-1} ±5 %)	d_{moy} (µm ±1)	Composé*
25	10,0	5	$Al(OH)_3$
25	35,0	20	$Al(OH)_3$
25	0,23**	25**	$Al(OH)_3$
100	0,40	n.e	
150	0,40	n.e	
250	282	n.e	
300	223	25	AlO(OH)
400	188	n.e	
700	93	n.e	
800	53	26	γ-Al_2O_3

Nota : T °, température de calcination, durée 24 h; S_{sp}, surface spécifique obtenue par BET à N_2; d_{moy}, diamètre moyen des particules; n.e, non effectué.

*Obtenu par DRX.

**Poudre de départ pour la calcination.

© 2002 CNRC Canada

Tableau 2. Rendements en hydrogénation électrocatalytique du cyclohexanone selon la surface spécifique à 1400 C.

Identification du catalyseur	Surface du catalyseur (BET) (m^2 g^{-1} ±5 %)	Taille moyenne (μm ±1)	Surface calculée (sphérique) (m^2 g^{-1} ±0,005)	Concentration Nickel (%p/p ±0,1)	Cyclohexanol formé (% relatif ±5)
A	0,23	25	0,051	1,1	56
B	35	20	0,064	1,1	66
C	10	5	0,258	0,7	86
D	—	2–3	—	100*	35

*200 mg de métal pur.

Fig. 7. Adsorption du phénanthrène sur l'hydroxyde ou l'oxyde d'aluminium calciné en fonction du poids (Q_e) et de la surface (S_e) dans le toluène (à partir de la référence 18).

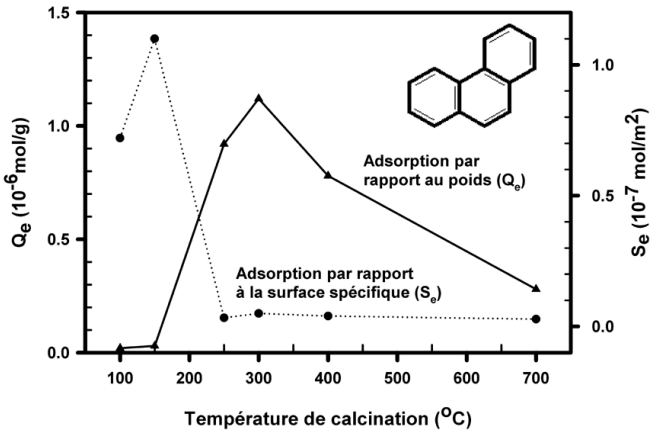

Fig. 8. Hydrogénation électrocatalytique du cyclohexanone sur l'hydroxyde d'aluminium de différentes surfaces spécifiques avec agrégats de nickel d'environ 1 % (p/p). Catalyseurs du tableau 2.

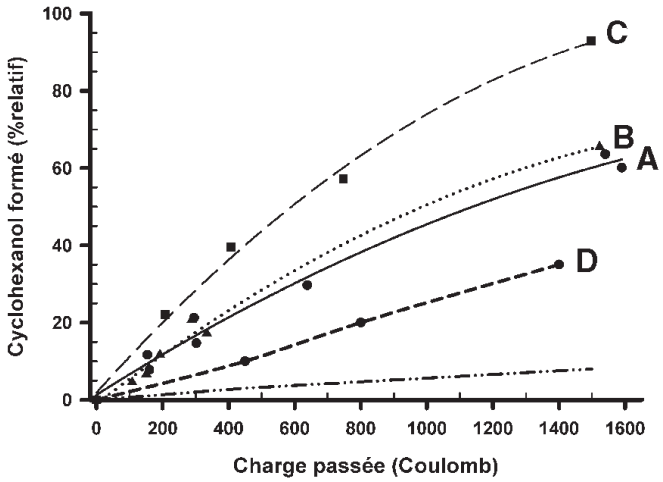

poudre, les résutats confirment que plus la surface spécifique est grande, plus l'adsorption est importante. D'autre part, cette figure illustre aussi que la nature des sites d'adsorption a une influence déterminante sur l'adsorption (en considérant une même aire de surface d'adsorption). Ainsi, la surface ayant des groupements hydroxydes (100°C et 150°C) a une adsorption plus importante que celle sur des surfaces de type oxydes (250°C à 700°C). Ces observations laissent croire que la nature des sites actifs d'adsorption est susceptible d'avoir une influence significative sur les rendements en HEC des composés organiques dans la mesure où l'étape limitante de la réaction est l'étape d'adsorption ou de désorption de la molécule organique à hydrogéner ou la désorption de la molécule après HEC.

Influence de la taille des particules et de la surface spécifique sur l'HEC

La quantité de cyclohexanol formé par HEC augmente en fonction du diamètre de l'électrocatalyseur composite d'hydroxyde d'aluminium et de nickel. Pour une quantité de 200 d'électrocatalyseur le meilleur rendement correspond à une surface spécifique BET de 10 m^2 g^{-1} (fig. 8). On suppose que les sites privilégiés pour l'HEC sont les interfaces métal-hydroxyde – oxyde d'aluminium où les sites métalliques contiennent H_{ads} et les sites non métalliques contiennent la molécule organique adsorbée. L'aire de la surface catalytique réelle semble dépendre de la technique de déposition des agrégats métalliques des catalyseurs employée. Ainsi, le rendement en HEC est susceptible de dépendre de l'importance de l'interface métal – hydroxyde – oxyde d'aluminium (IMHA) et non de la surface BET. On en déduit que la surface électrocatalytique est beaucoup plus petite que la surface BET.

Le tableau 2 présente un résumé des rendements en HEC pour une charge de 1400 C avec les électrocatalyseurs utilisés. On y retrouve le diamètre moyen des particules (Analysette 22) et la surface géométrique des catalyseurs (BET). L'électrocatalyseur C a une plus grande activité en HEC que les électrocatalyseurs A et B. L'utilisation de poudre de nickel pur (200 mg), notée D, donne des rendements inférieurs aux catalyseurs composites A, B et C.

Influence de la nature des sites d'adsorption sur l'HEC

La figure 9 montre que l'activité des électrocatalyseurs fabriqués à partir d'hydroxyde d'aluminium calciné ou non, dépend de la nature des composés d'aluminium formés. Pour l'hydroxyde d'aluminium non chauffé, électrocatalyseur A′, selon la diffraction des rayons-X, la surface est constituée majoritairement de groupements hydroxyl (Gibbsite). Pour les particules calcinées à 300°C, électrocatalyseur E, la surface est partiellement recouverte d'oxyde et d'hydroxyl (Boehmite) et à 800°C, électrocatalyseur F, on retrouve une surface d'oxyde (Alumine gamma). En phase aqueuse, la Gibbsite et la Boehmite ont déjà des hydroxydes de surface, mais il est connu que l'alumine gamma s'hydrate partiellement en surface. Les propriétés acido-basique des matériaux peuvent donc dépendre du degré d'hydratation en solution et de la structure cristalline interne : en effet, selon Pascal (19), l'acidité de Lewis varie comme ceci, alumine < Gibbsite < Boehmite. De plus, les oxydes et hydroxydes d'aluminium

© 2002 CNRC Canada

Fig. 9. Hydrogénation électrocatalytique du cyclohexanone sur l'hydroxyde d'aluminium calciné avec nickel d'environ 0,2 % (p/p).

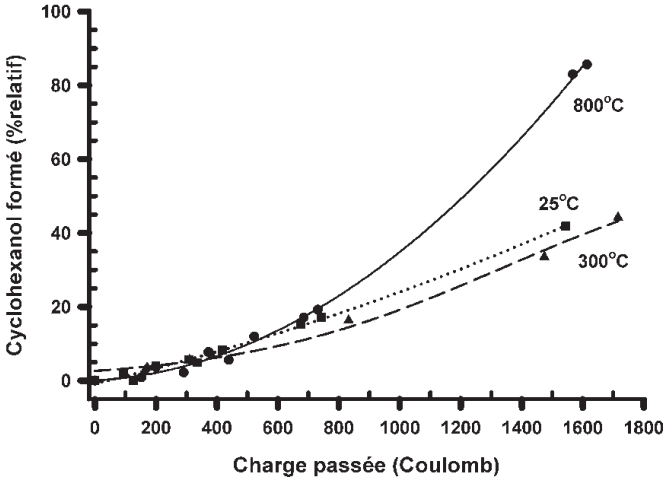

ont une forte capacité d'adsorption de l'eau et des molécules organiques polaires (20); cette tendance dépendant aussi du degré d'hydratation, il devient donc difficile de déterminer quel est l'effet prépondérant dans l'adsorption des molécules organiques. Toutes ces poudres après traitement thermique ont une taille moyenne similaire (tableau 1) ce qui facilite la comparaison, alors que les autres caractéristiques des électrocatalyseurs sont données au tableau 3. On observe pour une charge passée supérieure à 1400 C, un rendement en HEC bien meilleur dans le cas de l'électrocatalyseur F. L'électrocatalyseur F contient approximativement la même quantité de nickel que dans le cas des deux autres électrocatalyseurs. De plus, il ne semble pas y avoir de corrélation entre la surface BET de l'électrocatalyseur et son rendement en HEC. L'ensemble de ces observations indique le rôle clef joué par la nature du substrat non métallique sur l'adsorption ou la désorption des molécules organiques.

Conclusion

L'hydrogénation électrocatalytique du cyclohexanone a été réalisée en milieu aqueux à 25°C avec des électrodes composites de nickel déposé sur des substrats d'oxyde et d'hydroxyde d'aluminium. Les rendements en HEC dépendent étroitement de la nature du substrat d'aluminium utilisé; le substrat le plus favorable étant le γ-Al_2O_3. Ce qui met en évidence le rôle clef des étapes d'adsorption et de désorption des molécules organiques dans le procédé d'HEC.

Remerciements

Les auteurs remercient l'Alcan International limitée pour les échantillons d'hydroxyde d'aluminium fournis ainsi que le Conseil de recherches en sciences naturelles et en génie (CRSNG) et le fond de l'Université de Sherbrooke pour leur contribution financière.

Tableau 3. Hydrogénation électrocatalytique du cyclohexanone selon la température de cuisson à 1400 C.

Identification du catalyseur	Température de calcination (°C)	Surface du catalyseur* (m^2 g^{-1} ±5 %)	Concentration nickel (%p/p ±0,01)
A′	25	0,23	0,37
E	300	283	0,15
F	800	53	0,20

*Obtenue par BET.

Bibliographie

1. F. Haber. Z. Physik. Chem. **32**, 193 (1900).
2. L. Brossard. Int. J. Hydrogen Energy, **13**, 315 (1988).
3. T. Chiba et al. Bull. Chem. Soc. Jpn. **56**, 719 (1983).
4. U. Birkenstock, R. Holm, B. Reinfandt et S. Storp. J. Catal. **93**, 55 (1985).
5. Y. Choquette, L. Brossard et H. Ménard. J. Appl. Electrochem. **20**, 855 (1990).
6. V. Kirilyus, G.K. Murzatova et D.V. Sokol'skii. Sov. Electrochem. **15**, 1543 (1979).
7. R.M. Skomoroski et A. Schriesheim. J. Phys. Chem. **65**, 1340 (1961).
8. R.J. Kokes et P.H. Emmett. J. Am. Chem. Soc. **82**, 4497 (1960).
9. R.J. Kokes et P.H. Emmett. J. Am. Chem. Soc. **83**, 29 (1961).
10. B. Sen et J.L. Falconer. J. Catal. **113**, 444 (1988).
11. L.G. Hutchins et R.E. Pincock. J. Catal. **74**, 275 (1982).
12. C.A. Hassani et H. Ménard. Can. J. Chem. **77**, 1594 (1999).
13. F. Laplante et H. Ménard. Poster session, abstract No. 11. 197th meeting of the electrochemical society. The Electrochemical Society, Toronto, ON. mai 2000.
14. I. Horiuti et M. Polanyl. Trans. Faraday Soc. **30**, 1164 (1934).
15. P. Dubé, F. Kerdouss, P. Proulx, L. Brossard et H. Ménard. (En préparation).
16. P. Dubé et H. Ménard. Poster session, abstract No. 23. 197th meeting of the electrochemical society. The Electrochemical Society, Toronto, ON. mai 2000.
17. J. Fournier, H. Ménard et L. Brossard. J. Appl. Electrochem. **25**, 923 (1995).
18. C.A. Hassani. Étude de l'adsorption des hydrocarbures aromatiques polycycliques sur des matériaux particulaires et fibreux. Mémoire de maîtrise, Université de Sherbrooke. 1987. pp. 38–60.
19. P.V.H. Pascal. Nouveau traité de chimie minérale. Vol. 2. Masson, Paris. 1956. p. 586.
20. J. Bailar et al. *Dans* Comprehensive inorganic chemistry. Vol. 1. 1re éd. Pergamon Press, Oxford. 1975. pp. 1032 et 1033.

© 2002 CNRC Canada

Utilisation de vecteurs tournants pour l'optimisation de la formulation de mélanges de solvants

Serge Alex

Résumé : Cet article propose une stratégie simple qui permet d'optimiser la formulation de mélanges de solvants sans avoir recours à des modèles mathématiques et (ou) à des représentations graphiques sophistiqués. Les calculs peuvent être faits avec un chiffrier électronique (Excel, Lotus) et ne demandent pas de connaissance particulière, excepté quelques concepts de base en trigonométrie. Cette approche a été développée pour l'industrie du nettoyage et du dégraissage qui doit régulièrement reformuler des solutions de solvants à partir de composés purs. L'optimisation se fait en comparant soit visuellement soit par le calcul la somme des modules de vecteurs tournants normalisés, chacun d'eux représentant à la fois la composition chimique et un (ou plusieurs) des paramètres physico-chimiques à optimiser. Cette approche géométrique utilise une combinaison de coordonnées triangulaires et polaires permettant de ramener les nombreuses variables à représenter dans un espace à deux dimensions. La formulation d'une solution de solvants chlorés et bromés pour substituer des nettoyants purs sera utilisée afin d'illustrer les diverses étapes de calculs et l'intérêt de cette stratégie. La méthode présentée n'est pas restreinte à la problématique des solvants. Elle peut s'appliquer à tout problème de chimie impliquant des comparaisons de propriétés physico-chimiques de mélanges.

Mots clés : solvants, mélange, formulation, optimisation, dégraissage.

Abstract: A new strategy is proposed to optimize the design of solvent blends without using complex mathematical models and (or) graphical representations. All calculations are made with standard electronic programs, such as Excel, Lotus, etc. This approach was developed for the cleaning and degreasing industry, which has to find new recipes of solvent blends on a regular basis. The process relies on a visual analysis of the sum of normalized rotating vectors associated with the chemical composition and the physical properties of the individual components. This approach allows for representation of all parameters on a two-dimensional plot, including information about chemical composition, as well as the physical properties to be optimized. The research of a new mixture of halogenated solvents will be used as an example to illustrate the various steps of this technique. This method is not limited to solvent applications; it also applies to all problems that involve comparisons of physical and chemical properties of blends.

Key words: solvents, mixtures, components, optimization, cleaning.

Introduction

L'usage des solvants chlorés dans l'industrie entraîne de nombreux problèmes de pollution et d'atteinte à la santé (1–4). Ces dernières années des millions de dollars ont été dépensés pour trouver des produits pour les remplacer (5–7). Malgré cela, les alternatives ne sont pas toujours réalistes, car les produits de remplacement ont les défauts de leurs qualités, par exemple : (*i*) Les hydrocarbures et les cétones dégraissent bien et sont volatils, mais ils sont inflammables et pas toujours inoffensifs. (*ii*) Les formulations à base d'eau sont peu toxiques et peu inflammables, mais elles sont moins efficaces et laissent parfois une pellicule. (*iii*) Les dérivés à haut point d'ébullition telle que la *N*-méthylpyrrolidone dégraissent bien, sont peu toxiques, peu inflammables, mais s'évaporent mal. (*iv*) Enfin, nombre d'entre eux sont nocifs pour l'environnement global, car ils contribuent à la dégradation de la couche d'ozone, à l'augmentation de l'effet de serre, etc.

Aussi, une approche hybride est souvent choisie : les solvants chlorés sont conservés, car ils ne possèdent pas de point éclair, ne contribuent pas au réchauffement de la planète, n'attaquent pas la couche d'ozone, n'ont pas des temps de vie dans l'atmosphère très élevés et s'évaporent bien. Par contre pour réduire leur toxicité, ils sont souvent dilués avec une base compatible moins nocive. Cette astuce permet d'en limiter la toxicité, leur seul défaut, tout en conservant leur qualité exceptionnelle de solvant et leur coût peu élevé.

Par contre, trouver le mélange idéal oblige à essayer un nombre infini de combinaisons pour une application donnée si un plan d'expérience n'est pas choisi (8–10). Cette tâche est d'autant plus ardue qu'il faut optimiser des paramètres souvent antagonistes. Par exemple, dans l'industrie du nettoyage et du dégraissage, au moins quatre critères sont à concilier pour sélectionner une solution adéquate. Ce sont le taux d'évaporation, l'indice Kauri–Butanol ou tout autre indice de mesure de solubilité, la toxicité et le coût (1, 4, 5,

Reçu le 15 décembre 2000. Publié au site Web des Presses scientifiques du CNRC à http://revcanchimie.cnrc.ca le 3 avril 2002.

S. Alex. Centre d'études des procédés chimiques du Québec, 6220 Sherbrooke Est, Montréal, QC H1N 1C1, Canada (courriel : salex@cmaisonneuve.qc.ca).

 DOI: 10.1139/V02-036 © 2002 CNRC Canada

Tableau 1. Principales propriétés physico-chimiques des solvants cités.

Solvant	Chlorure de méthylène (M)	Trichloroéthylène (T)	Bromopropane (B)
Numéro CAS	75–09–2	79–01–6	106–94–5
Formule chimique	CH_2Cl_2	$HClC{=}CCl_2$	$CH_3CH_2CH_2Br$
Abréviation	MEC ou M	TCE ou T	BrP ou B
Masse molaire (g mol^{-1})	84,93	131,39	123,00
Densité à 20°C et masse volumique (lb gal^{-1})*	1,33 (11,0)	1,44 (12,1)	1,35 (11,1)
Indice de réfraction (à 20°C)	1,4240	1,4760	1,4336
Point d'ébullition (°C à 760 mm Hg)†	40	87	69
Tension de vapeur (mm Hg à 20°C)	352,1	57,8	110,8
Point éclair (°C)	Aucun	Aucun	Aucun
Taux d'évaporation normalisé (*n*-butyle acétate = 1 à 25°C)	14,5	3,9	4,5
Indice Kauri–Butanol	136	130	125
Paramètre d'Hansen (cal $cm^{-3})^{1/2}$‡	9,9	9,3	8,4
Limite d'exposition (ppm (8 h))	25	75	150
Contribution au réchauffement de la planète (GWP en années)	0,00	0,00	0,31
Pouvoir destructeur de la couche d'ozone (ODP avec CFC-11 = 1)	0,0090	0,0004	En cours d'évaluation
Potentiel photochimique de création d'ozone (POCP)	0,009	0,066	En cours d'évaluation
Composé organique volatil (COV)	NON	OUI/NON	OUI/NON
Temps de vie atmosphérique en jour	175	8	15

*1 lb = 0,453 kg; 1 gal (Imp.) = 4,546 L.
†1 mm Hg = 133,322 Pa.
‡1 cal = 4,186 J.

11). Les performances recherchées pour chacun d'eux sont : (*i*) Le taux d'évaporation : sa valeur doit être aussi élevée que possible pour limiter le temps de séchage. (*ii*) L'indice Kauri–Butanol (ou KB) : il faut un chiffre élevé pour assurer une bonne solubilisation des solutés. Certains formulateurs préfèrent utiliser les paramètres de Hansen (11) au lieu du KB, car ce dernier n'est pas applicable pour les composés oxygénés. Dans cette étude, le KB est particulièrement bien adapté et a donc été retenu, car expérimentalement il est facilement vérifiable. (*iii*) La toxicité : généralement, sauf exception, seule la toxicité des vapeurs de solvant est considérée. Ceci est justifié par le fait que le danger relié à l'ingestion et (ou) au contact cutané peut être facilement annulé par la pratique d'une hygiène appropriée ou par le port d'équipements individuels de protection. Aussi, le risque global ne dépend pas seulement de la toxicité intrinsèque de la substance, mais aussi de sa pression de vapeur qui renseigne sur la probabilité de la retrouver à l'état gazeux. Un produit est peu dangereux si sa nocivité et sa pression de vapeur sont faibles. (*iv*) Le coût : cette variable est importante pour les industriels, car à elle seule, elle peut déterminer le succès ou l'échec d'une formulation. Malgré, les programmes de plus en plus sophistiqués de recyclage de solvants avec pertes minimales, le prix des solvants demeure un élément déterminant dans le choix final.

Actuellement, il existe des programmes offerts par les fabriquants de solvants pour supporter la formulation tels que Arcocomp (Arco Chemical Company) qui optimise les paramètres de solubilité et le taux d'évaporation, Chemcomp (Dow Chemical Company) qui donne les profils d'évaporation, alors que Co-Act (Exxon Chemical Company) est surtout destiné à l'industrie des peintures et des polymères. Il est à noter que ce dernier renferme aussi une base de données qui contient les propriétés physico-chimiques de plus de 500 solvants (11). Shell Chemical et Eastman Chemical Company proposent aussi à leurs clients des programmes similaires. En dehors de ces produits spécialement conçus pour les formulateurs, il existe les méthodes d'optimisation classiques de recherche opérationnelle comme la méthode du Simplex, les arbres décisionnels de Taguchi ou encore les analyses en composantes principales, etc. (10, 12–14). Par contre, ces stratégies de calcul sont difficiles à appliquer dans ce cas de formulation, faute de modèle de base liant les critères de calculs ou de décision entre eux. Aussi, ce travail présente une approche qui a le mérite d'unifier et d'harmoniser les variables pour la sélection d'un bon solvant (c.-à-d. haut taux d'évaporation, indice Kauri–Butanol élevé, toxicité réduite et faible coût) malgré le manque de lien mathématique et physico-chimique entre les divers paramètres.

Un mélange pour le dégraissage de pièces métalliques de produits chlorés dilués par une base bromée moins toxique servira à illustrer cette technique d'optimisation. Les produits retenus pour le mélange sont le chlorure de méthylène (M), le trichloréthylène (T). Malgré leur toxicité discutable (et encore discutée), ils demeurent des produits très populaires (15). Le diluant est le 1-bromopropane (B) qui est considéré comme le produit de substitution idéal pour les dérivés chlorés et dont la nocivité est réduite.

Problématique

Une des difficultés première en formulation est de minimiser le nombre d'essais tout en étant sûr de couvrir toutes les possibilités de mélange offertes. De plus, il faut tenir compte de l'antagonisme des paramètres de sélection. Par exemple, si un solvant s'évapore bien, sa pression de vapeur est naturellement élevée, ce qui le rend potentiellement plus toxique comme il est plus probable de le retrouver sous forme vapeur. Pour le cas choisi, le tableau 1 résume les principales caractéristiques physico-chimiques des trois produits. Sans entrer dans les détails, le chlorure de méthylène

© 2002 CNRC Canada

Tableau 2. Pourcentages choisis pour les diverses solutions et angles formés par les vecteurs avec le repère dans la représentation de Fresnel.

	% En volume de chacun des solvants			% En volume combinés (coordonnées triangulaires)		Angle θ (sens horaire)
Cadran 1	M	T	B	M (axe *y*)	(T + B) (axe *x*)	θ
	1,000	0,000	0,000	1,000	0,000	0,00
	0,750	0,125	0,125	0,750	0,250	18,43
	0,660	0,170	0,170	0,660	0,340	27,26
	0,500	0,250	0,250	0,500	0,500	45,00
	0,333*	**0,333**	**0,333**	**0,333**	**0,666**	**63,43**
	0,250	0,375	0,375	0,250	0,750	71,56
	0,000	0,500	0,500	0,000	1,000	90,00
Cadran 2	M	T	B	–(M + T) (axe *y*)	B (axe *x*)	θ
	0,000	1,000	0,000	–1,000	0,000	180,00
	0,125	0,750	0,125	–0,875	0,125	171,86
	0,170	0,660	0,170	–0,830	0,170	168,42
	0,250	0,500	0,250	–0,750	0,250	161,56
	0,333*	**0,333**	**0,333**	**–0,666**	**0,333**	**153,43**
	0,375	0,250	0,375	–0,625	0,375	149,03
	0,500	0,000	0,500	–0,5000	0,500	135,00
Cadran 3	M	T	B	M (axe *y*)	–(T + B) (axe *x*)	θ
	0,000	0,000	1,000	0,000	–1,000	270,00
	0,125	0,125	0,750	0,125	–0,875	278,13
	0,170	0,170	0,660	0,170	–0,830	281,57
	0,250	0,250	0,500	0,250	–0,750	288,43
	0,333*	**0,333**	**0,333**	**0,333**	**–0,666**	**296,56**
	0,375	0,375	0,250	0,375	–0,625	300,96
	0,500	0,500	0,000	0,500	–0,500	315,00

Nota : Les angles sont mesurés dans le sens horaire à partir de l'axe +y du cercle trigonométrique. M, chlorure de méthylène; T, trichloréthylène; B, 1-bromopropane.

*Cette composition est volontairement ajoutée pour avoir un vecteur commun dans chaque cadran.

(M) est le solvant le plus performant mais malheureusement le plus toxique, alors que le 1-bromopropane (B) est le moins efficace, le plus cher des trois, mais aussi le moins dangereux. Quant au trichloréthylène (T), il se situe entre les deux aussi bien en termes d'efficacité que de santé sécurité.

Stratégie d'étude

Pour optimiser les mélanges, un processus décisionnel graphique est proposé. Il se décompose en trois étapes, soit : (1) Choisir la concentration des solutions des trois solvants pour que l'ensemble couvre au mieux toutes les possibilités. (2) Choisir un mode de représentation graphique qui permette de rapidement visualiser chacun des quatre paramètres physico-chimiques pour chaque mélange. (3) Développer un outil décisionnel pour sélectionner les meilleurs mélanges en fonction des contraintes d'usage, de production et environnementales.

Étape 1 : Choix de l'ensemble de solutions

Une série de solutions contenant divers pourcentages en volume (noté ϕ_v) de chacun des solvants est sélectionnée pour couvrir le maximum de possibilités. Les choix sont résumés dans les trois premières colonnes du tableau 2, les valeurs sont choisies et distribuées par permutation. Le premier set (cadran 1) représente le choix de base, et les deux suivants sont obtenus par permutation des valeurs. Le nombre de solutions retenues est au total de 19, ce chiffre pourrait être augmenté si un résultat plus fin était recherché. Cette étape ne présente aucune difficulté.

Étape 2 : Choix du mode de représentation

Les pourcentages volumiques de chaque substance doivent être représentés dans un espace à une ou deux dimensions pour être exploitables sur un graphique simple. De plus, une dimension doit rester libre pour représenter le (les) paramètre(s) à optimiser pour chaque constituant. Aussi, il faut impérativement réduire les trois pourcentages de la composition chimique en une coordonnée. La manière la plus simple d'y parvenir est de compresser ces variables en passant en coordonnées triangulaires pour supprimer une dimension, et finalement les reporter sur un graphique en coordonnées polaires pour libérer encore une autre dimension. Les colonnes 4 et 5 du tableau 2 illustrent cette opération. La procédure utilisée est détaillée dans les paragraphes suivants :

Dans le premier cadran : le pourcentage en volume ϕ_{v1} du chlorure de méthylène (M) est représenté en fonction de la somme de ceux du trichloréthylène (T) et du 1-bromopropane (B). Cette opération est appliquée pour les sept premières données de base. Puis, les coordonnées $\phi_{v1} = f(\phi_{v2} + \phi_{v3})$ sont reportées respectivement sur l'axe des y et des x du repère cartésien. En d'autres mots, l'axe des y

© 2002 CNRC Canada

Fig. 1. Représentation de Fresnel des solutions choisies.

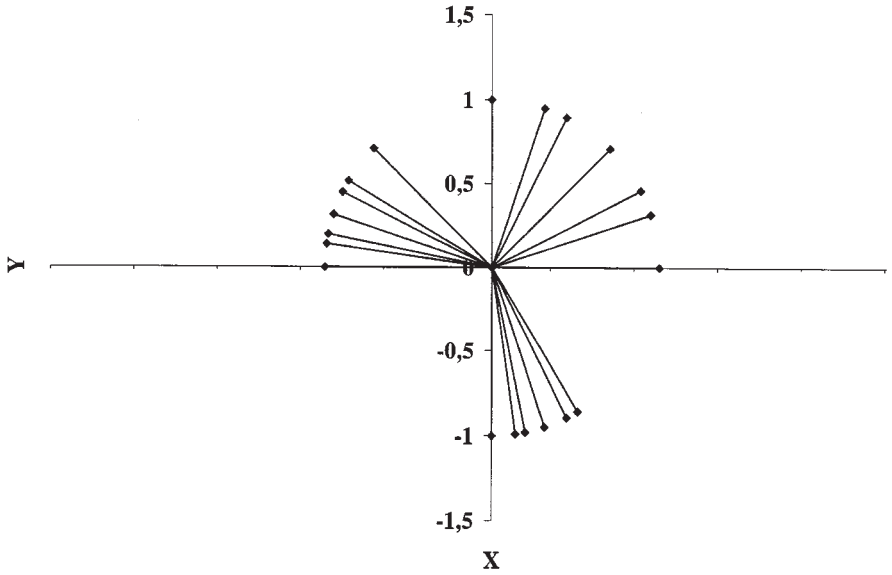

supporte le pourcentage en M et celui des x la somme des pourcentages en T et B.

Dans le second cadran : cette série est associée à la première permutation, donc il faut changer le mode de représentation des coordonnées triangulaires par rapport au précédent pour éviter les chevauchements entre valeurs induits par la compression triangulaire. Dans ce cadran, la somme complémentaire (signe négatif) du pourcentage de chlorure de méthylène ϕ_{v1} ajouté à celui du trichloréthylène ϕ_{v2} est représentée en fonction du pourcentage de 1-bromopropane ϕ_{v3}. Le tracé de $\phi_{v3} = f(-(\phi_{v1} + \phi_{v2}))$ permet de lever la dégénérescence entre les divers pourcentages. Ainsi, l'axe des y supporte la valeur négative de la somme des pourcentages M + T. Quant à l'axe des x, il correspond aux pourcentages associés à B.

Dans le troisième cadran : pour la dernière permutation, le changement de représentation est encore obligatoire. Dans ce cas, le pourcentage de chlorure de méthylène ϕ_{v1} est représenté en fonction de la somme complémentaire (signe négatif) du pourcentage de trichloréthylène ϕ_{v2} ajouté à celui du 1-bromopropane ϕ_{v3}, soit $\phi_{v1} = f(-(\phi_{v2} + \phi_{v3}))$. Dans cet espace, l'axe des y correspond au pourcentage en M, alors que l'axe des x est l'opposé de la somme des pourcentages de T et B. Cela clôture le graphique avec la seconde permutation des sept derniers nombres.

Lorsque les valeurs (ϕ_{vi}, $\pm (\phi v_j + \phi_{vk})$) sont reportées dans la figure 1 en suivant la recette établie ci-dessus, un faisceau de vecteurs est alors obtenu. Chaque segment correspond à un mélange particulier et forme un angle θ caractéristique qui est facilement accessible par le calcul en utilisant la tangente. Celle-ci se dérive à partir des valeurs des coordonnées triangulaires (à savoir, $tg(\theta)$ est le rapport du coté opposé sur le coté adjacent, tous deux sont connus car ils correspondent aux pourcentages de base ou à ceux combinés). Ainsi, le rapport (ϕ_{vi}, $\pm (\phi_{vj} + \phi_{vk})$) donne accès à l'angle que forme les diverses solutions avec le repère, et θ devient associé à une composition chimique fixée et unique. Ceci forme une base de coordonnées polaires, où la longueur du segment (ou le module) demeure encore inutilisée et peut servir de support pour les paramètres à optimiser. La figure 1 représente le faisceau de directions induites, et ces dernières sont tracées via la projection orthogonale d'un vecteur de module unitaire ($r = 1$) sur les axes, soit :

[1] $y = r \cos \theta$

[2] $x = r \sin \theta$

La figure 1 est un ensemble de vecteurs tournants ou de Fresnel de module égal à 1. L'angle formé entre la direction et le repère, θ, évolue dans le sens horaire et a pour origine le couple ($x = 0$; $y = +1$), soit le point confondu avec l'axe vertical correspondant aux valeurs y positives.

Les variables de concentration ayant été réduites, il reste à faire subir le même traitement aux quatre paramètres qui sont : le prix, le taux d'évaporation, l'indice Kauri–Butanol et la toxicité. Chacun d'eux doit être calculé pour chaque solution de composition différente. Ensuite, la valeur est reportée sur la direction vectorielle correspondant à la composition choisie et devient le module du vecteur. Dans un premier temps, quatre graphes indépendants associés respectivement au prix, au taux d'évaporation, à l'indice Kauri–Butanol et à la toxicité sont construits, tous supportant 21 vecteurs ou compositions chimiques (incluant deux répétitions). L'obtention de ces graphiques pour chacun des critères s'effectue comme suit.

Représentation graphique du prix

Le prix pour chaque solution est calculé en pondérant les prix de revient des composantes individuelles soit :

[3] $\mathbf{Pr}_j = \phi_{v1j}\mathrm{Pr}_1 + \phi_{v2j}\mathrm{Pr}_2 + \phi_{v3j}\mathrm{Pr}_3$

où $\mathbf{Pr}_j$ représente le prix résultant du j^e mélange. ϕ_{vij} et Pr_i sont respectivement le pourcentage volumique de la i^e composante du j^e mélange et le coût des solvants à l'état pur. Une fois l'ensemble $\mathbf{Pr}_j$ dérivé, les chiffres sont normalisés par rapport à **Prmin**, ce dernier étant le prix minimum, soit :

[4] $< \mathbf{Pr}_j > = \mathbf{Prmin}/\mathbf{Pr}_j$

© 2002 CNRC Canada

Fig. 2. Représentation des vecteurs tournants normalisés du paramètre prix.

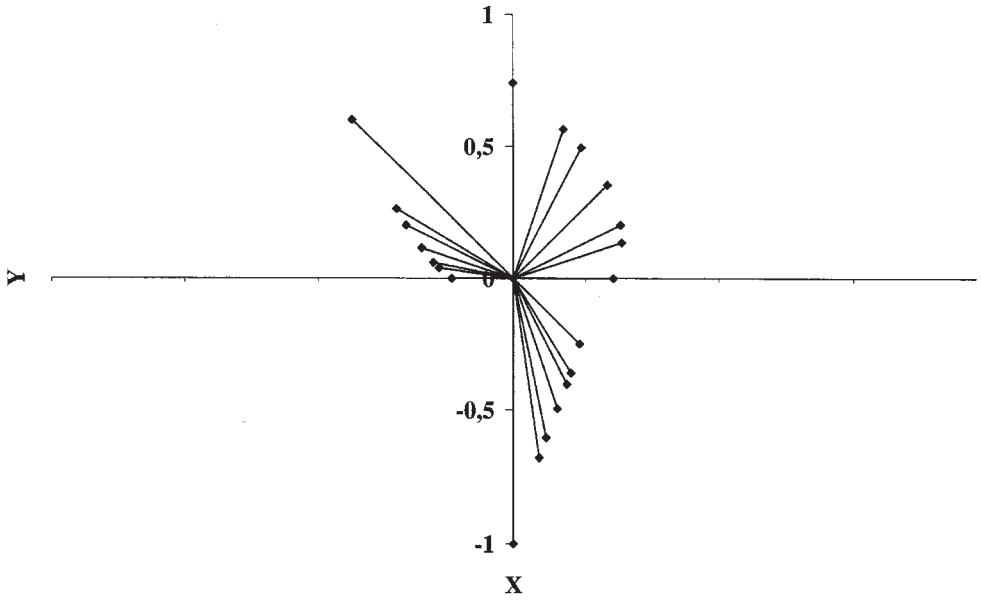

Finalement, les entrées < $\mathbf{Pr}_j$ > sont reportées sous forme de segments de longueur normalisée sur la direction associée au mélange choisi. Cette opération est effectuée en utilisant une relation identique aux équations [1] et [2] (projections orthogonales) :

[5] $y = < \mathbf{Pr}_j > \cos \theta$

[6] $x = < \mathbf{Pr}_j > \sin \theta$

Le résultat est montré dans la figure 2, graphe qui illustre sous forme géométrique le paramètre prix. Plus la longueur du vecteur est proche de l'unité, moins cher sera le mélange. L'étape de normalisation est obligatoire pour pouvoir comparer le prix avec les autres critères (c.-à-d. : toxicité, taux d'évaporation, etc.) qui n'ont pas les mêmes unités et qui eux aussi devront être harmonisés. La normalisation aurait pu s'effectuer par rapport à la valeur maximale au lieu de celle minimale. Ici, le choix est fait afin que le vecteur le plus long corresponde aux meilleures conditions. Ainsi, un segment de module (mod.) unitaire est la meilleure note (ou score) possible. Avec cet exemple, le trichloréthylène est le premier choix en terme de prix, suivi de près par la solution 0,50:0,50 v/v de trichloréthylène et de chlorure de méthylène avec un score de 0,85 (ou mod. = 0,85). Cela signifie que ce mélange rencontre uniquement 85 % des meilleures performances disponibles à partir des trois substances de base choisies.

Représentation graphique du taux d'évaporation

Le taux d'évaporation τ est une mesure relative qui se calcule par rapport à une substance de référence à une température donnée. Généralement, l'acétate de butyle sert de standard et l'expérience se fait à 25°C. Ce taux se mesure en normalisant le temps requis pour évaporer 90 % de la masse du solvant étudié par rapport à celui nécessaire pour évaporer la même masse d'acétate de butyle. Pour les solvants halogénés, il peut aussi s'obtenir en mesurant la vitesse de disparition de deux liquides (le solvant étudié et la référence) sur un plan incliné (16). Les valeurs sont connues pour les substances pures et sont reportées dans le tableau 1. Le taux d'évaporation des solutions est dérivé en assumant qu'il existe une relation linéaire entre celui des produits purs et celui des mélanges. Cette hypothèse est justifiée par le fait qu'il n'existe pas d'interactions fortes entre les diverses composantes du mélange comme des liaisons de type hydrogène. Aussi, l'équation [7] conduit au taux d'évaporation τ.

[7] $\tau_j = \phi_{m1j}\ \tau_1 + \phi_{m2j}\ \tau_2 + \phi_{m3j}\ \tau_3$

où τ_j représente le taux d'évaporation du j^e mélange et ϕ_{mij} correspond au pourcentage massique du i^e composé dans le j^e mélange. Dans cette équation, les fractions volumiques doivent être remplacées par les fractions massiques pour tenir compte de la définition du taux d'évaporation (voir ci-dessus). τ_i est le taux d'évaporation de la i^e substance pure à 25°C déterminé par rapport à l'acétate de butyle (τ = 1,0 par définition).

Le pourcentage massique est calculé à partir des pourcentages volumiques ϕ_{vij}. La fraction volumique étant égale à $\phi_{vij} = V_i/V_t$ (où V_i est le volume de la i^e substance pure et V_t est le volume total de la solution), alors ϕ_{mij} est dérivé grâce à la formule $\phi_{vi}\rho_i/\Sigma_i\phi_{vi}\rho_i$, où ρ_i est la masse volumique des produits purs. Les valeurs des taux d'évaporation de chaque mélange sont ensuite normalisées en faisant l'opération suivante :

[8] $< \tau_j > = \tau_j/\tau\mathbf{max}$

où τ_j est le taux d'évaporation du j^e mélange et $\tau\mathbf{max}$ est le taux d'évaporation le plus élevé. La figure 3 représente le faisceau de vecteurs correspondant en utilisant la relation habituelle :

[9] $y = < \tau_j > \cos \theta$

[10] $x = < \tau_j > \sin \theta$

© 2002 CNRC Canada

Fig. 3. Représentation des vecteurs tournants normalisés du taux d'évaporation.

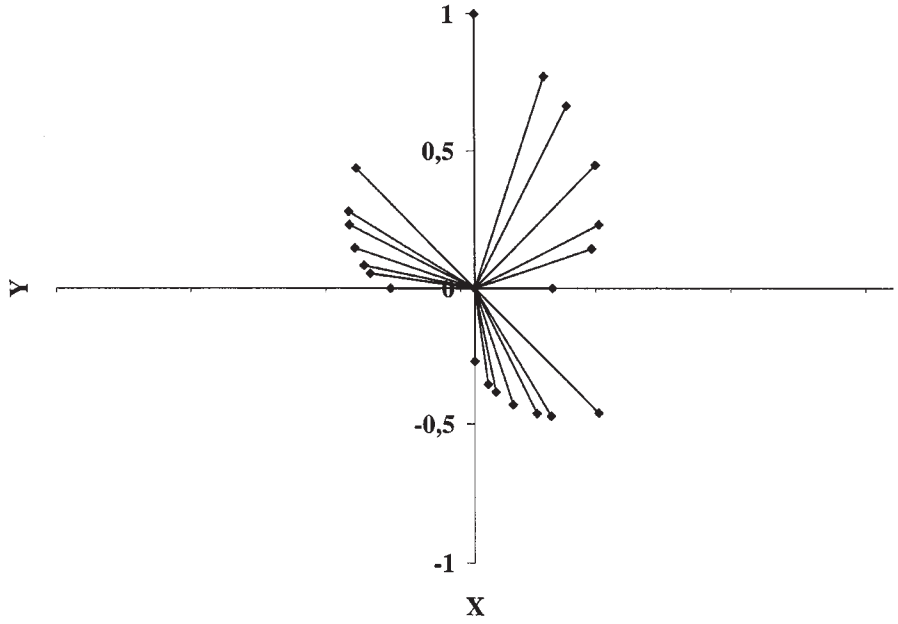

Le vecteur le plus long correspond au taux d'évaporation le plus rapide, et donc, au mélange le plus performant par rapport à ce paramètre. La solution de chlorure de méthylène pure sort gagnante (mod. = 1 ou 100 %), suivie du mélange 0,750:0,125:0,125 v/v/v en M–T–B, milieu très riche en chlorure de méthylène et qui obtient un score de 81 % (mod. = 0,81).

Représentation graphique de l'indice Kauri–Butanol

L'indice de Kauri–Butanol (KB) permet de mesurer le pouvoir solvant des composés chimiques. Ce test simple consiste à ajouter le solvant à tester dans un volume imposé d'une solution de gomme de Kauri dans du butanol jusqu'à l'apparition d'un trouble (17). Le volume de solvant versé est corrigé par des étalonnages avec des substances tests (le toluène et un mélange heptane–toluène (75:25)) et l'indice KB est dérivé à partir de ces mesures et d'une formule standardisée (17). Pour le mélange, le KB peut être considéré comme une combinaison linéaire des indices de chaque composé pur pondérée par leurs pourcentages volumiques respectifs, les solutions étant idéales comme déjà mentionné. Certains auteurs utilisent les paramètres de Hansen (δ) au lieu de l'indice KB pour évaluer le pouvoir solvant, ceux-ci étant souvent mieux connus et documentés (11, 18), et surtout applicables à toutes les catégories de solvants. Eux aussi sont calculés en supposant que le coefficient résultant du mélange est une combinaison linéaire des δ pondérés par le pourcentage volumique de chaque composé pur (11). Dans cette étude, l'indice KB est particulièrement bien choisi, car il est alors plus facile et rapide de faire des vérifications expérimentales si nécessaire.

$$[11] \quad \mathbf{KB}_j = \phi_{v1j}KB_1 + \phi_{v2j}KB_2 + \phi_{v3j}KB_3$$

où $\mathbf{KB}_j$ représente l'indice résultant du j^e mélange. ϕ_{vij} et KB_i sont respectivement le pourcentage volumique du i^e composant du j^e mélange, et l'indice KBi, celui des substances pures. Comme précédemment, les indices sont normalisés en divisant chaque $\mathbf{KB}_j$ par le **KBmax**, ce dernier correspondant au mélange ayant le pouvoir nettoyant le plus grand :

$$[12] \quad < \mathbf{KB}_j > = \mathbf{KB}_j/\mathbf{KBmax}$$

Ensuite, l'ensemble $< \mathbf{KB}_j >$ est porté en graphique (voir fig. 4) sous forme harmonisée. Cette opération est effectuée en utilisant les projections orthogonales :

$$[13] \quad y = < \mathbf{KB}_j > \cos\theta$$

$$[14] \quad x = < \mathbf{KB}_j > \sin\theta$$

Le vecteur de longueur unitaire représente le meilleur solvant. On notera que leurs performances étant tellement voisines, les pointes des vecteurs sont presque toutes inscrites dans un même cercle (voir fig. 4). Les modules sont tous compris entre 1 et 0,90, ce qui démontre que leurs capacités nettoyantes sont similaires et ce paramètre influencera peu le choix final dans cet exemple.

Représentation graphique de la toxicité

Il n'existe pas de modèle établi pour définir la toxicité. De plus, malgré des années d'existence et d'utilisation, de nombreux désaccords existent dans la littérature concernant les dangers et risques reliés aux solvants chlorés et bromés (1, 15). Les tableaux 3A et 3B illustrent bien ce point (1). Aussi, la toxicité est illustrée en créant un indice qui combine la dose moyenne d'exposition (TWA ou « time-weighted average ») sur un temps *t* et la pression de vapeur saturante du composé, soit :

$$[15] \quad \mathbf{ITOX} = P_i/(\mathrm{TWA})_i$$

où P_i est la pression de vapeur saturante en mm Hg (1 mm Hg = 133,322 Pa) à 20°C (ou autres unités (19)) de la substance *i*. $(\mathrm{TWA})_i$ représente la dose limite admise pour la concentration des vapeurs sur une période de temps définie (elle s'exprime en ppm pour une période de temps fixée,

© 2002 CNRC Canada

Fig. 4. Représentation des vecteurs tournants normalisés de l'indice Kauri–Butanol.

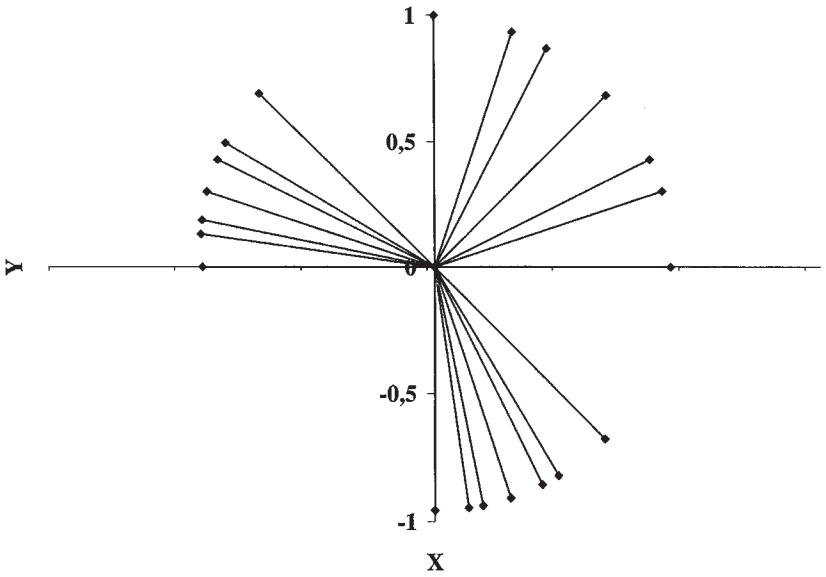

Tableau 3.

(A) Toxicité des solvants choisis et comparaison avec du carburant automobile.

Organisme ou règlement	Chlorure de méthylène	Trichloroéthylène	Bromopropane	Carburant automobile
EPA	B2	EV	EV	EV
IARC	2B	2A	NL	2B
MAK	B	B	NL	EV
NIOSH	X	X	EV	X
NTP	2B	NL	NL	NL
ACGIH	A3	A5	EV	A3
COV	NON	OUI	OUI/NON	OUI
SARA	OUI	OUI	NON	NON
HAP	OUI	OUI	NON	NON

(B) Limites d'exposition proposées.

Paramètre	Chlorure de méthylène	Trichloroéthylène	Bromopropane	Carburant automobile
8 h TWA (OSHA)	25 (25)[a]	75–100 (75)[a]	100–200 (150)[a]	ND
15 min STEL (OSHA)	125	ND	ND	ND
8 h TWA (ACGIH)	50	50	100–200	300
15 min STEL (ACGIH)	ND	100	ND	500

Nota : EPA, U.S. Environmental Protection Agency; **B2**, substance probablement cancérigène d'après les résultats obtenus sur des animaux; **EV**, en évaluation ou réévaluation; **IARC**, International Agency for Research on Cancer; **2A**, probablement cancérigène d'après les résultats obtenus sur des animaux. Résultats sur les humains limités; **2B**, substance probablement cancérigène, mais il manque des données aussi bien sur les humains que sur les animaux; **NL**, absent de la liste; **MAK**, Federal Republic of Germany Maximum Concentration Values in the Work Place; **B**, substance hautement suspectée cancérigène; **NIOSH**, National Institute for Occupational Safety and Health; **X**, cancérigène; **NTP**, National Toxicology Program; **2B**, le programme considère qu'il y a suffisamment de preuves pour affirmer que le produit est cancérigène; **ACGIH**, American Conference of Governmental Industrial Hygienists; **A3**, cancérigène pour les animaux, mais pas de preuves pour les humains; **A5**, non cancérigène pour les humains; **COV**, composés organiques volatils ou VOC en anglais; **OUI/NON**, actuellement considéré comme un COV, mais va être possiblement retiré de la liste; **SARA**, Superfund Amendments and Reauthorization Act; **HAP**, hazardous air pollutants; **OSHA**, Occupational Safety and Health Administration; **TWA**, *time-weighted average* (concentration moyenne d'exposition pour 8 h de travail exprimée en ppm); **STEL**, *short-term exposure limit* (dose à ne pas dépasser pendant plus de 15 min, même si la norme est respectée).

*La valeur entre parenthèse correspond à la valeur choisie dans ce travail.

généralement prise sur 8 h (voir tableau 3B)). ITOX tient compte à la fois de la toxicité via la grandeur TWA et de la probabilité que les vapeurs existent en introduisant la notion de pression de vapeur. En effet, si un composé chimique est dangereux à cause de sa toxicité intrinsèque, il l'est réellement uniquement si sa volatilité est notable. Pour le mélange des trois substances, l'indice de toxicité ITOX se calcule de la façon suivante :

© 2002 CNRC Canada

Fig. 5. Représentation des vecteurs tournants pour l'indice ITOX (voir texte pour la définition de l'indice ITOX).

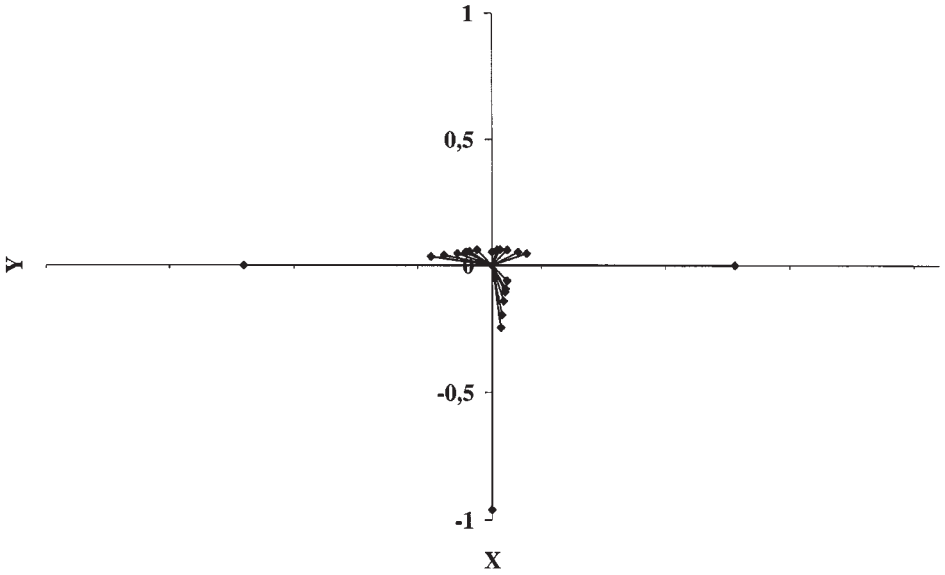

[16] $\mathbf{ITOX}_j = \Sigma_{i\,=\,1\ à\ 3}\ (\phi_{nij} P_i/(\mathrm{TWA})_i)$

où ϕ_{nij} est la fraction molaire de chacun des produits. Cette variable est dérivée de la fraction volumique calculée précédemment ($\phi_{nij} = \phi_{vi}\rho_i / M_{mi} / \Sigma_i \phi_{vi}\rho_i / M_{mi}$, où M_{mi} représente la masse molaire de la i^{e} espèce chimique exprimée en g mol^{-1}). Les termes P_i et $(\mathrm{TWA})_i$ ainsi que ϕ_{vi} et ρ_i ont déjà été définis plus haut. Dans ce modèle, la pression de vapeur au-dessus du liquide est supposée suivre la loi de Raoult (20), et donc la pression associée au mélange est directement reliée à la fraction molaire dans le liquide de chaque composé. Plus ITOX est élevé, plus le produit est dangereux. En effet si la pression est forte, ITOX croit avec ce terme. Simultanément, si TWA diminue, signe d'une grande toxicité, ITOX augmente alors, car le dénominateur chute. La figure 5 illustre les résultats obtenus. Une fois encore, les valeurs sont normalisées à l'unité par l'équation 17 pour pouvoir être comparées aux autres grandeurs.

[17] $< \mathbf{ITOX}_j > = \mathrm{ITOXmin}/\mathbf{ITOX}_j$

Les termes ont leur signification habituelle. Pour reporter les indices $< \mathbf{ITOX}_j >$ dans la figure 5, les équations habituelles sont nécessaires :

[18] $y = < \mathbf{ITOX}_j > \cos\theta$

[19] $x = < \mathbf{ITOX}_j > \sin\theta$

Plus le module du vecteur est grand, moins toxique sera le solvant. La forte volatilité et toxicité du chlorure de méthylène font que, dès qu'il est présent dans un mélange, celui-ci est grandement affecté. Aussi seules les compositions où il est absent obtiennent une note honorable. Notamment, il s'agit des solutions 0,00:0,00:1,00 v/v/v M–T–B (mod. = 1,00), 0,00:0,50:0,50 v/v/v M–T–B (mod. = 0,97) et 0,00:1,00:0,00 v/v/v M–T–B (mod. = 0,96). Les autres arrivent avec des scores nettement plus faibles, car le rapport *P*/TWA pour le chlorure de méthylène est environ 14 fois plus grand que celui des deux autres produits.

Optimisation des mélanges

Ce travail d'approche accomplit, les quatre paramètres importants sont supportés par des graphiques indépendants que l'on peut combiner par addition simple ou complexe pour réduire les variables. Ensuite, il existe plusieurs méthodes d'optimisation dépendant du mandat ou des contraintes imposées par l'usage ou le procédé. Avant de les présenter, le cas particulier où seul un paramètre est important permet de montrer que la représentation choisie fournit à la fois la meilleure solution et le degré de confiance.

Par exemple, si un formulateur doit impérativement optimiser la vitesse d'évaporation, seul ce critère est important, les autres facteurs étant secondaires. Dans ce cas, l'analyse peut consister non seulement à trouver le vecteur correspondant au taux d'évaporation le plus élevé, mais aussi à considérer des vecteurs moins performants mais acceptables. En effet, dépendant de l'usage recherché, des seuils d'acceptabilité représentant le pourcentage de performance du mélange acceptable par rapport à la situation idéale peuvent être imposés. Par exemple, si le formulateur recherche des mélanges avec des taux d'évaporation compris entre la perfection (mod. = 1) et ceux n'offrant que 80 % de la meilleure valeur : alors, cela signifie que tous vecteurs rencontrés dans la couronne incluse dans les rayons 1 et 0,8 seront des solutions. Ceci peut être résolu mathématiquement plutôt que graphiquement si on recherche l'économie d'une représentation graphique en se servant de l'équation du cercle :

[20] $x^2 + y^2 = R^2$

où R est le rayon du cercle et x et y sont les coordonnées cartésiennes. Alors, tous les mélanges dont les coordonnées (x,y) satisfont l'inéquation 19 :

[21] $1 \geq x^2 + y^2 \geq 0{,}64$

sont solutions. Les nombres 1 et 0,64 correspondent au carré des limites choisies (1 et 0,80). En effet, en regardant la fig. 3, rapidement on voit que seul le chlorure de méthylène pur (mod. = 1,00) et le mélange 0,750:0,125:0,125 v/v/v M–

© 2002 CNRC Canada

Fig. 6. Représentation de la somme simple des quatre paramètres.

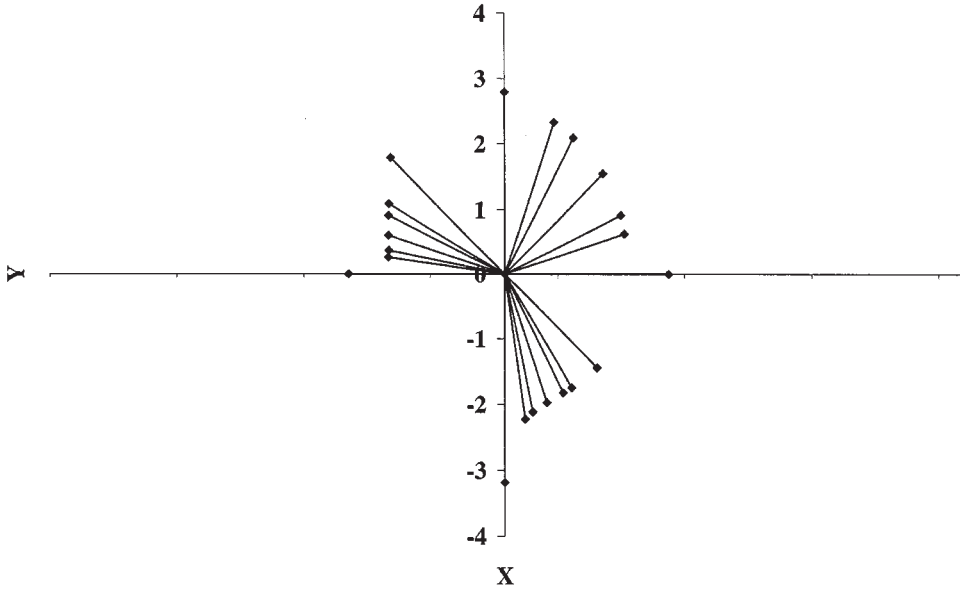

T–B (mod. = 0,81) sont capables de respecter les bornes choisies. La normalisation offre donc un espace probabilisé.

Si l'ensemble des contraintes est considéré, l'approche simple utilisée ci-dessus n'est plus possible. Il faut alors trouver un mode de combinaison des paramètres pour comprimer les variables tout en tenant compte de la réalité chimique. Pour cela, il existe deux voies possibles soit la sommation des vecteurs (union) ou leur superposition (intersection) comme chacune des représentations des paramètres se comporte comme un ensemble dans le sens mathématique du terme.

Combinaison simple (ou union simple)

Lorsque la combinaison simple est retenue, chaque facteur possède un poids statistique équivalent et la somme vectorielle conduit au graphique de la figure 6 :

$$[22] \quad V_t(\theta) = V_1(\theta) + V_2(\theta) + V_3(\theta) + V_4(\theta) \text{ ou } \Sigma_{i = 1 \text{ à } 4}\, V_i(\theta)$$

où $V_i(\theta)$ est le vecteur représentant un des quatre critères (c.-à-d. prix, taux d'évaporation, etc.) pour une composition fixée par l'angle θ (revoir le tableau 1). $V_t(\theta)$ est la somme des quatre grandeurs, où tous les vecteurs ont un poids statistique égal. Aussi, le score maximal est forcément compris entre ±4. Normalement le (ou les) vecteur(s) ayant la plus grande valeur numérique en valeur absolue sera(ont) le(s) meilleur(s) candidat(s).

Ici, les trois premières solutions affublées du module (ou score) le plus élevé sont :

(1) celle constituée de 0,00:0,50:0,50 v/v/v M–T–B (mod. = 3,18),

(2) celle contenant uniquement le chlorure de méthylène (mod. = 2,79),

(3) celle fabriquée à partir de 0,50/0,50/0,00 v/v/v M/T/B (mod. = 2,66).

Les trois premiers choix conduiraient à ces candidats. Ainsi, aucune combinaison ternaire appartient à ce bloc, et les produits purs demeurent encore dans le peloton de tête. Ceci n'est pas surprenant, car ils sont reconnus pour leur grande performance. Le 1-bromopropane, qui est considéré comme la substance de substitution par excellence des solvants chlorés (21), n'arrive qu'au quatrième rang, étant lourdement pénalisé par son prix beaucoup plus élevé.

À ce stade, le choix définitif peut être soit le mélange ayant la meilleure note (0,00:0,50:0,50 v/v/v M–T–B), soit tous ceux compris dans un intervalle de probabilité de performance imposée comme vu plus haut. Toutefois, en ajoutant cette contrainte, le problème peut s'avérer sans solutions. Par exemple, si seuls les solvants rencontrant 90 % du score maximal (mod. = 4) pour chacun des paramètres sont acceptés, alors le problème n'a pas de solution, car le premier mélange a uniquement un module de 3,18 (valeur plus petite que 0,90 * 4 = 3,60).

Cette approche décisionnelle, avec des niveaux de paramètres identiques, n'est pas toujours réaliste. Il est donc possible d'aménager des variantes à ce schéma pour tenir compte de réalités particulières courantes.

Variante 1 : cas de l'addition réduite

L'approche égalitaire n'est pas toujours représentative des situations rencontrées. En effet, l'optimisation de solutions nettoyantes dépend de facteurs propres à certains pays, à certaines coutumes de production ainsi que de la nature des lois et des procédés, etc. Par exemple en Allemagne, les solvants chlorés sont généralement confinés lors de leur usage, et le chargement et (ou) déchargement des machines se fait à l'aide de pompes et de circuits totalement isolés. Cette habitude de production supprime *de facto* l'aspect toxique du produit, car l'exposition des travailleurs aux vapeurs sont réduites, voire nulles. Aussi, il devient superflu de considérer la toxicité et seuls les trois autres facteurs méritent de la considération.

$$[23] \quad V_t(\theta) = V_1(\theta) + V_2(\theta) + V_3(\theta) \text{ ou } \Sigma_{i = 1 \text{ à } 3}\, V_i(\theta)$$

© 2002 CNRC Canada

Fig. 7. Représentation de la somme de trois paramètres (prix, taux d'évaporation et indice Kauri–Butanol).

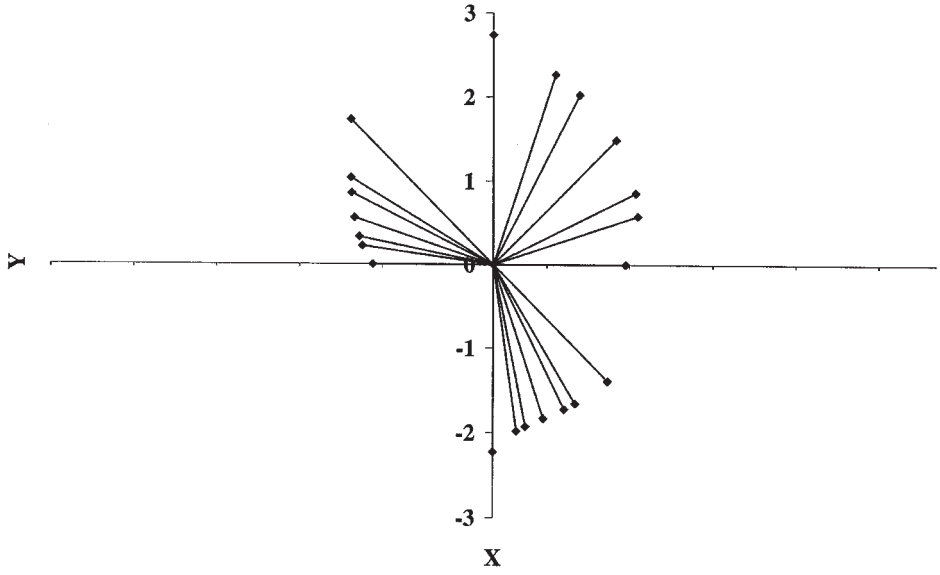

Alors, $V_t(\theta)$ correspond à la somme des contributions qui proviennent du taux d'évaporation, de l'indice Kauri–Butanol et du prix. Cela conduit à une valeur maximale de ±3 pour le graphique et seuls les vecteurs qui ont l'amplitude la plus proche de ce chiffre sont les meilleurs candidats. La figure 7 illustre ce cas. Le module le plus grand revient alors au chlorure de méthylène seul, car, hormis sa toxicité, il est le plus performant pour les autres paramètres, excepté pour le prix où seul le trichloréthylène est de quelques dollars meilleur marché.

De la même façon, s'il existe des programmes efficaces de recyclage comme c'est devenu le cas, le facteur coût peut être minimisé, car une partie des matières premières fonctionne en circuit fermé. L'équation 21 prendrait encore une expression plus simple, car les vecteurs associés à la toxicité et au prix pourraient être négligés.

Variante 2 : cas de l'addition pondérée

Dans le paragraphe précédent, l'équation 21 répondait à des situations particulières mais claires et précises. Malheureusement, il existe des cas où il est plus difficile de totalement négliger un facteur, et la pondération doit se faire avec des valeurs différentes de zéro ou un (tout ou rien). Par exemple, l'opérateur peut modifier la combinaison des vecteurs en pondérant la somme vectorielle par des nombres entiers positifs a_{ij} entiers ou décimaux pour souligner ou minimiser l'importance d'un paramètre :

$$[24] \quad V_t(\theta)_j = a_{1j}V_1(\theta) + a_{2j}V_2(\theta) + a_{3j}V_3(\theta) + a_{4j}V_4(\theta) \text{ ou } \Sigma_{i = 1 \text{ à } 4}\, a_{ij}V_{ij}(\theta)$$

Les coefficients a_{ij} sont alors des nombres entiers ou décimaux dont le choix est dicté par l'usage et la pratique. La figure 8 donne un exemple particulier où les nombres a_{ij} ont tous été pris égaux à un, excepté celui associé à la toxicité qui est de 6. Alors, le meilleur solvant ne peut pas donner un résultat supérieur à ±9 (voir fig. 8). Les meilleurs scores sont obtenus par la solution de trichloréthylène seul (mod. = 7,98) et par le mélange 0,00:1,00:1,00 v/v/v M–T–B (mod. = 7,47), les autres options restant très loin derrière (mod. = 3,48 pour la plus proche) à cause de la présence de chlorure de méthylène qui est dangereux. Cette amplification de la toxicité pourrait correspondre à la situation d'un utilisateur qui travaille dans un atelier où il n'y a pas de confinement des solvants. Cette pondération amplifie le critère toxicité par rapport aux autres pour tenir compte de cette réalité.

Variante alternative : cas de l'intersection des vecteurs

Jusqu'à présent le tri des vecteurs s'est effectué en recherchant le module maximum directement issu de la sommation simple ou combinée de ces derniers. Il existe une alternative, déjà en partie introduite, qui consiste à imposer une (des) valeur(s) minimale(s) à chaque paramètre en fixant des seuils de probabilité comme vu précédemment à partir des attentes d'usage ou (et) de production. Pour illustrer ce formalisme, on suppose qu'un formulateur désire un mélange avec les caractéristiques imposées suivantes :

- un indice Kauri–Butanol compris entre 136 et 122,4 (mod. : 1–0,9)
- un prix compris entre 168 $ et 336 $ pour un volume de 10 L de produit (mod. : 1–0,5)
- un taux d'évaporation variant de 14,5 à 10,15 (mod. : 1–0,7)
- une toxicité qui ne soit pas supérieure à 2,5 fois celle du mélange le moins nocif (mod. 1–0,4).

Le tableau 4 résume la situation obtenue avec ces contraintes. Le nombre de vecteurs vérifiant les contraintes dans les limites fixées pour chacun des paramètres est donné dans la deuxième colonne. Enfin, lorsqu'on fait l'intersection des ensembles de solutions, seul le trichloréthylène pur peut remplir les quatre critères énumérés. En effet, il est le seul produit ayant un vecteur commun dans chaque ensemble car il respecte toujours les seuils fixés.

Choix de la variante décisionnelle

Au niveau décisionnel, les conditions d'utilisation du solvant fixent laquelle des approches doit être sélectionnée

© 2002 CNRC Canada

Fig. 8. Représentation des paramètres avec pondération (voir texte).

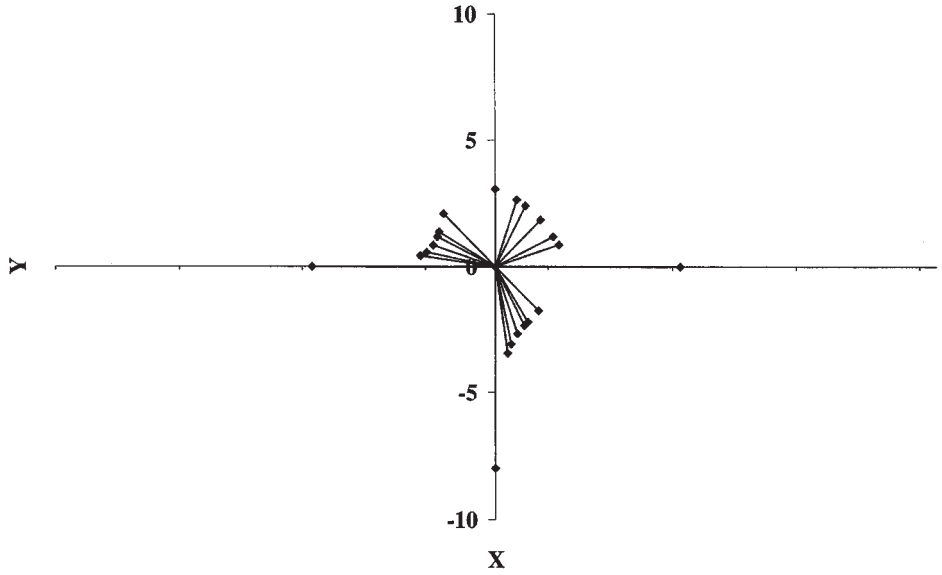

Tableau 4. Exemple de choix de mélange par intersection de vecteurs (voir texte).

Paramètre choisi et intervalle de tolérance	Nombre de mélanges respectant les critères	Paramètre de décision pour le choix des seuils
Indice KB Seuils : 1–0,9	19	Efficacité de nettoyage
Prix Seuils : 1–0,5	9	Budget
Taux d'évaporation Seuils : 1–0,7	3	Vitesse de lavage et temps de séchage
Indice ITOX Seuils : 1–0,4	2	Normes, lois et règlements
Intersection des quatre ensembles	1	Vecteur ayant rempli les quatre conditions (seul le trichloréthylène pur est acceptable)

entre (*i*) la « combinaison simple » (union d'un ensemble de vecteurs ayant le même poids statistique); (*ii*) l'« addition réduite » (union d'un nombre limité de vecteurs ayant le même poids statistique); (*iii*) l'« addition pondérée » (union de vecteurs pondérés) et (*iv*) l'« intersection des vecteurs » (sélection de vecteurs respectant des scores fixés).

(*i*) La combinaison simple a une tendance à favoriser les critères extrêmes. Notamment dans l'exemple traité, la toxicité du chlorure de méthylène et le coût élevé du bromopropane sont les facteurs qui ont le plus de poids sur le choix final. Cette approche est bien adaptée lorsque les contraintes d'usage ou de production du mélange sont inconnues ou floues, car aucun jugement ou prise de décision est nécessaire. Par contre, elle peut être trop discriminatoire pour les produits qui se démarquent.

(*ii*) L'addition réduite des paramètres, quand elle est possible, est la plus simple. Elle est une variante de la combinaison simple (certains coefficients sont nuls). Elle est particulièrement bien adaptée aux situations claires comme par exemple lorsque l'on rencontre des solvants confinés, des produits recyclés efficacement, etc. Dans ces cas de figures, il est facile de totalement ignorer un ou plusieurs paramètres avec certitude. Malheureusement, cela se limite aux cas simples comme mentionné dans le texte plus haut et peut être contestable, car il y a une part de subjectivité.

(*iii*) L'approche pondérée permet de favoriser une composante par rapport à une autre et elle atténue ou amplifie un ou plusieurs paramètres. Elle serait idéale, si le choix des coefficients de pondération ne serait pas parfois arbitraire lorsque les paramètres de choix ne sont pas connus ou calculables.

Ce défaut peut être compensé en sélectionnant un grand nombre de combinaisons de coefficients a_{ij} différents et ainsi créer une infinité de scénarios possibles. Alors, il est possible de construire une matrice V(*n*,*m*) de dimension égale au nombre de compositions *n* et de scénarios différents *m*, et elle devient à son tour le point de départ pour optimiser les mélanges en utilisant des méthodes classiques (Simplex, Analyse Factorielle, etc.).

(*iv*) Enfin, la méthode de superposition ou d'intersection des vecteurs n'est applicable que si les seuils de tolérance pour chaque paramètre sont connus ou faciles à fixer. Cette approche est très discriminatoire, mais conduit à des solutions fiables et indiscutables.

© 2002 CNRC Canada

Conclusion

La procédure de normalisation de vecteurs tournants offre un mode de représentation très souple et particulièrement bien adapté pour visualiser les propriétés physico-chimiques de mélanges ternaires et binaires. Peu importe, les variantes choisies comme outil de diagnostic, les résultats obtenus sont fiables et évitent de faire des mélanges inutiles. Par exemple, dans le cas traité, l'outil démontre que l'addition d'un solvant bromé à des solvants chlorés n'améliore rien à leurs performances, ce qui s'est avéré vrai sur le terrain, alors que cette pratique avait tenté de nombreux formulateurs.

Remerciements

Nous remercions la Fondation canadienne pour l'innovation (FCI-fonds de développement de la recherche volet collégial) et le ministère de l'éducation du Québec pour leur soutien financier.

Bibliographie

1. R. Reynolds. Parts Cleaning, **III**, 20 (1999).
2. J. Sherman, B. Chin, P.D.T. Huibers, R. Garcia-Valls et T.A. Hatton. Environ. Health Perspect. **106**, 253 (1998).
3. W.H. Ellis. Solvents in Federation series on coatings technology. Federation of Societies for Coating Technology, Philadelphia (1986).
4. M. Gérin, D. Begin, J. Goupil, R. Garneau et S. Sachs. Arch. Mal. Prof. **57**, 519 (1996).
5. A.F. Averill, J. Ingram et P.F. Nolan. Trans. Inst. Met. Finish., **76**, 81 (1998).
6. J.F. Certin. Comptes rendus de l'Académie des Sciences, Paris, Séance des 29 et 30 mai 1997, 271 (1997).
7. M. Gérin et D. Begin. Substitution des solvants en milieu de travail. Rapport A-098. Institut de Recherche en Santé et Sécurité au Travail du Québec, Montréal, Québec (1995).
8. D.C. Montgomery. Design and analysis of experiments, 3^{e} éd. John Wiley & Sons, New York (1991).
9. J. Goupy. La méthode des plans d'expérience. Dunod, Paris, (1988).
10. G.S. Peace. Taguchi methods : A hands-on approach. Addison-Wesley Company Inc., New York (1993).
11. W.L. Archer. Industrial solvents handbook. Marcel Dekker Inc., New York (1996).
12. P.G. Ciarlet. Introduction à l'analyse numérique matricielle et à l'optimisation. Masson, Paris (1982).
13. L. Lebart, A. Morineau et J.P. Fénelon. Traitement des données statistiques : Méthodes et programmes. Dunod, Paris (1982).
14. S. Alex et R. Savoie. Can. J. Spectrosc. **34**, 27 (1989).
15. J. Fauvarque. Info Chimie Magazine, **401**, 65 (1998).
16. Norm 1901–95. *Dans* Annual book of ASTM standards. West Conshohocken, PA **15.05**, 40 (1995).
17. Norm 1133–94. *Dans* Annual book of ASTM standards. West Conshohocken, PA **06.04**, 40 (1994).
18. P.A. Small. J. Appl. Chem. **3**, 71 (1953).
19. Norm 323–05. *Dans* Annual book of ASTM standards. West Conshohocken, PA **05.01**, 138 (1994).
20. P.W. Atkins. Éléments de chimie physique, chapitre 4. De Boeck, Paris. 116 (1998).
21. S. Scherrer. Precision Cleaning, **VIII**, 22, (2000).

© 2002 CNRC Canada

Asymmetric total synthesis of (+)-*exo*-brevicomin based on enantioconvergent biocatalytic hydrolysis of an alkene-functionalized 2,3-disubstituted epoxide

Sandra F. Mayer, Harald Mang, Andreas Steinreiber, Robert Saf, and Kurt Faber

Abstract: A short total asymmetric synthesis of (+)-*exo*- and (–)-*endo*-brevicomin ((+)-*exo*-**3** and (–)-*endo*-**3**), which are components of the attracting pheromone system of several bark-beetle species belonging to the genera *Dendroctonus* and *Dryocoetes*, was accomplished via a chemoenzymatic protocol. The key step consisted of biocatalytic hydrolysis by bacterial epoxide hydrolases of *cis*-configured 2,3-disubstituted oxiranes bearing olefinic side chains. This reaction proceeded in an enantioconvergent fashion, by affording a single enantiomeric *vic*-diol from the *rac*-epoxide in up to 92% ee and 83% isolated yield.

Key words: bacterial epoxide hydrolase, 2,3-disubstituted oxirane, enantioconvergent hydrolysis, (+)-*exo*-brevicomin, (–)-*endo*-brevicomin.

Résumé : Faisant appel à un protocole chimioenzymatique, on a réalisé une courte synthèse asymétrique totale des (+)-*exo*- et (–)-*endo*-brévicomines [(+)-*exo*-**3** et (–)-*endo*-**3**], des composants du système de phéromone d'attraction de plusieurs espèces de scolytes des genres *Dendroctonus* et *Dryocoetes*. L'étape clé implique une hydrolyse biocatalytique à l'aide d'hydrolases bactériennes d'époxyde d'oxiranes 2,3-disubstitués, de configuration *cis*- et portant des chaînes latérales oléfiniques. Cette réaction s'est produite de façon énantioconvergente en ne fournissant, à partir de l'époxyde racémique, qu'un seul énantiomère de diol vicinal, avec un rendement isolé de 83% et un e.e. de 92%.

Mots clés : hydrolase bactérienne d'époxyde, oxirane 2,3-disubstitué, hydrolyse énantioconvergente, (+)-*exo*-brévicomine, (–)-*endo*-brévicomine.

[Traduit par la Rédaction]

Introduction

Bacterial epoxide hydrolases have been shown to be highly versatile biocatalysts for the preparation of nonracemic *vic*-diols. In particular, bulky 2,2-disubstituted epoxides were hydrolyzed with excellent selectivities (*E* values up to > 200) via kinetic resolution (1). In addition, we recently reported the asymmetric biohydrolysis of (±)-*cis*-2,3-dialkyl oxiranes, which led to the formation of the corresponding internal *vic*-diols in high enantiomeric purities. In the case of haloalkyl-substituted derivatives, enzyme-triggered cascade reactions were observed (2, 3). The remarkable feature of these biotransformations is the fact that — depending on the relative stereochemistry of the substrate — they did not follow a kinetic-resolution pathway but proceeded in an enantioconvergent fashion by furnishing a single enantiomeric *vic*-diol as the sole product in 100% theoretical yield. In view of their considerably improved economic balance, such "deracemization" processes have recently gained considerable attention (4).

To extend the preparative utility of this method, we investigated more synthetically useful substrates bearing various functional groups to allow for further synthetic transformations. Our previous experience indicated that bacterial epoxide hydrolases generally do not accept substrates with polar functional groups (such as OH, N_3) (5). We therefore turned our attention to 2,3-disubstituted oxiranes, *rac*-*cis*-**1** and *rac*-*trans*-**1**, bearing olefinic side chains, which would serve as functional groups for further (oxidative) transformations (Scheme 1) (6). For this reason we investigated a short synthesis of (+)-*exo*-brevicomin. In addition, (–)-*endo*-brevicomin was also synthesized in moderate optical purity.

(+)-*Exo*- and (–)-*endo*-brevicomin ((+)-*exo*-**3** and (–)-*endo*-**3**, respectively) are components of the attracting pheromone system of several bark-beetle species belonging to the genera *Dendroctonus* and *Dryocoetes* (7). In several species, *endo*-**3** is a minor component accompanying (+)-*exo*-**3**. The (–)-*endo* isomer has been reported to be an anti-aggregation pheromone for the southern pine beetle *Dendroctonus frontalis*.

Received 23 November 2001. Published on the NRC Research Press Web site at http://canjchem.nrc.ca on 29 March 2002.

S.F. Mayer, H. Mang, A. Steinreiber, and K. Faber.[1] Department of Chemistry, Organic & Bioorganic Chemistry, University of Graz, Heinrichstrasse 28, A-8010 Graz, Austria.
R. Saf. Institute for Chemical Technology of Organic Materials, Graz University of Technology, Stremayrgasse 16, A-8010 Graz, Austria.

[1]Corresponding author: (e-mail: kurt.faber@uni-graz.at).

 DOI: 10.1139/V02-037 © 2002 NRC Canada

Scheme 1. Retrosynthetic analysis.

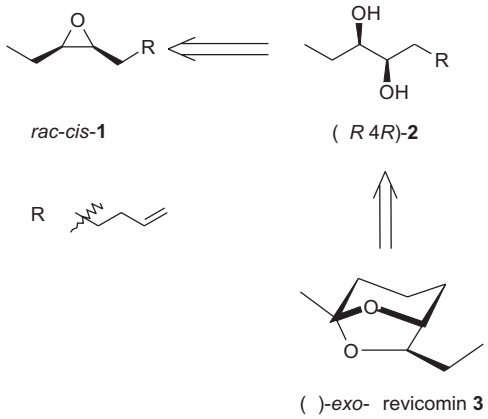

Fig. 1. Time-line of hydrolysis of *rac-cis*-**1** using *Mycobacterium paraffinicum* NCIMB 10420.

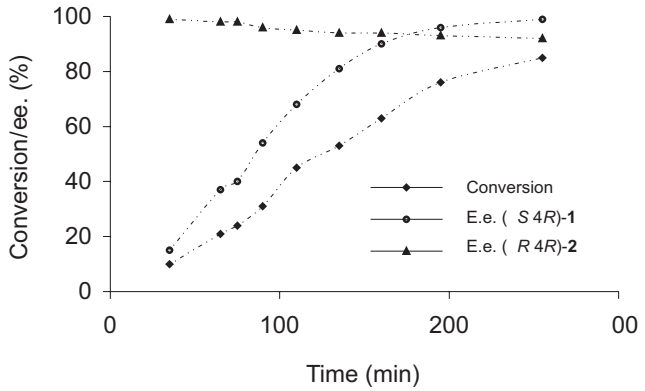

In contrast, (+)-*endo*-**3** increases aggregation (8). *Dentroctonus ponderosae* (Mountain Pine beetle) is known to produce (+)-*exo*-brevicomin with >98% ee, whereas the optical purities of the accompanying stereoisomer *endo*-**3** were reported in the range of 65–70% ee (9). Although a number of syntheses of brevicomin stereoisomers have been reported, few are satisfactory in terms of process simplicity (9). Herein, we wish to report a short chemoenzymatic synthesis of (+)-*exo*-brevicomin ((+)-*exo*-**3**) in 92% ee starting from diol (3*R*,*4R*)-**2**, obtained via biocatalytic hydrolysis of oxirane *rac-cis*-**1**. Because the latter process proceeded in an enantioconvergent fashion, the occurrence of an undesired stereoisomer was avoided, rendering this as a highly efficient synthetic sequence. In a related approach, (–)-*endo*-brevicomin ((–)-*endo*-**3**) was obtained in 72% ee starting from *rac-trans*-**1**.

Results and discussion

To provide insight into the factors governing the stereochemical course of the biohydrolysis that would facilitate the predictability of the reaction, 2,3-disubstituted alkene-functionalized oxiranes (*rac-cis*-**1** and *rac-trans*-**1**) were chosen as substrates. Oxiranes *rac-cis*-**1** and *rac-trans*-**1** were prepared from commercially available alcohols (*Z*)-**4** and (*E*)-**4** (Scheme 2). Conversion of the primary hydroxyl group of (*Z*)-**4** and (*E*)-**4** to the corresponding bromides was accomplished via the corresponding mesylates to furnish (*Z*)-**5** and (*E*)-**5**, respectively. The latter were transformed into the corresponding Grignard reagents and then were coupled to allyl bromide to give *cis*- and *trans*-configurated dienes, (*Z*)-**6** and (*E*)-**6**. Epoxidation of the electron-rich internal C=C bond using *m*-chloroperbenzoic acid proceeded regioselectively to furnish *rac-cis*-**1** and *rac-trans*-**1** in 37 and 44% yield, respectively, in three steps.

Substrates *rac-cis*-**1** and *rac-trans*-**1** were subjected to screening for biohydrolysis in Tris-buffer at pH 8.0 using various resting cells from *Actinomyces* spp. known to possess, in particular, strong secondary metabolic activity and strong epoxide hydrolase activity (5). The absence of any undesired spontaneous hydrolysis was verified under standard conditions in the absence of a biocatalyst within the anticipated reaction time of ~21 h. The only product formed during biohydrolysis was the desired diol, *threo*-**2** or *erythro*-**2**. The stereoselectivities (denoted as conversion (c) and enantiomeric purities of substrate (ee_S) and product (ee_P)) (10) obtained from the biohydrolysis of *rac-cis*-**1** and *rac-trans*-**1** are listed in Table 1.

Oxirane *rac-cis*-**1** was hydrolyzed with moderate to good selectivities by several bacterial strains with the predominant formation of diol (3*R*,4*R*)-**2** in up to 92% ee, except for *Rhodococcus equi* IFO 3730, which produced antipode (3*S*,4*S*)-**2** in moderate optical purity (Table 1, entry 7). Several data sets of c, ee_S, and ee_P clearly indicated that the transformation did not follow a kinetic-resolution pathway as indicated by a high ee_P at high conversion. This is most striking for entries 1–4 (Table 1).

The results obtained from *rac-trans*-**1** show a different pattern. Although this substrate was rapidly converted by several species of *Rhodococci* (Table 1, entries 1, 2, 5, and 7), the selectivities were significantly reduced in comparison with those of the corresponding *cis*-analogue *rac-cis*-**1**. The best result was with diol (3*R*,4*S*)-**2**, which was obtained in a moderate 72% ee (Table 1, entry 4).

An evaluation of the data obtained reveals the following general picture. (*i*) As can be deduced from the absolute configuration of the substrate and product, the enzymatic epoxide hydrolysis results in the inversion of configuration at the attacked oxirane carbon atom, and (*ii*) the biotransformation of *trans*-oxirane is faster, but hydrolysis of the *cis*-analogue is more enantioselective.

Any enantioconvergence of the reaction — indicated as a "deviation" from the classic kinetic-resolution protocol — can easily be detected if the ee of the product is beyond the benchmark of 50% conversion. This is most striking for *rac-cis*-**1** (ee of *threo*-**2** 92% at c 83%). The molecular reason for this phenomenon is that the hydrolysis of both enantiomers proceeds with opposite regioselectivity, i.e., the enzyme shows a predominant preference to attack an (*S*)-configurated oxirane carbon atom (2). For the *cis*-oxirane, *rac-cis*-**1** that consists of (3*R*,4*S*)- and (3*S*,4*R*)-enantiomers, an enantioconvergent hydrolysis is facilitated because each enantiomer has one "matching" (*S*)-center. This is not the case for the *trans*-isomer, *rac-trans*-**1**, which consists of(3*S*,4*S*)- and (3*R*,4*R*)-enantiomers, each possessing two "matching" or two "mismatching" centers.

The time line of a typical enantioconvergent transformation by *Mycobacterium paraffinicum* NCIMB 10420 is shown in Fig. 1. At the onset of the reaction, the faster-reacting (3*R*,4*S*)-

© 2002 NRC Canada

Scheme 2. Synthesis of substrates.

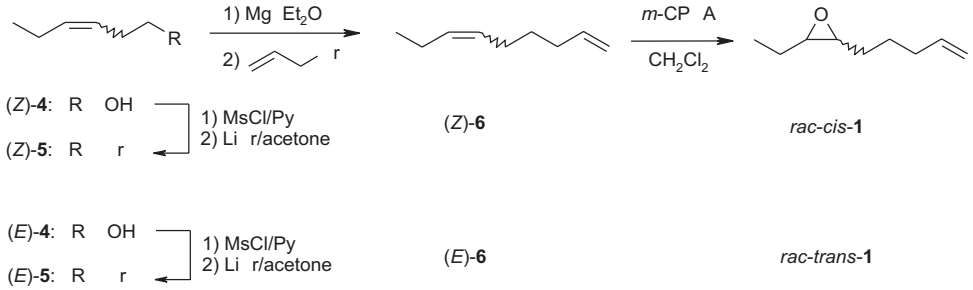

Scheme 3. Biocatalytic hydrolysis and synthesis of (+)-*exo*- and (–)-*endo*-brevicomin.

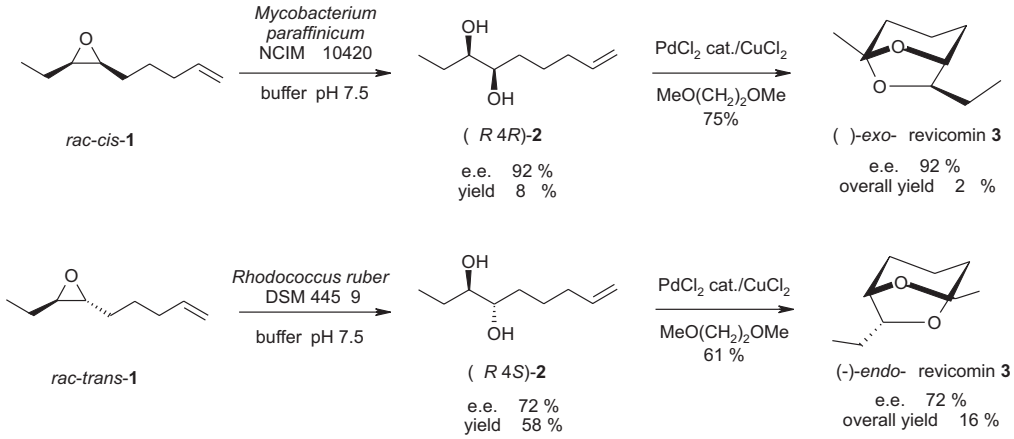

Table 1. Stereoselectivities from the biocatalytic hydrolysis of *rac-cis*-**1** and *rac-trans*-**1**.

		rac-cis-**1**			*rac-trans*-**1**		
Entry	Strain	ee_S (%)	ee_P (%)	Conversion[a] (%)	ee_S (%)[b]	ee_P (%)	Conversion[a] (%)
1	*Mycobacterium paraffinicum* NCIMB 10420	>99 (3*S*,4*R*)	92 (3*R*,4*R*)	83[c]	n.d.	36 (3*R*,4*S*)	90
2	*Rhodococcus sp.* R 312 (CBS 717.73)	59 (3*R*,4*S*)	85 (3*R*,4*R*)	79	n.d.	59 (3*R*,4*S*)	78
3	*Rhodococcus ruber* DSM 44540[d]	59 (3*R*,4*S*)	78 (3*R*,4*R*)	65	n.d.	71 (3*R*,4*S*)	54
4	*Rhodococcus ruber* DSM 44539	88 (3*R*,4*S*)	72 (3*R*,4*R*)	70	n.d.	72 (3*R*,4*S*)	58[e]
5	*Rhodococcus ruber* DSM 44541	51 (3*R*,4*S*)	76 (3*R*,4*R*)	19	n.d.	58 (3*R*,4*S*)	60
6	*Arthobacter* sp. DSM 312	22 (3*R*,4*S*)	86 (3*R*,4*R*)	10	n.d.	55 (3*R*,4*S*)	40
7	*Rhodococcus equi* IFO 3730	72 (3*S*,4*R*)	55 (3*S*,4*S*)	92	n.d.	29 (3*R*,4*S*)	96
8	*Streptomyces* sp. SM 4165	16 (3*R*,4*S*)	86 (3*R*,4*R*)	4	n.d.	67 (3*R*,4*S*)	27

[a]After 21 h.
[b]n.d. not determined (see *Experimental*).
[c]After 6 h.
[d]SM Numbers refer to the culture collection of the Institute of Biotechnology, Graz University of Technology.
[e]After 4 h.

enantiomer of *rac-cis*-**1** is preferentially hydrolyzed from the racemate, via attack at the stereochemically preferred C-3 position, to furnish diol (3*R*,4*R*)-**2** in high ee until a conversion of about 50% is reached. Beyond this point, the transformation of the slower-reacting (3*S*,4*R*)-enantiomer takes place with high but opposite regioselectivity (via attack at C-2), thus yielding the same enantiomeric diol (3*R*,4*R*)-**2**. The relative reaction rate of the enantiomers was calculated from the progress curves of c, ee_S, and ee_P vs. time, and was found to be $E = 6.7$ (11). As a consequence, the ee of *threo*-**2** remained high throughout the course of the biotransformation and (3*R*,4*R*)-**2** was formed as the sole product.

With the end goal being the asymmetric synthesis of (+)-*exo*- and (–)-*endo*-brevicomin, *Mycobacterium paraffinicum* NCIMB 10420 was chosen for the preparative-scale biohydrolysis of *rac-cis*-**1**. This reaction gave (3*R*,4*R*)-**2** as the sole product in 83% yield and 92% ee in an enantioconvergent fashion (Scheme 3). In contrast, the biotransformation of *rac-trans*-**1** underwent kinetic resolution. The hydrolysis of *rac-trans*-**1** using *Rhodococcus ruber* DSM 44539, however,

© 2002 NRC Canada

Table 2. Optical rotation values.

Compound	$[\alpha]_D^{20}$ [a]
(3*S*,4*R*)-**1**	–2.2 (*c* = 0.85, Et_2O, ee > 99%)
(3*R*,4*R*)-**2**	+21.8 (*c* = 0.65, CH_3Cl, ee 92%) [lit.: +25.3 (*c* = 1.0, CH_3Cl)] (16)
(3*R*,4*S*)-**2**	–11.8 (*c* = 0.42, CH_3Cl, ee 72%) [lit.: –14 (*c* = 6.0, CH_3Cl)] (20)
(+)-*exo*-**3**	+65.9 (*c* = 1.90, Et_2O, ee 92%) [lit.: 67.5 (*c* = 1.05, Et_2O, ee 98%)] (21)
(–)-*endo*-**3**	–59.3 (*c* = 0.41, Et_2O, ee 72%) [lit.: –79.5 (*c* = 1.17, Et_2O, ee 98%)] (22)
(*R*)-**7**	–8.1 (*c* = 1.87, $CHCl_3$, ee > 99%) [lit.: –8.4 (*c* = 1.5, MeOH)] (19)
(*R*)-**8**	+6.0 (*c* = 1.53, $CHCl_3$, ee > 99%)
(3*S*,4*R*)-**9**	–1.8 (*c* = 0.55, Et_2O, ee > 99%)

[a]References given in parentheses.

Table 3. GLC-data on a chiral stationary phase.

Compound	Column	Conditions	t_R (min) (absolute configuration)
rac-*cis*-**1**	A	14 psi, 80°C (iso)	3.0 (3*S*,4*R*), 3.2 (3*R*,4*S*)
rac-*threo*-**2**	B	14 psi, 110°C (iso)	11.2 (3*R*,4*R*), 11.6 (3*S*,4*S*)
rac-*erythro*-**2**	A	14 psi, 110°C (iso)	9.2 (3*R*,4*S*), 9.5 (3*S*,4*R*)
rac-*exo*-**3**	B	14 psi, 100°C (iso)	1.5 (–)-*exo*, 1.6 (+)-*exo*
rac-*endo*-**3**	B	14 psi, 100°C (iso)	1.8 (–)-*endo*, 1.9 (+)-*endo*
rac-**8**	A	14 psi, 90°C (iso)	3.6 (*S*), 4.2 (*R*)
rac-*cis*-**9**	A	14 psi, 80°C (iso)	2.8 (3*S*,4*R*), 2.9 (3*R*,4*S*)

Scheme 4. Determination of absolute configuration of epoxide (3*S*,4*R*)-**1**.

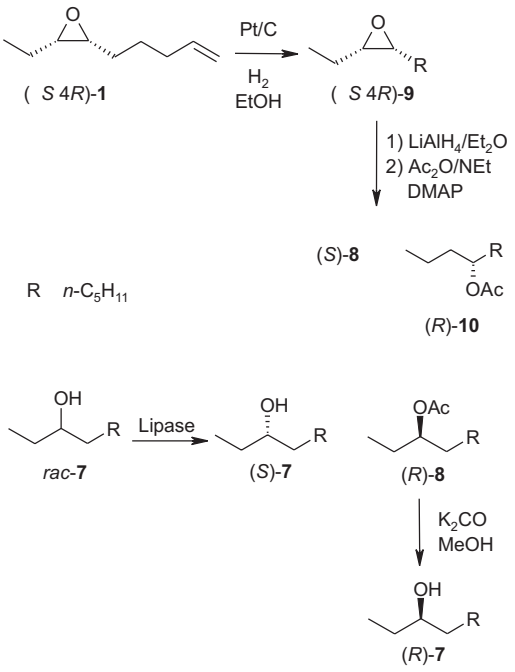

yielded (3*R*,4*S*)-**2** in 58% yield and 72% ee (Scheme 3). Because the ee of the precursor to (–)-*endo*-brevicomin was within the suitable range of 65–70%, the material was used for further synthesis (9). Wacker oxidation of (3*R*,4*R*)-**2** or (3*R*,4*S*)-**2**, employing $PdCl_2$ as the catalyst and $CuCl_2$ as the reoxidant, gave (+)-*exo*- and (–)-*endo*-brevicomin in 92% ee (23% overall yield) and 72% ee (16% overall yield), respectively (Scheme 3).

The absolute configuration of diols (3*R*,4*R*)-**2** and (3*R*,4*S*)-**2**, and (+)-*exo*- and (–)-*endo*-brevicomin stereoisomers were confirmed by comparison of their optical rotation with known values (Table 2, vide infra). The absolute configuration of the remaining non-hydrolyzed epoxide (3*S*,4*R*)-**1** was elucidated via the following sequence (Scheme 4). Hydrogenation of the alkene-moiety of (3*S*,4*R*)-**1** (Pt/C and H_2) gave oxirane (3*S*,4*R*)-**9**. $LiAlH_4$ reduction of (3*S*,4*R*)-**9** afforded a mixture of the corresponding alcohols, alkan-3-ol and alkan-4-ol, which were converted into their acetates (*S*)-**8** and (*R*)-**10**, respectively (Ac_2O/NEt_3/DMAP cat.). The absolute configuration of (*S*)-**8** was determined via GLC analysis on a chiral stationary phase by co-injection with an independently synthesized sample of (*R*)-**8** (Scheme 4, vide infra).

Enantiopure acetate (*R*)-**8** was obtained by kinetic resolution of alcohol (±)-**7** using *Candida antarctica* lipase B. The absolute configuration of (*R*)-**8** was confirmed via deprotection of the acetate moiety (K_2CO_3/MeOH) to yield (*R*)-3-nonanol (*R*)-**7**. The absolute configuration (*R*)-**7** was confirmed by comparison of its known optical-rotation value (Table 2).

In conclusion, we have demonstrated that the biohydrolysis of *cis*-2,3-disubstituted oxiranes bearing olefinic side chains using bacterial epoxide hydrolases proceeded in a highly selective and enantioconvergent manner, which provided the corresponding *vic*-diols in high ee and in almost quantitative yield. Although the yields of the *trans*-analogues were sufficient, the selectivities were moderate. The optically enriched diols were transformed into pheromones in a straightforward manner.

Experimental

General

NMR spectra were recorded in $CDCl_3$ using a Bruker AMX 360 at 360 (^{1}H) and 90 (^{13}C) MHz and a Bruker DMX Avance 500 at 500 (^{1}H) and 125 (^{13}C) MHz. Chemical shifts are reported relative to TMS (δ 0.00) with $CHCl_3$ as internal

© 2002 NRC Canada

standard (δ 7.23 (^{1}H) and 76.90 (^{13}C)), coupling constants (*J*) are given in Hz.

TLC plates were run on silica gel Merck 60 (F_{254}) and compounds were visualized by spraying with Mo-reagent ($(NH_4)_6Mo_7O_{24}\cdot 4H_2O$ (100 g L^{-1}) and $Ce(SO_4)_2\cdot 4H_2O$ (4 g L^{-1}) in H_2SO_4 (10%)) (detection I) or by dipping into a $KMnO_4$ reagent (2.5 g L^{-1} $KMnO_4$ in H_2O) (detection II). Compounds were purified either by flash chromatography on silica gel Merck 60 (230–400 mesh) or, for volatile substances, by Kugelrohr distillation. Petroleum ether (p.e.) had a boiling range of 60–90°C. GC analyses were carried out on a Varian 3800 gas chromatograph equipped with FID and either an HP1301 or a HP1701 capillary column (both 30 m, 0.25 mm, 0.25 μm film, N_2). Enantiomeric purities were analyzed on a Varian 3800 gas chromatograph equipped with FID, using a CP-Chirasil-DEX CB column (column A, 25 m, 0.32 mm, 0.25 μm film) or an Astec Chiraldex G-PN (column B, 30 m, 0.25 mm). H_2 was used as a carrier gas. For programs and retention times vide infra.

High resolution mass spectra were recorded on a double focussing Kratos Profile Mass Spectrometer with electron impact ionization (EI, +70 eV). Optical rotation values were measured on a PerkinElmer polarimeter 341 at 589 nm (Na-line) in a 1-dm cuvette and are given in units of 10^{-1} deg cm^2 g^{-1}.

Solvents were dried and freshly distilled by common practice. For anhydrous reactions, flasks were dried at 150°C and flushed with dry argon just before use. Organic extracts were dried over Na_2SO_4, and then the solvent was evaporated under reduced pressure. *m*-Chloroperbenzoic acid (*m*-CPBA, Fluka, 70%) was used. Olefinic alcohols (*Z*)-**4** and (*E*)-**4** were purchased from Lancaster. For biotransformations, lyophilized bacterial cells were used. The bacteria were obtained from culture collections. SM strain numbers refer to the culture collection of the Institute of Biotechnology, Graz University of Technology. All strains were grown as previously described (12–15).

Syntheses of substrates and reference materials

General procedure for the synthesis of (Z)-5 and (E)-5

Compounds (*Z*)-**5** and (*E*)-**5** were obtained via mesylation of alcohols (*Z*)-**4** and (*E*)-**4**, followed by halide exchange using Method A.

Method A: Alcohol (50 mmol) was dissolved in CH_2Cl_2 (50 mL) and pyridine (100 mmol) was added. The stirred solution was cooled to 0°C and methanesulfonyl chloride (75 mmol) was added in small portions. The reaction mixture was allowed to warm to room temperature. After the reaction reached completion (16 h), water (70 mL) was added and the resulting two-phase system was stirred for 1 h to destroy excess methanesulfonyl chloride. Then the two layers were separated and the aqueous layer was extracted with CH_2Cl_2. The combined organic layers were washed with 5% aq HCl (50 mL) and sat. aq $NaHCO_3$ (50 mL). The organic phase was dried and concentrated. The crude mesylate (50 mmol) was dissolved in anhydrous acetone (50 mL) and LiBr (75 mmol) was added. The reaction mixture was allowed to stir at room temperature until completion (ca. 20 h). Then, 5% aq HCl (70 mL) was added, the two layers were separated and the aqueous phase was extracted with CH_2Cl_2. The combined organic layers were washed with sat. aq $NaHCO_3$ (70 mL) and the organic phase was dried and concentrated. Flash chromatography afforded the pure haloalkenes (*Z*)-**5** and (*E*)-**5**, details and spectroscopic data being given below.

*cis-1-Bromo-hex-3-ene ((Z)-**5**)*

Method A was employed using alcohol (*Z*)-**4** (10 g, 99.84 mmol) and LiBr for the halogenation. Flash chromatography (pentane–Et_2O, 10:1) gave *cis*-1-bromo-hex-3-ene (*Z*)-**5** as a colorless liquid (9.82 g, 61% over 2 steps). R_f (p.e.–EtOAc, 5:1) = 0.83 (detection II). ^{1}H NMR (500.13 MHz, $CDCl_3$) δ: 0.98 (t, *J* = 7.5, 3H), 2.04–2.10 (m, 2H), 2.60–2.65 (m, 2H), 3.38 (t, *J* = 7.2, 2H), 5.33–5.35 (m, 1H), 5.53–5.56 (m, 1H). ^{13}C NMR (125.77 MHz, $CDCl_3$) δ: 14.1, 20.6, 30.6, 32.5, 125.1, 134.7.

*trans-1-Bromo-hex-3-ene ((E)-**5**)*

Method A was employed using alcohol (*E*)-**4** (10 g, 99.84 mmol) and LiBr for the halogenation. Flash chromatography (pentane–Et_2O, 10:1) gave *trans*-1-bromo-hex-3-ene (*E*)-**5** as a colorless liquid (10.5 g, 65% over 2 steps). R_f (p.e.–EtOAc, 5:1) = 0.80 (detection II). ^{1}H NMR (500.13 MHz, $CDCl_3$) δ: 0.99 (t, *J* = 7.5, 3H), 2.01–2.06 (m, 2H), 2.53–2.57 (m, 2H), 3.37 (t, *J* = 7.2, 2H), 5.35–5.41 (m, 1H), 5.57–5.61 (m, 1H). ^{13}C NMR (125.77 MHz, $CDCl_3$) δ: 13.6, 25.5, 32.8, 36.0, 125.3, 135.4.

General procedure for the synthesis of (Z)-6 and (E)-6 (Method B)

Method B: To a stirred solution of allyl bromide (9.1 g, 75.5 mmol) in anhydrous Et_2O (20 mL) under an Ar atmosphere, a Grignard reagent, prepared from (*Z*)-**5** or (*E*)-**5** (50 mmol) in 15 mL of anhydrous Et_2O, was added at room temperature. The mixture was heated at reflux until the reaction was completed (16 h). Then 5% aq HCl (20 mL) was added and after 10 min the product was extracted with Et_2O. The combined organic extracts were dried and concentrated. The residue was purified by flash chromatography to give (*Z*)-**6** or (*E*)-**6**, details and spectroscopic data are given below.

*(Z)-Nona-1,6-diene ((Z)-**6**)*

Method B was employed using (*Z*)-**5** (8.2 g, 50.3 mmol). Flash chromatography (pentane) gave (*Z*)-**6** as a colorless liquid (5.4 g, 87%). R_f (p.e.) = 0.85 (detection II). ^{1}H NMR (360.13 MHz, $CDCl_3$) δ: 0.98 (t, *J* = 7.2, 3H), 1.37–1.51 (m, 2H), 1.99–2.11 (m, 6H), 4.95–5.05 (m, 2H), 5.33–5.43 (m, 2H), 5.79–5.87 (m, 1H). ^{13}C (90.6 MHz, $CDCl_3$) δ: 14.4, 20.6, 26.6, 29.1, 33.3, 114.5, 128.9, 132.0, 139.0.

*(E)-Nona-1,6-diene ((E)-**6**)*

Method B was employed using (*E*)-**5** (8.5 g, 52.1 mmol). Flash chromatography (pentane) gave (*E*)-**6** as a colorless liquid (5.9 g, 91%). R_f (p.e.) = 0.85 (detection II). ^{1}H NMR (360.13 MHz, $CDCl_3$) δ: 0.98 (t, *J* = 7.3, 3H), 1.41–1.50 (m, 2H), 1.98–2.09 (m, 6H), 4.94–5.04 (m, 2H), 5.40–5.47 (m, 2H), 5.78–5.83 (m, 1H). ^{13}C (90.56 MHz, $CDCl_3$) δ: 14.0, 25.7, 28.9, 32.0, 33.3, 114.4, 128.9, 132.4, 139.0.

General procedure for the synthesis of rac-cis-1 and rac-trans-1

Substrates *rac-cis*-**1** and *rac-trans*-**1** were prepared by epoxidation of alkenes (*Z*)-**6** and (*E*)-**6** using *m*-chloroperbenzoic acid (*m*-CPBA) following Method C.

© 2002 NRC Canada

Method C: To a vigorously stirred solution of the alkene (40 mmol) in anhydrous CH_2Cl_2 (400 mL) was added NaH_2PO_4 (ca. 2.6 equiv). After the mixture was stirred for 15 min at room temperature, it was cooled to 0°C and *m*-CPBA (1.05 equiv) was added slowly. The reaction was allowed to warm to room temperature and stirred for an additional 8 h. The white suspension was filtered and the resulting solution was treated with 10% aq $Na_2S_2O_5$ (100 mL) to destroy the excess of peracid. The resulting two-phase system was stirred for 30 min, the layers were separated and the organic phase was washed with sat. aq $NaHCO_3$ (50 mL). The organic phase was dried and evaporated. Kugelrohr distillation afforded pure oxiranes *rac-cis*-**1** and *rac-trans*-**1**. Details and spectroscopic data are given below.

*cis-3,4-Epoxynon-8-ene (rac-cis-**1**)*

Method C was employed using (*Z*)-**6** (5 g, 40.3 mmol). Kugelrohr distillation gave *rac-cis*-**1** as a colorless liquid (3.9 g, 69%). R_f (p.e.–EtOAc, 5:1) = 0.55 (detection I). bp_{20mbar} (Kugelrohr): 80–90°C. ^{1}H NMR (360.13 MHz, $CDCl_3$) δ: 1.01 (t, *J* = 7.0, 3H), 1.49–1.58 (m, 6H), 2.08–2.12 (m, 2H), 2.84–2.92 (m, 2H), 4.94–5.04 (m, 2H), 5.75–5.83 (m, 1H). ^{13}C NMR (90.56 MHz, $CDCl_3$) δ: 10.6, 21.2, 25.9, 27.2, 33.6, 57.1, 58.4, 114.9, 138.4. Anal. calcd. for $C_9H_{16}O$: C 77.05, 11.50; found: C 77.12, H 11.51.

*trans-3,4-Epoxynon-8-ene (rac-trans-**1**)*

Method C was employed using (*E*)-**6** (6 g, 48.4 mmol). Kugelrohr distillation gave *rac-trans*-**1** as a colorless liquid (5.1 g, 75%). R_f (p.e.–EtOAc, 5:1) = 0.65 (detection I). bp_{20mbar} (Kugelrohr): 85–95°C. ^{1}H NMR (360.13 MHz, $CDCl_3$) δ: 0.98 (t, *J* = 7.0, 3H), 1.48–1.58 (m, 6H), 2.09 (d, *J* = 5.9, 2H), 2.62–2.67 (m, 2H), 4.94–5.03 (m, 2H), 5.76–5.84 (m, 1H). ^{13}C NMR (90.56 MHz, $CDCl_3$) δ: 9.94, 25.2, 25.4, 31.5, 33.5, 58.4, 60.0, 114.8, 138.4. Anal. calcd. for $C_9H_{16}O$: C 77.05, 11.50; found: C 77.08, H 11.55.

General procedure for the synthesis of reference material for racemic diols rac-threo-2 and rac-erythro-2

The *rac*-diols *rac-threo*-**2** and *rac-erythro*-**2** were obtained by acid-catalysed hydrolysis of *rac-cis*-**1** and *rac-trans*-**1** following Method D.

Method D: Racemic diols *rac-threo*-**2** and *rac-erythro*-**2** were obtained by hydrolysis of the corresponding racemic oxiranes of *rac-cis*-**1** and *rac-trans*-**1** (1.1 mmol) in a mixture of water and THF (10 mL, 4:1) under acidic conditions (6 M H_2SO_4, 10 drops). After the reaction reached completion (2 h), the solution was extracted with EtOAc (2 × 10 mL). The combined organic layers were dried and concentrated. The residue was purified by flash chromatography. Details and spectroscopic data are given below.

*rac-threo-8-Nonene-3,4-diol (rac-threo-**2**)*

Method D was employed using oxirane *rac-cis*-**1** (0.3 g, 2.1 mmol). Flash chromatography (p.e.–EtOAc, 3:1) gave pure *rac-threo*-8-nonene-3,4-diol *rac-threo*-**2** (0.25 g, 74%). R_f (p.e.–EtOAc, 1:1) = 0.42 (detection I). Spectroscopic data were in full agreement with those previously reported (16). HRMS calcd. for $C_9H_{18}O_2$: 158.1307 [M^+]; found: 158.1314 [M^+].

*rac-erythro-8-Nonene-3,4-diol (rac-erythro-**2**)*

Method D was employed using oxirane *rac-trans*-**1** (0.3 g, 2.1 mmol). Flash chromatography (p.e.–EtOAc, 3:1) gave pure *erythro*-8-nonene-3,4-diol *rac-erythro*-**2** (0.21 g, 63%). R_f (p.e.–EtOAc, 1:1) = 0.45 (detection I). Spectroscopic data were in full agreement with those previously reported (16). HRMS calcd. for $C_9H_{18}O_2$: 158.1307 [M^+]; found: 158.1303 [M^+].

General procedure for preparative-scale biohydrolysis of rac-cis-1 and rac-trans-1

Racemic epoxides *rac-cis*-**1** (0.7 g, 5 mmol) and *rac-trans*-**1** (0.3 g, 2.14 mmol) were hydrolyzed using rehydrated lyophilized microbial cells (1 g *Mycobacterium paraffinicum* NCIMB 10420 for *rac-cis*-**1**, 0.4 g of *Rhodococcus ruber* DSM 44539 for *rac-trans*-**1**) in Tris-buffer (30 mL for *rac-cis*-**1**, 15 mL for *rac-trans*-**1**, 0.05 M, pH 8.0) on an orbit shaker (120 rpm) at 30°C. When the starting material was consumed (after 6 h for *rac-cis*-**1**, 4 h for *rac-trans*-**1**, as judged by TLC and GLC), the mixture was extracted continuously with CH_2Cl_2 for 24 h. The organic layers were dried and evaporated. The residue was flash chromatographed (p.e.–EtOAc, 3:1) to give (3*R*,4*R*)-**2** (0.66 g, 83%, ee 92%) or (3*R*,4*S*)-**2** (0.20 g, 58%, ee 72%). Spectroscopic data of these products matched those of material obtained by acidic hydrolysis of the corresponding *rac*-oxiranes. Elemental analysis of (3*R*,4*R*)-**2**: Anal. calcd. for $C_9H_{18}O_2$: C 68.30, H 11.45; found: C 68.35, H 11.46. Elemental analysis of (3*R*,4*S*)-**2**: Anal. calcd. for $C_9H_{18}O_2$: C 68.30, H 11.45; found: C 68.38, H 11.48.

General procedure for the synthesis of (+)-exo- and (–)-endo-brevicomin [(+)-exo- and (–)-endo-3, respectively] via Wacker-oxidation of diols (3R,4R)-2 and (3R,4S)-2, respectively, following Method E

Method E: Nonracemic diol (3*R*,4*R*)-**2** or (3*R*,4*S*)-**2** (3.2 mmol) was dissolved in anhydrous 1,2-dimethoxyethane (10 mL). The solution was stirred at room temperature. $PdCl_2$ (0.10 g, 0.57 mmol) and $CuCl_2$ (0.43 g, 3.2 mmol) were added and stirring was continued for 10 h. The brown solution was diluted with H_2O and Et_2O (10 mL each). After phase separation, the aqueous layer was extracted with Et_2O (2 × 10 mL). The combined organic phases were dried (Na_2SO_4) and concentrated. The residue was purified by flash chromatography. Details and spectroscopic data are given below.

*(+)-exo-Brevicomin ((+)-exo-**3**)*

Method E was employed using (3*R*,4*R*)-**2** (0.5 g, 3.2 mmol). Flash chromatography (pentane–Et_2O, 10:1) gave pure (+)-*exo*-**3** (0.37 g, 75%, ee 92%). R_f (p.e.–EtOAc, 5:1) = 0.54 (detection I). ^{1}H NMR (360.13 MHz, $CDCl_3$) δ: 0.92 (t, *J* = 7.4, 3H), 1.43 (s, 3H), 1.57–1.84 (m, 8H), 3.94 (t, *J* = 6.4, 1H), 4.15 (s, 1H,). ^{13}C NMR (90.56 MHz, $CDCl_3$) δ: 9.8, 17.2, 25.1, 28.0, 28.6, 35.0, 78.4, 81.2, 107.7. HRMS calcd. for $C_9H_{16}O_2$: 156.1150 [M^+]; found: 156.1145 [M^+].

*(–)-endo-Brevicomin ((–)-endo-**3**)*

Method E was employed using (3*R*,4*S*)-**2** (0.15 g, 0.95 mmol). Flash chromatography (pentane–Et_2O, 10:1) gave pure (–)-*endo*-**3** (0.09 g, 61%, ee 72%). R_f (p.e.–EtOAc, 5:1) = 0.57 (detection I). ^{1}H NMR (360.13 MHz, $CDCl_3$) δ: 0.96 (t,

© 2002 NRC Canada

J = 7.4, 3H), 1.40 (s, 3H), 1.53–1.92 (m, 8H), 3.93–3.97 (m, 1H), 4.14–4.18 (m, 1H). ^{13}C NMR (90.56 MHz, $CDCl_3$) δ: 11.0, 17.6, 22.0, 23.7, 25.1, 34.5, 76.6, 81.7, 107.0. HRMS calcd. for $C_9H_{16}O_2$: 156.1150 [M^+]; found: 156.1159 [M^+].

General procedure for the screening of biocatalysts for the hydrolysis of rac-cis-1 and rac-trans-1

Racemic epoxides *rac-cis*-**1** and *rac-trans*-**1** (5 μL) were hydrolyzed using rehydrated lyophilized cells (50 mg) in Tris-buffer (1 mL, 0.05 M, pH 8.0) by shaking the mixture at 30°C with 120 rpm. The reactions were monitored by TLC. After 21 h and 42 h, a 0.4 mL aliquot was extracted with EtOAc (2 × 0.4 mL). To facilitate phase separation, the cells were removed by centrifugation. The combined organic layers were dried and analyzed by GC on a chiral stationary phase.

Determination of enantiomeric purities (Table 3)

All chiral materials could be analyzed directly by GC on a chiral stationary phase (see Table 3) except 3-nonanol **7** and *rac-trans*-**1**. In the case of alcohol **7**, derivatization to the acetate **8** was optimal, which gave satisfactory enantioseparation. For epoxide *rac-trans*-**1** no enantioseparation using four different chiral columns (columns A or B; Astec Chiraldex B-TA capillary column (column C, 30 m, 0.25 mm); or Astec Chiraldex G-PH (column D, 30 m, 0.32 mm)) was possible.

Syntheses of chiral reference material and determination of absolute configuration

All chiral compounds were diastereomerically pure. The absolute configuration of oxirane *trans*-**1** was not investigated because no enantioseparation on GC (with 4 different chiral columns) was achieved.

Determination of absolute configuration of oxirane (3S,4R)-1

The remaining non hydrolyzed epoxide from the biotransformation of *rac-cis*-**1** using *Mycobacterium paraffinicum* NCIMB 10420 (Scheme 4) was separated from the formed product (3*R*,4*R*)-**2** by flash chromatography (pentane–Et_2O, 10:1). The alkene-functionality of oxirane (3*S*,4*R*)-**1** (0.027 g, 0.2 mmol, ee > 99%) was hydrogenated with Pt/C (0.02 g, Pt on activated carbon, (5% w/w)) in anhydrous EtOH (5 mL) under H_2 at atmospheric pressure (30 min). The catalyst was removed by filtration through a plug of Celite-545 and the solvent was evaporated. After flash chromatography (pentane–Et_2O, 10:1) *cis*-(3*S*,4*R*)-epoxynonane (3*S*,4*R*)-**9** (0.021 g, 74%, >99% ee) was isolated. R_f (p.e.–EtOAc, 5:1) = 0.65 (detection I). ^{1}H NMR (360.13 MHz, $CDCl_3$) δ: 0.91 (t, *J* = 7.4, 3H), 1.04 (t, *J* = 7.2, 3H), 1.33–1.70 (m, 10H), 2.86–2.93 (m, 2H). ^{13}C NMR data match those previously described (17). Without affecting the chiral centers in position 2 and 3 of the oxirane, (3*S*,4*R*)-**10** was converted into the acetates (*S*)-**8** and (*R*)-**10**, using $LiAlH_4$ (0.015 g, 0.4 mmol) in anhydrous Et_2O (5 mL) at room temperature. After the reaction was complete (1 h), the reaction was quenched by addition of sat. aq NH_4Cl (10 mL). The combined organic phases were dried and concentrated. The residue was dissolved in Ac_2O and NEt_3 (0.040 g, 0.4 mmol) and then DMAP (5 mg, cat.) was added. The mixture was heated at reflux for 4 h and quenched by addition of water and Et_2O. The organic phase was dried and evaporated. Without further purification, the resulting mixture of (*S*)-**8** and (*R*)-**10** used directly for determination of the absolute configuration via coinjection with an independently synthesized sample of (*R*)-**8** on GC using a chiral stationary phase. Analysis was focussed on acetate **8**, since enantiopure acetate **10** was not available.

(R)-3-Nonanol ((R)-7)

Since enantioseparation for alcohol (±)-**7** was impossible, the corresponding acetate (±)-**8** was used for analysis. A reference sample of (*R*)-**7** was synthesized as follows: Lipase from *Candida antarctica* B (150 mg) was dispersed in heptane (25 mL) and after addition of (±)-**7** (1.0 g, 6.94 mmol) and vinyl acetate (2.0 g, 23.2 mmol) the mixture was agitated (120 rpm) on an orbit shaker at room temperature, while the progress of the reaction was monitored by GC. After 48 h, the conversion had reached ~50% and after filtration of the biocatalyst, the solution was concentrated in vacuo. After flash chromatography (p.e.–EtOAc, 5:1) (*R*)-3-nonyl acetate (*R*)-**8** (0.41 g, 64%, >99% ee) was isolated. R_f (p.e.–EtOAc, 3:1) = 0.80 (detection I). ^{1}H NMR (360.13 MHz, $CDCl_3$) δ: 0.86–0.90 (m, 6H), 1.23–1.27 (m, 8H), 1.42–1.54 (m, 4H), 2.04 (s, 3H), 4.77–4.82 (m, 1H). ^{13}C NMR (90.56 MHz, $CDCl_3$) δ: 9.55, 14.1, 21.2, 22.6, 25.3, 27.0, 29.3, 31.8, 33.6, 75.6, 171.0. Next, (*R*)-**8** (0.20 g, 1.07 mmol) was dissolved in MeOH (10 mL) and K_2CO_3 (0.30 g, 2.15 mmol) was added. After 30 min the reaction reached completion. The reaction was quenched by addition of water (10 mL) and Et_2O (20 mL). The combined organic phases were dried and concentrated. After flash chromatography (p.e. –EtOAc, 5:1) (*R*)-3-nonanol ((*R*)-**7**) (0.11 g, 71%, >99% ee) was isolated. R_f (p.e.–EtOAc, 3:1) = 0.50 (detection I). Spectroscopic data were in full agreement with those previously reported (18). The absolute configuration of (*R*)-**7** was confirmed by comparison of its known optical rotation value (Table 2) (19). Thus, the absolute configuration of C-3 of **8** was proven to be *R*.

The absolute configuration of diols (3*R*,4*R*)-**2** and (3*R*,4*S*)-**2**, and (+)-*exo*- and (–)-*endo*-brevicomin was determined by comparison of optical rotation values (Table 2) (16, 20–22).

Acknowledgments

We wish to express our thanks to H. Sterk (University of Graz) for skilful assistance in NMR-spectroscopy and NOVO Co. (Denmark) for their generous donation of *Candida antarctica* lipase B. This research was performed within the Spezialforschungsbereich Biokatalyse (SFB-A4, project no. F-104) and was financed by the Fonds zur Förderung der wissenschaftlichen Forschung and the Austrian Ministry of Science.

References

1. R.V.A. Orru and K. Faber. Curr. Opinion Chem. Biol. **3**, 16 (1999).
2. W. Kroutil, M. Mischitz, and K. Faber. J. Chem. Soc. Perkin Trans. 1 3629 (1997).
3. S.F. Mayer, A. Steinreiber, R.V.A. Orru, and K. Faber. Tetrahedron: Asymmetry, **12**, 41 (2001).
4. K. Faber. Chem. Eur. J. **7**, 5004 (2001).

© 2002 NRC Canada

5. A. Steinreiber, I. Osprian, S.F. Mayer, R.V.A. Orru, and K. Faber. Eur. J. Org. Chem. 3703 (2000).
6. A. Steinreiber, S.F. Mayer, and K. Faber. Synthesis, 2035 (2001).
7. S. Hu, S. Jayaraman and A.C. Oehlschlager. J. Org. Chem. **64**, 2524 (1999).
8. A.C. Oehlschlager and B.D. Johnston. J. Org. Chem. **52**, 940 (1987).
9. W. Francke and W. Schröder. Curr. Org. Chem. **3**, 407 (1999), and refs. cited therein.
10. Since the biocatalytic hydrolysis of 2,3-disubstituted epoxides is likely to proceed in an enantioconvergent fashion, the general use of *E*-values for the description of enantioselectivities is inapplicable.
11. W. Kroutil and K. Faber. In Press. A computer program will soon be released via Internet at http://borgc185.kfunigraz.ac.at; for a related mathematical treatment of the kinetics see: P. Moussou, A. Archelas, J. Baratti, and R. Furstoss. Tetrahedron: Asymmetry, **9**, 1539 (1998).
12. M. Mischitz, W. Kroutil, U. Wandel, and K. Faber. Tetrahedron: Asymmetry, **6**, 1261 (1995).
13. W. Kroutil, I. Osprian, M. Mischitz, and K. Faber. Synthesis, 156 (1997).
14. I. Osprian, W. Kroutil, M. Mischitz, and K. Faber. Tetrahedron: Asymmetry, **8**, 65 (1997).
15. W. Krenn, I. Osprian, W. Kroutil, G. Braunegg, and K. Faber. Biotechnol. Lett. **21**, 687 (1999).
16. H. Takahata, M. Kusunoki, Y. Takeda, and T. Momose. Tetrahedron: Asymmetry, **7**, 2093 (1996).
17. C. Chiappe, A. Cordoni, G.L. Moro, and C.D. Palese. Tetrahedron: Asymmetry, **9**, 341 (1998).
18. J. Spieler, O. Huttenloch, and H. Waldmann. Eur. J. Org. Chem. 391 (2000).
19. B. Weber and D. Seebach. Tetrahedron, **50**, 7473 (1994).
20. R. Bel-Rhlid, M.F. Renard, and H. Veschambre. Bull. Soc. Chim. Fr. **133**, 1011 (1996).
21. P.C. Bulman Page, C.M. Rayner, and I.O. Sutherland. J. Chem. Soc. Perkin Trans. 1, 1375 (1990).
22. H. Redlich, W. Bruns, W. Francke, V. Schurig, T.L. Payne, and J.P. Vité. Tetrahedron, **43**, 2029 (1987).

© 2002 NRC Canada

Comparative study of the thermodynamic behaviour of the binary mixtures dimethyl carbonate + (benzene, *n*-heptane, cyclohexane, or toluene)

José M. Pardo, Diego González-Salgado, Clara A. Tovar, Claudio A. Cerdeiriña, Enrique Carballo, and Luís Romaní

Abstract: Isobaric molar heat capacities at 288.15, 298.15, and 308.15 K and densities and speeds of sound at 288.15, 293.15, 298.15, and 308.15 K were determined for the dimethyl carbonate + benzene system over the whole composition range and at atmospheric pressure. In addition, speeds of sound at the same temperatures for the dimethyl carbonate + *n*-heptane system are reported. These experimental data were used to obtain molar volumes, isobaric thermal expansivities, isentropic and isothermal compressibilities, and isochoric molar heat capacities. Excess quantities of the above-mentioned properties were calculated using the Benson and Kiyohara criterion. The thermodynamic behaviour of the dimethyl carbonate + (*n*-heptane, cyclohexane, benzene, or toluene) systems is comparatively analyzed.

Key words: binary mixtures, excess properties, dimethyl carbonate, benzene, hydrocarbon.

Résumé : Opérant à pression atmosphérique, on a déterminé les capacités calorifiques molaires isobares à 288,15, 298,15 et 308,15 K ainsi que les densités et les vitesses du son à 288,15, 295,15, 298,15 et 308,15 K du système carbonate de diméthyle + benzène sur l'ensemble des compositions. On rapporte aussi les vitesses du son à la même température pour le système carbonate de diméthyle + heptane. On a utilisé ces données expérimentales pour en tirer les volumes molaires, les expansivités thermales isobares, les compressibilités isoentropiques et isothermales ainsi que les capacités calorifiques molaires isochoriques. On a calculé les propriétés en excès des quantités mentionnées en faisant appel au critère de Benson et Kiyohara. Le comportement thermodynamique des systèmes carbonate de méthyle + (heptane, cyclohexane, benzène ou toluène) a été analysé de façon comparative.

Mots clés : mélanges binaires, propriétés en excès, carbonate de diméthyle, benzène, hydrocarbure.

[Traduit par la Rédaction]

Introduction

Oils based on organic carbonates are suitable substances to be used as lubricants for stationary air conditioners that operate with HFCs refrigerants (1, 2). For this reason, the knowledge of the thermodynamic properties of mixtures containing dialkyl carbonates has been of great importance in recent years. Previous work related to the description of the thermodynamic behaviour of the dialkyl carbonates + (*n*-alkane, cyclohexane, benzene, or toluene) mixtures mainly dealt with the composition dependence of excess molar volumes (V_m^E) (3–7), excess molar enthalpies (H_m^E) (8, 9), and excess molar Gibbs free energies (G_m^E) (5, 10, 11), usually at 298.15 K. The temperature and pressure dependence of these properties has not been extensively analyzed; only the volumetric properties for the dialkyl carbonate + toluene (12) systems (278.15–328.15 K) and for the dimethyl carbonate + *n*–octane (13) system (in a broad range of temperatures and pressures) are available. In this context, the determination of first- and second-order excess derivatives at several temperatures of mixtures containing dimethyl or diethyl carbonate with hydrocarbons has been the subject of our research (14, 15). We have reported the V_m^E and $C_{p,m}^E$ (excess isobaric molar heat capacities) values at several temperatures and the partial derivatives of the excess molar volume with respect to temperature ($[\partial V_m^E/\partial T]_p$) at 298.15 K for dimethyl and diethyl carbonates mixtures with a linear hydrocarbon (*n*-heptane) (14). Dialkyl carbonate + cyclic hydrocarbon (cyclohexane) mixtures were also studied, and values for V_m^E and $C_{p,m}^E$ at different temperatures as well as the excess isentropic (κ_S^E) and isothermal (κ_T^E) compressibilities, excess isobaric thermal expansivities (α_p^E), and excess isochoric molar heat capacities ($C_{v,m}^E$) at 298.15 K were obtained (15).

In this paper, a comparative study of the excess thermodynamic properties (V_m^E and $C_{p,m}^E$ at several temperatures, and κ_S^E, κ_T^E, α_p^E, and $C_{v,m}^E$ at 298.15 K) for the dimethyl carbonate + (benzene, *n*-heptane, cyclohexane, or toluene) systems was carried out. To this end, the densities (ρ), speeds of sound (u) at 288.15, 293.15, 298.15, and 308.15 K, and iso-

Received 9 August 2001. Published on the NRC Research Press Web site at http://canjchem.nrc.ca on 3 April 2002.

J.M. Pardo, D. González-Salgado, C.A. Tovar, C.A. Cerdeiriña, E. Carballo, and L. Romaní.[1] Departamento de Física Aplicada, Universidad de Vigo, Facultad de Ciencias. Campus de Ourense, E-32004 Ourense, Spain.
[1]Corresponding author (e-mail: fisapor@uvigo.es).

 DOI: 10.1139/V02-030 © 2002 NRC Canada

Table 1. Densities (ρ, g cm^{-3}) for dimethyl carbonate(1)+ benzene(2) mixtures at different temperatures.

	Temperature (K)			
x_1	288.15	293.15	298.15	308.15
0.04990	0.89276	0.88735	0.88195	0.87114
0.10083	0.90155	0.89611	0.89065	0.87973
0.20109	0.91909	0.91354	0.90800	0.89688
0.30334	0.93748	0.93183	0.92617	0.91482
0.40283	0.95575	0.94997	0.94420	0.93264
0.50279	0.97460	0.96871	0.96280	0.95099
0.60513	0.99440	0.98833	0.98229	0.97026
0.70723	1.01472	1.00854	1.00238	0.99003
0.81193	1.03616	1.02983	1.02353	1.01091
0.90676	1.05621	1.04974	1.04328	1.03033
0.95606	1.06685	1.06024	1.05368	1.04064

baric molar heat capacities ($C_{p,m}$) at 288.15, 298.15, and 308.15 K dimethyl carbonate + benzene system, were also determined. Experimental data were obtained over the entire composition range and at atmospheric pressure. Results were used to calculate molar volumes, isothermal, and isentropic compressibilities, isobaric thermal expansivities, and isochoric molar heat capacities. The excess properties of these magnitudes were obtained using the criteria of Benson and Kiyohara (16). To complete the thermodynamic description for the dimethyl carbonate + *n*-heptane system, we also include values for *u* at 288.15, 293.15, 298.15, and 308.15 K. The results are discussed in terms of the different interactions between a polar solvent (dimethyl carbonate) and the hydrocarbons.

Experimental

Materials

All the chemicals were supplied from Aldrich (>99% mol). Their purity was checked by gas chromatography analysis, and all were degassed and dried by passage through molecular sieves (4 Å, Fluka) prior to use.

Apparatus and procedures

The density (ρ) and the speed of sound (*u*) were obtained using a combined densimeter–sound analyzer Anton-Paar DSA-48 equipped with temperature regulation to within 0.005 K via the Peltier effect. This instrument is equipped with a cell to measure the density and another cell, serially connected to the previous one, to measure the speed of sound. Calibration was done by using pure water (Milli-Q) and *n*-heptane as density standards, and the former as the speed of sound standard. The densities of pure water at several temperatures were obtained from Riddick et al. (17) and those of *n*-heptane were reported in previous work (18); the latter were obtained using certified density standards supplied by Deutscher Kalibrierdienst-Physikalisch Technische Bundesanstalt. The speeds of sound of pure water were obtained from the work of Bilaniuk and Wong (19, 20). The instrument is precise to within ±3 × 10^{-5} g cm^{-3} for density and ±0.05 m s^{-1} for speed of sound.

Isobaric heat capacities per unit volume (C_pV^{-1}) were measured with a Setaram micro DSC II differential scanning calorimeter, using the stepwise method. Isobaric molar heat capacities ($C_{p,m}$) values are obtained from C_pV^{-1} and ρ data using the relation $C_{p,m} = (C_pV^{-1})(M\rho^{-1})$, where *M* is the molar mass. Vacuum and *n*-heptane were used as heat capacity standards; the $C_{p,m}$ values of the latter were taken from literature (21). More experimental details are available elsewhere (22). The precision in $C_{p,m}$ was estimated to be ±0.03 J mol^{-1} K^{-1}. Mixtures were prepared by weighing, using a Mettler AE-240 balance, with a precision of ±1 × 10^{-5} g.

Table 2. Speeds of sound (*u*, m s^{-1}) for dimethyl carbonate(1)+ benzene(2) and dimethyl carbonate(1)+ *n*-heptane(2) mixtures at different temperatures.

	Temperature (K)			
x_1	288.15	293.15	298.15	308.15
Dimethyl carbonate(1)+ benzene(2)				
0.04990	1339.37	1315.78	1292.22	1245.79
0.10083	1331.77	1308.65	1285.37	1239.20
0.20109	1318.23	1295.01	1271.83	1226.11
0.30334	1304.30	1281.66	1258.85	1213.60
0.40283	1292.30	1269.48	1246.79	1202.02
0.50279	1280.94	1258.34	1235.79	1191.32
0.60513	1270.02	1247.83	1225.51	1181.39
0.70723	1261.02	1238.64	1216.43	1172.59
0.81193	1252.63	1230.52	1208.33	1164.79
0.90676	1246.56	1224.20	1202.07	1158.77
0.95606	1243.51	1221.20	1199.09	1155.93
Dimethyl carbonate(1)+ *n*-heptane(2)				
0.05195	1167.45	1145.76	1123.64	1080.82
0.10204	1162.42	1140.65	1118.57	1075.73
0.20450	1155.30	1133.02	1110.74	1067.81
0.30273	1150.74	1128.91	1106.78	1063.68
0.40489	1149.47	1127.60	1105.38	1062.46
0.50315	1151.20	1129.51	1107.43	1064.63
0.59734	1156.42	1134.81	1112.78	1070.01
0.70463	1167.23	1145.64	1123.56	1081.08
0.80119	1183.70	1162.04	1139.90	1097.30
0.90019	1208.31	1186.35	1164.02	1121.35
0.95026	1223.84	1201.85	1179.40	1136.60

Results and discussion

Results for the density (ρ, g cm^{-3}), speed of sound (*u*, m s^{-1}), and isobaric molar heat capacity ($C_{p,m}$, J mol^{-1} K^{-1}) are given in Tables 1–3. These data were fitted as a function of composition and temperature to the following expressions:

$$[1] \quad Y = \sum_{i=1}^{n} A_i x^{i-1}$$

$$[2] \quad A_i = \sum_{j=1}^{3} A_{ij} 10^{1-j} (T - T_0)^{j-1}$$

where *x* is the mol fraction of dimethyl carbonate, *T* is the absolute temperature (T_0 = 288.15 K), and *Y* can be ρ, *u*, or $C_{p,m}$. The fitting coefficients (A_{ij}) were obtained using the optimization method of Marquardt (23) and they are given in

© 2002 NRC Canada

Table 3. Isobaric molar heat capacities ($C_{p,m}$, J mol^{-1} K^{-1}) for dimethyl carbonate(1)+ benzene(2) system at different temperatures.

	Temperature (K)		
x_1	288.15	298.15	308.15
0.05109	135.19	137.15	139.33
0.10211	136.55	138.48	140.62
0.15297	—	139.79	141.94
0.20311	139.24	141.13	143.22
0.30551	142.12	143.91	145.99
0.35721	143.55	145.38	147.33
0.40717	145.00	146.77	148.70
0.45429	146.41	148.12	150.02
0.50135	—	149.47	151.32
0.55355	149.37	151.05	152.85
0.59834	—	152.37	154.13
0.64945	—	153.93	155.62
0.69915	153.97	155.48	157.03
0.80123	157.31	158.65	160.15
0.90275	160.67	161.95	163.28

Table 4, together with their respective standard deviations (s). The procedure to determine the number of parameters for each property has been described elsewhere (24).

The isentropic compressibility (κ_s) was calculated from ρ and u using the Laplace equation.

$$[3] \quad \kappa_s = 1/(\rho u^2)$$

The isobaric thermal expansivity (α_p) was obtained by analytical differentiation of the density-fitting equation. The procedure used to calculate α_p was previously validated (22) and allows the obtainment of data at an intermediate temperature of the working range (298.15 K in our case). The isothermal compressibility (κ_T) and the isochoric molar heat capacity ($C_{v,m}$) were obtained from the following equations:

$$[4] \quad \kappa_T = \kappa_S + \frac{T V_m \alpha_p^2}{C_{p,m}}$$

$$[5] \quad C_{v,m} = C_{p,m} \frac{\kappa_S}{\kappa_T}$$

Table 5 shows thermodynamic property data for the pure products compared with literature values. The density (ρ), speed of sound (u), isentropic compressibility (κ_S), and isobaric thermal expansivity (α_p) data of this work for dimethyl carbonate are similar to those found in literature. The scarcity of published data for heat capacities of organic carbonates does not permit a more comprehensive comparison, but it does, however, encourage new investigations to determine these thermodynamic properties at several temperatures. Good agreement between this work and literature values was also obtained for the ρ, u, and κ_S of benzene; a slight deviation was found for the α_p and κ_T. The value of u obtained for *n*-heptane is also close to the literature value and the deviation for the κ_T is less than 1%.

Excess properties were calculated by using the following expression:

$$[6] \quad Y^E = Y - Y^{id}$$

where Y^E is the excess quantity of the property Y, and Y^{id} its ideal value. Values for Y^{id} were calculated using the criterion of Benson and Kiyohara (16), and they are defined as follows:

$$[7] \quad V_m^{id} = xV_{m,1}^* + (1-x)V_{m,2}^*$$

$$[8] \quad C_{p,m}^{id} = xC_{p,m,1}^* + (1-x)C_{p,m,2}^*$$

$$[9] \quad \alpha_p^{id} = \phi\alpha_{p,1}^* + (1-\phi)\alpha_{p,2}^*$$

$$[10] \quad \kappa_T^{id} = \phi\kappa_{T,1}^* + (1-\phi)\kappa_{T,2}^*$$

$$[11] \quad \kappa_s^{id} = \kappa_T^{id} - \frac{TV_m^{id}(\alpha_p^{id})^2}{C_{p,m}^{id}}$$

$$[12] \quad C_{v,m}^{id} = C_{p,m}^{id} \frac{\kappa_s^{id}}{\kappa_T^{id}}$$

$$[13] \quad \phi = \frac{xV_{m,1}^*}{V_m^{id}}$$

where ϕ and x are the volume and mol fractions, respectively, of component 1 (dimethyl carbonate in this work) and superscript * denotes properties of the pure liquids.

The results using these criterion are shown in Figs. 1–4, where solid lines correspond to fitting polynomials of the Redlich–Kister-type equation.

$$[14] \quad Y = x(1-x)\sum_{i=1}^{n} A_i(2x-1)^{i-1}$$

The least-squares method was used to determine the polynomial coefficients (A_i), whose values for V_m^E, $C_{p,m}^E$, $C_{v,m}^E$, κ_S^E, κ_T^E, and α_p^E are given in Table 6, together with their respective standard deviations (s). The number of coefficients was determined in each case using an F-test.

The excess molar volumes (V_m^E) at 298.15 K of this work for the dimethyl carbonate + benzene system are in agreement with those of Rodriguez et al. (6) as can be seen in Fig. 1*a*. In addition, Fig. 1*a* shows the V_m^E values of this work at 288.15 K and 308.15 K. In all the cases, V_m^E values are positive and the fitted curves are parabolic and centred at equimolecular composition. Moreover, the V_m^E values slightly decrease with an increase of temperature. Figure 1*b* shows V_m^E at 298.15 K for the dimethyl carbonate + (benzene, *n*-heptane (14), cyclohexane (15), or toluene (12)) systems. In all cases, positive contributions (such as destruction of dipole–dipole interactions during the mixing process) overcome the negative contributions (e.g., free volume) resulting in positive V_m^E values. These values are higher for mixtures containing saturated hydrocarbons (*n*-heptane or cyclohexane), being especially important for the system containing cyclohexane, whose molecules behave as important order-destruction agents due to their globular forms (26–28). On the other hand, systems containing benzene or toluene, which have similar V_m^E values, display values that are significantly lower in relation to those of mixtures containing saturated hydrocarbons. Orye and Praustnitz (29) suggested the possibility of the formation of a charge-transfer complex between dimethyl carbonate and the unsaturated hydrocarbon (e.g., benzene or toluene). This interaction, which does not

© 2002 NRC Canada

Table 4. Smoothing coefficients (A_{ij}) and standard deviations (s) from eqs. [1] and [2].

		i						
	j	1	2	3	4	5	6	7
Dimethyl carbonate(1) + benzene(2) system								
ρ (g cm^{-3})	1	0.88429	0.16876	0.02214	– 0.00352	0.00489		
	2	– 0.01071	– 0.00123	–0.00414	0.00605	– 0.00336		
	3	– 0.00001	– 0.00025	0.00148	– 0.00253	0.00138		
		(s = 0.00003)						
u (m s^{-1})	1	1346.37	–143.93	7.20	46.64	–14.94		
	2	– 47.22	2.79	9.13	–17.23	7.66		
	3	0.14	1.20	–5.17	8.18	–3.83		
		(s = 0.11)						
$C_{p,m}$ (J mol^{-1} K^{-1})	1	133.87	25.46	4.70				
	2	1.85	– 0.09	– 0.79				
	3	0.11	– 0.11	0.08				
		(s= 0.03)						
Dimethyl carbonate(1) + *n*-heptane(2) system								
u (m s^{-1})	1	1173.96	–133.13	216.50	–49.40	–281.46	543.59	–228.68
	2	– 43.78	–7.34	6.01	49.46	–77.40	6.34	21.96
	3	0.25	3.42	–13.16	23.71	–38.45	47.51	–22.81
		(s = 0.19)						

Table 5. Properties of the pure liquids at different temperatures.

		Dimethyl carbonate		Benzene		*n*-Heptane	
Property	T (K)	This work	Lit.	This work	Lit.	This work	Lit.
ρ (g cm^{-3})	288.15	1.07660	1.07646[a]	0.88429			
	293.15	1.06992	1.07026[b]	0.87894	0.87900[c]		
	298.15	1.06329	1.06338[a]	0.87360	0.87360[c]		
	308.15	1.05011	1.05004[a]	0.86286			
u (m s^{-1})	288.15	1241.33		1346.32		1173.97	
	293.15	1219.17		1322.77		1152.33	
	298.15	1197.06	1196[d]	1299.32	1299[d]	1130.35	1133[e]
	308.15	1153.74		1252.50		1087.46	
$C_{p,m}$ (J mol^{-1} K^{-1})	288.15	164.03		133.84			
	298.15	165.02		135.84	135.76[c]		
	308.15	166.3		137.99			
κ_S (TPa^{-1})	288.15	602.80		623.89		1041.87	
	293.15	628.81		650.24		1094.35	
	298.15	656.32	656.8[d]	678.04	678.26[c]	1151.35	
	308.15	715.40		738.76		1259.75	
α_p (1 × 10^{-3}) (K^{-1})	298.15	1.246	1.241[a]	1.227	1.213[c]	1.241	
κ_T (TPa^{-1})	298.15	893.86		973.44	966.0[c]	1452.73	1440[c]
$C_{v,m}$ (J mol^{-1} K^{-1})	298.15	121.21		94.62		178.12	

[a]Reference 12.
[b]Reference 13.
[c]Reference 17.
[d]Reference 6.
[e]Reference 25.

© 2002 NRC Canada

Fig. 1. (*a*) Excess molar volumes (V_m^E) for dimethyl carbonate(1) + benzene(2) at (●) 288.15 K (this work); (▲) 298.15 K (this work); (□) 298.15 K (ref. 6); (◆) 308.15 K (this work). (—) Calculated values from eq. [14]. (*b*) V_m^E values at 298.15 K for dimethyl carbonate(1) + [benzene(2), *n*-heptane(2), cyclohexane(2), or toluene(2)]. Solid and dashed lines are calculated values: (—) benzene (eq. [14]); (···) *n*-heptane (14);(–··–) cyclohexane (15); and (–·–) toluene (12).

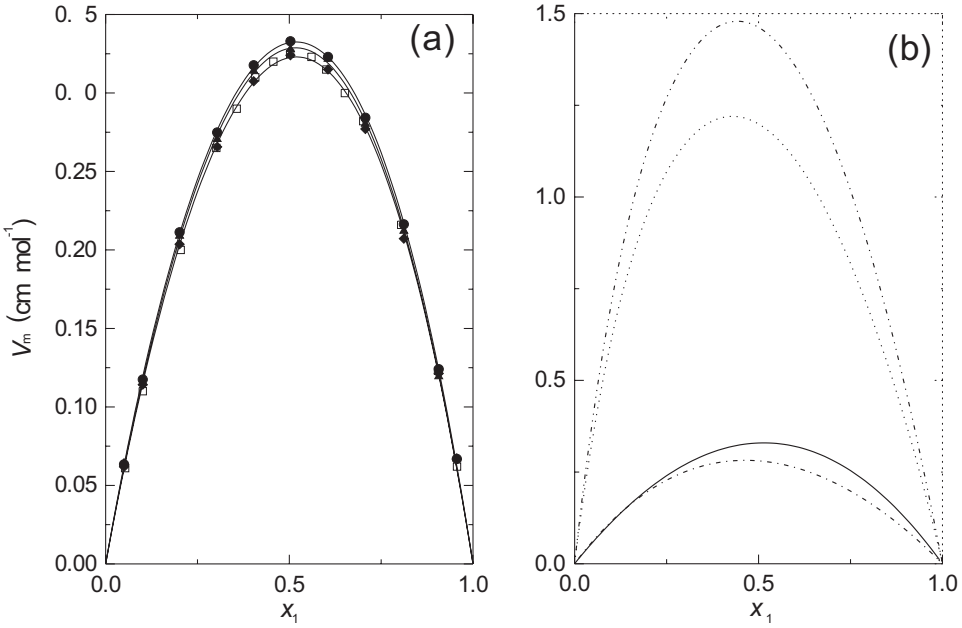

Fig. 2. (*a*) Excess isobaric molar heat capacities ($C_{p,m}^E$) for dimethyl carbonate(1) + benzene(2) at (●) 288.15 K; (▲) 298.15 K; (◆) 308.15 K. (—) Calculated values from eq. [14]. (*b*) $C_{p,m}^E$ values at 298.15 K for dimethyl carbonate(1) + [benzene(2), *n*-heptane(2), or cyclohexane(2)]. Solid and dashed lines, calculated values from: (—) benzene (eq. [14]); (···) *n*-heptane (14); and (–··–) cyclohexane (15).

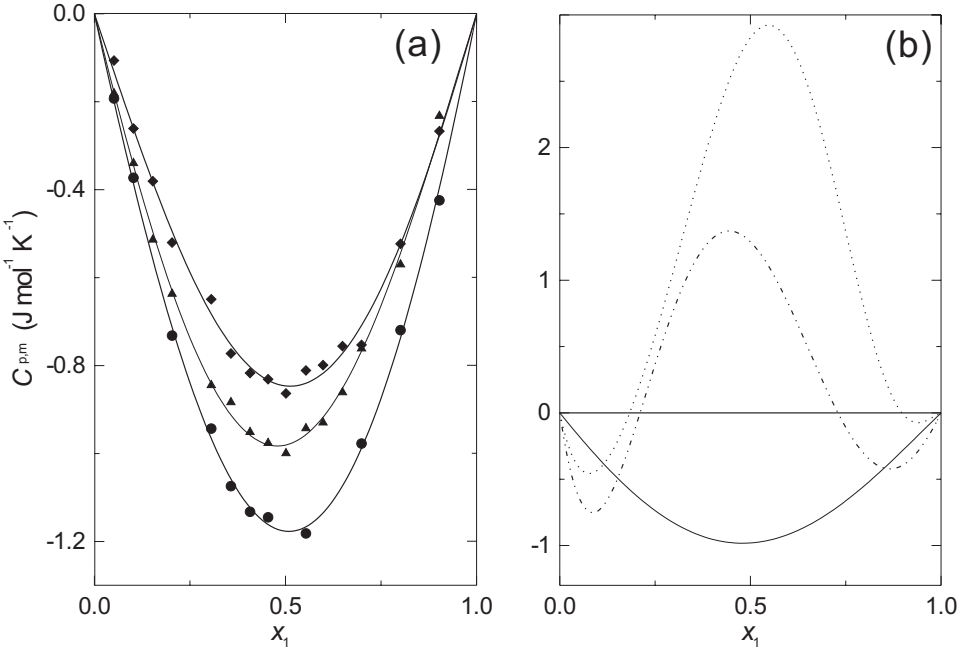

exist in mixtures containing saturated hydrocarbons, appears to be the main factor responsible for these smaller V_m^E values. Evidence of complex formation can also be observed when the values of H_m^E (9) at equimolecular composition for these mixtures are compared. The net energetic balance is more positive for the mixtures containing *n*-heptane (1997 J mol^{-1}) or cyclohexane (1938 J mol^{-1}) than for the mixtures containing benzene (400 J mol^{-1}) or toluene (512 J mol^{-1}).

Figure 2*a* shows the excess isobaric molar heat capacities ($C_{p,m}^E$) at the working temperatures together with the fitted

© 2002 NRC Canada

Fig. 3. (*a*) Excess isobaric thermal expansivities (α_p^E) and (*b*) excess isochoric molar heat capacities ($C_{v,m}^E$) values at 298.15 K for dimethyl carbonate(1) + [benzene(2), *n*-heptane(2), cyclohexane(2), or toluene(2)]. Points are experimental data: (●) benzene (this work) and (◆) *n*-heptane (this work). Solid and dashed lines are calculated values: (—) benzene (eq. [14]); (···) *n*-heptane (eq. [14]); (–··–) cyclohexane (15); and (–·–) toluene (12).

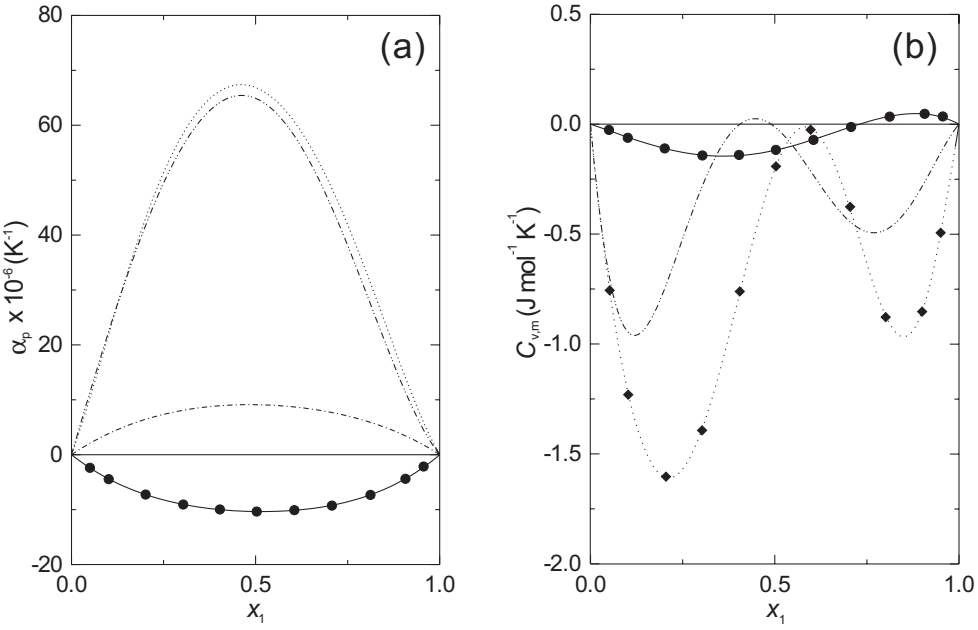

Fig. 4. (*a*) Excess isentropic (κ_S^E) and (*b*) isothermal (κ_T^E) compresibilities at 298.15 K for dimethyl carbonate(1) + [benzene(2), *n*-heptane(2), or cyclohexane(2)]. Points are experimental data: (●) benzene (this work) and (◆) *n*-heptane (this work). Solid and dashed lines are calculated values: (—) benzene (eq. [14]); (···) *n*-heptane (eq. [14]); and (–···–) cyclohexane (15).

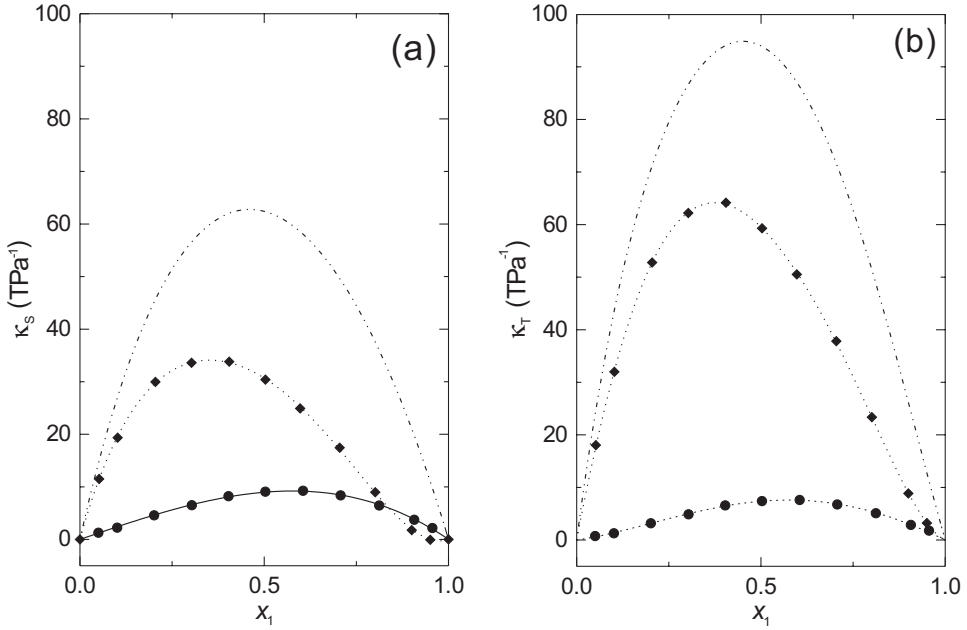

curves for the dimethyl carbonate + benzene system. As can be seen, $C_{p,m}^E$ values are negative, the fitted curves are parabolic, and $C_{p,m}^E$ values increase with an increase of temperature. Figure 2*b* compares the $C_{p,m}^E$ values at 298.15 K for the dimethyl carbonate + (benzene, *n*-heptane, or cyclohexane) systems. As can be seen, different composition dependence was found for the systems containing saturated hydrocarbons (W-shaped) with respect to that containing benzene. It is well-known that $C_{p,m}^E$ can be interpreted as a measure of the degree of non-randomness in the mixture. Saint-Victor and Patterson (30) showed in the framework of the Guggenheim quasi-chemical theory that non-randomness

© 2002 NRC Canada

Table 6. Smoothing coefficients (A_i) and standard deviations (s) of eq. [14] at different temperatures.

Property	T (K)	A_1	A_2	A_3	A_4	A_5	A_6	s
Dimethyl carbonate(1)+ benzene(2) system								
V^E_m (cm^3 mol^{-1})	288.15	1.3284	0.0714	0.0944	0.0520			0.0018
	293.15	1.314	0.085	0.077				0.003
	298.15	1.317	0.076					0.004
	308.15	1.290	0.094	0.084				0.003
$C^E_{p,m}$ (J mol^{-1} K^{-1})	288.15	– 4.707	– 0.190	0.542				0.018
	298.15	– 3.923	0.393	0.752				0.019
	308.15	– 3.385	– 0.199	0.603				0.03
α^E_p (1×10^{-6}) (K^{-1})	298.15	– 41.44	– 1.74	– 13.60				0.06
$C^E_{v,m}$ (J mol^{-1} K^{-1})	298.15	– 0.475	0.737	0.645				0.003
κ^E_S (TPa^{-1})	298.15	35.90	11.83					0.13
κ^E_T (TPa^{-1})	298.15	29.43	11.85	– 7.41				0.15
Dimethyl carbonate(1)+ *n*-heptane(2) system								
$C^E_{v,m}$ (J mol^{-1} K^{-1})	298.15	– 0.822	8.874	– 22.522	– 19.143	9.214	14.333	0.007
κ^E_S (TPa^{-1})	298.15	122.7	– 88.0	– 7.2	– 51.2			0.3
κ^E_T (TPa^{-1})	298.15	238.2	– 137.9	14.3	– 30.7	– 53.4		0.3

Table 7. Sign of the excess thermodynamic properties, value at equimolecular composition, and shape of their curves against mol fraction for all the systems at 298.15 K.

	n-Heptane	Dimethyl carbonate + cyclohexane	Benzene	Cyclohexane + *n*-tetradecane
V^E_m (cm^3 mol^{-1})	++	++	+	+
	1.194	1.473	0.327	0.450
H^E_m (J mol^{-1})	++	++	+	+
	1997	1938	400	512
α^E_p (1×10^{-6}) (K^{-1})	++	++	–	–
	66.80	64.93	–10.36	–24.95
κ^E_S (TPa^{-1})	++	++	+	+
	30.39	62.51	9.08	8.86
κ^E_T (TPa^{-1})	++	++	+	+
	59.30	94.18	7.39	3.37
$C^E_{p,m}$ (J mol^{-1} K^{-1})	W	W	–	–
$C^E_{v,m}$ (J mol^{-1} K^{-1})	W	W	0	–

Note: (++) Parabolic and high positive; (– –) parabolic and high negative; (+) parabolic and positive; (–) parabolic and negative; (W) W-shaped composition dependence; (0) nearly zero.

contributes positively to $C^E_{p,m}$, whereas its absence (randomness) it results in negative $C^E_{p,m}$ values. W-shaped $C^E_{p,m}$ have been found for a variety of polar + *n*-alkane systems (31, 32) and they can be explained from the above-mentioned ideas. At the extremes of the composition range ($C^E_{p,m} < 0$), the order of the diluted component is fully destroyed because the mean separation among its molecules is longer than the typical distances, resulting in randomness. On the contrary, at intermediate compositions ($C^E_{p,m} > 0$), the shorter mean separation between like molecules allows for attractive interactions. In addition, the absence of specific interactions between unlike molecules makes interactions between like molecules (primarily dipole–dipole interactions in dimethyl carbonate) to be much more energetically favourable than those between unlike molecules, resulting in non-randomness in the mixture. This situation becomes more important as temperature is lowered and is, ultimately, responsible for phase separation. In the case of dimethyl carbonate + benzene ($C^E_{p,m} < 0$), the formation of charge-transfer complexes causes the situation to change with respect to that of mixtures with a saturated hydrocarbon. The interactions between unlike molecules are, therefore, not as energetically unfavourable, which results in a more random distribution of the molecules in the mixture.

The excess isobaric thermal expansivities (α^E_p) values for the dimethyl carbonate + (benzene, *n*-heptane, cyclohexane, or toluene) systems are shown in Fig. 3*a*. For the dimethyl carbonate + benzene system, the α^E_p values are small and negative, which is in agreement with the decrease of positive V^E_m values as the temperature increases. For the remaining systems, α^E_p values are positive, with lower values being found for the system containing toluene and higher values being found for the mixtures with cyclohexane or *n*-heptane. The small values found for mixtures containing aromatic hy-

© 2002 NRC Canada

drocarbons with respect to those containing saturated hydrocarbons can be explained by the presence of charge-transfer complexes in the former, which make the mixture more packed and, consequently, less expansible. Figure 3*b*, compares the excess isochoric molar heat capacities ($C^{E}_{v,m}$) for the dimethyl carbonate + (benzene, *n*-heptane, or cyclohexane) systems. Similar to $C^{E}_{p,m}$, $C^{E}_{v,m}$ exhibits a different behaviour for the systems containing benzene (values are close to zero).

The excess isentropic (κ^{E}_{S}) and isothermal (κ^{E}_{T}) compressibilities for the dimethyl carbonate + (benzene, *n*-heptane, or cyclohexane) mixtures are compared in Fig. 4. Similar to α^{E}_{p}, H^{E}_{m}, and V^{E}_{m}, the κ^{E}_{S} and κ^{E}_{T} values are much lower for the benzene system. Again, because the dimethyl carbonate + benzene system is a more closely packed mixture, it makes them less compressible. The maximum values of κ^{E}_{S} or κ^{E}_{T} for the system containing benzene are similar but slightly higher for κ^{E}_{S} (9.5 vs. 8.5 TPa^{-1}, respectively). For the other systems, the κ^{E}_{S} values are lower than the κ^{E}_{T} values and the maxima are drastically different (e.g., 62 vs. 96 TPa^{-1}, respectively, for dimethyl carbonate + cyclohexane mixture). As a rule, high V^{E}_{m} values imply high κ^{E}_{S} and κ^{E}_{T} values. It is reasonable that if the system is expanded during the mixing process it is easier to compress it (33, 34).

Table 7 shows a qualitative description of the thermodynamic behaviour of the above-discussed mixtures together with the cyclohexane + *n*-tetradecane system (35). As mentioned earlier, while the *n*-heptane and cyclohexane systems show the same thermodynamic behaviour, this behaviour is quite different from that of mixtures containing aromatic hydrocarbons. Interestingly, the dimethyl carbonate + benzene system exhibits the same pattern of behaviour as those of the cyclohexane + long chain *n*-alkane systems, even though the nature of the interactions are very different. In both cases, the V^{E}_{m} and H^{E}_{m} values are positive, the α^{E}_{p} values are negative, and the curves of the negative $C^{E}_{p,m}$ values vs. mol fraction are parabolic. Negative values and parabolic curves of $C^{E}_{p,m}$ values are related to a tendency towards randomness in the mixture. In the dimethyl carbonate + benzene system, the charge-transfer complexation between the carbonate molecule and the aromatic ring of benzene is ultimately responsible for this behaviour. For the cyclohexane + *n*-alkane mixtures, however, randomness is due mainly to the loss of orientational order in the pure *n*-alkane by virtue of the presence of cyclohexane molecules.

Conclusions

The charge-transfer complex formation between dimethyl carbonate molecules and the aromatic ring of benzene appears to be the main reason for the different thermodynamic behaviour of this system with respect to the dimethyl carbonate + saturated hydrocarbons systems. In this way, excess molar volumes (V^{E}_{p}) are lower for the former system resulting in a more packed mixture, which is thus more difficult to expand (lower α^{E}_{m}) and to compress (lower κ^{E}_{S} and κ^{E}_{T}). The excess molar enthalpies (H^{E}_{m}) are also lower due to the formation of these complexes in solution. Excess isobaric molar heat capacities ($C^{E}_{p,m}$) of mixtures containing benzene indicate a tendency towards randomness in the mixture; this behaviour contrasts with that of mixtures containing saturated hydrocarbons, which are random at the extremes of the composition range and non-random at intermediate compositions. In this sense, the thermodynamic behaviour of dimethyl carbonate + benzene system is very similar to that of cyclohexane + long chain *n*-alkane systems, which are also characterized by randomness in the mixture.

Acknowledgments

This work is part of research project BFM2000–0597 of the "Programa Nacional de Promoción General del Conocimiento". The authors are indebted to the Dirección General de Investigación, Ministerio de Ciencia y Tecnología of Spain for financial support.

References

1. K. Takahata, M. Tanaka, T. Hayashi, and N. Sakamoto. Proceedings of 1994 international refrigeration conference at Purdue. Purdue University, W. Lafayette, IN. 1994. p. 141.
2. T. Hayashi, M. Tanaka, K. Takeuchi, K. Takahata, and N. Sakamoto. Proceedings of 1996 international refrigeration conference at Purdue. Purdue University, W. Lafayette, IN. 1996. p. 285.
3. I. García, J.A. González, J.C. Cobos, and C. Casanova. J. Solution Chem. **24**, 827 (1995).
4. J. García, L. Lugo, M.J. Comuñas, E.R. López, and J. Fernández. J. Chem. Soc. Faraday Trans. **94**, 1707 (1998).
5. L. Negadi, A. Blondel, I. Mokbel, A. Ait-Kaci, and J. Jose. Int. DATA Ser. Sel. Data Mixtures, Ser. A, **3**, 169, (1993).
6. A. Rodríguez, J. Canosa, and J. Tojo. J. Chem. Eng. Data, **44**, 1298 (1999).
7. I. García de la Fuente, J.A. González, J.C. Cobos, and C. Casanova. J. Chem. Eng. Data, **37**, 535 (1992).
8. I. García, J.A. González, J.C. Cobos, and C. Casanova. Int. DATA Ser. Sel. Data Mixtures, Ser. A, **3**, 164 (1987).
9. I. García, J.A. González, J.C. Cobos, and C. Casanova. Int. DATA Ser. Sel. Data Mixtures, Ser. A, **4**, 245 (1987).
10. M.J. Cocero, J.A. González, I. García, J.C. Cobos, and F. Mato. Int. DATA Ser. Sel. Data Mixtures, Ser. A, **2**, 112 (1991).
11. L. Negadi, G. Ghanem, and A. Ait-Kaci. J. Jose ELDATA: Int. Electron. J. Phys.-Chem. Data, **3 (1)**, 53 (1997).
12. E.R. López, L. Lugo, M.J.P. Comuñas, J. García, and J. Fernández. J. Chem. Thermodyn. **32**, 743 (2000).
13. L. Lugo, M.J.P. Comuñas, E.R. López, and J. Fernández. Fluid Phase Equilib. **186**, 235 (2001).
14. J.M. Pardo, C.A. Tovar, C.A. Cerdeiriña, E. Carballo, and L. Romaní. J. Chem. Thermodyn. **31**, 787 (1999).
15. J.M. Pardo, C.A. Tovar, C.A. Cerdeiriña, E. Carballo, and L. Romaní. Fluid Phase Equilib. **179**, 151 (2001).
16. G.C. Benson and O. Kiyohara. J. Chem. Thermodyn. **11**, 1061 (1979).
17. J.A. Riddick, W.A. Bunger, and T.K. Sakano. Organic solvents. Physical properties and methods of purification. 4th ed. Wiley, New York. 1986.
18. C.A. Cerdeiriña, C.A. Tovar, J. Troncoso, E. Carballo, and L. Romaní. Fluid Phase Equilib. **157**, 93 (1999).
19. N. Bilaniuk and G.S.K. Wong. J. Acoust. Soc. Am. **97**, 1609 (1993).
20. N. Bilaniuk and G.S.K. Wong. J. Acoust. Soc. Am. **9**9 3257 (1996).

© 2002 NRC Canada

21. D.C. Ginnings and G.T. Furukawa. J. Res. Natl. Bur. Stand. **75**, 522 (1953).
22. C.A. Tovar, E. Carballo, C.A. Cerdeiriña, J.L. Legido, and L. Romaní. Int. J. Thermophys. **18**, 761 (1997).
23. D.W. Marquardt. J. Soc. Ind. Appl. Math. **11**, 431 (1963).
24. D. González-Salgado, C.A. Tovar, C.A. Cerdeiriña, E. Carballo, and L. Romaní. Fluid Phase Equilib. accepted 2002.
25. T.M. Aminabhavi and V.B. Patil. J. Chem. Eng. Data, **42**, 641 (1997).
26. S.N. Bhattacharyya and D. Patterson. J. Phys. Chem. **83**, 2979 (1979).
27. S.N. Bhattacharyya and D. Patterson. J. Chem. Soc. Faraday Trans. **81**, 375 (1985).
28. M. Costas, S.N. Bhattacharyya, and D. Patterson. J. Chem. Soc. Faraday Trans. **81**, 387 (1985).
29. R.V. Orye and J.M. Prausnitz. Trans. Faraday Soc. **61**, 1338 (1965).
30. M-E Saint-Victor and D. Patterson. Fluid Phase Equilib. **35**, 237 (1987).
31. L.M. Trejo, M. Costas, and D. Patterson. J. Chem. Soc. Faraday Trans. **87**, 3001 (1991).
32. C.A. Tovar, E. Carballo, C.A. Cerdeiriña, M.I. Paz Andrade, and L. Romaní. J. Chem. Soc. Faraday Trans. **93**, 3505 (1997).
33. R.J. Fort and W.R. Moore. Trans. Faraday Soc. **61**, 2102 (1965).
34. G. Douhéret and M.I. Davis. Chem. Soc. Rev. **22**, 43 (1993).
35. C.A. Tovar, C.A. Cerdeiriña, D. González, E. Carballo, and L. Romaní. Fluid Phase Equilib. **169**, 209 (2000).

© 2002 NRC Canada

Multinuclear magnetic resonance studies of the aqueous products of the complexes *cis*- and *trans*-$Pt(Ypy)_2(NO_3)_2$ where Ypy = pyridine derivative

Fernande D. Rochon and Christian Tessier

Abstract: The hydrolyis or the aquation reactions of compounds of the types *cis*- and *trans*-$Pt(Ypy)_2(NO_3)_2$ (Ypy = pyridine derivative) were studied in D_2O and characterized by multinuclear (^{195}Pt, ^{13}C, and ^{1}H) NMR spectroscopy. In acidic pD, the product of the *cis* complexes is *cis*-$[Pt(Ypy)_2(D_2O)_2]^{2+}$, whereas in basic medium *cis*-$Pt(Ypy)_2(OD)_2$ is formed. The ^{195}Pt NMR resonances of the products containing ligands with an *ortho* substituent were observed at lower fields than the other complexes. The average coupling constant ($^3J(^{195}Pt–^1H)$ and $^3J(^{195}Pt–^{13}C)$) is 44 Hz for the diaqua species and 42 Hz for the dihydroxo compounds. At neutral pD, several hydrolyzed species were observed, except for the 2-picoline and 2,4-lutidine complexes, which contained only one compound, *cis*-$[Pt(Ypy)_2(D_2O)(OD)]^+$. The other hydrolyzed products for the ligands with no *ortho* substituent were identified as the dihydroxo-bridged dimer, the monohydroxo-bridged dimer, the trimer, and possibly the tetramer. The *trans* analogues have shown two signals in acidic pD corresponding to the diaqua monomer and the monohydroxo-bridged aqua dimer. Two species (the dihydroxo compound and the monohydroxo-bridged hydroxo dimer) were also observed in basic pD. In neutral medium, a third signal assigned to a longer chain hydroxo-bridged oligomer or polymer was detected.

Key words: platinum, pyridine derivative, nitrato, hydrolysis, NMR, aquation.

Résumé : Les réactions d'aquation et d'hydrolyse des complexes de types *cis*- et *trans*-$Pt(Ypy)_2(NO_3)_2$ (Ypy = dérivé de la pyridine) ont été étudiées dans D_2O et les produits ont été caractérisés par résonance magnétique multinucléaire (^{195}Pt, ^{13}C et ^{1}H). En milieu acide, le produit des complexes *cis* est *cis*-$[Pt(Ypy)_2(D_2O)_2]^{2+}$, tandis que *cis*-$Pt(Ypy)_2(OD)_2$ est formé en milieu basique. Les signaux en RMN du ^{195}Pt des complexes contenant des ligands substitués en position *ortho* ont été observés à plus bas champ que les autres. Les constantes de couplage moyennes $^3J(^{195}Pt–^1H)$ et $^3J(^{195}Pt–^{13}C)$ sont 44 Hz pour les espèces diaqua et 42 Hz pour les composés dihydroxo. À pD neutre, plusieurs espèces hydrolysées ont été observées, excepté pour les complexes contenant 2-picoline et 2,4-lutidine, qui ont montré une seule espèce, *cis*-$[Pt(Ypy)_2(D_2O)(OD)]^+$. Les autres produits hydrolysés pour les complexes contenant des ligands sans substituent *ortho* ont été identifiés comme le dimère à double ponts-hydroxo, le dimère à simple pont-hydroxo, le trimère et probablement le tétramère. Les composés analogues *trans* ont montré deux signaux à pD acide, correspondant au monomère diaqua et au dimère aqua à pont-hydroxo. Deux espèces (le composé dihydroxo et le dimère hydroxo à pont-hydroxo) ont aussi été observées en milieu basique. À pD neutre, un troisième signal attribué à un oligomère ou polymère à pont-hydroxo a été détecté.

Mots clés : platine, pyridine, nitrato, hydrolyse, RMN, aquation.

Introduction

The antitumor drug cisplatin (*cis*-$Pt(NH_3)_2Cl_2$) is one of the most widely used in chemotherapy. The complex remains unchanged in the plasma, because of the large chloride concentration (103 mM), but inside the cells, where the pH is neutral and the chloride ion concentration is much lower (4 mM), its mechanism of action involves aquation or hydrolysis reactions. In these conditions, *cis*-$Pt(NH_3)_2Cl_2$ produces different ionic species, especially the aqua-chloro complex *cis*-$[Pt(NH_3)_2(OH_2)Cl]Cl$. The latter can either bind to DNA (1), leading to the eventual destruction of the cell, or react with water to produce diaqua species. In neutral pH, it will exist mainly in the form of the monoaqua-monohydroxo complex *cis*-$[Pt(NH_3)_2(OH)(OH_2)]^+$ (2). This compound can also bind to DNA (1). It has also been shown in laboratories to produce different oligomeric species, which have been characterized by ^{195}Pt NMR (3–5) and by crystallographic methods (6–10).

Received 2 October 2001. Published on the NRC Research Press Web site at http://canjchem.nrc.ca on 5 April 2002.

F.D. Rochon[1] and C. Tessier. Département de chimie, Université du Québec à Montréal, C.P. 8888, Succ. Centre-ville, Montréal, QE H3C 3P8 Canada.

[1]Corresponding author (e-mail: rochon.fernande@uqam.ca).

 DOI: 10.1139/V02-043 © 2002 NRC Canada

Table 1. ^{195}Pt chemical shifts (ppm) for the monomeric *cis* complexes and $\Delta_{dihydroxo-diaqua}$.

Ypy	pK_a (YpyH$^+$)	$[Pt(Ypy)_2(D_2O)_2]^{2+}$	$Pt(Ypy)_2(OD)_2$	$\Delta_{dihydroxo-diaqua}$	$[Pt(Ypy)_2(D_2O)(OD)]^+$
2,4-Lutidine	6.63	–1440	–1487	–47	–1497
3,5-Lutidine	6.15	–1542	–1525	17	–1524
4-Picoline	5.98	–1522	–1512	10	–1507
2-Picoline	5.96	–1456	–1494	–38	–1495
3-Picoline	5.63	–1525	–1517	8	–1520
Pyridine	5.22	–1514	–1505	10	–1507

Some of these compounds are toxic to humans and could be partially responsible for the toxicity of cisplatin. It is therefore important to study the hydrolysis reactions of a complex prior to its development as a drug.

Recently, our research group has undertaken a systematic study of complexes of the types *cis*- and *trans*-$Pt(Ypy)_2X_2$, where Ypy = pyridine derivative and X = Cl^-, I^-, and NO_3^-. Platinum complexes with pyridine derivatives are potent antitumor agents. The complex *trans*-$Pt(py)_2Cl_2$ (py = pyridine) is active towards Leukemia L1210 cells (11, 12), whereas *cis*-$Pt(NH_3)$(2-pic)Cl_2 (pic = picoline) is currently in clinical trials (13, 14). The compounds *cis*- and *trans*-$Pt(Ypy)_2X_2$, have been studied in our laboratories by various spectroscopic techniques and by crystallography (15, 16). We have characterized these well-known products to study their hydrolysis reactions. The solubility of the dichloro and the diiodo complexes in water is very low, but substitution of the halides by nitrato ligands leads to a greater aqueous solubility. We have now completed our spectroscopic aqueous solution study on the *cis*-dinitrato compounds and the results are reported below. We have also done a similar preliminary study on some *trans* compounds. These are more difficult to study, since the *trans*-dinitrato compounds are less soluble in water than their *cis* analogues. Only one study in the literature has been reported on a *trans* compound, i.e., *trans*-$Pt(NH_3)_2Cl_2$ (17).

Experimental

$K_2[PtCl_4]$ was purchased from Johnson–Matthey and was recrystallized in water before use. The pyridine derivatives were obtained from Aldrich, and silver nitrate was purchased from Analar. Deuterated chloroform was purchased from CDN Isotopes and methylene chloride-d_2 from MSD Isotopes.

The NMR spectra were measured on a Varian Gemini 300BB in D_2O. The fields were 300.075, 75.462, and 64.400 MHz for ^{1}H, ^{13}C, and ^{195}Pt, respectively. For the ^{195}Pt NMR spectra, $K_2[PtCl_4]$ (–1628 ppm in D_2O with KCl) was the external standard. The low-field ^{1}H NMR spectra were measured on a Varian EM-360L at 60 MHz. A V-2048 Signal Averager was used for the accumulations.

The pH values were measured on a Radiometer Copenhagen pH Meter, using a combined electrode Ag/AgCl (Fisher Scientific) at room temperature. For the pD values, the pH values were increased by 0.4 (18). The conductivity measurements were performed on a Radiometer Copenhagen model CDM2e instrument with a Radiometer No. CDC114 electrode.

The dinitrato complexes were prepared and characterized as reported in our recent publication (16).

The aquation or hydrolysis of the dinitrato complexes were studied in three different pH conditions. (*i*) The dinitrato compounds were dissolved in water or D_2O (pH ~2.0) and the ^{195}Pt, ^{1}H, and ^{13}C NMR spectra were directly measured. (*ii*) The pH of another fresh solution was adjusted to about 7 with NaOD and then the NMR spectra were immediately measured. (*iii*) The pH of a fresh solution of the dinitrato complex was adjusted to about 10.6 and then the NMR spectra were recorded. In a typical experiment, the dinitrato compound was dissolved in D_2O by heating in a hot-water bath. Immediately, the ^{195}Pt NMR spectrum was measured for about 1–3 h, the ^{1}H spectrum was then recorded for 30–60 min, and then the ^{13}C spectrum was measured overnight (~15 h). At neutral pH, where the number of species in solution is usually greater, the accumulation time was longer.

Results and discussion

The dinitrato complexes were prepared by the reaction of the diiodo complexes with a slight excess (10%) of silver nitrate in acetone (16).

$$[1] \quad Pt(Ypy)_2I_2 + 2AgNO_3 \rightarrow Pt(Ypy)_2(NO_3)_2 + 2\,AgI\downarrow$$

The reaction takes more than 24 h before observing a clear colorless solution of $Pt(Ypy)_2(NO_3)_2$ and a yellow silver iodide precipitate. Complexes with Ypy = py, 2-pic, 3-pic, 4-pic, 3,-5-lut, and 2,4-lut (lut = lutidine) were prepared and their aquation and hydrolysis reactions were studied at three different pH conditions: acidic, neutral, and basic.

cis-$[Pt(Ypy)_2(D_2O)_2]^{2+}$

When the *cis*-dinitrato compounds are dissolved in water or D_2O (~0.02 M), heating in a water bath is required for most samples, and the pH of the solution is acidic (pH = ~2.0 or pD = ~2.4).

$$[2] \quad cis\text{-}Pt(Ypy)_2(NO_3)_2 + 2D_2O \rightarrow cis\text{-}[Pt(Ypy)_2(D_2O)_2](NO_3)_2$$

The molar conductivity of the complexes were measured in water and varied between 233 and 264 S cm^2 mol^{-1}. These values correspond to the presence of three ions in solution and are close to those reported for *cis*-$[Pt(NH_3)_2(H_2O)_2](NO_3)_2$ (264 S cm^2 mol^{-1}) (19). These solutions (in D_2O) were characterized by multinuclear (^{195}Pt, ^{1}H, and ^{13}C) NMR spectroscopy.

The ^{195}Pt NMR spectra of these solutions show the presence of only one signal, corresponding to the diaqua species.

© 2002 NRC Canada

Table 2. ^{1}H chemical shifts (ppm), $^3J(^{195}Pt–^1H)$ coupling constants (Hz) ($\Delta\delta$, ppm), and [$\Delta\delta_{ave}$ ppb, see text] for the complexes *cis*-$[Pt(Ypy)_2(D_2O)_2](NO_3)_2$ and *cis*-$Pt(Ypy)_2(OD)_2$.

Complex	H_2	H_3	H_4	H_5	H_6	CH_3	$^3J(^{195}Pt–^1H)$ [$\Delta\delta_{av.}$]
$[Pt(2,4\text{-lut})_2(D_2O)_2]^{2+}$		7.321 (0.297)		7.136d (0.124)	8.648d (0.486)	2.380, 3.220 (0.113, 0.810)	46 [302]
$Pt(2,4\text{-lut})_2(OD)_2$		7.173 (0.149)		7.008d (–0.004)	8.704d (0.542)	2.286, 3.012 (0.019, 0.602)	41 [229]
$[Pt(3,5\text{-lut})_2(D_2O)_2]^{2+}$	8.327 (0.260)		7.639 (0.286)		8.327 (0.260)	2.257 (0.044)	46 [269]
$Pt(3,5\text{-lut})_2(OD)_2$	8.257 (0.190)		7.545 (0.192)		8.257 (0.190)	2.229 (0.016)	44 [191]
$[Pt(4\text{-pic})_2(D_2O)_2]^{2+}$	8.441d (0.111)	7.335d (0.083)		7.335d (0.083)	8.441d (0.111)	2.443 (0.093)	45 [97]
$Pt(4\text{-pic})_2(OD)_2$	8.378d (0.048)	7.202d (–0.050)		7.202d (–0.050)	8.378d (0.048)	2.349 (–0.001)	40 [–4]
$[Pt(2\text{-pic})_2(D_2O)_2]^{2+}$		7.488d (0.209)	7.830t (0.110)	7.306dd (0.077)	8.883d (0.533)	3.296 (0.814)	47 [232]
$Pt(2\text{-pic})_2(OD)_2$		7.348d (0.069)	7.696t (–0.024)	7.181t (–0.048)	8.924 (0.574)	3.112 (0.630)	41 [143]
$[Pt(3\text{-pic})_2(D_2O)_2]^{2+}$	8.545 (0.230)		7.821d (0.165)	7.374dd (0.063)	8.474d (0.182)	2.309 (0.003)	40 [160]
$Pt(3\text{-pic})_2(OD)_2$	8.475 (0.160)		7.723d (0.067)	7.256t (–0.055)	8.406d (0.114)	2.278 (–0.028)	40 [72]
$[Pt(py)_2(D_2O)_2]^{2+}$	8.697d (0.187)	7.521t (0.077)	8.015t (0.154)	7.521t (0.077)	8.697d (0.187)		41 [136]
$Pt(py)_2(OD)_2$	8.613d (0.103)	7.383dd (–0.061)	7.906t (0.045)	7.383dd (–0.061)	8.613d (0.103)		40 [26]

The chemical shifts of the complexes *cis*-$[Pt(2\text{-pic})_2(D_2O)_2]^{2+}$ and *cis*-$[Pt(2,4\text{-lut})_2(D_2O)_2]^{2+}$, which contain ligands with *ortho* substituents, are observed at lower fields (av. –1448 ppm) than the others (av. –1526 ppm), as shown in Table 1. Downfield chemical shifts of the complexes containing ligands with *ortho* substituents have already been observed for $[Pt(Ypy)Cl_3]^-$ (measured in D_2O) (20) and *cis*- and *trans*-$Pt(Ypy)_2(NO_3)_2$ (16). These downfield shifts have been assigned to the solvent effect, also called the *ortho* effect (21). For square-planar complexes, the solvent molecules can normally approach and weakly bind to the Pt atom on both sides of the coordination plane. For complexes containing pyridine with *ortho* substituents, the planar pyridine ligands are nearly perpendicular to the coordination plane (to reduce the steric hindrance with the *cis* ligands) and the *ortho* substituents are almost on top of the Pt atom. This conformation is particularly important in the *cis* geometry. The methyl groups located in the *ortho* positions thus prevent the approach of the solvent water molecules, resulting in a decrease of the electronic density around the Pt nucleus. Downfield ^{195}Pt NMR shifts were thus observed for $[Pt(2\text{-pic})Cl_3]^-$ (–1796 ppm) and $[Pt(2,6\text{-lut})Cl_3]^-$ (–1754 ppm) (measured in D_2O) compared with the $[Pt(Ypy)Cl_3]^-$ complexes with no *ortho* substituents (av. –1816 ppm) (20). Similar results were reported for *cis*- and *trans*-$Pt(2\text{-pic})_2(NO_3)_2$ complexes (16), which were measured in deuterated chloroform or dichloromethane, solvents which are not known to coordinate as easily to Pt as water. But the average environments around the Pt atom are different whether there is almost-free or limited rotation of the ligand around the Pt–N bond. These results are different from those observed for the complexes *cis*- and *trans*-$Pt(Ypy)_2I_2$, where Ypy = 2-pic and 2,4-lut (measured in $CDCl_3$) (15). The Pt signals of the latter complexes were reported at higher fields than the other analogues containing Ypy with no *ortho* substituent. Diaqua or dihydroxo complexes seem to behave like dinitrato complexes.

Several factors can be responsible for these different results. The solvent probably plays a very important role. Water, which can coordinate to platinum, may be responsible for the solvent effect discussed above. The charge on the complex might also be an important factor, but this is difficult to evaluate, since the ionic compounds are normally studied in D_2O, whereas the spectra of the neutral complexes are measured in organic solvents. Besides the presence of *ortho* substituents, the orientation of the pyridine ring is also influenced by the other ligands. Nitrato ligands are more bulky than monoatomic ligands, which might prevent the ap-

© 2002 NRC Canada

Table 3. ^{13}C chemical shifts, ($\Delta\delta$ ppm), $^{3}J(^{195}Pt–^{13}C)$ coupling constants (Hz), and [$\Delta\delta_{av.}$, ppm (see text)] for the complexes *cis*-$[Pt(Ypy)_2(D_2O)_2](NO_3)_2$ and *cis*-$Pt(Ypy)_2(OD)_2$.

Complex	C_2	C_3	C_4	C_5	C_6	CH_3	$^{3}J(^{195}Pt–^{13}C)$ [$\Delta\delta_{av.}$]
$[Pt(2,4\text{-lut})_2(D_2O)_2]^{2+}$	163.71	130.69	155.17	127.75	156.36	27.63, 22.57	n.o.[a]
	(5.67)	(5.47)	(5.45)	(4.86)	(8.17)	(4.13, 1.62)	[6.17]
$Pt(2,4\text{-lut})_2(OD)_2$	163.55	129.69	153.58	126.80	155.53	27.62, 22.48	n.o.[a]
	(5.51)	(4.47)	(3.86)	(3.91)	(7.34)	(4.12, 1.53)	[5.24]
$[Pt(3,5\text{-lut})_2(D_2O)_2]^{2+}$	152.56	140.13	145.15	140.13	152.56	19.78	42
	(6.41)	(5.37)	(5.50)	(5.37)	(6.41)	(1.72)	[6.11]
$Pt(3,5\text{-lut})_2(OD)_2$	152.46	138.97	142.82	138.97	152.46	19.76	44
	(6.31)	(4.21)	(3.17)	(4.21)	(6.31	(1.70)	[5.26]
$[Pt(4\text{-pic})_2(D_2O)_2]^{2+}$	154.61	130.63	157.23	130.63	154.61	22.93	42
	(3.82)	(2.73)	(4.94)	(2.73)	(3.82)	(0.00)	[3.28]
$Pt(4\text{-pic})_2(OD)_2$	154.45	129.86	154.37	129.86	154.45	22.85	42
	(3.66)	(1.96)	(2.08)	(1.96)	(3.66)	(–0.08)	[2.81]
$[Pt(2\text{-pic})_2(D_2O)_2]^{2+}$	164.96	130.16	143.26	126.83	156.21	28.03	n.o.[a]
	(6.56)	(5.67)	(5.13)	(4.89)	(7.51)	(4.74)	[5.81]
$Pt(2\text{-pic})_2(OD)_2$	164.57	129.10	141.02	125.81	156.39	27.97	n.o.[a]
	(6.17)	(4.61)	(2.89)	(5.13)	(7.69)	(4.68)	[5.08]
$[Pt(3\text{-pic})_2(D_2O)_2]^{2+}$	155.45	141.02	143.78	129.19	152.86	19.99	46 (C_5)
	(5.87)	(6.32)	(5.58)	(4.69)	(6.42)	(1.59)	[5.64]
$Pt(3\text{-pic})_2(OD)_2$	155.32	139.78	142.15	128.44	152.54	19.98	45
	(5.74)	(5.08)	(3.95)	(3.95)	(6.10)	(1.58)	[4.93]
$[Pt(py)_2(D_2O)_2]^{2+}$	155.81	129.98	141.59	129.98	155.81		45
	(6.38)	(4.98)	(3.72)	(4.98)	(6.38)		[5.29]
$Pt(py)_2(OD)_2$	155.45	129.15	141.59	129.15	155.45		42
	(6.02)	(4.15)	(3.75)	(4.15)	(6.02)		[4.82]

[a]n.o. = Not observed.

proach of the molecules of solvent to a much greater extent than the Cl^- or I^- ligands. The Pt–O bonds are shorter than Pt–I bonds, which would enhance the effect. Free rotation around the Pt–N bonds is much more limited in the complexes containing two 2-pic and 2,4-lut ligands than in the other compounds, especially in the *cis* geometry. The crystal structure determination of *cis*-$Pt(2\text{-pic})_2(NO_3)_2$ has shown that the two nitrato ligands are on opposite sides of the Pt plane and that the methyl groups of the 2-picoline ligands are in *anti* positions with respect to each other (16). This is the least sterically demanding conformation of the molecules. No rotamers were observed in solution. The NMR spectra of the 2-pic and 2,4-lut diaqua complexes (similar to the dinitrato complexes) could, therefore, correspond to one conformer, while almost-free rotations around the Pt–N and Pt–O bonds could be present in the other complexes.

To study the nature of the Pt–Ypy bond, attempts have been made in the literature (15, 16, 20, 21) to correlate the ^{195}Pt chemical shifts with the basicity of the pyridine ligands. Pyridine possesses empty π^* orbitals, which could accept electron density from the metal. In addition to the $\sigma(Ypy\rightarrow Pt)$ bond, $\pi(Pt\rightarrow Ypy)$ back-donating bonding could, therefore, be present. In the formation of the $\sigma(Ypy\rightarrow Pt)$ bond, electronic density is transferred from the pyridine ligands to the platinum nucleus, resulting in a shielding effect on the ^{195}Pt nucleus and a deshielding on the ligands (^1H and ^{13}C signals). The presence of $\pi(Pt\rightarrow Ypy)$ bonding would lead to the opposite effect. For complexes of the type $[Pt(Ypy)Cl_3]^-$, which were measured in D_2O, the correlation $\delta(^{195}Pt)$–pK_a was not observed because the solvent effect is a much greater factor, especially in water (20). For these ionic complexes, the $\delta(^{195}Pt)$ was related to the presence of substituents in *ortho* positions on the pyridine ligand. In the case of the compounds *cis*-$Pt(Ypy)(DMSO)Cl_2$, *cis*-$[Pt(Ypy)(DMSO)_2Cl]^+$, and *cis*-$[Pt(Ypy)_2(DMSO)Cl]^+$, a $\delta(^{195}Pt)$–pK_a correlation was reported, but only for complexes containing *para* substituents on Ypy (21). The latter DMSO complexes were measured in DMSO, a coordinating solvent. A weak relation between $\delta(^{195}Pt)$ and the basicity of the ligands was reported for complexes of the type $Pt(Ypy)_2X_2$ (X = Cl^- or I^- measured in $CDCl_3$) (15), but the dispersion around the straight line was fairly large. For the dinitrato complexes, the ^{195}Pt chemical shifts (in $CDCl_3$) seem to depend more on the position of the CH_3 substituents than on the basicity of the ligand (16). For the diaqua complexes, except for the 2-pic and 2,4-lut complexes, where the *ortho*-solvent effect is important, the ^{195}Pt chemical shifts seem to vary slightly with the basicity (22) of the protonated ligands

© 2002 NRC Canada

Table 4. $\delta(^{195}Pt)$ of the different aqueous products of the *cis* complexes.

Complex	2-Picoline	2,4-Lutidine	3,5-Lutidine	4-Picoline	3-Picoline	Pyridine
$[PtL_2(D_2O)_2]^{2+}$	–1456	–1440	–1542	–1522	–1525	–1514
$PtL_2(OD)_2$	–1494	–1487	–1525	–1512	–1517	–1507
$[PtL_2(D_2O)(OD)]^+$	–1495	–1497	–1524	–1507	–1520	–1507
$[PtL_2(D_2O)(\mu\text{-}OD)PtL_2(OD)]^{2+}$			–1456	–1454	–1463	–1453
$[PtL_2(\mu\text{-}OD)]_3^{3+}$			–1426	–1421	–1436	–1431
$[PtL_2(\mu\text{-}OD)]_4^{4+}$					–1386	–1388
$[PtL_2(\mu\text{-}OD)]_2^{2+}$				–1130	–1142	–1121
Other peak					–1080	–1056
Other peak						–1249

(Table 1), although the differences in chemical shifts are small and the errors fairly large (~5 ppm).

Our δ(Pt) values (–1440 to –1542 ppm) correlate well with the reported value for the *cis*-$Pt(NH_3)_2$ analogue (–1584 ppm (23)), and are at lower field than those reported for primary amine complexes (e.g., –1721 ppm for $EtNH_2$ (24)) and at much lower fields than those reported for ethylenediamine and its derivatives (–1867 to –1999 ppm) (25, 26). Complexes containing bidentate ligands are known to produce signals at much higher fields than those containing monodentate ligands.

The ^{1}H NMR chemical shifts of the diaqua complexes are listed in Table 2, as well as the $^3J(^{195}Pt–^1H)$ coupling constants and the Δδ values ($\delta_{complex} - \delta_{free\ ligand}$). The Δδ values are all positive, showing a net decrease of electron density on the ligands upon coordination. No relation could be found with the pK_a values of the protonated ligands, probably because the ligands are too different. $\Delta\delta_{av.}$ was also calculated using all the Δδ values except those of the methyl groups. This value is shown in square brackets in Table 2. If we exclude the 4-picoline complex, a linear relationship was found between $\Delta\delta_{av.}$ and the pK_a values (r^2 = 0.947), suggesting that the σ bond is very important in these complexes.

The $^3J(^{195}Pt–^1H)$ coupling constants vary between 40 and 47 Hz and agree well with the reported values for *cis*-$Pt(Ypy)_2Cl_2$ (40–44 Hz (15)), *cis*-$Pt(Ypy)_2I_2$ (40–43 Hz (15)), and *cis*-$Pt(Ypy)_2(NO_3)_2$ (40–47 Hz (16)). These are usually larger than those in the corresponding *trans* isomers (15, 16). For the 2-pic and 2,4-lut complexes, the $^4J(^{195}Pt–^1H)$ coupling constants with the *ortho* methyl group were measured as 13 and 11 Hz, respectively.

The ^{13}C NMR chemical shifts, the Δδ values ($\delta_{complex} - \delta_{free\ ligand}$), and the $^3J(^{195}Pt–^{13}C)$ coupling constants are listed in Table 3. The fact that Δδ is always positive indicates a net decrease of electron density on the bonded pyridine ligand compared with the free pyridine derivative. The σ(Ypy→Pt) bond seems to be much more important than the π(Pt→Ypy) back donation, if the latter is present. It is not possible to choose a valid probe in ^{13}C NMR to find a correlation between Δδ and the basicity of the protonated ligands, since local effects caused by the presence of the methyl substituents are too important. If we exclude the 4-pic complex, which seems to behave differently, the $\Delta\delta_{av.}$ for the ring C atoms (neglecting those which have a methyl substituent) is directly related to the pK_a of the protonated ligand (r^2 = 0.925). The calculated values of $\Delta\delta_{av.}$ are shown in Table 3. These results seem to confirm that the σ(Ypy→Pt) bond is very important in these complexes and that the π-backdonating component is more limited.

The $^3J(^{195}Pt–^{13}C)$ coupling constants vary between 42 and 46 Hz. These values compare well with the values reported for *cis*-$Pt(Ypy)_2Cl_2$ (41–45 Hz (15)), *cis*-$Pt(Ypy)_2I_2$ (40–45 Hz (15)), and *cis*-$Pt(Ypy)_2(NO_3)_2$ (41–48 Hz (16)). The $^2J(^{195}Pt–^{13}C)$ coupling constants were not observed, as reported for other similar compounds, probably because of inadequate orientation of the orbitals (16, 20).

cis-$Pt(Ypy)_2(OD)_2$

When the pH of the diaqua complex is raised with NaOD to about 10.6, the dihydroxo species are formed. The ^{195}Pt NMR spectra of these solutions show the presence of a single signal. The chemical shifts of the complexes *cis*-$Pt(2\text{-}pic)_2(OD)_2$ and *cis*-$Pt(2,4\text{-}lut)_2(OD)_2$, which contain ligands with *ortho* substituents, are observed at slightly lower fields (av. –1491 ppm) than the others (av. –1515 ppm), as shown in Table 1. The signals of the dihydroxo complexes are observed at slightly lower fields than the corresponding diaqua compounds (Δδ ($\delta_{dihydroxo}$-δ_{diaqua}) = 8 to 17 ppm), except for the ligands 2-pic and 2,4-lut. For these *ortho*-substituted ligands, the dihydroxo complexes were observed at higher fields than the diaqua compounds (Δδ = –38 and –47 ppm, respectively). In the literature, the reported values on similar complexes show that the dihydroxo complexes are observed at slightly lower fields than the corresponding diaqua species. For *cis*-$Pt(NH_3)_2(OD)_2$, the δ(Pt) is –1572 ppm (23) (Δδ = 12 ppm), whereas for *cis*-$Pt(C_2H_5NH_2)_2(OD)_2$, the δ(Pt) is –1695 ppm (24) (Δδ = 26 ppm). The results on the 2-pic and 2,4-lut complexes are clearly different from all the published values for dihydroxo and diaqua species. The explanation must come from the presence of the *ortho* substituent.

The shielding of a heavy atom like the ^{195}Pt nucleus has been expressed in the Ramsey equation, which contains some C terms representing the metallic coefficients of the platinum *d* orbitals. A more covalent bond will result in a decrease in the C terms and hence a shielding of the ^{195}Pt signals. D_2O is a more polarizable molecule than OD^-, leading to a more covalent Pt–OD_2 bond (in the diaqua system) compared with the Pt–OD bond in the dihydroxo complex. A greater covalency leads to a reduction of the C terms on the Pt atom and, therefore, an increase in the shielding in the Ramsey equation. The diaqua compounds should, therefore, be observed at higher fields than the dihydroxo complexes,

© 2002 NRC Canada

Fig. 1. Structures of the different *cis*-oligomeric species.

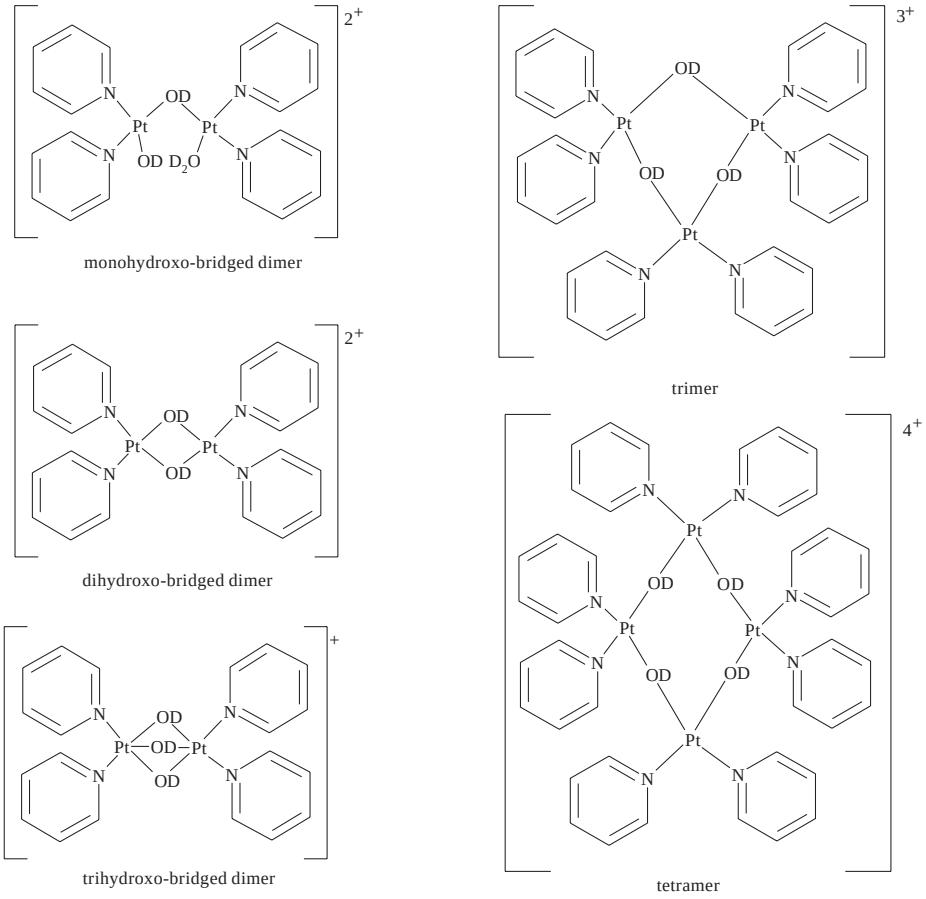

as observed in the literature and in our complexes, except for the ligands 2-pic and 2,4-lut. For the latter complexes, the *ortho* effect is probably a much greater factor. This behavior has not yet been reported in the literature. The solvent effect might also be quite different for an ionic complex like *cis*-$[Pt(Ypy)_2(D_2O)_2]^{2+}$ and for a neutral compound such as *cis*-$Pt(Ypy)_2(OD)_2$. The possibility that the *cis* compound containing 2-pic and 2,4-lut could isomerize to the *trans* complex in basic medium is not confirmed by the coupling constants observed in ^1H and ^{13}C NMR. These constants are usually smaller in the *trans* configuration (15, 16). Furthermore, the *trans* isomers with amines are usually observed at lower fields than the corresponding *cis* compounds.

The ^1H NMR spectra of the dihydroxo complexes are shown in Table 2. Similar to the diaqua species, a linear relationship was found between the $\Delta\delta_{av.}$ (in square brackets) and the pK_a values ($r^2 = 0.965$), except for the 4-picoline complex. The signals of the dihydroxo complexes are found at higher fields than the corresponding diaqua species, as seen by the smaller $\Delta\delta_{av.}$ values calculated for the dihydroxo compounds. The $^3J(^{195}Pt–^1H)$ coupling constants vary between 40 and 44 Hz and agree well with those observed for the diaqua complexes and those already reported and mentioned above (15, 16). For the 2-pic and 2,4-lut complexes, the $^4J(^{195}Pt–^1H)$ coupling constants with the *ortho*-methyl group are 11 Hz.

The ^{13}C NMR spectra of the dihydroxo complexes are shown in Table 3. The signals were observed at higher fields than those of the corresponding diaqua compounds (smaller $\Delta\delta_{av.}$ values for the dihydroxo compounds). Similar to the diaqua species, a linear relationship was found between the $\Delta\delta_{av.}$ (in square brackets) and the pK_a values ($r^2 = 0.952$), except for the 4-picoline complex. The $^3J(^{195}Pt–^{13}C)$ coupling constants vary between 42 and 45 Hz. They compared well with the values discussed above. The $^2J(^{195}Pt–^{13}C)$ coupling constants were not observed.

Hydrolysis of the *cis* complexes in neutral pH

The hydrolysis reactions were also studied in neutral medium. The dinitrato compounds were dissolved in D_2O (by heating in hot water) and the pH of the solution was raised with NaOD (1 M) to ca. 6.6 (pD = 7.0). The ^{195}Pt NMR spectra of these fresh solutions were immediately recorded. For most of the complexes, the spectra show several species in solution. These spectra were recorded using long accumulation times to reduce the background, but it was still quite significant. The presence of several peaks led to difficulties in the phase adjustment, and therefore, the determined proportion for each species is approximate, especially for the low-intensity signals.

The number of species seems to vary with the bulkiness of the ligand. For the most sterically hindered ligands, 2-pic and 2,4-lut, only one signal was observed, assigned to the

© 2002 NRC Canada

Fig. 2. Structure of the *trans*-diaqua dimer.

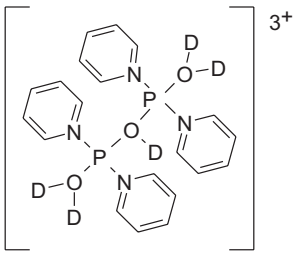

monoaqua–monohydroxo complex, *cis*-$[Pt(Ypy)_2(D_2O)(OD)]^+$, which is probably in equilibrium with some diaqua and dihydroxo species. For the 3,5-lut complex, two signals were observed at –1524 (80%) and –1426 (20%) ppm, while four peaks were found at –1507 (65%), –1454 (13%), –1421 (13%), and –1130 (9%) ppm for the for 4-pic compound. For the 3-pic complex, five signals were observed at –1520 (25%), –1463 (10%), –1436 (30%), –1386 (20%), and –1142 (15%) ppm. For the least sterically demanding ligand, pyridine, seven signals were observed at –1507 (25%), –1453 (30%), –1431 (10%), –1388 (10%), –1249 (5%), –1121 (5%), and –1056 (15%) ppm. These results are summarized in Table 4.

Our assignments for the different signals are based on published results for amine complexes, especially for the *cis*-$Pt(NH_3)_2$ system. The signals at highest field (–1496 ppm (av.) for the 2-pic and 2,4-lut complexes and at –1515 ppm (av.) for the other ligands) were assigned to the monoaquamohydroxo complex, *cis*-$[Pt(Ypy)_2(D_2O)(OD)]^+$. The next peak observed at an average value of –1457 ppm was assigned to the monohydroxo-bridged dimer *cis*-$[Pt(Ypy)_2(D_2O)(\mu\text{-}OD)Pt(Ypy)_2(OD)]^{2+}$ (see structure in Fig. 1), which is probably in equilibrium with its diaqua species *cis*-$[Pt(Ypy)_2(D_2O)(\mu\text{-}OD)Pt(Ypy)_2(D_2O)]^{3+}$ (or its dihydroxo analogue). This dimer was observed at 69 ppm (av.) from the *cis*-$[Pt(Ypy)_2(D_2O)_2]^{2+}$ species. A similar dimer has been reported (23) at –1547 ppm for *cis*-$[Pt(NH_3)_2(D_2O)(\mu\text{-}OD)Pt(NH_3)_2(D_2O)]^{3+}$, and at 47 ppm from the diaqua monomer *cis*-$[Pt(NH_3)_2(D_2O)_2]^{2+}$. The next signal observed at an average value of –1429 ppm (located at 97 ppm (av.) for the diaqua species) was attributed to the hydroxo-bridged cyclic trimer *cis*-$[Pt(Ypy)_2(\mu\text{-}OD)]_3^{3+}$ (Fig. 1). The corresponding trimer in the *cis*-$Pt(NH_3)_2$ system was observed at 74 ppm from the diaqua species (5). Crystal structures of the *cis*-$Pt(NH_3)_2$ trimer have been published (8, 9). The peak at –1387 ppm (139 ppm for the diaqua species), only observed with 3-pic and py, was assigned to the hydroxo-bridged cyclic tetramer, *cis*-$[Pt(Ypy)_2(\mu\text{-}OD)]_4^{4+}$. This species has not been reported in the literature for Pt–monodentate amine complexes, but it has been observed with ethylenediamine. The crystal structure of the Pt(en) tetramer has been published (27). The signal of the latter was reported at 202 ppm (26) from the diaqua species, but the $\Delta\delta$ are much larger in the Pt–bidentate systems. Another signal observed at much lower fields (av. –1131 ppm, at 395 ppm from the diaqua species) was assigned to the dihydroxo-bridged dimer *cis*-$[Pt(Ypy)_2(\mu\text{-}OD)]_2^{2+}$. In the *cis*-$Pt(NH_3)_2$ system, this dimer was observed at 423 ppm from the diaqua complex (3, 5). The crystal structures of several compounds of this type have been published (6, 7, 10). The chemical shifts for these species are found at much lower fields than the other compounds mentioned above because of the important strain of the four-membered ring. All of these structures are shown in Fig. 1. For pyridine, two other signals at –1249 and at –1056 ppm were observed (265 and 451 ppm from the diaqua compound). The origin of these resonances is not known. No such low field signal has been reported with monodentate amines. The only suggestion from the literature for a signal at such a low field was made for a trihydroxo-bridged dimer with bipyridine $[Pt(bipy)(\mu\text{-}OD)_3Pt(bipy)]^+$, as shown on Fig. 1. This signal was reported at 458 ppm from the dihydroxo species, but the authors could not confirm its structure. The color of this trihydroxo-bridged dimer (28) is red and our solution was colorless, but the red colour is probably associated with the presence of bipyridine. In a publication on the Pt(en) system (26), a signal was observed at very low field (636 ppm from $[Pt(en)(D_2O)_2]^{2+}$). The $\Delta\delta$ values are much larger for bidentate systems. The authors were unable to identify this peak, and we suggest that our signal observed at –1056 ppm for pyridine might have the same origin.

Table 5. $\delta(^{195}Pt)$ of the different aqueous products of the *trans* complexes.

Complex	Pyridine	3-Picoline
$[PtL_2(D_2O)_2]^{2+}$	–1425	–1430
$PtL_2(OD)_2$	–1478	–1473
$[PtL_2(D_2O)(OD)]^+$	–1474	–1471
$[PtL_2(D_2O)(\mu\text{-}OD)PtL_2(D_2O)]^{3+}$	–1319	–1308
$[PtL_2(OD)(\mu\text{-}OD)PtL_2(OD)]^+$	–1373	–1365
$[PtL_2(D_2O)(\mu\text{-}OD)PtL_2(OD)]^{2+}$	–1369	–1360
$[PtL_2(D_2O \text{ or } OD)(\mu\text{-}OD)]_n^+$	–1355	–1344

The ^{195}Pt NMR spectrum of the 3,5-lut complex dissolved in D_2O (neutral pH) was remeasured after one year. Three signals were observed, including a new species at –1456 ppm (15%), which was assigned to the presence of the monohydroxo-bridged dimer, that was not present in the fresh solution. The two other signals were observed at –1524 (*cis*-$[Pt(3,5\text{-}lut)_2(D_2O)(OD)]^+$, 75%), and –1426 ppm (*cis*-$[Pt(Ypy)_2(\mu\text{-}OD)]_3^{3+}$, 10%). The spectrum of the 3-pic complex was also measured after standing in D_2O for one year. Four species were observed at –1520 (20%), –1436 (35%), –1386 (15%), and a new peak at –1080 ppm (30%). The monohydroxo-bridged dimer and the cyclic dihydroxo-bridged dimer were no longer present. These results are listed in Table 4 along with their assignments.

The ^1H and ^{13}C NMR spectra of these solutions were measured, but could not be interpreted due to the great numbers of overlapping species. They are, therefore, not presented in this paper.

Study of the *trans* isomers

A similar study was attempted on the *trans* complexes. These compounds are much more difficult to dissolve than their *cis* analogues and heating in a water bath for a long time is required. Because of the aqueous insolubility of the other compounds, only the pyridine and the 3-picoline platinum complexes could be studied. In acidic media, two sig-

© 2002 NRC Canada

nals were observed at –1425 (~65%) and –1319 ppm for pyridine and at –1430 (~65%) and –1308 ppm for the 3-picoline compound. In basic media, one strong signal was observed at –1478 ppm for pyridine and at –1473 ppm for 3-picoline. There was also a second weaker signal (~10%) at slightly lower fields, –1373 and –1365 ppm, respectively. The most intense signals observed at higher fields probably correspond to the diaqua (acidic pD) and the dihydroxo species (basic pD), whereas the weaker signals have not been identified with certainty. These weaker signals are not, however, caused by a nitrato species (dinitrato, monoaqua-mononitrato, or monohydroxo-mononitrato), since the same two peaks (with identical intensities) were observed when the counter anions were changed to perchlorate, which are not known to coordinate to Pt in aqueous medium. The lower field peaks might be caused by the presence of the hydroxo-bridged dimers *trans*-$[Pt(D_2O)(Ypy)_2(\mu\text{-}OD)Pt(Ypy)_2(D_2O)]^{3+}$ (acidic pD) and *trans*-$[Pt(OD)(Ypy)_2(\mu\text{-}OD)Pt(Ypy)_2(OD)]^{+1}$ (basic pD) (Fig. 2). The study on the *trans*-$Pt(NH_3)_2$ system (17) shows only the presence of the diaqua species at low pH and the dihydroxo compound at high pH. At pH = 4 a second signal, assigned to the dimer $[\{trans\text{-}Pt(H_2O)(NH_3)_2\}_2(\mu\text{-}OH)]^{3+}$ was reported, while at pH = 9 the corresponding hydroxo compound $[\{trans\text{-}Pt(OH)(NH_3)_2\}_2(\mu\text{-}OH)]^{3+}$ was observed by Appleton et al. (17).

At neutral pD, our compounds showed the presence of three species at –1474 (65%), –1369 (30%), and –1355 (5%) ppm for the pyridine compound, and at –1471 (50%), –1360 (45%), and –1344 (5%) ppm for the 3-picoline complex. The higher-field signals correspond to the *trans*-$[Pt(Ypy)_2(D_2O)(OD)]^+$ compounds (in equilibrium with the diaqua and the dihydroxo species), the intermediate field signals correspond to the monohydroxo-bridged dimers (as discussed above), and the lower field signals probably correspond to the longer hydroxo-bridged oligomers or polymers, *trans*-$[Pt(Ypy)_2(D_2O \text{ or } OD)(\mu\text{-}OH)]_n^{n+}$, which could be cyclic or linear. For the $Pt(NH_3)_2$ system, Appleton et al. (17) have isolated a solid that formed after the solution was allowed to stand at pH = 5–6. The authors have formulated the solid as hydroxo-bridged polymeric cations, $[\{trans\text{-}Pt(\mu\text{-}OH)(NH_3)_2\}_n]^{n+}$ (the fourth ligand is probably H_2O or OH^-), which could be linear or cyclic. In our fresh solutions these polymers seem to be present in very small amounts (about 5%).

When the pyridine products in solution were remeasured after 7 months, the same three signals were observed, but the proportions of the three compounds were different: 20% for the monomer, 50% for the dimer, and 30% for the polymer.

Conclusion

When the complexes *cis*-$Pt(Ypy)_2(NO_3)_2$ were dissolved in D_2O, the diaqua complexes were observed in acidic media, while hydrolysis occurs in basic pH to produce the dihydroxo compounds. In ^{195}Pt NMR spectroscopy, the complexes containing the ligands 2-pic and 2,4-lut behave differently because of the *ortho* effect, which is probably a solvent effect. In acidic pH, monoaqua–mononitrato species were not detected, contrary to the results reported on the *cis*-$Pt(NH_3)_2$ system.

At neutral pH, several species can be observed. The δ(Pt) values of the different products are summarized in Table 5. The number of species depends on the bulkiness of the pyridine ligand. For the *ortho*-substituted ligands, only one complex is formed in solution, while for the least bulky ligand (pyridine), up to seven species were observed. The number and the structure of these species vary with time. The monoaqua–monohydroxo compound is the most important complex in fresh solutions. Different oligomeric ionic species are also formed, i.e., dihydroxo-bridged dimers, monohydroxo-bridged dimers, cyclic trimers, and probably cyclic tetramers. Two other unassigned signals were observed at lower fields. Attempts to crystallize these species were not successful.

The species in solution vary slightly with concentration and the time of heating to dissolve the dinitrato complexes. These complexes are not very soluble and must be heated in hot water before dissolving; it was difficult to reproduce the exact experimental conditions of sample preparation. Furthermore, there was, sometimes, a residue at the bottom of the NMR tube after the experiment was completed; therefore, there were some variations in the proportions of each species when the experiments were repeated.

The *trans* compounds are less soluble than the *cis* analogues and only the pyridine and 3-picoline complexes were studied. In acidic pH, the diaqua and the aqua monohydroxo-bridged dimer were observed, while at high pH, the dihydroxo monomer and the hydroxo monohydroxo-bridged dimer were identified. At neutral pH, a third signal assigned to a hydroxo-bridged cyclic or linear polymer was observed.

Acknowledgments

The authors are grateful to the Natural Sciences and Engineering Research Council of Canada (NSERC) for financial support of the project and for a scholarship to C.T.

References

1. S.E. Miller and D.A. House. Inorg. Chim. Acta, **173**, 53 (1990).
2. M.J. Cleare and J.D. Hoeschele. Bioinorg. Chem. **2**, 187 (1974).
3. B. Rosenberg. Biochimie, **60**, 859 (1978).
4. B. Rosenberg. Cancer Chemother. Rep. **63**, 1433 (1979).
5. C.J. Boreham, J.A. Broomhead, and D.P. Fairlie. Aust. J. Chem. **34**, 659 (1981).
6. R. Faggiani, B. Lippert, C.J.L. Lock, and B. Rosenberg. J. Am. Chem. Soc. **99**, 777 (1977).
7. B. Lippert, C.J.L. Lock, B. Rosenberg, and M. Zvagulis. Inorg. Chem. **17**, 2971 (1978).
8. R. Faggiani, B. Lippert, C.L.J. Lock, and B. Rosenberg. Inorg. Chem. **16**, 1192 (1977).
9. R. Faggiani, B. Lippert, C.L.J. Lock, and B. Rosenberg. Inorg. Chem. **17**, 1941 (1978).
10. J.A. Stanko, L.S. Hollis, J.A. Schreifels, and J.D. Hoeschele. J. Clin. Hematol. Oncol. **7**, 138 (1977).
11. N. Farrell, T.T.B. Ha, J.-P. Souchard, F.L. Wimmer, S. Cros, and N.P. Johnson. J. Med. Chem. **32**, 2240 (1989).
12. M.V. Beusichem and N. Farrell. Inorg. Chem. **31**, 634 (1992).
13. Y. Chen, Z. Guo, J.A. Parkinson, S. Parsons, and J.P. Sadler. Chem. Eur. J. **4**, 672 (1998).
14. J. Holford, F. Raynuad, B.A. Murrer, K. Grimaldi, J.A. Hartley, M. Abrams, and L.R. Kelland. Anti-Cancer Drug Des. **13**, 1 (1998).
15. C. Tessier and F.D. Rochon. Inorg. Chim. Acta, **195**, 25 (1999).

© 2002 NRC Canada

16. C. Tessier and F.D. Rochon. Inorg. Chim. Acta, **322**, 37 (2001).
17. T.G. Appleton, A.J. Bailey, K.G. Barnham, and J.R. Hall. Inorg. Chem. **31**, 3077 (1992).
18. P.K. Glasoe and F.A. Long. J. Phys. Chem. **64**, 188 (1960).
19. B. Lippert, C.J.L. Lock, B. Rosenberg, and M. Zvagulis. Inorg. Chem. **16**, 1525 (1977).
20. F.D. Rochon, A.L. Beauchamp, and C. Bensimon. Can. J. Chem. **74**, 2121 (1996).
21. L.G. Marzilli, Y. Hayden, and M.D. Reily. Inorg. Chem. **25**, 974 (1986).
22. D.D. Perrin. Dissociation of organic bases in aqueous solution. Butterworths, New York. 1965. pp.140–183.
23. T.G. Appleton, R.D. Berry, C.A. Davis, J.R. Hall, and H.A. Kimlin. Inorg. Chem. **23**, 3514 (1984).
24. S. Al-Baker and J.C. Dabrowiak. Inorg. Chem. **26**, 613 (1987).
25. F.D. Rochon and A. Morneau. Mag. Res. Chem. **29**, 120 (1991).
26. F.D. Rochon and A. Morneau. Mag. Res. Chem. **30**, 697 (1992).
27. F.D. Rochon, A. Morneau, and R. Melanson. Inorg. Chem. **27**, 10 (1988).
28. S. Wimmer, P. Castan, F.L. Wimmer, and N.P. Johnson. J. Chem. Soc. Dalton Trans. 403 (1989).

© 2002 NRC Canada

Size and temperature dependence of hydrocarbon solubility in concentrated aqueous solutions of urea and guanidine hydrochloride

Giuseppe Graziano

Abstract: At 25°C, methane and ethane are more soluble in water than in 7 M aqueous urea or 4.9 M aqueous guanidine hydrochloride (GuHCl); the reverse is true for larger hydrocarbons. In addition, the hydrocarbon solubility in 7 M aqueous urea or 4.9 M aqueous GuHCl increases compared with that in water on raising the temperature in the range of 5–45°C. These experimental data have not yet been rationalized. Using a well-founded theory of hydrophobic hydration, the present analysis indicates that the transfer of hydrocarbons from water to 7 M aqueous urea or to 4.9 M aqueous GuHCl is favored by the difference in the solute–solvent van der Waals interaction energy, and contrasted by the difference in the work of cavity creation. At room temperature, on increasing the hydrocarbon size, the first contribution rises in magnitude more rapidly than the second contribution, accounting for the threshold size occurrence. Moreover, the second contribution decreases in magnitude with an increase in temperature, becoming less unfavorable, while the first contribution is practically constant in the range of 5–45°C. The different temperature dependence of the work of cavity creation in such solvent systems is due to the fact that the density of 7 M aqueous urea and 4.9 M aqueous GuHCl decreases more rapidly than that of water when raising the temperature. The relationship between the density of a liquid and the work to create a cavity in it is discussed in detail.

Key words: work of cavity creation, solute–solvent van der Waals interaction energy, H-bond reorganization.

Résumé : À 25°C, le méthane et l'éthane sont plus solubles dans l'eau que dans des solutions aqueuses 7 M d'urée ou 4,9 M de chlorhydrate de guanidine, GuHCl; l'inverse est vrai pour les hydrocarbures à plus longues chaînes. De plus, dans l'intervalle de température allant de 5 à 45°C, une augmentation de la température provoque une augmentation de la solubilité des hydrocarbures dans des solutions aqueuses 7 M d'urée ou 4,9 M de GuHCl augmentent par rapport à celle dans l'eau. De telles données expérimentales n'ont pas été rationalisées jusqu'à maintenant. En se basant sur la théorie bien fondée de l'hydratation hydrophobe, l'analyse présentée ici indique que le transfert des hydrocarbures de l'eau vers des solutions aqueuses 7 M d'urée ou 4,9 M de GuHCl est favorisé par la différence d'énergie d'interaction de van des Waals soluté-solvant et que ceci est en opposition avec la différence dans le travail de création de la cavité. À la température ambiante, une augmentation de la taille de l'hydrocarbure, l'amplitude de la première contribution augmente plus rapidement que la seconde, ce qui explique l'existence du seuil de taille. De plus, l'amplitude de la deuxième contribution diminue avec la température, ce qui la rend moins favorable, alors que la première contribution est pratiquement constante dans l'intervalle de température de 5 à 45°C. Les différences dans la relation du travail de création d'une cavité avec la température, dans de tels systèmes de solvant, résulte du fait qu'une augmentation de la température s'accompagne d'une diminution plus rapide de la densité des solutions aqueuses 7 M d'urée ou 4,9 M de GuHCl que celle de l'eau. On discute en détail de la relation entre la densité d'un liquide et le travail de création d'une cavité.

Mots clés : travail de création d'une cavité, énergie d'interaction de van der Waals soluté-solvant, réorganisation des liaisons hydrogènes.

[Traduit par la Rédaction]

Introduction

About forty years ago, Wetlaufer et al. (1) determined the molar solubility of seven hydrocarbons (i.e., the first six compounds of the aliphatic series and toluene) in water, 7 M aqueous urea, and 4.9 M aqueous guanidine hydrochloride (GuHCl) over the temperature range 5–45°C. The Ben-Naim standard Gibbs energy change upon transfer from water to 7 M urea or to 4.9 M GuHCl is simply calculated from the relation (2)

$$[1] \qquad \Delta G^{\bullet} = RT \ln [C(H_2O)/C(\text{mix})]$$

where $C(H_2O)$ and C(mix) are the molar concentrations in water and in the mixed solvent system, respectively, and the filled circle denotes the Ben-Naim standard. The use of the Ben-Naim standard is strongly recommended because $\Delta G^{\bullet}$ is

Received 4 July 2001. Published on the NRC Research Press Web site at http://canjchem.nrc.ca on 8 April 2002.

G. Graziano. Dipartimento di Chimica, Università di Napoli "Federico II," Complesso Universitario di Monte S.Angelo, Via Cinthia, 45 – 80126 Napoli, Italy and Facoltà di Scienze, Università del Sannio, Via Port'Arsa, 11 – 82100 Benevento, Italy. (e-mail: graziano@chemistry.unina.it and graziano@unisannio.it).

 DOI: 10.1139/V02-041 © 2002 NRC Canada

Table 1. Ben-Naim standard Gibbs energy, enthalpy and entropy changes associated with the transfer of the seven hydrocarbons from water to 7 M urea; data from ref. 1.

	T (°C)	$\Delta G^{\bullet}$ (kJ mol^{-1})	$\Delta H^{\bullet}$ (kJ mol^{-1})	$\Delta S^{\bullet}$ (J K^{-1}mol^{-1})
CH_4	5	1.2		
σ = 3.70 Å	25	0.8	5.4	15.3
ASA = 152 Å^2	45	0.6		
C_2H_6	5	1.0		
σ = 4.38 Å	25	0.4	8.2	26.4
ASA = 192 Å^2	45	0		
C_3H_8	5	0.5		
σ = 5.06 Å	25	–0.1	7.2	24.3
ASA = 223 Å^2	45	–0.4		
i-C_4H_{10}	5	0.1		
σ = 5.55 Å	25	–0.5	6.5	23.3
ASA = 249 Å^2	45	–0.9		
n-C_4H_{10}	5	0.2		
σ = 5.65 Å	25	–0.5	7.8	27.8
ASA = 255 Å^2	45	–0.9		
$C(CH_3)_4$	5	0.3		
σ = 5.89 Å	25	–0.7	7.2	26.5
ASA = 270 Å^2	45	–1.2		
Toluene	5	–1.1		
σ = 5.93 Å	25	–1.5	6.3	26.2
ASA = 274 Å^2	45	–2.0		

Note: The hard-sphere diameter (12) and the *ASA* estimate (74) of each solute are also reported. For neopentane and toluene, the $\Delta G^{\bullet}$ values at 5°C were determined by extrapolation of the data at higher temperatures. Wetlaufer et al. (1) estimated an overall precision of ±2% for their molar solubility determinations; this should give rise to an uncertainty in the $\Delta G^{\bullet}$ values of about ±0.1 kJ mol^{-1} at 25°C. The hard-sphere diameter of toluene has been estimated from the *ASA* value.

directly obtained from the experimentally measured quantities, and it has a clear physical meaning (2, 3). In fact, $\Delta G^{\bullet}$ refers to the transfer of a solute molecule from a fixed position in liquid water to a fixed position in the mixed solvent. This is a rigorous statistical mechanical result that allows one to separate the contribution arising from the difference in translational degrees of freedom due to the different molar volume available to the solute molecule when the two phases have different densities (at 25°C the density is 0.99705 g cm^{-3} for water (4), 1.1044 g cm^{-3} for 7 M aqueous urea, and 1.1171 g cm^{-3} for 4.9 M aqueous GuHCl (5)). The corresponding thermodynamic quantities solely account for the difference in the solute–solvent coupling work for solutes that do not have conformational degrees of freedom. When the solute is flexible, the Ben-Naim standard also takes into account differences in the solute intramolecular energetics. From the temperature dependence of $\Delta G^{\bullet}$, it is possible to calculate the Ben-Naim standard enthalpy and entropy changes ($\Delta H^{\bullet}$ and $\Delta S^{\bullet}$, respectively) upon transfer at room temperature. The values of the thermodynamic functions for the transfer from water to 7 M urea and to 4.9 M GuHCl are presented in Tables 1 and 2, respectively, together with the hard-sphere diameters and accessible surface areas of the seven hydrocarbons.

For both transfer processes, the $\Delta G^{\bullet}$ values at 25°C are positive for methane and ethane, but negative for the other hydrocarbons, with the values increasing in magnitude when increasing the size of the solute molecule (see Tables 1 and 2). For the transfer, water→7 M urea, $\Delta G^{\bullet}$ (in kJ mol^{-1}) = 0.8 for methane, –0.1 for propane, –0.7 for neopentane, and –1.5 for toluene. For the transfer, water→4.9 M GuHCl, $\Delta G^{\bullet}$ (in kJ mol^{-1}) = 1.0 for methane, –0.1 for propane, –1.1 for neopentane, and –1.8 for toluene. Thus, there is a threshold size above which the presence of urea or GuHCl in water causes an enhancement of hydrocarbon solubility at room temperature; below this threshold size, the hydrocarbon solubility decreases. In contrast, all the $\Delta H^{\bullet}$ and $\Delta S^{\bullet}$ values at 25°C are positive, and do not show a clear trend as a function of the hydrocarbon size (see Tables 1 and 2). In addition, for both transfer processes, the $\Delta G^{\bullet}$ values become less positive (or more negative) with an increase in temperature. For the transfer, water→7 M urea, $\Delta G^{\bullet}$ (in kJ mol^{-1}) passes from 1.2 at 5°C to 0.6 at 45°C for methane, and from 0.3 at 5°C to –1.2 at 45°C for neopentane. For the transfer, water→4.9 M GuHCl, $\Delta G^{\bullet}$ (in kJ mol^{-1}) passes from 1.5 at 5°C to 0.8 at 45°C for methane, and from –0.3 at 5°C to –1.2 at 45°C for neopentane. This finding is not easy to rationalize because $\Delta G^{\bullet}$ becomes more positive with temperature for the transfer processes, gas→water and nonpolar liquid→water, of hydrocarbons (6). In fact, no reliable microscopic interpretation has been provided.

It should be noted that the values of $\Delta G^{\bullet}$ for the transfer of nonpolar amino acid side chains from water to 7 M urea and to 5 M GuHCl, determined by Nandi and Robinson (7)

© 2002 NRC Canada

Table 2. Ben-Naim standard Gibbs energy, enthalpy and entropy changes associated with the transfer of the seven hydrocarbons from water to 4.9 M GuHCl; data from ref. 1.

	T (°C)	$\Delta G^{\bullet}$ (kJ mol^{-1})	$\Delta H^{\bullet}$ (kJ mol^{-1})	$\Delta S^{\bullet}$ (J K^{-1}mol^{-1})
CH_4	5	1.5		
σ = 3.70 Å	25	1.0	6.2	17.5
ASA = 152 Å^2	45	0.8		
C_2H_6	5	1.1		
σ = 4.38 Å	25	0.5	8.0	25.0
ASA = 192 Å^2	45	0.1		
C_3H_8	5	0.5		
σ = 5.06 Å	25	–0.1	6.6	22.5
ASA = 223 Å^2	45	–0.4		
i-C_4H_{10}	5	0		
σ = 5.55 Å	25	–0.6	6.1	22.5
ASA = 249 Å^2	45	–0.9		
n-C_4H_{10}	5	0		
σ = 5.65 Å	25	–0.7	7.5	27.5
ASA = 255 Å^2	45	–1.1		
$C(CH_3)_4$	5	–0.3		
σ = 5.89 Å	25	–1.1	4.6	19.1
ASA = 270 Å^2	45	–1.2		
Toluene	5	–1.2		
σ = 5.93 Å	25	–1.8	3.7	18.4
ASA = 274 Å^2	45	–2.2		

Note: The hard-sphere diameter (12) and the *ASA* estimate (74) of each solute are also reported. For neopentane and toluene, the $\Delta G^{\bullet}$ values at 5°C were determined by extrapolation of the data at higher temperatures. Wetlaufer et al. (1) estimated an overall precision of ±2% for their molar solubility determinations; this should give rise to an uncertainty in the $\Delta G^{\bullet}$ values of about ±0.1 kJ mol^{-1} at 25°C. The hard-sphere diameter of toluene has been estimated from the *ASA* value.

from solubility measurements of several *N*-acetyl α-amino acid ethyl esters, are in semiquantitative agreement with those of Wetlaufer et al. (1). In fact, Nandi and Robinson (7) obtained, at 25°C, the following: (*i*) for the transfer, water→7 M urea, $\Delta G^{\bullet}$ (in kJ mol^{-1}) = 0.30 for Ala, 0.19 for Val, 0.15 for Leu, –0.06 for Nleu, and –0.66 for Phe; (*ii*) for the transfer, water→5 M GuHCl, $\Delta G^{\bullet}$ (in kJ mol^{-1}) = 0.48 for Ala, 0.27 for Val, –0.15 for Leu, –0.31 for Nleu, and –1.23 for Phe (7). Clearly, such values confirm the existence of a threshold size for the solubility enhancement due to urea or GuHCl. In addition, the data of Nandi and Robinson (7) show a temperature dependence resembling that obtained by Wetlaufer et al. (1) (see Tables IV and V in ref. 7). In contrast, from the solubility studies of α-amino acids by Tanford and co-workers (8), one determines, for nonpolar side-chains at 25°C, the following: (*i*) for the transfer, water→7 M urea, $\Delta G^{\bullet}$ (in kJ mol^{-1}) = 0.05 for Ala, –0.58 for Val, –1.06 for Leu, and –2.25 for Phe; (*ii*) for the transfer, water→4.9 M GuHCl, $\Delta G^{\bullet}$ (in kJ mol^{-1}) = –0.15 for Ala, –0.93 for Val, –1.70 for Leu, and –2.80 for Phe. Clearly, such values do not show the occurrence of a threshold size for the solubility enhancement. This is surely due to the presence of charges on the α-amino acid molecules that strengthen the interactions with urea and GuHCl, and limit the validity of the additivity principle.

On the other hand, Ben-Naim and Yaacobi (9), in accordance with the data of Wetlaufer et al., determined the following for the water→7 M urea transfer at 25°C: (*i*) for methane, $\Delta G^{\bullet}$ = 0.9 kJ mol^{-1}, $\Delta H^{\bullet}$ = 5.0 kJ mol^{-1}, and $\Delta S^{\bullet}$ = 13.8 J K^{-1}mol^{-1}; (*ii*) for ethane, $\Delta G^{\bullet}$ = 0.4 kJ mol^{-1}, $\Delta H^{\bullet}$ = 8.8 kJ mol^{-1}, and $\Delta S^{\bullet}$ = 28.0 J K^{-1}mol^{-1}. There was also agreement for the temperature dependence of the $\Delta G^{\bullet}$ values over the range of 10–30°C. Moreover, Breslow and Guo (10) found that $\Delta G^{\bullet}$ = –0.6 kJ mol^{-1} for the transfer of benzene from water to 5 M aqueous GuHCl at 20°C. Such experimental value agrees quantitatively with those determined by Wetlaufer et al. (1) for aliphatic hydrocarbons of similar size (i.e., isobutane and *n*-butane, see Table 2). The thermodynamic data of Tables 1 and 2, therefore, have to be considered reliable on a quantitative basis.

To the best of our knowledge, a complete rationalization of data of Wetlaufer et al. (1) has not yet been provided. No one has tried to perform this task with a convincing theoretical treatment. The analysis by Muller (11), limited to the water→7 M urea transfer, cannot be considered completely satisfactory. The model calculations of Muller did not reproduce the experimental data without the ad hoc introduction of eq. [11] in ref. 11, which has no physical justification. Recently, the author devised a simple but well-founded approach (12) that leads to a satisfactory rationalization for the occurrence of the threshold size at room temperature for the water→7 M urea transfer. In the present article, it will be shown that the same approach is able to account for all the nontrivial features of the data by Wetlaufer et al. (1), without the need of special assumptions.

© 2002 NRC Canada

Theory

The theoretical approach is described in detail in the accompanying paper[1]; this paper reports only the fundamental relationships to be used in this specific application. A liquid phase is a condensed state of matter and one should consider both the finite volume occupied by each molecule and the energetic interactions among molecules (i.e., both the repulsive and attractive parts of the intermolecular potential, as pioneered by van der Waals). On this basis, rigorous statistical mechanical approaches to solvation have been developed (13–15). The transfer of a solute molecule from a fixed position in water to a fixed position in the mixed-aqueous solvent system (both 7 M urea and 4.9 M GuHCl) can be dissected in the following subprocesses (12): (*i*) breaking solute–solvent attractive interactions in H_2O; (*ii*) closing the cavity therein; (*iii*) creating a cavity in the mixed solvent to accommodate the solute molecule; and (*iv*) turning on the solute–solvent attractive interactions in the mixed solvent. Accordingly, the Ben-Naim standard Gibbs energy change upon transfer is given by the following relation:

$$[2] \quad \Delta G^{\bullet} = [\Delta G_c(\text{mix}) - \Delta G_c(H_2O)] + [E_a(\text{mix}) - E_a(H_2O)] = \Delta\Delta G_c + \Delta E_a$$

where ΔG_c is the work of cavity creation and E_a is the average solute–solvent van der Waals interaction energy. These two terms represent the direct perturbation of each solvent system due to solute insertion. In response to the direct perturbation, a structural reorganization of solvent molecules occurs with associated enthalpy and entropy contributions (16). Since such structural reorganization is characterized by a rearrangement of H-bonds in H_2O, 7 M aqueous urea, and 4.9 M aqueous GuHCl, the corresponding enthalpy and entropy changes are indicated as ΔH^h and ΔS^h (note that in the accompanying paper[1] they are indicated as ΔH_r and ΔS_{nx} to be more general, given that there are no H-bonds in solvents such as benzene or *n*-hexane). The Ben-Naim standard enthalpy and entropy changes upon transfer are, therefore, given by

$$[3] \quad \Delta H^{\bullet} = [E_a(\text{mix}) - E_a(H_2O)] + [\Delta H^h(\text{mix}) - \Delta H^h(H_2O)] = \Delta E_a + \Delta\Delta H^h$$

$$[4] \quad \Delta S^{\bullet} = [\Delta S_x(\text{mix}) - \Delta S_x(H_2O)] + [\Delta S^h(\text{mix}) - \Delta S^h(H_2O)] = \Delta\Delta S_x + \Delta\Delta S^h$$

In the latter equation, ΔS_x is the entropy contribution due to the excluded volume effect associated with cavity creation in the solvent (16). It is exactly related to the work of cavity creation as follows:

$$[5] \quad \Delta S_x = -\Delta G_c/T$$

because ΔG_c, being a measure of the probability that a certain region of space in the solvent is devoid of solvent molecules, is purely of entropic origin (17).

According to eqs. [2]–[4], the Ben-Naim standard Gibbs energy change upon transfer is not affected by the reorganization of H-bonds in response to solute insertion. This is because the enthalpy–entropy compensation condition

$$[6] \quad \Delta H^h = T\Delta S^h$$

holds for the reorganization of H-bonds in such solvent systems. This is a very important topic which has been carefully analyzed and demonstrated by means of different theoretical approaches (18). For a general discussion on the occurrence of enthalpy–entropy compensation phenomena, see the review by Liu and Guo (19).

Ben-Naim was probably the first (20) to show that, for any reliable statistical mechanical definition of solvent structure, the standard solvation Gibbs energy change, being expressed as an ensemble average over the distribution function of pure solvent, depends upon the solvent structure, but does not derive any contribution from solvent structural changes induced by solute insertion (i.e., solvent structural changes correspond to a reorganization of H-bonds in the case of water and aqueous solutions). In addition, Ben-Naim pointed out that such solvent structural changes may dominate the standard solvation enthalpy and entropy changes, but in a compensating manner. From our point of view, the analysis devised by Lee (21) leads to a more clear physical interpretation. Lee demonstrated that enthalpy–entropy compensation is operative when the solute–solvent attractive interactions are weak in comparison to the solvent–solvent attractive interactions. This condition holds for hydrocarbons in both H_2O, 7 M aqueous urea, and 4.9 M aqueous GuHCl because van der Waals interactions are weak when compared with H-bonds.

Calculation procedure

The work of cavity creation is calculated using the theoretical equation provided by scaled particle theory (SPT) (22, 23) and reported in the accompanying paper[1].This theoretical equation is considered valid for calculating ΔG_c not only in pure liquids but also in the mixed-aqueous solvent systems (12). The author assumes that both 7 M aqueous urea and 4.9 M aqueous GuHCl can be treated as "uniform" solvents characterized by a single mean hard-sphere diameter and a single mean molar volume (12, 24). In this respect, Patterson wrote (25), "The simplest prescription is the one-fluid model where the mixture is taken to be equivalent to a single fluid with average molecular parameters. More complex two- and three-fluid models are available, but it is probable that they give no better results than the one-fluid." The reliability of the assumption was discussed in detail in previous work (12). It should be emphasized that, apart from the fundamental neutron-diffraction studies by Finney et al. (26) on aqueous urea solutions, further experimental measurements (27, 28) and computer simulations (29, 30) have confirmed that both GuHCl and urea, even at high molar concentrations, do not affect the H-bonding network of liquid water. This is simply due to the ability of guanidinium ions and urea molecules to form H-bonds in a pseudo-tetrahedral arrangement (31).

According to our assumption, the mean hard-sphere diameter of mixed-aqueous solvent systems is given by

[1] G. Graziano. Can. J. Chem. **80,** 401–412 (2002).

© 2002 NRC Canada

Table 3. Experimental densities of water, 7 M urea, and 4.9 M GuHCl; apparent molar volume of urea in 7 M urea, and of GuHCl in 4.9 M GuHCl; mean molar volume of 7 M urea and 4.9 M GuHCl; volume-packing densities of water, 7 M urea, and 4.9 M GuHCl.

	T (°C)	ρ (g cm^{-3})	Φv (cm^3 mol^{-1})	v (cm^3 mol^{-1})	ξ
H_2O	5	0.99996		18.02	0.364
	25	0.99705		18.07	0.363
	45	0.99021		18.20	0.360
7 M urea	5	1.1138	44.0	22.0	0.427
	25	1.1044	45.0	22.3	0.421
	45	1.0921	45.9	22.6	0.416
4.9 M GuHCl	5	1.1267	70.1	24.2	0.427
	25	1.1171	71.4	24.5	0.422
	45	1.1074	72.2	24.7	0.418

Note: The data for water are from ref. 4; those for 7 M aqueous urea are from ref. 40; those for 4.9 M aqueous GuHCl are from ref. 39; M_w = 18.02 for H_2O, 60.06 for urea, and 95.53 for GuHCl.

$$[7] \qquad \sigma(\text{mix}) = x_1\sigma_1 + x_2\sigma_2$$

where the subscript 1 refers to water, the subscript 2 refers to urea or GuHCl, and x is molar fraction. The molar fraction of water in 7 M urea is 0.846 at 5°C, 0.844 at 25°C, and 0.842 at 45°C; the molar fraction of water in 4.9 M GuHCl is 0.882 at 5°C, 0.880 at 25°C, and 0.879 at 45°C. For water, σ_{H_2O} = 2.75 Å (32) is used, close to the location of the first peak in the oxygen–oxygen pair correlation function of liquid water (33). The values of σ_{urea} and σ_{GuHCl} have to be properly selected.

The latter can be determined by addressing the concept of equivalent hard sphere (34). Consider, for instance, that the pair-correlation function of *N*-acetyl-leucine-amide (NALA) molecules in aqueous solution, determined from neutron-scattering measurements, can be satisfactorily reconstructed by assuming that each NALA molecule is equivalent to a hard-sphere of 6.0 Å diameter (35).

The molar volume of GuHCl, calculated from the crystal density (36), is 70.55 cm^3 mol^{-1}, corresponding to 117.2 Å^3 per molecule. The partial molar volume of GuHCl in 4.9 M aqueous GuHCl at 25°C is 72.47 cm^3 mol^{-1}, corresponding to 120.3 Å^3 per molecule (37, 38). The apparent molar volume of GuHCl in 4.9 M aqueous GuHCl at 25°C is 71.40 cm^3 mol^{-1}, corresponding to 118.6 Å^3 per molecule (39). All these values closely correspond to the volume of a sphere of 6.2 Å diameter, and σ_{GuHCl} is therefore fixed at 6.2 Å. A similar procedure led to σ_{urea} = 5.0 Å (12). Inserting these values into eq. [7], one obtains σ (7 M urea) = 3.10 Å and σ (4.9 M GuHCl) = 3.20 Å in the whole range of 5–45°C.

In the same way, the mean molar volume of mixed-aqueous solvent systems is given by

$$[8] \qquad v(\text{mix}) = x_1v_1 + x_2v_2$$

where for water we use the experimental values of molar volume at the different temperatures (4); for urea we use the values of the apparent molar volume of urea in 7 M aqueous urea solutions determined by Stokes (40); and for GuHCl we use the values of the apparent molar volume of GuHCl in 4.9 M aqueous GuHCl solutions determined by Makhatadze and co-workers (39). These simple calculations show the following: (*i*) v (7 M urea) = 22.0, 22.3, and 22.6 cm^3 mol^{-1} at 5, 25, and 45°C, respectively; (*ii*) v (4.9 M GuHCl) = 24.2, 24.5, and 24.7 cm^3 mol^{-1} at 5, 25, and 45°C, respectively. Correspondingly, the mean volume-packing densities are (*i*) ξ(7 M urea) = 0.427, 0.421, and 0.416 at 5, 25, and 45°C, respectively; (*ii*) ξ(4.9 M GuHCl) = 0.427, 0.422, and 0.418 at 5, 25, and 45°C, respectively. All these data are presented in Table 3. The two "uniform" solvent systems, 7 M aqueous urea and 4.9 M aqueous GuHCl, therefore, have both a mean hard-sphere diameter and a mean volume-packing density larger than those of water.

The physical validity of our approach and the reliability of eqs. [7] and [8] are supported by the following findings: (*i*) the volume change associated with the mixing of urea or GuHCl and water is negligible (39, 40); and (*ii*) computer simulations show that both urea and GuHCl, even at high molar concentrations, do not significantly affect the structure of water (29–31), which is in line with the results of neutron diffraction, IR, and NMR studies (26–28, 41).

Size dependence of hydrocarbon solubility

The SPT estimates of ΔG_c in water, 7 M aqueous urea, and 4.9 M aqueous GuHCl are reported in Table 4. They are larger in both 7 M urea and 4.9 M GuHCl than in water. For instance, at 25°C, for methane, ΔG_c (in kJ mol^{-1}) = 21.1 in H_2O, 23.9 in 7 M urea, and 22.9 in 4.9 M GuHCl; for neopentane, ΔG_c (in kJ mol^{-1}) = 46.3 in H_2O, 52.4 in 7 M urea, and 49.9 in 4.9 M GuHCl; for toluene, ΔG_c (in kJ mol^{-1}) = 46.8 in H_2O, 53.1 in 7 M urea, and 50.5 in 4.9 M GuHCl. The magnitude of ΔG_c, with a fixed temperature and cavity radius, is determined by two geometrical features of the solvent (14, 42), i.e., ΔG_c raises (*i*) on decreasing the value of the hard-sphere diameter of its molecules for a given ξ; and (*ii*) on increasing its volume-packing density for a given σ. By adding urea or GuHCl to water to make a 7 M urea or a 4.9 M GuHCl solution, there is an increase in both the mean hard-sphere diameter of the solvent (3.10 Å for 7 M urea, 3.20 Å for 4.9 M GuHCl, and 2.75 Å for H_2O) and the mean volume-packing density (at 25°C, 0.421 for 7 M urea, 0.422 for 4.9 M GuHCl, and 0.363 for H_2O). Even though the two factors act in opposite directions, the second factor (mean volume-packing density) prevails,

© 2002 NRC Canada

Table 4. Work of cavity creation and solute–solvent interaction energy in water (*a*); in 7 M urea (*b*); and 4.9 M GuHCl (*c*).

		T (°C)	CH_4	C_2H_6	C_3H_8	*i*-C_4H_{10}	*n*-C_4H_{10}	$C(CH_3)_4$	Toluene
a	ΔG_c	5	19.8	26.1	33.3	39.1	40.4	43.4	43.9
		25	21.1	27.8	35.5	41.7	43.0	46.3	46.8
		45	22.1	29.2	37.3	43.8	45.2	48.6	49.1
	E_a	25	–12.7	–20.2	–27.2	–32.3	–34.2	–36.0	–50.5
	E_a*	25	–12.1	–20.1	–27.6	–32.7	–34.7	–36.0	–50.6
b	ΔG_c	5	23.1	30.5	38.9	45.6	47.1	50.6	51.3
		25	23.9	31.6	40.3	47.3	48.8	52.4	53.1
		45	24.8	32.8	41.8	49.0	50.6	54.4	55.0
	E_a	25	–14.7	–23.6	–32.1	–38.4	–40.5	–42.8	–58.3
	E_a*	25	–14.0	–23.3	–32.0	–37.9	–40.2	–41.8	–58.7
c	ΔG_c	5	21.9	28.9	36.8	43.2	44.6	47.9	48.5
		25	22.9	30.1	38.4	45.0	46.4	49.9	50.5
		45	23.9	31.4	40.1	46.9	48.4	52.0	52.7
	E_a	25	–13.5	–22.0	–30.2	–36.2	–38.3	–40.7	–56.0
	E_a*	25	–14.1	–23.4	–32.1	–38.0	–40.3	–41.9	–58.8

Note: Values of ΔG_c were calculated by means of SPT; estimates of E_a were obtained from the difference $E_a = \Delta G^{\bullet} - \Delta G_c$, where $\Delta G^{\bullet}$ is the experimental solvation Gibbs energy. E_a* in H_2O are the values calculated by means of computer simulations (49, 50); E_a* in 7 M urea and 4.9 M GuHCl are the values calculated by means of eq. [10]. ΔG and E_a are in kJ mol^{-1}.

Table 5. Values of $\Delta\Delta G_c$, ΔE_a, $\Delta\Delta H^h$, $\Delta\Delta S_x$, and $\Delta\Delta S^h$ associated with the transfer of the seven hydrocarbons, at 25°C, from water to 7 M urea (*a*); and from water to 4.9 M GuHCl (*b*).

		$\Delta\Delta G_c$ (kJ mol^{-1})	ΔE_a (kJ mol^{-1})	$\Delta\Delta H^h$ (kJ mol^{-1})	$\Delta\Delta S_x$ (J K^{-1}mol^{-1})	$\Delta\Delta S^h$ (J K^{-1}mol^{-1})
a	CH_4	2.8	–2.0	7.4	–9.4	24.7
	C_2H_6	3.8	–3.4	11.6	–12.8	39.2
	C_3H_8	4.8	–4.9	12.1	–16.1	40.4
	i-C_4H_{10}	5.6	–6.1	12.6	–18.7	42.0
	n-C_4H_{10}	5.8	–6.3	14.1	–19.5	47.3
	$C(CH_3)_4$	6.1	–6.8	14.0	–20.5	47.0
	Toluene	6.3	–7.8	14.1	–21.1	47.3
b	CH_4	1.8	–0.8	7.0	–6.0	23.5
	C_2H_6	2.3	–1.8	9.8	–7.7	32.7
	C_3H_8	2.9	–3.0	9.6	–9.7	32.2
	i-C_4H_{10}	3.3	–3.9	10.0	–11.1	33.6
	n-C_4H_{10}	3.4	–4.1	11.6	–11.4	38.9
	$C(CH_3)_4$	3.6	–4.7	9.3	–12.1	31.2
	Toluene	3.7	–5.5	9.2	–12.4	30

Note: The $\Delta\Delta H^h$ estimates are obtained taking the difference $\Delta H^{\bullet} - \Delta E_a$; those of $\Delta\Delta S^h$ taking the difference $\Delta S^{\bullet} - \Delta\Delta S_x$, where the $\Delta\Delta S_x$ values are calculated using eq. [5].

so that ΔG_c in the two mixed-solvent systems is larger than in water.

This finding is correct from a physico-chemical point of view because (*i*) the addition of both urea and GuHCl to water causes an increase of the surface tension (10, 43); and (*ii*) there is a direct proportionality between the work of cavity creation in a solvent and its surface tension (44). In particular, following the proposal of Baldwin (45), we can consider that

$$[9] \qquad \Delta\Delta G_c = ASA\Delta\gamma$$

where *ASA* is the accessible surface area of the solute molecule and $\Delta\gamma$ is the increase in surface tension passing from pure water to 7 M urea or to 4.9 M GuHCl. Using the SPT estimates of $\Delta\Delta G_c$ at 25°C, shown in the second column of Table 5, and the *ASA* values listed in the first column of Table 1, estimates for $\Delta\gamma$ can be obtained. The average value of $\Delta\gamma$ is 21.5 J Å^{-2} mol^{-1} for 7 M urea and 12.9 J Å^{-2} mol^{-1} for 4.9 M GuHCl. The latter is close to the experimental value of 13.0 J Å^{-2} mol^{-1}, measured at 20°C by Breslow and Guo (10). The old data quoted by Timmermans (43), even though they do not allow a strictly quantitative comparison for 7 M urea because the surface tension was determined for less concentrated solutions, are in line with the above estimates. With respect to eq. [9], it should be noted that recent theoretical and computational approaches have demonstrated that the *ASA* significantly underestimates the macroscopic surface tension for molecular-sized solutes (46–48). A more appropriate procedure for aqueous solutions should use the van der Waals or molecular surface of the solutes. In any case,

© 2002 NRC Canada

computer simulations also indicate that ΔG_c should be larger in 7 M urea and 4.9 M GuHCl than in water (30).

Estimates of E_a at 25°C in water, 7 M urea, and 4.9 M GuHCl are determined with a "hybrid" procedure, using the relation $E_a = \Delta G^\bullet - \Delta G_c$, where $\Delta G^\bullet$ are the experimental data for the following solvation processes: gas→H_2O, gas→7 M urea, and gas→4.9 M GuHCl. The values of $\Delta G^\bullet$(gas→H_2O), $\Delta G^\bullet$(gas→7 M urea), and $\Delta G^\bullet$(gas→4.9 M GuHCl) come from the work of Wetlaufer et al. (1), using the relation $\Delta G^\bullet = RT \ln (C_g/C_l)$, where C_g and C_l are the molar concentrations in the gas and in the liquid, respectively (2). Note that, for the conditions adopted by Wetlaufer et al. (1), $C_g = 0.0409$ mol L^{-1} at 25°C for all hydrocarbons. The E_a estimates, determined with the hybrid procedure, are reported in Table 4, and show that E_a is larger, in absolute value, in both 7 M urea and 4.9 M GuHCl than in water. For instance, for methane, E_a (in kJ mol^{-1}) = –12.7 in H_2O, –14.7 in 7 M urea, and –13.5 in 4.9 M GuHCl; for neopentane, E_a (in kJ mol^{-1}) = –36.0 in H_2O, – 42.8 in 7 M urea, and –40.7 in 4.9 M GuHCl; for toluene, E_a (in kJ mol^{-1}) = –50.5 in H_2O, –58.3 in 7 M urea, and –56.0 in 4.9 M GuHCl.

To confirm this finding, the E_a values in water, at 25°C, calculated for aliphatic hydrocarbons by Jorgensen and co-workers (49), and that of toluene (obtained by adding to the estimate of Linse (50) for benzene the contributions of the methyl group), are listed in the last line of Table 4*a* (i.e., both Jorgensen and Linse performed calculations in TIP4P water). These values prove to be very close to those obtained with the hybrid procedure. In addition, the values of E_a in H_2O can be used to estimate E_a in the mixed-aqueous solvent systems by means of the following relation:

$$[10] \quad E_a(\text{mix}) = E_a(H_2O)\xi(\text{mix})/\xi(H_2O)$$

whose physical reliability is grounded in the general expression of the solute–solvent van der Waals interaction energy (23), which indicates that E_a is directly proportional to the solvent packing density (ξ). The values calculated by means of eq. [10] are listed in the last line of Table 4*b* for 7 M urea and Table 4*c* for 4.9 M GuHCl. These values qualitatively agree with those obtained using the hybrid procedure. The agreement is also quantitatively good for 7 M urea, but not for 4.9 M GuHCl. In such case, they are, on the average, too large by a magnitude of 2 kJ mol^{-1}. This is surely due to the fact that eq. [10], even though reliable and sound, cannot be quantitatively exact when there are charged species in solution, as in the case of GuHCl. The qualitative agreement, however, can be considered satisfactory, confirming that solute–solvent van der Waals interactions are stronger in both 7 M urea and 4.9 M GuHCl than in pure water. This point is supported by the fact that urea decreases the interfacial tension between alkanes and water (51) and by the results of computer simulations (30, 52). In addition, it is in accordance with the large polarizability of the urea molecule and guanidinium ion, due to the six π-electrons delocalized over the entire planar structure.

According to eq. [2], the $\Delta G^\bullet$ values for the transfer from water to the mixed solvent systems are governed by the balance between $\Delta\Delta G_c$ and ΔE_a. The first quantity is positive, whereas the second one is negative. Neither of these are large, but increase, in absolute value, with hydrocarbon size, and also remain close in magnitude (see the second and third columns of Table 5). In fact, the solubilities are similar (1), and the $\Delta G^\bullet$ values, regardless of the sign, are small and difficult to estimate by means of a purely theoretical approach. This is why we use the hybrid procedure to estimate E_a. It proves that ΔE_a increases in magnitude with hydrocarbon size more rapidly than $\Delta\Delta G_c$, in both 7 M urea and 4.9 M GuHCl, leading to the occurrence of a threshold size for the hydrocarbon solubility enhancement at 25°C.

This raises the question of why the increase in magnitude of ΔE_a is larger than that of $\Delta\Delta G_c$. A reliable explanation seems to be that for the transfer from H_2O to 7 M urea or to 4.9 M GuHCl, the increase of ΔG_c is simply a consequence of the change in the packing properties of the solvent system. The increase in magnitude of E_a reflects not only the change in the packing properties of the solvent system, but also direct-contact interactions between the solute molecule and urea molecules, or GuH^+ and Cl^- ions in the hydration shell (on this point see also *Appendix 1*). Molecular dynamics simulations (30) indicate that the number of urea molecules or GuH^+ and Cl^- ions located in the hydration shell of hydrocarbons increases with the size of the latter. This should be the molecular origin of the ΔE_a behavior.

We now analyze the Ben-Naim standard transfer enthalpy and entropy changes. The $\Delta\Delta S_x$ values are calculated using eq. [5], while those of $\Delta\Delta H^h$ and $\Delta\Delta S^h$ are obtained by calculating the differences $\Delta H^\bullet - \Delta E_a$ and $\Delta S^\bullet - \Delta\Delta S_x$, respectively. (Note that ΔH^h estimates could be directly calculated by means of computer simulations, but the associated uncertainty would be very large.) The obtained estimates of $\Delta\Delta H^h$, $\Delta\Delta S_x$, and $\Delta\Delta S^h$ are listed in the fourth, fifth, and sixth columns, respectively, of Table 5. They show that $\Delta H^\bullet$ and $\Delta S^\bullet$ are dominated by the contributions due to H-bond reorganization in both 7 M urea and 4.9 M GuHCl: $\Delta\Delta H^h > |\Delta E_a|$ and $\Delta\Delta S^h > |\Delta\Delta S_x|$. The reorganization of H-bonds upon solute insertion provides small positive values of ΔH^h and ΔS^h for the solvation of hydrocarbons in water (ref. 14; see also Table 5 of the accompanying paper[1]). The fact that $\Delta\Delta H^h$ and $\Delta\Delta S^h$ are positive for all hydrocarbons implies that ΔH^h and ΔS^h are positive and significantly larger in 7 M urea and 4.9 M GuHCl than in water. The H-bond reorganization upon solute insertion is, therefore, qualitatively similar in the three solvent systems, but it occurs to a far greater extent in the presence of urea or GuHCl. The geometric constraints imposed by the solute molecule on the surrounding solvent molecules should play the dominant role. When the latter are solely water molecules, the so-called straddling mechanism is able to minimize the waste of H-bonds (53); water molecules straddle the nonpolar solute by pointing in two or three tetrahedral directions tangential to the surface of the occupied volume. When there are also urea molecules or GuH^+ and Cl^- ions, the straddling mechanism is operative but cannot be as effective as in pure water because of geometric and energetic reasons. The planar structure of urea and GuH^+, and the presence of charges in the latter, affect the local configurations of water molecules.

These pictures of H-bond reorganization conflict with the iceberg or clathrate formation proposed by Frank and co-workers (54), Kauzmann (55), Nemethy and Scheraga (56), and others (57). They are, however, supported not only by theoretical approaches (13–16) and computer simulations

© 2002 NRC Canada

Table 6. Estimates of $\Delta\Delta G_c + \Delta E_a$ for the transfer from water to 7 M aqueous urea to be contrasted against the experimental $\Delta G^{\bullet}$ values over the range 5–45°C.

	T (°C)	$\Delta\Delta G_c$ (kJ mol^{-1})	$\Delta\Delta G_c + \Delta E_a$ (kJ mol^{-1})	$\Delta G^{\bullet}$ (kJ mol^{-1})
CH_4	5	3.3	1.3	1.2
ΔE_a = –2.0 kJ mol^{-1}	25	2.8	0.8	0.8
	45	2.7	0.7	0.6
C_2H_6	5	4.4	1.0	1.0
ΔE_a = –3.4 kJ mol^{-1}	25	3.8	0.4	0.4
	45	3.6	0.2	0
C_3H_8	5	5.6	0.7	0.5
ΔE_a = –4.9 kJ mol^{-1}	25	4.8	–0.1	–0.1
	45	4.5	–0.4	–0.4
i-C_4H_{10}	5	6.5	0.4	0.1
ΔE_a = –6.1 kJ mol^{-1}	25	5.6	–0.5	–0.5
	45	5.2	–0.9	–0.9
n-C_4H_{10}	5	6.7	0.4	0.2
ΔE_a = –6.3 kJ mol^{-1}	25	5.8	–0.5	–0.5
	45	5.4	–0.9	–0.9
$C(CH_3)_4$	5	7.2	0.4	0.3
ΔE_a = –6.8 kJ mol^{-1}	25	6.1	–0.7	–0.7
	45	5.8	–1.0	–1.2
Toluene	5	7.4	–0.4	–1.1
ΔE_a = –7.8 kJ mol^{-1}	25	6.3	–1.5	–1.5
	45	5.9	–1.9	–2.0

Note: For each alkane the ΔE_a estimate, considered temperature independent, is listed in the first column.

(58–60), but also by direct structural determinations from neutron scattering (61) and X-ray absorption spectroscopy measurements (62).

Temperature dependence of hydrocarbon solubility

We consider that the ΔE_a estimates are temperature independent in the range of 5–45°C, because the strength of the van der Waals interactions depends little on temperature when the solvent density does not markedly change (14, 63). This is the case for water, 7 M urea, and 4.9 M GuHCl, as indicated by the density values reported in Table 3. On the other hand, $\Delta\Delta G_c$ decreases with temperature (see the third column of Tables 6 and 7); this is the fundamental point. For instance, in the range of 5–45°C, $\Delta\Delta G_c$ (in kJ mol^{-1}) decreases (*i*) for methane, from 3.3 to 2.7 in 7 M urea, and from 2.1 to 1.7 in 4.9 M GuHCl; (*ii*) for isobutane, from 6.5 to 5.2 in 7 M urea, and from 4.1 to 3.0 in 4.9 M GuHCl; (*iii*) for neopentane, from 7.2 to 5.8 in 7 M urea, and from 4.5 to 3.3 in 4.9 M GuHCl. The calculated values of $\Delta\Delta G_c + \Delta E_a$ for both transfer processes are listed in the fourth column of Tables 6 and 7; they prove to be in satisfactory agreement with the experimental $\Delta G^{\bullet}$ data.

The temperature dependence of $\Delta G^{\bullet}$ is, therefore, due to the behavioral differences during cavity creation in water, 7 M urea, and 4.9 M GuHCl. The values reported in Table 4 indicate that ΔG_c increases with temperature in all three solvent systems, but the increase is larger in water than in 7 M urea and 4.9 M GuHCl. SPT indicates that ΔG_c depends on the hard-sphere diameter of solvent molecules and on the solvent-packing density. For all three solvent systems, the hard-sphere diameter is considered constant in the range of 5–45°C. Thus, the different temperature dependence of ΔG_c is because the solvent-packing density decreases a little more rapidly in 7 M urea and 4.9 M GuHCl than in water. In the range of 5–45°C, $\xi(H_2O)$ passes from 0.364 to 0.360, while ξ(7 M urea) passes from 0.427 to 0.416, and ξ(4.9 M GuHCl) passes from 0.427 to 0.418. In fact, in the temperature range considered, the densities of liquid water, 7 M aqueous urea, and 4.9 M GuHCl decrease by 1, 2, and 1.7%, respectively (see Table 3). In any case, a more fundamental discussion of ΔG_c is needed.

According to a general theorem of statistical mechanics (64), the work to create, in a solvent, a cavity suitable to host a given solute molecule is a measure of the probability that the requested region is devoid of solvent molecules (17). In other words, ΔG_c is related to the solvent density and can be directly computed from the density fluctuations of the pure solvent using computer simulations, i.e., by observing naturally occurring cavities in the pure liquid (65, 66). Specifically, ΔG_c is given by

$$[11] \quad \Delta G_c = -RT \ln P_0(\sigma) = -RT \ln [V_{avail}(\sigma)/V_{tot}]$$

where $P_0(\sigma)$ is the probability that a spherical region of diameter σ, centered at an arbitrary position, is not occupied by solvent molecules, and $P_0(\sigma)$ corresponds to the ratio of

© 2002 NRC Canada

Table 7. Estimates of $\Delta\Delta G_c + \Delta E_a$ for the transfer from water to 4.9 M aqueous GuHCl to be contrasted against the experimental $\Delta G^{\bullet}$ values over the range 5–45°C.

	T (°C)	$\Delta\Delta G_c$ (kJ mol^{-1})	$\Delta\Delta G_c + \Delta E_a$ (kJ mol^{-1})	$\Delta G^{\bullet}$ (kJ mol^{-1})
CH_4	5	2.1	1.3	1.5
ΔE_a = –0.8 kJ mol^{-1}	25	1.8	1.0	1.0
	45	1.7	0.9	0.8
C_2H_6	5	2.8	1.0	1.1
ΔE_a = –1.8 kJ mol^{-1}	25	2.3	0.5	0.5
	45	2.1	0.3	0.1
C_3H_8	5	3.5	0.5	0.5
ΔE_a = –3.0 kJ mol^{-1}	25	2.9	–0.1	–0.1
	45	2.6	–0.4	–0.4
i-C_4H_{10}	5	4.1	0.2	0
ΔE_a = –3.9 kJ mol^{-1}	25	3.3	–0.6	–0.6
	45	3.0	–0.9	–0.9
n-C_4H_{10}	5	4.2	0.1	0
ΔE_a = –4.1 kJ mol^{-1}	25	3.4	–0.7	–0.7
	45	3.1	–1.0	–1.1
$C(CH_3)_4$	5	4.5	–0.2	–0.3
ΔE_a = –4.7 kJ mol^{-1}	25	3.6	–1.1	–1.1
	45	3.3	–1.4	–1.2
Toluene	5	4.6	–0.9	–1.2
ΔE_a = –5.5 kJ mol^{-1}	25	3.7	–1.8	–1.8
	45	3.4	–2.1	–2.2

Note: For each alkane the ΔE_a estimate, considered temperature independent, is listed in the first column.

the volume available to insert such a cavity ($V_{avail}(\sigma)$) over the total volume of the system (V_{tot}). (Remember that the location of the cavity has to be fixed, but arbitrarily in the liquid volume because the liquid density is uniform at equilibrium.) Equation [11] is easily transformed to

$$[12] \quad \Delta G_c = -RT \ln [V_{empty}/V_{tot}] - RT \ln [V_{avail}(\sigma)/V_{empty}]$$

where V_{empty} is the empty space of the system. It is worth noting that V_{avail} is a function of σ, whereas both V_{tot} and V_{empty} do not depend on the cavity size. Equation [12] is important because it clarifies the difference between V_{empty} and V_{avail}. Even though the empty space in a typical liquid is large (i.e., 50–60% of the total volume), the actual volume available for the insertion of a molecular-sized cavity is many orders of magnitude smaller because the non-overlap condition has to be satisfied (i.e., the excluded volume effect produced by the finite size of the impenetrable cores of molecules). In fact, if the empty volume is not partitioned to provide cavities whose size is at least equal to σ, such an empty volume proves to be not available, as if it were occupied by solvent molecules.

This means that the distribution of empty space in a liquid is a fundamental issue. In view of the pivotal role played by packing effects in liquids (67), it can be argued that the empty space is partitioned in smaller pieces in a liquid constituted by small molecules than in a liquid constituted by large molecules (14). In other words, the size of solvent molecules defines the length scale of the system. The results of computer simulations by Pratt and Pohorille (68) on a series of model liquids quantitatively confirmed these expectations. Clearly, $P_0(\sigma)$, being a probability, is always smaller than one, going asymptotically to zero on increasing the cavity size. Correspondingly, ΔG_c proves to be very sensitive to this near-zero $P_0(\sigma)$, i.e., it is strongly dependent upon the size of solvent molecules and the solvent packing density. This reasoning has a general validity because eqs. [11] and [12] are exact, and it also explains why ΔG_c is so sensitive to liquid-density changes (69). In conclusion, the magnitude of ΔG_c is solely determined by pure-solvent properties. The solute molecule plays no role, except for the definition of the cavity size needed to host it.

On the other hand, detailed computer simulations have pointed out that, when the solvent density and molecular size are fixed, ΔG_c does not depend upon the nature of the interactions acting among solvent molecules, i.e., H-bonds or van der Waals interactions (58, 70). Such intermolecular interactions, however, are responsible for the actual density of the pure liquid solvent and its temperature dependence. In fact, the density of liquid water changes very little over the range of 0–100°C (4) due to the strength of H-bonds with respect to thermal energy. On the other hand, the density of common organic solvents changes significantly with temperature (71) due to the weakness of van der Waals interactions. As a consequence, the intermolecular interactions affect ΔG_c indirectly by determining the density of the pure liquid at each temperature.

© 2002 NRC Canada

Equation [11] also provides a general explanation for the temperature dependence of ΔG_c. The latter is given by the product of two terms: (*i*) the R*T* term accounts for the thermal energy of the solvent molecules bombarding the cavity surface and increases linearly with temperature; and (*ii*) the logarithmic term depends on liquid density and decreases with temperature, since the density of all liquids diminishes on increasing temperature. The first term prevails for water and aqueous solutions; the second term prevails for common organic solvents (14, 15).

Finally, it is clear that ΔG_c depends upon the physical and structural features of solvent molecules, but it is absolutely not affected by the reorganization of solvent molecules upon solute insertion. All of the above reasoning clarifies why SPT works well: (*i*) it was exactly aimed to evaluate $P_0(\sigma)$, using geometric and statistical arguments, and provided a physically consistent expression for ΔG_c (22); and (*ii*) the experimental values of the solvent density and molecular sizes are used as input parameters in calculating ΔG_c (23).

We can now return to the different temperature dependencies of ΔG_c in water, 7 M aqueous urea, and 4.9 M aqueous GuHCl. The density of 7 M urea and 4.9 M GuHCl solutions decreases with temperature a little more rapidly than that of water because the geometric constraints due to the planarity of urea molecules and guanidinium ions cause a distortion of surrounding H-bonds on increasing the random thermal energy. This does not, however, imply that urea and GuHCl are water-structure breakers, because the differences in the temperature dependence of liquid density and hydrocarbon solubility are small between water, 7 M urea, and 4.9 M GuHCl. In this regard, it should be recognized that 7 M aqueous urea is 38% urea by weight (36) and 4.9 M aqueous GuHCl is 42% GuHCl by weight (39).

Discussion

It should be emphasized that a change in a thermodynamic function, being a macroscopic quantity, cannot provide any microscopic information. The overall process has to be dissected in subprocesses, each having a well-defined physical meaning and a rigorous statistical mechanical description, to try to obtain a molecular interpretation. This is the approach adopted in the present study. To further emphasize the situation, we point out that the values of $\Delta G^\bullet$, $\Delta H^\bullet$, and $\Delta S^\bullet$ collected in Tables 1 and 2 provide no information on their molecular origin. One could say that both transfer processes are contrasted by enthalpic effects because they are endothermic and are favored by entropic effects because they cause an entropy increase. But such a statement does not clarify anything and would be, to say the least, misleading. In contrast, the performed analysis, based on rigorous statistical mechanical theories of hydrophobic hydration (13–15), clarifies the molecular processes involved and how they give rise to the overall experimentally measured thermodynamic changes. The results obtained seem reliable and allow one to rationalize an important question.

In this respect, it is worth noting that a similar rationalization was provided by Roseman and Jencks (72), albeit in a qualitative fashion (i.e., no calculations were performed). They hypothesized that the increased solubility of large hydrocarbons is due to a more favorable sum of the work of cavity creation and van der Waals interaction energy in the presence of GuHCl and urea, compared with pure water. Furthermore, in the case of polar solutes, Roseman and Jencks (72) suggested that the contribution due to the formation of multiple H-bonds by GuHCl and urea, in addition to the first two always operative, renders even more negative the transfer-Gibbs energy change. In fact, Nandi and Robinson (7) determined $\Delta G^\bullet$ = –0.5 and –0.9 kJ mol^{-1}, respectively, for the transfer from water to 7 M urea and to 5 M GuHCl, at 25°C, of the CH_2CONH group (it contains one more hydrogen atom than the repeating unit of protein backbone). These numbers are significantly larger in magnitude than those obtained for aliphatic side chains (see Tables 1 and 2), suggesting that the interactions of urea and GuHCl with the peptide group are responsible for their denaturing action.

Clearly, the use of the SPT-valid equation to calculate ΔG_c in pure liquids for aqueous solutions of GuHCl and urea may be seriously questioned. This important topic has been discussed in detail in the work on alkane solubility in 7 M aqueous urea at room temperature (12). Here we add only the following points. The SPT equation is used solely to obtain estimates of ΔG_c, which is a measure of the excluded volume effect caused by solute insertion into the solvent. If we assumed, more correctly, that 7 M urea and 4.9 M GuHCl are mixtures, we could use the SPT-valid relation for mixtures to calculate ΔG_c (73). The results would be quantitatively, but not qualitatively, different. The work of cavity creation is always larger in 7 M urea and 4.9 M GuHCl than in water (data not shown). The simple approach is preferred when considering 7 M aqueous urea and 4.9 M aqueous GuHCl as uniform solvent systems to render a more clear analysis and interpretation of the calculations. Clearly, such an approach does not allow the calculation of the squeezing force exerted by whatever surrounding solvent molecules on the cavity surface (68), nor the single contributions from water, urea, and GuH^+ and Cl^- ions. To perform this type of analysis, computer simulations have to be carried out. We believe, however, that our procedure provides qualitatively correct ΔG_c estimates (for more on this point, see Appendix 2).

In conclusion, in the whole range of 5–45°C, the transfer of hydrocarbons from water to 7 M urea or to 4.9 M GuHCl is contrasted by the difference in the work of cavity creation (i.e., the $\Delta\Delta G_c$ term), but is favored by the difference in the solute–solvent van der Waals interaction energy (i.e., the ΔE_a term). The latter contribution increases in magnitude with hydrocarbon size more rapidly than the first one, accounting for the occurrence of a threshold size for the solubility enhancement at room temperature. The H-bond reorganization upon solute insertion is a compensating process in all three solvent systems and does not affect the transfer-Gibbs energy change. Moreover, on raising the temperature, the hydrocarbon solubility in 7 M urea or 4.9 M GuHCl increases compared with that in water because the $\Delta\Delta G_c$ term becomes less unfavorable, while the ΔE_a term is practically constant. The temperature dependence of $\Delta\Delta G_c$ reflects the fact that the density of 7 M urea and that of 4.9 M GuHCl decrease a little more rapidly than the density of liquid water.

The analysis performed appears to be in accordance with Occam's razor: the fewest possible assumptions should be made in explaining a thing because the simplest explanation is usually the correct one.

© 2002 NRC Canada

Acknowledgment

The author wishes to thank reviewers for helpful comments.

References

1. D.B. Wetlaufer, S.K. Malik, L. Stoller, and R.L. Coffin. J. Am. Chem. Soc. **86**, 508 (1964).
2. A. Ben-Naim. Solvation thermodynamics. Plenum Press, New York. 1987.
3. B. Lee. Methods Enzymol. **259**, 555 (1995).
4. G.S. Kell. J. Chem. Eng. Data, **20**, 97 (1975).
5. K. Kawahara and C. Tanford. J. Biol. Chem. **241**, 3228 (1966).
6. P.L. Privalov and S.J. Gill. Adv. Protein Chem. **39**, 191 (1988); W. Blokzijl and J.B.F.N. Engberts. Angew. Chem. Int. Ed. Engl. **32**, 1545 (1993).
7. P.K. Nandi and D.R. Robinson. Biochemistry, **23**, 6661 (1984).
8. Y. Nozaki and C. Tanford. J. Biol. Chem. **238**, 4074 (1963); J. Biol. Chem. **245**, 1648 (1979); C.N. Pace. Methods Enzymol. **131**, 266 (1986).
9. A. Ben-Naim and M. Yaacobi. J. Phys. Chem. **78**, 170 (1974).
10. R. Breslow and T. Guo. Proc. Natl. Acad. Sci. U.S.A. **87**, 167 (1990).
11. N. Muller. J. Phys. Chem. **94**, 3856 (1990).
12. G. Graziano. J. Phys. Chem. B, **105**, 2632 (2001).
13. L.R. Pratt and D. Chandler. J. Chem. Phys. **67**, 3683 (1977); J. Chem. Phys. **73**, 3434 (1980).
14. B. Lee. Biopolymers, **24**, 813 (1985); Biopolymers, **31**, 993 (1991).
15. G. Graziano. J. Chem. Soc. Faraday Trans. **94**, 3345 (1998); Biophys. Chem. **82**, 69 (1999); an. J. Chem. **78**, 1233 (2000).
16. B. Lee and G. Graziano. J. Am. Chem. Soc. **118**, 5163 (1996); G. Graziano. J. Phys. Chem. B, **104**, 9249 (2000).
17. B. Lee. J. Chem. Phys. **83**, 2421 (1985); G. Graziano. J. Phys. Soc. Jpn. **69**, 1566 (2000).
18. R. Lumry, E. Battistel, and C. Jolicoeur. Faraday Symp. Chem. Soc. **17**, 93 (1982); E. Grunwald. J. Am. Chem. Soc. **108**, 5726 (1986); H.A. Yu and M. Karplus. J. Chem. Phys. **89**, 2366 (1988); H. Qian and J.J. Hopfield. J. Chem. Phys. **105**, 9292 (1996); H.S. Ashbaugh and M. Paulaitis. J. Phys. Chem. **100**, 1900 (1996).
19. L. Liu and Q.X. Guo. Chem. Rev. **101**, 673 (2001).
20. A. Ben-Naim. Biopolymers, **14**, 1337 (1975); J. Phys. Chem. **82**, 874 (1978).
21. B. Lee. Biophys. Chem. **51**, 271 (1994).
22. H. Reiss. Adv. Chem. Phys. **9**, 1 (1966).
23. R.A. Pierotti. Chem. Rev. **76**, 717 (1976).
24. N. Desrosiers and J.E. Desnoyers. Can. J. Chem. **54**, 3800 (1976).
25. D. Patterson. Pure Appl. Chem. **47**, 305 (1976).
26. J.L. Finney, A.K. Soper, and J.Z. Turner. Physica B, **156–157**, 151 (1989); J.Z. Turner, J.L. Finney, and A.K. Soper. Z. Naturforsch. **46a**, 73 (1991); J.L. Finney, A.K. Soper, and J.Z. Turner. Pure Appl. Chem. **65**, 2521 (1993).
27. A.J. Easteal. Can. J. Chem. **68**, 1611 (1990); K. Yoshida, K. Ibuki, and M. Ueno. J. Chem. Phys. **108**, 1360 (1998); M. Mayele and M. Holz. Phys. Chem. Chem. Phys. **2**, 2429 (2000).
28. K. Sharp, B. Madan, E. Manas, and J.M. Vanderkooi. J. Chem. Phys. **114**, 1791 (2001).
29. J. Tsai, M. Gerstein, and M. Levitt. J. Chem. Phys. **104**, 9417 (1996); F. Vanzi, B. Madan, and K. Sharp. J. Am. Chem. Soc. **120**, 10748 (1998).
30. P.E. Smith. J. Phys. Chem. B, **103**, 525 (1999); R. Chitra and P.E. Smith. J. Phys. Chem. B, **104**, 5854 (2000).
31. P.O. Astrand, A. Wallqvist, G. Karlstrom, and P. Linse. J. Chem. Phys. **95**, 8419 (1991).
32. R.A. Pierotti. J. Phys. Chem. **69**, 281 (1965).
33. J.M. Sorenson, G. Hura, R.M. Glaeser, and T. Head-Gordon. J. Chem. Phys. **113**, 9149 (2000).
34. A. Minton. Methods Enzymol. **295**, 127 (1998); Biophys. J. **78**, 101 (2000).
35. A. Pertsemlidis, A.K. Soper, J.M. Sorenson, and T. Head-Gordon. Proc. Natl. Acad. Sci. U.S.A. **96**, 481 (1999).
36. D.R. Lide. Handbook of chemistry and physics. 79th ed. CRC Press, Boca Raton, FL. 1998.
37. E. Reisler, and H. Eisenberg. Biochemistry, **8**, 4572 (1969).
38. H. Durchschlag. *In* Thermodynamic data for biochemistry and biotechnology. *Edited by* H.J. Hinz. Springer-Verlag, Berlin. 1986. Chap. 3. pp. 45–128.
39. G.I. Makhatadze, J. Fernandez, E. Freire, T.H. Lilley, and P.L. Privalov. J. Chem. Eng. Data, **38**, 83 (1993).
40. R.H. Stokes. Aust. J. Chem. **20**, 2087 (1967).
41. C.A. Swenson. Arch. Biochem. Biophys. **117**, 494 (1966); J.A. Glasel. J. Am. Chem. Soc. **92**, 372 (1970); S. Subramanian, T.S. Sarma, D. Balasubramanian, and J.C. Ahluwalia. J. Phys. Chem. **75**, 815 (1971).
42. M. Lucas. J. Phys. Chem. **80**, 359 (1976).
43. J. Timmermans. The physico-chemical constants of binary systems in concentrated solutions. Vol. 4. Interscience, New York. 1960. p. 118.
44. R.M. Jackson and M.J.E. Sternberg. Protein Eng. **7**, 371 (1994); F.M. Floris, M. Selmi, A. Tani, and J. Tomasi. J. Chem. Phys. **107**, 6353 (1997).
45. R.L. Baldwin. Biophys. J. **71**, 2056 (1996).
46. K. Lum, D. Chandler, and J.D. Weeks. J. Phys. Chem. B, **103**, 4570 (1999).
47. H.S. Ashbaugh and M.E. Paulaitis. J. Am. Chem. Soc. **123**, 10721 (2001).
48. M.P. Moody and P. Attard. J. Chem. Phys. **115**, 8967 (2001).
49. W.L. Jorgensen, J. Gao, and C. Ravimohan. J. Phys. Chem. **89**, 3470 (1985).
50. P. Linse. J. Am. Chem. Soc. **112**, 1744 (1990).
51. J.M. Corkill, J.F. Goodman, S.P. Harrold, and J.R. Tate. Trans. Faraday Soc. **63**, 240 (1967).
52. A. Wallqvist, D.G. Covell, and D. Thirumalai. J. Am. Chem. Soc. **120**, 427 (1998); A. Caflisch and M. Karplus. Structure, **7**, 477 (1999).
53. F.H. Stillinger. Science (Washington, D.C.), **209**, 451 (1980); K.A. Dill. Biochemistry, **29**, 7133 (1990).
54. H.S. Frank and M.W. Evans. J. Chem. Phys. **13**, 507 (1945); H.S. Frank and W.Y. Wen. Disc. Faraday Soc. **24**, 133 (1957); H.S. Frank and A.S. Quist. J. Chem. Phys. **34**, 604 (1961).
55. W. Kauzmann. Adv. Protein Chem. **14**, 1 (1959).
56. G. Nemethy and H.A. Scheraga. J. Chem. Phys. **36**, 3401 (1962); G. Nemethy. Angew. Chem. Int. Ed. **6**, 195 (1967).
57. B. Madan and K.A. Sharp. J. Phys. Chem. **100**, 7713 (1996); K.A. Sharp and B. Madan. J. Phys. Chem. B, **101**, 4343 (1997); K.A.T. Silverstein, A.D.J. Haymet, and K.A. Dill. J. Am. Chem. Soc. **120**, 3166 (1998).
58. A. Wallqvist and D.G. Covell. Biophys. J. **71**, 600 (1996); S.R. Durell and A. Wallqvist. Biophys. J. **71**, 1695 (1996).
59. K.E. Laidig and V. Daggett. J. Phys. Chem. **100**, 5616 (1996); R.L. Mancera. J. Chem. Soc. Faraday Trans. **94**, 3549 (1998); J. Phys. Chem. B, **103**, 3774 (1999).
60. E. Gallicchio, M.M. Kubo, and R.M. Levy. J. Phys. Chem. B, **104**, 6271 (2000).
61. A.K. Soper, and J.L. Finney. Phys. Rev. Lett. **71**, 4346 (1993); J.L. Finney and A.K. Soper. Chem. Soc. Rev. **23**, 1 (1994);

© 2002 NRC Canada

K.S. Sidhu, J.M. Goodfellow, and J.Z. Turner. J. Chem. Phys. **110**, 7943 (1999).
62. D.T. Bowron, A. Filipponi, C. Lobban, and J.L. Finney. Chem. Phys. Lett. **293**, 33 (1998); D.T. Bowron, A. Filipponi, M.A. Roberts, and J.L. Finney. Phys. Rev. Lett. **81**, 4164 (1998).
63. B. Guillot and Y. Guissani. J. Chem. Phys. **99**, 8075 (1993); T. Lazaridis, G. Archontis, and M. Karplus. Adv. Protein Chem. **47**, 426 (1995); T. Lazaridis. J. Phys. Chem. B, **104**, 4964 (2000).
64. R.C. Tolman. The principles of statistical mechanics. Oxford University Press, Oxford. 1938.
65. J.P. Kocher, M. Prevost, S.J. Wodak, and B. Lee. Structure, **4**, 1517 (1996); M. Prevost, I.T. Oliveira, J.P. Kocher, and S.J. Wodak. J. Phys. Chem. **100**, 2738 (1996).
66. B.J. Berne. Proc. Natl. Acad. Sci. U.S.A. **93**, 8800 (1996); G. Hummer, S. Garde, A.E. Garcia, A. Pohorille, and L.R. Pratt. Proc. Natl. Acad. Sci. U.S.A. **93**, 8951 (1996).
67. D. Chandler, J.D. Weeks, and H.C. Andersen. Science (Washington, D.C.), **220**, 787 (1983).
68. A. Pohorille and L.R. Pratt. J. Am. Chem. Soc. **112**, 5066 (1990); L.R. Pratt and A. Pohorille. Proc. Natl. Acad. Sci. U.S.A. **89**, 2995 (1992).
69. K.E.S. Tang and V.A. Bloomfield. Biophys. J. **79**, 2222 (2000).
70. B. Madan and B. Lee. Biophys. Chem. **51**, 279 (1994); M. Ikeguchi, S. Shimizu, S. Nakamura, and K. Shimizu. J. Phys. Chem. B, **102**, 5891 (1998).
71. B.D. Smith and R. Srivastava. Thermodynamic data for pure compounds. Part A, hydrocarbons and ketones. Elsevier, Amsterdam. 1986.
72. M. Roseman and W.P. Jencks. J. Am. Chem. Soc. **97**, 631 (1975).
73. J.L. Lebowitz, E. Helfand, and E. Praestgaard. J. Chem. Phys. **43**, 774 (1965).
74. R.B. Hermann. J. Phys. Chem. **76**, 2754 (1972).
75. M. Yaacobi and A. Ben-Naim. J. Solution Chem. **2**, 425 (1973).
76. A. Ben-Naim and M. Yaacobi. J. Phys. Chem. **79**, 1263 (1975).
77. A. Kalra, N. Tugcu, S.M. Cramer, and S. Garde. J. Phys. Chem. B, **105**, 6380 (2001).

Appendix 1. Solvation thermodynamics in water–ethanol and water–*p*-dioxane mixtures

We would like to apply the same approach to the analysis of $\Delta G^{\bullet}$ data for the solvation of methane in water–ethanol and water–*p*-dioxane mixtures at 25°C. The experimental data, which come from the works of Yaacobi and Ben-Naim (75, 76), covers all the composition range from pure water to pure ethanol and from pure water to pure *p*-dioxane, and are reported in the fifth column of Tables 1A and 2A, respectively. We also point out that the solvation thermodynamics of ethane in such mixtures were determined and proved to be similar in all respects to those of methane (75, 76). For this reason the data for ethane are not analyzed here.

For each mixture, we have calculated the mean value of σ, v, and ξ using eqs. [7] and [8] and data for pure liquids (i.e., the molar volumes have been used in view of the qualitative purpose of this Appendix). Such estimates are listed in the second, third, and fourth columns of Tables 1A and 2A. The values of ΔG_c are calculated using the SPT relationship valid for pure liquids (eq. [22] of the accompanying paper[1]), with σ = 3.70 Å for methane. They are listed in column six of Tables 1A and 2A. The values of E_a are determined using the hybrid procedure, performing the difference $\Delta G^{\bullet} - \Delta G_c$, and they are listed in column seven of Tables 1A and 2A. It is evident that both ΔG_c and E_a show a non-monotonous trend as a function of the molar fraction of either ethanol (x_{EtOH}) or *p*-dioxane ($x_{dioxane}$) in the mixture. The trend of ΔG_c is a consequence of the combined dependence of the ΔG_c magnitude upon the values of σ and ξ of the solvent, as already discused in the text. The trend of E_a parallels that of the mean volume-packing density of the solvent. In water–ethanol mixtures, E_a (in kJ mol^{-1}) decreases, in absolute value, from –12.7 in pure water (ξ = 0.363), to –9.3 at x_{EtOH} = 0.20 (ξ = 0.348), and then increases to –14.0 in pure ethanol (ξ = 0.439). In water–*p*-dioxane mixtures, E_a (in kJ mol^{-1}) decreases, in absolute value, from –12.7 in pure water (ξ = 0.363), to –8.1 at $x_{dioxane}$ = 0.20 (ξ = 0.343), and then increases to –17.5 in pure p-dioxane (ξ = 0.538).

Even though this finding confirms the qualitative correctness of eq. [10], the latter does not work quantitatively well, as can be easily verified. This is due to the fact that E_a depends also upon the number of solvent molecules in contact with the solute surface, the so-called contact density. We suggest, therefore, that water molecules preferentially interact with ethanol and *p*-dioxane molecules to form H-bonds, and this causes a decrease in the number of solvent molecules in contact with the surface of the methane molecule. In other words, a preferential desolvation of the solute surface should happen, and it appears to occur to a greater extent when the molar fraction of both ethanol and *p*-dioxane is around 0.2. Clearly, this suggestion should be tested by means of detailed computer simulations, determining the pair correlation function between the solute and solvent molecules.

Appendix 2. Work of cavity creation in aqueous salt solutions

We would like to further test the reliability of using the SPT-valid relationship for pure liquids (eq. [22] of the accompanying paper[1]) to calculate ΔG_c in aqueous salt solutions. To this end, we take advantage of the results reported by Garde and co-workers (77). The authors calculated ΔG_c estimates in water and aqueous solutions of three tetramethylammonium salts: TMAF, TMACl, and TMABI (BI stands for big ion). At room temperature, using the test-particle-insertion method coupled with molecular dynamics simulations, Garde and co-workers found that, to create a cavity of 4.0 Å diameter, ΔG_c (in kJ mol^{-1}) = 24.9 in water, 28.7 in 3 M TMACl, 30.7 in 3 M TMAF, and 23.4 in 3 M TMABI (see Fig. 3 in ref. 77). ΔG_c is, therefore, larger in 3 M TMAF and 3 M TMACl than in water, but smaller in 3 M TMABI than in water. From the numbers reported in Tables 1 and 2 in ref. 77, we have determined, for the three salts, the values of the hard-sphere diameter, the apparent molar volume, and molar fraction in a 3 M aqueous solution. Specifically, (*i*) for TMAF, σ = 6.7 Å, Φ_v = 46.3 cm^3 mol^{-1} and x = 0.05; (*ii*) for TMACl, σ = 8.0 Å, Φ_v = 88.8 cm^3 mol^{-1} and x = 0.07; (*iii*) for TMABI, σ = 9.7 Å, Φ_v = 164.2 cm^3 mol^{-1} and x = 0.10. Then, using eqs. [7] and [8], we have calculated the mean values of σ, v, and ξ for the 3 M aqueous salt solutions; specifically, (*i*) for 3 M TMAF, σ = 2.95 Å, v = 19.5 cm^3 mol^{-1}, and ξ = 0.415; (*ii*) for 3 M TMACl, σ = 3.12 Å, v = 23.0 cm^3 mol^{-1}, and ξ = 0.416;

© 2002 NRC Canada

Table 1A. Mean values of the hard-sphere diameter, molar volume, and volume-packing density for water–ethanol mixtures. Experimental $\Delta G^{\bullet}$ data from ref. 75; estimates of ΔG_c and E_a for the solvation of methane in water–ethanol mixtures at 25°C.

x_{EtOH}	σ (Å)	v (cm^3 mol^{-1})	ξ	$\Delta G^{\bullet}$ (kJ mol^{-1})	ΔG_c (kJ mol^{-1})	E_a (kJ mol^{-1})
0.00	2.75	18.07	0.363	8.4	21.1	–12.7
0.02	2.78	18.88	0.360	8.2	20.3	–12.1
0.03	2.80	19.29	0.358	8.1	19.9	–11.8
0.045	2.82	19.90	0.356	8.0	19.4	–11.4
0.06	2.85	20.51	0.354	8.0	18.9	–10.9
0.09	2.89	21.73	0.351	8.0	18.1	–10.1
0.12	2.94	22.94	0.350	7.8	17.6	–9.8
0.15	2.99	24.16	0.349	7.5	17.0	–9.5
0.20	3.07	26.19	0.348	6.9	16.2	–9.3
0.25	3.15	28.22	0.349	6.2	15.7	–9.5
0.40	3.39	34.31	0.358	4.5	14.7	–10.2
0.60	3.70	42.44	0.378	3.2	14.3	–11.1
0.80	4.02	50.56	0.406	2.3	14.7	–12.4
1.00	4.34	58.68	0.439	1.6	15.6	–14.0

Table 2A. Mean values of the hard-sphere diameter, molar volume, and volume-packing density for water–*p*-dioxane mixtures. Experimental $\Delta G^{\bullet}$ data from ref. 76; estimates of ΔG_c and E_a for the solvation of methane in water–*p*-dioxane mixtures at 25°C.

$x_{dioxane}$	σ (Å)	v (cm^3 mol^{-1})	ξ	$\Delta G^{\bullet}$ (kJ mol^{-1})	ΔG_c (kJ mol^{-1})	E_a (kJ mol^{-1})
0.00	2.75	18.07	0.363	8.4	21.1	–12.7
0.015	2.79	19.08	0.359	8.2	20.1	–11.9
0.03	2.83	20.09	0.356	8.2	19.3	–11.1
0.06	2.90	22.11	0.348	7.9	17.8	–9.9
0.09	2.98	24.13	0.346	7.6	16.8	–9.2
0.12	3.05	26.14	0.342	7.3	15.9	–8.6
0.15	3.13	28.16	0.343	6.9	15.3	–8.4
0.20	3.25	31.53	0.343	6.3	14.4	–8.1
0.40	3.75	44.98	0.370	4.5	13.5	–9.0
0.70	4.51	65.17	0.444	3.3	15.1	–11.8
1.00	5.26	85.35	0.538	2.3	19.8	–17.5

(*iii*) for 3 M TMABI, σ = 3.45 Å, v = 32.6 cm^3 mol^{-1}, and ξ = 0.397. Correspondingly, to create a cavity of 4.0 Å diameter at 25°C, ΔG_c (in kJ mol^{-1}) = 23.9 in water, 26.1 in 3 M TMACl, 28.5 in 3 M TMAF, and 20.0 in 3 M TMABI. Such ΔG_c estimates are in line with the results of Garde and co-workers. The value in water is close to that from computer simulations, whereas those in salt solutions are underestimated by about 2.5 kJ mol^{-1}. This finding emphasizes that our approach, notwithstanding its simplicity, provides reliable ΔG_c numbers also in aqueous salt solutions.

© 2002 NRC Canada

Size dependence of the solubility of nonpolar compounds in different solvents

Giuseppe Graziano

Abstract: At 25°C, plots of the standard Gibbs energy change associated with the solvation of noble gases and aliphatic hydrocarbons vs. the size of the solutes prove to be approximately linear with a negative slope for common organic solvents but not for water. In the latter case, the plot has a characteristic V-shape. The slope is negative for noble gases, methane, and ethane, but is positive for larger alkanes. This means that the solubility of nonpolar solutes increases with solute size in every solvent except water. The solvation thermodynamics of noble gases and aliphatic hydrocarbons in five solvents (water, ethanol, benzene, *c*-hexane, and *n*-hexane) are analyzed in detail by a general theory, which is rederived to avoid risky misunderstandings. The calculations are performed in the same manner for all solvents, using simple formulas where the physical reliability is well established and the results are consistent. The work of cavity creation increases with solute size in every solvent, but to a far greater extent in water. Additionally, the work to turn on the solute–solvent attractive interactions increases in magnitude with solute size in every solvent, but to a lesser extent in water. By combining these two factors a satisfactory explanation for experimental data obtained emerges. The microscopic origins of the difference between water and common organic solvents are discussed.

Key words: solvation, excluded-volume effect, solute–solvent interactions, enthalpy–entropy compensation, molecular size.

Résumé : À 25°C, les courbes reliant le changement d'énergie de Gibbs standard associé à la solvatation de gaz rares et d'hydrocarbures aliphatiques avec la taille des solutés sont approximativement linéaires et la pente est légèrement négative pour les solvants organiques habituels, mais ce n'est pas le cas pour l'eau. Dans ce dernier cas, la courbe présente une forme en V caractéristique: la pente est négative pour les gaz rares, le méthane et l'éthane, mais elle est positive pour les hydrocarbures à plus longue chaîne. Ces observations signifient que la solubilité des solutés non polaires augmente avec la taille du soluté dans tous les solvants, excepté l'eau. Faisant appel à une théorie générale qui a été complètement redérivée pour éviter toute conception erronée, on a analysé en détail les données thermodynamiques pour la solvatation de gaz rares et d'hydrocarbures aliphatiques dans cinq solvants, soit l'eau, l'éthanol, le benzène, l'hexane et le *c*-hexane. Les calculs ont été réalisés de la même manière pour chacun des solvants, en utilisant des formules simples dont la fiabilité est bien établie et qui donnent des résultats cohérents. Le travail de création d'une cavité augmente avec la taille dans chaque solvant, mais cette augmentation est beaucoup plus grande dans l'eau. De plus, l'amplitude du travail nécessaire pour provoquer le développement d'interactions d'attraction soluté–solvant augmente avec la taille du soluté pour chaque solvant, mais elle augmente moins dans l'eau. En combinant ces deux tendances, il se dégage une explication satisfaisante des données expérimentales. On discute des origines microscopiques de la différence entre l'eau et les solvants organiques habituels.

Mots clés : solvatation, effet du volume exclu, interactions soluté–solvant, compensation enthalpie–entropie, taille moléculaire.

[Traduit par la Rédaction]

Introduction

The analysis of the experimental values of the standard Gibbs energy of solvation at 25°C of noble gases and aliphatic hydrocarbons in a variety of solvents pointed out an unexpected situation (1). When the $\Delta G^{\bullet}$ values in a given solvent were plotted against the solute diameter, approximate linear trends were obtained for every solvent studied except water. In the latter case, a straight line was found only for the hydration of noble gases, whereas a V-shape trend was obtained by combining the data for noble gases and aliphatic hydrocarbons (1). A complete explanation of this experimental finding is still lacking, even though a reasonable answer has recently been suggested (2).

It is worth noting that the change in the standard solvation Gibbs energy is defined, according to Ben-Naim (3), as $\Delta G^{\bullet} = RT \ln (C_g/C_l)$, where C_g and C_l are the molar concentrations of the solute in the gas and liquid phases at equilibrium. The $\Delta G^{\bullet}$ values provide a direct measure of the solubility of a solute in a given solvent.

Received 16 November 2001. Published on the NRC Research Press Web site at http://canjchem.nrc.ca on 8 April 2002.

G. Graziano. Dipartimento di Chimica, Università di Napoli "Federico II," Complesso Universitario di Monte S.Angelo, Via Cinthia, 45 – 80126 Napoli, Italy and Facoltà di Scienze, Università del Sannio, Via Port'Arsa, 11 – 82100 Benevento, Italy. (e-mail: graziano@chemistry.unina.it and graziano@unisannio.it).

 DOI: 10.1139/V02-040 © 2002 NRC Canada

Table 1. Standard Gibbs energy change ($\Delta G^{\bullet}$) associated with the solvation at 25°C of noble gases and aliphatic hydrocarbons in five different solvents.

	$\Delta G^{\bullet}$(water) (kJ mol^{-1})	$\Delta G^{\bullet}$(ethanol) (kJ mol^{-1})	$\Delta G^{\bullet}$(benzene) (kJ mol^{-1})	$\Delta G^{\bullet}$(*c*-hexane) (kJ mol^{-1})	$\Delta G^{\bullet}$(*n*-hexane) (kJ mol^{-1})
He	11.5	8.5	9.6	8.9	7.5
Ne	11.2	7.7	8.6	8.0	6.6
Ar	8.4	3.3	3.5	2.7	1.9
Kr	6.9	1.0	0.7	–0.1	–0.7
Xe	5.5	—	–2.9	–3.8	–3.9
Rn	3.7	–4.2	–6.0	—	–6.5
CH_4	8.3	1.6	1.4	0.8	0.2
C_2H_6	7.6	–2.5	–3.5	–4.1	–4.3
C_3H_8	8.2	–5.2	–6.7	–7.6	–7.5
i-C_4H_{10}	9.7	–6.9	–8.7	–9.7	–9.8
n-C_4H_{10}	8.7	–8.1	–10.0	–11.1	–10.6
$C(CH_3)_4$	10.5	–8.6	–10.5	—	–11.6
n-C_5H_{12}	9.9	–10.1	–13.1	–13.8	–13.8

Note: The values for water are from ref. 2; those for ethanol, benzene, *c*-hexane, and *n*-hexane are from ref. 1, after correction for the Ben-Naim standard state.

Table 2. Standard enthalpy change ($\Delta H^{\bullet}$) associated with the solvation at 25°C of noble gases and aliphatic hydrocarbons in five different solvents.

	$\Delta H^{\bullet}$(water) (kJ mol^{-1})	$\Delta H^{\bullet}$(ethanol) (kJ mol^{-1})	$\Delta H^{\bullet}$(benzene) (kJ mol^{-1})	$\Delta H^{\bullet}$(*c*-hexane) (kJ mol^{-1})	$\Delta H^{\bullet}$(*n*-hexane) (kJ mol^{-1})
He	1.8	8.9	11.6	11.6	9.6
Ne	–1.3	7.6	14.1	7.9	7.0
Ar	–9.6	1.1	2.8	0.7	–1.2
Kr	–13.0	—	–0.1	–1.8	–3.2
Xe	–16.8	—	–5.6	–7.2	–9.2
Rn	–19.1	–10.2	–11.8	—	–11.2
CH_4	–10.9	–2.1	0.3	–0.9	–0.7
C_2H_6	–17.2	–7.1	–6.0	–9.3	–6.8
C_3H_8	–21.0	–12.4	–10.6	–13.9	–12.6
i-C_4H_{10}	–21.9	–16.1	–13.1	—	–17.3
n-C_4H_{10}	–23.6	–17.7	–16.0	—	–19.0
$C(CH_3)_4$	–22.8	—	—	—	–20.0
n-C_5H_{12}	–26.0	–23.4	–20.6	–23.9	–25.2

Note: The values for water are from ref. 2; those for ethanol, benzene, *c*-hexane, and *n*-hexane are from ref. 1, after correction for the Ben-Naim standard state.

The experimental values of the standard Gibbs energy of solvation at 25°C of noble gases and aliphatic hydrocarbons in five solvents (water, ethanol, benzene, *c*-hexane, and *n*-hexane) are listed in Table 1, and the corresponding standard enthalpy and entropy changes are reported in Tables 2 and 3, respectively (1, 2). Clearly, water as well as polar and nonpolar organic solvents are represented in our selection. Customary values of the hard-sphere diameters of both solvents and solutes are listed in the second column of Table 4 (4, 5). These values serve only to rank order of the relative size of the species considered, and do not imply that the molecules are really spheres.

Plots of $\Delta G^{\bullet}$ vs. σ are shown in Figs. 1–4 for the first four solvents. The plot for water has the characteristic V-shape, whereas the plots for ethanol, benzene, and *c*-hexane show approximately linear trends (*n*-hexane is not shown because it is qualitatively similar). The fundamental point is the sign of the slope of these plots — it is negative in all cases, except for large alkanes in water. This means that, at room temperature, on increasing the solute size, the solubility of both noble gases and alkanes increases in common organic solvents. It also increases for noble gases in water, but not for alkanes in water. This puzzling result is not simple to rationalize since the solvation mechanism of noble gases and aliphatic hydrocarbons in water cannot be different because all these solutes are nonpolar. A reliable explanation of the experimental data by means of a general theory of solvation, originally elaborated by Lee (6) and fruitfully applied by us to explain several aspects of hydrophobic hydration and solvation (7–9), will be provided. First, Lee's theory of solvation (6) will be described, followed by a detailed explanation of the procedures adopted to perform calculations. Finally,

© 2002 NRC Canada

Table 3. Standard entropy change ($\Delta S^\bullet$) associated with the solvation at 25°C of noble gases and aliphatic hydrocarbons in five different solvents.

	$\Delta S^\bullet$(water) (J K^{-1} mol^{-1})	$\Delta S^\bullet$(ethanol) (J K^{-1} mol^{-1})	$\Delta S^\bullet$(benzene) (J K^{-1} mol^{-1})	$\Delta S^\bullet$(*c*-hexane) (J K^{-1} mol^{-1})	$\Delta S^\bullet$(*n*-hexane) (J K^{-1} mol^{-1})
He	–32.5	1.3	6.7	9.1	7.0
Ne	–41.9	–0.3	18.5	–0.3	1.3
Ar	–60.4	–7.4	–2.4	–6.7	–1.0
Kr	–66.8	—	–2.7	–5.7	–8.4
Xe	–74.8	—	–9.1	–11.4	–17.8
Rn	–76.2	–20.1	–19.5	—	–15.8
CH_4	–64.4	–12.4	–3.7	–5.7	–3.0
C_2H_6	–83.2	–15.4	–8.4	–17.4	–8.4
C_3H_8	–97.9	–24.2	–13.1	–21.1	–17.1
i-C_4H_{10}	–106.0	–30.9	–14.8	—	–25.2
n-C_4H_{10}	–108.3	–32.2	–20.1	—	–28.2
$C(CH_3)_4$	–111.7	—	—	—	–28.2
n-C_5H_{12}	–120.4	–44.6	–25.2	–33.9	–38.2

Note: The values for water are from ref. 2; those for ethanol, benzene, *c*-hexane, and *n*-hexane are from ref. 1, after correction for the Ben-Naim standard state.

Table 4. Hard-sphere diameters and Lennard–Jones potential parameters (4,5) for the solvents and solutes considered in this work.

	σ (Å)	ε/*k* (K)
Water	2.75	100
Ethanol	4.34	330
Benzene	5.26	531
c-Hexane	5.63	573
n-Hexane	5.92	517
He	2.63	5
Ne	2.79	20
Ar	3.41	120
Kr	3.67	160
Xe	3.96	230
Rn	4.23	300
CH_4	3.70	150
C_2H_6	4.38	250
C_3H_8	5.06	300
i-C_4H_{10}	5.55	330
n-C_4H_{10}	5.65	350
$C(CH_3)_4$	5.89	350
n-C_5H_{12}	6.16	370

Note: Additional data at 25°C used for SPT calculations are: v = 18.07 cm^3 mol^{-1} (ξ = 0.363) for water; v = 58.68 cm^3 mol^{-1} (ξ = 0.439) for ethanol; v = 89.41 cm^3 mol^{-1} (ξ = 0.513) for benzene; v = 108.75 cm^3 mol^{-1} (ξ = 0.517) for *c*-hexane; v = 131.62 cm^3 mol^{-1} (ξ = 0.497) for *n*-hexane.

the solvation process of noble gases and aliphatic hydrocarbons in the five selected solvents is analyzed and an explanation is suggested.

Theory of solvation

Solvation, as suggested by Ben-Naim (3), refers to the transfer of a solute molecule from a fixed position in the ideal gas phase to a fixed position in a solvent at constant temperature and pressure. The process can be regarded as the insertion of an external perturbing potential ($\Psi(\boldsymbol{X})$), where $\boldsymbol{X}$ is a vector representing a single configuration of the N molecules of the liquid solvent. On the basis of Widom's potential distribution theorem (10), the Ben-Naim standard Gibbs energy change is

$$[1] \qquad \Delta G^\bullet = -RT \ln \langle \exp[-\Psi(\boldsymbol{X})/RT] \rangle_p$$

where the subscript p means that the ensemble average is performed over the pure-solvent configurations, assuming an NPT ensemble. The average is taken using the probability density function of the pure solvent

$$[2] \qquad \rho_p(\boldsymbol{X}) = \frac{\exp[-H(\boldsymbol{X})/RT]}{\int \exp[-H(\boldsymbol{X})/RT]\, d\boldsymbol{X}}$$

where $H(\boldsymbol{X}) = U(\boldsymbol{X}) + PV(\boldsymbol{X})$ is the enthalpy function of a configuration, $U(\boldsymbol{X})$ and $V(\boldsymbol{X})$ are the corresponding internal energy and volume, and the denominator is the isobaric partition function of the system. The fluctuations in the system volume occurring in an NPT ensemble are, therefore, correctly accounted for. It is important to realize that, in performing the ensemble average in eq. [1], one has to consider the configurations of the system before the insertion of the potential, so that the Boltzmann weights in the average do not include $\Psi(\boldsymbol{X})$, which acts as a ghost (10).

Since a liquid is a condensed state of matter, the insertion of a solute molecule requires the exclusion of the solvent molecules from the region of space that will be occupied by the solute. On this basis, simple physical considerations suggest that the perturbing potential has to be factorized in the following manner (6):

$$[3] \qquad \exp\left[\frac{-\Psi(\boldsymbol{X})}{RT}\right] = \zeta(\boldsymbol{X}) \exp\left[\frac{-\psi_a(\boldsymbol{X})}{RT}\right]$$

where $\zeta(\boldsymbol{X})$ can assume only the values of one or zero, depending on whether there is a suitable cavity to host the solute molecule in the given solvent configuration, and $\psi_a(\boldsymbol{X})$ represents the attractive potential between the solute molecule and the surrounding solvent molecules. Insertion of eq. [3] into eq. [1] leads to

© 2002 NRC Canada

Fig. 1. Experimental Ben-Naim standard Gibbs energy changes associated with the solvation of noble gases (■) and aliphatic hydrocarbons (●) in water at 25°C as a function of the solute's size.

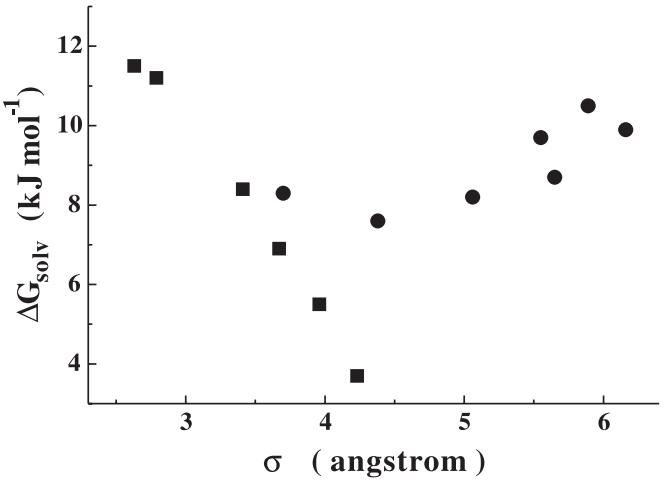

Fig. 2. Experimental Ben-Naim standard Gibbs energy changes associated with the solvation of noble gases (■) and aliphatic hydrocarbons (●) in ethanol at 25°C as a function of the solute's size.

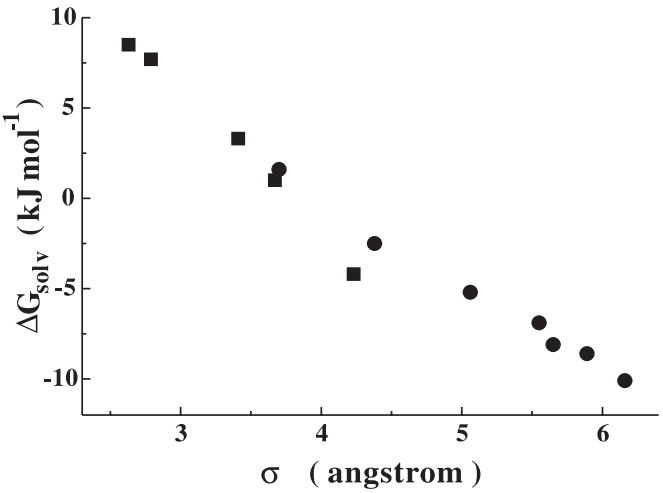

Fig. 3. Experimental Ben-Naim standard Gibbs energy changes associated with the solvation of noble gases (■) and aliphatic hydrocarbons (●) in benzene at 25°C as a function of the solute's size.

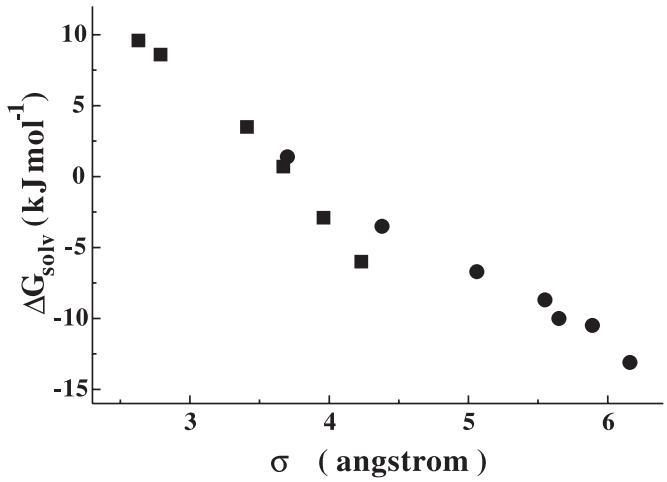

Fig. 4. Experimental Ben-Naim standard Gibbs energy changes associated with the solvation of noble gases (■) and aliphatic hydrocarbons (●) in *c*-hexane at 25°C as a function of the solute's size.

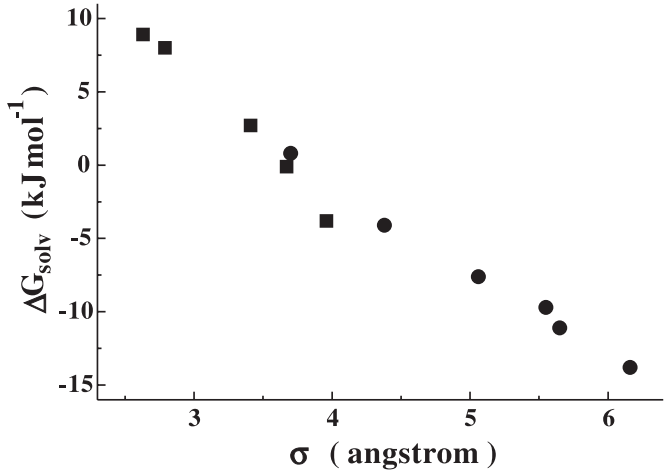

[4] $$\Delta G^{\bullet} = -RT \ln \langle \zeta(\boldsymbol{X}) \rangle_p - RT \ln \left\langle \exp\left[\frac{-\psi_a(\boldsymbol{X})}{RT}\right] \right\rangle_c$$

where the subscript c means that the ensemble average is performed over the solvent configurations possessing a suitable cavity to host the solute whose probability density function is

[5] $$\rho_c(\boldsymbol{X}) = \frac{\zeta(X)\ \exp[-H(\boldsymbol{X})/RT]}{\int \zeta(X)\ \exp[-H(\boldsymbol{X})/RT]d\boldsymbol{X}}$$

Clearly such configurations are only a small fraction of the total solvent configurations (i.e., those for which the function $\zeta(\boldsymbol{X})$ is equal to one). Equation [4] indicates that $\Delta G^{\bullet}$ is the sum of two terms: the work to create the cavity (ΔG_c) and the work to turn on the attractive solute–solvent potential (ΔG_a). The two subprocesses are analyzed in detail below.

Creation of the cavity

The work to create the cavity is given by the following:

[6] $$\Delta G_c = -RT \ln \langle \zeta(\boldsymbol{X}) \rangle_p$$

and corresponds to the work of selecting the configurations containing the cavity from the ensemble of pure-solvent configurations. This is an exact result of statistical mechanics because the ensemble average of $\zeta(\boldsymbol{X})$ corresponds to the probability of finding the desired cavity in the solvent (11, 12). Application of equilibrium thermodynamics leads to the following:

© 2002 NRC Canada

$$[7] \quad \Delta H_c = \langle H(\boldsymbol{X})\rangle_c - \langle H(\boldsymbol{X})\rangle_p$$

$$[8] \quad \Delta S_c = R \ln \langle \zeta(\boldsymbol{X})\rangle_p + (\Delta H_c/T) = \Delta S_x + (\Delta H_c/T)$$

The enthalpy change upon cavity creation is entirely due to solvent reorganization (12, 13), as is the entropy change upon cavity creation. The latter, however, consists of two parts: the first one, on the right-hand side of eq. [8], is due to the selection of the solvent configurations containing the cavity, and the second part is due to the reorganization of solvent molecules around the cavity. The latter contribution perfectly balances the change in enthalpy, so that ΔG_c is entirely entropic, and is due to the excluded-volume effect associated with the reduction in the size of the configuration space accessible to the solvent molecules (8, 14).

$$[9] \quad \Delta G_c = -T\Delta S_x$$

The excluded-volume effect is the entropic part of the perturbing potential.

Turning on the attractive potential

The work to turn on the attractive potential is defined as

$$[10] \quad \Delta G_a = -RT \ln \left\langle \exp\left[\frac{-\psi_a(\boldsymbol{X})}{RT}\right]\right\rangle_c$$

Application of the Gibbs–Helmholtz equation leads to

$$[11] \quad \Delta H_a = \langle \psi_a(\boldsymbol{X})\rangle_s + [\langle H(\boldsymbol{X})\rangle_s - \langle H(\boldsymbol{X})\rangle_c] = \langle \psi_a(\boldsymbol{X})\rangle_s + \Delta H_{ar}$$

where the subscript s means that the ensemble average is performed over the solution configurations whose probability density function is

$$[12] \quad \rho_s(\boldsymbol{X}) = \frac{\zeta(X)\, \exp\{-[\psi_a(\boldsymbol{X}) + H(\boldsymbol{X})]/RT\}}{\int \zeta(X)\, \exp\{-[\psi_a(\boldsymbol{X}) + H(\boldsymbol{X})]/RT\}\, d\boldsymbol{X}}$$

In other words, the solution configurations are the fraction of solvent configurations possessing the cavity occupied by the solute molecule that interacts with the surrounding solvent molecules. According to eq. [11], the enthalpy change consists of two parts: the average solute–solvent interaction energy, and the enthalpic contribution arising from the solvent reorganization upon turning on the attractive potential. The entropy change is

$$[13] \quad \Delta S_a = R \ln \left\langle \exp\left[\frac{-\psi_a(\boldsymbol{X})}{RT}\right]\right\rangle_c + [\langle \psi_a(\boldsymbol{X})\rangle_s/T] + (\Delta H_{ar}/T)$$

Using the inverse relationship demonstrated by Widom (10), eq. [13] becomes

$$[14] \quad \Delta S_a = -R \ln \left\langle \exp\left[\frac{-\psi_a(\boldsymbol{X})}{RT}\right]\right\rangle_s + [\langle \psi_a(\boldsymbol{X})\rangle_s/T] + (\Delta H_{ar}/T)$$

By setting $\kappa = \psi_a(\boldsymbol{X}) - \langle \psi_a(\boldsymbol{X})\rangle_s$, expanding the exponential function in power series, and keeping in mind that $\langle \kappa \rangle_s \equiv 0$, one obtains

$$[15] \quad -R \ln \left\langle \exp\left[\frac{-\psi_a(\boldsymbol{X})}{RT}\right]\right\rangle_s \approx -[\langle \psi_a(\boldsymbol{X})\rangle_s/T] - [\langle \kappa^2 \rangle_s/2RT^2]$$

When the attractive potential $\psi_a(\boldsymbol{X})$ is weak (15), the fluctuations in the value of $\langle \psi_a(\boldsymbol{X})\rangle_s$ are small, and the second term on the right-hand side of eq. [15] can be neglected. Thus

$$[16] \quad \Delta S_a \approx \frac{\Delta H_{ar}}{T}$$

and the solvent reorganization, associated with the process of turning on the attractive potential, is a compensating process. The condition of small fluctuations in the value of $\langle \psi_a(\boldsymbol{X})\rangle_s$ is verified for nonpolar compounds (16, 17), and the Gibbs energy change is simply given by the average solute–solvent interaction energy

$$[17] \quad \Delta G_a = \langle \psi_a(\boldsymbol{X})\rangle_s \equiv E_a$$

Recapitulation

The total solvation Gibbs energy change is

$$[18] \quad \Delta G^{\bullet} = \Delta G_c + \Delta G_a = \Delta G_c + E_a = -T\Delta S_x + E_a$$

It is given by the balance between two contrasting terms: ΔG_c, which is always positive and increases with the solute size, and E_a, which is always negative and increases, in absolute value, with the solute size. Their relative magnitude is the principle factor here. It is worth noting that this equation corresponds to that obtained by means of perturbative approaches using a hard-sphere fluid as the reference system (18). The derivation outlined above, however, originally devised by Lee (6), is more robust and convincing from a theoretical point of view (i.e., there is no need to consider a reference system of hard spheres). In any case, eq. [18] has to be considered of general validity (19), and is used in the present study to understand the solubility of nonpolar compounds in different solvents.

The total enthalpy change upon solvation is

$$[19] \quad \Delta H^{\bullet} = E_a + \Delta H_r$$

where E_a, the average solute–solvent interaction energy, is the enthalpic term for the perturbing potential. The term $\Delta H_r \equiv \Delta H_c + \Delta H_{ar}$ is the enthalpy change due to structural-solvent reorganization, which happens as a response to full perturbation.

The total entropy change upon solvation is given by

$$[20] \quad \Delta S^{\bullet} = \Delta S_r = \Delta S_x + \Delta S_{nx}$$

This change is due to solvent reorganization, because the solute molecule is fixed in space, adopting the standard state proposed by Ben-Naim (3), and its internal degrees of freedom are assumed to be unchanged on transfer. The excluded-volume effect for cavity creation is, however, the entropic part of the perturbing potential, and not a solvent response (14, 15); the ΔS_x term is the corresponding entropy

© 2002 NRC Canada

contribution. Solvent molecules further reorganize around the solute in response to the full perturbation (both volume exclusion and turning on solute–solvent interaction). ΔS_{nx} represents this non-excluded volume contribution to the total entropy change upon solvation. Finally, the following compensation relation:

[21] $T\Delta S_{nx} = \Delta H_r$

is operative for the solvent response.

Calculation procedure

The Gibbs energy cost to create a cavity is calculated with the following equation provided by scaled particle theory (SPT) (20, 21):

[22] $$\Delta G_c = RT\,[K_0 + K_1(\sigma_2/\sigma_1) + K_2(\sigma_2/\sigma_1)^2 + K_3(\sigma_2/\sigma_1)^3]$$

where $K_0 = -\ln(1-\xi)$; $K_1 = u = 3\xi/(1-\xi)$; $K_2 = u\,(u+2)/2$; and $K_3 = \xi P v_1/RT$.

In these equations, R is the gas constant; ξ is the volume packing density of pure solvent, which is defined as the ratio of the physical volume of a mole of solvent molecules over the molar volume of the solvent, v_1 (i.e., $\xi = \pi\sigma_1^3 N_{Av}/6v_1$); σ_1 and σ_2 are the hard-sphere diameters of the solvent and solute molecules, respectively; and P is the pressure. There is still debate, however, on what is the correct pressure to use in eq. [22]: the experimental value of the real liquid or the value of the corresponding hard-sphere fluid (22, 23). According to the above theoretical approach, ΔG_c is the work to create the cavity in the real liquid, not in the corresponding hard-sphere fluid. Therefore, as already claimed by other authors (21, 24, 25), P has to be the experimental value (1 atm), which is the hydrostatic pressure over the liquid. This value is used in all the SPT calculations.

The cavity size is defined as the diameter of the spherical region from which any part of any solvent molecules is excluded (i.e., it corresponds to the size of the solute molecule). It is well known that the SPT results are very sensitive to the σ values selected for both solvent and solute (26). For this reason, customary hard-sphere diameters are used for the solutes and solvents, which are listed in the second column of Table 4. For water, $\sigma = 2.75$ Å (27) is used, which is close to the location of the first peak in the oxygen–oxygen pair-correlation function of water (28). It should represent the distance of closest approach between two H-bonded water molecules. For the other four solvents, ethanol, benzene, *c*-hexane, and *n*-hexane, the σ values determined by Wilhelm and Battino (4) are used. They should be reliable; for instance, in the case of benzene, $\sigma = 5.26$ Å, which is close to the maximum of the ring center – ring center pair-correlation function of liquid benzene (29). In addition, the experimental values of the liquid densities at 25°C are used for all solvents (4, 30).

Ben-Naim (3) pointed out that SPT, as applied to real solvents, is not a true molecular theory because experimental values of the molecular diameter and molar volume are used as input data in the calculations. This, however, may be one of the reasons for its wide applicability, since some structural information on the liquid is implicitly taken into account. The application of SPT relies on treating molecularly detailed solutes as effective hard spheres, which is clearly an approximation. Nevertheless, both surface-area-based models (31) and statistical mechanically founded force fields (32), able to account for the subtleties of treating a molecular solute, seem to validate the spherical approximation.

The E_a term accounts for the van de Waals interactions of nonpolar molecules in the five solvents. It is estimated using a simple formula devised by Pierotti (21). He assumed that the solute–solvent dispersive interactions are represented by the Lennard–Jones potential and that the solvent density around the solute is uniform and equal to that of pure solvent. The formula of Pierotti (21) is:

[23] $E_a = -(64/3)\xi\,\varepsilon_{12}(\sigma_{12}/\sigma_1)^3$

where $\sigma_{12} = (\sigma_1 + \sigma_2)/2$, $\varepsilon_{12} = (\varepsilon_1\varepsilon_2)^{1/2}$, and ε_1 and ε_2 are the Lennard–Jones potential parameters for the solvent and solute, respectively, which measure the magnitude of the maximum attractive potential energy. Notwithstanding the simplifying assumptions, this formula is sound from a physico-chemical point of view, and should perform satisfactorily (33).

In benzene, *c*-hexane, and *n*-hexane the van der Waals interactions of nonpolar solutes consist purely of dispersive contributions. For these solvents, the ε_1/k values determined by Wilhelm and Battino (4) are used: 531 K for benzene, 573 K for *c*-hexane, and 517 K for *n*-hexane. In water and ethanol the van der Waals interactions of nonpolar solutes consist of both dispersive and dipole-induced dipole contributions. It is assumed that the latter can be absorbed into the parameterization of the dispersive contribution. This assumption is reasonable because both terms depend on the inverse sixth power of distance (34), and is usually employed in molecular mechanics force fields (35). The dipole-induced dipole contribution is taken into account by increasing the ε_1/k value of water and ethanol. Specifically, for water $\varepsilon_1/k = 100$ K instead of 85 K (21) is used, and for ethanol $\varepsilon_1/k = 330$ K instead of 324 K is used (4).

The ε_2/k values used for noble gases and alkanes are listed in the third column of Table 4. They do not correspond exactly to literature values; this should not be a problem because of the discrepancies that exist between the ε_2/k values obtained by different procedures (4). In addition, the ε_2/k values of noble gases are close to those reported by Pierotti (21); the values for the aliphatic hydrocarbons are lower than those reported by Abraham and Nasehzadeh (36), but in accordance with those quoted by Hirschfelder and co-workers (37).

It should be emphasized that both ΔG_c and E_a are not measurable quantities and that only their sum can be tested against experimental $\Delta G^\bullet$ data (38). In this paper, estimates of ΔG_c and E_a are obtained using several assumptions whose validity cannot be taken for granted. Computer simulations are also based on assumptions, where the results may be biased by the parameter values selected for the potential energy functions. The consistency of the assumptions can be checked by comparing the sum $\Delta G_c + E_a$ with the experimental $\Delta G^\bullet$ data. This procedure has been applied to this work.

Values for ΔH_r are obtained via eq. [19], where the E_a estimates are subtracted from the experimental $\Delta H^\bullet$ values.

© 2002 NRC Canada

Table 5. Estimates of ΔG_c, E_a, ΔH_r, ΔS_x, and ΔS_{nx} for the solvation at 25°C of noble gases and aliphatic hydrocarbons in water.

	ΔG^* (kJ mol^{-1})	ΔG_c (kJ mol^{-1})	E_a (kJ mol^{-1})	$\Delta G_c + E_a$ (kJ mol^{-1})	ΔH_r (kJ mol^{-1})	ΔS_x (J K^{-1} mol^{-1})	ΔS_{nx} (J K^{-1} mol^{-1})
He	11.5	12.4	–1.3	11.1	3.1	–41.6	9.1
Ne	11.2	13.5	–2.9	10.6	1.6	–45.3	3.4
Ar	8.4	18.5	–9.9	8.6	0.3	–62.0	1.6
Kr	6.9	20.8	–13.0	7.8	0	–69.8	3.0
Xe	5.5	23.5	–17.7	5.8	0.9	–78.8	4.0
Rn	3.7	26.2	–22.8	3.4	3.7	–87.9	11.7
CH_4	8.3	21.1	–12.7	8.4	1.8	–70.8	6.4
C_2H_6	7.6	27.8	–20.3	7.5	3.1	–93.2	10.0
			(–22.2)				
C_3H_8	8.2	35.5	–26.7	8.8	5.7	–119.1	21.2
			(–31.9)				
i-C_4H_{10}	9.7	41.7	–32.1	9.6	10.2	–139.9	33.9
			(–40.2)				
n-C_4H_{10}	8.7	43.0	–33.2	9.8	9.6	–144.2	35.9
			(–42.9)				
$C(CH_3)_4$	10.5	46.3	–36.2	10.1	13.4	–155.3	43.6
			(–46.7)				
n-C_5H_{12}	9.9	50.0	–39.7	10.3	13.7	–167.7	47.3
			(–52.7)				

Note: The values of $\Delta G_c + E_a$ have to be contrasted with the experimental ΔG^* values. From ethane up to *n*-pentane, two E_a estimates are reported for each solute: those in the first row are calculated using ε/k = 210 K, and those in the second row are calculated using the ε/k number reported in Table 4. See text for further details.

Table 6. Estimates of ΔG_c, E_a, ΔH_r, ΔS_x, and ΔS_{nx} for the solvation at 25°C of noble gases and aliphatic hydrocarbons in ethanol.

	ΔG^* (kJ mol^{-1})	ΔG_c (kJ mol^{-1})	E_a (kJ mol^{-1})	$\Delta G_c + E_a$ (kJ mol^{-1})	ΔH_r (kJ mol^{-1})	ΔS_x (J K^{-1} mol^{-1})	ΔS_{nx} (J K^{-1} mol^{-1})
He	8.5	9.6	–1.6	8.0	10.5	–32.2	30.9
Ne	7.7	10.4	–3.5	6.9	11.1	–34.9	34.6
Ar	3.3	13.8	–11.0	2.8	12.1	–46.3	38.9
Kr	1.0	15.4	–14.1	1.3	—	–51.7	—
Xe	—	17.3	–18.8	–1.5	—	–58.0	—
Rn	–4.2	19.1	–23.6	–4.5	13.4	–64.1	44.0
CH_4	1.6	15.6	–13.8	1.8	11.7	–52.3	39.9
C_2H_6	–2.5	20.2	–22.7	–2.5	15.6	–67.8	52.4
C_3H_8	–5.2	25.4	–31.1	–5.7	18.7	–85.2	61.0
i-C_4H_{10}	–6.9	29.6	–38.0	–8.4	21.9	–99.3	68.4
n-C_4H_{10}	–8.1	30.4	–40.3	–9.9	22.6	–102.0	69.8
$C(CH_3)_4$	–8.6	32.6	–43.3	–10.7	—	–109.3	—
n-C_5H_{12}	–10.1	35.2	–48.2	–13.0	24.8	–118.1	73.5

Note: The values of $\Delta G_c + E_a$ have to be contrasted with the experimental ΔG^* values obtained. See text for further details.

This procedure is appealing because it is very difficult to obtain a reliable estimate of ΔH_r, using both theoretical relations and computer simulations. This is because ΔH_r is the difference in the two large and fluctuating quantities: the enthalpy of the solvent after the solute insertion and that of the pure solvent. For the same reason, the values for ΔS_{nx} are obtained by means of eq. [20], where the ΔS_x estimates, calculated using eq. [9], are subtracted from the experimental ΔS^* values.

Analysis of the direct perturbation

The values of ΔG_c for noble gases and aliphatic hydrocarbons in the five solvents, calculated using eq. [22], are listed in the third column of Tables 5–9. It is readily evident that the work of cavity creation is larger in water than in the other four solvents. For instance, for methane, ΔG_c(in kJ mol^{-1}) = 21.1 in water, 17.3 in benzene, 16.0 in *c*-hexane, 15.6 in ethanol, and 13.4 in *n*-hexane; for *i*-butane, ΔG_c(in kJ mol^{-1}) = 41.7 in water, 32.6 in benzene, 29.8 in *c*-hexane, 29.6 in ethanol, and 24.6 in *n*-hexane. It is interesting to note that the order of ΔG_c corresponds to that of the surface tension of the five liquids. (The values for surface tension at 25°C, in dyne cm^{-1}, are 71.99 for water, 28.22 for benzene, 24.65 for *c*-hexane, 21.97 for ethanol, and 17.89 for *n*-hexane (39).) This agrees with the well-established correlation between the work of cavity creation and the surface tension of the liquid at room temperature (40). It must be noted, however, that the

© 2002 NRC Canada

Table 7. Estimates of ΔG_c, E_a, ΔH_r, ΔS_x, and ΔS_{nx} for the solvation at 25°C of noble gases and aliphatic hydrocarbons in benzene.

	$\Delta G^{\bullet}$ (kJ mol^{-1})	ΔG_c (kJ mol^{-1})	E_a (kJ mol^{-1})	$\Delta G_c + E_a$ (kJ mol^{-1})	ΔH_r (kJ mol^{-1})	ΔS_x (J K^{-1} mol^{-1})	ΔS_{nx} (J K^{-1} mol^{-1})
He	9.6	10.8	–2.0	8.8	13.6	–36.2	42.9
Ne	8.6	11.6	–4.2	7.4	18.3	–38.9	57.4
Ar	3.5	15.4	–12.9	2.5	15.7	–51.7	49.3
Kr	0.7	17.1	–16.2	0.9	16.1	–57.4	54.7
Xe	–2.9	19.1	–21.4	–2.3	15.8	–64.1	55.0
Rn	–6.0	21.2	–26.7	–5.5	14.9	–71.1	51.6
CH_4	1.4	17.3	–15.9	1.4	16.2	–58.0	54.3
C_2H_6	–3.5	22.3	–25.5	–3.2	19.5	–74.8	66.4
C_3H_8	–6.7	28.0	–34.3	–6.3	23.7	–93.9	80.8
i-C_4H_{10}	–8.7	32.6	–41.3	–8.7	28.2	–109.3	94.5
n-C_4H_{10}	–10.0	33.5	–43.8	–10.3	27.8	–112.4	92.3
$C(CH_3)_4$	–10.5	35.9	–46.7	–10.8	—	–120.4	—
n-C_5H_{12}	–13.1	38.7	–51.6	–12.9	31.0	–129.8	104.6

Note: The values of $\Delta G_c + E_a$ have to be contrasted with the experimental $\Delta G^{\bullet}$ values. See text for further details.

Table 8. Estimates of ΔG_c, E_a, ΔH_r, ΔS_x, and ΔS_{nx} for the solvation at 25°C of noble gases and aliphatic hydrocarbons in *c*-hexane.

	$\Delta G^{\bullet}$ (kJ mol^{-1})	ΔG_c (kJ mol^{-1})	E_a (kJ mol^{-1})	$\Delta G_c + E_a$ (kJ mol^{-1})	ΔH_r (kJ mol^{-1})	ΔS_x (J K^{-1} mol^{-1})	ΔS_{nx} (J K^{-1} mol^{-1})
He	8.9	10.0	–1.9	8.1	13.5	–33.5	42.6
Ne	8.0	10.8	–4.1	6.7	12.0	–36.2	35.9
Ar	2.7	14.2	–12.4	1.8	13.1	–47.6	40.9
Kr	–0.1	15.8	–15.6	0.2	13.8	–53.0	47.3
Xe	–3.8	17.7	–20.6	–2.9	13.4	–59.4	48.0
Rn	—	19.5	–25.5	–6.0	—	–65.4	—
CH_4	0.8	16.0	–15.3	0.7	14.4	–53.7	48.0
C_2H_6	–4.1	20.6	–24.4	–3.8	15.1	–69.1	51.7
C_3H_8	–7.6	25.7	–32.5	–6.8	18.6	–86.2	65.1
i-C_4H_{10}	–9.7	29.8	–39.0	–9.2	—	–99.9	—
n-C_4H_{10}	–11.1	30.7	–41.3	–10.6	—	–103.0	—
$C(CH_3)_4$	—	32.8	–44.0	–11.2	—	–110.0	—
n-C_5H_{12}	–13.8	35.3	–48.5	–13.2	24.6	–118.4	84.5

Note: The values of $\Delta G_c + E_a$ have to be contrasted with the experimental $\Delta G^{\bullet}$ values. See text for further details.

Table 9. Estimates of ΔG_c, E_a, ΔH_r, ΔS_x and ΔS_{nx} for the solvation at 25°C of noble gases and aliphatic hydrocarbons in *n*-hexane.

	$\Delta G^{\bullet}$ (kJ mol^{-1})	ΔG_c (kJ mol^{-1})	E_a (kJ mol^{-1})	$\Delta G_c + E_a$ (kJ mol^{-1})	ΔH_r (kJ mol^{-1})	ΔS_x (J K^{-1} mol^{-1})	ΔS_{nx} (J K^{-1} mol^{-1})
He	7.5	8.6	–1.7	6.9	11.3	–28.8	35.8
Ne	6.6	9.2	–3.6	5.6	10.6	–30.9	32.2
Ar	1.9	12.0	–10.7	1.3	9.5	–40.2	39.2
Kr	–0.7	13.3	–13.5	–0.2	10.3	–44.6	36.2
Xe	–3.9	14.8	–17.7	–2.9	8.5	–49.6	31.8
Rn	–6.5	16.3	–21.9	–5.6	10.7	–54.7	38.9
CH_4	0.2	13.4	–13.2	0.2	12.5	–44.9	41.9
C_2H_6	–4.3	17.1	–20.9	–3.8	14.1	–57.4	49.0
C_3H_8	–7.5	21.3	–27.7	–6.4	15.1	–71.4	54.3
i-C_4H_{10}	–9.8	24.6	–33.1	–8.5	15.8	–82.5	57.3
n-C_4H_{10}	–10.6	25.3	–35.0	–9.7	16.0	–84.9	56.7
$C(CH_3)_4$	–11.6	27.1	–37.2	–10.1	17.2	–90.9	62.7
n-C_5H_{12}	–13.8	29.1	–41.0	–11.9	15.8	–97.6	59.4

Note: The values of $\Delta G_c + E_a$ have to be contrasted with the experimental $\Delta G^{\bullet}$ values. See text for further details.

© 2002 NRC Canada

Fig. 5. Trend of ΔG_c in water at 25°C as a function of the solute's size, calculated by means of eq. [22]. The estimates of $-E_a$, calculated by means of eq. [23], for noble gases (■) and aliphatic hydrocarbons (●) in water are also shown.

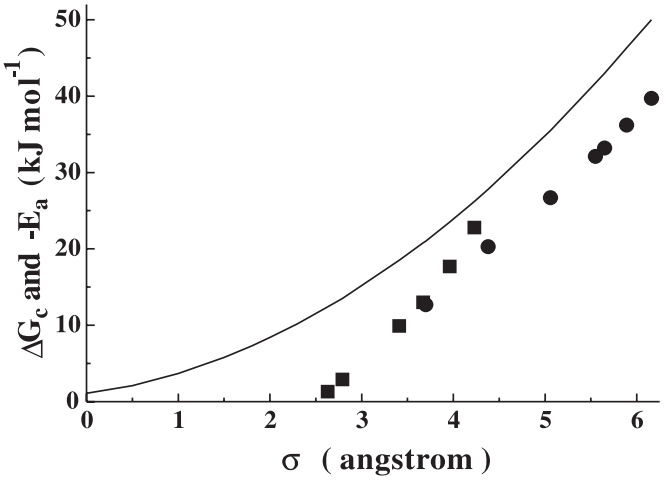

Fig. 6. Trend of ΔG_c in ethanol at 25°C as a function of the solute's size, calculated by means of eq. [22]. The estimates of $-E_a$, calculated by means of eq. [23], for noble gases (■) and aliphatic hydrocarbons (●) in ethanol are also shown.

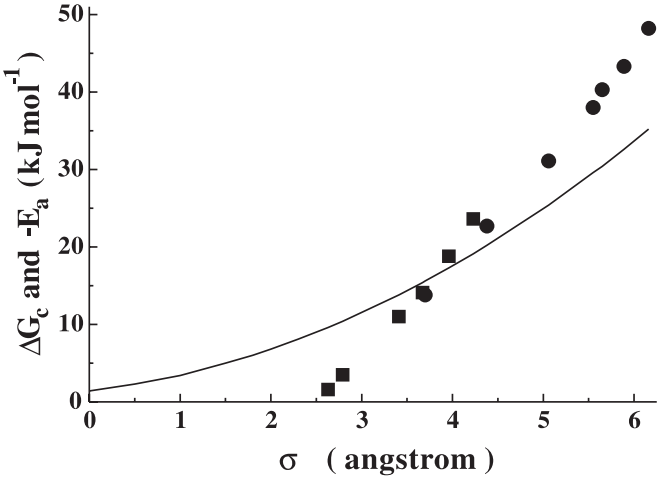

Fig. 7. Trend of ΔG_c in benzene at 25°C as a function of the solute's size, calculated by means of eq. [22]. The estimates of $-E_a$, calculated by means of eq. [23], for noble gases (■) and aliphatic hydrocarbons (●) in benzene are also shown.

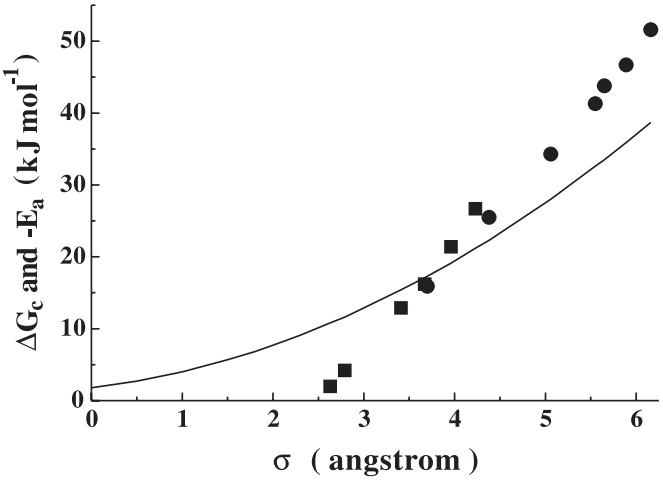

Fig. 8. Trend of ΔG_c in *c*-hexane at 25°C as a function of the solute's size, calculated by means of eq. [22]. The estimates of $-E_a$, calculated by means of eq. [23], for noble gases (■) and aliphatic hydrocarbons (●) in *c*-hexane are also shown.

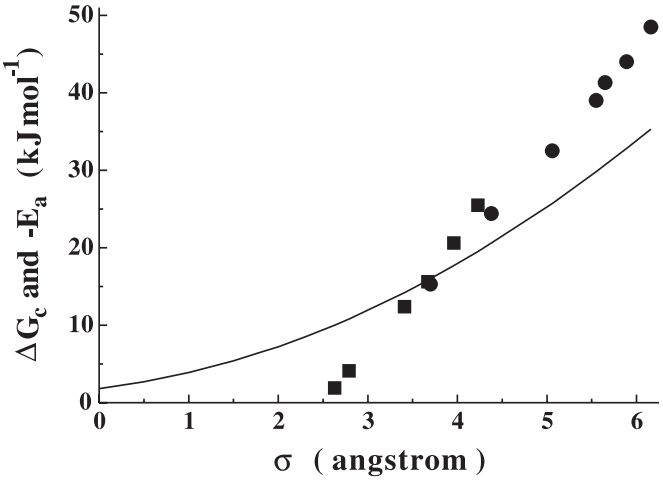

temperature dependence of ΔG_c in water does not agree with the macroscopic surface tension, i.e., with increasing temperature, the former exhibits a maximum (33), whereas the latter decreases monotonically (39). This implies a crossover from molecular cavities to macroscopic surfaces, which is perhaps buried in the non-trivial temperature dependence of the Tolman length (24, 41).

Analysis of the SPT formula shows that, at a fixed temperature and cavity radius, the magnitude of ΔG_c is determined by two geometrical properties of the solvent (6, 39): the size of its molecules (σ) and its volume-packing density (ξ). The work of cavity creation increases on decreasing the value of σ for a given ξ, and on increasing the value of ξ for a given σ. In general, the effect of the smallness of σ is dominant, and ΔG_c is larger in water compared with other solvents (6, 42–44). (Recall that the size of a water molecule is the smallest among all common solvents, i.e., it corresponds to the size of an oxygen atom.) It is worth noting that Lazaridis (45) recently claimed that it is the large cohesive energy density of liquid water, due to H-bonds, that are the fundamental cause of hydrophobicity and not the small size of water molecules. But this analysis seems to be a bit artificial, considering that the ΔG_c values determined in an isotropic single-site model of water, which lacks the attractive interactions due to H-bonds but retains the small molecular size, prove to be larger than those determined in water models, which take into account the presence of H-bonds (46).

In general, detailed computer simulations have confirmed the SPT predictions (47–50). At room temperature, the fractional-free volume is larger in water than in common organic liquids, as approximately indicated by the ξ values: 0.363 for water, 0.439 for ethanol, 0.513 for benzene, 0.517 for *c*-hex-

© 2002 NRC Canada

ane, and 0.497 for *n*-hexane (i.e., approximate because the ξ values refer to the packing of spheres, whereas the actual molecules are not spheres). Pohorille and Pratt (47) show, however, that this fractional-free volume is partitioned in a specific manner in each liquid, depending on the characteristic length scale of the liquid itself, i.e., the size of its molecules. As a consequence, the distribution of cavity sizes is significantly sharper in water than in other solvents (47), and the actual volume accessible to a solute is smaller in the former than in the latter. In addition, the contact density predicted by SPT, even though lower than that computed for TIP4P water, show a similar dependence on solute size (48). This quantitative discrepancy may be due to the directional nature of H-bonds, a feature neglected in SPT. The major role of the squeezing force exerted by water molecules on the cavity surface is, however, correctly explained by SPT. In conclusion, ΔG_c is larger in water than in common organic solvents because the empty space is partitioned in smaller packets due to the smaller size of water molecules (6, 49, 50).

The estimates of E_a, calculated using eq. [23], and the values for the sum $\Delta G_c + E_a$ are listed in the fourth and fifth columns of Tables 5–9, respectively. Good agreement with the experimental $\Delta G^•$ data for both noble gases and alkanes in ethanol, benzene, *c*-hexane, and *n*-hexane is seen. It is also observed for noble gases and methane in water, but not for large alkanes in water (see Table 5). For the latter, the estimates of E_a calculated using Pierotti's formula are too large; i.e., see the numbers reported in the second line of the fourth column of Table 5 from ethane to *n*-pentane. In particular, the calculated E_a values for neopentane and *n*-pentane are so large that they overwhelm the ΔG_c values from SPT. This result is clearly not correct, because experimental measurements unequivocally show that $\Delta G^•$ is a large positive quantity. Pierotti's formula, therefore, seems to fail for large alkanes in water.

The problem, however, is not in the formula itself, but the parameters that are used. Specifically, the ε/k values reported in the third column of Table 4 for large alkanes do not work well for water. This could be due to the fact that each water molecule, being very small, interacts only with a single methyl or methylene group and does not "feel" all of the electron density of an alkane molecule. This situation does not occur in the other four solvents, because their molecules have a size comparable or larger than that of all the solutes considered. It also does not happen for noble gases and methane in water for two physical reasons: first, these solutes are not large in comparison with a water molecule, except xenon and radon; second, they are spherical, and thus each water molecule in the hydration shell interacts with all the electrons of the solute.

If this reasoning is correct, Pierotti's formula should also work well for large alkanes in water by fixing a unique and constant ε/k value, which is intermediate in value, between methane and ethane. In fact, by using $\varepsilon/k = 210$ K for all the alkanes except methane, eq. [23] gives the values reported in the first line of the fourth column of Table 5 from ethane to *n*-pentane. When the latter are combined with the ΔG_c estimates from SPT, agreement with the experimental $\Delta G^•$ data is good. These E_a values are reliable because they are close to the solute–water interaction energies calculated at room temperature by Jorgensen et al. (16) for seven alkanes in TIP4P water by means of large-sample Monte Carlo simulations.

It is important to note that the magnitude of the van der Waals energetic contribution is different in each of the five solvents. The absolute value of E_a for each solute shows the following order: benzene > *c*-hexane > ethanol > *n*-hexane > water. For instance, in the case of methane, E_a (in kJ mol^{-1}) = –15.9 in benzene, –15.3 in *c*-hexane, –13.8 in ethanol, –13.2 in *n*-hexane, and –12.7 in water; in the case of *i*-butane, E_a (in kJ mol^{-1}) = – 41.3 in benzene, –39.0 in *c*-hexane, –38.0 in ethanol, –33.1 in *n*-hexane, and –32.1 in water.

Using a detailed continuum model approach, Floris and Tomasi (51) found that the magnitude of the dispersive energy follows the order: benzene > *c*-hexane > water, which is in accordance with the above findings. This is due to (*i*) the larger polarizability of the molecules of the organic solvents compared with water molecules; and (*ii*) the larger volume-packing density of the former compared with the latter. For large alkanes in water, however, the difference is amplified by the mechanism suggested above, i.e., given its small size, a single water molecule interacts with only a small part of an alkane molecule, whereas a single benzene molecule interacts with the whole alkane molecule. The size of solvent molecules is, therefore, a characteristic length scale of the solvent for both ΔG_c and E_a.

Since the calculations satisfactorily reproduce the experimental $\Delta G^•$ data, an understanding of the size dependence of the solubility of nonpolar compounds in the five different solvents is achievable. For this purpose, plots of ΔG_c and $-E_a$ vs. the hard-sphere diameter of noble gases and alkanes in the five solvents were constructed. The plot for water, shown in Fig. 5, indicates that the work of cavity creation dominates the solvation process, making the $\Delta G^•$ values large and positive for all of the solutes considered. Moreover, the $\Delta G^•$ values for noble gases decrease on increasing the molecular diameter because E_a increases in magnitude more rapidly than ΔG_c; the contrary is true for the large alkanes. The plots for ethanol, benzene, and *c*-hexane are shown in Figs. 6–8, respectively. (A plot for *n*-hexane is not shown because it is qualitatively similar.) These plots emphasize that the solvation process is dominated by ΔG_c up to $\sigma \approx 4.0$ Å. For $\sigma >$ 4.0 Å, the E_a term is larger in magnitude than ΔG_c, rendering the total Gibbs energy change negative. In benzene an increase in solute size results in an increase in ΔG_c, but the increase is smaller and slower than E_a. This supports the existence of critical sizes for solutes, above which the $\Delta G^•$ values are negative. This is also true for ethanol, *c*-hexane, and *n*-hexane.

General features emerge from the analysis of helium, the smallest extreme solute, and *n*-pentane, the largest one. The values of $\Delta G^•$ (in kJ mol^{-1}) at 25°C for He in the five solvents are positive and not dramatically different among each other: 11.5 in water, 8.5 in ethanol, 9.6 in benzene, 8.9 in *c*-hexane, and 7.5 in *n*-hexane. The corresponding ΔG_c and E_a estimates (in kJ mol^{-1}) are, respectively, 12.4 and –1.3 in water, 9.6 and –1.6 in ethanol, 10.8 and –2.0 in benzene, 10.0 and –1.9 in *c*-hexane, 8.6 and –1.7 in *n*-hexane. Clearly the difference among the five solvents is the ΔG_c term, which is larger in water than in the other four solvents. The E_a term plays no significant role because of the very small

© 2002 NRC Canada

polarizability of the helium atom. On the other hand, the value of $\Delta G^{\bullet}$ (in kJ mol^{-1}) at 25°C for *n*-C_5H_{12} in water is dramatically different compared with those in the other four solvents: 9.9 in water, –10.1 in ethanol, –13.1 in benzene, and –13.8 both in *c*-hexane and *n*-hexane. The corresponding ΔG_c and E_a estimates (in kJ mol^{-1}) are, respectively, 50.0 and –39.7 in water, 35.2 and –48.2 in ethanol, 38.7 and –51.6 in benzene, 35.3 and –48.5 in *c*-hexane, 29.1 and –41.0 in *n*-hexane. As expected, the ΔG_c term is larger in water than in the other four solvents, and there is also a difference in the E_a values. The two terms in eq. [18], therefore, account for the fundamental difference between water and common organic solvents for the solvation of alkanes.

Analysis of the solvent response

The standard solvation enthalpy changes are now analyzed. The E_a estimates for all solutes in the four solvents are larger in magnitude than the $\Delta H^{\bullet}$ values. For methane (in kJ mol^{-1}), E_a = –12.7, whereas $\Delta H^{\bullet}$ = –10.9 in water; in ethanol, E_a = –13.8, whereas $\Delta H^{\bullet}$ = –2.1 ; in benzene, E_a = –15.9, whereas $\Delta H^{\bullet}$ = 0.3; in *c*-hexane, E_a = –15.3, whereas $\Delta H^{\bullet}$ = –0.9; in *n*-hexane, E_a = –13.2, whereas $\Delta H^{\bullet}$ = –0.7. The van der Waals interactions of nonpolar solutes are so large that the purely structural solvent reorganization are, therefore, an endothermic process in all the solvents considered. The ΔH_r values, determined by eq. [19], which uses the experimental $\Delta H^{\bullet}$ values and the E_a estimates, are listed in the sixth column of Tables 5–9, and show that ΔH_r is small in water but large in the other solvents. For instance, in the case of methane, ΔH_r (in kJ mol^{-1}) = 1.8 in water, 11.7 in ethanol, 16.2 in benzene, 14.4 in *c*-hexane, and 12.5 in *n*-hexane; in the case of *i*-butane, ΔH_r (in kJ mol^{-1}) = 10.2 in water, 21.9 in ethanol, 28.2 in benzene, and 15.8 in *n*-hexane. In this regard, the purely structural solvent reorganization involves different intermolecular interactions in these solvents, i.e., van der Waals interactions in benzene, *c*-hexane, and *n*-hexane; H-bonds in water; and both types of interactions in ethanol.

In fact, this result is expected because a significant part of ΔH_r is due to the enthalpy change upon cavity creation, which, according to SPT (6, 21), is directly proportional to the thermal expansion coefficient of the solvent. The latter quantity, at room temperature, is very small for water with respect to all other solvents; at 25°C, $\alpha = 0.257 \times 10^{-3}$ K^{-1} for water compared with $\approx 1.2 \times 10^{-3}$ K^{-1} for common organic solvents (6, 21). These values can be rationalized by the statistical mechanical definition of $\alpha \equiv \langle \delta H\, \delta V \rangle / kT^2 \langle V \rangle$, where $\delta H = H - \langle H \rangle$, $\delta V = V - \langle V \rangle$, and the angle brackets represent ensemble average values (52). The thermal expansion coefficient is, therefore, directly proportional to the ensemble correlation between the fluctuations of enthalpy and those of volume. It is small in the case of water because there is little correlation between the enthalpy fluctuations and the volume fluctuations as a consequence of the strength of H-bonds, i.e., volume changes cause very little alteration in the number of H-bonds. On the other hand, α is large for common organic solvents because there is significant correlation between the enthalpy fluctuations and the volume fluctuations in view of the weakness of the van der Waals interactions and their strong dependence on the distance among interacting particles. This physical reasoning is also supported by the results of detailed computer simulations on water models and Lennard–Jones liquids (53).

The small positive values of ΔH_r for nonpolar solutes in water imply that there is no significant breakage of H-bonds. Water molecules in the hydration shell, exploiting their tetrahedral functionality, are able to form as many H-bonds as water molecules in the bulk, by straddling the surface of nonpolar groups (44). In fact, they point in two or three tetrahedral bonding directions (both the OH covalent bonds and the lone-pair directions) tangential to the surface of the occupied space, giving rise to disordered clathrate cages. This geometrical arrangement has been established by direct-neutron scattering and X-ray absorption spectroscopy measurements (54, 55). Similar results emerged from computer simulations (56), confirming the plasticity of the H-bonded network of water.

The two terms of the solvation entropy change are calculated by eqs [9] and [20]; the values obtained are listed in the seventh and eighth columns of Tables 5–9. The ΔS_x contribution is large and negative for all solutes in the five solvents. It is, however, significantly larger in water than in the others as a consequence of the difference in the ΔG_c estimates. For methane, ΔS_x (in J K^{-1} mol^{-1}) = –70.8 in water, –52.3 in ethanol, –58.0 in benzene, –53.7 in *c*-hexane, – 44.9 in *n*-hexane. These values unequivocally indicate that the excluded-volume effect is the physical cause explaining why the standard solvation entropies are negative for almost all the nonpolar solutes in the five solvents considered (see Table 3). The ΔS_{nx} contribution is always positive, i.e., the purely structural solvent reorganization leads to an entropy increase. This term is small in water but large in the other four solvents reflecting the behaviour of the ΔH_r contribution since the phenomenon of enthalpy–entropy compensation is operative.

Conclusion

The analysis performed shows that the solubility of nonpolar solutes in different solvents is always determined by the balance between the work spent to create the cavity and the work gained to turn on the solute–solvent interactions. The combination of SPT to estimate ΔG_c, with a simple formula to evaluate E_a allows one to rationalize the different size dependence found for the solubility of noble gases and alkanes in water compared with common organic solvents. The shortcomings of the calculation procedure adopted cannot detract from the general qualitative correctness of the results obtained.

Acknowledgment

The author wishes to thank reviewers for helpful comments.

References

1. M.H. Abraham. J. Am. Chem. Soc. **101**, 5477 (1979); J. Am. Chem. Soc. **104**, 2086 (1982).
2. G. Graziano. J. Chem. Soc. Faraday Trans. **94**, 3345 (1998).
3. A. Ben-Naim. Solvation thermodynamics. Plenum Press, New York. 1987.

© 2002 NRC Canada

4. E. Wilhelm and R. Battino. J. Chem. Phys. **55**, 4012 (1971).
5. G. Graziano. J. Phys. Chem. B, **105**, 2079 (2001).
6. B. Lee. Biopolymers, **24**, 813 (1985); Biopolymers, **31**, 993 (1991).
7. G. Graziano. Can. J. Chem. **76**, 437 (1998); Biophys. Chem. **82**, 69 (1999); Can. J. Chem. **78**, 1233 (2000).
8. G. Graziano. Phys. Chem. Chem. Phys. **1**, 1877 (1999); Phys. Chem. Chem. Phys. **1**, 3567 (1999); J. Phys. Chem. B, **104**, 9249 (2000).
9. G. Graziano. J. Phys. Soc. Jpn. **69**, 3720 (2000); Can. J. Chem. **79**, 105 (2001); Can. J. Chem. **79**, 1310 (2001).
10. B. Widom. J. Chem. Phys. **39**, 2808 (1963); J. Phys. Chem. **86**, 869 (1982).
11. R.C. Tolman. The principles of statistical mechanics. Oxford University Press, London. 1938. Chap. 14. p. 636.
12. B. Lee. J. Chem. Phys. **83**, 2421 (1985).
13. G. Graziano. J. Phys. Soc. Jpn. **69**, 1566 (2000).
14. B. Lee and G. Graziano. J. Am. Chem. Soc. **118**, 5163 (1996).
15. B. Lee. Biophys. Chem. **51**, 271 (1994).
16. W.L. Jorgensen, J. Gao, and C. Ravimohan. J. Phys. Chem. **89**, 3470 (1985).
17. P. Linse. J. Am. Chem. Soc. **112**, 1744 (1990).
18. R.O. Neff and D.A. McQuarrie. J. Phys. Chem. **77**, 413 (1973); J.P. Hansen and I.R. McDonald. Theory of simple liquids. Academic Press, New York. 1976.
19. L.R. Pratt and D. Chandler. J. Chem. Phys. **67**, 3683 (1977).
20. H. Reiss. Adv. Chem. Phys. **9**, 1 (1966).
21. R.A. Pierotti. Chem. Rev. **76**, 717 (1976).
22. S. Shimizu, M. Ikeguchi, S. Nakamura, and K. Shimizu. J. Chem. Phys. **110**, 2971 (1999).
23. K.E.S. Tang and V.A. Bloomfield. Biophys. J. **79**, 2222 (2000).
24. F.H. Stillinger. J. Solution Chem. **2**, 141 (1973).
25. D.M. Huang and D. Chandler. Phys. Rev. E, **61**, 1501 (2000); D.M. Huang, P.L. Geissler, and D. Chandler. J. Phys. Chem. B, **105**, 6704 (2001).
26. E. Wilhelm and R. Battino. J. Chem. Phys. **56**, 563 (1972); N. Morel-Desrosiers and.P. Morel. Can. J. Chem. **59**, 1 (1981).
27. R.A. Pierotti. J. Phys. Chem. **69**, 281 (1965).
28. A.H. Narten and H.A. Levy, Science, **165**, 447 (1969); J.M. Sorenson, G. Hura, M. Glaeser, and T. Head-Gordon. J. Chem. Phys. **113**, 9149 (2000).
29. M.I. Cabaco, Y. Danten, M. Besnard, Y. Guissani, and B. Guillot. J. Phys. Chem. B, **01**, 6977 (1997).
30. G.S. Kell. J. Chem. Eng. Data, **20**, 97 (1975).
31. H.S. Ashbaugh, E.W. Kaler, and M.E. Paulaitis. J. Am. Chem. Soc. **121**, 9243 (1999); H.S. Ashbaugh and M.E. Paulaitis. J. Am. Chem. Soc. **123**, 10721 (2001).
32. G. Hummer. J. Am. Chem. Soc. **121**, 6299 (1999).
33. S. Garde, A.E. Garcia, L.R. Pratt, and G. Hummer. Biophys. Chem. **78**, 21 (1999).
34. F. London. Trans. Faraday Soc. **33**, 8, (1937).
35. S.J. Weiner, P.A. Kollman, D.A. Case, U.C. Singh, C. Ghio, G. Alagona, S. Profeta, and P. Weiner. J. Am. Chem. Soc. **106**, 765 (1984).
36. M.H. Abraham and A. Nasehzadeh. J. Chem. Soc. Faraday Trans. **77**, 321 (1981).
37. J.O. Hirschfelder, C.F. Curtiss, and R.B. Bird. Molecular theory of gases and liquids. Wiley, New York. 1954.
38. J. Tomasi and M. Persico. Chem. Rev. **94**, 2027 (1994).
39. D.R. Lide. Handbook of chemistry and physics. 77th ed. CRC Press, Boca Raton, FL. 1996.
40. R.M. Jackson and M.J.E. Sternberg. Protein Eng. **7**, 371 (1994); F.M. Floris, M. Selmi, A. Tani, and J. Tomasi. J. Chem. Phys. **107**, 6353 (1997).
41. D.M. Huang and D. Chandler. Proc. Natl. Acad. Sci. U.S.A. **97**, 8324 (2000).
42. M. Lucas. J. Phys. Chem. **80**, 359 (1976); K. Soda. J. Phys. Soc. Jpn. **62**, 1782 (1993).
43. L.S.E. de Souza and D. Ben-Amotz. J. Chem. Phys. **101**, 9858 (1994).
44. W. Blokzijl and J.B.F.N. Engberts. Angew. Chem. Int. Ed. Engl. **32**, 1545 (1993).
45. T. Lazaridis. Acc. Chem. Res. **34**, 931 (2001).
46. S. Garde and H.S. Ashbaugh. J. Chem. Phys. **115**, 977 (2001).
47. A. Pohorille and L.R. Pratt. J. Am. Chem. Soc. **112**, 5066 (1990).
48. L.R. Pratt and A. Pohorille. Proc. Natl. Acad. Sci. U.S.A. **89**, 2995 (1992).
49. B. Madan and B. Lee. Biophys. Chem. **51**, 279 (1994).
50. A. Wallqvist and D.G. Covell. Biophys. J. **71**, 600 (1996); S.R. Durell and A. Wallqvist. Biophys. J. **71**, 1695 (1996).
51. F. Floris and J. Tomasi. J. Comput. Chem. **10**, 616 (1989).
52. T.H. Hill. An introduction to statistical thermodynamics. Addison-Wesley, Reading. 1960.
53. M. Ikeguchi, S. Shimizu, S. Nakamura, and K. Shimizu. J. Phys. Chem. B, **102**, 5891 (1998).
54. J.L. Finney and A.K. Soper. Chem. Soc Rev. **23**, 1 (1994); J.L. Finney. Faraday Discuss. Chem. Soc. **103**, 1 (1996); K.S. Sidhu, J.M. Goodfellow, and J.Z. Turner. J. Chem. Phys. **110**, 7943 (1999).
55. D.T. Bowron, A. Filipponi, C. Lobban, and J.L. Finney. Chem. Phys. Lett. **293**, 33 (1998); D.T. Bowron, A. Filipponi, M.A. Roberts, and J.L. Finney. Phys. Rev. Lett. **81**, 4164 (1998).
56. A. Wallqvist and B.J. Berne. J. Phys. Chem. **99**, 2893 (1995); R.D. Mountain and D. Thirumalai. Proc. Natl. Acad. Sci. U.S.A. **95**, 8436 (1998).

© 2002 NRC Canada

Assigning structures to diastereomeric aliphatic α,α′-dibromo ketones

Masood Parvez, S.M. Humayan Kabir, Ted S. Sorensen, Fang Sun, and Brian Watson

Abstract: X-ray crystal structures are reported for two symmetrical aliphatic α,α′-dibromo ketones: a *meso* diastereomer of 3,5-dibromo–2,2,6,6-tetramethylheptan-4-one, and a *rac* isomer of 4,6-dibromo–2,2,3,3,7,7,8,8-octamethylnonan-5-one. Using these secure assignments and a previously confirmed structure for the diastereomers of 2,4-dibromopentan-3-one, we show in this study that gas–liquid chromatography (GLC) retention times (*meso* > *rac*) can be used to confidently assign the diastereomers for a range of symmetrical and unsymmetrical aliphatic α,α′-dibromo ketones. ^{1}H NMR chemical shifts for the >CHBr hydrogen(s) can also be corroboratively used for assignment purposes ($\delta_{racH} > \delta_{mesoH}$).

Key words: α,α′-dibromo ketones, X-ray crystal structures, GLC retention times, isomer assignment

Résumé : Faisant appel à la diffraction des rayons X, on a déterminé les structures de deux α,α′-dibromocétones aliphatiques symétriques, un diastéréoisomère *méso* de la 3,5-dibromo-2,2,6,6-tétraméthylheptan-4-one et un isomère racémique de la 4,6-dibromo-2,2,3,3,7,7,8,8-octaméthylnonan-5-one. En se basant sur ces attributions certaines ainsi que sur une preuve de structure rapportée antérieurement pour les diastéréoisomères de la 2,4-dibromopentan-3-one, on démontre que les temps de rétention relatifs, en c.p.g., *méso* > *rac*, peuvent être utilisés avec confiance pour attribuer les configurations des diastéréoisomères pour un ensemble α,α′-dibromocétones aliphatiques symétriques et non-symétriques. Les déplacements chimiques en RMN du ^{1}H des hydrogènes >CHBr peuvent aussi être utilisés à des fins de corroboration des attributions, $\delta_{racH} > \delta_{mésoH}$.

Mots clés : α,α′-dibromocétones; diffraction des rayons X; structures; temps de rétention en c.p.g; attribution de structures d'isomères.

[Traduit par la Rédaction]

Introduction

Several years ago we reported (1, 2) the stereospecific conversion of a symmetrical acyclic α,α′-dibromo ketone (3,5-dibromo-2,2,6,6-tetramethylheptane-4-one) (**1**) to *cis*-2,3-di-*tert*-butylcyclopropanone (**2**). Dibromo ketone **1** was a crystalline single diastereomer, prepared directly in solution from the ketone and bromine, as previously described in the literature (3).

[1]

1 **2**

The question naturally arose as to whether the stereospecificity in the above reaction resided in the starting material (**1** *rac* vs. **1** *meso*), or in some later step in the overall mechanism. Unlike the diastereomeric mixtures found in many other α,α′-dibromination reactions, there was no evidence for a second diastereomer in the preparation of **1**.

There have been numerous reports in which symmetrical α,α′-dibromo ketones have been prepared, but where no consideration of stereochemistry needed to be taken into account. Föhlisch and Gottstein (4), however, made secure assignments for 2,4-dibromopentan-3-one, based on the reduction of the *rac* isomer to a single alcohol product, since in their studies it was important to assign the dibromo ketone stereochemistry.

The present paper extends and generalizes on these *rac* vs. *meso* assignments, and includes an X-ray structure of the di-*tert*-butyl system **1** (*meso* isomer). It also includes a predictive *rac* assignment in another system, which was subsequently verified by a second X-ray structure. We also discuss the stereochemical assignments for several unsymmetrical α,α′-dibromo ketones.

Results and discussion

Table 1 contains a summary of the relevant experimental data related to the *meso* vs. *rac* assignments for the symmetrical dibromo ketones. The first part of the table is based on gas–liquid chromatography (GLC) retention times and the

Received 28 August 2001. Published on the NRC Research Press Web site at http://canjchem.nrc.ca on 8 April 2002.

M. Parvez, S.M.H. Kabir, T.S. Sorensen,[1] F. Sun, and B. Watson. The Department of Chemistry, University of Calgary, Calgary, AB T2N 1N4, Canada.

[1]Corresponding author (e-mail: sorensen@ucalgary.ca).

 DOI: 10.1139/V02-033 © 2002 NRC Canada

Table 1. Symmetrical aliphatic α,α′-dibromo ketones. Assigned structure for *meso* and *rac* diastereomers based on polarity considerations and ^{1}H NMR chemical shifts

		GLC retention time (min)			^{1}H NMR shifts (δ) >CHBr	
Entry	R	Assigned *meso*	Assigned *rac*	Ratio *rac/meso*[a]	Assigned *meso*	Assigned *rac*
1	CH_3	**12.75**	**11.83**	0.93	**4.77**	**4.99**
2	Et	10.81	10.04	0.93	4.54	4.67
3	*n*-Pr	13.35	12.84	0.96	4.60	4.74
4	*i*-Pr	13.14	12.45	0.95	4.45[b]	4.41[b]
5	*t*-Bu	**8.73**	7.67	0.88	**4.40**	4.49
6	*t*-Amyl	15.8	14.4	0.91	4.48	4.58
7	$-CH(CH_3)_2CH(CH_3)_2$	11.92	11.35	0.95	4.69	4.83
8	$-C(CH_3)_2C(CH_3)_3$	21.27	**19.87**	0.93	4.86	**4.93**

[a]The values are slightly dependent on the actual retention times (variable settings used).

[b]Reversal, see text.

Fig. 1. ORTEP plot of *meso*-**3** (R = *t*-Bu).

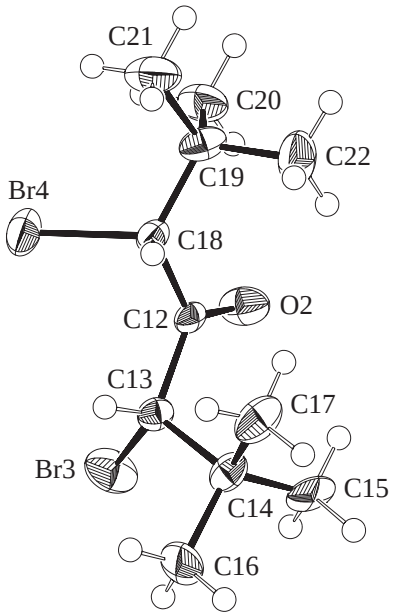

second on ^{1}H NMR chemical shifts for the >CHBr hydrogen. Note that the retention-time NMR-shift assignments are correlated, usually because one diastereomer in the mixture is dominant or because a complete or partial chromotographic separation of diastereomers was employed. The Föhlisch assignment for **3** (R = CH_3) is highlighted in bold as are the two X-ray structures reported in this work.

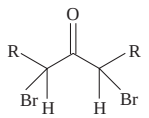

3

No data is given for the somewhat variable *meso–rac* product ratio observed for the direct bromination of the ketones in chlorinated hydrocarbon solvents. Since the HBr co-product of the reaction catalyzes *meso–rac* interconversion, the precise experimental procedure used undoubtedly plays a role in determining this ratio (kinetic vs. thermodynamic control). For entries 1–4 in Table 1, significant quantities of both diastereomers were obtained by direct bromination of the ketone. Somewhat inexplicably, however, only a single diastereomer for R = *t*-Bu was obtained (as previously noted). A small percentage of the other isomers could be obtained,[2] however, by direct bromination of the *cis*-cyclopropanone **2**. For entries 6–8 in Table 1, both diastereomers are obtained by direct bromination of the ketone.

In all cases, the *rac* and *meso* isomers have virtually identical mass-spectral fragmentation patterns. Hence, the identity of the peaks due to the α,α′-dibromo ketones are readily apparent in a GLC–MS determination, even when small amounts of the α,α-dibromo or tribromo impurities are present.

Early in the study, an X-ray crystal structure of the R = *t*-Bu isomer was obtained, and as is apparent from the ORTEP diagram (Fig. 1), this isomer has the *meso* configuration. Incorporating this information into Table 1, along with the Föhlisch R = CH_3 assignment, leads to the tentative conclusion that the *meso* isomer has the longer GLC retention time, and with the exception of R = *i*-Pr, it also has the higher-field chemical shift for the >CHBr hydrogen.

The Table 1 predictions could be readily tested because a pure crystalline shorter-retention-time isomer of R = $-C(CH_3)_2C(CH_3)_3$ could be obtained by column chromotography (first eluting fraction). The ORTEP X-ray crystal structure of this isomer is shown in Fig. 2, and indeed has the assigned (Table 1) *rac* stereochemistry. We therefore feel confident that all of the entries in Table 1 have the proper designated configurations.

It is possible that a chiral GLC column could be used to confirm the *rac* vs. *meso* assignments in Table 1. In unsym-

[2]Crystallographic information has also been deposited with the Cambridge Crystallographic Data Centre (CCDC No. 170983 for **3**, R = *t*-Bu; 170984 for **3**, R = 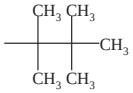 ($-C(CH_3)_2C(CH_3)_3$)).

Copies of the data can be obtained free of charge via www.ccdc.cam.ac.uk/conts/retrieving.html (or from the Cambridge Crystallographic Data Centre, 12, Union Road, Cambridge CB2 1EZ, UK; fax: +44 1223 336033; or deposit@ccdc.cam.ac.uk).

© 2002 NRC Canada

Fig. 2. ORTEP plot of *rac*-**3** (R = -C(CH$_3$)$_2$C(CH$_3$)$_3$).

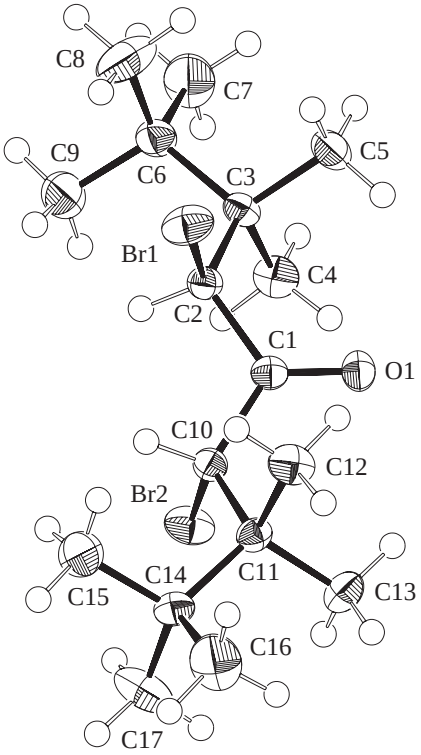

metrical dialkyl ketones, however, both diastereomers are racemates. Nevertheless one would expect that the diastereomer assignments would follow those of the symmetrical examples, i.e., the *meso* pair (*RS*(*SR*)) would have a longer GLC retention time and a higher-field ^{1}H NMR chemical shift for >C*H*Br than the racemic pair *RR*(*SS*).

Dibromination of 3-hexanone produces two isomers (**4**) with distinct GLC-retention behaviour (8.5 and 9.3 min, ratio 0.91), similar to the symmetrical examples in Table 1. Likewise, the longer- retention-time isomer has, on average, higher-field ^{1}H NMR shifts for the >CHBr hydrogens than the shorter retention diastereomer (δ 4.555 (dd) and 4.755 (q) vs. 4.74 (t) and 4.93 (q), respectively). Thus these isomers can be assigned as follows: the shorter-retention-time lower-field ^{1}H's to 2*R*,4*S*(2*S*,4*R*); and the longer-retention-time higher-field ^{1}H's to 2*R*,4*R* (2*S*,4*S*). Similarly, dibromination of the unsymmetrical ketone **5**, in which two alkyl groups are present on one α-carbon, one large (*t*-Bu), and one small (CH$_3$), again results in two diastereomers of **6**. The ^{1}H NMR shifts for >CHBr (a single ^{1}H peak) occur

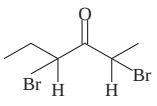

4

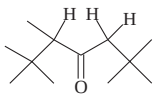

5

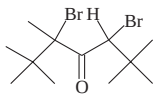

6

at δ 4.91 (longer-retention-time isomer) and at δ 5.22 (shorter-retention-time isomer), which is consistent with the assignment of 3*R*,5*S*(3*S*,5*R*) for the former and 3*R*,5*R*(3*S*,5*S*) for the latter. This assignment is based on the reasonable assumption that the steric interactions in A will somewhat resemble those in B.

Table 2. Experimental details for structure **3** (R = *t*-Bu).

Empirical formula	$C_{11}H_{20}Br_2O$
Formula weight	328.09
Crystal system	Triclinic
Lattice parameters	
a (Å)	10.916 (2)
b (Å)	15.013 (3)
c (Å)	9.3430 (18)
α (°)	92.97 (2)
β (°)	105.769 (17)
γ (°)	105.385 (16)
V (Å^3)	1408.0 (5)
Space group	$P\bar{1}$ (No. 2)
Z value	4
$D_{calcd.}$ (g cm^{-3})	1.548
Radiation	Mo Kα (λ = 0.71069 Å) Zr-filter
Temperature (°C)	–103.0
$2\theta_{max}$	50.0°
No. of reflections	Total: 5290 Unique: 5004 (R_{int} = 0.076)
No. of observations $I > 3.00\sigma(I)$	1836
Residuals: *R*; *wR*	0.043; 0.041
Max shift/error in final cycle	0.01
Max. peak in final diff. map (e Å^{-3})	0.48
Min. peak in final diff. map (e Å^{-3})	–0.63

(A) 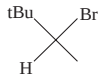

(B)

X-ray structures

Tables 2 and 3 contain X-ray parameters[2] for the structure determination of **3**, R = *t*-Bu, and **3**, R = -C(CH$_3$)$_2$C(CH$_3$)$_3$. The R = *t*-Bu crystal contains two independent molecules in the asymmetric unit, but the conformations of these are similar. One molecule is shown as an ORTEP diagram (Fig. 1) and is clearly a *meso* configuration. The methyl moieties of the *t*-Bu groups are staggered with respect to the >CHBr bonds. The most important features of this structure are, however, the Br1-C2-C1-O1 and Br2-C7-C1-O1 dihedral angles (56.5° and –110.8° respectively), and the Br1-C2-C7-Br2 dihedral angle of – 44.6°. Thus the two separate $C^{\delta+}$–$Br^{\delta-}$ dipoles are significantly aligned when the structure as a whole is taken into consideration. Individually, they are both almost perpendicular to the $>C^{\delta+}=O^{\delta-}$ dipole.

The R = -C(CH$_3$)$_2$C(CH$_3$)$_3$ crystal contains two independent molecules in the asymmetric unit of a centrosymmetric space group, again with very similar conformations. The structure for (4*S*,6*S*) is shown in Fig. 2, and as we had already predicted from the GLC–NMR data in Table 1, it is a *rac* configuration.

The methyl groups of the -C(CH$_3$)$_2$C(CH$_3$)$_3$ substituents are internally staggered, and are also staggered with respect to the >CHBr atoms. The Br1-C2-C1-O1 and Br2-C10-C1-O1 dihedral angles are –93.8° and –92.9°, respectively, and the

© 2002 NRC Canada

Table 3. Experimental details for structure **3**

R = 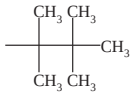

Empirical formula	$C_{17}H_{32}Br_2O$
Formula weight	412.25
Crystal system	Monoclinic
Lattice parameters	
a (Å)	10.79270 (10)
b (Å)	18.5538 (2)
c (Å)	18.8986 (3)
α (°)	90
β (°)	92.6860 (10)
γ (°)	90
Space group	$P2_1/c$
Z value	8
$D_{calcd.}$ (g cm^{-3})	1.449
Radiation	Mo Kα (λ = 0.71069 Å)
Temperature (°C)	–100.0 (1)
Independent reflections	8613 [*R*(int) = 0.021]
Final *R* indices [$I > 2\sigma(I)$]	R_1 = 0.028, wR_2 = 0.061
$(\Delta/\theta)_{max}$	0.001
Largest diff. peak and hole (e Å^{-3})	0.47 and –0.49

dihedral angle Br1-C2-C7-Br2 is 165.0°. Thus, in the molecule as a whole, the two $C^{\delta+}$–$Br^{\delta-}$ dipoles are nearly opposed, and both are nearly perpendicular to the $>C^{\delta+}=O^{\delta-}$ dipole.

The polarity behaviour of *cis*- and *trans*-2,6-dibromocyclohexanones (*cis* more polar than *trans*) has been discussed (5) in terms of the fixed orientation of the two $C^{\delta+}$–$Br^{\delta-}$ dipoles. In contrast, acyclic dibromoketones have free rotation around all of the bonds, but it seems clear that the *meso* conformations must have at least partially aligned $C^{\delta+}$–$Br^{\delta-}$ dipoles in the molecule as a whole, while the *rac* isomers involve some net cancellation of the two $C^{\delta+}$–$Br^{\delta-}$ dipoles. While it is somewhat dangerous to infer solution conformations from crystal structures, it should be noted that the two $C^{\delta+}$–$Br^{\delta-}$ dipoles are partially aligned in the more polar *meso* structure, compared with a cancellation of these dipoles in the *rac* structure, i.e., the crystal structure conformations sufficiently account well for the expected solution conformations.

There have been previous X-ray crystal structures of α,α′-dibromo ketones, but these have involved cyclic or bicyclic structures that do not have much conformational flexibility, the exception being a structure of dibromocyclododecanone (6).

Other possible *rac* vs. *meso* assignment parameters

The reduced polarity of the *rac* isomer is not confined to GLC retention times. In **3**, R = CH_3, the pure *rac* isomer can be obtained from a fractional distillation as the first fraction(4). TLC and flash chromotography will also separate the *rac* and *meso* isomers. We also looked at some of the ^{13}C NMR chemical shifts of the >CHBr carbons in the diastereomeric sets, but these do not correlate with the Table 1 assignments on a consistent basis.

Conclusions

Based on the two X-ray structures of α,α′-dibromo ketones, and a previous assignment of the the 3-pentanone system, it is clear that a combination of the GLC retention-time behaviour and the ^1H NMR chemical shifts (>CHBr) can be used to reliably assign the diastereomeric configuration of these compounds.

Experimental

^1H NMR spectra (δ values) were obtained in $CDCl_3$ at 200 MHz, using a Brucker ACE-200 spectrometer. All GLC–MS data was obtained on a Hewlett–Packard model 5890 gas chromatograph equipped with a model 5971 mass-selective detector. Split-mode injection was used employing 25 m × 0.25 mm i.d capilliary columns (DB5, DB17, or OV101). The intent of the Table 1 data is to show the large-retention-time differences for the diastereomeric pairs, under conditions where the retention times were in the range of 8–20 min.

α,α′-Dibromo ketones

Entries 5–8 in Table 1 involve compounds prepared in previous studies from this laboratory (2,7). Compound **3**, R = CH_3 (4), Et (8), *i*-Pr (8), and compound **4** (9) have been reported, often with no mention of diastereomeric possibilities. Compound **6** has also been reported (2). 4,6-Dibromononan-5-one (**3**, R = *n*-Pr) was prepared as a mixture of diastereomers, by adding Br_2 in CCl_4 at 20°C to a solution of 5-nonanone in CCl_4. For dibromides **3** (R = *i*-Pr) and **4**, the corresponding pure *rac* diastereomer was obtained by column chromatography (SiO_2). Our own preparations for entries 1–4 in Table 1 invariably contained small amounts of α,α-dibromo and tribromo impurities, which could be detected by GLC–MS.

X-ray structures

Compound 3 (R = t-Bu)

Pertinent data concerning the crystal structure determination of **3** (R = *t*-Bu) is summarized in Table 2.

Data Collection

A colorless prismatic crystal of $C_{11}H_{20}Br_2O$ having approximate dimensions of 0.42 × 0.40 × 0.39 mm was mounted on a glass fiber. All measurements were made on a Rigaku AFC6S diffractrometer using Mo Kα radiation monochromatized with a Zr filter.

The data were collected at a temperature of –103 ± 1°C using the ω–2θ scan technique to a maximum 2θ value of 50.0°. Omega scans of several intense reflections, made prior to data collection, had an average width at half height of 0.22°. Scans of (0.84 + 0.34 tan θ)° were made at a speed of 4.0° min^{-1} (in omega). The weak reflections ($I < 10.0\ \sigma(I)$) were re-scanned (maximum 4 scans) and the counts were accumulated to ensure good-counting statistics. Stationary background counts were recorded on each side of the reflection. The ratio of peak-counting time to background-counting time was 2:1. The diameter of the incident beam collimator was 1.0 mm, the crystal-to-detector distance

© 2002 NRC Canada

was 400 mm, and the aperture was 9.0 × 13.0 mm (horizontal × vertical).

Structure solution and refinement

The structure was solved by direct methods (10) and expanded using Fourier techniques (11). The non-hydrogen atoms were refined anisotropically. Hydrogen atoms were included at geometrically idealized positions and were not refined. The final cycle of full-matrix least-squares refinement was based on 1836 observed reflections ($I > 3.00\sigma(I)$) and 253 variable parameters and converged (largest parameter shift was 0.01 times its esd) with unweighted and weighted agreement factors of

$$[1] \qquad R = \sum \left| \frac{|F_0| - |F_c|}{F_0} \right| = 0.043$$

$$[2] \qquad R_w = \sqrt{\left(\sum w \frac{(|F_0 - F_c|)^2}{wF_0^2} \right)} = 0.041$$

The standard deviation of an observation of unit weight was 1.75. The weighting scheme was based on counting statistics and included a factor ($p = 0.015$) to downweight the intense reflections. Plots of $\Sigma w(|F_0| - |F_c|)^2$ vs. $|F_0|$, reflection order in data collection, $\sin\theta/\lambda$, and various classes of indices showed no unusual trends. The maximum and minimum peaks on the final difference Fourier map corresponded to 0.48 and –0.63 e Å^{-3}, respectively.

Neutral-atom scattering factors were taken from Cromer and Waber (12). Anomalous dispersion effects were included in F calcd. (13); the value for Δ and $\Delta f''$ were those of Creagh and McAuley (14). The values for the mass-attenuation coefficients are those of Creagh and Hubbel (15). All calculations were performed using the teXscan (16) crystallographic software package from the Molecular Structure Corporation.

Compound 3 (R = -C(CH$_3$)$_2$C(CH$_3$)$_3$)

Pertinent data concerning the crystal structure determination of **3** (R = -C(CH$_3$)$_2$C(CH$_3$)$_3$) is summarized in Table 3.

Data collection

A colorless prismatic crystal of $C_{17}H_{32}Br_2O$ was coated with paratone 8277 oil (Exxon) and mounted on a glass fibre. All measurements were made on a Nonius KappaCCD diffractrometer with graphite-monochromated Mo Kα radiation. Cell constants obtained from the refinement (17) of 8589 reflections in the range $1.0 < \theta < 27.5°$ corresponded to a primitive monoclinic cell. The space group was determined uniquely from the systematic absences. The data were collected (18) at –100(1)°C using the $\omega-\varphi$ scans to a maximum θ value of 27.5°. The data were corrected for Lorentz and polarization effects and for absorption using multi-scan methods (17). Since the crystal did not show any sign of decay during data collection, a decay correction was deemed unnecessary.

Structure solution and refinement

The structure was solved by the direct methods (10) and expanded using Fourier techniques (11). The non-hydrogen atoms were refined anisotropically. Hydrogen atoms were included at geometrically idealized positions and were not refined. The final cycle of full-matrix least-squares refinement using SHELXL97 (19) converged (largest parameter shift was <0.001 times its eds) with unweighted and weighted agreement factors, $R = 0.028$ [$I > 2\sigma(I)$] and $wR = 0.067$ (all data), respectively and goodness of fit, $S = 0.99$. The weighing scheme was based on counting statistics and the final difference Fourier map was essentially featureless. Figures 2 and 3 were plotted with the aid of ORTEPII (20).

Acknowledgment

We thank the Natural Sciences and Engineering Research Council of Canada (NSERC) for generous financial support.

References

1. T.S. Sorensen and F. Sun. J. Am. Chem. Soc. **117**, 5592 (1995).
2. T.S. Sorensen and F. Sun. Can. J. Chem. **75**, 1030 (1997).
3. J. Ciabattoni and E.C. Natham, III. J. Am. Chem. Soc. **91**, 4766 (1969).
4. B. Föhlisch and W. Gottstein. Liebigs Ann. Chem. 1768 (1979).
5. H.M.R. Hoffmann and J.G. Vinter. J. Org. Chem. **39**, 3921 (1974).
6. J. Delhi and P. Groth. Acta Chem. Scand. **23**, 587 (1969)
7. T.S. Sorensen and F. Sun. J. Chem. Soc. Perkin 2, 1053 (1998)
8. C. Lion and J.-E. Dubois. Tetrahedron, **31**, 1223 (1975).
9. L. Hegedus and M.S. Holden. J. Org. Chem. **50**, 3920 (1985)
10. SIR92: A. Altomare, M. Cascarano, C. Giacovazzo, and A. Guagliardi. H. Appl. Cryst. **26**, 343 (1993).
11. DIRDIF94: P.T. Beurskens, G. Admiraal, G. Beurskens, W.P. Bosman, R. de Gelder, R. Israel, and J.M.M. Smits. Technical report of the crystallography laboratory. University of Nijmegen, The Netherlands. 1994.
12. D.T. Cromer and J.T. Waber. International tables for X-ray crystallography. Vol IV. The Kynoch Press, Birmingham, England. 1974. Table 2.2A.
13. J.A. Ibers and W.C. Hamilton. Acta Cryst. **17**, 781 (1964).
14. D.C. Creagh and W.J. McAuley. International tables for crystallography. Vol. C. *Edited by* A.J.C. Wilson. Kluwer Academic Publishers, Boston. 1992. Table 4.2.6.8. pp. 219–222.
15. D.C. Creagh and J.H. Hubbell. International tables for crystallography. Vol C. *Edited by* A.J.C. Wilson. Kluwer Academic Publishers, Boston. 1992. Table 4.2.4.3. pp. 200–206.
16. teXscan; Crystal structure analysis package. Molecular Structure Corporation, The Woodlands, Texas, USA. 1985 and 1992.
17. Z. Otwinowski and W. Minor. Methods Enzymol. **276**, 307 (1997).
18. R. Hooft. COLLECT. Nonium BV, Delft, The Netherlands. 1998.
19. G.M. Sheldrick. SHELXL97. University of Göttingen, Germany. 1997.
20. C.K. Johnson. ORTEPII. Report ORNL-5138. Oak Ridge National Laboratory, Tennessee. 1976.

© 2002 NRC Canada

Aqueous nonelectrolyte solutions. Part XVIII. Equilibrium pressures of two methane hydrates with water. Formulae and dissociation thermodynamic functions for the structures I and II methane hydrates

David N. Glew

Abstract: Literature data for the saturation pressure $P(hl_1g)$ of methane hydrate with water, at 102 temperatures between –0.29 and 46.87°C, are properly represented by two distinct equations, with a quadruple point $Q(h_1h_2l_1g)$ transition temperature at 26.7°C with standard error (*SE*) 0.9°C and 55.5 MPa with *SE* 5.3 MPa. The structure I type methane hydrate phase h_1 is stable below 26.7°C and the structure II type methane hydrate phase h_2 is stable above 26.7°C. Between –0.29 and 25.54°C, 85 equilibrium pressures of methane hydrate with water are best represented, with *SE* 1.33% on a single pressure measurement, by a four-parameter thermodynamic equation. The corresponding equilibrium methane fugacities are represented, with *SE* 0.94% on a fugacity determination, by a five-parameter equation. Between 26.98 and 46.87°C, 17 equilibrium methane hydrate pressures with water are best represented, with *SE* 2.22% on a pressure measurement, by a three-parameter equation. Composition of the equilibrium aqueous phase is evaluated using methane fugacity with the solubility equation including a Poynting correction. Literature data between –2.22 and –14.10°C, for the saturation pressure $P(h_1s_1g)$ of structure I methane hydrate with ice, are properly represented by a two-parameter equation, with *SE* 1.1% on a single pressure measurement. Standard enthalpy change for structure I methane hydrate dissociation into ice and methane gas is found to be $\Delta H^{ot}(h_1 \rightarrow s_1g) = 18058$ J mol^{-1} with *SE* 608 J mol^{-1} at –8.28°C. The quadruple point $Q(h_1s_1l_1g)$ is estimated at –0.290°C with *SE* 0.0064°C and at 2.527 MPa with *SE* 0.053 MPa. Using the classical thermodynamic method, as described for deuterium sulfide D-hydrate, methane hydrate equilibrium fugacities define 85 equilibrium constants $Kp(h_1 \rightarrow l_1g)$ between –0.29 and 25.54°C for dissociation of structure I hydrate h_1 into liquid water l_1 and methane gas. Temperature dependence of ln $Kp(h_1 \rightarrow l_1g)$ is well-represented by a three-parameter thermodynamic equation that gives both estimates and their standard errors for (*i*) $\Delta H^{ot}(h_1 \rightarrow l_1g)$ and $\Delta Cp^{ot}(h_1 \rightarrow l_1g)$, the standard enthalpy and heat capacity changes, respectively, for hydrate h_1 dissociation, and for (*ii*) $n = r$, the approximate formula number of the hydrate $CH_4 \cdot nH_2O$ at each experimental temperature. The formula $CH_4 \cdot 6.205H_2O$ with *SE* $0.066H_2O$ is found for the structure I methane hydrate h_1 with water at quadruple point $Q(h_1s_1l_1g)$ –0.29°C; an approximate formula $CH_4 \cdot 5.759H_2O$ with *SE* $0.077H_2O$ is found at quadruple point $Q(h_1h_2l_1g)$ 26.7°C. Between 26.98 and 46.87°C, the 17-equilibrium constants $Kp(h_2 \rightarrow l_1g)$ for dissociation of structure II methane hydrate h_2 into liquid water l_1 and methane gas are represented by a constrained three-parameter thermodynamic equation. For structure II methane hydrate the formula $CH_4 \cdot 5.822H_2O$ with *SE* $0.064H_2O$ is found at quadruple point $Q(h_1h_2l_1g)$ 26.7°C and the formula $CH_4 \cdot 5.699H_2O$ with *SE* $0.064H_2O$ at 46.87°C. Molar volumes and cohesive energy densities of the methane hydrates are compared with equilibrium compressed water.

Key words: clathrate hydrates of methane, two methane gas hydrates, formula of structure I methane hydrate, thermodynamics of clathrate hydrate dissociation, dissociation equilibrium constants of structure I methane hydrate, standard enthalpy and heat capacity changes for dissociation of structure I methane hydrate, methane hydrates' transition temperature, formula of structure II methane hydrate, dissociation equilibrium constants of structure II methane hydrate, standard enthalpy change for dissociation of structure II methane hydrate, methane hydrates' cohesive energy density.

Résumé : Les données retrouvées dans la littérature pour la pression de saturation, $P(hl_1g)$ de l'hydrate de méthane avec l'eau, à 102 températures entre –0,29 et 46,87°C, peuvent être représentées correctement par deux équations distinctes, avec une température de transition à point quadruple, $Q(h_1h_2l_1g)$, à 26,7°C et une erreur standard (*ES*) de 0,9°C et une pression de 55,5 avec une *ES* de 5,3 MPa; avec une structure d'hydrate de méthane de type I, phase h_1, stable en-dessous de 26,7°C et une structure d'hydrate de méthane de type II, phase h_2, stable au-dessus de 26,7°C. Entre –0,29 et 25,54°C, la meilleure représentation de 85 pressions d'équilibre de l'hydrate de méthane avec l'eau est donnée par une équation thermodynamique à quatre paramètres, avec une *ES* de 1,33% sur une mesure de pression particulière; les fugacités correspondantes de l'équilibre du méthane sont représentées par une équation à cinq paramètres, avec une *ES*

Received 18 July 2001. Published on the NRC Research Press Web site at http://canjchem.nrc.ca on 10 April 2002.

D.N. Glew. 536 Highbury Park, Sarnia, ON N7V 2J9, Canada (telephone: (519) 337-3136).

 DOI: 10.1139/V02-017 © 2002 NRC Canada

de 0,94%. Entre 26,98 et 46,87°C, la meilleure représentation des 17 pressions d'équilibre de l'hydrate de méthane avec l'eau est donnée par une équation à trois paramètres, avec une *ES* de 2,22%. La composition de la phase aqueuse en équilibre est évaluée en utilisant la fugacité du méthane avec l'équation de solubilité et en y incluant la correction de Poynting. Les données de la littérature entre –2,22 et –14,10°C pour la meilleure représentation de la pression de saturation $P(h_1s_1g)$ de l'hydrate de méthane de structure I avec la glace est donnée par une équation à deux paramètres, avec une *ES* de 1,1% sur une mesure particulière de pression. On a trouvé que le changement d'enthalpie standard pour la dissociation de l'hydrate de méthane de structure I en glace et en méthane gazeux, $\Delta H^{ot}(h_1 \rightarrow s_1g) = 18058$ avec une *ES* de 608 J mol^{-1} à –8,28°C. On a évalué que le point quadruple se situe à une température de –0,290° avec une *ES* de 0,0064°C et une pression de 2,527 avec une *ES* de 0,053 MPa. Utilisant la méthode thermodynamique classique décrite pour le sulfure de deutérium et l'hydrate D, les fugacités d'équilibre de l'hydrate de méthane définissent 85 constantes d'équilibre $Kp(h_1 \rightarrow l_1g)$ entre –0,29 et 25,24°C pour la dissociation de l'hydrate h_1 de structure I en molécule d'eau liquide, l_1, et de méthane gazeux. La relation de ln $Kp(h_1 \rightarrow l_1g)$ avec la température est bien représentée une équation thermodynamique à trois paramètres qui fournit des évaluations, ainsi que leurs erreurs standards, pour (*i*) $\Delta H^{ot}(h_1 \rightarrow l_1g)$ et $\Delta Cp^{ot}(h_1 \rightarrow s_1g)$, les changements d'enthalpie standard et de capacité calorifique pour la dissociation de l'hydrate h_1, et pour *(ii)* $n = r$, le nombre de formule approximatif de l'hydrate $CH_4 \cdot nH_2O$ à chaque température expérimentale. Pour l'hydrate de méthane h_1 de structure I, on a trouvé que la formule est $CH_4 \cdot 6{,}205H_2O$, avec une *ES* de $0{,}066H_2O$, avec un point quadruple, $Q(h_1s_1l_1g)$, à –0,29°C; on a aussi détecté une formule approximative de $CH_4 \cdot 5{,}759H_2O$, avec une *ES* de $0{,}077H_2O$, avec un point quadruple, $Q(h_1h_2l_1g)$, à 26,7°C. Entre 26,98 et 46,87°C, la meilleure représentation des 17 constantes d'équilibre $Kp(h_2 \rightarrow l_1g)$ pour la dissociation de l'hydrate de méthane de structure II, h_2, en eau liquide et en méthane gazeux est donnée par une équation à trois paramètres contraints. Pour l'hydrate de méthane de structure II, on a trouvé que la formule est $CH_4 \cdot 5{,}822H_2O$, avec une *ES* de $0{,}064H_2O$, avec un point quadruple, $Q(h_1h_2l_1g)$, à 26,7°C et une formule de $CH_4 \cdot 5{,}699H_2O$, avec une *ES* de $0{,}064H_2O$, à 46,87°C. On a aussi comparé les volumes molaires et les densités de l'énergie cohésive des hydrates de méthane avec celles de l'équilibre de l'eau comprimée.

Mots clés : clathrate d'hydrates de méthane, deux hydrates du méthane gazeux, formule de l'hydrate de méthane de type I, thermodynamique de la dissociation du clathrate d'hydrate, constantes d'équilibres pour la dissociation de l'hydrate de méthane de structure I, changements d'enthalpie standard et d'entropie pour la dissociation de l'hydrate de méthane de structure I, température de transition des hydrates de méthane, formule de la structure de l'hydrate de méthane de structure II; constantes d'équilibre de dissociation de l'hydrate de méthane de structure II, changement d'enthalpie standard pour la dissociation de l'hydrate de méthane de structure II, densité de l'énergie cohésive des hydrates de méthane.

[Traduit par la Rédaction]

Introduction

Literature on the methane clathrate gas hydrate is large and extends from the pioneering pressure measurements of Villard in 1888 up to the calorimetric and spectroscopic studies of the present time (1–23). An excellent modern review of the clathrate hydrates of natural gases by Sloan (24) provides the background for the present work and has encouraged us to revisit methane hydrate (9).

Initially the data sets of methane hydrate measurements are examined separately, subsequently the data sets are combined to provide statistically valid models for all measurements.

Methane hydrate temperatures are converted to ITS-90 as described (25) and two digits are retained after the decimal point.

The temperature dependence of univariant equilibrium properties such as the total methane hydrate pressure $P(hl_1g)$, the hydrate methane fugacity $f_2(hl_1g)$, and the methane hydrate dissociation equilibrium constants $Kp(h \rightarrow l_1g)$ and $Kp(h \rightarrow s_1g)$ are represented by well-conditioned, unbiased, thermodynamic equations, similar to eq. [1*a*], which are fully described elsewhere (26).

The methane hydrate pressures (1–3, 6, 7, 10, 12–14, 17, 22) are combined with accurate aqueous methane solubility data including the Poynting correction (16) and the IUPAC equation of state for methane fugacity (27) to define the equilibrium composition of the aqueous phase l_1. The equilibrium constants for dissociation of the structures I and II methane hydrates use auxiliary properties of water (28–31).

Classical thermodynamic equations are used to define the dissociation equilibrium constant and formula for a methane hydrate of variable composition, as described in detail for the structure I deuterium sulfide D-hydrate and hydrogen sulfide hydrate (32–34).

All regression equations are evaluated using the method of weighted least-squares (35) and a predicted estimate is qualified by its standard error, written *SE*. Residuals for individual data sets from regression models for the combined data sets are qualified by their root mean-squared deviations, written *RMS*.

Results and discussion

Pressures of methane hydrate with aqueous liquid

The dependence on temperature of the total pressure $P(hl_1g)$ for methane hydrate with water is examined by individual data set first for internal consistency and then for attainment of equilibrium.

Because of the lack of agreement between the hydrate pressures from various data sets, each data set is fitted separately by eq. [1*a*] using the method of least-squares with unit

© 2002 NRC Canada

weights. In general, the lower the observed methane pressure at a given temperature, the nearer the measurement is to equilibrium.

Using this simple lower-pressure criterion, the four measurements of data set GRCK70 (13) are clearly shown to be nearest to thermodynamic equilibrium. To achieve proper phase equilibrium Kobayashi and co-workers (13) found it necessary to use the vigorous mixing of rolling stainless steel balls to triturate the methane hydrate slurry with the aqueous liquid. The earlier study of data set MSK64 (10) achieved equilibrium measurements for methane hydrate at higher pressures using a dynamic pressure–temperature variation method. Data sets D&F40 (2) and V74 (14) also exhibit lower methane hydrate pressures and are taken to be in equilibrium.

Using the lower-pressure criterion, the other seven data sets (1, 3, 6, 7, 12, 17, 22) of hydrate measurements are found to be near to, but not at equilibrium. It is found that the gentle rocking of a cell gauge for a short duration (6, 7, 12, 22), and the occasional stirring of a Caillitet tube (3, 17), are inadequate to achieve phase equilibrium for methane hydrate with its aqueous liquid.

The methane hydrate pressures of Villard (1) are consistently higher than those of the modern data sets with better phase agitation (2, 3, 6, 7, 10, 12–14, 17, 22). Six sets of modern measurements show slightly but significantly higher pressures than the four sets of equilibrium measurements (2, 10, 13, 14).

Individual data sets of pressure measurements below 26.7°C for methane hydrate, phase h_1, in contact with aqueous liquid, phase l_1, are represented by the general unbiased thermodynamic equation,

$$[1a] \quad \ln P(h_1l_1g) = b0 + b1.u1 + b2.u2 + b3.u3$$

which equation is mathematically equivalent (26) to the ill-conditioned thermodynamic equation

$$[1b] \quad \ln P(h_1l_1g) = A + B/T + C \ln T + DT.$$

Table 1 shows the results for representation of individual data sets of methane hydrate pressures by eq. [1*a*]. Column one lists abbreviated name(s) of the author(s) and the year of publication of the data set, together with the literature reference. Columns two and three list the temperature range of the hydrate measurements and their number *n*. Column four lists the estimate of the standard error of ln $P(h_1l_1g)$, abbreviated to *SE*(ln *P*), for a single hydrate pressure measurement, and the coefficient of determination R^2 for the least-squares fit of the data by eq. [1*a*]. Columns five to seven of Table 1 show the parameter estimates (*b*0, *b*1, *b*2) with their *SE* estimates, evaluated (26) at reference temperature θ = 25°C ≡ 298.15 K, for the 11 separate data sets.

No individual data set requires more than three parameters for a proper representation of the observed pressures, and all estimates of *b*1 and *b*2 are positive. The upper 11 rows of Table 1, for data at temperatures below 26.7°C, show values of *b*1 between 34.2 and 40.5 with values of *b*2 between 112.7 and 208.9. These parameters are characteristic of pressure measurements from the structure I type (36, 37) methane hydrate, which we define as phase h_1. Ideally all values of *b*1 should be equal and all values of *b*2 should be equal.

Estimates for the standard error, *SE*(ln *P*), of a single measurement vary from a minimum of 0.0028 for the most precise data set D&F40 (2), to a maximum of 0.0211 for the equilibrium data set MSK64 (10); standard errors of the other data sets are in the range between 0.0112 and 0.0186. Values of R^2 are greater than 0.9980 and indicate reasonable fits of the pressure data by eq. [1*a*].

In the 12th row of Table 1 parameters are shown for the fit of the combined set of 85 pressure measurements from the 11 data sets (1–3, 6, 7, 10, 12–14, 17, 22) plus one pressure datum evaluated in this work at the ice quadruple point, –0.29°C. This equation provides the best model with three parameters for the equilibrium pressure of methane hydrate with water below 26.7°C. The seven biases between the non-equilibrium data sets (1, 3, 6, 7, 12, 17, 22) and the four equilibrium data sets (2, 10, 13, 14) are removed in the weighted least-squares regression analysis. For the 85 data combined, the parameter and (*SE*) estimates are *b*1, 39.863 (0.241) and *b*2, 205.29 (5.12), values which confirm the reliability of the internal temperature differences within the data sets V1888 and J&R65 (1, 12). This contrasts with their large positive data set biases for *b*0 of 0.1072 (1) and 0.0456 (12), or biases of about +11.3% and +4.7% on their reported pressures. The overall *SE*(ln *P*) 0.0143 indicates a *SE* of 1.44% on a single pressure measurement of unit weight; this *SE* is significantly larger than the expected 0.1–0.4% using the upper 75% range of a precision Bourdon-type metal-tube pressure gauge. This relatively large *SE* estimate for pressure measurement indicates error contributions arising from other unknown factors, together with the inadequacy of eq. [1*a*] with three parameters. The coefficient of determination R^2 = 0.9998 indicates a good fit of the 85 data by eq. [1*a*].

When the combined 85 methane hydrate pressures are fitted by eq. [1*a*] without data set biases, the overall *SE*(ln *P*) estimate is 0.0291, giving a *SE* estimate of 2.95% on a single hydrate pressure measurement with 82 degrees of freedom. This model shows the data sets GRCK70, MSK64, D&F40, and V74 (13, 10, 2, 14) with large negative residuals and the data sets V1888, K&K49, and J&R65 (1, 6, 12) with large positive residuals. When the combined 85 hydrate pressures are fitted by eq. [1*a*], constrained to pass through the mean of the four measurements of data set GRCK70 (13), the overall *SE*(ln *P*) estimate is increased to 0.0477, giving a *SE* estimate of 4.88% for a single hydrate pressure measurement. Clearly these two models without data set biases do not provide an accurate representation of the equilibrium pressure for methane hydrate with water below 25.54°C.

Two methane hydrates

The seven methane hydrate pressure measurements of data set MSK64 (10) between 17.05 and 24.99°C are not continuous with the 13 higher-pressure measurements between 26.98 and 46.87°C.

The 13 hydrate pressure measurements between 15.49 and 25.54°C from data sets M&C61, MSK64, and GRCK70 (7, 10, 13) are represented by eq. [1*a*] with *SE*(ln *P*) 0.0243 on a single measurement, with parameter and (*SE*) estimates *b*0, 3.8046 (0.0108) and *b*1, 37.517 (0.531) and with R^2 0.9978. The 15 pressure measurements between 26.98 and 46.87°C from data sets M&C61 and MSK64 are represented by eq. [1*a*] with *SE*(ln *P*) 0.0243 on a single measurement, with

© 2002 NRC Canada

Table 1. Methane hydrate pressures with water, parameters, and standard errors for fit of separate data sets by eq. [1*a*].

Data set	Ref.	*t* Range (°C)	*n*	*SE*(ln *P*) R^2	*b*0 *SE*(*b*0)	*b*1 *SE*(*b*1)	*b*2 *SE*(*b*2)
V1888	1	0.0–20.3	11	0.0112 0.9998	3.9043 0.0163	40.483 0.716	202.96 13.92
D&F40	2	0.5–12.7	13	0.0028 0.9999	3.7319 0.0191	37.362 0.601	164.70 9.52
RBH40	3	0.0–13.6	4	0.0057 0.9999	3.6675 0.0419	34.326 1.453	112.73 23.63
K&K49	6	22.5–22.7	2				
M&C61	7	12.5–25.5	8	0.0146 0.9996	3.8239 0.0116	38.822 1.307	142.95 57.62
MSK64	10	17.1–25.0	7	0.0211 0.9980	3.7988 0.0122	38.215 0.775	
J&R65	12	0.0–21.2	8	0.0186 0.9996	3.8427 0.0281	40.170 1.282	208.88 25.57
GRCK70	13	10.0–15.6	4	0.0035 0.9999	3.5761 0.0077	30.528 0.176	
V74	14	2.0–18.0	7	0.0203 0.9995	3.7778 0.0645	38.516 2.944	171.35 58.03
dRPLD83	17	0.2–12.8	9	0.0170 0.9992	3.7382 0.1125	36.588 3.576	145.04 55.98
AFS91	22	0.2–12.5	11	0.0173 0.9989	3.6410 0.0999	34.208 3.265	116.71 53.01
11 Sets combined		−0.3–26.7	85	0.0143 0.9998	3.7971 0.0053	39.863 0.241	205.29 5.12
MSK64	10	27.0–46.9	13	0.0220 0.9991	3.8585 0.0209	28.572 1.310	56.04 33.07

parameters and (*SE*)s *b*0 3.8454 (0.0124) and *b*1 30.498 (0.280) and with R^2 0.9989. The point of intersection of the low- and the high-temperature equations indicates a quadruple point $Q(h_1h_2l_1g)$ transition temperature at 26.7°C with *SE* 0.9°C and a transition pressure of 55.5 MPa with *SE* 5.3 MPa for equilibrium of the low-temperature structure I methane hydrate phase h_1 with a different methane hydrate phase h_2 stable at higher temperature.

The bottom row of Table 1 shows the three parameters for the equation representing the 13 pressures of data set MSK64 (10) between 26.98 and 46.87°C for the high-temperature methane hydrate h_2. The significantly smaller values of the parameters *b*1 28.572 (1.310) and *b*2 56.04 (33.07) for the methane hydrate above 26.7°C indicate that it contains less water per mol of methane and is different from structure I methane hydrate (36–38) stable below 26.7°C.

The different methane hydrate h_2, stable above 26.7°C, explains why the authors (10) noted that above 68.9 MPa the methane hydrate–equilibrium locus became somewhat more concave down toward the temperature axis than had been expected. It also explains why the predicted (6) pressure of 275.8 MPa for methane hydrate at 37.78°C was too high, and was found experimentally (10) to be 165.5 MPa at 37.78°C.

Evaluation of equilibrium model for $P(h_1l_1g)$ for methane hydrate with water between −0.29 and 26.7°C

Table 2 presents 85 evaluations of $P(h_1l_1g)$ MPa, the equilibrium methane pressure for structure I methane hydrate h_1 in contact with water-rich liquid l_1 between −0.29 and 25.54°C.

The equilibrium pressure evaluations are defined by the best-weighted least-squares fit of the 85 corrected pressure measurements that are continuous from −0.29 to 25.54°C and are represented by eq. [1*a*] with four parameters.

Data sets D&F40 (2), MSK64 (10), GRCK70 (13), and V74 (14) are taken to be in thermodynamic equilibrium. The continuous equilibrium model for ln $P(h_1l_1g)$ with zero bias is defined to pass through the data-mean value of (the 13 ln $P(h_1l_1g)$ values of data set D&F40, plus the seven ln $P(h_1l_1g)$ values at lowest temperature of data set MSK64, plus four times the four ln $P(h_1l_1g)$ values of data set GRCK70, plus the seven ln $P(h_1l_1g)$ values of data set V74).

© 2002 NRC Canada

Table 2. Uncorrected and equilibrium pressures for structure I methane hydrate with water.

			Uncorrected $P_u(h_1l_1g)$		Equilibrium $P(h_1l_1g)$		
Temperature (°C)	Data set	$w^{1/2}$	Obsd (MPa)	Calcd (MPa)	Obsd (MPa)	Calcd (MPa)	Bias ln (P_u/P)
0.00	RBH40	1	2.64	2.66	2.57	2.59	0.0276
7.77	RBH40	1	5.85	5.79	5.69	5.64	0.0276
13.33	RBH40	1	10.63	10.63	10.34	10.34	0.0276
13.55	RBH40	1	10.80	10.90	10.51	10.60	0.0276
0.56	D&F40	1	2.76	2.73	2.76	2.73	0.0000
1.11	D&F40	1	2.90	2.88	2.90	2.88	0.0000
2.22	D&F40	1	3.24	3.21	3.24	3.21	0.0000
2.78	D&F40	1	3.42	3.39	3.42	3.39	0.0000
2.78	D&F40	1	3.43	3.39	3.43	3.39	0.0000
3.89	D&F40	1	3.81	3.79	3.81	3.79	0.0000
6.11	D&F40	1	4.77	4.74	4.77	4.74	0.0000
7.22	D&F40	1	5.35	5.32	5.35	5.32	0.0000
7.77	D&F40	1	5.71	5.64	5.71	5.64	0.0000
8.33	D&F40	1	6.06	5.98	6.06	5.98	0.0000
9.44	D&F40	1	6.77	6.73	6.77	6.73	0.0000
11.10	D&F40	1	8.12	8.06	8.12	8.06	0.0000
12.77	D&F40	1	9.78	9.71	9.78	9.71	0.0000
22.54	K&K49	1	33.99	34.31	31.94	32.24	0.0624
22.71	K&K49	1	35.30	35.08	33.17	32.96	0.0624
12.49	M&C61	1	9.62	9.65	9.38	9.41	0.0252
12.55	M&C61	1	9.62	9.71	9.38	9.47	0.0252
12.94	M&C61	1	10.10	10.14	9.85	9.89	0.0252
13.10	M&C61	1	10.31	10.34	10.05	10.08	0.0252
15.82	M&C61	1	13.96	14.18	13.61	13.82	0.0252
18.88	M&C61	1	21.13	20.57	20.61	20.06	0.0252
22.76	M&C61	1	34.75	34.06	33.88	33.21	0.0252
25.54	M&C61	1	48.68	49.93	47.46	48.68	0.0252
0.00	J&R65	1	2.65	2.69	2.55	2.59	0.0397
4.44	J&R65	1	4.17	4.17	4.01	4.00	0.0397
7.22	J&R65	1	5.58	5.53	5.37	5.32	0.0397
11.49	J&R65	1	8.67	8.75	8.33	8.41	0.0397
14.10	J&R65	1	11.65	11.76	11.20	11.30	0.0397
15.77	J&R65	1	14.06	14.29	13.51	13.73	0.0397
18.54	J&R65	1	20.11	20.02	19.32	19.24	0.0397
21.15	J&R65	1	28.56	27.92	27.45	26.83	0.0397
2.00	V74	0.001	3.02	3.14	3.02	3.14	0.0000
3.54	V74	1	3.69	3.66	3.69	3.66	0.0000
5.44	V74	1	4.39	4.43	4.39	4.43	0.0000
12.24	V74	1	9.19	9.15	9.19	9.15	0.0000
15.30	V74	1	13.04	12.99	13.04	12.99	0.0000
17.53	V74	1	16.96	16.98	16.96	16.98	0.0000
18.01	V74	1	18.55	18.00	18.55	18.00	0.0000
–0.29	QPsol	1	2.53	2.52	2.53	2.52	0.0000
0.15	dRPLD83	1	2.69	2.71	2.61	2.63	0.0320
2.26	dRPLD83	1	3.34	3.33	3.23	3.22	0.0320
2.80	dRPLD83	0.001	3.34	3.51	3.23	3.40	0.0320
6.34	dRPLD83	1	5.04	5.01	4.88	4.86	0.0320
8.14	dRPLD83	1	6.04	6.05	5.85	5.86	0.0320
9.65	dRPLD83	1	7.04	7.10	6.82	6.88	0.0320
10.83	dRPLD83	1	8.05	8.07	7.80	7.82	0.0320
11.83	dRPLD83	1	9.00	9.02	8.76	8.73	0.0320
12.83	dRPLD83	1	10.04	10.09	9.72	9.77	0.0320

© 2002 NRC Canada

Table 2 (*concluded*).

Temperature (°C)	Data set	$w^{1/2}$	Uncorrected $P_u(h_1l_1g)$		Equilibrium $P(h_1l_1g)$		Bias ln (P_u/P)
			Obsd (MPa)	Calcd (MPa)	Obsd (MPa)	Calcd (MPa)	
0.20	AFS91	1	2.68	2.71	2.61	2.64	0.0261
1.40	AFS91	1	3.05	3.04	2.97	2.96	0.0261
3.50	AFS91	1	3.72	3.74	3.62	3.64	0.0261
5.10	AFS91	1	4.39	4.39	4.28	4.28	0.0261
6.40	AFS91	1	5.02	5.02	4.89	4.89	0.0261
7.70	AFS91	1	5.77	5.74	5.62	5.59	0.0261
9.10	AFS91	1	6.65	6.66	6.48	6.49	0.0261
10.40	AFS91	1	7.59	7.66	7.39	7.46	0.0261
11.50	AFS91	1	8.55	8.64	8.33	8.42	0.0261
12.50	AFS91	0.001	9.17	9.66	8.93	9.41	0.0261
13.20	AFS91	1	10.57	10.46	10.30	10.19	0.0261
9.99	GRCK70	1	7.10	7.14	7.10	7.14	0.0000
10.05	GRCK70	1	7.12	7.18	7.12	7.18	0.0000
15.49	GRCK70	1	13.11	13.29	13.11	13.29	0.0000
15.55	GRCK70	1	13.11	13.38	13.11	13.38	0.0000
17.05	MSK64	1	15.93	16.01	15.93	16.01	0.0000
17.32	MSK64	1	15.94	16.55	15.94	16.55	0.0000
21.93	MSK64	1	29.92	29.72	29.92	29.72	0.0000
22.04	MSK64	1	29.99	30.16	29.99	30.16	0.0000
22.60	MSK64	1	33.75	32.48	33.75	32.48	0.0000
24.87	MSK64	1	44.31	44.33	44.31	44.33	0.0000
24.99	MSK64	1	43.78	45.03	43.78	45.03	0.0000
0.00	V1888	0.5	2.69	2.80	2.48	2.59	0.0789
1.10	V1888	0.5	3.04	3.11	2.81	2.88	0.0789
5.50	V1888	0.5	4.76	4.82	4.40	4.46	0.0789
8.49	V1888	0.5	6.43	6.58	5.95	6.08	0.0789
9.89	V1888	0.5	7.60	7.64	7.02	7.06	0.0789
10.79	V1888	0.5	8.41	8.43	7.77	7.79	0.0789
14.29	V1888	0.5	12.51	12.50	11.56	11.55	0.0789
16.09	V1888	0.5	15.40	15.44	14.23	14.27	0.0789
17.29	V1888	0.5	18.09	17.84	16.71	16.49	0.0789
19.29	V1888	0.5	23.51	22.86	21.72	21.12	0.0789
20.29	V1888	0.5	26.85	25.96	24.81	23.99	0.0789

The seven other data sets (1, 3, 6, 7, 12, 17, 22) show positive data-set biases ln (P_u/P) taken to be constant for each data set, above the continuous ln $P(h_1l_1g)$ model. The logarithm of the observed equilibrium pressure $P(h_1l_1g)$ is defined by eq. [2]

$$[2] \qquad \ln P(h_1l_1g) = \ln P_u(h_1l_1g) - \ln (P_u/P)$$

in which the data-set bias, ln (P_u/P), is subtracted from the logarithm of the observed uncorrected pressure $P_u(h_1l_1g)$ MPa.

The 85 uncorrected ln $P_u(h_1l_1g)$ data are fitted first by eq. [1*a*], the seven mean values of data-set bias ln (P_u/P) are evaluated and the 85 first-approximation equilibrium values of ln $P(h_1l_1g)$ are obtained from eq. [2]. The first-approximation equilibrium values are refitted by eq. [1*a*], the seven first-approximation data-set biases are evaluated, and the 85 second-approximation equilibrium values are obtained from eq. [2], and so on. This is continued for 18 cycles to convergence of better than 1×10^{-9} on each of the seven data-set biases.

The best fit of the final 85 ln $P(h_1l_1g)$ MPa equilibrium evaluations by eq. [1*a*] gives a *SE* estimate of 1.33% on a single equilibrium pressure datum of unit weight with 71 degrees of freedom. The coefficient of determination R^2 is 0.99982. Parameter and (*SE*) estimates at 25°C are the following: *b*0, 3.8093 (0.0059); *b*1, 41.713 (0.560); *b*2, 311.95 (30.0); *b*3, 1217.2 (338). The value of *b*3 could arise by random chance with a probability of less than 0.05%. The number of degrees of freedom for this weighted least-squares regression is 85 minus the 4 model parameters, minus the 3 low-weighted data, minus the 7 data-set biases, leaving the difference of 71.

We note that the three parameters (*b*1, *b*2, *b*3) for the temperature variation of methane hydrate pressure are positive at 25°C, as found for deuterium sulfide D-hydrate (32) and for hydrogen sulfide hydrate (34).

In Table 2 column one gives the observed hydrate temperature *t* (°C) (ITS-90) and column two indicates the data set.

Column three shows $w^{1/2}$, the square root of the weight of the measurement. Three data are assigned the low weight

© 2002 NRC Canada

$w^{1/2}$ = 0.001 because they deviate from the fitted model by more than 15-times their computed standard errors; this weighting reduces the degrees of freedom by three and ensures that these measurements do not bias the final representative model. The 11 measurements of data set V1888 (1) are assigned the weight $w^{1/2}$ = 0.5 because they are assessed to be four times less reliable than the modern measurements, which use improved phase agitation and automatic thermostatic control of the hydrate temperature. The remaining 71 measurements are given unit weight.

Column four gives the observed uncorrected hydrate pressure $P_u(h_1l_1g)$ MPa from the literature, uncorrected for bias of the data set from equilibrium conditions, and column five shows its calculated value.

Column six gives the observed equilibrium pressure $P(h_1l_1g)$ MPa, corrected for data-set bias from equilibrium conditions, and column seven shows its calculated value from eq. [1*a*] using the four best parameters.

Column eight lists the data-set bias from equilibrium conditions ln (P_u/P), which is the logarithm of the ratio of (uncorrected pressure/equilibrium pressure). The seven data-set biases are determined in the least-squares evaluation of the best model for the equilibrium methane pressure $P(h_1l_1g)$ as a continuous function of temperature over the data range −0.29 to 25.54°C.

The *RMS* (root mean squared) deviations of the unweighted residuals of ln $P(h_1l_1g)$ from eq. [1*a*] for the individual data sets are slightly larger than the (*SE*)s shown in Table 1 for the separate regressions. The *RMS* deviations for weighted (unweighted) residuals of ln $P(h_1l_1g)$ from eq. [1*a*] with four parameters are the following: V1888, 0.0116 (0.0232); D&F40, 0.0098; RBH40, 0.0077; K&K49, 0.0085; M&C61, 0.0174; MSK64, 0.0249; J&R65, 0.0134; GRCK70, 0.0141; V74, 0.0135 (0.0210); dRPLD83, 0.0052 (0.0185); and AFS91, 0.0071 (0.0182).

The very consistent equilibrium data set D&F40 (2), shows a relatively large *RMS* residual estimate of 0.0098, contributed mainly by a data set bias of 0.0091 combined with a very low internal standard deviation of 0.0028. Similarly the equilibrium data set GRCK70 (13), shows a large *RMS* residual estimate of 0.0141, contributed mainly by a data set bias of −0.0129 combined with a low internal standard deviation of 0.0056.

It should be noted that the total real error on each hydrate pressure measurement is equal to the square root of the sum of its data-set bias squared plus its random error squared.

Data set V1888 (1) shows the largest average data-set bias of ln (P_u/P) = 0.0789 above the equilibrium model, corresponding with observed uncorrected pressure measurements an average of 8.2% larger than their equilibrium values. This large bias, probably arising from lack of agitation, combined with an uncertain bias of the temperature scale, contributed to our final assignment of weight $w^{1/2}$ = 0.5 for each measurement of data set V1888.

The data set K&K49 (6), comprised of two measurements, shows a bias of 0.0624 above the equilibrium model, corresponding with observed uncorrected pressure measurements an average of 6.4% larger than the equilibrium values based on data sets (2, 10, 13, 14). This bias difference clearly highlights the nearer approach to equilibrium of the dynamic pressure–temperature variation method introduced by Kobayashi and co-workers (10) in MSK64.

The remaining five data sets (3, 7, 12, 17, 22) show data-set biases of between 0.0252 and 0.0397, with observed uncorrected pressure measurements between 2.6 and 4.0% larger than their equilibrium values.

Evaluation of equilibrium model for $f_2(h_1l_1g)$ for methane hydrate with water between −0.29 and 26.7°C

Table 3 presents 85 evaluations of $f_2(h_1l_1g)$ MPa, the equilibrium methane fugacity for structure I methane hydrate h_1 in contact with water-rich liquid l_1 between −0.29 and 25.54°C.

The equilibrium fugacity evaluations are defined by the best weighted least-squares fit of the 85 corrected fugacity measurements that are continuous from −0.29 to 25.54°C and are represented by eq. [1*a*] with five parameters and with ln $f_2(h_1l_1g)$ replacing ln $P(h_1l_1g)$.

Data sets D&F40, MSK64, GRCK70, and V74 (2, 10, 13, 14) are taken to be in thermodynamic equilibrium. The continuous equilibrium model for ln $f_2(h_1l_1g)$ with zero bias is defined to pass through the data mean value of (the 13 ln $f_2(h_1l_1g)$ values of data set D&F40, plus the seven ln $f_2(h_1l_1g)$ values at lowest temperature of data set MSK64, plus four times the four ln $f_2(h_1l_1g)$ values of data set GRCK70, plus the seven ln $f_2(h_1l_1g)$ values of data set V74).

The seven other data sets (1, 3, 6, 7, 12, 17, 22) show positive data-set biases, ln (f_{2u}/f_2), taken to be constant for each data set, above the continuous ln $f_2(h_1l_1g)$ model. The logarithm of the observed equilibrium fugacity ln $f_2(h_1l_1g)$ is defined by eq. [3]

$$\ln f_2(h_1l_1g) = \ln f_{2u}(h_1l_1g) - \ln (f_{2u}/f_2) \qquad [3]$$

in which the data-set bias ln (f_{2u}/f_2) is subtracted from the logarithm of the observed uncorrected fugacity $f_{2u}(h_1l_1g)$.

The observed uncorrected methane fugacity $f_{2u}(h_1l_1g)$ MPa is evaluated from the IUPAC fugacity equation for methane (27) using the observed uncorrected hydrate pressure $P_u(h_1l_1g)$ MPa and the observed thermodynamic temperature T (K) corrected to IPTS-68.

The 85 uncorrected ln $f_{2u}(h_1l_1g)$ data are fitted first by eq. [1*a*], the seven mean values of data-set bias ln (f_{2u}/f_2) are evaluated and the 85 first-approximation equilibrium values of ln $f_2(h_1l_1g)$ are obtained from eq. [3]. The first-approximation equilibrium values are refitted by eq. [1*a*], the seven first-approximation data-set biases are evaluated, and the 85 second-approximation equilibrium values are obtained from eq. [3], and so on. This is continued for 22 cycles to convergence of better than 1×10^{-9} on each of the seven data-set biases.

The best fit of the final 85 ln $f_2(h_1l_1g)$ equilibrium evaluations by eq. [1*a*] gives a *SE* estimate of 0.94% for a single equilibrium $f_2(h_1l_1g)$ observation of unit weight with 70 degrees of freedom. The coefficient of determination R^2 is 0.99989. Parameter and (*SE*) estimates at 25°C are the following: *b*0, 3.4550 (0.0047); *b*1, 42.185 (0.748); *b*2, 688.60 (71.0); *b*3, 8692.6 (1850); *b*4, 36663 (14100). The value of *b*4 could arise by random chance with a probability of about 0.65%, and could arise "not" by chance with a probability of 99.35%, with an odds on chance of being significant of about 154:1.

© 2002 NRC Canada

Table 3. Uncorrected and equilibrium fugacities for structure I methane hydrate with water.

			Uncorrected $f_{2u}(h_1l_1g)$		Equilibrium $f_2(h_1l_1g)$		
Temperature (°C)	Data set	$w^{1/2}$	Obsd (MPa)	Calcd (MPa)	Obsd (MPa)	Calcd (MPa)	Bias ln (f_{2u}/f_2)
0.00	RBH40	1	2.48	2.50	2.42	2.43	0.0268
7.77	RBH40	1	5.17	5.16	5.03	5.02	0.0268
13.33	RBH40	1	8.68	8.65	8.45	8.42	0.0268
13.55	RBH40	1	8.80	8.84	8.56	8.60	0.0268
0.56	D&F40	1	2.59	2.56	2.59	2.56	0.0000
1.11	D&F40	1	2.72	2.70	2.72	2.70	0.0000
2.22	D&F40	1	3.01	3.00	3.01	3.00	0.0000
2.78	D&F40	1	3.17	3.16	3.17	3.16	0.0000
2.78	D&F40	1	3.17	3.16	3.17	3.16	0.0000
3.89	D&F40	1	3.50	3.51	3.50	3.51	0.0000
6.11	D&F40	1	4.31	4.31	4.31	4.31	0.0000
7.22	D&F40	1	4.78	4.77	4.78	4.77	0.0000
7.77	D&F40	1	5.06	5.02	5.06	5.02	0.0000
8.33	D&F40	1	5.34	5.28	5.34	5.28	0.0000
9.44	D&F40	1	5.89	5.85	5.89	5.85	0.0000
11.10	D&F40	1	6.90	6.83	6.90	6.83	0.0000
12.77	D&F40	1	8.09	7.99	8.09	7.99	0.0000
22.54	K&K49	1	23.67	23.88	22.59	22.79	0.0467
22.71	K&K49	1	24.57	24.39	23.45	23.28	0.0467
12.49	M&C61	1	7.98	7.98	7.77	7.78	0.0255
12.55	M&C61	1	7.98	8.02	7.78	7.82	0.0255
12.94	M&C61	1	8.31	8.33	8.10	8.12	0.0255
13.10	M&C61	1	8.46	8.46	8.24	8.25	0.0255
15.82	M&C61	1	10.89	11.04	10.61	10.76	0.0255
18.88	M&C61	1	15.34	15.20	14.95	14.82	0.0255
22.76	M&C61	1	24.20	24.05	23.59	23.45	0.0255
25.54	M&C61	1	35.08	35.10	34.19	34.21	0.0255
0.00	J&R65	1	2.50	2.51	2.42	2.43	0.0323
4.44	J&R65	1	3.81	3.81	3.69	3.69	0.0323
7.22	J&R65	1	4.96	4.93	4.80	4.77	0.0323
11.49	J&R65	1	7.30	7.31	7.07	7.08	0.0323
14.10	J&R65	1	9.37	9.37	9.07	9.08	0.0323
15.77	J&R65	1	10.94	11.05	10.60	10.70	0.0323
18.54	J&R65	1	14.71	14.75	14.24	14.29	0.0323
21.15	J&R65	1	20.02	19.85	19.38	19.22	0.0323
2.00	V74	0.001	2.82	2.94	2.82	2.94	0.0000
3.54	V74	1	3.40	3.39	3.40	3.39	0.0000
5.44	V74	1	3.99	4.05	3.99	4.05	0.0000
12.24	V74	1	7.68	7.60	7.68	7.60	0.0000
15.30	V74	1	10.30	10.21	10.30	10.21	0.0000
17.53	V74	1	12.79	12.82	12.79	12.82	0.0000
18.01	V74	1	13.76	13.48	13.76	13.48	0.0000
−0.29	QPsol	1	2.38	2.36	2.38	2.36	0.0000
0.15	dRPLD83	1	2.53	2.54	2.46	2.46	0.0284
2.26	dRPLD83	1	3.10	3.10	3.01	3.01	0.0284
2.80	dRPLD83	0.001	3.10	3.26	3.01	3.17	0.0284
6.34	dRPLD83	1	4.52	4.53	4.40	4.40	0.0284
8.14	dRPLD83	1	5.32	5.34	5.17	5.19	0.0284
9.65	dRPLD83	1	6.09	6.14	5.92	5.97	0.0284
10.83	dRPLD83	1	6.85	6.85	6.66	6.66	0.0284
11.83	dRPLD83	1	7.56	7.52	7.35	7.31	0.0284
12.83	dRPLD83	1	8.27	8.26	8.04	8.03	0.0284

© 2002 NRC Canada

Table 3 (*concluded*).

Temperature (°C)	Data set	$w^{1/2}$	Uncorrected $f_{2u}(h_1l_1g)$		Equilibrium $f_2(h_1l_1g)$		Bias ln (f_{2u}/f_2)
			Obsd (MPa)	Calcd (MPa)	Obsd (MPa)	Calcd (MPa)	
0.20	AFS91	1	2.52	2.53	2.46	2.48	0.0218
1.40	AFS91	1	2.85	2.84	2.78	2.78	0.0218
3.50	AFS91	1	3.42	3.46	3.35	3.38	0.0218
5.10	AFS91	1	3.99	4.01	3.90	3.92	0.0218
6.40	AFS91	1	4.51	4.52	4.41	4.42	0.0218
7.70	AFS91	1	5.11	5.10	5.00	4.99	0.0218
9.10	AFS91	1	5.80	5.80	5.67	5.67	0.0218
10.40	AFS91	1	6.51	6.54	6.37	6.40	0.0218
11.50	AFS91	1	7.21	7.24	7.06	7.09	0.0218
12.50	AFS91	0.001	7.67	7.96	7.50	7.78	0.0218
13.20	AFS91	1	8.63	8.50	8.45	8.32	0.0218
9.99	GRCK70	1	6.14	6.16	6.14	6.16	0.0000
10.05	GRCK70	1	6.16	6.19	6.16	6.19	0.0000
15.49	GRCK70	1	10.34	10.40	10.34	10.40	0.0000
15.55	GRCK70	1	10.35	10.46	10.35	10.46	0.0000
17.05	MSK64	1	12.14	12.19	12.14	12.19	0.0000
17.32	MSK64	1	12.16	12.54	12.16	12.54	0.0000
21.93	MSK64	1	20.95	21.12	20.95	21.12	0.0000
22.04	MSK64	1	21.01	21.41	21.01	21.41	0.0000
22.60	MSK64	1	23.51	22.95	23.51	22.95	0.0000
24.87	MSK64	1	31.44	31.10	31.44	31.10	0.0000
24.99	MSK64	1	31.04	31.60	31.04	31.60	0.0000
0.00	V1888	0.5	2.52	2.59	2.37	2.43	0.0646
1.10	V1888	0.5	2.84	2.88	2.66	2.70	0.0646
5.50	V1888	0.5	4.29	4.34	4.03	4.07	0.0646
8.49	V1888	0.5	5.63	5.72	5.27	5.37	0.0646
9.89	V1888	0.5	6.51	6.51	6.10	6.10	0.0646
10.79	V1888	0.5	7.10	7.08	6.66	6.64	0.0646
14.29	V1888	0.5	9.93	9.86	9.30	9.24	0.0646
16.09	V1888	0.5	11.78	11.79	11.04	11.05	0.0646
17.29	V1888	0.5	13.44	13.33	12.60	12.50	0.0646
19.29	V1888	0.5	16.78	16.54	15.73	15.50	0.0646
20.29	V1888	0.5	18.88	18.52	17.70	17.36	0.0646

The *RMS* deviations of residuals for ln $f_2(h_1l_1g)$ from eq. [1*a*] for individual data sets are usually slightly smaller than those found for ln $P(h_1l_1g)$. The *RMS* deviations for weighted (unweighted) residuals of ln $f_2(h_1l_1g)$ from eq. [1*a*] with five parameters are the following: V1888, 0.0073 (0.0145); D&F40, 0.0082; RBH40, 0.0040; K&K49, 0.0088; M&C61, 0.0070; MSK64, 0.0198; J&R65, 0.0060; GRCK70, 0.0076; V74, 0.0117 (0.0201); dRPLD83, 0.0038 (0.0182); and AFS91, 0.0066 (0.0136).

The consistent equilibrium data set D&F40 (2), shows a *RMS* residual estimate of 0.0082, contributed mainly by a data set bias of 0.0067 together with an internal standard deviation of 0.0049. Similarly the equilibrium data set GRCK70 (13), shows a *RMS* residual estimate of 0.0076, contributed mainly by a data set bias of −0.0069 combined with a very small internal standard deviation of 0.0032.

The arrangement of Table 3 is similar to Table 2. Column eight shows values of the seven data-set biases ln (f_{2u}/f_2), evaluated together with the best weighted least-squares fit of the 85 equilibrium methane fugacities. The data-set biases for the best fugacity equation are slightly smaller than those for the best pressure equation. The five-parameter fugacity equation and the four-parameter pressure equation are mutually consistent and lie well within the real error limits of the pressure measurements.

Properties of gas and aqueous phases with methane hydrate

Intensive properties of the gas and aqueous phases in equilibrium with methane hydrate are assessed. The gas phase fugacity of methane for methane hydrate $f_2(h_1l_1g)$ is taken to be that of pure methane at equilibrium total pressure $P(h_1l_1g)$, because the water vapour pressure is less than 0.023% of the total pressure, while the accuracy of the methane hydrate pressures is not better than 1.3%. The methane fugacity is evaluated directly from the IUPAC fugacity equation (27).

The equilibrium methane solubility mol fraction in water x_2^{l1} is evaluated from the methane fugacity $f_2(h_1l_1g)$ divided by the Henry law constant H_2^P, which includes the Poynting

© 2002 NRC Canada

Table 4. Equilibrium properties of structure I methane hydrate with ice.

			$P(h_1s_1g)$				
Temperature (°C)	Data set	Ref.	Obsd (MPa)	Calcd (MPa)	Diff (%)	f_2 Obsd (MPa)	*Kp* Obsd (MPa)
–0.29	QPsol	this work	2.527	—	—	2.383	2.341
–2.22	F&D46	4	2.392	2.382	0.46	2.260	2.222
–4.55	F&D46	4	2.220	2.214	0.27	2.103	2.069
–6.66	F&D46	4	2.082	2.071	0.56	1.976	1.947
–8.94	F&D46	4	1.903	1.924	–1.08	1.812	1.787
–10.75	M&S94	23	1.798	1.813	–0.81	1.714	1.692
–10.77	F&D46	4	1.793	1.812	–1.04	1.710	1.688
–14.10	RBH40	3	1.648	1.620	1.69	1.575	1.556

correction at pressure $P(h_1l_1g)$; the solubility equation is from Rettich et al. (16). The equilibrium x_2^{l1} of methane in phase l_1 is listed in column eight of a later table.

Methane hydrate–ice–gas (h_1s_1g) equilibrium

Table 4 presents seven measurements of $P(h_1s_1g)$, the total pressure of structure I methane hydrate h_1 in contact with ice I_h s_1, at temperatures between –2.22 and –14.10°C. Column two lists the data sets and column three their references. Column four shows the observed $P(h_1s_1g)$ MPa, and column five the $P(h_1s_1g)$ calculated from the best (26) equation

$$[4] \qquad \ln P(h_1s_1g) = 9.2645 - 2275/T$$

with thermodynamic temperature T (K) (ITS-90). This equation gives a *SE* estimate of 1.1% for a single measurement of $P(h_1s_1g)$ and a *SE* estimate of 79 K on the parameter –2275. Column six shows the percentage difference of observed minus calculated pressures.

Seven hydrate pressure measurements between –29.95 and –82.95°C (15, 23) show significant positive-pressure deviations above eq. [4], of +4.7% at –30°C increasing to more than +20% below –75°C; these measurements are excluded from the regression to reduce possible bias of eq. [4].

Data set, denoted QPsol, is the quadruple point $Q(h_1s_1l_1g)$, evaluated at methane hydrate pressure from eq. [4] together with the fusion properties of ice (29–31) in equilibrium with its saturated aqueous solution of methane (16, 28).

Column seven in Table 4 shows the methane fugacity $f_2(h_1s_1g)$ abbreviated to f_2, evaluated using the IUPAC fugacity equation (27) at pressure $P(h_1s_1g)$ and at temperature T (K) corrected to IPTS-68.

Quadruple point $Q(h_1s_1l_1g)$

The quadruple point $Q(h_1s_1l_1g)$ is determined from first principles, by successive approximations, using the freezing-point depression (29–31) of ice at hydrate pressure $P(h_1s_1g)$ in equilibrium with an aqueous methane solution (16) having mol fraction x_1^{l1} of water. We find the estimated ice freezing-point depression for $t(h_1s_1l_1g)$ is –0.290°C with *SE* 0.0064°C and the estimated pressure $P(h_1s_1l_1g)$ is 2.527 MPa with *SE* 0.053 MPa, which is in agreement with the –0.30°C and 2.523 MPa by Falabella (15). The quadruple point temperature of –0.20°C given by de Roo et al. (17) is in error by 0.11°C, the effect of neglecting the methane solubility in water; their quadruple point pressure of 2.523 MPa agrees with Falabella (15).

Equilibrium constant for dissociation of methane hydrate into ice and methane gas

Thermodynamic equations from ref. 33 are used here without derivation since all have been discussed for the determination of the formula of deuterium sulfide D-hydrate.

Consider the standard dissociation of one gram mol (gram-molar mass) of methane hydrate h_1 of formula $CH_4{\cdot}nH_2O$ into n mol of ice s_1 plus one mol of methane gas g. The equilibrium constant $Kp(h_1{\rightarrow}s_1g)$ for this process is defined by the equation

$$[5] \qquad \ln Kp(h_1{\rightarrow}s_1g) = \ln f_2(h_1s_1g) + n(1/RT)\int_{0.1}^{P(h_1s_1g)}(V_1^{s1} - V_1^{h1})dP$$

in which $f_2(h_1s_1g)$ is the fugacity of methane, n the hydrate formula number, V_1^{s1} the molar volume of ice, and V_1^{h1} the molar volume of water in structure I hydrate, at total pressure $P(h_1s_1g)$ and thermodynamic temperature T (K). Values for $f_2(h_1s_1g)$ are given in Table 4 and the gaseous standard state is 1.0 MPa fugacity. The standard state of the condensed phases is 0.1 MPa pressure. Formula number $n = 6.2$ is assigned and is equal to its equilibrium value at $Q(h_1s_1l_1g)$. The molar volume of ice, its coefficient of expansion, and compressibility are from Lide (29).

The standard molar volume of water in structure I hydrate, V_1^{oh1} is evaluated from the methane D-hydrate lattice spacing 1.177 ± 0.001 nm at 5.2 K (38), expanded to 1.178 nm for the methane hydrate. Methane hydrate is taken to have the same coefficient of expansion as ethylene oxide hydrate between 18 and 260 K (39), and the same compressibility as ice (29). At pressure 0.1 MPa the standard molar volumes of structure I hydrate water V_1^{oh1} are 22.26, 22.31, and 22.35 $cm^3\ mol^{-1}$ at –14.10, –6.66, and –0.29°C, respectively.

The seven values of $\ln Kp(h_1{\rightarrow}s_1g)$ MPa between –2.22 and –14.10°C are best (26) represented by the equation

$$[6] \qquad \ln Kp(h_1{\rightarrow}s_1g) = 8.8110 - 2172/T$$

with thermodynamic temperature T (K). This equation gives a *SE* estimate of 1.05% for a single determination of $Kp(h_1{\rightarrow}s_1g)$ and a *SE* of 73 K on the parameter –2172. The coefficient of determination R^2 is 0.9944.

The standard enthalpy change derived for hydrate dissociation $\Delta H^{ot}(h_1{\rightarrow}s_1g)$ is 18058 J mol^{-1} with *SE* 608 J mol^{-1} methane at –8.28°C. This estimate of standard enthalpy change agrees with the calorimetric value 18130 J mol^{-1}

© 2002 NRC Canada

Table 5. Equilibrium constant for structure I methane hydrate with water.

			$Kp(h_1 \rightarrow l_1 g)$				
Data set	Temperature (°C)	$w^{1/2}$	Obsd (MPa)	Calcd (MPa)	Diff (%)	*SE Kp* calcd (%)	x_2^{11} (× 10^3)
RBH40	0.00	1	2.33	2.35	−0.92	0.22	1.07
RBH40	7.77	1	4.67	4.65	0.55	0.11	1.70
RBH40	13.33	1	7.44	7.43	0.04	0.12	2.32
RBH40	13.55	1	7.52	7.57	−0.62	0.12	2.34
D&F40	0.56	1	2.50	2.47	0.90	0.20	1.13
D&F40	1.11	1	2.61	2.60	0.39	0.18	1.16
D&F40	2.22	1	2.88	2.87	0.47	0.15	1.23
D&F40	2.78	1	3.02	3.01	0.39	0.14	1.27
D&F40	2.78	1	3.03	3.01	0.56	0.14	1.28
D&F40	3.89	1	3.33	3.32	0.27	0.12	1.36
D&F40	6.11	1	4.04	4.03	0.38	0.11	1.54
D&F40	7.22	1	4.45	4.43	0.48	0.11	1.65
D&F40	7.77	1	4.70	4.65	1.11	0.11	1.71
D&F40	8.33	1	4.94	4.87	1.27	0.11	1.77
D&F40	9.44	1	5.40	5.36	0.79	0.12	1.88
D&F40	11.10	1	6.23	6.17	0.99	0.12	2.07
D&F40	12.77	1	7.17	7.10	1.03	0.12	2.27
K&K49	22.54	1	15.71	15.75	−0.26	0.19	3.76
K&K49	22.71	1	16.09	15.96	0.82	0.20	3.82
M&C61	12.49	1	6.92	6.93	−0.21	0.12	2.21
M&C61	12.55	1	6.92	6.97	−0.66	0.12	2.21
M&C61	12.94	1	7.17	7.20	−0.32	0.12	2.27
M&C61	13.10	1	7.28	7.30	−0.23	0.12	2.29
M&C61	15.82	1	9.01	9.14	−1.48	0.12	2.63
M&C61	18.88	1	11.75	11.73	0.15	0.13	3.14
M&C61	22.76	1	16.07	16.03	0.22	0.20	3.80
M&C61	25.54	1	20.15	19.97	0.92	0.29	4.32
J&R65	0.00	1	2.33	2.35	−0.95	0.22	1.07
J&R65	4.44	1	3.49	3.48	0.21	0.12	1.40
J&R65	7.22	1	4.48	4.43	1.03	0.11	1.66
J&R65	11.49	1	6.36	6.38	−0.20	0.12	2.09
J&R65	14.10	1	7.91	7.93	−0.28	0.12	2.42
J&R65	15.77	1	9.00	9.10	−1.06	0.12	2.63
J&R65	18.54	1	11.35	11.42	.59	0.13	3.07
J&R65	21.15	1	14.14	14.10	0.33	0.16	3.53
V74	2.00	0.001	2.71	2.81	−3.78	0.16	1.17
V74	3.54	1	3.23	3.22	0.40	0.13	1.33
V74	5.44	1	3.76	3.80	−1.03	0.11	1.46
V74	12.24	1	6.84	6.79	0.82	0.12	2.20
V74	15.30	1	8.79	8.75	0.42	0.12	2.60
V74	17.53	1	10.46	10.51	−0.55	0.12	2.91
V74	18.01	1	11.06	10.93	1.13	0.12	3.03
QPsol	−0.29	1	2.30	2.29	0.26	0.23	1.07
dRPLD83	0.15	1	2.37	2.39	−0.72	0.21	1.08
dRPLD83	2.26	1	2.88	2.88	0.10	0.15	1.23
dRPLD83	2.80	0.001	2.88	3.02	−4.48	0.14	1.21
dRPLD83	6.34	1	4.12	4.11	0.34	0.11	1.56
dRPLD83	8.14	1	4.79	4.80	−0.02	0.11	1.73
dRPLD83	9.65	1	5.43	5.45	−0.47	0.12	1.88
dRPLD83	10.83	1	6.03	6.03	0.05	0.12	2.02
dRPLD83	11.83	1	6.59	6.56	0.48	0.12	2.14
dRPLD83	12.83	1	7.12	7.13	−0.08	0.12	2.26

© 2002 NRC Canada

Table 5 (*concluded*).

Data set	Temperature (°C)	$w^{1/2}$	$Kp(h_1 \rightarrow l_1 g)$ Obsd (MPa)	Calcd (MPa)	Diff (%)	*SE Kp* calcd (%)	x_2^{11} (× 10^3)
AFS91	0.20	1	2.38	2.40	−0.86	0.21	1.08
AFS91	1.40	1	2.67	2.67	0.19	0.17	1.17
AFS91	3.50	1	3.19	3.21	−0.58	0.13	1.31
AFS91	5.10	1	3.69	3.69	−0.09	0.11	1.45
AFS91	6.40	1	4.13	4.13	0.12	0.11	1.57
AFS91	7.70	1	4.65	4.62	0.59	0.11	1.69
AFS91	9.10	1	5.22	5.21	0.24	0.11	1.83
AFS91	10.40	1	5.80	5.81	−0.26	0.12	1.96
AFS91	11.50	1	6.36	6.38	−0.32	0.12	2.09
AFS91	12.50	0.001	6.71	6.94	–3.24	0.12	2.15
AFS91	13.20	1	7.44	7.35	1.14	0.12	2.33
GRCK70	9.99	1	5.61	5.62	−0.09	0.12	1.92
GRCK70	10.05	1	5.62	5.64	−0.39	0.12	1.92
GRCK70	15.49	1	8.82	8.89	−0.78	0.12	2.60
GRCK70	15.55	1	8.83	8.94	–1.18	0.12	2.60
MSK64	17.05	1	10.04	10.11	−0.62	0.12	2.81
MSK64	17.32	1	10.06	10.34	–2.66	0.12	2.79
MSK64	21.93	1	14.90	15.00	−0.69	0.18	3.55
MSK64	22.04	1	14.93	15.14	–1.37	0.18	3.54
MSK64	22.60	1	16.04	15.82	1.38	0.20	3.71
MSK64	24.87	1	19.17	18.95	1.18	0.27	4.05
MSK64	24.99	1	19.05	19.12	−0.35	0.27	4.02
V1888	0.00	0.5	2.28	2.35	–2.98	0.22	1.05
V1888	1.10	0.5	2.56	2.60	–1.55	0.18	1.13
V1888	5.50	0.5	3.80	3.82	−0.60	0.11	1.48
V1888	8.49	0.5	4.88	4.94	–1.22	0.11	1.74
V1888	9.89	0.5	5.58	5.57	0.15	0.12	1.91
V1888	10.79	0.5	6.04	6.01	0.42	0.12	2.02
V1888	14.29	0.5	8.08	8.05	0.29	0.12	2.46
V1888	16.09	0.5	9.31	9.34	−0.41	0.12	2.70
V1888	17.29	0.5	10.33	10.31	0.22	0.12	2.89
V1888	19.29	0.5	12.21	12.13	0.65	0.13	3.22
V1888	20.29	0.5	13.28	13.15	1.02	0.15	3.40
$Q(h_1h_2l_1g)$	26.7	—	—	21.87	—	7.27	4.57

with *SE* 270 J mol^{-1} methane at 0°C reported by Handa (18). The agreement of these two values for the standard enthalpy change confirms that the structure I methane hydrate pressure measurements between –2.22 and –14.10°C (3, 4, 23) are in thermodynamic equilibrium with ice. Hydrate pressures reported (15, 23) between –30 and –75°C do not agree with the values of the standard enthalpy change.

Definition of equilibrium constant for dissociation of structure I methane hydrate into water and methane gas between –0.29 and 26.7°C

Consider the standard dissociation of one gram mol of methane hydrate of formula $CH_4 \cdot nH_2O$ phase h_1 into n mol of pure water l_1 plus one mol of gaseous methane g. The equilibrium constant $Kp(h_1 \rightarrow l_1 g)$ for this process is defined by the equation

$$[7] \quad \ln Kp(h_1 \rightarrow l_1 g) = \ln f_2(h_1 l_1 g) + n \ln x_1^{11} + n(1/RT) \int_{0.1}^{P(h_1 s_1 g)} (V_1^{11} - V_1^{h1}) dP$$

in which V_1^{l1} is the molar volume of water at pressure $P(h_1 l_1 g)$ and temperature T (K). Equilibrium values of $P(h_1 l_1 g)$ are given in column six of Table 2, equilibrium values of $f_2(h_1 l_1 g)$ are given in column six of Table 3, and equilibrium values for $x_1^{11} = (1 - x_2^{11})$ are from x_2^{11} in column eight of Table 5. The formula number $n = 6.0$ is assumed initially, but this value changes with convergence and varies with temperature along the $(h_1 l_1 g)$ equilibrium line. The molar volume of water is from Haar et al. (28). At 0.1 MPa, the standard structure I hydrate water molar volumes V_1^{oh1} are 22.45 and 22.55 cm^3 mol^{-1} at 13.10 and 26.7°C, respectively.

© 2002 NRC Canada

Values of the 85 equilibrium constants ln $Kp(h_1 \rightarrow l_1g)$ MPa between −0.29 and 26.7°C are best (26) represented by the three-parameter thermodynamic equation,

[8*a*] $\ln Kp(h_1 \rightarrow l_1g) = d0 + d1.u1 + d2.u2$

which is mathematically equivalent to

[8*b*] $\ln Kp(h_1 \rightarrow l_1g) = A' + B'/T + C' \ln T$

Formula of methane hydrate at quadruple point $Q(h_1s_1l_1g)$

The formula of methane hydrate is evaluated by the method of Scheffer and Meyer (40) who first derived eq. [9] for *n*,

[9] $\Delta H^{oq}(h_1 \rightarrow l_1g) - \Delta H^{oq}(h_1 \rightarrow s_1g) = n\Delta H^{oq}(s_1 \rightarrow l_1)$

which is exact at −0.29°C of the quadruple point $Q(h_1s_1l_1g)$, with the equilibrium standard enthalpy changes denoted by superscript q.

Substitution into eq. [9], of 55 356 J mol^{-1} with *SE* 289 J mol^{-1} CH_4 for $\Delta H^{oq}(h_1 \rightarrow l_1g)$ from this work, of 18129 J mol^{-1} with *SE* 270 J mol^{-1} CH_4 for $\Delta H^{oq}(h_1 \rightarrow s_1g)$ from Handa (18), and of 6000 J mol^{-1} with *SE* 4 J mol^{-1} H_2O for $\Delta H^{oq}(s_1 \rightarrow l_1)$, evaluated from Osborne (31) and Giauque and Stout (30), yields $n = 6.205$ with *SE* 0.066 for the formula of structure I methane hydrate at $Q(h_1s_1l_1g)$ −0.29°C.

Using this method for hydrogen sulfide hydrate gives $n = 6.119$ with *SE* 0.029 (34) and for deuterium sulfide D-hydrate $n = 6.115$ with *SE* 0.018 (33) at their $Q(h_1s_1l_1g)$ quadruple points. The formula for methane hydrate at $Q(h_1s_1l_1g)$ is seen to be slightly richer in water than the formulae for the two sulfide hydrates.

A Student t-test of the formula difference [(6.205 − 6.119)/0.068] gives $t = 1.26$ with more than 40 degrees of freedom. The value of *t* indicates that this formula difference could arise by random chance with a probability of about 11%, could "not" arise by random chance with a probability of 89%, that is, the odds on this difference being significant is about 8:1.

The present study shows that the methane hydrate formula $CH_4 \cdot 5.765H_2O$ at 0°C reported earlier by us (9) is incorrect. The $\Delta H^{oo}(h_1 \rightarrow l_1g)$ is too small by 1707 J mol^{-1} and the $\Delta H^{oo}(h_1 \rightarrow s_1g)$ is too large by 920 J mol^{-1} leading to a total error on their difference of 2627 J mol^{-1} and a methane hydrate formula deficit of $0.433H_2O$.

The hydrate formula number *n* determined by Diepen and co-workers (17) at their $Q(h_1s_1l_1g)$ varies from 5.5 to 6.9, with a mean value of 6.3 and with three individual values of 6.1, 6.1, and 6.2: these are in rough agreement with our estimate of 6.205 with *SE* 0.066 at −0.29°C.

The equilibrium methane hydrate formula $CH_4 \cdot 6.205 \pm 0.066H_2O$ found at $Q(h_1s_1l_1g)$ −0.29°C contains significantly more water than the ice-free calorimetric sample $CH_4 \cdot 6.00 \pm 0.01H_2O$ prepared by direct synthesis under 2.6-times excess methane pressure at 253 K by Handa (18). Both formulae are probably correct and provide a clear confirmation of the variable stoichiometry of the structure I methane hydrate.

A similar positive difference of hydrate formula is reported by Davidson et al. (41) in their study on xenon hydrate. A xenon hydrate $Xe \cdot 6.286 \pm 0.030H_2O$ was found in equilibrium with water and xenon gas at 273 K, and a hydrate of formula $Xe \cdot 5.90 \pm 0.05H_2O$ was prepared under 27-times excess xenon pressure at 253 K (42).

Our equilibrium methane hydrate formula at the quadruple point $Q(h_1s_1l_1g)$ differs significantly from the NMR sample (20), conditioned for ~3 months at −40°C and then for one week at −13°C, presumably under excess methane pressure, and then measured as $CH_4 \cdot 6.05 \pm 0.06H_2O$ at −80°C. The variable stoichiometry of methane hydrate is again confirmed.

Our methane hydrate formula number at $Q(h_1s_1l_1g)$ agrees roughly with the NMR derived results of Collins et al. (43) who reported $H_2Se \cdot 6.21 \pm 0.13H_2O$ at 275 K, $D_2Se \cdot 6.21 \pm 0.18D_2O$ at 270 K, and $CO \cdot 6.22 \pm 0.24H_2O$ at 220 K.

Formula of structure I methane hydrate at temperatures between −0.29 and 26.7°C

We now extend eq. [9], valid at $Q(h_1s_1l_1g)$, for use at higher temperature *t* (°C) to evaluate an approximate formula number, defined as *r*, using the thermochemical identity eq. [10]

[10] $\Delta H^{ot}(h_1 \rightarrow l_1g) - \Delta H^{ot}(h_1 \rightarrow s_1g) = r\Delta H^{ot}(s_1 \rightarrow l_1)$

where superscript q in eq. [9] is replaced by t in eq. [10]. Values of $\Delta H^{ot}(h_1 \rightarrow s_1g)$ and $\Delta H^{ot}(s_1 \rightarrow l_1)$ at *t* are equal to their values at the quadruple point, plus the integral of their heat capacity changes from the quadruple point.

The first term in eq. [10] is derived from the 85 $Kp(h_1 \rightarrow l_1g)$ measurements (1–3, 6, 7, 10, 12–14, 17, 22) of this work.

The second term $\Delta H^{ot}(h_1 \rightarrow s_1g) = \Delta H^{oo}(h_1 \rightarrow s_1g) + \Delta Cp^{oo}(h_1 \rightarrow s_1g)t = (18130 + 4t)$ varies linearly with *t* (°C), where $\Delta H^{oo}(h_1 \rightarrow s_1g)$ is 18130 J mol^{-1} with *SE* 270 J mol^{-1} and $\Delta Cp^{oo}(h_1 \rightarrow s_1g)$ is 4 J mol^{-1} deg^{-1} with *SE* 3 J mol^{-1} deg^{-1}, taken directly from Handa (18).

The final term in eq. [10] is the standard molar enthalpy change for fusion of metastable ice H_2O s_1 into liquid water H_2O l_1 at *t* (°C). This is evaluated using the Taylor's series expansion

[11] $$\Delta H^{ot}(s_1 \rightarrow l_1) = \Delta H^{oo}(s_1 \rightarrow l_1) + \Delta Cp^{oo}(s_1 \rightarrow l_1)t + d\Delta Cp^{oo}(s_1 \rightarrow l_1)/dt(1/2)t^2 + d^2\Delta Cp^{oo}(s_1 \rightarrow l_1)/dt^2(1/6)t^3$$

at the normal freezing point 0°C, with $\Delta H^{oo}(s_1 \rightarrow l_1) = 6009$ J mol^{-1} with *SE* 4 J mol^{-1} (31). The standard molar heat capacity change and its temperature derivatives for fusion are evaluated at 0°C using (*i*) the heat capacities of ice between −74 and −2.6°C by Giauque and Stout (30); and (*ii*) the tabulated heat capacities of liquid water between 0 and 80°C by Haar et al. (28).

Method for evaluation of dissociation equilibrium constant of methane hydrate and its formula number *r*

The phase rule requires that the equilibrium water–methane two-component three-phase (h_1l_1g) system is univariant and that the intensive properties of the three equilibrium phases are continuous functions of temperature. In particular, the equilibrium hydrate composition and its component H_2O–CH_4 mol ratio $n = r$ is a continuous function of temperature only.

© 2002 NRC Canada

Table 6. Standard enthalpy and heat capacity changes for dissociation and the formula of structure I methane hydrate with water.

		Standard enthalpy		Standard heat capacity		Formula	
Data set	Temperature (°C)	$\Delta H^{ot}(h_1 \rightarrow l_1 g)$ (J mol^{-1})	*SE*	$\Delta Cp^{ot}(h_1 \rightarrow l_1 g)$ (J mol^{-1} deg^{-1})	*SE*	*r*	*SE*
RBH40	0.00	55389	283	112	23	6.198	0.065
RBH40	7.77	56259	123	112	23	6.047	0.050
RBH40	13.33	56880	98	112	23	5.951	0.048
RBH40	13.55	56905	100	112	23	5.948	0.048
D&F40	0.56	55451	271	112	23	6.187	0.064
D&F40	1.11	55513	258	112	23	6.175	0.062
D&F40	2.22	55637	234	112	23	6.153	0.060
D&F40	2.78	55699	222	112	23	6.141	0.058
D&F40	2.78	55699	222	112	23	6.141	0.058
D&F40	3.89	55824	198	112	23	6.120	0.056
D&F40	6.11	56072	153	112	23	6.077	0.052
D&F40	7.22	56197	133	112	23	6.057	0.050
D&F40	7.77	56259	123	112	23	6.047	0.050
D&F40	8.33	56321	115	112	23	6.037	0.049
D&F40	9.44	56445	100	112	23	6.017	0.048
D&F40	11.10	56632	88	112	23	5.988	0.048
D&F40	12.77	56818	93	112	23	5.960	0.048
K&K49	22.54	57912	273	112	23	5.814	0.065
K&K49	22.71	57931	277	112	23	5.812	0.065
M&C61	12.49	56787	91	112	23	5.965	0.048
M&C61	12.55	56793	91	112	23	5.964	0.048
M&C61	12.94	56837	94	112	23	5.958	0.048
M&C61	13.10	56855	95	112	23	5.955	0.048
M&C61	15.82	57160	134	112	23	5.912	0.051
M&C61	18.88	57502	194	112	23	5.866	0.056
M&C61	22.76	57937	278	112	23	5.811	0.066
M&C61	25.54	58248	341	112	23	5.774	0.074
J&R65	0.00	55389	283	112	23	6.198	0.065
J&R65	4.44	55886	187	112	23	6.109	0.055
J&R65	7.22	56197	133	112	23	6.057	0.050
J&R65	11.49	56675	88	112	23	5.982	0.048
J&R65	14.10	56967	107	112	23	5.939	0.049
J&R65	15.77	57154	133	112	23	5.913	0.051
J&R65	18.54	57465	187	112	23	5.871	0.055
J&R65	21.15	57757	243	112	23	5.833	0.061
V74	2.00	55612	239	112	23	6.157	0.060
V74	3.54	55785	206	112	23	6.126	0.057
V74	5.44	55997	167	112	23	6.090	0.053
V74	12.24	56759	89	112	23	5.969	0.048
V74	15.30	57101	125	112	23	5.920	0.050
V74	17.53	57351	167	112	23	5.886	0.054
V74	18.01	57404	176	112	23	5.879	0.054
QPsol	−0.29	55356	289	112	23	6.205	0.066
dRPLD83	0.15	55405	280	112	23	6.195	0.065
dRPLD83	2.26	55642	233	112	23	6.152	0.059
dRPLD83	2.80	55702	222	112	23	6.141	0.058
dRPLD83	6.34	56098	149	112	23	6.073	0.051
dRPLD83	8.14	56300	118	112	23	6.040	0.049
dRPLD83	9.65	56469	98	112	23	6.013	0.048
dRPLD83	10.83	56601	89	112	23	5.993	0.048
dRPLD83	11.83	56713	88	112	23	5.976	0.048

© 2002 NRC Canada

Table 6 (*concluded*).

Data set	Temperature (°C)	Standard enthalpy $\Delta H^{ot}(h_1 \rightarrow l_1 g)$ (J mol^{-1})	*SE*	Standard heat capacity $\Delta Cp^{ot}(h_1 \rightarrow l_1 g)$ (J mol^{-1} deg^{-1})	*SE*	Formula *r*	*SE*
dRPLD83	12.83	56825	93	112	23	5.959	0.048
AFS91	0.20	55411	279	112	23	6.194	0.065
AFS91	1.40	55545	252	112	23	6.169	0.062
AFS91	3.50	55780	207	112	23	6.127	0.057
AFS91	5.10	55959	173	112	23	6.096	0.053
AFS91	6.40	56105	148	112	23	6.072	0.051
AFS91	7.70	56250	125	112	23	6.048	0.050
AFS91	9.10	56407	104	112	23	6.023	0.048
AFS91	10.40	56553	91	112	23	6.000	0.048
AFS91	11.50	56676	88	112	23	5.982	0.048
AFS91	12.50	56788	91	112	23	5.965	0.048
AFS91	13.20	56866	96	112	23	5.953	0.048
GRCK70	9.99	56507	94	112	23	6.007	0.048
GRCK70	10.05	56514	94	112	23	6.006	0.048
GRCK70	15.49	57123	128	112	23	5.917	0.050
GRCK70	15.55	57129	129	112	23	5.916	0.050
MSK64	17.05	57297	157	112	23	5.893	0.053
MSK64	17.32	57328	162	112	23	5.889	0.053
MSK64	21.93	57844	260	112	23	5.822	0.063
MSK64	22.04	57856	262	112	23	5.821	0.064
MSK64	22.60	57918	275	112	23	5.813	0.065
MSK64	24.87	58173	326	112	23	5.783	0.072
MSK64	24.99	58186	328	112	23	5.781	0.072
V1888	0.00	55389	283	112	23	6.198	0.065
V1888	1.10	55512	259	112	23	6.175	0.062
V1888	5.50	56004	165	112	23	6.089	0.053
V1888	8.49	56340	112	112	23	6.034	0.049
V1888	9.89	56496	95	112	23	6.009	0.048
V1888	10.79	56597	89	112	23	5.994	0.048
V1888	14.29	56988	110	112	23	5.936	0.049
V1888	16.09	57190	139	112	23	5.908	0.051
V1888	17.29	57324	162	112	23	5.889	0.053
V1888	19.29	57548	203	112	23	5.860	0.057
V1888	20.29	57660	224	112	23	5.845	0.059
$Q(h_1h_2l_1g)$	26.7	58377	367	112	23	5.759	0.077

A method is given to evaluate the approximate formula number *r* for the structure I methane hydrate $CH_4 \cdot rH_2O$ and its dissociation equilibrium constant $Kp(h_1 \rightarrow l_1 g)$ at each experimental temperature on the univariant $(h_1 l_1 g)$ equilibrium line, between quadruple point $Q(h_1 s_1 l_1 g)$ at −0.29°C and quadruple point $Q(h_1 h_2 l_1 g)$ at 26.7°C.

The method of convergence to a stable solution depends on the temperature continuity of *r*, the approximate hydrate formula number. Initially we assume that $n = r = 6.0$ in eq. [7] for all measurements, giving a first approximation for the logarithm of the equilibrium constant, abbreviated ln *Kp*(1st). The ln *Kp*(1st) values are fitted as a proper function of temperature (26) by the method of least squares (35) to yield the best thermodynamic equation of the form of eq. [8*a*]. These measurements use two temperature variables (*u*1 *u*2) with $x = (T - 298.15)/298.15$, and define (26) three thermodynamic function parameters (*d*0, *d*1, *d*2) and their standard errors at 298.15 K.

Derived from (*d*1, *d*2) of eq. [8*a*], the first approximation standard enthalpy changes $\Delta H^{ot}(h_1 \rightarrow l_1 g)$, abbreviated ΔH(1st), for each measurement at its temperature *t* are substituted into eq. [10], to give a first approximation formula number *r*(1st).

Values of *r*(1st) are substituted for *n* in eq. [7] for each measurement to provide a second approximation for the logarithm of the equilibrium constant ln *Kp*(2nd); the ln *Kp*(2nd) values are refitted by eq. [8*a*], thence to obtain second approximation ΔH(2nd) values; these are substituted for $\Delta H^{ot}(h_1 \rightarrow l_1 g)$ in eq. [10] to give *r*(2nd) values, which are recycled for *n* in eq. [7], and so on. Iterations for 32 cycles give the converged values of $Kp(h_1 \rightarrow l_1 g)$ and of *r*, which are presented in Tables 5 and 6.

© 2002 NRC Canada

Values of equilibrium constant for dissociation of structure I methane hydrate into water and methane gas between –0.29 and 26.7°C

Table 5 lists 85 determinations between –0.29 and 25.54°C of the equilibrium constant, $Kp(h_1 \rightarrow l_1 g)$, for dissociation of structure I methane hydrate to liquid water and methane gas with $n = r$. Standard thermodynamic function changes refer to dissociation of one mol of $CH_4 \cdot rH_2O$ h_1 at 0.10 MPa to form r mol of pure water l_1 at 0.10 MPa plus one mol of methane g at 1.0 MPa fugacity.

Column one of Table 5 indicates the data set and column two lists the hydrate temperature. Column three lists the square root of the weights used. Column four lists $Kp(h_1 \rightarrow l_1 g)$ MPa observed and column five gives $Kp(h_1 \rightarrow l_1 g)$ calculated from the converged eq. [8*a*]. Column six shows the percentage differences between observed and calculated equilibrium constants, which yield an overall *SE* of 0.79% for a single $Kp(h_1 \rightarrow l_1 g)$ determination of unit weight with 72 degrees of freedom. Column seven shows the percentage error on the estimated equilibrium constant defined by eq. [8*a*]. Column eight of Table 5 lists the equilibrium mol fraction x_2^{11} of methane in the aqueous phase l_1.

Further investigation shows that the methane hydrate measurements are sufficiently accurate to evaluate only ($d0$, $d1$, $d2$) in eq. [8*a*], but are insufficiently accurate to define any value for $d3$.

The three parameters of the best converged eq. [8*a*] with their (*SE*)s are $d0 = 2.9516$ (0.0029), $d1 = 23.473$ (0.133), and $d2 = 13.46$ (2.82). The coefficient of determination R^2 is 0.99989.

The value of the least significant parameter $d2$ could arise by pure chance at a probability level of less than 0.05%. Estimates of $d1$ and $d2$ for structure I methane hydrate are 88 and 70%, respectively, of those found for hydrogen sulfide hydrate (34).

The *RMS* deviations of the residuals for ln $Kp(h_1 \rightarrow l_1 g)$ from eq. [8*a*] for the individual data sets are generally smaller than those for ln $P(h_1 l_1 g)$ and are about equal to those for ln $f_2(h_1 l_1 g)$. The *RMS* deviations for weighted (unweighted) residuals of ln $Kp(h_1 \rightarrow l_1 g)$ from eq. [8*a*] with three parameters are the following: V1888, 0.0063 (0.0126); D&F40, 0.0081; RBH40, 0.0066; K&K49, 0.0064; M&C61, 0.0073; MSK64, 0.0148; J&R65, 0.0073; GRCK70, 0.0079; V74, 0.0077 (0.0173); dRPLD83, 0.0037 (0.0167); and AFS91, 0.0056 (0.0120).

The very consistent equilibrium data set D&F40 (2), shows a *RMS* residual estimate of 0.0081, contributed mainly by a data set bias of 0.0071 combined with a low internal standard deviation of 0.0034. Similarly the equilibrium data set GRCK70 (13), shows a *RMS* residual estimate of 0.0079, contributed mainly by a data set bias of –0.0065 combined with a low internal standard deviation of 0.0044.

At 26.7°C with *SE* 0.9°C the estimate of equilibrium constant $Kp(h_1 \rightarrow l_1 g)$ is 21.87 MPa with *SE* 1.59 MPa, evaluated from eq. [8*a*].

The *SE* estimate of 0.79% for a single $Kp(h_1 \rightarrow l_1 g)$ datum of unit weight given by the best three-parameter eq. [8*a*] is seen to be about 60% of the *SE* estimate 1.33% for a single $P(h_1 l_1 g)$ measurement of unit weight given by the best four-parameter eq. [1*a*].

Standard enthalpy change $\Delta H^{ot}(h_1 \rightarrow l_1 g)$ and formula number r for structure I methane hydrate

Table 6 presents estimates and *SE*s for the standard enthalpy change $\Delta H^{ot}(h_1 \rightarrow l_1 g)$, for the standard heat capacity change $\Delta Cp^{ot}(h_1 \rightarrow l_1 g)$ and the approximate formula number r for the standard dissociation of structure I methane hydrate into water and methane gas. We note that the results listed in Tables 5 and 6 are biased estimates, except for those at –0.29°C, the ice quadruple point $Q(h_1 s_1 l_1 g)$, where eq. [10] is exact.

At higher temperatures a small bias may arise because it is assumed in eq. [10] that $\Delta H^{ot}(h_1 \rightarrow s_1 g) = (18130 + 4t)$ J mol^{-1} and that $\Delta Cp^{ot}(h_1 \rightarrow s_1 g)$ is a constant 4 J mol^{-1} deg^{-1} over the temperature range –0.29 to 25.54°C, where it is probable that $\Delta Cp^{ot}(h_1 \rightarrow s_1 g)$ may vary with temperature. The effect of this bias is assessed using the upper *SE* limit of (4 + 3) J mol^{-1} deg^{-1} for $\Delta Cp^{ot}(h_1 \rightarrow s_1 g)$ from (18). Evaluation of r at 25.54°C, using eq. [10] with $\Delta H^{ot}(h_1 \rightarrow s_1 g) = (18130 + 7t)$ at t (°C), gives a converged $r = 5.768$ with *SE* 0.074; a result not significantly different from that given in Table 6.

A second bias may arise because $\Delta H^{ot}(s_1 \rightarrow l_1)$ is given by the Taylor's series eq. [11] over the extrapolated temperature range –0.29 to 25.54°C. Classical error theory (35) indicates that the *SE* on r at 25.54°C, due to errors on the Taylor's series parameters of eq. [11], is less than 0.0004 and is not significant.

The *SE*s on the standard enthalpy changes for r at 25.54°C are 341 J mol^{-1} on $\Delta H^{ot}(h_1 \rightarrow l_1 g)$, 281 J mol^{-1} on $\Delta H^{ot}(h_1 \rightarrow s_1 g)$, and 8 J mol^{-1} on $\Delta H^{ot}(s_1 \rightarrow l_1)$.

The methane hydrate formula number n determined by method 1 of Galloway et al. (13) between 9.99 and 15.55°C has a mean value of 6.01 with *SE* 0.14, in approximate agreement with our mean value of 5.96 with *SE* 0.052 found using their four-equilibrium hydrate pressures. Unfortunately their temperature coefficient for n is of the wrong sign, which precludes a closer comparison.

In Table 6 the value of r decreases monotonously with increasing temperature and approaches its theoretical lower limit of 5.75, for a structure I hydrate (36–38), at a temperature above 25.54°C and very near to the quadruple point $Q(h_1 h_2 l_1 g)$ temperature of 26.7°C.

This requires a continuous increase with temperature in the number of methane guest molecules per unit cell of $46H_2O$, from 7.414 with *SE* 0.079 at –0.29°C, to 7.966 with *SE* 0.101 at 25.54°C, to about 7.987 with *SE* 0.107 at 26.7°C. Although these numbers may be slightly biased, the overall effect of increasing temperature remains unchanged. This shows that an increased fraction of cavities must be occupied by methane guests to stabilize the structure I hydrate lattice against thermal collapse up to $Q(h_1 h_2 l_1 g)$ at 26.7°C.

At 25.54°C and 48.6 MPa methane pressure the equilibrium hydrate lattice has 0.42% of empty cavities and 99.58% of occupied cavities with *SE* 1.26%. At 26.7°C and 55.5 MPa methane pressure the estimated hydrate lattice composition has 0.16% of empty and 99.84% of occupied cavities with *SE* 1.34%. These lattice compositions are less than, close to, and not significantly different from the theoretical formula limit $CH_4 \cdot 5.75H_2O$, for a cubic structure I methane clathrate hydrate.

This limiting hydrate composition found at 26.7°C, independently supports the discontinuity of the hydrate pressures

© 2002 NRC Canada

Table 7. Equilibrium pressure and fugacity for structure II methane hydrate with water.

			$P(h_2l_1g)$				
Data set	Temperature (°C)	$w^{1/2}$	Obsd (MPa)	Calcd (MPa)	Diff (%)	*SE* on *P* (%)	$f_2(h_2l_1g)$ (MPa)
$Q(h_1h_2l_1g)$	26.7	—	—	55.53	—	9.08	41.44
K&K49	27.82	1	60.89	61.86	–1.56	0.80	48.68
K&K49	28.82	0.001	72.81	68.12	6.89	0.71	63.62
M&C61	27.71	1	60.84	61.20	–0.59	0.82	47.18
M&C61	28.43	1	66.39	65.61	1.18	0.73	53.45
MSK64	26.98	1	56.92	57.08	–0.29	0.94	42.74
MSK64	28.37	1	65.43	65.26	0.26	0.74	51.82
MSK64	28.43	1	65.43	65.61	–0.28	0.73	51.84
MSK64	33.54	1	110.8	107.3	3.31	0.87	127.8
MSK64	37.15	1	152.7	151.6	0.71	0.92	264.5
MSK64	39.54	1	187.3	190.5	–1.70	0.82	460.6
MSK64	40.48	1	206.3	208.5	–1.04	0.76	617.1
MSK64	41.04	1	223.9	219.8	1.85	0.73	803.0
MSK64	41.87	1	237.5	238.0	–0.23	0.68	979.7
MSK64	43.65	1	271.7	281.9	–3.63	0.68	1596
MSK64	45.15	1	319.7	325.1	–1.66	0.84	3089
MSK64	46.42	1	367.8	367.0	0.22	1.09	5834
MSK64	46.87	1	397.0	382.8	3.72	1.19	8513

of data set MSK64 (10) and defines the $Q(h_1h_2l_1g)$ transition from the structure I methane hydrate phase h_1 stable below 26.7°C, to a different methane hydrate phase h_2 stable above 26.7°C.

At a temperature just above 26.7°C we expect that phase h_2 is a structure II methane clathrate hydrate similar to the structure II hydrates reported for Ar and Kr (38) and for O_2 (44).

Evaluation of equilibrium model for $P(h_2l_1g)$ for methane hydrate with water between 26.98 and 46.87°C

Table 7 presents 17 evaluations of $P(h_2l_1g)$, the equilibrium methane pressure for methane hydrate h_2 in contact with water-rich liquid l_1 between 26.98 and 46.87°C.

Column one of Table 7 indicates the data set and column two shows the hydrate temperature. Column three gives $w^{1/2}$, the square root of the assigned weight. Column four shows the observed equilibrium methane hydrate pressure $P(h_2l_1g)$ MPa, column five gives $P(h_2l_1g)$ calculated from eq. [1*a*], and column six shows the percent difference. Column seven lists the estimated percentage *SE* on the calculated hydrate pressure.

The measurement at 28.82°C of data set K&K49 is assigned the low weight $w^{1/2} = 0.001$ because its residual is greater than nine times its computed *SE*; the low weight eliminates bias of the regression model by this possibly deviant measurement.

The 13 measurements of data set MSK64 (10) are assumed to be in thermodynamic equilibrium and bias free, the two measurements of data set K&K49 (6) use the bias $\ln (P_u/P) = 0.0624$ and the two measurements of data set M&C61 (7) use the bias $\ln (P_u/P) = 0.0252$, the same biases found in Table 2. The equilibrium pressures, taken to be continuous between 26.98 and 46.87°C, are properly represented by their weighted least-squares fit by eq. [1*a*] with three parameters.

The best fit of the 17 $\ln P(h_2l_1g)$ equilibrium pressures by eq. [1*a*] gives a *SE* estimate of 2.2% on a single equilibrium pressure measurement of unit weight with 11 degrees of freedom. The coefficient of determination R^2 is 0.99983. The parameter and (*SE*) estimates at 25°C are the following: *b*0, 3.8527 (0.0163); *b*1, 28.835 (1.21); *b*2, 50.86 (31.7). The value of *b*2 could arise by random chance with a probability of about 7.5%, and could "not" arise by chance with a probability of 92.5%, giving an odds on chance of being significant of about 12:1.

We note that the estimates of the parameters *b*1 and *b*2 for methane hydrate h_2 are both positive and are significantly smaller than the 39.863 and 205.29 found for the structure I methane hydrate.

The *RMS* deviations for the weighted (unweighted) residuals of $\ln P(h_2l_1g)$ from eq. [1*a*] with three parameters are the following: K&K49, 0.0126 (0.0546); M&C61, 0.0105; and MSK64, 0.0218.

Column eight of Table 7 lists the equilibrium methane fugacity $f_2(h_2l_1g)$ MPa for methane hydrate h_2 with water. Measurements of data set MSK64 (10) are bias free, the two measurements of data set K&K49 (6) use the bias $\ln (f_{2u}/f_2) = 0.0467$ and the two measurements of data set M&C61 (7) use the bias $\ln (f_{2u}/f_2) = 0.0255$, the same biases given in Table 3. The observed uncorrected methane fugacity $f_{2u}(h_2l_1g)$ MPa is evaluated from the IUPAC fugacity equation for methane (27) using the observed uncorrected hydrate pressure $P_u(h_2l_1g)$ (MPa) and the observed thermodynamic temperature *T* (K) corrected to IPTS-68.

Equilibrium constant for dissociation of structure II methane hydrate into water and methane gas between 26.7 and 46.87°C

The equilibrium constant $Kp(h_2 \rightarrow l_1g)$ for dissociation of methane hydrate h_2 into pure water l_1 and methane gas g is the same as eq. [7] with h_1 replaced by h_2. Values of the equilibrium methane hydrate fugacity $f_2(h_2l_1g)$ and equilibrium pressure $P(h_2l_1g)$ are from columns eight and four, re-

© 2002 NRC Canada

Table 8. Equilibrium constant for structure II methane hydrate with water.

Data set	Temperature (°C)	$w^{1/2}$	$Kp(h_2 \rightarrow l_1 g)$ Obsd (MPa)	Calcd (MPa)	Diff (%)	Error on calcd *Kp* (%)	x_2^{11} ($\times 10^3$)
$Q(h_1h_2l_1g)$	26.7	—	—	21.25	—	7.31	4.57
K&K49	27.82	1	22.49	22.73	–1.05	0.36	5.13
K&K49	28.82	0.001	25.40	24.57	3.36	0.33	5.58
M&C61	27.71	1	22.42	22.53	–0.50	0.36	4.88
M&C61	28.43	1	23.81	23.84	–0.12	0.34	5.06
MSK64	26.98	1	21.62	21.29	1.53	0.38	4.61
MSK64	28.37	1	23.82	23.73	0.34	0.34	4.85
MSK64	28.43	1	23.83	23.84	–0.05	0.34	4.85
MSK64	33.54	1	35.34	35.35	–0.03	0.25	5.88
MSK64	37.15	1	46.08	46.47	–0.84	0.23	6.52
MSK64	39.54	1	54.87	55.57	–1.25	0.25	6.88
MSK64	40.48	1	59.49	59.61	–0.21	0.26	7.03
MSK64	41.04	1	63.47	62.12	2.18	0.27	7.14
MSK64	41.87	1	66.77	66.06	1.08	0.29	7.18
MSK64	43.65	1	74.69	75.28	–0.79	0.32	7.24
MSK64	45.15	1	84.07	84.00	0.09	0.36	7.19
MSK64	46.42	1	91.81	92.17	–0.39	0.39	6.99
MSK64	46.87	1	95.25	95.18	0.07	0.40	6.83

spectively, of Table 7. Values of $x_1^{11} = (1 - x_2^{11})$ are evaluated from the equilibrium aqueous methane solubility (16).

The standard molar volume of water in structure II methane hydrate V_1^{oh2} is evaluated from the oxygen D-hydrate lattice spacing of 1.707 ± 0.001 nm at 5.7 K (44), expanded to 1.708 nm for the methane hydrate. Structure II methane hydrate is taken to have the same coefficient of expansion as tetrahydrofuran hydrate between 18 and 260 K (45) and the same compressibility as ice (29). At standard pressure of 0.1 MPa, the structure II methane hydrate water molar volumes V_1^{oh2} are 22.96, 23.01, and 23.06 cm^3 mol^{-1} at 26.7, 37.15, and 46.87°C, respectively.

Temperature dependence of ln $Kp(h_2 \rightarrow l_1 g)$ MPa between 26.98 and 46.87°C is represented by a constrained three-parameter equation eq. [12]

$$[12] \quad \ln Kp(h_2 \rightarrow l_1 g) = d0 + d1(u1 + (d2/d1).u2) = d0 + d1(u1 + f.u2)$$

in which the constraint factor $f = (d2/d1)$ is assigned a constant value. Equation [12] is evaluated by the method of least-squares and is converged as a two-parameter equation, with $d0$ $d1$ unknown, using the combined temperature variable $(u1 + f.u2)$. The best value of f is determined to give the minimum *SE* for ln $Kp(h_2 \rightarrow l_1 g)$. The variability of the input measurements and the consequent large *SE* of $d2$ precluded use of an unconstrained three-parameter equation for ln $Kp(h_2 \rightarrow l_1 g)$.

The method of evaluation of the best model for the 17 $Kp(h_2 \rightarrow l_1 g)$ equilibrium constants is similar to that used for the structure I hydrate. Equation [7] initially uses $n = 6.0$ for all measurements but this changes with convergence. Equation [12] replaces [8*a*], and $d1$ and f values are used to determine the value of $\Delta H^{ot}(h_2 \rightarrow l_1 g)$ at each temperature. Equation [10] is used to determine r, with $\Delta H^{ot}(h_2 \rightarrow s_1 g)$ taken to be a constant 18130 J mol^{-1} with *SE* 270 J mol^{-1} for structure II methane hydrate. Equation [11] is used unchanged. After converging four models, each of 24 cycles, the best estimate of f is 0.7320 with *SE* 0.632.

Table 8, with the same arrangement as Table 5, shows best estimates of equilibrium constants $Kp(h_2 \rightarrow l_1 g)$ between 26.98 and 46.87°C. Differences between observed and calculated equilibrium constants yield an overall *SE* of 1.04% for a single $Kp(h_2 \rightarrow l_1 g)$ determination of unit weight with 12 degrees of freedom.

The two parameters of the best converged eq. [12] with their (*SE*)s are the following: $d0 = 2.9020$ (0.0048) and $d1 = 23.585$ (0.110). The estimate of $d2 = f.d1$ is 17.26 with an external *SE* estimate of 14.91. The coefficient of determination R^2 is 0.99993.

The *RMS* deviations for the weighted (unweighted) residuals of ln $Kp(h_2 \rightarrow l_1 g)$ from eq. [12] with two parameters are the following: K&K49, 0.0083 (0.0274); M&C61, 0.0041; and MSK64, 0.0104.

At 26.7°C with *SE* 0.9°C the estimate of equilibrium constant $Kp(h_2 \rightarrow l_1 g)$ is 21.25 MPa with *SE* 1.55 MPa, evaluated from eq. [12].

After some difficulty co-converging eqs. [7] and [12] for the structure II methane hydrate, we are surprised and reassured by the final good fit of the equilibrium constants, considering the extreme changes of the equilibrium methane fugacities above 40°C.

Standard enthalpy change $\Delta H^{ot}(h_2 \rightarrow l_1 g)$ and formula number r for structure II methane hydrate with water

Table 9, with the same arrangement as Table 6, presents estimates and *SE*s for the standard enthalpy and heat capacity changes $\Delta H^{ot}(h_2 \rightarrow l_1 g)$ and $\Delta Cp^{ot}(h_2 \rightarrow l_1 g)$ and for the ap-

© 2002 NRC Canada

Table 9. Standard enthalpy and heat capacity changes for dissociation and the formula of structure II methane hydrate with water.

		Standard enthalpy		Standard heat capacity		Formula	
Data set	Temperature (°C)	$\Delta H^{ot}(h_2 \rightarrow l_1 g)$ (J mol^{-1})	*SE*	$\Delta Cp^{ot}(h_2 \rightarrow l_1 g)$ (J mol^{-1} deg^{-1})	*SE*	*r*	*SE*
$Q(h_1h_2l_1g)$	26.7	58708	273	144	0	5.822	0.064
K&K49	27.82	58869	273	144	0	5.814	0.064
K&K49	28.82	59012	273	144	0	5.806	0.064
M&C61	27.71	58853	273	144	0	5.814	0.064
M&C61	28.43	58956	273	144	0	5.809	0.064
MSK64	26.98	58749	273	144	0	5.820	0.064
MSK64	28.37	58948	273	144	0	5.809	0.064
MSK64	28.43	58956	273	144	0	5.809	0.064
MSK64	33.54	59690	273	144	0	5.773	0.064
MSK64	37.15	60208	273	144	0	5.750	0.064
MSK64	39.54	60551	273	144	0	5.736	0.064
MSK64	40.48	60686	273	144	0	5.731	0.064
MSK64	41.04	60766	273	144	0	5.728	0.064
MSK64	41.87	60885	273	144	0	5.724	0.064
MSK64	43.65	61140	273	144	0	5.714	0.064
MSK64	45.15	61356	273	144	0	5.707	0.064
MSK64	46.42	61539	273	144	0	5.701	0.064
MSK64	46.87	61603	273	144	0	5.699	0.064

proximate formula number *r* for standard dissociation of structure II methane hydrate into water and methane gas. The constrained standard heat capacity change estimate is listed with zero *SE*.

At quadruple point $Q(h_1h_2l_1g)$ 26.7°C the formula of structure II methane hydrate is $CH_4 \cdot 5.822H_2O$ with *SE* $0.064H_2O$. This hydrate is in equilibrium with a structure I hydrate of formula $CH_4 \cdot 5.759H_2O$ with *SE* $0.077H_2O$. The formula difference of $0.063H_2O$ at 26.7°C is not significant compared with either the individual or the combined *SE*s. It is noted that the structure II methane hydrate at 37.15°C has the formula $CH_4 \cdot 5.750H_2O$ with *SE* $0.064H_2O$, at a significant higher temperature 10.45°C and pressure 97.2 MPa than the structure I methane hydrate.

In Table 9 the value of *r* decreases monotonously with increasing temperature and approaches the theoretical lower limit of 5.667, for a structure II hydrate (36–38), at some temperature above 46.84°C.

This requires a continuous increase with temperature in the number of methane guests per unit cell of $136H_2O$, from 23.36 with *SE* 0.26 at 26.7°C, to 23.87 with *SE* 0.27 at 46.87°C. Although these numbers may be slightly biased, the overall effect of increasing temperature remains unchanged. An increased fraction of cavities must be occupied by methane molecules to stabilize the structure II hydrate lattice against thermal collapse with increase of temperature from 26.7 to 46.87°C.

Expressed in terms of structure II hydrate lattice sites occupied by methane molecules, at 26.7°C there are 2.67% of empty and 97.33% of filled sites with *SE* 1.07%, and at 46.87°C there are 0.56% of empty and 99.44% of filled sites with *SE* 1.12%.

Quadruple point $Q(h_1h_2l_1g)$ and metastable quadruple point $Q(h_2s_1l_1g)$

Structure I methane hydrate undergoes a transition at 55.5 MPa and 26.7°C because all lattice sites are filled by methane and no empty site is available for additional methane. Additional volume is obtained by transition into the more open structure II hydrate water lattice, which can encage 1.47% more methane per mol lattice water.

Methane does not form a structure II hydrate with water at –0.29°C and 2.53 MPa because an approximate 70% occupancy by methane of the pentagonal dodecahedral sites of structure II is insufficient to stabilize a structure II methane hydrate of formula $CH_4 \cdot 7.083H_2O$. By contrast, under the same conditions the structure I methane hydrate has all six tetrakiadecahedral sites fully occupied by methane and the two pentagonal dodecahedral sites are at least 70.7% occupied by methane with *SE* 3.9%, stabilizing the structure I methane hydrate of formula $CH_4 \cdot 6.205H_2O$. As the equilibrium methane pressure and temperature are increased, methane completely fills the two pentagonal dodecahedral sites of structure I giving the extreme formula $CH_4 \cdot 5.75H_2O$ at 26.7°C and 55.5 MPa. Under these higher methane pressure conditions, the slightly smaller pentagonal dodecahedra of the structure II hydrate are at least 95.99% filled by methane with SE 0.40%, giving the structure II methane hydrate of formula $CH_4 \cdot 5.822H_2O$. Thus, it is seen that the methane "help gas" must occupy substantially more than 70% of the pentagonal dodecahedra to stabilize the structure II methane hydrate with methane in the large hexakiadecahedral sites.

Extrapolation of $P(h_2l_1g)$ to 0°C gives a methane gas pressure of 4.11 MPa with *SE* 1.00 MPa for formation of metastable structure II methane hydrate with water, having a for-

© 2002 NRC Canada

Table 10. Cohesive energy density of water and the methane hydrates

t (°C)	$P(hl_1g)$ (MPa)	V_1^{l1} (cm^3 mol^{-1})	p_i^{l1} (MPa)	a (nm)	V_1^{h} (cm^3 mol^{-1})	$p_i^{MT\,h}$ (MPa)	$p_i^{CH_4\,h}$ (MPa)
–0.29	2.53	18.00	2501	1.195	22.34	2283	2682
26.7	55.5	17.66	2435	1.196	22.38	2232	2685
26.7	55.5	17.66	2435	1.727	22.79	2193	2635
46.87	397	16.17	2303	1.701	21.80	2055	2551
46.87	397	16.17	2303	1.707	22.04	2032	2523

mula $CH_4{\cdot}6.113H_2O$ with *SE* $0.064H_2O$, with at least 89.05% occupancy of the dodecahedral sites by methane with *SE* 1.46%. The long extrapolation to 0°C is not very accurate, but the pressure should be correct within six *SE*s.

We note that the meta-stable structure II methane hydrate at 0°C has a higher methane pressure and a formula containing less water than the stable equilibrium structure I methane hydrate.

The meta-stable quadruple point $Q(h_2s_1l_1g)$ is estimated at –0.46°C with *SE* 0.11°C and at 3.93 MPa with *SE* 1.0 MPa.

Strictly, we need an equilibrium datum for $P(h_1h_2g)$ near 0°C, which is accessible by experiment, and which we estimate to be less than 40 MPa and more than 4.11 MPa methane pressure. Since the excess methane pressure required to form structure II methane hydrate from water is relatively small at 0°C, we expect that structure II methane hydrate will be produced by direct synthesis from ice with excess methane under higher methane pressure than used (18) for structure I methane hydrate. Even if structure I methane hydrate is formed first, it should equilibrate to form structure II methane hydrate with the excess methane gas at higher pressure.

Cohesive energy density of water and the methane hydrates

It is instructive to compare the cohesive energy density of the two equilibrium methane hydrates with their empty hydrate water lattices and with compressed water under the same conditions of temperature and pressure. The cohesive energy density of compressed water is evaluated from steam tables (28) as the specific enthalpy of vaporization of the liquid divided by its specific volume. Results are presented in Table 10. The cohesive energy density evaluated as J cm^{-3} is identical with the internal pressure listed in MPa.

For compressed water at –0.29°C and an external pressure of 2.53 MPa the cohesive-internal pressure of water p_i^{l1} is 2501 MPa, this value mainly reflects the strength of the hydrogen bonds in liquid water. With temperature increase to 46.87°C and external pressure to 397 MPa the water internal pressure p_i^{l1} is 2303 MPa, this is still 92% of the value at –0.29°C and indicates the relatively strong hydrogen bonds in water at 46.87°C.

Columns one and two in Table 10 give the equilibrium temperature and total pressure $P(hl_1g)$ for the methane hydrates at their quadruple points $Q(h_1s_1l_1g)$ and $Q(h_1h_2l_1g)$ and at the highest temperature of data set MSK64 (10). Column five lists the equilibrium-hydrate cubic-lattice spacing a in nm, and column six shows the equilibrium hydrate water molar volume V_1^{h} in cm^3 mol^{-1}. Column 7 is the internal pressure, $p_i^{MT\,h}$ in MPa, of the empty hydrate water lattices, and column eight is the internal pressure, $p_i^{CH_4\,h}$ in MPa, of the equilibrium methane hydrates.

At –0.29 and 26.7°C we find that 24 and 27% expansions of the liquid water volume are required to form the empty water lattice of structure I hydrate, this expansion reduces the water internal pressures by 8.7 and 8.3%, or by 218 and 203 MPa, respectively. Similarly at 26.7 and 46.87°C, liquid water expansions of 29% and 35%, are required to form the empty water lattice of structure II hydrate, this reduces the water internal pressures by 10.0 and 10.8%, or by 243 and 248 MPa, respectively. Despite these relatively large expansions the empty-hydrate water lattices have cohesive-internal pressures between 8.8 and 9.8 times larger than the 233 MPa internal pressure of liquid methane at 100 K (27).

The cohesive energy density of the equilibrium methane hydrates shown in column eight is found to be 7.2 and 10.3% greater than water for structure I hydrate at –0.29 and 26.7°C, respectively, and 8.2 and 10.8% greater than water for structure II hydrate at 26.7 and 46.87°C, respectively. The difference of column eight minus column seven gives the enhancement of stability due to the equilibrium methane within the two hydrate lattices. We note that the overall attractive methane–water enhancement of internal pressure runs from 399 to 453 MPa for structure I hydrate and from 443 to 496 MPa for structure II hydrate, and that the stability enhancement increases with equilibrium temperature and pressure. The encaged gaseous methane at these internal pressures has an estimated (27) methane molar volume of 33.32 and 33.05 cm^3 mol^{-1} in the structure I hydrate and 33.20 and 32.81 cm^3 mol^{-1} in the structure II hydrate; the lattice water partial molar volumes are correspondingly reduced to 16.97 and 16.63 cm^3 mol^{-1} in the structure I hydrate and to 17.09 and 16.04 cm^3 mol^{-1} in the structure II hydrate.

If the internal pressure enhancement for structure I hydrate is divided by an average coordination number 23 and that for structure II is divided by 22.667, the individual water–methane contributions are 17.3, 19.7 and 19.5, 21.9 MPa, respectively, from –0.29 to 46.87°C, which may be compared with the 19.4 MPa for methane–methane interactions assuming 12-fold coordination in liquid methane at 100 K.

It would appear that the filling of the "free volume" of each hydrate water molecule at separations between 0.278 and 0.454 nm, by three or four methane molecules, without breaking water–water H-bonds is responsible for the increased cohesive energy density of the methane hydrates relative to compressed water.

We may regard the formation of the methane gas hydrates as the efficient "pumping up" of the strongly self-adhering

© 2002 NRC Canada

water with individual methane molecules, and the data in Table 10 indicate the stabilization of the pumped up methane hydrate water lattices. In the equilibrium methane hydrates each water molecule has four nearest water neighbours, with 3 or 4 next-nearest neighbours which are methane, and then second nearest water molecules. It is the additional 3 or 4 next-nearest methane neighbours, giving the 7 or 8 coordination of each water molecule, that provide the extra attractive cohesive energy density of the methane hydrates. Equally the encaged methane guests provide the repulsive volume that efficiently fills the 4 regions between the H-bonds to nearest water neighbours.

We find that the equilibrium structure I hydrate lattice spacing a and hydrate water molar volume V_1^{h1} show the very small expansions of 0.054 and 0.162%, respectively, with temperature increase from –0.29 to 26.7°C; this clearly shows the balance between lattice thermal expansion and lattice compressibility.

We note that the highest external pressure of 397 MPa at 46.87°C is sufficient to reduce the structure II lattice spacing a to 1.701 nm and the hydrate water molar volume V_1^{h2} to 21.80 cm^3 mol^{-1}; this appears to be reasonable since the external pressure is now 80% of the internal pressure increment 496 MPa due to the encaged methane guests.

The last row of Table 10 shows the structure II hydrate internal pressures estimated using the lattice spacing a 1.707 nm, evaluated from the lattice spacing at 250 MPa and 25°C by Chou et al. (46). The hydrate water molar volume V_1^{h2} 22.04 cm^3 mol^{-1} at 46.87°C and 397 MPa remains smaller than at 26.7°C and 55.5 MPa. The hydrate lattice internal pressures $p_i^{MT\,h}$ of 2032 MPa and $p_i^{CH_4\,h}$ of 2523 MPa, are slightly reduced and the internal pressure increment due to the encaged methane guests becomes 491 MPa; these estimates are substantially the same as those given in row four of Table 10. Our estimate of the cubic structure II methane hydrate lattice spacing at about 250 MPa and 25°C is a = 1.7110 nm; 0.28% smaller than the value measured by Chou et al. (46).

Addendum after the referee's comments

We thank the referee for valuable suggestions and for the most recent references on the methane hydrates at high pressure.

After this work had been submitted for publication I was made aware of the elegant high-pressure studies by Chou et al. (46, 47), who had grown single crystals of structure II methane hydrate, in which the structure was confirmed by synchrotron X-ray diffraction analysis (46), and had indicated the structure II methane hydrate stability range in a phase diagram indicating invariant points.

This work is complementary to that of Chou et al. (46, 47) and provides independent and confirmatory estimates for (*i*) the equilibrium stability range and formulae of structure I methane hydrate with water and methane gas between quadruple point $Q(h_1s_1l_1g)$ at –0.29°C and 2.53 MPa and quadruple point $Q(h_1h_2l_1g)$ at 26.7°C and 55.5 MPa, and for (*ii*) the equilibrium stability range and formulae of structure II methane hydrate with water and methane gas between $Q(h_1h_2l_1g)$ at 26.7°C and 55.5 MPa and 46.87°C and 397 MPa. The reliability of this study depends on the accuracy of the primary (hl_1g) P–T measurements (1–4, 6, 7, 10, 12–14, 17, 22, 23): the accuracy on pressure is better than 1.5% and on temperature it is better than 0.10°C. Furthermore, (hl_1g) measurements, with phase mixing for long time periods in a thermostat, more closely attain equilibrium than unstirred condensed-phase measurements.

In Fig. 4. of reference 47 invariant point A is listed at 1.2 MPa and 0°C, whereas we find $Q(h_1s_1l_1g)$ at 2.53 MPa and –0.29°C. Invariant point C is listed at 137 MPa and 35.3°C, whereas we find $Q(h_1h_2l_1g)$ at 55.5 MPa and 26.7°C. The pure water isochore BC is listed (47) at 1046.8 kg m^{-3} cutting the ice Ih curve at –8.7°C and 99 MPa; we find the water isochore through $Q(h_1h_2l_1g)$ at density 1020.1 kg m^{-3} (28), which extrapolates to the ice Ih curve at about –3.5°C and 40 MPa. There is no evidence given to prove that the pure water isochore BC represents the equilibrium three-phase ($h_1h_2l_1$) curve, nor that the ice point B at –8.7°C is the equilibrium quadruple point $Q(h_1h_2s_1l_1)$.

The studies of methane hydrate by Dyadin et al. (48, 49) and by Nakano et al. (50), between 59 MPa at 27.6°C and 414 MPa at 46.65°C agree with the $P(h_2l_1g)$ measurements of Marshall et al. (10) for the equilibrium of structure II methane hydrate with water and methane gas.

References

1. P. Villard. Compt. Rend. **107**, 395 (1888).
2. W.M. Deaton and E.M. Frost, Jr. Proc. Amer. Gas Assoc. Houston, Texas. **May 6–10**, 122 (1940).
3. O.L. Roberts, E.R. Brownscombe, and L.S. Howe. Oil Gas J. **39**, 37 (1940).
4. E.M. Frost, Jr. and W.M. Deaton. Oil Gas J. **45**, 170 (1946).
5. W.M. Deaton and E.M. Frost, Jr. Gas hydrates and their relation to the operation of natural-gas pipe lines. U.S. Dept. of the Interior, Bureau of Mines Monograph 8. 1946.
6. R. Kobayashi and D.L. Katz. Trans. AIME, **186**, 66 (1949).
7. H.O. McLeod, Jr. and J.M. Campbell. J. Petrol. Tech. **222**, 590 (1961).
8. S.L. Miller. Proc. Nat. Acad. Sci. (U.S.), **47**, 1798 (1961).
9. D.N. Glew. J. Phys. Chem. **66**, 605 (1962).
10. D.R. Marshall, S. Saito, and R. Kobayashi. AIChE J. **10**, 202 (1964).
11. S. Saito, D.R. Marshall, and R. Kobayashi. AIChE J. **10**, 734 (1964).
12. J. Jhaveri and D.B. Robinson. Can. J. Chem. Eng. **43**, 75 (1965).
13. T.J. Galloway, W. Ruska, P.S. Chappelear, and R. Kobayashi. Ind. Eng. Chem. Fundam. **9**, 237 (1970).
14. V.K. Verma. Gas hydrates from liquid hydrocarbon – water systems. Ph.D. thesis. University of Michigan, Ann Arbor, Michigan. 1974.
15. B.J. Falabella. A study of natural gas hydrates. Ph.D. thesis. University of Massachusetts, Boston. 1975.
16. T.R. Rettich, Y.P. Handa, R. Battino, and E. Wilhelm. J. Phys. Chem. **85**, 3230 (1981).
17. J.L. de Roo, C.J. Peters, R.N. Lichtenthaler, and G.A.M. Diepen. AIChE J. **29**, 651 (1983).
18. Y.P. Handa. J. Chem. Thermodyn. **18**, 915 (1986).
19. J.L. Thakore and G.D. Holder. Ind. Eng. Chem. Res. **26**, 462 (1987).
20. J.A. Ripmeester and C.I. Ratcliffe. J. Phys. Chem. **92**, 337 (1988).
21. Y.P. Handa. J. Phys. Chem. **94**, 2652 (1990).

© 2002 NRC Canada

22. S. Adisasmito, R.J. Frank, III, and E.D. Sloan, Jr. J. Chem. Eng. Data, **36**, 68 (1991).
23. T.Y. Makogon and E.D. Sloan, Jr. J. Chem. Eng. Data, **39**, 351 (1994).
24. E.D. Sloan, Jr. Clathrate hydrates of natural gases. 2nd ed. Marcel Dekker, Inc., New York. 1997.
25. R.N. Goldberg and R.D. Weir. Pure Appl. Chem. **10**, 1545 (1992).
26. E.C.W. Clarke and D.N. Glew. Trans. Faraday Soc. **62**, 539 (1966).
27. S. Angus, B. Armstrong, and K.M. de Reuck. International thermodynamic tables of the fluid state-5 methane International Union of Pure and Applied Chemistry. Pergamon Press, Oxford. 1978.
28. L. Haar, J.S. Gallagher, and G.S. Kell. NBS/NRC steam tables. Hemisphere Publishing Corp., New York. 1984.
29. D.R. Lide. CRC handbook of chemistry and physics. 81st ed. 6–6. CRC Press, Boca Raton. 2000.
30. W.F. Giauque and J.W. Stout. J. Am. Chem. Soc. **58**, 1144 (1936).
31. N.S. Osborne. J. Res. Natl. Bur. Stand. **23**, 643 (1939).
32. C.W. Clarke and D.N. Glew. Can. J. Chem. **76**, 1119 (1998).
33. C.W. Clarke and D.N. Glew. Can. J. Chem. **78**, 1 (2000).
34. D.N. Glew. Can. J. Chem. **78**, 1204 (2000).
35. N.R. Draper and H. Smith. Applied regression analysis. 2nd ed. John Wiley & Sons, Inc., New York. 1981.
36. M. von Stackelberg and W. Jahns. Z. Elektrochem. **58**, 162 (1954).
37. D.W. Davidson. *In* Water: a comprehensive treatise. Vol. 2. *Edited by* F. Franks. Plenum Press, New York. 1973.
38. D.W. Davidson, Y.P. Handa, C.I. Ratcliffe, J.S. Tse, and B.M. Powell. Nature (London), **311**, 142 (1984).
39. J.S. Tse, W.R. McKinnon, and M. Marchi. J. Phys. Chem. **91**, 4188 (1987).
40. F.E.C. Scheffer and G. Meyer. Proc. K. Ned. Akad. Wet. **21**, 1338 (1919).
41. D.W. Davidson, Y.P. Handa, and J.A. Ripmeester. J. Phys. Chem. **90**, 6549 (1986).
42. Y.P. Handa. J. Chem. Thermodyn. **18**, 891 (1986).
43. M.J. Collins, C.I. Ratcliffe, and J.A. Ripmeester. J. Phys. Chem. **94**, 157 (1990).
44. J.S. Tse, Y.P Handa, C.I. Ratcliffe, and B.M. Powell. J. Inclus. Phenom. **4**, 235 (1986).
45. J.S. Tse. J. Physique, **48** C1, 543 (1987).
46. I.-M. Chou, A. Sharma, R.C. Burruss, J. Shu, H.-K. Mao, R.J. Hemley, A.F. Goncharov, L.A. Stern, and S.H. Kirby. PNAS, **97**, 13484 (2000).
47. I.-M. Chou, A. Sharma, R.C. Burruss, R.J. Hemley, A.F. Goncharov, L.A. Stern, and S.H. Kirby. J. Phys. Chem. A, **105**, 4664 (2001).
48. Y.A. Dyadin and E.Y. Aladko. *In* Proceedings of the 2nd International conference on natural gas hydrates. *Edited by* J.P. Monfort. Vol 2. Toulouse. 1996. p. 67.
49. Y.A. Dyadin, E.Y. Aladko, and E.G. Larionov. Mendeleev Commun. 34 (1997).
50. S. Nakano, M Moritoki, and K. Ohgaki. J. Chem. Eng. Data, **44**, 254 (1999).

© 2002 NRC Canada

Sampling variance as a function of single-increment size for estimation of bitumen in an oil-sand core

Zhi Gao and Byron Kratochvil

Abstract: The relationship between sampling variance and single-increment size for bitumen content in oil sand was investigated for a previously collected data set of 1468 contiguous 1-cm^2 IR measurements on a 15-m core. A variogram study showed that bitumen in the 15-m core is highly regionalized with a range of influence of 20 cm. For increment sizes lower than this range, the sampling variance as a function of increment size fits a logarithmic function but does not fit Visman's reciprocal function, which was also confirmed for a second oil-sand core with a range of influence of 100 cm. Visman's equation does, however, give good results for larger increment sizes. Computer randomization of the data reveals that Visman's equation is valid for either local or overall random distributions. Characterization by fractal dimension showed that Visman's equation is applicable to populations with higher fractal dimensions (equal or close to 2), whereas a logarithmic relationship is more applicable to populations with lower fractal dimensions.

Key words: Sampling, geostatistics, variogram, Visman's equation, oil sand.

Résumé : Utilisant un ensemble de données recueillies antérieurement pour 1468 mesures IR contiguës de 1 cm^3, sur une carotte de 15 m, on a étudié la relation entre la variance d'échantillonnage et des augmentations unitaires de leur taille pour le contenu en bitume de sables bitumineux. Une étude sous la forme de variogramme montre que le bitume, dans une carotte de 15 m, est fortement régionalisé avec un intervalle d'influence de 20 cm. Pour des augmentations de tailles inférieures à cette plage, la variance de l'échantillonnage en fonction des augmentations de la taille s'accommode bien dans une fonction logarithmique, mais elle ne peut pas être représentée par la fonction réciproque de Visman, ce qui a été confirmé par une deuxième carotte de sable bitumineux, avec un intervalle d'influence de 100 cm. Toutefois, l'équation de Visman donne de bons résultats pour augmentations de la taille plus importantes. Une distribution au hasard des données à l'aide d'un ordinateur révèle que l'équation de Visman est valide pour des distributions aléatoires locales ou globales. Une caractérisation par dimension fractale montre que l'équation de Visman peut être appliquée à des populations de dimensions fractales plus élevées (égales ou s'approchant de 2) alors qu'une relation logarithmique peut s'appliquer mieux à des populations de dimensions fractales plus faibles.

Mots clés : échantillonnage; géostatistiques; variogramme; équation de Visman; sable bitumineux.

[Traduit par la Rédaction]

Introduction

The overall analytical uncertainty of an analyte in a population is a combination of sampling and measurement errors. For bitumen in an oil-sand core, measurement is usually by Soxhlet extraction (1) or near-infrared diffuse-reflectance spectroscopy (2, 3). Both methods have reasonable analytical precision. As a result, the major part of the analytical uncertainty in bitumen analyses usually arises from sampling. Many factors affect sampling precision, but the primary factor is that bitumen is highly segregated in an oil-sand core. Additional factors include difficulties with sample collection, subsampling operations, and sample storage and handling in general. Due to the heterogeneous nature of oil sand, small samples do not give adequate sampling precision (3). On the other hand, large samples are more costly to obtain, process, and store. A better understanding of the relationship between sampling variance for bitumen and sample size would, therefore, be useful.

Among sampling equations (4), those of Ingamells (5) and Gy (6) are often applied to well-mixed particulate materials. Visman's equation for segregated populations is primarily empirical (7, 8). Although successfully used in some cases, its breadth of applicability has been questioned (9), and it should not be arbitrarily used.

This paper considers the relationship between single-sample increment size and sampling variance, using as a database a set of earlier measurements of bitumen content in an oil-sand core at 1-cm resolution by near-infrared diffuse-reflectance spectroscopy (3).

Received 10 March 2001. Published on the NRC Research Press Web site at http://canjchem.nrc.ca on 12 April 2002.

Z. Gao and B. Kratochvil.[1] Department of Chemistry, University of Alberta, Edmonton, AB T6G 2G2, Canada.

[1]Corresponding author (e-mail: ron.kratochvil@ualberta.ca).

 DOI: 10.1139/V02-039 © 2002 NRC Canada

Fig. 1. Distribution of bitumen content as a function of increment size over 15-meter core length. (*a*) L = 1 cm (from ref. 1); (*b*) L = 2 cm; (*c*) L = 10 cm; (*d*) L = 50 cm.

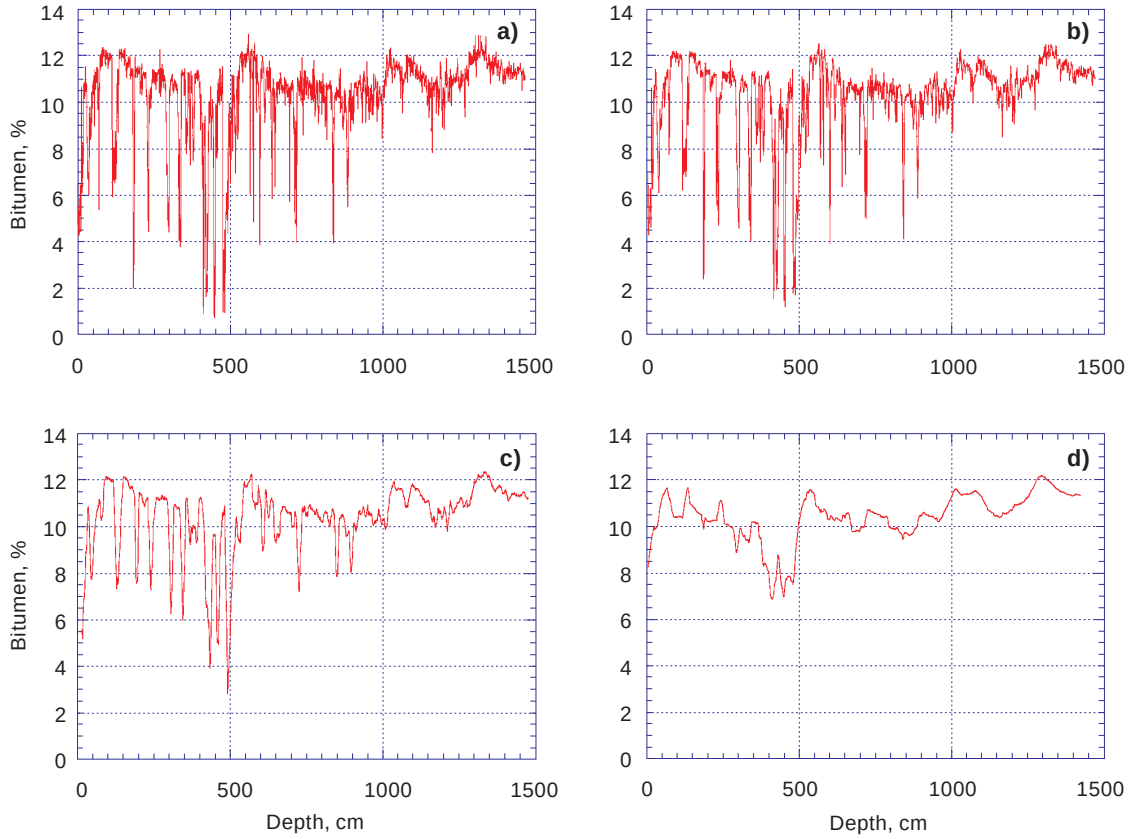

Experimental

The oil-sand analytical data used in this study was obtained by K. Donkor and reported earlier (3). A brief summary of the experimental details provided in that paper is repeated here. The original core, approximately 20 m long and 7 cm in diameter, was provided by Syncrude Canada from a region of the Athabasca oil-sand deposit near Fort McMurray, Alberta, Canada. A 15-m section, selected as typical of grade variations over a vertical transect within the deposit, was frozen and sawed in half longitudinally. This provided a uniformly textured flat surface for analysis by near-infrared diffuse-reflectance spectrometry. Spectra were recorded over the range of 1200–2400 nm at a rate of 5 scans per second with a resolution of 1 nm. The 15-m core was scanned at 1-cm intervals along its length in a 1-cm-wide strip, about 1.5 cm from one edge of the core casing. Fifty scans were taken and averaged for each reading of the 1-cm^2 sampling area for both samples and standards. All spectra were digitized and stored on a computer hard disk for processing. Standards were prepared by removal of 1- to 2-g samples from 96 1-cm^2 sections of the core and analyzed for bitumen by toluene extraction, evaporation of the solvent, and weighing. Calibration models were optimized by both principal-component regression and partial least-squares statistical data processing. Both models gave satisfactory results (residual values less than 1%).

All sample-increment sizes are expressed here in one dimension. For example, a L-cm increment represents a rectangle L cm in length and 1 cm in width. Thus the bitumen content in a L-cm increment sample is calculated as the average of L contiguous 1-cm^2 measurement units. Variation in the density of the oil sand was neglected for the purposes of this study. The relative standard deviation of the infrared analytical measurements was of the order of 0.2%, which is sufficiently small to be neglected in calculating sampling standard deviations from the data (2).

Results and discussion

Distribution of bitumen content as a function of increment size

The profile of bitumen content in the oil-sand core, at 1-cm resolution (1-cm increments), is shown in Fig. 1*a*. The upper 5 m of the core is generally more segregated than the middle 5 m, and the middle part is more segregated than the lower 5 m. Increasing the increment size changes the apparent bitumen distribution (Fig. 1*b–d*): the larger the increment size, the more homogeneous the distribution appears to be. Sampling precision therefore increases with increase in increment size. Quantification of this relationship for single increments collected from this population is investigated in the following sections.

Visman's equation

The sampling equation proposed by Visman relates sampling variance (s^2) to sample size through a random variability term (A/w) and a segregation term (B)

© 2002 NRC Canada

Fig. 2. Sampling variance of bitumen content as a function of sample size for various sections of core. circles, 0–15 m; squares, 0–5 m; diamonds, 5–10 m; crosses, 10–15 m.

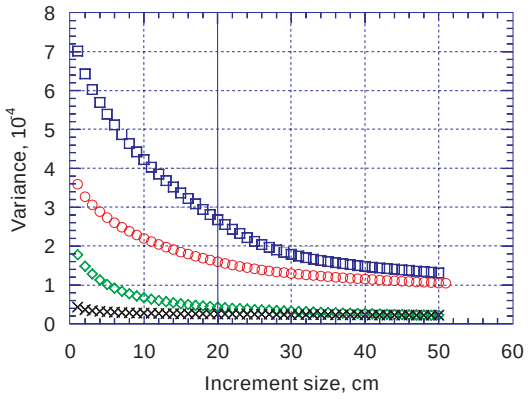

Table 1. Fit of Visman's equation to the relationship between sampling variance of bitumen content and sample size over 15-m length of oil-sand core and three 5-m subsections (100 points included in each fitting with increment sizes of 1, 2, …, 100 cm).

Oil-sand core	Sampling constants		Correlation coefficient, R
	A (1×10^{-4})	B (1×10^{-4})	
0–15m	4.00±0.31	1.07±0.04	0.792
0–5m	9.27±0.78	1.39±0.10	0.769
5–10m	2.21±0.12	0.21±0.02	0.878
10–15m	0.29±0.02	0.21±0.01	0.827

$$[1] \qquad s^2 = \frac{A}{Nw} + \frac{B}{N}$$

where w is the size of each increment, A and B are constants, and N is the number of increments collected from a population. Equation [1] shows that for a given increment size the sampling variance is proportional to the reciprocal of the number of increments. For $N = 1$, s^2 is the single-increment sampling variance. Figure 2 shows the sampling variance of bitumen content as a function of increment size for the entire core and for three 5-m sections, using eq. [1] to fit the relationship. Values calculated for A and B are shown in Table 1. From the correlation coefficients, it can be seen that Visman's equation does not work well under these conditions.

In Visman's equation, the constants A and B are usually estimated by a two-point method:

$$[2] \qquad A = \frac{w_{Lg} w_{Sm} (S^2_{Sm} - S^2_{Lg})}{w_{Lg} - w_{Sm}}$$

$$[3] \qquad B = S^2_{Lg} - \frac{A}{w_{Lg}}$$

where w_{Lg} and w_{Sm} are large and small increment sizes, respectively, and S^2_{Lg} and S^2_{Sm} are the corresponding sampling variances. This method can be misleading, however, because it will always give estimates for A and B even though the relationship between sampling variance and sample size may not follow Visman's equation. For a population such as the one considered here, an ideal equation should apply to all increment sizes with good correlation. As shown in Table 2, then, different values of w_{Lg} and w_{Sm} give different values for A and B. We conclude that Visman's equation is not generally applicable to this oil-sand core. Of interest, however, is to determine those distributions where Visman's equation is applicable and, if possible, to find a sampling expression that better fits populations such as the one under study.

Fig. 3. Bitumen distributions for regionally randomized core data. (*a*) Population I; (*b*) Population II; (*c*) Population III.

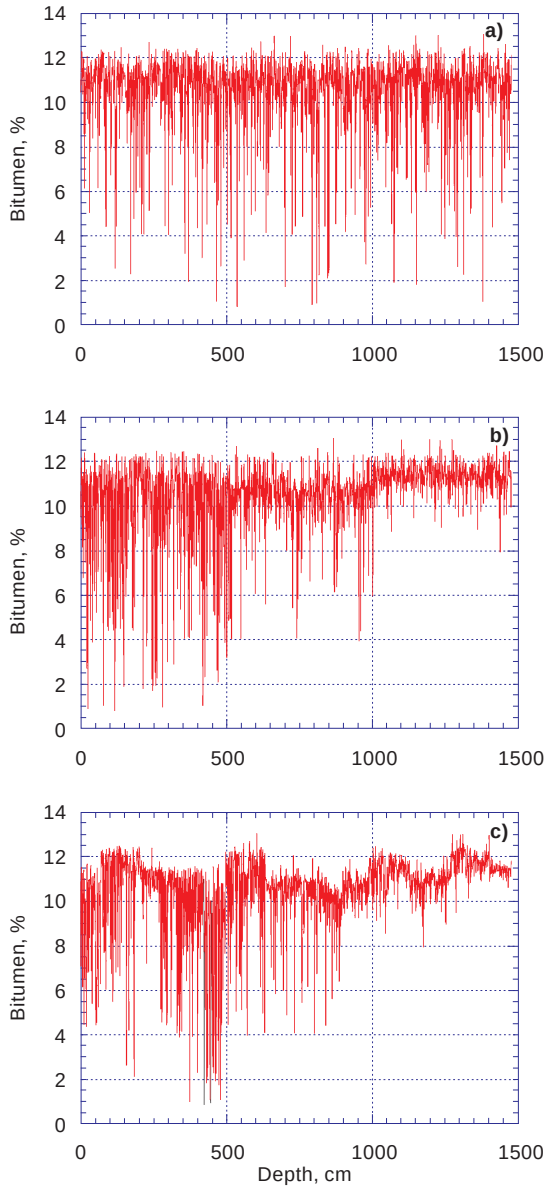

Different distributions of bitumen yield different populations, which affect sampling statistics. To assess this, the bitumen values for the 15-m core were redistributed into three different populations by computer (using the random-generation function in Microsoft Excel) and the applicability of Visman's equation to each was investigated. In Population I (Fig. 3*a*) the bitumen content was randomized over the whole core. In Population II (Fig. 3*b*) the initial oil-sand

© 2002 NRC Canada

Table 2. Estimated sampling constants *A* and *B* for Visman's equation using the two-point method for sampling of a 15-m length of oil-sand core for bitumen content.

Small sample size, L_{Sm} (cm)	s^2_{Sm} (1×10^{-4})	Large sample size, L_{Lg} (cm)	s^2_{Lm} (1×10^{-4})	Random variation factor, A (1×10^{-4})	Segregation factor, B (1×10^{-4})
1	3.59	10	2.20	1.55	2.04
2	3.27	10	2.20	2.69	1.93
2	3.27	20	1.60	3.72	1.41
5	2.74	50	1.05	9.37	0.86
10	2.20	50	1.05	14.35	0.76

Table 3. Fit of Visman's equation to the relationship between sampling variance of bitumen content and increment size for the case where content was randomly distributed within each section (Population II in text).

Sample size (cm)*	Random variation factor, A (1×10^{-4})	Segregation factor, B (1×10^{-4})	Correlation coefficient, R
1–10	3.15 ± 0.03	0.46 ± 0.01	0.9997
1–100	3.16 ± 0.02	0.47 ± 0.01	0.9987
10–100	3.76 ± 0.08	0.45 ± 0.01	0.9814
20–100	4.79 ± 0.10	0.43 ± 0.01	0.9836
30–100	5.68 ± 0.12	0.42 ± 0.01	0.9851
40–100	6.73 ± 0.10	0.40 ± 0.01	0.9930
100–500	26 ± 7	0.23 ± 0.04	0.9095

*All possible points were included in the fitting, e.g., sample sizes of 1–10 cm mean 1, 2, … 10 cm, except for sizes of 100–500 cm, which include only 100, 200, 300, 400, and 500 cm.

Table 4. Fit of Visman's equation to the relationship between sampling variance of bitumen content and increment size for the case where content was randomly distributed within each section (Population III in text).

Sample size (cm)*	Random variation factor, A (1×10^{-4})	Segregation factor, B (1×10^{-4})	Correlation coefficient, R
1–10	2.62 ± 0.01	0.98 ± 0.01	0.9999
1–50	2.76 ± 0.04	0.91 ± 0.01	0.9959
1–100	2.96 ± 0.07	0.83 ± 0.01	0.9747
10–100	6.55 ± 0.24	0.73 ± 0.01	0.9438
20–100	9.54 ± 0.31	0.68 ± 0.01	0.9609
30–100	12.41 ± 0.35	0.63 ± 0.01	0.9744
40–100	15.32 ± 0.34	0.59 ± 0.01	0.9864

*All possible points were included in the fitting, e.g., sample sizes of 1–10 cm mean 1, 2, … 10 cm.

core was divided into three sections (0–5 m, 5–10 m, and 10–14.68 m) and the bitumen content within each section was randomly distributed. In Population III (Fig. 3*c*) the initial oil-sand core was divided into 22 sections of 70 cm each (68 cm for the last section) and the bitumen content within each section was randomly distributed.

In Population I, where the bitumen is randomly distributed, the estimated Visman sampling constants for seven repetitions lie in the range of $(3.57–3.63) \times 10^{-4}$ with an average of 3.59×10^{-4} for *A*, and $(–0.21–0.22) \times 10^{-4}$ with an average of $–0.001 \times 10^{-4}$ for *B*. The correlation coefficients of the sampling variance as a function of increment size lie in the range of 0.9993–0.9998, with an average of 0.9996. The increment sizes used for the fitting are $L = 1, 2, \ldots, 100$ cm. These results show that in this case the sampling variance ($N = 1$) as a function of increment size fits Visman's equation well, with the segregation constant *B* approximately equal to zero, as expected for a random distribution. Changing the increment size over the range of 1–100 cm does not significantly affect the fitted results.

For Population II, the relationship between sampling variance and increment size fits Visman's equation well for small increment sizes, but as shown in Table 3, not so well for larger ones.

For Population III, sampling variance as a function of increment size again fits Visman's equation for small increment sizes (Table 4) but, similar to Population II, not for larger ones. The correlation coefficient drops with increasing large increment size (w_{Lg}) for a given small increment size (w_{Sm}), and vice versa. The range of increment sizes used to calculate the constants *A* and B can, therefore, significantly affect their values.

An alternate approach to estimation of Visman's sampling constants *A* and *B*

In this section we derive equations to estimate the constants *A* and *B* based on an assumed population distribution.

© 2002 NRC Canada

Consider a population divided into r sections, with the analyte randomly distributed within each section. If the increment size is very small relative to the size of the section from which it is taken, the theoretical random-sampling variance for a single increment can be estimated by

$$[4]\quad \sigma^2 = \frac{1}{N}\sum_{i=1}^{r}\sum_{j=1}^{N_i}(c_{ij}-\bar{c})^2 = \frac{1}{N}\sum_{i=1}^{r}\sum_{j=1}^{N_i}c_{ij}^2 - (\bar{c})^2$$

$$= \frac{1}{N}\sum_{i=1}^{r}N_i\left(\frac{1}{N}\sum_{j=1}^{N_i}c_{ij}^2 - (\bar{c}_i)^2\right) + \frac{1}{N}\sum_{i=1}^{r}N_i(\bar{c}_i)^2 - (\bar{c})^2$$

$$= \frac{1}{N}\sum_{i=1}^{r}N_i\sigma_i^2 + \frac{1}{N}\sum_{i=1}^{r}N_i(\bar{c}_i)^2 - (\bar{c})^2$$

where i is the serial number of sections, j is the serial number of increments from each section, N is the total number of increments, N_i is the number of increments taken from section i, c_{ij} is the analyte concentration in increment ij, $\bar{c}_i$ is the mean concentration of analyte in section i, $\bar{c}$ is the mean concentration of analyte in the overall population, and σ_i^2 is the theoretical single-increment variance for section i.

Since $N_i/N = f_i$, the fraction of section i in the population, when N and N_i are very large, eq. [4] gives

$$[5]\quad \sigma^2 = \sum_{i=1}^{r}f_i\sigma_i^2 + \sum_{i=1}^{r}f_i(\bar{c}_i-\bar{c})^2$$

Since Ingamells' sampling constant $K_{si} = 10^4\sigma_i^2 w/(\bar{c}_i)^2$ (5), eq. [5] becomes

$$[6]\quad \sigma^2 = \frac{1}{w}\sum_{i=1}^{r}10^{-4}K_{si}f_i(\bar{c}_i)^2 + \sum_{i=1}^{r}f_i(\bar{c}_i-\bar{c})^2$$

Letting

$$[7]\quad A = \sum_{i=1}^{r}10^{-4}K_{si}f_i(\bar{c}_i)^2$$

and

$$[8]\quad B = \sum_{i=1}^{r}f_i(\bar{c}_i-\bar{c})^2$$

eq. [6] becomes Visman's sampling equation (eq. [1]) when $N = 1$. Since all the quantities on the right-hand sides of eqs. [7] and [8] are constants for a given population, A and B are constants. A is characterized by the randomness of analyte within sections, and B by the difference between sections. From eqs. [7] and [8], the sampling constants for Population I were calculated to be $A = 3.59 \times 10^{-4}$ and $B = 0$; for Population II, $A = 3.13 \times 10^{-4}$ and $B = 0.47 \times 10^{-4}$; and for Population III, $A = 2.64 \times 10^{-4}$ and $B = 0.99 \times 10^{-4}$, all of which are in good agreement with experimental results for all increment sizes for Population I and for relatively small increment sizes for Populations II and III (Tables 3 and 4). We therefore conclude that Visman's equation is valid for segregated populations with randomly distributed values within subsections (or locally random distribution in general) and for increments of relatively small size.

Fig. 4. Semivariogram of bitumen content in oil-sand core (0–15 m).

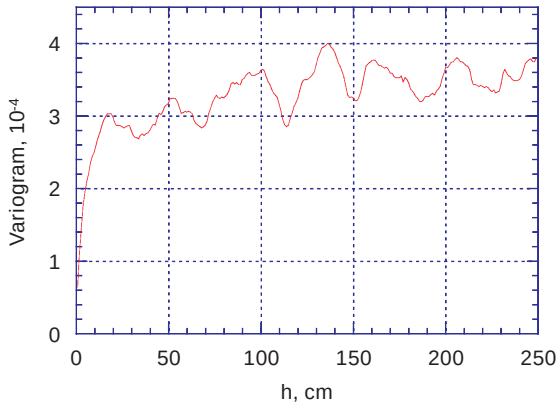

Evaluation of variogram approach

We have shown that Visman's equation is not applicable to sampling of the oil-sand core studied here because the bitumen is not randomly distributed at the local level. An alternative approach to characterize the relationship between sampling variance and increment size is therefore needed.

Geostatisticians commonly describe spatial correlation between sampling points by use of a semivariogram (10) or, for simplicity, a variogram ($\gamma(h)$) (11, 12) as follows:

$$[9]\quad \gamma(h) = \frac{1}{2n}\sum[c(x+h)-c(x)]^2$$

Here, $c(x)$ and $c(x + \mathrm{h})$ denote analyte content for sampling points x and x + h, and n is the number of pairs of sampling points distance h apart. Figure 4 shows the semivariance as a function of sampling interval h for the 15-m core studied. It shows that for $h \leq 20$ cm, $\gamma(h)$ monotonically increases with increase of sampling interval h, which indicates that points close to each other have more similarity than those far apart. For $h = 20$ cm, $\gamma(h)$ tends toward a plateau, with irregular variations over the sampling interval. This indicates that the bitumen in the 15-m core studied is highly regionalized, with a range of influence of 20 cm. At a scale larger than 20 cm, the bitumen distribution exhibits randomness; the sampling properties are therefore expected to be different for different sampling scales.

Evaluation of a logarithmic relationship between sampling variance and increment size

De Wijs (10) proposed a geostatistical dispersion model that relates log variance with log of sample size. Converting the bitumen contents in the oil-sand core into logarithmic values, we found that log variance as a function of increment size fitted de Wijs's equation very well. Although log variance is a useful parameter for geological study, for the purpose of evaluating the bitumen content in oil-sand core variance is still the commonly used parameter to reflect the sampling uncertainty, which (other than the logarithmic values) is calculated directly from the initial analyte contents. We therefore investigated the simpler expression

$$[10]\quad s^2 = K_1 - K_2 \log L$$

© 2002 NRC Canada

Table 5. Fit of logarithmic equation to the relationship between sampling variance of bitumen content and increment size over 15-m length of oil-sand core, three 5-m subsections and three randomized populations (50 points included with sample sizes of 1, 2, … 50 cm).

	Sampling constants		
Oil-sand core	K_1 (1×10^{-4})	K_2 (1×10^{-4})	Correlation coefficient, R
0–15m	3.58 ± 0.04	1.46 ± 0.02	0.988
0–5m	7.33 ± 0.11	3.45 ± 0.07	0.983
5–10m	1.45 ± 0.03	0.71 ± 0.02	0.969
10–15m	0.39 ± 0.01	0.10 ± 0.01	0.987
Population I	1.51 ± 0.11	0.83 ± 0.07	0.786
Population II	1.78 ± 0.09	0.73 ± 0.06	0.790
Population III	2.22 ± 0.07	0.78 ± 0.04	0.886

to relate sampling variance with increment size for the oil-sand core, where s^2 refers to variance calculated directly from initial bitumen content. Table 5 lists the fitted results of sampling constants using eq. [10], along with the correlation coefficients for the overall core population for the three 5-m subsections and for the idealized populations described earlier. The results confirm that eq. [10] gives a reasonable fit to the real oil-sand core, but not to the randomized populations I, II, or III. Considering different sampling scales, we found that for $L \leq 20$ cm (L = 1, 2, … 20 cm), eq. 10 becomes $s^2 = 3.78 \times 10^{-4} - 1.62 \times 10^{-4} \log L$ with $r = 0.993$, and for $L > 20$ cm (L = 21, … 100 cm), $s^2 = 2.80 \times 10^{-4} - 1.02 \times 10^{-4} \log L$ with $r = 0.991$. The equation for $L \leq 20$ cm does not differ much from the fitted result for increment sizes of 1–100 cm for the 15-m core (Table 5) because the points for small sample sizes contribute the most to regression results calculated by least squares. For larger increment sizes ($L \geq 20$ cm), the relationship fits Visman's equation better: $s^2 = 0.629 \times 10^{-4} + [(20.02 \times 10^{-4})/L]$ (r = 0.997, L = 20, 21, … 100 cm).

We conclude, therefore, that eq. [10] is more applicable for small increment sizes (L = 20 cm), which correspond to highly regionalized distribution, whereas Visman's equation is more applicable to large increment sizes ($L > 20$ cm), which correspond to relatively random distribution.

An additional test of eq. [10] was made by applying it to data obtained on an independent 4-m section of core, which was also analyzed with near-infrared diffuse-reflectance spectrometry (2). Bitumen content at 1-cm resolution for this core was in the range of 0–20%, for an average of 10.56%. A variogram for this core shows an increase with increase in sampling interval (h) up to 100 cm. For increment size $L \leq 100$ cm, the relationship between sampling variance and increment size fits eq. [10] well: $s^2 = 21.92 \times 10^{-4} - 7.66 \times 10^{-4} \log L$ (r = 0.986, L = 1, 2, …, 100 cm). It does not, however, fit Visman's equation: $s^2 = (18.47 \times 10^{-4})/L + 7.97 \times 10^{-4}$) ($r$ = 0.694, L = 1, 2, …, 100 cm). These results further verify that eq. [10] is applicable to the core for increment sizes smaller than the range of influence.

Fractal analysis of bitumen distribution in the oil-sand core

The preceding discussions reveal that whether Visman's equation or eq. [10] is applicable to a population depends on the distribution of the population. It is necessary, therefore, to characterize the distribution of a population prior to selecting the equation for sampling. Many geological structure or element distributions in geological or environmental areas exhibit self-similarity which can be characterized by fractal dimension (13–15). In this theory, a complicated environmental or geological data series can be depicted by a simple number called fractal dimension (D), which is related to the variogram expression by the following equation (14, 15):

$$[11] \quad \frac{d \log \gamma(h)}{d \log h} = 4 - 2D \qquad (h \rightarrow 0)$$

For a spatial-data series, since D is calculated by eq. [11] for $h \rightarrow 0$, fractal dimension is a parameter that reflects the local heterogeneity, or consistency, of a population (16). Data series that have a small fractal dimension imply that samples close to each other are more likely to be similar in composition, and heterogeneity can be found only over a longer range of scale. On the other hand, larger fractal dimension implies that samples close to each other are likely to be different in composition, and heterogeneity is dominant over a shorter range of scale. A fractal dimension of 2 as calculated by eq. [11] refers to a population with totally random distribution.

The fractal dimension for bitumen content distributed in the oil-sand core investigated here is estimated as 1.60. For the three 5-m sections of the core, the upper section (0–5 m) has a fractal dimension of 1.58, the middle section 1.61, and the lower section 1.82. These results show that the more random the population, the higher the fractal dimension would be. This conclusion is consistent with eq. [11]. The estimated fractal dimensions for ideal Populations I, II, and III are 2, 1.99, and 1.98, respectively.

By correlating the fractal dimension with the sampling equation, we therefore conclude that Visman's equation is more applicable to populations with higher fractal dimensions (equal or close to 2), whereas eq. [10] is more applicable to populations with lower fractal dimensions.

Conclusion

A study of the relationship between single-increment sampling variance and sample size for bitumen content in a 15-m length of an oil-sand core showed that a logarithmic equation is more useful for increment sizes lower than the range of influence in which the bitumen content is highly regionalized, and Visman's equation is more useful for larger increment sizes in which the bitumen content is relatively distributed. A random redistribution by computer of the initial bitumen content along the core showed that

© 2002 NRC Canada

Visman's equation is applicable to populations with local or overall random distributions. Characterization of the populations by the theory of fractal dimension reveals that Visman's equation is valid for populations with higher fractal dimensions (equal or close to 2), whereas eq. [10] applies for populations with lower fractal dimensions.

Acknowledgments

The support of the Natural Sciences and Engineering Research Council of Canada (NSERC) and of the Department of Chemistry, University of Alberta, is gratefully acknowledged.

References

1. J.T. Bulmer and T. Starr (*Editors*). Syncrude analytical methods for oil sand and bitumen processing. The Alberta Oil Sands Technology and Research Authority, Syncrude Canada Ltd. Research, Edmonton, Canada. 1979.
2. R.C. Shaw and B. Kratochvil. Anal. Chem. **62**, 167 (1990).
3. K.K. Donkor, B. Kratochvil, and G.R. Thompson. Analyst, **120**, 2713 (1995).
4. B. Kratochvil, D. Wallace, and J.K. Taylor. Anal. Chem. **56**, 113R (1984).
5. C.O. Ingamells and P. Switzer. Talanta, **20**, 547 (1973).
6. F.F. Pitard. Pierre Gy's sampling theory and sampling practice — heterogeneity, sampling correctness, and statistical process control. CRC Press, Boca Raton. 1993.
7. J. Visman. Mat. Res. Stds. **9**(11), 8 (1969).
8. D. Wallace and B. Kratochvil. Anal. Chem. **59**, 226 (1987).
9. A.J. Duncan. Mat. Res. Stds. **11**, 25 (1971).
10. D.G. Krige. Lognormal-de Wijsian geostatistics for ore evaluation. South African Institute of Mining and Metallurgy, Johannesburg. 1981.
11. E.H. Isaaks and R.M. Srivastava. Applied geostatistics. Oxford University Press, New York. 1989.
12. J.-P. Chiles and P. Delfiner. Geostatistics: modeling spatial uncertainty. John Wiley & Sons, New York. 1999.
13. J.H. Kruhl (*Editor*). Fractals and dynamic systems in geoscience. Springer-Verlag, Berlin Heidelberg. 1994.
14. P.A. Burrough. Principles of geographical information systems for land resources assessment. Clarendon Press, New York. 1988.
15. P.A. Burrough. Nature (London), **294**, 240 (1981).
16. R.C. Shaw. MSc thesis. Department of Chemistry, University of Alberta, Edmonton, Alberta. 1988.

© 2002 NRC Canada

An ab initio study of conformations and sigmatropic shifts in triazene and its mono-, di-, and trimethyl derivatives

Cory C. Pye, Keith Vaughan, and Julie F. Glister

Abstract: A computational study of triazene, methyltriazene, dimethyltriazene, and trimethyltriazene is presented. A number of different conformers are analyzed and rationalized using hyperconjugation and steric interaction arguments. The transition states for rotation, inversion, and proton and methyl shifts (including water-mediated) are found and the barriers determined.

Key words: triazene, ab initio, methyltriazene, 1,3-proton shift.

Résumé : On présente une étude théorique du triazène, du méthyltriazène, du diméthyltriazène et du triméthyltriazène. On a analysé un certain nombre de conformères différents qui ont été rationalisés sur la base de l'hyperconjugaison et d'arguments stériques. On a localisé les états de transition pour la rotation, l'inversion ainsi que pour les déplacements d'hydrogènes et de méthyles (y compris ceux qui s'effectuent sous l'influence de l'eau) et on en a déterminé les barrières.

Mots clés : triazène, calculs ab initio, méthyltriazène, déplacement-1,3 de proton.

[Traduit par la Rédaction]

Introduction

Triazene (NH_2-N=NH) is the fundamental reactive site in a number of molecules possessing antitumour properties, such as Dacarbazine, Temozolomide, and Mitozolomide (1–3). In addition, nitrogen–nitrogen bonds, found in high-energy compounds, are an important area of fuel and explosives research and new reports in this area still appear (4–10). Triazene itself, however, remains an elusive molecule, with reports sporadically appearing in the literature. Mass spectrometric evidence for triazene first appeared from a fast-flow apparatus in which hydrazine is subjected to an electrodeless discharge. The ionization energy was reported to be 9.6 ± 0.1 eV (11, 12). Triazene is also postulated to be an intermediate in the decomposition of hydrazine in aqueous solution by pulse radiolysis. After initial production of the hydroxyl radical, the following kinetic pathway was proposed, with protonated forms appearing at lower pH.

[1] $OH^{\bullet} + N_2H_4 \rightarrow H_2O + N_2H_3^{\bullet}$

[2] $2N_2H_3^{\bullet} \rightarrow N_4H_6$

[3] $N_4H_6 \rightarrow N_3H_3 + NH_3$

Triazene then decomposes with first-order kinetics. The pK_a of triazene was determined to be 7.0 ± 0.2 (13). In another study, the decomposition of triazene was shown to be dependent on the total phosphate buffer concentration, suggesting a second pathway for decomposition involving phosphate (14). The first and second pK_a of protonated triazene were determined to be 4.95 and 11.37, respectively. The isomer cyclotriazane (triaziridine) was found as a silver-ion complex after sorption of ammonia onto a completely silver-ion exchanged zeolite A and an X-ray structure was reported. The mass spectrum indicates that N_3H_3 can be degassed from the complex (15). The gas phase structure could be *cis*- or *trans*-triaziridine, the acyclic isomer azimine, which could be formed from triaziridine by ring opening, or *cis*- or *trans*-triazene, which could be formed from azimine via a 1,2-hydrogen shift.

Triazene and its isomers have also been studied by theoretical means. In a survey of all three-membered rings involving C, N, and O, the *cis* (C_{3v}) and *trans* (C_s) forms of triaziridine were examined using HF/STO-3G geometries and single-point Hartree–Fock calculations using the 4-31G and 6-31G* basis sets (16). Dipole moments and orbital energies were provided. In a HF/STO-3G study of substituted diazenes, the *trans* form of triazene was shown to be 20 kJ mol^{-1} more stable than the *cis* form (17). An approximate barrier of 312 kJ mol^{-1} was found between the two via an inversion mechanism at the central nitrogen, which was lower in energy than a rotation mechanism. Seven isomers of N_3H_3 were studied at the HF/3-21G, HF/6-31G, and HF/6-31G**//HF/3-21G levels (18). The two forms of triaziridine were higher in energy than the three forms of azimine, which were in turn higher in energy than the two forms of triazene. It is thus clear that triazene is the thermodynamically stable form. In addition, the transition states for conversion between the triaziridine forms, between the triazene forms, the 1,2-hydrogen shifts interconverting azimine and triazene, and the 1,3-hydrogen shift in triazene were investigated. This work was extended to the HF/6-31G* geometric

Received 24 Jan 2002. Published on the NRC Research Press Web site at http://canjchem.nrc.ca on 17 April 2002.

C.C. Pye,[1] K. Vaughan, and J.F. Glister. Department of Chemistry, Saint Mary's University, Halifax, NS B3H 3C3, Canada.

[1]Corresponding author (e-mail: cory.pye@stmarys.ca).

 DOI: 10.1139/V02-049 © 2002 NRC Canada

Table 1. ZPE-corrected energies (kJ mol^{-1}) of C_s structures of *trans*- and *cis*-triazene.

Level	C_s #1	C_s #2	C_s #3	C_1 *cis*
HF/STO-3G	17.48	30.51	41.68	18.39
HF/3-21G	–1.23	51.10	55.04	24.47
HF/6-31G*	3.64	48.22	54.37	26.74
HF/6-31+G*	2.37	58.07	55.76	32.25
MP2/6-31G*	2.67	54.21	58.98	21.25
MP2/6-31+G*	1.23	55.00	62.32	28.74

Note: Relative to C_1 *trans*-triazene.

Table 2. ZPE-corrected energies (kJ mol^{-1}) of C_s structures of *cis*-triazene.

Level	C_s #4	C_s #5	C_s #6
HF/STO-3G	17.80	6.19	49.10
HF/3-21G	–1.16	12.07	56.59
HF/6-31G*	4.15	18.23	55.91
HF/6-31+G*	3.48	16.86	55.28
MP2/6-31G*	3.08	22.39	58.68
MP2/6-31+G*	2.24	20.69	59.08

Note: Relative to C_1 *cis*-triazene.

and single-point HF and MP2/6-31G** energy levels (19) by the same authors, who also looked at barriers for double-proton transfer and amine rotation. Others have extended this work to the correlated level (MP2/DZP, CCSD-T/DZP) and supplied vibrational frequencies (20). Planar triazene was studied at the HF/3-21G* level in relation to double-bond conjugation in second- and third-period elements (21). Schmiedekamp et al. (22) investigated the protonation of triazenes at the HF/3-21G, HF/6-31G*//HF/3-21G, and MP3/6-31G*//HF/3-21G levels and later, with a multitude of basis sets at the HF, MP2-MP4, QCISD, and NL-DFT levels (23).

This paper comprises a computational examination of triazene itself, with a focus on conformational energetics and its rationalization, and the 1,3-proton shift. These results help us to interpret the following study of all methylated forms of triazene, which in principle can also undergo a methyl shift. It is intended that these studies will lay groundwork for future studies of triazene drugs used in chemotherapy, which are believed to act as methylating agents. A computational study of triazene drugs and smaller model systems is in progress and will be published separately.

Method

Calculations were performed using Gaussian 98 (24), using the 6-31G* (25) and 6-31+G* (26) basis sets. The MP2 calculations use the frozen-core approximation. The geometries were optimized using a stepping-stone approach, in which the geometries at the levels HF/STO-3G, HF/3-21G, HF/6-31G*, HF/6-31+G*, MP2/6-31G*, and MP2/6-31+G* were sequentially optimized.[2] Default optimization specifications were normally used. After each level, where possible, a frequency calculation was performed at the same level and the resulting Hessian was used in the following optimization. *Z*-matrix coordinates constrained to the appropriate symmetry were used as required to speed up the optimizations. If symmetry constraints led to a transition state or hilltop, instead of a minimum, this would show up as the presence of one or more imaginary frequencies not belonging to the totally symmetric irreducible representation. The Hessian was evaluated at the first geometry (opt = CalcFC) for the first level in a series to aid geometry convergence.

Results and discussion

Triazene

Conformational possibilities

Triazene itself can exist in either a *cis* or *trans* geometry about the N=N double bond (see Fig. 1).[3] For each of these isomers, there can exist three possible structures with C_s symmetry. The structures, whose hydrogens on the tricoordinate nitrogen are in the σ-plane, are labelled #1 and #4 for the *trans* and *cis* isomers, respectively. There are four structures whose hydrogens are bisected by the symmetry plane. Two of these are in an anticlinal arrangement with respect to the N=N double bond (*trans* (#2) and *cis* (#5)), and two are in a synclinal arrangement (*trans* (#3) and *cis* (#6)). None of these structures at any level was a minimum-energy structure. All possessed an imaginary frequency of irreducible representation A''. Of these structures, #1 and #4 were the lowest energy *trans* and *cis* structures, respectively. For these, the imaginary frequency corresponded to an NH_2 wagging motion. Desymmetrizing structures #2 and #3 invariably resulted in a *trans* structure with no symmetry (C_1 #1, see Fig. 1), while #5 and #6 led to the analogous *cis* structure (C_1 #2, see Fig. 1). The relative energies of the various *trans* and *cis* isomers relative to the most stable *trans* and *cis* isomers are given in Tables 1 and 2. The amine prefers this arrangement presumably because of the strong stabilizing hyperconjugation interaction between the nonbonding orbital of the sp^3 nitrogen and the π* orbital of the N=N bond.

The *trans* C_1 structure was the lowest in energy at all levels. We hypothesize that the repulsion between the sp^2 nitrogen lone pairs in the *cis* form destabilizes this structure. This is evident by the increase in the energy difference when

[2] A reviewer suggested that we elucidate the effect of adding polarization functions to hydrogen on N–H bond breaking. We re-examined *trans*-triazene and its transition state for proton transfer for the four highest levels investigated. Four single point calculations were done for each molecule, namely, HF/6-31G**//HF/6-31G*, HF/6-31+G**//HF/6-31+G*, MP2/6-31G**//MP2/6-31G*, and MP2/6-31+G**//MP2/6-31+G*. The barrier to proton transfer was about 11 kJ mol^{-1} lower at the HF level, but only 5 kJ mol^{-1} lower at the MP2 level. To examine trends in barriers in the substituted triazenes, the effect of the hydrogen polarization functions would most likely be consistent. Including them in, for example, Dacarbazine, would entail much additional computational expense, especially if geometry optimizations and frequency calculations were to be considered.

[3] The total electronic energies and the ZPE-uncorrected versions of the following tables are found in the supplementary material. Copies of material on deposit may be purchased from the Depository of Unpublished Data, Document Delivery, CISTI, National Research Council Canada, Ottawa, ON K1A 0S2, Canada.

© 2002 NRC Canada

Fig. 1. Structures associated with triazene.

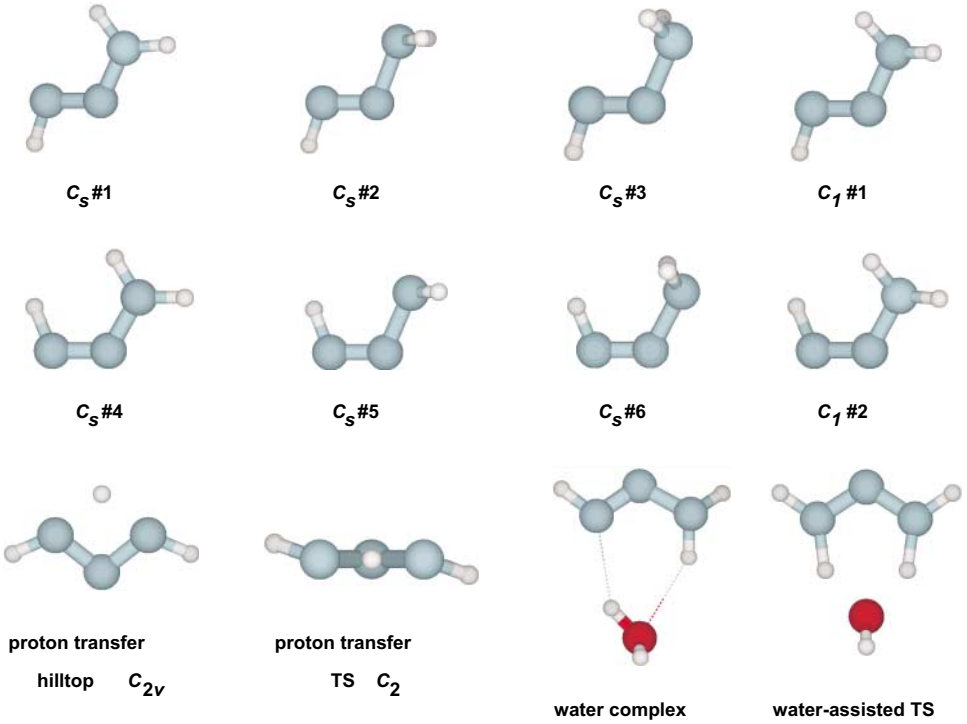

Fig. 2. Structures of triaziridine and azimine.

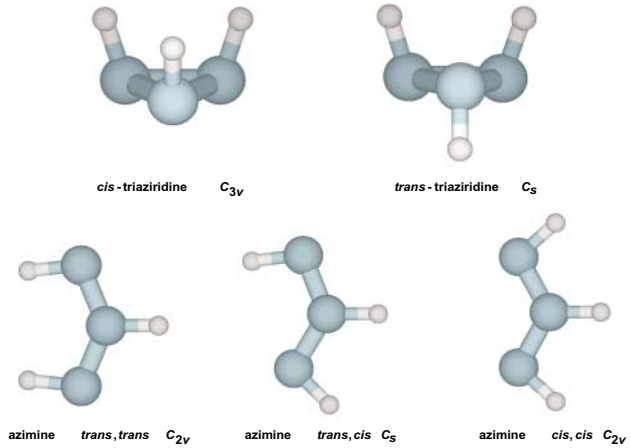

diffuse functions are added to the basis set, which give a better description of the lone pairs.

The C_s structures studied are assumed to be transition states for various transformations of the C_1 structures. The planar species #1 and #4 can be seen as transition states for the inversion of the sp^3 nitrogen of the C_1 structures to their mirror images, while the four remaining C_s structures, #2, #3, #5, and #6, can be seen as transition states for the transformations of the C_1 structures to their mirror images via rotation about the N–N single bond. These energies show that the inversion of the amine group is a more favorable reaction pathway than rotation since the barrier is lower. These barriers would be of importance in determining the high-resolution vibrational spectra because of hydrogen permutations and inversion doubling, especially with regard to tunnelling, and also to configurational stability for amines with chiral nitrogens.

Table 3. ZPE-corrected energies (kJ mol^{-1}) of azimines and triaziridines.

	Triaziridine		Azimine		
Level	*cis* C_{3v}	*trans* C_s	*tt* C_{2v}	*tc* C_s	*cc* C_{2v}
HF/STO-3G	150.64	90.90	220.43	230.57	265.96
HF/3-21G	267.92	200.27	158.99	168.01	214.27
HF/6-31G*	244.33	192.83	131.08	137.90	173.21
HF/6-31+G*	253.89	202.37	132.55	137.41	170.93
MP2/6-31G*	224.89	175.15	64.17	73.11	107.55
MP2/6-31+G*	238.25	187.80	67.81	73.75	105.22

Note: relative to C_1 *trans*-triazene.

It is of interest to compare the energies of triazene with that of other isomers, namely, triaziridine and azimine (see Fig. 2). We confirm the literature results (20) that the triazenes are more stable than the azimines, which, in turn, are more stable than the triaziridines (see Table 3).

Proton transfer via 1,3-hydrogen shift

Triazenes with an available proton on a nitrogen atom are able to undergo a proton transfer. Two possible structures of the transition state were studied. The first structure investigated possessed C_{2v} symmetry (see Fig. 1). This structure possessed two imaginary frequencies, indicating that it is not a true transition state. The first imaginary frequency was of irreducible representation B_2 and corresponded to the desired process, the proton transfer. The second imaginary frequency was of irreducible representation A_2 and corresponded to an out-of-plane amino hydrogen motion. To obtain the true transition state for the proton transfer, desymmetrization to a C_2 point group gave the structure shown in Fig. 1. This structure was coincident with the HF/3-21G and HF/6-31+G* representation and very close in energy to the HF/6-31G*

© 2002 NRC Canada

Fig. 3. Structures associated with methyltriazene.

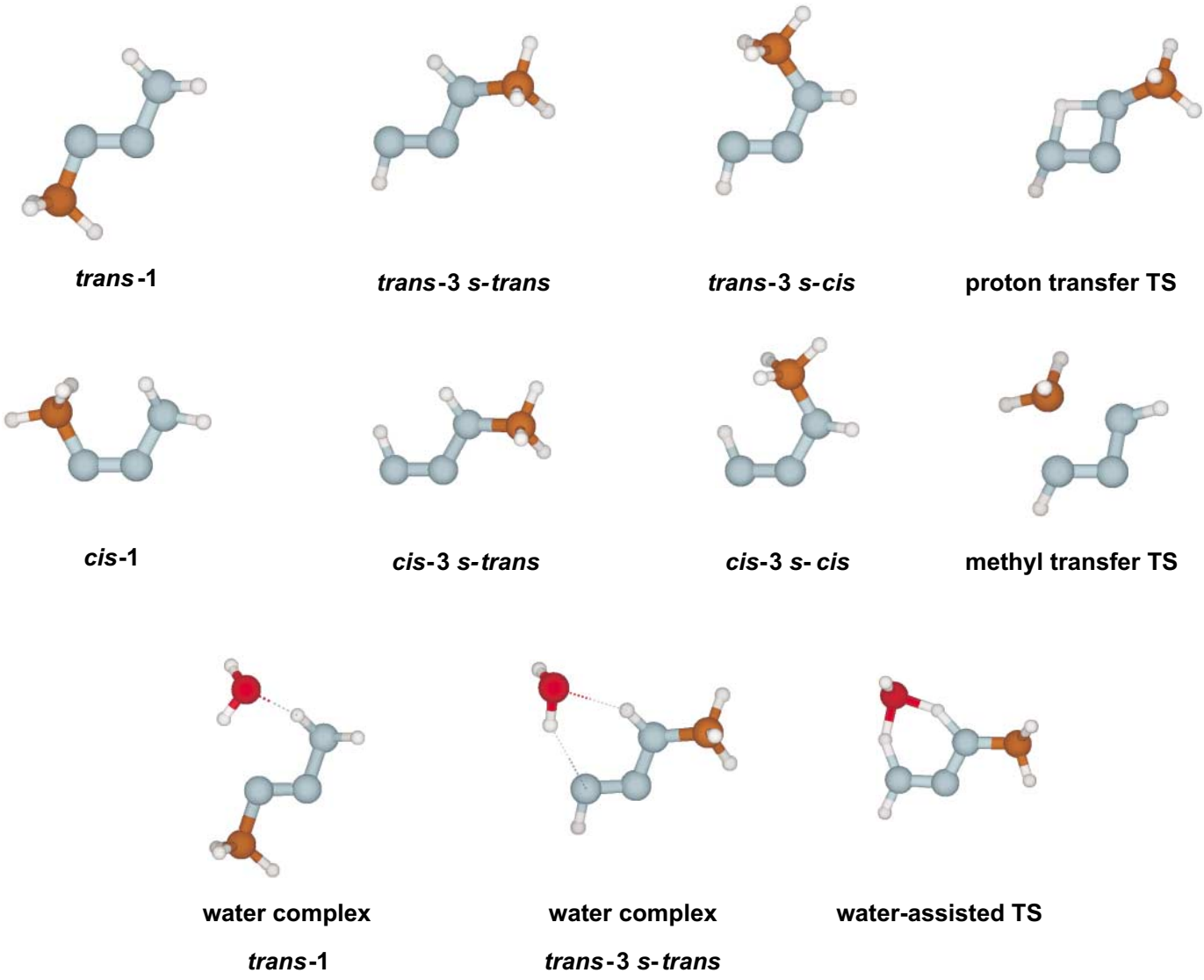

Table 4. ZPE-corrected activation barriers (kJ mol^{-1}) for proton transfer in *trans* C_1 structures with C_2 and C_{2v} transition states.

Level	C_2	C_{2v}
HF/STO-3G	241.31	242.88
HF/3-21G		207.34
HF/6-31G*	227.71	227.09
HF/6-31+G*		230.84
MP2/6-31G*	161.39	161.66
MP2/6-31+G*	173.11	164.81

Table 5. ZPE-corrected hydration energies and activation barriers (kJ mol^{-1}) for water-assisted proton transfer in *trans*–triazene.

Level	Hydration energy	Activation barrier
HF/STO-3G	–21.22	69.21
HF/3-21G	–52.59	64.99
HF/6-31G*	–21.19	136.64
HF/6-31+G*	–17.00	136.10
MP2/6-31G*	–35.84	74.85
MP2/6-31+G*	–29.24	76.81

representation of the C_{2v} structure. This structure possessed only one imaginary frequency of irreducible representation *B*, corresponding to the proton transfer. The activation barriers for this process for the C_{2v} and C_2 structures are shown in Table 4. This barrier is high, indicating that this process is not favored at room temperature in the gas phase.

In aqueous solution, water may facilitate the proton transfer by catalyzing the reaction. Triazene itself is stabilized by hydration to the effect of about 40 kJ mol^{-1}. Two different transition structures were tried with C_s and C_{2v} symmetry. At the lower levels, the C_{2v} structure was higher in energy than the C_s structure, and possessed two imaginary frequencies, the smaller of the two corresponding to an out-of-plane motion of the hydrogen to give the C_s structure. The C_{2v} structure was not investigated further.

The activation barriers decrease by a factor of two (see Table 5). To understand the reason for this, we consider the structures of hydrated triazene and the associated transition

© 2002 NRC Canada

Table 6. ZPE-corrected relative energies (kJ mol^{-1}) of methyltriazenes.

	trans[a]			*cis*		
		3-Methyl			3-Methyl[b]	
Level	1-Methyl	*s-trans*	*s-cis*	1-Methyl[a]	*s-trans*	*s-cis*
HF/STO-3G	0.00	14.07	17.33	27.95	4.57	14.69
HF/3-21G	0.00	12.37	8.48	33.47	2.63	4.58
HF/6-31G*	0.00	10.00	10.24	38.62	–2.01	4.07
HF/6-31+G*	0.00	11.33	10.88	43.04	0.18	5.18
MP2/6-31G*	0.00	11.67	7.90	27.16	5.91	8.37
MP2/6-31+G*	0.00	13.57	8.80	33.03	8.95	10.37

[a]Relative to *trans*-1-methyltriazene.
[b]Relative to *cis* 1-methyltriazene.

state for a water-assisted proton transfer in the *trans*-C_1 structure, as presented in Fig. 1. The N-N-N angle (MP2/6-31+G*) in *trans*-triazene is 112.4° (cf. experimental values in related compounds of 112.8–114.6° (28, 29)), while in the transition state it is 101.6°, resulting in a bending of 11.2°. In the hydrated forms, the corresponding angles are 115.0° and 113.3°, a change of only 1.7°. It is clear that a large part of the activation energy is removed if the triazene unit does not have to deform much to reach the transition state (27, 30).

Methyltriazenes

Conformation and isomerism

A methyl group can be located at either the 1- or the 3-position of either *cis*- or *trans*-triazene to give a total of four isomers. The results on triazene itself suggest that the amino group has a preferred orientation with respect to the double bond, and this does not change upon methyl substitution. Also, the *trans* structures remain more stable than the corresponding *cis* structures by approximately the same amount as in triazene itself. For *cis*- and *trans*-3-methyltriazene, the methyl group can take one of two possible minimum-energy conformations about the N–N bond corresponding to substitution of the two different hydrogens. These possibilities are enumerated in Fig. 3 and their relative energies are given in Table 6.

The orientation of the methyl group in *trans*-1-methyltriazene can be rationalized using hyperconjugation arguments. The methyl group has a moderately strong σ_{CH} donor and a moderately weak acceptor σ^*_{CH}. The N=N fragment has a strong lone-pair donor, a moderate σ_{NN} donor, a strong π^*_{NN} acceptor, and a moderate σ^*_{NN} acceptor. The strong lone pair donates into the σ^*_{CH}. In the *cis* isomer, the same interactions are possible, but the opposite orientation is preferred, suggesting that the hypercongugation preference is overridden by a steric interaction between one of the amine hydrogens and the methyl hydrogen in the less preferred conformation.

If we assume that the same interactions control the orientation about the N–N single bond as in triazene itself, we can then rationalize the stability of the conformers in the *trans* isomer by looking at the donation of the strong lone pair of the central nitrogen into either acceptor σ^*_{NH} or acceptor σ^*_{NC}. The latter should be the better acceptor, therefore the lone pair should be *trans* to the N–C bond, i.e., an *s-cis* conformation. In the *cis* structure, the steric interaction between the *cis* hydrogen and the methyl group cancels the hyperconjugation effect, causing the conformers to be closer in energy.

Table 7. ZPE-corrected energies (kJ mol^{-1}) of methyltriazene transition states.

Level	H TS[a]	Me TS[b]
HF/STO-3G	243.05	431.52
HF/3-21G	211.85	332.24
HF/6-31G*	232.46	349.86
HF/6-31+G*	236.10	343.34
MP2/6-31G*	159.61	284.18
MP2/6-31+G*	165.48	280.43

[a]Relative to *trans*-1-methyltriazene.
[b]Relative to *trans*-3-methyltriazene *s-cis*.

Proton and methyl transfer

trans-1-Methyltriazene can, in principle, undergo a 1,3-proton shift to give *trans*-3-methyltriazene in the *s-trans* conformation. Similarly, the *s-cis* conformer of 3-methyltriazene can undergo a degenerate 1,3-methyl shift. The transition state for these processes are shown in Fig. 3 and the barriers given in Table 7. There is no systematic difference between barriers to 1,3-proton shifting in triazene and in 1-methyltriazene. The barriers for methyl shifting are approximately 100 kJ mol^{-1} greater than those of the hydrogen shifting. It is clear that extremely high temperatures would be required to observe these processes in methyltriazene.

Again, water can catalyze the 1,3-hydrogen shift, as seen for triazene. The structures for water bound to *trans*-1-methyltriazene (*trans*-3-methyltriazene *s-trans*) and the 1,3-proton shift transition state are given in Fig. 3 and the relative energies are given in Table 8. The hydration energies of 1-methyltriazene are slightly less than those of triazene, by up to 3 kJ mol^{-1}. There are no systematic differences between the proton-shift barriers in triazene and in methyltriazene. The difference in energy between 1-methyltriazene and 3-methyltriazene, *s-trans* conformer, narrows somewhat as water is added, which suggests that the latter is better stabilized by water (by 2–4 kJ mol^{-1}).

Dimethyltriazenes

For dimethyltriazene, the methyl groups may be attached in either a 1,3- or 3,3- fashion. For the 1,3-dimethyl form, the methyl attached to the 3 position can be in one of two conformations, *s-cis* or *s-trans*. Along with the *cis–trans*

© 2002 NRC Canada

Fig. 4. Structures associated with dimethyltriazene.

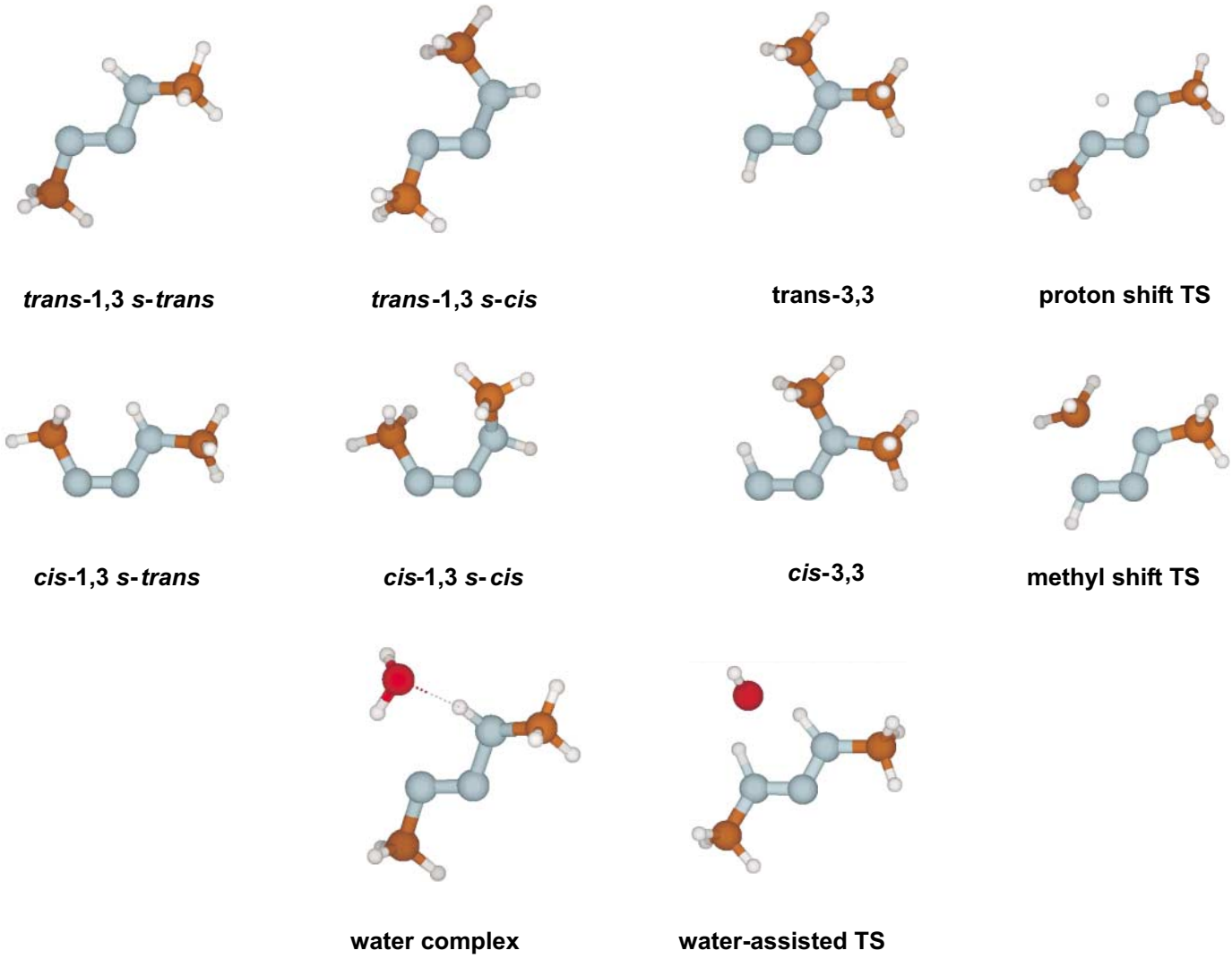

Table 8. ZPE-corrected energies (kJ mol^{-1}) of hydrated methyltriazene structures.

Level	1-Methyl[a]	3-Methyl *s-trans*[b]	TS[b]
HF/STO-3G	–19.15	12.58	76.61
HF/3-21G	–50.96	9.79	69.73
HF/6-31G*	–18.10	6.23	136.86
HF/6-31+G*	–14.88	8.35	135.18
MP2/6-31G*	–35.74	9.45	76.71
MP2/6-31+G*	–28.40	10.40	77.98

[a]Relative to separated fragments.
[b]Relative to hydrated *trans*-1-methyltriazene.

isomers about the double bond, this gives a total of four distinct possibilities for 1,3-dimethyltriazene. There are also two additional possibilities, *cis*- and *trans*-3,3-dimethyltriazene, for a total of six minimum-energy geometries, as shown in Fig. 4. The relative energies are presented in Table 9.

If the difference between the *trans s-cis* and *s-trans* conformers are compared between 3-methyltriazene and 1,3-dimethyltriazene, the same general trends are noted to within about 2 kJ mol^{-1}. Methyl substitution does seem to stabilize the *s-cis* conformation more (or destabilizes the *s-trans* conformation more) than the other isomer by 1.2–1.8 kJ mol^{-1}. The difference in energy between the *cis* and *trans* isomers of 1,3-dimethyltriazene parallels the difference for 1-methyltriazene. The main difference is the high energy of *cis*-1,3-dimethyltriazene *s-cis*. This is clearly due to a steric interaction between the methyl groups. This interaction is so strong that the amine moiety rotates significantly out of the position it normally would have in triazene, breaking some of the amine lone-pair antibonding-π hypercongugation.

Proton and methyl transfer

trans-1,3-Dimethyltriazene in the *s-trans* conformation can undergo a degenerate proton shift. The same molecule in the *s-cis* conformation can also undergo a methyl shift to form *trans*-3,3-dimethyltriazene. The structures of these transition states are shown in Fig. 4 and the activation energies for these processes are given in Table 10. The barriers for proton migration are all about 5–13 kJ mol^{-1} lower than methyltriazene. For methyl migration, at the HF level, the barriers are higher by between 5–10 kJ mol^{-1}, but at the

© 2002 NRC Canada

Table 9. ZPE-corrected relative energies (kJ mol^{-1}) of dimethyltriazenes.

	trans[a]			*cis*[b]		
	1,3-Dimethyl			1,3-Dimethyl		
Level	*s-trans*	*s-cis*	3,3-Dimethyl	*s-trans*[a]	*s-cis*	3,3-Dimethyl
HF/STO-3G	0.00	3.86	17.04	29.79	9.57	15.02
HF/3-21G	0.00	–2.10	6.65	33.28	14.08	3.45
HF/6-31G*	0.00	1.34	10.10	38.61	24.65	5.42
HF/6-31+G*	0.00	0.96	10.44	43.25	23.86	5.49
MP2/6-31G*	0.00	–2.73	0.57	27.40	24.94	2.57
MP2/6-31+G*	0.00	–3.10	0.49	32.66	23.25	3.18

[a]Relative to *trans*-1,3-dimethyltriazene *s-trans*.
[b]Relative to *cis*-1,3-dimethyltriazene *s-trans*, unless otherwise specified.

Fig. 5. Structures associated with trimethyltriazene.

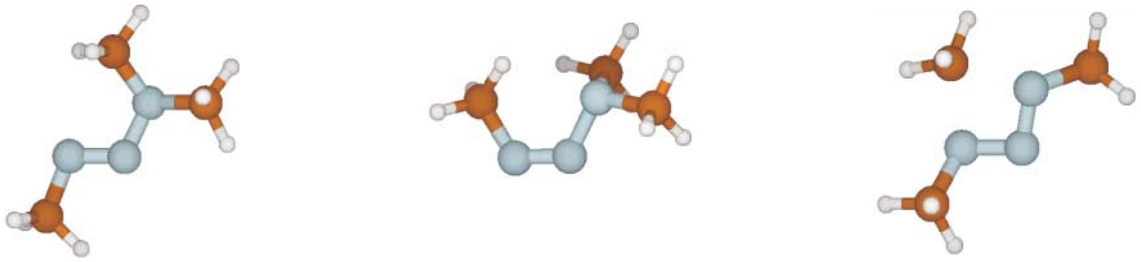

***trans*-1,3,3** ***cis*-1,3,3** **methyl shift TS**

Table 10. ZPE-corrected energies (kJ mol^{-1}) of dimethyltriazene transition states.

Level	H TS[a]	Me TS[b]
HF/STO-3G	230.66	431.00
HF/3-21G	205.53	337.24
HF/6-31G*	226.88	357.27
HF/6-31+G*	231.61	352.37
MP2/6-31G*	146.24	278.84
MP2/6-31+G*	151.81	275.49

[a]Relative to *trans*-1,3-dimethyltriazene *s-trans*.
[b]Relative to *trans*-1,3-methyltriazene *s-cis*.

Table 11. ZPE-corrected energies (kJ mol^{-1}) of hydrated dimethyltriazene structures.

Level	1,3-Dimethyl *s-trans*[a]	TS[b]
HF/STO-3G	–18.62	71.45
HF/3-21G	–50.96	65.15
HF/6-31G*	–19.97	133.08
HF/6-31+G*	–15.46	127.74
MP2/6-31G*	–37.49	69.27
MP2/6-31+G*	–30.37	69.26

[a]Relative to separated fragments.
[b]Relative to 1,3-dimethyl *s-trans*.

MP2 level, are lower by about 5 kJ mol^{-1}, compared with methyltriazene.

The water-catalyzed reactants and transition states are shown in Fig. 4, and the hydration energies and activation barriers to proton shift are given in Table 11. The hydration energies are very similar to those of *trans*-1-methyltriazene; however, the barriers to proton shift are lower than those of methyltriazene by 5–10 kJ mol^{-1}, a trend mirrored by the uncatalyzed reaction.

Table 12. ZPE-corrected energies (kJ mol^{-1}) of trimethyltriazene structures relative to *trans*-trimethyltriazene.

Level	*cis*	TS
HF/STO-3G	35.71	416.88
HF/3-21G	45.23	335.52
HF/6-31G*	60.96	355.98
HF/6-31+G*	64.27	353.50
MP2/6-31G*	56.04	270.39
MP2/6-31+G*	57.93	267.38

1,3,3-Trimethyltriazene

The only isomers of 1,3,3-trimethyltriazene are the *cis* and *trans* forms, whose structures are given in Fig. 5 and whose relative energies are given in Table 12. One very clear point to be made here is the difference between the *cis* and *trans* structures. This energy difference is much greater than that of triazene, by 20–30 kJ mol^{-1}. The steric interaction between the methyls is very significant in the *cis* form, causing one of the methyl groups to rotate severely out of its optimal hyperconjugation arrangement. The difference in energy between the *cis* and *trans* structures may be predicted to within about 3 kJ mol^{-1} by looking solely at the dimethyl case, i.e., by taking the difference in energy between the

© 2002 NRC Canada

cis-1,3-dimethyltriazene *s-cis* and *trans*-1,3-dimethyltriazene *s-cis* forms. Another way to predict these values is to add the value for *cis–trans* isomerization of triazene to that of rotating the amine moiety of *cis*-triazene to structure C_s #5. This method underestimates the value by 10–15 kJ mol^{-1}.

The barriers to methyl migration are also shown in Table 12. In general, the methyl barriers are lower than in dimethyltriazene. This effect is much more pronounced at the MP2 level.

Conclusions

The most stable form of triazene is the *trans* isomer. In the absence of steric interactions, the amine adopts a non-symmetric arrangement, which places the lone pair parallel to the π system. The barrier to inversion at the amine is much lower than the barrier to rotation about the nitrogen–nitrogen single bond. The barrier to proton transfer is high, but is cut in half when a water molecule mediates the transfer. The most stable form of methyltriazene is *trans*-1-methyltriazene. Methyl substitution does not affect systematically the proton shift barriers. The barrier to the 1,3-methyl shift is much higher than that of the 1,3-hydrogen shift. Similar conclusions regarding the hydrogen and methyl shift were reached for di- and trimethyltriazene.

Acknowledgments

The authors thank the Department of Astronomy and Physics, Saint Mary's University (AP-SMU), for providing access to computing facilities, in particular, to Cygnus, a 10-processor Sun server, purchased with assistance from the Canada Foundation for Innovation, Sun Microsystems, the Atlantic Canada Opportunities Agency, and SMU. CP also acknowledges the technical assistance of David Lane (AP-SMU). JG acknowledges support from the Student Employment Experience Program (Summer 2000), SMU. KV and CP acknowledge the support of the Natural Sciences and Engineering Research Council of Canada (NSERC).

References

1. K. Vaughan. *In* The chemistry of antitumour agents. *Edited by* D.E.V. Wilman. Blackie, Glasgow. 1990. Chap. 5. pp. 159–186.
2. E. Carvalho, A.P. Francisco, J. Iley, and E. Rosa. Bioorg. Med. Chem. **8**, 1719 (2000). This paper is Part 17 of a series entitled *Triazene Drug Metabolites*.
3. M. Ludwig and M. Kabickova. Coll. Czech. Chem. Commun. **61**, 355 (1996) and refs. therein.
4. K.O. Christe, W.W. Wilson, J.A. Sheehy, and J.A. Boatz. Angew. Chem. Int. Ed. **38**, 2004 (1999).
5. A. Vij, W.W. Wilson, V. Vij, F.S. Tham, J.A. Sheehy, and K.O. Christe. J. Am. Chem. Soc. **123**, 6308 (2001).
6. G.A. Olah, G.K.S. Prakash, and G. Rasul. J. Am. Chem. Soc. **123**, 3308 (2001).
7. Q.S. Li and L.J. Wang. J. Phys. Chem. A, **105**, 1203 (2001).
8. Q.S. Li and L.J. Wang. J. Phys. Chem. A, **105**, 1979 (2001).
9. S. Fau and R.J. Bartlett. J. Phys. Chem. A, **105**, 4096 (2001).
10. I. Morao, M.A. Vincent, and I.H. Hillier. J. Phys. Chem. A, **105**, 10689 (2001).
11. S.N. Foner and R.L. Hudson. J. Chem. Phys. **29**, 442 (1958).
12. S.N. Foner and R.L. Hudson. Adv. Chem. **36**, 34 (1962).
13. E. Hayon and M. Simic. J. Am. Chem. Soc. **94**, 42 (1972).
14. J.W. Sutherland. J. Phys. Chem. **83**, 789 (1979).
15. Y. Kim, J.W. Gilje, and K. Seff. J. Am. Chem. Soc. **99**, 7057 (1977).
16. W.A. Lathan, L. Radom, P.C. Hariharan, W.J. Hehre, and J.A. Pople. Topics Curr. Chem. **40**, 1 (1973).
17. J.M. Howell and L.J. Kirschenbaum. J. Am. Chem. Soc. **98**, 877 (1976).
18. M.-T. Nguyen, J. Kaneti, L. Hoesch, and A.S. Dreiding. Helv. Chim. Acta, **67**, 1918 (1984).
19. M.-T. Nguyen and L. Hoesch. Helv. Chim. Acta, **69**, 1627 (1986).
20. D.H. Magers, E.A. Salter, R.J. Bartlett, C. Salter, B.A. Hess, Jr., and L.J. Schaad. J. Am. Chem. Soc. **110**, 3435 (1988).
21. A.A. Korkin. Int. J. Quant. Chem. **38**, 245 (1990).
22. A.M. Schmiedekamp, R.H. Smith, Jr., and C.J. Michejda. J. Org. Chem. **53**, 3433 (1988).
23. A.M. Schmiedekamp, I.A. Topol, S.K. Burt, H. Razafinjanahary, H. Chermette, T. Pfaltzgraff, and C.J. Michejda. J. Comput. Chem. **15**, 875 (1994).
24. Gaussian 98. Revision A.9. M.J. Frisch, G.W. Trucks, H.B. Schlegel, G.E. Scuseria, M.A. Robb, J.R. Cheeseman, V.G. Zakrzewski, J.A. Montgomery, Jr., R.E. Stratmann, J.C. Burant, S. Dapprich, J.M. Millam, A.D. Daniels, K.N. Kudin, M.C. Strain, O. Farkas, J. Tomasi, V. Barone, M. Cossi, R. Cammi, B. Mennucci, C. Pomelli, C. Adamo, S. Clifford, J. Ochterski, G.A. Petersson, P.Y. Ayala, Q. Cui, K. Morokuma, D.K. Malick, A.D. Rabuck, K. Raghavachari, J.B. Foresman, J. Cioslowski, J.V. Ortiz, A.G. Baboul, B.B. Stefanov, G. Liu, A. Liashenko, P. Piskorz, I. Komaromi, R. Gomperts, R.L. Martin, D.J. Fox, T. Keith, M.A. Al-Laham, C.Y. Peng, A. Nanayakkara, M. Challacombe, P.M.W. Gill, B. Johnson, W. Chen, M.W. Wong, J.L. Andres, C. Gonzalez, M. Head-Gordon, E.S. Replogle, and J.A. Pople. Gaussian, Inc., Pittsburgh PA. 1999.
25. C-F 6-31G: W.J. Hehre, R. Ditchfield, and J.A. Pople. J. Chem. Phys. **56**, 2257 (1972); H, C-F polarization functions: P.C. Hariharan and J.A. Pople. Theor. Chim. Acta (Berlin), **28**, 213 (1973).
26. H, Li-F diffuse: T. Clark, J. Chandrasekhar, G.W. Spitznagel, and P.V.R. Schleyer. J. Comput. Chem. **4**, 294 (1983).
27. For water-catalyzed 1,2-shifts in methanol radical cation, see: J.W. Gauld, H. Audier, J. Fossey, and L. Radom. J. Am. Chem. Soc. **118**, 6299 (1996).
28. K. Biradha, M.B. Peori, K. Vaughan, and M.J. Zaworotko. J. Chem. Cryst. **29**, 145 (1999).
29. K. Biradha, H. Jenkins, M.B. Peori, K. Vaughan, and M.J. Zaworotko. J. Chem. Cryst. **29**, 1037 (1999).
30. R.A. Poirier, D. Yu, and P.R. Surjan. Can. J. Chem. **69**, 1589 (1991).

© 2002 NRC Canada

Experimental and theoretical study of the photochemical and thermal decomposition of maleic and dichloromaleic anhydrides

A. Ionescu, N. Piétri, M. Hillebrand, M. Monnier, and J.P. Aycard

Abstract: The photochemical and thermal behavior of maleic anhydride **1a** and dichloromaleic anhydride **1b**, in cryogenic matrix were investigated by means of FT-IR spectroscopy. The ketenylcarbenes represent the key intermediate in the decomposition processes of the anhydrides, even if they were not observed experimentally. The yields of the different products depend on the thermal or photochemical reaction conditions. The main photochemical products obtained from **1a** were cyclopropenone and acetylene, whereas the major products from **1b** were dichlorocyclopropenone and dichloroacetylene, along with small quantities of dichloropropadienone. The thermal reaction leads to dichloropropadienone, CO, and CO_2. MO calculations performed at the HF/6–31G*//HF/6–31G* level support the experimental mechanisms.

Key words: photolysis, thermolysis, ab initio calculations, cryogenic matrix, ketenylcarbenes.

Résumé : Le comportement photochimique et thermique de l'anhydride maléique **1a** et dichloromaléique **1b**, piégées en matrices cryogéniques est suivi par spectroscopie IRTF. Les intermédiaires clés dans le processus de décomposition des anhydrides sont des céténylcarbènes qui ne sont pas observés expérimentalement. La proportion des différents produits formés dépend des conditions de réaction. Les produits majoritaires obtenus photochimiquement à partir de l'anhydride maléique **1a** sont la cyclopropénone et l'acétylène tandis que l'anhydride dichloromaléique **1b** produit également une faible quantité de dichloropropadiénone. La décomposition thermique de l'anhydride dichloromaléique entraîne la formation de dichloropropadiénone, CO et CO_2. Les états de transitions des différentes réactions ont été modélisés en HF/6–31G*//HF/6–31G*.

Mots clés : photolyse, thermolyse, calculs ab initio, matrices cryogéniques, cétènes-carbenes.

Introduction

For many years our laboratory has been interested in the identification of highly reactive intermediate species produced by photochemical processes in cryogenic matrices (1). Attention was paid to the chemistry and reactivity of some conjugated carbenes, such as the ketenyl (2) and allenyl carbenes (3). Both carbenes can undergo several reactions, including ring closure, hydrogen or chlorine migration, and (or) CO elimination (ketenylcarbenes), which are the precursors of stable compounds. The presence of mono- or disubstituted ketenylcarbenes was postulated in the thermal and photochemical decomposition reactions of some cyclobutenediones and substituted maleic anhydride (4–9).

In our previous study (2) on the matrix photochemical decomposition of 3,4-dichloro-1,2-cyclobutenedione, both dichlorocyclopropenone (1896 cm^{-1}) and dichloropropadienone (2200 and 2260 cm^{-1}) were identified by FT-IR spectroscopy. A kinetic survey of the time evolution of the reaction reveals a ratio of about 13:1 for the respective formation rate constants — cyclopropenone is the major product. Under continuous irradiation, both compounds decomposed to dichloroacetylene (2232, 990, and 846 cm^{-1}). The mechanism of the reaction assumed the presence of the *syn*- and *anti*-dichloroketenylcarbenes, but attempts to identify them have failed.

In the case of difluoromaleic anhydride (R, R′ = F), Brahms and Dailey (4) reported that pyrolysis leads to difluoropropadienone, whereas photochemical decomposition predominantly gives difluorocyclopropenone. In contrast with this behaviour, the pyrolysis of the fluoromaleic anhydride (R = H, R′ = F) yields fluoroacetylene (7). For the two fluoromaleic anhydrides, irradiation initially produces cyclopropenones and, with time, produces the corresponding alkynes. In both cases, a ketenylcarbene was postulated as an intermediate, but only in the matrix photolysis of the fluoromaleic anhydride (7) was evidence found to support the presence of the fluoro–ketenylcarbene. The carbene was characterized by the IR bands at 2168, 1321, and 1102 cm^{-1}, the first value being the most intense.

Received 23 July 2001. Published on the NRC Research Press Web site at http://canjchem.nrc.ca on 17 April 2002.

A. Ionescu and M. Hillebrand. Department of Physical Chemistry, University of Bucharest, Bdul. Regina Elisabeta RO-7034, Romania.
N. Piétri,[1] M. Monnier, and J.P. Aycard. UMR CNRS 6633, Physique des Interactions Ioniques et Moléculaires, Equipe Spectrométrie et Dynamique Moléculaire, Université de Provence, Case 252, Centre de St. Jérôme, 13397 Marseille cedex 20, France.

[1]Corresponding author (e-mail: thalie@piimsdm8.univ-mrs.fr).

 DOI: 10.1139/V02-038 © 2002 NRC Canada

Fig. 1. Evolution of the FT-IR spectra of maleic anhydride **1a** isolated in an argon matrix at 10K during different irradiation times. (*a*) Spectrum after deposition t = 0 min; (*b*) t = 152 min; (*c*) t = 2800 min.

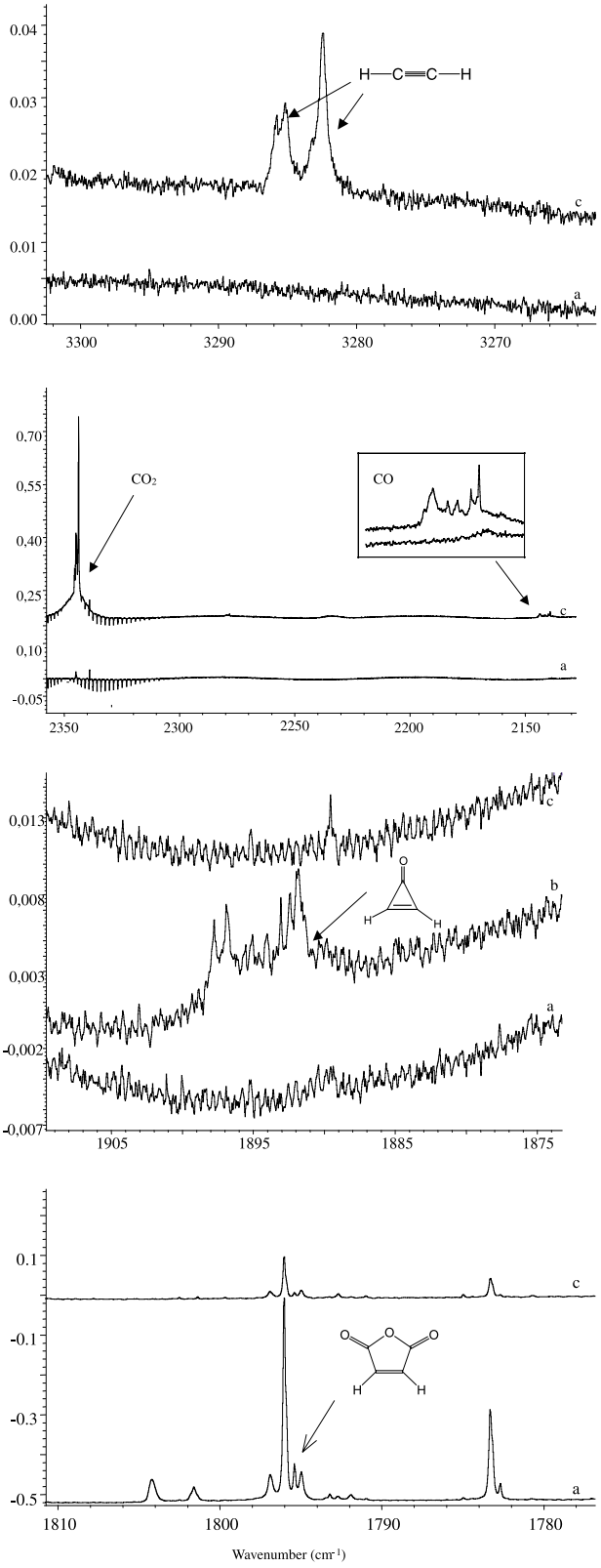

Fig. 2. Evolution of the FT-IR spectra of dichloromaleic anhydride **1b** isolated in an argon matrix at 10 K during different irradiation times. (*a*) Spectrum after deposition, t = 0 min; (*b*) t = 35 min; (*c*) t = 568 min.

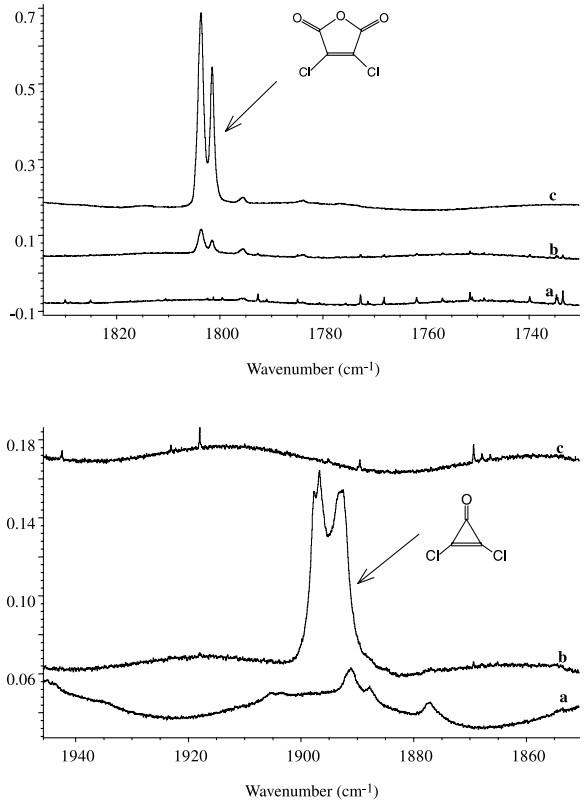

Taking into account the results of Dailey and co-workers (4, 7), it seems that the photolysis and thermolysis of maleic and dichloromaleic anhydrides could be a convenient method to confirm the presence and the role of the ketenylcarbenes in the reaction mechanism.

An extensive theoretical study on the formation of ketenylcarbenes starting from bisketenes, and of their reactivity in subsequent reactions of ring closure and further decarbonylation, was done by Tidwell and co-workers (10). In this study, they outlined the role of the substituents on the relative stability of the ketenes and the cyclopropenones.

In the present study, we report experimental and theoretical results on the photochemical and thermal decomposition of unsubstituted **1a** and dichloro derivative **1b** to provide more information on the different possible reaction pathways. In addition, ab initio MO calculations were performed to explain the chemical pathways.

Experimental

Dichloromaleic and maleic anhydride, supplied by Aldrich, were used after purification by vacuum sublimation.

Matrix-isolation experiments

The matrices were obtained by spraying anhydride–argon mixtures (1:750 and 1:360) onto a gold-copper plate cooled to 20 K in a closed-cycle helium refrigerator. The IR spectra were recorded at 10 K by reflectance with a Nicolet Series II

© 2002 NRC Canada

Scheme 1.

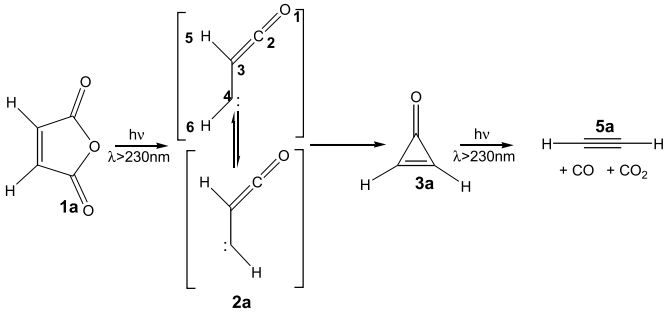

750 FT-IR in the 4000–400 cm^{-1} spectral range with a resolution of 0.12 cm^{-1}. The UV spectra were recorded in hexane and in the 200–600 nm range on an Unicam UV4 spectrometer. The spectrum of maleic anhydride shows an absorption band at 224 nm. In the case of the dichloromaleic anhydride, two absorption bands were observed at λ = 214 and 269 nm.

Irradiation techniques

Irradiation was carried out using an Osram 200 W high-pressure mercury lamp equipped with a quartz envelope. The broad band was filtered at λ > 230 nm. The light intensity was the same in all experiments and the irradiation area was wider than the surface used to record the spectrum.

MO calculations

Ab initio calculations at the HF/6–31G*//HF/6–31G* level were performed using the program Gamess (11). The critical points on the energy surface, minimum and saddle points, were characterized by the Hess matrix.

Ab initio calculations (on the lowest excited electronic states) using single-excitation CI (CI-single) at the 6–31G* level were also performed.

Results and discussion

Photolysis of maleic anhydride

The behavior of maleic anhydride (**1a**) with UV irradiation (λ > 230 nm) is shown in the IR spectra presented in Fig. 1. Broad-band irradiation (λ > 230 nm) of the matrix-isolated maleic anhydride causes a decrease in the absorption bands (the most intense located at ν = 1795.9 cm^{-1}) and the appearance of new bands in different areas of the spectrum.

The bands at 2139.1–2143.5 and 2343.8 cm^{-1} were assigned to CO and CO_2, respectively, while the intense bands at 3285.2 and 3282.4 cm^{-1} (due to the different matrix sites) and the less intense band at 742.3 cm^{-1} were assigned to acetylene (12).

Analysis of the spectra shows weak absorption bands at 1896.0–1891.9, 1628.7–1626.7, and 1035.8 cm^{-1}, which initially increase in intensity and then decrease after prolonged irradiation (Fig. 1). These bands, assigned to cyclopropenone, demonstrate the intermediary presence of this compound (13). The photochemical process is described in Scheme 1.

Table 1. Experimental vibrational frequencies of products obtained from photolysis of the dichloromaleic anhydride **1b**.

Observed frequencies (cm^{-1})		
Our work	Literature	Identification
2345.6		CO_2
2281.1–2279.1	2260[a]	**4b**
2142.7		CO
1896.7–1892.9	1896.3[a]	**3b**
1626.5	1629.9[a]	**3b**
1036.4	1029.9[a]	**3b**
993.1	993.6[a]	**5b**

Note: The main peak frequencies are indicated in italic font.
[a]See ref. 2.

Photolysis of dichloromaleic anhydride

The time evolution of the IR spectrum of the matrix-irradiated (λ > 230 nm) dichloromaleic anhydride (**1b**) is presented in Fig. 2, and the vibrational frequencies used for the identification of the products are listed in Table 1.

During irradiation, the bands of **1b** (1803.7, 1624.9, 1247.2, 1205.0, 1006.8, 934.1, 885.9, 727.8, 701.5 cm^{-1}) gradually diminish in intensity and completely disappear after 568 min.

With time, three new band systems with different intensities were observed in the 2400–2100 cm^{-1} region. The two most intense bands were assigned to CO (2142.7 cm^{-1}) and CO_2 (2345.6 cm^{-1}), while the band at 2281.1 cm^{-1}, of lower intensity, was assigned to dichloropropadienone (2).

The analysis of the whole range of frequencies revealed that a group of bands at 1895.7 (the most intense), 1626.5, and 1036.4 cm^{-1} have the same kinetic behavior: initially they increased in intensity and then they decreased in intensity. These bands were assigned to dichlorocyclopropenone (2), and correspond to the $\nu_{C=C}$, $\nu_{C=O}$, ν_{C-C} + β_{C-C-C} vibrations, respectively. With time, these bands disappeared and a band at 993.1 cm^{-1}, assigned to the most intense vibration mode of dichloroacetylene (2), gradually increased in intensity. The time evolution of the integrated absorbancies of the products is shown in Fig. 3. The experimental data are reported in Scheme 2. The relative intensities of the bands indicate that the major photochemical products are dichlorocyclopropenone and dichloroacetylene.

Thermolysis

The thermolysis of dichloromaleic anhydride at 450°C leads to the bands of the dichloropropadienone, CO, and CO_2 (Fig. 4). The reaction mechanism is also given in Scheme 2. The presence of CO in the matrix cage suggests formation of dichlorocyclopropenone. This compound, however, which is unstable in these temperature conditions, was not observed.

On heating maleic anhydride at 450°C, no spectral changes were observed. Apparently the thermal energy supplied was not sufficient for decomposition of the molecule.

Theoretical results

The experimental conditions used (irradiation of both compounds in their absorption-band regions) indicate that

© 2002 NRC Canada

Fig. 3. Evolution of integrated absorbance during photolysis of dichloromaleic anhydride **1b** at $\lambda > 230$ nm. The band at 2281.1 cm^{-1}, assigned to dichloropropadienone, is too small to follow its evolution.

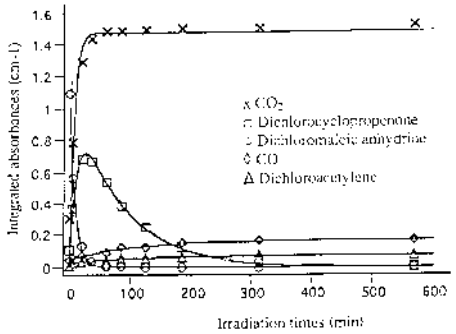

Scheme 2.

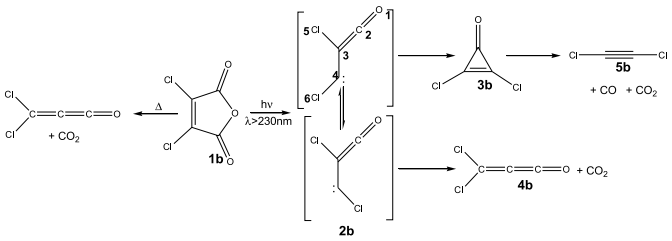

the first-excited singlet was populated. The energies of the Frank–Condon first-excited states depend on the number of included configurations and (or) the number of the required states. Their average value was approximately the energy of the experimental radiation, attesting that the singlet state was populated. We cannot tell if the energy furnished to the system is also sufficient to overcome the transition barriers in the excited state; we have considered that a radiationless deactivation process to the ground state could be taking place. Consequently, the reaction was based on the potential energy surface of the ground state.

Formation of ketenyl carbenes

The first step in the decomposition (either photochemical or thermal) of both anhydrides is CO_2 elimination, which yields ketenylcarbenes **2a** and **2b**. The localized transition states (TS1, Fig. 5) for this process are planar and have activation energies of 68.1 and 62.9 kcal mol^{-1} for **1a** and **1b**, respectively.

The differences between the lengths of the broken bonds in the anhydrides and the corresponding transition states for the CO_2 elimination are listed in Table 2. It may be seen that the bond breaking is asynchronous. In the transition state TS1, the increase of the O-C-O angle supports CO_2 formation.

After this first step, it is likely that an equilibrium mixture of *syn*- and *anti*-ketenylcarbene is present, as reported by Dailey (7).

Fig. 4. Spectrum of dichloromaleic anhydride **1b** after thermolysis at 450°C.

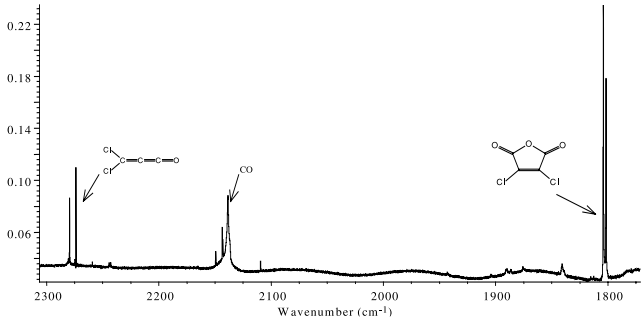

Fig. 5. Relevant optimized parameters (distances, Å; angles, deg) for the transition states of the CO_2 elimination from **1a** and **1b** (values in parentheses) and activation energies (kcal mol^{-1}) calculated with HF/ 6–31 G* basis set.

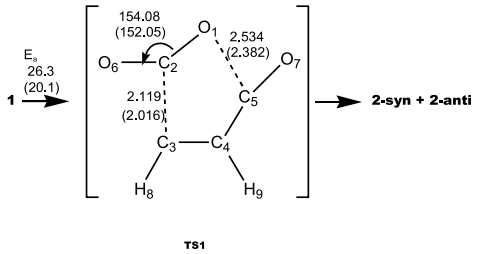

Reactivity of ketenyl carbenes

The previously discussed experimental data show that both ketenylcarbenes **2a** and **2b** undergo subsequent reactions leading to the corresponding cyclopropenone, propadienone, and alkyne.

The ketenylcarbenes **2a** and **2b** were optimized at the HF/6–31G*//HF/6–31G* level in the singlet and triplet states for both the *syn* and *anti* conformations (Table 3). For the unsubstituted ketenylcarbene, it was found that the ground state is a triplet for both conformers, whereas for dichloroketenylcarbenes, both conformers have singlet ground states, with the *syn* conformer more stable.

The optimized geometries reflect the features generally predicted for the singlet and triplet states of the *syn*-carbene conformers, i.e., an X-C-Y angle ($H_6C_4C_3$ (Scheme 1) and $Cl_6C_4C_3$ (Scheme 2)) of 109–115° for the singlet states and 130–131° for the triplet state. At the MP2 level, no minimum could be located for *syn*-**2a** or *syn*-**2b** due to spontaneous ring closure to cyclopropenone. The same results were observed by Tidwell and co-workers (10) for other *syn*-ketenylcarbenes.

Table 4 contains the compounds and transition-state energies modeled at the HF/6–31G* set level. The relevant geometric parameters of the transition states and the activation barriers for reactions of the *syn*- and *anti*-ketenylcarbenes are presented in Fig. 6.

Ring closure and cyclopropenone stabilities

With regard to the experimental data, the most important process (TS2) is the ring closure leading to the formation of cyclopropenones (**3**), which starts from the *syn*-

© 2002 NRC Canada

Table 2. Activation energies and relevant geometrical parameters (distances, angles) for the CO_2-elimination reaction from **1a** and **1b**.

	1a	TS1a	Δr	**1b**	TS1b	Δr
E (kcal mol^{-1})	0	68.1		0	62.9	
$r_{O\text{-}CO}$ (Å)	1.360	2.534	1.174	1.357	2.382	1.025
$r_{C\text{-}CO}$ (Å)	1.490	2.119	0.629	1.496	2.016	0.520
O-C-O (°)	123.34	154.08		124.02	152.05	

Table 3. Relative energies (kcal mol^{-1}) for the *syn* and *anti* conformers of ketenylcarbenes in the singlet and triplet states.

	^{1}*syn*	^{3}*syn*	^{1}*anti*	^{3}*anti*
2a	5.14	0.04	8.35	0.00
2b	0.00	7.90	6.86	7.03

ketenylcarbene conformers. The calculated energy barriers for this pathway are very low: 2.4 kcal mol^{-1} for *syn*-**2a** and 3.1 kcal mol^{-1} for the *syn*-**2b**.

The formation of acetylene in the decomposition reaction of **1a** and the accumulation of dichloroacetylene during prolonged irradiation of **1b** raises the question of the stability of the cyclopropenones. Two pathways to be considered are (*i*) concerted decarbonylation of the cyclopropenones leading directly to the alkynes; (*ii*) ring opening of cyclopropenones followed by decarbonylation of the *syn*-ketenylcarbenes, which are in competition with ring closure.

The optimized transition states (TS3) for the first process predicted high activation energies, 46.9 kcal mol^{-1} for **3a** and 53.9 kcal mol^{-1} for **3b**. These values indicate that there is a somewhat higher probability for the formation of the alkyne for unsubstituted carbene **2a** in comparison with substituted carbene **2b**. This is in agreement with the experimental findings.

For the second pathway, a larger activation energy was calculated for the ring opening of **3a** than for **3b**, 26.3 vs. 20.1 kcal mol^{-1}. (The transition state (TS2) is the same for the ring-closing and ring-opening reactions.) The transition states found for the CO elimination from the *syn*-ketenylcarbenes were identical (structure and energy) with those located in the previous path for the decarbonylation of cyclopropenones (TS3). This means that energetically both paths are equivalent.

Decarbonylation of the anti conformers

Assuming the *anti* conformers are present, they could be a source of the alkynes. The decarbonylation reaction starting from the *anti*-ketenylcarbenes and leading to the alkynes is characterized by the transition state TS4. The geometries of TS4 reflect the main features of the transition states for decarbonylation reactions in the ketenyl group, i.e., $r_{C\text{-}CO}$ values in the range 1.6–1.8 Å and C-C-O angles in the range 145–155°. There is a correlation between the activation energy and the length of the breaking C—CO bond in the TS4—the value in carbene **2a** ($r_{C\text{-}CO}$ = 1.680 Å (E_a = 17.6 kcal mol^{-1})) is lower than that found for Cl,Cl-disubstituted ketenylcarbene **2b** ($r_{C\text{-}CO}$ = 1.71 Å (E_a = 25.8 kcal mol^{-1})). The differences in the activation energies for the decarbonylation process indicate that the CO elimination is highly favored for **2a**.

Table 4. Total energies (Hartrees) of several compounds and transition states.

Maleic anhydride		Dichloromaleic anhydride	
Structure	Total energy	Structure	Total energy
^{1}***syn*-2a**	–189.49584	^{1}***syn*-2b**	–1107.29974
^{3}***syn*-2a**	–189.50397	^{3}***syn*-2b**	–1107.28714
^{1}***anti*-2a**	–189.49072	^{1}***anti*-2b**	–1107.28881
^{3}***anti*-2a**	–189.50404	^{3}***anti*-2b**	–11077.28852
TS2a	–189.49196	**TS2b**	1107.29476
3a	–189.53397	**3b**	–1107.32690
TS3a	–189.45918	**TS3b**	–1107.24081
TS4a	–189.46254	**TS4b**	–1107.24757
TS5a (S = 0)	–189.39443	**TS5b** (S = 0)	–1107.18066
TS5a (S = 1)	–189.41132	**TS5b** (S = 1)	–1107.24574

1,2–Substituent migration

This reaction is specific to the *anti*-ketenylcarbenes and may explain the formation of propadienones. The high probability of 1,2-halogen or 1,2-hydrogen migration in carbene chemistry is due to the interaction of the electrons of the migrating group with the vacant carbene orbital (14). This occurs only in cases in which the electrons of the migrating atom are located in an orbital quasi-parallel with the carbene vacant orbital. In such cases the overlap of orbitals is ensured and the repulsive interaction avoided.

For the singlet state **2a** and **2b**, the double-occupied carbene orbital is located in the molecular plane, whereas the first vacant orbital is a π orbital with a high degree of localization on the carbene and the ketene C=O group. It is therefore unlikely that such a migration, which might explain the formation of propadienone, can be favored, even assuming a nonplanar transition state.

The calculated results reveal that the activation energies are indeed very high; the larger value predicted for **2b** is in agreement with the assumption that the electronic repulsion between the chlorine lone pair and the carbene in-plane electrons prevents the migration. The structure of TS5 and the activation energies are similar to those found by Dailey (7) for the 1,2-fluorine migration in the fluoro-ketenylcarbene (E_a = 50 kcal mol^{-1}). It is apparent that the nature of the substituent does not have a large influence on this process.

An enhanced possibility for a 1,2 migration reaction could be expected starting from the triplet state, for which the carbene in-plane orbital is only single occupied, implying a decrease in electronic repulsions. The results in Fig. 6 indicate that for triplet ^{3}***anti*-2a** the 1,2-migration remains a high-energy process. For the triplet chlorine-disubstituted ketenylcarbene (^{3}***anti*-2b**), however, the 1,2-migration in the triplet state is a possible pathway and, therefore, the presence

© 2002 NRC Canada

Fig. 6. Relevant optimized parameters (distances, Å; angles, deg) for the transition states of the reactions of the *syn*- and *anti*-ketenyl carbenes **2a** and **2b**, respectively, (values in parentheses) and activation energies (kcal mol^{-1}) calculated with HF6–31G* basis set (τ=$H_5C_3C_4H_6$).

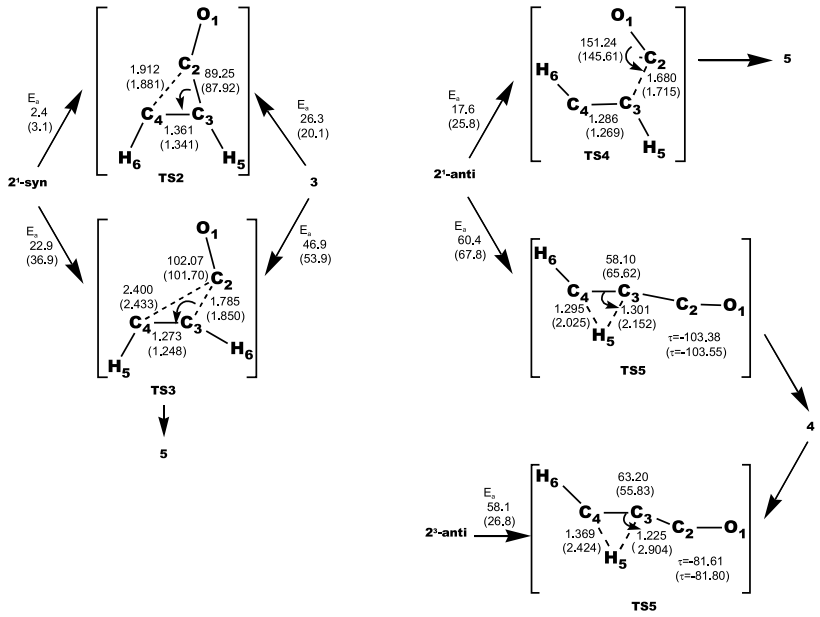

of small quantities of dichloropropadienone can be explained.

Summary

During the photolysis of maleic anhydride, only cyclopropenone, acetylene, CO, and CO_2 are observed as products. The transition-state structure calculations are consistent with these results. In fact, the cyclization process is spontaneous (2.4 kcal mol^{-1}) from *syn*-ketenylcarbene. From the *anti*-ketenylcarbene, decarbonylation is easier (17.6 kcal mol^{-1}) than the 1,2 migration process (63.5 kcal mol^{-1}). These results explain why the propadienone was not experimentally observed.

Photochemically, matrix-isolated dichloromaleic anhydride **1b** is converted to a mixture of *anti*- and *syn*-ketenylcarbene. The *syn* conformer undergoes rapid ring closure to dichlorocyclopropenone, while for the *anti* isomer there is competition between two possible pathways with similar activation barriers (25–26 kcal mol^{-1}) if we consider the 1,2-migration in the triplet state. The presence of small quantities of dichloropropadienone and dichloroacetylene can, therefore, be explained. The formation of the latter could also be produced from the *syn*-ketenylcarbene via dichlorocyclopropenone, a pathway which is calculated to have a lower barrier (37 kcal mol^{-1}).

The reaction mechanism is the same for the thermolysis and photolysis of dichloromaleic anhydride. The predicted facile ring opening to *syn*-ketenylcarbene (20.1 kcal mol^{-1}) explains the failure to isolate dichlorocyclopropenone in the matrix when **1b** was pyrolyzed at 450°C. (Dichlorocyclopropenone is not stable under these conditions.) Although the IR absorption bands seem intense, it is difficult to determine the quantity of dichloropropadienone produced because we cannot compare the relative intensities between this compound and the dichloropropenone, since the latter is not observed.

Acknowledgment

Financial support from CNCSIS-Romania is kindly acknowledged.

References

1. (*a*) C. Bachmann, T.Y. N'Guessan, F. Debu, M. Monnier, J. Pourcin, J.P. Aycard, and H. Bodot. J. Am. Chem. Soc. **112**, 7488 (1990); (*b*) M. Monnier, A. Allouche, P. Verlaque, and J.P. Aycard. J. Phys. Chem. **99**, 5977 (1995); (*c*) J.P. Aycard, M. Hnach, H. Zineddine, T.Y. N'Guessan, and E. Volanschi. J. Chem. Res. **346**, 2068 (1995); (*d*) F. Risi, L. Pizzala, M. Carles, P. Verlaque, and J.P. Aycard. J. Org. Chem. **61**, 666 (1996); (*e*) N. Pietri, I. Tamburelli, J.P. Aycard, and T. Chiavassa. J. Mol. Struct. **416**, 187 (1997); (*f*) J.P. Aycard, S. Dembele, and H. Bodot. Spectros. Letters, **30**, 1325 (1997); (*g*) N. Pietri, M. Monnier, and J.P. Aycard. J. Org. Chem. **63**, 2462 (1998).
2. I. Mincu, M. Hillebrand, P. Verlaque, A. Allouche, M. Cossu, J.P. Aycard, and J. Pourcin. J. Phys. Chem. **100**, 16045 (1996).
3. J.P. Aycard, A. Allouche, M. Cossu, and M. Hillebrand. J. Phys. Chem. A, **103**, 9013 (1999).
4. J.C. Brahms and W.P. Dailey. J. Am. Chem. Soc. **111**, 8940 (1989).
5. J.C. Brahms, W.P. Dailey, K. Beran, and M.D. Harmony. J. Am. Chem. Soc. **114**, 115 (1992).
6. W.J. Middleton and W.H. Sharkey. J. Am. Chem. Soc. **81**, 803 (1959).
7. W.P. Dailey. J. Org. Chem. **60**, 6737 (1995).
8. E.V. Dehmlow. Tetrahedron Lett. 1271 (1972).
9. A.D. Allen, J. Ma, T.T. Tidwell, and D.C. Zhao. Acc. Chem. Res. **23**, 265 (1995).

© 2002 NRC Canada

10. K. Sung, De.-C. Fang, D. Glenn, and T.T. Tidwell. J. Chem. Soc. Perkin Trans. 2, 2073 (1998).
11. M.W. Schmidt, K.K. Baldridge, J.A. Boatz, S.T. Elbert, M.S. Gordon, J.J. Jensen, S. Koseki, N. Matsunaga, K.A. Nguyen, S. Su, T.L. Windus, M. Dupuis, and J.A. Montgomery. J. Comput. Chem. **14**, 1347 (1993).
12. (*a*) A.A. Engdahl and B. Nelander. Chem. Phys. Letters, **100**, 129 (1983); (*b*) M.D. Newton and N.R. Kestner. Chem. Phys. Letters, **94**, 198 (1983).
13. R.C. Benson, W.H. Flygare, M. Oda, and R. Breslow. J. Am. Chem. Soc. **95**, 2772 (1973).
14. (*a*) M.T.H. Liu. Acc. Chem. Res. **27**, 287 (1994); (*b*) A.E. Keating, M.A. Garcia-Garibay, and K.N. Houk. J. Am. Chem. Soc. **119**, 10805 (1997); (*c*) A.E. Keating, M.A. Garcia-Garibay, and K.N. Houk. J. Phys. Chem. A, **102**, 8467 (1998); (*d*) M.T.H. Liu and R. Bonneau. J. Am. Chem. Soc. **118**, 8098 (1996).

© 2002 NRC Canada

Excess molar enthalpies of mixtures of methyl derivatives of polyethylene glycol with 1-alkanol at 298.15 K and 101.3 kPa

M.E.F. de Ruiz Holgado, J. Fernandez, M.I. Paz Andrade, and E.L. Arancibia

Abstract: Excess molar enthalpies (H^E) of the binary mixtures containing tetraethylene glycol dimethyl ether (TEGDME) or polyethylene glycol 350 monomethyl ether with a 1-alkanol (1-propanol, 1-butanol, or 1-pentanol) at 298.15 K and atmospheric pressure were measured using a Calvet microcalorimeter. All the H^E experimental values were positive and increase as the 1-alkanol length increases. The results are discussed qualitatively in terms of molecular interactions. The UNIFAC and DISQUAC group contribution models have been used to compare the predicted and the experimental values.

Key words: excess enthalpy, 1-alkanol, polyether, binary system.

Résumé : On présente les enthalpies molaires d'excès, H^E, des mélanges binaires de l'éther diméthylique du tétraéthylèneglycol ou de l'éther monométhylique du polyéthylèneglycol 350 avec un alcan-1-ol (propan-1-ol, butan-1-ol ou pentan-1-ol), à 298,15 K, à pression atmosphérique et mesurées à l'aide du microcalorimètre Calvet. Les valeurs de H^E de chacun des mélanges sont toutes positives et elles augmentent avec une augmentation de la longueur de la chaîne des alcanoles. On discute les résultats en fonction des interactions moléculaires. On a utilisé les modèles de contribution de groupes UNIFAC et DISQUAC pour comparer les résultats théoriques et expérimentaux.

Mots clés : enthalpie en excès, alcan-1-ol, polyéther, système binaire.

Introduction

In the last few years, interest in the thermophysical properties of polyethers and polyglycols with alkanols has increased. In the case of mixtures with methanol, these studies were undertaken to characterize new absorbent–refrigeration pairs, which could improve cycle performance (1, 2). Furthermore, mixtures containing ethers (-O- group) and alcohols (-OH group) are interesting because they are used as gasoline additives for their octane-enhancing and pollution-reducing properties (3).

In this work, excess enthalpies of tetraethylene glycol dimethyl ether (TEGDME) or polyethylene glycol 350 monomethyl ether (PEGMME) with an 1-alkanol (1-propanol, 1-butanol, or 1-pentanol) were determined to analyze the molecular interactions in the mixing process. The experimental results obtained for these mixtures were used to test the predictions of UNIFAC and DISQUAC models. For UNIFAC, we have used the Tassios et al. version, which uses the parameters of Dang and Tassios (4), the Larsen et al. version, which uses their parameters (5), and the Gmehling et al. version (6), which uses the parameters published in ref. 7. The parameters for the DISQUAC model (8) were determined by Delcros et al. (9). For mixtures containing PEGMME, we did not applied the DISQUAC model because not all of the required interaction parameters were available.

Received 30 November 2001. Published on the NRC Research Press Web site at http://canjchem.nrc.ca on 24 April 2002.

M.E.F. de Ruiz Holgado,[1] J. Fernandez, and M.I. Paz Andrade. Departamento de Física Aplicada, Universidad de Santiago, 15782 Santiago de Compostela, Spain.
E.L. Arancibia.[2] Departamento de Ingeniería Química, Facultad de Ciencias Exactas y Tecnología, Universidad Nacional de Tucumán. Avda. Independencia 1800- 4000 San Miguel de Tucumán – Argentina.

[1]Present address: Departamento de Ingeniería Química, Facultad de Ciencias Exactas y Tecnología, Universidad Nacional de Tucumán. Avda. Independencia 1800-4000 San Miguel de Tucumán – Argentina.
[2]Corresponding author (e-mail: earancibia@herrera.unt.edu.ar).

Experimental

1-Propanol, 1-butanol, and 1-pentanol were obtained from Merck (pro-analysis >99%) and TEGDME was obtained from Aldrich (99%). PEGMME (Sigma, 350 average molecular weight) was analyzed by gas chromatography and mass spectrometry, the mean molecular weight was 340.25 g mol^{-1}. All chemicals were used without further purification and were also kept over molecular sieves (4 Å). Density measurements (ρ) at 298.15 K and atmospheric pressure are given in Table 1, together with some values taken from the literature (Pal et al. (10), Carmona et al. (11), Reddick et al. (12), Shan and Asfour (13), and Aralaguppi et al. (14)).

Excess molar enthalpies (H^E) were determined with a standard Calvet microcalorimeter (1 μW precision) linked to a Philips voltmeter PM2525. The calorimeter is equipped with a batch-mixing cell with a small (<2%) vapour space. The microcalorimeter was calibrated electrically using a

 DOI: 10.1139/V02-044 © 2002 NRC Canada

Table 1. Comparison of experimental densities (ρ, g cm^{-3}) of pure liquids with literature values at 298.15 K.

Liquid	Expt.	Lit.
Tetraethylene glycol dimethyl ether (Aldrich >99%)	1.0059	1.0063,[a] 1.00653[b]
Polyethylene glycol 350 monomethyl ether (Sigma)	1.085	
1-Propanol (Merck p.a.)	0.7994	0.7996,[c] 0.7995,[d] 0.7995[e]
1-Butanol (Merck p.a.)	0.806	0.80575,[c] 0.8057,[d] 0.8059[e]
1-Pentanol (Merck p.a.)	0.8116	0.81080,[c] 0.8109,[d] 0.8107[e]

[a]Reference 10. [b]Reference 11. [c]Reference 12. [d]Reference 13. [e]Reference 14.

Table 2. Excess molar enthalpies (H^E, J mol^{-1}) in the TEGDME + 1-alkanol systems at 298.15 K and 101.3 kPa.

x_1	H^E	x_1	H^E	x_1	H^E
TEGDME (1) + 1-propanol (2)					
0.0178	17.6	0.1727	1230	0.7422	1071
0.0377	338	0.2468	1419	0.8328	746
0.0556	537	0.3455	1610	0.8903	507
0.0785	705	0.4245	1647	0.9135	405
0.1009	817	0.5718	1506		
0.1465	1093	0.6302	1392		
TEGDME (1) + 1-butanol (2)					
0.0475	492	0.304	1787	0.6371	1570
0.0988	922	0.3942	1918	0.7118	1344
0.1531	1252	0.4454	1925	0.7995	1011
0.2308	1583	0.5011	1860	0.886	610
0.2582	1678	0.559	1736	0.97	150
TEGDME (1) + 1-pentanol(2)					
0.0538	584	0.3312	1915	0.678	1584
0.1106	1070	0.3791	2015	0.7401	1371
0.1649	1383	0.4637	2012	0.8021	1079
0.1984	1573	0.5081	1983	0.8842	675
0.2296	1695	0.5348	1958		
0.2667	1792	0.6049	1811		

Table 3. Excess molar enthalpies (H^E, J mol^{-1}) in the PEGMME + 1-alkanol systems at 298.15 K and 101.3 kPa.

x_1	H^E	x_1	H^E	x_1	H^E
PEGMME (1) + 1-propanol (2)					
0,013	164	0.1921	1348	0.5802	1272
0.0257	315	0.2426	1483	0.5937	1249
0.0436	501	0.2781	1546	0.6511	1097
0.0696	724	0.3551	1547	0.7569	800
0.0805	811	0.4071	1545	0.7858	718
0.1308	1107	0.4231	1551	0.858	491
0.1498	1198	0.4959	1449	0.9084	314
PEGMME (1) + 1-butanol (2)					
0.0336	450	0.2648	1797	0.7284	1086
0.0403	523	0.3315	1859	0.8052	816
0.0882	950	0.4171	1840	0.9049	417
0.1399	1301	0.4931	1733	0.9544	190
0.173	1484	0.5899	1526		
PEGMME (1) + 1-pentanol (2)					
0.0184	276	0.2174	1795	0.6054	1731
0.035	494	0.3221	2044	0.6709	1500
0.052	683	0.3892	2083	0.7993	960
0.1025	1166	0.4608	2010	0.8781	588
0.1643	1555	0.5135	1938	0.9356	359

stabilized current source (EPJ-30, Setaram). More details of the apparatus and procedure have been described elsewhere (15).

Binary mixtures were prepared using a Mettler balance H51 (precision ±1 × 10^{-5} g) and air-tight stoppered bottles. The possible error in the mol fractions is estimated to be less than ±10^{-4}. Calibration of the calorimeter was performed using cyclohexane–hexane at 298.15 K. The results were compared with the literature (16) and agreed within ±1%.

Results and discussion

Tables 2 and 3 show the experimental values of H^E (J mol^{-1}) for the six binary mixtures studied in the present work. For each binary mixture, a Redlich–Kister function was used to correlate the experimental values.

$$[1] \qquad H^E = x_1 x_2 \sum_{i=1,\ldots n} A_i (2x_1 - 1)^{i-1}$$

The parameters A_i, and their standard deviation, obtained by a linear least-squares fitting procedure, are given in Table 4, together with the standard deviations (σ). The number of coefficients determined in each case were obtained using an *F*-test.

The root-mean-square deviations presented in this paper were computed using the following expression:

$$[2] \qquad \sigma = \left[\frac{\sum_{i=1}^{N} (H^E_{\text{exp}} - H^E_{\text{pred}})^2}{N - n} \right]^{1/2}$$

where N is the number of the experimental data points and n is the number of A_i coefficients.

Figures 1 and 2 show the measured values of H^E plotted against x_1, the mol fraction of glycol derivatives, together with the fitted curves. In Fig. 1, we have also included for comparison the excess enthalpies of TEGDME + methanol measured by Lopez et al. (17). The excess enthalpies of TEGDME + alkanol are positive, increasing with the length of the alkanol, and the $H^E(x)$ curves are slightly asymmetrical with a maximum in the polyether-poor region. The endothermicity of these mixtures shows that breaking the hydrogen bonds in the alkanol and the dipole–dipole interactions in the polyethers are energetically more important than the formation of hydrogen bonds between the unlike molecules.

© 2002 NRC Canada

Table 4. Coefficients A_i ($\sigma(A_i)$, J mol^{-1}) and $\sigma(H^E)$ (J mol^{-1}) standard deviations for the binary systems.

	1-Propanol	1-Butanol	1-Pentanol
TEGDME			
$A_1 \pm \sigma(A_i)$	6389 ± 38	7412 ± 32	7945 ± 25
$A_2 \pm \sigma(A_i)$	–1860 ± 140	–2330 ± 130	–1930 ± 100
$A_3 \pm \sigma(A_i)$	1230 ± 140	960 ± 150	1070 ± 120
$A_4 \pm \sigma(A_i)$	–1120 ± 290	–500 ± 330	1400 ± 280
$\sigma(H^E)$	17	18	14
PEGMME			
$A_1 \pm \sigma(A_i)$	5750 ± 20	6886 ± 36	7894 ± 33
$A_2 \pm \sigma(A_i)$	–3260 ± 69	–3650 ± 130	–3460 ± 120
$A_3 \pm \sigma(A_i)$	1220 ± 210	2070 ± 140	680 ± 350
$A_4 \pm \sigma(A_i)$	–1280 ± 170	–1060 ± 300	–1500 ± 260
$A_5 \pm \sigma(A_i)$	1580 ± 360	—	2050 ± 560
$\sigma(H^E)$	10	16	15

Figures 1 and 3 show that the excess enthalpies increase more from methanol to 1-propanol than from 1-propanol to 1-pentanol. This is in agreement with the H^E values of 2,5-dioxahexane and 3,6-dioxaoctane with alkanols (18–20). Excess volumes of polyether + alkanol mixtures present similar trends with the alkanol length, but for the shorter alkanols the excess volumes are negative because of the free-volume effect (11). Furthermore, if we compare our H^E results with those of the shorter glymes 2,5-dioxahexane (19) and 2,5,8-trioxaundecane (20) with alkanols, it can be concluded that the excess enthalpies increase as the number of OCH_2CH_2 groups increase.

Figure 2 shows that the excess enthalpies of PEGMME + alkanol systems are positive, increasing when the alcohol size increases. The $H^E(x)$ curves are quite asymmetrical with the maximum in the PEGMME-poor region. The breaking of the hydrogen bonds of both the alcohol and glycol derivatives, together with the formation of hydrogen bonds between the unlike molecules, is taking place in the mixing process. The endothermicity of these mixtures shows that the breaking of the hydrogen bonds is energetically more important that the formation of new hydrogen bonds, similar to the TEGDME mixtures.

In the application of the three versions of UNIFAC, there are three options for choosing the number and type of the different functional groups, because of the symmetry of the ether group (-O-). Thus, the types of molecules of TEGDME (CH_3O-$(CH_2$-$CH_2O)_4CH_3$) that can be considered are, option #1: $2CH_3O$, $5CH_2$, and $3CH_2O$. This option has been used by Delcros et al. (9) in the application of the Gmehling et al. version. Option #2: $1CH_3$, $4CH_2$, $4CH_2O$ and $1CH_3O$, in which the authors of the different versions of the UNIFAC model propose this option. Option #3: $2CH_3$, $3CH_2$, and $5CH_2O$, which was suggested by López et al. (17).

PEGMME 350 used in the present study is a commercial mixture of monomethyl polyethylene glycol ether (CH_3-$(OCH_2$-$CH_2)_n$OH with n = 5–9). Gas chromatography and mass spectrometry analysis yielded a molecular weight of 340.25 g mol^{-1} and pseudo n-value of 6.996. A value of n = 7.00 was assumed for the application of the group-contribution models, and we used option #1 ($1CH_3O$, $8CH_2$, $6CH_2O$, and 1OH) and option #2 ($1CH_3$, $7CH_2$, $7CH_2O$, and 1OH). Option #3 is not feasible because there is only one CH_3 group in the CH_3-$(OCH_2$-$CH_2)_7$OH molecule.

In Fig. 3, we have plotted the UNIFAC predictions with the different options for $H^E(x = 0.5)$ for TEGDME + 1-alkanol mixtures. The Larsen et al. version gives the poorest predictions (up to 85% of deviation for mixtures with methanol), while option #3 gives the best results. In the Tassios et al. version, the predictions for the longer alkanols can be considered good for options #2 and #3. In this version, however, methanol is not an independent group, and consequently, the predictions of Tassios et al. are poorest for

Fig. 1. H^E at 298.15 K and atmospheric pressure for TEGDME (1) + 1-alkanol (2) mixtures vs. x_1. Solid lines: results from the smoothing eq. [1] with the coefficients listed in Table 4. Experimental data: methanol (●) (14); 1-propanol (■); 1-butanol (▲); 1-pentanol (▼).

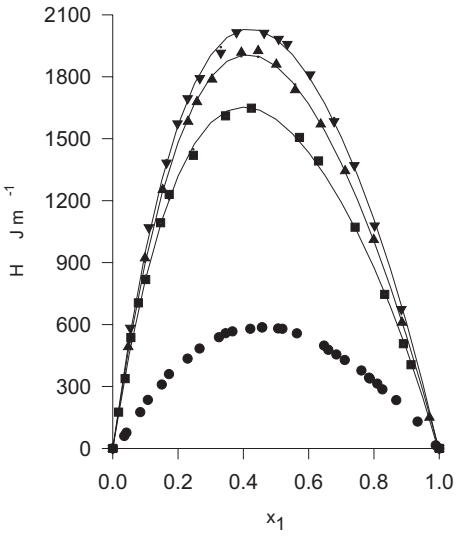

Fig. 2. H^E at 298.15 K and atmospheric pressure for PEGMME (1) + 1-alkanol (2) mixtures *vs.* x_1. Solid lines: results from the smoothing eq. [1] with the coefficients listed in Table 4. Experimental data: 1-propanol (■); 1-butanol (▲); 1-pentanol (▼).

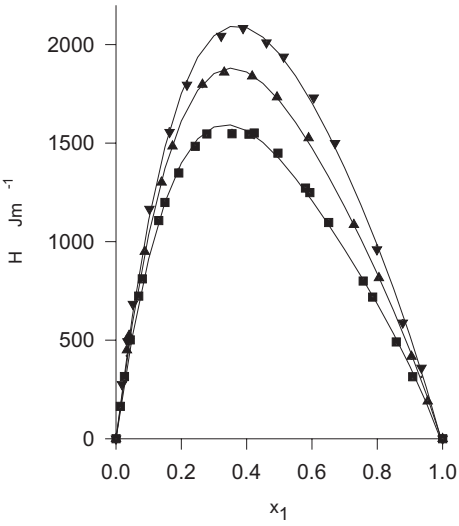

© 2002 NRC Canada

Fig. 3. Experimental and theoretical H^E (x = 0.5) at 298.15 K of the systems TEGDME + $C_nH_{2n+1}OH$ vs. n, the number of carbon atoms of the 1-alkanol. Experimental data: (○) DISQUAC model; (◆) UNIFAC model, version (*a*) Tassios et al., (*b*) Larsen et al., (*c*) Gmehling et al. Option #1 (■); #2 (▲); #3 (▼).

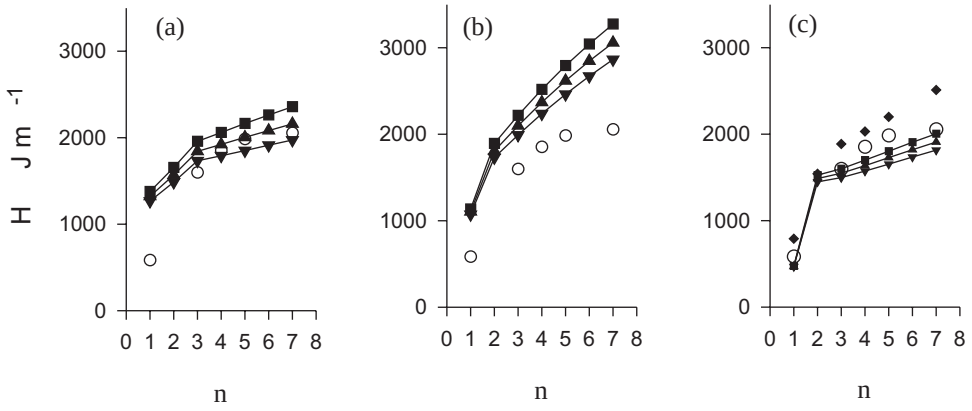

Fig. 4. Experimental and theoretical H^E (x = 0.5) at 298.15 K of the systems PEGMME + $C_nH_{2n+1}OH$ vs. n, the number of carbon atoms of the 1-alkanol. Experimental data: (○) UNIFAC model, version (*a*) Tassios et al., (*b*) Larsen et al., (*c*) Gmehling et al. Option #1 (■); #2 (▲).

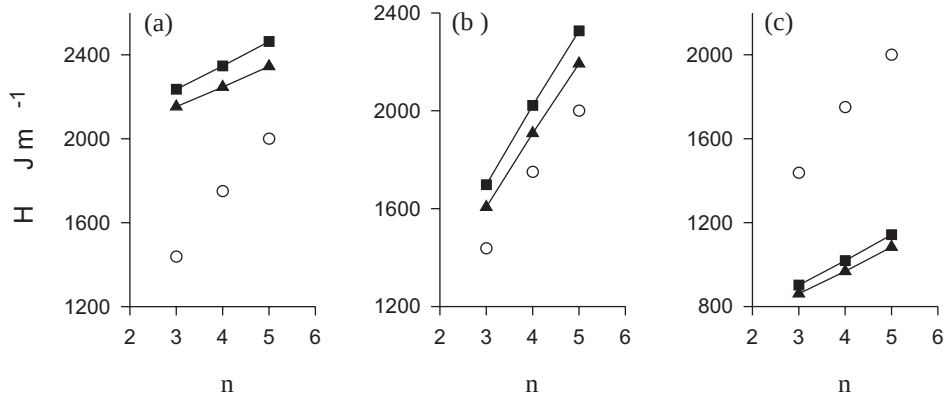

mixtures containing methanol. The Gmehling et al. version gives the best predictions because it correctly predicts both the trend of the excess enthalpies with the alkanol length and magnitude. The Gmehling et al. predictions, in contrast with the Tassios et al. and Larsen et al. versions, are quite independent of the options for choosing the type and number of groups. The symmetry of the $H^E(x)$ curves is well predicted with both the Gmehling et al. and Larsen et al. versions.

For the DISQUAC model, the parameters of González et al. (21) are used for alkanol–alkane interactions, while the parameters of Kehiaian et al. (22) are used for ether–alkane interactions and the parameters of Delcros et al. (9) are used for ether–alkanol interactions. Figure 3*c* shows that the DISQUAC model adequately reproduces the shape of the $H^E(x)$ curves with respect to the alkanol size. For the TEGDME + alkanol mixtures the global mean deviation of $H^E(x = 0.5)$ is around 19%.

Figures 4*a–c* shows the UNIFAC predictions for monomethyl polyethylene glycol ether + alkanol. Using the Larsen et al. version, the mean deviations for these mixtures are 10 and 17% for options #1 and #2, respectively. For the Tassios et al. version, the deviations are 38% for option #1 and 32% for option #2. The deviations using the Gmehling et al. versions are 41% for option #1 and 44% for option #2. Some of the interaction parameters needed to apply the DISQUAC model to this type of system are not available.

Conclusions

Data on H^E at 298.15 K and atmospheric pressure for TEGDME or polyethylene glycol 350 monomethyl ether + alkanols (from propanol to pentanol) are reported. Our results for H^E (x = 0.5) of TEGDME + alkanol follow a regular trend with those reported in the literature for mixtures with methanol and heptanol. In the comparison with the predictions with the UNIFAC model, the Gmehling version gives the best predictions for TEGDME + alkanol, whereas the Larsen version gives the best predictions for PEGMME + alkanol.

Acknowledgments

This work was partially financed by CIUNT. E.L.A. is member of CONICET. M.E.F.R.H. acknowledges the UNT fellowship to support her fellowship at Santiago de Compostela University.

© 2002 NRC Canada

References

1. D. Boer, M. Valles, and A. Coronas. Int. J. Refrig. **21**, 542 (1998).
2. M. Medrano, M. Bourouis, and A. Coronas. Appl. Energy, **68**, 173 (2001).
3. I. Hatzioannidis, E. Voutsas, E. Lois, and D.P. Tassios. J. Chem. Eng. Data, **43**, 386 (1998).
4. D. Dang and D. Tassios. Ind. Chem. Proc. Dev. **25**, 22 (1986).
5. B.L. Larsen, P. Rasmussen, and A. Fredenslund. Ind. Eng. Chem. Res. **26**, 2274 (1987).
6. U. Weidlich and J. Gmehling. Ind. Eng. Chem. Res. **26**, 1372 (1987).
7. J. Gmehling, J. Li, and M. Schiller. Ind. Eng. Chem. **32**, 178 (1993).
8. H.V. Kehiaian. Pure Appl. Chem. **57**, 15 (1985).
9. S. Delcros, J.R. Quint, J.-P.E. Grolier, and H.V. Kehiaian. Fluid Phase Equilib. **113**, 1 (1995).
10. A. Pal, G. Dass, and A. Kumar. J. Chem. Eng. Data, **44**, 2 (1999).
11. F.S. Carmona, I.J. Arroyo, I. Garcia de la Fuente, J.A. Gonzales, and J.C. Cobos. Can. J. Chem. **77**, 1608 (1999).
12. J.A. Riddick, W.B. Bunger, and T.K. Sakano. *In* Organic solvents. Physical properties and methods of purification. Wiley-Interscience, New York. 1986.
13. Z. Shan and A.-F.A. Asfour. J. Chem. Eng. Data, **44**, 118 (1999).
14. M.I. Aralaguppi, C.V. Jadar, and T.M. Aminabhavi. J. Chem. Eng. Data, **44**, 216 (1999).
15. M.I. Paz Andrade, E. Jiménez, and C. Hernández. Anal. Real. Soc. Esp. Fis. Quim. **68**, 33 (1972).
16. S.U. Gill and Y.J. Chen. Rev. Sci. Instrum. **43**, 774 (1972).
17. E.R. Lopez, J. García, A. Coronas, and J. Fernández. Fluid Phase Equilib. **133**, 229 (1997).
18. J. Cobos, M.A Villamañán, and C. Casanova. J. Chem. Thermodyn. **22**, 383 (1990).
19. M.A Villamañán, C. Casanova, A.H. Roux, and J.-P.E. Grolier. J. Chem. Thermodyn. **22**, 383 (1990).
20. M. Pintos and M.I. Paz Andrade. Int. Data. Ser. Sel. Data Mixtures Ser. A, **1**, 25 (1979).
21. J.A. González, I. García de la Fuente, J.C. Cobos, and C. Casanova. Ber. Bunsenges Phys. Chem. **95**, 1658 (1991).
22. H.V. Kehiaian, M.R. Tiné, L. Lepori, E. Matteoli, and B. Marongiu. Fluid Phase Equilib. **46**, 131 (1989).

© 2002 NRC Canada

Excess molar volumes and viscosities of binary mixtures of some polyethers with propylamine at 298.15 K

Amalendu Pal and Rakesh Kumar Bhardwaj

Abstract: Excess molar volumes (V^{E}_{m}) and dynamic viscosities (η) have been measured as a function of composition for binary liquid mixtures of propylamine with 2,5-dioxahexane, 2,5,8-trioxanonane, 2,5,8,11-tetraoxadodecane, 3,6,9-trioxaundecane, and 5,8,11-trioxapentadecane at 298.15 K. The excess volumes are positive over the entire range of composition for the systems propylamine + 2,5-dioxahexane, and + 3,6,9-trioxaundecane, negative for the systems propylamine + 2,5,8,11-tetraoxadodecane, and + 5,8,11-trioxapentadecane, and change sign from positive to negative for the remaining system propylamine + 2,5,8-trioxanonane. From the experimental data, deviations in the viscosity ($\Delta\ln\eta$) and excess energies of activation for viscous flow (ΔG^{*E}) have been derived. These values are positive for all mixtures with the exception of propylamine + 2,5-dioxahexane.

Key words : excess volume, viscosity, binary mixtures.

Résumé : On a mesuré les volumes molaires en excès (V^{E}_{m}) et les viscosités dynamiques (η) en fonction de la composition pour des mélanges liquides binaires de propylamine avec du 2,5-dioxahexane, du 2,5,8-trioxanonane, du 2,5,8,11-tétraoxadodécane, du 3,6,9-trioxoaundécane et du 5,8,11-trioxapentadécane, à 298,15 K. Les volumes en excès sont positifs sur toute la plage de compositions pour les systèmes propylamine + 2,5-dioxahexane et + 3,6,9-trioxoaundécane, ils sont négatifs pour les systèmes propylamine + 2,5,8,11-tétraoxadodécane et + 5,8,11-trioxapentadécane et ils changent de signe, de positif à négatif, pour le dernier système, celui de la propylamine + 2,5,8-trioxanonane. Utilisant les données expérimentales, on a dérivé les déviations dans la viscosité ($\Delta\ln\eta$) et dans les énergies d'activation en excès pour l'écoulement visqueux (ΔG^{*E}). Ces valeurs sont positives pour tous les mélanges, excepté celui de la propylamine + 2,5-dioxahexane.

Mots clés : volume en excès, viscosité, mélanges binaires.

[Traduit par la Rédaction]

Introduction

In recent years, we have been actively engaged in a systematic study of the thermodynamic, acoustic, and transport properties of some binary mixtures of polyethers with organic solvents (1–4), especially in terms of evaluation of various thermodynamic properties and functions that give a better understanding of the molecular interactions. Previously (5), we reported excess molar volumes and viscosities for binary mixtures of some alkoxyethanols with propylamine. From these results it was observed that there exist specific interactions between amine and alkoxyethanol, including the self association of both the amine and alkoxyethanol molecules, which influence the properties of the mixtures. As an extension of our studies and to understand the molecular interactions between amines and polyethers, here we report new experimental data for the excess molar volumes (V^{E}_{m}) and viscosities (η) of binary solvent mixtures containing 2,5-dioxahexane, 2,5,8-tetraoxanonane, 2,5,8,11-tetraoxadodecane, 3,6,9-trioxaundecane, and 5,8,11-trioxapentadecane with propylamine over the whole composition range at 298.15 K and atmospheric pressure. A survey of the literature reveals that binary mixtures of alkoxyethanols or amines with alkanol (6–11) and different amines with straight chain ethers (12) have mainly been studied. Recently, a few studies involving excess volumes and excess heat capacities of (polyethers + alkane or esters) (13–15), excess volumes and excess enthalpies of (alkanol + polyethers) (16–18) and excess volumes of (1–propanol, *n*-hexanol, or branched alkanols + polyethers) (19–21) have been reported. There is, however, no systematic study on the behavior of propylamine with polyethers.

Received 17 October 2001. Published on the NRC Research Press Web site at http://canjchem.nrc.ca on 8 May 2002.

A. Pal[1] and R.K. Bhardwaj.[2] Department of Chemistry, Kurukshetra University, Kurukshetra 136 119, India.

[1]Corresponding author (e-mail: search@vidya.kuk.ernet.in).
[2]Present address: Department of Chemistry, Dyal Singh College, Karnal 132 001, India.

Experimental

Materials

Propylamine, 3,6,9-trioxaundecane, and 5,8,11- trioxapentadecane were Merck–Schuchardt products with stated purities of 99, 98, and 98 mol%, respectively. 2,5-Dioxahexane, and 2,5,8-tetraoxanonane, Acros products with stated purities of 99 and 99 mol%, respectively, were dried and fractionally distilled (22, 23). 2,5,8,11-Tetraoxapentadecane

 DOI: 10.1139/V02-045 © 2002 NRC Canada

Table 1. Densities and viscosities of the pure components at 298.15 K.

	$\rho \times 10^{-3}$ (kg m^{-3})		η (mPa s)	
Component	Expt.	Lit.	Expt.	Lit.
Propylamine	0.7122	0.7121 (22)	0.356	0.353 (22)
2,5 Dioxahexane	0.8626	0.86262 (24) 0.86132 (25)	0.417	0.424 (25) 0.432 (26)
2,5,8-Trioxanonane	0.9391	0.93905 (27) 0.93873 (14) 0.93875 (19)	0.992	0.989 (22) 0.991 (28)
2,5,8,11-Tetraoxadodecane	0.9807	0.98067 (14) 0.98065 (19) 0.98058 (27)	1.960	1.960 (29)
3,6,9-Trioxaundecane	0.9035	0.90281 (19) 0.90390 (27) 0.9033 (30)	1.268	
5,8,11-Trioxapentadecane	0.8785	0.87830 (19)	2.160	

(Acros, 99 mol%) was used without further purification. Prior to measurements, however, all liquids were degassed and stored over with molecular sieves. The purities of the liquids were checked by measuring and comparing the densities and viscosities at 298.15 K with their corresponding literature values (24–30) as shown in Table 1. Densities (ρ) of pure solvents were measured with a bicapillary pycnometer. The pycnometer was calibrated at 298.15 K with doubly distilled water. The sensitivity of the pycnometer corresponded to a precision in density, 1×10^{-2} kg m^{-3}. The reproducibility of the density estimates was found to be within 1×10^{-1} kg m^{-3}. The mol fraction of each mixture was obtained with an uncertainty of 1×10^{-4} from the measured masses of the components. All masses were corrected for buoyancy.

The excess molar volumes were measured using a continuous-dilution dilatometer similar to that described by Dickinson et al. (31). The details pertaining to calibration, experimental set-up, and measuring procedure have been previously described (32). The measured excess molar volumes were reproducible to $\pm 0.003 \times 10^{-6}$ m^3 mol^{-1}. Each run covered just over half of the range of the ether mol fraction (x_1) so as to give an overlap between two runs.

Kinematic viscosities ν (= η/ρ) of the pure liquids and the mixtures were measured at 298.15 K with a calibrated Ubbelohde suspended-level viscometer. The detailed procedure has been previously reported (33, 34). The viscometer is filled with liquid or liquid mixtures, and its limbs are closed with Teflon caps, taking precautions to minimize evaporation losses. The flow-time measurements were made with an electronic stopwatch having a readability of ±0.01 s. Four- or five-flow times were averaged to evaluate the viscosity at each composition. The caps of the limbs are removed during the measurement of flow times. The measured kinematic viscosities were converted to dynamic viscosities (η) by multiplication with the density. The reproducibility of the viscosity was within ±0.003 mPa s. All measurements were carried out in a well-stirred water bath at a temperature controlled to ±0.01 K.

Results

Tables 2 and 3 give the experimental results of the excess molar volumes and viscosities at 298.15 K at various mol fractions. The plots of excess molar volumes ($V^{\mathrm{E}}_{\mathrm{m}}$) and viscosities (η) against the mol fraction of the polyether are given in Figs. 1 and 2. For compact and smooth representation of the results, the measured viscosities were fitted to a polynomial of type

$$[1] \qquad \eta = \sum_{i=0}^{n} a_i x_1^i$$

by the method of least squares with each point equally weighted. The values of coefficients a_i and standard deviations σ are listed in Table 4*a*.

From the measured values of the excess molar volumes, the densities of liquid mixtures were computed using the equation

$$[2] \qquad \rho = (x_1M_1 + x_2M_2)/(V^{\mathrm{E}}_{\mathrm{m}} + x_1V^*_1 + x_2V^*_2)$$

where M_1 and M_2 represent molar masses. The accuracy in ρ due to the estimated accuracy in excess molar volume ($\pm 0.003 \times 10^{-6}$ m^3 mol^{-1}) is 1×10^{-1} kg m^{-3}.

The deviation of the viscosity has been calculated from the following relationship (35, 36):

$$[3] \qquad \Delta \ln \eta = \ln \eta - (x_1 \ln \eta_1 + x_2 \ln \eta_2)$$

where x_1 and x_2 are the mol fractions, η is the dynamic viscosity of the mixture, and η_1 and η_2 are the viscosities of components 1 and 2, respectively.

The excess energies of activation for viscous flow were obtained with the following expression:

$$[4] \qquad \Delta G^{*\mathrm{E}} = RT\,[\ln(\eta V) - x_1 \ln(\eta_1 V^*_1) - x_2 \ln(\eta_2 V^*_2)]$$

where V, V^*_1, and V^*_2 are the molar volumes of the mixture and of the pure components 1 and 2, respectively. R and T are the gas constant and temperature, respectively. The

© 2002 NRC Canada

Table 2. Excess molar volumes (V^E_m, m^3 mol^{-1}) for polyether + propylamine systems at 298.15 K.

x_1	$V^E_m \times 10^6$	x_1	$V^E_m \times 10^6$	x_1	$V^E_m \times 10^6$
2,5-Dioxahexane (1) + propylamine (2)					
0.0086	0.012	0.3870	0.289	0.5887	0.319
0.0292	0.026	0.4035	0.294	0.6011	0.320
0.0657	0.059	0.4162	0.301	0.6151	0.316
0.1153	0.100	0.4426	0.304	0.6460	0.307
0.1601	0.139	0.4570	0.309	0.6507	0.304
0.2149	0.176	0.4755	0.310	0.6808	0.296
0.2474	0.199	0.4981	0.316	0.7406	0.259
0.2904	0.231	0.4985	0.314	0.7872	0.226
0.3328	0.261	0.5314	0.319	0.8330	0.192
0.3416	0.264	0.5393	0.317	0.8921	0.132
0.3653	0.280	0.5614	0.320	0.9308	0.087
0.3737	0.276	0.5725	0.319	0.9706	0.043
2,5,8-Trioxanonane (1) + propylamine (2)					
0.0071	0.003	0.2593	0.017	0.4409	0.002
0.0146	0.004	0.2688	0.018	0.4705	–0.002
0.0323	0.006	0.2904	0.016	0.4776	–0.003
0.0520	0.008	0.2982	0.016	0.5058	–0.009
0.0812	0.010	0.3170	0.016	0.5651	–0.016
0.1141	0.014	0.3352	0.015	0.6018	–0.020
0.1397	0.014	0.3570	0.013	0.6484	–0.028
0.1724	0.015	0.3693	0.012	0.7080	–0.035
0.2026	0.015	0.3865	0.011	0.7835	–0.037
0.2137	0.016	0.3951	0.008	0.8458	–0.036
0.2279	0.015	0.4122	0.006	0.9073	–0.027
0.2472	0.018	0.4260	0.002	0.9569	–0.016
2,5,8,11-Tetraoxadodecane (1) + propylamine (2)					
0.0073	–0.002	0.2647	–0.052	0.4608	–0.058
0.0326	–0.012	0.2922	–0.054	0.5223	–0.057
0.0625	–0.016	0.2957	–0.052	0.5935	–0.053
0.1367	–0.034	0.3275	–0.056	0.6598	–0.047
0.1775	–0.039	0.3290	–0.057	0.7590	–0.039
0.1913	–0.043	0.3614	–0.058	0.8244	–0.031
0.2169	–0.046	0.3822	–0.060	0.9055	–0.020
0.2459	–0.050	0.4069	–0.059	0.9783	–0.006
0.2536	–0.049	0.4205	–0.058		
3,6,9-Trioxaundecane (1) + propylamine (2)					
0.0079	0.002	0.2798	0.022	0.4692	0.031
0.0310	0.006	0.2918	0.024	0.4953	0.030
0.0511	0.010	0.3001	0.024	0.5560	0.032
0.1037	0.016	0.3272	0.025	0.6550	0.031
0.1446	0.018	0.3439	0.026	0.7715	0.028
0.2012	0.020	0.3663	0.026	0.8359	0.024
0.2101	0.016	0.4018	0.028	0.8952	0.015
0.2276	0.018	0.4113	0.028	0.9473	0.005
0.2504	0.023	0.4229	0.029		
0.2582	0.020	0.4514	0.030		
5,8,11-Trioxapentadecane (1) + propylamine (2)					
0.0098	–0.002	0.2589	–0.033	0.4805	–0.039
0.0407	–0.006	0.2702	–0.035	0.5520	–0.040
0.0839	–0.015	0.2847	–0.035	0.6220	–0.039
0.1298	–0.020	0.3153	–0.037	0.6608	–0.037
0.1683	–0.025	0.3182	–0.037	0.7210	–0.035
0.1798	–0.023	0.3310	–0.038	0.8293	–0.028
0.1939	–0.025	0.3627	–0.039	0.8904	–0.020
0.2117	–0.027	0.4127	–0.042	0.9451	–0.010
0.2251	–0.032	0.4176	–0.040		
0.2305	–0.031	0.4583	–0.042		

© 2002 NRC Canada

Table 3. Densities, viscosities, and excess energies of activation for viscous flow of polyether + propylamine systems at 298.15 K

x_1	$\rho \times 10^{-3}$ (kg m^{-3})	η (mPa s)	ΔG^{*E} (J mol^{-1})	x_1	$\rho \times 10^{-3}$ (kg m^{-3})	η (mPa s)	ΔG^{*E} (J mol^{-1})
2,5-Dioxahexane (1) + propylamine (2)							
0.0057	0.7132	0.356	1	0.4707	0.7889	0.378	–14
0.0115	0.7142	0.357	1	0.5131	0.7953	0.380	–18
0.0320	0.7178	0.358	5	0.5662	0.8031	0.381	–28
0.0568	0.7222	0.360	13	0.6099	0.8095	0.383	–33
0.0815	0.7264	0.362	19	0.6466	0.8148	0.386	–33
0.1075	0.7309	0.364	24	0.7017	0.8226	0.390	–31
0.1552	0.7389	0.368	34	0.7400	0.8280	0.392	–31
0.1871	0.7442	0.369	31	0.8022	0.8366	0.397	–32
0.2467	0.7539	0.372	31	0.8330	0.8408	0.399	–29
0.2882	0.7606	0.373	23	0.8785	0.8468	0.403	–28
0.3386	0.7686	0.374	15	0.9167	0.8519	0.408	–17
0.3526	0.7708	0.374	5	0.9436	0.8554	0.411	–9
0.3761	0.7744	0.374	–1	0.9811	0.8602	0.415	–5
0.4134	0.7802	0.375	–7				
2,5,8-Trioxanonane (1) + propylamine (2)							
0.0044	0.7139	0.359	13	03647	0.8252	0.613	506
0.0179	0.7192	0.368	45	0.3683	0.8261	0.615	508
0.0461	0.7298	0.385	95	0.4079	0.8355	0.644	524
0.0659	0.7370	0.400	145	0.4628	0.8478	0.679	516
0.0913	0.7459	0.417	192	0.5243	0.8608	0.721	507
0.1293	0.7587	0.443	260	0.5823	0.8723	0.757	478
0.1685	0.7712	0.472	327	0.6408	0.8833	0.796	447
0.1892	0.7775	0.487	355	0.7358	0.8998	0.840	325
0.2354	0.7911	0.518	404	0.7900	0.9086	0.873	272
0.2682	0.8003	0.541	431	0.8565	0.9189	0.908	184
0.2727	0.8015	0.544	437	0.8970	0.9248	0.935	147
0.3150	0.8127	0.575	471	0.9375	0.9306	0.955	83
0.3201	0.8140	0.579	476	0.9887	0.9376	0.985	15
2,5,8,11-Tetraoxadodecane (1) + propylamine (2)							
0.0076	0.7166	0.366	42	0.3623	0.8614	0.864	849
0.0166	0.7218	0.375	72	0.4044	0.8731	0.935	872
0.0296	0.7291	0.393	149	0.4583	0.8870	1.022	865
0.0659	0.7482	0.440	303	0.5139	0.9001	1.115	841
0.0954	0.7627	0.480	419	0.5761	0.9136	1.225	803
0.1298	0.7785	0.526	524	0.6483	0.9278	1.365	749
0.1596	0.7913	0.567	600	0.6867	0.9347	1.435	700
0.1909	0.8039	0.611	667	0.7450	0.9447	1.549	622
0.2265	0.8174	0.659	720	0.8308	0.9581	1.720	484
0.2351	0.8205	0.673	739	0.8787	0.9650	1.805	379
0.2622	0.8300	0.711	768	0.9203	0.9706	1.862	258
0.2681	0.8320	0.721	780	0.9618	0.9760	1.917	132
0.3073	0.8448	0.782	826				
3,6,9-Trioxaundecane (1) + propylamine (2)							
0.0050	0.7143	0.361	24	0.3686	0.8187	0.709	728
0.0106	0.7165	0.367	51	0.4053	0.8260	0.737	710
0.0197	0.7202	0.379	110	0.4615	0.8263	0.786	695
0.0413	0.7285	0.402	206	0.5261	0.8471	0.848	673
0.0623	0.7362	0.423	286	0.5564	0.8518	0.875	652
0.0897	0.7457	0.451	378	0.6025	0.8586	0.919	618
0.1329	0.7597	0.498	515	0.6358	0.8633	0.951	590
0.1762	0.7725	0.538	593	0.6749	0.8685	0.988	552
0.2138	0.7829	0.572	645	0.7261	0.8750	1.038	496
0.2434	0.7905	0.600	681	0.7852	0.8819	1.090	409
0.2446	0.7908	0.603	689	0.8437	0.8883	1.152	337
0.2849	0.8005	0.636	707	0.8917	0.8933	1.201	264

© 2002 NRC Canada

Table 3 (*Continued*)

x_1	$\rho \times 10^{-3}$ (kg m^{-3})	η (mPa s)	ΔG^{*E} (J mol^{-1})	x_1	$\rho \times 10^{-3}$ (kg m^{-3})	η (mPa s)	ΔG^{*E} (J mol^{-1})
0.2887	0.8014	0.640	710	0.9396	0.8979	1.235	159
0.3251	0.8096	0.672	726	0.9698	0.9008	1.248	73
5,8,11-Trioxapentadecane (1) + propylamine (2)							
0.0095	0.7169	0.375	107	0.3977	0.8229	1.129	1450
0.0288	0.7258	0.417	321	0.4621	0.8322	1.240	1391
0.0455	0.7330	0.450	470	0.5160	0.8390	1.330	1312
0.0845	0.7483	0.529	760	0.5979	0.8482	1.489	1194
0.1266	0.7627	0.622	1030	0.6482	0.8532	1.579	1090
0.1754	0.7771	0.719	1225	0.6986	0.8577	1.689	1001
0.2172	0.7879	0.806	1357	0.7471	0.8617	1.774	872
0.2531	0.7962	0.870	1408	0.7956	0.8655	1.869	748
0.2660	0.7990	0.904	1453	0.8618	0.8701	2.010	575
0.3172	0.8092	0.994	1479	0.9261	0.8742	2.093	327
0.3559	0.8161	1.055	1465	0.9641	0.8765	2.143	178

Fig. 1. Experimental excess molar volumes for propylamine (2) + 2,5-dioxahexane (1) (○); 2,5,8-trioxanonane (1) (Δ); 2,5,8,11-tetraoxadodecane (1) (□); 3,6,9-trioxundecane (1) (●); 5,8,11-trioxapentadecane (1) (⊗). Continuous curves were calculated from eq. [5].

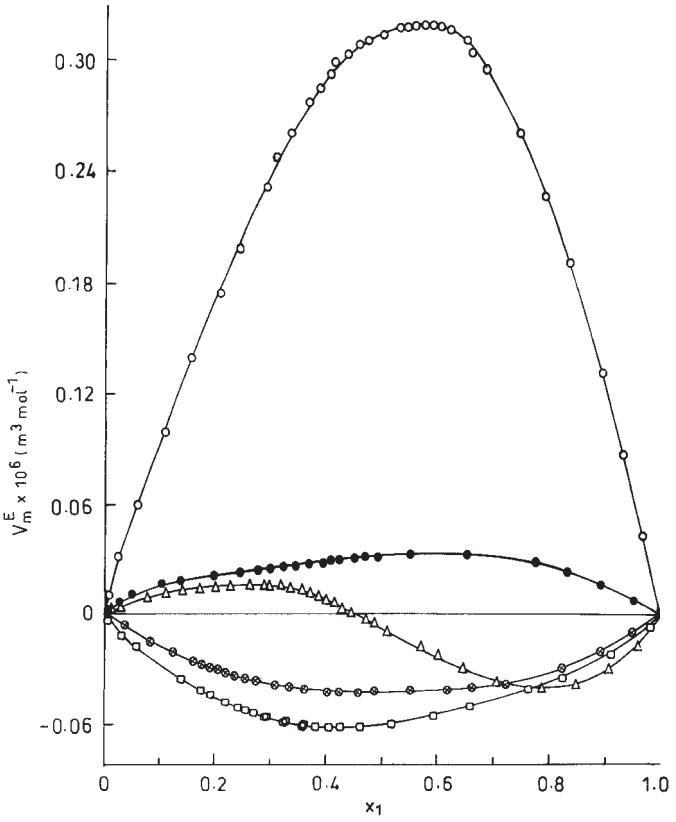

Fig. 2. Experimental viscosities for propylamine (2) + 2,5-dioxahexane (1) (○); 2,5,8-trioxanonane (1) (Δ); 2,5,8,11-tetraoxadodecane (1) (□); 3,6,9-trioxaundecane (1) (●); 5,8,11-trioxapentadecane (1) (⊗). Continuous curves were calculated from eq. [1].

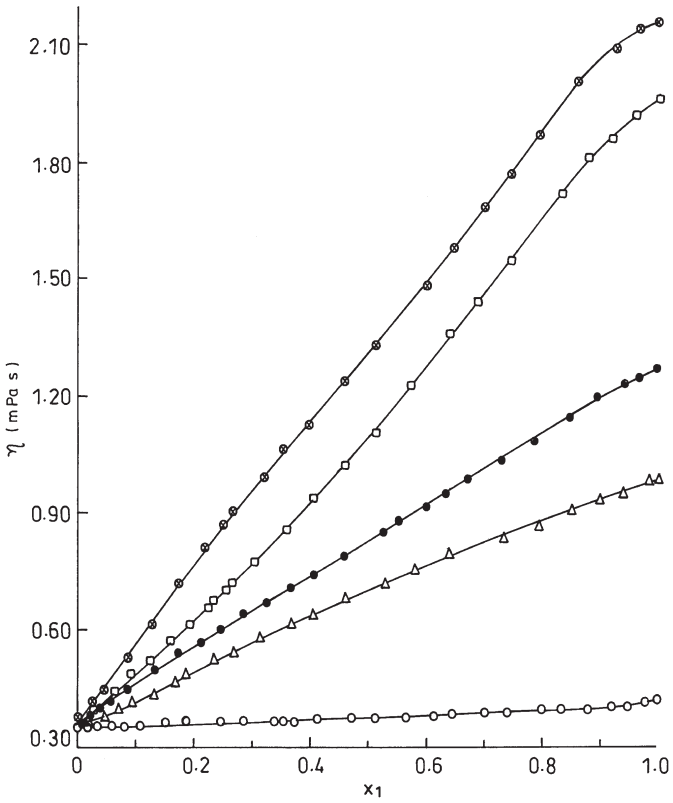

derived densities, viscosities, and excess energies of activation for viscous flow for the different binary mixtures at 298.15 K are given in Table 3.

The values of V_m^E, $\Delta \ln \eta$, and ΔG^{*E} for all mixtures were represented mathematically by the Redlich–Kister polynomial.

$$[5] \qquad Y(x) = x_1 x_2 \sum_{i=0}^{n} a_i (x_1 - x_2)^{i-1}$$

Values of the coefficients a_i and standard deviation σ are summarized in Table 4*b*. For all mixtures, $\sigma(V_m^E) \leq 0.003$, in accord with the precision attainable with the dilatometer

© 2002 NRC Canada

Table 4*a*. Coefficients a_i of eq. [1] for viscosity η (mPa s) and standard deviations σ

Propylamine (2) +	a_1	a_2	a_3	a_4	a_5	σ
2,5-Dioxhexane (1)	0.3560	0.0850	–0.1305	0.1082		0.001
2,5,8-Trioxanonane (1)	0.3574	0.5917	0.6318	–1.1192	0.5306	0.002
2,5,8,11-Tetraoxadodecane (1)	0.3507	1.4376	–0.8066	2.5938	–1.6026	0.005
3,6,9-Trioxaundecane (1)	0.3529	1.2533	–1.4676	2.2305	–1.0946	0.003
5,8,11-Trioxapentadecane (1)	0.3407	2.5957	–2.9613	4.3557	–2.1337	0.010

Table 4*b*. Coefficients a_i of eq. [5] and standard deviation σ.

Propylamine (2) +	a_1	a_2	a_3	a_4	a_5	σ
2,5-Dioxhexane (1)						
V^E_m x 10^6 (m^3 mol^{-1})	1.2709	0.2650	–0.1631			0.003
Δln η (mPa s)	–0.0678	–0.1234	0.0664	0.0108		0.002
ΔG^{*E} (J mol^{-1})	–81.7	–316.1	363.7	8.5	–339.6	3
2,5,8-Trioxanonane (1)						
V^E_m x 10^6 (m^3 mol^{-1})	–0.0233	–0.2887	–0.1161			0.001
Δln η (mPa s)	0.6828	–0.1820	–0.1121	–0.0169		0.003
ΔG^{*E} (J mol^{-1})	2053.7	–508.0	–271.9	–45.6		7
2,5,8,11-Tetraoxadodecane (1)						
V^E_m × 10^6 (m^3 mol^{-1})	–0.2308	0.0517	–0.0366			0.001
Δln η (mPa s)	1.0709	–0.2273	0.4500	0.0013		0.003
ΔG^{*E} (J mol^{-1})	3391.8	–751.5	1172.5	–11.7		6
3,6,9-Trioxaundecane (1)						
V^E_m × 10^6 (m^3 mol^{-1})	0.1206	0.0329	0.0521			0.002
Δln η (mPa s)	0.8095	–0.3671	0.5484	–0.0986		0.003
ΔG^{*E} (J mol^{-1})	2729.7	1088.9	1411.9	–263.2		7
5,8,11-Trioxapentadecane (1)						
V^E_m × 10^6 (m^3 mol^{-1})	–0.1655	–0.0066	–0.0352			0.001
Δln η (mPa s)	1.5924	–0.9230	1.1101	–0.1503		0.004
ΔG^{*E} (J mol^{-1})	5365.5	–2771.4	2953.8	–460.7		10

used. Literature values for V^E_m or η for these mixture are not available for comparison.

Comparison of experimental results with several empirical laws of mixing

Several relations have been proposed to evaluate the dynamic viscosity (η) of liquid mixtures by using several chemical laws of mixing representative of the viscosity of binary mixtures with an adjustable empirical parameter. The literature contains many laws of mixing, which can be defined according to the number of adjustable parameters used to account for the deviation from an ideal mixture. Thus, there are laws based on parameters of zero, one, two, three, and so forth

The equation of Kendall and Monroe (37), which has no adjustable parameters, is expressed as

$$[6] \qquad \eta = (x_1\eta_1^{1/3} + x_2\eta_2^{1/3})^3$$

The equations of Grunberg–Nissan (38), Tamura and Kurata (39), Hind (40), and Katti and Chaudhry (41) have one adjustable parameter. The single-parameter Grunberg–Nissan equation (38) reads

$$[7] \qquad \ln \eta = x_1 \ln \eta_1 + x_2 \ln \eta_2 + x_1x_2G_{12}$$

where G_{12} is a parameter proportional to the interchange energy. Tamura and Kurata (39) developed the following expression for the viscosity of binary mixtures:

$$[8] \qquad \eta = x_1\phi_1\eta_1 + x_2\phi_2\eta_2 + 2(x_1x_2\phi_1\phi_2)^{1/2}T_{12}$$

where T_{12} is the interaction parameter and ϕ_1 and ϕ_2 are the volume fractions. Hind et al. (40) proposed the following equation:

$$[9] \qquad \eta = x_1^2\eta_1 + x_2^2\eta_2 + 2x_1x_2H_{12}$$

where H_{12} is attributed to unlike-pair interactions. Katti and Chaudhry (41) derived the following equation:

$$[10] \qquad \ln (\eta V) = x_1 \ln (\eta_1 V_1^*) + x_2 \ln (\eta_1 V_1^*) + x_1x_2W_{vis}/RT$$

where W_{vis} is an adjustable parameter. The two-parameter Heric and Brewer equation (42) is of the form

$$[11] \qquad \ln \nu = x_1 \ln \nu_1 + x_2 \ln \nu_2 + x_1 \ln M_1 + x_2 \ln M_2 + \ln (x_1M_1 + x_2M_2) + x_1x_2[\alpha_{12} + \alpha_{21}(x_1 - x_2)]$$

where α_{12} and α_{21} are adjustable parameters and ν_i is the kinematic viscosity of pure component *i*. The two-parameter

© 2002 NRC Canada

Fig. 3. Experimental viscosity deviations for propylamine (2) + 2,5-dioxahexane (1) (○) ; 2,5,8-trioxanonane (1) (Δ); 2,5,8,11-tetraoxadodecane (1) (□); 3,6,9-trioxaundecane (1) (●); 5,8,11-trioxapentadecane (1) (⊗). Continuous curves were calculated from eq. [5].

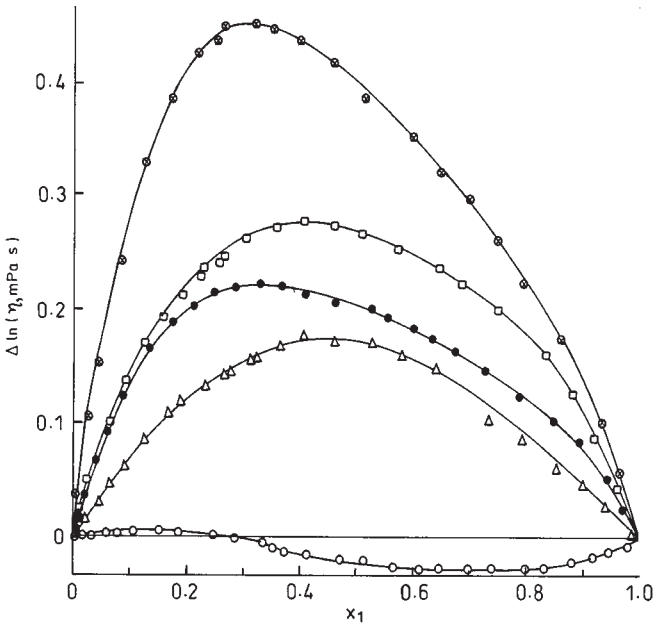

Fig. 4. Experimental excess energies of activation for viscous flow for propylamine (2) + 2,5-dioxahexane (1) (○); 2,5,8-trioxanonane (1) (Δ); 2,5,8,11-tetraoxadodecane (1) (□); 3,6,9-trioxaundecane (1) (●); 5,8,11–trioxapentadecane (1) (⊗). Continuous curves were calculated from eq. [5].

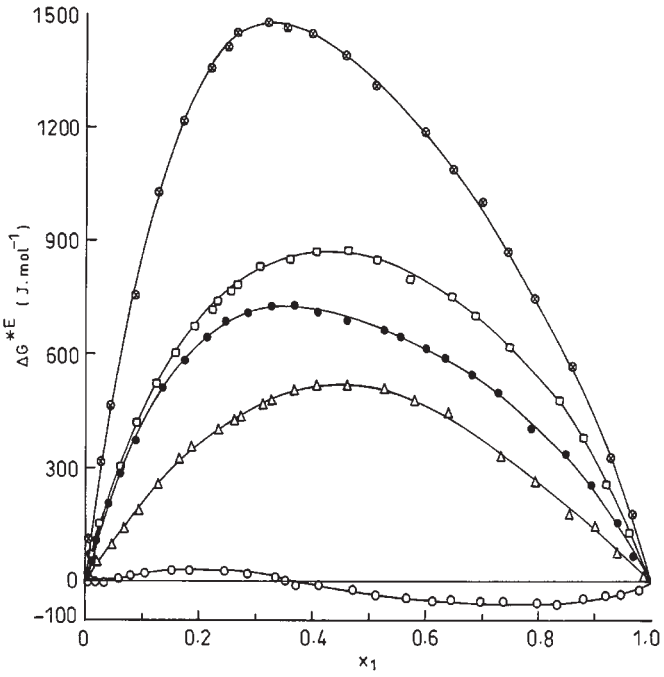

McAllister equation (43), based on Eyring's theory of absolute reaction rates (44), and the three-body interaction model is

$$[12]\quad \ln \nu = x_1^3 \ln \nu_1 + 3x_1^2x_2 \ln Z_{12} + 3x_1x_2^2 \ln Z_{21} + x_2^3 \ln \nu_2 - \ln [x_1 + x_2(M_2/M_1)] + 3x_1^2x_2 \ln [(2 + M_2/M_1)/3] + 3x_1x_2^2 \ln [(1 + 2M_2/M_1)/3] + x_2^3 \ln (M_2/M_1)$$

The four-body model gives

$$[13]\quad \ln \nu = x_1^4 \ln \nu_1 + 4x_1^3x_2 \ln Z_{1112} + 6x_1^2x_2^2 \ln Z_{1122} + 4x_1x_2^3 \ln Z_{2221} + x_2^4 \ln \nu_2 - \ln [x_1 + x_2(M_2/M_1)] + 4x_1^3x_2 \ln [(3 + M_2/M_1)/4] + 6x_1^2 2x_2^2 \ln [(1 + M_2/M_1)/2] + 4x_1x_2^3 \ln [(1 + 3M_2/M_1)/4] + x_2^4 \ln (M_2/M_1)$$

where Z_{12}, Z_{21}, Z_{1112}, Z_{1122}, and Z_{2221} are interaction parameters and M_i is the molecular mass of pure component *i*. The three-parameter Auslaender eq. [45] is of the form

$$[14]\quad \nu_1(x_1 + B_{12}x_2)(\nu - \nu_1) + A_{21}x_2(B_{21}x_2 + x_2)(\nu - \nu_2) = 0$$

where B_{12}, A_{21}, and B_{21} are the parameters representing binary *1 – 2* interactions. The correlating capability of eqs. [6]–[14] was tested by calculating the standard percentage deviation (σ%) between the experimental and the calculated viscosity using the following relation:

$$[15]\quad \sigma(\%) = [1/(p - k)\ \Sigma(100(\eta_{exp} - \eta_{cal})/\eta_{exp})^2]^{1/2}$$

where *p* represents the number of experimental points and *k* the number of numerical coefficients in the respective equations.

Discussion

From Fig. 1, it can be seen that V_m^E is large and positive for the 2,5-dioxahexane + propylamine mixtures at 298.15 K over the entire range of composition. For the same value of x_1, the magnitude of the V_m^E decreases with each additional -OC_2H_4- group in the parent molecule 2,5-dioxahexane. The behavior is similar to that of V_m^E for 2-methoxyethanol or propylamine with *n*-alkoxyethanol (5, 7, 46, 47), ethyl acetate with (mono and poly) ethers (14), and alkanols with polyethers (19, 27, 48), where V_m^E decreases with the increasing number of oxygen atoms in the ether chain. In Fig. 1, it can also be observed that V_m^E increases in the sequence 5,8,11-trioxapentadecane > 3,6,9-trioxundecane > 2,5,8- trioxanonane. This behavior may be compared with that of V_m^E for 2-(2-methoxyethoxy)ethanol, 2-(2-ethoxyethoxy)ethanol, or 2-(2-butoxyethoxy)ethanol with propylamine (5). The behavior of these mixtures is very complex and the overall values of V_m^E are attributable to the result of several opposing and diverse effects (49, 50): (*i*) a disruption of liquid order on mixing and unfavorable interactions between unlike molecules, which contribute positively to V_m^E; (*ii*) a volume decrease caused by the differences in molecular volumes and free volumes and possible interstitial accommodation of propylamine within larger molecules. Upon increasing the size of the polar-head group of the polyether, the interactions between unlike molecules become more important; V_m^E decreases and becomes more negative for the

© 2002 NRC Canada

Table 5. Values of the parameters in eqs. [7]–[10] and standard percentage deviations in eqs. [6]–[10] for polyether + propylamine systems.

	eq. [6]	eq. [7]		eq. [8]		eq. [9]		eq. [10]	
Propylamine (2) +	σ%	G_{12}	σ%	T_{12}	σ%	H_{12}	σ%	$W_{vis/RT}$	σ%
2,5-Dioxhexane (1)	1.32	0.06	0.85	0.37	0.93	0.37	0.88	–0.01	0.89
2,5,8-Trioxanonane (1)	8.39	0.69	1.29	0.65	0.97	0.72	0.78	0.84	1.44
2,5,8,11-Tetraoxadodecane (1)	10.94	1.17	2.26	0.79	1.46	1.01	1.93	1.49	2.76
3,6,9-Trioxaundecane (1)	10.84	0.89	3.36	0.74	0.94	0.86	1.09	1.19	3.86
5,8,11-Trioxapentadecane (1)	20.31	1.64	8.06	1.06	1.58	1.41	1.38	2.44	9.23

Table 6. Values of the parameters in eqs. [11]–[14] and standard percentage deviations in correlating viscosities of polyethers + propylamine systems.

	eq. [11]			eq. [12]			eq. [13]				eq. [14]			
Propylamine (2) +	α_{12}	α_{21}	σ%	Z_{12}	Z_{21}	σ%	Z_{1112}	Z_{1122}	Z_{2221}	σ%	B_{12}	B_{21}	A_{21}	σ%
2,5-Dioxhexane (1)	–1.17	6.67	0.22	0.46	0.50	0.25	0.47	0.56	0.51	0.16	1.21	1.29	1.33	0.29
2,5,8-Trioxanonane (1)	1.17	–0.71	0.49	0.94	0.83	0.38	0.94	1.27	0.71	0.24	–0.69	0.10	–0.54	0.54
2,5,8,11-Tetraoxadodecane (1)	1.84	–0.42	1.41	1.62	1.25	1.31	1.89	1.75	1.06	0.20	0.01	0.07	0.13	3.50
3,6,9-Trioxaundecane (1)	1.19	–0.52	1.54	1.13	1.10	1.54	1.35	1.30	0.99	0.27	–0.95	0.11	–0.75	1.52
5,8,11-Trioxapentadecane (1)	2.35	–1.23	3.25	1.79	2.29	3.47	2.52	1.96	1.92	0.42	–1.81	0.07	–1.3	1.71

larger polyethers. In the same homologous series, the algebraic values of V^E_m at $x_1 > 0.8$ for the three binary systems with propylamine vary in the following order: 5,8,11-trioxapentadecane < 2,5,8-trioxanonane < 3,6,9-trioxaundecane. The negative contribution to V^E_m for the 5,8,11-trioxapentadecane systems is caused by stronger interactions between unlike molecules giving higher negative values compared with those of the other two mixtures.

Figure 2 shows that η increases with the ether mol fraction (x_1) for all of the mixtures studied. The deviation in the viscosity (Δln η) and the excess energies of activation for viscous flow (ΔG^{*E}) are represented in Figs. 3 and 4. All of the mixtures show positive deviations from mol fraction linearity, except for the 2,5-dioxahexane + propylamine system at low ether mol fractions. Similar behavior is observed for ΔG^{*E}. The magnitude of η, Δln η, and ΔG^{*E} increase with increasing size of the polar-head group and with increasing alkyl chain length of polyether. The positive values of ΔG^{*E} are attributed to the large size and cohesive-energy difference between the two unlike molecules. The positive Δln η and ΔG^{*E} values are an indication of specific interactions (51, 52). Indeed, we observe positive deviations in the viscosity that regularly increase as the size or viscosity of the polyether is increased. This reveals that the strength of specific interaction is not the only factor influencing the viscosity deviation of liquid mixtures. The molecular size and shape of the components also play important roles.

The results of the correlating eqs. [6]–[14] are compiled in Tables 5 and 6. The fitting precision of eq. [6] (no adjustable parameters) and eqs. [7]–[10] (one adjustable parameter) are presented in Table 5. Table 6 gives the fitting results for the two-parameter Heric–Brewer equation (eq. [11]), the McAllister three-body model (eq. [12]), the three-parameter McAllister four-body model (eq. [13]), and the Auslaender equation (eq. [14]). The values of the different fittings parameters in eqs. [7]–[14] and the percentage standard deviation listed in Tables 5 and 6 were obtained from the experimental viscosity data using least squares with equal weights assigned to each point.

The values of σ are in the range from 1.3 to 20.3% for eq. [6] (no adjustable parameters); from 0.9 to 9.2% for the single-parameter fitting eqs. [7]–[10]; from 0.2 to 3.5% for the two-parameter eqs. [11] and [12]; and from 0.2 to 3.5% for the three-parameter eqs. (13] and [14]. Table 5 shows that, because of lower values of σ%, the equations of Tamura and Kurata (eq. [8]), and Hind et al. (eq. [9]), the behavior of the binary mixture satisfactorily compares with the equations of Grunberg–Nissan (eq. [7]) and Katti and Chaudhary (eq. [10]). The equations of Kendall and Monroe (eq. [6], with no adjustable parameters) has higher values of σ% than those of the single-parameter eqs. [7]–[10]. Use of the two-parameter eqs. [11] and [12] significantly reduces the σ% values below that of the single-parameter eqs. [8] and [9], except with 3,6,9-trioxaundecane and 5,8,11-trioxapentadecane. For all of the systems studied here, the three-parameter equation of McAllister (eq. [13]) gives very good results. The values of σ% are in the range of only 0.2–0.4%. Use of the three-parameter equation of Auslaender (eq. [14]), however, gives higher σ% values than that of the three-parameter equation of McAllister (eq. [13]).

From this study it can be concluded that all of the correlating equations considered are effective in the empirical fitting of viscosity data for (polyether + propylamine) mixtures. This is not surprising in view of the number of adjustable parameters in each equation, where a very large variability of the experimental measurements with composition of the solvent mixtures is observed. Thus it become very difficult to suggest any general rule in establishing the effectiveness of one fitting over the other. The comparisons are, however, more suitable with the same number of adjustable parameters. Thus the equations having one adjustable parameter (Tamura and Kurata, and Hind et al.) show a good correlating ability over the equation of Grunberg–Nissan and Katti and Chaudhry.

© 2002 NRC Canada

With respect to the three-parameter equations, it should be noted that the McAllister equation (eq. [13]) gives the best fit of the experimental values. Furthermore, the reproducibility of the experimental point is similar to those obtained by applying the two-parameter equations of Heric-Brewer and McAllister (eq. [11] and 12]).

Acknowledgment

RKB gratefully acknowledges the University Grants Commission (UGC), New Delhi, for awarding teacher fellowship (No. F.3–(TF 13)/98(NR)) and financial assistance for this study.

References

1. A. Pal and R. K. Bhardwaj. Int. J. Thermophysics, **22**, 769 (2001).
2. A. Pal and H. Kumar. Fluid Phase Equilib. **181**, 17 (2001).
3. A. Pal and G. Das. Can. J. Chem. **78**, 444 (2000).
4. A. Pal and S. Sharma. J. Chem. Thermodyn. **31**, 273 (1999).
5. A. Pal, S. Sharma, and H. Kumar. Can. J. Chem. **78**, 427 (2000).
6. T. M. Aminabhavi and B. Gopalakrishna. J. Chem. Eng. Data, **40**, 402 (1993).
7. J.C. Cobos, C. Casanova, J. Garcia, G. Roux–Desgranges, and J.-P.E. Grolier. Thermochim. Acta, **131**,73 (1988).
8. J.C. Cobos and C. Casanova. Fluid Phase Equilib. **20**, 155 (1985).
9. S.L. Oswal and H.S. Desai. Fluid Phase Equilib. **149**, 359 (1998).
10. I. Farnandez, M.I. Paz–Andrade, M. Pintos, F. Sarmiento, and R. Bravo. J. Chem. Thermodyn. **15**, 581 (1983).
11. D. Papaionnou and C. Panayiotou. J. Chem. Eng. Data, **40**, 202 (1995).
12. T.M. Letcher and U. Domanska. J. Chem. Thermodyn. **26**, 553 (1994); **26**, 1241 (1994).
13. C.A. Tovar, E. Carballo, C.A. Cerdeirina, J.L. Legido and L. Romani. Int. J. Thermophysics, **18**, 761 (1997).
14. C.A. Tovar, E. Carballo, C.A. Cerdeirina, and L. Romani. J. Chem. Eng. Data, **40**, 1085 (1997).
15. J. Peleterio, C.A. Tovar, E. Carballo, J.L. Legido, and L. Romani. Can. J. Chem. **72**, 454, (1994).
16. J.C. Cobos, I. Garcia, J.A. Gonzalez, and C. Casanova. J. Chem. Thermodyn. **22**, 383 (1990).
17. J.C. Cobos, M.A. Villamanan, and C. Casanova. J. Chem. Thermodyn. **16**, 861 (1984).
18. S. Mohren and A. Heintz. Fluid Phase Equilib. **133**, 247 (1997).
19. A. Serna, I. Garcia de la Fuente, J.A. Gonzalez, and J.C. Cobos. Fluid Phase Equilib. **133**, 187 (1997).
20. A. Serna, J.C. Cobos, I. Garcia de la Fuente, J.A. Gonzalez, and C. Casanova. The proceedings of the 13th IUPAC conference on chemical thermodynamics. Clermont, Ferrand, France. 1994. p. 80.
21. T.M. Aminabhavi and B Gopalakrishna. J. Chem. Eng. Data, **39**, 865 (1994).
22. J.A. Riddick, W.B. Bunger, and T.K. Sakano. Organic solvents: physical proprerties and method of purifications. 4th ed. Wiley Interscience, New York. 1986.
23. T.M. Letcher. J. Chem. Thermodyn. **4**, 159 (1972).
24. G. Douheret, M.I. Davis, M.E. Hernandez, and H. Flores. J. Indian Chem. Soc. **70**, 395 (1993).
25. P.K. Muhuri and D.K. Hazara. J. Chem. Eng. Data, **39**, 375 (1994).
26. W.J. Wallace and A.L. Methews. J. Chem. Eng. Data, **8**, 496 (1963).
27. F.J. Carmona, F.J. Arroyo, I. Garcia de la Fuente, J.A. Gonzalez, and J.C. Cobos. Can. J. Chem. **77**, 1608 (1999).
28. T.M. Aminabhavi and B. Gopalakrishna. J. Chem. Eng. Data, **40**, 462 (1995).
29. W.J. Wallace, C.S. Shephard, and C. Underwood. J. Chem. Eng. Data, **13**, 11 (1968).
30. G. Roux, G. Perron, and J.E. Desnoyers. Can. J. Chem. **56**, 2808 (1978).
31. E. Dickinson, D.C. Hunt, and I.A. McLure. J. Chem. Thermodyn. **7**, 731 (1975).
32. A. Pal and Y.P. Singh. J. Chem. Thermodyn. **26**, 1063 (1994).
33. A. Pal and W. Singh. J. Chem. Eng. Data, **42**, 234 (1997).
34. A. Pal and A. Kumar. J. Chem. Eng. Data, **43**, 143 (1998).
35. A. Aucejo, M.C. Burguet, R. Munoz, and M. Sanchotello. J. Chem. Eng. Data, **41**, 508 (1996).
36. R.S. Ramadevi, P. Venkatesu, and M.V.P. Rao. J. Chem. Eng. Data, **41**, 479 (1996).
37. J. Kendall and K.P. Monroe. J. Am. Chem. Soc. **39**, 1787 (1917).
38. L. Grunberg and A.H. Nissan. Nature (London), **164**, 799 (1949).
39. M. Tamura and M. Kurata. Bull. Chem. Soc. Jpn. **25**, 32 (1952).
40. R.K. Hind, E. McLaughlin, and U.R. Ubbelohde. Trans. Faraday Soc. **56**, 328 (1960).
41. P.K. Katti and M.M. Chaudhry. J. Chem. Eng. Data, **9**, 442 (1964).
42. E.L. Heric and J.C. Brewer. J. Chem. Eng. Data, **12**, 574 (1967).
43. R.A. McAllister. AIChE J. **6**, 427 (1960).
44. S. Glasstone, K.J. Laidler, and H. Eyring. The theory of rate processes. McGraw–Hill, New York. 1941.
45. G. Auslaender. Br. Chem. Eng. **10**, 196 (1965).
46. A. Pal and W. Singh. J. Chem. Thermodyn. **28**, 227 (1996).
47. A. Pal and W. Singh. J. Chem. Eng. Data, **41**, 888 (1996).
48. A. Pal and A. Kumar. Fluid Phase Equlib. **161**, 153 (1999).
49. S.N. Vinogradov and R.H. Linell. Hydrogen bonding. Van–Nostrand, Reinhold, New York. 1971. p. 136.
50. G.C. Benson, C.J. Halpin, and A.J. Treszczanowicz. J. Chem. Thermodyn. **13**, 1175 (1981).
51. R.J. Fort and W.R. Moore. Trans. Faraday. Soc. **62**, 1112 (1996).
52. R. Palepu, J. Oliver, and B. Mackinnon. Can. J. Chem. **63**, 1024 (1985).

© 2002 NRC Canada

Thermodynamics of mixtures containing a very strongly polar compound. Part II. Solid–liquid equilibria for sulfolane + nitrile systems and characterization of the sulfolane–nitrile and sulfolane–1-alkyne interactions in terms of DISQUAC

Urszula Domanska and Juan Antonio Gonzalez

Abstract: Equilibrium temperatures for solid–liquid transitions of mixtures formed by sulfolane and ethanenitrile, propanenitrile, butanenitrile, or pentanenitrile were measured by a dynamic method. The solid–liquid equilibria phase diagrams show positive deviations from Raoult's law, except for the system with ethanenitrile, which is nearly ideal. The sulfolane–nitrile and sulfolane–1-alkyne interactions have been characterized in terms of the DISQUAC group contribution model. DISQUAC properly represents a complete set of thermodynamic properties: solid–liquid equilibria, molar excess enthalpies, and natural logarithms of activity coefficients. DISQUAC predictions are valid over a wide temperature range.

Key words: solid–liquid equilibria, thermodynamics, mixtures, interactions.

Résumé : Faisant appel à une méthode dynamique, on a mesuré les températures d'équilibre de transitions solide–liquide de mélanges formés de sulfolane et d'éthanenitrile, de propanenitrile, de butanenitrile ou de pentanenitrile. Les diagrammes de phase pour les équilibres solide–liquide présentent des déviations positives par rapport à la loi de Raoult, excepté pour le système de l'éthanenitrile qui est pratiquement idéal. Les interactions sulfolane–nitrile et sulfolane–alk-1-yne ont été caractérisées en fonctions du modèle DISQUAC de contribution des groupes. Le modèle DISQUAC représente assez bien un ensemble complet de propriétés thermodynamiques: équilibre solide-liquide, enthalpies molaires en excès ou logarithmes naturels des coefficients d'activité. Les prédictions découlant du modèle DISQUAC sont valides sur un large éventail de températures.

Mots clés : équilibre solide–liquide, thermodynamique, mélanges, interactions.

[Traduit par la Rédaction]

Introduction

We are engaged in a systematic study of solutions containing a component with a very high dipolar moment (μ) in the gas phase, e.g., propylene carbonate (μ = 4.94 D (1)), 1-methyl-2-pyrrolidinone (μ = 4.09 D (1)), dimethyl sulfoxide (DMSO; μ = 4.06 D (1)), or sulfolane (μ = 4.80 D (1)).

Sulfolane is a globular molecule in which only the negative end of its large dipole moment is exposed (2, 3) and thus it cannot act as a proton acceptor–donor (4, 5). Also, because of the steric hindrance of its globular shape, sulfolane does not easily interact with other molecules (2, 3, 6, 7). Below its melting point (301.60 K (1)), it is also a weakly structured substance (8). This conclusion may be drawn from the insensivity to temperatures of its dipole moment in the liquid phase and below the melting point (9, 10) — that is, in the stability range of the mesophase crystal (crystal I) (11), in which molecules can freely rotate, until a transition temperature (288.6 K (2, 8)) is gained at which an ordinary nonrotational phase (crystal II) is formed.

Due to these properties, mixtures of sulfolane are very interesting from a theoretical point of view. Systems with benzene, CCl_4, or 1,4-dioxane are almost regular (12) since volumes or dielectric constants on mixing scarcely exhibit noticeable deviations from ideal values (13–16). The activity coefficients of components obtained from solid–liquid equilibrium measurements are also close to 1 (14–16). Nevertheless, solid–liquid equilibrium phase diagrams for sulfolane + CCl_4 or 1,4-dioxane mixtures indicate the presence of complexes (15, 16). Their formation has been attributed more to favourable packing rather to strong interactions (15, 16). On the other hand, sulfolane is almost insoluble with many

Received 1 November 2001. Published on the NRC Research Press Web site at http://canjchem.nrc.ca on 27 April 2002.

U. Domanska. Physical Chemistry Division, Faculty of Chemistry, Warsaw University of Technology, 00–664 Warsaw, Poland.
J.A. Gonzalez.[1] G.E.T.E.F., Departamento de Física Aplicada y Termodinámica, Universidad de Valladolid, 47071 Valladolid, Spain.

[1]Corresponding author (e-mail: jagl@termo.uva.es).

 DOI: 10.1139/V02-066 © 2002 NRC Canada

Table 1. Experimental solid–liquid equilibrium temperatures (T, K) for the sulfolane(1) + ethanenitrile(2) system.

x_1	T (K)	x_1	T (K)
0.0000	231.56[a]	0.3223	226.06
0.0556	227.83	0.3528	230.30
0.1035	224.49	0.3624	229.71
0.1435	222.35	0.4680	241.90
0.1781	220.33	0.5721	252.53
0.1989	219.14	0.6720	262.62
0.2207	218.12	0.7581	270.42
0.2511	217.38	0.8541	278.44
0.2800	219.40	1.0000	301.15[b]

[a] $T_{fus\ 2}$ = 229.31 K (1).
[b] $T_{fus\ 1}$ = 301.60 K (1).

Table 2. Experimental solid–liquid equilibrium temperatures (T, K) for the sulfolane(1) + propanenitrile(2) system.

x_1	T (K)	x_1	T (K)
0.0000	180.37[a]	0.5946	258.82
0.1668	210.57	0.7654	271.03
0.2256	220.84	0.8371	276.85
0.3146	231.15	0.9123	282.59
0.4341	245.15	0.9536	285.53
0.5050	251.38	1.0000	301.15[b]

[a] Reference 1.
[b] $T_{fus\ 1}$ = 301.60 K (1).

organic liquids, such as *n*-alkanes, cycloalkanes, or long chain 1-alkanols (17–22). These systems show strong positive deviations from Raoult's law.

In this work, we report solid–liquid equilibrium measurements for sulfolane + nitrile systems. Moreover, we characterize solutions with these compounds and sulfolane + 1-alkyne mixtures in terms of DISQUAC (23, 24), an extended-group contribution model based on the rigid-lattice theory developed by Guggenheim (25). Previously, we have reported solid–liquid and liquid–liquid equilibria data on sulfolane + 1-alkanol mixtures (26). Binary systems formed by sulfolane and one organic solvent, such as alkane, benzene, toluene, CCl_4, or 1-alkanol have been also characterized in terms of DISQUAC (26).

Experimental

Materials

Sulfolane was supplied by Aldrich (98% reagent) and was twice vacuum distilled at a pressure below 2.7 kPa to yield a colourless and odourless product. To minimize the contact of this deliquescent reagent with moist air, the product was kept in sealed bottles in a dessicator. Ethanenitrile (99.93% HPLC), propanenitrile (99%), butanenitrile (>99%), and pentanenitrile (99.5% GC) from Aldrich, were stored over molecular sieves (4 Å) and used without further purification.

Procedure

The solubilities were determined using a dynamic method described elsewhere (27). The mixtures of solute and solvent were prepared by mass, with weighings accurate to 0.0002 g. Conversion to molar quantities was based on the relative atomic mass table issued by IUPAC (28). The mixtures were well stirred using a magnetic stirrer and heated very slowly with a heating rate that did not exceed 2 K h^{-1} near the equilibrium temperature. The temperature at which the last set of crystals disappeared was taken as the temperature of the solution–crystal equilibrium. The temperature was measured using a calibrated platinum-resistance thermometer (Authoterm2 by Gallenkamp), with an accuracy of 0.01 K. The reproducibility of the measurements was better than 0.1 K, which corresponded to an estimated error in mol fraction of Δx = 0.001.

Table 3. Experimental solid–liquid equilibrium temperatures (T, K) for the sulfolane(1) + butanenitrile(2) system.

x_1	T (K)	x_1	T (K)
0.0000	161.30[a]	0.5843	260.04
0.1765	220.84	0.6530	264.45
0.2392	230.60	0.7397	270.57
0.2992	237.86	0.8410	277.28
0.3545	243.31	0.9297	283.74
0.4600	252.45	0.9750	286.89
0.5301	256.52	1.0000	301.15[b]

[a] Reference 1.
[b] $T_{fus\ 1}$ = 301.60 K (1).

Table 4. Experimental solid–liquid equilibrium temperatures (T, K) for the sulfolane(1) + pentanenitrile(2) system.

x_1	T (K)	x_1	T (K)
0.0000	177.00[a]	0.7617	274.21
0.1929	233.39	0.7756	275.61
0.3001	245.80	0.7949	276.05
0.3826	252.96	0.8067	277.68
0.4628	258.23	0.8471	279.00
0.5218	261.75	0.8865	281.41
0.5643	264.12	0.9176	283.35
0.5985	265.35	0.9269	284.75
0.6111	266.72	0.9409	284.82
0.6482	268.17	0.9686	286.68
0.6651	269.58	0.9839	289.79
0.6929	270.54	1.0000	301.15[b]
0.7258	272.88		

[a] Reference 1.
[b] $T_{fus\ 1}$ = 301.60 K (1).

Results

Experimental solid–liquid equilibrium temperatures of the sulfolane(1) + nitrile(2) systems considered in this work are collected in Tables 1– 4. There are no data in the literature for comparison. The sulfolane(1) + ethanenitrile(2) system presents an eutectic point (determined graphically (29)): x_{1e} = 0.253, T_e = 217.03 K. This solution is nearly ideal (Fig. 1). The remaining mixtures show positive deviations from Raoult's law, which increase with the size of the nitrile (Fig. 2).

© 2002 NRC Canada

Fig. 1. SLE phase diagram for the sulfolane(1) + butanenitrile(2) mixture. Filled circles, experimental results (this work). Solid line, DISQUAC calculation; dashed line, ideal solubility curve.

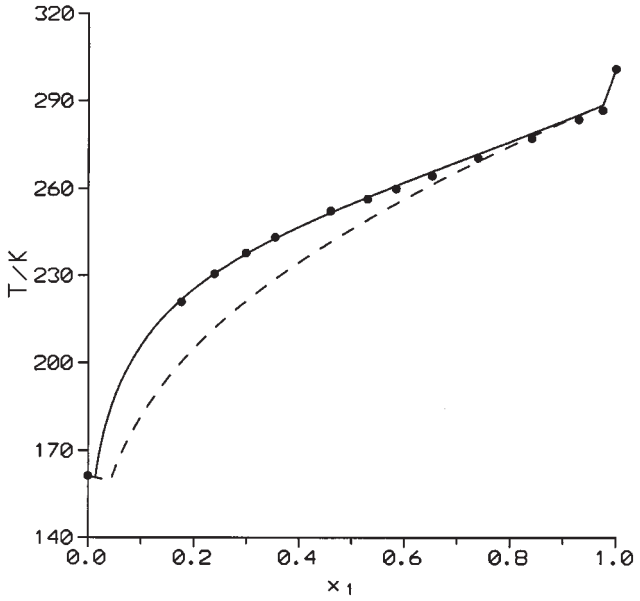

Fig. 2. SLE phase diagram for the sulfolane(1) + 1-heptyne(2) mixture. Filled circles, experimental values (72). Solid line, DISQUAC calculation; dashed line, ideal solubility curve.

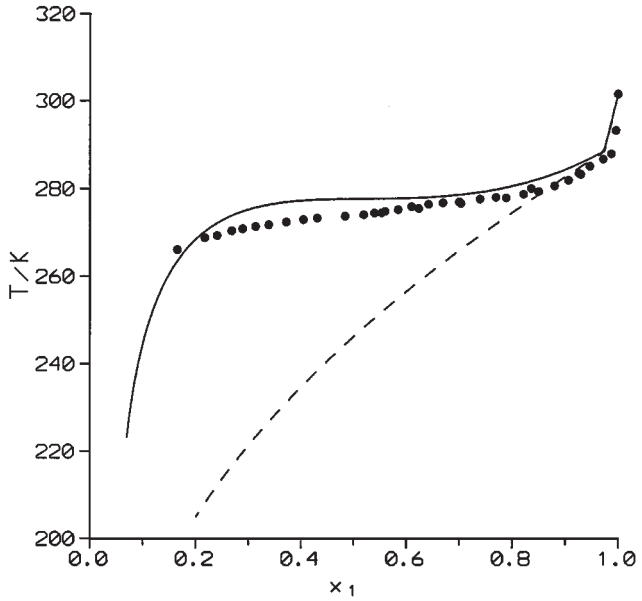

DISQUAC

Assessment of geometrical parameters

When DISQUAC is applied, the total relative molecular volumes (r_i), surfaces (q_i), and molecular surface fractions (α_{si}), of the compounds present in the mixture are usually calculated additively on the basis of the group volumes (R_G) and surfaces (Q_G), recommended by Bondi (30). As volume and surface units, the volume R_{CH_4} and Q_{CH_4} of methane are arbitrarily taken (31). For the sulfolane group, r_{c-SO_2} = 1.18574; q_{c-SO_2} = 0.89655 (26). The geometrical parameters for other groups referred to in this work are given elsewhere (31–33).

Equations

The equations used to calculate molar Gibbs energies (G^E_m) and molar excess enthalpies (H^E_m) are the same as in other applications (34). The interactional terms in the excess thermodynamic properties G^E_m and H^E_m contain a DIS and a QUAC contribution, which are calculated independently by classical formulas and then simply added. The degree of nonrandomness is thus expressed by the relative amounts of dispersive and quasichemical terms

$$[1] \qquad G^E_m = G^{E,COMB}_m + G^{E,DIS}_m + G^{E,QUAC}_m$$

$$[2] \qquad H^E_m = H^{E,DIS}_m + H^{E,QUAC}_m$$

where $G^{E,COMB}_m$ is the Flory–Huggins combinatorial term (31, 35). For the QUAC contribution, the reference value z = 4 was chosen for the coordination number.

The temperature dependence of the interaction parameters g_{st}, h_{st}, and c_{pst} has been expressed in terms of the DIS and QUAC interchange coefficients (34), $C^{DIS}_{st,1}$ and $C^{QUAC}_{st,1}$, where s and t are the two groups present in the solution (s ≠ t); and l = 1 (Gibbs energy; $C^{DIS/QUAC}_{st,1} = g^{DIS/QUAC}_{st}(T_0)/RT_0$); l = 2 (enthalpy; $C^{DIS/QUAC}_{st,2} = h^{DIS/QUAC}_{st}(T_0)/RT_0$); and l = 3 (heat capacity; $C^{DIS/QUAC}_{st,3} = c^{DIS/QUAC}_{stp}(T_0)/R$). T_0 = 298.15 K is the scaling temperature.

The equation of the solid–liquid equilibrium curve of a pure-solid component 1, including one first-order transition (as in the case of sulfolane (2, 8)) is (29, 36):

$$[3] \qquad -\ln x_1 = (\Delta H_{fus1}/R)\,[1/T - 1/T_{fus1}] + (\Delta H'_{trs1}/R)\,[1/T - T'_{trs1}] + \ln \gamma_1$$

Conditions at which eq. [3] is valid have been specified elsewhere (37). In eq. [3], x_1 is the mole fraction and γ_1 the activity coefficient of component 1 in the solvent mixture, at temperature T. In this work, DISQUAC is used to calculate γ_1. $\Delta H_{fus\,1}$ and $T_{fus\,1}$ are the molar enthalpy of fusion and the the melting temperature, respectively, of component 1, while $\Delta H'_{trs1}$ and T'_{trs1} represent the molar enthalpy of transition and transition temperature, respectively. For sulfolane, ΔH_{fus1} = 1428 J mol (1), T'_{trs1} = 288.6 K (2,8), and $\Delta H'_{trs1}$ = 7860 J mol^{-1} (38). For nitriles, ΔH_{fus} values were taken from ref. 1.

Estimation of DISQUAC interaction parameters

The general procedure applied for the fitting of the DISQUAC interaction parameters has been explained in detail in the first article of this series (26) and will not be repeated. Some remarks are given below. Sulfolane + nitrile or 1-alkyne mixtures are characterized by the following four types of surfaces: type *a*, CH_3 or CH_2 in nitriles or 1-alkynes; type *c*, *c*-CH_2 in sulfolane; type *w*, *c*-SO_2 in sulfolane; type *s*, *s* = *n*, CN in nitriles or *s* = *y*, HC≡C in 1-alkynes. We therefore have six types of contacts: (*a*, *c*), (*a*, *w*), (*c*, *w*), (*a*, *s*) (*c*, *s*), and (*s*, *w*) with *s* = *n* or *y*.

Because sulfolane is a five-membered ring, the (*a*, *c*) contacts must be fitted to experimental data for cyclopentane +

© 2002 NRC Canada

Table 5. Dispersive ($C^{DIS}_{st,1}$) and quasichemical ($C^{QUAC}_{st,1}$) interchange coefficients,[a] determined in this work for (s, t) contacts present in cyclopentane + nitrile systems, or in sulfolane + nitrile and sulfolane + 1-alkyne mixtures.

Solvent	$C^{DIS}_{st,1}$	$C^{DIS}_{st,2}$	$C^{QUAC}_{st,1}$	$C^{QUAC}_{st,2}$
(s, t) = (*c*, *n*)[b] contacts in cyclopentane + nitrile				
Ethanenitrile	0.65	1.35	6.10	7.45
Propanenitrile	1.00	2.05	5.30	5.80
≥Butanenitrile	1.00	2.05	5.00	5.60
(s, t) = (*n*, *w*)[c] contacts in sulfolane + nitrile				
Ethanenitrile	5.15	3.47	–0.75	0.20
Propanenitrile	4.35	2.62	–0.75	0.20
Butanenitrile	3.90	1.22	–0.75	0.20
≥Pentanenitrile	3.90	–0.38	–0.75	0.20
(s, t) = (*n*, *y*)[d] contacts in sulfolane + 1-alkyne				
1-Hexyne	2.00	3.70	3.00	–5.30
1-Heptyne	2.00	1.00	3.00	–5.30
≥1-Octyne	2.00	–1.75	3.00	–5.30

[a] l = 1, Gibbs energy; l = 2, enthalpy.
[b] Type *c*, *c*-CH_2 in cyclopentane or sulfolane; type *n*, CN in alkanenitriles
[c] Type *w*, *c*-SO_2 in sulfolane.
[d] Type *y*, HC≡C in 1-alkynes.

n-alkane systems, which are described only by dispersive parameters (26). In our previous work (26), the interchange coefficients for the (*a*, *w*) and (*c*, *w*) contacts were determined assuming that $C^{DIS}_{ac,1}$ (l = 1, 2, 3) = 0. This is reasonable in view of the low values of the excess functions of cyclopentane + *n*-alkane systems (26). Here, we have proceeded in a similar manner.

The interaction parameters for the (*a*, *n*) contacts are known from experimental data for nitrile + *n*-alkanes mixtures (33). The $C^{DIS/QUAC}_{cn,1}$ coefficients should be determined using data for nitrile + cyclopentane systems (see above). Unfortunately, for this class of solutions there are no data available in the literature. We therefore estimated the mentioned coefficients (Table 5) taking into consideration the liquid–liquid equilibria measurements for nitrile + alkane mixtures (39–41), and assuming, as in many other applications (42–54) that $C^{QUAC}_{an,1} = C^{QUAC}_{cn,1}$. These coefficients are well known from the DISQUAC analysis of nitrile + (*n*-alkane or cyclohexane) systems (33).

The interaction parameters for the (*a*, *y*) and (*c*, *y*) contacts have been previously estimated by us on the basis of experimental data for 1-alkyne + (*n*-alkane or cyclohexane) mixtures (32).

Now, the $C^{DIS/QUAC}_{cw,1}$ and $C^{DIS/QUAC}_{wy,1}$ (l = 1, 2, 3) coefficients must be determined. The former were obtained using experimental data for sulfolane + nitrile systems; the latter were calculated from data for sulfolane + 1-alkyne mixtures (Table 5). Due to the lack of H^E_m measurements at different temperatures for the solutions under study, the third DIS and QUAC coefficients were neglected.

Results and discussion

DISQUAC predictions for the mixtures are compared with experimental data in Tables 6–8. Graphical comparison are shown in Figs. 1–4.

In view of these results, we can conclude that DISQUAC favorably represents the thermodynamic properties of the mixtures under study. It is noteworthy that the same interaction parameters can be used to describe solutions with isomeric nitriles (Table 7). The model can be applied over a rather wide range of temperature. Note the good results obtained for solid–liquid equilibria of sulfolane(1) + nitrile(2) systems are at very low temperatures (Table 6). DISQUAC predicts eutectic points (Table 6). For the mixture with ethanenitrile, $x_{1e} = 0.261$ and $T_e = 218.03$ K, which compare well with the experimental values ($x_{1e} = 0.253$, $T_e = 217.03$ K).

Table 6. Comparison of experimental results with DISQUAC predictions on solid–liquid equilibrium temperatures for sulfolane(1) + organic solvent(2) mixtures obtained using interchange coefficients listed in Table 5.

		Deviations			
Solvent	N[a]	I[b]	II[c]	T_e(K)[d]	x_{1e}[e]
Acetonitrile	16	0.006	1.2	218.03	0.261
Propanenitrile	10	0.004	1.0	177.93	0.048
Butanenitrile	12	0.004	1.1	160.71	0.014
Pentanenitrile	23	0.006	1.5	175.95	0.019
1-Heptyne[f]	36	0.012	3.0		

[a] Number of experimental data points.
[b] Deviation = $\{1/N \Sigma[(T^{exp}_{SLE} - T^{calcd.}_{SLE}) / T_{SLE}]^2\}^{1/2}$.
[c] Deviation/K = $\Sigma| T^{exp}_{SLE} - T^{calcd.}_{SLE}|/N$.
[d] DISQUAC prediction for the temperature of the eutectic point.
[e] DISQUAC prediction for the mole fraction of the eutectic point.
[f] Reference 72.

The modified UNIFAC model (55, 56) has been applied to characterize mixtures formed by sulfolane and nitrile, or by sulfolane and 1-alkynes assuming that sulfolane is an homogeneous molecule (57). DISQUAC, however, substantially improves the results for sulfolane + nitrile systems, because the UNIFAC parameters were determined using only H^E data for the solutions (57).

Discussion

It is interesting to compare experimental results of mixtures containing sulfolane, DMSO, or acetonitrile. These

© 2002 NRC Canada

Table 7. Molar excess functions (F^E_m) at equimolar composition and temperature T of sulfolane(1) + organic solvent(2) mixtures. Comparison of experimental results (exp) with DISQUAC (DQ) values obtained using the coefficients from Table 5.

			F^E_m (J mol^{-1})		Deviation		
Solvent	T (K)	N[a]	Exp	DQ	Exp	DQ	Ref.
1-Heptyne	353.15	10	1480[b]	1404	0.004	0.075[d]	73
CH_3CN	303.15	12	–14[c]	–14	0.05	0.07[e]	68
CH_3CH_2CN	303.15	9	174[c]	176	0.017	0.022[e]	68
$CH_3(CH_2)_2CN$	303.15	9	322[c]	326	0.016	0.019[e]	68
$CH_3CH(CH_3)CN$	303.15	9	340[c]	323	0.009	0.059[e]	69
$CH_2(CH_2)_3CN$	303.15	9	459[c]	460	0.006	0.098[e]	68
$CH_3C(CH_3)_2CN$	303.15	9	461[c]	513	0.011	0.030[e]	69
1-Heptyne	303.15	21	347[c]	345	0.026	0.043[e]	71
1-Octyne	303.15	15	333[c]	334	0.024	0.057[e]	71

[a]Number of experimental data points.
[b]$F^E_m = G^E_m$, molar excess energy.
[c]$F^E_m = H^E_m$, molar excess enthalpy.
[d]Deviation = $\{1/N\ \Sigma[(P_{exp} - P_{calcd.})/P_{exp}]^2\}^{1/2}$, where P is the pressure.
[e]deviation = $\{1/N\ \Sigma[(H^E_{m,\,exp} - H^E_{m,\,calcd.})/H^E_{m,\,exp}\ (x = 0.5)]^2\}^{1/2}$.

Fig. 3. H^E_m for sulfolane(1) + alkanenitrile(2) mixtures at 303.15 K. Solid lines, DISQUAC calculations. Experimental results (68): ▼, ethanenitrile; ●, propanenitrile; ■, butanenitrile; ▲, pentanenitrile.

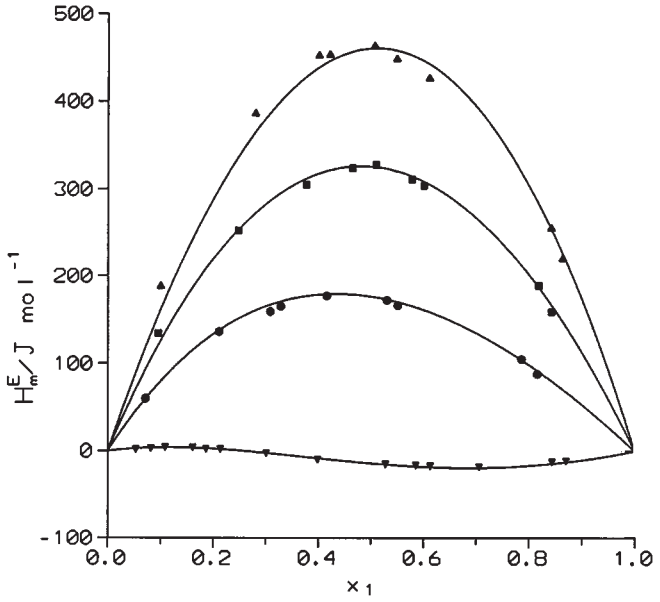

Fig. 4. H^E_m for the sulfolane(1) + 1-octyne(2) mixture at 303.15 K. Solid lines, DISQUAC calculations. Filled circles, experimental results (71).

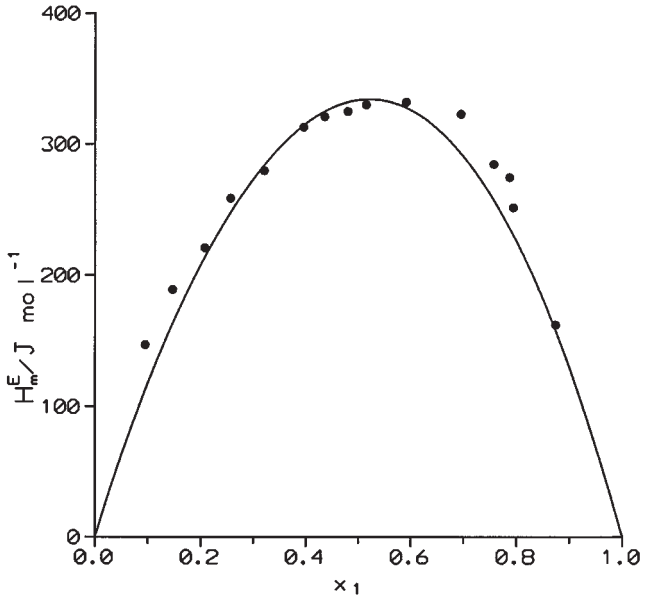

compounds have different dipole moments, but similar effective dipole moments (Table 9). This quantity is defined as (58–62)

$$[4] \qquad \mu = [\mu^2 N_A/(4\pi\varepsilon_o\ V k_B T)]^{1/2}$$

where N_A is Avogadro's number, k_B is Boltzmann's constant, ε_o is the permittivity of vacuum, and V is the molar volume. The effective dipole moment is a very useful property for characterizing the impact of polarity on bulk properties. Moreover, it gives an indication of the ratio between dipolar and nonpolar interactions (63).

For ethanenitrile(1) + *n*-hexane(2), the upper critical solution temperature (UCST) is 350.15 K (39). For sulfolane(1) + *n*-hexane(2), the UCST must be much higher. Note that the liquid–liquid equilibrium temperature at $x_1 = 0.013$ is 373.15 K (18). DISQUAC predicts 476.6 K for the UCST and 475 K for DMSO(1) + *n*-hexane(2) (64).

On the other hand, for ethanenitrile(1) + ethanol(2), H^E_m ($x_1 = 0.5$; 298.15 K) = 1496 J mol^{-1} (65). For sulfolane(1) + ethanol(2), H^E_m ($x_1 = 0.5$; 303.15 K) = 1971 J mol^{-1} (66), and for DMSO(1) + ethanol(2), H^E_m ($x_1 = 0.5$; 298.15 K) = 411 J mol^{-1} (67). These data reveal that sulfolane–alkane and sulfolane–1-alkanol interactions are very weak. The positive and relatively low H^E_m values of sulfolane + nitrile or 1-alkyne systems (except for the solution with ethanenitrile, Table 7) might be attributed to strong interactions between unlike molecules. The excess enthalpy of this class of solutions and the observed increase in H^E_m for sulfolane + nitrile mixtures when the effective dipole moment of the nitrile

© 2002 NRC Canada

Table 8. Natural logarithms of the activity coefficients at infinite dilution ($\ln \gamma_1^\infty$) in sulfolane(1) + 1-alkyne(2) mixtures at various temperatures (T). Comparison of experimental results (exp) (74) with DISQUAC values obtained using the coefficients from Table 5.

		$\ln \gamma_1^\infty$		$\ln \gamma_2^\infty$	
Solvent	T (K)	Exp	DQ	Exp	DQ
1-Hexyne	303.15		1.58	1.75	1.87
	313.15		1.55	1.73	1.86
1-Heptyne	303.15		2.13	2.09	2.10
	313.15		2.08	2.05	2.08
1-Octyne	303.15		2.64	2.48	2.32
	313.15		2.62	2.42	2.30

decreases have, however, been mainly ascribed to the breaking of the dipole–dipole interactions between nitrile molecules in presence of sulfolane (68, 69). The solid–liquid equilibrium measurements carried out in this work also show that sulfolane + nitrile systems present positive deviations from Raoult's law. Note that the mixture with ethanenitrile is nearly ideal.

Finally, it should be noted that the excess molar volumes (V_m^E) of sulfolane + nitrile or 1-alkyne systems are large and negative. At equimolar composition and 303.15 K, $V_m^E = -0.726$ cm^3 mol^{-1} and –1.36 cm^3 mol^{-1} for the systems with butanenitrile (70) and 1-heptyne (71), respectively. In addition, V_m^E decreases with increasing temperature (6, 70). It has been proposed by assuming that, in the case of mixtures with nitriles, nitrile–nitrile interactions predominate over weak sulfolane–nitrile interactions (6, 70) as well as in terms of packing effects (6, 70).

It is therefore possible to conclude that sulfolane may play the role of an almost inert diluent and thus limits its action to a disturbing effect of the other component; this is probably due to the steric hindrance of this globular molecule (2, 3, 6, 7, 17, 26, 68, 70).

Conclusions

Equilibrium temperatures for solid–liquid transitions of mixtures formed by sulfolane and ethanenitrile, propanenitrile, butanenitrile, or pentanenitrile mixtures are reported. The solid–liquid equilibrium phase diagrams show positive deviations from Raoult's law, except for the system with acetonitrile, which is nearly ideal.

DISQUAC interaction parameters are given for binary systems of sulfolane with nitriles or 1-alkynes. DISQUAC reasonably represents a complete set of thermodynamic properties (solid–liquid equilibria, molar excess enthalpies, natural logarithms of activity coefficients at infinite dilution) over a wide temperature range.

Sulfolane may play the role of an almost inert diluent — probably due to the steric hindrance of this globular molecule.

Acknowledgments

J.A.G. acknowledges the financial support from the Programa Nacional de I+D+I del Ministerio de Ciencia y Technología under project PPQ2001-1664 and the Consejería de Educación y Cultura de la Junta de Castilla y León F.S.E. under Project VA039/01.

Table 9. Critical constants: pressure (P_c), temperature (T_c), molar volume (V_{mol}), dipole moment (μ), and effective dipole moment ($\bar{\mu}$) of compounds referred to in this work.

Compound	P_c (bars)	T_c (K)	V_{mol} (cm^3 mol^{-1})	μ (D)	$\bar{\mu}$ (D)
Acetonitrile	48.3[a]	545.5[a]	52.87[a]	3.53[a]	1.86
Propanenitrile	41.8[a]	564.4[a]	70.90[a]	3.50[a]	1.59
Butanenitrile	37.9[a]	582.3[a]	87.87[a]	3.50[a]	1.43
Pentanenitrile	35.8[b]	610.3[b]	104.57[a, e]	3.57[a]	1.34
Sulfolane	49.9[c]	776[c]	95.34[a]	4.8[a]	1.88
DMSO	57.04[d]	729.6[d]	71.28[a]	4.06[a]	1.84

[a]Reference 1.
[b]Reference 75.
[c]Reference 73.
[d]Calculated using Lyndersen's method (76).
[e]At 301.15 K.

References

1. J.A. Riddick, W.B. Bunger, and T.K. Sakano. Organic solvents. *In* Techniques of chemistry. Vol. II. *Edited by* A. Weissberger. Wiley, N.Y. 1986.
2. M. Della Monica, L. Jannelli, and U. Lamanna. J. Phys. Chem. **72**, 1068 (1968).
3. M. Pansini and L. Jannelli. J. Chem. Eng. Data, **31**, 157 (1986).
4. J. Martinmaa. The chemistry of non-aqueous solvents. Academic Press, N.Y. 1976.
5. E.M. Arnett and C.F. Douty. J. Am. Chem. Soc. **86**, 409 (1964).
6. L. Jannelli, A. López, and S. Saiello. J. Chem. Eng. Data, **25**, 259 (1980).
7. L. Jannelli, A. Azzi, A. López, and S. Saiello. J. Chem. Eng. Data, **25**, 77 (1980).
8. L. Jannelli, A. López, R. Jalenti, and L. Silvestri. J. Chem. Eng. Data, **27**, 28 (1982).
9. O. Sciacovelli, L. Jannelli, and A. Della Monica. Gazz. Chim. Ital. **97**, 1012 (1967).
10. U. Lamanna, O. Sciacovelli, and L. Jannelli. Gazz. Chim. Ital. **96**, 114 (1966).
11. L. Jannelli, M. Della Monica, and A. Della Monica. Gazz. Chim. Ital. **94**, 552 (1964).
12. J.H. Hildebrand and R.L. Scott. Regular solutions. Englewood Cliffs, N.J. 1962.
13. A. Sacco and L. Jannelli. J. Chem. Thermodyn. **4**, 191 (1972).
14. L. Jannelli and A. Sacco. J. Chem. Thermodyn. **4**, 715 (1972).
15. A. Sacco, A. Inglese, P. Ciani, A. Dell'Atti, and A.K. Rakshit. Thermochim. Acta, **15**, 71 (1976).
16. L. Jannelli, A. Inglese, A. Sacco, and P. Ciani. Z. Naturforsch, **30A**, 87 (1975).
17. L. Jannelli, A.K. Rakshit, and A. Sacco. Z. Naturforsch, **29A**, 355 (1974).
18. R.M. De Fré and L.A. Verhoeye. J. Appl. Chem. Biotechnol. **26**, 469 (1976).
19. A. Masohau, J.M. Nanoti, K.G. Sharma, S.N. Puri, P. Gupta, and B.S. Rawat. Fluid Phase Equilib. **61**, 89 (1990).
20. T.M. Letcher, G.G. Redhi, S.E. Radloff, and U. Domanska. J. Chem. Eng. Data, **41**, 634 (1996).
21. Ch.-F. Kao and W.-Ch. Lin. Fluid Phase Equilib. **163**, 9 (1999).
22. Ch.F. Kao and W.-Ch. Lin. J. Chem. Eng. Data, **44**, 338 (1999).
23. H.V. Kehiaian. Fluid Phase Equilib. **13**, 243 (1983).

© 2002 NRC Canada

24. H.V. Kehiaian. Pure and Appl. Chem. **57**, 15 (1985).
25. E.A. Guggenheim. Mixtures. Oxford University Press, U.K. 1952.
26. J.A. González and U. Domanska. Phys. Chem. Chem. Phys. **3**, 1034 (2001).
27. U. Domanska. Fluid Phase Equilib. **114**, 175 (1996).
28. IUPAC. Quantities, units, and symbols in physical chemistry. 2nd ed. Blackwell Science Ltd. 1993.
29. P.B. Choi and E. McLaughlin. AIChE J. **29**, 150 (1983).
30. A. Bondi. Physical properties of molecular crystals, liquids, and glasses. Wiley, U.S.A. 1968.
31. H.V. Kehiaian, J.-P.E. Grolier, and G.C. Benson. J. Chim. Phys. **75**, 1031 (1978).
32. J.A. González, S. Villa, N. Riesco, I. García de la Fuente, and J.C. Cobos. Thermochim. Acta, **381**, 103 (2002).
33. B. Marongiu, B. Pittau, and S. Porcedda. Thermochim. Acta, **221**,143 (1993).
34. J.A. González, I. García de la Fuente, J.C. Cobos, and C. Casanova. Ber. Bunsenges. Phys. Chem. 9**5**, 1658 (1991).
35. J.A. González, I. García de la Fuente, J.C. Cobos, C. Casanova, and A. Ait-Kaci. Fluid Phase Equilib. **112**, 63 (1995).
36. R.F. Weimer and J.M. Prausnitz. J. Chem. Phys. **42**, 3643 (1965).
37. U. Domanska and J.A. González. Fluid Phase Equilib. **119**, 131 (1996).
38. J. Ahlers, J. Lohmann, and J. Gmehling. J. Chem. Eng. Data, **44**, 727 (1999).
39. I.A. McLure, A.T. Rodríguez, P.A. Ingham, and J.F. Steele. Fluid Phase Equilib. **8**, 271 (1982).
40. J.N. Ott, J.B. Purdy, B.J. Neely, and R.A. Harris. J. Chem. Thermodyn. **20**, 1079 (1988).
41. V. Vani, S. Gupta, and E.S.R. Gopal. J. Chem. Phys. **84**, 3999 (1986).
42. H.V. Kehiaian, M.R. Tiné, L. Lepori, E. Matteoli, and B. Marongiu. Fluid Phase Equilib. **46**, 131 (1989).
43. H.V. Kehiaian and B. Marongiu. Fluid Phase Equilib. **40**, 23 (1988).
44. M.J. Soriano, I. Velasco, S. Otín, and H.V. Kehiaian. Fluid Phase Equilib. **45**, 205 (1989).
45. H.V. Kehiaian, S. Porcedda, B. Marongiu, L. Lepori, and E. Matteoli. Fluid Phase Equilib. **63**, 231 (1991).
46. J.A. González, I. García de la Fuente, J.C. Cobos, C. Casanova, and H.V. Kehiaian. Thermochim. Acta, **217**, 57 (1993).
47. J.A. González, I. García de la Fuente, J.C. Cobos, and C. Casanova. Fluid Phase Equilib. **99**, 19 (1994).
48. J.A. González, I. García de la Fuente, J.C. Cobos, and C. Casanova. J. Solution Chem. **23**, 399 (1994).
49. J.A. González, I. García de la Fuente, and J.C. Cobos. Ber. Busnsenges Phys. Chem. **101**, 219 (1997).
50. J.A. González, I. García de la Fuente, and J. C. Cobos. Fluid Phase Equilib. **123**, 39 (1996).
51. J.A. González, I. García de la Fuente, J.C. Cobos, and U. Domanska. Fluid Phase Equilib. **119**, 81 (1996).
52. J.A. González, I. García de la Fuente, and J.C. Cobos. Thermochim. Acta, **278**, 57 (1996).
53. J.A. González, I. García de la Fuente, and J.C. Cobos. Ber. Bunsenges. Phys. Chem. **100**, 1476 (1996).
54. J.A. González, I. García de la Fuente, and J.C. Cobos. Can. J. Chem. **78**, 1272 (2000).
55. J. Gmehling, J. Li, and M. Schiller. Ind. Eng. Chem. Res. **32**, 178 (1993).
56. J. Gmehling, J. Lohmann, A. Jakob, J. Li, and R. Joh. Ind. Eng. Chem. Res. **37**, 4876 (1998).
57. W.C. Moollan, U. Domanska, and T.M. Letcher. Fluid Phase Equilib. **128**, 137 (1997).
58. J.A. González, F.J. Carmona, N. Riesco, I. García de la Fuente, and J.C. Cobos. Phys. Chem. Chem. Phys. **2**, 2587 (2000).
59. J.A. González, I. García de la Fuente, and J.C. Cobos. Fluid Phase Equilib. **168**, 31 (2000).
60. J.S. Rowlinson and F.L. Swinton. Liquids and liquids mixtures. 3rd ed. Butterworths, London. 1982.
61. E. Wilhelm, A. Laínez, and J.-P.E. Grolier. Fluid Phase Equilib. **49**, 233 (1989).
62. Th. Kraska and K.E. Gubbins. Ind. Eng. Chem. Res. **35**, 4727 (1996).
63. M.E. van Leewen. Fluid Phase Equilib. **99**, 1 (1994).
64. J.A. González. Unpublished results
65. V. Dohnal, F. Vesely, R. Holub, and J. Pick. Collect. Czech. Chem. Commun. **47**, 3177 (1982).
66. E. Tommila, E. Lindell, M.L. Virtalaine, and R. Laakso. Suom. Kemistil. **42**, 95 (1969).
67. J.P. Chao, M. Dai, and Y.X. Wang. J. Chem. Thermodyn. **21**, 1169 (1989).
68. A. López, M. Pansini, and L. Jannelli. J. Chem. Eng. Data, **28**, 173 (1983).
69. A. López, L. Jannelli, and M. Pansini. J. Chem. Eng. Data, **28**, 176 (1983).
70. A. López, L. Jannelli, and L. Silvestri. J. Chem. Eng. Data, **27**, 183 (1982).
71. T.M. Letcher, W.C. Moollan, J.A. Nevines, and U. Domanska. J. Chem. Thermodyn. **32**, 579 (2000).
72. U. Domanska, W.C. Mollan, and T.M. Letcher. J. Chem. Eng. Data, **41**, 261 (1996).
73. U. Domanska, A. Sporzynski, W.C. Moollan, and T.M. Lecher. J. Chem. Eng. Data, **41**, 624 (1996).
74. T.M. Letcher, and P.G. Whitehead. J. Chem. Thermodyn. **28**, 843 (1996).
75. CRC Handbook of chemistry and physics. 75th ed. *Edited by* D.R. Lide. CRC Press, U.S.A. 1995.
76. R.C. Reid, J.M. Prausnitz, and B.E. Poling. The properties of gases and liquids. 4th ed. McGraw-Hill, U.S.A. 1987.

© 2002 NRC Canada

Ryanoids and related compounds — Isolation and characterization of 11 new minor ryanoids from the plant *Ryania Speciosa* Vahl

Luc Ruest, Marco Dodier, Hélène De Sève, Christian Lessard, and Pascal Mongrain

Abstract: In a search for minor ryanoids from the plant *Ryania Speciosa* Vahl, we recently characterized 11 new members of that family of natural compounds. Most of them represent ryanodine (**1**) and dehydroryanodine (**2**) with a modified stage of oxidation in ring C. A second member of the new 4-deoxy series has been identified.

Key words: minor natural ryanoids, ryanodine, dehydroryanodine, deoxyryanoids.

Résumé : En cherchant à identifier les ryanoïdes mineurs de la plante *Ryania Speciosa* Vahl, nous avons caractérisé récemment onze nouveaux membres de cette famille de produits naturels. La plupart de ces composés représentent la ryanodine (**1**) et la déhydroryanodine (**2**) avec un degré d'oxydation modifié dans le cycle C. Un deuxième membre de la série 4-déoxyryanoïde a été identifié.

Mots clés : ryanoïdes mineurs naturels, ryanodine, déhydroryanodine, déoxyryanoïde.

Introduction

Ryanodine (**1**) (Scheme 1) is known to be a potent modulator of the sarcoplasmic reticulum calcium release channel (1). After ryanodine's structure elucidation by Wiesner (2), groups (3–14) have reported that this complex polycyclic, polyhydroxylic compound was not the sole insecticidal component in the plant *Ryania Speciosa* Vahl. In a recent review on the pharmacology of ryanodine and related compounds (1), 18 structurally related compounds, the ryanoids, were reported. More recently (13), four other minor ryanoids have been identified. These structures have been elucidated by extensive NMR analysis and also by X-ray diffraction. These natural compounds represent a very interesting family of molecules, in which the parent structure is slightly modified by the different orientations of the functional groups and the nature of the functional groups. Most of the natural ryanoids would be relatively difficult to obtain by multistep transformations of ryanodine (**1**) or 9,21-didehydroryanodine (**2**), the two most abundant ryanoids in that plant. The total synthesis of ryanodol (**3**) (15) and 3-epiryanodine (not shown) (16) from ryanodol (**3**) have been reported.

The biological activities of these metabolites and of several of their derivatives have been studied (1, and refs. therein). A number of hypotheses have been formulated on the effects of specific structural moieties on the binding affinity of these compounds in the ryanodine binding site (1, 17–29).

In a search for other members of this family, we have very recently identified new ryanoids **4**–**14** (Fig. 1) in the extracts of the plant. Compound **5** represents a second known member of a novel series — the 4-deoxyryanoids (13). These 11 metabolites are very minor components, each one representing ~0.1–5.0 ppm quantities (w/w) of the dried powdered wood, compared with approximately 500–800 ppm for **1** and **2**. With the 11 new ryanoids, this family of natural compounds presently has 32 identified metabolites.

Results and discussion

The discovery of the new ryanoids came after the usual separation of the known major compounds (1). In this paper, we will present, for each new compound, the arguments (mainly NMR data) that led us to propose the nature, the position, and the orientation of the substituents. In the experimental section, we will list the new compounds in order of their increasing polarity on silica gel, when mixtures of chloroform and methanol are used as the solvent.

The ^{1}H NMR spectrum of diester **4** shows two series of pyrrole aromatic hydrogens together with the usual singlet at δ 5.53 for the C3 hydrogen and a doublet (J = 10.5 Hz) at δ 5.44 for the C10 hydrogen. Synthetically, acylation of ryanodine (**1**) (Scheme 1) with α-pyrrole carboxylic acid and dicyclocarbodiimide (30) afforded compound **4** in low yield (10%).

The ^{1}H NMR spectrum of compound **5** shows that the C21 hydrogens (at δ 4.91) are magnetically equivalent and that they are coupled (J = 1.8 Hz) with the axial hydrogen at C8 (allylic coupling). The configuration at C10 was deduced by irradiating the equatorial C8 hydrogen (at δ 2.20): this

Received 7 February 2002. Published on the NRC Research Press Web site at http://canjchem.nrc.ca on 17 April 2002.

L. Ruest,[1] M. Dodier,[2] H. De Sève, C. Lessard, and P. Mongrain. Département de Chimie, Université de Sherbrooke, Sherbrooke, QC J1K 2R1, Canada.

[1]Corresponding author (e-mail: Luc.Ruest@courrier.usherb.ca).
[2]Taken in part from MSc thesis, 1996.

 DOI: 10.1139/V02-048 © 2002 NRC Canada

Fig. 1. Eleven new ryanoids from *Ryania Speciosa* Vahl.

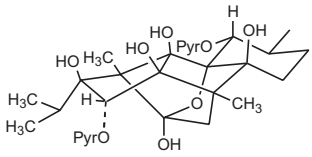

4: **10-*O*-Pyrrolecarbonylryanodine**

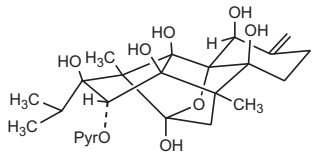

5: **10-Epi-9,21-didehydroryanodine**

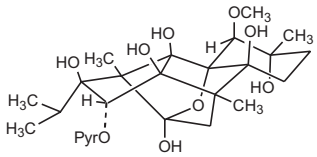

6: **9α-Hydroxy-10-*O*-methyl-10-epiryanodine**

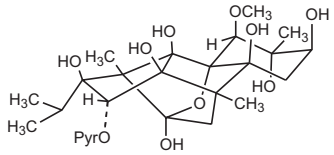

7: **8β, 9α-Dihydroxy-10-*O*-methyl-10-epiryanodine**

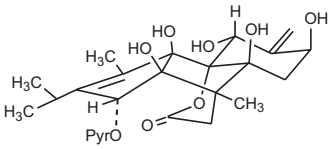

8: **8β-Hydroxy-9,21-didehydro-anhydroryanodine**

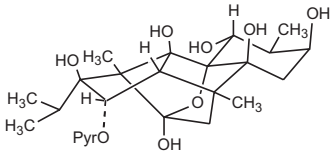

9: **4-Deoxy-8β-hydroxy ryanodine**

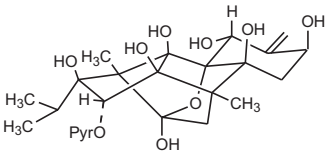

10: **8β-Hydroxy-9,21-didehydroryanodine**

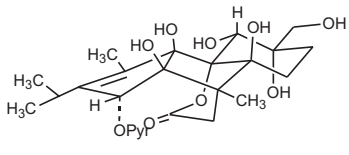

11: **9,21-Dihydroxy-anhydroryanodine**

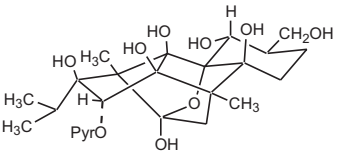

12: **21-Hydroxyryanodine**

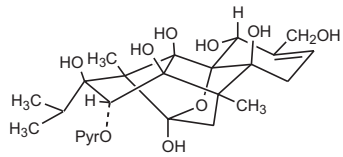

13: **21-Hydroxy-8,9-didehydroryanodine**

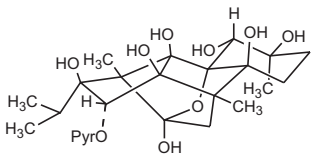

14: **9β-Hydroxyryanodine**

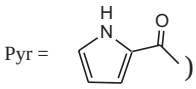

Scheme 1. Structures of two major ryanoids: ryanodine (**1**) and 9,21-didehydroryanodine (**2**), and synthesis of the new natural ryanoid **4** from **1**. Reaction conditions: (*a*) pyrrole-2-carboxylic acid, DCC, DMAP, Et_3N, CH_2Cl_2, THF, 25 h, 10%.

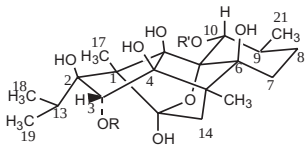

a → **1**: Ryanodine (R = Pyr; R' = H)
3: Ryanodol (R = R' = H)
4: 3,10-Di-*O*-pyrrolecarbonyl-ryanodol (R = R' = Pyr)

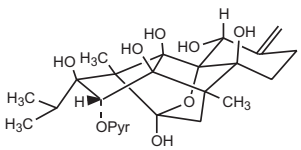

2: 9,21-Didehydroryanodine

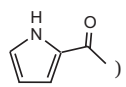

operation resulted in a 20% enhancement of the signal at δ 4.26 (W coupling), indicating the equatorial orientation of that hydrogen.

For compound **6**, the C10 hydrogen appears as a broad singlet at δ 3.27. The intensity of this signal was increased 30% by irradiating at δ 1.54 (equatorial C8 hydrogen). This result is consistent with a W coupling and an equatorial orientation of the C10 hydrogen. The absence of the usual multiplet for the C9 hydrogen, together with the downfield shift of the C9 methyl group (now a singlet at δ 1.35), indicates the presence of a hydroxyl group at position 9. The equatorial orientation of the C9 methyl group was deduced by the absence of W coupling between the methyl group and the axial C8 hydrogen. An axial methyl group at that position indeed shows a W coupling with axial hydrogens at the C8 and (or) C10 positions (vide infra for compound **14**).

The ^{1}H NMR spectrum of ryanoid **7** is consistent with the proposed structure: the axial hydroxyl groups at positions 8 and 9 account for a broad singlet at δ 3.73 (this is the equatorial hydrogen at C8) and a methyl singlet at δ 1.39 that overlaps the CH_3-C1 signal (this is the equatorial methyl group at C9). The signal at δ 3.35 is increased by 50% upon

© 2002 NRC Canada

Fig. 2. ORTEP perspective view of crystalline **11** and **14**: two minor natural ryanoids from *Ryania Speciosa* Vahl. 30% probability thermal ellipsoids are shown for the nonhydrogen atoms.

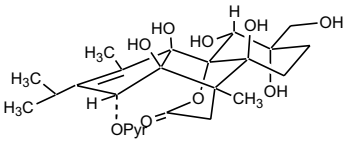

11: 9,21-Dihydroxy-anhydroryanodine

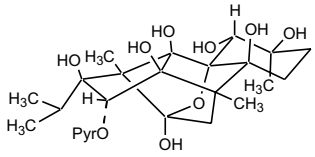

14: 9β-Hydroxyryanodine

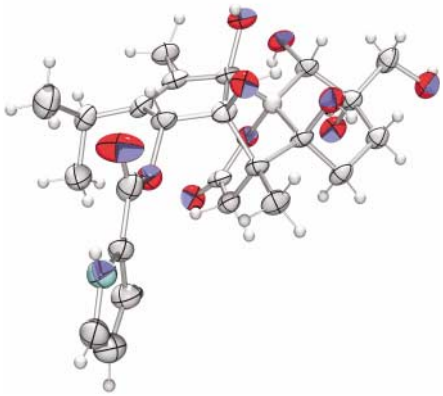

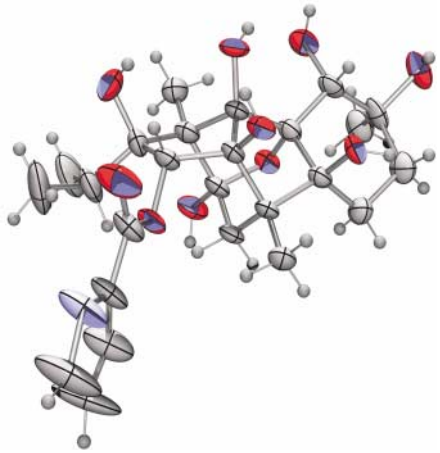

irradiation of the signal at δ 3.73. This increment shows a significant coupling between these two hydrogens due to a mutual W orientation. Ryanoid **8** shows the usual ^{1}H NMR signals of the anhydro-9,21-dehydroryanodine series, with the C3 hydrogen as a quartet at δ 6.20 and narrow multiplets at δ 5.45 and 5.25 for the C21 hydrogens. The axial orientation of the hydroxyl group at position 8 is revealed by the small coupling constants between $H_{eq}C8$ (δ 4.63) and H_2C7 (J = 2.3 and 3.7 Hz). The axial orientation of HC10 was revealed by a COSY experiment, which clearly showed an allylic coupling with both C21 hydrogens. No W coupling between HC10 and HC8 was observed under selective irradiation.

Compound **9** represents the second known member of the 4-deoxyryanoid series (13). An unusual doublet (J = 8.4 Hz) at δ 5.65 for the C3 hydrogen suggests the presence of a vicinal hydrogen at C4 — this new hydrogen signal appears at δ 3.20 as a doublet of doublets (J = 8.4 and 1.5 Hz). The small coupling constant (1.5 Hz) is due to a mutual W orientation of HC4 with one hydrogen at C14, which also appears as a doublet of doublets at δ 1.71. A narrow multiplet at δ 3.99 accounts for the equatorial hydrogen at C8, and the axial hydrogen at C10 appears as a doublet (J = 10.7 Hz) at δ 3.97, in accordance with an equatorial orientation of the methyl group at C9.

Ryanoid **10** is the "ryanodine version" of compound **8**. The axial orientation of the hydroxyl group at C8 is revealed by a narrow signal at δ 4.54, which represents the equatorial hydrogen at that position. This is confirmed by the small coupling constants of that hydrogen with the C7 hydrogens appearing at δ 2.24 and 1.65. Our assigned stereochemistry at C10 follows the same arguments used for compound **8** — strong allylic coupling between axial HC10 and H_2C21, and no W coupling with the equatorial C8 hydrogen.

New compound **11** belongs to the anhydroryanodine series, with HC3 (m) at δ 6.17, the C1 methyl group at δ 1.87, and the C14 methylene as two doublets (J = 19.7 Hz) at δ 3.44 and 2.58. The unequivalent hydrogens at C21 appear as two sharp doublets (J = 10.8 Hz) centered at δ 3.44, suggesting the presence of two hydroxyls at positions 9 and 21. The very sharp singlet at δ 4.46 is consistent with an axial hydrogen at C10 (no W coupling with the C8 equatorial hydrogen nor with the C21 hydrogens) and an equatorial orientation of the hydroxymethyl at C9. In Fig. 2 the ORTEP view for this natural crystalline ryanoid confirms the deductions made by the preceeding NMR analysis.

Compound **12** shows a doublet (J = 10.4 Hz) at δ 4.07, which is consistent with a diaxial relationship between HC10 and HC9. An ABX pattern centered at δ 3.66 represents the equatorial H_2C21 bearing a hydroxyl group. The remaining signals in the ^{1}H NMR spectrum are easily assigned.

The ^{1}H NMR spectrum of ryanoid **13** shows an olefinic hydrogen at δ 5.62 (broad singlet) near the HC3 signal (δ 5.63). Irradiation at δ 5.62 produced a noticeable sharpening of the broad doublets at δ 4.25 and 4.08, which thus represents a hydroxymethyl group attached to C9. It also revealed vicinal coupling, with two doublets of doublets located at δ 2.66 and 1.84 that represent H_2C7. In addition, this irradiation revealed the position and orientation of the axial allylic HC10: it appears as a broad singlet at δ 4.86 and is partly obscured by the solvent signal, which appears at δ 4.87. This broad singlet is enhanced by 15% upon the same irradiation, which allows us to deduce a β pseudoaxial orientation for HC10. Identification of the other signals in ^{1}H NMR spectrum of compound **13** was not a problem.

New ryanoid **14**, actually the most polar known ryanoid, was shown to be the epimer of known 9-hydroxyryanodine

© 2002 NRC Canada

(11). Its ^{1}H NMR spectrum shows, in particular, a singlet (δ 4.21) whose intensity is enhanced by 15% upon irradiation of the methyl singlet appearing at δ 1.35. Alternatively, irradiation of the singlet at δ 4.21 enhanced the intensity of this methyl group by 25% (W coupling). This situation clearly illustrates the diaxial relationship between HC10 and CH_3-C9. The ORTEP view of this crystalline material (Fig. 2) corroborates the proposed structure deduced from ^{1}H NMR analysis.

The biological activities of the new ryanoids and their affinities for ryanodine binding sites are currently under analysis in the laboratories of Professor William Welch, Department of Biochemistry, University of Nevada, Reno, Nevada.

Experimental

Melting points were recorded on a Reichert hot stage apparatus and are uncorrected. Mass spectra (MS) and peak matching (HRMS) data were determined at 70 eV on a VG Micromass ZAB-1F spectrometer. The ^{1}H (300 MHz) NMR spectra were recorded on a Bruker AC-300 instrument (with CHD_2OD as internal standard centered at δ 3.30). The usual abbreviations have been used to indicate the multiplicity of the proton signals. Analytical and preparative thin layer chromatography were performed with glass plates (0.25 or 0.5 mm) precoated with silica gel 60F-250 (Merck). The typical solvent was 5–15% of methanol in chloroform, to which 0.5–2.0% of commercial 40% aqueous methylamine may be added. For some special cases, we also used mixtures of ethyl acetate in hexane (40–80%). Column chromatography (flash) was performed with Merck silica gel (200–400 mesh). High performance liquid chromatography (HPLC) used a Waters model 510 instrument equipped with a Vydac C18 reverse-phase preparative column (15 μm, 2.5 × 25 cm) and a Waters 484 tunable UV detector set at 254 nm. The typical solvent for HPLC preparative separation was 40% methanol in water. All reactions were performed under argon atmosphere and in solvents purified by standard methods. Reaction mixtures were extracted with at least five portions of distilled ethyl acetate. Solutions in organic solvents were washed with brine, dried over anhydrous sodium sulfate, filtered, and then stripped of solvents with a rotatory evaporator connected to a water aspirator.

Isolation of the new ryanoids

Extraction of powdered Ryania wood was done as previously described (11). The isolation of each of the new ryanoids was done as described above. After numerous chromatographic separations and purification operations, we isolated each of the new ryanoids **4**–**14** in quantities of approximately 3 to 100 mg, starting from a lot of ~100 g of crude extract (obtained from ~ 100 kg of dry powder wood). The presentation of these new ryanoids follows their *increasing polarities* — the first compound (**4**) in the following is therefore the least polar one. Occasionally, polarities relative to already known ryanoids (1, 4, 6, 12, 13) will be given to locate these new compounds by thin layer chromatography.

New ryanoids less polar than ryanodine (1)

*3,10-Di-*O*-Pyrrolecarbonylryanodol (10-*O*-pyrrolecarbonylryanodine) (4)*

By TLC analysis, compound **4** is slightly less polar than the known Ester A (8β-hydroxy-10-*O*-methyl-10-epiryanodine), (1, 4, 6) but slightly more polar than 4-deoxyester A (13). Amorphous solid: ^{1}H NMR (CD_3OD) δ: 7.03, 6.86, 6.23 and 6.96, 6.91, 6.19 (two series of doublets of doublets for pyrrole rings hydrogens), 5.57 (s, 1H, HC3), 5.44 (d, J = 10.5 Hz, 1H, HC10), 2.58 (d, J = 13.8 Hz, 1H, H_AC14), 2.23 (m, 1H, HC13), 2.22–2.05 (m, 2H, $H_{ax}C7$, HC9), 1.98 (d, J = 13.8 Hz, 1H, H_BC14), 1.62 (m, 2H, $H_{eq}C7$, $H_{ax}C8$), 1.33 (m, 1H, $H_{eq}C8$), 1.31 (s, 3H, CH_3C1), 1.08 (d, J = 6.7 Hz, 3H, H_3C18), 0.91 (s, 3H, CH_3C5), 0.86 (d, J = 6.6 Hz, 3H, CH_3C9), 0.71 (d, J = 6.4 Hz, 3H, H_3C19). MS *m*/*z*: 475 ([M – $C_5H_5O_2N$]$^+$). HRMS calcd. for $C_{25}H_{33}NO_8$ ([M – $C_5H_5O_2N$]$^+$): 475.2206; found: 475.2201.

Synthesis of diester 4 from ryanodine

At ambient temperature, a solution of dicyclohexylcarbodiimide (230 mg, 1.11 mmol) in dry dichloromethane (3 mL) was transferred (canula) to a solution of ryanodine (133 mg, 0.27 mmol), pyrrole-2 carboxylic acid (128 mg, 1.15 mmol), 4-dimethylaminopyridine (1 mg), and triethylamine (5 μL) in dry THF (5 mL) (30). After 40 h, the reaction mixture was poured into aqueous sodium bicarbonate and extracted. The crude product was chromatographed to give a low yield (17 mg, 10%) of diester **4** together with unreacted starting ryanodine (93 mg).

10-Epi-9,21-didehydroryanodine (5)

This compound was obtained from the extracts by HPLC techniques combined with careful multi-elution preparative thin layer chromatography using a mixture of chloroform–methanol (95:5) as the solvent. It is slightly more polar than ester A (1, 4, 6), but less polar than the known 3-*O*-benzoylryanodol (13); mp 198–200°C. ^{1}H NMR (CD_3OD) δ: 7.03, 6.86, and 6.23 (3 dd for pyrrole ring hydrogens), 5.67 (s, 1H, HC3), 4.91 (d, J = 1.8 Hz, 2H, H_2C21), 4.26 (s, 1H, $H_{eq}C10$; this signal is increased by ~20% upon irradiation at 2.20 ppm), 2.65 (m, 1H, $H_{ax}C8$), 2.58 (d, J = 13.8 Hz, 1H, H_AC14), 2.18 (m, 3H, HC13, $H_{ax}C7$ and $H_{eq}C8$), 1.87 (d, J = 13.8 Hz, 1H, H_BC14), 1.50 (m, 2H, $H_{eq}C7$), 1.33 (s, 3H, CH_3C1), 1.07 (d, J = 6.8 Hz, 3H, H_3C18), 0.91 (s, 3H, CH_3C5), 0.73 (d, J = 6.4 Hz, 3H, H_3C19). MS *m*/*z*: 492 ([M + H]$^+$). HRMS calcd. for $C_{25}H_{34}NO_9$, MH$^+$): 492.2233; found: 492.2243.

*9α-Hydroxy-10-*O*-methyl-10-epiryanodine (6)*

This compound was obtained as above after HPLC techniques combined with careful multi-elution preparative thin layer chromatography using a mixture of chloroform–methanol (97:3) as the solvent. It is slightly more polar than the known ester B (1, 4), but less polar than ester C_2 (1, 4); mp 212–215°C. ^{1}H NMR (CD_3OD) δ: 7.02, 6.85, and 6.23 (3 dd for pyrrole ring hydrogens), 5.66 (s, 1H, HC3), 3.63 (s, 3H, OCH_3), 3.27 (s, 1H, $H_{eq}C10$; this signal is increased by ~30% upon irradiation at 1.54 ppm), 2.58 (d, J = 13.8 Hz, 1H, H_AC14), 2.21 (m, 1H, HC13), 2.04 (m, 1H, $H_{ax}C8$), 1.88 (m, 1H, $H_{ax}C7$), 1.84 (d, J = 13.8 Hz, 1H, H_BC14),

© 2002 NRC Canada

1.54 (m, 1H, $H_{eq}C8$), 1.39 (s, 3H, CH_3C1), 1.35 (s, 3H, CH_3C9) (this signal shows no enhancement by irradiation at δ 2.04), 1.31 (m, 1H, $H_{eq}C7$), 1.07 (d, *J* = 6.8 Hz, 3H, H_3C18), 0.89 (s, 3H, CH_3C5), 0.72 (d, *J* = 6.4 Hz, 3H, H_3C19). MS *m/z*: 505 ($[M - H_2O]^+$). HRMS calcd. for $C_{26}H_{35}NO_9$ ($[M - H_2O]^+$): 505.2312; found: 505.2322.

8*β,*9*α-*Dihydroxy-10*-O-*methyl-10-epiryanodine (7)

This compound was obtained as above after HPLC techniques combined with careful multi-elution preparative thin layer chromatography using a mixture of chloroform–methanol (97:3) as the solvent. It is slightly more polar than the known ester G (3-*O*-nicotinoylryanodol) (1), but less polar than 10-*O*-acetylryanodol (13). Amorphous solid; ^{1}H NMR (CD_3OD) δ: 7.03, 6.86, and 6.23 (3 dd for pyrrole ring hydrogens), 5.64 (s, 1H, HC3), 3.73 (br s, 1H, HC8), 3.55 (s, 3H, CH_3-O-C10), 3.35 (s, 1H, HC10; this signal is increased by 50% upon irradiation at 3.73), 2.63 (d, *J* = 13.9 Hz, 1H, H_AC14), 2.43 (dd, *J* = 12.0 and 3.4Hz, 1H, $H_{ax}C7$), 2.21 (m, 1H, HC13), 1.90 (d, *J* = 13.7 Hz, 1H, H_BC14), 1.69 (dd, *J* = 12.0 and 1.5 Hz, 1H, $H_{eq}C7$), 1.39 (s, 6H, CH_3C1 and CH_3C9), 1.08 (d, *J* = 6.8 Hz, 3H, H_3C18), 0.95 (s, 3H, CH_3C5), 0.74 (d, *J* = 6.4 Hz, 3H, H_3C19). MS *m/z*: 539 ($[M]^+$). HRMS calcd. for $C_{26}H_{37}NO_{11}$: 539.2366; found: 539.2379.

8*β-*Hydroxy-9,21-didehydroanhydroryanodine (8)

This compound was obtained as above after HPLC techniques combined with careful multi-elution preparative thin layer chromatography using a mixture of chloroform–methanol (95:5) as a solvent. It is slightly more polar than 10-*O*-acetylryanodol (13), but less polar than ester D (1, 4, 6); mp 180–185°C (dec.). ^{1}H NMR (CD_3OD) δ: 7.05, 6.85, and 6.24 (3 dd for pyrrole ring hydrogens), 6.19 (m, 1H, HC3), 5.43 (apparent t, *J* = 2.0 Hz, H_AC21), 5.26 (apparent t, *J* = 2.0 Hz, H_BC21), 5.19 (br s, 1H, $H_{ax}C10$), 4.63 (br s, 1H, $H_{eq}C8$), 3.46 (d, *J* = 19.8 Hz, 1H, H_AC14), 2.76 (m, 1H, HC13), 2.54 (d, *J* = 19.8 Hz, 1H, H_BC14), 1.89 (dd, *J* = 14.5 and 2.3 Hz, 1H, $H_{eq}C7$), 1.88 (d, *J* = 2.2 Hz, 3H, CH_3C1), 1.68 (dd, *J* = 14.5 and 3.7 Hz, 1H, $H_{ax}C7$), 1.07 (d, *J* = 7.1 Hz, 3H, H_3C18), 1.01 (s, 3H, CH_3C5), 0.98 (d, *J* = 7.0 Hz, 3H, H_3C19). MS *m/z*: 471 ($[M - H_2O]^+$). HRMS calcd. for $C_{25}H_{29}NO_8$: 471.1893; found: 471.1896.

New ryanoids more polar than ryanodine (1)

4-Deoxy-8*β-*hydroxyryanodine (9)

This compound was obtained as above after HPLC techniques combined with careful multi-elution preparative thin layer chromatography using a mixture of chloroform-methanol (90:10) as the solvent. It is slightly more polar than 9-hydroxyryanodine (11), but less polar than 19-hydroxyryanodine (1, 12). Amorphous solid; ^{1}H NMR (CD_3OD) δ: 7.00, 6.84, and 6.21 (3 dd for pyrrole ring hydrogens), 5.65 (d, *J* = 8.4 Hz, 1H, HC3), 3.99 (br s, 1H, $H_{eq}C8$), 3.97 (d, *J* = 10.7 Hz, 1H, HC10), 3.20 (dd, *J* = 8.4 and 1.5 Hz, 1H, HC4), 2.40 (m, 1H, HC13), 2.34 (d, *J* = 13.6 Hz, 1H, H_AC14), 2.16 (dd, *J* = 13.7 and 3.3 Hz, 1H, $H_{ax}C7$), 2.00 (m, 1H, HC9), 1.71 (dd, *J* = 13.6 and 1.5 Hz, 1H, H_BC14), 1.52 (dd, *J* = 13.4 and 2.3 Hz, 1H, $H_{eq}C7$), 1.34 (s, 3H, CH_3C1), 1.14 (apparent t, *J* = 7.1 Hz, 6H, H_3C18 and CH_3C9), 0.82 (d, *J* = 6.4 Hz, 3H, H_3C19), 0.80 (s, 3H, CH_3C5). MS *m/z*: 450 ($[M - C_3H_7]^+$). HRMS calcd. for $C_{22}H_{28}NO_9$ ($[M - C_3H_7]^+$): 450.1764; found: 450.1756.

8*β-*Hydroxy-9,21-didehydroryanodine (10)

This compound was obtained as above after HPLC techniques combined with careful multi-elution preparative thin layer chromatography using a mixture of chloroform–methanol (88:12) as solvent. It is slightly more polar than the known 18-hydroxy-9,21-didehydroryanodine (1, 12). Amorphous solid; ^{1}H NMR (CD_3OD) δ: 7.01, 6.86, and 6.23 (3 dd for pyrrole ring hydrogens), 5.65 (s, 1H, HC3), 5.30 and 5.15 (two apparent t, *J* = 2.0 Hz, 1H each, H_AH_BC21), 4.95 (br s, 1H, HC10), 4.54 (br s, 1H, $H_{eq}C8$), 2.60 (d, *J* = 13.8 Hz, 1H, H_AC14), 2.24 (dd, *J* = 13.6 and 4.3 Hz, 1H, $H_{ax}C7$), 2.23 (m, 1H, HC13), 1.85 (d, *J* = 13.8 Hz, 1H, H_BC14), 1.64 (dd, *J* = 13.6 and 2.0 Hz, 1H, $H_{eq}C7$), 1.40 (s, 3H, CH_3C1), 1.09 (d, *J* = 6.7 Hz, 3H, H_3C18), 0.95 (s, 3H, CH_3C5), 0.73 (d, *J* = 6.4 Hz, 3H, H_3C19). MS *m/z*: 471 ($[M - 2H_2O]^+$). HRMS calcd. for $C_{25}H_{29}NO_8$ $[M - 2H_2O]^+$): 471.1893; found: 471.1901.

9*α,*21-Dihydroxyanhydroryanodine (11) (X-ray)

This compound was obtained as above after HPLC techniques combined with careful multi-elution preparative thin layer chromatography using a mixture of chloroform–methanol (85:15) as the solvent. It is slightly more polar than compound **10**; mp: 210–214°C (dec., MeOH–CH_2Cl_2). ^{1}H NMR (CD_3OD) δ: 7.06, 6.87, and 6.25 (3 dd for pyrrole ring hydrogens), 6.17 (m, 1H, HC3), 4.46 (s, 1H, HC10), 3.59 (d, *J* = 10.8 Hz, 1H, H_AC21), 3.44 (d, *J* = 19.7 Hz, 1H, H_AC14), 3.32 (d, *J* = 10.8 Hz, 1H, H_BC21), 2.76 (m, 1H, HC13), 2.58 (d, *J* = 19.7 Hz, 1H, H_BC14), 2.18 (m, 1H, $H_{ax}C8$), 1.87 (d, *J* = 2.3 Hz, 3H, CH_3C1), 1.80 (m, 1H, $H_{ax}C7$), 1.61 (m, 1H, $H_{eq}C8$), 1.49 (m, 1H, $H_{eq}C7$), 1.08 (d, *J* = 7.1 Hz, 3H, H_3C18), 0.99 (d, *J* = 7.0 Hz, 3H, H_3C19), 0.98 (s, 3H, CH_3C5). MS *m/z*: 489 ($[M - H_2O]^+$). HRMS calcd. for $C_{25}H_{31}NO_9$: 489.1999; found: 489.2010. This material was analyzed by X-ray diffraction (see Fig. 2).

21-Hydroxyryanodine (12)

This compound was obtained as above after HPLC techniques combined with careful multi-elution preparative thin layer chromatography using a mixture of chloroform–methanol (85:15) as the solvent. It is slightly more polar than compound **11**. Amorphous solid: ^{1}H NMR (CD_3OD) δ: 7.02, 6.87, and 6.23 (3 dd for pyrrole ring hydrogens), 5.62 (s, 1H, HC3), 4.07 (d, *J* = 10.4 Hz, 1H, HC10), 3.74 (dd, *J* = 10.6 and 4.1 Hz, 1H, H_AC21), 3.56 (dd, *J* = 10.6 and 6.3 Hz, 1H, H_BC21), 2.56 (d, *J* = 13.7 Hz, 1H, H_AC14), 2.26 (m, 1H, HC13), 2.10 (m, 1H, $H_{ax}C7$), 1.93 (d, *J* = 13.7 Hz, 1H, H_BC14), 1.92 (m, 1H, HC9), 1.60 (m, 2H, $H_{ax}C8$ and $H_{eq}C7$), 1.39 (s, 3H, CH_3C1), 1.30 (m, 1H, $H_{ax}C8$), 1.10 (d, *J* = 6.7 Hz, 3H, H_3C18), 0.89 (s, 3H, CH_3C5), 0.74 (d, *J* = 6.4 Hz, 3H, H_3C19). MS *m/z*: 491 ($[M - H_2O]^+$). HRMS calcd. for $C_{25}H_{33}NO_9$ ($[M - H_2O]^+$): 491.2155; found: 491.2158.

21-Hydroxy-8,9-didehydroryryanodine (13)

This compound was obtained as above after HPLC techniques combined with careful multi-elution preparative thin

© 2002 NRC Canada

layer chromatography using a mixture of chloroform–methanol (80:20) as the solvent. It is slightly more polar than compound **12**. Amorphous solid: ^{1}H NMR (CD_3OD) δ: 7.03, 6.87, and 6.23 (3 dd for pyrrole ring hydrogens), 5.63 (br s, 2H, HC3 and HC8), 4.86 (br s, partly obscured by water signal, 1H, HC10), 4.25 (br d, J = 13.1 Hz, 1H, H_AC21), 4.08 (br d, J = 13.1 Hz, 1H, H_BC21), 2.66 (br d, J = 10.1 Hz, 1H, $H_{ax}C7$), 2.65 (d, J = 13.9 Hz, 1H, H_AC14), 2.27 (m, 1H, HC13), 1.99 (d, J = 13.7 Hz, 1H, H_BC14), 1.84 (dd, J = 10.1 and 4.9 Hz, 1H, $H_{eq}C7$), 1.39 (s, 3H, CH_3C1), 1.10 (d, J = 6.7 Hz, 3H, H_3C18), 0.92 (s, 3H, CH_3C5), 0.75 (d, J = 6.4 Hz, 3H, H_3C19). MS *m/z*: 471 ($[M - 2H_2O]^+$). HRMS calcd. for $C_{25}H_{29}NO_8$ ($[M - 2H_2O]^+$): 471.1893; found: 471.1901.

9β-Hydroxyryanodine (14) (X-ray)

This compound was obtained as above after HPLC techniques combined with careful multi-elution preparative thin layer chromatography using a mixture of chloroform–methanol (80:20) as the solvent. It is slightly more polar than compound **13**; mp 165–168°C (dec.). ^{1}H NMR (CD_3OD) δ: 7.03, 6.86, and 6.23 (3 dd for pyrrole ring hydrogens), 5.63 (s, 1H, HC3), 4.21 (s, 1H, HC10; this signal is increased by 15% upon irradiation at 1.35), 2.56 (d, J = 13.7 Hz, 1H, H_AC14), 2.25 (m, 1H, HC13), 2.10 (m, 1H, $H_{ax}C8$), 2.02 (m, 1H, $H_{ax}C7$), 1.88 (d, J = 13.7 Hz, 1H, H_BC14), 1.51 (m, 1H, $H_{ax}C7$), 1.39 (s, 3H, CH_3C1), 1.35 (s, 3H, H_3C9), 1.31 (m, 1H, $H_{eq}C8$), 1.09 (d, J = 6.8 Hz, 3H, H_3C18), 0.89 (s, 3H, CH_3C5), 0.74 (d, J = 6.4 Hz, 3H, H_3C19). MS *m/z*: 491 ($[M - H_2O]^+$). HRMS calcd. for $C_{25}H_{33}NO_9$ ($[M - H_2O]^+$): 491.2155; found: 491.2148. This material was analyzed by X-ray diffraction (see Fig. 2).

Acknowledgments

We are grateful to Professor W. Welch, Department of Biochemistry, University of Nevada, Reno, who allowed us to do this work as subcontracts of projects funded by the National Science Foundation (NSF) and the American Heart Association (AHA). We also thank Professor Alan J. Williams, Department of Cardiac Medicine, Imperial College School of Medicine at NHLI, London, U.K., for a research contract from the British Heart Foundation. We also thank the Université de Sherbrooke for financial support from the Fonds de Recherche à Allocation Interne (FRAI). We wish to thank Dr. N. Pothier, Mr. G. Boulé, and Mr. M. Drouin, Département de Chimie, Université de Sherbrooke, for their technical assistance (NMR spectroscopy, mass spectrometry, and X-ray diffraction analysis).

References

1. J.L. Sutko, J.L. Airey, W. Welch, and L. Ruest. Pharmacol. Rev. **49**, 53 (1997).
2. K. Wiesner. Adv. Org. Chem. **8**, 295 (1972).
3. A.L. Waterhouse, I. Holden, and J.E. Casida. J. Chem. Soc. Chem. Commun. 1265 (1984).
4. L. Ruest, D.R. Taylor, and P. Deslongchamps. Can. J. Chem. **63**, 2840 (1985).
5. A.L. Waterhouse, I. Holden, and J.E. Casida. J. Chem. Soc. Perkin Trans. 2, 1011 (1985).
6. A.L. Waterhouse, I.N. Pessah, A.O. Francini, and J.E. Casida. J. Med. Chem. **30**, 710 (1987).
7. R.A. Humerickhouse, J. Paschal, T. Elvey, D. Berry, and H.R. Besch, Jr. Pharmacologist, **31**, 185 (1989) (Program and Abstracts ASPET, Abstracts 363).
8. P.R. Jefferies, R.F. Toia, and J.E. Casida. J. Nat. Products, **54**, 1147 (1991).
9. P.R. Jefferies, R.F. Toia, B. Brannigan, I.N. Pessah, and J.E. Casida. J. Agric. Food Chem. **40**, 142 (1992).
10. P.R. Jefferies, W.-W. Lam, R.F. Toia, and J.E. Casida. J. Agric. Food Chem. **40**, 509 (1992).
11. R.A. Humerickhouse, H.R. Besch, Jr., K. Gerzon, L. Ruest, J.L. Sutko, and J.T. Emmick. Mol. Pharmacol. **44**, 412 (1993).
12. L. Ruest and M. Dodier. Can. J. Chem. **74**, 2424 (1996).
13. L. Ruest, C. Berthelette, M. Dodier, L. Dubé, and D. St-Martin. Can. J. Chem. **77**, 12 (1999).
14. M. Drouin, M. Dodier, and L. Ruest. Acta Cryst. **C54**, 687 (1998).
15. (*a*) A. Bélanger, D.J.F. Berney, H.J. Borschberg, R. Brousseau, A. Doutheau, R. Durand, H. Katayama, R. Lapalme, D.M. Leturc, C.C. Liao, F.N. MacLachlan, J.P. Maffrand, F. Marazza, R. Martino, C. Moreau, L. St-Laurent, R. Saintonge, P. Soucy, L. Ruest, and P. Deslongchamps. Can. J. Chem. **57**, 3348 (1979); (*b*) P. Deslongchamps, A. Bélanger, D.J.F. Berney, H.J. Borschberg, R. Brousseau, A. Doutheau, R. Durand, H. Katayama, R. Lapalme, D.M. Leturc, C.C. Liao, F.N. MacLachlan, J.P. Maffrand, F. Marazza, R. Martino, C. Moreau, L. Ruest, L. St-Laurent, R. Saintonge, and P. Soucy. Can. J. Chem. **68**, 115 (1990) (a series of four papers).
16. L. Ruest and P. Deslongchamps. Can. J. Chem. **71**, 634 (1993).
17. D.E. Mais, N. Bowling, and A.M. Watanabe. Biochem. Biophys. Res. Commun. **183**, 462 (1992).
18. P.R. Jefferies, E. Lermberg, W.-W. Lam, and J.E. Casida. J. Med. Chem. **36**, 1128 (1993).
19. R.A. Humerickhouse, K.R. Bidasee, K. Gerzon, J.T. Emmick, S. Kwon, J.L. Sutko, L. Ruest, and H.R. Besch, Jr. J. Biol. Chem. **269**, 30242 (1994).
20. W. Welch, S. Ahmad, J.A. Airey, K. Gerzon, R.A. Humerickhouse, H.R. Besch, Jr., L. Ruest, P. Deslongchamps, and J.L. Sutko. Biochemistry, **33**, 6074 (1994).
21. D.R. Witcher, P.S. McPherson, S.D. Kahl, T. Lewis, P. Bentley, M.J. Mullinnix, J.D. Windass, and K.P. Campbell. J. Biol. Chem. **269**, 13076 (1994).
22. S.D. Kahl, P.S. McPherson, T. Lewis, P. Bentley, M.J. Mullinnix, J.D. Windass, and K.P. Campbell. Anal. Biochemistry, **218**, 55 (1994).
23. K.R. Bidasee, H.R. Besch, Jr., K. Gerzon, and R.A. Humerickhouse. Mol. Cell. Biochem. **149/150**, 145 (1995).
24. W. Welch, J.L. Sutko, K.E. Mitchell, J. Airey, and L. Ruest. Biochemistry, **35**, 7165 (1996).
25. S. Tinker, J.L. Sutko, L. Ruest, P. Deslongchamps, W. Welch, J.A. Airey, K. Gerzon, K.R. Bidasee, H.R. Besch, Jr., and A.J. Williams. Biophys. J. **70**, 2110 (1996)
26. W. Welch, A.J. Williams, A. Tinker, K.E. Mitchell, P. Deslongchamps, J. Lamothe, K. Gerzon, K.R. Bidasee, H.R. Besch, Jr., J.A. Airey, J.L. Sutko, and L. Ruest. Biochemistry, **36**, 2939 (1997).
27. P.R. Jefferies, P. Yu, and J.E. Casida. Pest. Sci. **51**, 33 (1997)
28. B. Tanna, W. Welch, L. Ruest, J.L. Sutko, and A.J. Williams. J. Gen. Physiol. **112**, 55 (1998).
29. B. Tanna, W. Welch, L. Ruest, J.L. Sutko, and A.J. Williams. J. Gen. Physiol. **116**, 1 (2000).
30. B. Neisses and W. Steglich. Angew. Chem. Int. Ed. Eng. Suppl. **117**, 522 (1978).

© 2002 NRC Canada

Catalytic reduction of benzoate esters and lactones in the presence of $PhMeSiH_2$ and a titanocene-based catalyst

Ronghua Shu, John F. Harrod, and Anne-Marie Lebuis

Abstract: $PhMeSiH_2$ reduces ethyl benzoate in the presence of a Cp_2TiMe_2 (Cp = η^5-cyclopentadienyl) catalyst to give $PhMeSi(OEt)(OCH_2Ph)$ (**1**). Small to moderate amounts of toluene are also produced, depending on the reaction conditions. Under 40 psi of H_2 the same reaction gives quantitative reduction of the ester to toluene. PhCHO is reduced, under the same conditions as the ester, to a mixture of $PhMeSi(OCH_2Ph)_2$ and toluene in proportions similar to that observed with the ester. A stoichiometric reaction of $PhMeSiH_2$, PhCOOEt, and Cp_2TiMe_2 resulted in the formation of known $[Cp_2Ti(OEt)]_2$ (**2**) in 75% isolated yield. A mechanism is proposed in which the C=O of the ester inserts into a Ti–H bond. A Ti-mediated transfer of the ethoxy group from the resulting (α-ethoxy)benzyloxytitanium intermediate to silicon produces PhMeSi(OEt)H and PhCHO. **1** is generated via hydrosilation of PhCHO by PhMeSi(OEt)H. Both β- and γ-butyrolactones react with $PhMeSiH_2$ in the presence of a catalytic amount of Cp_2TiMe_2 to produce copolymers $-[O\text{-}PhMeSi\text{-}O(CH_2)_3CHR]_n-$ (R = H, **3**; R = Me, **4**) ($M_w \approx 1 \times 10^3$; $M_w/M_n \approx 1.3$). A mechanism analogous to that proposed for the ethyl benzoate reduction is proposed. A reaction of $PhMeSiH_2$ and γ-butyrolactone with a stoichiometric amount of Cp_2TiMe_2 in the presence of tetrahydofuran (THF) produces $Cp_2Ti(\mu\text{-}H)(\mu\text{-}\eta^1,\eta^5\text{-}C_5H_4)Ti(OC_4H_8)Cp$ **(5)** (65% isolated yield) whose structure is determined by X-ray crystallography.

Key words: hydrosilation, esters, lactones, titanocene, catalysis.

Résumé : En présence d'un catalyseur de Cp_2TiMe_2 (Cp = η^5-cyclopentadiényle), le $PhMeSiH_2$ réduit le benzoate d'éthyle en conduisant à la formation de $PhMeSi(OEt)(OCH_2Ph)$, **1**. Suivant les conditions expérimentales utilisées, il y a aussi formation de faibles quantités de toluène. À une pression de H_2 de 40 << psi >>, la même réaction conduit à une réduction quantitative de l'ester en toluène. Dans les mêmes conditions de réduction, le PhCHO fournit un mélange de $PhMeSi(OCH_2Ph)_2$ et de toluène dont les proportions sont semblables à celles observées avec l'ester. Une réaction stoechiométrique de $PhMeSiH_2$, PhCOOEt et de Cp_2TiMe_2 conduit à la formation du $[Cp_2Ti(OEt)]_2$, **2**, déjà connu, avec un rendement isolé de 75%. On propose un mécanisme dans lequel le C=O de l'ester s'insère dans une liaison Ti-H. Un transfert du groupe éthoxy, sous l'influence du Ti, de l'intermédiaire (α-éthoxy)benzoyloxytitane vers le silicium conduit à la formation de PhMeSi(OEt)H et de PhCHO. Le produit **1** est généré par le biais d'une hydrosilation du PhCHO par le PhMeSi(OEt)H. Les β- et γ-butyrolactones réagissent toutes les deux avec le $PhMeSiH_2$, en présence d'une quantité catalytique de Cp_2TiMe_2 pour conduire à la formation de copolymères $-[O\text{-}PhMeSi\text{-}O(CH_2)_3CHT]_n-$ (R = H, **3**; R Me, **4**) ($M_w \approx 10^3$; $M_w/M_n \approx 1{,}3$). On propose un mécanisme semblable à celui suggéré pour la réduction du benzoate d'éthyle. Une réaction du $PhMeSiH_2$ avec la γ-butyrolactone et une quantité stoechiométrique de Cp_2TiMe_2 dans du tétrahydrofurane (THF) conduit à la formation de $Cp_2Ti(\mu\text{-}H)(\mu\text{-}\eta^1,\eta^5\text{-}C_5H_4)Ti(OC_4H_8)Cp$, **5** (rendement de 65% en produit isolé) dont on a déterminé la structure par diffraction des rayons X.

Mots clés : hydrosilation, esters, lactones, titanocène, catalyse.

[Traduit par la Rédaction]

Introduction

Titanocene derivatives have been widely applied as catalysts for the hydrogenation and hydrosilation of carbonyl compounds (1). Hydrosilation of ketones (2) has received the most attention, but Buchwald and co-workers have also developed procedures for the reduction of both lactones (3) and esters (4). A variety of esters, including those containing bromo-, phenoxy-, amino-, alkenyl- or cyclopropyl-groups, as well as α,β-unsaturated esters, can be reduced with triethoxysilane and catalytic amounts of titanocene dichloride, preactivated with butyllithium (4*a*). This procedure can also be used for the selective reduction of methyl esters in the presence of *tert*-butyl esters. For substrates containing a terminal olefin, or an epoxide, a more hindered titanocene dichloride species, such as ethylene-1,2-bis(tetrahydroindenyl)titanium dichloride ($[EBTHI]TiCl_2$), is required. Other procedures involving safer and cheaper reagents, such as poly(methylhydrosiloxane) instead of $(EtO)_3SiH$ and EtMgBr instead of *n*-BuLi, were also reported (4*c*).

Received 9 August 2001. Published on the NRC Research Press Web site at http://canjchem.nrc.ca on 30 April 2002.

R. Shu, J.F. Harrod,[1] and A.-M. Lebuis. Chemistry Department, McGill University, 801 Sherbrooke St. W. Montreal, QC H3A 2K6, Canada.

[1]Corresponding author (e-mail: john.harrod@mcgill.ca).

 DOI: 10.1139/V02-047 © 2002 NRC Canada

Most of the reported work on the hydrosilation of esters and lactones, catalyzed by titanocene derivatives, has been focused on its use for synthesis of alcohols, while little is known of the mechanism or the nature of the intermediates in the reactions. On the other hand, our interest in hydrosilation chemistry has been focused on the organosilicon products and the titanocene intermediates (5). In the present paper, we describe a detailed analysis of the intermediates and products for some titanocene catalyzed hydrosilations of esters and lactones. The results of these studies provide the first direct evidence for the participation of Cp_2Ti in a catalytic hydrosilation reaction catalyzed by Cp_2TiMe_2. Our interest in these reactions evolved from an earlier study of hydrosilation–hydrogenation of pyridine carboxylic esters (6).

Results and discussion

Reduction of ethyl benzoate under hydrosilation conditions

To remove the complications arising from the presence of the ring nitrogen in isonicotinate esters, we re-investigated the reduction of ethyl benzoate under hydrosilation conditions (eq. [1] — this equation is not balanced but shows the observed reactants and products). Under most conditions studied, benzyloxysilane (**1**) was the major product. Toluene was generally a minor product, but was the only product when the reaction was carried out under a hydrogen atmosphere.

[1] $$PhCOOEt + PhMeSiH_2 \xrightarrow{Cp_2TiMe_2} \underset{\mathbf{1}}{MePhSi(OCH_2Ph)(OEt)]} + PhMe$$

The results of a number of reactions carried out under a range of conditions are summarized in Table 1. It is difficult to derive any conclusion from the results under Ar due to the scatter in the data. Nevertheless, it is reasonable to conclude that the C–O bond reduction is favored by higher temperatures and by the presence of H_2.

An isolated sample of **1** did not react with $PhMeSiH_2$ in the presence of Cp_2TiMe_2. Reactions of benzaldehyde and anisole were also briefly studied as substrates for the reaction with $PhMeSiH_2$ in the presence of Cp_2TiMe_2. A reaction of benzaldehyde at room temperature for 1 h, with a ratio of PhCHO–$PhMeSiH_2$–Cp_2TiMe_2 of 1:2:0.15, gave roughly equal amounts of $PhMeSi(OCH_2Ph)_2$ and $PhCH_3$. Under the same conditions, anisole gave only a trace of product ($PhCH_3$, ca. 0.5%). After an additional 4 h at 60°C, the yield of $PhCH_3$ increased to ca. 10%.

A reaction of $PhMeSiH_2$, PhCOOEt, and Cp_2TiMe_2 in a molar ratio of 2:1:1 gave a 75% isolated yield of the known ethoxy titanocene(III) dimer, $[Cp_2Ti(OEt)]_2$ (**2**, ref. 7). This pale green complex reacts slowly with $PhMeSiH_2$ at room temperature to give a blue product that exhibits a catalytic activity similar to that of Cp_2TiMe_2 for reduction of PhCOOEt to **1**, but with no detectable production of toluene.

Reactions of lactones with $PhMeSiH_2$ and Cp_2TiMe_2

Both γ- and β-butyrolactone reacted with $PhMeSiH_2$ in the presence of a Cp_2TiMe_2 catalyst to yield the ring-opened copolymers **3** (eq. [2]) and **4** (eq. [3]), respectively.

Table 1. Yields of toluene from reactions of ethyl benzoate with $PhMeSiH_2$ and Cp_2TiMe_2 under various conditions.

Cp_2TiMe_2/PhCOOEt (%)	*T* (°C)	Yield of toluene (%)[a]
5	20	5
10	20	10
20	20	19
30	20	11
40	20	13
10	0	2
20[b]	20	4
20[c]	20	3
20	40	40
20[d]	40	100

Note: Except where indicated, reactions were run under Ar with 10 mol% catalyst, based on $PhMeSiH_2$. All reactants were added to the reactor at the same time. Conversions were quantitative and the balance of the product was **1**.

[a]Based on ^1H NMR integration.

[b]Ethyl benzoate was added dropwise after the reaction of $PhMeSiH_2$ and Cp_2TiMe_2 was complete.

[c]$PhMeSiH_2$ (0.10 mL, 0.7 mmol) was added to the mixture of Cp_2TiMe_2 (0.088 g, 0.43 mmol) and ethyl benzoate (0.30 mL, 2.13 mmol). After the solution color changed from orange to dark violet blue an additional 0.50 mL of $PhMeSiH_2$ was added dropwise to the mixture.

[d]The reaction was run under 40 psi H_2.

[2] 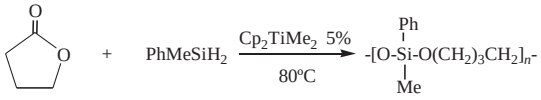

3

[3] 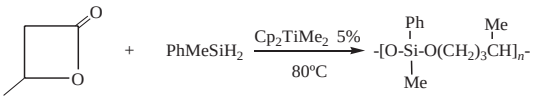

4

The polymers were recovered in ca. 30% yields, as amorphous white solids, by precipitation of the reaction mixtures with excess methanol. Molecular weights, determined by GPC, were in the range of 2–4 × 10^3 D, with polydispersities in the range of 1.2–1.3. The balance of the reaction products was not fully characterized, but from their IR and NMR spectra appeared to be a mixture of lower molecular-weight oligomers of the same structure as the isolated solid.

Stoichiometric reactions of Cp_2TiMe_2, $PhMeSiH_2$, and either γ- or β-butyrolactone, in a molar ratio of 1:2:1 in hexane–THF (15:2 v/v), yielded dark grayish-brown crystals. Given the reaction of ethyl benzoate, described above, and the known oxophilicity of Ti, a product containing Ti–O bonds was expected. To our surprise, a structure determination by X-ray crystallographic analysis showed the product to be **5** (Fig. 1).

Molecule **5** contains two inequivalent Ti atoms. One, Ti1, is coordinated to a η^5-C_5H_5 ligand, a bridging η^5-C_5H_4 ligand, and a THF molecule. The other, Ti2, is η^1-bonded to the bridging C_5H_4 ligand and to two η^5-C_5H_5 ligands. More importantly, a hydrogen-atom bridge, located in the difference map, connects the two Ti atoms. The mean distance

© 2002 NRC Canada

Fig. 1. The structure of **5**, showing thermal ellipsoids at the 30% probability level.

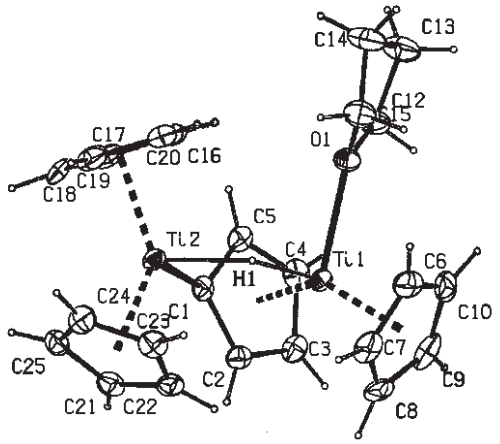

between the titaniums and the carbon atoms of the η-C_5H_5 rings (2.388 Å) and the distance between C1 and Ti1 (2.207(5) Å) agree with the assignment that three of the C_5 rings are coordinating to Ti1 and Ti2 in η^5-mode, while the fourth bridging ring is coordinating η^5 to Ti1 and η^1 to Ti2. The formula of **5** ($C_{24}H_{28}OTi_2$) corresponds to a dimer of Cp_2Ti coordinated to a molecule of THF. The crystal structure also reveals that in the lattice there is half a molecule of THF per formula unit of **5**.

The values of the molecular parameters for **5** (a number of which are compared in Table 2) are essentially the same as those reported by Pez (8) for compound **5′**, which differed only in the absence of the hydride bridge. We believe these compounds to be the same. Small differences in the parameter values are attributed to the fact that our data were collected at –60°C, while those of Pez were collected at 23°C. In addition, our measurements were carried out with Cu Kα radiation in order to favour detection of the hydride, while Pez used Mo Kα radiation. In a preliminary study, we also failed to detect the bridging hydride using Mo Kα radiation. Finally, there is a slight difference due to the fact that the Pez structure is reported in the monoclinic space group *I*2/*a*, which is a non-conventional orientation of the *C*2/*c* group used by us.

Solutions of **5** in THF are strongly paramagnetic. NMR spectra of such solutions are very broad and strongly shifted, and give essentially no clue to the structure. Their EPR spectra also consist of a very broad single peak, which gives no structural information. Pez also concluded that his compound was paramagnetic on the basis of the temperature dependence of the ^{1}H NMR chemical shift. The originally proposed structure, without a bridging hydrogen atom, is an odd- electron count system and therefore would be expected to have one unpaired electron. Addition of the bridging hydrogen atom results in an even-electron count and the molecule is expected to be diamagnetic. A simple rationalization of these observations is that **5** dissociates in the weakly coordinating THF solvent to give a titanocene(II) complex (**6**), as in eq. [4]. Although Cp_2TiL_2 complexes are well known for strong-field ligands such as PR_3 (9) and CO (10), the ground states of such complexes are normally spin singlets. The bipyridyl complex is unusual, in that it has a spin-triplet ground state, interpreted to be the result of a Ti(III) coordinated to a bipyridyl radical anion ligand (11). It is not unreasonable however to assume that a Ti(II)-centered triplet ground state could be preferred with a σ-bonding weak-field ligand such as THF that coordinates through O. Indeed, both theoretical (12) and experimental (13) results support the conclusion that the ground state of *uncomplexed* Cp_2Ti is a triplet. We are continuing to study the magnetochemistry and EPR properties of solutions of **5** in order to resolve this question.

Table 2. A comparison of some selected molecular parameters for compounds **5** and **5′**.

5		**5′**	
Bond lengths (Å)			
Ti1—O1	2.239(3)	Ti1—O1	2.26(1)
Ti1—Ti2	3.329(2)	Ti1—Ti2	3.363(2)
Ti2—C1	2.207(5)	Ti1—C5	2.19(2)
Ti1—C1	2.325(5)	Ti1—C1	2.34(2)
Ti1—C2	2.307(5)	Ti1—C5	2.32(2)
Ti1—C3	2.363(5)	Ti1—C4	2.32(2)
Ti1—C4	2.365(5)	Ti1—C3	2.37(2)
Ti1—C5	2.333(5)	Ti1—C2	2.37(2)
Ti1—(C6–10)	2.3796[a]	Ti1—(C10–14)	2.38
Bond angles (deg)			
Ti2-Ti1-O1	95.65(10)	Ti2-Ti1-O1	96.1(30)
Ti2-C1-C5	125.3(4)	Ti2-C5-C1	125.6(12)
Ti2-C1-C2	123.3(3)	Ti2-C5-C4	124.2(13)

Note: The numbering schemes for the two structures are slightly different. Those for **5′** are those used in ref. 8.

[a]These values are the average values for the five Ti–C distances of the η^5-C_5H_5 ring attached to Ti2.

[4] 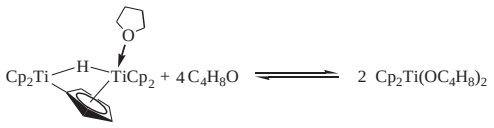

5 **6**

The two titanium atoms in **5** can be formally assigned either as Ti(II) and Ti(IV), or both as Ti(III). This oxidation-state ambiguity, and the structural motif of a hydride bridge accompanying another more-complex bridging group, is now a common feature of titanocene chemistry (6, 14–16).

The mechanism of ester hydrosilation–reduction

Earlier studies of hydrosilation–reduction of esters (17) and lactones (18) in the presence of titanocene-based catalysts were carried out from the perspective of their usefulness in organic synthesis. In no case was the intermediate organosilicon compound identified or isolated. Nevertheless, a reasonable mechanism involving addition of a Ti–H bond across the carbonyl group, followed by release of the alkoxy silicon product was proposed. A similar mechanism is shown in Scheme 1.

The cycle shown in Scheme 1 rationalizes all of the features of the hydrosilation reaction. There is ample evidence from earlier studies for the generation of Cp_2TiH by reaction of Cp_2TiMe_2 with a hydrosilane (5*a* and refs. therein). Step **a** is a plausible insertion of C=O into a Ti–H bond. The

© 2002 NRC Canada

Scheme 1. A catalytic cycle for the hydrosilation of benzoate esters.

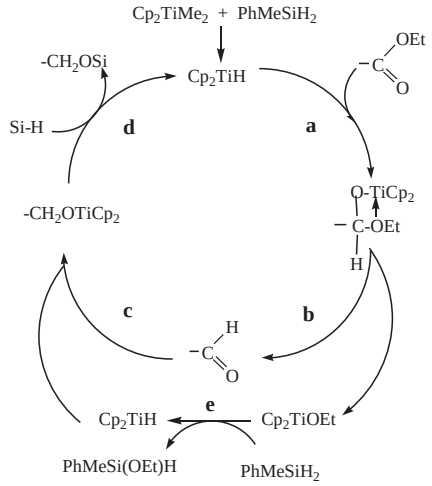

Scheme 2. A cycle for the titanocene-hydride catalyzed co-polymerization of γ-butyrolactone–$PhMeSiH_2$.

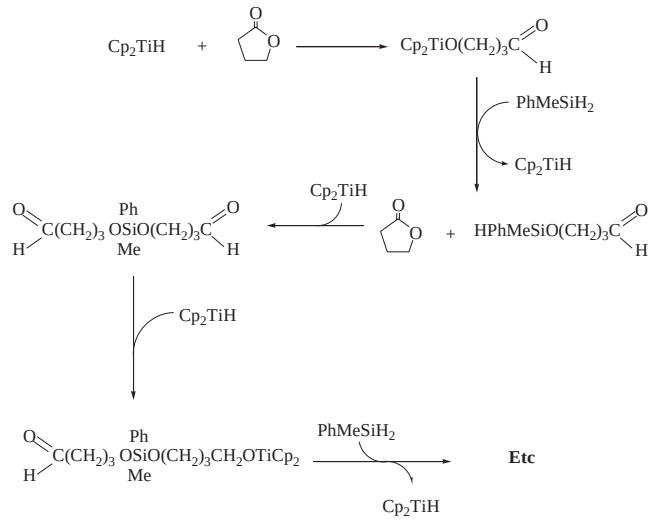

observation that a stoichiometric reaction of Cp_2TiMe_2, $PhMeSiH_2$, and PhCOOEt gives **2** in high yield is explained by the assumption that the initially formed (1-phenyl-1-ethoxy)methoxy titanocene is unstable with respect to transfer of the ethoxy group to the Ti, perhaps by an initial intramolecular coordination of the EtO oxygen to the metal. The intermediate benzaldehyde was not detected under catalytic conditions, perhaps because of an additional rapid reaction. It was however shown that benzaldehyde is reduced under these conditions to give $PhMeSi(OCH_2Ph)_2$ (presumably by step **c**) and toluene in proportions similar to those observed in the reaction with PhCOOEt. For the benzaldehyde reaction, there is no possibility of EtO transfer to the Si and hence it raises the question as to why the observed product in the ester reaction (step **d**, Scheme 1) is $PhMeSi(OEt)(OCH_2Ph)$ rather than $PhMeHSi(OCH_2Ph)$, or $PhMeSi(OCH_2Ph)_2$. A problem is also presented by the fact that $PhMeSiH_2$ does react with $[Cp_2Ti(OEt)]_2$ (step **e** Scheme 1), and the latter is also a precatalyst for the hydrosilation of PhCOOEt. Neither of these reactions, however, are fast enough to account for the rate of the Cp_2TiMe_2 catalyzed hydrosilation of PhCOOEt.

Both of these problems would be resolved if the slowness of the reaction of **2** with $PhMeSiH_2$ was due to a slow dissociation of the dimer, which masks the intrinsic reactivity of monomeric $Cp_2Ti(OR)$. The assumption of the production of a highly reactive monomeric $Cp_2Ti(OEt)$ in step **c** permits the rapid recycling of this intermediate through loop **d**, to allow for the transfer of the EtO group to silicon and regeneration of the catalyst, Cp_2TiH. Finally, once the reaction is underway, the Si–H in the σ-bond metathesis in step **d** would have to be mainly PhMe(EtO)SiH, rather than $PhMeSiH_2$.

Although the steps in the catalytic loop of Scheme 1 can explain the features of the hydrosilation reaction of PhCOOEt, they fail to explain the complete reduction (deoxygenation) to toluene. The fact that toluene is the only product when the reaction is carried out under moderate pressure of H_2 suggests that high concentrations of Ti–H favour complete deoxygenation. Reactions of hydrosilanes with Cp_2TiMe_2 produce a mixture of $CpTiSiR_3$ and Cp_2TiH, which have been isolated and characterized as bridged dimers (5*b*, 15). The balance between the amounts of silyl and hydride complexes is a function of the silane concentration, with the silyl species being favored by high silane concentration. It is also likely that H_2 is in equilibrium with these species as shown in eq. [5] (although this has never been unequivocally demonstrated). The fact that $PhMeSi(OEt)(OCH_2Ph)$ does not react under the catalytic reduction conditions excludes it as an intermediate in the production of toluene. On the other hand, the similarity of the products from the PhCOOEt and PhCHO reductions suggests that $Cp_2Ti(OCH_2Ph)$ is a plausible intermediate in the production of toluene.

[5] $Cp_2TiH + R_3SiH \rightleftharpoons Cp_2TiSiR_3 + H_2$

The mechanism of lactone–silane co-polymerization

A plausible mechanism for the titanocene-hydride mediated co-polymerization of γ-butyrolactone and $PhMeSiH_2$ is shown in Scheme 2. This scheme couples two of the steps proposed in Scheme 1 for the reduction of ethylbenzoate; namely, the addition of Cp_2TiH to an aldehyde and a σ-bond metathesis between Ti–O and Si–H to give Si–O and Ti–H. In this case the ring-opening step is an intramolecular version of steps **a** and **b** in Scheme 1. In the lactone reactions no cleavage of C–O bonds was observed.

The mechanism of formation of 5

Compound **5** is expected to be formed from the dimerization of bis(η^5-cyclopentadienyl)Ti. The manner in which the latter species may be generated by reaction of Cp_2TiMe_2 with a hydrosilane has been discussed at length elsewhere (5*b* and refs. therein). It is our belief that titanocene(II), or its dimer (**5**) is normally present in reactions involving Si–H and Cp_2TiMe_2, but its detection in solution is precluded by its electronic structure. (Its paramagnetism interferes with NMR measurements and a triplet ground state can be very difficult to observe by EPR.)

© 2002 NRC Canada

Scheme 3. In **A**, one molecule of Cp_2Ti inserts into a C–H bond of a second molecule. In **B**, a second intramolecular insertion of Ti into a C–H bond of the Cp_2Ti unit of **5** occurs, followed by coupling of the two C_5H_4 fragments. In **C**, a molecule of H_2 reacts with two Cp_2Ti molecules, perhaps by initial formation of the Cp_2TiH_2, followed by reaction with the second Cp_2Ti molecule.

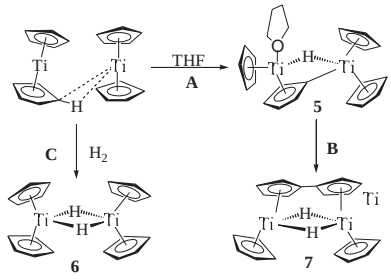

It has also been postulated that titanocene, as a result of its carbene-like character, will insert into X–H bonds and, in the absence of other choices, it will insert into one of its own C–H bonds (19). Pez (8) recognized this possibility when he first isolated and characterized **5**. A second similar-intramolecular insertion takes **5** to the hydride-bridged fulvalenyl dititanium complex (**7**), originally reported by Bercaw and co-workers (20) and structurally characterized by Troyanov et al. (21). The relationship between the various titanocene hydrides is shown in Scheme 3.

Conclusions

The titanocene-catalyzed hydrosilation of esters to the alkoxide level can be rationalized by a conventional Ti–H mediated reduction of the ester, followed by alkoxide transfer to Si. Further reduction to the hydrocarbon level occurs under unusually mild conditions, particularly in the presence of a hydrogen atmosphere. Although the mechanism is not known, it is likely that this reaction occurs via X–H (X = H or Ti) induced C–O cleavage of a benzyloxy-Ti complex.

Experimental

General manipulations and materials

All manipulations were performed under an atmosphere of nitrogen or argon using Schlenk techniques. Dry oxygen-free solvents were employed throughout. Glassware was flame-dried or oven-dried before use. γ-Butyrolactone and (±)-β-butyrolactone were purchased from Aldrich and distilled prior to use. Ethyl benzoate, benzaldehyde, and benzyl alcohol were purchased from Aldrich and purified by distillation over calcium hydride before use. Dimethyltitanocene (22) and phenylmethylsilane (23) were prepared by the procedures described in the literature.

Benzylmethyl ether was prepared by a Williamson synthesis using the following procedure: sodium (2.3 g, 0.1 mol) was added in small pieces to benzyl alcohol (11 g, 0.1 mol) in ether (50 mL). After the sodium had dissolved, CH_3I (16 g, 0.11 mol) was added dropwise from a syringe. A white solid precipitated during the addition of CH_3I. The suspension was stirred for 1 h and then dilute HCl (5 mL concentrated HCl in 30 mL H_2O) was added dropwise. The organic phase was washed with distilled water three times and then dried with $MgSO_4$. Pure benzylmethyl ether was obtained in 80% isolated yield by distillation.

^{1}H NMR spectra were recorded on a Varian XL-200, Varian XL-300, Gemini-200, or Unity-500 spectrometer using an internal solvent as a reference. ^{13}C NMR spectra were recorded on a Unity-500 spectrometer using C_6D_6 (128.0 ppm) as a reference. GPC analyses were run with THF as solvent and calibrated relative to polystyrene standards.

Reaction of ethyl benzoate with $PhMeSiH_2$ catalyzed by Cp_2TiMe_2

$PhMeSiH_2$ (0.20 mL, 1.4 mmol) and ethyl benzoate (0.10 mL, 0.70 mmol) were added to Cp_2TiMe_2 (14 mg, 0.07 mmol). After a while, the solution color changed to dark blue then brown with vigorous gas evolution. After stirring at room temperature for 1 h, quantitative conversion of ethyl benzoate to a mixture of toluene and **1** was observed by ^{1}H NMR (molar ratio 1:9). ^{1}H NMR (300 MHz, C_6D_6) for **1**: 0.34 (s, 3H, Si-C*H*$_3$), 1.15 (t, 3H, OCH_2CH_3), 3.70 (q, 2H, OCH_2CH_3), 4.78 (m, 2H, $PhCH_2O$-), 6.9–8.0 (m, Ph-*H*).

All of the experiments to obtain the data in Table 1 were carried out following the above general procedure, with the exception of the last entry, which was carried out in a stirred mini-autoclave rather than a Schlenk tube and with all of the reactants scaled up by a 10-fold.

Preparation of $[Cp_2Ti(\mu\text{-}OEt)]_2$

$PhMeSiH_2$ (0.70 mL, 4.9 mmol) and ethyl benzoate (0.40 mL, 2.5 mmol) were added to a solution of Cp_2TiMe_2 (0.50 g, 2.4 mmol in 40 mL toluene and 10 mL benzene). The solution turned dark green with precipitation of green crystals of $[Cp_2Ti(\mu\text{-}OEt)]_2$, which were filtered, washed with hexane, and dried in vacuo (0.40 g, 75% isolated yield). The identity of the product was confirmed by comparison of its IR spectrum and X-ray diffraction pattern to those of an authentic sample (7).

Reaction of ethyl benzoate and $PhMeSiH_2$ in the presence of $[Cp_2Ti(\mu\text{-}OEt)]_2$

$PhMeSiH_2$ (0.34 mL, 2.60 mmol) was added to $[Cp_2Ti(\mu\text{-}OEt)]_2$ (50 mg, 0.11 mmol). The mixture was stirred at room temperature for 24 h (during this time the formation of some 1,2-dimethyl-1,2-diphenyldisilane was observed by ^{1}H NMR). Ethyl benzoate (0.17 mL, 1.06 mmol) was then added. Gas evolution was observed in 5 min, while the solution changed from green to yellow-green. Conversion (86%) of the ester to **1** was obtained in 12 h. No toluene was detected by ^{1}H NMR.

Reaction of benzaldehyde and $PhMeSiH_2$ in the presence of Cp_2TiMe_2

$PhMeSiH_2$ (0.40 mL, 3.06 mmol) and benzaldehyde (0.20 mL, 1.97 mmol) were added to Cp_2TiMe_2 (55 mg, 0.28 mmol) at room temperature. After a while, the solution color changed to purple then dark blue accompanied by gas evolution. After 1 h toluene was observed in a 50% yield (based on ester, by ^{1}H NMR). The reaction mixture was diluted with C_6D_6 (1.0 mL) and saturated with gaseous HCl to destroy the presumed $Cp_2Ti(OCH_2Ph)$. Volatiles were

© 2002 NRC Canada

removed under vacuum and collected in an NMR tube. The resulting mixture contained toluene and $PhCH_2OH$ in roughly equal amounts, as shown by spiking the mixture with authentic samples.

Reaction of $PhCH_2OMe$ and $PhMeSiH_2$ in the presence of Cp_2TiMe_2

$PhMeSiH_2$ (0.60 mL, 4.20 mmol) and $PhCH_2OMe$ (0.30 mL, 2.46 mmol) were added to Cp_2TiMe_2 (0.10 g, 0.48 mmol). The solution color changed from orange to dark blue, accompanied by gas evolution. After stirring at 60°C for 4 h, toluene was detected in the solution by ^1H NMR in an amount equivalent to 10% of the reactant ether.

In the absence of Cp_2TiMe_2, reactions of $PhCH_2OMe$ with $PhMeSiH_2$ or $(EtO)Me_2SiH$ at 60°C for 12 h yield no toluene.

Reaction of γ-butyrolactone and $PhMeSiH_2$ catalyzed by Cp_2TiMe_2

γ-Butyrolactone (0.30 mL, 3.9 mmol) and $PhMeSiH_2$ (0.60 mL, 4.2 mmol) were added to a solution of Cp_2TiMe_2 (0.05 g, 0.24 mmol in 1 mL THF). After thorough mixing, the solution was stirred for 10 h at 80°C. The product was added dropwise to 10 mL of well-stirred dry methanol; 0.3 g of a white precipitate were obtained. The compound was assigned as $-[OSiPhMeO(CH_2)_4]_n-$ based on ^1H and ^{13}C NMR spectra. GPC analysis indicated a $M_w = 4.9 \times 10^3$, $M_w/M_n = 1.3$. ^1H NMR (300 MHz, C_6D_6) δ: 0.40 (s, 3H, Si-CH_3), 1.7 (m, 4H, $CH_2(CH_2)_2CH_2$), 3.75 (m, 4H, $CH_2(CH_2)_2CH_2$), 7.0–8.0 (m, 5H, Ph-*H*). ^{13}C NMR (500 MHz, C_6D_6) δ: –5 (1C, SiCH_3), 29 (2C, $CH_2(CH)2CH$), 62 (2C, $CH_2(CH_2)_2CH_2$), 130, 134 (6C, C_6H_5).

Reaction of (±)-β-butyrolactone and $PhMeSiH_2$ in the presence of Cp_2TiMe_2

(±)-β-Butyrolactone (0.30 mL, 3.7 mmol) and $PhMeSiH_2$ (0.55 mL, 3.8 mmol) were added to a solution of Cp_2TiMe_2 (0.05 g, 0.24 mmol, in 1 mL THF). After thorough mixing, the solution was stirred for 8 h at 80°C. The product was added dropwise to 10 mL of well-stirred methanol. A white precipitate (0.28 g) was obtained. The compound was identified as $-[OSiPhMeO(CH_2)_2CH(CH_3)]_n-$ based on its ^1H NMR spectrum. GPC analysis indicated a $M_w = 1.8 \times 10^3$ with $M_w/M_n = 1.2$. ^1H NMR (300 MHz, C_6D_6) δ: 0.40 (s, 3H, Si-CH_3), 1.1 (m, 3H, $CH_2CH_2CH(CH_3)$), 1.4 (m, 2H, $CH_2CH_2CH(CH_3)$), 3.6 (m, 2H, CH_2 $CH_2CH(CH_3)$), 3.9 (m, 1H, $CH_2CH_2CH(CH_3)$), 7.1–7.9 (m, 5H, Ph-*H*).

Sythesis of crystalline $C_{26}H_{32}O_{1.5}Ti_2$ (5)

γ-Butyrolactone (0.02 mL, 0.26 mmol) and $PhMeSiH_2$ (0.07 mL, 0.49 mmol) were added to a Cp_2TiMe_2 in hexane–THF solution (50 mg, 0.24 mmol, in 15 mL hexane and 2 mL THF). After thorough mixing, the flask was left undisturbed for 24 h. Dark gray plates of **5** (33 mg) crystallized from the solution (65% isolated yield). Anal. calcd. for $C_{26}H_{32}O_{1.5}Ti_2$: C 67.86, H 6.96, O 4.35, Ti 20.84; found: C 67.58, H 6.75. The low CH analysis is probably due to loss of lattice THF during sample isolation. The IR spectrum of **5** showed the same features as that of the compound described by Pez (8). Despite several attempts, we were not able to assign an IR band due to the bridging hydride of **5**, or to its deuterated analogue, prepared with $PhMeSiD_2$.

Collection of X-ray data and structure determination of 5

Data were collected on a crystal of **5** of dimensions of 0.52 × 0.29 × 0.01 mm mounted in a glass capillary under argon.[2] *Crystal data*: $C_{24}H_{28}O_1Ti_2 \cdot 1/2C_4H_8O_1$; FW = 456.299; monoclinic, *C*2/*c*; a = 31.232(13), b = 7.998(3), c = 19.603(9) Å, β = 116.78(3)°; Z = 8, Z' = 1; D_c = 1.387 g cm^{-3}. Data were collected on a CAD4 diffractometer using Cu Kα radiation. In all, 29561 reflections were measured, of which 4145 unique (R_{int} 14.9%) reflections were used for structure solution and refinement. Data were corrected for absorption (μ = 63.48 cm^{-1}; transmission range: 0.2708–0.9287). Final agreement factors: R_1: (obsd./all) 0.059/0.094; wR_2: 0.143/0.157. The structure was solved by SHELXLS-96 (24) and refined in SHELXL-96 (25). All nonhydrogen atoms are anisotropic. Hydrogen atoms are calculated except the bridging hydride, which was located in the difference map and refined isotropically with the restraint that both Ti–H distances be similar.

Acknowledgments

Financial support from NSERC of Canada and Fonds FCAR du Québec are gratefully acknowledged.

References

1. N.A. Petasis and Y.H. Hu. Current Org. Chem. **1**, 249 (1997).
2. (*a*) F. Sato, T. Jinbo, and M. Sato. Tetrahedron Lett. **21**, 2171 (1980); (*b*) T. Nakano and Y. Nagai. Chem. Lett. 481 (1988); (*c*) R.L. Halterman, T.M. Ramsey, and Z.-L. Chen. J. Org. Chem. **59**, 2642 (1994); (*d*) S.-X. Xin and J.F. Harrod. Can. J. Chem. **73**, 999 (1995); (*e*) M.B. Carter, B. Schiøtt, A. Gutiérrez, and S.L. Buchwald. J. Am. Chem. Soc. **116**, 11667 (1994).
3. (*a*) X. Verdaguer, S.C. Berk, and S.L. Buchwald. J. Am. Chem. Soc. **117**, 12641 (1995); (*b*) X. Verdaguer, M.C. Hansen, S.C. Berk, and S.L. Buchwald. J. Org. Chem. **62**, 8522 (1997).
4. (*a*) S.C. Berk, K.A. Kreutzer, and S.L. Buchwald. J. Am. Chem. Soc. **113**, 5093 (1991); (*b*) S.C. Berk and S.L. Buchwald. J. Org. Chem. **57**, 3751 (1992); (*c*) K.J. Barr, S.C. Berk, and S.L. Buchwald. J. Org. Chem. **59**, 4323 (1994); (*d*) M.T. Reding and S.L. Buchwald. J. Org. Chem. **60**, 7884 (1995).
5. (*a*) L. Hao, J.F. Harrod, A.-M. Lebuis, Y. Mu, R. Shu, E. Samuel, and H.-G. Woo. Angew. Chem. Int. Ed. Engl. **37**, 3126 (1998); (*b*) J.F. Harrod. Coord. Chem. Rev. **206–207**, 541 (2000).

[2] Supplementary material may be purchased from the Depository of Unpublished Data, Document Delivery, CISTI, National Research Council Canada, Ottawa, ON K1A 0S2, Canada. For information on obtaining material electronically go to http://www.nrc.ca/cisti/irm/unpub_e.shtml. Crystallographic information has also been deposited with the Cambridge Crystallographic Data Centre (CCDC No. 169316). Copies of the data can be obtained free of charge via www.ccdc.cam.ac.uk/conts/retrieving.html (or from the Cambridge Crystallographic Data Centre, 12, Union Road, Cambridge CB2 1EZ, UK; fax: +44 1223 336033; or deposit@ccdc.cam.ac.uk).

© 2002 NRC Canada

6. J.F. Harrod, R. Shu, H.-G. Woo, and E. Samuel. Can. J. Chem. **79**, 1075 (2001).
7. E. Samuel, J.F. Harrod, D. Gourier, Y. Dromzee, F. Robert, and Y. Jeannin. Inorg. Chem. **31**, 3252 (1992).
8. G.P. Pez. J. Am. Chem. Soc. **98**, 8072 (1976).
9. (*a*) L.B. Kool, M.D. Rausch, M. Alt, M. Heberhold, U. Thewalt, and B. Wolf. J. Organomet. Chem. **310**, 27 (1986); (*b*) D.J. Sikora, J.W. Macomber, and M.D. Rausch. Adv. Organomet. Chem. **25**, 316 (1986).
10. (*a*) L.P. Battaglia, M. Nardelli, C. Pelizzi, G. Predieri, and G.P. Chiusoli. J. Organomet. Chem. **259**, 301 (1983); (*b*) M.D. Fryzuk, T.S. Haddad, and D.J. Berg. Coord. Chem. Rev. **90**, 137 (1990).
11. R. Gyepes, P.T. Witte, M. Horcek, I. Císarová, and K. Mach. J. Organomet. Chem. **551**, 207 (1998).
12. J.F. Harrod, T. Ziegler, and V. Tschinke. Organometallics, **9**, 890 (1990)
13. P.B. Hitchcock, F.M. Kerton, and F.M. Lawless. J. Am. Chem. Soc. **120**, 10264 (1998).
14. L.J. Guggenberger and F.N. Tebbe. J. Am. Chem. Soc. **95**, 7870 (1973)
15. C. Aitken, J.F. Harrod, and E. Samuel. J. Am. Chem. Soc. **108**, 4059 (1986).
16. S. Xin, H.-G. Woo, J.F. Harrod, E. Samuel, and A.-M. Lebuis. J. Am Chem. Soc. **119**, 5307 (1997).
17. (*a*) S.C. Berk, K.A. Kreutzer, and S.L. Buchwald. J. Am. Chem. Soc. **113**, 5093 (1991); (*b*) S.C. Berk and S.L. Buchwald. J. Org. Chem. **57**, 3751 (1992); (*c*) K.J. Barr, S.C. Berk, and S.L. Buchwald. J. Org. Chem. **59**, 4323 (1994); (*d*) M.T. Reding and S.L. Buchwald. J. Org. Chem. **60**, 7884 (1995).
18. (*a*) X. Verdaguer, S.C. Berk, and S.L. Buchwald. J. Am. Chem. Soc. **117**, 12641 (1995); (*b*) X. Verdaguer, M.C. Hansen, S.C. Berk, and S.L. Buchwald. J. Org. Chem. **62**, 8522 (1997).
19. J.W. Lauher and R. Hoffmann. J. Am. Chem. Soc. **98**, 1729 (1976).
20. (*a*) J. Bercaw and H.H. Brintzinger. J. Am. Chem. Soc. **91**, 7301 (1969); (*b*) H.H. Brintzinger and J. Bercaw J. Am. Chem. Soc. **92**, 6182 (1970).
21. S.I. Troyanov, H. Antropiusová, and K.J. Mach. J. Organomet. Chem. **49**, 427 (1992).
22. K. Claus and K. Bestiam. Liebigs Ann. Chem. **8**, 654 (1962).
23. R.A. Benkeser, H. Landesman, and D.J. Foster. J. Am. Chem. Soc. **74**, 648. (1952).
24. G.M. Sheldrick. SHELXS-96. Program for the solution of crystal structures. University of Gottingen, Germany. 1996.
25. G.M. Sheldrick. SHELXL-96. Program for structure analysis. University of Göttingen, Germany. 1996.

© 2002 NRC Canada

Solution and solid-state characterization of a dicopper receptor for large substrates

Greg J.E. Davidson, Andrew J. Baer, Adrien P. Côté, Nicholas J. Taylor, Garry S. Hanan, Yasutaka Tanaka, and Masashi Watanabe

Abstract: Ligand **2** contains two metal-binding domains separated by a rigid spacer and assembles into a dicopper receptor with a large central cavity with no evidence of catenation.

Key words: copper complex, coordination, X-ray crystallography, molecular recognition.

Résumé : Le ligand **2** contient deux groupement pour coordonner des métaux séparer par un espaceur rigide et s'auto-assemble avec le cuivre(II) pour former un récepteur avec un grand cavité centrale avec aucune evidence pour la formation de caténane.

Mots clés : complex de cuivre, coordination, crystallographie rayons-X, reconnaissance moléculaire.

Introduction

The metal-directed self-assembly of discrete supramolecular structures, e.g., triangles (1), squares (2), and grids (3), has attracted considerable interest in recent years. When properly designed, discrete supramolecular structures may serve as metalloreceptors for small organic and bio-organic molecules (4). A key advantage of metallomacrocycles over similarly sized organic receptors is the higher yields associated with metal-directed self-assembly compared with conventional macrocycle synthesis (5). One drawback, however, is that dimetallic receptors have a tendency to form interlocking rings depending on their concentration and the size of the receptor site (6). Although templation of the metalloreceptor around a guest molecule(s) may eliminate catenation, it may in turn diminish or eliminate further guest binding by occupying the receptor site.

Since metalloreceptors capable of binding functionalized substrate can perform catalysis and behave as artificial enzymes (7), receptors for larger substrate would increase the diversity of possible substrate and, therefore, products obtained. Early work with dimetallic receptors proved the importance of metal-directed self-assembly; however, it focused on systems with small receptor sites (8). Thus the binding of substrates larger than a single heterocycle was precluded, and the formation of catenanes was impossible. Although reports of dimetallic receptors with large cavities have recently appeared in the literature, no confirmation of host–guest binding in the solid state was presented (9). Herein we present solution and solid-state evidence for the assembly of a dimetallic receptor with a large cavity that displays no evidence of catenation, yet requires no template for its formation.

Results and discussion

The organic framework for our dimetallic receptor is based on *m*-terphenyl, synthesized by the uncatalyzed reaction of aryllithium or arylmagnesium reagents with *m*-dichlorobenzene (the Hart reaction) (10). The Hart reaction allows facile entry into large substructures suitable for further functionalization, since R groups may be readily incorporated in the ligand framework (Scheme 1). Thus, 4,4′-bis(bromomethyl)-1,1′:3′,1″-terphenyl (**1**) was synthesized from 4,4′-dimethyl-1,1′:3′,1″ -terphenyl by radical bromination with NBS in 67% yield (11). Allowing **1** to react with two equivalents of potassium acetylacetonate in *tert*-butanol afforded ligand **2** in 91% yield after extraction with methanol (Scheme 1).[2] In solution, ligand **2** exists in its keto and enol forms. Integration of the two methyl peaks at 2.12 and 2.17 ppm supports an approximate 1:1 of the two forms. A singlet and doublet for H-3 and H-3′, respectively, and a triplet for H-2, also supports this assignment. In the IR region, both O–H and C–O stretches confirm the keto–enol formulation.

The dicopper receptor is readily synthesized in near quantitative yield from **2** and $Cu(NH_3)_4SO_4$ in a biphasic H_2O–$CHCl_3$ reaction mixture (8).[3] Upon layering **2** in chlo-

Received 16 February 2002. Published on the NRC Research Press Web site at http://canjchem.nrc.ca on 30 April 2002.

G.J.E. Davidson, A.J. Baer, A.P. Côté, N.J. Taylor, and G.S. Hanan.[1] Department of Chemistry, University of Waterloo, Waterloo, ON, Canada N2L-3G1.
Y. Tanaka and M. Watanabe. Faculty of Engineering, Shizuoka University, Hamamatsu, 432–8561, Japan.

[1]Corresponding author (e-mail: ghanan@uwaterloo.ca).

[2]Selected data for **2**: ^{1}H NMR ($CDCl_3$) δ: 2.12 (s, 3H, H-1, keto), 2.17 (s, 3H, H-1, enol), 3.21 (d, 2H, H-3, keto), 3.72 (s, 2H, H-3, enol), 4.03 (t, 1H, H-4, keto), 7.23–7.75 (m, 12H, H-4,) 16.8 (s, 1H, H-7, -OH enol). FAB-MS *m*/*z*: 455.0 $[M + H]^+$.
[3]Selected data for **3**: ESI-MS *m*/*z*: 1055.46 $[M + Na]^+$ Anal. calcd. for **3**·0.5$CHCl_3$: C 66.31, H 5.56; found: C 66.60, H 5.48.

 DOI: 10.1139/V02-065 © 2002 NRC Canada

Scheme 1. Synthesis of ligand **2** and metallomacrocycle **3** (R = H). Reagents and conditions: (*a*) KO-*t*-Bu and 2,4-pentanedione in *t*-BuOH; (*b*) $Cu(NH_3)_4SO_4 \cdot H_2O$ in H_2O–$CHCl_3$.

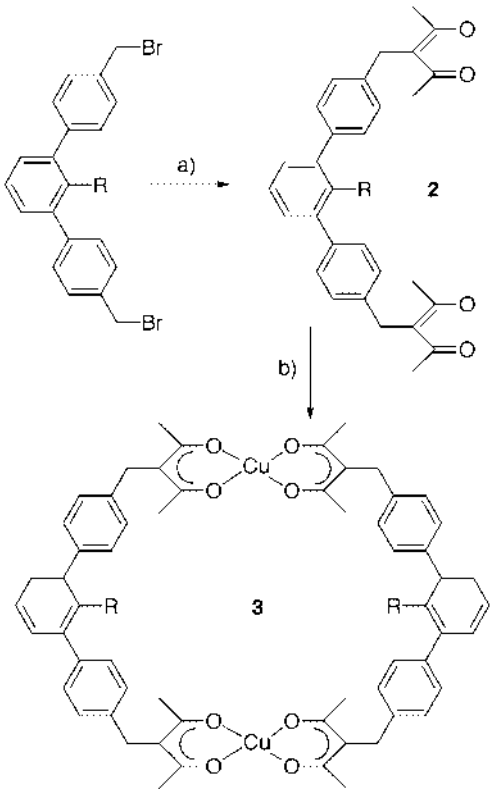

roform with $Cu(NH_3)_4SO_4$ in H_2O, the organic-soluble olive-green $Cu_2\mathbf{2}_2$ complex (**3**) is produced (Scheme 1). The IR spectrum of **3** confirms the presence of metal-bound acetylacetonate moieties, while electrospray mass spectrometry verified the molecular structure of complex **3**. Since the complex is charge neutral, the molecular ion was obtained as the Na^+ adduct of the complex.[3]

The electronic absorption spectrum of **3** contains an absorption band at 644 nm associated with metal-based *d–d* transitions. The addition of nitrogen-containing bases to a chloroform solution of **3** produces a turquoise solution and a concomitant shift in the metal-based transition to higher energy. (An isosbestic point in the titration is an indication of a two-species system.) A more detailed binding study with 4,4′-bipyridine reveals a binding constant of 250 M^{-1}. Monoaza guests, such as pyridine and substituted pyridines, bind much more poorly to the dicopper complex, with binding constants of ≈1.

X-ray quality crystals of **3** as its 4,4′-bipyridine adduct (**4**) are obtained by slow evaporation of a 1:1 mixture of 4,4′-bipyridine and **3** in $CHCl_3$ (Scheme 1, Fig. 1).[4] The solid-state structure of **4** clearly delineates the size of the cavity

Fig. 1. X-ray crystal structure of **4** showing 50% probability ellipsoids for all nonhydrogen atoms. H atoms and $CHCl_3$ have been omitted for clarity. Only the N, O, and Cu of the asymmetric unit are labelled. Selected bond distances (Å) and angles (°): Cu(1)—N(1): 2.338(5); Cu(1)—O(1): 1.926(4); Cu(1)—O(2): 1.921(4); Cu(1)—O(3): 1.921(5); Cu(1)—O(4): 1.912(4); O(1)-Cu(1)-O(2): 91.61(17)°; O(3)-Cu(1)-O(4): 90.8(2)°.

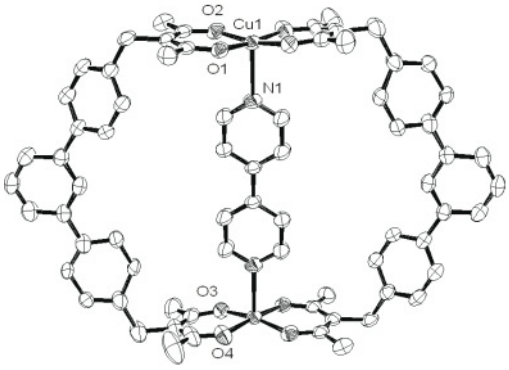

produced by the assembly of the complex: the Cu—Cu distance is 11.8 Å, while the cross-cavity distance, measured from the central benzene 2-positions, is 14.0 Å, and the peripheral phenyl groups are separated by 12.6 Å. The metal ions are not only directing the assembly of the receptors, but they are also binding the substrate, 4,4′-bipyridine, into their primary coordination sphere. The Cu—N bond length is 2.338 Å, and the Cu—O bond lengths vary between 1.912 and 1.926 Å. The Cu(II) ions are pulled slightly out of the basal plane (0.15 Å), maintaining a typical metal–metal distance for 4,4′-bipyridine bridged-metal ions. The angle at the benzyl carbon that connects the acetylacetonate and terphenyl moieties is distorted from a tetrahedral geometry to 115°. The unit cell is over 2500 $Å^3$; ten chloroform molecules are also present.

The large hexagonal cavity delineated by the two terphenyl groups and the $Cu(acac)_2$ moieties encompasses a volume of approximately 400 $Å^3$ when extended to the acetylacetonate methyl groups (Fig. 2). Crystallization solvent (10 × $CHCl_3$) is also found within this cavity. The $Cu(acac)_2$ moieties are approximately perpendicular to the central phenyl ring, whereas the two other phenyl rings are tilted away from the plane. Molecular modelling based on the $Cu_2\mathbf{2}_2$ framework suggests that the $Cu(acac)_2$ moities are sufficiently bulky to preclude catenane formation in **4**. This bodes well for the use of this framework in secondary sphere coordination studies, since R groups such as -CO_2H, -CO_2Me, and -$CONH_2$ may be readily introduced using existing methodology (Scheme 1). Furthermore, extending the cavity volume may also be possible by introducing bulkier aliphatic groups to the metal-binding acetylacetonate

[4] Crystal data for **4**: $C_{70}H_{64}N_2O_8Cu_2$ (10 × $CHCl_3$), M = 2381.99, triclinic, space group $P\bar{1}$; a = 12.0488(5), b = 14.5721(6), c = 15.0139(6) Å; α = 104.141(1), β = 95.203(1), γ = 95.569(1)°; V = 2526.20(18) $Å^3$; Z = 1; D_c = 1.566 g cm^{-3}; μ = 1.265 mm^{-1}; T = 180(1) K; R_1 = 0.0880 for 8929 data with $I > 2\sigma(I)$. Supplementary material may be purchased from the Depository of Unpublished Data, Document Delivery, CISTI, National Research Council Canada, Ottawa, ON K1A 0S2, Canada. For information on obtaining material electronically go to http://www.nrc.ca/cisti/irm/unpub_e.shtml. Crystallographic information has also been deposited with the Cambridge Crystallographic Data Centre (CCDC No. 179443). Copies of the data can be obtained free of charge via www.ccdc.cam.ac.uk/conts/retrieving.html (or from the Cambridge Crystallographic Data Centre, 12, Union Road, Cambridge CB2 1EZ, U.K.; fax: +44 1223 336033; or deposit@ccdc.cam.ac.uk).

© 2002 NRC Canada

Fig. 2. View of the X-ray crystal structure of **4** along the plane containing the *m*-terphenyl framework. Eight of the 10 chloroform solvent molecules are shown. The solvent is found above and below a cavity delineated by the acetylacetonate groups of the metallomacrocycle.

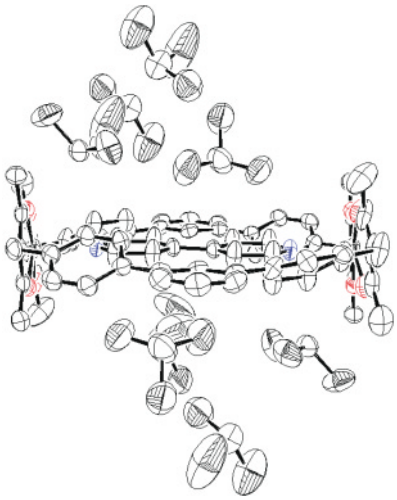

moities. We are currently pursuing these two avenues and will present our results in due course.

Acknowledgments

G.S.H. thanks the Natural Sciences and Engineering Research Council (NSERC) of Canada, the Research Corporation (Tucson, AZ), and the Province of Ontario for financial support. A.J.B. thanks the Davies Charitable Foundation for financial support. Y.T. thanks PRESTO (Precursory Research for Embryonic Science and Technology) of Japan Science and Technology Corporation.

References

1. (*a*) S. Leininger, B. Olenyuk, and P.J. Stang. Chem. Rev. **100**, 853 (2000); (*b*) J.A.R. Navarro and B. Lippert. Coord. Chem. Rev. **185–186**, 653 (1999); (*c*) B. Olenyuk, A. Fechtenkotter, and P.J. Stang. J. Chem. Soc. Dalton Trans. 1707 (1998); (*d*) A. Sautter, D.G. Schmid, G. Jung, and F. Wuerthner. J. Am. Chem. Soc. **123**, 5424 (2001); (*e*) R.-D. Schnebeck, E. Freisinger, and B. Lippert. Chem. Commun. 675 (1999); (*f*) R.-D. Schnebeck, E. Freisinger, F. Glahe, and B. Lippert. J. Am. Chem. Soc. **122**, 1381 (2000).
2. (*a*) S.-S. Sun and A.J. Lees. J. Am. Chem. Soc. **122**, 8956 (2000); (*b*) S.-S. Sun and A.J. Lees. Inorg. Chem. **40**, 3154 (2001); (*c*) S.-S. Sun, A.S. Silva, I.M. Brinn, and A.J. Lees. Inorg. Chem. **39**, 1344 (2000); (*d*) P.J. Stang, D.H. Cao, S. Saito, and A.M. Arif. J. Am. Chem. Soc. **117**, 6273 (1995); (*e*) M. Fujita, J. Yazaki, and K. Ogura. J. Am. Chem. Soc. **112**, 5645 (1990).
3. (*a*) L. Zhao, Z. Xu, L.K. Thompson, and D.O. Miller. Polyhedron, **20**, 1359 (2001); (*b*) P.N.W. Baxter, J.-M. Lehn, G. Baum, and D. Fenske. Chem. Eur. J. **6**, 4510 (2000); (*c*) J. Rojo, F.J. Romero-Salguero, J.-M. Lehn, G. Baum, and D. Fenske. Eur. J. Inorg. Chem. 1421 (1999); (*d*) D.M. Bassani, J.-M. Lehn, K. Fromm, and D. Fenske. Angew. Chem. Int. Ed. **37**, 2364 (1998); (*e*) G.S. Hanan, D. Volkmer, U.S. Schubert, J.-M. Lehn, G. Baum, and D. Fenske. Angew. Chem. Int. Ed. Engl. **36**, 1842 (1997).
4. (*a*) J.A. Whiteford, C.V. Lu, and P.J. Stang. J. Am. Chem. Soc. **119**, 2524 (1997); (*b*) M. Fujita, J. Yazaki, and K. Ogura. Tetrahedron Lett. **32**, 5589 (1991).
5. (*a*) M. Fujita. *In* Comprehensive supramolecular chemistry. Vol. 9. *Edited by* J.A. Atwood and J.-M. Lehn. Pergamon Press, New York. 1996. p. 25; (*b*) D.H. Cao, K. Chen, J. Fan, J. Manna, B. Olenyuk, J.A. Whiteford, and P.J. Stang. Pure Appl. Chem. **69**, 1979 (1997).
6. (*a*) W.J. Hunks, M.C. Jennings, and R.J. Puddephatt. Inorg. Chem. **39**, 2699 (2000); (*b*) W.J. Hunks, M.-A. MacDonald, M.C. Jennings, and R.J. Puddephatt. Organometallics, **19**, 5063 (2000); (*c*) M. Fujita and K. Ogura. Coord. Chem. Rev. **148**, 249 (1996); (*d*) M. Fujita and K. Ogura. Supramol. Sci. **3**, 37 (1996); (*e*) M. Fujita, M. Aoyagi, F. Ibukuro, K. Ogura, and K. Yamaguchi. J. Am. Chem. Soc. **120**, 611 (1998); (*f*) C. Dietrich-Buchecker, J.-P. Sauvage, N. Geum, A. Hori, M. Fujita, S. Sakamoto, and K. Yamaguchi. Chem. Commun. 1182 (2001); (*g*) G.J.E. Davidson, S.J. Loeb, N.A. Parekh, and J.A. Wisner. J. Chem. Soc. Dalton Trans. 3135 (2001).
7. (*a*) W.B. Motherwell, M.J. Bingham, and Y. Six. Tetrahedron, **57**, 4663 (2001); (*b*) J. Suh. Adv. Supramol. Chem. **6**, 245 (2000).
8. (*a*) A.W. Maverick and F.E. Klavetter. Inorg. Chem. **23**, 4129 (1984); (*b*) A.W. Maverick, S.C. Buckingham, Q. Yao, J.R. Bradbury, and G.G. Stanley. J. Am. Chem. Soc. **108**, 7430 (1986).
9. (*a*) L.H. Uppadine, J.M. Weeks, and P.D. Beer. J. Chem. Soc. Dalton Trans. 3367 (2001); (*b*) K. Fujimoto and S. Shinkai. Tet. Lett. **35**, 2915 (1994).
10. (*a*) T.K. Vinod, P. Rajakumar, and H. Hart. Tetrahedron, **51**, 2267(1995); (*b*) A. Saednya and H. Hart. Synthesis, 1455 (1996).
11. H. Hart and P. Rajakumar. Tetrahedron, **51**, 1313 (1995).

© 2002 NRC Canada

Gas-phase pyrolysis of thiopheneacetic acids, thienylethanols, and related compounds — protophilicity of ring π-electrons and relative acidities of hydrogen-bond donors of hydroxyl groups

Ibtehal A. Al-Juwaiser, Nouria A. Al-Awadi, and Osman M.E. El-Dusouqui

Abstract: Based on kinetic data of thermal gas-phase elimination reactions, the following Arrhenius log A (s^{-1}) and E_a (kJ mol^{-1}) values, respectively, are obtained: 10.76 and 153.5 for 3-thiopheneacetic acid (**1**), 10.08 and 149.4 for 2-thiopheneacetic acid (**2**), 12.04 and 207.1 for 2-(3-thienyl)ethanol (**3**), 11.55 and 203.3 for 2-(2-thienyl)ethanol (**4**), 10.91 and 123.4 for 2-thiopheneglyoxylic acid (**5**), 11.05 and 223.8 for 1-(2-thienyl)propan-1-one (**6**), and 10.33 and 149.8 for 3-thiophenemalonic acid (**7**). The products of these pyrolytic reactions were either carbon dioxide or formaldehyde in addition to methylthiophene or thiophenecarboxaldehyde. Both positional and molecular reactivities of the substrates and related compounds are compared, and the results are rationalized on the basis of a reaction pathway involving a concerted six-membered transition state.

Key words: thiophenes, gas-phase, pyrolysis, kinetics, mechanism.

Résumé : Sur la base de données cinétiques de réactions d'élimination thermiques en phase gazeuse, on a déterminé les valeurs suivantes d'Arrhenius suivantes log A (s^{-1}) et E_a (kJ mol^{-1}) pour respectivement l'acide 3-thiophèneacétique (**1**, 10,76 et 153,5), l'acide 2-thiophèneacétique (**2**, 10,08 et 149,4), le 2-(thién-3-yl)éthanol (**3**, 12,04 et 207,1), le 2-(thién-2-yl)éthanol (**4**, 11,55 et 203,3), l'acide 2-thiophèneglyoxylique (**5**, 10,91 et 123,4), la 1-(thién-2-yl)propan-1-one (**6**, 11,05 et 223,8) et l'acide 3-thiophènemalonique (**7**, 10,33 et 149,8). Les produits de ces réactions de pyrolyse sont le bioxyde de carbone ou le formaldéhyde ainsi que le méthylthiophène ou le thiophènecarboxaldéhyde. On a comparé les réactivités positionnelles ainsi que moléculaires des substrats examinés ici ainsi que celles de composés apparentés et on rationalise les résultats en se basant sur une voie réactionnelle impliquant un état de transition concerté à six chaînons.

Mots clés : thiophènes, phase gazeuse, pyrolyse, cinétique, mécanisme.

[Traduit par la Rédaction]

Introduction

Thiophene is classified as an electron-rich (π-excessive) heteroaromatic compound, with its aromaticity between that of furan and benzene, and reactivity towards electrophiles ca. 10^3- to 10^5-fold higher relative to benzene (1, 2). The structural effects associated with the 2,3-conjugative interaction and the high 2:3-bond order superimposed upon an intrinsic 2 > 3 positional reactivity serve to explain the relative rates and partial rate factors obtained in electrophilic aromatic substitution reactions of thiophene and its N, O, and Se analogues and monosubstituted derivatives (3–5). Hammett substituent-replacement constants reported for both solution and gas-phase reactions suggest that the 2- and 3-thienyl ring systems act as electron withdrawing and electron donating groups, respectively (6). An electron withdrawing effect would be expected to augment the electrophilic nature of the hydroxyl hydrogen of both the alcohol and carboxylic acid moieties of substituted thiophenes. The present study involves thiophenes substituted at the 2- and 3-positions with groups in which terminal O-H moieties serve as H-bond donor acids, and where a protonic hydrogen is available for intramolecular electrophilic H-exchange processes. Reactions of this nature, for which a concerted six-membered transition state (TS) is postulated, are expected to have favourable conformations and effective intramolecular pre-organization. A representative example is the thermal gas-phase elimination reaction of 2-thiopheneglyoxylic acid, the final product of which is 2-thiophenecarboxaldehyde (Scheme 1).

Previous studies on comparable reactions have lead to the conclusion that, during the development of the TS of the elimination process, either bond **a**, **b**, or **d** (Scheme 1) could be effectively displaced further away from the reacting site compared with the other two bonds, or that a combined

Received 16 September 2001. Published on the NRC Research Press Web site at http://canjchem.nrc.ca on 30 April 2002.

I.A. Al-Juwaiser, N.A. Al-Awadi,[1] and O.M.E. El-Dusouqui. Department of Chemistry, University of Kuwait, P.O. Box 5969, Safat 13060, Kuwait.

[1]Corresponding author (e-mail: nouria@kuc01.kuniv.edu.kw).

 DOI: 10.1139/V02-067 © 2002 NRC Canada

Scheme 1. Reaction pathway, concerted six-membered TS, and final product of thermal gas-phase elimination.

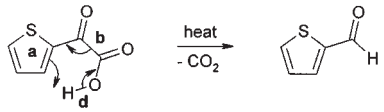

effect on the observed reactivity involves either two or all three of the bonds (7–11). The effect of the double bond (**a**) is associated with the lability (protophilicity) of its π-electrons, the effect of **b** depends on bond polarity, and that of **d** results from the relative acidity of the H-bond donor and the magnitude of the positive charge developing on the hydrogen. In addition, an important factor in these elimination reactions is the relative thermodynamic stability of the incipient moieties leading to the products (10*a*, *c*). It is noteworthy that a six-membered TS has also been proposed for decarboxylation reactions of heteroarylacetic acids in aqueous media (12).

Results and discussion

Kinetics

The kinetic data of the gas-phase elimination reactions of the seven compounds (**1**–**7**) under study are given in Table 1. Each rate constant represents an average from a set of three values obtained in three separate kinetic runs; all three values were measured at the same temperature. The agreement between the rate-constant values in each set is within ±2%. Each elimination process was monitored until 90–95% of reaction was completed. The temperature range (54 ± 7 K) over which each compound was investigated is a prerequisite for reliable kinetic studies (9–11). Arrhenius parameters were obtained using the results from Table 1. The Arrhenius plots were linear over the temperature range studied, with correlation coefficients of the order of 0.990 ± 0.009. For example, for 3-thiopheneacetic acid (**1**) at 53.5 K the correlation coefficient is 0.9994. Arrhenius log A (s^{-1}), $\Delta S^{\#}$ (J mol^{-1} K^{-1}), the energy of activation (E_a, kJ mol^{-1}), and the first-order rate constants (k, s^{-1}) of the elimination reactions at 600 K are recorded in Table 2. The values of log A (s^{-1}) show a narrow range for each set of compounds (10.5 ± 0.4 for the acids and 11.8 ± 0.2 for the alcohols), but a wider range for the E_a (kJ mol^{-1}) values, an indication of dependence of the reaction on E_a. This seems to be a common feature of polar thermal gas-phase elimination processes (13). The values for $\Delta S^{\#}$ (J mol^{-1} K^{-1}) are negative and relatively large, which might be the result of considerable pre-organization leading to the formation of the six-membered TS postulated for such gas-phase reaction pathways (7). It is to be noted that an earlier but independent preliminary study by our group on the present substrates gave almost identical reaction rate factors at 450 K; however, only the rates for pyrolysis at 600 K are reported here.

Reaction products

Reaction products for complete pyrolysis were obtained for all substrates except 1-(2-thienyl)-1-propanone, since its complete pyrolysis required temperatures beyond the operating temperatures of the reactors. Pyrolyses were carried out either in a flow reactor or in a sealed-tube pyrolyzer at temperatures comparable with those used in the kinetic investigations. The reactions were allowed ample residence time to ensure maximum pyrolysis. The constituents of the pyrolysates were analyzed using GC–MS, FT-IR, and ^1H NMR techniques. Conversion of the acid and alcohol starting materials into reaction products was monitored in part by observing the absence of the characteristic FT-IR absorption peaks of the substrates. Pyrolysis of 2-thiopheneacetic acid (**2**) and 2-(2-thienyl)ethanol (**4**) gave 2-methylthiophene (*m*/*z*: $M^{\bullet+}$ = 98 and base peak at 97; the corresponding values for their precursor substrates are $M^{\bullet+}$ = 142 and $M^{\bullet+}$ = 128, respectively). On the other hand, pyrolysis of 3-thiopheneacetic acid (**1**) and 2-(3-thieny)ethanol (**3**) produced 3-methylthiophene with *m*/*z* values identical to those of their 2-substituted analogues. Differentiation between 2-methylthiophene and 3-methylthiophene was derived from their respective ^1H NMR spectra (2-methylthiophene ($CDCl_3$) δ: 3.2–3.5 (s, 3H, CH_3), 6.8–7.7 (m, 3H, HAr); 3-methylthiophene ($CDCl_3$) δ: 2.1–2.3 (s, 3H, CH_3), 6.9–7.5 (m, 3H, HAr)). Pyrolysis of 2-thiopheneglyoxylic acid (**5**) gave 2-thiophenecarboxaldehyde (*m*/*z*: $M^{\bullet+}$ = 112, and fragment ions at 111 and 83; ν_{max}: 1655 (C=O); and δ ($CDCl_3$): 7.3–8.3 (m, 3H, HAr), 10.0 (s, 1H, HCO)). It is noteworthy

Table 1. Kinetic data for pyrolysis of compounds **1**–**7**.

Compd.	T (K)	$k \times 10^4$ (s^{-1})	Compd.	T (K)	$k \times 10^4$ (s^{-1})
1	564.3	3.303	**5**	443.4	1.574
	574.2	6.171		453.5	4.747
	584.1	9.986		463.5	12.25
	588.8	15.13		473.2	23.47
	593.8	22.74		477.2	25.59
	603.4	28.43		483.4	41.20
	613.0	45.07		493.0	68.35
	617.8	50.98		503.1	83.67
2	563.2	1.795	**6**	774.9	0.894
	573.3	2.627		785.1	1.748
	583.8	5.749		795.2	2.506
	593.4	8.984		805.5	3.853
	603.4	13.31		813.4	4.755
	613.2	20.07		821.9	4.932
	623.4	31.63			
3	684.8	1.574	**7**	563.3	2.069
	695.1	3.229		573.8	5.866
	705.1	5.149		583.7	8.515
	715.3	7.390		594.6	15.00
	720.8	11.78		599.0	18.82
	725.2	16.64		604.4	25.24
	735.3	20.75		613.9	37.30
	745.6	32.85			
4	704.5	3.003			
	714.9	4.191			
	725.1	9.145			
	735.2	9.865			
	745.2	17.66			
	755.4	31.49			
	765.3	45.79			

© 2002 NRC Canada

Table 2. Arrhenius parameters and rate coefficients (k, s^{-1}) at 600 K and $\Delta S^{\#}$ values for pyrolysis of compounds **1**–**7**.

Compd.	T (K)	E_a (kJ mol^{-1})	log A (s^{-1})	$\Delta S^{\#}$ (J $mol^{-1}K^{-1}$)	Corr. Coeff.	k (s^{-1})
1	53.5	153.5	10.76	–44.8	0.9994	2.51×10^{-3}
2	60.2	149.4	10.08	–57.7	0.9866	1.20×10^{-3}
3	60.8	207.1	12.04	–20.3	0.9943	1.03×10^{-6}
4	60.8	203.3	11.55	–29.6	0.9906	7.08×10^{-7}
5	59.7	123.4	10.91	–41.8	0.9918	1.48
6	47.0	223.8	11.05.	–39.2	0.9814	3.72×10^{-9}
7	50.6	149.8	10.33	–53.0	0.9827	1.95×10^{-3}

Scheme 2. Concerted four-membered TS (*a*) and six-membered TS (*b*) for pyrolysis of 3-thiopheneacetic acid.

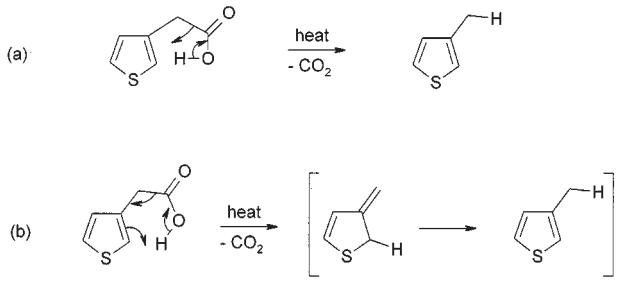

that 3-thiophenemalonic acid (**7**) gave pyrolysis products and a rate constant similar to those of 3-thiopheneacetic acid, an indication that the latter seems to be the primary decomposition product, which then pyrolyzes further into 2-methylthiophene and CO_2.

Reaction pathway and molecular reactivity

The present results for substrates **1**–**7** suggest a homogeneous unimolecular first-order elimination process. Moreover, the magnitudes of the Arrhenius-parameter values are in the range expected for such reactions (7, 13–16). The homogeneous nature and the lack of reactor-surface effects were proven by increasing the available surface area for reaction using tubes packed with glass helices. An increase of ca. 50% in surface area produced no noticeable change in the reaction rates. Kinetic runs were also conducted in the presence and absence of cyclohexene (free-radical scavenger). The rates, however, remained the same within experimental error. Additional analysis of the pyrolysates gave no indication of a radical-based reaction product.

Product formation can be rationalized either (*i*) on the basis of a mechanism involving a concerted four-membered TS or (*ii*) by a pathway with a concerted six-membered TS. The two mechanisms are shown in Scheme 2 for the gas-phase elimination reaction of 3-thiopheneacetic acid.

Although it is much simpler to explain product formation using the four-membered TS mechanism (Scheme 2*a*), theoretical and experimental evidence favour the six-membered TS (Scheme 2*b*). This evidence includes the following: (*i*) the conformation of the cyclic six-membered structure is known to be much more stable compared with the highly strained four-membered counterpart. (*ii*) The development of the six-membered TS requires a more facile intramolecular transfer of the electrophilic hydrogen to the protophilic thiophene ring positions, which are amenable to electrophilic attack. (*iii*) Theoretical ab initio calculations on the mechanism of similar thermal gas-phase elimination reactions gave results based on a six-membered TS that agree well with experimental values. In addition, these calculations have replaced the proposed four- and five-membered TS with five- and six-membered structures, respectively (17, 18).

Scheme 3. Calculated reaction mechanism for thermal gas-phase elimination of diacetamide.

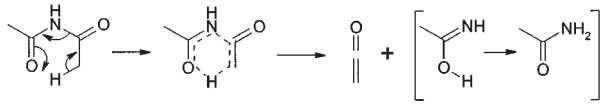

The theoretical studies used analytical gradients at the MP2//RHF/6–31G* level of theory, optimization routines, and microcanonical probability fluxes through TS to map PES and to calculate activation barriers and rate constants for the thermal reactions. The compounds whose elimination reactions were assigned a concerted six-membered TS include diacetamide, β-hydroxyketones, acetic anhydride, and methyl benzoylformate (17). Concerted five-membered TS were calculated for the pyrolysis of pyruvic acid, benzoyl formic acid, 3-hydroxy-3-methyl-2-butanone (α-oxoacids and α-hydroxyketone), and a large number of α-substituted carboxylic acids (17, 18). The theoretical calculations further confirm that the development of the TS involves intramolecular hydrogen transfer to a protophilic site and concomitant formation and breaking of the other bonds in the concerted structure. Typically, the reaction pathway calculated for the thermal gas-phase elimination reaction of diacetamide shown in Scheme 3 reproduces the cyclic six-membered TS, which accounts for the kinetic values and the reaction products reported in the experimental study of this substrate (17*a*, 19).

The six-membered TS mechanism (Scheme 2*b*), presently adopted to account for the kinetic results and reaction products of the thiophene compounds (**1**–**7**), has also been proposed for the thermal elimination reaction of 3-butenoic acid (**8**), 3-buten-1-ol (**9**), and the π-deficient 2-(2-ethoxy)pyridine systems (7, 15). The values of the Arrhenius parameters reported for the latter systems are comparable to those obtained in the present study.

The gas-phase molecular and positional reactivities of the thiophene compounds (**1**–**7**) and related systems (**8**–**10**) given in Scheme 4 allow for the following comparisons to be made:

(*i*) the thiopheneacetic acids **1**, **2** are more reactive than their thienylethanol analogues (**3**, **4**) by a factor ca. 2×10^3.

© 2002 NRC Canada

Scheme 4. Rate coefficients (k, s^{-1}) at 600 K and selected rate ratios for pyrolysis of present substrates (**1**–**7**) and related compounds (**8**–**10**).

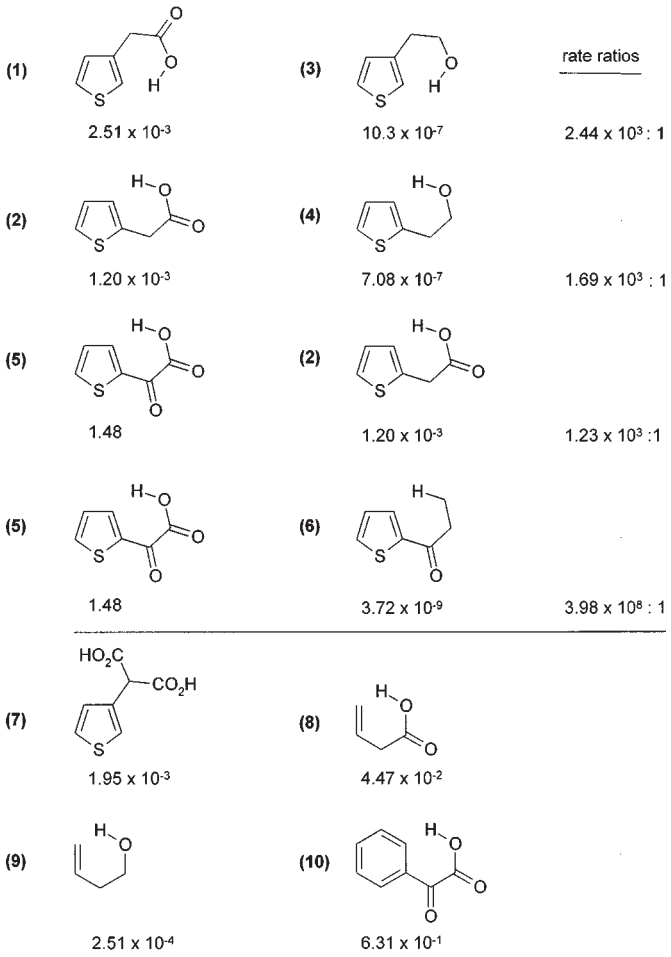

This large difference in molecular reactivity is ascribed to a more acidic H-bond (bond **d**, Scheme 1) and to the magnitude of the positive charge developing on the incipient hydrogen of the OH group of substrates **1**, **2**. The difference in reactivity becomes much larger (a factor of 4×10^8) when the O–H moiety of **5** is compared with a C–H bond of related ketone **6**.

(*ii*) 2-Thiopheneglyoxylic acid (**5**) is 1.2×10^3 more reactive than 2-thiopheneacetic acid (**2**). This is a consequence of the effect of the relative bond polarity (bond **b**, Scheme 1) on molecular reactivity, and on the repulsion between the positive charge on the carbon atoms of the adjacent carbonyl groups of **2**, which result in a more polar bond (**b**) in **2**.

(*iii*) Aliphatic 3-butenoic acid (**8**) and 3-buten-1-ol (**9**) are both more reactive than their heteroaromatic thienyl counterparts (3- and 2-thiopheneaceatic acid (**1**, **2**) and 1-(3-thienyl)- and 1-(2-thienyl)ethanol (**3**, **4**), respectively). The rate factors involved are, respectively, 18 and 37 for the former, and 244 and 355 for the latter pair of analogues. This pattern of relative reactivities indicates that although the thiophene ring is π-excessive in nature, its π bonds (bond **a**, Scheme 1) are still less protophilic than the aliphatic π bonds. Comparative protophilicity of bond **a** also explains why the rate of the elimination reaction of 3-buten-1-ol ($k = 2.5 \times 10^{-4}$ s^{-1} at 600 K, protophilic alkene π bond) is much lower than that of 4-hydroxy-2-butanone ($k = 1.5 \times 10^{-2}$ s^{-1} at 600 K, protophilic carbonyl moiety) (15). The effect of aromaticity on molecular reactivity is demonstrated when thiopheneglyoxylic acid (**5**) is shown to be twofold more reactive than benzoylformic acid (**10**); the latter being the more aromatic in nature (20).

(*iv*) 3-Thiopheneacetic acid (**1**) is more reactive than its 2-isomer (**2**) by a factor of ca. 2, whereas the corresponding relative rate factor for the thienylethanols (**3** and **4**) is 1.5. These rate factors, though moderate, are nevertheless consistent with the accepted intrinsic 2 > 3 positional reactivities of π-excessive five-membered aromatic heterocycles (4, 5). In the present systems, the protonic H of the group at the 3-position is reacting with the more protophilic π-bond at the nuclear 2-position.

(*v*) 3-Thiophenemalonic acid (**7**) has two equivalent carboxylic acid groups that are equally susceptible to decarboxylation during pyrolysis, whereas 3-thiopheneacetic acid (**1**) only has one such group. Statistically, **7** would be expected to be twice as reactive as **1**; however, the rate constants of the elimination reaction of the two acids are comparable (2.0×10^{-3} s^{-1} and 2.5×10^{-3} s^{-1}, respectively). The reason that the higher reactivity expected for **7** is not observed might be due to intramolecular H-bonding involving the two acid groups, with an adverse effect on the molecular reactivity of acid **7**.

Experimental

Materials, techniques, and instrumentation

The acids, alcohols, and ketone (**1**–**7**) under investigation are commercially available from Aldrich. The substrates and the constituents of their pyrolysates were characterized using GC–MS, FT-IR, and ^{1}H NMR spectroscopy. Instrumentation included a Finnigan Mat INCOSXL for GC–MS studies, a PerkinElmer 2000 for the FT-IR, and a Bruker AC80 for the NMR analysis. Kinetic runs were conducted in a Chemical Data System (CDS) custom-made pyrolyzer comprising an insulated aluminium block fitted with a platinum-resistance thermometer and a thermocoupler connected to a Comark microprocessor thermometer. The temperature of the aluminium block was controlled by a digital Eurotherm 093 precision temperature regulator. It is to be noted that aluminium was chosen for its low temperature gradient and resistance to elevated temperatures. HPLC analysis of kinetic runs was carried out on a Bio-rad Model 2700 coupled with a Bio-rad 1740 UV–vis detector.

Kinetic measurements and product analysis

Procedures for kinetic measurements and data treatment and analysis of pyrolysates using flow-reactors have been described in detail elsewhere (9*a*, 10*b*, 19). Reaction products were obtained in sealed-tube pyrolyzers. Acetonitrile was used as the solvent for both kinetic and reaction product studies, and either benzene or 1,2,3-trichlorobenzene as the internal standard in the quantitative chromatography measurement of the extent of the reaction.

© 2002 NRC Canada

Acknowledgments

We wish to thank Tommy Mathew for a preliminary kinetic study on the present compounds. The support of the University of Kuwait received through research grant SC 088 and the facilities of ANALAB/SAF is gratefully acknowledged.

References

1. T.L. Gilchrist. Heterocyclic chemistry. Pergamon, New York. 1977.
2. D.I. Davies. Aromatic heterocyclic chemistry. OUP, New York. 1991.
3. A.R. Katritzky. Handbook of heterocyclic chemistry. Pergamon, New York. 1985.
4. A.R. Katritzky and R. Taylor. *In* Advances in heterocyclic chemistry. Vol. 47. *Edited by* A.R. Katritzky. Academic Press, London. 1990. p. 1.
5. M.R. Grimmett. *In* Advances in heterocyclic chemistry. Vol. 57. *Edited by* A.R. Katritzky. Academic Press, London. 1993. p. 292.
6. N.A. Al-Awadi, R.F. Al-Bashir, and O.M.E. El-Dusouqui. Tetrahedron Lett. **30**, 1699 (1989); Tetrahedron, **46**, 2911 (1990).
7. D.B. Bigley and M.J. Clarke. J. Chem. Soc. Perkin Trans. 2, 1 (1982).
8. R.T. Arnold and G. Smolinsky. J. Am. Chem. Soc. **81**, 2126 (1959).
9. (*a*) N.A. Al-Awadi, K. Kaul, and O.M.E. El-Dusouqui. J. Phys. Org. Chem. **13**, 499 (2000); (*b*) N.A. Al-Awadi, O.M.E. El-Dusouqui, K. Kaul, and H.H. Dib. Int. J. Chem. Kinet. **32**, 407 (2000).
10. (*a*) N.A. Al-Awadi, K. Kaul, and O.M.E. El-Dusouqui. Can. J. Chem. **76**, 1922 (1998); (*b*) N.A. Al-Awadi, M.H. Elnagdi, H.A. Al-Awadhi, and O.M.E. El Dusouqui. Int. J. Chem. Kinet. **30**, 457 (1998); (*c*) R. Taylor. *In* The chemistry of functional groups: supplement B. *Edited by* S. Patai. John Wiley, Chichester. 1979. p. 876.
11. N.A. Al-Awadi, M.H. Elnagdi, K. Kaul, S. Ilingovan, and O.M.E. El-Dusouqui. Tetrahedron, **54**, 4622 (1998); J. Phys. Org. Chem. **12**, 645 (1999).
12. P.J. Taylor. J. Chem. Soc. Perkin Trans. 2, 1077 (1972).
13. W.H. Saunders and A.F. Cockerill. Mechanism of elimination reactions. John Wiley, New York. 1973. p. 377.
14. G.G. Smith and F.W. Kelly. *In* Progress in physical organic chemistry. Vol. 8. *Edited by* A. Streitwieser and R.W. Taft. 1971. p. 75.
15. R. Taylor. J. Chem. Soc. Perkin Trans. 2, 809 (1983).
16. K.A. Holbrook. *In* The chemistry of functional groups, supplement B: chemistry of acid derivatives. *Edited by* S. Patai. John Wiley, Chichester. 1992. p. 703.
17. (*a*) S-W. Zhang, Y. Wang, and W-L. Feng. J. Mol. Struct. (Theochem), **488**, 29 (1999); (*b*) W-L. Feng, Y. Wang, and S-W. Zhang. Int. J. Quantum Chem. **62**, 297 (1997); (*c*) Y. Wang et al. CA. 131:58534s, 131:2992058, 131:322298j, 132:165862q (1999).
18. J. Anders, G. Chuchani, L.R. Domingo, V. Molliner, A. Rotinov, and V.S. Safont. J. Phys. Chem A, **101**, 1859 (1997); J. Am. Chem. Soc. **119**, 6415 (1997); Phys. Lett. **274**, 422 (1997); J. Phys. Chem. A, **103**, 3935 (1999); Chem. Phys. **246**, 1 (1999).
19. N.A. Al-Awadi, R.F. Al-Bashir, and O.M.E. El-Dusouqui. J. Chem. Soc. Perkin Trans. 2, 579 (1989).
20. R. Taylor. Int. J. Chem. Kinet. **23**, 247 (1991); **19**, 709 (1987).

© 2002 NRC Canada

A facile methodology for the synthesis and detection of N7-guanine adduct of sulfur mustard as a biomarker

Mula Kameswara Rao, Pinaki S. Bhadury, Mamta Sharma, Rajinder S. Dangi, Appanabhotla S.B. Bhaskar, Syed K. Raza, and Devendra K. Jaiswal

Abstract: A simple and convenient method has been developed for the synthesis of a N7-guanine adduct of sulfur mustard (SM), which can serve as an efficient biomarker for alleged exposure to SM. The adduct obtained in high yields (~78%) was characterized on the basis of its physical properties and spectral data. In addition, HPLC and LC–MS conditions have been standardized for the detection of the adduct in both in vitro and in vivo samples, which is useful for retrospective detection of exposure to SM in biological samples.

Key words: sulfur mustard, biomarker, N7-guanine adduct, in vitro, in vivo, HPLC, LC–MS, electrospray, 2D NMR.

Résumé : On a développé une méthode simple et pratique de synthétiser l'adduit de la N7-guanine avec la moutarde au soufre (MS) qui peut servir de biomarqueur efficace dans les cas supposés d'exposition à la MS. L'adduit qui a été obtenu avec des rendements élevés (environ 78 %) a été caractérisé sur la base de données physiques et spectroscopiques. De plus, on a développé des conditions standards de chromatographie liquide à haute performance (CLHP) et de spectrométrie de masse couplée à la chromatographie liquide (SM–CL) pour la détection de l'adduit dans des échantillons in vitro ainsi que in vivo; celles-ci seront très utiles pour la détection rétrospective d'expositions à la MS dans des échantillons biologiques.

Mots clés : moutarde au soufre, biomarqueur, adduit de la N7-guanine, in vitro, in vivo, CLHP, SM–CL, électronébulisation, RMN 2D.

[Traduit par la Rédaction]

Introduction

Sulfur mustard (SM) is a carcinogen because of its ability to alkylate DNA (1, 2). The primary site of alkylation is the N7 position of guanine (3, 4) resulting in the formation of N7-[2-[(2-hydroxyethyl)thio]ethyl]guanine (**V**). This is the most abundant adduct arising out of alkylation of DNA with SM (4, 5). The adduct can be formed in the skin, blood, and urine of animals allegedly exposed to SM and can, therefore, serve as a biomarker for the retrospective detection of exposure to SM in alleged exposure to the agent (6, 7). Attempts have, therefore, been made to develop a synthetic method for the preparation of synthetic standard of N7-guanine–SM adduct to be used as reference material for its detection in real biological samples obtained from the patients allegedly exposed to SM.

The reported method for the synthesis of N7-guanine–SM adduct from guanosine-5′-monophosphate (GMP) and SM involves a cumbersome procedure with poor yields (15%) (3). Furthermore, in these studies, attempts were not made to understand the underlying chemistry and structures of the intermediates formed during the reaction. We have developed a simplified and improved methodology for the synthesis of N7-guanine–SM adduct, based on the techniques adopted for the methylation of certain purine nucleosides (8). In this paper, we discuss the mechanism, the probable structures of the pH-sensitive intermediates, and the underlying chemistry behind the improved and facile synthesis of the adduct, which has been fully characterized on the basis of its physical properties and its spectral data. Furthermore, a methodology for the detection of the adduct by HPLC and LC–MS with electrospray ionization has also been standardized, and has been successfully applied for the analysis of the adduct obtained from in vitro and in vivo samples.

Received 24 August 2001. Published on the NRC Research Press Web site at http://canjchem.nrc.ca on 3 May 2002.

M.K. Rao, P.S. Bhadury, M. Sharma, R.S. Dangi, A.S.B. Bhaskar, S.K. Raza,[1] and D.K. Jaiswal. Defence Research & Development Establishment, Gwalior-474002, India.

[1]Corresponding author (e-mail: skraza2k@hotmail.com).

Results and discussion

We have developed a simplified and improved methodology for the synthesis of the N7-guanine–SM adduct. This method is analogous to the techniques adopted for the methylation of certain purine nucleosides (8). It is well documented that alkylation of guanosine using methyl iodide generates N7-methyl guanosine as an iodide salt. This salt on treatment with concentrated aqueous ammonia is converted into a water-soluble betaine 7-methyl guanosine intermediate. It should be noted that this internal betaine (which is not a salt) is characteristic of N7-alkylated guanosine derivatives. Both N7-methyl guanosine and its iodide salt, i.e.,

 DOI: 10.1139/V02-058 © 2002 NRC Canada

Scheme 1. Stepwise formation of N7-guanine–SM adduct.

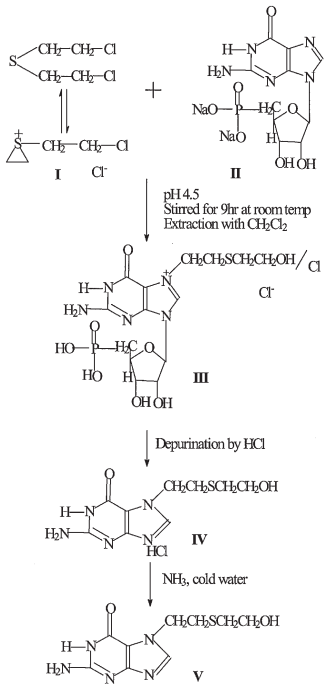

Scheme 2. Fragmentation mechanism under electron impact (EI) conditions.

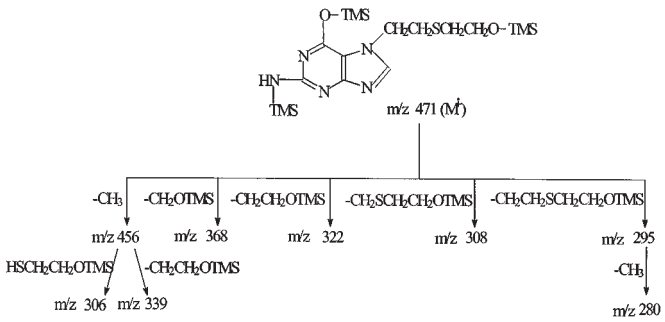

N7-methyl guanine hydro iodide, can be hydrolyzed or depurinated by acid to yield 7-methyl guanine.

Using the same analogy, we reacted sulphur mustard (SM, **I**) with guanonsine-5′-monophosphate (GMP) (**II**) in aqueous medium to generate the chloride salt of N-7-[2-[(2-hydroxy/chloro-ethyl)thio]ethyl]guanosine monophosphate (**III**). This salt was formed via the interaction between the N7 nitrogen atom of the purine base and sulphur mustard, presumably existing as a sulfonium species, through a S_Ni rearrangement. The pH of the reaction mixture was maintained at 4.5. The hydrochloride salt was then purified by careful extraction with dichloromethane to remove the organic impurities, mainly thiodiglycol. The salt thus obtained was subjected to direct depurination by hydrochloric acid to afford the hydrochloride salt of the desired N7-guanine–SM adduct (**IV**). Since GMP was totally consumed as indicated by HPLC and the organic impurities removed by extraction, the aqueous extract, containing soluble hydrochloride of N7-guanine–SM adduct, was neutralized with ammonia resulting in the formation of the free insoluble organic base (N-7-[2-[(2-hydroxyethyl)thio]ethyl]guanine, **V**), which was precipitated out and collected (Scheme 1).

Fig. 1. 2D COSY (HETCOR) spectrum of N7-guanine–SM adduct.

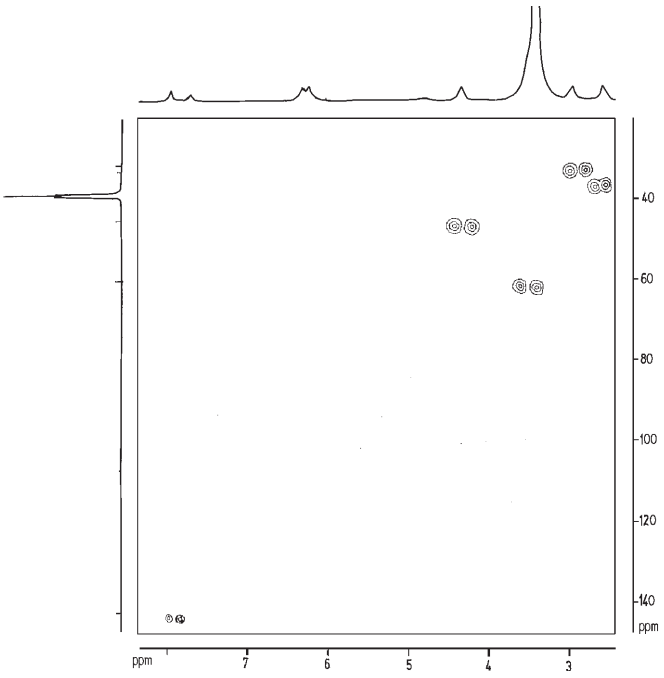

Experiments showed that hydrolysis was achieved at the salt stage (Scheme 1, ensuring the absence of any unreacted GMP) and that this method of hydrolysis did not involve any binding or retention of the product on the column. Furthermore, since this type of hydrolysis does not contain any inorganic salts or thiodiglycols, the purification technique employing sephadex G-10 column as used in earlier methods was also avoided. This resulted in the development of a synthetic method that not only is drastically simplified but also results in excellent yields of the final product. The purity of the final product was confirmed by HPLC (99%).

It should be noted that, the solvent, the pH, and the substrate play a major role in the selective synthesis of the N7-monoalkylated guanine adduct of sulphur mustard. The selection of GMP over guanosine is based on its solubility in water — pH 4.5 has been found to be the most effective for exclusively obtaining the N-7 adduct. Alkylation at position 9 through other tautomeric forms of the imidazole ring or the formation of a dialkylated product in the ring or a mixture of both is avoided by blocking position 9 with a sugar moiety. Moreover, under this steric model, N7 is the only position favoured for alkylation that is not involved in hydrogen bonding in the Watson–Crick model of DNA (4). At pH 4.5, not only is the nucleophilicity of N-7 nitrogen maintained, but depurination of GMP is also avoided. On the other hand, at an alkaline pH, SM is converted into thiodiglycol via the interaction of nucleophilic water with an intermediate sulphonium species. Thus alkylation of water is preferred over N7-purine at alkaline pH and hence reaction conditions at pH 4.5 are preferred. In addition, an excess of SM is added to avoid the formation of a di-adduct of purine and SM.

© 2002 NRC Canada

Fig. 2. Direct-probe EI (above) and CI (below) mass spectra of the silylated N7-guanine–SM adduct.

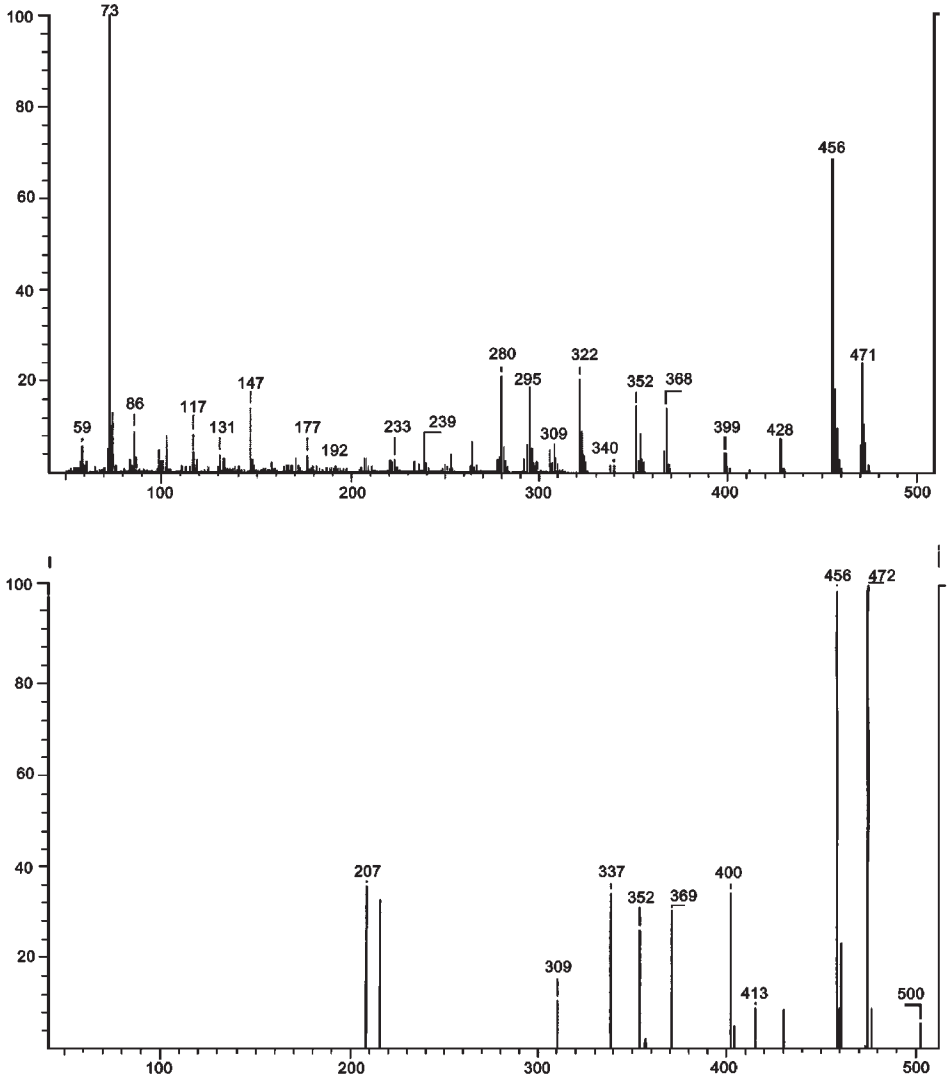

Fig. 3. Reverse-phase HPLC chromatogram for the N7-guanine–SM adduct dissolved in DMSO. The adduct eluted at 3.9 min.

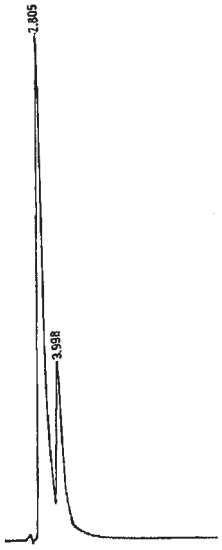

The adduct has been characterized on the basis of its physical properties and its spectral data. The melting point, the UV absorbance, and ^{1}H and ^{13}C NMR data of the adduct were in full agreement with the reported values (5). In addition, we also recorded the 2D NMR spectrum (Fig. 1) of the adduct, which clearly showed long-range coupling (4 Hz and 3 Hz for C-8 and C-5, respectively) between N7-CH_2 and C-8 and C-5 carbons. This long-range coupling is indicative of CH_2 being attached to the N7 position of the guanine. The adduct was not amenable to GC–MS even after derivatization (3, 12, 13). Since the compound was pure, analysis by direct probe MS was attempted. The adduct however failed to give a reasonable spectrum under these conditions. Analysis of the silylated derivative of the adduct with a direct probe, however, provided a spectrum showing a strong molecular-ion peak at *m*/*z* 471 (Fig. 2). The molecular weight of the adduct was further confirmed by recording a CI-MS spectrum of the compound, which showed an $[M + H]^{+}$ ion peak at *m*/*z* 472 (Fig. 2). Fragment ions in EI-MS were observed at *m*/*z* 456, 399, 368, 352, 322, 339, 295, 280, 264, 239, 177, 147, 131, 117, 103, and 73. The genesis of the formation of some of the significant ions is shown in

© 2002 NRC Canada

Fig. 4. ESI-MS spectrum (top) of the N7-guanine–SM adduct showing a $[M + H]^+$ peak at *m*/*z* 256 and ion chromatogram (bottom) for the adduct at *m*/*z* 256.

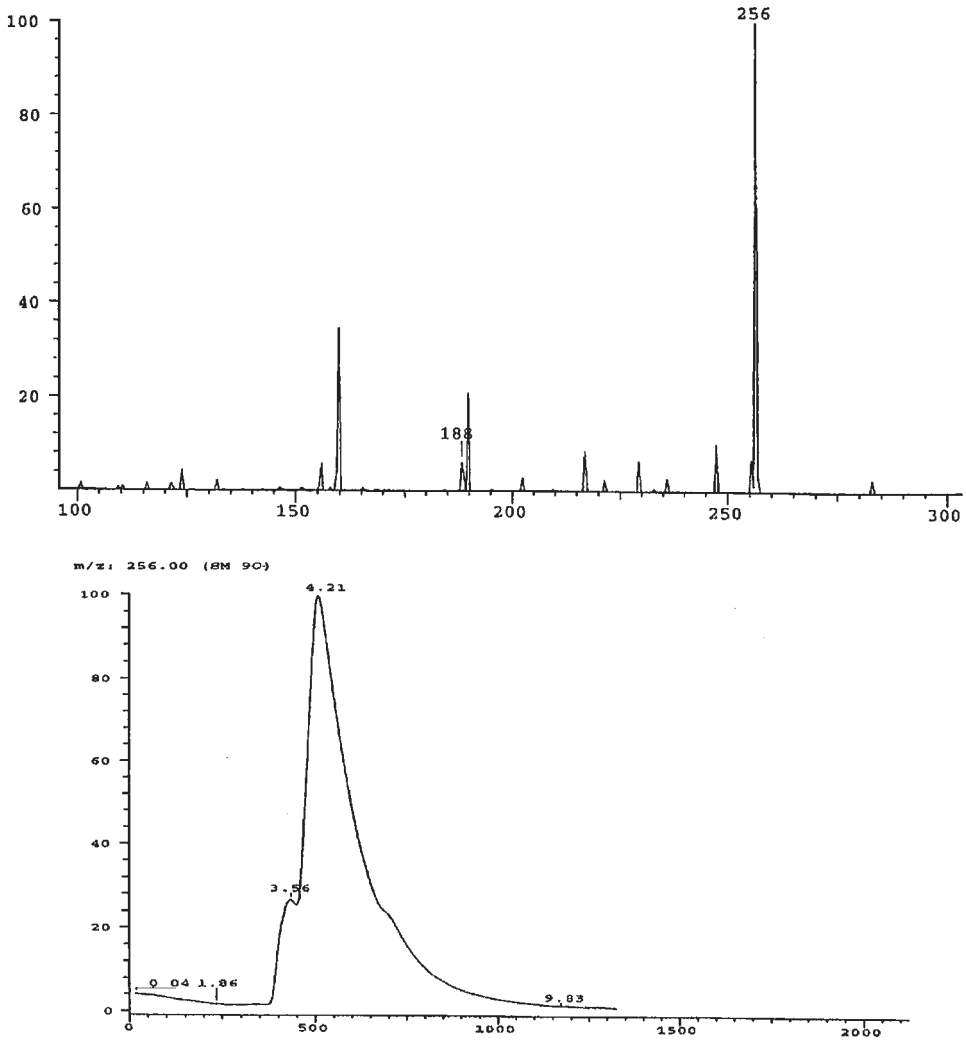

Scheme 2. The mechanism proposed has been confirmed by performing MS–MS experiments in daughter-ion mode.

A method based on HPLC and LC–MS using electrospray ionization has also been optimized for easy detection of the adduct. HPLC analysis was performed on a PG C-18 column using 25 mM NH_4HCO_3 in 20% methanol (v/v) (pH 8) as the mobile phase at a flow rate of 1 mL min^{-1}. The adduct was detected by UV at 280 nm. The adduct was well separated under these conditions and showed an excellent response. The results were reproducible (Fig. 3). The adduct was also subjected to LC–MS analysis using electrospray ionization and gave an $[M + H]^+$ ion peak at *m*/*z* 256 (Fig. 4). The detection limit achieved using LC–ESI-MS was 10 ng.

The HPLC and LC–MS methods developed for the synthetic standard has been successfully used for the detection of adduct in various in vitro and in vivo samples. The adduct formed in vitro by reacting calf thymus DNA with SM has been analyzed by HPLC using the same conditions as optimized for synthetic standard. The results are shown in Fig. 5. These samples were also analyzed by direct-probe MS after silylation, and LC–MS and the spectra matched well with those obtained from the synthetic standard.

For in vivo samples, SM was given percutaneously to rats. Liver and spleen were collected after 7 days. The DNA content in these tissues was estimated for the analysis of N7-guanine–SM adduct and was found to be 38 μg in spleen and 56 μg in liver. Previously, our laboratory showed that there is time- and dose-dependent DNA damage in various organs after percutaneous or inhalation exposure of SM (14). We observed persistent DNA damage in liver, spleen, and thymus even after 7 days exposure and liver was the major organ affected in terms of DNA damage by either dermal or inhalation exposure. In the present study, N7-guanine–SM adduct was detected in both types of tissues 7 days after a single dermal exposure (Fig. 6).

Conclusion

The method developed for the synthesis of N7-guanine–SM adduct as a biomarker for the verification of alleged exposure to SM is simple and convenient. The purification stages

© 2002 NRC Canada

Fig. 5. Reverse-phase HPLC chromatogram for synthetic standard (A) and in-vitro formed N7-guanine–SM adduct from calf thymus DNA (B).

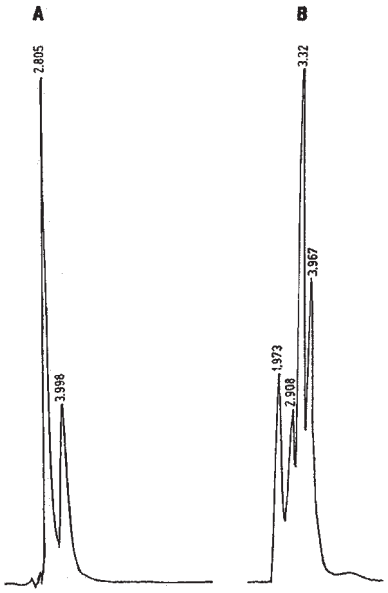

Fig. 6. Reverse-phase HPLC chromatogram for synthetic standard (A) and in-vivo formed N7-guanine–SM adduct from liver (B) and spleen (C).

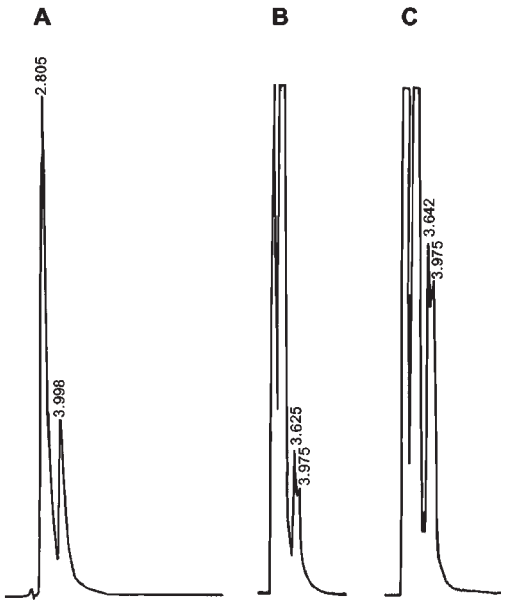

do not employ Q-sepharose or sephadex G-10 and hence the yields are much better than those previously reported. The chemistry behind the synthesis was explained in detail. A detection methodology based on HPLC and LC–MS with electrospray ionization was also developed for the easy detection of adduct, which is useful when monitoring the biomarker in biological samples obtained from the patients allegedly exposed to SM.

Experimental

Chemicals

Sulphur mustard (2,2′-bis(2-chloroethyl)sulphide, SM) is a carcinogen and cytotoxic agent. All operations involving this compound should be carried out only in a well-ventilated fume cupboard by experienced personnel. Guanosine monophosphate (disodium salt), CT DNA, and the enzymes used for the hydrolysis of DNA adduct were purchased from Sigma (St. Louis, MO). The solvents used were from E. Merck (India).

Synthesis of sulfur mustard

Sulfur mustard used in this study was synthesized in our laboratory according to the standard procedure (9) and found to be 99% pure by GC.

Synthesis of N7-[2-[(2-hydroxyethyl)thio]ethyl]guanine

A solution of guanosine-5′-monophosphate (GMP) disodium salt monohydrate (814 mg, 2 mmol) in water (20 mL) was adjusted to pH 4.5 with 1 N HCl. The mixture was transferred into a two-necked flask (100 mL) and stirred at room temperature for 5 min. One end of the flask was connected to a U-shaped tube filled with active carbon. Sulfur mustard (0.50 mL, 4 mmol) was then added into the reaction mixture by means of a micropipette in one shot through the second neck of the flask. The pH of the reaction mixture immediately decreased due to the liberation of HCl, which was readjusted to 4.5 with 0.1 N NaOH solution. The reaction mixture was stirred vigorously at room temperature and continuously monitored by HPLC for the complete consumption of GMP. The reaction mixture was then neutralized with 0.1 N NaOH solution and stirred for an additional 10 min. The organic impurities (mainly thiodiglycol) were then removed by careful extraction with dichloromethane (3 × 20 mL). The aqueous extract containing the chloride salt of the GMP–SM adduct was concentrated on a speed vacuum lyophiliser. The adduct was then dissolved in 1 N HCl (50 mL) and subjected to direct depurination on a boiling water bath for 2 h. The resulting adduct was a soluble hydrochloride. The reaction mixture was then concentrated to a small volume (10 mL) under reduced pressure and neutralized with ammonia. The free insoluble organic base (N7-guanine–SM adduct) immediately precipitated out from the reaction mixture. The material was filtered under suction, washed repeatedly with cold water, and dried in a vacuum desiccator. The isolated yield of the adduct was 400 mg (~78%). Melting point: >280°C (dec.). UV λ_{max} (nm, pH 7): 284. ^{1}H NMR (DMSO-d_6) δ: 10.79 (br s, H, NH), 7.93 (s, 1H, H-8), 6.17 (s, 2H, NH_2), 4.89 (t, 1H, OH), 4.32 (t, 2H, CH_2OH), 3.52 (t, 2H, CH_2OH) 2.94 (t, 2H, $NCCH_2S$), 2.56 (t, 2H, SCH_2COH). ^{13}C NMR (DMSO-d_6) δ: 160.1 (C_4), 154.7 (C_6), 153.2 (C_2), 143.5 (C_8), 107.9 (C_5), 60.8 (CH_2OH), 46.0 (NCH_2), 33.8 (SCH_2COH), 32.2 ($NCCH_2S$). EI-MS *m/z* (%): 471 (M^+, 24), 456 (65), 399 (6.6), 368 (18), 352 (18), 339 (7), 322 (22.6), 308 (7.9), 306 (5.3), 295 (18.6), 280 (24), 264 (6.6), 239 (8), 177 (6.6), 147 (17.3), 131 (8), 103 (9.3), 73 (100). CI-MS *m/z* (%): 472 ($[M + H]^+$, 100), 456 ($[M - 15]^+$).

In-vitro SM–CT DNA adduct formation

A solution of double stranded calf thymus DNA (1 mg mL^{-1} in phosphate-buffered saline) was treated with

© 2002 NRC Canada

SM in acetone (1 mM) for 24 h at 37°C. The G + C content obtained in 1 mg CT DNA was 40%, which is similar to the published G + C content (42%) (10, 11). The reaction was stopped by precipitating DNA from the reaction medium on ice with a mixture of 3 M sodium acetate and ice cold ethanol (0.1:3 v/v) and centrifuging for 15 min at 3000 rpm. The supernatant was removed and the pellet was washed with ice cold 70% aqueous ethanol and the wash was added to the supernatant. The pellet was air dried for 15 min and dissolved in 50 mM Tris buffer. The DNA was then enzymatically hydrolyzed (10) at 37°C overnight using nuclease P1 (24 U mL^{-1}), alkaline phosphatase (3 U mL^{-1}), DNase (10 U mL^{-1}), and phosphodiesterase (0.3 U mL^{-1}). The enzymatic hydrolysis was stopped by heating the sample at 100°C for 5 min, followed by centrifugation and filtration to remove the denatured enzyme proteins. Acidic hydrolysis of the reaction mixture was also performed by adding 0.1 N HCl to the alkylated DNA in Tris buffer and the sample was heated at 75°C for 20 min to release the purine bases. The sample was then cooled to room temperature and the pH was adjusted to 7.2 with potassium hydroxide solution and stored at 4°C until analysis. The samples in each case were concentrated by speed-vacuum lyophilization prior to analysis by HPLC and LC–MS. The sample was dried, silylated, and analyzed by direct-probe MS. The yield of the adduct based on guanine residue in the CT DNA and the SM added was 24%.

In-vivo formation of N7-guanine–SM adduct

The tissues selected for the in vivo formation of N7-guanine–SM adduct were spleen and liver. Female albino rats of weight range of 230–250 g were used in this study. SM dose was 3 mg kg^{-1} dissolved in PEG 300, and applied (100 μL) percutaneously after clipping the hairs on the back. Animals were observed for 7 days. On 7th day animals were sacrificed, the liver and spleen were quickly excised in cold PBS, and stored at –70°C. Genomic DNA was isolated from tissue sample using QIAamp DNA mini kit (QIAGEN GmbH, Germany). Genomic DNA was collected in deionized water and DNA content was estimated using spectrofluorimetry. The DNA content estimated for the analysis of N7-G–SM adduct was 38 μg in spleen and 56 μg in liver. Acid hydrolysis was employed for the release of adduct from the backbone of DNA (10). After hydrolysis samples were centrifuged at 500 × *g* for 20 min, supernatants collected and freeze dried. Just before HPLC analysis samples were redissolved in acidic methanol (50 μL), centrifuged again at 500 × *g* . Clear supernants were injected in to HPLC.

Instrumentation

HPLC analysis was carried out on a reverse-phase C-18 column using Shimadzu LC-6A. The mobile phase used was 25 mM NH_4HCO_3 in 20% methanol (v/v) (pH 8) at a flow rate of 1 mL min^{-1}. The UV detection was at 280 nm. ^1H, ^{13}C, and 2D NMR spectra were recorded on a Bruker Avance 400 MHz spectrophotometer. Chemical shifts are given in ppm relative to TMS. The solvent signal at 2.51 ppm (residual DMSO in DMSO-d_6) served as a reference for ^1H NMR spectroscopy, whereas the solvent signal at 39.59 ppm (DMSO-d_6) was used as a reference for ^{13}C NMR spectroscopy. UV spectra were recorded on a Speccord 200 (Analytical Jena, Carl Zeiss Technology, Germany). Direct-probe MS (EI and CI) and LC–MS experiments were carried out on a TSQ 7000 mass spectrometer (Finnigan Mat, U.K.) using electrospray ionization in positive-ion mode. The samples in LC–MS were introduced through HP 1100 HPLC system using PG C-18 column with 25 mM NH_4HCO_3 in 20% methanol (v/v) (pH 8) as the mobile phase at a flow rate of 1 mL min^{-1}. The sheath gas (nitrogen) pressure was 60 psi and the capillary temperature was set at 200°C. The spray needle was held at 4.5 KV. MS–MS experiments in daughter-ion mode was performed by using argon as the collision gas at a pressure of 2 torr.

Acknowledgments

The authors are thankful to Dr. R.V. Swamy, ex-director, DRDE, Gwalior and Chief Controller, DRDO, New Delhi for his keen interest in the work and to Dr. B.S. Batra for providing sulphur mustard used in these studies. M.K. Rao thanks DRDO for providing financial assistance in the form of research fellowship.

References

1. P. Brookes and P.D. Lawley. J. Biochem. **77**, 478 (1960).
2. P. Brookes and P.D. Lawley. Brit. Med. Bull. **20**, 91 (1964).
3. A. Fidder, G.W.H. Moes, A.G. Scheffer, G.P. Vanderschans, R.A. Bann, L.P.A. DeJong, and H.P. Benschop. Chem. Res. Toxicol. **7**, 199 (1994).
4. B. Papirmeister, A. Fiester, S.I. Robinson, and R.D. Ford (*Editors*). Chemistry of sulphur mustard, in medical defence against mustard gas: Toxic mechanism and pharmacological implications. CRC Press, Boca Raton, FL. 1991. p. 91.
5. S.M. Somani and S.R. Babu. Int. J. Clin. Pharamcol. Ther. Toxicol. **27**, 419 (1989).
6. A. Fidder, D. Noort, L.P.A. DeJong, and H.P. Benschop. Arch. Toxicol. **70**, 854 (1996).
7. G.P. Vanderschans, A.G. Scheffer, R.H. Mars-Groenendijk, A. Fidder, H.P. Benschop, and R.A. Bann. Chem. Res. Toxicol. **7**, 408 (1994).
8. J.W. Jones and R.K. Robins. J. Am. Chem. Soc. **81**, 193 (1963).
9. H.T. Clarke. J. Chem. Soc. **101**, 1583 (1912).
10. R.R. Selzer and A.A. Elfarra. Carcinogenesis, **20**, 285 (1999).
11. J. Marmur and P. Doty. J. Mol. Biol. **5**, 109 (1962).
12. D.E.G. Shuker, E. Bailey, S.M. Gorf, J.H. Lamb, and P.B. Farmer. Anal. Biochem. **140**, 270 (1984).
13. J.R. Cushnir, S. Naylor, J.H. Lamb, and P.B. Farmer. Org. Mass Spectrom. **28**, 552, (1993).
14. P.V. Lakshman Rao, R. Vijayaraghavan, and A.S.B. Bhaskar. Toxicology, **139**, 39 (1999).

© 2002 NRC Canada

Medium-size cyclophanes. Part 60[1]: Synthesis and conformational studies of 9-substituted [3.3]metacyclophane-2,11-diones and conversion to the corresponding [3.3]metacyclophanes

Takehiko Yamato, Koji Tsuchihashi, Noriko Nakamura, Mai Hirahara, and Kan Tanaka

Abstract: Various *syn*- and *anti*-9-substituted [3.3]metacyclophane-2,11-diones are obtained by the coupling reaction of the corresponding 2,6-bis(bromomethyl)benzenes (**3**) with 2,6-bis[2-cyano-2-(toluenesulfony)ethyl]-4-*tert*-butyl-1-substituted benzenes (**4**) in dimethylformamide (DMF) with an excess of sodium hydride. Depending on the substituents at positions 1 and 4 on **3**, different yields (inversion of selectivity) of *anti*-**5** and *syn*-**5** were achieved.

Key words: metacyclophanes, cyclization, conformation, CH–π interaction, through-space interaction, charge-transfer-type interaction.

Résumé : Le couplage des 2,6-bis(bromométhyl)benzènes correspondants (**3**) et des 2,6-bis[2-cyano-2-toluènesulfonyl)éthyl]-4-*tert*-butylbenzènes substitués en position 1 (**4**) effectué dans le diméthylformamide (DMF) avec un excès d'hydrure de sodium permet d'obtenir diverses [3.3]métacyclophane-2,11-diones portant des substituants *syn*- et *anti*- en position 9. Les rendements (avec inversion de sélectivité) en composés *anti*-**5** et *syn*-**5** varient avec la nature des substituants dans les positions 1 et 4 des divers 2,6-bis(bromométhyl)benzènes (**3**).

Mots clés : métacyclophanes, cyclisation, conformation, interaction CH–π, interaction à travers l'espace, interaction de type transfert de charge.

[Traduit par la Rédaction]

Introduction

The synthesis and stereochemical aspects of conformationally mobile [3.3]MCPs (MCP= metacyclophane) have been of interest for the past decade, with particular attention (2) paid to dithia[3.3]MCPs, which possess an *anti*-stepped conformation. The pioneering conformational investigation of 2,11-dithia[3.3]MCPs was reported by Vögtle and Schunder (3). While Shinmyozu and co-workers (4) reported the first preparation and conformational behavior of carbocyclic [3.3]MCPs **1** and their analogues. The [3.3]MCP **1** exist in the crystal state in a *syn* geometry with the trimethylene chains in a chair–chair arrangement (Fig. 1). The preferred geometry of **1** in solution is also *syn* on the basis of the ^{1}H NMR spectrum, in which **1** shows a strong temperature-dependent phenomenon at low temperatures (5, 6).

Shinmyozu and co-workers (4) prepared [3.3]MCP **1** using (*p*-tolylsulfonyl)methyl isocyanide (TosMIC) as the cyclization reagent, followed by a Wolff–Kishner reduction (4). They also performed studies on the *syn–anti* conversions in other [3.3]MCPs, especially in relation to the size of the substituents such as halogens (7). Like the parent compound, 9-halo[3.3]MCPs prefer the *syn* conformation but the corresponding 2,11-diones favour the *anti* arrangement. Even one internal halogen substituent is sufficient to allow the isolation of a discrete *syn* or *anti* isomer. Although the effect on the ratio of *syn* and *anti* conformers of [3.3]MCPs was reported, it is still not clear what the effects are — including not only the properties of the internal substituents, but also the presence of unsymmetrically substituted benzene rings arising from charge-transfer-type interactions between two benzene rings, as well as the steric effects of substituents at the 6 and 15 positions.

All of the previous compounds are internally unsubstituted [3.3]MCP-2,11-diones and it is surprising that there are very few reports (8) on the preparation of 9-methyl- or 9-methoxy-analogues despite the fact that the chemical shift of the internal substituents, such as the methyl and the methoxy group, provides a convenient probe for ^{1}H NMR studies of any possible conformational changes. We report here the synthesis and stereochemical assignments of 9-substituted [3.3]MCP-2,11-diones and conversion to the

Received 7 January 2002. Published on the NRC Research Press Web site at http://canjchem.nrc.ca on 10 May 2002.

T. Yamato,[2] K. Tsuchihashi, N. Nakamura, and M. Hirahara. Department of Applied Chemistry, Faculty of Science and Engineering, Saga University, Honjo-machi 1, Saga-shi, Saga 840–8502, Japan.
K. Tanaka. Department of Industrial Chemistry, Faculty of Science and Engineering, Tohwa University, 1–1-1 Chikushigaoka, Minami-ku, Fukuoka-shi, Fukuoka 815–8510, Japan.

[1]Part 59. See Ref. 1.
[2]Corresponding author (e-mail: yamatot@cc.saga-u.ac.jp).

 DOI: 10.1139/V02-072 © 2002 NRC Canada

Fig. 1. *syn*- and *anti*-Confomers of [3.3]metacyclophane **1**.

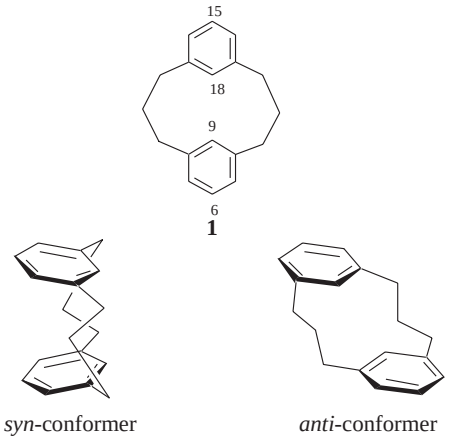

Scheme 1.

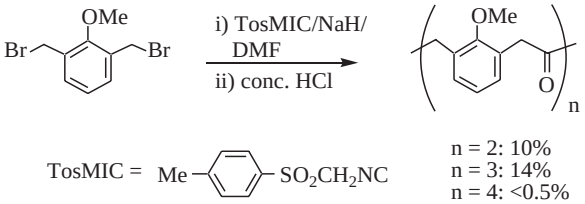

Scheme 2.

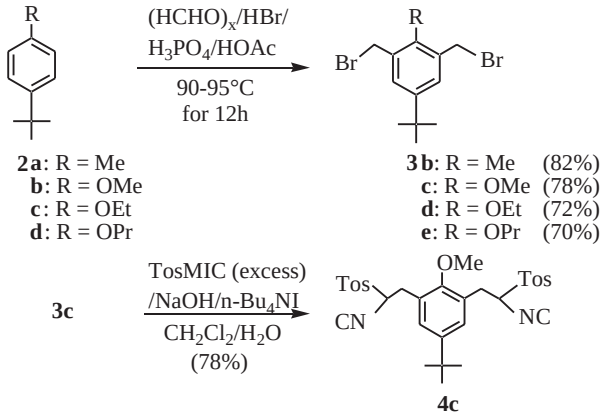

corresponding [3.3]MCPs by Wolff-Kishner reduction. The substituent effects on the formation of the *syn*- and *anti*-conformations are discussed.

Results and discussion

Vögtle and co-workers reported (9) the preparation of carbocyclic [3$_n$]MCPs using TosMIC (10) as the cyclization reagent, which was applied in a new cyclization procedure without phase-transfer conditions (Scheme 1) (11).

This strategy can be employed for the preparation of [3.3]MCP containing two benzene rings. The preparation of [3.3]MCPs using the TosMIC method is, however, difficult because of its low yield as well as the difficulty of the product separation from the other macrocyclic oligoketones, i.e., trimer and tetramer. It has, therefore, been very difficult to obtain sufficient amounts of the above compounds to investigate their chemical behavior.

Scheme 3.

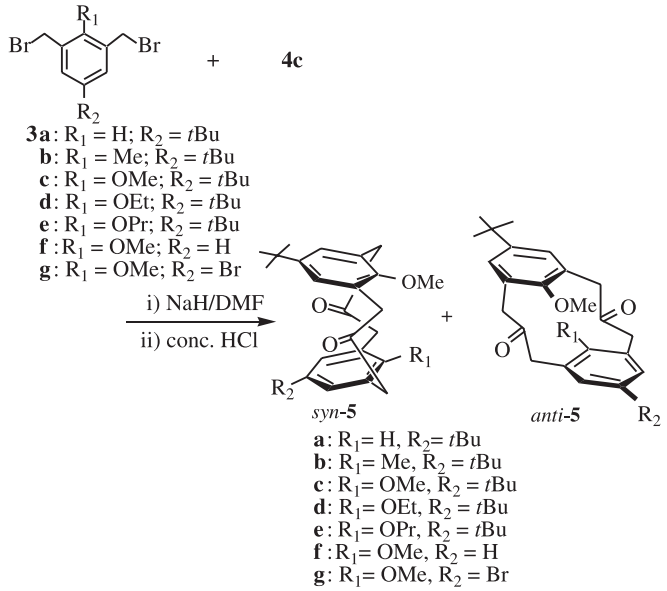

Table 1. Ratios of *anti*-*to*-*syn* in TosMIC cyclization of **3** with **4c**.

				Distribution (%)[b]	
	R_1	R_2	Product (%)[a]	*anti*	*syn*
3a	H	*t*-Bu	**5a** (72)	100	0
3b	Me	*t*-Bu	**5b** (71)	50	50
3c	OMe	*t*-Bu	**5c** (53)	30	70
3d	OEt	*t*-Bu	**5d** (50)	28	72
3e	OPr	*t*-Bu	**5e** (50)	25	75
3f	OMe	H	**5f** (53)	5	95
3g	OMe	Br	**5g** (70)	0	100

[a]Isolated yields.
[b]Ratios of *anti*-to-*syn* determined by ^{1}H NMR spectroscopy at 20°C.

We therefore have selected the stepwise cyclization of the TosMIC adduct **4** with 2,6-bis(bromomethyl)-4-*tert*-butyl-1-substituted benzenes (**3**) to prepare the desired cyclic dimer **5**. The starting compounds, 2,6-bis(bromomethyl)-4-*tert*-butyl substituted benzenes (**3**), are easily prepared by bromomethylation of 4-*tert*-butyltoluene (**2a**) and 4-*tert*-butylalkoxybenzenes (12) using the *tert*-butyl group as a positional protecting group on the aromatic ring (Scheme 2) (13). Although TosMIC adduct **4c** was obtained in 78% yield by the reaction of **3c** with TosMIC as a mixture of two isomers, i.e., *meso* and *dl*, the attempted separation of these isomers of **4c** pure failed.

The cyclic diketones (**5**) were synthesized by coupling **3** with TosMIC adduct **4c** under highly diluted conditions in DMF with an excess of sodium hydride as shown in Scheme 3. We have improved the addition procedure in Vögtle's method (9) — thus, to a suspension of NaH in DMF was added dropwise a solution of **3** and TosMIC adducts **4c** in DMF at room temperature. This method not only improves the yield of the desired ketones but also makes the handling of the base (solid NaH) easier (Table 1). The ^{1}H NMR spectrum of **5** shows two kinds of methoxy protons, each as a singlet. By careful column chromatography (silica gel, Wako C-300), the two conformers, *anti*-**5** and *syn*-**5**, are

© 2002 NRC Canada

Table 2. ^{1}H NMR spectral data for 6,15-di-*tert*-butyl-9-methoxy[3.3]MCP-2,11-diones **5a**.

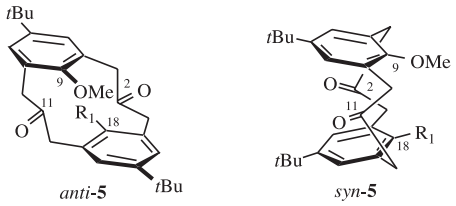

Compound	Methoxy protons	Protons of internal substituent (R_1)		Benzene protons	*tert*-Butyl protons
anti-**5a**	3.26	H	5.29	7.08, 7.19	1.27, 1.36
anti-**5b**	3.15	Me	0.94	7.19, 7.21	1.27, 1.35
anti-**5c**	3.15	OMe	—	7.14	1.31
anti-**5d**	3.13	OEt	0.98, 3.26	7.15	1.30, 1.32
anti-**5e**	3.12	OPr	0.79, 1.35,[a] 3.17	7.14, 7.15	1.30, 1.32
syn-**5b**	3.43	Me	2.50	6.64, 6.70	1.07, 1.14
syn-**5c**	3.52	OMe	—	6.68	1.08
syn-**5d**	3.54	OEt	1.37	6.66, 6.67	1.07
syn-**5e**	3.54	OPr	1.18, 1.85,[a] 3.50	6.67	1.08

Note: Determined in $CDCl_3$ by using $SiMe_4$ as a reference and expressed in ppm given.
[a]Midpoint value of multiplet.

separated. They are thermally stable and do not interconvert at 150°C in DMSO solution and at 400°C in the solid state.

The structures of **5** have been elucidated by elemental analyses and spectral data. For instance, the mass spectral data for *anti*-**5c** (M^+ = 436) strongly support cyclic dimeric structure. The IR spectrum of *anti*-**5c** shows the absorption of the carbonyl stretching vibration around 1706 cm^{-1}. The ^{1}H NMR spectrum (in $CDCl_3$) of *anti*-**5c** exhibits a set of doublets at δ = 3.22 and 3.73 (*J* = 14.7 Hz) for the Ar*CH*$_2$CO*CH*$_2$Ar methylene protons and a singlet for the internal methoxy group at an upfield shift δ = 3.15 from that of anisole (δ = 3.75) due to the ring current of the opposing aromatic ring (13*a, b*, 14). This observation strongly suggests that compound *anti*-**5c** adopts the *anti*-conformation.

In contrast, the methoxy protons of *syn*-**5c** are observed at δ 3.52. Furthermore, the aryl hydrogens can clearly be seen to be shielded (δ 6.68) by the adjacent ring, a common consequence of a face-to-face benzene ring (14, 15). Also the *tert*-butyl protons were observed at higher field (δ 1.09) compared with that of the *anti*-**5c** (δ 1.31) due to the strong shielding effect of the benzene ring. These observations strongly suggest that compound *syn*-**5c** adopts *syn*-conformation. Similarly, the assignments of structures for other *anti* and *syn* conformers were readily apparent from their ^{1}H NMR spectra. The chemical shifts (δ) of the internal methoxy protons, the protons of internal substituents at the 18 position, aromatic protons, and the *tert*-butyl protons of *anti*- and *syn*-9-methoxy[3.3]MCP-2,11-diones **5a**–**e** are compiled in Table 2.

Dependent on R_1 and R_2 of 2,6-bis(bromomethyl)-1-substituted benzenes (**3**), different yields (inversion of selectivity) of *anti*-**5** and *syn*-**5** were formed. Thus, the 18-unsubstituted analogue is exclusively formed in the *anti*-conformer, but other 18-methyl- and 18-alkoxy-analogues are formed in a mixture of *syn*- and *anti*-conformers. Interestingly, the 18-methyl analogue decreases the ratio of *syn*-to-*anti* conformers of [3.3]MCP-2,11-diones. The effect of the bulkiness of the alkyl group in alkoxy substituents on the ratio of *syn*-to-*anti* conformers was not, however, observed.

Fig. 2. Reaction intermediate for the cyclization to form [3.3]MCP-2,11-diones.

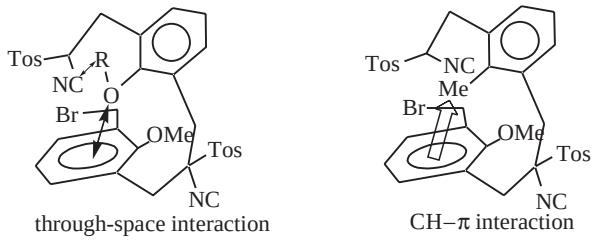

These findings suggest that in the case of the 18-methyl analogue the aromatic π–π interaction of two opposite benzene rings and the steric crowdedness at internal positions 9 and 18 may inhibit the formation of the *syn*-conformer in the [3.3]MCP-2,11-diones system and in turn the CH–π interaction (16) between methyl groups, and the opposite aromatic π-electrons may favour the formation of *anti*-conformer in the cyclization process. The CH–π interaction involving aliphatic CH moieties is well documented (16*a*) as either a conformation-controlling intramolecular process or a crystal-structure controlling intermolecular force, especially for inclusion complexes of calixarene derivatives (16*b–h*). In contrast, in the case of the 18-alkoxy analogue, the through-space interaction between the nonbonding electron pairs of the oxygen atom of the alkoxy groups and the opposite aromatic π-electrons of the *anti*-conformer may disfavour the formation of the latter (Fig. 2).

On treatment of 2,6-bis(bromomethyl)anisole (**3f**) with **4c** a preferential formation of *syn*-[3.3]MCP-2,11-dione (*syn*-**5f**) in the ratio of 95:5 was observed, which is different from the result of that of **5c** (the *syn*-to-*anti* ratio; 70:30). This result might be attributed to the bulkiness of the *tert*-butyl groups, which would inhibit the formation of *syn*-**5c**. Accordingly, the ratio of *syn* conformer is observed to increase with decreasing bulkiness of the substituents at the 15-position, as shown in Fig. 3. Furthermore, the effect on the

© 2002 NRC Canada

Fig. 3. Steric effect and π–π stacking charge-transfer-type interaction on the reaction intermediate for the cyclization to form *syn*-[3.3]MCP-2,11-diones.

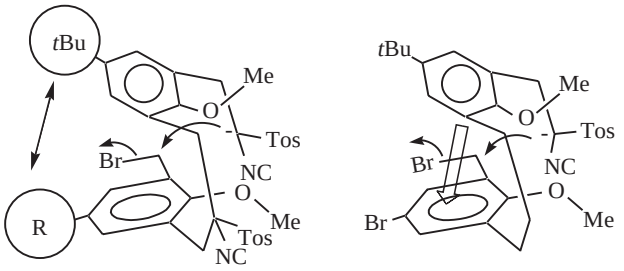

Scheme 4.

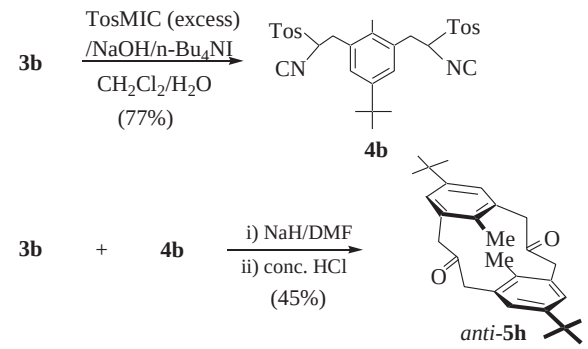

ratio of *syn*-to-*anti* conformers of MCP-2,11-diones might be also governed by charge-transfer-type interactions between the two benzene rings in the case of unsymmetrically substituted benzene rings. In fact, in the case of *syn*-6-bromo-15-*tert*-butyl-9,18-dimethoxy[3.3]MCP-2,11-dione (**5g**) the *syn*-conformer was exclusively formed due to π–π stacking charge-transfer-type interactions, as shown in Fig. 3.

To study in more detail the effects on the reaction intermediates in the cyclization to form [3.3]MCP-2,11-diones attributable to through-space interactions, we have attempted to investigate the cyclization of the TosMIC adduct **4b** with 2,6-bis(bromomethyl)-4-*tert*-butyltoluene (**3b**). Thus, the cyclization of **3b** and **4b**, carried out under the same conditions as described above, afforded exclusively the *anti*-[3.3]MCP-2,11-dione (*anti*-**5h**) in 45% yield (Scheme 4). No formation of the *syn*-conformer was observed. This result strongly suggests that the CH–π interactions play an important role in the *syn*–*anti* conformer distribution during the cyclization reaction.

In conclusion, we have demonstrated for the first time a through-space interaction between the nonbonding electron pairs of the oxygen atom of the methoxy group and the opposite aromatic π-electrons, which may disfavour formation of the *anti*-conformer during the coupling reaction of the corresponding 2,6-bis(bromomethyl)alkoxybenzenes and TosMIC adduct **4c** to preferentially afford *syn*-9-methoxy[3.3]MCP-2,11-diones (**5**).

The Wolff-Kishner reduction of *syn*- and *anti*-diketone **5c** afforded the desired *syn*- and *anti*-6,15-di-*tert*-butyl-9,18-dimethoxy[3.3]MCP (**6c**) in 86 and 90% yields, respectively. Similar results were obtained in the case of reduction of **5f** to afford **6f**. No *syn*–*anti* isomerization was observed under the reaction conditions used (Scheme 5).

Scheme 5.

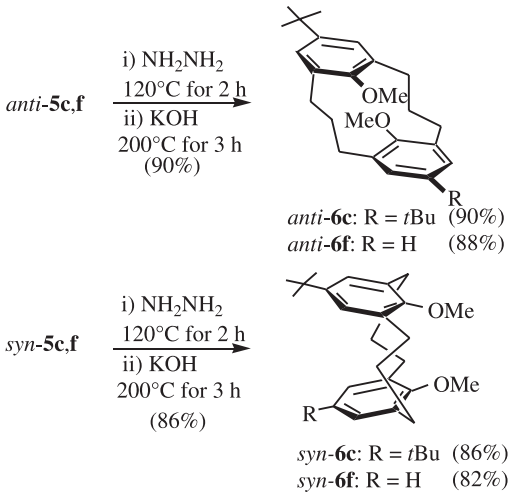

Scheme 6.

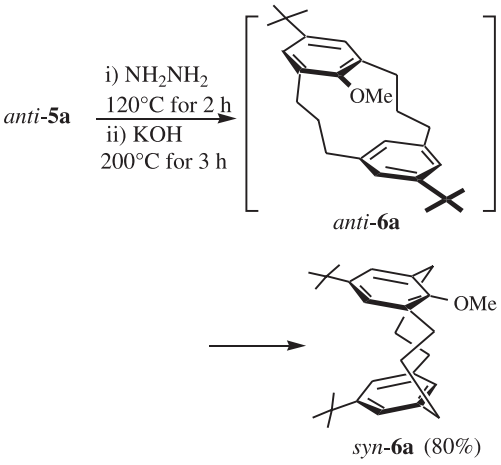

In contrast, attempted Wolff-Kishner reduction of *anti*-diketone **5a**, carried out under the same reaction conditions as **5c**, led to *syn*-9-9-methoxy[3.3]MCP *syn*-**6a** in 80% yield (Scheme 6). No formation of the corresponding *anti* conformer has been observed under the reaction conditions used. This finding strongly suggests that the ring inversion to the thermodynamically more stable *syn* conformation is possible in the 9-methoxy[3.3]MCP **6a**. On the other hand, as previously mentioned, we have reported that of *anti*-**5a** is thermally stable and does interconvert at 150°C in DMSO solution and at 400°C in the solid state. Although a detailed mechanistic conclusion to rationalize the present observation of *anti*-to-*syn*-conversion is not clear, one might assume the similar behaviour that the [3.3]MCP **1** exists in the *syn* geometry with a chair–chair arrangement of the trimethylene chains. Further studies on the chemical properties of the two conformers *syn*- and *anti*-**5** and **6** are now in progress.

Experimental

All melting points (Yanagimoto MP-S1) were uncorrected. ^{1}H NMR spectra were recorded on a Nippon Denshi JEOL FT-270 spectrometer. Chemical shifts are reported as δ values (ppm) relative to internal Me_4Si. Mass spectra were obtained

© 2002 NRC Canada

on a Nippon Denshi JMS-01SG-2 mass spectrometer at an ionization energy of 70 eV using a direct-inlet system through GLC; *m*/*z* values reported include the parent ion peak. Infrared (IR) spectra were obtained on a Nippon Denshi JIR-AQ2OM spectrophotometer as KBr disks. Elemental analyses were performed by Yanaco MT-5. Gas–liquid chromatograph (GLC) analyses were performed by Shimadzu gas chromatograph, GC-14A; silicone OV-1, 2 m; programmed temperature rise, 12°C min^{-1}; carrier gas nitrogen, 25 mL min^{-1}.

Materials

The preparations of 2,6-bis(bromomethyl)-4-*tert*-butylbenzene (**3a**), 2,6-bis(bromomethyl)anisole (**3f**), and 2,6-bis(bromomethyl)-4-bromoanisole (**3g**) were previously described (17).

Bromomethylation of 4-*tert*-butyltoluene (2a)

A mixture of **2a** (37 g, 0.23 mol), paraformaldehyde (45 g, 1.5 mol), acetic acid (55 mL), H_3PO_4 (85%, 110 mL), and concentrated HBr (48%, 164 mL) was heated at 85–90°C with vigorous stirring for 14 h, and then the reaction mixture was extracted with benzene (3 × 200 mL). The combined extracts were neutralized with a 10% aqueous Na_2CO_3 solution, washed with water, dried with Na_2SO_4, and the solvent was evaporated in vacuo to leave a residue, which was chromatographed on silica gel with hexane as the eluent to give a colorless solid. Recrystallization from hexane afforded 2,6-bis(bromomethyl)-4-*tert*-butyltoluene (**3b**) (63.6 g, 82%) as colorless prisms, mp 89–91°C. ^{1}H NMR ($CDCl_3$) δ: 1.30 (s, 9H), 2.41 (s, 3H), 4.54 (s, 4H), 7.30 (s, 2H). MS *m*/*z*: 332, 334, 336 (M^+). Anal. calcd. for $C_{13}H_{18}Br_2$: C 46.73, H 5.43; found: C 46.72, H 5.52.

Compounds **3c**, **3d**, and **3e** were similarly prepared. The yields are listed in Scheme 2.

*2,6-Bis(bromomethyl)-4-*tert*-butylanisole (3c)*

Colorless prisms (hexane), mp 88–89°C. ^{1}H NMR ($CDCl_3$) δ: 1.31 (s, 9H), 4.01 (s, 3H), 4.56 (s, 4H), 7.36 (s, 2H). MS *m*/*z*: 348, 350, 352 (M^+). Anal. calcd. for $C_{13}H_{18}Br_2O$: C 44.60, H 5.18; found: C 45.30, H 4.99.

*2,6-Bis(bromomethyl)-4-*tert*-butylethoxybenzene (3d)*

Colorless prisms (hexane), mp 65–66°C. ^{1}H NMR ($CDCl_3$) δ: 1.31 (s, 9H), 1.51 (t, *J* = 7.32 Hz, 3H), 4.16 (q, *J* = 7.32 Hz, 2H), 4.56 (s, 4H), 7.36 (s, 2H). MS *m*/*z*: 362, 364, 366 (M^+). Anal. calcd. for $C_{14}H_{20}Br_2O$: C 46.18, H 5.54; found: C 45.95, H 5.39.

*2,6-Bis(bromomethyl)-4-*tert*-butylpropoxybenzene (3e)*

Colorless prisms (hexane), mp 108.5–109.5°C. ^{1}H NMR ($CDCl_3$) δ: 1.13 (t, *J* = 7.32 Hz, 3H), 1.31 (s, 9H), 1.85–2.00 (m, 2 H), 4.05 (t, *J* = 6.83 Hz, 2H), 4.56 (s, 4H), 7.36 (s, 2H). MS *m*/*z*: 376, 378, 380 (M^+). Anal. calcd. for $C_{15}H_{22}Br_2O$: C 47.64, H 5.86; found: C 47.98, H 5.89.

Preparation of the TosMIC adduct 4

Typical procedure

To a mixture of 20% aqueous NaOH (40 mL) and CH_2Cl_2 (50 mL) was added *n*-Bu_4NI (700 mg, 1.9 mmol) followed by a solution of TosMIC (8 g, 41 mmol) in CH_2Cl_2 (50 mL). After the reaction mixture was stirred at room temperature for 30 min, a solution of dibromide **3b** (4.0 g, 11 mmol) in CH_2Cl_2 (50 mL) was added. The reaction mixture was stirred at room temperature for 2 h, quenched with water (100 mL), and extracted with CH_2Cl_2 (3 × 100 mL). It was washed with water (100 mL), dried with Na_2SO_4, and concentrated in vacuo to leave a residue. To this residue methanol (100 mL) was added and left overnight in the refrigerator to give 2,6-bis[2-cyano-2-(toluenesulfonyl)ethyl]-4-*tert*-butyltoluene (**4b**) (4.90 g, 77%) as pale brown prisms, mp 176°C (dec.). IR (KBr) υ_{max} (cm^{-1}): 2135 (CN). ^{1}H NMR ($CDCl_3$) δ: 1.26, 1.27 (each s, 9H), 2.26, 2.27 (each s, 3H), 2.50 (s, 6H), 3.00–4.52 (m, 6H), 7.16 (s, 2H), 7.46 (d, *J* = 8.3 Hz, 4H), 7.92 (d, *J* = 8.3 Hz, 4H). MS *m*/*z*: 436 (M^+). Anal. calcd. for $C_{31}H_{34}N_2O_4S_2$: C 66.16, H 6.09, N 4.98; found: C 65.95, H 6.06, N 4.73.

Compound **4c** was similarly prepared in 78% yield.

*2,6-Bis[2-cyano-2-(toluenesulfony)ethyl]-4-*tert*-butylanisole (4c)*

Pale brown prisms (hexane), mp 150–151°C (dec.). IR (KBr) υ_{max} (cm^{-1}): 2134 (CN). ^{1}H NMR ($CDCl_3$) δ: 1.26, 1.27 (each s, 9H), 2.49, 2.50 (each s, 6H), 2.87, 2.99 (each dd, *J* = 11.7 and 13.7 Hz, 2H), 3.66, 3.77 (each dd, *J* = 2.9 and 13.7 Hz, 2H), 3.76, 3.80 (each s, 3H), 4.73, 4.83 (each dd, *J* = 2.9 and 11.7 Hz, 2H), 7.19, 7.20 (each s, 2H), 7.44, 7.46 (each d, *J* = 8.3 Hz, 4H), 7.87, 7.93 (each d, *J* = 8.3 Hz, 4H). MS *m*/*z*: 578 (M^+). Anal. calcd. for $C_{31}H_{34}N_2O_5S_2$: C 64.34, H 5.92, N 4.84; found: C 64.56, H 5.87, N 4.73.

Stepwise cyclization of TosMIC adduct 4 and dibromide 3

Typical procedure

To a suspension of NaH (2.1 g, 51 mmol) in DMF (150 mL) a solution of **3c** (4.7 g, 8.5 mmol) and **4c** (5.0 g, 8.5 mmol) in DMF (35 mL) was added dropwise over a period of 6 h. After the suspension was stirred for an additional 5 h at room temperature, it was quenched with ice water (300 mL). The reaction mixture was extracted with CH_2Cl_2 (3 × 100 mL), washed with water (200 mL), dried with Na_2SO_4, and concentrated in vacuo to 15 mL. Conc. HCl (15 mL) was added, and the solution was stirred for 15 min. The organic layer was again extracted with CH_2Cl_2 (3 × 100 mL), washed with water (2 × 100 mL), dried with Na_2SO_4, and concentrated and condensed under reduced pressure. The residue was chromatographed on silica gel using $CHCl_3$ as eluents to give crude *anti*-**5c** and *syn*-**5c** as a pale yellow solid. Recrystallization from hexane afforded *anti*-**5c** (592 mg, 16%) and *syn*-**5c** (1.37 g, 37%).

anti-*6,15-Di*-tert-*butyl-9,18-dimethoxy[3.3]metacyclophane-2,11-dione (*anti-*5c)*

Colorless prisms (hexane), mp 210–211°C. IR (KBr) υ_{max} (cm^{-1}): 1706 (C=O). ^{1}H NMR ($CDCl_3$) δ: 1.31 (s, 18H), 3.15 (s, 6H), 3.22 (d, *J* = 14.7 Hz, 4H), 3.73 (d, *J* = 14.7 Hz, 4H), 7.14 (s, 4H). MS *m*/*z*: 436 (M^+). Anal. calcd. for $C_{28}H_{36}O_4$: C 77.03, H 8.31; found: C 76.66, H 8.37.

syn-*6,15-Di*-tert-*butyl-9,18-dimethoxy[3.3]metacyclophane-2,11-dione (*syn-*5c)*

Colorless prisms (hexane), mp 22–23°C. IR (KBr) υ_{max} (cm^{-1}): 1701 (C=O). ^{1}H NMR ($CDCl_3$) δ: 1.08 (s, 18H), 3.28 (d, *J* = 12.7 Hz, 4H), 3.52 (s, 6H), 4.24 (d, *J* = 12.7 Hz,

© 2002 NRC Canada

4H), 6.68 (s, 4H). MS *m*/*z*: 436 (M^+). Anal. calcd. for $C_{28}H_{36}O_4$: C 77.03, H 8.31; found: C 76.83, H 8.34.

Compounds **5a**–**b** and **5d**–**g** were similarly prepared. The yields are listed in Table 1.

anti-*6,15-Di*-tert-*butyl-9-methoxy[3.3]metacyclophane-2,11-dione* (anti-*5a*)

Colorless prisms (hexane), mp 142–144°C. IR (KBr) υ_{max} (cm^{-1}): 1688 (C=O). ^1H NMR ($CDCl_3$) δ: 1.27 (s, 9H), 1.36 (s, 9H), 3.26 (s, 3H), 3.29 (d, *J* = 15.6 Hz, 2H), 3.39 (d, *J* = 13.7 Hz, 2H), 3.51 (d, *J* = 13.7 Hz, 2H), 3.73 (d, *J* = 15.6 Hz, 2H), 5.29 (s, 1H), 7.08 (s, 2H), 7.19 (s, 2H). MS *m*/*z*: 406 (M^+). Anal. calcd. for $C_{27}H_{34}O_3$: C 79.77, H 8.43; found: C 79.75, H 8.47.

anti-*6,15-Di*-tert-*butyl-9-methoxy-18-methyl[3.3]metacyclophane-2,11-dione* (anti-*5b*)

Colorless prisms (hexane), mp 252–254°C. IR (KBr) υ_{max} (cm^{-1}): 1699 (C=O). ^1H NMR ($CDCl_3$) δ: 0.94 (s, 3H), 1.27 (s, 9H), 1.35 (s, 9H), 3.15 (s, 3H), 3.18 (d, *J* = 13.2 Hz, 2H), 3.40 (d, *J* = 15.6 Hz, 2H), 3.63 (d, *J* = 15.6 Hz, 2H), 3.85 (d, *J* = 13.2 Hz, 2H), 7.19 (s, 2H), 7.21 (s, 2H). MS *m*/*z*: 420 (M^+). Anal. calcd. for $C_{28}H_{36}O_3$: C 79.96, H 8.63; found: C 79.84, H 8.56.

syn-*6,15-Di*-tert-*butyl-9-methoxy-18-methyl[3.3]metacyclophane-2,11-dione* (syn-*5b*)

Colorless prisms (hexane), mp 118–120°C. IR (KBr) υ_{max} (cm^{-1}): 1689 (C=O). ^1H NMR ($CDCl_3$) δ: 1.07 (s, 9H), 1.14 (s, 9H), 2.50 (s, 3H), 3.30 (d, *J* = 13.2 Hz, 2H), 3.43 (s, 3H), 3.50 (d, *J* = 13.7 Hz, 2H), 3.92 (d, *J* = 13.7 Hz, 2H), 4.14 (d, *J* = 13.2 Hz, 2H), 6.64 (s, 2H), 6.70 (s, 2H). MS *m*/*z*: 420 (M^+). Anal. calcd. for $C_{28}H_{36}O_3$: C 79.96, H 8.63; found: C 79.78, H 8.53.

anti-*6,15-Di*-tert-*butyl-9-ethoxy-18-methoxy[3.3]metacyclophane-2,11-dione* (anti-*5d*)

Colorless prisms (hexane), mp 198–199°C. IR (KBr) υ_{max} (cm^{-1}): 1702 (C=O). ^1H NMR ($CDCl_3$) δ: 0.98 (t, *J* = 7.33 Hz, 3H), 1.30 (s, 9H), 1.32 (s, 9H), 3.13 (s, 3H), 3.14 (d, *J* = 14.6, 4H), 3.26 (q, *J* = 7.33 Hz, 2H), 3.63 (d, *J* = 14.6 Hz, 2H), 3.65 (d, *J* = 14.6, 2H), 7.15 (s, 4H). MS *m*/*z*: 450 (M^+). Anal. calcd. for $C_{29}H_{38}O_4$: C 77.30, H 8.50; found: C 77.54, H 8.46.

syn-*6,15-Di*-tert-*butyl-9-ethoxy-18-methoxy[3.3]metacyclophane-2,11-dione* (syn-*5d*)

Colorless oil. IR (NaCl) υ_{max} (cm^{-1}): 1701 (C=O). ^1H NMR ($CDCl_3$) δ: 1.07 (s, 18H), 1.37 (t, *J* = 7.33 Hz, 3H), 3.28 (d, *J* = 12.7 Hz, 2H), 3.30 (d, *J* = 12.7 Hz, 2H), 3.54 (s, 3H), 3.60 (q, *J* = 7.33 Hz, 2H), 4.27 (d, *J* = 12.7 Hz, 2H), 4.30 (d, *J* = 12.7 Hz, 2H), 6.66 (s, 2H), 6.67 (s, 2H). MS *m*/*z*: 450 (M^+). Anal. calcd. for $C_{29}H_{38}O_4$: C 77.30, H 8.50; found: C 77.45, H 8.63.

anti-*6,15-Di*-tert-*butyl-9-methoxy-18-propoxy[3.3]metacyclophane-2,11-dione* (anti-*5e*)

Colorless prisms (hexane), mp 123–124°C. IR (KBr) υ_{max} (cm^{-1}): 1685 (C=O). ^1H NMR ($CDCl_3$) δ: 0.79 (t, *J* = 7.33 Hz, 3H), 1.30 (s, 9H), 1.32 (s, 9H), 1.30–1.40 (m, 2H), 3.12 (s, 3H), 3.17 (t, *J* = 7.33 Hz, 2H), 3.21 (d, *J* = 14.16 Hz, 4H), 3.73 (d, *J* = 14.16 Hz, 2H), 3.74 (d, *J* = 14.16 Hz, 2H), 7.14 (s, 2H), 7.15 (s, 2H). MS *m*/*z*: 464 (M^+). Anal. calcd. for $C_{30}H_{40}O_4$: C 77.55, H 8.68; found: C 77.35, H 8.64.

syn-*6,15-Di*-tert-*butyl-9-methoxy-18-propoxy[3.3]metacyclophane-2,11-dione* (syn-*5e*)

Colorless oil. IR (NaCl) υ_{max} (cm^{-1}): 1703 (C=O). ^1H NMR ($CDCl_3$) δ: 1.08 (s, 18H), 1.18 (t, *J* = 7.33 Hz, 3H), 1.80–1.90 (m, 2H), 3.27 (d, *J* = 12.7 Hz, 2H), 3.30 (d, *J* = 12.7 Hz, 2H), 3.50 (q, *J* = 7.33 Hz, 2H), 3.54 (s, 3H), 4.29 (d, *J* = 12.7 Hz, 2H), 4.33 (d, *J* = 12.7 Hz, 2H), 6.67 (s, 4H). MS *m*/*z*: 464 (M^+). Anal. calcd. for $C_{30}H_{40}O_4$: C 77.55, H 8.68; found: C 77.41, H 8.47.

anti-*6*-tert-*Butyl-9,18-dimethoxy[3.3]metacyclophane-2,11-dione* (anti-*5f*)

Colorless prisms (hexane), mp 198–199°C. IR (KBr) υ_{max} (cm^{-1}): 1685 (C=O). ^1H NMR ($CDCl_3$) δ: 1.32 (s, 9H), 3.16 (s, 3H), 3.17 (s, 3H), 3.23 (d, *J* = 14.6 Hz, 4H), 3.60 (d, *J* = 14.6 Hz, 2H), 3.63 (d, *J* = 14.6 Hz, 2H), 6.93–6.99 (m, 1H), 7.16–7.18 (m, 4H). MS *m*/*z*: 380 (M^+). Anal. calcd. for $C_{24}H_{28}O_4$: C 75.76, H 7.42; found: C 75.55, H 7.54.

syn-*6*-tert-*Butyl-9,18-dimethoxy[3.3]metacyclophane-2,11-dione* (syn-*5f*)

Colorless oil. IR (NaCl) υ_{max} (cm^{-1}): 1688 (C=O). ^1H NMR ($CDCl_3$) δ: 1.12 (s, 9H), 3.32 (d, *J* = 12.7 Hz, 4H), 3.55 (s, 3H), 3.56 (s, 3H), 4.30 (d, *J* = 12.7 Hz, 4H), 6.48–6.54 (m, 1H), 6.65–6.68 (m, 4H). MS *m*/*z*: 380 (M^+). Anal. calcd. for $C_{24}H_{28}O_4$: C 75.76, H 7.42; found: C 75.62, H 7.35.

syn-*6-Bromo-15*-tert-*butyl-9,18-dimethoxy[3.3]metacyclophane-2,11-dione* (syn-*5g*)

Colorless prisms (hexane), mp 150–153°C. IR (KBr) υ_{max} (cm^{-1}): 1700 (C=O). ^1H NMR ($CDCl_3$) δ: 1.18 (s, 9H), 3.27 (d, *J* = 13.0 Hz, 2H), 3.34 (d, *J* = 13.0 Hz, 2H), 3.54 (s, 3H), 3.55 (s, 3H), 4.21 (d, *J* = 13.0 Hz, 2H), 4.27 (d, *J* = 13.0 Hz, 2H), 6.71 (s, 2H), 6.79 (s, 2H). MS *m*/*z*: 458. 460 (M^+). Anal. calcd. for $C_{24}H_{27}BrO_4$: C 62.75, H 5.92; found: C 62.65, H 5.85.

anti-*6,15-Di*-tert-*butyl-9,18-dimethyl[3.3]metacyclophane-2,11-dione* (anti-*5h*)

Colorless prisms (hexane), mp 282–284°C. IR (KBr) υ_{max} (cm^{-1}): 1698 (C=O). ^1H NMR ($CDCl_3$) δ: 0.95 (s, 6H), 1.30 (s, 18H), 3.26 (s, 3H), 3.30 (d, *J* = 14.7 Hz, 4H), 3.67 (d, *J* = 14.7 Hz, 4H), 7.25 (s, 4H). MS *m*/*z*: 404 (M^+). Anal. calcd. for $C_{28}H_{36}O_2$: C 83.12, H 8.97; found: C 82.98, H 8.88.

Wolff-Kishner reduction of 5

Typical procedure

A mixture of *anti*-**5c** (1.20 g, 2.75 mmol), KOH (1.28 g, 23.0 mmol), 100% hydrazine hydrate (0.35 mL, 6.2 mmol), and triethylene glycol (35 mL) was heated at 120°C for 2 h and then at 220°C for 3 h. The cooled mixture was poured into water (50 mL), acidified with diluted HCl, and then extracted with CH_2Cl_2 (3 × 50 mL), washed with water (2 × 20 mL), dried with Na_2SO_4, and concentrated under reduced pressure. The residue was chromatographed on silica gel using hexane–benzene (1:1) as eluents to give crude *anti*-**6c** as a colorless solid. Recrystallization from hexane afforded

© 2002 NRC Canada

anti-6,15-di-*tert*-butyl-9,18-dimethoxy[3.3]metacyclophane (*anti*-**6c**) (1.02 g, 90%) as colorless prisms, mp 220–222°C. ^{1}H NMR ($CDCl_3$) δ: 1.32 (s, 18H), 2.08–2.15 (m, 4H), 2.30–2.39 (m, 4H), 2.57–2.67 (m, 4H), 3.11 (s, 6H), 6.95 (s, 4H). MS *m*/*z*: 408 (M^+). Anal. calcd. for $C_{28}H_{40}O_2$: C 82.30, H 9.87; found: C 81.99, H 9.94.

Compounds *syn*-**6c**, *syn*-**6a**, *anti*-**6f**, and *syn*-**6f** were similarly prepared. The yields are listed in Scheme 6.

syn-*6,15-Di*-tert-*butyl-9,18-dimethoxy[3.3]metacyclophane (syn-*6c*)

Colorless prisms (hexane), mp 116–118°C. ^{1}H NMR ($CDCl_3$) δ: 1.11 (s, 18H), 1.59–1.76 (m, 2H), 2.28–2.52 (m, 5H), 3.00–3.11 (m, 4H), 3.47 (s, 6H), 6.53 (s, 4H). MS *m*/*z*: 408 (M^+). Anal. calcd. for $C_{28}H_{40}O_2$: C 82.30, H 9.87; found: C 82.06, H 9.92.

syn-*6,15-Di*-tert-*butyl-9-methoxy[3.3]metacyclophane (syn-*6a*)

Colorless oil. ^{1}H NMR ($CDCl_3$) δ: 1.06 (s, 9H), 1.14 (s, 9H), 2.25–2.38 (m, 4H), 2.48–2.65 (m, 4H), 2.61–2.73 (m, 4H), 3.66 (s, 3H), 6.57 (s, 2H), 6.58 (s, 1H), 6.69 (s, 1H), 7.10 (s, 1H). MS *m*/*z*: 378 (M^+). Anal. calcd. for $C_{27}H_{38}O$: C 85.66, H 10.12; found: C 85.36, H 9.99.

anti-*6*-tert-*Butyl-9,18-dimethoxy[3.3]metacyclophane (anti-*6f*)

Colorless prisms (hexane), mp 220–222°C. ^{1}H NMR ($CDCl_3$) δ: 1.34 (s, 18H), 2.05–2.15 (m, 4H), 2.31–2.42 (m, 4H), 2.57–2.69 (9m, 4H), 3.10 (s, 3H), 3.15 (s, 3H), 6.85–6.88 (m, 1H), 6.95–6.97 (m, 4H). MS *m*/*z*: 352 (M^+). Anal. calcd. for $C_{24}H_{32}O_2$: C 81.77, H 9.15; found: C 81.69, H 9.04.

syn-*6*-tert-*Butyl-9,18-dimethoxy[3.3]metacyclophane (syn-*6f*)

Colorless prisms (hexane), mp 82–84°C. ^{1}H NMR ($CDCl_3$) δ: 1.15 (s, 9H), 1.81–1.89 (m, 2H), 2.45–2.52 (m, 6H), 3.03–3.13 (m, 4H), 3.48 (s, 6H), 6.48–6.56 (m, 5H). MS *m*/*z*: 352 (M^+). Anal. calcd. for $C_{24}H_{32}O_2$: C 81.77, H 9.15; found: C 81.58, H 9.11.

References

1. (*a*) T. Yamato, K. Noda, and K. Tanaka. J. Chem. Res. Synop. 62 (2002); (*b*) J. Chem. Res. Miniprint 256 (2002).
2. (*a*) F. Vögtle. Cyclophane chemistry: synthesis, structures, and reactions. John Wiley & Sons, New York. 1993; (*b*) M.F. Semmelhack, J.J. Harrison, D.C. Young, A. Gutiérrez, S. Rafii, and J. Clardy. J. Am. Chem. Soc. **107**, 7508 (1985).
3. F. Vögtle and L. Schunder. Chem. Ber. **102**, 2677 (1969).
4. T. Shinmyozu, T. Inazu, and T. Yoshino. Chem. Lett. 1405 (1976).
5. (*a*) K. Sako, T. Hirakawa, N. Fujimoto, T. Shinmyozu, T. Inazu, and H. Horimoto. Tetrahedron Lett. **29**, 6275 (1988); (*b*) K. Sako, T. Shinmyozu, H. Takemura, M. Suenaga, and T. Inazu. J. Org. Chem. **57**, 6536 (1992).
6. (*a*) J. Nishimura, A. Ohbayashi, Y. Horiuchi, Y. Okada, Y. Namanaka, and A. Oku. J. Org. Chem. **57**, 6536 (1987); (*b*) Y. Fukazawa, Y. Takeda, S. Usui, and M. Kodama. J. Am. Chem. Soc. **110**, 7842 (1988); (*c*) L. Ernst. Progr. Nucl. Magn. Reson. Spectrosc. **37**, 47 (2000).
7. T. Shinmyozu, T. Inazu, and T. Yoshino. Mem. Fac. Sci. Kyushu Univ. Ser. C, **15**, 79 (1985).
8. (*a*) S. Osada, Y. Miyahara, T. Shinmyozu, and T. Inazu. Mem. Fac. Sci. Kyushu Univ. Ser. C, **19**, 39 (1993); (*b*) S. Osada, Y. Miyahara, N. Shimizu, and T. Inazu. Chem. Lett. 1103 (1995).
9. (*a*) J. Breitenbach and F. Vögtle. Synthesis, 41 (1992); (*b*) J. Breitenbach, F. Ott, and F. Vögtle. Angew. Chem. **104**, 360 (1992); Angew. Chem. Int. Ed. Engl. **31**, 307 (1992); (*c*) F. Ott, J. Breitenbach, M. Nieger, and F. Vögtle. Chem. Ber. **126**, 97 (1993).
10. (*a*) O. Possel and A.M. van Leusen. Tetrahedron Lett. 4229 (1977); (*b*) D. van Leusen and A.M. van Leusen. Tetrahedron Lett. 4233 (1977).
11. (*a*) K. Kobiro, M. Takashi, N. Nishikawa, K. Kikuchi, Y. Tobe, and Y. Odaira. Tetrahedron Lett. **28**, 3825 (1987); (*b*) K. Kurosawa, M. Suenaga, T. Inazu, and T. Yoshino. Tetrahedron Lett. **23**, 5335 (1982); (*c*) T. Shinmyozu, Y. Hirai, and T. Inazu. J. Org. Chem. **51**, 1551 (1986); (*e*) T. Meno, K. Sako, M. Suenaga, M. Mouri, T. Shinmyozu, T. Inazu, and H. Takemura. Can. J. Chem. **68**, 440 (1990); (*g*) K. Sako, T. Meno, H. Takemura, T. Shinmyozu, and T. Inazu. Chem. Ber. **123**, 630 (1990).
12. M. Tashiro and T. Yamato. Org. Prep. Proced. Int. **13**, 1 (1981).
13. (*a*) M. Tashiro and T. Yamato. J. Org. Chem. **46**, 4556 (1981); (*b*) M. Tashiro and T. Yamato. J. Org. Chem. **48**, 1461 (1983); (*c*) M. Tashiro and T. Yamato. J. Org. Chem. **50**, 2939 (1985); (*d*) T. Yamato, J. Matsumoto, K. Tokuhisa, M. Kajihara, K. Suehiro, and M. Tashiro. Chem. Ber. **125**, 2443 (1992); (*e*) T. Yamato, J. Matsumoto, K. Tokuhisa, K. Tsuji, K. Suehiro, and M. Tashiro. J. Chem. Soc. Perkin Trans. 1, 2675 (1992); (*f*) T. Yamato, A. Miyazawa, and M. Tashiro. J. Chem. Soc. Perkin Trans. 1, 3127 (1993); (*g*) T. Yamato, A. Miyazawa, and M. Tashiro. Chem. Ber. **126**, 2505 (1993).
14. (*a*) B.H. Smith. *In* Bridged aromatic compounds. Academic Press, New York. 1964; (*b*) F. Vögtle and P. Neumann. Angew. Chem. **84**, 75 (1972); Angew. Chem. Int. Ed. Engl. **11**, 73 (1972); (*c*) F. Vögtle and P. Neumann. Synthesis, 85 (1973); (*d*) F. Vögtle and G. Höhner. Top. Curr. Chem. **74**, 1 (1978); (*e*) P.M. Keehn and S.M. Rosenfield. Cyclophanes. Vol. 1. Academic Press, New York. 1983.
15. (*a*) R.H. Mitchell and V. Boekelheide. Tetrahedron Lett. 1197 (1970); (*b*) R.H. Mitchell and V. Boekelheide. J. Chem. Soc. Chem. Commun. 1555 (1970); (*c*) W. Anker, G.W. Bushnell, and R.H. Mitchell. Can. J. Chem. **57**, 3080 (1979); (*d*) R.H. Mitchell, R.J. Carruther, L. Mazuch, and T.W. Dingle. J. Am. Chem. Soc. **104**, 2544 (1982); (*e*) R.H. Mitchell and V. Boekelheide. J. Am. Chem. Soc. **96**, 1547 (1974).
16. (*a*) M. Nishio and M. Horita. Tetrahedron, **45**, 7201 (1989); (*b*) C.D. Andreetti, R. Ungaro, and A. Pochini. J. Chem. Soc. Chem. Commun. 1005 (1979); (*c*) R. Ungaro, A. Pochini, C.D. Andreetti, and O. Domiano. J. Chem. Soc. Perkin Trans. 2, 197 (1985); (*d*) M.A. McKervey, E.M. Seward, G. Ferguson, and B.L. Ruhl. J. Org. Chem. **51**, 3581 (1986); (*e*) D.J. Cram, S. Karbach, H.-E. Kim, C.B. Knobler, E.F. Marverick, J.L. Ericson, and R.C. Helgeson. J. Am. Chem. Soc. **110**, 2229 (1988); (*f*) P. Soncini, S. Bonsignore, E. Dalcanale, and F. Ugozzoli. J. Org. Chem. **57**, 4608 (1992); (*g*) J.L. Atwood, S.G. Bott, C. Jones, and C.L. Raston. J. Chem. Soc. Chem. Commun. 1349 (1992); (*h*) K. Kobayashi, Y. Asakawa, Y. Kikuchi, H. Toi, and Y. Aoyama. J. Am. Chem. Soc. **115**, 2648 (1993).
17. M. Tashiro and T. Yamato. J. Org. Chem. **46**, 1543 (1981).

© 2002 NRC Canada

Kinetics of glycoluril template-directed Claisen condensations and mechanistic implications

Mohammad Rahimizadeh, Karen Kam, Stephen I. Jenkins, Robert S. McDonald, and Paul H.M. Harrison

Abstract: Eight *N*-acetyl-*N*-aroyl-glycolurils were prepared and found to undergo efficient *tert*-butoxide-promoted Claisen-like condensation between the two acyl moieties. The kinetics for formation of each of the *N*-(aroylacetyl)glycoluril products were monitored by UV spectroscopy. The reactions exhibited pseudo-first-order kinetics in substrate in the presence of excess base. For the parent benzoyl compound the observed first-order rate constant (k_{obs}) was linearly dependent on the concentration of the base, *tert*-butoxide. A Hammett plot of the resulting apparent second-order rate constants (k_{app}) vs. σ for each of the eight aroyl derivatives was linear and had a positive ρ value 1.04 ± 0.04), demonstrating that the substituent on the aromatic ring exerts a significant effect upon the condensation reaction. The corresponding plot for three [D_3]acetyl analogues was also linear, but the slope was reduced by 20% relative to the protonated compounds. The isotope effect (k^{H}_{app}/k^{D}_{app}) thus increased from 1.4 (benzoyl) to 2.6 (*p*-nitrobenzoyl). The results are consistent with a three-step mechanism in which both deprotonation of the acetyl entity and the ensuing nucleophilic attack of the resulting enolate on the benzoyl group are partially rate-determining steps. The tetrahedral intermediate thus produced rapidly collapses to the product. For the [D_3]acetyl benzoyl derivative, exchange of substrate deuterium with solvent hydrogen due to reprotonation of the enolate intermediate occurs at a rate that is similar to that of condensation, but the enolate partitions towards the product when electron withdrawing groups are present in the aroyl ring. Thus, despite the presence of a large excess of co-solvent *tert*-butanol, the efficiency with which the enolate undergoes condensation remains high. The clean kinetics observed allows further exploration of the details of this intramolecular Claisen-like condensation process.

Key words: Claisen condensation, glycoluril, kinetics, Hammett, mechanism.

Résumé : On a préparé huit *N*-acétyl-*N*-aroylglycolurils et on a observé que les deux portions acyles subissent facilement une condensation de type Claisen, catalysée par l'ion *tert*-butylate. La cinétique de formation de chacun des *N*-(aroylacétyl)glycolurils produits a été suivie par spectroscopie UV. En présence d'un excès de base, les réactions présente une cinétique de pseudo-premier ordre en substrat. Pour le composé benzoylé fondamental, la constante de vitesse du premier ordre observée (k_{obs}) varie de façon linéaire avec la concentration du *tert*-butylate utilisé comme base. La courbe de Hammett des constantes de vitesse du deuxième ordre apparentes qui en résultent (k_{app}) en fonction de σ est linéaire pour chacun des huit dérivés aroylés et la valeur de ρ est légèrement positive (1,04 ± 0,04) ce qui démontre que le substituant du noyau aromatique exerce un effet important sur la réaction de condensation. La courbe correspondante pour les trois analogues [D_3]acétylés est aussi linéaire, mais la pente est réduite de 20% par rapport à celle des composés protiés. L'effet isotopique (k^{H}_{app}/k^{D}_{app}) augmente donc de 1,4 (benzoyle) à 2,6 (*p*-nitrobenzoyle). Les résultats sont en accord avec un mécanisme en trois étapes dans lequel la déprotonation de l'entité acétyle ainsi que l'attaque nucléophile subséquente de l'énolate qui en résulte sur le groupe benzoyle sont les étapes partiellement cinétiquement limitantes. L'intermédiaire tétraédrique ainsi produit se décompose rapidement en produit. Pour le dérivé [D_3]acétyle benzoyle, l'échange de deutérium du substrat avec l'hydrogène du solvant causé par la reprotonation de l'intermédiaire énolate se produit à une vitesse similaire à celle de la condensation, mais l'énolate se partitionne vers le produit quand le noyau aroyle comporte des groupes électroattracteurs. Ainsi, malgré la présence d'un large excès du *tert*-butanol qui agit comme solvant, l'efficacité avec laquelle l'énolate donne lieu à une condensation demeure élevée. Les cinétiques bien définies observées permettent d'explorer plus à fond les détails du processus de condensation intramoléculaire de type Claisen.

Mots clés : condensation de Claisen, glycoluril, cinétique, Hammett, mécanisme.

[Traduit par la Rédaction]

Received 5 November 2001. Published on the NRC Research Press Web site at http://canjchem.nrc.ca on 13 May 2002.

M. Rahimizadeh,[1] K. Kam, S.I. Jenkins, and P.H.M. Harrison.[2,3] Department of Chemistry, McMaster University, 1280 Main Street West, Hamilton, ON L8S 4M1, Canada.
R.S. McDonald.[3] Department of Chemistry, Mount St. Vincent University, Halifax, NS B3M 2J6, Canada.

[1]On sabbatical leave from Ferdowsi University of Mashad, Iran.
[2]Corresponding author (e-mail: pharriso@mcmaster.ca).
[3]Joint principal corresponding authors.

 DOI: 10.1139/V02-071 © 2002 NRC Canada

Introduction

The fatty acids (1, 2) and polyketides (1, 3) are two large and diverse groups of natural products. Both sets of metabolites are assembled in vivo by sequential "head-to-tail" condensations of acyl units in a series of Claisen-like condensation steps on the surface of multifunctional fatty acid- (FAS) or polyketide synthases (PKS) (1–3). Synthetically, these compounds are frequently accessed by a sequence of aldol condensations, often mediated by catalysts and (or) chiral auxiliaries. Another approach involves using Claisen-like condensations to mimic the biosynthetic assembly process (4). In this context, we developed a method using a glycoluril auxiliary: two acyl units are attached to the N-1 and N-6 positions of 3,4,7,8-tetramethylglycoluril (**1**, Scheme 1) to give **2**. An ensuing intramolecular base-promoted Claisen-like condensation furnishes β-ketoacylglycolurils **3** under relatively mild conditions and in high yield (5–7).

Furthermore, the resulting β-ketoacylglycolurils **3** can be chemically modified through a sequence of reactions, which is analogous to those that occur on FAS or PKS. The ensuing product can then undergo repetitive cycles of acylation, condensation, and functional group manipulations, resembling the head-to-tail assembly of acyl units by FAS or PKS (6–8). Thus, **1** acts as a functional small-molecule model of some of the features of these giant enzymes.

A study of the mechanism of the condensation reaction of **2** to give **3** would provide further insight into the effects that contribute to the efficiency of the process. As part of our earlier studies, we showed that when the 1-acetyl-6-[D_3]acetyl analogue **2b** was treated with lithium *tert*-butoxide, the base preferred to remove protium over deuterium by a factor of 4.6:1 (7). We invoked a primary kinetic isotope effect (KIE) and proposed a slow proton removal followed by fast intramolecular trapping of the resulting enolate by the other acceptor acyl entity, in accord with our strategy for the design of **1**. Subsequent work, however, showed that changing the reaction conditions caused a small but significant change in the magnitude of the isotope effect, suggesting that deprotonation may not be the sole rate-limiting step (unpublished data).

We have not previously been able to quantify the rate of transformation of diacylglycolurils **2** into **3**, and thus little is known about the critical carbon–carbon bond-forming step. To re-examine the rate-limiting step(s), to further probe the details of the mechanism of this intriguing process, and to provide a quantitative measure of the efficiency of the condensation and the factors that govern it, we chose the acetyl benzoyl glycoluril **2c** for monitoring the progress of the condensation reaction by UV spectroscopy. Herein, the results of this experiment as well as further quantitative studies of the effects of substituents on the aroyl ring, and of deuterium substitution in the acetyl group in **2c**, are described. Mechanistic implications are then discussed, and the results compared with those from the literature for intramolecular Claisen and aldol condensations.

Results

Treatment of monoacetylglycoluril **4a** (7) with *n*-BuLi in THF, then benzoyl chloride, using the method previously reported for preparation of diacylglycolurils readily afforded acetyl benzoylglycoluril **2c** in 92% yield (Scheme 1). Compound **2c** was fully characterized by X-ray crystallography, as will be described elsewhere (9). In a similar manner, a range of *meta*- and *para*-substituted acetyl aroyl glycolurils (**2d**–**j**) were prepared from the appropriate acid chloride. In all cases, little apparent difference in ease of reaction was observed when compared with the aliphatic diacylglycolurils that we have previously reported (5–8). Deuterated monoacetylglycoluril **4b** was prepared from **1** and $(CD_3CO)_2O$, or from **1** and *n*-BuLi–CD_3COCl, as has been previously described for the protonated analogue (7). Conversion of **4b** to **2k**, **2l**, and **2m** followed as for **2c**, **2e**, and **2g**, respectively.

Treatment of **2c** with lithium *tert*-amylate or potassium *tert*-butoxide under preparative conditions in THF at 0°C resulted in rapid rearrangement to product **3c**, the result of an intramolecular Claisen-like condensation, in 98% isolated yield. The structure of **3c** was also unambiguously confirmed by X-ray crystallographic analysis (9). Each of the compounds (**2d**–**g**) was also subjected to the same condensation

Scheme 1. Reagents and conditions: (*i*) $(CX_3CO)_2O$, reflux or *n*-BuLi, THF, reflux then CX_3COCl, rt; (*ii*) *n*-BuLi, THF, 0°C then RCOCl, 0°C to rt; (*iii*) 50:50 *t*-BuOH:THF, 0°C, then *n*-BuLi, 0°C to rt.

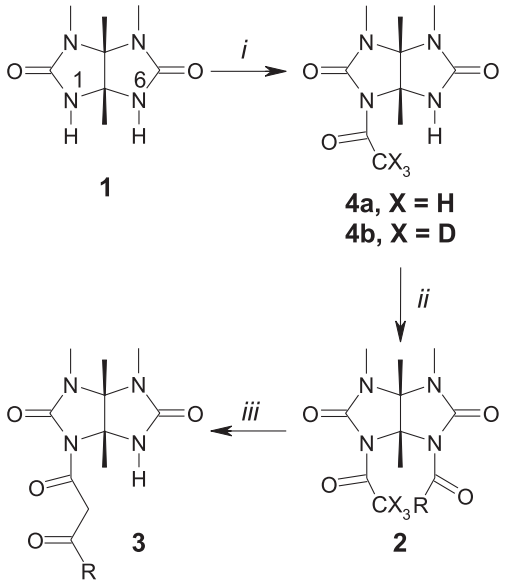

Compound	R	X
a	Me	H
b	CD_3	H
c	Ph	H
d	4-$OMeC_6H_4$	H
e	3-ClC_6H_4	H
f	4-MeC_6H_4	H
g	4-$NO_2C_6H_4$	H
h	3-$NO_2C_6H_4$	H
i	4-ClC_6H_4	H
j	4-$CF_3C_6H_4$	H
k	Ph	D
l	3-ClC_6H_4	D
m	4-$NO_2C_6H_4$	D

© 2002 NRC Canada

Table 1. Chemical yields for formation of compounds **2c**–**m** and **3c**–**g**, UV data for **3** before and after treatment with potassium *tert*-butoxide, and calculated values of the observed second-order rate constants for conversion of **2c**–**m** into enolates of **3c**–**m**.

Compound	Yield **2** (%)	Yield **3** (%)	λ_{max} **3** (nm)	λ_{max} enolate **8** (nm)	k_{app} (L mol^{-1}sec^{-1})[a]
c	92	98	313	335[b]	19.8,[e] 10.3[f]
d	61	30	326	335[b]	8.0
e	43	74	323	325[b,g]	31.6,[e] 37.6[f]
f	55	69	322	331[b]	8.2
g	24	35	335	404[b]	122,[e] 155[f]
h	42	ND[d]	ND[d]	339[d]	72
i	94	ND	ND	341[c]	27
j	12	ND	ND	348[c]	51
k	33	ND	ND	335[c,h]	7.5
l	71	ND	ND	337[c,h]	18.1
m	21	ND	ND	404[c,h]	59

[a]Second-order rate constant, calculated from observed rate constant and base concentration (see text).
[b]Determined by treatment of synthetic **3** with potassium *tert*-butoxide (5–10 equiv.).
[c]Determined from a preliminary kinetic run.
[d]Not determined, compound was not prepared.
[e]Value obtained during comparison of **2c**–**j**.
[f]Value obtained during comparison of **2k**–**m** with protonated analogues. See text for discussion of the discrepancy between these values.
[g]Kinetics observed at 337 nm.
[h]Values as for protonated analogs.

conditions to afford β-ketones **3d**–**g** (Table 1). In each case, condensation proceeded within minutes, and no detectable side-products were observed. All the compounds for subsequent kinetic work were recrystallized under identical conditions to those for **2c** and **3c**. Furthermore, although the chemical yields for formation of **2c** and **3c** were improved through a degree of optimization of conditions, no attempt was made to optimize the yields for the remaining compounds. Thus, the reported yields of recrystallized material are not indicative of the efficiency of either step. Each product **3c**–**g** was found by NMR to be a mixture of the tautomeric keto and enol forms. These reactions thus proceed analogously to those of the aliphatic acyl derivatives and similarly provide good yields with no detectable side-products. The results clearly show that the template-directed condensation may be extended with high efficiency to aroyl groups.

Preliminary experiments to evaluate conditions for monitoring the kinetics of these intriguing condensations were conducted with **2c**. It was found that the solid potassium *tert*-butoxide base was not readily soluble in THF, while the substrate was poorly soluble in *tert*-butanol. For this reason, we chose a mixed solvent system of 50:50 v/v *tert*-butanol–THF for kinetics experiments. Both **2c** and potassium *tert*-butoxide were readily soluble in this mixture at concentrations of interest, i.e., up to several millimolar. All stock solutions were prepared in rigorously dried solvents. Control UV spectra of a 1–2 × 10^{-4} M solution of each substrate **2c**–**j** in this solvent were recorded. Similarly, control spectra for each of the products **3c**–**g** were obtained. Finally, control spectra of each of the putative enolates resulting from deprotonation of products **3c**–**g** were obtained by treatment of the solutions of **3c**–**g** in situ with a five- to tenfold excess of base. The λ_{max} values were determined for each species (Table 1 and *Experimental*). For **3h**–**j**, the enolate λ_{max} was determined by scanning the solution within the UV cell after a preliminary kinetic experiment. It was found that the starting solutions **2c**–**j** showed essentially no absorbance at the λ_{max} of the deprotonated products.

For the first kinetics experiments, a solution of **2c** in a stoppered quartz cuvette was treated with a freshly prepared solution of potassium *tert*-butoxide (5–10 equiv.) in the standard solvent. After magnetic mixing within the cuvette, the increase in absorbance at the predetermined λ_{max} of the presumed enolate of the product was monitored with time until no further change was observed. Formation of product was then confirmed by recording the UV spectrum of the final solution, which showed a λ_{max} identical to within 2–3 nm to that of the authentic deprotonated product. Attempts to monitor the disappearance of starting material were unsuccessful because both the starting and the final solutions were found to absorb in the same region. These experiments show that the reaction proceeds within minutes at 25°C under these conditions.

The absorbance values at λ_{max} vs. time were fit to the equation for pseudo-first-order kinetics by the spectrometer computer, giving the pseudo-first-order rate constant k_{obs}. For each run, excellent fits were obtained ($\sigma < 0.001$). Errors in rate constants were, therefore, estimated from variance in replicate runs (≤10%). A series of experiments was next performed on **2c** in which the concentration of base was varied. A plot of k_{obs} vs. [base] was found to be linear over the range examined (Fig. 1); no curvature was observed, implying that saturation did not occur, at least at the low concentrations used in this study. The reaction is, therefore, first order for both **2c** and base. The overall second-order rate constant (k_{app}) was then determined by division of k_{obs} by the concentration of base, as determined during stock solution preparation.

Each of the substituted compounds **2d**–**j** was monitored by the same procedure. In all cases, excellent fits were obtained for pseudo-first-order kinetics ($\sigma < 0.001$). The rate law is, therefore, first order for substrate concentration for all substrates **2c**–**j**. Values of k_{app} were then obtained as for

© 2002 NRC Canada

Fig. 1. Plot of apparent pseudo-first-order rate constant k_{obs} for formation of **3c** from **2c** vs. concentration of potassium *tert*-butoxide base. The line was generated by linear regression (R^2 = 0.9635).

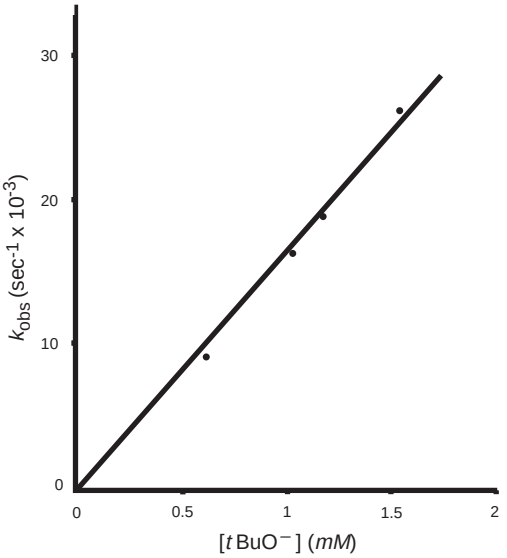

Fig. 2. Successive scans performed on the acetyl *p*-methylbenzoyl glycoluril **2f**. UV spectra were recorded sequentially at a scan rate of 600 nm min^{-1}. The direction of change in absorbance with time is indicated by the arrows. The peak due to the enolate **8f** of product **3f** at 336 nm was used to monitor reaction progress in further kinetic runs.

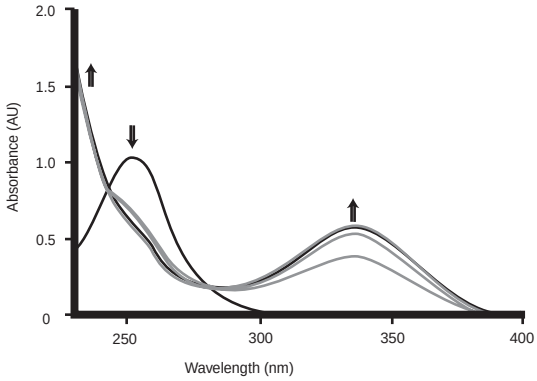

2c, with the assumption that the reactions are all first order for base concentration. A series of successive scans was performed during the reaction of both **2c** and **2f**. A smooth increase in absorption with time at the λ_{max} of the product enolate as well as at low wavelengths, accompanied by a net decrease in absorbance at intermediate wavelengths, was found (Fig. 2). The scans clearly show two isosbestic points for each of the reactions monitored.

The results of the experiments on **2c**–**j** may be shown in the form of a Hammett plot (Fig. 3) (10). When log k_{app} is plotted against the substituent constant σ (11), a linear relationship is seen, with positive slope ρ = 1.05 ± 0.05.

In a separate series of experiments, the rates of condensation for **2c**, **2e**, **2g**, **2k**, **2l**, and **2m** were compared under identical conditions. When the values for k_{app} are plotted on

Fig. 3. Hammett plot showing the logarithm of the observed bimolecular rate constant (log k_{app}) plotted against the substituent constant σ for the eight acetyl aroyl glycoluril substrates **2c**–**j** that were studied. Linear regression gives a slope ρ = 1.05 ± 0.05 and R^2 = 0.9952.

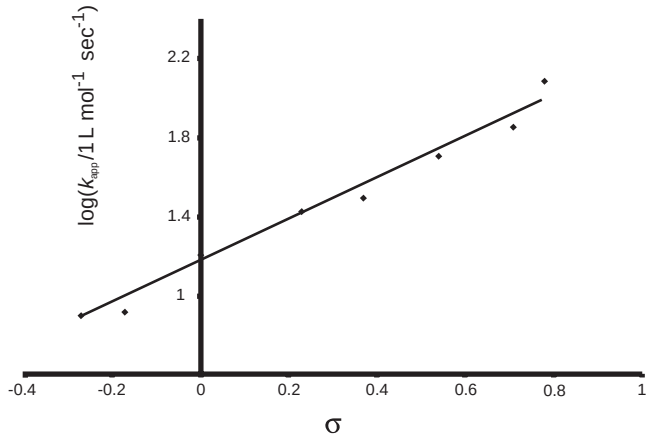

a Hammett plot, it was found that protio-compounds **2c**, **2e**, and **2g** again correlated well with the Hammett equation, in this case with ρ = 1.55 ± 0.02. When the corresponding deuterated substrates **2k**–**m** were investigated by the same UV spectroscopic method, they were also found, at first approximation, to obey pseudo-first-order kinetics. Each data set could be fit to predicted curves to give values of k_{app}, although the errors were higher for these fits than for the protonated analogues. The deviation from the first-order fit was highest for **2k**, less for **2l**, and negligible for **2m**. The resulting values of log K_{app} also varied in a linear manner with σ on the Hammett plot, and gave a slope ρ = 1.20 ± 0.06, a value significantly different from the former plot for the protio analogues (Fig. 4). The apparent isotope effect on k_{app} (k^H_{app}/k^D_{app}) varied from 1.4 for the benzoyl moiety (**2c** vs. **2k**), to 2.6 for *p*-nitrobenzoyl acetyl glycoluril (**2g** vs. **2m**).

When a typical data set for **2k** was analyzed in greater detail, a small deviation from pseudo-first-order behaviour was observed. It was found that the value of the parameter *n* as determined by curve fitting to the equation d[**3k**]/dt = *n*[**2k**] increased as the time at which curve fitting was initiated increased. This result is illustrated in Fig. 5, where the value of *n* is plotted against the start time for curve fitting; in each case the curve was fit to the same stop time, a time where the absorbance had essentially reached a steady value (8 min). By contrast, a similar analysis of the protonated analogue revealed that the value of *n* remained essentially constant regardless of which part of the absorbance-time curve was analyzed; thus this reaction is truly first order and *n* = k_{obs} (Fig. 5). The [D_3]acetyl *m*-chlorobenzoyl derivative **2l** followed a similar but less dramatic trend, with *n* increasing from 0.027 to 0.038 sec^{-1}. The [D_3]acetyl *p*-nitrobenzoyl derivative **2m** gave an absorbance-time plot that fit much better to first-order kinetics and no significant change in *n* with time was observed. The changing values of *n* imply that another process must be included in the deuterated compounds; this is interpreted as isotope exchange (see *Discussion*).

© 2002 NRC Canada

Fig. 4. Hammett plots showing log k_{app} plotted against σ for three acetyl aroyl glycoluril substrates **2c**, **2e**, and **2g**; and for the trideutero isotopomers **2k**, **2l**, and **2m**. Linear regression gives slopes ρ = 1.55 ± 0.02 and 1.20 ± 0.06 for the two respective series. Correlation coefficients R^2 are 0.9994 and 0.9901, respectively. The isotope effect, k^H_{app}/k^D_{app}, is given by the difference in rate between pairs of points for the same substituent, and varies from 1.4 for the benzoyl moiety (σ = 0), to 2.6 for the 4-nitrobenzoyl case (σ = 0.77).

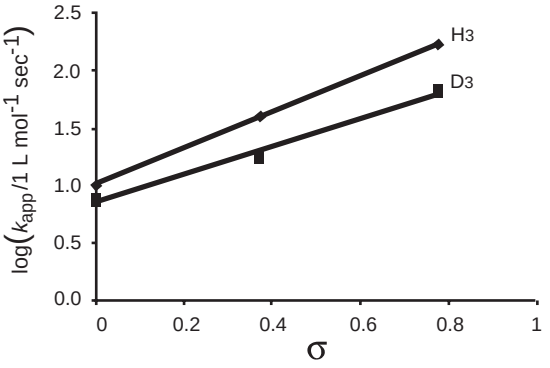

Fig. 5. For [D_3]acetyl benzoyl glycoluril **2k**, different values of parameter *n* are obtained when the absorbance vs. time data are analysed over different portions of the curve. The data were fit between different starting times *t* and an arbitrary but constant final time at which the absorbance remained essentially unchanged. The resulting values of *n* from the equation d[**3k**]/dt = *n* [**2k**] are then plotted against start time *t* (▲). Comparison of the calculated curves and the experimental data showed that this procedure emphasized the data around, and hence gave a good fit at, time *t*. By contrast, a corresponding analysis for [H_3]acetyl benzoyl glycoluril **2c**, gave values for *n* which were independent of *t* (■), and $n = k_{obs}$. The starting concentration for **2c** and **2k** was 28.8 μM; [KO-*t*-Bu] = 1.43 mM.

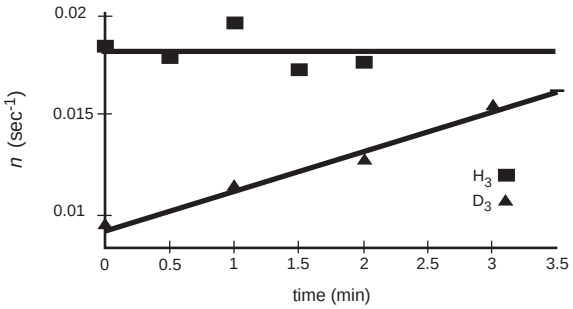

Discussion

A minimal scheme for the condensation reaction of diacylglycolurils **2** to give β-ketoacylglycolurils **3**, in accord with the classical mechanism for Claisen (12, 13) and Dieckmann (14) condensations, is presented in Scheme 2. A potentially reversible deprotonation of **2** by the *tert*-butoxide base forms enolate **5**. Rate constants k_1 and k_{-1} characterize this step. Intramolecular nucleophilic attack forms tetrahedral intermediate **6** with rate constant k_2, while k_{-2} reflects the potential reverse reaction. Intermediate **6** collapses to the amide anion of the product β-ketoacylglycoluril **7**, and finally, proton transfer generates enolate **8** of product **3**. It is the rate of formation of **8** that is monitored in the kinetics experiments. Product **3** is formed during acidic work-up, but is fully deprotonated by the excess base present in the reactions, as shown by the change in the UV spectra of authentic **3c**–**g** when treated with potassium *tert*-butoxide under the conditions of the kinetics experiments. The presence of isosbestic points during analysis of reaction progress by scanning kinetics illustrates that there is no significant build-up of intermediates as the reaction proceeds. Consideration of pK_a values for **5**–**8** suggests that each of the forward steps connecting these species would be thermodynamically favorable, and hence effectively irreversible. In addition, the proton transfer step of **7** to **8** is likely to be rapid, leaving step(s) 1 and (or) 2 as the most likely possibilities for the rate-limiting steps. Indeed, these ideas are fully consistent with the experimental data described below.

The observation of a clear, positive ρ value in the Hammett plot of rate constant k_{app} for **2c**–**k** vs. the substituent constant σ shows that the aromatic system must be involved in a rate-limiting step. The rates for formation of **8** increase over a range of more than tenfold from the electron donating *p*-OMe group to the electron withdrawing *p*-NO_2 group. The relationship is linear, suggesting no fundamental change in mechanism as the substituent is varied. The simplest explanation of the results involves invoking step 2 as at least partially rate limiting. When the aroyl substituent is electron withdrawing, it activates the electrophilic carbonyl group and enhances the rate constant k_{app} relative to the benzoyl compound **2c**. Conversely, electron donating substituents in the aromatic ring reduce k_{app} through loss of resonance between the carbonyl and aromatic π systems in the transition state leading to **6**. Although k_1 might be influenced by the aroyl substituent through steric effects, and marginally through electronic effects at the anomeric carbon C-7, which we have previously invoked to explain the geometry of diacylglycolurils (15–17), it seems improbable that these effects can explain the good fit to the Hammett equation and the magnitude of the Hammett constant ρ.

The electron withdrawing and electron donating substituents may influence the rate constant for step 2 in either of two ways: activating or deactivating the carbonyl group to nucleophilic attack, or altering the conformation of the aroyl entity, for example by altering the twist angle τ around the amide N–C bond (15–17). The crystal structure shows that for the parent system **2c**, the amidic twist of the benzoyl group is substantial (9). It is possible that the twist may be further influenced by the aromatic substituent as more electron donation allows greater C=O π stability despite a putatively larger twist and hence less resonance stabilization of the aroyl carbonyl group by nitrogen. A study of how the substituents influence τ through X-ray crystallography is currently underway to resolve this issue and determine if τ has an influence on transition state structure and energy.

While the results with deuterated substrates **2k**–**m** reconfirm the sensitivity of k_{app} to the benzoyl substituent, they also demonstrate a substantial isotope effect in this reaction. The magnitude of this effect for the *p*-nitrobenzoyl compounds (2.6) is indicative of a primary kinetic isotope effect, and suggests that in this case the reaction is sensitive to the

© 2002 NRC Canada

Scheme 2. Proposed mechanism for intramolecular Claisen-like condensation of **2** to give **3**.

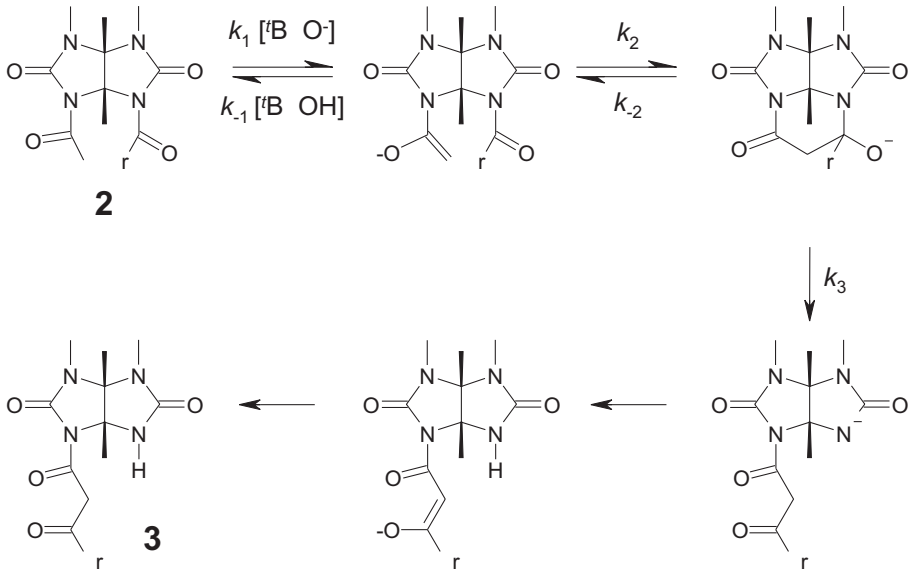

rate of deprotonation as well as to the substituent on the aroyl ring. This set of results may be rationalized by invoking a mechanism in which both steps 1 and 2 are partially rate limiting and thus k_1[**2**][base] ≈ k_2[enolate]. The other results are consistent with this interpretation: as the substituent becomes less electron-withdrawing, the rate becomes dominated by step 2 and therefore it is less sensitive to step 1 and hence to the isotopic substitution. Nonetheless, a substantial and reproducible isotope effect remains even in the acetyl benzoyl case. Conversely, substitution with deuterium slows step 1 and the sensitivity of step 2 to the aroyl substituent is reduced, resulting in a lower ρ value for the deuterated series compared with the protonated analogues. Furthermore, comparison of the two independent Hammett plots for the protonated series shows that ρ varies with the conditions. In the former series, ρ ≈ 1, while the second determination gives ρ ≈ 1.5. This change in Hammett slope is consistent with the difference in base concentration between the two experiments (5–10 × 10^{-4} vs. 1.43 × 10^{-3} M). At the lower base concentration used in the former experiments, bimolecular step 1 is slower, step 2 becomes less dominant in determining the rate, and the overall rate of reaction is less sensitive to the aromatic substituent.

In prior work with **2b** (7) it was concluded that step 1 was at least primarily rate limiting because of the presence of a significant primary kinetic isotope effect as the base discriminates between abstraction of hydrogen from the acetyl entity versus deuterium from the CD_3 group. This result now becomes consistent with the overall mechanism as presented, if the preparative reaction of **2b** proceeds under conditions where step 1 is dominant. The kinetic experiments contrast with this earlier preparative work in several ways, each of which might contribute to this influence on the rate-limiting step. First, the structure of the substrate has changed. Second, the absolute concentration of substrate has been dramatically reduced for the kinetics work. Third, the solvent has changed from THF with a trace of excess *tert*-butanol to a 50:50 mixture of these two solvents; as a result, all of the base is in solution, a situation which does not occur in the preparative work. Fourth, there is a relatively larger molar excess of base in the kinetics experiments. Finally, the temperature has been changed from 0 to 25°C. Thus, although the lower concentration of substrate in the kinetics work will dramatically reduce the rate of the bimolecular step 1 relative to unimolecular step 2, this may be compensated by the reduction of k_2 due to any or all of the greater stability of the benzoyl group over acetyl; the higher relative concentration of base and its availability in solution, accelerating step 1; stabilization of intermediates and transition states by the polar protic alcohol co-solvent; and the higher temperature accelerating the bimolecular step. Although the current experiments do not yet allow for a definitive answer to the question of how each of these effects influence the reaction, experiments to resolve these issues become possible as a result of the ability to quantitate the rates described in this paper, and are now underway.

While a further study is needed to perform a complete mathematically correct analysis of the deviation from first-order kinetics for the deuterated acetyl benzoyl compound **2k**, the current data are fully consistent with a slow exchange of deuterium for hydrogen in the substrate. The increase in parameter *n* (formally k_{obs} in a pure first-order reaction) with time as the process progresses would result from the reprotonation of the substrate enolate intermediate **5** by solvent *tert*-butanol, yielding first mono-, then di-, and then tri-protioacetyl substrate. As the reaction proceeds, the original trideutero substrate is depleted and partially deuterated substrates form; these react at a greater rate due to the isotope effect. Near the end of the reaction, the value of *n* approaches, but still does not reach, that for **2c**. The results show that most molecules overall react through loss of deuterium, and hence the first-order approximation used to evaluate k_{app} for this compound is valid. On this basis, qualitative information on the rate of enolate reprotonation, k_{-1}, may be obtained. The time needed for *n* to increase by 33% of the difference between its initial value and the constant value for **2c** is approximately 1.5 min. Assuming that this time approximates the average time required to exchange

© 2002 NRC Canada

one deuteron for a proton, it may be compared with the half-life for the overall condensation reaction (1.75 min) as measured by k_{app}. Thus molecules of the enolate of **2c** partition roughly equally between protonation to regenerate substrate and condensation to generate product, and k_{-1}[*t*-BuOH] ≈ k_2. This analysis illustrates the remarkable efficiency of trapping of the enolate by the proximal electrophilic carbonyl group — despite the availability of solvent *tert*-butanol as a proton donor, the enolate still has a strong tendency to condense to give product. A similar analysis for **2l** shows that the half-life for deuterium exchange is approx. 1.3 min, essentially unchanged from the value for **2k**. This is consistent with the aromatic substituent exerting little effect on the deprotonation–reprotonation step, as expected and discussed above. By contrast, the half-life for condensation in **2l** is reduced to 0.63 min. Hence, the substituent accelerates the rate of step 2 relative to **2k**, and the enolate partitions towards condensation by approx. 2:1 over reprotonation. For **2m**, step 2 is still further accelerated and reprotonation only rarely occurs; thus the plot of absorbance vs. time fits well to the equation for pseudo-first-order kinetics.

It should be noted that the results cannot rigorously exclude a concerted deprotonation–condensation process (i.e., steps 1 and 2 in Scheme 2 are concerted), although similar concerted mechanisms have been excluded in both chemical enolization (18) and enzymatic mechanistic (19, 20) studies. In such a process, both a variable isotope effect and a substituent effect in the aroyl ring would be expected, as the extent of C–H bond breaking and C–C bond making in the transition state varies with substrate structure. The tetrahedral intermediate **6** would, however, have to partition between retro-Claisen reaction to give **2** and conversion to **7** in order to explain the deuterium exchange in the substrate (i.e., $k_{-2} \approx k_3$); this is counter to the thermodynamic stability arguments (above).

Ashby and Park (21) proposed a mechanism involving a single electron transfer (SET) followed by coupling of the resulting radical anion–radical pair for the C–C bond-forming step of the Claisen-like condensation of pinacolone enolate with ethyl *p*-nitrobenzoate, although this mechanism was refuted by Arnett and co-workers (22). In the present case, the good correlation with σ suggests a polar one-step mechanism (23); there was a significantly worse correlation of our data with σ^+ (R^2 = 0.895, data not shown), a parameter which has been shown to give a better correlation than σ for SET reactions such as reduction of aceto- and benzophenones (24). The data for **2g** also lie on the Hammett line, suggesting that there is no change in mechanism for the *p*-nitro compound compared with other members of the series. We conclude that there is no reason to invoke a SET in the conversion of **2** to **3**.

The magnitude and sign of the Hammett slope ρ for the current data set also favorably compare with published values for intermolecular additions of ketone enolates to aroyl esters (ρ = 2–3) (25) or ketones (ρ = 1–2.2) (26, 27), under conditions where the second C–C bond-forming step is slow. For the latter, aldol condensations, the classic work of Bell and co-workers (28, 29) showed that, as in the current case, one or both of the ketone deprotonation and condensation steps may be rate limiting. Furthermore, Guthrie and Guo (30) and Richard and co-workers (31) examined intramolecular aldol condensations in exquisite kinetic detail, and concluded that either step may be rate limiting. Notably, in their study of the intramolecular aldol condensation of 2-(2-oxopropyl)benzaldehyde, Richard and Nagorski (32) observed that the extent of enolate reprotonation to effect reversal of step 1 depended on the acidity of the proton donor and the relative rates k_{-1} and k_2, a result which compares with the explanation offered herein for the deviation from first-order kinetics observed with **2k**. Thus, the current study correlates with a substantial body of mechanistic data from the literature, which supports a general mechanism for addition of enolates to carbonyl compounds, and extends this work to the Claisen-like conversion of **2** into **3**.

It should be pointed out, however, that the current work does not offer any direct evidence for tetrahedral intermediate **6**, or its protonated analogue. It is not possible to rigorously exclude collapse of **6** (step 3) as the rate-limiting step, because the value of ρ in such a scheme would be an aggregate of the effect on both earlier steps and on step 3, making it hard to predict (33). We are currently exploring this reaction further to clarify these details.

Overall, the data give a clear and fully consistent picture of the events occurring as compounds **2** are converted to **3** by base. For these compounds, the rates of deprotonation and condensation are comparable, as seen by the presence of an isotope effect in deprotonation and a substituent effect in the condensation step(s). Additionally, enolate reprotonation (step 1) and condensation are competitive in some cases. As the substituent is changed and (or) hydrogen is replaced by deuterium in the acetyl group, the relative importance of deprotonation vs. condensation, and of enolate reprotonation vs. condensation change in a consistent and rational manner. This analysis supports the classic mechanism for the Claisen condensation in this case, and has various implications for structural variation of the substrate, and the effect of variations in conditions (e.g., *tert*-butanol solvent concentration on rate, the effect of base concentration on the magnitude of the isotope effect); these aspects are currently being explored.

Conclusion

That each acyl aroyl glycoluril underwent efficient condensation on the preparative scale, irrespective of the presence of electron withdrawing or electron donating substituents, shows that the glycoluril-directed condensation process is rugged, and can tolerate various substituents. It is shown that conditions can be arranged under which the condensation of diacylglycolurils to give β-ketoacylglycolurils proceeds with clean bimolecular kinetics and short half-lives. This work shows that both the deprotonation of substrate and a condensation step, probably the second, key C–C bond formation process, are partially rate limiting. Once formed, the enolate partitions approximately halfway between condensation and reprotonation by solvent under these conditions. These two observations imply roughly equal rates for substrate deprotonation, enolate reprotonation, and enolate condensation steps in **2c**; as the substrate structure is changed, the rate of each step alters in a consistent and rational manner. Hence, the door is opened to find conditions in which a single step may be made fully rate

© 2002 NRC Canada

determining, thus allowing further studies of these key steps of the reaction. Such results may lead to better understanding of the mechanistic details, geometric requirements and transition state structure for enolate addition reactions onto carbonyl groups.

Experimental

General

THF was dried over potassium–benzophenone, then distilled. *tert*-Butanol was dried over calcium oxide and distilled. All glassware was dried in the oven and cooled under an atmosphere of dry nitrogen. All solvent transfers were by syringe. Quartz UV cells bearing a screw cap and septum were from Aldrich; they were dried by evacuation over phosphorus pentoxide in the desiccator.

UV spectroscopy was performed on a Cary 500 spectrophotometer with the temperature controlled to 25°C. NMR spectra were recorded on a Bruker AM-200 spectrometer. IR spectra were recorded on a Biorad FTS-40 spectrophotometer, or on the probe of an ASI in situ reaction monitoring system. Mass spectra were determined on a Finnigan 4500 mass spectrometer.

General procedure for kinetic determinations

Stock solutions of each pre-dried acetyl aroyl glycoluril (**2c**–**m**) were prepared under argon by dissolution of a carefully determined mass (ca. 20 mg) in 1:1 v/v anhydrous THF–*tert*-butanol in a dried volumetric flask (25 mL). Serial dilution was employed to give final concentrations of 5–10 × 10^{-5} M. Stock solutions of the condensation products were prepared similarly, giving final concentrations of 1–10 × 10^{-5} M. Stock solutions of potassium *tert*-butoxide were prepared in the same manner by dissolution of a carefully determined mass (ca. 20 mg) in the same solvent (25 mL). Final concentrations were 2–5 × 10^{-3} M.

To a dried quartz UV cell equipped with a magnetic stir bar and a septum, and which had been purged with dry nitrogen, was added 2.0 mL of stock solution of **2** by syringe. The reference cell contained 1:1 v/v anhydrous THF–*tert*-butanol. After equilibration of the temperature to 25°C within the spectrophotometer, the UV spectrum was recorded in scanning mode. Base solution (0.1–0.5 mL) was added by syringe with rapid stirring. The reaction was monitored, beginning within 5 s, either by following the absorbance at a set wavelength with time, or in some cases by rapid scanning of the spectrum. The observation wavelengths used were: **2c**, **2d**, and **2k**: 335; **2e** and **2l**: 337; **2f**: 336; **2g** and **2m**: 404; **2h**: 339; **2i**: 341; and **2j**: 348 nm. After there was no further change in absorbance, the UV spectrum of the final solution was recorded.

The absorbance–time plot was analyzed on the spectrometer computer by a best-fit approach for pseudo-first-order kinetics. The resulting values of k_{obs} were converted to k_{app} by dividing by the calculated base concentration within the sample. Standard deviations in k_{app} which were generated by the program were evaluated in each experiment; these were always small (<0.001) for **2c**–**j**, and thus errors in k_{app} were calculated from variations between replicate experiments.

General procedure for preparation of acetyl aroyl glycolurils 2c–m

To a solution of **4a** or **4b** in anhydrous THF (15 mL per mmol **4**), which had been cooled to 0°C, was added 1.05 equivalents of *n*-butyllithium in hexane (1.6 M). The mixture was stirred for 15 min, then the aroyl chloride (1.2 equiv.) was added and stirring was continued for 1 h. After quenching with 1 M $NaHSO_4$ (3 mL per mmol **4**), most of the THF was removed on the rotary evaporator and the aqueous residue was extracted three times with $CHCl_3$. The combined organic layers were washed with an equal volume of water and then brine, dried over Na_2SO_4, filtered, and concentrated. The product was purified by recrystallization from $CHCl_3$–hexanes.

Acetyl benzoyl glycoluril 2c

Compound **4a** (708 mg, 2.95 mmol) and benzoyl chloride (410 μL) gave 855 mg (92%) of pure **2c** as a yellowish foam. UV (THF) λ_{max} (nm) (ε, M^{-1} cm^{-1}): 242 (6 300). IR (NaCl disks, cm^{-1}): 3020 (C-H str.), 1728 (C=O), 1408, 1333, 1216, 1114. ^{1}H NMR (200 MHz, $CDCl_3$) δ: 7.51–7.42 (m, 3H, *m*-, *p*-C_6H_5), 7.37–7.24 (m, 2H, *o*-C_6H_5), 3.00 (3H, s, N-CH_3), 2.82 (s, 3H, N-CH_3), 2.47 (s, 3H, O=C-CH_3), 2.03 (s, 3H, CH_3), 1.53 (s, 3H, CH_3). ^{13}C NMR (50 MHz, $CDCl_3$) δ: 170.04 (C=O), 169.91 (C=O), 153.14 (C=O), 152.61 (C=O), 135.02, 132.00, 129.04 (2C), 127.51 (2C, benzoyl), 80.03, 78.04 (*C* bridgehead), 27.04, 25.18, 20.92, 19.09, 15.01. EI-MS *m*/*z*: 344 [M^+], 301, 229, 126, 105 (base), 77, 56. HRMS calcd. for $C_{17}H_{20}N_4O_4$: 344.1484, found: 344.1492.

Acetyl 4-methoxybenzoyl glycoluril 2d

Compound **4a** (960 mg, 4 mmol) and 4-methoxybenzoyl chloride (715 mg) gave 920 mg (61%) of **2d**; mp 182–183°C. UV (50:50 THF–*t*-BuOH) λ_{max} (nm) (ε, M^{-1} cm^{-1}): 273 (14 400). IR ($CHCl_3$ cast, cm^{-1}): 3018 (Ar-H str.), 2941 (C-H str.), 1721 (C=O), 1698 (C=O), 1603, 1329, 1254, 1167. ^{1}H NMR (200 MHz, $CDCl_3$) δ: 7.53 (d, *J* = 7 Hz, 2H, Ar*H*), 6.85 (d, *J* = 7 Hz, 2H, Ar*H*), 3.81 (s, 3H, OCH_3), 3.05 (s, 3H, N-CH_3), 2.86 (s, 3H, N-CH_3), 2.47 (s, 3H, O=C-CH_3), 2.04 (s, 3H, CH_3), 1.58 (s, 3H, CH_3). EI-MS *m*/*z*: 374 [M^+], 346, 135 (base), 77, 56, 43. HRMS calcd. for $C_{18}H_{22}N_4O_5$: 374.1590, found: 374.1587.

Acetyl 3-chlorobenzoyl glycoluril 2e

Compound **4a** (720 mg, 3 mmol) and 3-chlorobenzoyl chloride (577 mg) gave 485 mg (43%) of **2e**; mp 154–156°C. UV (50:50 THF–*t*-BuOH) λ_{max} (nm) (ε, M^{-1} cm^{-1}): 237, 287 (11 000, 2 200). IR ($CHCl_3$ cast, cm^{-1}): 3018 (Ar-H str.), 2944 (C-H str.), 1725 (C=O), 1702 (C=O), 1573, 1407, 1329, 1115, 1094, 942. ^{1}H NMR (200 MHz, $CDCl_3$) δ: 7.22–7.46 (m, 4H, Ar*H*), 3.02 (s, 3H, N-CH_3), 2.83 (s, 3H, N-CH_3), 2.49 (s, 3H, O=C-CH_3), 2.02 (s, 3H, CH_3), 1.55 (s, 3H, CH_3). ^{13}C NMR (50 MHz, $CDCl_3$) δ: 170.34 (2 O=C), 153.01, 152.65 (urea C=O), 136.87, 133.73, 132.01, 129.15, 128.92, 127.26 (aroyl), 80.14, 78.16 (*C* bridgehead), 27.09, 26.82, 25.12, 19.25, 15.24. EI-MS *m*/*z*: 378, 380 [M^+], 336, 156, 141, 139, 135, 126, 111, 56, 43 (base). HRMS calcd. for $C_{17}H_{19}{}^{35}ClN_4O_4$: 378.1095, found: 378.1089.

© 2002 NRC Canada

Acetyl 4-methylbenzoyl glycoluril 2f

Compound **4a** (720 mg, 3 mmol) and 4-methylbenzoyl chloride (437 μL) gave 590 mg (55%) of **2f**; mp 111–114°C dec. UV (50:50 THF–*t*-BuOH) λ_{max} (nm) (ε, M^{-1} cm^{-1}): 253 (13 500). IR ($CHCl_3$ cast, cm^{-1}): 3010 (Ar-H str.), 2944 (C-H str.), 1721 (C=O), 1702 (C=O), 1609, 1407, 1329, 1277, 1115, 1094. ^{1}H NMR (200 MHz, $CDCl_3$) δ: 7.42 (d, *J* = 8 Hz, 2H, Ar*H*), 7.14 (d, *J* = 8 Hz, 2H, Ar*H*), 3.04 (s, 3H, N-CH_3), 2.85 (s, 3H, N-CH_3), 2.47 (s, 3H, O=C-CH_3), 2.34 (s, 3H, ArCH_3), 2.04 (s, 3H, CH_3), 1.57 (s, 3H, CH_3). EI-MS *m*/*z*: 358 [M^+], 330, 243, 126, 119 (base), 91, 56, 43. HRMS calcd. for $C_{18}H_{22}N_4O_4$: 358.1641, found: 358.1618.

Acetyl 4-nitrobenzoyl glycoluril 2g

Compound **4a** (720 mg, 3 mmol) and 4-nitrobenzoyl chloride (555 mg) gave 277 mg (24%) of **2g**; mp 212–218°C dec. UV (50:50 THF–*t*-BuOH) λ_{max} (nm) (ε, M^{-1} cm^{-1}): 269 (12 500). IR ($CHCl_3$ cast, cm^{-1}): 3018 (Ar-H str.), 2946 (C-H str.), 1727 (C=O), 1710 (C=O), 1605, 1524 (NO_2), 1407, 1333, 1115, 1094. ^{1}H NMR (200 MHz, $CDCl_3$) δ: 8.45 (d, *J* = 8 Hz, 2H, Ar*H*), 7.65 (d, *J* = 8 Hz, 2H, Ar*H*), 3.05 (s, 3H, N-CH_3), 2.85 (s, 3H, N-CH_3), 2.55 (s, 3H, O=C-CH_3), 2.05 (s, 3H, CH_3), 1.60 (s, 3H, CH_3). EI-MS *m*/*z*: 389 [M^+], 347, 240, 141, 126 (base), 56, 43. HRMS calcd. for $C_{17}H_{19}N_5O_6$: 389.1335, found: 389.1355.

Acetyl 3-nitrobenzoyl glycoluril 2h

Compound **4a** (720 mg, 3 mmol) and 3-nitrobenzoyl chloride (577 mg) gave 493 mg (42%) of **2h**; mp 192–194°C. UV (50:50 THF–*t*-BuOH) λ_{max} (nm) (ε, M^{-1} cm^{-1}): 259 (sh, 10 900), 225 (sh). IR ($CHCl_3$ cast, cm^{-1}): 3018 (Ar-H str.), 2944 (C-H str.), 1725 (C=O), 1706 (C=O), 1615, 1530 (NO_2), 1331, 1115, 1092. ^{1}H NMR (200 MHz, $CDCl_3$) δ: 8.31 (ddd, *J* = 8, 2, 1 Hz, 1H, Ar*H*), 8.27 (dd, *J* = 2, 1 Hz, 1H, Ar*H*), 7.82 (ddd, *J* = 8, 2, 2 Hz, 1H, Ar*H*), 7.54 (ddd, *J* = 8, 8, 1 Hz, 1H, Ar*H*), 3.07 (s, 3H, N-CH_3), 2.86 (s, 3H, N-CH_3), 2.51 (s, 3H, O=C-CH_3), 2.05 (s, 3H, CH_3), 1.60 (s, 3H, CH_3). EI-MS *m*/*z*: 389 [M^+], 374, 272, 150, 135 (base), 126, 56, 43. HRMS calcd. for $C_{17}H_{19}N_5O_6$: 389.1335, found: 389.1345.

Acetyl 4-chlorobenzoyl glycoluril 2i

Compound **4a** (720 mg, 3 mmol) and 4-chlorobenzoyl chloride (420 μL) gave 1.07 g (94%) of **2i**; mp 186–188°C. UV (50:50 THF–*t*-BuOH) λ_{max} (nm) (ε, M^{-1} cm^{-1}): 250 (11 900). IR ($CHCl_3$ cast, cm^{-1}): 3014 (Ar-H str.), 2943 (C-H str.), 1721 (C=O), 1702 (C=O), 1590, 1329, 1279, 1115, 1090. ^{1}H NMR (200 MHz, $CDCl_3$) δ: 7.43 (d, *J* = 8 Hz, 2H, Ar *H*), 7.30 (d, *J* = 8 Hz, 2H, Ar*H*), 3.04 (s, 3H, N-CH_3), 2.84 (s, 3H, N-CH_3), 2.48 (s, 3H, O=C-CH_3), 2.02 (s, 3H, CH_3), 1.57 (s, 3H, CH_3). EI-MS *m*/*z*: 378, 380 [M^+, base], 352, 350. HRMS calcd. for $C_{17}H_{19}{}^{35}ClN_4O_4$: 378.1095, found: 378.1074.

Acetyl 4-(trifluoromethyl)benzoyl glycoluril 2j

Compound **4a** (1.05 g, 4.36 mmol) and 4-(trifluoromethyl)benzoyl chloride (1 g) gave 222 mg (12%) of **2j**; mp 193–195°C. UV (50:50 THF–*t*-BuOH) λ_{max} (nm) (ε, M^{-1} cm^{-1}): 238, 276 (sh) (12 400, 1 090). IR ($CHCl_3$ cast, cm^{-1}): 3018 (Ar-H str.), 2943 (C-H str.), 1725 (C=O), 1708 (C=O), 1407, 1332, 1297, 1111, 1065, 1017, 936, 851. ^{1}H NMR (200 MHz, $CDCl_3$) δ: 7.62 (m, 4H, Ar*H*), 3.08 (s, 3H, N-CH_3), 2.88 (s, 3H, N-CH_3), 2.53 (s, 3H, O=C-CH_3), 2.08 (s, 3H, CH_3), 1.61 (s, 3H, CH_3). EI-MS *m*/*z*: 412 [M^+, base], 370, 297, 172, 125, 56, 43. HRMS calcd. for $C_{18}H_{19}F_3N_4O_4$: 412.1358, found: 412.1368.

[D_3]Acetyl benzoyl glycoluril 2k

Compound **4b** (see below, 176 mg, 724 μmol) and benzoyl chloride (91 μL) gave 83.3 mg (33%) of **2k**. ^{1}H NMR as for **2c**, except that the resonance due to the acetyl group was absent. EI-MS *m*/*z*: 347 [M^+, base], 319, 229, 105, 43.

[D_3]Acetyl 3-chlorobenzoyl glycoluril 2l

Compound **4b** (134 mg, 550 μmol) and 3-chlorobenzoyl chloride (96 mg) gave 160 mg (71%) of **2l**. ^{1}H NMR as for **2e**, except that the resonance at 2.49 ppm due to the acetyl group was absent. EI-MS *m*/*z*: 381, 383 [M^+, base], 337, 263, 139, 127, 84, 56, 49.

[D_3]Acetyl 4-nitrobenzoyl glycoluril 2m

Compound **4b** (243 mg, 1.0 mmol) and 4-nitrobenzoyl chloride (185 mg) gave 82 mg (21%) of **2m**. ^{1}H NMR as for **2g**, except that the resonance at 2.55 ppm due to the acetyl group was absent. EI-MS *m*/*z*: 392 [M^+, base], 348, 150, 127, 56, 46.

Benzoylacetyl glycoluril 3c with KO-*t*-Bu

To a solution of compound **2c** (100 mg, 0.29 mmol) in THF (10 mL) at 0°C was added potassium *tert*-butoxide (43 mg, 1.3 equiv.), and the mixture was stirred for 30 min. The reaction mixture was quenched over 3 h with ammonium bicarbonate, then filtered through celite. Solvent was removed in vacuo to give **3c** as a foam (98 mg, 98%). UV (50:50 THF–*t*-BuOH) λ_{max} (nm) (ε, M^{-1} cm^{-1}): 240, 313 (9 650, 6 950); when treated with excess KO-*t*-Bu: λ_{max} = 335 (15 800). IR (NaCl disks, cm^{-1}): 3020 (C-H), 1728 (C=O), 1408, 1333, 1216, 1114. ^{1}H NMR (200 MHz, $CDCl_3$, 2.6:1 mixture of keto–enol tautomers) δ: 8.10–7.40 (m, 5H, Ar*H*), 6.11 (br s, 1H, N*H* enol), 6.09 (br s, 1H, N*H* keto), 4.94 (d, *J* = 16 Hz, 1H, O=C-C*H*H keto), 4.05 (d, *J* = 16 Hz, 1H, O=CCH*H* keto), 3.02 (s, 3H, N-CH_3 enol), 2.92 (s, 3H, N-CH_3 keto), 2.86 (s, 3H, N-CH_3 enol), 2.84 (s, 3H, N-CH_3 keto), 1.79 (s, 3H, CH_3 keto), 1.76 (s, 3H, CH_3 enol), 1.56 (s, 3H, CH_3 enol), 1.55 (s, 3H, CH_3 keto). ^{13}C NMR (125 MHz, $CDCl_3$, keto and some enol signals) δ: 193.67 (O=*C*-Ph), 167.91 (C=O), 167.23 (C=O), 152.79 (C=O), 136.06, 133.73, 131.58, 128.73, 128.16, 126.48, 88.24, 78.80, 48.15, 28.10, 26.44, 20.05, 19.32, 15.71. EI-MS *m*/*z*: 344 [M^+], 272, 198, 125, 105 (base), 77, 56. HRMS calcd. for $C_{17}H_{20}N_4O_4$: 344.1484, found: 344.1492. Anal. calcd. for $C_{17}H_{20}N_4O_4$: C 59.24, H 5.85, N 16.27; found C 59.16, H 6.05, N 16.58.

General procedure for preparative condensations of acetyl aroyl glycolurils 2d–g giving 3d–g

The acetyl aroyl glycoluril was dissolved in anhydrous THF and *t*-BuOH, and the mixture cooled to 0°C. A solution of *n*-butyllithium in hexane (1.6 M) was added and the mixture was stirred for 30 min at 0°C then for 30 min at room temperature. The reaction mixture was quenched with

© 2002 NRC Canada

1 M $NaHSO_4$ (5 mL), then organic solvents were removed on the rotary evaporator, and the residue extracted with $CHCl_3$. The extracts were dried, filtered, concentrated, and where needed, purifed from unreacted starting material by flash column chromatography in 1% then 2% MeOH–$CHCl_3$.

4-Methoxybenzoylacetyl glycoluril 3d

Compound **2d** (930 mg, 2.49 mmol) in THF (12 mL) and *t*-BuOH (8 mL) with *n*-BuLi (2 mL) gave 275 mg (30%) of **3d**; mp 187–191°C dec. UV (50:50 THF–*t*-BuOH) λ_{max} (nm) (ε, M^{-1} cm^{-1}): 271, 326 (10 800, 4 900); when treated with excess KO-*t*-Bu: λ_{max} = 271, 335 (7 300, 14 400). IR ($CHCl_3$ cast, cm^{-1}): 3327 (br, OH and NH str.), 2999, 2944 (C-H str.), 1710 (C=O), 1673 (C=O), 1601, 1408, 706. ^{1}H NMR (200 MHz, $CDCl_3$, keto form ca. 75%) δ: 7.84 (d, *J* = 9 Hz, 2H, Ar*H* keto), 7.78 (d, *J* = 9 Hz, 2H, Ar*H* enol), 7.30 (d, *J* = 9 Hz, 2H, Ar*H* enol), 7.15 (s, 1H, C*H*=C enol), 6.88 (d, *J* = 9 Hz, 2H, Ar*H* keto), 6.15 (br s, 1H, N*H* enol), 6.11 (br s, 1H, N*H* keto), 4.88 (d, *J* = 16 Hz, 1H, O=C-C*H*H keto), 4.00 (d, *J* = 16 Hz, 1H, O=CCH*H* keto), 3.81 (s, 3H, OCH_3 keto), 3.79 (s, 3H, OCH_3 enol), 2.99 (s, 3H, N-CH_3 enol), 2.90 (s, 3H, N-CH_3 enol), 2.89 (s, 3H, N-CH_3 keto), 2.81 (s, 3H, N-CH_3 keto), 1.75 (s, 3H, CH_3 keto), 1.72 (s, 3H, CH_3 enol), 1.57 (s, 3H, CH_3 enol) 1.52 (s, 3H, CH_3 keto). EI-MS *m*/*z*: 374 [M^+], 176, 135 (base), 56. HRMS calcd. for $C_{18}H_{22}N_4O_5$: 374.1590, found: 374.1573.

3-Chlorobenzoylacetyl glycoluril 3e

Compound **2e** (82 mg, 217 μmol) in THF–*t*-BuOH (50:50, 15 mL) with *n*-BuLi (0.53 mL) gave 60.6 mg (74%) of **3e**; mp 148–151°C dec. UV (50:50 THF–*t*-BuOH) λ_{max} (nm) (ε, M^{-1} cm^{-1}): 323 (7 960); when treated with excess KO-*t*-Bu: λ_{max} = 325, 348 (sh) (17 800). IR ($CHCl_3$ cast, cm^{-1}): 3430, 3316 (br, OH and NH str.), 3015 (Ar-H str.), 2935 (C-H str.), 1708 (br, C=O), 1407, 1214, 1109, 746. ^{1}H NMR (200 MHz, $CDCl_3$, keto form ca. 66%) δ: 7.66–8.05 (m, 2H, Ar*H*), 7.24–7.55 (m, 2H, Ar*H*), 6.23 (br s, 1H, N*H* enol), 6.18 (br s, 1H, N*H* keto), 4.87 (d, *J* = 16 Hz, 1H, O=C-C*H*H keto), 4.02 (d, *J* = 16 Hz, 1H, O=C-CH*H* keto), 3.03 (s, 3H, N-CH_3 enol), 2.92 (s, 3H, N-CH_3 keto), 2.86 (s, 3H, N-CH_3 enol), 2.84 (s, 3H, N-CH_3 keto), 1.78 (s, 3H, CH_3 keto), 1.76 (s, 3H, CH_3 enol), 1.57 (s, 3H, CH_3 enol), 1.55 (s, 3H, CH_3 keto). EI-MS *m*/*z*: 378, 380 [M^+], 308, 306, 141, 139, 125, 111, 56, 43 (base). HRMS calcd. for $C_{17}H_{19}{}^{35}ClN_4O_4$: 378.1095, found: 378.1095.

4-Methylbenzoylacetyl glycoluril 3f

Compound **2f** (90 mg, 250 μmol) in THF–*t*-BuOH (50:50, 15 mL) with *n*-BuLi (0.53 mL) gave 62 mg (69%) of **3f**; mp 202–203°C. UV (50:50 THF–*t*-BuOH) λ_{max} (nm) (ε, M^{-1} cm^{-1}): 322 (8 900); when treated with excess KO-*t*-Bu: λ_{max} = 331 (17 800). IR ($CHCl_3$ cast, cm^{-1}): 3325 (br, OH and NH str.), 3005, 2927 (C-H str.), 1715 (C=O), 1607, 1406, 1328, 1104, 803. ^{1}H NMR (200 MHz, $CDCl_3$) (keto form ca. 75%) δ: 7.79 (d, *J* = 8 Hz, 2H, Ar*H* keto), 7.72 (d, *J* = 8 Hz, 2H, Ar*H* enol), 7.24 (m, 2H, Ar*H* keto and enol, enol C*H*=C), 6.12 (br s, 1H, N*H* enol), 6.02 (br s, 1H, N*H* keto), 4.94 (d, *J* = 16 Hz, 1H, O=C-C*H*H keto), 4.02 (d, *J* = 16 Hz, 1H, O=CCH*H* keto), 3.02 (s, 3H, N-CH_3 enol), 2.92 (s, 3H, N-CH_3 keto), 2.86 (s, 3H, N-CH_3 enol), 2.85 (s, 3H, N-CH_3 keto), 2.39 (s, 3H, ArCH_3 keto), 2.37 (s, 3H, ArCH_3 enol), 1.79 (s, 3H, CH_3 keto), 1.75 (s, 3H, CH_3 enol), 1.56 (s, 3H, CH_3 enol), 1.55 (s, 3H, CH_3 keto). ^{13}C NMR (50 MHz, $CDCl_3$, keto and some enol signals) δ: 168.11, 152.82, 144.42, 133.71, 129.43 (2C), 129.24, 128.30 (2C), 126.52, 87.58, 78.80, 48.05, 27.11, 26.46, 21.64, 19.34, 15.73. EI-MS *m*/*z*: 358 [M^+], 330, 119 (base), 91, 56, 43. HRMS calcd. for $C_{18}H_{22}N_4O_4$: 358.1641, found: 358.1628.

4-Nitrobenzoylacetyl glycoluril 3g

Compound **2g** (195 mg, 501 μmol) in THF–*t*-BuOH (50:50, 20 mL) with *n*-BuLi (0.41 mL) gave 67.9 mg (35%) of **3g**; mp 167–169°C. UV (50:50 THF–*t*-BuOH) λ_{max} (nm) (ε, M^{-1} cm^{-1}): 271, 335 (11 200, 4 800); when treated with excess KO-*t*-Bu: λ_{max} = 286, 404 (15 000, 4 000). IR ($CHCl_3$ cast, cm^{-1}): 3395 (br, OH and NH str.), 2942 (C-H str.), 1705 (br, C=O), 1593, 1523, 1105, 759. ^{1}H NMR (200 MHz, $CDCl_3$, ca. 50% keto form) δ: 8.08–8.16 (m, 2H, enol and keto Ar*H*), 7.80–7.93 (m, 2H, enol and keto Ar*H*), 6.0 and 5.9 (br s, 1H, enol and keto N*H*), 4.75 (d, *J* = 16 Hz, 1H, O=CCH*H* keto), 3.95 (d, *J* = 16 Hz, 1H, O=CCH*H* keto), 2.91, 2.79, 2.74 and 2.72 (s, 6H, keto and enol N-CH_3), 1.66, 1.64, 1.45, and 1.43 (s, 6H, keto and enol C-CH_3). EI-MS *m*/*z*: 389 [M^+, weak], 150, 125, 56.

[D_3]Monoacetylglycoluril 4b

Method A: Glycoluril **1** (0.5 g, 2.5 mmol) and [D_6]acetic anhydride (5 mL) were heated at reflux for 20 h. Work-up as previously described (7) gave [D_3]monoacetylglycoluril **4b** (50 mg, 9%).

Method B: Glycoluril **1** (2 g, 10 mmol) in THF (200 mL) was treated with *n*-BuLi (7.0 mL of 1.6 M solution in hexane) and [D_3]acetyl chloride (1.07 mL, 15 mmol) was added as previously described (7). Work-up as previously reported gave [D_3]monoacetylglycoluril **4b** (0.64 g, 26%). ^{1}H NMR data were as previously reported for **4**, except that the resonance due to the acetyl group was absent.

Acknowledgments

The authors gratefully acknowledge financial support from NSERC. M.R. was supported on sabbatical leave by Ferdowsi University, Iran. R.M. acknowledges the Committee for Research and Publication at Mount St. Vincent University (MSVU) for financial support. We also wish to thank Verna MacKinnon for many initial kinetic trials during her honours research project at MSVU.

References

1. T.J. Simpson. *In* Biosynthesis: Polyketides and vitamins. *Edited by* F.J. Leeper and J.C. Vederas. Springer, Berlin. 2000. pp. 1–48; J. Staunton and B. Wilkinson. *In* Biosynthesis: Polyketides and vitamins. *Edited by* F.J. Leeper and J.C. Vederas. Springer, Berlin. 2000. pp. 49–92.
2. For recent reviews, see: B.J. Rawlings. Nat. Prod. Rep. **14**, 335 (1997); B.J. Rawlings. Nat. Prod. Rep. **15**, 275 (1998).
3. For a selection of recent reviews, see: J. Staunton and K.J. Weissman. Nat. Prod. Rep. **18**, 380 (2001); B.J. Rawlings. Nat. Prod. Rep. **18**, 190 (2001); **18**, 231 (2001); R. Bentley and J.W. Bennett. Annu. Rev. Microbiol. **53**, 411 (1999); B.J. Rawlings. Nat. Prod. Rep. **14**, 523 (1997); C.W. Carreras, R.

© 2002 NRC Canada

Pieper, and C. Khosla. Top. Curr. Chem. **188**, 85 (1997); also see the thematic issue: Polyketide and nonribosomal polypeptide biosynthesis. Chem. Rev. **7** (1997); and refs. therein.
4. For a biomimetic, decarboxylative Claisen-like condensation, see: A.I. Scott, C.J. Wiesner, S. Yoo, and S.K. Chung. J. Am. Chem. Soc. **97**, 6277 (1975).
5. S. Sun and P.H.M. Harrison. Tetrahedron Lett. **33**, 7715 (1992).
6. S. Sun and P.H.M. Harrison. J. Chem. Soc. Chem. Commun. 2235 (1994).
7. S. Sun, L. Edwards, and P.H.M. Harrison. J. Chem. Soc. Perkin Trans. 1, 437 (1998).
8. C. Cow, D. Valentini, and P. Harrison. Can. J. Chem. **75**, 884 (1997).
9. Details of these crystal structures will be reported elsewhere.
10. L.P. Hammett. J. Am. Chem. Soc. **59**, 96 (1937).
11. C.D. Ritchie and W.F. Sager. Prog. Phys. Org. Chem. **2**, 323 (1964); C. Hansch, A. Leo, S. Unger, K.H. Kim, D. Nikaitani, and E.J. Liem. J. Med. Chem. **16**, 1207 (1973).
12. C.R. Hauser and B.E. Hudson, Jr. Org. React. **1**, 266 (1942).
13. F. Garst. J. Chem. Educ. **56**, 721 (1979).
14. J.P. Schaefer and J.J. Bloomfield. Org. React. **1**, 1 (1942).
15. P.A. Duspara, C.F. Matta, S.I. Jenkins, and P.H.M. Harrison. Org. Lett. **3**, 495 (2001).
16. C. Matta, C. Cow, S. Sun, J.R. Britten, and P.H.M. Harrison. J. Mol. Struct. **523**, 241 (2000).
17. C. Cow, J.F. Britten, and P.H.M. Harrison. J. Chem. Soc. Chem. Commun. 1147 (1998).
18. T. Amyes and J.P. Richard. J. Am. Chem. Soc. **114**, 10297 (1992).
19. M.J.S. Dewar and K.M. Dieter. Biochemistry, **27**, 3302 (1988).
20. J.D. Clark, S.J. O'Keefe, and J.R. Knowles. Biochemistry, **27**, 5961 (1988).
21. E.C. Ashby and W.-S. Park. Tetrahedron Lett. **24**, 1667 (1983).
22. C.A. Palmer, C.A. Ogle, and E.M. Arnett. J. Am. Chem. Soc. **114**, 5619 (1992).
23. W.A. Pryor, T.H. Lin, J.P. Stanley, and R.W. Henderson. J. Am. Chem. Soc. **95**, 6993 (1973).
24. W.J. Leigh, D.R. Arnold, R.W.R. Humphreys, and P.C. Wong. Can. J. Chem. **58**, 2537 (1980).
25. S.S.-W. Leung and A. Streitwieser. J. Am. Chem. Soc. **120**, 10557 (1998).
26. S. Kandlikar, B. Sethuram, and T.N. Rao. J. Prakt. Chem. **321**, 131 (1979).
27. E.I. Gasull, J.J. Silber, S.E. Blanco, F. Tomas, and F.H. Ferretti. J. Mol. Struct. (THEOCHEM) **503**, 131 (2000).
28. R.P. Bell and M.J. Smith. J. Chem. Soc. 1691 (1958).
29. R.P. Bell and P.T. McTigue. J. Chem. Soc. 2983 (1960).
30. J.P. Guthrie and J. Guo. J. Am. Chem. Soc. **118**, 11472 (1996), and refs. therein.
31. R.W. Nagorski, T. Mizerski, and J.P. Richard. J. Am. Chem. Soc. **117**, 4718 (1995).
32. J.P. Richard and R.W. Nagorski. J. Am. Chem. Soc. **121**, 4763 (1999).
33. See for example, B.M. Anderson and W.P. Jencks. J. Am. Chem. Soc. **82**, 1773 (1960).

© 2002 NRC Canada

National Research Council Canada
Ottawa, Canada K1A 0R6

Conseil national de recherches Canada
Ottawa, Canada K1A 0R6

Postage paid at Ottawa
Publications mail
Registration No. 40062591

Port payé à Ottawa
Poste-publication
Enregistrement n° 40062591

USPS periodical postage paid at Champlain, N.Y.

Canadian Journal of Chemistry

Revue canadienne de chimie

Volume 80, Number 6, June 2002

Volume 80, numéro 6, juin 2002

This issue is dedicated to Professor J. Bryan Jones
Ce tirage est dédié au Professeur J. Bryan Jones

Dedication iii
Biography v

Dédicace iii
Biographie v

Selective reduction and chemical modification of oxidized lipase cysteine mutants

Eva M.K. Hedin, Shamkant A. Patkar, Jesper Vind, Allan Svendsen, Karl Hult, and Per Berglund

529–539

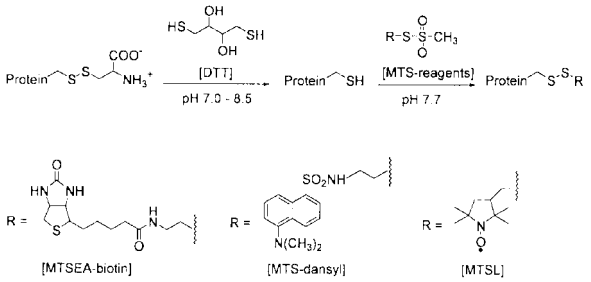

Chemo-enzymatic synthesis of trimeric sialyl Lewis^x pentadecasaccharide

Yeuk Chuen Liu, Hong Li, Albin Otter, Vivekanand P. Kamath, Markus B. Streiff, and Monica M. Palcic

540–545

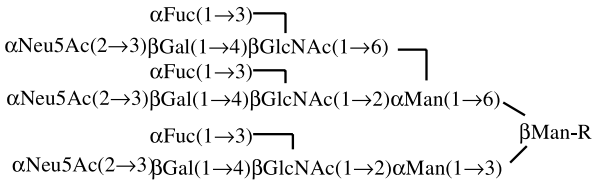

Biomimetic reactions in organic synthesis: Semi-pinacol rearrangements of some spirocyclic epoxyalcohols derived from Juliá–Colonna asymmetric epoxidations

Bernhard Hauer, Jamie F. Bickley, Julien Massue, Paula C.A. Pena, Stanley M. Roberts, and John Skidmore

546–550

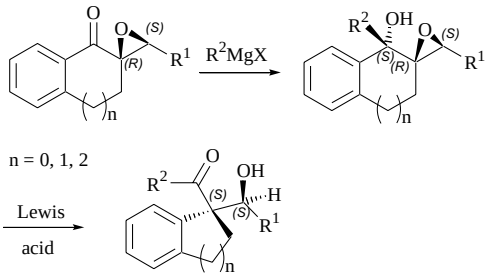

Discriminating between dispersion and lyoprotection effects in biocatalysis in organic media

Francesco Secundo, Giacomo Carrea, and Francesco Maria Veronese

551–554

Continued on inside back cover / Suite au verso

Canada

Printed in Canada by / Imprimé au Canada par
University of Toronto Press Inc.
Typesetting by / Typographie par
NRC Research Press / Presses scientifiques du CNRC

0008-4042(200206)80:6;1-I

Towards an unprotected self-activating glycosyl donor system: Bromobutyl glycosides

Benjamin G. Davis, Steven D. Wood, and Michael A.T. Maughan

555–558

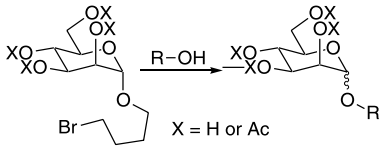

Rationalization of enzyme enantioselectivity by active-site cubic-space models

Gianluca Ottolina and Giacomo Carrea

559–564

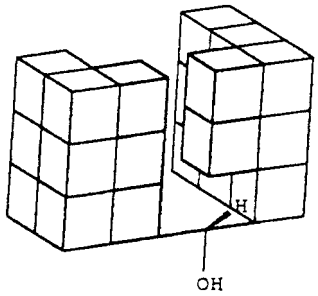

Structural effects on chemo- and enantio-selectivity of *Candida antarctica* lipase B — Resolution of β-amino esters

Szilvia Gedey, Arto Liljeblad, László Lázár, Ferenc Fülöp, and Liisa T. Kanerva

565–570

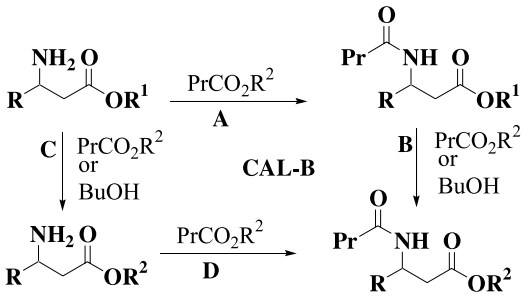

Chemo-enzymatic synthesis of the C_{15}–C_{23} unit of Leptomycin B

Michael Scheck and Herbert Waldmann

571–576

Water content influences the selectivity of CALB-catalyzed kinetic resolution of phenoxymethyl-substituted secondary alcohols

Elisabeth Egholm Jacobsen and Thorleif Anthonsen

577–581

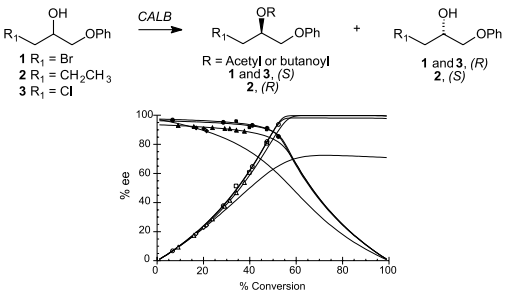

Continued on facing page / Suite au la page précédente

Biocatalytic oxidation of 4-vinylphenol by *Nocardia*

Kyung-Seon Lee and John P.N. Rosazza

582–588

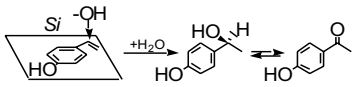

Dioxygenase-catalyzed *cis*-dihydroxylation of pyridine-ring systems

Derek R. Boyd, Narain D. Sharma, Ludmila V. Modyanova, Jonathan G. Carroll, John F. Malone, Christopher C.R. Allen, John T.G. Hamilton, David T. Gibson, Rebecca E. Parales, and Howard Dalton

589–600

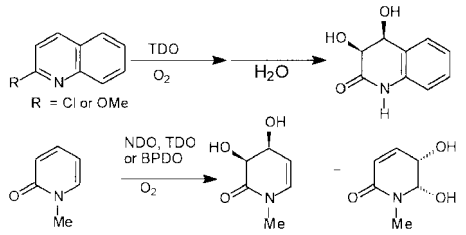

Biomimetic decarboxylative condensation between malonate and acetate units attached to a glycoluril template

Hao Chen and Paul H.M. Harrison

601–607

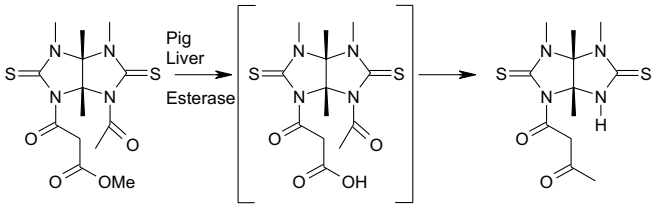

Enantioselective enzymatic aminolysis of a racemic 2-isoxazolylacetate alkyl ester

Amy E. Sigmund, Kenneth C. McNulty, Dzuy Nguyen, Charlotte E. Silverman, Philip Ma, Jaan A. Pesti, and Robert DiCosimo

608–612

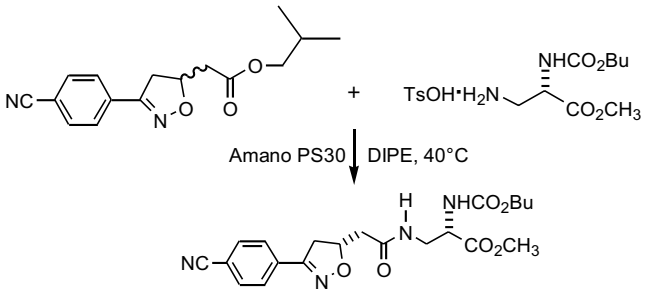

Baeyer-Villiger oxidations catalyzed by engineered microorganisms: Enantioselective synthesis of δ-valerolactones with functionalized chains

Shaozhao Wang, Gang Chen, Margaret M. Kayser, Hiroaki Iwaki, Peter C.K. Lau, and Yoshie Hasegawa

613–621

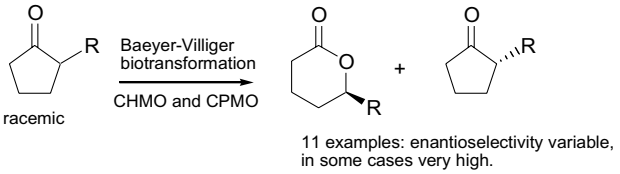

Metal substitution in thermolysin: Catalytic properties of tungstate thermolysin in sulfoxidation with H_2O_2

Martin Bakker, Fred van Rantwijk, and Roger A. Sheldon

622–625

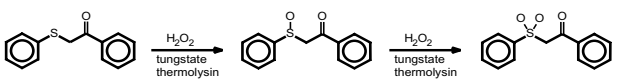

Continued on facing page / Suite au la page précédente

Second-generation MS-based high-throughput screening system for enantioselective catalysts and biocatalysts

Wolfgang Schrader, Andreas Eipper, D. Jonathan Pugh, and Manfred T. Reetz

626–632

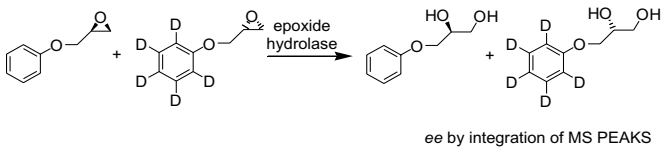

Chloroperoxidase-catalyzed oxidation of methionine derivatives

Herbert L. Holland, Frances M. Brown, Damian Lozada, Benjamin Mayne, W. Rick Szerminski, and Aaron J. van Vliet

633–639

Formation of single diastereomers of β-hydroxy-sulfoxides by biotransformation of β-ketosulfides using *Helminthosporium* species NRRL 4671

Herbert L. Holland, Nancy Ihasz, and Brendan J. Lounsbery

640–642

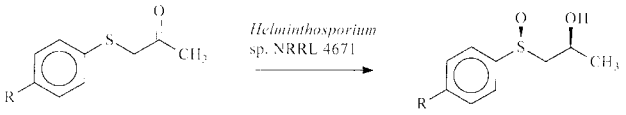

Structure-based rationalization of aldolase-catalyzed asymmetric synthesis

Junjie Liu, Grace DeSantis, and Chi-Huey Wong

643–645

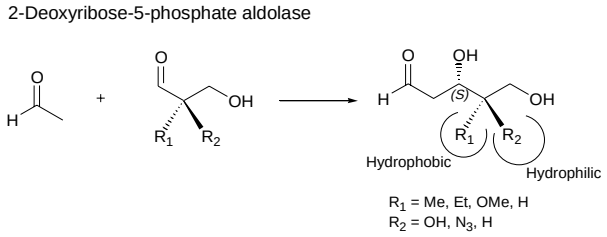

Efficient synthesis of the optically active dihydropyrimidinone of a potent α_{1A}-selective adrenoceptor antagonist

Daniel R. Sidler, Nancy Barta, Wenjie Li, Essa Hu, Louis Matty, Nori Ikemoto, Jeffrey S. Campbell, Michel Chartrain, Kozo Gbewonyo, Russell Boyd, Edward G. Corley, Richard G. Ball, Robert D. Larsen, and Paul J. Reider

646–652

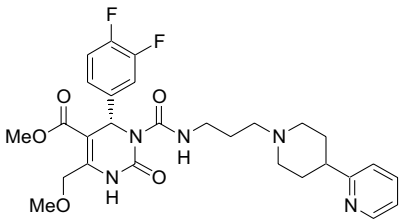

Continued on facing page / Suite au la page précédente

Enzymatic synthesis of octyl glucoside catalyzed by almond β-glucosidase in organic media

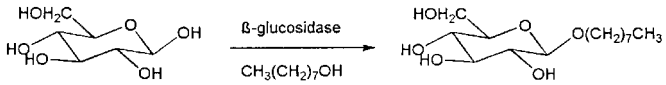

Amélie Ducret, Jean-François Carrière, Michael Trani, and Robert Lortie

653–656

Optimized production of the Diels–Alderase antibody 1E9 as a chimeric Fab

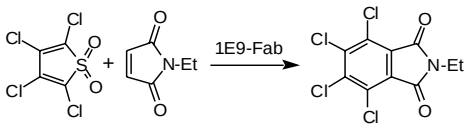

Andrea Piatesi and Donald Hilvert

657–664

Methylamine adenine dinucleotide (MAD): A co-factor to turn alcohol dehydrogenases into aldolases

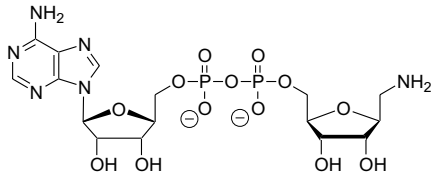

Denis Wahler and Jean-Louis Reymond

665–670

Hydroxynitrile lyase-catalyzed addition of HCN to 4-substituted cyclohexanones: stereoselective preparation of tetronic acids

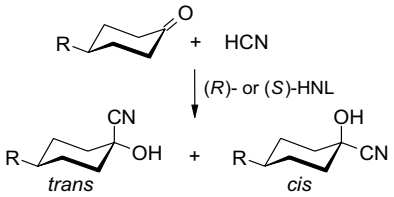

Franz Effenberger, Jürgen Roos, Christoph Kobler, and Holger Bühler

671–679

Tailoring the substrate specificity of secondary alcohol dehydrogenase

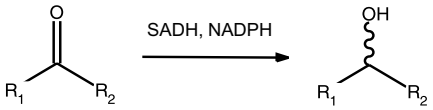

Robert S. Phillips

680–685

Kinetic resolution of oxime esters with lipases — synthesis of enantiomerically enriched building blocks with quaternary carbon centers and formal total synthesis of perhydro histrionicotoxin

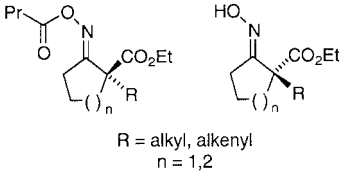

Nicole Diedrichs, Ralf Krelaus, Ina Gedrath, and Bernhard Westermann

686–691

Continued on facing page / Suite au la page précédente

Novel esterase activity of dihydrolipoamide acetyltransferase AcoC of *Pseudomonas putida* identified by mutation of the *acoR* regulator

Paola Pedroni, Thomas Friedrich, Michael Breuer, Dani McBeth, and Bernhard Hauer

692–698

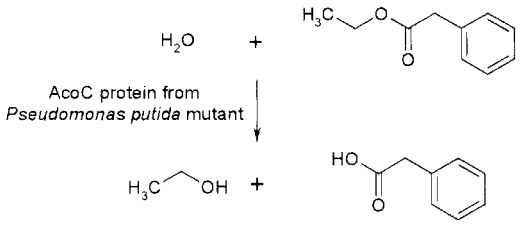

Enzymatic hydrolysis of β-lactam antibiotics at low pH in a two-phase "aqueous solution – water-immiscible organic solvent" system

Ghermes G. Chilov and Vytas K. Švedas

699–707

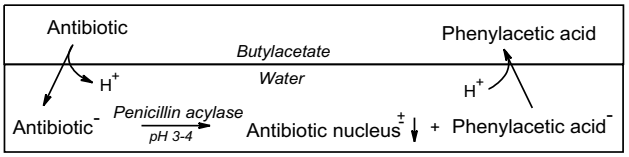

Enzymatic oxidation of cyclopropylbenzene: structures of new metabolites and possible mechanistic implications

Vu P. Bui, Minh Nguyen, Jeff Hansen, John Baker, and Tomas Hudlicky

708–713

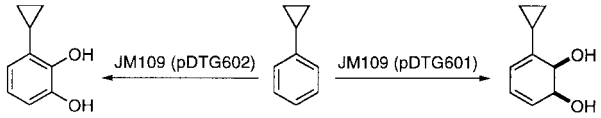

Bio-catalyzed preparation of the optically enriched stereoisomers of 4-methyl-2-phenyl-tetrahydro-2*H*-pyran (Doremox®)

Elisabetta Brenna, Claudio Fuganti, Sabrina Ronzani, and Stefano Serra

714–723

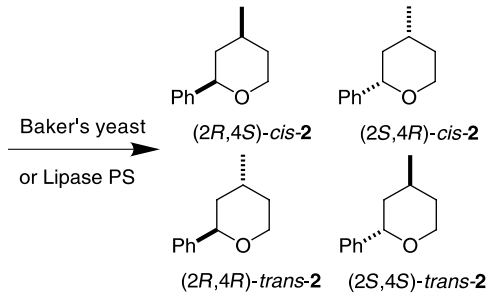

Selective biotransformation of substituted alicyclic nitriles by *Rhodococcus equi* A4

Ludmila Martínková, Norbert Klempier, Margit Preiml, Mária Ovesná, Marek Kuzma, Veronika Mylerová, and Vladimír Křen

724–727

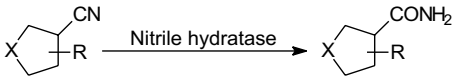

X: CH_2, R: *trans*-2-OH

X: $(CH_2)_2$, R: *trans*-2-OH, *cis*-3-OBz, *trans*-4-OBz

Concluded on facing page / Suite et fin à la page précédente

Exploratory synthetic investigations related to 12a-deoxypillaromycinone

Lan Wang, Sanath K. Meegalla, Cheng-Lin Fang, Nicholas Taylor, and Russell Rodrigo

728–738

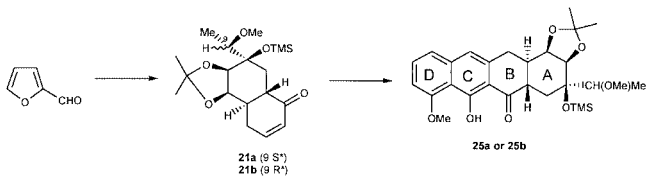

Regiospecific synthesis of lactose analog Gal-(β 1,4)-Xyl by transgalactosylation

Wolf-Dieter Fessner and Juan Manuel Juárez Ruiz

739–742

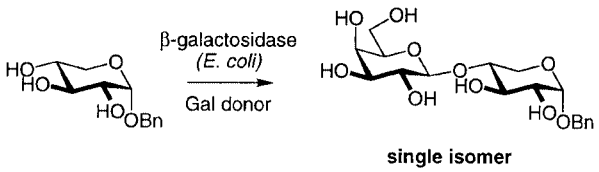

Glucosyltransferases acting on starch or sucrose for the synthesis of oligosaccharides

Francisco J. Plou, M. Teresa Martín, Aránzazu Gomez de Segura, Miguel Alcalde, and Antonio Ballesteros

743–752

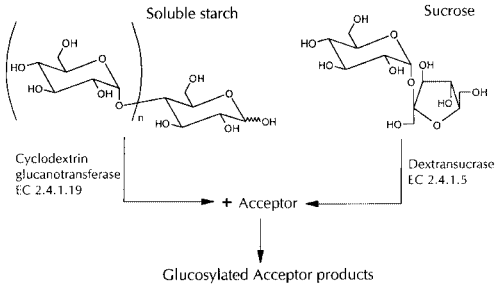

Asymmetric total synthesis of (+)-*exo*-brevicomin based on enantioconvergent biocatalytic hydrolysis of an alkene-functionalized 2,3-disubstituted epoxide

Sandra F. Mayer, Harald Mang, Andreas Steinreiber, Robert Saf, and Kurt Faber

Previously published in Can. J. Chem. 80, 362–369 (2002).

The Canadian Journal of Chemistry is affiliated with the Canadian Society for Chemistry and publishes papers in all areas of chemistry.

La Revue canadienne de chimie est affiliée à la Société canadienne de chimie et publie des articles dans tous les domaines de la chemie.

Selective reduction and chemical modification of oxidized lipase cysteine mutants

Eva M.K. Hedin, Shamkant A. Patkar, Jesper Vind, Allan Svendsen, Karl Hult, and Per Berglund

Abstract: Thirteen single-cysteine mutants of the 33 kDa fungal triacylglycerol lipase *Thermomyces* (formerly *Humicola*) *lanuginosa* lipase (TLL, EC 3.1.1.3) were produced and characterized for the purpose of site-directed chemical modification with spectroscopic reporter groups. All cysteine mutants were found to be predominantly blocked by oxidation to disulfides with endogenous cysteine during production. The fraction of lipase molecules with free sulfhydryl groups was analyzed by labeling with *N*-biotinylaminoethyl methanethiosulfonate, followed by a novel dot-blot method based on biotin–streptavidin interactions. A non-invasive method for the reduction of the introduced cysteine was elaborated for this protein containing three native disulfide bridges. The site-specifically reduced TLL mutants were then labeled with the sulfhydryl-specific reagents 2-(5-dimethylaminonaphth-1-ylsulfonamido)ethyl methanethiosulfonate or (1-oxyl-2,2,5,5-tetramethyl-Δ^3-pyrroline-3-methyl) methanethiosulfonate, and studied by fluorescence and electron spin resonance (ESR) spectroscopy.

Key words: lipase, cysteine mutant, selective reduction, chemical modification, methanethiosulfonate.

Résumé : Dans le but d'obtenir des modifications chimiques orientées vers les sites au contact de groupes rapporteurs, on a préparé et caractérisé 13 mutants de la lipase fongique du triacétylglycérol, la lipase *Thermomyces* (antérieurement *Humicola*) *lanuginosa* (TLL, EC 3.1.1.3), de masse 33 kDa, qui ne comportent qu'une seule cystéine. On a trouvé que, durant la production, tous les mutants à la cystéine sont bloqués principalement par une oxydation en disulfures avec la cystéine endogène. On a analysé la fraction de molécules de lipase comportant des groupes sulfhydryles libres en les marquant avec du méthanethiosulfonate de *N*-biotinylaminoéthyle, suivi d'une nouvelle méthode à point sur papier buvard qui est basée sur les interactions entre la biotine et la streptavidine. On a élaboré une méthode non invasive de réduction de la cystéine introduite pour la protéine qui contient trois ponts disulfures d'origine. Par la suite, les mutants de TLL réduits spécifiquement en fonction du site ont été marqués avec des réactifs spécifiques aux sulfhydryles, le méthanethiosulfonate de 2-(5-diméthylaminonapht-1-ylsulfamido)éthyle ou de (1-oxyl-2,2,5,5-tétraméthyl-Δ^3-pyrroline-3-méthyle) et on les a étudiés par fluorescence et par spectroscopie de résonance paramagnétique électronique (RPE).

Mots clés : lipase, mutant à cystéine, réduction sélective, modification chimique, méthanethiosulfonate.

[Traduit par la Rédaction]

Introduction

The combination of site-directed mutagenesis and covalent chemical modification has, during the last decades, emerged as a powerful tool in the study of protein structure, function, and dynamics. Introducing probes, such as fluorescent groups or spin labels, at predetermined sites in a protein enables detailed information on protein structure and interactions to be obtained through spectroscopic studies (1, 2). For example, advances in the field of site-directed spin labeling and electron spin resonance (ESR) spectroscopy have allowed the elucidation of protein topology and function for several proteins (3–5), as well as of protein–membrane interactions (6, 7). With the technique of chemical modification of mutated proteins (CMM technology), enzymes with new functionalities or enhanced activities have also been prepared (for a review, see ref. 8). An example of altering the activity and specificity of an enzyme by this approach is reported by Jones and co-workers (9), in which the introduction of various alkyl- and aryl-side chains in the S_1 and S'_1 specificity pockets of subtilisin *Bacillus lentus* cysteine mutants created enzymes with greater activity than the wild-type enzyme.

The success of studying proteins using CMM technology is ultimately dependent on the specificity of the chemical-modification reaction. Although chemical modification can be targeted to various amino-acid side chains, it often results in multiple labeling due to the occurrence of several copies of the target amino acid. Cysteine, however, is very rarely present as free cysteine in protein structures, and possesses a unique reactivity among the amino acids. Consequently, the

Received 5 December 2001. Published on the NRC Research Press Web site at http://canjchem.nrc.ca on 24 April 2002.

Dedicated to Professor J. Bryan Jones on the occasion of his 65th birthday.

E.M.K. Hedin, K. Hult, and P. Berglund.[1] Department of Biotechnology, Royal Institute of Technology, Stockholm Center for Physics, Astronomy and Biotechnology, SE-106 91 Stockholm, Sweden.
S.A. Patkar, J. Vind, and A. Svendsen. Novozymes A/S, Smørmosevej 25, DK-2880 Bagsvaerd, Denmark.

[1]Corresponding author (e-mail: per.berglund@biochem.kth.se).

 DOI: 10.1139/V02-046 © 2002 NRC Canada

Scheme 1.

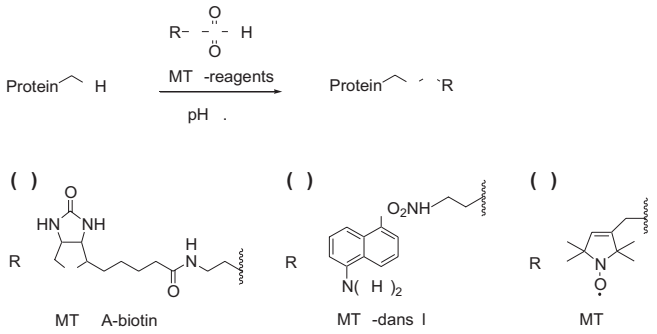

introduction of cysteine by mutagenesis at a preselected site in a protein, in combination with sulfhydryl-specific labeling reagents, has emerged as a highly specific modification process that is extensively employed. Several classes of reagents exist for the modification of cysteine (reviewed in ref. 10), of which the methanethiosulfonate (MTS) reagents have surfaced as the most specific, and are routinely used (10, 11). The MTS reagents react specifically and quantitatively with sulfhydryl groups under mild reaction conditions with no large excess of reagent required, and their reactivity is independent of the nature of the group to be attached (12, 13).

Unfortunately, due to the intrinsic reactivity of cysteine, it is prone to oxidation, especially when introduced at surface-exposed parts of a protein, which may result in disulfide formation with endogenous sulfur-containing compounds or in protein dimerization (14, 15). As a result, reduction of cysteine disulfides must often precede any chemical modification. An interesting study was recently reported, in which several single-cysteine mutants of subtilisin were produced, and the oxidation state of the introduced cysteine was analyzed by mass spectrometry (MS), employing protein digestion and sub-digestion techniques (15). In particular, a striking correlation was found between oxidation and surface accessibility of the cysteines. Most of the cysteine mutants that had been oxidized, however, were also found to contain a small fraction of free sulfhydryl groups.

In the present study, we report the detection and quantitation of free sulfhydryl groups in recombinant single-cysteine mutants of a triacylglycerol lipase. Specifically, the oxidation state of the introduced cysteine was studied for this lipase that contains three native disulfide bridges. Furthermore, a procedure for selective and non-invasive reduction of the oxidized recombinant proteins has been developed, to enable site-specifically labeled lipases as the end product. This was performed on a series of single-cysteine mutants of *Thermomyces* (formerly *Humicola*) *lanuginosa* lipase (TLL). This 33 kDa fungal glycosylated triacylglycerol lipase (EC 3.1.1.3) is a well-characterized enzyme with interesting industrial applications (16), and displays classical interfacial activation (17). TLL has been cloned, overexpressed, and purified (16, 18), and several high-resolution crystal structures of TLL have been reported (19, 20). Furthermore, the dynamics and the kinetic behaviour of TLL have been well characterized (18, 21–24), although the mechanistic details of interfacial activation have not yet been elucidated. In this paper, 13 TLL single-cysteine mutants are presented, in which the cysteine has been introduced at the surface of the enzyme. The cysteine variants were studied through labeling with different MTS reagents (Scheme 1). A dot-blot method for the detection of free sulfhydryl groups in the protein (employing reagent **A**) was developed and evaluated. This method requires only small quantities of protein and is based on the strong ligand interaction between biotin and streptavidin. A selective reduction method for the oxidized TLL cysteine mutants is then presented, which distinguishes between the three structural disulfide bridges in TLL and the introduced cysteine. The selectively reduced TLL mutants were labeled with spectroscopic probes (**B** and **C**, Scheme 1), which afforded varying degrees of label insertion in each of the different mutants. The labeled mutants were studied by fluorescence- and ESR spectroscopy. The correlation between spectral signatures, yield of label insertion, and local structural features at the mutation site is discussed, as is the applicability of the dot-blot method and the optimized selective-reduction method.

Results

Preparation of functional TLL mutant proteins

Thirteen single-cysteine mutants of TLL were produced for the purpose of site-directed labeling with various spectroscopic probes. The mutations were made on the surface of TLL by replacement of a selected residue with cysteine. Every target site was preselected to provide a coverage around the surface of the molecule, using the TLL X-ray structure for reference. A structure of TLL in the open conformation, complexed with an *n*-dodecyl (C12) phosphonate inhibitor, was used (the TLL-C12 atomic coordinates were provided by Lawson et al., ref. 25). The TLL mutants created can be divided into two groups. In the first group, only single-cysteine mutations were made, which afforded 11 different mutants with a cysteine introduced at one of the following positions: P42C (proline 42 exchanged for cysteine), G61C, K74C, D96C, T123C, D137C, T192C, R209C, T231C, I252C, and T267C. The second group included two variants where, in addition to the cysteine mutation, three tryptophans were removed, leaving only the tryptophan residing in the lid of TLL (Trp-89). This was done for the purpose of fluorescence spectroscopy studies to allow Trp-89 to be monitored without any interference from the other tryptophans. Furthermore, these mutants had the glycosylation site removed, which yielded two TLL variants containing the following mutations: G61C/W117F/W221H/W260H/N33Q and R209C/W117F/W221H/W260H/N33Q (which henceforth shall be referred to as "G61C-singleW" and "R209C-singleW," respectively).

The ribbon structure in Fig. 1 shows the relative positions of all single-point cysteine mutations prepared in TLL, with the substituted amino acids highlighted in yellow. In addition, the four tryptophans are indicated, of which Trp-89, together with the rest of the α-helical lid, is colored green. The catalytic triad (Ser-146, His-258, Asp-201), which is next to the lid, is displayed in cyan/red. Five cysteine mutations were placed around the lid and the active site (T267C, I252C, R209C, D96C, and G61C). A ring of residues were mutated around the lower third of the molecule (P42C, T231C, T192C, and T123C), and opposite to the active site,

© 2002 NRC Canada

Fig. 1. A ribbon representation of *Thermomyces lanuginosa* lipase, showing the open conformation (the complexed *n*-dodecyl (C12) phosphonate inhibitor has been omitted in this figure for clarity). The relative positions of all single-point cysteine mutations are shown, where the substituted residues are marked in yellow spacefill (single amino-acid codes used). In addition, the four tryptophans in TLL are indicated, the lid is highlighted in green and the catalytic triad in cyan/red. The TLL-C12 atomic coordinates were kindly provided by Lawson and Brzozowski (25). The figure was generated using VMD (39) and POV-Ray.

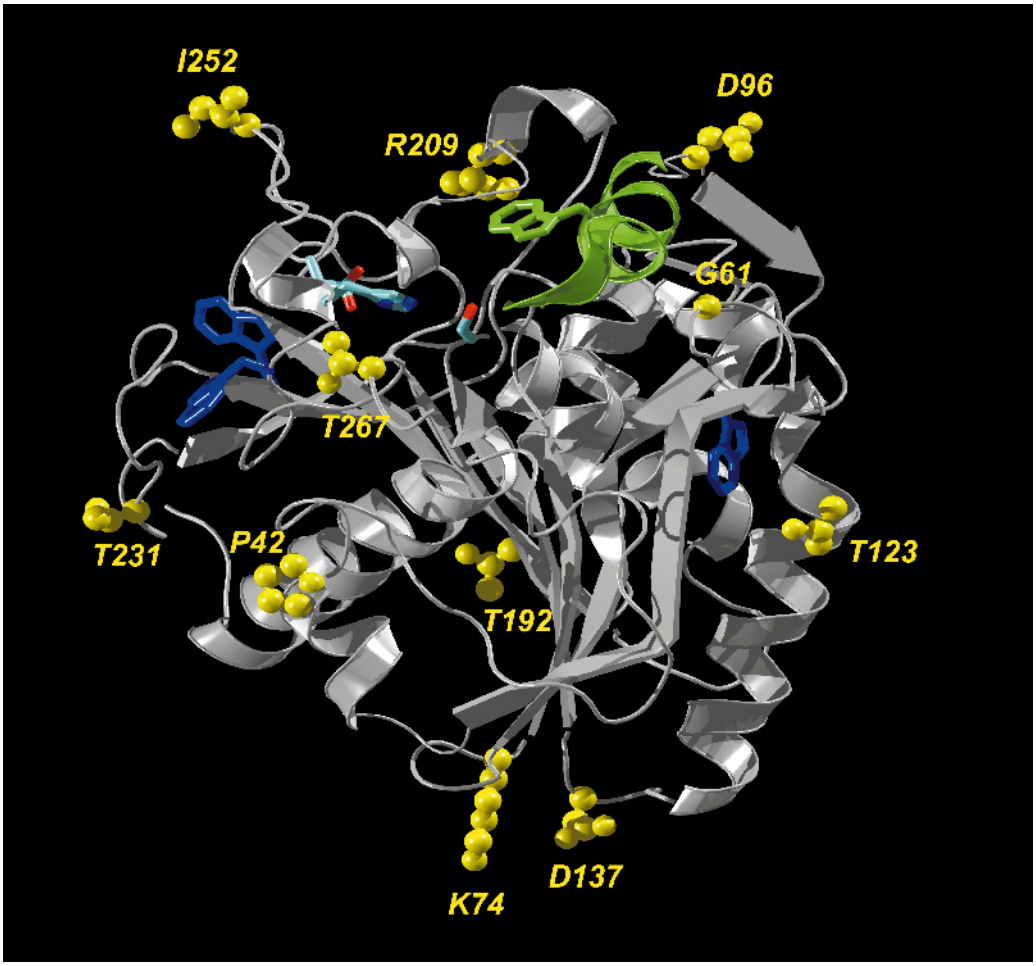

two mutations were placed close to each other but positioned at the turns of two different hairpin loops (K74C and D137C). Although all of these mutations are at the surface of TLL, some are situated on more exposed and flexible segments of the protein, such as loops, whereas others are located on the surface of α-helices and β-sheets.

All created TLL proteins produced one band of approximately 33 kDa on SDS-PAGE. The tryptophan fluorescence spectra of the variants containing only the single-cysteine mutation were effectively identical to that of the wild-type enzyme. This was also the case for G61C-singleW and R209C-singleW, indicating the strong contribution to the total TLL tryptophan fluorescence by Trp-89 in the lid, in agreement with previously reported work (21). The specific hydrolytic activity of the TLL mutants was measured on an emulsion of glyceryl tributanoate using a pH-stat method (16). All mutants displayed high hydrolytic activity comparable to that of the wild-type enzyme, where G61C-singleW and R209C-singleW were the least active (Table 1). The specific activity of the TLL mutants varied between 53–118% of that of the wild-type enzyme. As seen in Table 1, the mutants I252C and T267C have slightly lower activity than the rest of the single-cysteine mutants, which may be due to the proximity of the mutation to the lid and the active site in TLL. Finally, it should also be noted that the specific activity of the mutants was found to vary slightly between different batches. Altogether, the above data show that the mutations performed on TLL did not significantly perturb the protein structure or activity.

Detection of free protein-sulfhydryl groups by the dot-blot method

In the present study, a dot-blot method for the detection of free protein-sulfhydryl groups was developed. This method requires only small quantities of protein (50–200 μL) at concentrations of 1–3 mg mL^{-1}, and is based on the strong ligand interaction between biotin and avidin or streptavidin. Accordingly, the produced TLL cysteine mutants were labeled with the sulfhydryl-specific reagent MTSEA–biotin (**A**, Scheme 1) and purified by dialysis. The biotinylated proteins were then applied on a nitrocellulose membrane by a Bio-Dot® microfiltration apparatus, together with a series of biotinylated protein standards. The membrane was subsequently incubated with a streptavidin-AP (alkaline

© 2002 NRC Canada

Table 1. Specific hydrolytic activity of TLL wild-type enzyme and variants.

Variant	Specific activity (LU/mg)[a]
Wild type	6470 ± 250
P42C	5820 ± 70
G61C	6660 ± 10
K74C	7480 ± 60
D96C	7120 ± 400
T123C	7640 ± 520
D137C	7130 ± 300
T192C	6070 ± 140
R209C	7640 ± 10
T231C	6050 ± 340
I252C	5360 ± 230
T267C	4090 ± 280
G61C-singleW	3540 ± 40
R209C-singleW	3890 ± 10

Note: Activity mesured by the pH-stat method on a 16 mM emulsion of glyceryl tributanoate. The error in each sample was estimated from the standard deviation of triplicate measurements.

[a]A lipase unit (LU) equals one μmol of released titratable acid per min.

phosphatase) conjugate at 30°C and developed with the substrate BCIP–NBT (5-bromo-4-chloro-3-indolyl phosphate – nitro blue tetrazolium), which afforded dots of varying intensities, proportional to the AP activity. The intensities of the developed dots were analyzed by densiometry. The densiometrically determined quantities of the TLL biotin content were normalized by protein concentration, which revealed the amount of free cysteine for each variant. The "biotinylated" TLL wild-type control always gave a negative result in the dot-blot assay (data not shown). A representative dot-blot membrane is shown in Fig. 2. The results from the dot-blot quantitation are summarized in the second column of Table 2. As seen, the dot-blot method showed that for all TLL cysteine variants analyzed, the sulfhydryl group of the introduced cysteine was predominantly blocked. Four variants contained only 1–2% of free cysteine (mol of free cysteine per mol of protein, in percent), three contained around 15%, and one variant displayed 37% free cysteine (T231C). Nevertheless, these results are not unexpected for cysteine mutations positioned on the surface of a protein (15). The dot-blot method was evaluated by comparison with three other methods of sulfhydryl detection: titration with Ellman's reagent (DTNB, 26), labeling with a dansyl fluorescent probe (**B**, Scheme 1), and labeling with a nitroxide spin label (**C**, Scheme 1). The population of variants labeled with **B** or **C** was then estimated by fluorescence spectroscopy or ESR spectroscopy against dansyl- and nitroxide-standard solutions, respectively. The results obtained by the different methods, including the dot-blot method, are compared in Table 2. It is generally seen that the four independent techniques agree well in determining the free sulfhydryl content of the TLL cysteine mutants, even though very low contents were measured in most cases. As indicated by the majority of the methods, only two of the 11 TLL variants contained any substantial fraction of free cysteine (10–15%), whereas the rest contained 5% or less. It is also noted that the dot-blot method appeared to overestimate the biotin content in two cases (P42C and T231C), but was otherwise in good agreement with the other methods.

Fig. 2. The dot-blot method performed on biotinylated TLL cysteine variants. Dots number 1–12 are standards (biotinylated BSA) with the following biotin concentrations: 730, 360, 180, 90, 45, 23, 11, 6, 3, 1.4, 0.7, and 0.4 nM. The biotinylated TLL variants are applied in triplicates vertically (protein concentrations in parenthesis) in the following order: A, D96C (340 nM); B, K74C (650 nM); C, T123C (290 nM); D, T267C (590 nM); E, I252C (500 nM); F, P42C (300 nM); G, T231C (250 nM); and H, R209C (180 nM). Positive control: biotinylated Rat-IgM. Negative control: I252C (not biotinylated).

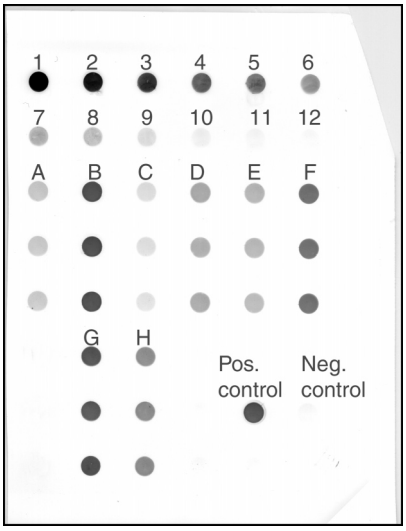

On the other hand, Ellman's reagent underestimated the free sulfhydryl content in R209C.

Selective reduction of blocked TLL cysteine mutants

All methods indicated that the sulfhydryl groups of the TLL cysteine mutants were predominantly blocked from reaction. Electrospray MS revealed that this was due to oxidation by disulfide coupling to free cysteine (presumably during protein expression, ref. 15). It was, therefore, desirable to increase the yield of labeled proteins by prior reduction of the oxidized cysteine on the enzyme surface. Since the native protein contains three disulfide bridges, however, a procedure for selective reduction of the surface cysteine had to be elaborated. This was done in two steps:

(*i*) the limiting reduction conditions were analyzed on the wild-type enzyme by varying the concentration of reducing agent (DL–dithiothreitol, DTT). In addition, reduction on a column was tested (Reduce-Imm™ column, Pierce). The reactions were performed at pH 8.5 and 8.0, for reduction in solution and on the column, respectively. The effect of the reduction was assessed by Ellman's reagent, activity measurements, and dansyl labeling. Table 3 shows the results from the reduction experiments on the wild-type enzyme. As can be seen, non-invasive reduction conditions for TLL were found only as low as with 0.1 mM DTT. For any higher concentrations of DTT, the decrease in residual specific activity and the presence of free sulfhydryl groups suggest that disulfide bridges were reduced to some extent. This is also supported by the insertion of dansyl seen after reduction with higher DTT concentrations, and the further decrease of the already diminished activity after labeling. Reduction on the column afforded fractions with different quantities of

© 2002 NRC Canada

Table 2. Results from analysis of free sulfhydryl content of TLL cysteine mutants.

Variant	Dot-blot (mol%)[a]	Ellman's (mol%)[a, b]	Dansyl flourescence (mol%)[a]	ESR spectroscopy (mol%)[a]
P42C	18.3 ± 0.3	3.4 ± 0.1	n.d.	1.8 ± 0.2
G61C	n.d.	3.4 ± 0.5	6.5 ± 1.0	n.d.
K74C	16.4 ± 0.6	14.4 ± 0.9	9.5 ± 1.5	11.5 ± 1.5
D96C	1.3 ± 0.1	1.4 ± 0.1	n.d.	2.7 ± 0.5
T123C	1.2 ± 0.1	1.4 ± 0.1	n.d.	1.9 ± 0.2
D137C	n.d.	0 ± 0	0 ± 0	n.d.
T192C	n.d.	3.4 ± 0.6	n.d.	1.9 ± 0.5
R209C	14.1 ± 0.8	5.0 ± 2.5	13.5 ± 3.5	12.4 ± 2.0
T231C	36.6 ± 5	4.4 ± 0.4	n.d.	3.2 ± 0.5
I252C	1.9 ± 0.1	2.4 ± 0.3	n.d.	3.7 ± 0.7
T267C	2.1 ± 0.1	2.4 ± 0.2	n.d.	2.1 ± 0.2

Note: The different methods for determining the content of free protein-sulfhydryl groups are described in the *Experimental* section. n.d. = not determined.

[a]Mol of free sulfhydryl groups per mol of protein, in percent, for the TLL cysteine mutants.

[b]Ellman's reagent was titrated with DTT to verify that one mol of free sulfhydryl groups corresponded to one mol of released thiolate anion at 412 nm.

Table 3. Reduction of TLL wild type at pH 8.5.

Reduction method (mM DTT)	Residual activity I[a] (%)	Ellman's reagent (free-SH/protein) (mol%)	Dansyl insertion[b] (mol%)	Residual activity II[c] (%)
0	100	0	0	100
0.1	100	0	85	95
0.5	100	0	65	90
1	95	30	85	90
Red-Imm™ column	85–100[d]	30–170[d]	250–300[d]	30–35[d]
10	50	160–180	>200	20
25	60	130–140	>200	32
50	67	160–200	>200	17

Note: The reduction conditions are described in the *Experimental* section. The Red-Imm column was pre-equilibrated with a 10 mM DTT solution. Activity was measured by the pH-stat method.

[a]Residual specific hydrolytic activity after reduction and removal of DTT (dialysis).

[b]Dansyl labeling performed after reduction and removal of DTT (dialysis). Insertion of dansyl estimated by fluorescence spectroscopy against dansyl standard solutions.

[c]Residual specific hydrolytic activity after reduction, dansyl labeling and purification.

[d]Range of values for the different fractions eluted from the column.

free sulfhydryl content as analyzed by Ellman's reagent. It seems peculiar that substantial dansyl insertion was seen also after reduction with 0.1, 0.5, and 1 mM DTT, which is contradicted by the findings with Ellman's reagent and the specific activity. The fluorescence noted may originate from hydrophobically attached dansyl reagent still present after purification. Interestingly, this was not observed with the unreduced wild-type control.

(*ii*) A systematic variation of several parameters, such as pH, DTT concentration, time of reduction, and inert reaction atmosphere was performed on the wild-type enzyme and a cysteine mutant (G61C) in parallel. Furthermore, efforts were made to remove all residual dansyl reagent after the reaction. The results from this second optimization are summarized in Table 4. The optimal reduction conditions were found where the dansyl insertion in G61C was as close to quantitative as possible, with minimal insertion into the wild-type enzyme. This was encountered at pH 7.7 with a DTT concentration of 0.3 mM and a reduction time of 30 min, affording a 36% yield of dansyl insertion for the mutant. Table 4 shows that the effect of increasing the pH by one unit approximately equaled a 10-fold increase in DTT concentration. Furthermore, increasing the reduction time apparently allowed the DTT to act on the disulfide bridges, which was seen for both the wild-type and the mutant enzymes. This implies a kinetic discrimination between the structural cysteines and the cysteine introduced at the protein surface. The most harsh reduction conditions attempted, at pH 8.5 with 10 mM DTT for 90 min, reduced all disulfide bridges as well as the blocked surface cysteine in the mutant, resulting in 7 dansyl groups incorporated per enzyme. Other variables, such as performing the reactions under an atmosphere of N_2 or adding the DTT to the dialysis buffer, were found to be of less importance. These optimized conditions for selective reduction and labeling allowed the production of various selectively and site-directed labeled TLL mutants containing different functional groups, with no or minimal (1–2%) insertion of label in the wild-type controls.

Preparation of functional labeled TLL-mutant proteins

Fluorescence-labeled TLL variants

By employing the optimized reduction method prior to chemical modification, a selection of mutants were labeled

© 2002 NRC Canada

Table 4. Optimization of reduction parameters on TLL wild type and G61C. The optimal conditions are marked in bold.

[DTT] (mM)	pH	Reduction time (min)	Under N_2	Dansyl insertion WT (mol%)	Dansyl insertion G61C (mol%)
0.1[a]	7	60	No	0	3
0.1[b]	7	80	Yes	0	6
0.1[a]	8.5	60	No	2	17
0.3[a]	**7.7**	**30**	**Yes**	**2**	**36**
0.3[a]	7.7	60	Yes	10	39
1[b]	7	80	Yes	3	17
2[b]	7	30	Yes	5	35
2[b]	7	60	Yes	8	29
2[b]	7	100	Yes	50	170
2[a]	7.7	30	Yes	20	44
4[b]	7	100	Yes	100	190
10[b]	7	90	Yes	30	460
10[b]	8.5	90	Yes	240	700

Note: Reduction was monitored by estimating the insertion of dansyl into TLL. Dansyl labeling was performed after reduction and removal of DTT (dialysis). Insertion of dansyl was quantified by fluorescence spectroscopy against dansyl standard solutions.
[a]DTT reduction carried out directly in protein solution.
[b]DTT reduction performed by dialysis against DTT in buffer.

with the fluorescent reagent MTS–dansyl (**B**, Scheme 1). The dansyl labeling was performed on a few of the single-cysteine variants, and on the cysteine variants containing only one tryptophan (G61C-singleW and R209C-singleW). Interestingly, the latter mutants required milder reduction conditions, and the DTT concentration had to be reduced threefold. This is consistent with the lowered resistance to thermal denaturation observed for G61C-singleW and R209C-singleW, displaying a T_m of 62.1 and 60.3°C, respectively, compared with 75.0°C for the wild-type enzyme, at pH 7.0. This decrease in stability after removal of the three tryptophans has been previously reported in studies of thermal and chemical denaturation of similar TLL tryptophan variants without the cysteine mutation (27, 28). Generally, the yield of dansyl insertion (after reduction and labeling) for the mutants employed was around 30%, as determined by fluorescence spectroscopy. An accurate determination of the dansyl content was difficult to obtain, however, since the quantum yield for the attached dansyl is unknown and its extinction coefficient is quite low for detection through UV spectroscopy (approximately 4200 cm^{-1} M^{-1} in methanol, 29). Furthermore, it has been reported that the quantum yield of a fluorophore may decrease as much as 60% by covalent attachment to a protein (29) and, moreover, the local environment of the label position in each TLL mutant will differ, effecting further variations in the quantum yield. The fluorescence spectra of dansyl-labeled TLL K74C and G61C-singleW are shown in Fig. 3. The emission maxima were 518 and 498 nm for the two variants, respectively. This 20 nm blue shift in dansyl emisson for G61C-singleW, compared with K74C, is in good agreement with the relative positions of the cysteine mutation in the two variants. K74C is positioned on the turn of a hairpin loop, exposed to the aqueous surroundings, whereas G61C is proximal to a β-sheet quite close to the lid in TLL, and should be more restricted in the protein structure.

The dansyl-labeled TLL mutants were analyzed by SDS-PAGE and a Western blot, which was developed with antibodies directed against dansyl. A representative gel and

Fig. 3. Fluorescence emission spectra of dansyl-labeled *Thermomyces lanuginosa* lipase variants K74C (solid line) and G61C-singleW (broken line). The spectra were recorded with the excitation set at 340 nm. The protein concentrations were 15 and 20 μM (K74C and G61C-singleW, respectively) in 20 mM HEPES, pH 7.0.

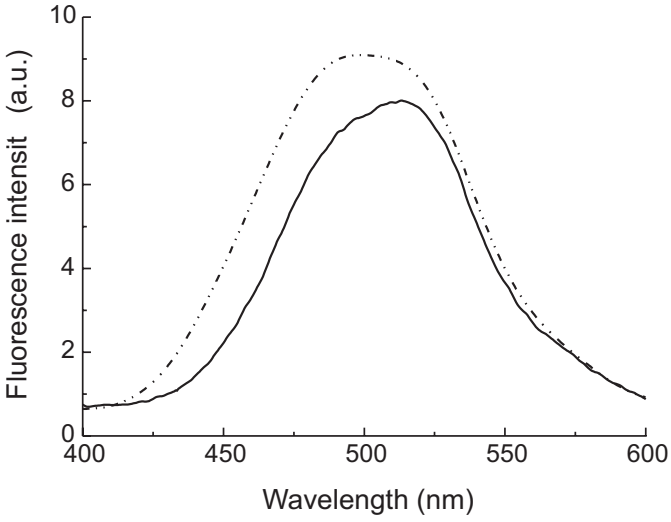

Western blot are shown in Fig. 4, with the dansyl-labeled mutants G61C-singleW, R209C-singleW, and two controls from the labeling reaction. The controls were singleW (the tryptophan mutant without the cysteine mutation) and the wild-type enzyme. Each protein was prepared in both a reducing and a non-reducing loading buffer before application on the gel (panel A). As seen, the bands appear somewhat higher than 33 kDa. It is also seen that the non-reduced proteins have migrated slightly farther on the gel. Upon illumination of the gel with UV light (302 nm), only the labeled cysteine mutants loaded in the non-reducing buffer displayed dansyl fluorescence (panel B). A Western blot was performed (panel C), where the membrane was incubated

© 2002 NRC Canada

Fig. 4. SDS-PAGE and Western blot performed on dansyl-labeled *Thermomyces lanuginosa* lipase variants and wild-type (wt) enzyme showing the Coomassie-stained gel (panel A), fluorescent dansyl bands of the UV-illuminated gel (panel B), and the Western blot developed with anti-dansyl IgG (panel C). The dansyl-labeled proteins were loaded on the gel in the following order (prepared in reducing and non-reducing loading buffers, respectively): 1, G61C-singleW reduced; 2, G61C-singleW not reduced; 3, R209C-singleW reduced; 4, R209C-singleW not reduced; 5, singleW-control reduced; 6, singleW-control not reduced; 7, wt-control reduced; 8, wt-control not reduced. Molecular weight markers (from top): 112, 81, 49.9, 36.2, 29.9, and 21.3 kDa.

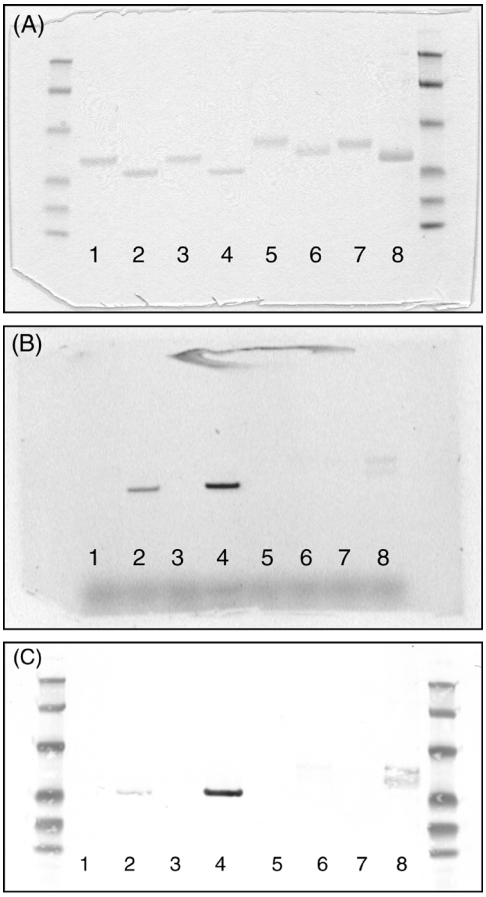

with antibodies directed against dansyl (anti-dansyl rabbit IgG) and with a secondary antibody-AP conjugate (anti-rabbit goat IgG-AP). The membrane was developed with BCIP–NBT, which afforded positive bands only for the non-reduced labeled cysteine mutants, consistent with the UV-illuminated gel. A weak signal was seen for the wild-type control in lane 8, however, which indicates that there was a slight unspecific insertion of dansyl in this control (but not in the singleW-control). Nevertheless, the lack of fluorescence in the UV-illuminated gel suggests that this dansyl content was insignificant. It is also seen in panel C that G61C-singleW only displayed a weak band on the blot, but was clearly fluorescent on the gel (panel B), indicating a steric restriction for the antibody in binding to the dansyl at position G61. The results from the SDS-PAGE and Western blot confirmed that the dansyl was covalently attached to the protein via a disulfide bond.

Table 5. Spin-label incorporation and residual specific activity for TLL variants.

Variant	Spin-label incorporation[a] (mol%)	Residual specific activity[b] (%)	Mutation position
P42C	21 ± 3	91 ± 2	α-Helix[c]
G61C	13 ± 1	51 ± 1	β-Turn
K74C	13 ± 2	68 ± 2	β-Hairpin
D96C	53 ± 6	47 ± 5	Loop
T123C	23 ± 2	51 ± 1	α-Helix
D137C	52 ± 8	92 ± 7	β-Turn
T192C	8 ± 0.9	86 ± 6	β-Sheet
R209C	26 ± 3	85 ± 2	α-Helix
T231C	52 ± 5	64 ± 5	β-Hairpin
I252C	100 ± 12	105 ± 9	Loop
T267C	14 ± 2	121 ± 7	Loop[c]

Note: Spin labeling performed after selective reduction with DTT.
[a]Determined by CW ESR spectroscopy against nitroxide standard solutions. The error in each sample was estimated from the standard deviation of triplicate measurements.
[b]Residual activity after reduction, spin labeling and purification. Activity was measured by the pH-stat method on a 16 mM emulsion of glyceryl tributanoate. The error in each sample was estimated from the standard deviation of triplicate measurements.
[c]Positioned next to a disulfide bridge.

Spin-labeled TLL variants

Eleven TLL single-cysteine mutants were specifically reduced and labeled with the nitroxide spin-label reagent MTSL (**C**, Scheme 1). The degree of spin-label insertion was estimated by continuous wave (CW) ESR spectroscopy against nitroxide standard solutions. The yield of spin-label insertion varied between 10–100% for the different mutants. Table 5 shows the degree of spin-label incorporation, the residual specific activity after the labeling, and the secondary structure at the mutation site. As seen in Table 5, there was no severe effect of the spin labeling on the activity of the lipases, and in some instances there was even a slight increase of activity (I252C, T267C), which may be ascribed to the reduction of covalent dimers.[2] The variations in spin-label incorporation was consistent with the relative steric accessibility of the cysteines (30, 31) but did not correspond with the variations in the residual specific activity. First derivative CW ESR spectra for the spin-labeled mutants are presented in Fig. 5, where the spectral amplitude has been normalized by the central resonance line. The variants are arranged according to low and high spin-label insertion (panels A and B, respectively), where the high spin-label insertion provided a better signal-to-noise ratio. All spectra are distinctive for moderately immobilized nitroxides with rotational correlation times (τ_R) of approximately 1 ns (2, 4), which is equivalent with rapid internal motion of the nitroxide side chain, caused by unrestricted bond rotation when attached to the protein surface. It can be seen in the

[2] In addition to being oxidized by linkage to a free cysteine, a small content of covalent dimers was seen for some TLL cysteine mutants on SDS-PAGE.

© 2002 NRC Canada

Fig. 5. First derivative CW ESR spectra retrieved in the X-band at 9.75 GHz of site-specific spin-labeled *Thermomyces lanuginosa* lipase cysteine variants, grouped according to low spin-label insertion (panel A) and high spin-label insertion (panel B). The resonance amplitudes were normalized with respect to the central $m_{I=0}$ resonance line. The scale of the magnetic field is indicated by a bar and the identity of the variants is specified in the figure.

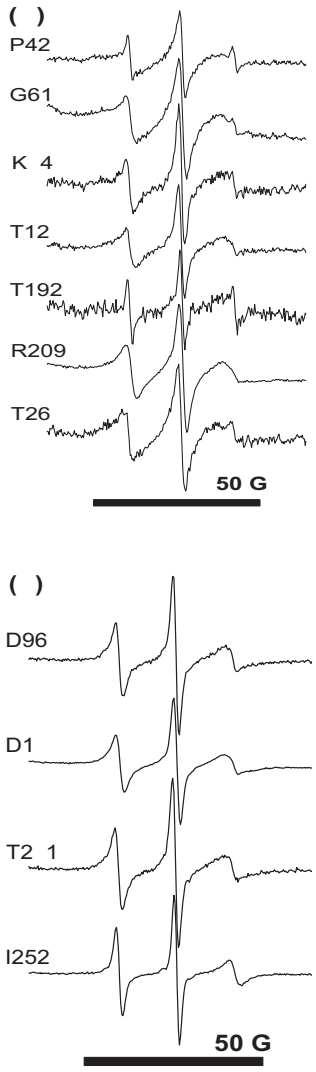

linewidth, however, that the spectra in panel A display more constrained nitroxide mobility, whereas the spectra in panel B reflect more rapid isotropic motion.[3] This is characteristic for spin-label side chains on the surface of α-helices or β-sheets (panel A), while the narrower line widths (panel B) are characteristic of spin-label side chains attached to highly flexible protein segments, such as hairpin loops (4). Altogether, this points toward a correlation between cysteine steric accessibility in the protein and the yield of spin-label insertion. In conclusion, the different lineshapes of the ESR spectra and the variable incorporation of spin label in each of the different TLL mutants were found to correlate well with the local structural features near the cysteine mutations.

Discussion

In the present study, 13 single-cysteine mutants of TLL were created that were fully functional and displayed specific hydrolytic activities comparable to that of the wild-type enzyme. This is consistent with previous work that has shown that single or multiple mutations on the surface of proteins do not perturb protein structure and function (3, 32, 33). Substitution of three tryptophans in the TLL variants G61C-singleW and R209C-singleW, however, caused a decrease in activity and resistance to thermal denaturation, in good agreement with previous studies on similar TLL mutants (27, 28).

It is recognized that cysteines introduced at surface-exposed parts of proteins are prone to oxidation, and furthermore, that for such proteins only a small fraction of unoxidized cysteines may exist (14, 15). Presumably, unwanted oxidation takes place during fermentation or purification (34, 35). When producing cysteine mutant proteins, it may be desirable to detect post-translational modifications of the cysteine at an early stage. Early detection could enable changes in fermentation conditions to be made, such as employing expression systems with reducing conditions (bacterial periplasmatic expression) or modulating the pH. Alternatively, one might choose to use the small fraction of free cysteines in the batch, if present in acceptable amounts. In the present paper, a dot-blot method for the quantitation of free protein-sulfhydryl groups was developed. This method has a picomole detection limit and should, therefore, be convenient to use as a diagnostic tool in the production of recombinant proteins. The method could present an alternative to using Ellman's reagent, which, although useful, requires substantial amounts of protein (1–3 mL, approximately 10 μM), where the detection limit is set by the extinction coefficient of the produced thiolate anion. The method could also be useful with glycosylated proteins, for which the oxidation state of the sulfhydryl groups is complex to detect and quantify by mass spectrometry due to the glycosylation patterns. The dot-blot method was found to be sensitive and accurate in protein sulfhydryl determination.

All TLL cysteine mutants created were found to be oxidized to a major extent. Through a careful optimization of the reduction conditions, however, it was shown that the oxidized surface cysteine could be selectively reduced, in varying degrees for the different mutants, without damaging any of the native disulfide bridges. It is unambiguous that creating cysteine mutants is more suitable with a protein that contains no disulfide bridges; however, this would severely limit the scope of proteins that can be studied.

Several of the selectively reduced TLL variants were labeled with a fluorescent probe (dansyl) or a spin label (a nitroxide). It was verified by SDS-PAGE and Western blot that the dansyl group was covalently attached to the protein via a disulfide bridge. In addition, it was shown that the reduction and labeling had little or no effect on the activity of the lipases. By means of the selective reduction, the spin labeling afforded insertion between 10–100%. The quantitative yield achieved for I252C suggests that the reduction conditions were optimized. Furthermore, the correlation found

[3] It should be noted that only qualitative information in the ESR spectra was used to draw conclusions on protein structure. A more detailed analysis of the lineshapes by simulation was not attempted in the present paper.

© 2002 NRC Canada

between spin-label insertion and ESR spectral linewidths suggested a dependency on cysteine steric availability for the yield of labeling, which has previously been seen (30, 31).

In conclusion, the development of a novel dot-blot method enabled the detection and quantitation of oxidized sulfhydryl groups in lipase cysteine mutants, with a high sensitivity. A process for selective reduction of the oxidized surface cysteine enabled the production of specifically labeled and functional proteins. The methods presented in this paper should prove useful in the production and modification of other related cysteine-mutant proteins.

Experimental

General

Unless stated otherwise, all chemical reagents (DTT, Ellman's reagent, BCIP–NBT, anti-rabbit goat IgG alkaline phosphatase conjugate, biotinylated BSA), organic solvents, and buffers were purchased from Sigma–Aldrich Sweden AB (Stockholm, Sweden). PD-10 desalting columns were purchased from Amersham Pharmacia Biotech (Uppsala, Sweden). Streptavidin-AP was purchased from Roche Diagnostics Scandinavia AB (Bromma, Sweden). The ReduceImm™ column and Slide-A-Lyzer® dialysis cassettes (10 kDa molecular weight cut-off) were purchased from Pierce (Boule Nordic AB, Stockholm, Sweden). MTSL, MTSEA–biotin, and MTS–dansyl were purchased from Toronto Research Chemicals Inc. (Ontario, Canada), and anti-dansyl rabbit IgG from Molecular Probes Europe BV (Leiden, The Netherlands).

Construction, fermentation, and purification of TLL lipase variants

All *Thermomyces lanuginosa* lipase variants were constructed by the USE method according to the manufacturer (Stratagene). The template was pAHL (WO lipase patent number EP 305.216), and the selection oligos were P-GAATGACTTGGTTGACGCGTCACCAGTCAC (changing the ScaI site into the MluI site in the Amp gene) and P-TCTAGCCCAGAATACTGGATCAAATC (changing the ScaI site in the lipase gene without changing the amino acids). The variants were sequenced across the whole gene, transformed into *Aspergillus oryzae* and fermented as reported previously (36). The fermentation supernatant was sterile-filtered using 0.22 μm EKS filters (Seitz-Schenk, Waldstetten, Germany), solid NaCl was added to a final concentration of 1 M, and the supernatant was filtered again using 0.45 μm Millipore filters (Millipore, Molsheim, France). The succeeding chromatographic steps were carried out using an ÄKTA explorer (Amersham Pharmacia Biotech). Hydrophobic interaction chromatography was performed using Decyl Agarose 6XL (Affinity Chromatography Ltd, Freeport, Isle of Man) packed in a XK50 column (Amersham Pharmacia Biotech). The column was equilibrated with a buffer consisting of 50 mM Tris-acetate and 1 M NaCl at pH 7.0, after which the supernatant was applied. Elution was made with ultrapure water (resistivity, $\rho \geq 18.2$ MΩ cm^{-1}). Fractions with high absorbance at 280 nm were pooled and assayed for lipase activity using the pH-stat method (described below). Pools displaying activity were diluted with ultrapure water to a final conductivity of <4 mSi and the pH was adjusted to 7.5. Anion-exchange chromatography was performed with Fast Flow Q-Sepharose (Amersham Pharmacia Biotech) packed in an XK50 column and equilibrated with 50 mM Tris-acetate, pH 7.5. The pools containing activity were applied on the column and eluted with a linear salt gradient using the 1 M NaCl Tris-buffer.

Characterization of TLL lipase variants

The purity of the produced TLL proteins was verified by SDS–PAGE. The protein concentration was determined from the absorbance at 280 nm using an extinction coefficient of 35 920 cm^{-1} M^{-1} (18 850 cm^{-1} M^{-1} for the tryptophan mutants) based on amino acid composition (37). The specific hydrolytic activity was measured by the pH-stat method on an emulsion of glyceryl tributanoate (a modification of the method described in ref. 16), where one lipase unit is defined as one μmol of released titratable acid per min. The assay was performed at pH 7.0 and 25°C on a sonicated (Branson Sonifier W-250; 10 W min^{-1} for 30 mL substrate) 16 mM emulsion of glyceryl tributanoate (0.5% w/v) in a 2% aqueous solution of gum arabicum and 0.2 M $CaCl_2$. Typically, 10 μL of enzyme (1 μM) was added to 1.5 mL stirred emulsion and the activity was monitored using an ABU91 Autoburette together with a TIM900 Titralab station and software TimTalk 9, v1.4 (Radiometer, Copenhagen, Denmark). The tryptophan–cysteine variants and wild-type enzyme were analyzed by differential scanning calorimetry (DSC) using a MicroCal (Tm) VP microcalorimeter (MicroCal, Northampton, MA, U.S.A.), using 1.3 mg mL^{-1} TLL in 50 mM HEPES–NaOH, pH 7.0. The scan rate was 90°C h^{-1}.

The dot-blot method

The TLL cysteine mutants (200 μL, 1.5–3 mg mL^{-1} in 100 mM Tris-HCl, pH 8.5) were incubated with MTSEA–biotin (**A**, Scheme 1, 25–50 μL, 5.5 mM in DMF) in Eppendorf tubes and rotated slowly end-over-end for 1 h. The reaction mixture was purified by dialysis against 20 mM HEPES–NaOH, pH 7.0 (three buffer exchanges) at 4°C. A nitrocellulose membrane (0.45 μm, Bio-Rad Laboratories AB, Sundbyberg, Sweden) was pre-wet in Tris-buffered saline (TBS; 20 mM Tris-HCl, 150 mM NaCl, pH 8.0) for 10 min and fitted onto a Bio-Dot® Microfiltration Apparatus (Bio-Rad) according to the manufacturer's instructions. A dilution series of biotinylated bovine serum albumin (BSA, approximately 9 mol of biotin per mol BSA) was prepared in TBS ranging from 0.04 to 73 μM biotin. All samples (standards, controls, or biotinylated TLL variants) were diluted (1:100) in TBS. The samples were loaded in the applicator, 100 μL per well, and applied to the membrane by gravitation (vacuum not used), after which the wells were washed several times with TBS. The membrane was dried, then treated with the blotting procedure, performed with gentle rocking at 30°C as follows: Blocking of membrane in a 2% solution of nonfat milk powder in TBS for 30 min, washing with 0.1% Tween 20 in TBS (3 × 5 min), incubation with the streptavidin–AP conjugate (diluted 1:20 000 in TBS–Tween) for 90 min, washing again, and lastly, development with BCIP–NBT (5-bromo-4-chloro-3-indolyl phosphate and nitro blue tetrazolium) prepared according to the

© 2002 NRC Canada

manufacturer (Sigma). The membrane was dried and scanned. The intensities of the dots were quantified against the standards by densiometric analysis, using the public domain NIH Image software (developed at the U.S. National Institutes of Health and available on the Internet at http://rsb.info.nih.gov/nih-image/). It should be mentioned that application by manual auto pipet was also performed with the dot-blot method (3 μL undiluted protein applied per dot), which afforded similar results in quantifying the biotinylated TLL variants (data not shown).

Selective reduction of oxidized TLL cysteine mutants

In the first optimization, reduction was performed for 60 min on the TLL wild-type enzyme (1.5–2 mg mL^{-1} in 100 mM Tris-NaOH, pH 8.5) by adding DTT from freshly prepared stocks (in the same buffer) of appropriate concentrations (250 μL stock solution added to 2.5 mL protein) to the gently stirred protein in a round bottom flask. The following final DTT concentrations were employed: 0.1, 0.5, 1, 10, 25, and 50 mM. The reaction was terminated by gel filtration on a PD-10 desalting column equilibrated with deoxygenated Tris buffer, and the proteins were further purified by dialysis against the same buffer (three buffer exchanges) under an atmosphere of nitrogen. Reduction with the Reduce-Imm™ column was performed with 10 mM DTT at pH 8.0 in a 20 mM sodium phosphate buffer containing 2 mM EDTA, according to the protocol (Pierce). Wild-type enzyme (1 mL, 5.6 mg mL^{-1}) was incubated on the column for 60 min after which ten 1-mL fractions were collected and analyzed without further purification. The reduced and purified (or eluted) proteins were assayed with Ellman's reagent (10 mM DTNB freshly prepared in the phosphate buffer) by adding 100 μL reagent to 1 mL protein solution (10 μM) and measuring the absorption at 412 nm using a Cary 50 Bio UV-vis spectrophotometer (Varian AB, Solna, Sweden) for 15–30 min. The concentration of free sulfhydryl groups was determined using an extinction coefficient of 14 150 cm^{-1} M^{-1} (at pH 8.0).

The second optimization of reduction conditions was performed on the wild-type enzyme and the variant G61C in parallel (1.0 mg protein per mL). DTT was added from a freshly prepared stock either to the protein solution (as described in the previous paragraph) or to the dialysis buffer, against which the protein was dialyzed. The reduction was performed either at pH 8.5 (in 100 mM Tris-NaOH), at pH 7.0 (in 20 mM HEPES–NaOH or 20 mM sodium acetate), or at pH 7.7 (in 50 mM Tris-acetate and 2 mM EDTA) for 30–100 min. The protein was purified by dialysis against Tris buffer, with or without an atmosphere of nitrogen.

Site-directed labeling of TLL variants with spectroscopic probes

Chemical labeling with the fluorescent probe MTS–dansyl and the nitroxide spin-label MTSL (**B** and **C**, Scheme 1, respectively) was performed with or without prior reduction of the TLL single-cysteine mutants. TLL wild-type or the mutant singleW were used as controls in all reactions. The labeling reagent was added to the protein (1–3 mg mL^{-1} in 100 mM Tris-NaOH, pH 8.5, or 50 mM Tris-acetate, 2 mM EDTA, pH 7.7); 45 or 15 molar equivalents, from a freshly prepared stock in ethanol or acetonitrile (for MTSL and MTS–dansyl, respectively). The final content of organic solvent in the sample was 1.5% (v/v). MTSL remained totally soluble under these conditions, while MTS–dansyl had the tendency to partially precipitate and was, therefore, spun down after the reaction. After 1 h the reaction mixture was subjected to gel filtration on a PD-10 column preequilibrated with 20 mM HEPES–NaOH, pH 7.0 and was further purified by extensive dialysis against the same buffer at 4°C. The entire reaction with MTS–dansyl was performed with minimal exposure to light.

The dansyl-labeled variants (1 μg per band, each sample prepared in reducing (containing 50 mM DTT) and nonreducing Novex LDS loading buffers) were analyzed by SDS-PAGE, using a Novex NuPAGE™ precast 4–12% Bis Tris gel (1.0 mm × 10 well) and a Novex MES running buffer, performed in a Novex XCell II™ Mini-Cell electrophoresis equipment (Labora Chemicon, Sollentuna, Sweden). Low-range prestained SDS-PAGE molecular-weight standards (Bio-Rad) were used. After separation at 200 V and 35 min, the gels were analyzed for fluorescence on a Gel Doc 2000 gel documentation system, illuminated with UV light at 302 nm and employing the Quantity One imaging software (Bio-Rad). The gels were then Coomassie stained (50% (v/v) methanol, 10% (v/v) acetic acid, and 0.1% (w/v) Coomassie Brilliant Blue R-250 in ultrapure water) or subjected to a Western blot. The proteins were transferred with a Trans-Blot SD semidry transfer cell (Bio-Rad) at 15 V for 15 min onto a nitrocellulose membrane (0.45 μM, Bio-Rad), using a Towbin transfer buffer (25 mM Tris, 19.2 mM glycine, 20% (v/v) methanol, pH 8.3). The immunoblot was performed at 30°C as follows: Blocking of the membrane with a 5% (w/v) solution of nonfat milk powder in TBS for 30 min, incubation with anti-dansyl rabbit IgG (12.5 μg mL^{-1} in TBS containing 5% milk, 0.1% (w/v) Tween 20, and 33 μg TLL wild type) for 90 min, washing of the membrane with 0.1% Tween 20 in TBS (3 × 5 min), incubation with anti-rabbit goat IgG-AP conjugate (diluted 1:20 000 in TBS containing 5% milk, 0.1% Tween 20 and 7 μg TLL wild type) for 90 min, washing (4 × 5 min), and development with BCIP–NBT.

Fluorescence spectroscopy

Fluorescence spectra were recorded on a PerkinElmer LS50B spectrofluorimeter at room temperature, using slit widths of 10 nm and a scan range of 500 nm min^{-1}. The tryptophan emission spectra were recorded with the excitation set at 280 nm, and the dansyl emission spectra were recorded with the excitation set at 340 nm. Protein concentrations were 1–20 μM (in 20 mM HEPES–NaOH, pH 7.0). The yield of dansyl incorporation for the TLL variants was quantified against dansyl standards in acetonitrile, and normalization by protein concentration. A Bradford assay (Pierce) was used for reconfirmation of the protein concentration of the dansyl-labeled variants.

ESR spectroscopy

The ESR spectra were recorded on a Bruker EMX EPR spectrometer with a 12 kW 10″ magnet in the X-band at 9.75 GHz, using a Bruker ER 4102 ST standard cavity and a microwave power up to 10 mW. The spectra were recorded at room temperature using 1 G, 100 kHz magnetic field

© 2002 NRC Canada

modulation for phase-sensitive detection, which ensures a well-defined signal. The line broadening due to overmodulation is less than 10% (38). All measurements were performed under critical coupling conditions and the spectra were recorded several times for improvement of signal-to-noise ratio. Quartz tubes (i.d. = 1 mm) were used and the sample size was 50 μL. The spin-label incorporation for the enzymes (15 μM in 20 mM HEPES–NaOH, pH 7.0) was determined by quantitation against nitroxide standard solutions and normalization by protein concentration.

Acknowledgments

This work was supported by the European Commission (contract number BIO4-CT972365). We thank Dr. Pernille Høyrup for helping us with the ESR measurements. Dr. Harry Brumer III is thanked for help in preparing the molecular graphics figure of *Thermomyces lanuginosa* lipase.

References

1. I.D. Campbell and R.A. Dwek. Biological spectroscopy. Benjamin/Cummings, Menlo Park, CA. 1984.
2. W.L. Hubbell, D.S. Cafiso, and C. Altenbach. Nat. Struct. Biol. **7**, 735 (2000).
3. C. Altenbach, T. Marti, H.G. Khorana, and W.L. Hubbell. Science (Washington, D.C.), **248**, 1088 (1990).
4. H.J. Merianos, N. Cadieux, C.H. Lin, R.J. Kadner, and D.S. Cafiso. Nat. Struct. Biol. **7**, 205 (2000).
5. O. Kensch, T. Restle, B.M. Wohrl, R.S. Goody, and H.J. Steinhoff. J. Mol. Biol. **301**, 1029 (2000).
6. Y. Lin, R. Nielsen, D. Murray, W.L. Hubbell, C. Mailer, B.H. Robinson, and M.H. Gelb. Science (Washington, D.C.), **279**, 1925 (1998).
7. A. Kostrzewa, T. Pali, W. Froncisz, and D. Marsh. Biochemistry, **39**, 6066 (2000).
8. G. DeSantis and J.B. Jones. Curr. Opin. Biotechnol. **10**, 324 (1999).
9. P. Berglund, G. DeSantis, M.R. Stabile, X. Shang, M. Gold, R.R. Bott, T.P. Graycar, T.H. Lau, C. Mitchinson, and J.B. Jones. J. Am. Chem. Soc. **119**, 5265 (1997).
10. J. Brocklehurst. Int. J. Biochem. **10**, 259 (1979).
11. R. Wynn and F.M. Richards. Methods Enzymol. **251**, 351 (1995).
12. G.L. Kenyon and T.W. Bruice. Methods Enzymol. **47**, 407 (1977).
13. T.W. Bruice and G.L. Kenyon. J. Protein Chem. **1**, 47 (1982).
14. W.W. Cleland. Biochemistry, **3**, 480 (1964).
15. T.W. Keough, Y. Sun, B.L. Barnett, M.P. Lacey, M.D. Bauer, E.S. Wang, and C.R. Erwin. *In* Methods in molecular biology. Vol. 61. *Edited by* J.R. Chapman. Humana Press, New Jersey. 1996. pp. 171–183.
16. A. Svendsen, I.G. Clausen, S.A. Patkar, K. Borch, and M. Thellersen. Methods Enzymol. **284**, 317 (1997).
17. L. Sarda and P. Desnuelle. Biochim. Biophys. Acta, **30**, 513 (1958).
18. M. Holmquist, M. Martinelle, I.G. Clausen, S. Patkar, A. Svendsen, and K. Hult. Lipids, **29**, 599 (1994).
19. D.M. Lawson, A.M. Brzozowski, S. Rety, C. Verma, and G.G. Dodson. Protein Eng. **7**, 543 (1994).
20. A.M. Brzozowski, H. Savage, C.S. Verma, J.P. Turkenburg, D.M. Lawson, A. Svendsen, and S. Patkar. Biochemistry, **39**, 15071 (2000).
21. Y. Cajal, A. Svendsen, V. Girona, S.A. Patkar, and M.A. Alsina. Biochemistry, **39**, 413 (2000).
22. A. Jutila, K. Zhu, S.A. Patkar, J. Vind, A. Svendsen, and P.K.J. Kinnunen. Biophys. J. **78**, 1634 (2000).
23. K. Zhu, A. Jutila, E.K.J. Tuominen, and P.K.J. Kinnunen. Protein Sci. **10**, 339 (2001).
24. A. Tiss, F. Carriere, and R. Verger. Anal. Biochem. **294**, 36 (2001).
25. D.M. Lawson, A.M. Brzozowski, S. Rety, C. Verma, and G.G. Dodson. Protein Eng. **7**, 543 (1994).
26. G.L. Ellman. Arch. Biochem. Biophys. **82**, 70 (1959).
27. K. Zhu, A. Jutila, and P.K.J. Kinnunen. Protein Sci. **9**, 598 (2000).
28. K. Zhu, A. Jutila, E.K.J. Tuominen, S.A. Patkar, A. Svendsen, and P.K.J. Kinnunen. Biochim. Biophys. Acta, **1547**, 329 (2001).
29. R.P. Haugland. Handbook of fluorescent probes and research chemicals. 6th ed. Molecular Probes, Eugene, OR. 1996.
30. J.J. Falke, A.F. Dernburg, D.A. Sternberg, N. Zalkin, D.L. Milligan, and D.E. Koshland. J. Biol. Chem. **263**, 14850 (1988).
31. A.P. Todd, J.P. Cong, F. Levinthal, C. Levinthal, and W.L. Hubbell. Proteins: Struct. Funct. Genet. **6**, 294 (1989).
32. B.W. Matthews. *In* Advances in protein chemistry. Vol. 46. Academic Press, San Diego. 1995. pp. 249–278.
33. C. Altenbach, K. Yang, D.L. Farrens, Z.T. Farahbakhsh, H.G. Khorana, and W.L. Hubbell. Biochemistry, **35**, 12470 (1996).
34. R.G. Briggs and J.A. Fee. Biochim. Biophys. Acta, **537**, 100 (1978).
35. M.W. Pantoliano, M. Whitlow, J.F. Wood, S.W. Dodd, K.D. Hardman, M.L. Rollence, and P.N. Bryan. Biochemistry, **28**, 7205 (1989).
36. T. Christensen, H. Woeldike, E. Boel, S.B. Mortensen, K. Hjortshoej, L. Thim, and M.T. Hansen. Bio/Technology, **6**, 1419 (1988).
37. C.N. Pace, F. Vajdos, L. Fee, G. Grimsley, and T. Gray. Protein Sci. **4**, 2411 (1995).
38. C.P. Poole. Electron spin resonance: A comprehensive treatise on experimental technique. Interscience Publishers, New York. 1967.
39. W. Humphrey, A. Dalke, and K. Schulten. J. Molec. Graphics, **14.1**, 33 (1996).

© 2002 NRC Canada

Chemo-enzymatic synthesis of trimeric sialyl Lewis^x pentadecasaccharide

Yeuk Chuen Liu, Hong Li, Albin Otter, Vivekanand P. Kamath, Markus B. Streiff, and Monica M. Palcic

Abstract: The enzymatic synthesis of trimeric sialyl Lewis^x pentadecasaccharide (**6**), a 15-mer, from a trimannoside precursor required six different glycosyltransferase enzymes and four nucleotide donor sugars. Three *N*-acetylglucosaminyl residues were transferred from UDP-*N*-acetylglucosamine to a trimannoside by *N*-acetylglucosaminyltransferases I, II, and V, respectively. Galactosylation using β(1→4) galactosyltransferase and UDP-galactose gave three *N*-acetyllactosamine units in nonasaccharide **4**. Sialylation of **4** with α(2→3) sialyltransferase and CMP-*N*-acetylneuraminic acid was followed by fucosylation with α(1→3) fucosyltransferase and GDP-fucose giving the 15-mer **6** in mg quantities. Compound **4** was also converted to a trimeric Lewis^x dodecasaccharide 12-mer with α(1→3) fucosyltransferase and GDP-fucose and to a trimeric α-2,6-sialyl *N*-acetyllactosamine dodecasaccharide 12-mer with α(2→6) sialyltransferase and CMP-*N*-acetylneuraminic acid.

Key words: glycosyltransferases, pentadecasaccharide, sialyl Lewis^x.

Résumé : La synthèse enzymatique du pentadécasaccharide trimère sialyl Lewis^x (**6**), un 15-mère, a été réalisée à partir d'un trimannoside en utilisant six glycosyltransférases différentes et quatre nucléotides comme donneurs de sucre. Trois résidus *N*-acétylglucosaminyles ont été transférés de la UDP-*N*-acétylglucosamine à un trimannoside par les *N*-acétylglucosaminyltransférases I, II et V respectivement. La galactosylation utilisant une β(1→4) galactotransférase et du UDP-galactose ont conduit à trois unités de *N*-acétyllactosamine dans le nonasaccharide **4**. Le sialylation de **4** à l'aide de la α(2→3) sialyltransférase et d'acide CMP-*N*-acétylneuraminique a été suivie d'une fucosylation à l'aide de la α(1→3) fucosyltransférase et de GDP-fucose conduisant à quelques milligrammes du 15-mère **6**. Le composé **4** a aussi été transformé en dodécasaccharide trimère 12-mère de Lewis^x à l'aide de la α(1→3) fucosyltransférase et de GDP-fucose et en un α-2,6-sialyl *N*-acétylactosamine dodécasaccharide trimère 12-mère à l'aide de α(2→6) sialyltransférase et d'acide CMP-*N*-acétylneuraminique.

Mots clés : galactotransférase, pentadécasaccharide, sialyl Lewis^x.

[Traduit par la Rédaction]

Introduction

Interest in the preparation of oligosaccharides and their analogs stems from demonstrations of their roles in diverse biological recognition events (1). Cell-surface oligosaccharides are attachment sites for the binding of bacteria, viruses, toxins, and hormones and they also are involved in cell–cell adhesion. Characteristic changes in complex carbohydrates also occur during cellular differentiation, development, and malignant transformation. Oligosaccharides are required not only for basic glycobiology research but also for developing leads to new therapeutics for the treatment of infectious diseases, inflammation, and cancer (2).

The chemical synthesis of oligosaccharides is well established. It is, however, a multistep endeavor requiring the preparation of selectively protected building blocks, their coupling and then deprotection to obtain the desired stereochemistry and regiochemistry in the final product (3). Biocatalytic approaches for oligosaccharide production are increasingly being used employing engineered cells or isolated enzymes, either glycosyltransferases or glycosidases (4). Glycosyltransferases catalyze the transfer of a monosaccharide from a donor (usually a nucleotide donor) to saccharide, protein, or lipid acceptors (5). These transfers are regiospecific and stereospecific thus eliminating the need for the protection and deprotection steps required in chemical synthesis.

The tetrasaccharide sialyl Lewis^x (α-Neu5Ac(2→3)β-Gal(1→4)[α-Fuc(1→3)]β-GlcNAc-) is an example of a biologically important oligosaccharide. It is found on the termini of glycoproteins where it binds to selectins, a class of calcium-dependent carbohydrate-binding proteins (6).

Received 29 January 2002. Published on the NRC Research Press Web site at http://canjchem.nrc.ca on 7 May 2002.

This paper is dedicated to J. Bryan Jones on the occasion of his 65th birthday in recognition of his contributions to biocatalysis.

Y.C. Liu, H. Li, A. Otter, V.P. Kamath, and M.M. Palcic.[1] Department of Chemistry, University of Alberta, Edmonton, AB T6G 2G2, Canada.
M.B. Streiff. Novartis Pharma, CH-4002 Basel Switzerland.

[1]Corresponding author (e-mail: monica.palcic@ualberta.ca).

 DOI: 10.1139/V02-073 © 2002 NRC Canada

Scheme 1.

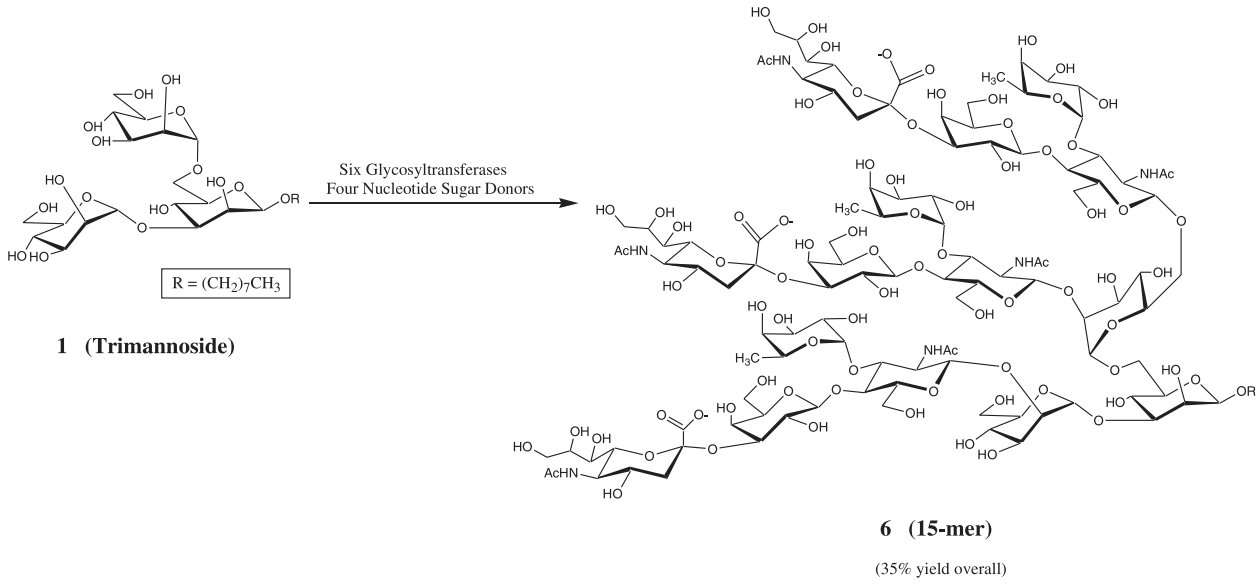

Scheme 2.

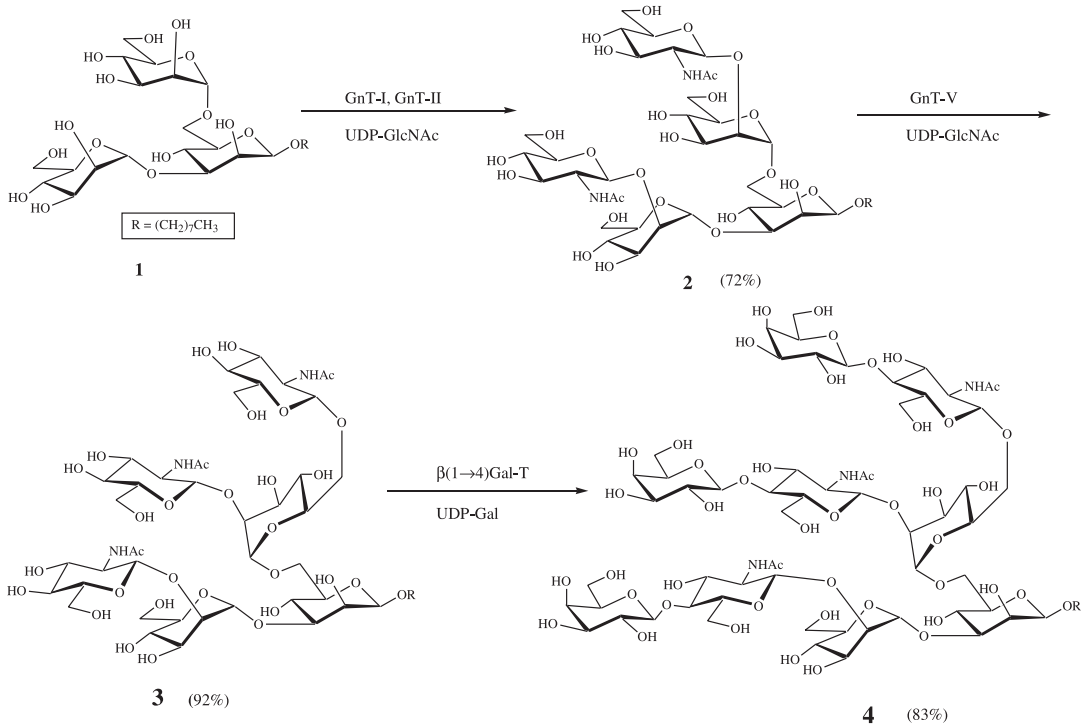

Selectins are found on vascular cell surfaces where they mediate leukocyte capture to endothelial cells, an early step in the inflammatory response. The use of sialyl Lewis^x to inhibit the interaction of E-selectin with it's physiological ligand represents a potential treatment for inflammatory disorders. Monovalent carbohydrate–protein interactions are, however, usually weak interactions with dissociation constants typically in the mM range. High affinity binding has been achieved by multivalent presentation of carbohydrate ligands including sialyl Lewis^x (6, 7). In this paper we report the chemo-enzymatic synthesis of a multivalent (trimeric) sialyl Lewis^x containing pentadecasaccharide (**6**) (Scheme 1) for use in probing selectins and other carbohydrate-binding proteins. This is a natural multivalent sequence found on asparagine-linked oligosaccharides in glycoproteins.

Results and discussion

The enzymatic synthesis of trimeric sialyl Le^x **6** from trimannoside **1** required six glycosyltransferase enzymes and four different nucleotide donor sugars (Schemes 2 and 3). Trimannoside **1** is easily prepared by chemical synthesis (8) and is the conserved core present on all *N*-linked oligosaccharides. In the natural structures, a chitobiose unit is present rather than the octyl group. The hydrophobic octyl moiety facilitates the isolation of reaction products by solid-phase

© 2002 NRC Canada

Scheme 3.

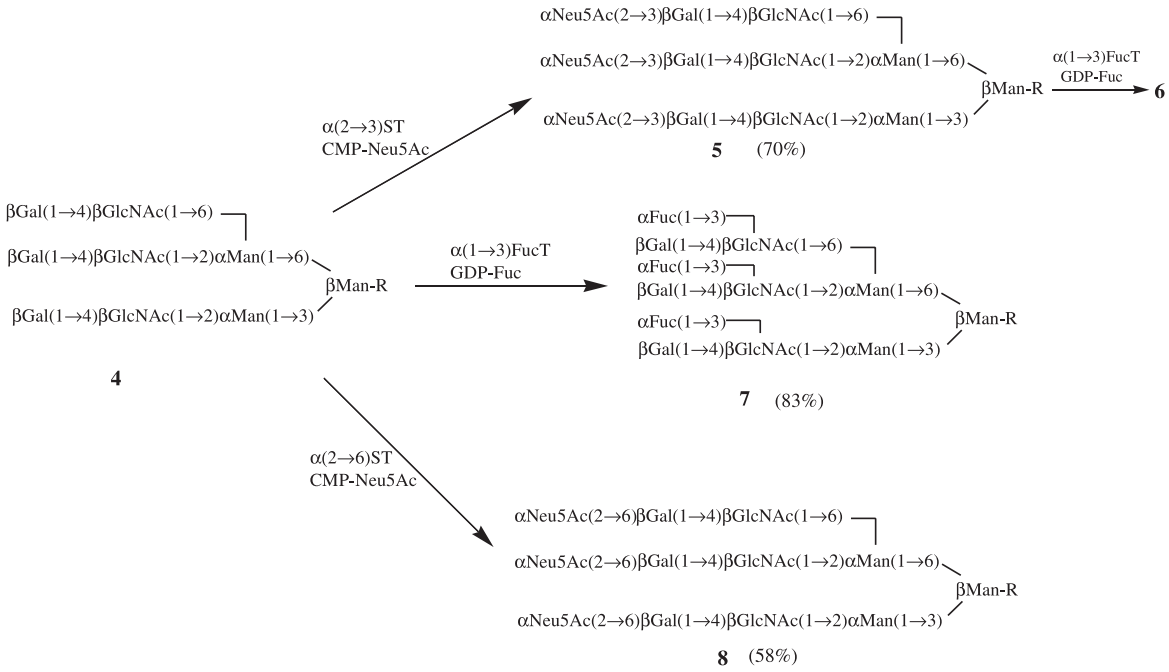

extraction on reverse-phase cartridges as well the monitoring of reaction progress by MALDI mass spectrometry (9).

Each of the *N*-acetylglucosamine residues is transferred from UDP-GlcNAc to a specific mannose by a different *N*-acetylglucosaminyltransferase enzyme. *N*-acetylglucosaminyltransferase I (GnT-1) first transfers GlcNAc to the α-1,3-Man branch, which is followed by *N*-acetylglucosaminyltransferase II (GnT-II) transfer to the α-1,6-Man arm (Scheme 2). While the isolated yield of the GnT-I and GnT-II product **2** was 70%, this yield is variable and will depend on the purity of the original trimannoside (8). Although the chemical synthesis of the trimannoside is straightforward, a mixture of trimannosides is produced, only one of which is a substrate for GnT-I enzyme. The conversion of the trimannoside **1** to pentasaccharide **2** was likely quantitative since unreacted starting material was not a substrate for either GnT-1 or GnT-II when re-assayed with these enzymes. Compound **3** was obtained in good yield after the *N*-acetylglucosaminyltransferase V (GnT-V) reaction.

Unlike the strict branch specificity of the *N*-acetylglucosaminyltransferases, galactosylation using β(1→4) galactosyltransferase (Gal-T) and UDP-Gal will give all three *N*-acetyllactosamine residues in nonasaccharide **4**. This is a key compound, because it can be employed not only for probing galactose and *N*-acetyllactosamine binding proteins such as galectins (10), but it can also be further elaborated to trimeric sialosides and fucosides.

Sialylation of **4** with recombinant rat liver α(2→3) sialyltransferase (ST) and CMP-Neu5Ac was followed by fucosylation with milk α(1→3) fucosyltransferase (Fuc-T) and GDP-Fuc giving mg quantities of the trimeric sialyl Lewis^x **6** (Scheme 3). Compound **6** was obtained in 35% yield after the six enzyme reactions starting from trimannoside **1**. The ^{1}H NMR spectrum of the final product is shown in Fig. 1, where the characteristic resonances for fucose (δ 1.17 and 4.83, methyl and H-5, respectively) and sialic acid (δ 1.80 and 2.77, for H-3$_{ax}$ and H-3$_{eq}$, respectively) are clearly seen. No peaks corresponding to partially glycosylated intermediates were observed in any of the electrospray mass spectra. This indicated essentially complete glycosylation as verified by the integration in the ^{1}H NMR spectra. Assignments for anomeric protons given in the experimental section are in agreement with literature values. Mammalian biosynthesis requires that sialylation precede fucosylation since **7**, the product of the fucosyltransferase reaction, is not a substrate for rat sialyltransferase. In addition to α-2,3-sialylLacNAc, compound **4** was also converted to Lewis^x **7** and to α-2,6-sialyl *N*-acetyllactosamine **8** (Scheme 3). These were produced on mg scale, which is sufficient material for use in glycobiology applications to inhibit sialosides on cellular receptors for influenza and other viruses (11).

In summary, the trimeric sialyl Lewis^x containing 15-mer **6** and its precursors were conveniently obtained in highly purified form because the glycosyltransferases employed are regiospecific and stereospecific. The hydrophobic octyl aglycon facilitated the purification processes by solid-phase extraction using reverse-phase cartridges. Since glycosyltransferase enzymes are becoming increasingly commercially available and more are being cloned and overexpressed, multistep syntheses such as those described here could easily be scaled up to the gram scale.

Experimental

General

Trimannoside **1** was chemically synthesized as previously reported (8). Uridine 5′-diphosphate-*N*-acetylglucosamine (UDP-GlcNAc, disodium salt) and cytidine 5′-monophosphate-*N*-acetylneuraminic acid (CMP-Neu5Ac, sodium salt) were from the Sigma Chemical Co. Sequencing-grade calf intestine alkaline phosphatase and UDP-galactose (UDP-Gal,

© 2002 NRC Canada

Fig. 1. The ^{1}H NMR spectrum (500 MHz, deuterium oxide) of sialyl Lewis^x 15-mer **6**.

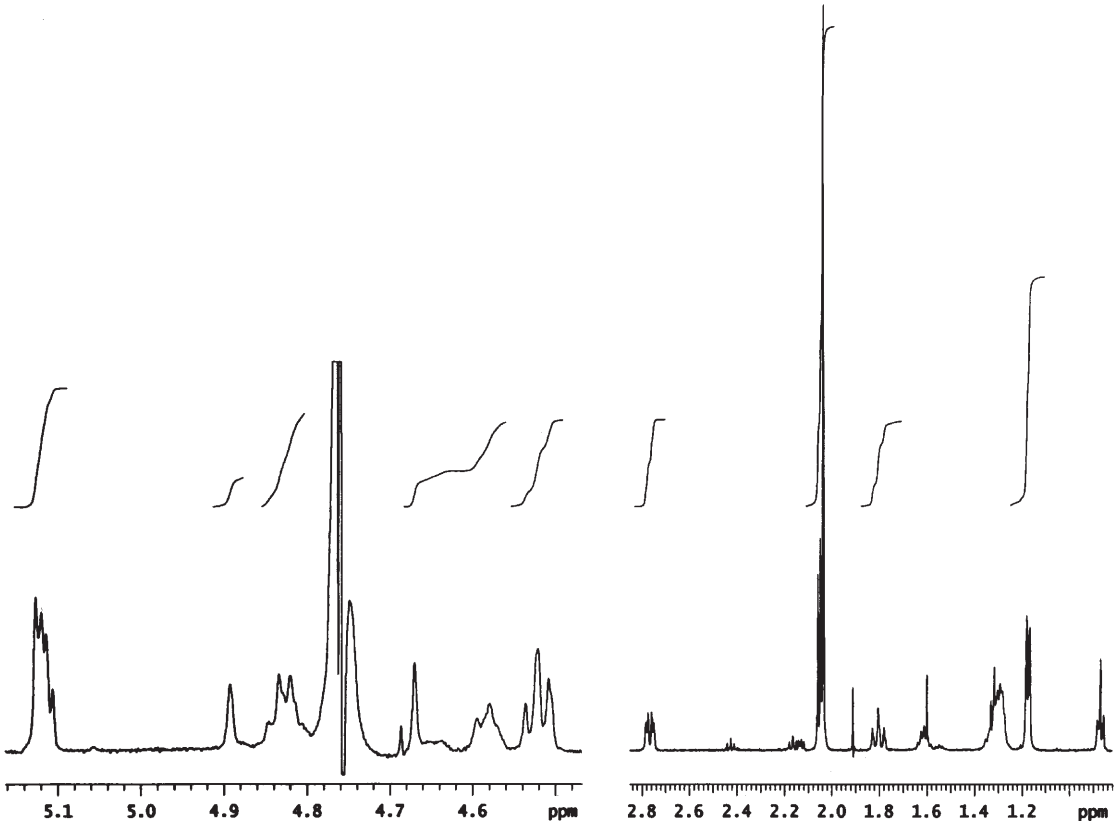

dipotassium salt) were obtained from Boehringer-Mannheim, and guanosine 5′-diphosphate-fucose (GDP-Fuc, disodium salt) was from Calbiochem. A mixture of *N*-acetylglucosaminyltransferase I and II (GnT-I and GnT-II) was isolated from rabbit liver acetone powder (Sigma) by modification of literature procedures (12). Briefly, a 1% Triton X-100 extract of 150 g of the acetone powder was applied to a UDP-hexanolamine affinity column equilibrated with 50 mM sodium cacodylate buffer, pH 6.5, containing 10 mM $MnCl_2$ and 1% of Triton X-100. The column was washed with equilibration buffer until the column eluant contained background levels of protein. GnT-I and GnT-II were both eluted from the column with equilibration buffer containing 3 M NaCl. The following enzymes were isolated and assayed by previously reported methods: recombinant human *N*-acetylglucosaminyltransferase V (GnT-V) (13), bovine milk $\beta(1\rightarrow4)$ galactosyltransferase (9), recombinant rat liver $\alpha(2\rightarrow3)$ sialyltransferase (9, 14), rat liver $\alpha(2\rightarrow6)$ sialyltransferase (15), and human milk $\alpha(1\rightarrow3)$ fucosyltransferase (9, 14). A unit of enzyme activity is the amount that catalyzes the formation of 1 μmol of product per min. Millex GV filters (0.22 μm) and Sep-Pak Plus C_{18} cartridges were from Millipore. The cartridges were preconditioned immediately before use by washing with 20 mL HPLC-grade methanol and then 20 mL of Milli-Q water. Centriprep concentrators were obtained from Amicon. TLC was performed on silica gel 60-F254 (Merck, Darmstadt) with detection by charring with 5% phenol–H_2SO_4. Iatrobead, a beaded silica gel 6RS-8060 was obtained from Iatron Laboratories Tokyo. ^{1}H NMR spectra were recorded in D_2O with a Varian Unity 500 spectrometer at 500 MHz. Only partial NMR data are reported, the remaining data were in accordance with the proposed structures. Chemical shifts in ppm are relative to external acetone at 2.225 ppm. Due to the complex nature of the molecules, spectral overlap is common and therefore ranges for chemical shifts are given where appropriate. The fast atom bombardment mass spectra (FAB-MS) were recorded on a modified Kratos AEI MS-9 instrument using Cleland's matrix and electrospray (ESI-MS) on a Micromass ZabSpec hybrid Sector-TOF. A Kratos Kompact MALDI I was used to monitor enzyme reaction progress (9).

Synthesis of pentasaccharide 2

A mixture (30 mL) containing trimannoside **1** (50 mg, 81 μmol), UDP-GlcNAc (100 mg, 150 μmol), 27 mU GnT-I, 16 mU GnT-II, alkaline phosphatase (40 U), 50 mM sodium cacodylate buffer, pH 6.5, 1% Triton X-100, and 10 mM $MnCl_2$ was incubated for ten days at rt. UDP-GlcNAc (35 mg, 54 μmol) was added daily for six days. Additional enzyme (5 mU of GnT-I and 4 mU of GnT-II) was added after six days. The reaction mixture was filtered through a Millex filter and divided into four portions, each of which was applied to two Sep-Pak C_{18} cartridges in tandem. The cartridges were washed with Milli-Q water (100 mL) and then the product was eluted with HPLC grade MeOH (35 mL). The combined methanol eluants were evaporated to dryness under reduced pressure. The residue was dissolved in CH_2Cl_2–MeOH (9:1), applied to an Iatrobead column (15 g), and eluted with CH_2Cl_2–MeOH (9:1) to remove Triton X-100 detergent. Product eluted with CH_2Cl_2–MeOH–H_2O (65:35:6), the fractions containing product were

© 2002 NRC Canada

combined and evaporated to dryness. The residue was dissolved in Milli-Q H_2O, filtered through a Millex filter, and the filtrate was lyophilized to dryness giving **2** as a white powder (60 mg, 72% yield). ^{1}H NMR δ: 5.13 (br s, Manα1,3-H1), 4.92 (br s, Manα1,6-H1), 4.67 (s, Manβ-H1), 4.58 (d, *J* = 8.6 Hz, GlcNAcα1,3-H1)[a], 4.56 (d, *J* = 8.2 Hz, GlcNAcα1,6-H1)[a]. [a]The two GlcNAc resonances might be interchanged. FAB-MS calcd. *m/z* for $[M + Na]^+$ $C_{42}H_{74}N_2O_{26}Na$: 1045.4; found: 1045.2.

Synthesis of hexasaccharide 3

A mixture containing pentasaccharide (**2**, 25 mg, 24 μmol), UDP-GlcNAc (16 mg, 25 μmol), GnT-V (10 mU), alkaline phosphatase (20 U), and *N*-acetyl glucosamine (10 mg) in 25 mL of 50 mM sodium cacodylate buffer, pH 7.0, was incubated at 37°C for 3 days. Additional UDP-GlcNAc (16 mg) was added after 24 and 48 h. The reaction mixture was filtered through a Millex filter, divided into four portions, and each portion was applied to three Sep-Pak C_{18} cartridges in tandem for isolation as described for the preparation of **2**. The residue was further purified by Iatrobead column chromatography (6 g) using CH_2Cl_2–MeOH (7:3) for column loading and CH_2Cl_2–MeOH–H_2O (40:40:8) for product elution. The fractions containing product were evaporated to dryness, dissolved in water, filtered, and lyophilized giving **3** as a white powder (27 mg, 92% yield). ^{1}H NMR δ: 5.14 (br s, Manα1,3-H1), 4.88 (br s, Manα1,6-H1), 4.68 (s, Manβ-H1), 4.60 (d, *J* = 8.5 Hz, GlcNAcα1,3-H1)[a], 4.56 (d, *J* = 8.5Hz, GlcNAcα1,6-H1)[a], 4.50 (d, *J* = 8.1 Hz, GlcNAcα1,6-H1′). [a]The three GlcNAc resonances might be interchanged. FAB-MS calcd. *m/z* for $[M + Na]^+$ $C_{50}H_{87}N_3O_{31}Na$: 1248.5; found: 1248.3.

Synthesis of nonasaccharide 4

A mixture containing hexasaccharide (**3**, 12 mg, 9.8 μmol), UDP-Gal (20 mg, 31 μmol), β(1→4) galactosyltransferase (2 U), alkaline phosphatase (30 U) in 3 mL of 20 mM sodium cacodylate buffer, pH 7.1, and 20 mM $MnCl_2$ was incubated at rt for 25 h. Additional UDP-Gal (10 mg) was added after 18 h. The reaction mixture was divided into five portions, each of which was applied to three Sep-Pak C_{18} cartridges in tandem for isolation as described for **2**. The residue was dissolved in H_2O, filtered through a Millex filter, and the filtrate was lyophilized to dryness. Compound **4** was obtained as white powder (14 mg, 83% yield). ^{1}H NMR δ: 5.14 (d, *J* = 1.4 Hz, Manα1,3-H1), 4.89 (d, *J* = 1.2 Hz, Manβ-H1), 4.68 (s, Manβ-H1), 4.62 (d, *J* = 8.2 Hz, GlcNAcα1,3-H1), 4.58 (d, *J* = 8.0 Hz, 2 GlcNAcα1,6-H1), 4.48 (d, *J* = 7.8 Hz, 1 Gal-H1), 4.47 (d, *J* = 7.8 Hz, 2 Gal-H1), 4.19 (Manα1,3-H2)[b], 4.15–4.12 (Manα1,6-H2[b] and Manβ-H2), 3.92 (Manα1,3-H3), 3.83 (Manα1,6-H3), 3.75 (Manβ-H3), 2.06–2.04 (s, 3 NAc-CH3). [b]The typical dd (ca. 3.4 and 1.8 Hz) coupling pattern for Man-H2 is visible but precise values cannot be measured due to spectral overlap. FAB-MS calcd. *m/z* for $[M + Na]^+$ $C_{68}H_{117}N_3O_{46}Na$: 1734.7; found: 1734.9.

Synthesis of dodecasaccharide 5

A mixture containing nonasaccharide (**4**, 10.0 mg, 5.8 μmol), CMP-Neu5Ac (11 mg, 17 μmol), α(2→3) sialyltransferase (120 mU), alkaline phosphatase (20 U) in 1 mL of 50 mM sodium cacodylate buffer, pH 6.5, and 20 mM $MnCl_2$ was incubated at 37°C for 3 days. Additional CMP-Neu5Ac was added — 12 mg after 20 h and 6 mg at 38 and 58 h. α(2→3) Sialyltransferase (45 mU) was added after 58 h. The reaction mixture was filtered through a Centriprep concentrator (30 000 D cut-off), divided into five portions, each of which was applied to three Sep-Pak C_{18} cartridges in tandem. The cartridges were washed with water (60 mL) and then the product was eluted in 50% MeOH–H_2O (60 mL). The combined MeOH fractions were evaporated to dryness, the residue was dissolved in H_2O, filtered through a Millex filter, and the filtrate was lyophilized. Compound **5** was obtained as a white powder (10.5 mg, 70% yield). ^{1}H NMR δ: 5.14 (br s, Manα1,3-H1), 4.91 (br s, Man α1,6-H1), 4.69 (s, Manβ-H1), 4.64–4.54 (3 GlcNAc-H1 and 3 Gal-H1), 2.76 (dd, *J* = 12.5 and 4.5 Hz, 3 NeuNAc-H3eq), 1.81 (t, *J* = 12.5 Hz, 3 NeuAc-H3ax). ESI-MS *m/z* calcd. for $[M + 2Na]^+$ $C_{101}H_{166}N_6O_{70}Na_2$: 2628.9; found: 2629.1.

Synthesis of pentadecasaccharide 6

A mixture containing dodecasaccharide (**5**, 5.5 mg, 2.1 μmol), GDP-Fuc (3.7 mg, 5.7 μmol), α(1→3) fucosyltransferase (80 mU), and alkaline phosphatase (20 U) in 50 mM sodium cacodylate buffer (5 mM $MnCl_2$, 25% glycerol, pH 6.5, 1 mL) was incubated at rt for 30 h. Additional GDP-Fuc was added after 10 h (3.8 mg) and 20 h (1.6 mg). The reaction mixture was filtered through a Centriprep concentrator (30 000 D cut-off), the filtrate was diluted with water to 1% glycerol, and divided into five portions, each of which was applied to three tandem Sep-Pak C_{18} cartridges for isolation as described for the preparation of **5**. Compound **6** was obtained as a white powder (5.6 mg, 90% yield). ^{1}H NMR δ: 5.14–5.10 (3 Fuc-H1 and 1 Manα1,3-H1), 4.90 (br s, Manα1,6-H1), 4.85–4.80 (br q, 3 Fuc H-5), 4.67 (s, Manβ-H1), 4.66–4.56 (3 GlcNAc-H1), 4.54–4.50 (3 Gal-H1), 2.77 (dd, *J* = 12.5 and 4.5 Hz, 3 NeuNAc-H3eq), 2.07–2.02 (s, 6 NAc-CH3), 1.80 (t, *J* = 12.5 Hz, 3 NeuNAc-H3ax), 1.17 (d, *J* = 6.5 Hz, 3 Fuc-H6). ESI-MS *m/z* calcd. for $[M + 2Na]^+$ $C_{119}H_{196}N_6O_{82}Na_2$: 3067.1; found: 3066.9.

Synthesis of dodecasaccharide 7

A reaction mixture containing nonasaccharide (**4**, 2 mg, 1.2 μmol), GDP-Fuc (1.8 mg, 2.8 μmol), α(1→3) fucosyltransferase (40 mU), and alkaline phosphatase (20 U) in 50 mM sodium cacodylate buffer (5 mM $MnCl_2$, 25% glycerol, pH 6.5, 1.2 mL) was gently stirred at rt for 30 h. Additional GDP-Fuc was added after 8 h (1.8 mg) and 20 h (1 mg). The reaction mixture was filtered through a Centriprep concentrator (30 000 D cut-off), the filtrate was diluted with Milli-Q water to 1% glycerol, divided into three portions, each of which were applied to three Sep-Pak C_{18} cartridges in tandem for isolation as described for the preparation of **5**. Compound **7** was obtained as a white powder (2.2 mg, 83% yield). ^{1}H NMR δ: 5.16–5.12 (3 Fuc-H1 and 1 Manα1,3-H1), 4.88 (br s, Manα1,6-H1), 4.87–4.83 (br q, 3 Fuc-H5), 4.68 (s, Manβ-H1), 4.60–4.56 (3 GlcNAc-H1), 4.47–4.42 (3 Gal-H1), 1.18 (d, *J* = 6.5 Hz, 3 Fuc-H6). ESI-MS *m/z* calcd. for $[M + Na]^+$ $C_{86}H_{147}N_3O_{58}Na$: 2172.9; found: 2173.1.

Synthesis of dodecasaccharide 8

A reaction mixture containing nonasaccharide (**4**, 2.0 mg, 1.2 μmol), CMP-Neu5Ac (2.3 mg, 3.6 μmol), α(2→6)

© 2002 NRC Canada

sialyltransferase (40 mU), and alkaline phosphatase (20 U) in 2 mL of 50 mM sodium cacodylate buffer, pH 6.5, was gently stirred at ambient temperature for 8 days. Additional CMP-Neu5Ac (1 mg) was added daily. The reaction mixture was then filtered through a Centriprep concentrator (10 000 D cut-off), and the filtrate divided into three portions, each of which was applied to three tandem Sep-Pak C_{18} cartridges for isolation as described for the preparation of **5**. Compound **8** was obtained as a white powder (1.8 mg, 58% yield). ^{1}H NMR δ: 5.15 (br s, Manα1,3-H1), 4.93 (br s, Man α1,6-H1), 4.68 (s, Manβ-H1), 4.64–4.60 (3 GlcNAc-H1), 4.46–4.42 (3 Gal-H1), 2.68 (dd, J = 12.5 and 4.5 Hz, 3 NeuNAc-H3eq), 1.72 (t, J = 12.5 Hz, NeuAc-H3ax). ESI-MS m/z calcd. for $[M + 2Na]^+$ $C_{101}H_{166}N_6O_{70}Na_2$: 2628.9; found: 2629.2.

Acknowledgments

This work was supported by the Natural Sciences and Engineering Research Council of Canada (NSERC). We thank Dr. Suzanne C. Crawley for providing *N*-acetylglucosaminyltransferase V enzyme and Mr. Yves Henriquez for the isolation of the α-2,3 sialyltransferase enzyme.

References

1. A. Varki. Glycobiology **3**, 97 (1993); R.A. Dwek. Chem. Rev. **96**, 683 (1996); P. Sears and C.-H. Wong. Cell. Mol. Life Sci. **54**, 223 (1998); T. Kolter and K. Sandhoff. Angew. Chem. Int. Ed. Eng. **38**, 1532 (1999).
2. J. Alper. Science (Washington, D.C.), **291**, 2338 (2001); J.C. McAuliffe and O. Hindsgaul. *In* Molecular and cellular glycobiology. *Edited by* M. Fukuda and O. Hindsgaul. Oxford University Press, Oxford; New York. 2000. pp. 249; J.W. Dennis, M. Granovsky, and C.E. Warren. Biochim. Biophys. Acta, **1473**, 21 (1999).
3. Carbohydrates in chemistry and biology. Vol 1. *Edited by* B. Ernst, G. W. Hart, and P. Sinay. Wiley-VCH, Verlag, Weinheim. 2000; R.R. Schmidt and K.-H. Jung Carbohydr. Eur. **27**, 13 (1999); G.-J. Boons. Tetrahedron, **52**, 1095 (1996).
4. D.H.G. Crout and G. Vic. Curr. Opin. Chem. Biol. **2**, 98 (1999); M.M. Palcic. Curr. Opin. Biotechnol. **10**, 616 (1999); R. Ohrlein. Top. Curr. Chem. **200**, 227 (1999); K.M. Koeller and C.–H. Wong. Chem. Rev. **100**, 4465 (2000); N. Wymer and E.J. Toone. Curr. Opin. Chem. Biol. **4**, 110 (2000).
5. R. Kleene and E.G. Berger. Biochim. Biophys. Acta, **1154**, 283, (1994); H. Schachter. *In* Molecular and cellular glycobiology. *Edited by* M. Fukuda and O. Hindsgaul. Oxford University Press, Oxford; New York. 1994. pp. 88; M.M. Palcic. Methods Enzymol. **230**, 300 (1994).
6. D. Vestweber and J.E. Blanks. Physiol. Rev. **79**, 181 (1999); D.D. Manning, X. Hu, P. Beck, and L.L. Kiessling. J. Am. Chem. Soc. **119**, 3161 (1997); G. Thoma, R.O. Duthaler, J.L. Magnani, and J.T. Patton. J. Am. Chem. Soc. **123**, 10113 (2001) and refs. 4–8 in this article.
7. Y.C. Lee and R.T Lee. Acc. Chem. Res. **28**, 321 (1995); M. Mammen, S.-K Choi, and G.M. Whitesides. Angew. Chem. Int. Ed. **37**, 2754 (1998); R. Roy. Curr. Opin. Struct. Biol. **6**, 692 (1996); L.L. Keisslilng and N.L. Pohl. Chem. Biol. **3**, 71 (1996); K. Drickamer. Struct. Biol. **2**, 437 (1995).
8. K.J. Kaur and O. Hindsgaul. Glycoconjugate J. **8**, 90 (1991).
9. M.M. Palcic, H. Li, D. Zanini, R.S. Bhella, and R. Roy. Carbohydr. Res. **305**, 433 (1998).
10. R.C. Hughes. Biochim. Biophys. Acta, **1473**, 172 (1999).
11. J.J. Skehel and D.C. Wiley. Annu. Rev. Biochem. **69**, 531 (2000); J.L. Connolly, E.S. Barton, and T.S. Dermody. J. Virol. **75**, 4029 (2001).
12. C.L. Oppenheimer and R.L. Hill. J. Biol. Chem. **256**, 799 (1981); K.J. Kaur, G. Alton, and O. Hindsgaul. Carbohydr. Res. **210**, 145 (1991).
13. B. Zhang, M.M. Palcic, D.C. Schriemer, G. Alvarez-Manilla, M. Pierce, and O. Hindsgaul. Anal. Biochem. **299**, 173 (2001).
14. S. Gosselin, M. Alhussaini, M.B. Streiff, K. Takabayashi, and M.M. Palcic. Anal. Biochem. **220**, 92 (1994).
15. K.B. Wlasichuk, M.A. Kashem, P.V. Nikrad, P. Bird, C. Jiang, and A.P. Venot. J. Biol. Chem. **268**, 13971 (1993).

© 2002 NRC Canada

Biomimetic reactions in organic synthesis: Semi-pinacol rearrangements of some spirocyclic epoxyalcohols derived from Juliá–Colonna asymmetric epoxidations

Bernhard Hauer, Jamie F. Bickley, Julien Massue, Paula C. A. Pena, Stanley M. Roberts, and John Skidmore

Abstract: Epoxy *tert*-alcohols have been prepared from (*E*)-enones in a two-step approach consisting of Juliá–Colonna asymmetric epoxidation followed by Grignard alkylation of the epoxyketone. On treatment with sub-stoichiometric amounts of $Yb(OTf)_3$ these *trans*-epoxyalcohols underwent efficient stereoselective semi-pinacol rearrangement to afford *anti*-α-phenyl-β-hydroxy-ketones (aldols). Under the same conditions, spirocyclic epoxyalcohols derived from 1-tetralone and 1-benzosuberone undergo either ring contraction (via semi-pinacol rearrangement) or fragmentation. A mechanistic rationale is presented to explain the formation of the various products.

Key words: Juliá–Colonna reaction, asymmetric epoxidation, epoxy *tert*-alcohols, semi-pinacol rearrangement.

Résumé : Faisant appel à l'approche en deux étapes de Juliá–Colonna impliquant une époxydation asymétrique suivie d'une alkylation de Grignard de l'époxycétone, on a préparé des époxy *tert*-alcools à partir de (*E*)-énones. Le traitement de ces *trans*-époxyalcools avec des quantités sous-stoechiométriques d'$Yb(OTf)_3$ provoque un réarrangement semi-pinacolique stéréosélectif et efficace qui conduit aux *anti*-α-phényl-β-hydroxycétones (aldols). Dans les mêmes conditions, les époxyalcools spirocycliques obtenus à partir de la 1-tétralone et de la 1-benzosubérone donnent lieu soit à une contraction de cycle (par le biais d'un réarrangement semi-pinacolique) ou à une fragmentation. On propose un mécanisme qui permet de rationaliser la formation des divers produits.

Mots clés : réaction de Juliá–Colonna, époxydation asymétrique, époxy *tert*-alcools, réarrangement semi-pinacolique.

[Traduit par la Rédaction]

Introduction

Epoxides are among the most widely used functional groups in modern synthetic chemistry. This reflects the existence of numerous reliable, highly enantioselective methods for epoxidation, and the wealth of chemistry that epoxides can undergo, allowing a wide range of compounds to be prepared in an efficient and stereoselective manner (1). Amongst the reactions of epoxides, rearrangements have been widely used as key steps in the synthesis of biologically active targets and natural products. Several different modes of epoxide rearrangement have been identified (2); in substrates where the epoxide is flanked by an alcohol, or a silyl-protected alcohol, treatment with a suitable Lewis acid can lead to a semi-pinacol rearrangement (3), in which 1,2-migration of one of the alcohol substituents opens the epoxide, generating an α-substituted-β-hydroxyketone (aldol) in a stereoselective manner. Various Lewis acids have been used, in stoichiometric quantities, to facilitate this rearrangement, including $TiC1_4$ (4), $BF_3{\cdot}OEt_2$ (3, 5, 6), $Ti(i\text{-}PrO)_2C1_2$ (5), $Ti(i\text{-}PrO)_3C1$ (7), and $SnC1_4$ (8). Until recently, catalytic variants of this rearrangement required a silyl-protected epoxyalcohol, using either TMSI or TMSOTf as the Lewis acid (9). Our recent report (10) and that of Tu et al. (11) have shown, however, that rare-earth triflates and $ZnBr_2$ are capable of catalyzing semi-pinacol rearrangements of unprotected epoxyalcohols.

Some of the epoxy *tert*-alcohol substrates used in semi-pinacol rearrangements may be prepared in enantiomerically enriched form by a five-step Sharpless AE–oxidation–alkylation–oxidation–alkylation strategy (4, 5). An alternative approach to prepare such substrates is the use of a polyleucine-catalyzed asymmetric epoxidation of an enone (Juliá–Colonna epoxidation) (12–14) followed by a

Received 20 November 2001. Published on the NRC Research Press Web site at http://canjchem.nrc.ca on 30 April 2002.

Dedicated to Professor J. Bryan Jones on the occassion of his 65th birthday.

B. Hauer. BASF AG, GVF B9, D67056, Ludwigshafen, Germany.
J.F. Bickley, J. Massue, P.C.A. Pena, S.M. Roberts,[1] and J. Skidmore. Department of Chemistry, Liverpool University, Liverpool, U.K., L69 7ZD.

[1]Corresponding author (e-mail: smrsm@liv.ac.uk).

 DOI: 10.1139/V02-061 © 2002 NRC Canada

Scheme 1. (*a*) Asymmetric epoxidation; (*b*) Grignard alkylation; (*c*) $Yb(OTf)_3$ catalyzed rearrangement.

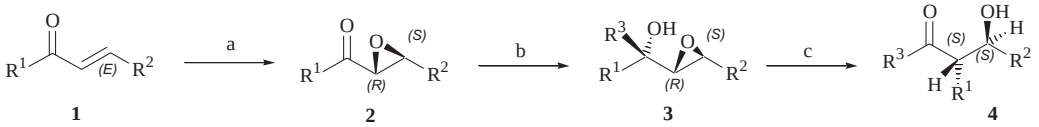

Scheme 2. (*a*) Asymmetric epoxidation; (*b*) Grignard alkylation; (*c*) $Yb(OTf)_3$ catalyzed rearrangement.

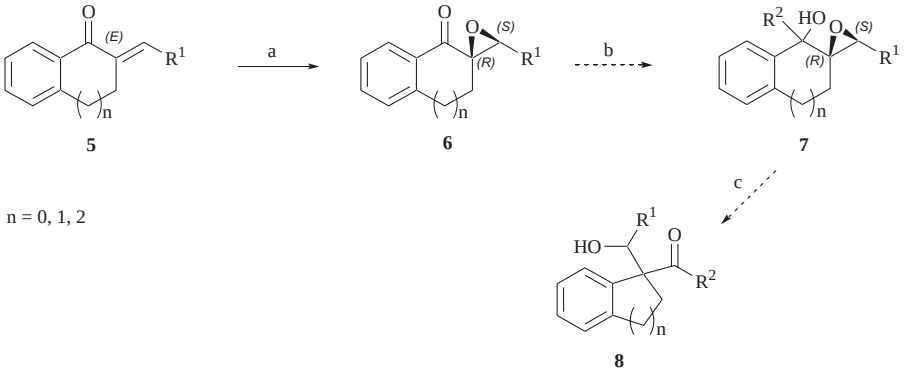

Scheme 3. Reagents and conditions: (*i*) urea–H_2O_2, BEMP, SiO_2-poly-L-leucine, THF, room temp.

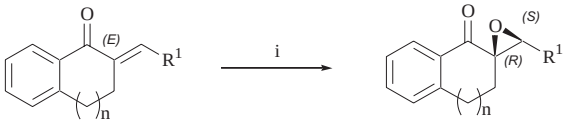

5a	n = 1, R^1 = Et	**6a**
5b	n = 0, R^1 = *i*-Pr	**6b**
5c	n = 2, R^1 = *i*-Pr	**6c**
5d	n = 1, R^1 = Ph	**6d**

Scheme 4. Reagents and conditions: (*i*) R^2MgBr, Et_2O–THF, –78°C.

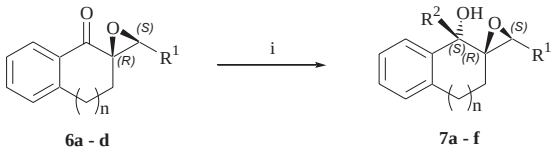

diastereoselective Grignard alkylation of the resultant epoxyketone (15, 16). This method entails conversion of achiral enones **1** into optically active epoxides **2**, which are transformed with high stereoselectivity into enantiomerically enriched diastereomerically pure epoxyalcohols **3**. We have shown that such epoxyalcohols are efficiently rearranged to afford aldols **4** in reactions catalyzed by rare-earth triflates (Scheme 1) (10).

Recent work has extended the Juliá–Colonna epoxidation to cyclic enones possessing an exocyclic olefin unit; thus epoxidation of ketones **5** using urea–H_2O_2 and DBU in the presence of poly-L-leucine affords spirocyclic epoxides **6** in 63–85% yield and 59–94% ee (Scheme 2) (17).

It was anticipated that alkylation of spirocyclic epoxyketones **6** would afford epoxy alcohols **7** (step b) in which the aromatic ring is the group with the highest migratory aptitude in a semi-pinacol rearrangement unless stereochemical constraints become dominant. Thus, treatment of 1,2,3,4-tetrahydronaphthalene epoxyalcohols (**7**, *n* = 1) with rare-earth triflates was expected to result in ring contraction to afford indans (**8**, *n* = 1) bearing a quaternary chiral center (step c); such systems are not readily accessible, in enantiomerically enriched form, using conventional methodology. We report herein the outcome of Lewis acid catalyzed rearrangements of compounds of type **7**.

Results

E-3,4-Dihydro-2-propylidene-2*H*-naphthalen-1-one (**5a**) was converted into the epoxide **6a** in 75% yield and 85% ee employing silica-supported poly-L-leucine as the catalyst with urea–H_2O_2 (UHP) as the oxidant and sub-stoichiometric quantities of BEMP as the base (Scheme 3). Using similar reaction conditions,indanone epoxide **6b** was prepared from enone **5b** with good stereoselectivity (74% yield, 81% ee), whilst the epoxidation of alkylidene–benzosuberone **5c** under these conditions proved to be very slow and to generate racemic product **6c** (62% yield). This result contrasts with our previously reported asymmetric epoxidation of **5c** (under different conditions), which generated the product in 74% yield and 59% ee. The synthesis of epoxide **6d** (76% yield and 84% ee) was reported previously, employing poly-L-leucine as the catalyst, UHP as the oxidant in isopropyl acetate containing DBU (17). The alternative use of sub-stoichiometric quantities of BEMP as the base and silica-supported poly-L-leucine as the catalyst led to a quantitative yield of **6d** having the same optical purity.

Epoxyketones **6a**–**d** were alkylated with methylmagnesium bromide to afford the epoxyalcohols **7a**–**d**, respectively; compounds **6a** and **6d** were also reacted with phenylmagnesium bromide to afford the tertiary alcohols **7e** and **7f** (Scheme 4 and Table 1).

All the ketones gave the appropriate product as a single diastereoisomer. The operation of a Cram-chelate mode of

© 2002 NRC Canada

Table 1. Reaction of epoxyketones **6a**–**d** with Grignard reagents R^2MgBr.

Epoxyketone	R^1	R^2	*n*	Epoxyalcohol (yield %)
6a	Et	Me	1	**7a** (82)
6b	*i*-Pr	Me	0	**7b** (66)
6c	*i*-Pr	Me	2	**7c** (57)
6d	Ph	Me	1	**7d** (97)
6a	Et	Ph	1	**7e** (69)
6d	Ph	Ph	1	**7f** (94)

Scheme 5. Reagents and conditions: (*i*) $Yb(OTf)_3$, CH_2Cl_2, room temp., 1 h.

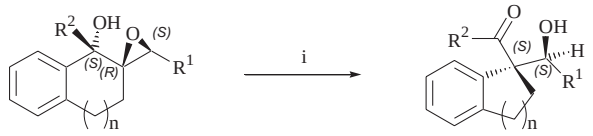

7a	n = 1, R^1 = Et, R^2 = Me	**8a**
7c	n = 2, R^1 = *i*-Pr, R^2 = Me	**8c**
7e	n = 1, R^1 = Et, R^2 = Ph	**8e**

addition (16) was confirmed by X-ray analysis of the epoxyalcohol **7d** (Fig. 1).[2]

To effect the desired semi-pinacol rearrangement, tertiary alcohol **7a** was treated with Yb $(OTf)_3$ (20 mol %) in dichloromethane for 1 h. The formation of the expected methyl ketone **8a** (Scheme 5) was supported by NMR spectroscopy (three-proton singlet at δ 2.03 inter alia) and by a strong signal at 1693 cm^{-1} in the IR spectrum. Under the same reaction conditions, indan-epoxide **7b** gave a complex mixture, whereas treatment of the benzosuberan-epoxide **7c** with $Yb(OTf)_3$ gave the ring-contracted product **8c** in 60% yield.

Similarly, treatment of **7e** with $Yb(OTf)_3$ (20 mol %) in dichloromethane, followed by purification of the crude product by chromatography over silica gel led to the isolation of a rearranged product. The structure of the isolated product **8e** (58% yield) was initially suggested by IR spectroscopy (λ_{max} = 1661 cm^{-1}), corroborated by NMR spectroscopy, and firmly established by X-ray crystallography (Fig. 2). As expected, the epoxide ring opening had occurred with inversion of configuration.

Treatment of alcohol **7f** with $Yb(OTf)_3$ (20 mol %) gave a mixture of products from which the indan-1-yl phenyl ketone (**9**) was isolated in 63% yield (Scheme 6). Ketone **9** is most probably formed by retroaldol fragmentation of the initially formed ring-contracted product **8f**. To try to provide proof for this hypothesis, the reaction was repeated but quenched after a much shorter period of time. Purification of the crude material led to the isolation of a major product — the ^1H NMR spectrum of which was closely analogous to those of the ring-contracted products **8a** and **8e**. FAB mass spectrometry displayed a molecular-ion peak corresponding to compound **8f**. This material was unstable (decomposing readily but cleanly to ketone **9** and benzaldehyde), which prevented more extensive characterization. With this additional evidence, however, it seems highly likely that the well-precedented semi-pinacol rearrangement forms during the first part of the reaction.

Fig. 1. X-ray crystal structure of compound **7d**.

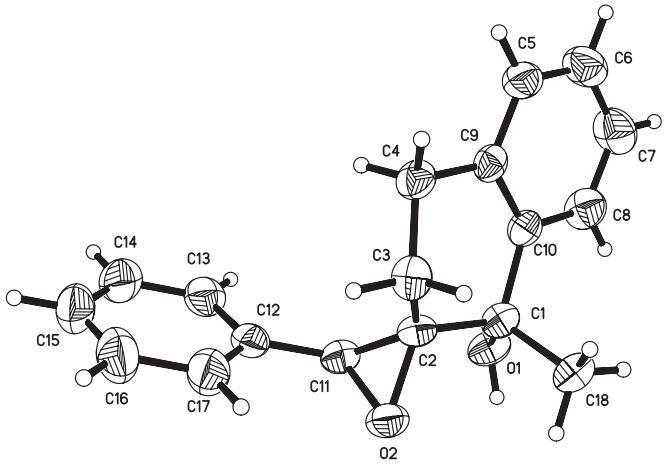

Surprisingly, epoxyalcohol **7d** did not produce ring-contracted material, but instead, formed two major products, 1-methyl-2-tetralone (**10**) (40% yield) and benzaldehyde, which were identified by ^1H NMR and by comparison with authentic materials (10).

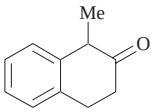

10

Discussion

Indans **8a** and **8e** are clearly formed by the expected ring-contraction process, whilst the fragmentation product **9** is assumed to be generated from indan **8f**. The fact that indan-epoxide **7b** fails to undergo ring contraction is presumably due to a high-energy transition state caused by ring strain. The key stereoelectronic requirement for the semi-pinacol rearrangement is that the migrating group should be anti-periplanar to the breaking C–O bond. Note that compound **7e** undergoes ring contraction rather than phenyl migration. Although no crystal structure data are available for **7e**, inspection of the X-ray crystal structure of the analogous methyl substituted epoxyalcohol **7d** (Fig. 1) suggests an origin for the selectivity. Thus whilst the dihedral angle between the epoxide C–O and the methyl group C–C [O(2)-

[2] Supplementary material may be purchased from the Depository of Unpublished Data, Document Delivery, CISTI, National Research Council Canada, Ottawa, ON K1A 0S2, Canada. For information on obtaining material electronically go to http://www.nrc.ca/cisti/irm/unpub_e.shtml. Crystallographic information has also been deposited with the Cambridge Crystallographic Data Centre (CCDC Nos. 181123 and 181124). Copies of the data can be obtained free of charge via www.ccdc.cam.ac.uk/conts/retrieving.html (or from the Cambridge Crystallographic Data Centre, 12, Union Road, Cambridge CB2 1EZ, U.K.; fax: +44 1223 336033; or deposit@ccdc.cam.ac.uk).

© 2002 NRC Canada

Scheme 6. Reagents and conditions: (*i*) $Yb(OTf)_3$, CH_2Cl_2, room temp.

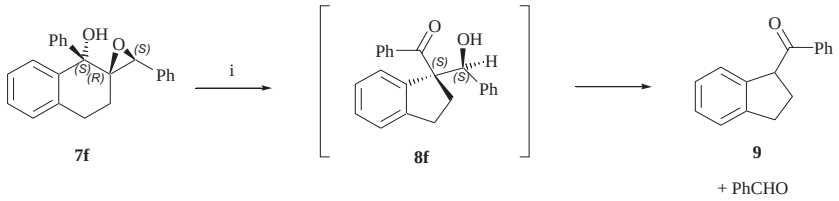

Fig. 2. X-ray crystal structure of compound **8e**.

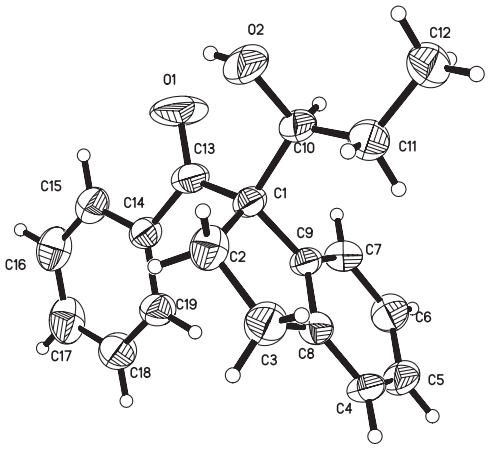

C(2)-C(1)-C(18)] is 61.0°, the dihedral angle between the epoxide C–O and the migrant C–C [O(2)-C(2)-C(1)-C(10)] is 178.45°, i.e., anti-periplanar. The required alignment of the migrating C–C with the C–O s^* of the epoxide dictates the outcome of these semi-pinacol rearrangements.

The mechanism by which 1-methyl-2-tetralone (**10**) is formed from epoxyalcohol **7d** is less clear; two possibilities are outlined in Scheme 7. Coordination of the $Yb(OTf)_3$ to the epoxide moiety should assist ring opening to reveal benzylic carbocation **11** (Scheme 7, path a). It is possible that this cation can rearrange via oxetane **12** to generate tertiary benzylic carbocation **13**. This would readily undergo a fragmentation reaction to generate benzaldehyde and the enolate (**14**) of 1-methyl-2-tetralone. An alternative approach to benzylic carbocation **13** is via a Lewis acid-catalyzed Payne rearrangement generating epoxyalcohol **15** followed by epoxide opening (Scheme 7, path b).

Work is in progress to try to distinguish between these two possibilities and the outcome of these experiments will be reported in a full paper.

Conclusions

Application of Juliá–Colonna asymmetric epoxidation followed by Grignard alkylation has been used to prepare epoxyalcohols in enantiomerically enriched form, both from acyclic enones and from cycloalkanones bearing exocyclic olefin units. The spirocyclic epoxyalcohols prepared from the latter substrates undergo either ring contraction or fragmentation processes, depending on the substituents present and the size of the ring. $Yb(OTf)_3$ has been shown to be an excellent catalyst for epoxyalcohol semi-pinacol rearrangements.

Scheme 7.

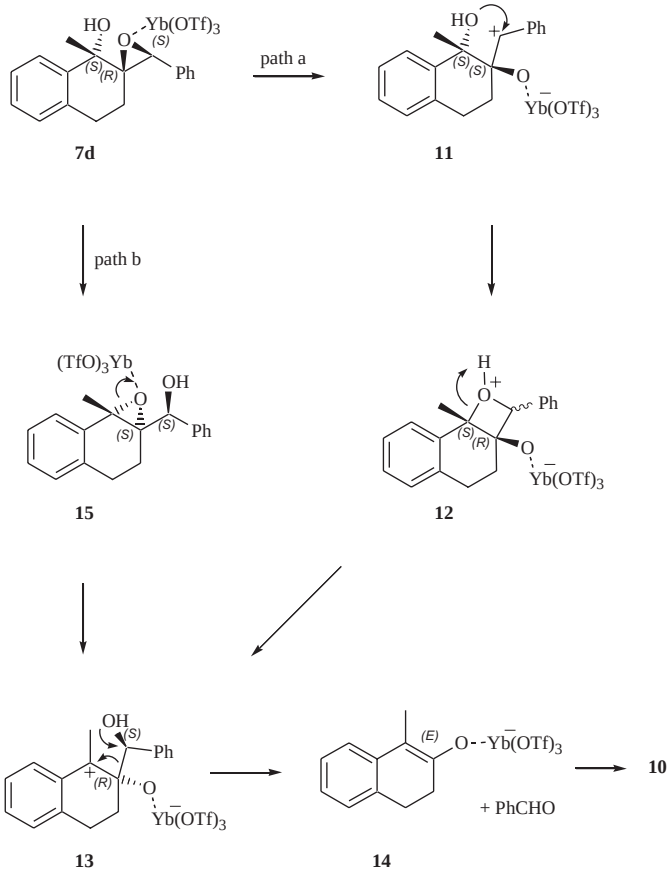

Acknowledgments

Financial support was gratefully received from the Fundação para a Ciência e Tecnologia (FCT) and BASF (for PCAP). JM received support from the University of Rennes. We thank Dr. M. J. Porter (U.C., London) for insightful discussions.

References

1. E.N. Jacobsen, A. Pfaltz, and H. Yamamoto. *In* Comprehensive asymmetric catalysis. *Edited by* Springer-Verlag, Berlin. 1999.
2. B. Rickborn. *In* Comprehensive organic synthesis. Vol. 3. *Edited by* B.M. Trost and I. Fleming. Pergamon Press, Oxford. 1991. pp. 733–775.
3. C.J. Cheer and C.R. Johnson. J. Am. Chem. Soc. **90**, 178 (1968).

© 2002 NRC Canada

4. K. Maruoka, M. Hasagavia, and H. Yamamoto. J. Am. Chem. Soc. **108**, 3827 (1986).
5. M. Shimazaki, H. Hara, H.K. Suzuki, and G. Tsuchihashi. Tetrahedron Lett. **28**, 5891 (1987).
6. K. Suzuki, M. Miyazawa, M. Shimazaki, and G. Tsuchihashi. Tetrahedron, **44**, 4061 (1988).
7. S.W. Baldwin, P. Chen, N. Nikolic, and D.C. Weinselmer. Org. Lett. **2**, 1193 (2000).
8. C.M. Marson, A.J. Walker, J. Pickering, A.D. Hobson, R. Wrigglesworth, and S.J. Edge. J. Org. Chem. **58**, 5944 (1993).
9. K. Suzuki, M. Miyazawa, and G. Tsuchihashi. Tetrahedron Lett. **28**, 3515 (1987).
10. J.F. Bickley, B. Hauer, P.C.A. Pena, S.M. Roberts, and J. Skidmore. J. Chem. Soc. Perkin Trans. 1, 1253 (2001).
11. Y.Q. Tu, C.A. Fan, S.K. Ren, and A.S.C. Chan. J. Chem. Soc. Perkin Trans. 1, 3791 (2000).
12. S. Juliá, J. Guixer, J. Masana, J. Rocas, S. Colonna, R. Annuziata, and H. Molinari. J. Chem. Soc. Perkin Trans. 1, 1317 (1982).
13. B.M. Adger, J.V. Barkley, S. Bergeron, M.W. Cappi, B.E. Flowerdew, M.P. Jackson, R. McCague, T.C. Nugent, and S.M. Roberts. J. Chem. Soc. Perkin Trans. 1, 3501 (1997).
14. M.J. Porter, S.M. Roberts, and J. Skidmore. Bioorg. Med. Chem. **7**, 2145 (1999).
15. A.T. Gillmore, S.M. Roberts, M.B. Hursthouse, and K.M. Abdul. Tetrahedron Lett. **39**, 3315 (1998).
16. J.F. Bickley, A.T. Gillmore, S.M. Roberts, J. Skidmore, and A. Steiner. J. Chem. Soc. Perkin Trans. 1, 1109 (2001).
17. P.A. Bentley, J.F. Bickley, S.M. Roberts, and A. Steiner. Tetrahedron Lett. **42**, 3741 (2001).

© 2002 NRC Canada

Discriminating between dispersion and lyoprotection effects in biocatalysis in organic media

Francesco Secundo, Giacomo Carrea, and Francesco Maria Veronese

Abstract: The increment of activity and solubility in 1,4-dioxane of lipase B from *Candida antarctica*, lipase from *Pseudomonas cepacia*, and subtilisin, were investigated as a function of the methoxypoly(ethylene glycol)–protein (PEG–protein) ratio employed during lyophilization. Both activity and solubility markedly increased as the PEG–protein ratio was increased. The increment of activity at low PEG–protein ratios, however, was much higher than that of solubility. These data suggest that the PEG-induced activation effect is due mainly to a lyoprotection effect rather than to relaxation of diffusional limitations.

Key words: hydrolases, activity, dispersion, lyoprotection, circular dichroism.

Résumé : On a étudié l'augmentation de l'activité et de la solubilité de la lipase B de la *Candida antartica*, de la lipase de *pseudomonas cepacia* et de la subtilisine dans le 1,4-dioxane en fonction du rapport méthoxypoly(éthylèneglycol)/protéine (PEG/protéine) utilisé lors de la lyophilisation. L'activité ainsi que la solubilité augmentent toutes les deux de façon remarquable avec une augmentation du rapport PEG/protéine. Toutefois, l'augmentation de l'activité à des rapports PEG/protéine faibles est beaucoup plus grande que celle de la solubilité. Ces données suggèrent que l'effet d'activation induite par le PEG résulte principalement d'un effet de lypoprotection que d'une relaxation des limitations diffusionnelles.

Mots clés : hydrolases, activité, dispersion, lyoprotection, dichroïsme circulaire.

[Traduit par la Rédaction]

Introduction

Biocatalysis in non-aqueous media has been widely studied and employed, as shown by its numerous applications in the areas of synthesis, food, and even analysis (1–3). Although this methodology has numerous advantages, its main drawback is the lower catalytic efficiency of enzymes in organic solvents than in aqueous solutions. This phenomenon can be ascribed to different causes, including restricted protein flexibility, low stabilization of the transition state of the enzyme–substrate intermediate, partial-enzyme denaturation by lyophilization, non-optimal acid–base conditions in the surrounding of the enzyme molecule, or poor catalyst dispersion (4). Several methods, such as the dispersion of the biocatalyst by immobilization on solid supports (5–9), the use of lyoprotectants (10, 11) or protein dissolution in the organic media by ion-pair forming surfactants (12), amphipatic lipids (13), or poly(ethylene glycol) (PEG) (14), were employed to increase enzymatic activity.

Although PEG was found to markedly improve the enzymatic activity of some hydrolytic enzymes in organic solvents, it has not been determined if the activation is due to lyoprotection or to biocatalyst dispersion–dissolution (15, 16). Here, we try to shed light on this issue by correlating the increment of activity and solubility of two lipases and subtilisin, in 1,4-dioxane, at different PEG–protein ratios.

Received 31 October 2001. Published on the NRC Research Press Web site at http://canjchem.nrc.ca on 17 April 2002.

Dedicated to Professor J. Bryan Jones on the occasion of his 65th birthday.

F. Secundo[1] and G. Carrea. Istituto di Chimica del Riconoscimento Molecolare, via Mario Bianco 9, 20131 Milano, Italy.
F.M. Veronese. Dipartimento di Scienze Farmaceutiche, Università di Padova, via Marzolo 5, 35131, Padova, Italy.

[1]Corresponding author (e-mail: secundo@ico.mi.cnr.it).

Experimental

Materials

Lipase B from *Candida antarctica* (CALB) was purified, as reported by Secundo et al. (16), from a crude preparation (experimental product SP 525) kindly provided by Novo Nordisk. Lipase from *Pseudomonas cepacia* (lipase PC) was purified, as reported by Secundo et al. (15), from a commercial crude preparation of lipase PS (Amano). Subtilisin and PEG (MW 5000) were purchased from Sigma and 1,4-dioxane of spectrophotometric grade from Aldrich. All other reagents and compounds were of analytical grade.

Preparation of enzyme samples

Purified CALB (0.2 mg) and lipase PC (0.2 mg) were dissolved in potassium phosphate buffer (1 mL, 5 mM, pH 7), divided into 20-μg portions, and added to PEG (0.05–5 mg) dissolved in water (0.4 mL) (PEG–protein ratio (w/w) 2.5–250); final volume 0.5 mL. Subtilisin (3 mg) was

 DOI: 10.1139/V02-026 © 2002 NRC Canada

dissolved in potassium phosphate buffer (1 mL, 5 mM, pH 7), divided into 0.3-mg portions, and added to PEG (2.5–125 mg) dissolved in water (0.4 mL) (PEG–protein ratio (w/w) 8–417); final volume 0.5 mL. The samples were then frozen and lyophilized. Each sample was prepared in double to allow for the measurement of activity and to record the circular dichroism spectrum. Control samples were analogously prepared, but without PEG. The protein content was determined by Biorad Protein Assay.

Circular dichroism spectra

Far-UV circular dichroism (CD) spectra were recorded with a Jasco 500 A spectropolarimeter over the range of 200–250 nm for the sample dissolved in water and 210–250 nm for the samples dissolved in dioxane. (Below 210 nm, the high absorbance of dioxane causes a low signal-to-noise ratio that prevents the measurements.) All spectra were recorded at 25°C. The optical path was 0.5 cm in the case of lipases and 0.1 cm in the case of subtilisin. The PEG–enzyme samples were added to 1 mL of 1,4-dioxane (or water), vigorously shaken, and immediately used for CD analysis. All spectra were baseline corrected.

Measurements of catalytic activity

The transesterification between 1-octanol and vinyl acetate to give 1-octyl acetate and acetaldehyde was used as model reaction for the three enzymes considered. In all cases, 1 mL of 1,4-dioxane containing 1-octanol (0.19 M) and vinyl acetate (1.1 M) was added to the different enzyme samples. All the reagents, enzyme samples, and 1,4-dioxane were equilibrated against molecular sieves ($a_w < 0.1$) before being used. The reaction mixtures were shaken at 200 rpm and 25°C. At scheduled times, aliquots were withdrawn from the reaction mixtures and the conversion determined by GLC. (HP-1 Crosslinked Methyl Silicone Gum, 25 m, 0.32 mm ID, Hewlett-Packard; conditions: oven temperature from 35°C (initial time 10 min) to 160°C with a heating rate of 15°C min^{-1}, H_2 as carrier gas.) The retention times for vinyl acetate, acetic acid, 1-octanol, and 1-octyl acetate were 1.8, 2.2, 11.5, and 13.0 min, respectively. Using these reaction conditions, the catalytic activity for CALB, lipase PC, and subtilisin was, respectively, 2.20, 0.16, and 0.028 μmol min^{-1} for the samples without PEG, whereas it was 6.75, 0.68, and 0.098 μmol min^{-1} for the samples at the highest PEG–protein ratio tested (250 for lipases and 417 for subtilisin).

The possibility that PEG could affect the enzymatic activity by competing as a nucleophile with octanol seems very unlikely because, as shown in Fig. 2, the activity increased as a function of PEG concentration or, when the plateau value was reached, remained constant.

Results and discussion

Figure 1 shows that CALB, at a PEG–protein ratio higher than 125 (w/w), is fully solubilized in 1,4-dioxane, as shown by the almost complete overlap between the spectra recorded in the organic solvent and in water. In addition, the similarity between the spectra outside the range typical for a protein, in our case from 350 to 250 nm (data not shown), should rule out the presence of scattering phenomena usually caused by sizeable aggregates or very fine protein dispersions (17). Moreover, it is worth noting that the enzyme only showed a CD signal in dioxane when it was previously lyophilized from an aqueous solution containing PEG. When the enzyme was suspended in dioxane, it did not give a CD signal in the 210–350 nm range, even when PEG was subsequently added (up to 5 mg mL^{-1}) to the protein suspension. This result, which is in agreement with previous observations on other proteins (14), demonstrates that CALB is soluble in 1,4-dioxane and its secondary structure is the same as in water. On the other hand, the spectra obtained for CALB at PEG–protein ratios lower than 125 showed a proportionally lower signal, which can be attributed to a decrease in the solubility of the protein (14). Analogous behavior was observed for lipase PC and subtilisin (spectra not shown).

Fig. 1. Circular dichroism spectra, in water and 1,4-dioxane, of CALB colyophilized with PEG. PEG–protein ratio of 250 for the spectrum recorded in water (*g*) and 2.5 (*a*); 5 (*b*); 25 (*c*); 50 (*d*); 125 (*e*); and 250 (*f*) for those recorded in 1,4-dioxane.

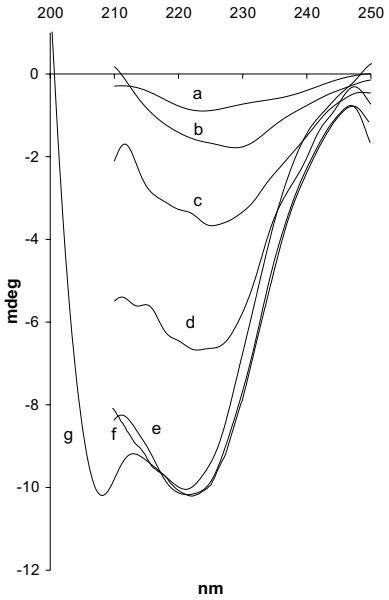

Figure 2 compares the increment of activity and solubility of the three enzymes as a function of the PEG–protein ratio. From zero to the highest ratio tested, not only did the activity increase 3.1-, 4.3-, and 3.5-fold for CALB (*a*); lipase PC (*b*); and subtilisin (*c*), respectively, but the enzymes were also fully solubilized. Nevertheless, it is evident that for all the enzymes the initial increment of activity was much steeper than that of solubility. Table 1 reports the increments of activity and solubility for CALB, lipase PC, and subtilisin at low PEG–protein ratios. It can be seen that the increment of activity was for all the enzymes much higher than the increment of solubility. For example, passing from 0 to a PEG–protein ratio of 2.5 for the lipases or 8 for protease, the increment of activity was 4.4-, 7.1-, and 4.1-fold higher than that of solubility for CALB, lipase PC, and subtilisin, respectively.

These data prove that the activating effect of PEG is not directly correlated to enzyme solubility. As a consequence, the activity increase should be due to a lyoprotective effect

© 2002 NRC Canada

Fig. 2. Increment of activity (■) and solubility (□) of CALB (*a*); lipase PC (*b*); and subtilisin (*c*) as a function of the PEG–protein ratio. The increment value (Δ) for activity and solubility is defined as $\Delta = (x - x_o)/(x_{max} - x_o)$, where x is the initial reaction rate or, for solubility, the CD signal at 220 nm obtained at a given PEG–protein ratio; x_o and x_{max} are the values obtained in the absence of PEG and at the highest PEG–protein ratio tested, respectively. For solubility, x_o was considered 0. (There was no CD signal for all the enzymes tested.) Each point was the average of three measurements.

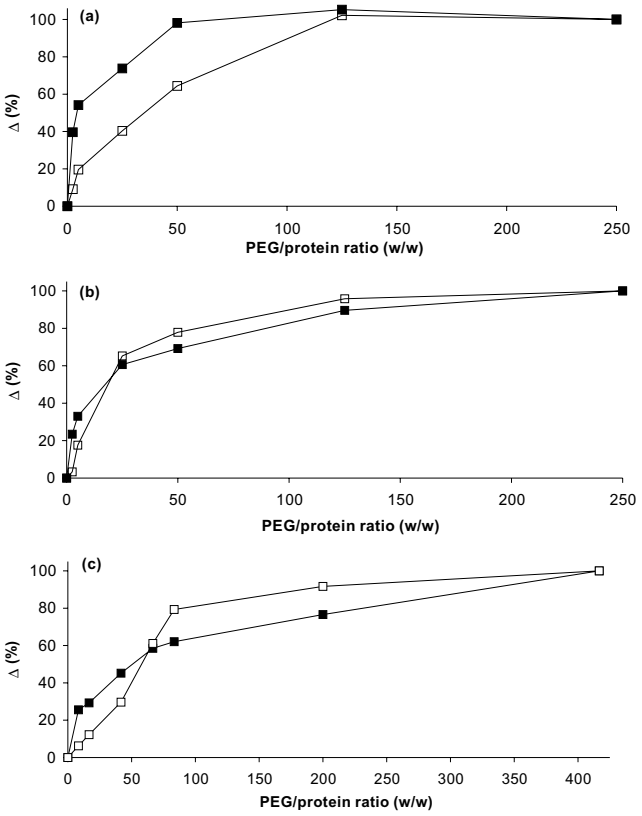

of PEG on the secondary structure of the enzyme (18, 19), rather than to the relaxation of diffusional limitations obtained through the solubilization of the enzyme in the organic medium. It is worth pointing out that the data reported here are in agreement with our previous findings (16), which, through the method proposed by Wescott and Klibanov (20) and Bedell et al. (21) (a method that correlates the catalytic activity with the relative percentage of active and chemically inactivated enzyme present in a given amount of enzyme protein), proved that the activating effect of PEG on CALB is not due to the relaxation of diffusional limitations. Furthermore, we have previously found that different formulations of lipase from *Pseudomonas cepacia* (crude powder, Celite adsorbed, or PEG modified) have very similar K_M values (22). This result also suggests the absence of diffusion limitations. Concerning this point, however, it should be emphasized that a recent study by Rees and Halling (23) demonstrated that both of these approaches (K_M determination and use of mixtures of active and inactivated enzyme) were unable to explain the severe "solid-phase" mass-transfer limitations that occur in lyophilized enzymes in organic media. In conclusion, the present work indicates that the lyoprotectant effect of PEG plays a major role in improving biocatalyst performance in organic solvents. Furthermore, the comparison of the effects produced by different concentrations of a given additive on the activity and solubility of an enzyme in organic solvents appears to be a simple and general approach to distinguish between the lyoprotective and dispersive action of the additive itself.

Table 1. Increments of activity and solubility for CALB, lipase PC, and subtilisin at low PEG–protein values.

Enzyme	PEG–protein ratio	Increment of activity (%)[a]	Increment of solubility (%)[a]
CALB	2.5	39.6	9.1
CALB	5	54.2	19.6
Lipase PC	2.5	23.5	3.3
Lipase PC	5	33.0	17.6
Subtilisin	8	25.6	6.3
Subtilisin	17	29.3	12.3

[a]For the definition of increment see the legend of Fig. 2.

Acknowledgment

We thank the CNR Target project on Biotechnology for financial support.

References

1. Enzyme catalysis in organic synthesis. Vol. I and II. *Edited by* K. Drauz, and H. Waldmann. VCH, Weinheim. 1995.
2. Enzymatic reactions in organic media. *Edited by* A.M.P. Koskinen and A.M. Klibanov. Blackie Academic & Professional. London. 1996.
3. G. Carrea and S. Riva. Angew. Chem. Int. Ed. Engl. **39**, 2226 (2000).
4. A.M. Klibanov. Trends Biotechnol. **15**, 97 (1997).
5. A.R. Macrae. *In* Biocatalysts in organic synthesis. *Edited by* J. Tramper, H.C. van der Plas, and P. Linko. Elsevier, Amsterdam. 1985. pp 195–208.
6. G. Ottolina, G. Carrea, S. Riva, L. Sartore, and F.M. Veronese. Biotechnol. Lett. **14**, 947 (1992).
7. Y.L. Khmelnitsky, S.H. Welch, D.S. Clark, and J.S. Dordick. J. Am. Chem. Soc. **116**, 2647 (1994).
8. M.T. Reetz, A. Zonta, and J. Simpelkamp. Biotechnol. Bioeng. **49**, 527 (1996).
9. G. Pencreac'h and J.C. Baratti. Appl. Microbiol. Biotech. **47**, 630 (1997).
10. K. Dabulis and A.M. Klibanov. Biotechnol. Bioeng. **41**, 566 (1993).
11. A.O. Triantafyllou, E. Wehtje, P. Adlercreutz, and B. Mattiason. Biotechnol. Bioeng. **54**, 67 (1997).
12. V.M. Paradkar and J.S. Dordick, Biotechnol. Bioeng. **43**, 529 (1994).
13. Y. Okahata, Y. Fujimoto, and K. Ijiro. J. Org. Chem. **60**, 2244 (1995).
14. F. Secundo, G. Carrea, G. Vecchio, and F. Zambianchi. Biotechnol. Bioeng. **64**, 624 (1999).
15. F. Secundo, S. Spadaro, G. Carrea, and P.L.A. Overbeeke. Biotechnol. Bioeng. **62**, 554 (1999).
16. F. Secundo, G. Carrea, D. Varinelli, and C. Soregaroli. Biotechnol. Bioeng. **73**, 157 (2001).

© 2002 NRC Canada

17. W.C. Johnson Jr., *In* Circular dichroism and the conformational analysis of biomolecules. *Edited by* G.D. Fasman. Plenum Press, New York. 1996. p. 648.
18. K. Griebenow and A.M. Klibanov. Proc. Natl. Acad. Sci. U.S.A. **92**, 10969 (1995).
19. G. Vecchio, F. Zambianchi, P. Zacchetti, F. Secundo, and G. Carrea. Biotechnol. Bioeng. **64**, 545 (1999).
20. C.R. Wescott and A.M. Klibanov. J. Am. Chem. Soc. **115**, 1629 (1993).
21. B.A. Bedell, V.V. Mozhaev, D.S. Clark, and J.S. Dordick. Biotechnol. Bioeng. **58**, 654 (1998).
22. R. Bovara, G. Carrea, G. Ottolina, and S. Riva. Biotechnol. Lett. **15**, 937 (1993).
23. D.G. Rees and P.J. Halling. Enzyme Microb. Technol. **27**, 549 (2000).

© 2002 NRC Canada

Towards an unprotected self-activating glycosyl donor system: Bromobutyl glycosides

Benjamin G. Davis, Steven D. Wood, and Michael A.T. Maughan

Abstract: Bromobutyl mannopyranosides have been successfully used as both protected and unprotected glycosyl donors both with and without the use of an external activator.

Key words: glycosylation, unprotected glycosyl donors, oligosaccharides.

Résumé : On a utilisé avec succès des mannopyranosides de bromobutyle comme donneurs, tant protégés que non protégés, de glycosyles et avec ou sans l'aide d'activateur externe.

Mots clés : glycosylation, donneurs de glycosyles non protégés, oligosaccharides.

[Traduit par la Rédaction]

Oligosaccharides and glycoconjugates are essential tools for the investigation of the enormous variety of biological functions that require specific carbohydrate-containing structures (1). Furthermore, their potential as therapeutic agents is clear (2). As a result, the formation of the glycosidic linkage continues to be a dominant theme in carbohydrate chemistry (3). Yet despite the development of many elegant strategies, there is still no generally efficient and stereoselective method available. To this end, a number of glycosyl-donor systems have been developed, but few chemical systems allow the use of unprotected glycosyl donors; one exception has been Hanessian's 3-methoxypyridyl (MOP) glycoside system (4). It has been estimated that, on average, the need for protecting groups introduces an additional six steps to each overall glycoside bond formation. If the use of protecting groups could, therefore, be avoided or limited, while maintaining control of reactivity, then overall efficiencies may be improved. To this end, and as part of an ongoing programme to develop novel glycosylation systems and strategies (5), we have begun to investigate a new class of glycosyl donors: 4-bromobutyl glycosides. This communication describes our first results in this area.

Our goal was to create a glycosylation system that (*i*) uses sufficiently stable donors to allow preparation in unprotected form but that can still be activated; and (*ii*) may self-activate or activate under mild conditions. We reasoned that spontaneous 5-*exo* cyclization (Scheme 1) through nucleophilic attack of the C-1 oxygen atom in **1**, for example, would yield an anomeric furanosyl cation, which would closely resemble those postulated as intermediates in the activation of Fraser-Reid's powerful pentenyl glycoside class of glycosyl donors. (6) This would not only yield THF as a volatile, non-nucleophilic leaving group, but such a cyclization would also be favoured over any potentially competing cyclic ether formation with the free hydroxyls of the unprotected donor through, for example, 8-*exo* cyclization of OH-2 onto the primary bromide of the aglycon.

Clearly, the use of activation conditions that are compatible with the presence of free hydroxyl groups is essential to the use of unprotected glycosyl donors. We chose to investigate two potential activation conditions: self-activation and soft Lewis acid activation (e.g., Hal^+, Ag^+).

Our first target donor, mannoside **1**, was prepared as shown in Scheme 2. Penta-*O*-acetyl-D-mannose **6** was synthesized in quantitative yield using well-established methods from D-mannose and acetic anhydride with pyridine as a catalyst. Our strategy for creating **1** relied on the different hard and soft Lewis basicities of the anomeric *O*-1 and the aglycon primary bromide of bromobutyl glycosides, respectively (Scheme 1). Formation of 4-bromobutyl tetra-*O*-acetyl-α-D-mannopyranoside **2** was accomplished through a glycosidation using pentaacetate **6** and 4-bromobutanol, in which the hard Lewis acid $BF_3{\cdot}Et_2O$ catalysed the loss of the acetate group from the anomeric position of **6** without affecting the soft Lewis base aglycon primary bromide or indeed without activating **2** as a glycosyl donor through the mechanism envisaged in Scheme 1. In this regard, an additional aiding factor is that because of the disarmed (7) nature of **2,** this should be less reactive than the target unprotected donor **1**. 4-Bromobutanol was readily prepared through the

Received 31 October 2001. Published on the NRC Research Press Web site at http://canjchem.nrc.ca on 17 April 2002.

Dedicated to Professor J. Bryan Jones on the occasion of his 65th birthday.

B.G. Davis,[1] and M.A.T. Maughan.[2] Dyson Perrins Laboratory, University of Oxford, South Parks Road, Oxford OX1 3QY UK.
S.D. Wood. Department of Chemistry, University of Durham, South Road, Durham DH1 3LE U.K.

[1]Corresponding author (e-mail: Ben.Davis@chem.ox.ac.uk).
[2]Present address: Department of Chemistry, University of Durham, South Road, Durham DH1 3LE U.K.

 DOI: 10.1139/V02-029 © 2002 NRC Canada

Scheme 1.

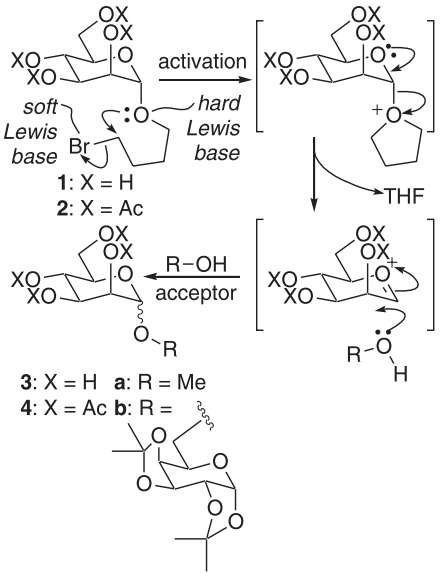

reaction of THF with 48% HBr (aq.) (8), which was preferred for large-scale work over the use of Me_2BBr (9). More than five equivalents of $BF_3{\cdot}Et_2O$ were required for effective conversion of **6** to the α-anomer **2**[3] (the sole product); the exclusive stereoselectivity for this *trans*-glycoside may be attributed to neighbouring group participation by the C-2 acetate group. While higher conversions were obtained through the use of a large excess of 4-bromobutanol, the 43% yield of **2** obtained through the use of 1.1 equivalents represents an efficient 83% yield when based on recovered starting material and was, therefore, the preferred procedure for scale-up. The use of higher equivalents of Lewis acid or increased reaction times led to no significant change in the yield of **2**.

The final step in the formation of fully deprotected donor 4-bromobutyl tetra-*O*-acetyl-α-D-mannopyranoside **1**[4] was carried out in a single efficient (87% yield) Zemplén deacetylation. Small amounts of methyl glycoside **1** (7% yield) were also recovered, encouragingly suggesting that through its action as a glycosyl donor, substitution of the anomeric 4-bromobutoxy group by MeOH had occurred at some point during the deprotection process. Since methyl glycosides are not products of the deprotection of mannosides (for example, the corresponding 3-bromopropyl mannoside (vide infra)), the formation of these methanolysis products under conditions not typically associated with lability of the glycosidic bond gave us our first indication of the successful action of 4-bromobutyl glycosides as glycosyl donors. As a consequence of this methanolysis, care was required during deacetylation of **2**. As might be anticipated, removal of the disarming effect of the acetyl groups meant that **1** would potentially prove more reactive as a glycosyl donor than **2** and that, similarly, each of the intervening partially deacetylated intermediates would prove even more reactive than the previous. After extensive screening, the use of a ~0.017 M methoxide solution freshly prepared from anhydrous MeOH and reaction times of 18 h proved optimal; shorter reactions times led to incomplete deprotection, whereas extended reaction times led to significant accumula-

Scheme 2. Reagents and conditions: (*i*) Ac_2O, py (3:2), 100%; (*ii*) $Br(CH_2)_{3+n}OH$, DCM, $BF_3{\cdot}Et_2O$, 43% for **2**, 39% for **8**; (*iii*) MeONa, MeOH, 87% for **1**, 98% for **7**; (*iv*) $Br(CH_2)_{3+n}OH$, $BF_3{\cdot}Et_2O$, 18% for **1**, 25% for **7**.

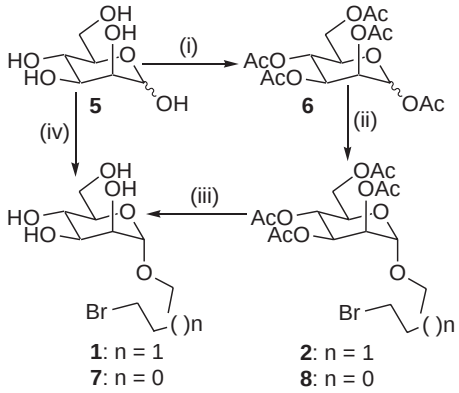

[3] **2**: $BF_3{\cdot}Et_2O$ (6.00 g, 42.3 mmol, 5.5 equiv.) was added dropwise to a solution of **6** (3.00g, 7.69 mmol) and 4-bromobutanol (1.30 g, 8.47 mmol, 1.1 equiv.) in dry DCM (20 mL) at 0°C under N_2. After 1.5 h, the reaction solution was warmed to room temperature and stirred for a further 16.5 h, when TLC (EtOAc–hexane, 50:50) showed conversion of starting material (R_f = 0.5) to a major product (R_f = 0.65). The reaction mixture was poured into ice water (10 mL) and extracted with DCM (3 × 20 mL). The organic extracts were combined, washed with water (15 mL), dried ($MgSO_4$), filtered, and the solvent removed. The residue was purified by flash chromatography (EtOAc–hexane, 40:60) to give recovered bromobutanol, starting material **6** and product **2** (1.61 g, 43% yield, 83% based on recovered starting material) as a white solid; mp 61–62°C. $[\alpha]_D^{22}$ = + 46.4 (*c*, 0.34 in $CHCl_3$). IR (cm^{-1}): 1747 (C=O). ^1H NMR (300 MHz, $CDCl_3$) δ: 1.78 (m, 2H, $OCH_2CH_2CH_2CH_2Br$), 1.88 (m, 2H, $OCH_2CH_2CH_2CH_2Br$), 2.00, 2.05, 2.11, 2.16 (4s, 4 × 3H, 4 × Ac), 3.46 (m, 2H, CH_2Br), 3.72 (m, 2H, $OCH_2CH_2CH_2CH_2Br$), 3.96 (ddd, *J* = 10, 6, 3 Hz, 1H, H-5), 4.14 (dd, *J* = 12, 3 Hz, 1H, H-6), 4.29 (dd, *J* = 12, 6 Hz, 1H, H-6′), 4.81 (d, *J* = 2 Hz, 1H, H-1), 5.23–5.33 (m, 3H, H-2, H-3, H-4). ^{13}C NMR (300 MHz, $CDCl_3$) δ: 20.7, 20.7, 20.8, 20.9 (4 × CH_3CO-), 27.9, 29.3 ($OCH_2CH_2CH_2CH_2Br$), 33.3 (CH2Br), 62.5, 66.1, 67.4, 68.6, 69.0, 69.6 ($OCH_2CH_2CH_2CH_2Br$, C-2, C-3, C-4, C-5, C-6), 97.6 (C-1), 169.8, 170.2, 170.3, 170.6 (4 × CH_3CO-). ES-MS *m*/*z* (MeOH): 505, 507 ($M+Na^+$). ES-HRMS calcd. for $C_{18}H_{31}BrNO_{10}$: 500.1131; found: 500.1131 ($[M + NH_4]^+$).

[4] **1**: A freshly prepared solution of NaOMe–MeOH (3 mL, 0.1 M) was added to a solution of **2** (1.00 g, 2.07 mmol) in dry methanol (15 mL) at room temperature under nitrogen. After 18 h, TLC (ethyl acetate–hexane, 50:50) showed the conversion of **2** (R_f = 0.65) to **1** (R_f = 0.05). The mixture was run through a Dowex 50W (H^+) plug (1 × 4 cm, eluant MeOH) and the solvent removed. The residue was purified by flash chromatography (15% MeOH–$CHCl_3$) to yield **1** (0.57 g, 1.82 mmol, 87%); mp 104–105°C. $[\alpha]_D^{22}$ = + 36.0 (*c*, 0.2 in MeOH). ^1H (250 MHz, CD_3OD) δ: 1.78 (m, 2H, $OCH_2CH_2CH_2CH_2Br$), 1.98 (m, 2H, $OCH_2CH_2CH_2CH_2Br$), 3.50 (m, 2H, CH_2Br), 3.70 (m, 2H, $OCH_2CH_2CH_2CH_2Br$), 3.60–3.90 (m, 5H, H-2, H-3, H-4, H-5, H-6), 3.96 (dd, *J* = 12, 3 Hz, 1H, H-6′), 4.78 (d, *J* = 2 Hz, 1H, H-1). ^{13}C (250 MHz, CD_3OD) δ: 30.0, 31.9 ($OCH_2CH_2CH_2CH_2Br$), 35.1 (CH_2Br), 63.8, 68.5, 69.5, 73.1, 73.5, 75.6 ($OCH_2CH_2CH_2CH_2Br$, C-2, C-3, C-4, C-5, C-6), 102.4 (C-1). ES-MS *m*/*z* (MeOH): 337, 339 ($[M + Na]^+$, 100%). ES-HRMS calcd. for $C_{10}H_{23}BrNO_6$: 332.0709; found: 332.0716 ($[M + NH_4]^+$). Anal. calcd. for $C_{10}H_{19}BrO_6$: C 38.11, H 6.08; found: C 37.95, H 6.04.

© 2002 NRC Canada

Table 1. Results of glycosylation reactions using bromobutylglycosides **1** and **2** as donors.

Donor	Activator[a]	Solvent	Reaction time (h)	Acceptor	Product	Yield(%)[b]	Product α:β ratio
1	—	DMF	10	MeOH[c]	**3a**	20	9:1
1	—	DMF	60	MeOH[c]	**3a**	53	9:1
1	IBr	DMF	12	MeOH[c]	**3a**	36	8:1
1	AgOTf	DMF	24	MeOH[c]	**3a**	66	9:1
1	AgOTf	DMF	20	DAG[d]	**3b**	60	5:1
2	—	DCM	60	MeOH[c]	—	—	—
2	IBr	DCM	60	MeOH[c]	—	—	—
2	AgOTf	DCM	24	MeOH[c]	**4a**	43	α only
2	AgOTf	DCM	20	DAG[d]	**4b**	51	α only

[a]All reactions at room temperature.
[b]All yields are for isolated products.
[c]5 equivalents used.
[d]1 equivalent used.

tion of methyl mannoside products. The anomeric mixture of glycosides formed (the formation of some methyl β-D-mannopyranoside suggests that there was a lack of neighbouring group participation and therefore the lack of a C-2 acetate) and the disarming effect (7) of the acyl groups in **2**, likely means that methanolysis occurred when the donor was fully deprotected as **1**. It should be noted that although **1** is an effectively active glycosyl donor, it is nonetheless stable even to flash column chromatography on silica: an unusual and highly convenient stability that may be attributed to silica as a mild, hard rather than soft, Lewis acidic medium. As an alternative direct method for the direct synthesis of **1** from D-mannose **5**, Fischer glycosidation was also investigated. Treatment of a suspension of **5** in neat 4-bromobutanol with $BF_3{\cdot}Et_2O$ gave, after extensive purification, a low yield (18%) of **1**; although this was only a one-step procedure, inferior overall yield and use of large quantities of 4-bromobutanol meant preparation via **2** was selected as a superior route.

The results of glycosylation reactions[5] with **1** and **2** are shown in Table 1. We were delighted to see that simply by stirring **1** with MeOH as a glycosyl acceptor and *without activator*, methyl mannoside **3a** (10) was formed in a low 20% yield after 10 h, but in a fair 53% yield after 60 h. The α:β stereoselectivity (9:1) observed is consistent with the stereoselectivities of other non-participatory mannosyl donors. (3) Although these results were encouraging, we reasoned that use of a soft Lewis acid might increase rate and (or) efficiency because of the differing nature of the Lewis basicities of **1** (Scheme 1). Thus, the use of IBr (11) led after 12 h to increased rate and yield when compared with glycosylations without an activator. Unfortunately, prolonged reaction times with IBr did not lead to enhanced yield and so AgOTf was tested as an alternative halophilic Lewis acid. Using AgOTf, we were extremely pleased to observe a yield of 66% of **3a**. These improved conditions were also successfully applied to the synthesis of disaccharide **3b** (60% yield) through the use of diacetone galactose (DAG) as an acceptor, thereby demonstrating potential for oligosaccharide synthesis and confirming the compatibility of the method with acid-sensitive protecting groups. The possibility exists that although none was isolated, self-condensation of **1** may account for the only fair yield of **3b**, and we are now investigating the use of *O*-6 protected donors.

Having demonstrated the ability of **1** to act as a glycosyl donor, peracetylated **2** was examined next. Consistent with our earlier hypothesis (vide supra) and with the disarmed (7) nature of **2**, glycosylation did not proceed either in the absence of an activator or in the presence of IBr. Through the use of AgOTf, however, fair yields of methyl mannoside **4a** (12) (43%) and disaccharide **4b** (51%) were obtained. The exclusive α-stereoselectivity that was observed for **4a**,**b** may be attributed to neighbouring group participation by the C-2 acetate group.

Finally, to test the hypothesis that cyclization to form a furanosyl oxonium leaving group is an essential precursor step in the mechanism of glycosylation, two analogous peracetylated (**8**) and deprotected (**7**) 3-bromopropyl mannopyranosides were prepared using analogous routes to those used for the preparation of **1** and **2** (Scheme 2). Consistent with the need for cyclization, neither **7** or **8** were able to act as glycosyl donors under the conditions that had proved successful for **1** or **2**.[6]

In summary, this communication describes the first examples of a new class of glycosyl donor: bromobutylglycosides (BBGs). Deprotected BBG **1** appears to possess a remarkably balanced reactivity that allows its ready preparation and

[5]General procedure for glycosylation reactions: To a solution of **1** (100 mg, 0.32 mmol, 1 equiv.) in DMF (5 mL) under nitrogen, was added acceptor MeOH (64 μL, 1.6 mmol, 5 equiv.). The solution was stirred at room temperature for 60 h, any precipitate removed by centrifugation and the solvent removed. The residue was purified by flash chromatography (15% MeOH– $CHCl_3$) to yield **3a** (33 mg, 53%, α:β = 9:1) as a white solid. Parallel reactions were repeated under similar conditions using, IBr (66 mg, 0.32 mmol, 1 equiv.) or silver triflate (82 mg, 0.32 mmol, 1 equiv.) to yield 22 mg (α:β, 8:1, 36%, after 12 h) or 41 mg (α:β, 9:1, 66%, after 24 h) of **3a**, respectively.

[6]As usefully highlighted by a referee, the inactivity of 3-bromopropyl glycosides does not exclude the possibility of direct Fischer glycosylation that could be catalyzed by the equivalent of HBr (in spontaneous and IBr-activated reactions) or TfOH (in AgOTf-activated reactions) that is liberated. To test this hypothesis, **1** was used to glycosylate MeOH activated with AgOTf in the presence of the hindered base 2,4,6-tri-*tert*-butylpyridine (TTBP) [D. Crich D, M. Smith, Q.J. Yao, J. Picione, Synthesis, 323 (2001).] and yielded 64% of **3a** after 24h; near identical to that obtained without base. Other aspects of the mechanism, including the detection of THF, are currently in progress.

© 2002 NRC Canada

purification and yet is sufficiently reactive to act as an *unprotected* glycosyl donor *even in the absence of activator*. In addition, although **1** is strongly activated by soft Lewis acid catalysis its relative resistance to hard Lewis acid catalysis allows, for example, its direct preparation through Fischer glycosidation. Although the yields for glycosylations using BBGs are thus far only fair or low,[7] the potential to avoid the use of protecting groups might offset overall glycosylation efficiencies. The breadth of the utility of **1** with other acceptors and the investigation of bromobutyl-glycosides of other parent carbohydrates is underway, the results of which will be presented in due course.

Acknowledgments

We would like to thank HEFCE (SDW), the Royal Society (BGD), and the University of Oxford for funding and the EPSRC for access to the Mass Spectrometry Service at Swansea and the Chemical Database Service at Daresbury. Last but not least we would like to thank Prof. J. Bryan Jones for his constant inspiration and encouragement.

References

1. A. Varki. Glycobiology, **3**, 97 (1993); R.A Dwek. Chem. Rev., **96**, 683 (1996); B.G. Davis. J. Chem. Soc. Perkin Trans. 1, 3215 (1999).
2. J.C. McAuliffe and O. Hindsgaul. Chem. Ind. 170 (1997); B.G. Davis. Chem. Ind. 134 (2000); K.M. Koeller and C.-H. Wong. Nature Biotechnol. **18**, 835 (2000).
3. H. Paulsen. Angew. Chem. Int. Ed. Engl., **21**, 155 (1982); K. Toshima and K. Tatsuta. Chem. Rev. **93**, 1503 (1993); G.J. Boons. Contemp. Org. Synth. **3**, 173 (1996); G.J. Boons. Tetrahedron, **52**, 1095 (1996); B.G. Davis. J. Chem. Soc. Perkin Trans. 1, 2137 (2000).
4. S. Hanessian and B.L. Lou. Chem. Rev. **100**, 4443 (2000).
5. R.J. Tennant-Eyles, B.G. Davis, and A.J. Fairbanks. Chem. Commun. 1037 (1999); R.J. Tennant-Eyles, B.G. Davis, and A.J. Fairbanks. Tetrahedron: Asymmetry, **11**, 231 (2000); B.G. Davis. J. Chem. Soc. Perkin Trans. 1, 2137 (2000); B.G. Davis, S.J. Ward, and P.M. Rendle. Chem. Commun. 189 (2001).
6. B. Fraser-Reid, U.E. Udodong, Z.F. Wu, H. Ottosson, J.R. Merritt, C.S. Rao, C. Roberts, and R. Madsen. Synlett, 927 (1992).
7. For the background to the use of armed–disarmed donors (in which the reactivity is increased or decreased by the use of electron donating or withdrawing protecting groups, respectively), see: D.R. Mootoo, P. Konradsson, U. Udodong, and B. Fraser-Reid. J. Am. Chem. Soc. **110**, 5583 (1988); G.J. Boons, P. Grice, R. Leslie, S.V. Ley, and L.L. Yeung. Tetrahedron Lett. **34**, 8523 (1993).
8. E. Vedejs, M. J. Arnost, and J. P. Hagen. J. Org. Chem. **44**, 3230 (1979).
9. Y. Guindon, M. Therien, Y. Girard, and C. Yoakim. J. Org. Chem. **52**, 1680 (1987).
10. E. Fischer and L. Beensch. Chem. Ber. **29**, 2927 (1896).
11. K.P.R. Kartha and R.A. Field. Tetrahedron Lett. **38**, 8233 (1997).
12. J.K. Dale. J. Am. Chem. Soc. **46**, 1046 (1924).

[7] The possibility of competing 1,6-anhydromannose formation was raised by a referee as a reason for the moderate yields. Although none was isolated as a by-product, the synthesis of 6-*O*-protected donors to test this hypothesis is underway.

© 2002 NRC Canada

Rationalization of enzyme enantioselectivity by active-site cubic-space models

Gianluca Ottolina and Giacomo Carrea

Abstract: Active-site models of enzymes are important tools that help researchers in understanding and predicting the stereochemical outcome of enzymatic reactions. In this article, various active-site models for dehydrogenases, hydrolases, oxygenases, and oxynitrilases have been reviewed.

Key words: Active-site model, cubic space, enzyme model, dehydrogenases, hydrolases, oxygenases, oxynitrilases.

Résumé : Les modèles de sites actifs d'enzymes sont des instruments précieux pour aider aux chercheurs à comprendre et à prédire le résultat stéréochimique de réactions enzymatiques présentant de l'intérêt. Dans cet article, on passe en revue une variété de modèles de sites actifs de déshydrogénases, d'hydrolases, d'oxygénases et d'oxynitrilatases.

Mots clés : modèle de site actif, espace cubique, modèle d'enzyme, déshydrogénases, hydrolases, oxygénases; oxynitrilatases.

[Traduit par la Rédaction]

Introduction

For an enzyme to be a useful catalyst, it is desirable to understand the factors controlling its selectivity; in particular how the selectivities of specific enzymes can be correlated with the structural features of the substrate they process. In absence of such data, one must rely upon arbitrary screening to find an enzyme suitable for a given reaction. Knowledge of the enzyme–substrate interactions that regulate and control enzyme selectivity will permit the development of active-site models capable of accurately predicting both whether an enzyme will accept a new structure as a substrate and what the stereochemical outcome of the reaction will be.

In 1964, Nobel Laureate Vladimir Prelog devised an active-site model for horse liver alcohol dehydrogenase (HLADH), based on diamond-lattice section approach (1). This model, which was very successful for interpreting the steric reaction course of six-membered ring ketones and alcohols, was derived from previous observations made for the reduction of carbonyl compounds by *Curvularia falcata* (Prelog's rule, Fig. 1). The HLADH model was updated by Jones and Beck (2) as depicted in Fig. 2, but was not further refined for several reasons, including (*i*) the model cannot rationalize the *cis–trans* ratios of the 4-alkylcyclohexanols obtained by the reduction of the corresponding 4-alkylcyclohexanones; (*ii*) the substituent in (3*R*)-3-alkylcyclohexanones must be in an axial position before reaction can occur; (*iii*) the forbidden positions are rather scattered, which is inconsistent with an extensive enzyme surface.

To overcome this weakness, Jones and Jakovac (3) proposed a model based on cubic space (Fig. 3). The model described the active site of HLADH and was proposed as a complementary way to reliably predict enzyme specificity after the X-ray structure of HLADH was solved. The information gained from the diamond-lattice section was introduced in the new model along with newly acquired data. This information was used to identify the active-site regions open to substrate occupation (allowed regions) and those where substrate binding was precluded (forbidden regions) (Fig. 4). The use of a cubic framework eliminated many of the chemical and conformational disadvantages of previous models based on carbon-bond lengths and angles, and the cubic section could be made as specific and flexible as needed by appropriate selection of the unit volume. Jones and co-workers (4) also proposed an active-site model, based again on the cubic-space approach, for pig liver esterase (PLE, Fig. 5).

Several active-site models based on the cubic-space approach have been developed; many are well defined while others are simple sketches of enzyme-active sites. These models are used by many researchers to predict the stereochemical outcome of enzymatic reactions. In the following report, we will briefly review these models and discuss their applications.

Cubic-space approach

The cubic-space approach is principally adopted in the absence of a three-dimensional structure of the enzyme, and is an empirical method based on substrate selectivity. To build a new model, it is necessary to collect experimental data from numereous substrates with high selectivity (chemo-, regio-, or enantio-) and well-defined or unique conformations. The substrates are then aligned along the reactive moi-

Received 7 December 2001. Published on the NRC Research Press Web site at http://canjchem.nrc.ca on 6 May 2002.

Dedicated to Professor J. Bryan Jones on the occasion of his 65th birthday.

G. Ottolina[1] and G. Carrea. Istituto di Chimica del Riconoscimento Molecolare, CNR, Via Mario Bianco 9, 20131 Milano, Italy.

[1]Corresponding author (e-mail: ottolina@ico.mi.cnr.it).

 DOI: 10.1139/V02-056 © 2002 NRC Canada

Color profile: Generic CMYK printer profile
Composite Default screen

Fig. 1. Steric course of the microbial reduction of carbonyl compounds by *Curvularia falcata*.

Fig. 2. Diamond-lattice model for HLADH. F, forbidden positions; U, undesirable positions.

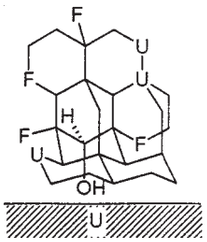

Fig. 3. A perspective (left-front viewpoint) of the HLADH cubic-space model.

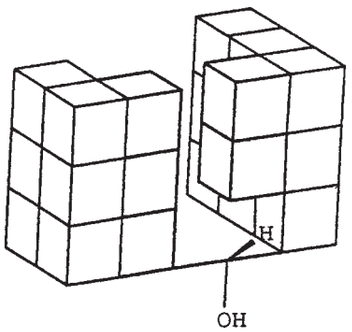

ety of interest (e.g., the ester group for hydrolysis, sulfur for sulfoxidation) and overlaid to identify the components that can occupy common volumes. The overlapping moieties, of course, whether polar or nonpolar, have to be coincident, and the selectivity predicted in the formation of the products must agree with the experimental product. The emerging three-dimensional picture is inserted inside a "cage" composed of several cubes (the cubic space) of a convenient edge (usually 1.54 Å). The cubes not occupied by the common volumes of the substrates are removed and the final cage thus obtained is identified as the active-site model.

To correctly use the model, the substrate must be placed inside the cage following a few simple rules such as alignment of the carbonyl or hydroxyl group along the C–OH bond. The rules concerning substrate positioning inside the active-site models reflect the chemical logic used to construct such models. Since these models are kept as simple as possible they cannot predict the kinetic and quantitative features of the reactions such as V_{max}, K_M, or yield.

Dehydrogenases

Alcohol dehydrogenases, which catalyze the oxidoreduction of a broad structural range of aldehydes, ketones, and alcohols, are among the most useful enzymes for organic synthetic purposes. The active-site model for HLADH has been proposed by Jones and Jakovac (3) and is depicted in Fig. 3. Hydride is delivered to, or removed from, the coenzyme at the front of the model (as shown in Fig. 3), with the C–OH bond, which projects downward to coordinate with the active-site Zn^{2+} atom in the region below, forbidden to the substrates. The rules governing the correct positioning of the substrates inside the active-site model are described in detail in the original paper (3).

Fig. 4. Front view of the HLADH model. Top covers the 2*R*-alkylcyclohexanones and the bottom the 2*S*. The cyclohexanone rings are shown in the conformations required for correct orientation of the carbonyl group at the hydride delivery site.

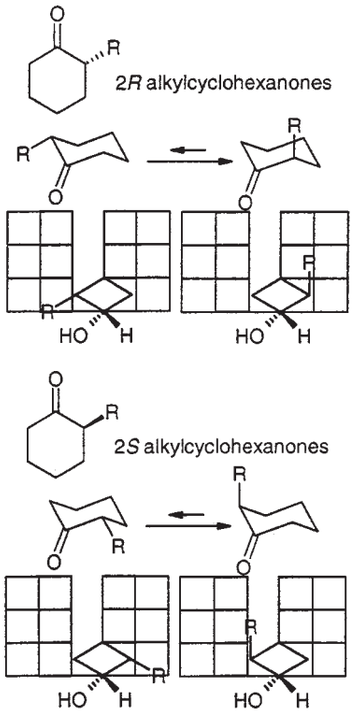

Figure 4 shows the picture for 2-alkylcyclohexanones, where all the possible absolute configurations and conformations for the substrates are taken into account and every structure is separately placed inside the model and evaluated. For the (2*R*)-series, reduction is strongly disfavored because the required binding of both conformations (Fig. 4, top left and top right) would place the R substituent in the forbidden region of the model. The same situation holds for the thermodynamically preferred conformer of the (2*S*)-series (Fig. 4, bottom left). The disfavored conformer (Fig. 4, bottom right) can, however, effectively bind to give a productive enzyme–substrate complex since the axial substituent can be accommodated at the boundary of the limited region. Reduction would therefore lead to (1*S*,2*S*)-2-alkylcyclohexanol. The experimental results were in full agreement with this prediction. For branched 2-*iso*-propyl and 2-*tert*-butylcyclohexanones, it was experimentally demonstrated that they are not substrates — this was also predicted by the HLADH model because the substituent at C-2 overlaps in the forbidden region in all possible conformations.

© 2002 NRC Canada

I:\cjc\cjc80\cjc-06\V02-056.vp
Monday, May 13, 2002 2:45:02 PM

Color profile: Generic CMYK printer profile
Composite Default screen

Fig. 5. A perspective (right-front viewpoint) of the PLE cubic-space model. The hydrophobic large (H_L), hydrophobic small (H_S), polar front (P_F), and polar back (P_B) pockets are depicted. The catalytic region (serine) is encircled.

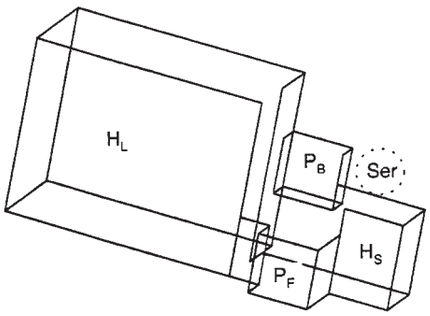

This HLADH model has been successfully applied to many substrates, such as monocyclic and bicyclic ketones or alcohols, including the desymmetrization of meso compounds.

Hydrolases

Pig liver esterase (PLE) is a serine hydrolase, which catalyzes the hydrolysis of various ester structures with high selectivity. Numerous stereoselective modifications of prochiral substrates and the resolution of racemates have been reported. As already mentioned, Jones and co-workers (4–6) developed a cubic-space model for this enzyme, which after some refinements (taking into account the increased quantity of experimental data subsequently produced), was defined as shown in Fig. 5. This suggests that a model could in principle be based on a minimal set of substrates and then amplified to accommodate new substrates. (Obviously the amplified model cannot contradict previous predictions of substrate selectivity.) One point raised during the development of the PLE model was that PLE contains several isozymes. It has been demonstrated, however, that all the isozymes act in a more or less similar manner and that for preparative purposes PLE can be used as though it were a single species. Thus, the active-site model holds for all the isozymes that, from a selectivity point of view, behave as a single species. PLE is quite sensitive to reaction conditions; in fact, in many reactions enantioselectivity is influenced by temperature and by the presence of organic co-solvents such as acetone, dioxane, acetonitrile added to solubilize the substrates. These observations suggest that when designing an enzyme active-site model the reaction conditions must be carefully taken into account. Reliable predictions from the model can, therefore, only be expected for reactions carried out under the conditions adopted for its development. Figure 6 illustrates that the model can explain the high stereoselectivity of PLE in the hydrolysis of a biphenylyl malonate substrate to give the half-ester with the expected (*R*) absolute configuration. When the malonate is positioned within the active-site model as dictated by the guidelines, an ES-complex is formed, where the pro-*S* methyl ester is within the radius of action of the serine group, the second nonhydrolyzed methyl ester is located in the P_F pocket, the C-2 methyl extends into the empty space above the active site, and the biphenylyl group is directed into the H_L pocket.

Fig. 6. Fitting of dimethyl 2-(3-biphenylyl)-2-methyl-malonate into PLE model is shown from the right-front perspective.

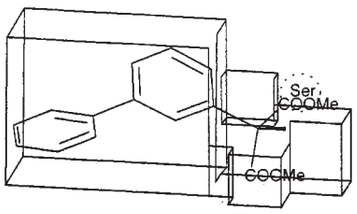

Fig. 7. A perspective (right-front viewpoint) of the lipase PS cubic-space model according to Lemke et al. (9). In the figure the serine of the catalytic triad is also localized.

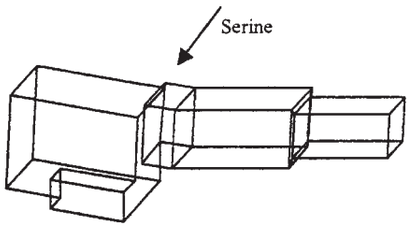

Several groups have applied this predictive model for numerous new substrates such as the hydrolysis to the half-ester of benzene-1,2-diacetic ester chromium carbonyl (7) or the resolution of racemic methylsulfinylacetates (8).

One of the most popular lipases for synthetic applications is lipase PS (Amano Pharmaceutical) from *Pseudomonas cepacia*. This lipase has been used for the regio- and stereoselective hydrolysis and alcoholysis of carboxylic esters and anhydrides and for the regio- and stereoselective transesterification of alcohols. Lipase PS shows a broad range of substrate acceptability and thus has stimulated the development of a cubic-space model for the enzyme. Two models have been independently devised by Lemke et al. (9) and Grabuleda et al. (10) and they are shown in Figs. 7 and 8, respectively. For the first model, a set of 61 3-(aryloxy) propan-2-ols acetylated with vinyl acetate in THF by lipase PS were used. For the second model, the data were collected from the literature and refer to various substrates acylated with vinyl acetate in different organic solvents. It is interesting to note that even if the models were based on two different sets of molecules they share some similarity. The model in Fig. 7 (9) shows that the substrate is oriented mainly by two hydrophobic pockets with very different shapes: one is a tube-like pocket with a very limited diameter, while the other has a cube-like shape; both are located close to the active serine. The other model (Fig. 8), also shows two hydrophobic pockets that accommodate the large and the small hydrophobic substituents and also a hydrophilic pocket that essentially accommodates the hydroxyl group (10). Interestingly, the small hydrophobic pocket is tube-shaped as in the Lemke et al. model (9), while the total volume of the second model is smaller, which probably reflects the different structures of the two sets of substrates. When developing their model, Grabuleda et al. (10) took into consideration only those compounds that displayed very high selectivity with lipase PS and were, therefore, rather insensitive to variations in the reaction conditions. Indeed the enantiomeric ratio (*E*)

© 2002 NRC Canada

I:\cjc\cjc80\cjc-06\V02-056.vp
Monday, May 13, 2002 2:45:03 PM

Color profile: Generic CMYK printer profile
Composite Default screen

Fig. 8. A perspective (right-front viewpoint) of the lipase PS cubic-space model according to Grabuleda et al. (10). Important substrate-binding regions are identified as the following: $H_{L,}$ large hydrophobic pocket; H_S, small tunnel-shaped hydrophobic pocket; and H_H, hydrophilic pocket for hydroxyl group.

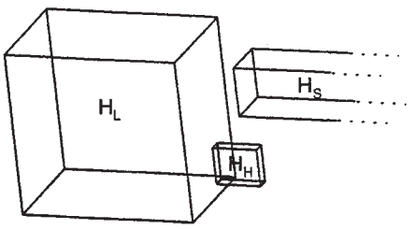

for this set of substrates ranged from 45 to over 300, where binding inside the active site was not heavily influenced by the nature of the medium. This choice, however, is also a limit of the model that cannot predict the influence of variations with the reaction medium on enzyme stereoselectivity.

The cubic-space approach has also been used to simulate the active site of other lipases. These models, however, were mainly two-dimensional with the active site not fully described; still, some important predictive features were retained. These models, which are not described here, refer to lipase YS (11), lipase AK (12), lipase QL (13), and *Rhizopus delemar* lipase (14).

Oxygenases

The enantioselective sulfoxidation of sulfides to sulfoxides has been accomplished with different microrganisms and free enzymes. Among these, cyclohexanone monooxygenase (CHMO) from *Acinetobacter calcoaceticus* NCIMB 9871 has been the most investigated. This flavoenzyme catalyzes the sulfoxidation of numerous alkyl aryl sulfides, dialkyl sulfides, alkyl disulfides, and cyclic organic sulfites to optically active sulfoxides and sulfates (15, 16). The structure of the sulfides dramatically influence not only the enantioselectivity, but also the stereochemical outcome of the reaction, giving sulfoxides ranging from 99% ee with (*R*)-configuration to 93% ee with (*S*)-configuration (16). To explain the puzzling behavior of CHMO, an active-site model starting from a set of 31 substrates has been developed (17). Figure 9 depicts the active-site model, where it is possible to see the three-binding pockets that accommodate the substrates and an example of the applicability of this model. The series of *o*-, *m*-, and (*p*-methyl)-phenyl methyl sulfides display an interesting reversal in stereoselectivity yielding products that go from (*R*)-sulfoxide for *o*- and *m*-substrates to (*S*)-sulfoxide for the *p*-substrates. At the bottom of Fig. 9, the binding modes for these three substrates are depicted. It appears that the methyl group for the *p*-substituent in the (*R*)-conformation protrudes outside the M pocket in a forbidden position, which therefore precludes oxidation. The *p*-substituted phenyl ring can, however, be accommodated in the H_L pocket, leading to (*S*)-(*p*-methyl)-phenyl methyl sulfoxide.

CHMO also catalyzes another mechanistically different reaction within the confines of the same active site, i.e., the Baeyer-Villiger oxidation of ketones to esters or lactones. Thus, the same active-site model of CHMO should also explain the stereoselectivity of enzymatic Baeyer-Villiger oxidations. In fact, the model was shown to be applicable to this type of reaction and has provided useful insight to understanding the behavior of the enzyme (18, 19). In the Baeyer-Villiger oxidation reaction, the priority rules for the migrating group are strictly respected. In the enzymatic reaction, however, an "abnormal" oxygen insertion (with reversal of the priority rules) is observed along with the "normal" oxygen insertion. This behavior can be explained by the model, as illustrated for the oxidation of racemic bicyclo[3.2.0]hept-2-en-6-one (Fig. 10). With the (1*R*,5*S*)-enantiomer, oxygen insertion takes place exclusively on the more substituted C–C bond ("normal" mode), because the "abnormal" oxygen insertion is prevented by steric–enzymatic constraints. The opposite is true for the (1*S*,5*R*)-enantiomer, even though the selectivity is lower because of less stringent steric hindrances.

Fig. 9. Top: A perspective (right-front viewpoint) of the CHMO cubic-space model. Important binding regions for substrates are identified as the following: M, main hydrophobic pocket; H_L, large hydrophobic pocket; H_S, small hydrophobic pocket. Bottom: Top perspective view of the preferred binding modes of *o*-, *m*-, and (*p*-methyl)-phenyl methyl sulfide.

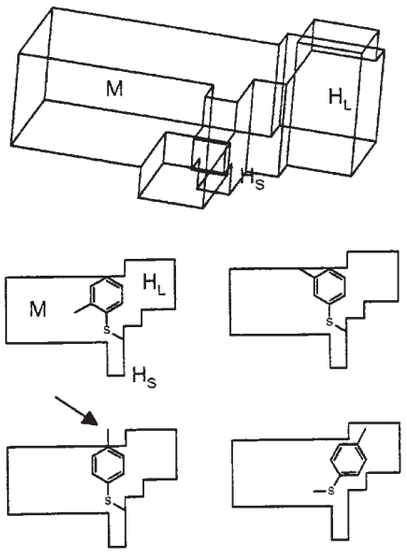

The model also holds with cyclic thiolactones, which are known to be suicide inhibitors of CHMO. The substrates (sulfides or ketones) examined so far are mainly oriented inside the active-site model by hydrophobic interactions and steric hindrances. The contribution of polar substrates also has to be taken into consideration by locating the electon-rich and electron-poor regions inside the active-site model (20).

The fungi *Helminthosporium* sp. NRRL 4671 and *Mortierella isabellina* ATCC 42613 convert a wide range of prochiral sulfides to the corresponding chiral sulfoxides, the former with a preference for the (*S*) configuration at sulfur and the latter for the opposite configuration. Active-site models for enzymes capable of this type of biotransformations have been developed by Holland and co-workers (21–23) and are shown in Figs. 11 and 12. These models, which can

© 2002 NRC Canada

I:\cjc\cjc80\cjc-06\V02-056.vp
Monday, May 13, 2002 2:45:04 PM

Color profile: Generic CMYK printer profile
Composite Default screen

Fig. 10. Top perspective binding modes of racemic bicyclo[3.2.0] hept-2-en-6-one in the active site of CHMO. The bold arrows indicate the preferred (or exclusive) oxidation pathways.

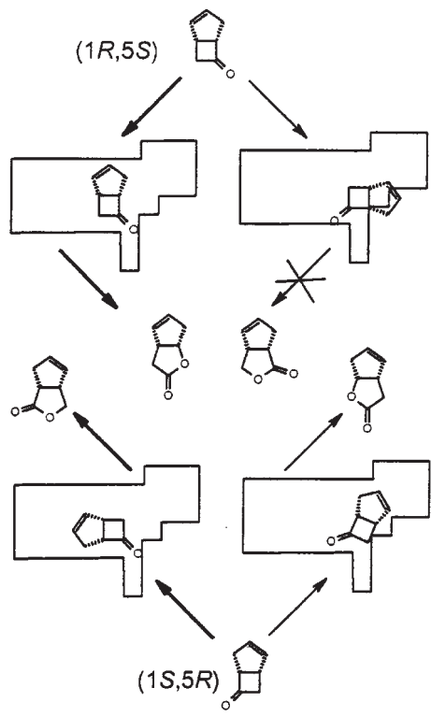

predict and correlate substrate–product relationships for the reactions catalyzed by these whole-cell biocatalysts, have as a common feature a binding site for polar substrate moieties. The model for *Mortierella isabellina* can also be applied to other reactions catalyzed by this enzyme, such as benzylic hydroxylations and epoxidation of suitable substrates.

Two models have also been proposed for sulfide oxidations catalyzed by 2,5-diketocamphane 1,2-monooxygenase and 3,5-diketocamphane 1,6-monooxygenase from *Pseudomonas putida* NCIMB 10007. These models, which are based on 23 different phenyl-, benzyl-, methyl-, and ethyl-alkyl sulfides appear, however, exceedingly detailed, which makes their application rather laborious (24).

Oxynitrilase

A model for (*R*)-oxynitrilase has been developed from a small set of substrates. The active site, which essentially appears as a wide parallelepiped, lacks detail (25). The model is, therefore, only useful as an approximate guide to predict whether a substrate, on the basis of its encumbrance, can bind to oxynitrilase.

Conclusion

The empirical approach based on cubic space has demonstrated its validity as a general tool to quickly get answers for a specific enzyme–substrate combination. We have shown several examples using this methodology and also how to build and use the cubic-space enzyme model. The accessibility and the chemo-, regio-, and enantioselectivity are

Fig. 11. A perspective of the cubic-space model for sulfoxidation by *Helminthosporium*. The oxidation centre and the polar binding region (P) are indicated. The preferred binding mode for benzyl alkyl sulfides is also displayed.

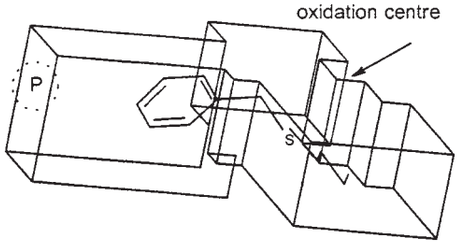

Fig. 12. A perspective of the cubic-space model for the sulfoxidation by *Mortierella isabellina*. The oxidation centre and the polar binding region (P) are indicated. The preferred binding mode for bycyclic sulfides is also displayed.

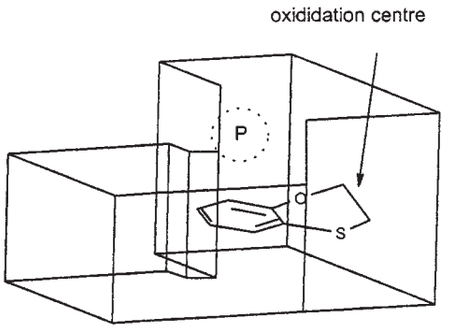

predicted for the compounds of interest with a good confidence. Unfortunately, this approach cannot give information on the kinetic parameters that govern enzyme catalysis.

The cubic-space approach is also challenged by the increased availability of computer power, which makes the extensive use of molecular modelling and (or) chemometric techniques possible.

Molecular dynamic simulations, used in conjunction with appropriate thermodynamics-based models, allow qualitative predictions on the selectivity of many reaction types; however, the application of quantum mechanical – molecular mechanical methods is required for the development of quantitative models of actual reactivity patterns (26–30). Unfortunately, these methods require the 3D structure of the enzyme, are very computer-time demanding, and the results obtained might not be fully supported by the experimental data. On the other hand, chemometric techniques such as 3D-QSAR are becoming more popular and various methodologies are used. This last approach is, however, so far mostly applied in the pharmacological area; few reports deal with the biocatalytic area (31–33).

References

1. V. Prelog. Pure Appl. Chem. **9**, 119 (1964).
2. J.B. Jones and J.B. Beck. Techiques of Chemistry. N.Y. **10**, 107 (1976).
3. J.B. Jones and I.J. Jakovac. Can. J. Chem. **60**, 19 (1982).

© 2002 NRC Canada

I:\cjc\cjc80\cjc-06\V02-056.vp
Monday, May 13, 2002 2:45:06 PM

Color profile: Generic CMYK printer profile
Composite Default screen

4. E.J. Toone, M.J. Werth, and J.B. Jones. J. Am. Chem. Soc. **112**, 4946 (1990).
5. L. Provencher, H. Wynn, J.B. Jones, and A.R. Krawczyk. Tetrahedron: Asymmetry, **4**, 2025 (1993).
6. L. Provencher and J.B. Jones. J. Org. Chem. **59**, 2729 (1994).
7. J.A.S. Howell, M.G. Palin, G. Jaouen, B. Malezieux, S. Top, J.M. Cense, J. Salaün, P. McArdle, D. Cunningham, and M. O'Gara. Tetrahedron: Asymmetry, **7**, 95 (1996).
8. P. Kielbasinski. Tetrahedron: Asymmetry, **11**, 911 (2000).
9. K. Lemke, M. Lemke, and F. Theil. J. Org. Chem. **62**, 6268 (1997).
10. X. Grabuleda, C. Jaime, and A. Guerrero. Tetrahedron: Asymmetry, **8**, 3675 (1997).
11. K. Naemura, R. Fukuda, M. Murata, M. Konishi, K. Hirose, and Y. Tobe. Tetrahedron: Asymmetry, **6**, 2385 (1995).
12. K. Burgess and L.D. Jennings. J. Am. Chem. Soc. **113**, 6129 (1991).
13. K. Naemura, M. Murata, R. Tanaka, M. Yano, K. Hirose, and Y. Tobe. Tetrahedron: Asymmetry, **7**, 3285 (1996).
14. M. Tanaka, M. Yoshioka, and K. Sakai. Tetrahedron: Asymmetry, **4**, 981 (1993).
15. S. Colonna, N. Gaggero, L. Casella, P. Pasta, and G. Ottolina. Chem. Commun. 2303 (1996)
16. G. Carrea, B. Redigolo, S. Riva, S. Colonna, N. Gaggero, E. Battistel, and D. Bianchi. Tetrahedron: Asymmetry, **3**, 1063 (1992).
17. G. Ottolina, P. Pasta, G. Carrea, S. Colonna, S. Dallavalle, and H.L. Holland. Tetrahedron: Asymmetry, **6**, 1375 (1995).
18. G. Ottolina, G. Carrea, S. Colonna, and A. Rückemann. Tetrahedron: Asymmetry, **7**, 1123 (1996).
19. F. Zambianchi, P. Pasta, G. Ottolina, G. Carrea, S. Colonna, N. Gaggero, and J.M. Ward. Tetrahedron: Asymmetry, **11**, 3653 (2000).
20. G. Ottolina, P. Pasta, D. Varley, and H.L. Holland. Tetrahedron: Asymmetry, **7**, 3427 (1996).
21. H.L. Holland, F.M. Brown, G. Lakshmaiah, B.G. Larsen, and M. Patel. Tetrahedron: Asymmetry, **8**, 683 (1997).
22. H.L. Holland, L.J. Allen, M.J. Chernishenko, M. Diaz, A. Kohl, J. Ozog, and J.-X. Gu. J. Mol. Cat. B: Enzym. **3**, 311 (1997).
23. H.L. Holland, C.D. Turner, P.R. Andreana, and D. Nguyen. Can. J. Chem. **77**, 463 (1999).
24. J. Beecher, and A. Willetts. Tetrahedron: Asymmetry, **9**, 1899 (1998).
25. V.I. Ognyanov, V.K. Datcheva, and K.S. Kyler. J. Am. Chem. Soc. **113**, 6992 (1991).
26. G. Colombo, G. Ottolina, G. Carrea, A. Bernardi, and C. Scolastico. Tetrahedron: Asymmetry, **9**, 1205 (1998).
27. F. Haeffner, T. Norin, and K. Hult. Biophys. J. **74**, 1251 (1998).
28. G. Colombo, S. Toba, and K.M. Merz, Jr. J. Am. Chem. Soc. **121**, 3486 (1999).
29. G. Colombo, G. Ottolina, G. Carrea, and K.M. Merz, Jr. Chem. Commun. 559 (2000).
30. D.G. Gascoyne, H.L. Finkbeiner, K.P. Chan, J.L. Gordon, K.R. Stewart, and R.J. Kazlauskas. J. Org. Chem. **66**, 3041 (2001).
31. K. Faber, H. Griengl, H. Honig, and J. Zuegg. Biocatalysis, **9**, 227 (1994).
32. M. Botta, E. Cernia, F. Corelli, F. Manetti, and S. Soro. Biochim. Biophys. Acta, **1296**, 121 (1996).
33. H.P. Deigner, C. Blencowe, and C.E. Freyberg. J. Mol. Cat. B: Enzym. **1**, 61 (1996).

© 2002 NRC Canada

I:\cjc\cjc80\cjc-06\V02-056.vp
Monday, May 13, 2002 2:45:06 PM

Structural effects on chemo- and enantioselectivity of *Candida antarctica* lipase B — Resolution of β-amino esters

Szilvia Gedey, Arto Liljeblad, László Lázár, Ferenc Fülöp, and Liisa T. Kanerva

Abstract: The *Candida antarctica* lipase B-catalyzed reactions of five β-amino esters with neat butyl butanoate and with 2,2,2-trifluoroethyl butanoate in diisopropyl ether were studied, as were the reactions of the same β-amino esters and their *N*-butanamides with neat butanol. The possibility for sequential resolution, where the amino and ester functions of the substrate both react with an achiral butanoate, became less likely with increasing size of the substrate from ethyl 3-aminobutanoate (**1a**) to pentanoate (**1b**) or larger. On the other hand, the alcoholyses of *N*-acylated β-amino esters successfully proceeded in butanol with $E > 100$. Gram-scale resolution of the *N*-butanoylated **1a** was performed to demonstrate the usefulness of the method.

Key words: lipase, interesterification, acylation, alcoholysis, resolution, β-amino esters.

Résumé : On a étudié les réactions, catalysées par la lipase B de *Candida antartica*, de cinq esters β-aminés avec du butanoate de butyle pur et avec du butanoate de 2,2,2-trifluoroéthyle dans l'éther diisopropylique ainsi que les réactions des mêmes esters β-aminés et des leurs *N*-butanamides avec du butanol pur. La possibilité d'une résolution séquentielle, dans laquelle les fonctions aminées et esters du substrat réagissent toutes les deux avec le butanoate achiral, diminue avec une augmentation de la taille du substrat en passant de 3-aminobutanoate (**1a**) à 3-aminopentanoate d'éthyle (**1b**) ou plus long. Par ailleurs, les alcoolyses des esters *N*-acétyl-β-amino effectuées dans le butanol se produisent avec succès, avec $E > 100$. Afin de démontrer l'utilité de la méthode, on a réalisé une résolution du *N*-butanoyl-3-aminobutanoate d'éthyle (**1a**) à l'échelle du gramme.

Mots clés : lipase, interestérification, acylation, alcoolyse, résolution, esters β-aminés.

[Traduit par la Rédaction]

Introduction

In recent years, there has been increased interest in β-amino acids, in consequence of their unique pharmacological properties, their ability to modify biologically active peptides, their importance in the preparation of peptidomimetics and natural products, and so on (1–5). A number of syntheses and transformations leading to both racemic and enantiomeric β-amino acids and esters were previously reviewed (6–11).

Received 24 October 2001. Published on the NRC Research Press Web site at http://canjchem.nrc.ca on 6 May 2002.

Dedicated to Professor J. Bryan Jones on the occasion of his 65th birthday.

S. Gedey,[1] A. Liljeblad, and L.T. Kanerva.[2] Laboratory of Synthetic Drug Chemistry and Department of Chemistry, University of Turku, Lemminkäisenkatu 2, FIN-20520 Turku, Finland.
L. Lázár and F. Fülöp. Institute of Pharmaceutical Chemistry, University of Szeged, H-6701, Szeged, PO Box 121, Hungary.

[1]Present address: Institute of Pharmaceutical Chemistry, University of Szeged, H-6701, Szeged, PO Box 121, Hungary.
[2]Corresponding author (e-mail: lkanerva@utu.fi).

The pioneering works of Jones and Klibanov on understanding enzymatic possibilities beyond biology have efficiently encouraged synthetic chemists in using enzymes to cause chiral induction in the preparation of a wide variety of enantiopure compounds (12, 13). Effective enzymatic methods to prepare β-amino acid enantiomers include the lipase-catalyzed enantioselective acylation of amino esters and β-lactam derivatives as well as penicillin or the penicillin G acylase-catalyzed enantioselective hydrolyses of *N*-acylated amino acids (14–26).

The properties and the wide application area of *Candida antarctica* lipase B (CAL-B) as a regio- and enantioselective catalyst in organic synthesis are widely described (14, 26–30). These procedures include highly enantioselective reactions of monofunctional alcohols and amines as well as highly regio- and enantioselective reactions of bifunctional diols and dicarboxylic acid esters. On the other hand, in the previous CAL-B-catalyzed reactions of ethyl 3-aminobutanoate (**1a**) with achiral esters, low chemoselectivity led to the simultaneous *N*-acylation and interesterification of the ethyl ester function and finally to the formation of a highly enantiopure product **4a** through the sequential steps A + B and C + D (Scheme 1) (21). The prevailing reaction route was A + B in the case of alkyl-activated 2,2,2-trifluoroethyl butanoate and C + D in the case of butyl butanoate as achiral acyl donors. To our knowledge, this work was the first time when 2,2,2-trifluoroethyl esters ((*R*)-**4a** ($R^2 = CH_2CF_3$) from

 DOI: 10.1139/V02-015 © 2002 NRC Canada

Scheme 1.

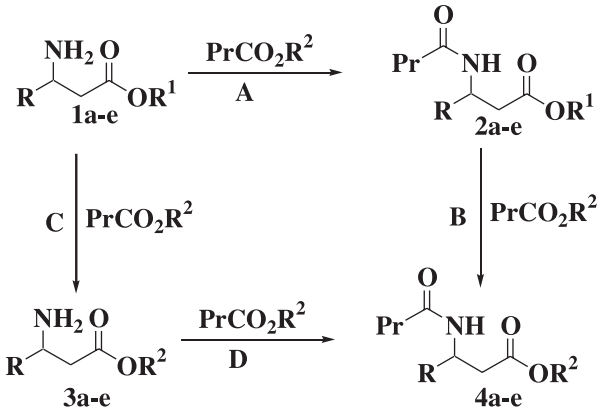

	R	R^1	R^2
a	Me	Et	Bu/ CH_2CF_3
b	Et	Et	Bu/ CH_2CF_3
c	^{i}Pr	Et	Bu/ CH_2CF_3
d	Ph	Et	Bu
e	CO_2Me	Me	Bu

(*R*)-**2a** and (*R*)-**3a** (R^2 = CH_2CF_3) from *rac*-**1a**) were obtained as resolution products, although the quasiirreversible nature of such esters as acyl donors has been well attributed. As previously shown, 2,2,2-trifluoroethyl ester rather than 2,2,2-trifluoroethanol was needed for the formation of the products. The above observations awoke our interest to study the structural effects of β-amino ester substrates on the chemo- and enantioselectivity of CAL-B. In the present work, amino esters **1b**–**1e** and *N*-butanoylated dimethyl aspartate **2e** were subjected to CAL-B-catalyzed reactions with neat butyl butanoate (R^2 = Bu) and with 2,2,2-trifluoroethyl butanoate (R^2 = CH_2CF_3) in diisopropyl ether (Scheme 1).

Additionally, the CAL-B-catalyzed alcoholyses of **1a**–**1e** and those of the *N*-butanoylated **2a–2e** in neat butanol were studied as an one-step resolution possibility (Scheme 2). Gram-scale resolution of **2a** was performed to illustrate the usefulness of CAL-B-catalyzed alcoholysis.

Results and discussion

Reactions of 3-substituted 3-aminopropanoates with achiral esters

In the case of compounds **1a**–**1e**, the reaction with butyl and 2,2,2-trifluoroethyl butanoates can take place at the ester (interesterification) and amino (*N*-acylation) groups of the substrates. On this basis and on the basis of the previous results for **1a** (21), low chemoselectivity for the transformations of **1b**–**1e** by CAL-B was expected. However, the present results indicate magnificent structural effects on enzymatic chemoselectivity toward step C and reduction in the number of observed reaction steps from maximal four (steps A–D) to only one (step C) with increasing size of R (Table 1). Chiral GLC analysis and the comparison of the results to those of the previous works (21, 22) predict that the same enantiomer reacts faster in every step. Thus, the *R*-enantiomer is more reactive for the reactions starting from **1a** and **1b** and the *S*-enantiomer for those starting from **1c**–**1e** in such a way that the same steric demand at the stereocenter becomes fulfilled. Some uncertainty about enantiopreference exists in the case of very low concentrations of almost racemic products **2d**–**4d** (Table 1, row 4).

Scheme 2.

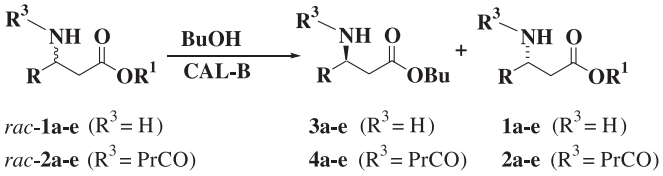

	R	R^1
a	Me	Et
b	Et	Et
c	^{i}Pr	Et
d	Ph	Et
e	CO_2Me	Me

For the CAL-B-catalyzed reactions of **1a**–**1e** (Scheme 1) with neat butyl butanoate (R^2 = Bu) and with 2,2,2-trifluoroethyl butanoate (R^2 = CH_2CF_3) in diisopropyl ether, the substitution of R with methyl (**1a**), ethyl (**1b**), and further with isopropyl (**1c**) causes the acylation step A to become progressively less favorable as compared to the interesterification step C. Thus, when 2,2,2-trifluoroethyl butanoate (R^2 = CH_2CF_3) is an acyl donor, enhanced chemoselectivity toward the formation of the corresponding products **3a**-**3c** (R^2 = CH_2CF_3) is best seen from the area ratios of the GLC chromatograms, leading to the product distribution (**2**:**3**:**4**) of 12:2:10 for **1a** (R = Me) and that of 2:10:1 for **1b** (R = *i*-Pr) at 52% total conversion. The predominance of interesterification is even more clearly seen for the reactions in butyl butanoate (R^2 = Bu) where the acylation products **2b**, **2c**, and **2e** and **4c** and **4e** were not detected at all during the course of the reaction (Table 1, rows 2, 3 and 5), except that traces of **2b** (R^1 = Et) appeared when the reaction approached 90% total conversion. Those traces are evidently due to the enzymatic interesterification between **4b** (R^2 = Bu) and ethyl butanoate (another interesterification product) rather than to the acylation of **1b** through step A. Moreover, the drop in ee of **4a** (R^2 = Bu, Δ solid line) and **4b** (R^2 = Bu, ▲ dotted line, Fig. 1) starts at 80–90% total conversion. Thus, e.g., the $ee_{(R)\text{-}\mathbf{4b}}$ of >99% at 50% and that of only 92% at 97% total conversions are observed. It is reasonable to propose that the reaction of the less reactive (*S*)-**3** to (*S*)-**4** affects the enantiopurities of (*R*)-**4** at longer reaction times.

The enzymatic interesterification of **3b** (R^2 = Bu) with ethyl butanoate back to **1b** explains the drop in $ee_{(S)\text{-}\mathbf{1b}}$ (■ dotted line, Fig. 1) starting at around 80% total conversion. In the case of **1a** (□ solid line), only a minor drop in ee is observed. The different behavior of the two compounds (**1a** and **1b**) is easily deduced from Fig. 1. Thus, the products **3a** (○ solid line) and **3b** (● dotted line) are first enriched with

© 2002 NRC Canada

Table 1. CAL-B-catalyzed (40 mg mL^{-1}) reactions of **1a**–**1e** (0.1 M) in butyl butanoate (R^2 = Bu) and with 2,2,2-trifluoroethyl butanoate (0.2 M, R^2 = CH_2CF_3) in diisopropyl ether at room temperature.

	R/R^1	R^2	Conversion *(%)*	Time (h)	ee_1 (%)	ee_2 (%)	ee_3 (%)	ee_4 (%)
1a	Me/Et	Bu	47	0.5	64 (*S*)	41 (*R*)	40 (*R*)	>99 (*R*)
1b	Et/Et	Bu	50	0.75	89 (*S*)	—[a]	80 (*R*)	>99 (*R*)
1c	*i*-Pr/Et	Bu	51	5	76 (*R*)	—[a]	73 (*S*)	—[a]
1d	Ph/Et	Bu	—[b]	55	32 (*R*)	9	4	16 (*S*)
1e	CO_2Me/Me	Bu	41	0.08	3	—[a]	Regioisomers[c]	—[a]
2e	CO_2Me/Me[d]	Bu	55	6	—[a]	95 (*R*)	—[a]	79 (*S*)
1a	Me/Et[e]	CH_2CF_3	52	4	78 (*S*)	87 (*R*)	5	>99 (*R*)
1b	Et/Et[e]	CH_2CF_3	50	7	80 (*S*)	81 (*R*)	34 (*R*)	99 (*R*)
1c	*i*-Pr/Et	CH_2CF_3	52	24	43 (*R*)	rac[f]	41 (*S*)	rac[f]

[a]Product not observed.
[b]Insufficient accuracy in the GLC analysis of the slow reaction; enzyme content 100 mg mL^{-1}.
[c]87% (ee 6%) of α- and 13% (ee 23%) of β-butyl ester; enzyme content 75 mg mL^{-1}.
[d]Enzyme content 75 mg mL^{-1}.
[e]Enzyme content 30 mg mL^{-1}.
[f]Amount negligible.

Fig. 1. Enantiomeric excess vs. conversion for the CAL-B-catalyzed (40 mg mL^{-1}) reactions of **1a** (0.1 M) and **1b** (0.1 M) in butyl butanoate: (solid lines) **1a** (□), **3a** (○), **4a** (△) and (dotted lines) **1b** (■), **3b** (●), **4b** (▲).

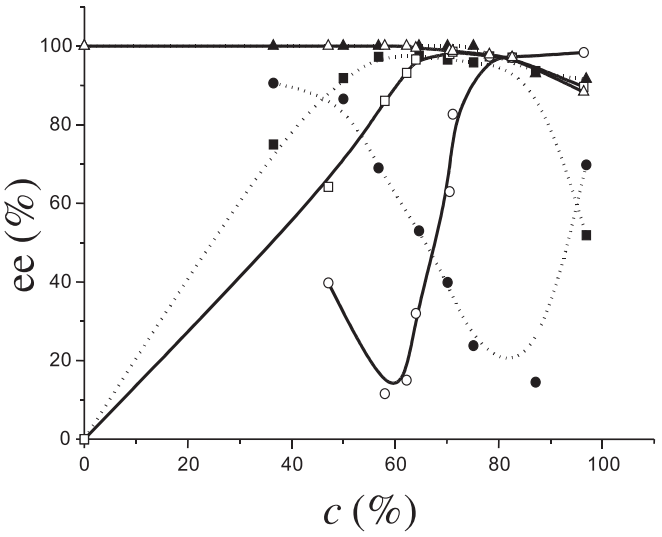

respect to the more reactive *R*-enantiomer. There is a change to the less reactive *S*-enantiomer (and minima in the figure) with total conversion when the more reactive *R*-enantiomer reacts further to the product (*R*)-**4**. As a result, **3a** is already of high (*S*)-enantiopurity (ee > 95%) whereas **3b** is almost racemic (ee close to 20%) at 80% total conversion. Accordingly, the *R*-enantiomer of **3b** is available for enzymatic reaction with ethyl butanoate back to (*R*)-**1b** leading to a drop of $ee_{(S)\text{-}\mathbf{1b}}$.

The phenyl substituent in **1d** allows CAL-B-catalyzed acylation with butyl butanoate in parallel with interesterification, leading to the formation of **4d** (R^2 = Bu) through routes A + B and C + D (Table 1, row 4). The reaction is extremely slow, leading to the product distribution (**2d**:**3d**:**4d**) of 20:100:7 (the ratios of the relative amounts) after 55 h. Enantioselectivity is negligible, as can be concluded from the low ee values in general and for **4d** (R^2 = Bu, ee = 16) in particular.

The CAL-B-catalyzed reaction of **1e** in butyl butanoate (Table 1, row 5) proceeds with high chemoselectivity (66 h is needed before amide formation is detected), low regioselectivity now complicating the situation. Thus, both the α- and β-methyl ester functions are highly reactive, the regioselectivity somewhat favoring the reaction at the α-ester group. Moreover, the reactions continue from the mixed esters to the dibutyl ester, poor enantiopurities being observed at every stage of the sequence. The methods for the determination of regioselectivity were based on our previous works (26, 31).

For considering how substrate structure can affect the chemoselective outcome of CAL-B-catalyzed reactions, the binding modes for the enantiomers of secondary alcohols is useful (30). Accordingly, for acylation reactions (steps A and D) the medium size group R of β-amino esters **1** and **3** binds to the so-called stereospecificity pocket of the enzyme as is shown for the anionic tetrahedral intermediate leading to products **2** and **4**, respectively, in Fig. 2. Holding in this model, it is concluded that the fit of group R into the pocket becomes less likely the bigger it is in size. Finally, the multistep reaction in Scheme 1 turns to a single-step resolution through step C as is the case for the reaction of **1c** (R = *i*-Pr) in butyl butanoate (Table 1, row 3). Structural effects on CAL-B-catalyzed interesterification reactions (and alcoholysis reactions below) are more difficult to explain because, e.g., binding modes for recognizing chirality in the acyl site of the enzyme are not available. Moreover, the number of usable experimental data is limited. The work is continuing to get more insight into the chemoselectivity control that could favor acylation over interesterification.

To conclude, CAL-B poorly recognizes stereocenters at the acyl part of substrates **1**, leading to moderate enantioselectivities (*E* 10–15) for the formation of **3** (R^2 = CH_2CF_3 or R^2 = Bu) as was calculated in the cases where the formation of products **2** and (or) **4** was slow enough or not observed at all. Excellent enantioselectivities for the acylation step D (and A) can be expected on the basis of high ee values (>99% for **4a** and **4b**, Table 1) and on *E* > 100

© 2002 NRC Canada

Table 2. CAL-B-catalyzed (40 mg mL^{-1}) butanolysis of **1a**–**1e** or **2a**–**2e** (0.1 M) in butanol at room temperature.

		rac-**1**			rac-**2**		
	R/R^1	*c* (%)	Time (h)	*E* (*R*/*S*)[a]	*c* (%)	Time (h)	*E* (*R*/*S*)[a]
a	CH_3/Et	55	19	8 ± 2/(*R*)	50	9	>100/(*R*)
b	C_2H_5/Et	49	5	70 ± 5/(*R*)	—[b]	—	—
c	*i*-Pr/Et	53	48	10 ± 1/(*S*)	34	504	>100/(*S*)
d	Ph/Et	<1	24	1/(*S*)	15	96	>100/(*S*)
e	CO_2Me/Me	84[c]	17	—	44[d]	26	55/(*S*)

[a]The faster reacting enantiomer.
[b]Not studied.
[c]87% (ee = 4%) of α- and 13% (ee = 35%) of β-butyl ester, enzyme content 75 mg mL^{-1}.
[d]Substrate **2e** (26).

Fig. 2. Substrate and (or) active site model for the anionic tetrahedral intermediate of the faster reacting enantiomer in *N*-acylation.

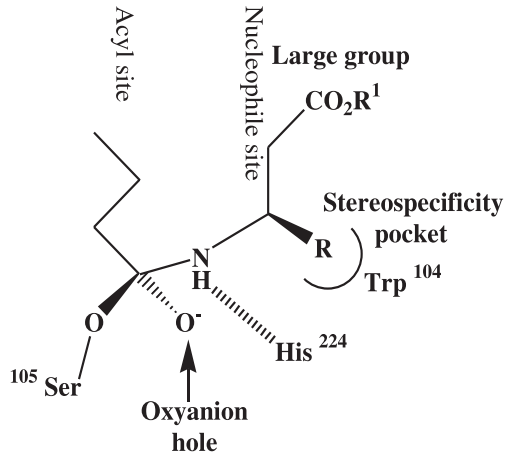

previously observed for the CAL-B-catalyzed reaction of **3a** in neat butyl butanoate (21). It is worth mentioning that *E* values are not available for all transformations due to the sequential course of the reactions. Although with increasing R the same trend toward enhanced chemoselectivity for the formation of products **3** is evident for the reactions of substrates **1** with butyl and 2,2,2-trifluoroethyl butanoates, the stereochemical outcome in the terms of product enantiopurities is more appropriate in the former case. Thus, e.g., the transformation of racemic **1a** to two highly enantiopure fractions ((*S*)-**3a** (R^2 = Bu) + (*S*)-**1a** (R^1 = Et)) and ((*R*)-**4a** (R^2 = Bu)), is possible at ca. 80% total conversion (Fig. 1, solid lines). This was performed in a gram-scale in the previous work (21). The enantiomers (*S*)-**1b** (ee 96%) and (*R*)-**4b** (R^2 = Bu, ee > 99%) can also be obtained by the same procedure at ca. 70% total conversion (dotted lines) but at that point the product ratio (**1b**:**3b**:**4b**) of 3:10:2 (the ratios of the relative amounts) strongly disfavors the chemical yields.

Resolution of β-amino and *N*-butanoylated β-amino esters in butanol

CAL-B was previously shown to catalyze the alcoholysis of **2e** smoothly in a neat alcohol as a solvent (26). In the present work, the alcoholysis of **1a**–**1d** (R^2 = H) and **2a**–**2d** (R^2 = PrCO) in butanol was utilized to study substrate effects on enzymatic enantioselectivity (Scheme 2). The results are presented in Table 2. As above, the (*R*)-enantiomer is the faster-reacting enantiomer for **1a** and **1b**, while the (*S*) counterpart reacts faster in the other cases. Low enantioselectivities are obvious for the substrates **1** with free amino groups, **1b** being an exception (Table 2). Moreover, there is almost no reactivity in the case of compound **1d**. The reactions differ from the interesterification reactions of route C in Scheme 1 by solvent effects, but evidently in some mechanistic ways, too. In support of this and as already mentioned in introduction, alcoholysis between **1a** and the slightly nucleophilic 2,2,2-trifluoroethanol (0.1 M) in diisopropyl ether or in neat 2,2,2-trifluoroethanol does not proceed in the presence of CAL-B, although products **3a**–**3c** (R^2 = CH_2CF_3) were readily detected for the reactions with 2,2,2-trifluoroethyl butanoate (Table 1) (21).

The results in Table 2 clearly indicate that the CAL-B-catalyzed alcoholyses of *N*-butanoylated compounds **2** (R^2 = PrCO) all proceed in a highly enantioselective manner. This result shows that CAL-B is able to recognize stereocenters at the acyl part of an ester when a proper substrate structure is available. Unreasonably long reaction times needed for the resolution of **2c** and **2d** can be seen as limitations, however. To this end, the gram-scale resolution of **2a** by CAL-B catalysis was performed. As reported in the experimental section, the products (*S*)-**2a** and (*R*)-**4a** were both obtained with ee = 99% from one reaction at 50% conversion.

Experimental

Racemic ethyl (**1a**–**1d**) and butyl (**3a**–**3d**, R^2 = Bu) 3-aminoalkanoates were prepared from the corresponding acids using thionyl chloride and dry ethanol or butanol and were available from the previous work (22). Dimethyl aspartate **1e** was prepared from commercial dimethyl aspartate hydrochloride (26). The *N*-butanoylated counterparts **2a**–**2e** and **4a**–**4e** (R^2 = Bu) were prepared from **1a**–**1e** and **3a**–**3e** (R^2 = Bu) using butanoyl chloride in the presence of triethyl amine. GLC–MS was used to detect the products **3a**–**3c** and **4a**–**4c** (R^2 = CH_2CF_3). Acyl donors were prepared from the corresponding acid chlorides and alcohols. CAL-B (Chirazyme L2) was purchased from Boehringer–Mannheim. The solvents were of the best analytical grade from Lab Scan.

^{1}H NMR spectra were recorded using a Bruker AM 400 spectrometer. Multiplicities were recorded as s (singlet), d (doublet), dd (double doublet), t (triplet), q (quartet), m (multiplet), and om (overlapping multiplet). MS spectra

© 2002 NRC Canada

were obtained on a VG Analytical 7070E instrument equipped with a Vaxstation 3100 M 76 computer. Elemental analyses were performed with a PerkinElmer CHNS-2400 Ser II elemental analyzer. Optical rotations were measured with a JASCO DIP-360 polarimeter, and $[\alpha]_D$ values are given in units of 10^{-1} deg cm^2 g^{-1}.

Enzymatic resolutions

In a typical small-scale experiment, one of compounds **1a**–**1e** (0.1 M) was dissolved in butyl butanoate (2 mL) or in diisopropyl ether (2 mL) containing 2,2,2-trifluoroethyl butanoate (0.2 M). As another possibility, one of compounds **1a**–**1e**, **2a**–**2e** (0.1 M) was dissolved in butanol (2 mL), which served as a nucleophile and a solvent. For the reactions with achiral acyl donors, conversion was determined by using hexadecane (0.01 M) as an internal standard. In the case of butanolysis reactions conversion was obtained by equation $c = ee_s/(ee_s + ee_p)$ (32). The enzyme preparation (30 or 40 mg mL^{-1}) was added to start the reaction. The reaction mixture was shaken at room temperature. The progress of the reaction was followed by taking samples (0.1 mL) at intervals and analysing them by gas chromatography on a Chrompack CP-Chirasil-DEX CB column (25 m), except in the cases of **1d**, **1e**, or **2e** as substrates. A Chrompack CP-Chirasil-L-Val column (25 m) was then used. For good baseline separation, the unreacted amines in the sample were derivatized with acetic or butanoic anhydride in the presence of pyridine containing 1% 4-*N*,*N*-dimethylaminopyridine.

Gram-scale butanolysis of *N*-butanoylated ethyl 3-aminobutanoate 2a

Racemic **2a** (2.28 g, 11.3 mmol) was dissolved in butanol (113 mL) and CAL-B (5.65 g, 50 mg mL^{-1}) was added. The reaction was stirred at room temperature until 50% conversion was reached after 11.5 h. The enzyme was filtered off and the solvent was evaporated. The resolution products (the unreacted (*S*)-**2a** and the (*R*)-**4a** (R^2 = Bu) formed) were purified by column chromatography, using elution with petroleum ether:propan-2-ol (100:6), the elution sequence being product (*R*)-**4a** before the unreacted (*S*)-**2a**.

(*S*)-**2a**: 0.99 g, 4.92 mmol. $[\alpha]_D^{20}$ –17.9 (c = 1.0, MeOH), ee 99%. M = 201 according to MS. ^{1}H NMR (400 MHz, $CDCl_3$, Me_4Si) δ: 0.94 (3H, t, *J* = 7.4, $CH_2CH_2CH_3$), 1.23 (3H, d, *J* = 6.6, $CHCH_3$), 1.27 (3H, t, *J* = 7.2, OCH_2CH_3), 1.65 (2H, m, $CH_2CH_2CH_3$), 2.14 (2H, t, *J* = 7.4, $CH_2CH_2CH_3$), 2.52 (2H, dd, *J* = 5.4, 1.4, $CHCH_2CO$), 4.15 (2H, q, *J* = 7.2, OCH_2CH_3), 4.37 (1H, m, CH), 6.22 (1H, broad s, NH). $C_{10}H_{19}NO_3$ requires (%): C 59.68, H 9.52, N 6.96; found (%): C 59.44, H 9.72, N 6.64.

(*R*)-**4a** (R^2 = Bu): 1.18 g, 5.15 mmol. $[\alpha]_D^{20}$ +16.0 (c = 1.0, MeOH), ee 99%. M = 229 according to MS. ^{1}H NMR (400 MHz, $CDCl_3$, Me_4Si) δ: 0.94 (6H, t, *J* = 7.3, $COCH_2CH_2CH_3$, $CH_2CH_2CH_2CH_3$), 1.22 (3H, d, *J* = 6.8, $CHCH_3$), 1.38 (2H, m, $CH_2CH_2CH_2CH_3$), 1.51–1.71 (4H, om, $CH_2CH_2CH_2CH_3$, $COCH_2CH_2CH_3$), 2.14 (2H, t, *J* = 7.4, $COCH_2CH_2CH_3$), 2.52 (2H, d, *J* = 5.4, $CHCH_2CO$), 4.09 (2H, m, $OCH_2CH_2CH_2CH_3$), 4.37 (1H, m, CHNH), 6.26 (1H, broad s, NH). $C_{12}H_{23}NO_3$ requires (%): C 62.85, H 10.11, N 6.11; found (%): C 62.51, H 10.22, N 5.94.

Conclusions

In the presence of CAL-B, the reactions of β-amino esters **1a**–**1e** with neat butyl butanoate and with 2,2,2-trifluoroethyl butanoate in diisopropyl ether have been studied (Scheme 1, Table 1). CAL-B mediates interesterification between achiral and amino esters over the *N*-acylation of the amino group, increasing size of the R and the nature of an achiral acyl donor strongly affecting the behavior. The equilibrium (**1** + $PrCO_2Bu$) ⇌ (**3** + $PrCO_2Et$) of step C decreases the enantiopurities of **1** at high total conversions and therefore excludes the possibility for successful sequential resolution except in the case of **1a**. 2,2,2-Trifluoroethyl butanoate as an acyl donor is expected to be worse in this respect.

In an attempt to find a useful method for the resolution of the present amino esters by CAL-B, the butanolyses of **1a**–**1e** and that of the *N*-butanoylated derivatives **2a**–**2e** in neat butanol were studied. The latter system led to excellent enantioselectivities (*E* > 100) in all cases except when the aspartate **2e** was used as substrate (*E* = 55, Scheme 2, Table 2).

Acknowledgements

S.G. is grateful for a grant from the Centre for International Mobility (CIMO) in Finland. Support from the Technology Development Centre (TEKES) in Finland and from the MKM (FKFP 0535/1999) and OTKA (T030452) in Hungary are also gratefully acknowledged.

References

1. Y. Hamuro, J.P. Schneider, and W. DeGrabo. J. Am. Chem. Soc. **121**, 12 200 (1999).
2. K. Gademann, T. Hintermann, and J.V. Schreiber. Current Med. Chem. **6**, 905 (1999).
3. I. Ojima, S. Lin, and T. Wang. Current Med. Chem. **6**, 927 (1999).
4. R.M. Scarborough. Current Med. Chem. **6**, 971 (1999).
5. D. Ma and H. Sun. Org. Lett. **2**, 2503 (2000).
6. D.C. Cole. Tetrahedron, **50**, 9517 (1994).
7. E. Juaristi. Enantioselective synthesis of β-amino acids. Wiley–VHC, New York. 1997.
8. J.C.A. Hunt, C. Lloyd, C.J. Moody, A.M.Z. Slawin, and A.K. Takle. J. Chem. Soc. Perkin Trans. 1, 3443 (1999).
9. A.F. Abdel-Magid, J.H. Cohen, and C.A. Maryanoff. Current Med. Chem. **6**, 955 (1999).
10. E. Juaristi and H. López-Ruiz. Current Med. Chem. **6**, 983 (1999).
11. F. Fülöp. Chem. Rev. **101**, 2181 (2001).
12. A. Zaks and A.M. Klibanov. Science (Washington, D.C.), **224**, 1249 (1984); A.M. Klibanov. Chemtech. **16**, 324 (1986).
13. J.B. Jones. Tetrahedron, **42**, 3351 (1986).
14. U.T. Bornscheuer and R.J. Kazlauskas. Hydrolysis in organic synthesis, regio- and stereoselective biotransformations. Wiley–VHC, Weinheim. 1999.
15. P. Csomós, L.T. Kanerva, G. Bernáth, and F. Fülöp. Tetrahedron: Asymmetry, **7**, 1789 (1996).
16. J. Kámán, E. Forró, and F. Fülöp. Tetrahedron: Asymmetry, **11**, 1593 (2000).
17. E. Forró, J. Árva, and F. Fülöp. Tetrahedron: Asymmetry, **12**, 1593 (2001).

© 2002 NRC Canada

18. L.T. Kanerva, E. Vänttinen, and E. Kiljunen. Recent research developments in organic & bioorganic chemistry. Vol. 1. Transworld Research Network, India. 1997. pp. 55.
19. V.M. Sánchez, F. Rebolledo, and V. Gotor. Tetrahedron: Asymmetry, **8**, 37 (1997).
20. L.T. Kanerva, P. Csomós, O. Sundholm, G. Bernáth, and F. Fülöp. Tetrahedron: Asymmetry, **7**, 1705 (1996).
21. S. Gedey, A. Liljeblad, F. Fülöp, and L.T. Kanerva. Tetrahedron: Asymmetry, **10**, 2573 (1999).
22. S. Gedey, A. Liljeblad, L. Lázár, F. Fülöp, and L.T. Kanerva. Tetrahedron: Asymmetry, **12**, 105 (2001).
23. G. Cardillo, A. Tolomelli, and C. Tomasini. J. Org. Chem. **61**, 8651 (1996).
24. G. Cardillo, A. Tolomelli, and C. Tomasini. Eur. J. Org. Chem. 155 (1999).
25. V.A. Soloshonok, I.V. Soloshonok, V.P. Kukhar, and V.K. Svedas. J. Org. Chem. **63**, 1878 (1998).
26. A. Liljeblad and L.T. Kanerva. Tetrahedron: Asymmetry, **10**, 4405 (1999).
27. P. Virsu, A. Liljeblad, A. Kanerva, and L.T. Kanerva. Tetrahedron: Asymmetry, **12**, 2447 (2001).
28. T.B. Nielsen, M. Ishii, and O. Kirk. Biotechnol. Appl. Cold-Adapted Org. *Edited by* R. Margesin and F. Schinner. 1999. p. 49.
29. E.M. Anderson, K.M. Larsson, and O. Kirk. Biocat. Biotransform. **16**, 181 (1998).
30. C. Orrenius, F. Hæffner, D. Rotticci, N. Öhrner, T. Norin, and K. Hult. Biocat. Biotransform. **16**, 1 (1998).
31. A. Liljeblad and L.T. Kanerva. Tetrahedron: Asymmetry, **11**, 3957 (2000).
32. $E = \ln [(1 - ee_S)/(1 - ee_S/ee_P)]/\ln [(1 - ee_S)/(1 + ee_S/ee_P)]$ with $c = ee_S/(ee_S + ee_P)$, as derived from the original equations in C.-S. Chen, Y. Fujimoto, G. Girdaukas, and C.J. Sih. J. Am. Chem. Soc. **104**, 7294 (1982).

© 2002 NRC Canada

Chemo-enzymatic synthesis of the C_{15}–C_{23} unit of Leptomycin B

Michael Scheck and Herbert Waldmann

Abstract: The asymmetric synthesis of the C_{15}–C_{23} unit of Leptomycin B (LMB) is described. All four stereocenters of the C_{15}–C_{23} unit were prepared from one building block exhibiting only one stereocenter. This building block was synthesized via either an enzymatic transformation or starting from a chiral reagent.

Key words: Leptomycin, natural product synthesis, enzymatic transformation, Aldol reaction, *Pseudomonas fluorescence* lipase (PFL).

Résumé : On décrit la synthèse asymétrique de l'unité C_{15}–C_{23} de la leptomycine B. Les quatre stéréocentres de l'unité C_{15}–C_{23} ont été préparés à partir d'un seul bloc ne comportant qu'un seul stéréocentre. Ce bloc a été synthétisé par le biais d'une transformation enzymatique ou à partir d'un ensemble chiral.

Mots clés : leptomycine, synthèse d'un produit naturel, transformation enzymatique, réaction aldolique, lipase *Pseudomonas fluorescence* (PFL).

[Traduit par la Rédaction]

Introduction

Leptomycin B (LMB, **1**) is an unsaturated branched-chain polyketide isolated from *Streptomyces sp* (1, 2), which was found to induce arrest of the eukaryotic cell cycle at G1 and G2 phases (3). LMB is a specific inhibitor of proteins containing a nuclear-export signal and has been used as an important tool in the study of this phenomenon (4). It inhibits nucleo-cytoplasmic translocation of molecules such as the HIV-1 Rev protein and Rev-dependent export of mRNA, thereby inhibiting the propagation of HIV-1 in low nanomolar concentrations (5, 6). LMB also interacts with the nuclear-export signal of Hepatitis B Virus X and causes the virus to accumulate in the nucleus (7). Other proteins that are influenced by LMB are actin (8), c-Abl (9), cyclin B1 (10), MDM2/p53 (11), IκB (12), MPF (13), and PKA (14). The suggested inhibition mechanism involves the direct binding of LMB to CRM1 (chromosomal region maintenance), which blocks the binding of CRM1 to proteins containing the nuclear-export signal (6, 15), via the interaction with a cysteine residue in CRM1 (16).

Due to these outstanding properties, LMB is an interesting target for total synthesis. The absolute stereochemistry was proven through the only known total synthesis by Kobayashi et al. (17) Herein we report the synthesis of the C_{15}–C_{23} fragment employing a substrate-controlled diastereoselective aldol reaction to assemble two smaller subunits, which are both derived from monoprotected chiral diol **6**.

Received 6 December 2001. Published on the NRC Research Press Web site at http://canjchem.nrc.ca on 7 May 2002.

Dedicated to Professor J. Bryan Jones on the occasion of his 65th birthday.

M. Scheck and H. Waldmann.[1] Max-Planck Institut für molekulare Physiologie, Otto-Hahn-Strasse 11, 44227 Dortmund, Germany; and Institut für Organische Chemie, Universität Dortmund, Otto-Hahn-Strasse 8, 44227 Dortmund, Germany.

[1]Corresponding author (e-mail: herbert.waldmann@mpi-dortmund.mpg.de).

Results and discussion

The retrosynthetic analysis of LMB (**1**) described in Scheme 1 dissects the molecule at the central diene moiety (C-13 and C-14) using the Stille transformation to provide two fragments of nearly equal size and structural complexity. The northern half (**3**) contains a polypropionate unit with four stereocenters, which can be derived from fragments **4** and **5** by a diastereoselective aldol reaction. In turn, both fragments can be synthesized from the same building block (**6**). Through this sequence all four stereocenters in **3** can be traced back to a single stereocenter in **6**.

Synthesis of the key building block **6** begins from methylmalonic acid diethyl ester (**7**), which was first reduced with borane and then acetylated to afford diacetate **8** (Scheme 2). Via an enzymatic resolution with *Pseudomonas fluorescens* lipase (PFL), the selective hydrolysis of diacetate **8** to monoacetate **9** could be achieved with an enantiomeric excess of 95% (18, 19). Protection of the free hydroxy function of **9** as a TBS-ether and cleavage of the acetate with potassium carbonate in methanol provided the central building block **6**. (*R*)-Methyl-3-hydroxy-2-methylpropanoate (**10**) also yielded **6** after TBS-protection and reduction with diisobutylaluminiumhydride (DIBAH).

Swern oxidation of alcohol **6**, followed by Grignard addition of ethylmagnesium bromide to the resulting aldehyde furnished alcohol **11**, which was oxidized with tetrapropylammonium perruthenate (TPAP) and *N*-methylmorpholine *N*-oxide (NMO) to ketone **5** (Scheme 3). The second building block (**4**) for the asymmetric aldol reaction was also synthesized from **6**. After transformation of the hydroxy

 DOI: 10.1139/V02-070 © 2002 NRC Canada

Scheme 1. Retrosynthetic analysis of Leptomycin B (LMB, **1**).

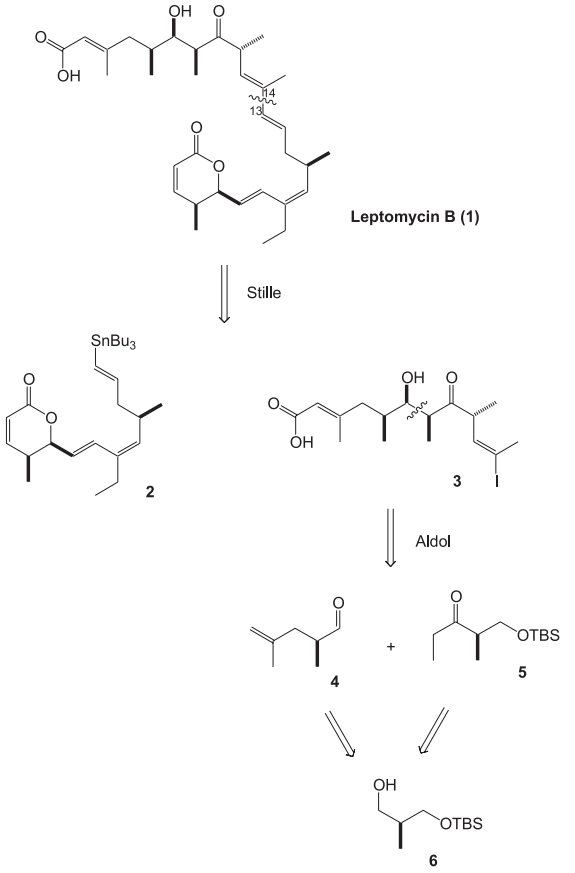

function of **6** into an iodide (**12**) a Cu(I)-catalyzed cross-coupling with 2-propenylmagnesium bromide led to silyl-protected alcohol **13** (19). Deprotection of the silyl ether **13** with tetrabutylammonium fluoride buffered with acetic acid and subsequent Swern oxidation provided aldehyde **4**.

Coupling of fragments **4** and **5** was achieved by a diastereoselective substrate-controlled Aldol-addition of a Ti(IV)-enolate (Scheme 4) (20). Although this represents a mismatched case between the influence of the C-20 and the C-16 stereocenters, Felkin–Anh control by C-20 is slightly favored affording an approximate 1.8:1 mixture of *syn* diastereomers, with the desired diastereomer predominating (21). The desired product could be readily separated by preparative HPLC. Finally, the keto function was protected as a 1,3 dioxolane and the hydroxy function as a methoxymethyl ether (**15**).

Compound **15**, which represents the C_{15}–C_{23} fragment of LMB, was synthesized in a highly convergent fashion using **6**. The terminal olefin provides a handle for extension to the desired carboxylic acid, while the TBS protected alcohol should allow conversion to the desired trisubstituted vinyl iodide.

Experimental

General methods

All reactions were carried out under argon unless water was used.

Solvents were dried by distillation prior to use. Tetrahydrofuran was distilled from sodium–benzophenone and

Scheme 2. Reagents and conditions: (*a*) BH_3, Et_2O, rt, 87%; (*b*) Ac_2O, pyridine, reflux, 95%; (*c*) *Pseudomonas fluorescence* lipase, pH 7, rt, 31%, ee ≥ 95%; (*d*) TBSCl, imidazole, DMF, rt, 99%; (*e*) K_2CO_3, MeOH, reflux, 69%; (*f*) TBSCl, imidazole, DMF, rt, quant.; (*g*) DIBAH, THF, –78°C, 96%.

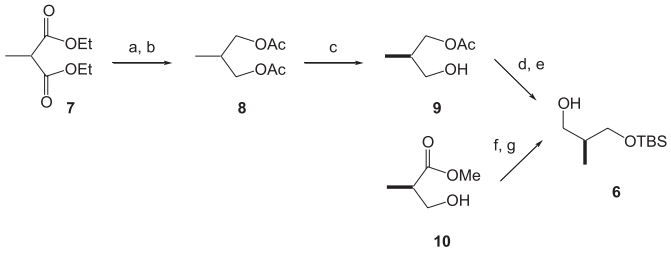

Scheme 3. Reagents and conditions: (*a*) $(COCl)_2$, DMSO, NEt_3, DCM, –78°C, 68%; (*b*) EtMgBr, Et_2O, reflux, 94%; (*c*) TPAP, NMO, 4 Å MS, DCM, rt, 78%; (*d*) I_2, PPh_3, imidazole, toluene, rt, 100%; (*e*) 2-propenyl–MgBr, CuI (2.5 mol%), DMPU, THF, –20°C to 0°C, 93%; (*f*) TBAF, HOAc, 4 Å MS, THF, rt, 72%; (*g*) $(COCl)_2$, DMSO, NEt_3, DCM, –78°C, 75%.

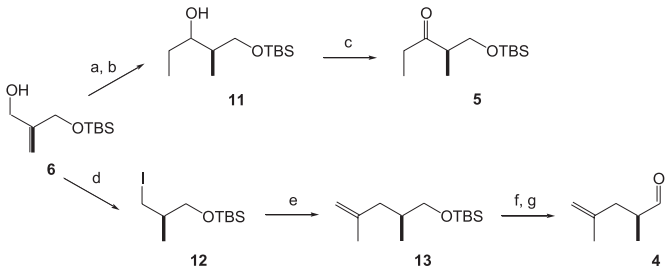

Scheme 4. Reagents and conditions: (*a*) DIPEA, $TiCl_4$, THF, –78°C, 42%, diastereomers: 1.8:1 *RS*:*SR*, *syn*–*anti*: 10:1; (*b*) $HOCH_2CH_2OH$, TMSCl, rt, 84%; (*c*) MOMCl, DIPEA, DCM, 0°C, 29%.

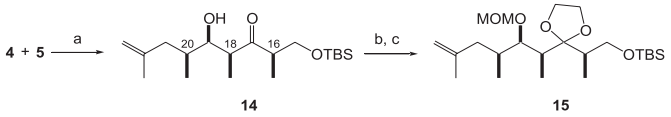

methylene chloride over CaH_2 immediately prior to use. ^1H and ^{13}C NMR spectra were recorded in $CDCl_3$ on Bruker AC-250, AM-400, or DRX-500 spectrometers (250, 400, and 500 MHz, respectively). The enantiomeric excess was determined with gas chromatography, which was carried out on a Hewlett Packard 5890 Series II gas chromatograph with a capillary column Lipodex E (with chiral stationary phase) from Macherey&Nagel, a mass selective detector Hewlett Packard MSD 5972 A, and using the racemate as the reference. All measurements were carried out with helium as carrier gas. Optical rotations were measured with a PerkinElmer 241 polarimeter at ambient temperature. TLC was conducted on Merck aluminum slides coated with silica gel 60 F254. Flash column chromatography was performed using Baker silica gel 60 (corn size 30–60 μm). HPLC was carried out with a L-6000A-HPLC from Merck/Hitachi with diode-array detector L-3000. A EC 250/4 Nucleosil (100–5) PPN from Macherey&Nagel was used as column. Mass

© 2002 NRC Canada

spectrometry and high resolution mass spectrometry were carried out with a Finnigan MAT 90.

2-Methyl-1,3-propanediol

To a solution of 2.17 g (12.5 mmol) of methylmalonic acid diethyl ester (**7**) in 20 mL of THF was added 12.5 mL (18.8 mmol) of a 1.5 M solution of borane in THF at –78°C. The mixture was allowed to warm to room temperature and stirred overnight. A 10% aqueous solution of citric acid was added until a clear solution was obtained. The solvent was removed under reduced pressure and the resulting white solid was dissolved in water. The solution was extracted with methylene chloride (4 × 50 mL) and the combined organic layers were dried over $MgSO_4$. Column chromatography (cyclohexane–ethyl acetate 1:1) afforded 0.98 g (10.9 mmol, 87%) of the title compound as a colorless oil. ^{1}H NMR (250 MHz, $CDCl_3$) δ: 0.88 (d, J = 7.8 Hz, 3H, CH_3), 1.63–1.70 (m, 1H, CH), 3.40–3.63 (m, 4H, CH_2), 3.71 (br s, 2H, OH). The ^{1}H NMR data is in concordance with literature (18).

2-Methyl-1,3-propanediyl diacetate (8)

To a solution of 1.0 g (11.0 mmol) of 2-methyl-1,3-propane diol in 20 mL of THF was added 16.6 g (54.5 mmol) of acetic acid anhydride and 6.6 mL (82 mmol) of pyridine and the mixture was stirred at room temperature for 2 days. The solvent was removed under reduced pressure and the resulting white solid was dissolved in 30 mL of water. The solution was extracted with diethyl ether (3 × 40 mL) and dried over $MgSO_4$. After solvent removal in vacuo, 1.83 g (10.5 mmol, 95%) of the title compound were obtained as a colorless oil ^{1}H NMR (250 MHz, $CDCl_3$) δ: 1.02 (d, J = 7.5 Hz, 3H, CH_3), 2.01 (s, 6H, CO-CH_3), 2.14–2.21 (m, 1H, CH), 4.01 (d, J = 4.9 Hz, 4H, CH_2). The ^{1}H NMR data is in concordance with literature (18).

(2*R*)-Acetic acid-3-hydroxy-2-methyl-propyl ester (9)

To a suspension of 1.83 g (10.35 mmol) of 2-methyl-1,3-propane diacetate (**8**) in 100 mL phosphate buffer (0.1 M, pH 7) was added 900 mg of *Pseudomonas fluorescens* lipase immobilized on Sol-Gel-AK and the mixture was stirred at 30°C for 2.5 h. Diethyl ether (100 mL) was added and the solution was filtered to recover the enzyme. The solution was extracted with diethyl ether (2 × 100 mL), the organic layers were combined and dried over $MgSO_4$. Column chromatography (cyclohexane–ethyl acetate 1:1) afforded 0.43 g (3.26 mmol, 31%) of the title compound as a colorless oil. $[\alpha]_D^{20}$ +7.1 (c = 0.9, $CHCl_3$). ^{1}H NMR (250 MHz, $CDCl_3$) δ: 0.98 (d, J = 8.6 Hz, 3H, CH_3), 2.01 (s, 3H, CO-CH_3), 2.04–2.11 (m, 1H, CH), 2.27 (s, 1H, OH), 3.43–3.54 (m, 2H, CH_2-OH), 4.01–4.12 (m, 2H, CH_2-O-CO). The ^{1}H NMR data is in concordance with literature (18).

(2*R*)-Acetic acid-3-([*tert*-butyldimethylsilyl]oxy)-2-methyl-propyl ester

To a solution of 430 mg (3.26 mmol) of (2*R*)-acetic acid-3-hydroxy-2-methyl-propyl ester (**9**) in 1.5 mL of dry *N*,*N*-dimethylformamide were added 0.60 g (9.8 mmol) of imidazole and 0.72 g (4.6 mmol) of *tert*-butyldimethylsilyl chloride, and the mixture was stirred at room temperature for 2 days. Water (2 mL) and diethyl ether (10 mL) were added and the aqueous phase was extracted with diethyl ether (4 × 20 mL). The combined organic layers were washed with 10 mL of a 5% aqueous sodium hydrogencarbonate solution and dried over $MgSO_4$. Column chromatography (cyclohexane–ethyl acetate 50:1) afforded 0.79 g (3.23 mmol, 100%) of the title compound as a colorless oil. $[\alpha]_D^{20}$ +5.0 (c = 0.8, CH_2Cl_2). ^{1}H NMR (250 MHz, $CDCl_3$) δ: 0.02 (s, 6H, Si-CH_3), 0.87 (s, 9H, Si-C$(CH_3)_3$), 0.97–1.03 (m, 3H, CH-CH_3), 1.90–1.98 (m, 1H, CH), 2.02 (s, 3H, CO-CH_3), 3.42 (d, J = 6.4 Hz, 2H, CH_2-O-Si), 3.87–4.02 (m, 2H, CH_2-O-CO). The ^{1}H NMR data is in concordance with literature (18).

(2*S*)-3-([*tert*-Butyldimethylsilyl]oxy)-2-methyl-1-propanol (6)

To a solution of 0.75 g (3.04 mmol) of (2*R*)-acetic acid-3-([*tert*-butyldimethylsilyl]oxy)-2-methyl-propyl ester in 5 mL of methanol was added 5 mL of a 10% aqueous potassium carbonate solution. The mixture was heated at reflux for 5 h and the then solvent was removed under reduced pressure. The resulting white solid was dissolved in 10 mL of water and extracted with methylene chloride (4 × 20 mL). The combined organic layers were dried over $MgSO_4$. Column chromatography (cyclohexane–ethyl acetate 4:1) afforded 0.43 g (2.09 mmol, 69%) of the title compound as a colorless oil. $[\alpha]_D^{20}$ +11.0 (c = 1.2, $CHCl_3$). ^{1}H NMR (250 MHz, $CDCl_3$) δ: 0.02 (s, 6H, Si-CH_3), 0.84 (d, J = 7.8 Hz, 3H, CH-CH_3), 0.87 (s, 9H, C$(CH_3)_3$), 1.89–2.04 (m, 1H, CH), 2.68 (br s, 1H, OH), 3.29–3.74 (m, 4H, CH_2-O-Si and CH_2-OH). The ^{1}H NMR data is in concordance with literature (22).

(2*R*)-3-([*tert*-Butyldimethylsilyl]oxy)-2-methyl propanoate

To a solution of 1.0 mL (9.02 mmol) of (*R*)-methyl-3-hydroxy-2-methyl propanoate (**10**) in 5 mL of dry *N*,*N*-dimethylformamide were added 1.87 g (27.3 mmol) of imidazole and 2.30 g (14.7 mmol) of *tert*-butyldimethylchlorsilane. The mixture was stirred for 3 h at room temperature, then 40 mL of water and 40 mL of diethyl ether were added and the aqueous phase was extracted with diethyl ether (4 × 40 mL). The combined organic extracts were washed with 40 mL of a 5% aqueous sodium hydrogencarbonate solution and dried over $MgSO_4$. Column chromatography (cyclohexane–ethyl acetate 5:1) afforded 2.09 g (9.00 mmol, quantitative) of the title compound as a colorless oil. $[\alpha]_D^{20}$ +18.1 (c = 4.0, $CHCl_3$). ^{1}H NMR (250 MHz, $CDCl_3$) δ: 0.02 (s, 6H, Si-CH_3), 0.87 (s, 9H, C$(CH_3)_3$), 1.11 (d, J = 6.8 Hz, 3H, CH-CH_3), 2.43–2.54 (m, 1H, CH), 3.22–3.46 (m, 2H, CH_2), 3.56 (s, 3H, O-CH_3). The ^{1}H NMR data is in concordance with literature (23).

(2*S*)-3-([*tert*-Butyldimethylsilyl]oxy)-2-methyl-1-propanol (6)

To a solution of 1.94 g (8.40 mmol) of methyl-(2*R*)-3-([*tert*-butyldimethylsilyl]oxy)-2-methyl propanoate in 25 mL of THF was added 18.5 mL of a 1.0 M solution of diisobutylaluminiumhydride in heptane at –78°C. The solution was stirred for 2 h at that temperature and additional 15 h at room temperature. The mixture was quenched with 40 mL of methanol and 15 mL of brine at –78°C. After stirring for 1 hour the mixture was dried over $MgSO_4$ and

© 2002 NRC Canada

filtered through Celite. After solvent removal 1.64 g (8.06 mmol, 96%) of the title compound was obtained as a colorless liquid. $[\alpha]_D^{20}$ +11.0 (*c* = 2.0, CH_2Cl_2). ^{1}H NMR (250 MHz, $CDCl_3$) δ: 0.02 (s, 6H, Si-CH_3), 0.84 (d, *J* = 7.3 Hz, 3H, CH-C*H*$_3$), 0.87 (s, 9H, $C(CH_3)_3$), 1.89–2.04 (m, 1H, CH), 2.68 (br s, 1H, OH), 3.29–3.74 (m, 4H, C*H*$_2$-O-Si and C*H*$_2$-OH). The ^{1}H NMR data is in concordance with literature (22).

(2*S*)-3-([*tert*-Butyldimethylsilyl]oxy)-2-methyl-1-propanal

To a solution of 0.67 mL (7.8 mmol) of oxalyl chloride in 60 mL of methylene chloride was added 0.74 mL (10.4 mmol) of dimethyl sulfoxide at –78°C. After stirring for 20 min, 1.05 g (5.17 mmol) of (2*S*)-3-([*tert*-butyldimethylsilyl]oxy)-2-methyl-1-propanol (**6**) was added and after 30 min 5.1 mL (36.2 mmol) of triethylamine. After stirring for additional 5 min at –78°C, the solution was allowed to warm to room temperature and stirred for 1 hour. After cooling to –78°C water (25 mL) was added, the mixture was allowed to warm to room temperature and the aqueous layer was extracted with methylene chloride (4 × 60 mL). The organic layers were combined and dried over $MgSO_4$. Column chromatography (cyclohexane–ethyl acetate 10:1) afforded 0.71 g (3.51 mmol, 68%) of the title compound as a colorless oil. $[\alpha]_D^{20}$ +25.5 (*c* = 2.2, $CHCl_3$). ^{1}H NMR (250 MHz, $CDCl_3$) δ: 0.02 (s, 6H, Si-CH_3), 0.87 (s, 9H, $C(CH_3)_3$), 1.06 (d, *J* = 5.3 Hz, 3H, CH-C*H*$_3$), 2.42–2.48 (m, 1H, CH), 3.41–3.51 (m, 2H, CH_2), 9.63 (s, 1H, COH). The ^{1}H NMR data is in concordance with literature (24).

(2*R*)-1-([*tert*-Butyldimethylsilyl]oxy)-2-methyl-3-pentanol (11)

To a mixture of 1.6 g (65 mmol) of magnesium fillings in 10 mL of diethyl ether was added approx. 5% of 7.1 g (65 mmol) of bromoethane in 20 mL of diethyl ether. After the solution had turned cloudy the rest of the bromoethane was slowly added and the mixture was heated at reflux for 1 h. A solution of 6.62 g (32.6 mmol) of (2*S*)-3-([*tert*-butyldimethylsilyl]oxy)-2-methyl-1-propanal in 15 mL of diethyl ether was slowly added and the mixture was heated at reflux for 2 h. The mixture was then poured on ice and acetic acid was added until the magnesium had completely dissolved. The layers were separated and the aqueous layer was extracted with methylene chloride (4 × 60 mL). The organic layers were combined and dried over $MgSO_4$. Column chromatography (cyclohexane–ethyl acetate 10:1) afforded 7.14 g (30.7 mmol, 94%) of the title compound as a colorless oil. $[\alpha]_D^{20}$ +18.3 (*c* = 2.1, $CHCl_3$). ^{1}H NMR (400 MHz, $CDCl_3$) δ: 0.02 (s, 6H, Si-CH_3), 0.86 (s, 9H, $C(CH_3)_3$), 0.89–0.92 (m, 3H, CH-C*H*$_3$), 0.93–0.97 (m, 3H, CH_2-C*H*$_3$), 1.41–1.52 (m, 2H, C*H*$_2$-CH_3), 1.60–1.71 (m, 1H, CH), 2.85 (br s, 1H, OH), 3.45–3.50 (m, 2H, O-CH_2), 3.65–3.73 (m, 1H, C*H*-OH). ^{13}C NMR (100.6 MHz, $CDCl_3$) δ: – 0.03 (Si-CH_3), 9.90 (CH_2-*C*H$_3$), 10.59 (CH-*C*H$_3$), 13.82 (*C*-$(CH_3)_3$), 26.85 (C-(*C*H$_3$)$_3$), 27.90 (*C*H$_2$-CH_3), 39.26 (*C*H-CH_3), 67.13 (CH_2-O), 76.03 (CH-OH). MS (70 eV) *m*/*z* (%): 232 (3.1) $[M]^+$, 205 (2.1) $[M - C_2H_5]^+$, 190 (15.4), 189 (94.8), 147 (13.0), 131 (17.8), 117 (7.8) $[M - CH_3 - CH_3 - C(CH_3)_3 - Si]^+$, 89 (15.6), 83 (11.1), 75 (5.3) $[HO{=}Si(CH_3)_2]^+$, 73 (12.3) $[C_4H_9O]^+$, 71 (25.5), 59 (100) $[C_3H_7O]^+$, 57 (47.4) $[C(CH_3)_3]^+$, 55 (12.9), 43 (33.5)$[C_3H_7]^+$, 42 (49.6), 41 (36.1). FAB-HRMS: calcd. for $C_{12}H_{28}O_2Si$: 232.4351; found: 232.4379.

(2*R*)-1-([*tert*-Butyldimethylsilyl]oxy)-2-methyl-3-pentanone (5)

To a mixture of 6.91 g (29.8 mmol) of (2*R*)-1-([*tert*-butyldimethylsilyl]oxy)-2-methyl-3-pentanol (**11**), 6.11 g (44.7 mmol) of *N*-methylmorpholin *N*-oxide and 14.9 g of molecular sieves (4 Å) in 100 mL of methylene chloride was added 209 mg (0.59 mmol) of tetrapropylammonium perruthenate. The mixture was stirred for 1 day at room temperature, tetrapropylammonium perruthenate was filtered off, and the resulting brown solution was consecutively washed with 100 mL of a saturated solution of ammonium chloride, sodium chloride, and copper sulfate. The organic layer was then dried over $MgSO_4$. Column chromatography (cyclohexane–ethyl acetate 10:1) afforded 5.36 g (23.2 mmol, 78%) of the title compound as a colorless oil. $[\alpha]_D^{20}$ +4.3 (*c* = 0.2, CH_2Cl_2). ^{1}H NMR (400 MHz, $CDCl_3$) δ: 0.01 (s, 6H, Si-CH_3), 0.85 (s, 9H, $C(CH_3)_3$), 0.99–1.03 (m, 6H, CH-C*H*$_3$ and CH_2-C*H*$_3$), 2.49 (q, *J* = 7.1 Hz, 2H, C*H*$_2$-CH_3), 2.74–2.79 (m, 1H, CH), 3.56–3.60 (m, 2H, O-CH_2). ^{13}C NMR (100.6 MHz, $CDCl_3$) δ: –5.60 (Si-CH_3), 7.43 (CH_2-*C*H$_3$), 13.06 (CH-*C*H$_3$), 18.15 (*C*-$(CH_3)_3$), 25.77 (C-(*C*H$_3$)$_3$), 35.95 (*C*H$_2$-CH_3), 48.26 (*C*H-CH_3), 65.71 (CH_2-O), 214.44 (C=O). MS (70 eV) *m*/*z* (%): 230 (8.0) $[M]^+$, 215 (3.1) $[M - CH_3]^+$, 189 (31.0), 174 (12.6), 173 (100) $[M - C(CH_3)_3]^+$, 147 (13.3), 143 (16.9) $[M - CH_3 - CH_3 - C(CH_3)_3]^+$, 131 (10.0), 115 (34.8) $[M - CH_3 - CH_3 - C(CH_3)_3 - Si]^+$, 99 (4.3) $[M - CH_3 - CH_3 - C(CH_3)_3 - Si - O]^+$, 75 (63.5) $[HO{=}Si(CH_3)_2]^+$, 73 (25.7) $[C_4H_9O^+]^+$, 69 (11.1), 57 (12.9) $[C(CH_3)_3]$. HRMS (FAB): calcd. for $C_{12}H_{26}O_2Si$: 230.4193; found: 230.4181.

(2*R*)-1-(*tert*-Butyldimethylsilyloxy)-3-iodo-2-methylpropane (12)

To a solution of 1.11 g (5.50 mmol) of (2*S*)-3-([*tert*-butyldimethylsilyl]oxy)-2-methyl-1-propanol (**6**) in 30 mL of toluene were added 2.2 g (8.3 mmol) of triphenylphosphine, 1.1 g (16.5 mmol) of imidazole, and 1.9 g (7.6 mmol) of iodine. The flask was protected against light and the mixture was stirred for 1 day at room temperature. The liquid was decanted and the bronze colored solid was extracted with ether (3 × 20 mL). The combined organic layers were washed with 50 mL of a concentrated solution of sodium hydrogen carbonate, sodium thiosulfate, and sodium chloride. The organic layer was dried over $MgSO_4$. Column chromatography (cyclohexane–ethyl acetate 10:1) afforded 1.71 g (5.47 mmol, 100%) of the title compound as a yellow oil. $[\alpha]_D^{20}$ +12.2 (*c* = 0.6, CH_2Cl_2). ^{1}H NMR (250 MHz, $CDCl_3$) δ: 0.02 (s, 6H, Si-CH_3), 0.87 (s, 9H, $C(CH_3)_3$), 0.96 (d, *J* = 7.3 Hz, 3H, CH-C*H*$_3$), 1.47–1.59 (m, 1H, CH), 3.14–3.23 (m, 2H, CH_2-I), 3.31–3.53 (m, 2H, CH_2-O).

(2*S*)-5-(*tert*-Butyldimethylsilyloxy)-2,4-dimethyl-1-pentene (13)

To a solution of 0.86 g (2.75 mmol) of (2*R*)-1-(*tert*-butyldimethylsilyloxy)-3-iodo-2-methylpropane (**12**) in 10 mL of THF were added 60 mg (0.30 mmol) of copper(I) iodide and 1.33 mL (10.9 mmol) of 1,3-dimethyl-3,4,5,6-

© 2002 NRC Canada

tetrahydro-2(1*H*)-pyrimidinone (DMPU). The mixture was cooled to –20°C and a freshly prepared solution of 2-propenylmagnesium bromide (6.85 mmol) in THF (7 mL) was added over 20 min. After stirring for 2 h at –20°C, the mixture was stirred for 1 h at 0°C and then quenched with 10 mL of saturated ammonium chloride solution. The layers were separated and the aqueous phase was extracted with ether (3 × 20 mL). The combined organic layers were washed with 20 mL of a concentrated solution of ethylene diamine tetraacetate and sodium chloride. The organic layer was dried over $MgSO_4$. Column chromatography (cyclohexane–ethyl acetate 8:1) afforded 581 mg (2.54 mmol, 93%) of the title compound as a colorless oil. $[\alpha]_D^{20}$ –3.4 (*c* = 0.9, CH_2Cl_2). ^{1}H NMR (250 MHz, $CDCl_3$) δ: 0.02 (s, 6H, Si-CH_3),), 0.83 (d, *J* = 6.5 Hz, 3H, CH-C*H*$_3$), 0.87 (s, 9H, C(CH_3)$_3$), 1.63 (s, 3H, CH_2=C-C*H*$_3$), 1.83–1.88 (m, 2H, C*H*$_2$-C=CH_2), 2.09–2.15 (m, 1H, CH), 3.35–3.41 (m, 2H, CH_2-O), 4.65 (d, *J* = 10.5 Hz, 2H, CH_2=C).

(2*S*)-2,4-Dimethyl-4-pentenol

To a solution of 6.57 g (28.8 mmol) of (2*S*)-5-(*tert*-butyldimethylsilyloxy)-2,4-dimethyl-1-pentene (**13**) in 10 mL of THF were added 85 mL (85 mmol) of a 1.0 M solution of tetrabutylammonium fluoride in THF, 11.0 g of molecular sieves (4 Å), 5 mL of acetic acid, and 5 g of glass splinters. The mixture was stirred for 2 days at room temperature. The solution was then filtered and 50 mL of water was added to the filtrate. The layers were separated and the aqueous phase was extracted with diethyl ether (3 × 50 mL). The combined organic layers were washed with 50 mL of a concentrated solution of sodium hydrogen carbonate and sodium chloride. The organic layer was dried over $MgSO_4$ and the solvent was removed under reduced pressure. The resulting oil was distilled under reduced pressure (*p* = 3 mbar, bp = 42°C) to afford 2.36 g (20.7 mmol, 72%) of the title compound as a colorless oil. $[\alpha]_D^{20}$ –3.9 (*c* = 0.7, $CHCl_3$). ^{1}H NMR (250 MHz, $CDCl_3$) δ: 0.90 (d, *J* = 7.3 Hz, 3H, CH-C*H*$_3$), 1.62 (s, 1H, OH), 1.76 (s, 3H, C-CH_3), 1.84–1.96 (m, 2H, CH-C*H*$_2$-C), 2.09–2.15 (m, 1H, CH), 3.42–3.53 (m, 2H, C*H*$_2$-OH), 4.65 (d, *J* = 11.6 Hz, 2H, CH_2=C). The ^{1}H NMR data is in concordance with literature (25).

(2*S*)-2,4-Dimethyl-4-pentenal (4)

To a solution of 0.67 mL (7.77 mmol) of oxalyl chloride in 60 mL of methylene chloride was added 0.74 mL (10.4 mmol) of dimethyl sulfoxide at –78°C and the resulting solution was stirred for 20 min. Next, 0.59 g (5.17 mmol) of (2*S*)-2,4-dimethyl-4-penten-1-ol was added and the solution was stirred for another 30 min. Then 5.06 mL (36.2 mmol) of triethylamine was added and the mixture was stirred for 5 min at –78°C. The reaction mixture was allowed to warm to room temperature and stirred for another hour. The solution was cooled to –78°C, water (25 mL) was added, and the mixture was allowed to warm to room temperature again. The aqueous layer was extracted with methylene chloride (4 × 60 mL). The organic layers were combined, washed consecutively with a saturated aqueous solutions of ammonium chloride and sodium chloride, and then dried over $MgSO_4$. Removal of the solvent under reduced pressure afforded 435 mg (3.88 mmol, 75%) of the title compound. $[\alpha]_D^{20}$ +3.3 (*c* = 0.1, $CHCl_3$). ^{1}H NMR (250 MHz, $CDCl_3$) δ: 1.06 (d, *J* = 8.3 Hz, 3H, CH-C*H*$_3$), 1.78 (s, 3H, C-C*H*$_3$), 2.06–2.33 (m, 2H, C-C*H*$_2$), 2.43–2.61 (m, 1H, CH), 4.81 (s, 1H, C=CH_2), 4.85 (s, 1H, C=CH_2), 9.63 (s, 1H, COH). The ^{1}H NMR data is in concordance with literature (25).

(2*R*,4*S*,5*R*,6*S*)-1-([*tert*-Butyldimethylsilyl]oxy)-5-hydroxy-2,4,6,8-tertamethyl-8-nonen-3-one (14)

To a solution of 1.39 g (6.00 mmol) of (2*R*)-1-([*tert*-butyldimethylsilyl]oxy)-2-methyl-3-pentanone (**5**) in 70 mL of methylene chloride was added at –78°C 18 mL (18 mmol) of a 1.0 M solution of $TiCl_4$ in methylene chloride. After 30 min, 2.21 mL (13.0 mmol) of *N*-ethyl-diisopropylamine was added dropwise and after 70 min a solution of 0.60 g (5.36 mmol) of (2*S*)-2,4-dimethyl-4-pentenal (**4**) in 5 mL methylene chloride was added. After strirring at –78°C for 1 h, the reaction mixture was allowed to warm slowly to –5°C. Saturated ammonium chloride solution (15 mL) and 20 mL buffer solution (pH 7) were added, the layers were separated, and the aqueous layer was extracted with diethyl ether (3 × 70 mL). The organic layers were combined, washed with 150 mL of a concentrated solution of sodium hydrogencarbonate and 150 mL of brine. After drying over $MgSO_4$, column chromatography (cyclohexane–ethyl acetate 10:1) afforded 780 mg (2.28 mmol, 42%) of crude product as a slightly red oil. The diastereomers were separated by HPLC, which lead to the desired diastereomer as a slight yellow oil. The diastereomers were found in a ratio of 1.8:1 and with a *syn–anti* ratio of 10:1. $[\alpha]_D^{20}$ +14.1 (*c* = 1.3, $CHCl_3$). ^{1}H NMR (500 MHz, $CDCl_3$) δ: 0.03 (s, 6H, Si-CH_3), 0.88 (s, 9H, Si-C(CH_3)$_3$), 0.91–0.92 (m, 3H, C-CH_2-CH-C*H*$_3$), 1.11 (d, *J* = 6.1 Hz, 3H, O-CH-CH-C*H*$_3$), 1.16–1.18 (m, 3H, CH-CH-CO-CH-C*H*$_3$), 1.73 (s, 3H, C=C-CH_3), 2.02–2.04 (m, 3H, C=C-CH_3), 2.07 (dd, *J* = 7.4 and 14.2 Hz, 1H, C-CH_2-C*H*-CH_3), 2.66–2.68 (m, 1H, O-CH-C*H*-CH_3), 2.93–2.99 (m, 1H, CH-CO-C*H*-CH_3), 3.47–3.53 (m, 2H, O-CH_2), 3.68–3.69 (m, 1H, CH-O), 4.61 (s, 1H, C=CH_2), 4.69 (s, 1H, C=CH_2). ^{13}C NMR (125.6 MHz, $CDCl_3$) δ: –5.56 (Si-CH_3), 13.10 (CH-CH-CO-CH-*C*H_3), 14.21 (O-CH-CH-*C*H_3), 17.73 (C-CH_2-CH-*C*H_3), 19.37 (*C*(CH_3)$_3$), 22.15 (C=C-*C*H_3), 25.66 (C(*C*H_3)$_3$), 28.30 (C-CH_2-*C*H-CH_3), 41.53 (C-*C*H_2-CH-CH_3), 42.41 (CH-CO-*C*H-CH_3), 48.30 (O-CH-*C*H-CH_3), 65.16 (CH_2-O), 65.73 (CH-OH), 112.24 (*C*H_2=C), 142.95 (CH_2=*C*), 214.46 (C=O). MS (70 eV) *m*/*z* (%): 342 (0.1) $[M]^+$, 327 (0.1) $[M - CH_3]^+$, 285 (3.7) $[M - C(CH_3)_3]^+$, 271 (14.7), 259 (2.2) $[M - C_6H_{11}]^+$, 227 (1.7) $[M - CH_3 - CH_3 - C(CH_3)_3 - Si]^+$, 201 (5.7) $[M - C_9H_{17}O]^+$, 185 (60.0), 174 (12.8), 173 (100.0), 169 (0.8) $[M - C_3H_6O - CH_3 - CH_3 - C(CH_3)_3 - Si]^+$, 115 (6.5) $[Si(CH_3)_2C(CH_3)_3]^+$, 113 (22.1) $[C_7H_{13}O]^+$, 81 (12.3), 75 (25.7), 73 (16.4), 57 (9.1) $[C(CH_3)_3]^+$. FAB-HRMS calcd. for $C_{19}H_{38}O_3Si$: 342.2590; found: 342.2587.

(2*R*,4*S*,5*R*,6*S*)-1-([*tert*-Butyldimethylsilyl]oxy)-5-hydroxy-2,4,6,8-tetramethyl-8-nonene-3-[1,3]dioxolane

To a solution of 240 mg (0.70 mmol) of (2*R*,4*S*,5*R*,6*S*)-1-([*tert*-butyldimethylsilyl]oxy)-5-hydroxy-2,4,6,8-tertamethyl-8-nonen-3-one (**14**) in 10 mL of ethylene glycol was added 0.89 mL (0.76 g, 7.01 mmol) of chlorotrimethylsilane and the resulting solution was stirred overnight. A 5% aqueous sodium hydrogencarbonate solution (15 mL) was then

© 2002 NRC Canada

added, the layers were separated, and the aqueous phase was extracted with ether (3 × 75 mL). The organic layers were combined, washed twice with brine, and dried over $MgSO_4$. Column chromatography (cyclohexane–ethyl acetate 10:1) afforded 227 mg (0.59 mmol, 84%) of the title compound as a slightly yellow oil. $[\alpha]_D^{20}$ +24.4 (*c* = 2.59, MeOH). ^{1}H NMR (400 MHz, $CDCl_3$) δ: 0.02 (s, 6H, Si-CH_3), 0.88 (s, 9H, Si-C(CH_3)$_3$), 0.91–0.92 (m, 3H, C-CH_2-CH-C*H*$_3$), 1.14 (d, *J* = 6.1 Hz, 3H, O-CH-CH-C*H*$_3$), 1.16 (d, *J* = 6.9 Hz, 3H, CH-CH-CO-CH-C*H*$_3$), 1.73 (s, 3H, C=C-CH_3), 2.02–2.04 (m, 3H, C=C-CH_3), 2.07 (dd, *J* = 7.4 and 14.2 Hz, 1H, C-CH_2-C*H*-CH_3), 2.34–2.42 (m, 1H, O-CH-C*H*-CH_3), 2.63–2.73 (m, 1H, CH-CO-C*H*-CH_3), 3.62 (t, *J* = 4.7 Hz, 4H, O-CH_2-CH_2), 3.65–3.69 (m, 2H, O-CH_2), 3.88–3.91 (m, 1H, CH-O), 4.67 (s, 1H, C=CH_2), 4.74 (s, 1H, C=CH_2). ^{13}C NMR (125.6 MHz, $CDCl_3$) δ: –5.12 (Si-CH_3), 17.04 (CH-CH-CO-CH-*C*H_3), 17.88 (O-CH-CH-*C*H_3), 18.54 (C-CH_2-CH-*C*H_3), 22.32 (*C*(CH_3)$_3$), 25.86 (C=C-*C*H_3), 26.11 (C(*C*H_3)$_3$), 33.37 (C-CH_2-*C*H-CH_3), 37.93 (C-*C*H_2-CH-CH_3), 42.08 (CH-CO-*C*H-CH_3), 49.18 (O-CH-*C*H-CH_3), 63.91 (CH_2-O), 64.03 (CH-OH), 64.29 and 64.33 (O-*C*H_2-*C*H_2-O), 112.55 (*C*H_2=C), 122.08 (*C*-O-CH_2-CH_2-O), 142.93 (CH_2=*C*). FAB-HRMS: calcd. for $C_{21}H_{42}O_4Si$: 386.6459; found: 386.6461.

(2*R*,4*S*,5*R*,6*S*)-1-([*tert*-Butyldimethylsilyl]oxy)-5-methoxymethoxy-2,4,6,8-tertamethyl-8-nonene-3-[1,3]dioxolane (15)

To a solution of 81 mg (0.19 mmol) of (2*R*,4*S*,5*R*,6*S*)-1-([*tert*-butyldimethylsilyl]oxy)-5-hydroxy-2,4,6,8-tetramethyl-8-nonene-3-[1,3]dioxolane in 3 mL of methylene chloride were added 0.33 mL (1.9 mmol) of *N*,*N*-diisopropylamine and 72 μL (0.95 mmol) of chloromethyl methyl ether, and the solution was stirred overnight. Saturated aqueous sodium hydrogencarbonate solution (10 mL) was then added, the layers were separated, and the aqueous phase was extracted with ether (3 × 20 mL). The organic layers were combined and dried over $MgSO_4$. Column chromatography (cyclohexane–ethyl acetate 10:1) afforded 23 mg (55 μmol, 29%) of the title compound as a yellow oil. $[\alpha]_D^{20}$ +21.3 (*c* = 2.33, MeOH). ^{1}H NMR (400 MHz, $CDCl_3$) δ: 0.08 (s, 6H, Si-CH_3), 0.86 (s, 9H, Si-C(CH_3)$_3$), 0.92–0.93 (m, 3H, C-CH_2-CH-C*H*$_3$), 1.14 (d, *J* = 6.1 Hz, 3H, O-CH-CH-C*H*$_3$), 1.16 (d, *J* = 6.9 Hz, 3H, CH-CH-CO-CH-C*H*$_3$), 1.72 (s, 3H, C=C-CH_3), 2.03–2.07 (m, 3H, C=C-CH_3), 2.35–2.43 (m, 1H, O-CH-C*H*-CH_3), 2.61–2.70 (m, 1H, CH-CO-C*H*-CH_3), 2.71 (dd, *J* = 7.4 and 14.3 Hz, 1H, C-CH_2-C*H*-CH_3), 3.52 (s, 3H, O-CH_3), 3.62 (t, *J* = 4.7 Hz, 4H, O-C*H*$_2$-C*H*$_2$-O), 3.64–3.67 (m, 2H, O-CH_2), 4.71 (s, 1H, C=CH_2), 4.76 (s, 1H, C=CH_2), 5.47 (s, 2H, O-CH_2-O). ^{13}C NMR (125.6 MHz, $CDCl_3$) δ: –5.27 (Si-CH_3), 17.32 (CH-CH-CO-CH-*C*H_3), 18.47 (O-CH-CH-*C*H_3), 18.83 (C-CH_2-CH-*C*H_3), 22.48 (*C*(CH_3)$_3$), 25.16 (C=C-*C*H_3), 25.32 (C(*C*H_3)$_3$), 31.46 (C-CH_2-*C*H-CH_3), 38.14 (C-*C*H_2-CH-CH_3), 42.37 (CH-CO-*C*H-CH_3), 45.53 (O-CH-*C*H-CH_3), 53.21 (CH-O-CH_2-O-*C*H_3), 62.71 (CH-OH), 63.97 (CH_2-O), 64.30 and 64.34 (O-*C*H_2-*C*H_2-O), 112.61 (*C*H_2=C), 113.94 (CH-O-*C*H_2-O), 122.89 (*C*-O-CH_2-CH_2-O), 142.96 (CH_2=*C*). FAB-HRMS calcd. for $C_{23}H_{46}O_5Si$: 430.6989; found: 430.6987.

References

1. T. Hammamoto, S. Gunji, H. Tsuji, and T. Beppu. J. Antibiot. **36**, 639 (1983).
2. T. Hammamoto, S. Gunji, H. Tsuji, and T. Beppu. J. Antibiot. **36**, 646 (1983).
3. M. Yoshida, M. Nishikawa, K. Nishi, K. Abe, S. Horinouchi, and T. Beppu. T. Exp. Cell. Res. **187**, 150 (1990).
4. K.S. Ullman, M.A. Powers, and D.J. Forbes. Cell, **90**, 967 (1997).
5. B. Wolff, J.-J. Sanglier, and Y. Wang. Chem. & Biol. **4**, 139 (1997).
6. K. Nishi, M. Yoshida, D. Fujiwara, M. Nishikawa, S. Horinouchi, and T. Beppu. J. Biol. Chem. **269**, 6320 (1994).
7. M. Forgues, A.J. Marrogi, A.E. Spillare, C.-G. Wu, Q. Yang, M. Yoshida, and X.W. Wang. J. Biol. Chem. **276**, 22797 (2001).
8. A. Wada, M. Fukuda, M. Mishima, and E. Nishida. EMBO J. **17**, 1635 (1998).
9. S. Taagepera, D. McDonald, J.E. Loeb, L.L. Whitaker, A.K. McElroy, J.Y.K. Wang, and T. Hope. J. Proc. Natl. Acad. Sci. U.S.A. **95**, 7457 (1998).
10. J. Yang, E.S.G. Bardes, J.D. Moore, J. Brennan, M.A. Powers, and S. Kornbluth. Genes Dev. **12**, 2131 (1998).
11. D.A. Freedman and A.J. Levine. Mol. Cell. Biol. **18**, 7288 (1998).
12. T.T. Huang, N. Kudo, M. Yoshida, and S. Miyamoto. Proc. Natl. Acad. Sci. U.S.A. **97**, 1014 (2000).
13. A. Hagting, C. Karlsson, P. Clute, M. Jackman, and J. Pines. EMBO J. **17**, 4127 (1998).
14. W. Wen, A.T. Harootunian, S.R. Adams, J. Feramisco, R.Y. Tsien, J.L. Meinkoth, and S.S. Taylor. J. Biol. Chem. **269**, 32214 (1994).
15. B.R. Henderson and A. Eleftheriou. Exp. Cell Res. **256**, 213 (2000).
16. N. Kudo, N. Matsumori, H. Taoka, D. Fujiwara, E.P. Schreiner, B. Wolff, M. Yoshida, and S. Horinouchi. Proc. Natl. Acad. Sci. U.S.A. **96**, 9112 (1999).
17. M. Kobayashi, W. Wang, Y. Tsutsui, M. Sugimoto, and N. Murakami. Tetrahedron Lett. **39**, 8291 (1998).
18. Z.F. Xie, H. Suemune, and K. Sakai. Tetrahedron: Asymmetry, **4**, 973 (1993).
19. J. Tamura and A. Kochi. J. Am. Chem. Soc. **93**, 1485 (1971).
20. I. Paterson and M.V. Perkins. Tetrahedron, **52**, 1811 (1996).
21. D.A. Evans, M.J. Dart, J.L. Duffy, and D.L. Rieger. J. Am. Chem. Soc. **117**, 9073 (1995).
22. P. Grisenti, P. Ferraboschi, A. Manzocchi, and E. Santaniello. Tetrahedron, **48**, 3827 (1992).
23. E.J. Thomas and J.W.F. Whitehead. J. Chem. Soc. Perkin Trans. 1, **507** (1989).
24. W. Roush, A.D. Palkowitz, and K. Ando. J. Am. Chem. Soc. **112**, 6348 (1990).
25. D.A. Evans, R.P. Polniaszek, K.M. De Vries, M. Keith, D.E. Guinn, and D.J. Mathre. J. Am. Chem. Soc. **113**, 7613 (1991).

© 2002 NRC Canada

Water content influences the selectivity of CALB-catalyzed kinetic resolution of phenoxymethyl-substituted secondary alcohols

Elisabeth Egholm Jacobsen and Thorleif Anthonsen

Abstract: Derivatives of 1-phenoxy-2-alkanols were kinetically resolved by esterification with irreversible and reversible acyl donors using lipase B from *Candida antarctica* (Novozyme 435) as a catalyst. To optimize the relative rate of reaction (the *E*-value), esterifications in eight different solvents with different water activities were performed. For 3-bromo-1-phenoxy-2-propanol (**1**), the *E*-values in all the solvents were higher when the water activity was increased, while the *E*-values for 1-phenoxy-2-pentanol (**2**) and 3-chloro-1-phenoxy-2-propanol (**3**) decreased by increasing water activity. The water content of the various reaction media with the same water activity was determined. Solvents such as 1,4-dioxane, acetonitrile, and tetrahydrofuran contained much more water than hexane, carbon tetrachloride, cyclohexane, toluene, and benzene. At high-water activity, the high-water content of the former group of solvents resulted in termination of the reaction at low conversion. The reason seemed to be that the acyl donor and possibly also the produced esters were hydrolyzed. This was not the case when the esterification was performed in water-immiscible solvents with the same water activity.

Key words: kinetic resolution, *E*-value, solvents, water activity, water content.

Résumé : Des dérivés de 1-phénoxyalcan-2-ols ont été résolus de façon cinétique par estérification avec des donneurs irréversibles et réversibles de groupes acyles, sous l'influence de la lipase B de *Candida antartica* (Novozyme 435) comme catalyseur. Afin d'optimiser la vitesse relative de réaction (la valeur *E*), on a effectué les estérifications dans huit solvants différents avec des activités aqueuses différentes. Pour le 3-bromo-1-phénoxypropan-2-ol (**1**), les valeurs *E* dans chacun des solvants augmentent avec une augmentation de l'activité aqueuse alors que les valeurs *E* pour le 1-phénoxypentan-2-ol (**2**) et 3-chloro-1-phénoxypropan-2-ol (**3**) diminuent avec une augmentation de l'activité aqueuse. On a déterminé la teneur en eau de divers milieux réactionnels de même activité aqueuse. Des solvants tels que le 1,4-dioxane, l'acétonitrile et le tétrahydrofurane contiennent plus d'eau que l'hexane, le tétrachlorure de carbone, le cyclohexane, le toluène et le benzène. À des activités aqueuses élevées, la teneur en eau du premier groupe de solvant provoque une terminaison de la réaction à des taux de conversion faibles. Il semble que ce résultat soit attribuable à une hydrolyse du donneur acyle et possiblement des esters produits. Ceci ne se produit pas lorsque l'estérification est réalisée dans des solvants immiscibles avec l'eau de teneur en eau similaire.

Mots clés : résolution cinétique, valeur *E*, solvants, activité aqueuse, teneur en eau.

[Traduit par la Rédaction]

Introduction

Resolution of racemic mixtures is a very popular method to produce enantiopure compounds. Resolution may be obtained either via diastereomeric complexes or by kinetic resolution. In a kinetic resolution, one enantiomer reacts faster than the other to form a product that is separable from the unreactive enantiomer. Kinetic resolutions may be catalyzed by enzymes. If the reaction is suboptimal it may be improved by changing the medium. When resolution is conducted as an enantioselective esterification in an organic medium, the water content of the reaction medium may be important. The influence of the water content of the reaction medium on the enantioselectivity (the *E*-value) of kinetic resolutions were studied in many different systems such as lipase-catalyzed esterifications. In some cases the value of *E* was unaffected by the water activity (1–3), whereas in other examples the *E*-value increased with increasing water activity (4). It has also been observed that the *E*-value decreased with increasing water activity (5, 6). Transesterification of sulcatol with porcine pancreatic lipase gave a tenfold increase in the *E*-value when the enzyme was dehydrated before use (7). The water-activity effect, however, has to be seen in connection with the solvent used in the reaction. It is

Received 11 December 2001. Published on the NRC Research Press Web site at http://canjchem.nrc.ca on 15 May 2002.

Dedicated to Professor J. Bryan Jones on the occasion of his 65th birthday.

E.E. Jacobsen and T. Anthonsen.[1] Department of Chemistry, Norwegian University of Science and Technology, N-7491 Trondheim, Norway.

[1]Corresponding author (e-mail: thorleif.anthonsen@chembio.ntnu.no).

 DOI: 10.1139/V02-068 © 2002 NRC Canada

Scheme 1.

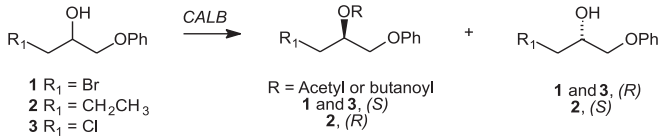

Fig. 1. Esterifications of 3-bromo-1-phenoxy-2-propanol (**1**) with vinyl butanoate in CCl_4 with a_w = 0.18 (-○-) and a_w = 0.65 (-□-) and in THF with a_w = 0.18 (-△-) and a_w = 0.39 (-◇-). Open symbols represent the ee values of the substrates; the corresponding filled symbols are the ee values of the products. Esterification of **1** did not take place in THF with a_w = 0.65.

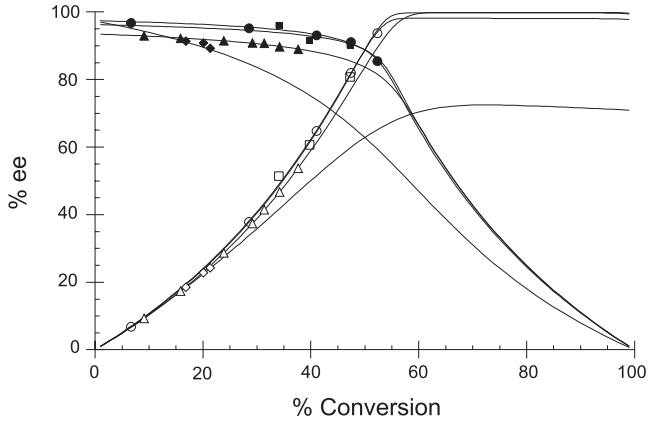

reported that better enantioselectivity is obtained in hydrophilic solvents than in hydrophobic ones, although hydrophobic solvents yield higher reaction rates than hydrophobic solvents (6). Although different substrates and enzymes were used under varying conditions in all these experiments, no general conclusions have been obtained. To determine the amount of water actually bound to the enzyme, the water activity of a system is more relevant than the total water content (8, 9) — addition of different salt hydrate pairs to the organic solvents is a simple method to vary the water activity in low-water media (10–12).

Results and discussion

The racemic secondary alcohols **1**–**3** (Scheme 1) were resolved by esterification catalyzed by immobilized lipase B from *Candida antarctica* (Novozyme 435). To increase the relative rate of reaction of the enantiomers (the *E*-value), medium engineering was performed.

The *E*-values of **1** increased with increasing a_w, Table 1. In the reactions of **1** in 1,4-dioxane, acetonitrile, and THF, a significant increase in the *E*-value was observed on going from a_w = 0.18 to 0.39; the reactions with a_w = 0.39, however, stopped at 30% conversion. When a_w = 0.65 the reactions did not exceed 1% conversion. When water-immiscible solvents were used, the *E*-values showed a moderate increase as a_w was increased from 0.18 to 0.65. The reactions were slow when a_w = 0.65, but did not stop until ca. 40–50% conversion was achieved (Fig. 1).

Water content can affect the enzyme-catalyzed kinetic resolution by esterification in organic solvents either by influencing the relative rate of formation of the two enantiomers

Table 1. *E*-values from kinetic resolution of **1** catalyzed by CALB with vinyl butanoate in different solvents with different water activity.

Solvent	Log *P*	a_w = 0.18	a_w = 0.39	a_w = 0.65
1,4-Dioxane	–1.1	25	47	Conv. <1%
Acetonitrile	–0.3	40	69	Conv. <1%
THF	0.5	30	73	Conv. <1%
Et_2O	0.9	23	24	Conv. <1%
Hexane	3.5	16	25	55
CCl_4	3.0	52	63	69
Toluene	2.5	35	42	52
Benzene	2.0	22	31	48

Table 2. Water content (μg water per g solvent) at different water activity in different solvents, measured at 30°C.

Solvent	Log *P*	a_w = 0.18	a_w = 0.39	a_w = 0.65
1,4-Dioxane	–1.1	360.1	433.0	5820.5
Acetonitrile	–0.3	1641.0	1862.0	12391.1
THF	0.5	882.7	904.2	13003.0
Et_2O	0.9	471.4	543.3	7980.2
Hexane	3.5	27.9	28.2	74.1
CCl_4	3.0	45.0	55.6	84.4
Toluene	2.5	138.4	142.3	510.4
Benzene	2.0	134.6	179.1	627.2

or by influencing the different equilibria of the system (18). The reason for the different reaction-rate patterns in the esterifications of **1** is that the water content at the same water activity is conciderably higher in 1,4-dioxane, acetonitrile, THF, and Et_2O compared with water-immiscible solvents, although the water activity is set by salt-hydrate pairs to be the same (Table 2). Compared with nonpolar solvents, polar solvents need higher water content to reach the same water activity (19). Solvents with high ability to solvate water have the lowest log *P* values. Other solvent parameters were not considered in this case.

The reaction system will consist of five different equilibria. If the esterification of a racemic mixture of alcohols is performed using an acyl donor, which is irreversible, e.g., vinyl butanoate (X = -CH=CH_2), there will be two irreversible esterification rxns. [1] and [2] and three reversible hydrolysis rxns. [3]–[5], Scheme 2. The reaction-progress graphs for the esterifications of rxn. [1] in CCl_4 with a_w = 0.65 and in THF with a_w = 0.39 reveal a large difference in the rate of the reactions, Fig. 2. From the figure it is also clear that the faster-reacting enantiomer (*S*) reacts much faster in CCl_4 than in THF. The relative rate of the two enantiomers in these media is, however, similar (*E* = 69 and 73, respectively).

The reactions are irreversible due to the nature of the acyl donor. Water in the medium can catalytically hydrolyze the formed esters, again with different rates. Thus the ester that was formed at a higher rate will also be hydrolyzed at a higher rate. Hence the ee of both the product (ester) and the remaining substrate (alcohol) will decrease. If the acyl donor is hydrolyzed (rxn. [5]), the esterifications (rxns. [1] and [2]) will slow down and will virtually stop. This was observed

© 2002 NRC Canada

Table 3. *E*-values from kinetic resolution of **2** and **3** catalyzed by CALB in hexane and toluene with different water activity and esterified with 2-chloroethyl butanoate (2-ceb), 2,2,2-trichloroethyl butanoate (2,2,2-tceb), 2,2,2-trifluoroethyl butanoate (2,2,2-tfeb), vinyl butanoate (vb), or vinyl acetate (va).

Solvent	Substrate	Acyl donor	a_w = 0.18	a_w = 0.39	a_w = 0.65
Hexane	**2**	2-ceb	20	17	Conv. <1%
Hexane	**2**	vb	12	15	16
Hexane	**2**	2,2,2-tceb	30	32	9
Hexane	**2**	2,2,2-tfeb	23	19	Conv. <1%
Toluene	**3**	vb	33	25	21
Toluene	**3**	va	13	n.d.	11

Scheme 2.

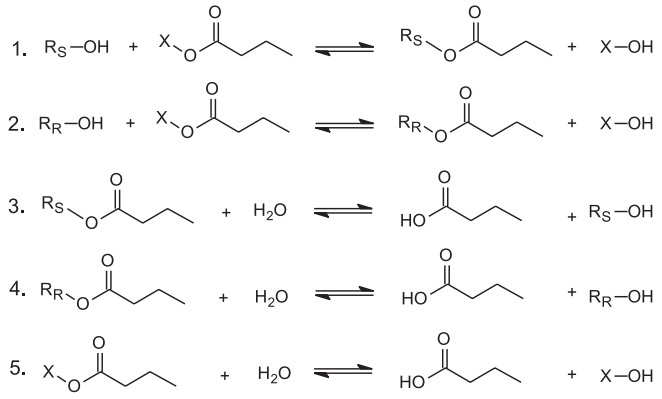

when **1** was esterified in 1,4-dioxane, acetonitrile, THF, and Et_2O with a_w = 0.65, Table 1. Even after an extra addition (10 equivalents) of acyl donor in acetonitrile, the degree of conversion did not exceed 6%. Moreover, formation of butanoic acid will take place (rxns. [3]–[5]).

It was shown that the *E*-value of the kinetic resolutions may depend on the acyl donor (20). In some cases, reversible or quasi-reversible acyl donors based on halogenated ethanols (X = CH_2CH_2Cl, CH_2CCl_3, CH_2CF_3 in Scheme 2) give higher *E*-values than the irreversible ones. When these acyl donors are used, however, all of the five reactions are reversible.

Pentanol **2**, when esterified with vinyl butanoate (vb) in hexane at a_w = 0.18, 0.39, and 0.65 showed the same tendency as **1** — an increased *E*-value with increasing water activity (Table 3). But when the acyl donors 2-chloroethyl butanoate (2-ceb), 2,2,2-trichloroethyl butanoate (2,2,2-tceb), and 2,2,2-trifluoroethyl butanoate (2,2,2-tfeb) were used, the *E*-value decreased with increasing water activity. From the esterification of **2** with different acyl donors it is clear that the acyl donor also can affect the rate of reaction. Esterification of **2** with vb is much faster than with 2-ceb, and when **2** was esterified with vb and 2-ceb in hexane, the reaction was faster when a_w = 0.18 compared with the same reaction in a_w = 0.39 (Fig. 3).

Esterifications of **3** with vinyl butanoate in toluene showed a moderate *E*-value; however, it decreased with increasing water activity. Reactions of **3** with 2-chloroethyl butanoate and vinyl acetate gave moderate *E*-values, but decreased with increasing a_w. Since **1**–**3** are different substrates, it was expected that the *E*-values would be different. In addition to different solvents, water activity and acyl donors are contributing factors to the difference in enantioselectivity. Previously we have reported that the size limitation for a secondary alcohol similar to **2** in the stereospecificity pocket of CALB is a propyl group connected to the stereocenter. When the alkyl chain is longer, CALB will not catalyze the reaction (21). The electronic effects of the small group will also play a role in orientation of the substrate, thus affecting both the reaction rate and the enantioselectivity.

Fig. 2. Reaction progress of the esterification of the two enantiomers of **1** with vinyl butanoate (vb) in CCl_4 with a_w = 0.65 show the faster-reacting enantiomer (-●-) and the slower-reacting enantiomer (-○-). The same esterification performed in THF with a_w = 0.39 shows the faster-reacting enantiomer (-◆-) and the slower-reacting enantiomer (-◇-).

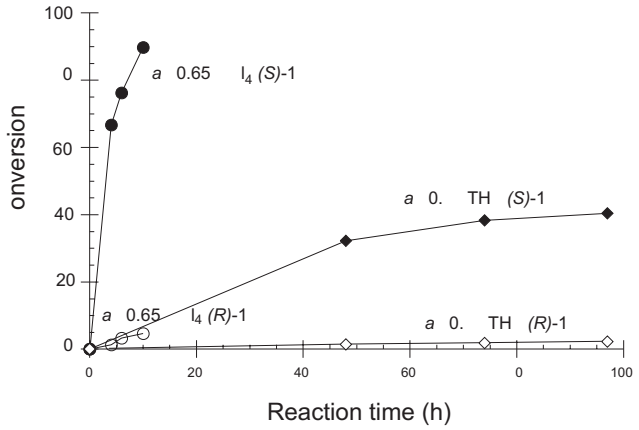

Conclusions

The *E*-value increased with increasing water activity in esterifications of substrate **1** (R_1 = Br) with vinyl butanoate as acyl donor. Reactions in 1,4-dioxane, acetonitrile, THF, and Et_2O gave optimal *E*-values when a_w = 0.39, but the reactions stopped or reversed at a low degree of conversion. Esterifications in hexane, toluene, CCl_4, and benzene also proceeded as normal when the water activity was high (a_w = 0.65). The water content at the same water activity varies considerably depending on solvents. This causes the produced esters and the acyl donor to be hydrolyzed and thus terminates the reactions at a low degree of conversion in polar solvents. Esterifications of substrate **2** (R_1 = Et) and **3** (R_1 = Cl) with 2-ceb, 2,2,2-tceb, and 2,2,2-tfeb in toluene and hexane gave decreasing *E*-values with increasing water activity. Optimal conditions for resolution of substrates **1**–**3**

© 2002 NRC Canada

Fig. 3. Esterification of **2** with vinyl butanoate (vb) in hexane with a_w = 0.18 (-◆-) and a_w = 0.39 (-●-), and esterification of **2** with 2-chloroethyl butanoate (2-ceb) in hexane with a_w = 0.18 (-▲-) and a_w = 0.39 (-■-).

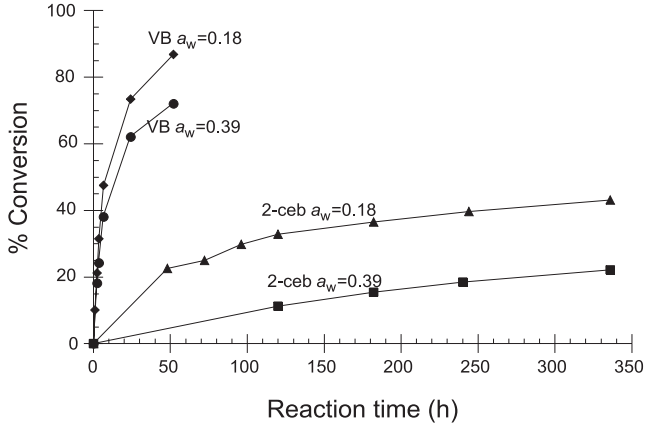

seem to be nonpolar solvents, irreversible acyl donor, and water activity between 0.39 and 0.65.

Experimental

General

Immobilized lipase B from *Candida antarctica* (CALB, Novozyme 435) from Novozymes, Denmark, has an activity of 19 PLU mg^{-1} for substrates **2** and **3** and 7 PLU mg^{-1} substrate **1**, and a water content of 2.16% w/w. All chemicals were purchased from Fluka except for vinyl butanoate, which was purchased from Aldrich. Petroleum ether has a boiling point range of 60–80°C. Column and flash chromatography were performed using silica gel 60 from Fluka, with pore sizes 0.0663–0.2000 mm and 0.035–0.070 mm, respectively.

Analyses

Optical rotations were determined using an Optical Activity Ltd. AA-10 automatic polarimeter; concentrations are given in grams per 100 mL. Chiral analyses were performed using a Varian 3400 gas chromatograph equipped with CP-Chirasil-Dex CB columns from Chrompack (25 m, 0.25 or 0.32 mm i.d., 0.25 μm film density). For chromatographic parameters, see individual compounds. NMR experiments were performed in $CDCl_3$ solutions, using Bruker DPX 300 and 400, operating at 300 and 400 MHz for ^1H and 75.4 and 100.6 MHz for ^{13}C, respectively. Chemical shifts are in ppm relative to TMS. Enantiomeric ratios (*E*) were calculated based on ping-pong bi-bi kinetics using the computer program E&K Calculator, version 2.03 (13). The *E*-values were determined from at least three experiments, with standard deviations less than 4. The water content in reaction mixtures was measured by the Karl Fischer method by a Metrohm 756 KF coulometer.

Determination of absolute configurations

The absolute configurations of the faster-reacting enantiomers of **1** and **2** were verified by comparison of optical rotation and retention times on GLC with authentic (*S*)-**1**, (*R*)-**2**, and (*R*)-**3** synthesized by a two-step procedure from (*R*)-phenyl glycidyl ether made from (*S*)-epichlorohydrin and phenol (14, 15). The synthesized alcohols had the following properties: (*S*)-**1** ee = 96%, $[\alpha]_D^{22}$ = + 5.26 (*c* 1.71, EtOH), (*R*)-**2**: ee > 99%, $[\alpha]_D^{20}$ = 6.86 (*c* 1.17, $CHCl_3$). The absolute configuration of **3** was assigned by comparing relative retention times on chiral GLC and supported by the known enantiopreference of CALB (16).

Enzymatic and nonenzymatic synthesis

Transesterifications

Substrate (**1**–**3**, 1.31 × 10^{-4} mol) and acyl donor (6.55 × 10^{-4} mol) were added to hexane (3 mL). Salt hydrates Na_2HPO_4 2/0 hydrate, $CaSO_4$ 2/0.5 hydrate, and Na_2HPO_4 7/2 hydrate (0.17 g of each) were added to give water activity values of 0.18, 0.39, and 0.65 at 30°C, respectively. The reactions were started by addition of lipase (20 mg) and performed in a shaker incubator at 30°C. Chiral GLC analyses gave ee_s and ee_p values from which the degree of conversion was determined according to $c = ee_s/(ee_s + ee_p)$. In control experiments (reaction conditions with no enzyme) no acylation was observed.

3-Bromo-1-phenoxy-2-propanol (1)

Phenyl glycidyl ether (1.19 g, 0.00793 mol) and AcOH (2.25 g, 0.0375 mol) were dissolved in dry THF (12.5 mL). Dry LiBr (1.74 g, 0.02 mol) was added and the mixture stirred at rt for 5 h. Water (12.5 mL) was added and the mixture extracted with Et_2O (5 × 10 mL). The extract was washed with water, dried over $MgSO_4$, filtered, and concentrated. The reaction product was purified by flash chromatography (pet. ether–acetone, 8:2), yield 1.56 g (85%), purity 99% (GLC). R_f = 0.38 (hexane–EtOH, 1:1). GLC (CP Chirasil DEX CB, 25 m, 0.32 mm i.d., 0.25 μm film density, 140–150°C, 0.5°C min^{-1}, 7.5 psi, 60 mL min^{-1}); acetate R_t(*R*): 16.96 min, R_t(*S*): 17.90 min, R_S= 3.40 (R_S is the resolution of the enantiomers (17)); butanoate: R_t(*R*): 29.61 min, R_t(*S*): 30.14 min, R_S = 2.37. ^1H NMR (300 MHz, $CDCl_3$) δ: 2.52 (br, 1H, OH), 3.62 (1H), 3.56 (1H), 4.15 (1 H), 4.02 (1H), 4.06 (1H), 6.90 (m, 3H), 7.25 (m, 2H, Ph). ^{13}C NMR (75.4 MHz, $CDCl_3$) δ: 33.1, 67.0, 67.8, 112.2 (2C), 119.2, 127.6 (2C), 156.0.

1-Phenoxy-2-pentanol (2)

Activated Mg (7.29 g, 0.30 mol) and EtBr (22.8 g, 0.21 mol) in dry Et_2O (100 mL) were stirred at 80°C under reflux. The reaction mixture was cooled to –78°C and Li_2CuCl_4 dissolved in THF (0.2 M, 6.5 mL) and dry Et_2O (200 mL) were added. Phenyl glycidyl ether (10.96 g, 0.073 mol) was added over a period of 1 h, the mixture was stirred at –78°C for 3 h, and left at rt overnight. Solvents were removed in vacuo and sat. NH_4Cl (250 mL) was added. After stirring at rt for 1/2 h, the mixture was extracted with Et_2O (150 mL), dried over $MgSO_4$, filtered, and concentrated. The reaction product was purified by flash chromatography (acetone–hexane, 3:7), yield 6.37 g (48.5%), purity 100% (GLC). R_f = 0.37 (acetone–hexane, 3:7). GLC (CP Chirasil DEX CB, 25 m, 0.25 mm i.d., 0.25 μm film density, 120–150°C, 1°C min^{-1}, 7.5 psi, 60 mL min^{-1}) acetate; R_t(*S*): 36.63 min, R_t(*R*): 37.29 min, R_S = 2.6; butanoate: R_t(*S*): 44.99 min, R_t(*R*): 45.59 min, R_S = 2.74. ^1H NMR (400 MHz,

© 2002 NRC Canada

$CDCl_3$) δ: 0.97 (t, 3H), 1.45 (m, 2H), 1.55 (m, 2H), 2.24 (br s, 1H, OH), 3.82 and 3.98 (dd, 1H each, -CH_2O-), 4.05 (m, 1H, -CHO-), 6.89 (m, 3H), 7.30 (m, 2H, Ph). ^{13}C NMR (100.6 MHz, $CDCl_3$) δ: 14.0, 18.7, 35.1, 69.9, 72.1, 114.5 (2C), 121.0, 129.5 (2C), 158.6.

3-Chloro-1-phenoxy-2-propanol (3)

A solution of Li_2CuCl_4 in dry THF (300 mL, 0.5 M) was added to a stirred solution of phenyl glycidyl ether (18.02 g, 0.12 mol) in dry THF (100 mL). The reaction mixture was stirred under N_2 for 18 h at rt and was stopped by addition of phosphate buffer (pH 7.0, 0.05 M, 150 mL). THF was evaporated to avoid emulsifying in the extraction with EtOAc (5 × 100 mL). The organic phase was washed with sat. NaCl solution, dried over $MgSO_4$, filtered, and concentrated by Kugelrohr distillation (0.1 mm Hg, 94°C). Yield 19.31 g (86.3%), purity 99% (GLC). R_f = 0.80 (acetone–hexane, 1:1). GLC (CP Chirasil DEX CB, 25 m, 0.32 mm i.d., 0.25 μm film density, 140–151°C, 0.5°C min^{-1}, 5 min hold time, 8.0 psi, 90 mL min^{-1}); acetate: R_t(*R*): 25.21 min, R_t(*S*): 26.63 min, R_S = 5.9; butanoate: R_t(*R*): 39.46 min, R_t(*S*): 40.15 min, R_S = 2.4. ^{1}H NMR (400 MHz, $CDCl_3$) δ: 2.12 (s, 1H, OH), 3.74 (m, 1H), 3.79 (m, 1H), 4.08 (m, 1H), 4.11 (m, 1H), 4.23 (m, 1H), 6.90 (m, 3H), 7.33 (m, 2H, Ph). ^{13}C NMR (100.6 MHz, $CDCl_3$) δ: 46.4, 68.8, 70.3, 114.9 (2C), 121.9, 130.0 (2C), 158.6.

Acknowledgment

We thank Novozymes, Bagsværd, Denmark for their gift of immobilized CALB.

References

1. R. Bovara, G. Carrea, G. Ottolina, and S. Riva. Biotechnol. Lett. **15**, 169 (1993).
2. R. Bovara, G. Carrea, G. Ottolina, and S. Riva. Biotechnol. Lett. **15**, 937 (1993).
3. E. Wehtje, D. Costes, and P. Adlercreutz. J. Mol. Catal. B, **3**, 221 (1997).
4. H.-E. Högberg, H. Edlund, P. Berglund, and E. Hedenström. Tetrahedron: Asymmetry, **4**, 2123 (1993).
5. C. Orrenius, T. Norin, K. Hult, and G. Carrea. Tetrahedron: Asymmetry, **6**, 3023 (1995).
6. A. Ducret, M. Trani, and R. Lortie. Enzyme Microb. Technol. **22**, 212 (1998).
7. T. Stokes and A. Oehlschlager. Tetrahedron Lett. **28**, 2091 (1987).
8. A. Zaks and A.M. Klibanov. J. Biol. Chem. **263**, 8017 (1998).
9. P.J. Halling. Biotechnol. Bioeng. **35**, 691 (1990).
10. B. Sjursnes, L. Kvittingen, T. Anthonsen, and P. Halling. Biocatalysis in non-conventional media. *Edited by* J. Tramper, M. Vermüe, H. Beeftink, and U. Stockar. Elsevier Science, Amsterdam. 1992. p. 451.
11. P. Kuhl and P. Halling. Biochim. Biophys. Acta, **1078**, 326 (1991).
12. L. Kvittingen, B. Sjursnes, T. Anthonsen, and P. Halling. Tetrahedron, **48**, 2793 (1992).
13. H.W. Anthonsen. http://Bendik.chembio.ntnu.no. 1996–97.
14. S. Takano, Y. Sekiguchi, M. Setho, T. Yoshimuts, K. Inomata, M. Takahasi, and K. Ogasawara. Heterocycles, **31**, 1715 (1990).
15. V. Partali, V. Waagen, T. Alvik, and T. Anthonsen. Tetrahedron: Asymmetry, **4**, 961 (1993).
16. B.H. Hoff and T. Anthonsen. Chirality, **11**, 760 (1999).
17. S. Mayer and V. Schurig. J. High Resol. Chromatog. **15**, 129 (1992).
18. C.J. Sih and S.-H. Wu. Topics Stereochem. **19**, 63 (1989).
19. P. Halling. TIBTECH, **7**, 50 (1989).
20. B.H. Hoff, H.W. Anthonsen, and T. Anthonsen. Tetrahedron: Asymmetry, **7**, 3187 (1996).
21. E.E. Jacobsen, B.H. Hoff, and T. Anthonsen. Chirality, **12**, 654 (2000).

© 2002 NRC Canada

Biocatalytic oxidation of 4-vinylphenol by *Nocardia*

Kyung-Seon Lee and John P.N. Rosazza

Abstract: *Nocardia* species NRRL 5646 stereospecifically hydrates 4-vinylphenol (**15**) to *S*-1-(4′-hydroxyphenyl)ethanol (**17**), and further oxidizes **17** to 4′-hydroxyacetophenone (**18**). Labeled metabolites **17** and **18** obtained from incubations in D_2O and $H_2{}^{18}O$ support initial enzymatic tautomerization of **15** to a reactive quinone methide (**16**), which adds water in the first reaction. Commitment to catalysis is high in the hydration reaction, while the alcohol dehydrogenation reaction appears to be reversible. The stereochemical features of water addition, alcohol oxidations, and ketone reductions with growing culture biocatalysis were established by chiral HPLC. Alcohol oxidations or ketone reductions in 12 000 × *g* supernatants preferentially require $NADP^+$–$NADPH,H^+$ as co-factors. The alcohol dehydrogenase has broad substrate specificity, favoring the oxidation of primary alkanols and 4-hydroxybenzyl alcohols.

Key words : 4-vinylphenol, *Nocardia* sp., enantiospecific hydration, 1-(4′-hydroxyphenyl)ethanol, 4′-hydroxyacetophenone

Résumé : L'espèce *Nocardia* NRRL 5446 hydrate stéréospécifiquement le 4-vinylphénol (**15**) en *S*-1-(4′-hydroxyphénnyl)éthanol (**17**) qu'il oxyde aussi en 4′-hydroxyacétophénone (**18**). Les métabolites **17** et **18** marqués obtenus par incubation dans D_2O et $H_2{}^{18}O$ sont en accord avec un mécanisme impliquant une tautomérisation enzymatique initiale de **15** en une méthoquinone réactive (**16**) qui fixe de l'eau dans la première étape de la réaction. Dans la réaction d'hydratation, le degré de catalyse est élevé alors que la réaction de déshydrogénation de l'alcool semble réversible. Faisant appel à la CLHP chirale, on a déterminé les caractéristiques stéréochimiques de l'addition d'eau, des oxydations de l'alcool et des réductions de cétone par la catalyse de cultures en croissance. Les oxydations d'alcool ou réductions de cétones dans des liquides surnageant 12,000 x *g* requièrent le coupe $NADP^+$–$NADPH,H^+$ comme cofacteurs. La déshydrogénase de l'alcool possède une grande spécificité par rapport au substrat qui favorise l'oxydation d'alcools primaires et d'alcools 4-hydroxybenzyliques.

Mots clés : 4-vinylphénol, *Nocardia* sp., hydratation spécifique, 1-(4′-hydroxyphényl)éthanol, 4′-hydroxyacétophénone.

[Traduit par la Rédaction]

Introduction

Microbial and enzymatic transformations have been developed for nearly every class of natural and synthetic chemical products (1). Microorganisms and their enzymes are biocatalysts, which are now widely used as "reagents" in synthetic organic chemistry. Biocatalysts are valued for their intrinsic abilities to bind organic substrates and to catalyze highly specific and selective reactions under the mildest of reaction conditions. Biocatalytic transformations of abundant renewable natural chemicals afford attractive "green chemistry" alternatives to synthetic chemical approaches, which rely on petrochemically derived starting materials.

Green chemistry (2) presents a continuing need for the discovery of new biocatalysts capable of catalyzing useful chemical transformations by novel mechanisms. An ideal biocatalyst has few technical hurdles, such as the requirement for co-factors. They should be robust, stable, and recyclable, and ultimately be amenable to large-scale adaptation to bioreactor use, even under unusual reaction conditions (3).

p-Coumaric acid (4), ferulic acid (5), and caffeic acid are abundantly occurring phenolic acids commonly found in plants in their esterified or free-acid forms. The acids *p*-coumaric and ferulic compose nearly 4% of the dry weight of maize plant parts, rendering them available in the billions of pounds annually from this source alone (5). The large quantities of these natural compounds render them useful for the biocatalytic production of value-added aromatic natural chemicals. Systematic screening of microorganisms showed that the major and most common biocatalytic reaction with hydroxycinnamates is decarboxylation to the corresponding vinylphenols (hydroxystyrenes) (5, 6). Deuterium-labeling experiments showed that non-oxidative decarboxylations occurred by enzymatic tautomerization of *p*-hydroxycinnamates to doubly vinylogous β-keto acid intermediates that spontaneously decarboxylated (5, 6*a*). Phenolic cinnamate decarboxylation is capable of providing potentially huge quantities of oxygenated styrenes, which are difficult to produce by ordinary chemical means (5, 6*a*, *b*). Phenolic styrenes are valuable starting materials for oxygenated biodegradable polymers, fragrances, and flavors, and chiral intermediates for organic synthesis.

Biocatalytically unsubstituted styrene (**1**) is usually converted to styrene epoxides (**2**) of varying enantiomeric

Received 23 November 2001. Published on the NRC Research Press Web site at http://canjchem.nrc.ca on 23 April 2002.

Dedicated to Professor J. Bryan Jones on the occasion of his 65th birthday.

K.-S. Lee and J.P.N. Rosazza.[1] Division of Medicinal and Natural Products Chemistry, and Center for Biocatalysis and Bioprocessing, College of Pharmacy, University of Iowa, Iowa City, Iowa 52242, U.S.A.

[1]Corresponding author: (e-mail: john-rosazza@uiowa.edu).

 DOI: 10.1139/V02-034 © 2002 NRC Canada

Scheme 1. A summary diagram of known styrene bioconversions. Solid arrows indicate aerobic conditions and dashed arrows indicate anaerobic conditions.

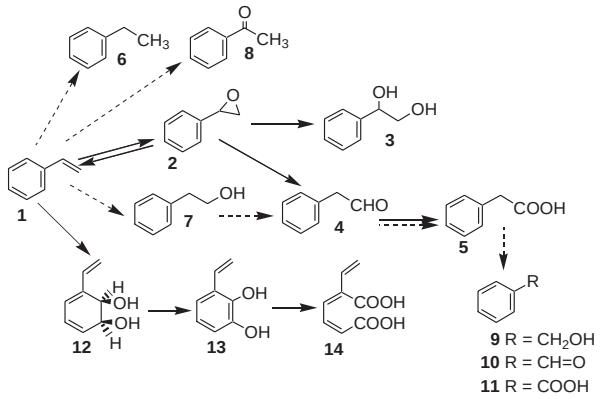

purities by enzymatic activation and insertion of molecular oxygen into the unsaturated styrene side-chain (7–9). Styrene epoxides (**2**) are also formed by hydrogen peroxide dependent-peroxidase mediated epoxidations (10). Styrene epoxides (**2**) are hydrolytically converted to diols (**3**) by epoxide hydrolases (8, 11), to phenylacetaldehyde (**4**) and phenylacetic acid (**5**) (9, 12), and to alkenes in a "reversal" of the epoxidation reaction (13). With anaerobic consortia, after water addition to the double bond, styrene (**1**) is oxidized through the phenylacetate route to yield various products, including ethylbenzene (**6**), phenylethanol (**7**), 1-phenylethanone (**8**), phenylacetaldehyde (**4**), phenylacetic acid (**5**), benzyl alcohol (**9**), benzaldehyde (**10**), and benzoic acid (**11**) (14). Styrene (**1**) is also metabolized via styrene *cis*-glycol (**12**) to 3-vinylcatechol (**13**) and 2-vinylmuconate (**14**), demonstrating double-bond and aromatic-ring oxygenation prior to ring fission (15) (Scheme 1).

Much less is known about biocatalytic transformations of phenolic styrenes such as **15**. The introduction of oxygen into the styrene side-chain olefin by a hydration mechanism is a novel and relatively unexplored biocatalytic reaction. In this study, we examined the mechanism and disposition of **15** by growing cultures, induced resting cells and cell-free enzyme preparations of the *Nocardia* species, that afforded *S*-1-(4′-hydroxyphenyl)ethanol (**17**) by vinylphenol hydratase, and subsequently, 4′-hydroxyacetophenone (**18**) by an $NADP^+$-dependent alcohol dehydrogenase (Scheme 2).

Experimental

Chemicals

4-Vinylphenol (**15**) (10% solution in propylene glycol), 4′-hydroxyacetophenone (**18**), cinnamyl alcohol (3-phenyl-2-propen-1-ol), 2-hydroxybenzyl alcohol, 3-hydroxybenzyl alcohol, 4-hydroxybenzyl alcohol, oleyl alcohol, and vinyl acetate were obtained from Lancaster Synthesis Inc. (Windham, NH, U.S.A.). D_2O (99.9 atom% D), vanillyl alcohol (4-hydroxy-3-methoxybenzyl alcohol), cyclohexanol, tetralol (1,2,3,4-tetrahydro-1-naphthol), 4-methoxybenzyl alcohol, benzyl alcohol, 1-phenyl-1-propyl alcohol, 1-phenyl-2-propyl alcohol, and 3-phenyl-1-propyl alcohol were purchased from Aldrich (Milwaukee, WI, U.S.A.). Methanol, ethanol, 1-propanol, 1-butanol, 2-butanol, 2-phenylethyl alcohol, β-NAD^+ (99%), β-$NADP^+$ (sodium salt, 98%), and β-NADPH (tetrasodium salt, 95%) were obtained from Sigma (St. Louis, MO, U.S.A.). Coomassie Plus protein assay reagent and Albumin Standard (bovine serum album fraction V, 2 mg mL^{-1} in a 0.9% aqueous NaCl solution containing sodium azide) were obtained from Pierce (Rockford, IL, U.S.A.). $H_2{}^{18}O$ (96 atom% ^{18}O) and NMR solvents were purchased from Cambridge Isotope Laboratories, Inc. (Andover, MA, U.S.A.). HPLC solvents were obtained from Fisher Scientific (Fair Lawn, NJ, U.S.A.), and other reagents were analytical grade from Fisher Scientific unless otherwise indicated.

Scheme 2. Oxidation of 4-vinylphenol (**15**) to **17** and **18** by *Nocardia* sp.

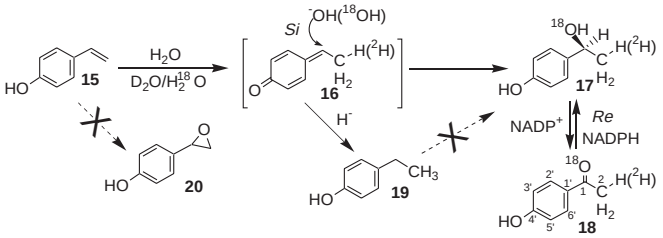

Racemic 1-(4′-hydroxyphenyl)ethanol (**17**) was prepared as described by the $NaBH_4$ reduction of 4′-hydroxyacetophenone (**18**) in CH_3OH (16).

S-(–)-**17** was prepared by a modification of Reeve et al. (17), where the lipase mediated enantioselective esterification of *R*-(+)-**17** occurs, leaving unreacted *S*-(–)-**17** behind. Racemic **17** (4 mg) was dissolved in vinyl acetate (4 mL) as the acyl donor and as the solvent and lipase (4 mg, *Pseudomonas fluorescens* lipase, EC 3.1.1.3, 3097 units mg^{-1}, Fluka Chemical Co., Milwaukee, WI, U.S.A.) were added. After incubation for 12 h at 28°C, lipase was filtered off and the filtrate was evaporated. The residue was dissolved in CH_3OH (2 mL), filtered, and subjected to chiral HPLC analysis, where the enantiomeric excess of unreacted **17** was 98.8% ee of the *S*-(–)-isomer (Fig. 1B).

Analytical methods and instrumentation

TLCs were carried out on 0.25 mm layers of silica gel GF_{254} (Sigma) precoated on polyester plates (20 × 20 cm). The developing solvent was a mixture of CH_2Cl_2–CH_3OH–HOAc (95:5:0.5, v/v/v). Developed chromatograms were directly visualized under 254 and 366 nm UV light for fluorescence quenching or fluorescence. Plates were then spayed with diazotized sulfanilic acid reagent, which consisted of solution A (0.5% sulfanilic acid in 1 N HCl), solution B (0.5% $NaNO_2$ in water), and solution C (0.5% NaOH in 50% (v/v) C_2H_5OH–H_2O). Developed plates were first sprayed with a fresh mixture of equal volumes of solutions A and B, warmed with a heat gun, followed by spraying with solution C to develop the colors. Under these conditions, **15**, **17**, and **18** gave R_f values of 0.7 (scarlet), 0.3 (yellow), and 0.5 (orange), respectively.

HPLC was performed with a Shimadzu liquid chromatograph (Shimadzu Corporation, Kyoto, Japan) equipped with dual pumps (LC-6A) and a variable wavelength UV detector (SPD-6AV). Eluted peaks were detected at 280 nm and identified by comparison with standard compounds. Separations were carried out under isocratic

© 2002 NRC Canada

Fig. 1. Chiral HPLC resolution of *R*-(+)- and *S*-(–)-1-(4′-hydroxyphenyl)ethanol (**17**): (A) racemic **17**; (B) *S*-(–)-**17** resolved by *Pseudomonas fluorescens* lipase; (C) **17** isolated from reaction of *Nocardia* cultures with 4-vinylphenol (**15**).

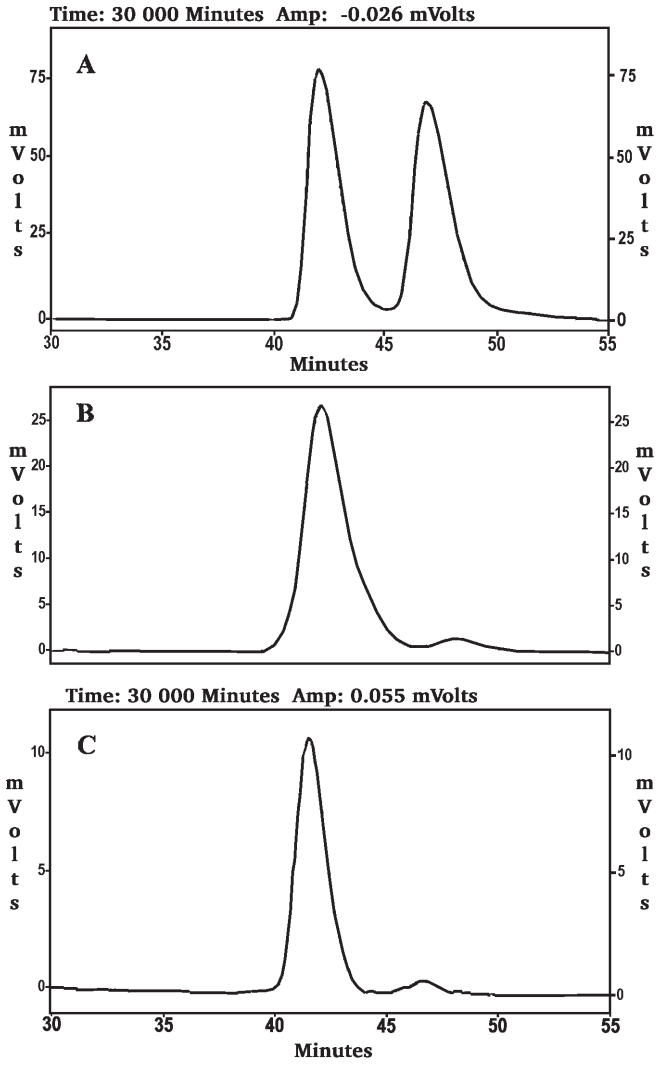

conditions over a Hypersil C18 column (250 × 4.6 mm ID, 5 μm particle size, Alltech Associates, Inc., Deerfield, IL, U.S.A.) protected with a guard column (10 × 4.6 mm ID, 5 μm particle size, Alltech) eluted with CH_3OH–CH_3CN–H_2O (7:3:10, v/v/v) at a flow rate of 0.8 mL min^{-1} to give retention volumes (*Rv*) of 3.6 mL for **17**, 4.5 mL for **18**, and 10.1 mL for **15**. Standard curves were established over the range of 1–10 μg for **15**, 1–8 μg for **17**, and 0.2–0.8 μg for **18**.

Chiral HPLC was carried out with a Chiralcel OJ column (250 × 4.6 mm ID, 10 μm particle size, Chiral Technoloies Inc., Exton, PA, U.S.A.) linked to a Chiralcel OJ guard column (50 × 4.6 mm ID, 10 μm particle size) at a flow rate of 0.8 mL min^{-1} with *n*-hexane–2-propanol (9:1, v/v), which gave retention volumes (*Rv*, mL) of 16.6 for **15**, 16.8 for **18**, 33.6 for *S*-(–)-**17**, and 37.5 for *R*-(+)-**17**.

Flash column chromatography was conducted over silica gel, 40 μm for flash columns (J.T. Baker, Phillipsburg, NJ, U.S.A.).

Mass spectra were obtained by direct inlet probe mass spectrometry (DIPMS) performed on a Voyager mass spectrometer (ThermoQuest, Manchester, England). One dimensional ^1H and ^{13}C NMR spectra were obtained with a Bruker DMX-400 (operating at 400 MHz for ^1H and 100 MHz for ^{13}C) or an AMX-600 spectrometer (operating at 600 MHz for ^1H, Karlsruhe, Germany), equipped with an IBM Aspect 2000 processor and with VNMR version 4.1. Impurities in deuterated NMR solvents were used as internal standards. Chemical shift values (δ) are reported in parts per million (ppm) and coupling constants (*J* values) are given in Hz. Abbreviations for NMR are s, singlet; d, doublet; and q, quartet.

Fermentation and biocatalysis

Nocardia sp. NRRL 5646 was grown and maintained on slants of Sabouraud-dextrose agar or sporulation agar (ATCC No. 5 medium) (18). For analytical scale reactions, cultures were grown by a two-stage protocol (19) in 25 mL of sterile soybean meal-glucose medium held in stainless steel-capped 125-mL DeLong culture flasks. The medium contained 2% glucose, 0.5% yeast extract, 0.5% soybean meal, 0.5% NaCl, and 0.5% K_2HPO_4 in doubly distilled water, and was adjusted to pH 7.0 with 6 N HCl before being autoclaved at 121°C for 15 min. Cultures were incubated with shaking at 250 rpm at 28°C on an Innova 5000 Gyrotory tier Shaker (New Brunswick Scientific Co., Edison, NJ, U.S.A.). A 10% inoculum derived from a 72-hour-old first-stage culture was used to initiate the second-stage cultures, which were incubated as above for 24 h. For bioconversions, **15** and **17** were added directly, usually at concentrations of 1 mg mL^{-1}, and **18** was added at 0.4 mg mL^{-1} of media.

Induced *Nocardia* resting cells were prepared by adding 1 mg mL^{-1} **15** to 24-hour-old stage-two cultures. After an additional 24 h, incubations were filtered through a cheese cloth to remove soybean meal solids, and the cells were concentrated by centrifugation (Sorvall RC 26 Plus centrifuge with a SLA-600TC rotor, Kendro Laboratory Products, Newton, CT, U.S.A.) at 10 000 × *g* at 4°C for 20 min. Cell pellets were suspended and washed in cold phosphate buffer (pH 7.0, 0.1 M) and centrifuged again. Typical wet cell yields ranged from 20 to 24 g L^{-1}.

Cell-free extracts were prepared from induced cells. Typically, 15 g wet weight of cells were suspended in cold phosphate buffer (45 mL, pH 7.0, 0.1 M) containing dithiothreitol (1 mM) (Aldrich) and disrupted by a Sonifier Cell Disrupter 350 (Branson Sonic Power Co., Danbury, CT, U.S.A.) operating at 10 W with a 60% intermittent duty cycle for 5 min. Cell debris was removed by centrifugation at 12 000 × *g* for 30 min at 4°C to provide a supernatant as the cell-free extract. The cell-free extract was assayed for total-protein content by the Bradford protein microassay (20) with bovine serum albumin as the standard.

For preparative-scale conversions, stage-two incubations were carried out in 200 mL of medium held in 1-L DeLong flasks. After 24 h of incubation in the second stage, **15** was added as the substrate and incubated with shaking at 250 rpm at 28°C for 24 h. The reaction mixture was harvested, acidified to pH 2 with 6 N HCl, followed by centrifugation at 10 000 × *g* at 4°C for 20 min to remove

© 2002 NRC Canada

Table 1*a*. ^{1}H NMR and mass spectral analyses for 1-(*4′*-hydroxyphenyl)ethanol (**17**) isolated from reactions of 4-vinylphenol (**15**) with *Nocardia* conducted in H_2O- or D_2O-containing buffers.

	Relative intensity at *m/z* (%)					
D_2O amount (%)	138 $[M]^+$	139 $[M + 1]^+$	140 $[M + 2]^+$	123 $[M - CH_3]^+$	124 $[M + 1 - CH_3]^+$	^{1}H NMR relative intensity – C-2H at δ 1.35
0	100	9	1	100	14	3.0
50	100	18	2	100	9	2.7
100	100	69	11	100	8	1.6

Table 1*b*. ^{1}H NMR and mass spectral analyses for 4′-Hydroxyacetophenone (**18**) isolated from reactions of 4-vinylphenol (**15**) with *Nocardia* conducted in H_2O- or D_2O-containing buffers.

	Relative intensity at *m/z* (%)					
D_2O amount (%)	136 $[M]^+$	137 $[M + 1]^+$	138 $[M + 2]^+$	121 $[M - CH_3]^+$	122 $[M + 1 - CH_3]^+$	^{1}H NMR relative intensity – C-2H at δ 2.51
0	100	24	7	100	9	3.0
50	100	23	6	100	8	2.8
100	100	83	18	100	10	1.6

cells. The supernatant was extracted wiht EtOAc (3 × 200 mL), the combined EtOAc extracts were dried over anhydrous Na_2SO_4 and concentrated by rotary evaporation to give 431 mg of crude extract. The extract was dissolved in CH_3OH (5 mL), adsorbed onto 2 g of silica gel, and loaded onto a flash column (2 × 25 cm). The column was eluted stepwise with $CHCl_3$ and $CHCl_3$–CH_3OH (99:1 to 97:3) to give fraction A (39 mg) and fraction B (173 mg). These fractions were separately resolved by flash column chromatography over silica gel using mixtures of *n*-hexane–EtOAc (95:5) for fraction A, and *n*-hexane–EtOAc (8:2 to 7:3) for fraction B. The resulting pure products were subjected to chromatographic and spectral analyses.

Induced resting cell conversions of 4-vinylphenol

Induced resting-cell reactions were performed by suspending 0.6 g wet weight of *Nocardia* cells in phosphate buffer (25 mL, pH 7.0, 0.1 M) containing glucose (0.5%) and **15** (25 mg). Samples of 2.0 mL were diluted with CH_3OH (2.0 mL), filtered through 0.2-μm nylon membrane filters, and 10 μL of the filtrates were injected for HPLC analysis. The same procedure was used in induced cell conversions of **17** at 1 mg mL^{-1} and **18** at 0.4 mg mL^{-1}.

Reactions of 4-vinylphenol with *Nocardia* sp. in D_2O and 20% $H_2{}^{18}O$

Deuterium-incorporation experiments used induced resting cells of *Nocardia* sp. as described, except that flasks held phosphate buffer (25 mL, pH 7.0, 0.1 M) containing glucose (0.5%, prepared with 50 and 100% D_2O) and **15** (1 mg mL^{-1}). For each reaction, incubations were stopped after 24 h, acidified and pelleted as before, and supernatants were extracted with EtOAc (3 × 25 mL). The combined extracts were dried over anhydrous Na_2SO_4 and evaporated to dryness. The extracts were purified on glass preparative-TLC plates coated with 1-mm layers of silica gel GF_{254} (20 × 20 cm, Sigma). UV-quenching bands were scraped from plates, extracted with CH_3OH (3 × 20 mL), and the extracts were evaporated to dryness for ^{1}H NMR and MS analysis.

Labeled-oxygen incorporation experiments also used induced *Nocardia* resting cells that were suspended in a phosphate buffer (10 mL, pH 7.0, 0.1 M) containing glucose (0.5%, prepared with 20% $H_2{}^{18}O$) and contained in 50-mL DeLong flasks. After addition of **15** (30 mg), the incubation was carried out at 28°C with spinning at 250 rpm. The control consisted of an identical reaction mixture, except the buffer was prepared with unlabeled H_2O. The 24-hour-old culture solutions were extracted with EtOAc (10 mL), the extracts were concentrated and purified by preparative TLC, as previously mentioned, to give products that were subjected to spectral analysis.

Enantiospecificity of 4-vinylphenol hydration

The enantiospecificity of the hydration reaction was evaluated by adding **15** (25 mg) to 25 mL volumes of 24-hour-old stage-two cultures. Incubations were conducted in 125-mL DeLong flasks. Samples of 3 mL were taken after 24, 48, 72, and 144 h and each was extracted with EtOAc (3 mL). After evaporation, crude extracts were redissolved in CH_3OH to concentrations of 2 mg mL^{-1}, passed through syringe filters (Acrodisc 13 mm with 0.45 μm nylon membrane filter, Gelman Science, Ann Arbor, MI, U.S.A.), and the filtrate samples (20 μL) were injected for chiral HPLC analysis.

Substrate specificity of alcohol dehydrogenase in *Nocardia* cell-free extracts

Incubations in quartz cuvettes were conducted in phosphate buffer (1.0 mL, pH 7.0, 0.1 M) containing the substrates (3 mM), $NADP^+$ or NAD^+ (0.25 mM), and cell-free extract (500 μL, 1.70 mg protein). Substrates were dissolved in dimethylformamide (DMF), and 10 μL of the DMF solutions were added to incubation mixtures. Reactions were

© 2002 NRC Canada

Table 2*a*. Mass spectral data for 1-(4′-hydroxyphenyl)ethanol (**17**) isolated from reactions of 4-vinylphenol (**15**) with *Nocardia* conducted in H_2O- and 20% $H_2{}^{18}O$-containing buffers.

	138	139	140	123	125
	$[M]^+$	$[M + 1]^+$	$[M + 2]^+$	$[M - CH_3]^+$	$[M + 2 - CH_3]^+$
Control H_2O	100	10	0	100	2
20% $H_2{}^{18}O$	100	23	18	100	23

Table 2*b*. Mass spectral data for 4′-hydroxyacetophenone (**18**) isolated from reactions of 4-vinylphenol (**15**) with *Nocardia* conducted in H_2O- and 20% $H_2{}^{18}O$-containing buffers.

	136	137	138	121	123
	$[M]^+$	$[M + 1]^+$	$[M + 2]^+$	$[M - CH_3]^+$	$[M + 2 - CH_3]^+$
Control H_2O	100	11	3	100	3
20% $H_2{}^{18}O$	100	16	17	100	20

monitored under initial-rate conditions by measuring changes in absorbance at 340 nm for 5 min at 20°C (Shimadzu 2101-PC equipped with UVPC Optional Kinetics Software v 2.5). The molar extinction coefficient used for NADPH at pH 7.0 was $\varepsilon_{340} = 6.22\ mM^{-1}\ cm^{-1}$.

Results and discussion

Conversion of 4-vinylphenol by *Nocardia* sp.

The reaction of *Nocardia* sp. with 4-vinylphenol (**15**) gave two major products identified as **17** and **18**. Characterization data for **17**: R_f = 0.3. ^1H NMR (CD_3OD) δ: 7.19 (d, ^2J = 8.4 Hz, 2H, Ar-2′, 6′H), 6.76 (d, ^2J = 8.4 Hz, 2H, Ar-3′, 5′H), 4.73 (q, ^2J = 6.5 Hz, 1H, C-1H), 1.35 (d, ^2J = 6.5 Hz, 3H, C-2H); identical to the results of Everhart and Craig (21). MS *m*/*z* (%): 138 ($[M]^+$, 15.4), 123 ($[M - CH_3]^+$, 63.5). Characterization data for **18**: R_f = 0.5. ^1H NMR (CD_3OD) δ: 7.87 (d, ^2J = 8.8 Hz, 2H, Ar-2′, 6′H), 6.82 (d, ^2J = 8.8 Hz, 2H, Ar-3′, 5′H), 2.51 (s, 3H, C-1H); spectrum was identical to that for authentic **18**. MS *m*/*z* (%): 136 ($[M]^+$, 35.2), 121 ($[M - CH_3]^+$, 100).

With induced resting cells, **15** was transformed to **17** (25%) and **18** (1%) within 48 h. Trace amounts of 4-ethylphenol (**19**) were detected as a peak at *Rv* 12.1 mL, but only after 144 h, indicating this to be a very minor biotransformation pathway. With racemic **17**, induced resting cells gave **18** in 10% yield, while **15** was undetectable. In the reverse direction, 4′-hydroxyacetophenone (**18**) gave **17** (33%) in 48 h, again producing trace amounts of 4-ethylphenol (**19**). Neither **17** nor **18** gave **15** as a product, indicating the irreversibility of the initial hydration reaction.

Resting cell incubations in 50% D_2O, 100% D_2O, and 20% $H_2{}^{18}O$ containing buffers were conducted to examine the source of oxygen and the mechanism by which *Nocardia* oxidized **15** to **17** and **18**. Reaction products isolated from these incubations were analyzed by mass spectrometry and ^1H NMR spectroscopy to determine the extent and positions of isotope incorporations. Tables 1*a* and 1*b* show the results of deuterium incorporation. For **17**, when compared with control reactions conducted in H_2O-containing buffer, ions at *m*/*z* 139 and 140 for $[M + 1]^+$ and $[M + 2]^+$ were enhanced by 9% and 1%, respectively, from 50% D_2O-containing buffer reaction, and 60% and 10%, respectively, from the 100% D_2O-containing buffer reaction. Fragment ions at *m*/*z* 123 and 124, where methyl groups were lost from the molecular ions, were essentially identical to those from unlabeled **17**, showing that all the deuterium in labeled **17** resided in the methyl groups. ^1H NMR of relative peak intensities for C-2H showed approximately 10 and 47% deuterium incorporations vs. signals for Ar-2′ and 6′-H, respectively, similar to the mass spectral findings. Similar analyses of **18** showed that all deuterium labeling resided in the C-2 methyl group. Deuterium incorporations of 59 and 11%, respectively, for $[M + 1]^+$ and $[M + 2]^+$ from 100% D_2O-containing reactions matched very well with the results for **17** from 100% D_2O. ^1H NMR results for **18** again gave 6.6% incorporation from the 50% D_2O reaction and 47% from the 100% D_2O buffer reaction. Results of deuterium incorporation from 50% D_2O buffers were inexplicably lower than expected.

Comparisons of $[M + 2]^+$ ions for **17** and **18** from reactions conducted in buffers prepared with 20% $H_2{}^{18}O$ (Tables 2*a* and 2*b*) revealed oxygen-incorporation levels of 18 and 14%, respectively. Relative intensities of $[M + 2 - CH_3]^+$ ions revealed 21 and 17% increases in similar ions vs. unlabeled **17**. Both results are consistent with complete incorporation of oxygen from water and not from molecular oxygen.

Labeling results permit a description of the reaction process as shown in Scheme 2. *Nocardia* contains a hydratase that binds and tautomerizes 4-vinylphenol (**15**) to a quinoid intermediate (**16**), which adds water to afford **17**. The tautomerization reaction is apparently partially reversible, because both **17** and its oxidation product **18** contain 1.4 deuterium atoms on the C-2 methyl group. Addition of oxygen from water and not air was clearly confirmed by the $H_2{}^{18}O$ labeling experiment, which gave nearly theoretical incorporations of ^{18}O into **17** and **18**. Slightly lower values than expected in deuterium and $H_2{}^{18}O$ incorporations can be explained by dilutions of isotopically labeled water by intracellular stores of water during the hydration reaction. Reactions conducted under an argon atmosphere with induced resting cells and in cell free extracts without cofactors gave similar products (data not shown), supporting

© 2002 NRC Canada

Table 3. Influence of time on ee% of **17** from hydration of 4-vinylphenol (**15**), reduction of 4′-hydroxyacetophenone (**18**), and oxidation of racemic **17** by *Nocardia* cultures.

	From hydration of **15**		From reduction of **18**		From oxidation of *R*,*S*-**17**	
Time (h)	*S*-(–)-**17** ee%	Yield (%)	*S*-(–)-**17** ee%	Yield (%)	*R*-(+)-**17** ee%	Yield of **18** (%)
24	90	4	98	0.5	1.4	16
48	90	10	90	1.6	2.2	29
72	88	13	90	2.4	4.9	36
144	84	24.6	86	5.7	7.7	52

Table 4. Substrate specificity of *Nocardia* sp. alcohol dehydrogenase.

Substrate (3 mM)	Relative activity (%)[a]
Primary alcohols	
Vanillyl alcohol	100
Benzyl alcohol	10
2-Hydroxybenzyl alcohol	15
3-Hydroxybenzyl alcohol	20
4-Hydroxybenzyl alcohol	65
4-Methoxybenzyl alcohol	11
2-Phenylethyl alcohol	4
Cinnamyl alcohol	23
3-Phenyl-1-propyl alcohol	2
Methanol	59
Ethanol	25
1-Propanol	39
1-Butanol	39
Oleyl alcohol	0
Secondary alcohols	
1-(4′-Hydroxyphenyl)ethanol	12
2-Butanol	9
Cyclohexanol	9
1-Phenyl-1-propyl alcohol	2
1-Phenyl-2-propyl alcohol	3
Tetralol	3

[a]Vanillyl alcohol was oxidized by cell free extracts containing $NADP^+$ at a rate of 101.2 μM sec^{-1} with a ΔmAbs sec^{-1} of 0.630.

the proposed hydration mechanism. The addition of water to a styrene double bond through a hydration mechanism and not by activation and insertion of molecular oxygen through an epoxide intermediate has not been observed before, except with a mixed anaerobic microbial consortium (14).

Hopper and co-workers (22) reported **17** and **18** as the products of *Pseudomonas* sp. derived, flavoprotein-catalyzed oxidations of 4-ethylphenol (**19**). 4-Ethylphenol methylenehydroxylase, *p*-cresol methylhydroxylase, and vanillyl alcohol oxidase (17, 22, 23) are all flavoproteins that oxidize 4-ethylphenol (**19**) to a proposed quinoid intermediate (**16**) similar to that proposed here for *Nocardia* sp. with **15**. The *R* vs. *S* stereochemistry of **17** produced in flavoprotein-mediated reactions varies with the enzyme used, and may be affected by the addition of electron acceptors (17). Heresztyn (24) and Eldin et al. (25) showed that 4-vinylphenol (**15**) could be microbiologically reduced to 4-ethylphenol (**19**). To rule out a combination of the 4-vinylphenol reduction and coupled flavoprotein oxidation of 4-ethylphenol (**19**) to **17**, *Nocardia* sp. was incubated with **19**. No metabolites were obtained, thus ruling out this oxidative pathway and the benzylic hydroxylation of **19** to **17**.

Enantiospecificity of 4-vinylphenol hydration

The stereospecificity of *Nocardia* 4-vinylphenol hydration was established by chiral HPLC comparison of **17** formed by *Nocardia* cultures to *S*-(–)-**17** prepared by *Pseudomonas fluorescens* lipase resolution of racemic **17** (17, 26). Chromatograms (Fig. 1) for racemic **17** (Fig. 1A), lipase resolved *S*-(–)-**17** (Fig. 1B), and **17** from incubation reactions (Fig. 1C.) clearly show that **17** produced by *Nocardia* is predominantly *S*-(–)-**17**. We then compared the enantiomeric purity of **17** formed by hydration of **15** vs. time (Table 3). From 24 to 144 h, yields of **17** ranged from 4% to about 25%, while the ee of *S*-(–)-**17** decreased from 90% at 24 h to 84% at 144 h. Over time, the reduction of **18** to **17**, a less favorable reaction over all, progressed from 0.5% at 24 h to about 6% at 144 h, while the ee of *S*-(–)-**17** ranged from 98 to 86% (Table 3). These results indicate that hydration occurs preferentially by *si*-face delivery of water to **16**, and that the reduction of **18** occurs preferentially by *re*-face hydride delivery. As both reactions progressed, the ee% decreased, suggesting the enhancement of *R*-(+)-**17** by reaction reversibility, or the involvement of more than one alcohol dehydrogenase with varying enantiospecificity or selectivity. In this regard, when racemic **17** was oxidized to **18**, small excesses of *R*-(+)-**17** (7.7% ee) accumulated as the reaction time and yield progressed (52% yield at 144 h) (Table 3).

Substrate specificity of alcohol dehydrogenase in cell-free *Nocardia* extracts

Both $NADP^+$ and NAD^+ were co-factors in the oxidation of **17** to **18** in *Nocardia* cell free extracts. The alcohol oxidation reaction, however, was nearly 17 times more favorable with $NADP^+$. The range of substrates used by the crude enzyme preparation was broad, as shown in Table 4. Among the primary alcohols, phenolic benzyl alcohols were favorable substrates with vanillyl alcohol giving the highest relative oxidation rates. Among the mono-phenolic benzyl alcohols, 4-hydroxybenzyl alcohol was most readily oxidized, indicating a preference for and a possible participation of the 4-phenolic moiety in the oxidation reaction. As a group of compounds, aliphatic alcohols including methanol, ethanol, 1-propanol, and 1-butanol were oxidized more readily than secondary alcohols. We compared the relative rates of oxidation vs. reduction of 4-hydroxybenzaldehyde–4-hydroxybenzyl alcohol and benzaldehyde–benzyl alcohol using crude cell free *Nocardia* extracts prepared from cells induced with 4-vinylphenol (**15**). In these preparations, the rate of alcohol oxidation was 13 times greater than aldehyde reduction, while the benzaldehyde reduction was greater by 14 times than the alcohol oxidation of benzyl

© 2002 NRC Canada

alcohol. We have initiated the purification and characterization of vinylphenol hydratase.

Acknowledgments

We are grateful for the inspirational and pioneering efforts of Professor J. Bryan Jones in applying enzymes in synthetic organic chemistry. His infectious enthusiasm and chemical excellence has influenced a generation of chemists and has fostered the widespread application of enzymes in green chemistry approaches in the field. This work was supported by the USDA through the Iowa Biotechnology Byproducts Consortium.

References

1. (*a*) F.S. Sariaslani and J.P.N. Rosazza. Enz. Microbial Technol. **6**, 242 (1984); (*b*) U.T. Bornscheuer and R.J. Kazlauskas. Hydrolases in organic synthesis: Regio and stereoselective biotransformations. Wiley-VCH, New York. 1999; (*c*) H.G. Davies, R.H. Green, D.R. Kelly, and S.M. Roberts. Biotransformations in preparative organic chemistry. Academic Press Inc., San Diego. 1989; (*d*) K. Faber. Biotransformations in organic chemistry. 3rd ed. Springer Verlag, Berlin-Heidelberg. 1999; (*e*) S.M. Roberts, K. Wiggins, and G. Casy. Preparative biotransformations: Whole cells and isolated enzymes in organic synthesis. John Wiley & Sons Inc., New York. 1993; (*f*) J.P.N. Rosazza and M.W. Duffel. The alkaloids. *Editied by* R.H.F. Manske and R.G.A. Rodrigo. Academic Press Inc., San Diego. 1986. pp. 324 – 400.
2. (*a*) P.T. Anastas and J.C. Warner. Green chemistry: Theory and practice. Oxford University Press, New York. 1998; (*b*) K.M. Manoj, A. Archelas, J. Baratti, and R. Furstoss. Tetrahedron, **57**, 695 (2001); (*c*) M.T. Bustad, J.G. Burgess, V. Meeyoo, and P.C. Wright. J. Chem. Technol. Biotechnol. **75**, 1095 (2000).
3. (*a*) A.M. Klibanov. Nature (London), **409**, 241 (2001); (*b*) J.A.M. de Bont. Trends Biotechnol. **16**, 493 (1998); (*c*) B. Schulze and M.G. Wubbolts. Curr. Opin. Biotechnol. **10**, 609 (1999).
4. (*a*) M.N. Clifford. J. Sci. Food Agric. **79**, 362 (1999); (*b*) R.D. Hartley and C.W. Ford. Plant cell wall polymers. *Editied by* N.G Lewis and M.G. Paice. American Chemical Society, Washington D.C. 1989. pp. 137–145.
5. J.P.N. Rosazza, Z. Huang, L. Dostal, T. Volm, and B. Rousseau. J. Indust. Microbiol. **15**, 457 (1995).
6. (*a*) J.L. Torres y Torres and J.P.N. Rosazza. J. Nat. Prod. **64**, 1408 (2001); (*b*) L. Barthelmebs, C. Divies, and J. Cavin. Appl. Environ. Microbiol. **66**, 3368 (2000); (*c*) Y. Hashidoko and S. Tahara. Arch. Biochem. Biophys. **359**, 225 (1998); (*d*) J. Cavin, L. Barthelmebs, J. Guzzo, J. van Beeumen, B. Samyn, J. Travers, and C. Diviès. FEMS Microbiol. Lett. **147**, 291 (1997); (*e*) Z. Huang, L. Dostal, and J.P.N. Rosazza. J. Biol. Chem. **268**, 23954 (1993).
7. (*a*) I. Linhart, I. Gut, J. Smejkal, and J. Novák. Chem. Res. Toxicol. **13**, 36 (2000); (*b*) I. Linhart, J. Smejkal, and I. Mládková. Toxicol. Lett. **94**, 127 (1998); (*c*) S. Panke, B. Witholt, A. Schmid, and M.G. Wubbolts. Appl. Environ. Microbiol. **64**, 2032 (1998).
8. (*a*) S. Bernasconi, F. Orsini, G. Sello, A. Colmegna, E. Galli, and G. Bestetti. Tetrahedron Lett. **41**, 9157 (2000); (*b*) S. Bernasconi, F. Orsini, G. Sello, A. Colmegna, E. Galli, and G. Bestetti. Appl. Environ. Microbiol. **65**, 2794 (1999).
9. H.H.J. Cox, B.W. Faber, W.N.M. van Heiningen, H. Rodhoe, H.J. Doddema, and W. Harder. Appl. Environ. Microbiol. **62**, 1471 (1996).
10. (*a*) T. Hirata, S. Izumi, M. Ogura, and T. Yawasta. Tetrahedron, **54**, 15993 (1998); (*b*) A. Tuynman, J.L. Spelberg, I.M. Kooter, H.E. Schoemaker, and R. Wever. J. Biol. Chem. **275**, 3025 (2000).
11. (*a*) F. Zocher, M.M. Enzelberger, U.T. Bornscheuer, B. Hauer, W. Wohlleben, and R.D. Schmid. J. Bacteriol. **77**, 287 (2000); (*b*) P. Moussou, A. Archelas, J. Baratti, and R. Furstoss. J. Org. Chem. **63**, 3532 (1998); (*c*) N.A.E. Kronenburg and J.A.M. de Bont. Enzyme Microb. Technol. **28**, 210 (2001).
12. (*a*) S. Hartmans, J.P. Smits, M.J. Van der Werf, F. Volkering, and J.A.M. de Bont. Appl. Environ. Microbiol. **55**, 2850 (1989); (*b*) S. Hartmans, M.J. Van der Werf, and J.A.M. de Bont. Appl. Environ. Microbiol., **56**, 1347 (1990).
13. S. Kitamura, M. Mita, K. Matsuda, S. Ohta, and K. Tatsumi. Xenobiotica, **30**, 359 (2000).
14. D. Grbic-Galic, N. Churchman-Eisel, and I. Mrakovic. J. Appl. Bacteriol. **69**, 247 (1990).
15. A.M. Warhurst, K.F. Clarke, R.A. Hill, R.A. Holt, and C.A. Fewson. Appl. Environ. Microbiol. **60**, 1137 (1994).
16. F.P. Drijfhout, M.W. Fraaije, M. Jongejan, W.J.H. van Berkel, and M.C.R. Franssen. Biotechnol. Bioeng. **59**, 171 (1998).
17. C.D. Reeve, M.A. Carver, and D.J. Hopper. Biochem. J. **269**, 815 (1990).
18. R. Gherna, P. Pienta, and R. Cote. ATCC catalogue of bacteria & bacteriophages. 18th ed. American Type Culture Collection, Rockville, MD, U.S.A. 1992. p. 415.
19. R.E. Betts, D.E. Walters, and J.P. Rosazza. J. Med. Chem. **17**, 599 (1974).
20. M.M. Bradford. Anal. Biochem. **72**, 248 (1976).
21. E.T. Everhart and J.C. Craig. J. Chem. Soc. Perkin Trans. 1, 1701 (1991).
22. W. McIntire, D.J. Hopper, J.C. Craig, E.T. Everhart, R.V. Webster, M.J. Causer, and T.P. Singer. Biochem. J. **224**, 617 (1984).
23. R.H.H. van den Heuvel, M.W. Fraaije, and W.J.H. van Berkel. FEBS Lett. **481**, 109 (2000).
24. T. Heresztyn. Arch. Microbiol. **146**, 96 (1986).
25. D.A.N. Eldin, A. Narbad, J.R. Dickinson, and D. Lloyd. FEMS Microbiol. Lett. **125**, 311 (1995).
26. F. Hæffner and T. Norin. Chem. Pharm. Bull. **47**, 591 (1999).

© 2002 NRC Canada

Dioxygenase-catalyzed *cis*-dihydroxylation of pyridine-ring systems

Derek R. Boyd, Narain D. Sharma, Ludmila V. Modyanova, Jonathan G. Carroll, John F. Malone, Christopher C.R. Allen, John T.G. Hamilton, David T. Gibson, Rebecca E. Parales, and Howard Dalton

Abstract: Toluene dioxygenase-catalyzed dihydroxylation, in the carbocyclic rings of quinoline, 2-chloroquinoline, 2-methoxyquinoline, and 3-bromoquinoline, was found to yield the corresponding enantiopure *cis*-5,6- and -7,8-dihydrodiol metabolites using whole cells of *Pseudomonas putida* UV4. *cis*-Dihydroxylation at the 3,4-bond of 2-chloroquinoline, 2-methoxyquinoline, and 2-quinolone was also found to yield the heterocyclic *cis*-dihydrodiol metabolite, (+)-*cis*-(3*S*,4*S*)-3,4-dihydroxy-3,4-dihydro-2-quinolone. Heterocyclic *cis*-dihydrodiol metabolites, resulting from dihydroxylation at the 5,6- and 3,4-bonds of 1-methyl 2-pyridone, were isolated from bacteria containing toluene, naphthalene, and biphenyl dioxygenases. The enantiomeric excess (ee) values (>98%) and the absolute configurations of the carbocyclic *cis*-dihydrodiol metabolites of quinoline substrates (benzylic *R*) and of the heterocyclic *cis*-diols from quinoline, 2-quinolone, and 2-pyridone substrates (allylic *S*) were found to be in accord with earlier models for dioxygenase-catalyzed *cis*-dihydroxylation of carbocyclic arenes. Evidence favouring the dioxygenase-catalyzed *cis*-dihydroxylation of pyridine-ring systems is presented.

Key words: dioxygenases; *cis*-dihydroxylation, pyridines, 2-pyridones, absolute configurations.

Résumé : On a trouvé que la dihydroxylation des carbocycles de la quinoléine, de la 2-chloroquinoléine, de la 2-méthoxyquinoléine et de la 3-bromoquinoléine, catalysée par la dioxygénase du toluène en utilisant des cellules complètes de *Pseudomonas putida* UV4, conduit aux métabolites correspondants énantiopurs, les *cis*-5,6- et 7,8-dihydrodiols. On a aussi observé que la *cis*-dihydroxylation de la liaison 3,4 de la 2-chloroquinoléine, de la 2-méthoxyquinoléine et de la quinoléin-2-one conduit au métabolite hétérocyclique *cis*-dihydrodiol (+)-*cis*-(3*S*,4*S*)-3,4-dihydroxy-3,4-dihydroquinoléin-2-one. Lorsqu'on a utilisé des bactéries contenant des dioxygénases du toluène, du naphtalène et du biphényle, on a isolé des métabolites hétérocycliques *cis*-dihydrodiols qui résultent d'une dihydroxylation aux niveaux des liaisons 5,6- et 3,4- de la 1-méthylpyridin-2-one. Les valeurs des excès énantiomériques (ee) (>98%) et les configurations absolues des métabolites des *cis*-dihydrodiols carbocycliques des substrats à base de quinoléine (groupe benzylique étant *R*) et des *cis*-diols hétérocycliques dérivés de substrats à base de quinoléine, de quinoléin-2-one et de pyridin-2-one (groupe allylique étant *S*) sont en accord avec les modèles antérieurs pour les réactions de *cis*-dihydroxylation des arènes carbocycliques catalysées par la dioxygénase. On présente des données favorisant la *cis*-dihydroxylation catalysée par la dioxygénase de systèmes à noyau pyridine.

Mots clés : dioxygénase, *cis*-dihydroxylation, pyridines, pyridin-2-ones, configurations absolues.

[Traduit par la Rédaction]

Introduction

The initial step in the bacterial metabolism of aromatic rings often proceeds via dioxygenase-catalyzed asymmetric dihydroxylation to yield *cis*-dihydrodiol metabolites (1–5). Polycyclic arenes and azaarenes (Scheme 1) are amongst the wide range of substrates (> 400) found to yield carbocyclic *cis*-dihydrodiol metabolites (2, 3).

To date, however, only a small number of *cis*-dihydrodiols has been obtained from enzymatic *cis*-dihydroxylation of

Received 9 January 2002. Published on the NRC Research Press Web site at http://canjchem.nrc.ca on 23 May 2002.

Dedicated to Professor J. Bryan Jones on the occasion of his 65th birthday.

D.R. Boyd,[1] N.D. Sharma, L.V. Modyanova,[2] J.G. Carroll, J.F. Malone, and C.C.R. Allen. School of Chemistry and the QUESTOR Centre, The Queen's University of Belfast, Belfast BT9 5AG, U.K.
J.T.G. Hamilton. Department of Agriculture and Rural Development for Northern Ireland and School of Agriculture and Food Science, Newforge Lane, Belfast BT9 5PX, U.K.
D.T. Gibson and R.E. Parales Department of Microbiology and Center for Biocatalysis and Bioprocessing, University of Iowa, Iowa City, Iowa 52242, U.S.A.
H. Dalton. Department of Biological Sciences, University of Warwick, Coventry, CV4 5AL, U.K.

[1]Corresponding author (e-mail: dr.boyd@qub.ac.uk).
[2]Present address: Department of Pharmacology, Medical College of Ohio, 3035 Arlington Ave., Toledo, Ohio 43614, U.S.A.

 DOI: 10.1139/V02-062 © 2002 NRC Canada

Scheme 1.

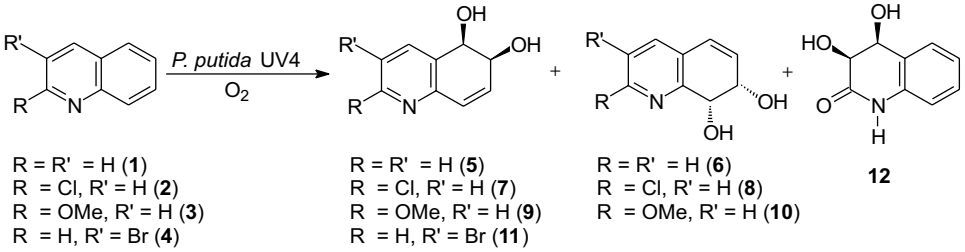

Scheme 2.

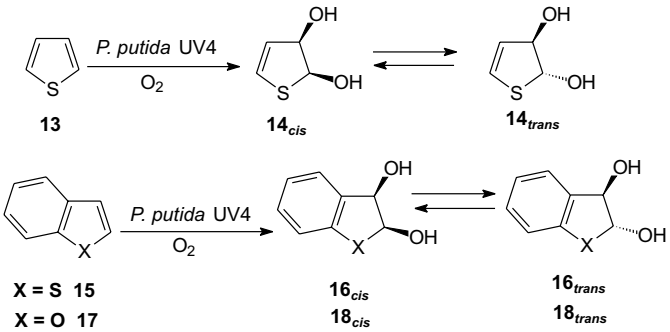

aromatic heterocyclic rings. These are generally derived from electron-rich five-membered aromatic heterocycles including thiophenes (e.g., **13**), benzothiophenes (e.g., **15**), and benzofurans (e.g., **17**) (Scheme 2).

Heterocyclic *cis*-diols $\mathbf{14}_{cis}$, $\mathbf{16}_{cis}$, and $\mathbf{18}_{cis}$ were found to spontaneously isomerize to the corresponding *trans*-isomers, $\mathbf{14}_{trans}$, $\mathbf{16}_{trans}$, and $\mathbf{18}_{trans}$ (6, 7). No direct evidence of dioxygenase-catalyzed *cis*-dihydroxylation of electron-poor heterocyclic arenes such as pyridine and quinoline has been reported (8–12). Alternative pathways for the bacterial metabolism of pyridine and quinoline rings, including azaarene hydration and monohydroxylation have, however, been discovered (8–12).

cis-Dihydroxylation of the carbocyclic ring and monohydroxylation of the azaarene ring in quinoline (**1**), isoquinoline, quinoxaline, and quinazoline substrates has been reported in *Pseudomonas putida* UV4 (12, 13). Unfortunately, the yields of *cis*-dihydrodiols obtained were generally low. A preliminary study from these laboratories on the biotransformation of quinoline substrates containing a substituent at C-2, such as azaarenes **2** and **3**, has shown that the yield of the corresponding carbocyclic *cis*-dihydrodiols **7**–**10** can be significantly increased (Scheme 1) (14). An unexpected heterocyclic *cis*-diol **12** was also isolated from quinoline substrates **2** and **3**. The possibility of *cis*-dihydroxylation occurring in the heterocyclic ring, either via the corresponding *cis*-dihydrodiols **20** and **21** or via benzo-fused 2-pyridone intermediate **24** as a precursor of metabolite **12**, was also briefly addressed (Scheme 3) (14).

Direct evidence of the stereoselective *cis*-dihydroxylation of a monocyclic 2-pyridone ring (**28**) to yield heterocyclic *cis*-diols **29** and **30** has recently been reported by Modyanova and Azerad (Scheme 4) (15, 16).

Results and discussion

A major objective of the present study was to conduct a more comprehensive search for evidence of dioxygenase-catalyzed *cis*-dihydroxylation of pyridine-ring systems — a topic that has received little attention in the literature (8–12). In this context, the reported bacterial *cis*-dihydroxylation of the benzo-fused pyridines **2**–**4** (14) and 2-pyridones **24** and **28** (15, 16) has now been re-examined. This extension of earlier work (12–16) involves a wider range of dioxygenases and substrates, with emphasis on the absolute configurations and enantiopurities of metabolites formed by *cis*-dihydroxylation of either the carbocyclic or the heterocyclic ring.

The biotransformation studies were carried out using mutant and recombinant strains of bacteria containing different types of ring-hydroxylating dioxygenase enzymes (Rieske-type nonheme iron oxygenases) (4), devoid of the corresponding *cis*-diol dehydrogenase enzymes, which are responsible for dehydrogenation of *cis*-dihydrodiols to the corresponding catechols. These mutant strains included *Pseudomonas putida* UV4 (a source of toluene dioxygenase, TDO) (17), *P. putida* 9816/11 (a source of naphthalene dioxygenase, NDO) (18), and *Sphingomonas yaniokuyae* B8/36 (a source of biphenyl dioxygenase, BPDO) (19). Recombinant strains used included *Escherichia coli* pKST11 (a source of TDO) (20) and *E. coli* JM 109 (DE3) pDTG141 (a source of NDO) (21) (Table 1).

Earlier studies of the biotransformation of parent quinoline substrate **1** with *P. putida* UV4 showed that diols could be formed by *cis*-dihydroxylation at the 5,6-bond (to yield the major *cis*-diol **5**) and the 7,8-bond (to yield minor *cis*-diol **6**) of the carbocyclic ring (12, 13) in relatively low yields (<10%). Other bioproducts of quinoline (**1**) included 3-hydroxy quinoline (**25**) and anthranilic acid, which could have resulted from *cis*-dihydroxylation at the 3,4-bond in the pyridine ring followed by decompositon of unstable 3,4-*cis*-diol **19** (Scheme 3, path A) (12, 13). When 2-chloroquinoline (**2**) was added as a substrate to the same strain, *cis*-dihydroxylation was found to occur preferentially within the carbocyclic ring at the 7,8-bond to give dihydrodiol **8** (20% yield) and also at the 5,6-bond to yield diol **7** (9% yield). A

© 2002 NRC Canada

Scheme 3.

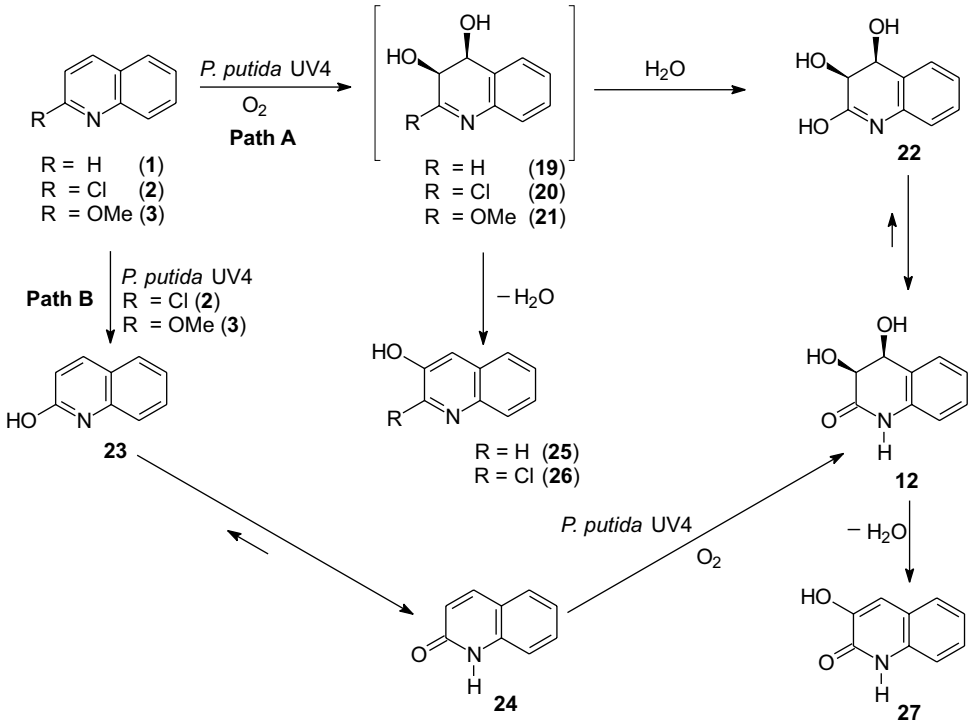

Scheme 4.

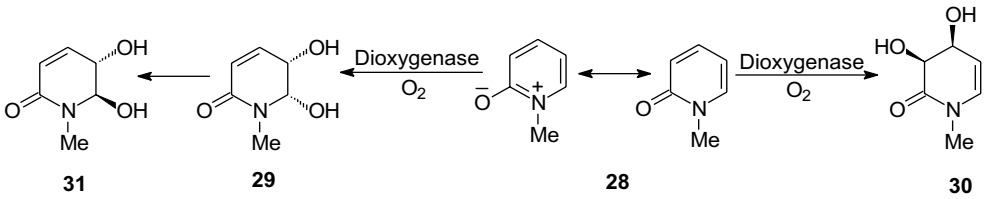

similar trend was found using the TDO-containing recombinant strain (*E. coli* pKST11), where diols **8** (11% yield) and **7** (4% yield) were isolated. The bacterial strains containing NDO showed a preference for *cis*-dihydroxylation at the 7,8-bond to give diol **8** (15% yield using *P. putida* 9816/11 and 5% yield using *E. coli* JM 109). 5,6-Dihydrodiol **7** was also produced using *P. putida* 9816/11 (6% yield). *S. yanoikuyae* B8/36 and *P. fluorescens* Q1 (a wild-type strain grown on quinoline as a carbon source) only yielded *cis*-7,8-dihydrodiol **8** (15% and 1% yields, respectively, Table 1). These results are similar to those reported earlier on the bacterial biotransformation of **1** using *P. putida* 86 (a wild-type strain grown on quinoline as a carbon source) (22). In the latter example, compound **8**, of unspecified ee and absolute configuration, was reported to be the sole *cis*-dihydrodiol metabolite (22).

cis-Diol bioproducts **7** and **8**, obtained from TDO-, NDO-, and BPDO-catalyzed asymmetric dihydroxylation of 2-chloroquinoline (**2**), were all found to be enantiopure (>98% ee) based on the ^{1}H NMR spectral analyses of the corresponding cyclic-boronate derivatives formed by using (–)-(*S*)- and (+)-(*R*)-2-(1-methoxyethyl)benzeneboronic acid (MEBBA). This method has previously been used to determine the absolute configurations of both mono- and polycyclic *cis*-dihydrodiol metabolites (23–25). From a comparison of the characteristic chemical-shift values of the MeO signals in the ^{1}H NMR spectra of the MEBBA esters (23–25) and the circular dichroism (CD) spectral data (compared with parent *cis*-dihydrodiols **5** and **6** of known configurations), metabolites **7** and **8** were assigned the 5*R*,6*S* and 7*S*,8*R* configurations, respectively.

The two major carbocyclic *cis*-dihydrodiols **7** (R_f = 0.3, 8% yield) and **8** (R_f = 0.45, 18% yield), isolated from the biotransformation of **2** using *P. putida* UV4, were accompanied by a more polar metabolite, **12** (R_f = 0.14, 2% yield). X-ray crystallographic analysis, using the anomalous dispersion method, confirmed that bioproduct **12** was an enantiopure sample of (3*S*,4*S*)-3,4-dihydroxy-3,4-dihydro-2-quinolone (**12**) (14). While neither the corresponding MEBBA-boronate derivatives nor the corresponding diMTPA esters could be synthesized, the enantiopurity of *cis*-diol **12** was confirmed as >98% ee (^{1}H NMR analysis) by the formation of a single diastereoisomer of the monocamphanate ester at C-4. It is noteworthy that, with the exception of *P. putida* UV4, no evidence of the more polar *cis*-dihydrodiol metabolite **12** was found with the other five dioxygenase-containing strains. When the biotransformation of **2** was repeated on a larger scale (50 g substrate **2** in 100-L fermenter using *P. putida* UV4) and a more rigorous extraction procedure involving total removal of water prior to extraction was

© 2002 NRC Canada

Table 1. Substrate (arene), bacterial strain (strain), dioxygenase (enzyme), product (diol), % isolated yield (yield), and absolute configuration (Ab. con.) of *cis*-dihydrodiol metabolites (**7**–**12**)[a] obtained from the quinoline substrates **2**–**4** and 2-quinolone (**24**).

Arene	Strain	Enzyme	Diol	Yield	Ab.con.
2	UV4	TDO	**7**	9	5*R*,6*S*
			8	20	7*S*,8*R*
			12	6	3*S*,4*S*
2	pKST11	TDO	**7**	4	5*R*,6*S*
			8	11	7*S*,8*R*
2	9816/11	NDO	**7**	6	5*R*,6*S*
			8	15	7*S*,8*R*
2	JM109	NDO	**8**	5	7*S*,8*R*
2	B8/36	BPDO	**8**	15	7*S*,8*R*
2	Q1	QDO	**8**	1	7*S*,8*R*
			9	2	5*R*,6*S*
3	UV4	TDO	**10**	7	7*S*,8*R*
			12	13	3*S*,4*S*
3	9816/11	NDO	**10**	54	7*S*,8*R*
3	JM109	NDO	**10**	5	7*S*,8*R*
3	B8/36	BPDO	**10**	47	7*S*,8*R*
4	UV4	TDO	**11**	23	5*R*,6*S*
24	UV4	TDO	**12**	10	3*S*,4*S*

[a]All *cis*-dihydrodiols were enantiopure (>98% ee).

adopted, two additional metabolites were found. Carbocyclic *cis*-dihydrodiols **7** (ca. 5.4 g, 9%) and **8** (ca. 12.0 g, 20%) and the heterocyclic *cis*-diol **12** (ca. 3.1 g, 6%), were again the major bioproducts; the new metabolites were identified as 2-chloro-3-hydroxyquinoline (**26**) (ca. 0.5 g, 1%) and 3-hydroxy-2-quinolone (**27**) (ca. 1.5 g, 3%). It is probable that **27** was obtained by dehydration of the *cis*-diol **12** during the work-up procedure, since its dehydration was observed upon treatment with acid or at elevated temperatures. The presence of the minor phenolic metabolite (**26**) could be accounted for by the spontaneous dehydration of the transient *cis*-dihydrodiol **20**. When the total yields of 2-chloroquinoline metabolites **12**, **26**, and **27** are combined, the dioxygenase-catalyzed oxidation in the heterocyclic ring clearly emerges as a significant metabolic pathway (ca. 10% yield) compared with the total yield (ca. 29%) of carbocyclic ring *cis*-dihydroxylation products **7** and **8** (Scheme 3, path A).

2-Methoxyquinoline (**3**) also proved to be a substrate for *P. putida* UV4; it yielded, from dihydroxylation at the 5,6- and 7,8-positions, the anticipated carbocyclic *cis*-dihydrodiols **9** (R_f = 0.30, 2% yield) and **10** (R_f = 0.40, 7% yield), respectively (Scheme 1). Formation of the corresponding MEBBA derivatives, and CD comparison with *cis*-dihydrodiols **5** and **6**, indicated that metabolites **9** and **10** were enantiopure (>98% ee) and of the 5*R*,6*S* and 7*S*,8*R* configurations, respectively. The major metabolite (R_f = 0.14, 13% yield), formed from 2-methoxyquinoline (**3**) as the substrate and *P. putida* UV4 as a dioxygenase source, was *cis*-diol metabolite **12** of identical configuration (3*S*,4*S*) and enantiopurity (>98% ee) to that found earlier using **2** as substrate. Only 7,8-*cis*-dihydrodiol **10**, of identical ee value and absolute configuration, was obtained using NDO (*P. putida* 9816/11, *E. coli* JM 109) or BPDO (*S. yanoikuyae* B8/36) as the biocatalysts and **3** as the substrate (Table 1).

Fig. 1. X-ray structure of *cis*-diol **11**.

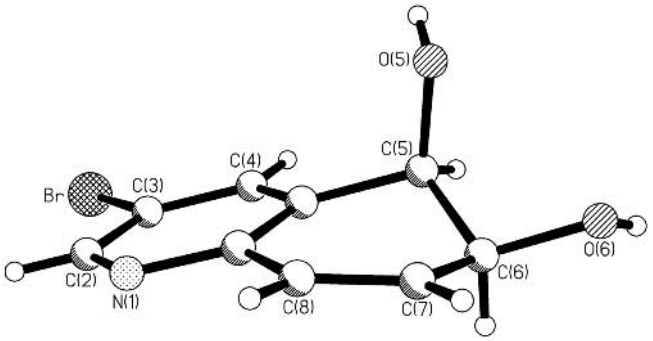

To decrease the possibility of dioxygenase-catalyzed *cis*-dihydroxylation of the heterocyclic ring, 3-bromoquinoline (**4**) was examined as a substrate with TDO (*P. putida* UV4). As anticipated, no hydroxylation occurred at the blocked 3,4-bond in the pyridine ring; the sole metabolite, *cis*-dihydrodiol **11** (23% yield) was enantiopure (>98% ee, (NMR analysis of the MEBBA-boronate derivatives), and resulted from attack at the 5,6-bond. The structure and absolute stereochemistry of *cis*-diol **11** was determined by X-ray crystallography using the anomalous dispersion method (Fig. 1). It again confirmed that 3-bromo-*cis*-5,6-dihydroxy-5,6-dihydroquinoline (**11**) was a single enantiomer and had a 5*R*,6*S* configuration, similar to the other 5,6-*cis*-dihydrodiol metabolites of substituted quinolines (e.g., **7** and **9**). The crystal structure of diol **11** showed no evidence of intramolecular H-bonding, but six intermolecular H-bonding interactions to four neighbouring molecules were observed.

Two feasible mechanisms could account for the formation of heterocyclic *cis*-dihydrodiol metabolite **12** during biotransformation of **2** and **3** in cultures of *P. putida* UV4. The first mechanism assumes that unstable *cis*-dihydrodiols **20** and **21** are the initial products of the direct dihydroxylation of the pyridine rings in the corresponding 2-substituted quinoline substrates, **2** and **3**, respectively (Scheme 3, path A). The postulated intermediates, imidoyl halide **20** and imidate **21**, are likely to spontaneously hydrolyze to yield trihydroxy product **22**, which exists preferentially as 2-quinolone tautomer **12**. Initial metabolites **20** (from **2**) and **19** (from **1**) (12, 13) could also dehydrate yielding the corresponding 3-hydroxyquinolines **26** and **25**, respectively. This evidence, based on the isolation of metabolites **12**, **25**, and **26**, is consistent with the mechanism shown in path A (Scheme 3).

The observation of the "NIH shift" has recently been shown to occur when aromatic hydroxylation proceeds via ei-

© 2002 NRC Canada

Scheme 5.

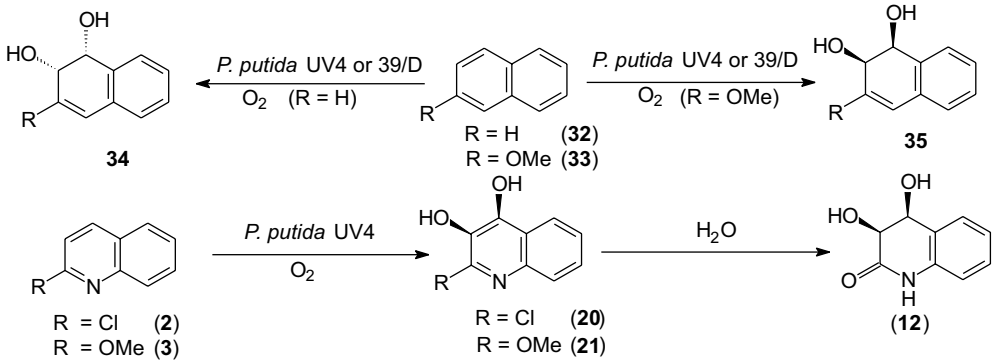

ther arene oxide isomerization (monooxygenase pathway) or *cis*-dihydrodiol dehydration (dioxygenase pathway) (26). Biotransformation of 3-deuterioquinoline (**1**) using *P. putida* UV4 yielded 3-hydroxyquinoline (**25**), with concomitant migration and retention of the deuterium atom (20% D) at an adjacent carbon atom, i.e., the NIH shift was observed (26). This provides further evidence in support of the formation of unstable *cis*-dihydrodiol **19** derived from the pyridine ring in substrate **1** (Scheme 3, path A).

A comparison of the enantiopurity and absolute configuration of *cis*-dihydrodiol metabolites **34** and **35**, obtained from naphthalene (**32**) and 2-methoxynaphthalene (**33**), respectively (27), with *cis*-dihydrodiol intermediates **20** and **21** from **2** and **3**, respectively, showed striking similarities (Schemes 1 and 5). The major *cis*-dihydrodiol metabolites from **33** were formed at the 5,6- and 7,8- bonds in the unsubstituted ring with TDO (using both *P. putida* 39/D and UV4) as biocatalyst (27); these *cis*-diols, derived from a carbocyclic ring, were of the normal benzylic *R* configuration as found in other bicyclic arenes, such as *cis*-diols **5**–**11** and **34**. Enantiopure *cis*-dihydrodiol **35**, a minor metabolite of **33** (27) was, however, found to have the opposite absolute configuration (benzylic *S*) to that normally found in carbocyclic rings (Schemes 1 and 5).

2-Substituted quinoline substrates **2** and **3** may be considered as isosteres of **33** and, when accepted as substrates by the TDO enzyme, would be expected to form *cis*-diols **20** and **21**, respectively, having the same absolute configuration (benzylic *S*) and enantiopurity as *cis*-diol **35** (>98% ee). As reported earlier, heterocyclic *cis*-diol metabolite **12** was a single enantiomer of identical absolute configuration (benzylic *S*). This observation provides additional indirect evidence favouring dioxygenase-catalyzed *cis*-dihydroxylation of the pyridine ring of substrates **2** and **3** to form the corresponding unstable metabolites **20** and **21**, respectively, as precursors of *cis*-diol **12** (Scheme 3, path A).

Direct evidence of the involvement of *cis*-dihydrodiol intermediates in the initial TDO-catalyzed biotransformation step of electron-rich five-membered aromatic rings was presented earlier (Scheme 2) (6, 7). Indirect evidence of dioxygenase-catalyzed dihydroxylation of the pyrrole ring in indole is also available. Thus, in the manufacture of indigo dye (28, 29), the spontaneous dehydration of the transient *cis*-dihydrodiol metabolite of indole to yield indoxyl (which further undergoes autoxidation) is assumed to occur. Until recently, it was not possible to find direct evidence of *cis*-dihydrodiol formation in the pyridine ring. The electron-poor pyridine-ring system has generally proved to be extremely resistant to dioxygenase-catalyzed *cis*-dihydroxylation where alternative metabolic routes are available. In the case of pyridine-substituted thioethers and arenes, dioxygenase-catalyzed oxidation has been observed only at the sulfur atom (sulfoxidation) (30) or at the carbocyclic ring (*cis*-dihydroxylation) (unpublished data).

In the light of recent direct evidence for *cis*-dihydroxylation of 1-methyl-2-pyridone (**28**) (15, 16), a second mechanism, to account for the formation of *cis*-dihydrodiol **12** from the 2-substituted quinolines **2** and **3**, was considered (Scheme 3, path B). Chemical or enzyme-catalyzed hydrolysis of the quinoline substrates could, in principle, occur in the aqueous-culture medium prior to the *cis*-dihydroxylation process yielding 2-hydroxyquinoline (**23**), which exists mainly as the 2-quinolone tautomeric form (**24**). The halogen and alkoxy substituents at C-2 in the pyridine ring of compounds **2** and **3** are susceptible to hydrolysis via an addition–elimination mechanism normally under acidic conditions. An aqueous–methanolic solution (D_2O–CD_3OD) of **2**, when heated (~45°C) for an extended period, did not undergo hydrolysis, suggesting that it was unlikely that more than a small proportion of substrates **2** and **3** would have hydrolyzed under the relatively mild aqueous conditions that existed during the biotransformation. GC–MS analysis, conducted during the course of the biotransformation of quinoline substrate **2**, showed minute traces of 2-quinolone (**24**) among the bioproducts, which could be due to chemical and (or) enzyme-catalyzed hydrolysis.

To test if **24** was a substrate, it was added to whole cells of *P. putida* UV 4. The corresponding *cis*-dihydrodiol (**12**) was found as the sole metabolite with an identical ee value (>98%) and absolute configuration (3*S*,4*S*) to that isolated from 2-substituted quinoline substrates **2** and **3**, but in a relatively low yield (10%). This observation confirms that metabolite **12** could be derived from **24**. Despite the latter result, the balance of evidence appears to favour path A and involvement of the transient *cis*-diol metabolites **20** and **21** as precursors of heterocyclic *cis*-diol **12**. A recent report of the TDO-catalyzed 3-hydroxylation of 4-picoline (4-methylpyridine) has assumed, without evidence, the initial formation of an unstable *cis*-dihydrodiol metabolite of the pyridine ring (31); the results presented in this study support this conclusion.

The NDO-catalyzed dihydroxylation of the pyridone ring in **28** has recently been found to yield two interesting and

© 2002 NRC Canada

Table 2. Bacterial strains and dioxygenases used in the *cis*-dihydroxylation of 1-methyl 2-pyridone (**28**) and relative (isolated) combined yields of *cis*-diols **29** and **30**.

Strain	Enzyme	% Relative yield of diols **29**:**30**[a]
P. putida 9816/11[b,c]	NDO	93:7 (41)
E. coli JM109(DE3) (pDTG141)[d,e]	NDO	96:4 (52)
E. coli JM109(DE3) (pDTG141-F352V)[d,f]	NDO_{352V}	100:0 (10)
S. yanoikuyae B8/36[b,g]	BPDO	90:10 (2)
P. putida UV4[b,h]	TDO	95:5 (<1)

[a]Relative yield based on the peak ratio obtained after GC–MS analysis.
[b]Without the corresponding *cis*-diol dehydrogenase enzyme activity.
[c]Salicylate inducer.
[d]IPTG inducer, ampicillin resistant.
[e]Recombinant-strain encoding NDO from *P. putida* 9816–4.
[f]Site-directed recombinant NDO with valine at 352.
[g]*m*-Xylene inducer.
[h]Constitutive mutant.

Fig. 2. X-ray structure of *cis*-diol **29**.

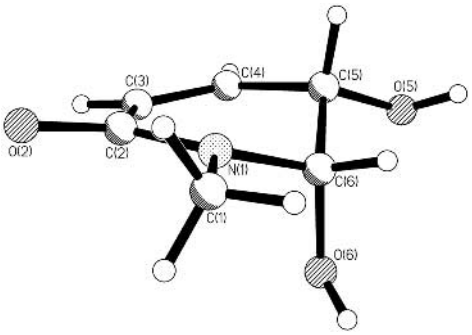

Fig. 3. X-ray structure of *cis*-diol **12**.

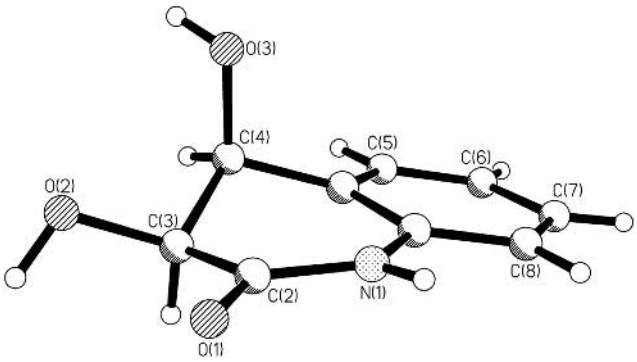

relatively stable *cis*-diol metabolites, **29** and **30** (Scheme 4) (16).

In an extension of our earlier work on TDO-catalyzed formation of heterocyclic *cis*-diol **12** from substituted 2-pyridone **24** (14), a programme was undertaken to examine the range of dioxygenases capable of producing *cis*-diols **29** and **30** from pyridone **28**. It was hoped that this would result in higher yields (particularly of the very minor regioisomer **30**), and would allow absolute configurations to be assigned to *cis*-diols **29** and **30**. These *cis*-diol metabolites may be considered as synthetic precursors of polyhydroxylated piperidines, several of which have already been identified as potent inhibitors of glycosidases (32).

An evaluation of the relative merits of the NDO, BPDO, and TDO enzyme systems in the *cis*-dihydroxylation of 1-methyl-2-pyridone (**28**) was carried out by GC–MS analysis. Both of the *cis*-dihydrodiols, **29** and **30**, were found to be detectable and separable as the corresponding bis-trimethylsilyl ethers (*m*/*z* 287). Some evidence of the isomerization of *cis*-diol **29** to *trans*- isomer **31** was found during the analytical process. The yield of the initially formed major diol metabolite **29** from **28** was estimated from the combined yields of *cis*-and *trans*-diols **29** and **31**, respectively.

A range of mutant (*P. putida* 9816/11, *S. yaniokuyae* B8/36, *P. putida* UV 4) and recombinant strains (*E. coli* JM 109 (DE3) pDTG141) (which had previously been used with bicyclic substrates **2** and **3**) and a site-directed mutant (*E. coli* JM 109 (DE3) pDTG141 strain 352V), were applied to the monocyclic substrate **28**; the relative ratios of products are given in Table 2.

Naphthalene dioxygenase, present in *P. putida* 9816/11 and *E. coli* JM 109 (DE3) pDTG141, was found to give a similar ratio of *cis* isomers favouring 5,6-regioisomer **29** (93–96%) and a comparable isolated yield (41–52%). When a site-directed mutant strain was used, where phenylalanine 352 had been replaced by valine (352-V), the isolated yield decreased (10%) but the regioselectivity increased to exclusively yield metabolite **29**. Although the highest proportion of the minor *cis*-diol regioisomer **30** (10% relative yield) was obtained with the BPDO enzyme system, this was offset by a much lower isolated yield (2%). The observation that a monocyclic compound, having a significant degree of aromatic character, was a substrate for both the NDO and BPDO systems was surprising, since only a small number of monocyclic arene derivatives have proved to be substrates for these enzymes. In contrast, more than 200 monocyclic arenes have proved to be acceptable substrates with TDO (2, 3). Surprisingly, when **28** was added as a substrate to *P. putida* UV4, *cis*-diol **29** was detected in very low yield (<1%); the substitution pattern and polarity of substrate **28** may have been contributing factors to the low yield.

The structure and relative stereochemistry of 2-pyridone *cis*-dihydrodiols **29** and **30** were established earlier on the basis of rigorous NMR spectral analysis (16). Similar spectral data was obtained during the current study. In addition, the structure of major *cis*-diol **29** ($[\alpha]_D$ +40, MeOH) was confirmed by X-ray crystallography (Fig. 2); it showed that the C-5 and C-6 hydroxyl groups were in a *cis* relationship with pseudo-equatorial and pseudo-axial conformations, re-

© 2002 NRC Canada

Scheme 6.

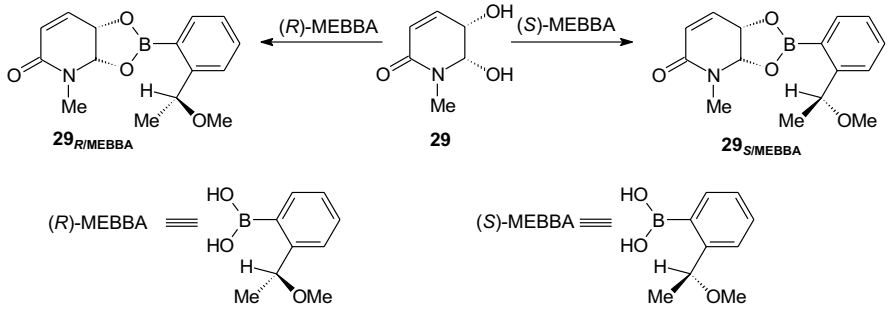

Fig. 4. CD spectra of the *cis*-diols (3*S*,4*S*)-**12**, **(**5*S*,6*S*)-**29** and **(3***S*,4*S*)-**30**.

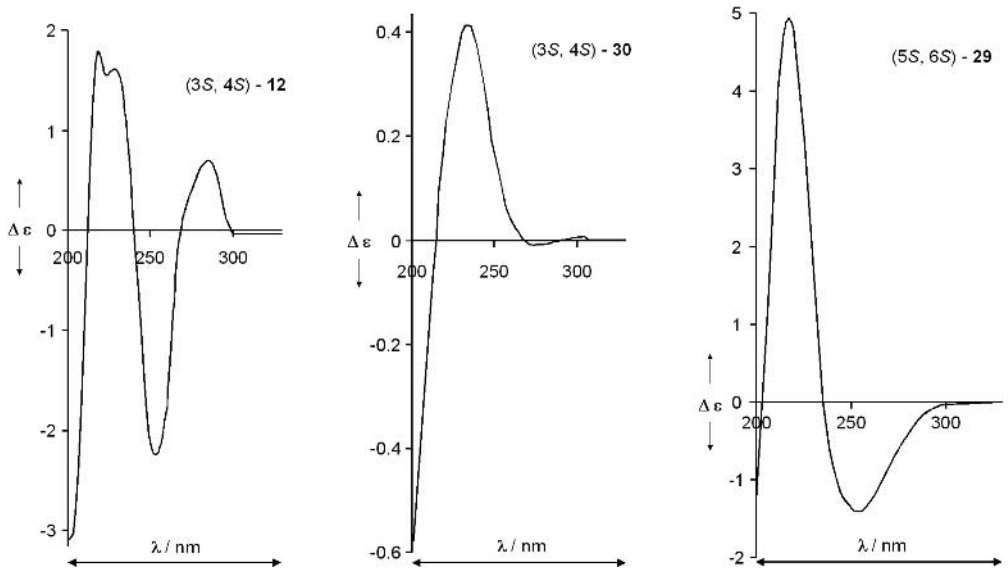

spectively. The adoption of a pseudo-axial conformation by the OH group at C-6 appears to be the result of steric interaction with the *N*-methyl group. The pseudo-axial conformation of the OH group proximate to a substituent and the formation of a single enantiomer are common features of *cis*-dihydrodiol metabolites of monosubstituted benzene substrates (14, 30). For comparison purposes, the X-ray crystal structure of heterocyclic *cis*-diol **12** is shown in Fig. 3 (14). The OH group at C-4 in **12** and at C-6 in **29** are both pseudo-axial due to steric constraints.

The crystal structure analysis also showed that the sample was enantiopure. There was no evidence of intramolecular H-bonding, but five intermolecular H-bonding interactions to four neighbouring molecules were observed.

From the relative chemical shift positions of methoxyl signals of the cyclic boronate derivatives $\mathbf{29}_{R/\text{MEBBA}}$ (δ_{MeO} 3.24) and $\mathbf{29}_{S/\text{MEBBA}}$ (δ_{MeO} 3.22), a 5*S*,6*S* absolute configuration was tentatively assigned (23–25) to major *cis*-diol **29**; the boronates also confirmed its enantiopurity (>98% ee) (Scheme 6).

In the determination of absolute stereochemistry via analysis of the X-ray crystal structure (using the anomalous dispersion method), the refinement of the Flack (33) absolute-structure parameter (*x*) ideally yields a value of zero for the correct enantiomer and a value of unity for the incorrect enantiomer. In the analysis of *cis*-diol **29**, using the anomalous dispersion method, *x* was refined to a final value of 0.24 (35) for the 5*S*,6*S* enantiomer. This implies that, at a confidence level above 2σ (i.e., >95%), the inverse 5*R*,6*R* structure can be rejected, and hence the true configuration has to be 5*S*,6*S*. Although this indicates an emphatic preference, it fails to meet the commonly accepted level (3σ, 99.8%), which is regarded as equating to statistical certainty. (An independent refinement of the inverse structure (5*R*,6*R*) gave $x = 0.76$ (35), which also independently implies that this configuration can be rejected at better than the 2σ level, albeit not at the preferred 3σ level.)

The circular dichroism (CD) spectra of the bicyclic 3*S*,4*S*-*cis*-diol **12** and monocyclic diols **29** and **30** provided strong supporting evidence for the stereochemical assignments (Fig. 4). Based on a comparison of CD spectra of *cis*-diols **12**, **29**, and **30**, where a strong positive CD absorption was found at lower wavelengths (210–250 nm) and a weaker negative CD absorption at longer wavelengths (235–300 nm), a similar absolute configuration can be assigned to each of the *cis*-diol metabolites. Since the 3*S*,4*S* configuration of (+)-*cis*-diol **12** was rigorously established by X-ray crystallography, monocyclic *cis*-diols **29** and **30** should thus have the 5*S*,6*S* and 3*S*,4*S* configurations, respectively. Since the major *cis*-diol (**29**) was found to be a single enantiomer of 5*S*,6*S* configuration, *trans* isomer (+)-**31** ($[\alpha]_D$ +207, MeOH), obtainable upon gentle heating at ca. 50°C (16) (via

© 2002 NRC Canada

Scheme 7.

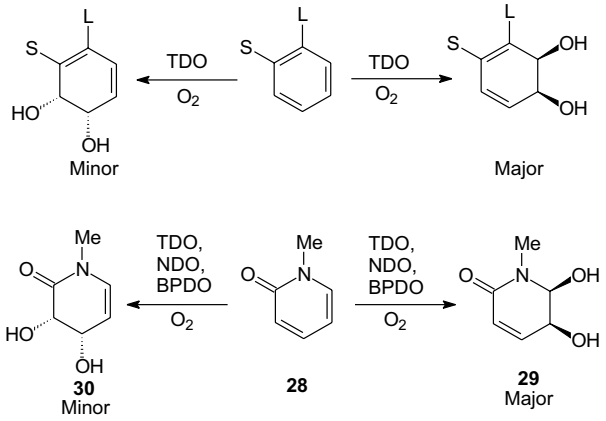

reversible ring opening to the corresponding aldehyde) must have a 5*S*,6*R* configuration.

Due to the very low relative yield (<10%) of the minor *cis*-diol (**30**) (Table 2), it was not possible to carry out its complete characterization. The presence of **30** was confirmed by ^{1}H NMR, MS, and GC–MS analysis. Unfortunately neither the corresponding diMTPA esters (from *R*- or *S*-α-methoxy-α-(trifluoromethyl)phenylacetic acid) nor the chiral boronate (MEBBA) derivatives (from *R*- or *S*-2-(1-methoxyethyl)phenylboronic acid) could be formed from *cis*-diols **12** and **30**. In both cases, this may have been due to intramolecular hydrogen bonding between the OH group on C-3 and the adjacent carbonyl group. As stated in the preceding paragraph, however, it was assumed from a comparison of the CD specta that minor *cis*-diol **30** was a single enantiomer of 3*S*,4*S* configuration.

The absolute configurations of *cis*-dihydrodiol metabolites **29** and **30** were found to be in accord with a stereochemical model based on the preferred *cis*-dihydrodiol enantiomers obtained from 1,2-disubstituted benzene substrates with TDO as biocatalyst (Scheme 7) (2). Earlier studies of the TDO-catalyzed *cis*-dihydroxylation of a range of mono-, 1,2-, 1,3-, and 1,4-di-substituted benzene substrates have shown that stereo and regioselectivity can be predicted by considering the substituent size (L = large, S = small) (2). If the *cis*-dihydroxylation of **28** (L = Me, S = O) is considered to occur in a similar manner to 1,2-disubstituted benzene substrates (including polycyclic systems) using several dioxygenase enzymes, then the observed relative yields, ee values, and absolute configurations are in accord with the stereochemical template used earlier (Scheme 7) (2). This premise also supports the view that **28** has a considerable degree of aromatic character and an appreciable resonance energy (34).

The heterocyclic *cis*-dihydrodiols from the quinoline and 2-pyridone substrates have potential as chiral ligands (**5**–**11**) and as precursors for the synthesis of azasugars, alkaloids (**29**, **30**), and enzyme inhibitors (**5**–**11**). Studies are currently in progress to evaluate their potential in these areas.

Conclusion

The biotransformation of quinoline ring systems to yield *cis*-dihydrodiol metabolites appears to be a relatively common metabolic pathway and eight examples (**5**–**12**) have been found. Carbocyclic *cis*-dihydrodiol metabolites **7**–**10**, obtained by TDO-catalyzed dihydroxylation, were single enantiomers of identical configuration (benzylic *R*) to *cis*-diols (e.g., **34**) derived from other polycyclic arenes (e.g., **32**) using TDO, NDO, and BPDO as biocatalyst. A novel enantiopure heterocyclic *cis*-dihydrodiol (**12**) was isolated as a metabolite from 2-chloroquinoline (**2**), 2-methoxyquinoline (**3**), and 2-quinolone (**24**). No direct evidence could be obtained for the formation of *cis*-diol metabolites **20** and **21** from *cis*-dihydroxylation of the pyridine ring of substrates **2** and **3**. Strong indirect evidence has, however, been found for the formation of *cis*-diols **19**–**21** as unstable metabolites of a pyridine ring. The absolute configurations of *cis*-diol metabolites **29** and **30**, derived from 1-methyl-2-pyridone (**28**), are consistent with the dioxygenase enzymes being able to accept substrate **28** as a pyridine derivative having a structure similar to 1,2-disubstituted benzene substrates.

Experimental

^{1}H NMR spectra of compounds were recorded on Bruker Avance DPX-300 and DRX-500 instruments. Mass spectra were recorded using a double-focusing triple-sector VG Autospec instrument. Accurate mass measurements were obtained by the peak-matching method using perfluorokerosene as the standard reference and were accurate to within ±0.006 amu. Flash chromatography and PLC were performed on Merck Kieselgel type 60 (250–400 mesh) and $PF_{254/366}$, respectively. Merck Kieselgel $60F_{254}$ analytical plates were used for TLC. Optical rotation ($[\alpha]_D$) measurements were carried out with a PerkinElmer 214 polarimeter at ambient temperature (ca. 20°C) and are given in units of 10^{-1} deg cm^2 g^{-1}. CD spectra were recorded using a JASCO J-720 instrument and spectroscopic-grade methanol as solvent.

GC–MS analysis of the crude EtOAc extract of *cis*-diol metabolites **29** and **30** was carried out after concentration under a stream of dry N_2 and treatment with *N*-methyl-*N*-(trimethylsilyl)trifluoroacetamide to yield the corresponding bis-trimethylsilyl ethers. The GC–MS instrument used consisted of a Hewlett Packard 6890 gas chromatograph directly attached to a Hewlett Packard 5973 Mass Selective Detector. The GC oven was equipped with a Hewlett Packard 7683 autosampler and fitted with a wall-coated open-tubular capillary column (12 m × 0.2 mm) with 100%

© 2002 NRC Canada

dimethyl polysiloxane (0.33 μm) as the bonded phase. The injector port was held at 250°C and the oven was programmed at 100°C for 1 min and then ramped to 300°C at 10°C min^{-1}. Helium was employed as carrier gas at a flow rate of 0.8 mL min^{-1} and the sample (1 μL) was injected at a split ratio of 25:1. Under these conditions the *cis*-diols **29** and **30** and the *trans*-diol **31** were eluted at 7.34, 6.96, and 6.00 min, respectively. The mass-selective detector was operated in the full-scan mode measuring ion currents between *m*/*z* 30 and 450 amu. The relative yields of diols were calculated by comparing the relative peak areas of diols (**29**/**31** and **30**).

Substrates **2**, **4**, **24**, and **28** were obtained from commercial sources. Substrate **3** (35) and (–)-(*S*)- and (+)-(*R*)-2-(1-methoxyethyl)benzene boronic acids were synthesized and used according to literature methods (23–25, 36).

Substrates were metabolized using growing cultures of *P. putida* UV4, a constituent mutant strain devoid of *cis*-diol dehydrogenase activity, according to the reported method (30). *P. putida* 9816/11, an inducible mutant, without the corresponding *cis*-diol dehydrogenase enzyme activity, was grown on minimal-salts medium containing 0.05% sodium succinate. The naphthalene dioxygenase (NDO) present was induced by addition of 0.5% sodium salicylate at the late exponential phase of growth. *S. yanoikuyae*, also an inducible mutant without the corresponding *cis*-diol dehydrogenase enzyme activity, was grown on minimal-salts medium with 0.5% sodium pyruvate and 0.05% of yeast extract; the late exponential phase of growth the biphenyl dioxygenase (BPDO) was again induced by the addition of *m*-xylene (0.05 mL L^{-1}) every 1/2 h for 7 h. When the cells were grown in a 100-L fermenter, continuous addition of the volatile inducer (*m*-xylene) was necessary since it was constantly depleted by the air supply. *E. coli* pKST11 biotransformations were carried on cells grown on minimal-salts medium supplemented with glucose (20 mM), thiamin (1 mM), and ampicillin (100 μg mL^{-1}) at 37°C. TDO activity was induced by the addition of 1 mM isopropyl-β-thiogalactopyranoside (IPTG). The NDO in *E. coli* JM109 was similarly induced by the addition of IPTG. *P. putida* Q1 was grown on minimal-salts medium supplemented with quinoline (0.3 mg mL^{-1}) as the carbon source.

Biotransformation of substrates: isolation and identification of metabolites

2-Chloroquinoline 2 with P. putida *UV4*

Biotransformation (10-L fermenter) of 2-chloroquinoline (**2**) (7.5 g) by *P. putida* UV4, repeated extraction of the aqueous biotransformed material with EtOAc, and removal of solvent from the extract under reduced pressure (Procedure 1), yielded a crude mixture of three *cis*-diols **12**, **7**, and **8**; these were separated by a combination of column chromatography ($CHCl_3$ → 10% MeOH–$CHCl_3$) and PLC (7% MeOH–$CHCl_3$). A larger-scale biotransformation (100-L fermenter) of 2-chloroquinoline **2** (50 g) was also carried out. The bioproducts were isolated by removal of water (reduced pressure) from the biotransformed material followed by hot extraction (45°C) of the residual material with 20% MeOH–EtOAc (Procedure 2). Column chromatography and PLC separations yielded five metabolites: **12**, **7**, **8**, **26**, and **27**. The yields obtained from the small and larger scale biotransformations, respectively, are shown together.

(+)-cis-*(3*S*,4*S*)-3,4-Dihydroxy-3,4-dihydro-2-quinolone (**12**)*

Colourless crystals (0.164 g, 2.0% and 3.10 g, 5.7%); mp 177–179°C (MeOH–hexane). R_f = 0.14 (7% MeOH–$CHCl_3$). $[\alpha]_D$ +6.0 (*c* 0.72, pyridine). CD λ (nm): 285.20 (Δε = +0.683), 252.40 (Δε = –2.237), 217.50 (Δε = +1.760), 200.40 (Δε = –3.258). IR ν_{max} (cm^{-1}): 3220 (OH), 1674 (CONH). ^{1}H NMR (500 MHz, $(CD_3)_2CO$) δ: 4.05 (d, *J* = 3.0 Hz, 1H, OH), 4.13 (d, *J* = 3.0 Hz, 1H, OH), 4.34 (d, $J_{3,4}$ = 3.7 Hz, 1H, H-3), 4.77 (d, $J_{4,3}$ = 3.7 Hz, 1H, H-4), 7.03 (m, 2H, H-6 and H-8), 7.30 (m, 1H, H-7), 7.36 (m, 1H, H-5), 9.36 (br s, 1H, NH): NOE enhancement of H-3 (1%) and H-5 (2%) from irradiation of H-4; NOE enhancement of H-4 (1%) from irradiation of H-3. ^{13}C NMR (125 MHz, $(CD_3)_2CO$) δ: 70.0, 71.1, 105.2, 116.1, 123.0, 129.8, 130.1, 137.8, 171.0. MS *m*/*z* (%): 179 (M^+, 77), 161 ([M – H_2O]$^+$, 54), 122 (100). Anal. calcd. for $C_9H_9NO_3$: C 60.3, H 5.1, N 7.8; found: C 59.8, H 4.9, N 7.6.

(+)-cis-*(5*R*,6*S*)-2-Chloro-5,6-dihydroquinoline-5,6-diol (**7**)*

Colourless crystals (0.66 g, 8% and 5.4 g, 9%); mp 120–122°C (EtOAc–hexane). R_f = 0.30 (7% MeOH–$CHCl_3$). $[\alpha]_D$ +140 (*c* 0.55, MeOH). CD λ (nm): 294.60 (Δε = –1.891), 254.40 (Δε = +7.648), 226.00 (Δε = +8.017), 195.60 (Δε = –3.821). IR ν_{max} (cm^{-1}): 3402 (OH). ^{1}H NMR (500 MHz, $(CD_3)_2CO$) δ: 4.00 (m, 1H, OH), 4.18 (dd, $J_{6,5}$ = 4.9, $J_{6,7}$ = 4.6 Hz, 1H, H-6), 4.24 (m, 1H, OH), 4.55 (d, $J_{5,6}$ = 4.9 Hz, 1H, H-5), 6.27 (dd, $J_{7,6}$ = 4.6, $J_{7,8}$ = 9.9 Hz, 1H, H-7), 6.37 (d, $J_{8,7}$ = 9.9 Hz, 1H, H-8), 7.13 (d, $J_{3,4}$ = 8.1 Hz, 1H, H-3), 7.71 (d, $J_{4,3}$ = 8.1 Hz, 1H, H-4); NOE enhancement of H-4 (1%) from irradiation of H-5. ^{13}C NMR (125 MHz, $(CD_3)_2CO$) δ: 67.3, 70.5, 123.6, 130.0, 133.5, 136.8, 138.8, 150.5, 153.5. MS *m*/*z* (%): 197 (M^+(^{35}Cl), 34), 179 ([M – H_2O]$^+$, 8), 168 (100). Anal. calcd. for $C_9H_8ClNO_2$: C 54.7, H 4.1, N 7.1; found: C 54.2, H 3.8, N 6.9.

(+)-cis-*(7*S*,8*R*)-2-Chloro-7,8-dihydroquinoline-7,8-diol (**8**)*

Colourless crystals (1.63 g, 18% and 12.0 g, 20%); mp 110–111°C (EtOAc–hexane). R_f = 0.45 (7% MeOH–$CHCl_3$). $[\alpha]_D$ +148° (*c* 0.55 in MeOH). CD λ (nm): 309.80 (Δε = –0.932), 252.20 (Δε = +3.750), 246.80 (Δε = +3.665), 210.00 (Δε = +7.257). ^{1}H NMR (500 MHz, $(CD_3)_2CO$) δ: 4.01 (d, *J* = 5.8 Hz, 1H, OH), 4.49 (dd, $J_{7,8}$ = 5.0, $J_{7,6}$ = 4.2 Hz, 1H, H-7), 4.59 (m, 1H, OH), 4.61 (d, $J_{8,7}$ = 5.0 Hz, 1H, H-8), 6.17 (dd, $J_{6,7}$ = 4.2, $J_{6,5}$ = 9.6 Hz, 1H, H-6), 6.57 (d, $J_{5,6}$ = 9.6 Hz, 1H, H-5), 7.34 (d, $J_{3,4}$ = 8.0 Hz, 1H, H-3), 7.61 (d, $J_{4,3}$ = 8.0 Hz, 1H, H-4); NOE enhancement of H-4 (3%) and H-6 (3%) from irradiation of H-5. ^{13}C NMR (125 MHz, $(CD_3)_2CO$) δ: 68.2, 72.4, 124.6, 126.2, 128.3, 133.3, 137.7, 149.6, 158.4. MS *m*/*z* (%): 197 (M^+(^{35}Cl), 37), 179 ([M – H_2O]$^+$, 6), 168 (100). Anal. calcd. for $C_9H_8ClNO_2$: C 54.7, H 4.1, N 7.1; found: C 54.2, H 3.8, N 6.7.

*2-Chloro-3-hydroxyquinoline (**26**)*

White crystalline solid (0.5 g, 1%); mp 311–312°C (EtOAc–hexane) (lit. (37) mp > 210°C). R_f = 0.55 (EtOAc–hexane, 1:1). ^{1}H NMR (500 MHz, $(CD_3)_2CO$) δ: 7.41 (ddd, $J_{7,6}$ = 8.3, $J_{7,8}$ = 8.3, $J_{7,5}$ = 1.4 Hz, 1H, H-7), 7.45 (ddd, $J_{6,5}$ = 8.3, $J_{6,7}$ = 8.3, $J_{6,8}$ = 0.6 Hz, 1H, H-6), 7.60 (s, 1H, H-4), 7.68 (dd, $J_{5,6}$ = 8.3, $J_{5,7}$ = 1.4 Hz, 1H, H-5), 7.73 (dd, $J_{8,7}$ = 8.3, $J_{8,6}$ = 0.6 Hz, 1H, H-8). The physical and spectral data

© 2002 NRC Canada

(IR, NMR, MS) of chlorohydroxy compound **26** and its methoxy derivative were similar to the data reported in the literature (37, 38).

*3-Hydroxy-2-quinolone (**27**)*

Colourless crystals (1.5 g, 3%); mp 261–263°C (EtOAc) (lit. (37) mp > 220°C). R_f = 0.2 (EtOAc–hexane, 1:1). ^{1}H NMR (500 MHz, $(CD_3)_2CO$) δ: 7.02 (s, 1H, H-4), 7.06 (ddd, $J_{6,5}$ = 7.8, $J_{6,7}$ = 7.0, $J_{6,8}$ = 1.3 Hz, 1H, H-6), 7.23 (ddd, $J_{7,6}$ = 7.0, $J_{7,8}$ = 7.0, $J_{7,5}$ = 1.3 Hz, 1H, H-7), 7.42 (dd, $J_{5,6}$ = 7.8, $J_{5,7}$ = 1.3 Hz, 1H, H-5), 7.45 (dd, $J_{8,7}$ = 7.0, $J_{8,6}$ = 1.3 Hz, 1H, H-8), 8.07 (br s, 1H, NH). Anal. calcd. for $C_9H_7NO_2$: C 67.1, H 4.35, N 8.7; found: C 67.2, H 4.0, N 8.5. The physical and spectral data (IR, NMR, MS) of hydroxyquinolone **27** was similar to the data reported in the literature (37).

2-Chloroquinoline 2 with* E. coli *pKST11

Biotransformation of **2** (0.6 g) with *E. coli* pKST11, extraction (Procedure 1), and purification by PLC (7% MeOH–$CHCl_3$) yielded (+)-*cis*-(5*R*,6*S*)-2-chloro-5,6-dihydroquinoline-5,6-diol (**7**) (0.029 g, 4%) and (+)-*cis*-(7*S*,8*R*)-2-chloro-7,8-dihydroquinoline-7,8-diol (**8**) (0.080 g, 11%).

2-Chloroquinoline 2 with* P. putida *9816/11

Biotransformation of **2** (0.2 g) with *P. putida* 9816/11, extraction (Procedure 1), and separation by PLC (7% MeOH–$CHCl_3$), yielded (+)-*cis*-(5*R*,6*S*)-2-chloro-5,6-dihydroquinoline-5,6-diol (**7**) (0.014 g, 6%) and (+)-*cis*-(7*S*,8*R*)-2-chloro-7,8-dihydroquinoline-7,8-diol (**8**) (0.036 g, 15%).

2-Chloroquinoline 2 with* E. coli *JM109

Biotransformation of **2** (0.05 g) with *E. coli* JM109, extraction (Procedure 1), and PLC purification (7% MeOH–$CHCl_3$), yielded (+)-*cis*-(7*S*,8*R*)-2-chloro-7,8-dihydroquinoline-7,8-diol (**8**) (0.003 g, 5%).

2-Chloroquinoline 2 with* S. yanoikuyae *B8/36

Biotransformation of **2** (0.5 g) with *S. yanoikuyae* B8/36, extraction (Procedure 1), and PLC purification (7% MeOH–$CHCl_3$), gave (+)-*cis*-(7*S*,8*R*)-2-chloro-7,8-dihydroquinoline-7,8-diol (**8**) (0.091 g, 15%).

2-Chloroquinoline 2 with* P. fluorescens *Q1

Biotransformation of **2** (0.5 g) with *P. fluorescens* Q1, extraction (Procedure 1), and PLC purification (7% MeOH–$CHCl_3$) only yielded (+)-*cis*-(7*S*,8*R*)-2-chloro-7,8-dihydroquinoline-7,8-diol (**8**) (0.006 g, 1%).

2-Methoxyquinoline 3 with* P. putida *UV4

Biotransformation (10-L fermenter) of 2-methoxyquinoline (**3**) (7.0 g) with *P. putida* UV4 and extraction (Procedure 1) of bioproducts followed by separation of the crude mixture through a combination of column chromatography (0 → 10% MeOH–$CHCl_3$) and PLC (7% MeOH–$CHCl_3$) gave three compounds. The most abundent component (1.02 g, 13%) was found to be (+)-*cis*-(3*S*,*4S*)-3,4-dihydroxy-1,2,3,4-tetrahydro-2-quinolinone (**12**), which was indistinguishable from the sample obtained from substrate **3**. The other two components were identified as (+)-*cis*-(5*R*,6*S*)-2-methoxy-5,6-dihydroquinoline-5,6-diol (**9**) and (+)-*cis*-(7*R*,8*S*)-2-methoxy-7,8-dihydroquinoline-7,8-diol (**10**).

*(+)-*cis*-(5R,6S)-2-Methoxy-5,6-dihydroquinoline-5,6-diol (**9**)*

White crystalline solid (0.170 g, 2%); mp 182–184°C (MeOH–$CHCl_3$). R_f = 0.30 (7% MeOH–$CHCl_3$). $[\alpha]_D$ +80 (*c* 0.81, MeOH). CD λ (nm): 320.30 (Δε = –0.309), 274.70 (Δε = –0.810), 228.10 (Δε = +3.031), 199.40 (Δε = –4.009). IR ν_{max} (cm^{-1}): 3220 (OH). ^{1}H NMR (500 MHz, $(CD_3)_2CO$) δ: 4.00 (m, 1H, OH), 4.18 (dd, $J_{6,5}$ = 4.9, $J_{6,7}$ = 4.6 Hz, 1H, H-6), 4.24 (m, 1H, OH), 4.55 (d, $J_{5,6}$ = 4.9 Hz, 1H, H-5), 6.27 (dd, $J_{7,6}$ = 4.6, $J_{7,8}$ = 9.9 Hz, 1H, H-7), 6.37 (d, $J_{8,7}$ = 9.9 Hz, 1H, H-8), 7.13 (d, $J_{3,4}$ = 8.1 Hz, 1H, H-3), 7.71 (d, $J_{4,3}$ = 8.1 Hz, 1H, H-4); NOE enhancement of H-4 (1%) from irradiation of H-5. ^{13}C NMR (125 MHz, $CDCl_3$) δ: 53.9, 68.2, 70.1, 109.9, 125.4, 130.9, 133.5, 138.5, 149.3, 167.1 MS *m/z* (%): 193 (M^+, 57), 164 (100). Anal. calcd. for $C_{10}H_{11}NO_3$: C 62.2, H 5.7, N 7.3; found: C 62.0, H 5.4, N 6.9.

*(+)-*cis*-(7S,8R)-2-Methoxy-7,8-dihydroquinoline-7,8-diol (**10**)*

White crystalline solid (0.595 g, 7%); mp 80–82°C (MeOH–$CHCl_3$). R_f = 0.40 (7% MeOH–$CHCl_3$). $[\alpha]_D$ +200 (*c* 0.53, MeOH). IR ν_{max} (cm^{-1}): 3367 (OH). ^{1}H NMR (500 MHz, $(CD_3)_2CO$) δ: 3.55 (d, *J* = 5.0 Hz, 1H, OH), 3.82 (s, 3H, OMe), 4.23 (m, 1H, OH), 4.24 (dd, $J_{7,6}$ = 4.7, $J_{7,8}$ = 5.0 Hz, 1H, H-7), 4.41 (d, $J_{8,7}$ = 5.0 Hz, 1H, H-8), 5.87 (dd, $J_{6,7}$ = 4.7, $J_{6,5}$ = 9.9 Hz, 1H, H-6), 6.37 (d, $J_{5,6}$ = 9.9 Hz, 1H, H-5), 6.52 (d, $J_{3,4}$ = 8.1 Hz, 1H, H-3), 7.47 (d, $J_{4,3}$ = 8.1 Hz, 1H, H-4); NOE enhancement of H-4 (1%) from irradiation of H-5. ^{13}C NMR (125 MHz, $CDCl_3$) δ: 54.2, 64.8, 71.2, 109.7, 120.2, 125.0, 128.9, 137.5, 152.5, 163.9. MS *m/z* (%): 193 (M^+, 96), 164 (100). Anal. calcd. for $C_{10}H_{11}NO_3$: C 62.2, H 5.7, N 7.3; found: C 62.2, H 5.7, N 6.8.

2-Methoxyquinoline 3 with* P. putida *9816/11

Biotransformation of **3** (0.5 g) with *P. putida* 9816/11, extraction (Procedure 1), and PLC purification (7% MeOH–$CHCl_3$), yielded (0.328 g, 54%) (+)-*cis*-(7*S*,8*R*)-2-methoxy-7,8-dihydroquinoline-7,8-diol (**10**).

2-Methoxyquinoline 3 with* S. yanoikuyae *B8/36

Biotransformation of **3** (0.5 g) with *S. yanoikuyae* B8/36, extraction (Procedure 1), and PLC purification (7% MeOH–$CHCl_3$), yielded (0.285 g, 47%) (+)-*cis*-(7*S*,8*R*)-2-methoxy-7,8-dihydroquinoline-7,8-diol (**10**).

2-Methoxyquinoline 3 with* E. coli *JM109

Biotransformation of **3** (0.05 g) with *E. coli* JM109, extraction (Procedure 1), and PLC purification (7% MeOH–$CHCl_3$), yielded (0.003 g, 5%) (+)-*cis*-(7*S*,8*R*)-2-methoxy-7,8-dihydroquinoline-7,8-diol (**10**).

2-Quinolone (24) with* P. putida *UV4

Biotransformation of **24** (0.5 g) with *P. putida* UV4, extraction (Procedure 1), and PLC purification (7% MeOH–$CHCl_3$), yielded (0.062 g, 10%) (+)-*cis*-(3*S*,*4S*)-3,4-dihydroxy-1,2,3,4-tetrahydro-2-quinolinone (**12**).

3-Bromoquinoline (4) with* P. putida *UV4

Biotransformation of **4** (7.5 g) with *P. putida* UV4, extraction (Procedure 1), and purification by column chromatography ($CHCl_3$ and then 10% MeOH–$CHCl_3$) furnished a single compound, which was identified as (+)-*cis*-(5*R*,6*S*)-3-bromo-5,6-dihydroquinoline-5,6-diol (**11**).

© 2002 NRC Canada

(+)-cis-*(5*R*,6*S*)-3-Bromo-5,6-dihydroxy-5,6-dihydroquinoline (**11**)*

Pale yellow crystalline solid (1.7 g, 23%); mp 171°C (MeOH-CH_2Cl_2). R_f = 0.2 (5% MeOH–$CHCl_3$). $[\alpha]_D$ +220 (*c* 0.69, MeOH). CD λ (nm): 318.70 (Δε = –0.016), 260.10 (Δε = +1.439), 214.5 (Δε = +6.222), 197.90 (Δε = –3.931). IR ν_{max} (cm^{-1}): 3392 (OH). ^{1}H NMR (500 MHz, $CDCl_3$) δ: 1.56 (br s, 2H, OH,), 4.35 (dd, $J_{6,5}$ = 4.8, $J_{6,7}$ = 5.1 Hz, 1H, H-7), 4.77 (d, $J_{5,6}$ = 4.8 Hz, 1H, H-5), 6.46 (dd, $J_{7,8}$ = 9.9, $J_{7,6}$ = 5.1 Hz, 1H, H-7), 6.73 (d, $J_{8,7}$ = 9.9 Hz, 1H, H-8), 8.04 (s, 1H, H-2), 8.48 (s, 1H, H-4); NOE enhancement of H-4 (2%) from irradiation of H-5. ^{13}C NMR (125 MHz, $CDCl_3$) δ: 65.6, 69.6, 120.0, 131.0, 132.2, 133.9, 137.2, 149.1, 149.5. MS *m*/*z* (%): 241 (M^+(^{79}Br), 37), 212 ([M(^{79}Br) – C_2H_5]$^+$, 100). Anal. calcd. for $C_9H_8BrNO_2$: C 44.7, H 3.3, N 5.8; found: C 44.5, H 2.8, N 5.6.

X-ray crystal data for cis-*diol* **11**[3]

$C_9H_8BrNO_2$, M_w = 242.1, orthorhombic, *a* = 4.4973(6), *b* = 11.5223(14), *c* = 17.5491(18) Å, *V* = 909.4(2) Å^3, *T* = 293 K, Cu Kα radiation, λ = 1.54178 Å, space group $P2_12_12_1$, *Z* = 4, D_x = 1.768 g cm^{-3}, 0.50 × 0.50 × 0.25 mm, μ = 5.89 mm^{-1}, *F(000)* = 480, Bruker P3/V2000 diffractometer, ω scan, 9 < 2θ < 110°, measured/independent reflections: 1440/1440, direct methods solution, full matrix least squares refinement on F_0^2, anisotropic displacement parameters for non-hydrogen atoms, hydrogens located in difference Fourier but included at positions calculated from the geometry of the molecule using the riding model, R_1 = 0.037 for 1334 data with $F_0 > 4\sigma(F_0)$, 122 parameters, wR_2 = 0.095 (all data), GoF = 1.13, Flack absolute structure parameter *x* = –0.05(5), $\Delta\rho_{min,max}$ = –0.67/0.31 e Å^{-3}.

*X-ray crystal data for cis-diol **12***

Previously deposited as CCDC 182/770.

1-Methyl-2-pyridone (28) with a range of dioxygenases

Biotransformation of 1-methyl-2-pyridone (**28**) was first carried out using *E. coli* JM109(DE3) pDTG141 an ampicillin-resistant recombinant-strain encoding NDO from *P. putida* 9816–4 and using IPTG as inducer under conditions previously reported (16). This biotransformation was then carried out using the other strains listed in Table 2 employing essentially the same conditions as for substrate **2**. Biotransformation of pyridone **28** with site-directed mutant-strain *E. coli* JM109(DE3) (pDTG141–352V) was carried out as reported (36).

Biotransformations of **28** (0.10 g, dissolved in 1 L of buffer) using strains listed in Table 2, were followed by removal of water by freeze-drying or evaporation under reduced pressure at ~30°C. Extraction of the residue with acetone, yielded a mixture of *cis*-diols **29** and **30**, which were separated by a combination of column chromatography and TLC (MeOH–MeCOMe–$CHCl_3$, 1:1:8). The yields of purified *cis*-diols **29** (major) and **30** (minor) were in the range of 15–20% and 0.7–1.5%, respectively.

(+)-cis-*(5*S*,6*S*)-1-Methyl-5,6-dihydroxy-5,6-dihydro-2-pyridone (**29**)*

Colourless crystals; mp 86–88°C (from CH_2Cl_2). $[\alpha]_D$ +40 (*c* 0.42, MeOH) (lit. (16) $[\alpha]_D$ +41, MeOH). CD λ (nm): 252.0 (Δε = –1.500), 216.2 (Δε = +5.47). ^{1}H NMR (500 MHz, $CDCl_3$) δ: 3.08 (s, 3H, Me), 4.61 (dd, $J_{5,6}$ = 4.4, $J_{5,4}$ = 2.2, $J_{5,3}$ = 2.2 Hz, 1H, H-5), 4.92 (dd, $J_{6,5}$ = 4.8, $J_{6,4}$ = 1.8 Hz, 1H, H-6), 5.70 (dd, $J_{3,4}$ = 10.0, $J_{3,5}$ = 2.2 Hz, 1H, H-3), 6.37 (dt, $J_{4,3}$ = 10.0, $J_{4,5}$ = 2.2, $J_{4,6}$ = 1.8 Hz, 1H, H-4). Anal. calcd. for C_6H_9NO: 125.04768 ([M – H_2O]$^+$); found: 125.04835.

*X-ray crystal data for cis-diol **29***[3]

$C_6H_9NO_3$, M_w = 143.1, orthorhombic, *a* = 4.627(1), *b* = 10.605(1), *c* = 14.041(2) Å, *V* = 689.0(1) Å^3, *T* = 293 K, Cu Kα radiation, λ = 1.54178 Å, space group $P2_12_12_1$, *Z* = 4, D_x = 1.380 g cm^{-3}, elongated hexagonal prism, 0.40 × 0.12 × 0.12 mm, μ = 0.95 mm^{-1}, Bruker P4 diffractometer, ω scan, 10 < 2θ < 110°, measured/independent reflections: 3381/863, analytical absorption correction, direct methods solution, full matrix least squares refinement on F_0^2, anisotropic displacement parameters for non-hydrogen atoms, hydrogens located in difference Fourier but included at positions calculated from the geometry of the molecule using the riding model, R_1 = 0.027 for 827 data with $F_0 > 4\sigma(F_0)$, 95 parameters, wR_2 = 0.076 (all data), GoF = 1.14, Flack absolute structure parameter *x* = 0.24(35), $\Delta\rho_{min,max}$ = –0.10/0.13 e Å^{-3}.

cis-*(3*S*,4*S*)-1-Methyl-3,4-dihydroxy-3,4-dihydro-2-pyridone (**30**)*

Semi-solid. CD λ (nm): 233.40 (Δε = +0.417). ^{1}H NMR (300 MHz, $(CD_3)_2CO$) δ: 2.90 (s, 3H, Me), 3.77 (br s, 1H, OH), 3.92 (br s, 1H, OH), 4.03 (m, 2H, H-3 and H-4), 5.20 (dd, $J_{5,6}$ = 7.8, $J_{5,4}$ = 5.7 Hz, 1H, H-5), 6.17 (d, $J_{6,5}$ = 7.8 Hz, 1H, H-6). Anal. calcd. for C_6H_9NO: 125.04768 ([M – H_2O]$^+$); found: 125.04748.

Acknowledgments

We wish to thank Miss P.L. Loke for assistance with the isolation of metabolites **26** and **27**, and Dr. A.F. Drake (Kings College London) for assistance with the CD spectral analysis. Financial support was provided by the BBSRC (NDS) and by the European Social Fund (JGC).

References

1. S.M. Resnick, K. Lee, and D.T. Gibson. J. Ind. Microbiol. **17**, 438 (1996).
2. D.R. Boyd and G.N. Sheldrake. Nat. Prod. Rep. **15**, 309 (1998).
3. T. Hudlicky, D. Gonzalez, and D.T. Gibson. Aldrichim. Acta, **32**, 35 (1999).
4. D.T. Gibson and R.E. Parales. Curr. Opin. Biotechnol. **11**, 236 (2000).

[3] Supplementary material may be purchased from the Depository of Unpublished Data, Document Delivery, CISTI, National Research Council Canada, Ottawa, ON K1A 0S2, Canada. For information on obtaining material electronically go to http://www.nrc.ca/cisti/irm/unpub_e.shtml. Crystallographic information has also been deposited with the Cambridge Crystallographic Data Centre (CCDC Nos. 183535 and 183536). Copies of the data can be obtained free of charge via www.ccdc.cam.ac.uk/conts/retrieving.html (or from the Cambridge Crystallographic Data Centre, 12, Union Road, Cambridge CB2 1EZ, UK; fax: +44 1223 336033; or deposit@ccdc.cam.ac.uk).

© 2002 NRC Canada

5. D.R. Boyd, N.D. Sharma, and C.C.R. Allen. Curr. Opin. Biotechnol. **12**, 564 (2001).
6. D.R. Boyd, N.D. Sharma, I.N. Brannigan, D.A. Clarke, H. Dalton, S.A. Haughey, and J.F. Malone. Chem. Commun. 2361 (1996).
7. D.R. Boyd, N.D. Sharma, R. Boyle, B.T. McMurray, T.A. Evans, J.F. Malone, H. Dalton. J. Chima, and G.N. Sheldrake. J. Chem. Soc. Chem. Commun. 49 (1993).
8. N.S. Zefirov, S.R. Agapova, P.B. Terentiev, I.M. Bulakhova, N.I. Vasyukova, and L.V. Modyanova. FEMS Microbiol. Lett. **118**, 71 (1994).
9. J-P. Kaiser, Y. Feng, and J-M. Bollag. Microbiol. Rev. **60**, 483 (1996).
10. S. Fetzner, B. Tshisuaka, F. Lingens, R. Kappl, and J. Huttermann. Angew. Chem. Int. Ed. **37**, 576 (1998).
11. S. Fetzner. Appl. Microbiol. Biotechnol. **49**, 237 (1998).
12. D.R. Boyd, R.A.S. McMordie, H.P. Porter, H. Dalton, R.O. Jenkins, and O.W. Howarth. Chem. Commun. 1722 (1987).
13. D.R. Boyd, N.D. Sharma, M.R.J. Dorrity, M.V. Hand, R.A.S. McMordie, J.F. Malone, H.P. Porter, H. Dalton, J. Chima, and G.N. Sheldrake. J. Chem. Soc. Perkin Trans. 1, 1065 (1993).
14. D.R. Boyd, N.D. Sharma, J.G. Carroll, J.F. Malone, D.G. Mackerracher, and C.C.R. Allen. Chem. Commun. 683 (1998).
15. L. Modyanova and R. Azerad. 4th International symposium on biocatalysis and biotransformation. Biotrans '99 Abstracts, 265 (1999).
16. L. Modyanova and R. Azerad. Tetrahedron Lett. **41**, 3865 (2000).
17. D.G.H. Ballard, A. Courtis, I.M. Shirley, and S.C. Taylor. J. Chem. Soc. Chem. Commun. 954 (1983).
18. G.M. Lecka and D.T. Gibson. Biochem. J. **180**, 639 (1979).
19. W.R. Mahaffy, D.T. Gibson, and C. Cerniglia. Appl. Environ. Microbiol. **54**, 2415 (1988).
20. D.R. Boyd, N.D. Sharma, S.A. Haughey, M.A. Kennedy, B.T. McMurray, G.N. Sheldrake, C.C.R. Allen, H. Dalton, and K. Sproule. J. Chem. Soc. Perkin Trans. 1, 1929 (1998).
21. S.M. Resnick and D.T. Gibson. Appl. Environ. Microbiol. **62**, 3355 (1996).
22. S. Fetzner, B. Vogler, and F. Lingens. FEMS Microbiol. Lett. **112**, 151 (1993).
23. S.M. Resnick, D.S. Torok, and D.T. Gibson. J. Org. Chem. **60**, 3546 (1995).
24. D.R. Boyd, N.D. Sharma, F. Hempenstall, M.A. Kennedy, J.F. Malone, C.C.R. Allen, S.M. Resnick, and D.T. Gibson. J. Org. Chem. **64**, 4005 (1999).
25. D.R. Boyd, N.D. Sharma, J.S. Harrison, M.A. Kennedy, C.C.R. Allen, and D.T. Gibson. J. Chem. Soc. Perkin Trans. 1, 1264 (2001).
26. S.C. Barr, N. Bowers, D.R. Boyd, N.D. Sharma, L. Hamilton, R.A.S. McMordie, and H. Dalton. J. Chem. Soc. Perkin Trans 1, 3443 (1998).
27. T. Hudlicky, S.P. Fearnley, H.F. Olivo, D. Parker, G.M. Whited, C.J. Downie, and T. Dudding. J. Biorg. Med. Chem. **2**, 727 (1994).
28. B.D. Ensley, B.J. Ratzkin, T.D. Osslund, M.J. Simon, L.P. Wackett, and D.T. Gibson. Science (Washington, D.C.), **222**, 167 (1983).
29. D. Murdoch, B.D. Ensley, C. Serdar, and M. Thalen. BioTechnology, **11**, 381 (1993).
30. D.R. Boyd, N.D. Sharma, S.A. Haughey, J.F. Malone, A.W.T. King, B.T. McMurray, A. Alves-Areias, C.C.R. Allen, R. Holt, and H. Dalton. J. Chem. Soc. Perkin Trans. 1, 3288 (2001).
31. T. Sakamoto, J.M. Joern, A. Arisawa, and F.H. Arnold. Appl. Environ. Microbiol. **67**, 3882 (2001).
32. M. Bols. Acc. Chem. Res. **31**, 1 (1998).
33. H.D. Flack. Acta Cryst. **A39**, 876 (1983).
34. T.L. Gilchrist. *In* Heterocyclic chemistry. 3rd ed. Longman, Harlow. 1997. p. 33.
35. U.C. Yoon, S.L. Quillen, P.S. Mariano, R. Swanson, J.L. Stavinoha, and E. Bay. J. Am. Chem. Soc. **105**, 1204, (1983).
36. R.E. Parales, S.M. Resnick, C-L. Yu, D.R. Boyd, N.D. Sharma, and D.T. Gibson. J. Bacteriol. **182**, 5495 (2000).
37. F. Marsais, A. Godard, and G. Queguiner. J. Heterocycl. Chem. **26**, 1589 (1989).
38. M. Yutaka, T. Sakae, N. Yashiharu, and H. Masatomo. Heterocycles, **32**, 1579 (1991).

© 2002 NRC Canada

Biomimetic decarboxylative condensation between malonate and acetate units attached to a glycoluril template

Hao Chen and Paul H.M. Harrison

Abstract: Compound **10** (3,4,7,8-tetramethyl-2,5-dithioglycoluril) was converted in two steps to **12a**, which contains a malonate and acetate unit attached to N1 and N6, respectively. These two groups are held in proximity in a manner analogous to the loaded ketosynthase domain of polyketide and fatty acid synthases. After cleavage of the methyl ester by pig liver esterase (PLE), a polar intermediate assigned to acid **15** was separated. This material undergoes conversion to acetoacetylglycoluril **18** upon attempted isolation. The overall conversion thus resembles the decarboxylative condensation catalyzed by ketosynthase. Furthermore, isotope labeling and product studies support a mechanism in which decarboxylation of **15** precedes an intramolecular Claisen-like condensation, as it is believed to occur for the ketosynthase enzymic case. The system thus provides a functional chemical model of the key carbon–carbon bond-forming step in fatty acid and polyketide biosynthesis.

Key words: biomimetic, decarboxylation, polyketide, esterase, Claisen condensation.

Résumé : Le 3,4,7,8-tétraméthyl-2,5-dithioglycouril (**10**) a été transformé en deux étapes en **12a** qui contient des unités malonate et acétate attachées respectivement en N1 et en N6. Ces deux groupes sont maintenus à proximité l'un de l'autre d'une façon analogue de celle que l'on retrouve dans le domaine chargé de la cétosynthase de synthases de polycétides et d'acides gras. Après clivage de l'ester méthylique par une estérase de foie de cochon, on a pu séparer un intermédiaire polaire attribué à l'acide **15**. Lorsqu'on essaye de l'isoler, ce produit se transforme en acétoacétylglycouril, **18**. La conversion globale est donc semblable à une condensation décarboxylante catalysée par la cétosynthase. De plus, un marquage isotopique et une étude des produits sont en accord avec un mécanisme dans lequel la décarboxylation du produit **15** se produit par une condensation intramoléculaire de type Claisen selon l'hypothèse généralement retenue pour le cas de la cétosynthase enzymatique. Le système fournit donc un modèle chimique fonctionnel de l'étape clé de la formation de la liaison carbone–carbone dans la synthèse des acides gras et des polycétides.

Mots clés : biomimétique, décarboxylation, polycétide, estérase, condensation de Claisen.

[Traduit par la Rédaction]

Introduction

The polyketides are a diverse group of natural products that includes many commercially important antibiotics such as erythromycin and monensin (1). The carbon skeletons of these secondary metabolites are derived from repetitive "head-to-tail" condensations of multiple acyl groups, commonly acetate and propionate. Studies on the giant multifunctional polyketide synthases (PKS), and the closely related fatty acid synthases (FAS) have revealed several classes of enzyme (2). The key carbon–carbon bond forming steps catalyzed by the ketosynthase (KS) component(s) of these enzymes, however, always involve the decarboxylative condensation of a malonate or 2-alkylmalonate unit onto an acyl moiety (Fig. 1). These two chemical groups are temporarily attached to KS via covalent thioester bonds that presumably hold and orient the two condensing entities in proximity. Based on early observations that include inversion of configuration at the malonate α-carbon and a lack of solvent isotope exchange, a concerted decarboxylative condensation was proposed (3). More recent data, however, including computational calculations for FAS (4) and experimental results for colletoketol and monocerin (5), support a mechanism in which decarboxylation of the malonate entity furnishes a transient enolate intermediate that is then efficiently trapped by the acyl electrophile. This process thus resembles that of other Claisen enzymes. For example, Knowles and co-workers (6) used the double-isotope fractionation test to establish a sequential deprotonation–condensation mechanism for malate synthase.

A chemical model of this intricate biochemical system could provide a test for the implications of these two distinct mechanisms, and might have use in natural product synthesis. There are, however, few examples of such a biomimic. Scott et al. (7) showed that base-promoted condensation of catechol acetate malonate provides acetoacetyl–catechol in

Received 22 January 2002. Published on the NRC Research Press Web site at http://canjchem.nrc.ca on 16 May 2002.

Dedicated to Professor J. Bryan Jones on the occasion of his 65th birthday.

H. Chen and P.H.M. Harrison.[1] Department of Chemistry, McMaster University, 1280 Main St. W., Hamilton, ON L8S 4M1, Canada.

[1]Corresponding author (e-mail pharriso@mcmaster.ca).

 DOI: 10.1139/V02-059 © 2002 NRC Canada

Fig. 1. Decarboxylative condensation of malonate and acetate units catalyzed by the ketosynthase domain of fatty acid- and polyketide-synthases.

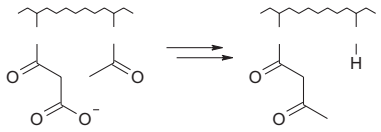

Scheme 1. Intramolecular Claisen-like condensation promoted by glycoluril template **1**.

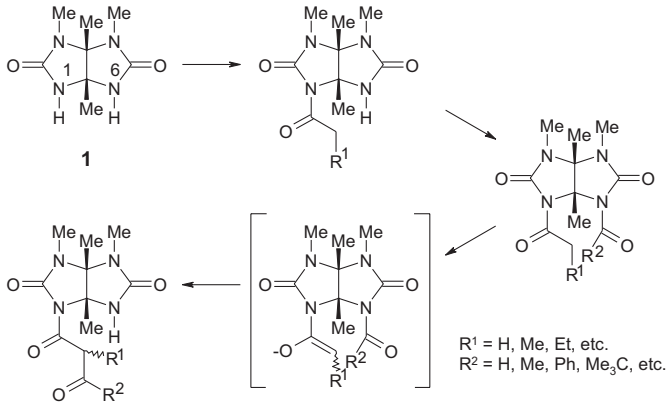

30% yield, but little mechanistic work or extension to effect repetitive cycles of acylation and condensation reactions was reported.

We have previously described the use of 3,4,7,8-tetramethylglycoluril (**1**) (8) as a template to promote intramolecular Claisen-like condensations between two acyl units. Thus, **1** could be converted via monoacyl derivatives **2** to symmetrically or asymmetrically substituted diacylglycolurils **3** (Scheme 1) (9–13). Treatment of **3** with base gives β-ketoacylglycolurils **4** in high yield. Labeling (10) and kinetic (13) studies support a mechanism in which the base abstracts a proton from one acyl group and the resulting enolate **5** is efficiently trapped by the second electrophilic acyl moiety. Subsequent rapid collapse of the ensuing tetrahedral intermediate, and proton transfers, followed by work-up generate **4**. Asymmetric diacylglycolurils afford moderate regioselectivity (ca. 83:17 for acetyl propionyl): the base removes a proton from the less-substituted acyl unit (9–12). The products **4** can be manipulated through a sequence of chemical steps to mimic the functional-group transformations that occur on FAS and PKS. Then, attachment of another acyl group leads to repetitive cycles of condensation and functional group manipulation at the ketone centre, affording fatty acids and polyketides through an iterative biomimetic synthetic sequence (10–12).

Although this system models many facets of the overall assembly of these natural products, the generation of the enolate through a base-promoted deprotonation contrasts with the biosynthetic events in which malonate is decarboxylated. We therefore investigated whether a glycoluril loaded with malonate and acyl groups would undergo decarboxylative condensation (*i*) to test such a system from a mechanistic standpoint; (*ii*) to examine whether enhanced regioselectivity could be obtained through such a method, and (*iii*) to apply the methodology to the synthesis of natural products. Herein we describe our first investigations of such a process and the key role of pig liver esterase in achieving this goal.

Scheme 2. Reagents and conditions: (*a*) KO-*t*-Bu, THF, 0°C, 20 min; (*b*) *n*-BuLi, then AcCl, THF; (*c*) *n*-BuLi, then $MeOC(O)CH_2COCl$ (**8**), THF.

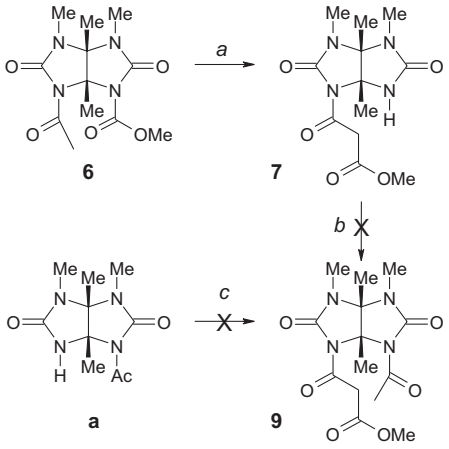

Results

Although we had previously shown that condensation of 1-acetyl-6-carbomethoxyglycoluril (**6**) provides the monomethyl ester of malonylglycoluril **7** (Scheme 2) (10), attempts to acylate **7** with acid chlorides (e.g., AcCl) proved unsuccessful. Presumably, the NH site is less acidic than the malonate α-protons. The reaction of 1-acetylglycoluril with base followed by monomethylmalonyl chloride **8** also failed to furnish target compound **9**.

We therefore investigated the attachment of **8** to thio analog **10**, which had previously been shown to be more readily acylated than **1**. Treatment of **10** with *n*-BuLi followed by **8** furnished **11** in 40% yield (unoptimized; see Scheme 3). Acetylation of **11** at the N6 position with AcCl readily gave **12a** (66%). The reverse sequence, acetylation of **10** followed by acylation with **8**, failed to give **12a**, for reasons that remain unclear. Acylation of **11** with isobutyryl chloride or benzoyl chloride proceeded similarly, to furnish **13** and **14**, respectively.

We then turned our attention to the hydrolysis of the methyl ester functionality in **12a** to afford malonic acid **15**. Various chemical agents, including aqueous acidic or basic conditions, as well as TMSI (14), KO-*t*-Bu–DMSO (15), and KOTMS (16) failed to cleave the methyl ester, resulting in decomposition or partial conversion to products of acyl–nitrogen cleavage (**10** and **11**). We therefore examined the milder conditions and higher selectivity offered by enzymatic hydrolysis (17). Thus **11** and **12a** were separately treated with pig liver esterase (PLE) (18), an enzyme that has been extensively applied in synthesis as illustrated by the pioneering work of J.B. Jones (19).

Initial experiments with ester **11** and PLE demonstrated a relatively clean conversion to acid **16**, which was isolated and fully characterized, along with recovered starting material (Scheme 4). In contrast, when **12a** was subjected to the same

© 2002 NRC Canada

Scheme 3. Reagents and conditions: (*a*) *n*-BuLi, then $MeOC(O)CH_2COCl$ (**8**), THF, 40%; (*b*) RCOCl, proton sponge, CH_2Cl_2, rt, **12a**: 67%; **12b**: 32%; **13**: 49%; **14**: 74%.

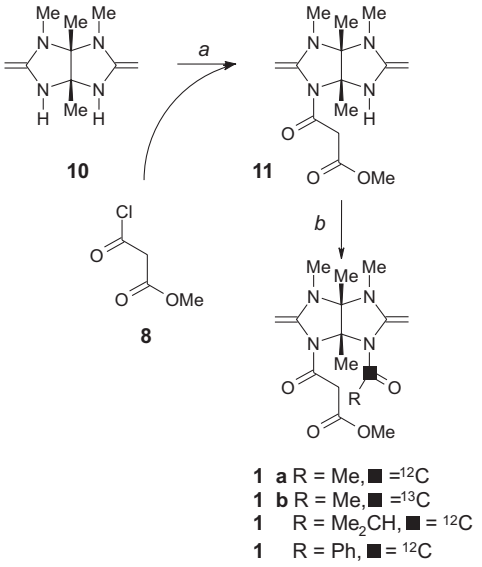

conditions, several products were observed, isolated by preparative TLC, and characterized. These products included (*i*) recovered **12a** (43%) that was identical to starting material by NMR, but which was no longer converted to products by repeated incubation with PLE, and which was optically active. (*ii*) Compounds **10** (15%) and (*iii*) **11** (21%), which were both observed in active-enzyme incubations as well as boiled controls and controls lacking the enzyme. (*iv*) Traces of diacetyldithioglycoluril **17**, identified by TLC comparison with authentic material (20); and (*v*) a polar component, tentatively assigned to acid **15**. Compounds **13** and **14** gave only unreacted starting material and **10** and **11** as products with PLE under similar conditions.

When elution of putative acid **15** from the TLC plate was attempted, condensation product **18**, which is much less polar than **15**, was obtained instead (5% unoptimized yield from **12a**), along with small amounts of **17**. Product **18** was spectroscopically identical to authentic material prepared by the previously reported base-catalyzed condensation of **17** (20), except that a strong positive band was observed in the CD spectrum, and a small but significant optical activity was seen. Efforts to purify **15** for full characterization have to date proved unsuccessful, despite using various media (Sephadex LH20, ion exchange resins, etc.).

To further probe the details of the observed overall transformation of **12a** to **18**, the result of the net putative ester hydrolysis, decarboxylation, and Claisen-like condensation, and to clarify the order of these events, we prepared the [1-^{13}C]acetyl derivative **12b** from **11** and [1-^{13}C]acetyl chloride. Treatment with PLE, separation of the presumed malonic acid, and condensation during isolation gave a sample of **18** (9% overall yield). Analysis by ^{13}C NMR spectroscopy revealed that most of the isotopic label was present at the ketonic carbonyl carbon site (δ 200.9), while some isotopic label was located at the amidic acyl carbonyl (δ 181.0) (Scheme 5). The ratio of enrichment at these two sites was ca. 86:14, as judged by the relative intensities of these two

Scheme 4. Products observed from separate incubations of (*a*) **11** and (*b*) **12a** with pig liver esterase.

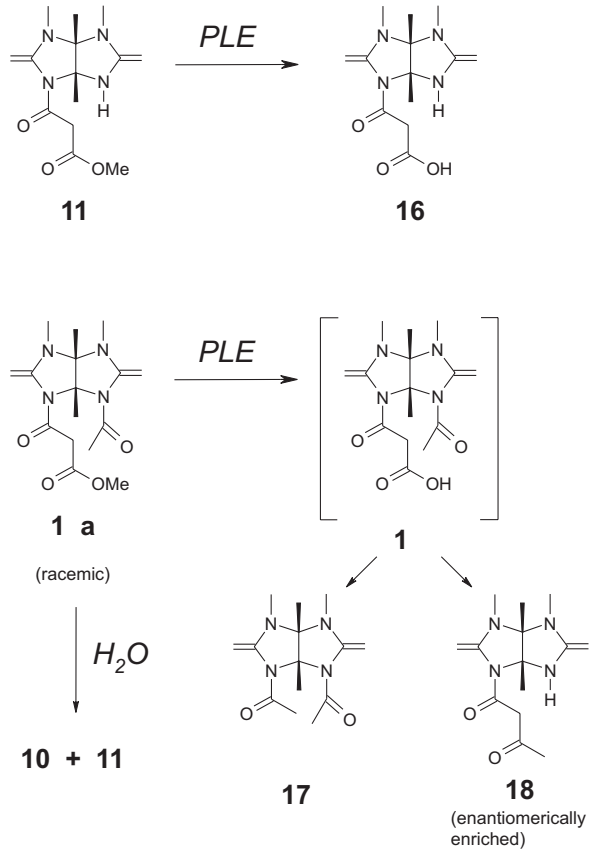

peaks compared with their relative intensities in unlabeled **18**. All the product molecules were labeled within the limits of detection (<10% unlabeled), as shown by the presence of two-bond ^{13}C–^{1}H couplings at the α-carbon of the β-ketoacyl group in the ^{1}H NMR spectrum. By contrast, no molecules were detected that contained two labels, as judged by the lack of two-bond ^{13}C–^{13}C coupling between the two carbonyl carbon atoms.

Discussion

This investigation was initiated to determine whether a biomimetic decarboxylative condensation of a malonate unit with an acyl moiety could be promoted on a glycoluril template. Use of the readily acylated dithioglycoluril **10** and commercially available half-ester half-acid chloride of malonic acid **8** allowed the first direct attachment of a malonate group, protected as the half-methyl ester, to a glycoluril. With the subsequent straightforward attachment of an acetyl group at the N6 position, it only remained to remove the methyl ester protection in **12a** to provide substrate **15** for the study of the decarboxylation reaction.

Deprotection of the methyl ester proved challenging: several chemical reagents failed. We thus considered switching to a protecting group that could be more readily cleaved. However, such a process would require the preparation of an appropriate half-ester half-chloride of malonic acid, and we wished to establish the viability of the decarboxylative approach prior to undertaking this work. In the present study,

© 2002 NRC Canada

Scheme 5. Distribution of isotope in product **18** formed from: (*a*) incubation of **12b** with pig liver esterase; (*b*) separation on silica gel and elution with methanol.

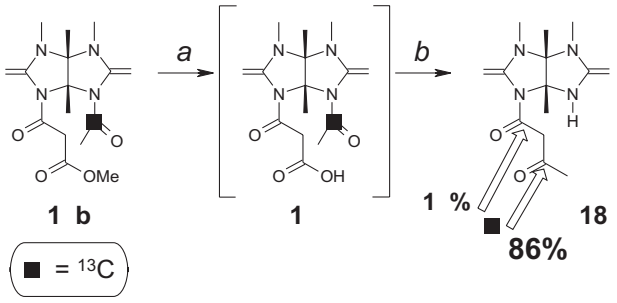

we show that, despite several side-reactions, **12a** can be converted to **18** by PLE, a result consistent with the desired sequence. Other protecting groups, which can be removed chemically under nonaqueous conditions, and which might be expected to avoid these side-reactions, are therefore currently being evaluated.

The major side-products, **10** and **11**, are probably produced by spontaneous hydrolysis of substrate **12a**, since they are also formed in control incubations lacking the active enzyme. This result is consistent with several observations of spontaneous hydrolysis under nonideal conditions, which we have made during our prior work with acylated glycolurils. This effect may be due to acyl group activation as the result of a twist around the amidic N–C bond, which we have observed to be substantial in X-ray crystallographic studies of related structures (21–23).

The remaining two products, putative acid **15** and traces of diacetyl derivative **17**, are only formed when active PLE is incubated with **12a**. Results that support this conclusion include (*i*) boiled controls do not give these products. (*ii*) Although the absolute configuration and enantiomeric excess remains to be determined, product **18** is formed as one predominant enantiomer, as shown by CD and optical activity. Starting material **12a** prior to incubation is racemic, and thus product **18** must have been formed using the enzyme at some point. (*iii*) Although **12a** isolated from the incubation failed to give a CD spectrum, this recovered sample of **12a** is essentially inert as a substrate for PLE, implying that one enantiomer has been processed with a substantive preference, leaving the other enantiomer unchanged. This conclusion is qualitatively supported by the observed optical activity of the sample. The established specificity of PLE thus suggests that ester hydrolysis is obligatory in the pathway to **18**. Two additional observations imply that this reaction precedes the condensation step, and that malonic acid **15** is the initial product. First, monoester **11**, which lacks the acetyl group for condensation, gives acid **16**, the product of the expected esterase activity. That **11** appears to be a better substrate than **12a**, coupled with the observation that **13** and **14** failed to act as substrates for PLE, suggests that the enzyme is sensitive to the size of the acyl group at N6. Second, the high polarity of **15** on TLC, greater than that of the other products and comparable to that of **16**, also supports the structure.

Although **15** was not characterized, there is an obligate reaction intermediate between **12a** and **18**, since the polar product assigned structure **15** was purified by TLC and

Scheme 6. Five possible mechanisms for conversion of **15** to **18**. The structure of the glycoluril has been abbreviated for clarity.

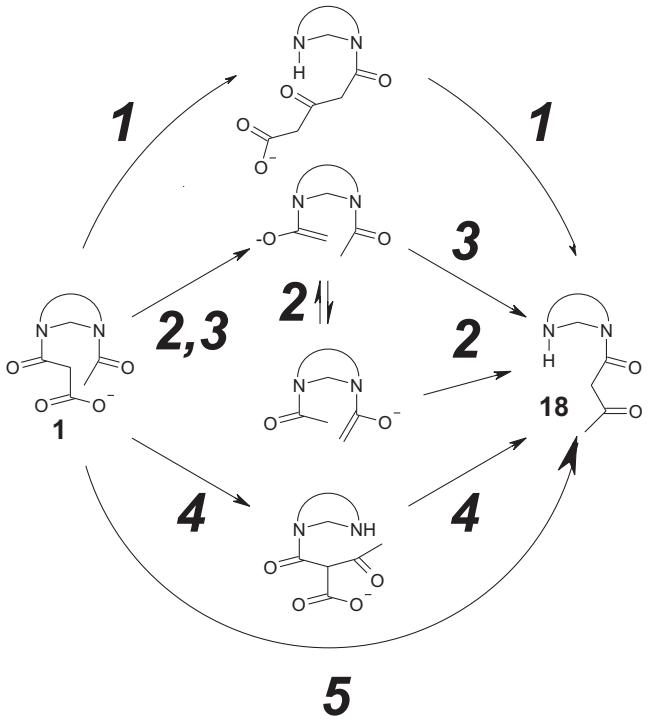

shown to furnish **18** only when eluted with methanol. It is unlikely that condensation of the malonate with the acetyl group precedes via ester hydrolysis and decarboxylation, since **12a** failed to undergo any apparent condensation reaction when treated with base, again pointing towards the proposed structure for **15**. That **18** is formed after preparative TLC supports its formation in a chemical process; thus PLE is not required to catalyze the condensation reaction.

There are several mechanisms by which **15** can be converted to **18** (Scheme 6). The results with isotopically labeled **12b** exclude a pathway in which the acetyl group is deprotonated and the resulting enolate attacks the malonate carbonyl (path 1, Scheme 6), at least as the dominant route. Pathway 4, involving condensation prior to decarboxylation, and concerted pathway 5, are consistent with the observed major location of the isotope at the ketonic position, but cannot account for the 14% of isotope that has scrambled to the amidic carbonyl during this reaction. These two routes would thus require a separate path (e.g., 1 or 2) to operate in competition.

While the present study cannot rigorously exclude these mechanistic possibilities, we prefer to invoke pathway 3, in which the desired malonate **15** is produced by PLE, and then undergoes a facile decarboxylation. The resulting enolate predominantly undergoes direct intramolecular nucleophilic attack to furnish the major isotopomer of **18** (path 3). A minor pathway, however, perhaps the intramolecular proton transfer (path 2), accounts for the partial scrambling of labeling between two sites, since this process interconverts nucleophilic enolate and electrophilic acyl acceptor sites. Nonetheless, the incomplete scrambling of the isotopic label in **12b** shows that this equilibration process cannot be complete. Finally, the formation of diacetyl glycoluril **17** may result from trapping of the enolate by water. That **17** is

© 2002 NRC Canada

a side-product, rather than an intermediate is shown by the incomplete scrambling of the isotopic label in **18** derived from **12b**. Further experiments to delineate the sequence of events in this system are currently underway.

Conclusion

Treatment with PLE converts compound **12a** to **18**, the result of overall ester hydrolysis, decarboxylation, and intramolecular condensation. The results are fully consistent with a mechanism in which the esterase selectively acts on one enantiomer of **12a**, to generate an intermediate, suggested to be malonic acid **15**. Upon isolation, intermediate **15** undergoes facile conversion to enantiomerically enriched **18**. Isotope labeling is consistent with the stepwise formation of an enolate intermediate that undergoes fast intramolecular nucleophilic attack onto the acetyl carbonyl carbon atom. Under the reaction conditions, partial isotope scrambling occurs as labeled **12b** is converted into **18**, in accord with a competing intramolecular proton transfer. Also, enolate protonation under the protic conditions results in trace amounts of the side-product diacetylglycoluril **17**. The results are therefore comparable with the proposed mechanism for decarboxylative condensation on the ketosynthase component of FAS and PKS, and provide an intriguing model of this fascinating biochemical system. Work to find a protective group for the malonate moiety that can be removed by a chemical reagent, allowing for isolation of the malonic acid intermediate and hence better control of the decarboxylative condensation process, is now underway.

Experimental

General

All reactions were performed in flame-dried glassware, under a positive pressure of nitrogen, unless otherwise noted. Air- and moisture-sensitive compounds were transferred by syringe. THF was freshly distilled under nitrogen protection from potassium–benzophenone. Flash column chromatography was performed with Kieselgel 60 (230–400 mesh ASTM) according to the method of Still et al. (24). Melting points are uncorrected. ^{1}H and ^{13}C NMR spectra were obtained on Bruker AC-200, AV-200, and AV-500 spectrometers. The reference for NMR chemical shifts was TMS. Data are given as chemical shift (δ), multiplicity (s = singlet, d = doublet, t = triplet, q = quartet, m = multiplet), coupling constant(s) (Hz), and integral. Fourier transform infrared (FT-IR) spectra were recorded on a Bio-Rad SPC 3200 spectrophotometer. Mass spectra were recorded on a VG analytical ZAB-E machine using electron impact (EI-MS), chemical ionization (CI-MS), and electrospray MS. High resolution mass spectra were also recorded on the same spectrometer.

1-(*O*-Methylmalonyl)-3,4,7,8-tetramethyl-2,5-dithioglycoluril 11

To a stirred suspension of finely powdered 3,4,7,8-tetramethyl-2,5-dithioglycoluril **(10)** (1 g, 4.35 mmol) in dry THF (200 mL) at room temperature was added *n*-BuLi (1.6 M in hexanes, 3 mL, 1.1 equiv, 4.78 mmol). The mixture was heated at reflux for 2 h. After cooling to room temperature, methyl malonyl chloride **8** (0.7 mL, 6.54 mmol) was added. The resulting solution was heated at reflux for 30 min, cooled, and filtered. The filtrate was concentrated to give crude product. Flash chromatography on silica gel in EtOAc–hexanes (30:70) gave pure **11** as a colorless powder (500 mg, 35%); mp 103–105°C. ^{1}H NMR ($CDCl_3$, 200 MHz) δ: 7.29 (s, 1H), 4.67 (d, *J* = 17 Hz, 1H), 4.11 (d, *J* = 17 Hz, 1H), 3.70 (s, 3H), 3.30 (s, 3H), 3.15 (s, 3H), 1.75 (s, 3H), 1.62 (s, 3H). ^{13}C NMR ($CDCl_3$, 50 MHz) δ: 180.0, 177.5, 167.8, 167.5, 86.0, 83.5, 52.7, 45.9, 32.1, 30.2, 18.8, 16.1. EI-MS *m/z*: 330 [M^+], 142 (base), 109, 84, 56, 41. HRMS calcd. for $C_{12}H_{18}N_4O_3S_2$: 330.0820; found: 330.0819.

1-Acetyl-6-(*O*-methylmalonyl)-tetramethyl-2,5-dithioglycoluril 12a

A mixture of **11** (400 mg, 1.21 mmol) and proton sponge (389 mg, 1.82 mmol) dissolved in dichloromethane (40 mL) was stirred at room temperature for 30 min. Acetyl chloride (143 mg, 1.82 mmol) was added over 30 min at room temperature. The reaction mixture was quenched with 1 M HCl (2 mL) and the resulting organic layer washed with 3 portions of water. The organic extracts were dried over anhydrous Na_2SO_4, filtered, and concentrated in vacuo. The product **12a** (300 mg, 67%) was isolated as a white solid after flash column chromatography on silica gel in EtOAc–hexanes (30:70). ^{1}H NMR ($CDCl_3$, 200 MHz) δ: 4.57 (d, *J* = 17 Hz, 1H), 4.15 (d, *J* = 17 Hz, 1H), 3.69 (s, 3H), 3.24 (s, 3H), 3.22 (s, 3H), 2.72 (s, 3H), 1.91 (s, 3H), 1.58 (s, 3H). ^{13}C NMR ($CDCl_3$, 50 MHz) δ: 178.1, 177.7, 173.1, 167.6, 167.5, 87.5, 85.4, 52.6, 46.3, 31.6, 31.3, 29.3, 18.7, 15.1. EI-MS *m/z*: 372 [M^+], 142, 56, 43 (base). HRMS calcd. for $C_{14}H_{20}N_4O_4S_2$: 372.0926; found: 372.0923.

1-([1′-^{13}C]Acetyl)-6-(*O*-Methylmalonyl)-tetramethyl-2,5-dithioglycoluril 12b

Compound **12b** was similarly prepared from **11** (500 mg, 1.52 mmol), proton sponge (486.5 mg, 2.27 mmol), and [1-^{13}C]acetyl chloride (178 mg, 2.27 mmol). Yield: 180 mg, 32%. ^{1}H NMR ($CDCl_3$, 200 MHz) as for **12a** except: δ: 2.73 (d, *J* = 7 Hz, 3H). ^{13}C NMR ($CDCl_3$, 50 MHz) as for **12a** except: δ: 173.0 enhanced. EI-MS *m/z*: 373 [M^+], 273, 142 (base), 109, 56, 44. HRMS calcd. for $C_{13}{}^{13}C_1H_{20}N_4O_4S_2$: 373.0959; found: 373.0966.

General procedure for pig liver esterase (PLE) incubations

To a solution of substrate in acetone and 0.1 M phosphate buffer (pH 8) was added PLE. The mixture was incubated for 5 h at 30°C, and then acidified to pH 4 with 1 M HCl and extracted with $CHCl_3$. The organic layer was washed with water, dried over Na_2SO_4, and concentrated in vacuo to afford crude product which was purified by preparative TLC (50:50 EtOAc–hexanes).

1-(3′-Oxobutanoyl)-3,4,7,8-tetramethyl-2,5-dithioglycoluril 18 from 12a

Compound **12a (**120 mg, 0.32 mmol) in 2 mL acetone and 20 mL buffer with 34 mg (680 units) PLE afforded crude product as a light brown solid. Preparative TLC of this solid gave recovered **12a** (51.6 mg, 43%, $[\alpha]_D^{20}$ – 4 ± 0.5 (*c* = 0.28,

© 2002 NRC Canada

$CHCl_3$)), **10** (9.5 mg, 15%), **11** (22.2 mg, 21%), and a polar product (**15**) that gave desired product **18** (5 mg, 5%) and **14** (traces as judged by TLC) after elution with methanol. Compound **18** was identical to material reported previously, except for optical activity: $[\alpha]_D^{20} - 4 \pm 1$ (c = 0.10, $CHCl_3$). mp: >260°C dec. ^{1}H NMR ($CDCl_3$, 200 MHz) δ: 7.26 (s, 1H), 5.09 (d, J = 17 Hz, 1H), 3.90 (d, J = 17 Hz, 1H), 3.30 (s, 3H), 3.17 (s, 3H), 2.26 (s, 3H), 1.78 (s, 3H), 1.63 (s, 3H). ^{13}C NMR ($CDCl_3$, 125 MHz) δ: 200.8, 181.0, 177.6, 168.6, 85.9, 83.5, 54.0, 32.0, 30.2 (overlapped), 18.8, 16.0. CI-MS (NH_3) m/z: 315 $[M + H]^+$, 231.

Rearrangement of 12b

Compound **12b** (161 mg, 0.43 mmol) was treated with PLE (45 mg, 900 units) and the products were separated by preparative TLC to give recovered **12b** (64 mg, 40%), labeled **10** (11.9 mg, 14%), **11** (28 mg, 20%), and **18** as a pair of isotopomers (12 mg, 9%) as well as traces of labeled **14**. For **18**: ^{1}H NMR ($CDCl_3$, 200 MHz) δ: 7.26 (s, 1H), 5.08 (dd, J = 6, 17 Hz, 1H), 3.90 (dd, J = 6, 17 Hz, 1H), 3.29 (s, 3H), 3.16 (s, 3H), 2.26 (d, J = 6 Hz, 3H), 1.78 (s, 3H), 1.62 (s, 3H). ^{13}C NMR ($CDCl_3$, 125 MHz) δ: 200.9 (enhanced), 181.0 (enhanced), 177.7, 168.7, 85.9, 83.6, 54.1 (d, J = 37 Hz), 32.0, 30.3 (d, J = 43 Hz), 30.3, 18.9, 16.1. CI-MS (NH_3) m/z: 316 $[M + H]^+$, 231, 171. HRMS calcd. for $C_{11}{}^{13}C_1H_{18}O_2S_2$: 315.0904; found: 315.0880.

1-Malonyl-tetramethyl-2,5-dithioglycoluril 16

Compound **11** (200 mg, 0.6 mmol) was treated with PLE (60 mg, 1200 units) in buffer (30 mL), and the product separated by flash column chromatography (washed with EtOAc–hexanes 50:50, then eluted with methanol) to give **16** (76 mg, 40%); $[\alpha]_D^{20}$ +2 ± 0.5 (c = 0.15, DMSO). FT-IR (cm^{-1}): 3275 (NH), approx. 3000 (v br, CO_2H), 2995, 2932 (CH), 1730 (C=O), 1689 (C=O). ^{1}H NMR (DMSO-d_6, 200 MHz) δ: 9.46 and 9.41 (br s, 2H), 4.41 (d, J = 16 Hz, 1H), 4.07 (d, J = 16 Hz, 1H), 3.24 (s, 3H), 3.03 (s, 3H), 1.66 (s, 3H), 1.61 (s, 3H). ^{13}C NMR ($CDCl_3$, 50 MHz) δ: 180.0, 176.8, 168.0, 166.8, 86.1, 83.5, 45.7, 31.7, 29.5, 18.2, 15.0. EI-MS m/z: 272 $[M - CO_2]^+$, 230, 184, 142 (base).

1-(*O*-Methylmalonyl)-6-isobutyryl-3,4,7,8-tetramethyl-2,5-dithioglycoluril 13

A mixture of **11** (20 mg, 64 μmol) and proton sponge (22.17 mg, 1.2 equiv.) was stirred in CH_2Cl_2 (3 mL) for 10 min. Isobutyryl chloride (73 μL, 1.2 equiv.) was added and stirring continued for 30 min. The reaction mixture was quenched with 1 M HCl (0.5 mL). The organic layer was washed with water (3 mL), dried over anhydrous Na_2SO_4, filtered, and concentrated in vacuo. The product **13** (12 mg, 49%) was isolated by flash column chromatography on silica gel in 30% EtOAc–hexanes. ^{1}H NMR ($CDCl_3$, 200 MHz) δ: 4.97 (d, J = 17 Hz, 1H), 4.27 (m, 1H), 3.81 (d, J = 17 Hz, 1H), 3.70 (s, 3H), 3.32 (s, 3H), 3.18 (s, 3H), 1.97 (s, 3H), 1.60 (s, 3H), 1.19 (d, J = 7 Hz, 3H), 1.07 (d, J = 7 Hz, 3H).

1-Benzoyl-6-(*O*-methylmalonyl)-tetramethyl-2,5-dithioglycoluril 14

Compound **11** (150 mg, 0.46 mmol) was treated with proton sponge (148 mg, 1.5 equiv., 0.69 mmol) and benzoyl chloride (97 mg, 1.5 equiv., 0.69 mmol), similar to the procedure for **12a**, to afford **14** (148 mg, 74%). ^{1}H NMR ($CDCl_3$, 200 MHz) δ: 7.77 (d, J = 7 Hz, 2H), 7.46 (m, 3H), 4.63 (d, J = 17 Hz, 1H), 4.06 (d, J = 17 Hz, 1H), 3.64 (s, 3H), 3.36 (s, 3H), 3.24 (s, 3H), 2.07 (s, 3H), 1.73 (s, 3H). ^{13}C NMR ($CDCl_3$, 50 MHz) δ: 180.1, 177.1, 170.6, 167.7, 167.4, 134.6, 133.5, 130.7, 128.5, 87.2, 86.6, 52.6, 45.9, 31.9, 31.1, 18.8, 16.6. EI-MS m/z: 434 $[M^+]$, 334, 142, 105 (base), 77, 42. CI-MS (NH_3) m/z: 435 $[M + H]^+$, 335 (base).

References

1. T.J. Simpson. *In* Biosynthesis: Polyketides and vitamins. *Edited by* F.J. Leeper and J.C. Vederas. Springer, Berlin. 2000. pp. 1–48; J. Staunton and B. Wilkinson. *In* Biosynthesis: Polyketides and vitamins. *Edited by* F.J. Leeper and J.C. Vederas. Springer, Berlin. 2000. pp. 49–92.
2. For recent reviews of fatty acid biosynthesis, see: B.J. Rawlings. Nat. Prod. Rep. **14**, 335 (1997); B.J. Rawlings. Nat. Prod. Rep. **15**, 275 (1998). For selected recent reviews of polyketide biosynthesis, see: J. Staunton and K.J. Weissman. Nat. Prod. Rep. **18**, 380 (2001); B.J. Rawlings. Nat. Prod. Rep. **18**, 190 (2001); B.J. Rawlings. Nat. Prod. Rep. **18**, 231 (2001); R. Bentley and J.W. Bennett. Annu. Rev. Microbiol. **53**, 411 (1999); C.W. Carreras, R. Pieper, and C. Khosla. Top. Curr. Chem. **188**, 85 (1997); also see the thematic issue of: Polyketide and nonribosomal polypeptide biosynthesis. Chem. Rev. **7** (1997) and refs. therein.
3. K.-I. Arnstad, G. Schindlbeck, and F. Lynen. Eur. J. Biochem. **55**, 561 (1975); B. Sedgwick, C. Morris, and S.J. French. J. Chem. Soc. Chem. Commun. 193 (1978).
4. M.J.S. Dewar and K.M. Dieter. Biochemistry, **27**, 3302 (1988).
5. See results in T.J. Simpson and H. Floss. Biosynthesis: Polyketides and vitamins. *Edited by* F.J. Leeper and J.C. Vederas. Springer, Berlin. 2000. pp. 23–25.
6. For a review of Claisen enzymes, see: K.R. Hanson and I.A. Rose. Acc. Chem. Res. **8**, 1 (1975); J.D. Clark, S.J. O'Keefe, and J.R. Knowles. Biochemistry, **27**, 5961 (1988).
7. A.I. Scott, C.J. Wiesner, S. Yoo, and S.K. Chung. J. Am. Chem. Soc. **97**, 6277 (1975).
8. H. Biltz. Chem. Ber. **40**, 4806 (1907).
9. S. Sun and P. Harrison. Tetrahedron Lett. **33**, 7715 (1992).
10. S. Sun, L. Edwards, and P. Harrison. J. Chem. Soc. Perkin Trans. 1, 437 (1998).
11. S. Sun and P. Harrison. J. Chem. Soc. Chem. Commun. 2235 (1994).
12. C. Cow, D. Valentini, and P. Harrison. Can. J. Chem. **75,** 884 (1997).
13. M. Rahimizadeh, K. Kam, S.I. Jenkins, R.S. MacDonald, and P.H.M. Harrison. Can. J. Chem. **80**, 517 (2002).
14. E. Haslam. Tetrahedron, **36**, 2409 (1980).
15. P.A. Bartlett and W.S. Johnson. Tetrahedron Lett. 4470 (1970).
16. E.D. Lagamis and B.L. Chenard. Tetrahedron Lett. 5831 (1984).
17. For a recent review of enzymes in organic synthesis, see: B.G. Davis and V. Boyer. Nat. Prod. Rep. **18**, 618 (2001). For reviews of PLE, see: C. Tamm. Pure Appl. Chem. **64**, 1187 (1992); L. Zhu and M.C. Tedford. Tetrahedron, **46**, 6587 (1990).
18. For the specific procedure employed, see: E. Alvarez, T. Cuvigny, C. Herve, and M. Julia. Tetrahedron, **44**, 119 (1988).
19. For selected reviews, see: J.B. Jones. Aldrichim. Acta, **26**, 105 (1993); J.B. Jones. Can. J. Chem. **71**, 1273 (1993); J.B. Jones. Pure Appl. Chem. **62**, 1445 (1990). For examples of malonate ester hydrolysis, see: L. Provencher and J.B. Jones. J. Org. Chem. **59**, 2729 (1994); L. Provencher, H. Wynn, J.B. Jones,

© 2002 NRC Canada

and A.R. Krawczyk. Tetrahedron: Asymmetry, **4**, 2025 (1993); E.J. Toone and J.B. Jones. Tetrahedron: Asymmetry, **2**, 1041 (1991).
20. C.N. Cow and P.H.M. Harrison. J. Org. Chem. **62**, 8834 (1997).
21. C.N. Cow, J.F. Britten, and P.H.M. Harrison. Chem. Commun. 1147 (1998).
22. P.A. Duspara, C.F. Matta, S.I. Jenkins, and P.H.M. Harrison. Org. Lett. **4**, 495 (2001).
23. C.F. Matta, C.N. Cow, S. Sun, J.F. Britten, and P.H.M. Harrison. J. Mol. Struct. **523**, 241 (2000).
24. W. Still, M. Kahn, and A. Mitra. J. Org. Chem. **43**, 2923 (1978).

© 2002 NRC Canada

Enantioselective enzymatic aminolysis of a racemic 2-isoxazolylacetate alkyl ester

Amy E. Sigmund, Kenneth C. McNulty, Dzuy Nguyen, Charlotte E. Silverman, Philip Ma, Jaan A. Pesti, and Robert DiCosimo

Abstract: *Pseudomonas cepacia* lipase or *Candida antartica* lipase B catalyzes the enantioselective aminolysis of a racemic 2-isoxazolylacetate alkyl ester, isobutyl 2-[3-(4-cyanophenyl)-4,5-dihydro-5-isoxazolyl]acetate, by 3-amino-*N*-(butoxycarbonyl)-L-alanine methyl ester, mono(4-methylbenzenesulfonate) to produce the corresponding amide, (*R*)-methyl-3-[[[3-(4-cyanophenyl)-4,5-dihydro-5-isoxazolyl]acetyl]amino]-*N*-(butoxycarbonyl)-L-alanine, which is an intermediate in the preparation of an isoxazoline-based platelet glycoprotein IIb/IIIa antagonist.

Key words: enantioselective aminolysis, *Pseudomonas cepacia* lipase, *Candida antartica* lipase B.

Résumé : La lipase de *Pseudomonas cepacia* ou la lipase B de *Candida antartica* catalyse l'aminolyse énantiosélective d'un ester 2-isoxazolylylacétate d'alkyle, le 2-[3-(4-cyanophényl)-4,5-dihydro-5-isoxazolyl]acétate d'isobutyle, par le mono(4-méthylbenzènesulfonate) de l'ester méthylique du 3-amino-*N*-(butoxycarbonyl)-L-alanine pour conduire à la formation de l'amide correspondant, la (*R*)-méthyl-3-[[[3-(4-cyanophényl)-4,5-dihydro-5-isoxazolyl]acétyl]amino]-*N*-(butoxycarbonyl)-L-alanine, un intermédiaire dans la préparation d'un antagoniste IIb/IIIa glycoprotéinique des plaquettes à base d'isoxazoline.

Mots clés : aminolyse énantiosélective, lipase de *Pseudomonas cepacia*, lipase B de *Candida antartica*.

[Traduit par la Rédaction]

Introduction

A variety of enzymes catalyze the enantioselective ammoniolysis or aminolysis of racemic esters. Several lipases have been used for the enantioselective ammoniolysis of free amino acid esters (1), and *Candida antartica* lipase B (CAL B) catalyzed the kinetic resolution of a racemic ester via ammoniolysis (2). D-Aminopeptidase (3), thiolsubtilisin (4), and papain (5) each catalyzed the aminolysis of α-amino acid esters to produce the corresponding chiral α-amino acid amides.

The lipase-catalyzed enantioselective aminolysis of racemic esters to produce chiral amides has been reviewed (6). Aminolysis of racemic 2-methyloctanoate by (*R*)-1-phenylethylamine in the presence of CAL B produced (*R*)-2-methyloctanoic-(*R*)-1-phenylethylamide in 30–40% diastereomeric excess (de) at ca. 100% conversion (7). Resolution of chiral amines by reaction with an isoalkyl ester in the presence of CAL B produced the corresponding chiral amides in high enantiomeric excess (8). A systematic study of the enzymatic aminolysis of racemic 2-methyl butyrate by benzylamine found that CAL B and the lipases from *Rhizopus niveus* and porcine pancreas were highly enantioselective (84–87% ee), while *Candida rugosa* and *Pseudomonas cepacia* lipases were neither highly active nor enantioselective (15% ee and 12% ee, respectively) (9). CAL B (Novo SP435) catalyzed the enantioselective aminolysis of racemic 3-hydroxyesters (10), or racemic 2-alkylesters or 2-haloesters (11), by aliphatic amines, where the degree of enantioselectivity was dependent on the substrate and nucleophile. For the enzymatic aminolysis of dimethyl 3-hydroxyglutarate by aliphatic and aromatic amines (12), CAL B yielded enantiopure monoamidation products in very high yield, while no amidation products were observed in the presence of lipases from *Candida cylindracea* and *P. cepacia* under identical reaction conditions.

An enantioselective enzymatic aminolysis of a racemic 2-isoxazolylacetate alkyl ester has now been employed to produce an intermediate in the preparation of roxifiban ((*R*)-methyl-3-[[[3-[4-(aminoiminomethyl)phenyl]-4,5-dihydro-5-isoxazolyl]acetyl]amino]-*N*-(butoxycarbonyl)-L-alanine monoacetate (Scheme 1)), a non-peptide platelet glycoprotein IIb/IIIa antagonist that has antithrombotic activity (13, 14). The aminolysis reaction produces the desired product with

Received 16 October 2001. Published on the NRC Research Press Web site at http://canjchem.nrc.ca on 10 April 2002.

Dedicated to Professor J. Bryan Jones on the occasion of his 65th birthday.

A.E. Sigmund and R. DiCosimo.[1] DuPont Central Research and Development, Experimental Station, P.O. Box 80328, Wilmington, DE 19880-0328, U.S.A.
K.C. McNulty, D. Nguyen, C.E. Silverman, P. Ma, and J.A. Pesti. Chemical Process Research and Development, Bristol-Meyers Squibb Co., Chambers Works, Deepwater, NJ 08023, U.S.A.

[1]Corresponding author (e-mail: Robert.DiCosimo@usa.dupont.com).

 DOI: 10.1139/V02-004 © 2002 NRC Canada

Scheme 1.

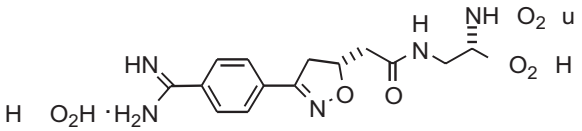

Roxifiban

high selectivity and de, despite the presence of a second alkyl ester functionality on both the reacting amine and the product amide.

Results and discussion

The 2-isoxazolylacetate alkyl ester intermediate (*R*)-methyl-3-[[[3-(4-cyanophenyl)-4,5-dihydro-5-isoxazolyl]acetyl]amino]-*N*-(butoxycarbonyl)-L-alanine ((*R*,*S*)-**1**) is currently synthesized in two steps (Scheme 2) (13*b*). Racemic isobutyl 2-[3-(4-cyanophenyl)-4,5-dihydro-5-isoxazolyl]acetate ((*R*/*S*)-**2**) is first converted into the chiral acid (*R*)-2-[3-(4-cyanophenyl)-4,5-dihydro-5-isoxazolyl]acetic acid ((*R*)-**3**) in an aqueous reaction mixture using *P. cepacia* (formerly *Pseudomonas sp.)* lipase (15), leaving the chiral isobutyl ester (*S*)-**2** unreacted. After isolation, (*R*)-**3** is reacted with thionyl chloride and diamine (*S*)-**4** (3-amino- *N*-(butoxycarbonyl)-L-alanine methyl ester, mono(4-methylbenzenesulfonate)), followed by the addition of diisopropylethylamine (DIEA) to produce (*R*,*S*)-**1**. In a separate step, recovered (*S*)-**2** is racemized for recycle by a catalytic amount of potassium *tert*-butoxide in toluene. This sequence of reactions provides (*R*)-**3** in 70% yield (after one recycle) from racemate (*R*/*S*)-**2**, and (*R*)-**3** is subsequently converted to (*R*,*S*)-**1** in 82% yield.

As an alternative to the two-step procedure described above, the lipase-catalyzed aminolysis of racemic (*R*/*S*)-**2** by diamine (*S*)-**4** to directly produce (*R*,*S*)-**1** was examined (Scheme 3). Several potential by-product-forming reactions which could have resulted in yield loss or a decrease in de of (*R*,*S*)-**1** included: (*i*) nonenzymatic aminolysis of (*R*/*S*)-**2** by (*S*)-**4**; (*ii*) enzymatic hydrolysis of (*R*/*S*)-**2** to (*R*)-**3** (if water is present in the organic solvent); (*iii*) enzymatic hydrolysis of the product (*R*,*S*)-**1** (if water is present in the organic solvent); (*iv*) enzyme-catalyzed aminolysis of (*S*)-**4** by an additional equivalent of (*S*)-**4**; or (*v*) enzymatic or nonenzymatic aminolysis of the product (*R*,*S*)-**1** to produce an aminated by-product. Regioselective aminolysis of non-chiral diesters catalyzed by PS30 lipase has been reported, where regioselectivity was attributed to a preference for aminolysis of a β-alkoxy ester relative to the remaining ester functionality (16).

The free amine of (*S*)-**4** was unstable, and readily dimerized and trimerized in both aqueous solution and in organic solvents in the absence of lipase. As a *p*-toluenesulfonate salt, (*S*)-**4** was stable in organic solvents, and it was first demonstrated that in the presence or absence of *P. cepacia* lipase (Amano PS30) or CAL B there was no significant change in concentration of (*S*)-**4** in diisopropyl ether (DIPE), methyl-*tert*-butyl ether (MTBE), heptane, dioxane, or toluene after 24 h at 25°C. In aqueous solution, a significant (>75%) decomposition of the *p*-toluenesulfonate salt of (*S*)-**4** occurred at 25°C in 0.40 M sodium phosphate buffer (pH 8.0) after 24 h, whereas the salt was stable for at least 18 h in aqueous 5 mM methanesulfonic acid (pH 2.5).

Prior to use in aminolysis reactions, a solution of 30–60 mg mL^{-1} of lipase in 0.10 M sodium phosphate buffer was adjusted to pH 8.0, and then lyophilized to obtain a "dry" enzyme catalyst. This catalyst was subsequently used in aminolysis reactions to produce (*R*,*S*)-**1**, where 52 mM (*R*/*S*)-**2** and from 37.5 to 100 mM (*S*)-**4** were reacted with the dried lipase in DIPE, MTBE, heptane, toluene, or acetonitrile, at temperatures of from 24– 40°C. Initially, the resulting product mixtures contained significant amounts of the ester hydrolysis product (*R*)-**3** as the sole reaction by-product, indicating that water was available in the reaction mixtures, possibly originating from the solvent, enzyme preparation, and (or) starting materials. None of the other potential reaction by-products described above occurred in significant amounts (<1%). Drying the solvents over activated molecular sieves prior to use improved selectivity to (*R*,*S*)-**1** over (*R*)-**3**, and the inclusion of 10–35 mg mL^{-1} of powdered, activated molecular sieves in the reaction mixture (17) further improved selectivity to (*R*,*S*)-**1**.

Table 1 lists the conversion of (*R*/*S*)-**2**, selectivity to (*R*,*S*)-**1** (vs. hydrolysis to produce (*R*)-**3**), and the corresponding de of (*R*,*S*)-**1** (where there was significant conversion) obtained using lyophilized PS30 lipase in dry DIPE, MTBE, heptane, toluene, or acetonitrile. There was no significant conversion of (*R*/*S*)-**2** in the absence of lipase under the reported reaction conditions. With lipase present, there was very little conversion of starting material in toluene or acetonitrile relative to the other solvents, and the reaction rate was considerably slower in heptane relative to MTBE or DIPE. The solubilities of (*R*/*S*)-**2**, (*R*,*S*)-**1**, and reaction by-products were low in all of these solvents, and reactions were run as heterogeneous mixtures (18). Following the progress of a reaction by sampling the heterogeneous mixture over time gave inconsistent results, so measurements of selectivity and de vs. conversion of (*R*/*S*)-**2** were performed by setting up a series of identical reactions, then working up individual reactions for analysis at predetermined times.

The de and selectivity for production of (*R*,*S*)-**1** at conversions of (*R*/*S*)-**2** between 20 and 55% in either DIPE or MTBE are depicted in Fig. 1. The selectivity to (*R*,*S*)-**1** in DIPE averaged ca. 95% at conversions of up to 45%, whereas in MTBE the selectivity was only ca. 90% at conversions of up to 52%. The de of (*R*,*S*)-**1** at a given conversion was similar in either solvent; for MTBE, the de decreased from 86 to 78% as conversion increased from 27 to 46%, and in DIPE, the de decreased from 86 to 74% as the conversion increased from 23 to 44%.

CAL B (19) also produced the desired diastereomer (*R*,*S*)-**1** in high de (Table 2), while *C. antartica* lipase A (CAL A) had the opposite enantioselectivity for (*R*/*S*)-**2** (producing (*S*,*S*)-**1** instead of (*R*,*S*)-**1**), demonstrating that not all enzymes capable of catalyzing the aminolysis of (*R*,*S*)-**1** by (*S*)-**4** produce the desired diastereomer. Although the de obtained using CAL B was moderately higher than that obtained with PS30 lipase in the same solvent (ca. 8% higher de at 35% conversion), the selectivity to the aminolysis product relative to hydrolysis product was significantly lower (81 vs. 89% at 35% conversion); all attempts to improve selectivity by removal of additional water from the

© 2002 NRC Canada

Scheme 2.

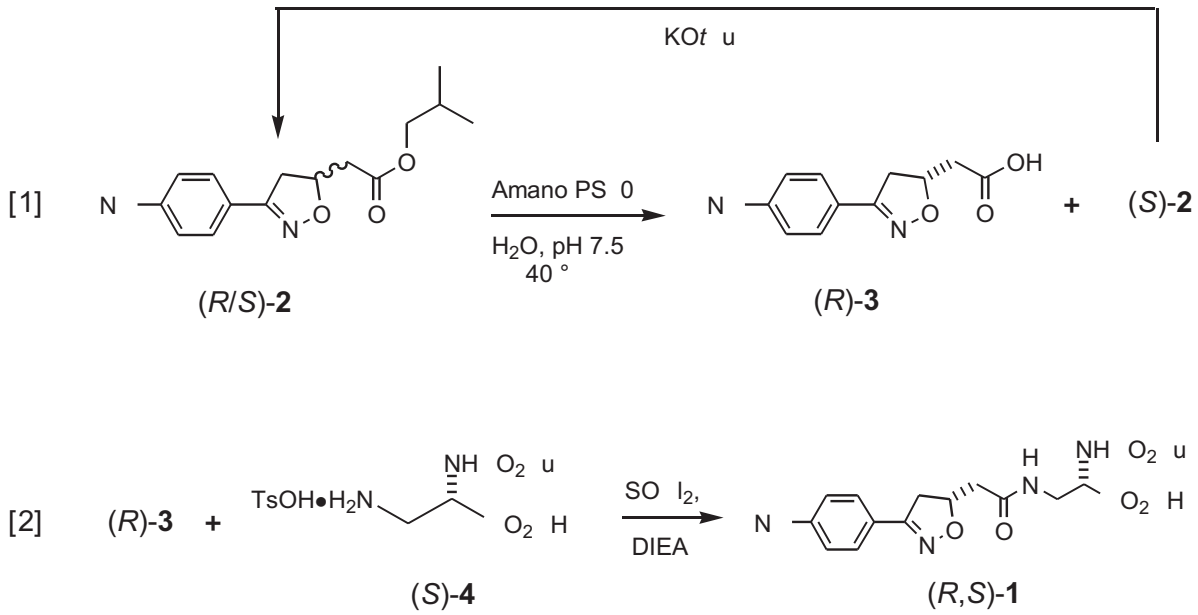

Scheme 3.

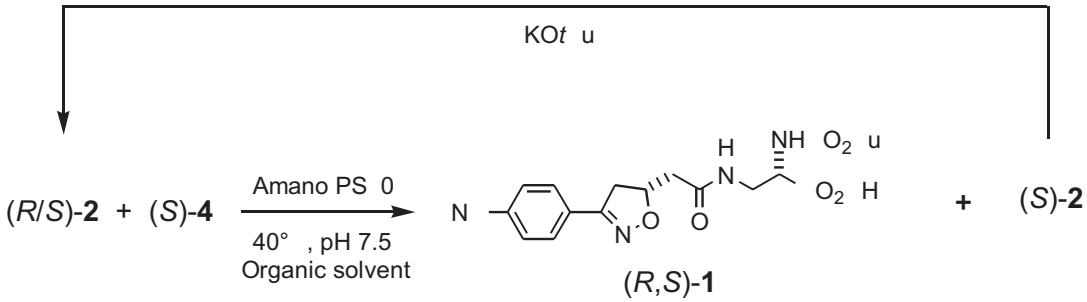

individual components of the reaction mixture, or from the reaction mixture itself, were unsuccessful. *Pseudomonas fluorescens* lipase (Fluka or Amano AK) gave no significant conversion of (*R*/*S*)-**2** to (*R*,*S*)-**1** under these same reaction conditions.

The PS30 or CAL B lipase-catalyzed aminolysis of racemic (*R*/*S*)-**2** by (*S*)-**4** to directly produce (*R*,*S*)-**1** has several advantages when compared to the two-step, resolution and aminolysis method. The reaction proceeds with significant enantioselectivity, reduces the number of process steps, eliminates several costly reagents, generates less waste, and permits facile product recovery. The heterogeneous product mixture can be diluted with additional solvent, which will dissolve (*R*,*S*)-**1** and unreacted (*R*)-**2** and (*S*)-**2**, and leave unreacted (*S*)-**4** (as the *p*-toluenesulfonate salt), molecular sieves, and the enzyme as filterable solids. The product (*R*,*S*)-**1** can then be isolated by column chromatography, selective precipitation, or fractional crystallization. Unreacted (*R*)-**2** and (*S*)-**2** can be recovered and racemized (13*b*) and this racemate recycled in a second enzymatic aminolysis reaction, thereby increasing the overall yield of (*R*,*S*)-**1** produced, and decreasing the amount of waste. (*R*,*S*)-**1** was produced in 78– 86% de, which corresponds to a yield of the desired diastereomer of 89–93%, respectively, (based on total (*R*,*S*)-**1** and (*S*,*S*)-**1** produced); the subsequent separation of these two diastereomers is readily performed by recrystallization, and produces the desired diastereomer in very high purity. Further improvement in de might be obtained by examining the dependence of enantioselectivity on the choice of alkyl ester substituent of (*R*/*S*)-**2**.

Experimental section

Starting materials ((*R*/*S*)-**2** and (*S*)-**4**) and products ((*R*,*S*)-**1**, (*S*,*S*)-**1**, (*S*)-**2**, (*R*)-**3**, and (*S*)-**3**) for the enzymatic aminolysis reactions were prepared and characterized according to published procedures (13*b*), or obtained from commercial sources. Enzymes were obtained from Amano, Sigma, Fluka, or Roche Molecular Biochemicals, and were used as received without further purification. Relative specific activities of commercial enzyme preparations were determined by measuring the rate of hydrolysis of *p*-nitrophenyl acetate (PNPA) (20).

HPLC analysis of reaction components

Analysis of mixtures of (*R*/*S*)-**2**, (*R*,*S*)-**1**, and (*S*,*S*)-**1**, and (*R*)-**3** and (*S*)-**3** (without separation of enantiomers or diastereomers) were performed by HPLC using UV detection at 260 nm on an Eclipse XDB-C8 column (4.6 ×

© 2002 NRC Canada

Table 1. Enantioselective amination of (*R*/*S*)-**2** by (*S*)-**4** using *P. cepacia* lipase in different organic solvents.

Solvent	Time (h)	(*R*/*S*)-**2** Conversion (%)	(*R*,*S*)-**1**, (*S*,*S*)-**1** Selectivity (%)[a]	(*R*,*S*)-**1**:(*S*,*S*)-**1**	de (*R*,*S*)-**1** (%)
DIPE[b]	24	23	95	93:7	86
MTBE[c]	24	24	95	91:9	82
Heptane[b]	72	24	90	86:14	72
Toluene[b]	72	4	—	—	—
Acetonitrile[b]	72	3	—	—	—

[a]Selectivity = 100([(*R*,*S*)-**1** + (*S*,*S*)-**1**]/[(*R*,*S*)-**1** + (*S*,*S*)-**1** + (*R*)-**3** + (*S*)-**3**]).
[b]Reaction conditions: 40°C, 3 Å sieves (20 mg mL^{-1}), 30 mg lyophilized PS30 mL^{-1}.
[c]Reaction conditions: 24°C, 3 Å sieves (25 mg mL^{-1}), 30 mg lyophilized PS30 mL^{-1}.

Table 2. Enantioselective amination of (*R*/*S*)-**2** by (*S*)-**4** in MTBE using *C. antartica* lipase A or B (CAL A or CAL B).

Enzyme	(*R*/*S*)-**2** Conversion (%)	(*R*,*S*)-**1**, (*S*,*S*)-**1** Selectivity (%)	(*R*,*S*)-**1**:(*S*,*S*)-**1**	de (*R*,*S*)-**1** (%)	de (*S*,*S*)-**1** (%)
CAL A	35	86	12:88	—	76
CAL B	31	81	96:4	92	—

Note: Reaction conditions: 24 h, 24°C, 3 Å sieves (20 mg mL^{-1}), 30 mg lyophilized CAL A or CAL B mL^{-1}.

Fig. 1. Selectivity and de for the conversion of (*R*/*S*)-**2** to (*R*,*S*)-**1** using *P. cepacia* lipase (PS30) in DIPE or MTBE: selectivity (DIPE (■), MTBE (●)); de (DIPE (□), MTBE (○)). Reaction conditions: (*a*) DIPE, 40°C, 3 Å sieves (20 mg mL^{-1}), 30 mg lyophilized PS30 mL^{-1}; (*b*) MTBE, 40°C, 3 Å sieves (20–25 mg mL^{-1}), 60 mg lyophilized PS30 mL^{-1}.

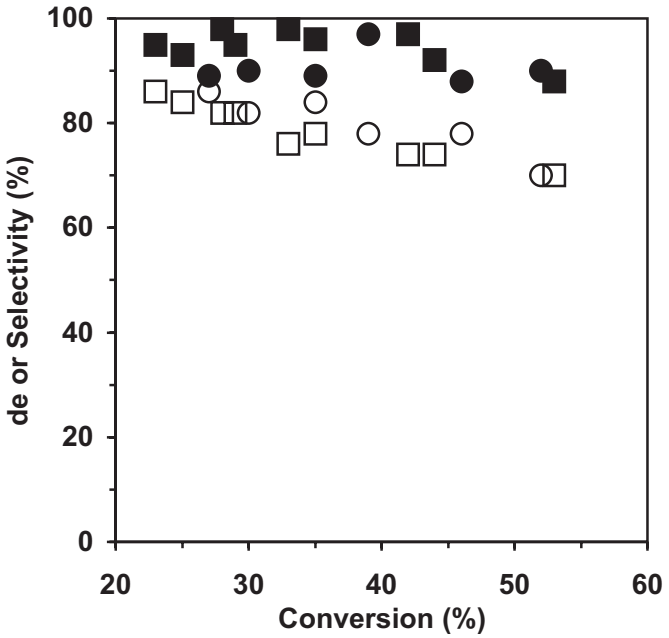

250 mm) at 40°C and a flow rate of 1.0 mL min^{-1}, using a gradient of two eluents: mobile phase A (0.1% trifluoroacetic acid – 0.1% triethylamine in distilled deionized water), mobile phase B (0.1% trifluoroacetic acid in THF (unstabilized)). The mobile phase gradient employed was: t = 0 min, 85% A, 15% B; t = 10 min, 85% A, 15% B; t = 32 min, 50% A, 50% B; t = 40 min, 50% A, 50% B; t = 42 min, 85% A, 15% B; t = 52 min, 85% A, 15% B.

Chiral HPLC analysis of (*R*)-**2** and (*S*)-**2**, and (*R*)-**3** and (*S*)-**3**, was performed using UV detection at 280 nm on a Daicel Chiralcel OJ column (4.6 × 250 mm) at 38°C and a flow rate of 0.90 mL min^{-1} of 0.25% trifluoroacetic acid in 81% hexane – 19% ethanol.

Chiral HPLC analysis of (*R*,*S*)-**1** and (*S*,*S*)-**1** was performed using UV detection at 280 nm on two Daicel Chiralcel OJ columns (4.6 × 250 mm) in series at 40°C and a flow rate of 0.75 mL min^{-1} of 80% heptane – 20% ethanol. The production of (*R*,*S*)-**1** and (*S*,*S*)-**1** as aminolysis reaction products was confirmed by preparing authentic samples of (*R*,*S*)-**1**, (*S*,*S*)-**1**, (*S*,*R*)-**1**, and (*R*,*R*)-**1**, separating all four diastereomers by chiral HPLC, and comparing product retention times with the authentic standards.

Lipase-catalyzed aminolysis of racemic isobutyl 2-[3-(4-cyanophenyl)-4,5-dihydro-5-isoxazolyl]acetate ((*R*/*S*)-2) by 3-amino-*N*-(butoxycarbonyl)-L-alanine methyl ester, mono(4-methylbenzenesulfonate) ((*S*)-4)

In a typical procedure, a series of 4 mL glass vials were charged with 30–60 mg of lipase and 1.0 mL of 100 mM NaH_2PO_4 (pH 8.0, adjusted with 50% aq NaOH), and the resulting solution was frozen and lyophilized. To each vial was then added 15 mg of (*S*)-**4** (38.3 mM), 15.0 mg of (*R*,*S*)-**2** (52.3 mM), 10–35 mg of powdered, activated 3 Å molecular sieves, 1.0 mL of diisopropyl ether (dried over activated 3 Å molecular sieves), and a magnetic stir bar. The vials were capped and the reaction mixtures stirred at 24–40°C for 18–48 h.

After the desired reaction time, the individual reactions were prepared for analysis by cooling the product mixtures to 24°C and then evaporating the solvent by flowing a

© 2002 NRC Canada

stream of dry nitrogen over the product mixture. The resulting solid was mixed with: (*i*) 18.0 mL of a 1:1 (v/v) mixture of tetrahydrofuran and 0.1% (v/v) acetic acid in distilled, deionized water (adjusted to pH 2.0 with 6.0 N HCl); (*ii*) 2.0 mL of 30 mM *p*-toluamide (HPLC external standard) in a 1:1 (v/v) mixture of tetrahydrofuran and 0.1% (v/v) acetic acid in distilled, deionized water (adjusted to pH 2.0 with 6.0 N HCl); and (*iii*) 0.108 mL of 6.0 N HCl. A 1 mL sample of the resulting mixture (mixture A) was centrifuged to remove undissolved solids, and the supernatant analyzed for (*R*/*S*)-**2**, (*R*,*S*)-**1**, and (*R*/*S*)-**3** by HPLC.

A second 2.0 mL sample of mixture A was evaporated to dryness under vacuum, then 1 mL of ethanol was added to the resulting solid and the suspension heated at 50°C for 1.0 min. The resulting suspension was filtered (0.45 μm) and analyzed by chiral HPLC for (*R*)-**2** and (*S*)-**2**, (*R*,*S*)-**1** and (*S*,*S*)-**1**, and (*R*)-**3** and (*S*)-**3**.

Acknowledgment

The authors thank Michael B. D'Amore for helpful discussions regarding lipase-catalyzed reactions.

References

1. (*a*) P. Lopez-Serrano, M.A. Wegman, F. van Rantwijk, and R.A. Sheldon. Tetrahedron: Asymmetry, **12**, 235 (2001); (*b*) M.A. Wegman, M.A.P.J. Hacking, J. Rops, P. Pereira, F. Van Rantwijk, and R.A. Sheldon. Tetrahedron: Asymmetry, **10**, 1739 (1999); (*c*) M.A.P.J. Hacking, M.A. Wegman, J. Rops, F. van Rantwijk, and R.A. Sheldon. J. Mol. Catal. B: Enzym. **5**, 155 (1998).
2. E. Garcia-Urdiales, F. Rebolledo, and V. Gotor. Tetrahedron: Asymmetry, **10**, 721 (1999).
3. (*a*) Y. Kato, Y. Asano, A. Nakazawa, and K. Kondo. Tetrahedron, **45**, 5743 (1989); (*b*) Y. Asano, A. Nakazawa, Y. Kato, and K. Kondo. J. Biol. Chem. **264**, 14 233 (1989).
4. T. Nakatsuka, T. Sasaki, and E.T. Kaiser. J. Am. Chem. Soc. **109**, 3808 (1987).
5. Y.V. Mitin, N.P. Zapevalova, and E.Y. Gorbunova. Int. J. Pept. Protein Res. **23**, 528 (1984).
6. V. Gotor. Bioorg. Med. Chem. **7**, 2189 (1999).
7. C. Vörde, H.E. Högsberg, and E. Hedenström. Tetrahedron: Asymmetry, **7**, 1507 (1996).
8. C.D. Reeve. PCT Int. Appl. WO 9931264 A1 (1999).
9. M.S. de Castro and J.V.S. Gago. Tetrahedron, **54**, 2877 (1998).
10. M.J. Garcia, F. Rebolledo, and V. Gotor. Tetrahedron: Asymmetry, **4**, 2199 (1993).
11. M. Quiros, V.M. Sanchez, R. Brieva, F. Rebolledo, and V. Gotor. Tetrahedron: Asymmetry, **4**, 1105 (1993).
12. S. Puertas, F. Rebolledo, and V. Gotor. J. Org Chem. **61**, 6024 (1996).
13. (*a*) L.-H. Zhang, L. Anzalone, P. Ma, G.S. Kauffman, L. Storace, and R. Ward. Tetrahedron Lett. **37**, 4455 (1996); (*b*) L.-H. Zhang, J.C. Chung, T.D. Costello, I. Valvis, P. Ma, G.S. Kauffman, and R. Ward. J. Org. Chem. **62**, 2466 (1997).
14. (*a*) J. Wityak, T.M. Sielecki, D.J. Pinto, G. Emmett, J.Y. Sze, J. Liu, E. Tobin, S. Wang, B. Jiang, P. Ma, S.A. Mousa, R.A. Wexler, and R.E. Olson. J. Med. Chem. **40**, 50 (1997); (*b*) C.B. Xue and S.A. Mousa. Drugs Future, **23**, 707 (1998); (*c*) C.B. Xue, J. Wityak, T.M. Sielecki, D.J. Pinto, D.G. Batt, G.A. Cain, M. Sworin, A.L. Rockwell, J.J. Rodercik, S. Wang, M.J. Orwat, W.E. Frietze, L.L. Bostrom, J. Liu, C.A. Higley, F.W. Rankin, A.E. Tobin, G. Emmett, G.K. Lalka, J.Y. Sze, S.V. Di Meo, S.A. Mousa, M.J. Thoolen, A.L. Racanelli, E.A. Hausner, T.M. Reilly, W.F. DeGrado, R.R. Wexler, and R.E. Olson. J. Med. Chem. **40**, 2064 (1997).
15. S.A. Patkar, F. Bjoerking, M. Zundel, M. Schulein, A. Svendsen, H.P. Heldt-Hansen, and E. Gormsen. Indian J. Chem. Sect. B: Org. Chem. Incl. Med. Chem. **32B**, 76 (1993).
16. M. Adamczyk and J. Grote. Bioorg. Med. Chem. Lett. **9**, 245 (1999).
17. (*a*) W. Lu and C.J. Sih. Tetrahedron Lett. **40**, 4965 (1999); (*b*) S. Conde, P. Lopez-Serrano, M. Fierros, M.I. Biezma, A. Martinez, and M.I. Rodriguez-Franco. Tetrahedron, **53**, 11 745 (1997).
18. A. Wolff, V. von Asperen, A.J.J. Straathof, and J.J. Heijnen. Biotechnol. Prog. **15**, 216 (1999).
19. U. Bornscheuer, O.W. Reif, R. Lausch, R. Freitag, T. Scheper, K.N. Fragiskos, and U. Menge. Biochim. Biophys. Acta, **1201**, 55 (1994).
20. (*a*) J. Anderson, T. Byrne, K.J. Woelfel, J.E. Meany, G.T. Spyridis, and Y. Pocker. J. Chem. Ed. **71**, 715 (1994); (*b*) T. Furutani, R. Su, H. Ooshima, and J. Kato. Enzyme Microb. Technol. **17**, 1067 (1995); (*c*) J. Zhou, R.J. Ain, C.M. Riley, and R.L. Schowen. Anal. Biochem. **231**, 265 (1995).

© 2002 NRC Canada

Baeyer-Villiger oxidations catalyzed by engineered microorganisms: Enantioselective synthesis of δ-valerolactones with functionalized chains

Shaozhao Wang, Gang Chen, Margaret M. Kayser, Hiroaki Iwaki, Peter C.K. Lau, and Yoshie Hasegawa

Abstract: Cyclohexanone monooxygenase (CHMO) from *Acinetobacter* sp NCIMB 9871 expressed in baker's yeast and in *E. coli* and cyclopentanone monooxygenase (CPMO) from *Comamonas* (previously *Pseudomonas*) sp. NCIMB 9872 expressed in *E. coli* are new bioreagents for Baeyer-Villiger oxidations. These engineered microorganisms, requiring neither biochemical expertise nor equipment beyond that found in chemical laboratories, were evaluated as reagents for Baeyer-Villiger oxidations of cyclopentanones substituted at the 2-position with polar and nonpolar chains suitable for further modifications. Two such functionalized substrates that can be transformed into highly enantiopure lactones were identified. The performance and the potential of these bioreagents are discussed.

Key words: enantioselective Baeyer-Villiger oxidations, biotransformations, cyclohexanone monooxygenase, cyclopentanone monooxygenase, engineered baker's yeast, recombinant *E. coli*, optically pure 2-substituted cyclopentanones, optically pure lactones.

Résumé : La monooxygénase de la cyclohexanone (« CHMO ») obtenue à partir d'*Acinetobacter* sp NCIMB 9871 extraite de la levure pâtissière et d'*E. coli* et la monooxygénase de la cyclopentanone (« CPMO ») de *Comamonas* (antérieurement *Pseudomonas*) sp. NCIMB 9872 extraite d'*E. coli* sont les nouveaux bioréactifs pour les oxydations de Baeyer-Villiger. Ces microorganismes, qui ne nécessitent ni expertise biochimique ni équipement supplémentaire par rapport à ce que l'on retrouve dans les laboratoires chimiques, ont été évalués comme réactifs pour des oxydations de Baeyer-Villiger de cyclopentanones substituées en position 2 par des chaînes polaires ainsi que non polaires susceptibles d'être modifiées ultérieurement. On a identifié deux de ces substrats fonctionnalisés qui peuvent être éventuellement transformés en lactones de grande pureté énantiomérique. On discute de la performance et du potentiel de ces bioréactifs.

Mots clés : oxydations de Baeyer-Villiger, biotransformations, monooxygénase de la cyclohexanone, monooxygénase de la cyclopentanone, levure pâtissière, *E. coli* recombinant, cyclopentanone substituée en position 2 optiquement pure, lactones optiquement pures.

[Traduit par la Rédaction]

Introduction

The transformation of cyclic ketones to lactones is most frequently performed using peroxyacids. The lactones are important intermediates in organic synthesis, and hence the reaction has been studied and extensively employed for over a hundred years since its discovery in 1899 by Baeyer and Villiger (1). Many developments and changes to the reaction occurred over the years (2), and the accepted two-step mechanism is familiar to chemists (2, 3). In general, this is a successful reaction and problems only arise when scaling-up is required because peracid oxidants are toxic and intrinsically unstable. For this reason, new oxidizing agents continue to be investigated and several have been introduced over the years (4). The growing interest in the preparation of optically pure compounds has stimulated interest in creating enantioselective Baeyer-Villiger oxidations, and a number of transition-metal-based oxidants have been described (5). The yields and enantiomeric excesses (ee) of the lactone products varied, but were typically in the order of 30–70% ee. "Biological" Baeyer-Villiger oxidants, recognized for their use for several decades, perform these oxidations on a broad variety of compounds, frequently with good yields and with superior enantioselectivity (6). Although many microorganisms produce enzymes that perform Baeyer-Villiger reactions, two bacterial species *Acinetobacter* sp. and *Pseudomona*, have received the most attention in recent years. These

Received 20 November 2001. Published on the NRC Research Press Web site at http://canjchem.nrc.ca on 17 May 2002.

We would like to dedicate this paper to J. Bryan Jones whose vision inspired us all.

S. Wang, G. Chen,[1] and M.M. Kayser.[2] Department of Physical Sciences, University of New Brunswick, Saint John, NB E2L 4L5, Canada.
H. Iwaki, and P.C.K. Lau. Biotechnology Research Institute, N.R.C., Montreal, QC H4P 2R2, Canada.
Y. Hasegawa. Department of Biotechnology, Kansai University,Yamate-cho, Suita, Osaka 564–8680, Japan.

[1]Parts of this work stem from Gang Chen's Ph.D. thesis. University of New Brunswick. 1999.
[2]Corresponding author (e-mail: kayser@unbsj.ca).

 DOI: 10.1139/V02-035 © 2002 NRC Canada

Scheme 1.

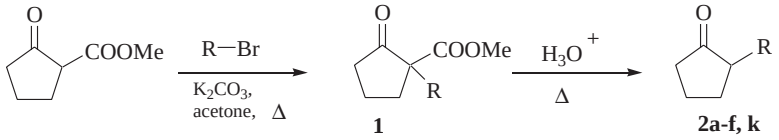

R : a = allyl
b = n-butyl
c = cyclopentyl
d = isobutyl
e = benzyl
f = 3-bromopropyl
g = hydroxymethyl
h = methoxymethyl
i = allyloxymethyl
j = acetoxymethyl
k = ethoxycarbonylmethyl

organisms and (or) the Baeyer-Villiger enzymes (flavin monooxygenases) that they produce are biological reagents of real value in organic synthesis.

Pseudomonas sp. NCIMB 10007, which carries genes inducible by growth on (+)- or (–)-camphor to produce the camphore flavin monooxygenase enzymes, has been investigated in numerous reactions. The crude-enzyme extracts from this organism were separated on the basis of the co-factor requirement to give two fractions: NADH-dependent MO1 and NADPH-dependent MO2. These fractions were used as selective catalysts in reactions with various unnatural substrates (6*b*, *c*, 7, 8). Elective culture grown on cyclohexanol allowed Donoghue and Trudgill (9) to identify *Acinetobacter* sp. NCIMB 9871. Since then, CHMO has been the subject of several mechanistic and biochemical studies (10–12). Extraction of cyclohexanone monooxygenase from this strain (CHMO EC 1.14.13.22) was optimized by Trudgill (13), and both the microorganism and enzyme continued to be extensively investigated (see reviews listed in ref. 6). The high enantioselectivity and broad spectrum of substrate acceptability made the enzyme and the organism the most widely used bioreagents for Baeyer-Villiger oxidations. Since, however, *Acinetobacter* sp. NCIMB 9871 is a class 2 pathogen and the isolated CHMO enzyme is relatively unstable and requires the NADPH co-factor, these biotransformations were not embraced enthusiastically by nonspecialists. The recently constructed recombinant strains of baker's yeast [15C(pKR001)] and *E. coli* [BL21(DE3)(pMM4)] overexpressing CHMO, which can be used to perform enantioselective Baeyer-Villiger oxidations in ordinary shake flasks in any organic laboratory (14, 15), should place these versatile reagents at the disposal of all organic chemists.

Elective culture grown on cyclopentanol yielded *Pseudomonas* sp. NCIMB 9872, now identified as *Comamonas* (16). This organism was able to oxidize cyclopentanol, via cyclopentanone and δ-valerolactone, to glutarate and, presumably, to acetate by an inducible set of enzymes (17). Purified cyclopentanone monooxygenase (CPMO; EC 1.14.13.16) is NADPH-specific (17*b*, *c*). Compared with NCIMB 9871, it has been studied relatively little in Baeyer-Villiger oxidations of unnatural substrates, probably because it was assumed to have stereoselectivity similar to that of cyclohexanone monooxygenase from *Acinetobacter* (6*b*, *c*, 7, 18, 19). We have now cloned and overexpressed the gene for cyclopentanone monooxygenase in the laboratory *E. coli* strain DH5α, [*E. coli* (CPMO)] making it as accessible as *E. coli* (CHMO) for development as another reagent for biological Baeyer-Villiger oxidations (16).

In an earlier paper, we reported several successful Baeyer-Villiger oxidations of 2-alkyl cyclopentanones mediated by the recombinant yeast (CHMO) (20). Our objective in the current project was to evaluate the recombinant CHMO- and CPMO-expressing strains as reagents for Baeyer-Villiger oxidations of 2-substituted cyclopentanones with functional groups on the side chain. Several such substrates were prepared and subjected to biotransformations. The stereochemical results of this work are discussed in this paper.

Results

2-Cyclopentylcyclopentanone (**2c**) was purchased from Aldrich, and compounds **2d**–**f** were prepared in good yields by alkylation and decarboxylation of methyl cyclopentanone-2-carboxylate as shown in Scheme 1. 2-Allylcyclopentanone (**2a**) was prepared by direct alkylation of cyclopentanone. 2-Oxocyclopentyl-1-methanol (**2g**) and 2-alkoxymethylcyclopentanones **2h** and **2i** were synthesized in 3 and 4 steps, respectively, from methyl cyclopentanone-2-carboxylate. In these reactions, the ketone was protected as an ethylene ketal, and the ester group was reduced by $LiAlH_4$ to give hydroxyketal **4**. Subsequent hydrolysis of the ketal with a mild Lewis acid catalyst preserved the hydroxyl group and yielded hydroxyketone **2g**. Alkylation of **4** followed by hydrolysis with a dilute aqueous acid gave alkoxyketones **2h** and **2i** (Scheme 2). The synthesis of ester **2k** paralleled that for simple alkyl side chains. Coupling of ethyl cyclopentanone-2-carboxylate with bromoacetate, followed by acidic hydrolysis and decarboxylation, afforded the desired product **2k** (Scheme 1).

Whole-cell mediated oxidations were carried out in shake flasks as previously described (15*a*, 21). In most cases, one equivalent of β-cyclodextrin (relative to the ketone) was included in the reaction medium to diminish any of the toxic effects of the substrates. The reactions were monitored by chiral GC, and the concentrations of the ketone and the lactone were measured against an internal standard (methyl benzoate). Only the results that were consistent in terms of conversion, enantioselectivity, time, and isolated yields over the course of several fermentations are listed in Tables 1*a* and 1*b*. Controlled chemical-oxidation experiments were performed for all substrates, and it was possible to achieve baseline resolution for the majority of ketones and (or) lactones. The absolute configuration of ketones **2a** and **2b** were deduced by comparison with literature values as described in our earlier paper (20). The absolute configurations for **2c**–**f** were tentatively assigned by analogy with prior results (22)

© 2002 NRC Canada

Scheme 2.

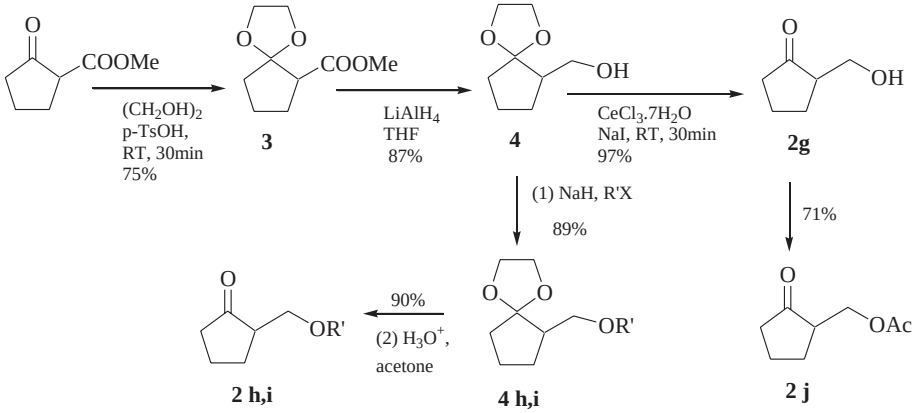

and with the demonstrated selectivity of the CHMO for (*S*)-cyclohexanones and cyclopentanones substituted with *n*-alkyl chains (6, 23). It should be noted that because of changes in numbering priority the *R*/*S* nomenclature is reversed for compounds **2a** and **2c**–**k**.

A majority of the reactions reported in Tables 1*a* and 1*b* were performed with the recombinant *E. coli* (CHMO); however, the same reactions that were re-investigated with the yeast (CHMO) gave virtually identical results, apart from small variations in the isolated yields. Compound **2d** appeared to be toxic to *E. coli* even in the presence of cyclodextrin and the successful transformation could only be achieved with the yeast (CHMO) strain. As can be seen in Table 1*a*, branching and increased bulk of the 2-substituents (**2c**–**e**) resulted in diminished selectivity of the CHMO oxidations. Parallel *E. coli* (CPMO) catalyzed reactions were generally faster and the lactones were isolated in excellent yields; however, the enantioselectivity of the transformation was consistently lower than that with CHMO. Extending the three-carbon chain by a bromine atom in compound **2f** restored CHMO's selectivity and the racemic ketone was kinetically resolved to give the lactone **5f** ($[\alpha]_D^{25}$ –63 (*c* 0.4, EtOAc), 95% ee) and the unreacted ketone **2f** ($[\alpha]_D^{25}$ –144 (*c* 1.65, CH_2Cl_2), 92% ee) in excellent isolated yields. The (*S*)-**2f** ketone was subsequently chemically oxidized to the corresponding lactone without loss of optical purity. Thus, readily prepared racemic 2-(3′-bromopropyl)-cyclopentanone (**2f**) introduces the possibility of further modification of the highly enantiopure δ-valerolactones.

The *E. coli* (CPMO) catalyzed oxidations, shown in Table 1*a*, were intentionally interrupted at low conversion levels to estimate the enantioselectivity values (*E*) (24), which turned out to be low, but consistently showed a slight preference for the *same* ketone enantiomer as the CHMO-catalyzed transformations. Uninterrupted *E. coli* (CPMO) mediated reactions rapidly produced racemic lactones in excellent yields. All starting materials were generally consumed, and neither by-products nor metabolites were evident in the GC traces of the crude-reaction mixtures. Only in the case of ketone **2f** did the CPMO-mediated transformation show significant enantioselectivity.

The 2-cyclopentanones substituted with polar oxygen-containing groups on the side chain were acceptable substrates for both CHMO and CPMO (Table 1*b*). Ketone **2g**, with an unprotected hydroxy group on the side chain, reacted very slowly with yeast (CHMO) to give (*R*)-**5g** (34% ee, $[\alpha]_D^{25}$ –11 (*c* 4.5, EtOAc)). The absolute configuration for this compound was confirmed by comparison with the previously reported rotation (25). The difficulty in transporting the more polar substrates across cell membranes could be partially responsible for the sluggishness of this transformation. When the hydroxy group in **2g** was masked in the form of its ether derivatives **2h** and **2i,** the oxidations were faster, which supports the transport-through-membranes hypothesis. Furthermore, the enantioselectivity of the latter transformations was improved, particularly in the case of ketone **2i** bearing a long allyloxy chain. In this case, the lactone product (*R*)-**5i** was obtained in 93% ee. When the allyl group in lactone **5i** was removed (Pd/C in *p*-toluenesulfonic acid–H_2O), the product **5g** was shown to have the same configuration (*R*) as the major lactone enantiomer obtained from the oxidation of ketone **2g** by yeast (CHMO) or *E. coli* (CPMO). Again, the two enzymes showed a preference for the *same* enantiomer, and again, the CHMO enzyme proved to be the more selective of the two. Ketone **2j** was transformed by *E. coli* (CPMO) to the known lactone (*R*)-**5j** (26). At 41% conversion and 53% ee the reaction was stopped, the lactone product was isolated, and the optical rotation was determined ($[\alpha]_D^{25}$ –15 (*c* 2.5, EtOAc)). In a parallel reaction catalyzed by *E. coli* (CHMO), the **2j** substrate was also consumed and at 49% conversion an unidentified optically active product was formed in 74% ee. Lactone **5j** from the CPMO oxidation was subsequently chemically hydrolyzed ($NaHCO_3$, MeOH, pH 11) to (*R*)-**5g** without a change in optical purity. Ketone **2k** was rapidly oxidized by *E. coli* (CPMO), but the *E*-value was only 8. At 52% conversion, the product mixture consisted of lactone **5k** (61% ee, $[\alpha]_D^{25}$ –10 (*c* 1.2, EtOAc)) and residual ketone **2k** (66% ee, $[\alpha]_D^{25}$ –12.5 (*c* 0.8, EtOAc)). The transformation with *E. coli* (CHMO) was very slow and apparently nonselective and, since large quantities of by-products and metabolites were formed in the early stages of the reaction, we did not pursue this transformation any further.

Discussion

Cyclopentanones substituted at the 2-position with alkyl chains of five carbons or longer are substrates to several Baeyer-Villiger monooxygenases. *Acinetobacter* species NCIB 9871 and TD 63 (23), *Pseudomonas* sp. NCIMB

© 2002 NRC Canada

Table 1a. Biological Baeyer-Villiger oxidations of 2-substituted cyclopentanones.

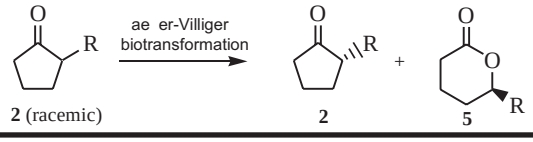

2 (racemic) **2** **5**

		Organism	Time (hours)	Conv. %[a]	Ketone **2** yield %[b] (ee %)[c]	Lactone **5** yield %[b] (ee %)[c]	E[d]
2a	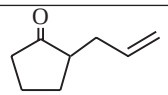	*E. coli* / **CHMO**	8	27	10 (51 *S*)	54 (34 *R*)	2.3
		E. coli / **CPMO**	3	95	5[a] (- -)	95[a] (- -)	0
2b	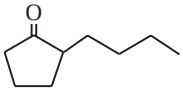	*E. coli* / **CHMO**	12	50	32 (98 *R*)	18 (95 *S*)	200
		E. coli / **CPMO**	2.5	11	89[a] (2 *R*)	11[a] (19 *S*)	1.5
2c	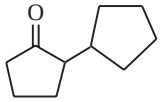	*E. coli* / **CHMO**	33	37	28 (--)[e]	20 (9)	1.3
		E. coli / **CPMO**	24	46	54[a] (--)[e]	46[a] (16)	1.6
2d	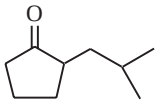	*Yeast* / **CHMO**	19	35	18 (--)[e]	23 (83)	16
		E. coli / **CPMO**	--	ND			
2e	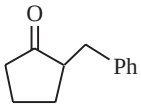	*E. coli* / **CHMO**	16	34	56 (58)	28 (--)[e]	7.3
		E. coli / **CPMO**	16	85	15[a] (26)	85[a] (--)[e]	1.3
2f	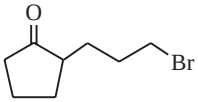	*Yeast* / **CHMO**	24	49	47 (92)	47 (95)	128
		E. coli / **CPMO**	36	36	64[a] (34)	36[a] (61)	5.7

[a] Conversion from G.C.; [b] Isolated yield of chromatographically purified product; [c] Determined from chiral G.C.(Supelco β-Dex 225 column); [d] Calculated according to Ref.(24); [e] Not resolved on chiral GC; **Note** that because of change in numbering priority the R/S nomenclature for ketones and and lactones **a**, c-f is reversed *vis a vis* that of **2b** and **5b**; also absolute configurations indicated are only tentatively assigned for compounds c-f (see text).

10007, and enzyme fractions MO1 and MO2 from that organism were used in oxidations of these compounds. The highest enantioselectivities were reported in reactions catalyzed by the MO2 fraction (7). *Acinetobacter*-catalyzed reactions were found to be highly enantioselective in several of the compounds studied, but the yields were low because the lactonic products were further metabolized by a hydrolase present in the organism. The problem was minimized by adding tetraethyl pyrophosphate to the reaction medium to inhibit the hydrolytic enzyme, and the reactions were re-investigated using *Acinetobacter* TD 63, a related species, which does not produce lactone hydrolase (23). Using our nonpathogenic yeast (CHMO) strain, we were able to achieve excellent kinetic resolution of the 2-alkylcyclopentanones, provided that the chains were at least four-carbon atoms long (20). It was previously observed that cyclohexanone monooxygenase exhibits virtually complete enantioselectivity for the (*S*)-enantiomer of 2-alkyl cyclohexanones, with the exception of 2-methyl cyclohexanone (10, 23, 27). With cyclopentanones, however, the chains must be longer to obtain comparable enantioselectivities. Cyclopentanones and cyclohexanones with functionalized chains have not been evaluated as substrates for either *Acinetobacter* sp. or the isolated cyclohexanone monooxygenase enzyme, but they were used as substrates in oxidations with the MO2 fraction from the species NCIMB 10007 (7, 19) and NCIMB 9872 (7, 18, 19). These compounds were of particular interest to us, since the oxidations with our easy-to-use bioreagents could provide convenient routes to optically pure lactones, ready for further modification through classical chemical reactions.

Our earlier experiments (20) with the yeast (CHMO) have shown that, although 2-*n*-butylcyclopentanone was fully kinetically resolved over the course of the Baeyer-Villiger oxidation, the 2-allylcyclopentanone was not, giving at best the (*R*)-lactone with 51% ee. To investigate the effect of branching and of polar substituents on the selectivity of CHMO and CPMO, we evaluated several potential substrates

© 2002 NRC Canada

Table 1b. Biological Baeyer-Villiger oxidations of 2-substituted cyclopentanones.

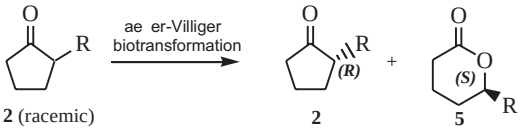

2 (racemic) **2** **5**

		Organism	Time (hours)	Conv. %[a]	Ketone **2** yield %[b] (ee %)[c]	Lactone **5** yield %[b] (ee %)[c]	E[d]
2g	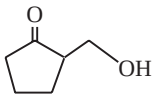	*Yeast* / **CHMO**	96	24	20 (11 *S*)	10 (34 *R*)	2.3
		E. coli / **CPMO**	4	5	95[a] (12 *S*)	5[a] (43 *R*)	2.8
2h	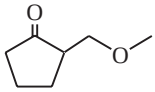	*E. coli* / **CHMO**	36	14	66 (--)[e]	14 (44)	2.8
		E. coli / **CPMO**	6	78	22[a] (--)[e]	78[a] (56)	3.7
2i	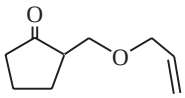	*E. coli* / **CHMO**	36	45	19 (-- *S*)[e]	33 (93 *R*)	69
		E. coli / **CPMO**	19	30	70[a] (-- *S*)[e]	30[a] (81 *R*)	13
2j	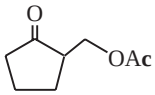	*E. coli* / **CHMO**	--	--	--	--	--
		E. coli / **CPMO**	5	41	59[a] (-- *S*)[e]	41[a] (53 *R*)	4.6
2k	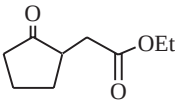	*E. coli* / **CHMO**	--	--	--	--	--
		E. coli / **CPMO**	10	52	48[a] (66)	52[a] (61)	8
					Ketone **6a,b** yield %[b] (ee %)	Lactone **7a,b** yield %[b] (ee %)	
6	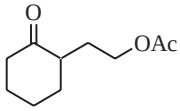	*purified* **MO2**[f]	3.5	--	13 (75 *S*)	34 (83 *R*)	17
		purified **CPMO**[g]	0.5	61	37 (68 *R*)	59 (42 *S*)	5

[a] Conversion from G.C.; [b] Isolated yield of chromatographically purified product; [c] Determined from chiral G.C.(Supelco β-Dex 225 column); [d] Calculated according to Ref.(24); [e] Not resolved on GC; [f] Ref. 23; [g] Ref. 7, 19. Note that because of change in numbering priority the R/S nomenclature for ketones and lactones **g-k** is reversed *vis a vis* that of compounds **2b** and **5b.**

listed in Table 1. The ability of CHMO to accommodate polar chains was intimated by the fact that both isolated enzyme (28) and our recombinant organisms successfully oxidized cyclohexanones with polar chains in the 3- and 4-positions (29). To the best of our knowledge, however, these compounds have not been tested as substrates for CPMO.

The point that needs to be stressed involves generalizations applied to the enantioselectivity trends of various oxygenases. Although these can be useful when one chooses an enzyme or an organism for a specific transformation, wide speculation, resulting in nonconfirmed assignments of absolute configuration, are unwarranted. We experienced this when comparing oxidations by CHMO and CPMO with those performed by MO2. In an earlier study, Adger et al. (18) showed that monooxygenase MO2 from camphor-grown NCIMB 10007 species converted racemic 2-(2′-acetoxyethyl)cyclohexanone (**6**) to the corresponding *R*-(–)-lactone **7a** (40% conversion, 83% ee), while purified CPMO from cyclopentanol-grown NCIMB 9872 transformed the same substrate to its *S*-(+) antipode **7b** (59% conversion, 42% ee), as shown in Table 1*b*. The rotations were reported and the absolute configurations were unambiguously confirmed after the two lactones were converted to the (*R*)- and (*S*)-lipoic acids. MO2 was also used to oxidize cyclopentanones **2j** and **2k** to lactones **5j** and **5k**, respectively, in better than 98% ee (7). The two lactones were reported as having the *R* configuration. Unfortunately, neither rotations nor references were specified. We were able to unambiguously identify lactone **5j** from the CPMO oxidation as the (*R*) enantiomer (vide supra), but the absolute configuration

© 2002 NRC Canada

of lactone **5k** has not yet been confirmed. Although it was shown (19) that enantioselectivity of CPMO (NCIMB 9872) can be opposite to that of MO2 (Table 1*b*, example 6), it appears that, at least for cyclopentanone **2j**, the enantioselectivities are the same and that both enzymes preferentially oxidize the (*R*) ketone.

In summary, the goals of this project were to determine (*i*) if cyclopentanones with more polar functionalized substituents in the 2-position are substrates for CHMO and CPMO; (*ii*) if highly optically enriched lactone (or lactones) suitable for further chain modifications could be identified; and (*iii*) if the performance of CPMO was adequately different from the CHMO to attempt its development as an alternative bioreagent for biological Baeyer-Villiger reactions. From the results reported here it is clear that while Baeyer-Villiger oxidations of 2-substituted cyclopentanones by CHMO- and CPMO-expressing strains are frequently nonselective, some compounds are oxidized with a very high enantiselectivity; in the present survey three of the candidates investigated (**2b**, **2f**, and **2i**) were found to meet the selectivity criteria. In general, of the two enzymes studied, CHMO was shown to be the more selective. On the other hand, oxidations with CPMO are appealing for another reason: these transformations are fast, clean, and there are no by-products or metabolites. Where enantioselectivity is not a primary concern, the *E. coli* (CPMO) strain (16) can serve as an excellent biological equivalent of organic peracids.

In conclusion, the results presented here indicate that "designer microbes" expressing various Baeyer-Villiger monooxygenases can contribute significantly to "developing synthetic methodology and "green" processes that meet criteria of a sustainable, environmentally conscious development (30)."

Experimental

Optical rotations were measured on a PerkinElmer 241 polarimeter operating at room temperature. IR spectra were recorded from thin films on a Mattson Satellite FT-IR spectrometer. ^{1}H and ^{13}C NMR spectra were recorded on Varian XL-200 or Bruker AMX-400 FT-NMR spectrometers. All spectra were recorded in $CDCl_3$ solutions unless otherwise specified. Chemical shifts are reported in ppm with TMS as internal standard. EI-MS spectra and HRMS were obtained on Kratos MS 50 mass spectrometer. Packed-column gas chromatography was performed on a Shimadzu GC-9A gas chromatograph employing a customer-packed column (1/8" × 1 m, 5% OV-101 on 100/120 Supelcoport, Supelco Inc.). Capillary gas chromatography was performed on a Hewlett Packard 5890 instrument employing a 0.54 μm × 1.00 mm × 15 m DB-1301 column (J&W) or Shimadzu GC-9A using a 0.32 μm × 0.25 mm × 30 m β-Dex 225 column (Supelco). All the GC instruments used flame-ionization detectors and helium as the carrier gas. The injector and detector temperatures were maintained at 225°C and 300°C, respectively. Thin-layer chromatography was performed on precoated silica gel 60 plates (Aldrich). Flash chromatography was performed on silica gel (200–425 mesh, Fisher Scientific or SiliCycle). Tetrahydrofuran was distilled from Na in the presence of benzophenone. Acetone was dried over $CaSO_4$ and distilled from $KMnO_4$. Methylene chloride was dried over anhydrous potassium carbonate, distilled, and stored over 3 Å molecular sieves. All solvents were purified by fractional distillation. Other reagents were obtained from commercial suppliers and used as received.

Protocols for biotransformations

Preparation of yeast cells (pKR001) and the general procedure for yeast-catalyzed Baeyer-Villiger oxidations were previously described (14, 21, 22). Maintenance and biotranformation protocols for the reactions with *E. coli* [BL21(DE3)(pMM4)] are outlined in refs. 15 and 29.

Protocol for *E. coli*-(CPMO) mediated oxidations

The *E. coli* strain DH5α[pCMP201] was streaked from a frozen stock on LB-ampicillin plates and incubated at 37°C until colonies were 1–2 mm in size. One colony was used to inoculate 10 mL of LB-ampicillin medium in a 50-mL Erlenmeyer flask and was shaken at 30°C and 250 rpm overnight. This culture was used at a 1:100 (v/v) ratio to inoculate an LB-ampicillin medium supplemented with 10% glucose in a baffled-Erlenmeyer flask. The culture was incubated at 30°C and 250 rpm until OD_{600} was approximately 1. IPTG (isopropyl thio-β-D-galactoside) stock solution (200 mg per mL in water) was added (0.1 μL per mL of medium) and the flask was shaken for another 30 min. The substrate was then added, and, if solubility was a problem, cyclodextrin was introduced at this stage. The culture was agitated at 30°C at 250 rpm and monitored by GC or TLC. The culture was saturated with NaCl and extracted with ethyl acetate. Combined extracts were washed once with brine and dried with anhydrous Na_2SO_4 or $MgSO_4$. The solvent was removed on a rotary evaporator and the residue was purified by flash chromatography.

Compounds 2d and 2e

Compounds **2d** and **2e** were prepared according to modified literature procedure (31). Anhydrous K_2CO_3 (5.5 g, 40 mmol) and acetone (20 mL) were placed in a three-neck round-bottom flask equipped with reflux condenser. After flushing the system with nitrogen, methyl cyclopentanone-2-carboxylate (20 mmol) and alkyl halide (20 mmol) were added, and the stirred reaction mixture, maintained under nitrogen, was gently heated at reflux for two days until all starting material was consumed or a significant amount of by-product was formed as shown by GC. The mixture was cooled to room temperature and poured into ice water. The aqueous phase was extracted with ethyl acetate (3 × 200 mL) and the combined extracts were washed with brine and dried over anhydrous Na_2SO_4. After removal of the solvent on a rotary evaporator the crude product **1d** (or **1e**) was purified by flash chromatography on silica gel using a mixture of hexane and ethyl acetate as eluent. The resulting 2-alkylketoester (**1d** or **1e**, 10 mmol) was dissolved in a mixture of glacial acetic acid (20 mL) and HCl (6 M, 10 mL) and gently heated at reflux under nitrogen until all starting material was consumed as shown by GC (usually 4–6 h). The reaction mixture was cooled to room temperature, poured into ice water, and extracted with ethyl acetate or petroleum ether (3 or 4 × 150 mL). The combined extracts were washed with water and then with saturated $NaHCO_3$. After drying over anhydrous Na_2SO_4, the solvent was

© 2002 NRC Canada

removed and the crude product **2** was purified by vacuum distillation.

2*-iso-*Butyl cyclopentanone (2d)

bp 120–140°C (18–25 Torr). IR ν_{max} (neat) (cm^{-1}): 2957.5 (s), 2869.1 (m), 1739.4 (s), 1467.1 (m), 1154.0 (m). ^{1}H NMR δ: 2.20 (m, 2H), 2.10 (m, 1H), 2.09–1.90 (m, 3H), 1.72 (m, 1H), 1.58 (m, 1H) 1.42 (m, 1H), 1.08, (m, 1H), 0.86 (d, *J* = 3.2 Hz, 3H), 0.82 (d, *J* = 3.0 Hz, 3H). ^{13}C NMR δ: 221.8, 47.4, 38.9, 37.9, 30.0, 26.1, 23.3, 21.4, 20.7.

2-Benzylcyclopentanone (2e)

Obtained after chromatography (hexane–ethyl acetate 10:1) in 85% yield as pale yellow oil: IR υ_{max} (neat) (cm^{-1}): 3000 (m), 2960 (s), 2870 (m), 1730 (vs), 1600 (w), 1490 (m), 1450 (s), 1400 (m), 1150 (s), 690 (s). ^{1}H NMR δ: 7.27 (m, 2H), 7.17 (m, 3H), 3.15 (dd, *J* = 7 and 3 Hz, 1H), 2.54 (dd, *J* = 7 and 6 Hz, 1H), 2.37 (m, 2H), 2.12 (m, 2H), 1.97 (m, 1H), 1.71 (m, 1H), 1.60 (m, 1H). ^{13}C NMR δ: 220.1, 140.0, 128.8, 128.4, 126.1, 51.0, 38.2, 35.6, 29.1, 20.5.

2-(3′-Bromopropyl)cyclopentanone (2f)

The racemic ketone (32) was purified by flash chromatography on silica gel using 10:1 petroleum ether–acetone as the eluant to give **2f** as colourless oil (2.6 g, 41% yield after two steps). IR ν_{max} (neat) (cm^{-1}): 2960 (m), 2875 (m), 1743 (s), 1374 (w), 1242 (m), 1157 (w). ^{1}H NMR δ: 4.00 (t, *J* = 3 Hz, 2H), 2.23 (m, 2H), 2.03 (m, 1H), 1.80–1.60 (m, 4H), 1.46 (m, 2H), 1.27 (m, 2H). ^{13}C NMR δ: 220.7, 64.1.3, 48.6, 38.0, 29.5, 26.6, 26.0, 20.6. MS *m*/*z* (%): 204/206 (1), 125 (100), 107 (38), 83 (26), 67 (37), 55 (85).

6-Cyclopentyltetrahydropyran-2-one (5c)

Ketone **2c** (100 mg, 0.66 mmol) was oxidized using *E. coli* (CHMO) and was purified by flash chromatography on silica gel (petroleum ether–ethyl acetate, 5:1) to afford **5e** (22 mg, 20%, 9% ee). IR ν_{max} (neat) (cm^{-1}): 2952 (s), 2869 (m), 1731 (s), 1243 (m), 1176 (m). ^{1}H NMR δ: 4.10, (m, 1H), 2.57 (m, 1Ha), 2.45 (m, 1Hb); 2.07 (m, 2H), 1.90 (m, 3H), 1.75–1.50 (m, 4H), 1.42 (m, 2H), 1.28 (m, 2H). ^{13}C NMR δ: 172.3, 84.5, 45.2, 29.7, 28.9, 28.8, 27.1, 25.6, 25.5, 18.7.

6-*iso*-Butyltetrahydropyran-2-one (5d)

Biotransformation of **2d** using *E. coli* (CHMO) followed by flash chromatography (petroleum ether–acetone, 7:1 then 5:1) gave **5d** (23%, 83% ee). IR ν_{max} (neat) (cm^{-1}): 2928 (s), 2855 (m), 1741 (s), 1463 (w), 1246 (m), 1047(m). ^{1}H NMR δ: 4.31 (m, 1H), 2.51 (m, 1H), 2.43 (m, 1H), 1.87 (m, 4H), 1.63 (m, 1H), 1.47 (m, 1H), 1.28 (m, 1H), 0.90 (d, *J* = 1 Hz, 3H), 0.88 (d, *J* = 1 Hz, 3H). ^{13}C NMR δ: 172.0, 78.7, 44.9, 29.4, 28.3, 23.9, 23.0, 22.0, 18.4.

6-Benzyltetrahydropyran-2-one (5e)

Biotransformation of **2e** (100 mg, 0.57 mmol) using *E. coli* (CHMO) followed by flash chromatography (petroleum ether–ethyl acetate, 4:1) gave **5e** pale yellow oil (28%, 61% ee). IR ν_{max} (neat) (cm^{-1}): 3060 (w), 3027 (w), 2951 (m), 2874 (m), 1733 (vs), 1496 (m), 1455 (m), 1238 (s), 1178 (m), 1040 (m), 749 (w), 700 (m). ^{1}H NMR δ: 7.33–7.14 (m, 5H), 4.51 (m, 1H), 3.09–2.88 (d ABquartet, *J* = 27 and 11 Hz, 2H), 2.57 (m, 1H), 2.44 (m, 1H), 1.89 (m, 2H), 1.52 (m, 2H). ^{13}C NMR δ: 171.6, 136.4, 129.5, 128.5, 126.8, 81.0, 42.1, 29.4, 27.0, 18.4.

(*R*)-6-(3′-Bromopropyl)tetrahydropyran-2-one (5f) (33)

Ketone **2f** (100 mg, 0.45 mmol) and γ-cyclodextrin (0.5 g) were added to YP-Gal (100 mL) in a 250-mL baffled-conical flask. The mixture was then shaken at 30°C at 250 rpm for 5–10 min to obtain a uniform dispersion. A 1-mL portion of yeast cells was added to the reaction flask and the culture was shaken at 30°C (250 rpm). The reaction monitored by GC and chiral-GC, and was stopped at 50% conversion. After saturating the mixture with NaCl, the organic layer was extracted with ethyl acetate (3 × 100 mL). The combined organic extracts were dried over anhydrous sodium sulfate and concentrated by rotary evaporation. Separation of chiral lactone and ketone by flash chromatography (hexane–acetone, 3:1) gave lactone **5f** as colorless oil (51 mg, 47% yield, 94% ee) and ketone (*S*)-**2f** also as colorless oil (53 mg, 47% yield, 92% ee). (*R*)-**5f**: $[\alpha]_D^{25}$ –63 (*c* 0.4, EtOAc, 95% ee (GC)). IR ν_{max} (neat): 2956, 1734 (s), 1242, 1944. ^{1}H NMR δ: 4.29 (m, 1H), 4.08 (m, 2H), 2.57 (m, 1H) 2.42 (m, 1H), 1.88–1.71 (dm, 6H), 1.51 (m, 2H). ^{13}C NMR δ: 171.3, 80.0, 64.1, 32.5, 28.0, 25.1, 24.5, 18.7. MS *m*/*z*: 223 ($[M + 1]^+$), 141, 112, 99, 55. HRMS calcd. for $C_8H_{13}BrO_2$: 220.0099 / 222.0078; found: 220.0099 / 222.0079. Unreacted ketone (42 mg, 42%) (*S*)-**2f**: $[\alpha]_D^{25}$ –144 (*c* 1.65, CH_2C1_2, 92% ee (GC)). An analytical sample of (*S*)-**2d** was oxidized with *m*-chloproperbenzoic acid (TFA, CH_2Cl_2) to give (*S*)-**5f** 92% ee (GC).

1,4-Dioxa-spiro[4.4]nonane-6-carboxylic acid methyl ester (3)

Methyl cyclopentanone-2-carboxylate (5.0 mL, 40 mmol) was added to a solution of *p*-toluene sulfonic acid (5.6 g, 40 mmol) in ethylene glycol (20 mL) and stirred at room temperature for 30 min. The mixture was poured into 50 mL 1 M KOH solution saturated with NaCl and extracted with ether (4 × 50 mL). The combined organic extracts were washed with brine and dried over anhydrous Na_2SO_4. The solvent was removed on a rotary evaporator to give **3** as a colourless oil, 4.73 g (75%). IR ν_{max} (neat) (cm^{-1}): 2950 (s), 2890 (m), 1700 (vs), 1480 (m), 1350 (m), 1210 (s), 1040 (m). ^{1}H NMR δ: 4.05–4.00 (m, 1H), 3.97–3.88 (m, 3H), 3.70 (s, 3H), 2.92 (t, *J* = 7.7 Hz, 1H), 2.12 (m, 1H), 1.98–1.79 (m, 4H), 1.67 (m, 1H). ^{13}C NMR δ: 172.8, 118.3, 65.1, 64.5, 52.2, 51.7, 51.6, 36.7, 26.9, 22.0.

1,4-Dioxa-spiro[4.4]non-6-yl-methanol (4)

1,4-Dioxa-spiro[4.4]nonane-6-carboxylic acid methyl ester (**3**, 3.8 g in 10 mL THF, 20 mmol) was added to a vigorously stirred suspension of $LiAlH_4$ (0.8 g, 21 mmol) in THF (60 mL) at 0°C. The mixture was stirred for 1.5 h and allowed to warm up to room temperature. The reaction was quenched by pouring it into an ice cold saturated tartaric acid solution and was then extracted with ethyl acetate (5 × 40 mL). The combined organic extracts were dried over anhydrous Na_2SO_4 and the solvent was removed on a rotary evaporator to give **4** as a colourless oil, 2.81 g (87%). IR ν_{max} (neat) (cm^{-1}): 3500 (m, br), 2950 (s), 2890 (s), 2390 (s), 2280 (m), 1460 (m), 1390 (m), 1330 (m), 1160 (s), 1100 (m), 1020 (s). ^{1}H NMR δ: 3.96–3.84 (m, 4H), 3.66–3.54 (m,

© 2002 NRC Canada

2H), 2.64 (br s, 1H), 2.34–2.05 (m, 1H), 1.84–1.76 (m, 1H), 1.74–1.46 (m, 5H). ^{13}C NMR δ: 119.0, 64.5, 64.0, 62.5, 47.0, 35.6, 25.6, 21.3.

2-Hydroxymethylcyclopentanone (2g) (34)

$CeCl_3 \cdot 7H_2O$ (1.86 g, 5 mmol) and KI (0.3 g, 1.8 mmol) were mixed with 18 g silica gel (200–425 mesh) in acetone (30 mL) and ground in a mortar. Compound **4** (0.96 g, 6 mmol) was added and the mixture was stirred at room temperature for 30 min. The silica was filtered off and the solid was washed with acetone. The solvent was removed on a rotary evaporator and the residue was purified by flash chromatography (hexane–ethyl acetate, 3:1) to give **2g** as a colourless oil, 0.67 g (97%). IR ν_{max} (neat) (cm^{-1}): 3427 (s, br), 2966 (s), 2877 (s), 1734 (vs), 1404 (m), 1154 (m), 1054 (m). ^{1}H NMR (acetone-d_6) δ: 3.73–3.64 (m, 3H, including an overlapping OH peak), 2.26–2.12 (m, 3H), 2.10–1.95 (m, 2H), 1.96–1.75 (m, 2H). ^{13}C NMR (acetone-d_6) δ: 219.5, 61.6, 51.7, 39.0, 27.1, 21.4.

6-Hydroxymethyltetrahydropyran-2-one ((*R*)-5g)

Ketone **2g** oxidized using yeast (CHMO) was purified by flash chromatography (petroleum ether–acetone, 2:1) to give colorless oil (16 mg, 14%, 34% ee). $[\alpha]_D^{25}$ –11 (*c* 4.5, EtOAc. Lit. (25) (*R*)-enantiomer: $[\alpha]_D^{25}$ –32 (*c* 1.3, $CHC1_3$)). IR ν_{max} (neat) (cm^{-1}): 3394 (m, br), 2947 (m), 2881 (w), 1723 (vs), 1249 (s), 1058 (s). ^{1}H NMR δ: 4.42–4.35 (m, 1H), 3.76 (dd, *J* = 12.1 and 3.2 Hz, 1H), 3.66 (dd, *J* = 12.3 and 5.5 Hz, 1H), 2.64–2.54 (m, 1H), 2.48–2.39 (m, 1H), 2.00–1.90 (m, 1H), 1.90–1.81 (m, 2H), 1.81–1.64 (m, 2H). ^{13}C NMR δ: 171.4, 81.0, 64.9, 29.6, 23.6, 18.3.

6-Methoxymethyl-1,4-dioxa-spiro[4.4]nonane (4h)

NaH (2 g, 50% dispersion in mineral oil, excess) was added to a 100-mL two-neck round-bottom flask and the system was flushed with nitrogen. NaH was washed 3 times with THF, and then was finally suspended in THF (10 mL). MeI (2 mL, excess) was added, followed by 1,4-dioxa-spiro[4.4]non-6-yl-methanol **4** (1.58 g in 40 mL THF, 10 mmol) with vigorous stirring. After reacting overnight, the mixture was poured onto ice cubes and extracted with ethyl acetate (3 × 35 mL). The combined extracts were washed once with 0.2 M KOH, once briefly with 0.5 M HCl, and once with brine. After drying over anhydrous K_2CO_3, the solvent was removed on a rotary evaporator to give the title product as a colourless oil, 1.11 g (89%). IR ν_{max} (film) (cm^{-1}): 2950 (vs), 2870 (vs), 1450 (s), 1380 (s), 1320 (s), 1200 (s), 1100 (vs), 750 (s). The crude product was used in the next step without further characterizations.

2-Methoxymethylcyclopentanone (2h)

6-Methoxymethyl-1,4-dioxa-spiro[4.4]nonane (**4h**, 0.8 g, 4.7 mmol) was dissolved in acetone (10 mL). In a separate flask $PdCl_2$ (30 mg) was dissolved in acetone (1 mL) and acetonitrile (0.5 mL). The two solutions were combined and TFA (1 mL) was added. The mixture was stirred at room temperature for 3 h, poured into brine, and extracted with ethyl acetate (3 × 35 mL). The combined extracts were dried over anhydrous Na_2SO_4 and the solvent was removed on a rotary evaporator. The residue was purified by flash chromatography (hexane–ethyl acetate, 10:1) to give **2h** as a colourless oil, 0.56 g (94%). IR ν_{max} (neat) (cm^{-1}): 2970 (s), 2920 (s), 2870 (s), 1730 (s), 1150 (m), 1120 (m). ^{1}H NMR δ: 3.53 (m, 2H), 3.30 (s, 3H), 2.34–1.96 (m, 5H), 1.80 (m, 2H). ^{13}C NMR δ: 219.5, 71.5, 59.0, 49.4, 38.6, 27.1, 20.8.

6-Methoxymethyltetrahydropyran-2-one (5h)

Ketone **2h** was oxidized using *E. coli* (CHMO) to give **5h**, which was purified by flash chromatography (petroleum ether–acetone, 5:1, then petroleum ether–acetone, 3:1) to give a colorless oil (16 mg, 14%, 44% ee). IR ν_{max} (neat) (cm^{-1}): 2940 (m), 2881 (m), 2815 (w), 1736 (vs), 1249 (s), 1071 (s). ^{1}H NMR δ: 4.46–3.90 (m, 1H), 3.55–3.47 (m, 1H), 3.36 (s, 3H), 3.28–3.18 (m, 1H), 2.62–2.53 (m, 1H), 2.43–2.34 (m, 1H), 1.98–1.87 (m, 2H), 1.74–1.62 (m, 2H). ^{13}C NMR δ: 172.6, 79.0, 74.4, 59.4, 29.6, 24.5, 18.3. The unreacted **2h** was also isolated: 7% ee; $[\alpha]_D^{25}$ –17 (*c* 1.3, CH_2Cl_2).

6-Allyloxymethyl-1,4-dioxa-spiro[4.4]nonane (4i)

Compound **4i** was synthesized according to the same protocol as **4h**, except allyl bromide was used instead of methyl iodide. The crude product was used in the following step without purification.

2-Allyloxymethylcyclopentanone (2i)

Crude **4i** dissolved in a mixture of acetone (20 mL) and HCl (5 mL, 2 M) was stirred at room temperature for 2 h. Acetone was removed by rotary evaporation and the residue was extracted with CH_2Cl_2. Combined extracts were dried over anhydrous Na_2SO_4 and the solvent was removed by rotary evaporation. The crude product was purified by flash chromatography (hexane–ethyl acetate, 6:1) to give **2j** as a colorless oil, 0.35 g (90% from **4i**). IR ν_{max} (neat): 3081 (w), 2967 (s), 2877 (s), 1737 (vs), 1647 (w), 1152 (s), 1088 (s), 926 (s). ^{1}H NMR δ: 5.84–5.73 (m, 1H), 5.20–5.04 (m, 2H), 3.87 (dt, *J* = 5.5 and 1.4 Hz, 2H), 3.57–3.48 (m, 2H), 2.31–2.10 (m, 3H), 2.12–2.00 (m, 1H), 2.00–1.91 (m, 1H), 1.88–1.76 (m, 1H), 1.76–1.65 (m, 1H). ^{13}C NMR δ: 219.3, 134.5, 116.6, 71.9, 68.9, 49.2, 38.5, 27.0, 20.7.

6-Allyloxymethyltetrahydropyran-2-one ((*R*)-5i)

Ketone **2i** oxidized using *E. coli* (CHMO) was purified by flash chromatography (petroleum ether–acetone 5:1 followed by petroleum ether–acetone, 3:1). $[\alpha]_D^{25}$ = –14.1 (*c* 2.2, $CDCl_3$). IR ν_{max} (neat) (cm^{-1}): 3078 (w), 2947 (m), 2876 (m), 1726 (vs), 1453 (m), 1347 (m), 1240 (s), 1062 (s), 932 (m). ^{1}H NMR δ: 5.91–5.80 (m, 1H), 5.25 (dq, *J* = 17.3 and 1.5 Hz, 1H), 5.16 (qd, *J* = 10.4 and 1.2 Hz, 1H), 4.46–4.39 (m, 1H), 4.01 (dd, *J* = 5.5 and 1.5 Hz, 2H), 3.56 (m, 2H), 2.60–2.52 (m, 1H), 2.48–2.39 (m, 1H), 1.98–1.88 (m, 2H), 1.87–1.76 (m, 1H), 1.75–1.63 (m, 1H). ^{13}C NMR δ: 171.2, 134.2, 117.3, 79.1, 72.5, 71.8, 29.6, 24.6, 18.2. MS *m*/*z* (%): 171 ($[M + 1]^+$, 0.2), 114 (48), 99 (58), 71 (100), 55 (28). The isolated chiral ketone **2i**, 19% yield, 81% ee: $[\alpha]_D^{25}$ – 56 (*c* 1.9, $CH_2Cl_{2)}$. Lactone (*R*)-**5i** was hydrogenated (5% Pd/C in methanol–water (2:1) containing 1% *p*-toluene sulfonic acid, 5 h) to give (*R*)-**5g** (60%, 93% ee) (25).

Acknowledgments

Support by the Natural Sciences and Engineering Research Council of Canada (NSERC) is gratefully acknowledged

© 2002 NRC Canada

(M.M.K.). The NMR spectra were recorded at the Atlantic Regional Magnetic Resonance Centre at Dalhousie University, Halifax, Canada, and we would particularly like to express our thanks for the Centre's help. The authors also thank Cerestar Inc. for supplying the cyclodextrin used in this study.

References

1. A. Baeyer and V. Villiger. Chem. Ber. **32**, 3625 (1899).
2. (*a*) G.H. Krow. Org. Reactions, **43**, 251 (1993); (*b*) G.H. Krow. Tetrahedron, **37**, 2697 (1981).
3. R. Criegee. Liebigs Ann. Chem. **560**, 127 (1948).
4. (*a*) M. Suzuki, H. Takeda, and R. Noyori. J. Org. Chem. **47**, 902 (1982); (*b*) M.Hirano, S. Yakabe, A. Satoh, J.H. Clark, and T. Morimoto. Synth. Commun. 4591 (1996); (*c*) T. Yamada and T. Mukaiyama. Bull. Chem. Soc. Jpn. **68**, 17 (1995); (*d*) T. Yamada, K. Takahashi, K. Kato, T. Takai, S. Inoki, and T. Mukaiyama. Chem. Lett. 641 (1991); (*e*) A. Corma, L.T. Nemeth, M. Renz, and S. Valencia. Nature (London), **412**, 473 (2001).
5. (*a*) C. Bolm, G. Schlingloff, and K Weickhardt. Ang. Chem. Int. Ed. Engl. **33**, 1848 (1994); (*b*) C. Bolm and G. Schlingloff. J. Chem. Soc. Chem. Commun. 1247 (1995); (*c*) C. Bolm, G. Schlingloff, and F. Bienewald. J. Mol. Catal. A: Chem. **117**, 347, (1997); (*d*) C. Bolm, T.K.K. Luong, and G. Schlingloff. Synlett, 1151 (1997); (*e*) C. Paneghetti, R. Gavagnin, F. Pinna, and G. Strukul. Organometallics, **18**, 5057 (1999); (*f*) C. Bolm, O. Beckmann, T. Kühn, C. Palazzi, W. Adam, P.B. Rao, and C.R. Saha-Möller. Tetrahedron: Asymmetry, **12**, 2441 (2001); (*g*) T. Uchida and T. Katsuki. Tetrahedron Lett. **42**, 6911 (2001).
6. Reviews: (*a*) J.D. Stewart. Curr. Org. Chem. **2**, 195 (1998); (*b*) D.R. Kelly, P.W.H. Wan, and J. Tang. Biotransformations I. *In* Biotechnology. Vol 8a. *Edited by* H.-J. Rehm and G. Reed. Wiley-VCH, Weinheim. 1998. pp. 536–587; (*c*) S.M. Roberts and P.W.H. Wan. J. Mol. Cat. B: Enzym. **4**, 111 (1998); (*d*) A. Willetts. Trends Biotech. **15**, 55 (1997).
7. B. Adger, M.T. Bes, G. Grogan, R. McCague, S. Pedragosa-Moreau, S.M. Roberts, R. Villa, P.W.H. Wan, and A.J. Willetts. J. Chem. Soc. Chem. Commun. 1563 (1995).
8. R. Gagnon, G. Grogan, M.S. Levitt, S.M. Roberts, P.W.H. Wan, and A.J. Willetts. J. Chem. Soc. Perkin Trans. 1, 2537 (1994).
9. N.A. Donoghue and P.W. Trudgill. Eur. J. Biochem. **60**, 1 (1975).
10. (*a*) Y.C. Chen, O.P. Peoples, and C.T. Walsh. J. Bacteriol. **170**, 781 (1988); (*b*) B.P. Branchaud and C.T. Walsh. J. Am. Chem. Soc. **107**, 2153 (1985); (*c*) O. Abril, C.C. Ryerson, C. Walsh, and G.M. Whitesides. Bioorg. Chem. **17**, 41 (1989).
11. H. Iwaki, Y. Hasegawa, M. Teraoka, T. Tokuyama, H. Bergeron, and P.C. Lau. Appl. Environ. Microbiol. **65**, 5158, (1999).
12. M.B. Kneller, J. Cheesman, and A.E. Rettie. Biochem. Biophys. Res. Commun. **282**, 899 (2001).
13. P.W. Trudgill. Methods Enzymol. **188**, 70 (1990).
14. M.M. Kayser, G. Chen, and J.D. Stewart. Synlett, 153 (1999).
15. (*a*) G. Chen, M.M. Kayser, M.D. Mihovilovic, M.E. Mrstik, C.A. Martinez, and J.D. Stewart. New J. Chem. 827 (1999); (*b*) For the most recent CHMO expressions in *E. coli.*, see. S.D. Doig, L.M. O'Sullivan, S. Patel, J.M. Ward, and J.M. Woodley. Enzyme Microb. Tech. **28**, 265 (2001); (*c*) M.B. Kneller, M.J. Cheesman, and A.E. Rettie. Biochem. Biophys. Res. Commun. **282**, 899 (2001).
16. H. Iwaki, Y. Hasegawa, P.C.K. Lau, S. Wang, and M.M. Kayser. Submitted.
17. (*a*) M. Griffin and P.W. Trudgill. Biochem. J. **129**, 595 (1972); (*b*) M. Griffin and P.W. Trudgill. Eur. J. Biochem. **63**, 199 (1976); (*c*) P.W. Trudgill. Methods Enzymol. **188**, 77 (1990).
18. B. Adger, M.T. Bes, G. Grogan, R. McCague, S. Pedragosa-Moreau, S.M. Roberts, R. Villa, P.W.H. Wan, and A.J. Willetts. Bioorg. Med. Chem. **5**, 253 (1997).
19. M.T. Bes, R. Villa, S.M. Roberts, P.W.H. Wan, and A.J. Willetts. J. Mol. Catal. B: Enzym. **1**, 127 (1996).
20. M.M. Kayser, G. Chen, and J.D. Stewart. J. Org. Chem. **63**, 7103 (1998).
21. J.D. Stewart, K.W. Reed, and M.M. Kayser. J. Chem. Soc. Perkin Trans. 1, 755 (1996).
22. J.D. Stewart, K.W. Reed, C.A. Martinez, J. Zhu, G. Chen, and M.M. Kayser. J. Am. Chem. Soc. **120**, 3541 (1998).
23. V. Alphand, A. Archelas, and R. Furstoss. J. Org. Chem. **55**, 347 (1990).
24. For the original reference, see: C.-S. Chen, Y. Fujimoto, G. Girdaukas, and C.J. Sih. J. Am. Chem. Soc. **104**, 7294 (1982). The programme for the calculation is available free of charge at: http://www-org.tu-graz.ac.at
25. (*a*) Ph. Coutrot, C. Grison, and C. Bômont. Tetrahedron Lett. **35**, 8381 (1994). (*R*)-5-Hydroxy δ-valerolactone $[\alpha]_D$ –32 (*c* 1.3, $CHCl_3$); (*b*) E.J. Corey, S.G. Pyne, and W. Su. Tetrahedron Lett. **24**, 4883 (1983). (*S*)-5-Hydroxy δ-valerolactone $[\alpha]_D$ +34.68 (*c* 1.3, $CHCl_3$).
26. S.-K. Kang, J.-H. Jeon, T. Yamaguchi, R.-K. Hong, and B.-S. Ko. Tetrahedron: Asymmetry, **6**, 97 (1995): (*S*)-enantiomer $[\alpha]_D$ +29.4 (*c* 0.48, $CHCl_3$).
27. J.D. Stewart, KW. Reed, J. Zhu, G. Chen, and M.M. Kayser. J.Org. Chem. **61**, 7652 (1996).
28. M.J. Taschner, D.J. Black, and Q.-Z. Chen. Tetrahedron: Asymmetry, **4**, 1387 (1993).
29. (*a*) M.D. Mihovilovic, G. Chen, S. Wang, B. Kyte, F. Rochon, M.M. Kayser, and J.D. Stewart. J. Org. Chem. **66**, 733 (2001).
30. W.-D. Fessner and J.B. Jones. Curr. Opinion Chem. Biol. **5**, 103 (2001).
31. K.F. Bernady, J.F. Poletto, J. Nocera, P. Mirando, R.E. Schaub, and M.J. Weiss. J. Org. Chem. **45**, 4702 (1980).
32. Racemic 2-(3′-bromopropyl)cyclopentanone, **2f**: W.H. Pearson, R. Walavalkar, J.M. Schkeryantz, W. Fang, and J.D. Blickensdorf. J. Am. Chem. Soc. **115**, 10183 (1993).
33. Racemic 6-(3′-bromopropyl)tetrahydropyran-2-one, **5f**: (*a*) G.A. Molander and J.A. McKie. J. Org. Chem. **58**, 7216 (1993); (*b*) J.K. Crandall, H.S. Magaha, M.A. Henderson, R.K. Widener, and G.A. Tharp. J. Org. Chem. **47**, 5372 (1982).
34. E. Marcantoni, F. Nobili, G. Bartoli, M. Bosco, and L. Sambri. J. Org. Chem. **62**, 4183 (1997).

© 2002 NRC Canada

Metal substitution in thermolysin: Catalytic properties of tungstate thermolysin in sulfoxidation with H_2O_2

Martin Bakker, Fred van Rantwijk, and Roger A. Sheldon

Abstract: The catalytic Zn^{2+} ion was extracted from thermolysin, which had been covalently bound to Eupergit C. The apo-enzyme incorporated the oxometallate anions MoO_4^{2-}, SeO_4^{2-}, and WO_4^{2-} with partial restoration of the proteolytic activity. Tungstate thermolysin was moderately active in the sulfoxidation of thioanisole by hydrogen peroxide, whereas its activity towards phenylmercaptoacetophenone, which was designed to bind well in the active site of thermolysin, was much higher.

Key words: thermolysin, metal substitution, sulfoxidation.

Résumé : On a pu extraire l'ion catalytique Zn^{2+} de la thermolysine qui avait été liée de façon covalente à Eupergit C. L'apoenzyme incorpore alors les anions oxométallates MnO_4^{2-}, SeO_4^{2-} et WO_4^{2-} avec restauration partielle de l'activité protéolytique. La thermolysine au tungstate est modérément active dans la réaction de sulfoxydation du thioanisole par le peroxyde d'hydrogène alors que son activité est beaucoup plus élevée vis-à-vis de la phénylmercaptoacétophénone qui avait été choisie pour bien se lier dans le site actif de la thermolysine.

Mots clés : thermolysine, substitution d'un métal, sulfoxydation.

[Traduit par la Rédaction]

Introduction

Post-translational modification of the active site is a powerful tool for modifying the catalytic activity of enzymes (1). Yamamura and Kaiser (2) proved the validity of this notion by substituting the catalytic Zn^{2+} ion in the active site of carboxypeptidase A by Cu^{2+}, transforming the peptidase into an oxidase. More recently, the serine hydrolase subtilisin has been transformed into selenosubtilisin, which mimics glutathione peroxidase (3). We selected the neutral zinc-dependent protease thermolysin (4) from *Bacillus proteolyticus rokko* (E.C. 3.4.24.4) as an attractive candidate for metal substitution, because it is readily available and highly stable (5, 6). We were surprised to find that apothermolysin (7, 8), upon reconstitution with oxometallate anions, regained a part of its proteolytic activity. We present here our results on sulfoxidation in the presence of this tungstate thermolysin.

Results and discussion

Metal substitution in immobilized thermolysin

Thermolysin was fixed to Eupergit C (an acrylic copolymer containing an oxirane functionality) using a standard procedure recommended by the supplier. The catalytic Zn^{2+} ion was extracted from the Eupergit-fixed thermolysin by repeated treatment with an EDTA solution (7*a*) until the residual activity was lower than 1%. Treatment of the carrier-fixed apo-enzyme with Co^{2+} or Mn^{+2} ions resulted in a partial recovery of the proteolytic activity. We note, inter alia, that a twofold activation of thermolysin upon incorporation of a Co^{2+} ion has been reported (8), but our procedure was not optimized. Even the incorporation of the bulky oxometallate ions MoO_4^{2-}, SeO_4^{2-}, and WO_4^{2-}, which do not display proteolytic activity when freely dissolved, into apothermolysin partially restored the proteolytic activity of the latter (Table 1). We tentatively conclude that the oxometallate anions are correctly bound in the active site, in spite of their size.

Sulfoxidation mediated by tungstate(IV) thermolysin

Tungstate is known to catalyze various oxidations with H_2O_2 (9), and we surmized that incorporation of tungstate in the active site could transform thermolysin into an oxidation catalyst. We therefore investigated the use of Eupergit-bound tungstate thermolysin in sulfoxidation reactions with H_2O_2 (Fig. 1). The reactions were performed in *tert*-butyl alcohol at 40°C; the biocatalyst showed a high stability under these conditions. The aromatic sulfides **1**–**5** were selected as substrates for tungstate thermolysin because native thermolysin

Received 10 January 2002. Published on the NRC Research Press Web site at http://canjchem.nrc.ca on 22 May 2002.

This paper is dedicated to J. Bryan Jones on the occasion of his 65th birthday in recognition of his contributions to biocatalysis.

M. Bakker, F. van Rantwijk, and R.A. Sheldon.[1] Laboratory of Biocatalysis and Organic Chemistry, Julianalaan 136, 2628 BL Delft, The Netherlands.

[1]Corresponding author (e-mail: secretariat-OCK@tnw.tudelft.nl).

 DOI: 10.1139/V02-082 © 2002 NRC Canada

Table 1. Metal exchange in Eupergit C immobilized thermolysin.

Metal ion	Activity (U mg^{-1})	Relative activity (%)
Zn^{2+} (untreated)	12	100
Co^{2+}	10	85
Cu^{2+}	0.7	6
Mn^{2+}	9	83
MoO_4^{2-}	8	69
SeO_4^{2-}	6	50
WO_4^{2-}	7	58

Fig. 1. Sulfides and sulfoxidation.

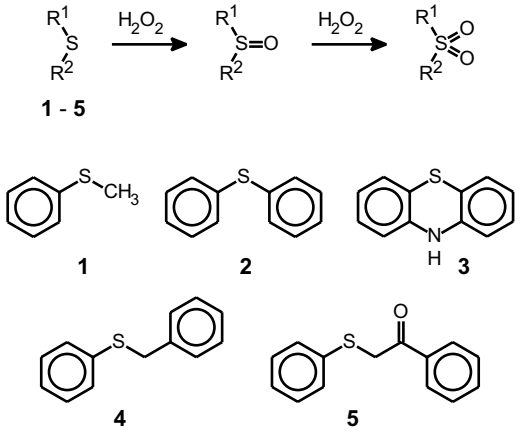

is known to favour reactants with bulky hydrophobic groups (10).

Thioanisole (**1**) was slowly converted into its racemic sulfoxide in the presence of tungstate(VI) thermolysin (Table 2). The further reaction to the sulfone, which is generally not observed in peroxidase-mediated sulfoxidation, was much slower and took 24 h to reach complete conversion. The reaction was much slower in the absence of any catalyst and did not progress beyond the sulfoxide stage; addition of sodium tungstate had no effect. We also performed a reaction in the presence of tungstate thermolysin and removed the catalyst by filtration after 2.5 h (9% conversion). The reaction slowly continued in the filtrate, at a rate comparable with that of the uncatalyzed reaction, to reach 55% conversion into the sulfoxide after 7 h.

The conversion of diphenyl sulfide (**2**) was insignificant, regardless of the presence of tungstate thermolysin. Phenothiazine (**3**), which has a planar and rigid structure, reacted much faster than **2** and was completely converted in 20 h. The uncatalyzed reaction was much slower, but in contrast with all of the other sulfides, sodium tungstate exerted a significant catalytic effect. Benzyl phenyl sulfide (**4**) was converted at a comparable rate.

The highest reaction rate was observed with phenylmercaptoacetophenone (**5**). Within 2 h a complete conversion into a mixture of the sulfoxide and the sulfone was observed. The reaction continued to complete conversion into the sulfone after 5 h (Fig. 2). The uncatalyzed reaction was much slower and no formation of the sulfone was observed. We tentatively attribute the high reactivity of **5** to its resemblance to the natural (peptide) subtrates of thermolysin.

Fig. 2. Time course of the tungstate thermolysin-mediated oxidation of **5**. ● (**5**); ■ (sulfoxide); ▲ (sulfone).

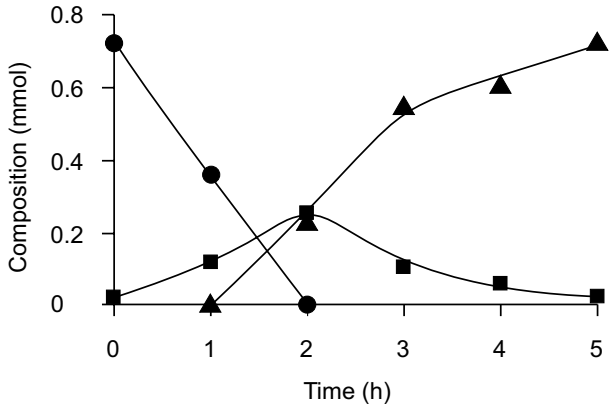

Hence, this result also supports the hypothesis that tungstate is incorporated into the active site.

Conclusion

The reconstitution of Eupergit C fixed apo-thermolysin with a range of metal and oxometal ions results in a partial recovery of the proteolytic activity. Incorporation of tungstate(IV) transforms thermolysin into a peroxidase, which is a moderately active catalyst for the oxidation of sulfides into their sulfoxides and sulfones. It accepts much bulkier substates than common peroxidases, but the sulfoxides are racemic. This surprising lack of enantioselectivity will be the subject of further investigation.

Experimental

Materials

Thermolysin from *Bacillus thermoproteolyticus rokko* (E.C. 3.4.24.4) was received from DSM Research (Geleen, The Netherlands) as a gift. Eupergit C (an acrylic copolymer containing an oxirane functionality) was kindly donated by Röhm GmbH (Darmstadt, Germany). 3-(2-Furylacryloyl)-glycyl-L-leucine amide (FAGLA) was purchased from Sigma. Thioanisole, diphenyl sulfide, diphenyl sulfoxide, diphenyl sulfone, phenyl benzyl sulfide, phenothiazine, disodium molybdate(IV), disodium selenate(VI), vanadium trioxide, disodium tungstate(VI), manganese(II) acetate, cobalt(II) chloride, zinc acetate, and copper(II) chloride were obtained from Aldrich. Ethylenediamine-(*N*,*N*,*N*′,*N*′)tetra-acetic acid (EDTA) was purchased from Acros.

Thermolysin was immobilized on Eupergit C by dissolving dialyzed and concentrated thermolysin (100 mg) in Hepes buffer (1.0 M, 50 mL) containing $CaCl_2$ (1 mM). Eupergit C (1 g) was added and the suspension was shaken for 72 h at 4°C. The solids were collected by filtration and washed (4 h) with Tris buffer (100 mM, 3 × 100 mL) containing 0.5% $CaCl_2$, to destroy any unreacted epoxide groups. 16.7 mg thermolysin was bound per g of carrier material.

© 2002 NRC Canada

Table 2. Oxidation of the sulfides **1**–**5**.

			Conversion (%)			
	Specific activity		WO_4^{2-} thermolysin		No catalyst	Na_2WO_4
Reactant	(μmol mg^{-1} min^{-1})	Time (h)	Sulfoxide	Sulfone	Sulfoxide	Sulfoxide
1	5	7	97	3	48	47
2	—	24	1	0	1	3
3	450	2	82	18	26	47
4	0.3	24	86	11	n.d.	n.d.
5	1800	2	53	47	4	5

Analysis and equipment

Proteolytic assay

The proteolytic activity of thermolysin was measured during the hydrolysis of FAGLA, according to the method developed by Feder (11). FAGLA (76.6 mg, 2.49 mmol) was dissolved in Tris buffer (50 mM, pH 7.5), containing $CaCl_2$ (10 mM, 100 mL). The FAGLA solution (3 mL) was mixed with a thermolysin sample (5–10 mg thermolysin on Eupergit C; 1–5 mg native enzyme) in a 3-mL quartz cuvette, stirred for 3 s, and placed in a UV spectrophotometer (Varian Cary 3). The absorbance at 345 nm was monitored while stirring. The data points were fitted to first-order kinetics and V_{max} was calculated using K_m = 30 μM (11). One unit (U) will hydrolyze 1 μmol FAGLA per min under V_{max} conditions.

Reaction monitoring

The sulfoxidation reactions of **1**, **2**, **4**, and **5** were monitored by reversed-phase HPLC, using a custom-packed 7 μ Symmetry C18 cartridge (Waters Radial-Pak, 8 × 100 mm) contained in a Waters RCM 8 × 10 compression unit at 1 mL min^{-1} eluent flow and UV detection (Waters 486) at 220 nm with Waters Millennium[32] software. Further analysis conditions are summarized in Table 3. The oxidation of **3** was more conveniently monitored by HPLC over a Chiralcel OD column.

Samples for analyzing the enantiomeric excess of the sulfoxides were diluted with hexane–isopropyl alcohol (75:25, v/v) and dried over Na_2SO_4. After centrifugation, the samples were analyzed by chiral HPLC, using a Chiralcel OD column (Diacel Chemical Industries, Ltd., 250 × 4.6 mm), hexane–isopropyl alcohol (75:25, v/v) at 0.6 mL min^{-1} as the eluent, and UV detection (Waters 486) at 220 nm with Waters Millennium[32] software. The same technique was used for monitoring the oxidations of **3**; eluent hexane–isopropyl alcohol (80:20, v/v).

Metal substitution in immobilized thermolysin

Thermolysin on Eupergit C (1 g) was shaken for 3 h in a solution of EDTA (2 mM, 100 mL), NaCl (1 M), and Tris buffer (50 mM, pH 7.5) at 4°C. The solids were collected by filtration and the treatment was repeated until the residual activity was less than 1%. Any excess of EDTA was removed from the immobilized apo-enzyme by washing 1 M NaCl (3 × 200 mL) containing Tris buffer (50 mM, pH 7.5).

The apo-enzyme was reconstituted by treatment with a 1 mM metal ion solution in Tris buffer (50 mM, pH 7.5) for 1 h at room temperature. The volume was measured and the Ca^{2+} concentration was increased to 10 mM. The resulting suspension was agitated overnight at 4°C and the proteolytic activity of the reconstituted catalyst was measured.

Table 3. HPLC conditions.

Reactant	Internal standard	Eluent composition (v/v)
1	1,2,3-Trimethoxybenzene	ACN–H_2O (35:65)
2	1,3-Dimethoxybenzene	ACN–H_2O (40:60)
4	1,2,3-Trimethoxybenzene	ACN–H_2O (45:55)
5	2-Oxindole	ACN–H_2O (40:60)

Synthesis of substrates and products

Phenylmercaptoacetophenone (**3**) was prepared by dissolving 2-bromoacetophenone (5 g, 25 mmol) in cold ethanol (50 mL). K_2CO_3 (6.9 g, 50 mmol) was added, and then thiophenol (2.75 g, 25 mmol) was slowly titrated over 2 h. The resulting mixture was stirred for 12 h and the solids were removed by filtration. The filtrate was washed with water and the aqueous layer was extracted with ethyl acetate. The combined organic layers were dried over Na_2SO_4 and concentrated in vacuo. Yellow crystals were obtained and recrystallized from an ethyl acetate–diethyl ether mixture. Yield 83%, purity (HPLC) 99%. mp: 227–229°C. ^{1}H NMR (400 MHz, $CDCl_3$) δ: 4.25 (s, 2H), 7.25–8.22 (m, 10H). MS *m*/*z*: 228 ($C_{14}H_{12}OS$).

The sulfoxides and sulfones that were not commercially available were prepared from the sulfides by oxidation with H_2O_2 (12) and $KHSO_5$ (13), respectively, according to published procedures.

Oxidation procedure

Sulfide (0.8 mmol) and wet immobilized tungstate thermolysin (200 mg) were mixed in *tert*-butyl alcohol and stirred at 40°C in a sealed vessel until the reactant was dissolved. A 1 M aqueous H_2O_2 solution (1.6 mmol) was added to the reaction mixture over 2 h, using a Metrohm 665 Dosimat syringe-pump system, while stirring. Samples were withdrawn at regular intervals, treated with Na_2SO_3 (catalase in the case of phenylmercaptoacetophenone) to destroy the excess of H_2O_2, and analyzed by HPLC.

Acknowledgments

The authors express their thanks to DSM Research (Geleen, The Netherlands) for the kind gift of thermolysin. A generous donation of Eupergit C by Röhm GmbH (Darmstadt, Germany) is also gratefully acknowledged.

© 2002 NRC Canada

References

1. G. DeSantis and J.B. Jones. Curr. Opin. Chem. Biol. **10**, 324 (1999), and refs. cited therein.
2. K. Yamamura and E.T. Kaiser. J. Chem. Soc. Chem. Commun. 830 (1967).
3. Z.P. WU and D. Hilvert. J. Am. Chem. Soc. **111**, 4513 (1989).
4. T. Hofman. *In* Metalloproteins. Part 2. Metal proteins with non-redox roles. *Edited by* P.M. Harrison. Verlag Chemie, Weinheim. 1985. p. 1.
5. K. Okayama, S. Nishimura, Y. Nonaka, I. Kahara, and T. Hashimoto. J. Org. Chem. **46**, 631 (1981).
6. K. Faber. Pure Appl. Chem. **69**, 1613 (1997).
7. (*a*) D.S. Auld. Methods Enzymol. **158**, 71 (1988); (*b*) D.S. Auld. Methods Enzymol. **248**, 228 (1995).
8. B. Holquist and B.L. Vallee. J. Biol. Chem. **249**, 4601 (1974).
9. For leading refs. see: (*a*) K. Sato, M. Aoki, M. Ogawa, T. Hashimoto, and R. Noyori. J. Org. Chem. **61**, 8310 (1996); (*b*) K. Sato, M. Aoki, J. Takagi, and R. Noyori. J. Am. Chem. Soc. **119**, 12386 (1997); (*c*) K. Sato, M. Aoki, and R. Noyori. Science (Washington, D.C.), **281**, 1646 (1998); (*d*) E. Antonelli, R. D'Aloisio, M. Gambaro, T. Fiorani, and C. Venturello. J. Org. Chem. **63**, 7190 (1998).
10. I. Gill, R. López-Fandino, X. Jorba, and E.N. Vulfson. Enzyme Microb. Technol. **18**, 162 (1996).
11. J. Feder. Biochem. Biophys. Res. Commun. **32**, 326 (1968).
12. W.J. Kenney, J.A. Walsh, and D.A. Davenport. J. Am. Chem. Soc. **83**, 4019 (1961).
13. B.M. Trost and D.P. Curran. Tetrahedron Lett. **22**, 1287 (1981).

© 2002 NRC Canada

Second-generation MS-based high-throughput screening system for enantioselective catalysts and biocatalysts

Wolfgang Schrader, Andreas Eipper, D. Jonathan Pugh, and Manfred T. Reetz

Abstract: A high-throughput method is described, where the enantioselectivity of approximately 10 000 catalysts or biocatalysts can be determined per day. The method is based on electrospray mass spectrometric techniques using an eight-channel multiplexed (MUX) sprayer system connected to a time-of-flight mass spectrometer. The inlet of the ion source is controlled by a stepping rotor that is continuously moving from one sprayer to the next with a recording time of 100 ms for each channel and a delay time of 50 ms, thus allowing a spectrum to be obtained from each channel every 1.2 s. One cycle, where eight samples are being sprayed in parallel, requires around 70 s, which allows a 96-well microtiter plate to be screened in 14 min. Integration of two pseudo-enantiomers (*S*)-glycidyl phenyl ether and (*R*)-D_5-glycidyl phenyl ether is necessary to quantify the enantiomeric excess (ee-value), where one enantiomer is isotopically labeled to allow easy identification of the mass spectrometric signals. Errors of ~2% for the ee-values indicate that in addition to the significant improvement in sample throughput this is also a precise method for high-throughput screening. This second-generation assay is useful for combinatorial enantioselective transition-metal catalysis and in the directed evolution of enantioselective enzymes.

Key words: multiplexed ESI-MS, high-throughput screening, enantioselectivity, combinatorial catalysis, directed evolution.

Résumé : On décrit une méthode à grand débit à l'aide de laquelle on peut déterminer l'énantiosélectivité d'environ 10,000 catalyseurs ou biocatalyseurs par jour. La méthode est basée sur des techniques de spectrométrie de masse avec électronébulisation à l'aide d'un système de nébulisation multiplex à huit canaux relié à un spectromètre de masse à temps de vol. L'insertion dans la source ionique est contrôlée par un rotor variable qui se déplace continuellement d'un nébulisateur au suivant, avec un temps d'enregistrement de 100 ms pour chaque canal et un délai de 50 ms qui permet d'obtenir un spectre pour chaque canal toutes les 1,2 s. Un cycle, dans lequel on soumet huit échantillons à la nébulisation en parallèle, requiert 70 s; il est donc possible de traiter un bloc de 96 échantillons en 14 min. Quand un énantiomère est marqué d'un isotope, il est nécessaire d'introduire deux pseudo-énantiomères, l'oxyde de (*S*)-glycidyle et de phényle et l'oxyde de (*R*)-D_5-glycidyle et de phényle, pour identifier rapidement les signaux de spectrométrie de masse et pour quantifier les excès énantiomériques (valeur ee). Des erreurs d'environ 2% dans les valeurs ee indiquent que, en plus d'être une amélioration sensible au débit des échantillons, cette méthode s'avère aussi très précise pour une évaluation à grand débit. Cette méthode de deuxième génération est utile dans le domaine de la catalyse énantiosélective combinatoire par les métaux de transition et dans l'évolution orientée des enzymes énantiosélectifs.

Mots clés : spectrométrie de masse avec électronébulisation multiplex, évaluation à grand débit, énantiosélectivité, catalyse combinatoire, évolution orientée.

[Traduit par la Rédaction]

Introduction

The importance of enantiomerically pure or enriched organic compounds in pharmaceutical, agricultural, synthetic organic, and natural products chemistry is undisputed (1). Although classical separation of enantiomers is still used in industry (1*d*), in the future the most economically and ecologically attractive strategy is likely to be enantioselective catalysis. The two options are synthesized catalysts such as chiral transition-metal complexes (2) or biocatalysts (3). The former involves ligand tuning, a process requiring design, molecular modelling, and usually a great deal of trial and error. Recently, an alternative approach to the traditional development of chiral transition-metal catalysts has emerged,

Received 18 December 2001. Published on the NRC Research Press Web site at http://canjchem.nrc.ca on 22 May 2002.

This paper is dedicated to Professor J. Bryan Jones on the occasion of his 65th birthday in recognition of his contributions to biocatalysis.

W. Schrader, A. Eipper, and M.T. Reetz.[1] Max-Planck-Institut für Kohlenforschung, Kaiser-Wilhelm-Platz 1, D-45470 Mülheim/Ruhr, Germany.
D.J. Pugh. Micromass (U.K. Ltd.), Atlas Park, Simonsway, Manchester, M22 5PP, U.K.

[1]Corresponding author (e-mail: reetz@mpi-muelheim.mpg.de).

 DOI: 10.1139/V02-069 © 2002 NRC Canada

Scheme 1. (*a*) Asymmetric transformation of a mixture of pseudo-enantiomers involving cleavage of the functional groups FG and labeled FG*. (*b*) Asymmetric transformation of a mixture of pseudo-enantiomers involving either cleavage or bond formation at the functional group FG; isotopic labeling at R^2 is indicated by the asterisk. (*c*) Asymmetric transformation of a pseudo-meso substrate involving cleavage of the functional groups FG and labeled FG*. (*d*) Asymmetric transformation of a pseudo-prochiral substrate involving cleavage of the functional groups FG and labeled FG*.

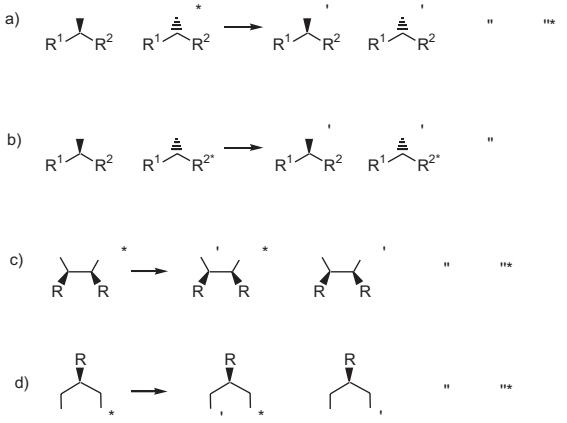

namely combinatorial methods in which large numbers of catalysts are produced in a parallel manner (4, 5). The challenges in this new field of endeavour are twofold because novel synthetic strategies as well as efficient high-throughput screening systems need to be developed. In the case of enzymes as asymmetric catalysts in organic chemistry, the method of directed evolution (6) has recently been applied for the first time (7). This entailed the creation of thousands of mutant enzymes, which were screened for enantioselectivity in a given synthetic transformation. Several cycles of mutagenesis screening resulted in highly enantioselective catalysts — knowledge of the structure or of the mechanism of the enzyme is not necessary.

Both approaches to asymmetric catalysis rely on the availability of analytical systems capable of assaying the enantiomeric excess (ee) of large numbers of samples within a reasonable time span, and hence why various high-throughput and super high-throughput ee-assays have been recently developed (5). These assays have been based on color tests (7, 8), capillary-array electrophoresis (9), IR thermography (10), fluorescence (11), circular dichroism (12), or other systems (13–18). Mass spectrometry (MS) is a particularly powerful method for high-throughput analysis of products arising from general catalytic reactions (19), in the rapid LC–MS screening of chiral stationary phases (20), and in the FAB-MS study of crown ether complexes (21). Finn and co-workers (22) have recently developed an MS system for high-throughput determination of enantioselectivity based on the formation of diastereomers.

We have previously described an ee-assay based on the use of isotopically labeled substrates, detection being possible by MS using standard ionization methods such as electrospray ionization (ESI) or matrix-assisted laser-desorption ionization (MALDI) (23). Two fundamentally different stereochemical processes can be monitored by our method: (*i*) the kinetic resolution of racemates and (*ii*) the desymmetrization of prochiral compounds bearing enantiotopic groups (Scheme 1).

Scheme 2. Reaction of a pseudo-meso-compound (**1**) with formation of pseudo-enantiomers **2** and **3**.

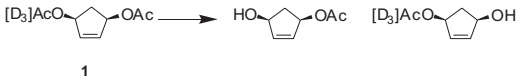

Scheme 3. Kinetic resolution of glycidyl phenyl ether (**4**) by an epoxide hydrolase.

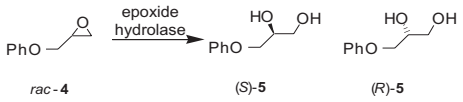

Scheme 4. Enzymatic hydrolysis of the pseudo-enantiomers (*S*)-glycidyl phenyl ether and (*R*)-D_5-glycidyl phenyl ether.

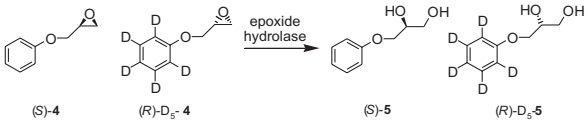

For kinetic resolution, pseudo-enantiomeric substrates must also be used, i.e., one of the enantiomers has to be isotopically labeled (23). After the reaction with the proposed enantioselective catalyst, the mixture can be analyzed using MS. Because of the isotopical labeling, the two pseudo-enantiomers are adequately separated with respect to their mass-to-charge ratios to allow for quantitative determination of their respective signals, while being chemically indifferent so as not to influence their catalytic conversion. In each case a simple kinetic experiment was necessary to exclude possible kinetic isotope effects in the actual reaction. The quantitative determination of both pseudo-enantiomers allows one to determine the enantioselectivity of a given catalytic or biocatalytic transformation.

We recently initiated a project concerning the directed evolution of an epoxide hydrolase obtained from *Aspergillus niger*, which had previously been used in the kinetic resolution of certain epoxides (24). Our goal was to perform several cycles of random mutagenesis to create an enantioselective enzyme mutant, which catalyzes the kinetic resolution of glycidyl phenyl ether (*rac*-**4**) (Scheme 3). The wild-type enzyme shows, however, only a slight degree of

© 2002 NRC Canada

Fig. 1. MUX interface developed by Micromass, Manchester, U.K.

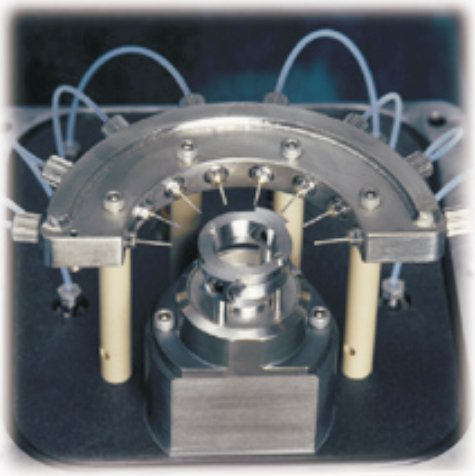

enantioselectivity, which is unfortunate because substrates of this kind are of great synthetic interest.

To evaluate thousands of mutant epoxide hydrolases, we envisioned the use of our ESI-MS-based assay (23). Accordingly, one of the enantiomeric epoxides needs to be labeled with deuterium and mixed with the nonlabeled enantiomer forming a pseudo-racemate (Scheme 4). We anticipated that the integration of the MS peaks of the nonlabeled (*S*)-diol ((*S*)-**5**) and the labeled (*R*)-diol ((*R*)-D_5-**5**) would provide a measure of enantioselectivity, and that it should also be possible to screen about 1000 reactions per day. In this paper we show that this is indeed the case. Moreover, we demonstrate that throughput can be increased by one order of magnitude by adapting and using a parallel eight-channel multiplexed ESI-MS system. Thus, the new ee-assay is capable of screening about 10 000 samples per day.

Experimental

Synthesis

The D_5-labeled glycidyl phenyl ether ((*R*)-D_5-**4**) was prepared analogously to the known procedure for the nonlabeled substrate (25). Model samples were prepared for analysis by mixing nonlabeled and D_5-labeled compounds to give a pseudo-racemate.

Multiplexed ESI-MS system

Electrospray mass spectrometry was carried out using an eight-channel parallel multiplexed (MUX) LC–MS system (Micromass, Manchester, U.K.). The analytical system combines a Waters 600 HPLC pump (Waters, Milford, MA, U.S.A.), one Gilson 215/889 eight-channel liquid autosampler equipped with a multi-injection module using 20 μL injection loops (Gilson, Middleton, WI, U.S.A.), eight reverse-phase columns (2.1 × 20 mm, Waters Symmetry, C8), and an eight-channel MUX ESI system (see Fig. 1) connected to a time-of-flight mass spectrometer (5*b*) (Micromass, Manchester, U.K.).

The MUX sprayer system, which consists of eight-electrospray nebulizers, was installed instead of the standard single-electrospray probe into the existing *Z*-spray ion source. This system sprays the fluids that arrive from the eight columns in a parallel manner. The inlet of the LCT is controlled by a stepping rotor, which opens to each sprayer in rapid succession. Each channel has a 100 ms recording time, with a 50-ms time delay before switching to the next channel. The data are written separately into eight different data files for each sample, thus acquiring a mass spectrum for each channel every 1.2 s. This "indexing" set-up means that only one channel is being analyzed at one time and that the data is written into the corresponding file, before the stepping rotor moves on to the next channel. Spectra were obtained in the scan mode between 100 to 800 mass units. Flow rates of 1 mL min^{-1} (MeOH–H_2O, 90:10) from the HPLC pump were adjusted to 100 μL min^{-1} for each channel through a Valco zero-dead-volume split system.

GC experiments

Control experiments to determine the ee-values were carried out using gas chromatography (GC). Accordingly, a RTX-5 column of 30 m length was used in combination with a flame-ionization detector. Product separation was achieved by using the following temperature program: start: 80°C, heating rate 8 K min^{-1} to 340°C, 10 min isotherm. This results in a retention time of 43.4 min for (*R*)-D_5-**5** and 44.8 min for (*S*)-**5**. The temperature of the injector was kept constant at 220°C.

For each sample the ee-value was determined three times. All data were averaged for each concentration (error < 0.1%).

Results and discussion

High-throughput screening ideally involves very fast, accurate, reliable, precise, and reproducible analysis. Depending on the information content that is required, limitations in any of these requirements can be accepted, provided that the overall gain in information is sufficiently satisfactory and that the main goal of high-sample throughput is achieved. Mass spectrometric methods using electrospray ionization are known to be not only fast enough, but also accomplish the other requirements for high-throughput screening systems (19).

For the determination of the enantiomeric excess, we previously developed an MS-based concept that used pseudo-enantiomers — one of the enantiomers was isotopically labeled (23). To test the feasibility of increasing throughput by using an eight-channel parallel multiplexed mass spectrometric (MUX HPLC – ESI-MS) system for high-throughput analysis of enantioselective reactions, a 96-deep-well microtiter plate was filled with 12 different samples containing the pseudo-enantiomers as shown in Scheme 4. These samples all have different ee-values as measured in control experiments using standard GC. All 12 samples were measured eight times in parallel with each of the channels spraying the same sample, thus allowing a direct comparison. The microtiter plate was scanned repeatedly overnight without operator intervention. Adequate statistical data were obtained.

For quantitative analysis, the areas below mass traces at *m/z* 191 and 196 for the nonlabeled and labeled enantiomers, respectively (both as Na^+ adducts) were integrated automatically (see Fig. 2) and then transferred into an Excel spread

© 2002 NRC Canada

Fig. 2. Total ion current (TIC) and mass traces 191 and 196 of pseudo-enantiomers (both as Na^+ adducts), mass trace at 228 is of the internal standard; integration as shown.

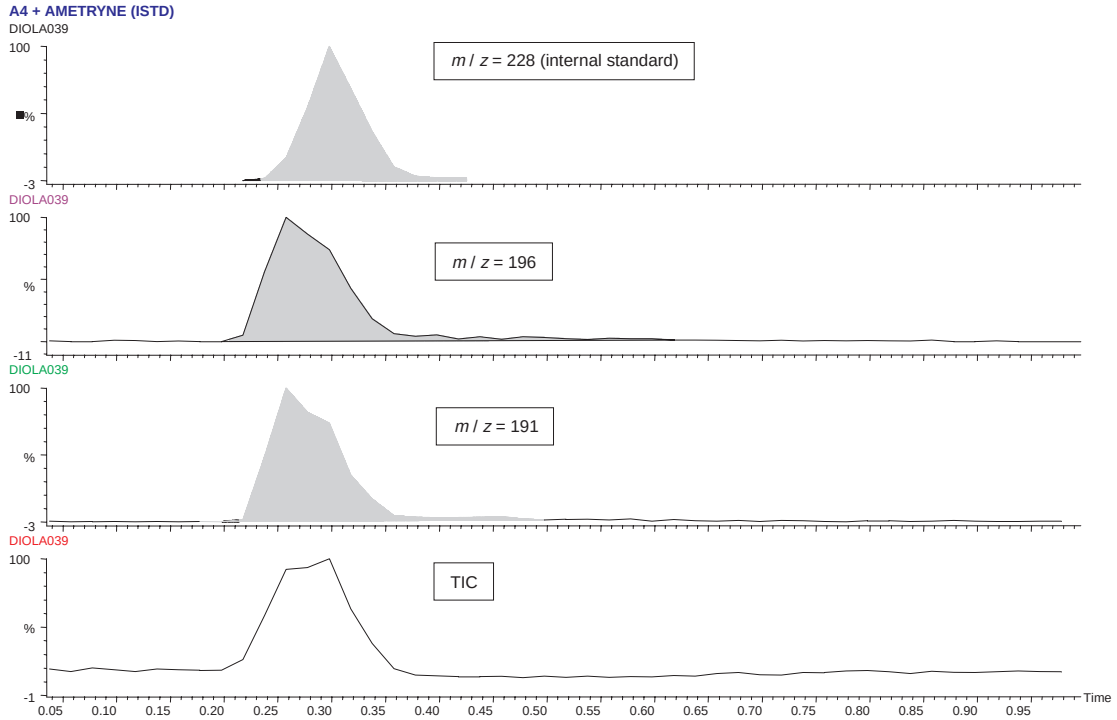

Fig. 3. Typical mass spectra of reaction products (*S*)-**5** and (*R*)-D_5-**5** with internal standard ametryne; corresponding spectrum to Fig. 1.

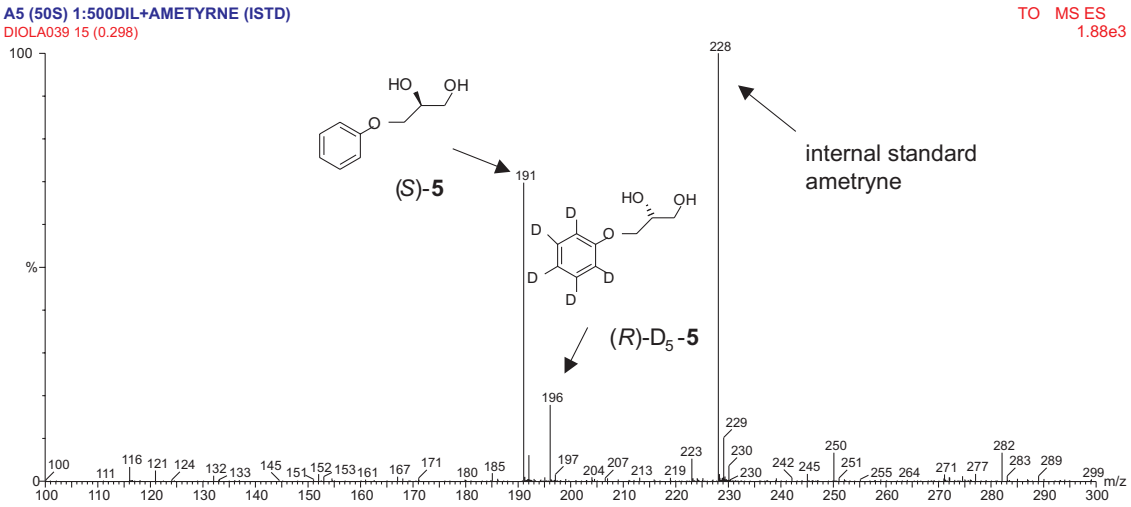

sheet (26) for processing. A representative mass spectrum is shown in Fig. 3.

The enantiomeric purity of a given sample is generally defined by the enantiomeric excess (ee-value). Here the ee-values were derived by integrating the MS-peak areas of pseudo-enantiomeric diols (*S*)-**5** and (*R*)-D_5-**5**. The samples were prepared by mixing these two components to give a pseudo-racemate. In the actual application of the assay for the directed evolution of an enantioselective epoxide hydrolase, the reaction mixture contained not only (*S*)-**5** and (*R*)-D_5-**5**, but also the starting pseudo-enantiomeric epoxides (*S*)-**4** and (*R*)-D_5-**4**. We have ensured that the ratio of the starting epoxides was also reliably derived by the MS assay by integration of the relevant peaks at *m*/*z* = 173 and 178, respectively. According to the formula developed by Chen and Sih (27), the integration values of the products and the starting compounds allows for the determination of selectivity factors (*E*) in the kinetic resolution. Alternatively, the ee-value of the diol product in combination with an internal standard such as ametryne also allows for the determination of *E*, again using the formula of Chen and Sih (27). High accuracy in quantification is observed (see below). In the real application of the assay described here we used the latter method (28). Control experiments showed that no kinetic-isotopic effects were observed in the enzyme-catalyzed ring-opening reactions.

© 2002 NRC Canada

Table 1. *ee*-Values of one microtiter plate compared with GC results; standard deviation (σ) calculated from data.

			ee (LC–MS)								Avg. for	
Sample	Configuration	ee (GC)	Run 1	Run 2	Run 3	Run 4	Run 5	Run 6	Run 7	Run 8	runs 1–8	σ
A1	(*S*)	99.4	98.2	97.8	97.7	97.6	98.8	97.8	98.0	97.8	98.0	0.4
A2	(*S*)	22.0	22.2	23.5	23.1	21.0	22.2	21.1	22.9	21.9	22.2	0.9
A3	(*S*)	42.6	44.3	42.1	43.5	42.5	42.2	42.4	43.3	40.6	42.6	1.1
A4	(*S*)	50.2	51.5	52.2	48.6	49.2	52.8	49.9	52.9	48.6	50.7	1.8
A5	(*S*)	56.6	58.4	55.7	58.1	55.4	55.1	53.6	59.0	54.2	56.2	2.0
A6	(*S*)	66.2	67.1	68.6	68.5	65.2	64.6	66.9	68.6	66.0	66.9	1.6
A7	(*S*)	82.1	82.0	82.4	82.7	84.7	83.6	80.4	81.6	83.1	82.6	1.3
A8	(*S*)	26.0	26.7	24.2	26.9	26.5	26.7	26.2	27.1	29.0	26.7	1.3
A9	(*S*)	64.2	66.7	66.1	66.7	64.6	63.8	67.0	64.6	66.3	65.7	1.2
A10	(*R*)	17.6	19.3	20.4	17.9	18.8	18.9	16.4	17.1	17.6	18.3	1.3
A11	(*R*)	18.4	17.2	20.4	20.1	18.9	17.3	19.4	19.6	19.9	19.1	1.2
A12	(*R*)	73.6	76.4	77.6	76.9	73.8	71.1	77.1	76.8	76.6	75.8	2.2

Fig. 4. Comparison of actual GC vs. average determined MS ee-values over the whole concentration range.

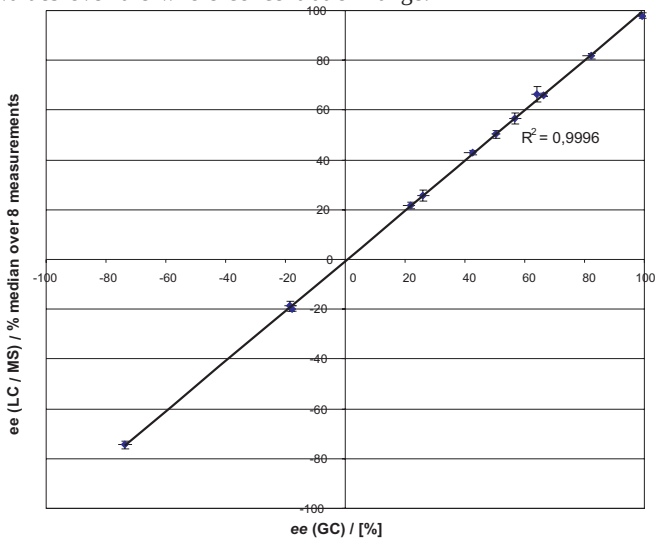

Rapid analysis was achieved using the MUX ESI-MS system. In the current setup the mass spectrometer can analyze eight parallel samples in about 70 s, thus allowing a 96-microtiter plate to be analyzed in 14 min. This corresponds to an overall analytical capability of ca. 10 000 ee- or *E*-determinations per day.

The use of a short HPLC column has the benefit of condensing the sample, which in turn reduces the effects of peak tailing, interference, and injection pressure fluctuations associated with simple direct-infusion analysis. In general, the more Gaussian-shaped the peak, the better the reliability of integration and therefore the greater the quantification of the method. Overall, the sample throughput is not compromised since analyte retention times of less than 30 s were observed and could be reduced further.

One of the major problems for high-throughput systems is that although they produce a high number of analytical data, the precision and accuracy is sometimes poor. In the present study, the MUX ESI-MS system provides very precise data, as can be seen in Fig. 4, where the MS-determined average ee-values are plotted against the GC values over the whole range. Moreover, accurate mass data using a time-of-flight analyzer have become available. This makes it possible to screen large libraries not only qualitatively, but also quantitatively. Table 1 shows typical results from measurements of samples in the wells of a microtiter plate. The average observed values correlate well with the corresponding GC values. The error of only 2% is quite acceptable for a high-throughput system.

The long-term stability of the sprayer system is also good. While evaluating the microtiter plate a series of 96 measurements were performed overnight on a given sample and compared with the standard values. In Fig. 5 three of such series are displayed. Difficulties can arise due to pressure fluctuations in the flow provided by the HPLC pump because the flow is divided into eight different channels supporting eight different electrosprays. Nonetheless, even though the sprayer of the ESI-MS system fluctuates, which results in larger differences in the total ion current, the ee-values remain unaffected. This is because the determination of the ee-values are based on the calculation of the ratio of the two main signals of the spectrum; the fluctuations are equal for both pseudo-enantiomers and thus do not affect the ratio.

The one limiting factor in this analysis is the dynamic range of the detector in the time-of-flight mass spectrometer (TOF-MS). The dynamic range of the multichannel plate detector (MCP) is linear over three orders of magnitude when the dead-time correction-software algorithm is applied. In absolute terms this corresponds to a maximum centroided-peak area of the monoisotopic MS peak of interest of 30 000 counts per second. Dead time arises because when an ion has been detected by the MCP there is a recovery time of approximately 4 ns before another ion arrival can be recorded. It should be noted that the presence of an intense MS peak in another region of the spectrum will have no local effect on the MS peak(s) of interest. This means that for direct quantitative analysis of the samples, the concentration range must be considered or an additional dilution step needs to be included. If necessary, a better dynamic range can be achieved by using another type of analyzer, such as a quadrupole MS instrument, which typically provides four to five orders of magnitude linear response. Quadrupole

© 2002 NRC Canada

Fig. 5. Reproducibility of three different sets of ee-determinations over 96 runs each, compared with the corresponding GC values; standard deviation (σ) calculated from data.

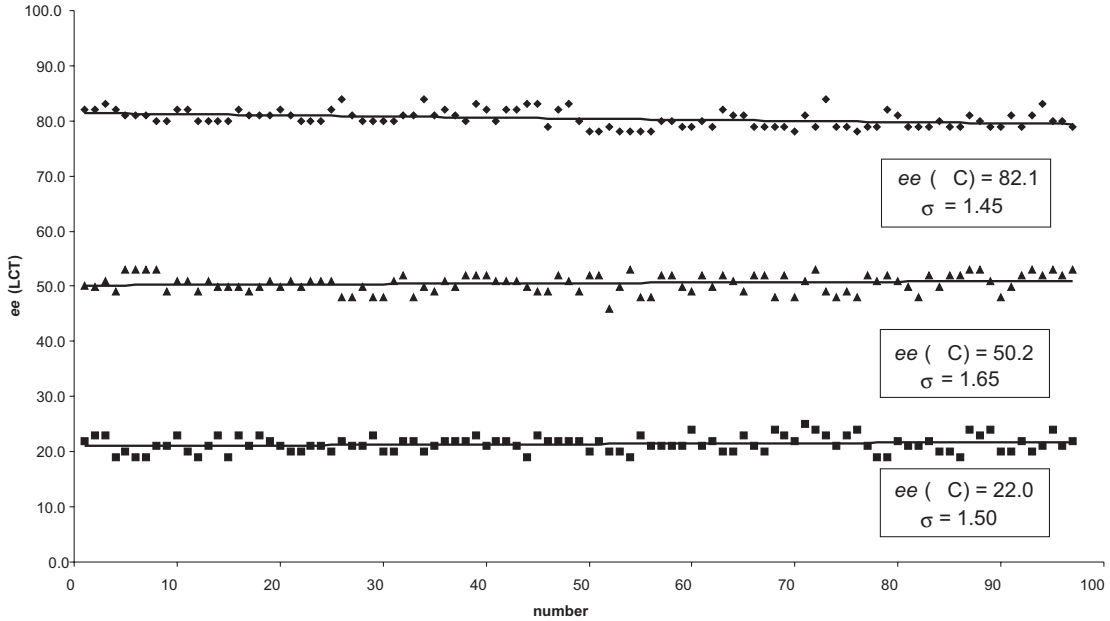

instruments are currently limited to four-channel multiplexed ESI systems, which effectively reduces the analytical throughput by half (29). The eight-channel MUX ESI system is only compatible with time-of-flight instruments, where the necessary high spectrum acquisition rates are possible.

Conclusion

We have developed a high-throughput ee-assay based on the MS detection of isotopically labeled pseudo-enantiomers. Our results show that the multiplexed HPLC–ESI-MS system is capable of acquiring up to 10 000 ee- or *E*-determinations per day by having a cycle time of around 70 s for eight parallel experiments. The standard deviation for the observed ee-values is around 2%, thus allowing quantitative analysis of chemical catalyst or biocatalyst libraries with high precision and excellent reproducibility. This was demonstrated using a specific substrate of interest in the kinetic resolution of a chiral epoxide. Moreover, the assay can be expected to have general applications for analyzing kinetic resolutions and for analyzing the desymmetrization of prochiral compounds containing enantiotopic groups. Finally, it is likely that the system can be used to simultaneously assay the catalytic transformation of two or more substrates without carrying out any separation.

With an improved communication link between the MS operating software and the autosampler, the analysis of even larger libraries should be possible, since the actual flow of the sample through the column requires around 30 s, and a cycle time of 40–50 s seems possible even when a washing step of the autosampler is included.

Acknowledgement

Parts of this research were funded by EC projects BIO4-CT98–0249, QLK3–2000–00426, and QLK3-CT-2001–00519.

References

1. (*a*) Chirality in industry: The commercial manufacture and applications of optically active compounds. *Edited by* A.N. Collins, G.N. Sheldrake, and J. Crosby. Wiley, Chichester. 1992; (*b*) Chirality in industry II: Developments in the commercial manufacture and applications of optically active compounds. *Edited by* A.N. Collins, G.N. Sheldrake, and J. Crosby. Wiley, Chichester. 1997; (*c*) R.A. Sheldon. Chirotechnology: Industrial synthesis of optically active compounds. Dekker, New York. 1993; (*d*) S.C. Stinson. Chem. Eng. News, Oct. 1, 79 (2001).
2. (*a*) Comprehensive asymmetric catalysis. Vols. I–III. *Edited by* E.N. Jacobsen, A. Pfaltz, and H. Yamamoto. Springer, Berlin. 1999; (*b*) H. Brunner and W. Zettlmeier. Handbook of enantioselective catalysis with transition metal compounds. Vols. I and II. VCH, Weinheim. 1993; (*c*) R. Noyori. Asymmetric catalysis in organic synthesis. Wiley, New York. 1994; (*d*) Catalytic asymmetric synthesis. *Edited by* I. Ojima. VCH, Weinheim. 1993; (*e*) D.J. Berrisford, C. Bolm, and K.B. Sharpless. Angew. Chem. **107**, 1159 (1995); Angew. Chem. Int. Ed. Engl. **34**, 1059 (1995).
3. (*a*) J.B. Jones. Tetrahedron, **42**, 3351 (1986); (*b*) H.G. Davies, R.H. Green, D.R. Kelly, and S.M. Roberts. Biotransformations in preparative organic chemistry: The use of isolated enzymes and whole cell systems in synthesis. Academic Press, London. 1989; (*c*) C.H. Wong and G.M. Whitesides. Enzymes in synthetic organic chemistry (Tetrahedron organic chemistry series. Vol. 12). Pergamon, Oxford. 1994; (*d*) Enzyme catalysis in organic synthesis: A comprehensive handbook. Vols. I and II. *Edited by* K. Drauz and H. Waldmann. VCH, Weinheim. 1995; (*e*) K. Faber. Biotransformations in organic chemistry. 3rd ed. Springer, Berlin. 1997.
4. See for example: (*a*) M.B. Francis and E.N. Jacobsen. Angew. Chem. **111**, 987 (1999); Angew. Chem. Int. Ed. **38**, 937(1999); (*b*) S.R. Gilbertson and C.-W.T. Chang. Chem. Commun. 975 (1997); (*c*) C. Gennari, S. Ceccarelli, U. Piarulli, C.A.G.N. Montalbetti, and R.F.W. Jackson. J. Org. Chem. **63**, 5312 (1998); (*d*) K. Burgess, H.-J. Lim, A.M. Porte, and G.A. Sulikowski. Angew. Chem. **108**, 192(1996); Angew. Chem.

© 2002 NRC Canada

Int. Ed. Engl. **35**, 220 (1996); (*e*) C.A. Krueger, K.W. Kuntz, C.D. Dzierba, W.G. Wirschun, J.D. Gleason, M.L. Snapper, and A.H. Hoveyda. J. Am. Chem. Soc. **121**, 4284 (1999).
5. For reviews of high-throughput ee-screening systems, see: (*a*) M.T. Reetz. Angew. Chem. **113**, 292 (2001); Angew. Chem. Int. Ed. **40**, 284 (2001); (*b*) M.T. Reetz. Angew. Chem. **114**, 1391 (2202); Angew. Chem. Int. Ed. **41**, 1335 (2002).
6. (*a*) D.W. Leung, E. Chen, and D.V. Goeddel. Technique, **1**, 11 (1989); (*b*) F.H. Arnold. Acc. Chem. Res. **31**, 125 (1998); (*c*) W.P.C. Stemmer. Nature (London), **370**, 389 (1994); (*d*) R.C. Cadwell and G.F. Joyce. PCR Methods Appl. **2**, 28 (1992).
7. (*a*) M.T. Reetz, A. Zonta, K. Schimossek, K. Liebeton, and K.-E. Jaeger. Angew. Chem. **109**, 2961 (1997); Angew. Chem., Int. Ed. Engl. **36**, 2830 (1997); (*b*) M.T. Reetz and K.-E. Jaeger. Chem. Eur. J. **6**, 407 (2000); (*c*) M.T. Reetz, S. Wilensek, D. Zha, and K.-E. Jaeger. Angew. Chem. **113**, 3701 (2001); Angew. Chem. Int. Ed. **40**, 3589 (2001).
8. (*a*) L.E. Janes and R.J. Kazlauskas. J. Org. Chem. **62**, 4560 (1997); (*b*) L.E. Janes, A.C. Löwendahl, and R.J. Kazlauskas. Chem. Eur. J. **4**, 2324 (1998); (*c*) F. Morís-Varas, A. Shah, J. Aikens, N.P. Nadkarni, J.D. Rozzell, and D.C. Demirjian. Bioorg. Med. Chem. **7**, 2183 (1999); (*d*) F. Zocher, M.M. Enzelberger, U.T. Bornscheuer, B. Hauer, and R.D. Schmid. Anal. Chim. Acta, **391**, 345 (1999).
9. M.T. Reetz, K.M. Kühling, A. Deege, H. Hinrichs, and D. Belder. Angew. Chem. **112**, 4049 (2000); Angew. Chem. Int. Ed. **39**, 3891 (2000).
10. M.T. Reetz, M. Hermes, and M.H. Becker. Appl. Microbiol. Biotechnol. **55**, 531 (2001).
11. (*a*) G.T. Copeland and S.J. Miller. J. Am. Chem. Soc. **121**, 4306 (1999); (*b*) M.T. Reetz and S. Sostmann. Tetrahedron, **57**, 2515 (2001).
12. T. Hattori, Y. Minato, S. Yao, M.G. Finn, and S. Miyano. Tetrahedron Lett. **42**, 8015 (2001).
13. G.A. Korbel, G. Lalic, and M.D. Shair. J. Am. Chem. Soc. **123**, 361 (2001).
14. R.A. van Delden and B.L. Feringa. Angew. Chem. **113**, 3298 (2001); Angew. Chem. Int. Ed. **40**, 3198 (2001).
15. P. Abato and C.T. Seto. J. Am. Chem. Soc. **123**, 9206 (2001).
16. M.T. Reetz. K.M. Kühling, S. Wilensek, H. Husmann, U.W. Häusig, and M. Hermes. Catal. Today, **67**, 389 (2001).
17. M. Baumann, R. Stürmer, and U.T. Bornscheuer. Angew. Chem. **113**, 4329 (2001); Angew. Chem. Int. Ed. **40**, 4201 (2001).
18. F. Taran, C. Gauchet, B. Mohar, S. Meunier, A. Valleix, P.Y. Renard, C. Créminon, J. Grassi, A. Wagner, and C. Miokowski. Angew. Chem. **114**, 132 (2002); Angew. Chem. Int. Ed. **41**, 124 (2002).
19. (*a*) B. Jandeleit, D.J. Schaefer, T.S. Powers, H.W. Turner, and W.H. Weinberg. Angew. Chem. **111**, 2648 (1999); Angew. Chem. Int. Ed. **38**, 2494 (1999); (*b*) W.F. Maier. Angew. Chem. **111**, 1294 (1999); Angew. Chem. Int. Ed. **38**, 1216 (1999); (*c*) P.P. Pescarmona, J.C. van der Waal, I.E. Maxwell, and T. Maschmeyer. Catal. Lett. **63**, 1 (1999); (*d*) S. Senkan. Angew. Chem. **113**, 322 (2001); Angew. Chem. Int. Ed. **40**, 312 (2001); (*e*) M.-J. Kang, A. Tholey, and E. Heinzle. Rapid Commun. Mass Spectrom. **15**, 1327 (2001); (*f*) C. Felten, F. Foret, M. Minarik, W. Goetzinger, and B.L. Karger. Anal. Chem. **73**, 1449 (2001).
20. C.J. Welch, S.D. Pollard, D.J. Mathre, and P.J. Reider. Org. Lett. **3**, 95 (2001).
21. M. Sawada, Y. Takai, H. Yamada, S. Hirayama, T. Kaneda, T. Tanaka, K. Kamada, T. Mizooku, S. Takeuchi, K. Ueno, K. Hirose, Y. Tobe, and K. Naemura. J. Am. Chem. Soc. **117**, 7726 (1995).
22. J. Guo, J. Wu, G. Siuzdak, and M.G. Finn. Angew. Chem. **111**, 1868 (1999); Angew. Chem. Int. Ed. **38**, 1755 (1999).
23. M.T. Reetz, M.H. Becker, H.-W. Klein, and D. Stöckigt. Angew. Chem. **111**, 1872 (1999); Angew. Chem. Int. Ed. **38**, 1758 (1999).
24. M. Arand, H. Hemmer, H. Dürk, J. Baratti, A. Archelas, R. Furstoss, and F. Oesch. Biochem. J. **344**, 273 (1999).
25. J.M. Klunder, T. Onami, and K.B. Sharpless. J. Org. Chem. **54**, 1295 (1989).
26. Microsoft-Excel is commercially available from Mircosoft (Unterschleissheim, Germany).
27. C.-S. Chen and C.J. Sih. Angew. Chem. **101**, 711 (1989); Angew. Chem. Int. Ed. Engl. **28**, 695 (1989).
28. M.T. Reetz and C. Torre. Unpublished results.
29. V. de Biasi, N. Haskins, A. Organ, R. Bateman, K. Giles, and S. Jarvis. Rapid Commun. Mass Spectrum. **13**, 1165 (1999).

© 2002 NRC Canada

Chloroperoxidase-catalyzed oxidation of methionine derivatives

Herbert L. Holland, Frances M. Brown, Damian Lozada, Benjamin Mayne, W. Rick Szerminski, and Aaron J. van Vliet

Abstract: Treatment of *N*-methoxycarbonyl *C*-carboxylate ester derivatives of L- and D-methionine and L-ethionine by chloroperoxidase–hydrogen peroxide resulted in oxidation at sulfur to produce the (R_S) sulfoxide in moderate to high diastereomeric excess. The (R_S) sulfoxide of methionine was also obtained in moderate to high diastereomeric excess from $(\pm)_{SO}$-*N*-methoxycarbonyl-L-methionine methyl ester sulfoxide by ester hydrolysis using α-chymotrypsin, *Aspergillus* sp. protease or subtilisin Carlsberg.

Key words: amino acid oxidation, biocatalysis, biotransformation, chloroperoxidase, enzyme catalysis, lipase, sulfoxidation.

Résumé : Le traitement de dérivés *N*-méthoxycarbonyle *C*-carboxylates des L- et D-méthionines et de la L-éthionine par de la chloroperoxydase et du peroxyde d'hydrogène conduit à l'oxydation au niveau du soufre et à la formation de sulfoxydes (R_S), avec des excès diastéréomériques qui vont de modérés à élevés. Le (R_S) sulfoxyde de la méthionine a aussi été obtenu avec un excès diastéréomérique élevé à partir de l'ester méthylique du de sulfoxyde $(\pm)_{SO}$-*N*-méthoxycarbonyl-L-méthionine, par hydrolyse de l'ester à l'aide d'α-chymotrypsine, de protéase d'*Aspergillus* sp. ou de subtilisine Carlsberg.

Mots clés : oxydation d'acide aminé, biocatalyse, biotransformation, chloroperoxydase, catalyse enzymatique, lipase, sulfoxydation.

[Traduit par la Rédaction]

Introduction

Sulfoxides of the sulfur-containing amino acids possess various biological properties. Oxidation of methionine residues in proteins is the target of continued interest, and can result in structural and functional changes in protein (1) and (or) cellular oxidative-stress properties (2). The reversible oxidation of methionine (**1**) can also be involved in other biological functions such as the modulation of potassium-channel activity (3) and the oxidation of high- density lipoproteins (4, 5). It is also implicated in ageing processes by the effect of methionine sulfoxidation on the activity of the human keratinocyte growth factor (6) and on the immunopeptide thymosin β-4 (7); the in vivo oxidation of methionine to the sulfoxide is an age-dependent process in humans (8). The carcinogenic properties of ethionine (**2**) have been linked to its in vivo oxidation to sulfoxide (9), while *S*-methylcysteine sulfoxide (**3**-sulfoxide) is responsible for the antibacterial action of cabbage (10) and possesses the ability to lower serum-cholesterol levels (11, 12).

Received 23 November 2001. Published on the NRC Research Press Web site at http://canjchem.nrc.ca on 17 April 2002.

This paper is dedicated to Professor J. Bryan Jones, whose introductory work, continued research, and present-day creations are all fundamental areas of biocatalysis.

H.L. Holland,[1] F.M. Brown, D. Lozada, B. Mayne, W.R. Szeminski, and A.J. van Vliet. Department of Chemistry, Brock University, St. Catharines, ON L2S 3A1, Canada.

[1]Corresponding author (e-mail holland@chemiris.labs.brocku.ca).

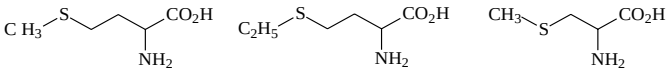

1 **2** **3**

With the exception of L-methionine sulfoxide isolated from the blowfly *Phormia regina* (13), and *S*-methyl-L-cysteine sulfoxide from cabbage (14), both of which have the (S_S) configuration, no data are available on the configuration at sulfur in naturally occurring amino acid sulfoxides.

The stereoselective chemical oxidation at sulfur of a thia-amino acid has not been reported, and only recently have other chemical routes for the preparation of diastereomerically defined amino acid sulfoxides been systematically investigated (14). The value of biocatalytic oxidation for the stereoselective oxidation of sulfides to sulfoxides, however, is well established (15, 16), and was used for the oxidation of methionine by *Penicillium citreoviride*, but no stereochemical details were reported (17). Fungal biocatalysts oxidize various prochiral sulfides to chiral sulfoxides. The use of *Beauveria bassiana* ATCC 7159 and *B. caledonica* ATCC 64970 for the stereoselective oxidation of *N*-phthaloyl-methionines and -ethionines to the (S_S) methionine and ethionine sulfoxides has recently been reported (18, 19). The application of isolated enzymes for chiral sulfoxidation is less common, but chloroperoxidase (CPO) from *Caldariomyces fumago* has been systematically used for the oxidation of various sulfides (16, 20–22). Cyclohexanone monooxygenase (CMO) from *Acinetobacter* species has also been employed for moderate diastereomeric sulfoxidation of *S*-allylcysteine (alliin) (23).

 DOI: 10.1139/V02-025 © 2002 NRC Canada

Table 1. CPO-catalyzed oxidations of L-methionine derivatives.

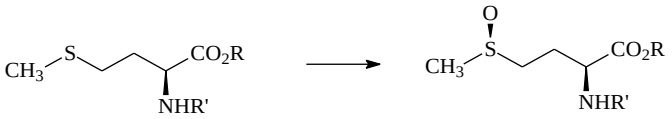

R	R′	Conversion (%)	de (%)	Sulfoxide stereochemistry
H	Ac	0	—	—
	MOC	2	—	—
	Phthaloyl	0	—	—
CH_3	Ac	20	72	*R*
	MOC	84	82	*R*
	ClAc	85	12	*R*
	CHO	25	30	*R*
	t-Boc	10	72	*R*
C_2H_5	MOC	60	72	*R*
n-C_3H_7	MOC	72	84	*R*
n-C_4H_9	MOC	60	48	*R*
n-C_5H_{11}	MOC	50	60	*R*

With the latter exception, the present paper describes the first use of isolated enzymes, particularly the oxidizing species chloroperoxidase–hydrogen peroxide, for the stereoselective oxidation at sulfur in methionine and ethionine derivatives.

Results and discussion

Table 1 summarizes the optimum use of substrate-protecting groups for the chloroperoxidase-catalyzed oxidation of L-methionine derivatives, where maximum yield and diastereomeric excesses were obtained with the *N*-methoxycarbonyl (*N*-MOC) *C*-carboxylate methyl ester derivatives.

The configurations at sulfur of the sulfoxides listed in Table 1 were obtained by analysis of their ^{13}C NMR spectra. Although the ^{1}H NMR spectra of the two diastereomers (S_SS_C) and (R_SS_C) were essentially identical, the signals in ^{13}C NMR spectra from the α and β carbons to the sulfoxide sulfur were separable in methanol. Comparison with ^{13}C NMR spectra from diastereomerically pure L-methionine sulfoxide standards with similar protection groups (19), were then used to assign the configurations obtained by the CPO-catalyzed oxidations. The sulfoxides listed in Table 1 were predominantly (R_SS_C) configurations, and illustrate a consistent excess of the upfield-signal intensity in the stereochemically dependent pairs of signals at ca. δ 24 (C-3), 37 (S(O)-CH_3), and 50 (C-4). Confirmation that the diastereomeric pairs of all the sulfoxide products (possessing both (R_SS_C) and (S_SS_C) configurations) exhibited base-line peak separation in the ^{13}C NMR spectra was obtained from the ^{13}C NMR spectra of such products obtained using hydrogen peroxide as the oxidation reagent for the *N*-MOC ester derivatives.

The results obtained from CPO-catalyzed oxidation of D-methionine derivatives are listed in Table 2. The configuration at sulfur was again determined to be (R_S) by ^{13}C NMR spectral analysis of the α and β carbons to the sulfoxide sulfur (ca. δ 24 (C-3), 37 (S(O)-CH_3), and 50 (C-4)). The predominant (R_SR_C) configurations of the products illustrate a consistent excess of the downfield ^{13}C NMR signals in the stereochemically dependent pairs.

Table 2. CPO-catalyzed oxidations of D-methionine derivatives.

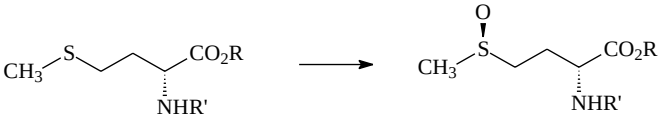

R	R′	Conversion (%)	de (%)	Sulfoxide stereochemistry
CH_3	MOC	42	50	*R*
	t-Boc	6	—	—
C_2H_5	MOC	22	50	*R*
n-C_3H_7	MOC	28	46	*R*
n-C_4H_9	MOC	19	24	*R*
n-C_5H_{11}	MOC	10	0	—

Table 3. CPO-catalyzed oxidations of L-and D-ethionine derivatives.

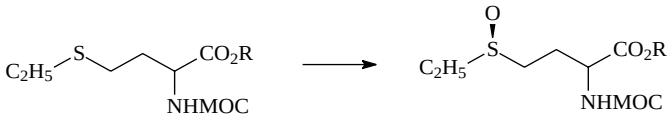

C-2 configuration	R	Conversion (%)	de (%)	Sulfoxide stereochemistry
L (*S*)	CH_3	30	91	*R*
L (*S*)	C_2H_5	40	80	*R*
D (*R*)	CH_3	8	0	—

Table 3 illustrates that only the L-ethionine derivatives were effective substrates for CPO-catalyzed oxidation at sulfur. The configurations at sulfur were determined as described above, i.e., using ^{13}C NMR spectral analysis of α carbons to the sulfoxide sulfur (ca. δ 24 (C-3) and 51 (SCH_2CH_3)), and by comparison with the ^{13}C NMR spectra of stereochemically known samples (19). The predominant signal from the (R_SS_C) configurations of both diastereomerically enriched sulfoxides occurs as the upfield component of the stereochemically dependent pair of signals.

The formation of diastereomerically enriched sulfoxides by stereoselective hydrolysis of the methyl ester from diastereomeric *N*-MOC-L-methionine sulfoxides (1:1) is summarized in Table 4.

Of the hydrolytic enzymes that were successful in the stereoselective hydrolysis of this diastereomeric pair, subtilisin Carlsberg was the most efficient and gave both the acid and the unreacted ester products in moderate yield and high diastereomeric excess. Again, configuration at sulfur of both products was determined by ^{13}C NMR spectral analysis of the α and β carbons to the sulfoxide sulfur (ca. δ 24 (C-3), 37 (S(O)-CH_3), and 50 (C-4)), with (R_SS_C) configurations of diastereomerically enriched sulfoxides occurring as the upfield component of the stereochemically dependent signal pair and (S_SS_C) configurations with the predominant peak as the downfield component.

The CPO-catalyzed oxidations of a series of methionine-containing dipeptides are summarized in Table 5. Although the enzyme was capable of the oxidation of several of these substrates in acceptable yields, only one sulfoxide, from the

© 2002 NRC Canada

Table 4. Stereoselective hydrolysis of *N*-MOC-L-methionine methyl ester sulfoxides.

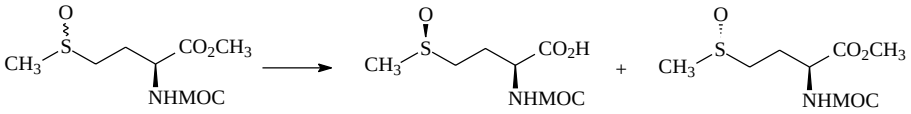

Enzyme	Time (min)	Yield (%)	de (%)	Sulfoxide stereochemistry	Yield (%)	de (%)	Sulfoxide stereochemistry
α-Chymotrypsin	10	42	82	*R*	35	80	*S*
Aspergillus sp. protease	5	39	40	*R*	46	28	*S*
Subtilisin Carlsberg	15	41	90	*R*	38	86	*S*
Aspergillus lipase	10	25	0	—	58	0	—

Table 5. CPO-catalyzed oxidations of L-methionine-containing protected dipeptides

N-MOC-Me-ester dipeptide	Yield (%)	de (%)	Sulfoxide stereochemistry
MET-GLY	90	0	—
MET-ALA	80	0	—
MET-LEU	90	0	—
MET-PRO	17	0	—
MET-PHE	<5	0	—
GLY-MET	95	0	—
ALA-MET	90	98	*R*
LEU-MET	16	0	—
PRO-MET	33	5	—
PHE-MET	<5	0	—

methyl ester of *N*-MOC, ALA-MET, was produced in a stereochemically acceptable form.

In the absence of a stereochemical standard for this product, the assignment of the configuration at sulfur was again based on ^{13}C NMR spectral analysis of the α and β carbons to the sulfoxide sulfur (ca. δ 24 (C-3), 37 (S(O)-CH_3), and 50 (C-4)), with the assumption that the (R_SS_C) configuration of *N*-MOC-ALA-MET methyl ester sulfoxide presumably resulted in signal intensities consistent with the standard L-methionine products. Nevertheless, the description of the methionine sulfoxide configuration of the dipeptide product as (R_SS_C) must be considered tentative.

The removal of both *N*-MOC- and methyl ester protecting groups from the diastereomerically enriched L-methionine, D-methionine, and L-ethionine sulfoxide enzyme-catalyzed products was performed in moderate yield by routine hydrolysis with barium hydroxide, generating the appropriate free amino-acid sulfoxides.

Experimental

Materials and methods

Melting points were determined on a Kofler hot stage and are uncorrected. The ^{1}H NMR spectra were recorded on a Bruker Advance series 300 spectrometer in $CDCl_3$ using residual $CHCl_3$ as the internal standard or CD_3OD using CH_3OH as the internal standard unless otherwise stated; chemical shifts are reported in ppm (δ) and the signals quoted as s (singlet), d (doublet), t (triplet), q (quartet), or m (multiplet). The ^{13}C NMR spectra were recorded at 75 MHz on the same spectrometer in $CDCl_3$, CD_3OD, or D_2O. Diastereomeric excess (de) was determined by ^{13}C NMR analysis of signals α and β to sulfur. Mass spectra were obtained using a Kratos 1S spectrometer. Optical rotations were recorded at ambient temperature in the stated solvent using a Rudolph Autopol 3 polarimeter. TLC was performed on Merck silica gel F_{254} plates, 0.2 mm, and column chromatography used Merck silica gel 9385, 230–400 mesh.

Chloroperoxidase from *Caldariomyces fumago* was obtained from the Sigma Chemical Co. (catalogue no. C-0278). α-Chymotrypsin, *Aspergillus* sp. protease, subtilisin Carlsberg, and *Aspergillus* lipase were obtained from Altus Biologics Inc.

Preparation of substrates

N-*Protection*

N-*t*-Boc-L- and D-methionines, *N*-acetyl-L-methionine, and *N*-formyl-L-methionine are commercial samples. *N*-chloroacetyl-L-methionine (24) and *N*-phthaloyl-L-methionine (19) were prepared from the amino acids as previously described.

N-MOC-L- and D-methionines, *N*-MOC-L- and -D- ethionines, and *N*-MOC-dipeptides were prepared by the following standard procedure. A stirred solution of L-methionine (2.08 g) in aqueous sodium hydroxide (40 mL, 2 M) at 0°C was treated with methyl chloroformate (10.4 mL) in 1 mL increments over 1 h. The pH was maintained above 10.5 by addition of 2 M sodium hydroxide as required. After the final aliquot of methyl chloroformate (0.4 mL) was added, the reaction mixture was allowed to reach room temperature and was then washed with an equal volume of ether. The aqueous layer was then cooled to 0°C, acidified to pH 2–3 with 10% HCl, and extracted with ethyl acetate (3 × 100 mL). The extract was dried ($MgSO_4$) and evaporated to yield *N*-MOC-L-methionine (2.34 g, 84%) as an oil. NMR data are listed below. Unless stated otherwise all products gave *m*/*z* MH^+ ions using FAB-NBA spectra.

N-*MOC-L- and D-methionines*

^{1}H NMR ($CDCl_3$) δ: 1.95–2.26 (m, 2H), 2.10 (s, 3H, SCH_3), 2.59 (t, 2H), 3.70 (s, 3H, OCH_3), 4.50 (q, 1H), 5.39

© 2002 NRC Canada

(d, 1H), 6.47 (d, 1H). ^{13}C NMR ($CDCl_3$) δ: 15.6 (SCH_3), 30.2 (SCH_2), 31.9 (CH_2), 53.0 (OCH_3), 53.3 (CH), 157.5 (CO), 176.2 (CO). EI-MS *m*/*z* (%): 207 (26), 175 (40), 133 (47), 115 (58), 75 (66), 61 (100).

N-*MOC-L- and D- ethionines*

^{1}H NMR ($CDCl_3$) δ: 1.21 (t, 3H), 1.81–2.17 (m, 4H, $2CH_2$) 3.71 (s, 3H, OCH_3), 4.34 (q, 1H), 4.84 (s, 1H), 7.35 (d, 1H). ^{13}C NMR (CD_3OD) δ: 14.1 (CH_3), 25.4 (SCH_2), 27.3 (SCH_2), 31.6 (CH_2), 52.6 (CH), 53.3 (OCH_3), 163.5 (CO), 173.4 (CO).

N-*MOC-MET-GLY*

^{1}H NMR (CD_3OD) δ: 1.8–2.1 (m, 2H, CH_2), 2.08 (s, 3H, SCH_3), 2.55 (m, 2H), 3.34 (s, 3H, OCH_3), 3.67 (br s, 2H), 4.28 (m, 1H), 5.6 (br s, 1H), 6.8 (br s, 1H). ^{13}C NMR (CD_3OD) δ: 14.1 (SCH_3), 30.0, 31.8, 40.9, 54.4, 56.4, 158.1, 171.9, 173.8.

N-*MOC-MET-ALA*

^{1}H NMR (D_2O) δ: 1.22 (d, 3H), 1.88 (m, 2H, CHC*H*$_3$), 2.0 (s, 3H, SCH_3), 2.51 (m, 2H), 3.57 (s, 3H, OCH_3), 4.05 (q, 1H, C*H*CH_3), 4.16 (m, 1H). ^{13}C NMR (D_2O) δ: 14.5, 17.8, 29.7, 31.0, 51.3, 53.0, 54.3, 159.3, 172.6, 173.2.

N-*MOC-MET-LEU*

^{1}H NMR (CD_3OD) δ: 0.75 (d, 3H, CHC*H*$_3$), 0.81 (d, 3H, CHC*H*$_3$), 1.55 (m, 2H), 1.95–2.2 (m, 2H), 2.08 (s, 3H, SCH_3), 2.85 (m, 1H), 3.20 (m, 2H), 3.56 (s, 3H, OCH_3), 4.17 (m, 1H), 4.34 (t, 1H). ^{13}C NMR (D_2O) δ: 13.8, 20.9 (2), 22.6, 24.5, 30.5, 39.9, 52.6, 52.9, 158.5, 173.8, 175.1.

N-*MOC-MET-PRO*

^{1}H NMR (CD_3OD) δ: 1.88–2.15 (m, 6H), 2.09 (s, 3H, SCH_3), 2.25 (m, 2H), 2.60 (t, 2H), 3.62 (s, 3H, OCH_3), 4.49 (m, 1H), 4.62 (m, 1H). ^{13}C NMR (CD_3OD) δ: 14.3, 24.9, 29.0, 29.8, 31.1, 51.7, 59.4, 78.5, 156.8, 172.1, 173.0.

N-*MOC-MET-PHE*

^{1}H NMR ($CDCl_3$) δ: 1.8–2.0 (m, 2H), 2.08 (s, 3H, SCH_3), 2.50 (m, 2H), 3.03 (m, 2H), 3.64 (s, 3H, OCH_3), 4.22 (m, 1H), 4.72 (m, 1H), 7.23 (m, 5H). ^{13}C NMR (CD_3OD) δ: 14.2, 29.9, 31.9, 37.2, 51.7, 54.1, 54.3, 126.9, 128.5, 129.3, 137.0, 155.9, 172.2, 173.2.

N-*MOC-GLY-MET*

^{1}H NMR (CD_3OD) δ: 1.9–2.2 (m, 2H), 2.07 (s, 3H, SCH_3), 2.5–2.7 (m, 4H), 3.68 (s, 3H, OCH_3), 4.57 (q, 1H). ^{13}C NMR (CD_3OD) δ: 14.2, 30.1, 31.1, 43.8, 51.5, 51.8, 157.7, 171.5, 171.8.

N-*MOC-ALA-MET*

^{1}H NMR (CD_3OD) δ: 1.32 (d, 3H), 1.9–2.2 (m, 2H), 2.09 (s, 3H, SCH_3), 2.50 (m, 2H), 3.66 (s, 3H, OCH_3), 4.12 (m, 1H), 4.58 (m, 1H). ^{13}C NMR (CD_3OD) δ: 14.2, 17.3, 30.1, 31.3, 50.9, 51.1, 51.6, 157.0, 173.8, 174.7.

N-*MOC-LEU-MET*

^{1}H NMR (CD_3OD) δ: 0.96 (d, 3H), 0.98 (d, 3H), 1.58 (m, 2H), 1.70 (m, 1H), 1.9–2.2 (m, 2H), 2.05 (s, 3H, SCH_3), 2.55 (m, 2H), 3.66 (s, 3H, OCH_3), 4.16 (m, 1H), 4.57 (m, 1H). ^{13}C NMR (CD_3OD) δ: 14.2, 20.9, 22.3, 24.7, 30.1, 31.2, 41.0, 51.5, 51.6, 53.8, 156.8, 173.2, 174.6.

N-*MOC-PRO-MET*

^{1}H NMR (CD_3OD) δ: 1.8–2.3 (m, 8H), 2.09 (s, 3H, SCH_3), 2.60 (m, 2H), 3.64 (s, 3H, OCH_3), 4.28 (m, 1H), 4.58 (m, 1H). ^{13}C NMR (CD_3OD) δ: 14.3, 24.4, 30.1, 30.4, 31.1, 51.7, 51.8, 60.2, 60.5, 156.3, 172.6, 174.3.

N-*MOC-PHE-MET*

^{1}H NMR (CD_3OD) δ: 1.82–2.12 (m, 2H), 2.04 (s, 3H, SCH_3), 2.52 (m, 2H), 2.88 and 3.14 (m, total 2H), 3.58 (s, 3H, OCH_3), 4.35 (m, 1H), 4.60 (m, 1H), 7.07 (d, 1H, NH), 7.24 (m, 5H), 8.40 (d, 1H, NH). ^{13}C NMR (CD_3OD) δ: 14.2, 30.0, 31.0, 38.0, 51.6, 51.7, 56.6, 126.7, 128.4 (2), 129.3 (2), 137.5, 157.3, 172.5, 173.4.

Esterification

The esters of *N*-protected amino acids and dipeptides were all obtained by the following standard procedure using the appropriate alcohol. *N*-MOC-L-methionine (2.34 g) was dissolved in methanol (50 mL) and a catalytic amount of hydrochloric acid added to adjust the solution to pH 3.0. The solution was heated under reflux for 12 h, then evaporated. Water (50 mL) was added and the product extracted with ethyl acetate. The solution was washed with saturated $NaHCO_3$, dried, and evaporated to give *N*-MOC-L-methionine methyl ester as an oil (2.03 g, 81%). NMR data are listed below. Unless listed otherwise, all products gave *m*/*z* MH^+ ions using FAB-NBA spectra.

N-*Acetyl-L-methionine methyl ester*

^{1}H NMR (CD_3OD) δ: 1.9–2.2 (m, 2H), 1.94 (s, 3H), 2.08 (s, 3H, SCH_3), 2.42 (m, 2H), 3.60 (s, 3H, OCH_3), 4.58 (m, 1H), 6.72 (d, 1H, NH). ^{13}C NMR (CD_3OD) δ: 14.3, 21.4, 30.1, 31.0, 51.8, 51.9, 172.4, 173.0.

N-*Chloroacetyl-L-methionine methyl ester*

^{1}H NMR ($CDCl_3$) δ: 1.98–2.25 (m, 2H), 2.1 (s, 3H, SCH_3), 2.50 (t, 2H), 3.78 (s, 3H, OCH_3), 4.08 (2H, s), 4.70 (m, 1H). ^{13}C NMR ($CDCl_3$) δ: 15.9, 30.2, 31.7, 42.8, 52.2, 53.1, 166.3, 172.1.

N-*Formyl-L-methionine methyl ester*

^{1}H NMR ($CDCl_3$) δ: 1.9–2.2 (m, 2H), 2.05 (s, 3H, SCH_3), 2.52 (t, 2H), 3.73 (s, 3H, OCH_3), 4.70 (m, 1H), 4.80 (s, 1H, NH), 8.10 (s, 1H). ^{13}C NMR ($CDCl_3$) δ: 15.9, 30.2, 32.0, 50.6, 53.1, 161.1, 172.4.

N-*MOC-L- and D-methionine methyl esters*

^{1}H NMR ($CDCl_3$) δ: 1.92–2.24 (m, 2H), 2.10 (s, 3H, SCH_3), 2.54 (t, 2H), 3.70 (s, 3H, OCH_3), 3.79 (s, 3H, OCH_3), 4.51 (q, 1H), 5.35 (d, 1H, NH). ^{13}C NMR ($CDCl_3$) δ: 15.0, 29.6, 31.4, 52.0, 52.1, 52.8, 156.4, 172.4.

N-*MOC-L- and D-methionine ethyl esters*

^{1}H NMR ($CDCl_3$) δ: 1.26 (t, 3H), 1.90–2.2 (m, 2H), 2.11 (s, 3H, SCH_3), 2.52 (m, 2H), 3.67 (s, 3H, OCH_3), 4.20 (2H, q), 4.45 (m, 1H), 5.36 (m, 1H, NH). ^{13}C NMR ($CDCl_3$) δ: 14.5, 15.8, 30.2, 32.4, 52.7, 53.6, 62.0, 156.9, 172.4.

N-*MOC-L- and D-methionine n-propyl esters*

^{1}H NMR ($CDCl_3$) δ: 0.92 (t, 3H), 1.67 (sextet, 2H), 1.90–2.15 (m, 2H), 2.08 (s, 3H, SCH_3), 2.51 (t, 2H), 3.68 (s, 3H, OCH_3), 4.08 (q, 2H), 4.42 (m, 1H), 5.39 (m, 1H, NH).

© 2002 NRC Canada

^{13}C NMR ($CDCl_3$) δ: 10.7, 15.8, 22.3, 30.3, 32.5, 52.7, 53.6, 67.6, 156.9, 172.5.

N-*MOC-L- and D-methionine n-butyl esters*

^{1}H NMR ($CDCl_3$) δ: 0.92 (t, 3H), 1.33 (sextet, 2H), 1.60 (sextet, 2H), 1.87–2.15 (m, 2H), 2.07 (s, 3H, SCH_3), 2.50 (t, 2H), 3.66 (s, 3H, OCH_3), 4.10 (q, 2H), 4.41 (m, 1H), 5.40 (m, 1H, NH). ^{13}C NMR ($CDCl_3$) δ: 14.0, 15.8, 19.4, 30.3, 30.9, 32.5, 52.7, 53.6, 65.8, 156.9, 172.5.

N-*MOC-L- and D-methionine n-pentyl esters*

^{1}H NMR ($CDCl_3$) δ: 0.87 (t, 3H), 1.30 (m, 6H), 1.62 (m, 2H), 1.85–2.18 (m, 2H), 2.07 (s, 3H, SCH_3), 2.49 (m, 2H), 3.64 (s, 3H, OCH_3), 4.08 (q, 2H), 4.40 (m, 1H), 5.38 (m, 1H, NH). ^{13}C NMR ($CDCl_3$) δ: 14.3, 15.8, 22.6, 28.3, 28.6, 30.3, 32.5, 52.7, 53.6, 66.1, 156.9, 172.5.

N-*MOC-L- and D- ethionine methyl esters*

^{1}H NMR (CD_3OD) δ: 1.21 (t, 3H), 1.80–2.15 (m, 2H), 2.52 (m, 4H), 3.62 (s, 3H, OCH_3), 3.72 (s, 3H, OCH_3), 4.33 (m, 1H), 7.35 (m, 1H, NH). ^{13}C NMR (CD_3OD) δ: 14.1, 25.1, 27.5, 31.6, 51.7, 51.8, 53.3, 158.3, 173.4.

N-*MOC-L-ethionine ethyl ester*

^{1}H NMR (CD_3OD) δ: 1.22 (t, 3H), 1.30 (t, 3H), 1.90–2.16 (m, 2H), 2.55 (m, 4H), 3.68 (s, 3H, OCH_3), 4.21 (q, 2H), 4.35 (m, 1H). ^{13}C NMR (CD_3OD) δ: 13.5, 14.1, 25.5, 27.5, 31.6, 51.8, 71.6, 158.3, 173.0.

N-*MOC-MET-GLY methyl ester*

^{1}H NMR ($CDCl_3$) δ: 1.86–2.18 (m, 2H), 2.07 (s, 3H, SCH_3), 2.56 (m, 2H), 3.64 (s, 3H, OCH_3), 3.76 (s, 3H, OCH_3), 4.02 (m, 2H), 4.42 (m, 1H), 5.76 (m, 1H, NH), 6.98 (m, 1H, NH). ^{13}C NMR (CD_3OD) δ: 15.1, 31.0, 32.8, 41.8, 52.6, 52.8, 55.4, 159.1, 171.6, 175.1. EI-MS *m/z* (%): 278 (8), 246 (11), 204 (60), 172 (22), 90 (64), 61 (100),

N-*MOC-MET-ALA methyl ester*

^{1}H NMR (D_2O) δ: 1.38 (d, 3H), 1.82–2.04 (m, 2H), 2.01 (s, 3H, SCH_3), 2.50 (m, 2H), 3.57 (s, 3H, OCH_3), 3.68 (s, 3H, OCH_3), 4.12 (q, 1H), 4.33 (m, 1H). ^{13}C NMR (D_2O) δ: 14.5, 16.3, 29.5, 31.0, 49.1, 53.0, 53.3, 54.2, 158.9, 174.6, 175.2.

N-*MOC-MET-LEU methyl ester*

^{1}H NMR (CD_3OD) δ: 0.74 (d, 3H, CHCH_3), 0.81 (d, 3H, CHCH_3), 1.55 (m, 2H), 1.95–2.2 (m, 2H), 2.10 (s, 3H, SCH_3), 2.85 (m, 1H), 3.24 (m, 2H), 3.55 (s, 3H, OCH_3), 3.60 (s, 3H, OCH_3), 4.17 (m, 1H), 4.35 (t, 1H). ^{13}C NMR (D_2O) δ: 13.6, 20.9 (2), 22.6, 24.5, 30.5, 39.9, 52.6, 52.9, 53.3, 158.8, 173.8, 175.1.

N-*MOC-MET-PRO methyl ester*

^{1}H NMR (CD_3OD) δ: 1.88–2.15 (m, 6H), 2.10 (s, 3H, SCH_3), 2.25 (m, 2H), 2.60 (t, 2H), 3.62 (s, 3H, OCH_3), 3.80 (s, 3H, OCH_3), 4.49 (m, 1H), 4.62 (m, 1H). ^{13}C NMR (CD_3OD) δ: 14.3, 24.9, 29.0, 29.8, 30.1, 31.1, 51.7 (2), 59.4, 78.5, 158.1, 172.1, 173.0.

N-*MOC-MET-PHE methyl ester*

^{1}H NMR (CD_3OD) δ: 1.7–2.1 (m, 2H), 2.02 (s, 3H, SCH_3), 2.48 (m, 2H), 3.05 (m, 2H), 3.64 (s, 3H, OCH_3), 3.70 (s, 3H, OCH_3), 4.22 (m, 1H), 4.72 (m, 1H), 7.25 (m, 5H). ^{13}C NMR (CD_3OD) δ: 14.2, 29.9, 31.9, 37.2, 51.7 (2), 54.1, 54.3, 126.9, 128.5, 129.3, 137.0, 157.9, 172.2, 173.2.

N-*MOC-GLY-MET methyl ester*

^{1}H NMR (CD_3OD) δ: 1.94–2.2 (m, 2H), 2.07 (s, 3H, SCH_3), 2.56 (m, 2H), 3.67 (s, 3H, OCH_3), 3.72 (s, 3H, OCH_3), 4.61 (m, 1H). ^{13}C NMR (CD_3OD) δ: 14.2, 30.0, 30.9, 43.7, 51.6, 51.8, 158.7, 171.3, 172.7.

N-*MOC-ALA-MET methyl ester*

^{1}H NMR (CD_3OD) δ: 1.33 (d, 3H), 1.9–2.18 (m, 2H), 2.07 (s, 3H, SCH_3), 3.64 (s, 3H, OCH_3), 3.73 (s, 3H, OCH_3), 4.16 (m, 1H), 4.59 (m, 1H). ^{13}C NMR (CD_3OD) δ: 14.2, 17.3, 30.1, 31.3, 50.9, 51.1, 51.6 (2), 157.9, 173.8, 174.7.

N-*MOC-LEU-MET methyl ester*

^{1}H NMR (CD_3OD) δ: 0.92 (d, 3H), 0.94 (d, 3H), 1.54 (m, 2H), 1.70 (m, 1H), 1.9–2.18 (m, 2H), 2.05 (s, 3H, SCH_3), 2.52 (m, 2H), 3.60 (s, 3H, OCH_3), 3.71 (s, 3H, OCH_3), 4.12 (m, 1H), 4.58 (m, 1H), 7.0 (d, 1H, NH), 8.35 (d, 1H, NH). ^{13}C NMR (CD_3OD) δ: 14.2, 21.0, 22.3, 24.8, 30.0, 30.9, 41.0, 51.6, 51.7, 53.7, 158.1, 172.6, 174.7.

N-*MOC-PRO-MET methyl ester*

^{1}H NMR (CD_3OD) δ: 1.82–2.3 (m, 8H), 2.1 (s, 3H, SCH_3), 2.60 (m, 2H), 3.64 (s, 3H, OCH_3), 3.73 (s, 3H, OCH_3), 4.28 (m, 1H), 4.58 (m, 1H). ^{13}C NMR (CD_3OD) δ: 14.3, 24.4, 30.1, 30.4, 31.1, 51.7, 51.8, 52.2, 60.2, 60.5, 156.0, 172.6, 174.3.

N-*MOC-PHE-MET methyl ester*

^{1}H NMR (CD_3OD) δ: 1.82–2.1 (m, 2H), 2.06 (s, 3H, SCH_3), 2.52 (m, 2H), 2.87 (m, 1H), 3.14 (m, 1H), 3.58 (s, 3H, OCH_3), 3.70 (s, 3H, OCH_3), 4.35 (m, 1H), 4.60 (m, 1H), 7.25 (m, 5H), 8.39 (d, 1H, NH). ^{13}C NMR (CD_3OD) δ: 14.2, 30.0, 31.0, 38.0, 51.6, 51.7, 51.8, 56.6, 126.7, 128.4, 129.3, 137.4, 157.9, 172.5, 173.4.

Preparation of standard protected sulfoxides

Standard diastereomeric sulfoxide mixtures of esters of *N*-protected amino acids and dipeptides were prepared using the following representative procedure: *N*-MOC-L-methionine methyl ester (2.03 g) was dissolved in methanol (40 mL) in an Erlenmeyer flask (100 mL). In a separate flask, hydrogen peroxide (1.13 g of 30% aqueous solution, 1.1 molar equivalents) was dissolved in methanol (15 mL). Both solutions were cooled to –20°C, then mixed and allowed to stand at –20°C overnight. The solvent was then removed by vacuum to give a quantitative yield of a 1:1 diastereomeric mixture of *N*-MOC-L-methionine methyl ester sulfoxides (oil).

N-*Acetyl-L-methionine methyl ester, sulfoxide*

^{1}H NMR (CD_3OD) δ: 1.94 (s, 3H, $COCH_3$), 2.2–2.4 (m, 2H), 2.52 (s, 3H, $SOCH_3$), 2.8–3.0 (m, 2H), 3.60 (s, 3H, OCH_3), 4.62 (m, 1H). ^{13}C NMR (CD_3OD) δ: 21.4, 24.8, 37.2/37.3, 49.9, 51.6, 52.0, 172.0, 173.0.

N-*Chloroacetyl-L-methionine methyl ester, sulfoxide*

^{1}H NMR (CD_3OD) δ: 2.15 (m, 1H), 2.35 (m, 1H), 2.76 (s, 3H, $SOCH_3$), 2.88 (m, 2H), 3.78 (s, 3H, OCH_3), 4.10 (s, 2H), 4.60 (m, 1H). ^{13}C NMR (CD_3OD) δ: 24.7, 37.1/37.2, 41.9, 49.9, 52.0, 52.6, 166.8, 171.4.

© 2002 NRC Canada

N-*Formyl-L-methionine methyl ester, sulfoxide*

^{1}H NMR (CD_3OD) δ: 2.0–2.3 (m, 2H), 2.62 (s, 3H, $SOCH_3$), 2.80 (m, 2H), 3.80 (s, 3H, OCH_3), 4.80 (m, 1H), 8.22 (s, 1H). ^{13}C NMR (CD_3OD) δ: 25.8, 38.1/38.2, 50.71/50.75, 51.0, 53.1, 163.7, 172.4.

N-*MOC-L- and D-methionine methyl esters, sulfoxides*

^{1}H NMR (CD_3OD) δ: 2.2–2.6 (m, 2H), 2.66 (s, 3H, $SOCH_3$), 2.90 (m, 2H), 3.62 (s, 3H, OCH_3), 3.73 (s, 3H, OCH_3), 4.30 (m, 1H). ^{13}C NMR (CD_3OD) δ: 24.82/24.94, 37.1/37.25, 49.96/50.06, 52.0, 52.1, 53.2, 158.2, 172.4.

N-*MOC-L- and D-methionine ethyl esters, sulfoxides*

^{1}H NMR (CD_3OD) δ: 1.28 (t, 3H), 2.2–2.58 (m, 2H), 2.60 (s, 3H, $SOCH_3$), 2.94 (m, 2H), 3.68 (s, 3H, OCH_3), 4.18 (q, 2H), 4.30 (m, 1H). ^{13}C NMR (CD_3OD) δ: 13.4, 24.72/24.95, 37.12/37.27, 48.8, 50.1, 51.73/51.83, 61.7, 158.3, 172.0.

N-*MOC-L- and D-methionine n-propyl esters, sulfoxides*

^{1}H NMR (CD_3OD) δ: 0.94 (t, 3H), 1.67 (m, 2H), 2.2–2.5 (m, 2H), 2.68 (s, 3H, $SOCH_3$), 2.80 (m, 2H), 3.62 (s, 3H, OCH_3), 4.08 (q, 2H), 4.44 (m, 1H), 7.32 (m, 1H, NH). ^{13}C NMR (CD_3OD) δ: 9.8, 22.3, 24.70/24.94, 37.11/37.27, 51.71/51.80, 52.7, 53.6, 67.1, 158.3, 172.0.

N-*MOC-L- and D-methionine n-butyl esters, sulfoxides*

^{1}H NMR (CD_3OD) δ: 0.95 (t, 3H), 1.40 (sextet, 2H), 1.60 (sextet, 2H), 2.2–2.6 (m, 2H), 2.68 (s, 3H, $SOCH_3$), 2.90 (t, 2H), 3.70 (s, 3H, OCH_3), 4.13 (q, 2H), 4.32 (m, 1H). ^{13}C NMR (CD_3OD) δ: 13.0, 19.4, 24.68/24.92, 32.5, 37.12/37.27, 50.2, 51.7, 53.4, 65.4, 158.3, 172.0.

N-*MOC-L- and D-methionine n-pentyl esters, sulfoxides*

^{1}H NMR (CD_3OD) δ: 0.87 (t, 3H), 1.30 (m, 6H), 1.62 (m, 2H), 2.22–2.5 (m, 2H), 2.63 (s, 3H, $SOCH_3$), 2.65 (m, 2H), 3.62 (s, 3H, OCH_3), 4.15 (q, 2H), 4.33 (m, 1H). ^{13}C NMR (CD_3OD) δ: 14.2, 22.3, 24.69/24.93, 28.4, 31.0, 37.13/37.29, 50.10/50.16, 51.7, 53.4, 65.7, 157.6, 172.0.

N-*MOC-L- and D- ethionine methyl esters, sulfoxides*

^{1}H NMR (CD_3OD) δ: 1.33 (t, 3H), 2.11 (m, 1H), 2.33 (m, 1H), 2.72–2.97 (m, 4H), 3.64 (s, 3H, OCH_3), 3.77 (s, 3H, OCH_3), 4.34 (m, 1H). ^{13}C NMR (CD_3OD) δ: 6.2, 24.89/25.12, 45.3, 51.93/52.11, 52.3, 53.29, 53.62, 158.2, 172.5.

N-*MOC-L-ethionine ethyl ester, sulfoxides*

^{1}H NMR (CD_3OD) δ: 1.22 (t, 3H), 1.30 (t, 3H), 2.15 (m, 1H), 2.33 (m, 1H), 2.7–2.95 (m, 4H), 3.68 (s, 3H, OCH_3), 4.20 (q, 2H), 4.36 (m, 1H). ^{13}C NMR (CD_3OD) δ: 6.1, 13.5, 24.88/25.11, 45.26/45.35, 51.71/51.81, 53.4, 53.5, 71.6, 158.3, 172.0.

N-*MOC-MET-GLY methyl ester, sulfoxides*

^{1}H NMR (CD_3OD) δ: 2.0–2.32 (m, 2H), 2.66 (s, 3H, $SOCH_3$), 2.92 (t, 2H), 3.67 (s, 3H, OCH_3), 3.73 (s, 3H, OCH_3), 3.95 (q, 2H), 4.30 (m, 1H). ^{13}C NMR (CD_3OD) δ: 25.5, 37.08/37.14, 40.8, 49.63/49.77, 51.6, 51.8, 53.9, 157.9, 171.8, 173.0.

N-*MOC-MET-ALA methyl ester, sulfoxides*

^{1}H NMR (CD_3OD) δ: 1.30 (d, 3H), 1.98 (m, 1H), 2.10 (m, 1H), 2.58 (s, 3H, $SOCH_3$), 2.75–2.90 (m, 2H), 3.55 (s, 3H, OCH_3), 3.60 (s, 3H, OCH_3), 4.16 (d, 1H), 4.30 (q, 1H). ^{13}C NMR (CD_3OD) δ: 16.0, 24.71/24.79, 36.69/36.78, 49.65/49.74, 52.90, 53.07, 53.64/53.86, 158.2, 172.3, 173.5.

N-*MOC-MET-LEU methyl ester, sulfoxides*

^{1}H NMR (CD_3OD) δ: 0.75 (d, 3H), 0.81 (d, 3H), 1.50–1.60 (m, 3H), 2.58 (s, 3H, $SOCH_3$), 2.75–2.90 (m, 2H), 3.53 (s, 3H, OCH_3), 3.62 (s, 3H, OCH_3), 4.16 (d, 1H), 4.34 (q, 1H). ^{13}C NMR (CD_3OD) δ: 20.6, 22.3 (2), 24.52/24.68, 37.06/37.13, 40.0, 50.6, 51.3, 51.8, 53.4, 157.9, 172.4, 173.5.

N-*MOC-MET-PRO methyl ester, sulfoxides*

^{1}H NMR (CD_3OD) δ: 1.88–2.15 (m, 4H), 2.40–2.60 (m, 2H), 2.60 (t, 2H), 2.70 (s, 3H, $SOCH_3$), 2.90 (m, 2H), 3.62 (s, 3H, OCH_3), 3.80 (s, 3H, OCH_3), 4.50 (m, 1H), 4.62 (m, 1H). ^{13}C NMR (CD_3OD) δ: 24.8, 24.9, 29.0, 31.1, 37.23/37.34, 51.7 (2), 51.8, 59.4, 78.4, 158.1, 171.0, 172.9.

N-*MOC-MET-PHE methyl ester, sulfoxides*

^{1}H NMR (CD_3OD) δ: 2.2–2.6 (m, 2H), 2.62 (s, 3H, $SOCH_3$), 2.88 (m, 2H), 3.06 (m, 2H), 3.65 (s, 3H, OCH_3), 3.72 (s, 3H, OCH_3), 4.22 (m, 1H), 4.72 (m, 1H), 7.25 (m, 5H). ^{13}C NMR (CD_3OD) δ: 25.56/25.61, 37.2, 37.31/37.39, 49.87/49.92, 51.7 (2), 54.1, 54.3, 126.9, 128.5, 129.3, 136.8, 157.9, 172.2, 173.3.

N-*MOC-GLY-MET methyl ester, sulfoxides*

^{1}H NMR (CD_3OD) δ: 2.16 (m, 1H), 2.36 (m, 1H), 2.68 (s, 3H, $SOCH_3$), 2.77–2.97 (m, 2H), 3.68 (s, 3H, OCH_3), 3.78 (s, 3H, OCH_3), 3.80 (2H, s), 4.22 (m, 1H), 4.60 (m, 1H). ^{13}C NMR (CD_3OD) δ: 24.8, 37.16/37.23, 43.8, 49.9, 51.3, 51.7/51.8, 52.0, 158.7, 171.7, 171.8.

N-*MOC-ALA-MET methyl ester, sulfoxides*

^{1}H NMR (CD_3OD) δ: 1.35 (d, 3H), 2.10 (m, 1H), 2.36 (m, 1H), 2.68 (s, 3H, $SOCH_3$), 2.87 (m, 2H), 3.65, (s, 3H, OCH_3), 3.74 (s, 3H, OCH_3), 4.10 (m, 1H), 4.60 (m, 1H). ^{13}C NMR (CD_3OD) δ: 17.1, 24.67/24.90, 37.18/37.27, 49.9, 50.8, 51.57/51.69, 52.0, 157.9, 171.6, 174.9.

N-*MOC-LEU-MET methyl ester, sulfoxides*

^{1}H NMR (CD_3OD) δ: 0.92 (d, 3H), 0.94 (d, 3H), 1.54 (m, 2H), 1.70 (m, 1H), 2.2–2.45 (m, 2H), 2.66 (s, 3H, $SOCH_3$), 2.82 (m, 2H), 3.63 (s, 3H, OCH_3), 3.73 (s, 3H, OCH_3), 4.15 (m, 1H), 4.58 (m, 1H). ^{13}C NMR (CD_3OD) δ: 21.6, 22.0, 25.5, 25.7, 38.14/38.20, 42.0, 50.9, 51.6, 51.7, 54.6, 159.1, 173.6, 175.6.

N-*MOC-PRO-MET methyl ester, sulfoxides*

^{1}H NMR (CD_3OD) δ: 1.82–2.3 (m, 6H), 2.68 (s, 3H, $SOCH_3$), 2.80 (m, 2H), 3.62 (s, 3H, OCH_3), 3.73 (s, 3H, OCH_3), 4.30 (m, 1H), 4.58 (m, 1H). ^{13}C NMR (CD_3OD) δ: 23.5, 24.37/24.46, 30.4, 37.19/37.23, 49.97, 51.4, 51.8, 52.2, 60.2, 60.5, 156.3, 172.6, 174.4.

N-*MOC-PHE-MET methyl ester, sulfoxides*

^{1}H NMR (CD_3OD) δ: 2.25–2.60 (m, 2H), 2.66 (s, 3H, $SOCH_3$), 2.88 (m, 2H), 2.87 (m, 1H), 3.14 (m, 1H), 3.63 (s, 3H, OCH_3), 3.75 (s, 3H, OCH_3), 4.45 (m, 1H), 4.60 (m, 1H), 7.25 (m, 5H). ^{13}C NMR (CD_3OD) δ: 24.62/24.76, 37.51/37.60, 38.0, 50.08/50.16, 51.6 (2), 51.8, 56.8, 126.6, 128.4, 129.5, 137.6, 158.3, 172.3, 173.6.

© 2002 NRC Canada

Biotransformation procedures

Chloroperoxidase-catalyzed oxidations

The reactions were carried out using the following standard procedure: *N*-MOC-L-methionine methyl ester (33 mg, 0.15 mM) was dissolved in disodium citrate buffer (16.6 mL, 0.1 M, pH 5.0) in a 50 mL flask. The solution was stirred slowly at room temperature, and chloroperoxidase (2000 units) was added. A solution of hydrogen peroxide (56.6 μL of 30% aqueous solution) in disodium citrate buffer (1.6 mL, 0.1 M, pH 5.0) was then added via a syringe pump over 70 min, with addition occurring directly below the surface level of the reaction mixture. The reaction was stirred for a further 5 min, quenched by addition of aqueous saturated sodium sulfite (0.5 mL), and then continuously extracted with dichloromethane for 3 d. Evaporation of the extract gave a quantitative recovery of amino acid material, which was directly analyzed by ^{1}H and ^{13}C NMR. Configuration at sulfur of *N*-MOC-L-methionine ester sulfoxides was identified by ^{13}C NMR analysis.

Ester hydrolysis of N-MOC-L-methionine methyl ester sulfoxides

The diastereomeric mixture of chemically prepared *N*-MOC-L-methionine methyl ester sulfoxide (100 mg) was dissolved in phosphate buffer (0.1 M, pH 7.0, 20 mL), and then the stirred solution was treated with the appropriate Altus Chiroclec® enzyme (100 mg for each of α-chymotrypsin, *Aspergillus* sp. protease, subtilisin Carlsberg, or *Aspergillus* lipase in four separation experiments), each suspended in phosphate buffer (5 mL). The resulting reaction mixture was then stirred at room temperature for 5–60 min, monitored by TLC (silica gel, EtOAc–MeOH–AcOH, 79:20:1), and on ca. 50% completion the reaction was quenched by the addition of ethanol (5 mL) and then filtered. The filtrate was acidified to pH 3 by the addition of 10% HCl, then continuously extracted with dichloromethane for 3 d. Evaporation of the extract gave a quantitative recovery of amino acid material, which was directly analyzed by ^{1}H and ^{13}C NMR, and separated by chromatography using silica gel with 10% gradient elution (EtOAc–MeOH, 80:20 to MeOH). Spectral data are quoted above for *N*-MOC-L-methionine methyl ester sulfoxide and *N*-MOC-L-methionine sulfoxide products. Configuration at sulfur of *N*-MOC-L-methionine methyl ester sulfoxides was identified by ^{13}C NMR analysis.

Removal of *N*-MOC and ester-protecting groups

The following standard reaction procedure was used: *N*-MOC-L-methionine methyl ester sulfoxide (120 mg), prepared by CPO-catalyzed oxidation of *N*-MOC-L-methionine methyl ester, was dissolved in a mixture of distilled water (4 mL) and methanol (1 mL). Barium hydroxide (300 mg) was added, and the mixture stirred and heated at reflux for 4 h. Water (10 mL) was added and the mixture was cooled and adjusted to pH 5.75 with sulfuric acid (0.1 M), filtered (celite), and evaporated to yield a semi-solid (100 mg), which was then dissolved in distilled water (1 mL), filtered, and the filtrate diluted with acetone (7 mL). The resulting cloudy mixture was refrigerated overnight to produce crystals of L-methionine sulfoxide (62 mg, 76%), identified by ^{13}C NMR and other analytical comparisons with authentic samples (19) as (R_SS_C) material; mp230–235°C (lit. (25, 26) mp 239°C). $[\alpha]_D$ –75 (c = 0.5, H_2O) (lit. (25) $[\alpha]_D$ –77 (c = 0.5, H_2O)).

Acknowledgments

This work was funded by the Natural Sciences and Engineering Research Council of Canada (NSERC) and by a grant from the American Chemical Society Petroleum Research Fund B. We are grateful to Mr. T. Jones of Brock University for help with the acquisition of spectral data.

References

1. J.O. Konz, J. King, and C.L. Cooney. Biotechnol. Prog. **14**, 393 (1998).
2. J. Moskovitz, B.S. Berlett, J.M. Poston, and E.R. Stadtman. Proc. Natl. Acad. Sci. **94**, 9585 (1997).
3. M.A. Ciorba, S.H. Heinemann, H. Weissbach, N. Brot, and T. Hoshi. Proc. Natl. Acad Sci. **94**, 9932 (1997).
4. B. Garner, P.K. Witting, A.R. Waldeck, J.K. Christinson, M. Raftery, and R. Stocker. J. Biol. Chem. **273**, 6080 (1998).
5. B. Garner, A.R. Waldeck, P.K. Witting, K.-A. Rye, and R. Stocker. J. Biol. Chem. **273**, 6088 (1998).
6. C.S. Spar, L.O. Narhi, J. Speakman, S. Hieng, and Y.-R. Hsu. Tech. Protein Chem. VIII. 10th symposium of the Protein Society. Academic Press, San Diego. 1997. p. 299.
7. T. Huff and E. Hannappel. Anal. Chim. Acta, **352,** 249 (1997).
8. V.S. Sharov and C. Schöneich. Free Rad. Biol. Med. **29**, 986 (2000).
9. Z. Brada, S. Bulba, and J. Cohen. Cancer Res. **35**, 2674 (1975).
10. K.H. Kyung, D.C. Han, and H.P. Fielding. J. Food Sci. **62**, 406 (1997).
11. W. Komatsu, Y. Miura, and K. Yagasaki. Lipids, **33**, 499 (1998).
12. H.W. Chin and R.C. Lindsay. J. Agric. Food Chem. **42**, 1529 (1994).
13. F. Lucas and L. Levenbrook. Biochem. J. **100**, 473 (1966).
14. V.G. de la Rosa, M. Ordonez, and J.M. Llera. Tetrahedron: Asymmetry, **12**, 1615 (2001).
15. H.L. Holland. Chem. Rev. **88**, 473 (1988).
16. H.L. Holland. Nat. Prod. Rep. **18**, 171 (2001).
17. M. Uyeda, S. Takenobu, and M. Hongo. Agric. Biol. Chem. **38**, 1797 (1974).
18. H.L. Holland and F. M. Brown. Tetrahedron: Asymmetry, **9**, 535 (1998).
19. H.L. Holland, P.R. Andreana, and F. M. Brown. Tetrahedron: Asymmetry, **10**, 2833 (1999).
20. R.R. Vargas, E.J.H. Bechara, L. Marzorati, and B. Wladislaw. Tetrahedron: Asymmetry, **10**, 3219 (1999).
21. F. van der Velde, M. Bakker, F. van Rantwijk, G.P. Rai, L.P. Hager, and R.A. Sheldon. J. Mol. Cat. B: Enzymat. **11**, 765 (2001).
22. G.P. Rai, S. Sakai, A.M. Flórez, L. Mogollon, and L.P. Hager. Adv. Synth. Catal. **343**, 658 (2001).
23. I. Koch and M. Keusen. Pharmazie, **53**, 668 (1998).
24. A.F. Cook and D.T. Maichuk. J. Org. Chem. **35**, 1940 (1970).
25. J.P. Greenstein and M. Winitz. Chemistry of the amino acids. Vol. 3. Wiley, New York. 1961. p. 2145.
26. F. Lucas and L. Levenbook. Biochem. J. **100**, 473 (1966).

© 2002 NRC Canada

Formation of single diastereomers of β-hydroxy-sulfoxides by biotransformation of β-ketosulfides using *Helminthosporium* species NRRL 4671

Herbert L. Holland, Nancy Ihasz, and Brendan J. Lounsbery

Abstract: Single biotransformations of 1-(phenylthio)-2-propanone and 1-(*p*-methoxyphenylthio)-2-propanone by the fungus *Helminthosporium* species NRRL 4671 resulted in both sulfur oxidation to the sulfoxide and carbonyl reduction to the alcohol. The corresponding (S_S,S_C)-1-sulfinyl-2-propanols were obtained as single diastereomers following simple crystallization.

Key words: biocatalysis, biotransformation, carbonyl reduction, *Helminthosporium* sp. NRRL 4671, sulfoxidation.

Résumé : Des biotransformations uniques de la 1-(phénylthio)propan-2-one et de la 1-(4-méthoxyphénylthio)propan-2-one sous l'influence de champignons de l'espèce *Helminthosporium* NRRL 4761 provoquent à la fois une oxydation du soufre en sulfoxyde et une réduction du groupement carbonyle en alcool. Après une simple cristallisation, on a obtenu les ($S_S S_C$)-1-sulfinylpropano-2-ols sous la forme d'un seul diastéréomère.

Mots clés : biocatalyse, biotransformation, réduction d'un groupe carbonyle, *Helminthosporium* NRRL 4671, sulfoxydation.

[Traduit par la Rédaction]

Introduction

One of the key features of biocatalytic reactions is their ability to produce chiral products from non-chiral starting materials. This is particularly common for carbonyl groups, which can be reduced to secondary alcohols (1) or converted to cyanohydrins (2), and the oxidation of sulfides to generate sulfoxides (3). In contrast, however, the generation of two or more independent chiral centres from a non-chiral starting material in a single biotransformation is unusual. The formation of two chiral centres is primarily achieved by either the reduction of diketones to chiral diols (4), the use of an aromatic dioxygenase enzyme to produce an arene dihydrodiol (5), or the conversion of ketones into chiral diols by a combination of carbonyl reduction and hydroxylation reactions (6). The latter process, requiring the combined activity of two different enzymes, is carried out only by whole-cell biocatalysts.

Even more unusual is the formation of a product with two different chiral centres from a single non-chiral substrate. It has recently been reported that the dioxygenase activity of *Pseudomonas putida* results in the formation of dihydrodiol sulfoxides from aryl sulfides, products possessing three chiral centres (two of which are alcohols) that are formed by the activity of a single enzyme (7). The combined application of two or more different enzymes to generate two different chiral centres from a non-chiral substrate is also unusual, but has been reported in the whole-cell biocatalysis of conjugated unsaturated carbonyl substrates to give saturated alcohol products, which involves a combination of enoate reductase and alcohol dehydrogenase activities (8).

The present communication presents a new combined biocatalysis reaction, involving both the oxidation of sulfides and reduction of carbonyls in a single biotransformation process, resulting in the formation of chiral sulfoxide alcohols in high diastereomeric excess (de). Potential values of such 1,3-sulfoxide alcohols lie in their use as chiral synthons and reagents, the latter in the presence of metal catalysts with which they can execute hydrogen-bonding interactions.

Received 19 February 2002. Published on the NRC Research Press Web site at http://canjchem.nrc.ca on 23 May 2002.

This communication is dedicated to Professor J. Bryan Jones as both a pioneer and a current expert in fundamental areas of biocatalysis.

H.L. Holland,[1] N. Ihasz, and B.J. Lounsbery. Department of Chemistry, Brock University, St. Catharines, ON L2S 3A1, Canada.

[1]Corresponding author (e-mail: holland@chemiris.labs.brocku.ca).

Results and discussion

Biotransformation of 1-(phenylthio)-2-propanone (**1a**) and 1-(*p*-methoxyphenylthio)-2-propanone (**1b**) by *Helminthosporium* species NRRL 4671 resulted in the formation of the corresponding sulfoxide alcohols **2a** and **2b** as illustrated in Scheme 1 and summarized in Table 1. The configurations at the carbon and sulfur of **2a** and **2b** were determined independently by conversion to the sulfone alcohols (*S*)-**3a** and (*S*)-**3b** and the sulfoxide ketones **4a** and **4b** as shown in Scheme 2. Optical rotations of sulfones **3** were identical with those reported for stereochemically pure versions produced by biotransformation of the corresponding sulfone ketones (9). Enantiomeric purity was confirmed as ≥95% ee

 DOI: 10.1139/V02-091 © 2002 NRC Canada

Table 1. Biotransformations of 1-(phenylthio)-2-propanone (**1a**) and 1-(*p*-methoxyphenylthio)-2-propanone (**1b**) by *Helminthosporium* sp.

Substrate	Product	Yield (%)	Original de (%)[a]	Final de (%)	Configuration
1a	**2a**	90	89	≥95	(S_S,S_C)
1b	**2b**	70	85	≥95	(S_S,S_C)

[a]Diastereomeric excess obtained directly from biotransformation and prior to crystallization.

Scheme 1. Biotransformations by *Helminthosporium* sp.

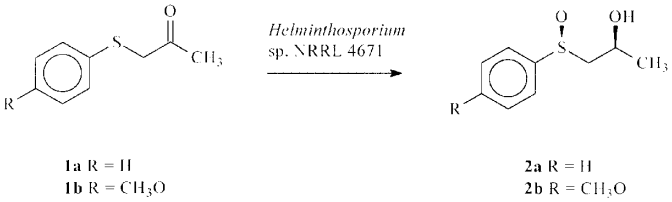

1a R = H
1b R = CH_3O

2a R = H
2b R = CH_3O

Scheme 2. Conversions to determine configurations at C and S.

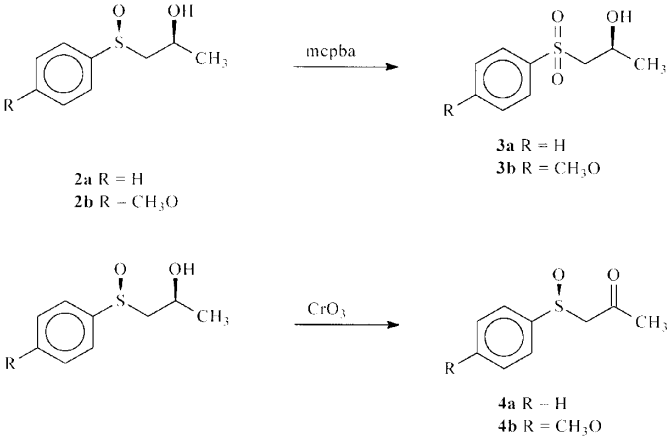

2a R = H
2b R = CH_3O

3a R = H
3b R = CH_3O

4a R = H
4b R = CH_3O

by ^{1}H NMR analysis using Eu(thfc)$_3$ as a chiral-shift reagent.

Stereochemical analyses of sulfoxides (*S*)-**4** were carried out by ^{1}H NMR analyses using the Kagan chiral-shift reagent (*R*)-(–)-*N*-(3,5-dinitrobenzoyl)-α-methylbenzylamine (10, 11), confirming that the materials were 85-89% ee, which corresponds with the estimated original de values of products **2a** and **2b** that were determined by their ^{1}H NMR analyses (see *Experimental*). The (*S*)-configurations of **4** were determined by their optical rotations (negative) (3, 12, 13) and by the ^{1}H NMR shifts in the presence of Kagan reagent (10, 11).

Crystallization of products **2a** and **2b** gave samples with ≥95% de; it is apparent from the stereochemical analysis presented above that these arose from materials with a single configuration (*S*) at the carbon and a mixed configuration (ca. *S*:*R* = 93:7) at the sulfur. Both (*S*)-configurations are consistent with those produced by biotransformations of ketones (12) and sulfides (3) by *Helminthosporium*.

The biotransformation of β-ketosulfides to produce chiral β-hydroxysulfoxides represents a new version of single biocatalysis for the formation of molecules with two different chiral centres from non-chiral starting materials. This process is now under investigation using a variety of such substrates for microbial biocatalysts known for their ability to carry out both sulfide oxidation and carbonyl reduction reactions when applied to different independent substrates.

Experimental

Maintenance, growth, and biotransformations using *Helminthosporium* species NRRL 4671 were carried out as previously described (13). Isolated yields of products from 1 g of substrate were obtained as presented in Table 1. Preparations of **3a** and **3b** in yields of 85 and 97%, respectively, were performed by oxidations of **2a** and **2b** by the standard procedure using 1.5 equivalents of *m*-chlorobenzoic acid in CH_2Cl_2 at room temperature for 48 h. Preparations of **4a** and **4b** were performed by standard Jones oxidations at 0°C of **2a** and **2b** in yields of 71 and 60%, respectively.

Analytical data for biotransformation products **2** and their derivatives **3** and **4** are listed below.

(S_S,S_C)-1-(Phenylsulfinyl)-2-propanol (2a)

mp 55–57°C. $[\alpha]_D$ –260 (*c* 1.0, $CHCl_3$). ^{1}H NMR ($CDCl_3$) δ: 1.32 (d, 3H), 2.74 and 3.0 (m of ABX, 2H), 3.63 (br s, 1H, OH), 4.45 (m, 1H), 7.52 (m, 3H), 7.70 (d, 2H). ^{13}C NMR ($CDCl_3$) δ: 23.7, 64.1, 65.5, 124.2, 129.9, 131.9, 144.0. The (R_S,S_C) isomer produced two different sets of ^{1}H NMR peaks, located at δ 1.25 (d) (cf. 1.32 (d)) and 4.30 (m) (cf. 4.45 (m)), integration of which peaks together with the major ones at δ 1.32 and 4.45 was used to determine the initial de of 89%.

(S_S,S_C)-1-(*p*-Methoxyphenylsulfinyl)-2-propanol (2b)

mp 84–86°C. $[\alpha]_D$ –267 (*c* 1.0, $CHCl_3$). ^{1}H NMR ($CDCl_3$) δ: 1.32 (d, 3H), 2.73 and 3.0 (m of ABX, 2H), 3.73 (br s, 1H, OH), 3.82 (s, 3H), 4.45 (m, 1H), 7.02 and 7.58 (q of AB, 4H). ^{13}C NMR ($CDCl_3$) δ: 23.7, 56.0, 64.1, 65.4, 115.4, 126.5, 134.8, 162.7. The (R_S,S_C) isomer produced two different sets of ^{1}H NMR peaks located at δ 1.25 (d) (cf. 1.32 (d)) and 4.30 (m) (cf. 4.45 (m)), integration of which peaks together with the major ones at δ 1.32 and 4.45 was used to determine the initial de of 85%.

(*S*)-1-(Phenylsulfonyl)-2-propanol (3a)

Oil. $[\alpha]_D$ +19.8 (*c* 1.0, $CHCl_3$) (Lit. (9) $[\alpha]_D$ + 15.7 (*c* 1.0, $CHCl_3$, 95% ee) ≥95% ee. ^{1}H NMR ($CDCl_3$) δ: 1.19 (d, 3H), 3.14 and 3.24 (m ABX, 2H), 3.87 (br s, 1H, OH), 4.27 (m, 1H), 7.5–7.9 (m, 5H). ^{13}C NMR ($CDCl_3$) δ: 23.1, 62.8, 63.7, 128.3, 129.8, 134.1, 139.6.

(*S*)-1-(*p*-Methoxyphenylsulfonyl)-2-propanol (3b)

mp 53–55°C. $[\alpha]_D$ +14.8 (*c* 1.0, $CHCl_3$) (Lit. (9) $[\alpha]_D$ + 15.7 (*c* 1.0, $CHCl_3$, 95% ee), ≥95% ee. ^{1}H NMR ($CDCl_3$) δ: 1.21 (d, 3H), 3.10 and 3.19 (m of ABX, 2H), 3.87 (s, 3H), 4.27

© 2002 NRC Canada

(m, 1H), 7.02 and 7.83 (q of AB, 4H). ^{13}C NMR ($CDCl_3$) δ: 22.9, 56.2, 62.8, 64.0, 115.1, 130.6, 130.9, 164.4.

(*S*)-1-(Phenylsulfinyl)-2-propanone (4a)

mp 61–63°C. $[\alpha]_D$ –176 (*c* 1.0, $CHCl_3$), 88% ee. ^{1}H NMR ($CDCl_3$) δ: 2.20 (s, 3H), 3.7 and 3.9 (q of AB, 2H), 7.5–7.63 (5H, m). ^{13}C NMR ($CDCl_3$) δ: 32.4, 69.0, 124.4, 129.9, 132.1, 143.2, 199.8.

(*S*)-1-(*p*-Methoxyphenylsulfinyl)-2-propanone (4b)

mp 58–60°C. $[\alpha]_D$ –169 (*c* 1.0, $CHCl_3$), 85% ee. ^{1}H NMR ($CDCl_3$) δ: 2.21 (s, 3H), 3.80 (m, 5H), 7.02 and 7.58 (q of AB, 4H). ^{13}C NMR ($CDCl_3$) δ: 32.5, 56.0, 69.1, 115.4, 126.4, 135.4, 162.8, 199.9.

Acknowledgments

This work was funded by the Natural Sciences and Engineering Research Council of Canada (NSERC). We are grateful to Mr. T. Jones of Brock University for help with the acquisition of spectral data.

References

1. S.M. Roberts. J. Chem. Soc. Perkin Trans. 1, 1475 (2001); 1485 (2001).
2. D.V. Johnson and H. Griengl. Adv. Biochem. Eng. Biotechnol. **63**, 31 (1999).
3. H.L. Holland. Nat. Prod. Rep. **18**, 171 (2001).
4. R. Csuk and B.I. Glänzer. *In* Stereoselective biocatalysis. *Edited by* R.N. Patel. Marcel Dekker, N.Y. 2000. p. 527.
5. D.R. Boyd, N.D. Sharma, and C.C.R. Allen. Curr. Op. Biotechnol. **12**, 564 (2001).
6. S.A. Selifonov. Biochem. Biophys. Commun. **186**, 1429 (1992).
7. D.R. Boyd, N.D. Sharma, S.A. Haughey, J.F. Malone, A.W.T. King, B.T. McMurray, A. Alves-Areias, C.C.R. Allen, R. Holt, and H. Dalton. J. Chem. Soc. Perkin Trans. 1, 3288 (2001).
8. M. Utaka, S. Konishi, and A. Takeda. Tetrahedron Lett. **27**, 4737 (1986).
9. R.L. Crumbie, B.S. Deol, J.E. Nemorin, and D.D. Ridley. Aust. J. Chem. **31**, 1965 (1978).
10. P.H. Buist, D. Marecak, H.L. Holland, and F.M. Brown. Tetrahedron: Asymmetry, **6**, 7 (1995).
11. M. Deshmukh, E. Dunach, S. Juge, and K. Kagan. Tetrahedron Lett. **25**, 3467 (1984).
12. H.L. Holland, E.J. Bergen, P.C. Chenchaiah, S.H. Khan, B. Munoz, R.W. Ninniss, and D. Richards. Can. J. Chem. **65**, 502 (1987).
13. H.L. Holland, M.J. Bornmann, and G. Lakshmaiah. J. Mol. Cat. B: Enzym. **1**, 97 (1996).

© 2002 NRC Canada

Structure-based rationalization of aldolase-catalyzed asymmetric synthesis

Junjie Liu, Grace DeSantis, and Chi-Huey Wong

Abstract: This paper describes a structure-based approach to elucidate the stereospecificity, including inversion of enantioselectivity, of the 2-deoxyribose-5-phosphate aldolase-catalyzed asymmetric aldol addition reaction using unnatural substrates designed for the total synthesis of epothilones. In addition, an aldolase variant with Ser-238 being altered for Asp was found to be 2.5 times more effective than the wild type in accepting the unphosphorylated substrate D-glyceraldehyde. A new H-bonding interaction between the Asp-238 carboxylate and the 3-hydroxyl of the substrate was identified and was used to rationalize the rate enhancements.

Key words: aldol reaction, 2-deoxyribose-5-phosphate aldolase, mutagenesis, inversion of enantioselectivity.

Résumé : Cette communication décrit une approche basée sur la structure d'élucider la stéréospécificité, y compris l'inversion d'énantiosélectivité, de la réaction d'addition aldolique asymétrique catalysée par l'aldolase de 2-désoxyribose-5-phosphate; cette étude fait appel à des substrats qui ne sont pas naturels et qui ont été développés pour la synthèse totale des épothilones. De plus, on a observé qu'une variante de l'aldolase, portant une Asp au lieu de la Ser-238, est 2,5 fois plus efficace que la forme naturelle pour accepter le substrat d-glycéraldéhyde non phosphorylé. On a identifié une nouvelle interaction par liaison hydrogène entre le carboxylate de l'Asp-238 et l'hydroxyle en position 3 du substrat; elle permet de rationaliser les augmentations de vitesses de réaction.

Mots clés : réaction aldolique, aldolase de 2-désoxyribose-5-phosphate, mutagénèse, inversion d'énantiosélectivité.

[Traduit par la Rédaction]

Introduction

Over the past 20 years, enzymes have been exploited as catalysts in large-scale organic synthesis. Recent advances in molecular genetics, protein engineering, and site-specific modification of enzymes have further expanded the scope of enzyme catalysis with regard to its synthetic application (1). Most of these new developments are based on the inspiring work of a few pioneers in the field, particularly that of Professor Bryan Jones (2). To date, many useful transformations based on enzymes have been developed on large scales for the chemical and pharmaceutical industries, and new developments based on biocatalysis continue to evolve (1, 3).

One subject of current interest to us is the use of enzyme-structure information to design new protein catalysts or new substrates for enzymatic reactions with altered stereoselectivity. The enzyme employed in this study is 2-deoxyribose-5-phosphate aldolase (DERA, EC 4.1.2.4), which catalyzes the aldol reaction between acetaldehyde and D-glyceraldehyde 3-phosphate to form D-2-deoxyribose-5-phosphate (4). The structure of this enzyme has been solved at the atomic level (~1 Å resolution) and the reaction mechanism has been studied in detail (Scheme 1) (5). The enzyme forms a Schiff base with acetaldehyde to generate an enamine intermediate, which then attacks the *Re*-face carbonyl of the incoming acceptor to form a new C–C bond with a new stereogenic center in the *R*-configuration. Both the Schiff base and the carbinol amine intermediates have been trapped and the structures have been determined (5). According to the structure, the C-3 phosphate of the acceptor substrate has H-bonding interactions with a hydrophilic site composed of Ser-238, Ser-239, and Gly-205, and the C-2 hydroxyl group has H-bonding interactions (5) through a water molecule with another hydrophilic site composed of Thr-170 and Lys-172. The C-2 hydrogen is positioned in a hydrophobic pocket (Fig. 1). The enzyme also accepts the corresponding unphosphorylated substrate and related structures with a much weaker affinity and activity (4).

Results and discussion

In an effort to find new substrates, we found that the enzyme catalyzes the aldol reaction with racemic 2-methyl-3-hydroxypropanal **1a** to give the pyranose **2a** (Scheme 2) (6). Characterization of the product by oxidative conversion to the lactone with Br_2 indicates that the enzyme exhibits a re-

Received 17 December 2001. Published on the NRC Research Press Web site at http://canjchem.nrc.ca on 29 May 2002.

Dedicated to Professor J. Bryan Jones on the occasion of his 65th birthday.

J. Liu, G. DeSantis, and C.-H. Wong.[1] Department of Chemistry and the Skaggs Institute for Chemical Biology, The Scripps Research Institute, 10550 N. Torrey Pines Road, La Jolla, CA 92037, USA.

[1]Corresponding author (e-mail: wong@scripps.edu).

 DOI: 10.1139/V02-094 © 2002 NRC Canada

Scheme 1. Highlights of the mechanism of DERA catalyzed aldol addition reaction. Shown are those steps associated with C–H cleavage and C–C bond formation. Asp-102 and Lys-201 act as a proton relay system to assist the proton abstraction and carbonyl protonation mediated by the conserved water molecule. The enzyme side chains interacting with the phosphate group and the C-4 hydroxyl (corresponding to the C-2 OH of acceptor) have been identified and designated each as a hydrophilic pocket. The C-4 hydrogen is located in a small hydrophobic pocket without interaction with side chains.

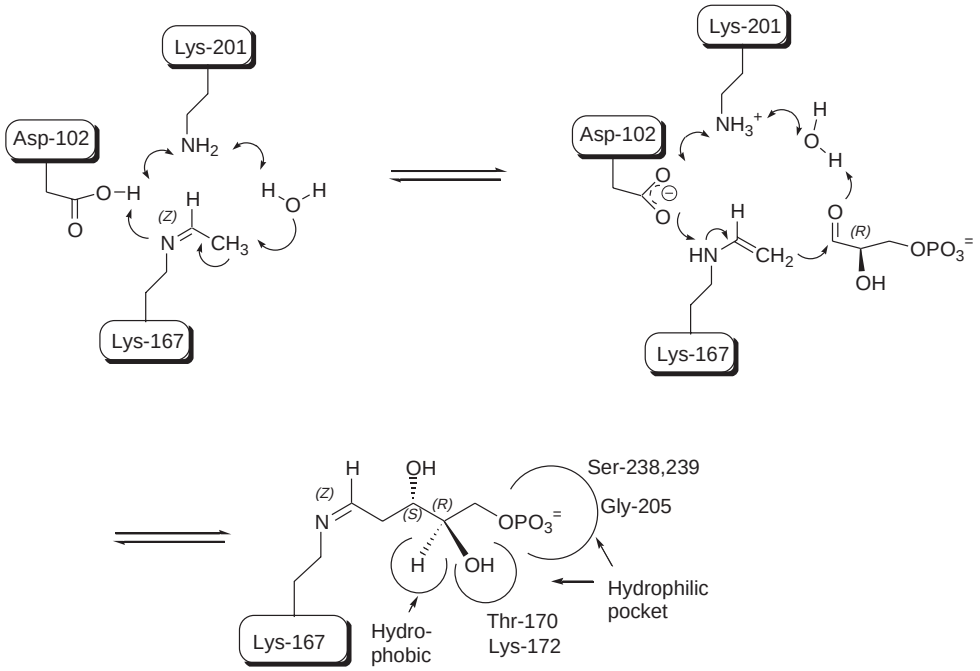

Scheme 2. Enantioselective aldol reaction catalyzed by DERA. A reversal of enantioselectivity was observed with acceptor substrates with small hydrophobic substituents at C-2 as indicated in the conversions of **1a–c** to **2a–c**, respectively.

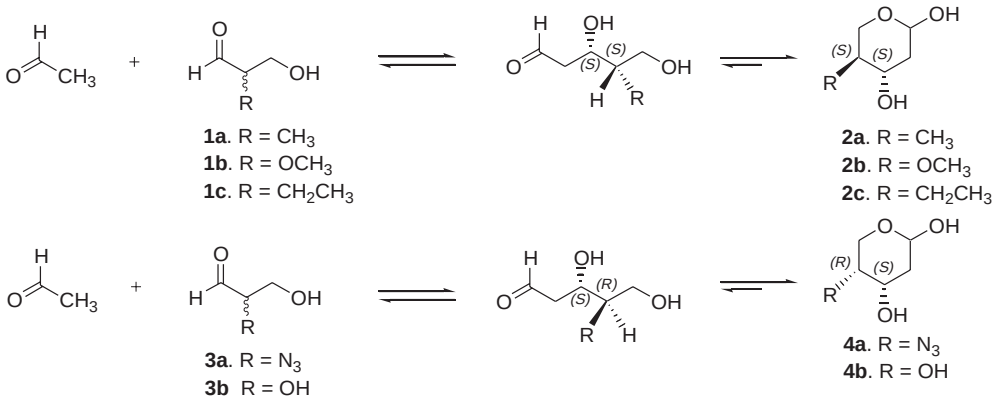

versal of enantioselectivity in the aldol reaction, accepting the L-aldehyde as an acceptor. Similarly, reverse enantioselectivity was observed with the 2-methoxy and 2-ethyl derivatives **1b** and **1c**, respectively. Alternatively, when the racemic 2-azido or 2-hydroxy derivative was used (**3a** and **3b**, respectively), enantioselectivity that followed that of the natural reaction was observed, i.e., the D-enantiomer was converted to the pyranose product (**4a** and **4b**). In all cases, no change in facial selectivity was observed (6). The equilibrium of the reaction is driven by the formation of the pyranose ring in favor of condensation (Fig. 2). With the enzyme structure now available, the results can be rationalized such that the 2-methyl, 2-methoxy, or 2-ethyl groups is bound to the hydrophobic pocket and the C-2 hydrogen is in the hydrophilic pocket. If the methyl, methoxy, or ethyl group was in the hydrophilic pocket, it would have a close contact with the water molecule and the carbonyl oxygen of Thr-170, resulting in a less favorable binding. Since the azide or the hydroxy group is considered to be hydrophilic, it fits into the hydrophilic pocket (Scheme 3).

In another effort to engineer the enzyme to accept unphosphorylated neutral substrates more effectively, Ser-238 was exchanged for Asp. It was anticipated that this change would still retain the hydrophilic nature of the C-3

© 2002 NRC Canada

Table 1. Kinetic parameters of wild-type DERA and the Ser238Asp variant in the retroaldol reaction.

Enzyme[a]	Substrate[b]	k_{cat} (s^{-1})	K_m (mM)	k_{cat}/K_m (s^{-1} mM^{-1})
WT	DERP	68 ± 1	0.64 ± 0.01	106 ± 2
	DER	0.107 ± 0.005	57 ± 7	0.0020 ± 0.0003
Ser238Asp	DERP	0.58 ± 0.05	61 ± 11	0.01 ± 0.001
	DER	0.21 ± 0.01	39 ± 6	0.005 ± 0.0009

Note: Enzymes and kinetic parameters were determined according to the procedures previously described (5)
[a]WT, wild-type DERA.
[b]DERP, D-2-deoxyribose-5-phosphate; DER, D-2-deoxyribose.

Scheme 3. (*a*) Acceptor model of wild-type DERA; (*b*) acceptor model of the Ser238Asp variant.

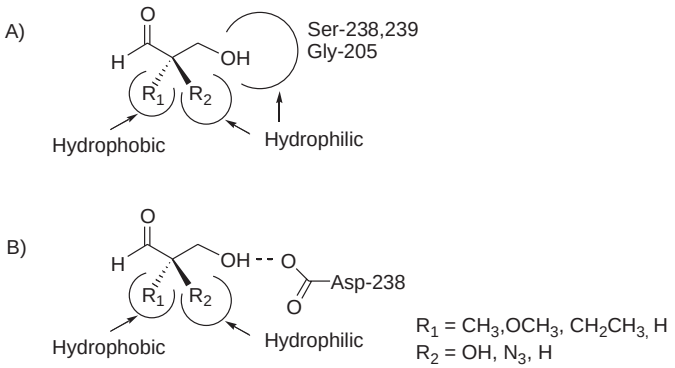

binding pocket, but substrates with a negative charge in the C-3 position would be disfavored. Indeed, the Ser238Asp-mutant enzyme is 2.5 times more active (based on the k_{cat}/K_m value of the retroaldol reaction) than the wild-type to D-glyceraldehyde as a substrate, as indicated in Table 1. Molecular modeling indicates that the C-3 hydroxy hydrogen forms a 2.9–3.2 Å hydrogen bond with the Asp-238 carboxylate, accounting for the increase in reactivity (Fig. 3).

In summary, this study has demonstrated that with a well-defined enzyme structure, one can effectively alter the substrate specificity of an enzyme by protein engineering or substrate design. Methyl pyranose **2a** has been used as a key synthon in the total synthesis of the anti-cancer agents epothilones (6, 7).[2] Work is in progress to further utilize the structural information to design new substrates for DERA-catalyzed aldol addition reactions.

Acknowledgment

We thank the National Institutes of Research for support of this research.

Reference

1. For a recent special issue on this subject, see: Nature (London), **409**, 226 (2001).
2. J.B. Jones. Tetrahedron, **42**, 3351 (1986); G. DeSantis and J.B. Jones. Curr. Opin. Biotechnol. **10**, 324 (1999).
3. R.N. Patel. *In* Stereoselective biocatalysis. Dekker, New York. 2000, and refs. cited therein.
4. T.D. Machajewski and C.-H. Wong. Angew. Chem. Int. Ed. **39**, 1352 (2000), and refs. cited therein.
5. A. Heine, G. DeSantis, J.G. Luz, M. Mitchell, C.-H. Wong, and I.A. Wilson. Science (London), **294**, 369 (2001).
6. For details, see: J. Liu and C.-H. Wong. Angew. Chem. Int. Ed. **41**, 1404 (2002).
7. K.M. Koeller and C.-H. Wong. Nature (London), **409**, 232 (2001).

[2] General enzymatic synthesis: To a 100 mL buffer solution (0.1 M KH_2PO_4, pH 7.5) containing 0.1 M acceptor aldehyde and 0.3 M donor acetaldehyde was added 3000 units of DERA. The resulting solution was stirred in the dark for 3–6 days under argon. The reaction was quenched by addition of 2 volumes of acetone. The mixture was then stirred at 0°C for 1 h and centrifuged to remove the precipitated enzyme. The aqueous phase was concentrated in vacuo, and the residue was purified by flash chromatography (silica, 1:2 to 4:1 EtOAc–hexane) to yield 31% of **2c**. Characterized by its lactone form: $[\alpha]_D$ = 30.2 (*c* 0.7, $CHCl_3$). IR (film) (cm^{-1}): 3424.6, 2970.0, 1719.2, 1190.4, 1114.0, 1055.2. ^{1}H NMR (600 MHz, $CDCl_3$) δ: 4.43 (dd, *J* = 4.4, 11.4 Hz, 1H), 3.97 (dd, *J* = 7.9, 11.4 Hz, 1H), 3.96 (m, 1H), 2.85 (dd, *J* = 5.7, 17.1 Hz, 1H), 2.74 (d, *J* = 3.9 Hz, 1H), 2.55 (dd, *J* = 6.2, 17.6 Hz, 1H), 1.79 (m, 1H), 1.64 (m, 1H), 1.35 (m, 1H), 1.01 (t, *J* = 7.1 Hz, 3H). ^{13}C NMR (150 MHz, $CDCl_3$) δ: 171.07, 69.21, 67.81, 42.32, 38.03, 21.63, 11.23. HRMS *m*/*z* calcd. for $C_7H_{12}O_3$ (M^+): 144.0786; found: 167.0678 ([M + Na]$^+$). D-aldehyde product; 3% yield. Characterized by its lactone form: $[\alpha]_D$ = –1.0 (*c* 0.6, $CHCl_3$). ^{1}H NMR (600 MHz, $CDCl_3$) δ: 4.37 (t, *J* = 10.9 Hz, 1H), 4.25 (dd, *J* = 4.9, 11.0 Hz, 1H), 4.22 (br s, 1H), 2.73 (dd of AB, *J* = 3.1, 18.0 Hz, 1H), 2.68 (dd of AB, *J* = 4.4, 18.4 Hz, 1H), 2.37 (br s, 1H), 1.86 (m, 1H), 1.48 (m, 1H), 1.35 (m, 1H), 1.00 (t, *J* = 7.4 Hz, 3H). ^{13}C NMR (150 MHz, $CDCl_3$) δ: 170.30, 68.91, 64.50, 39.28, 39.18, 19.60, 11.25. **4a**; 47% yield. ^{1}H NMR (500 MHz, $CDCl_3$) δ major isomer): 5.14 (dt, *J* = 2.6, 7.7 Hz, 1H), 4.22 (m, 1H), 4.13 (dd, *J* = 10.1, 11.9 Hz, 1H), 3.71 (dd, *J* = 4.8, 11.8 Hz, 1H), 3.58 (ddd, *J* = 2.9, 4.8, 9.9 Hz, 1H), 2.93 (d, *J* = 5.2 Hz, 1H), 2.10 (ddd, *J* = 2.6, 10.2, 19.3Hz, 1H), 1.92 (dt, *J* = 3.3, 16.8 Hz); minor isomer: 5.32 (q, *J* = 3.3 Hz, 1H), 4.24 (m, 1H), 4.10 (dd, *J* = 2.6, 12.5 Hz, 1H), 3.84 (dd, *J* = 4.8, 12.1 Hz, 1H), 3.77 (q, *J* = 3.3 Hz, 1H), 1.98 (ddd, *J* = 3.0, 9.9, 12.8 Hz), 1.88 (dt, *J* = 4.0, 13.2 Hz, 1H). ^{13}C NMR (125 MHz, $CDCl_3$) δ major isomer: 92.28, 67.12, 58.97, 56.83, 35.14; minor isomer: 91.74, 64.92, 61.07, 60.63, 35.33.

© 2002 NRC Canada

Efficient synthesis of the optically active dihydropyrimidinone of a potent α_{1A}-selective adrenoceptor antagonist

Daniel R. Sidler, Nancy Barta, Wenjie Li, Essa Hu, Louis Matty, Nori Ikemoto, Jeffrey S. Campbell, Michel Chartrain, Kozo Gbewonyo, Russell Boyd, Edward G. Corley, Richard G. Ball, Robert D. Larsen, and Paul J. Reider

Abstract: The convergent synthesis of a potent α_{1A}-selective adrenoceptor antagonist is described. Salient features of the synthesis include the enzymatic resolution of a racemic dihydropyrimidinone and the use of a palladium coupling reaction in the synthesis of 2,4′-dipyridyl.

Key words: dihydropyrimidinone, enzymatic resolution, palladium coupling.

Résumé : Voici la description de la synthèse convergente d'un puissant antagoniste α_{1A}-sélectif au récepteur adrénergique (adrénorécepteur). Les principales caractéristiques de cette synthèse incluent notamment la résolution enzymatique d'un dihydropyrimidinone racémique et l'utilisation d'une réaction de couplage catalysée par le palladium dans la synthèse du 2,4′-dipyridyle.

Mots clés : dihydropyrimidinone, résolution enzymatique, couplage par le palladium.

[Traduit par la Rédaction]

Introduction

Benign prostatic hyperplasia (BPH) is a common condition afflicting men over the age of 40, with symptoms characterized by urinary obstruction resulting from enlargement of the prostate gland and increased noradrenergic tone in the hyperplastic prostate. Currently, transurethral prostatectomies are the second most common operation performed on males over the age of 65. To avoid surgery, pharmacological approaches are increasingly becoming the first option in treatment (1). Current treatment options include treatment with a 5-α reductase inhibitor, such as finasteride, for relief of symptoms through inhibition of the transformation of testosterone to dihydrotestosterone which results in reduction of prostatic mass (1*f*). The prostate is innervated with adrenergic nerves, which determine smooth muscle tone. The α_1 adrenoceptor has been identified as a target to alleviate the symptoms of BPH through decreasing the adrenergic tone of smooth muscle in the prostate (2). Three subtypes for the α_1 adrenoceptors have been identified (α_{1A}, α_{1B}, and α_{1D}). Selective antagonists for the α_{1A} receptor are expected to be more efficacious and to exhibit fewer side effects (3). The nonselective antagonists terazosin and doxazosin, and more recently tamsulosin, a subtype (α_{1A}/α_{1D})-selective antagonist, are currently in use.

Recently, Merck and Synaptic (4) reported candidate **1** as a new, potent, and selective α_{1A}-adrenoceptor antagonist. The dihydropyrimidinone moiety of **1** is a particularly interesting pharmacophore (3*a*, 5) in that this heterocycle has shown activity in a number of medicinal applications. Here we describe our work on the development of a highly efficient synthesis of the enantiomerically pure form of clinical candidate **1**. Retrosynthetically, the logical approach to **1** would involve the formation of a urea linkage (4,5) between the two penultimate building blocks **2** and **3** (Scheme 1). The preparations of non-racemic dihydropyrimidinone **2** and amine side chain **3**, as well as the formation of the urea linkage, and isolation of a crystalline form of the drug are also described.

Results and discussion

Typically, dihydropyrimidinones are constructed through variations of the Biginelli reaction (6). This reaction is a three-component coupling of an aromatic aldehyde, urea, and an acetoacetate to afford the heterocycle in generally moderate yields. The Biginelli reaction has been used in one form or another for over a century using Bronsted acids in protic media (7). In the last decade a number of improvements have been reported for this reaction using polyphosphate esters (8*a*, 8*i*), microwave-assisted synthesis (8*b*, 8*c*),

Received 16 January 2002. Published on the NRC Research Press Web site at http://canjchem.nrc.ca on 5 June 2002.

Dedicated to Professor J. Bryan Jones on the occasion of his 65th birthday.

D.R. Sidler,[1] N. Barta,[2] W. Li, E. Hu, L. Matty, N. Ikemoto, J.S. Campbell, M. Chartrain, K. Gbewonyo, R. Boyd, E.G. Corley, R.G. Ball, R.D. Larsen, and P.J. Reider. Department of Process Research, Department of Bioprocess R&D, Merck & Co., Inc., Rahway, NJ 07065, U.S.A.

[1]Corresponding author (e-mail: rick_sidler@merck.com).
[2]Present address: Pfizer Global Research & Development, Ann Arbor, Michigan, U.S.A.

 DOI: 10.1139/V02-079 © 2002 NRC Canada

Scheme 1.

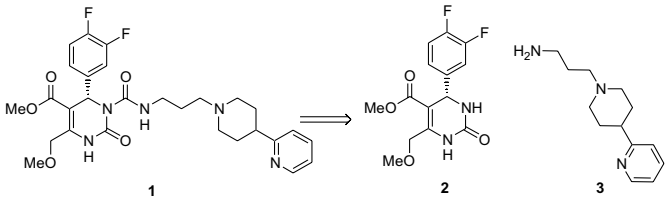

Scheme 2.

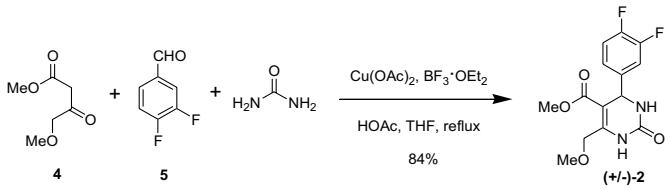

Scheme 3.

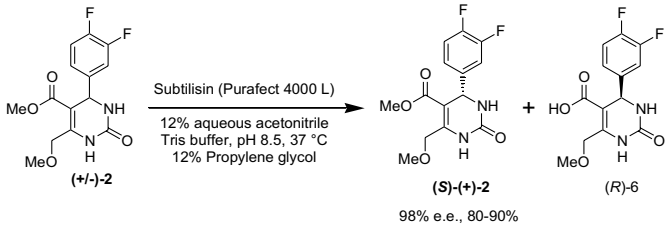

solid-phase synthesis (8*d*, 8*e*), solid-acid catalysis (8*f*), and fluorous synthesis (8*g*, 8*h*). A major improvement in the traditional Biginelli protocol was recently reported by us through the application of a Lewis acid catalysis which afforded much improved yields (9*a*). A combination of boron trifluoride etherate with a catalytic amount of acetic acid and a metal salt in THF has vastly improved the reaction. Metal salts such as $Cu(OAc)_2$, CuCl, $CuCl_2$, Cu_2O, $NiBr_2$, and $Pd(OAc)_2$ can be used equally well in this reaction. Alternative Lewis acids, such as $Ln(OTf)_3$ (9*b*), $FeCl_3$ (9*c*), or $InCl_3$ (9*d*) have also been reported for this three-component condensation. We determined that 1.7 equivalents of $BF_3{\cdot}Et_2O$ in combination with 10 mol% acetic acid and 10 mol% $Cu(OAc)_2$ gave the best overall results for this reaction. Heating a mixture of methyl 4-methoxyacetoacetate (**4**), 3,4-difluorobenzaldehyde (**5**), and urea with the acid mixture in THF afforded an 84% isolated yield of the desired dihydropyrimidinone (±)-**2** (Scheme 2).

The only preparation of an optically pure dihydropyrimidinone through an asymmetric variant of the Biginelli reaction was reported by Overman and co-workers (10). Our attempts at diastereoselective Biginelli reactions through cyclization of chiral ester derivatives of methoxyacetoacetate afforded only modest diastereoselectivity. A brief investigation of chiral ligands used in conjunction with the Lewis acid mixture of the boron–copper-mediated Biginelli reaction afforded no enantioselectivity. Most reports on the preparation of non-racemic dihydropyrimidinones have employed either classical resolution through diastereomeric salt crystallization (11) or chiral HPLC separation (12). For our needs, the former would require hydrolysis of the ester to the acid, resolution, and re-esterification, reducing the overall efficiency of the process, and the latter would not be amenable to large-scale preparation.

Fig. 1. Crystal structure of dihydropyrimidinone·D-*threo*-2-amino-1-(4-nitrophenyl)-1,3-propanediol salt (**6**).

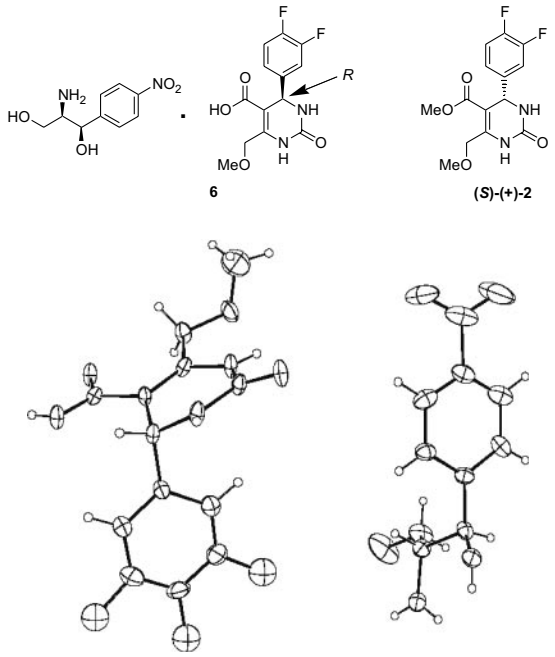

A more effective approach for the resolution of **2** would be an enzymatic hydrolysis of the unwanted methyl ester to the acid, allowing easy separation of the enantiomers (Scheme 3) (13). A number of esterases, lipases, and proteases were screened for this reaction. Interestingly, none of the esterases or lipases tested were successful for this procedure (14). The protease enzyme Proteinase K (Sigma), however, gave excellent selectivity for conversion of the undesired methyl ester to the acid. Unfortunately, this enzyme is not widely available and is quite expensive to use in a bulk process. The search for a less expensive, commercially available protease led to the discovery of Subtilisin (Genencor Purafect 4000L) as a highly effective biocatalyst for the resolution of **2** to the desired (+)-methyl ester of the dihydropyrimidinone.

At the time of this work, only the rotation of the desired ester was known, since this material was previously resolved by chiral HPLC (4). Upon successful hydrolysis of the (–)-methyl ester to the free acid, we were able to evaluate the absolute configuration of the 6-aryl moiety. The acid was recovered from the aqueous phase of the resolution after workup, which was then crystallized from ethanol as a D-*threo*-2-amino-1-(4-nitrophenyl)-1,3-propanediol salt **6**. A crystal structure was obtained and the absolute stereochemistry of the 6-position of the acid was assigned as *R* relative to the stereocenters of the amine (Table 1).

By inference we could assign the desired enantiomer of **2** as the (*S*)-(+)-isomer (Fig. 1).

The optimization of the resolution procedure provided the desired (S)-(+)-methyl ester in 40–45% yield or 80–90% of the available enantiomer. The reaction was run with an enzyme loading of 40–50 wt% at ~6 g L^{-1} in a medium of 12% acetonitrile. Acetonitrile was needed to solubilize the ester. Without the co-solvent the reaction was very sluggish

© 2002 NRC Canada

Table 1. Summary of crystal data for **6**.

Formula	$C_{23}H_{28}F_2N_4O_9$	Diffractometer	Rigaku AFC5
Fw	542.498	Reflections measured	5888
Crystal colour	Colorless	Data Octants	
Crystal dimen. (mm)	0.08 × 0.33 × 0.35	Scan type	ω–2θ
Lattice symmetry	Orthorhombic	Resolution (Å)	0.80
Space group	$P2_12_12_1$	Unique reflections	5888
a (Å)	18.148(3)	Absorp. corr.	none
b (Å)	22.282(4)	Reflections used	5888
c (Å)	13.372(2)	Refl. obsd. criterion	$>2\sigma(I)$
α (°)	90	Obsd. Reflections	2725
β (°)	90	Variables	648
γ (°)	90	Refined on	F^2
V (Å^3)	5407(3)	*R*	0.105
Z	8	R_w	0.293
$D_{calcd.}$ (Mg m^{-3})	1.328	*S*	0.97
Radiation	Kα Cu	Residual peak (e Å^{-3})	0.8(1)
Wavelength (Å)	1.541838	Computer programs:	
Temperature (K)	294	Solution	SHELXS-86
μ (mm^{-1})	0.96	Refinement	SHELXL-97

(>15 days reaction time); however, as the concentration of acetonitrile was increased to >20%, the enzyme was deactivated. Subtilisin was purchased as a solution containing propylene glycol as a stabilizer. By adjusting the concentration of the glycol to 12% an increased stability in reaction solution was obtained, but as the volume percent was increased to >15%, the additive slowed the rate significantly. The system was buffered at pH 8.5 using a Tris buffer and the reaction required 10–12 days at 37°C to complete. The reaction was stopped once the ee of the unhydrolyzed ester reached 98%. During the course of the reaction the pH of the mixture dropped due to the liberation of acid; therefore, aqueous sodium hydroxide was added to maintain the pH. Interestingly, during the course of the enzymatic resolution very little of the desired (+)-methyl ester was hydrolyzed by the enzyme. There was, however, a small amount of background chemical hydrolysis leading to a slight loss in yield. Upon reaching 98% ee, the reaction was worked up by adding toluene and extracting the methyl ester into the organic phase. The undesired free acid remained in the aqueous phase. The toluene was concentrated and the product was isolated in >40% yield by crystallization from toluene–heptane, with an increase in optical purity to >99% ee.

Synthesis of the second penultimate building block (**3**) required the preparation of the two-ring heterocycle. The original synthesis (4) of **3** was improved to afford a process capable of preparing multi-kilogram quantities of the side chain. Although 2,4′-dipyridyl (**7**) is commercially available, only gram quantities could be obtained. We therefore set out to prepare **7** through a selective coupling process (Scheme 4).

Traditionally, the synthesis of bipyridines has involved the construction of one pyridine ring upon an existing substituted pyridine (15). In recent years, cross coupling through organometallic species has increasingly become more practical (16), especially with the advent of the palladium-catalyzed cross-coupling reactions (17). The preparation of a dipyridyl is often encumbered by the selection of the coupling partners. Generally, the halides are available, which has been exploited by the use of Ullmann-like couplings to

Scheme 4.

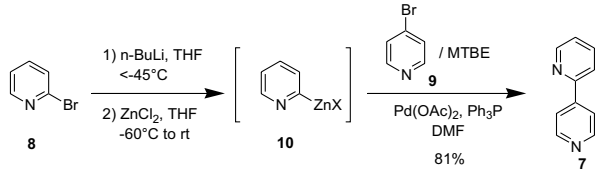

prepare the symmetrical bipyridines (18). In the case of unsymmetrical bipyridines, one of the halopyridines needs to be converted to a suitable coupling partner, such as a stannane (19), borane (20), or zinc halide (21). We sought to avoid the synthesis of an intermediate, as is necessary with the stannanes or boranes, and in the case of the former to avoid the use of tin reagents on a large scale. The Negishi coupling protocol (22) provided a straightforward approach using a zinc halide intermediate. Surprisingly, 2,4′-dipyridyl has not been previously prepared with this procedure. Both 2- and 4-bromo pyridines are available, but the better substrate for conversion to the zinc reagent is 2-bromopyridine (**8**). Previous reports show that 2-pyridyl zinc halide can be generated by halogen–metal exchange with either Rieke's zinc (21*d*) or with an alkyl lithium reagent followed by transmetalation with zinc chloride (21*e*, 22*b*). Accordingly, the metal–halogen exchange was carried out on **8** with *n*-BuLi at <–45°C. 2-Pyridyl–lithium was then transmetalated with zinc chloride in THF to afford intermediate **10**. 4-Bromopyridine (**9**) was purchased as its hydrochloride salt, which was partitioned between *tert*-butyl methyl ether (MTBE) and aqueous sodium carbonate to afford the free base in MTBE. The azeotropically dried MTBE solution was added directly to zinc reagent **10** followed by addition of palladium acetate and triphenylphosphine. The coupling reaction was carried out at 50°C. If the temperature exceeded 50°C, an exotherm occurred causing the reaction to reflux. Upon completion of the coupling, the reaction mixture was quenched with ammonium hydroxide and the solvent was concentrated and displaced with DMF. 2,4′-Dipyridyl **7** was obtained as a DMF solution in 81% yield. Alternatively,

© 2002 NRC Canada

Scheme 5.

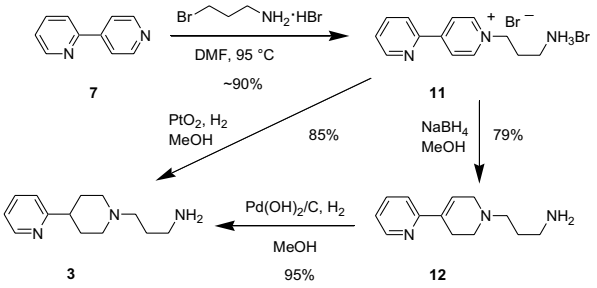

rather than preparing a DMF solution, **7** could be isolated as a solid; however, large losses were incurred during the isolation procedure.

The first step in the conversion of 2,4′-dipyridyl (**7**) to side chain **3** was the selective alkylation at the 4′-position. Heating a mixture of dipyridyl **7** and bromopropylamine hydrobromide in DMF at 95°C resulted in a high conversion to pyridinium salt **11**, with no competing alkylation at the 2-position. Alkylation reactions run at 1 M concentrations in DMF became quite thick, because the pyridinium salt started to crystallize. To alleviate stirring problems, the reaction was run at 0.5 M, but the reaction rate and yield suffered. By adding 10–15% water to the reaction mixture, however, the concentration and rate of reaction was maintained. At the end of the reaction, the water was removed by distillation and pyridinium salt **11** could be isolated in 95% yield after cooling and addition of MTBE.

At this stage, the piperidine ring (**3**) could be obtained by either a one- or two-step reduction process (Scheme 5). In the two-step process, pyridinium salt **11** was dissolved in methanol and 3.3 equivalents of $NaBH_4$ was added to produce tetrahydropiperidine **12** in 79% yield. The remaining olefin was then reduced at 40 psi hydrogen and 20% $Pd(OH)_2/C$ in methanol to afford **3** in 95% assay yield. Unfortunately, amine **3** was not crystalline. To facilitate isolation and handling of the product as a solid it was crystallized as the L-tartrate salt from ethanol in 93% recovery. Alternatively, pyridinium intermediate **11** could be reduced directly to **3** using PtO_2 as catalyst in methanol. In this case, the product could be isolated by crystallization as the dihydrobromide salt in 85% yield upon switching the solvent to a mixture of 2-propanol–hexanes (1:1).

The final coupling step used 1,1′-carbonyldiimidazole (CDI) as the urea linking agent (Scheme 6). The (*S*)-dihydropyrimidinone **2** was deprotonated with LDA in THF at <–55°C. CDI was then added and the mixture was warmed to complete the acylation to **13**. The mixture was then recooled to –60°C and the free base of **3** as an IPAc solution was added. The reaction proceeded regioselectively, with no acylation or coupling observed at the unprotected N-1 position. Following an aqueous work-up, the coupled product was isolated from 2-propanol by addition of L-tartaric acid. A sample of the salt was hydrolyzed and the free base was analyzed by chiral HPLC showing the product **1** to be >99% optically pure. The product L-tartrate salt was obtained as a 2-propanol solvate in 80% yield. Interestingly, this salt was reluctant to crystallize without the presence of 2-propanol. Fortunately, the 2-propanol solvate could be removed by aging the solid as a suspension in ethanol for a few hours. Upon filtration, unsolvated salt **1** was isolated in 80% yield.

Scheme 6.

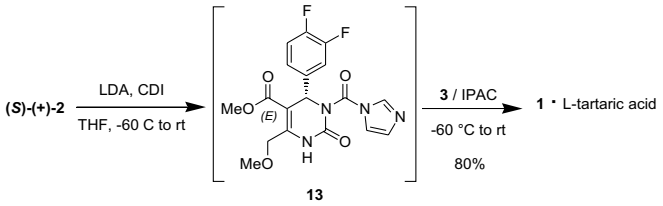

In conclusion, a highly effective preparation of drug candidate **1** for the treatment of BPH has been designed and demonstrated. The key chiral dihydropyrimidinone was easily prepared in two steps using a Lewis acid-modified Biginelli reaction and a very efficient enzymatic hydrolysis to afford the resolved heterocycle in 67–75% overall theoretical yield. An improved process for preparing the side chain and coupling procedure have also been developed, which allows for the construction of the material in multi-kilogram quantities.

Experimental

(±)-4-(3,4-Difluorophenyl)-1,2,3,4-tetrahydro-6-(methoxymethyl)-2-oxo-5-pyrimidinecarboxylic acid methyl ester (2)

A mixture of 3,4-difluorobenzaldehyde (670 g, 4.7 mol), methyl 4-methoxyacetoacetate (702 g, 4.8 mol), urea (433 g, 7.2 mol), boron trifluoride diethyl etherate (1126 g, 7.9 mol), copper(II) acetate (94 g, 0.5 mol), and acetic acid (36 mL) in THF (7.5 L) was heated at reflux for ~8 h. The mixture was cooled to room temperature and ethyl acetate (8 L) and aqueous citric acid (10%, 7.5 kg) were added. The layers were separated and the aqueous layer was washed with ethyl acetate (4 L). The combined organic layers were washed with aqueous 10% Na_2CO_3 (2 × 5 kg) and 5% brine (5 kg). The organic layer was concentrated to 4.3 L, then toluene (5 L) was added, and the batch was concentrated to ~4 L. The batch was heated to 80°C to dissolve the solids and then cooled to room temperature, whereupon the product crystallized. Hexanes (450 mL) were added and the slurry was aged for 18 h. The solid was filtered and washed with toluene (2.5 L) and dried to afford 1.2 kg of racemic dihydropyrimidinone **2** in 84% yield; mp 92–94°C. IR (cm^{-1}): 3232, 3114, 293, 1695, 1652, 1515, 1435, 1093. ^1H NMR ($CDCl_3$) δ: 7.65 (s, 1H), 7.00 (m, 3H), 6.63 (s, 1H), 5.34 (s, 1H), 4.63 (m, 2H), 3.64 (s, 3H), 3.45 (s, 3H). ^{13}C NMR ($CDCl_3$) δ: 165.0, 152.2, 150.3 (dd, J = 249, 13 Hz), 149.8 (dd, J = 249, 13 Hz), 147.5, 140.2, 122.3, 117.4 (d, J = 18 Hz), 115.5 (d, J = 18 Hz), 98.3, 68.4, 59.0, 54.4, 51.3. Anal. calcd. for $C_{14}H_{14}F_2N_2O_4$: C 53.85, H 4.52, N 8.97; found: C 53.80, H 4.48, N 8.84.

(*S*)-4-(3,4-Difluorophenyl)-1,2,3,4-tetrahydro-6-(methoxymethyl)-2-oxo-5-pyrimidinecarboxylic acid methyl ester ((*S*)-2)

A suspension of the racemic dihydropyrimidinone (3.1 kg, 10.2 mol), Trizma hydrochloride (1.3 kg), Trizma base (5.5 kg) in water (992 L), and acetonitrile (110 kg) was heated to 37°C. Purafect 4000L (362 kg) was added and the

© 2002 NRC Canada

suspension was agitated for 10 d. The extent of the optical enrichment was followed by chiral SFC: Chiralcel OD-H (4.6 mm × 25 cm), isocratic elution at 30°C (290 bar), CO_2 with 6% methanol, 2 mL min^{-1}, 280 nm, retention times: (+)-DHP ester = 4.6 min, (–)-DHP ester = 5.3 min, (–)-DHP acid = 11 min; or chiral HPLC: Chiracel OD-H, isocratic elution at ambient temperature with 15% isopropanol in hexanes, 1 mL min^{-1}, 280 nm, retention times: (+)-DHP ester = 7.6 min, (–)-DHP ester = 9.1 min. The reaction was stopped once the DHP methyl ester (*S*)-(+)-**2** had been enriched to >96% ee. The batch was cooled to 20°C, and then toluene (182 kg) was added. The layers were separated and the aqueous layer was washed with toluene (133 kg). The combined organic layers were washed with water (132 L) containing NaCl (32 kg). The organic layer was concentrated to a volume of 4 L and filtered. Toluene was added to bring the volume to 11 L. Heptane (15.8 L) was added to the batch over 10 h with seeding (2 wt%) with pure (*S*)-**2** and aged for 18 h. The solids were filtered, washed with toluene–heptane (40:60, 5.7 L), and dried to afford 1.3 kg of (*S*)-**2** in 40% yield. The optical purity was assayed at >99% (*S*)-(+)-**2**; mp 92–94°C. $[\alpha]_D^{25}$ +89 (*c* 0.5, $CHCl_3$). IR (cm^{-1}): 3232, 3114, 293, 1695, 1652, 1515, 1435, 1093. Anal. calcd. for $C_{14}H_{14}F_2N_2O_4$: C 53.85, H 4.52, N 8.97; found: C 53.76, H 4.34, N8.81.

Dihydropyrimidinone·D-*threo*-2-amino-1-(4-nitrophenyl)-1,3-propanediol salt (6)

Crystals grew from an ethanol solution of **6** held at room temperature. A suitable crystal was selected and reflection data were collected on a point-detector diffractometer. The structure was solved by direct methods and determined to have two independent molecules of **6** present in the lattice along with ethanol molecules and disordered water molecules of solvation. Refinement proceeded normally with the final model using 648 parameters. All non-hydrogen atoms were refined with anisotropic thermal displacements except for the fluorine atoms (one of which is disordered) and those of the solvent molecules. The weighting scheme used was the standard SHELXL function with P^2 and *P* coefficients of 0.2562 and 0.0 respectively. Final agreement statistics are: $R = 0.105$, $wR = 0.371$, $S = 0.97$, $(\Delta/\sigma)_{max} = 0.01$. The maximum peak height in a final difference Fourier map is 0.80 e $Å^{-3}$ and it has no chemical significance.[3]

Preparation of 2,4′-Bipyridine (7)

Lithiation–transmetalation

n-BuLi in hexanes (2.5 M, 4.16 L, 10.4 mol) was added to THF (9.4 L) at <–45°C. 2-Bromopyridine (**8**) (881.4 mL, 9.24 mol) was added to the *n*-BuLi in THF at <–45 C and the mixture was aged for 1.5 h at –55°C. A suspension of zinc chloride (1352 g, 9.92 mol) in THF (9.9 L), previously heated at reflux over molecular sieves in a Soxhlet extractor for 2 h, was added to the batch and the mixture was warmed to room temperature and aged for 2 h.

Salt break of 4-bromopyridine hydrochloride

In a separate flask, 4-bromopyridine hydrochloride (**9**) (1300 g, 6.62 mol) was partitioned between methyl *tert*-butyl ether (MTBE) (6.5 L) and water (1 L). Aqueous Na_2CO_3 (2 M, 4.7 L, 9.4 mol) was added carefully over 10 min and the mixture was well-agitated for 10 min. The layers were separated and the organic phase was diluted with MTBE (6.5 L). The combined organics were azeotropically dried by concentrating to ~6.5 L at 48–54°C.

Coupling

The solution of **8** was added to the 2-pyridyl zinc mixture (**10**) over 10 min. Triphenylphosphine (177 g, 0.67 mol) was added followed by palladium(II) acetate (34.8 g, 0.15 mol). The mixture was then heated and maintained at 50°C. The reaction is exothermic above 50°C. The heating was discontinued, but the reaction temperature rose to 60°C over 10 min. The reaction mixture was cooled to room temperature and concentrated ammonium hydroxide (5 L) was slowly added and the mixture was stirred for 30 min. The layers were separated and the organic layer was washed with brine (4 L). DMF (5 L) was added and the mixture was concentrated to ~2 L. The concentrate contained 837 g of 2,4′-dipyridyl (**7**) (81% assay yield).

1-(3-Aminopropyl)-2,4′-bipyridinium bromide monohydrobromide (11)

To a solution of 2,4′-dipyridyl (**7**) in DMF (1.85 L, 444 mg mL^{-1}, 5.25 mol) was added 3-bromopropylamine-hydrobromide (1400 g, 6.39 mol) and DMF (3.5 L). The mixture was heated to 95°C and aged for 8 h. The reaction mixture was cooled to room temperature and MTBE (3.7 L) was added over 3 h, whereupon the pyridinium salt crystallized. The slurry was aged for 1 h and filtered. The solid was washed with MTBE–DMF (1:1, 4.2 L) and dried to afford 1866 g (95%) of the pyridinium salt **11**; mp 253–256°C. IR (cm^{-1}): 3030, 2933, 1638, 1558, 1506, 1216, 1185, 1149. ^1H NMR (DMSO-d_6) δ: 9.33 (d, J = 6.8 Hz, 2H), 8.82 (d, J = 6.8 Hz, 3H), 8.46 (d, J = 8.1 Hz, 1H), 8.10 (m, 4H), 7.63 (dd, J = 7.5, 4.8 Hz, 1H), 4.87 (t, J = 6.8 Hz, 2H), 2.93 (m, 2H), 2.33 (m, 2H). ^{13}C NMR (DMSO-d_6) δ: 152.8, 150.5, 149.6, 145.2, 138.2, 126.6, 124.4, 123.4, 57.0, 35.5, 34.1, 28.5. Anal. calcd. for $C_{13}H_{17}Br_2N_3$: C 41.63, H 4.57, N 11.20; found: C 41.40, H 4.46, N 11.10.

4-(2-Pyridinyl)-1-piperidinepropanamine (3)

Method A

Pyridinium salt **11** (1840 g, 4.9 mol) was dissolved in methanol (18 L). The slurry was cooled to 5°C and $NaBH_4$ (612 g, 16.2 mol) was added over 2 h. The mixture was concentrated in vacuo and MTBE (10 L) and 20% aqueous NaOH (20 L) were added. The layers were well-stirred and then separated. The aqueous layer was washed with MTBE (10 L). The combined organics were concentrated to afford **12** as a thick oil (836 g, 79% yield). The crude tetrahydropiperidine **12** was dissolved in methanol (8 L). To the methanol solution of crude **12** (812 g, 3.70 mol) was added 20%

[3] Crystallographic information has also been deposited with the Cambridge Crystallographic Data Centre (CCDC No. 177624). Copies of the data can be obtained free of charge via www.ccdc.cam.ac.uk/conts/retrieving.html (or from the Cambridge Crystallographic Data Centre, 12, Union Road, Cambridge CB2 1EZ, UK; fax: +44 1223 336033; or deposit@ccdc.cam.ac.uk).

© 2002 NRC Canada

$Pd(OH)_2$ (81 g) and the tetrahydropiperidine was hydrogenated at 40 psi hydrogen. The catalyst was removed by filtration through Celite 521 and the solids were rinsed with methanol (3 × 300 mL). The combined filtrates were concentrated to afford amine **3** as a yellow oil (755 g, 93%). Amine **3** (755 g, 3.4 mol) was dissolved in ethanol (8 L) and the solution was warmed to 65°C. A solution of L-tartaric acid (596 g, 3.97 mol) in ethanol (2.1 L) was added over ~1 h with seeding to crystallize the **3**-tartrate salt. The slurry was slowly cooled to ambient temperature over 18 h. The solids were filtered and washed with ethanol (2 × 1 L) and dried to afford the amine **3**-tartrate salt containing 11 wt% residual solvent (1401 g, 97% corrected yield); mp 101–103°C. IR (cm^{-1}): 3372, 2980, 1589, 1386, 1201, 1118. ^1H NMR ($CDCl_3$) δ: 8.48 (d, *J* = 0.3 Hz, 1H), 7.57 (dt, *J* = 7.7, 1.8 Hz,1H), 7.14 (d, *J* = 7.9 Hz, 1H), 7.07 (m, 1H), 3.03 (d, *J* = 11.5 Hz, 2H), 2.70 (m, 3H), 2.40 (m, 2H), 2.1–1.5 (m, 10H). ^{13}C NMR ($CDCl_3$) δ: 165.2, 149.1, 136.3, 121.2, 120.5, 56.8, 54.2, 44.7, 41.0, 32.1, 30.9.

Method B

Di-hydrobromide salt: Pyridinium bromide salt **11** (50 g, 0.13 mol) was dissolved in methanol (500 mL) and hydrogenated over PtO_2 (1.0 g) at 40 psi and 20°C. After 6 h, the slurry was filtered through Solka-floc® (powdered-cellulose filter aid) on a sintered glass funnel. The solids were rinsed with methanol (2 × 50 mL), and the solution was concentrated and turned over to 2-propanol by distillation at ambient pressure to a concentration of ca. 7.5 mL 2-propanol per g for a final volume of ca. 375 mL. The suspension was cooled to 20°C, and *n*-heptane (15 mL g^{-1}, 750 mL) was added over 1 h. The resulting slurry was filtered, rinsed with 2-propanol–heptane (1:2, 50 mL) and dried at 40°C in vacuo to afford of the dihydrobromide salt (45.5 g, 90% yield); mp 200–204°C. IR (cm^{-1}): 3411, 2934, 1589, 1472, 1435, 1200, 1146. ^1H NMR (DMSO-d_6) δ: 8.51 (m, 1H), 7.75 (dt, *J* = 7.5, 2.0 Hz, 1H), 7.30 (d, *J* = 7.5 Hz, 1H), 7.25 (m, 1H), 3.5–3.0 (br m, 10H), 2.92 (m, 3H), 2.08 (m, 6H). ^{13}C NMR (DMSO-d_6) δ: 162.7, 149.4, 137.3, 122.4, 121.9, 53.5, 52.2, 45.0, 36.7, 28.8, 22.0. Anal. calcd. for $C_{13}H_{23}Br_2N_3 \cdot H_2O$: C 39.12, H 6.31, N 10.53; found: C 39.22, H 6.11, N 10.47.

Salt break

The L-tartrate or dihydrobromide salt of **3** (3.0 mol) was added to 50% NaOH (2.29 kg) diluted with water (6 L). The free amine was extracted with isopropyl acetate (3 × 18 L) and the combined extracts were concentrated to afford 594.1 g of **3** as an oil (90% recovery), which was used without further purification in the following step.

(*S*)-6-(3,4-Difluorophenyl)-1,2,3,6-tetrahydro-4-(methoxymethyl)-2-oxo-1-[[[3-[4-(2-pyridinyl)-1-piperidinyl]propyl]amino]carbonyl]-5-pyrimidinecarboxylic acid methyl ester – tartrate salt

A solution of LDA (2 M in heptane–THF–ethylbenzene, 184 mL, 0.4 mol) was added to a –65°C solution of (*S*)-(+)-**2** (100 g, 0.4 mol) in THF (1 L). After 15 min, carbonyl diimidazole (62.3 g, 0.38 mol) was added in one portion. The resulting slurry was aged at –60°C for 15 min and then warmed to 20°C. After 1 h, the mixture was re-cooled to –60°C. A solution of amine **3** (100 g, 0.45 mol) in isopropyl acetate (IPAc) (300 mL) was added at <–45°C. The mixture was slowly warmed to 20°C. The reaction was quenched with water (1.5 L) and IPAc (1.5 L). The layers were separated and the organic layer was washed with water (2 × 1.5 L). The combined aqueous layers were washed with IPAc (0.5 L). The combined organic layers were extracted with 2 N HCl (1 × 1 L and 1 × 0.5 L). The combined acid extracts were neutralized with solid $NaHCO_3$ (450 g). IPAc (1 L) and water (1 L) were added and the layers were mixed and separated. The aqueous layer was extracted with IPAc (1 L). The combined organic layers were washed with water (2 × 1 L) and concentrated to an oil. The oil was dissolved in 2-propanol (1.27 L). The solution was warmed to 50°C. A solution of L-tartaric acid (38 g, 0.2 mol) in ethanol (175 mL) was added and the mixture was aged for 1 h, whereupon crystals formed. The slurry was cooled to 20°C, aged for 18 h, cooled to 0°C, and then aged for an additional 1 h. The solid was filtered, washed with 2-propanol (300 mL), and dried to afford 195 g of the **1** tartrate salt as a 2-propanol solvate (80% yield). The solvate was broken by stirring the solid in ethanol (975 mL) at 0°C for 2 h. The solid was filtered and dried to afford the L-tartrate salt of **1** (156 g, 80% yield); mp 145–148°C. $[\alpha]_{589}^{20}$ +127.5 (*c* 1.0, CH_3OH). Optical purity >99.9% by chiral HPLC assay. IR (cm^{-1}): 3295, 2946, 1709, 1645, 1516, 1436, 1393. ^1H NMR (DMSO-d_6) δ: 9.98 (br s, 1H), 8.82 (t, *J* = 5.5 Hz, 1H), 8.49 (d, *J* = 4.0 Hz, 1H), 7.72 (dt, *J* = 7.5, 1.5 Hz, 1H), 7.42 (m, 1H), 7.28 (d, *J* = 7.5 Hz, 1H), 7.21 (m, 2H), 7.08 (m, 1H), 6.56 (s, 1H), 4.63 (d, *J* = 13.0 Hz, 1H), 4.42 (d, *J* = 13.0 Hz, 1H), 4.07 (s, 2H), 3.67 (s, 3H), 3.29 (s, 3H), 3.25 (m, 4H), 2.77 (m, 1H), 2.65 (m, 1H), 2.49 (m, 7H), 1.90–1.60 (m, 6H). ^{13}C NMR (DMSO-d_6) δ: 173.9, 164.4, 163.2, 152.9, 152.1, 148.8, 146.7, 138.0, 136.6, 123.1, 123.0, 122.9, 121.6, 121.2, 118.0, 117.7, 115.4, 115.2, 103.1, 71.8, 66.7, 62.0, 58.1, 54.2, 52.1, 51.7, 41.7, 38.0, 29.4, 25.4, 24.7. Anal calcd. for $C_{32}H_{39}F_2N_5O_{11}$: C 54.31, H 5.55, N 9.90; found: C 54.12, H 5.64, N 9.80.

References

1. (*a*) For a recent review of the classes of drugs used for the treatment of BPH, see: B. Kenney, S. Ballard, J. Blagg, and D. Fox. J. Med. Chem. **40**, 1293 (1997); (*b*) H.J. Lepor. Urol. **141**, 1283 (1989); (*c*) M. Jonler, M. Reihmann, and R.C. Bruskewitz. Drugs, **47**, 66 (1994); (*d*) C.R. Chapple. Brit. J. Urol. **76**, 47 (1995); (*e*) L.M. Eri and K.J. Tveter. J. Urol. **154**, 923 (1995); (*f*) J.D. McConnell, J.D. Wilson, F.W. George, J. Geller, F. Pappas, and E. Stoner. J. Clin. Endocrinol. Metab. **74**, 505 (1992).
2. For a review of the adrenergic class of drug candidates, see: C. Forray and S.A. Noble. Exp. Opin. Invest. Drugs, **8**, 2073 (1999).
3. (*a*) J.C. Barrow, K.L. Glass, H.G. Selnick, R.M. Freidinger, R.S.L. Chang, S.S.O. O'Malley, and C. Woyden. Bioorg. Med. Chem. Lett. **10**, 1917 (2000); (*b*) B. Lagu, D. Tian, M.R. Nagarathnam, W.C. Wong, S.W. Miao, F. Zhang, W. Sun, G. Chiu, J. Fang, C. Forray, R.S.L. Chang, R.W. Ransom, T.B. Chen, S. O'Malley, K. Zhang, K.P. Vyas, and C. Gluchowski. J. Med. Chem. **42**, 4794 (1999); (*c*) S. Furuya, Y. Kumamoto, E. Yokoyama, T. Tsukamoto, T. Izumi, and Y. Abiko. J. Urol. **128**, 836 (1982).
4. (*a*) R.S.L. Chang, T.-B. Chen, S.S. O'Malley, D.J. Pettibone, J. DiSalvo, B. Francis, M.G. Bock, R. Freidinger, D.

© 2002 NRC Canada

Nagarathnam, S.W. Miao, Q. Shen, B. Lagu, T.G.M. Dhar, S. Tyagarajan, M.R. Marzabadi, W.C. Wong, C. Gluchowski, and C. Forray. Eur. J. Pharm. **409**, 301 (2000).

5. (*a*) J.M. Wetzel, S.W. Miao, C. Forray, L.A. Borden, T.A. Branchek, and C. Gluchowski. J. Med. Chem. **38**, 1579 (1995); (*b*) J.C. Barrow, P.G. Nantermet, H.G. Selnick, K.L. Glass, K.E. Rittle, K.F. Gilbert, T.G. Steele, C.F. Homnick, R.M. Freidinger, R.W. Ransom, P. Kling, D. Reiss, T.P. Broten, T.W. Schorn, R.S.L. Chang, S.S. O'Malley, T.V. Olah, J.D. Ellis, A. Barrish, K. Kassahun, and P. Leppert. J. Med. Chem. **43**, 2703 (2000); (*c*) B. Lagu, D. Tian, G. Chiu, D. Nagarathnam, J. Fang, Q. Shen, C. Forray, R.W. Ransom, R.S.L. Chang, K.P. Vyas, K. Zhang, and C. Gluchowski. Bioorg. Med. Chem. Lett. **10**, 175 (2000); (*d*) D. Nagarathnam, S.W. Miao, B. Lagu, G. Chiu, J. Fang, T.G.M. Dhar, J. Zhang, S. Tyagarajan, M.R. Marzabadi, F. Zhang, W.C. Wong, W. Sun, D. Tian, J.M. Wetzel, C. Forray, R.S.L. Chang, T.P. Broten, R.W. Ranson, T.W. Schorn, T.B. Chen, S. O'Malley, P. Kling, K. Schneck, R. Bendesky, C.M. Harrell, K.P. Vyas, and C. Gluchowski. J. Med. Chem. **42**, 4764 (1999); (*e*) T.G.M. Dhar, D. Nagarathnam, M.R. Marzabadi, B. Lagu, W.C. Wong, G. Chiu, S. Tyagarajan, S.W. Miao, F. Zhang, W. Sun, D. Tian, Q. Shen, J. Zhang, J.M. Wetzel, C. Forray, R.S.L. Chang, T.P. Broten, T.W. Schorn, T.B. Chen, S. O'Malley, R. Ransom, K. Schneck, R. Bendesky, C.M. Harrell, K,P. Vyas, K. Zhang, J. Gilbert, D.J. Pettibone, M.A. Patane, M.G. Bock, R.M. Freidinger, and C. Gluchowski. J. Med. Chem. **42**, 4778 (1999); (*f*) B. Lagu, D. Tian, D. Nagarathnam, M.R. Marzabadi, W.C. Wong, S.W. Miao, F. Zhang, W. Sun, G. Chiu, J. Fang, C. Forray, R.S.L. Chang, R.W. Ransom, T.B. Chen, S. O'Malley, K. Zhang, K.P. Vyas, and C. Gluchowski. J. Med. Chem. **42**, 4794 (1999); (*g*) W.C. Wong, W. Sun, B. Lagu, D. Tian, M.R. Marzabadi, F. Zhang, D. Nagarathnam, S.W. Miao, J.M. Wetzel, J. Peng, C. Forray, R.S.L. Chang, T.B. Chen, R. Ransom, S.S. O'Malley, T.P. Broten, P. Kling, K.P. Vyas, K. Zhang, and C. Gluchowski. J. Med. Chem. **42**, 4804 (1999); (*h*) P.G. Nantermet, J.C. Barrow, H.G. Selnick, C.F. Homnick, R.M. Freidinger, R.S.L. Chang, S.S. O'Malley, D.R. Reiss, T.P. Broten, R.W. Ransom, D.J. Pettibone, T. Olah, and C. Forray. Bioorg. Med. Chem. Lett. **10**, 1625 (2000).
6. (*a*) C.O. Kappe. Acc. Chem. Res. **33**, 879 (2000); (*b*) C.O. Kappe Tetrahedron, **49**, 6937 (1993).
7. For an excellent investigation into the mechanism of this reaction, see: (*a*) C.O. Kappe. J. Org. Chem. **62**, 7201 (1997); (*b*) C.O. Kappe, S.F. Falsone, W.M.F. Fabian, and F. Belaj. Heterocycles, **51**, 77 (1999).
8. (*a*) C.O. Kappe and S.F. Falsone. Synlett, 718 (1998); (*b*) C.O. Kappe, D. Kumar, and R.S. Varma. Synthesis, 1799 (1999). c) H.A. Stefani and P.M. Gatti. Synth. Commun. **30**, 2165 (2000); (*d*) C.O. Kappe. Bioorg. Med. Chem. Lett. **10**, 49 (2000); (*e*) P. Wipf and A. Cunningham. Tetrahedron Lett. **36**, 7819 (1995); (*f*) F. Bigi, S. Carloni, B. Frullanti, R. Maggi, and G. Sartori. Tetrahedron Lett. **40**, 3465 (1999); (*g*) A. Studer, P. Jeger, P. Wipf, and D.P. Curran. J. Org. Chem. **62**, 2917 (1997); (*h*) A. Studer, S. Hadida, R. Ferrito, S.-Y. Kim, P. Jeger, P. Wipf, and D.P. Curran.Science (Washington, D.C.), **275**, 823 (1997); (*i*) C.O. Kappe and S.F. Falsone. Synlett, 718 (1998).
9. (*a*) E.H. Hu, D.R. Sidler, and U.-H. Dolling. J. Org. Chem. **63**, 3454 (1998); (*c*) J. Lu and H. Ma. Synlett, 63 (2000); (*b*) Y. Ma, C. Qian, L. Wang, and M. Yang. J. Org. Chem. **65**, 3864 (2000); (*d*) B.C. Ranu, A. Hajra, and U. Jana. J. Org. Chem. **65**, 6270 (2000).
10. (*a*) F. Cohen, L.E. Overman, and S.K.L. Sakat. Org. Lett. **1**, 2169 (1999); (*b*) D.S. Coffey, A.I. McDonald, L.E. Overman, and F. Stappenbeck. J. Am. Chem. Soc. **121**, 6944 (1999); (*c*) A.S. Franklin, S.K. Ly, G.H. Macklin, L.E. Overman, and A.J. Shaka. J. Org. Chem. **64**, 1512 (1999); (*d*) A.I. McDonald and L.E. Overman. J. Org. Chem. **64**, 1520 (1999); (*e*) L.E. Overman, and M.H. Rabinowitz J. Org. Chem. **58**, 3235 (1993).
11. C.O. Kappe, G. Uray, P. Roschger, W. Lindner, C. Kratky, and W. Keller. Tetrahedron, **48**, 5473 (1992).
12. O.P. Kleidernigg and C.O. Kappe. Tetrahedron: Asymmetry, **8**, 2057 1997.
13. Since the development of our enzymatic resolution another such process was reported: B. Schnell, W. Krenn, K. Faber, and C.O. Kappe. J. Chem. Soc. Perkin Trans. 1, 4382 (2000).
14. A complete report on the studies of the enzymatic resolution of **2** will be reported elsewhere: M. Chartrain, C. Roberge, D.R. Sidler, C. Taylor, N. Ikemoto, K. Goklen, R.D. Larsen, R. Buccino, B. Buckland, and R. Greasham. Manuscript in preparation.
15. (*a*) L.A. Summers. Adv. Heterocycl.Chem. **35**, 281 (1984); (*b*) K. Oda, R. Nakagami, N. Nishizono, and M. Machida. Chem. Commun. 2371 (1999); (*c*) M. Hasebe, K. Kogawa, and T. Tsuchiya. Tetrahedron Lett. **25**, 3887 (1984); (*d*) H. Bonnemann and R. Brinkmann. Synthesis, 600 (1975).
16. (*a*) M.-J. Shiac and K.-Y. Tarng. Heterocycles, **31**, 637 (1990); (*b*) N. Furukawa, T. Shibutani, and H. Fujihara. Tetrahedron Lett. **28**, 5845 (1987); (*c*) A.G. Osborne, K.J. Glass, and M.L. Staley. Tetrahedron Lett. **30**, 3567 (1989).
17. (*a*) T. Sakamoto, Y. Kondo, N. Murata, and H. Yamanaka. Tetrahedron, **49**, 9713 (1993); (*b*) S. Mukhopadhyay, G. Rothenberg, D. Gitis, M. Baidossi, D.E. Ponde, and Y. Sasson. J. Chem. Soc. Perkin Trans 2, 1809 (2000); (*c*) A.F. Littke, C. Dai, and G.C. Fu. J. Am. Chem. Soc. **122**, 4020 (2000); (*d*) O. Lohse, P. Thevenin, and E. Waldvogel. Synlett, 45 (1999); (*e*) H. Zhang, F.Y. Kwong, Y. Tian, and K.S. Chan. J. Org. Chem. **63**, 6886 (1998); (*f*) K. Inada and N. Miyaura. Tetrahedron, **56**, 8661 (2000); (*g*) D. Villemin and F. Caillot. Tetrahedron Lett. **42**, 639 (2001); (*h*) N. Zhang, L. Thomas, and B. Wu. J. Org. Chem. **66**, 1500 (2001); (*i*) H. Zhang, F. Xue, T.C.W. Mak, and K.S. Chan. J. Org. Chem. **61**, 8002 (1996); (*j*) A.O. Aliprantis and J.W. Canary. J. Am. Chem. Soc. **116**, 6985 (1994).
18. (*a*) Y. Hassan, V. Penalva, L. Lavenot, C. Gozzi, and M. Lemaire. Tetrahedron, **54**, 13793 (1998); (*b*) H. Hagelin, B. Hedman, I. Orabona, T. Akermark, B. Akermark, and C.A. Klug. J. Mol. Catal. A: Chem. **164**, 137 (2000).
19. (*a*) Y. Yamamoto, Y. Azuma, and H. Mitoh. Synthesis, 564 (1986); (*b*) J. Mathieu, P. Gros, and Y. Fort. Tetrahedron Lett. **42**, 1879 (2001); (*c*) S. Gronowitz, P. Bjork, J. Malm, and A.-B. Hornfeldt. J. Organomet. Chem. **460**, 127 (1993); (*d*) J. Malm, P. Bjork, S. Gronowitz, and A.-B. Hornfeldt. Tetrahedron Lett. **33**, 2199 (1992); (*e*) P. Gros and Y. Fort. Synthesis, 754 (1999).
20. M. Ishikura, T. Ohta, and M. Terashima. Chem. Pharm. Bull. **33**, 4755 (1985).
21. (*a*) T. Sakamoto, Y. Kondo, N. Murata, and H. Yamanaka. Tetrahedron Lett. **33**, 5373 (1992); (*b*) P. Gros and Y. Fort. Synthesis, 754 (1999); (*c*) A.S. Bell, D.A. Roberts, and K.S. Ruddock. Synthesis, 843 (1987); (*d*) T. Sakamoto, Y. Kondo, N. Murata, and H. Yamanaka. Tetrahedron Lett. **49**, 9713 (1993); (*e*) A.S. Bell, D.A. Roberts, and K.S. Ruddock. Synthesis, 843 (1987).
22. (*a*) E. Negishi, A.O. King, and N. Okukado. J. Org. Chem. **42**, 1821 (1977); (*b*) E. Negishi, F.-T. Luo, R. Frisbee, and H. Matsushita. Heterocycles, **18**, 117 (1982).

© 2002 NRC Canada

Enzymatic synthesis of octyl glucoside catalyzed by almond β-glucosidase in organic media

Amélie Ducret, Jean-François Carrière, Michael Trani, and Robert Lortie

Abstract: The synthesis of *n*-octyl-β-D-glucopyranoside can be performed by direct condensation of 1-octanol and glucose, catalyzed by immobilized almond β-glucosidase, using solid glucose suspended in 1-octanol as a reaction media. Both the rate of reaction and the conversion could be enhanced by using acetonitrile and *N*,*N*-dimethylformamide (DMF) as co-solvents, the latter giving the best results. The rate of reaction was dependent on the concentration of DMF and on the initial water activity (a_w), with higher water activity fostering faster reactions. The rate increased with DMF concentration, up to 20% DMF, but diminished rapidly at higher concentrations. Product concentration could be increased from 40 to 100 mM by going from 0 to 20% DMF; however, it was not sensitive to the initial water activity.

Key words: β-glucosidase, alkyl glycosides, reverse hydrolysis, water activity, organic solvent.

Résumé : La synthèse du *n*-octyl-β-D-glucopyranoside a été effectuée par condensation du octane-1-ol et du glucose, catalysée par la β-glucosidase d'amande immobilisée, en suspendant le glucose solide dans l'octane-1-ol. La vitesse de réaction de même que le taux de conversion ont été améliorés par addition de co-solvants tels que l'acétonitrile et le *N*,*N*-diméthylformamide (DMF), ce dernier permettant d'obtenir de meilleurs résultats. La vitesse de réaction dépendait de la concentration en DMF et de l'activité de l'eau initiale, des activités élevées favorisant des réactions plus rapides. La vitesse de réaction augmentait avec la concentration en DMF, jusqu'à 20% de DMF, mais diminuait rapidement à des concentrations supérieurs. On a pu augmenter la concentration en produit, de 40 à 100 mM en passant de 0 à 20% de DMF; cependant, elle n'était pas fonction de l'activité de l'eau.

Mots clés : β-glucosidase, glycosides d'alkyles, hydrolyse inversée, activité de l'eau, solvant organique.

Introduction

The use of enzymes in organic synthesis is now widely accepted and documented (1, 2). Simple enzymes like hydrolases have also found applications in synthesis (3). They are especially interesting because they do not require cofactors and many of them display good stability. Their use has expanded with the recognition that they can catalyze the reverse reaction, condensation, if the thermodynamic conditions are favourable, by, for instance, lowering the water activity (a_w) by working in organic solvents. This fact has been known for some time (4, 5), but became more prominent in the last 20 years or so (6, 7), and some rationalizations were made about the choice of solvent and the role of water (8, 9).

This approach can be used in the preparation of alkyl glycosides. These non-ionic surfactants obtained from renewable feedstock are stable under alkaline conditions (10) and completely biodegradable. They show antimicrobial properties and low toxicity (11), and they have numerous applications in areas such as cosmetics, pharmaceuticals, food, and detergents. As a good alternative to chemical syntheses, which require protection and deprotection of the hydroxyl groups, the use of glycosidases in the enzymatic synthesis of such compounds was emphasized since it permits the regio- and stereoselectivity to be obtained in one step under mild reaction conditions. Enzymatic synthesis of alkyl glycosides can be achieved by either a kinetically (transglycosylation) or a thermodynamically (condensation) controlled approach (12). In spite of numerous studies performed on the subject (13), only poor yields have been obtained, mostly because glycosidases lose activity at low water activity (14, 15).

In the present work, we report the effect of water and co-solvent on the activity of almond β-glucosidase in the synthesis of octyl-β-D-glucoside by direct condensation of glucose and 1-octanol. Almond β-glucosidase was selected because it is readily available, relatively inexpensive, and shows no inhibition by glucose when compared with various microbial glycosidases (16).

Received 8 November 2001. Published on the NRC Research Press Web site at http://canjchem.nrc.ca on 30 May 2002.

Dedicated to Professor J. Bryan Jones on the occasion of his 65th birthday.

A. Ducret, J.-F. Carrière, M. Trani, and R. Lortie.[1]
Microbial and Enzyme Technology Group, Bioprocess Sector, Biotechnology Research Institute, National Research Council, 6100 Royalmount Ave., Montreal, QC H4P 2R2, Canada.

[1]Corresponding author (e-mail: robert.lortie@nrc.ca).

Materials and methods

Materials

Almond β-glucosidase (2.8 U mg^{-1}), *n*-octyl-β-D-glucopyranoside, *p*-nitrophenyl-β-D-glucopyranoside (*p*NPG), and 2-methyl-2-butanol were purchased from Sigma (St. Louis,

 DOI: 10.1139/V02-081 © 2002 NRC Canada

MO, U.S.A.). Glucose, Amberlite XAD-4 resin, sodium acetate, and $MgCl_2$ were purchased from BDH (Montreal, Quebec, Canada). The solvents used were always from the highest grade available and were used without further purification. Acetonitrile, 1-octanol, and the molecular sieves (3 Å) were purchased from Fisher Scientific (Nepean, Ontario, Canada). *N*,*N*-dimethylformamide (DMF), $BaCl_2$, and $Mg(NO_3)_2$ were purchased from Aldrich (Milwaukee, WI, U.S.A.). Methanol was purchased from J.T. Baker (Phillipsburgh, NJ, U.S.A.) and sulphuric acid from Anachemia (Montreal). NaCl was purchased from ACP Chemicals Inc. (Montreal). MilliQ+ water was used.

Immobilization of almond β-glucosidase on Amberlite XAD-4

Almond β-glucosidase (483 mg) was dissolved in sodium acetate buffer (2 mL, 50 mM, pH 5.0) and gently mixed with XAD-4 resin (2 g), which was previously washed and dried according to the procedure of Vulfson et al. (17). The mixture was then dried under vacuum for 20 h. The immobilized enzyme preparation contains 194.5 mg protein per g of dry weight. The immobilization yield was measured by suspending the preparation (3.5 mg) in a buffer (50 mL) containing *p*NPG (1.67 mM). Aliquots (0.75 mL) were taken, diluted with glycine buffer (1.0 mL, 0.4 M, pH 10.8), and the amount of *p*-nitrophenol released was measured at 430 nm.

HPLC analysis

HPLC analyzes were performed using a Waters Millennium[32] liquid chromatography system equipped with a Waters 600E solvent delivery system, a Waters 717 autosampler, and a Waters 410 refractive index detector, all purchased from Waters Scientific (Montreal).

The analysis of octyl glucoside was performed using a reversed-phase column CSC-Inertsil, 150 Å/ODS2, 5 μm, 25 × 0.46 cm (CSC, Montreal). Periodically, 12 μL of reaction sample were dissolved in acetonitrile (320 μL) and 25 μL were injected. A mixture of acetonitrile–water (60:40, v:v) was used as the mobile phase. The flow rate was maintained constant at 1.0 mL min^{-1} and the column temperature at 25°C. The retention times of *n*-octyl-β-D-glucopyranoside and 1-octanol were 3.53 and 9.08 min, respectively.

Glucose analysis was accomplished on an ion-exclusion column ICSep ICE-ION-300, 8 μm, 30 × 0.78 cm preceded by the guard column ICSep ICE-GC-801 (Transition Technologies Inc., Toronto, Ontario, Canada). A sample of the mixture (100 μL) was dissolved in methanol (200 μL) and 10 μL were injected into the column. Sulphuric acid (0.0042 M) was used as the mobile phase. The flow rate was maintained constant at 0.5 mL min^{-1} and the column temperature at 60°C; 10 μL of each sample were injected. The retention times of glucose, methanol, acetonitrile, 2-methyl-2-butanol, DMF, and *n*-octyl-β-D-glucopyranoside were 13.1, 25.5, 28.2, 46.0, 62.2, and 80.5 min, respectively. The system was washed periodically with the mobile phase to elute 1-octanol (which has a retention time of several hours).

Enzymatic synthesis

Before starting the reactions, the immobilized enzyme (207 mg, corresponding to 40.3 mg of protein) and reaction media (300 mg glucose and 2 mL of a mixture of 1-octanol–DMF) were equilibrated separately in chambers containing saturated salt solutions to preset the water activity ($BaCl_2$, a_w = 0.90; NaCl, a_w = 0.75; $Mg(NO_3)_2$, a_w = 0.53; $MgCl_2$, a_w = 0.33). Equilibration of the different reaction media was followed by measuring their water content by coulometric Karl Fischer titration using a Metrohm 684 KF coulometer (Herisau, Switzerland). After addition of the enzyme in the reaction mixture, the vials were hermetically closed and the reactions were run at 50°C. In the reaction mixture, most of the glucose was present as a solid phase. It was verified that all the octyl glucoside formed during the reaction was soluble in the liquid phase. Aliquots of the liquid phase were taken periodically through a Mininert® valve (Supelco, Bellefonte, PA, U.S.A.) for HPLC analysis. The initial reaction rates were determined by linear regression over 4–7 points.

Fig. 1. Synthesis of octyl-β-D-glucoside with a_w = 0.90 (300 mg D-glucose, 2 mL 1-octanol–DMF, 207 mg immobilized enzyme).

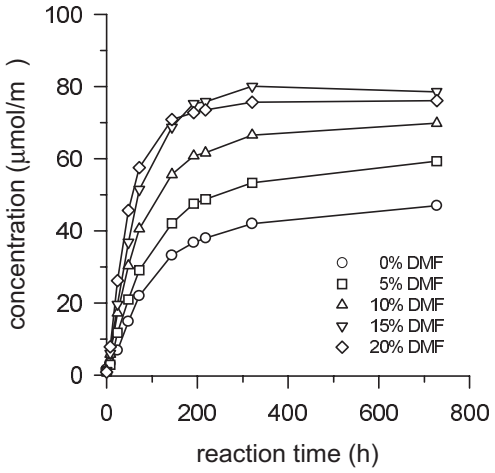

Solubility measurement

The solid glucose as well as each solvent were previously equilibrated separately in chambers containing a saturated NaCl solution to preset the a_w to 0.75. Glucose (0.30–0.35 g) was then added to 2 mL of a mixture of 1-octanol–co-solvent. The hermetically closed vials containing the mixtures were kept under constant agitation at 50°C for several days and then transferred to an oven at the same temperature. The liquid phase was filtered (0.45 μm, Millipore, Bedford, MA, U.S.A.) and diluted with methanol for HPLC analysis. To prevent precipitation, all the equipment used was previously heated to 50°C. A second determination was performed by simply diluting the settled liquid phase in methanol before HPLC analysis. Both methods gave identical results.

Results and discussion

The immobilized preparation and the enzyme in solution both catalyzed the hydrolysis of *p*NPG at a rate of 2.1 and 1.9 μmol per min per mg protein, respectively. The immobilization yield is therefore around 100%. When the solid was filtrated from the reaction, the rate dropped to 20% of that observed without filtration. This indicates that in water only 20% of the enzyme desorbs from the resin, even with a very

© 2002 NRC Canada

Fig. 2. Effect of various co-solvents on the initial reaction rate (*a*) and on the maximum concentration of octyl glucoside (*b*) (300 mg D-glucose, 2 mL 1-octanol–co-solvent, 207 mg immobilized enzyme, a_w = 0.75).

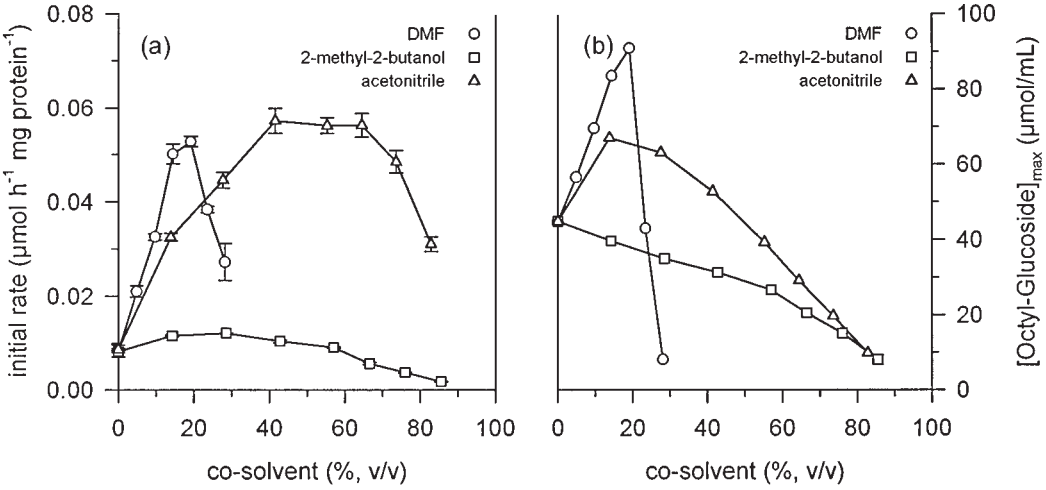

Fig. 3. Effect of co-solvent on the glucose solubility at a_w = 0.75.

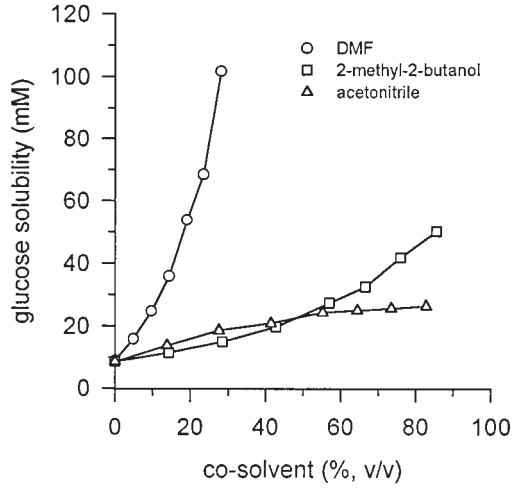

high liquid–solid ratio. In a much smaller volume of octanol, the enzyme should remain adsorbed (even in the presence of hydrophilic solvents).

A typical time course of the β-glucosidase-catalyzed condensation of glucose and octanol, at an initial a_w = 0.90 and various DMF concentrations, is presented in Fig. 1. As can be seen, the presence of the solvent affects both the initial rate and the equilibrium-product concentration. As shown in Fig. 2, other solvents at a_w = 0.75 have a different effect on the rate and equilibrium. The presence of 2-methyl-2-butanol impairs the synthesis by diminishing the maximum concentration of octyl glucoside reached as well as the initial rates at high concentrations (>50%). Conversely, addition of DMF or acetonitrile to the media increases the production of octyl glucoside — with a different maximum for each solvent. A sharp optimum concentration of DMF in the media (20%) led to the highest rate as well as the highest concentration of octyl glucoside at equilibrium (0.053 µmol per h per mg protein and 91 mM, respectively). Identical high values for the initial rates can be obtained with a broad concentration range of acetonitrile (40–65%); high concentrations of octyl glucoside, however, are only obtained with low percentages of acetonitrile (15–30%) and then rapidly diminish as the concentration of acetonitrile increases. When acetonitrile and DMF were used as co-solvents in water for the synthesis of 2-hydroxybenzyl-β-D-glucopyranoside catalyzed by almond β-glucosidase, the effect was not as favourable (18). In this case, acetonitrile had a positive effect on the product concentration between 80 and 95% (v/v), while DMF had no real positive effect.

The addition of polar co-solvents increases the solubility of glucose in the reaction medium (Fig. 3), which could be responsible for the observed increase in the reaction rates upon the addition of small amounts of the co-solvent. The fact that the addition of 2-methyl-2-butanol and acetonitrile has a similar effect on the solubility of glucose, but a very different effect on the initial reaction rates indicates that an increase in glucose solubility is not a determining factor.

It is possible that the low reaction rate in octanol is partly caused by its low dielectric constant (8.1), which results in higher electrostatic interactions between the polar and the charged residues, thus decreasing the flexibility of the protein. Addition of co-solvents with higher dielectric constants such as DMF (38.2) or acetonitrile (36.6) (or increasing the water content) raises the dielectric constant, which leads to lower electrostatic interactions and higher protein flexibility and activity, whereas 2-methyl-2-butanol, with its low dielectric constant (5.8) has little impact on the activity. This is in agreement with previous observations for subtilisin suspended in tetrahydrofuran (19) and for α-chymotrypsin suspended in various solvents (20).

Since DMF fosters higher reaction rates and product concentrations at a_w = 0.75, a study of its effect at various water activities was performed. As can be seen in Fig. 4, the positive effect of DMF on the reaction rates observed at a_w = 0.75 is present at other water activities up to a concentration of 20%, after which the rates drop dramatically. The presence of DMF, up to 20%, fosters higher octyl glucoside equilibrium concentrations. For instance, at a_w = 0.53, nearly 100 mM (~30 g L^{-1}) of octyl glucoside is obtained at equilibrium, which is greater than the amount obtained without the addition of co-solvents (40–50 mM); the amount measured by Ljunger et al. (14) was the same. Furthermore, this

© 2002 NRC Canada

Fig. 4. Effect of water activity on the initial reaction rate (*a*) and effect of DMF on the equilibrium concentration of octyl-β-D-glucopyranoside (*b*) (same conditions as Fig. 1).

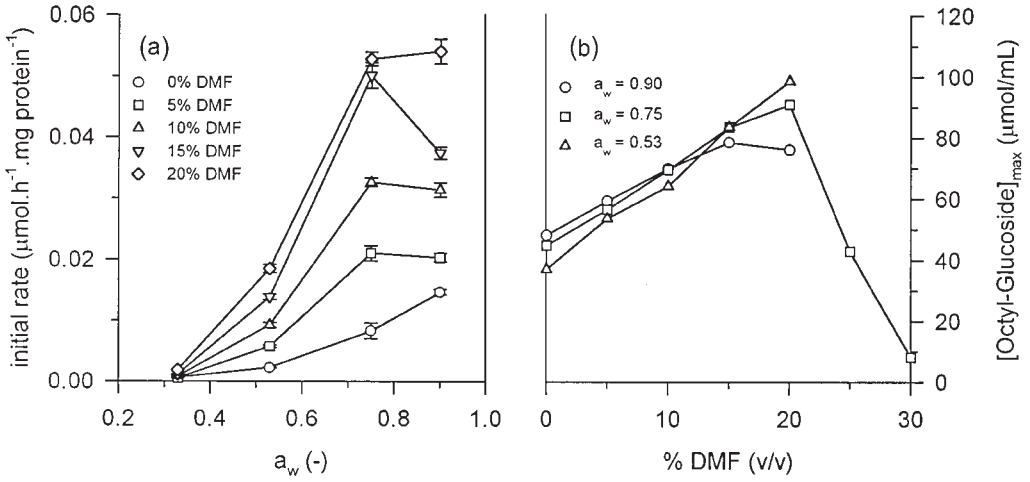

result has been obtained with a reaction rate superior to the highest rates observed without DMF. This high conversion is probably caused by the higher solubility of octyl glucoside in the presence of DMF (8). The solubility of glucose does not have to be taken into account, since the solution is always saturated, due to the presence of an excess of solid glucose, leading to small variations in the thermodynamic activity of glucose. It is difficult to explain the drop in conversion at concentrations higher than 20% DMF. We believe that equilibrium was reached, since addition of fresh catalyst does not change concentrations.

It should be noticed that the maximum concentration of octyl glucoside obtained increases only with the percentage of added DMF and, surprisingly, does not seem to be influenced by a_w (Fig. 4*b*). This is contrary to observations for 1-octanol without addition of co-solvent (14) and for 1-hexanol using various glycoside donors (21), where in both cases, the lowering of a_w induces higher octyl glucoside concentrations. The synthesis of 2-hydroxybenzyl-β-D-glucopyranoside in an aqueous-organic media was also favoured by low water activities (18). The presence of most of the glucose as a solid phase, on which water molecules can adsorb, may play a role, which should be investigated.

References

1. J.B. Jones. Tetrahedron, **42**, 3351 (1986).
2. G.M. Whitesides and C.H. Wong. Angew. Chem. Int. Ed. Engl. **24**, 617 (1985).
3. U.T. Bornscheuer and R.J. Kazlauskas. *In* Hydrolases in organic synthesis: Regio- and stereoselective biotransformations. Wiley-VCH, Weinheim. 1999.
4. J.H. Kastle and A.S. Loevenhart. Am. Chem. J. **24**, 491 (1900).
5. E.A. Sym. Biochem. J. **30**, 609 (1936).
6. A.M. Klibanov. ChemTech, 354 (1986).
7. A.M. Klibanov. Acc. Chem. Res. **23**, 114 (1990).
8. P.J. Halling. Enzyme Microbial Technol. **16**, 178 (1994).
9. P.J. Halling. Trends Biotechnol. **7**, 50 (1989).
10. K. Holmberg. *In* Novel surfactants: Preparation, applications, and biodegradablity. *Edited by* K. Holmberg. Marcel Dekker, N.Y. 1998. p. 333.
11. S. Matsumura, K. Imai, S. Yoshikawa, K. Kawada, and T. Uchibori. J. Am. Oil Chem. Soc. **67**, 996 (1990).
12. V. Kasche. Enzyme Microbial Technol. **8**, 4 (1986).
13. F. van Rantwijk, M. Woudenberg-van Oosterom, and R.A. Sheldon. J. Mol. Catal. B: Enzym. **6**, 511 (1999).
14. G. Ljunger, P. Adlercreutz, and B. Mattiasson. Enzyme Microbial Technol. **16**, 751 (1994).
15. M. Garcia-Garibay, A. Lopez-Mungia, and E. Barzana. Biotechnol. Bioeng. **70**, 647 (2000).
16. A. Ducret, M. Trani, and R. Lortie. Biotechnol. Bioeng. **77**, 752 (2002).
17. E.N. Vulfson, R. Patel, and B.A. Law. Biotech. Lett. **12**, 397 (1990).
18. G. Vic, D. Thomas, and D.H.G. Crout. Enzyme Microbial Technol. **20**, 597 (1997).
19. R. Affleck, Z.F. Xu, V. Suzawa, K. Focht, D.S. Clark, and J.S. Dordick. Proc. Natl. Acad. Sci. U.S.A. **89**, 1100 (1992).
20. R. Affleck, C.A. Haynes, and D.S. Clark. Proc. Natl. Acad. Sci. U.S.A., **89**, 5167 (1992).
21. M. Andersson and P. Adlercreutz. J. Mol. Catal. B: Enzym. **14**, 69 (2001).

© 2002 NRC Canada

Optimized production of the Diels–Alderase antibody 1E9 as a chimeric Fab

Andrea Piatesi and Donald Hilvert

Abstract: Monoclonal antibody 1E9, which catalyzes the [4+2] cycloaddition between tetrachlorothiophene dioxide and *N*-ethylmaleimide, has been re-engineered for production as a chimeric human–murine Fab fragment in *Escherichia coli*. Stabilizing point mutations in the variable regions of the antibody were identified by replacing residues that rarely occur at individual positions in aligned immunoglobulin sequences with their consensus counterparts. By combining favorable substitutions, double ($Met^{H87}Thr–Gly^{L63}Ser$) and triple ($Met^{H87}Thr–Gly^{L63}Ser–Phe^{L95}Pro$) mutants were created, which can be produced in good yield (4 and 17 mg L^{-1} cell culture, respectively). The triple mutant exhibits a modest fourfold drop in the apparent k_{cat} value for the cycloaddition reaction, but the kinetic properties of the double mutant are indistinguishable from those of the parent murine IgG. The availability of recombinant versions of this catalytic antibody will facilitate efforts to determine the origins of its selectivity and catalytic efficiency through mutagenesis.

Key words: catalytic antibody, Fab fragment, bacterial production.

Résumé : L'anticorps catalytique monoclonal 1E9, qui catalyse la cycloaddition [4+2] entre le dioxide de tétrachlorothiophène et le *N*-éthylmaleimide, a été modifié afin de permettre la production d'un fragment chimérique (humain–murine) Fab dans l'*Escherichia coli*. L'identification des mutations ponctuelles stabilisantes dans les régions variables de l'anticorps, a été réalisée en remplaçant les résidus rarement présents dans les alignements des séquences d'immunoglobulines par les résidus de plus grande occurrence. En combinant les substitutions favorables, on a créé les mutants double ($Mer^{H87}Thr–Gly^{L63}Ser$) et triple ($Met^{H87}Thr–Gly^{L63}Ser–Phe–^{L95}Pro$) qui ont été produits avec de bons rendements (respectivement de 4 et 17 mg L^{-1} de culture cellulaire). Alors que le mutant triple présente, pour la réaction de cycloaddition, une diminution d'un facteur 4 de la valeur du k_{cat} apparent, les propriétés cinétiques du mutant double sont identiques à celles de la murine originelle. L'accessibilité à des versions recombinantes de cet anticorps permettra, par le biais de la mutagenèse, de déterminer les origines de l'activité catalytique de 1E9 ainsi que sa sélectivité.

Mots clés : anticorps catalytique, fragment Fab, production bactérienne.

[Traduit par la Rédaction]

Introduction

Over the last decade, tailored antibody molecules have been engineered to catalyze a wide range of chemical reactions, including transformations that are rare or unknown in nature (1–4). For example, antibodies raised in response to bicyclic compounds that mimic the highly ordered boat-like geometry of the Diels–Alder reaction promote [4+2] cycloadditions with significant rate accelerations (5–8). They also exert considerable control over the *exo–endo* selectivity and absolute stereochemistry of such reactions (6, 8, 9).

Antibody 1E9 is currently the most efficient Diels–Alderase known (7). It was raised against the *endo*-hexachloronorbornene compound (**1**) and catalyzes the cycloaddition of tetrachlorothiophene dioxide (**2**, TCTD) and *N*-ethylmaleimide (**3**, NEM) with multiple turnovers (Fig. 1). The initially formed adduct (**4**) spontaneously eliminates sulfur dioxide to give the dihydrophthalimide derivative **5**, and the latter spontaneously oxidizes in situ to yield *N*-ethyl tetrachlorophthalimide (**6**) as the final product. A k_{cat}/k_{uncat} value in excess of 1000 M has been determined for 1E9 (10), making this catalyst substantially more active than other Diels–Alderase antibodies for which effective molarities rarely exceed 10 M. It is also considerably more efficient than ribozymes selected for their ability to promote cycloadditions (11, 12) and several natural Diels–Alderase enzymes that have been recently characterized (13–15).

The crystal structure of 1E9 complexed with its hapten reveals almost perfect shape complementarity between protein and ligand (10). Molecular recognition is achieved through extensive van der Waals contacts, π-stacking interactions, and a strategically placed hydrogen bonding interaction to one of the succinimide carbonyl groups. Although originally

Received 17 January 2002. Published on the NRC Research Press Web site at http://canjchem.nrc.ca on 24 May 2002.

Dedicated to Professor J. Bryan Jones on the occasion of his 65th birthday.

Abbreviations: BSA: bovine serum albumin; CDR: complementarity determining region; ELISA: enzyme-linked immunosorbent assay; NEM: *N*-ethylmaleimide; PBS: phosphate-buffered saline solution; PCR: polymerase chain reaction; HEPES: *N*-2-hydroxyethylpiperazine-*N′*-2-ethanesulfonic acid; SPR: surface plasmon resonance; TCTD: tetrachlorothiophene dioxide.

A. Piatesi and D. Hilvert.[1] Laboratorium für organische Chemie, Swiss Federal Institute of Technology, ETH-Hönggerberg, CH-8093 Zurich, Switzerland.

[1]Corresponding author (e-mail: hilvert@org.chem.ethz.ch).

 DOI: 10.1139/V02-057 © 2002 NRC Canada

Fig. 1. Diels–Alder cycloaddition catalyzed by 1E9. The antibody was elicited in response to the tetrachloronorbornene derivative **1** (7). It catalyzes the reaction between tetrachlorothiophene dioxide (**2**, TCTD) and *N*-ethylmaleimide (**3**, NEM) to give the high-energy intermediate **4**, which subsequently breaks down to yield *N*-ethyltetrachlorophthalimide (**6**).

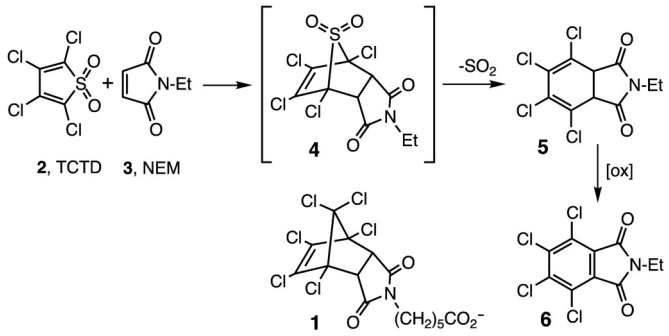

designed as an entropy trap, computational results suggest that enthalpic stabilization of the transition state through an unusually close fit to the apolar binding surface of the antibody active site and a strong hydrogen bond between the side chain of Asn^{H35} and the carbonyl of the dienophile component are responsible for catalysis (16).

In order to test these ideas and explore the relationship between binding energy and catalysis through systematic variation of antibody structure, recombinant versions of 1E9 are needed. This antibody has been successfully produced in a mammalian cell line as a recombinant chimeric murine–human IgG, but attempts to generate a more conveniently manipulated Fab fragment or a single-chain Fv in bacteria were unsuccessful (17, and unpublished results). Here we describe the design and characterization of variants of 1E9 that can be readily produced as Fab proteins in bacteria.

Experimental

Materials

Hapten **1** (7) and TCTD (18) were synthesized according to published protocols. NEM was purchased from *Aldrich*. The expression plasmid p4xH-M13 (19) was generously provided by Prof. P.G. Schultz. *E. coli* XL1-blue and TOPP2 strains were obtained from Stratagene (La Jolla, CA). Restriction enzymes and T4 ligase were purchased from New England Biolabs (Beverly, MA) and Fermentas (Vilnius, Lithuania), respectively. Polymerase chain reactions (PCRs) were carried out with thermostable HotStarTaq DNA polymerase from Qiagen (Basel, Switzerland). Oligonucleotides for mutagenesis and sequencing were prepared by Microsynth (Balgach, Switzerland). All nucleic acid manipulations were according to standard procedures (20). DNA sequencing was performed on an ABI PRISM 310 Genetic Analyzer from PE-Applied Biosystems (Foster City, CA).

Expression constructs

Poly(A)$^+$ mRNA was isolated from the hybridoma cells that produce antibody 1E9 and reverse transcribed to cDNA with avian myeloblastosis virus reverse transcriptase using oligo(dT) as a primer (17). The V_L and V_H genes were amplified by the polymerase chain reaction (PCR) using the following primers:

V_L-sense (5′-GCGTACGCTGAGCTCGTGATGACCCAGACTCCACTCTCC-3′, *Sac* I site underlined);
V_L-antisense (5′-TTTGATCTCAAGCTTGGTGCCACCACCGAACGTCGGAAA-3′, *Hin*d III site underlined);
V_H-Glu^{H6} sense (5′-CAGGTTCAGCTGCTCGAGTCTGGACCTGAACTGAAGAAG-3′, *Xho* I site underlined);
V_H-Gln^{H6} sense (5′-GTGTTAAGCTGGGGATCCTCTAGAGGTTGA-3′, *Bam*H I site underlined);
V_H-antisense (5′-TGAGGAGACGGTGACCGAGGTTCCTTGACCCCAGTAGTC-3′, *Bst*E II site underlined).

The amplified fragments were purified and inserted into vector p4xH (19) to give the expression plasmid p4xH-1E9.

The heavy chain was sequenced with primers HSEQF (5′-AGCAAAGCAGACTACGAGAAA-3′) and HSEQB (5′-GGGTGCCAGGGGGAAGAC-3′). The light chain was sequenced with the primer LSEQB (5′-CATCAGATG-GCGGGAAGATG-3′).

Site-directed mutagenesis

Mutations were introduced into p4xH-1E9 by a standard overlap-extension PCR technique (21). The flanking primers for the Phe^{L46}Leu, Gly^{L63}Ser, and Ile^{L72}Thr mutations were the V_L-sense and the V_L-antisense primers. For the Phe^{L95}Pro mutation, the flanking primers V_L-sense and 5′-CATCAGATGGCGGGAAGATG-3′ (antisense) were used. The flanking primers for the Leu^{H5}Val–Glu^{H6}Gln, Lys^{H12}Val, Met^{H28}Thr, Lys^{H46}Glu, Phe^{H59}Tyr, and Met^{H87}Thr mutations were 5′-GTGTTAAGCTGGGGATCCTCTAGAGGTTGA-3′ (sense) and 5′-TGAGGAGACGGTGACCGAGGTTCCTTG-ACCCCAGTAGTC-3′ (antisense).

The following mutation-containing primers were used together with the corresponding antisense sequences:

Phe^{L46}Leu (sense), 5′-GGCCAGTCTCCAAAG**CTG**CTGATCTACAAAGTT-3′;
Gly^{L63}Ser (sense), 5′-GTCCCAGACAGGTTC**AGC**GGCAGTGGATCA-3′;
Ile^{L72}Thr (sense), 5′-TCAGGGACAGATTTC**ACT**CTCAAGATCAGCAGA-3′;
Phe^{L95}Pro (sense), 5′-CAAAGTACACATTTT**CCG**CCGACGTTCGGT-3′;
Leu^{H5}Val/Glu^{H6}Gln (sense), 5′-CAGGTTCAGCTG**GTCCAG**TCTGGACCTGAA-3′;
Lys^{H12}Val (sense), 5′-CCTGAACTG**GTG**AAGCCTGGAGAGA-3′;
Met^{H28}Thr (sense), 5′-AAGGCCTCTGGATAT**ACT**TTCACAAATTATGGA-3′;
Lys^{H46}Glu (sense), 5′-AGGAAAGGCTTTA**GAA**TTGATGGGCTGGATA-3′;
Phe^{H59}Tyr (sense), 5′-ACTGGAGAGTCAACA**TAT**GCTGATGACTTCAAG-3′;
Met^{H87}Thr (sense), 5′-CTCAAAAATGAGGAC**ACT**GCTACATATTTCTGT-3′.

Mutagenized positions are denoted in bold. Mutant codons were chosen to exploit the most frequently used codon for a particular amino acid among highly expressed genes in *E. coli* (Wisconsin Sequence Analysis package, version 8, Genetics Computer Group, Inc.). The presence of the correct mutations was confirmed by DNA sequencing using the HSEQF, HSEQB, and LSEQB primers.

ELISA measurements

Antibody production was screened by enzyme-linked immunosorbent assay (ELISA) (22). The TOPP2 strain of *E. coli* was transformed with p4xH-1E9 and its derivatives, and the individual Fab variants were produced in 100 mL shake-flask cultures as previously described (19).

© 2002 NRC Canada

Periplasmic lysates were prepared, and after normalizing the total protein concentration, the samples were diluted 100-fold in PBS buffer containing 1% bovine serum albumin (BSA). Standard ELISA measurements were performed by immobilizing BSA–**1** conjugates on microtiter plates blocked with 3% BSA in PBS and titrating the crude lysates by serial dilution. Bound Fab was detected using goat anti-human IgG heavy and light-chain antibodies conjugated to horseradish peroxidase (Calbiochem, La Jolla, CA). The plates were developed with 2,2′-azino-bis(3-ethylbenzthiazoline-6-sulfonic acid) (ABTS), 0.02% H_2O_2 in 0.1 M citrate buffer (pH 4.0). Absorbance at 405 nm was recorded following color development.

Production and purification of chimeric 1E9 Fabs

Large-scale antibody production was achieved by culturing the transformed TOPP2 *E. coli* strains in shake-flasks (6 L) or by high-density fermentation (2 L) in a BIOFLO 3000 bioreactor (New Brunswick Scientific, Edison, NJ) as previously described (19). The chimeric Fab fragments were purified from crude periplasmic lysates by protein G affinity chromatography, followed by Mono S cation-exchange chromatography. Sample purity was assessed by sodium dodecyl sulfate polyacrylamide gel electrophoresis (SDS-PAGE). Protein concentration was determined spectroscopically at 280 nm, using molar absorption coefficients calculated as described by Pace et al. (23). An ε_{280} of 59 000 M^{-1} cm^{-1} was employed for all the Fab fragments except the triple mutant, which had a value of 57 500 M^{-1} cm^{-1}. Proteins were stored at 4°C in 20 mM Tris-HCl (pH 7.2) containing 0.5 mM EDTA and 100 mM NaCl.

Fluorescence titrations

Thermodynamic dissociation constants were determined as previously described (24). Titration curves were recorded by stepwise addition of a hapten stock solution (15 μM) to a diluted solution of the chimeric Fab fragment (26 nM) and subsequent measurement of the fluorescence. The excitation and emission wavelengths were 290 nm and 340 nm, respectively, and the corresponding bandpasses were 8 and 16 nm. The high voltage of the detector was set to 900 V. These measurements were carried out in 20 mM sodium acetate (pH 5.5) and 100 mM NaCl at 15°C.

The dissociation constant (K_d) for the Fab–hapten complex is given by $K_d = (E_T - EL)(L_T - EL)/(EL)$, where L_T represents the total hapten concentration, E_T is the total Fab concentration, and EL is the concentration of the Fab–hapten complex. This equation can be rearranged into $(L_T)(1/R - 1) = K_d + E_T(1 - R)$ for Scatchard analysis, where R denotes the ratio of the Fab–hapten complex concentration to the total Fab concentration (EL/E_T). Since $EL = (F_E - F)$ and $E_T = (F_E - F_{EL})$, where F_E represents the initial fluorescence of the Fab solution, F the observed fluorescence and F_{EL} the fluorescence of the protein at infinite hapten concentration, it is possible to plot $L_T(1/R - 1)$ vs. $(1 - R)$ and get K_d from the intercept and the total Fab concentration from the slope (24).

BIAcore measurements

The binding process between 1E9 Fab mutants and the hapten was monitored by the surface plasmon resonance (SPR) technique using a BIAcore 3000 instrument (Pharmacia, Uppsala, Sweden) (25, 26). All experiments were performed at 25°C. The surface of the dextran-chip was activated with 1-[3-dimethylamino)propyl]-3-ethylcarbodiimide hydrochloride and *N*-hydroxysuccinimide in 10 mM acetate (pH 4.0) and covalently linked to the BSA-hapten conjugate (SPR response: 400 RU). Fab samples were diluted in 10 mM HEPES buffer (pH 7.4) containing 150 mM NaCl, 3.4 mM EDTA, and 0.005% Tween 20 prior to SPR analysis. The Fab fragments were injected in the presence of the immobilized hapten at a flow rate of 5 μL min^{-1}. The association rate constant (k_{on}) was determined by measuring the rate of binding to the hapten at three different Fab concentrations (1, 0.6, and 0.4 μM). The dissociation phase (k_{off}) was monitored after the association process was complete. The dextran matrix was regenerated after each injection using 10 mM HCl. Rate constants were calculated from the SPR data using BIAevaluation 3.1 software (Pharmacia, Uppsala, Sweden). A single-site binding model (A + B = AB) was assumed for the analysis. The apparent dissociation constant ($K_d = k_{off}/k_{on}$) was calculated from the individual association and dissociation rate constants.

Kinetic assays

The reaction between TCTD and NEM was carried out at 25°C in 50 mM sodium acetate buffer (pH 5.5) containing 20 mM NaCl in the presence and absence of the antibody (1 μM). The substrates were diluted from stock solutions in acetonitrile; the final concentration of acetonitrile in the reaction mixture was 2% by volume. Initial velocities were determined by starch-I_2 bleaching at 606 nm (10, 17) at several concentrations of NEM while holding the concentration of TCTD constant at 150 μM. The data were corrected for the uncatalyzed reaction (7) and fitted to the Michaelis–Menten equation, $v_o/[Ab] = (k_{cat}[NEM])/(K_m + [NEM])$, where v_o is the initial rate, [Ab] and [NEM] are the active site and substrate concentrations, respectively, and k_{cat} and K_m are the catalytic rate and the Michaelis constants, respectively, at a fixed concentration of TCTD.

Thermal denaturation experiments

Thermal denaturation of the Fab variants was monitored by circular dichroism (CD) on an AVIV Circular Dichroism spectropolarimeter, Model 202 (AVIV Instruments, Lakewood, NJ) equipped with a single-position thermoelectric cuvette holder. CD spectra were recorded at 25°C in PBS (pH 7.4), with a protein concentration of 0.2 mg mL^{-1}. Spectra were obtained by averaging three wavelength scans from 260 to 200 nm in 1-nm steps, with a signal averaging time of 1 s and a bandwidth of 1 nm. Thermal denaturation curves were obtained using these samples in a 0.1-cm cuvette. The ellipticity at 216 nm was monitored as a function of temperature from 25 to 95°C in 1°C steps. For each point, the sample was first equilibrated for 2 min and then the signal was averaged for 3 s before moving to the next temperature.

Results

Production of 1E9 as a chimeric Fab fragment

Antibody production in microorganisms is often problematic. In some cases, fusion of the murine V_L and V_H variable

© 2002 NRC Canada

Fig. 2. Amino acid sequence of the variable regions of 1E9 (17). Active site residues are shown with underlined boldface type; nonconsensus residues are shown with lightface type (red and blue, respectively, in the electronic version of this article). The most frequently encountered amino acid in aligned immunoglobulin sequences is shown at the corresponding position below the 1E9 sequence (c1E9) together with the relative frequency of the nonconsensus residue and its consensus conterpart (from the Kabat database, http://immuno.bme.nwu.edu). FR: framework region; CDR: complementarity determining region.

```
LIGHT CHAIN (VARIABLE REGION)
                FR1                CDR1          FR2       CDR2              FR3                  CDR3      FR4
                                                          L46          L63      L72                  L95
 1E9  DVVMTQTPLSLPVSLGDQASISCRSSQSLVHSNGNTYLHWYLQKPGQSPKFLIYKVSNRFSGVPDRFGGSGSGTDFILKISRVEAEDLGVYFCFQSTHFPTFGGGTKLEIK
 c1E9 EL----------------------------------------------------L----------------S--------T---------------------P------------
                                                 0.006/0.760      0.004/0.844 0.011/0.671          0.003/0.838

HEAVY CHAIN (VARIABLE REGION)
                  FR1             CDR1     FR2             CDR2                    FR3                    CDR3       FR4
           H6    H12              H28               H46           H59                          H87
 1E9  QIQLVQSGPELKKPGETVKISCKASGYMFTNYGMNWVKQAPGKALKLMGWINPYTGESTFADDFKGRFAFFLETSATTAYLQINNLKNEDMATYFCARGTTIVRAMDYWGQGTSLTVSS
 c1E9 -V---------V---------------T-----------------E-------------Y-----------------------------T----------------------V----
           0.125/0.699     0.002/0.564        0.013/0.959   0.017/0.931                    0.007/0.721
```

regions with the C_L and C_H1 regions of a human κ_1 and IgG1 antibody, respectively, can greatly increase the efficiency of expression in *E. coli* (19). Preliminary attempts to engineer 1E9 as a chimeric murine – human Fab fragment, however, only gave very low yields of protein (17, and unpublished results).

In retrospect, these disappointing results appear to be largely due to the introduction of an *Xho* I restriction site during cloning, which resulted in the replacement of Gln^{H6} with Glu. Although the sequence database shows that Gln and Glu occur with similar frequency at position H6 (27), comparison of known structures with these two residues at the H6 position reveals that the Gln and Glu side chains participate in distinct and highly conserved hydrogen-bonding networks with surrounding residues (28, 29). Not surprisingly, therefore, swapping these amino acids can have a significant deleterious effect on antibody production (28). Indeed, in the case of 1E9, reversion to the wild-type sequence greatly increases the yield of the chimeric Fab (≈ 20- to 30-fold determined by ELISA). Under fermentative conditions, this protein can be produced in sufficient amounts (0.7 mg L^{-1} cell culture) for kinetic and binding studies.

Nevertheless, detailed characterization of 1E9 would be facilitated by the availability of a more efficiently produced Fab. Steipe et al. (30) have compiled amino acid distributions in aligned immunoglobulin sequences and successfully used these distributions to predict stabilizing point mutations in the variable domains. They showed that replacement of nonconsensus residues with their consensus counterparts can greatly increase the stability and yields of recombinant antibodies (30–33). Moreover, the beneficial effects of these mutations are often additive. We have applied this approach to the optimization of the 1E9 Fab chimera.

Comparison of the 1E9 variable regions with the Kabat database of antibody sequences (27) identified several residues that appear rarely in antibodies (Fig. 2), making them good targets for mutagenesis. They include Phe^{L46}, Gly^{L63}, Ile^{L72}, and Phe^{L95} in the light chain and Lys^{H12}, Met^{H28}, Lys^{H46}, Phe^{H59}, and Met^{H87} in the heavy chain. With the exception of Phe^{L95}, which is in the L3 complementarity determining region (CDR), these residues are distant from the active site (Fig. 3) and were not expected to significantly influence binding or catalysis.

To optimize antibody production, the nonconsensus residues in 1E9 were individually replaced by their consensus counterparts (i.e., Phe^{L46}Leu, Gly^{L63}Ser, Ile^{L72}Thr, and Phe^{L95}Pro in the light chain and Lys^{H12}Val, Met^{H28}Thr, Lys^{H46}Glu, Phe^{H59}Tyr, and Met^{H87}Thr in the heavy chain) via standard mutagenesis protocols (20). In each case, the mutations were introduced into the human–murine chimeric Fab containing the wild-type Gln residue at position H6. The variants were produced on a small scale in *E. coli*, and the relative amount of active Fab in crude periplasmic lysates was determined by ELISA (data not shown) (22). Most of the targeted changes had little or no effect on protein production. The Met^{H87}Thr, Gly^{L63}Ser, and Phe^{L95}Pro mutations, however, gave approximately 2-, 4- and 16-fold higher titers, respectively, than the parent chimera.

Fig. 3. Crystal structure of the murine Fab fragment of 1E9 complexed with its transition state analogue (10). Noncanonical residues that were examined in this study are highlighted. Heavy chain: red; light chain: blue.

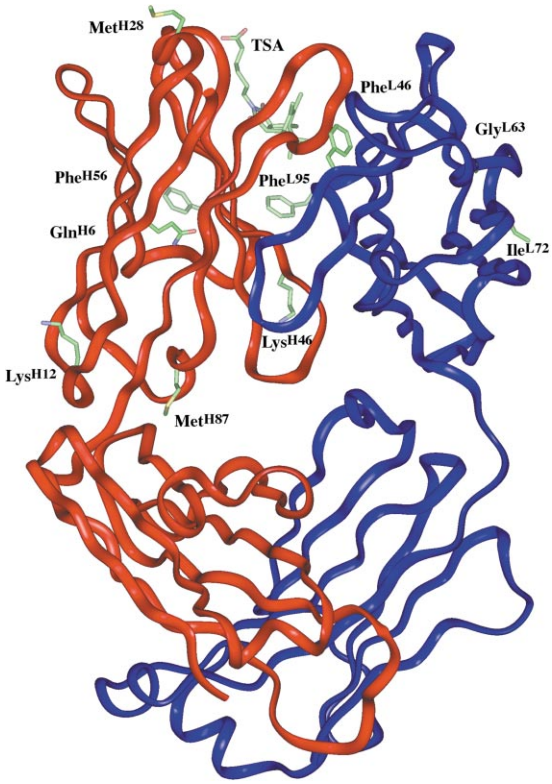

© 2002 NRC Canada

Fig. 4. SPR sensograms obtained with the chimeric Fab 1E9 double mutant. (A) 1 μM Fab; (B) 0.6 μM Fab; (C) 0.4 μM Fab. All measurements were carried out at 25°C at a flow rate of 5 μL min^{-1}. The BSA-hapten conjugate was covalently linked to the activated dextran surface of the chip. Regeneration of the chip surface was done with 10 mM HCl. The k_{on} and k_{off} values were calculated from the association and dissociation phases, respectively.

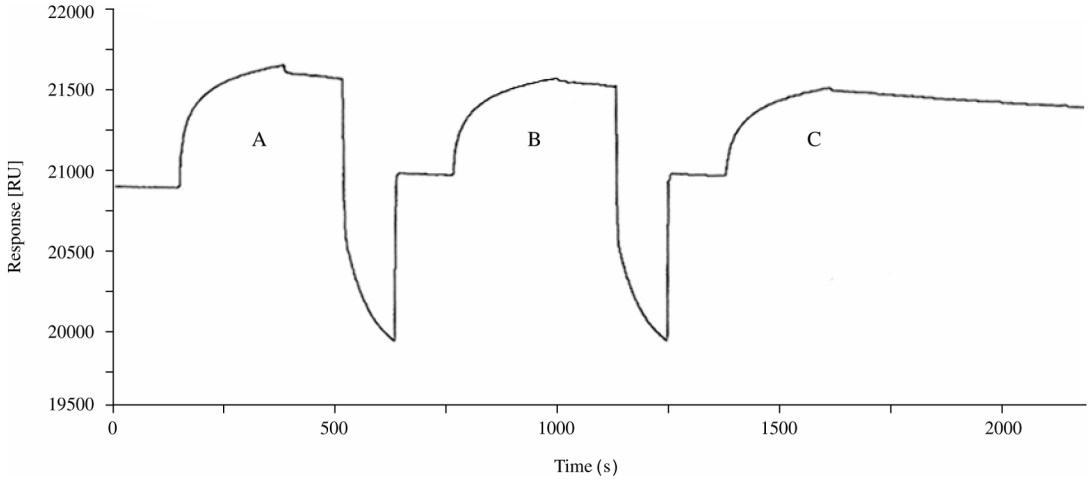

Table 1. Yields of chimeric 1E9 Fab variants.

Variant[a]	Shake-flask yield (mg L^{-1})	Fermentor yield (mg L^{-1})
1E9 IgG	n.d.	n.d.
Chimeric 1E9 Fab	n.d.	0.7
$G^{L63}S$	0.03	2
$M^{H87}T$–$G^{L63}S$	0.05	4
$M^{H87}T$–$G^{L63}S$–$F^{L95}P$	0.1	17

[a]All recominant proteins contained the wild-type Gln residue at H6.

The additivity of these substitutions was examined by construction of a double ($Met^{H87}Thr$–$Gly^{L63}Ser$) and a triple ($Met^{H87}Thr$–$Gly^{L63}Ser$–$Phe^{L95}Pro$) mutant. These variants were produced in parallel with the wild-type chimera and the $Gly^{L63}Ser$ single mutant in the TOPP2 strain of *E. coli* (19). All proteins were isolated and purified as previously described (19). Yields of Fab obtained from shake-flask and high-density fermentation experiments are compared in Table 1. In general, fermentation provides ca. 100-fold more antibody protein per liter of cell culture than the shake-flask cultures. The single-point mutation $Gly^{L63}Ser$ improves the yield by more than twofold compared with the parent Fab. A further twofold increase in production is obtained by adding the $Met^{H28}Thr$ mutation. The triple mutant is the most efficiently produced protein examined (17 mg L^{-1}), and can be obtained in ca. 25-fold higher yield than the wild-type 1E9 Fab.

Binding and catalytic properties

The chimeric 1E9 Fab fragments retain the recognition properties of the original IgG as revealed by ELISA. Dissociation constants were determined by fluorescence titrations of the recombinant proteins with hapten **1** (24). As summarized in Table 2, the chimeric Fab as well as the $Gly^{L63}Ser$ single and $Met^{H87}Thr$–$Gly^{L63}Ser$ double mutants appear to bind the ligand approximately one order of magnitude more tightly than the original IgG molecule. This gain in affinity, however, is lost in the $Met^{H87}Thr$–$Gly^{L63}Ser$–$Phe^{L95}Pro$ triple mutant. Although the side chain of the L95 residue is distant from the bound hapten (10), this residue is located in the CDR L3 loop, and the Phe→Pro substitution may slightly alter the shape of the active site.

Similar overall trends were observed in surface plasmon resonance (SPR) measurements with the recombinant proteins (Fig. 4, Table 2). The on rate for all the proteins examined is very similar (k_{on} ~ 6×10^4 M^{-1} s^{-1}). The off rate for the chimeric 1E9 Fab fragment and the single and double mutants is also similar (k_{off} ~ 3 to 4×10^{-4} s^{-1}) but roughly five times faster than the off rate determined for the full-length IgG and about seven times slower than k_{off} for the triple mutant. The SPR results thus confirm that the triple mutant binds the hapten significantly less tightly than the other Fab fragments. They also show that the Fab–hapten complex is relatively long-lived with a $\tau_{1/2}$ (= ln $2/k_{off}$) of 35 min in the case of the chimeric 1E9 Fab. Nevertheless, the dissociation constants calculated from these data ($K_d = k_{off}/k_{on}$) are about two orders of magnitude larger than the K_d values determined by fluorescence. This is due in part to the fact that the SPR experiments were carried out at higher temperature (25°C rather than 15°C), but similar discrepancies have been observed before and also likely reflect the different nature of interactions between the antibody and a solid support and between the antibody and a ligand free in solution (34). Avidity effects (34) probably account for the comparable affinity of the bivalent IgG and the recombinant Fab in the SPR experiment, a conclusion supported by the low k_{off} value determined for the IgG.

The 1E9 variants also all catalyze the Diels–Alder reaction between TCTD and NEM. The apparent k_{cat} and $(K_m)_{NEM}$ values obtained at 150 μM TCTD are summarized in Table 2 and are compared with the kinetic parameters of the murine IgG protein assayed under identical conditions. Within experimental error, the human–murine chimeric Fab and the $Gly^{L63}Ser$ single and $Met^{H87}Thr$–$Gly^{L63}Ser$ double mutants are indistinguishable from the IgG. In contrast, the

© 2002 NRC Canada

Table 2. Dissociation constants and kinetic parameters of chimeric 1E9 Fab variants.

Variant[a]	K_d[b] (nM)	K_d[c] (nM)	$k_{on} \times 10^{-4}$ (m^{-1} s^{-1})	$k_{off} \times 10^{4}$ (s^{-1})	$(k_{cat})_{app}$ (min^{-1})	$(K_m)_{NEM}$ (mM)
1E9 IgG	0.57 ± 0.03	1.2 ± 0.2	6.0 ± 1.0	0.73 ± 0.23	3.97 ± 0.10	8.4 ± 0.5
Chimeric 1E9 Fab	0.05 ± 0.03	5.5 ± 0.9	6.1 ± 1.8	3.3 ± 0.31	4.45 ± 0.18	10.0 ± 1.0
$G^{L63}S$	0.05 ± 0.02	6.9 ± 1.4	5.8 ± 1.9	4.0 ± 0.2	4.01 ± 0.10	9.4 ± 0.6
$M^{H87}T$–$G^{L63}S$	0.10 ± 0.04	6.4 ± 1.1	6.3 ± 1.9	4.0 ± 0.3	3.71 ± 0.11	9.0 ± 0.6
$M^{H87}T$–$G^{L63}S$–$F^{L95}P$	0.36 ± 0.04	35 ± 0.8	7.6 ± 2.5	27 ± 1	1.07 ± 0.04	8.7 ± 0.9

Note: Kinetic measurements were determined at 25°C in 50 mM sodium acetate buffer (pH 5.5) containing 20 mM NaCl and 2% acetonitrile.
[a]All variants were constructed with the wild-type Gln residue at H6.
[b]Fluorescence measurements at 15°C
[c]SPR measurements at 25°C.

$Met^{H87}Thr$–$Gly^{L63}Ser$–$Phe^{L95}Pro$ triple mutant exhibits a fourfold decrease in k_{cat}, consistent with its diminished affinity for transition state analog **1**.

The murine immunoglobulin scaffold of 1E9 thus appears to be quite tolerant to substitutions of nonconsensus residues and to replacement of the mouse constant regions with human constant regions. The modest differences in binding and catalysis exhibited by the chimeric Fab fragments presumably reflect small adjustments in the variable domains, rather than dramatic changes in structure or mechanism.

Thermal denaturation experiments

Steipe et al. (30) have argued that consensus residues in antibodies are selected in part for the stability they confer to the immunoglobulin scaffold. The relative stability of the four chimeric Fab 1E9 variants generated in this work was therefore assessed by thermal denaturation. The CD spectrum of these proteins, like other proteins composed mainly of β-sheets, is characterized by a negative minimum at 216 nm and a positive maximum at 202 nm (Fig. 5*a*). Thermal unfolding can be readily assessed by monitoring increases in ellipticity at 216 nm as a function of increasing temperature. The resulting curves are complex, with an apparent gradual loss of some β-sheet structure below 65°C, followed by a major, irreversible transition between 70 and 80°C (Fig. 5*b*). Similar behavior has been previously observed for the denaturation of a nucleic acid-binding Fab (35). In that study, no evidence for unfolding below 70°C was found using differential scanning calorimetry, and the pretransition reduction in ellipticity was ascribed to temperature-induced changes in the β-sheet structure due to Fab solvent interactions or aggregation state.

From the thermal unfolding patterns shown in Fig. 5*b*, it appears that the wild-type Fab is significantly less stable than the other mutants. It has a T_m value of roughly 76°C, which is approximately 5°C lower than that of the $Gly^{L63}Ser$ single and $Met^{H87}Thr$–$Gly^{L63}Ser$ double mutants. The latter two proteins exhibit essentially superimposable unfolding profiles, with a much less pronounced pretransitional loss of ellipticity than for the chimeric 1E9 Fab, consistent with overall higher stability. The $Met^{H87}Thr$–$Gly^{L63}Ser$–$Phe^{L95}Pro$ triple mutant, which has an apparent T_m of 83°C, appears to be the most stable variant examined.

Fig. 5. (A) Circular dichroism (CD) spectra of the chimeric Fab variants. Spectra were measured in PBS buffer at pH 7.4 and 25°C. All the Fab concentrations were 0.2 mg mL^{-1}. Data are reported as molar ellipticity [θ]. (●) Wild-type chimeric 1E9 Fab; (O) $Gly^{L63}Ser$; (X) $Met^{H87}Thr$–$Gly^{L63}Ser$; (△) $Met^{H87}Thr$–$Gly^{L63}Ser$–$Phe^{L95}Pro$. (B) Thermal denaturation curves monitored by CD. All the spectra were obtained in PBS buffer at pH 7.4 and an Fab concentration of 0.2 mg mL^{-1}. CD data were recorded at 216 nm between 25 and 95°C in 1°C steps. Values are reported as molar ellipticity [θ]. (●) Wild-type chimeric 1E9 Fab; (O) $Gly^{L63}Ser$; (X) $Met^{H87}Thr$–$Gly^{L63}Ser$; (△) $Met^{H87}Thr$–$Gly^{L63}Ser$–$Phe^{L95}Pro$. T_m values were estimated from the midpoint of the irreversible transition that is observed between 75 and 85°C.

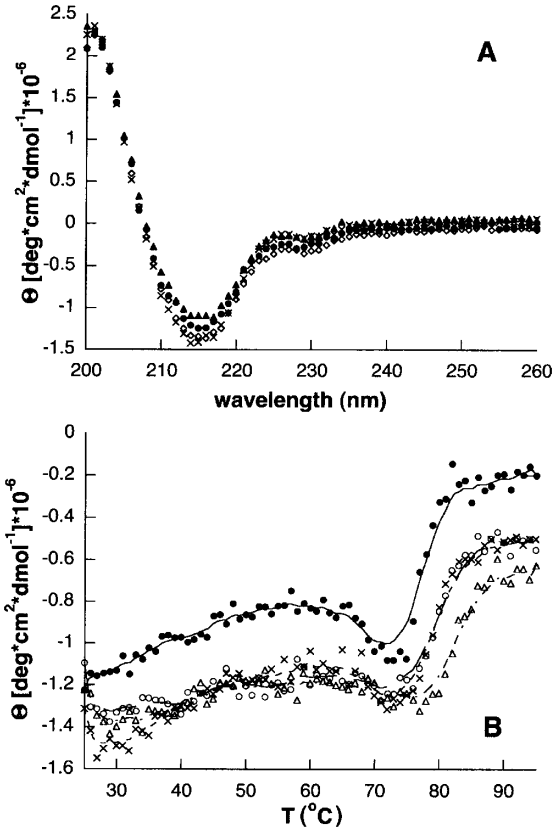

Discussion

In this study, we show that the catalytic antibody 1E9 can be produced conveniently in bacteria as a human–murine chimera and that the yields of functional protein are significantly improved when two or three noncanonical-framework residues in the heavy and light chain variable domains are

© 2002 NRC Canada

replaced with their consensus counterparts. The $Met^{H87}Thr–Gly^{L63}Ser$ double and $Met^{H87}Thr–Gly^{L63}Ser–Phe^{L95}Pro$ triple mutants are obtained in useful amounts by fermentation (4 and 17 mg L^{-1} cell culture, respectively) and exhibit binding and kinetic properties similar to those of the original murine IgG. Antibody 1E9 is closely related to other structurally characterized antibodies that bind hydrophobic ligands (10, 17), and the availability of this protein in recombinant form will greatly facilitate investigations of the evolution of shape complementarity and catalytic efficiency from a promiscuous primordial germ-line template. The triple mutant is the most efficiently produced protein examined, although a modest decrease in hapten affinity and catalytic efficiency compared with the double mutant suggests that the latter will be the best starting point for such studies.

Steipe et al. (30) originally developed the strategy employed here to predict stabilizing mutations in the V_κ domain of the anti-phosphorylcholine antibody McPC603, and subsequently exploited it in the construction of hyperstable V_L and V_H domains, which can be produced as soluble proteins in the cytoplasm of *E. coli* (31, 33). This approach has also been adopted to engineer stable heterodimeric Fv (32) and single-chain Fv fragments (36). Our results show that the canonical sequence approximation can aid the production of soluble, chimeric human–murine Fab fragments as well, and as seen in the earlier studies, yield appears to correlate with protein stability. Although a relatively small fraction of the canonical mutations we investigated (3 out of 9) have a beneficial effect on Fab yield — substantially lower than the 60% success rate reported for the prediction of stabilizing mutations in the McPC603 V_κ domain (30), the canonical sequence approximation provides a valuable approach for rationally optimizing the properties of immunoglobulin proteins in the absence of other information.

Given the large number of homolog and paralog sequences being generated in whole genome sequencing projects, this approach is likely to become a more valuable tool for enhancing the properties of proteins. The preparation of highly stable consensus versions of phytase (37), apomyoglobin (38), the DNA binding domain of the tumor suppressor p53 (39), and a functional GroEL minichaperone (40) illustrate its promise.

Acknowledgments

This work was supported in part by the ETH Zürich and Novartis Pharma AG. We thank J. Haugstetter for carrying out some preliminary experiments, D. Neri for assistance with BIAcore measurements, and J. Goldberg for useful discussions.

References

1. P.G. Schultz and R.A. Lerner. Acc. Chem. Res. **26**, 391 (1993).
2. P.G. Schultz and R.A. Lerner. Science (Washington, D.C.), **269**, 1835 (1995).
3. D. Hilvert. Top. Stereochem. **22**, 83 (1999).
4. D. Hilvert. Annu. Rev. Biochem. **69**, 751 (2000).
5. A.C. Braisted and P.G. Schultz. J. Am. Chem. Soc. **112**, 7430 (1990).
6. V.E. Gouverneur, K.N. Houk, B. de Pascual-Teresa, B. Beno, K.D. Janda, and R.A. Lerner. Science (Washington, D.C.), **262**, 204 (1993).
7. D. Hilvert, K.W. Hill, K.D. Nared, and M.-T.M. Auditor. J. Am. Chem. Soc. **111**, 9261 (1989).
8. J.T. Yli-Kauhaluoma, J.A. Ashley, C.-H. Lo, L. Tucker, M.M. Wolfe, and K.D. Janda. J. Am. Chem. Soc. **117**, 7041 (1995).
9. M. Resmini, A.A.P. Meekel, and U.K. Pandit. Pure Appl. Chem. **68**, 2025 (1996).
10. J.A. Xu, Q.L. Deng, J.G. Chen, K.N. Houk, J. Bartek, D. Hilvert, and I.A. Wilson. Science (Washington, D.C.), **286**, 2345 (1999).
11. B. Seelig and A. Jäschke. Chem. Biol. **6**, 167 (1999).
12. T.M. Tarasow, S.L. Tarasow, and B.E. Eaton. Nature (London), **389**, 54 (1997).
13. K. Watanabe, T. Mie, A. Ichihara, H. Oikawa, and M. Honma. J. Biol. Chem. **275**, 38393 (2000).
14. K. Auclair, A. Sutherland, J. Kennedy, D.J. Witter, J.P. van den Heever, C.R. Hutchinson, and J.C. Vederas. J. Am. Chem. Soc. **122**, 11519 (2000).
15. K. Katayama, T. Kobayashi, H. Oikawa, M. Honma, and A. Ichihara. Biochim. Biophys. Acta. **1384**, 387 (1998).
16. J.G. Chen, Q.L. Deng, R.X. Wang, K.N. Houk, and D. Hilvert. ChemBioChem. **1**, 255 (2000).
17. M.R. Haynes, M. Lenz, M.J. Taussig, I.A. Wilson, and D. Hilvert. Isr. J. Chem. **36**, 151 (1996).
18. M.S. Raasch. J. Org. Chem. **45**, 856 (1980).
19. H.D. Ulrich, P.A. Patten, P.L. Yang, F.E. Romesberg, and P.G. Schultz. Proc. Natl. Acad. Sci. U.S.A. **92**, 11907 (1995).
20. J. Sambrook, E.F. Fritsch, and T. Maniatis. Molecular cloning. A laboratory manual. Cold Spring Harbor Laboratory Press, Cold Spring Harbor, New York. 1989.
21. A. Aiyar, Y. Xiang, and J. Leis. Methods Mol. Biol. **57**, 177 (1996).
22. B.R. Clark and E. Engvall. Enzyme-immunoassay. CRC Press Inc., Boca Raton, Fla. 1980.
23. C.N. Pace, F. Vajdos, L. Fee, G. Grimsley, and T. Gray. Protein Sci. **4**, 2411 (1995).
24. K. Taira and S.J. Benkovic. J. Med. Chem. **31**, 129 (1988).
25. H. Kobayashi, H. Morioka, K. Tobisawa, T. Torizawa, K. Kato, I. Shimada, O. Nikaido, J. D. Stewart, and E. Ohtsuka. Biochemistry, **38**, 532 (1999).
26. U. Jönsson, L. Fägerstam, B. Ivarsson, B. Johnsson, R. Karlsson, K. Lundh, S. Löfäs, B. Persson, H. Roos, I. Rönnberg, S. Sjölander, E. Stenberg, R. Stählberg, C. Urbaniczky, H. Östlin, and M. Malmqvist. Biotechniques, **11**, 620 (1991).
27. E.A. Kabat, T.T. Wu, H.M. Perry, K.S. Gottesman, and C. Foeller. Sequences of proteins of immunological interest. 5th ed. U.S. Public Health Service, National Institutes of Health, Bethesda, MD. 1991.
28. K. Hotta, I.A. Wilson, and D. Hilvert. Biochemistry, **41**, 772 (2002).
29. A. Honegger and A. Plückthun. J. Mol. Biol. **309**, 687 (2001).
30. B. Steipe, B. Schiller, A. Plückthun, and S. Steinbacher. J. Mol. Biol. **240**, 188 (1994).
31. E.C. Ohage and B. Steipe. J. Mol. Biol. **291**, 1119 (1999).
32. E.C. Ohage, P. Wirtz, J. Barnikow, and B. Steipe. J. Mol. Biol. **291**, 1129 (1999).
33. P. Wirtz and B. Steipe. Protein Sci. **8**, 2245 (1999).
34. A. Huber, S. Demartis, and D. Neri. J. Mol. Recognit. **12**, 198 (1999).
35. S.L. Deutscher, M.E. Crider, J.A. Ringbauer, A.A. Komissarov, and T.P. Quinn. Arch. Biochem. Biophys. **333**, 207 (1996).

© 2002 NRC Canada

36. A. Knappik, L. Ge, A. Honegger, P. Pack, M. Fischer, G. Wellnhofer, A. Hoess, J. Wölle, A. Plückthun, and B. Virnekas. J. Mol. Biol. **296**, 57 (2000).
37. M. Lehmann, D. Kostrewa, M. Wyss, R. Brugger, A. D'Arcy, L. Pasamontes, and A. van Loon. Protein Eng. **13**, 49 (2000).
38. E.E. Scott, E.V. Paster, and J.S. Olson. J. Biol. Chem. **275**, 27129 (2000).
39. P.V. Nikolova, J. Henckel, D.P. Lane, and A.R. Fersht. Proc. Natl. Acad. Sci. U.S.A. **95**, 14675 (1998).
40. Q.H. Wang, A.M. Buckle, N.W. Foster, C.M. Johnson, and A.R. Fersht. Protein Sci. **8**, 2186 (1999).

© 2002 NRC Canada

Methylamine adenine dinucleotide (MAD): a co-factor to turn alcohol dehydrogenases into aldolases

Denis Wahler and Jean-Louis Reymond

Abstract: Methylamine adenine dinucleotide (MAD) was prepared in seven steps and 15.3% overall yield from 1-acetoxy-2,3,5-tri-*O*-benzoyl-D-ribose by chemoenzymatic synthesis. The key step was the phosphate–phosphate coupling between adenosine monophosphate and 2,5-anhydro-1-deoxy-1-phenylacetamide-6-phosphate-D-allitol (**3**) mediated by carbonyl diimidazole (CDI), followed by the removal of the phenylacetamido group by penicillin G acylase. The MAD co-factor provided a primary amine functionality that was suitably positioned to promote the enamine aldolization of 2-oxopropionamide with aldehydes within the active site of alcohol dehydrogenases, which should lead to the transformation of these stereoselective enzymes into aldolases. Preliminary investigations did not reveal any activity with horse liver alcohol dehydrogenase or yeast alcohol dehydrogenase.

Key words: aldolases, alcohol dehydrogenases, co-factor enginering, nucleosides, acylases.

Résumé : On a réalisé une synthèse chimioenzymatique du dinucléotide de méthylamine et d'adénine (« MAD »), en sept étapes et avec un rendement global de 15,3%, en utilisant le 1-acétoxy-2,3,5-tri-*O*-benzoyl-D-ribose comme produit de départ. L'étape clé est le couplage phosphate–phosphate entre le monophosphate d'adénosine et le 2,5-anhydro-1-désoxy-1-phénylacétamide-6-phosphate-D-allitol (**3**) catalysée par le carbonyldiimidazole (CDI), suivie de l'élimination du groupe phénylacétamido par l'acylase de la pénicilline G. Le cofacteur MAD fournit une fonction amine primaire positionnée de façon appropriée pour favoriser une aldolisation de l'énamine du 2-oxopropanamide avec les aldéhydes dans le site actif des déshydrogénases de l'alcool, ce qui devrait conduire à une transformation de ces enzymes stéréosélectifs en aldolases. Des études préliminaires indiquent qu'il n'y a pas d'activité avec la déshydrogénase du foie de cheval ou la déshydrogénase d'alcool de la levure.

Mots clés : aldolases, déshydrogénases d'alcool, cofacteur d'ingénierie, nucléosides, acylases.

[Traduit par la Rédaction]

Introduction

Co-factor engineering is a purely chemical approach to enzyme modification, which offers the possibility to turn a given enzyme into a completely different biocatalyst by changing the nature of the reaction being catalyzed (1). Impressive examples of this approach include the transformation of phytases into peroxidases by combining them with vanadate (2), and the alkylation of the active-site cysteine residue in cysteine proteases such as papain with various co-factors to create novel enzyme activities (3). Herein we describe the synthesis and preliminary evaluation of methylamine adenine dinucleotide (MAD) as a co-factor to turn alcohol dehydrogenases into aldolases. This type of co-factor engineering should enable one to take advantage of the substrate versatility and high and predictable stereoselectivity of alcohol dehydrogenases, as has been explored in depth by Jones and co-workers (4), to achieve stereoselective aldol reactions. The work draws on the structural analogy between the transition states for hydride transfer and aldol addition to carbonyl compounds.

Results and discussion

The aldol reaction efficiently combines carbon–carbon bond formation with the creation of asymmetric centers. Aldol products are useful synthons appearing either as synthetic intermediates or in the final structures of many natural products. Natural aldolase enzymes provide biocatalytic aldolization routes to polyhydroxylated compounds, in essence carbohydrates and close derivatives (5). By contrast, less oxygenated aldols, such as polypropionates, remain the domain of pure synthetic chemistry (6). One notable exception is the aldolase catalytic antibodies developed by Wagner et al. (7), which allow for the preparation of optically and stereochemically pure non-carbohydrate aldols through

Received 15 January 2002. Published on the NRC Research Press Web site at http://canjchem.nrc.ca on 28 May 2002.

This paper is dedicated to J. Bryan Jones on the occasion of his 65th birthday in recognition of his contributions to biocatalysis.

D. Wahler and J.-L. Reymond.[1] Department of Chemistry & Biochemistry, University of Bern, Freiestrasse 3, 3012 Bern, Switzerland.

[1]Corresponding author (e-mail: jean-louis.reymond@ioc.unibe.ch).

 DOI: 10.1139/V02-074 © 2002 NRC Canada

Scheme 1. Analogy between the targeted enamine-mediated aldolization with **1** and the hydride transfer process with NAD.

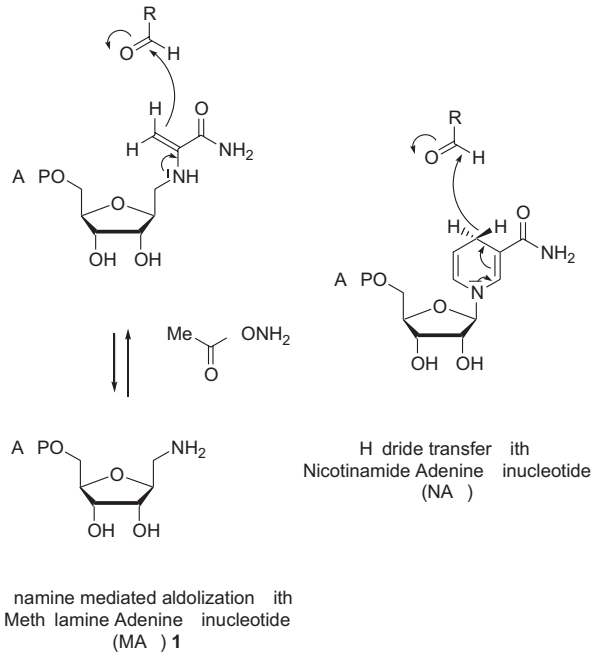

Scheme 2. Retrosynthetic analysis.

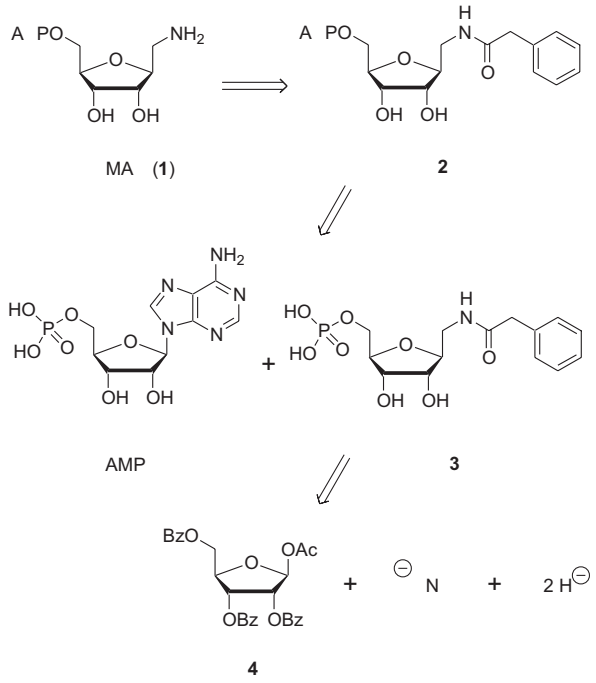

kinetic resolution of aldols by enantio- and stereoselective retro-aldolization (8). These catalytic antibodies demonstrate the versatility of the enamine mechanism for the aldol reaction. We have shown earlier that enamine-mediated aldolization by catalytic antibodies is possible using a co-factor approach by combining antibodies raised against a quaternary benzyl ammonium ion with the corresponding benzylamine (9).

Co-factor design

Drawing on the mechanistic analogy between the aldol reaction and the reduction of aldehydes, where in both cases a nucleophile is added to an electrophilic carbonyl group, we envisioned that co-factor engineering might convert alcohol dehydrogenases into aldolases. Thus MAD is expected to promote an enamine-mediated cross-aldolization between oxo-propionamide and an aldehyde within the binding pocket of an alcohol dehydrogenase (Scheme 1). The enzyme binding pocket should provide the correct relative positioning of the reactants and induce an electrophilic activation of the aldehyde carbonyl group, thus catalyzing the carbon–carbon bond formation using the primary amine functional group of the co-factor as a chemical catalyst. Aldol reactions readily occur under amine catalysis in aqueous environments (10). It should be noted that a catalytic effect on the rate-limiting carbon–carbon bond forming step should be sufficient to induce an observable catalysis of the overall process. Indeed, catalysis of the enamine formation step, which is not rate-limiting in enamine-mediated aldolization catalysis (11), is not required, but it might become necessary to optimized the catalyst.

Retrosynthetic analysis

Various nicotinamide adenine dinucleotide (NAD) analogs have been prepared by enzyme-catalyzed exchange of nicotinamide against modified nicotinamides (12). We approached the synthesis from a completely different and purely synthetic angle. MAD (**1**) could be obtained from deprotection of the protected MAD precursor (**2**), which would itself be the product of phosphate–phosphate coupling between adenosine monophosphate and a suitably protected synthetic monophosphate (**3**) (Scheme 2). Similar phosphate–phosphate coupling reactions have been described for the preparation of UDP-sugars (13). The phenacetyl group on the primary amine was planned for technical reasons as a hydrophobic and UV-active group to facilitate the isolation, purification, and identification of the coupling product **1**. Furthermore, the phenacetyl group could be removed enzymatically under mild aqueous conditions, which do not affect the labile diphosphate and glycosidic linkages present in the target molecule (14).

Synthesis

Intermediate **3** was first prepared from the commercially available 1-acetoxy-2,3,5-tri-*O*-benzoyl-D-ribose (**4**) (Scheme 3). Thus, reaction with trimethylsilyl cyanide and catalytic $SnCl_4$ gave cyanide **5** (15), which was selectively reduced using sodium tris(trifluoroacetoxy)borohydride in tetrahydrofuran to give primary amine **6** as described by Sauer and Schneller (16). Amine **6** was then directly acylated with phenacetyl chloride to give amide **7**. The benzoyl groups were removed under basic conditions to afford triol **8**. Direct phosphorylation of the primary alcohol in **8** with phophorus oxychloride in triethylphosphate solvent, a common method in nucleoside chemistry (17), gave intermediate **3** in 69% yield. Activation to the imidazolide and coupling with the tributylammonium salt of adenosine monophosphate yielded protected dinucleotide **2**. Finally, treatment with penicillin G acylase gave free-methylamine adenine dinucleotide **1**,

© 2002 NRC Canada

Scheme 3. Synthesis of MAD.

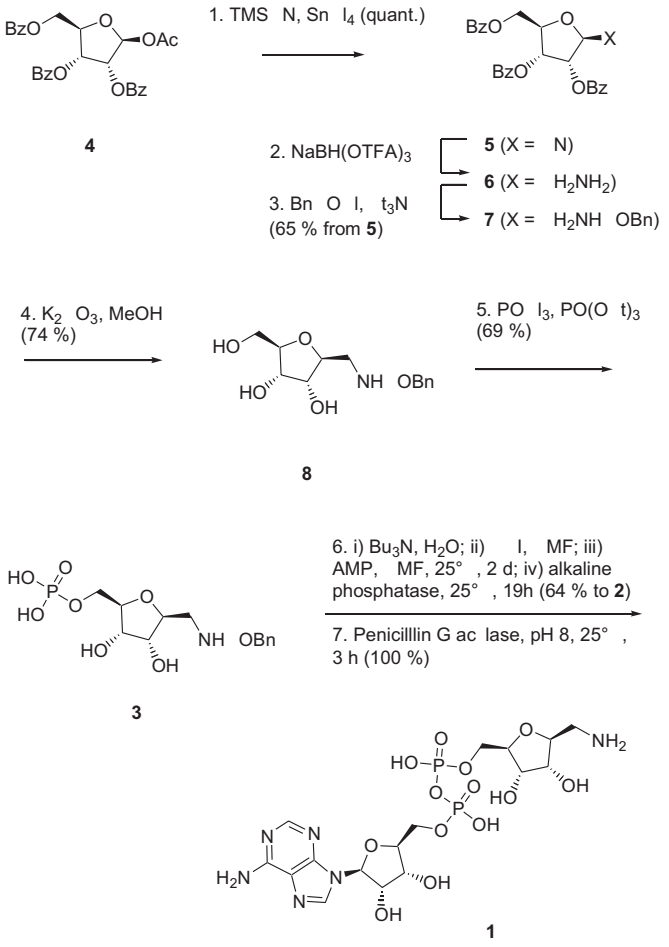

Scheme 4. Fluorogenic assays used to detect alcohol dehydrogenase and aldolase activities.

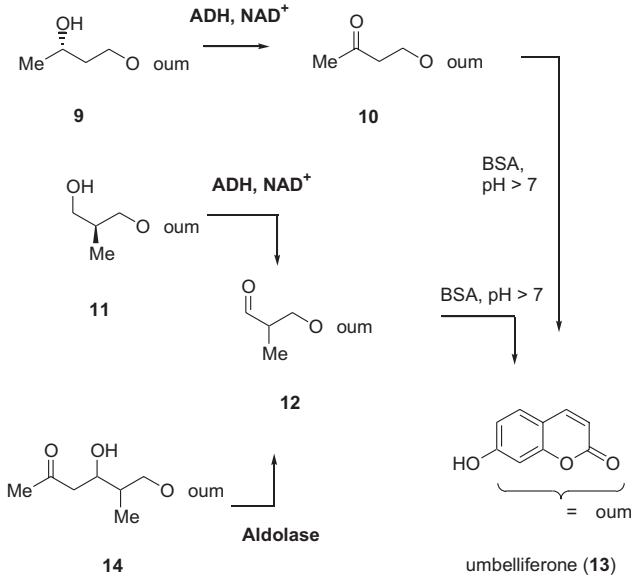

Table 1. Inhibition constants for **1** and **2** with alcohol dehydrogenases.

Inhibitor	ADH	Apparent K_i (μM)
1	Horse liver	850
1	Yeast	1400
2	Horse liver	3.0
2	Yeast	2000

Note: In competition with NAD^+ for the oxidation of substrate **9**. Conditions: 20 mM aq. borate, pH 8.8, 2 mg mL^{-1} BSA, 100 μM substrate **9**, 0.1 mM and 1 mM NAD^+.

which was isolated as the trifluoroacetate salt by reversed-phase HPLC.

Interactions between MAD and alcohol dehydrogenases

Horse liver alcohol dehydrogenase and yeast alcohol dehydrogenase, both of which are commercially available and represent a broad spectrum of alcohol dehydrogenases, were selected as the target enzymes. We first tested whether MAD could inhibit the redox activity of the enzymes, and thus could bind to the active site. The alcohol dehydrogenase activity was measured using the fluorogenic oxidation of the chiral alcohols (*S*)-**9** and (*S*)-**11** (Scheme 4) (18). The oxidation products **10** and **12** undergo a rapid β-elimination in the presence of bovine serum albumin (BSA) to give strongly fluorescent umbelliferone **13**, which is readily detected at micromolar concentrations in microtiter plates.

Inhibition experiments of alcohol oxidation showed that our primary amine co-factor MAD (**1**) bound to the alcohol dehydrogenases, albeit weakly (Table 1). Only protected precursor **2** showed a good affinity for horse liver alcohol dehydrogenase. The inhibition of the ADH oxidation activity by **1** (1 mM) was unaffected by the presence of carbonyl compounds such as phenacetaldehyde, benzaldehyde, anisaldehyde, 1,2,3,6-tetrahydrobenzaldehyde, acetaldehyde, acetylacetone, crotonaldehyde, cinnamaldehyde, or 2-oxopropionamide (1 mM each). Since imine formation occurs spontaneously between amines and aldehydes with a pH-independent equilibrium constant of approximately 10 mM (19), the experiment showed that the binding pocket of the alcohol dehydrogenases did not strongly bind to the imines formed between these carbonyls and our primary amine co-factor.

Evaluation of MAD as an aldolization co-factor

Aldolization activity was investigated using a series of fluorogenic aldols such as **14** and close derivatives under the same conditions as those used for the ADH-activity assay (Table 2). Under these experimental conditions, these substrates undergo clean retro-aldolization in the presence of aldolase catalysts such as antibody 38C2 (20). Although these aldols do not posess the oxoamide carbonyl that would make them optimally suited to alcohol dehydrogenases according to our design, the approximation was judged close enough considering that alcohol dehydrogenases also easily accept various redox co-factors where the carboxamide group has been changed to other groups. There was no observable retro-aldolization catalysis with MAD and the dehydrogenases for these substrates, despite the fact that corresponding alcohol **11** is a good oxidation substrate for these enzymes. Direct aldolization was also tested for the cross-aldolization between 2-oxopropionamide and acetaldehyde, as well as for the direct dimerization of acetaldehyde

© 2002 NRC Canada

Table 2. Assays for aldolization activity of MAD (**1**).

Entry	Substrate	Conditions	MAD (**1**)	Detection	Reaction
1	Fluorogenic aldol (**14**)	0.1 mM, 2 mg mL^{-1} BSA	1 mM	Fluorescence[a]	n.r.
2			None		n.r.
3	2-Oxopropionamide, acetaldehyde	10 mM each	1 mM	RP-HPLC, 214 nm[b]	n.r.
4			None		n.r.
5	Acetaldehyde	10 mM	1 mM	RP-HPLC, 230 nm[b]	No catalysis
6			None		Spontaneous

Note: All assays in 20 mM aq. borate pH 8.8, 25°C, were followed over 48 h.
[a]λ_{ex} = 360 nm, λ_{em} = 460 nm
[b]Analytical column: Vydac 218TP-54 (C_{18}, pore size 300 Å), 0.45 × 22 cm, detection by UV at 214 or 230 nm, isocratic elution at 1.5 mL min^{-1}, A = 0.1 % TFA in H_2O, B = 50:50 CH_3CN–H_2O). t_R (2-oxopropionamide) = 3.9 min at 5% B, t_R (crotonaldehyde) = 5.2 min at 15% B.

Table 3. Analytical RP-HPLC conditions for MAD and intermediates.

Compound	% A	% B	t_R (min)
8	70	30	3.0
3	90	10	5.2
2	95	5	10.0
1	98	2	2

Note: Isocratic elution at 1.5 mL min^{-1}, detection by UV at 254 nm, A = 0.1% TFA in H_2O, B = 50:50 CH_3CN–H_2O, analytical column: Vydac 218TP-54 (C_{18}, pore size 300 Å), 0.45 × 22 cm.

to crotonaldehyde. In both cases there was no observable product formation.

Conclusion

MAD (**1**) has been prepared in seven steps by an efficient chemoenzymatic synthesis from protected D-ribose derivative **4**. Penicillin G acylase provided the key to remove the phenacetyl-protecting group of the primary amine function, which was used as a hydrophobic, UV-visible tag to facilitate the purification of intermediates. The structural and mechanistic analogy between the putative aldolization chemistry of MAD and the redox chemistry of the natural NAD co-factor suggests that our synthetic co-factor should be able to transform alcohol dehydrogenases into stereoselective aldolases. Our preliminary investigation using the alcohol dehydrogenases from horse liver and from yeast, however, do not seem to indicate any activity of this type. Although the enzyme preparations used might not contain a high concentration of active protein, we must conclude that aldolization catalysis as designed does not occur within the active site of these enzymes at a level that is detectable under our conditions. Further experiments with other alcohol dehydrogenases and other aldolization substrates may, however, afford different results. MAD also offers an attractive opportunity for enzyme evolution, which should be obtainable using fluorogenic substrates such as **14** as screening tools.

Experimental

All reagents and enzymes were purchased from Aldrich or Fluka. Chromatographies (flash) were performed with Merck Silicagel 60 (0.040–0.063 mm). CH_2Cl_2 was distilled from P_2O_5 prior to use. Preparative HPLC was done with HPLC-grade acetonitrile and MilliQ de-ionized water using a Waters prepak cartridge 500 g (RP-C18 20 μm, 300 Å pore size) installed on a Waters Prep LC 4000 system from Millipore, flow rate 100 mL min^{-1}, gradient +0.5% min^{-1} CH_3CN, detection by UV at 214 nm. TLC were performed with fluorescent F254 glass plates. MS and HRMS (high resolution mass spectra) were provided by Dr. Thomas Schneeberger (University of Bern). Fluorescence measurements were carried out using a Cytofluor II Plate-Reader from Perseptive Biosystems.

2,5-Anhydro-3,4,6-tri-*O*-benzoyl-1-deoxy-1-phenylacetamide-D-allitol (7)

As described in literature (15), a solution of $NaBH_3(O_2CCF_3)$ (1.0 g, 6.6 mmol) was prepared by adding under nitrogen pure trifluoroacetic acid (0.51 mL, 6.7 mmol) to an ice-bath-cooled, stirred suspension of $NaBH_4$ (0.26 g, 6.8 mmol) in dry THF (20 mL). A solution of cyanide **5** (2.2 g, 4.7 mmol) in dry THF (13 mL) was added at 0°C, and the mixture was stirred at 25°C for 18 h. The reaction was quenched with de-ionized water (5 mL) and concentrated to dryness. The residue was partitioned between EtOAc (20 mL) and sat. aq. $NaHCO_3$ (7 mL), and cooled in an ice bath. BnCOCl (2 mL, 14.7 mmol) was added, and the mixture was vigorously stirred at 0°C for 3 h. The layers were separated, the organic phase was washed once with water, dried over Na_2SO_4, and concentrated to dryness. The residue was purified by flash chromatography on silica gel (Hex–EtOAc, 50:50) to give **7** (1.8 g, 3 mmol, 65 % over the two steps) as a yellow syrup. IR (neat) (cm^{-1}): 3013, 1727, 1654, 1601, 1584, 1522, 1496, 1452, 1316, 1269, 1216, 1178, 1124, 1070, 1026. ^{1}H NMR ($CDCl_3$) δ: 8.09–7.22 (m, 20H), 6.03 (NH), 5.56 (dd, *J* = 4.4, 5.9 Hz, 1H), 5.32 (dd, *J* = 6.3 Hz, 1H), 4.45 (m, 4H), 3.60 (dd, *J* = 5.2, 5.5 Hz, 2H), 3.51 (s, 2H). ^{13}C NMR ($CDCl_3$) δ: 172.1, 169.9, 167.0, 166.1, 135.4, 134.1, 134.0, 130.4, 130.0, 129.6, 129.3, 129.1, 128.0, 80.8, 80.5, 73.3, 73.2, 64.8, 44.2, 41.2. MS *m/z*: 594 (M^+).

2,5-Anhydro-1-deoxy-1-phenylacetamide-D-allitol (8)

To a solution of K_2CO_3 (0.24 g, 1.68 mmol) in methanol (20 mL) and water (4 mL) was added a solution of compound **7** (1.0 g, 1.68 mmol) in methanol (20 mL). The mixture was stirred vigorously overnight at 25°C, and the solvent was removed in vacuo. The residue was dissolved in dichloromethane and water, and extracted several times with

© 2002 NRC Canada

water. The aqueous phase was then purified by preparative HPLC to afford **8** (0.35 g, 1.24 mmol, 74 %) as a light yellow syrup (Table 3). ^{1}H NMR (CD_3OD) δ: 7.28 (m, 5H), 3.85 (m, 4H), 3.69 (dd, *J* = 2.9, 11.8 Hz, 1H), 3.53 (dd, *J* = 2.9, 11.8 Hz, 1H), 3.51 (s, 2H), 3.40 (m, 2H). ^{13}C NMR (CD_3OD) δ: 173.9, 136.2, 129.7, 129.3, 127.6, 85.1, 82.9, 73.2, 72.0, 62.6, 43.7, 42.1.

2,5-Anhydro-1-deoxy-1-phenylacetamide-6-phosphate-D-allitol (3)

To a solution of **8** (0.430 g, 1.53 mmol) in $(EtO)_3PO$ (15 mL) was added under N_2 a solution of $POCl_3$ (0.8 mL, 8.7 mmol) and H_2O (0.080 mL) in $(EtO)_3PO$ (10 mL), in a bath cooled with acetone–ice. The mixture was stirred at 0°C for 3 h, and then $POCl_3$ (0.8 mL) and H_2O (0.070 mL) in $(EtO)_3PO$ (10 mL) were added at 0°C. The reaction mixture was then stored at 4°C for the night, and $NaHCO_3$ (4.8 g) in H_2O (40 mL) was added at 0°C. After one night at 4°C, the solution was extracted several times with CH_2Cl_2 to remove $(EtO)_3PO$. The aqueous phase was purified by preparative RP-HPLC to afford **3** (0.38 g, 1.05 mmol, 69 %) as a colorless syrup. ^{1}H NMR (CD_3OD) δ: 7.25 (m, 5H), 4.00 (m, 6H), 3.54 (s, 2H), 3.41 (d, *J* = 4.8 Hz, 2H). ^{13}C NMR (CD_3OD) δ: 174.4, 137.0, 130.2, 129.6, 127.9, 83.7, 83.3, 73.7, 72.8, 67.5, 43.8, 42.4.

6-Adenosine-diphosphate-2,5-anhydro-1-deoxy-1-phenylacetamide-D-allitol (2)

Tri-*n*-butylammonium-AMP (0.165 g, 0.3 mmol) was dissolved in dry DMF (0.5 mL) at 25°C under N_2. A solution of carbonyl diimidazole (CDI, 0.102 g, 0.63 mmol) in dry DMF (1 mL) was added, and the mixture was stirred at 25°C for 2 h. The excess CDI was destroyed by adding MeOH (0.026 mL), and the excess MeOH was removed under high vacuum. A solution of compound **8** (0.100 g, 0.28 mmol) in dry DMF (2.5 mL) was added, and the reaction was stirred at 25°C for 2 days. The solvent was removed in vacuo, and the residue taken in aq. 50 mM Tris buffer (10 mL, pH 7.45). The mixture was treated with ~150 U (0.067 mL) of calf intestinal alkaline phosphatase at 25°C overnight. After concentration in vacuo, the crude product was purified by preparative HPLC to give **2** (0.122 g, 0.18 mmol, 64 %) as a colorless solid; mp 132–133°C. ^{1}H NMR (D_2O–CD_3OD) δ: 8.64 (s, 1H), 8.34 (s, 1H), 7.23 (m, 5H), 6.09 (s, 1H), 4.03–3.81 (m, 9H), 3.55–3.39 (m, 6H). ^{13}C NMR (D_2O–CD_3OD) δ: 172.2, 151.0, 146.0, 136.1, 130.0, 129.9, 129.6, 127.9, 89.0, 85.3, 83.1, 82.5, 75.8, 73.1, 72.2, 71.3, 67.7, 66.2, 43.3, 41.8. ^{31}P NMR (D_2O) δ: –10.5, –14.8. MS *m/z*: 713 ($[M + Na]^+$), 691 ($[M + H]^+$). HRMS *m/z*: calcd. for $C_{24}H_{33}N_6O_{14}P_2$: 691.1530; found: 691.1547.

6-Adenosine-diphosphate-1-amino-2,5-anhydro-1-deoxy-D-allitol (1)

Compound **2** (0.060 g, 0.087 mmol) is dissolved in MeOH (1 mL), water (2.5 mL), and NaOH (0.1 M, 2.7 mL, pH 8) at 25°C. Penicillin G acylase immobilized on Eupergit C[14] (15 U, 0.140 g) was added and the suspension was stirred at 25°C for one day. After filtration, the solution was lyophilized, and the residue purified by preparative HPLC (A–B, 1.5 mL min^{-1}) to afford 0.050 g (0.087 mmol, quant.) of 6-adenosine-diphosphate-1-amino-2,5-anhydro-1-deoxy-D-allitol (**1**) as a colorless solid; mp 128°C. ^{1}H NMR (D_2O) δ: 8.60 (s, 1H), 8.35 (s, 1H), 6.07 (br d, 1H), 4.60–4.00 (m, 11H), 2.96 (m, 2H). ^{13}C NMR (D_2O–CD_3OD) δ: 151.5, 149.1, 146.3, 143.3, 119.5, 89.0, 85.3, 84.0, 79.3, 75.7, 73.2, 72.3, 71.4, 66.1, 41.8. ^{31}P NMR (D_2O) δ: –10.5. MS *m/z*: 632 ($[M – 2H + Na + K]^+$), 616 ($[M – 2H + 2Na]^+$), 610 ($[M – H + K]^+$), 594 ($[M – H + Na]^+$), 572 (M^+).

Acknowledgments

This work was supported by the University of Bern, the Swiss National Science Foundation, the European COST program (Action D12) and the Swiss Office Fédéral de l'Education et de la Science.

References

1. (*a*) J.A. Duine. Trends Biotechnol. **9**, 343 (1991); (*b*) E.T. Kaiser, D.S. Lawrence, and S.E. Rokita. Ann. Rev. Biochem. **54**, 565 (1985); (*c*) E.T. Kaiser. Angew. Chem. **100**, 945 (1988); Angew. Chem. Int. Ed. Engl. **27**, 913 (1988).
2. (*a*) F. van de Velde, L. Könemann, F. van Rantwijk, and R.A. Sheldon. Chem. Commun. 1891 (1998); (*b*) F. van de Velde, I.W.C.E. Arends, and R.A. Sheldon. J. Inorg. Biochem. **80**, 81 (2000); (*c*) F. van de Velde, L. Könemann, F. van Rantwijk, and R.A. Sheldon. Biotechnol. Bioeng. **67**, 87 (2000); (*d*) F. van de Velde, I.W.C.E. Arends, and R.A. Sheldon. Top. Catal. **13**, 259 (2000).
3. (*a*) H.L. Levine, Y. Nakagawa, and E.T. Kaiser. Biochem. Biophys. Res. Commun. **76**, 64 (1977); (*b*) H.L. Levine and E.T. Kaiser. J. Am. Chem. Soc. **100**, 7670 (1978); (*c*) J.T. Slama, S.R. Oruganti, and E.T. Kaiser. J. Am. Chem. Soc. **103**, 6211 (1981); (*d*) J.T. Slama, C. Radziejewski, S.R. Oruganti, and E.T. Kaiser. J. Am. Chem. Soc. **106**, 6778 (1984).
4. (*a*) J.B. Jones and I.J. Jakovac. Can. J. Chem. **60**, 19 (1982); (*b*) A.R. Krawczyk and J.B. Jones. J. Org. Chem. **54**, 1795 (1989).
5. T.D. Machajewski and C.H. Wong. Angew. Chem. **112**, 1406 (2000); Angew. Chem. Int. Ed. Engl. **39**, 1352 (2000).
6. (*a*) T. Mukaiyama, K. Banno, and K. Narasaka. J. Am. Chem. Soc. **96**, 7503 (1974); (*b*) D.A. Evans, J.V. Nelson, and T.R. Taber. Top. Stereochem. **13**, 1 (1982); (*c*) I. Paterson. Pure Appl. Chem. **64**, 1821 (1992); (*d*) E.M. Carreira, R.A. Singer, and W. Lee. J. Am. Chem. Soc. **116**, 8837 (1994).
7. J. Wagner, R.A. Lerner, and C.F. Barbas. Science, **270**, 1797 (1995).
8. G. Zhong, R.A. Lerner, and C.F. Barbas. Angew. Chem. **111**, 3957 (1999); Angew. Chem. Int. Ed. Engl. **38**, 3738 (1999).
9. (*a*) J.-L. Reymond and Y. Chen. Tetrahedron Lett. **36**, 2575 (1995); (*b*) J.-L. Reymond. Angew. Chem. **107**, 2471 (1995); Angew. Chem. Int. Ed. Engl. **34**, 2285 (1995).
10. For aldol condensations catalyzed by primary and secondary amines in water, see: (*a*) F.G. Fischer and A. Marschall. Chem. Ber. **64**, 2825 (1931); (*b*) W. Langenbeck and G. Borth. Chem. Ber. **75**, 951 (1942); (*c*) T.A. Spencer, H.S. Neel, T.W. Flechtner, and R.A. Zayle. Tetrahedron Lett. **6**, 3889 (1965); (*d*) C.D. Gutsche, D. Redmore, R.S. Buriks, K. Nowotny, H. Grassner, and C.W. Armbruster. J. Am. Chem. Soc. **89**, 1235 (1967). For Schiff base mechanism of aldolases, see: (*e*) E. Grazi, P.T. Rowley, T. Cheng, O. Tchola, and B.L. Horecker. Biochem. Biophys. Res. Commun. **9**, 38 (1962).
11. J.-L. Reymond and Y. Chen. J. Org. Chem. **60**, 6970 (1995).
12. S. Tono-Oka. Bull. Chem. Soc. Jpn. **55**, 1531 (1982).

© 2002 NRC Canada

13. G. Baisch and R. Öhrlein. Bioorg. Med. Chem. **5**, 383 (1997).
14. H. Waldmann. Tetrahedron Lett. **29**, 1131 (1988).
15. P.D. Cook and D.J. McNamara. J. Heterocyclic Chem. **23**, 155 (1986).
16. D.R. Sauer and S.W. Schneller. Synthesis, **9**, 747 (1991).
17. (*a*) M. Yoshikawa, T. Kato, and T. Takenishi. Bull. Chem. Soc. Jpn. **42**, 3505 (1969); (*b*) P. Franchetti, L. Cappellacci, P. Perlini, H.N. Jayaram, A. Butler, B.P. Schneider, F.R. Collart, E. Huberman, and M. Grifantini. J. Med. Chem. **41**, 1702 (1998).
18. G. Klein and J.-L. Reymond. Helv. Chim. Acta, **82**, 400 (1999).
19. J. Hine, B.C. Menon, J.H. Jensen, and J. Mulders. J. Am. Chem. Soc. **88**, 3367 (1966).
20. R. Pérez Carlòn, N. Jourdain, and J.-L. Reymond. Chem. Eur. J. **6**, 4154 (2000).

© 2002 NRC Canada

Hydroxynitrile lyase-catalyzed addition of HCN to 4-substituted cyclohexanones: stereoselective preparation of tetronic acids

Franz Effenberger, Jürgen Roos, Christoph Kobler, and Holger Bühler

Abstract: The addition of HCN to 4-alkylcyclohexanones **1** to give cyanohydrins **2** is strongly catalyzed by hydroxynitrile lyases (HNLs). With PaHNL, from bitter almond, *trans*-addition occurs almost exclusively, yielding *trans*-**2**. With MeHNL, from cassava, *cis*-addition is preferred to give *cis*-**2**. *cis*-Selectivity is nearly quantitative, especially for cyclohexanones with larger 4-substituents. Comparable results with respect to the stereoselectivity were observed in the HNL-catalyzed addition of HCN to 4-alkoxycyclohexanones **3a**–**g**. In contrast, the stereoselectivity in the HNL-catalyzed addition to 4-alkanoyloxycyclohexanones **3h**–**k** is very poor. The transformation of *cis*-4-propylcyclohexanone cyanohydrin (**2c**) into the corresponding *cis*-spirotetronic acid **7** occurs without any isomerization.

Key words: enzyme, hydroxynitrile lyase, cyclohexanones, cyanohydrins, *cis*/*trans*-stereoselectivity.

Résumé : L'addition du HCN sur les 4-alkylcyclohexanones (**1**) conduisant à la formation de cyanohydrines (**2**) est fortement catalysée par les lyases d'hydroxynitriles (« HNL »). Sous l'influence d'une PaHNL obtenue à partir de l'amande amère, l'addition se fait pratiquement exclusivement de façon *trans*, conduisant aux *trans*-2. Avec une MeHNL tirée de cassava, l'addition se fait préférentiellement de façon *cis* pour conduire aux *cis*-2. Dans les cas de cyclohexanones portant des substituants encombrants en position 4, la sélectivité *cis* est pratiquement quantitative. Des résultats de stéréosélectivités comparables sont aussi obtenus lors de l'addition de HCN, catalysée par une lyase d'hydroxynitrile, aux 4-alcoxycyclohexanones (**3a-g**). Par opposition, la stéréosélectivité de l'addition de HCN, catalysée par une lyase d'hydroxynitrile, sur les 4-alcanoyloxycyclohexanones (**3h-k**) est très faible. La transformation de la cyanohydrine de la *cis*-4-propylcyclohexanone (**2c**) en acide *cis*-spirotétronique correspondant (**7**) se réalise sans épimérisation.

Mots clés : enzyme, lyase d'hydroxynitrile, cyclohexanones, cyanohydrines, stéréosélectivité *cis/trans*.

[Traduit par la Rédaction]

Introduction

Tetronic acids **C** derived from 1-hydroxy-4-alkoxycyclohexane-1-carboxylic acids are of particular interest as herbicides and insecticides (1). The simplest approach to hydroxycarboxylic acids of this type would be the hydrolysis of cyanohydrins **B** accessible from the corresponding 4-substituted cyclohexanones **A** (Chart 1). The common chemical addition of HCN to 4-substituted cyclohexanones results in a *cis*/*trans*-isomeric mixture of cyanohydrins **B**, and the tetronic acids thus obtained would also be *cis*/*trans* isomers. Since the different stereoisomers of tetronic acids **C** reveal very distinct biological activities (1), the exclusive stereoselective preparation of one isomer, *cis* or *trans*, of 4-substituted cyclohexanone cyanohydrins **B** is an important target. Until now this could not be realized, and therefore the mixture of isomeric tetronic acids had to be separated by crystallization. This procedure is not only time-consuming but also the accumulation of the non-desired isomer is disadvantageous.

In this paper, we report on the enzyme-catalyzed addition of HCN to 4-substituted cyclohexanones, which stereoselectively yields the corresponding *cis*- or *trans*-cyanohydrins. Hydroxynitrile lyases (HNLs) have been applied as biocatalysts. By using PaHNL from bitter almond (*Prunus amygdalus*) *trans* isomers are preferentially formed, while with MeHNL from cassava (*Manihot esculenta*) *cis* isomers are the major products.

In a previous communication (2), a mainly mechanistic explanation of this unexpected *cis*/*trans*-selectivity is described and interpreted based on the X-ray crystal structure of the MeHNL (3), while the synthetic potential of the reaction is

Received 12 February 2002. Published on the NRC Research Press Web site at http://canjchem.nrc.ca on 29 May 2002.

Dedicated to Professor J. Bryan Jones — a good friend and an excellent scientist.

F. Effenberger,[1] J. Roos,[2] C. Kobler,[3] and H. Bühler.[4] Institut für Organische Chemie, Universität Stuttgart, Pfaffenwaldring 55, D-70569 Stuttgart, Germany.

[1]Corresponding author (e-mail: franz.effenberger@po.uni-stuttgart.de).
[2]Taken in part from Ph.D. thesis. Universität Stuttgart, Germany. January 1999.
[3]Taken from Diplomarbeit. Universität Stuttgart, Germany. September 2000.
[4]Taken in part from Ph.D. thesis. Universität Stuttgart, Germany. November 2000.

 DOI: 10.1139/V02-087 © 2002 NRC Canada

Table 1. Formation of 4-alkylcyclohexanone cyanohydrins **2** by (*S*)-MeHNL- and (*R*)-PaHNL-catalyzed addition of HCN to 4-substituted cyclohexanones **1**.

	(*S*)-MeHNL			(*R*)-PaHNL			Chemical addition	
Substrate	*t* (h)	Conv. (%)	*cis*:*trans* (%)	*t* (h)	Conv. (%)	*cis*:*trans* (%)	Conv. (%)	*cis*:*trans* (%)
1a	2	80	35:65	1.5	99	3:97	4	17:83
1b	5	quant	74:26	22	99	2:98	0.5	16:84
1c	5	93	96:4	31	83	2:98	<1	15:85
1d	5	quant	97:3	22	94	1:99	<1	13:87
1e	3	82	99:1	216	50	10:90	2	13:87
1f	9	99	98:2	24	99	1:99	2.5	11:89
1g	3	95	99:1	264	71	4:96	28	9:91

Chart 1.

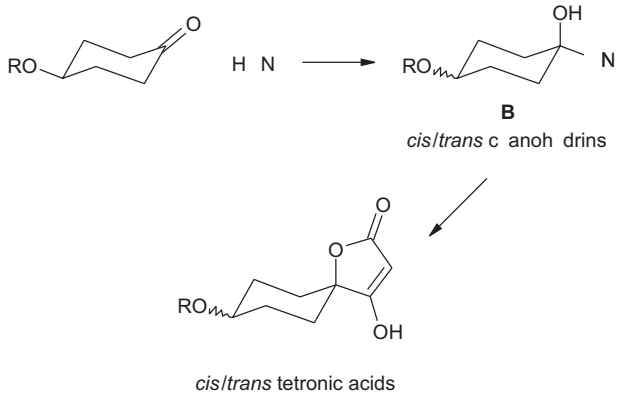

not comprehensively examined. The MeHNL-catalyzed HCN addition to 4-substituted cyclohexanones (2) is mechanistically comparable with the hydrogenation of cyclohexanones to the corresponding alcohols using NADH-depending alcohol dehydrogenases (4).

Only very few samples of 4-substituted cyclohexanone cyanohydrins have been reported in the literature (5–9). In all cases, mixtures of *cis*/*trans* isomers are obtained. For the 4-methyl compound the *cis*:*trans* ratio is 1:2, while for the 4-*tert*-butyl-substituted derivative the *cis*:*trans* ratio is 1:3. Because these ratios are also found under base catalysis (8), it can be assumed that these ratios correspond to the thermodynamic equilibria.

In recent times, HCN is often replaced by trimethylsilyl cyanide in the addition to carbonyl compounds, giving the corresponding *O*-trimethylsilyl cyanohydrins (10). With 4-substituted cyclohexanones only the cyanosilylation of *tert*-butyl- and benzyloxycyclohexanone was performed, yielding in both cases the *trans* isomer as major product. With various catalysts the percentage of the *trans* product in the reaction of 4-*tert*-butylcyclohexanone with trimethylsilyl cyanide could be increased up to 90% (11), compared with 80% *trans* isomer obtained with 4-benzyloxycyclohexanone using ZnI_2 as catalyst (12).

Results and discussion

Hydroxynitrile lyase-catalyzed HCN addition to 4-alkylcyclohexanones 1 (2)

To investigate the scope of the *cis*/*trans* selectivity of the enzyme-catalyzed HCN addition to 4-substituted cyclohexanones, the 4-alkyl-substituted compounds **1a**–**g** (13*a*–*c*) were investigated.

Scheme 1.

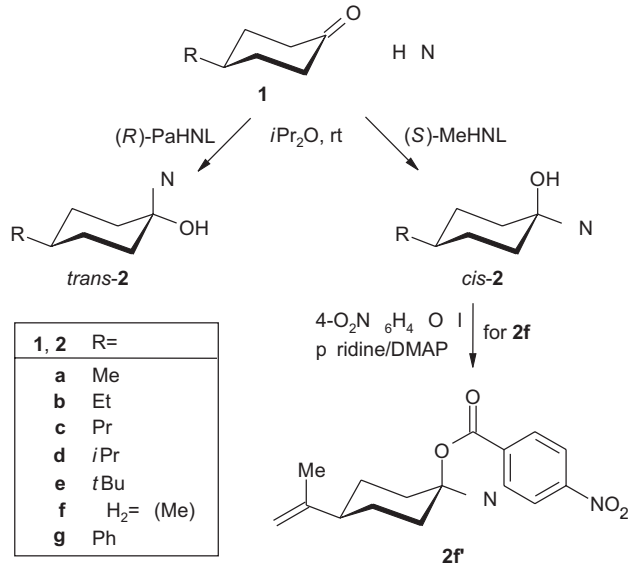

For the enzymatic reactions of the ketones **1**, the hydroxynitrile lyases (*R*)-PaHNL from almond and (*S*)-MeHNL from cassava were used. The results of the HNL-catalyzed addition of HCN to the 4-alkyl substituted cyclohexanones **1** (Scheme 1) are summarized in Table 1.

All investigated cyclohexanones **1** were found to be good substrates for both enzymes. The PaHNL-catalyzed conversion selectively afforded the *trans*-cyanohydrins (*trans*-**2**), while with catalyst MeHNL the corresponding *cis* isomers (*cis*-**2**) were formed almost exclusively for the larger 4-substituents. As can be seen from Table 1, the substituent R clearly influences the reactivity of the (*R*)-PaHNL-catalyzed reaction: with increasing steric demand of the R group the conversion rate is markedly diminished. The stereoselectivity, however, is fairly high in all cases with one exception; the *tert*-butyl derivative **1e** reacts very slowly, therefore the chemical addition becomes more dominant, causing diminished stereoselectivity (*cis*:*trans* = 10:90).

With the recombinant MeHNL from cassava, all substrates **1** were converted faster to the cyanohydrins compared with PaHNL (whose selectivity is almost independent of the steric demand of R) (Table 1). In contrast to PaHNL,

© 2002 NRC Canada

Table 2. Experimental crystallographic data for compounds **2f′**, **4b′**, and **4h′**.[5]

Compd	**2f′**	**4b′**	**4h′**
Formula	$C_{17}H_{18}N_2O_4$	$C_{15}H_{16}N_2O_5$	$C_{16}H_{16}N_2O_6$
Crystal size (mm)	0.65 × 0.25 × 0.01	0.8 × 0.8 × 0.07	1.1 × 0.1 × 0.07
FW (g mol^{-1})	314.33	304.30	332.31
Space group	$P\bar{1}$	$P2_1/n$	$P2_1/c$
Cell parameters			
a (Å)	6.8616(8)	6.9275(12)	10.923(3)
b (Å)	7.1533(14)	7.1416(13)	6.436(2)
c (Å)	17.564(3)	30.957(4)	23.184(3)
α (°)	80.622(12)	90.00	90.00
β (°)	80.239(11)	90.952(12)	91.721(14)
γ (°)	83.077(10)	90.00	90.00
V (Å^3)	834.4(2)	1531.3(4)	1629.0(6)
Z	2	4	4
$\rho_{calcd.}$ (g cm^{-3})	1.251	1.320	1.355
Data collection[a]			
Total reflections	2390	3276	2544
Unique reflections	2173	3018	2400
Refinement			
R/R_w (*F*)	0.081/0.2178	0.0586/0.1297	0.0595/0.1239
No. of variables	236	200	218
GoF	1.040	1.077	1.193
$\Delta\rho_{min}$ (e Å^{-3})	–0.241	–0.235	–0.190
$\Delta\rho_{max}$ (e Å^{-3})	0.300	0.308	0.209

[a] *T* = 293 K, Nicolet P3 diffractometer, MoKα (λ = 0.71073) or Siemens P4 diffractometer, Cu Kα (λ = 1.54178) radiation.

Fig. 1. ORTEP view of 4-isopropenyl-1-(4-nitrobenzoyloxy)cyclohexanecarbonitrile (**2f′**).

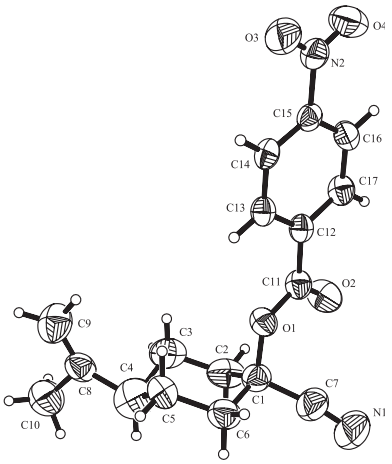

Fig. 2. ORTEP view of (*a*) 4-methoxy-1-(4-nitrobenzoyloxy)cyclohexanecarbonitrile (**4b′**); (*b*) 4-acetoxy-1-(4-nitrobenzoyloxy)cyclohexanecarbonitrile (**4h′**).

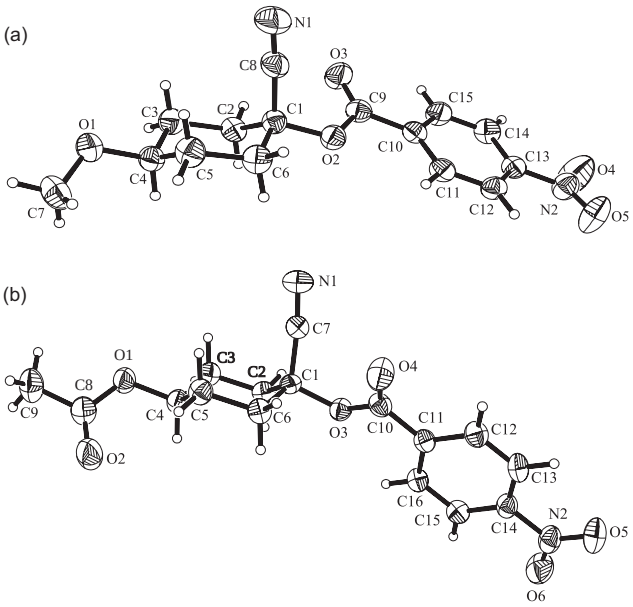

MeHNL is *cis*-selective and the stereoselectivity of the HCN addition strongly depends on the size of R, as can be clearly seen in the reactions of the homologues **1a**–**c** (R = Me, Et, Pr, respectively).

The structural assignment of the isomers by ^{13}C NMR spectroscopy followed from comparison with literature data (13*b*). The C-1 atom signal in the *cis* isomer is clearly shifted to a higher field compared with that of the *trans* isomer (see Table 4). Furthermore, the X-ray structure (14) of the nitrobenzoyl derivative **2f′** (Fig. 1, Table 2), obtained by nitrobenzoylation of the MeHNL-derived main isomer **2f** (Scheme 1), unequivocally confirms the assignment.

[5] Supplementary material has been deposited with the Cambridge Crystallographic Data Centre. Copies of the data can be obtained, free of charge, on quoting the depository number CCDC-174989 (**2f′**), CCDC-169991 (**4b′**), and CCDC-179064 (**4h′**) from CCDC, 12 Union Road, Cambridge CB2 1EZ, U.K. (Fax: 44–1223–336033 or e-mail: deposit@ccdc.cam.ac.uk).

© 2002 NRC Canada

Table 3. Formation of 4-alkoxy- and 4-alkanoyloxycyclohexanone cyanohydrins **4** by (*R*)-PaHNL and (*S*)-MeHNL-catalyzed addition of HCN to 4-substituted cyclohexanones **3**.

	(*S*)-MeHNL			(*R*)-PaHNL			Chemical addition	
Substrate	*t* (h)	Conv. (%)	*cis*:*trans* (%)	*t* (h)	Conv. (%)	*cis*:*trans* (%)	Conv. (%)	*cis*:*trans* (%)
3a	1	80	43:57	1	90	39:61	52	45:55
3b	1	quant	28:72	2	97	9:91	21	45:55
3c	1	99	61:39	7	82	11:89	34	43:57
3d	2.5	quant	87:13	48	60	14:86	17	46:54
3e	46	52	90:10	46	18	16:84	2	47:53
3f	22	99	87:13	22	97	8:92	2	45:55
3g	96	45	82:18	19	99	2:98	9	45:55
3h	1	92	66:34	1	97	5:95	8	57:43
3i	2	92	69:31	2	85	9:91	17	60:40
3j	5	76	60:40	5	99	9:91	4	63:37
3k	7	71	58:42	7	98	4:96	7	61:39
3l	7	72	88:12	72	89	29:71	24	71:29

Scheme 2.

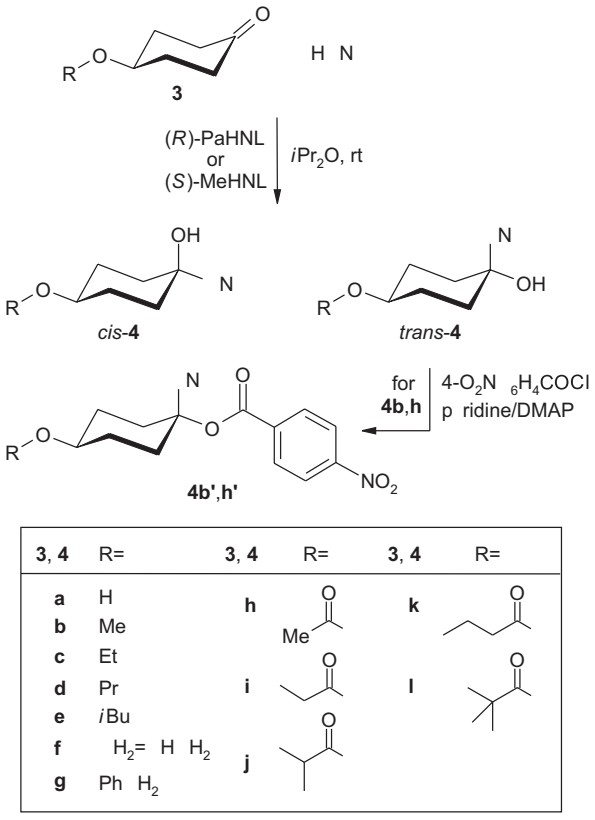

3, 4	R=	3, 4	R=	3, 4	R=
a	H	**h**		**k**	
b	Me				
c	Et				
d	Pr	**i**		**l**	
e	*i*Bu				
f	H_2= H H_2	**j**			
g	Ph H_2				

Scheme 3.

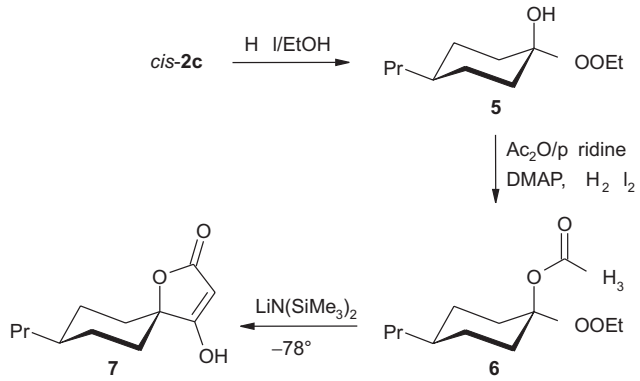

Hydroxynitrile lyase-catalyzed HCN addition to 4-alkyloxy- and 4-alkanoyloxycyclohexanones 3

In addition, to known cyclohexanones **3a**–**h** and **3l** (13*d*–*i*), the 4-alkanoyloxycyclohexanones **3i**–**k** had to be prepared. For this purpose, 4-hydroxycyclohexanone (**3a**) was acylated in the presence of pyridine and catalytic amounts of dimethylaminopyridine (DMAP) with either the respective acid chloride or anhydride to give the cyclohexanones **3i**–**k** in 45–65% yields (not optimized; see *Experimental*).

The HNL-catalyzed HCN addition to the 4-alkyloxy- and 4-alkanoyloxycyclohexanones **3** is depicted in Scheme 2, and the results are listed in Table 3.

Analogous to cyclohexanones **1**, compounds **3** were also converted using PaHNL as the catalyst with moderate to high stereoselectivity to *trans* isomers **4**. The *trans* selectivity of PaHNL with the substrates **3b**–**l** is comparable with the behavior of alkylcyclohexanones **1**. In the case of 4-hydroxycyclohexanone **3a**, both enzymes (PaHNL and MeHNL) show only a very low stereoselectivity. The MeHNL-catalyzed addition of HCN to compounds **3** again results in the preferred formation of the *cis* isomers (*cis*-**4**), with one exception. In the conversion of **3b** (R = MeO) the *trans* isomer dominates. For benzyloxycyclohexanone **3g** a long reaction time is required and a slight decrease of the *cis* stereoselectivity at low conversion was also observed.

The isomers were assigned by the chemical shift of the C-4 atom in ^{13}C NMR spectra and, due to deficiency of literature data, the structure was also determined by X-ray crystallographic analysis (14). The isomers *trans*-**4b** and *trans*-**4h**, obtained in the PaHNL-catalyzed HCN addition, were crystallized as nitrobenzoyl derivatives **4b′** and **4h′** (Scheme 2, Fig. 2, Table 2). As can be seen from Fig. 2, both compounds exist as *trans* isomers, confirming the assignment.

© 2002 NRC Canada

Table 4. Spectroscopic data of the 4-substituted cyclohexanone cyanohydrins **2c**, **2f**, and **4a–l**.

Compd	^{1}H NMR (250 MHz) (J in Hz)	^{13}C NMR (63 MHz)
trans-**2c**	0.89 (t, J = 6.9, 3H, CH_3), 1.26–1.47 (m, 7H, 2 CH, 4-CH, $(CH_2)_2CH_3$), 1.53–1.64 (m, 2H, 2 CH), 1.83–1.87 (m, 2H, 2 CH), 2.16–2.21 (m, 2H, 2 CH), 2.91 (br s, 1H, OH)	14.24 (CH_3), 20.10 ($CH_2CH_2CH_3$), 29.60 (CH_2), 35.79, 38.28 (C4, $CH_2CH_2CH_3$), 38.03 (CH_2), 70.68 (C1), 121.69 (CN)
cis-**2c**	0.89 (t, J = 7.0, 3H, CH_3), 1.13–1.39 (m, 7H, 2 CH, 4-CH, $(CH_2)_2CH_3$), 1.60–1.67 (m, 2H, 2 CH), 1.78–1.90 (m, 2H, 2 CH), 2.03–2.10 (m, 2H, 2 CH), 2.39 (br s, 1H, OH)	14.23 (CH_3), 19.90 ($CH_2CH_2CH_3$), 26.40 (CH_2), 35.14, 38.11 (C4, $CH_2CH_2CH_3$), 36.16 (CH_2), 67.29 (C1), 122.78 (CN)
trans-**2f**	1.48–1.72 (m, 4H, 4 CH), 1.74 (s, 3H, CH_3), 1.86–1.99 (m, 3H, 3 CH), 2.23–2.29 (m, 2H, 2 CH), 3.16 (br s, 1H, OH), 4.74–4.76 (m, 2H, $=CH_2$)	20.82 (CH_3), 28.28, 38.03 (CH_2), 43.56 (C4), 70.32 (C1), 109.66 ($=CH_2$), 121.54 (CN), 148.14 (C=)
cis-**2f**	1.64–1.67 (m, 4H, 4 CH), 1.72 (s, 3H, CH_3), 1.82–2.01 (m, 3H, 3 CH), 2.13–2.20 (m, 2H, 2 CH), 2.79 (br s, 1H, OH), 4.71–4.74 (m, 2H, $=CH_2$)	20.84 (CH_3), 24.98, 36.48 (CH_2), 43.23 (C4), 66.56 (C1), 109.40 ($=CH_2$), 122.83 (CN), 148.70 (C=)
trans-**4a**[a]	1.53–2.13 (m, 6H, 6 CH), 2.21–2.35 (m, 2H, 2 CH), 2.86 (s, 1H, OH), 2.93 (s, 1H, OH), 3.79 (d, J = 2.0, 1H, 4-CH)	29.63, 33.36 (CH_2), 66.34, 67.43 (C1, C4), 121.68 (CN)
cis-**4a**[a]	1.47–2.39 (m, 8H, 4 CH_2), 2.59 (br s, 2H, OH), 3.81–3.94 (m, 1H, 4-CH)	28.70, 31.56 (CH_2), 62.64 (C1), 65.29 (C4), 121.18 (CN)
trans-**4b**[a]	1.64–2.22 (m, 8H, 4 CH_2), 3.00 (br s, 1H, OH), 3.28–3.33 (m, 1H, 4-CH), 3.34 (s, 3H, CH_3O)	26.20, 33.99 (CH_2), 55.95 (CH_3O), 68.37 (C1), 75.39 (C4), 121.80 (CN)
cis-**4b**	1.60–2.23 (m, 8H, 4 CH_2), 3.08 (br s, 1H, OH), 3.28–3.41 (m, 1H, 4-CH), 3.32 (s, 3H, CH_3O)	26.38, 33.32 (CH_2), 55.80 (CH_3O), 68.89 (C1), 73.75 (C4), 121.80 (CN)
trans-**4c**[a]	1.20 (t, J = 7.0, 3H, CH_3CH_2O), 1.63–1.76 (m, 4H, 4 CH), 1.89–2.06 (m, 2H, 2 CH), 2.19–2.23 (m, 2H, 2 CH), 3.36–3.40 (m, 2H, OH, 4-CH), 3.50 (q, J = 7.0, 2H, CH_3CH_2O)	15.58 (CH_3), 26.89, 34.28 (CH_2), 63.56 (CH_3CH_2O), 68.51 (C1), 73.82 (C4), 121.89 (CN)
cis-**4c**[a]	1.21 (t, J = 7.0, 3H, CH_3CH_2O), 1.63–1.76 (m, 3H, 3 CH), 1.88–2.23 (m, 6H, OH, 5 CH), 3.36–3.43 (m, 1H, 4-CH), 3.46–3.52 (m, 2H, CH_3CH_2O)	15.56 (CH_3), 26.78, 33.41 (CH_2), 63.34 (CH_3CH_2O), 68.50 (C1), 72.02 (C4), 121.91 (CN)
trans-**4d**[a]	0.92 (t, J = 7.6, 3H, $CH_3(CH_2)_2O$), 1.54–2.23 (m, 10H, $CH_3CH_2CH_2O$, 4 CH_2), 3.33–3.47 (m, 4H, $CH_3CH_2CH_2O$, 4-CH, OH)	10.65 (CH_3), 23.27 ($CH_3CH_2CH_2O$), 26.74, 34.18 (CH_2), 68.41 (C1), 70.10 ($CH_3CH_2CH_2O$), 73.83 (C4), 121.97 (CN)
cis-**4d**[a]	0.92–0.96 (m, 3H, $CH_3(CH_2)_2O$), 1.53–2.23 (m, 10H, $CH_3CH_2CH_2$, 4 CH_2), 3.20–3.50 (m, 4H, $CH_3CH_2CH_2$, 4-CH, OH)	10.68 (CH_3), 23.24 ($CH_3CH_2CH_2O$), 26.74, 34.18 (CH_2), 68.41 (C1), 70.10 ($CH_3CH_2CH_2O$), 73.83 (C4), 121.97 (CN)
trans-**4e**	0.90 (d, J = 6.6, 6H, CH_3), 1.13–2.23 (m, 9H, 4 CH_2, $CH(CH_3)_2$), 3.00 (br s, 1H, OH), 3.17 (d, J = 6.0, 2H, CH_2CH), 3.33–3.36 (m, 1H, 4-CH)	19.42 (CH_3), 25.60 (CH_2), 28.76 (CH_2CH), 34.04 (CH_2), 69.06 (C1), 73.84 (C4), 75.28 (CH_2CH), 121.99 (CN)
cis-**4e**	0.90 (d, J = 6.6, 6H, CH_3), 1.13–2.23 (m, 9H, 4 CH_2, $CH(CH_3)_2$), 3.00 (br s, 1H, OH), 3.15 (d, J = 6.5, 2H, CH_2CH), 3.44 (m, 1H, 4-CH)	19.42 (CH_3), 26.88 (CH_2), 28.76 (CH_2CH), 33.32 (CH_2), 67.96 (C1), 71.85 (C4), 75.03 (CH_2CH), 121.90 (CN)
trans-**4f**	1.64–2.24 (m, 8H, 4 CH_2), 2.99 (br s, 1H, OH), 3.43–3.49 (m, 1H, 4-CH), 3.97–4.00 (m, 2H, $CH_2CH=$), 5.17–5.34 (m, 2H, $=CH_2$), 5.88–5.95 (m, 1H, $CH_2CH=$)	26.62, 34.06 (CH_2), 68.33 (C1), 69.19 ($CH_2CH=$), 73.31 (C4), 117.78 ($=CH_2$), 121.79 (CN), 134.98 ($CH_2CH=$)
cis-**4f**	1.71–2.15 (m, 8H, 4 CH_2), 2.94 (br s, 1H, OH), 3.48–3.58 (m, 1H, 4-CH), 3.96–4.01 (m, 2H, $CH_2CH=$), 5.14–5.32 (m, 2H, $=CH_2$), 5.83–5.98 (m, 1H, $CH_2CH=$)	26.78, 33.37 (CH_2), 68.83 (C1), 69.00 ($CH_2CH=$), 71.56 (C4), 116.70 ($=CH_2$), 121.79 (CN), 134.98 ($CH_2CH=$)
trans-**4g**	1.67–1.81 (m, 4H, 4 CH), 1.95–2.03 (m, 2H, 2 CH), 2.93 (br s, 1H, OH), 3.45–3.54 (m, 1H, 4-CH), 4.51–4.56 (m, 2H, CH_2Ph), 7.25–7.38 (m, 5H, Ph)	26.54, 33.99 (CH_2), 68.34 (C1), 70.17 (CH_2Ph), 73.27 (C4), 121.78 (CN), 127.46, 127.63, 128.45, 138.48 (Ph)

© 2002 NRC Canada

Table 4 (*concluded*).

Compd	^{1}H NMR (250 MHz) (*J* in Hz)	^{13}C NMR (63 MHz)
cis-**4g**	1.67–2.33 (m, 8H, 4 CH_2), 3.50 (br s, 1H, OH), 3.57–3.60 (m, 1H, 4-CH), 4.50–4.52 (m, 2H, C*H*$_2$Ph), 7.25–7.37 (m, 5H, Ph)	26.81, 33.35 (CH_2), 68.79 (C1), 70.13 (*C*H$_2$Ph), 71.64 (C4), 121.84 (CN), 127.39, 127.56, 128.40, 138.47 (Ph)
trans-**4h**	1.68–1.85 (m, 4H, 4 CH), 1.87–2.10 (m, 5H, 2 CH, CH_3), 2.13–2.25 (m, 2H, 2 CH), 3.13 (br s, 1H, OH), 4.81–4.88 (m, 1H, 4-CH)	21.29 (CH_3), 26.32, 34.05 (CH_2), 67.96 (C1), 69.33 (C4), 121.61 (CN), 170.78 (C=O)
cis-**4h**	1.68–2.24 (m, 11H, 4 CH_2, CH_3), 3.79 (br s, 1H, OH), 4.91–5.00 (m, 1H, 4-CH)	21.32 (CH_3), 26.53, 33.47 (CH_2), 68.02 (C1), 68.30 (C4), 121.57 (CN), 170.80 (C=O)
trans-**4i**[a]	1.15 (t, *J* = 7.6, 3H, C*H*$_3$CH$_2$), 1.64–1.78 (m, 2H, 2 CH), 1.82–1.87 (m, 2H, 2 CH), 1.93–2.04 (m, 2H, 2 CH), 2.17–2.22 (m, 2H, 2 CH), 2.34 (q, *J* = 7.6, 2H, CH$_3$C*H*$_2$), 3.46 (br s, 1H, OH), 4.85 (tt, *J* = 7.7, 3.6, 1H, 4-CH)	9.15 (CH_3), 26.29 (CH_2), 27.88 (CH$_3$*C*H$_2$), 33.97 (CH_2), 67.89 (C1), 69.14 (C4), 121.73 (CN), 174.27 (C=O)
cis-**4i**[a]	1.15 (t, *J* = 7.6, 3H, C*H*$_3$CH$_2$), 1.81–1.88 (m, 2H, 2 CH), 1.92–2.04 (m, 5H, 5 CH), 2.17–2.22 (m, 1H, CH), 2.32–2.37 (m, 2H, CH$_3$C*H*$_2$), 3.52 (br s, 1H, OH), 4.85 (tt, *J* = 5.6, 3.3, 1H, 4-CH)	9.15 (CH_3), 26.61 (CH_2), 27.89 (CH$_3$*C*H$_2$), 33.48 (CH_2), 67.88 (C1), 68.17 (C4), 121.49 (CN), 174.03 (C=O)
trans-**4j**	1.17 (d, *J* = 7.0, 6H, (C*H*$_3$)$_2$CH), 1.67–1.96 (m, 4H, 4 CH), 1.97–2.05 (m, 2H, 2 CH), 2.14–2.24 (m, 2H, 2 CH), 2.56 (q, *J* = 7.0, 1H, (CH$_3$)$_2$C*H*), 3.69 (br s, 1H, OH), 4.84 (tt, *J* = 7.4, 3.6, 1H, 4-CH)	18.96 (CH_3), 26.17, 33.86 (CH_2), 34.21 (CH), 67.81 (C1), 68.96 (C4), 121.81 (CN), 176.99 (C=O)
cis-**4j**	1.17 (d, *J* = 7.0, 6H, (C*H*$_3$)$_2$CH), 1.64–2.24 (m, 8H, 4 CH_2), 2.50–2.63 (m, 1H, (CH$_3$)$_2$C*H*), 3.84 (br s, 1H, OH), 4.91–5.04 (m, 1H, 4-CH)	18.96 (CH_3), 26.64, 33.48 (CH_2), 34.21 (CH), 67.59 (C1), 68.16 (C4), 121.81 (CN), 176.49 (C=O)
trans-**4k**	0.96 (t, *J* = 7.4, 3H, CH_3), 1.58–1.89 (m, 6H, 4 CH, CH$_3$C*H*$_2$CH$_2$), 1.96–2.06 (m, 2H, 2 CH), 2.10–2.24 (m, 2H, 2 CH), 2.30 (t, *J* = 7.4, 2H, CH$_3$CH$_2$C*H*$_2$), 3.80 (br s, 1H, OH), 4.94 (tt, *J* = 7.5, 3.6, 1H, 4-CH)	13.61 (CH_3), 18.53 (CH$_3$*C*H$_2$), 26.32, 33.95 (CH_2), 36.49 (CH$_3$CH$_2$*C*H$_2$), 67.86 (C1), 69.15 (C4), 121.78 (CN), 173.58 (C=O)
cis-**4k**	0.94–0.99 (m, 3H, CH_3), 1.63–1.71 (m, 2H, CH$_3$C*H*$_2$CH$_2$), 1.81–2.12 (m, 8H, 4 CH_2), 2.27–2.39 (m, 2H, CH$_3$CH$_2$C*H*$_2$), 3.82 (br s, 1H, OH), 4.94 (tt, *J* = 5.7, 3.4, 1H, 4-CH)	13.62 (CH_3), 18.53 (CH$_3$*C*H$_2$), 26.66, 33.53 (CH_2), 36.47 (CH$_3$CH$_2$*C*H$_2$), 67.76 (C1), 68.29 (C4), 121.57 (CN), 173.02 (C=O)
trans-**4l**[a]	1.20 (s, 9H, (CH$_3$)$_3$C), 1.71–1.78 (m, 1H, CH), 1.81–1.89 (m, 2H, 2 CH), 1.93–2.09 (m, 4H, 4 CH), 2.13–2.20 (m, 1H, CH), 3.32 (br s, 1H, OH), 4.81–4.85 (m, 1H, 4-CH)	26.68 (CH_2), 27.14 (CH_3), 33.45 (CH_2), 38.89 (*C*(CH$_3$)$_3$), 67.76 (C1), 68.75 (C4), 121.81 (CN), 178.18 (C=O)
cis-**4l**[a]	1.21 (s, 9H, (CH$_3$)$_3$C), 1.71–2.16 (m, 8H, 4 CH_2), 3.60 (br s, 1H, OH), 4.93 (s, 1H, 4-CH)	26.69 (CH_2), 27.18 (CH_3), 33.42 (CH_2), 38.91 (*C*(CH$_3$)$_3$), 67.31 (C1), 68.00 (C4), 121.41 (CN), 177.75 (C=O)

[a]500 MHz spectra.

Preparation of spirotetronic acids

As mentioned in the introduction, isomerically pure cyclohexanone cyanohydrins are important as starting compounds in the stereoselective synthesis of tetronic acids known as potent insecticides or herbicides (1). In a recent publication (15), we described the preparation of optically active 5,5-disubstituted tetronic acids starting from chiral ketone cyanohydrins. This reaction sequence, involving a Pinner reaction of the cyanohydrin to give the corresponding hydroxy ester, acylation of the hydroxyl group, and subsequent hexamethyldisilazanide (LiN(SiMe$_3$)$_2$) mediated ring closure at –78°C following a known procedure (16), could be applied also for the preparation of spirotetronic acids. The synthetic route to *cis*-spirotetronic acid **7** from cyanohydrin *cis*-**2c** is shown in Scheme 3.

In the (*S*)-MeHNL-catalyzed HCN addition to 4-propylcyclohexanone **1c**, cyanohydrin **2c** was isolated in an isomeric ratio *cis*:*trans* = 96:4 (Table 1). Compound **2c** was directly converted to hydroxy ester **5** by treatment with HCl in ethanol at 90–100°C with 84% yield (15). Acetylation of hydroxy ester **5** with acetic anhydride–pyridine and DMAP in dichloromethane gave acetoxy carboxylate **6** in 83% yield. The cyclization of **6**, resulting in the spirotetronic acid **7** with 73% yield, was performed by using LiN(SiMe$_3$)$_2$ in THF at –78°C. Recrystallization of **7** from chloroform gave a single crystal suitable for X-ray crystallographic analysis

© 2002 NRC Canada

Table 5. Elemental analysis of silylated cyanohydrins **4a**–**l**.

Compd	Mol. formula (Mol. weight)	Calcd./found C	H	N	Compd	Mol. formula (Mol. weight)	Calcd./found C	H	N
4a	$C_{13}H_{27}NO_2Si_2$	54.68	9.53	4.91	**4g**	$C_{17}H_{25}NO_2Si$	67.28	8.30	4.62
	(285.5)	54.53	9.47	5.08		(303.5)	67.19	8.21	4.58
4b	$C_{11}H_{21}NO_2Si$	58.11	9.31	6.16	**4h**	$C_{12}H_{21}NO_3Si$	56.44	8.29	5.48
	(227.4)	58.18	9.31	6.10		(255.4)	56.60	8.23	5.43
4c	$C_{12}H_{23}NO_2Si$	59.71	9.60	5.80	**4i**	$C_{13}H_{23}NO_3Si$	57.96	8.60	5.20
	(241.4)	59.53	9.65	5.79		(269.4)	58.04	8.60	5.05
4d	$C_{13}H_{25}NO_2Si$	61.13	9.86	5.48	**4j**	$C_{14}H_{25}NO_3Si$	59.33	8.89	4.94
	(255.4)	61.01	9.89	5.41		(283.4)	59.47	8.86	4.89
4e	$C_{14}H_{27}NO_2Si$	62.40	10.10	5.20	**4k**	$C_{14}H_{25}NO_3Si$	59.33	8.89	4.94
	(269.5)	62.48	10.01	5.34		(283.4)	59.31	8.85	4.70
4f	$C_{13}H_{23}NO_2Si$	61.61	9.15	5.53	**4l**	$C_{15}H_{27}NO_3Si$	60.56	9.15	4.71
	(253.4)	61.53	9.27	5.46		(297.5)	60.62	9.17	4.62

(17). The crystal structure unambiguously shows the *cis* conformation of the spirotetronic acid **7** (17).

Mechanistic interpretation of the *cis*/*trans* selectivity of MeHNL-catalyzed reactions

The stereoselectivity of the (*S*)-MeHNL-catalyzed reaction of 4-alkylcyclohexanones **1** can be explained as follows (2). From the X-ray crystal structure of (*S*)-MeHNL it is known that the active site is accessible via a narrow channel and consists of a small (S_1) and a larger (S_2) binding pocket (3*a*). In the active site the carbonyl group of the incoming substrate is fixed by hydrogen bonds from Thr11 and Ser80, as shown in the acetone-complexed MeHNL crystal structure (3*a*). The superposition of the catalytically inactive mutant MeHNL-Ser80Ala complexed with acetone cyanohydrin onto the MeHNL–acetone structure clearly reveals that the cyanohydrin is fixed in an analogous manner (3*b*). Cyclohexanones **1** are assumed to bind to the enzyme's active site in the channel either in an upright or a flat mode (2). In both cases, the cyanide ion attacks the substrate from the same direction, namely from below, giving either the *cis* isomer from the upright position or the *trans* isomer from the flat position. Taking into account the hydrogen bonding of the substrate and the chair-form of the cyclohexane ring with preferred equatorial 4-substituent R, in the case of cyclohexanones with a small R substituent, especially **1a** with R = Me, both positions in the channel are possible without unfavourable steric interactions between the substrate and the channel wall. Hence, the formation of both *cis* and *trans* isomers is possible. In this case, the percentage of the isomers varies and depends on enzyme activity and general reaction conditions. With increasing size of R, however, the upright binding mode is favored. As demonstrated by molecular modeling calculations of 4-*tert*-butylcyclohexanone cyanohydrin (**2e**), the flat position would lead to severe steric interactions between the substrate and the channel wall, whereas vertically arranged **2e** fits perfectly in the channel without unfavourable interactions (2). Hence, the formation of the *cis* isomer dominates.

Stereoselectivity of cyanohydrin formation from 4-alkoxy- and 4-alkanoyloxycyclohexanones 3

The improved *cis* stereoselectivity with increasing size of the R substituent is also observed for the MeHNL-catalyzed reactions of 4-alkyloxy-substituted homologues **3c**–**f**. Alkanoyloxy-substituted derivatives **3h**–**k**, however, gave only low *cis* selectivity in this addition reaction. A plausible interpretation of this result so far is not possible. Polar interactions and hydrogen bonding of the alkanoyloxy substituents with amino acids in the surrounding of the active site of the enzyme are assumed to be responsible for the different behavior in comparison with 4-alkylcyclohexanones **1**.

Since the reactions of the 4-isobutyloxy and the 4-benzyloxy derivatives (**3e** and **3g**) occur with relatively high *cis* selectivity, stereoisomerically pure *cis*-4-hydroxycyclohexanone cyanohydrin **4a** can be prepared either by hydrolysis or by hydrogenolytic cleavage of **3e** and **3g**, respectively.

As can be seen from Tables 1 and 3 and in contrast to MeHNL, the PaHNL-catalyzed addition of HCN to 4-substituted cyclohexanones **1** as well as **3** gives, in most cases, high *trans* selectivity independent of the kind of substituent. An explanation for PaHNL's high *trans* selectivity is not possible, since too little is known about its X-ray structure (18); a substrate–enzyme complex would be very helpful for the interpretation of our experimental results.

Experimental

General procedure for the preparation of cyclohexanones 3i–k

To a solution of **3a** (11.5 mmol) in CH_2Cl_2 (20 mL) or neat **3a** (13.1–15.4 mmol) was added pyridine (20–25 mL), DMAP (30–50 mg), and the respective acid chloride propionyl chloride and isobutyryl chloride (2 equiv) or butyric anhydride (2 equiv), and the reaction mixture was stirred for 3 h (**3i**, **3j**) or 5 h (**3k**) at room temperature. Then water (120 mL) was added, and the aqueous layer was extracted with diethyl ether (3 × 70 mL). The combined extracts were

© 2002 NRC Canada

washed with diluted HCl until neutral, dried (Na_2SO_4), and concentrated. The crude products were distilled.

4-Propionyloxycyclohexanone (3i)

Yield: 45%; bp 80–82°C (0.1 Torr). ^{1}H NMR (250 MHz, $CDCL_3$) δ: 1.18 (t, J = 7.6 Hz, 3H, C*H*$_3$CH$_2$), 2.00–2.17 (m, 4H, 4 CH), 2.30–2.43 (m, 4H, 4 CH), 2.49–2.62 (m, 2H, CH$_3$C*H*$_2$), 5.19 (quin, J = 4.8 Hz, 1H, 4-CH). ^{13}C NMR (63 MHz, $CDCL_3$) δ: 9.17 (CH_3), 27.84 (CH_3*C*H$_2$), 30.44, 37.27 (CH_2), 68.33 (C4), 173.81 (CO_2), 209.95 (CO).

4-Isobutyryloxycyclohexanone (3j)

Yield: 64%; bp 84–86°C (0.1 Torr). ^{1}H NMR (250 MHz, $CDCL_3$) δ: 1.20 (d, J = 7.0 Hz, 6H, 2 CH_3), 1.98–2.18 (m, 4H, 4 CH), 2.31–2.42 (m, 2H, 2 CH), 2.50–2.68 (m, 3H, (CH$_3$)$_2$C*H*, CH_2), 5.17 (tt, J = 5.6, 3.9 Hz, 1H, 4-CH). ^{13}C NMR (63 MHz, $CDCL_3$) δ: 19.01 (CH_3), 30.42 (CH_2), 34.21 (*C*H(CH$_3$)$_2$), 37.23 (CH_2), 68.10 (C4), 176.42 (CO_2), 209.94 (CO).

4-Butyryloxycyclohexanone (3k)

Yield: 65%; bp 91–93°C (0.1 Torr). ^{1}H NMR (250 MHz, $CDCL_3$) δ: 0.97 (t, J = 7.4 Hz, 3H, CH_3), 1.60–1.76 (m, 2H, CH$_2$C*H*$_2$CH$_3$), 1.96–2.17 (m, 4H, 4 CH), 2.31–2.42 (m, 4H, 4 CH), 2.49–2.61 (m, 2H, C*H*$_2$CH$_2$CH$_3$), 5.19 (quin, J = 4.8 Hz, 1H, 4-CH). ^{13}C NMR (63 MHz, $CDCL_3$) δ: 13.66 (CH_3), 18.56 (CH$_2$*C*H$_2$CH$_3$), 30.49 (CH_2), 36.46 (*C*H$_2$CH$_2$CH$_3$), 37.29 (CH_2), 173.02 (CO_2), 209.92 (CO).

General procedure for the (*R*)-PaHNL-catalyzed preparation of cyclohexanone cyanohydrins 2 and 4

A solution of (*R*)-PaHNL (19) (100 U per 100 mg support, total 200 U, 78 μL) was added to cellulose (Elcema-Cellulose P100PSC (Degussa); 1 g soaked in 10 mL of 0.02 M sodium citrate buffer, pH 3.3, for 2 h, and filtered off) followed by addition of diisopropyl ether (5 mL), substrate **1** or **3** (1 mmol), and HCN (20) (150 μL, 3.9 mmol). After stirring at room temperature for the times given in Tables 1 and 3, the support was filtered off, washed twice with diethyl ether, and the combined filtrates were concentrated under vacuum. For physical data see Tables 4 and 5.

General procedure for the (*S*)-MeHNL-catalyzed preparation of cyclohexanone cyanohydrins 2 and 4

A solution of (*S*)-MeHNL (21) (100 U per 100 mg support, total 180–200 U, 92–93 μL) was added to nitrocellulose [Blotting-Membrane (Schleicher & Schuell); 1 g, soaked in 50 mL of 0.02 M sodium citrate buffer, pH 3.3, for 0.5 h; the buffer was decanted and nitrocellulose centrifuged (5700 × *g* for 30 min) and dried under high vacuum for 5 h], followed after 15 min by addition of diisopropyl ether (5 mL), substrate **1** or **3** (1 mmol), and HCN (150 μL, 3.9 mmol). The reaction was performed as described above. For physical data see Tables 4 and 5.

Chemical reaction (blank experiment)

The chemical HCN addition was performed analogously with the enzymatic reaction, however, the enzyme solution was replaced by the same volume of 0.02 M sodium acetate buffer, pH 5.4. The reaction times correspond with those of the (*R*)-PaHNL-catalyzed reaction.

Determination of conversion and isomeric ratio

To a solution of crude **2** or **4** (10 μL) in CH_2Cl_2 (500 μL) was added acetic anhydride (50 μL) and DMAP (15 mg), and the reaction mixture was allowed to stand at room temperature for 15 min. The mixture was then filtered through a silica gel column (3 × 0.5 cm) with CH_2Cl_2 (4 mL). Conversion and isomeric ratio were directly determined from the filtrate by gas chromatography.

General procedure for the preparation of the nitrobenzoylated derivatives 2f′, 4b′, and 4h′

To a solution of **2f**, **4b**, or **4h** (0.35 mmol or 3.2–3.8 mmol, isomeric ratio given in Tables 1 and 3) in pyridine (5–30 mL) was added DMAP (ca. 0.1 equiv) and *p*-nitrobenzoyl chloride (1.5–2.0 equiv), and the reaction mixture was stirred for the given time. Then water (10 or 100 mL) was added, the layers were separated, and the aqueous layer was extracted with diethyl ether (3 × 50 mL). The combined extracts were washed with diluted HCl until neutral, dried (Na_2SO_4), and concentrated. The residue was chromatographed on silica gel with petroleum ether–ethyl acetate (3:1 to 10:1).

cis-*4-Isopropenyl-1-(4-nitrobenzoyloxy)cyclohexanecarbonitrile (2f′)*

Reaction time: 7 d at room temperature; mp 107°C (EtOH–CH_2Cl_2). ^{1}H NMR (500 MHz, $CDCL_3$) δ: 1.52–1.60 (m, 2H, 2 CH), 1.73 (s, 3H, CH_3), 1.84–1.87 (m, 2H, 2 CH), 2.02–2.08 (m, 3H, 3 CH), 2.75 (d, J = 13.2 Hz, 2H, 2 CH), 4.72 and 4.78 (each s, 1H, =CH_2), 8.21–8.35 (m, 4H, Ph). ^{13}C NMR (126 MHz, $CDCL_3$) δ: 20.98 (CH_3), 25.50, 34.26 (CH_2), 42.62 (C4), 71.51 (C1), 109.75 (=CH_2), 118.76 (CN), 123.86, 130.90, 134.44, 150.97 (Ph), 147.91 (C=), 162.38 (C=O).

trans-*4-Methoxy-1-(4-nitrobenzoyloxy)cyclohexanecarbonitrile (4b′)*

Reaction time: 3 h at 50°C; mp 146°C (MeOH). ^{1}H NMR (250 MHz, $CDCL_3$) δ: 1.81–2.57 (m, 8 H, 4 CH_2), 3.35–3.45 (m, 1H, 4-CH), 3.37 (s, 3H, CH_3O), 8.18–8.35 (m, 4H, Ph). ^{13}C NMR (63 MHz, $CDCL_3$) δ: 25.77, 30.81 (CH_2), 56.03 (CH_3O), 72.91 (C1), 74.19 (C4), 117.95 (CN), 123.78, 130.95, 134.40, 150.98 (Ph), 162.48 (C=O). Anal. calcd. for $C_{15}H_{16}N_2O_5$: C 59.21, H 5.30, N 9.21; found: C 59.29, H 5.37, N 8.97.

trans-4-Acetoxy-1-(4-nitrobenzoyloxy)cyclohexanecarbonitrile (4h′)

Reaction time: 7 d at room temperature; mp 173°C (EtOH). ^{1}H NMR (250 MHz, $CDCL_3$) δ: 1.84–2.10 (m, 4H, 4 CH), 2.10 (s, 3H, CH_3), 2.17–2.28 (m, 2H, 2 CH), 2.51–2.62 (m, 2H, 2 CH), 4.92 (tt, J = 7.4, 3.9 Hz, 1H, 4-CH), 8.18–8.36 (m, 4H, Ph). ^{13}C NMR (63 MHz, $CDCL_3$) δ: 21.22 (CH_3), 26.26, 31.45 (CH_2), 68.41 (C4), 72.55 (C1), 117.61 (CN), 123.82, 131.00, 134.15, 151.06 (Ph), 162.48 (PhC=O), 170.38 (CH_3C=O). Anal. calcd. for $C_{16}H_{16}N_2O_6$: C 57.83, H 4.85, N 8.43; found: C 57.66, H 4.89, N 8.34.

Ethyl *cis*-1-hydroxy-4-propylcyclohexanecarboxylate (5)

A solution of *cis*-**2c** (5.0 g, 29.9 mmol) in ethanolic HCl solution (60 mL) was stirred at 90–100°C for 16 h in a pressure vessel. To open the vessel, it was cooled with ice water.

© 2002 NRC Canada

The reaction mixture was diluted with diethyl ether (40 mL) and ice water was added until the white precipitate dissolved. The layers were separated and the aqueous layer was extracted three times with diethyl ether. The combined organic layers were washed with sat. $NaHCO_3$ solution, dried (Na_2SO_4), and concentrated. The residue was distilled under vacuum to give 5.4 g (84%) of **5**; bp 84°C (0.01 mm Hg). ^{1}H NMR (500 MHz, $CDCL_3$) δ: 0.88 (t, J = 7.3 Hz, 3H, CH_3CH_2), 1.19–1.38 (m, 10H), 1.60–1.81 (m, 6H), 2.92 (s, 1H, OH), 4.22 (q, J = 7.0 Hz, 2H, CH_3CH_2). ^{13}C NMR (126 MHz, $CDCL_3$) δ: 14.19, 14.34, 19.89, 27.54, 36.63, 39.34 (CH_3, CH_2), 61.66 (CH_3CH_2O), 73.99 (C-OH), 177.76 (C=O). Anal. calcd. for $C_{12}H_{22}O_3$: C 67.26, H 10.35; found: C 67.04, H 10.43.

Ethyl *cis*-1-acetyloxy-4-propylcyclohexanecarboxylate (6)

A solution of **5** (5.4 g, 25.2 mmol), pyridine (2 equiv), acetic anhydride (2 equiv), and a catalytic amount of DMAP in CH_2Cl_2 was heated under reflux for 1 h (GC control). The reaction mixture was concentrated, the residue was taken up in diethyl ether, and washed with 10% HCl solution, sat. $NaHCO_3$, and sat. NaCl solution, and then dried (Na_2SO_4) and concentrated. The residue was distilled under vacuum to give 5.4 g (83%) of **6**; bp 105°C (0.01 mm Hg). ^{1}H NMR (500 MHz, $CDCL_3$) δ: 0.88 (t, J = 7.2 Hz, 3H, CH_3CH_2), 1.12–1.35 (m, 10H), 1.63–1.76 (m, 4H), 2.09 (s, 3H, CH_3CO), 2.23 (dd, J = 14.9, 2.3 Hz, 2H, 2,6-CH_{eq}), 4.17 (q, J = 7.0 Hz, 2H, CH_3CH_2). ^{13}C NMR (126 MHz, $CDCL_3$) δ: 14.06, 14.31, 19.89, 21.14, 27.63, 31.85, 36.17, 39.16 (CH_3, CH_2), 61.08 (CH_3CH_2), 79.87 (C-O), 169.90, 172.89 (C=O). Anal. calcd. for $C_{14}H_{24}O_4$: C 65.60, H 9.44; found: C 65.58, H 9.43.

***cis*-4-Hydroxy-8-propyl-1-oxaspiro[4.5]dec-3-en-2-one (7)**

To a solution of $LiN(SiMe_3)_2$ [prepared from hexamethyldisilazane (3.3 mL, 16 mmol) and a 1.6 M solution of *n*-BuLi in hexane (10 mL, 16 mmol)] in THF (60 mL) at –78°C was added a solution of **6** (2.0 g, 7.8 mmol) in THF (20 mL) over 15 min. After stirring for 2 h (TLC control), water (20 mL) was added and the reaction mixture was allowed to warm to room temperature. The organic layer was extracted twice with sat. $NaHCO_3$ solution. The combined aqueous layers were adjusted to pH 1 with conc. HCl and extracted three times with ethyl acetate. The combined extracts were dried (Na_2SO_4) and concentrated. The residue was recrystallized from chloroform to give 1.2 g (73%) of **7** as colorless crystals; mp 218°C. ^{1}H NMR (250 MHz, DMSO-d_6) δ: 0.87 (t, J = 6.8 Hz, 3H, CH_3), 1.09–1.83 (m, 13H), 4.79 (s, 1H, =CH), 12.65 (br s, 1H, OH). ^{13}C NMR (126 MHz, DMSO-d_6) δ: 14.13, 19.28, 28.01, 32.35, 34.90 (CH_3, CH_2, CH), 82.57 (C-O), 86.33 (=CH), 172.04, 185.15 (C=O, C-OH). Anal. calcd. for $C_{12}H_{18}O_3$: C 68.55, H 8.63; found: C 68.46, H 8.70.

Acknowledgments

This work was supported by the Fonds der Chemischen Industrie and the Degussa AG. The authors thank the Bayer AG for donation of 4-alkylcyclohexanones, Dr. Wolfgang Frey for X-ray crystallographic analysis, and Dr. Angelika Baro for preparing the manuscript.

References

1. R. Fischer, B.W. Krüger, H.-J. Santel, M. Dollinger, U. Wachendorff-Neumann, and C. Erdelen. (Bayer AG). Ger. Offen. DE 4 337 853 (1995); Chem. Abs. **123**, 32947p (1995).
2. F. Effenberger, J. Roos, and C. Kobler. Angew. Chem. **114**, in print, (2002); Angew. Chem. Int. Ed. **41**, in print (2002).
3. (*a*) H. Lauble, S. Förster, B. Miehlich, H. Wajant, and F. Effenberger. Acta Crystallogr. **D57**, 194 (2001); (*b*) H. Lauble, B. Miehlich, S. Förster, H. Wajant, and F. Effenberger. Protein Sci. **10**, 1015 (2001).
4. (*a*) V. Prelog. Pure Appl. Chem. **9**, 119 (1964); (*b*) J.M.H. Graves, A. Clark, and H.J. Ringold. Biochemistry, **4**, 2655 (1965); (*c*) J.B. Jones. *In* Applications of biochemical systems in organic chemistry. Part 1. Wiley, N.Y. 1976. p. 15.
5. R.D. Desai, R.F. Hunter, G. Khan, and G.S. Saharia. J. Chem. Soc. 416 (1936).
6. G.A. Kraus and K. Frazier. J. Org. Chem. **45**, 4820 (1980).
7. L. Munday. J. Chem. Soc. 1413 (1964).
8. R.W. Freerksen and D.S. Watt. Synth. Commun. **6**, 447 (1976).
9. H. Ohno, A. Mori, and S. Inoue. Chem. Lett. 375 (1993).
10. (*a*) D.A. Evans and L.K. Truesdale. Tetrahedron Lett. 4929 (1973); (*b*) W. Lidy and W. Sundermeyer. Chem. Ber. **106**, 587 (1973); (*c*) D.A. Evans, J.M. Hoffman, and L.K. Truesdale. J. Am. Chem. Soc. **95**, 5822 (1973).
11. (*a*) D.A. Evans, G.L. Carroll, and L.K. Truesdale. J. Org. Chem. **39**, 914 (1974); (*b*) S. Matsubara, T. Takai, and K. Utimoto. Chem. Lett. 1447 (1991); (*c*) J.W. Faller and L.-L. Gundersen. Tetrahedron Lett. **34**, 2275 (1993).
12. S. Kaneko, N. Nakajima, T. Katoh, and S. Terashima. Chem. Pharm. Bull. **45**, 43 (1997).
13. (*a*) J.-C. Richer and R. Bisson. Can. J. Chem. **47**, 4399 (1969); (*b*) M. Mousseron, J.-M. Kamenka, and M.R. Darvich. Bull. Soc. Chim. Fr. 208 (1970); (*c*) O.H. Wheeler. J. Org. Chem. **29**, 3634 (1964); (*d*) A.S. Bloss, P.R. Brook, and R.M. Ellam. J. Chem. Soc. Perkin Trans 2, 2165 (1973); (*e*) R.A. Moss and C.B. Mallon. J. Org. Chem. **40**, 1368 (1975); (*f*) J.H. Rigby and C. Senanayake. J. Org. Chem. **53**, 440 (1988); (*g*) M. Majewski and J. MacKinnon. Can. J. Chem. **72**, 1699 (1994); (*h*) M. Haslanger and R.G. Lawton. Synth. Commun. **4**, 155 (1974); (*i*) H.C. Brown and F.G.M. Vogel. Liebigs Ann. Chem. 695 (1978).
14. (*a*) G.M. Sheldrick. SHELXL-93. Programm for refining crystal structures. University of Göttingen, Germany. 1993; (*b*) G.M. Sheldrick. Acta Crystallogr. **A46**, 467 (1990).
15. H. Bühler, A. Bayer, and F. Effenberger. Chem. Eur. J. **6**, 2564 (2000).
16. (*a*) T. Hiyama, H. Oishi, Y. Suetsugu, K. Nishide, and H. Saimoto. Bull. Chem. Soc. Jpn. **60**, 2139 (1987); (*b*) H. Ohta, Y. Kimura, and Y. Sugano. Tetrahedron Lett. **29**, 6957 (1988).
17. H. Bühler. Dissertation. University of Stuttgart, Germany. 2000.
18. I. Dreveny, K. Gruber, A. Glieder, A. Thompson, and C. Kratky. Structure (Cambridge), **9**, 803 (2001).
19. H. Lauble, K. Müller, H. Schindelin, S. Förster, and F. Effenberger. Proteins: Structure, Function, and Genetics, **19**, 343 (1994).
20. P. Kurtz. *In* Houben-Weyl, Methoden der Organischen Chemie. Vol. 8. 4th ed. Thieme, Stuttgart. 1952. p. 255.
21. S. Förster, J. Roos, F. Effenberger, H. Wajant, and A. Sprauer. Angew. Chem. **108**, 493 (1996); Angew. Chem. Int. Ed. Engl. **35**, 437 (1996).

© 2002 NRC Canada

Tailoring the substrate specificity of secondary alcohol dehydrogenase

Robert S. Phillips

Abstract: Our research with the thermophilic secondary-alcohol dehydrogenase (SADH) from *Thermoanaerobacter ethanolicus* has provided novel information regarding the physical basis of enzyme substrate specificity and stereospecificity. We demonstrated that oxidation of secondary alcohols catalyzed by *T. ethanolicus* SADH exhibits temperature-dependent enantiospecificity. In other studies, we found that the structure of co-factor analogs also significantly affects the stereochemistry of the SADH reaction. More recently, we demonstrated that pH can also have a modest effect on SADH enantiospecificity. Organic solvents have also been shown by others to affect the stereochemistry of SADH reactions. We designed and prepared S39T and C295A mutant forms of SADH by site-directed mutagenesis, and we evaluated the effects of the mutations by analysis of the temperature dependence of the enantiomeric ratio (*E*) for simple chiral alcohols such as 2-butanol. This procedure allows for the determination of the differential Eyring parameters ($\Delta\Delta H^{\ddagger}$ and $\Delta\Delta S^{\ddagger}$) for the reaction. We demonstrated that this technique is a sensitive method for analysis of the effects of mutation on enzyme stereospecificity. S39T and C295A SADH exhibit significant changes in substrate specificity and stereospecificity consistent with the changes in the volume of the alkyl-binding pockets. Thus, it is possible to alter the substrate specificity and stereospecificity of alcohol dehydrogenase by changing either the reaction medium or the protein structure.

Key words: alcohol dehydrogenase, substrate specificity, stereospecificity, temperature dependence, site-directed mutagenesis.

Resumé : Dans le cadre de nos travaux sur la déshydrogénase d'alcools secondaires thermophile (« SADH ») provenant de *Thermoanaerobacter ethanolicus*, on a obtenu de nouvelles informations concernant la base physique pour la spécificité et la stéréospécificité de l'enzyme vis-à-vis des substrats. On a démontré que l'oxydation d'alcools secondaires catalysées par la déshydrogénase d'alcools secondaires provenant de *T. ethanolicus* présente une énantiospécificité qui dépend de la température. Dans d'autres études, on a trouvé que la structure des analogues du cofacteur affecte aussi de façon significative la stéréochimie de la réaction de la « SADH ». Plus récemment, on a démontré que le pH peut aussi avoir un modeste effet sur l'énantiospécificité des réactions de la « SADH ». On a mis au point et préparé les formes mutantes S39T et C295A de la « SADH » en faisant appel à de la mutagénèse orientée vers le site et, à l'aide d'alcools chiraux simples tel le butan-2-ol, on a évalué les effets des mutations par l'analyse du rapport énantiomérique sur la dépendance de la température, E. Cette procédure permet de déterminer les paramètres différentiels d'Eyring, $\Delta\Delta H^{\ddagger}$ et $\Delta\Delta S^{\ddagger}$ pour la réaction. On a démontré que cette technique s'avère une méthode sensible pour l'analyse des effets de mutation sur la stéréospécificité des enzymes. Les formes S39T et C295A de la « SADH » présentent des différences significatives de spécificité et de stéréospécificité qui sont en accord avec des changements dans le volume des poches qui lient les groupes alkyles. Il est donc possible de modifier la spécificité du substrat et la stéréospécificité de la déshydrogénase d'alcool en changeant le milieu réactionnel ou la structure de la protéine.

Mots clés : déshydrogénase d'alcool, spécificité du substrat, stéréospécificité, dépendance sur la température, mutagénèse orientée vers le site.

[Traduit par la Rédaction]

Introduction

Enzymes are remarkable not only for their catalytic efficiencies, but also for their high stereospecificities. This stereospecificity has been studied for more than a century, and in 1894 was central in the formulation of Emil Fisher's (1) seminal "lock and key" hypothesis for enzyme action. More recently, Ogston (2) developed his "three-point attachment" hypothesis to explain enzymatic stereospecificity. It is now recognized, however, that stereospecificity can be explained by only a single-point contact between two asymmetric molecules (3).

Alcohol dehydrogenases (ADHs) have served as a paradigm for the study of stereochemistry of enzymatic reactions.

Received 13 December 2001. Published on the NRC Research Press Web site at http://canjchem.nrc.ca on 29 May 2002.

Dedicated to Professor J. Bryan Jones on the occasion of his 65th birthday.

R.S. Phillips. Departments of Chemistry and of Biochemistry and Molecular Biology and Center for Metalloenzyme Studies, University of Georgia, Athens, GA 30602–2556, U.S.A.
(e-mail: rsphillips@chem.uga.edu).

 DOI: 10.1139/V02-103 © 2002 NRC Canada

The seminal work of Vennesland and co-workers (4) and Westheimer et al. (5) with yeast ADH demonstrated that the enzyme is stereospecific for the faces of the NADH dihydropyridine ring, as well as for the enantiotopic C–H bonds of ethanol. Prelog (6) studied the stereoselectivities of horse liver and microbial ADHs in cyclic ketone reduction, and found that most ADHs reduce ketones by hydride transfer to the pro-*R* face of the carbonyl, producing (*S*)-alcohols. This generalization, known as "Prelog's Rule," is still in widespread use. An empirical structural model of the horse liver ADH (HLADH) active site, known as the "diamond lattice section," was developed by Prelog (6) and further extended by Jones and co-workers (7). This model was used quite successfully by Jones (8) in predicting substrate activity and the stereochemistry of ADH. HLADH, however, has low activity toward most acyclic ketones, is not thermally stable or stable to immobilization, and is unstable in the presence of organic solvents. There has therefore been a need for more active and robust ADHs for synthetic applications. In this regard, ADHs isolated from thermophilic microorganisms have been especially interesting, since they are highly active with ketones, exhibit high thermal stability, and are stable upon immobilization and (or) in the presence of organic solvents. Thus, the thermophilic *Thermoanaerobacter brockii* ADH (TBADH) has been successfully used to synthesize several chiral compounds of interest (9–11).

Discussion

Effects of physical variables on stereochemistry of alcohol dehydrogenases — reaction medium engineering

We have been studying the effects of temperature and other physical variables on stereochemistry of enzymatic reactions. The stereospecificity of any enzymatic reaction can be defined by the enantiomeric ratio (*E*, eq. [1]) (12). (Note that the term "stereospecific" as used in organic chemistry refers to the difference between the reaction rates or products arising from pre-existing isomers (13). On the other hand, if a chiral center is formed during the reaction, and if the product favors one enantiomer, it is said to be "stereoselective" (13). By this definition, ADHs are stereospecific in the oxidation direction, but stereoselective in the reduction direction.) Under kinetic control, the ratio of observed products is equivalent to the ratio of the rate constants (k_{cat}/K_m) of formation (or reaction) of the enantiomers. The differential free energy of activation ($\Delta\Delta G^{\ddagger}$) is given by eq. [2]. The temperature dependence of $\Delta\Delta G^{\ddagger}$ can be given by the thermodynamic relationship in eq. [3]. Combining eqs. [2] and [3], one can write eq. [4].

$$[1] \qquad E = R/S = (k_{cat}/K_m)_R/(k_{cat}/K_m)_S$$

$$[2] \qquad \Delta\Delta G^{\ddagger} = -RT \ln E = \Delta G^{\ddagger}_R - \Delta G^{\ddagger}_S$$

$$[3] \qquad \Delta\Delta G^{\ddagger} = \Delta\Delta H^{\ddagger} - T\Delta\Delta S^{\ddagger}$$

$$[4] \qquad -RT \ln E = \Delta\Delta H^{\ddagger} - T\Delta\Delta S^{\ddagger}$$

$$[5] \qquad T_r = \Delta\Delta H^{\ddagger}/\Delta\Delta S^{\ddagger}$$

Thus, a plot of $-RT \ln E$ vs. T for the reaction of a pair of enantiomers is predicted to be linear, with a slope of $\Delta\Delta S^{\ddagger}$ and an intercept of $\Delta\Delta H^{\ddagger}$ (14, 15). If there is no enantiospecificity in a reaction, $E = 1$ and therefore $\Delta\Delta G^{\ddagger} = 0$. Equation [3] then can be rearranged to eq. [5], where T_r is the "racemic temperature," at which there will be no stereochemical discrimination in the reaction. If the differential activation enthalpy and activation entropy have the same sign (and thus favor different enantiomers), at temperatures below T_r, the stereochemical course of the reaction is dominated by the activation enthalpy difference, and the stereochemical purity of products is expected to decrease with increasing temperature. At temperatures above T_r, the reaction is controlled by the activation entropy difference, and the stereochemical purity of the reaction products increases with increasing temperature. The major product obtained at $T > T_r$ will, however, be the antipode to that obtained at $T < T_r$, and a temperature-dependent reversal of stereochemical configuration is predicted.

We demonstrated that 2-butanol oxidation catalyzed by *Thermoanaerobacter ethanolicus* SADH exhibits temperature-dependent enantiospecificity (14, 15). The T_r is 26°C for 2-butanol; at lower temperatures, the preferred substrate is (*S*)-2-butanol, but at higher temperatures (*R*)-2-butanol is preferred. For 2-pentanol, T_r is ~100°C, so the preferred substrate is the (*S*)-enantiomer throughout the normal range of the study. Thus, our work established the physical basis of the substrate size-dependent reversal of stereochemical configuration previously observed empirically at a single temperature by Keinan and co-workers (9). This temperature dependence of enantiospecificity is due to a dichotomy between the activation enthalpies and activation entropies for the enantiomers. (*S*)-Alcohols exhibit lower activation enthalpies, probably due to better van der Waals surface contacts with the active site. In contrast, (*R*)-alcohols have lower activation entropies, and they may become the favored substrates (or products in the reduction direction) at higher temperatures. This lower entropy may be either the result of less restricted freedom of movement of the substrate and enzyme side chains in the complex, and hence in the transition state(s) of the reaction, or the result of differences in active-site desolvation upon binding of the enantiomeric substrates. These results demonstrated that the stereoselectivity of enzymatic reactions is not solely due to enthalpic factors, and that the activation entropy may be equally important. This work was the first analysis of this kind performed for an enzymatic reaction. In recent years, a number of investigators have applied our method to other enzymes, especially lipases, and it was observed that entropy is often the main contributor to the differential activation free energy ($\Delta\Delta G^{\ddagger}$) (16–18).

In other studies, we found that the structure of the co-factor analogs also significantly affects the stereochemistry of the SADH reaction (19). For 2-butanone reduction at 37°C, the stereochemical purity of the (*R*)-2-butanol product increases from $E = 1.9$ with NADP as the co-factor to $E = 9$ using the co-factor analog, 3-acetylpyridineadeninedinucleotide phosphate (APADP). As expected, *E* values increase when (*R*)- and (*S*)-2-butanol oxidations are followed using APADP or thio-NADP as the co-factor, rather than NADP. Even NAD shows a significant increase in the (*R*)-preference compared with NADP, although the activity is relatively low. The effects of co-factor and temperature are additive; reactions catalyzed using co-factor analogues show a linear

© 2002 NRC Canada

Fig. 1. Sequence alignment of alcohol dehydrogenases. Human liver ADH β (huladhb); human liver ADH γ (huladhg); human liver ADH α (huladha); *T. ethanolicus* SADH (S71131); *T. brockii* SADH (P14941); *C. beijerinckii* SADH (P25984). This figure was prepared using PILEUP (30).

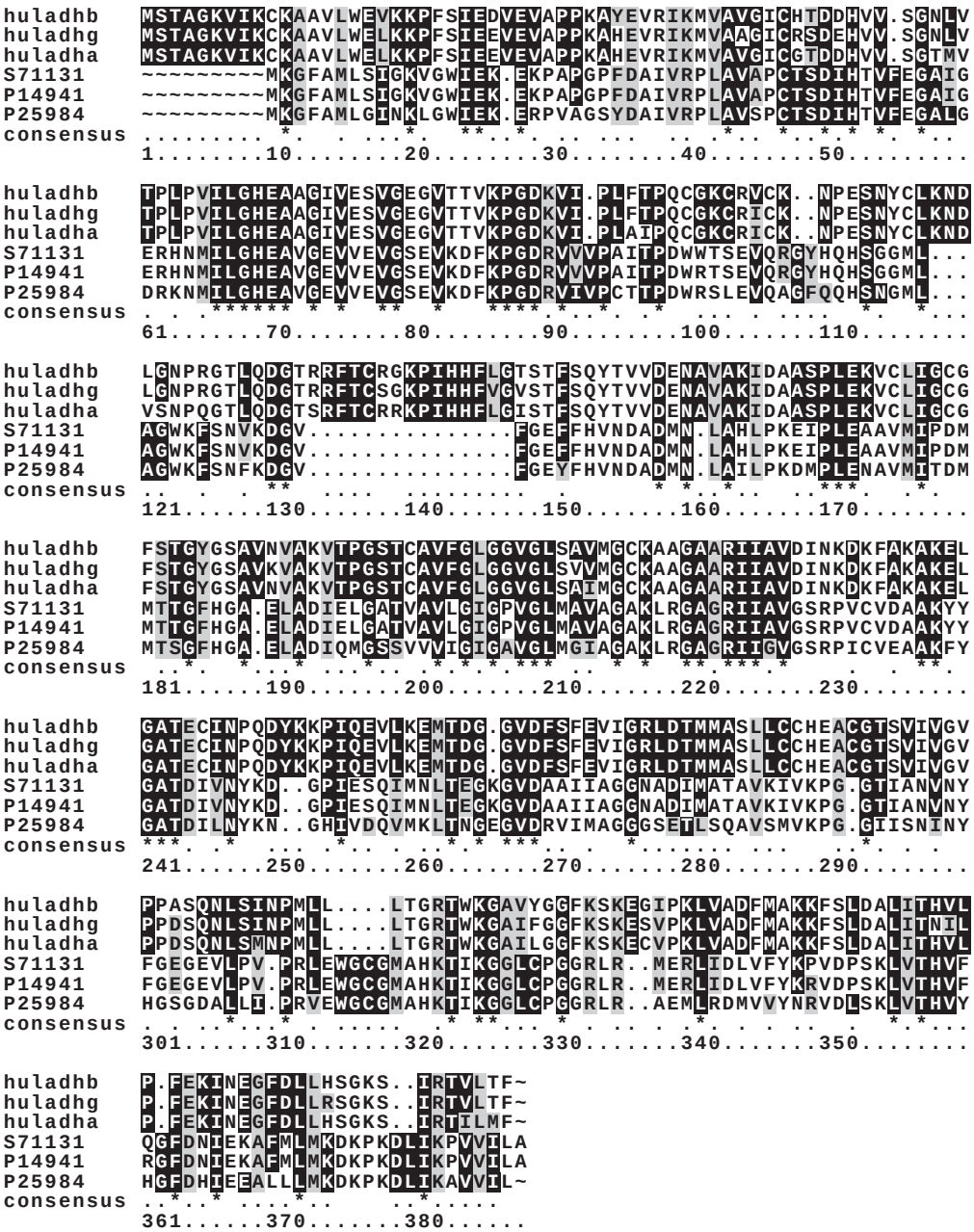

dependence of –RT ln E vs. T, similar to that in the presence of NADP but shifted to more negative values (19).

We also evaluated the effects of chain length on k_{cat}/K_m for a series of (*R*)- and (*S*)-alcohols (15). For the (*S*)-alcohols, a linear free-energy relationship holds when ln (k_{cat}/K_m) is plotted against chain length of the large substituent. This result implies a constant mechanism for the (*S*)-alcohols. In contrast, the (*R*)-alcohols exhibit a convex plot, which implies that the rate-determining step changes with chain length. The slope of the (*S*)-alcohols plot gives $\Delta\Delta G_n^{\ddagger}$, which is the change in activation free energy per methylene group. This parameter was calculated between 20 to 60°C, and $\Delta\Delta H_n^{\ddagger}$ and $\Delta\Delta S_n^{\ddagger}$ were determined. $\Delta\Delta H_n^{\ddagger}$ was –3.3 kcal mol^{-1}, indicating that each methylene contributes binding energy toward the reaction, and that there are no unfavorable steric contacts. $\Delta\Delta S_n^{\ddagger}$ was –13 cal mol^{-1} deg^{-1}, and hence contributes negatively to catalysis. The decreasing rate for the (*S*)-alcohols with increasing chain length is due to this unfavorable entropy, which in turn is likely due to restricted freedom of rotation of the longer chains in the bound substrate. Thus, entropy emerges as a controlling factor for both stereospecificity and substrate specificity of SADH.

More recently, we demonstrated that pH can also have a modest effect on SADH enantiospecificity (20). For a simple enzyme mechanism using a general base catalytic group, where only the unprotonated enzyme can productively bind

© 2002 NRC Canada

Fig. 2. Active site of *T. brockii* ADH showing the surface of the small alkyl-binding pocket, located behind and to the left of the nicotinamide ring (thick-stick structure in the center). This figure was prepared using PyMOL (DeLano Scientific) with the coordinates of 1YKF.pdb.

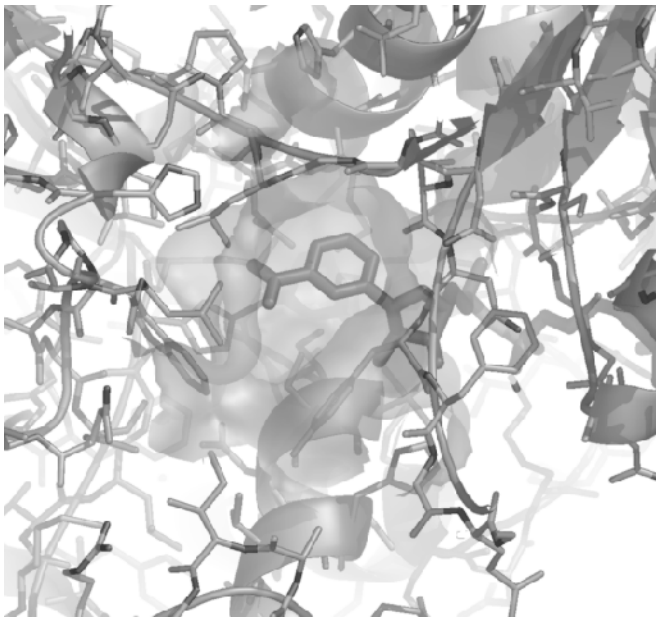

the substrate, k_{cat}/K_m is expected to vary with pH according to eq. [6], where K_1 is the acidity constant of the ionizable basic catalytic group on the protein.

$$[6] \qquad (k_{cat}/K_m)_{obs} = (k_{cat}/K_m)K_1/([H^+] + K_1)$$

If, however, the complete kinetic mechanism is operating so substrates can bind to either the protonated or unprotonated enzyme, and substrates are "sticky" (i.e., reaction to products is as fast as or faster than release of unreacted substrate), the apparent ionization constant (K_1) will shift by a factor of ($1 + C$), where C is the ratio of the rate constant of conversion of enzyme-bound substrate to product over the rate constant of the substrate released from the enzyme. The effect of this commitment is a shifting of the observed pK_a to lower pH by log ($1 + C$)[(pK_a)$_{obs}$ = pK_a – log ($1 + C$)]. In the presence of a catalytic commitment, the pH dependence is described by eq. [7]. For the reaction of enantiomeric substrates under kinetically controlled conditions, the enantiomeric ratio (E) is given by eq. [1]. Substitution of eq. [7] into eq. [1] gives eq. [8], which describes the effect of pH on E.

$$[7] \qquad (k_{cat}/K_m)_{obs} = (k_{cat}/K_m)K_1(1 + C)/([H^+] + K_1(1 + C))$$

$$[8] \qquad E = \left[\frac{(k_{cat}/K_m)_R K_1(1 + C_R)}{([H^+] + K_1(1 + C_R)}\right] \div \left[\frac{(k_{cat}/K_m)_S K_1(1 + C_S)}{([H^+] + K_1(1 + C_S)}\right]$$

$$[9] \qquad E = [(k_{cat}/K_m)_R(1 + C_R)]/[(k_{cat}/K_m)_S(1 + C_S)]$$

At $[H^+] << K_1$, eq. [8] reduces to eq. [1], which is the intrinsic ratio of the k_{cat}/K_m values. But at $[H^+] >> K_1$, eq. [8] will reduce to eq. [9], which contains the commitment ratio $[(1 + C_R)/(1 + C_S)]$ as well as the k_{cat}/K_m ratio. C_R and C_S are used to designate the commitments for substrate (R)- and (S)-enantiomers, respectively. Thus, if commitments for the enantiomeric substrates are significantly different, E can be pH dependent, varying between the values defined by eqs. [1] and [9]. Horse liver ADH does not show any effect of pH on enantiospecificity (E = 0.26) in the reaction of (R) and (S)-2-butanol, since identical pK_as of 8.0 are seen for both enantiomers (20). In contrast, the reaction of SADH with these alcohols shows a modest but significant influence of pH on enantiospecificity. At 65°C, the pK_a for the reaction of SADH with 1-propanol, which is a poor substrate and hence has a low commitment, is 6.82 ± 0.11. This pK_a value should be the true thermodynamic value. At 65°C, the reaction of (R)-2-butanol exhibits a pK_a of 6.60 ± 0.10, while that of (S)-2-butanol exhibits a pK_a of 6.85 ± 0.15. As a result, the E value for 2-butanol increases from 2.5 at pH 9 to 4.2 at pH 5.5.

The effects of solvents on the stereoselectivity of ADH reactions have been examined by two groups. Simpson and Cowan (21) examined the effects of polar water-miscible solvents, such as acetonitrile, methanol, and dimethylformamide, on the reduction of ketones by a secondary ADH from *Thermoanaerobacterium sp*. Addition of

Table 1. Reduction of ethynyl ketones by C295A and wild-type SADH.

Entry	Substrate	Yield[a] (%)	Abs. conf.[a]	E [a,b]
1	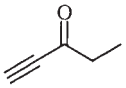	39 (32)	*S* (*S*)	0.14 (0.10)
2	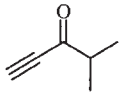	88 (50)	*S* (*S*)	<0.01 (<0.01)
3	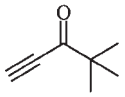	39 (0)	*S* (*S*)	0.08 (0.08)
4	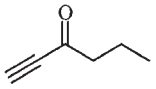	51 (28)	*S* (*S*)	0.14 (0.32)
5	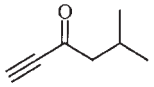	42 (20)	*S* (*R*)	0.28 (3.0)
6	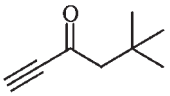	0 (0)	— (*R*)	— (4.88)
7	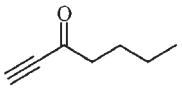	60 (32)	*S* (*R*)	0.20 (2.45)
8	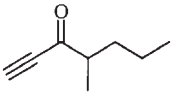	43 (0)[c]	*S* (–)	<0.01 (–)
9	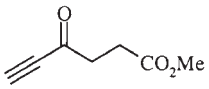	23 (35)	*R* (*R*)	4.0 (10.1)

Note: Data from ref. 29.
[a]Values for wild-type SADH are given in parentheses.
[b]$E = R/S$.
[c]The product is a 2:1 mixture of (2*S*,3*S*) and (2*S*,3*R*) diastereomers.

© 2002 NRC Canada

Table 2. Differential Eyring parameters for C295A, wild-type, and S39T SADH with secondary alcohols.

	C295A SADH		Wild-type SADH		S39T SADH	
Substrate	$\Delta\Delta H^{\ddagger}$ (kcal mol^{-1})	$\Delta\Delta S^{\ddagger}$ (cal mol^{-1} deg^{-1})	$\Delta\Delta H^{\ddagger}$ (kcal mol^{-1})	$\Delta\Delta S^{\ddagger}$ (cal mol^{-1} deg^{-1})	$\Delta\Delta H^{\ddagger}$ (kcal mol^{-1})	$\Delta\Delta S^{\ddagger}$ (cal mol^{-1} deg^{-1})
2-Butanol	–0.6 ± 0.5	–1.2 ± 1.5	8.2 ± 1.0	27.6 ± 3.4	1.9 ± 0.4	10.4 ± 1.3
2-Pentanol	0.7 ± 0.3	2.4 ± 1.2	2.8 ± 0.4	7.3 ± 1.2	0.60 ± 0.15	2.9 ± 0.5
2-Hexanol	0.3 ± 0.4	–0.5 ± 1.1	5.8 ± 0.2	11.4 ± 0.7	—	—

Fig. 3. Temperature dependence of stereospecificity for wild-type and C295A SADH (29). 2-Butanol (circles); 2-pentanol (squares); 2-hexanol (diamonds). Wild-type SADH (open symbols and dashed lines); C295A SADH (filled symbols and solids lines).

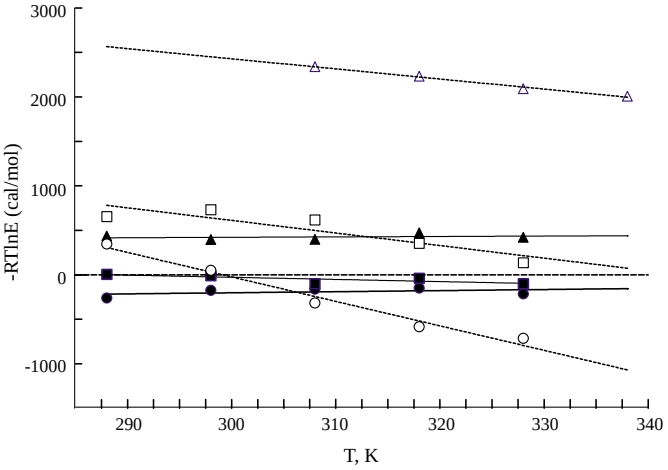

acetonitrile was found to increase the (*R*)-specificity for 2-butanol, from $E = 1.8$ without acetonitrile to $E = 4.7$ at 40% (v/v) acetonitrile. Jonsson et al. (22) studied the reduction of 2-pentanone by TBADH in hexane, hexane–water biphasic medium, and water. They found that the activity was much lower, and the stereoselectivity for reduction of 2-pentanone to 2-pentanol was considerably reduced in hexane at a low water activity ($a = 0.53$). The low enzyme activity at low water activity is associated with a large negative reaction entropy. The authors attributed these solvent effects to decreased flexibility of the enzyme in the non-aqueous medium.

Preparation of mutant SADHs with altered substrate specificity and stereospecificity — protein engineering

The ADH from mammalian liver and the SADHs from microorganisms are members of the "medium-chain" family of ADHs. Figure 1 shows the sequence alignment of human α, β, and γ forms of liver ADH, and the *T. ethanolicus*, *T. brockii*, and *Clostridium beijerinckii* ADHs. There is a relatively high-sequence identity between human and bacterial ADHs, with the residues of the catalytic zinc site especially conserved. The zinc is bound to Cys-47 in the consensus sequence and to His-69, both of which are conserved. The third zinc ligand, however, is consensus residue 179, which is Cys for the mammalian enzymes, but Asp for the bacterial enzymes. The structural zinc site seen in mammalian ADHs is not found in the microbial enzymes. The SADH S39T mutation was performed and the mutant protein was characterized (23). Ser-39 in SADH corresponds to Ser-49 in the sequence of horse liver ADH and Thr-49 in the sequence of α-human liver ADH (Fig. 1). This serine–threonine residue (49 in the consensus sequence in Fig. 1) is conserved in all members of this ADH family, and it is apparently required as part of a proton shuttle to allow protons to go in and out of the active site and facilitate substrate binding and catalysis (24). Mutation of this conserved serine–threonine to alanine results in the complete loss of activity in human liver ADH (25). We were interested in the effect of the S39T mutation on SADH stereospecificity, since there was a report that α-human liver ADH has greater (*R*)-specificity than horse liver ADH or β-human liver ADH (26). Interestingly, the specific activity of S39T SADH is about 50% higher than wild-type SADH with 2-propanol (23). This result is consistent with the report that the corresponding T40S mutation in *B. stearothermophilus* ADH reduced its activity by about 30% (24). Furthermore, the mutation of this threonine of β-human liver ADH to serine results in significantly greater reactivity with cyclohexanol and steroidal alcohols than the wild-type enzyme (26). Analysis of the temperature dependence of stereospecificity of S39T SADH for 2-butanol demonstrated a dramatic decrease in the T_r, from 26 to –110°C (23). Correspondingly, the (*R*)-selectivity for 2-butanone reduction has increased at 50°C from $E = 2.3$ to $E = 19$. This is consistent with the location in the crystal structure of Ser-39 in the large alkyl-group binding pocket, so the mutation to Thr increases the steric restraints in the large pocket, favoring the reaction of the (*R*)-alcohol. In the case of 2-pentanol, the effect of the S39T mutation is even more dramatic, reversing the preferred configuration from (*S*) to (*R*) throughout the temperature range studied (20–60°C). Interestingly, the value of k_{cat}/K_m of both enantiomers of 2-pentanol is greater with S39T SADH than with the wild-type enzyme, but the activity of (*R*)-2-pentanol is increased to a greater extent than (*S*)-2-pentanol.

Recently, we prepared the C295A mutant SADH, based on the results of modeling studies of the wild-type crystal structure with ethynyl ketoester substrates (28). Cys-295 was predicted to make up part of the putative small alkyl-group binding pocket, together with Ala-85 and Ile-86. As expected, these residues are not highly conserved, since they are not directly involved in catalysis. Cys-295 (residue 329 in the consensus sequence in Fig. 1) is replaced by the bulkier Tyr, Phe, or Leu in the human liver enzymes. The crystal structure of TBADH, showing the position of the small hydrophobic pocket as the surface just behind and to the left of the nicotinamide ring, is shown in Fig. 2. C295A SADH has specific activity with 2-propanol, which is about half that of wild-type SADH, but exhibits significant differences in both substrate specificity and stereospecificity, as shown in Table 1 (28). Wild-type SADH will reduce ethynyl ketones to (*R*)-alcohols if the alkyl group is propyl, isopropyl, or

© 2002 NRC Canada

smaller (Table 1) (27). Ethynyl ketones with butyl or larger alkyl groups provide (*S*)-alcohols upon reduction. Thus, the small alkyl pocket can only comfortably accommodate alkyl groups with three carbons or less. The stereoselectivity of C295A SADH is reversed for *n*-butyl and isobutyl ethynyl ketones, demonstrating that the C295A mutant enzyme has a larger hydrophobic pocket (Table 1). Even more striking, wild-type SADH does not reduce ketones with large α-branched substituents, such as 4-methyl-1-heptyn-3-one, at a rate that is synthetically useful. This racemic ketone, however, is an excellent substrate of C295A SADH, and is rapidly reduced to give a 2:1 mixture of enantiomerically pure (2*S*,3*S*) and (2*S*,3*R*) diastereomers of 4-methyl-1-heptyn-3-ol, in good chemical yield (Table 1) (28). Thus, the result shows that α-branching is not tolerated by wild-type SADH in the large alkyl substituent, likely due to unfavorable steric interactions with the nicotinamide ring of NADP, but in the C295A mutant SADH, the *sec*-pentyl substituent can fit into the small hydrophobic pocket. These results demonstrate that dramatic changes in substrate specificity of SADH can be achieved with only single-point mutations.

Remarkably, in sharp contrast to wild-type and S39T SADH, C295A SADH shows much lower temperature dependence of *E* values for 2-butanol, 2-pentanol, and 2-hexanol (Fig. 3) (29). The $\Delta\Delta H^{\ddagger}$ and $\Delta\Delta S^{\ddagger}$ values for 2-butanol with C295A SADH are dramatically reduced (Table 2). While the change in $\Delta\Delta H^{\ddagger}$ was expected as a result of the C295A mutation, the change in $\Delta\Delta S^{\ddagger}$ was unexpected. Close examination of the crystal structures of *T. brockii* ADH revealed a water molecule bound in the small alkyl binding pocket, 4 Å from the cysteinyl sulfur of Cys-295. This water molecule will evidently be expelled to the bulk solvent by the binding of a large substituent in the small pocket. Thus, the entropy term is likely due at least in part to the differential expulsion of this water by substrate (*R*)-enantiomers. Mutation of Cys-295 to alanine apparently prevents the binding of this water in the small alkyl binding pocket, eliminating the entropy. This result, together with the reversal of stereochemistry observed in the reduction of isobutyl ketones, provides strong evidence that Cys-295 is in the small hydrophobic pocket of SADH. The study of mutations of Cys-295 of SADH to other amino acids is currently in progress.

Conclusions

The stereospecificity of SADH from *T. ethanolicus* is influenced by temperature, co-factor structure, pH, and organic solvents. Furthermore, mutations of the amino acids in the proposed alkyl-group binding pockets can change both substrate specificity and stereospecificity, consistent with the changes in the volume of the alkyl-binding pockets. It is therefore possible to alter the substrate specificity and stereospecificity of alcohol dehydrogenases by changing either the reaction medium or the protein structure.

References

1. E. Fischer. Ber. Dt. Chem. Ges. **27**, 2985 (1894).
2. A.G. Ogston. Nature (London), **162**, 963 (1948).
3. S. Topiol. Chirality, **1**, 69 (1989).
4. F.A. Loewus, F.H.Westheimer, and B.Vennesland. J. Am. Chem. Soc. **75**, 5018 (1951).
5. F.H. Westheimer, H.F. Fischer, E.E. Conn, and B. Vennesland. J. Am. Chem. Soc. **73**, 2403 (1951).
6. V. Prelog. Pure Appl Chem. **9**, 119 (1964).
7. A.J. Irwin, K.P. Lok, K.W. Huang, and J.B. Jones. J. Chem. Soc. Perkin 1, 1636 (1978).
8. J.B. Jones. Tetrahedron Lett. **42**, 3351 (1986).
9. E. Keinan, E.K. Hafeli, K.K. Seth, and R. Lamed. J. Am. Chem. Soc. **108**, 162 (1986).
10. D.G. Drueckhammer, C.F. Barbas, III, K. Nozaki, C.-H. Wong, C.Y. Wood, and M.A. Ciufolini. J. Org. Chem. **53**, 1607 (1988).
11. C.-H. Wong, D.G. Drueckhammer, and H.M. Sweers. J. Am. Chem. Soc. **107**, 4028 (1985).
12. C.-S. Chen, Y. Fujimoto, G. Girdaukas, and C.J. Sih. J. Am. Chem. Soc. **104**, 7294 (1982).
13. E.L. Eliel and S.H. Wilen. *In* Stereochemistry of organic compounds. Wiley-Interface, New York. 1994. p. 837.
14. V.T. Pham, R.S. Phillips, and L.G. Ljungdahl. J. Am. Chem. Soc. **111**, 1935 (1989).
15. V.T. Pham and R.S. Phillips. J. Am. Chem. Soc. **112**, 3629 (1990).
16. P.L.A. Overbeeke, S.C. Orrenius, J.A. Jongejan, and J.A. Duine. Chem. Phys. Lipids, **93**, 81 (1998).
17. T. Sakai, T. Kishimoto, Y. Tanaka, T. Ema, and M. Utaka. Tetrahedron Letts. **39**, 7881 (1998).
18. A. Avdagic, A. Lesac, Z. Majer, M. Hollosi, and V. Sunjic. Helv. Chim. Acta, **81**, 1567 (1998).
19. C. Zheng and R.S. Phillips. J. Chem. Soc. Perkin Trans. 1, 1083 (1992).
20. F. Secundo and R.S. Phillips. Enz. Microb. Technol. **19**, 487 (1996).
21. H.D. Simpson and D.A. Cowan. Prot. Pept. Letters, **4**, 25 (1997).
22. A. Jonsson, E. Wehtje, P. Adlercreutz, and B. Mattiasson. Biochim. Biophys. Acta, **1430**, 313 (1999).
23. A.E. Tripp, D.S. Burdette, J.G. Zeikus, and R.S. Phillips. J. Am. Chem. Soc. **120**, 5137 (1998).
24. H. Sakoda and T. Imanaka. J. Bacteriol. **174**, 1397 (1992).
25. J.-O. Hoog, H. Eklund, and H. Jornvall. Eur. J. Biochem. **205**, 519 (1992).
26. C.L. Stone, T.-K. Li, and W.F. Bosron. J. Biol. Chem. **264**, 11112 (1989).
27. C. Heiss and R.S. Phillips. J. Chem. Soc. Perkin Trans. 1, 2821 (2000).
28. C. Heiss, M. Laivenieks, J.G. Zeikus, and R.S. Phillips. Bioorg. Med. Chem. **9**, 1659 (2001).
29. C. Heiss, M. Laivenieks, J.G. Zeikus, and R.S. Phillips. J. Am. Chem. Soc. **123**, 345 (2001).
30. J. Devereux, P. Haeberli, and O. Smithies. Nucleic Acids Res. **12**, 387 (1984).

© 2002 NRC Canada

Kinetic resolution of oxime esters with lipases — synthesis of enantiomerically enriched building blocks with quaternary carbon centers and formal total synthesis of perhydro histrionicotoxin

Nicole Diedrichs, Ralf Krelaus, Ina Gedrath, and Bernhard Westermann

Abstract: Enantiomerically enriched oximes bearing stereogenic quaternary carbon centers can be obtained by lipase-catalyzed kinetic resolution of oxime esters. Substrate specificity, solvent effects, and the use of different lipases are discussed. Kinetic resolution of butyrylated oximes by lipase PS in the presence of *n*-butanol gave the best ee-values of both the saponified oxime and the residual oxime ester. Subsequent stereospecific Beckmann rearrangement of an enantiomerically enriched oxime provided lactams, which could be employed for the synthesis of optically active perhydro histrionicotoxin.

Key words: oxime, lipase, kinetic resolution, Beckmann rearrangement, perhydro histrionicotoxin.

Résumé : Le dédoublement cinétique d'esters d'oximes catalysé par une lipase permet d'obtenir des oximes énantiomériquement enrichies, portant des centres carbonés quaterneraires stéréogéniques. On discute de la stéréospécificité des substrats, des effets de solvant et de l'utilisation de diverses lipases. Le dédoublement cinétique d'oximes portant un groupe butyryle sous l'influence de la lipase PS, en présence de butanol, donne les meilleurs valeurs d'ee pour l'oxime saponifiée et pour l'ester d'oxime résiduel. Une transposition de Beckmann stéréospécifique subséquente d'une oxime énantiomériquement enrichi fournit des lactames qui peuvent être utilisés pour la synthèse de la perhydrohistrionicotoxine optiquement active.

Mots clés : oxime, lipase, dédoublement cinétique, transposition de Beckmann, perhydrohistrionicotoxine.

[Traduit par la Rédaction]

Introduction

Enzymes are used in organic chemistry for their numerous advantages as mild and easy-to-handle catalysts (1). Their exquisite chemo-, regio-, and stereoselectivity has been demonstrated numerous times. Most reported reactions are hydrolytic reactions, e.g., lipase-catalyzed esterifications, transesterifications, and saponifications of esters. In an overwhelming number of studies, employment of irreversible transacylating reagents has had a major impact in diversifying the use of hydrolytic enzymes (2). In this context, oxime esters have been used as irreversible acyl transfer agents, sometimes exhibiting superior activity compared with their anhydride or vinyl-derived congeners (3). Despite these advantages, the resolution of racemic oximes or oxime esters have been studied infrequently (4).

Oximes **1** are involved in many different reactions, the Beckmann rearrangement being one of the most prominent. Due to its stereospecificity, the synthesis of natural product precursors **3** (spirocyclic framework of histrionicotoxins) or products of pharmaceutical interest **4** (non-natural amino acids) via lactams **2** can be accomplished (Scheme 1). All oximes employed bear a common stereogenic quaternary-carbon center adjacent to the oxime functionality. Although other methods to provide enantiomerically pure building blocks possessing quaternary-carbon centers have been published, there is still a need for widely applicable procedures (5).

Herein we describe a general method to obtain enantiomerically enriched oximes **1** via kinetic resolution of racemic oxime esters with lipase PS. In addition, the application of these intermediates in the synthesis of the enantiomerically pure spirocyclic framework of histrionicotoxin is reported. The synthesis of non-natural amino acids has been described elsewhere (6).

Received 17 January 2002. Published on the NRC Research Press Web site at http://canjchem.nrc.ca on 29 May 2002.

Dedicated to my teacher and mentor J.B. Jones on the occasion of his 65th birthday.

N. Diedrichs, R. Krelaus, I. Gedrath, and B. Westermann.[1] Department of Organic Chemistry, 33095 Paderborn, University of Paderborn, Germany.

[1]Corresponding author (e-mail: bw@fb13n.uni-paderborn.de).

Results and discussion

Synthesis of *E*-oximes

Racemic oximes (±)-**1** can be obtained from alkylated β-ketoesters (±)-**5** by treatment with hydroxyl ammonium chloride in pyridine–ethanol (Scheme 2) (6*a*). The reaction is carried out at 0°C to afford almost exclusively the *E*-oximes in quantitative yields (the ratio of *E*:*Z* stereoisomers is always >50:1 as determined by GLC analysis). The *E*-configuration of the oximes has been established by subsequent

 DOI: 10.1139/V02-097 © 2002 NRC Canada

Table 1. Influence of the carboxylic acid moiety R′ in oxime ester (±)-**7a**–**11a**.

			ee-Value (%)[a]		Yield (%)[b]	
	R′	Reaction time (h)	(–)-Ester	(+)-Oxime	Ester	Oxime
7a	CH_3	47	92	96	94	90
8a	$ClCH_2$	Fast	Unselective reaction			
9a	CH_3OCH_2	Fast	Unselective reaction			
10a	$(CH_3)_3C$	No reaction				
11a	C_3H_7	130	94	96	88	90

[a]Determined by GLC (Hydrodex β-PM) and HPLC (Chiralcel OB-H).
[b]Isolated yields.

Scheme 1.

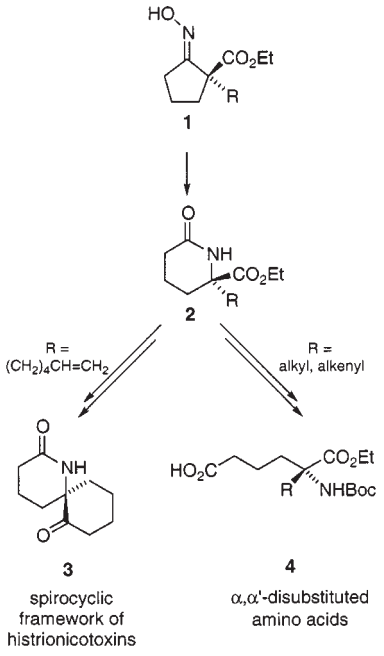

Beckmann rearrangements, which afforded lactams **2** as the sole products in high yields. The isoxazolidinone (±)-**6** is formed in quantitative yield, if the reaction is carried out under thermodynamic control (e.g., boiling chloroform).

Lipase-catalyzed kinetic resolution of oximes (±)-1

Lipase-catalyzed kinetic resolutions can be carried out in two ways, either employing irreversible transacylating agents like vinyl acetate in the presence of racemic oximes or using racemic oxime esters in transesterification reactions. In our initial experiments, the kinetic resolution of oxime (±)-**1a** was carried out with lipase PS in the presence of vinyl acetate (Scheme 3). Kinetic resolution was achieved by stirring the oxime in diisopropyl ether with lipase PS. While high selectivities (ee-values > 90%) were obtained, the reactions took about one month. Optimization and screening of various lipases showed no significant effect. (The employed lipases were all of microbial origin: *Aspergillus niger*, *Candida antarctica*, *Candida cylindracea*, *Mucor miehei*, *Pseudomonas cepacia*, *Pseudomonas fluorescens* and *Mucor javanicus*.). We therefore abandoned this approach and envisioned carrying out kinetic resolution reactions starting from the corresponding racemic oxime esters (±)-**7a** and derivatives thereof.

Scheme 2.

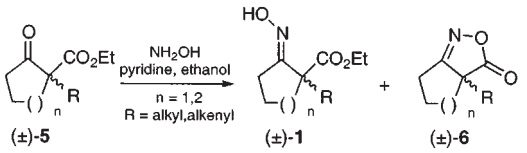

Scheme 3.

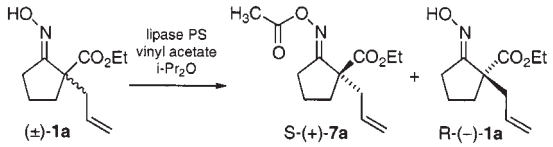

All enzyme catalyzed reactions reported in this publication have been monitored by GLC (cyclodextrin-modified stationary phase for oximes) and HPLC (Daicel stationary phases for oxime esters). Using these materials, base-line separation of the racemic substrates was achieved in all cases. The respective assignment of the absolute (*S*)- and (*R*)-configurations of the quaternary stereogenic centers in (+)-**7a** and (–)-**1a** were based on chemical correlation to products obtained by PLE-catalyzed saponification of β-ketoesters (±)-**5** (7). The enantiomerically pure β-ketoesters obtained by this method have been employed in the total synthesis of the alkaloids (+)-nitramine and (–)-isonitramine. Thus, the stereogenic center in (+)-**7a** is (*S*)-configured, and in (–)-**1a** it is (*R*)-configured.

Lipase-catalyzed kinetic resolution of oxime esters

To identify the best stereodifferentiation by the enzyme, several carboxylic esters of the allylated oxime (±)-**1a** were reacted in diisopropyl ether as solvent containing *n*-butanol. The methoxy- and the chloro-substituted acetic acid derivatives (±)-**8a** and (±)-**9a**, respectively, were hydrolyzed very quickly, yet unselectively (Table 1). In addition, lipase PS did not accept the pivalic acid oxime ester (±)-**10a**. Further experiments showed that acetic acid oxime ester (±)-**7a** and butyrylated oxime ester (±)-**11a** were good substrates and the products were obtained with high enantiomeric excess (Table 1).

In polar solvents such as acetonitrile or acetone, only low ee-values were obtained. High ee-values were observed using

© 2002 NRC Canada

Table 2. Results of lipase-catalyzed transesterification of (±)-**11a–f**.

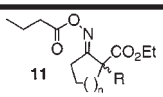

Substrate	R/n	Oxime ester $[\alpha]_D^{20}$ (*c*)[a]	Oxime ester ee/yield (%)[b]	Oxime $[\alpha]_D^{20}$ (*c*)[a]	Oxime ee/yield (%)[b]	Reaction time (h)
a	-$CH_2CH{=}CH_2$/1	–0.9 (1.4)	96/85	+14.6 (1.1)	92/85	91
b	-CH_3/1	–4.3 (0.7)	57/75	+8.6 (0.9)	33/119	70
c	-$(CH_2)_2CH{=}CH_2$/1	–11.8 (1.0)	93/83	+21.5 (0.72)	89/90	120
d	-$(CH_2)_4CH{=}CH$/1	–12.6 (0.9)	96/87	+22.1 (1.2)	95/89	145
e	-$CH_2CH{=}CH_2$/2	–116.6 (0.87)	97/92	+107.2 (1.2)	89/96	70
f	-CH_3/2	–106.8 (1.6)	96/87	+165.5 (1.8)	95/78	100

[a]In $CHCl_3$.
[b]Isolated yields, calculated for 100% (*R*)- and (*S*)-enantiomer.

Scheme 4.

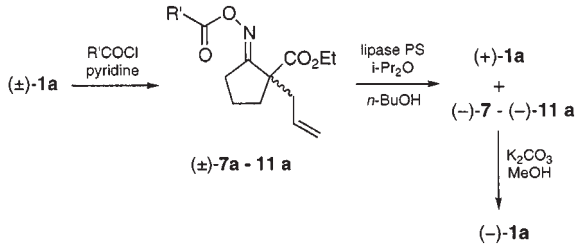

Fig. 1. Structures of histrionicotoxin and perhydro histrionicotoxin.

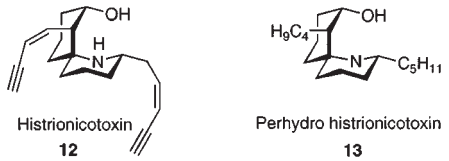

toluene and hexane, but prolonged reaction times (up to 20 d) were required for good conversion. We achieved the best results by using ethers as solvents; amongst the ones screened, diisopropyl ether proved to be most suitable for our purposes in terms of reaction times and selectivity.

Based on these initial results, we synthesized racemic butyrylated oxime esters (±)-**11a–f** (Scheme 4, Table 2). Kinetic resolution of these substrates was achieved over 3–5 days. Thus, stirring the oxime esters in diisopropyl ether with lipase PS in the presence of *n*-butanol gave rise to highly stereoselective saponifications of the substrates. No striking difference was observed on starting from cyclopentane (**11a–d**) or cyclohexane derivatives (**11e**, **f**). Similarly, the size of the alkyl side chain at the quaternary carbon center does not play a major role in stereodifferentiation. All products were isolated in high yields with good ee-values after column chromatography. The butyrylated oxime esters (–)-**11a–f** were saponified quantitatively in 10 min by stirring with potassium carbonate in methanol. The ester moiety at the quaternary center remains intact during the two-step procedure (kinetic resolution and hydrolysis).

Synthesis of the spirocyclic framework of histrionicotoxin (–)-3

Histrionicotoxin **12** and their hydrogenated congeners **13** (Fig. 1) are well-known neurotoxins used by natives of South America as arrow poisons. They have been isolated from skin extracts of the neotropical frog *Dendrobates histrionicus.* These spirocyclic alkaloids influence neurophysiological ion transport and their action on the acetylcholine receptor is of considerable biological interest (8). The total synthesis of racemic perhydro histrionicotoxin **13** was achieved by Kishi et al. (9*a*) and Corey et al. (9*b*); however, the total synthesis of enantiomerically pure histrionicotoxin was achieved only recently by an ingenious route reported by Stork and Zhao (10*a*).

Scheme 5.

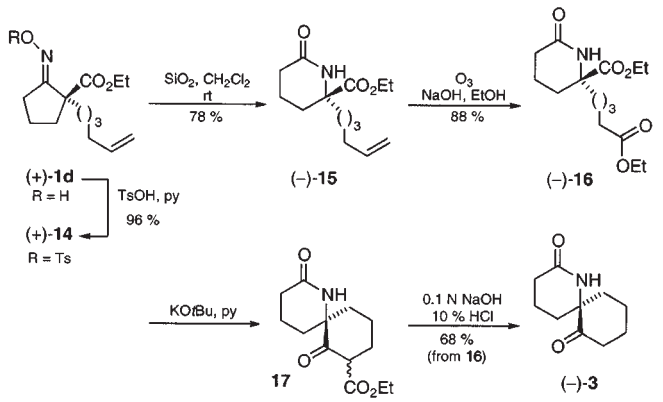

Our route towards the enantiomerically pure spirocyclic framework is related to the methodology reported by Witkop and Kiessing (11) (Scheme 5). In this synthesis, the key step towards the spirocyclic framework is a Dieckmann reaction. To obtain suitable starting materials for this step, we chose to elaborate the enantiomerically pure oxime (+)-**1d**. The corresponding tosylate (+)-**14** was synthesized quantitatively by using tosyl chloride in pyridine. Rearrangement took place while stirring the tosylate in the presence of silica gel. Lactam (–)-**15** was isolated in 78% yield as the only regio- and stereoisomer. It is well known that the Beckmann rearrangement occurs with retention of the configuration at a migrating stereogenic center, and indeed, NMR experiments employing $Eu(hfc)_3$ proved that no racemization had taken place. (The racemic lactam (±)-**15** exhibits two triplets for the methyl group of the ethyl ester moiety at 1.32 and 1.64 ppm, whereas the homochiral lactam (–)-**15** shows only one triplet at 1.26 ppm (12).)

Ozonolysis of the double bond was carried out as described by Marshall et al. (13). Reaction with solid NaOH in

© 2002 NRC Canada

ethanol at –78°C provided the diester (–)-**16** in 88% yield. Subsequently, a Dieckmann reaction was carried out in the presence of potassium *tert*-butylate, affording the spirocycle **17** as a crystalline product. Without further characterization, saponification and decarboxylation was carried out leading to (–)-**3** in 68% yield (from **16**). Because racemic ketone (±)-**3** was used to synthesize perhydro histrionicotoxin, this synthesis represents a formal total asymmetric synthesis of this alkaloid (9). Currently we are exploring the synthesis of histrionicotoxin.

Conclusions

We have demonstrated that oxime esters are valuable substrates for kinetic resolution with lipases. Transesterification of the butyrylated oximes gave products containing a quaternary stereocenter adjacent to the oxime functionality; this method is therefore a valuable tool to provide building blocks with this structural feature. The configuration at the stereocenter could be unambigously determined by chemical correlation, which is based on the synthesis of known natural products.

The oximes were employed in Beckmann rearrangements leading to enantiomerically pure lactams. These lactams can be used for the synthesis of non-natural amino acids and for the preparation of spirocyclic alkaloids as demonstrated in the case of perhydro histrionicotoxin.

Experimental

All reagents were of commercial quality. Lipases were purchased from Fluka (Switzerland) and were provided by Amano (Japan). All solvents were distilled prior to use. Silica gel 60 F_{254} plates from Merck (Germany) were used for TLC. Column chromatography was performed using silica gel 60/230–400 mesh from Merck. NMR spectra were measured on a Bruker ARX 200 spectrometer (^{1}H 200 MHz and ^{13}C 50 MHz). IR spectra were measured on an FT-IR spectrometer NICOLET 510 P. Mass spectra were obtained with a FINNIGAN MAT 8430. The optical rotations were recorded on a PerkinElmer 241 polarimeter. For HPLC a Merck-Hitachi chromatograph equipped with an OB-H column from Daicel Chemical Industries (25 × 0.46 cm) was used. For GLC measurements an HP 8890 gas chromatograph with a Lipodex E cyclodextrin column (12.5 m, Macherey & Nagel, Germany) was used. Elemental analyses were carried out on a PerkinElmer analytical analyzer 241.

General procedure for the preparation of racemic oxime esters (±)-11a–f

To a solution of oxime (±)-**1** (5.0 mmol) in dry pyridine (25 mL), was added dropwise butyric acid chloride (5.0 mmol) over a period of 10 min at 0°C under an argon atmosphere. The reaction mixture was stirred for 1 h at this temperature and an additional 3 h at room temperature. After adding 5% hydrochloric acid (30 mL) the aqueous layer was extracted with diethyl ether (3 × 70 mL). The combined organic layers were washed with 10% hydrochloric acid (10 mL), saturated sodium bicarbonate solution (2 × 40 mL), and finally with saturated brine. The organic layer was dried over $MgSO_4$, filtered, and evaporated to dryness under reduced pressure. After column chromatography with dichloromethane–methanol (95:5) or distillation, the desired products were obtained in 81–94% yield.

General procedure for kinetic resolution of oxime esters (±)-11a–f

Lipase PS (500 mg) and *n*-butanol (5 mL) were added to a solution of (±)-**11** (2 mmol) in diisopropyl ether (15 mL). The reaction was monitored by HPLC. After the reaction, the enzyme was filtered through Celite™ and washed with diethyl ether. The crude residue was subjected to column chromatography using dichloromethane–methanol (98:2) as the eluent.

General procedure for saponification of oxime esters (–)-11a–f

To a saturated solution of K_2CO_3 in methanol (20 mL) was added oxime ester (±)-**11** (1 mmol) and the solution was stirred for 10 min. After evaporation to dryness, the residue was dissolved in water (45 mL). The aqueous layer was extracted with diethyl ether (3 × 50 mL). The combined organic layers were washed with 5% hydrochloric acid (10 mL) and saturated brine. After drying over $MgSO_4$, filtration and evaporation of the solvent gave the oximes (–)-**1** in quantitative yield.

Ethyl 1-allyl-2-[(butyryloxy)imino]cyclopentane carboxylate (11a)

^{1}H NMR ($CDCl_3$) δ: 0.94 (t, ^3J = 7.3 Hz, 3H, CH_3), 1.21 (t, ^3J = 7.1 Hz, 3H, CH_3), 1.66 (q, ^3J = 7.4 Hz, 2H, CH_2), 1.76–1.90 (m, 3H, CH_2), 2.15–2.83 (m, 7H, CH_2), 4.13 (q, ^3J = 7.1 Hz, 2H, OCH_2), 5.02–5.11 (m, 2H, $=CH_2$), 5.67–5.87 (m, 1H, =CH). ^{13}C NMR ($CDCl_3$) δ: 14.2, 14.5, 18.8, 22.0, 29.9, 35.2, 39.9, 57.3, 61.9, 72.8, 119.4, 133.9, 171.7, 172.9, 174.2. EI-HRMS calcd. for $C_{15}H_{23}NO_4$: 281.1627; found: 281.1625.

Ethyl 1-methyl-2-[(butyryloxy)imino]cyclopentane carboxylate (11b)

^{1}H NMR ($CDCl_3$) δ: 1.00 (t, ^3J = 7.3 Hz, 3H, CH_3), 1.26 (t, ^3J = 7.1 Hz, 3H, CH_3), 1.29 (s, 3H, CH_3) 1.63–2.02 (m, 5H, CH_2), 2.19–2.45 (m, 3H, CH_2), 2.58–2.76 (m, 2H, CH_2), 4.19 (q, ^3J = 7.1 Hz, 2H, OCH_2). ^{13}C NMR ($CDCl_3$) δ: 14.1, 14.5, 18.8, 21.9, 22.0, 29.7, 35.2, 39.4, 53.6, 61.8, 171.6, 174.0, 175.5. EI-HRMS calcd. for $C_{13}H_{21}NO_4$: 295.1471; found: 295.1488.

Ethyl 1-(but-3-enyl)-2-[(butyryloxy)imino]cyclopentane carboxylate (11c)

^{1}H NMR ($CDCl_3$) δ: 0.99 (t, ^3J = 7.4 Hz, 3H, CH_3), 1.26 (t, ^3J = 7.1 Hz, 3H, CH_3), 1.71 (q, ^3J = 7.4 Hz, 2H, CH_2), 1.78–2.81 (m, 12H, CH_2), 4.19 (q, ^3J = 7.1 Hz, 2H, OCH_2), 4.92–5.06 (m, 2H, $=CH_2$), 5.70–5.90 (m, 1H, =CH). ^{13}C NMR ($CDCl_3$) δ: 14.1, 14.4, 18.7, 22.0, 27.8, 29.8, 34.9, 36.2, 37.5, 57.7, 61.9, 115.2, 138.2, 172.0, 172.9, 174.5. EI-HRMS calcd. for $C_{16}H_{25}NO_4$: 295.1784; found: 295.1790.

Ethyl 1-(hex-5-enyl)-2-[(butyryloxy)imino]cyclopentane carboxylate (11d)

^{1}H NMR ($CDCl_3$) δ: 1.02 (t, ^3J = 7.4 Hz, 3H, CH_3), 1.24 (t, ^3J = 7.1 Hz, 3H, CH_3), 1.62 (q, ^3J = 7.4 Hz, 2H, CH_2), 1.68–2.73 (m, 16H, CH_2), 4.17 (q, ^3J = 7.1 Hz, 2H, OCH_2), 4.76–4.98 (m, 2H, $=CH_2$), 5.56–5.78 (m, 1H, =CH).

© 2002 NRC Canada

^{13}C NMR ($CDCl_3$) δ: 14.0, 14.4, 18.3, 21.7, 24.6, 27.3, 29.1, 33.4, 34.6, 36.5, 37.8, 54.5, 61.1, 114.4, 138.7, 172.6, 173.1, 174.8. EI-HRMS calcd. for $C_{18}H_{29}NO_4$: 323.2097; found: 323.2110.

Ethyl 1-allyl-2-[(butyryloxy)imino]cyclohexane carboxylate (11e)

^{1}H NMR ($CDCl_3$) δ: 1.00 (t, ^3J = 7.3 Hz, 3H, CH_3), 1.25 (t, ^3J = 7.1 Hz, 3H, CH_3), 1.35–1.98 (m, 8H, CH_2), 2.09–2.83 (m, 5H, CH_2), 3.18–3.28 (m, 1H, CH_2), 4.17 (q, ^3J = 7.1 Hz, 2H, OCH_2), 5.01–5.09 (m, 2H, $=CH_2$), 5.81–6.02 (m, 1H, =CH). ^{13}C NMR ($CDCl_3$) δ: 14.1, 14.6, 18.7, 23.0, 26.2, 26.3, 35.3, 36.2, 40.5, 55.1, 61.6, 118.6, 134.0, 167.5, 172.0, 172.7. EI-HRMS calcd. for $C_{16}H_{25}NO_4$: 295.1784; found: 295.1792.

Ethyl 2-[(butyryloxy)imino]-1-methylcyclohexane carboxylate (11f)

^{1}H NMR ($CDCl_3$) δ: 0.98 (t, ^3J = 7.3 Hz, 3H, CH_3), 1.25 (t, ^3J = 7.1 Hz, 3H, CH_3), 1.31–1.41 (m, 2H, CH_2), 1.45 (s, 3H, CH_3), 1.52–2.02 (m, 6H, CH_2), 2.39–2.46 (m, 3H, CH_2), 3.19–3.28 (m, 1H, CH_2), 4.17 (q, ^3J = 7.1 Hz, 2H, OCH_2). ^{13}C NMR ($CDCl_3$) δ: 14.1, 14.5, 18.7, 22.9, 23.1, 25.9, 26.1, 35.3, 38.6, 51.2, 61.6, 168.5, 172.0, 174.3. EI-HRMS calcd. for $C_{14}H_{23}NO_4$: 269.1627; found: 269.1681.

Ethyl 2-[(acetyloxy)imino]-1-allylcyclopentane carboxylate (7a)

$[\alpha]_D^{20}$ –2.0 (*c* 1.0, $CHCl_3$, ee > 98%). ^{1}H NMR ($CDCl_3$) δ: 1.23 (t, ^3J = 7.1 Hz, 3H, CH_3), 1.73–1.91 (m, 3H, CH_2), 2.04–2.83 (m, 5H, CH_2), 2.16 (s, 3H, CH_3), 4.16 (q, ^3J = 7.1 Hz, 2H, OCH_2), 5.04–5.13 (m, 2H, $=CH_2$), 5.66–5.85 (m, 1H, =CH). ^{13}C NMR ($CDCl_3$) δ: 14.5, 20.2, 22.0, 29.9, 35.2, 39.8, 57.2, 61.9, 119.4, 133.8, 169.5, 172.8, 174.1. EI-HRMS calcd. for $C_{13}H_{19}NO_4$: 253.1314; found: 253.1288.

Ethyl 1-allyl-2-{[(2,2-dimethylpropanoyl)oxy]imino}cyclopentane carboxylate (10a)

^{1}H NMR ($CDCl_3$) δ: 1.22 (s, 9H, CH_3), 1.26 (t, ^3J = 7.1 Hz, 3H, CH_3), 1.14–1.26 (m, 2H, CH_2), 1.77–1.87 (m, 2H, CH_2), 2.23–2.79 (m, 4H, CH_2), 4.08–4.20 (m, 2H, OCH_2), 5.02–5.11 (m, 2H, $=CH_2$), 5.73–5.82 (m, 1H, =CH). ^{13}C NMR ($CDCl_3$) δ: 14.5, 21.9, 27.6, 29.7, 35.1, 39.8, 57.3, 61.9, 119.3, 133.9, 169.0, 172.7, 175.2 (one quaternary center could not be determined). EI-HRMS calcd. for $C_{16}H_{25}NO_4$: 295.1784; found: 295.1812.

Ethyl 1-allyl-2-(hydroxyimino)cyclopentane carboxylate (1a)

^{1}H NMR ($CDCl_3$) δ: 1.21 (t, ^3J = 7.1 Hz, 3H, CH_3), 1.67–1.93 (m, 3H, CH_2), 2.19–2.80 (m, 5H, CH_2), 4.12 (q, ^3J = 7.1 Hz, 2H, OCH_2), 5.00–5.09 (m, 2H, $=CH_2$), 5.63–5.84 (m, 1H, =CH). ^{13}C NMR ($CDCl_3$) δ: 14.4, 22.1, 27.9, 34.5, 41.1, 56.3, 61.7, 118.9, 134.0, 165.8, 173.2. EI-HRMS calcd. for $C_{11}H_{17}NO_3$: 211.1208; found: 211.1207.

Ethyl 2-(hydroxyimino)-1-methylcyclopentane carboxylate (1b)

^{1}H NMR ($CDCl_3$) δ: 1.27 (t, ^3J = 7.1 Hz, 3H, CH_3), 1.43 (s, CH_3, 3H), 1.62–2.65 (m, 6H, CH_2), 4.17 (q, ^3J = 7.1 Hz, 2H, OCH_2), 9.10 (br s, 1H, OH). ^{13}C NMR ($CDCl_3$) δ: 14.5, 22.1, 22.8, 27.6, 38.6, 52.6, 61.6, 167.5, 174.6. Anal. calcd. for $C_9H_{15}NO_3$ (185.22): C 58.36, H 8.16, N 7.56; found: C 58.18, H 8.34, N 7.80.

Ethyl 1-(3-butenyl)-2-(hydroxyimino)cyclopentane carboxylate (1c)

^{1}H NMR ($CDCl_3$) δ: 1.26 (t, ^3J = 7.1 Hz, 3H, CH_3), 1.63–2.69 (m, 10H, CH_2), 4.15 (q, ^3J = 7.1 Hz, 2H, OCH_2), 4.88–5.09 (m, 2H, $=CH_2$), 5.65–5.88 (m, 1H, =CH), 9.54 (s, 1H, OH). ^{13}C NMR ($CDCl_3$) δ: 14.4, 22.2, 27.7, 30.0, 35.1, 36.3, 56.6, 61.7, 115.2, 138.3, 166.0, 173.3. EI-HRMS calcd. for $C_{12}H_{19}NO_3$: 225.136; found: 225.1379.

Ethyl 1-(5-hexenyl)-2-(hydroxyimino)cyclopentane carboxylate (1d)

^{1}H NMR ($CDCl_3$) δ: 1.32 (t, ^3J = 7.1 Hz, 3H, CH_3), 1.54–2.79 (m, 14H, CH_2), 4.22 (q, ^3J = 7.1 Hz, 2H, OCH_2), 4.92–5.12 (m, 2H, $=CH_2$), 5.65–5.88 (m, 1H, =CH), 9.28 (s, 1H, OH). ^{13}C NMR ($CDCl_3$) δ: 14.0, 21.7, 24.6, 27.3, 29.1, 33.4, 34.6, 36.5, 54.5, 61.1, 114.4, 138.7, 165.9, 173.1. Anal. calcd. for $C_{14}H_{23}NO_3$ (253.17): C 66.36, H 9.16, N 5.53; found: C 66.03, H 9.33, N 5.82.

Ethyl 1-allyl-2-(hydroxyimino)cyclohexane carboxylate (1e)

^{1}H NMR ($CDCl_3$) δ: 1.26 (t, ^3J = 7.1 Hz, 3H, CH_3), 1.34–1.98 (m, 6H, CH_2), 2.33–2.48 (m, 2H, CH_2), 2.66–2.76 (m, 1H, CH_2), 3.17–3.24 (m, 1H, CH_2), 4.18 (q, ^3J = 7.1 Hz, 2H, OCH_2), 5.02–5.08 (m, 2H, $=CH_2$), 5.71–5.91 (m, 1H, =CH), 9.21 (s, 1H, OH). ^{13}C NMR ($CDCl_3$) δ: 14.6, 22.9, 23.6, 25.9, 35.5, 40.1, 54.0, 61.4, 118.6, 133.9, 160.4, 173.4. EI-HRMS calcd. for $C_{12}H_{19}NO_3$: 225.1365; found: 225.1370.

Ethyl 2-(hydroxyimino)-1-methylcyclohexane carboxylate (1f)

mp 64.7°C. ^{1}H NMR ($CDCl_3$) δ: 1.29 (t, ^3J = 7.1 Hz, 3H, CH_3), 1.39 (s, CH_3, 3H), 1.55–2.70 (m, 8H, CH_2), 4.15 (q, ^3J = 7.1 Hz, 2H, OCH_2), 8.25 (br s, 1H, OH). ^{13}C NMR ($CDCl_3$) δ: 14.6, 23.0, 23.3, 23.4, 25.9, 38.4, 50.4, 61.5, 161.1, 175.0. Anal. calcd. for $C_{10}H_{17}NO_3$ (253.17): C 60.28, H 8.60, N 7.03; found: C 60.13, H 8.72, N 7.12.

Ethyl 1-(5-hexenyl)-2-([tosyloxy]imino)cyclopentane carboxylate ((+)-14)

Oxime (+)-**1d** (0.30 g, 1,2 mmol) was dissolved in pyridine (2.0 mL) and *p*-toluene sulfonic acid (0.23 g, 1.2 mmol) was added. The solution was stirred for 20 h at room temperature. After addition of $NaHCO_3$ (5 mL of a 5% solution), the reaction mixture was extracted with CH_2Cl_2 (3 × 20 mL). The combined organic extracts were washed with 5% $NaHCO_3$, water, and brine, dried over $MgSO_4$, filtered and the organic solvent evaporated under reduced pressure to furnish an oily residue (0.42 g, 87%). Further purification was not required. $[\alpha]_D^{20}$ +16.8 (*c* 1.33, $CHCl_3$). ^{1}H NMR ($CDCl_3$) δ: 1.22 (t, ^3J = 7.1 Hz, 3H, CH_3), 1.25–2.40 (m, 12H, CH_2), 2.51 (s, 3H, CH_3), 2.70 (m, 2H, CH_2), 4.13 (q, ^3J = 7.1 Hz, 2H, OCH_2), 5.05 (m, 2H, CH_2=), 5.84 (m, 1H, CH=), 7.38 (m, 2H, Ar-H), 7.93 (m, 2H, Ar-H). ^{13}C NMR ($CDCl_3$) δ: 13.9, 21.5, 21.6, 24.3, 29.1, 29.5, 33.4, 35.0, 35.6, 57.9, 61.3, 114.4, 128.9, 129.3, 133.0, 138.6, 144.6, 172.1, 174.9. Anal. calcd. for $C_{14}H_{29}NO_3S$ (407.18): C 61.89, H 7.18, N 3.44; found: C 61.69, H 7.40, N 3.79.

© 2002 NRC Canada

R-(–)-Ethyl 2-(hex-5-enyl)-6-oxo-piperidine-2-carboxylate ((–)-15)

Tosyloxime **14** (0.20 g, 0.49 mmol) was dissolved in CH_2Cl_2 (15 mL) and silica gel (10 g) was added. The reaction slurry was stirred for 16 h, after which TLC control showed no starting material. The silica gel was filtered off and washed several times with a methanol–CH_2Cl_2 mixture. Residual toluene sulfonic acid was removed by washing with water, if necessary. The combined organic extracts were dried over $MgSO_4$, filtered, and evaporated under reduced pressure to afford slightly yellow crystals (0.97 g, 78%); mp 46.6°C. $[\alpha]_D^{20}$ –8.83 (*c* 1.22, $CHCl_3$). ^{1}H NMR ($CDCl_3$) δ: 1.26 (t, ^3J = 7.1 Hz, 3H, CH_3), 1.32–2.46 (m, 14H, CH_2), 4.18 (q, ^3J = 7.1 Hz, 2H, OCH_2), 4.82 (m, 2H, CH_2=), 5.78 (m, 1H, CH=), 6.13 (s, 1H, NH). ^{13}C NMR ($CDCl_3$) δ: 14.0, 17.8, 22.5, 28.5, 30.4, 30.8, 3.1, 40.0, 61.6, 62.7, 114.7, 138.0, 171.5, 173.1. Anal. calcd. for $C_{14}H_{23}NO_3$ (253.17): C 66.36, H 9.16, N 5.53; found: C 66.12, H 9.13, N 5.72.

R-(–)-Ethyl 2-(5-ethoxy-5-oxopentyl)-6-oxo-piperidine-2-carboxylate ((–)-16)

Ozone was passed through a mixture of lactam **15** (0.12 g, 0.47 mmol) dissolved in CH_2Cl_2 (4 mL) and ethanolic NaOH (2.5 mL, 2.5 M) at –78°C. This process was stopped when the characteristic blue color appeared. The reaction mixture was warmed to room temperature and diluted with water and ether. The organic layer was separated and the aqueous phase was extracted with ether (3 × 50 mL). The combined organic extracts were dried over $MgSO_4$, filtered, and the organic solvent was evaporated under reduced pressure to afford a colorless oil (0.13 g, 88%), which was analytically pure. $[\alpha]_D^{20}$ –6.60 (*c* 2.0, $CHCl_3$). ^{1}H NMR ($CDCl_3$) δ: 1.22 (t, ^3J = 7.1 Hz, 3H, CH_3), 1.26 (t, ^3J = 7.1 Hz, 3H, CH_3), 1.50–2.30 (m. 14H, CH_2), 4.09 (q, ^3J = 7.1 Hz, 2H, OCH_2), 4.18 (q, ^3J = 7.1 Hz, 2H, OCH_2), 6.30 (s, 1H, NH). ^{13}C NMR ($CDCl_3$) δ: 13.9, 14.0, 17.7, 22.7, 24.6, 30.2, 30.7, 33.7, 39.4, 60.1, 61.6, 62.5, 171.8, 172.8, 173.0. Anal. calcd. for $C_{15}H_{25}NO_5$ (299.36): C 60.18, H 8.42, N 4.68; found: C 60.32, H 8.11, N 4.71.

(–)-1-Azaspiro[5.5]undecane-2,7-dione ((–)-3)

To potassium *tert*-butoxide (0.17 g, 1.6 mmol) dissolved in pyridine (3 mL) under an argon atmosphere was added dropwise diester **16** (0.20 g, 0.7 mmol) in pyridine (3 mL). The reaction mixture was stirred for 2 h at 20°C. Diluted HCl was added and then brine (10 mL) was added. After extraction with ethyl acetate (3 × 40 mL), the combined organic extracts were washed with 5% HCl, water, 5% $NaHCO_3$, and brine, and then dried over $MgSO_4$, filtered, and evaporated. The remaining oily residue (0.12 g, 75%) was stirred with 1% NaOH (3 mL) overnight at room temperature, after which the reaction mixture was cooled to 0°C and 10% HCl (5 mL) was added. β-ketoacid **17** crystallized and was filtered off, dried over P_2O_5 (67 mg, 75%), and used without further purification. The β-ketoacid was dissolved in xylene (2 mL) and after addition of a small amount of *p*-toluene sulfonic acid was heated at reflux for 2 h. The organic solvent was removed under reduced pressure to afford colorless crystals (0.48 g, 90%); mp 148°C; $[\alpha]_D^{20}$ –36.0 (*c* 2.0, $CHCl_3$). ^{1}H NMR ($CDCl_3$) δ: 1.58–2.68 (m, 14H, 7 × CH_2), 6.60 (s, 1H, NH). ^{13}C NMR ($CDCl_3$) δ: 23.0, 24.7, 26.2, 35.3, 35.6, 35.7, 36.5, 66.3, 174.4, 211.3. Anal. calcd. for $C_{10}H_{15}NO_2$ (181.23): C 66.27, H 8.34, N 7.73; found: C 66.12, H 8.76, N 7.72.

Acknowledgments

N. Diedrichs and I. Gedrath would like to thank the Fonds der Chemischen Industrie for a doctoral scholarship. R. Krelaus has been awarded the Graduiertenförderung, for which he is very grateful. The work has been supported by the Fonds der Chemischen Industrie and by gifts from Amano.

References

1. (*a*) K. Drauz and H. Waldmann. *In* Enzyme catalysis in organic synthesis. VCH, Weinheim. 1995; (*b*) K. Faber. *In* Biotransformations in organic chemistry. VCH, Weinheim. 1992; (*c*) J.B. Jones. Tetrahedron, **42**, 3351 (1986).
2. (*a*) A.M. Klibanov. Chem. Tech. 354 (1986); (*b*) G. Carrea and S. Riva. Angew. Chem. Int. Ed. **39**, 2226 (2000).
3. (*a*) A. Ghogare and G.S. Kumar. J. Chem. Soc. Chem. Commun. 1533 (1989); (*b*) A. Ghogare and G.S. Kumar. J. Chem. Soc. Chem. Commun. 134 (1990); (*c*) R. Pulido, F.L. Ortiz, and V. Gotor. J. Chem. Soc. Perkin Trans. 1, 2891 (1992); (*d*) S.T. Chen, C.F. Tsai, and K.T. Wang. Chem. Commun. 165 (1996).
4. (*a*) C. Baldoli, S. Maiorana, G. Carrea, and S. Riva. Tetrahedron: Asymmetry, **4**, 767 (1993); (*b*) M. Murakata, M. Imai, M. Tamura, and O. Hoshino. Tetrahedron: Asymmetry, **5**, 2019 (1994).
5. (*a*) S.F. Martin. Tetrahedron, **36**, 419 (1980); (*b*) D. Romo and A.I. Meyers. Tetrahedron, **47**, 9503 (1991); (*c*) J. d'Angelo, D. Desmaele, F. Dumas, and A. Guingant. Tetrahedron: Asymmetry, **3**, 459 (1992); (*d*) K. Fuji. Chem. Rev. **93**, 2037 (1993); (*e*) E.J. Corey and A. Guzman-Perez. Angew. Chem. Int. Ed. **37**, 388 (1998); (*f*) J. Christoffers and A. Mann. Chem. Eur. J. **7**, 1014 (2001).
6. (*a*) B. Westermann and I. Gedrath. Synlett, 665 (1996); (*b*) B. Westermann, A. Walter, and N. Diedrichs. Angew. Chem. Int. Ed. **38**, 3384 (1999).
7. (*a*) B. Westermann, H.G. Scharmann, and I. Kortmann. Tetrahedron: Asymmetry, **4**, 2119 (1993); (*b*) B. Westermann and I. Kortmann. Biocatalysis, **10**, 289 (1994).
8. J.W. Daly. *In* New Aspects of organic chemistry. Vol 1. *Edited by* Z. Yoshida, T. Shiba, and Y. Oshiro. VCH, Weinheim. 1989. pp. 385–412.
9. (*a*) M. Aratani, L.V. Dunkerton, T. Fukujama, Y. Kishi, K. Kakoi, S. Suhiura, and S. Inoue. J. Org. Chem. **40**, 2009 (1975); (*b*) E.J. Corey, J.F. Arnett, and G.N. Widiger. J. Am. Chem. Soc. **97**, 430 (1975); (*c*) Synform, **2**, 1 (1984); (*d*) Y. Inubushi and T. Ikuba. Heterocycles, **17**, 507 (1982).
10. (*a*) G. Stork and K. Zhao. J. Am. Chem. Soc. **112**, 5875 (1990); (*b*) S. Carey, C. Aratani, and Y. Kishi. Tetrahedron Lett. **26**, 5887 (1985); (*c*) G.M. Williams, S.D. Roughley, J.E. Davies, A.B. Holmes, and J.P. Adams. J. Am. Chem. Soc. **121**, 4900 (1999).
11. W. Kiessing and B. Witkop. Chem. Ber. **108**, 1623 (1975).
12. (*a*) R.E. Gawley. Org. React. **35**, 1 (1988); (*b*) P.A. Evans and A.B. Holmes. Tetrahedron, **47**, 9131 (1991).
13. J.A. Marshall, A.W. Garafolo, and G.C. Sedrani. Synlett, 643 (1992).

© 2002 NRC Canada

Novel esterase activity of dihydrolipoamide acetyltransferase AcoC of *Pseudomonas putida* identified by mutation of the *acoR* regulator

Paola Pedroni, Thomas Friedrich, Michael Breuer, Dani McBeth, and Bernhard Hauer

Abstract: A mutant strain of *Pseudomonas putida* (LU2201) expressing a novel ethylphenylacetate (EPA) esterase was isolated after mutagenesis of *P. putida* LU6456. The DNA fragment conferring the EPA^+ phenotype was cloned and characterized. It included the structural genes of the 2,3-butanediol catabolic pathway, including *acoC*, which catalyzes the acetyl transfer step (i.e., dihydrolipoamide acetyltransferase). The *acoC* gene product from LU2201 was expressed in *E. coli* and shown to be responsible for the novel EPA-esterase activity. Biochemical characterization revealed that the enzyme still retained the natural dihydrolipoamide acetyltransferase activity. Sequence comparison with the corresponding wild-type gene indicated a single-base pair change leading to a I238V replacement in the respective protein. Biochemical characterization of wild-type AcoC enzyme showed that it too was able to catalyze EPA hydrolysis despite the apparent absence of this activity in cells grown in the presence of EPA. Unlike the wild type, EPA serves as an inducer in the mutant strain. Inverse PCR was used to clone the putative regulator *acoR* from the *aco* operon in both wild type and mutant strains. Sequence analyses indicated an S14R exchange in the AcoR from the *P. putida* mutant. This mutation was located in the *N*-terminal region responsible for regulatory functions, presumably by interaction with signal molecules. This may account for the ability of EPA to induce expression of *acoC* only in the mutant strain.

Key words: *Pseudomonas putida*, ethylphenylacetate esterase, acetoin cleaving system, *acoC* gene, dihydrolipoamide acetyl-transferase, E2 component, *acoR* gene.

Résumé : À la suite d'une mutagénèse de *P. putida* LU6456, on a isolé une nouvelle souche mutante de *Pseudomonas putida* (LU2201) qui exprime une nouvelle estérase du phénylacétate d'éthyle (« EPA »). On a cloner et caractériser le fragment d'ADN qui confère le phénotype EPA. Il comporte des gènes structuraux de la voie catabolique du butane-2,3-diol, y compris l'*aco*C catalyse l'étape de transfert du groupe acétyle (soit l'acétyltransférase dihydrolipoamide). Le gène *aco*C produit à partir du LU2201 est exprimé en *E. coli* et il a été démontré qu'il est responsable de la nouvelle activité estérase EPA. La caractérisation biochimique montre que l'enzyme a conservé l'activité acétyltransférase dihydrolipoamide naturelle. Une comparaison de la séquence avec celle du gène correspondant de type sauvage montre qu'il ne s'est produit qu'un seul changement de paire de bases qui conduit à un remplacement 1238V dans la protéine respective. La caractérisation biochimique de l'enzyme *aco*C de type sauvage a permis de montrer qu'il est aussi capable de catalyser l'hydrolyse EPA malgré l'absence apparente de cette activité dans les cellules cultivées en présence d'EPA. À l'inverse du produit de type sauvage, l'EPA est un inducteur dans la souche mutante. On a utilisé une « PCR » inverse pour cloner le régulateur putatif *aco*R à partir de l'opéron *aco* des souches mutantes ou de type sauvage. Une analyse de la séquence indique qu'un échange S14R s'est produit dans l'*Aco*R provenant du *P. putida* mutant. Cette mutation est localisée dans la région *N*-terminale responsable des fonctions de régulation, probablement par interaction avec les molécules qui signalent. Ceci pourrait expliquer l'habilité de l'EPA à n'induire une expression d'*aco*C qu'à partir de la variété mutante.

Mots clés : *Pseudomonas putida*, estérase de phénylacétate d'éthyle, système clivant l'acétoïne, gène d'*aco*C, transférase d'acétyle dihydrolipoamide, composant E2, gène d'*aco*R.

[Traduit par la Rédaction]

Received 20 November 2001. Published on the NRC Research Press Web site at http://canjchem.nrc.ca on 29 May 2002.

Dedicated to Professor J. Bryan Jones on the occasion of his 65th birthday.

P. Pedroni,[1] T. Friedrich, M. Breuer, and B. Hauer.[2] Fine Chemicals and Biocatalysis Research, BASF, D-67056 Ludwigshafen, Germany.
D. McBeth. Department of Microbiology, CUNY Medical School, New York.

[1]Present address: Enitecnologie S.p.a., Via F. Maritano, 26 20097, San Donato Milanese, Milan, Italy.
[2]Corresponding author (e-mail: bernhard.hauer@basf-ag.de).

 DOI: 10.1139/V02-080 © 2002 NRC Canada

Table 1. Bacterial strains and plasmids used in this study.

Strain or plasmid	Relevant characteristics	Source or reference
Pseudomonas putida		
LU6456-PpS338	Wild-type, Trp,[a] EPA[b]	25
LU2201	Derivative from LU6456-PpS338 by UV radiation and carrying the pDM101 plasmid, Trp$^-$, EPA$^+$	This study
Escherichia coli		
SURE	e14$^-$(McrA$^-$) Δ(*mcrCB-hsdSMR-mrr*)*171 endA1 supE44 thi-1 gyrA96 relA1 lac recB recJ sbcC umuC::*Tn*5* (Kan^r) *uvrC* [F′ *proAB lacI*^{q}*Z*Δ*M15* Tn*10* (Tet^r)]	Stratagene
XL1-Blue	Δ(*mcrA*)*183* Δ(*mcrCB-hsdSMR-mrr*)*173 endA1 supE44 thi-1 recA1* gyrA96 *relA1lac* [F′ *proAB lacI*^{q}*Z*Δ*M15* Tn*10* (Tet^r)]	Stratagene
Plasmids		
pDM101	Tc^r, carrying the CAM-OTC UV genes	8
pUC19	Ap^r, *lacPOZ′*	Boehringer
pQE-8	Ap^r, T5 promoter, His-tag expression vector	Qiagen
pREP4	Km^r, *lacI* gene repressor plasmid	Qiagen
pLAFR1		20
p12/5	pUC19 harboring the EPA$^+$ 5.1 kb EcoRI genomic fragment from *P. putida* LU2201	This study
pΔSalI	Derivative from p12/5, deleted in the 1.4 kb SalI fragment	This study
pΔApaI	Derivative from p12/5, deleted in the 1.1 kb ApaI fragment	This study
pΔHindIII	Derivative from p12/5, deleted in the 3.6 kb HindIII fragment	This study
p*acoC* 2	pQE-8 harboring the amplified *acoC* gene from *P. putida* LU2201	This study
p*acoC* 3	pQE-8 harboring the amplified *acoC* gene from *P. putida* LU6456-PpS338	This study

[a]Trp, tryptophan.
[b]EPA, ethyl-phenylacetate.

Introduction

Hydrolases are biocatalysts that have various industrial applications. In particular, lipases and esterases are employed for the synthesis of enantiomerically pure compounds (1), where they have been used for the resolution of more than 1000 different compounds including alcohols, carboxylic acids, and lactones by hydrolysis or transesterification. To develop industrial biocatalytic processes, suitable microbes or enzymes must be found and developed. The classical enrichment technique is still successful, but it is a time-consuming and labour-intensive task, even though novel screening approaches have accelerated the screening process (2). To alter an enzyme, various approaches involving both rational and non-rational design have been successfully used (3). We are interested in using natural-evolutionary processes to obtain new catalytic activities under selective pressure (4).

Pseudomonas is biochemically very versatile and shows a remarkable metabolic diversity. Members of this genus produce a number of lipases and esterases (5–7). The strain *Pseudomonas putida* LU6456, however, cannot hydrolyze phenylacetic acid or lactic or methylpropionic acid esters. Instead of screening for these activities in different strains, we explored the potential of adaptating *Pseudomonas putida* LU6465, by growing it on the above substrates and thereby acquiring the potential to hydrolyze them.

To increase the isolation frequency of *Pseudomonas putida* derivatives capable of using these esters as their sole carbon source, we used a 25-kb fragment of *Pseudomonas* plasmid (CAM-OCT DNA) encoding a DNA-repair gene or genes (8).

In this paper, we describe the isolation and the molecular characterization of the gene locus providing *P. putida* mutant strain LU2201 with a novel ethylphenylacetate (EPA) esterase activity. The results show that this enzymatic function is an inherent property of the *acoC* gene product, the dihydrolipoamide acetyltransferase enzyme of the acetoin cleaving system. Comparative studies with the wild-type strain indicate that *P. putida* LU2201 carries a regulatory mutation in the *N*-terminal domain of the putative positive activator AcoR, which accounts for the EPA$^+$ phenotype.

Material and methods

Bacterial strains and growth conditions

Bacterial strains and plasmids used in this study are listed in Table 1. *P. putida* was cultivated at 30°C as previously described (8). EPA (0.1%, w/v), glucose (0.2%, w/v), acetoin (0.2% w/v), glycerol (0.4%, w/v) or succinate (0.2% w/v, pH 7) were used as different carbon sources to analyze the induction of EPA-esterase activity. *E. coli* was grown in an LB medium at 37°C.

Mutagenesis and isolation of the *P. putida* EPA$^+$ mutant strain

Before UV mutagenesis, *P. putida* wild-type strain LU6456 was transformed with pDM101, a plasmid which increases UV-mutagenesis frequency (8), and bacterial colonies containing the plasmid were selected on NB plates. Cells were collected, suspended in NaCl 0.9% (w/v), and spread onto M9 plates containing tryptophan and EPA to identify the EPA$^+$ phenotype (9). After one day incubation at 30°C, plates were subjected to UV radiation at 254 nm, with 1500 Erg intensity for 10 s. Plates were then incubated at 30°C for two days and then at room temperature for several days more.

© 2002 NRC Canada

Fig. 1. Molecular organization of the 8.55 kb DNA fragment carrying the *P. putida* (LU2201 and LU6456) genes involved in the degradation of 2,3-butanediol and acetoin. Restriction map of the DNA region analyzed and physical organization of the genes is included. Indicated are the putative promoters (P_1: σ^{70}-type, P_2: σ^{54}-type) and the putative transcriptional terminators (stem-loops). Relevant DNA fragments used in this study. Triangles indicate the amplification directions of PCR and IPCR primers.

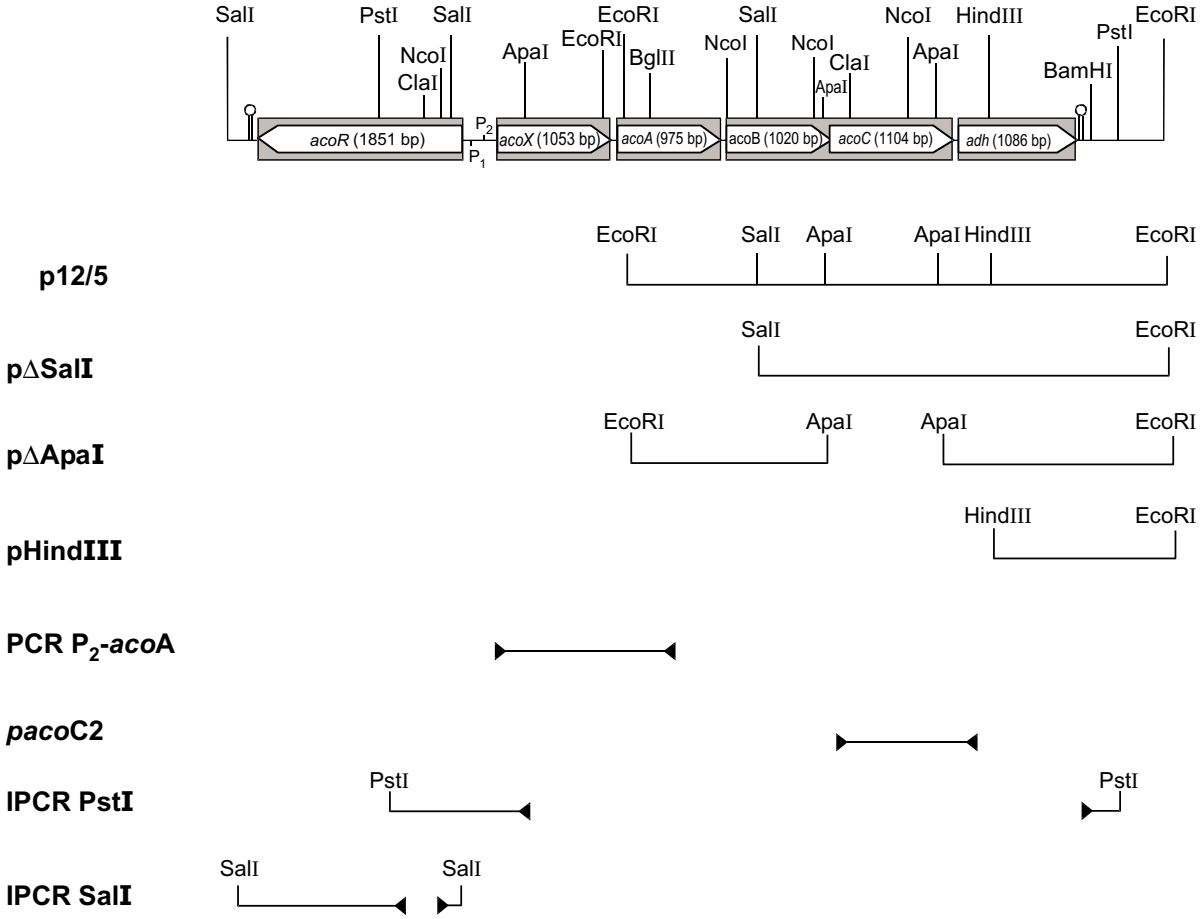

Recombinant DNA techniques, DNA sequencing, and PCR

Recombinant DNA techniques and PCR were performed according to standard protocols (9, 10). To clone the DNA fragment conferring the EPA^+ phenotype, total genomic DNA from *P. putida* LU2201 (0.5 μg) was digested with EcoRI and ligated to pUC19 vector. Approximately 3500 transformants were selected and screened for esterase activity.

IPCR amplifications

Inverse PCR (IPCR) reactions were carried using the Expand™ Long Template PCR System (Roche Biochemicals) according to Ochman et al. (11). The following amplification program was applied: initial denaturation at 95°C for 2 min, 30 cycles of denaturation at 95°C for 20 s, annealing at 65°C for 30 s, elongation at 68°C for 3 min, and a final elongation at 68°C for 8 min.

Expression of *acoC* gene in *E. coli* and purification of the recombinant enzyme

E. coli XL1-Blue transformed with *acoC* plasmids (Table 1) were grown in LB medium at 37°C. The expression of the *acoC* gene was induced by adding isopropyl-β-D-thiogalactoside (IPTG) to a final concentration of 1 mM. Cells were collected by centrifugation (10 min at 8000 × *g* at 4°C) and resuspended in 40 mL of homogenization buffer (20 mM NaH_2PO_4, 1% octylglucopyranoside, 0.05% NaN_3, pH 7). Cells were disrupted by sonication using a Branson Sonifier (1 × 8 min pulse 60% s^{-1} at 0°C) and the lysate was then centrifuged 10 min at 16 000 × *g* at 4°C to remove the cellular debris. The soluble extract was applied to a Chelating-Sepharose 6B column (1.5 × 12 cm, Pharmacia) loaded with Cu^{2+} and equilibrated with buffer A (20 mM NaH_2PO_4, 0.5% octylglucopyranoside, and 0.5 M NaCl, pH 7.7). The column was washed with 80 mL of buffer A and the adsorbed proteins were eluted with a linear gradient of 0 to 0.2 M imidazole-buffer A (pH 6.6). Elution was ended with 60 mL of buffer B. Fractions (5 mL) were collected at a flow rate of 1 mL min^{-1}. Esterase-containing fractions eluted at 0.16 M imidazole. Fractions with high EPA-esterase activity were pooled and concentrated. Purified samples were analyzed by SDS-PAGE and Western blotting and used in enzyme activity assays performed by HPLC.

Esterase activity assay

EPA-esterase production by cells containing suitable plasmids was directly tested on agar plates as described by

© 2002 NRC Canada

Sakimae et al. (12). HPLC analysis was used to determine the EPA-esterase activity in the soluble extracts, in purified samples of the recombinant enzyme, or in bacterial cell suspensions from different growth conditions. In the first two cases, the assay mixture contained 100 μL 1 M sodium phosphate (pH 7), 20 μL of EPA (1 g diluted in 10 mL of ethanol, 10% Triton X-100), and 100 μL of cell-free extract (in homogenization buffer, v.s.) or 0.2 to 6 μg of purified protein sample in a final volume of 1.0 mL. The reaction mixture was incubated at room temperature for 30 min and terminated by the addition of 0.1 mL of HCl (1 N). In the latter case, bacterial cells were collected from agar plates, suspended in 2 mL 100 mM KH_2PO_4 and diluted in H_2O to an OD_{600} value of 2.0. 100 μL of the diluted cultures were added to the same EPA-assay mixture described above. HPLC analysis was performed using a Lichrosorb RP15 column (4 × 250 mm; Merck, Darmstadt).

One unit (U) of EPA-esterase activity was defined as the amount of enzyme releasing 1 μmol of phenyl acetic acid per min.

Cleavage of ethyl-(*S*)-lactate (MEE) and methyl-(*R*,*S*)-ethylbutyrate (MBEE) was analyzed in the same way as EPA cleavage, using filter paper soaked with 0.1% of ethyl-(*S*)-lactate or methyl-(*R*,*S*)-ethylbutyrate, respectively.

Dihydrolipoamide acetyl transferase

Dihydrolipoamide acetyl transferase (DHLAT) activity was assayed by loading purified protein sample (8.5 μg) onto 10% polyacrylamide gels containing 0.2% SDS. The active protein band was visualized by precipitation of $Ca_3(PO_4)_2$ in the presence of acetylphosphate, coenzyme A, phosphotransacetylase from *Bacillus stearothermophilus*, and dihydrolipoamide during incubation of the gel as previously described (13).

Protein methods

Protein concentrations were determined using the method of Bradford (14), with bovine serum albumin as the standard. SDS-PAGE was carried out as described elsewhere (15).

Expression in pQE-8 plasmids yields recombinant protein with an *N*-terminal histidine tag. Immunoblot analyzes of purified preparations were performed using the QIA*express* Detection System (Qiagen GmbH, Hilden, Germany), which specifically identifies this tag. Using purified mouse monoclonal anti-$MRGS(H)_4$ antibodies according to manufacturer's instructions recombinant protein was detected.

Nucleotide sequence accession number

The nucleotide and amino acid sequence data reported in this paper have been submitted at the EMBL nucleotide sequence database under accession number Y11136.

Results

Cloning and characterization of the *P. putida* LU2201 DNA fragment conferring the EPA$^+$ phenotype

Using a method for enhanced UV-induced mutagenesis, we isolated a strain of *P. putida* LU6456 able to use EPA as the sole carbon source (EPA$^+$). This mutant strain designated LU2201 exhibited novel EPA-esterase activity not expressed in the wild type.

Fig. 2. (*a*) In vivo, AcoC (dihydrolipoamide *S*-acetyltransferase, EC 2.3.1.12) catalyzes the transfer of the acetyl group of *S*-acetyldihydrolipoamide to co-enzyme A. (*b*) Hydrolysis of ethyl-phenylacetate (1), ethyl-(*S*)-lactate (MEE) (2), and methyl-(*R*,*S*)-ethylbutyrate (MBEE) (3) by AcoC.

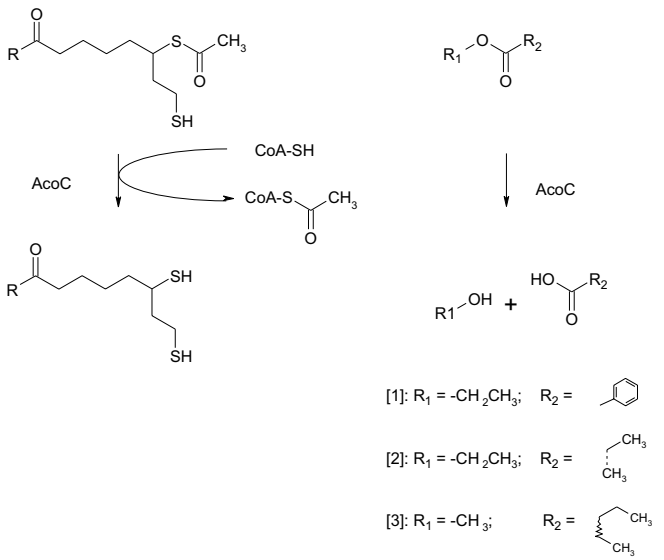

A genomic-DNA library was constructed from LU2201 in *E. coli* and screened for esterase activity by an EPA filter-paper assay and HPLC analysis. Nine (0.26%) EPA-positive transformants were obtained. The EPA-esterase activity measured in cell suspensions was approximately 0.9 U L^{-1}. All clones contained a pUC19 vector containing the same 5.1 kb EcoRI DNA insert. This plasmid was designated p12/5.

The nucleotide sequence of the 5.1-kb EcoRI DNA fragment was determined. DNA database searches revealed strong homologies to structural genes and proteins of the acetoin (3-hydroxy-2-butanone) cleaving systems from different bacteria. In particular, a nearly complete sequence identity to the *acoABC* genes and *adh* gene from *P. putida* strain PpG2 (16) was detected.

The 5.1-kb fragment lacks the putative σ^{54}-type promoter of the operon, the entire *acoX* gene, and the 5′ portion of *acoA*. (Fig. 1).

Identification of *acoC* as the gene responsible for EPA-esterase activity

To determine which gene was responsible for EPA-esterase expression, a deletion analysis of the p12/5 DNA insert was performed.

Three plasmids, pΔSalI, pΔApaI, and pΔHindIII were constructed (Fig. 1). EPA-esterase filter- paper assays showed that the only positive clone was pΔSalI, indicating that the EPA-esterase activity was associated with the *acoC* gene, which encodes dihydrolipoamide acetyltransferase (DHLAT). In vivo this enzyme transfers the acetyl-group of *S*-acetyldihydrolipoamide to coenzyme A (Fig. 2*a*).

The *acoC* gene was subcloned to the expression vector pQE-8 (Qiagen GmbH, Hilden, Germany) to express and

© 2002 NRC Canada

Fig. 3. Expression of *P. putida* LU2201 *acoC* gene in *E. coli* XL1-Blue. Coomassie Blue-stained 10% SDS-PAGE (**A**) and Western blot analysis (**B**) of soluble fractions and purified protein sample. Molecular mass standards (lane 1): 113, 92, 52.3, 35, 29.9, and 21 kDa. (*a*) Soluble proteins of the cell-free extract from *E. coli* XL1-Blue (lane 2, negative control), from *E. coli* carrying p*acoC* 2 plasmid (lane 3). Lane 4, purified AcoC enzyme from *E. coli* cells containing the p*acoC* 2 plasmid. (*b*) Purified AcoC enzyme from *E. coli* cells containing p*acoC* 2 (lane 2).

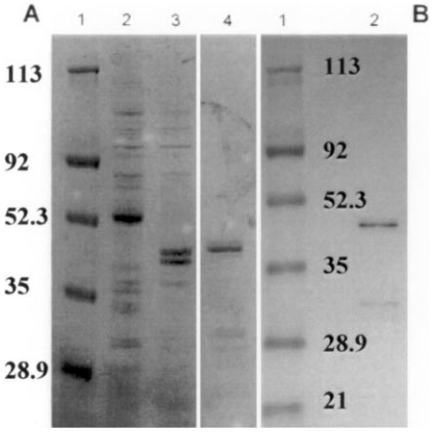

study the protein in *E. coli*. The resulting EPA^+ plasmids p*acoC* 2, (Table 1 and Fig. 1) leads to an EPA-esterase activity of 100.8 U L^{-1}, which is 112-fold higher than *E. coli* bearing the p12/5 plasmid.

Purification and biochemical properties of the recombinant AcoC enzyme

Purification of the recombinant enzyme expressed by p*acoC* 2 was accomplished in a one-step procedure as described above. SDS-PAGE and Western blot analyses of the purified protein sample are shown in Fig. 3.

Activity staining for DHLAT was carried out to verify that the purified AcoC enzyme still catalyzed its physiological reaction (Fig. 3). Protein degradation results in an additional signal with a smaller molecular weight visible in lane 2 of Figs. 3*b* and 4*b*. The positive result shows that the *acoC*-encoded polypeptide from the *P. putida* mutant is a bifunctional enzyme catalyzing both the cleavage of EPA esters and performing its natural reaction as DHLAT.

Sequence comparison to the *acoC* gene product from wild-type *P. putida* LU6456

A comparison of the mutant *acoC* gene to the wild type showed a single-base pair change. This mutation results in a conservative substitution of I238 for V in the mutated AcoC (Fig. 5). The amino acid sequences of the AcoC proteins from *P. putida* LU2201 and LU6456 strains were compared with various AcoC enzymes. The alignment shows that in the protein region where the I238V substitution occurred, AcoC sequences do not show a high degree of conservation.

EPA-esterase activity of *P. putida* wild-type AcoC enzyme

The *acoC* gene from the wild-type strain was cloned on plasmid p*aco*C3 and expressed in *E. coli*. The EPA-activity filter-paper assay also gave a positive response for extracts

Fig. 4. Dihydrolipoamide acetyl transferase (DHLAT) activity assay of the recombinant *P. putida* LU2201 *acoC* gene product. Coomassie Blue-stained 10% SDS-PAGE (*a*) and corresponding DHLAT activity staining gel (*b*) of purified protein sample. Lane 1, molecular mass standards: 106, 80, 49.5, 32.5, and 27.5 kDa; lane 2, purified AcoC enzyme from *E. coli* cells carrying p*acoC* 2 plasmid.

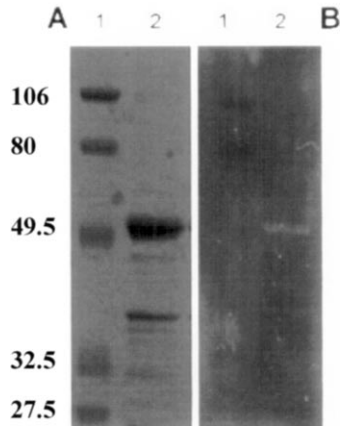

from strains carrying the wild-type gene. Expression experiments indicated that the product of the structural gene *acoC*, from both *P. putida* strains, is a bifunctional enzyme establishing that the I238V substitution alone cannot account for the EPA-esterase activity of LU2201.

Induction of EPA-esterase activity

We investigated the possibility that EPA-esterase activity could also be induced in the *P. putida* wild type using different substrates in addition to acetoin, the direct inducer of *aco* genes. Both strains were grown under different conditions and then bacterial-cell suspensions, collected from agar plates, were assayed for EPA-esterase activity by HPLC (Table 2). Several substrates were able to induce EPA-esterase activity in the *P. putida* wild type. In minimal medium, acetoin acted as the strongest inducer for both strains.

MEE and MBEE esterase activity of AcoC enzyme

MEE and MBEE esterase activities of AcoC enzyme were assayed in both *P. putida* and *E. coli* cells bearing different expression plasmids in which the genes were singularly and constitutively expressed. Both mutated and wild-type AcoC enzymes expressed in *E. coli* were able to hydrolyze MEE and MBEE esters in addition to EPA.

In both *P. putida* LU2201 and LU6456 there is no expression of the *acoC* gene when either MEE or MBEE esters are added as inducers, whereas EPA induces *acoC* expression in LU2201.

Identification and characterization of the regulatory gene *acoR*

To verify whether additional mutations might be present in the *P. putida* LU2201 genome, we characterized the remainder of the *aco* operon and the promoter region not included in the 5.1-kb DNA fragment originally cloned.

On the basis of the molecular organization of the *aco* gene cluster in *P. putida* strain PpG2, a 1.3-kb DNA fragment encompassing the putative σ^{54}-type promoter and the 5′ end of

© 2002 NRC Canada

Fig. 5. Partial amino-acid sequence comparison of AcoC proteins. Sequence comparison of *P. putida* LU2201 and LU6456 AcoC proteins with the corresponding enzymes from different sources. GenBank entries are referenced by the respective accession numbers. *P.p., P. putida* GB L35343; *A.e., Alcaligenes eutrophus* GB M66060; *P.c., Pelobacter carabinolicus* GB L24124; *K.p., Klebsiella pneumoniae* GB U00985; *C.m., Clostridium magnum* GB L31844. Numbers indicate the positions of the respective amino acids within the protein. Regions of identity are boxed. The position of the I238V change is indicated by an asterisk.

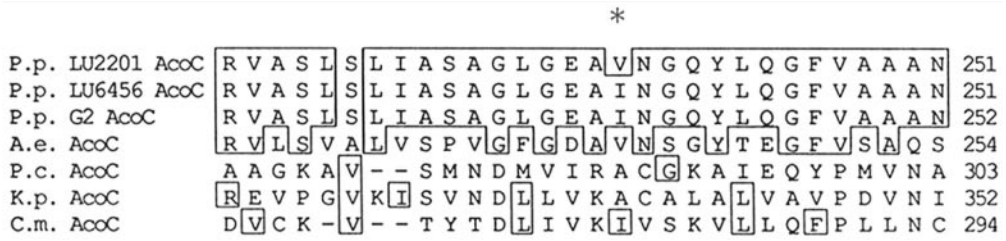

Table 2. Comparison of EPA-esterase activity in cell suspensions from *P. putida* wild type and mutant strain grown in different conditions.

Cultivation	*P. putida* LU6456 wild type EPA-esterase activity (U L^{-1})	*P. putida* LU2201 mutant EPA-esterase activity (U L^{-1})
MM + EPA	n.d.	141.1
MM + acetoin	18.93	303.1
MM + glucose	0.5	12.51
MM + glycerol	2.19	35.7
MM + succinate	0.28	4.3
LB	0.19	0.7
LB + EPA	0	2.1
LB + acetoin	2.42	27.1

Note: *P. putida* strains were grown on mineral medium (MM) + tryptophan (41 μg mL^{-1}) plates in the presence of EPA (0.1%, w/v), acetoin (0.2% w/v), glucose (0.2%, w/v), glycerol (0.4%, w/v) or succinate (0.2% w/v, pH 7) at 30°C. In MM + EPA, *P. putida* LU6456 is not able to grow.

the *aco* operon was isolated by PCR from both *Pseudomonas* strains (Fig. 1). Nucleotide sequence of PCR product P_2-acoA analysis showed the two DNA fragments isolated from *P. putida* wild type and the mutant strain were absolutely identical.

Regulatory genes (designated *acoR* or *acoK*) for the respective *aco* operons have been identified in *A. eutrophus*, *C. magnum*, and *K. pneumoniae* (17–19). In *P. putida* an *acoR*-like gene has not yet been identified. In both *P. putida* strains the DNA region upstream from the putative σ^{54}-type promoter of the *aco* operon was isolated by IPCR. Two IPCR-fragments of 1.2 and 1.6 kb were isolated (Fig. 1). These fragments comprise a total of 2.2 kb of DNA located upstream from the *aco* operon promoter. Nucleotide sequence comparison between the two *P. putida* genomic fragments identified a single-base pair change in the DNA from mutant strain LU2201. This mutation results in an S14R exchange in the corresponding polypeptide.

To study the function of the mutant gene *acoR*S14R in the wild type, we subcloned it in the HindIII site of the plasmid pLAFR1 (20). By conjugation, this construct was introduced into *P. putida*. Exconjugants containing pLAFR::*acoR*S14R had a EPA^+ phenotype. When grown on minimal medium containing EPA, theses strains had an EPA activity of 14.8 U L^{-1}.

Discussion

In the present paper, we isolated and characterized the gene locus conferring the capability to hydrolyze EPA-esters by a novel esterase from *P. putida*. The *P. putida* LU2201 genomic fragment responsible for the EPA^+ phenotype was cloned in *E. coli*. Sequencing analysis revealed that the cloned DNA encodes the structural genes involved in the cleavage of acetoin. Subcloning of the fragment showed that EPA-esterase activity was solely due to the *acoC* gene product DHLAT. Heterologous expression of the *acoC* gene from the *P. putida* mutant revealed that in addition to the cleavage of EPA esters the recombinant enzyme still catalyzes its physiological reaction. By comparative sequence analysis of *acoC* from wild type and LU2201, a single-base pair change causing a conservative I238V replacement in the *C*-terminal region of the mutant *acoC* was determined. Expression of the wild-type *acoC* gene in *E. coli* led to the detection of EPA-esterase activity in the wild-type enzyme as well.

Our findings show that the mutation detected in the AcoC protein from strain LU2201 does not account for the EPA^+ phenotype of this mutant. Rather, the *acoC*-encoded polypeptide from *P. putida* is a bifunctional enzyme and possesses the entire catalytic machinery required to perform both the hydrolysis of the EPA-ester bond and the acetyltransfer step to co-enzyme A. Other enzymes having bi- or even multifunctionalities are well known. For example, an enzyme from *Amycolatopsis* species, which was prematurely identified as an *N*-acylamino acid racemase turned out to be an *O*-succinylbenzoate synthase after a thorough investigation of its genetic environment (21).

In essence, our observations can be considered a snapshot in the course of enzyme evolution. Due to a mutation in the regulatory mechanism of an organism, a thus-far cryptic-catalytic function of an enzyme becomes apparent. In the course of evolution, this enzyme may evolve further away from its original ancestor. In this case, a situation may develop as we find it in the enolase superfamily, where a number of enzymes with different specificities evolved from the same molecular scaffold (12, 22, 23).

Expression experiments indicate that *P. putida* strain LU2201 is altered in its inducer specificity, since the mutant strain, unlike the wild type, is capable of recognizing EPA. This is likely due to a mutation in the regulatory apparatus of the *acoC* gene. This assumption is corroborated by the induction of EPA-esterase activity in *P. putida* wild type by

© 2002 NRC Canada

acetoin (Table 2). Isolation of the DNA region located upstream from the *aco* operon in both *Pseudomonas* strains enabled us to identify *acoR*, the product of which exhibited a striking homology to *A. eutrophus* and *C. magnum* AcoR polypeptides and to other transcriptional activators from different sources (17–19). In the AcoR of the mutant strain, we find an S14R substitution in the *N*-terminal part of the molecule. In similar regulatory proteins, this region was shown to be essential for the interaction with the respective signal molecules. We therefore suggest that mutation of *acoR*S14R alters the specificity of the respective protein in such a way that it can interact with EPA. The EPA–AcoRS14R complex acts as inducer for the *aco* operon, ultimately enabling AcoC to catalyze the hydrolysis of the non-natural substrate EPA. This hypothesis is supported as well by the results from the transformation experiments with pLAFR::*acoR*S14R.

Regulatory mutations may be important events for the in vivo development of new enzyme activities. A mutation in the regulatory apparatus of β-galactosidase is described to precede the evolution of this enzyme (24). In this case, however, the biocatalyst does not have bifunctional properties as in the case of AcoC.

The EPA-esterase activity of the bifunctional AcoC was not predictable from the structure of the protein. Rational approaches to identify the esterase from sequence data would likely have failed. This work describes a novel approach to identify biocatalysts. Regulatory mutants are generated, resulting in a deregulation of otherwise tightly repressed genes. This leads to the production of proteins, which normally would not have been detectable. By screening with the desired substrate, novel enzymes can de identified. This approach broadens the potential of screening for natural diversity; traditional techniques rely on the genes expressed under the respective growth conditions. Non-natural substrates, which are often targets of industrial biocatalysis, may not trigger the appropriate regulatory mechanism in vivo. Thus, potentially useful enzymes remain concealed. As shown for the EPA-esterase from *P. putida*, deregulation by mutation can give access to those hidden genes.

Acknowledgments

We thank Daniela Burkhardt, Uwe Ruffer, Annette Hübner, Andreas Schädler, and Monika Scheidel for their technical assistance.

References

1. U.T. Bornscheuer and R.J. Kazlauskas. *In* Hydrolases in organic synthesis. Wiley-VCH, Weinheim. 1999.
2. D.E. Robertson, E.J. Mathur, R.V. Swanson, B.L. Marrs, and J.M. Short. SIM News, **46**, 3 (1996).
3. R. Chen. Trends Biochem. Sci. **19**, 13 (2001).
4. B.G. Hall and B. Hauer. Methods Enzymol. **224**, 603 (1993).
5. A. Schlacher, T. Stanzer, I. Osprian, M. Mischitz, E. Klingsbichel, K. Faber, and H. Schwab. J. Biotechnol. **62**, 47 (1998).
6. V. Khalameyzer, I. Fischer, U.T. Bornscheuer, and J. Altenbuchner. Appl. Environ. Microb. **65**, 477 (1999).
7. E. Ozaki and A. Sakimae. J. Ferment. Bioeng. **83**, 535 (1997).
8. D.L. McBeth and B. Hauer. Appl. Environ. Microbiol. **62**, 3538 (1996).
9. J. Sambrook, E.F. Fritsch, and T. Maniatis. *In* Molecular cloning: a laboratory manual. CSH Laboratory Press, Cold Spring Harbor, N.Y. 1989.
10. H. Ochman, M.M. Medhora, D. Garza, and D.L. Hartl. PCR protocols. *Edited by* M.A. Innis, D.H. Gelfand, J.J. Sninsky, and T.J. White. Academic Press, San Diego. 1990.
11. H. Ochman, M.M. Medhora, D. Garza, and D.L. Hart. *In* PCR protocols. *Edited by* M.A. Innis, D.H. Gelfand, J.J. Sninsky, and T.J. White. Academic Press, San Diego. 1990.
12. A. Sakimae, A. Hosoi, E. Kobayashi, N. Ohsuga, R. Numazawa, I. Watanabe, and H. Ohnishi. Biosci. Biotechnol. Biochem. **56**, 1252 (1992).
13. H. Priefert, S. Hein, N. Kruger, K. Zeh, B. Schmidt, and A. Steinbuchel. J. Bacteriol. **173**, 4056 (1991).
14. M.M. Bradford. Anal. Biochem. **72**, 248 (1976).
15. U.K. Laemmli. Nature (London), **227**, 680 (1970).
16. M. Huang, F.B. Oppermann, and A. Steinbüchel. FEMS Microbiol. Lett. **124**, 141 (1994).
17. N. Krüger and A. Steinbüchel. J. Bacteriol. **174**, 4391 (1992).
18. N. Krüger, F.B. Oppermann, H. Lorenzl, and A. Steinbüchel. J. Bacteriol. **176**, 3614 (1994).
19. W.L. Deng, H.Y. Chang, and H.L. Peng. J. Bacteriol. **176**, 3527 (1994).
20. S.R. Long, W.J. Buikema, and F.M. Ausubel. Nature (London) **298**, 485 (1982).
21. D.R. Palmer, J.B. Garrett, V. Sharma, R. Meganathan, P.C. Babbitt, and J.A. Gerlt. Biochemistry, **38**, 4252 (1999).
22. J.A. Gerlt and P.C. Babbitt. Curr. Opin. Chem. Biol. **2**, 607 (1998).
23. B.K. Hubbard, M. Koch, D.R.J. Palmer, P.C. Babbitt, and J. A. Gerlt. Biochemistry, **37**, 14369 (1998).
24. B.G. Hall. Bioessays, **12**, 551 (1990).
25. M. Benedik, M. Fennewald, and J. Shapiro. J. Bacteriol. **129**, 809 (1977).

© 2002 NRC Canada

Enzymatic hydrolysis of β-lactam antibiotics at low pH in a two-phase "aqueous solution – water-immiscible organic solvent" system

Ghermes G. Chilov and Vytas K. Švedas

Abstract: The application of the two-phase "aqueous solution – water-immiscible organic solvent" system is suggested not for effective biocatalytic synthesis, but for hydrolytic purposes. Enzymatic hydrolysis of benzylpenicillin and *N*-phenylacetamidodesacetoxycephalosporanic acid to corresponding antibiotic nuclei 6-aminopenicillanic and 7-aminodesacetoxycephalosporanic acids in a two-phase water–butylacetate system at pH 3–4 is proposed as an alternative to the biocatalytic hydrolysis in an alkaline medium. An experimental study has been performed and a model has been developed, which describes the influence of pH, phase volume ratio, thermodynamic constants, and initial antibiotic concentration on the effectiveness of their hydrolysis in a two-phase "aqueous solution – water-immiscible organic solvent" system. The thermodynamic evaluation of penicillin G and 7-phenylacetamidodesacetoxycephalosporanic acid hydrolysis at low pH in a two-phase aqueous solution – water-immiscible organic solvent system has demonstrated high practical potential. The suggested approach allows for the exclusion of several technological steps during the transformation of natural β-lactam antibiotics to their semi-synthetic analogues: alkaline extraction of the biosynthetic antibiotic from butylacetate followed by its enzymatic hydrolysis at pH 7.5–8.0 and further acidification of the reaction mixture, which results in the precipitation of the antibiotic nucleus. Experimental observations also revealed a specific feature of this process: the kinetic supersaturation of the antibiotic nucleus slows down the attainment of the equilibrium, which should be taken into account when further developing this approach.

Key words: enzymatic hydrolysis, β-lactam antibiotic nuclei, two-phase systems, supersaturation, penicillin acylase.

Résumé : On propose l'utilisation du système à deux phases « solution aqueuse – solvant organique immiscible dans l'eau », non pas pour des synthèses biocatalytiques efficaces, mais pour des fins d'hydrolyse. On propose une hydrolyse enzymatique dans le système à deux phases eau–acétate de butyle à un pH allant de 3 à 4 comme alternative à l'hydrolyse biocatalytique en milieu alcalin de la benzylpénicilline et de l'acide *N*-phénylacétamidodésacétoxycéphalosporanique conduisant aux noyaux des antibiotiques correspondants, les acides 6-aminopénicillanique et 7-aminodésacétoxycéphalosporanique. On a effectué une étude expérimentale et on a développé un modèle qui permet de décrire l'influence du pH, du rapport des volumes dans la phase, des constantes thermodynamiques et de la concentration initiale d'antibiotique sur l'efficacité de leurs hydrolyses dans un système à deux phases « solution aqueuse – solvant organique à deux phases ». L'évaluation thermodynamique de l'hydrolyse de la pénicilline G et de l'acide 7-phénylacétamidodésacétoxycéphalosporanique à faible pH, dans un un système à deux phases « solution aqueuse – solvant organique à deux phases » a permis de démontrer le caractère très pratique de ce système. L'approche suggérée permet d'exclure plusieurs étapes technologiques de la transformation des antibiotiques β-lactames naturels en leurs analogues semi-synthétiques, telle l'extraction alcaline de l'antibiotique biosynthétique de l'acétate de butyle, suivie de son hydrolyse enzymatique à pH de 7,5 à 8,0 et de l'acidification subséquente du milieu réactionnel pour précipiter le noyau de l'antibiotique. Une réalisation expérimentale de cette approche a aussi permis de mettre en évidence une caractéristique spécifique du procédé: dans le développement de cette approche, on doit tenir compte du fait que la sursaturation cinétique du noyau antibiotique ralentit l'obtention de l'équilibre.

Mots clés : hydrolyse enzymatique, noyau antibiotique β-lactame, systèmes à deux phases, sursaturation, acylase de pénicilline.

[Traduit par la Rédaction]

Received 14 January 2002. Published on the NRC Research Press Web site at http://canjchem.nrc.ca on 5 June 2002.

Dedicated to Professor J. Bryan Jones on the occasion of his 65th birthday.

G.G. Chilov and V.K. Švedas.[1] Department of Biokinetics, Belozersky Institute of Physicochemical Biology, Lomonosov Moscow State University, 119899 Moscow, Russia.

[1]Corresponding author (e-mail: vytas@belozersky.msu.ru).

 DOI: 10.1139/V02-096 © 2002 NRC Canada

Fig. 1. Penicillin acylase catalyzed hydrolysis of benzylpenicillin (Pen G) and 7-phenylacetamidodesacetoxycephalosporanic acid (CephG) to antibiotic nuclei (6-APA and 7-ADCA, respectively) and phenylacetic acid (PAA).

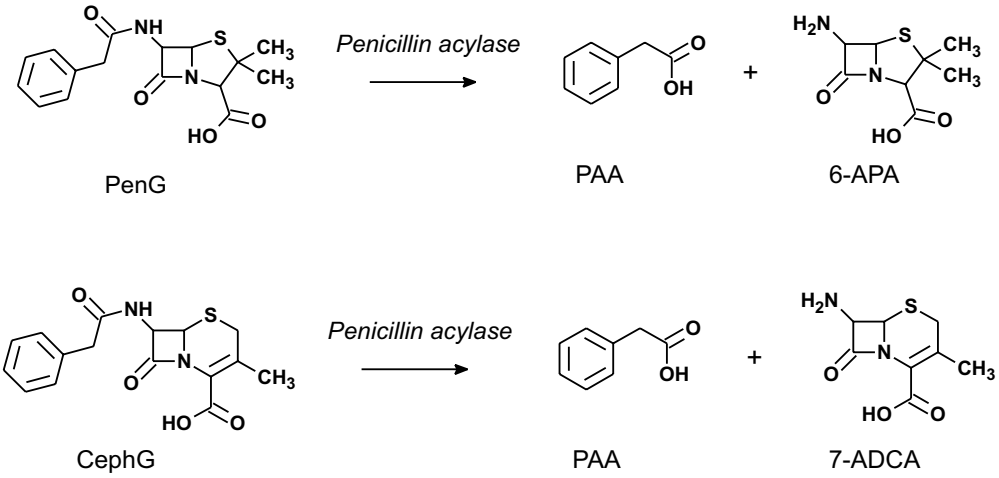

Introduction

In a technological scheme of natural penicillin conversion to its semi-synthetic analogues, penicillin G (Pen G) is first extracted from the fermentation broth by organic solvent (butylacetate, amylacetate) at pH 2.0–2.5 (1). After back-extraction into aqueous solution, it is enzymatically hydrolyzed at pH 7–8 (Fig. 1). After acidification of the reaction mixture, the antibiotic nucleus is isolated by precipitation at its isoelectric point (pH 3.5) (2). Attractiveness of such process stems mainly from thermodynamic considerations, where antibiotic hydrolysis could reach nearly quantitative yields above pH 7 (3). Moreover, the optimum pH (7.5–8.0) of penicillin acylase catalytic activity coincides well with these conditions (4). The major shortcomings of the above-mentioned Pen G conversion to 6-aminopenicillanic acid (6-APA) include numerous pH shifts leading to formation of waste inorganic salts and degradation of a β-lactam ring in an alkaline medium. Additionally, kinetic factors such as strong product inhibition (competitive by phenylacetic acid and non-competitive by 6-APA) should be borne in mind (5). These drawbacks can, however, be avoided in the process presented in this work — the hydrolysis of biosynthetic β-lactam antibiotics Pen G and 7-phenylacetamidodesacetoxycephalosporanic acid (Ceph G) at pH 3–4 in a two-phase water–butylacetate system. Butylacetate containing the acidic form of the antibiotic can be directly added to an aqueous phase containing penicillin acylase, which is followed by partitioning of antibiotic between two phases, hydrolysis of the antibiotic in an aqueous phase, precipitation of an antibiotic nucleus (whose solubility in the considered pH range is the lowest possible), and partitioning of the second reaction product (phenylacetic acid) between the two phases. In addition to the reduction of technological steps, the suggested process can improve the quality and the yield of the reaction product since several factors leading to the degradation of β-lactam ring are excluded. It is worth noting that two-phase water-immiscible organic solvent systems have so far only been evaluated for performing synthetic reactions (6, 7), while the hydrolytic potential of these systems has been deprived of proper attention. For practical implementation of this process in hydrolysis (e.g., in the countercurrent biocatalytic reactor, as recently proposed by Straathof et al. (8)), it is necessary to conceive the thermodynamic and kinetic parameters of the system, which influence the effectiveness of this process. Here, a more detailed analysis of thermodynamic model of β-lactam antibiotic hydrolysis in a two-phase aqueous solution – water-immiscible organic solvent system is described and some kinetic features of the process are shown to be crucial. Critical evaluation of the experimental results and mathematic modeling demonstrate the potential of the proposed process.

Theoretical aspects

Thermodynamics of hydrolysis in a two-phase system at low pH

Thermodynamic regularities of antibiotic hydrolysis in a two-phase aqueous solution – water-immiscible organic solvent system should take into account the following physicochemical processes:

(*i*) Partition of acidic form of antibiotic (ABH) between two phases:

$$[1] \qquad ABH_{org} \Leftrightarrow ABH$$

with a partition constant of

$$[2] \qquad K_{P,ABH} = \frac{[ABH_{org}]}{[ABH]}$$

(*ii*) Dissociation of ABH in an aqueous phase (p*K* of the carboxylic group of β-lactam antibiotics is close to 2.5):

$$[3] \qquad ABH \Leftrightarrow AB^- + H^+$$

with a dissociation constant of

$$[4] \qquad K_{a,ABH} = \frac{[H^+][AB^-]}{[ABH]}$$

(*iii*) Enzymatic hydrolysis in an aqueous phase:

$$[5] \qquad AB^- + H_2O \Leftrightarrow AH + B^-$$

and the corresponding equilibrium constant:

© 2002 NRC Canada

$$[6] \quad K_{synth,AB} = \frac{[AB^-]}{[AH][B^-]}$$

where AH is a protonated form of phenylacetic acid and B^- is an anionic form of antibiotic nucleus.

(*iv*) Partition of a protonated form of phenylacetic acid between two phases:

$$[7] \quad AH \Leftrightarrow AH_{org}$$

with a partition constant of

$$[8] \quad K_{P,AH} = \frac{[AH_{org}]}{[AH]}$$

(*v*) Dissociation of phenylacetic acid in an aqueous phase:

$$[9] \quad AH \Leftrightarrow A^- + H^+$$

with a dissociation constant (p*K* 4.3) of

$$[10] \quad K_{a,AH} = \frac{[H^+][A^-]}{[AH]}$$

(*vi*) Protonation of an amino group of the antibiotic nucleus (p*K* about 4.7):

$$[11] \quad B^- + H^+ \Leftrightarrow BH^{\pm}$$

with a dissociation constant of

$$[12] \quad K_{a2,BH} = \frac{[B^-][H^+]}{[BH^{\pm}]}$$

(*vii*) Protonation of a carboxylic group of the nucleus (p*K* 2.5):

$$[13] \quad BH^{\pm} + H^+ \Leftrightarrow BH_2^{\pm}$$

with a dissociation constant of the Zwitter-ionic form of

$$[14] \quad K_{a1,BH} = \frac{[BH^{\pm}][H^+]}{[BH_2^+]}$$

(*viii*) Precipitation of the Zwitter-ionic form of antibiotic nucleus:

$$[15] \quad BH^{\pm} \Leftrightarrow BH^+_{ppt}$$

which should make its concentration in an aqueous phase equal to its solubility:

$$[16] \quad [BH^{\pm}] = [BH^{\pm}_{sol}]$$

Bearing in mind the relations mentioned above, we can trace the factors that determine the yield of antibiotic nucleus in the corresponding hydrolysis. Reserving η for the reaction yield, the total content of each component (i.e., concentrations of all ionic forms in the co-existing phases) can be represented as

$$[17] \quad [AB] = (1 - \eta)[AB]_0$$

$$[18] \quad [A] = \eta[AB]_0$$

$$[19] \quad [B] = \eta[AB]_0$$

Concentration of a certain ionic species in an aqueous medium can be expressed as

$$[20] \quad [AB^-] = [AB]F_{AB^-}$$

$$[21] \quad [AH] = [A]F_{AH}$$

where

$$[22] \quad F_{AB} = \frac{1}{1 + \frac{[H^+]}{K_{a,ABH}}(1 + \alpha K_{P,ABH})}$$

$$[23] \quad F_{AH} = \frac{1}{1 + \frac{[H^+]}{K_{a,AH}}(1 + \alpha K_{P,AH})}$$

which follow from the eqs. [2], [4], [8], and [10], respectively (where α is the phase-volume ratio). If concentration of the Zwitter-ionic form is confined by its solubility $[BH^{\pm}_{sol}]$,

$$[24] \quad [B] = [BH^{\pm}_{sol}]\frac{K_{a1,B}}{[H^+]}$$

then the thermodynamic equilibrium of hydrolysis can be expressed in the following way:

$$[25] \quad K_{synth,AB} = \frac{(1-\eta)[AB]_0 F_{AB}}{\eta[AB]_0 F_{AH}[BH^{\pm}_{sol}]\frac{K_{a1,B}}{[H^+]}}$$

The final expression for the reaction yield can be written as

$$[26] \quad \eta = \frac{1}{1 + K_{synth,AB}[BH^{\pm}_{sol}]\frac{K_{a1,B}}{[H^+]}\frac{F_{AH}}{F_{AB}}}$$

Factors that influence the yield of hydrolysis

As seen from the previous paragraph, the yield of the antibiotic nucleus is a complex parameter determined by the thermodynamic constant of hydrolysis, the dissociation and partition constants, and the solubility of the product. Using eq. [26], we can estimate their impact on the outcome of the process.

The effectiveness of the hydrolysis in a two-phase system under a given set of conditions does not depend on the initial antibiotic concentration. Such a conclusion might seem strange, especially if one takes into consideration that in the industrial processing of penicillin, hydrolysis at pH 7–8 (its starting concentration) does not exceed 0.25 M — because of the thermodynamic limitations. A further increase of the substrate concentration would lead to the decrease in the yield of 6-APA (9). But this conclusion is only valid for homogeneous solutions. If precipitation of the product(s) occurs, such a dependence on the initial substrate concentration would also disappear. From a practical point of view, the larger the substrate concentration converted, the higher the productivity of the process.

In evaluating the influence of different factors on the degree of antibiotic conversion, it is important to note that when some characteristics of the two-phase system (thermo-

© 2002 NRC Canada

dynamic constant of hydrolysis, dissociation and partition constants of certain reaction components) are fixed, parameters such as pH and phase volume ratio (α) represent extra degrees of freedom, which must be taken into account when looking for optimal processing conditions.

The pH dependence of a conversion is stipulated by the presence of ionogenic groups capable of dissociation in a pH range of 3–4. It follows from thermodynamic considerations that hydrolysis in an alkaline medium is nearly irreversible. Degradation of β-lactam rings at higher pH, however, limits its application for the biocatalytic process in this pH range, making the biocatalytic process optimal in a pH range of 7–8. In a two-phase system, the situation is quite different. Removal of both reaction products out of the reaction sphere (i.e., precipitation of 6-APA and partition of phenylacetic acid) promotes enzymatic hydrolysis, making the biocatalytic process optimal in acidic medium. In a two-phase system, a pH increase above pH 4.4 hampers extraction of phenylacetic acid into the organic phase, prevents 6-APA precipitation, and, in contrast to homogeneous reactions, does not improve hydrolysis. Analysis of eq. [26] shows that with a pH decrease, antibiotic conversion approaches a definite value:

$$[27]\quad \eta_{\mathrm{pH}\to 0} = \frac{1}{1 + K_{synth,\mathrm{AB}}\,[\mathrm{BH}^{\pm}_{\mathrm{sol}}]\dfrac{K_{a1,\mathrm{B}}}{K_{a,\mathrm{AB}}}\dfrac{1 + K_{P,\mathrm{ABH}}\,\alpha}{1 + K_{P,\mathrm{AH}}\,\alpha}}$$

It is quite clear that the optimal yield is determined both by thermodynamic characteristics and phase volume ratio (α). The influence of the latter parameter, however, is quite limited. Generally, the values of the partition constants are several tens in its magnitude, and hence under reasonable values of α the value of $K_P\alpha$ sufficiently exceeds the unity. Taking this into consideration, eq. [27] may be reduced to

$$[28]\quad \eta_{\mathrm{pH}\to 0} = \frac{1}{1 + K_{synth,\mathrm{AB}}\,[\mathrm{BH}^{\pm}_{\mathrm{sol}}]\dfrac{K_{a1,\mathrm{B}}}{K_{a,\mathrm{AB}}}\dfrac{K_{P,\mathrm{ABH}}}{K_{P,\mathrm{AH}}}}$$

Finally, within the set of thermodynamic parameters and their combinations (which determine the yield), we can distinguish three basic parameters: (*i*) The product of the thermodynamic antibiotic synthesis constant and the solubility of the Zwitter-ionic form of the nucleus ($K_{synth,\mathrm{AB}}[\mathrm{BH}^{\pm}_{\mathrm{sol}}]$). It should be emphasized that the impact of these two parameters on the yield is reciprocal, i.e., any deterioration of the thermodynamics of the hydrolysis could, in principle, be compensated for by lowering the product solubility. (*ii*) The difference in the p*K* of the amino group of antibiotic nuclei and the carboxylic group of the substrate, where protonation of the former leads to the domination of the Zwitter-ionic form (low solubility), while deprotonation of the latter assists in the extraction of the substrate into aqueous phase. (*iii*) The ratio of the partition constants of antibiotic and the phenylacetic acid, where partition of the substrate into the aqueous phase and product withdrawal to the organic phase favors conversion.

Of particular interest is determining the degree of conversion under given conditions. This is especially intriguing, since biocatalytic hydrolysis at pH 7.5–8 was already shown to be quite acceptable. To illustrate this point, we first analyzed the dependence of the yield of 6-APA, calculated on the basis of the model presented above (Fig. 2), using thermodynamic parameters from the literature (Table 1).

Fig. 2. Dependence of 6-APA yield during Pen G hydrolysis in a two-phase system, calculated with the eq. [18] on the basis of constants given in Table 1. Dashed line $\alpha = 1$; solid line $\alpha = 5$; dotted line $\alpha = 0.2$.

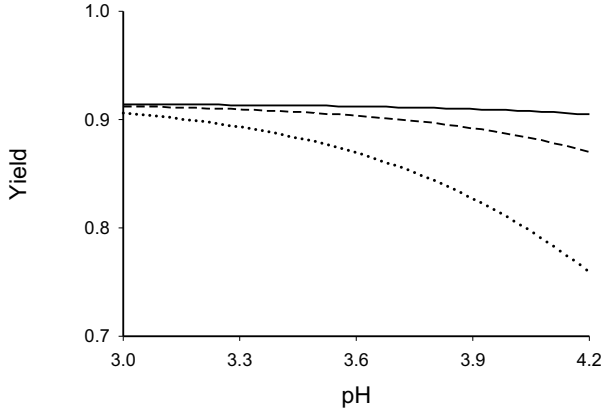

According to thermodynamic predictions, the yield of 6-APA under pH 3–4 with a single hydrolytic step is close to 90%, which may be considered quite satisfactory. But one should determine whether such yields are achievable in practice and if the kinetics of the thermodynamically controlled hydrolysis of antibiotics under a given set of conditions is achievable. The aim of this paper is to report the results of Pen G and Ceph G hydrolysis in a two-phase aqueous solution – water-immiscible organic solvent system at acidic pH.

Materials and methods

Materials

6-APA, 7-ADCA, Pen G-K salt, Ceph G, and penicillin acylase from *E. coli* (ATCC 11105) were kind gifts from DSM (the Netherlands). The concentration of the enzyme-active sites was determined by titration with PMSF (15) and found to be 3.2×10^{-4} M. PAA was from Aldrich, butyl acetate from Fluka, acetonitrile (HPLC grade) from Kriochrom (Russia), sodium dodecylsulfate, the components of the buffer systems, and all other reagents were from Merck. In all experiments MilliQ (Millipore) water was used.

Enzymatic hydrolysis in a two-phase system

Each experiment was performed in a series of microtubes (Eppendorf) in a shaker at 20°C. The total reaction volume was 500 μL. A stock solution of Pen G (0.1 M) was prepared by dissolving the corresponding amount of Pen G–K salt in water. Equal volumes of BuAc and Pen G stock solutions (250 μL of each) were placed in a microtube and the pH was adjusted to a required value with phosphoric acid (less than 5 μL). At cephalosporin hydrolysis, a definite amount of Ceph G (acidic form) was placed in 250 μL of BuAc, the suspension was then treated in an ultrasonic bath (Branson 2510) for 10 min to dissolve the substrate, the required volume of water was added, the system was stirred in the centrifuge, and the pH was adjusted with a KOH solution.

© 2002 NRC Canada

Table 1. Thermodynamic parameters of the processes involved in antibiotic hydrolysis in a two-phase system under acidic pH.

	Pen G	Ceph G	PAA	6-APA	7-ADCA
K_{synth} (M^{-1})	680[a]	n.d.	—	—	—
pK_{COOH}	2.5[b]	2.5[b]	4.3[b]	2.6[c]	2.2[d]
pK_{NH2}	—	—	—	4.7[c]	4.9[d]
K_P	47[e]	n.d.	28[e]	0	0
Solubility (M)	—	—	—	0.01[c]	0.001[d]

[a]Values from ref. 10.
[b]Values from ref. 11.
[c]Values from ref. 12.
[d]Values from ref. 13.
[e]Values from ref. 14.

Reactions were started by adding 7.8 μL of stock PA solution.

Reactions in close-to-equilibrium systems

Reaction conditions (e.g., total reaction volume, temperature, phase volume ratio) were similar to those described above. Stock solutions were prepared by dissolving definite amounts of antibiotic and phenylacetic acid in water; after mixing with BuAc, a required amount of solid 6-APA (or 7-ADCA) was added, and the pH was adjusted with phosphoric acid.

Analysis

To analyze the total content of both the aqueous and organic phases, 10 mL of the stop-reagent (50% of HPLC eluent (v/v) and acetonitrile) was added to the reaction mixture (500 μL) at a definite moment. An aliquot of the obtained solution was diluted with the eluent [potassium phosphate buffer (0.68 g L^{-1}, pH 3.0), sodium dodecylsulfate (100 mg L^{-1}), and CH_3CN (24%, v/v)] and analyzed by HPLC using a Waters system with a Chrompack Nucleosil-C18 4.6 × 250 mm column, Waters Lambda-Max Model 481 detector at 210 nm, and a Waters 6000A pump with a flow of 1 mL min^{-1}. Once the 6-APA concentration in an aqueous phase was determined, the reaction mixture was centrifuged for 1 min at 13 200 rpm (Eppendorf 5415D), and then 10 μL of the aqueous phase were added to 1 mL of the stop-reagent. After dilution with the eluent, an aliquot was subjected to HPLC analysis.

Results and discussion

Hydrolysis of antibiotics

Antibiotic hydrolysis in a two-phase aqueous solution – water-immiscible organic solvent system could be complicated by several factors, with the most negative ones being enzyme inactivation in the organic phase at low pH and β-lactam degradation.

The presence of a water-immiscible organic phase did not influence the activity or stability of native penicillin acylase: the loss of activity during the characteristic time of reaction (1–3 h) did not exceed 10%, which is quite acceptable for the thermodynamic evaluation of the system. Stabilized enzyme preparations should therefore be used in a preparative biocatalytic process to meet the economic and technological demands. In this study, we focused primarily on a thermodynamic evaluation of the new approach, and hence, did not apply standard techniques for PA stabilization (16, 17).

Fig. 3. Integral curves of Pen G (*a*) and Ceph G (*b*) hydrolysis in a two-phase system. (*a*) pH 3.8, 10 μM PA; (*b*) pH 3.5, 10 μM PA; (■), antibiotic (●), antibiotic nucleus.

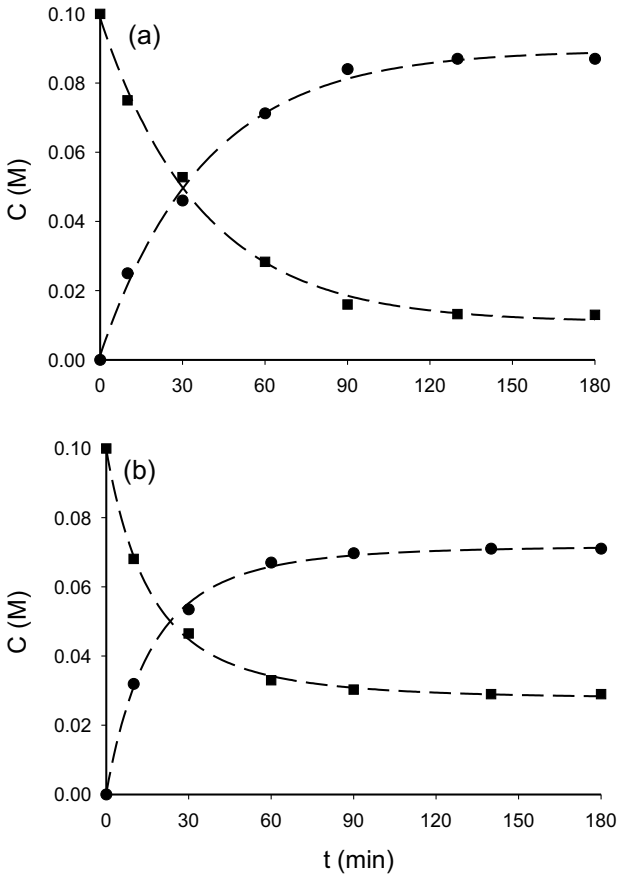

Penicillin degradation was studied by Reschke and Schugerl (1), who observed lower stability of penicillin in an aqueous phase under pH 3–4 and no degradation in the organic phase. Based on their experimental data and accounting for the partition of antibiotic in a two-phase system (Table 1), we determined the chance of penicillin degradation at the stated experimental conditions to be less than 1%. In fact, we did not observe Pen G decomposition within an hour in a two-phase system at pH 3.5. Since Ceph G is known to be more stable in an acidic medium, there was no danger of decomposition.

Typical experimental integral curves of penicillin acylase-catalyzed β-lactam antibiotic hydrolysis in a two-phase system are given in Fig. 3. Effective enzymatic hydrolysis of both biosynthetic antibiotics Pen G and Ceph G took place at pH 3.8, followed by precipitation of corresponding antibiotic nuclei, which is in good agreement with the preliminary thermodynamic evaluation.

Withdrawal of both reaction products out of reaction sphere, i.e., precipitation of 6-APA (or 7-ADCA) and extraction of phenylacetic acid into the organic phase, is favorable from both a thermodynamic and a kinetic point of view. The pH dynamics during the course of hydrolysis must, however, being taken into consideration. Starting from the initial pH (3–4), there was no significant change in pH over the course

© 2002 NRC Canada

Fig. 4. Experimental dependence of conversion degrees in hydrolysis of 0.1 M antibiotic in a two-phase system. (▼), 6-APA; (▲), 7-ADCA.

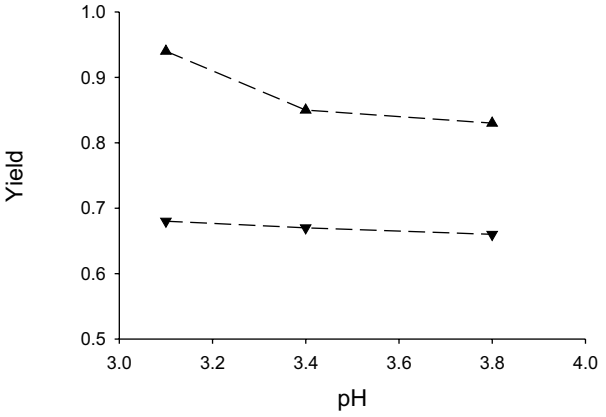

of the reaction due to the balance of the dissociation and partition constants, which prevented formation of unwanted inorganic salts in a reaction mixture.

Experimental antibiotic nuclei yield dependence on pH

Hydrolysis of Pen G and Ceph G in a two-phase system (water–BuAc, 1:1) at pH 3–4 was carried out and the pH dependencies of the antibiotic conversion were obtained (Fig. 4).

In a chosen interval, the yield of hydrolysis (70% for 6-APA and 90% for 7-ADCA) was weakly dependent on pH. It should be noted that the yield of 6-APA evaluated on the basis of reported parameters (Fig. 2) exceeds the experimental yields by 20%. The discrepancy could arise from slightly different experimental conditions used in different laboratories when determining the numerous constants used for the evaluation (eq. [27] contains several parameters determined by different scientists). For example, there is a remarkable discrepancy for the Pen G synthesis constant: Švedas et al. (3) reported a value of 4300 M^{-1}, while Tewari and Goldberg (10) determined the value to be 680 M^{-1}. Bearing this in mind, we tested the thermodynamic model presented above, but initially sought to characterize the equilibrium state during the course of antibiotic hydrolysis in a two-phase system.

It is interesting to compare antibiotic hydrolysis under studied conditions in a biphasic system with that in a monophasic one at the same acidic pH and at traditionally used alkaline conditions (pH 8). Pen G and Ceph G hydrolysis in a monophasic aqueous system at low pH is thermodynamically unfavorable (see corresponding values of equilibrium constants) and is not practical due to very low product yield (less than 30%) as well as low conversion rates due mainly to very strong product inhibition at these conditions (data not shown). Thus, in comparison with the corresponding monophasic aqueous system, the biphasic system (where both reaction products are removed out of the reaction sphere due to extraction of phenylacetic acid into the organic phase and precipitation of 6-APA or 7-ADCA) favors the hydrolytic reaction with thermodynamic and kinetic feasibility.

Compared with the traditional hydrolysis of Pen G and Ceph G at pH 8, the suggested approach is subjected to less

Fig. 5. Supersaturation at antibiotic nucleus formation in the course of Pen G (*a*) and Ceph G (*b*) hydrolysis. (■), total antibiotic nucleus content; (●), concentration in aqueous phase; (……), saturation level.

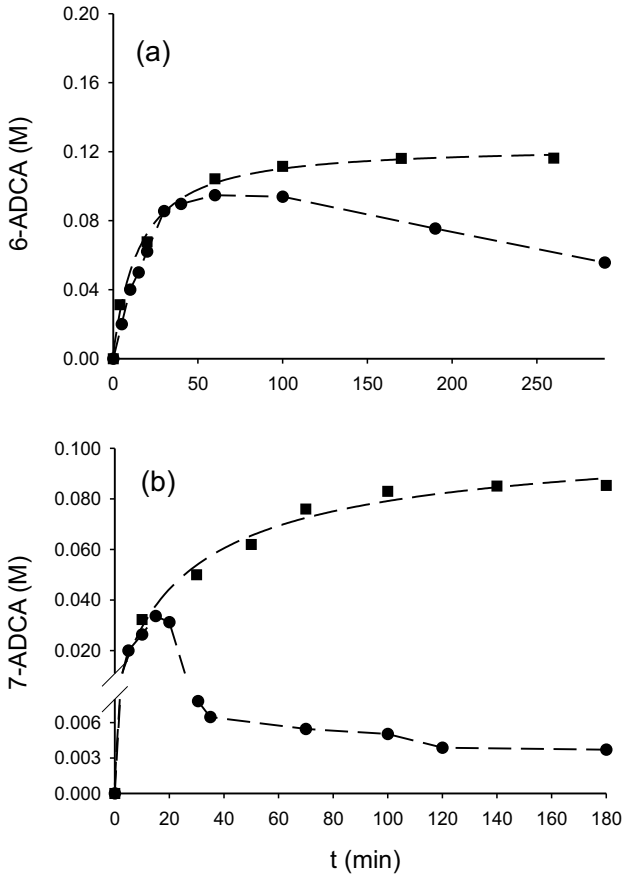

product inhibition, and therefore is just 5 to 6 times slower. The total turnover rate is good enough for preparative conversion. Moreover, the conversion rate can be further increased by the appropriate choice of "acidic" PA, since enzymes of this family are remarkably different in their pH dependencies of catalytic activity (18). Furthermore, the overall antibiotic conversion in a suggested technological process can be increased up to the stoichiometric value by applying a continuous downstream processing scheme. Antibiotic extraction from a cultural broth can be coupled with further conversion in the biphasic system, which allows for downstreaming in the feed-countercurrent reactor, and thus, the possibility of reaching conversions that are close to unity (19). When comparing traditional hydrolysis with a putative one, the overall balance should take into account factors such as the decrease in the number of the technological steps, the formation of waste inorganic salt during numerous pH shifts in the traditional procedure, and the economic gains. It should also be done on the experimental process at the preparative scale.

Dependence of the antibiotic conversion on its initial concentration

The basic qualitative feature of the thermodynamic model of β-lactam antibiotic hydrolysis in a two-phase system with precipitation of the antibiotic nucleus is the independence of

© 2002 NRC Canada

Fig. 6. Reaction in a two-phase system under close-to-equilibrium conditions. (*a*) (▲), 87 mM 6-APA, 87 mM PAA, 13 mM Pen G; (■), 89 mM 6-APA, 89 mM PAA, 11 mM Pen G; (●), 95 mM 6-APA, 95 mM PAA, 5 mM Pen G; (*b*) (▲), 98 mM 7-ADCA, 98 mM PAA, 2 mM Ceph G; (■), 99 mM 7-ADCA, 99 mM PAA, 1 mM Ceph G; (●), 100 mM 7-ADCA, 100 mM PAA, 0 mM Ceph G.

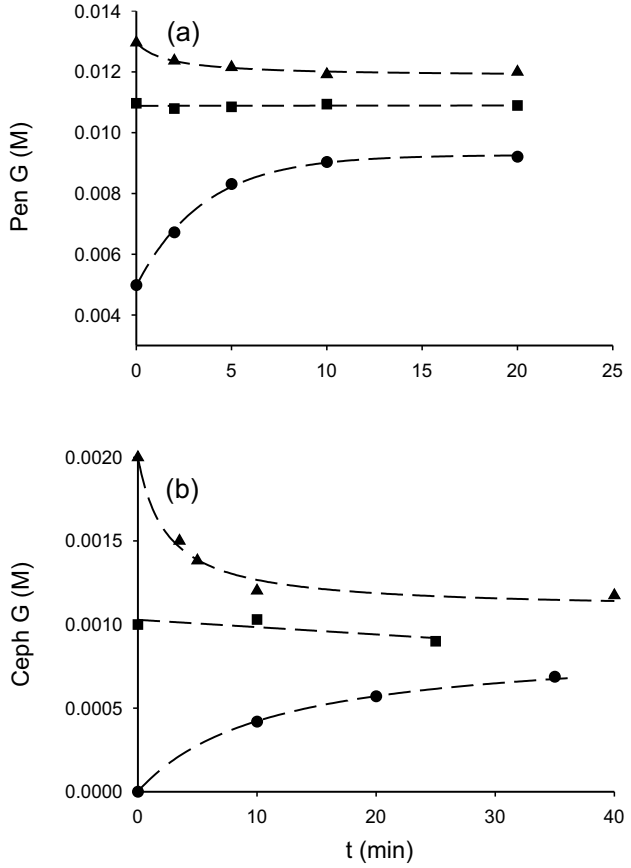

Fig. 7. Dependence of thermodynamically controlled antibiotic conversion degree in a two-phase system. (▼), 6-APA; (▲), 7-ADCA.

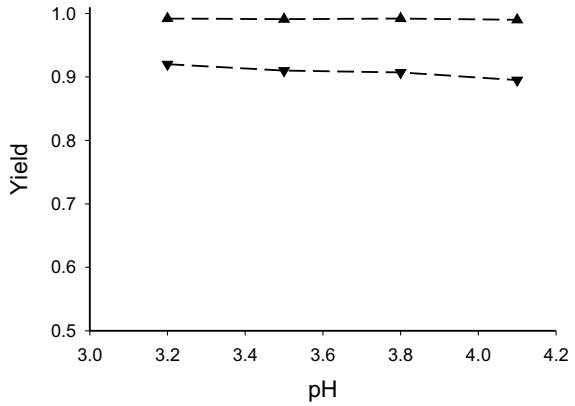

the conversion on the initial substrate concentration. Experimental study shows that this is a case for Ceph G hydrolysis, where the yield of 7-ADCA does not depend on the Ceph G concentration up to the 0.1 M (solubility limit of Ceph G under these conditions). An increase in the Pen G concentration from 0.1 to 0.2 M, however, decreases the yield of 6-APA from 67 to 57%. This fact pointed out one more discrepancy between the thermodynamic model and the experimental data. To solve this apparent contradiction, one might change the model, but there was no sufficient reason for such a change, and we wanted to be sure that the experimental data reflected a true equilibrium state. (Most of the doubts were related to the precipitation of 6-APA.)

Dynamic supersaturation of 6-APA in the course of reaction

Investigation of supersaturation effects was carried out by comparing the composition of aqueous phase with that of the whole system. Results are presented in Fig. 5.

Supersaturation takes place in both cases, and its scale is impressive: 12-fold for 6-APA and 35-fold for 7-ADCA. It therefore makes sense to consider these results in more detail. Normally, supersaturated solutions are usually unstable and supersaturation dissipates within several minutes, but this is not the case in this particular system. The process of antibiotic nuclei crystallization is complicated by various factors such as contact with the organic phase, presence of other reagents (Pen G and PAA), and the enzyme. In a separate experiment, we observed that addition of 6-APA or 7-ADCA crystals into the corresponding reaction mixture does not influence precipitation, which emphasizes the peculiarity of solid-phase formation under these experimental conditions. We noted that 6-APA supersaturation dissipates very slowly (tens of hours) and within the reasonable time interval, one cannot expect the concentration of antibiotic nuclei in aqueous phase to reach equilibrium. Despite a more sharp precipitation for 7-ADCA, equilibrium solubility is also not reached, and fourfold of oversaturation is left. Thus the stability of supersaturated solutions of antibiotic nuclei is most probably responsible for the discrepancy between the experimental and thermodynamic modeling presented above.

True equilibrium state of hydrolysis in a two-phase system

It is nevertheless important to know what yields could be expected if the problems with precipitation of the nuclei were solved. In other words, it is important to determine the true equilibrium state of hydrolysis in a two-phase system. For this purpose, we investigated the direction of the reaction in systems with designed composition of reagents (Pen G, 6-APA, PAA). By tracing the reaction direction it can be concluded where the equilibrium, the state of no macroscopic reagent conversion, is situated. At the same time there is no need to wait for the end of the reaction — it is enough just to check the initial direction and then again with each iteration step as the reaction approaches those concentrations that characterize the system at equilibrium. An analogous method is well known in mathematics as the method of division by half for root estimation, where the sign of a function is checked at each iteration step. If the sign changes, the size of the interval, which contains the root or the equilibrium (as in our case), is reduced. This method is even more attractive because only the initial interval of reaction is taken into account and thus supersaturation, reagent degradation, and other dynamic effects can be omitted.

© 2002 NRC Canada

Fig. 8. Expected degrees of conversion in a two-phase system after formal elimination of supersaturation in accordance with eq. [21]. (▼), 6-APA; (▲), 7-ADCA.

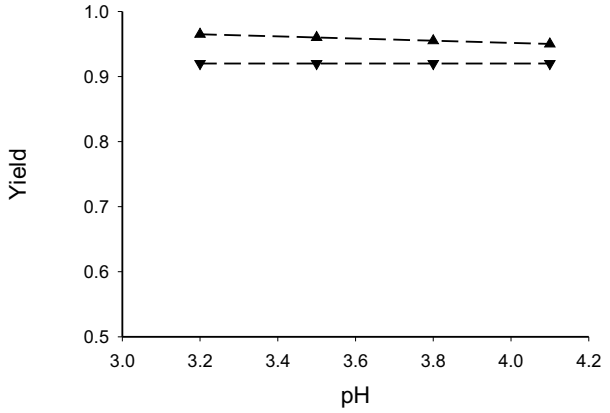

Several typical dependencies are given in Fig. 6 to illustrate this proposed approach.

As can be seen, loading the system with 0.087 M 6-APA, 0.087 M PAA, and 0.013 M Pen G (which corresponds to 87% yield) leads to further hydrolysis of the antibiotic, affording equilibrium yields exceeding 87%. On the other hand, designing a yield of 95% causes a synthetic reaction, and thus the equilibrium value is less than 95%. Finally, in the system containing 0.089 M 6-APA, 0.089 M PAA, and 0.011 M Pen G (89% yield), no macroscopic changes in the concentrations were observed, which suggests a good approach to achieving equilibrium conditions.

A series of measurements under pH 3.2–4.1 was conducted and the thermodynamic equilibrium state of Pen G and Ceph G hydrolysis in a two-phase system (water–BuAc) was found. Results are presented in Fig. 7.

Correspondence of true equilibrium state and practical conversions

In the case of Pen G, thermodynamically estimated yields of hydrolysis (Fig. 2) are in good agreement with experimental values obtained under close-to-equilibrium conditions (Fig. 7). Moreover, the latter values also agreed with the yields in non-equilibrium (as far as nucleus precipitation is concerned) reactions. In fact, if the crystallization process is considered relatively slow in comparison with the chemical reaction, the yield will be determined by eq. [26], where the equilibrium solubility should be replaced by the current concentration (determined by supersaturation) in the aqueous phase. Then, other thermodynamic parameters being equal, the difference between thermodynamically and kinetically controlled yields will be stipulated only by the ratio of saturated and current concentrations according to eq. [26]. After several transformations, we obtain the following parametric relation between the conversion degrees and the ratio of concentrations of precipitating component:

$$[29]\quad \frac{[BH^{\pm}_{eq}]}{[BH^{\pm}_{kin}]} = \frac{\frac{1}{\eta_{eq}} - 1}{\frac{1}{\eta_{kin}} - 1}$$

where $[BH^{\pm}_{eq}]$ is the saturated (equilibrium) level and $[BH^{\pm}_{kin}]$ is the supersaturated (kinetically stipulated) concentration; η_{eq} and η_{kin} are the respective yields. Thus, on the basis of supersaturations observed, one can recalculate expected yields with the use of eq. [29]. Results of these calculations are presented in Fig. 8.

As can be seen, after formal elimination of supersaturation, the expected yields approximate the equilibrium values with good accuracy. This fact highlights that both the experimental results and the theoretical conceptions intrinsically agree.

Conclusion

A process of Pen G and Ceph G hydrolysis is studied in a two-phase system (water–BuAc) at pH 3–4. The thermodynamic model of the process is analyzed, incorporating the influence of pH, phase volume ratio, initial substrate concentration, and parameters of hydrolytic reaction (acid-base and interphase equilibria). For effective hydrolysis, we emphasize the crucial role of product withdrawal from the reaction sphere in a two-phase system: extraction of the emerging phenylacetic acid as well as precipitation of the antibiotic nucleus during the course of hydrolysis result in high yields. Experimental tests also revealed the formation of antibiotic-nucleus supersaturated solutions. For these solutions, being rather stable, the yield in hydrolytic reactions is smaller than predicted by the thermodynamic model. To study the true thermodynamic equilibrium state, a method is proposed where the initial reagent concentrations in an experimental system are set close to the equilibrium concentration values. Depending on whether hydrolysis or synthesis takes place, the interval of equilibrium concentrations is returned. Supersaturation effect is shown to decrease 6-APA yield from 90%, as it is set by thermodynamics, to 67%, and 7-ADCA yield from 99 to 90%, correspondingly.

Acknowledgments

This work was supported by the Russian Foundation for Basic Research (Grants 00–04–48658 and 01–04–06616). We thank T. Van der Does for fruitful discussions and DSM for donated reagents.

References

1. M. Reschke and K. Schugerl. Chem. Eng. J. **28**, B1 (1984).
2. P.S. Nys, L.M. Elizarovskaya, N.N. Shellenberg, and E.M. Savitskaya. Antibiotiki (Rus), **24**, 895 (1979).
3. V.K. Švedas, A.L. Margolin, and I.V. Berezin. Enzyme Microb. Technol. **2**, 138 (1980).
4. I.V. Berezin, A.A. Klyosov, A.L. Margolin, P.S. Nys, E.M. Savitskaya, and V.K. Švedas. Antibiotiki (Rus), **21**, 411 (1976).
5. I.V. Berezin, A.A. Klyosov, V.K. Švedas, P.S. Nys, and E.M. Savitskaya. Antibiotiki (Rus), **19**, 880 (1974).
6. J.B. Jones. Tetrahedron, **42**, 3351 (1986).
7. Y.L. Khmelnitsky, I.N. Zharinova, I.V. Berezin, A.V. Levashov, and K. Martinek. Ann. N.Y. Acad. Sci. **501**, 161 (1987).
8. A.J.J. Straathof, M.B. Diender, J.L. den Hollander, T. van der Does, L.A.M. van der Wielen, and J.J. Heijnen. *In* Integration of biotransformation and downstream processing applied to

© 2002 NRC Canada

β-lactam antibiotic synthesis. Abstracts. 5th Int. Symp. Biocat. Biotrans. Darmstadt. 2001. p. 151.
9. V.K. Švedas. *In* Advances in science and technology. Ser. Biotechnol. *Edited by* P.S. Nys and Yu.V. Mitin. VINITI Press. Moscow. 1988.
10. Y.B. Tewari and R.N. Goldberg. Biophys. Chem. **29**, 245 (1988).
11. M.B. Diender, A.J.J. Straathof, and J.J. Heijnen. Biocatal. Biotransform. **16**, 275 (1998).
12. B.P. Bruns, E.M. Savitskaya, N.N. Shellenberg, G.S. Libinson, T.S. Kolygina, and E.N. Druzhinina. Antibiotiki (Rus), **7**, 440 (1962).
13. P.S. Nys, E.V. Koltsova, N.N. Shellenberg, E.M. Savitskaya, and M.M. Levitov. Antibiotiki (Rus), **21**, 391 (1976).
14. M. Reschke and K. Schugerl. Chem. Eng. J. **28**, B11 (1984).
15. V.K. Švedas, A.L. Margolin, S.F. Sherstiuk, A.A. Klyosov, and I.V. Berezin. Bioorg. Khim. **3**, 546 (1977).
16. G. Alvaro, R. Fernandez-Lafuente, R.M. Blanco, and J.M. Guisan. Appl. Biochem. Biotechnol. **26**, 181 (1990).
17. J. Masarova, D. Mislovicova, P. Gemeiner, and E. Michalkova. Biotechnol. Appl. Biochem. **34**, 127 (2001).
18. V. Švedas, D. Guranda, L. van Langen, F. van Rantwijk, and R. Sheldon. FEBS Lett. **417**, 414 (1997).
19. L.A.M. van der Wielen, K. Ch, and A.M. Luyben. Curr. Opin. Biotechnol. **3**, 130 (1992).

List of symbols

α	Phase volume ratio (V_{org}/V_{aq})
$C(X)$	Cconcentration of species X (mol L^{-1})
$C_0(X)$	Initial concentration of X (mol L^{-1})
$F(X)$	Mol fraction of species X
K_a	Acidity dissociation constant (mol L^{-1})
pK	Negative logarithm of acidity dissociation constant
K_P	Partitioning constant
K_{synth}	Equilibrium synthesis constant (mol^{-1} L)
V	Volume (L)
η	Yield

Sub- or superscript

app	Apparent
aq	Aqueous
eq	Equilibrium
kin	Kinetic
org	Organic
sol	Solubility
ppt	Precipitate

© 2002 NRC Canada

Enzymatic oxidation of cyclopropylbenzene: structures of new metabolites and possible mechanistic implications

Vu P. Bui, Minh Nguyen, Jeff Hansen, John Baker, and Tomas Hudlicky

Abstract: Cyclopropylbenzene was subjected to whole-cell fermentation with either *Escherichia coli* JM109 (pDTG601) or *E. coli* JM109 (pDTG602), expressing toluene dioxygenase and toluene dioxygenase – dihydrodiol dehydrogenase enzymes, respectively. The corresponding metabolites, 3-cyclopropylcyclohexa-3,5-diene-1,2-diol (**3**) and 3-cyclopropylbenzene-1,2-diol (**5**) have been isolated in yields of 2.5 and 1 g L^{-1}, respectively. The absolute stereochemistry correlation for **3** is provided, along with a preliminary discussion of its potential in asymmetric synthesis. Possible mechanistic implications are indicated for the enzymatic oxygenation through the use of calculations. Experimental data are provided for all new compounds.

Key words: cyclopropylbenzene, bio-oxidation, *cis*-diene diol, catechol, JM109 (pDTG601), JM109 (pDTG602), dioxygenase.

Résumé : On a soumis le cyclopropylbenzène à une fermentation à l'aide de cellules entières d'*Escherichia coli* JM109 (pDTG601) ou d'*E*. coli JM109 (pDTG602) qui laissent écouler respectivement les enzymes dioxygénase du toluène et dioxygénase du toluène/déshydrogénase du dihydrodiol. On a isolé les métabolites correspondants, le 3-cyclopropylcyclohexa-3,5-diène-1,2-diol (**3**) et le 3-cyclopropylbenzène-1,2-diol (**5**) avec des rendements respectifs de 2,5 g/L et 1 g/L. On présente une corrélation absolue de la stéréochimie du produit **3** ainsi qu'une discussion préliminaire de son potentiel éventuel en synthèses asymétriques. En se basant sur des calculs théoriques, on indique les implications mécanistiques possibles pour l'oxygénation enzymatique. On rapporte les données expérimentales relatives à tous les nouveaux composés.

Mots clés : cyclopropylbenzène, biooxydation, *cis*-dièneediol, catéchol, JM109 (pDTG601), JM109 (pDTG602), dioxygénase.

[Traduit par la Rédaction]

Introduction

The historically significant disclosure of isolation of the first homochiral *cis*-cyclohexadiene diol by Gibson and coworkers (1) in 1968 was soon followed by detailed studies of the degradation pathways employed by soil organisms that grow on aromatic compounds. Gibson provided the first blocked mutants of *Pseudomonas putida*, whose use led to isolation of homochiral diols of type **1** (2). Eventually, the elucidation of the degradation pathway (Fig. 1) allowed the protein synthesis of the first two enzymes employed in the pathway, namely, toluene dioxygenase (TDO) and dihydrodiol dehydrogenase (DHDH), to be expressed in recombinant clones of *Escherichia coli* JM109 (3). Similar organisms have also been constructed to express the topologically similar enzymes, naphthalene (4) and biphenyl dioxygenase (5). The X-ray crystal structure has been solved for naphthalene dioxygenase (6).

Fig. 1. Natural degradation pathway of aromatics by eukaryotic organisms, and mutation points for specific enzyme expression.

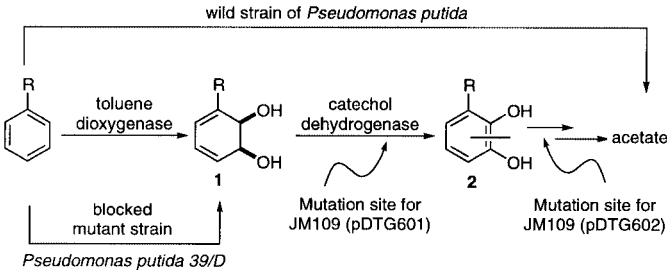

Metabolites of type **1** have been extensively used in asymmetric synthesis (7) since 1987, when the first such application was disclosed by Ley et al. (8). Recently, we reported the synthetic applications of *E. coli* JM109 (pDTG602) to the practical preparation of substituted catechols (**2**), compounds which are difficult to prepare efficiently by traditional means (9). Although cyclopropyl catechol has been previously reported (10), the corresponding diene diol was unknown.

In this paper we report the results of the oxidation of cyclopropylbenzene with the organisms that express TDO

Received 15 March 2002. Published on the NRC Research Press Web site at http://canjchem.nrc.ca on 3 June 2002.

This paper is dedicated to Professor Bryan Jones in recognition and appreciation of his many contributions to the field of biocatalysis.

V.P. Bui, M. Nguyen, J. Hansen, J. Baker, and T. Hudlicky.[1] Department of Chemistry, University of Florida, Gainesville, FL 32611–7200, U.S.A.

[1]Corresponding author (e-mail: hudlicky@chem.ufl.edu).

 DOI: 10.1139/V02-098 © 2002 NRC Canada

Scheme 1. Reagents: (*i*) JM109 (pDTG601); (*ii*) JM109 (pDTG602).

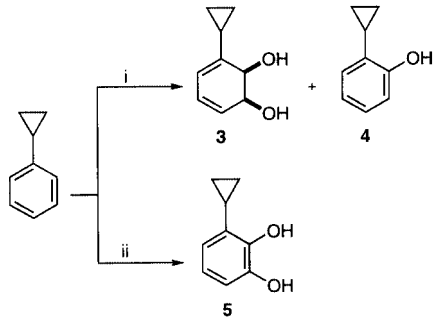

and TDO–DHDH. The isolation of the metabolites may provide clues to the mechanism by which oxygen is introduced into the aromatic nucleus. In addition, the vinylcyclopropanes generated by such means may serve as versatile intermediates for asymmetric syntheses.

Results and discussion

Whole-cell fermentation of either *E. coli* JM109 (pDTG601), expressing toluene dioxygenase (TDO) or *E. coli* JM109 (pDTG602) expressing both TDO and dihydrodiol dehydrogenase (DHDH), was performed in either a 10-L or 15-L fermentor, as previously described (9*b*, 11). When the cells were grown to optimum optical density (OD = 50–60 at 640 nm) (9*b*, 11), the substrate was introduced at a rate of 5 g h^{-1} and the biotransformation allowed to proceed for 5–6 h. After the separation of cells from the broth, diol **3** was isolated in a yield of 2.5 g L^{-1}. Diol **3** is essentially pure after extraction from the broth, but is somewhat unstable and soon thereafter begins to dehydrate to phenol **4** (Scheme 1).

Since this dehydration is greatly accelerated by the presence of acid, it is essential to use base-washed solvents when isolating **3**. The amount of **4** produced varies depending on the time and the amount of acid present. The dehydration process is self-catalytic, insofar as **4** is sufficiently acidic to catalyze further dehydration. Diol **3** can be stored for several weeks at –78°C.

Exposure of cyclopropylbenzene to *E. coli* JM109 (pDTG602) led to the formation of cyclopropyl catechol **5** in an isolated yield of 1 g L^{-1}. The identity of the metabolites was established by spectroscopic techniques. The absolute stereochemistry of diol **3** was confirmed by an independent synthesis of vinylcyclopropane **9** from diol **6** whose absolute stereochemistry is known (Scheme 2). Compound **9** was prepared by the selective reduction of diol **3** with potassium azadicarboxylate (PAD) in 73% yield. Diol **6** was also reduced with PAD (86%) and then protected to provide acetonide **7** (78%) (12). Grignard reagent **11**, derived from cyclopropyl bromide **10**, was coupled with **7** via a modified Corey–House synthesis (13) to give **8** in a low yield (16%). Deprotection of this material with THF–H_2O–TFA (4:1:1) afforded diol **9**, whose $[\alpha]_D$ (–126°) matched that of the material obtained via fermentation of cyclopropylbenzene.

Scheme 2. Reagents and conditions: (*i*) PAD, AcOH, MeOH; (*ii*) DMP, *p*-TsOH; (*iii*) Mg, I_2, Et_2O; (*iv*) $Pd(PPh_3)_4$, THF, reflux; (*v*) THF–H_2O–TFA (4:1:1); (*vi*) Ac_2O, pyridine, DMAP, CH_2Cl_2; (*vii*) JM109 (pDTG601).

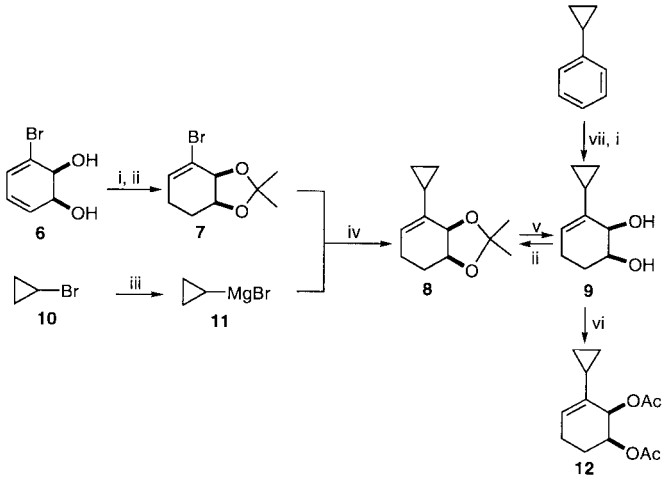

Fig. 2. Exploration of reactivity of oxygenated cyclopropylhexenyl systems.

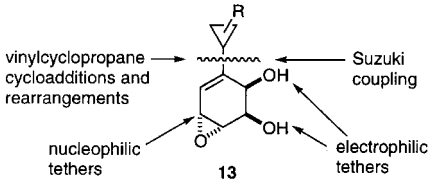

Diol **3** offers new opportunities for asymmetric synthesis through further transformations of the reactive vinylcyclopropane moiety. Two obvious applications are the tethered [5+2] annulation to 7-membered ring systems, discovered and developed by Wender et al. (14), simple thermolysis to cyclopentenes (15), or cascade radical cyclizations with concomitant unraveling of the cyclopropylcarbinyl system (Fig. 2). The electrochemical behavior of the vinylcyclopropane moiety will also be investigated (16).[2]

The development of such new technology also depends on our ability to efficiently couple cyclopropyl units to the vinyl bromide in **6** or **7** via a Suzuki-type process. The research on the synthesis of cyclopropyl boronates is ongoing and will be reported in due course.

Mechanistic implications

The mechanism of aromatic dioxygenation remains unknown, except for initial proposals by Gibson (17), who suggested dioxetane **14** as an intermediate. This proposal would account for the *cis*-configuration of diols **1** found in metabolites from biotransformation by prokaryotic organisms (Fig. 3) (18) and was supported by incorporation of ^{18}O from labeled dioxygen into both hydroxyl groups of the diol

[2] The vinylcyclopropane to cyclopentene rearrangement has been shown to be greatly accelerated by catalytic amounts of triarylaminium ions via a one-electron oxidation (16). We are investigating the initiation of the rearrangement by a one-electron electrochemical oxidation. Cyclic voltammetry of vinylcyclopropane **9** indicates an irreversible oxidation at $E_{1/2}$ = 1.2 V (0.15 M $LiClO_4$ in MeOH). Initial attempts at oxidative rearrangement consumed **9** and produced products that do not contain a cyclopropane ring and may contain a cyclopentene ring.

© 2002 NRC Canada

Fig. 3. Oxygenation of aromatics by prokaryotic and eukaryotic systems.

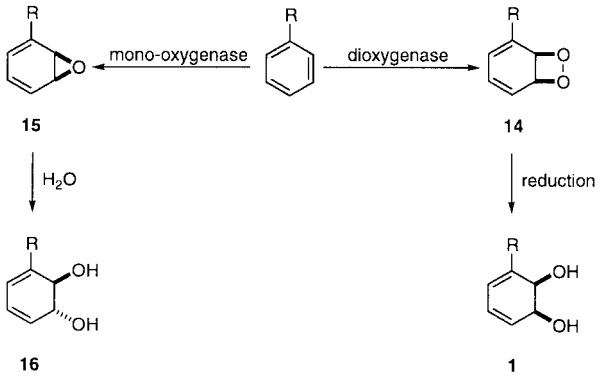

(19). On the other hand, eukaryotic oxidations are much better understood and known to proceed via arene oxides **15** (incorporation of only one oxygen from O_2), which are hydrolyzed to *trans* diols **16** (20).

The suggestion of a dioxetane as an intermediate would require the participation of a singlet oxygen-type species. Alternatively, radical species such as iron-bound peroxy radicals or anionic species (peroxides) of either type **18** or **19** might lead to a stepwise formation of C–O bonds for the former cases or synchronous formation of cycloadducts of type **20** in the latter, as indicated in a very speculative way in Fig. 4 (21).

Since the full structure of naphthalene dioxygenase (NDO) has been determined (6), Gibson and co-workers (21*a*) provided further details on an alternative mechanism of dioxygenation by an iron-peroxide species either of a radical nature or as a partially reduced metal-bound peroxide. Intermediates analogous to **18** or **19** have been observed in the oxidation of indole by NDO in crystals grown in a rich medium containing indole.

Cyclopropylcarbinyl-type rearrangements have been observed during the investigation of the mechanism in the isopenicillin *N*-synthase reaction (22). Iron(IV)–sulfur-bound species have been proposed to account for the results, where trapping of the butenyl radical by the sulfur atom has been observed.

We therefore wished to compare the reactive tendency of a conjugated cyclopropylcarbinyl radical such as **19** to the well-known cyclopropylcarbinyl rearrangement (23). Since unrestricted Becke's hybrid three-parameter functional theory (UB3LYP) (24) provides a reliable level of theory for examining the cyclopropylcarbinyl radical system (25), the density functional theory methodology was used to examine the kinetics of the ring opening of the cyclopropylcarbinyl radical system (**22**) to the conjugated butenyl system (**23**) (Fig. 4). Calculations were performed using the Gaussian 98 program package (26). Structures were optimized and vibrational frequency calculations were performed using UB3LYP level of theory and the 6–31G(*d*) basis set (27). The transition structure was characterized by a single imaginary frequency, and thermochemical information was obtained using unscaled frequencies. Single-point energies were calculated using UB3LYP level of theory using the 6–311+G(2df,2p) basis set (28). At 35°C the ring opening of the cyclopropylcarbinyl radical **(17)** ($k_r = 1.4 \times 10^8$ s^{-1}) (29) is 10^8 times

Fig. 4. Mechanistic possibilities for *cis*-dihydroxylation.

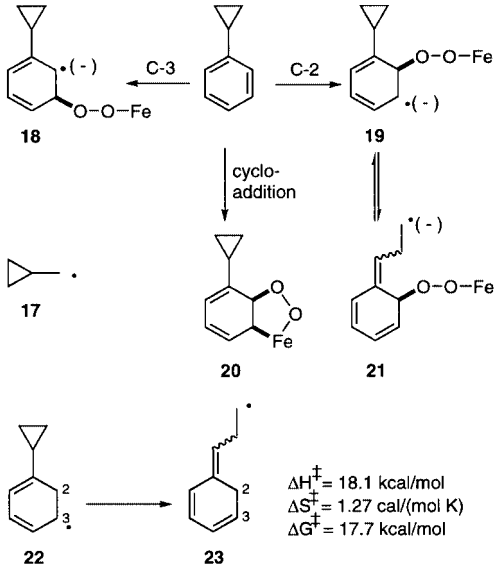

faster than that of radical **22** ($k_r^{calcd} = 1.1$ s^{-1}). Radical stabilizing substituents at the carbinyl position are known to retard the rates of ring opening (30). Even if a radical is formed at C3, ring opening may not occur if the radical has a short lifetime.

Conclusions

The calculation described here for species such as **19** does not eliminate the possibility of intermediates of this type in the oxidation of cyclopropyl benzene even though products derived from the ring opening of the cyclopropane have not been observed in the reaction mixtures. While the nature of the *cis*-dihydroxylation remains a mechanistic enigma, recent evidence by Gibson points to a possible stepwise mechanism for this unique reaction. Whether the mechanism involves radical or anionic iron-bound species is at the moment unknown.

From a synthetic viewpoint, the cyclopropyl system further offers various synthetic manipulations and can be viewed as a chiral vinylcyclopropane synthon for incorporation into future synthetic schemes. Such endeavors will be reported in due course.

Experimental

3-Cyclopropylcyclohexa-3,5-diene-1,2-diol (3)

3-Cyclopropylcyclohexa-3,5-diene-1,2-diol was isolated from the crude mixture collected from the biotransformation of cyclopropyl benzene. This was accomplished by centrifugation of the cells and extraction of the broth with base-washed ethyl acetate. This process provides essentially pure diene diol, which can be further purified by flash column chromatography (hexanes–EtOAc, 4:1) to afford a white solid; mp 45–46°C (dec); $[\alpha]_D^{28}$ +11.39 (*c* 1.75, CD_3OD); R_f = 0.4 (hexanes–EtOAc, 1:1). IR (film) (cm^{-1}): 3274, 3008, 2911, 1453, 1090, 992, 804. ^1H NMR (300 MHz, acetone-d_6) δ: 5.75–5.85 (m, 1H), 5.54–5.66 (m, 2H), 4.17–4.26 (m, 1H), 3.63–3.81 (m, 2H), 3.40–3.51 (d, J = 7 Hz, 1H), 1.48–1.62 (m, 1H), 0.40–0.79 (m, 4H). ^{13}C NMR (75 MHz,

© 2002 NRC Canada

acetone-d_6) δ: 130.2, 127.4, 124.7, 118.7, 71.2, 69.0, 15.8, 7.6, 6.6.

2-Cyclopropylphenol (4)

2-Cyclopropylphenol was isolated from the crude mixture collected from the biotransformation of cyclopropyl benzene. The phenol was purified by distillation to afford a clear oil; R_f = 0.42 (hexane–EtOAc, 8:1). IR (film) (cm^{-1}): 3536, 1609, 1580, 1491, 752. ^{1}H NMR (300 MHz, DMSO-d_6) δ: 9.26 (s, 1H), 6.86–6.92 (m, 1H), 6.63–6.76 (m, 3H), 2.02–2.12 (m, 1H), 0.80–0.87 (m, 2H), 0.55–0.61 (m, 2H). ^{13}C NMR (75 MHz, $CDCl_3$) δ: 155.8, 129.4, 125.9, 124.5, 119.0, 114.6, 9.3, 7.7. EI-MS *m*/*z*: 136 (23), 134 (100), 133 (24), 115 (27), 107 (39), 106 (21), 105 (28), 91 (34), 89 (41), 78 (24), 77 (96), 61 (43). EI-HRMS calcd. for $C_9H_{10}O$ (M^+): 134.0732; found: 134.0732.

3-Cyclopropylbenzene-1,2-diol (5)

Metabolite **5** was prepared by biotransformation of the corresponding arene with *E. coli* JM109 (pDTG602); mp 41–42°C; R_f = 0.52 (hexane–EtOAc, 3:2). IR (film) (cm^{-1}): 3418, 1622, 1592, 1477, 775. ^{1}H NMR (300 MHz, DMSO-d_6) δ: 9.11 (s, 1H), 8.11 (s, 1H), 6.50–6.58 (m, 1H), 6.49 (t, J = 7.8 Hz, 1H), 6.16–6.21 (m, 1H), 2.01–2.12 (m, 1H), 0.79–0.86 (m, 2H), 0.50–0.57 (m, 2H). ^{13}C NMR (75 MHz, $CDCl_3$) δ: 143.4, 142.9, 128.8, 120.6, 119.7, 113.5, 9.4, 6.1. EI-MS *m*/*z* (%): 150 (100), 149 (6), 107 (26), 77 (44). EI-HRMS calcd. for $C_9H_{10}O_2$ (M^+): 150.0681; found: 150.0675. Anal. calcd. for $C_9H_{10}O_2$: C 71.98, H 6.71; found: C 72.07, H 6.69.

7-Cyclopropyl-2,2-dimethyl-3a,4,5,7a-tetrahydrobenzo[1,3]dioxole (8)

To a well-stirred solution of diol **9** (0.150 g, 1.0 mmol) in 2,2-dimethoxypropane (DMP) (20 mL), a catalytic amount of *p*-toluenesulfonic acid was added. The reaction mixture was stirred for 30 min and then quenched with 5% $NaHCO_3$ (2 mL). Solvent was removed under reduced pressure. The residue was diluted with brine (20 mL) and extracted with CH_2Cl_2 (3 × 30 mL). The organic layers were combined, dried ($MgSO_4$), and concentrated under reduced pressure. The crude residue was purified by flash silica gel chromatography (hexane–EtOAc, 8:1) to afford **8** (0.151 g, 80%); $[\alpha]_D^{20}$ +58.99 (*c* 1.0, CH_3OH); R_f = 0.57 (hexane–EtOAc, 8:1). IR (film) (cm^{-1}): 3082, 2985, 1456, 1367, 870. ^{1}H NMR (300 MHz, $CDCl_3$) δ: 5.51 (t, J = 3.9 Hz, 1H), 4.37 (d, J = 4 Hz, 1H), 4.25–4.31 (m, 1H), 2.09–2.22 (m, 1H), 1.75–1.96 (m, 2H), 1.60–1.72 (m, 2H), 1.42 (d, J = 5 Hz, 6H), 0.32–0.71 (m, 4H). ^{13}C NMR (75 MHz, $CDCl_3$) δ: 137.3, 123.4, 108.5, 74.5, 73.8, 28.2, 26.8, 25.9, 20.9, 14.6, 5.9, 5.1. EI-MS *m*/*z* (%): 179 (57), 137 (33), 136 (66), 121 (29), 108 (25), 107 (28), 95 (21), 91 (100), 79 (45), 77 (23), 55 (26). EI-HRMS calcd. for $C_{12}H_{18}O_2$ (M^+): 194.1307; found: 194.1317.

3-Cyclopropylcyclohex-3-ene-1,2-diol (9)

Method A*: *From diol 3

To a well-stirred and ice-cooled solution of diol **3** (17 g, 0.11 mol) in methanol (50 mL), potassium azadicarboxylate (PAD) (76 g, 0.35 mol) was added. A solution of acetic acid (64 mL, 1 mol) in methanol (50 mL) was added dropwise to the reaction mixture at such a rate that 1–2 bubbles were produced per second. The mixture was allowed to warm to ambient temperature, with the color changing from yellow to milky white. The reaction mixture was stirred overnight and then quenched with saturated $NaHCO_3$ until effervescence ceased. Methanol was removed under reduced pressure. The residue was diluted with brine (20 mL) and extracted with ethyl acetate (4 × 40 mL). The combined organic phases were dried ($MgSO_4$) and concentrated to yield a reddish oil. The crude product was purified by flash silica gel chromatography (hexane–EtOAc, 3:2) to afford **9** (12.411 g, 73%); as a white solid; mp 96–98°C; $[\alpha]_D^{29}$ –126.0 (*c* 1.0, CH_3OH); R_f = 0.20 (hexane–EtOAc, 3:2). IR (film) (cm^{-1}): 3272, 3012, 1461, 989. ^{1}H NMR (300 MHz, DMSO-d_6) δ: 5.32 (s, 1H), 4.32–4.36 (m, 1H), 3.65 (t, J = 4 Hz, 1H), 3.35–3.42 (m, 2H), 1.92–1.99 (m, 2H), 1.52–1.63 (m, 1H), 1.38–1.46 (m, 2H), 0.33–0.56 (m, 4H). ^{13}C NMR (75 MHz, $CDCl_3$) δ: 138.6, 123.4, 70.0, 68.9, 25.3, 24.2, 14.9, 5.6. FAB-MS *m*/*z* (%): 137 (8), 93 (100). FAB-HRMS calcd. for $C_9H_{13}O$ ([MH – H_2O]$^+$): 137.0966; found: 137.0967. Anal. calcd. for $C_9H_{14}O_2$: C 70.1, H 9.15; found: C, 70.17, H 9.18.

Method B: From vinyl bromide 7

A 50-mL round-bottom flask equipped with a condenser and an addition funnel under argon atmosphere was charged with magnesium metal (0.76 g, 31.2 mmol) and a crystal of iodine. The addition funnel was charged with a solution of cyclopropyl bromide (0.76 g, 6.24 mmol) in anhydrous diethyl ether (10 mL) and this solution was added dropwise into the reaction flask. Once the reaction proceeded on its own, the addition was continued to maintain a constant reflux. After the addition was completed the reaction flask was heated to reflux for an additional 45 min. Grignard reagent **11** was then transferred into another reaction flask containing bromoacetonide **7** (1.29 g, 5.61 mmol) and tetrakis(triphenylphosphine) palladium (0.194 g, 0.17 mmol) in THF (25 mL). The reaction was heated at reflux for 5 h and then the reaction mixture was filtered through a thin layer of silica. The filtrate was concentrated under reduced pressure. Flash chromatography provided the coupled product **8** (0.174 g, 16%). Acetonide **8** was deprotected using a THF–H_2O–TFA (4:1:1, 10 mL) solvent mixture to afford diol **9** (0.104 g, 75%) whose physical data matched the compound obtained via the biotransformation of cyclopropylbenzene followed by PAD reduction.

Acetic acid 6-acetoxy-2-cyclopropylcyclohex-2-enyl ester (12)

To a well-stirred solution of diol **9** (0.105 g, 0.68 mmol) in CH_2Cl_2 (20mL), pyridine (0.16 g, 2.0 mmol) was added. Addition of acetic anhydride (0.21 g, 2.0 mmol) was followed by dimethylaminopyridine catalyst (0.2 mg, 0.20 mol%). The reaction mixture was allowed to stir for 20 h and quenched with saturated citric acid (2 mL). The reaction mixture was diluted with brine (20 mL) and extracted with CH_2Cl_2 (3 × 30 mL). The organic layers were combined, dried (Na_2SO_4), and concentrated under reduced pressure. The crude residue was purified by flash silica gel chromatography (hexane–EtOAc, 3:2) to afford **12** (0.156 g, 96%) as a white solid; mp 80.5–81.5°C; $[\alpha]_D^{29}$ –196.9 (*c* 1.0,

© 2002 NRC Canada

CH_3OH); R_f = 0.79 (hexane–EtOAc, 3:2). IR (film) (cm^{-1}): 1739, 1460, 1248. ^1H NMR (300 MHz, $CDCl_3$) δ: 5.82 (t, J = 3.2 Hz, 1H), 5.52 (d, J = 3.2 Hz, 1H), 4.92–4.99 (m, 1H), 2.14–2.22 (m, 2H), 2.10 (s, 3H), 2.01 (s, 3H), 1.84–1.91 (m, 1H), 1.70–1.74 (m, 1H), 1.22–1.28 (m, 1H), 0.50–0.64 (m, 2H), 0.30–0.47 (m, 2H). ^{13}C NMR (75 MHz, $CDCl_3$) δ: 170.9, 170.6, 135.6, 125.5, 70.8, 68.4, 24.3, 22.6, 21.3, 21.2, 14.8, 5.6, 5.0. EI-MS *m/z* (%): 179 (100), 119 (92), 91 (24). EI-HRMS calcd. for $C_{13}H_{19}O_4$ (MH^+): 239.1283; found: 239.1289. Anal. calcd. for $C_{13}H_{18}O_4$: C 65.63, H 7.61; found: C, 65.43, H 7.60.

Acknowledgments

The generous research support from the National Science Foundation (CHE-9910412), TDC Research, Inc., and TDC Research Foundation is acknowledged. We thank Professor William Dolbier (UF) and his group for assistance with the calculations performed by John M. Baker.

References

1. D.T. Gibson, J.R. Koch, C.L. Schuld, and R.E Kallio. Biochemistry, **7**, 3795 (1968).
2. D.T. Gibson, M. Hensley, H. Yoshioka, and T.J. Mabry. Biochemistry, **9**, 1626 (1970).
3. G.J. Zylstra and D.T. Gibson. J. Biol. Chem. **264**, 14940 (1989).
4. J.J. Simon, T.D. Osslund, R. Saunders, B.D. Ensley, S. Suggs, A. Harcourt, W.C. Suen, D.L. Cruden, D.T. Gibson, and G.J. Zylstra. Gene, **127**, 31 (1993).
5. F.J. Mondello. J. Bacteriol. **171**, 1725 (1989).
6. B. Kauppi, K. Lee, E. Carredano, R.E. Parales, D.T. Gibson, H. Eklund, and S. Ramaswamy. Structure, **6**, 571 (1998).
7. (*a*) T. Hudlicky, D. Gonzalez, and D.T. Gibson. Aldrich. Acta, **32**, 35 (1999); (*b*) D.R. Boyd and G.N. Sheldrake. Nat. Prod. Rep. **15**, 309 (1998); (*c*) T. Hudlicky. *In* Green chemistry: Frontiers in benign chemical syntheses and process. *Edited by* P.T. Anastas and T.C. Williamson. Oxford University Press, Oxford. 1998. Chap. 10. p. 166; (*d*) T. Hudlicky. *In* Green chemistry: Designing chemistry for the environment. Vol. 626. *Edited by* P.T. Anastas and T.C Williamson. ACS Symposium Series, American Chemical Society, Washington, DC. 1996. p. 180; (*e*) T. Hudlicky, D.A. Entwistle, K.K. Pitzer, and A.J. Thorpe. Chem. Rev. **96**, 1195 (1996); (*f*) T. Hudlicky. Chem. Rev. **96**, 3 (1996); (*g*) T. Hudlicky and A.J. Thorpe. Chem. Commun. 1993 (1996); (*h*) T. Hudlicky and J.W. Reed. *In* Advances in asymmetric synthesis. *Edited by* A. Hassner. JAI Press, Greenwich, CT. 1995. p. 271; (*i*) A.D. Grund. SIM News, **45**, 59 (1995); (*j*) S.M. Brown and T. Hudlicky. *In* Organic synthesis: Theory and applications. Vol. 2. *Edited by* T. Hudlicky. JAI Press, Greenwich, CT. 1993. p. 113; (*k*) H.A.J. Carless. Tetrahedron: Asymmetry, **3**, 795 (1992); (*l*) G.N. Sheldrake. *In* Chirality and industry. *Edited by* A.N. Collins, G.N. Sheldrake, and J. Crosby. John Wiley and Sons, Chichester, U.K. 1992. p. 127; (*m*) D.A. Widdowson, D.W. Ribbons, and S.D. Thomas. Janssen Chimica Acta, **8**, 3 (1990).
8. S.V. Ley, F. Sternfeld, and S. Taylor. Tetrahedron Lett. **28**, 225 (1987).
9. (*a*) V.P. Bui, T.V Hansen, Y. Stenstrom, and T. Hudlicky. Green Chem. **2**, 263 (2000); (*b*) for an up-to-date description of the medium-scale fermentation procedure see: M.A. Endoma, V.P. Bui, J. Hansen, and T. Hudlicky. Org. Process Res. Dev. In press (2002); (*c*) V.P. Bui, T. Hudlicky, T.V. Hansen, and Y. Stenstrom. Tetrahedron Lett. **43**, 2839 (2002).
10. (*a*) J.B. Johnston and V. Renganathan. Enzyme Microb. Technol. **9**, 706 (1987); (*b*) J.B. Johnston and V. Renganathan. Applied Microb. Biotechnol. **31**, 419 (1989).
11. (*a*) V.P. Bui, T.V. Hansen, Y. Stenstrom, T. Hudlicky, and D.W. Ribbons. New J. Chem. **25**, 116 (2001); (*b*) V.P. Bui, T.V. Hansen, Y. Stenstrom, D.W. Ribbons, and T. Hudlicky. J. Chem. Soc. Perkin Trans 1, 1669 (2000); (*c*) T. Hudlicky, M.R. Stabile, D.T. Gibson, and G.M. Whited. Org. Synth. **76**, 77 (1999).
12. D.R. Boyd, M.R. Hand, N.D. Sharma, J. Chima, H. Dalton, and G.N. Sheldrake. J. Chem. Soc. Chem. Commun. 1630 (1991).
13. M. Yamamura, I. Moritani, and S.I. Murahashi. J. Organomet. Chem. **91**, C39 (1975).
14. (*a*) P.A. Wender, H. Takahashi, and B. Witulski. J. Am. Chem. Soc. **117**, 4720 (1995); (*b*) P.A. Wender, J.M. Nuss, D.B. Smith, A. Suarez-Sobrino, J. Vagberg, D. Decosta, and J. Bordner. J. Org. Chem. **62**, 4908 (1997); (*c*) P.A. Wender and A.J. Dyckman. Org. Lett. **1**, 2089 (1999); (*d*) P.A. Wender, M. Fuji, C.O. Husfeld, and J.A. Love. Org. Lett. **1**, 137 (1999); (*e*) P.A. Wender, A.J. Dyckman, C.O. Husfeld, and M.J. Scanio. Org. Lett. **2**, 1609 (2000); (*f*) P.A. Wender, F.C. Bi, M.A. Brodney, and F. Gosselin. Org. Lett. **3**, 2105 (2001); (*g*) P.A. Wender, C.M. Barzilay, and A.J. Dyckman. J. Am. Chem. Soc. **123**, 179 (2001).
15. T. Hudlicky. J.W. Reed. *In* Comprehensive organic synthesis: Selectivity, stategy and efficiency in modern organic chemistry. Vol. 5. *Edited by* B.M. Trost. Pergamon Press, Oxford. 1991. p. 899.
16. (*a*) J.P. Dinnocenzo and D.A. Conlon. J. Am. Chem. Soc. **110**, 2324 (1988); (*b*) J.P. Dinnocenzo and D.A. Conlon. Tetrahedron Lett. **36**, 7415 (1995).
17. D.T. Gibson. Zentralbl. Bakt. P. 157 (1976).
18. D.T Gibson. *In* Microbial degradation of organic compounds. Vol 13. *Edited by* D.T. Gibson. Marcell Dekker, Inc., New York, NY. 1984. Chap. 7. p. 181.
19. D.T. Gibson, G.E. Cardini, F.C. Maseles, and R.E. Kallio. Biochemistry, **9**, 1631, (1970).
20. D.M. Jerina and J.W. Daly. *In* Natl. Inst. Arthritis Metab. Dis. *Edited by* T. E. King. Natl. Inst. Health, Bethesda, MD, U.S.A. Oxidases Relat. Redox Syst., Proc. Int. Symp. 2nd (1973), Meeting Date 1971, 1, 143.
21. (*a*) Gibson has recently reported evidence suggesting a stepwise mechanism. E. Carredano, A. Karlsson, B. Kauppi, D. Choudhury, R.E. Parales, J.V. Parales, K. Lee, D.T. Gibson, H. Eklund, and S. Ramaswamy. J. Mol. Biol. **296**, 701 (2000); For a review of dioxygenase-type enzymes see: (*b*) K. Chen and L. Que, Jr. Angew. Chem. Int. Ed. **38**, 2227 (1999); (*c*) L. Que, Jr. and R.Y.N. Ho. Chem. Rev. **96**, 2607 (1996).
22. J.E. Baldwin, R.M. Adlington, B.P. Domayne-Hayman, G. Knight, and H.H. Ting. J. Chem. Soc. Chem. Commun. 1661 (1987)
23. L. Birladeanu, T. Hanafusa, B. Johnson, and S. Winstein. J. Am. Chem. Soc. **88**, 2316 (1966); (*b*) C.D. Poulter and S. Winstein. J. Am. Chem. Soc. **91**, 3649 (1969); (*c*) C.D. Poulter and S. Winstein. J. Am. Chem. Soc. **91**, 3650 (1969).
24. A.D. Becke. J. Chem. Phys. **98**, 5648 (1993).
25. D.M. Smith, A. Nicolaides, B.T. Golding, and L. Radom. J. Am. Chem. Soc. **120**, 10223 (1998).
26. M.J.T. Frisch, G.W. Trucks; H.B. Schlegel, G.E. Scuseria, M.A. Robb, J.R. Cheeseman, V.G. Zakrzewski, J.A. Montgomery, Jr., R.E. Stratmann, J.C. Burant, S. Dapprich, J.M. Millam, A.D. Daniels, K.N. Kudin, M.C. Strain, O. Farkas, J. Tomasi, V. Barone, M. Cossi, R. Cammi, B. Mennucci, C. Pomelli,

© 2002 NRC Canada

C. Adamo, S. Clifford, J. Ochterski, G.A. Petersson, P.Y. Ayala, Q. Cui, K. Morokuma, D.K. Malick, A.D. Rabuck, K. Raghavachari, J.B. Foresman, J. Cioslowski, J.V. Ortiz, A.G. Baboul, B.B. Stefanov, G. Liu, A. Liashenko, P. Piskorz, I. Komaromi, R. Gomperts, R.L. Martin, D.J. Fox, T. Keith, M.A. Al-Laham, C.Y. Peng, A. Nanayakkara, C. Gonzalez, M. Challacombe, P.M.W. Gill, B. Johnson, W. Chen, M.W. Wong, J.L. Andres, C. Gonzalez, M. Head-Gordon, E.S. Replogle, and J.A. Pople. Gaussian 98. Revision A.7. Gaussian, Inc., Pittsburgh PA. 1998.

27. P.C. Hariharan and J.A. Pople. Theor. Chem. Acta, **28**, 213 (1973).
28. K. Raghavachari and G.W. Trucks. J. Chem. Phys. **91**, 1062 (1989).
29. (*a*) M. Newcomb and A.G. Glenn. J. Am. Chem. Soc. **111**, 275 (1989); (*b*) J.M. Tanko and R.E. Drumright. J. Am. Chem. Soc. **112**, 5362 (1990); (*c*) J.M. Tanko, R.E. Drumright, N.K. Suleman, and L.E. Brammer, Jr. J. Am. Chem. Soc. **116**, 1785 (1994); (*d*) J.M. Tanko and J.P. Phillips. J. Am. Chem. Soc. **121**, 6078 (1999).
30. A.L.J. Beckwith and V.W. Bowry. J. Am. Chem. Soc. **116**, 2710 (1994).

© 2002 NRC Canada

Biocatalyzed preparation of the optically enriched stereoisomers of 4-methyl-2-phenyl-tetrahydro-2*H*-pyran (Doremox®)

Elisabetta Brenna, Claudio Fuganti, Sabrina Ronzani, and Stefano Serra

Abstract: The four stereoisomers of the rose oxide analogue Doremox® were prepared in enantiomerically enriched form by enantiospecific bakers' yeast reduction of suitable derivatives and by lipase-mediated kinetic resolution of diol precursors.

Key words: yeast, lipase, odorant, reduction, kinetic resolution.

Résumé : Faisant appel à une réduction énantiospécifique de dérivés appropriés à l'aide de levure de boulanger ou à une résolution cinétique de diols précurseurs à l'aide de lipase, on a préparé une forme énantiomériquement enrichie des quatre stéréoisomères du Doremox®, un analogue de l'oxyde de rose.

Mots clés : levure, lipase, odorant, réduction, résolution cinétique.

[Traduit par la Rédaction]

Introduction

The use of cyclic ethers as fragrant ingredients for the preparation of perfuming compositions and perfumed articles originated with the two diastereoisomeric rose oxides (2*S*,4*R*)-*cis*-**1** and (2*R*,4*R*)-*trans*-**1**, after their discovery in rose oil (1) and geranium oil (2) and their availability through efficient synthetic procedures (3).

In the aim of improving the olfactory properties of **1**, several structural modifications were realized. For example, the isobutenyl unit was elongated to produce sesquiterpenoid homologues showing a rather complex odour profile (4), or one carbon atom of the tetrahydropyrane ring was substituted with an oxygen atom, to afford chiral 3-oxa analogues (5).

In 1993, 4-methyl-2-phenyl-tetrahydro-2*H*-pyran (Doremox®, **2**) was obtained by Firmenich (6) as a mixture of the two racemic *cis*- and *trans*-diastereoisomers, by hydrogenation of 5,6-dihydro-4-methyl-2-phenyl-2*H*-pyran in the presence of Pd on charcoal. This preparation represented a further evolution in the structure–activity study of the olfactory properties of rose oxide. The isobutenyl fragment of **1** was substituted with a phenyl group, to increase the substantivity of rose scent, i.e the persistence of the perfume material on blotters, skin, or in the intended application (7). Substantivity is mainly determined by vapor pressure, which depends in turn on molecular weight. The phenyl group increases the mass, without a substantial change of the shape of the molecule, and thus without affecting the main odour characteristics (8).

Received 9 January 2002. Published on the NRC Research Press Web site at http://canjchem.nrc.ca on 31 May 2002.

This paper is dedicated to J. Bryan Jones on the occasion of his 65th birthday in recognition of his contributions to biocatalysis.

E. Brenna,[1] C. Fuganti, S. Ronzani, and S. Serra. Dipartimento di Chimica, Materiali, ed Ingegneria Chimica del Politecnico, Centro CNR per lo Studio delle Sostanze Organiche Naturali, Via Mancinelli 7, I-20131 Milano.

[1]Corresponding author (e-mail: elisabetta.brenna@polimi.it).

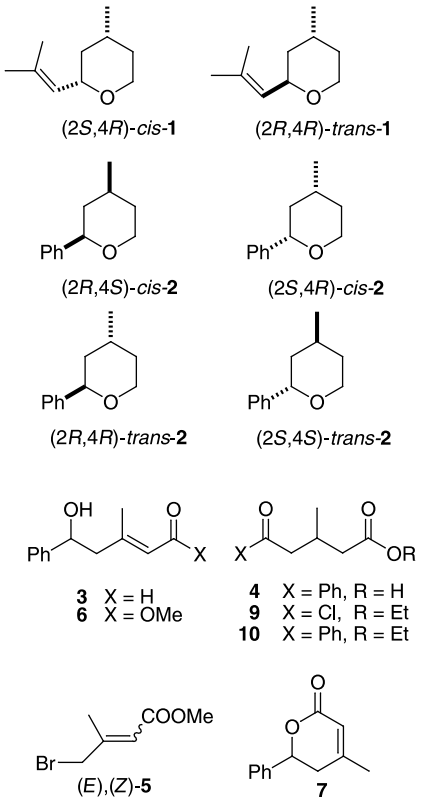

The two isomers (*cis*-**2** and *trans*-**2**) were separated by preparative gas chromatography, and their odour properties

 DOI: 10.1139/V02-042 © 2002 NRC Canada

Scheme 1. (*i*) Diisobutylaluminum hydride in toluene; (*ii*) MnO_2 in hot DMF; (*iii*) baker's yeast; (*iv*) $CHCl_3$, TosCl, pyridine; (*v*) MeONa, MeOH.

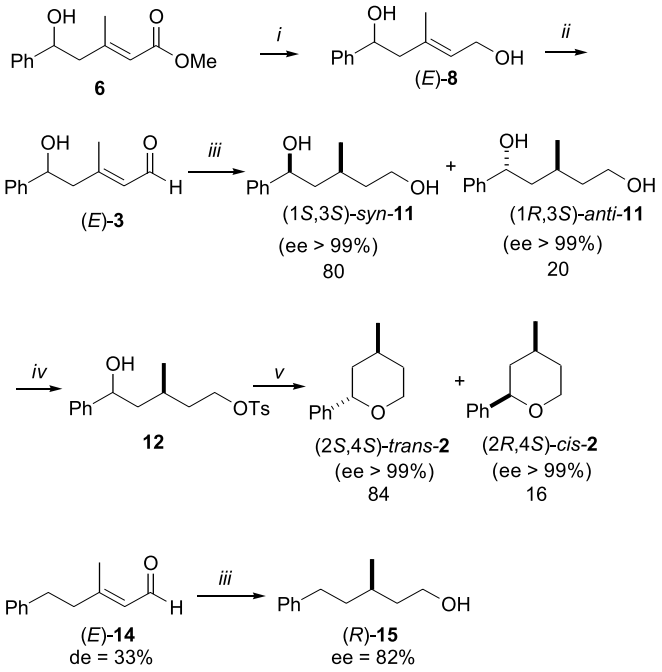

were described (6). The racemic *cis*-diastereoisomer was found to be very powerful and to have a green, rose oxide – diphenyl oxide type note. The racemic *trans*-isomer had a much weaker odour, with a green, vegetable, slightly dirty and minty character and a floral undertone. Both of them were described to be useful in the preparation of perfumes and concentrated perfuming bases, as well as of a variety of articles, such as soaps, bath or cosmetic formulations, air and body deodorants, detergents, fabric softeners, and household products.

Neither enantioselective synthesis of the four stereoisomers of Doremox®, nor olfactory evaluation of each distinct isomer have been performed so far. The wide diffusion of this fragrant component in many commercial preparations induced us to investigate the possibility of obtaining the enantiomerically enriched isomers of *cis*-**2** and *trans*-**2**, to select those showing the most powerful and interesting odour properties. Now we wish to report on the outcome of this investigation, which is part of a research project aimed at the preparation of the olfactory active stereoisomers of commercial fragrances (9), via biocatalyzed methods.

Results and discussion

Two different approaches to optically active Doremox® isomers were chosen on the basis of our past experience: (*i*) enantioselective synthesis based on bakers' yeast (BY) reduction; (*ii*) lipase-mediated kinetic resolution of suitable precursors.

Bakers' yeast approach

We had successfully developed synthetic methods for the preparation of enantiomerically enriched rose oxide (10) and Aerangis lactone (11), based on BY-enantiospecific and

Scheme 2. (*i*) Baker's yeast; (*ii*) $LiAlH_4$, THF; (*iii*) $CHCl_3$, TosCl, pyridine; (*iv*) MeONa, MeOH.

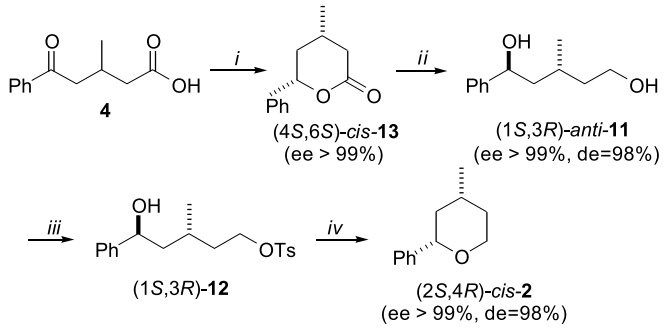

diastereoselective reduction of 1,5- and 1,4-difunctionalized synthons. Thus, as for the synthesis of **2**, we envisaged hydroxy aldehyde **3** and keto acid **4** as substrates for yeast fermentation.

Compound **3** was prepared according to this synthetic scheme. Reformatsky reaction of bromo derivative **5** (12) with benzaldehyde afforded a mixture of hydroxy ester **6** and lactone **7** (13) which were easily separated by column chromatography. DIBAL reduction of compound **6** in toluene solution gave unsaturated diol (*E*)-**8** (Scheme 1), which was straightforwardly oxidized to the desired aldehyde (*E*)-**3** (14) with MnO_2 in hot DMF; no oxidation of the benzylic hydroxylic group was observed in this reaction condition.

Keto acid **4** was prepared according to the following route. Friedel–Crafts acylation of benzene with the monochloride monomethyl ester of 3-methyl glutaric acid (**9**) (15) in the presence of aluminum(III) chloride gave mainly keto ester **10** (16), which was hydrolyzed with potassium hydroxide in methanol to afford keto acid **4** (17). Derivatives (*E*)-**3** and **4** were incubated with BY for 24 h, and, interestingly enough, the two reactions took different stereochemical courses.

Reduction of the double bond of derivative **3** (Scheme 1), in the presence of the benzylic stereocentre previously created without steric control, gave mainly (80%, GC–MS) diol (1*S*,3*S*)-*syn*-**11** (ee > 99%, chiral HPLC) and a minor quantity (20%, GC–MS) of diol (1*R*,3*S*)-*anti*-**11** (ee > 99%, chiral HPLC). The mixture of the two diastereoisomeric diols was converted into the corresponding monotosylate derivative **12** and, after treatment with sodium methylate in methanol, a sample of Doremox® with the following composition was obtained: (2*S*,4*S*)-*trans*-**2**, 86%, ee = 99% (chiral GC); (2*R*,4*S*)-*cis*-**2**, 14%, ee > 99%, $[\alpha]_D^{20}$ + 18.1 (*c* = 0.75, $CHCl_3$).

Reduction of the carbonyl function of racemic **4** (Scheme 2) gave lactone (4*S*,6*S*)-**13**, which was recovered in pure form after column chromatography, and reduced with $LiAlH_4$ to give diol (1*S*,3*R*)-*anti*-**11** (ee > 99%, de = 97%, chiral HPLC). This latter was then converted into (2*S*,4*R*)-*cis*-**2** (ee > 99%, de = 98%, $[\alpha]_D^{20}$ –54.1 (*c* = 1.05, $CHCl_3$)) according to the mentioned procedure, via the corresponding tosylate derivative (1*S*,3*R*)-*anti*-**12**.

In both cases the preferred isomer was produced enantiospecifically, but with different diastereoselection: *syn*-diastereoisomer prevailed when BY promoted the reduction of the double bond, while *anti*-diastereoisomer was obtained

© 2002 NRC Canada

Scheme 3. (*i*) $LiAlH_4$, THF, then AcOEt; (*ii*) $NaBH_4$, MeOH–CH_2Cl_2; (*iii*) MeOH–HCl; (*iv*) $LiAlH_4$, THF, then MeOH.

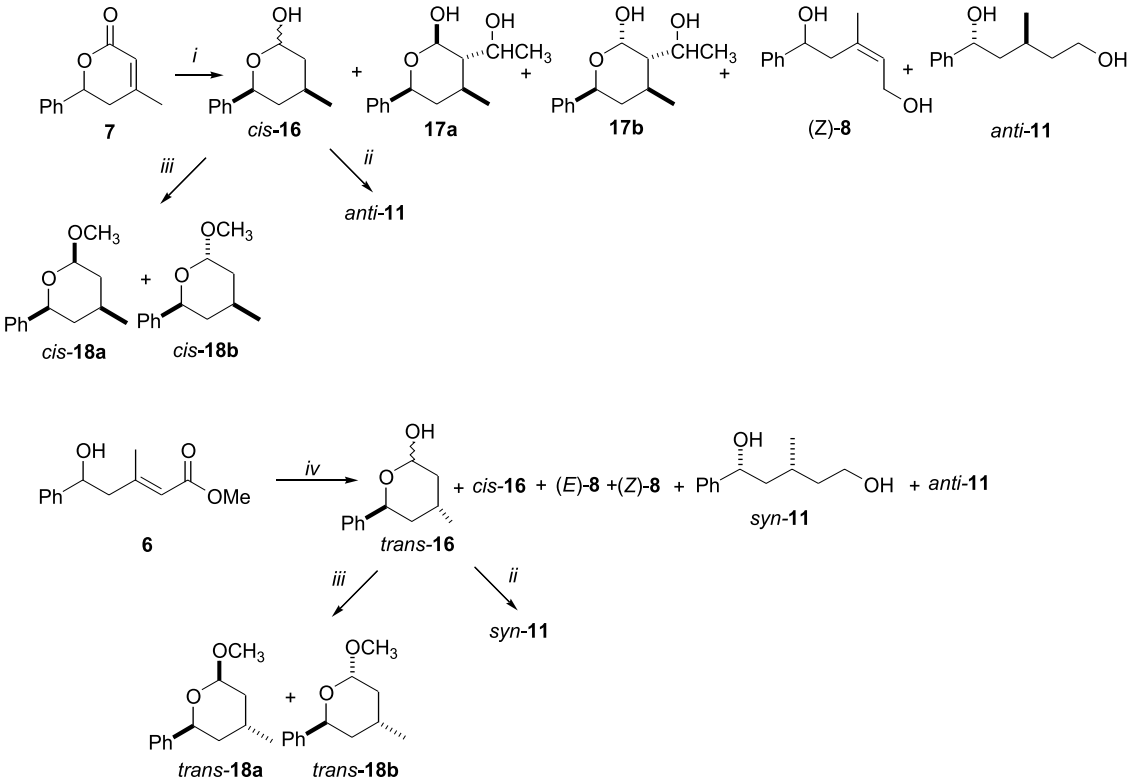

when the reduction of the carbonyl was involved. As for diol *anti*-**11**, opposite enantioselection was observed: (1*R*,3*S*)-*anti*-**11** was the product of BY reduction of hydroxy aldehyde **3**, while its enantiomer (1*S*,3*R*)-*anti*-**11** was the result of yeast fermentation of keto acid **6**.[2]

Lipase-mediated kinetic resolution

A second approach to optically active Doremox® was investigated, to prepare all the four possible stereoisomers in enantiomerically enriched form. For this purpose the preparation of the two racemic diols *anti*-**11** and *syn*-**11** was optimized.

Lactone **7** was treated with lithium aluminum hydride in THF (Scheme 3). When the reaction mixture was quenched with ethyl acetate, a complex mixture of products was obtained. The following compounds could be isolated and identified: tetrahydropyranol *cis*-**16** (1:1 mixture of the two possible epimers at C-2, 40%), substituted tetrahydropyranols **17a** (11%) and **17b** (10%),[3] unsaturated diol (*Z*)-**8** (8%) (20), and diol *anti*-**11** (12%). The structural assignment to *cis*-**16** was based on ^{1}H NMR and mass spectrometry data, and on its chemical reactivity; it afforded diol *anti*-**11** upon $NaBH_4$ reduction, and it was transformed into the mixture of the epimeric methyl glycosides *cis*-**18a** and *cis*-**18b** by treatment with MeOH–HCl.

Low diastereoselection was obtained when hydroxy ester **6** was reduced (Scheme 3). GC–MS analysis of the reduction mixture allowed us to detect *cis*-**16** (25%) and *trans*-**16** (20%), *syn*-**11** (14%) and *anti*-**11** (10%), (*E*)-**8** (12%) and (*Z*)-**8** (6%) (20), and a complex system of compounds with retention times and mass spectra resembling those of **17a** and **17b** (12%). The reaction was then repeated using methanol to consume the excess of $LiAlH_4$ and the residue was chromatographed, to yield a nearly 1:1 mixture of *cis*-**16** and *trans*-**16** and a 2:1 mixture of *syn*-diol **11** and *anti*-diol **11**. The saturated diol fraction was enriched in the *syn*-diasteroisomer (de = 83%) by column chromatography. An analytical sample of *trans*-**16** was obtained by careful column chromatography and recrystallization from ether. This sample was reduced to *syn*-**11** with $NABH_4$ and converted into methyl glycosides *trans*-**18a** and *trans*-**18b** with MeOH–HCl.

Racemic diols *anti*-**11** (de > 99%) and *syn*-**11** (de = 83%) were acetylated with Ac_2O–Py, and the corresponding acetyl derivatives *anti*-**19** and *syn*-**19** were submitted separately to enzymic saponification, at pH 7.8 in the presence of lipase PS. As for diacetate *anti*-**19** (Scheme 4), the first enzymic saponification (monitored by chiral HPLC) afforded monoacetate (1*R*,3*S*)-*anti*-**20** showing 55% ee (chiral HPLC). This latter was acetylated and submitted again to lipase-mediated hydrolysis, to give (1*R*,3*S*)-*anti*-**20** with ee = 95% (chiral HPLC). Treatment with KOH in methanol gave (1*R*,3*S*)-*anti*-**11** (ee = 95%, chiral HPLC). Diacetate (1*S*,3*R*)-*anti*-**19** (ee = 41%), chiral HPLC of the corresponding diol), recovered

[2] When unsaturated aldehyde **14** (18*a*) (*E*:*Z*, 2:1) (Scheme 1) was submitted to yeast fermentation, saturated alcohol (+)-(*R*)-**15** (19) (ee 82%, chiral HPLC) was obtained. BY reduction of the conjugated double bond thus showed the same preferred enantioselectivity in structurally related compounds (CIP descriptors are different because the group priority changes from (*E*)-**3** to **14**).

[3] The formation of derivatives **17a** and **17b** was unexpected and unusual. ^{1}H NMR spectra showed that in both compounds the substituent $CH(OH)CH_3$ was located in the equatorial position (**17a** $J_{(H\text{-}3,H\text{-}4)}$ = 11.5 Hz, **17b** $J_{(H\text{-}2,H\text{-}3)}$ = 8.9 Hz).

© 2002 NRC Canada

Scheme 4. (*i*) Acetic anhydride, pyridine; (*ii*) lipase PS, THF–water, pH 7.8, 0.025 M NaOH; column chromatography; (*iii*) KOH, MeOH; (*iv*) TosCl, pyridine, then MeONa in methanol; (*v*) Jones' reactive acetone.

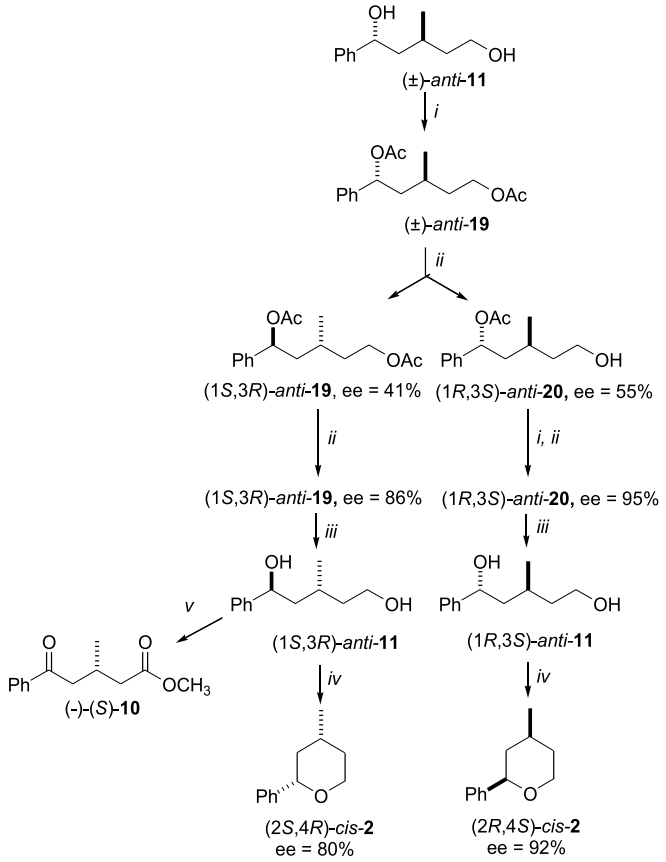

Scheme 5. (*i*) Acetic anhydride, pyridine; (*ii*) lipase PS, THF–water, pH 7.8, 0.025 M NaOH; column chromatography; (*iii*) KOH, MeOH; (*iv*) TosCl, pyridine, then MeONa in methanol; (*v*) Jones' reactive acetone.

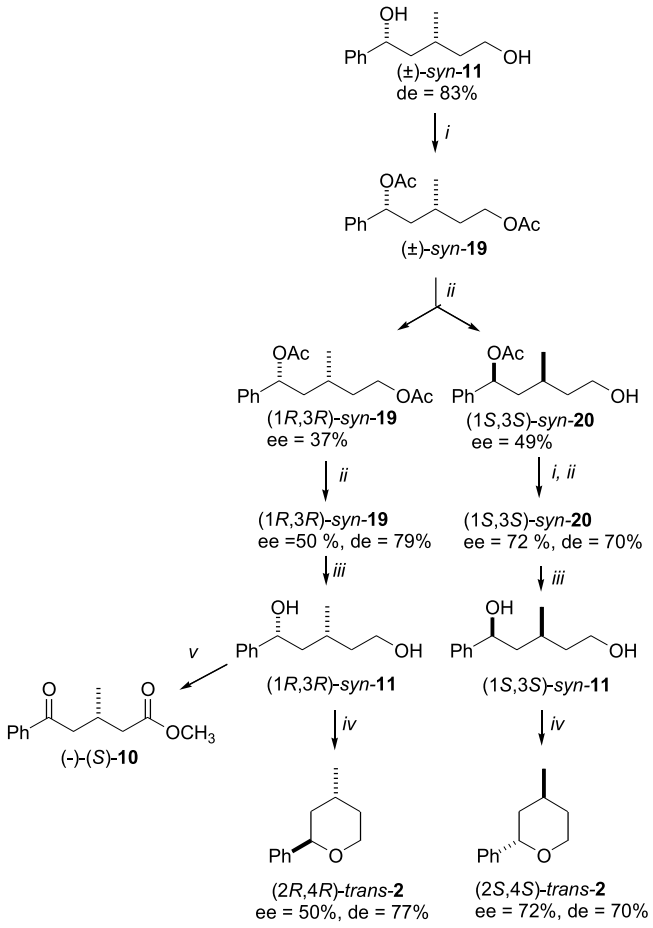

unreacted from the first saponification, was depleted of the (1*R*,3*S*) enantiomer as much as possible by prolonged enzymic reaction. Finally, it afforded diol (1*S*,3*R*)-*anti*-**11** with ee = 86% (chiral HPLC) by reaction with KOH in methanol.

The same procedure was applied to diacetate *syn*-**19** (Scheme 5). (1*S*,3*S*)-*syn*-**11** (ee = 72%, de = 70%) and (1*R*,3*R*)-*syn*-**11** (ee = 50%, de = 79%) were obtained from monoacetate *syn*-**20** and survived diacetate *syn*-**19**, respectively.

The four enantiomerically enriched diols were treated with tosyl chloride and pyridine, then with sodium methylate in methanol, to promote ring closure. The following samples of Doremox® were obtained: (*i*) (2*R*,4*S*)-*cis*-**2** (from (1*R*,3*S*)-*anti*-**11**): ee = 92%, de > 99% (chiral GC), $[\alpha]_D^{20}$ +52 (*c* = 0.27, $CHCl_3$); (*ii*) (2*S*,4*R*)-*cis*-**2** (from (1*S*,3*R*)-*anti*-**11**): ee = 80%, de > 99% (chiral GC), $[\alpha]_D^{20}$ – 42 (*c* = 1.2, $CHCl_3$); (*iii*) (2*S*,4*S*)-*trans*-**2** (from (1*S*,3*S*)-*syn* -**11**): ee = 72%, de = 70% (chiral GC), $[\alpha]_D^{20}$ + 14.6 (*c* = 0.3, $CHCl_3$); this sample contained 15% of (+)-*cis*-**2** with ee = 73%; (*iv*) (2*R*,4*R*)-*trans*-**2** (from (1*R*,3*R*)-*syn*-**11**): ee = 50%, de = 77% (chiral GC), $[\alpha]_D^{20}$ – 9.8 (*c* = 1.15, $CHCl_3$); this sample contained 11.5% of (–)-*cis*-**2** with ee = 65%.

Configurational assignment

The absolute configurations of the two stereocentres of diols *anti*-**11** and *syn*-**11** and of *cis*-**2** and *trans*-**2** were assigned by chemical correlation on the basis of these data: (*i*) ^{1}H NMR spectra of *cis*-**2** and *trans*-**2** had been described, so the relative configurations of Doremox® isomers and those of the diol precursors could be defined; (*ii*) samples of (–)-*anti*-**11** (ee > 99%) and of (+)-*syn*-**11** (ee = 50%, de = 79%) were oxidized to the corresponding keto acids upon treatment with Jones' reactive in acetone solution. These latter derivatives were purified by column chromatography of the correponding methyl esters (diazomethane). In both cases, (–)-(*S*)-**10** (lit. value (21*a*) $[\alpha]_D^{20}$ – 5.65 (*c* = 1.24, benzene) for the (*S*)-isomer, ee = 90%; lit. value (21*b*) $[\alpha]_D^{20}$ +9.25 (neat) for the (*R*)-isomer, ee > 96%) was obtained showing optical rotation values of –5.02 (*c* = 0.85, benzene; prepared from *anti*-**11**) and –3.21 (*c* = 0.73, benzene; prepared from *syn*-**11**). (*R*)-Configuration was assigned to C-3 in (–)-*anti*-**11** and (+)-*syn*-**11** (the CIP descriptor of the stereogenic carbon atom changes because the order of group priority is different). The absolute configurations of all the derivatives involved in the synthetic scheme was then deduced.

Thus, it was possible to verify that lipase PS promoted the saponification of both the diol isomers showing (*S*)-configuration at the carbon atom nearer to the reactive site.

© 2002 NRC Canada

Olfactory descriptions

Olfactory evaluation of Doremox® samples gave the following results: (*i*) (2*R*,4*S*)-*cis*-**2**, ee = 92%, de > 99%: rose oxide, diphenyl oxide, metallic, slightly plastic; (*ii*) (2*S*,4*R*)-*cis*-**2**, ee = 80%, de > 99%: rose oxide, powerful, nice; (*iii*) (2*S*,4*S*)-*trans*-**2**, ee = 72%, de = 70%: weak, rosy, plastic, citronellol, a rose oxide note is also present; (*iv*) (2*R*,4*R*)-*trans*-**2**, ee = 50%, de = 77%: rosy, rose oxide, metallic, off-note.

Experimental

Lipase PS *Pseudomonas cepacia* (Amano Pharmaceuticals Co., Japan) was employed in this work. GC–MS analyses were performed on a HP 6890 gas chromatograph equipped with a 5973 mass detector, using a HP-5MS column (30 m × 0.25 mm × 0.25 μm). The following temperature program was employed: 60°C (for 1 min)/6°/min to 150°C (for 1 min)/12°/min to 280°C (for 5 min). Chiral GC analyses of Doremox® stereoisomers were performed on a DeTBuSiBETA (086) 25 m × 0.25 mm column (Mega, Italy), installed on a DANI HT 86.10 gas chromatograph, with the following temperature program: 45°C (3′)/5°C/min to 75°C/0.5°C/min to 100°C/10°C/min to 180°C (5′): t_R (2*S*,4*R*)-**1a** = 45.4 min, t_R (2*R*,4*S*)-**1a** = 46.5 min, t_R (2*R*,4*R*)-**1b** = 49.2 min, t_R (2*S*,4*S*)-**1b** = 49.7 min. Chiral HPLC analyses were performed on a Chiralcel OD column (Daicel, Japan) installed on a Merck–Hitachi L-6200 apparatus: 0.6 mL min^{-1}, UV detector (254 nm), hexane:isopropanol (95:5). The following retention times were observed: (1*RS*,3*SR*)-*anti*-**19** (single peak) t_R = 11.4 min; (1*R*,3*S*)-*anti*-**20** t_R = 21.7 min; (1*S*,3*R*)-*anti*-**20** t_R = 28.9 min; (1*R*,3*S*)-*anti*-**11** t_R = 29.8 min; (1*S*,3*R*)-*anti*-**11** t_R = 30.6 min; (1*S*,3*S*)-*syn*-**19** t_R = 10.6 min; (1*R*,3*R*)-*syn*-**19** t_R = 11.1 min; (1*S*,3*S*)-*syn*-**20** t_R = 17.2 min; (1*R*,3*R*)-*syn*-**20** t_R = 23.9 min; (1*R*,3*R*)-*syn*-**11** t_R = 30.8 min; (1*S*,3*S*)-*syn*-**11** t_R = 41.9 min; (*R*)-**15** t_R = 14.9 min; (*S*)-**15** t_R = 17.2 min. ^{1}H NMR spectra were recorded at room temperature (r.t.) on a Bruker AC-250 spectrometer (250 MHz ^{1}H). The chemical shift scale was based on internal tetramethylsilane. Optical rotations were measured on a Dr. Kernchen Propol digital automatic polarimeter. Microanalyses were determined on a Carlo Erba 1106 analyzer. TLC analyses were performed on Merck Kieselgel 60 F_{254} plates. All the chromatographic separations were carried out on silica gel columns.

The mixture of (*E*)- and (*Z*)-methyl 4-bromo-3-methyl-2-butenoate (**5**) was prepared as described in ref. 12. The monochloride mono methyl ester of 3-methyl glutaric acid was prepared according to ref. 15. Aldehyde **14** was prepared according to ref. 18*a*, and the diasteroisomeric excess (33%) was determined on the basis of ^{1}H NMR spectra of (*E*)-**14** and (*Z*)-**14** in ref. 18*b*.

5-Hydroxy-3-methyl-5-phenyl-pent-2-enoic acid methyl ester (6) (13) and 4-methyl-6-phenyl-5,6-dihydropyran-2-one (7) (13)

A solution of bromo derivative **5** (38.4 g, 0.20 mol) and benzaldehyde (2.12 g, 0.20 mol) in 100 mL THF was added dropwise to a suspension of zinc (14.3 g, 0.22 mol) in 300 mL THF at 0°C. The reaction was refluxed for 2 h, poured into ice, and extracted with ethyl acetate. The organic layer was washed with a solution of ammonium chloride, dried (Na_2SO_4), and concentrated. Column chromatography (hexane–EtOAc, 9:1) provided hydroxy ester **6** (16.7 g, 38%) and lactone **7** (17.7 g, 47%).

6

GC–MS (t_R = 21.80 min) *m*/*z*: 186 (M^+ – 34) (50), 158 (100), 129 (40), 77 (25). ^{1}H NMR ($CDCl_3$, ppm): 7.32 (m, 5H, C_6H_5), 5.76 (q, *J* = 1.1 Hz, 1H, H-C_2), 4.89 (dd, *J* = 4.6, 8.1 Hz, 1H, H-C_5), 3.68 (s, 3H, $COOCH_3$), 2.53 (m, 2H, CH_2), 2.22 (d, *J* = 1.1 Hz, 3H, CH_3-C=C).

7

mp 60°C. GC–MS (t_R = 21.80 min) *m*/*z*: 188 (M^+) (10), 105 (8), 82 (100). ^{1}H NMR ($CDCl_3$, ppm): 7.35 (m, 5H, C_6H_5), 5.87 (m, 1H, H-C_3), 5.37 (dd, *J* = 3.9, 11.8 Hz, 1H, H-C_6), 2.62 (ddm, *J* = 11.8, 18.0 Hz, 1H, H-C_5), 2.42 (dd, *J* = 3.9, 18.0 Hz, 1H, H-C_5), 1.99 (m, 3H, CH_3-C=C).

(*E*)-3-Methyl-5-phenyl-2-pentene-1,5-diol ((*E*)-8)

A 1.5 M solution of diisobutyl aluminum hydride in toluene (69 mL, 0.103 mol) was added dropwise to a solution of hydroxy ester **6** (10.0 g, 0.045 mol) in 100 mL toluene at –10°C. The reaction was allowed to warm to 25°C, treated with water, filtered through a Celite cake, and extracted with ethyl acetate. The residue was chromatographed (hexane:EtOAc, 6:4) to give unsaturated diol (*E*)-**8** (6.82 g, 79%). GC–MS (t_R = 20.89 min) *m*/*z*: 174 (M^+ – 18) (0.04), 107 (71), 105 (83), 68 (100). ^{1}H NMR ($CDCl_3$, ppm): 7.25 (m, 5H, C_6H_5), 5.50 (tq, *J* = 6.7, 1.2 Hz, 1H, H-C_2), 4.76 (t, *J* = 6.7 Hz, 1H, H-C_5), 4.09 (m, 2H, CH_2OH), 2.35 (d, *J* = 6.7 Hz, 2H, CH_2), 1.71 (d, *J* = 1.2 Hz, 3H, CH_3-C=C). Anal. calcd. for $C_{12}H_{16}O_2$: C 74.97, H 8.39; found: C 74.75, H 8.53.

(*E*)-5-Hydroxy-3-methyl-5-phenyl-pent-2-enal ((*E*)-3) (14)

Manganese(IV) oxide (1.5 equiv) was added to a solution of unsaturated diol (*E*)-**8** (6.70 g, 0.035 mol) in 50 mL DMF. The suspension was heated at 80°C for 4 h, then filtered poured into water, and extracted with EtOAc. The organic phase was dried (Na_2SO_4), and concentrated in vacuo. The residue was chromatographed (hexane–EtOAc, 7:3) to afford (*E*)-**3** (6.05 g, 91%). GC–MS (t_R = 21.20 min) *m*/*z*: 190 (M^+) (0.01), 172 (6), 107 (92), 84 (100). ^{1}H NMR ($CDCl_3$, ppm): 9.99 (d, *J* = 7.9 Hz, 1H, CHO), 7.35 (m, 5H, C_6H_5), 5.95 (dt, *J* = 7.9, 1.1, 1H, H-C_2), 4.94 (dd, *J* = 4.9, 8.7 Hz, 1H, H-C_5), 2.68 (dd, *J* = 14.0, 8.7 Hz, 1H, H-C_4), 2.57 (dd, *J* = 14.0, 4.9 Hz, 1H, H-C_4), 2.22 (d, *J* = 1.1 Hz, 3H, CH_3-C=C).

Methyl 3-methyl-5-oxo-5-phenyl-pentanoate (10) (16)

Aluminum trichloride (15.9 g, 0.12 mol) was added to a solution of derivative **9** (17.8 g, 0.10 mol) in 300 mL benzene at 10°C. The reaction mixture was refluxed for 2 h, poured into ice and 10% HCl, and extracted with EtOAc. The organic phase was dried (Na_2SO_4), concentrated, and chromatographed (hexane–EtOAc, 95:5), to give keto ester **10** (14.1 g, 64%). GC–MS (t_R = 21.01 min) *m*/*z*: 220 (M^+) (1.4), 189 (7.1), 120 (75), 105 (100). ^{1}H NMR ($CDCl_3$, ppm): 7.97 (m, 2H, aromatic hydrogens), 7.40 (m, 3H, aromatic hydrogens), 3.67 (s, 3H, COOMe), 3.11 (dd, *J* = 16.0, 5.8 Hz, 1H), 2.84 (dd, *J* = 16.0, 7.3 Hz, 1H), 2.66 (m, 1H,

© 2002 NRC Canada

H-C_3), 2.44 (dd, J = 15.4, 6.1 Hz, 1H), 2.31 (dd, J = 15.4, 7.3 Hz, 1H), 1.05 (d, J = 6.6 Hz, CH_3).

3-Methyl-5-oxo-5-phenyl-pentanoic acid (4) (17)

Keto ester **10** (14.0 g, 0.064 mol) was hydrolysed with KOH (5.38 g, 0.096 mol) in 70 mL MeOH to afford, after the usual work-up, keto acid **4** (12.4 g, 93%). ^{1}H NMR ($CDCl_3$, ppm): 7.95 (m, 2H, aromatic hydrogens), 7.40 (m, 3H, aromatic hydrogens), 2.98 (m, 2H), 2.67 (m, 1H), 2.45 (m, 2H), 1.09 (d, J = 6.3 Hz, CH_3).

$LiAlH_4$ reduction of lactone 7

Procedure A

A solution of lactone **7** (18.8 g, 0.10 mol), in 30 mL THF was added dropwise to a suspension of $LiAlH_4$ (7.6 g, 0.20 mol), in 250 mL THF. The reaction mixture was stirred at r.t. for 12 h, then EtOAc was added to consume the excess $LiAlH_4$. The reaction mixture was poured into ice, extracted with Et_2O, dried (Na_2SO_4), and chromatographed (from hexane–EtOAc (95:5) to hexane–EtOAc (1:1)). The following products, in order of progressive elution, were isolated.

*(2*RS*,4*RS*,6*RS*)-4-Methyl-6-phenyl-tetrahydro-2*H*-pyran-2-ol and (2*RS*,4*SR*,6*SR*)-4-methyl-6-phenyl-tetrahydro-2*H*-pyran2-ol (*cis*-**16**, 1:1 mixture of the two epimers at C-2)*

7.68 g (40%), mp 67°C (diethyl ether). GC–MS (t_R = 19.34 min, single peak) m/z: 192 (M^+) (1.7), 174 (13), 159 (17), 104 (100). ^{1}H NMR ($CDCl_3$, ppm): 7.32 (m, 10H, $2C_6H_5$), 5.40 (m, 1H, H-C_2 of one epimer), 4.98 (dd, 1H, J = 11.8, 2.1 Hz, H-C_2 of one epimer), 4.74 (dd, 1H, J = 9.6, 2.1 Hz, H-C_6 of one epimer), 4.74 (dd, 1H, J = 11.3, 1.7 Hz, H-C_6 of one epimer), 2.16 (m, 1H), 1.78 (m, 5H), 1.39–0.97 (m, 4H), 0.94 (d, J = 6.6 Hz, 3H, CH_3 of one epimer), 0.90 (d, J = 6.6 Hz, 3H, CH_3 of one epimer). Anal. calcd. for $C_{12}H_{16}O_2$: C 74.97, H 8.39; found: C 75.13, H 8.48.

A sample of *cis*-**16** was treated with MeOH–HCl to give the mixture of the corresponding *O*-methyl glycosides *cis*-**18a** and *cis*-**18b** (3:1 mixture of the two epimers at C-2). GC–MS major epimer (t_R = 17.61 min) m/z: 206 (M^+) (2), 174 (41), 104 (94), 58 (100); minor epimer (t_R = 18.17 min): 174 (M^+ – 32) (3), 146 (27), 104 (100), 58 (50). ^{1}H NMR ($CDCl_3$, ppm): 7.32 (m, $2C_6H_5$), 4.90 (m, 1H of the major epimer), 4.74 (dd, J = 11.8, 1.9 Hz, 1H of the major epimer), 4.48 (dd, J = 9.8, 1.9 Hz, 1H of the minor epimer), 4.43 (dd, J = 11.3, 1.4 Hz, 1H of the minor epimer), 3.52 (s, OCH_3 of the minor epimer), 3.39 (s, OCH_3 of the major epimer), 2.16 (m, 1H), 1.83 (m), 1.45–1.10 (m), 1.00 (d, J = 6.3 Hz, CH_3 of the minor epimer), 0.93 (d, J = 6.8 Hz, CH_3 of the major epimer).

*(2*RS*,3*SR*,4*SR*,6*SR*)-3-(1-Hydroxyethyl)-4-methyl-6-phenyl-tetrahydro-2*H*-pyran-2-ol (**17a**, stereochemistry undefined at the stereogenic carbon atom in the substituent group)*

2.59 g (11%). GC–MS (t_R = 24.12 min) m/z: 218 (M^+ – 18) (1.7), 200 (1), 174 (17), 159 (25), 104 (100). ^{1}H NMR ($CDCl_3$, ppm): 7.28 (m, 5H, C_6H_5), 5.43 (d, J = 3.1 Hz, 1H, H-C_2), 5.02 (dd, 1H, J = 12.0, 2.9 Hz, H-C_6), 4.02 (dq, J = 3.1, 6.7 Hz, 1H, *CH*CH_3OH), 2.32 (m, 1H, H-C_4), 1.84 (dt, J = 12.0, 2.9 Hz, 1H, H-C_5), 1.36 (q, J = 12.0 Hz, 1H, H-C_5), 1.29 (dt, J = 11.5, 3.1 Hz, H-C_3), 1.12 (d, J = 6.7 Hz, 3H, *CH*$_3$CHOH), 0.94 (d, J = 6.7 Hz, 3H, CH_3-C_4). Anal. calcd. for $C_{14}H_{20}O_3$: C 71.16, H 8.53; found: C 70.89, H 8.77.

An analytical sample of **17a** was treated with Ac_2O and pyridine to give the corresponding diacetyl derivative. GC–MS (t_R = 25.56 min) m/z: 200 (M^+ – 2 × 60) (47), 104 (100). ^{1}H NMR ($CDCl_3$, ppm): 7.32 (m, 5H, C_6H_5), 6.52 (d, J = 3.1 Hz, 1H, H-C_2), 5.14 (dq, J = 3.1, 6.6 Hz, *CH*CH_3OAc), 4.89 (dd, 1H, J = 12.0, 2.9 Hz, H-C_6), 2.12 (m + s, 4H, H-C_4 + CH_3COO), 2.04 (s, 3H, CH_3COO), 1.95 (dt, J = 12.0, 2.9 Hz, 1H, H-C_5), 1.72 (dt, J = 11.5, 3.1 Hz, H-C_3), 1.40 (q, J = 12.0 Hz, 1H, H-C_5), 1.32 (d, J = 6.6 Hz, 3H, *CH*$_3$CHOAc), 1.01 (d, J = 6.6 Hz, 3H, CH_3-C_4).

*(2*RS*,3*RS*,4*RS*,6*RS*)-3-(1-Hydroxyethyl)-4-methyl-6-phenyl-tetrahydro-2*H*-pyran-2-ol (**17b**, stereochemistry undefined at the stereogenic carbon atom in the substituent group)*

2.35 g (10%). GC–MS (t_R = 24.15 min) m/z: 218 (M^+ – 18) (1.4), 200 (3.5), 174 (8.5), 159 (14), 104 (100). ^{1}H NMR ($CDCl_3$, ppm): 7.30 (m, 5H, C_6H_5), 4.92 (d, J = 8.9 Hz, 1H, H-C_2), 4.50 (dd, 1H, J = 11.2, 2.2 Hz, H-C_6), 4.11 (dq, J = 2.9, 6.7 Hz, *CH*CH_3OH), 1.80 (dt, J = 12.6, 2.2 Hz, 1H, H-C_5), 1.66–1.25 (m, 3H, H-C_5, H-C_3, H-C_4), 1.19 (d, J = 6.7 Hz, *CH*$_3$CHOH), 0.98 (d, J = 6.7 Hz, 3H, CH_3-C_4). Anal. calcd. for $C_{14}H_{20}O_3$: C 71.16, H 8.53; found: C 71.55, H 8.78.

An analytical sample of **17b** was treated with Ac_2O and pyridine to give the corresponding diacetyl derivative. GC–MS (t_R = 24.50 min) m/z: 200 (M^+ – 2 × 60) (50), 104 (100). ^{1}H NMR ($CDCl_3$, ppm): 7.33 (m, 5H, C_6H_5), 5.94 (d, J = 8.5 Hz, 1H, H-C_2), 5.23 (dq, J = 2.0, 6.7 Hz, *CH*CH_3OAc), 4.61 (dd, J = 11.6, 2.0 Hz, 1H, H-C_6), 2.14–2.02 (m + 2s, 7H, 1H + 2CH_3COO), 1.94–1.4 (m, 3H), 1.29 (d, J = 6.9 Hz, 3H, *CH*$_3$CHOAc), 1.17 (d, J = 6.2 Hz, 3H, CH_3-C_4).

*(Z)-3-Methyl-5-phenyl-2-penten-1,5-diol ((Z)-**8**) (20)*

1.53 g (8%). GC–MS (t_R = 21.04 min) m/z: 174 (M^+ – 18) (2.8), 159 (3), 105 (86), 68 (100). ^{1}H NMR ($CDCl_3$, ppm): 7.29 (m, 5H, C_6H_5), 5.72 (t, J = 7.2 Hz, 1H, H-C_2), 4.75 (dd, J = 3.4, 9.4 Hz, 1H, H-C_5), 4.09 (dd, J = 11.7, 7.2 Hz, 1H, H-C_1), 3.86 (dd, J = 11.7, 7.2 Hz, 1H, H-C_1), 2.74 (dd, J = 13.4, 9.4 Hz, 1H, H-C_4), 2.22 (dd, J = 13.4, 3.4 Hz, 1H, H-C_4), 1.81 (s, 3H, CH_3-C_3).

*(1*RS*,3*SR*)-3-Methyl-1-phenyl-pentane-1,5-diol (*anti-**11**)*

2.33 g (12%), mp 76°C. GC–MS (t_R = 20.89 min) m/z: 194 (M^+) (9), 176 (15), 107 (100). ^{1}H NMR ($CDCl_3$, ppm): 7.33 (m, 5H, C_6H_5), 4.79 (m, 1H, H-C_1), 3.69 (m, 2H, CH_2OH), 1.87 (m, 2H), 1.55 (m, 2H), 1.42 (m, 1H), 1.01 (d, J = 6.4 Hz, 3H, CH_3-C_3). Anal. calcd. for $C_{12}H_{18}O_2$: C 74.19, H 9.34; found: C 73.93, H 9.15.

Procedure B

A solution of lactone **7** (18.8 g, 0.10 mol), in 30 mL THF was added dropwise into a suspension of $LiAlH_4$ (7.60 g, 0.20 mol), in 250 mL THF. The reaction mixture was stirred at r.t. for 12 h, then MeOH was added to consume the excess $LiAlH_4$. The reaction mixture was poured into ice, extracted with Et_2O, dried (Na_2SO_4), and chromatographed (from hexane–EtOAc (95:5) to hexane:EtOAc (1:1)). The following products, in order of progressive elution, were isolated: *cis*-**16** (8.64 g, 45%), (*Z*)-**8** (1.15 g, 6%), *anti*-**11** (3.49 g, 18%).

© 2002 NRC Canada

cis-**16** (8.50 g, 0.045 mol) was treated with $NaBH_4$ (2.56 g, 0.067 mol) in 50 mL CH_2Cl_2–MeOH (2:1) solution, to afford, after the usual work-up, *anti*-**11** (7.59 g, 87%).

$LiAlH_4$ reduction of hydroxy ester 6

Procedure A

The reduction of **6** (22.0 g, 0.10 mol), followed by treatment with EtOAc, gave the following mixture of products (GC–MS identification only): *cis*-**16** (25%, t_R = 19.35 min), *trans*-**16** (20%, t_R = 19.59 min), *syn*-**11** (14%, t_R = 20.80 min), *anti*-**11** (10%, t_R = 20.89 min), (*Z*)-**8** (6%, t_R = 21.03 min), (*E*)-**8** (12.5%, t_R = 21.19 min), unidentified products 12%, 23.72–24.12 min.

Procedure B

The reduction of **6** (22.0 g, 0.10 mol), followed by treatment with MeOH, gave a residue which was chromatographed, to give (after column chromatography) a 1:1 mixture of *cis*- and *trans*-**16** (2.96 g, 15%), a 9:1 mixture of (*E*)- and (*Z*)-**8** (1.82 g, 9%), and a 2:1 mixture of *syn*- and *anti*-**11** (12.4 g, 64%).

*(2*RS*,4*RS*,6*SR*)-4-Methyl-6-phenyl-tetrahydro-2*H*-pyran-2-ol and (2*RS*,4*SR*,6*RS*)-4-methyl-6-phenyl-tetrahydro-2*H*-pyran-2-ol (*trans*-**16***, mixture of two epimers)*

The 1:1 mixture of *cis*- and *trans*-**16** (2.96 g) was chromatographed (hexane–EtOAc, 9:1), to give, after crystallization from ether, *trans*-**16** (1.03 g), mp 72°C. GC–MS (t_R = 19.57 min (single peak)) *m*/*z*: 192 (M^+) (3.3), 174 (42), 159 (83), 104 (100). ^1H NMR ($CDCl_3$, ppm): 7.35 (m, $2C_6H_5$), 5.15 (m), 5.07 (dd, *J* = 9.1, 3 Hz, 1H), 4.74 (dd, *J* = 11.7, 2.3 Hz), 2.27 (m), 2.11–1.29 (m), 1.17 (d, *J* = 6.9 Hz, $2CH_3$). Anal. calcd. for $C_{12}H_{16}O_2$: C 74.97, H 8.39; found: C 75.26, H 8.11.

A sample of *trans*-**16** was treated with MeOH–HCl, to afford the mixture of the corresponding *O*-methyl glycosides *trans*-**18a** and *trans*-**18b** (2:1 mixture of the two epimers at C-2). GC–MS major epimer (t_R = 17.88 min) *m*/*z*: 174 (M^+ – 32) (23), 146 (25), 104 (100), 58 (85); minor epimer (t_R = 18.53 min) *m*/*z*: 174 (M^+ – 32) (4), 146 (21), 104 (100), 58 (50). ^1H NMR ($CDCl_3$, ppm): 7.35 (m, $2C_6H_5$), 4.96 (dd, *J* = 3.9, 9.3 Hz), 4.78 (t, *J* = 3.9 Hz), 4.71 (m), 3.50 (s, OCH_3 of the minor epimer), 3.39 (s, OCH_3 of the major epimer), 2.31 (m), 2.06–1.43 (m), 1.22 (d, *J* = 6.9 Hz, CH_3 of the major epimer), 1.21 (d, *J* = 6.7 Hz, CH_3 of the minor epimer).

*(*E*)-3-Methyl-5-phenyl-2-pentene-1,5-diol ((*E*)-**8**)*

Yield 1.82 g (9)%.

*(1*RS*,3*RS*)-3-Methyl-1-phenyl-pentane-1,5-diol (*syn-**11**)*

12.4 g (64%), de = 33%. The de was increased by column chromatography (hexane–EtOAc, 8:2), with *syn*-**11** eluting first. *syn*-**11** with de = 83% was obtained (8.71 g, 70%). GC–MS (t_R = 20.80 min) *m*/*z*: 194 (M^+) (7), 176 (9), 107 (100). ^1H NMR ($CDCl_3$, ppm): 7.29 (m, 5H, C_6H_5), 4.81 (t, *J* = 5.4 Hz, 1H, H-C_1), 3.66 (m, 2H, CH_2OH), 1.70 (m, 4H), 1.39 (m, 1H), 0.96 (d, *J* = 6.1 Hz, 3H, CH_3-C_3). Anal. calcd. for $C_{12}H_{18}O_2$: C 74.19, H 9.34; found: C 73.89, H 9.10.

Yeast reduction

A suspension of bakers' yeast (0.5 kg) and D-glucose (0.4 kg) in tap water (1.5 L) was stirred for 30 min at 32°C. A solution of the suitable substrate (0.03 mol) in ethanol (20 mL) was then added. After 48 h at r.t., Celite (200 g) was added, and the reaction mixture filtered, washing the Celite pad with ethyl acetate. The filtrate was adjusted to pH 4 with 2 N HCl, and extracted with ethyl acetate. The organic layer was dried (Na_2SO_4) and concentrated under reduced pressure. The residue was chromatographed on a silica gel column. The following derivatives were obtained upon BY reduction.

*(1*S*,3*S*)-3-Methyl-1-phenyl-pentane-1,5-diol ((1*S*,3*S*)-syn-**11**)*

2.99 g (44%) (from (*E*)-**3** (6.60 g, 0.035 mol)), ee > 99% (chiral HPLC), de = 60% (GC–MS). The sample contained 20% of (1*R*,3*S*)-*anti*-**11** (ee > 99%, chiral HPLC). ^1H NMR and GC–MS spectra were in agreement with those of (±)-*syn*-**11**.

*(4*S*,6*S*)-4-Methyl-6-phenyl-tetrahydropyran-2-one (**13**) (23)*

4.27 g (31%) (from **4**). $[\alpha]_D^{20}$ –12.1 (*c* = 1.26, $CHCl_3$). GC–MS (t_R = 21.65 min) *m*/*z*: 190 (M^+) (28), 104 (100), 56 (95). ^1H NMR ($CDCl_3$, ppm): 7.37 (m, 5H, C_6H_5), 5.31 (dd, *J* = 3.7, 12.0 Hz, 1H, H-C_6), 2.81 (m, 1H), 2.30–2.10 (m, 3H), 1.53 (m, 1H), 1.08 (d, *J* = 6.0 Hz, 3H, CH_3-C_4). This derivative (4.20 g, 0.022 mol) was reduced with $LiAlH_4$ (0.841 g, 0.044 mol) in 50 mL THF, to afford, after the usual work-up, (1*S*,3*R*)-*anti*-**11** (3.03 g, 71%), ee = 99% (chiral HPLC), de = 99% (GC–MS). $[\alpha]_D^{20}$ –60.2 (*c* = 1.05, $CHCl_3$). ^1H NMR and GC–MS spectra were in agreement with those of (±)-*anti*-**11**.

*(*R*)-3-Methyl-5-phenyl-pentan-1-ol ((*R*)-**15**)*

2.99 g (29%) (from (*E*)-**14** (de = 33%, 10.1 g, 0.058 mol)), ee = 82% (chiral HPLC). $[\alpha]_D^{20}$ +11.2 (*c* = 11.4, $CHCl_3$) (lit. (19) $[\alpha]_D^{20}$ –2 (neat) for the (*S*)-isomer). GC–MS (t_R = 16.60 min) *m*/*z*: 178 (M^+) (30), 160 (35), 104 (91%), 91 (100). ^1H NMR ($CDCl_3$, ppm): 7.21 (m, 5H, C_6H_5), 3.68 (m, 2H, CH_2OH), 2.61 (m, 2H, CH_2Ph), 1.62 (m, 3H), 1.49 (m, 2H), 0.98 (d, *J* = 6.0 Hz, 3H, CH_3-C_3).

(1*RS*,3*SR*)-Acetic acid 5-acetoxy-3-methyl-1-phenyl-pentyl ester (*anti-**19**)

Diol *anti*-**11** (11.4 g, 0.056 mol) was treated with 6 mL Ac_2O and 6 mL pyridine, to afford, after the usual work-up, diacetate *anti*-**19** (14.5 g, 92%). GC–MS (t_R = 22.92 min) *m*/*z*: 278 (M^+) (1), 235 (31), 175 (92), 143 (75), 107 (100). ^1H NMR ($CDCl_3$, ppm): 7.30 (m, 5H, C_6H_5), 5.85 (dd, *J* = 4.6, 9.2 Hz, 1H, H-C_1), 4.10 (m, 2H, CH_2OAc), 2.06 (s, 3H, CH_3COO), 2.03 (s, 3H, CH_3COO), 1.98 (m, 1H), 1.81–1.44 (m, 4H), 0.97 (d, *J* = 6.2 Hz, 3H, CH_3-C_3). Anal. calcd. for $C_{16}H_{22}O_4$: C 69.04, H 7.97; found: C 69.27, H 7.81.

(1*RS*,3*RS*)-Acetic acid 5-acetoxy-3-methyl-1-phenyl-pentyl ester (*syn-**19**)

Diol *syn*-**11** (8.60 g, 0.044 mol) was treated with 5 mL Ac_2O and 5 mL pyridine, to afford, after the usual work-up, diacetate *syn*-**19** (11.1 g, 90%). GC–MS (t_R = 22.83 min) *m*/*z*: 235 (M^+ – 43) (33), 175 (94), 143 (73), 107 (100). ^1H NMR ($CDCl_3$, ppm): 7.30 (m, 5H, C_6H_5), 5.82 (t, *J* = 7.3 Hz, 1H, H-C_1), 4.06 (m, 2H, CH_2OAc), 2.05 (s, 3H, CH_3COO), 1.99

© 2002 NRC Canada

(s, 3H, CH_3COO), 1.86–1.38 (m, 5H), 0.98 (d, J = 6.2 Hz, 3H, CH_3-C_3). Anal. calcd. for $C_{16}H_{22}O_4$: C 69.04, H 7.97; found: C 68.85, H 8.21.

General procedure of lipase-mediated kinetic resolution

A solution of the suitable diacetate (10.0 g, 0.036 mol) in 2 mL THF was added to a suspension of lipase PS (5 g) in 100 mL water at pH 7.8 at room temperature. The pH was kept constant by means of a pH-Stat. The reaction was monitored by chiral HPLC. When the mono alcohol mono acetate formed upon saponification reached ee ~ 50%, the reaction was stopped. The mixture was filtered, extracted with EtOAc, and chromatographed (hexane–EtOAc, 9:1). The mono alcohol mono acetate was acetylated with Ac_2O and pyridine, and submitted again to enzymic saponification to enhance ee.

*(1*R,*3*S*)-Acetic acid 5-hydroxy-3-methyl-1-phenyl-pentyl ester ((1*R,*3*S*)*-anti-***20)** *(from (±)-*anti-***19)***

1.53 g (18%), ee = 95% (chiral HPLC), de > 99% (GC–MS). $[\alpha]_D^{20}$ +67 (c = 1.4, $CHCl_3$). GC–MS (t_R = 21.73 min) m/z: 193 (M^+ – 43) (67), 175 (11), 107 (100). ^{1}H NMR ($CDCl_3$, ppm): 7.30 (m, 5H, C_6H_5), 5.86 (dd, J = 4.9, 9.4 Hz, 1H, H-C_1), 3.68 (m, 2H, CH_2OH), 2.04 (s + m, 4H, 1H + CH_3COO), 1.78–1.36 (m, 4H), 0.96 (d, J = 6.4 Hz, 3H, CH_3-C_3). Anal. calcd. for $C_{14}H_{20}O_3$: C 71.16, H 8.53; found: C 71.33, H 8.32.

*(1*S,*3*S*)-Acetic acid 5-hydroxy-3-methyl-1-phenyl-pentyl ester ((1*S,*3*S*)*-syn-***20)** *(from (±)-*syn-***19)***

1.36 g (16%), ee = 72% (chiral HPLC), de = 70% (GC–MS). $[\alpha]_D^{20}$ –19.2 (c = 0.92, $CHCl_3$). GC–MS (t_R = 21.65 min) m/z: 193 (M^+ – 43) (73), 175 (89), 107 (100). ^{1}H NMR ($CDCl_3$, ppm): 7.32 (m, 5H, C_6H_5), 5.86 (dd, J = 6.8, 7.9 Hz, 1H, H-C_1), 3.64 (m, 2H, CH_2OH), 2.05 (s, 3H, CH_3COO), 1.85–1.30 (m, 5H), 0.97 (d, J = 6.5 Hz, 3H, CH_3-C_3). Anal. calcd. for $C_{14}H_{20}O_3$: C 71.16, H 8.53; found: C 70.91, H 8.37.

The diacetate (recovered unreacted) was submitted again to enzymic saponification to increase ee.

*(1*S,*3*R*)-Acetic acid 5-acetoxy-3-methyl-1-phenyl-pentyl ester ((1*S,*3*R*)*-anti-***19)** *(from (±)-*anti-***19)***

2.30 g (23%), ee = 86% (chiral HPLC), de > 99% (GC–MS). $[\alpha]_D^{20}$ – 45 (c = 1.18, $CHCl_3$). ^{1}H NMR and GC–MS spectra were in agreement with those of (±)-*anti*-**19**.

*(1*R,*3*R*)-Acetic acid 5-acetoxy-3-methyl-1-phenyl-pentyl ester ((1*R,*3*R*)*-syn-***19)** *(from (±)-*syn-***19)***

2.38 g (28%), ee = 50%, de = 79%. $[\alpha]_D^{20}$ +13.5 (c = 1.51, $CHCl_3$). ^{1}H NMR and GC–MS spectra were in agreement with those of (±)-*syn*-**19**.

(1*R,*3*S*)-3-Methyl-1-phenyl-pentane-1,5-diol ((1*R,*3*S*)*-anti-*11)

Mono alcohol mono acetate (1*R*,3*S*)-*anti*-**20** (1.50 g, 6.36 mmol) was hydrolysed with KOH (0.533 g, 9.54 mmol) in 10 mL MeOH, to afford diol (1*R*,3*S*)-*anti*-**11** (1.16 g, 94%), ee = 95% (chiral HPLC), de > 99% (GC–MS). $[\alpha]_D^{20}$ +54.8 (c = 0.5, $CHCl_3$). ^{1}H NMR and GC–MS spectra were in agreement with those of (±)-*anti*-**11**.

(1*S,*3*R*)-3-Methyl-1-phenyl-pentane-1,5-diol ((1*S,*3*R*)*-anti-*11)

Diacetate (1*S*,3*R*)-*anti*-**19** (2.20 g, 7.91 mmol) was hydrolysed with KOH (0.644 g, 0.012 mol) in 10 mL MeOH, to afford diol (1*S*,3*R*)-*anti*-**11** (1.39 g, 91%), ee = 86% (chiral HPLC), de > 99% (GC–MS). $[\alpha]_D^{20}$ –53.4 (c = 0.55, $CHCl_3$). ^{1}H NMR and GC–MS spectra were in agreement with those of (±)-*anti*-**11**.

(1*S,*3*S*)-3-Methyl-1-phenyl-pentane-1,5-diol ((1*S,*3*S*)*-syn-*11)

Mono alcohol mono acetate (1*S*,3*S*)-*syn*-**20** (1.30 g, 5.51 mmol) was hydrolysed with KOH (0.464 g, 8.26 mmol) in 10 mL MeOH, to afford diol (1*S*,3*S*)-*syn*-**11** (1.01 g, 95%), ee = 70% (chiral HPLC), de = 72% (GC–MS). $[\alpha]_D^{20}$ –15.5 (c = 1.05, $CHCl_3$). ^{1}H NMR and GC–MS spectra were in agreement with those of ((±)-*syn*-**11**.

(1*R,*3*R*)-3-Methyl-1-phenyl-pentane-1,5-diol ((1*R,*3*R*)*-syn-*11)

Diacetate (1*R*,3*R*)-*syn*-**19** (2.30 g, 8.27 mmol) was hydrolysed with KOH (0.694 g, 0.012 mol) in 10 mL MeOH, to afford diol (1*R*,3*R*)-*syn*-**11** (1.41 g, 88%), ee = 50% (chiral HPLC), de = 77% (GC–MS). $[\alpha]_D^{20}$ +11.05 (c = 1.05, $CHCl_3$). ^{1}H NMR and GC–MS spectra were in agreement with those of (±)-*syn*-**11**.

General procedure for the preparation of Doremox®

p-Toluene-sulfonyl chloride (1.47 g, 7.73 mmol) was added to a solution of the suitable diol (1.00 g, 5.15 mmol), in 10 mL CH_2Cl_2 and 2 mL pyridine at 0°C. The reaction mixture was stirred at room temperature for 3 h, then poured into water and extracted with CH_2Cl_2. The residue, obtained upon concentration, was dissolved in 10 mL MeOH, and treated with MeONa in MeOH (1 M, 8 mL). The reaction mixture was stirred at r.t. for 2 h, poured into water, and extracted with EtOAc. The organic phase was dried (Na_2SO_4), concentrated, and chromatographed (hexane–EtOAc, 95:5), to afford *cis* or *trans*-**2**.

*(2*R,*4*S*)-*cis-***2** *(from (1*R,*3*S*)-*anti-***11** *(1.1 g, 5.67 mmol))*

0.668 g (67%), ee = 92%, de > 99% (chiral GC). $[\alpha]_D^{20}$ +52 (c = 0.27, $CHCl_3$). GC–MS (t_R = 15.59 min) m/z: 176 (M^+) (100), 175 (90), 105 (73). ^{1}H NMR ($CDCl_3$, ppm): 7.31 (m, 5H, C_6H_5), 4.31 (dd, J = 1.9, 11.2 Hz, 1H, H-C_2), 4.15 (ddd, J = 1.5, 4.2, 11.2, 1H, C-H_6), 3.60 (m, 1H, H-C_6), 1.82 (m, 2H), 1.58 (m, 1H), 1.26 (m, 2H), 0.98 (d, J = 6.2 Hz, 3H, CH_3-C_4).

*(2S,4R)-cis-***2** *(from (1S,3R)-anti-***11** *(1.30 g, 6.70 mmol))*

0.778 g (66%), ee = 80%, de > 99% (chiral GC). $[\alpha]_D^{20}$ – 42 (c = 1.2, $CHCl_3$). ^{1}H NMR and GC–MS spectra were in agreement with those of (+)-*cis*-**2**.

*(2*S,*4*S*)-*trans-***2** *(from (1*S,*3*S*)-*syn-***11** *(0.981 g, 5.05 mmol))*

0.577 g (65%), ee = 72%, de = 70% (chiral GC). $[\alpha]_D^{20}$ +14.6 (c = 0.3, $CHCl_3$); this sample contained 13% of (+)-*cis*-**2** and 2% of (–)-*cis*-**2**. GC–MS (t_R = 16.05 min) m/z: 176 (M^+) (100), 175 (89), 105 (80). ^{1}H NMR ($CDCl_3$, ppm): 7.31 (m, 5H, C_6H_5), 4.67 (dd, J = 3.1, 9.6 Hz, 1H, H-C_2), 3.83 (m, 2H, CH_2-O), 2.10 (m, 1H), 1.92 (m, 2H), 1.61 (m, 1H), 1.34 (m, 1H), 1.17 (d, J = 7.1 Hz, 3H, CH_3-C_4).

© 2002 NRC Canada

*(2*R*,4*R*)*-trans-***2** *(from (1*R*,3*R*)*-syn-***11** *(1.30 g, 6.70 mmol))*

0.743 g (63%), ee = 50%, de = 77% (chiral GC). $[\alpha]_D^{20}$ –9.8 (*c* = 1.15, $CHCl_3$); this sample contained 9.5% of (–)-*cis*-**2** and 2% of (+)-*cis*-**2**. ^{1}H NMR and GC–MS spectra were in agreement with those of (+)-*trans*-**2**.

*(2*S*,4*R*)*-cis-***2** *(from (1*S*,3*R*)*-anti-***11** *(1.50 g, 7.73 mmol, obtained by reduction of (4*S*,6*S*)-***13**))*

0.925 g (68%), ee = 98%, de > 99% (chiral GC). $[\alpha]_D^{20}$ –54.1 (*c* = 1.05, $CHCl_3$). ^{1}H NMR and GC–MS spectra were in agreement with those of (+)-*cis*-**2**.

*(2*S*,4*S*)*-trans-***2** *(from (1*S*,3*S*)*-syn-***11** *(obtained by BY reduction of (*E*)-***3**))*

ee = 99%, de = 72% (chiral GC). $[\alpha]_D^{20}$ +18.1 (*c* = 0.75, $CHCl_3$); this sample contained 14% of (+)-*cis*-**2** with ee > 99%. ^{1}H NMR and GC–MS spectra were in agreement with those of (+)-*trans*-**2**.

Configurational assignment

Two samples of (–)-*anti*-**11** (ee = 86%, de > 99%) and (+)-*syn*-**11** (ee = 50%, de = 79%) were oxidized with Jones' reagent in acetone. The corresponding keto acids were treated with diazomethane in Et_2O, and the corresponding methyl ester derivatives were purified by column chromatography (hexane). The following samples of keto ester **10** were obtained: (*i*) (–)-**10** (from (–)-*anti*-**11**): chemical purity (GC–MS) = 98%. $[\alpha]_D^{20}$ –5.02 (*c* = 0.85, benzene) lit. value (21*a*) $[\alpha]_D^{20}$ –5.65 (*c* = 1.24, benzene) for (*S*)-isomer ee = 90%; lit. value (21*b*) $[\alpha]_D^{20}$ +9.25 (neat) for (*R*)-isomer ee > 96%; (*ii*) (–)-**10** (from (+)-*syn*-**11**): chemical purity (GC–MS) = 97%. $[\alpha]_D^{20}$ –3.21 (*c* = 0.73, benzene).

Conclusion

The preparation of the four stereoisomers of Doremox® in enantiomerically enriched form was accomplished. BY reduction of suitable precursors **3** and **4** resulted in enantiospecific and highly diastereoselective compounds. Diol precursors of (–)-*cis*-**2** (ee > 99%, de = 98%) or of (+)-*trans*-**2** (ee > 99%, de = 72%) were obtained when a carbonyl or a carbon–carbon double bond was reduced by yeast, under the influence of a preexisting stereocentre in position β. Thus, an interesting, unpredictable stereochemical feature of BY reduction was highlighted.

Lipase PS-mediated kinetic resolution of diol *anti*-**11** and *syn*-**11** was less efficient, but it allowed us to obtain both the enantiomers of the *cis* and *trans* series. The high reactivity of primary acetate groups towards saponification prevented the accomplishment of higher enantiomeric excesses. However, the enzymic reaction of diacetate derivatives enriched in the most reactive enantiomer allowed us to reach quite satisfactory enantiomeric excesses. Biocatalyzed reactions are once again the most effective in the optical activation of such scarcely functionalised substrates as diols *anti*-**11** and *syn*-**11**.

The whole work put into evidence the supremacy of yeast reduction with respect to lipase-mediated hydrolysis. Once the substrate has been accepted by yeast, the whole-cell reductive system always assures enantiospecific transformations, which greatly compensate for the troublesome work-up. Lipases are of much wider application, showing less demanding requisites on the substrate acceptance, but their stereochemical course is sometimes less satisfactory, and strongly dependent on structural factors.

The unusual behaviour of hydroxy ester **6** and lactone **7** under hydride reduction was fully described. Lactols were isolated, as well as products of a diastereoselective addition of some intermediates on EtOAc, followed by reduction.

Olfactory evaluation of optically enriched Doremox samples clearly showed that (2*S*,4*R*)-*cis*-**2** is the nicest and the most powerful isomer of the series. This stereoisomer, incidentally, has the same absolute configuration of the most appreciated of rose oxide isomers (22) (i.e., (2*S*,4*R*)-*cis*-**1**).

Acknowledgement

COFIN-Murst is acknowledged for financial support. The authors would like to thank Dr. Philip Kraft and Mrs. Caroline Denis (Givaudan Dübendorf AG, Fragrance Research) for the olfactory descriptions of Doremox® samples.

References

1. (*a*) C.F. Seidel and M. Stoll. Helv. Chim. Acta, **42**, 1830 (1959); (*b*) C.F. Seidel, D. Felix, A. Eschenmoser, K. Biemann, E. Paully, and M. Stoll. Helv. Chim. Acta, **44**, 598 (1961).
2. Y.R. Naves, D. Lamparsky, and P. Ochsner. Bull. Soc. Chim. Fr. 645 (1961).
3. (*a*) G. Ohloff, E. Klein, and G.O. Schenck. Angew. Chem. **73**, 578 (1961); (*b*) G. Ohloff. Pure Appl. Chem. **43**, 481 (1975).
4. G. Ohloff, W. Giersch, R. Decorzant, and G. Büchi. Helv. Chim. Acta, **63**, 1589 (1980).
5. G. Ohloff and W. Giersch. Helv. Chim. Acta, **63**, 1598 (1980).
6. Firmenich. U.S. Patent 005 219 836A, June 15, 1993.
7. P. Kraft, J.A. Bajgrowicz, C. Denis, and G. Frater. Angew. Chem. Int. Ed. **39**, 2980 (2000).
8. (*a*) W. Sturm. Parfuem. Kosmet. **55**, 351 (1974); (*b*) W. Sturm. H&R Contact, **21**, 20 (1978).
9. (*a*) E. Brenna, C. Fuganti, S. Serra, and P. Kraft. Eur. J. Org. Chem. 967 (2002); (*b*) E. Brenna, C. Fuganti, G. Fronza, L. Malpezzi, A. Righetti, and S. Serra. Helv. Chim. Acta, **82**, 2246 (1999); (*c*) E. Brenna, M. Delmonte, C. Fuganti, and S. Serra. Helv. Chim. Acta, **84**, 69 (2001); (*d*) E. Brenna, C. Fuganti, S. Ronzani, and S. Serra. Helv. Chim. Acta, **84**, 3650 (2002).
10. G. Fronza, C. Fuganti, P. Grasselli, and M. Terreni. Tetrahedron, **48**, 7363 (1992).
11. E. Brenna, C. Dei Negri, C. Fuganti, and S. Serra. Tetrahedron: Asymmetry, **12**, 1871 (2001).
12. J.E. Safaryn, J. Chiarello, K.-M. Chen, and M.M. Joullie. Tetrahedron, **42**, 2635 (1986).
13. M. Bellassoued, F. Habbacht, and M. Gaudemar. Tetrahedron, **43**, 1785 (1987).
14. P. Duhamel, D. Cahard, and J.-M. Poirier. J. Chem. Soc. Perkin Trans. 1, 2509 (1993).
15. J. Cason, H.J. Wolfhagen, W. Tarpey, and R.E. Adams. J. Org. Chem. **14**, 152 (1949).
16. M. Periasamy, M.R. Reddy, U. Radhakrishnan, and A. Devasagayaraj. J. Org. Chem. **58**, 4997 (1993).
17. J. Mulzer, G. Brüntrup, G. Hartts, U. Kühl, U. Blaschek, and G. Böhrer. Chem. Ber. **114**, 3701 (1981).
18. (*a*) S. Kojima, S. Maki, T. Hirano, Y. Ohmiya, and H. Niwa. Tetrahedron Lett. **41**, 4409 (2000); (*b*) K. Narasaka, H. Kusama, and Y. Hayashi. Tetrahedron, **48**, 2059 (1992).

© 2002 NRC Canada

19. H. Levene. J. Biol. Chem. **111**, 725 (1935).
20. T. Fujiwara, K. Yanai, K. Shimane, M. Takamori, and T. Takeda. Eur. J. Org. Chem. 155 (2001).
21. (*a*). Y. Shi, W.D. Wulff, G.P.A. Yap, and A.L. Rheingold. Chem. Commun. 2601 (1996); (*b*) D. Enders and K. Papadopoulos. Tetrahedron Lett. **24**, 4967 (1983).
22. Takasago. EP 770 670, October 13, 1995.
23. A. Barbero, D.C. Blakemore, I. Fleming, and R.N. Wesley. J. Chem. Soc. Perkin Trans. 1, 1329 (1997).

© 2002 NRC Canada

Selective biotransformation of substituted alicyclic nitriles by *Rhodococcus equi* A4

Ludmila Martínková, Norbert Klempier, Margit Preiml, Mária Ovesná, Marek Kuzma, Veronika Mylerová, and Vladimír Křen

Abstract: Nitrile hydratase from *Rhodococcus equi* A4 discriminated between geometric isomers of substituted alicyclic nitriles. The enzyme transformed *trans*-4-benzoyloxycyclohexanecarbonitrile (*trans*-**1a**), *cis*-3-benzoyloxycyclohexanecarbonitrile (*cis*-**2a**), *trans*-2-hydroxycyclohexanecarbonitrile (*trans*-**3a**), and *trans*-2-hydroxycyclopentanecarbonitrile (*trans*-**4a**) into the corresponding amides. On the contrary, *cis*-2-hydroxycyclohexanecarbonitrile (*cis*-**3a**) and *cis*-2-hydroxycyclopentanecarbonitrile (*cis*-**4a**) were not converted to a significant extent. *cis*-4-Benzoyloxycyclohexanecarbonitrile (*cis*-**1a**) was also a substrate of the enzyme but reacted slowly. Diequatorial arrangement of the substituents in *trans*-**1a**, *cis*-**2a**, and *trans*-**3a** appears to positively influence the activity of the nitrile hydratase.

Key words: nitrile hydratase, substituted cyclohexanecarbonitriles, substituted cyclopentanecarbonitriles.

Résumé : L'hydratase des nitriles obtenue à partir de *Rhodococcus equi* A4 donne lieu à de la discrimination entre des isomères géométriques de nitriles alicyliques substitués. L'enzyme a transformé les *trans*-4-benzoyloxycyclohexanecarbonitrile (*trans*-**1a**), *cis*-3-benzoyloxycyclohexanecarbonitrile (*cis*-**2a**), *trans*-2-hydroxycyclohexanecarbonitrile (*trans*-**3a**) et *trans*-2-hydroxycyclopentanecarbonitrile *(trans*-**4a**) en amides correspondants. Au contraire, le degré de conversion des *cis*-2-hydroxycyclohexanecarbonitrile (*cis*-**3a**) et *cis*-2-hydroxycyclopentanecarbonitrile (*cis*-**4a**) est faible. Comme substrat de cet enzyme, le *cis*-4-benzoyloxycyclohexanecarbonitrile (*cis*-**1a**) ne réagit que lentement. L'arrangement diéquatorial des substituants dans les isomères *trans*-**1a**, *cis*-**2a** et *trans*-**3a** semble influencer positivement l'activité de l'hydratase des nitriles.

Mots clés : hydratase des nitriles, cyclohexanecarbonitriles substitués, cyclopentanecarbonitriles substitués.

[Traduit par la Rédaction]

Introduction

The use of bacterial nitrile-converting enzymes for enantio-, regio-, and chemoselective hydration and hydrolysis of nitriles has been described in numerous works (1). This work reports the resolution of geometric isomers using a nitrile hydratase.

Different affinities of this enzyme for geometric isomers of *trans*-1,4-dicyanocyclohexane (DCC) were shown using *Corynebacterium* sp. C5 cells containing both nitrile hydratase and amidase. The relative specific activity of the biocatalyst for the *cis* isomer of DCC was only 6% of that for the *trans* isomer (2). The conversion of *trans*-DCC to *trans*-4-cyanocyclohexane-1-carboxylic acid was involved in the chemoenzymatic synthesis of the pharmaceutically important *trans*-4-aminomethylcyclohexanecarboxylic acid (tranexamic acid) (3).

The hydrolysis of alicyclic mono- and dinitriles and amides of *cis* configuration was reported to be catalyzed by *Rhodococcus rhodochrous* IFO 15564 with enantioselectivity in some cases (4), but the biotransformation of the corresponding *trans* isomers was not studied.

Whole-cell biocatalyst SP 409 (Novo Industri, not available commercially) hydrolyzed both *cis*- and *trans*-2-hydroxycyclohexanecarbonitrile and *cis*-2-hydroxycyclopentanecarbonitrile (5).

Here we report the discrimination of *trans* and *cis* isomers of the 3- and 4-benzoyloxy- and 2-hydroxy derivatives of cyclohexanecarbonitriles as well as 2-hydroxycyclopentanecarbonitriles by the nitrile hydratase from *Rhodococcus equi* A4.

Received 4 September 2001. Published on the NRC Research Press Web site at http://canjchem.nrc.ca on 4 June 2002.

Dedicated to Professor J. Bryan Jones on the occasion of his 65th birthday.

L. Martínková,[1] M. Ovesná, M. Kuzma, V. Mylerová, and V. Křen. Institute of Microbiology, Academy of Sciences of the Czech Republic, Laboratory of Biotransformation, Vídeňská 1083, CZ-142 20 Prague 4, Czech Republic.
N. Klempier and M. Preiml. Institute of Organic Chemistry, Technical University Graz, Stremayrgasse 16, A-8010 Graz, Austria.

[1]Corresponding author (e-mail: martinko@biomed.cas.cz).

Results and discussion

Hydrolysis of alicyclic nitriles, 2-hydroxycyclohexanecarbonitrile, 2-hydroxycyclopentanecarbonitrile (5), cyclopentanecarbonitrile (6), and 2-arylcyclopropanecarbonitriles (7), or the regioselective hydrolysis of DCC (2, 3, 8), *trans*-cyclohexane-1,4-diacetonitrile (9), and other saturated and unsaturated dinitriles (4) was the subject of few reports regarding enzymatic nitrile conversion. The present work demonstrated that the nitrile hydratase from *R. equi* A4, which showed a broad substrate specificity for aromatic,

 DOI: 10.1139/V01-205 © 2002 NRC Canada

Scheme 1.

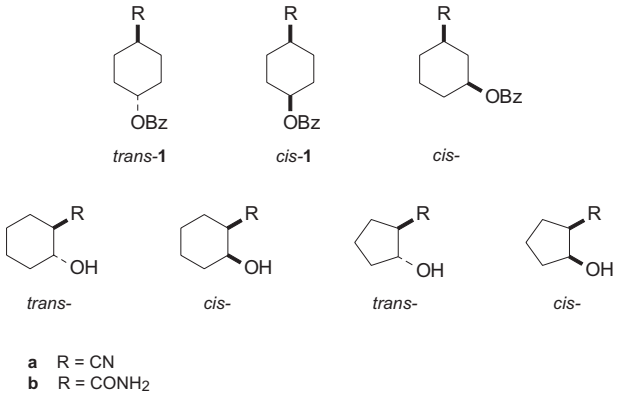

Table 1. Biotransformations of 2-hydroxycyclohexanecarbonitriles, 2-hydroxycyclopentanecarbonitriles, and 3-, 4-benzoyloxycyclohexanecarbonitriles by the nitrile hydratase of *Rhodococcus equi* A4.

Substrate[a]	Reaction time (h)	Product	Conversion (%)[b]	Isolated yield (%)
trans-**1a**	2	*trans*-**1b**	100	91
cis-**1a**	48	*cis*-**1b**	85	74
cis-**2a**	5	*cis*-**2b**	86	79
trans-**3a**	3.5	*trans*-**3b**	100	48
cis-**3a**	24	*cis*-**3b**	<5[c]	—
trans-**4a**	3	*trans*-**4b**	100	51
cis-**4a**	24	no reaction	—	—

[a]The structures (see Scheme 1) represent single enantiomers of *trans*-**1a**, *cis*-**1a**, *cis*-**2a**, *trans*-**3a**, *cis*-**3a**, *trans*-**4a**, and *cis*-**4a**, whereas the biotransformations were carried out with racemates.
[b]Determined by TLC (for compound **4a**) or HPLC (for other compounds).
[c]Traces of amide detected by NMR.

arylaliphatic, and aliphatic nitriles (10), is also useful for the hydration of alicylic nitriles. The use of the purified enzyme afforded 2-, 3-, and 4-substituted (hydroxy-, benzoyloxy-) alicyclic amides. On the contrary, whole-cell biocatalyst SP 409 exhibiting nitrile hydratase and amidase activities gave 2-hydroxycyclohexane- and 2-hydroxycyclopentanecarboxylic acids as the only products (5).

The syntheses of *cis*- and *trans*-2-hydroxycyclohexanecarboxamide (11), 2-hydroxycyclopentanecarboxamide (11), as well as *cis*- (12, 13) and *trans*-4-hydroxycyclohexanecarboxamide (13) have been published previously. Hydroxycyclohexanecarboxamides, both the *cis*- and *trans*-3-isomers, were reported as the respective *O*-acetyl derivatives only (12); however, no NMR data were given for these compounds.

All examined *trans* isomers of 2- and 4-substituted alicyclic nitriles (Scheme 1) were readily converted into the corresponding amides by the nitrile hydratase from *R. equi* A4 (Table 1). *trans*-4-Benzoyloxycyclohexanecarbonitrile (*trans*-**1a**) was transformed at a substantially higher rate than *cis*-**1a**. The reaction rate of *cis*-3-benzoyloxycyclohexanecarbonitrile (*cis*-**2a**) was somewhat lower than that of *trans*-**1a** (Table 1). The *trans* isomer of **2a** was not available.

An even more striking difference than between *trans*-**1a** and *cis*-**1a** was observed when comparing the activities of the nitrile hydratase towards *trans* and *cis* isomers of 2-hydroxycyclohexanecarbonitriles (*trans*-**3a** and *cis*-**3a**) or 2-hydroxycyclopentanecarbonitriles (*trans*-**4a** and *cis*-**4a**) (Table 1). In both pairs of nitriles, the compounds bearing *trans*-substituents were totally converted within 3 h to afford corresponding amides *trans*-**3b** and *trans*-**4b**, respectively. On the contrary, only traces of *cis*-**3b** were formed from *cis*-**3a**, and nitrile *cis*-**4a** was not transformed by the enzyme at all.

It is apparent that the enzyme prefers an equatorial position for both substituents, which can be adopted by the *trans*-1,2- and *trans*-1,4-isomers of the investigated substituted cyclohexanecarbonitriles. Nevertheless, this diequatorial arrangement of the substituents is also in accordance with *cis*-3-benzoyloxycyclohexanecarbonitrile (*cis*-**2a**), which is readily converted to the amide. The two large coupling constants J_{aa} = 9.2 and 9.7 Hz and J_{aa} = 8.7 and 8.8 Hz for H-1 and H-3, respectively, and the ^{1}H coupling pattern clearly reveal a diequatorial substituent position in *cis*-**2a**.

Impairment of the activity of the nitrile hydratase from *R. equi* A4 by steric effects, for example by nitriles with bulky groups such as 2-(3-benzoylphenyl)propionitrile, 2,6-dichlorobenzonitrile, and some 2-substituted benzonitriles, was previously observed (10). Its inefficient hydration of 2- and 4-substituted cyclohexane(pentane)carbonitriles with a *cis*-configuration suggested that this enzyme is more sensitive to steric hindrances than biocatalyst SP 409.

Experimental

NMR spectra of substrates were recorded on a Varian Gemini 200 spectrometer (200 and 50.3 MHz for ^{1}H and ^{13}C, respectively) in $CDCl_3$. NMR spectra of products of the biotransformation were recorded on a Unity Inova 400 MHz spectrometer (399.90 MHz for ^{1}H, 100.57 MHz for ^{13}C) in DMSO-d_6 at 30°C. The assignment was based on COSY, HMQC, and HMBC experiments performed using the manufacturer's software. Residual solvent signals (DMSO: δ_H 2.50 ppm, δ_C 39.60 ppm; $CDCl_3$: δ_H 7.27 ppm, δ_C 77.27 ppm) were used as internal standards.

Synthesis of substrates

Nitriles *trans*-**1a** (14), *cis*-**1a** (14), *cis*-**2a** (15), *trans*-**3a** (16), *cis*-**3a** (17), *trans*-**4a** (18), and *cis*-**4a** (17) were prepared according to literature reported procedures. ^{13}C and ^{1}H NMR data were previously reported for *trans*-**1a** (19), *cis*-**1a** (19), *trans*-**3a** (16, 20), *cis*-**3a** (20–22), *trans*-**4a** (18), and *cis*-**4a** (20–22) but no ^{1}H–^{1}H coupling constants were given.

trans-*1a*

^{1}H NMR δ: 1.70–1.84 (m, 4H, H-2, H-3, H-5, H-6), 2.06–2.16 (m, 4H, H-2, H-3, H-5, H-6), 2.71 (tt, *J* = 7.8, 4.4 Hz, 1H, H-1), 5.11 (tt, *J* = 7.6, 3.7 Hz, 1H, H-4), 7.44 (m, 2H, H-*meta*), 7.56 (m, 1H, H-*para*), 8.02 (m, 2H, H-*ortho*).

cis-*1a*

^{1}H NMR δ: 1.83–2.11 (m, 8H, H-2, H-3, H-5, H-6), 2.77 (tt, *J* = 7.4, 3.7 Hz, 1H, H-1), 5.10 (tt, *J* = 7.4, 3.7 Hz, 1H,

© 2002 NRC Canada

H-4), 7.46 (m, 2H, H-*meta*), 7.58 (m, 1H, H-*para*), 8.05 (m, 2H, H-*ortho*).

cis-*2a*

^{1}H NMR δ: 1.40–2.10 (m, 7H), 2.31 (m, 1H), 2.72 (tt, *J* = 3.5, 5.9, 9.2, 9.7 Hz, 1H, H-1), 5.04 (tt, *J* = 3.5, 5.0, 8.7, 8.8 Hz, 1H, H-3), 7.44 (m, 2H, H-*meta*), 7.53 (m, 1H, H-*para*), 8.06 (m, 2H, H-*ortho*). ^{13}C NMR δ: 21.68 (C-5), 26.22 (C-6), 28.95 (C-4), 30.56 (C-2), 33.98 (C-1), 70.36 (C-3), 121.88 (CN), 128.62 (C-*meta*), 129.95 (C-*ortho*), 130.32 (C-ipso), 133.33 (C-*para*), 165.98 (C=O).

trans-*3a*

^{1}H NMR δ: 1.10–1.44 (m, 4H, H-3, H-4, H-5, H-6), 1.51–1.84 (m, 3H, H-4, H-5, H-6), 2.06 (m, 1H, H-3), 2.42 (ddd, *J* = 11.5, 9.3, 3.8 Hz, 1H, H-1), 3.03 (br s, 1H, OH), 3.69 (dt, *J* = 9.4, 4.2 Hz, 1H, H-2).

cis-*3a*

^{1}H NMR δ: 1.13–2.20 (m, 8H, H-3/3, H-4/4, H-5/5, H-6/6), 3.01 (q, *J* = 3.1 Hz, 1H, H-1), 3.10 (br s, 1H, OH), 3.75 (dt, *J* = 8.4, 4.1, Hz, 1H, H-2).

trans-*4a*

^{1}H NMR δ: 1.48–2.30 (m, 6H), 2.65 (m, Σ *J* = 13.2 Hz, 1H, H-1), 3.68 (d, *J* = 3.5 Hz, 1H, OH), 4.37 (m, Σ *J* = 11.9 Hz, 1H, H-2).

cis-*4a*

^{1}H NMR δ: 1.46–2.10 (m, 6H), 2.71 (dt, *J* = 8.3, 4.8 Hz, 1H, H-1), 3.65 (br s, 1H, OH), 4.35 (dt, *J* = 5.3, 3.5 Hz, 1H, H-2).

General procedure of the biotransformation

The nitrile hydratase from *Rhodococcus equi* A4 (10) was diluted with KH_2PO_4–Na_2HPO_4 buffer (54 mM, pH 7.5) to a concentration of 22 μg of protein mL^{-1} (42 μg of protein mL^{-1} for *cis*-**2a**) and the substrates were added from stock solutions in methanol to make up final concentrations of 1.25 mM of *trans*-**1a**, *cis*-**1a**, and *cis*-**2a** and 5 mM of *trans*-**3a**, *cis*-**3a**, *trans*-**4a**, and *cis*-**4a**. Methanol did not exceed 5% (v/v) of the reaction mixture. The reactions were carried out in shaken vessels (850 rpm, Thermomixer Compact Eppendorf) at 30°C. At intervals, samples were withdrawn, the reaction was quenched with 1 M HCl (0.1 mL per 1 mL of sample) and the precipitated protein was removed by centrifugation. The supernatants were analyzed by HPLC as described below or by TLC on silica gel plates (Merck) developed with chloroform–ethyl acetate (10:1) (for substrates *trans*-**3a**, *cis*-**3a**, *trans*-**4a**, and *cis*-**4a**); the spots were visualized by charring with 5% sulphuric acid in ethanol.

Analytical HPLC

The concentrations of substrates and products were determined using an HPLC system consisting of a solvent-delivery system 600 (Waters), a photo-diode array detector 996 (Waters), and a refractive-index detector 2410 (Waters) and a Nova-Pak C_{18} column (5 μm, 3.9 × 150 mm, Waters). As mobile phases, 50% (v/v) acetonitrile (for compounds *trans*-**1a**, *trans*-**1b**, *cis*-**1a**, *cis*-**1b**, *cis*-**2a**, and *cis*-**2b**) or 10% (v/v) acetonitrile (for other compounds) in water plus 0.1 % (v/v) H_3PO_4 were employed at a flow rate of 1.0 mL min^{-1}. Compounds *trans*-**1a**, *trans*-**1b**, *cis*-**1a**, *cis*-**1b**, *cis*-**2a**, and *cis*-**2b** (retention times 5.6, 2.2, 5.0, 1.8, 5.5, and 2.1 min, respectively) were detected at 230 nm. Compounds *cis*-**3a**, *trans*-**4a**, and *cis*-**4a** (retention times 5.4, 3.5, and 2.9 min, respectively) were detected by the refractive-index detector.

Isolation and identification of products

Amides *trans*-**1b**, *cis*-**1b**, and *cis*-**2b** were extracted from supernatants of the reaction mixtures with ethyl acetate at pH 8.5–8.8 (NaOH). The reaction mixtures from the biotransformations of substrates *trans*-**3a** and *trans*-**4a** were lyophilized and extracted with methanol to give the respective amides *trans*-**3b** and *trans*-**4b**.

trans-*1b*

^{1}H NMR δ: 1.41–1.55 (m, 4H, H-2a, H-3a, H-5a, H-6a), 1.85 (m, 2H, H-2b, H-6b), 2.05 (m, 2H, H-3b, H-5b), 2.14 (m, Σ *J* = 29.7 Hz, 1H, H-1), 4.82 (m, Σ *J* = 29.7 Hz, 1H, H-4), 6.71 (br s, 1H, NH), 7.25 (br s, 1H, NH), 7.52 (m, 2H, H-*meta*), 7.64 (m, 1H, H-*para*), 7.94 (m, 2H, H-*ortho*). ^{13}C NMR δ: 27.17 (t, C-2 and C-6), 30.60 (t, C-3 and C-5), 42.44 (d, C-1), 73.01 (d, C-4), 128.82 (d, C-*meta*), 129.19 (d, C-*ortho*), 130.25 (s, C-ipso), 133.33 (d, C-*para*), 165.29 (s, O*C*OPh), 176.80 (s, $CONH_2$).

cis-*1b*

^{1}H NMR δ: 1.60–1.80 (m, 6H, H-2, H-6, H-3a, H-5a), 1.93 (m, 2H, H-3b, H-5b), 2.22 (m, Σ *J* = 28.6 Hz, 1H, H-1), 5.14 (m, Σ *J* = 13.9 Hz, 1H, H-4), 6.71 (br s, 1H, NH), 7.23 (br s, 1H, NH), 7.55 (m, 2H, H-*meta*), 7.66 (m, 1H, H-*para*), 7.99 (m, 2H, H-*ortho*). ^{13}C NMR δ: 23.96 (t, C-2 and C-6), 28.77 (t, C-3 and C-5), 42.10 (d, C-1), 69.64 (d, C-4), 128.76 (d, C-*meta*), 129.06 (d, C-*ortho*), 130.38 (s, C-ipso), 133.20 (d, C-*para*), 165.01 (s, O*C*OPh), 176.78 (s, $CONH_2$).

cis-*2b*

^{1}H NMR δ: 1.27 (m, 1H, H-6a), 1.37 (m, 1H, H-4a), 1.38 (m, 1H, H-5a), 1.52 (d, *J* = 12.2 Hz, 1H, H-2a), 1.74 (m, 1H, H-6b), 1.86 (m, 1H, H-5b), 2.01 (m, 1H, H-4b), 2.08 (m, Σ *J* = 23.6 Hz, 1H, H-2b), 2.30 (dd, *J* = 3.5, 11.9 Hz, 1H, H-1), 4.88 (dd, *J* = 4.4, 11.0 Hz, 1H, H-3), 6.73 (br s, 1H, NH), 7.25 (br s, 1H, NH), 7.52 (m, 2H, H-*meta*), 7.65 (m, 1H, H-*para*), 7.95 (m, 2H, H-*ortho*). ^{13}C NMR δ: 23.07 (t, C-5), 28.19 (t, C-6), 31.01 (t, C-4), 34.33 (t, C-2), 41.97 (d, C-1), 72.92 (d, C-3), 128.71 (d, C-*meta*), 129.10 (d, C-*ortho*), 130.13 (s, C-ipso), 133.22 (d, C-*para*), 165.11 (s, O*C*OPh), 175.75 (s, $CONH_2$).

trans-*3b*

^{1}H NMR δ: 1.01–1.24 (m, 3H, H-3a, H-4a, H-5a), 1.27 (m, 1H, H-6a), 1.54–1.72 (m, 3H, H-4b, H-5b, H-6b), 1.81 (m, 1H, H-3b), 1.94 (ddd, *J* = 3.7, 9.8, 12.2 Hz, 1H, H-1), 3.46 (m, 1H, H-2), 4.57 (d, *J* = 5.1 Hz, 1H, OH), 6.61 (br s, 1H, NH), 7.13 (br s, 1H, NH). ^{13}C NMR δ: 24.39 (t, C-4), 24.84 (t, C-5), 28.73 (t, C-6), 35.16 (t, C-3), 52.10 (d, C-1), 69.80 (d, C-2), 176.67 (s, $CONH_2$).

trans-*4b*

^{1}H NMR δ: 1.42 (m, 1H, H-3a), 1.50–1.64 (m, 3H, H-4a, H-4b, H-5a), 1.68–1.83 (m, 2H, H-3b, H-5b), 2.39 (m, 1H,

© 2002 NRC Canada

H-1), 4.08 (m, 1H, H-2), 6.67 (br s, 1H, NH), 7.20 (br s, 1H, NH). ^{13}C NMR δ: 22.50 (t, C-4), 27.90 (t, C-5), 34.96 (t, C-3), 53.01 (d, C-1), 75.42 (d, C-2), 176.54 (s, $CONH_2$).

Acknowledgments

Financial support of this work from the Grant Agency of the Academy of Sciences of the Czech Republic (project A4020802/1998), by the Grant Agency of the Czech Republic (project 524/00/1275), by the grant AKTION 17p12 from the Austrian and Czech Ministries of Education and by the Österreichische Nationalbank (project No. 7241) is gratefully acknowledged. Authors wish to thank Dr. Petr Sedmera for critically reading the manuscript and Ms. Magdalena Balvínová for her excellent technical assistance.

References

1. T. Sugai, T. Yamazaki, M. Yokoyama, and H. Ohta. Biosci. Biotech. Biochem. **61**, 1419 (1997).
2. Y. Tani, M. Kurihara, and H. Nishise. Agric. Biol. Chem. **53**, 3151 (1989).
3. K. Yamamoto, Y. Ueno, K. Otsubo, H. Yamane, K.-I. Komatsu, and Y. Tani. J. Ferment. Bioeng. **73**, 125 (1992).
4. K. Matoishi, A. Sano, N. Imai, T. Yamazaki, M. Yokoyama, T. Sugai, and H. Ohta. Tetrahedron: Asymmetry, **9**, 1097 (1998).
5. N. Klempier, A. de Raadt, K. Faber, and H. Griengl. Tetrahedron Lett. **32**, 341 (1991).
6. J.C.T. Dias, R.P. Rezende, C.A. Rosa, M.-A. Lachance, and V.R. Linardi. Can. J. Microbiol. **46**, 525 (2000).
7. M.X. Wang and G.C. Feng. Tetrahedron Lett. **41**, 6501 (2000).
8. Y. Tani, M. Kurihara, H. Nishise, and K. Yamamoto. Agric. Biol. Chem. **53**, 3143 (1989).
9. O. Meth-Cohn and M.-X. Wang. Chem. Commun. 1041 (1997).
10. I. Přepechalová, L. Martínková, A. Stolz, M. Ovesná, K. Bezouška, J. Kopecký, and V. Křen. Appl. Microbiol. Biotechnol. **55**, 150 (2001).
11. G. Bernáth, K.L. Láng, G. Göndös, P. Márai, and K. Kovács. Acta Chim. Hung. **74**, 479 (1972).
12. D.S. Noyce, B.N. Bastian, P.T.S. Lau, R.S. Monson, and B. Weinstein. J. Org. Chem. **34**, 1247 (1969).
13. R. Krieg, M. Schierhorn, H. Altmann, and H.J. Deutscher. J. Prakt. Chem. **329**, 1123 (1987).
14. J.P. Aycard, R. Lafrance, and B. Boyer. Can. J. Chem. **57**, 2823 (1979).
15. M.P. Mertes, A.A. Ramsey, P.E. Hanna, and D.D. Miller. J. Med. Chem. **13**, 789 (1970).
16. H. Hönig, P. Seufer-Wasserthal, and F. Fülöp. J. Chem. Soc. Perkin Trans. 1, 2341 (1989).
17. P. Kozikowski and M. Adamczyk. J. Org. Chem. **48**, 366 (1983).
18. F. Fülöp, I. Huber, G. Bernáth, H. Hönig, and P. Seufer-Wasserthal. Synthesis, 43 (1991).
19. K. Praefcke and D. Schmidt. Z. Naturforsch. **35b**, 1451 (1980).
20. de Raadt, N. Klempier, K. Faber, and H. Griengl. J. Chem. Soc. Perkin Trans. 1, 137 (1992).
21. P.A. Wade and J.F. Bereznak. J. Org. Chem. **52**, 2973 (1987).
22. E. Forró, K. Lundell, F. Fülöp, and L.T. Kanerva. Tetrahedron: Asymmetry, **8**, 3095 (1997).

© 2002 NRC Canada

Exploratory synthetic investigations related to 12a-deoxypillaromycinone

Lan Wang, Sanath K. Meegalla, Cheng-Lin Fang, Nicholas Taylor, and Russell Rodrigo

Abstract: Furfural is converted to suitably substituted AB synthon **21** for 12a-deoxypillaromycinone in 10 steps by a sequence involving the following key steps: intramolecular Diels-Alder reaction of a furan, *5-endo-trig* cleavage of the oxabicyclo adducts **18**, and catalytic hydrogenation of the double bond of a tetrasubstituted enone to produce **19**. Enones **21a** and **21b** obtained by dehydrogenation of **19a** and **19b**, respectively, are then annulated with ethyl 2-methoxy-6-methylbenzoate in a four-step procedure to generate tetracyclic products **25** in 14 steps from furfural.

Key words: antibiotics, furan, intramolecular Diels-Alder, retro Diels-Alder.

Résumé : Le furfural peut être transformé par une séquence de synthèse en dix étapes en un synthon AB (**21**) portant des substituants appropriés pour la 12a-désoxypillaromycocinone; les étapes clés sont une réaction de Diels-Alder intramoléculaire sur le furane, un clivage *5-endo-trig* des adduits oxabicycliques (**18**) et une hydrogénation catalytique de la double liaison de l'énone tétrasubstituée conduisant au produit **19**. Les énones **21a** et **21b** été obtenues par déshydrogénation des produits **19a** et **19b** ont été soumises à une annellation en quatre étapes avec le 2-méthoxy-6-méthylbenzoate d'éthyle qui génère les produits tétracycliques **25** en 14 étapes à partir du furfural.

Mots clés : antibiotiques, furane, Diels-Alder intramoléculaire, rétro Diels-Alder.

[Traduit par la Rédaction]

Introduction

Pillaromycin A, isolated from a culture of *Streptomyces flavovirens* in 1970 (1), is an anti-neoplastic antibiotic that is structurally related to the anthracyclines and tetracyclines but with significantly reduced cardiotoxicity. The aglycone pillaromycinone was assigned the linear tetracyclic structure (**1**) characteristic of this group of antibiotics, by a combination of spectroscopic, degradative, and X-ray crystallographic studies (2). More recently, a re-investigation of the biosynthetic pathway to the aureolic acid group of antibiotics resulted in the isolation of premithramycinone **2** from a blocked mutant of *S. argillaceus*. This antibiotic aglycone, structurally similar to pillaromycinone, is the suggested precursor for the aureolic acid group, and is shown to arise by "tetracycline-type" folding of the initial decaketide (3).

All these tetracyclic antibiotic aglycones have been attractive synthetic targets, and although successful routes to the anthracyclinones and the tetracyclines have been developed, no synthesis of pillaromycinone has been reported. The AB *cis*-ring junction of the antibiotic coupled with the *cis* disposition of the A ring hydroxyl groups and the *peri* positioning of the phenolic hydroxyl groups in rings C and D constitute serious stereochemical and regiochemical problems that must be overcome in any synthetic endeavour. Two attempts have been made (4, 5), and both focused on solving the problem of the AB *cis*-ring fusion. In both instances, the C-12a hydroxyl group was omitted from the target and the desired stereochemistry was achieved by Diels-Alder cycloadditions.

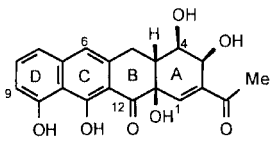

1

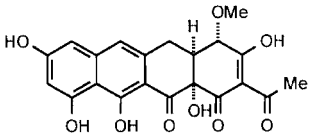

2

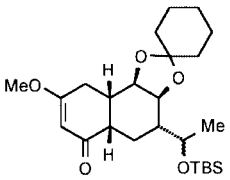

3

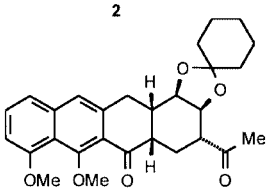

4

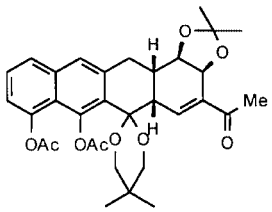

5

Received 16 January 2002. Published on the NRC Research Press Web site at http://canjchem.nrc.ca on 4 June 2002.

L. Wang, S.K. Meegalla, C.-L. Fang, N. Taylor, and R. Rodrigo.[1] Guelph-Waterloo Centre for Graduate Work in Chemistry and Biochemistry, Department of Chemistry, University of Waterloo, Waterloo, ON N2L 3G1, Canada.

[1]Corresponding author (e-mail: rrodrigo@uwaterloo.ca).

 DOI: 10.1139/V02-105 © 2002 NRC Canada

Scheme 1.

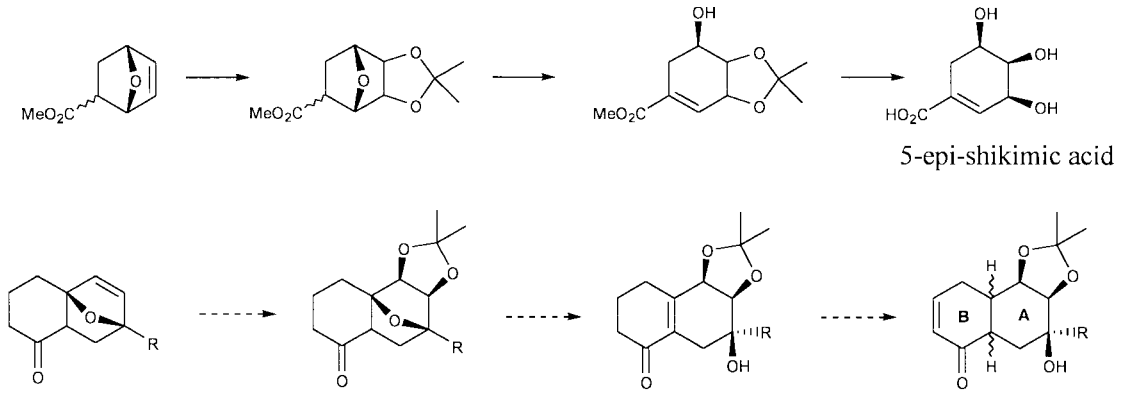

The latter synthesis (5) commenced with a homochiral diacetate derived from L-rhamnose in three steps. By incorporating a chiral centre from the starting material in the linker of an intramolecular Diels-Alder (IMDA) reaction stereochemical control was achieved in the cycloaddition to eventually obtain the desired *cis*-4a,12a ring fusion with the 4a*R* configuration of natural pillaromycinone. This was an elegant demonstration of fidelity in the transmission of stereochemical information in the IMDA reaction, but the "cost" of this strategy was paid for in separation of isomeric intermediates and in the 17 steps needed to obtain AB synthon **3** from L-rhamnose. The regio-controlled attachment of rings C and D to form the tetracyclic core of 12a-deoxypillaromycinone was effected by the Staunton–Weinreb procedure and the synthesis concluded with the 1,2-dihydro-2,3-cyclohexylidenyl-10,11-dimethyl derivative (**4**) of deoxypillaromycinone in 21 steps from L-rhamnose. The earlier synthetic work (4) also concentrated on the establishment of the *cis* AB-ring fusion, but this time by means of an intermolecular Diels-Alder reaction. Much experience with protection and deprotection sequences for the oxygen functional groups was gained, but this effort also ended short of the target at the tetracyclic intermediate (**5**) after 27 steps.

Our synthetic planning for this project relied on earlier work on the synthesis of the shikimic acids (6) and (±)-daunomycinone (7), and used a similar *5-endo-trig* cleavage of a 7-oxabicyclo[2.2.1]heptane adduct as the key step in the rapid production of a prospective AB synthon from furfural (Scheme 1).

Clearly, the major issues that had to be addressed by this investigation were (*i*) the relative stereochemistry of the AB-ring junction that ensues from saturation of the 4a–8a enone double bond; (*ii*) the exact nature of the acetyl group surrogate R, and its compatibility with the experimental conditions of the individual synthetic steps; and (*iii*) the attachment of rings CD at the 2,3-enone double bond of the AB segment. In this paper we report the outcome of our work and discuss its applicability to the future synthesis of (±)-12a-deoxypillaromycinone.

Results and discussion

Elaboration of a suitably substituted AB fragment

Furfural was treated with methyllithium, and resulting alcohol **6** was methylated with sodium hydride–iodomethane. 1′-Methoxyethyl furan **7** was deprotonated at the remaining α-position with *n*-butyl lithium, a 10% molar excess of 1,3-dibromopropane was then added rapidly at –78°C, and the solution was allowed to reach room temperature overnight. Chromatography of the resulting products provided 62% yield of desired bromopropylfuran **8**, a smaller amount of the dehydrobrominated allyl furan (5%), and 7% of the symmetrical dimer arising from substitution at both ends of the 1,3-dibromopropane. Inverse addition of the reagents did not significantly improve the yield of **8**. Iodide **9** was obtained in 95% yield from **8** by nucleophilic displacement with potassium iodide in purified (HPLC grade) acetone containing a small amount of sodium bicarbonate. These four routine transformations were conducted on ~20-g scales to furnish **9** in 30% overall yield (Scheme 2).

It was now necessary to set the stage for the IMDA reaction with the furan ring as the diene by appending a vinyl ketone residue (the dienophile) at the end of the three-carbon substituent. Various methods are available for accomplishing the transformation of **9** to desired enone **10**; these usually involve the addition of an organolithium or magnesium species to an acrolein (or substituted acrolein) followed by oxidation of the resulting alcohol (8). In our case, the alcohol obtained from **9** in this manner was much more sensitive to the oxidative conditions than alcohols from simple α-methyl furans, and hence the yields were poor and the enone was accompanied by products of decomposition and polymerization. We therefore sought an alternative that did not require oxidative conditions for the conversion of **9** to **10**. Although cyanide **11** could be prepared, it failed to react with vinyl lithium or vinyl magnesium bromide. Amide **12** prepared from acryloyl chloride and *N*,*O*-dimethyl hydroxylamine (9) seemed to be a promising option for this transformation. The conjugated double bond of **12** was "masked" by reacting it with furan (1.1 equiv zinc iodide, 50°C, 10 days) to produce *exo* adduct **13** exclusively. This compound was prepared on a large scale as a crystalline solid after column chromatography. Reaction of iodide **9** with 2.2 equiv of *tert*-butyllithium at –78°C followed by addition of the amide (1.5 equiv in ether) at –78°C provided ketone **14** after work-up in 75% yield. It was heated in dry benzene for 12 h to induce the retro Diels-Alder reaction and the solvent was removed under reduced pressure to leave crude enone **10**. Cyclization of **10** by treatment with a stoichiometric quantity of methyl aluminum dichloride in

© 2002 NRC Canada

Scheme 2.

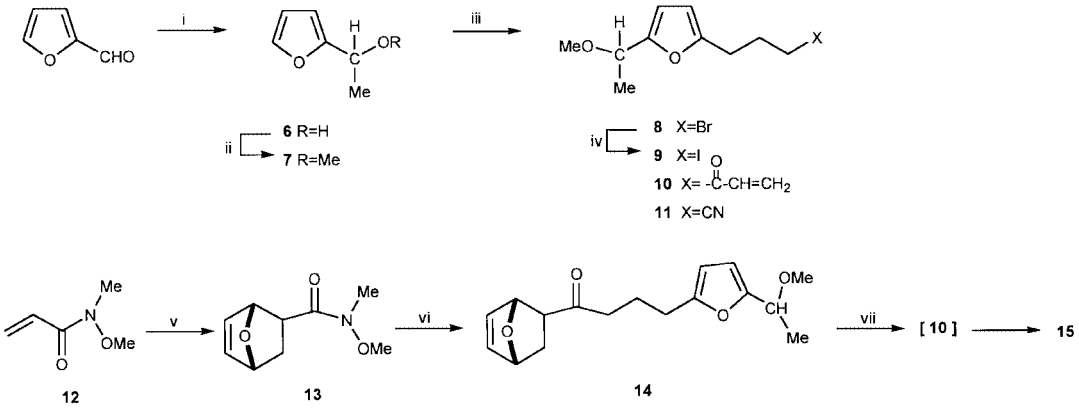

i. MeLi, THF, 85% ii. NaH, MeI, 60% iii.BuLi, -78°C -> -20°C, $C_3H_6Br_2$, 61% iv. KI, Me_2CO, 91% v. Furan, ZnI_2, reflux, 10 days, 67% vi. **9**, *t*-BuLi, -78°C, 75% vii. PhH, reflux, 12h, PhH removed; CH_2Cl_2, $MeAlCl_2$, -78°C, 76%

dry methylene chloride at –78°C to produce a ~1:1 mixture of two IMDA *exo* adducts (8) (diastereomeric at C-9) in an overall yield of 68% (15.3% from furfural in six steps). This was an important but unavoidable consequence of the chirality at C-9 in our surrogate acetyl group; furthermore, the approximately equal amounts of diastereomers produced in the reaction indicated that the configuration at C-9 did not have any influence on the stereochemical outcome of the cycloaddition. The diastereomers were separated by chromatography on silica in 30% ethyl acetate–hexane to provide individual racemic ketones 2*S**,4a*S**,8a*R**,9*S** (**15a**, higher R_f), and 2*S**,4a*S**,8a*R**,9*R** (**15b**, lower R_f). The chirality at C-9 is immaterial as it must eventually be lost in the conversion of this group to the desired C-2 acetyl substituent, but it was convenient to separate the diastereomers at this stage and process them separately (as the 9*S** series from **15a** and the 9*R** series from **15b**) to accurately monitor the stereochemical integrity of each succeeding intermediate. The 500 MHz ^{1}H NMR spectra of the individual diastereomers, though complex in the δ 1.8–2.6 region, displayed the resonance of H-1α as a clear doublet of doublets at ca δ 1.5–1.65 with J = 12.4, 8.9 Hz (9*S** isomer) and 11.7, 8.2 Hz (9*R** isomer). These values of J_{gem} and J_{vic}, respectively, imply that the adjacent H-8a proton is in an α configuration; therefore, these signals are diagnostic for *exo* cycloaddition in the IMDA reaction. Similar observations have been recorded (8) for such adducts by other authors.

The alkene double bond of each isomer was hydroxylated with osmium tetroxide in pyridine to install the vicinal dihydroxy function (80%), which was then protected as the acetonide (70%) by treatment with 2,2-dimethoxypropane and *p*-toluene sulfonic acid in methylene chloride (Scheme 3). An X-ray crystallographic structure (Fig. 1) of acetonide **17a** (9*S** series) confirmed the earlier stereochemical assignments as well as the subsequent *exo* hydroxylation common in these oxabicyclo analogues of norbornene (6). Treatment of each of these acetonides with methoxide in methanol resulted in the expected (10) 5-*endo-trig* oxygen-bridge cleavage to produce the respective enones **18a** and **18b** in 72% yield. Many attempts were made to saturate the tetrasubstituted double bond of these enones. Catalytic hydrogenation (Pd, ethylacetate) of each isomer gave complex mixtures of stereoisomeric ketones as well as allylic alcohols of undefined stereochemistry. Use of dissolving metal reductions (sodium amalgam or Birch reduction) gave product mixtures lacking resonances attributable to the acetonide. Complexed tin hydrides and copper hydrides only returned the starting materials. A recent report (11) of the beneficial effects of DBU in the catalytic hydrogenation of the tetrasubstituted double bond of an enone was relevant to this problem. Thus, the hydrogenation of **18a** with hydrogen at atmospheric pressure, 20% palladium hydroxide on carbon, and 0.33 molar proportions of DBU in methanol containing 3% water produced single decalone **19a** in good yield. Furthermore, we were able to combine the reverse Michael oxygen-bridge cleavage with the hydrogenation by treating **17a** with 2 molar proportions of sodium methoxide under the above hydrogenation conditions for four days at room temperature. This resulted in the formation of **19a** in one pot and in 60% yield. Its ^{1}H NMR spectrum had a diagnostic signal for H-8a: an apparent triplet of doublets at δ 2.75 with two diaxial coupling constants ($J_{8,8a} \approx J_{4a,8a} \approx 11.8$ Hz) and one axial–equatorial coupling ($J_{8,8a} \approx 2.3$ Hz). This result suggested that hydrogenation of the tetrasubstituted enone double bond occurred from the α-face, which was followed by equilibration of the *cis*-fused decalone to the less crowded *trans*-isomer **19a** by base catalyzed epimerization at C-8a. In the expectation that the haptophilic influence (12) of the neighboring hydroxyl groups would promote hydrogenation from the β-face, we attempted the same reaction with bridged diol **16b**. The major constituent, estimated to be at least 80% of the crude product mixture, from this reaction displayed a similar triplet of doublets in its ^{1}H NMR spectrum at δ 2.75 with two diaxial couplings (J = 12.1 Hz) and one equatorial–axial coupling (J = 3.1 Hz) to the neighboring protons at C-8 and C-4a, respectively. The structure and relative stereochemistry of that material was confirmed as **20b** by an X-ray crystallographic determination (Fig. 2). 9*R** acetonide **17b** was treated with DBU, aqueous methanol, methoxide, $Pd(OH)_2$, and H_2 as before to produce a mixture of two inseparable isomers, the *trans*-decalone and presumably the α-*cis*-decalone, which were stirred without hydrogen for an additional three days to produce *trans*-decalone **19b** with a similar triplet of doublets (J = 11.9, 2.3 Hz) for

© 2002 NRC Canada

Scheme 3.

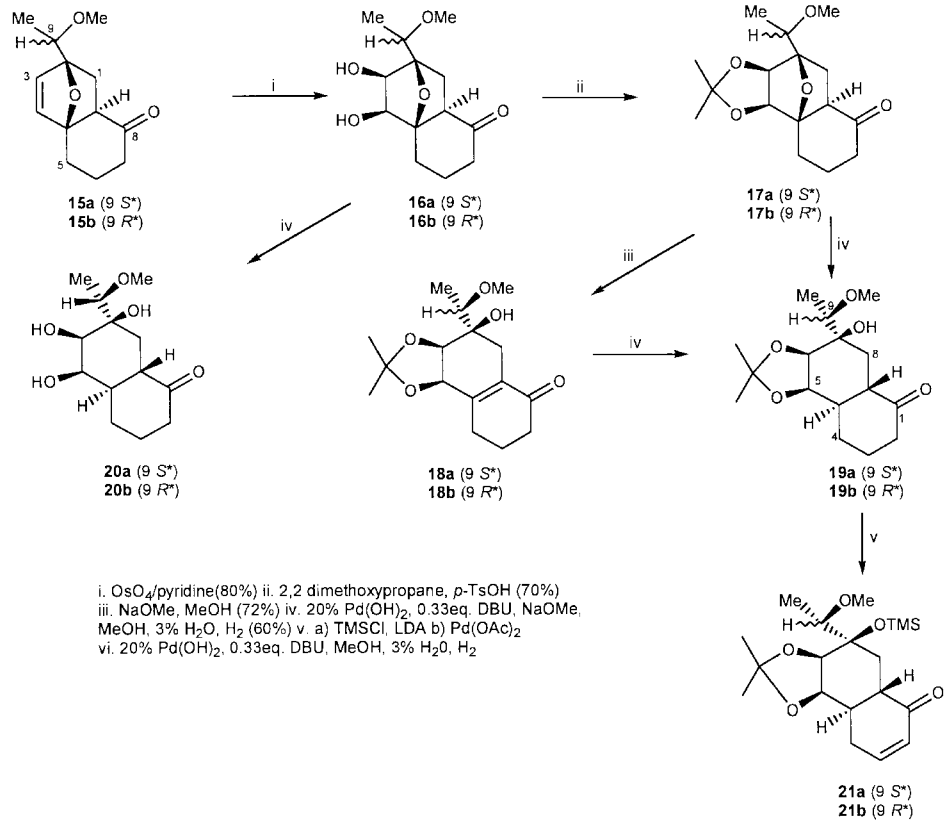

Fig. 1. The X-ray crystal structure of **17a**.

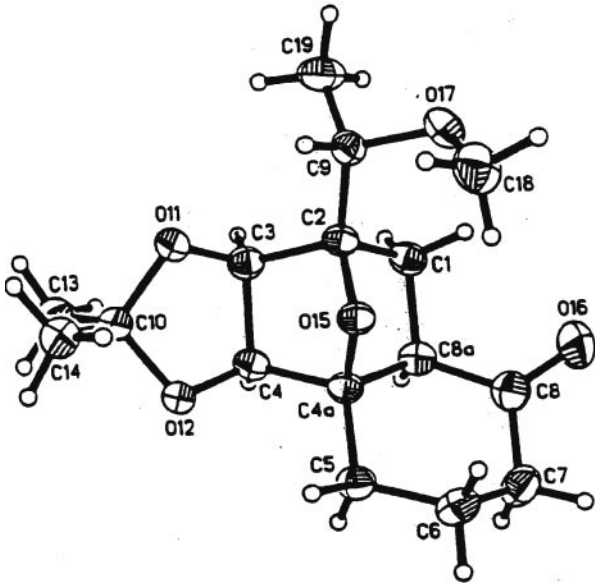

Fig. 2. The X-ray crystal structure of **20b**.

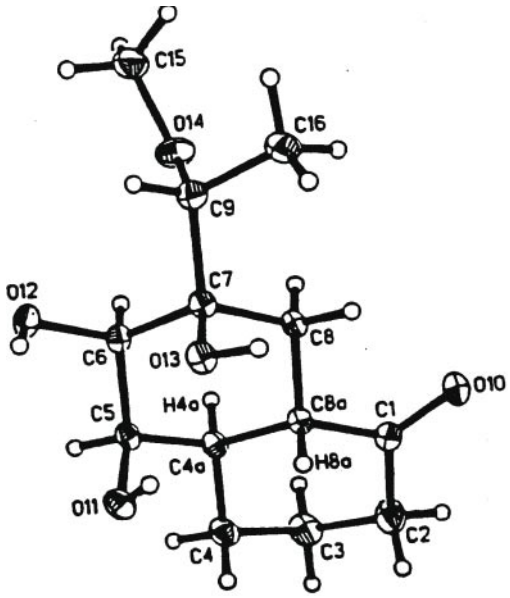

the β-oriented C-8a proton. The unfortunate but inescapable conclusion is that heterogeneous hydrogenation of these intermediates takes place predominantly from the α-face of the molecule and the expected haptophilic effect does not operate in these substrates.

In spite of this serious setback, we decided to continue with the final steps of the synthesis to test the viability of the plan for eventual synthesis of a tetracycle with the corrected AB *cis* ring fusion (vide infra). Dehydrogenation (13) of the kinetic enol silanes derived from **19a** and **19b** at C_2–C_3 was achieved with palladium acetate in 56% yield. Our synthesis of properly functionalized enones **21a** and **21b** was thus completed in ten steps from furfural in an overall yield of ~3%.

© 2002 NRC Canada

Scheme 4.

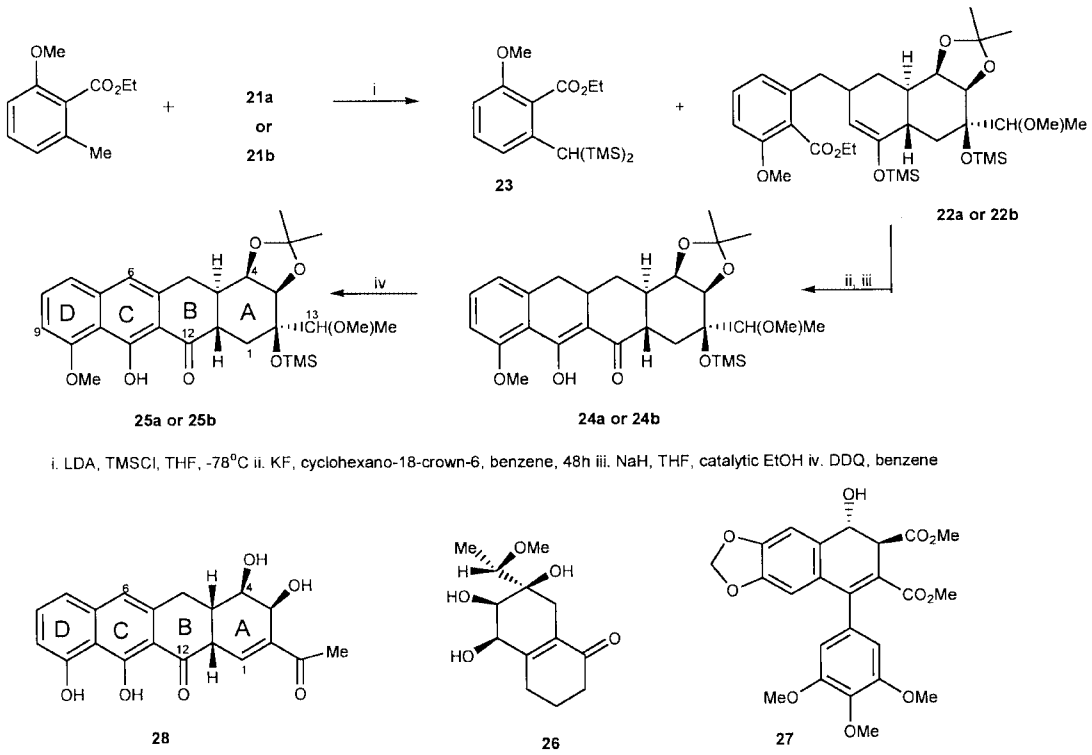

Attachment of the CD rings

After some experiments with 2-cyclohexenone (serving as a model for bicyclic enones **21**), we settled on a four-step conjugate addition–cyclization procedure to achieve the AB + CD connection with the proper regiochemical outcome. Deprotonation of ethyl 2-methoxy-6-methylbenzoate (14) with excess LDA at –78°C in THF–HMPA and reaction of the ensuing anion with each enone **21a** and **21b** separately at this temperature for 1 h was followed by quenching the reaction mixture with TMS chloride. Standard work-up and flash chromatography gave the crude silyl enol ethers **22** as yellow oils in 48% yield. The optimum ratio of reagents for this step was 4.5:1:0.5 (LDA–benzoate–enone) and the excess benzoate was recovered as its disilylated derivative **23**. The crude enol silanes were desilylated and subjected to a Dieckmann condensation with a catalytic amount of sodium ethoxide to produce the tetracycles **24**, which were dehydrogenated with DDQ in benzene to the desired naphthacenones **25** in 18% overall yield each for the four-step sequence (Scheme 4). These tetracycles are therefore obtainable in 14 steps from furfural. The 500 MHz ^{1}H NMR spectra provide conclusive support for the structure and stereochemistry of each compound. Thus **25b** displays an apparent triplet of doublets at δ 3.18 (J ~ 13–14, 3–4 Hz) for H-12a, representing two approximately equal diaxial and one small equatorial coupling (to H-1$_{eq}$). The other AB ring-junction proton, H-4a appears (superficially) as a triplet of triplets at δ 2.21 with two diaxial couplings (13–14 Hz each) and two axial–equatorial couplings (4–5 Hz each) to the neighbouring "equatorial" protons at C-4 and C-5. The 13-*S** isomer **25a** has a very similar spectrum, but the signals for H-12a overlap with the quartet for H-13 so that the approximate coupling constants cannot be measured. The signal for H-4a is, however, a similar triplet of triplets at δ 2.19 with coupling constants of 12.7 and 4.4 Hz.

This investigation has demonstrated that the plan outlined in Scheme 1 delivers a short synthesis (14 steps) of tetracycles **25** with all but one stereocentre (C-4a) correctly established for (±)-12a-deoxypillaromycinone. A method for rectifying the AB stereochemistry still remains to be developed, but now that the structure and stereochemistry of every intermediate has been conclusively established by this work our next goal will be the evaluation of hydroxyl-directed homogeneous hydrogenation methods using cationic Rh and Ir complexes (15). Substrates like **18** and **26** seem to be particularly appropriate for such explorations in view of the recently reported (16) hydrogenation of the tetrasubstituted double bond of α,β-unsaturated ester **27** containing an α-homoallylic hydroxyl group with a Rh(I) cationic complex to produce an 85% yield of hydrogenated products, in which α-hydrogen delivery predominated in a 20:1 ratio. We have already obtained **26** by extended treatment of **16a** with trifluoroacetic acid and confirmed its structure and stereochemistry by X-ray analysis. These investigations will commence shortly, and if successful, the CD annulation procedure developed here will be used to obtain an AB *cis*-fused tetracycle akin to **25**. Subsequent transformations, desilylation, dehydration, demethylation, oxidation at C-13, and acetonide hydrolysis are expected to lead to the first synthesis of (±) 12a-deoxypillaromycinone (**28**).

Experimental

General

Reactions that were expected to be sensitive to air or moisture were performed under an inert atmosphere of

© 2002 NRC Canada

argon. All glassware and syringes were dried in an oven, and then cooled in a dry box before use. All temperatures are in °C. Tetrahydrofuran (THF), diethyl ether, and benzene were distilled from sodium benzophenone ketyl. Dichloromethane, hexane, diisopropylamine, and HMPA were distilled from CaH_2. All reagents were purchased from Aldrich.

Thin layer chromatography was carried out on Merck 5554 precoated silica gel 60 F_{254} aluminum sheets. After development, the sheets were viewed under UV light or with an oxidizing stain solution consisting of ceric ammonium sulfate and hexammonium heptamolybdate in 1.8 M H_2SO_4. Flash chromatography was performed using Merck 9385 silica gel 60 (230–400 mesh). Fourier transform infrared spectra (FT-IR) were recorded on a Bomem MB-100 spectrometer as neat films between NaCl plates, or as KBr discs. ^1H and ^{13}C NMR spectra were obtained on Bruker AM-250, AM-300, and AMX-500 instruments. Samples were prepared in $CDCl_3$ unless otherwise stated. Chemical shifts for NMR were determined relative to the internal standard tetramethylsilane (δ 0.00) or $CHCl_3$ (δ 7.24) for ^1H spectra, and $CDCl_3$ (δ 77.0) for ^{13}C spectra. All ^1H NMR data listed have the following order: chemical shift (ppm), (multiplicity, coupling constants, number of protons, assignment). ^1H assignments were confirmed by decoupling. Mass spectra were run at the McMaster Regional Centre for Mass Spectrometry, McMaster University, Hamilton, Ontario. Elemental analysis were performed by MHW Laboratories, Phoenix, Arizona.

1-Furylethanol (6)

Methyllithium (300 mL, 1.4 M solution in ether, 4.2 mol) was added dropwise to a solution of 2-furfural (34 mL, 0.4 mol) in dry THF (400 mL) at –78°C under argon over 1.5 h. The solution was allowed to warm to –20°C while stirring for 3 h. Saturated NH_4Cl solution was added and the THF layer was separated and concentrated. The aqueous layer was extracted with EtOAc (3 × 100 mL) and the combined organic extracts were dried and concentrated in vacuo. Distillation under reduced pressure (water aspirator) gave a clear liquid (bp 70–74°C, 43 g, 85%). IR (neat) (cm^{-1}): 3350, 1150, 1009, 738. ^1H NMR (250 MHz) δ: 1.53 (d, J = 6.6 Hz, 3H, CHCH_3), 2.24 (br s, 1H, OH), 4.86 (q, J = 6.6 Hz, 1H, CHCH$_3$), 6.22, 6.31, and 7.36 (m each, 3H, furan-H).

2-(1′-Methoxy)ethylfuran (7)

Alcohol **6** (16.1 g, 0.14 mol) in THF (100 mL) was added dropwise to a suspension of NaH (9.0 g, 60% dispersion in mineral oil, 0.22 mol) in THF (50 mL) at 0°C under argon. The solution was stirred for 30 min and iodomethane (18 mL, 0.29 mol) was added dropwise over 15 min. The reaction was stirred overnight. Saturated NH_4Cl solution (100 mL) was added dropwise and the THF layer was separated and concentrated in vacuo. The residue was dissolved in ether (200 mL), dried, and concentrated to give a dark brown oil, which was distilled under reduced pressure (oil pump) to give a colourless liquid (bp 50–55°C, 10.5 g, 60%). ^1H NMR (250 MHz) δ: 1.50 (d, J = 6.6 Hz, 3H, CH_3), 3.27 (s, 3H, OCH_3), 4.36 (q, J = 6.6 Hz, 1H, CH), 6.33 (m, 2H, H-3 and H-4), 7.38 (m, 1H, H-5). HRMS calcd. for $C_7H_{10}O_2$: 126.0681; found: 126.0679. Anal. calcd. for $C_7H_{10}O_2$: C 66.66, H 7.93; found: C 66.61, H 7.91.

2-(3-Bromopropyl)-5-(1′-methoxy)ethylfuran (8)

n-BuLi (62.5 mL, 0.1 mol) was added dropwise to a solution of methyl ether **7** (12.6 g, 0.1 mol) in THF (100 mL) at –78°C under argon. The solution was allowed to warm to –20°C over 1 h, then stirred for 3 h. The reaction was cooled to –78°C and 1,3-dibromopropane (11.2 mL, 0.11 mol) was added and stirring continued overnight at ambient temperature. The solution was warmed to room temperature and saturated NH_4Cl was added, the organic layer was washed with brine, dried, and concentrated in vacuo. Chromatography using 3–5% EtOAc–hexane gave product **8** as a pale yellow oil (15.1 g, 61%), the dehydrobrominated product (5%), and the dimer (7%). IR (neat) (cm^{-1}): 1558, 1445, 1249, 1102, 1013, 790. ^1H NMR (250 MHz) δ: 1.48 (d, J = 6.6 Hz, 3H, CH_3), 2.18 (m, 2H, $CH_2CH_2CH_2Br$), 2.80 (t, J = 7.2 Hz, 2H, $CH_2CH_2CH_2Br$), 3.27 (s, 3H, OCH_3), 3.42 (t, J = 6.6 Hz, 2H, CH_2Br), 4.29 (q, J = 6.6 Hz, 1H, CH), 5.98 and 6.15 (d each, J = 3.1 Hz, 2H, H-3 and H-4). EI-MS m/z (%): 248, 246 (M^+, 1), 245 (7), 231 (31), 229 (31), 216 (27), 214 (27), 139 (34), 123 (78). HRMS calcd. for $C_{10}H_{15}{}^{79}BrO_2$: 246.0197; found: 246.0198.

2-(3-Iodopropyl)-5-(1′-methoxy)ethylfuran (9)

Bromide **8** (15.1 g, 0.061 mol), KI (25 g, 0.153 mol), and $NaHCO_3$ (0.5 g, 6 mmol) were dissolved in HPLC-grade acetone, and heated to reflux for 24 h under argon. The reaction was cooled, and the solvent was removed in vacuo. The residue was dissolved in diethyl ether and water was added. The aqueous layer was extracted with diethyl ether (3 × 200 mL), the combined organic layers were dried over Na_2SO_4, filtered, and concentrated in vacuo to give the crude iodide. Flash chromatography using 10% EtOAc–hexane provided pure iodide **9** as a pale yellow oil (16.3 g, 91%). IR (neat) (cm^{-1}): 1557, 1442, 1234, 1114, 1087, 789. ^1H NMR (250 MHz) δ: 1.50 (d, J = 6.6 Hz, 3H, CH_3), 2.18 (m, 2H, $CH_2CH_2CH_2I$), 2.76 (t, J = 7.2 Hz, 2H, $CH_2CH_2CH_2I$), 3.24 (t, J = 6.6 Hz, 2H, CH_2I), 3.30 (s, 3H, OCH_3), 4.32 (q, J = 6.6 Hz, 1H, CH), 5.98 and 6.15 (d each, J = 3.1 Hz, 2H, H-3 and H-4). HRMS calcd. for $C_{10}H_{14}O_2$: 166.0990 ($[M - HI]^+$); found: 166.0989 ($[M - HI]^+$).

2-(3-Cyanopropyl)-5-(1′-methoxy)ethylfuran (11)

Bromide **8** (2 g, 8.1 mmol) and tetrabutylammonium chloride (0.5 g, 1.8 mmol) were dissolved in CH_2Cl_2 and mixed with a saturated KCN solution (2.2 g, 33 mmol); the mixture was stirred at room temperature for 24 h and monitored by TLC while the color of the reaction turned to red-brown. Once the reaction was completed, the organic and aqueous layers were separated, the aqueous layer was extracted with ether (2 × 20 mL), the combined organic layers were dried over Na_2SO_4, and concentrated in vacuo to give a dark brown oil. Flash chromatography using 10% EtOAc–hexane provided pure nitrile **11** as a pale yellow oil (1.32 g, 84%). IR (neat) (cm^{-1}): 2246, 1114, 1087, 794. ^1H NMR (250 MHz) δ: 1.50 (d, J = 6.6 Hz, 3H, CH_3), 2.04 (m, 2H, $CH_2CH_2CH_2CN$), 2.39 (t, J = 7.2 Hz, 2H, $CH_2CH_2CH_2CN$), 2.80 (t, J = 6.6 Hz, 2H, $CH_2CH_2CH_2CN$), 3.30 (s, 3H, OCH_3), 4.32 (q, J = 6.6 Hz, 1H, CH), 5.98 and 6.15 (d each, J = 3.1 Hz, 2H, H-3 and H-4). HRMS calcd. for $C_{11}H_{15}NO_2$: 193.1103; found: 193.1112.

© 2002 NRC Canada

2β-(*N*-Methyl-*N*-methoxyamido)-7-oxabicyclo[2.2.1]hept-5-ene (13)

N,O-Dimethylhydroxylamine

N,*O*-Dimethylhydroxylamine hydrochloride (80 g) was added to a cooled (0°C) solution of KOH (80 g) in water (120 mL). *N*,*O*-dimethylhydroxylamine was distilled from the mixture to give a clear liquid (47 g); bp 41–43°C.

Reaction with acryloyl chloride (12)

N,*O*-Dimethylhydroxylamine (14.0 g, 0.24 mol) and pyridine (18.9 mL, 0.24 mol) in ether (100 mL) was added dropwise to a cooled (–78°C) solution of acryloyl chloride (19 mL, 0.24 mol) in ether (400 mL) under argon over a period of 1 h. The mixture was allowed to warm to 0°C while stirring for 3 h. The ether was decanted from the solid and the solid was washed with dry ether. The combined ether solutions were concentrated in vacuo to give a pale yellow liquid, which was distilled under reduced pressure (oil pump) to give a clear liquid (10.3 g); bp 45°C (0.05 mm Hg). IR (neat) (cm^{-1}): 1664, 1619. ^1H NMR (250 MHz) δ: 3.26 (s, 3H), 3.71 (s, 3H), 5.74 (dd, *J* = 10.35, 2.1 Hz, 1H), 6.41 (dd, *J* = 17.1, 2.1 Hz, 1H), 6.72 (dd, *J* = 17.1, 10.35 Hz, 1H). Anal. calcd. for $C_5H_9NO_2$: C 52.17, H 7.88, N 12.17; found: C 51.90, H 8.00, N 12.28 (17).

Diels-Alder addition to furan (13)

N,*O*-Dimethylacryloylamide **12** (10.33 g, 89 mmol) and zinc iodide (28.7 g, 90 mmol) were heated at reflux in distilled furan (90 mL) for 10 days. The reaction mixture was diluted with EtOAc (400 mL) and washed with H_2O (200 mL). The organic layer was separated, washed with brine, dried, and concentrated in vacuo (bath < 35°C) to give a yellow oil. Chromatography over silica using 80% EtOAc–hexane gave a colourless oil (**13**), which crystallized on refrigeration (mp 46–47°C; yield 67%). IR (neat) (cm^{-1}): 1660, 1440, 1381, 1317, 1032, 908, 704. ^1H NMR (250 MHz) δ: 1.57 (dd, *J* = 11.3, 8.4 Hz, 1H, H-6α), 2.12 (dt, *J* = 11.3, 4.5 Hz, 1H, H-6β), 2.67 (dd, *J* = 8.4, 4.1 Hz, 1H, H-5α), 3.22 and 3.68 (s each, 6H, NCH_3 and OCH_3), 5.07 (d, *J* = 4.5 Hz, 1H, H-1), 5.13 (s, 1H, H-4), 6.39 (ABq, *J* = 4.5 Hz, 2H, H-5 and H-6). HRMS calcd. for $C_9H_{13}NO_3$: 183.0896; found: 183.1074. Anal. calcd. for $C_{19}H_{13}NO_3$: C 59.03, H 7.15; found: C 59.13, H 7.13.

4-[5-(1-Methoxyethyl)furan-2-yl]-1-(7-oxabicyclo-[2.2.1]hept-5-en-2-yl)butan-1-one (14)

Iodide **9** (11.2 g, 38 mmol) was dissolved in anhydrous Et_2O (200 mL), and the solution was cooled to –78°C in a dry ice – acetone bath. *tert*-Butyllithium (52 mL, 1.7 M in pentane, 88.4 mmol) was added dropwise to the cooled solution, and the reaction was stirred for 1 h at –78°C. Amide **13** (10.5 g, 57 mmol) in Et_2O was purged with argon for 15 min and added to the reaction by cannulation at –78°C. The reaction was continued for a further 4 h, and was then quenched at low temperature with saturated NH_4Cl (100 mL). After warming to room temperature, the aqueous layer was extracted with Et_2O (3 × 50 mL) and CH_2Cl_2 (2 × 50 mL). The combined organic layers were dried over Na_2SO_4, filtered, and concentrated in vacuo. Flash chromatography of the crude ketone using 30% EtOAc–hexane provided pure product **14** as a yellow oil (8.2 g, 75%). IR (neat) (cm^{-1}): 1707, 1557, 1100, 793. ^1H NMR (250 MHz) δ: 1.48 (d, *J* = 6.6 Hz, 3H, CH_3), 1.95 (m, 3H, $CH_2CH_2CH_2CO$ and H-3β), 2.65 (m, 6H, $CH_2CH_2CH_2CO$, H-3α, and H-2α), 3.26 (s, 3H, OCH_3), 4.29 (q, *J* = 6.6 Hz, 1H, C*H*OMe), 5.08 (m, 2H, H-1 and H-4), 5.95 and 6.15 (d each, *J* = 3.0 Hz, 2H, furan-H), 6.38 (ABq, *J* = 5.7, 1.3 Hz, 2H, H-5 and H-6). HRMS calcd. for $C_{17}H_{22}O_4$: 290.1512; found: 290.1510.

2*H*-2-(1′-Methoxyethyl)-2,4a-epoxy-8aβ,4aα-1,8a,5,6,7,8-hexahydro-naphthalen-8-one (15a and 15b)

Ketone **14** (8.2 g, 37 mmol) was dissolved in dry benzene (50 mL) and heated to reflux for 12 h. Benzene was removed by distillation under reduced pressure (water aspirator, bath temperature 40°C). Enone **10** generated in situ was dissolved in dry CH_2Cl_2 (50 mL), and the solution was cooled to –78°C. Methylaluminum dichloride (41 mmol, 1.0 M in hexane) was added to the cooled enone solution, and the reaction was stirred for a further 1 h at –78°C. The reaction was quenched with 10% $NaHCO_3$, and warmed until no frozen material remained. The aqueous layer was extracted with CH_2Cl_2, and the combined organic layers were washed with H_2O, dried over Na_2SO_4, filtered, and concentrated in vacuo without external heat to provide a mixture of two stereoisomers. Flash chromatography using 30% EtOAc–hexane gave the C9-*S** isomer **15a** and C9-*R** isomer **15b** as pale yellow oils (total yield: 76%).[2]

C9-S* isomer 15a (R_f = 0.41)

IR (neat) (cm^{-1}): 1701, 1446, 1375, 1062, 715. ^1H NMR (500 MHz) δ: 1.23 (d, *J* = 6.4 Hz, 3H, Me), 1.61 (dd, *J* = 12.4, 8.9 Hz, 1H, H-1α), 1.8–2.31 (m, 2H), 2.22 (ddd, *J* = 14.8, 12.6, 5.0 Hz, 1H, H-5α), 2.37 (dd, *J* = 12.4, 3.2 Hz, 1H, H-1β), 2.39–2.44 (m, 2H), 2.45 (dd, *J* = 8.9, 3.1 Hz, 1H, H-8a), 2.52 (dtd, *J* = 14.0, 3.5, 1.6 Hz, 1H, H-7β), 3.42 (s, 3H, OMe), 3.66 (q, *J* = 6.4 Hz, 1H, H-9), 6.16 and 6.40 (d each, *J* = 5.8 Hz, 2H, H-3 and H-4). ^{13}C NMR (63 MHz) δ: 15.2, 21.8, 28.4, 31.4, 41.6, 53.0, 57.4, 76.8, 90.7, 91.8, 137.5, 138.5, 209.5. EI-MS *m*/*z* (%): 190 ($[M - CH_3OH]^+$, 41), 152 (20), 137 (80), 121 (100), 108 (69), 59 ($[Me - O{=}CHMe]^+$, 80). CI-MS *m*/*z* (%): 240 ($[M + NH_4]^+$, <2), 191 (100). HRMS calcd. for $C_{12}H_{15}O_3$: 207.1021; found: 207.1040 ($[M - Me]^+$). Anal. calcd. for $C_{13}H_{18}O_3$: C 70.27, H 8.11; found: C 70.12, H 8.02.

C9-R* isomer 15b (R_f = 0.31)

IR (neat) (cm^{-1}): 1710, 1449, 1322, 1102, 714. ^1H NMR (500 MHz) δ: 1.28 (d, *J* = 6.5 Hz, 3H, Me), 1.51 (dd, *J* = 11.7, 8.2 Hz, 1H, H-1α), 1.90–2.02 (m, 2H), 2.18–2.25 (m,

[2] Supplementary material (^1H NMR spectra of compounds **15a**, **b**, **19a**, **b**, **21a**, **b** and **25a**, **b**; and X-ray crystallographic data for **17a** and **20b**) may be purchased from the Depository of Unpublished Data, Document Delivery, CISTI, National Research Council Canada, Ottawa, ON K1A 0S2, Canada. For information on obtaining material electronically go to http://www.nrc.ca/cisti/irm/unpub_e.shtml. Crystallographic information has also been deposited with the Cambridge Crystallographic Data Centre. Copies of the data can be obtained free of charge via www.ccdc.cam.ac.uk/conts/retrieving.html (or from the Cambridge Crystallographic Data Centre, 12, Union Road, Cambridge CB2 1EZ, UK; fax: +44 1223 336033; or deposit@ccdc.cam.ac.uk).

© 2002 NRC Canada

1H), 2.28 (dd, *J* = 11.7, 3.0 Hz, 1H, H-1β), 2.36 (dd, *J* = 8.0, 3.0 Hz, 1H, H-8a), 2.38–2.53 (m, 3H), 3.41 (s, 3H, OMe), 3.66 (q, *J* = 6.4 Hz, 1H, H-9), 6.19 and 6.46 (d each, *J* = 5.8 Hz, 2H, H-3 and H-4). ^{13}C NMR (63 MHz) δ: 15.0, 21.5, 28.2, 31.1, 41.3, 52.5, 56.95, 76.5, 90.6, 92.0, 137.0, 137.5, 209.1. EI-MS *m*/*z* (%): 191 ([M – OCH_3]$^+$, 38), 190 (52), 152 (24), 137 (76), 121 (100), 108 (71), 59 (80). CI-MS *m*/*z* (%): 240 ([M + NH_4]$^+$, <2), 191 (100). HRMS calcd. for $C_{12}H_{15}O_3$: 207.1021; found: 207.1061 ([M – Me]$^+$). Anal. calcd. for $C_{13}H_{18}O_3$: C 70.27, H 8.11; found: C 70.12, H 8.36.

2*H*-2-(1′-Methoxyethyl)-3β,4β-dihydroxy-2,4a-epoxy-8aβ,4aα-octahydro-naphthalen-8-one (16a and 16b)

OsO_4 (4.0 g, 15.6 mmol) and bicyclic ketone **15a** or **15b** (3.46 g, 15.6 mmol) were dissloved in pyridine (40 mL) and stirred at room temperature under argon for 48 h. The resulting dark solution was stirred with a mixture of $NaHSO_3$ (8.4 g), pyridine (88 mL), and water (140 mL) for a further 4 h. The reaction was continuously extracted with EtOAc (600 mL) for 48 h. The organic layer was dried over Na_2SO_4, and EtOAc and pyridine were removed under reduced pressure. Flash chromatography using 70% EtOAc–hexane gave each diol as a white solid (3.2 g, 80%).

C9-S* isomer 16a

mp 132–134°C. IR (KBr) (cm^{-1}): 3380, 1714, 1383, 1110, 946, 826. ^{1}H NMR (250 MHz) δ: 1.29 (d, *J* = 6.3 Hz, 3H, CH_3), 1.30 (dd, *J* = 13.2, 8.9 Hz, 1H, H-1α), 2.29 (dd, *J* = 8.9, 3.2 Hz, 1H, H-1β), 2.00 and 2.46 (m each, 6H, H-5, H-6, and H-7), 2.51 (dd, *J* = 13.2, 3.3 Hz, 1H, H-8a), 3.43 (s, 3H, OMe), 3.60 (d, *J* = 6.8 Hz, 1H, OH), 3.82 (dd, *J* = 6.6, 5.9 Hz, 1H, OHC*H*CHOH), 3.96 (q, *J* = 6.3 Hz, 1H, H-9), 4.01 (dd, *J* = 5.9, 3.2 Hz, 1H, HOCHC*H*OH), 5.14 (d, *J* = 3.5 Hz, 1H, OH). ^{13}C NMR (63 MHz) δ: 14.1, 22.2, 25.2, 28.7, 41.2, 51.7, 56.9, 75.7, 76.7, 77.3, 86.9, 91.1, 208.6. CI-MS *m*/*z* (%): 257 ([M + 1]$^+$, 67), 207 (30), 197 (36), 195 (44), 179 (27), 165 (24), 59 (100). Anal. calcd. for $C_{13}H_{20}O_5$: C 60.94, H 7.81; found: C 60.72, H 7.68.

C9-R* isomer 16b

mp 114–116°C. IR (KBr) (cm^{-1}): 3377, 1710, 1458, 1106, 942, 835. ^{1}H NMR (250 MHz) δ: 1.37 (d, *J* = 6.6 Hz, 3H, CH_3), 1.42 (dd, *J* = 13.1, 8.8 Hz, 1H, H-1α), 2.16 (dd, *J* = 13.1, 3.7 Hz, 1H, H-8a), 2.01 and 2.45 (m each, 6H, H-5, H-6, and H-7), 2.28 (dd, *J* = 8.9, 3.7 Hz, 1H, H-1β), 3.44 (s, 3H, OMe), 3.80 (m, 3H, OH, H-9, and OHCHC*H*OH), 4.11 (dd, *J* = 5.7, 3.8 Hz, 1H, OHC*H*CHOH), 5.17 (d, *J* = 3.7 Hz, 1H, OH). ^{13}C NMR (75 MHz) δ: 15.2, 21.2, 24.4, 31.4, 40.6, 51.8, 57.9, 74.1, 75.6, 79.4, 87.9, 91.8, 208.9. HRMS calcd. for $C_{13}H_{21}O_5$: 257.1388; found: 257.1376 ([M + 1]$^+$, 10). Anal. calcd. for $C_{13}H_{20}O_5$: C 60.94, H 7.81; found: C 61.05, H 7.63.

2*H*-2-(1′-Methoxyethyl)-3β,4β-di-*O*-isopropylidene-2,4a-epoxy-8aβ,4aα-octahydro-naphthalen-8-one (17a and 17b)

A mixture of each diol **16** (0.6 g, 2.34 mmol), 2,2-dimethoxypropane (6 mL, 49 mmol), and TsOH (6 mg) was stirred in CH_2Cl_2 for 12 h under argon. Anhydrous K_2CO_3 (1.5 g) was added to the reaction and stirred for a further 3 h. The solution was filtered and concentrated in vacuo. Flash chromatography using 20% EtOAc–hexane gave the pure acetonide as a white solid (0.478 g, 69%).

C9-S* isomer 17a

mp 109–110°C. IR (KBr) (cm^{-1}): 1714, 1458, 1380, 1207, 1101, 873, 606. ^{1}H NMR (250 MHz) δ: 1.23 (d, *J* = 6.6 Hz, 3H, CH_3), 1.31 (dd, *J* = 13.0, 9.2 Hz, 1H, H-1α), 1.30 and 1.48 (s each, 6H, CH_3CCH_3), 1.96, 2.38, and 2.50 (m each, 6H, H-5, H-6, and H-7), 2.18 (dd, *J* = 9.1, 4.1 Hz, 1H, H-1β), 2.57 (dd, *J* = 13.1, 4.1 Hz, 1H, H-8a), 3.36 (s, 3H, OMe), 3.79 (q, *J* = 6.6 Hz, 1H, H-9), 4.20, 4.24 (ABq, *J* = 5.56 Hz, 2H, H-3 and H-4). ^{13}C NMR (75 MHz) δ: 16.5, 21.7, 25.3, 25.5, 25.9, 26.1, 41.3, 50.4, 58.1, 74.3, 84.3, 84.4, 88.8, 90.0, 112.4, 208.6. CI-MS *m*/*z* (%): 297 ([M + 1]$^+$, 14), 239 (10), 206 (13), 59 (100). Anal. calcd. for $C_{16}H_{24}O_5$: C 64.86, H 8.11; found: C 64.77, H 7.97. Crystal data: Colourless bicapped prism, 0.30{100} × 0.66{101} mm, $C_{16}H_{24}O_5$, *M* = 296.4, tetragonal, *a* = 25.901(2), *c* = 9.458(1) Å, *U* = 6344.9(11) Å^3, space group $I4_1/a$ (No. 88), *Z* = 16, μ(Mo Kα) = 0.091 mm^{-1}, 2945 reflections measured, 2804 unique (R_{int} = 1.33%), 1915 observed ($F > 6.0\sigma(F)$). Final *R* and R_w values were 3.18 and 3.19%, respectively (based on *F*).

C9-R* isomer 17b

mp 98–101°C. IR (KBr) (cm^{-1}): 1718, 1456, 1374, 1164, 1096, 870, 669. ^{1}H NMR (250 MHz) δ: 1.16 (d, *J* = 6.3 Hz, 3H, CH_3), 1.30 (dd, *J* = 13.5, 9.0 Hz, 1H, H-1α), 1.32 and 1.46 (s each, 6H, CH_3CCH_3), 2.22 (dd, *J* = 9, 3.7 Hz, 1H, H-1β), 1.95 and 2.40 (m each, 6H, H-5, H-6, and H-7), 2.46 (dd, *J* = 13.5, 3.7 Hz, 1H, H-8a), 3.39 (s, 3H, OMe), 3.88 (q, *J* = 6.3 Hz, 1H, H-9), 4.24, 4.35 (AXq, *J* = 5.55 Hz, 2H, H-3 and H-4). ^{13}C NMR (75 MHz) δ: 13.5, 22.0, 25.2, 25.5, 25.8, 26.1, 41.3, 50.6, 57.0, 73.2, 83.0, 84.5, 87.7, 89.0, 112.2, 208.6. HRMS calcd. for $C_{16}H_{25}O_5$: 297.1702 ([M + 1]$^+$); found: 297.1684. Anal. calcd. for $C_{16}H_{24}O_5$: C 64.86, H 8.11; found: C 65.12, H 8.03.

7-(1′-Methoxyethyl)-5β,6β,7β-trihydroxy-8aβ,4aα-octahydro-naphthalen-1-one (20b)

Palladium hydroxide on carbon (17.4 mg, 20% palladium by dry weight) was added to the argon-flushed solution of the diol **16b** (100 mg, 0.39 mmol), DBU (15 mg), CH_3OH (16 mL), and H_2O (0.5 mL). The flask was evacuated and backfilled with H_2 three times and then maintained at 1 atm H_2 for 2 days. TLC analysis indicated formation of two isomers. The resulting solution was then filtered through a thin layer of celite and concentrated. The residue was diluted with CH_2Cl_2 (50 mL), washed with 1N HCl; the organic layer was dried with Na_2SO_4 and concentrated in vacuo to give a pale yellow oil. Flash chromatography of the crude material using 7:3 EtOAc–hexane gave (*a*) a single isomer as colourless crystals **20b** and (*b*) mixture of two isomers (total yield 72%). ^{1}H NMR (250 MHz) δ: 1.22 (d, *J* = 6.4 Hz, 3H, CH_3), 1.41 (dd, *J* = 14.4, 12.1, 1H, H-8α), 1.5–1.8 (m, 3H), 1.85 (dd, *J* = 14.4, 3.4 Hz, 1H, H-8β), 1.9–2.24 (m, 2H), 2.38 (m, 2H, H-2), 2.75 (td, *J* = 12.1, 3.1 Hz, 1H, H-8a), 3.37 (q, *J* = 6.5 Hz, 1H, H-9), 3.42 (s, 3H, OCH_3), 3.65 and 3.90 (d and br m, 4H, H-5, H-6, and two OH). ^{13}C NMR (63 MHz) δ: 13.4, 26.2, 27.6, 31.4, 41.6, 43.2, 46.8, 57.9, 70.2, 74.6, 76.9, 83.3, 212.4. Crystal data:

© 2002 NRC Canada

Colourless prism fragment, 0.38{100} × 0.66{010} × 0.42{001} mm, $C_{13}H_{22}O_5$, M = 258.3, monoclinic, a = 24.4438(17), b = 5.8361(4), c = 17.8409(13) Å, β = 101.287(4)°, U = 2495.9(4) Å^3, T = 180 K, space group $C2/c$ (No. 15), Z = 8, μ(Mo Kα) = 0.104 mm^{-1}, 3712 reflections measured, 3636 unique (R_{int} = 1.35%), 2974 observed ($F > 6.0\sigma(F)$). The final R and R_w values were 3.08 and 3.87%, respectively (based on F).

7-(1′-Methoxyethyl)-7β-hydroxy-5β,6β-di-*O*-isopropylidene-8aβ,4aα-octahydro-naphthalen-1-one (19a and 19b)

Synthesis of C9-S isomer 19a*

Palladium hydroxide on carbon (100 mg, 20% palladium by dry weight) was added to the argon-flushed solution of the acetonide **17a** (500 mg, 1.69 mmol), DBU (50 mg, 0.33 mol), CH_3ONa (183 mg, 3.4 mmol), CH_3OH (128 mL), and H_2O (4 mL). The flask was evacuated and backfilled by H_2 three times and then maintained at 1 atm H_2 for 4 days. The resulting solution was then filtered, and the filtrate was neutralized by adding dry ice, then concentrated. The residue was dissolved in EtOAc and the precipitate was filtered. EtOAc solution was concentrated in vacuo to give a dark oil which was chromatographed using EtOAc–hexane–methanol (1:4:0.5) to give colourless crystals (304 mg, 60%); mp 110–112°C. IR (KBr) (cm^{-1}): 3527, 2948, 1703, 1435, 1379, 1100, 1030, 881. ^{1}H NMR (500 MHz) δ: 1.11 (d, J = 6.3 Hz, 3H, CH_3), 1.36 and 1.52 (s each, 6H, CH_3CCH_3), 1.47 (dd, J = 14.9, 12.2 Hz, 1H, H-8α), 1.61(m, 1H, H-3α), 1.68 (tt, J = 12.4, 3.6 Hz, 1H, H-4a), 1.78 (m, 1H, H-4β), 1.91 (qt, $J \approx$ 13.3, 3.8 Hz, 1H, H-4α), 2.01 (dd, J = 14.5, 2.4 Hz, 1H, H-8β), 2.14 (m, 1H, H-3β), 2.38 (m, 2H, H-2), 2.76 (td, J = 11.9, 2.3 Hz, 1H, H-8a), 2.90 (br s, 1H, OH), 3.02 (q, J = 6.3 Hz, 1H, H-9), 3.34 (s, 3H, OMe), 4.11 (d, J = 6.3 Hz, 1H, H-6), 4.30 (dd, J = 6.3, 3.9 Hz, 1H, H-5). ^{13}C NMR (75 MHz) δ: 12.5, 25.1, 26.1, 26.4, 27.7, 31.9, 41.7, 42.9, 44.1, 57.2, 71.5, 73.9, 83.4 (2 × C), 108.7, 212.8. CI-MS m/z (%): 299 ([M + 1]$^+$, 15), 241 (25), 239 (30), 191 (10), 181 (41), 135 (14), 91 (11), 81 (14), 59 (100). Anal. calcd. for $C_{16}H_{26}O_5$: C 64.43, H 8.72; found: C 64.20, H 8.53.

Synthesis of C9-R isomer 19b*

Palladium hydroxide on carbon (120 mg, 20% palladium by dry weight) was added to the argon flushed solution of the acetonide 1**7b** (600 mg, 2.03 mmol), DBU (60 mg, 0.4 mmol), CH_3ONa (219 mg, 4.1 mmol), CH_3OH (128 mL), and H_2O (4 mL). The flask was evacuated and backfilled with H_2 three times and then maintained at 1 atm for 24 h. The hydrogen source was then turned off and the reaction was stirred at room temperature for further 3 days. The resulting solution was then filtered, and the filtrate was neutralized by adding dry ice, then concentrated. The residue was dissolved in EtOAc (250 mL) and the precipitate was filtered. EtOAc solution was concentrated in vacuo to give a dark oil which was chromatographed using EtOAc–hexane (1:4) to give colourless crystals (420 mg, 70%); mp 140–142°C. IR (KBr): 3516, 2955, 1763, 1443, 1373, 1158, 1041, 873. ^{1}H NMR (250 MHz) δ: 1.10 (d, J = 6.3 Hz, 3H, CH_3), 1.18 (dd, J = 14.6, 11.7 Hz, 1H, H-8α), 1.35 and 1.48 (s each, 6H, CH_3CCH_3), 1.53 (m, 1H, H-3α), 1.64 (m, 1H, H-4a), 1.68–1.97 (m, 2H, H-4), 2.07 (dd and m, J = 14.4, 2.2 Hz, 1H, H-8β and H-3β), 2.32 (m, 2H, H-2), 2.55 (br s, 1H, OH), 2.70 (td, J = 11.8, 2.3 Hz, 1H, H-8a), 3.03 (q, J = 6.3 Hz, 1H, H-9), 3.24 (s, 3H, OMe), 4.15 (d, J = 6.24 Hz, 1H, H-6), 4.29 (dd, J = 6.23, 4.04 Hz, 1H, H-5). ^{13}C NMR (75 MHz) δ: 11.7, 25.2, 26.3, 26.4, 27.2, 27.7, 41.6, 42.8, 43.9, 57.0, 71.5, 74.1, 81.1 (2 × C), 108.7, 212.2. CI-MS m/z (%): 299 ([M + 1]$^+$, 28), 241 (20), 239 (31), 209 (12), 181 (33), 163 (12), 135 (11), 59 (100). Anal. calcd. for $C_{16}H_{26}O_5$: C 64.43, H 8.72; found: C 64.49, H 8.64.

7-(1′-Methoxyethyl)-7β-trimethylsiloxy-5β,6β-di-*O*-isopropylidene-8aβ,4aα-hexahydro-naphthalen-1-one (21a and 21b)

A fresh LDA solution was prepared from *n*-BuLi (6.6 mL, 1.36 M in hexane, 9.0 mmol) and diisopropylamine (1.25 mL, 8.9 mmol) at 0°C in dry THF.

A solution of hydroxy ketone **19** (210 mg, 0.71 mmol) in dry THF was slowly added to the LDA solution at –78°C under argon. The mixture was stirred for 1 h at –78°C. TMSCl (1.8 mL, 14.2 mmol) was then added. The reaction was stirred for 30 min at –78°C and then allowed to warm to room temperature. The THF was evaporated under reduced pressure and the residue was diluted with dry hexane, white precipitates were filtered, and the hexane solution was concentrated in vacuo to give the crude silyl enol ether. The silyl enol ether was heated at reflux with $Pd(OAc)_2$ (177 mg, 0.78 mmol) in CH_3CN (20 mL) for 1 h under argon. The reaction mixture was filtered through a thin pad of Celite and the solvent was concentrated in vacuo to give a dark brown oil. Flash chromatography using 20% EtOAc–hexane of the crude mixture gave colourless crystals (116 mg, 56%) in each case.

C9-S isomer 21a*

^{1}H NMR (500 MHz) δ: 0.12 (s, 9H, $OSiMe_3$), 1.21 (d, J = 6.4 Hz, 3H, CH_3), 1.31 and 1.51 (s each, 6H, CH_3CCH_3), 1.52 (dd, J = 14.7, 11.8 Hz, 1H, H-8α), 2.09 (m, 1H, H-4a), 2.27 (dd, J = 14.8, 3.1 Hz, 1H, H-8β), 2.33 (dt, J = 19.1, 5.1 Hz, 1H, H-4α), 2.66 (td, J = 11.8, 2.9 Hz, 1H, H-8a), 2.7 (m, 1H, H-4β), 3.16 (q, J = 6.4 Hz, 1H, H-9), 3.28 (s, 3H, OMe), 4.07 (d, J = 5.7 Hz, 1H, H-6), 4.19 (t, J = 5.4 Hz, 1H, H-5), 5.78 (dd, J = 10, 2.2 Hz, 1H, H-2), 6.97 (ddd, J = 10, 6, 2.2, 1H, H-3). ^{13}C NMR (75 MHz) δ: 2.9 (3 × C), 13.8, 26.0, 26.2, 28.4, 32.0, 39.5, 40.6, 56.7, 74.5, 75.6, 76.6, 104.9, 108.6, 129.1, 149.3, 201.1. EI-MS m/z (%): 309, 251 (17), 161 (12), 131 (19), 89 ([Me_3SiO]$^+$, 15), 73 ([Me_3Si]$^+$, 100), 59 ([Me-CH=OMe]$^+$, 96). HRMS calcd. for $C_{16}H_{25}O_4Si$: 309.1522; found: 309.1525 ([M – MeCHOMe]$^+$, 7).

C9-R isomer 21b*

^{1}H NMR (500 MHz) δ: 0.11 (s, 9H, $OSiMe_3$), 1.1 (dd, J = 14.8, 11.4 Hz, 1H, H-8α), 1.16 (d, J = 6.3 Hz, 3H, CH_3), 1.33 and 1.52 (s each, 6H, CH_3CCH_3), 2.11 (m, 1H, H-4a), 2.32 (dt, J = 19.1, 5.2 Hz, 1H, H-4α), 2.61 (td, J = 11.4, 3.4 Hz, 1H, H-8a), 2.65 (m, 1H, H-4β), 2.68 (dd, J = 14.6, 3.4 Hz, 1H, H-8β), 3.0 (q, J = 6.3 Hz, 1H, H-9), 3.29 (s, 3H, OMe), 3.78 (d, J = 5.8 Hz, 1H, H-6), 4.20 (t, J = 5.3 Hz, 1H, H-5), 5.99 (dd, J = 10, 2.3 Hz, 1H, H-2), 6.97 (ddd, J = 10, 6, 2.1, 1H, H-3). ^{13}C NMR (75 MHz) δ: 3.0 (3 × C), 13.1, 25.5, 26.4, 28.1, 32.0, 39.3, 41.1, 56.3, 75.8, 77.5, 77.8, 78.5, 109.9, 128.3, 148.1, 199.8. EI-MS m/z (%): 353 ([M –

© 2002 NRC Canada

Me]$^+$, 8), 309 ([M – MeCHOMe]$^+$, 63), 279 ([M – $OSiMe_3$]$^+$, 41), 251 (72), 73 ([Me_3Si]$^+$, 51), 59 ([MeCH=OMe]$^+$, 100). HRMS calcd. for $C_{19}H_{33}O_5Si$: 369.2097 ([M + 1]); found: 369.2084.

11-Hydroxy-10-methoxy-2-trimethylsilyloxy-2-[1′-(1′-methoxyethyl)]-3β,4β-di-*O*-isopropylidene-1,2,3,4,4a,5,12,12a-octahydronaphthacene-12-one (25a and 25b) from 21a and 21b, separately

The LDA solution was prepared by adding *n*-BuLi (6.1 mL, 4.75 mmol) to freshly distilled diisopropylamine (0.66 mL, 4.75 mmol) in THF at 0°C under argon.

Ethyl 2-methoxy-6-methylbenzoate (0.208 mg, 1.08 mmol) in THF was added to the LDA solution under argon at –78°. The resulting dark red solution was stirred for 15 min and HMPA (0.169 mL, 0.978 mmol) was added. After 5 min, enone **21** (180 mg, 0.489 mmol) was slowly added and the solution was stirred for 1 h. TMSCl (0.5 mL, 3.91 mmol) was added and the mixture was allowed to warm to room temperature. The reaction mixture was slowly added to a solution of saturated $NaHCO_3$ (20 mL) and stirred for 15 min. The aqueous layer was extracted with EtOAc (3 × 25 mL). The combined organic layer was dried over Na_2SO_4, and concentrated in vacuo. Flash chromatography of the crude product using 20% EtOAc–hexane gave silyl enol ether **22** as a yellow oil (150 mg, 48%).

The silyl enol ether **22** (150 mg, 0.237 mmol) was dissolved in benzene (20 mL) and stirred with KF (30 mg, 0.52 mmol) and dicyclohexano-18-crown-6 (194 mg, 0.52 mmol) under argon for 48 h. The reaction was quenched by H_2O (15 mL), the aqueous layer was extracted with Et_2O (3 × 20 mL). The combined organic layer was dried over Na_2SO_4, and concentrated in vacuo. Flash chromatography of the crude product using 20% EtOAc–hexane gave a pale yellow oil (96 mg, 72%).

NaH (13.6 mg in 60% mineral oil, 0.34 mmol) was washed with dry hexane, which was then removed by Pasteur pipette. A solution of the above product (96 mg, 0.17 mmol) in THF was slowly added to a stirring suspension of NaH and a drop of ethanol in THF (10 mL). The reaction mixture was stirred at room temperature for 3 h, and then water (15 mL) was added. The resulting solution was neutralized with dry ice, and extracted with Et_2O (3 × 10 mL) and EtOAc (2 × 15 mL). The combined organic layer was dried over Na_2SO_4, and concentrated in vacuo. Flash chromatography of the crude product using 20% EtOAc–hexane gave yellow crystals of **24** (48 mg, 55%).

DDQ (21 mg, 0.093 mmol) was slowly added to a solution of **24** (48 mg, 0.093 mmol) in benzene (10 mL) under argon at room temperature. The reaction was stirred for 1 h, H_2O (10 mL) and ether (10 mL) were added to the solution, and the aqueous layer was separated and extracted with ether (3 × 10 mL). The combined organic layers were dried over Na_2SO_4 and concentrated in vacuo to give a dark oil. Flash chromatography of the crude product using 20% EtOAc–hexane gave naphthacenone **25** as a yellow solid (46 mg, 96%).

C9-S* isomer 25a (18% overall)

mp 182–184°C (dec.). IR (KBr) (cm^{-1}): 2935, 1624, 1575, 1370, 1259, 1103, 840, 757. ^{1}H NMR (500 MHz) δ: 0.16 (s, 9H, $OSiMe_3$), 1.24 (d, J = 6.32 Hz, 3H, CH_3), 1.37 and 1.55 (s each, 3H each, CH_3CCH_3), 1.66 (dd, J = 14.6, 11.6 Hz, 1H, H-1α), 2.19 (tt, J = 12.7, 4.4 Hz, 1H, H-4a), 2.49 (dd, J = 14.6, 3 Hz, 1H, H-1β), 2.96 (m, 2H, H-5), 3.22 (m, 2H, H-13 and H-12a overlapping), 3.30 (s, 3H, CH-OCH_3), 3.99 (s, 3H, Ar-OCH_3), 4.15 (d, J = 5.77 Hz, 1H, H-3), 4.33 (t, J = 5.36 Hz, 1H, H-4), 6.77 (d, J = 7.84 Hz, 1H, H-9), 6.95 (s, 1H, H-6), 7.19 (d, J = 7.97 Hz, 1H, H-7), 7.45 (t, J = 7.98 Hz, 1H, H-8) 8.23 (s, 1H, Ar-OH). ^{13}C NMR (125 MHz) δ: 2.9 (3 × C), 13.7, 25.9, 26.2, 32.1, 32.4, 38.9, 41.5, 56.1, 56.6, 74.6, 75.9, 82.1, 77.4, 105.4, 108.6, 111.1, 115.1, 116.4, 119.7, 130.8, 138.1, 140.1, 159.8, 165.7, 205.9. CI-MS *m*/*z* (%): 515 ([M + 1]$^+$, 11), 397 (19), 281 (11), 253 (10), 239 (12), 74 (15), 59 (100). Anal. calcd. for $C_{28}H_{38}O_7Si$: C 65.36, H 7.39; found, C 65.32, H 7.44.

C9-R* isomer 25b: (18% overall)

mp 176–178°C (dec.). IR (KBr) (cm^{-1}): 2939, 1622, 1573, 1099, 841, 761. ^{1}H NMR (500 MHz) δ: 0.15 (s, 9H, $OSiMe_3$), 1.19 (d, J = 6.22 Hz, 3H, CH_3), 1.28 (m, 2H, H-1), 1.38 and 1.55 (s each, 3H each, CH_3CCH_3), 2.21 (tt, J = 12.2, 5.28 Hz, 1H, H-4a), 2.87 (m, 2H, H-5), 3.07 (q, J = 6.14 Hz, 1H, H-13), 3.18 (td, 1H, H-12a), 3.29 (s, 3H, CH-OCH_3), 3.88 (d, J = 5.82 Hz, 1H, H-3), 4.00 (s, 3H, Ar-OCH_3), 4.33 (t, J = 5.28 Hz, 1H, H-4), 6.77 (d, J = 8.02 Hz, 1H, H-9), 6.95 (s, 1H, H-6), 7.19 (d, J = 7.85 Hz, 1H, H-7), 7.45 (t, J = 8 Hz, 1H, H-8), 8.23 (s, 1H, Ar-OH). ^{13}C NMR (125 MHz) δ: 2.9 (3 × C), 12.8, 25.5, 26.3, 29.6, 31.5, 38.9, 41.7, 56.1, 56.2, 75.9, 77.1, 78.2, 82.9, 105.4, 108.1, 111.1, 115.1, 116.4, 119.6, 130.8, 138.5, 140.1, 159.8, 165.7, 205.9. CI-MS *m*/*z* (%): 515 ([M + 1]$^+$, 16), 397 (26), 253 (11), 89 ([Me_3SiO]$^+$, 18), 73 ([Me_3Si]$^+$, 93), 59 ([MeO=CHMe]$^+$, 100).

Acknowledgment

We thank the Natural Sciences and Engineering Research Council of Canada (NSERC) for support of this work.

References

1. M. Asai. Chem. Pharm. Bull. **18**, 1699, (1970).
2. (*a*) M. Asai. Chem. Pharm. Bull. **18**, 1706, (1970); (*b*) K. Kamiya, M. Asai, M. Nishikawa, K. Mizuno, Y, Tomiie, and I. Nitta. Chem. Pharm. Bull. **18**, 1724 (1970); (*c*) J.O. Pezzanite, J. Clardy, P.Y. Lau, G. Wood, D.L. Walker, and B. Fraser-Reid. J. Am. Chem. Soc. **97**, 6250 (1975).
3. J. Rohr, U. Weissbach, C. Beninga, E. Kunzel, K. Siems, K.U. Bindseil, F. Lombo, L. Prado, A.F. Brana, C. Mendez, and J.A. Salas. Chem. Commun. 437 (1998).
4. B.M. Trost, C.G. Caldwell, E. Murayama, and D. Heissler. J. Org. Chem. **48**, 3252 (1983).
5. J.D. White, E.G. Nolen, Jr., and C.H. Miller. J. Org. Chem. **51**, 1151 (1986).
6. D. Rajapaksa, B.A. Keay, and R. Rodrigo. Can. J. Chem. **62**, 826 (1984).
7. B.A. Keay and R. Rodrigo. Tetrahedron, **40**, 4597 (1984).
8. (*a*) C. Rogers and B.A. Keay. Can. J. Chem. **71**, 611 (1993); (*b*) **70**, 2929 (1992); (*c*) P.J. de Clercq and L.A. Van Royen. Synth. Commun. **9**, 771 (1979).
9. S. Nahm and S.M. Weinreb. Tetrahedron Lett. **23**, 3815 (1982).

© 2002 NRC Canada

10. B.A. Keay, D. Rajapaksa, and R. Rodrigo. Can. J. Chem. **62**, 1093 (1984).
11. L.E. Overman and A.L. Tomasi. J. Am. Chem. Soc. **120**, 4039 (1998).
12. J.E. Baldwin, A.M. Fryer, G.J. Pritchard, M.R. Spyree, R.C. Whitehead, and M.E. Wood. Tetrahedron Lett. **39**, 707, (1998).
13. Y. Ito, T. Hirao, and T. Saegusa. J. Org. Chem. **43**, 1011 (1978).
14. F.M. Hauser and S.A. Pogany. Synthesis, **814**, (1980).
15. A.H. Hoveyda, D.A. Evans, and G.C. Fu. Chem. Rev. **93**, 1307 (1993).
16. T. Kuroda, M. Takahashi, K. Kondo, and T. Iwasaki. J. Org. Chem. **61**, 9560 (1996).
17. J.V. Raman, Ph.D. thesis. University of Waterloo, Waterloo, Ontario. 1990. p. 159.

© 2002 NRC Canada

Regiospecific synthesis of lactose analog Gal-(β 1,4)-Xyl by transgalactosylation

Wolf-Dieter Fessner and Juan Manuel Juárez Ruiz

Abstract: A short enzymatic synthesis of disaccharide 4-*O*-β-D-galactopyranosyl-D-xylose (**1**) has been developed, which is of interest as a lactose analog for a non-invasive medicinal determination of lactose intolerance. The starting material, benzyl α-D-xyloside, was obtained by a Fischer-type glycosidation of D-xylose with benzyl alcohol, followed by anomeric differentiation of mixed glycosides using a glycosidase from *Aspergillus oryzae*. From several commercial β-galactosidases, which were screened for their transgalactosylation capacity, the enzyme from *Escherichia coli* was found to catalyze a virtually regio- and stereospecific galactosyl transfer from donor compounds *o*-nitrophenyl β-D-galactoside or lactose to the α-D-xyloside. Subsequent hydrogenolytic deprotection furnished desired disaccharide **1**.

Key words: oligosaccharide synthesis, β-galactosidase, lactose intolerance.

Résumé : On a mis au point une courte synthèse du disaccharide 4-*O*-β-D-galactopyranosyl-D-xylose qui présente de l'intérêt comme analogue de lactose pour procéder à une évaluation médicinale non invasive de l'intolérance au lactose. On a obtenu le produit de départ, l'α-D-xyloside de benzyle, par une glycosylation de type Fischer du D-xylose par l'alcool benzylique suivie d'une différentiation anomérique des glycosides mixtes à l'aide d'une glycosidase provenant d'*Aspergillus oryzae*. Diverses β-galactosidases commerciales ont été évaluées pour leur capacité à provoquer une transgalactosylation; on a trouvé que l'enzyme provenant d'*Escherichia coli* catalyse le transfert du galactosyle d'une façon virtuellement régio- et stéréospécique à partir de β-D-galactoside d'*o*-nitrophényle ou de lactose agissant comme composés donneurs vers l'α-D-xyloside. Une déprotection hydrogénolytique subséquente conduit au disaccharide **1** recherché.

Mots clés : oligosaccharide, synthèse, β-galactosidase, intolérance au lactose.

[Traduit par la Rédaction]

Introduction

Lactose is a milk disaccharide produced by nearly all mammalian species. For digestion, it must be hydrolyzed to D-galactose and D-glucose by lactase, an enzyme which is present on the brush border of small intestinal enterocytes. Evaluation of an enzyme deficiency (lactase insufficiency, lactose intolerance) (1, 2) is important in pediatrics and gastroenterology due to the high frequency of a genetic disposition. Because many of the standard diagnostic procedures are invasive, quite drastic, and unacceptable or dangerous for the testing of infants and young children, a non-invasive method for lactase determination has been proposed on the basis of 4-*O*-β-D-galactopyranosyl-D-xylose (**1**) (3), which can be administered as a substrate analog to lactose (4, 5). The xylose released from small quantities of this disaccharide by lactase activity is eliminated in the urine where it can be quantified colorimetrically. The β-Gal-(1,4)-Xyl disaccharide (**1**) is also well known as a fragment of the highly conserved linkage region between the core protein and the polysaccharide chain (glycosaminoglycan) in proteoglycans of connective tissue (6).

Chemical syntheses of **1** require a judicious installation of protective groups and suffer from long, tedious reaction sequences with little overall productivity (7–9). For a choice of alternative enzymatic strategies, the biosynthetic route involving specific UDP-Gal dependant galactosyltransferase enzymes (e.g., β4GalT7) (10) is burdened by technical difficulties, high costs, and the ambident reactivity of xylose (11, 12). On the other hand, glycosidases have been shown by numerous examples to allow the facile formation of glycosides by transglycosylation at low cost (13, 14). Disadvantages of this approach, however, include yield limitations due to competing hydrolysis reactions, and separation problems because of the formation of regioisomers and other by-products with similar physical properties, which is due to the low acceptor selectivity of glycosidases. For example, attempts to form Gal-(β 1,4)-linkages by transglycosylation to D-xylose (15, 16) or to different aryl- or alkyl-β-D-xylosides (17–20) as acceptors were generally met by concomitant

Received 15 March 2002. Published on the NRC Research Press Web site at http://canjchem.nrc.ca on 5 June 2002.

Dedicated to J. Bryan Jones on the occasion of his 65th birthday in recognition of his pioneering contributions to preparative biocatalysis.

W.-D. Fessner[1] and J.M. Juárez Ruiz. Darmstadt University of Technology, Department of Organic Chemistry, Petersenstr. 22, D-64287 Darmstadt, Germany.

[1]Corresponding author (e-mail: fessner@tu-darmstadt.de).

 DOI: 10.1139/V02-106 © 2002 NRC Canada

formation of the corresponding (β 1,3)-disaccharides in significant proportions.

Here we report a new enzymatic synthesis of **1** based on a successful regiospecific transgalactosylation to α-configurated benzyl D-xyloside.

Results and discussion

The synthetic strategy for constructing free-reducing disaccharide **1** (for possible use in clinical diagnosis) called for an anomeric protection group that ideally should confer several important properties to the synthetic intermediates: (*i*) it needs to be easily introduced in the starting material at low cost; (*ii*) it needs to be efficiently removed in the last step with avoidance of toxic reagents; (*iii*) it should facilitate monitoring of conversion and characterization at intermediate stages; (*iv*) it should simplify purification of the intermediates by a sufficiently high tendency to crystallize (particularly in view of a larger scale synthesis); and (*v*) it should exert pronounced stereoelectronic effects for substrate recognition during the transglycosylation process for an enhanced regioselectivity. Thus, from a choice of allyl, 4-pentenyl, and benzyl protection, the latter was given preference because it was expected to best meet these criteria.

Recently, we have developed a simple and efficient procedure for the anomeric differentiation of mixed α,β-glycosides using the hydrolytic function of glycosidases (21). Such anomeric mixtures are readily obtainable by acid-catalyzed Fischer-type glycosidation. Because many glycosidases with suitable substrate specificity and complementary anomeric preference are readily available from various sources (14), pure unprotected glycosides are efficiently accessible. Specifically, the α-configurated anomeric form of benzyl xylopyranoside **1** (Scheme 1) can be isolated in high yield at low cost using crude commercial enzyme preparations from *Aspergillus oryzae* (21).

Since prior attempts for D-xylopyranoside transgalactosylation were mainly performed on the β-configurated benzyl glycoside with unsatisfactory regioselectivity (17–20), α-anomer **1** was chosen for our study. Several commercial β-galactosidases (EC 3.2.1.23, e.g., from *A. oryzae*, *E. coli*, and CloneZyme® library enzymes of undisclosed origin) were screened for transgalactosylation activity in phosphate buffer at pH 7.0 using **1** as the acceptor component and *o*-nitrophenyl β-D-galactoside (*o*-NPG) as the donor component. Because individual regioisomers were not revealed upon TLC analyses using various solvents, crude product mixtures were analyzed by NMR spectroscopy for composition. Practically all enzymes tested were found to catalyze the desired reaction to a varying extent, producing disaccharide mixtures composed of **2** and considerable fractions of the undesired (β 1,3)-regioisomer. No formation of the (β 1,2)-disaccharide was observed, which is probably due to the steric inaccessibility to the biocatalysts. The enzyme from *E. coli* was unique, however, because it yielded the desired 1,4-regioisomer **2** as the only disaccharide product detectable by high-resolution NMR spectroscopy (de ≥ 95%).

Although the transgalactosylation proceeded with excellent regioselectivity, the presence of unreacted acceptor glycoside and free galactose from competing hydrolysis of the donor complicated product purification by silica gel column chromatography. Residual acceptor **1** could, however, be easily removed by selective extraction with ethyl acetate, while the more hydrophilic disaccharide derivative **2** remained in the aqueous phase. Further purification was performed by column filtration through a plug of reversed-phase silica gel. Free galactose was readily removed upon washing with water, while ethanol elution furnished pure benzyl-protected disaccharide **2** in 23% yield as a crystalline solid. Unambiguous structural proof was obtained by full characterization of corresponding peracetate **3**.

Scheme 1. Chemoenzymatic synthesis of disaccharide **4**. Reagents and conditions: (*a*) crude β-galactosidase from *A. oryzae*, H_2O, >60%; (*b*) β-galactosidase from *E. coli*, 23%; (*c*) Ac_2O, pyridine, 95%; (*d*) H_2–Pd/C, aq. EtOH, 80%.

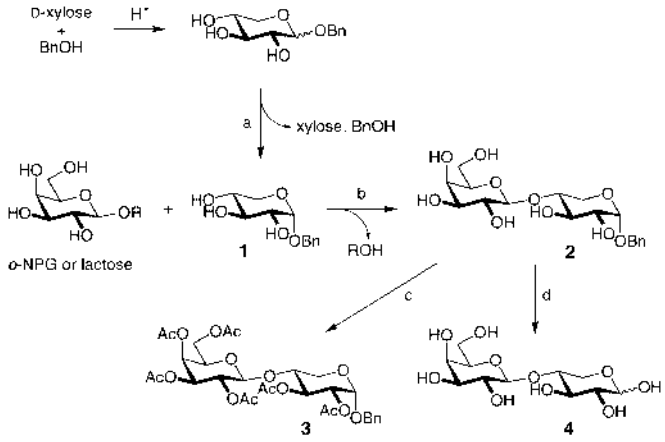

It should be emphasized that the judicious choice of benzyl protection did indeed strongly facilitate product recovery and purification by easily scalable extractive manipulations and thus obviated the need for an exacting high-performance chromatographic separation. Although reaction conditions have not been further optimized, the yield is within the range commonly obtainable by preparative-scale transglycosylations (13, 14). An improvement may be expected from applications of glycosynthases that have been engineered to prevent product hydrolysis (22). Concerning the regioselectivity of the galactosyl transfer, it should be compared with the unfavorable 5:2 ratio of 3-/4-regioisomers obtained for the corresponding benzyl β-xyloside with the same enzyme. The unusually high regioselectivity in the case of α-xyloside may be due to a pronounced bend in the molecular shape of **1** induced by the steric bulk of the α-anomeric benzyl group. Rather than the linearly extended geometry of the β-xyloside, this seems to render the relative setting of the 3- and 4-hydroxyl groups sufficiently different from each other to facilitate discrimination by the galactosidase in favor of the desired compound.

The transgalactosylation was also tested using lactose as an alternative, inexpensive galactosyl donor. As expected, the reactions proceeded more slowly compared with those with the highly reactive *o*-NPG donor. Following the same work-up procedure, pure disaccharide **2** was obtained in 15% yield. The lower yield, as compared with the *o*-NPG donor, is in line with the relatively lower conversion rate because of the increasing likelihood of product hydrolysis at longer reaction times. Attempts were also made for an extended usage of the biocatalyst. Because a continuous operation

© 2002 NRC Canada

of the transglycosylation would be difficult to achieve given the propensity of the product to be hydrolyzed under the reaction conditions, batchwise recycling of the enzyme offered a better solution. Indeed, when the protein was recovered from the reaction mixture by ultrafiltration, it could be reused for at least four identical consecutive runs without noticeable detrimental effects on the reaction velocity or product yield.

Hydrogenolytic cleavage of the benzyl protection group in **2** was performed on 10% Pd/C catalyst. Complete conversion was only achieved by applying quite forcing conditions (60 bar H_2, 50°C), which may be related to the lower reactivity of an α-glycoside. The resultant product was purified by filtration through reversed-phase silica gel column using water as the eluent to furnish the free disaccharide **4** in 80% yield. The spectroscopic data of this compound was identical to values published for the disaccharide from chemical synthesis (7).

Conclusions

A short, versatile enzymatic synthesis has been developed for the lactose analog Gal-(β 1,4)-Xyl **4** by a highly regio- and stereoselective transgalactosylation of benzyl α-D-xyloside **1** as the acceptor. Unlike the situation for free xylose or the corresponding β-D-xyloside, the β-galactosidase from *E. coli* efficiently directs galactosyl transfer to 4-OH of the acceptor, which is likely supported by the steric influence of the bulky α-anomeric substituent that is presumed to restrict a competing access to 3-OH. The benzyl group is of further advantage for simple and effective isolation of the target disaccharide **2** from complex product mixtures by allowing group-specific extraction procedures. Thus, this synthesis is promising for the preparation of larger disaccharide quantities.

Experimental

General

NMR spectra were recorded on Bruker ARX-300 and Bruker AVANCE 500 spectrometers; chemical shifts are referenced to internal TMS ($CDCl_3$) or TSP (D_2O; 0.00 ppm). Mass spectra were recorded on a Bruker Esquire-LC system (ESI), and elemental analyses were performed on a Heraeus CHN-O-Rapid system. Optical rotations were measured with a PerkinElmer 241 apparatus in a 10-cm cuvette at λ = 589 nm. For ultrafiltration, an Amicon 8400 cell equipped with a YM 10 membrane was used. Column chromatography was performed on Merck 60 silica gel (0.063–0.200 mesh), and analytical thin-layer chromatography was performed on Merck silica gel plates 60 GF_{254} using anisaldehyde stain for detection. C_{18}-silica gel 100 (Fluka, 0.040–0.063 mm) was used for reversed-phase (RP) adsorption. β-Galactosidases from *A. oryzae* (Sigma, G-5160 or G-7138) and from *E. coli* (Roche Molecular Biochemicals, 150797 or Sigma, G-6008) were used as commercially supplied. The CloneZyme® glycosidase kit from Recombinant Biocatalysts Inc. (now Diversa) was used for transglycosylation screening.

Benzyl α-D-xylopyranoside (1)

The glycosidation mixture (21) from acidic equilibration of D-xylose with benzyl alcohol (0.1 M) was hydrolyzed in phosphate buffer (0.2 M, pH 4.5) at 37°C using the crude β-galactosidase preparation from *A. oryzae* with TLC monitoring. The unreacted benzyl α-D-xyloside (**1**) was isolated according to the published procedure (21) as a colorless crystalline solid in >60% absolute yield.

Benzyl β-D-galactopyranosyl-(1,4)-α-D-xylopyranoside (2)

o-NPG donor

Compound **1** (100 mg, 0.4 mmol) and *o*-nitrophenyl β-D-galactoside (250 mg, 0.8 mmol) were dissolved in phosphate buffer (8.0 mL, 50 mM; 1.0 mM $MgCl_2$, 5.0 mM mercaptoethanol, pH 7.0), and the mixture was incubated with β-galactosidase from *E. coli* (130 μL, 215 U) on a rotary shaker (50 rpm) at room temperature. Reaction was monitored for product formation by TLC (MeOH–toluene, 2:1, R_f (**2**) = 0.50). After 4 h, an additional equivalent of *o*-NPG was added to the solution, and agitation was continued for 1 h. The enzyme was removed by heating the solution at 80°C for 3 min, followed by centrifugation. Free nitrophenol and residual acceptor were removed by extraction with ethyl acetate (3 × 10 mL), and the aqueous phase was filtered through a plug of RP-silica gel (5.0 g). After washing with water (20 mL), the product was eluted with ethanol to furnish **2** as a colorless solid (37 mg, 23%).

Lactose donor

Compound **1** (23 mg, 0.1 mmol) and D-lactose (65 mg, 0.2 mmol) were dissolved in phosphate buffer (2.0 mL, 50 mM; 1.0 mmol L^{-1} $MgCl_2$, 5.0 mM mercaptoethanol, pH 7.0), and the mixture was incubated with β-galactosidase from *E. coli* (30 μL, 50 U) with shaking. After 3 h, a further equivalent of lactose was added to the solution, and agitation was continued for 2 h. The product was isolated as above to give pure **2** (4 mg, 15%).

Repetitive-batch operation

To a solution containing D-lactose (3.7 g, 10.8 mmol) in phosphate buffer (20 mL, 50 mM; 1.0 mmol L^{-1} $MgCl_2$, 5.0 mM mercaptoethanol, pH 7.0) was added a solution of **1** (1.00 g, 4.2 mmol) in acetonitrile (1.0 mL). The mixture was placed in an ultrafiltration cell and was incubated with β-galactosidase from *E. coli* (1.3 mL, 2150 U) at room temperature for 3.5 h with slow stirring. The product-containing solution was collected by pressure application, and the enzyme that was retained by the membrane was re-used for a subsequent, identical conversion.

The combined reaction volumes from consecutive batches were processed by extractive removal of **1** using ethyl acetate (3 × 30 mL), followed by solid-phase extraction of **2** on RP-silica gel essentially as described above. Isolated yield 334 mg (10%); $[\alpha]_D^{20}$ +63.7 (*c* 1.0, water); R_f = 0.42 (EtOAc–isopropanol–H_2O, 9:4:2). ^1H NMR (500 MHz, D_2O) δ: 7.49–7.41 (m, 5H, H_{ar}), 5.00 (d, 1H, 1′-H), 4.77 (d, 1H, 1-H_a), 4.62 (d, 1H, 1-H_b), 4.46 (d, 1H, 1″-H), 3.92 (d, 1H, 4″-H), 3.87–3.78 (m, 4H, 3′-H, 5′-H_a, 5″-H, 6″-H_a), 3.75 (dd, 1H, 5′-H_b), 3.70 (dd, 1H, 4′-H), 3.66–3.63 (m, 2H, 3″-, 6″-H_b), 3.60 (dd, 1H, 2′-H), 3.52 (dd, 1H, 2″-H) ($J_{1a,1b}$ =

© 2002 NRC Canada

11.7, $J_{1',2'}$ = 3.7, $J_{2',3'}$ = 9.3, $J_{3',4'}$ = 8.1, $J_{4',5b'}$ = 3.9, $J_{5a',5b'}$ = 11.8, $J_{1',2''}$ = 7.8, $J_{2',3''}$ = 9.8, $J_{3',4''}$ = 3.3 Hz). ^{13}C NMR (125.7 MHz, D_2O) δ: 139.8 (C_i), 131.6 (C_o), 131.3 (C_m), 131.16 (C_p), 104.6 (C-1″), 100.3 (C-1′), 79.6 (C-3′), 78.1 (C-4′), 75.5 (C-3″), 74.3 (C-5″), 74.0 (C-2′), 73.5 (C-2″), 72.6 (C-1), 71.5 (C-4″), 63.9 (C-5′), 62.0 (C-6″). MS *m*/*z* (%): 425.3 ([M + Na]$^+$100).

Benzyl 2,3,4,6-tetra-*O*-acetyl-β-D-galactopyranosyl-(1,4)-2,3-di-*O*-acetyl-α-D-xylopyranoside (3)

Disaccharide **2** (40 mg, 0.1 mmol) was taken up in dry pyridine (3.0 mL), acetic anhydride (2.0 mL) was added, and the solution was stirred at room temperature for 24 h. Water was added (20 mL), and the mixture was extracted with EtOAc (3 × 10 mL). The combined organic phases were washed consecutively with water, 1.0 N HCl, sat. $NaHCO_3$, and brine, and then dried over Na_2SO_4. The solvent was removed in vacuo, and the residue recrystallized from Et_2O–petrol ether mixtures to give peracetate **3** as colorless crystals (95 mg, 95%); mp 102°C; R_f = 0.47 (chloroform–MeOH, 40:1). ^{1}H NMR (300 MHz, $CDCl_3$) δ: 7.35–7.23 (m, 5H, H_{ar}), 5.42 (t, 1H, 3′-H), 5.33 (dd, 1H, 4″-H), 5.06 (dd, 1H, 2″-H), 4.96 (dd, 1H, 3″-H), 4.93 (d, 1H, 1′-H), 4.73 (dd, 1H, 2′-H), 4.71 (d, 1H, 1-H_a), 4.47 (d, 1H, 1-H_b), 4.46 (d, 1H, 1″-H), 4.08 (m, 2H, 6″-H) 3.86 (dd, 1H, 5″-H), 3.78 (dd, 1H, 4′-H), 3.62 (d, 2H, 5′-H_{ab}) 2.13, 2.02, 2.01, 2.00, 1.99, 1.95 (6 × s, 18H, Ac) ($J_{1a,1b}$ = 12.2, $J_{1',2'}$ = 3.3, $J_{2',3'}$ = 10.2, $J_{3',4'}$ 9.4, $J_{4',5a'}$ = 7.6, $J_{5a',5b'}$ = 8.0, $J_{1',2''}$ = 7.6, $J_{2',3''}$ = 10.4, $J_{3',4''}$ 3.4, = $J_{4',5''}$ = 0.9, $J_{5',6a'}$ = 6.6, $J_{5',6b'}$ = 7.1 Hz) ^{13}C NMR (75.4 MHz, $CDCl_3$) δ: 172.2 (C=O), 138.9 (C_i), 130.4 (C_o), 129.9 (C_m), 129.7 (C_p), 103.1 (C-1″), 96.9 (C-1′), 79.1 (C-4′), 73.1 (C-5″), 72.9 (C-2′), 72.8 (C-3″), 72.1 (C-3′), 71.6 (C-1), 71.1 (C-2″), 68.9 (C-4″), 63.2 (C-6″), 61.4 (C-5′), 22.5, 22.6, 22.8 (6 × CH_3). Anal. calcd. for $C_{30}H_{38}O_{16}$ (654.61): C 55.04, H 5.85; found C 55.12, H 5.88.

β-D-Galactopyranosyl-(1,4)-D-xylose (4)

To a solution of benzyl disaccharide **2** (160 mg, 0.4 mmol) in 50% aqueous ethanol (10 mL) containing acetic acid (0.25 mL) was added Pd/C catalyst (10%; 400 mg), and the suspension was stirred in an autoclave under hydrogen (60 bar) at 50°C. After 24 h (TLC control EtOAc–isopropanol–water, 3:2:2), the reaction mixture was filtered through Celite, and the solution was concentrated in vacuo. The resultant residue was taken up in water (10 mL) and filtered through a plug of RP silica gel (2.0 g). After further elution with water (20 mL), the combined aqueous phases were freeze-dried to provide free disaccharide **4** as a colorless solid, which could be recrystallized from acetone. Yield 99 mg (80%); mp 164°C (mp 160–168°C (7)); $[\alpha]_D^{20}$ +21.5 (*c* 1.0, water; $[\alpha]_D^{20}$ +22 (7)). ^{1}H NMR (300 MHz, D_2O) δ: 4.56 (d, $J_{1',2'}$ = 7.3 Hz, 1″-H), 3.97–3.56 (m, 12H). ^{13}C NMR (75.4 MHz, D_2O) δ: 105.19 (C-1″), 82.91 (C-1′), 77.95, 75.40, 74.71, 73.76, 72.70, 71.45, 65.48, 63.89, 63.44.

Acknowledgments

This work was partially supported by the Fonds der Chemischen Industrie. J.M.J.R. thanks the Consejo Nacional de Ciencia y Tecnologia (CONACYT) México, for a research fellowship. We are grateful to Dr. P. Rasor from Roche Molecular Biochemicals for a generous gift of the β-galactosidase from *E. coli*.

References

1. E.H. Rings, R.J. Grand, and H.A. Buller. Curr. Opin. Pediatr. **6**, 562 (1994).
2. H.Y. Naim. Histol. Histopathol. **16**, 553 (2001).
3. J.J. Aragon, A. Fernandez-Mayoralas, J. Jimenez-Barbero, M. Marin-Lomas, A. Rivera-Sagredo, and D. Villanueva. Clin. Chim. Acta, **210**, 221 (1992).
4. A. Rivera-Sagredo, F.J. Canada, O. Nieto, J. Jimenez-Barbero, and M. Martin-Lomas. Eur. J. Biochem. **209**, 415 (1992).
5. P. Fernandez, F.J. Canada, J. Jimenez-Barbero, and M. Martin-Lomas. Carbohydr. Res. **271**, 31 (1995).
6. S.B. Selleck. Trends Genet. **16**, 206 (2000).
7. A. Rivera-Sagredo, A. Fernandez-Mayoralas, J. Jimenez-Barbero, M. Martin-Lomas, D. Villanueva, and J.J. Aragon. Carbohydr. Res. **228**, 129 (1992).
8. B. Lindberg, L. Roden, and B.G. Silvander. Carbohydr. Res. **2**, 413 (1966).
9. B. Erbing, B. Lindberg, and T. Norberg. Acta Chem. Scand. Ser. B, **32**, 308 (1978).
10. R. Almeida, S.B. Levery, U. Mandel, H. Kresse, T. Schwientek, E.P. Bennett, and H. Clausen. J. Biol. Chem. **274**, 26165 (1999).
11. T. Wiemann, Y. Nishida, V. Sinnwell, and J. Thiem. J. Org. Chem. **59**, 6744 (1994).
12. Y. Hara and K. Suyama. Eur. J. Biochem. **267**, 830 (2000).
13. K.G.I. Nielsson. *In* Modern methods in carbohydrate synthesis. *Edited by* S.H. Khan and R.A. O'Neill. Harwood Academic, Amsterdam. 1996. p. 518.
14. M. Scigelova, S. Singh, and D.H.G. Crout. J. Mol. Catal. B: Enzym. **6**, 483 (1999).
15. E. Montero, J. Alonso, F.J. Canada, A. Fernandez-Mayoralas, and M. Martin-Lomas. Carbohydr. Res. **305**, 383 (1998).
16. J.J. Aragon, F.J. Canada, A. Fernandez-Mayoralas, R. Lopez, M. Martin-Lomas, and D. Villanueva. Carbohydr. Res. **290**, 209 (1996).
17. R. Lopez and A. Fernandez-Mayoralas. J. Org. Chem. **59**, 737 (1994).
18. R. Lopez and A. Fernandez-Mayoralas. Tetrahedron Lett. **33**, 5449 (1992).
19. T. Yasukochi, C. Inaba, K. Fukase, and S. Kusumoto. Tetrahedron Lett. **40**, 6585 (1999).
20. T. Yasukochi, K. Fukase, Y. Suda, K. Takagaki, M. Endo, and S. Kusumoto. Bull. Chem. Soc. Jpn. **70**, 2719 (1997).
21. J.M. Juarez Ruiz, G. Oβwald, M. Petersen, and W.-D. Fessner. J. Mol. Catal. B: Enzym. **11**, 189 (2001).
22. L.F. Mackenzie, Q. Wang, R.A.J. Warren, and S.G. Withers. J. Am. Chem. Soc. **120**, 5583 (1998).

© 2002 NRC Canada

Glucosyltransferases acting on starch or sucrose for the synthesis of oligosaccharides

Francisco J. Plou, M. Teresa Martín, Aránzazu Gomez de Segura, Miguel Alcalde, and Antonio Ballesteros

Abstract: In this work we review the extraordinary biotechnological potential of two glycosyltransferases, cyclodextrin glucanotransferase and dextransucrase, especially their utility in the synthesis of oligosaccharides. Both enzymes are non-Leloir transferases that require neither co-factors nor activated substrates, as they directly employ the free energy of cleavage of starch and sucrose, respectively. Cyclodextrin glucanotransferase is able to produce cyclodextrins from starch. In the presence of appropriate acceptors (e.g., carbohydrates), this enzyme furnishes oligosaccharides containing $\alpha(1\rightarrow4)$ bonds. Thus, we have found that glucose, maltose, and sucrose readily serve as acceptors to form the corresponding [Glc-$\alpha(1\rightarrow4)]_n$- oligosaccharides, with the degree of polymerization being controlled by the starch:acceptor ratio. The ability of other sugars and related compounds to act as acceptors is also reviewed. Dextransucrase is a glycansucrase that synthesizes dextran using sucrose as glucosyl donor. The formation of dextrans can be quantitatively replaced with the formation of novel oligosaccharides by adding alternative carbohydrate acceptors to the reaction medium. With the dextransucrase from *Leuconostoc mesenteroides* B-1299, we have investigated the synthesis of gluco-oligosaccharides containing $\alpha(1\rightarrow2)$ bonds using methyl 1-*O*-α-D-glucopyranoside as the acceptor. These products constitute a class of nondigestible nutraceutical oligosaccharides with prebiotic properties relating to the stabilization and enhancement of gastrointestinal tract flora, and are being increasingly used by the food industry.

Key words: glycansucrases, cyclodextrin glucanotransferase, cyclodextrin glucosyltransferase, dextransucrase, acceptor products, gluco-oligosaccharides, malto-oligosaccharides, coupling sugar, nutraceuticals, functional foods, prebiotics.

Résumé : Dans ce travail, on passe en revue le potentiel biotechnologique extraordinaire de deux glycosyltransférases, la glucanotransférase de la cyclodextrine et de la sucrase de dextrane, en particulier de leurs utilités dans la synthèse d'oligosaccharides. Les deux enzymes sont des transférases non Lenoir qui ne nécessitent pas de cofacteurs ou de substrats activés puisqu'ils utilisent directement l'énergie libre de clivage de l'amidon et du sucrose respectivement. La glucanotransférase de la cyclodextrine peut produire des cyclodextrines à partir de l'amidon. En présence d'accepteurs appropriés (par exemple des carbohydrates), cet enzyme conduit à la formation d'oligosaccharides contenant des liaisons $\alpha(1\rightarrow4)$. On a ainsi observé que le glucose, le maltose et le sucrose peuvent facilement servir d'accepteurs pour former les oligosaccharides [Glc-$\alpha(1\rightarrow4)]_n$- correspondants dans lesquels le degré de polymérisation est déterminé par le rapport amidon/accepteur. On a aussi passé en revue la possibilité d'autres sucres et de composés apparentés à agir comme accepteurs. La sucrase du dextrane est une sucrase de glycane qui synthétise du dextrane à partir du sucrose agissant comme donneur de glycosyle. La formation des dextranes peut être remplacée quantitativement par la formation de nouveaux oligosaccharides par l'addition de carbohydrates accepteurs dans le milieu réactionnel. Avec la sucrase de dextrane provenant du *Leuconostos mesentoroides* B-1299, nous avons étudié la synthèse de glucooligosaccharides contenant des liaisons $\alpha(1\rightarrow2)$ en faisant appel au 1-*O*-α-D-glucopyranoside de méthyle comme accepteur. Ces produits constituent une classe d'oligosaccharides nutraceutiques non digestibles possédant des propriétés prébiotiques découlant d'une stabilisation et d'une augmentation de la flore intestinale et qui sont de plus en plus utilisés dans l'industrie alimentaire.

Mots clés : sucrases de glycane, cyclodextrine, glucanotransférase, glucosyltransférase de la cyclodextrine, sucrase de dextrane, produits accepteurs, glucooligosaccharides, maltooligosaccharides, sucre qui se couple, nutraceutique, aliments fonctionnels, prébiotique.

[Traduit par la Rédaction]

Received 14 January 2002. Published on the NRC Research Press Web site at http://canjchem.nrc.ca on 5 June 2002.

This paper is dedicated to J. Bryan Jones on the occasion of his 65th birthday, in recognition of his pioneering role in the use of biocatalysts in organic synthesis.

F.J. Plou, M.T. Martín, A. Gomez de Segura, M. Alcalde, and A. Ballesteros.[1] Departamento de Biocatálisis, Instituto de Catálisis, CSIC, Cantoblanco, 28049 Madrid, Spain.

[1]Corresponding author (e-mail: aballesteros@icp.csic.es).

 DOI: 10.1139/V02-104 © 2002 NRC Canada

Table 1. Enzymes that synthesize oligosaccharides using sucrose as substrate (glycansucrases).

Enzyme	EC Number	Classification	Producer microorganism	Bonds (polysaccharide formed)	Branching	Ref.
Dextransucrase	2.4.1.5	Glucansucrase	*Leuconostoc mesenteroides*	α-(1→6) (Dextran)	α-(1→2) α-(1→3)	3
Mutansucrase	2.4.1.5	Glucansucrase	*Streptococcus* strains	α-(1→3) (Mutan)	α-(1→6)	4
Amylosucrase	2.4.1.4	Glucansucrase	*Neisseria polysaccharea*	α-(1→4) (Amylose-like)	—	5
Alternansucrase	2.4.1.140	Glucansucrase	*Leuconostoc mesenteroides*	α-(1→3) alternating with α-(1→6) (Alternan)	α-(1→3)	6
Inulosucrase	2.4.1.9	Fructansucrase	*Streptococcus* mutants *Lactobacillus reuteri*	β-(2 →1) (Inulin)	β-(2 →6)	7
Levansucrase	2.4.1.10	Fructansucrase	*Bacillus subtilis, Rahnella aquatilis*, Oral bacteria	β-(2 →6) (Levan)	β-(2 →1)	8

Introduction

Oligosaccharides are generally considered to be carbohydrates consisting of 3–10 monosaccharide units. (However, from a dietary point of view, disaccharides such as leucrose or lactulose are also included in this group because of their similar properties.) There is increasing interest in developing efficient and scalable synthetic routes to oligosaccharides for addressing applications in the food (sweeteners, stabilizers, bulking agents, functional foods, etc.) and pharmaceutical industries (e.g., in prevention of infection, neutralization of toxins, immunotherapies for cancer) (1).

Considering this structural diversity of oligosaccharides (three different amino acids allow the synthesis of only six different peptides, while three different hexopyranose units will yield 720 trisaccharides), the stereo- and regioselectivity of biological catalysts may be considered a valuable and complementary aid to chemical synthesis (which needs complex protection and deprotection steps) for the preparation of structurally well-defined oligosaccharides.

Enzymatic oligosaccharide synthesis can be catalyzed by two different types of enzymes: glycosidases (EC 3.2) and glycosyltransferases (EC 2.4) (2). Glycosidases are widely available enzymes which in nature mediate the hydrolytic cleavage of glycosidic bonds and exhibit high stereoselectivities. To revert the in vivo hydrolytic function of glycosidases towards glycosidic bond synthesis, thermodynamic control (using low-water environments) and (or) kinetic control (using activated glycosyl donors) have been successfully employed. Despite the broad specificity of glycosidases and their numerous synthetic applications, the application of these catalysts is often limited by low yields and poor regioselectivity.

To the subclass of glycosyltransferases or transglycosylases belong all enzymes capable of transferring glycosyl groups. Some of these enzymes also have hydrolytic activity, which can be regarded as transfer of a glycosyl group from the donor to water. This subclass is further subdivided, according to the nature of the sugar residue being transferred, into hexosyltransferases (EC 2.4.1), pentosyltransferases (EC 2.4.2), and those transferring other glycosyl groups (EC 2.4.99). Within the sub-subclass 2.4.1, several related enzymes are worth mentioning. Under the term glycansucrases are considered glucansucrases and fructansucrases, bacterial enzymes acting on sucrose and utilizing it as the sole energy source for sugar synthesis (3). Glycansucrases share the same substrate specificity but catalyze the synthesis of a variety of oligo- and polysaccharides (Table 1). For example, they may transfer the glucosyl moiety of sucrose to dextran (i.e., dextransucrase, EC 2.4.1.5) or the fructosyl group to inulin (inulosucrase).

Other bacterial 2.4.1. enzymes (cyclodextrin glucanotransferases (CGTases), EC 2.4.1.19), cyclize part of an α-(1→4)-amylose chain by formation of an α-(1→4)-glucosidic bond yielding cyclodextrins (CDs).

In our laboratory we are currently studying two bacterial glucosyltransferases with considerable potential for oligosaccharide synthesis: cyclodextrin glucanotransferase and dextransucrase (a glycansucrase). These enzymes require neither sugar nucleotides (glycosyltransferases of the Leloir pathway, e.g., UDP-glucosyltransferase) nor sugar-1-phosphates (most glycosyltransferases of the non-Leloir pathway, e.g., phosphorylases) as donors (9). The synthesis of these activated substrates is rather difficult and expensive, as is the regeneration of sugar nucleotides. Rather, CGTase and dextransucrase use the free energy of cleavage of the readily available substrates starch and sucrose, respectively.

Cyclodextrin glycosyltransferase

Cyclodextrin glucanotransferases (CGTases) catalyze the formation of cyclodextrins (CDs) from starch by way of an intramolecular transglycosylation reaction (cyclization). CDs are cyclic oligosaccharides composed of α(1→4)-linked glucose residues, that possess a hydrophilic exterior and a hydrophobic cavity, and have numerous applications in food, pharmaceutical, chemical, and cosmetic industries (10). CDs form inclusion complexes with a wide variety of organic molecules of suitable size (guest molecules). CGTases usually produce a mixture of α-, β-, and γ-CDs (structures containing six, seven, and eight D-glucose units, respectively) and are accordingly classified as α-, β-, or γ-CGTases (11).

Besides this cyclization process, CGTases catalyze three different reactions (Fig. 1): (*i*) coupling (the CD molecule is cut open and combined with a linear oligosaccharide to produce a longer linear oligosaccharide); (*ii*) disproportionation (transfer of part of a linear oligosaccharide chain to another linear oligosaccharide); (*iii*) and hydrolysis of starch (12).

Several highly thermostable CGTases have been isolated from thermophilic microorganisms, belonging to the species *Bacillus stearothermophilus* (13), *Thermococcus* sp. (14), *Thermoanaerobacterium thermosulfurigenes EM1* (15), and

© 2002 NRC Canada

Fig. 1. Reactions catalyzed by CGTase.

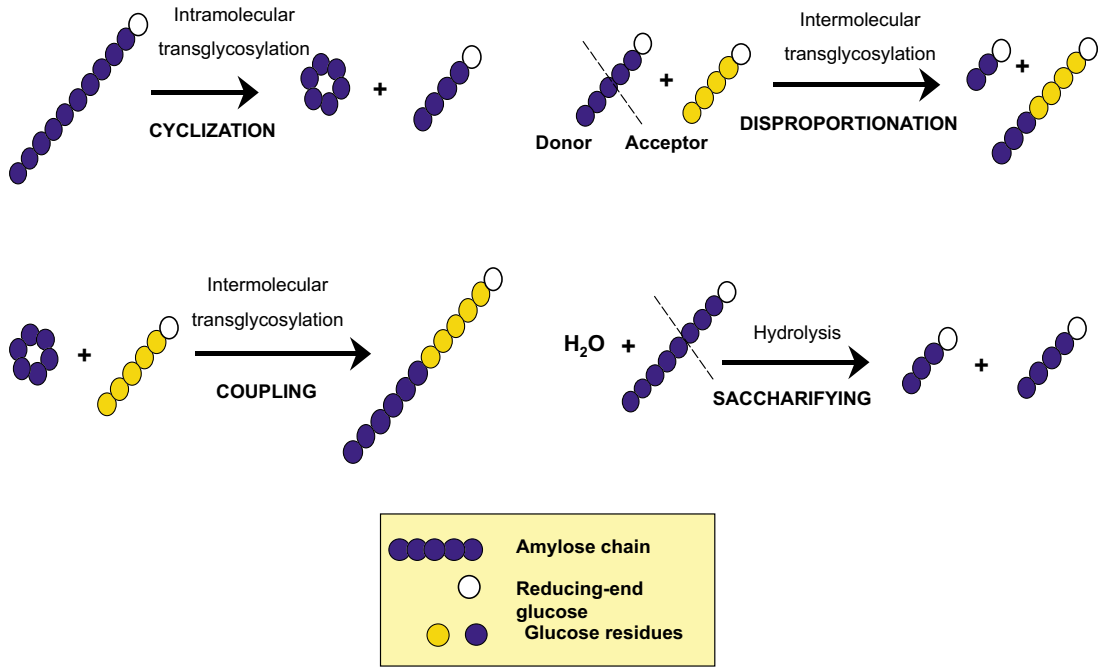

Thermoanaerobacter sp. (16). The two latter exhibit similar biochemical properties and are able to degrade starch into CDs under jet-cooking industrial conditions, thus avoiding the use of α-amylase pretreatment for the liquefaction of starch (17). In this way, the enzymatic synthesis of CDs starting from starch can be performed using one single enzyme (CGTase).

In our laboratory, we are studying the commercially available CGTase from *Thermoanaerobacter* sp., whose optimum temperature is 85°C at pH 5.5 (18). This enzyme is able to convert about 30% of a 25% (w/v) starch-slurry into a mixture of CDs, with a ratio α–β–γ of 3:5:2 (16).

The acceptor specificity of CGTase is rather broad. It is able to use various carbohydrates and related compounds such as natural glycosides, sugar alcohols, or vitamins as acceptors by way of intermolecular α-glucosylation reactions (coupling or disproportionation) (19). The transglycosylation capability of CGTase seems to be very dependent on the sources of CGTase (20).

The requirement for strong or moderately strong acceptor properties of a certain carbohydrate is a D-glucopyranose structure (chair form) with equatorial hydroxyl groups at C-2, C-3, and C-4 (21). Among monosaccharides, D-glucose, D-xylose, and L-sorbose are the most effective acceptors. As shown in Fig. 2, these compounds share the same configuration at the C-2, C-3, and C-4 of the pyranose moiety. CGTase transfers a glucosyl residue to the hydroxyl group at the C-4 of D-glucose and D-xylose, but to the 3-OH of L-sorbose. Monosaccharide derivatives such as methyl-α-D and methyl-β-D-glucosides are also efficient acceptors. On the contrary, D-galactose, D-ribose, D-mannose, D-arabinose, and D-fructose — which lack the above mentioned configuration of 2-OH, 3-OH and 4-OH — give rise to very low or even negligible yields of acceptor products.

The transglycosylation to disaccharides containing a nonreducing-end glucose residue occurs mainly or exclusively at the C-4 hydroxyl group of this glucose moiety (Fig. 2). Nakamura et al. (22) demonstrated that maltose and cellobiose have higher acceptor specificity than glucose for the transglycosylation reaction of CGTase. It is now well-documented that CGTase has a higher affinity to disaccharides compared with monosaccharides (20). This suggests that the acceptor-binding site can recognize at least two glucopyranose moieties. Disaccharides such as isomaltose, gentiobiose, turanose, maltulose, isomaltulose, cellobiose, and sucrose act as good CGTase acceptors, yielding the corresponding oligosaccharides. When these acceptors are present in the reaction mixture, they inhibit the formation of cyclodextrins because the glucosyl donor (starch) is deviated towards the acceptor reaction (19). The disaccharides α,α-trehalose and melibiose, despite having an available glucose moiety, are unexpectedly not acceptors.

A steric factor possibly plays a major role in diminishing the acceptor of malto-oligosaccharides larger than maltose (e.g., maltotriose). With increasing polymerization degree, the ability of the unsubstituted glucopyranosyl moiety to occupy a binding site of the enzyme must be lower.

Other carbohydrate derivatives such as glycosides, sugar alcohols, some vitamins, etc. have been also reported to act as acceptors (Table 2), in many cases with very notable yields. Transglycosylation often results in new properties (stability, solubility, etc.) of the glycosylated compound. Though mainly found in plants, there are numerous glycosides which occur in nature (e.g., aminoglycosidic antibiotics, glycosinolates, saponins, carotenoid glycosides, or terpenoid glycoside sweeteners). They are currently at the forefront of scientific investigation and already have a variety of uses including the treatment of congestive heart failure, lowering cholesterol, flavourings, antibiotics, and sweeteners. Stevioside, as isolated from the plant *Stevia rebaudiana*, has bitter taste and low solubility (26). CGTase-catalyzed glycosylation of stevioside decreases its bitterness and increases its solubility. The

© 2002 NRC Canada

Fig. 2. Carbohydrates with good acceptor properties of CGTase. The arrows indicate the hydroxyl group where the glucose moiety of the donor is transferred.

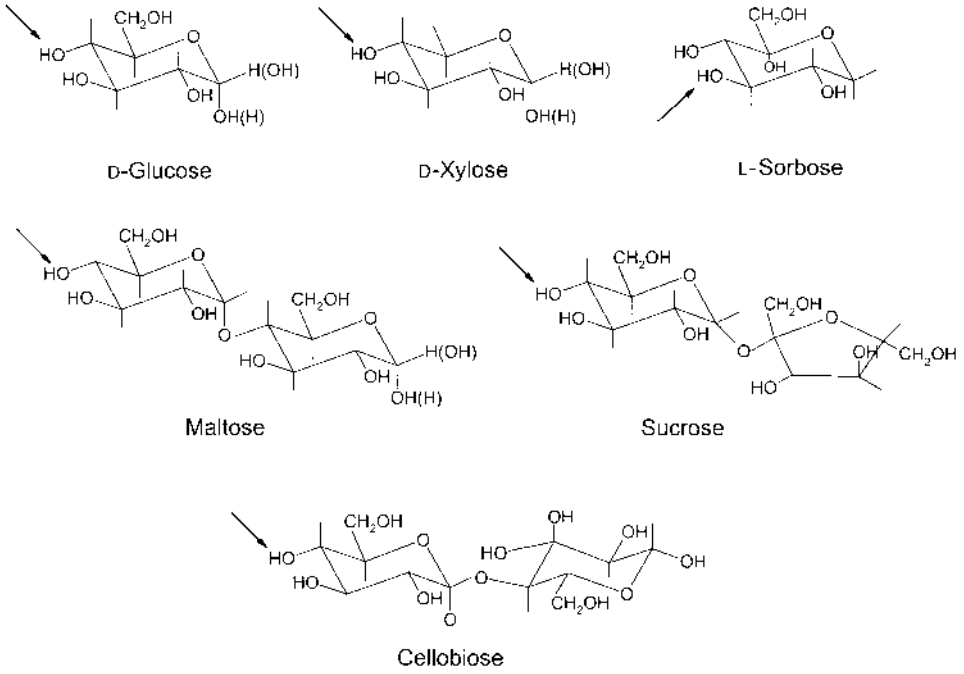

Table 2. Carbohydrate derivatives and other compounds that have been reported as acceptors for CGTase.

Type of compound	Acceptor	Microorganism producing CGTase	Ref.
Sugar alcohols	*Myo*-inositol	*Bacillus ohbensis*	23
	Sorbitol	*Bacillus macerans*	24
	Lactitol	*Bacillus macerans*	24
	Xylitol	*Bacillus macerans*	24
	Maltitol	*Bacillus macerans*	24
Glycosides	Rutin	*Bacillus stearothermophilus*	25
	Stevioside	*Bacillus macerans*	26
	Salicin	*Bacillus macerans*	20
Vitamins	Ascorbic acid	*Bacillus stearothermophilus*	27
Polyols	Trimethylolpropane	*Bacillus stearothermophilus*	28
	Trimethyloletane	*Bacillus stearothermophilus*	28
	Pentaerythritol	*Bacillus stearothermophilus*	28
Flavonoids	Hesperidin	*Bacillus macerans*, *Bacillus* sp.	20, 29

glucosylation of another glycoside, rutin, increases its solubility in water 3×10^4 times (25).

Flavonoids can be used as protectors against UV radiation; however, their use is limited because of their low solubility (29). CGTase is able to transglycosylate starch to the flavonoid hesperidin (which presents vitamin-like activity).

In our laboratory, we have examined glucose, maltose, and sucrose as acceptors of CGTase. When using maltose or glucose as acceptors (30), and starch as donor, linear malto-oligosaccharides (MOS), composed of α-D-glucose residues linked by α(1→4) glycosidic bonds, are produced (Fig. 3). A homologous series of MOS was obtained, as shown in the HPLC chromatogram of Fig. 4. Malto-oligosaccharides constitute an important class of functional oligosaccharides in the food industry (10 000 metric tons/year), and appear to exert their nutraceutical effect by reducing the levels of undesirable anaerobic bacteria such as *Clostridium perfringens* in the intestinal tract (31).

The degree of polymerization of malto-oligosaccharides formed could be modulated by the ratio (w/w) starch–D-glucose provided. Figure 5 shows the effect of this ratio on product distribution, using 10% (w/v) soluble starch and varying D-glucose concentration. In the absence of D-glucose, the consumption of starch was directed preferentially to CDs (34% conversion after 48 h incubation, with a ratio α–β–γ, 2.2:3.6:1), whereas only 4.5% of initial starch was transformed into MOS. In the presence of a twofold weight excess of D-glucose with respect to soluble starch, the formation of CDs was negligible (30). The higher the percentage of D-glucose in the medium, the higher the selectivity to low-molecular-weight oligosaccharides (Fig. 5 illustrates this effect on selectivity to maltose).

© 2002 NRC Canada

Fig. 3. Scheme of the acceptor reaction using soluble starch as donor and D-glucose as acceptor, catalyzed by CGTase.

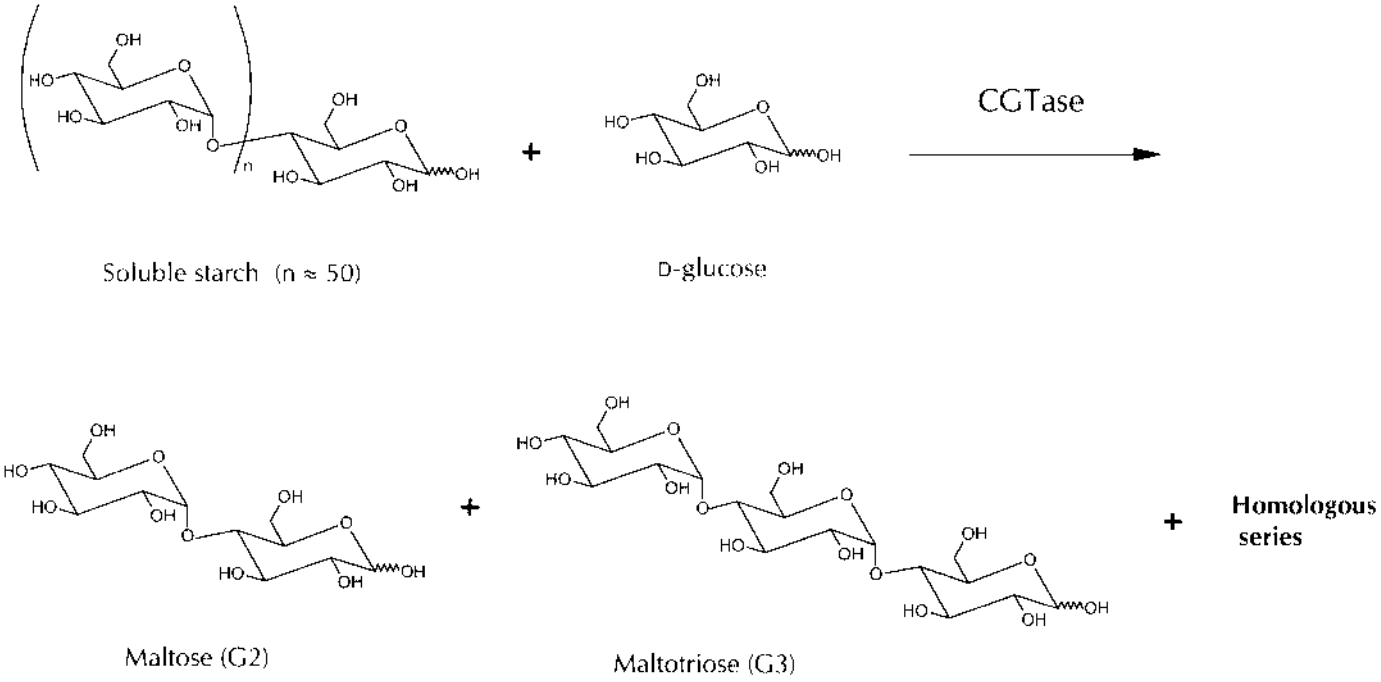

Fig. 4. HPLC chromatogram of the reaction mixture using soluble starch as donor and maltose as acceptor catalyzed by CGTase. Conditions: 10% soluble starch (w/v), ratio starch–maltose 1:2 (w/w), 10 mM sodium citrate buffer (pH 5.5) containing 0.15 mM $CaCl_2$, 60°C. HPLC conditions: two Aminex HPX-42A columns (300 × 7.8 mm, BioRad) put in series, water as mobile phase (0.7 mL min^{-1}), 85°C, refraction-index detector.

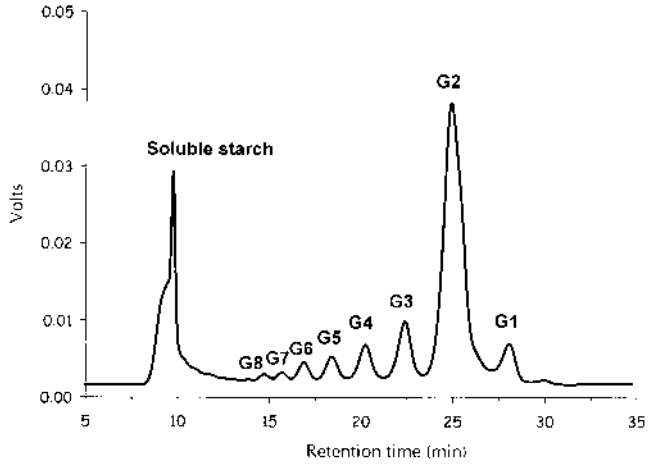

Fig. 5. Distribution of products of the acceptor reaction catalyzed by the CGTase from *Thermoanaerobacter* sp. using starch as the donor and D-glucose as the acceptor. The percentage of initial starch transformed into cyclodextrins (CDs) and malto-oligosaccharides (MOS) after 48 h incubation is represented as a function of the ratio starch–D-glucose (w/w). The percentage of maltose (G2) formed in the MOS series is also shown. Data from ref. 30.

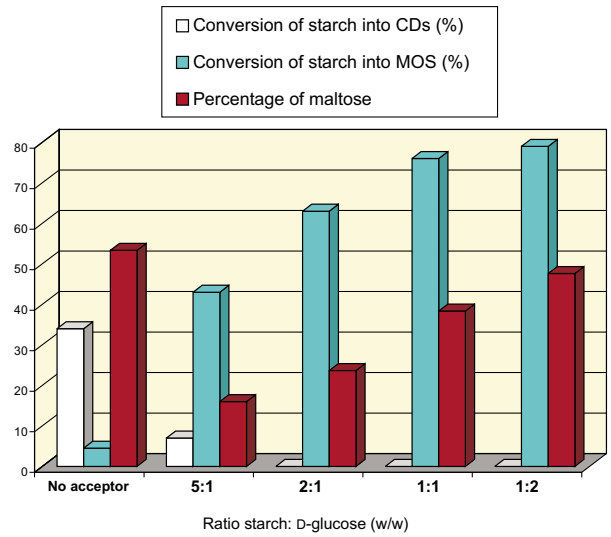

When using sucrose, glucosyl-sucrose (α-D-Glu-(1→4)-α-D-Glu-(1→2)-β-D-Fru) (Fig. 6) and higher polymerization products of the homologous series (called coupling sugar) are obtained (32). Coupling sugar is used as a non-cariogenic sweetener and viscosity control agent, with its higher chemical and thermal stability as compared to other sweeteners containing reducing sugars being notable (33).

The 3D structure of several CGTases has been reported (12, 15). This information can be very useful: (*i*) to predict if a certain molecule can become a CGTase acceptor; and (*ii*) to design mutants with modified selectivity.

For these acceptor reactions, the immobilization of the transferases constitutes an interesting strategy to achieve their stabilization and (or) the separation of the biocatalyst from the reaction mixture. Different approaches have been applied for the immobilization of CGTases, based on adsorption onto inorganic supports or covalent coupling to aminated resins (Table 3). However, the recovery of activity in the immobilized biocatalyst is generally low, especially

© 2002 NRC Canada

Table 3. Immobilization of CGTase.

Support	Immobilization method	Microorganism producing CGTase	Reference
Capillar membrane	Covalent	*Bacillus macerans*	34
Porous glass (Trisoperl)	Covalent	*Bacillus macerans*	35
Polyacrylamide	Covalent	*Bacillus macerans*	36
Aminated PVC	Covalent	*Paenibacillus macerans*	37
Epoxy-sepharose	Covalent	*Bacillus macerans*	38
Ionic-exchange resin	Adsorption	*Bacillus* sp. ATCC 21783	39
DEAE-celullose	Adsorption	*Bacillus macerans*	36
Amberlite IRA 900	Adsorption	*Thermoanaerobacter* sp.	40
Alginate	Entrapment	*Bacillus macerans*	36

Fig. 6. Structure of glucosyl-sucrose (α-D-Glu-(1→4)-α-D-Glu-(1→2)-β-D-Fru).

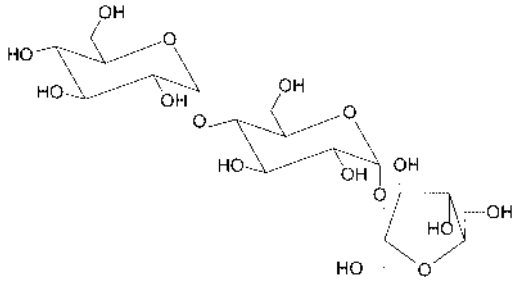

when compared with structurally related enzymes such as the glycosidases. This can be attributed to the complexity of CGTase structure (five domains) and mechanism (four possible reactions). We are currently investigating the covalent coupling of CGTase to epoxy-activated acrylic polymers with different morphologies.

Dextransucrase

Dextransucrase (sucrose:1,6-α-D-glucan 6-α-D-glucosyltransferase, EC 2.4.1.5) polymerizes the glucosyl moiety of sucrose to form dextran, an α(1→6) linked glucan, also with α(1→2), α(1→3), or α(1→4) branch linkages depending on the producing enzyme. When, in addition to sucrose, other carbohydrates (such as maltose, isomaltose, etc.) are present, some of the glucosyl groups are transferred to the carbohydrates ("acceptor reaction") and are diverted from forming dextran to yield acceptor products (Fig. 7). The three reactions catalyzed by dextransucrase: (*i*) polymerization of the glucose moiety of sucrose; (*ii*) glucose transfer to acceptors; and (*iii*) sucrose hydrolysis, are competitive, indicating that they take place at the same active site (41).

In our laboratory, we have studied the dextransucrases from two different strains of *Leuconostoc mesenteroides* (NRRL B-512F and B-1299). The dextransucrase from *L. mesenteroides* NRRL B-512F synthesizes a dextran containing 95% α(1→6) and 5% α(1→3) osidic bonds, while the *L. mesenteroides* B-1299 dextran contains 65% α(1→6), 30% α(1→2) and 5% α(1→3)-branching linkages (42, 43).

Numerous sugars can act as acceptors of dextransucrase. The acceptors can be subdivided in: (*i*) the strong acceptors, such as maltose or isomaltose, that have an activator effect on the reaction rate (measured as fructose liberated) and

Fig. 7. Scheme of reactions catalyzed by dextransucrase.

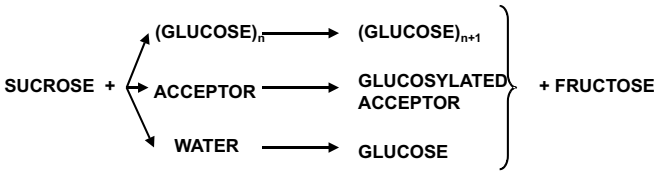

strongly inhibit the synthesis of dextran; and (*ii*) the weak acceptors, like fructose or melibiose, that have an inhibitory effect on glucan formation but yield a low amount of acceptor products (44).

The acceptors can be also classified according to the acceptor products obtained, in: (*i*) those that give a homologous series of oligosaccharides, each differing one from the other by one glucose residue (e.g., maltose); and (*ii*) those acceptors that only form a single acceptor product containing one glucose residue more than the acceptor (41). The latter is the case of fructose, which is a major product in all the dextransucrase-catalyzed reactions (Fig. 7). There are two products formed, depending on the ring form of the fructose acceptor (pyranose or furanose): leucrose (5-*O*-α-D-glucopyranosyl-D-fructopyranose) and the minor product, isomaltulose (4-*O*-α-D-glucopyranosyl-D-fructofuranose). The leucrose synthesis process becomes particularly important at the final stages of the glucan synthesis reaction when the fructose concentration is high. A process for leucrose production by action of dextransucrase in the presence of sucrose and fructose has been developed on a pilot scale (45).

When using acceptors such as glucose, methyl 1-*O*-α-D-glucopyranoside, maltose or isomaltose, the glucose unit from sucrose is transferred to the C-6 hydroxyl of the monosaccharide or to the 6-OH of the nonreducing-end glucose of a disaccharide. This yields a series of isomaltodextrins of degree of polymerization of two to seven attached to the acceptor. Similar homologous series are obtained from 1,5-anhydro-D-glucitol, nigerose, and turanose (46).

Cellobiose gives an unusual series in which the first product is 2-α-D-glucopyranosyl cellobiose with glucose attached to the C-2 of the reducing end of cellobiose. With the cellobiose analog, lactose, only the first acceptor product is formed, but with similar regiospecificity (47).

An analysis of the data on acceptor reactions with dextransucrases suggests that a specificity of recognition exists. However, to extend this reaction to the synthesis of

© 2002 NRC Canada

Fig. 8. Mechanism of dextran synthesis and acceptor reaction of dextransucrase.

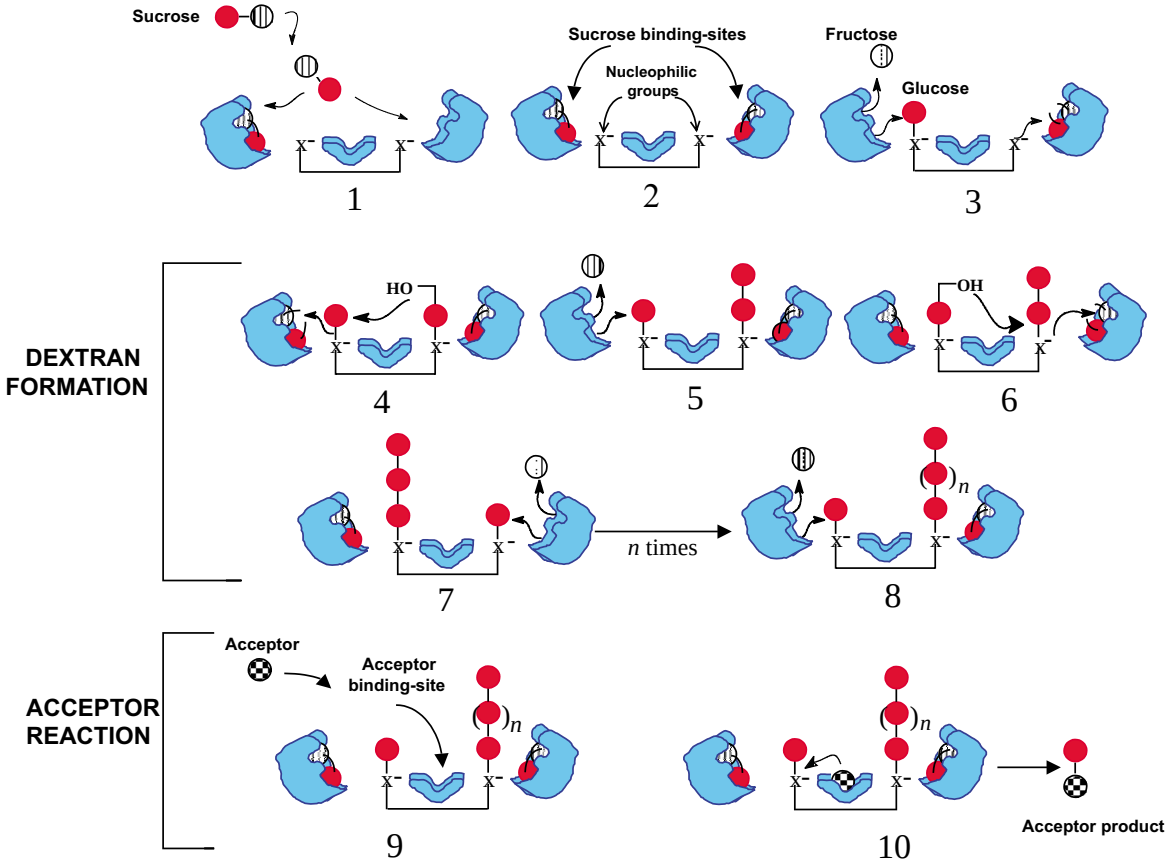

new glucoconjugates, it is necessary to progress in the understanding of the mechanism of the acceptor reaction (48). It is desirable to have a better knowledge of the protein determinants involved in: (*i*) the selectivity towards a given acceptor molecular structure; and (*ii*) in the regiospecificity of the enzyme.

The active site of *L. mesenteroides* B-512F dextransucrase is described as having two sucrose binding-sites and one acceptor binding-site (49). Figure 8 illustrates the proposed mechanism of dextran synthesis and acceptor reaction catalyzed by dextransucrase (50). The transfer of glucose units to yield dextrans supposes first the formation of two covalent glucosyl-enzyme complexes (41). Oligosaccharides can be synthesized by a nucleophilic attack of the hydroxyl group located at the nonreducing-end of the acceptor to the C-1 of one of the two glucosyl residues involved in the two covalent glucosyl-enzyme complexes. Various experiments tried to demonstrate that the acceptor binding-site is really unique and separated from the two active sites, but up to now there is no direct evidence that a separate acceptor binding-site exists (44). Kobayashi and Matsuda (50) suggested that one of the two sucrose binding sites may also be an acceptor binding-site.

Dextransucrases have not been reported as capable of transferring glucose to alcohols or polyols (51). This contrast with levansucrases, which are capable of transferring fructose to glycerol, although in low yield. However, nonconventional acceptors can be used with dextransucrase. Bucholz's group (52), using dextransucrase from *L. mesenteroides* B-512F, reported the glucosylation of D-sorbitol, α-D-glucosyl-1,6-D-sorbitol, α-D-glucosyl-1,6-D-arabonic acid, and D-glucal.

In our laboratory, we have investigated the acceptor reaction with maltose using B-512F dextransucrase (53). The first acceptor product which is formed, the trisaccharide panose, may also act as an acceptor, and a homologous series of products having isomaltodextrin residues attached through 6-*O* to the nonreducing glucosyl moiety of maltose were obtained. We observed that the lower the percentage of maltose, the higher the degree of polymerization of the acceptor products (but the concentration of the products decreases).

We have recently investigated the acceptor reaction using methyl 1-*O*-α-D-glucopyranoside as acceptor (54). To control the polymerization degree, the ratio sucrose–methyl 1-*O*-α-D-glucopyranoside was varied (from 5:1 to 1:5 w/w). The first acceptor product formed is 1-*O*-α-D-methyl-isomaltoside; this may also act as an acceptor, and a homologous series of products is formed (Fig. 9). In addition to isomalto-oligosaccharides, dextransucrase B-1299 afforded a series of glucooligosaccharides containing α(1→2) bonds. A great demand exists for glucooligosaccharides containing α(1→2) osidic bonds. These molecules — which belong to the group of prebiotics — are now produced on industrial scale (40 metric tons/year) for their dermocosmetic and nutritional (animal and human) applications (Fig. 10).

One of the most explored alternatives to stabilize dextransucrase is its entrapment in alginate beads (42, 55).

© 2002 NRC Canada

Fig. 9. Acceptor reaction with methyl 1-*O*-α-D-glucopyranoside catalyzed by dextransucrases from *L. mesenteroides*.

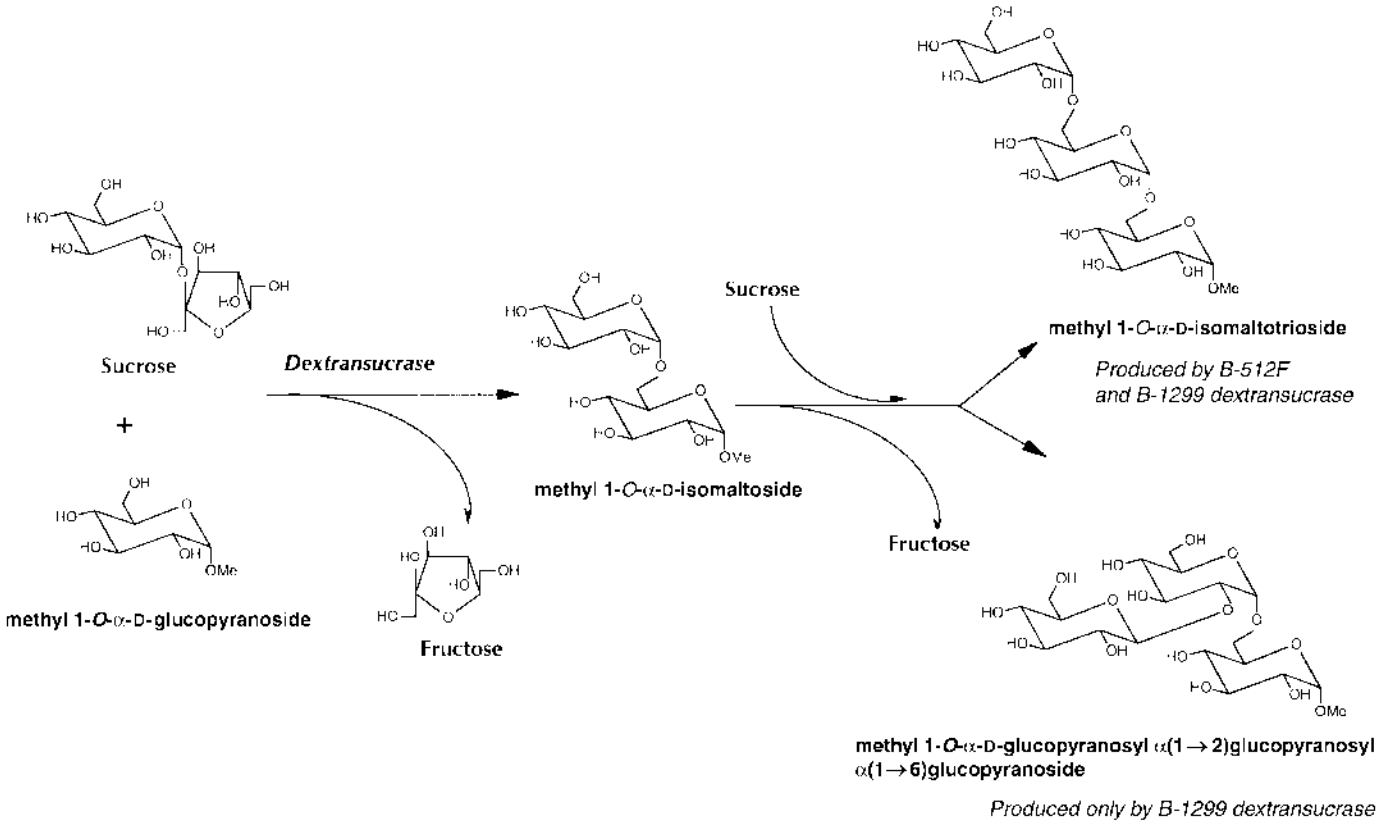

Fig. 10. Oligosaccharides with prebiotic properties currently commercialized.

Enzymatic synthesis
Fructo-oligosaccharides
Inulin
Galacto-oligosaccharides
Isomalto-oligosaccharides
Lactosucrose
Gluco-oligosaccharides containing α(1→2) bonds
Chemical synthesis
Lactulose
Soybean oligosaccharides

Although this method is normally more suitable for the immobilization of whole cells than for globular proteins, it is useful for dextransucrase, probably because the dextran layer that covers the protein surface prevents leakage of the enzyme through the matrix pores. We found that native and alginate-entrapped dextransucrases yielded similar gluco-oligosaccharides production in the acceptor reaction with maltose. However, the operational stability of the alginate-entrapped dextransucrase was found to be higher compared with the soluble enzyme, with the immobilized form retaining 100% of its initial activity after seven cycles of 24 h (53). Other methods have been tested by different groups to immobilize dextransucrase (e.g., in porous phenoxyacetyl cellulose, alkylamine porous silica, DEAE Sephadex, polyacrylamide, etc.) but either the immobilization yields were low or the enzyme was not stable (56).

Prebiotic Oligosaccharides

The main role of food is to provide nutrients for the metabolic requirements and well-being of humans. However, investigations in the last decade support the concept that, in addition to satisfying nutrition needs, diet may modulate various biochemical processes in the body and may play deleterious or beneficial roles in aging and disease. This hypothesis is becoming a kind of new frontier in nutrition sciences.

In this context, the concept of functional foods (other synonyms are nutraceuticals or pharmafoods) has appeared. In 1998, European experts approved that "a food can be regarded as functional if it is satisfactorily demonstrated to affect beneficially one or more target functions in the body, beyond adequate nutritional effects in a way which is relevant to either the state of well-being and health or the reduction of the risk of disease" (57). A functional food may be a macro- or a micronutrient, essential or not (58).

It was only in 1995 when the concept of prebiotic was introduced (59). Prebiotic is a nondigestible food ingredient (i.e., resistant to the action of human digestive enzymes) that affects beneficially the host by stimulating selectively the growth and (or) activity of one or a limited number of endogenous bacteria in the colon (mainly bifidobacteria and

© 2002 NRC Canada

lactic acid bacteria), and (or) inhibiting the proliferation of pathogenic microbes (60–62).

Several food-grade oligosaccharides that can be regarded as prebiotics are being currently commercialized (Fig. 10). Most of them are obtained by enzymatic methods. Because of their high solubility in water, they are easily incorporated into processed foods as functional ingredients. Apart from their prebiotic effect, there are reports of positive effects such as the enhancement of calcium absorption, stimulation of immune functions, reduction of cancer risk, modulation of lipid metabolism, etc. (60). In 1995, the world production of food-grade oligosaccharides was over 85 000 tons, most of them using biological catalysts (31).

In view of the functional effects of oligosaccharides, many companies and academic laboratories are examining novel compounds (second generation oligosaccharides) with new and (or) improved bioactivities, especially in terms of reduction of intestinal gas, tailoring the in vivo fermentation activity of desirable flora, and extended persistence throughout the colon (63).

We are particularly interested in glucooligosaccarides containing $\alpha(1\rightarrow2)$ bonds (GOS). They are not hydrolysed in the gastrointestinal tract and reach the colon promoting the growth of certain beneficial bacteria (*Bifidobacterium*, *Lactobacillus*) as opposed to pathogenic flora (64). It has also been suggested that some GOS can block colonization sites often occupied by pathogens (65). Furthermore, GOS are non-cariogenic, since salivary enzymes cannot hydrolyse the $\alpha(1\rightarrow2)$ bonds. By stabilizing intestinal floras and this protection against the proliferation of pathogenic microbes, it is envisaged that the use of such novel oligosaccharides may reduce the current excessive use of antibiotics in human and animal health.

Acknowledgments

We are very grateful to our European colleagues Dr. S. Pedersen (Novozymes A/S, Bagsvaerd), Dr. P. Monsan (INSA, Toulouse), and Dr. L. Dijkhuizen (University of Groningen), for very valuable help with this work, and to Dr. I.S. Gill (U.S.A.) for critical reading of the manuscript. This research was supported by the Comunidad de Madrid (Project 07G/0042/2000) and the Spanish CICYT (Project PPQ 2001–2294). We thank Instituto Danone, Gobierno Vasco, and Ministerio de Educacion, Cultura y Deporte for research fellowships.

References

1. K.G. Nilsson. Trends Biotechnol. **6**, 256 (1998).
2. P. Monsan and F. Paul. FEMS Microbiol. Rev. **16**, 187 (1995).
3. P. Monsan, S. Bozonnet, C. Albenne, G. Joucla, R.M. Willemot, and M. Remaud-Simeon. Int. Dairy J. **11**, 675 (2001).
4. G. Mooser. *In* The enzymes. Vol. 20. *Edited by* P.D. Boyer. Academic Press, London. 1992. p. 187.
5. G. Potocki de Montalk, M. Remaud-Simeon, R.M. Willemot, P. Sarcabal, V. Planchot, and P. Monsan. FEBS Lett. **471**, 219 (2000).
6. M.A. Argüello-Morales, M. Remaud-Simeon, S. Pizzut, P. Sarcabal, R.M. Willemot, and P. Monsan. FEMS Microbiol. Lett. **182**, 81 (2000).
7. G.H. van Geel-Schutten. *In* Exopolysaccharide synthesis by *Lactobacillus reuteri*. Ph.D. thesis. University of Groningen, The Netherlands. 2000.
8. M.G. Kim, C.H. Kim, J.S. Lee, K.B. Song, and S.K. Rhee. Enzyme Microb. Technol. **27**, 646 (2000).
9. V. Kren and J. Thiem. Chem. Soc. Rev. **26**, 463 (1997).
10. J. Szejtli. Carbohyd. Polym. **12**, 375 (1990).
11. A. Tonkova. Enzyme Microb. Technol. **22**, 678 (1998).
12. B.A. van der Veen, G.J.W.M van Alebeek, J.C.M. Uitdehaag, W. Dijkstra, and L. Dijkhuizen. Eur. J. Biochem. **267**, 658 (2000).
13. H.J. Chung, S.H. Yoon, M.J. Lee, M.J. Kim, K.S. Kweon, I.W. Lee, J.W. Kim, B.H. Oh, H.S. Lee, V.A. Spiridonova, and K.H. Park. J. Agric. Food Chem. **46**, 952 (1998).
14. Y. Tachibana, A. Kuramura, N. Shirasaka, Y. Suzuki, T. Yamamoto, S. Fujiwara, M. Takagi, and T. Imanaka. Appl. Environ. Microbiol. **65**, 1991 (1999).
15. R.D. Wind, R.M. Buitelaar, and L. Dijkhuizen. Eur. J. Biochem. **253**, 598 (1998).
16. R.L. Starnes, C.L. Hoffman, V.M. Flint, P.C. Trackman, D.J. Duhart, and D.M. Katkocin. *In* Enzymes in biomass conversion. *Edited by* G.F. Leathman and M.E. Himmel. American Chemical Society, Washington. 1991. p. 384.
17. S. Pedersen, L. Dijkhuizen, B.W. Dijkstra, B.F. Jensen, and S.T. Jorgensen. Chem.Tech. 19 (Dec. 1995).
18. M. Alcalde, F.J. Plou, C. Andersen, M.T. Martín, S. Pedersen, and A. Ballesteros. FEBS Lett. **445**, 333 (1999).
19. J.A. Rendleman. Biotechnol. Appl. Biochem. **24**, 121 (1996).
20. D.C. Park, T.K. Kim, and Y.H. Lee. Enzyme Microb. Technol. **22**, 217 (1998).
21. S. Kobayashi. *In* Enzymes for carbohydrate engineering. *Edited by* K.H. Park, J.F. Robyt, and D. Choi. Elsevier Science, Amsterdam. 1996. p. 23.
22. A. Nakamura, K. Haga, and K. Yamame. FEBS Lett. **337**, 66 (1994).
23. M. Sato, T. Matsuo, N. Orita, and Y. Yagi. Biotechnol. Lett. **13**, 69 (1991).
24. T.K. Kim, D.C. Park, and Y.H. Lee. J. Microbiol. Biotechnol. **7**, 310 (1997).
25. Y. Suzuki and K. Suzuki. Agric. Biol. Chem. **55**, 181 (1991).
26. Y.H. Lee, S.G. Baek, H.D. Shin, and D.C. Park. Kor. J. Appl. Microbiol. Biotechnol. **21**, 461 (1993).
27. H. Aga, M. Yoneyama, S. Sakai, and I. Yamamoto. Agric. Biol. Chem. **55**, 1751 (1991).
28. H. Nakano, S. Kitahata, Y. Tominaga, Y. Kiku, K. Ando, Y. Kawashima, and S. Takenishi. J. Ferm. Bioeng. **73**, 237 (1992).
29. T. Kometani, Y. Terada, T. Nishimura, H. Takh, and S. Okada. Biosci. Biotechnol. Biochem. **58**, 1990 (1994).
30. M.T. Martín, M. Alcalde, F.J. Plou, L. Dijkhuizen, and A. Ballesteros. Biocatal. Biotransform. **19**, 21 (2001).
31. R.G. Crittenden and M.J. Playne. Trends Food Sci. Technol. **7**, 353 (1996).
32. S. Pedersen and E. Reesens. WO Patent 92/13962 (1992).
33. T. Ozawa and H. Hattori. EP Patent 0 102 032 (1990).
34. T. Okada, M. Ito, and K. Hibino. J. Ferment. Bioeng. **77**, 259 (1994).
35. J. Steighardt and R. Kleine. Appl. Microbiol. Biotechnol. **39**, 63 (1993).
36. S.H. Lee, H.D. Shin, and Y.H. Lee. J. Microbiol. Biotechnol. **1**, 54 (1991).
37. M.A. Abdel-Naby. Process Biochem. **34**, 399 (1999).
38. T.E. Abraham. Biocatal. Biotransform. **12**, 137 (1995).
39. N. Nakamura and K. Horikoshi. Biotechnol. Bioeng. **19**, 87 (1977).

© 2002 NRC Canada

40. P.S. Kim, H.D. Shin, J.K. Park, and Y.H. Lee. Biotechnol. Bioprocess, **5**, 174 (2000).
41. J.F. Robyt. *In* Enzymes for carbohydrate engineering. *Edited by* K.H. Park, J.F. Robyt, and Y.D. Choi. Elsevier Science, Amsterdam. 1996. p. 1.
42. M. Remaud, A. López, V. Pelenc, F. Paul, and P. Monsan. Appl. Biochem. Biotechnol. **44**, 101 (1994).
43. M. Dols, M. Remaud-Simeon, R.M. Willemot, M. Vignon, and P. Monsan. Carbohydr. Res. **305**, 549 (1998).
44. V. Monchois, R.M. Willemot, and P. Monsan. FEMS Microbiol. Rev. **23**, 131 (1999).
45. K. Buchholz, M. Noll-Borchers, and D. Schwengers. Starch, **50**, 164 (1998).
46. J.F. Robyt and S.H. Eklund. Carbohydr. Res. **121**, 279 (1983).
47. F. Yamamuchi and Y. Ohwada. Agric. Biol. Chem. **33**, 1295 (1969).
48. M. Remaud-Simeon, R.M. Willemot, P. Sarcabal, G. Potocki de Montalk, and P. Monsan. J. Mol. Catal. B: Enzym. **10**, 117 (2000).
49. D. Su and J.F. Robyt. Arch. Biochem. Biophys. **308**, 471 (1994).
50. M. Kobayashi and K. Matsuda. Carbohydr. Res. **66**, 277 (1978).
51. F. González-Muñoz, A. Pérez-Oseguera, J. Cassani, M. Jiménez-Estrada, R. Vazquez-Duhalt, and A. López-Munguía. J. Carbohydr. Chem. **18**, 275 (1999).
52. K. Heincke, B. Demuth, H.J. Jördening, and K. Buchholtz. Ann. N.Y. Acad. Sci. **864**, 203 (1998).
53. M. Alcalde, F.J. Plou, A. Gómez de Segura, M. Remaud-Simeon, R.M. Willemot, P. Monsan, and A. Ballesteros. Biotechnol. Tech. **13**, 749 (1999).
54. A. Gómez de Segura, F.J. Plou, M. Alcalde, M. Remaud-Simeon, R.M. Willemot, P. Monsan, and A. Ballesteros. Abstracts Enzyme Engineering Conference XVI, 244 (2001).
55. M. Alcalde, F.J. Plou, M.T. Martín, M. Remaud, P. Monsan, and A. Ballesteros. *In* Stability and stabilization of biocatalysts. *Edited by* A. Ballesteros, F.J. Plou, J.L. Iborra, and P. Halling. Elsevier, Amsterdam. 1998. p. 535.
56. A. Tanriseven and S. Dogan. Process Biochem. **37**, 1111 (2002).
57. R.B. Roberfroid. Am. J. Clin. Nutr. **7** (Suppl), 1660S (2000).
58. G.E. Inglett. Chem.Tech. 38 (Oct. 1999).
59. G. R. Gibson and M.B. Roberfroid. J. Nutr. **125**, 1401 (1995).
60. G.R. Gibson, P.B. Ottaway, and R.A. Rastall. Prebiotics: New developments in functional foods. Chandos Publishing, Oxford. 2000.
61. M. Roberfroid and J. Slavin. Crit. Rev. Food Sci. Nutr. **40**, 461 (2000).
62. P. Simmering and M. Blaut. Appl. Microbiol. Biotechnol. **55**, 19 (2001).
63. B. Rastall. Food Sci. Technol. Int. 17 (2001)
64. P. Valette, V. Pelenc, Z. Djouzi, C. Andrieux, F. Paul, P. Monsan, and O. Szylit. J. Sci. Food. Agric. **62**, 121 (1993).
65. A. Nash and G. Gibson. Food Sci. Technol. Int. 17 (1998).

© 2002 NRC Canada

Canadian Journal of Chemistry

Author Index
Volume 80, 2002

Revue canadienne de chimie

Index des auteurs
Volume 80, 2002

Al-Awadi, N.A., 499
Al-Juwaiser, I.A., 499
Alcalde, M., 743
Alex, S., 350
Allen, C.C.R., 589
Amat-Guerri, F., 62
Andraos, J., 141
Anthonsen, T., 577
Arancibia, E.L., 462
Arévalo, E.A., 76
Aycard, J.P., 455
Azad, M., 148
Baer, A.J., 496
Baker, J., 708
Bakker, M., 622
Ball, R.G., 646
Ballesteros, A., 743
Barta, N., 646
Bazzi, L., 106
Benrahmoune, M., 333
Berglund, P., 529
Bertolotti, S., 62
Bhadury, P.S., 504
Bhardwaj, N., 141
Bhardwaj, R.K., 467
Bhaskar, A.S.B., 504
Bickley J.F., 546
Bonal, C., 163
Bottomley, F., 55
Boyd, D.R., 589
Boyd, R., 646
Brenna, E., 714
Breuer, M., 692
Bridson, J.N., 155
Brion, C.E., 222
Brossard, L., 345
Brown, F.M., 633
Brown, G.R., 89
Brown, R.S., 183
Brunet, E., 169
Buchanan, G.W., 148
Bühler, H., 671
Bui, V.P., 708
Bunce, N.J., 200
Campbell, J.S., 646
Carballo, E., 370
Cargnoni, F., 235
Carrea, G., 551, 559
Carrière, J.-F., 653
Carroll, J.G., 589
Cerdeiriña, C.A., 370
Chapados, C., 113
Chartrain, M., 646
Chen, G., 613
Chen, H., 601
Chiang, Y., 82
Chilov, G.G., 699
Chong, D.P., 222
Cobos, J.C., 292
Cole, J.G., 46
Cooper, G., 222
Corley, E.G., 646
Côté, A.P., 496
Dalton, H., 589
Daneault, S., 113
Dangi, R.S., 504
Davidson, G.J.E., 496
Davis, B.G., 555
de Ruiz Holgado, M.E.F., 462
DeSantis, G., 643
De Sève, H., 483
Decken, A., 31, 55
Delamere, C., 94
Detellier, C., 163
DiCosimo, R., 608
Diedrichs, N., 686
Dodier, M., 483
Domanska, U., 476
Dubé, P., 345
Ducret, A., 653
Dyker, C.A., 55
Edwards, J.P., 31
Effenberger, F., 671
Eipper, A., 626
El-Dusouqui, O.M.E., 499
El Issami, S., 106
Faber, K., 362
Fang, C.-L., 728
Fernandez, J., 462
Fessner, W.-D., 739
Filali-Mouhim, A., 68, 333
Friedrich, T., 692
Fuganti, C., 714
Fülöp, F., 565
Gadosy, T.A., 302
Gao, Z., 440
Galley, W.C., 89
García, N.A., 62
Garcia de la Fuente I., 292
García-Losada, P., 169
Gbewonyo, K., 646
Gedey, S., 565
Gedrath, I., 686
Gibson, D.T., 589
Glew, D.N., 418
Glister, J.F., 447
Gomez de Segura, A., 743
Gonzalez, J.A., 292, 476
González-Salgado, D., 370
Graziano, G., 388, 401
Green, D.F., 281
Haggi, E., 62
Hamilton, J.T.G., 589
Hammouti, B., 106
Hanan, G.S., 496
Hansen, J., 708
Harrison, P.H.M., 517, 601
Harrod, J.F., 489
Hasegawa, Y., 613
Hauer, B., 546, 692
He, W., 263
Hedin, E.M.K., 529
Hillebrand, M., 455
Hilvert, D., 657
Hirahara, M., 207, 510
Holland, H.L., 633, 640
Hu, C.Y., 222
Hu, E., 646
Hudlicky, T., 708
Hult, K., 529
Ihasz, N., 640
Ikemoto, N., 646
Ingham, A.M., 155
Ionescu, A., 455
Israëli, Y., 163
Iwaki, H., 613
Jaiswal, D.K., 504
Jacobsen, E.E., 577
Jakins, C., 94
Janzen, M.C., 41
Jay-Gerin, J.-P., 68, 333
Jenkins, H.A., 281
Jenkins, S.I., 517
Jennings, M.C., 41

© 2002 NRC Canada

Jiang, F., 281
Jiang, X., 263
Juanes, O., 169
Juárez Ruiz, J.M., 739
Kabir, S.M.H., 413
Kam, K., 517
Kamath, V.P., 540
Kamerling, J.P., 76
Kanerva, L.T., 565
Kayser, M.M., 613
Kertit, S., 106
Kinastowski, S., 192
Klempier, N., 724
Kluger, R., 217
Kobler, C., 671
Koerner, T.B., 183
Kratochvil, B., 440
Krelaus, R., 686
Křen, V., 724
Kresge, A.J., 82
Kuzma, M., 724
Larsen, R.D., 646
Lau, P.C.K., 613
Lázár, L., 565
Lebuis, A.-M., 489
Lee, K.-S., 582
Lefeber, D.J., 76
Lessard, C., 483
Lewandowska, E., 192
Lewars, E., 94
Leznoff, C.C., 141
Li, H., 540
Li, W., 646
Liljeblad, A., 565
Liu, J., 643
Liu, X., 263
Liu, Y.C., 540
Loncke, P.G., 302
Lortie, R., 653
Lounsbery, B.J., 640
Lozada, D., 633
Lu, J., 263
Lu X., 228
Ma, P., 608
Mahiuddin, S., 175
Malone, J.F., 589
Mang, H., 362
Mankhetkorn, S., 68
Martín, M.T., 743
Martínková, L., 724
Massue, J., 546
Matty, L., 646
Maughan, M.A.T., 555
Max, J.-J., 113
Mayer, P.M., 25
Mayer, S.F., 362
Mayne, B., 633
McAuley, A., 155
McBeth, D., 692
McClelland, R.A., 269
McDonald, R.S., 517
McNulty, K.C., 608
Meegalla, S.K., 728
Meesungnoen, J., 68
Ménard, H., 345
Meng, Q., 82
Miller, R.J.D., 1
Miskoski, S., 62
Modyanova, L.V., 589
Mongrain, P., 483
Monnier, M., 455
Morel, J.-P., 163
Morel-Desrosiers, N., 163
Mylerová, V., 724
Nakamura, N., 207, 510
Neil, M.A., 55
Nguyen, D., 608
Nguyen, M., 708
Norman, D.W., 31
Oniciu, L., 315
Otter, A., 540
Ottolina, G., 559
Ovesná, M., 724
Pal, A., 467
Palcic, M.M., 540
Parales, R.E., 589
Pardo, J.M., 370
Parvez, M., 245, 413
Patkar, S.A., 529
Paz Andrade, M.I., 462
Pedroni, P., 692
Pena, P.C.A., 546
Peslherbe, G.H., 302
Pesti, J.A., 608
Phillips, R.S., 680
Piatesi, A., 657
Piétri, N., 455
Plou, F.J., 743
Pomeroy, R.K., 281
Poon, C., 25
Popescu, I.C., 315
Preiml, M., 724
Puddephatt, R.J., 41
Pugh, D.J., 626
Pye, C.C., 447
Rahimizadeh, M., 517
Rao, M.K., 504
Raza, S.K., 504
Reetz, M.T., 626
Reider P.J., 646
Reymond, J.-L., 665
Roberts, S.M., 546
Rochon, F.D., 379
Rodrigo, R., 728
Rodríguez-Ubis, J.-C., 169
Rolke, J., 222
Romaní, L., 370
Ronzani, S., 714
Roos, J., 671
Rosazza, J.P.N., 582
Ruest, L., 483
Saf, R., 362
Salghi, R., 106
Sanchez, C., 269
Sánchez, V., 133
Sauer, E., 269
Sauro, V.A., 250
Scavini, M., 235
Scheck, M., 571
Schrader, W., 626
Secundo, F., 551
Serra, S., 714
Sharma, M., 504
Sharma, N.D., 589
Sheldon, R.A., 622
Shi, Z., 222
Shu, R., 489
Sidler, D.R., 646
Sigmund, A.E., 608
Silverman, C.E., 608
Skidmore, J., 546
Sorensen, T.S., 245, 413
Steinreiber, A., 362
Stephan, W., 125
Stock, N.L., 200
Storr, A., 133
Streiff, M.B., 540
Sun, F., 245, 41
Švedas, V.K., 699
Svendsen, A., 529
Szerminski, W.R., 633
Tanaka, K., 510
Tanaka, Y., 496
Taylor, N., 728
Taylor, N.J., 496
Tessier, C., 379
Thompson, R.C., 133
Tovar, C.A., 370
Trani, M., 653
Tsuchihashi, K., 207, 510
Tsuzuki, H., 207
Turdean, G., 315
van Rantwijk, F., 622
van Vliet, A.J., 633
Vaughan, K., 447
Veronese, F.M., 551
Vind, J., 529
Vliegenthart, J.F.G., 76

© 2002 NRC Canada

Vogels, C.M., 31
Vukovic, S., 269
Wahab, A., 175
Wahler, D., 665
Waldmann, H., 571
Wan, P., 46
Wang, L., 728
Wang, S., 613
Watanabe, M., 496
Warkentin, J., 228
Watson, B., 413
Westcott, S.A., 31
Westermann, B., 686
Whitcombe, T.W., 155
Williams, C.K., 89
Wnuk, S.F., 192
Wolfe, S., 222
Wong, C.-H., 643
Wood, S.D., 555
Workentin, M.S., 250
Xie, Y., 263
Xu, C., 155
Xu, C., 155
Yamato, T., 207, 510
Yap, G.P.A., 148, 281
Zheng, Y., 222
Zhu, L., 263
Zine, E., 106

© 2002 NRC Canada

This issue is dedicated to

Professor J. Bryan Jones

This special issue is dedicated to Professor Bryan Jones, on the occasion of his 65th birthday, to honour his outstanding contributions to organic chemistry, especially to recognize his pioneering use of enzymes in organic synthesis and pharmaceutical chemistry.

The paper by Mayer and co-workers entitled "Asymmetric total synthesis of (+)-exo-brevicomin based on enantioconvergent biocatalytic hydrolysis of an alkene-functionalized 2,3-disubstituted epoxide," that was dedicated to Bryan Jones, was published in the April issue and is reprinted here for completeness.

Associate Editors: R. Green and R. Kazlauskas

Le présent numéro est dédié au

Professeur J. Bryan Jones

Ce numéro spécial est dédié au professeur Bryan Jones, à l'occasion de son 65^{e} anniversaire de naissance, en reconnaissance de ses contributions exceptionnelles au domaine de la chimie organique et, en particulier, en reconnaissance de son utilisation novatrice des enzymes dans la synthèse organique et dans la chimie pharmaceutique.

L'article de Mayer *et al.* intitulé « Asymmetric total synthesis of (+)-exo-brevicomin based on enantioconvergent biocatalytic hydrolysis of an alkene-functionalized 2,3-disubstituted epoxide », dédié à Bryan Jones, a été publié dans le numéro du mois d'avril et il est reproduit ici pour compléter le recueil.

Directeurs scientifiques associés : R. Green et R. Kazlauskas

© 2002 NRC Canada

Professor J. Bryan Jones

Professor J. Bryan Jones

John Bryan Jones was born in the coastal town of Colwyn Bay in North Wales. He began his undergraduate education at the University of Wales, Cardiff, and remained there to obtain a Ph.D. in alkaloid chemistry under the supervision of Dr. A.R. Pinder in 1958. His first post-doctoral work was carried out as an ICI fellow, investigating polyacetylene synthesis with Professor Sir Ewart Jones at the University of Oxford, for which he was awarded a second doctoral degree, the D.Phil. Bryan Jones' next post-doctoral work was with Professor A.C. Cope at MIT, where he worked on amine oxides, after which he moved to Caltech and worked with Professor C. Niemann. In the latter project he was able to perform his first reaction using an enzyme (α-chymotrypsin), opening a research field that is still active 40 years later. Bryan Jones returned to Oxford as an ICI fellow, and in 1963 moved to the Chemistry Department at the University of Toronto, where he was appointed as a full Professor of Chemistry in 1974.

Professor Jones has been a pioneer in the application of enzymes as practical catalysts for organic synthesis. His basic work in this area was broadly focused on alcohol dehydrogenases and hydrolytic enzymes. The results obtained by his research group have demonstrated the unique benefits and broad applicability that the use of enzymes can bring to the production of chiral synthons, including key intermediates for antibiotics, insecticides, and pheromones. From an area that virtually did not exist when he began his work seriously in the early 1970s, the synthetic applications of enzymes has now become one of the most active research fields in chemistry. Furthermore, he has created an electronic database on the applications of enzymes and microorganisms in organic chemistry, which has now been converted into a state-of-the-art, fully structured and keyword-searchable database by Accelrys, a leading chemical software company in the U.K. This database, the only one in its field, is comprehensive for both journal and patent citations, and is now widespread in most of the important pharmaceutical and enzyme companies around the world, as well as in academic institutions.

More recently, he has addressed other frontiers of the field, involving the investigation of factors determining and controlling the catalytic activities and specificities of the enzymes of asymmetric synthetic value, using molecular modeling and graphics, molecular dynamics, and site-directed mutagenesis, in addition to organic chemistry methods. He applied the same strategy to design and synthesize compounds that can act as drugs by inhibiting medicinally important enzymes such as cysteine proteases and β-lactamases, and also to pro-drugs that can be activated in situ at targeted sites of disease. Part of this research was carried out within the Protein Engineering Network of the Federal Centres of Excellence program. A further area of related research was that of catalytic antibody activation of pro-drugs at a specifically targeted disease site.

Most recently, he has initiated a totally new area — that of creating unnatural and novel enzyme catalysts

Professeur J. Bryan Jones

Le professeur John Bryan Jones est né dans la ville côtière de Colwyn Bay, du nord du pays de Galles. Il a commencé ses études sous-graduées à l'Université de Wales, à Cardiff, où il a aussi obtenu son Ph.D. pour des travaux sur la chimie des alcaloïdes, sous la direction du Dr. A.R. Pinder, en 1958. Son premier travail post-doctoral a été réalisé à titre de boursier ICI, à étudier la synthèse des polyacétylènes avec le professeur Ewart Jones à l'Université d'Oxford; ces travaux lui ont valu un deuxième doctorat, le D.Phil. Bryan Jones a ensuite effectué un autre stage post-doctoral au cours duquel il a travaillé sur les oxydes d'amines, sous la direction du professeur A.C. Cope, au MIT, d'où il est passé à Caltech où il a travaillé avec le professeur C. Niemann. Au cours de ce dernier projet, il a réalisé sa première réaction à l'aide d'un enzyme (α-chymotrypsine), ce qui lui a ouvert le champ de recherches dans lequel il est encore actif après 40 ans. Bryan Jones est retourné à Oxford comme boursier ICI et, en 1963, il a déménagé au département de chimie de l'Université de Toronto où il a été nommé professeur titulaire de chimie en 1974.

Le professeur Jones a été un pionnier dans l'application des enzymes comme catalyseurs pratiques en chimie organique. Ses travaux fondamentaux dans ce domaine ont été orientés principalement sur les déshydrogénases de l'alcool et sur les enzymes permettant des hydrolyses. Les résultats obtenus par son groupe de recherches ont démontré les bénéfices uniques et le large spectre des domaines d'application qui peuvent être ouverts par l'utilisation des enzymes dans la production de synthons chiraux, y compris des intermédiaires clés pour les antibiotiques, les insecticides et les phéromones. Alors que ce domaine n'existait pratiquement pas lorsqu'il a débuté sérieusement ses travaux au début des années 1970, les applications synthétiques des enzymes sont maintenant devenues l'un des champs de recherches les plus actifs de la chimie. De plus, il a créé une banque de données électroniques sur l'application des enzymes et des microorganismes en chimie organique; la compagnie Accelrys, R.-U., un chef de fil dans le domaine des logiciels chimiques, l'a maintenant transformée en banque de pointe dans laquelle on peut faire des recherches par structures ainsi que par mots-clés. Cette banque de données est la seule dans son domaine, elle couvre entièrement les citations tirées des journaux et des brevets et elle est maintenant largement utilisée dans les compagnies pharmaceutiques et d'enzymes les plus importantes ainsi que dans les institutions académiques.

Plus récemment, il s'est intéressé à d'autres frontières du domaine, dont l'étude des facteurs qui déterminent et qui contrôlent les activités catalytiques et les spécificités des enzymes ayant une valeur en synthèse asymétrique; il a réalisé ces études à l'aide de modelage et de graphiques moléculaires, de dynamiques moléculaires, de mutagénèses orientées vers les sites ainsi qu'à l'aide de méthodes de la chimie organique. Il a appliqué la même stratégie à la conception et à la synthèse de composés qui peuvent agir comme médicaments par inhibition médicinale d'enzymes importants comme les protéases de la cystéine et les β-lactamases ainsi qu'aux prodrogues qui peuvent être activées *in situ* au niveau des sites ciblés de la maladie. Une partie de ces travaux a été réalisée dans le cadre du « Réseau de génie des protéines » créé dans le cadre du programme des centres d'excellence du gouvernement fédéral. Il s'est aussi intéressé à un autre domaine de recherches apparenté, celui de l'activation

© 2002 NRC Canada

via highly controlled chemical modification in combination with site-directed mutagenesis. This new strategy is at the cutting edge of the enzyme frontier and permits previously unattainable control and modulation of enzyme properties and selectivity, including stereoselectivity. It has also opened up a totally new strategy for pharmaceutical and drug development, involving targeting and then selectively destroying enzymes, proteins, and receptors that are involved in the mediation and promotion of diseases.

Professor Jones is recognized as one of the leading authorities on the synthetic uses of enzymes, a fact reflected by his numerous plenary lectures at international meetings. His work in this area has already attracted some 55 specialized papers in the journal "Bioorganic and Medicinal Chemistry" (Nos. **6** and **7**, 1994) in commemoration of his 60th birthday, in addition to the 35 papers in this special issue.

Professor Jones is a Fellow of the Royal Society of Canada and of the Chemical Institute of Canada, and a Killam Fellow of the Canada Council. Other honours include the Perlman award of the American Chemical Society (Microbial Chemistry Division), the Labatt Award and the Bader Award of the Canadian Society of Chemistry, the Chemical Institute of Canada Medal (1995), the Lemieux Award of the Canadian Society of Chemistry (1998), and the Steacie Award of the Canadian Society of Chemistry (2000). He was also awarded the Henry Marshall Tory Medal of the Royal Society of Canada in 2001, following the Chairman Medal of the Royal Society of Chemistry (London), and appointments as Dow Lecturer at the Ottawa-Carleton Institute, Suisse Romande Lecturer (Switzerland), and Austrian Chemical Society Lecturer. In 1994, Bryan Jones was named University Professor, the University of Toronto's highest academic rank, and celebrated his retirement from the University of Toronto in 1997.

He has published over 200 papers and book chapters, and co-authored and edited two Techniques of Chemistry volumes on "Applications of Biochemical Systems In Organic Chemistry" that have become the reference standards in the field.

We, together with all the contributors of this special issue, have the honour of congratulating Professor Jones for his research activities, and collectively celebrating his retirement from the University of Toronto after 34 years of magnificent service.

H.L. Holland
R. Kazlauskas

catalytique d'anticorps de prodrogues au niveau d'un site de maladie spécifiquement ciblé.

Tout récemment, il a initié une voie de recherches complètement nouvelle — celle de créer de nouveaux catalyseurs enzymatiques, non naturels, par le biais de modifications chimiques hautement contrôlées en combinaison avec de la mutagénèse orientée vers le site. Cette nouvelle stratégie est à la fine pointe de l'étude des enzymes et elle permet d'atteindre des niveaux de contrôles, de modulation des propriétés des enzymes et de sélectivité, y compris la stéréosélectivité, que l'on ne pouvait obtenir antérieurement. Il a aussi permis l'ouverture d'une toute nouvelle stratégie pour le développement de drogues et de médicaments, y compris la possibilité de cibler et ensuite de détruire sélectivement des enzymes, des protéines et des récepteurs impliqués dans la promotion des maladies.

Le professeur Jones est reconnu comme l'une des sommités dans l'utilisation synthétique des enzymes, un fait qui est reflété par ses nombreuses présentations plénières à des réunions internationales. Son travail dans ce domaine a déjà permis d'attirer environ 55 présentations dans le journal « Bioorganic and Medicinal Chemistry », Nos. **6** et **7** (1994), pour commémorer son soixantième anniversaire de naissance, en plus des 35 regroupés dans ce numéro spécial.

Le professeur Jones est un membre de la Société royale du Canada et de l'Institut de chimie du Canada et un Associé Killam du Conseil du Canada. Il a aussi reçu le prix Perlman de la Société américaine de chimie (Division de chimie microbiologique), les prix Labatt et Bader de la Société canadienne de chimie, la Médaille de l'Institut de chimie du Canada (1995), le prix Lemieux de la Société canadienne de chimie (1998) et le prix Steacie de la Société canadienne de chimie (2000). On lui a aussi octroyé la Médaille Henry Marshall Tory de la Société royale du Canada en 2001, la Médaille du président de la « Royal Society of Chemistry (London) » et il a aussi été Dow Lecturer à l'Institut Ottawa-Carleton, conférencier invité de la Suisse Romande et conférencier de la Société autrichienne de chimie. En 1994, Bryan Jones a été nommé « University Professor », le niveau académique le plus élevé de l'Université de Toronto et il a célébré sa retraite de cette université en 1997.

Il est l'auteur de plus de deux cents publications et de chapitres de livres et il est le coauteur et l'éditeur de deux volumes de Techniques de chimie sur les « Applications des systèmes biochimiques en chimie organique » qui sont devenus des volumes de référence standards dans ce domaine.

Avec tous ceux qui ont contribué à ce numéro spécial, nous avons l'honneur de féliciter le professeur Jones pour ses activités de recherches et pour célébrer ensemble sa retraite de l'Université de Toronto après trente-quatre ans de superbes services.

H.L. Holland
R. Kazlauskas

© 2002 NRC Canada

Previously published / Prédémment paru

Asymmetric total synthesis of (+)-*exo*-brevicomin based on enantioconvergent biocatalytic hydrolysis of an alkene-functionalized 2,3-disubstituted epoxide

Sandra F. Mayer, Harald Mang, Andreas Steinreiber, Robert Saf, and Kurt Faber

Abstract: A short total asymmetric synthesis of (+)-*exo*- and (–)-*endo*-brevicomin ((+)-*exo*-**3** and (–)-*endo*-**3**), which are components of the attracting pheromone system of several bark-beetle species belonging to the genera *Dendroctonus* and *Dryocoetes*, was accomplished via a chemoenzymatic protocol. The key step consisted of biocatalytic hydrolysis by bacterial epoxide hydrolases of *cis*-configured 2,3-disubstituted oxiranes bearing olefinic side chains. This reaction proceeded in an enantioconvergent fashion, by affording a single enantiomeric *vic*-diol from the *rac*-epoxide in up to 92% ee and 83% isolated yield.

Key words: bacterial epoxide hydrolase, 2,3-disubstituted oxirane, enantioconvergent hydrolysis, (+)-*exo*-brevicomin, (–)-*endo*-brevicomin.

Résumé : Faisant appel à un protocole chimioenzymatique, on a réalisé une courte synthèse asymétrique totale des (+)-*exo*- et (–)-*endo*-brévicomines [(+)-*exo*-**3** et (–)-*endo*-**3**], des composants du système de phéromone d'attraction de plusieurs espèces de scolytes des genres *Dendroctonus* et *Dryocoetes*. L'étape clé implique une hydrolyse biocatalytique à l'aide d'hydrolases bactériennes d'époxyde d'oxiranes 2,3-disubstitués, de configuration *cis*- et portant des chaînes latérales oléfiniques. Cette réaction s'est produite de façon énantioconvergente en ne fournissant, à partir de l'époxyde racémique, qu'un seul énantiomère de diol vicinal, avec un rendement isolé de 83% et un e.e. de 92%.

Mots clés : hydrolase bactérienne d'époxyde, oxirane 2,3-disubstitué, hydrolyse énantioconvergente, (+)-*exo*-brévicomine, (–)-*endo*-brévicomine.

[Traduit par la Rédaction]

Previously published in Can. J. Chem. **80**, 362–369 (2002).

© 2002 NRC Canada

PREVIEW / APERÇU

Forthcoming special issues / Numéros spécials à paraître

August 2002	In honour of Professor Ray Lemieux
November 2002	In honour of Professor Tris Chivers
June 2003	In honour of Professor Don Arnold

Forthcoming articles / Articles à paraître

A partial-molar volume study of electrolytes in propylene carbonate-based lithium battery electrolyte solutions at 298.15 K	J. Wang, Y. Zhao, and K. Zhuo
Effect of pH on the mechanism of $OClO^{\bullet}$ oxidation of aromatic compounds	D. Svenson, J.F. Kadla, H.-m. Chang, and H. Jameel
Fixed stereochemical control in the synthesis of new mono- and disubstituted 2-phenyl-6-aza-1,3-dioxa-2-borabenzocyclononenes	H.I. Beltrán, S.J. Alas, R. Santillan, and N. Farfán
On the temperature dependence of the primary yield and the product $G\varepsilon_{max}$ of hydrated electrons in the low-LET radiolysis of liquid water	J. Meesungnoen, J.-P. Jay-Gerin, A. Filali-Mouhim, and S. Mankhetkorn
Peptide model XXVIII: An exploratory ab initio and density-functional study on the side-chain/backbone interaction in *N*-acetyl-L-cysteine-*N*-methylamide and *N*-formyl-L-cysteinamide in their γ_L backbone conformations	M.A. Zamora, H.A. Baldoni, A.M. Rodriguez, R.D. Enriz, C.P. Sosa, A. Perczel, A. Kucsman, O. Farkas, E. Deretey, J.C. Vank, and I.G. Csizmadia
Sodium borohydride: A versatile reagent in the reductive *N*-monoalkylation of α-amino acids and α-amino methyl esters	G. Verardo, P. Geatti, E. Pol, and A.G. Giumanini
The determination of stereochemistry of epoxides located at the 5,6-positions of decalinic systems: An empirical method based on ^{13}C NMR chemical shifts	R.M. Cravero, G.R. Labadie, and M.G. Sierra
Vibrational spectroscopic studies of aqueous solutions of *tert*-butyl alcohol and *tert*-butylamine	P.K. Kipkemboi and A.J. Easteal

© 2002 NRC Canada

A partial-molar volume study of electrolytes in propylene carbonate-based lithium battery electrolyte solutions at 298.15 K

Jianji Wang, Yang Zhao, Kelei Zhuo, and Ruisen Lin

Abstract: Apparent molar volumes ($V_{2,\phi}$) and standard partial-molar volumes ($V^0_{2,\phi}$) of $LiClO_4$ and LiBr at 298.15 K have been determined from precise density measurements in solvent mixtures of propylene carbonate (PC) with dimethylformamide (DMF), tetrahydrofuran (THF), acetonitrile (AN), and methyl formate (MF). The scaled particle theory is used to calculate the contributions of the cavity formation and the electrolyte–solvent interactions to the standard partial-molar volumes. It is shown that $V^0_{2,\phi}$ is strongly dependent on the nature of the solvents, and the trends in $V^0_{2,\phi}$ with composition of the solvent mixtures are determined by the interaction volumes of electrolytes with solvents. The results are discussed in terms of ionic preferential solvation, packing effect of solvents in the solvation shell, and electrostriction of solvents by ion.

Key words: partial-molar volume, scaled particle theory, lithium salts, propylene carbonate, solvent mixtures, lithium battery electrolytes.

Résumé : En se basant sur des mesures précises de densité dans des mélanges de solvants de carbonate de propylène (PC) avec du diméthylformamide (DMF), du tétrahydrofurane (THF), de l'acétonitrile (AN) et de formiate de méthyle (MF), on a déterminé les volumes molaires apparents ($V_{2,\phi}$) et les volumes molaires partiels standards, ($V^0_{2,\phi}$) du $LiClO_4$ et du LiBr, à 298,15 K. On a utilisé la théorie de la particule pour calculer les contributions de la formation de la cavité et de l'interaction de l'électrolyte-solvant aux volumes molaires partiels standards. On a démontré que la valeur de $V^0_{2,\phi}$, dépend fortement de la nature des solvants et les tendances dans les valeurs de $V^0_{2,\phi}$ avec la composition des mélanges de solvant sont déterminées ceux qui sont présents dans les volumes d'interaction des électrolytes avec les solvants. On discute des résultats sur la base de la solvatation ionique préférencielle, de l'effet du tassement des solvants dans la couche de solvatation et de l'électrostriction des solvants par l'ion.

Mots clés : volume molaire partiel, théorie de la particule scalaire, sels de lithium, carbonate de propylène, mélanges de solvants, électrolytes de piles au lithium.

[Traduit par la Rédaction]

Introduction

Lithium batteries are often considered the future leaders in the battery industry, mainly because of their high energy and low environmental impact. As an important part of the battery, the quality of the electrolyte solution is one of the main factors for determining the performance, operating temperature range, and shelf life of batteries (1, 2). In widely produced commercial lithium batteries, liquid electrolytes are the most commonly used. These electrolyte solutions must be stable and highly conductive, and display low viscosity and perfect cycle efficiency. A great variety of solvents and electrolytes have been employed in an effort to improve battery characteristics. Among the solvents, propylene carbonate (PC) is widely used because of its high dielectric constant, wide liquid range, and good solubilizing power for lithium salts. Nevertheless, its viscosity is high and the Li-cycling efficiency using Li metal as anode is poor in the absence of additives. Addition of low-viscosity ethers like tetrahydrofuran (THF) and dimethoxyethane (DME), or linear carbonate like dimethyl carbonate (DMC) and diethyl carbonate (DEC), significantly increase the conductivity of the electrolyte solutions.

Molar volumes of electrolytes affect the properties of lithium-battery electrolyte solutions, such as conductivity and viscosity (2). They also influence the behavior of the electrodes during the cycling (3). Studies on volumetric properties are, therefore, important for developing an understanding of solute–solvent and solute–solute interactions in lithium batteries. A literature survey reveals that there have been numerous studies on conductivity and viscosity for lithium-battery electrolyte solutions. Very little investigation, however, has been carried out on the related volumetric properties. Zana et al. (4) have obtained the ionic volume of electrolytes in PC from the measurements of densities, ultrasonic vibration potentials, and transference numbers of electrolytes at 298.15 K. It was found that the electrostriction in

Received 24 January 2002. Published on the NRC Research Press Web site at http://canjchem.nrc.ca on 7 June 2002.

J. Wang,[1] Y. Zhao, and K. Zhuo. Department of Chemistry, Henan Normal University, Xinxiang, Henan 453002, People's Republic of China.
R. Lin. Department of Chemistry, Zhejiang University, Hangzhou, Zhejiang 310027, People's Republic of China.

[1]Corresponding author (e-mail: jwang@henannu.edu.cn).

 DOI: 10.1139/V02-092 © 2002 NRC Canada

PC is close to that in water, ethylene glycol, ethanol, and dimethyl sulfoxide. Perron et al. (5) determined the apparent molar volumes of $LiClO_4$ and LiBr in aprotic solvents (DME, acetonitrile (AN), γ-butyrolactone, dioxolane, and to a lesser extent PC), together with other properties, such as solid–liquid phase equilibrium, heat capacities, conductivities, and viscosities. The solvation effect was discussed based on the low-concentration thermodynamic data. The volumes, heat capacities, and specific conductivities of $LiClO_4$ and LiBr, measured in mixtures of γ-butyrolactone (BUTY) with DME and of PC with BUTY, have been reported by Couture et al. (6). These results are compared with those of the electrolytes in the pure solvents. The properties of water in DME, BUTY, or the mixtures of the two solvents are modified significantly in the presence of LiBr but only slightly with $LiClO_4$. Brouillette et al. (7) characterized lithium bis(trifluoromethylsulfone)imide (LiTFSI) in solution, which is a promising electrolyte for high-energy lithium batteries. Its conductance, apparent volume, and heat capacity were measured over a wide range of concentration in glymes, tetraethylsulfamide, AN, BUTY, and PC at 298.15 K. Atkins et al. (8) reported the apparent molar volumes of several electrolytes in solvent mixtures of PC with AN, DME, or THF, but the volumes were measured at an electrolyte concentration of 0.05 mol dm^{-3}. No standard partial-molar volumes were reported for these systems. Recently, Naejus et al. (9) determined the standard partial-molar volumes of $LiClO_4$, $LiCF_3SO_3$, and $LiPF_6$ in PC, EC, or DMC, and of $LiClO_4$ in some mixtures of EC with DMC or PC. Partial-molar volumes of Li^+ and associated anions have been deduced.

All of these studies seem scarce considering that technologically advanced electrolytes have been used in the development of lithium batteries. In this paper, we studied the partial-molar volumes of $LiClO_4$ and LiBr in the mixtures of PC with *N*,*N*-dimethylformamide (DMF), THF, AN, and methyl formate (MF). LiBr was chosen to study the anion effect. The solvent mixtures selected are either currently used in the developmental secondary batteries, such as PC + THF (10), or show potential as battery solvents, such as PC + AN (11), PC + MF (12), and PC + DMF (13). The results have been discussed from ion–solvent interaction with the help of the scaled particle theory.

Experimental

Materials

$LiClO_4 \cdot 3H_2O$ (Beijing Baili Chem. Co., A.R.) was recrystallized twice from ethanol or acetonitrile, and dried at 453 K under vacuum for 4 days. $LiBr \cdot 2H_2O$ (Beijing Chem. Co., A.R.) was recrystallized from ethanol, and dried at 423 K under vacuum for 3 days.

Propylene carbonate (Luoyang Chemical Factory, A.R.) was dried over molecular sieves (4 Å) for several days, heated at reflux for 5 h in the presence of sodium, and then distilled at reduced pressure. The middle fraction of the distillate was collected. *N*,*N*-Dimethylformamide (Tianjin Chemical Factory, A.R.) was mixed with 10% (v/v) of benzene (Beijing Chemical Factory, A.R.). The azeotrope was distilled off under atmospheric pressure at about 353 K. The product was dried over a silica-gel drier and distilled at reduced pressure. Acetonitrile (Beijing Chem. Co., A.R.) was distilled after being stored over activated molecular sieves (3 Å) for several days. Tetrahydrofuran (Zhengzhou Chem. Co., A.R.) was stored over fine sodium wire for several days until no gas evolved upon introduction of fresh sodium. Methyl formate (Shanghai Chem. Co., C.R.) was distilled twice after being heated at reflux over P_2O_5.

Since all these solvents are highly hygroscopic, the purified solvents are stored over P_2O_5 in desiccators before use. The water content, determined by the Karl–Fischer method, was less than 100 ppm.

Measurements

All solutions were prepared by weight, and concentration of the salts is expressed by molality (mol kg^{-1}). Every precaution was taken to minimize contamination by water. The composition of binary solvents is always represented by mole fraction (x) of the co-solvent in the PC-based solvent mixtures.

Solution densities were determined to $\pm 1.5\times10^{-5}$ g cm^{-3} with an Anton Paar DMA 60/602 vibrating-tube digital densimeter. The temperature around the density-meter cell was controlled to 298.15 ± 0.005 K using a CT-1450 temperature controller and a CK-100 ultracryostat. The densimeter was calibrated with known densities of pure water and dry air every day. The other details have been described previously (14).

Results and discussion

Apparent molar volumes of the lithium salts in a given solvent mixture were calculated from the solution densities by

$$[1] \qquad V_{2,\phi} = M/\rho - 10^3(\rho - \rho_0)/(m\rho\rho_0)$$

where M and m are, respectively, the molar mass and molality of the lithium salts, and ρ and ρ_0 are the densities of the ternary solutions and the binary solvents, respectively. Apparent molar volumes of the lithium salts in PC-based solvent mixtures are given in Tables 1 and 2.

It was found that $V_{2,\phi}$ varied linearly with the square root of the molalities of lithium salts, and could be analyzed by least-square fitting to

$$[2] \qquad V_{2,\phi} = V^0_{2,\phi} + S_v m^{1/2}$$

where $V^0_{2,\phi}$ is the infinite dilution of the apparent molar volume that is equal to the standard partial-molar volume, and S_v is the experimental slope. The $V^0_{2,\phi}$ values obtained by least-square analysis for $LiClO_4$ and LiBr in PC-based solvent mixtures are listed in Table 3, along with their standard deviations.

The standard partial-molar volumes of $LiClO_4$ and LiBr have been reported in PC (4) (36.77, 15.32 cm^3 mol^{-1}, respectively) and in AN (5) (15.0, −4.8 cm^3 mol^{-1}, respectively). The present values (37.15, 15.26 cm^3 mol^{-1} in PC and 15.31, −4.90 cm^3 mol^{-1} in AN) are in reasonable agreement with those reported in literature. Atkins et al. (8) reported the apparent molar volume of 0.05 mol dm^{-3} $LiClO_4$ in THF (23.3 cm^3 mol^{-1}), which is in excellent agreement with the present value (23.43 cm^3 mol^{-1}). No literature data can be found for comparison in the mixed solvents.

© 2002 NRC Canada

Table 1. Solution density (ρ) and apparent molar volume ($V_{2,\phi}$) for electrolytes in PC + DMF and PC + MF mixtures at 298.15 K as a function of molality of the electrolytes.

x = 0			x = 0.2500			x = 0.5000			x = 0.7500			x = 1.00		
m (mol kg^{-1})	ρ (g cm^{-3})	$V_{2,\phi}$ (cm^3 mol^{-1})	m (mol kg^{-1})	ρ (g cm^{-3})	$V_{2,\phi}$ (cm^3 mol^{-1})	m (mol kg^{-1})	ρ (g cm^{-3})	$V_{2,\phi}$ (cm^3 mol^{-1})	m (mol kg^{-1})	ρ (g cm^{-3})	$V_{2,\phi}$ (cm^3 mol^{-1})	m (mol kg^{-1})	ρ (g cm^{-3})	$V_{2,\phi}$ (cm^3 mol^{-1})
$LiClO_4$ + PC + DMF														
0.0000	1.19944		0.0000	1.13863		0.0000	1.07678		0.0000	1.01095		0.0000	0.94402	
0.01378	1.20045	37.60	0.01259	1.13957	36.54	0.01318	1.07776	34.66	0.01439	1.01203	31.87	0.01473	0.94514	26.88
0.02963	1.20161	37.57	0.02953	1.14080	36.84	0.02673	1.07875	34.98	0.02271	1.01623	32.05	0.02951	0.94625	27.57
0.04994	1.20309	37.74	0.04949	1.14225	37.01	0.04858	1.08035	35.19	0.03356	1.01345	32.18	0.04853	0.94768	27.92
0.06953	1.20450	37.92	0.06485	1.14336	37.14	0.06252	1.08137	35.31	0.04730	1.01446	32.47	0.06391	0.94881	28.36
0.09969	1.20666	38.10	0.07980	1.14436	37.96	0.08297	1.08284	35.60	0.07628	1.01660	32.60	0.07460	0.94959	28.63
0.1536	1.21048	38.39	0.1018	1.14600	37.37	0.1013	1.08416	35.64	0.1088	1.01896	32.86	0.09904	0.95140	28.85
0.2127	1.21466	38.48	0.1511	1.14949	37.68	0.1508	1.08774	35.72	0.1703	1.02341	33.25	0.1494	0.95508	29.24
LiBr + PC + DMF														
0.01499	1.20042	15.87	0.01541	1.13985	14.55	0.01766	1.07835	11.67	0.01489	1.01216	6.93	0.01282	0.94506	0.48
0.03048	1.20166	16.39	0.03020	1.14103	14.70	0.02972	1.07931	12.01	0.02902	1.01330	7.56	0.02845	0.94632	0.95
0.05002	1.20320	16.80	0.04947	1.14255	14.92	0.04824	1.08078	12.05	0.04890	1.01485	7.86	0.04792	0.94788	1.37
0.08114	1.20564	17.17	0.06580	1.14385	14.91	0.06495	1.08210	12.08	0.06439	1.01608	7.93	0.06347	0.94910	1.74
0.1080	1.20773	17.37	0.08019	1.14498	14.99	0.07765	1.08310	12.17	0.08004	1.01732	8.08	0.07799	0.95025	2.19
0.1520	1.21113	17.70	0.1014	1.14666	15.00	0.1046	1.08521	12.39	0.1012	1.01898	8.24	0.1023	0.95216	2.58
0.2294	1.21700	18.20	0.1240	1.14841	15.27	0.1709	1.09035	18.88	0.1880	1.02563	9.40	0.1414	0.95517	3.40
$LiClO_4$ + PC + MF														
0.0000	1.19938		0.0000	1.15835		0.0000	1.03996		0.0000	1.01713		0.0000	0.96542	
0.01378	1.20045	37.60	0.01557	1.15973	25.78	0.02512	1.11214	21.00	0.03109	1.05003	16.44	0.01161	0.96640	19.28
0.02963	1.20161	37.57	0.03004	1.16087	29.27	0.04533	1.11382	24.18	0.05029	1.05158	20.74	0.03116	0.96804	20.00
0.04994	1.20309	37.74	0.04968	1.16240	30.94	0.05875	1.11493	25.23	0.07385	1.05351	22.65	0.04861	0.96948	20.41
0.06953	1.20450	37.92	0.06541	1.16360	31.91	0.07234	1.11602	26.15	0.09864	1.05543	24.66	0.06504	0.97085	20.45
0.09969	1.20666	38.10	0.08504	1.16489	34.34	0.1017	1.11820	28.80	0.1240	1.05737	25.97	0.08103	0.97217	20.66
0.1536	1.21048	38.39	0.1038	1.16636	34.17	0.1573	1.12216	31.83	0.1470	1.05911	26.93	0.09878	0.97362	20.89
0.2127	1.21466	38.48	0.1574	1.17005	36.09							0.1568	0.97837	21.27
LiBr + PC + MF														
0.01499	1.20042	15.87	0.03123	1.16079	7.06	0.02613	1.11153	0.48	0.02750	1.04868	–4.82	0.02766	0.96664	3.10
0.03048	1.20166	16.39	0.04700	1.16216	8.21	0.04938	1.11355	3.86	0.04554	1.05027	–1.86	0.04804	0.96827	3.49
0.05002	1.20320	16.80	0.06385	1.16356	9.43	0.05984	1.11446	4.42	0.06541	1.05198	–0.02	0.06376	0.96950	3.98
0.08114	1.20564	17.17	0.07685	1.16462	10.20	0.08162	1.11625	6.37	0.07915	1.05309	1.60	0.07656	0.97050	4.18
0.1080	1.20773	17.37	0.09080	1.16565	11.67	0.1009	1.11774	8.05	0.1012	1.05480	3.80	0.1004	0.97237	4.66
0.1520	1.21113	17.70	0.1553	1.17049	14.65	0.1367	1.12043	10.35	0.1528	1.05870	7.15	0.1619	0.97717	5.19

© 2002 NRC Canada

Table 2. Solution density (ρ) and apparent molar volume ($V_{2,\phi}$) for electrolytes in PC + THF and PC + AN mixtures at 298.15 K as a function of molality of the electrolytes.

x = 0			x = 0.2000			x = 0.4000[a]			x = 0.6000[b]			x = 1.00		
m (mol kg^{-1})	ρ (g cm^{-3})	$V_{2,\phi}$ (cm^3 mol^{-1})	m (mol kg^{-1})	ρ (g cm^{-3})	$V_{2,\phi}$ (cm^3 mol^{-1})	m (mol kg^{-1})	ρ (g cm^{-3})	$V_{2,\phi}$ (cm^3 mol^{-1})	m (mol kg^{-1})	ρ (g cm^{-3})	$V_{2,\phi}$ (cm^3 mol^{-1})	m (mol kg^{-1})	ρ (g cm^{-3})	$V_{2,\phi}$ (cm^3 mol^{-1})
$LiClO_4$ + PC + THF														
0	1.19937		0.0000	1.13876		0.0000	1.08152		0.0000	1.01117		0.0000	0.88201	
0.01378	1.20045	37.60	0.01470	1.14006	25.54	0.01424	1.08278	22.93	0.01431	1.01242	20.40	0.01417	0.88310	22.22
0.02963	1.20161	37.57	0.02972	1.14121	29.96	0.02935	1.08407	24.18	0.02935	1.01360	24.29	0.02894	0.88420	23.32
0.04994	1.20309	37.74	0.04866	1.14267	31.38	0.04877	1.08561	26.70	0.04884	1.01514	25.61	0.03755	0.88485	23.41
0.06953	1.20450	37.92	0.06674	1.14409	31.71	0.06495	1.08694	26.96	0.06608	1.01655	25.54	0.05001	0.88579	23.43
0.09969	1.20666	38.10	0.08369	1.14509	34.96	0.08520	1.08817	31.52	0.09059	1.01804	30.88	0.06506	0.88690	23.89
0.1536	1.21048	38.39	0.1039	1.14672	34.15	0.1041	1.08971	30.87	0.1014	1.01947	24.98	0.07059	0.88732	23.84
0.2127	1.21466	38.48	0.1430	1.14948	35.30	0.1502	1.09307	32.34	0.1265	1.02082	30.34	0.1019	0.88964	24.25
LiBr+ PC + THF														
0.01499	1.20042	15.87	0.01520	1.13961	14.52	0.02882	1.08338	8.81	0.02672	1.01320	4.75	0.03881	0.88480	7.54
0.03048	1.20166	16.39	0.02835	1.14065	14.83	0.04854	1.08495	10.30	0.04480	1.01461	6.76	0.05163	0.88568	8.12
0.05002	1.20320	16.80	0.04903	1.14227	15.21	0.06365	1.08613	11.03	0.06733	1.01631	8.48	0.06840	0.88684	8.44
0.08114	1.20564	17.17	0.06432	1.14345	15.54	0.07884	1.08730	11.65	0.09224	1.01796	11.85	0.08165	0.88770	9.21
0.1080	1.20773	17.37	0.08294	1.14480	16.59	0.1060	1.08939	12.27	0.1038	1.01899	10.36	0.1024	0.88913	9.58
0.1520	1.21113	17.70	0.1017	1.14638	15.57	0.1275	1.09091	13.56	0.1565	1.02271	12.49	0.1828	0.89443	11.26
0.2294	1.21700	18.20	0.1898	1.15295	16.88									
$LiClO_4$ + PC + AN														
0	1.19939		0.0000	1.14452		0.0000	1.03996		0.0000	0.90360		0.0000	0.77652	
0.01378	1.20045	37.60	0.01535	1.14567	36.18	0.01490	1.04107	34.00	0.01466	0.90471	25.51	0.01543	0.77764	16.90
0.02963	1.20161	37.57	0.03936	1.14742	36.63	0.02099	1.04151	34.12	0.03616	0.90630	26.42	0.02533	0.77835	17.75
0.04994	1.20309	37.74	0.04990	1.14818	36.95	0.02961	1.04214	34.25	0.05019	0.90731	27.10	0.02965	0.77864	18.67
0.06953	1.20450	37.92	0.06574	1.14935	36.74	0.04896	1.04353	34.87	0.07799	0.90932	27.77	0.04633	0.77981	19.44
0.09969	1.20666	38.10	0.08118	1.15043	37.24	0.07192	1.04516	35.37	0.1022	0.91107	27.94	0.05029	0.78008	19.71
0.1536	1.21048	38.39	0.1016	1.15186	37.63	0.09824	1.04698	36.02	0.1235	0.91246	29.58	0.1015	0.78361	21.15
0.2127	1.21466	38.48	0.1263	1.15362	37.70	0.1302	1.04920	36.41	0.1603	0.91506	29.82	0.1549	0.78727	21.70
LiBr + PC + AN														
0.01499	1.20042	15.87	0.01952	1.14552	19.51	0.02076	1.04127	22.15	0.01559	0.90344	19.76	0.01510	0.77756	–2.86
0.03048	1.20166	16.39	0.03540	1.14672	18.92	0.03679	1.04239	20.91	0.03608	0.90488	14.07	0.03489	0.77891	–1.71
0.05002	1.20320	16.80	0.05045	1.14790	17.94	0.04099	1.04276	18.89	0.05264	0.90604	12.78	0.04871	0.77977	–1.25
0.08114	1.20564	17.17	0.06709	1.14918	17.78	0.05261	1.04361	18.27	0.06533	0.90690	12.72	0.05004	0.77993	–1.05
0.1080	1.20773	17.37	0.08352	1.15046	17.43	0.1001	1.04709	16.98	0.07836	0.90782	12.27	0.07342	0.78147	–0.35
0.1520	1.21113	17.70	0.1013	1.15183	17.29	0.1030	1.04738	16.22	0.09829	0.90923	11.63	0.1027	0.78342	0.55
0.2294	1.21700	18.20	0.1248	1.15360	17.49	0.1553	1.05131	15.38	0.1433	0.91240	10.63	0.1230	0.78474	1.07

[a] x = 0.5000 for PC + AN.
[b] x = 0.8000 for PC + AN.

© 2002 NRC Canada

Table 3. Standard partial-molar volumes ($V^0_{2,\phi}$, cm^3 mol^{-1}) of $LiClO_4$ and LiBr in PC based binary solvents at 298.15 K as a function of mole fraction of the co-solvent.

	PC + DMF		PC + AN		PC + THF		PC + MF	
x	$LiClO_4$	LiBr	$LiClO_4$	LiBr	$LiClO_4$	LiBr	$LiClO_4$	LiBr
0	37.15±0.08	15.26±0.11	37.15±0.08	15.26±0.11	37.15±0.08	15.26±0.11	37.15±0.08	15.26±0.11
0.2000			35.30±0.23	20.68±0.51	25.35±0.58	13.60±0.21		
0.2500	36.11±0.03	14.23±0.09					24.06±0.27	0.56±0.42
0.4000					18.23±0.35	4.93±0.43		
0.5000	34.30±0.10	11.19±0.12	32.56±0.12	25.26±0.35			14.24±0.48	–6.93±0.38
0.6000					16.57±0.33	–0.35±0.43		
0.7500	31.36±0.06	5.97±0.16					11.95±0.52	–13.46±0.41
0.8000			23.48±0.44	17.10±0.42				
1.00	25.97±0.20	–0.92±0.16	15.31±0.23	–4.90±0.11	21.60±0.26	4.41±0.23	18.74±0.16	1.58±0.18

Fig. 1. Dependence of standard partial-molar volume of the lithium salts on the mole fraction of the co-solvent in PC based binary solvents: (*a*) PC + DMF; (*b*) PC + AN; (*c*) PC + THF; (*d*) PC + MF.

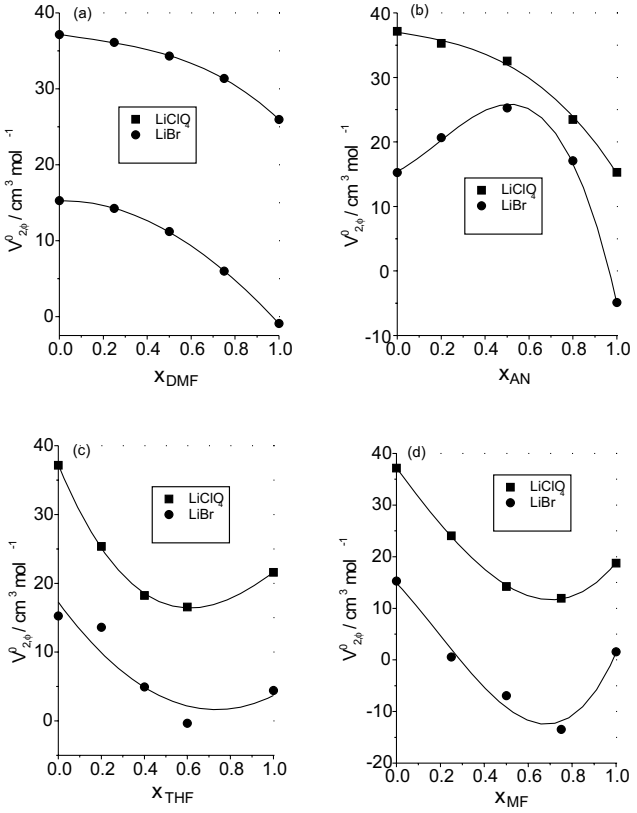

Dependence of $V^0_{2,\phi}$ on the composition of the mixed solvents

Figure 1 shows the variation of $V^0_{2,\phi}$ for $LiClO_4$ and LiBr with mole fraction of the co-solvent (DMF, AN, THF, MF) in the solvent mixtures. It can be seen that all values of $V^0_{2,\phi}$ for the electrolytes decrease with addition of the co-solvent, except for those of LiBr in the PC-rich region of PC + AN mixtures. The trends in $V^0_{2,\phi}$ with composition of the binary solvents are, however, different. They can generally be divided into two groups: one is characterized by the monotonous and slow decrease of $V^0_{2,\phi}$ over the entire solvent composition range, such as in PC + DMF and PC + AN mixtures; the other is reflected by an abrupt decrease in the PC-rich region and a minimum in the curve, such as in PC + THF and PC + MF mixtures. This suggests that the nature of the solvents and their interaction with electrolytes play an important role in the variation of $V^0_{2,\phi}$. The significant difference among the studied solvents is the dielectric property, as shown in Table 4. THF and MF have much lower dielectric constant values (ε) than PC, DMF, and AN. The electrostatic field of ions can penetrate much deeper into these low dielectric-constant solvents, leading to the increased electrostriction of the solvent and the decreased standard partial-molar volume of the electrolytes (5). We therefore conclude that dielectric property has an important influence on the variation of $V^0_{2,\phi}$ in the low dielectric solvents.

Table 4. Selected physical properties of the solvents at 298.15 K.

Property	PC	DMF	AN	THF	MF
V_m (cm^3 mol^{-1})[a]	85.2	77.4	52.9	81.6	62.3
ε[a]	66.1	36.7	36.01	7.58	8.5
D_N[b]	15.1	26.6	14.1	20.0	13.8
A_N[b]	18.3	13.6	19.3	8.0	—
V_w (cm^3 mol^{-1})[c]	53.68	46.61	27.68	47.00	34.25

[a]Ref. 23.
[b]Ref. 24.
[c]Ref. 19.

In addition, it is interesting to note that $\Delta V^0_{2,\phi}$ (difference between the two salts) varies with the mole fraction of the co-solvent, but the extent (not shown) is different in different solvent mixtures. Since both salts have the same cation, it appears that the anion effect is of some importance. Differences in molecular size and charge density between Br^- and ClO_4^- would result in different abilities of the solvent collapsing around them, which would affect the $\Delta V^0_{2,\phi}$ values in mixed solvents.

To get more information about electrolyte–solvent interaction, the scaled particle theory is applied later in the *Discussion*.

Application of scaled particle theory

The scaled particle theory (15, 16) was used to evaluate the measured particle volume as a sum of the geometric volume of solute molecule and the change in the solvent due to its interaction with the solute. That is,

$$[3] \qquad V^0_{2,\phi} = V_c + V_{in} + \beta RT$$

© 2002 NRC Canada

Table 5. Values of V_c (I) and V_{in} (II) for the electrolytes in PC based binary solvents calculated from SPT at 298.15 K.

	PC + DMF				PC + AN				PC + THF				PC + MF			
	$LiClO_4$		LiBr		$LiClO_4$		LiBr		$LiClO_4$		LiBr		$LiClO_4$		LiBr	
x	I	II	I	II	I	II	I	II	I	II	I	II	I	II	I	II
0	40.15	−3.00	38.27	−23.01	40.15	−3.00	38.27	−23.01	40.15	−3.00	38.27	−23.01	40.15	−3.00	38.27	−23.01
0.2000					41.12	−5.82	38.86	−18.18	41.39	−16.04	39.12	−25.52				
0.2500	40.95	−4.84	38.70	−24.47									41.12	−17.06	38.86	−38.30
0.4000									41.95	−23.72	39.66	−34.73				
0.5000	41.22	−6.92	38.96	−27.77	42.11	−9.55	39.81	−14.55					42.16	−27.92	39.87	−46.80
0.6000									43.18	−26.61	40.85	−41.20				
0.7500	41.56	−10.20	39.28	−33.31									44.16	−32.21	41.80	−55.26
0.8000					43.24	−19.76	40.91	−23.81								
1.00	42.16	−16.19	29.87	−40.79	45.03	−29.72	42.63	−47.53	45.03	−23.43	42.63	−38.22	44.04	−25.30	41.68	−40.10

where V_c is the partial-molar volume of cavity formation, and V_{in} is the volume change associated with the solute–solvent interactions, namely the "interaction volume." This term is introduced to describe the difference in volume arising from the difference between the real potential of intermolecular interaction and the potential of the absolutely rigid core. β is the isothermal compressibility of the solvent. The term βRT describes the volume effect of the ideal part of the solute dissolution. It is equal to 1.1 $cm^3\ mol^{-1}$ in aqueous solution at 298.15 K and is often neglected.

Assuming the solute molecule can be approximated by hard sphere with radius r_3 and the thickness of the void space between solute and solvent is Δ, the cavity volume can be estimated from

$$[4] \qquad V_c = (4\pi N_0/3)(r_3 + \Delta)^3$$

where N_0 is Avogadro's number. The Δ value was determined by Glueckauf (17) as follows:

$$[5] \qquad \Delta = (3V_1/4\pi N_0)^{1/3} - r_1$$

where V_1 and r_1 are molar volume and radius of the solvent molecule, respectively. When binary solvents are used, Δ can be obtained from

$$[6] \qquad V_{1,2} = 4\pi N_0\, x(r_2 + \Delta)^3/3 + 4\pi N_0(1 - x)(r_1 + \Delta)^3/3$$

where $V_{1,2}$ is the molar volume of mixed solvents, which is equal in value to the molar mass of mixed solvent divided by its density, x is the mole fraction of co-solvent in the solvent mixtures, and r_1 and r_2 are radii of the solvent and co-solvent, respectively.

In this work, the values of V_c for Li^+, Br^-, and ClO_4^- were calculated by means of eqs. [4]–[6] on the basis of the small spherical ions in the study. Pauling's crystal radii (18) are used as ionic radii (r_3) in the calculations, and radii of the solvents were calculated from van der Waals volume using the method proposed by Bondi (19). The interaction volumes of the lithium salts with solvent mixtures were then calculated by eq. [3] and reported in Table 5, along with the partial-molar volumes of cavity formation. In the calculations, the term βRT is neglected.

It can be seen from Table 5 that in every mixed solvents, values of V_c vary slightly with the mole fraction of the co-solvent. In fact, V_c consists of two terms:

$$[7] \qquad V_c = V_g + V_v$$

where V_g is the geometric volume occupied by the solute molecule itself, and V_v is the "empty" volume, namely the volume of the void space surrounding the solute molecules (20), which is of great importance for highly structured solvents like water, but is negligible in the case of unstructured solvents like carbonate. As a first approximation for low molecular-weight substances, the value of V_g can be taken as the van der Waals volume (V_w), which is considered to be independent of the nature of solvent and the composition of solvent mixtures. It is therefore understandable that no significant changes were observed for V_c of the lithium salts in different solvents.

The interaction volumes, however, are found to be sensitive to the mole fraction of the co-solvent. Their negative values originated mainly from the electrostriction of solvent

© 2002 NRC Canada

Fig. 2. Dependence of interaction volume on the mole fraction of the co-solvent in PC based binary solvents: (*a*) PC + DMF; (*b*) PC + AN; (*c*) PC + THF; (*d*) PC + MF.

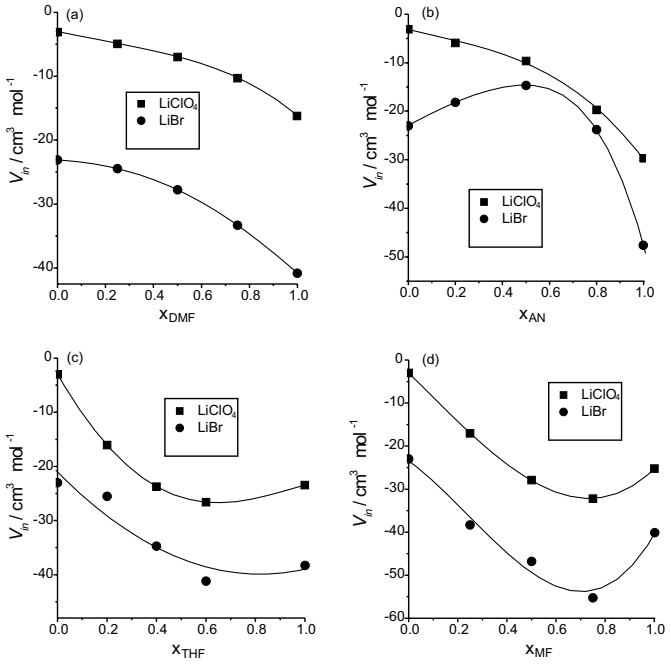

by electrolytes. The dependence of V_{in} for $LiClO_4$ and LiBr on the composition of the solvent mixtures is illustrated in Fig. 2. It is interesting to note that the trends in V_{in} with the mole fraction of the co-solvent are almost the same with those in $V^0_{2,\phi}$. We can, therefore, conclude that the trends in $V^0_{2,\phi}$ with composition of the solvent mixtures are determined by the interaction volumes of electrolytes with solvents.

Interactions of electrolytes with solvents

Volumetric properties are quite informative about solute–solvent interactions. Changes in the interaction volumes reflect the relative electrostriction (negative contribution) of the solvent in the presence of a given electrolyte. The contribution to the interaction of the electrolytes with solvents is essentially due to the following five factors: (*i*) steric effects of the solvent, which may force the solvent shell further from the ion and decrease the interaction of the cation with solvent (21); (*ii*) power of ion solvation, which can be expressed directly by the solvation number of ions. (Any decrease in the solvation number will allow tighter packing, i.e., greater electrostriction of the nearby but uncoordinated solvent molecules.); (*iii*) dielectric property of solvent. (According to the Drude–Nernst equation (22), the electrostatic field of an ion can penetrate much deeper into a low dielectric solvent, leading to the increased electrostriction of the solvent.); (*iv*) donor and acceptor ability of solvent, where the donor number (D_N) can be used to judge the interaction between cation and solvent (24), whereas the A_N number is considered to be a measure of solvating ability of anion (24); (*v*) the ability of solvent to collapse around an anion exerts a large influence on the interaction volume. The above related factors are combined to affect the electrostriction of the solvent by the ion.

Previous studies using IR, Raman, and ^{7}Li NMR (25–27) suggest that in the PC + DMF mixed solvents, the interaction between Li^+ and DMF is much stronger than that between Li^+ and PC, and the anion does not influence the solvation of Li^+. At the same time, a coordination number of 4 has been reported for Li^+ in PC (25), DMF, and AN (26). It can be seen in Table 4 that PC has the biggest molecular size in the studied solvents, indicating significant steric crowing of PC around the cation. When PC molecules are replaced by DMF in the solvation shell of the cation, the steric crowding of the solvent is reduced because of the smaller molecular size of DMF. This leads to the increased interaction of the cation with the solvent and the decreased interaction volumes. Since no great difference in molecular size and solvation properties toward Li^+ was observed between PC and DMF, it is not surprising that the variation in interaction volume is not significant from PC to PC + DMF mixtures.

Data on Gibbs energies of transfer (8) indicate that cations are solvated preferentially by PC in PC + AN mixed solvents. As shown in Fig. 2*b*, significant changes in V_{in} are observed when $x_{AN} > 0.5$, indicating significant displacement of PC by AN from the coordination sphere of the cation in this composition range. Although the preferential solvation of Li^+ in this binary solvent is different from that in PC + DMF, a similar solvation mechanism is operative in PC (25) and AN (26). Steric effect resulting from the large difference in molecular size between PC and AN (Table 4) is also a dominant factor for the decreased trend of V_{in} in PC + AN mixed solvents.

Both the D_N value and the Gibbs energies of transfer (8) indicate that cations are in general preferentially solvated by THF in PC + THF mixed solvents. Interaction volume values appear to broadly reflect the effect of preferential solvation as illustrated in Fig. 2*c*. At the initial addition of THF, V_{in} immediately decreases and a minimum value is observed at $x_{THF} \approx 0.6$. At this mixing ratio ($x_{THF} \approx 0.6$), a maximum conductivity of electrolytic solution was reported (28). It was found that this optimum mixing ratio does not depend on the concentration or kind of solutes; the solvation number of Li^+ is estimated to be unity in this mixing ratio (29). This suggests that it is the smaller radius of the solvated Li^+ that contributes to the increased conductivity. It is clear that the electrostriction increases and reaches a maximum with the decrease in the Li^+ solvation number from 4 (PC) to 1 ($x_{THF} \approx 0.6$). On the other hand, the dielectric property of the solvents also has an important effect on the electrostriction. THF has a much lower dielectric constant than DMF and AN, thus ions can penetrate much further into this solvent causing an increase in electrostriction and a decrease in V_{in}. These two contributing factors determine the trend of V_{in} in PC + THF to be much different from that in PC + DMF and PC + AN.

Similar dielectric effect is seen in PC + MF. In addition, MF has a stronger positive center on the formyl proton, which results in a stronger interaction with the anion (30, 31). This attractive interaction is also responsible for the increased electrostriction and the decreased interaction volumes. Except for MF, the other solvents are usually considered as weak anion solvators. Steric crowding of solvent around the anions will not occur to the same extent as

© 2002 NRC Canada

with the cations because of the much larger size of the anions and the weaker interactions with the solvents. Thus solvent molecules always collapse around the anion. It can be expected that the larger the anion, the less steric hindrance there would be to the packing of the solvent molecules. But this effect decreases because of the decreased charge field around the larger anion (ClO_4^-). Moreover, taking into account the difference of structure between the tetrahedral ClO_4^- and Br^-, a steric hindrance for the penetration of the solvent will occur for the first ion in the bulky solvent molecules and thus a higher value for V_{in} is expected. It can be seen from Table 5 that the values of V_{in} for $LiClO_4$ are higher than that of LiBr in every mixed solvent system. Thus, the ability of solvent to collapse around an anion is also a contributing factor to solvent electrostriction.

Conclusions

Addition of co-solvents like DMF, THF, AN, and MF to PC causes a significant decrease in the partial-molar volume of the electrolytes, the magnitude of which depends not only on the nature but also on the amount of the added co-solvent to the mixtures. Thus a noticeable solvent effect on the performance behavior of lithium batteries containing these solvents is expected.

The partial-molar volume of cavity formation is not sensitive to the nature of solvent and the composition of solvent mixtures, whereas the interaction volume is. The interaction volumes of the electrolytes with solvents determine the trends in the standard partial-molar volume of the electrolytes with the composition of solvent mixtures.

It is suggested that steric effects are a dominant factor for the interaction volume of electrolytes in PC + DMF and PC + AN. The large decrease in the solvation number of Li^+ and the dielectric effect are mainly responsible for the interaction volume in PC + THF and PC + MF, while the stronger anion–MF interaction has an additional contribution in PC + MF.

Acknowledgments

We wish to acknowledge the financial support from the National Natural Science Foundation of China (Grant No. 29973009) and the Research Foundation of Ministry of Education of China.

References

1. J. Barthel and H.J. Gores. Pure Appl. Chem. **57**, 1071 (1985).
2. G.E. Blomgren. *In* Lithium batteries. *Edited by* J.P. Gabano. Academic Press, New York. 1983. Chap. 2.
3. J.O. Besenhard and G. Eivhinger. J. Electroanal. Chem. **68**, 1 (1976).
4. R. Zana, J.E. Desnoyers, G. Perron. R.L. Key, and K. Lee. J. Phys. Chem. **56**, 3996 (1982).
5. G. Perron, L. Couture, D. Lambert, and J.E. Desnoyer. J Electroanal. Chem. **355**, 277 (1993).
6. L. Couture, J.E. Desnoyers, and G. Perron. Can. J. Chem. **74**, 153 (1996)
7. D. Brouillette, G. Perron, and J.E. Desnoyers. J. Solution Chem. **27**, 151 (1998).
8. P. Atkins, G.T. Hefter, and P. Singh. J. Solution Chem. **20**, 1059 (1991).
9. R. Naejus, R. Coudert, P. Willmann, and D. Lemordant. Electrochimica Acta, **43**, 275 (1998).
10. E.A. Gomaa. Thermochim. Acta, **50**, 355 (1984).
11. K. Cedzynska, A.J. Parker, and P. Singh. J. Power Sources, **10**, 13 (1983).
12. Y. En-Eli, S.R. Thomas, and R. Chadha. Electrochim. Acta, **144**, 823 (1997).
13. V.R. Korch and J.H. Young. Science (Washington, D.C.), **204**, 499 (1979).
14. Y. Zhao, J. Wang, X. Xuan, and J. Lu. J. Chem. Eng. Data, **45**, 440 (2000**)**.
15. H. Reiss. Adv. Chem. Phys. **9**, 1 (1964).
16. F.H. Stillinger. J. Solution Chem. **2**, 141 (1973).
17. E. Glueckauf. Trans. Faraday Soc. **61**, 915 (1965).
18. F. Hirata and K. Arakawa. Bull. Chem. Soc. Jpn. **46**, 3367 (1973).
19. A. Bondi. J. Phys. Chem. **68**, 44 (1964).
20. D.P. Kharakoz. J. Solution Chem. **21**, 569 (1992).
21. M.R.J. Dack, K.J. Bird, and A.J. Parker. Aust. J. Chem. **28**, 955 (1975).
22. F.J. Millero. Chem. Rev. **71**, 147 (1971).
23. Y. Marcus. *In* Ion solvation. Wiley, New York. 1985.
24. V. Gutmann. *In* The donor–acceptor approach to molecular interactions. Plenum Press, New York. 1978.
25. X. Xuan, J. Wang, and J. Lu. Spectrochim. Acta, **A56**, 2131 (2000).
26. I.S. Perelygin and M.A. Klimchuk. Russ. J. Chem. **47**, 1138 (1973).
27. Y.M. Cahen, R.R. Handy, E.T. Roach, and A.I. Popov. J. Phys. Chem. **79**, 80 (1975).
28. S.Tobishima and A. Yamaji. Electrochim. Acta, **28**, 1067 (1983).
29. C.H. Hammonds and M.C. Day. J. Phys. Chem. **77**, 3089 (1973).
30. E. Plichta, M. Salomon, S. Slame, and M. Uchiyama. J. Solution. Chem. **16**, 225 (1987).
31. M. Salomon. J. Solution Chem. **22**, 715 (1993).

© 2002 NRC Canada

Effect of pH on the mechanism of OClO• oxidation of aromatic compounds

Doug Svenson, John F. Kadla, Hou-min Chang, and Hasan Jameel

Abstract: Contrary to previous reports, the reaction mechanism of chlorine dioxide (OClO•) with benzyl alcohols involves both radical cation and benzyl radical mechanisms dependent on pH. The primary reaction product between OClO• and 1-(3,4-dimethoxy-phenyl) ethanol at pH 8 is 3,4-dimethoxyacetophenone. At pH 4 no acetophenone was observed; the majority of the degradation products were chlorinated and aromatic ring-oxidized compounds. A primary kinetic isotope effect (k_H/k_D = 2.05) was observed in the reaction of OClO• with 1-(3,4-dimethoxy-phenyl)-(1-^{2}H) ethanol at pH 8, but was absent at pH 4 ($k_H/k_D \approx 1$). Similarly, the corresponding methyl ether (4-(1-methoxy)ethyl-1,2-dimethoxybenzene) was substantially less reactive at pH > 6. On the basis of these results, competing pH-dependent reaction mechanisms have been proposed, where at high pH OClO• reacts with benzyl alcohols via a OClO•–benzyl alcohol complex.

Key words: chlorine dioxide, mechanism, kinetic isotope effect, aromatic radical cation, benzyl radical.

Résumé : Contrairement à ce qui a été rapporté antérieurement, le mécanisme de réaction du dioxyde de chlore (OClO•) avec les alcools benzyliques varie avec le pH et il comporte des mécanismes avec cation radicalaire ainsi le radical benzyle. Le produit primaire de la réaction du OClO• et le 1-(3,4-diméthoxyphényl) éthanol à un pH de 8 est la 3,4-diméthoxyacétophénone. À un pH de 4, on n'observe aucune formation d'acétophénone; la majorité des produits de dégradation était formée de produits chlorés et de produits à noyau aromatique oxydé. On a observé un effet isotopique cinétique primaire (k_H/k_D = 2,05) dans la réaction du OClO• avec le 1-(3,4-diméthoxyphényl)-(1-^{2}H) éthanol, à un pH de 8, mais il est absent à un pH de 4 ($k_H/k_D \approx 1$). De la même manière, l'éther méthylique correspondant (4-(2-méthoxyéthyl)-1,2-diméthoxybenzène) est beaucoup moins réactif à des pH supérieurs à 6. Sur la base de ces résultats, on a proposé des mécanismes réactionnels en compétition qui dépendent du pH; à des pH élevés, les alcools benzyliques réagissent avec le OClO• par le biais d'un complexe OClO•–alcool benzylique.

Mots clés : dioxyde de chlore, mécanisme, effet isotopique cinétique, cation radicalaire aromatique, radical benzylique.

[Traduit par la Rédaction]

Introduction

The reactivity of chlorine dioxide (OClO•) is an area of intense research due to the environmental and industrial importance of this oxidant. Chlorine dioxide is extensively used in the bleaching of wood pulps in the manufacturing of paper (1–4), in food processing (5–9), and water purification (10–16). The mechanism of chlorine dioxide oxidation of aromatic compounds has been well documented (17–25). It is reported to involve two consecutive one-electron transfer processes leading to the formation of various oxidation and substitution products. The rate-determining step (RDS) is the formation of the intermediate aromatic radical cation (26), with concomitant formation of chlorite ($OClO^-$). A second molecule of OClO• rapidly reacts with the radical cation forming the corresponding chlorous ester that, depending on the point of substitution, leads to various oxidation and substitution products (18).

In addition to the radical cation mechanism, benzyl radical formation during OClO• oxidation of aromatic compounds has been proposed. Brage et al. (18) reported a diphenylmethane product from the reaction of OClO• with 2-methoxy-4-methylphenol, and suggested that a benzyl radical intermediate was involved. Similarly, studies with allylic structures and conjugated aromatics (e.g. styrene) undergo hydrogen atom extraction or electrophilic additions of OClO• to form allyl and benzyl radical intermediates, respectively (27, 28). Molecular orbital calculations for veratryl alcohol show that benzyl hydrogen atoms should be labile toward free-radical induced reactions in the presence of OClO• (29). This is determined by the ΔH_f calculation of a benzyl radical vs. an aromatic radical cation. Calculations indicate that the formation of a benzyl radical requires approximately 11.7 kcal mol^{-1} less energy than that of an aromatic radical cation. Moreover, the stability of the radical cation intermediate will be pH-dependent and decrease with increasing pH (30–32). It is therefore expected that a benzyl radical intermediate may be involved in the reaction of aromatic compounds; the role of which is dependent on the compound structure and reaction conditions.

Received 1 March 2002. Published on the NRC Research Press Web site at http://canjchem.nrc.ca on 12 June 2002.

D. Svenson, J.F. Kadla,[1] H.-m. Chang, and H. Jameel. College of Natural Resources, North Carolina State University, Raleigh, NC 27695-8005, U.S.A.

[1]Corresponding author (e-mail: jfkadla@ncsu.edu).

 DOI: 10.1139/V02-089 © 2002 NRC Canada

Table 1. Inorganic material balance after 60 min of reacting $OClO^{\bullet}$ with **1**. Reaction conditions: **1**–$OClO^{\bullet}$ (1:1 mol), temp = 25°C, $[\mathbf{1}]_o$ = 37.5 mM in HPLC-grade H_2O, constant pH.

	pH 4 (mol%)	pH 8 (mol%)
Cl^-	42 ± 5	17 ± 3
$OClO^-$	3 ± 1	48 ± 4
$OClO_2^-$	15 ± 3	16 ± 3
$OClO^{\bullet}$	—	18 ± 3
Cl_{org}	38 ± 4	—

Recently, Gunnarsson and Ljunggren (23) reported that in the reaction of $OClO^{\bullet}$ with 1-(3,4-dimethoxy-phenyl) ethanol the reaction rate and the products produced were dependent on the pH of the reaction system. Under acidic conditions (pH 2–4) various oxidation–substitution products were detected, whereas at mildly alkaline conditions (pH 8) the primary reaction product was 3,4-dimethoxy-acetophenone. Reaction mechanisms involving the initial formation of a radical cation intermediate were proposed. The oxidation and substitution at the benzyl carbon proceeded via a series of complex molecular rearrangements in which an initially formed aromatic radical cation is converted into an oxygen-centered radical (23). Based on the shift in oxidation product distribution over the pH range studied, we believe, however, that more than one oxidation mechanism may be taking place. In the present study, we investigate the reaction of benzyl alcohols with $OClO^{\bullet}$ and the effect of pH on the reaction mechanism.

Results and discussion

Effect of pH on the reaction of $OClO^{\bullet}$ with 1-(3,4-dimethoxyphenyl) ethanol

1-(3,4-Dimethoxyphenyl) ethanol (**1**) was reacted with equimolar amounts of $OClO^{\bullet}$ at 25°C and constant pH. The extent of the reaction increased with decreasing pH. At pH 8, ~25% of **1** was degraded after 60 min of reaction, compared with more than 80% at pH 4. The primary organic degradation product at pH 8 (>94%) was 3,4-dimethoxy-acetophenone (**4**), and the predominant inorganic product was chlorite ($OClO^-$). In fact, two equivalents of $OClO^-$ were generated for every equivalent of **1** reacted (Table 1). The large amount of $OClO^-$ produced and the decreased reactivity of **1** at pH 8 is consistent with the loss of oxidation power of the $OClO^{\bullet}$ system due to $OClO^-$ formation (33). The major remaining oxidation product at pH 8 (<6 mol%) was (2-methyl-6-oxo-6*H*-pyran-3-ylidene) acetic acid methyl ester (**5**). No chlorinated organic compounds were detected (34).

At pH 4, various oxidation–substitution products and chlorinated compounds were detected (Fig. 1), along with a large amount of chloride (Cl^-) ions (Table 1). At low pH, chloride ions arise from hypochlorous acid (HOCl) decomposition of chlorite (35). As illustrated in Scheme 1, aromatic ring oxidation–substitution via a radical cation intermediate generates one equivalent of chlorite and one equivalent of HOCl, which then rapidly reacts with $OClO^-$ to produce Cl^- according to eq. [1] (36–40).

[1] $$2OClO^- + HOCl \rightarrow 2OClO^{\bullet} + Cl^-$$

Fig. 1. Oxidation products identified from $OClO^{\bullet}$ reactions with **1** at pH 4 are (2-methyl-6-oxo-6*H*-pyran-3-ylidene) acetic acid methyl ester (**5**), 2-methoxy-1,4-benzoquinone (**6**), 4-chloro-1,2-dimethoxy-benzene (**7**), and 1-(2-chloro-4,5-dimethoxy-phenyl) ethanol (**8**).

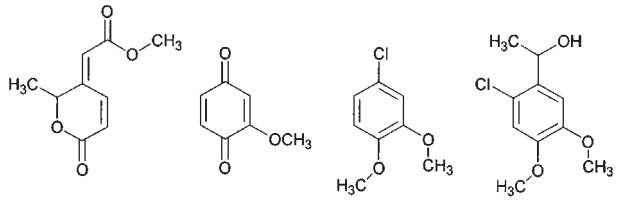

5 **6** **7** **8**

Scheme 1.

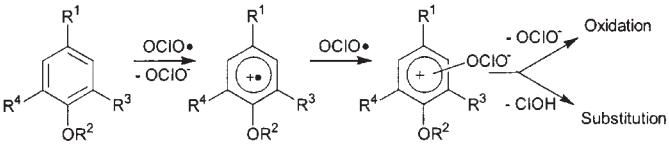

R^1, R^2 = alkyl
R^3, R^4 = alkyl, aryl, alkoxyl

HOCl is in equilibrium with elemental chlorine (Cl_2) through a hydrolysis reaction (eq. [2]):

[2] $$H^+ + Cl^- + HOCl \rightleftharpoons Cl_2 + H_2O$$

The rate of the hydrolysis is pH dependent, and increases with decreasing pH. The presence of Cl_2 explains the large amount of chlorinated organic products detected (**7**, **8**) at pH 4. In agreement with the findings of Gunnarsson and Ljunggren (23), aromatic oxidation (**5**, **6**) and chlorination (**7**, **8**) products dominate the reaction at lower pH. These products can be rationalized by a reaction mechanism involving a radical cation intermediate (Scheme 1). Likewise, the detection of **5** at pH 8 confirms the presence of a radical cation intermediate mechanism. The detection of **4**, with concurrent generation of 2 equivalents of $OClO^-$, which is consistent with two consecutive one-electron transfer reactions, suggests, however, the possibility of another mechanism, perhaps involving a benzyl radical. In the reactions of **1** with $OClO^{\bullet}$ at pH 8, Gunnarsson and Ljunggren (23) proposed a reaction mechanism in which an initially formed radical cation intermediate was converted into an oxygen-centered radical. This radical intermediate subsequently reacts with $OClO^{\bullet}$ to form a chlorate ester, followed by rearrangement to the acetophenone. No experimental evidence of an oxygen-centered radical was provided. The possibility of a benzyl radical intermediate was eliminated on the basis of reactions performed in the presence of $Br_2^{\bullet -}$ and oxygen. Based on the shift in oxidation-product distribution with increasing pH and the lack of substantial evidence that a benzyl radical is not involved, we believe that more than one oxidation mechanism is taking place. Scheme 2 depicts a competing pH-dependent reaction scheme for the production of the detected products from the reaction of $OClO^{\bullet}$ with **1**.

We propose that both a benzyl radical and an aromatic radical cation mechanism are taking place, with the extent of

© 2002 NRC Canada

Scheme 2.

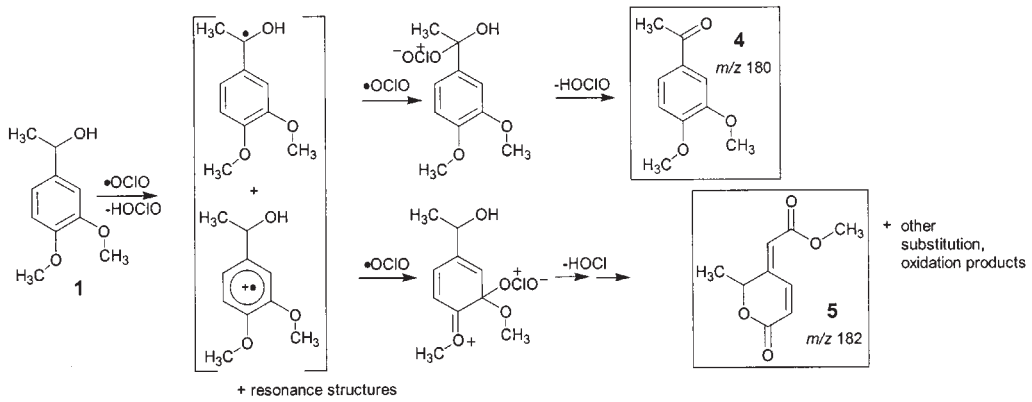

Scheme 3.

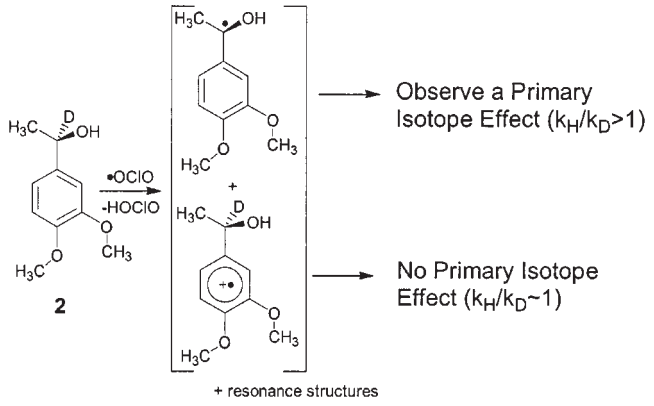

each mechanism determined by compound structure and reaction conditions (pH, solvent, etc.).

Fig. 2. Kinetic isotope effect for the reaction of OClO• and 1-(3,4-dimethoxy-phenyl) ethanol (◆) and 1-(3,4-dimethoxy-phenyl)-(1-^{2}H) ethanol (○). Pseudo-first-order reaction conditions: $[substrate]_o$ = 3 mM, $[OClO^•]_o$ = 100 mM, 25°C, pH 8, H_2O.

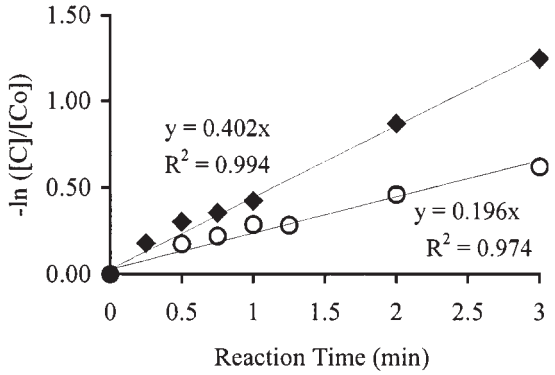

Investigation of a benzyl radical mechanism

A common method used to probe reaction mechanisms involves isotope labeling and the observance of an isotope effect (41). A primary isotope effect can be detected by kinetic measurements if the bond to the isotopically labeled atom is broken during the RDS. The presence (or absence) and the magnitude of such an effect can provide important information about the geometry of the transition state and its position along the reaction coordinate. The involvement of a benzyl radical intermediate in the OClO• oxidation of aromatic substrates was studied using deuterium-labeled 1-(3,4-dimethoxy-phenyl)-(1-^{2}H) ethanol (**2**). In this reaction system, the formation of an aromatic radical cation intermediate would not exhibit a primary isotope effect, whereas that involving a benzyl radical would (Scheme 3).

Under psuedo-first-order reaction conditions ($[substrate]_o$ = 3 mM, $[OClO^•]_o$ = 100 mM, 25°C), rate constants were determined for both **1** and **2** at pH 4 and pH 8. Figure 2 shows a plot of ln ([**1**]/[**1**]$_o$) and ln ([**2**]/[**2**]$_o$) vs time for the reactions run at pH 8. A primary kinetic isotope effect (k_H/k_D = 2.05) was observed in the reactions run at pH 8. No kinetic isotope effect was observed in the acidic media (pH 4, $k_H/k_D \approx 1$).

In a reaction system in which a three-bodied transition state (C···H···O) is linear, theory predicts $k_H/k_D \approx 1$ for reactions in which C–H cleavage occurs after the RDS and k_H/k_D = 6.9 for reactions in which C–H cleavage occurs before or during the RDS (42). Depending on the transition state, the value of k_H/k_D will vary. A maximum kinetic isotope effect (k_H/k_D = 6.9) will be observed when the transition state is symmetrical. Very exothermic or endothermic reactions (in which the transition state tends to occur early or late in the reaction coordinate, respectively) have smaller values of k_H/k_D (43). Accordingly, the results presented here indicate that in the reaction between OClO• and **1** at pH 8 the bond to the benzylic hydrogen is either only slightly or nearly completely broken at the transition state. That is, the transition state must occur quite close to the reactant or to the product.

To further investigate the reaction mechanism of OClO• at high pH, methyl ether 4-(1-methoxy)ethyl-1,2-dimethoxybenzene (**3**) was studied. At pH 8, the reaction between **3** and OClO• was extremely slow. The observed pseudo-first-order rate was more than an order of magnitude lower than that for the same reaction conditions with **1** (Table 2).

In a reaction mechanism involving an initial radical cation intermediate, methylation of the benzyl hydroxyl group should not affect the rate of the reaction, only the product distribution. The dramatic decrease in observed reaction rate, therefore, supports a benzyl radical mechanism. Moreover, these results indicate that the benzyl hydroxyl group is required to facilitate the oxidation.

© 2002 NRC Canada

Table 2. Pseudo-first-order rate constants for the reaction of $OClO^{\bullet}$ with various 1,2-dimethoxy-phenyl) ethanol derivatives.

Compound	pH	k (s^{-1})
1	8	0.402 ± 0.039
2	8	0.196 ± 0.015
3	8	0.029 ± 0.005

Chlorine dioxide has been reported to form complexes with various compounds. For example, $OClO^{\bullet}$ and $OClO^{-}$ form a well-characterized chlorine oxide association complex [$Cl_2O_4^-$] (44); H_2O–$OClO^{\bullet}$ complexes have also been well characterized (45, 46). It is therefore possible that $OClO^{\bullet}$ complexes react with the benzyl alcohol to form a chlorite ester as illustrated in Scheme 4. This association complex may lower the activation energy required for benzyl hydrogen atom removal, thus facilitating oxidation by a second $OClO^{\bullet}$ molecule.

This proposed reaction scheme would explain the small k_H/k_D (2.05), in which an asymmetrical transition state occurs. The RDS is the removal of the benzyl hydrogen atom.

Conclusions

Contrary to previous reports, the reaction mechanism of $OClO^{\bullet}$ with benzyl alcohols involves both radical cation and benzyl radical mechanisms. The rate and extent of each mechanism is dependent on the pH and the benzyl alcohol structure. The reaction rate decreases with increasing pH; at pH 8, the reaction of 1-(3,4-dimethoxyphenyl) ethanol is dramatically lower than at pH 4. Similarly, the reaction products are substantially different at pH 8 compared with those at pH 4. At pH 8 the primary product is 3,4-dimethoxyacetophenone, whereas at pH 4 no acetophenone was detected, and the majority of the degradation products were aromatic-ring oxidized and chlorinated compounds.

Methylation of the benzyl alcohol severely decreases the rate and extent of reaction with $OClO^{\bullet}$ at pH 8, indicating the involvement of the benzyl hydroxyl group in the reaction mechanism. Chlorine dioxide appears to react with benzyl alcohols via an association complex. These results, in combination with an observed kinetic isotope effect (k_H/k_D = 2.05), indicate a transition state in which complex formation likely lowers the energy required to remove the benzyl hydrogen atom thus facilitating oxidation. We therefore propose that two competing reaction mechanisms are taking place — at low pH a radical cation mechanism is involved in the rate-determining step, whereas at pH 8 a benzyl radical mechanism dominates.

Experimental

Materials

3,4-Dimethoxy acetophenone, sodium borohydride ($NaBH_4$), sodium borodeuteride ($NaBD_4$), *p*-dibromobenzene, biphenyl, and all solvents were purchase from Aldrich and used as received. Chlorine dioxide was produced by reacting 80% stabilized sodium chlorite (ACROS) with 1.5 equivalents of potassium persulfate (Fluka) in distilled water at room temperature. The resulting solution was stripped with UHP-nitrogen. Nitrogen gas containing

Scheme 4.

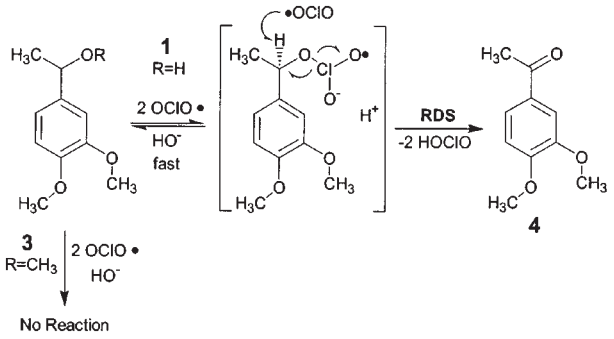

stripped chlorine dioxide was passed through a column of sodium chlorite (Aldrich), then scrubbed in cold HPLC water, and pH adjusted to 4 with 0.1% wt. aqueous sulfuric acid.

Compound synthesis

1-(3,4-Dimethoxyphenyl) ethanol (1)

1-(3,4-Dimethoxyphenyl) ethanol was prepared by reacting 3,4-dimethoxy acetophenone (**6**) with 2 equivalents of $NaBH_4$. The reaction was carried out in MeOH–H_2O (3:1) and heated at reflux for 3 h. The reaction mixture was neutralized with carbon dioxide, and extracted with 1,2-dichloroethane. A quantitative conversion of the acetophenone was obtained. ^{1}H NMR δ: 1.48 (d, 3H), 3.90 (d, 6H), 4.83 (q, 1H), 6.84 (q, 1H), 6.86 (q, 1H), 6.93 (d, 1H). MS *m*/*z* (%): 182 (M^+, 59), 167 (87), 153 (47), 139 (100), 124 (32), 108 (21), 93 (50), 77 (21), 65 (25), 51 (11), 43 (41).

1-(3,4-Dimethoxy-phenyl)-(1-^{2}H) ethanol (2)

1-(3,4-Dimethoxy-phenyl)-(1-^{2}H) ethanol was prepared similar to **1** using 1.5 equivalents of $NaBD_4$. ^{1}H NMR δ: 1.48 (d, 3H), 3.83 (d, 6H), 6.56 (q, 1H), 6.59 (q, 1H), 6.63 (d, 1H). MS *m*/*z* (%): 183 (M^+, 65), 168 (8), 167 (83), 151 (8), 139 (100), 124 (29), 108 (16), 95 (7), 79 (13), 77 (20), 43 (45).

4-(1-Methoxy)ethyl-1,2-dimethoxybenzene (3)

4-(1-Methoxy)ethyl-1,2-dimethoxybenzene (**3**) was quantitatively prepared by heating at reflux **1** in methanol with catalytic amounts of H_2SO_4 for 4 h. ^{1}H NMR: δ: 1.48 (d, 3H), 3.34 (s, 3H), 3.76 (s, 6H), 4.31 (s, 1H), 6.59 (d, 1H), 6.71 (d, 1H), 6.93 (m, 1H).

Reaction conditions

All reactions were run at 25 ± 1°C in a constant-temperature oil bath. The pH of the chlorine dioxide reactions was kept constant by using a pH-control feedback loop. Reactions were run in a 100-mL four-necked flask. An Omega™ pH controller (model PHCN-37) was connected to a Milton-Roy micro-chemical metering pump (model A771-155S). A sodium hydroxide solution (0.8 M) was delivered to the reaction vessel from a burette via Nalgene® PVC tubing. Volumetric addition of alkali did not exceed 1% of the total reaction volume. The reaction mixture was stirred with a Teflon-coated stir bar on a magnetic stir plate. Water and chlorine dioxide were pH adjusted using aqueous sodium

© 2002 NRC Canada

hydroxide (5 wt%) or sulfuric acid (5 wt%) to achieve a desired final pH and mixed for one minute prior to injection of an aqueous solution of the soluble model compound. Samples of the reaction were taken with a syringe through a rubber septum. In the kinetic experiments sampling was done every 15 s over the first few minutes, then at 2–5 min intervals over the next 30–60 min. The reaction was monitored until all of the model compound or chlorine dioxide was consumed.

Work-up procedures for the reaction mixtures

Organic compound concentrations were determined by gas chromatography. Samples (20 μL) of the reaction mixture were quenched either by adding ascorbic acid (0.5 mL, 0.4 M) or a saturated aqueous sodium thiosulfate solution (500 μL). The quenched samples were extracted with ethylacetate (0.5 mL) containing *p*-dibromobenzene or biphenyl (0.6 mg L^{-1}) as an internal standard. Thereafter, the samples were dried over anhydrous sodium sulfate and made up to 2 mL prior to GC analysis.

All compound analyses were carried out with a HP 5890 (splitless injection) instrument equipped with a flame ionization detector, using He as the carrier gas. Injector and detector temperatures were 240 and 280°C, respectively. Separations were achieved on a J&W DB-5 fused silica capillary column (30 m × 0.32 mm × 0.25 μm). Typical temperature programs were from 45 to 250°C at a rate of 10°C min^{-1} with an initial time delay of 1 min, and from 100 to 270°C at 10–20°C min^{-1}. In quantitative studies, *p*-dibromobenzene or biphenyl was used as an internal standard and the relative peak areas and corresponding response factors were used to calculate model-compound concentrations.

All GC–MS analyses were conducted as per GC analysis on a HP 5985B GC–MS, equipped with a DB-5 capillary column and using the same temperature program as per GC-analysis. In the EI mode, the electron energy used was 70 eV.

^{1}H NMR spectra were determined using a GE 300 MHz instrument. Samples were dissolved in $CDCl_3$. Chemical shifts are given in ppm downfield from TMS (tetramethylsilane).

Inorganic compound (chlorite, chlorate, and chloride) concentrations were measured using both a Waters Capillary Ion Analyzer (CIA) and iodometric titrations. A Waters AccuSep™ capillary (100 cm × 75 μm i.d.) and a chromate electrolyte were used for CIA analysis of anions. Chlorine dioxide concentrations were determined using a PerkinElmer UV/Vis spectrophotometer (model Lambda 3B) containing no organic compounds. The spectrometric wavelength was set at 380 nm (λ_{max} of ClO_2 = 357 nm) (17). In reactions containing organic compounds, chlorine dioxide was determined by iodometric titration.

The quantity of hypochlorous acid in a reaction medium was determined by trapping with aqueous solutions of dimethylsulfoxide (DMSO). Accordingly, samples (100 μL) of the reaction mixture were injected into cold aqueous solutions (0.5 mL) containing excess DMSO (0.25 M, pH adjusted to 8). Trapped samples were quenched after 15 s with a saturated sodium thiosulfate solution. The resulting dimethylsulfone content was determined by GC using cyclohexanol as an internal standard.

Reaction product characterization

3,4-Dimethoxyacetophenone (4)

^{1}H NMR: δ: 2.58 (s, 3H), 3.89 (s, 3H), 4.00 (s, 3H), 6.89 (d, 1H), 7.50 (d, 1H), 7.62 (m, 1H). MS *m*/*z* (%): 180 (M^+, 46), 165 (100), 137 (9), 122 (8), 107 (5), 77 (12), 43 (9).

(2-Methyl-6-oxo-6H-pyran-3-ylidene) acetic acid methyl ester (5)

^{1}H NMR δ: 1.57 (d, 3H), 3.76 (s, 3H), 5.21 (m, 1H), 5.89 (m, 1H), 6.21 (m, 1H), 8.2 (m, 1H). MS *m*/*z* (%): 182 (M^+, 1), 167 (8), 151 (7), 150 (8), 139 (57), 138 (79), 108 (43), 95 (17), 80 (24), 79 (47), 51 (46), 43 (100).

2-Methoxy-[1,4]-benzoquinone (6)

^{1}H NMR: δ: 3.56 (s, 3H), 5.71 (d, 1H), 6.78 (m, 2H). MS *m*/*z* (%): 138 (M^+, 44), 123 (8), 110 (33), 108 (47), 85 (27), 82 (28), 79 (13), 69 (100), 54 (42), 53 (43), 39 (23), 18 (17).

4-Chloro-1,2-dimethoxy-benzene (7)

^{1}H NMR δ: 3.89 (s, 3H), 4.00 (s, 3H), 6.60 (d, 1H), 6.67 (d, 1H), 6.72 (m, 1H). MS *m*/*z* (%): 174 ($[M + 2]^+$, 28), 172 (M^+, 100), 159 (19), 157 (55), 129 (29), 111 (19), 107 (8), 93 (35), 79 (29), 65 (36), 51 (25), 43 (10).

1-(2-Chloro-4,5-dimethoxy-phenyl) ethanol (8)

^{1}H NMR δ: 1.47 (d, 3H), 3.76 (d, 6H), 4.68 (q, 1H), 6.51 (s, 1H), 6.58 (s, 1H). MS *m*/*z* (%): 218 ($[M + 2]^+$, 14), 216 (M^+, 51), 203 (35), 201 (100), 173 (19), 158 (12), 138 (81), 100 (9), 77 (22), 43 (54).

References

1. H. Rapson, C.B. Anderson, and D. Reeve. Pulp Pap.-Can. **78**, 111 (1977).
2. D.W. Reeve and W.H. Rapson. Pulp Pap.-Can. **82**, 123 (1981).
3. D. Lachenal, M.J. Joncourt, P. Froment, and C. Chirat. J. Pulp Pap. Sci. **24**, 14 (1998).
4. Y. Ni, G.J. Kubes, and A.R.P. Vanheiningen. J. Pulp Pap. Sci. **20**, J103 (1994).
5. C.I. Wei, W.S. Otwell, and M.R. Marshall. Abstr. Pap. Am. Chem. Soc. **211**, 42 (1996).
6. C.N. Cutter and W.J. Dorsa. J. Food Prot. **58**, 1294 (1995).
7. S. Zhang and J.M. Farber. Food Microbiol. **13**, 311 (1996).
8. C. Komosuwelack, L. Acker, and E. Schulte. Z. Lebensm. Unters. For. **176**, 285 (1983).
9. C. Komosuwelack, E. Schulte, and L. Acker. Z. Lebensm. Unters. For. **176**, 173 (1983).
10. A.D. Andreadakis, G.H. Kristensen, A. Papadopoulos, and C. Oikonomopoulos. Water Sci. Technol. **32**, 75 (1995).
11. G. Gordon, B. Slootmaekers, S. Tachiyashiki, and D.W. Wood. J. Am. Water Work Assoc. **82**, 160 (1990).
12. G. Gordon and B. Bubnis. Prog. Nucl. Energy, **37**, 37 (2000).
13. M.H. Griese, J.J. Kaczur, and G. Gordon. J. Am. Water Work Assoc. **84**, 69 (1992).
14. E. Hamilton, D.V. Seal, and J. Hay. J. Hosp. Infect. **32**, 156 (1996).
15. C. Morissette, M. Prevost, and B. Langlais. J. Water Supply Res. Technol. Aqua, **45**, 232 (1996).

© 2002 NRC Canada

16. F. Zanetti, S. Stampi, G. DeLuca, O. Varoli, and E. Tonelli. Zbl. Hyg. Umweltmed. **198**, 567 (1996).
17. E. Grimley and G. Gordon. J. Inorg. Nucl. Chem. **35**, 2383 (1973).
18. C. Brage, T. Eriksson, and J. Gierer. Holzforschung, **45**, 23 (1991).
19. J. Hoigne and H. Bader. Water Res. **28**, 45 (1994).
20. Y. Ni, X. Shen, and A.R.P. Vanheiningen. J. Wood Chem. Technol. **14**, 243 (1994).
21. C. Brage, T. Eriksson, and J. Gierer. Holzforschung, **49**, 127 (1995).
22. G. Gellerstedt, E.L. Lindfors, M. Pettersson, and D. Robert. Res. Chem. Intermed. **21**, 441 (1995).
23. N.P.I. Gunnarsson and S.C.H. Ljunggren. Acta Chem. Scand. **50**, 422 (1996).
24. P.S. Rajan, C.L. Chen, and J.S. Gratzl. Holzforschung, **50**, 165 (1996).
25. M.J. Joncourt, P. Froment, and D. Lachenal. J. Wood Chem. Technol. **18**, 159 (1998).
26. J. Fossey, D. Lefort, and J. Sorba, *In* Free radicals in organic chemistry. Vol. X. *Edited by* Wiley, New York. 1995.
27. J.J. Kolar and B.O. Lindgren. **36**, 599 (1982).
28. B.O. Lindgren and C.M. Svahn. Acta Chem. Scand. **20**, 211 (1966).
29. T. Elder. Holzforschung, **51**, 47 (1997).
30. A. Ronlan, J. Coleman, O. Hammeric, and V.D. Parker. J. Am. Chem. Soc. **96**, 845 (1974).
31. F.G. Bordwell and J.P. Cheng. J. Am. Chem. Soc. **111**, 1792 (1989).
32. G.T.R. Palmore, D.K. Smith, and M.S. Wrighton. J. Phys. Chem. B, **101**, 2437 (1997).
33. W.H. Rapson and C.B. Anderson. **61**, 97 (1978).
34. D. Svenson. Ph.D. thesis. North Carolina State University, Releigh, North Carolina. 2001.
35. J.J. Kolar, B.O. Lindgren, and B. Pettersson. Wood Sci. Technol. **17**, 117 (1983).
36. H. Dodgen and H. Taube. J. Am. Chem. Soc. **71**, 2501 (1949).
37. H. Taube and H. Dodgen. J. Am. Chem. Soc. **71**, 3330 (1949).
38. F. Emmenegg and G. Gordon. Inorg. Chem. **6**, 633 (1967).
39. G. Gordon and S. Tachiyashiki. Environ. Sci. Technol. **25**, 468 (1991).
40. V. Csordas, B. Bubnis, I. Fabian, and G. Gordon. Inorg. Chem. **40**, 1833 (2001).
41. H. Zollinger. **2**, 163 (1964).
42. F.H. Westheimer. Chem. Rev. **61**, 265 (1961).
43. R.B. Timmons, J. Deguzman, and R.E. Varnerin. J. Am. Chem. Soc. **90**, 5996 (1968).
44. G. Gordon and F. Emmenegger. Inorg. Nucl. Chem. Letters, **6**, 395 (1966).
45. V. Vaida, E.C. Richard, A. Jefferson, L.A. Cooper, R. Flesch, and E. Ruhl. Ber. Bunsen-Ges. Phys. Chem. **96**, 391 (1992).
46. S. Aloisio and J.S. Francisco. Chem. Phys. **254**, 1 (2000).

© 2002 NRC Canada

On the temperature dependence of the primary yield and the product $G\varepsilon_{max}$ of hydrated electrons in the low-LET radiolysis of liquid water

Jintana Meesungnoen, Jean-Paul Jay-Gerin, Abdelali Filali-Mouhim, and Samlee Mankhetkorn

Abstract: Monte-Carlo simulations are performed to calculate the temperature dependence of the primary hydrated electron yield ($G_{e^-_{aq}}$) for liquid water irradiated by low linear-energy-transfer radiation (LET ~ 0.3 keV μm^{-1}) in the range 25–325°C. Calculations are carried out by taking properly into account the effect of the time and temperature dependencies of the water dielectric constant on the electron–cation geminate recombination. Our computed $G_{e^-_{aq}}$ values slightly increase with increasing temperature, in good agreement with experiment. The product $G_{e^-_{aq}}\varepsilon_{max}(e^-_{aq})$, estimated by using existing experimental data of the maximum molar extinction coefficient $\varepsilon_{max}(e^-_{aq})$, remains nearly constant or slightly increases, depending on the temperature dependence chosen for ε_{max}. Our $G_{e^-_{aq}}\varepsilon_{max}(e^-_{aq})$ values compare generally well with most experimental data, as well as with the predictions of deterministic diffusion-kinetic model calculations. Moreover, our results indicate that the static dielectric constant of water (ε_s) does not play any significant role on the electron–cation recombination at early times. Such a finding is inconsistent with the interpretation, proposed by certain authors in the literature, that $G_{e^-_{aq}}$ should in fact decrease as temperature is increased because of an increased electron–cation geminate recombination due to a lowering of ε_s. Finally, the temperature dependence of the hydrated electron yields, calculated at various times between 10 ps and 1 μs, shows that at low LET, the time required to establish homogeneous chemistry in the bulk of the solution is ~10^{-6} s in the range ~25–100°C, and that this time diminishes to ~10^{-7} s at higher temperatures.

Key words: liquid water, radiolysis, temperature, hydrated electron (e^-_{aq}), radiolytic yields, electron–cation geminate recombination, dielectric constant, molar extinction coefficient of e^-_{aq}, homogenization time.

Résumé : À l'aide des méthodes de simulation Monte-Carlo, nous calculons la dépendance en température du rendement primaire en électrons hydratés ($G_{e^-_{aq}}$) produit lors de la radiolyse de l'eau liquide par un rayonnement de faible transfert d'énergie linéique (TEL ~ 0,3 keV μm^{-1}) dans la gamme 25–325°C. Les calculs sont effectués en prenant convenablement en compte l'effet des variations de la constante diélectrique de l'eau en fonction du temps et de la température sur la recombinaison géminée électron-cation. Les valeurs de $G_{e^-_{aq}}$ ainsi calculées augmentent légèrement avec la température, en bon accord avec l'expérience. Le produit $G_{e^-_{aq}}\varepsilon_{max}(e^-_{aq})$, estimé à partir de nos valeurs de $G_{e^-_{aq}}$ et des données expérimentales disponibles du coefficient d'extinction molaire maximal $\varepsilon_{max}(e^-_{aq})$, reste sensiblement constant ou augmente légèrement, dépendant du choix adopté pour la dépendance en température de ε_{max}. Nos valeurs de $G_{e^-_{aq}}\varepsilon_{max}(e^-_{aq})$ s'accordent bien en général avec la plupart des données expérimentales, ainsi qu'avec les prédictions de calculs modèles diffusionnels déterministes. De plus, nos calculs indiquent que la constante diélectrique statique (ε_s) de l'eau ne joue pas de rôle significatif sur la recombinaison électron-cation à temps court. Un tel résultat contredit l'interprétation, proposée par certains auteurs dans la littérature, que $G_{e^-_{aq}}$ devrait en fait décroître lorsque la température augmente à cause d'une recombinaison géminée électron-cation augmentée due à une diminution de ε_s. Enfin, la dépendance en température du rendement en électrons hydratés, calculée à différents temps entre 10 ps et 1 μs, suggère qu'à faible TEL, le temps au bout duquel le stade de chimie homogène s'établit au sein de la solution est de ~10^{-6} s dans la gamme ~25–100°C, et que ce temps diminue à ~10^{-7} s aux températures plus élevées.

Mots clés : eau liquide, radiolyse, température, électron hydraté (e^-_{aq}), rendements radiolytiques, recombinaison géminée électron-cation, constante diélectrique, coefficient d'extinction molaire de e^-_{aq}, durée de l'étape hétérogène.

Received 27 February 2002. Published on the NRC Research Press Web site at http://canjchem.nrc.ca on 18 June 2002.

J. Meesungnoen, J.-P. Jay-Gerin,[1] and A. Filali-Mouhim. Département de médecine nucléaire et de radiobiologie, Faculté de médecine, Université de Sherbrooke, Sherbrooke, QC J1H 5N4, Canada.
J. Meesungnoen and S. Mankhetkorn. Laboratory of Physical Chemistry, Molecular and Cellular Biology, Faculty of Science, Burapha University, Bangsaen, Chonburi 20131, Thailand.

[1]Corresponding author (e-mail: jaygerin@courrier.usherb.ca).

 DOI: 10.1139/V02-088 © 2002 NRC Canada

Introduction

Recently, Wu et al. (1) reported the temperature dependence of the product $G_{e^-_{aq}}\varepsilon_{max}(e^-_{aq})$, where $G_{e^-_{aq}}$ is the "primary" yield[2] and ε_{max} is the maximum molar extinction coefficient of the hydrated electron (e^-_{aq}), in light and heavy liquid water over the range 25–400°C, including the supercritical water regime. Using pulse-radiolysis experiments with 100-ns electron pulses, these authors observed that $G_{e^-_{aq}}\varepsilon_{max}(e^-_{aq})$ continuously decreases with increasing temperature above ~100°C, going from ~0.55×10^5 to ~0.1×10^5 (molec./100 eV) × (M^{-1} cm^{-1}) for D_2O between 100 and 400°C.[3] Wu et al. (1) argued that such a decrease of $G_{e^-_{aq}}\varepsilon_{max}(e^-_{aq})$ at high temperatures may result from an increased electron–cation geminate recombination due to the decrease of the static dielectric constant (ε_s) of water with increasing temperature (ε_s goes from ~79 at 25°C, density 1 g cm^{-3} to ~8 at 400°C, density 0.45 g cm^{-3}). These results are consistent with those measured by Dixon and Lopata (3), but in disagreement with most other experimental data (4–8), which show that $G_{e^-_{aq}}\varepsilon_{max}(e^-_{aq})$ is nearly constant or even slightly increases with increasing temperature (Fig. 1).

From their pulse-radiolysis experiments performed in alkaline solutions under hydrogen pressure, Christensen and Sehested (6) concluded that most of the increase of $G_{e^-_{aq}}\varepsilon_{max}(e^-_{aq})$ should be ascribed to an increase in ε_{max} rather than to an increase in $G_{e^-_{aq}}$. In contrast, Elliot et al. (9, 10) found for light and heavy liquid water that $\varepsilon_{max}(e^-_{aq})$ decreases linearly with increasing temperature up to 200°C, which is in agreement with the work of Shiraishi et al. (11), who estimated $\varepsilon_{max}(e^-_{aq})$ values for H_2O of 2.0×10^4 and 1.7×10^4 M^{-1} cm^{-1} at 25 and 200°C, respectively. In previous studies using γ-rays and dilute solutions of various scavengers, Burns and Marsh (12) found that $G_{e^-_{aq}}$ decreased from 2.7 molec./100 eV at ambient temperature to 0.4 ± 0.1 molec./100 eV at 400°C and density 0.45 g cm^{-3}. These authors argued that such a decrease of $G_{e^-_{aq}}$ with temperature was consistent with the low-static dielectric constant of water at high temperature, compared with its value at 25°C. This result, however, is markedly different from those of our previous Monte-Carlo simulations of water radiolysis (13) and also of the deterministic diffusion–kinetic model calculations of Swiatla-Wojcik and Buxton (14), which only show a slight increase of $G_{e^-_{aq}}$ with increasing temperature up to 300°C.

To gain further insights into the influence of temperature (in the range 25–325°C) on $G_{e^-_{aq}}$ and $G_{e^-_{aq}}\varepsilon_{max}(e^-_{aq})$, we extend in this work our previous Monte-Carlo calculations (13) of the temperature dependence of $G_{e^-_{aq}}$ to properly take into account the effect of the time and temperature dependencies of the water dielectric constant on the early time electron–cation recombination. Values of $G_{e^-_{aq}}\varepsilon_{max}(e^-_{aq})$ are calculated by using our computed $G_{e^-_{aq}}$ values and the temperature dependence of $\varepsilon_{max}(e^-_{aq})$ reported by Elliot et al. (9, 10) and that estimated from the data of Shiraishi et al. (7). Finally, we compare our values of $G_{e^-_{aq}}\varepsilon_{max}(e^-_{aq})$ with available experimental data, as well as with the predictions of previous deterministic diffusion–kinetic calculations.

Fig. 1. Effect of temperature on the product $G_{e^-_{aq}}\varepsilon_{max}$ [in (molec./100 eV) × (M^{-1} cm^{-1})] of hydrated electrons. The solid and dashed curves represent the values of $G_{e^-_{aq}}\varepsilon_{max}(e^-_{aq})$ obtained for light water, from our computed $G_{e^-_{aq}}$ values at 10^{-7} s, using the $\varepsilon_{max}(e^-_{aq})$ values of Elliot and Ouellette (eq. [I] of ref. 9, revised upward by 4.6% as described in ref. 10, and linearly extrapolated to 325°C) and those estimated from the data of Shiraishi et al. (7), respectively (see text). Experiments are from ref. 1: (●), H_2O and (○), D_2O; ref. 3: (▽), D_2O; ref. 4: (▲), H_2O and (△), D_2O; ref. 5: (■), H_2O; ref. 6: (◆), H_2O (alkaline solutions under hydrogen pressure); ref. 7: (▶), H_2O; ref. 8: (★), H_2O. For the sake of comparison, the products $G_{e^-_{aq}}\varepsilon_{max}(e^-_{aq})$ obtained from the deterministic diffusion-kinetic model calculations of $G_{e^-_{aq}}$ of Swiatla-Wojcik and Buxton for H_2O (– -- – -- –) (14) and D_2O (------) (45), using $\varepsilon_{max}(e^-_{aq})$ from Elliot and Ouellette (eq. [I] of ref. 9, revised as described in ref. 10, and linearly extrapolated to 300°C) and Elliot et al. (eq. [I] of ref. 10), respectively, are also included.

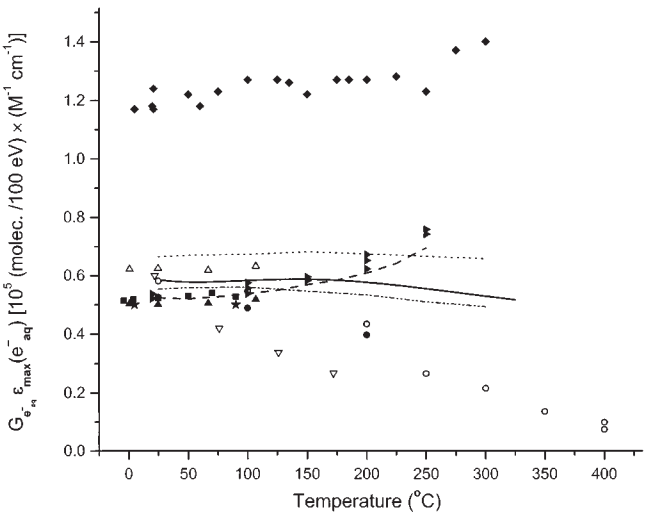

Monte-Carlo simulations

A detailed description of our Monte-Carlo modeling of the radiolysis of liquid water has been given previously (13, 15–18). In brief, the energy deposition by the incident radiation (high-energy protons) and by all the low-energy electrons (collectively named "secondary electrons") that it has generated occurs through the slowing down of those particles via various inelastic scattering processes, such as ionization, electronic and (or) vibrational excitation of single water molecules, and excitation of plasmon-type collective modes ("physical stage"). The species created during this stage rapidly reorganize and produce the "initial" radical (e^-_{aq}, $H^•$, $^•OH$, $HO^•_2/O^{•-}_2$) and molecular (H_2, H_2O_2) products of the radiolysis, distributed in a highly non-homogeneous

[2] The so-called "primary" (or "escaped") e^-_{aq} yield, denoted here $G_{e^-_{aq}}$, represents the number of hydrated electrons formed per 100 eV of absorbed energy that remain after spur expansion is complete. See, for example, ref. 2.

[3] The units for the radiation chemical yields used throughout in this paper are molecules per 100 eV (molec./100 eV). For conversion into SI units: 1 molec./100 eV ≈ 1.0364×10^{-7} mol J^{-1}. As for the maximum molar extinction coefficient $\varepsilon_{max}(e^-_{aq})$, the units used here are M^{-1} cm^{-1}.

© 2002 NRC Canada

track structure composed of small, spatially isolated regions of high ionization and excitation densities, commonly referred to as "spurs" ("physicochemical stage"). These two stages are handled by our simulation codes TRACPRO and TRACELE (16). The complex spatial distribution of reactants at ~10^{-13} s, which is provided as an output of the program TRACELE, is then used directly as the starting point for the so-called "stage of non-homogeneous chemistry." This third and final stage, during which the various species diffuse and react with one another until all spur reactions are complete, is covered by our TRACIRT simulation code (13, 15, 17, 18), using the "independent reaction times" (IRT) method (19) to model the non-homogeneous reaction kinetics.[4]

To reproduce the effects of ^{60}Co γ-rays or fast electrons, we use short (100-μm) segments of one hundred fifty 300-MeV proton tracks, over which the average linear-energy-transfer (LET) value obtained in the simulations is ~0.3 keV μm^{-1} at 25°C.[5] As for the calculation of $G_{e^-_{aq}}$ as a function of temperature, we use here an extended version of our computer code, which has recently been developed to include the effects of high temperature on water radiolysis (13). In this version, the thermalization distances (r_{th}) of subexcitation electrons[6] are assumed to decrease linearly with increasing temperature by a factor of 2 between 25 and 300°C (13). This choice was shown to offer the best agreement of $G_{e^-_{aq}}$ and G_{H_2} with experimental data at elevated temperatures in the case of low-LET radiation (13). Physically, such a decrease in r_{th} as the temperature increases[7] could be linked to an increase in the low-energy electron-scattering cross sections, which arise from the corresponding loss of structural order in liquid water owing to the increase in breaking of hydrogen bonds with temperature.

In the course of its thermalization, a subexcitation electron can encounter its geminate H_2O^+ partner and recombine to form H_2O^* (16).[8] To account for the effect of the Coulomb field of the geminate positive charge on the early time electron–cation recombination (22), we use in our simulations the following form for the time-dependent water dielectric constant ε(t) (23)

$$[1] \qquad \frac{1}{\varepsilon} = \frac{1}{\varepsilon_s} + \left(\frac{1}{\varepsilon_\infty} - \frac{1}{\varepsilon_s}\right) \exp\left(\frac{-t}{\tau_L}\right)$$

where ε_s and ε_∞ are the static (long-time) and high-frequency (short-time) dielectric constants, respectively, $\tau_L = (\varepsilon_\infty/\varepsilon_s)\tau_D$ is the longitudinal dielectric relaxation time, and τ_D is the Debye relaxation time. The temperature dependencies for ε_s and τ_D up to 325°C are described by polynomial and exponential fits to available experimental data (24–33), as shown in Figs. 2*a* and 2*c*, respectively. For ε_∞, whose data are rather scattered below 50°C and scarce at higher temperatures (24, 32), we assume the linear temperature dependence empirically described by Kaatze (24) between – 4.1 and 60°C, namely,

$$[2] \qquad \varepsilon_\infty = 5.77 - 2.74 \times 10^{-2}(T - 273.15)$$

where T is the absolute temperature in degrees Kelvin. In the model adopted here (34), this line (eq. [2]) is extrapolated to higher temperatures until it connects to $\varepsilon_\infty = 1$, and afterwards ε_∞ is assumed to remain constant at 1 up to 325°C (Fig. 2*b*).

Results and discussion

The results of the temperature dependence of our $G_{e^-_{aq}}$ values, computed at 10^{-7} s after the ionizing event,[9] are shown in Fig. 3. As can be seen, $G_{e^-_{aq}}$ increases with increasing temperature, going from ~2.8 molec./100 eV at 25°C to ~3.7 molec./100 eV at 325°C. Good overall agreement is observed with most available experimental data (7, 11, 35, 37–43), as well as with the predictions of the deterministic-spur diffusion-model calculations of Swiatla-Wojcik and Buxton (14). In fact, such an increase of $G_{e^-_{aq}}$ with temperature can readily be explained from the fact that many important spur reactions are not diffusion controlled and therefore have rate constants that increase less steeply with temperature than do the diffusion coefficients of the individual species; under those conditions, these reactions occur less as the temperature increases, which leads to more hydrated electrons being available to escape the spurs (13, 44). Our computed yields, however, are markedly different from the data of Burns and Marsh (12), who, as mentioned above, reported a dramatic decrease of $G_{e^-_{aq}}$ at 400°C.

The effect of temperature on the product $G_{e^-_{aq}}\varepsilon_{max}(e^-_{aq})$ can readily be obtained from our $G_{e^-_{aq}}$ values at 10^{-7} s and by using the values of $\varepsilon_{max}(e^-_{aq})$ reported by Elliot et al. (9, 10) and those estimated from the data of Shiraishi et al. (7). As far as the latter authors are concerned, they in fact measured

[4] The IRT simulation methodology has the advantage over deterministic-modeling calculations in that, instead of using the "typical, average spur" concept, it correctly incorporates reactants from the same ionization or excitation in their actual non-homogeneous spatial distribution. See, for example, refs. 14 and 20.

[5] Typically, about 5000 species are produced in those simulated track segments, thus ensuring only small statistical fluctuations in the determination of average yields.

[6] Subexcitation electrons are those that have kinetic energies lower than the first-electronic excitation threshold of the medium (~7.3 eV in liquid water) (21). They lose energy relatively slowly, the dominant mode of energy loss being the excitation of molecular vibrations.

[7] At 25°C, our calculated mean electron thermalization distance, averaged over the energy spectrum of the subexcitation electrons ("entry spectrum") (22), is ~88 Å, whereas at 325°C it is taken to be ~40 Å.

[8] Our simulations show that only electrons whose energy is below the subexcitation energy limit have an appreciable probability to recombine with their parent water cation prior to thermalization (22). In fact, the electrons that recombine tend to be the ones that, in the absence of cation, would thermalize relatively close to their starting position.

[9] Consistently with our previous Monte-Carlo simulations of the radiolysis of liquid water at elevated temperatures (13), the time scale of 10^{-7} s is chosen in accordance with the scavenging powers of solutes used by Elliot et al. (35) to measure their yields. Recall that the "scavenging power" is defined as the product of a solute (or scavenger) concentration and its rate constant for the scavenging reaction (k[S]), with units of s^{-1}. The reciprocal of the scavenging power gives a measure of the time scale over which the scavenging is occurring. See, for example, ref. 36.

© 2002 NRC Canada

Fig. 2. Temperature dependencies of the static (ε_s) and high-frequency (ε_∞) dielectric constants, and the Debye relaxation time (τ_D) of liquid water. (*a*) The solid line is a polynomial fit to the available experimental data of ε_s. Experiments for ε_s are from ref. 24: (■); ref. 25: (+); ref. 26: (○); ref. 27: (×); ref. 28: (△). (*b*) The solid line represents ε_∞ from eq. [2] up to 60°C, as described by Kaatze (24). The dotted line denotes the curve extrapolated so that it connects to $\varepsilon_\infty = 1$ and remains constant at this value at higher temperatures (34). Experiments for ε_∞ are from ref. 24: (▲); ref. 32: (*). (*c*) The solid line is a third-order exponential decay fit to the available experimental data of τ_D. Experiments for τ_D are from ref. 24: (□); ref. 29: (●); ref. 30: (△); ref. 31: (◆); ref. 32: (▶); ref. 33: (◁).

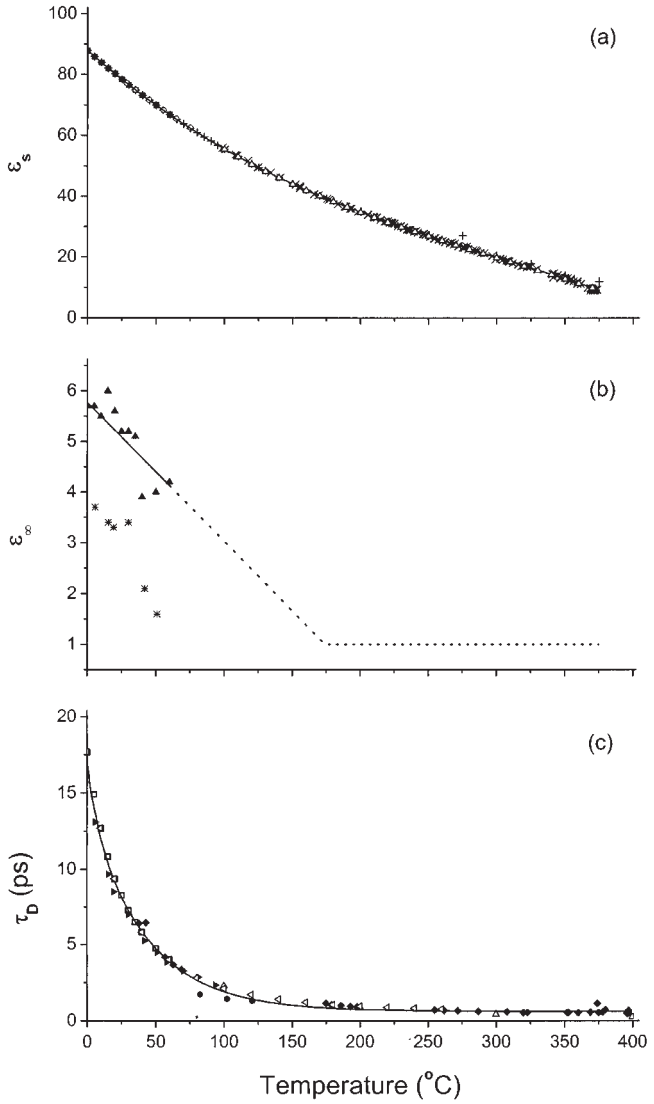

$G(e^-_{aq})\,\varepsilon_{max}(e^-_{aq})$ at 5 ns as a function of temperature between 20 and 250°C (7).[10] Here, $\varepsilon_{max}(e^-_{aq})$ is estimated from these $G(e^-_{aq})\,\varepsilon_{max}(e^-_{aq})$ values by using our values of $G(e^-_{aq})$ computed at 5 ns and by assuming that $\varepsilon_{max}(e^-_{aq})$ does not change as a function of time. The corresponding plots of $\varepsilon_{max}(e^-_{aq})$ against temperature obtained from the data of these two groups are shown in Fig. 4. Using the $\varepsilon_{max}(e^-_{aq})$ values of

Fig. 3. Temperature dependence of the primary hydrated-electron yield ($G_{e^-_{aq}}$, in molec./100 eV) of the radiolysis of liquid water, over the range 25–325°C. The solid curve represents our Monte-Carlo calculations at 10^{-7} s (see text). Experiments are from ref. 7: (★); ref. 11: (■); ref. 12: (◇); ref. 35: (▽); ref. 37: (×); ref. 38: (*); ref. 39: (◀); ref. 40: (▲); ref. 41: (◁); ref. 42: (○); ref. 43: (●). For the sake of comparison, the deterministic spur diffusion model calculations of $G_{e^-_{aq}}$ (– – – -) from ref. 14 are also included.

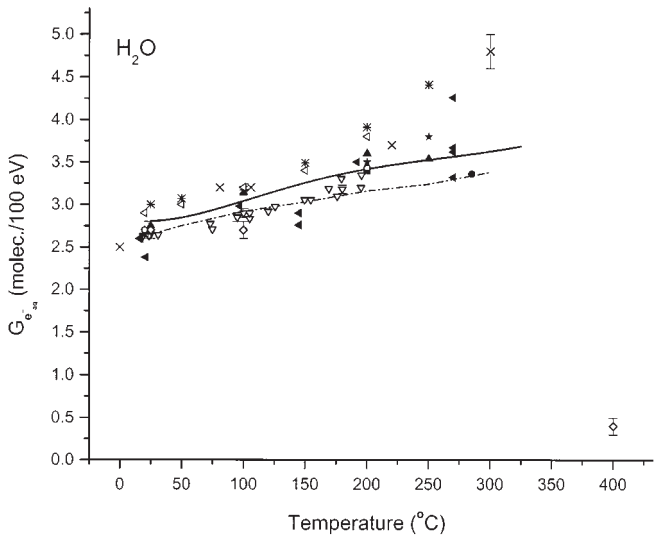

Fig. 4. Plots of the maximum molar extinction coefficient of the hydrated electron $\varepsilon_{max}(e^-_{aq})$ vs. temperature. The solid line represents $\varepsilon_{max}(e^-_{aq})$ obtained by Elliot and Ouellette (eq. [I] of ref. 9, revised upward by 4.6% as described in ref. 10, and linearly extrapolated to 325°C). The dashed line represents a polynomial fit to the data of $\varepsilon_{max}(e^-_{aq})$ (■) obtained by using the measured values of the product $G(e^-_{aq})\,\varepsilon_{max}(e^-_{aq})$ at 5 ns of Shiraishi et al. (7) and our computed values of $G(e^-_{aq})$ at 5 ns (see text).

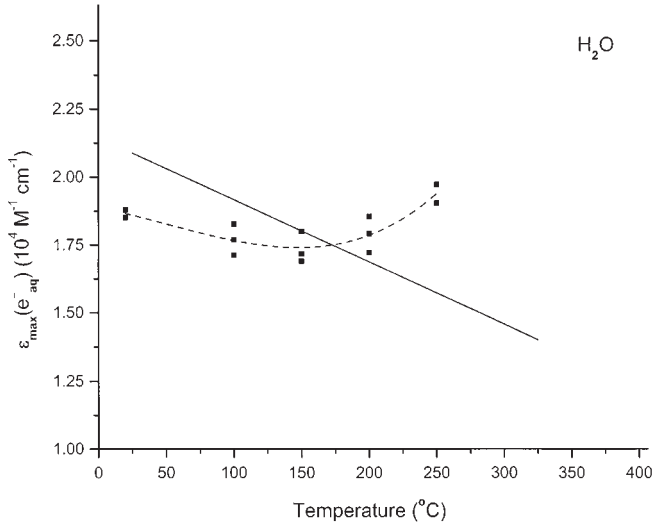

Elliot et al. (9, 10), which decrease linearly with increasing temperature, $G_{e^-_{aq}}\,\varepsilon_{max}(e^-_{aq})$ is found to be nearly constant below ~150°C and to slightly decrease at higher temperatures

[10]The symbol $G(e^-_{aq})$ is used in this paper for the yield of hydrated electrons measured or calculated at any specific time.

© 2002 NRC Canada

Fig. 5. Time dependence of the water dielectric constant $\varepsilon(t)$ computed from eq. [1] (23) using ε_s, ε_∞, and τ_D as described in Fig. 2, at 25, 100, and 300°C. At 25°C, for the sake of comparison of the various time scales involved, the electron thermalization time (obtained from our calculations), as well as the corresponding electron "trapping" and "hydration" times (46), are also indicated on the figure by arrows labelled e^-_{th} (thermalized electron), e^-_{tr} (trapped electron), and e^-_{aq} (hydrated electron), respectively. Note that geminate electron–cation recombination occurs before thermalization is complete (see ref. 22).

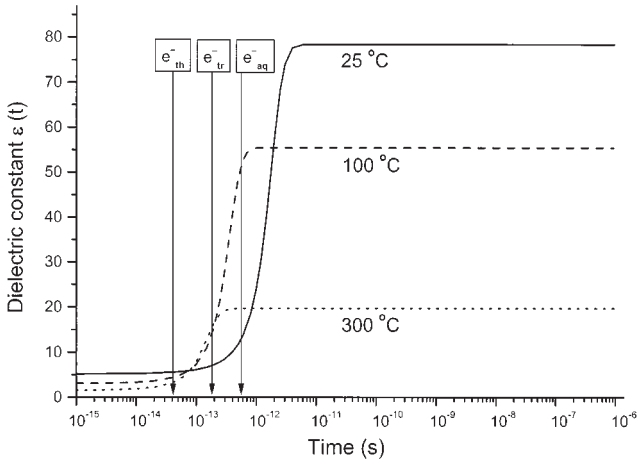

Fig. 6. Temperature dependencies of the hydrated electron yields $G(e^-_{aq})$ (in molec./100 eV) calculated from our Monte-Carlo simulations of the radiolysis of liquid water for various times from 10 ps to 1 μs, in the range 25–325°C.

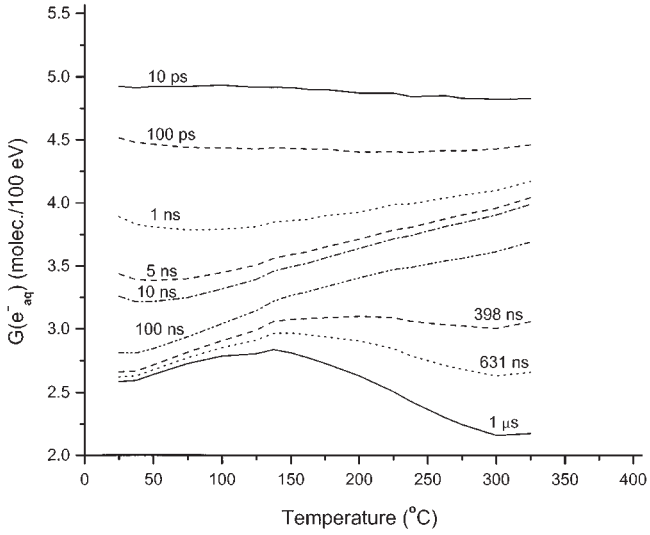

(see Fig. 1). In contrast, with the values of $\varepsilon_{max}(e^-_{aq})$ estimated from the data of Shiraishi et al. (7), there is an overall increase of $G_{e^-_{aq}}\varepsilon_{max}(e^-_{aq})$ with temperature over the whole range of temperatures considered. As can be seen from Fig. 1, our calculated temperature dependencies of $G_{e^-_{aq}}\varepsilon_{max}(e^-_{aq})$ are in good agreement with most available experimental data (4, 5, 7, 8). Moreover, our $G_{e^-_{aq}}\varepsilon_{max}(e^-_{aq})$ values agree well with those obtained from the deterministic diffusion-kinetic calculations of $G_{e^-_{aq}}$ of Swiatla-Wojcik and Buxton for H_2O (14) and D_2O (45), using the $\varepsilon_{max}(e^-_{aq})$ values in light and heavy liquid water reported by Elliot et al. (refs. 9 and 10 and ref. 10, respectively). Our results, however, notably differ from the experimental data of Wu et al. (1) and Dixon and Lopata (3), as well as from those of Christensen and Sehested (6) (see Fig. 1).

To better understand the influence of the water dielectric constant on the early time electron–cation recombination, and hence on $G_{e^-_{aq}}$, as a function of temperature, it is of interest to see the time dependence of ε at different temperatures. This is shown in Fig. 5, where ε, calculated from eq. [1] using ε_s, ε_∞, and τ_D as described above (Fig. 2), is plotted against time at 25, 100, and 300°C. As can be seen at 25°C, ε essentially reduces to ε_∞ at times lower than the longitudinal dielectric relaxation time of water ($\tau_L \approx 540$ fs). Since, at that temperature, the average electron thermalization time (22) is equal to ~41 fs (calculated from our simulations),[11] it follows that ε_s does not practically affect the recombination probability of an electron–cation pair.[12] The same conclusion should likely also apply at 100 and 300°C (where $\tau_L \approx$ 103 and 31.5 fs, respectively), even if the electron thermalization time is not well known at elevated temperatures.[13] These results show that the previous conclusion invoked by some authors (1, 12) that a decrease in $G_{e^-_{aq}}$ or $G_{e^-_{aq}}\varepsilon_{max}(e^-_{aq})$ at high temperatures would result from an increased electron–cation recombination due to the decrease of ε_s with increasing temperature, can hardly be justified. In parallel to these calculations, we have also computed $G_{e^-_{aq}}$ by using the square of the refractive index of liquid water for ε_∞, which is a smooth, slowly varying function of temperature, going from 1.77 at 25°C to 1.47 at 325°C (47). The values of $G_{e^-_{aq}}$ obtained (data not shown here) are similar to those calculated above by using the temperature dependence of ε_∞ given in Fig. 2*b*. As a result, the early time electron–cation recombination remains practically unaffected by the Coulombic attraction of the positive H_2O^+ ion. Similar conclusions were also obtained in our previous calculations of the thermalization distances and times of subexcitation electrons in solid water (22).

Figure 6 shows the temperature dependence of our $G(e^-_{aq})$ values over the range 25–325°C, calculated at different times from 10 ps to 1 μs. As can be seen in the time scale 10–100 ps, the yield of hydrated electrons remains nearly constant with temperature. In the range 1–10 ns, $G(e^-_{aq})$ initially decreases with increasing temperature, reaches a minimum around 40–100°C, and then increases at higher temperatures. Noteworthily, the temperature dependence of our computed $G(e^-_{aq})$ values at 5 ns agrees well with that of the product

[11]For the sake of comparison, it is interesting to recall here that, in liquid water at 25°C, the time scale for electron "trapping" is ~110–300 fs, while the electron "hydration" time is ~240–620 fs (46).
[12]Based on the fact that the recombination process of a subexcitation electron with its parent cation occurs before thermalization is complete (22).
[13]In fact, as we have mentioned above, the electron thermalization distance at 300°C is decreased by a factor of ~2 with respect to its value at 25°C. We can thus expect that the corresponding electron thermalization time, equal to ~41 fs at 25°C, will also be decreased by a similar amount.

© 2002 NRC Canada

$G(e^-_{aq})$ $\varepsilon_{max}(e^-_{aq})$ at 5 ns measured by Shiraishi et al. (7), which exhibits a minimum around 100°C. At 100 ns, $G(e^-_{aq})$ increases monotonically with temperature over all the temperature range considered (see also Fig. 3). At longer times, $G(e^-_{aq})$ first increases with temperature over the range ~25–140°C and then decreases at higher temperatures in the order 398 ns < 631 ns < 1 μs. At these latter times, the observed decrease in $G(e^-_{aq})$ above ~140°C is due to the reactions of e^-_{aq} with H_2O and with H^+ ions distributed homogeneously in the solution (13, 48, 49). At 1 μs, the influence of those two reactions already shows itself from ~100°C by a marked weakening in the slope of the curve of $G(e^-_{aq})$ vs. temperature. Consequently, for temperatures below ~100°C, we can consider that homogeneous chemistry takes over in the bulk of the solution at ~1 μs,[14] whereas at higher temperatures, this time diminishes to ~100 ns. This result agrees well with our previous Monte-Carlo simulation studies of water radiolysis at elevated temperatures (13, 48, 49).

Conclusions

In this paper, Monte-Carlo simulations of the low-LET radiolysis of liquid water are carried out to calculate the primary hydrated electron yields as a function of temperature, in the range 25–325°C. In the calculations, the effect of the time and temperature dependencies of the water dielectric constant on the electron–cation geminate recombination is properly taken into account. The product $G_{e^-_{aq}}\varepsilon_{max}(e^-_{aq})$ is estimated by using our computed $G_{e^-_{aq}}$ values with the maximum molar extinction coefficient $\varepsilon_{max}(e^-_{aq})$ obtained from existing experimental data. The results show that our values of $G_{e^-_{aq}}\varepsilon_{max}(e^-_{aq})$ are in good agreement with most experimental data, as well as with the predictions of deterministic diffusion-kinetic model calculations. Moreover, contrary to the interpretation proposed by certain authors in the literature, the static dielectric constant of water is found not to play any significant role on the electron–cation recombination at early times. However, more experimental work is required to better specify the temperature dependence of $G_{e^-_{aq}}$, especially above 300°C and in the supercritical regime of water (> 374°C, > 22.1 MPa or 218 atm) (1, 50). Finally, the temperature dependence of our $G(e^-_{aq})$ values, calculated at various times between 10 ps and 1 μs, shows that at low LET, the time required to establish homogeneous chemistry in the bulk of the solution is ~10^{-6} s in the range ~25–100°C, whereas this time diminishes to ~10^{-7} s at higher temperatures.

Acknowledgments

We thank M. Yusa Muroya (Nuclear Engineering Research Laboratory, University of Tokyo, Japan) for valuable discussions. Financial support from the Canadian Institutes of Health Research (Grant No. MT-14617) is gratefully acknowledged.

References

1. G. Wu, Y. Katsumura, Y. Muroya, X. Li, and Y. Terada. Chem. Phys. Lett. **325**, 531 (2000); see also G. Wu, Y. Katsumura, Y. Muroya, X. Li, and Y. Terada. Radiat. Phys. Chem. **60**, 395 (2001).
2. J.W.T. Spinks and R.J. Woods. An introduction to radiation chemistry. 3rd ed. Wiley, New York. 1990. p. 243; C. Ferradini and J.-P. Jay-Gerin. Can. J. Chem. **77**, 1542 (1999).
3. R.S. Dixon and V.J. Lopata. Radiat. Phys. Chem. **11**, 135 (1978).
4. F.-Y. Jou and G.R. Freeman. J. Phys. Chem. **83**, 2383 (1979).
5. B.D. Michael, E.J. Hart, and K.H. Schmidt. J. Phys. Chem. **75**, 2798 (1971).
6. H. Christensen and K. Sehested. J. Phys. Chem. **90**, 186 (1986); see also K. Sehested and H. Christensen. *In* Proceedings of the 8th international congress of radiation research, Edinburgh, July 19–24, 1987. Vol. 2. *Edited by* E.M. Fielden, J.F. Fowler, J.H. Hendry, and D. Scott. Taylor and Francis, London. 1987. p. 199.
7. H. Shiraishi, Y. Katsumura, D. Hiroishi, K. Ishigure, and M. Washio. J. Phys. Chem. **92**, 3011 (1988).
8. W.C. Gottschall and E.J. Hart. J. Phys. Chem. **71**, 2102 (1967); E.J. Hart and M. Anbar. The hydrated electron. Wiley-Interscience, New York. 1970. p. 40.
9. A.J. Elliot and D.C. Ouellette. J. Chem. Soc. Faraday Trans. **90**, 837 (1994).
10. A.J. Elliot, D.C. Ouellette, and C.R. Stuart. The temperature dependence of the rate constants and yields for the simulation of the radiolysis of heavy water. Report AECL-11658. Atomic Energy of Canada Ltd., Chalk River, Ontario. 1996.
11. H. Shiraishi, Y. Katsumura, and K. Ishigure. Radiat. Phys. Chem. **34**, 705 (1989).
12. W.G. Burns and W.R. Marsh. J. Chem. Soc. Faraday Trans. 1, **77**, 197 (1981).
13. M.-A. Hervé du Penhoat, T. Goulet, Y. Frongillo, M.-J. Fraser, Ph. Bernat, and J.-P. Jay-Gerin. J. Phys. Chem. A, **104**, 11757 (2000).
14. D. Swiatla-Wojcik and G.V. Buxton. J. Phys. Chem. **99**, 11464 (1995); J. Chem. Soc., Faraday Trans. **94**, 2135 (1998).
15. Y. Frongillo, M.-J. Fraser, V. Cobut, T. Goulet, J.-P. Jay-Gerin, and J.P. Patau. J. Chim. Phys. **93**, 93 (1996).
16. V. Cobut, Y. Frongillo, J.P. Patau, T. Goulet, M.-J. Fraser, and J.-P. Jay-Gerin. Radiat. Phys. Chem. **51**, 229 (1998).
17. Y. Frongillo, T. Goulet, M.-J. Fraser, V. Cobut, J.P. Patau, and J.-P. Jay-Gerin. Radiat. Phys. Chem. **51**, 245 (1998).
18. T. Goulet, M.-J. Fraser, Y. Frongillo, and J.-P. Jay-Gerin. Radiat. Phys. Chem. **51**, 85 (1998).
19. P. Clifford, N.J.B. Green, M.J. Pilling, and S.M. Pimblott. J. Phys. Chem. **91**, 4417 (1987); N.J.B. Green, M.J. Pilling, S.M. Pimblott, and P. Clifford. J. Phys. Chem. **94**, 251 (1990); S.M. Pimblott, M.J. Pilling, and N.J.B. Green. Radiat. Phys. Chem. **37**, 377 (1991).
20. S.M. Pimblott and J.A. LaVerne. Radiat. Res. **122**, 12 (1990).
21. R.L. Platzman. Radiat. Res. **1**, 558 (1954); **2**, 1 (1955); J. Weiss. Nature (London), **174**, 78 (1954); J. Chim. Phys. **52**, 539 (1955); M. Michaud, P. Cloutier, and L. Sanche. Phys. Rev. A: At. Mol. Opt. Phys. **44**, 5624 (1991). See also A. Mozumder. Fundamentals of radiation chemistry. Academic Press, San Diego. 1999. p. 247.

[14]Noteworthily, in the temperature range ~25–100°C, our calculations show that there is only a little change (~8–9%) in the yields of e^-_{aq} between 10^{-7} and 10^{-6} s. See refs. 13 and 49.

© 2002 NRC Canada

22. T. Goulet, J.P. Patau, and J.-P. Jay-Gerin. J. Phys. Chem. **94**, 7312 (1990); Radiat. Prot. Dosim. **31**, 33 (1990); T. Goulet, J.-P. Jay-Gerin, Y. Frongillo, V. Cobut, and M.-J. Fraser. J. Chim. Phys. **93**, 111 (1996).
23. A. Mozumder. J. Chem. Phys. **50**, 3153 (1969); see also G.R. Freeman. *In* Kinetics of nonhomogeneous processes. *Edited by* G.R. Freeman. Wiley, New York. 1987. p. 277.
24. U. Kaatze. J. Chem. Eng. Data, **34**, 371 (1989); see also U. Kaatze. J. Solution Chem. **26**, 1049 (1997).
25. D.G. Archer and P. Wang. J. Phys. Chem. Ref. Data, **19**, 371 (1990).
26. G.S. Anderson, R.C. Miller, and A.R.H. Goodwin. J. Chem. Eng. Data, **45**, 549 (2000).
27. D.P. Fernández, Y. Mulev, A.R.H. Goodwin, and J.M.H. Levelt Sengers. J. Phys. Chem. Ref. Data, **24**, 33 (1995).
28. G.C. Akerlof and H.I. Oshry. J. Am. Chem. Soc. **72**, 2844 (1950).
29. N. Agmon. J. Phys. Chem. **100**, 1072 (1996).
30. C.-N. Yang and H.J. Kim. J. Chem. Phys. **113**, 6025 (2000).
31. K. Okada, M. Yao, Y. Hiejima, H. Kohno, and Y. Kajihara. J. Chem. Phys. **110**, 3026 (1999).
32. C. Rønne, L. Thrane, P.-O. Åstrand, A. Wallqvist, K.V. Mikkelsen, and S.R. Keiding. J. Chem. Phys. **107**, 5319 (1997).
33. O.A. Nabokov and Yu.A. Lubimov. Mol. Phys. **65**, 1473 (1988).
34. K. Okada, Y. Imashuku, and M. Yao. J. Chem. Phys. **107**, 9302 (1997).
35. A.J. Elliot, M.P. Chenier, and D.C. Ouellette. J. Chem. Soc. Faraday Trans. **89**, 1193 (1993); A.J. Elliot, M.P. Chenier, D.C. Ouellette, and V.T. Koslowsky. The temperature dependence of *g*-values for aqueous solutions irradiated with a 23 MeV $^2H^+$ beam. Report AECL-10659. Atomic Energy of Canada Ltd., Chalk River, Ontario. 1992.
36. D.R. McCracken, K.T. Tsang, and P.J. Laughton. Aspects of the physics and chemistry of water radiolysis by fast neutrons and fast electrons in nuclear reactors. Report AECL-11895. Atomic Energy of Canada Ltd., Chalk River, Ontario. 1998.
37. K.N. Jha, T.G. Ryan, and G.R. Freeman. J. Phys. Chem. **79**, 868 (1975).
38. S.A. Kabakchi and V.L. Bugaenko. High Energy Chem. **26**, 319 (1992), and refs. therein.
39. M.C. Kent and H.E. Sims. *In* Proceedings of the 6th international conference on water chemistry of nuclear reactor systems. British Nuclear Energy Society, London. 1992. p. 153. See also M.C. Kent and H.E. Sims. The yield of γ-radiolysis products from water at temperatures up to 270°C. Report AEA-RS-2302. Atomic Energy Authority, Didcot, Oxfordshire, U.K. 1992.
40. G.R. Sunaryo, Y. Katsumura, D. Hiroishi, and K. Ishigure. Radiat. Phys. Chem. **45**, 131 (1995); K. Ishigure, Y. Katsumura, G.R. Sunaryo, and D. Hiroishi. Radiat. Phys. Chem. **46**, 557 (1995); Y. Katsumura, G. Sunaryo, D. Hiroishi, and K. Ishigure. Prog. Nucl. Energy **32**, 113 (1998).
41. H. Shiraishi, G.V. Buxton, and N.D. Wood. Radiat. Phys. Chem. **33**, 519 (1989); G.V. Buxton. *In* Proceedings of the 5th international conference on water chemistry of nuclear reactor systems. British Nuclear Energy Society, London. 1989. p. 123.
42. G.V. Buxton, N.D. Wood, and S. Dyster. J. Chem. Soc. Faraday Trans. 1, **84**, 1113 (1988).
43. H. Christensen, A. Molander, A. Lassing, and H. Tomani. Experimental studies of radiolysis in an in-core loop in the Studsvik R2 reactor. Report STUDSVIK/M-97/87. Studsvik Material AB, 611 82 Nyköping, Sweden. 1997; H. Christensen. Nucl. Technol. **109**, 373 (1995).
44. A.J. Elliot. Rate constants and *g*-values for the simulation of the radiolysis of light water over the range 0–300°C. Report AECL-11073. Atomic Energy of Canada Ltd., Chalk River, Ontario. 1994; A.J. Elliot, M.P. Chenier, D.C. Ouellette, and V.T. Koslowsky. J. Phys. Chem. **100**, 9014 (1996).
45. D. Swiatla-Wojcik and G.V. Buxton. Phys. Chem. Chem. Phys. **2**, 5113 (2000).
46. A. Migus, Y. Gauduel, J.L. Martin, and A. Antonetti. Phys. Rev. Letters, **58**, 1559 (1987); F.H. Long, H. Lu, and K.B. Eisenthal. Phys. Rev. Lett. **64**, 1469 (1990); X. Shi, F.H. Long, H. Lu, and K.B. Eisenthal. J. Phys. Chem. **100**, 11903 (1996); A. Reuther, A. Laubereau, and D.N. Nikogosyan. J. Phys. Chem. **100**, 16794 (1996); C. Pépin, T. Goulet, D. Houde, and J.-P. Jay-Gerin. J. Phys. Chem. A, **101**, 4351 (1997); J.-P. Jay-Gerin. Can. J. Chem. **75**, 1310 (1997), and refs. therein; R. Laenen, T. Roth, and A. Laubereau. Phys. Rev. Lett. **85**, 50 (2000); see also A. Mozumder. Radiat. Phys. Chem. **32**, 287 (1988).
47. A.H. Harvey, J.S. Gallagher, and J.M.H. Levelt Sengers. J. Phys. Chem. Ref. Data, **27**, 761 (1998).
48. J. Meesungnoen, J.-P. Jay-Gerin, A. Filali-Mouhim, and S. Mankhetkorn. Chem. Phys. Lett. **335**, 458 (2001).
49. M.-A. Hervé du Penhoat, J. Meesungnoen, T. Goulet, A. Filali-Mouhim, S. Mankhetkorn, and J.-P. Jay-Gerin. Chem. Phys. Lett. **341**, 135 (2001).
50. D.R. Lide (*Editor*). CRC handbook of chemistry and physics. 75th ed. CRC Press, Boca Raton, Florida. 1994. p. 6.54.

© 2002 NRC Canada

The determination of the stereochemistry of epoxides located at the 5,6-positions of decalinic systems: An empirical method based on ^{13}C NMR chemical shifts

Raquel M. Cravero, Guillermo R. Labadie, and Manuel González Sierra

Abstract: The ^{13}C NMR spectra of a series of 5,6-epoxides in decalinic systems were studied. The interpretation of the chemical shifts allowed us to formulate an empirical rule to predict the epoxide stereochemistry. A discussion of the scope and limitations of this method and its extension to larger carbon skeletons is also presented.

Key words: epoxide stereochemistry, ^{13}C NMR, NMR, decalinic systems, oxiranes.

Résumé : On a étudié les spectres RMN du ^{13}C d'une série de systèmes décaliniques portant un époxyde en 5,6. L'interprétation des déplacements chimique a permis de formuler une règle empirique permettant de prédire la stéréochimie de l'époxyde. On présente aussi une discussion relative à la portée et aux limitations de cette méthode et de son extension aux squelettes carbonés plus importants.

Mots clés : stéréochimie des époxydes, RMN du ^{13}C, RMN, systèmes décaliniques, oxiranes.

[Traduit par la Rédaction]

Introduction

^{1}H and ^{13}C NMR techniques are the most convenient methods for the elucidation of the oxiranic-ring stereochemistry in condensed polycyclic systems, and have been widely used in the structural analyses of epoxides isolated from natural sources (1–4).

Generally, the stereochemical assignment of the epoxides is achieved by observing the change in the chemical shift of the γ-carbons upon introduction of the oxiranic ring. Although several explanations regarding the mechanism of the γ-effects have been offered, no general agreement has been reached thus far about the factors that contribute to this effect. Nevertheless, semi-empirical rules have been developed to estimate the changes in the ^{13}C NMR chemical shifts, and they have been used successfully to predict the configuration of the epoxides within rigid-ring systems (5–8).

Recently, we have been investigating the epoxidation of highly substituted decalinic systems, and we wanted to examine further the stereochemical outcome of the process. Specifically, we were introducing an oxirane ring at the 5,6-position of the decalin, with one of the carbons of the oxirane being incorporated into the ring juncture (Fig. 1). A preliminary communication on this subject has been previously reported (9).

Fig. 1. General structure of the studied epoxides.

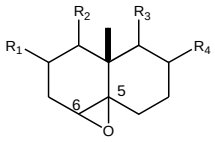

Experimental

The epoxides were prepared through a sequence involving a Birch-reductive alkylation with or without carbonyl-group reduction followed by treatment with *m*-CPBA in a heterogeneous phase as reported in the literature (10).

^{13}C NMR (50.3 MHz) spectra were recorded on a Bruker AC-200 E spectrometer in $CDCl_3$ solutions using standard conditions in 5-mm probe tubes at room temperature. The chemical shifts were recorded in δ (ppm). A complete report of the ^{1}H and ^{13}C NMR chemical shifts for the decalinic systems used in the present analysis were previously published (10, 11).

Results and discussion

In studies examining the synthetic preparation of Saudin, a series of angularly substituted synthetic decalins containing an oxirane moiety in the C_5–C_6 position were prepared (Scheme 1). It was deemed necessary to establish the stereochemistry of the epoxide in a straightforward and simple manner.

Received 30 November 2001. Published on the NRC Research Press Web site at http://canjchem.nrc.ca on 18 June 2002.

R.M. Cravero, G.R. Labadie, and M.G. Sierra.[1]
Departamento de Química Orgánica, Instituto de Química Orgánica de Síntesis, Facultad de Ciencias Bioquímicas y Farmacéuticas, Universidad Nacional de Rosario, Casilla de Correo 991, S2000WAJ-Rosario, Argentina.

[1]Corresponding author (e-mail: mgsierra@fbioyf.unr.edu.ar).

 DOI: 10.1139/V02-107 © 2002 NRC Canada

Scheme 1.

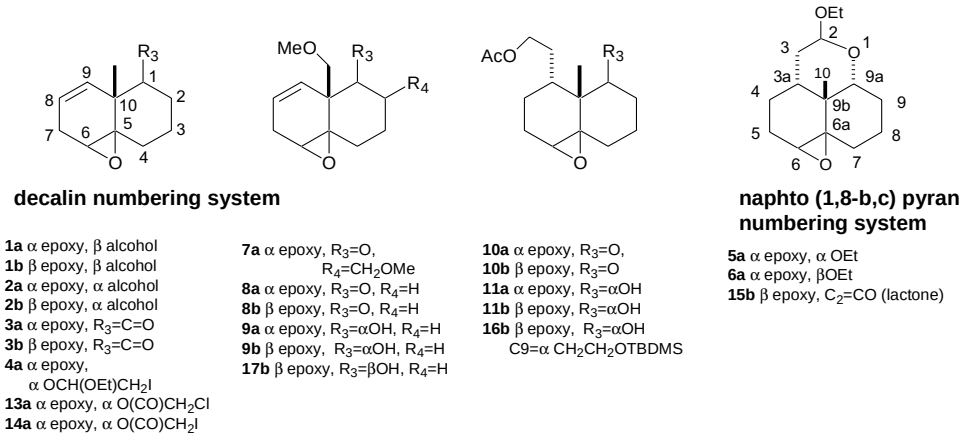

Table 1. Comparison of ^{13}C NMR data for C8 and C3 of epoxides and related olefins.

Compd	$\delta_{C\text{-}8}$ (olefin)	$\delta_{C\text{-}8}$ (epoxide)	$\Delta\delta$	$\delta_{C\text{-}3}$ (olefin)	$\delta_{C\text{-}3}$ (epoxide)	$\Delta\delta$
10a	23.46	19.08	–4.38	30.35	26.77	–3.58
10b	23.46	22.35	–1.11	30.35	28.40	–1.95
11a	24.66	17.86	–6.80	26.04	22.76	–3.28
11b	24.66	22.96	–1.70	26.04	23.19	–2.85
5a	24.32	19.99	–4.33	26.22	20.77	–5.45
6a	24.32	19.64	–4.68	26.22	20.22	–6.00
15b	24.49	20.64	–3.85	26.04	24.40	–1.64
16b	24.86	20.68	–4.18	26.51	25.39	–1.12

Fig. 2. Optimized computer generated structures of the α- and β-epoxides of the simpler decalinic model.

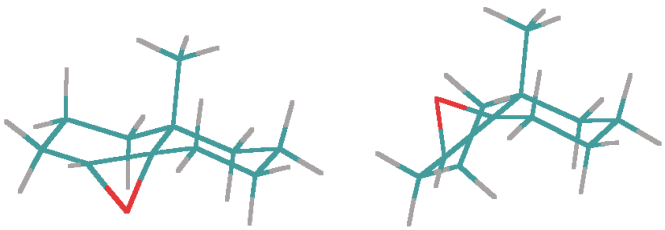

This problem resembled the one encountered by Carda et al. (1), who were dealing with a series of natural and synthetic epoxides of eudesmanolides, and we anticipated the same difficulties. It was therefore not unexpected to find that, regardless of the stereochemistry of the epoxides, the γ-effects on carbons C_8 and C_3 were mostly shielding effects, and were of no use as markers for the stereochemical assignment (Table 1).

We attribute these results mainly to the fact that, in this particular position, the α or β stereochemistry of the epoxides also determines the change in the *cis*/*trans*-ring fusion of the decalinic rings.

Optimized computer-generated structures[2] of the α- and β-epoxides of simpler decalinic models are shown in Fig. 2. It can be seen that the change in the stereochemistry of the ring junction induces changes in the conformation of the A ring in both series, and that such changes could explain the abnormal responses found for the chemical shifts of the γ-carbons.

Thus, taking in consideration the computed α- and β-epoxide structures and those of the parent olefins, we estimated the expected chemical shifts of the γ-carbons (C_8) for the epoxides using the parameters described in refs. 6 and 7 (Scheme 2). To calculate this, the following formulas were used: for the α-epoxides: $\delta_{C\text{-}8} = \delta_{C\text{-}8}$, olefin – (HC) + $(HC)_e$ + γ(OH); for the β-epoxides: $\delta_{C\text{-}8} = \delta_{C\text{-}8}$ olefin – (HC) + $(HC)_e$ + γ(OH).

A similarity is noticeable in the calculated increments for both series [$\delta_{C\text{-}8}$, olefin – (HC) + $(HC)_e$ + γ(OH)], giving an estimated shielding value of –3.83 ppm. The average experimental-shielding value found was –3.83 ppm for the α series and –3.34 ppm for the β series (Table 1).

In view of the impossibility of extracting any valuable information from the γ-effects, we focused on the observation of the behavior of the ^{13}C NMR chemical shifts of the oxirane carbons. Our attempts to relate the stereochemistry of oxiranes to the C_5 or C_6 chemical shifts in each series, through the use of the semi-empirical calculation rules available (6, 7), as well as the introduction of additional parameters into the semi-empirical calculation formula, also failed. We believed this failure could be attributed to the conformational changes produced by remote substituents on a rather flexible decalinic system, since such structural

[2] All the lowest energy conformations were found using the conformational search procedure with the MM+ molecular mechanics force field, as implemented in Hyperchem Pro 6.0. Each structure was then re-minimized with the AM1 semi-empirical method.

© 2002 NRC Canada

Table 2. Dihedral angles (°) in fragments containing C5 and (or) C6 in the center of a butane moiety.

Compds	C8-7-6-5	C7-6-5-4	C7-6-5-10	C6-5-10-11	C6-5-10-1	C6-5-10-9	C6-5-4-3
α-epoxide	–5.45	158.52	2.28	93.60	–145.85	–26.70	145.33
1a	17.03	156.39	1.26	98.70	–140.11	–19.54	162.95
9a	22.86	157.17	–0.014	97.70	–144.37	–23.11	142.46
10a	–7.61	158.68	4.64	90.52	–154.31	–28.28	145.19
11a	30.56	163.97	3.99	108.69	–134.91	–8.37	135.26
β-epoxide	16.87	–155.44	0.37	131.58	–107.68	13.09	104.64
1b	–7.24	–156.80	0.99	126.19	–111.99	6.07	108.27
9b	15.14	–177.85	–2.88	105.89	–138.15	–11.36	135.79
10b	10.05	–154.48	–0.42	141.50	–101.33	23.02	100.58
11b	16.49	–155.14	1.39	131.34	–108.67	13.02	110.11

Scheme 2.

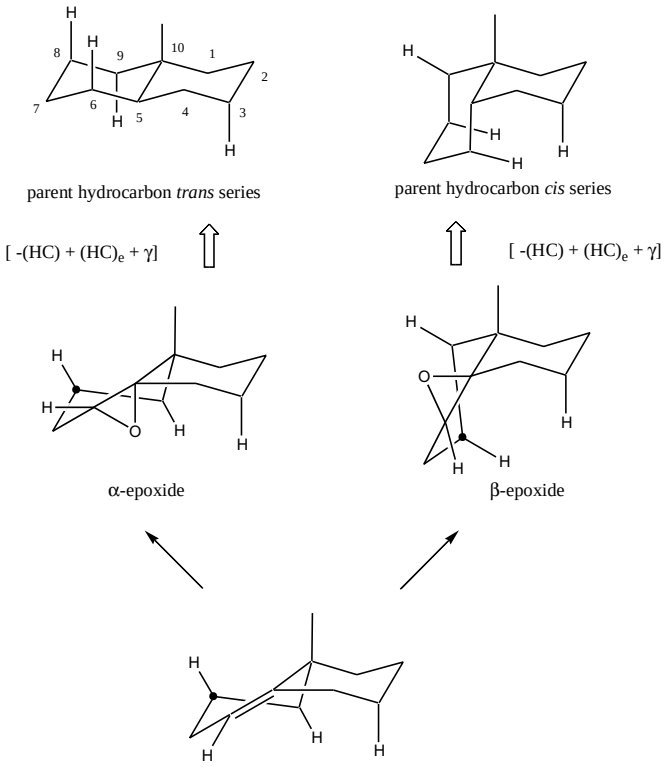

variations can be neither predicted nor adequately quantified. They might affect the validity of the semi-empirical parameters.

Because there is a great deal of overlap among the hydrogen signals, a conclusion about the shape of the rings in the various compounds could not be obtained from the spectral data. We therefore resorted to a computer-assisted conformational analysis to predict the conformational preferences of the ring system. This analysis showed different degrees of distortion in the dihedral angles and significant variations in the interatomic distances for the different substitution patterns of some decalinic derivatives.[3]

Table 2 shows the results of the dihedral-angle calculations for the A ring of some representative molecules, including the model α- and β-epoxides.

As expected, the C_7-C_6-C_5-C_{10} fragment shows an almost eclipsed relationship (dihedral angle of the α series: +2.53 ± 1.56°, and β series: –0.75 ± 1.48°) within a narrow degree of tolerance for both series. Fragments C_8-C_7-C_6-C_5 (dihedral angle of the α series: +11.48 ± 17.14°, and β series: +10.26 ± 10.15°) and C_6-C_5-C_{10}-C_9 C_5 (dihedral angle of the α series: –21.20 ± 7.92°, and β series: –0.44 ± 16.09°) show slightly larger dihedral angles, indicating that ring A resembles the half chair of cyclohexene, with the C_8 and C_9 carbons flipping above or below the equatorial plane of the cyclohexene ring according to the substitution pattern. Overall, there is no significant difference in the conformational behavior for both series.

We also considered using the ^{1}H NMR chemical shifts of some distinctive protons such as the oxirane -CH-O- and the angular C_{10}-methyl, but again, the observed values were not useful as stereochemical markers (2).

Comparing ^{13}C NMR chemical-shift differences between C_5 and C_6 in the *trans*- and *cis*-10-methyl decalins, however, showed a $[\Delta\delta_{5,6}]_{trans}$ = 16.80 for the *trans*-fused decalin and a $[\Delta\delta_{5,6}]_{cis}$ = 12.1 for the *cis*-fused decalin, rendering a relative $\Delta_{(trans\text{-}cis)}$ value of 4.7 ppm. Similar analyses of the ^{13}C NMR data for the synthetic epoxides (Table 3), showed that $[\Delta\delta_{5,6}]_{trans}$ = 6.71 ± 0.64 for the *trans* series and $[\Delta\delta_{5,6}]_{cis}$ = 1.96 ± 1.16 for the *cis* series, which produces a relative $\Delta_{(trans\text{-}cis)}$ value of 4.8 ppm.

It therefore seemed possible to predict the *trans* or *cis* stereochemistry of the ring fusion and, consequently, the α or β orientation relative to the C_{10}-substituent by using the ^{13}C NMR chemical-shift differences between the oxirane carbons.

By computing for each epoxide, the following rule was formulated:

$$\Delta\delta = \delta_{(\text{quaternary carbon})} - \delta_{(\text{tertiary carbon})}$$

The difference between the ^{13}C NMR chemical shifts of both oxirane carbon signals predicts that:

$$\Delta\delta_{\alpha\text{-epoxide}} > 5 \text{ ppm and } \Delta\delta_{\beta\text{-epoxide}} < 3.8 \text{ ppm}$$

[3] Supplementary material (tables of distances, dihedral angles, and $J_{6,7}$ values of epoxides) may be purchased from the Depository of Unpublished Data, Document Delivery, CISTI, National Research Council Canada, Ottawa, ON K1A 0S2, Canada. For information on obtaining material electronically go to http://www.nrc.ca/cisti/irm/unpub_e.shtml.

© 2002 NRC Canada

Table 3. ^{13}C NMR data (ppm) for synthetic epoxides **1–17**.

Compd	C-epoxide	CH-epoxide	Δδ	Compd	C-epoxide	CH-epoxide	Δδ
1a	64.88	58.28	6.60	**1b**	63.44	59.70	3.74
2a	64.43	56.73	7.70	**2b**	61.70	59.92	1.78
3a	65.41	57.80	7.61	**3b**	62.82	59.71	3.11
4a	62.78	55.71	7.07	**8b**	61.64	59.23	2.41
5a	62.90	56.16	6.74	**9b**	59.97	58.79	1.18
6a	63.32	56.48	6.84	**10b**	64.10	61.39	2.71
7a	64.53	58.10	6.43	**11b**	62.92	62.68	0.24
8a	63.96	58.07	5.90	**15b**	61.74	60.07	1.67
9a	62.60	57.30	5.30	**16b**	62.95	62.72	0.23
10a	64.80	57.75	7.05	**17b**	61.22	58.67	2.55
11a	66.36	59.95	6.41				
13a	62.48	55.79	6.69				
14a	62.60	55.64	6.96				

Note: According to Scheme 1, **a** is related to α-epoxide and **b** is related to β-epoxide.

Table 4. ^{13}C NMR data (ppm) for C5 and C6 of representative epoxides from the literature (12–14).

Compd	C_5	C_6	Δδ	Compd	C_5	C_6	Δδ
18	64.1	57.3	6.8	**27**	62.5	63.5	–1
19	65.7	59.1	6.6	**28**	62.6	63.6	–1
20	65.2	59.0	6.2	**29**	62.4	63.4	–1
21	65.9	58.9	7.0	**30**	62.5	63.5	–1
22	65.2	58.7	6.5	**31**	62.5	63.5	–1
23	65.2	58.9	6.3	**32**	62.5	63.5	–1
36	62.8	53.4	9.4	**33**	62.4	63.5	–1.1
24	63.1	64.4	–1.3	**34**	62.5	63.1	–0.6
25	63.1	63.1	0	**35**	62.4	63.3	–0.9
26	62.2	63.3	–1.1				

Scheme 3.

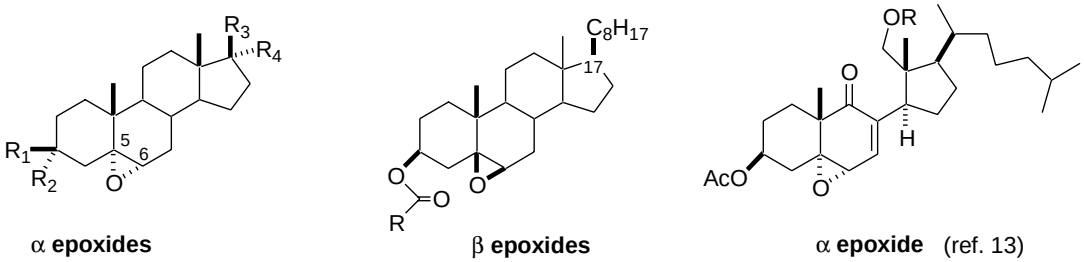

α **epoxides**

18 R_1=R_2=OCH_2CH_2O, R_3=OH, R_4=H
19 R_1=OH, R_2=H, R_3=R_4=OCH_2CH_2O
20 R_1=OAc, R_2=H, R_3=$COCH_3$, R_4=H
21 R_1=OH, R_2=H, R_3=R_4=O
22 R_1=OAc, R_2=H, R_3=R_4=O
23 R_1=OAc, R_2=H, R_3=OAc, R_4=H

β **epoxides**

24 R_1=OH, R_2=H, R_3=R_4=O
25 R_1=R_2=OCH_2CH_2O, R_3=OH, R_4=H

β **epoxides**

26 R=H
27 R=CH_3
28 R=nC_5H_{11}
29 R=nC_8H_{17}
30 R=$nC_{17}H_{35}$
31 R=*ter* C_4H_9
32 R=Ph
33 R=OCH_2CH_3
34 C_{17}=C=O
35 C_{17}=b $COCH_3$

α **epoxide** (ref. 13)

36 R=H

Finally, to test the scope and reliability of this observation, this calculation was performed on some representative examples from the literature (12–14) (Scheme 3, Table 4). It was found that this empirical rule may be used with confidence within the limits stated above. Notably, there is a larger Δδ for most of the examples chosen from the literature, which is clearly related to the rigidity of the steroidal skeletons.

Conclusions

In this study, we looked for a marker that could be used to correlate the ^{13}C NMR chemical shift of various epoxides, located at the C_5-C_6 position of decalins with their stereochemistry. We found that the effect of the oxiranic ring on the γ carbons described previously in the literature does not apply, and attempted to rationalize the abnormal

© 2002 NRC Canada

behavior of the γ-carbons chemical shifts for the α and β series. We also discovered that the set of parameters used by semi-empirical methods known in the literature to predict chemical shifts cannot be used with confidence in this situation for such flexible systems. Finally, we found a correlation involving the chemical-shift difference between both α carbons of the oxirane that, within reasonable limits, can be used for the prediction of the stereochemistry of epoxides.

Acknowledgments

Financial support to the authors from Universidad Nacional de Rosario, Consejo Nacional de Investigaciones Científicas y Tecnológicas (CONICET) and Agencia de Promoción Científica y Tecnológica (ANPCYT) are gratefully acknowledged. Thanks are also due to CONICET for a GRL fellowship.

References

1. M. Carda, J.F. Sanz, and J.A.M. J. Org. Chem. **57**, 804 (1992), and refs. cited therein.
2. A.M. Pohlit and H.M.C. Ferraz. Quimica Nova, **18**, 160 (1995).
3. K. Tori, T. Komeno, M. Sangaré, B. Septe, B. Delpech, A. Ahond, and G. Luckacs. Tetrahedron Lett. 1157 (1974).
4. M. Sangaré, B. Septe, G. Berenger, and G. Luckacs. Tetrahedron Lett. 699 (1977).
5. A.D. Cross. J. Am. Chem. Soc. **84**, 3206 (1962).
6. (*a*) H. Beierbeck and J.K. Saunders. Can. J. Chem. **54**, 632 (1976); (*b*) H. Beierbeck and J.K. Saunders. Can. J. Chem. **54**, 2985 (1976).
7. M.I. Colombo, D.A. Bustos, M. González Sierra, A.C. Olivieri, and E.A. Rúveda. Can. J. Chem. **61**, 552 (1986).
8. (*a*) G.C. Levy and G.L. Nelson. *In* Carbon-13 nuclear magnetic resonance for organic chemists. Wiley Interscience, New York. 1972. Chap 3; (*b*) T.P. Forrest amd J.G.K Webb. Org. Magn. Reson. **12**, 371 (1979).
9. R.M. Cravero, G.R. Labadie, and M. González Sierra. Molecules, **5**, 323 (2000).
10. G.R. Labadie, R.M. Cravero, and M. González Sierra. Synthesis, **5**, 708 (2001).
11. G.R. Labadie, R.M. Cravero, and M. González Sierra. Synth. Commun. **30**, 4065 (2000).
12. H.L. Holland, P.R.P. Diakow and G.J. Taylor. Can. J. Chem. **56**, 3121 (1978).
13. J.-C. Marchon and R. Ramasseul. Synthesis, 389 (1989).
14. S. De Rosa, A. De Giulio, A. Crispino, C. Iodice, and G. Tommonaro. Nat. Prod. Lett. **13**, 15 (1999).

© 2002 NRC Canada

Sodium borohydride: A versatile reagent in the reductive *N*-monoalkylation of α-amino acids and α-amino methyl esters

Giancarlo Verardo, Paola Geatti, Elena Pol, and Angelo G. Giumanini

Abstract: α-Amino acids and α-amino methyl esters are easily converted to their *N*-monoalkyl derivatives by a reductive condensation reaction using several carbonyl compounds in the presence of sodium borohydride. This reducing agent has shown a wide versatility with minor but essential procedural variations. The reaction allows the α-monodeuterium labeling of the new *N*-substituent by use of sodium borodeuteride.

Key words: α-amino acid, α-amino methyl esters, sodium borohydride, reductive *N*-monoalkylation, carbonyl compounds.

Résumé : Les acides α-aminés et leurs esters peuvent facilement être transformés en leurs dérivés *N*-monoalkylés par le biais d'une réaction de condensation réductrice faisant appel à divers composés carbonylés, en présence de borohydrure de sodium. Il a été démontré que ce réactif présente une grande versatilité par rapport aux variations mineures, mais essentielles, dans les procédures. L'utilisation de borodeutérure de sodium permet d'obtenir les dérivés portant un atome de deutérium en position α de l'azote portant le nouveau substituant.

Mots clés : acide α-aminé, esters méthyliques d'acide α-aminé, borohydrure de sodium, *N*-monoalkylation réductrice, composés carbonylés.

[Traduit par la Rédaction]

Introduction

The use of peptides as drugs is often hampered by their poor bioavailability because of their enzymatic degradation by proteases (1), poor adsorption after oral ingestion, and rapid excretion through liver and kidneys. The introduction of modified amino acids or the use of peptidomimetics (2) can be a solution for these drawbacks. Amino acids may be modified by *N*-alkylation: peptoids (3), an important class of peptidomimetics, express *N*-alkylated glycine residues.

The synthesis of *N*-alkylated amino acids and amino esters has been extensively studied and a number of procedures are available. One interesting approach is the alkylation of sulfonamides (Mitsunobu reaction) both in solution using, e.g., 2,4-dinitrobenzenesulfonyl (4) or 2,2,5,7,8-pentamethylchroman-6-sulfonyl (5) as protecting groups, and in the solid phase with 2-nitrobenzenesulfonyl (6) as the protecting group. These methods require long reaction times, three or more reaction steps, and occasional racemization is observed. The alkylation of *N*-unprotected amino acids and esters was also reported (7), but is limited to *N*-benzylation. Alternatively, the desired amino function can be directly introduced by a S_N2 reaction with appropriate α-substituted carboxylic acid derivatives e.g., α-trifluoromethanesulfonyloxy carboxylate (8) or α-halo acids (9). The problems with these reactions are the availability of the suitable starting materials and, in the case of the α-halo acids, the fact that racemization and elimination are prominent side reactions. *N*-Alkylated amino acids were also prepared by acid hydrolysis of 2-amino nitriles, according to the Strecker synthesis using primary amines (10) or by the oxidation of allylamines obtained from the enantioselective reaction of an allylic substrate with benzylamine in the presence of a palladium catalyst bearing chiral ferrocenylphosphine ligands (11). Examples of catalytic hydrogenation of preformed imines obtained from the condensation reaction of amino acids and carbonyl compounds (9, 12) or benzylamine and α-keto acids (13) were also reported.

Reductive *N*-alkylation of amino acids and amino esters is a method widely used to synthesize the corresponding *N*-benzyl derivatives: $NaBH(OAc)_3$ (14), NaHTe (15), $NaBH_3CN$ (16), and $NaBH_4$ (12*c*, 17) were the reducing agents employed. Sodium triacetoxyborohydride has also been used to reduce imines derived from the reaction between α-keto esters and benzylamine (18). The last two reactants showed a larger range of applicability: in fact, they were used with carbonyl compounds (other than benzaldehyde), but sodium cyanoborohydride had to be used under inert atmosphere. Moreover, long reaction times (16–20 h) with amino acids (19) and large excess of the carbonyl compounds and the reducing agent with amides of amino acids (20) were needed. Sodium borohydride, on the other hand, has been used in water only on amino acids (12*e*) but, even when the reaction was carried out in the presence of large excess of reactants, yields were not satisfactory.

Received 8 January 2002. Published on the NRC Research Press Web site at http://canjchem.nrc.ca on 18 June 2002.

G. Verardo,[1] P. Geatti, E. Pol, and A.G. Giumanini. Department of Chemical Sciences and Technologies, University of Udine, I-33100 Udine, Italy.

[1]Corresponding author (e-mail: gverardo@tin.dstc.uniud.it).

 DOI: 10.1139/V02-083 © 2002 NRC Canada

Scheme 1.

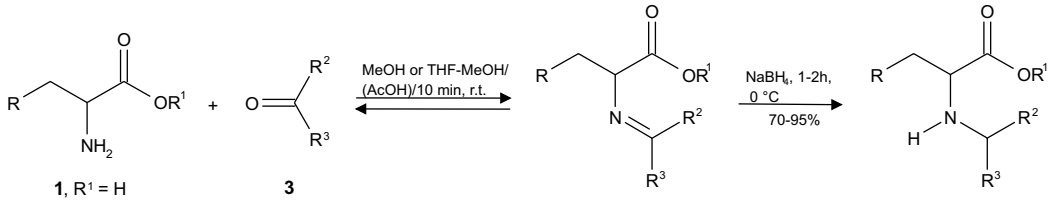

1, R^1 = H
2, R^1 = Me

3

4, R^1 = H
5, R^1 = Me

6, R^1 = H
7, R^1 = Me

1	R	**2**	R	**3**	R^2	R^3
a	H	**a**	H	**a**	H	Et
b	Me_2CH	**b**	Me_2CH	**b**	H	Pr
c	Ph	**c**	Ph	**c**	H	tert-Bu
d	4-HO-C_6H_4	**d**	4-HO-C_6H_4	**d**	H	Ph
e	indolyl	**e**	indolyl	**e**	Me	Me
f	CH_2CO_2H	**f**	CH_2CO_2Me			
h	imidazolyl					
i	CH_2CONH_2					
j	CH_2SMe					

6	R	R^2	R^3	**7**	R	R^2	R^3
ab	H	H	Pr	**ad**	H	H	Ph
bb	Me_2CH	H	Pr	**bb**	Me_2CH	H	Pr
cb	Ph	H	Pr	**bd**	Me_2CH	H	Ph
cc	Ph	H	tert-Bu	**ca**	Ph	H	Et
cd	Ph	H	Ph	**cb**	Ph	H	Pr
ce	Ph	Me	Me	**cc**	Ph	H	tert-Bu
dd	4-HO-C_6H_4	H	Ph	**cd**	Ph	H	Ph
eb	Indolyl	H	Pr	**ce**	Ph	Me	Me
ec	Indolyl	H	tert-Bu	**db**	4-HO-C_6H_4	H	Pr
ed	Indolyl	H	Ph	**dd**	4-HO-C_6H_4	H	Ph
fb	CH_2CO_2H	H	Pr	**ea**	indolyl	H	Et
fd	CH_2CO_2H	H	Ph	**ec**	indolyl	H	tert-Bu
ha	imidazolyl	H	Et	**ed**	indolyl	H	Ph
hb	imidazolyl	H	Pr	**ee**	indolyl	Me	Me
hd	imidazolyl	H	Ph	**fa**	CH_2CO_2Me	H	Et
ib	CH_2CONH_2	H	Pr	**fc**	CH_2CO_2Me	H	tert-Bu
jb	CH_2Sme	H	Pr	**fd**	CH_2CO_2Me	H	Ph
				fe	CH_2CO_2Me	Me	Me

Results and discussion

On the basis of the knowledge we have acquired on the applications of sodium borohydride as reducing agent in the reductive *N*-alkylation of amines (21), we have now extended its use to α-amino acids (**1**) and α-amino methyl esters (**2**) in combination with several carbonyl compounds (**3**) (Scheme 1).

The carbonyl compound (**3**) was added at room temperature to a methanolic solution of **1** or a hydrochloride of **2** after its neutralization in situ with a slight excess of finely powdered NaOH. After 10 min, a time sufficient to form imine **4** or **5**, the reaction mixture was cooled to 0°C and solid $NaBH_4$ was added. GC–MS analysis of the reaction mixture before the addition of $NaBH_4$ indicated that higher temperatures and (or) longer contact times between **2** and **3** did not improve the formation of **5**; moreover, the conversion into the corresponding *N*-alkylated compounds **7** was lower. Since our goal was the use of $NaBH_4$ as the reducing agent in the reductive alkylation of both **1** and **2**, the physical form (pellets or granular) of the reductant and minor but essential procedural variations were found to be very important.

The reaction between the amino acids (**1**) and all the carbonyl substrates (**3**) was carried out in MeOH using $NaBH_4$ pellets (Method A). Unlike water (12*e*), this solvent, was able to solubilize all the species initially present and the species eventually forming in the process, and it also made the $NaBH_4$ reactive enough to reduce the imine **4**. The methanolic mixture obtained was acidified with 37% aqueous HCl up to the isoelectric point of the starting amino acid (**1**) and, after removal of the solvent and addition of acetone, a solid was obtained composed of a mixture of the *N*-alkyl amino acids (**6**) and NaCl as determined by ^1H and ^{13}C NMR and by qualitative analysis. To eliminate NaCl, the solid was washed with water, but unfortunately, all the *N*-alkyl derivatives of glutamic acid (**1f**) and, particularly, histidine (**1h**) were found to be widely soluble in water. For

© 2002 NRC Canada

Table 1. Yields and some properties of *N*-alkyl amino acids (**6**).

Product	Isolated yield (%)[a]	mp (°C)	Lit. mp (°C)	Anal. calcd. (found)	$[\alpha]_D$ (1 M HCl)
6ab $C_7H_{15}NO_2$	82	>260	286 (12*a*)	C 57.90 (57.88) H 10.41 (10.40) N 9.65 (9.67)	+19.0 (*c* 1.0)
6bb $C_{10}H_{21}NO_2$	86	>260	267 (12*a*)	C 64.13 (64.16) H 11.30 (11.28) N 7.48 (7.47)	+33.0 (*c* 1.0)
6cb $C_{13}H_{19}NO_2$	85	>260		C 70.56 (70.58) H 8.65 (8.68) N 6.33 (6.36)	+44.0 (*c* 1.0)
6cb-*d* $C_{13}H_{18}DNO_2$	80	>260		C 70.23 (70.20) H 8.16 (8.18) N 6.30 (6.28)	+43.8 (*c* 1.0)
6cc $C_{14}H_{21}NO_2$	83	205		C 71.46 (71.48) H 8.99 (8.98) N 5.95 (5.96)	+68.7 (*c* 0.8)
6cd $C_{16}H_{17}NO_2$	91	245	243 (19), 225–227 (9)	C 75.27 (75.25) H 6.71 (6.74) N 5.49 (5.46)	+44.0 (*c* 1.0)
6ce $C_{12}H_{17}NO_2$	63	260 dec.	260–263 (19)	C 69.54 (69.55) H 8.27 (8.25) N 6.76 (6.78)	+58.7 (*c* 1.0)
6dd $C_{16}H_{17}NO_3$	92	259 dec.		C 70.83 (70.85) H 6.32 (6.35) N 5.16 (5.18)	+68.7 (*c* 0.7)
6eb $C_{15}H_{20}N_2O_2$	82	248 dec.		C 69.20 (69.23) H 7.74 (7.75) N 10.76 (10.78)	+48.0 (*c* 2.0)
6ec $C_{16}H_{22}N_2O_2$	90	234 dec.		C 70.04 (70.01) H 8.08 (8.05) N 10.21 (10.25)	+34.5 (*c* 2.0)
6ed $C_{18}H_{18}N_2O_2$	94	249 dec.	248–250 (9)	C 73.45 (73.48) H 6.16 (6.15) N 9.52 (9.55)	+48.0 (*c* 0.9)
6fb $C_9H_{17}NO_4$	73 (91)	185		C 53.19 (53.18) H 8.43 (8.45) N 6.89 (6.86)	+31.3 (*c* 2.0)
6fd $C_{12}H_{15}NO_4$	78 (89)	165	156–157 (19)	C 60.75 (60.77) H 6.37 (6.35) N 5.90 (5.89)	+19.6 (*c* 1.0)
6ha $C_9H_{15}N_3O_2$	73 (92)	198		C 54.81 (54.78) H 7.67 (7.65) N 21.30 (21.33)	+49.0 (*c* 1.0)
6hb $C_{10}H_{17}N_3O_2$	75 (90)	166		C 56.85 (56.88) H 8.11 (8.14) N 19.89 (19.91)	+48.2 (*c* 0.9)
6hd $C_{13}H_{15}N_3O_2$	84 (90)	191		C 63.66 (63.68) H 6.16 (6.14) N 17.13 (17.11)	+39.0 (*c* 1.0)
6ib $C_9H_{18}N_2O_3$	89	205	198–199 (12*e*)	C 53.45 (53.48) H 8.97 (8.94) N 13.85 (13.88)	+22.7 (*c* 1.5)
6jb $C_9H_{19}NO_2S$	90	260 dec.		C 52.65 (52.68) H 9.33 (9.34) N 6.82 (6.80)	+52.0 (*c* 1.0)

[a]All the reactions were carried out according to Method A; yields in parentheses were determined by ^{1}H NMR using phenylacetic acid as internal standard.

Table 2. Yields and some properties of *N*-alkyl amino acid methyl ester hydrochlorides (**7**).

Product	Isolated yield (%)	Method	mp (°C)	Lit. mp (°C)	Anal. calcd. (found)	$[\alpha]_D$ (MeOH)
7ad $C_{11}H_{16}NO_2Cl$	70	C	184		C 57.52 (57.48) H 7.02 (7.00) N 6.10 (6.15)	+27.3 (*c* 1.0)
7bb $C_{11}H_{24}ClNO_2$	91	B	83		C 55.57 (55.58) H 10.17 (10.09) N 5.89 (5.91)	+16.0 (*c* 1.5)
7bd $C_{14}H_{22}ClNO_2$	89	C	169	167–168 (17*b*)	C 61.87 (61.83) H 8.16 (8.13) N 5.15 (5.11)	+25.4 (*c* 1.0)
7ca $C_{13}H_{20}ClNO_2$	97	B	128		C 60.58 (60.55) H 7.82 (7.83) N 5.43 (5.43)	+47.5 (*c* 2.0)
7cb $C_{14}H_{22}ClNO_2$	90	B	104		C 61.87 (61.85) H 8.16 (8.18) N 5.15 (5.13)	+46.0 (*c* 2.0)
7cc $C_{15}H_{24}ClNO_2$	72	C	143		C 63.04 (63.05) H 8.46 (8.48) N 4.90 (4.93)	+61.0 (*c* 1.0)
7cd $C_{17}H_{20}ClNO_2$	87	C	153	151–152 (7*b*)	C 66.77 (66.75) H 6.59 (6.58) N 4.58 (4.55)	+39.0 (*c* 1.0)
7cd-*d* $C_{17}H_{19}ClDNO_2$	82	C	150		C 66.55 (66.57) H 6.24 (6.26) N 4.57 (4.55)	+39.6 (*c* 1.0)
7ce $C_{13}H_{20}ClNO_2$	87	D	154		C 60.58 (60.57) H 7.82 (7.80) N 5.43 (5.41)	+60.4 (*c* 1.2)
7db $C_{14}H_{22}ClNO_3$	88	B	96		C 58.43 (58.45) H 7.71 (7.70) N 4.87 (4.89)	+43.8 (*c* 2.0)
7dd $C_{17}H_{20}ClNO_3$	85	C	195		C 63.45 (63.45) H 6.26 (6.28) N 4.35 (4.33)	+57.3 (*c* 0.8)
7ea $C_{15}H_{21}ClN_2O_2$	95	B	109		C 60.70 (60.72) H 7.13 (7.15) N 9.44 (9.43)	+22.5 (*c* 2.0)
7ec $C_{17}H_{25}ClN_2O_2$	87	C	>260		C 62.86 (62.83) H 7.76 (7.75) N 8.62 (8.63)	+16.5 (*c* 2.0)
7ed $C_{19}H_{21}ClN_2O_2$	82	C	101		C 66.18 (66.16) H 6.14 (6.15) N 8.12 (8.10)	+23.3 (*c* 1.5)
7ee $C_{15}H_{21}ClN_2O_2$	93	D	105		C 60.70 (60.71) H 7.13 (7.12) N 9.44 (9.45)	+40.0 (*c* 1.5)
7fa $C_{10}H_{20}ClNO_4$	74	B	121		C 47.34 (47.35) H 9.95 (9.98) N 5.52 (5.53)	+20.0 (*c* 2.0)
7fc $C_{12}H_{24}ClNO_4$	89	C	122		C 51.15 (51.16) H 8.58 (8.56) N 4.97 (4.99)	+25.5 (*c* 1.8)
7fd $C_{14}H_{20}ClNO_4$	83	C	103		C 55.72 (55.75) H 6.68 (6.68) N 4.64 (4.63)	+19.5 (*c* 2.0)
7fe $C_{10}H_{20}ClNO_4$	78	D	116		C 47.34 (47.37) H 9.95 (9.94) N 5.52 (5.50)	+57.8 (*c* 1.0)

this reason the yield of *N*-butyl- (**6fb**), *N*-benzyl- (**6fd**) glutamic acid, *N*-propyl- (**6ha**), *N*-butyl- (**6hb**), and *N*-benzyl histidine (**6hd**) were also determined by ^{1}H NMR using phenylacetic acid as internal standard (Table 1). This acid, as sodium salt in D_2O–NaOH, exhibited a singlet at $\delta = 3.54$, which was far away from all the other signals.

The use of acetone during the work-up of the reaction provided a solid that, freed from unreacted **3** and (or) the corresponding alcohol, happened to be less soluble in water during the elimination of NaCl.

N-Isopropyl phenylalanine (**6ce**) was obtained only in 63% isolated yield; however, a large excess (3 mol equiv) of acetone (**3e**) was used.

When propanal (**3a**) or butanal (**3b**) were used in combination with **2**, Method A was followed but granular $NaBH_4$ was added (Method B). These aldehydes reacted very quickly with **2**; therefore excess granular $NaBH_4$ was used to promote the reduction of **3a** or **3b**, which in turn caused the *N*,*N*-dialkylation of **2** as shown by the GC–MS analysis of the reaction mixture.

© 2002 NRC Canada

Table 3. Infrared, ^{1}H and ^{13}C NMR spectra, and EI-MS spectra of *N*-alkyl amino acids (**6**).

Product	IR (KBr) ν (cm^{-1})	^{1}H NMR (D_2O–NaOH–DSS) δ (*J* in Hz)	^{13}C NMR (D_2O–NaOH–DSS) δ (*J* in Hz)	EI-MS (70eV) *m*/*z* (%)
6ab	3200–2000, 1570, 1460, 1383, 1360, 1280, 1210, 1142, 1100, 1090, 1052, 980, 890, 835, 774, 670	0.82 (t, J = 7.1, 3H, CH_3), 1.31 (sext, J = 7.1, 2H, CH_3CH_2), 1.37 (d, J = 7.1, 3H, *CHCH_3) 1.46–1.67 (m, 2H, CH_2), 2.81–3.03 (app t, 2H, NCH_2), 3.55 (q, J = 7.1, 1H, *CH)	15.3, 17.6, 21.7, 30.3, 48.5, 60.3, 177.5	145 (M^+, 2), 111 (1), 102 (19), 100 (100), 74 (6), 56 (11), 44 (20)
6bb	3300–2000, 1580, 1165, 1390, 1294, 1273, 1230, 1150, 1130, 1063, 1009, 885, 849, 805, 782, 742, 683	0.82–0.95 (m, 9H, 3×CH_3), 1.15–1.65 (m, 7H, 3×CH_2 + CH), 2.30–2.52 (m, 2H, NCH_2), 3.05 (dd, J_1 = 8.3, J_2 = 6.6, 1H, *CH)	15.8, 22.3, 24.2, 25.2, 27.3, 33.4, 40.1, 49.3, 65.0, 185.9	187 (M^+, 2), 172 (1), 143 (12), 142 (100), 130 (11), 88 (30), 86 (8)
6cb	3300–2000, 1578, 1460, 1390, 1361, 1305, 1087, 1060, 851, 788, 752, 707, 680, 530	0.82 (t, J = 7.1, 3H, CH_3), 1.11–1.48 (m, 4H, 2×CH_2), 2.28–2.54 (m, 2H, NCH_2), 2.81 and 2.86 (AB of ABX, J_{AB} = 13.5, J_{AX} = 7.5, J_{BX} = 6.1, 2H, *CHCH_2), 3.24 (dd, J_1 = 7.5, J_2 = 6.1, 1H, *CH), 7.17–7.35 (m, 5H, H_{arom})	15.9, 22.3, 33.3, 41.5, 49.3, 67.7, 129.1, 131.0, 131.8, 140.7, 183.9	222 ([M+1]$^+$, 1], 221 (M^+, 1), 176 (24), 132 (17), 130 (100), 120 (30), 91 (33), 88 (30), 84 27), 74 (11), 57 (27)
6cb-*d*	3300–2000, 1580, 1456, 1398, 1381, 1301, 1085, 1060, 844, 784, 747, 701, 676, 533	0.80 (t, J = 7.1, 3H, CH_3), 1.13–1.44 (m, 4H, 2×CH_2), 2.27–2.53 (m, 1H, NCD*H*), 2.79 and 2.84 (AB of ABX, J_{AB} = 13.5, J_{AX} = 7.5, J_{BX} = 6.1, 2H, *CHCH_2), 3.22 (dd, J_1 = 7.5, J_2 = 6.1, 1H, *CH), 7.17–7.35 (m, 5H, H_{arom})	15.8, 22.2, 33.2, 41.4, 48.8 (t, J = 21.2), 67.5, 129.0, 131.0, 131.7, 140.5, 183.9	223 ([M+1]$^+$, 1), 222 (M^+, 1), 177 (22), 133 (11), 131 (100), 120 (32), 91 (18), 89 (12), 74 (9), 58 (15)
6cc	3280–2000, 1611, 1495, 1482, 1382, 1374, 1342, 1284, 1266, 845, 790, 749, 702, 536, 475	0.73 (s, 9H, 3×CH_3), 2.08 and 2.11 (AB, J_{AB} = 11.0, 2H, NCH_2), 2.67 and 2.79 (AB of ABX, J_{AB} = 13.2, J_{AX} = 8.8, J_{BX} = 5.3, 2H, *CHCH_2), 3.07 (dd, J_1 = 8.8, J_2 = 5.3, 1H, *CH), 7.04–7.28 (m, 5H, H_{arom})	29.8, 32.3, 41.3, 62.1, 68.8, 129.2, 131.1, 131.9, 140.7, 184.1	236 ([M+1]$^+$, 1), 220 (9), 190 (21), 178 (17), 144 (100), 132 (45), 120 (28), 91 (19), 74 (16), 71 (24)
6cd	3220–2030, 1618, 1459, 1451, 1437, 1394, 1334, 1205, 1084, 868, 746, 697, 586, 532	2.52 and 2.60 (AB of ABX, J_{AB} = 13.4, J_{AX} = 7.7, J_{BX} = 6.2, 2H, *CHCH_2), 3.00 (dd, J_1 = 7.7, J_2 = 6.2, 1H, *CH), 3.23 and 3.42 (AB, J_{AB} = 12.6, 2H, NCH_2), 6.84–7.13 (m, 10H, H_{arom})	41.5, 53.5, 66.9, 129.1, 129.9, 131.0, 131.1, 131.2, 131.7, 140.5, 141.3, 183.7	256 ([M+1]$^+$, 1), 210 (5), 164 (34), 120 (4), 91 (100), 65 (7)
6ce	3230–2000, 1574, 1392, 1374, 1339, 846, 745, 700, 539	0.56 (app t, J = 7.3, 6H, 2×CH_3), 2.05–2.52 (m, 3H, NCH + *CHCH_2), 2.91 (app t, J = 7.3, 1H, *CH), 6.50–6.90 (m, 5H, H_{arom})	22.8, 25.0, 41.6, 48.5, 65.0, 128.9, 130.9, 131.6, 140.6, 183.9	208 ([M+1]$^+$, 1), 207 (M^+, 1), 192 (2), 162 (19), 146 (7), 120 (40), 116 (100), 103 (8), 91 (20), 74 (39), 65 (5), 43 (10)
6dd	3330–2020, 1591, 1518, 1464, 1439, 1401, 1334, 1259, 1213, 1178, 1109, 1087, 1061, 968, 864, 832, 753, 702, 642, 571, 540	2.47 (app d, J = 6.2, 2H, *CHCH_2), 2.98 (app t, J = 6.6, 1H, *CH), 3.22 and 3.38 (AB, J_{AB} = 13.2, 2H, NCH_2), 6.32 (app d, J = 8.3, 2H, H_{arom}), 6.67 (app d, J = 8.3, 2H, H_{arom}), 6.91–7.23 (m, 5H, H_{arom})	40.6, 53.5, 67.2, 121.2, 126.2, 131.2, 131.3, 133.2, 141.5, 166.9, 184.2	272 ([M+1]$^+$, 1), 271 (M^+, 1), 226 (5), 164 (49), 107 (31), 91 (100), 77 (5), 65 (4)
6eb	3410, 3200–2000, 1640, 1450, 1385, 1356, 1300, 1267, 1230, 1098, 1070, 1053, 1010, 995, 861, 813, 760, 755, 653	0.56 (t, J = 7.3, 3H, CH_3), 0.84–1.25 (m, 4H, 2×CH_2), 2.05–2.36 (m, 2H, NCH_2), 2.83 (app d, J = 6.3, 2H, *CHCH_2), 3.17 (dd, J_1 = 13.2, J_2 = 6.8, 1H, *CH), 6.82–7.08 (m, 3H, H_{arom}), 7.15–7.28 (m, 1H, H_{arom}), 7.40–7.54 (m, 1H, H_{arom})	15.9, 22.4, 31.2, 33.4, 49.4, 66.8, 113.2, 114.3, 121.3, 121.5, 124.2, 126.5, 129.8, 138.6, 184.6	260 (M^+, 1), 215 (1), 214 (1), 171 (1), 159 (2), 158 (1), 157 (1), 144 (2), 143 (1), 142 (1), 130 (100), 115 (2), 77 (2)

© 2002 NRC Canada

Table 3 (*Continued*).

Product	IR (KBr) ν (cm^{-1})	^1H NMR (D_2O–NaOH–DSS) δ (J in Hz)	^{13}C NMR (D_2O–NaOH–DSS) δ (J in Hz)	EI-MS (70eV) *m/z* (%)
6ec	3410, 3290–2000, 1613, 1492, 1444, 1459, 1360, 1341, 1287, 1024, 1007, 854, 739, 582, 533, 514	0.79 (s, 9H, 3×CH_3), 2.20 (app s, 2H, NCH_2), 2.99 and 3.05 (AB of ABX, J_{AB} = 14.3, J_{AX} = 8.1, J_{BX} = 5.7, 2H, *CHCH_2), 3.29 (dd, J_1 = 8.1, J_2 = 5.7, 1H, *CH), 7.04–7.23 (m, 3H, H_{arom}), 7.39–7.47 (m, 1H, H_{arom}), 7.63–7.72 (m, 1H, H_{arom})	29.8, 30.9, 32.8, 62.3, 67.9, 113.3, 114.3, 121.4, 121.6, 124.3, 126.6, 129.8, 138.7, 184.7	274 (M^+, 1), 259 (1), 229 (1), 188 (1), 159 (2), 144 (8), 130 (100), 115 (2)
6ed	3415, 3150–2000, 1602, 1489, 1457, 1449, 1392, 1353, 1348, 1316, 1213, 1082, 893, 802, 744, 701, 608, 584, 544, 510	2.72 and 2.84 (AB of ABX, J_{AB} = 14.5, J_{AX} = 7.7, J_{BX} = 6.1, 2H, *CHCH_2), 3.06–3.37 (m, 3H, *CH + NCH_2), 6.53–6.90 (m, 3H, H_{arom}), 6.95–7.08 (m, 1H, H_{arom}), 7.18–7.28 (m, 1H, H_{arom})	31.3, 53.4, 65.4, 113.2, 114.2, 121.2, 121.5, 124.1, 126.4, 129.5, 129.6, 130.7, 130.9, 138.6, 141.3, 184.1	294 (M^+, 2), 248 (1), 164 (1), 130 (100), 91 (19), 77 (3), 65 (2)
6fb	3300–2100, 1727, 1690, 1580, 1457, 1390, 1125, 1230, 1152, 1080, 1040, 861, 815, 800, 680, 625	0.69 (t, J = 7.2, 3H, CH_3), 0.96–1.37 (m, 4H, 2×CH_2), 1.40–1.77 (m, 2H, *CHCH_2), 1.82–2.10 (m, 2H, $COCH_2$), 2.13–2.41 (m, 2H, NCH_2), 2.81 (dd, J_1 = 8.1, J_2 = 5.6, 1H, *CH)	15.8, 22.4, 32.3, 33.4, 36.8, 49.5, 66.2, 185.0, 185.2	203 (M^+, 1), 185 (9), 158 (37), 142 (12), 140 (100), 114 (19), 98 (23), 84 (92)
6fd	3300–2070, 1706, 1632, 1468, 1456, 1370, 1348, 1274, 1089, 1069, 1020, 989, 819, 760, 699, 555, 509	1.71–2.07 (m, 2H, *CHCH_2), 2.25 (app t, J = 8.6, 2H, $COCH_2$), 3.13 (dd, J_1 = 7.7, J_2 = 5.7, 1H, *CH), 3.61 and 3.77 (AB, J_{AB} = 12.5, 2H, NCH_2), 7.33–7.54 (m, 5H, H_{arom})	32.4, 36.9, 53.9, 65.6, 130.2, 131.4, 141.6, 184.6, 185.4	238 ([M+1]$^+$, 1), 219 (23), 192 (24), 174 (56), 164 (2), 146 (35), 130 (8), 118 (8), 106 (12), 91 (100), 65 (12)
6ha	3670–2000, 1578, 1457, 1398, 1138, 1111, 984, 940, 841, 811, 752, 667, 628, 553	0.64 (t, J = 7.5, 3H, CH_3), 1.08–1.39 (m, 2H, CH_2), 2.11–2.36 (m, 2H, NCH_2), 2.63 (app d, J = 6.6, 2H, *CHCH_2), 3.11 (app t, J = 6.6, 1H, *CH), 6.65 (s, 1H, H_{arom}), 7.40 (s, 1H, H_{arom})	13.8, 24.6, 33.0, 51.6, 66.4, 121.5, 136.2, 139.8, 184.4	198 ([M+1]$^+$, 2), 197 (M^+, 1), 152 (37), 140 (25), 124 (10), 122 (14), 116 (17), 110 (21), 109 (9), 95 (27), 82 (100), 74 (5), 54 (10), 43 (10)
6hb	3670–2000, 1580, 1448, 1387, 1334, 1260, 1220, 1180, 1110, 1050, 999, 929, 885, 850, 830, 792, 743, 720, 665	0.64 (t, J = 7.3, 3H, CH_3), 0.90–1.44 (m, 4H, 2×CH_2), 2.10–2.38 (m, 2H, NCH_2), 2.62 (app d, J = 6.8, 2H, *CHCH_2), 3.08 (app t, J = 6.8, 1H, *CH), 6.60–6.70 (m, 1H, H_{arom}), 7.38–7.44 (m, 1H, H_{arom})	15.8, 22.3, 32.7, 33.3, 49.4, 66.3, 120.5, 135.6, 138.2, 184.1	211 (M^+, 1), 166 (13), 140 (6), 130 (3), 124 (4), 122 (10), 110 (7), 95 (15), 82 (100), 81 (20), 74 (2), 57 (3)
6hd	3630–2000, 1621, 1500, 1430, 1396, 1330, 1291, 1215, 1191, 1104, 1089, 961, 940, 869, 840, 810, 750, 702, 657, 631, 533	2.44 and 2.53 (AB of ABX, J_{AB} = 14.7, J_{AX} = 6.8, J_{BX} = 6.8, 2H, *CHCH_2), 2.97 (app t, J = 6.8, 1H, *CH), 3.15 and 3.32 (AB, J_{AB} = 12.7, 2H, NCH_2), 6.41 (app d, J = 1.0, 1H, H_{arom}), 6.81–7.04 (m, 5H, H_{arom}), 7.15 (app d, J = 1.0, 1H, H_{arom})	33.2, 53.5, 65.5, 122.4, 129.8, 131.0, 131.1, 136.5, 141.3, 141.4, 184.0	246 ([M+1]$^+$, 1), 200 (13), 140 (33), 122 (22), 110 (37), 106 (24), 91 (100), 82 (83), 65 (8)
6ib	3403, 3300–2000, 1641, 1625, 1574, 1458, 1380, 1314, 1037, 858, 810, 775, 684, 639, 587, 559	0.53 (t, J = 7.5, 3H, CH_3), 0.83–1.24 (m, 4H, 2×CH_2), 1.28–1.68 (m, 2H, *CHCH_2), 1.73–1.90 (m, 2H, $COCH_2$), 1.95–2.23 (m, 2H, NCH_2), 2.65 (dd, J_1 = 8.1, J_2 = 5.5, 1H, *CH)	15.8, 22.3, 31.3, 33.3, 34.3, 49.3, 65.6, 181.3, 184.4	203 ([M+1]$^+$, 1), 185 (6), 184 (6), 169 (10), 157 (24), 142 (26), 140 (100), 130 (13), 128 (8), 114 (16), 98 (16), 84 (55), 72 (8), 70 (8), 57 (11)
6jb	3280–2000, 1575, 1460, 1390, 1315, 1232, 1187, 1151, 1065, 980, 955, 858, 796, 760, 740, 700, 675	0.86 (t, J = 6.8, 3H, CH_3), 1.14–1.57 (m, 4H, 2×CH_2), 1.67–1.94 (m, 2H, *CHCH_2), 2.09 (s, 3H, SCH_3), 2.32–2.60 (m, 4H, SCH_2 + NCH_2), 3.09 (app t, J = 7.1, 1H, *CH)	16.0, 16.9, 22.5, 32.4, 33.5, 35.0, 49.6, 65.5, 184.6	205 (M^+, 3), 187 (40), 172 (28), 160 (100), 157 (21), 144 (18), 130 (26), 112 (78), 88 (80), 74 (16), 61 (31)

© 2002 NRC Canada

Table 4. Infrared, ^{1}H and ^{13}C NMR spectra, and EI-MS spectra of *N*-alkyl amino acid methyl ester hydrochlorides (**7**).

Product	IR (KBr) ν (cm^{-1})	^{1}H NMR (DMSO-d_6/TMS) δ (*J* in Hz)	^{13}C NMR (DMSO-d_6/TMS) δ (*J* in Hz)	MS (70 eV) *m*/*z* (%)
7ad	3200–2200, 1745, 1548, 1450, 1250, 1208, 1137, 1093, 990, 758, 695, 664	1.58 (d, J = 7.2, 3H, CH_3), 3.74 (s, 3H, OCH_3), 4.06 (q, J = 7.2, 1H, *CH), 4.16 and 4.21 (AB, J_{AB} = 13.1, 2H, CH_2), 7.35–7.50 (m, 3H, H_{arom}), 7.56–7.70 (m, 2H, H_{arom}), 10.20 (br s, 2H, NH)	14.4, 48.4, 52.7, 54.1, 128.4, 128.8, 130.2, 131.7, 169.5	194 ([M+1]$^+$, 2), 192 (2), 178 (1), 134 (100), 106 (36), 92 (30), 91 (95), 65 (21)
7bb	3200–2200, 1749, 1559, 1470, 1392, 1372, 1245, 1211, 1058, 959, 846, 750	0.80–1.15 (m, 9H, 3×CH_3), 1.39 (sext, J = 7.3, 2H, CH_3CH_2), 1.77 (sept, J = 6.4, 1H, CH), 1.87–2.12 (m, 4H, 2×CH_2), 2.88–3.17 (m, 2H, NCH_2), 3.78–3.97 (m, 4H, *CH + OCH_3), 9.82 (br s, 1H, NH), 10.16 (br s, 1H, NH)	13.3, 19.9, 21.1, 22.8, 24.7, 27.6, 37.9, 46.1, 52.8, 58.2, 168.6	202 ([M+1]$^+$, 2), 201 (M$^+$, 1), 158 (3), 144 (9), 142 (100), 130 (4), 102 (13), 88 (7), 86 (8), 84 (7), 57 (9)
7bd	3200–2100, 1734, 1557, 1463, 1416, 1382, 1360, 1284, 1219, 1182, 1066, 1026, 1001, 944, 742, 702	0.87 (d, J = 6.5, 6H, 2×CH_3), 1.59–2.04 (m, 3H, CH + CH_2), 3.72 (s, 3H, OCH_3), 3.84 (dd, J_1 = 9.2, J_2 = 4.8, 1H, *CH), 4.12 and 4.22 (AB, J_{AB} = 13.0, 2H, NCH_2), 7.35–7.46 (m, 3H, H_{arom}), 7.60–7.71 (m, 2H, H_{arom}), 10.42 (br s, 2H, NH)	21.0, 22.8, 24.1, 37.6, 48.7, 52.5, 56.9, 128.3, 128.8, 130.4, 131.4, 169.1	236 ([M+1]$^+$, 2), 235 (M$^+$, 1), 234 (2), 220 (3), 192 (1), 190 (1), 178 (10), 176 (100), 106 (19), 91 (81), 65 (11)
7ca	3300–2150, 1747, 1599, 1500, 1458, 1442, 1428, 1362, 1348, 1329, 1285, 1251, 1216, 1172, 1043, 951, 750, 704, 607, 524, 501	0.90 (t, J = 7.3, 3H, CH_3), 1.62–1.89 (m, 2H, CH_3CH_2), 2.73–3.02 (m, 2H, NCH_2), 3.13 and 3.52 (AB of ABX, J_{AB} = 13.5, J_{AX} = 9.6, J_{BX} = 4.5, 2H, *$CHCH_2$), 3.58 (s, 3H, OCH_3), 4.18 (dd, J_1 = 9.6, J_2 = 4.5, 1H, *CH), 7.18–7.36 (m, 5H, H_{arom}), 9.68 (br s, 1H, NH), 10.47 (br s, 1H, NH)	10.8, 18.8, 34.8, 47.5, 52.3, 60.3, 127.1, 128.4, 129.1, 134.8, 168.4	222 ([M+1]$^+$, 2), 221 (M$^+$, 1), 190 (3), 162 (28), 160 (8), 132 (7), 130 (100), 128 (17), 120 (15), 103 (11), 91 (14), 88 (12), 43 (8)
7cb	3200–2200, 1750, 1568, 1445, 1350, 1338, 1245, 1215, 1180, 1049, 848, 753, 708, 670	0.89 (t, J = 7.3, 3H, CH_3), 1.25–1.46 (m, 2H, CH_3CH_2), 1.65–1.85 (m, 2H, CH_2CH_2), 2.80–3.12 (m, 2H, NCH_2), 3.16 and 3.52 (AB of ABX, J_{AB} = 13.7, J_{AX} = 9.6, J_{BX} = 4.6, 2H, *$CHCH_2$), 3.60 (s, 3H, OCH_3), 4.19 (dd, J_1 = 9.6, J_2 = 4.6, 1H, *CH), 7.20–7.30 (m, 5H, H_{arom}), 10.20 (br s, 2H, NH)	13.2, 19.3, 25.0, 27.4, 35.0, 45.8, 52.3, 60.5, 127.1, 128.4, 129.2, 134.8, 168.6	236 ([M+1]$^+$, 4), 235 (M$^+$, 1), 192 (6), 176 (91), 144 (100), 132 (18), 120 (33), 103 (18), 102 (57), 91 (29), 88 (30), 57 (21), 41 (20)
7cc	3290–2200, 1750, 1533, 1472, 1455, 1441, 1377, 1311, 1275, 1235, 1187, 1172, 1080, 1040, 1009, 835, 774, 753, 710, 519	1.05 (s, 9H, 3×CH_3), 2.68 and 2.96 (AB, J_{AB} = 12.2, 2H, NCH_2), 3.08 and 3.68 (AB of ABX, J_{AB} = 13.2, J_{AX} = 10.9, J_{BX} = 4.2, 2H, *$CHCH_2$), 3.55 (s, 3H, OCH_3), 4.09 (dd, J_1 = 10.9, J_2 = 4.2, 1H, *CH), 7.18–7.38 (m, 5H, H_{arom}), 10.32 (br s, 2H, NH)	27.1, 30.3, 34.7, 52.1, 56.6, 61.4, 126.9, 128.2, 128.9, 135.4, 168.4	250 ([M+1]$^+$, 1), 248 (1), 234 (19), 192 (30), 190 (50), 174 (10), 164 (19), 158 (100), 132 (81), 120 (51), 103 (11), 91 (22), 88 (52), 71 (25), 43 (30)
7cd	3200–2080, 1753, 1541, 1502, 1496, 1457, 1442, 1266, 1255, 1213, 1180, 1086, 1064, 1041, 1026, 756, 702, 492	3.12 and 3.57 (AB of ABX, J_{AB} = 13.0, J_{AX} = 10.2, J_{BX} = 4.1, 2H, *$CHCH_2$), 3.53 (s, 3H, OCH_3), 4.15 (dd, J_1 = 10.2, J_2 = 4.1, 1H, *CH), 4.23 (AB, J_{AB} = 13.0, 2H, NCH_2), 7.15–7.36 (m, 5H, H_{arom}), 7.37–7.52 (m, 3H, H_{arom}), 7.55–7.73 (m, 2H, H_{arom}), 10.33 (br s, 2H, NH)	35.1, 49.2, 52.3, 60.0, 127.1, 128.4, 128.9, 129.1, 130.4, 131.4, 134.7, 168.4	270 ([M+1]$^+$, 1), 268 (1), 210 (55), 178 (100), 118 (9), 117 (8), 91 (81), 77 (11), 65 (15)
7cd-*d*	3220, 2070, 1756, 1566, 1498, 1472, 1453, 1429, 1380, 1262, 1209, 1175, 1079, 1053, 1029, 985, 754, 656, 521, 493	3.11 and 3.59 (AB of ABX, J_{AB} = 13.3, J_{AX} = 10.2, J_{BX} = 4.1, 2H, *$CHCH_2$), 3.52 (s, 3H, OCH_3), 4.13 (dd, J_1 = 10.2, J_2 = 4.1, 1H, *CH), 4.24 (s, 1H, NCD*H*), 7.18–7.36 (m, 5H, H_{arom}), 7.38–7.48 (m, 3H, H_{arom}), 7.58–7.70 (m, 2H, H_{arom}), 10.01 (br s, H, NH), 10.08 (br s, H, NH)	35.1, 48.8 (t, J = 22.3), 52.4, 60.0, 127.2, 128.5, 129.0, 129.2, 130.5, 131.4, 134.9, 168.5	271 ([M+2]$^+$, 1), 270 (M$^+$, 1), 211 (39), 179 (86), 178 (50), 119 (3), 92 (100), 91 (76), 77 (3), 65 (8)

© 2002 NRC Canada

Table 4 (*continued*).

Product	IR (KBr) ν (cm^{-1})	^{1}H NMR (DMSO-d_6/TMS) δ (*J* in Hz)	^{13}C NMR (DMSO-d_6/TMS) δ (*J* in Hz)	MS (70 eV) *m*/*z* (%)
7ce	3220–2150, 1748, 1568, 1498, 1459, 1389, 1322, 1294, 1233, 1180, 1152, 1135, 1063, 961, 851, 773, 751, 705, 516	1.34 (d, J = 6.7, 6H, 2×CH_3), 3.15 and 3.59 (AB of ABX, J_{AB} = 13.7, J_{AX} = 10.2, J_{BX} = 4.5, 2H, *CHCH_2), 3.35 (sept, J = 6.7, 1H, NCH), 3.58 (s, 3H, OCH_3), 4.17 (dd, J_1 = 10.2, J_2 = 4.5, 1H, *CH), 7.20–7.46 (m, 5H, H_{arom}), 9.70 (br s, 1H, NH), 10.53 (br s, 1H, NH)	18.0, 19.0, 35.3, 49.1, 52.3, 58.0, 127.0, 128.3, 129.0, 134.7, 168.3	222 ([M+1]$^+$, 1), 220 (1), 206 (3), 162 (69), 146 (18), 130 (100), 120 (49), 103 (10), 91 (14), 88 (45), 43 (9)
7db	3280, 3200–2300, 1737, 1617, 1594, 1521, 1445, 1352, 1326, 1271, 1246, 1212, 1182, 1108, 1062, 960, 854, 827, 780, 656, 563, 526	0.83 (t, J = 6.9, 3H, CH_3), 1.05–1.45 (m, 4H, 2×CH_2), 1.90 (br s, 1H, NH), 2.25–2.55 (m, 2H, NCH_2), 2.68 and 2.74 (AB of ABX, J_{AB} = 13.4, J_{AX} = 7.5, J_{BX} = 5.9, 2H, *CHCH_2), 3.21 (dd, J_1 = 7.5, J_2 = 5.9, 1H, *CH), 3.54 (s, 3H, OCH_3), 6.49–6.59 (m, 2H, H_{arom}), 6.92–7.03 (m, 2H, H_{arom}), 9.02 (br s, 1H, OH)[a]	13.6, 19.6, 31.6, 38.7, 46.6, 50.8, 62.8, 114.8, 127.6, 129.7, 155.7, 174.5[a]	252 ([M+1]$^+$, 2), 208 (3), 192 (56), 144 (100), 107 (28), 102 (51), 91 (10), 88 (21), 57 (16), 41 (11)
7dd	3280, 3200–2400, 1734, 1614, 1596, 1521, 1450, 1437, 1370, 1324, 1309, 1284, 1260, 1230, 1214, 1184, 1109, 1033, 980, 843, 830, 754, 702, 653	3.02 and 3.40 (AB of ABX, J_{AB} = 13.8, J_{AX} = 9.7, J_{BX} = 4.6, 2H, *CHCH_2), 3.40 (br s, 1H, NH), 3.55 (s, 3H, OCH_3), 4.05 (dd, J_1 = 9.7, J_2 = 4.6, 1H, *CH), 4.14 and 4.24 (AB, J_{AB} = 13.1, 2H, NCH_2), 6.70–6.80 (m, 2H, H_{arom}), 6.95–7.07 (m, 2H, H_{arom}), 7.36–7.46 (m, 3H, H_{arom}), 7.54–7.65 (m, 2H, H_{arom}), 9.02 (br s, 1H, OH)[a]	34.4, 49.2, 52.5, 60.3, 115.4, 124.4, 128.6, 129.1, 130.2, 130.5, 131.4, 156.7, 168.6[a]	286 ([M+1]$^+$, 2), 285 (M$^+$, 1), 226 (12), 178 (100), 118 (5), 107 (10), 91 (83), 77 (5), 65 (7)
7ea	3415, 3300–2300, 1745, 1619, 1566, 1461, 1438, 1360, 1341, 1261, 1224, 1100, 1071, 748	0.89 (t, J = 7.6, 3H, CH_3), 1.62–1.86 (m, 2H, CH_2), 2.75–3.05 (m, 1H, NCH_2), 3.29–3.43 (m, 1H, *CHCHH), 3.47–3.61 (m, 4H, OCH_3 + *CHCHH), 4.14 (dd, J_1 = 9.2, J_2 = 4.3, 1H, *CH), 6.96–7.13 (m, 2H, H_{arom}), 7.26 (d, J = 2.2, 1H, H_{arom}), 7.33–7.42 (m, 1H, H_{arom}), 7.53–7.62 (m, 1H, H_{arom}), 9.49 (br s, 1H, NH), 10.42 (br s, 1H, NH), 11.16 (s, 1H, NH_{arom})	10.9, 18.8, 25.2, 47.5, 52.4, 59.8, 106.4, 111.4, 118.0, 118.4, 120.9, 124.5, 126.7, 136.1, 168.8	260 (M$^+$, 2), 201 (9), 144 (8), 130 (100), 115 (8), 102 (13), 88 (17), 77 (15), 70 (18), 43 (32), 41 (13)
7ec	3380, 3300–2400, 1747, 1476, 1457, 1433, 1368, 1355, 1284, 1202, 1178, 1124, 1098, 1068, 1024, 975, 828, 802, 780, 741, 624	0.84 (s, 9H, 3×CH_3), 2.15 and 2.33 (AB, J_{AB} = 11.1, 2H, NCH_2), 3.05 (app d, J = 6.4, 2H, *CHCH_2), 3.47 (app t, J = 6.4, 1H, *CH), 3.54 (s, 3H, OCH_3), 6.33 (s, 1H, NH), 6.48 (s, 1H, NH), 6.92–7.09 (m, 2H, H_{arom}), 7.11 (d, J = 2.2, 1H, H_{arom}), 7.36 (app d, J = 7.6, 1H, H_{arom}), 7.51 (app d, J = 7.3, 1H, H_{arom}), 10.87 (s, 1H, NH_{arom})	27.3, 28.7, 31.2, 51.0, 55.9, 63.1, 119.8, 111.3, 118.1, 118.2, 120.7, 123.3, 122.7, 127.2, 136.0, 174.7	288 (M$^+$, 5), 273 (3), 229 (25), 202 (8), 160 (11), 158 (100), 144 (56), 143 (11), 132 (25), 131 (89), 130 (99), 102 (11), 88 (62), 71 (25), 43 (29)
7ed	3420, 3300–2300, 1746, 1622, 1566, 1457, 1434, 1344, 1259, 1212, 1184, 1098, 1075, 746, 701	3.36 and 3.64 (AB of ABX, J_{AB} = 14.5, J_{AX} = 9.2, J_{BX} = 4.3, 2H, *CHCH_2), 3.50 (s, 3H, OCH_3), 4.11 (dd, J_1 = 9.1, J_2 = 4.3, 1H, *CH), 4.18 and 4.27 (AB, J_{AB} = 13.0, 2H, NCH_2), 6.94–7.14 (m, 2H, H_{arom}), 7.25 (d, J = 2.4, 1H, H_{arom}), 7.35–7.46 (m, 4H, H_{arom}), 7.49–7.56 (m, 1H, H_{arom}), 7.59–7.67 (m, 2H, H_{arom}), 10.00 (br s, 1H, NH), 10.71 (br s, 1H, NH), 11.11 (s, 1H, NH_{arom})	25.4, 49.1, 52.4, 59.3, 106.5, 111.5, 118.0, 118.4, 121.0, 124.5, 126.7, 128.4, 128.9, 130.4, 131.3, 136.1, 168.7	308 (M$^+$, 5), 249 (12), 206 (5), 178 (66), 131 (89), 130 (100), 103 (13), 91 (99), 77 (11), 65 (8)

© 2002 NRC Canada

Table 4 (*concluded*).

Product	IR (KBr) ν (cm^{-1})	^{1}H NMR (DMSO-d_6/TMS) δ (*J* in Hz)	^{13}C NMR (DMSO-d_6/TMS) δ (*J* in Hz)	MS (70 eV) *m*/*z* (%)
7ee	3394, 3300–2150, 1745, 1622, 1578, 1453, 1397, 1384, 1353, 1330, 1236, 1184, 1105, 1065, 1046, 1013, 950, 835, 746, 625, 564	1.32 (d, *J* = 6.2, 6H, 2×CH_3), 3.25–3.48 (m, 2H, NCH + *CHCH*H*), 3.48–3.72 (m, 4H, *CHC*H*H + OCH_3), 4.14 (dd, J_1 = 9.7, J_2 = 4.1, 1H, *CH), 6.93–7.18 (m, 2H, H_{arom}), 7.28 (d, *J* = 1.6, 1H, H_{arom}), 7.34–7.43 (m, 1H, H_{arom}), 7.52–7.63 (m, 1H, H_{arom}), 9.36 (br s, 1H, NH), 10.43 (br s, 1H, NH), 11.12 (s, 1H, NH_{arom})	17.9, 19.0, 25.7, 49.2, 52.4, 57.4, 106.5, 111.4, 117.9, 118.5, 121.0, 124.4, 126.7, 136.1, 168.9	260 (M^+, 8), 201 (17), 159 (6), 131 (81), 130 (100), 115 (8), 103 (8), 88 (57), 77 (7), 43 (8)
7fa	3150–2300, 1742, 1565, 1442, 1388, 1301, 1281, 1254, 1217, 1180, 1078, 1003, 981, 784, 722	0.90 (t, *J* = 7.3, 3H, CH_3), 1.71 (sext, *J* = 7.6, 2H, CH_2), 2.02–2.36 (m, 2H, *CHCH_2), 2.42–2.68 (m, 2H, $COCH_2$), 2.71–2.97 (m, 2H, NCH_2), 3.61 (s, 3H, OCH_3), 3.74 (s, 3H, OCH_3), 3.98 (dd, J_1 = 7.6, J_2 = 5.3, 1H, *CH), 9.60 (br s, 2H, NH)	10.8, 18.9, 23.9, 29.0, 47.4, 51.3, 52.6, 57.9, 168.8, 171.9	218 ($[M+1]^+$, 2), 217 (M^+, 1), 202 (1), 188 (5), 186 (13), 158 (100), 130 (9), 128 (11), 126 (31), 98 (11), 84 (16)
7fc	3250–2300, 1755, 1743, 1544, 1476, 1434, 1382, 1336, 1274, 1259, 1236, 1205, 1092, 1040, 992, 963, 887, 827, 746	1.03 (s, 9H, 3×CH_3), 2.10–2.28 (m, 2H, *CHCH_2), 2.49–2.60 (m, 2H, $COCH_2$), 2.67 and 2.86 (AB, J_{AB} = 10.5, 2H, NCH_2), 3.61 (s, 3H, OCH_3) 3.74 (s, 3H, OCH_3), 3.98 (dd, J_1 = 7.7, J_2 = 4.6, 1H, *CH), 9.13 (br s, 1H, NH), 9.75 (br s, 1H, NH)	23.5, 27.1, 29.5, 30.3, 51.3, 52.6, 56.8, 59.0, 168.4, 172.0	246 ($[M+1]^+$, 3), 245 (M^+, 1), 230 (8), 214 (9), 198 (5), 188 (100), 186 (75), 156 (15), 144 (8), 128 (46), 84 (28), 68 (14)
7fd	3200–2200, 1740, 1544, 1470, 1438, 1370, 1315, 1289, 1276, 1260, 1222, 1194, 1100, 1015, 950, 858, 765, 712	2.05–2.40 (m, 2H, CH_2), 2.45–2.62 (m, 2H, $COCH_2$), 3.60 (s, 3H, OCH_3), 3.72 (s, 3H, OCH_3), 4.01 (dd, J_1 = 7.9, J_2 = 4.9, 1H, *CH), 4.14 and 4.21 (AB, J_{AB} = 12.9, 2H, NCH_2), 7.36–7.49 (m, 3H, H_{arom}), 7.53–7.66 (m, 2H, H_{arom}), 10.28 (br s, 2H, NH)	24.0, 29.0, 49.1, 51.4, 52.8, 57.6, 128.5, 128.9, 130.3, 131.4, 168.5, 171.9	266 ($[M+1]^+$, 1), 233 (15), 206 (82), 174 (100), 146 (21), 106 (20), 92 (29), 91 (91), 65 (20)
7fe	3200–2300, 1744, 1561, 1474, 1438, 1388, 1360, 1314, 1230, 1189, 1156, 1139, 1072, 977, 959, 834, 750	1.29 (d, *J* = 6.4, 3H, CH_3), 1.31 (d, *J* = 6.4, 3H, CH_3), 2.02–2.39 (m, 2H, *CHCH_2), 2.42–2.68 (m, 2H, $COCH_2$), 3.32 (sept, *J* = 6.4, 1H, NCH), 3.62 (s, 3H, OCH_3), 3.75 (s, 3H, OCH_3), 4.07 (dd, J_1 = 8.2, J_2 = 4.9, 1H, *CH), 9.51 (br s, 2H, NH)	18.0, 18.9, 24.1, 28.9, 48.9, 51.3, 51.7, 52.7, 55.3, 168.7, 171.9	218 ($[M+1]^+$, 2), 217 (M^+, 1), 202 (7), 174 (21), 158 (100), 144 (14), 142 (14), 88 (10), 84 (68), 56 (16)

[a]Spectrum obtained after neutralization.

When sterically hindered 2,2,2-trimethylacetaldehyde (**3c**) or benzaldehyde (**3d**) were used in connection with **2**, the addition of acetic acid (1 mol equiv) and the less reactive pelletized $NaBH_4$ were found to be beneficial to the reaction (Method C). In fact, under these experimental conditions, carbonyl compounds (**3c**) and (**3d**) and imine **5** are more reactive towards **2** and $NaBH_4$, respectively, because they are partially protonated.

The reaction of **2** with acetone (**3e**), the least reactive carbonyl compound considered, required more acetic acid (2 mol equiv) than Method C. In addition, THF was added to reduce the reactivity of pelletized $NaBH_4$ towards **3e** (Method D).

With the sterically hindered and (or) less electrophilic 2,2,2-trimethylacetaldehyde (**3c**), benzaldehyde (**3d**), and acetone (**3e**), GC–MS analysis sometimes showed the presence of unreacted **2** or **5**. A further addition of **3** and $NaBH_4$ or $NaBH_4$ alone (see *Experimental*) was used to bring the reaction to completion. The results of the reactions involving **2** are listed in Table 2.

When $NaBD_4$ was used instead of $NaBH_4$, a deuterium atom was introduced in the α position of the entering *N*-substituent. This procedure was successfully employed in the synthesis of *N*-(1-deuterio)butyl phenylalanine (**6cb-*d***) and *N*-(α-deuterio)benzyl phenylalanine methyl ester hydrochloride (**7cd-*d***).

The mass spectra (EI positive ion at 70 eV) of some of *N*-alkyl derivatives of **6** and **7** showed the presence of the $[M + 1]^+$ peak (Tables 3 and 4) and the almost complete absence of the parent ion. This species might be produced by an ion–molecule reaction, as invoked to explain the behaviour of substituted malonic acids (22).

Data pertinent to the synthesized *N*-alkyl amino acids (**6**) and amino methyl esters hydrochlorides (**7**) are collected in Tables 3 and 4, respectively.

© 2002 NRC Canada

The GC–MS analyses of **7ad**, **7cb**, **7ec**, and **7fa** performed using a chiral column showed that the enantiomeric purity of the original α-amino acid methyl ester was retained.

Conclusions

In conclusion, the method described here is very simple, fast, and inexpensive, with respect to both the handling of chemicals and the equipment required. It is also applicable both to amino acids and amino methyl esters with various carbonyl compounds, and the preformation and isolation of the imine is not required. It appears essential, however, to find the most suitable conditions for successful experimentations.

Experimental

General

All the L-amino acids (**1a**–**j**), the L-amino acid methyl ester hydrochlorides (**2a**–**f**), the carbonyl compounds (**3a**–**e**), and $NaBD_4$ powder (96 atom% D, pelletized with an IR die) were purchased from Aldrich, Italy; $NaBH_4$ (Venpure®) caplets and granular was kindly donated by Morton International S.p.A. (now Rohm and Haas; Mozzate, Como, Italy). Thin layer chromatography was performed on silica gel (Kieselgel 60 F_{254} Merck, Darmstadt, Germany) and EtOAc–hexane (50:50) was used as the eluent. Solvents were used as received. GC–MS analyses were performed with a Fisons TRIO 2000 gas chromatograph–mass spectrometer, working in the positive-ion 70 eV electron-impact mode. Spectra were recorded in the range 35–450 u. Injector temperature was kept at 250°C and the column (Supelco SPB™-5, 30 m long, 0.25 mm i.d.) temperature was programmed from 60 to 300°C with a gradient of 10°C min^{-1}. Direct-inlet mass spectra (DI-MS) were obtained on the same instrument: temperatures between 150 and 250°C were found suitable to volatilize all the compounds into the ion source. The enantiomeric purity of **7ad**, **7cb**, **7ec**, and **7fa** was determined using chiral-GC analysis, upon comparison with the racemic mixtures obtained from the reaction of the corresponding D,L-amino acid methyl esters under the same conditions (using a Chrompack 7495 WCOT column, liquid phase Chirasil-val-L, 26 m long, 0.22 mm i.d.). IR spectra were obtained with a Nicolet FT-IR Magna 550 spectrophotometer using the KBr technique for solids and recorded in the range 4000–400 cm^{-1}. ^1H and ^{13}C NMR spectra were recorded at room temperature on a Bruker AC-F 200 spectrometer at 200 and 50 MHz, respectively, using D_2O–NaOH for the *N*-alkyl amino acids (**6**) and DMSO-d_6 for the *N*-alkyl amino acids methyl ester hydrochlorides (**7**) as solvents. NMR peak locations are reported as δ values from DSS (2,2-dimethyl-2-silapentane-5-sulfonate) and TMS, respectively. Some ^1H NMR multiplets are characterized by the term app (apparent): this refers only to their appearance and may be an oversimplification. Optical rotations were determined at 21°C using a POLAX-D polarimeter purchased from ATAGO (Japan). Elemental analyses were performed with a Carlo Erba Mod. 1106 elemental analyser and were in satisfactory agreement with calculated values. Melting points were determined with an automatic Mettler (Mod. FP61) melting point apparatus and are not corrected.

Method A

N-*Alkyl amino acids (6)*

The aldehyde (**3a**–**d**, 14.0 mmol) was added to a stirred solution of the amino acid (**1**, 10.0 mmol) in MeOH (25 mL) neutralized with finely powdered NaOH (0.42 g, 10.5 mmol). After 10 min at room temperature, the solution was cooled with an ice bath and $NaBH_4$ pellets (0.49 g, 13.0 mmol) were added. The reaction mixture was stirred for 120 min at 0°C, then acidified with 37% HCl up to the isoelectric point of starting amino acid **1**. The solvents were distilled off and the residue was triturated in acetone and filtered. The solid was washed with H_2O to remove NaCl and pure *N*-alkyl amino acid **6** was obtained.

With tyrosine (**1d**) and glutamic acid **(1f**), twice the amount of NaOH (0.84 g, 20.1 mmol) was used to neutralize all the acid centers.

When acetone **3e** was used as the carbonyl compound, the procedure was the same, but 30.0 mmol (2.20 mL) of **3e** was used.

Method B

N-*Propyl and* N-*butyl amino acid methyl ester hydrochlorides (7)*

Propanal or butanal (**3a** or **3b**, respectively, 14.0 mmol) was added to a stirred solution of the amino acid methyl ester hydrochloride (**2**, 10.0 mmol) in MeOH (50 mL) neutralized with finely powdered NaOH (0.42 g, 10.5 mmol). After 10 min at room temperature, the solution was cooled with an ice bath and granular $NaBH_4$ (0.30 g, 8.0 mmol) was added. The reaction mixture was stirred for 60 min at 0°C, then MeOH was distilled off, the residue re-dissolved in EtOAc, and NaCl filtered off. The organic phase was washed with brine and dried over Na_2SO_4. EtOAc was removed in vacuo and the residue, dissolved in Et_2O, was treated with ethereal HCl (2 M, 5 mL, 10 mmol); *N*-alkyl amino acid methyl ester hydrochloride **7** was filtered and washed with Et_2O. If the residue was insoluble in Et_2O, it was dissolved in EtOAc, treated with ethereal HCl and, after elimination of solvents under reduced pressure, **7** was crystallized from Et_2O.

Method C

N-*Benzyl and* N-*neopentyl amino acid methyl ester hydrochlorides (7)*

2,2,2-Trimethylacetaldehyde or benzaldehyde (**3c** or **3d**, respectively, 15.0 mmol) and acetic acid (0.57 mL, 10.0 mmol) were added to a stirred solution of the amino acid methyl ester hydrochloride (**2**, 10.0 mmol) in MeOH (50 mL) neutralized with finely powdered NaOH (0.42 g, 10.5 mmol). After 10 min at room temperature, the solution was cooled with an ice bath and $NaBH_4$ pellets (0.38 g, 10.0 mmol) were added. The reaction mixture was stirred for 60 min at 0°C and if the GC–MS analysis of the reaction mixture showed the presence of unreacted imine **5**, granular $NaBH_4$ (0.19 g, 5.0 mmol) was added. The reaction mixture was stirred for an additional 30 min, then MeOH was distilled off, the residue dissolved in EtOAc, and NaCl filtered

© 2002 NRC Canada

off. The organic phase was washed with saturated Na_2CO_3 solution and dried over Na_2SO_4. EtOAc was removed in vacuo and the residue, dissolved in Et_2O, was treated with ethereal HCl (2 M, 5 mL, 10.0 mmol); *N*-alkyl amino acid methyl ester hydrochloride **7** was filtered and washed with Et_2O. If the residue was insoluble in Et_2O, it was dissolved in EtOAc, treated with ethereal HCl and, after the elimination of solvents under reduced pressure, **7** was crystallized from Et_2O.

Method D

N-*Isopropyl amino acid methyl ester hydrochlorides (7)*

A solution of acetone (**3e**, 1.47 mL, 20.0 mmol) and acetic acid (1.14 mL, 20.0 mmol) in THF (6 mL) was added to a stirred solution of amino acid methyl ester hydrochloride **2** (10.0 mmol) in MeOH (18 mL) and THF (35 mL) neutralized with NaOH (0.42 g, 10.5 mmol). After 10 min at room temperature, the solution was cooled with an ice bath and $NaBH_4$ pellets (0.38 g, 10.0 mmol) were added. The reaction mixture was stirred for 60 min at 0°C and if the GC–MS analysis of the reaction mixture showed the presence of unreacted amino ester **2**, a solution of acetone (**3e**, 0.73 mL, 10. 0 mmol) and acetic acid (0.57 mL, 5.0 mmol) in THF (3 mL), and after 10 min $NaBH_4$ pellets (0.19 g, 5.0 mmol), were added. The reaction mixture was stirred for additional 30 min, then solvents were distilled off, the residue was dissolved in EtOAc, and NaCl filtered off. The organic phase was washed with saturated Na_2CO_3 solution and dried over Na_2SO_4. EtOAc was removed in vacuo and the residue, dissolved in Et_2O, was treated with ethereal HCl (2 M, 5 mL, 10.0 mmol); *N*-isopropyl amino acid methyl ester hydrochloride **7** was filtered and washed with Et_2O. If the residue was insoluble in Et_2O, it was dissolved in EtOAc, treated with ethereal HCl and, after the elimination of solvents under reduced pressure, **7** was crystallized from Et_2O.

Acknowledgments

Financial support was obtained from the Italian Ministry of University, Sciences and Technology (MURST 40% 2000 and 2001 to GV). PG is the recipient of a three-year scholarship from the Ministry of Agriculture. The authors are grateful to Dr. P. Martinuzzi for recording ^1H and ^{13}C NMR spectra and Mr P. Padovani for expert instrumental maintenance.

References

1. A.E.P Adang, P.H.H. Hermkens, J.T.M. Linders, H.C.J. Ottenheijm, and C.J. van Staveren. Recl. Trav. Chim. Pays-Bas, **113**, 63 (1994).
2. (*a*) A. Giannis and T. Kolter. Angew. Chem. Int. Ed. Engl. **32**, 1244 (1993); (*b*) J. Gante. Angew. Chem. Int. Ed. Engl. **33**, 1699 (1994).
3. R.J. Simon, R.S. Kania, R.N. Zuckermann, V.D. Huebner, D.A. Jewell, S. Banville, S. Wang, S. Rosenberg, C.K. Marlowe, D.C. Spellmeyer, R. Tan, A.D. Frankel, D.V. Santi, F.E. Cohen, and P.A. Bartlett. Proc. Natl. Acad. Sci. U.S.A. **89**, 9367 (1992).
4. T. Fukuyama, M. Cheung, C.-K. Jow, Y. Hidai, and T. Kan. Tetrahedron Lett. **38**, 5831 (1997).
5. K. Wisniewski and A.S. Kolodziejczk. Tetrahedron Lett. **38**, 483 (1997).
6. J.F. Reichwein and R.M.J. Liskamp. Tetrahedron Lett. **39**, 1243 (1998).
7. (*a*) S. Kanao and Y. Sakayori. Yakuga. Zasshi, **86**, 1105 (1966); (*b*) J. Baker and T.L. Little. J. Med. Chem. **28**, 46 (1985); (*c*) S. Okamoto, M. Iwakubo, K. Kobayashi, and F. Sato. J. Am. Chem. Soc. **119**, 6984 (1997); (*d*) H.-W. Shao, Y. Wu, and R. Li. Synth. Commun. **30**, 1911 (2000).
8. (*a*) F. Effenberger and U. Burkard. Angew. Chem. Int. Ed. Engl. **22**, 65 (1983); (*b*) F. Effenberger, U. Burkard, and J. Willfahrt. Liebigs Ann. Chem. 314 (1986).
9. A.N. Kost, A.F. Sviridov, R.S. Sagitullin, and S.A. Fedorova. Khim.-Farm. Zh. **1**, 3 (1967).
10. N.A. Hassan, E. Bayer, and J.C. Jochims. J. Chem. Soc. Perkin Trans. 1, 3747 (1998).
11. T. Hayashi, A. Yamamoto, Y. Ito, E. Nishioka, H. Miura, and K. Yanagi. J. Am. Chem. Soc. **111**, 6301 (1989).
12. (*a*) R.E. Bowman. J. Am. Chem. Soc. **72**, 1346 (1950); (*b*) L. Velluz, G. Amiard, and R. Heymès. Bull. Soc. Chim. Fr. 1012 (1954); (*c*) P. Quitt, J. Hellerbach, and K. Vogler. Helv. Chim. Acta, **46**, 327 (1963); (*d*) J.W. Davis, Jr., and A. Furst. Anal. Chem. **40**, 1910 (1968); (*e*) E. Davidov, H. Spiegelstein-Klarfeld, O. Gizri-Yaron, E. Naim, and N. Lichtenstein. Isr. J. Chem. **7**, 487 (1969); (*f*) N. Lichtenstein. Israeli Patent. No. 23 768 (1969); (*g*) N. Galeotti, J. Poncet, L. Chiche, and P. Jouin. J. Org. Chem. **58**, 5370 (1993); (*h*) N.K. Nayyar, D.R. Hutchison, and M.J. Martinelli. J. Org. Chem. **62**, 982 (1997).
13. V.I. Tararov, R. Kadyrov, T.H. Riermeier, and A. Börner. Chem. Commun. 1867 (2000).
14. (*a*) B.A. Kulkarni and A. Ganesan. Angew. Chem. Int. Ed. Engl. **36**, 2454 (1997); (*b*) D.L. Boger, J. Zhou, R.M. Borzilleri, S. Nukui, and S.L. Castle. J. Org. Chem. **62**, 2054 (1997); (*c*) B. Cao, D. Xiao, and M.M. Joullié. Org. Lett. **1**, 1799 (1999).
15. (*a*) D. Zhou, Y. Guan, and S. Jin. Chin. Chem. Lett. **1**, 209 (1990); (*b*) D. Zhou, Y. Guan, and S. Jin. Beijing Daxue Xuebao Ziran Kexueban, **29**, 428 (1993).
16. (*a*) J. Bastide, C. Coste, and J.-L. Marty. C.R. Hebd. Seances Acad. Sci. Ser. C, **287**, 471 (1978); (*b*) S. Laschat, R. Fröhlich, and B. Wibbeling. J. Org. Chem. **61**, 2829 (1996); (*c*) A. Nefzi, J.M. Ostresh, and R.A. Houghten. Tetrahedron Lett. **38**, 4943 (1997).
17. (*a*) D. Soerens, J. Sandrin, F. Ungemach, P. Mokry, G.S. Wu, E. Yamanaka, L. Hutchins, M. DiPierro, and J.M. Cook. J. Org. Chem. **44**, 535 (1979); (*b*) T.J. Cheeseright, A.J. Edwards, D.T. Elmore, J.H. Jones, M. Raissi, and E.C. Lewis. J. Chem. Soc. Perkin Trans. 1, 1595 (1994); (*c*) M. Weigl and B. Wünsch. Org. Lett. **2**, 1177 (2000).
18. A. Abdel-Magid, K.G. Carson, B.D. Harris, C.A. Maryanoff, and R.D. Shah. J. Org. Chem. **61**, 3849 (1996).
19. Y. Ohfune, N. Kurokawa, N. Higuchi, M. Saito, M. Hashimoto, and T. Tanaka. Chem. Lett. 441 (1984).
20. A.K. Szardenings, T.S. Burkoth, G.C. Look, and D.A. Campbell. J. Org. Chem. **61**, 6720 (1996).
21. (*a*) A.G. Giumanini, G. Verardo, M.H. Gei, and L. Lassiani. J. Labelled Compd. Radiopharm. **24**, 255 (1987); (*b*) G. Verardo, A.G. Giumanini, G. Favret, and P. Strazzolini. Synthesis, 447 (1991); (*c*) G. Verardo, A.G. Giumanini, P. Strazzolini, and M. Poiana. Synthesis, 121 (1993); (*d*) G. Verardo, A.G. Giumanini, and P. Strazzolini. Synth. Commun. **24**, 609 (1994); (*e*) G. Verardo, A. Dolce, and N. Toniutti. Synthesis, 74 (1999).
22. R.I. Reed and W.K. Reid. J. Chem. Soc. 5933 (1963).

© 2002 NRC Canada

Vibrational spectroscopic studies of aqueous solutions of *tert*-butyl alcohol and *tert*-butylamine

Pius K. Kipkemboi and Allan J. Easteal

Abstract: Raman and FT-IR absorption spectra of aqueous *tert*-butyl alcohol (*t*-BuOH) and *tert*-butylamine (*t*-$BuNH_2$) in the region of the O–H and NH_2 stretching and bending modes have been measured as a function of organic co-solvent concentration in the whole co-solvent mole fraction region. The major observed changes of the aqueous binary solution spectra compared with the solvent spectra are a loss or gain of band intensity. In particular, the observed changes in intensities and linewidths of some bands were significantly more pronounced at low concentrations of organic co-solvents in water, where *t*-BuOH and *t*-$BuNH_2$ tend to integrate into the water structure. Clear evidence of structural enhancement of the network is obtained in dilute solutions as well as destruction of the network by hydrophobic interactions as the concentration is increased. Generally, the interpretation of the spectra is in agreement with the capacity of the hydrophobic co-solvent to break the structure of water in the more concentrated aqueous solutions and to enhance the structure in dilute solutions. Vibrational intensities and frequency shifts of some bands show definite trends with varying the concentration of the solutions. In the concentration-dependence study, unusual linewidth changes of certain bands were observed.

Key words: infrared, Raman spectra, aqueous, *tert*-butanol, *tert*-butylamine.

Résumé : On a mesuré les spectres d'absorption Raman et infrarouges en transformée de Fourier de solutions aqueuses de *tert*-butanol (*t*-BuOH) et de *tert*-butylamine (*t*-$BuNH_2$), dans la région des modes d'élongation et de déformation du O–H et du NH_2, en fonction de la concentration du cosolvant organique, sur toute la plage des fractions molaires du cosolvant. Les changements principaux observés dans les spectres en solutions aqueuses binaires par rapport à ceux des spectres du solvant sont des gains ou des pertes dans l'intensité de la bande. En particulier, les changements observés dans les intensités et les largeurs de quelques bandes sont beaucoup plus prononcés à de faibles concentrations des cosolvants organiques dans l'eau vers laquelle le *t*-BuOH et la *t*-$BuNH_2$ ont tendance de migrer dans la structure de l'eau. On a obtenu des données claires en faveur d'une augmentation de la structure du réseau en solutions diluées ainsi que de la destruction du réseau par les interactions hydrophobes avec une augmentation de la concentration. En général, l'interprétation des spectres est en accord avec la capacité du cosolvant hydrophobe à briser la structure de l'eau dans les solutions aqueuses plus concentrées et à les augmenter en solutions diluées. Les intensités vibrationnelles et les déplacements dans les fréquences de quelques bandes présentent des tendances bien définies avec les variations dans les concentrations dans les solutions. Dans l'étude sur la dépendance sur la concentration, on a observé des changements inhabituels dans la largeur de certaines bandes.

Mots clés : infrarouge, spectre Raman, aqueux, *tert*-butanol, *tert*-butylamine.

[Traduit par la Rédaction]

Introduction

Vibration spectra are, in general, sensitive to the local environment of a molecule, and information concerning the relative position of the molecule in quite a short time can be obtained from the spectra. Vibrational spectra of water or aqueous solutions have received considerable attention in relation to the liquid structure of water. Although numerous papers have been presented reporting spectra of inorganic electrolytes in aqueous solution, there are few studies on the vibrational spectra of organic molecules in water (1–10). It is of interest to interpret vibrational spectra of organic molecules in aqueous solution and to discuss the intermolecular interactions and liquid structures in the these systems.

In the present investigation, FT-IR and Raman spectra of aqueous *tert*-butanol and *tert*-butylamine in the O–H stretching and bending regions were measured at room temperature as a function of co-solvent concentration in the entire co-solvent mole fraction region. The purpose of this study was to investigate the structural changes brought about by a change in the concentration of co-solvent. It was anticipated that FT-IR and Raman spectroscopy of aqueous solutions of the aforementioned compounds would provide insights into the structural perturbations of bulk water, which are caused by hydrophobic co-solvents, and provide a structure-oriented conceptual framework for evaluating various hydrophobic effects. In the present study, the two co-solvents, *tert*-butyl alcohol (*t*-BuOH) and *tert*-butylamine (*t*-$BuNH_2$), were used

Received 14 December 2001. Published on the NRC Research Press Web site at http://canjchem.nrc.ca on 20 June 2002.

P.K. Kipkemboi.[1] Department of Chemistry, Moi University, P.O. Box 1125, Eldoret, Kenya,
A.J. Easteal. Department of Chemistry, The University of Auckland, Private Bag 92019, Auckland, New Zealand.

[1]Corresponding author (e-mail: keronei@yahoo.com).

 DOI: 10.1139/V02-102 © 2002 NRC Canada

because they are relatively hydrophobic yet completely miscible with water in all proportions. H_2O + *t*-BuOH and H_2O + *t*-$BuNH_2$ mixtures provide a useful opportunity for investigating the interactions of a non-electrolyte with water. Both *t*-BuOH and *t*-$BuNH_2$ hydrophobic co-solvents may serve as model compounds for more complicated aqueous systems like surfactants, emulsions, and biopolymers.

Most of the essential functions of macromolecules in living materials are determined by the hydrogen-bonded structures. The vibrational modes of NH- and OH-stretch character, therefore, carry valuable function-related structural information. Since life is inseparably connected with the presence of water, water as a solvent should be used to study biological molecules (3). Overlap of the vibrational bands of water with those of solutes is inevitable, resulting in broad-band contours, which cannot usually be deconvoluted into their constituents (11, 12). In this study, we explored the fact that vibrational spectra of solvent water are very sensitive to the nature of solute. Network-perturbing hydrophobic organic co-solvents can provide useful information about aqueous solutions of non-electrolytes, but the interpretation is complicated by the different stretching frequencies for N–H···O bonds compared with O–H···O bonds.

Our previous work focussed on investigating the thermodynamic and mass transport behaviour of such systems (13–17). Studies of aqueous solutions of *t*-BuOH and *t*-$BuNH_2$ showed an "enhancement" of the water structure by the co-solvent (*t*-BuOH or *t*-$BuNH_2$) at very low concentrations. In contrast, at higher concentrations, both co-solvents disrupt the structure of the water, behaving as "structure breakers." In this work such previous data are extended and consolidated with Raman and FT-IR spectra. Although the vibrational spectra of the H_2O + *t*-BuOH system were previously reported (5), there are few data available for the H_2O + *t*-$BuNH_2$ system.

Experimental

Materials

tert-Butyl alcohol was supplied by Riedel-de Haën and *tert*-butylamine by Aldrich. The stated purity of both solvents exceeded 99.0 mol%. The solvents were dried using thermally activated molecular sieves (3 Å). Ultra-pure water from a milli-Q purification system was used.

Binary mixtures were prepared by weighing appropriate amounts of the components into fine glass vials using a balance with accuracy ±0.1 mg.

Apparatus and procedures

Raman spectra were recorded with a Jobin-Yvon V1000 spectrometer, a double monochromator instrument equipped with holographic gratings (1600 grooves per mm) for high resolution and good stray-light rejection. A Spectra-Physics Model 2016 argon ion laser was used as the excitation source and non-lasing plasma lines were removed with a Laser III premonochromator. The filtered laser light was diverted to the macro sampling chamber using a flip mirror. The Raman scattered radiation was detected with a gallium–arsenide photomultiplier tube (PMT), which was cooled by a Peltier-effect device to ca. 250 K to reduce the thermal noise. A spectralink module, connected to the PMT and interfaced to an IBM PC-compatible computer, provided photon counting, data acquisition, and monochromator drive. Liquid samples in glass vials were attached to a motor drive unit situated in the macrochamber of the spectrometer. The vial was then spun to enhance the Raman signal and to reduce the risk of sample decomposition. Typically 40–100 mW of focused-laser light was used. The Jobin-Yvon Prism software package was employed to operate the spectrometer. All data manipulations and spectral plottings were performed with Spectra Calc (Galactic Industries Corp.) software. The spectrometer was calibrated using the 514.5 nm line of the argon ion laser, and the spectra were reproducible to ±1 cm^{-1}. The spectra were obtained at a spectral resolution of 5 cm^{-1}, the data being collected at 2 cm^{-1} intervals. The scanning speed of the spectrometer was 1.0 cm^{-1} s^{-1} and the integration time was 0.5 s per data point. The acquisition time was 30 min. The spectral range covered was 4000–400 cm^{-1}. All the Raman spectra were recorded with the samples at room temperature.

Mid-IR spectra were recorded on a Digilab FTS-60 Fourier transform infrared spectrometer employing a Globar source, a KBr beam splitter, and an uncooled DTGS detector. The spectrometer was interfaced to a computer and a 68020 processor with Digilab software. The main body of the spectrometer was purged with dry nitrogen. Samples were examined as thin films using an attenuated internal

Fig. 1. Raman spectra of water, *t*-BuOH, and two *t*-BuOH aqueous solutions in the frequency range of 400–4000 cm^{-1}; mol% of *t*-BuOH are noted on each curve. Spectra are plotted as recorded but shifted in a vertical direction.

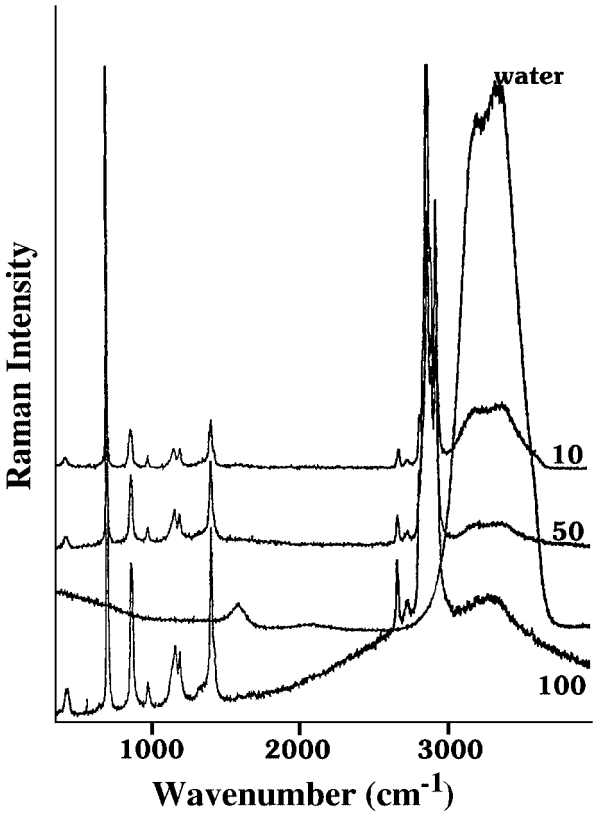

© 2002 NRC Canada

Fig. 2. Raman spectra as a function of composition for H_2O + *t*-BuOH mixtures in the region 2700–3800 cm^{-1}; mol% of *t*-BuOH are noted on each curve. Spectra are plotted as recorded but shifted in a vertical direction.

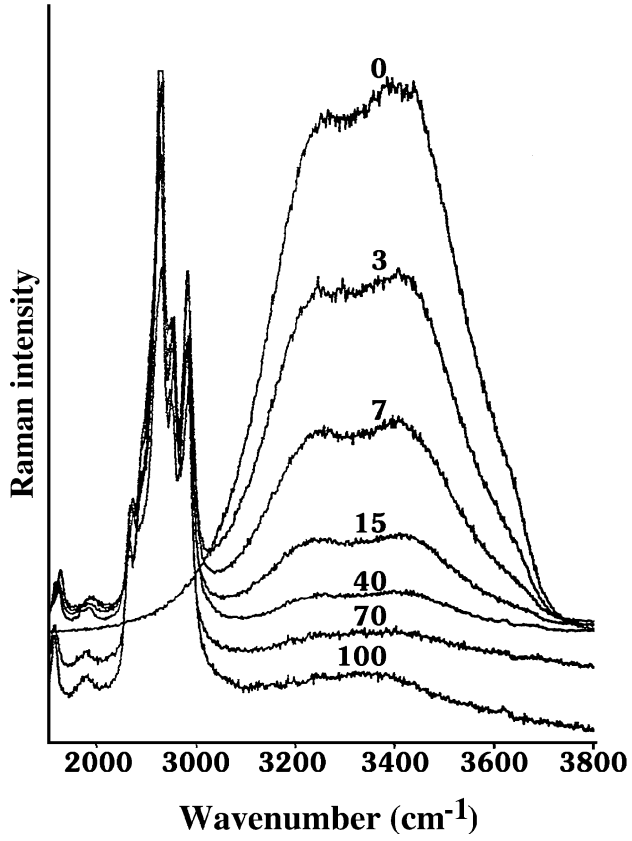

Fig. 3. IR spectra of H_2O + *t*-BuOH mixtures as a function of composition in the region 2800–3600 cm^{-1}; mol% of *t*-BuOH are noted on each curve. Spectra are plotted as recorded but shifted in a vertical direction.

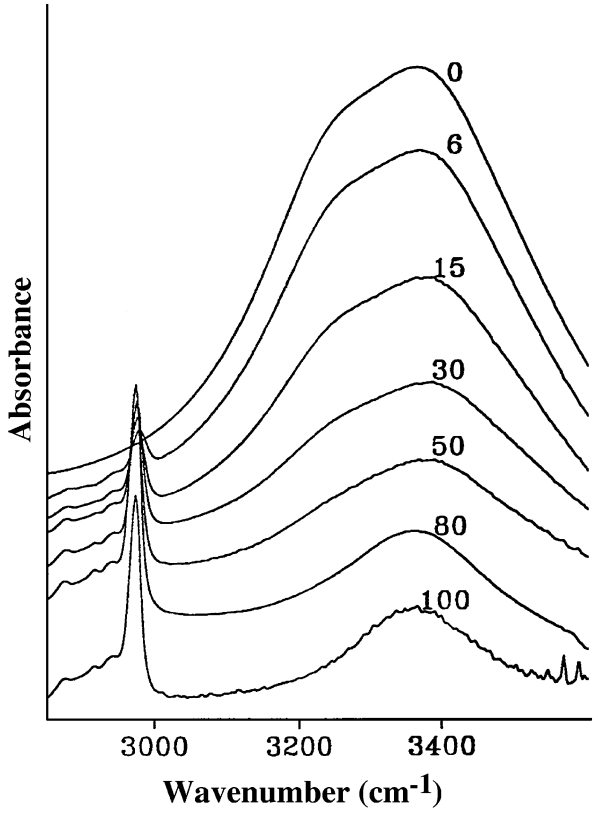

reflectance (ATR) accessory. Internal reflection spectroscopy was performed using multiple-reflection ATR parallelogram with a 45° angle of reflection. A clean dry Silicon ATR element was used to obtain a single-beam background spectrum. The ATR cell was then filled with a sample solution using syringe pressure and scanned to obtain absorbance spectra. The sample in the ATR cell was purged for at least 5 min with nitrogen gas before spectra were recorded. Between sample runs, the cell was flushed with water and acetone and then dried with ambient air. Thirty interferograms were collected, co-added, apodized with a triangular function, and Fourier transformed to give spectra of 4 cm^{-1} resolution. Spectral manipulations were performed with Spectra Calc. All spectra reported here were obtained using a Silicon ATR cell at room temperature. The spectral range covered was 4000–1050 cm^{-1}.

Results and discussion

Vibrational spectra of H_2O + *t*-BuOH mixtures

Figure 1 represents the Raman spectra of water, *t*-BuOH, and two *t*-BuOH solutions of different concentrations recorded in the frequency range of 400–4000 cm^{-1}. In Fig. 2, the Raman spectra of various H_2O + *t*-BuOH mixtures in the 2700–3800 cm^{-1} region are shown in more detail and compared with the spectrum of water. These spectra were recorded with the same incident-laser power and no further corrections, such as for refractive index, were made. Figure 2 allows us to follow the effect of *t*-BuOH concentration on the water organization. The broad feature dominating the spectrum is due to the O–H stretching mode of water. The strongest Raman band observed for liquid *t*-BuOH is polarized and found at ~752 cm^{-1}. This band is attributed to the in-phase C_3C–O stretching mode. A CH_3 stretching band for *t*-BuOH appears in the 2800–3000-cm^{-1} region and is clearly seen even in systems with high water content. In pure liquid *t*-BuOH only one broad O–H stretching vibration band appears in the high-frequency region centred around 3360 cm^{-1}, which has an antisymmetric contour. The band is very strong in the IR spectrum but very weak in the Raman spectrum. The small shoulder observed at ~3600 cm^{-1} in pure water seems to disappear as the concentration of *t*-BuOH increases. Nevertheless, it is difficult to determine if this apparent disappearance is due to the reduction in the intensity of this band or to the overlapping of the adjacent strong band. Needless to say, *t*-BuOH as well as *t*-$BuNH_2$ are not unique in this respect. For instance, hydrogen peroxide also suppresses the high-frequency shoulder in water (18). Electrolytes are also known to suppress the high-frequency shoulder in water (19).

In contrast, the position and shape of the O–H stretching vibrations of the two bands centred at ~3250 and 3400 cm^{-1} remain almost constant with an increase in the concentration

© 2002 NRC Canada

Fig. 4. IR spectra of H_2O + *t*-BuOH mixtures as a function of composition in the region 1100–1750 cm^{-1}; mol% of BuOH are noted on each curve. Spectra are plotted as recorded but shifted in a vertical direction.

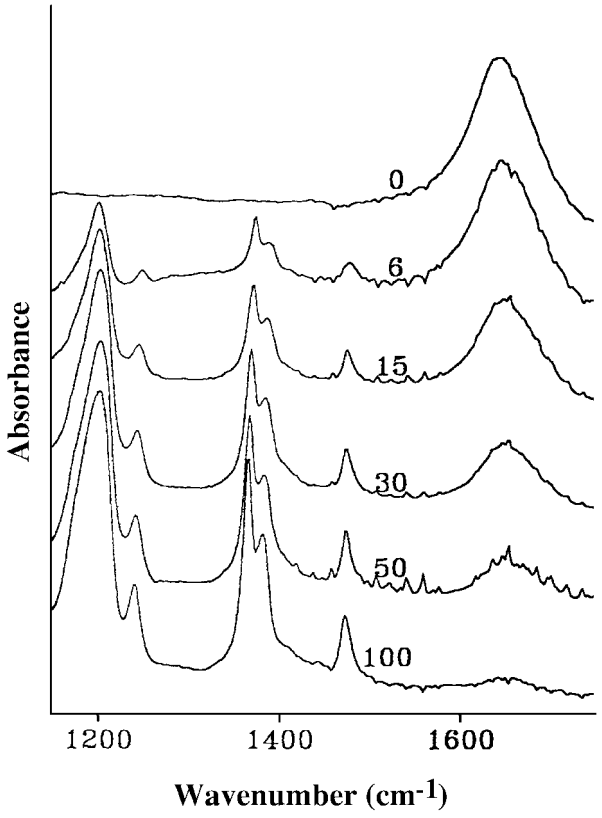

Fig. 5. Raman spectra of water, *t*-$BuNH_2$, and two *t*-$BuNH_2$ aqueous solutions in the frequency range of 400–4000 cm^{-1}; mol% of *t*-$BuNH_2$ are noted on each curve. Spectra are plotted as recorded but shifted in a vertical direction.

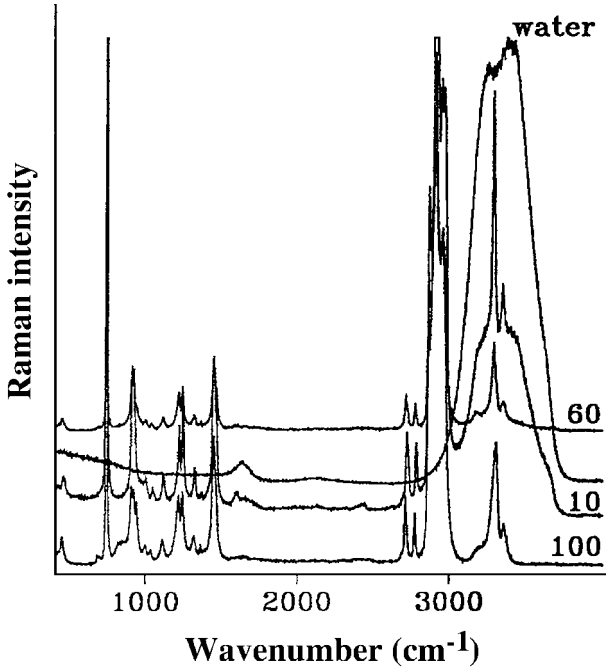

of *t*-BuOH. At low concentrations (≤15 mol% *t*-BuOH), however a sharp decrease in the intensity of the O–H stretching mode of water is observed. Thus, Figs. 1 and 2 show that the primary effect of the addition of *t*-BuOH is the reduction in the intensity of the two bands. The decrease in intensity of the two peaks at moderately high concentrations of *t*-BuOH (i.e., >15 mol%) is less noticeable indicating that the network structure of bulk water has been significantly disrupted at these concentrations.

The IR spectra of several H_2O + *t*-BuOH systems with increasing mole fractions of *t*-BuOH are presented in Fig. 3. The position of the low-frequency shoulder at ~3250 cm^{-1} remains relatively constant. It can be seen, however, that the prominence of the low-frequency shoulder continuously decreases with increasing *t*-BuOH content and eventually vanishes at high concentrations. It is difficult to follow the absorption profile of the high-frequency broad band centred at ~3400 cm^{-1} of water because it occurs in the same region as the strong broad absorption band of *t*-BuOH. It is noteworthy that the peak shows a frequency shift towards higher wavenumbers with increasing concentration of *t*-BuOH, at least up to 50 mol% co-solvent.

With the exception of the water bending mode at 1650 cm^{-1}, there were no significant changes in the Raman or IR spectra of the H_2O–*t*-BuOH system in the region below 2800 cm^{-1} with change in composition. But, as shown in Figs. 1 and 4, the intensity of the vibrational bending mode of water in both Raman and IR decreases considerably with increasing *t*-BuOH concentration until it vanishes at high concentrations, but its position seems to be invariant.

Vibrational spectra of H_2O + *t*-$BuNH_2$ mixtures

Figure 5 represents the Raman spectra of water, *t*-$BuNH_2$, and two solutions of *t*-$BuNH_2$ in water recorded in the frequency range of 400–4000 cm^{-1}. These spectra were recorded with the same incident-laser power and no further corrections, such as for refractive index, were made. The strongest Raman band observed for *t*-$BuNH_2$ is polarized and found at ~750 cm^{-1}. This band is attributed to the symmetric C_3C–N stretching mode. The CH_3 stretching bands of *t*-$BuNH_2$ appear in the 2800–3000 cm^{-1} region and are clearly seen even in systems with high water content. The vibrational spectrum of pure liquid *t*-$BuNH_2$ contains two peaks between 3200 and 3400 cm^{-1}. In this region of the Raman spectrum, the strongest band at 3310 cm^{-1} is polarized and it is assigned to the symmetric NH_2 stretching mode, while the weak depolarized band at 3360 cm^{-1} is assigned to the corresponding antisymmetric stretching mode. In the IR spectrum, the band at 3360 cm^{-1} is fairly strong, whereas the peak at 3310 cm^{-1} is very weak. Figure 6 shows in more detail the variations in the Raman-band profiles of the NH_2 stretching modes as a function of the concentration of *t*-$BuNH_2$ in water. The high-frequency band at ~3360 cm^{-1} attributed to the NH_2 antisymmetric stretch is generally weak and very broad, making it difficult to follow its variation in intensity with composition. Our interest is therefore directed toward the much stronger NH_2 symmetric peak at 3310 cm^{-1}.

The low-frequency band centred at ~3310 cm^{-1} exhibits a frequency shift to higher wavenumbers with increasing concentration of *t*-$BuNH_2$ and its intensity changes in a

© 2002 NRC Canada

Fig. 6. Raman spectra for H_2O + *t*-$BuNH_2$ mixtures as a function of composition in the region 2700–3700 cm^{-1}; mol% of *t*-$BuNH_2$ are noted on each curve. Spectra are plotted as recorded but shifted in a vertical direction.

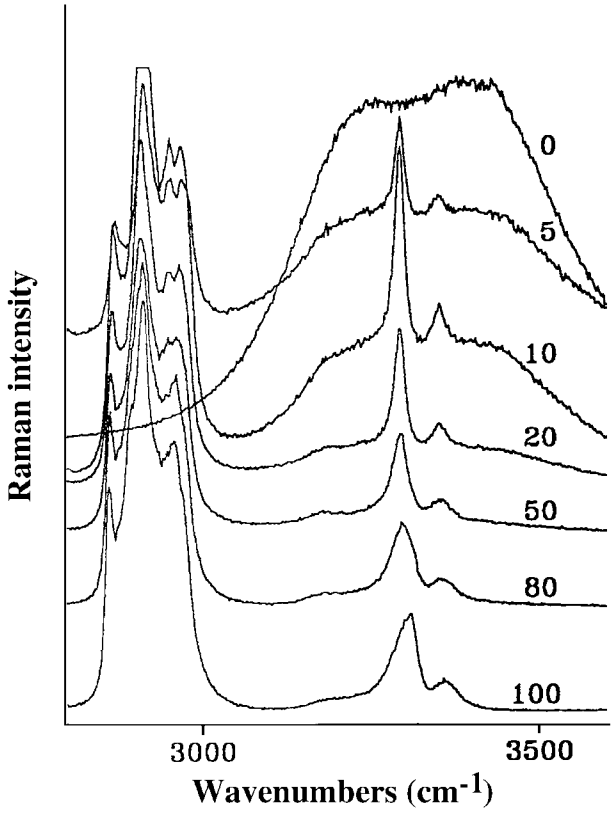

peculiar manner. As observed in Figs. 5 and 6, the intensity of the band seems to increase sharply as the concentration of *t*-$BuNH_2$ rises, passing through a maximum value in the water-rich region, and then shows a decreasing trend. To quantitatively follow the apparent change in peak intensity as a function of composition, the peaks were integrated. The CH_3 symmetric band at 2920 cm^{-1} was chosen as the reference band as it is very strong in Raman and its intensity does not seem to change significantly with the variation in the concentration of water, and furthermore, it is close to the band of interest. The band maxima of the NH_2 and CH_3 symmetric stretching vibrations were baseline corrected, and integration of the spectral profiles of their areas were determined using the Spectra Calc software. In Fig. 7, the variation of the integrated Raman intensity ratio ($I[3296cm^{-1}]_{NH_2}/I[2920cm^{-1}]_{CH_3}$) with composition is presented, where the peaks at 3296 and 2920 cm^{-1} are baseline corrected and the integrated intensity of the NH_2 and CH_3 components are measured. The concentration dependence of the integrated Raman intensity ratio is unique and characteristic. The ratio of integrated Raman intensity of the bands at 3296 and 2920 cm^{-1} as a function of *t*-$BuNH_2$ content is in qualitative agreement with previous results obtained with other techniques (13–16) — the intensity ratio shows a maximum around 10 mol% of *t*-$BuNH_2$. This demonstrates that *t*-$BuNH_2$ exhibits a strong hydrophobic hydration at low mole fractions, and that this hydration structure is broken down at higher mole fractions. We have followed the effect

Fig. 7. Ratio of Raman integrated intensity of the bands around 3296 and 2920 cm^{-1} as a function of composition.

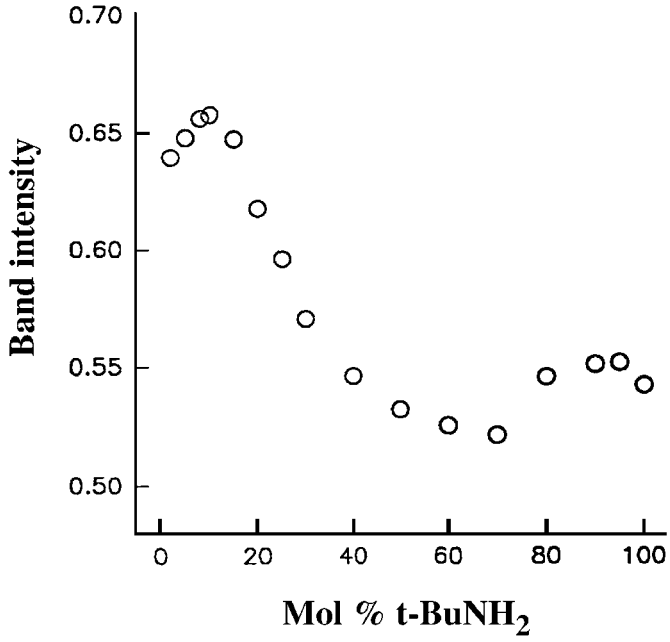

Table 1. Observed frequency and line width at half-maximum (FWHM) of the NH_2 symmetric stretch in the Raman spectra of *t*-$BuNH_2$ mixtures as a function of composition.

mol% *t*-$BuNH_2$	Frequency (cm^{-1})	FWHM (cm^{-1})
5.0	3294	17.3
10.0	3294	18.1
15.0	3294	18.2
20.0	3294	18.2
25.0	3296	21.8
30.0	3296	25.5
40.0	3296	26.4
50.0	3296	31.4
60.0	3296	34.9
70.0	3296	40.0
80.0	3298	44.5
90.0	3300	49.1
95.0	3305	50.5
100	3310	52.3

of concentration on the full width at half-maximum (FWHM) of the NH_2 symmetric stretching band at ~3296 cm^{-1}. The variation in apparent frequency shifts and line widths at half-maximum with concentration are presented in Table 1. As seen in Table 1, the line width at half-maximum below 20 mol% *t*-$BuNH_2$ does not depend on the concentration in water-rich solutions, being nearly constant in the water-rich region, but the dependence is remarkable above this concentration, showing a continuous and virtually linear change of line width from 18.2 to 52.3 cm^{-1} on going from 20 to 100 mol% *t*-$BuNH_2$.

It can be assumed that in the water-rich region (presumably below 15 mol% *t*-$BuNH_2$), the structure of the solution corresponds to the structure of pure water and the amine

© 2002 NRC Canada

Fig. 8. IR spectra of H_2O + *t*-$BuNH_2$ mixtures as a function of composition in the region 2600–4000 cm^{-1}; mol% of *t*-$BuNH_2$ are noted on each curve. Spectra are plotted as recorded but shifted in a vertical direction.

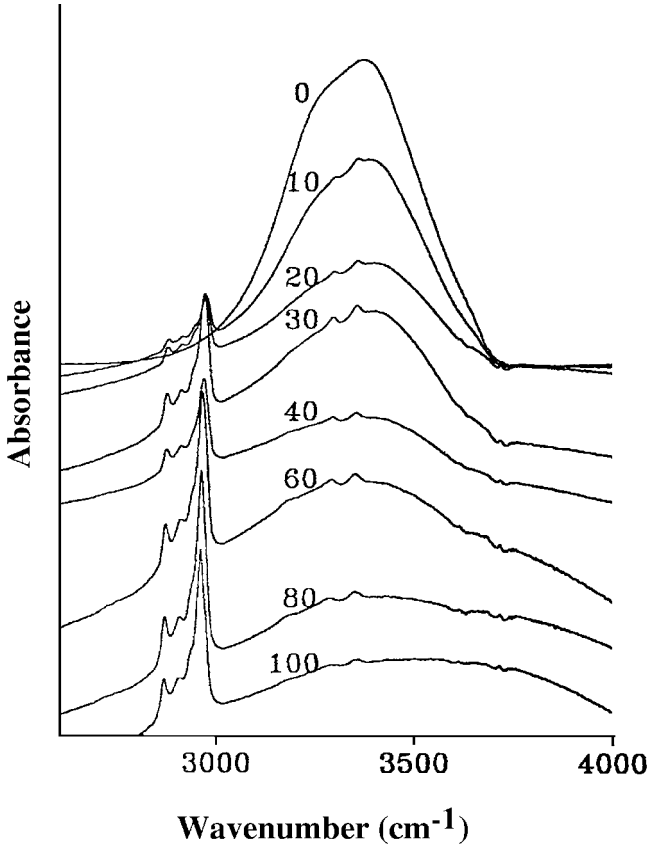

Fig. 9. IR spectra of H_2O + *t*-$BuNH_2$ mixtures as a function of composition in the region 1150–1750 cm^{-1}; mol% of *t*-$BuNH_2$ are noted on each curve. Spectra are plotted as recorded but shifted in a vertical direction.

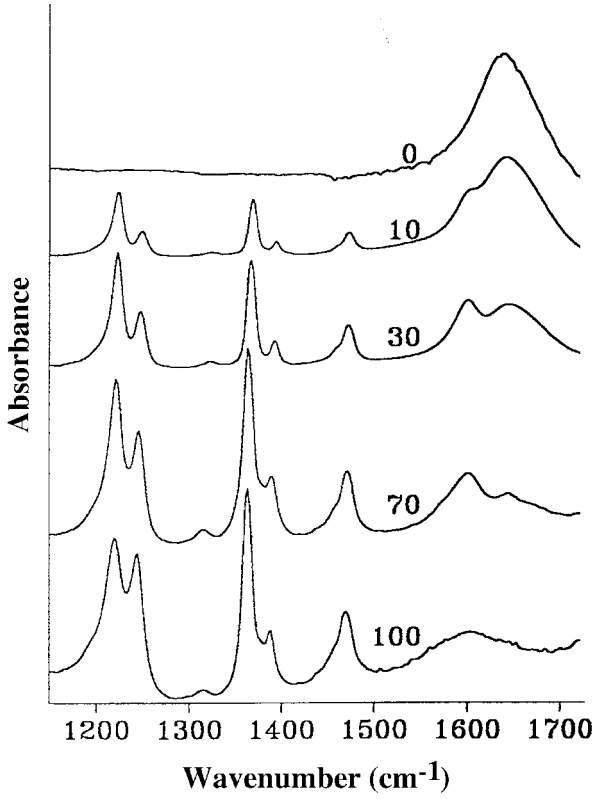

molecules are incorporated into the network structure of bulk water by cavity filling, thereby enhancing the water structure because of water–co-solvent hydrophobic interactions. But at higher concentrations of co-solvent the enhanced structure of water is gradually broken down by the organic co-solvent as the *t*-$BuNH_2$ molecules form hydrogen-bonds with water molecules. The formation of such hydrogen bonds between *t*-$BuNH_2$ and water gives rise to large line widths, similar to those in neat liquid *t*-$BuNH_2$. At relatively higher concentration of *t*-$BuNH_2$, the hydrogen bonds between *t*-$BuNH_2$ molecules are dominant — the more hydrogen-bonded the *t*-$BuNH_2$ molecules become the larger the observed line widths.

Good IR spectra of aqueous solutions of *t*-$BuNH_2$ were difficult to obtain due to the broad, intense water absorption bands, which obscure much of the mid-IR spectrum (the NH_2 stretching vibrations of *t*-$BuNH_2$, which are comparatively weak, occur in the same region). The O–H stretching region from 3100 to 3500 cm^{-1} is essentially opaque in the highly water-rich solvent (<10 mol% *t*-$BuNH_2$), and hence, the weak NH_2 stretching vibrations are completely masked.

As the concentration increases above 10 mol% *t*-$BuNH_2$, the broad O–H profile-band contour observed for water decreases gradually in intensity and the NH_2 stretching bands become more noticeable with no apparent shifts in their band positions. The band corresponding to the symmetric NH_2 stretching mode of *t*-$BuNH_2$, is a fairly intense band in Raman, but is much weaker in IR in comparison with the high-frequency band at ~3360 cm^{-1} attributed to the characteristic antisymmetric NH_2 stretching vibration. Changes in the relative intensities of these two bands were found to parallel the Raman intensity of the low-frequency component at ~3296 cm^{-1} (Figs. 6 and 7), since they seem to initially increase passing through maxima before apparently decreasing again with increasing concentration of *t*-$BuNH_2$. In Fig. 8, the variation in IR-band profiles of the OH and NH_2 stretching modes are shown as a function of concentration of *t*-$BuNH_2$ in water.

The bands at ~1645 and 1600 cm^{-1}, which are weak in the Raman but fairly strong in the IR, correspond to the bending vibrations of water and the NH_2 component of *t*-$BuNH_2$, respectively. The two bands are very sensitive to concentration. It is noteworthy that the peak absorbancies of the two bands vary in a nearly linear fashion with concentration, and can be used for analytical purposes. The trends of their absorbancies with concentration are shown in Fig. 9. It can be seen that the absorbance of the bending mode of water at ~1645 cm^{-1} decreases with the addition of *t*-$BuNH_2$ to water. The NH_2 bending mode initially appears as a shoulder at low concentrations of *t*-$BuNH_2$. As the mole fraction of *t*-$BuNH_2$ increases, this shoulder develops into a band centred at ~1600 cm^{-1}. Finally, the 1600 cm^{-1} band dominates the spectrum at high concentrations of *t*-$BuNH_2$, leaving the band at 1645 cm^{-1} as a shoulder.

© 2002 NRC Canada

Acknowledgments

The authors are indebted to the New Zealand government for the award of a Commonwealth Scholarship to Pius Kipkemboi, and to the University of Auckland Research Committee for equipment funding.

References

1. S. Singh and P.J. Krueger. J. Raman Spectrosc. **13**, 178 (1982).
2. Zh.S. Nickolov, J.C. Earnshaw, J.J. McGarvey, and G.M. Georgiev. J. Raman Spectrosc. **25**, 837 (1994).
3. W.B. Fischer, H.H. Eysel, O.F. Nelsen, and J.E. Bertie. Appl. Spectosc. **48**, 107 (1994).
4. D. Jamroz, J. Stangret, and J. Lindgren. J. Am. Chem. Soc. **115**, 6165 (1993).
5. J.L. Green, A.R. Lacey, and M.G. Sceats. Chem. Phys. Lett. **137**, 537 (1987).
6. C.H. Spink and J.C. Wyckoff. J. Phys. Chem. **76**, 1660 (1972).
7. R.T. Yang and M.J. Low. Spectrochim. Acta, **30A**, 1787 (1974).
8. O.D. Bonner and Y.S. Choi. J. Sol. Chem. **4**, 457 (1975).
9. K. Tanabe and S. Tsuzuki. Spectrochim. Acta, **42A**, 611 (1986).
10. I. Auzanneau, D. Combes, and A. Zwick. J. Raman Spectrosc. **22**, 227 (1991).
11. H.J. Himmler and H.H. Eysel. Spectrochim. Acta, **45A**, 1077 (1989).
12. M. Moskovitis and K.H. Michaaelian. J. Am. Chem. Soc. **102**, 2209 (1980).
13. P.K. Kipkemboi and A.J. Easteal. Can. J. Chem. **72**, 1937 (1994).
14. P.K. Kipkemboi and A.J. Easteal. Aust. J. Chem. **47**, 1771 (1994).
15. P.K. Kipkemboi and A.J. Easteal. Bull. Chem. Soc. Jpn. **67**, 2956 (1994).
16. P.K. Kipkemboi and L.A. Woolf. J. Chem. Eng. Data, **40,** 943 (1995).
17. P.K. Kipkemboi and A.J. Easteal. J. Kenya Chem. Soc. **1**, 20 (1999).
18. P.A. Giguére and M. Pigeon-Gosselin. J. Raman Spectrosc. **17**, 341 (1986).
19. F. Rull and J.A. de Saja. J. Raman Spectrosc. **17**, 167 (1986).

© 2002 NRC Canada

Baker's yeast-catalyzed synthesis of optically pure 4-*tert*-butyl-3-hydroxy β-lactam *cis*-(3*R*,4*S*) and *trans*-(3*R*,4*R*) diastereomers

Margaret M. Kayser, Yan Yang, Marko D. Mihovilovic, Anton Feicht, and Fernande D. Rochon

Abstract: Baker's yeast (*Saccharomyces cerevisiae*) reductions were applied to the synthesis of the paclitaxel C-13 side-chain analogue. An easily synthesized α-keto-β-lactam (1-(4-methoxyphenyl)-4-*tert*-butylazetidin-2,3-dione, **4**) was reduced by yeast cells to give a mixture of enantiomerically pure *cis* and *trans* isomers. Both compounds were isolated and characterized, and their absolute configurations were confirmed by X-ray crystallographic analysis.

Key words: Taxol®, C-13 side-chain, paclitaxel analogues, optically pure α-hydroxy-β-lactams, baker's yeast-catalyzed reductions.

Résumé : On a fait appel à des réductions à l'aide de levure de bière (*Saccharomyces cerevisiae*) pour réaliser la synthèse un analogue du paclitaxel portant une chaîne latérale en C-13. Un α-céto-β-lactame facilement accessible par synthèse (1-(4-méthoxyphényl)-4-*tert*-butylazétidine-2,3-dione, **4**) a été réduit par des cellules de levure pour conduire à un mélange d'isomères *cis*- et *trans*-énantiomériquement purs. On a isolé et caractérisé les deux composés et on a confirmé leurs configurations absolues par une analyse cristallographique par diffraction des rayons-X.

Mots clés : Taxol® à chaîne latérale en C-13, analogue du paclitaxel, α-hydroxy-β-lactames optiquement purs, réductions catalysées par la levure de bière.

[Traduit par la Rédaction]

Introduction

Taxol® (paclitaxel), an important cancer chemotherapeutic agent, is produced through a semi-synthetic route involving the condensation of a natural precursor (10-deacetylbaccatin III) with a synthetic phenylisoserine side-chain (C-13 side-chain). The side-chain is essential for paclitaxel's biological activity (1), but a wide range of modifications is tolerated. For example, replacement of the phenyl group with aliphatic groups provides highly bioactive analogues (2–4). One of the most efficient coupling protocols for grafting the side-chain onto the taxane ring system uses the activated β-lactam derivative of phenylisoserine (5, 6). This methodology allows the introduction of various modified chains into the analogues. Promising results from the bioactivity studies with paclitaxel analogues (4, 6) prompted the search for new enantioselective routes to 3-hydroxy-β-lactams with various substituents in the 4-position (7). The most challenging aspect of these syntheses revolves around obtaining the correct (or desired) absolute configuration at the two stereogenic centres. Our strategy has been to use yeast-mediated reduction of racemic α-keto-β-lactam **1** as a way of introducing the required chirality into the side-chain precursors (8). The same methodology can be applied to the synthesis of various paclitaxel C-13 chain analogues.

We anticipated that the rigid skeleton of **1** might contribute to the enantioselectivity of the carbonyl reduction. Reduction of **1** (R = Ph) with commercial baker's yeast gave a mixture of *cis* and *trans* isomers. The natural paclitaxel side-chain (*cis*-(3*R*,4*S*)) was formed with 57% enantiomeric excess (ee), but its diastereomer (*trans*-(3*R*,4*R*)) was essentially optically pure (>98% ee) (Scheme 1). Kinetic data for the reductions with the fatty acid synthase (FAS)-deficient mutant suggested that two principal enzymes were involved in the reductions of this substrate: a fatty acid synthase that kinetically resolved the racemic mixture, leading to the formation of **2** (*trans*-(3*R*,4*R*)), and another, as yet unidentified reductase that produced *cis*-isomer **3** with low enantioselectivity (8).

We speculated that the low enantioselectivity in the latter case could be due to the nearly symmetrical structure of substrate **1**, where the 4-phenyl substituent resembles the *para*-methoxyphenyl (PMP) protective group on the nitrogen (8). The calculated structures of the two enantiomers can be overlaid on one another so that the aromatic groups are nearly coincident. The hydride transfers to one or the other are separated by only 0.5 Å. Thus, in principle, the enzyme's active site can accommodate both enantiomers (8). To test the validity of our reasoning, we wanted to investigate a less symmetrically substituted substrate such as 4-*tert*-butyl-3-oxo-β-lactam **4**. Additionally, this compound was of interest

Received 21 March 2002. Published on the NRC Research Press Web site at http://canjchem.nrc.ca on 26 June 2002.

M.M. Kayser,[1] Y. Yang, M.D. Mihovilovic, and A. Feicht. Department of Physical Sciences, University of New Brunswick, Saint John, NB E2L 4L5, Canada.
F.D. Rochon. Department of Chemistry, Université du Québec à Montréal, Montréal, QC H3C 3P8, Canada.

[1]Corresponding author (e-mail: kayser@unbsj.ca).

 DOI: 10.1139/V02-108 © 2002 NRC Canada

Table 1. Crystal data and structure refinement for **5** and **6**.

Crystal	**5**	**6**
Empirical formula	$C_{14}H_{19}NO_3$	$C_{14}H_{19}NO_3$
Formula weight	249.302	249.302
Wavelength (Å)	1.54178	1.54178
Crystal system	Orthorhombic	Orthorhombic
Space group	$P2_12_12_1$	$P2_12_12_1$
a (Å)	6.51(2)	6.405(2)
b (Å)	10.427(5)	11.554(6)
c (Å)	20.949(9)	18.627(6)
Volume (Å^3)	1387.3(10)	1378.5(9)
Z	4	4
$D_{calcd.}$ (Mg m^{-3})	1.194	1.2013
Absorption coefficient (mm^{-1})	0.679	0.684
F(000)	536	536
θ range for data collection (°)	4.22 to 69.92	4.50 to 69.80
Reflections collected	19847	14614
Independent reflections	2634 [R_{int} = 0.046]	2596 [R_{int} = 0.053]
Data/restraints/parameters	2632/0/168	2596/0/169
Goodness-of-fit on F^2	1.013	0.776
Final *R* indices [$I > 2\sigma(I)$]	R_1 = 0.0359, wR_2 = 0.0730	R_1 = 0.0378, wR_2 = 0.0740
R indices (all data)	R_1 = 0.0417, wR_2 = 0.0772	R_1 = 0.0641, wR_2 = 0.0805
Absolute structure parameter	–0.1(3)	0.1(3)
Extinction coefficient	0.0249(7)	0.0107(4)
Largest diff. peak and hole (e Å^{-3})	0.134 and –0.133	0.109 and –0.112

Scheme 1.

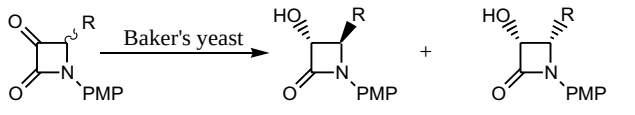

PMP: *p*-methoxyphenyl

Scheme 2.

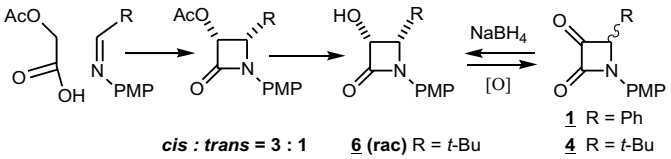

in its own right, since the structure–activity studies on butitaxel analogues have shown them to possess excellent cytotoxicity and improved water solubility (9, 10).

Results and discussion

Racemic 4-*tert*-butyl-3-oxo-β-lactam **4** was assembled in three steps from readily available starting materials, as shown in Scheme 2 (11). Its baker's yeast-catalyzed transformation followed by TLC and GC showed an essentially complete reduction (>99%). A mixture of compounds identified as *trans* and *cis* isomers was isolated in 97% yield. The two products, cleanly resolved by GC, were separated by chromatography, purified by crystallization from EtOAc, and characterized. According to chiral HPLC, the *cis* diastereomer was formed in 95% ee, while the *trans* compound was optically pure (>98% ee).[2]

Sodium borohydride reduction of racemic **4** gave the *cis* alcohol as the only product. Conversely, alcohol *rac*-**6**, from the condensation–hydrolysis reactions (Scheme 2), was found to be a mixture of isomers (75% *cis* and 25% *trans*). NMR experiments performed on *rac*-**6** with a chiral solvating agent (*R*-(–)-2,2,2-trifluoro-1-(9-anthryl)ethanol (CSA)) demonstrated that the *cis* and *trans* isomers were resolvable. Under identical experimental conditions, the *cis* and *trans* products from the yeast-catalyzed reduction were not resolved, indicating that diastereomers *trans*-**5** and *cis*-**6** were optically pure. This was confirmed by chiral HPLC analyses of all products. To establish the absolute configurations, the crystal structures of **5** and **6** were studied by X-ray diffraction methods. The two compounds belong to the chiral $P2_12_12_1$ space group. Table 1 contains the crystal data and the experimental details of the structure refinement for **5** and **6**, while selected bond distances and angles are listed in Table 2. Labeled diagrams of the two compounds are illustrated in Figs. 1 and 2. The same labeling system was chosen for both crystals to facilitate comparison between the two structures.

[2] For all HPLC analyses the Chiracel OD-H column (Daicel Chemical Industries, Ltd.) was used and the solvent system was hexane–*iso*-propanol (9:1). The two diastereomers appeared as well-separated peaks on the capillary GC (capillary column 15 m × 0.53 mm, DB-1301, J & W Scientific).

© 2002 NRC Canada

Table 2. Selected bond lengths (Å) and angles (°).

	5	6
Bond lengths (Å)		
O1—C1	1.220(2)	1.216(3)
O2—C2	1.392(2)	1.398(2)
O3—C14	1.370(2)	1.369(3)
O3—C8	1.417(2)	1.418(3)
N—C1	1.353(3)	1.352(3)
N—C11	1.425(2)	1.416(3)
N—C3	1.488(2)	1.491(3)
C1—C2	1.524(3)	1.520(3)
C2—C3	1.558(2)	1.567(3)
C3—C4	1.525(2)	1.519(3)
C4—C6	1.532(3)	1.526(3)
C4—C7	1.515(3)	1.533(3)
C4—C5	1.538(3)	1.534(3)
Bond angles (°)		
C14-O3-C8	117.8(2)	117.7(2)
C1-N-C11	131.9(2)	129.8(2)
C1-N-C3	95.24(13)	95.55(18)
C11-N-C3	132.32(14)	134.3(2)
O1-C1-N	132.6(2)	130.5(2)
O1-C1-C2	135.0(2)	137.2(2)
N-C1-C2	92.35(14)	92.3(2)
O2-C2-C1	118.1(2)	115.6(2)
O2-C2-C3	118.1(2)	121.2(2)
C1-C2-C3	85.93(13)	86.12(17)
N-C3-C4	117.4(2)	115.76(19)
N-C3-C2	86.11(12)	85.41(17)
C4-C3-C2	119.1(2)	120.3(2)
C3-C4-C6	109.8(2)	109.5(2)
C3-C4-C7	111.8(2)	112.5(2)
C6-C4-C7	109.6(2)	108.6(2)
C3-C4-C5	106.8(2)	107.7(2)
C6-C4-C5	108.7(2)	109.2(2)
C7-C4-C5	110.1(2)	109.3(2)

The crystallographic results clearly show the configuration at the two stereogenic centres. In **5** (Fig. 1), the *tert*-butyl and hydroxyl groups are on the opposite sides of the plane of the four-member ring (*trans*), while in **6** (Fig. 2), the two groups are on the same side of the plane, indicating a *cis* configuration. Since the measurements were made with Cu Kα radiation and the data was collected on the entire sphere (all the Friedel pairs were measured), the absolute configurations of the two compounds were unambiguously determined (12). The values of the Flack parameters are in agreement with the assigned configurations. In each structure, the four-member ring is planar with a mean deviation of 0.029(4) Å for **5** and 0.038(1) Å for **6** from the calculated best plane. The carbonyl oxygen atom O1 (deviation of –0.128(4) Å for **5** and –0.112(5) Å for **6**) and C11 (deviation of –0.030(4) Å (**5**) and 0.283(4) Å (**6**) are also close to the plane. The best plane was also calculated through the six atoms of the phenyl ring. The mean deviation is 0.005(1) Å for **5** and 0.002(2) Å for **6**. The atoms O3 (deviation of –0.011(3) Å for **5** and 0.031(3) Å for **6**) and N (deviation of –0.033(3) Å for **5** and 0.062(3) Å for **6**) are also in the phenyl plane. The dihedral angles between the phenyl and the four-member ring planes are very similar in the two structures: 47.2(1)° in **5** and 49.1(1)° in **6**.

Fig. 1. Labeled diagram of the *trans*-**5**.

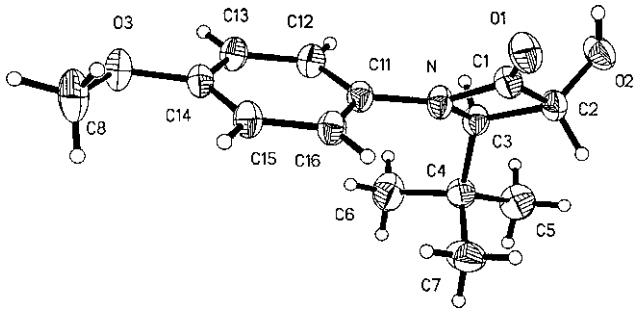

Fig. 2. Labeled diagram of the *cis*-**6**.

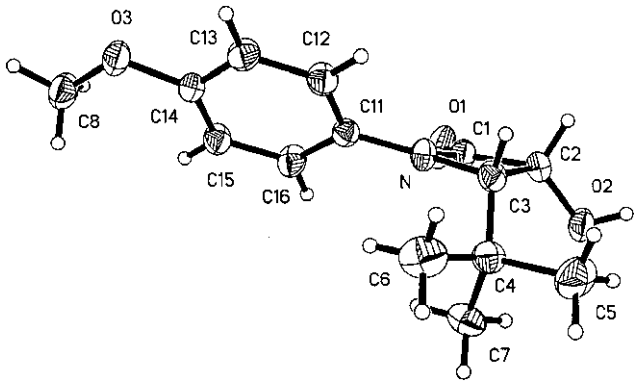

The torsion angles are listed in Table 3, confirming the configuration of the molecules. For example, we can compare the values of the torsion angles O2-C2-C3-C4 (116.6(2)° for *trans*-**5** and –5.8(3)° for *cis*-**6**), C1-N-C3-C4 (125.6(2)° for **5** and –115.4(2)° for **6**), C1-C2-C3-C4 (–123.5(2)° for **5** and 111.9(2)° for **6**), while N-C1-C2-O2 are very similar (124.4(2)° for **5** and 128.9(2)° for **6**).

The bond distances and angles are normal. In the four-member ring, the C—C bonds are as expected, while the N—C1 bond attached to the carbonyl group is shorter (av 1.353(3) Å) than the N—C3 bond (av 1.490(3) Å). The internal angles vary between 85.41(17) and 95.55(18)°. The angles at N (av 95.40(16)°) and at the carbonyl C atom (av 92.3(2)°) are larger than the others (av 85.89(15)°). The carbonyl bonds are 1.220(2) Å (**5**) and 1.216(3) Å (**6**).

The molecules are held together in the crystals by van der Waals forces and by intermolecular H-bonding between the hydroxyl group and the carbonyl O atom. The O··O distance in **5** is 2.760(2) Å, while the C2-O2··O1 and O2-H2··O1 angles are 101.4(1) and 145.6°, respectively. For **6**, the O··O distance is 2.728(2) Å (5), with the C2-O2··O1 and O-H··O angles 103.3(1) and 170.8°.[3]

[3] The crystallographic data for the structural analyses have been deposited with the Cambridge Crystallographic Data Centre (CCDC Nos. 171073 and 171074). Copies of this information may be obtained free of charge from The Director, CCDC, 12 Union Road, Cambridge CB2 1EZ, U.K. (Fax: +44-1223-336033; e-mail: deposit@ccdc.cam.ac.uk or www: http://www.ccdc.cam.ac.uk).

© 2002 NRC Canada

Table 3. Selected torsion angles (°).

Angle	**5**	**6**
C11-N-C1-O1	1.9(4)	–11.4(5)
C3-N-C1-O1	173.7(2)	175.2(3)
C11-N-C1-C2	–176.6(2)	167.1(2)
C3-N-C1-C2	–4.8(2)	–6.3(2)
O1-C1-C2-O2	–54.0(3)	–52.8(4)
N-C1-C2-O2	124.4(2)	128.8(2)
O1-C1-C2-C3	–173.8(3)	–175.7(3)
N-C1-C2-C3	4.6(2)	5.93(18)
C1-N-C3-C4	125.6(2)	–115.4(2)
C11-N-C3-C4	–62.7(3)	71.7(3)
C1-N-C3-C2	4.7(2)	6.08(19)
C11-N-C3-C2	176.4(2)	–166.8(2)
O2-C2-C3-N	–124.0(2)	–123.1(2)
C1-C2-C3-N	–4.15(14)	–5.39(17)
O2-C2-C3-C4	116.6(2)	–5.8(3)
C1-C2-C3-C4	–123.5(2)	111.9(2)
N-C3-C4-C6	79.5(2)	–70.2(3)
C2-C3-C4-C6	–178.9(2)	–170.5(2)
N-C3-C4-C7	–42.4(3)	50.6(3)
C2-C3-C4-C7	59.2(2)	–49.7(3)
N-C3-C4-C5	–162.9(2)	171.1(2)
C2-C3-C4-C5	–61.3(2)	70.8(3)
C1-N-C11-C12	126.5(2)	–127.1(3)
C3-N-C11-C12	–42.4(3)	43.6(4)
C1-N-C11-C16	–52.6(3)	50.0(4)
C3-N-C11-C16	138.5(2)	–139.3(3)

Having confirmed the optical purity and absolute configurations, we attempted to scale up the synthesis of the two compounds. Using a small 500-mL fermenter capable of maintaining vigorous agitation and adequate aeration, we performed several transformations on the 1–2-g scale. In these reactions, all the substrate was consumed in 24–44 h and the isolated yields of the two diastereomers (*cis*–*trans* = 57:43) were consistently between 86–92%. The isolated products were almost completely metabolite-free. Most of the *cis*-(3*R*,4*S*) isomer crystallized from EtOAc as white needles. The remaining mixture, consisting of *cis*-(3*R*,4*S*) and *trans*-(3*R*,4*R*) (20:80), was separated by flash chromatography to give additional pure *cis*-(3*R*,4*S*) and *trans*-(3*R*,4*R*). The best total isolated yields of pure *cis*-(3*R*,4*S*) and *trans*-(3*R*,4*R*) were 96 and 89%, respectively.

In conclusion, the results described in this paper provide a simple protocol for the preparation of two optically pure diastereomers of *tert*-butyl substituted C-13 paclitaxel side-chain analogues. The absolute configuration of both compounds was established by X-ray crystallographic analysis. The *cis* isomer was previously prepared in an optically pure form via chemical synthesis involving several steps (11). Access to the *trans* isomer is difficult via chemical routes, and, to our knowledge, the biological activities of paclitaxel analogues with *trans* C-13 side-chains have not been extensively investigated. Our simple methodology makes both compounds easily available for further structure–activity studies. Although the natural stereochemistry (2′*R*,3′*S*) appears to be the most biologically active form of natural paclitaxel (13), it may not be the optimum stereochemistry for all analogues, and the availability of **5** (3*R*,4*R*) and other chains with that absolute configuration will allow us to study the impact of *erythro*-chains on the activity of paclitaxel analogues.

The results from small-scale fermentations suggest that this reaction can be adapted for a large-scale multigram fermentation, and that the two products can be easily isolated as optically pure compounds.

Finally, we would like to add a word of caution: It should not be assumed that the formation of alcohol **6** (*cis*-(3*R*,4*S*)), in an almost optically pure form, unambiguously supports our original speculation (8) that the parent ketone **4** with a bulky *tert*-butyl substituent is selectively reduced by a single yeast reductase, while the same enzyme is not selective compared with the more symmetrical phenyl-substituted compound **1.** Recent results showing that baker's yeast harbor a large number of reductases, which may compete for the same substrates, make such conclusions unwarranted without further studies leading to the identification of enzyme or enzymes involved in reduction of a particular substrate (14).

Experimental

Melting points were determined on a Fisher-Johns melting point apparatus and are uncorrected. Optical rotations were measured on a PerkinElmer 241 polarimeter operating at room temperature. IR spectra were recorded as thin films on NaCl plates on a Mattson Satellite FT-IR spectrometer. ^{1}H and ^{13}C NMR spectra were recorded in $CDCl_3$ solution at room temperature on a Bruker 200 FT-NMR spectrometer; chemical shifts are reported in ppm using Me_4Si as internal standard. *J* values are expressed in Hertz. Chiral-phase HPLC analyses were performed on a Chiracel OD-H column (4.6 × 150 mm) using hexane–isopropanol (90:10) as the mobile phase. A UV detector set at 254 nm was used to monitor the reactions. Commercial baker's yeast was obtained from a local grocery chain.

Micro baker's yeast reduction of 4-*tert*-butyl-3-oxo-β-lactam 4

Fresh baker's yeast (3 g) was added to a solution of sucrose (12 g) in sterilized water (150 mL) in a 500-mL Erlenmeyer flask. The mixture was shaken (200 rpm) for 30 min at 30°C to activate the yeast. Finely ground *tert*-butyl-β-lactam (150 mg) with β-cyclodextrin (1.2 g)[4] was added to initiate the reaction. After 32 h, the reaction mixture was saturated with NaCl and centrifuged at 3000 × *g* for 10 min to remove the yeast cells. The supernatant was extracted with EtOAc (120 mL, 2 × 80 mL). The cell pellet was also extracted with EtOAc (2 × 20 mL). The combined organic layer was washed with brine, dried over anhydrous $MgSO_4$, and concentrated in vacuum. Purification of the crude product by column chromatography on silica gel (hexane–EtOAc, 2:1) gave a mixture of diastereomers **6** and **5** (57:43, respectively, 146 mg, 97%). Separation by spinning

[4] It is possible to perform this transformation without β-cyclodextrin; however, the reaction is slower and thus more metabolites are present in the product mixture.

© 2002 NRC Canada

chromatotron using hexane–EtOAc (4:1 to 3:1) as the eluent gave **6** (66 mg), **5** (15 mg), and a mixture **6** and **5** (65 mg, 27:73). Recrystallization from EtOAc and hexane yielded optically pure product **6** as white needles and optically pure **5** as colourless cubic crystals.

Small-scale fermentation

Dry baker's yeast (10 g) was added to a solution of sucrose (40 g) in sterilized water (400 mL) contained in a 500-mL fermenter. The mixture was stirred vigorously at 30°C for 30 min to activate the yeast. The aeration was maintained at 230 mL min^{-1}. Finely ground 4-*tert*-butyl-3-oxo-β-lactam (1 g) with β-cyclodextrin (200 mg)[4] was added to the fermenting yeast and the reaction was monitored by GC. After 26 h, the conversion was 98% and the reaction was stopped since prolonging the transformation results in the formation of metabolites. The reaction mixture was saturated with NaCl and centrifuged at 3000 × *g* for 10 min to remove yeast cells. The cell pellet was washed with EtOAc. The supernatant was extracted continuously with EtOAc for 24 h and the combined extracts were washed with brine and dried over anhydrous $MgSO_4$. After removing the solvent under reduced pressure, the crude product was crystallized from EtOAc to yield (4*R*,3*S*)-4-*tert*-butyl-3-hydroxy-β-lactam (439 mg) as white crystals (>95% ee). The remaining mixture consisting of *cis*-(3*R*,4*S*) and *trans*-(3*R*,4*R*) (in a 20:80 ratio) was separated by flash chromatography using hexane–EtOAc (5:1 then 2:1) as the eluent to give an additional 59 mg of *cis*-(3*R*,4*S*) and 349 mg of *trans*-(3*R*,4*R*). The total isolated yields of pure *cis*-(3*R*,4*S*) and *trans*-(3*R*,4*R*) were 96% and 87%, respectively.

(*R*,*R*)-4-*tert*-Butyl-3-hydroxy-β-lactam (5)

mp 120–121.5°C; $[\alpha]_D^{20}$ = +90 (*c* 0.2, CH_2Cl_2). IR λ_{max} (cm^{-1}): 3365, 3011, 2964, 1733, 1512, 1248. ^{1}H NMR δ: 0.98 (s, 9H, $CHC(CH_3)_3$), 3.79 (s, 3H, $ArOCH_3$), 3.84 (d, *J* = 1.2 Hz, 1H, $CHCMe_3$), 4.66 (br s, 1H, $CHOHCHCMe_3$), 6.83 (d, *J* = 9.2 Hz, 2H, Ar*H*), 7.17 (d, *J* = 8.9 Hz, 2H, Ar*H*). ^{13}C NMR δ: 26.6 ($C(CH_3)_3$), 33.3 (CMe_3), 55.4 (OCH_3), 72.2 ($NCHCMe_3$), 75.9 (HO*C*H), 114.2, 123.5, 129.5, 157.5, 175.6 (*C*O).

(*R*,*S*)-4-*tert*-Butyl-3-hydroxy-β-lactam (6)

mp 215.5–216.0°C; $[\alpha]_D^{20}$ = +84 (*c* 1.2, CH_2Cl_2). IR λ_{max} (cm^{-1}): 3349, 3010, 2959, 1734, 1512, 1247. ^{1}H NMR δ: 1.08 (s, 9H, $CHC(CH_3)_3$), 3.79(s, 3H, $ArOCH_3$), 4.11 (d, *J* = 5.5 Hz, 1H, $CHCMe_3$), 5.09 (t, *J* = 5.5 Hz, 1H, $CHOHCHCMe_3$), 6.87 (d, *J* = 9.2 Hz, 2H, Ar*H*), 7.30 (d, *J* = 9.2 Hz, 2H, Ar*H*). ^{13}C NMR δ: 27.2 ($C(CH_3)_3$), 35.3 (CMe_3), 55.5 (OCH_3), 67.8 ($NCHCMe_3$), 75.7 (HO*C*H), 114.2, 121.9, 130.3, 157.0, 175.6 (*C*O).

X-ray crystal structure analysis

The two compounds were crystallized from a diisopropylether–dichloromethane mixture. They were measured on an Enraf-Nonius CAD-4 diffractometer operating with the Cu Kα radiation. The intensity data were collected at room temperature (whole sphere) and were corrected for the effects of Lorentz and polarization. Crystal **6** was also corrected for absorption (integration). The SHELXTL system was used for all calculations and drawings. The coordinates of the first set of atoms were determined by direct methods and the positions of all the other atoms were found by the standard Fourier method. The structures were refined on F_o^2 using all reflections. The H atoms were fixed in idealized positions using a riding model with displacement parameters (U_{eq}) of 1.2U_{eq} (1.5 for methyl or hydroxyl groups) of the parent atom.

The Flack parameters (–0.1(3) for **5** and 0.1(3) for **6**) confirmed the absolute configuration of the two compounds.

Acknowledgments

Financial support (FDR and MMK) by the Natural Sciences and Engineering Research Council (NSERC) of Canada and Medical Research Fund of New Brunswick (MMK) are gratefully acknowledged. The NMR spectra were recorded at the Atlantic Regional Magnetic Resonance Centre at Dalhousie University, Halifax, Canada. The authors thank Dr. D.L. Hooper for the spectra with chiral solvating agents.

References

1. M.C. Wani, H.L.Taylor, M.E. Wall, P. Coggon, and A.T. McPhail. J. Am. Chem. Soc. **93**, 2325 (1971).
2. Taxane anticancer agents: Basic science and current status. *Edited by* G.I. Georg, T.T. Chen, I. Ojima, and D.M. Vyas. ACS Symposium Series 583, American Chemical Society, Washington DC. 1995. pp. 264–275.
3. I. Ojima, O. Duclos, M. Zucco, and F. Lavelle. J. Med. Chem. **37**, 2602 (1994).
4. I. Ojima, S. Lin, J.C. Slater, T. Wang, P. Pera, R.J. Bernacki, C. Ferlini, and G. Scambia. Bioorg. Med. Chem. **8**, 1619 (2000); T. Yamaguchi, N. Harada, K. Ozaki, H. Arakawa, K Oda, N. Nakanishi, K. Tsujihara, and T. Hashiyama. Bioorg. Med. Chem. Lett. **9**, 1639 (1999).
5. I. Ojima and S. Lin. J. Org. Chem. **63**, 224 (1998).
6. Review: G.I. Georg, T.C. Boge, Z.S. Cheruvallath, J.S. Clowers, G.C. Harrieman, M. Hepperle, and H. Park. *In* Taxol: Science and applications. *Edited by* M. Suffness. CRS, Boca Raton, FL. 1995. pp. 317–375.
7. S. Lin, X. Geng, C. Qu, R. Tynebor, D.J. Gallagher, E. Pollina, J. Rutter, and I. Ojima, Chirality, **12**, 431 (2000); I. Ojima, T. Wang, M.L. Miller, S. Lin, C.P. Borella, X. Geng, P. Pera, and R.J. Bernacki. Bioorg. Med. Chem. Lett. **9**, 3423 (1999).
8. M.M. Kayser, M.D. Mihovilovic, J. Kearns, A. Feicht, and J.D. Stewart. J. Org. Chem. **64**, 6603 (1999).
9. S.M. Ali, M.Z. Hoemann, J. Aubé, L.A. Mitscher, G.I. Georg, R. McCall, and L.R. Jayasinghe. J. Med. Chem. **38**, 3821 (1995).
10. S.M. Ali, M.Z. Hoemann, J. Aubé, G.I. Georg, L.A. Mitscher, and L.R. Jayasinghe. J. Med. Chem. **40**, 236 (1997).
11. M.D. Mihovilovic, A. Feicht, and M.M. Kayser. J. Prakt. Chem. **342**, 585 (2000).
12. H.D. Flack and G. Bernardinelli. J. Appl. Cryst. **33**, 1143 (2000); H.D. Flack and G. Bernardinelli. Acta Cryst. **A55**, 908 (1999).
13. F. Guéritte-Voegelein, D. Guénard, F. Lavalle, M.-T Le Goff, L. Mangatel, and P. Potier. J. Med. Chem. **34**, 992 (1991).
14. S. Rodriguez, M.M. Kayser, and J.D. Stewart, J. Am. Chem. Soc. **123**, 1547 (2001); J.D. Stewart, S. Rodriguez, and M.M. Kayser. Cloning, structure and activity of ketone reductases. *In* Enzyme technology for pharmaceutical and biotechnological applications. *Edited by* H.A. Kirst, W-K. Yeh, and M. Zmijewski. Marcel Dekker, Inc., New York. 2001. pp. 175–207.

© 2002 NRC Canada

Fixed stereochemical control in the synthesis of new mono- and disubstituted 2-phenyl-6-aza-1,3-dioxa-2-borabenzocyclononenes

Hiram I. Beltrán, S. Jesús Alas, Rosa Santillan, and Norberto Farfán

Abstract: Five new boronates of the type 2-phenyl-6-aza-1,3-dioxa-2-borabenzocyclononenes (**6a**–**e**) were prepared from substituted 2-[(2-hydroxyethylamino)methyl]phenols (**4a**–**e**) and phenylboronic acid (**5**) in benzene–EtOH (4:1) mixtures. Tridentate ligands **4a**–**e** and boronates **6a**–**e** were characterized by ^{1}H, ^{13}C, ^{15}N, and 2D-NMR (HETCOR, NOESY, and COLOC) experiments, FT-IR, mass spectra, and elemental analysis, as well as ^{11}B NMR for the boron derivatives. Suitable monocrystals of 2-[(2-hydroxyethylamino)methyl]phenol hydrochloride (**4a**), *cis*-2-phenyl-6-aza-1,3-dioxa-2-borabenzocyclononene (**6a**), (2*S*,5*R*,6*S*)-2,5-diphenyl-6-aza-1,3-dioxa-2-borabenzocyclononene (**6b**), and (2*S*,4*R*,5*R*,6*S*)-2,4-diphenyl-5-methyl-6-aza-1,3-dioxa-2-borabenzocyclononene (**6e**) were obtained and their structures are discussed. The X-ray structures of **6a**, **6b**, and **6e**, as well as the NMR data established that the configurations at the nitrogen and boron atoms are both "*S*" and the transannular fusion is *cis*. A semi-empirical (SAM1) study was used to calculate the energy for all possible stereoisomers, showing that the stabilization increases as the THC (tetrahedral character of the boron atom) increases and also as the N→B bond distance decreases, in agreement with the experimental results and previous work related to amino acid boronates.

Key words: boron compounds, X-ray structures, NMR, boronates, synthesis.

Résumé : On a préparé cinq nouveaux boronates du type 2-phényl-6-aza-1,3-dioxa-2-borabenzocyclononènes (**6a**–**e**) en faisant réagit des 2-[(2-hydroxyéthylamino)méthyl]phénols substitués (**4a**–**e**) avec de l'acide phénylboronique (**5**) dans des mélanges 4:1 de benzène–éthanol. Les ligands tridentates (**4a**–**e**) et les boronates (**6a**–**e**) ont été caractérisés par les analyses élémentaires, par infrarouge à transformée de Fourier, par des expériences de RMN du ^{1}H, du ^{13}C, du ^{15}N et par RMN-2D (HETCOR, NOESY et COLOC) ainsi que par RMN du ^{11}B pour les dérivés du bore. On a obtenu des monocristaux appropriés du chlorhydrate du 2-[(2-hydroxyéthylamino)méthyl]phénol (**4a**), du *cis*-2-phényl-6-aza-1,3-dioxa-2-borabenzocyclononène (**6a**), du (2*S*,5*R*,6*S*)-2,5-diphényl-6-aza-1,3-dioxa-2-borabenzocyclononène (**6b**) et du (2*S*,4*R*,5*R*,6*S*)-2,4-diphényl-5-méthyl-6-aza-1,3-dioxo-2-borabenzo-cyclononène (**6e**) et on discute de leurs structures. Les structures des composés **6a**, **6b** et **6e** déterminées par diffraction des rayons-X ainsi que les données de la RMN ont permis d'établir que les configurations au niveau des atomes d'azote et du bore sont toutes les deux *S* et que la fusion transannulaire est *cis*. On a fait appel à des calculs semi-empiriques (SAM1) pour calculer l'énergie des tous les stéréoisomères possibles; ils montrent que la stabilisation augmente avec une augmentation du caractère tétraédrique de l'atome de bore ainsi qu'avec une diminution de la longueur de la distance N→B, en accord avec les données expérimentales obtenues ici et avec celles obtenues dans un travail antérieur sur des boronates apparentés d'acides aminés.

Mots clés : composés du bore, structures par diffraction des rayons X, RMN, boronates, synthèse.

[Traduit par la Rédaction]

Introduction

In previous studies we described the syntheses of a series of mono-, di-, tri-, and tetrameric boronates derived from tridentate ligands (1–8). These ligands possess one nitrogen and two oxygen donor atoms with several variations in the main skeleton, which allowed for the evaluation of the steric and electronic effects (Fig. 1). The studies showed that, in all cases, the boron atom is tetracoordinated and forms a coordinative bond with the nitrogen atom (6), which is responsible for the self-assembly of the macrocycles, whereby the oxygens build up five- or six-membered rings as well as intermolecular boron–oxygen bonds. Moreover, the reaction product is mainly dependent on the structure of the ligand and, to a lesser extent, on the steric and electronic factors. The use of a tridentate ligand such as 2,6-pyridinedimethanol lead to a tetrameric compound containing four 5-membered- and one 20-membered ring by self-assembly (1). The stabilization of all these compounds is due to tetracoordination of the boron atom.

It has been reported that the formation of dimeric and monomeric structures is highly dependent on reaction conditions as well as the structure of the salicylidenimino alcohol. It is therefore possible in certain cases to obtain either the

Received 26 January 2002. Published on the NRC Research Press Web site at http://canjchem.nrc.ca on 28 June 2002.

H.I. Beltrán, S.J. Alas, R. Santillan, and N. Farfán.[1] Departamento de Química, Centro de Investigación y de Estudios Avanzados del Instituto Politécnico Nacional, Apdo. Postal 14–740, 07000 México, México, D.F.

[1]Corresponding author (e-mail: jfarfan@mail.cinvestav.mx).

 DOI: 10.1139/V02-109 © 2002 NRC Canada

Fig. 1. Mono-, di-, tri-, and tetrameric boronates.

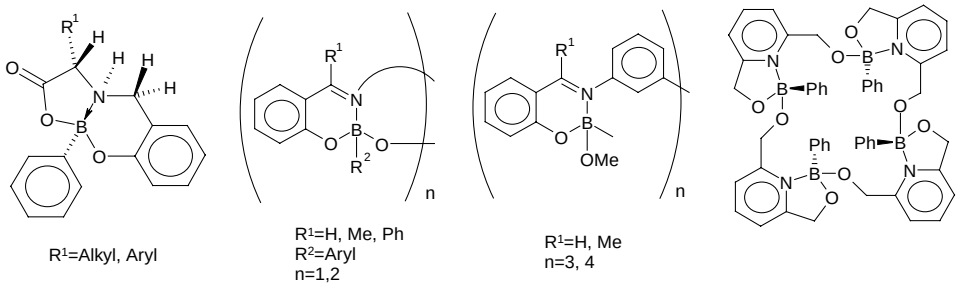

Fig. 2. Formation of monomers and dimers.

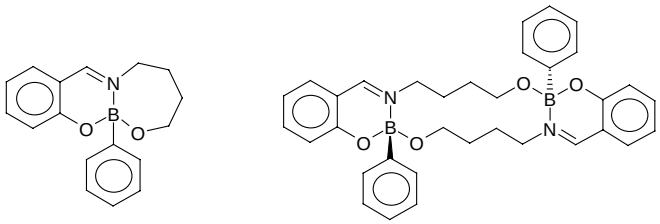

Fig. 3. Stereochemistry for the fused rings in amino acid boronates.

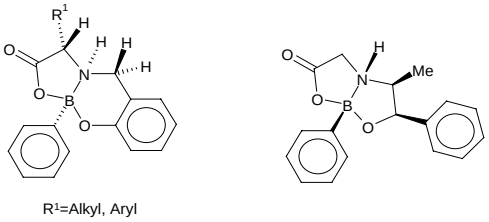

dimeric or monomeric derivatives in high yields by using kinetic or thermodynamic control (Fig. 2) (7). The use of long reaction times leads to monomeric structures (7, 8). In general, the N→B bond distances are between 1.6 and 1.7 Å, characteristic for dative nitrogen–boron bonds (1–13), and the boron atom shows a distorted tetrahedral geometry.

Regarding the stereochemistry of these compounds, a literature search showed preference for *cis*-fused transannular N→B bond (8–30). Moreover, the presence of a stereogenic center in the five-membered ring induces formation of the *cis–cis* isomer (8, 12) (Fig. 3).

Continuing in our investigations, we describe herein the preparation and complete characterization of five new 4,5-disubstituted-2-phenyl-6-aza-1,3-dioxa-2-borabenzocyclononenes (**6a**–**e**) prepared from 2-[(2-hydroxyethylamino)methyl]phenols (**4a**–**e**) and phenylboronic acid (**2**). Some of the phenols have found application as chelating agents for Cu(II) (31) and in catalytic enantioselective hydrogenation of ketones with ruthenium (32). Analogous compounds have been prepared by reduction of the corresponding Schiff base (33) and hydrogen-bonded structures for these derivatives have been reported (31, 34).

The aim of this work is to investigate the influence of nitrogen hybridization and the acidity of the amino alcohol to selectively form monomeric or dimeric boronates, since increased flexibility in the ligand should lead to release of strain at the fused bicyclic structure. In addition, it was desirable to establish the stereochemistry of these new boronates, which possess two fixed chiral atoms (nitrogen and boron) and to compare the theoretical and experimental results.

Tridentate ligands **4a**–**e** and monomeric boronates **6a**–**e** were characterized by ^{1}H, ^{13}C, ^{15}N, and 2D-NMR (HETCOR, NOESY, and COLOC) experiments, FT-IR, mass spectra, and additionally for boronates, the ^{11}B NMR spectra were recorded. Suitable monocrystals of 2-[(2-hydroxyethylamino)methyl]phenol hydrochloride (**4a**), *cis*-2-phenyl-6-aza-1,3-dioxa-2-borabenzocyclononene (**6a**), (2*S*,5*R*,6*S*)-2,5-diphenyl-6-aza-1,3-dioxa-2-borabenzocyclononene (**6b**) and (2*S*,4*R*,5*R*,6*S*)-2,4-diphenyl-5-methyl-6-aza-1,3-dioxa-2-borabenzocyclononene (**6e**) were obtained. The theoretical calculations (SAM1) support that compounds **6a**–**e** are energetically favored and indeed all the products obtained show *cis–cis* stereochemistry.

Results and discussion

Synthesis of 2-[(2-hydroxyethylamino)methyl]phenol hydrochlorides (4a–e)

The synthetic route to prepare 2-[(2-hydroxyethylamino)methyl]phenols **4a**–**e** involved the reaction of β-aminoalcohols **1a**–**e** with an equimolecular ratio of salicylaldehyde **2** under reflux of THF–MeOH (1:1) for 4 h to give corresponding Schiff bases **3a**–**e**, followed by reduction with sodium borohydride (Scheme 1). The products were obtained in moderate to high yields.

Synthesis of 4,5-disubstituted 2-phenyl-6-aza-1,3-dioxa-2-borabenzocyclononenes (6a–e)

The condensation of 2-[(2-hydroxyethylamino)methyl]phenol hydrochlorides **4a**–**e** with phenylboronic acid **5** in the presence of an excess of sodium bicarbonate was carried out at reflux in benzene–EtOH mixtures to yield the corresponding (2*S*,5*S*,6*R*)-2-phenyl-6-aza-1,3-dioxa-4,5-(*R*,*R*′)-2-borabenzocyclononenes **6a**–**e** in yields from 69 to 89%. These tricyclic derivatives show transannular N→B bonds with a tetrahedral geometry for the boron and nitrogen atoms (35) as well as five- and six-membered fused rings. In all cases, the configurations at positions 2, 5, and 6 are *S*, *R*, and *S*, respectively (Scheme 1).

Spectroscopic data

The ^{1}H NMR data of 2-[(2-hydroxyethylamino)methyl] phenol hydrochlorides **4a**–**e** is summarized in Table 1; ^{13}C and ^{15}N NMR are given in Table 2. For 4,5-disubstituted-2-phenyl-6-aza-1,3-dioxa-2-borabenzocyclononenes **6a**–**e**, the

© 2002 NRC Canada

Scheme 1. Synthetic route for the preparation of 4,5-disubstituted-2-phenyl-6-aza-1,3-dioxa-2-borabenzocyclononenes (**6a**–**e**).

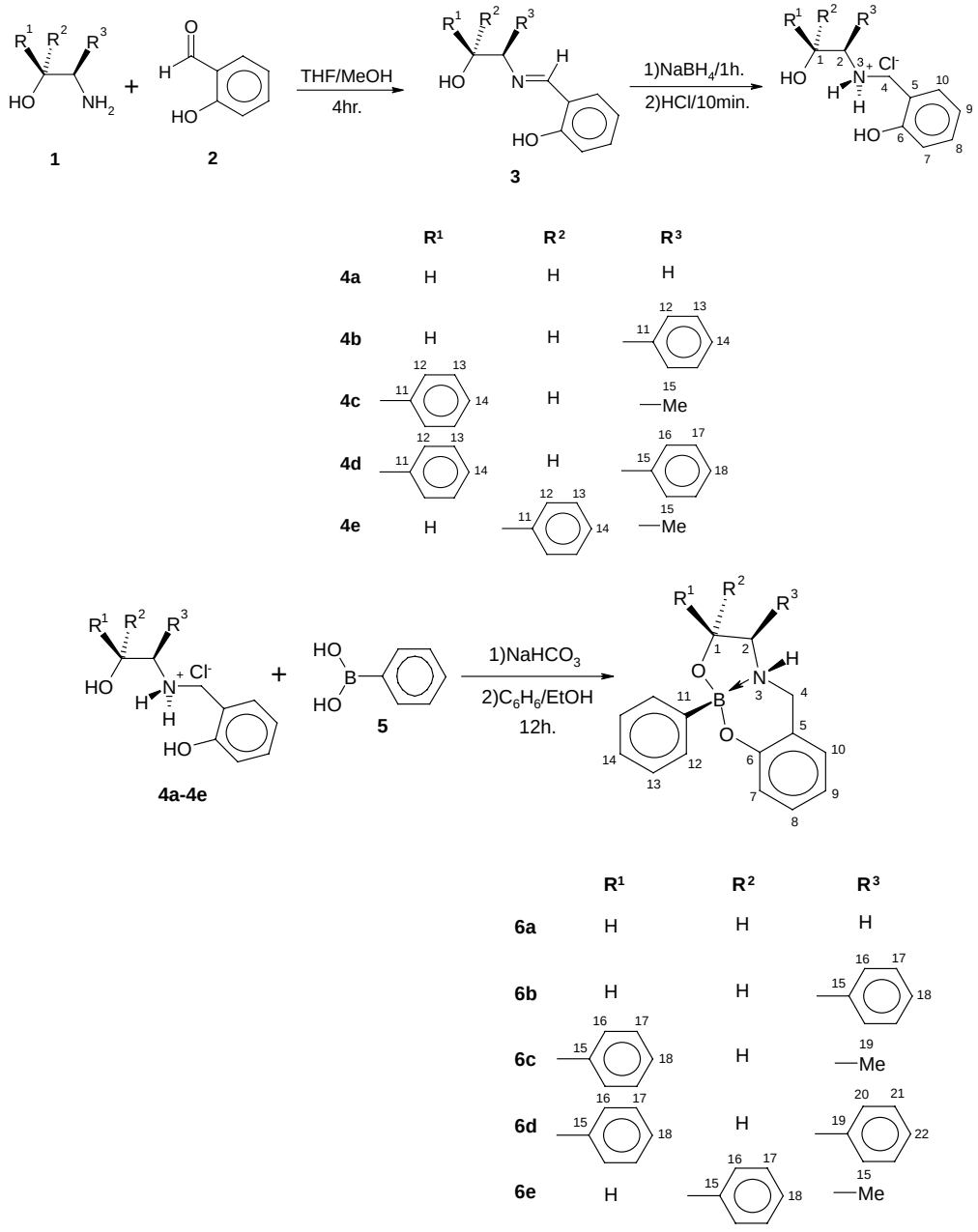

^{1}H and ^{13}C NMR data are given in Tables 3 and 4, respectively. Table 5 summarizes the ^{15}N and ^{11}B NMR data.

NMR data of 2-[(2-hydroxyethylamino)methyl]phenol hydrochlorides (4a–e)

The ^{1}H NMR spectra show the phenolic OH between 10.42 and 9.68 ppm, followed by the nitrogen protons (H-3a and H-3b) in the range from 10.10 to 8.05 ppm — these protons are diastereotopic in **4b**–**e** and the proton antiperiplanar to the substituent is shifted to higher frequencies and labeled as H-3a. The salicylidene fragment shows an ABCD system, with H-10 observed as a double of doublets at higher frequency, followed by H-8 (ddd or t), H-7 (ddd), and H-9 (ddd or t). The protons in position 4 are diastereotopic for compounds **4b** and **4c**, showing an AB system with coupling constants of 13.2 Hz; for the remaining compounds these protons give rise to broad signals. Hydrogens in positions 1 and 2 are shifted according to substitution; for example, the signals for **4b** give an ABX system for protons H-1a, H-1b, and H-2 with a geminal coupling constant of 11.4 Hz and AX and BX couplings of 5.1 and 7.0 Hz, respectively.

The ^{13}C NMR spectra show the following trends: the resonance for C-6 always appears at higher frequencies (156.6 and 155.7 ppm) followed by C-10 (132.1–131.4 ppm), and C-8 (131.2–130.2 ppm); C-9 shows chemical shifts between 120.4 and 119.0 ppm, C-5 between 118.6 and 116.5 ppm, and C-7 is the most shielded at 116.6 to 115.4 ppm. The chemical shifts for C-1 and C-2 depend on substitution: a phenyl group at position 1 shifts the signal to higher frequencies ($\Delta\delta$ = 18.2 and 13.5 ppm, respectively) and a

© 2002 NRC Canada

Table 1. ^{1}H NMR data for 2-[(2-hydroxyethylamino)methyl]phenol hydrochlorides (**4a**–**e**).

Compd	OH_{aliph}	H-1a	H-1b	H-2	H-3a	H-3b	H-4a	H-4b	OH_{phenol}	H-7	H-8	H-9	H-10
4a	5.30 br s 1H	3.67 t J = 5.0 1H	3.67 t J = 5.0 1H	2.92 br s 2H	9.05 br s 1H	9.05 br s 1H	4.07 br s 1H	4.07 br s 1H	10.36 br s 1H	7.00 dd J_o = 8.0 J_m = 0.9 1H	7.21 ddd J_o = 8.0 J_o = 7.4 J_m = 1.6 1H	6.81 ddd J_o = 7.5 J_o = 7.4 J_m = 0.9 1H	7.41 dd J_o = 7.5 J_m = 1.6 1H
4b[a]	5.65 br s 1H	3.96 ABX J_{AB} = 11.4 J_{AX} = 5.1 1H	3.79 ABX J_{AB} = 11.4 J_{BX} = 7.0 1H	4.26 br s 1H	9.59 br s 1H	9.37 br s 1H	3.95 AB J_{AB} = 13.2 1H	3.89 AB J_{AB} = 13.2 1H	10.34 br s 1H	6.97 d J_o = 7.7 1H	7.19 t J_o = 7.7 1H	6.78 dd J_o = 7.7 J_o = 7.4 1H	7.32 d J_o = 7.4 1H
4c[b]	6.14 d J = 4.0 1H	5.29 br s 1H	—	3.31 br q J = 6.6 1H	9.09 br s 1H	9.05 br s 1H	4.27 AB J_{AB} = 13.2 1H	4.20 AB J_{AB} = 13.2 1H	10.42 br s 1H	7.04 d J_o = 7.7 1H	7.22 ddd J_o = 7.7 J_o = 6.6 J_m = 1.3 1H	6.84 dd J_o = 7.5 J_o = 6.6 1H	7.55 dd J_o = 7.5 J_m = 1.3 1H
4d[c]	6.36 d J = 3.8 1H	5.62 br s 1H	—	4.40 br s 1H	10.10 br s 1H	9.39 br s 1H	4.02 br s 1H	4.02 br s 1H	10.31 br s 1H	7.00 dd J_o = 8.1 J_m = 1.0 1H	7.22 ddd J_o = 8.1 J_o = 7.4 J_m = 1.5 1H	6.82 ddd J_o = 7.6 J_o = 7.4 J_m = 1.0 1H	7.43 dd J_o = 7.6 J_m = 1.5 1H
4e[d]	—	4.73 d J = 8.8 1H	—	3.06 br s 1H	9.55 br s 1H	8.05 br s 1H	4.35 br s 1H	3.97 br s 1H	9.68 br s 1H	7.28–7.12 m 1H	7.28–7.12 m 1H	6.79 m 1H	7.28–7.12 m 1H

Note: ^{1}H NMR at 400 MHz. Solvent: DMSO-d_6 (δ in ppm, J in Hz). br s = broad singlet, d = doublet, q = quartet, m = multiplet.
[a]**4b**: 7.59 (d, J_o = 7.3, 2H, H-12, H-16), 7.45–7.40 (m, 2H, H-13, H-15), 7.45–7.40 (m, 1H, H-14).
[b]**4c**: 7.36–7.31 (m, 2H, H-12), 7.36–7.31 (m, 2H, H-13), 7.25 (td, J_o = 6.2, J_m = 1.4, 1H, H-14), 1.00 (d, J = 6.6, 3H, H-15).
[c]**4d**: 7.21 (m, 2H, H-12), 7.21 (m, 2H, H-13), 7.30–7.26 (m, 1H, H-14), 7.01 (d, J_o = 7.0, 2H, H-16), 7.18 (d, J_o = 7.0, 2H, H-17), 7.15 (m, 1H, H-18).
[d]**4e**: 7.04 (d, J_o = 6.0, 2H, H-12), 7.28–7.12 (m, 2H, H-13), 7.28–7.12 (m, 1H, H-14), 1.06 (d, J = 4.1, 3H, H-15).

© 2002 NRC Canada

Table 2. ^{13}C and ^{15}N NMR data of 2-[(2-hydroxyethylamino)methyl]phenol hydrochlorides (**4a**–**e**).

Compd	C-1	C-2	C-4	C-5	C-6	C-7	C-8	C-9	C-10	^{15}N
4a	56.3	48.4	45.0	118.0	156.2	115.5	130.3	119.0	131.7	–335.2
4b[a]	62.5	63.8	44.5	118.4	156.5	115.8	130.7	119.4	131.9	–326.1
4c[b]	69.8	58.5	43.3	118.6	156.6	116.1	130.7	119.5	132.1	–324.0
4d[c]	70.6	66.6	44.1	118.0	156.1	115.4	130.2	119.0	131.5	–324.3
4e[d]	74.5	58.7	46.0	116.5	155.7	116.6	131.2	120.4	131.4	–327.4

Note: ^{13}C NMR at 100 MHz, ^{15}N NMR at 40.515 MHz. Solvent: DMSO-d_6 (δ in ppm).
[a]**4b**: 134.0 (C-11), 129.2 (C-12), 129.2 (C-13), 129.4 (C-14).
[b]**4c**: 141.7 (C-11), 126.2 (C-12), 128.6 (C-13), 127.7 (C-14), 9.8 (C-15).
[c]**4d**: 131.1 (C-11), 129.9 (C-12), 127.7 (C-13), 128.6 (C-14), 140.6 (C-16), 126.0 (C-16), 127.7 (C-17), 127.2 (C-18).
[d]**4e**: 139.5 (C-11), 127.2 (C-12), 128.8 (C-13), 128.7 (C-14), 12.1 (C-15).

Fig. 4. Molecular structure of **4a**.

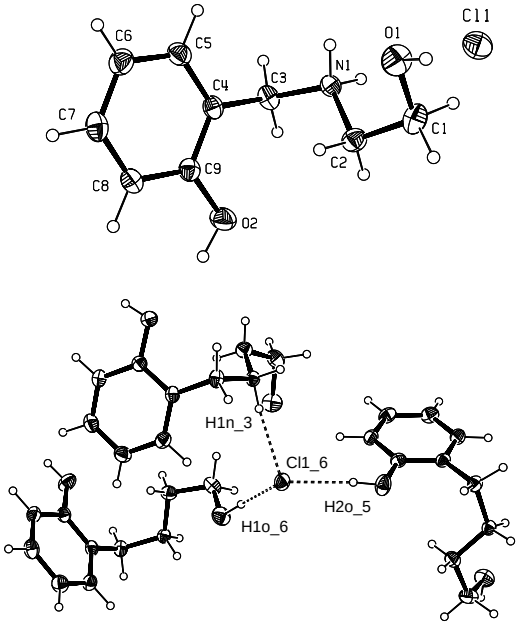

similar behavior is observed for C-2. The shift induced by a methyl group is less than for phenyl substituents, thus C-4 appears between 46.0 and 43.3 ppm, showing no significant variations due to substitution.

Since all ^{15}N NMR spectra were determined on HCl derivatives, their chemical shifts are shifted to lower frequencies. Substituents at the β position show an additive effect with respect to compound **4a**. The ^{15}N chemical shift for **4a** is shifted to lower frequencies with respect to compounds **4b**–**e**, which show $\Delta\delta \approx 10$ ppm.

NMR data of 4,5-disubstituted 2-phenyl-6-aza-1,3-dioxa-2-borabenzocyclononenes (6a–e)

The ^{1}H NMR data for compounds **6a**–**e** show that H-12 is the most deshielded signal (7.72–7.48 ppm), followed by H-13 and H-14 (7.34 and 7.20 ppm, respectively). The chemical shift for the benzylidene fragment and the hydrogens at positions 1, 2, and 4 are very similar to those of the Schiff bases, while that of H-3 depends on the anisotropy of the vicinal group (7.29 (**6a**), 7.27 (**6b**), 6.87 ppm (**6c**)). The existence of two phenyl groups in **6d** shifts the signal to 4.07 ppm. In **6e**, methyl substitution at the opposite side of H-3 modifies the conformation at the five-membered ring in such a way that both phenyl groups affect its environment and there is an extra anisotropic contribution (4.32 ppm). For compound **6a**, the couplings for these signals were difficult to assign and selective decoupling experiments were carried out. Hydrogens at the 3 and 4 positions appear as an ABC system, with an additional coupling between H-4a and H-3.

The difference in chemical shifts with respect to the Schiff bases is approximately 1 ppm and the most shielded signal is C-6. The ipso (to boron) carbon (C-11) is observed in the range between 146.2 and 144.6 ppm, followed by the *ortho* (C-12), *meta* (C-13), and *para* carbons (C-14), which were assigned using HETCOR experiments.

The ^{15}N NMR chemical shifts of **6a**–**e** (–331.8 to –312.1) and those of tridentate ligands **4a**–**e** (Table 2), are in the characteristic range for tetracoordinated nitrogen atoms (36). In ^{11}B NMR, the signals are observed from 5.1 to 6.0 ppm, characteristic for tetracoordinated boron atoms (37).

IR and MS data of 4a–e and 6a–e

The IR spectra of compounds **4a**–**e** show strong N–H and O–H stretching bands, while the IR spectra of compounds **6a**–**e** show only the N–H band. The mass spectra of **4a**–**e** show the molecular ion peak, along with the loss of hydrochloric acid, and the hydroxytropylium and cycloheptatrienone ions. In most cases M^+, $[M - C_6H_5]^+$, and $[M - C_6H_6]^+$ are observed.

Molecular structures of 4a, 6a, 6b, and 6e

Crystallographic data for **4a**, **6a**, **6b**, and **6e** are listed in Table 6; selected bond lengths, bond angles, torsion angles, and plane deviations are summarized in Table 7. The molecular structures are shown in Figs. 4–7.

For **4a** all distances are in agreement with reported values (31, 34). The salicylidene and β-amino alcohol fragments have *gauche* conformations, with C(2)-N(1)-C(3)-C(4) and O(1)-C(1)-C(2)-N(1) torsion angles of 60.63(21)° and 58.17(22)°, respectively. There are two hydrogen-bonding interactions in the asymmetric unit, one intramolecular contact between H(1n) and O(1) with a magnitude of 2.359(23) Å (which is mostly responsible for the *gauche* conformation in this fragment), and a second intramolecular contact between Cl(1) and H(1o) with a value of 2.295(29) Å. There are also important interactions with the neighboring molecules. The first is for both hydrogens attached to nitrogen (H(1n)···Cl(1) = 2.376(25) Å, H(2n)···Cl(1) = 2.241(24) Å), and the second one between chlorines at opposite sides of the molecule and the phenolic hydrogen (H(2o)···Cl(1) = 2.202(33) Å).

© 2002 NRC Canada

Table 3. ^{1}H NMR data of 4,5-disubstituted-2-phenyl-6-aza-1,3-dioxa-2-borabenzocyclononenes (**6a**–**e**).

Compd	H-1a	H-1b	H-2a	H-2b	H-3	H-4a	H-4b	H-7	H-8	H-9	H-10	H-12	H-13	H-14
6a	3.76 ddd $J_{1a,1b}$ = 11.4 $J_{1a,2a}$ = 5.5 $J_{1a,2b}$ = 6.9 1H	3.73 ddd $J_{1a,1b}$ = 11.4 $J_{1b,2a}$ = 5.5 $J_{1b,2b}$ = 6.9 1H	3.76 ddd $J_{2a,2b}$ = 11.0 $J_{2a,NH}$ = 6.2 $J_{2a,1}$ = 5.5 1H	3.76 ddd $J_{2a,2b}$ = 11.0 $J_{2b,NH}$ = 7.0 $J_{2b,1}$ = 6.9 1H	7.29 br s 1H	4.04 dd $J_{4a,4b}$ = 14.5 $J_{4a,NH}$ = 3.5 1H	3.83 dd $J_{4a,4b}$ = 14.5 $J_{4b,NH}$ = 2.0 1H	6.78 d J_o = 7.7 1H	7.18 dd J_o = 8.4 J_o = 7.7 1H	6.76 dd J_o = 8.4 J_o = 7.0 1H	7.11 d J_o = 7.0 1H	7.48 dd J_o = 7.4 J_m = 1.5 2H	7.22–7.20 m 2H	7.22–7.20 m 1H
6b[a]	4.12 dd $J_{1a,1b}$ = 9.2 $J_{1a,2}$ = 6.6 1H	3.93 dd $J_{1a,1b}$ = 9.2 $J_{1b,2}$ = 8.8 1H	4.04 ddd $J_{2,1a}$ = 6.6 $J_{2,1b}$ = 8.8 $J_{2,NH}$ = 5.2 1H	—	7.27 m 1H	4.05 dd $J_{4a,4b}$ = 15.0 $J_{4a,NH}$ = 3.6 1H	3.65 d $J_{4a,4b}$ = 15.0 1H	6.84 d J_o = 8.4 1H	7.22 m 1H	6.81 dd J_o = 7.7 J_o = 7.3 1H	6.84 d J_o = 7.3 1H	7.58 dd J_o = 7.3 J_m = 1.4 2H	7.24–7.21 m 2H	7.24–7.21 m 1H
6c[b]	5.12 d $J_{1,2}$ = 6.8 1H	—	3.51 dq $J_{2,1}$ = 6.8 $J_{2,19}$ = 6.8 $J_{2,NH}$ = 5.9 1H	—	6.87 br s 1H	4.07 dd $J_{4a,4b}$ = 15.0 $J_{4a,NH}$ = 3.0 1H	3.98 d $J_{4a,4b}$ = 15.0 1H	6.76 dd J_o = 7.7 J_m = 1.8 1H	7.14 dd J_o = 7.7 J_o = 7.0 1H	6.79 ddd J_o = 7.7 J_o = 7.0 J_m = 1.8 1H	7.19 d J_o = 7.7 1H	7.58 dd J_o = 7.3 J_m = 1.3 2H	7.24 dd J_o = 7.3 2H	7.22 dd J_o = 7.0 J_m = 1.3 1H
6d[c]	5.42 d $J_{1,2}$ = 7.7 1H	—	4.73 dd $J_{2,1}$ = 7.7 $J_{2,NH}$ = 8.2 1H	—	4.07 dd $J_{NH,2}$ = 8.2 $J_{NH,4a}$ = 2.8 1H	4.29 dd $J_{4a,4b}$ = 15.6 $J_{4a,NH}$ = 2.8 1H	3.98 d $J_{4a,4b}$ = 15.6 1H	6.86 d J_o = 7.6 1H	7.22 ddd J_o = 7.6 J_o = 7.2 J_m = 1.4 1H	6.79 dd J_o = 7.4 J_o = 7.2 1H	7.15–7.00 dd J_o = 7.4 J_m = 1.4 1H	7.72 dd J_o = 7.3 J_m = 1.6 2H	7.34–7.27 d J_o = 7.3 2H	7.34–7.27 d J_m = 1.6 1H
6e[d]	4.38 d $J_{1,2}$ = 9.5 1H	—	2.84 ddq $J_{2,1}$ = 9.5 $J_{2,19}$ = 6.6 $J_{2,NH}$ = 10.3 1H	—	4.32 dd $J_{NH,2}$ = 10.3 $J_{NH,4a}$ = 2.6 1H	4.01 dd $J_{4a,4b}$ = 14.1 $J_{4a,NH}$ = 2.6 1H	3.55 d $J_{4a,4b}$ = 14.1 1H	7.07 dd J_o = 8.0 J_m = 0.8 1H	7.29 ddd J_o = 8.0 J_o = 7.3 J_m = 1.5 1H	6.82 ddd J_o = 7.3 J_o = 7.2 J_m = 0.8 1H	6.92 dd J_o = 7.2 J_m = 1.5 1H	7.58 dd J_o = 7.0 J_m = 1.8 2H	7.34 d J_o = 7.0 2H	7.33 m 1H

Note: ^{1}H NMR at 399.784 MHz. Solvent: DMSO-d_6 (δ in ppm, J in Hz).
[a]**6b**: 7.42–7.37 (m, 2H, H-16), 7.42–7.37 (m, 2H, H-17), 7.42–7.37 (m, 1H, H-18).
[b]**6c**: 7.39 (dd, J_o = 7.5, 2H, H-16), 7.34 (dd, J_o = 7.5, J_o = 6.6, 2H, H-17), 7.25 (dd, J_o = 6.6, 1H, H-18), 0.69 (d, J = 6.8, 3H, H-19).
[c]At 270.167 MHz. **6d**: 7.15–7.00 (m, 2H, H-16), 7.15–7.00 (m, 2H, H-17), 7.15–7.00 (m, 1H, H-18), 7.15–7.00 (m, 2H, H-20), 7.15–7.00 (m, 2H, H-21), 7.15–7.00 (m, 1H, H-22).
[d]In $CDCl_3$. **6e**: 7.22 (dd, J_o = 7.7, J_m = 1.8, 2H, H-16), 7.26 (dd, J_o = 7.0, J_m = 1.8, 2H, H-17), 7.24 (dd, J_o = 7.0, J_m = 1.8, 1H, H-18), 1.14 (d, J = 6.6, 3H, H-19).

© 2002 NRC Canada

Table 4. ^{13}C NMR data of 2-phenyl-6-aza-1,3-dioxa-4,5-(*R*,*R′*)-2-borabenzocyclononenes (**6a**–**e**).

Compd	C-1	C-2	C-4	C-5	C-6	C-7	C-8	C-9	C-10	C-11	C-12	C-13	C-14
6a	62.1	48.1	46.7	119.8	157.5	118.5	130.0	118.8	128.8	146.2	132.7	127.4	127.2
6b[a]	68.9	63.0	44.8	118.5	156.8	118.7	129.9	119.0	128.9	145.7	133.0	127.4	127.3
6c[b]	77.4	59.1	46.1	118.8	157.6	118.2	128.6	118.6	129.7	145.9	132.7	127.5	127.3
6d[c]	78.7	68.0	46.3	117.5	157.1	118.4	129.8	118.8	128.8	145.3	133.0	127.6	127.6
6e[d]	82.4	61.1	45.1	117.9	156.2	119.4	127.9	119.2	128.1	144.6	132.3	127.9	130.3

Note: ^{13}C NMR at 100.535 MHz. Solvent: DMSO-d_6 (δ in ppm).
[a]**6b**: 134.6 (C-15), 129.2 (C-16), 129.2 (C-17), 129.2 (C-18).
[b]**6c**: C141.7 (C-15), 127.2 (C-16), 128.3 (C-17), 127.5 (C-18), 14.4 (C-19).
[c]**6d**: 134.7 (C-15), 129.1 (C-16), 128.3 (C-17), 128.1 (C-18), 141.1 (C-19), 127.2 (C-20), 127.8 (C-21), 127.2 (C-22).
[d]In $CDCl_3$. **6e**: 141.1 (C-15), 126.9 (C-16), 128.4 (C-17), 128.0 (C-18), 13.2 (C-19).

Table 5. ^{15}N and ^{11}B NMR data for 4,5-disubstituted-2-phenyl-6-aza-1,3-dioxa-2-borabenzocyclononenes (**6a**–**e**).

Compd	^{15}N	^{11}B
6a[a]	–331.8	5.1
6b[a]	–318.8	5.7
6c[b]	–320.7	5.3
6d[b]	–324.0	5.3
6e[c]	–312.1	6.0

Note: ^{15}N NMR data at 30.423 MHz. ^{11}B NMR data at 128.266 MHz. Solvent: DMSO-d_6 (δ in ppm).
[a]^{15}N NMR at 40.515 MHz.
[b]^{11}B NMR at 128.7 MHz.
[c]In $CDCl_3$.

With respect to the boronates, compounds **6a** and **6b** are shown in Fig. 5, while compound **6e** is shown in Fig. 6. Compound **6e** crystallized with a molecule of benzene and there are three different molecules in the unit cell. The concluding remarks of the obtained X-ray structures are as follows: (*i*) the N→B distances found are 1.647(2) Å for **6a**, 1.635(3) Å for **6b**, and 1.615(6), 1.643(3), 1.620(6) Å for **6e**, in agreement with the distances found in similar derivatives described in the literature (1–30). (*ii*) The B—$O_{aliphatic}$ distances are 1.465(2) Å for **6a**, 1.455(3) Å for **6b**, and 1.447(6), 1.454(6), 1.457(5) Å for **6**,which are also in agreement with values found for similar compounds (7, 8). (*iii*) The B—$O_{phenolic}$ distances are 1.462(2) Å for **6a**, 1.463(3) Å for **6b**, and 1.475(6), 1.459(6), 1.472(6) Å for **6e**, in agreement with the literature values for the same fragment (8). The structures possess similar dihedral angles for the H-N(1)→B(1)-C(10) fragment; the differences are due to the nature of the R^3 substituent in position 2 and, to a lesser extent, to the R^1 and R^2 substituents in position 1, resulting in dihedral angles of 18.16(126)° for **6a**, –38.72(172)° for **6b**, and –47.60(47)°, –48.79(44)°, –49.85(45)° for **6e**. Additionally, there are intermolecular hydrogen bonds between the NH proton and the aliphatic oxygen O(1) with magnitudes of 1.906(20) Å for **6a**, 2.256(24) Å for **6b**, and 2.313(3) and 2.327(3) Å for **6e**. In all cases, the six-membered ring containing the B-N-C(3)-C(4)-C(5)-O(3) fragment has a twisted boat conformation, the five-membered ring formed by the B-N-C(2)-C(1)-O(1) moiety (**6a** and **6b**) are in the half-chair conformation, with C(1) and C(2) out of the plane, and the three molecules in **6e** have envelope conformations with N(1) out of the plane.

Fig. 5. Molecular structures of **6a** and **6b**.

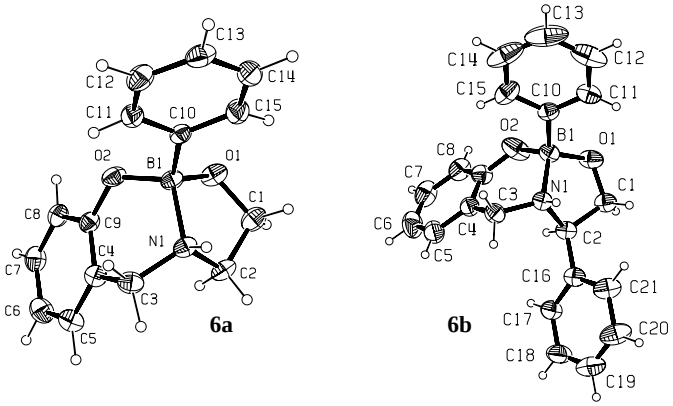

Fig. 6. Unit cell for compound **6e**.

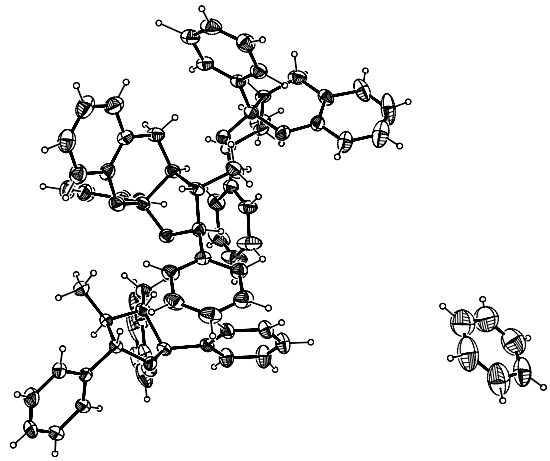

The tetrahedral character (THC) of the boron atom (38) is a useful parameter to evaluate the geometry of the boron atom for crystalline boronates (**6a**, **6b**, and **6e**). The THC was calculated from the boron-bond angles obtained by X-ray analysis as described by Höpfl (38), whereby a value of 100% corresponds to a perfect tetrahedral structure for boron. The values of THC (%) are 80.13 for **6a**, 76.86 for **6b**, and 74.44, 70.08, and 71.39 for **6e**. It is important to mention that the lower bond angle measured corresponds to the O(1)-B(1)-N(1) angle with THC values of 100.37(14)° for **6a**, 101.23(19)° for **6b**, and 101.1(4)°, 99.64(28)°, and 99.89(29)° for **6e**. This can be attributed to ring fusion.

© 2002 NRC Canada

Table 6. Crystallographic data of **4a**, **6a**, **6b**, and **6e**.

Compd	**4a**	**6a**	**6b**	**6e**
Molecular formula	$C_9H_{14}ClNO_2$	$C_{15}H_{16}BNO_2$	$C_{21}H_{20}BNO_2$	$C_{24}H_{24}BNO_2 \cdot 1/3C_6H_6$
Molecular Weight	203.66	253.10	329.19	369.25
Crystal Lattice	Orthorhombic	Monoclinic	Orthorhombic	Orthorhombic
Space Group	*Pcab*	$P2_1/n$	$P2_12_12_1$	$P2_12_12_1$
Cell Dimensions				
a (Å)	7.7036(2)	8.639(5)	9.149(19)	13.255(5)
b (Å)	15.8161(4)	9.038(5)	10.885(5)	18.261(5)
c (Å)	16.9502(5)	16.745(5)	18.133(2)	26.097(5)
β (°)	90	91.061(5)	90	90
Volume (Å^3)	2065.23(10)	1307.2(11)	1805.9(42)	6317.0(30)
Z	8	4	4	12
$D_{calcd.}$ (g m^{-3})	1.310	1.286	1.211	1.165
μ (mm^{-1})	0.339	0.084	0.076	0.073
Parameters	174	237	280	827
Collected reflections	4362	2454	3520	6822
Independent reflections	2363	2293	3150	6822
R (int.)	0.0261	0.0206	0.0762	0.0000
GoF	1.073	1.024	1.048	1.135
R	0.0378	0.0378	0.0369	0.0514
R_w	0.1111	0.0779	0.0970	0.1218

Note: $R = \Sigma||F_o|-|F_c||/\Sigma|F_o|$. $R_w(F_o)^2 = [\Sigma w(F_o^2 - F_c^2)^2/\Sigma wF_o^4]^{1/2}$.

Table 7. Selected distances, angles, and plane deviation for **6a**, **6b**, and **6e**.

			6e		
Compd	**6a**	**6b**	Molecule 1	Molecule 2	Molecule 3
Bond distances (Å)					
N(1)—B(1)	1.647(2)	1.635(3)	1.615(6)	1.643(3)	1.620(6)
C(10)—B(1)	1.604(3)	1.584(4)	1.589(7)	1.589(7)	1.596(7)
B(1)—O(1)	1.465(2)	1.455(3)	1.447(6)	1.454(5)	1.457(5)
B(1)—O(2)	1.462(2)	1.463(3)	1.475(6)	1.459(6)	1.472(6)
N(1)—H(1N)	0.899(20)	0.819(23)	0.910	0.910	0.910
Bond angles (°)					
O(1)-B(1)-O(2)	112.06(15)	109.0(2)	109.1(3)	109.95(35)	109.88(35)
N(1)-B(1)-C(10)	109.46(14)	112.56(18)	113.1(3)	113.31(35)	113.73(35)
N(1)-B(1)-O(1)	100.37(14)	101.23(19)	101.1(4)	99.64(28)	99.89(29)
N(1)-B(1)-O(2)	109.39(15)	107.4(2)	106.4(4)	105.25(31)	105.68(31)
O(1)-B(1)-C(10)	114.57(16)	113.9(2)	114.0(4)	114.54(35)	114.64(35)
O(2)-B(1)-C(10)	110.47(15)	112.0(2)	112.5(4)	113.02(36)	112.07(36)
Torsion angles (°)					
H(1N)-N(1)-B(1)-C(10)	18.16(126)	–38.72(172)	–47.60(47)	–48.79(44)	–49.85(45)
N(1)-C(2)-C(1)-O(1)	36.24(20)	–37.67(23)	–26.04(40)	–30.40(37)	–26.14(37)
Plane of deviation (Å)					
B(1)-N(1)-C(2)					
O(1)	0.2840(45)	–0.7222(53)	0.8989(90)	–0.9157(84)	–0.9454(87)
C(1)	0.6912(49)	–0.9686(55)	0.9392(97)	–0.9930(88)	–0.9697(88)
C(3)-C(4)-C(5)-C(6)-C(7)-C(8)-C(9)-O(2)					
B(1)	0.8019(26)	–0.1901(40)	0.1883(70)	–0.4483(63)	0.1559(64)
N(1)	0.9649(23)	–0.6854(30)	0.4482(57)	0.2050(57)	–0.5134(53)
THC B (%)	80.13	76.86	74.44	70.08	71.39

Semi-empirical calculations of boronates 6–9

To evaluate the influence of steric factors on this reaction, the geometry for all possible stereoisomers was determined by using a theoretical (AM1) approach (Fig. 8).

The computational study for semi-empirical calculations (AM1 method) was performed with Hyperchem (39). A full set of semi-empirical optimizations was carried out to determine the main preferences to obtain just the 2(*R*), N(*S*), B(*S*)

© 2002 NRC Canada

Fig. 7. Molecular structure of **6e**.

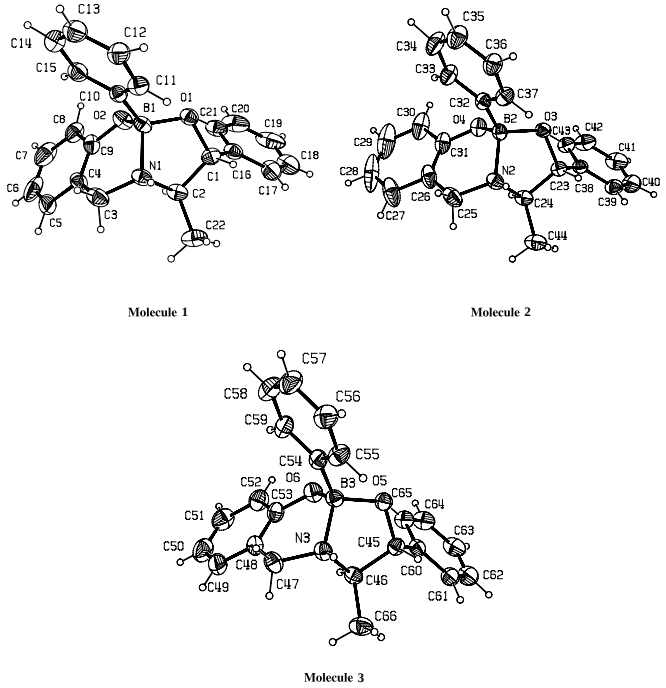

products (**6a**–**e**); all the stationary points were classified as minima by Hessian-matrix calculations with the same method (AM1). The coordinates used to obtain SAM1 results were obtained from X-ray analyses.

The data for compounds **6a**–**e**, **7a**–**e**, **8a**–**e**, and **9a**–**e** have been deposited as supplementary material.[2] All possible stereoisomers were minimized. In the case of compound **6a**, which was determined experimentally, there is only one counterpart (compound **8a**), while the remaining compounds have four possible stereoisomers. The data confirm that the compounds obtained experimentally are enthalpically favored, and there is an important steric effect controlling the formation of these fused compounds. The energy gap between stereoisomers **6** and **7** is between 5.2 and 3.1 kcal mol^{-1}, and they show two eclipsed interactions, while stereoisomers **8** and **9** show four *gauche* interactions. The deviation of the fused structure (*cis* or *trans*) depends directly on the substituent effect, as evidenced by the H-N-B-Ph torsion angles.

The calculated properties for each stereoisomeric series show that both the N→B bond length and the energy are inversely proportional to the THC values (supplementary material).[2]

Conclusions

In conclusion, boron compounds derived from the tridentate ligands **4a**–**e** yield fused five- and six-membered rings due to N→B bond formation (**6a**–**e**). In all cases, the ring fusion for the H-N→B-Ph fragment is *cis*, and the reaction is highly stereoselective yielding structures with "*S*" configuration at both the boron and the nitrogen atoms (**6b**–**e**). This was demonstrated by 2D-NMR NOESY experiments and confirmed by the X-ray analysis of compounds **6a**, **6b**, and **6e**. There is an increased tension at the five-membered ring; hence, the deviation of the boron atom from the idealized tetrahedral geometry is on average 77.5%. The theoretical calculations are in good agreement with the experimental data. These compounds show the same behavior as those containing tridentate ligands derived from amino acids. THC is a powerful tool to evaluate the stabilization of these types of molecules. The results show that the greater the stabilization of the compounds, the greater the THC value. In addition, there is a significant influence on the configuration of these newly formed stereogenic centers associated with the N→B bond lengths.

Fig. 8. Possible stereoisomers relative to the R^3 position.

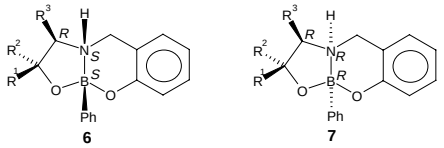

	R^1	R^2	R^3
a	H	H	H
b	H	H	C_6H_5
c	C_6H_5	H	CH_3
d	C_6H_5	H	C_6H_5
e	H	CH_3	C_6H_5

Experimental

NMR experiments were performed on a Jeol Eclipse+400 spectrometer at room temperature. All ^1H and ^{13}C resonances are reported relative to TMS, ^{15}N resonances are relative to neat $MeNO_2$, ^{11}B spectra were obtained relative to $BF_3 \cdot OEt_2$, and all the samples were determined in DMSO-d_6 as solvent. The IR spectra were recorded as KBr pellets on a PerkinElmer 16F PC FT-IR spectrometer. Mass spectra were recorded on a Hewlett-Packard 59940-A spectrometer at 20 eV electron impact. Melting points were measured in open capillary tubes on a Gallenkamp MFB 595 apparatus and have not been corrected. Elemental analyses were determined on an Eager 300 equipment.

Preparation of 2-[(2-hydroxyethylamino)methyl]phenols (4a–e)

2-[(2-Hydroxyethylamino)methyl] phenol hydrochloride (4a)

Compound **4a** was prepared from 0.50 g (8.18 mmol) of ethanolamine (**1a**) and 1.00 g (8.18 mmol) of

[2] Supplementary material may be purchased from the Depository of Unpublished Data, Document Delivery, CISTI, National Research Council Canada, Ottawa, ON K1A 0S2, Canada. For information on obtaining material electronically go to http://www.nrc.ca/cisti/irm/unpub_e.shtml. Crystallographic information has also been deposited with the Cambridge Crystallographic Data Centre (CCDC Nos. 176548 for **4a**, 176549 for **6a**, 176550 for **6b**, and 176551 for **6e**.). Copies of the data can be obtained free of charge via www.ccdc.cam.ac.uk/conts/retrieving.html (or from the Cambridge Crystallographic Data Centre, 12, Union Road, Cambridge CB2 1EZ, UK; fax: +44 1223 336033; or deposit@ccdc.cam.ac.uk).

© 2002 NRC Canada

salicylaldehyde (**2**) under reflux in a THF–MeOH mixture for 4 h to give **3a**, followed by reduction with 0.62 g (16.36 mmol) of sodium borohydride, and addition of 3.4 mL (40.90 mmol) of hydrochloric acid, to obtain a white solid. Suitable crystals were obtained from methanol. Yield 94% (1.57 g, 7.71 mmol); mp 152–154°C. IR ν_{max} (KBr, cm^{-1}): 3402, 3198, 3082, 2964, 2882, 2842, 2794, 2778, 1594, 1590, 1458, 1440, 1404, 1364, 1260, 1246, 1108, 1076, 922, 762. MS (20 eV) *m*/*z* (%): 167 (27), 136 (77), 107 (100), 77 (15). Anal. calcd. for $C_9H_{14}ClNO_2$: C 53.08, H 6.93, N 6.88; found: C 53.17, H 6.97, N 6.84.

*(***R***)-2-[(2-Hydroxy-1-phenylethylamino)methyl]phenol hydrochloride (4b)*

Compound **4b** was prepared from 0.50 g (3.64 mmol) of (*R*)-(–)-2-phenylglycinol (**1b**) and 0.45 g (3.64 mmol) of salicylaldehyde (**2**), to obtain a highly hygroscopic yellow powder. Yield 77% (0.79 g, 2.82 mmol); mp 83–85°C. IR ν_{max} (NaCl, cm^{-1}): 2928, 1596, 1458, 1420, 1264, 758, 734, 700, 496, 460, 454. MS (20 eV) *m*/*z* (%): 212 ([M^+], 41), 122 (2), 107 (29), 106 (100), 77 (4). Anal. calcd. for $C_{15}H_{18}ClNO_2$: C 64.40, H 6.49, N 5.01; found: C 64.25, H 6.53, N 5.16.

*(1***R***,2***S***)-2-[(2-Hydroxy-1-methyl-2-phenylethylamino)methyl]phenol (4c)*

Compound **4c** was prepared from 0.50 g (3.30 mmol) of (1*R*,2*S*)-(–)-norephedrine (**1c**) and 0.40 g (3.30 mmol) of salicylaldehyde (**2**), to give the product as a white solid. Yield 64% (0.62 g, 2.11 mmol); mp 164–166°C. IR ν_{max} (KBr, cm^{-1}): 3398, 3274, 3072, 2956, 2846, 1598, 1462, 1404, 1352, 1266, 1244, 748, 702. MS *m*/*z* (%): 293 ([M^+], 0.1), 257 (1.4), 150 (100), 122 (0.6), 107 (46.2), 106 (5.4), 77 (5.6). Anal. calcd. for $C_{16}H_{20}ClNO_2$: C 65.41, H 6.86, N 4.77; found: C 65.41, H 6.87, N 5.03.

*(1***S***,2***R***)-2-[(2-Hydroxy-1,2-diphenylethylamino)methyl]phenol (4d)*

Compound **4d** was prepared from 0.50 g (2.34 mmol) of (1*S*,2*R*)-(+)-2-amino-1,2-diphenylethanol (**1d**) and 0.29 g (2.34 mmol) of salicylaldehyde (**2**), to afford **4d** as a white powder. Yield 93% (0.78 g, 2.19 mmol); mp 188–190°C. IR ν_{max} (KBr, cm^{-1}): 3302, 3174, 3064, 3032, 2924, 2850, 1458, 758, 750, 700. MS *m*/*z* (%): 319 (0.4), 212 (87.2), 122 (0.9), 107 (32.9), 106 (100), 77 (5.9). Anal. calcd. for $C_{21}H_{22}ClNO_2$: C 70.88, H 6.23, N 3.94; found: C 70.85, H 6.25, N 3.95.

*(1***R***,2***R***)-2-[(2-Hydroxy-1-methyl-2-phenylethylamino)methyl]phenol (4e)*

Compound **4e** was prepared from 0.50 g (3.30 mmol) of (1*R*,2*R*)-(–)-norpseudoephedrine (**1e**) and 0.40 g (3.30 mmol) of salicylaldehyde (**2**), to give **4e** as a white hygroscopic solid. Yield 71% (0.69 g, 2.35 mmol); mp 50–52°C. IR ν_{max} (KBr, cm^{-1}): 3190, 2940, 1610, 1598, 1458, 1388, 1352, 1262, 1040, 1024, 758, 702. MS *m*/*z* (%): 257 (1.3), 150 (100), 122 (0.7), 107 (53.7), 106 (4.4), 77 (5.7). Anal. calcd. for $C_{16}H_{20}ClNO_2$: C 65.41, H 6.86, N 4.77; found: C 65.66, H 6.74, N 4.62.

Preparation of 4,5-disubstituted 2-phenyl-6-aza-1,3-dioxa-2-borabenzocyclononenes (6a–e)

cis-*2-Phenyl-6-aza-1,3-dioxa-2-borabenzocyclononene (6a)*

Compound **6a** was prepared by the reaction of 0.50 g (2.45 mmol) of **4a**, 0.30 g (2.45 mmol) phenylboronic acid (**5**), and 0.31 g (3.68 mmol) of sodium bicarbonate in a benzene–EtOH mixture for 12 h, to give a white solid; yield 69% (0.43 g, 1.70 mmol). Suitable monocrystals were obtained from a CH_2Cl_2–hexane mixture (4:1) ; mp 239–241°C. IR ν_{max} (KBr, cm^{-1}): 3068, 2962, 2944, 2928, 2900, 2870, 2740, 2664, 2620, 2552, 1608, 1488, 1462, 1452, 1432, 1378, 1368, 1292, 1266, 1248, 1216, 1202, 1180, 1112, 1082, 1038, 1016, 994, 982, 958, 938, 874, 822, 760, 738, 704. MS *m*/*z* (%): 253 ([M^+], 0.9), 222 (5.0), 176 (100), 175 (60.1), 174 (36.6), 147 (11.4), 146 (8.1), 107 (5.4), 91 (5.7), 77 (1.1). Anal. calcd. for $C_{15}H_{16}BNO_2$: C 71.18, H 6.37, N 5.53; found: C 71.45, H 6.41, N 5.76.

*(2***S***,5***R***,6***S***)-2,5-Diphenyl-6-aza-1,3-dioxa-2-borabenzocyclononene (6b)*

Compound **6b** was prepared from 0.30 g (1.07 mmol) of **4b**, 0.13 g (1.07 mmol) of phenylboronic acid (**5**), and 0.14 g (1.61 mmol) of sodium bicarbonate, to give **6b** as a brown solid; yield 74% (0.26 g, 0.80 mmol). Suitable monocrystals were obtained from a CH_2Cl_2–acetone–hexane mixture (2:1:4); mp 251–253°C. IR ν_{max} (KBr, cm^{-1}): 3066, 3004, 2954, 2928, 2870, 1608, 1490, 1460, 1448, 1432, 1300, 1286, 1238, 1214, 1186, 1114, 1080, 1062, 1042, 1034, 1004, 994, 970, 946, 872, 754, 740, 700. MS *m*/*z* (%): 329 ([M^+], 2), 298 (2), 252 (100), 251 (47), 250 (13), 174 (3), 146 (4), 107 (2), 91 (44), 77 (1). Anal. calcd. for $C_{21}H_{20}BNO_2$: C 76.62, H 6.12, N 4.25; found: C 76.33, H 6.05, N 4.12.

*(2***S***,4***S***,5***R***,6***S***)-2,4-Diphenyl-5-methyl-6-aza-1,3-dioxa-2-borabenzocyclononene (6c)*

Compound **6c** was prepared from 0.30 g (1.02 mmol) of **4c**, 0.12 g (1.02 mmol) of phenylboronic acid (**5**), and 0.13 g (1.53 mmol) of sodium bicarbonate, to give **6c** as a white solid; yield 89% (0.31 g, 1.27 mmol); mp 90–92°C. IR ν_{max} (KBr, cm^{-1}): 1488, 1462, 1432, 1300, 1284, 1266, 1220, 1112, 1102, 1080, 1042, 1026, 1010, 998, 956, 742, 700. MS *m*/*z* (%): 343 ([M^+], 3), 299 (1), 266 (100), 265 (40), 264 (8), 236 (9), 194 (42), 107 (2), 106 (1), 105 (10), 91 (4), 90 (8). Anal. calcd. for $C_{22}H_{22}BNO_2$: C 76.99, H 6.46, N 4.08; found: C 76.76, H 6.71, N 3.79.

*(2***S***,4***S***,5***R***,6***S***)-2,4,5-Triphenyl-6-aza-1,3-dioxa-2-borabenzocyclononene (6d)*

Compound **6d** was prepared from 0.30 g (0.84 mmol) of **4d**, 0.10 g (0.84 mmol) of phenylboronic acid (**5**), and 0.11 g (1.26 mmol) of sodium bicarbonate, to give **6d** as a white solid; yield 80% (0.27 g, 0.67 mmol); mp 204–206°C. IR ν_{max} (KBr, cm^{-1}): 1490, 1462, 1452, 1300, 1282, 1222, 1208, 1112, 1076, 1054, 1038, 1028, 1010, 960, 744, 724, 698. MS *m*/*z* (%): 405 ([M^+], 6), 328 (65), 327 (19), 300 (21), 299 (100), 222 (24), 194 (59), 193 (23), 192 (13), 106 (31), 78 (2), 77 (1). Anal. calcd. for $C_{27}H_{24}BNO_2$: C 80.01, H 5.97, N 3.46; found: C 79.96, H 5.94, N 3.45.

© 2002 NRC Canada

(2S,4R,5R,6S)-2,4-Diphenyl-5-methyl-6-aza-1,3-dioxa-2-borabenzocyclononene (6e)

Compound **6e** was prepared from 0.30 g (1.02 mmol) of **4e**, 0.12 g (1.02 mmol) of phenylboronic acid (**5**), and 0.13 g (1.53 mmol) of sodium bicarbonate, to give **6e** as a white solid; yield 87% (0.30 g, 0.88 mmol). Suitable monocrystals were obtained from a CH_2Cl_2–acetone–hexane mixture (2:1:4); mp 160–162°C. IR ν_{max} (KBr, cm^{-1}): 1490, 1286, 1212, 1040, 1026, 1006, 756, 744, 704. MS *m*/*z* (%): 343 ([M^+], 3), 266 (100), 265 (44), 264 (10), 236 (3), 194 (14), 107 (2), 106 (2), 105 (18), 91 (5), 90 (5). Anal. calcd. for $C_{22}H_{22}BNO_2$: C 76.99, H 6.46, N 4.08; found: C 76.81, H 6.80, N 3.82.

X-ray structures of boronates 4a, 6a, 6b, and 6e

X-ray diffraction analyses were determined on an Enraf Nonius-CAD4 diffractometer ($\lambda_{Mo\ K\alpha}$ = 0.71073 Å, graphite monochromator, T = 293 K, ω–2θ scan mode) and on an Enraf Nonius FR590 Kappa-CCD diffractometer ($\lambda_{Mo\ K\alpha}$ = 0.71073 Å, graphite monochromator, *T* = 293 K, CCD rotation images). The crystals were mounted in Lindeman tubes. For compounds **6a** and **6b**, an absorption correction was performed with SHELX-A(40); whereas for **4a** and **6e**, an absorption correction was not necessary due to the systematic scaling integration of the reflections. For all structures, corrections were made for the Lorentz and Polarization effects. The X-ray data was obtained through SHELXS-97 for the structure solution and through SHELXL-97 ver. 34 (40) for the refinement and data output; both programs are included in WIN-GX program set (41). The corresponding images were prepared with ORTEP 3 (42). All non-hydrogen atoms were found by Fourier map differences and were fully refined by anisotropic thermal parameters. Most of hydrogen atoms were determined by difference Fourier maps and refined with one overall isotopic thermal parameter, the other non-found hydrogens were added by geometrical situation and calculation.

Acknowledgments

Financial support and scholarship to H.I. Beltrán from the Consejo Nacional de Ciencia y Teconología (CONACyT, México) is acknowledged. The authors would like to thank Q.F.I. Dolores Castillo for IR spectra, Q.I. Victor González and Q.I. Guillermo Uribe for NMR spectra, and I.Q. Geiser Cuéllar for mass spectra determinations.

References

1. H. Höpfl and N. Farfán. J. Organomet. Chem. **547**, 71 (1997).
2. H. Höpfl, M .Sánchez, N. Farfán, S. Rojas, and R. Santillan. Inorg. Chem. **37**, 1679 (1998).
3. V. Barba, D. Cuahutle, M.E. Ochoa, R. Santillan, and N. Farfán. Inorg. Chim. Acta, **303**, 7 (2000).
4. N. Farfán, H. Höpfl, V. Barba, M.E. Ochoa, R. Santillan, E. Gómez, and A. Gutierrez. J. Organomet. Chem. **581**, 70 (1999).
5. V. Barba, R. Luna, D. Castillo, R. Santillan, and N. Farfán. J. Organomet. Chem. **604**, 273 (2000).
6. N. Farfán, R. Santillan, and H. Höpfl. Main Group Chem. News, **7**, 3 (1999).
7. V. Barba, E. Gallegos, R. Santillan, and N. Farfán. J. Organomet. Chem. **622**, 259 (2001).
8. H.I. Beltrán, L.S. Zamudio-Rivera, T. Mancilla, R. Santillan, and N. Farfán. J. Organomet. Chem. In press. (2002).
9. R. Contreras, C. García, and T. Mancilla. J. Organomet. Chem. **246**, 213 (1983).
10. T. Mancilla, R. Contreras, and B. Wrackmeyer. J. Organomet. Chem. **307**, 1 (1986).
11. T. Mancilla and R. Contreras. J. Organomet. Chem. **321**, 191 (1987).
12. N. Farfán, T. Mancilla, D. Castillo, G. Uribe, L. Carrillo, P. Joseph-Nathan, and R. Contreras. J. Organomet. Chem. **381**, 381 (1990).
13. V. Barba, D. Cuahutle, R. Santillan, and N. Farfán. Can. J. Chem. **79**, 1229 (2001).
14. E.B. Fleischer and R. Dewar. Tetrahedron Lett. 363 (1970).
15. W. Kliegel, S.J. Rettig, and J. Trotter. Can. J. Chem. **62**, 515 (1984).
16. W. Kliegel, D. Nanninga, S.J. Rettig, and J. Trotter. Can. J. Chem. **62**, 845 (1984).
17. S.M.S.V. Doidge-Harrison, O.C. Musgrave, and J.L. Wardell. J. Chem. Crystallogr. **28**, 361 (1998).
18. N. Farfán, P. Joseph-Nathan, L.M. Chiquete, and R. Contreras. J. Organomet. Chem. **348**, 149 (1988).
19. W. Kliegel, G. Lubkowitz, S.J. Rettig, and J. Trotter. Can. J. Chem. **71**, 2129 (1993).
20. P.D. Woodgate, G.M. Hornel, N.P. Maynard, and C.E.F. Rickard. J. Organomet. Chem. **592**, 188 (2000).
21. P.D. Woodgate, G.M. Hornel, N.P. Maynard, and C.E.F. Rickard. J. Organomet. Chem. **595**, 215 (2000).
22. T. Mancilla, H. Höpfl, G. Bravo, and L. Carrillo. Main Group Met. Chem. **20**, 31 (1997).
23. S.J. Rettig and J. Trotter. Can. J. Chem. **53**, 1393 (1975).
24. S. Caron and J.M. Hawkins. J. Org. Chem. **63**, 2054 (1998).
25. R.A. Howie, O.C. Musgrave, and J.L. Wardell. Main Group Met. Chem. **20**, 723 (1997).
26. H. Arnt, W. Kliegel, S.J. Rettig, and J. Trotter. Can. J. Chem. **68**, 1791 (1990).
27. S.J. Rettig, J. Trotter, W. Kliegel, and H. Becker. Can. J. Chem. **54**, 3142 (1976).
28. W. Kliegel, G. Lubkowitz, S.J. Rettig, and J. Trotter. Can. J. Chem. **70**, 2015 (1992).
29. W. Kliegel, G. Lubkowitz, S.J. Rettig, and J. Trotter. Can. J. Chem. **70**, 2027 (1992).
30. W. Kliegel, G. Lubkowitz, S.J. Rettig, and J. Trotter. Can. J. Chem. **70**, 2809 (1992).
31. Y. Xie, W. Bu, A.S.-Ch. Chan, X. Xu, Q. Liu, Z. Zhang, J. Yu, and Y. Fan. Inorg. Chim. Acta, **310**, 257 (2000).
32. C.G. Frost and P. Mendonca. Tetrahedron: Asymmetry, **11**, 1845 (2000).
33. (*a*) J.G. Wilson. Aust. J. Chem. **43**, 1283 (1990); (*b*) **41**, 173 (1988); (*c*) **43**, 783 (1990); (*d*) H.I. Beltrán, A. Abreu, L.S. Zamudio-Rivera, T. Mancilla, R. Santillan, and N. Farfán. Rev. Soc. Quim. Mex. **45**, 152 (2001).
34. E.D. Bergmann, E. Gil-Av, and S. Pinchas. J. Am. Chem. Soc. **75**, 68 (1953).
35. A. Haaland. Angew. Chem. Int. Ed. Engl. **28**, 992 (1989).
36. L. Stefaniak, G.A. Webb, and M. Witanowski. Ann. Rep. NMR Spectros. **18**, 72 (1986).
37. H. Nöth and B. Wrackmeyer. Nuclear magnetic resonance spectroscopy of boron compounds. Springer-Verlag, Berlin. 1978. p. 461.
38. H. Höpfl. J. Organomet. Chem. **581**, 129 (1999).

© 2002 NRC Canada

39. HyperChem V.5. Hypercube Inc. Gainesville FL, U.S.A.
40. G.M. Sheldrick. SHELX97. A program for crystal structure solution. University of Göttingen, Germany. 1993.
41. Win GX program set. L.J. Farrugia. J. Appl. Cryst. **32**, 837 (1999).
42. ORTEP 3. L.J. Farrugia. J. Appl. Cryst. **30**, 837 (1997).

© 2002 NRC Canada

X-ray diffraction, Raman spectroscopic, and solid-state NMR studies of the group 14 metal–(tetracarbonyl)cobalt complexes $Ph_3MCo(CO)_4$ (M = Si, Sn, Pb)

J.M. Geller, J.H. Wosnick, I.S. Butler, D.F.R. Gilson, F.G. Morin, and F. Bélanger-Gariépy

Abstract: Single-crystal X-ray diffraction studies illustrate that the three title compounds are isomorphous, belonging to the triclinic space group $P\bar{1}$, with slightly distorted trigonal bipyramidal geometry about cobalt. The solid-state ^{29}Si, ^{119}Sn, and ^{207}Pb cross-polarization magic angle spinning (CP MAS) NMR spectra are presented. The indirect spin–spin coupling constant (J), quadrupolar–dipolar shift (d), direct dipolar coupling constant (D'), anisotropy in spin–spin coupling (ΔJ), and the chemical shift tensor were extracted. A plot of the reduced coupling constant vs. *s*-electron densities at the nucleus indicates that the Fermi contact term may be dominant for the tin and lead complexes; however, the large ΔJ for all complexes indicate that there are also significant anisotropic terms. Trends in the Raman scattering spectra are also discussed.

Key words: ^{29}Si, ^{119}Sn, and ^{207}Pb CP MAS NMR, tetracarbonyl cobalt, spin–spin coupling, chemical shift tensor, quadrupole coupling, Fermi contact, cobalt–group 14.

Résumé : Des études par diffraction des rayons X par des cristaux uniques permettent d'illustrer que les trois composés mentionnés dans le titre sont isomorphes, appartenant au groupe d'espace triclinique $P\bar{1}$, avec une géométrie bipyramidale trigonale légèrement déformée autour du cobalt. On présente des études de RMN du ^{29}Si, ^{119}Sn et du ^{207}Pb à l'état solide avec polarisation croisée à l'angle magique de rotation. On en a déduit la constante de couplage spin-spin indirecte (J), le déplacement quadripolaire–dipolaire (d), la constante de couplage dipolaire directe (D'), l'anisotropie du couplage spin–spin (ΔJ) ainsi que le tenseur du déplacement chimique. Une courbe de la constante de couplage réduite en fonction des densités des électrons s au niveau du noyau indique que le terme de contact de Fermi peut être dominant pour les complexes de l'étain et du plomb; toutefois, les valeurs importantes de ΔJ pour tous les complexes indiquent que les termes anisotropiques ont aussi une grande importance. On discute aussi des tendances dans les spectres de diffusion Raman.

Mots clés : RMN, polarisation croisée, angle magique de rotation ^{29}Si, ^{119}Sn et ^{207}Pb, cobalt tétracarbonyle, couplage spin–spin, tenseur du déplacement chimique, couplage quadripolaire, contact de Fermi, cobalt groupe 14.

[Traduit par la Rédaction]

Introduction

The study of transition metal complexes by NMR is widespread since the technique can give information about the electronic environment and bonding, but studies of many transition metals have been limited because they have nuclear spins >1/2 and large quadrupole moments, which lead to increased linewidths and low sensitivity. From an NMR perspective, the ^{59}Co (spin = 7/2) nucleus is attractive due to its high magnetogyric ratio ($\gamma = 6.3175 \times 10^7$ rad T^{-1} s^{-1}) and its 100% natural abundance, both of which are helpful for high receptivity. The major drawback in the study of cobalt NMR comes from the large quadrupole moment (0.4×10^{-28} m^2), which often leads to rapid relaxation. Thus, in solution, direct observation of the ^{59}Co nucleus is limited to compounds with octahedral symmetry, i.e., with low quadrupolar coupling constants. The spin-lattice relaxation times, chemical shifts, and linewidths have been reported for a series of octahedral Co(III) complexes (1).

Cobalt complexes have also been studied in solution by observing a spin –1/2 nucleus bonded to the cobalt. Solution-phase NMR studies of ^{13}CO-enriched tetracarbonyl cobalt – group 14 complexes have illustrated that a downfield shift occurs for the axial carbonyl with respect to the radial CO on going down the group, and an axial–radial exchange process occurs that can be resolved at lower

Received 14 December 2001. Published on the NRC Research Press Web site at http://canjchem.nrc.ca on 28 June 2002.

J.M. Geller, J.H. Wosnick, I.S. Butler,[1] D.F.R. Gilson,[1] and F.G. Morin. Department of Chemistry, McGill University, 801 Sherbrooke Street West, Montreal, QC H3A 2K6, Canada.
F. Bélanger-Gariépy. Université de Montréal, Département de chimie, C.P. 6128 Succursale Centre-ville, Montréal QC H3C 3J7, Canada.

[1]Corresponding authors (e-mail: denis.gilson@mcgill.ca and ian.butler@mcgill.ca).

 DOI: 10.1139/V02-110 © 2002 NRC Canada

temperatures (2). Compounds of the form $(C_6H_5)_3MCo(CO)_4$, where M is a group 14 element, have been extensively studied (3–6). The solution ^{207}Pb NMR spectra were studied for the series $R_3PbCo(CO)_4$ (R = methyl, ethyl, phenyl), and the ^{207}Pb chemical shifts display a difference of over 200 ppm on changing the R group from methyl to phenyl (7).

Solid-state NMR spectroscopy allows for a wider variety of compounds to be studied since the quadrupolar relaxation is slower in the solid phase. Similarly, complexes with axial symmetry are also amenable to examination. Direct excitation of the ^{59}Co central transition (+1/2 to –1/2) in solids has been reported; ^{59}Co NMR static spectra have been obtained for cobaltophthalocyanines (8), porphyrins (9, 10), and vitamin B_{12} (11). Most recently, the chemical shift tensors and orientations of the electric field gradients (EFG) were determined for a series of octahedral Co(III) complexes (12). In a number of porphyrin systems with axial symmetry, the ^{59}Co magic angle spinning (MAS) spectra were acquired directly because the quadrupolar–dipolar broadening was small (9). Both solid- and solution-state ^{59}Co NMR have been recently reviewed (13).

The ^{59}Co nuclear quadrupole coupling constants (χ) of the triphenyl silicon, tin, and lead tetracarbonyl cobalt complexes have been determined from single-crystal NMR studies. Differences in $d\pi$–$p\pi$ back-bonding to the group 14 metal (M) were postulated to influence the amount of paramagnetic shielding experienced by the ^{59}Co nucleus (14). These quadrupole coupling constants were in good agreement with the pure nuclear quadrupole resonance (NQR) frequencies reported by Brown et al. (15).

Various compounds can be examined if the ^{59}Co nucleus is studied indirectly through a spin 1/2 nucleus probe (*I*). The interest in *I*–Co spin pairs stems from the measurement of indirect spin–spin couplings ($J_{I,Co}$), which are not observed in analogous solution NMR experiments due to rapid relaxation and "self-decoupling" of the quadrupolar nucleus. The ^{31}P–^{59}Co and ^{15}N–^{59}Co spin pairs have been studied by this method (16–21). Residual dipolar coupling is also manifested in the MAS NMR spectrum of nucleus *I* by a skewing of the multiplet resulting from the *J* coupling between the *I* and *S* nuclei. More specifically, instead of observing $2S + 1$ evenly spaced peaks in the multiplet, the peaks are shifted so that the spacings are uneven. Analysis of spectra exhibiting quadrupolar-induced dipolar splitting can also yield information on the EFG tensor at the quadrupolar nucleus, the magnitude and sign of the quadrupolar coupling constant (χ), the direct dipolar coupling constant (*D*), anisotropy in spin–spin coupling (ΔJ), and the chemical shift tensor of nucleus *I*. A treatment based on first-order perturbation theory has been developed to interpret the MAS spectra of nucleus *I* (22–24).

In this paper, we present the ^{29}Si, ^{119}Sn, and ^{207}Pb solid-state CP MAS NMR spectra of the triphenyl-substituted group-14 cobalt(I) tetracarbonyls. These compounds were chosen because they contain a spin–spin (*I*–Co) pair with axial symmetry surrounding the cobalt nucleus. This work follows from our previous study on triaryl silicon–, tin–, and lead–managanese pentacarbonyls, where we illustrated that the Fermi contact term was the dominant mechanism in spin–spin coupling (25). We now make a comparison between this ^{59}Co series and the ^{55}Mn series to determine if the Fermi contact dominance in spin–spin coupling can also be established for the *I*–Co spin pairs.

Fig. 1. ORTEP diagram of $Ph_3SiCo(CO)_4$ showing 30% thermal probability ellipsoids.

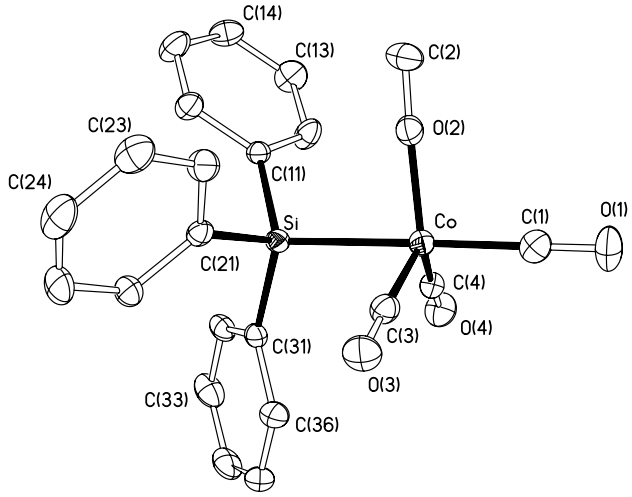

Single-crystal X-ray diffraction methods were used to determine accurate molecular geometries for this series of compounds. The structure of the triphenylsilyl complex has been reported previously by McIndoe and Nicholson (26).

The approximate C_{3v} symmetry of the carbonyl groups around the cobalt nucleus led to an early interest in the vibrational spectra, with IR spectral studies of the carbonyl stretching frequencies (5), force constant calculations (6), and additional calculations by ^{12}C–^{16}O direct CO-factored methods (27). In this work, the Raman scattering spectra for the three complexes are reported.

Results and discussion

X-ray crystallography

Complexes **I**–**III** are isomorphous, crystallize in the space group $P\bar{1}$, and have one molecule per asymmetric unit. The ORTEP (36) diagrams are shown in Figs. 1–3, and details of the crystal data and structure refinements are given in Table 1. There are very few reports of Si–Co bond lengths studied by X-ray diffraction methods. In the trichlorosilyl and trifluorosilyl tetracarbonyl cobalt complexes, the Si—Co bond lengths are 2.254(3) and 2.226(5) Å, respectively (37, 38). These are significantly shorter than the Si—Co bond lengths for **I** (2.3799(14) Å) that we obtained, or the value of 2.3810(7) Å previously reported (26) for the same compound. The Co—Sn bond length in **II** (2.5950(8) Å) is within the range reported for the series $Cl_{4-x}Sn[Co(CO)_4]_x$ (x = 1–4), where the Sn—Co distances increase from 2.477(1) Å for $Cl_3SnCo(CO)_4$ (39) to 2.669(1) Å for $Sn[Co(CO)_4]_4$ (39). The Pb—Co distance in **III** is 2.667(2) Å; the only other Pb—Co bond lengths reported are 2.761(5) and 2.738(5) Å for the two independent Pb—Co distances in $Pb[Co(CO)_4]_4$ (40).

The geometry around the Co atom in all three complexes is a slightly distorted trigonal bipyramidal. For **I**–**III**, the M-Co-CO_{ax} angles are linear: 179.07(9), 178.9(2), and 179.1(5)°, respectively. There is some distortion of the equatorial carbonyls towards the Ph_3M ligand and away from the axial

© 2002 NRC Canada

Fig. 2. ORTEP diagram of $Ph_3SnCo(CO)_4$ showing 30% thermal probability ellipsoids.

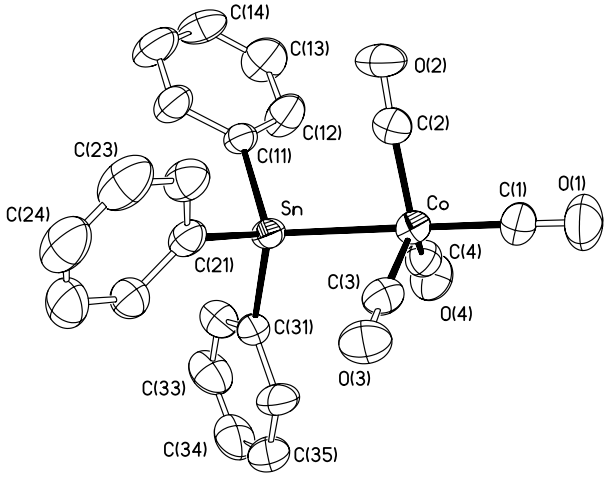

Fig. 3. ORTEP diagram of $Ph_3PbCo(CO)_4$ showing 30% thermal probability ellipsoids.

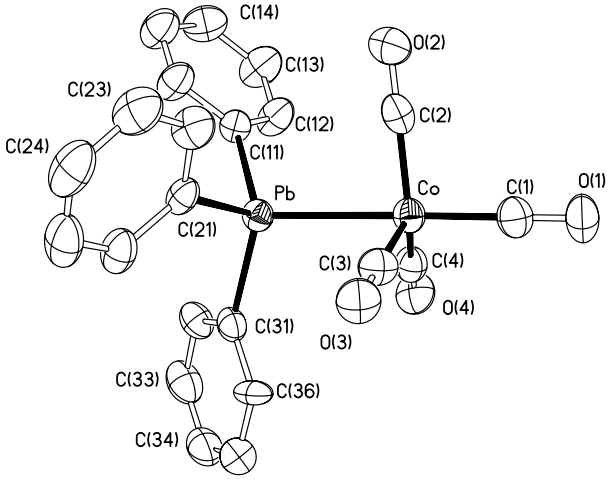

Table 1. Crystal structure data and structural refinements.

	I (Si)	**II** (Sn)	**III** (Pb)
Formula	$C_{22}H_{15}CoO_4Si$	$C_{22}H_{15}CoO_4Sn$	$C_{22}H_{15}CoO_4Pb$
MW (g mol^{-1})	430.360	520.960	609.470
Crystal color, habit	Colourless, needle	Pale yellow, block	Pale yellow, block
Crystal Size (mm)	0.40 × 0.09 × 0.04	0.27 × 0.17 × 0.15	0.27 × 0.11 × 0.08
Crystal System	Triclinic	Triclinic	Triclinic
Space group	$P\bar{1}$	$P\bar{1}$	$P\bar{1}$
a (Å)	9.859(8)	10.1203(1)	10.110(5)
b (Å)	10.311(5)	10.5225(1)	10.500(8)
c (Å)	10.681(5)	11.0554(1)	10.956(4)
α (°)	85.64(4)	85.40(1)	84.62(5)
β (°)	69.25(5)	69.03(6)	69.71(3)
γ (°)	81.57(5)	81.93(5)	81.45(6)
V (Å^3)	1004.0(11)	1087.92(1)	1077.6(11)
Z	2	2	2
$D_{calcd.}$ (Mg m^{-3})	1.4235	1.5903	1.8783
λ (Å)	1.54056	1.54178	1.54056
μ (mm^{-1})/T (K)	7.484/220(2)	15.296/293(2)	21.534/293(2)
Diffractometer	Nonius CAD-4	Bruker AXS SMART 2K	Nonius CAD-4
Scan type	ω–2θ	ω	ω–2θ
Measured reflections,	28853	13172	15142
Unique reflections, R_{int}	3802, 0.047	4147, 0.0413	4081, 0.053
Observed data, criterion	2572, $I > 2\sigma(I)$	3688, $I > 2\sigma(I)$	3421, $I > 2\sigma(I)$
Absorption correction	Analytical[a]	Multiscan[b]	Analytical[a]
Transmission range	0.2740–0.7528	0.0590–0.2210	0.0816–0.3022
θ_{max} (°)	69.80	72.72	69.80
Range measured	$-12 < h < 12$	$-11 < h < 9$	$-12 < h < 12$
	$-12 < k < 12$	$-12 < k < 12$	$-12 < k < 12$
	$-13 < l < 13$	$-13 < l < 13$	$-13 < l < 13$
Refinement on	F^2	F^2	F^2
R_1 (obs/all)	0.0304/0.0492	0.0403/0.0439	0.0520/0.0631
wR_2 (obs/all)	0.0516/0.0545	0.1059/0.1086	0.1318/0.1514
Refined parameters	254	254	254
S	0.866	1.018	1.002
Extinction coefficient	0.0030(1)	0.0010(2)	0.0052(4)

Note: $R_1 = \sum(|F_o| - |F_c|)/\sum|F_o|$; $wR_2 = \{\sum[w(F_o^2 - F_c^2)^2]/\sum[w(F_o^2)^2]\}^{1/2}$; $w = 1/\sigma^2(F_o^2)$. $S = \{\sum[w(F_o^2 - F_c^2)^2]/(n - p)\}^{1/2}$; n = number of data; p = number of refined parameters.

[a]Reference 34.

[b]Reference 35.

© 2002 NRC Canada

Table 2. Selected bond lengths (Å) and angles (°) determined from X-ray diffraction.

	I (Si)	**II** (Sn)	**III** (Pb)
Bond lengths (Å)			
M—Co	2.3799(14)	2.5953(7)	2.667(2)
Co—C1	1.809(3)	1.808(6)	1.813(13)
Co—C2	1.776(3)	1.790(5)	1.750(15)
Co—C3	1.786(3)	1.790(5)	1.785(13)
Co—C4	1.788(3)	1.792(5)	1.798(12)
M—C11	1.878(2)	2.152(4)	2.202(10)
M—C21	1.876(3)	2.139(4)	2.205(9)
M—C31	1.873(3)	2.144(4)	2.217(11)
Bond angles (°)			
C1-Co-C2	96.67(12)	97.4(3)	97.1(6)
C1-Co-C3	96.47(12)	98.0(3)	97.5(6)
C1-Co-C4	95.49(13)	96.2(3)	96.9(6)
C2-Co-C3	117.20(12)	116.6(3)	116.0(6)
C2-Co-C4	117.99(12)	118.3(3)	119.0(6)
C3-Co-C4	121.38(12)	120.5(2)	120.3(6)
C1-Co-M	179.07(9)	179.2(2)	179.1(5)
C2-Co-M	84.34(9)	83.2(2)	83.7(4)
C3-Co-M	83.28(9)	82.2(2)	81.8(4)
C4-Co-M	83.89(10)	83.0(2)	82.9(4)
C11-M-C21	107.60(11)	107.9(2)	108.8(4)
C11-M-C31	108.72(11)	108.7(2)	110.0(4)
C21-M-C31	108.87(11)	109.2(2)	110.5(4)
Co-M-C11-C12	45.8(2)	44.7(5)	48.7(12)
Co-M-C21-C22	53.4(2)	53.5(4)	54.4(10)
Co-M-C31-C32	–129.1(2)	–131.6(3)	–129.7(8)
C2-Co-M-C11	39.03(12)	44.3(2)	39.2(5)
C3-Co-M-C21	37.42(11)	38.4(2)	37.0(5)
C4-Co-M-C31	39.67(12)	40.1(2)	38.7(5)

carbonyl group, so that the average M-Co-CO_{eq} angles for the three complexes are 83.8(5), 82.8(5), and 83(1)°, respectively. Such a distortion from a trigonal bipyramidal structure towards a capped tetrahedron has been previously discussed (41). The average CO_{eq}-Co-CO_{eq} angles in the three complexes are 119(2), 118(2), and 118(2)°, respectively, further confirming the threefold symmetry surrounding the Co nucleus. In the three complexes, the ipso-carbon atoms of the triphenyl groups are rotated 37–43° (Table 2) from the ideal staggered position of 60° with respect to the triangle formed by the three equatorial carbonyl groups. This difference is attributed to the steric interaction between carbonyl carbons and the *ortho*-carbon atom of the phenyl rings. The closest intermolecular non-bonded C_{ortho}—$C_{carbonyl}$ distances are between 3.4 and 3.6 Å. The important bond lengths and angles for complexes **I**–**III** are listed in Table 2.

Raman spectroscopy

The IR spectra of **I**–**III** have been previously reported in the C–O stretching (5, 6, 27) and far-IR (42) regions, and the Raman spectra (Table 3) complement these IR data. Only the tin–cobalt IR stretching frequency has been previously assigned (42) and appears at 171 cm^{-1}. Based on this assignment, the $\nu_{M\text{-}Co}$ values for the silicon and lead complexes have been assigned as shown in Table 3. For the ν_{CO} vibrations, there is a decrease in wavenumber on going down group 14. The small decrease in the average of the ν_{CO} frequencies on going from silicon to lead suggests a decrease in multiple bond character for the M–Co bonds. The ν_{CO} *e*-mode is split due to crystal effects.

Table 3. Raman vibrational frequencies of solid compounds (cm^{-1}).

Mode/bond	**I** (Si)	**II** (Sn)	**III** (Pb)
	85 s	84 s	83 m
	112 m	109 s	107 s
ν_{M-Co}	189 w	171 m	155 m
	206 w	212 m	202 m
	239 w	237 w	221 w
	422 m	422 m	418 m
	539 w	549 w	544 w
	619 w	617 w	615 w
	675 w	655 m	646 m
	706 w	699 w	695 w
ν_{CO} *e*	1994, 2008 m	1989, 2001 m	1988, 1997 m
ν_{CO} $a_1^{(1)}$	2037 s	2030 s	2023 s
ν_{CO} $a_1^{(2)}$	2093 m	2087 m	2080 m

Solid-state CP MAS NMR

A treatment based on first-order pertubation theory has been developed by Olivieri (23), which is valid in the limit $\chi/[4S(2S-1)\nu_s] << 1$, where ν_s is the Larmor frequency of the quadrupolar nucleus. Thus, for ^{59}Co ($S = 7/2$), provided that $\chi/84\nu_s << 1$, the splittings observed in the solid-state spectra under MAS can be treated by first-order perturbation theory. With the assumption that that the *J* tensor is co-linear with the internuclear dipole vector, the line splittings are given by eq. [1],

$$[1]\qquad \Delta\nu_m = -m_s J_{IS} + (3\chi D'/20\nu_s)(3\cos^2\beta^D - 1 + \eta\sin^2\beta^D\cos 2\alpha^D)[\{S(S+1) - 3m_s^2\}/\{S(2S-1)\}]$$

where $D' = (D - \Delta J/3)$ and the second-order quadupolar–dipolar splitting (*d*) is $3\chi D'/20\nu_s$. *D* is the direct dipolar coupling constant ($D = (\mu_o/4\pi)\gamma_s\gamma_I h^2/(4\pi(r_{IS})^3)$ and ΔJ is the anisotropy in the spin–spin coupling. α^D and β^D are, respectively, the azimuthal and polar angles relating the internuclear vector to the principle axis of the EFG and η is the asymmetry in the field gradient. Equation [1] assumes that the *J* tensor is co-linear with the internuclear dipole vector. From NQR studies (15), η was found to be 0.05 or less, indicating a near axially symmetric EFG about cobalt for all three complexes. The ^{59}Co ($S = 7/2$) resonance frequency at 7.05 T is 71.2 MHz, and the nuclear quadrupole coupling constants for these complexes range from 101 to 110 MHz at 298 K (14, 15). Thus, the first-order perturbation treatment is applicable for the three complexes studied here.

The local symmetry about the M–Co bonds (approximately C_{3v}) is sufficiently high and η is close enough to zero that it can be assumed that the angle β^D is 0° and the value of α^D is undefined, because it is multiplied by $\sin^2\beta^D$, which is 0. Hence, eq. [1] is reduced to the simple form

$$[2]\qquad \Delta\nu_m = -m_s J_{IS} + (3\chi D'/10\nu_s)[3/4 - 1/7m_s^2]$$

© 2002 NRC Canada

Table 4. NMR data for the silicon, tin, and lead complexes.

	I (^{29}Si)	**II** (^{119}Sn)	**III** (^{207}Pb)
δ_{iso} (solution) (ppm)	26.0(0.2)	20.5(0.2)	127(1)
δ_{iso} (solid) (ppm)	26.3(0.2)	35.3(0.5)	193(1)
$^1J_{M,Co}$ (Hz)	57(1)	57(2)	110(1)
$^1K_{M,Co}$ (T^2 J^{-1})	-8.92×10^{20}	-5.39×10^{20}	1.85×10^{21}
D (Hz)	47(2)	127(5)	–2(2)
δ_{11} (ppm)	—	92(4)	360(5)
δ_{22} (ppm)	—	52(1)	138(10)
δ_{33} (ppm)	—	–41(5)	80(5)
Span ($\delta_{11}-\delta_{33}$) (ppm)	—	132(9)	280(5)
χ (MHz)[a]	101.09	104.11	110.82
D' (Hz)[b]	–417(4)	–606(3)	314(4)
ΔJ (Hz)[c]	–1580(20)	–2690(30)	950(10)

[a]From ref. 14. The frequencies are ±0.05 MHz.
[b]Calculated from the M–Co bond lengths given in Table 2, errors calculated using $\pm 5\sigma$.
[c]Standard deviation propagated from *d*.

Fig. 4. CP MAS NMR spectra of **I–III** at 7.05 T. The three spectra were plotted on the same horizontal axis (in ppm) to illustrate the increase in span on going from ^{29}Si to ^{207}Pb. For the chemical shifts, see Table 4.

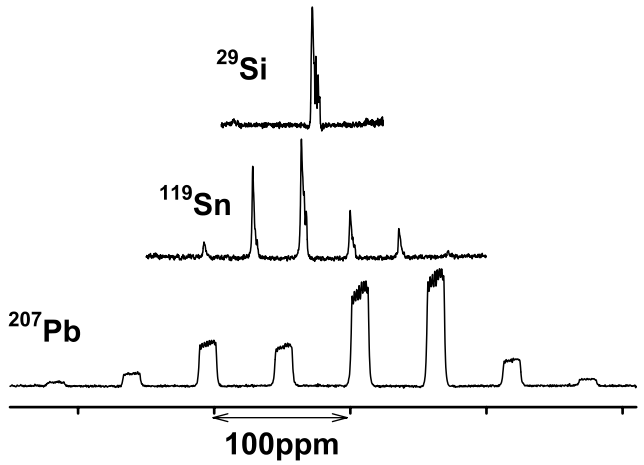

and the second-order quadupolar-dipolar splitting (*d*) given by $3\chi D'/10\nu_s$, can be obtained.

The NMR data for **I–III**, are given in Table 4, and the full spectra of all of the compounds are given in Fig. 4. In all cases, only a single chemical shift was observed, which is consistent with the crystal structures. In the case of the triphenylsilyl complex, the spectrum has only a centreband at the spinning speeds used. The ($\delta_{11}-\delta_{33}$) span of the spectrum is therefore very small, as was observed previously for the triphenylsilyl(pentacarbonyl)manganese(I) complex (25). The centreband should exhibit eight lines, but the downfield lines overlap, which is characteristic of a d/J ratio that is close to, or greater than, one. Since the lines overlap in the downfield region, the sign of *d* is positive.

The ^{119}Sn CP MAS spectrum of the triphenyltin complex has a much larger span and the components of the chemical shift tensor could be calculated, using the Herzfeld–Berger method, from the relative intensities of the spinning sidebands (28, 43). The span of the spectrum (133 ppm) is smaller than the values reported (25) for $Ph_3SnMn(CO)_5$ (187–209 ppm) and for the less-symmetrical diaryl complexes (44, 45). The centreband shows an overlap of the downfield lines, characteristic of a d/J ratio close to one.

Since ^{207}Pb spectra usually show a very wide range of chemical shifts, it is surprising that the span of the triphenyl lead complex is only 280 ppm. This value is similar to those obtained for the triphenylplumbyl(pentacarbonyl)manganese(I) complex (25), where the spans ranged from 268 to 329 ppm. It is notable that both the lead–cobalt and the lead–manganese complexes have smaller spans than the more symmetrical hexaorganyldiplumbanes, which have spans ranging from 484 to 996 ppm (46). Comparison of the spans for the tin and lead complexes showed the expected increase as the size of the valence *p*-electron radius ($\langle r^{-3}\rangle_{np}$) increases. According to the expression for paramagnetic shielding suggested by Ramsey (47–49), the ratio of the spans should correlate well with the $\langle r^{-3}\rangle_{6p}/\langle r^{-3}\rangle_{5p}$ ratio of 1.4 previously reported (50). The span of the lead complex is 2.1 times greater than that of the tin complex. Our results are not inconsistent with the greater-than-expected chemical shielding range of ^{207}Pb previously obtained (51) from a plot of $\delta(^{207}Pb)$ vs. $\delta(^{119}Sn)$ isotropic chemical shifts, where a slope of 3.0 was obtained. Unexpectedly large chemical shielding ranges for heavy nuclei have been previously discussed (52).

The spectrum of **III** is quite different from the spectra of **I** and **II**, showing an almost symmetric octet. The lines of the octet are almost evenly spaced, which is indicative of a small *d* value. The quadrupolar–dipolar shift term is small because the effective D' is small. Since the value χ for **III** was determined (110.82 MHz), D' can be obtained using eq. [1], and because the direct dipolar coupling constants can be calculated from the measured bond lengths, ΔJ can be extracted from eq. [2].

The differences between the isotropic solid and solution chemical shifts are greatest for the lead complex and smallest for silicon. This trend can be attributed to the larger range of observed chemical shifts for ^{207}Pb and ^{119}Sn rather than structural differences between the three complexes.

Very few instances of direct measurement of the spin–spin couplings of *I*–Co spin pairs have been reported. The compounds most frequently studied are highly symmetric with octahedral or tetrahedral symmetry, e.g., $Na[Co(CO)_4]$ (53) and $Na_3[Co(CN)_6]$ (54). Coupling between ^{59}Co and ^{13}C and ^{31}P has been indirectly measured by T_1 relaxation measurements in solution (55, 56) and in the solid state (57). The one-bond coupling constants to cobalt reported here are rare because these complexes have large quadrupole coupling constants, and are less symmetrical than the complexes previously reported.

The contributions to the spin–spin coupling constant arise from the diamagnetic spin-orbit (DSO), paramagnetic spin-orbit (PSO), spin-dipolar term (SD), Fermi contact (FC), and a spin-dipolar – Fermi contact (SD–FC) cross term. The DSO and PSO contributions are usually small, have opposite signs to each other, and tend to cancel, leaving the latter major terms (58). To compare the spin–spin coupling constants of different nuclei, the reduced coupling con-

© 2002 NRC Canada

stants ($K_{I,J} = 4\pi^2 J_{I,J}/(h\gamma_I\gamma_J)$) are used. For the FC term, $K_{I,J}$ is proportional to the product of the *s*-electron densities at the nuclei and the *s*-character of the hybrid orbitals used to form the bond, all divided by an average excitation energy (ΔE) (59, 60). Using the *s*-electron densities given by Pyykkö and Weisenfeld (61), with a non-relativistic value for silicon and relativistic values for the heavier elements, a plot of the reduced coupling constants against the *s*-electron densities ($|\psi(0)|^2$) for the silicon, tin, and lead nuclei showed a linear relationship, passing through the origin, for the triphenyl complexes with manganese pentacarbonyl (25). In the present series of compounds, the reduced coupling constants for the tin and lead complexes also showed a linear dependence extrapolating to the origin, but the silicon value was too high (Table 4). This, combined with the large ΔJ values for all complexes, suggests that, in addition to the FC term, there are appreciable anisotropic contributions to the *J* tensor most probably from the SD–FC term. Large ΔJ values were also observed for the manganese pentacarbonyl complexes (25) and for other heavy-atom cases, such as ^{199}Hg–^{31}P coupling (62–65). Theoretical calculations of ΔJ have been limited to light-atom systems, but even in the case of ^{13}C–^{13}C coupling in benzene, ethane, ethene, and ethyne (66, 67) there is appreciable anisotropy, but the FC term is still the major contribution.

Experimental

General

All reactants were used as received from Aldrich or Strem [$Co_2(CO)_8$]. With the exception of THF (which was dried over sodium with benzophenone indicator), solvents were not dried before use,. All reactions were performed under nitrogen with subsequent work-up under air.

IR spectra were measured (100 scans) in either CH_2Cl_2 or hexanes solutions between KBr plates on a Bruker IFS-48 FT-IR spectrometer at 1.0 cm^{-1} resolution. Raman spectra were recorded (100 scans) on a Bruker IFS-88 FT-Raman spectrometer with samples contained in a metal cup at 4.0 cm^{-1} resolution. Solution-state ^{13}C, ^{29}Si, and ^{119}Sn proton-decoupled NMR spectra were measured in $CDCl_3$ solutions at room temperature (21°C), on a Varian XL-400 spectrometer operating at a field strength of 9.40 T. The ^{207}Pb spectrum was measured on a JEOL 270 MHz spectrometer operating at 6.34 T. Solid-state proton-decoupled CP MAS spectra were obtained on a Chemagnetics CMX-300 spectrometer operating at 59.52 MHz (^{29}Si), 111.73 MHz (^{119}Sn), and 63.10 MHz (^{207}Pb). Experimental conditions **I**: contact time 2 ms; pulse delay 750 s; 128 transients. **II**: contact time 2 ms; pulse delay 20 s; 700 transients. **III**: contact time 2 ms; pulse delay 3 s; 18644 transients. Chemical shifts were externally referenced to tetramethylsilane (^{29}Si), tetramethyltin (^{119}Sn), and tetramethyllead (^{207}Pb), respectively. Powdered samples were contained in 7.5-mm diameter zirconia pencil-type rotors. FIDs on the CMX-300 were zero-filled to 8K data points. Spinning rates ranging from 2–4 kHz were used to identify isotropic chemical shifts. The chemical shifts of ^{207}Pb resonances can be temperature-dependent, but the centre band position did not vary with spinning speed and, therefore, no heating effects occurred. The resonance lines in all sidebands were fitted with Lorentzian line shapes using the program Peakfit (Jandel Scientific) and the errors given are from the averages of the fitted parameters. Calculation of the chemical shift tensors were performed with the aid of a computational package developed by Eichele and Wasylishen (28).

$Ph_3SiCo(CO)_4$ (I)

Compound **I** was synthesized using the reaction first described by Chalk and Harrod (3) and later improved by McIndoe and Nicholson (26). $Co_2(CO)_8$ (2.38 g, 6.95 mmol) and Ph_3SiH (6.79 g, 6.95 mmol) were reacted in hexanes (30 mL) at room temperature for 90 min. After cooling to 0°C (ice bath), an off-white solid was precipitated. The solid was isolated by Buchner filtration and washed with cold hexanes. Recrystallization from hot hexanes yielded clear crystals of the desired compound (3.71 g, 62%); mp 138–140°C (lit. (1) 135–140°C). IR ν_{CO} (hexanes, cm^{-1}): 2093 (m), 2033 (m), 2005 (s); (CH_2Cl_2, cm^{-1}): 2094 (s), 2033 (m), 1993 (s). ^{13}C NMR δ: 198.7 (s, CO), 138.2 (s, ipso), 135.4 and 127.9 (s, *ortho* and *meta*), 129.6 (s, *para*). The IR and ^{13}C NMR spectra were in agreement with previously published results (26).

$Ph_3SnCo(CO)_4$ (II)

Compound **II** was synthesized according to the method described by Darensbourg (6). $Co_2(CO)_8$ (4.00 g, 11.7 mmol) was dissolved in methanol and the solution was gently warmed to 50°C and stirred until the pink colour of $[Co^{2+}][Co(CO)_4^-]_2$ was observed and gas evolution ceased. The reaction mixture was then cooled to 0°C (ice bath) and a methanolic solution of Ph_3SnCl (4.20 g, 10.9 mmol) was added. The reaction mixture was stirred for 1 h at room temperature and then cooled to 0°C, which resulted in the precipitation of a white solid. The solid was isolated, washed with cold methanol, and then dried by vacuum filtration. Recrystallization from hot hexanes yielded large yellow crystals (3.97 g, 70%); mp 118–121°C (lit. (5) 119–121°C). IR ν_{CO} (hexanes, cm^{-1}): 2087 (m), 2026 (m), 1997 (s); (CH_2Cl_2, cm^{-1}): 2088 (s), 2026 (m), 1994 (s). ^{13}C NMR δ: 198.8 (s, CO), 140.2 (ipso, $^1J_{^{119}Sn,C}$ = 459, $^1J_{^{117}Sn,C}$ = 439 Hz), 128.8 (*meta*, $^3J_{Sn,C}$ = 53.4 Hz), 136.16 (*ortho*, $^2J_{Sn,C}$ = 41.2 Hz), 129.4 (*para*, $^4J_{Sn,C}$ = 12.2 Hz).

$Ph_3PbCo(CO)_4$ (III)

Compound **III** was synthesized in an analogous manner to complex **II** from $Co_2(CO)_8$ (4.00 g, 8.19 mmol) and Ph_3PbCl (5.07 g, 10.7 mmol), as described by Patmore and Graham (5). Upon recrystallization from hexanes, light-yellow block-shaped crystals were obtained (4.69 g, 72% yield); mp 102°C (lit. (6) 100–102°C). IR ν_{CO} (hexanes, cm^{-1}): 2079 (s), 2020 (m), 1993 (s); (CH_2Cl_2, cm^{-1}): 2082 (s), 2020 (m), 1994 (s). ^{13}C NMR δ: 199.4 (s, CO), 152.9 (ipso, $^1J_{Pb,C}$ = 314 Hz), 129.8 (*meta*, $^3J_{Pb,C}$ = 80.5 Hz), 136.5 (*ortho*, $^2J_{Pb,C}$ = 72.1 Hz), 128.9 (*para*, $^4J_{Pb,C}$ = 19.2 Hz).

X-ray crystallography

All complexes were recrystallized by dissolving in boiling hexanes and then cooling to –30°C, where, after several days, X-ray quality crystals were obtained. Details of the crystal data and structure refinements are given in Table 1.

© 2002 NRC Canada

Data for **I** and **III** were processed using a locally modified version of the NRC-2 program (29) and data for **II** was processed by SAINT (30).[2] All structures were solved by direct methods using SHELXS-97 (31) and refined using SHELXL-96 (32). Non-hydrogen atoms were refined with anisotropic thermal parameters. The hydrogen atoms were included in calculated positions. Scattering factors were from the usual sources (33). **I** was run at low temperature (220 K) because it was prone to decomposition under X-rays at room temperature.

Acknowledgments

This work was supported by grants from the Natural Sciences and Engineering Research Council of Canada (NSERC) and Fonds pour la formation de chercheurs et l'aide à la recherche (Québec) (FCAR).We thank Dr. A.-M. Lebuis for assistance in examining the crystal structures and Professor R.E. Wasylishen for the HBA program.

References

1. C.W. Kirby, C.M. Puranda, and W.P. Power. J. Phys. Chem. **100**, 14618 (1996).
2. D.L. Lichtenberger and T.L. Brown. J. Am. Chem. Soc. **99**, 8187 (1977).
3. A.J. Chalk and J.F. Harrod. J. Am. Chem. Soc. **87**, 1133 (1965).
4. F. Hein, P. Kleinert, and W. Jehn. Naturwissenschaften, **44**, 34 (1957).
5. D.J. Patmore and W.A.G. Graham. Inorg. Chem. **5**, 981 (1967).
6. D.J. Darensbourg. Inorg. Chim. Acta, **4**, 597 (1970).
7. K.H. Pannell, J.M. Rozell, S. Cortez, and R. Kapoor. Organometallics, **9**, 1322 (1990).
8. A. Medek, V. Frydman, and L. Frydman. J. Phys. Chem. A, **103**, 4830 (1999).
9. A. Medek, V. Frydman, and L. Frydman. J. Phys. Chem. B, **101**, 8959 (1997).
10. X. Xiao-Ping and S.C.F. Au-Yeung. J. Am. Chem. Soc. **122**, 6468 (2000).
11. A. Medek and L. Frydman. J. Am. Chem. Soc. **122**, 684 (2000).
12. C.W. Kirby and W.P. Power. Can. J. Chem. **79**, 296 (2001).
13. J.C.C. Chan and S.C.F. Au-Yeung. Ann. Rep. NMR Spec. **41**, 1 (2000).
14. H.W. Spiess and R.K. Sheline. J. Chem. Phys. **53**, 3036 (1970).
15. T.L. Brown, P.A. Edwards, C.B. Harris, and J.L. Kirsch. Inorg. Chem. **4**, 763 (1969).
16. R.W. Schurko, R.E. Wasylishen, and J.H. Nelson. J. Phys Chem. **100**, 8057 (1996).
17. F. Asaro, R. Gobetto, L. Lorenza, and G. Pellizer. Chem. Phys. Lett. **300**, 414 (1999).
18. R.W. Schurko, R.E. Wasylishen, S.J. Moore, and L.G. Marzilli. Can. J. Chem. **77**, 1973 (1999).
19. R.W. Schurko and R.E. Wasylishen. J. Phys. Chem. A, **104**, 3410 (2000).
20. R. Gobetto, R.K. Harris, and D.C. Apperley. J. Magn. Reson. **96**, 119 (1992).
21. D. Rentsch, R. Hany, and W.V. Philipsborn. Magn. Reson. Chem. **35**, 832 (1997).
22. A.C. Olivieri, L. Frydman, and L.E. Diaz. J. Magn. Reson. **75**, 50 (1987).
23. A.C. Olivieri. J. Magn. Reson. **81**, 201 (1989).
24. R.K. Harris and A.C. Olivieri. Prog. Nucl. Magn. Reson. Spectrosc. **24**, 534 (1992).
25. D. Christendat, I.S. Butler, D.F.R. Gilson, and F.G. Morin. Can. J. Chem. **77**, 1892 (1999).
26. J.S. McIndoe and B.K. Nicholson. J. Organomet. Chem. **577**, 181 (1999).
27. C. Kaya. J. Organomet. Chem. **2**, 586 (1999).
28. HBA, version 1.44. K. Eichele and R.E. Wasylishen. Dalhousie University, Halifax. 2001.
29. F. Ahmed, S.R. Hall, M.E. Pippy, and C.P. Huber. NRC crystallographic computer Programs for the IBM/360. Accession Nos. 133–147. J. Appl. Cryst. **6**, 309 (1973).
30. SAINT Release 6.06. Integration software for single crystal data. Bruker AXS Inc., Madison, WI. 1999.
31. G.M. Sheldrick. SHELXS-97. Program for the solution of crystal structures. University of Gottingen, Germany. 1997.
32. G.M. Sheldrick. SHELXL-96. Program for the refinement of crystal structures. University of Gottingen, Germany. 1997.
33. International tables for crystallography. Vol. C. 4. Kluwer Acacdemic Publishers, Dordrecht. 1992. Tables 4.2.6.8 and 6.1.1
34. E.J. Gabe, Y. Le Page, J.-P. Charland, F.L. Lee, and P.S. White. J. Appl. Cryst. **22**, 384 (1989).
35. G.M. Sheldrick. SADABS. Bruker area detector absorption corrections. Bruker AXS Inc., Madison, WI. 1996.
36. C.K. Johnson. ORTEPII. Report ORNL-5138. Oak Ridge National Laboratory, Tennessee, U.S.A.
37. W.T. Robinson and J.A. Ibers. Inorg. Chem. **6**, 1209 (1967).
38. K. Emerson, P.R. Ireland, and W.T. Robinson. Inorg. Chem. **9**, 436 (1970).
39. P.Z. Klufers. Naturforsch. Teil B, **46**, 187 (1991).
40. J.S. Leigh and K.H. Whitmire. Acta Crystallogr. Sect. C, **46**, 732 (1990).
41. S.A. Jackson, O. Eisenstein, J.D. Martin, A.C. Albeniz, and R.H. Crabtree. Organometallics, **10**, 3062 (1991).
42. L.F. Wuyts and G.P. van der Kelen. Spectrochim. Acta, **32A**, 689 (1976).
43. J. Herzfeld and A.E. Berger. J. Chem. Phys. **73**, 6021 (1980).
44. R.K. Harris, S.E. Lawrence, S.-W. Oh, and V.G. Kumar Das. J. Mol. Struct. **347**, 309 (1995).
45. D. Christendat, J.H. Wosnick, I.S. Butler, D.F.R. Gilson, A.-M. Lebuis, and F.G. Morin. J. Mol. Struct. **559**, 235 (2001).
46. A. Sebald and R.K. Harris. Organometallics, **9**, 2096 (1990).
47. N.F. Ramsey. Phys Rev. **77**, 567 (1950).
48. N.F. Ramsey. Phys Rev. **78**, 699 (1950).
49. N.F. Ramsey. Phys Rev. **83**, 540 (1951).
50. R.G. Barnes and W.V. Smith. Phys. Rev. **93**, 95 (1954).
51. J.D. Kennedy, W. McFarlane, and G.S. Payne. J. Chem. Soc. Dalton Trans. 2332 (1977).
52. C.J. Jameson. *In* Multinuclear NMR spectroscopy. *Edited by* J. Mason. Plenum, New York. 1987. pp. 64–65.

[2] Crystallographic information has also been deposited with the Cambridge Crystallographic Data Centre (CCDC Nos. 169557, 169556, 169558 for **I**–**III**, respectively). Copies of the data can be obtained free of charge via www.ccdc.cam.ac.uk/conts/retrieving.html (or from the Cambridge Crystallographic Data Centre, 12, Union Road, Cambridge CB2 1EZ, UK; fax: +44 1223 336033; or deposit@ccdc.cam.ac.uk).

© 2002 NRC Canada

53. E.A.C. Lucken, K. Noack, and D.F. Williams. J. Chem. Soc. A, 148 (1967).
54. V.P. Chacko and R.G. Bryant. J. Magn. Reson. **57**, 79 (1984).
55. P. Kofod, P. Harris, and S. Larsen. Inorg. Chem. **36**, 2258 (1997).
56. A. Fioretta, L. Lorenza, and G. Pellizer. Phys. Chem. Chem. Phys. **1**, 4981 (1999).
57. C. Sizun, P. Kempgens, J. Raya, K. Elbayed, P. Granger, and J. Rose. J. Organomet. Chem. **604**, 27 (2000).
58. J.A. Gonzalez, G.A. Aucar, M.C. Ruiz, and R.H. Contreras. Int. J. Quantum Chem. **66**, 823 (1997).
59. C. Juan and H.S. Gutowsky. J. Chem. Phys. **37**, 2198 (1962).
60. C.J. Jameson. *In* Multinuclear NMR spectroscopy. *Edited by* J. Mason. Plenum, New York. 1987. Chap. 4.
61. P. Pyykkö and L. Weisenfeld. Mol. Phys. **43**, 557 (1981).
62. M.D. Lumsden, K. Eichele, R.E. Wasylishen, T.S. Cameron, and J.F. Britten. J. Am. Chem. Soc. **116**, 11129 (1994).
63. M.D. Lumsden, R.E. Wasylishen, and J.F. Britten. J. Phys. Chem. **99**, 16602 (1995).
64. G. Wu and R.E. Wasylishen. J. Phys. Chem. **97**, 7863 (1993).
65. S. Koeker, J.V. Hanna, R.E. Wasylishen, E.W. Ainscough, and A.M. Brodi. J. Magn. Reson. **135**, 208 (1994).
66. J. Kaski, P. Lantto, J. Vaara, and J. Jokisaari. J. Am. Chem. Soc. **120**, 3993 (1998).
67. J. Kaski, J. Vaara, and J. Jokisaari. J. Am. Chem. Soc. **118**, 8879 (1996).

© 2002 NRC Canada

Syntheses and X-ray structures of boraamidinate complexes of lithium, phosphorus, and tellurium

Tristram Chivers, Chantall Fedorchuk, Gabriele Schatte, and Justin K. Brask

Abstract: The dilithiated boraamidinate complexes $\{Li_2[RB(N\text{-}t\text{-}Bu)_2]\}_2$ (**1a**, R = Ph; **1b**, R = *t*-Bu), prepared by the reaction of $B[N(H)\text{-}t\text{-}Bu]_3$ with three equivalents of LiR, are shown by X-ray crystallography to have dimeric structures consisting of a distorted Li_4N_4 cube capped on two opposite faces by RB units. Reactions of **1a** with $TeCl_4$ or PX_3 (X = Cl, Br) yielded complexes $PhB(\mu\text{-}N\text{-}t\text{-}Bu)_2TeCl_2$ (**2**) and $PhB(\mu\text{-}N\text{-}t\text{-}Bu)_2PX$ (**4a**, X = Cl; **4b**, X = Br), respectively. The structures of **2** and **4b** were determined by X-ray crystallography. In the solid state, complex **2** forms a dimer with weak Te···Cl contacts (3.2411(6) Å). Complex **4b** is monomeric with a P—Br bond length of 2.3047(11) Å. The reactions of **2** and **4a** with the appropriate amounts of Li[N(H)-*t*-Bu] produce the monomeric tellurium imide $PhB(\mu\text{-}N\text{-}t\text{-}Bu)_2Te{=}N\text{-}t\text{-}Bu$ and the amido derivative $PhB(\mu\text{-}N\text{-}t\text{-}Bu)_2PN(H)\text{-}t\text{-}Bu$ (**4c**), respectively. The X-ray structure of **4c** was determined. Deprotonation of **4c** with *n*-BuLi produces the dimeric monolithium derivative $\{Li[PhB(\mu\text{-}N\text{-}t\text{-}Bu)_2PN\text{-}t\text{-}Bu]\}_2$ (**5**), which was shown by X-ray crystallography to have a centrosymmetric structure with a central transoid Li_2N_2 ring.

Key words: boraamidinates, lithium, tellurium, phosphorus, X-ray structures.

Résumé : Faisant appel à la diffraction des rayons X, on a montré que les structures des complexes boraamidinates dilithiés $\{Li_2[RB(N\text{-}t\text{-}Bu)_2]\}_2$ (**1a**, R = Ph; **1b**, R = *t*-Bu) préparés par réaction du $B[N(H)\text{-}t\text{-}Bu]_3$ avec trois équivalents de LiR sont des dimères formés d'un cube Li_4N_4 déformé et portant des unités RB sur deux faces opposées. Les réactions de métathèse du composé **1a** avec le $TeCl_4$ ou le PX_3 (X = Cl, Br) fournissent respectivement les complexes $PhB(\mu\text{-}N\text{-}t\text{-}Bu)_2TeCl_2$ (**2**) et $PhB(\mu\text{-}N\text{-}t\text{-}Bu)_2PX$ (**4a**, X Cl; **4b**, X = Br). Les structures des composés **2** et **4b** ont été déterminées par diffraction des rayons X. Le complexe **2** forme un dimère avec de faibles contacts Te···Cl (3,2411(6) Å) à l'état solide. Le complexe **4b** est un monomère dans lequel la longueur de la liaison P—Br est de 2,3047(11) Å. Les réactions des composés **2** et **4a** avec des quantités appropriées de Li[N(H)N-*t*-Bu)] conduisent à la formation respectivement de l'imide de tellure monomère $PhB(\mu\text{-}N\text{-}t\text{-}Bu)_2Te{=}N\text{-}t\text{-}Bu$ et du dérivé amido $PhB(\mu\text{-}N\text{-}t\text{-}Bu)_2PN(H)\text{-}t\text{-}Bu$ (**4c**). On a déterminé la structure du composé **4c** par diffraction des rayons X. La déprotonation du composé **4c** à l'aide de *n*-BuLi conduit à la formation du dérivé monolithié dimère $\{Li[PhB(\mu\text{-}N\text{-}t\text{-}Bu)_2PN\text{-}t\text{-}Bu]\}_2$ (**5**) dont structure, telle que déterminé par diffraction des rayons X, est centrosymétrique avec un cycle central Li_2N_2 transoïde.

Mots clés : boraamidates, lithium, tellure, phosphore, structures par diffraction des rayons X.

[Traduit par la Rédaction]

Introduction

Amidinate ligands $(RC(NR')_2]^-$ (**A**) have been investigated extensively as ligands for *p*- and *d*-block metals (1). Recent studies have focused on the application of aluminum (2) and early transition-metal (3) complexes as catalysts for alkene polymerization. By contrast, the isoelectronic boraamidinate dianions $(RB(NR')_2]^{2-}$ (**B**) have received restricted attention. The known complexes of **B** are limited almost exclusively to elements from groups 4, 14, or 16 (4).

The most straightforward route to such complexes involves metathesis between a halide and the reagent $\{Li_2[PhB(N\text{-}t\text{-}Bu)_2]\}_2$, prepared in situ by dilithiation of $PhB[N(H)\text{-}t\text{-}Bu]_2$ with *n*-BuLi (5). This method has been used for the synthesis of complexes of the type $PhB(\mu\text{-}N\text{-}t\text{-}Bu)_2ML_n$ (where ML_n = Pb(II) (5), $ZrCp_2$ (6), and $SnMe_2$ (6)) as well as the spirocyclic compounds $[PhB(\mu\text{-}N\text{-}t\text{-}Bu)_2]_2M$ (where M = Ge, Sn, Ti, or Zr (6), Te (7)). The fluorinated compound $C_6F_5B(\mu\text{-}N\text{-}t\text{-}Bu)_2SnMe_2$ has been obtained in a similar manner (8). Less direct methods have been employed for the synthesis of the following boraamidinates: $[MeB(\mu\text{-}NSiMe_3)_2Sn]_2$ (9), *t*-$BuB(\mu\text{-}N\text{-}t\text{-}Bu)_2P(N\text{-}t\text{-}Bu)\text{-}t\text{-}Bu$ (10), $RB(\mu\text{-}NR')_2S$ (R = alkyl, aryl, C_6F_5; R′ = *t*-Bu or $SiMe_3$) (11), $MeB[\mu\text{-}N(2,6\text{-}Me_2CH)_2C_6H_3]_2SiMe_2$ (12), $MesB(\mu\text{-}N\text{-}t\text{-}Bu)_2Si(SiMe_3)(Mes)$ (13), and $PhB(\mu\text{-}N\text{-}t\text{-}Bu)_2TeN\text{-}t\text{-}Bu$ (14).

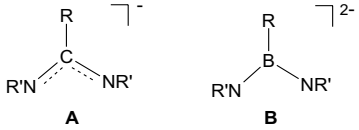

More recently, we have reported an alternative and potentially more versatile route to boraamidinates that involves the reaction of $B(NH\text{-}t\text{-}Bu)_3$ with three equivalents of an

Received 3 April 2002. Published on the NRC Research Press Web site at http://canjchem.nrc.ca on 26 June 2002.

T. Chivers,[1] C. Fedorchuk, G. Schatte, and J.K. Brask. Department of Chemistry, University of Calgary, Calgary, AB T2N 1N4, Canada.

[1]Corresponding author (e-mail: chivers@ucalgary.ca).

 DOI: 10.1139/V02-111 © 2002 NRC Canada

alkyl-lithium reagent (15). The dilithium salts $\{Li_2[RB(N\text{-}t\text{-}Bu)_2]\}_x$ obtained in this way form either dimeric (R = *n*-Bu; *x* = 2, **1c**) or trimeric (R = Me; *x* = 3) clusters (15). In this article we describe (*i*) the synthesis and X-ray structures of $\{Li_2[RB(N\text{-}t\text{-}Bu)_2]\}_2$ (R = Ph, *t*-Bu); (*ii*) the preparation and X-ray structure of $PhB(\mu\text{-}N\text{-}t\text{-}Bu)_2TeCl_2$ and a new route to the monomeric tellurium imide $PhB(\mu\text{-}N\text{-}t\text{-}Bu)_2TeN\text{-}t\text{-}Bu$; and (*iii*) the preparation, spectroscopic characterization, and X-ray structure (X = Br) of the P(III) boraamidinates $PhB(\mu\text{-}N\text{-}t\text{-}Bu)_2PX$ (X = Cl, Br, N(H)-*t*-Bu), and the dimeric lithium derivative $\{Li[PhB(\mu\text{-}N\text{-}t\text{-}Bu)_2PN\text{-}t\text{-}Bu]\}_2$.

Experimental

Reagents and general procedures

The compounds $PhBCl_2$ (Aldrich, 97%), PCl_3 (Aldrich, 98%), PBr_3 (Aldrich, 99.99+%), and $TeCl_4$ (Alfa Aesar, 99.9%) were used as received. Li[N(H)-*t*-Bu] was prepared by the addition of *n*-BuLi (2.5 M solution in hexanes, 200 mL, 0.5 mol; Aldrich) to a solution of anhydrous *t*-$BuNH_2$ (65 mL, 0.609 mol; Aldrich, 98%) in *n*-hexane (170 mL) at –10°C and its purity was checked by ^{1}H NMR spectroscopy (δ in C_7D_8, 1.37 (*t*-Bu) and in THF-d_8, 1.07 (*t*-Bu), –1.55 (NH)). The compound $\{Li_2[n\text{-}BuB(N\text{-}t\text{-}Bu)_2]\}_2$ (**1c**) (15) was obtained in 70% yield from the reaction of B[N(H)-*t*-Bu]$_3$ (16) with three equivalents of *n*-BuLi. Solvents were dried with appropriate drying agents and distilled onto molecular sieves before use. All reactions and the manipulation of moisture-sensitive products were carried out under an atmosphere of argon or under vacuum. All glassware was carefully dried prior to use.

Instrumentation

^{1}H NMR spectra were recorded on Bruker AC 200 and DRX 400 spectrometers, and chemical shifts are reported relative to Me_4Si in $CDCl_3$. ^{13}C, ^{11}B, ^{31}P, ^{125}Te, and ^{7}Li NMR spectra were measured at 23°C in C_6D_6, $CDCl_3$, or C_4D_8O on a Bruker DRX 400 spectrometer using a 5-mm broadband probe operating at 100.613, 128.377, 161.975, 126.429, and 155.505 MHz, respectively. The samples were externally referenced to $BF_3{\cdot}Et_2O$ in C_6D_6, H_3PO_4 in D_2O, K_2TeO_3 in D_2O (referenced to Me_2Te), and 1.0 M LiCl in D_2O, respectively. Line-broadening parameters, used in the exponential multiplication of the free induction decays, were 50–0.5 Hz. Chemical shifts with a positive sign are correlated with shifts to high frequencies (downfield) of the reference compound. EPR spectra were recorded at 20°C on a Buker EMX 10/12 EPR spectrometer equipped with a microwave X-Band bridge (9.1–9.9 GHz), a 10-inch magnet, and a 12-kW power supply ER083CS. Samples of **1a** and **1c** were loaded into a 4-mm glass tube in a glovebox and dissolved in oxygen-free toluene. After brief exposure of these solutions to dry air, the EPR spectra were recorded. Mass spectra were obtained with a VG Micromass spectrometer VG7070 (70 eV). Infrared spectra were obtained as Nujol mulls between KBr plates on a Nicolet Nexus 470 FT-IR spectrometer in the range of 4000–350 cm^{-1}. Elemental analyses were provided by the Analytical Services Laboratory of the Department of Chemistry, University of Calgary.

Preparation of $\{Li_2[PhB(N\text{-}t\text{-}Bu)_2]\}_2$ (1a)

From B[N(H)-t-Bu]$_3$ and 3 equivalents of LiPh

A solution of LiPh in cyclohexane–ether (1.8 M, 3.70 mL, 6.67 mmol) was added slowly to a solution of B[N(H)-*t*-Bu]$_3$ (0.50 g, 2.22 mmol) in Et_2O (50 mL) at 23°C and the mixture was stirred for 18 h. Concentration by removal of solvent in vacuo, and subsequent cooling (0°C for 18 h) of the resulting yellow solution (~20 mL) yielded colourless hexagonal blocks of $\{Li_2[PhB(N\text{-}t\text{-}Bu)_2]\}_2$ (0.82 g, 1.69 mmol, 76%); mp. 158–160°C (dec.). ^{1}H NMR (C_6D_6) δ: 7.38–7.18 (m, 5H, C_6H_5), 1.09 (s, 18H, C_4H_9). ^{13}C NMR (C_6D_6) δ: 133.85, 126.41, 125.12 (C_6H_5), 51.52 (CMe_3), 35.33 (CMe_3). ^{11}B NMR (C_6D_6) δ: 35.4 (br). ^{7}Li NMR (C_6D_6) δ: +2.24 (s). Anal. calcd. for $C_{28}H_{46}B_2Li_4N_4$: C 68.90, H 9.50, N 11.48; found: C 67.76, H 9.50, N 10.47.

A 1-mL aliquot of the initial Et_2O reaction mixture was pumped to dryness in vacuo and taken up in C_6D_6. The ^{1}H and ^{7}Li NMR spectra indicated the presence of Li[N(H)-*t*-Bu]: ^{1}H NMR δ: 1.36 (s, C_4H_9), cf. lit.: 1.37 (17). ^{7}Li NMR δ: 0.14 (s).

From PhB[N(H)-t-Bu]$_2$ and two equivalents of n-BuLi

PhB[N(H)-*t*-Bu]$_2$ is obtained by adding a solution of $PhBCl_2$ (2.000 g, 64 mL, 12.54 mmol) in *n*-hexane (20 mL) to a slurry of Li[N(H)-*t*-Bu] (3.900 g, 49.32 mmol)[2] in *n*-hexane (30 mL) at –20°C. The reaction mixture was stirred for 4 h at 23°C and then filtered twice using a glass-sintered frit (8 μm) and then a PTFE filter disk (Acrodisc syringe filter; diameter: 25 mm; pore size: 0.45 μm). The volatile materials were removed under vacuum to give PhB[N(H)-*t*-Bu]$_2$ as a golden yellow oil (2.600 g, 11.20 mmol, 89%). IR (cm^{-1}): 3429 (NH). ^{1}H NMR (C_6D_6) δ: 7.54–7.17 (m, 5H, C_6H_5), 2.80 (br s, 2H, N*H*), 1.12 (s, 18H, C_4H_9). ^{13}C NMR (C_6D_6) δ: 133.12, 127.81, 127.61 (C_6H_5), 49.32 (CMe_3), 33.63 (CMe_3). ^{11}B NMR (C_6D_6) δ: 29.6.

The product was dissolved in *n*-hexane (20 mL) and the solution was cooled to –10°C. Then *n*-BuLi in hexane (2.5 M, 9 mL, 22.20 mmol) was added, and the reaction mixture was heated at reflux for 17 h. The white precipitate of **1a** was allowed to settle and the yellow solution was removed via a cannula and discarded. The product was washed twice with *n*-hexane (~5 mL) at 0°C giving **1a** (2.220 g, 4.55 mmol, 81%). The ^{1}H, ^{13}C, and ^{11}B NMR spectral parameters were in good agreement with those obtained for **1a** prepared by method A.

An increase in the scale of the reaction of $PhBCl_2$ with Li[N(H)-*t*-Bu] by a factor of two results in lower yields (60–80%) of PhB[N(H)-*t*-Bu]$_2$.

Preparation of $\{Li_2[t\text{-}BuB(N\text{-}t\text{-}Bu)_2]\}_2$ (1b)

tert-Butyllithium (3.30 mL, 5.61 mmol) was added slowly to a solution of B[N(H)-*t*-Bu]$_3$ (0.425 g, 1.87 mmol) in *n*-pentane (10 mL) at 23°C and stirred for 2.5 h. Concentration by removal of solvent in vacuo and subsequent cooling (0°C

[2] It is necessary to use an excess of Li[N(H)-*t*-Bu] to optimize the yield of PhB[N(H)-*t*-Bu]$_2$. Unreacted Li[N(H)-*t*-Bu] is readily removed by filtration.

© 2002 NRC Canada

for 3 h) of the resulting solution (~2 mL) yielded colourless rods of **1b** (0.342 g, 0.76 mmol, 81%). ^{1}H NMR (C_6D_6) δ: 1.48 (s, 9H, BC_4H_9), 1.38 (s, 18H, NC_4H_9). ^{7}Li NMR (C_6D_6) δ: –0.55 (s). ^{11}B NMR (C_6D_6) δ: 35.1 (s). Anal. calcd. for $C_{12}H_{27}BLi_2N_2$: C 64.33, H 12.15, N, 12.50; found: C 64.70, H 11.32, N 12.58.

Preparation of PhB(μ-N-*t*-Bu)$_2$TeCl$_2$ (2)

The addition of a colourless solution of **1a** (1.000 g, 2.049 mmol) in toluene (10 mL) to a yellow solution of $TeCl_4$ (1.104 g, 4.098 mmol) in toluene (15 mL) at –78°C produced a dark red solution, which became black upon warming to 23°C. After 1 h, the volatiles were removed under vacuum and the solid black residue was extracted with acetonitrile (2 × 10 mL). Elemental tellurium (50 mg) was separated by filtration through an Acrodisc syringe filter (PTFE membrane, pore size 0.45 μm) to give an orange solution. Removal of solvent under vacuum produced PhB(μ-N-*t*-Bu)$_2$TeCl$_2$ (1.604 g, 3.742 mmol, 91%) as an orange-yellow solid; mp 110–114°C dec. ^{1}H NMR (C_6D_6) δ: 7.51–7.16 (m, 5H, C_6H_5), 1.22 (s, 18H, C_4H_9); ($CDCl_3$) δ: 7.60–7.38 (m), 1.29 (s). ^{13}C NMR (C_6D_6) δ: 131.08, 129.75, 128.49 (C_6H_5), 55.76 (CMe_3), 33.70 (CMe_3). ^{11}B NMR (C_6D_6) δ: 43.5; ($CDCl_3$) δ: 43.3. ^{125}Te NMR ($CDCl_3$) δ: 1677.1; (C_6D_6) δ: 1673.9. Anal. calcd. for $C_{14}H_{23}BCl_2N_2Te$: C 39.23, H 5.41, N 6.53; found: C 37.42, H 5.35, N 6.05.

Preparation of PhB(μ-N-*t*-Bu)$_2$TeN-*t*-Bu (3)

A slurry of Li[N(H)-*t*-Bu] (0.222 g, 2.800 mmol) in *n*-hexane (15 mL) was added to a yellow-orange solution of **2** (0.600 g, 1.400 mmol) in *n*-hexane (20 mL) cooled to –78°C. The reaction mixture was allowed to reach room temperature after 15 min, whereupon an orange solution containing a white solid (LiCl) was obtained. The mixture was stirred for 18 h, after which time the colour of the solution had changed to dark orange. The solution was filtered and the volatile materials were removed under vacuum to give a sticky red solid. Et_2O (5 mL) was added and at –60°C PhB(μ-N-*t*-Bu)$_2$TeN-*t*-Bu (**3**) crystallized from this solution. The red supernatant was removed via cannula, and the remaining yellow-brown solid was washed with Et_2O (2 × 5 mL) at –60°C to give **3** (0.233 g, 0.543 mmol, 39%). The final product was LiCl-free (^{7}Li NMR). ^{1}H NMR (C_6D_6) δ: 7.50–7.10 (m, 5H, C_6H_5), 1.71 (s, 9H, C_4H_9), 1.11 (s, 18H, C_4H_9); cf. lit. (14) δ: 7.6–7.2, 1.70, 1.11 (in C_6D_6). ^{13}C NMR (THF-d_8) δ: 132.03, 128.15, 128.00 (C_6H_5), 64.71 (CMe_3), 53.91 (CMe_3), 34.85 (CMe_3), 34.48 (CMe_3). ^{11}B NMR (THF-d_8) δ: 33.4 (br). ^{125}Te NMR (THF-d_8) δ: 1491.5 (s).

Preparation of PhB(μ-N-*t*-Bu)$_2$PCl (4a)

A colourless solution of **1a** (2.000 g, 4.098 mmol) in THF (15 mL) was added to a solution of PCl_3 (0.72 mL, 1.125 g, 8.195 mmol) in toluene (15 mL) at –78°C. The reaction mixture was allowed to reach room temperature after 0.5 h, whereupon a pale yellow solution containing a white solid (LiCl) was obtained. After 4 h, the reaction mixture was filtered through a PTFE filter disk (0.45 μm). The volatile materials were removed under vacuum to give a white solid. After addition of Et_2O (5 mL), the solution was filtered to remove LiCl. Further purification was achieved by sublimation at 100°C (10^{-3} torr) to give **4a** (2.028 g, 6.848 mmol, 84%) as a white solid; mp 104°C. ^{1}H NMR (C_6D_6) δ: 7.4–7.0 (m, 5H, C_6H_5), 1.15 (d, $^4J_{H,P}$ = 1.20 Hz, 18H, C_4H_9); (THF-d_8) δ: 7.44–7.30 and 7.13–7.08 (m, 5H, C_6H_5), 1.16 (d, $^4J_{H,P}$ = 0.96 Hz, 18H C_4H_9). ^{13}C NMR (THF-d_8) δ: 131.93, 129.54, 128.65 (3s, C_6H_5), 52.77 (d, $^2J_{C,P}$ = 6.10 Hz, CMe_3), 32.28 (d, $^3J_{C,P}$ = 6.90 Hz, CMe_3). ^{11}B NMR (THF-d_8) δ: 35.4 (s). ^{31}P NMR (THF-d_8) δ: 181.2 (s). MS *m*/*z*: 281 ([M – Me]$^+$), 225 ([M – N-*t*-Bu]$^+$). Anal. calcd. for $C_{14}H_{23}BClN_2P$: C 56.69, H 7.82, N 9.44; found: C 56.13, H 7.34, N 9.28.

Preparation of PhB(μ-N-*t*-Bu)$_2$PBr (4b)

A colourless solution of **1a** (0.500 g, 1.024 mmol) in THF (15 mL) was added to a solution of PBr_3 (0.195 mL, 0.555 g, 2.049 mmol) in toluene (10 mL) at –40°C. After 5 min, the reaction mixture was allowed to reach room temperature, whereupon a pale yellow solution containing a yellow-orange solid (LiBr) was obtained. The reaction mixture was filtered through a PTFE filter disk after 3.5 h. The volatile materials were removed under vacuum to give a pale sticky yellow solid. *n*-Hexane (~10 mL) was added and the cloudy solution was transferred into another Schlenk vessel leaving a microcrystalline yellow solid (0.293 g) (mainly LiBr). After removal of the solvent from the decanted solution an off-white, slightly sticky solid was recovered. The solid was identified as [PhB(μ-N-*t*-Bu)$_2$]PBr (**4b**, 0.600 g, 1.764 mmol, 86%) by multinuclear NMR spectroscopy and single crystal X-ray structure analysis. Two 20-mg samples of **4b** were dissolved in Et_2O and in a mixture of Et_2O–*n*-pentane (1:1) (~3 mL) in test tubes and colourless prism-like crystals were obtained from both samples after four days at –19°C. ^{1}H NMR (C_6D_6) δ: 7.6–7.2 (m, 5H, C_6H_5), 1.22 (d, $^4J_{H,P}$ = 1.00 Hz, 18H, C_4H_9); (THF-d_8) δ: 7.44 (m, 2H, C_6H_5), 7.34 (m, 3H, C_6H_5), 1.19 (d, $^4J_{H,P}$ = 1.12 Hz, 18H, C_4H_9). ^{13}C NMR (THF-d_8) δ: 131.88, 129.76, 128.62 (3s, C_6H_5), 53.21 (d, $^2J_{C,P}$ = 5.84 Hz, CMe_3), 32.07 (d, $^3J_{C,P}$ = 6.65 Hz, CMe_3). ^{11}B NMR (THF-d_8) δ: 34.5 (s). ^{31}P NMR (THF-d_8) δ: 199.5 (s). MS *m*/*z*: 340 (M$^+$), 325 ([M – Me]$^+$), 261 ([M – N-*t*-Bu]$^+$). Anal. calcd. for $C_{14}H_{23}BBrN_2P$: C 49.30, H 6.80, N 8.21; found: C 48.57, H 8.63, N 7.81.

Preparation of PhB(μ-N-*t*-Bu)$_2$P[N(H)-*t*-Bu] (4c)

A colourless solution of Li[N(H)-*t*-Bu] (0.133 g, 1.688 mmol) in THF (10 mL) was added to a solution of **4a** (0.500 g, 1.688 mmol) in THF (15 mL) at –20°C. The reaction mixture was allowed to reach room temperature after 10 min. The volatile materials were removed under vacuum after 4 h to give a white solid. *n*-Hexane (10 mL) was added and the resulting solution was filtered through a PTFE filter disk to remove LiCl. The solvent was removed under vacuum to give **4c** as a white solid (0.454 g, 1.362 mmol, 81%); mp 60°C. IR (cm^{-1}): 3347 (NH). ^{1}H NMR (C_7D_8) δ: 7.5–7.0 (m, 5H, C_6H_5), 2.37 (s, 1H, N*H*), 1.90 (d, $^4J_{H,P}$ = 0.90 Hz, 9H, C_4H_9), 1.25 (s, 18H, C_4H_9); (THF-d_8) δ: 7.36–7.30 and 7.27–7.20 (m, 5H, C_6H_5), 3.26 (d, $^2J_{H,P}$ = 6.0 Hz, 1H, N*H*), 1.31 (d, $^4J_{H,P}$ = 1.07 Hz, 9H, C_4H_9), 1.12 (s, 18H, C_4H_9). ^{13}C NMR (THF-d_8) δ: 132.09, 128.01, 127.96 (3s, C_6H_5), 51.74 (s, CMe_3), 51.67 (s, CMe_3), 33.27 (d, $^3J_{C,P}$ = 6.14 Hz, CMe_3), 33.03 (d, $^3J_{C,P}$ = 9.34 Hz, CMe_3). ^{11}B NMR (THF-d_8) δ: 32.66 (s). ^{31}P NMR (THF-d_8) δ: 94.02 (s). Anal.

© 2002 NRC Canada

calcd. for $C_{18}H_{33}BN_3P$: C 64.87, H 9.98, N 12.61; found: C 63.06, H 9.69, N 11.90.[3]

Preparation of {Li[PhB(μ-N-*t*-Bu)$_2$N-*t*-Bu]}$_2$ (5)

A solution of *n*-BuLi (2.5 M, 0.60 mL, 1.50 mmol) in hexanes was added to a solution of **4c** (0.500 g, 1.50 mmol) in *n*-hexane (10 mL) at –78°C. After 2.5 h, the solvent was removed from the golden yellow solution under vacuum to give **5** as a white solid (0.443 g, 1.306 mmol, 87%); mp 151°C (dec.). The ^{1}H, ^{13}C, ^{7}Li, and ^{11}B NMR spectra of THF-d_8 solutions of this product at 23°C indicate the presence of two components (**5A** and **5B**) in the approximate molar ratio 3:1.

5A: ^{1}H NMR δ: 7.38–7.14 (m, 5H, C_6H_5), 1.24 (d, $^4J_{H,P}$ = 1.13 Hz, 9H, *exo*-C_4H_9), 1.13 (s, 18H, *endo*-C_4H_9). ^{13}C NMR δ: 127.59, 127.41, 127.21 (3s, C_6H_5), 53.09 (d, $^2J_{C,P}$ = 25.6 Hz, *exo*-*C*Me$_3$), 52.13 (d, $^2J_{C,P}$ = 7.7 Hz, *endo*-*C*Me$_3$), 36.47 (d, $^3J_{C,P}$ = 6.5 Hz, *exo*-C*Me*$_3$), 33.49 (d, $^3J_{C,P}$ = 6.5 Hz, *endo*-C*Me*$_3$). ^{7}Li NMR δ: 0.39 (s).[4] ^{11}B NMR δ: 31.68 (s). ^{31}P NMR δ: 129.89 (s).

5B: ^{1}H NMR δ: 7.38–7.14 (m, 5H, C_6H_5), 1.32 (s, 9H, *exo*-C_4H_9), 1.18 (s, 18H, *endo*-C_4H_9). ^{13}C NMR δ: 133.03, 132.49, 132.18 (3s, C_6H_5), 56.84 (d, $^2J_{C,P}$ = 18.7 Hz, *exo*-*C*Me$_3$), 51.58 (d, $^2J_{C,P}$ = 8.2 Hz, *endo*-*C*Me$_3$), 35.92 (d, $^3J_{C,P}$ = 10.9 Hz, *exo*-C*Me*$_3$), 33.38 (d, $^3J_{C,P}$ = 4.8 Hz, *endo*-C*Me*$_3$). ^{11}B NMR δ: 37.21 (s). ^{31}P NMR δ: 68.10 (s). X-ray quality crystals were obtained from a solution of this solid (0.040 g) in C_7D_8 after 5 days at –19°C in an NMR tube. Satisfactory CHN analyses could not be obtained because of the extremely moisture-sensitive crystalline samples of **5**.

X-ray analyses

Crystals suitable for X-ray diffraction were obtained from solutions of the desired compounds in *n*-pentane at 23°C (**1a**, **1b**), in $CDCl_3$ at 23°C (**2**), in Et_2O or Et_2O–*n*-pentane at –19°C (**4b**), in *n*-hexane at –19°C (**4c**), and in C_7D_8 at –19°C (**5**). Single crystals of **1a**, **1b**, **2, 4b**, **4c**, and **5** were coated with Paratone oil, mounted on thin glass fibres, and frozen in the cold nitrogen stream of the goniometer or on a CryoLoop (nylon fibre).

Measurements for **1a** and **1b** were made on a Bruker AXS SMART/Platform 1000 CCD (ω-scans) and on a Bruker AXS SMART/PY/RA/SMART 1000 CCD (ϕ- and ω-scans) diffractometer, respectively. The data were reduced with SAINT (18*a*), which corrects for Lorentz and polarization effects, and corrected for absorption with SADABS (18*b*).

X-ray data for **2**, **4b**, **4c**, and **5** were collected on a Nonius Kappa CCD 4-circle Kappa FR540C diffractometer using ϕ- and ω-scans. Data reduction was performed with the HKL, DENZO, and SCALEPACK (18*c*) software, which corrects for beam non-homogeneity, possible crystal decay, and *Lp* effects, respectively. A multiscan absorption correction was applied (SCALEPACK) (18*c*).

Relevant parameters for the data collections and crystallographic data for **1a**, **1b**, **2**, **4b**, **4c**, and **5** are summarized in Tables 1 and 2.[5]

All structures were solved using direct methods (**1a**, **1b**, **4b**: SHELXS-97 (19*a*); **4c**: SHELXS-97–2 (19*b*); **2**: SIR-92 (20*a*); **6**: SIR-97 (20*b*)) and refined by full-matrix least-squares methods on F^2 with SHELXL97–2 (19*b*). The non-hydrogen atoms were refined anisotropically. Hydrogen atoms were included at geometrically idealized positions (C—H and N—H bond distances 0.95 Å) and were not refined. The isotropic thermal parameters of the hydrogen atoms were fixed at 1.2 times that of the corresponding carbon or nitrogen atom.

Two of the carbon atoms (C(50) and C(53)) of the *t*-Bu group attached to B(1) in **1b** were disordered around the mirror plane with partial occupancy factors of 0.5 each, leading to two possible orientations of the disordered *t*-Bu group: C(52), C(50), C(51), C(53) and C(53)*, C(50)*, C(52), C(51) (*: *x*, *–y* + 1/2, *z*).

In **4b**, one of the carbon atoms (C(13), C(13′) of one of the *t*-Bu groups was disordered around the mirror plane with partial occupancy factors of 0.62(2) and 0.38(2), respectively. In **4c**, the hydrogen atom connected to N(3) was located from the Fourier difference map.

Results and discussion

Synthesis and X-ray structures of {Li$_2$[RB(N-*t*-Bu)$_2$]}$_2$ (1a, R = Ph; 1b, R = *t*-Bu)

In a preliminary communication (15), we reported that the dilithio boraamidinate complexes {Li$_2$[RB(N-*t*-Bu)$_2$]}$_x$ (R = *n*-Bu, *x* = 2 (**1c**); R = Me, *x* = 2,3) were obtained by treatment of B[N(H)-*t*-Bu]$_3$ with three equivalents of the appropriate organolithium reagent. In this transformation the alkyl-lithium reagent functions as a base to dilithiate B[N(H)-*t*-Bu]$_3$ and as a nucleophile to displace the third *t*-BuNH group with an alkyl substituent.[6] Here we have demonstrated that aryl-lithium reagents can also be used in this new synthesis of boraamidinates. Thus {Li$_2$[PhB(N-*t*-Bu)$_2$]}$_2$ (**1a**) is obtained in 76% yield via eq. [1]. The preferred synthesis of **1a**, however, is the dilithiation of PhB[N(H)-*t*-Bu]$_2$, for which an improved procedure is described in the *Experimental* section (eq. [2]). The overall yield of **1a** from $PhBCl_2$ is ~73%; it is not necessary to separate the product from Li[N(H)-*t*-Bu] (cf. eq. [1]).

[3] Slightly low CHN values were obtained for three different samples. The product was, however, spectroscopically pure (^{1}H, ^{13}C, and ^{31}P NMR spectra) and showed no resonance for LiCl in the ^{7}Li NMR spectrum.

[4] Two very weak resonances were also observed in the ^{7}Li NMR spectrum at δ 1.07 and 1.60, but neither of these resonances were sufficiently intense to be attributable to **5B**. It is possible that the ^{7}Li NMR resonance for **5B** is hidden under the resonance at δ 0.39 for **5A**.

[5] Supplementary material may be purchased from the Depository of Unpublished Data, Document Delivery, CISTI, National Research Council Canada, Ottawa, ON K1A 0S2, Canada. For information on obtaining material electronically go to http://www.nrc.ca/cisti/irm/unpub_e.shtml. Crystallographic information has also been deposited with the Cambridge Crystallographic Data Centre (CCDC Nos. 181868 (**1a**), 181864 (**1b**), 181865 (**2**), 181866 (**4b**), 181867 (**4c**), and 181863 (**5**)). Copies of the data can be obtained free of charge via www.ccdc.cam.ac.uk/conts/retrieving.html (or from the Cambridge Crystallographic Data Centre, 12, Union Road, Cambridge CB2 1EZ, UK; fax: +44 1223 336033; or deposit@ccdc.cam.ac.uk).

[6] A similar transformation has been reported by Nöth et al. (21) for the lithiation of MesP(NH-*t*-Bu)$_2$ with *n*-BuLi, which produces {*n*-BuP[N(Li)-*t*-Bu]$_2$}$_2$·(OEt$_2$)$_2$ via the nucleophilic substitution of the mesityl group at the phosphorus(III) centre by an *n*-butyl group.

© 2002 NRC Canada

Table 1. Crystallographic data for **1a**, **1b**, and **2**.

	1a	**1b**	**2**
Formula	$C_{24}H_{54}B_2Li_4N_4$	$C_{28}H_{46}B_2Li_4N_4$	$C_{14}H_{23}BCl_2N_2Te$
FW	448.09	488.07	428.65
Crystal size (mm)	0.39 × 0.30 × 0.13	0.48 × 0.21 × 0.15	0.30 × 0.30 × 0.25
Colour and habit	Colourless prism	Colourless prism	Orange plate
T (K)	193(2)	193(2)	173(2)
Wavelength (Å)	0.71073	0.71073	0.71073
Crystal system	Monoclinic	Monoclinic	Orthorhombic
Space group	$P2_1/m$	$C2/c$	$Pbca$
a (Å)	10.1301(11)	19.844(4)	14.8178(2)
b (Å)	11.0986(12)	8.9232(18)	11.5449(2)
c (Å)	13.4048(13)	17.876(4)	21.3800(3)
β (°)	100.8559(19)	100.970(3)	
V (Å^3)	1480.1(3)	3107.6(11)	3657.48(10)
Z	2	4	8
$D_{calcd.}$ (g cm^{-3})	1.005	1.043	1.557
μ (cm^{-1})	0.55	0.58	19.11
No. of reflns. collected	5783	7320	10310
No. of indep. reflns./R_{int}	2624/0.0446	3177/0.0529	5226/0.0196
Reflns. with $I > 2\sigma(I)$	1650	1784	4140
S (GoF) on F^2 [a]	1.025	0.923	1.021
R $[I \geq 2\sigma(I)]$[b]	0.0571	0.0543	0.0265
wR (all data)[c]	0.1652	0.1452	0.0655
Largest diff. peak/hole (e Å^{-3})	0.188/–0.136	0.293/–0.220	0.625/–0.583

[a] $S = \{\Sigma[w(F_o^2 - F_c^2)^2]/(n-p)\}^{1/2}$.
[b] $R = \Sigma||F_o| - |F_c||/\Sigma|F_o|$.
[c] $wR = \{[\Sigma w(F_o^2 - F_c^2)^2]/[\Sigma w(F_o^2)^2]\}^{1/2}$.

Table 2. Crystallographic data for **4b**, **4c**, and **5**.

	4b	**4c**	**5**
Formula	$C_{14}H_{23}BBrN_2P$	$C_{18}H_{33}BN_3P$	$C_{36}H_{64}B_2Li_2N_4P_2$
FW	341.02	333.25	678.37
Crystal size (mm)	0.30 × 0.30 × 0.20	0.15 × 0.15 × 0.10	0.12 × 0.12 × 0.05
Colour and habit	Colourless prism	Colourless plate	Colourless plate
T (K)	223(2)	173(2)	173(2)
Wavelength (Å)	0.71073	0.71073	0.71073
Crystal system	Monoclinic	Monoclinic	Monoclinic
Space group	$P2_1/m$	$C2/c$	$P2_1/n$
a (Å)	6.2890(1)	36.1860(6)	11.2310(2)
b (Å)	13.8520(3)	6.0030(2)	10.4010(2)
c (Å)	10.0331(2)	25.2640(6)	18.4790(4)
β (°)	91.306(2)	131.0551(11)	107.2790(8)
V (Å^3)	873.80(3)	4138.35(18)	2061.18(7)
Z	2	8	2
$D_{calcd.}$ (g cm^{-3})	1.296	1.070	1.093
μ (cm^{-1})	24.33	1.36	1.37
No. of reflns. collected	4064	6619	9039
No. of indep. reflns./R_{int}	2423/0.0139	3507/0.0371	4695/0.0264
Reflns. with $I > 2\sigma(I)$	1785	2520	3703
S (GoF) on F^2 [a]	1.042	1.030	1.030
R $[I \geq 2\sigma(I)]$[b]	0.0517	0.0381	0.0419
wR (all data)[c]	0.1442	0.0998	0.1146
Largest diff. peak/hole (e Å^{-3})	0.800/–0.949	0.210/–0.262	0.563/–0.382

[a] $S = \{\Sigma[w(F_o^2 - F_c^2)^2]/(n-p)\}^{1/2}$.
[b] $R = \Sigma||F_o| - |F_c||/\Sigma|F_o|$.
[c] $wR = \{[\Sigma w(F_o^2 - F_c^2)^2]/[\Sigma w(F_o^2)^2]\}^{1/2}$.

© 2002 NRC Canada

Table 3. Selected bond lengths and bond angles (deg) for **1a** and **1b**.

Bond lengths (Å)		Bond angles (deg)			
1a					
B(1)—N(1)	1.448(3)	B(1)-N(1)-Li(1)′	132.46(18)	Li(2)-N(2)-Li(1)	88.65(16)
B(1)—N(2)	1.449(3)	B(1)-N(1)-Li(1)	75.12(15)	Li(1)-N(2)-Li(2)′	68.34(15)
B(1)—C(31)	1.598(3)	B(1)-N(2)-Li(2)	78.15(16)	N(1)-B(1)-N(2)	109.50(18)
N(1)—Li(1)′	2.017(4)	B(1)-N(2)-Li(1)	75.93(16)	N(1)′-Li(1)-N(2)	110.64(18)
N(1)—Li(2)	2.027(4)	B(1)-N(1)-Li(2)	78.02(16)	N(1)′-Li(1)-N(1)	109.59(17)
N(1)—Li(1)	2.077(4)	B(1)-N(2)-Li(2)′	131.29(17)	N(2)-Li(1)-N(1)	69.93(14)
N(2)—Li(2)	2.022(4)	Li(1)′-N(1)-Li(2)	69.94(15)	N(2)-Li(2)-N(1)	71.52(13)
N(2)—Li(1)	2.052(4)	Li(1)′-N(1)-Li(1)	69.62(17)	N(2)-Li(2)-N(2)′	109.94(18)
N(2)—Li(2)′	2.074(4)	Li(2)-N(1)-Li(1)	87.84(16)	N(1)-Li(2)-N(2)′	109.34(18)
1b					
B(1)—N(1)	1.476(4)	N(1)-B(1)-N(2)	105.2(2)	Li(2)-N(3)-Li(3)	85.51(17)
B(1)—N(2)	1.479(4)	N(1)-B(1)-C(50)	126.6(3)	N(1)-Li(1)-N(2)	72.41(13)
B(1)—C(50)	1.660(5)	N(2)-B(1)-C(50)	126.4(3)	N(1)-Li(1)-N(3)	112.25(17)
B(2)—N(3)	1.476(2)	N(3)-B(2)-N(3)′	105.5(2)	N(2)-Li(1)-N(3)	111.41(17)
B(2)—C(60)	1.662(4)	N(3)-B(2)-C(60)	127.25(11)	N(1)-Li(2)-N(3)	111.22(19)
N(1)—Li(1)	1.980(4)	B(1)-N(1)-Li(1)	78.33(15)	N(3)-Li(2)-N(3)′	72.94(18)
N(1)—Li(2)	2.154(5)	B(1)-N(1)-Li(2)	132.1(2)	N(2)-Li(3)-N(3)	113.23(19)
N(2)—Li(1)	1.996(4)	Li(1)-N(1)-Li(2)	67.43(14)	N(3)-Li(3)-N(3)′	71.99(18)
N(2)—Li(3)	2.080(5)	B(2)-N(3)-Li(2)	79.65(15)	Li(1)-N(1)-Li(1)′	86.4(2)
N(3)—Li(1)	2.125(4)	B(2)-N(3)-Li(3)	76.36(16)	B(1)-N(2)-Li(1)	77.73(15)
N(3)—Li(2)	1.976(4)	B(2)-N(3)-Li(1)	131.94(15)	B(1)-N(2)-Li(3)	132.1(2)
N(3)—Li(3)	1.999(4)	Li(1)-N(3)-Li(2)	68.07(16)	Li(1)-N(2)-Li(3)	67.74(14)
		Li(1)-N(3)-Li(3)	66.79(15)	Li(1)-N(2)-Li(1)′	85.5(2)

Note: Symmetry transformations used to generate equivalent atoms ′: $-x + 1/2, y, -z$.

[1] $B[N(H)\text{-}t\text{-}Bu]_3 + 3LiPh \rightarrow 1/2\{Li_2[PhB(N\text{-}t\text{-}Bu)_2]\}_2 + Li[N(H)\text{-}t\text{-}Bu] + 2C_6H_6$

[2] $PhBCl_2 + 2LiN(H)\text{-}t\text{-}Bu \rightarrow PhB[N(H)\text{-}t\text{-}Bu]_2 + 2LiCl \xrightarrow{2n\text{-}BuLi} 1/2\{Li_2[PhB(N\text{-}t\text{-}Bu)_2]\}_2 + 2H\text{-}n\text{-}Bu$

We have also shown that the *tert*-butyl derivative $\{Li_2[t\text{-}BuB(N\text{-}t\text{-}Bu)_2]\}_2$ (**1b**) can be prepared in 81% yield by the reaction of $B[N(H)\text{-}t\text{-}Bu]_3$ with three equivalents of *t*-BuLi. It is interesting to compare this result with the related chemistry of transition-metal amides. The amido–niobium complex $[(THF)_2Li]_2[Nb(NMes)_3(NHMes)]$ (Mes = 2,4,6-$Me_3C_6H_2$) is lithiated by *t*-BuLi to give the tetrakisimidoniobate $(THF)_4Li_3[Nb(NMes)_4]$ (22*a*), whereas the reaction of the same complex with *n*-BuLi results in nucleophilic displacement of the amido ligand to give the alkyl–niobium complex $[[(THF)_2Li]_2n\text{-}BuNb(NMes)_3]$ (22*b*).

An intriguing observation, which was not reported in the earlier work (5, 6), is the appearance of persistent bright pink solutions when **1a**–**c** are exposed to air.[7] This transformation is reminiscent of the behaviour of solutions of the related dimeric clusters $\{Li_2[E(N\text{-}t\text{-}Bu)_3]\}_2$ (E = S, Se), which form deep blue (E = S) or green (E = Se) solutions upon air oxidation (23–25). These colours were attributed to the radicals $\{Li_3[E(N\text{-}t\text{-}Bu)_3]_2\}^{\bullet}$ on the basis of their EPR spectra, which consisted of a septet of decets with the appropriate relative intensities for the coupling of the unpaired electron with three nitrogen (^{14}N, 99.6%, $I = 1$) and three lithium

Fig. 1. ORTEP drawing of $\{Li_2[PhB(N\text{-}t\text{-}Bu)_2]\}_2$ (**1a**) (30% probability ellipsoids). Primed atoms are related by the symmetry transformation: $-x + 1/2, y, -z$.

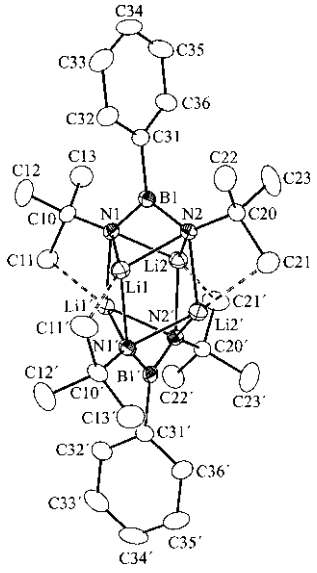

(^7Li, 92.6%, $I = 3/2$) nuclei (24, 25). These neutral radicals are comprised of the radical anion $[E(N\text{-}t\text{-}Bu)_3]^{\bullet-}$ and the dianion $[E(N\text{-}t\text{-}Bu)_3]^{2-}$ bridged by three Li^+ ions. The pink solution of air-oxidized **1a** in toluene at 23°C exhibits a five-line EPR spectrum, but the hyperfine coupling with

[7] T. Chivers, C. Fedorchuk, G. Schatte, J.K. Brask, and R.T. Boeré. Unpublished results.

© 2002 NRC Canada

Table 4. Selected bond lengths (Å) and bond angles (deg) for **2**.

Bond lengths (Å)		Bond angles (deg)			
Te(1)—N(2)	1.9954(16)	Cl(2)-Te(1)···Cl(2)*	78.29(2)	B(1)-N(1)-C(10)	137.35(18)
Te(1)—N(1)	1.9998(16)	Cl(1)-Te(1)···Cl(2)*	94.53(2)	B(1)-N(1)-Te(1)	92.21(13)
Te(1)—Cl(1)	2.4356(6)	Cl(2)*-Te(1)-N(1)	168.06(2)	C(10)-N(1)-Te(1)	127.02(14)
Te(1)—Cl(2)	2.6452(6)	Cl(2)*-Te(1)-N(2)	108.97(2)	B(1)-N(2)-C(20)	136.69(18)
N(1)—B(1)	1.447(3)	Cl(1)-Te(1)-Cl(2)	172.73(2)	B(1)-N(2)-Te(1)	92.41(13)
N(2)—B(1)	1.447(3)	N(2)-Te(1)-N(1)	69.33(7)	C(20)-N(2)-Te(1)	129.46(14)
C(1)—B(1)	1.563(3)	N(2)-Te(1)-Cl(1)	94.48(5)	N(2)-B(1)-N(1)	103.49(19)
		N(1)-Te(1)-Cl(1)	97.38(5)	N(2)-B(1)-C(1)	127.08(18)
Te(1)···Cl(2)*	3.2411(6)	N(2)-Te(1)-Cl(2)	88.98(5)	N(1)-B(1)-C(1)	129.23(18)
		N(1)-Te(1)-Cl(2)	89.82(5)		

Note: Symmetry transformations used to generate equivalent atoms *: *–x, –y, –z*.

Scheme 1.

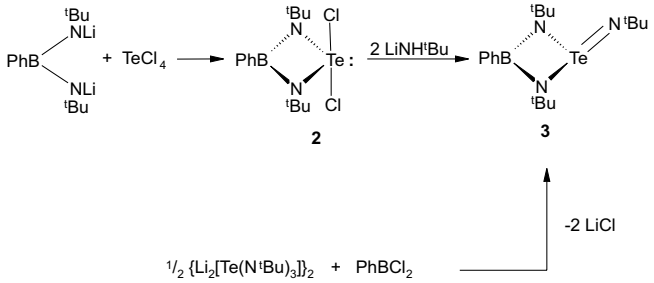

lithium centres is not resolved.[7] Consequently, we will not speculate on the identity of the radical species.

Because the structures of **1a** and **1b** were shown by X-ray crystallography to be similar, only the drawing of **1a** is shown (see Fig. 1). Pertinent structural parameters are compared in Table 3. The dimeric arrangement of **1a** and **1b** is similar to that previously reported for $\{Li_2[n\text{-BuB(N-}t\text{-Bu)}_2]\}_2$ (**1c**) (15); a detailed discussion here of the structures of **1a** and **1b** is therefore not warranted. All three structures consist of a distorted Li_4N_4 cube capped on two opposite faces by RB units, which are in a trigonal planar environment. Molecule **1b**, however, crystallizes in the space group $P2_1/m$ (cf. $P2_1/n$ for **1c**), imposing a mirror plane that bisects the cluster core at the atoms B(1), B(2), Li(2), Li(3), N(1), and N(2). Carbon atoms C(50) and C(53) of the *t*-Bu group attached to B(1) are disordered over two positions, each with site occupancy factors of 0.5. The replacement of the *n*-Bu groups attached to the boron atoms in **1c** with bulkier *t*-Bu groups results in lengthening of the B—N and B—C bonds (by ~0.02 and 0.05 Å, respectively) and contraction of the N-B-N angles (by ~3°). The weighted mean Li—N distance of 2.032 Å in **1b** is similar to that found for **1c** (2.037 Å), but the range of Li—N distances (1.976(4)–2.154(5) Å) is broader. The weighted mean distance of 2.226 Å for the agostic C–H···Li interactions in **1b** is significantly shorter (by ~0.2 Å) than that in **1c**, presumably as a result of the influence of the bulky *t*-Bu groups. Consistently, the mean C–H···Li contacts in **1a** (2.421 Å) are similar to the corresponding interaction exhibited by **1c** (2.440 Å).

Fig. 2. ORTEP drawing of $[PhB(\mu\text{-N-}t\text{-Bu})_2TeCl_2]_2$ (**2**) (30% probability ellipsoids). Starred atoms are related by the symmetry transformation: *–x, –y, –z*.

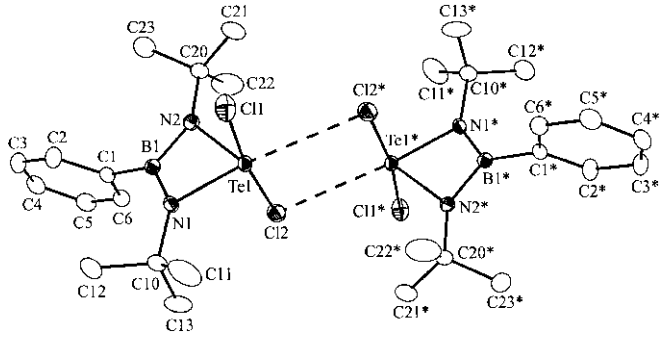

Phenylboraamidinate complexes of tellurium(IV)

We have shown earlier that a boraamidinate ligand stabilizes a monomeric tellurium imide in the complex $PhB(\mu\text{-N-}t\text{-Bu})_2Te{=}N\text{-}t\text{-Bu}$ (**3**) (14); however, the yield of this complex in the synthesis from $PhBCl_2$ and $\{Li_2[Te(N\text{-}t\text{-Bu})_3]\}_2$ was only 29%. Consequently, an alternative route to **3**, as depicted in Scheme 1, was investigated. The reaction of the monomer of **1a** with $TeCl_4$ in a 1:1 molar ratio produces $PhB(\mu\text{-N-}t\text{-Bu})_2TeCl_2$ (**2**) in 91% yield. The spirocyclic complex $[PhB(\mu\text{-N-}t\text{-Bu})_2]_2Te$ is obtained in 43% yield when a 2:1 stoichiometry is used for this reaction (7). Complex **2** was characterized by CHN analyses, multinuclear (^1H, ^{13}C, ^{11}B, and ^{125}Te) NMR spectroscopy,[8] and by an X-ray structural determination (vide infra). The subsequent reaction of **2** with two equivalents of Li[N(H)-*t*-Bu] produced **3** in ~40% yield. Although the improvement in the yield of **3** is modest, this new synthesis is preferable to the existing method using $\{Li_2[Te(N\text{-}t\text{-Bu})_3]\}_2$, (14) in view of the easier preparation of the reagents.

The structure of **2** was determined by X-ray crystallography (see Fig. 2). Selected bond lengths and bond angles are given in Table 4. Complex **2** forms a centrosymmetric dimer linked by weak Te···Cl interactions of 3.2411(6) Å (cf. sum of van der Waals radii for Te and Cl of 3.81 Å (27*a*) or 4.0 Å (27*b*)). Several bisamido or bisimido–tellurium dichloride complexes have been structurally characterized, including monomeric $[(Ph_3PN)_2TeCl_2$ (28), $(Ph_2CN)_2TeCl_2$ (29)],

[8] The ^{125}Te NMR resonance for **2** appears at δ 1677, which may be compared with the ^{125}Te chemical shifts of δ 1575 and 1693 observed for the inequivalent tellurium atoms in $t\text{-BuNTe}(\mu\text{-N-}t\text{-Bu})_2TeCl_2$ (26).

© 2002 NRC Canada

Fig. 3. ORTEP drawing of [PhB(μ-N-*t*-Bu)$_2$PBr] (**4b**) (30% probability ellipsoids).

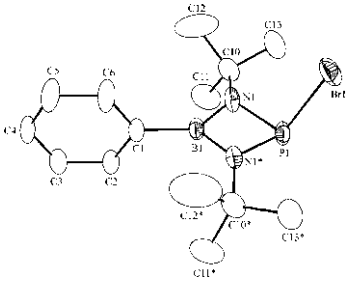

dimeric [(Me$_3$PN)$_2$TeCl$_2$ (30), CF$_3$SNTeCl$_2$·THF (31)], or extended structures [{Cl$_2$Te(μ-N-*t*-Bu)$_2$TeCl$_2$}$_3$ (26), [(Me$_3$Si)$_2$N]$_2$TeCl$_2$ (32), MeN[PhBN(Me)]$_2$TeCl$_2$ (7), (Ph$_2$SN)$_2$TeCl$_2$ (29), and *t*-BuN(H)Sb(μ-N-*t*-Bu)$_2$TeCl$_2$ (33)[9]. The different degrees of oligomerization observed for closely related molecules suggest that packing considerations, influenced by subtle steric effects, are responsible for the presence (or absence) of association.

The boraamidinate ligand in **2** is symmetrically bonded to tellurium with equal B–N and Te–N bond lengths. The relevant bond angles (N(2)-Te(1)-N(1) = 69.33(7)°, Cl(2)*-Te(1)-N(1) = 168.06(2)°, Cl(2)*-Te(1)-N(2) = 108.97(2)°, Cl(1)-Te(1)-Cl(2) = 172.73(2)°) indicate that the tellurium atom in **2** is in a distorted pseudo-octahedral environment, with the lone pair occupying an octahedral site. The Te—N bond lengths (av 1.997 Å) can be compared with the values of 2.036 and 2.147 Å reported for the equatorial and axial bonds, respectively, in the spirocyclic compound [PhB(μ-N-*t*-Bu)$_2$]$_2$Te, which is a distorted trigonal bipyramid (7). The Te—Cl bond distances in **2** are significantly different (2.4356(6) and 2.6452(6) Å) as a result of the weak Te···Cl contacts, which are reflected by the non-linearity of the Cl-Te-Cl unit (172.73(2)°) and the Cl(2)-Te(1)···Cl(2)* bond angle (78.29(2)°) in the Te$_2$Cl$_2$ rectangle.

Phenylboraamidinate complexes of phosphorus(III)

We have also obtained boraamidinate complexes containing a phosphorus(III)–halogen bond in 85–95% yields by the reaction of **1a** with phosphorus trihalides (eq. [3]). The only previously reported P(III) complex is MeB(μ-N-*t*-Bu)$_2$PMe prepared by treatment of MeBBr$_2$ with (LiN-*t*-Bu)$_2$PMe (34). The complexes PhB(μ-N-*t*-Bu)$_2$PX (**4a**, X = Cl; **4b**, X = Br) were characterized by CHN analyses, multinuclear (^{1}H, ^{13}C, ^{11}B, and ^{31}P) NMR spectroscopy, mass spectrometry, and an X-ray structure determination of **4b**. The ^{1}H NMR spectra of **4a** or **4b** in C$_6$D$_6$ or THF-d_8 show resonances for the Ph and N-*t*-Bu groups with the appropriate intensities. The latter appears as a doublet owing to the four-bond ^{1}H–^{31}P coupling. ^{31}P NMR resonances are observed at δ 181 (**4a**) and 199 (**4b**) in THF-d_8 solution (cf. XP(μ-N-*t*-Bu)$_2$PX (δ 211, X = Cl; δ 224, X = Br)) (34). Surprisingly, the mass spectra of **4a** and **4b** show fragment ions corresponding to [M – Me]$^+$ and [M – N-*t*-Bu]$^+$ rather than [M – X]$^+$ implying a relatively strong covalent P–X (X = Cl, Br) bond. A molecular ion is observed for **4b**.

Table 5. Selected bond lengths (Å) and bond angles (deg) for **4b**.

Bond lengths (Å)		Bond angles (deg)	
Br(1)—P(1)	2.3047(11)	N(1)-P(1)-N(1)*	80.09(17)
P(1)—N(1)	1.688(3)	N(1)-P(1)-Br(1)	103.67(10)
N(1)—B(1)	1.440(4)	B(1)-P(1)-Br(1)	112.85(11)
N(1)—C(10)	1.470(5)	B(1)-N(1)-P(1)	90.41(19)
C(1)—B(1)	1.567(5)	B(1)-N(1)-C(10)	136.3(2)
		C(10)-N(1)-P(1)	130.6(2)
		N(1)*-B(1)-N(1)	97.9(3)
		N(1)-B(1)-C(1)	131.03(15)

Note: Symmetry transformations used to generate equivalent atoms *: *x*, –*y* + 1/2, *z*.

Fig. 4. ORTEP drawing of [PhB(μ-N-*t*-Bu)$_2$PN(H)-*t*-Bu] (**4c**) (30% probability ellipsoids).

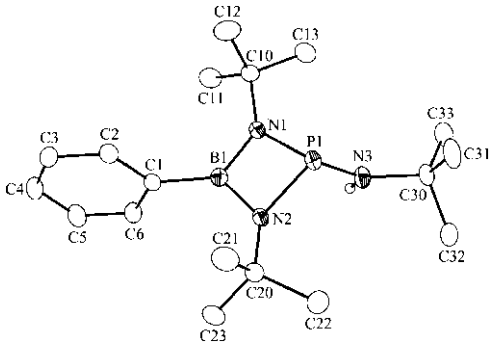

[3] $$1/2\{Li_2[PhB(N\text{-}t\text{-}Bu)_2]\}_2 + PX_3 \rightarrow PhB(\mu\text{-}N\text{-}t\text{-}Bu)_2PX \quad (X = Cl, Br)$$

The X-ray structure of **4b** is illustrated in Fig. 3 and selected bond lengths and bond angles are given in Table 5. The four-membered PNBN ring is slightly puckered (P(1)-N(1)-B(1)-N(1)* = 8.8(3)°) with symmetrically bridging N-*t*-Bu groups. The B–N bond lengths are in the typical range for phenylboraamidinate complexes (14) and the geometry at nitrogen is essentially planar. A search of the Cambridge Crystal Data Base revealed no structural information for cyclic P(III)–N compounds with exocyclic P–Br bonds. For example, the structure of the cyclodiphosph(III) azane BrP(μ-N-*t*-Bu)$_2$PBr is unknown (34). The P—N bond distance of 1.688(3) Å can be compared with values in the range 1.674(3)–1.689(9) Å for cyclodiphosph(III) azanes with Cl substituents attached to phosphorus (35, 36). The P—Br distance of 2.3047(11) Å is only slightly longer than the sum of the covalent radii for P and Br (2.24 Å) (27*b*), consistent with a strong covalent contribution to the P–Br bond.

The nucleophilic substitution reaction of **4a** with one equivalent of Li[N(H)-*t*-Bu] produced PhB(μ-N-*t*-Bu)$_2$PN(H)-*t*-Bu (**4c**) in ~80% yield. Amido derivative **4c** (see Table 6) was characterized by multinuclear (^{1}H, ^{13}C, ^{11}B, and ^{31}P) NMR and by X-ray crystallography (Fig. 4). The geometrical parameters of the phenylboraamidinate ligand in **4c** are similar to those discussed above for **4b**, although the four-membered ring is more puckered (torsion angle P(1)-N(1)-B(1)-N(2) = –12.50(13)°). The exocyclic P—N bond length of 1.6544(16) Å is ~0.1 Å shorter than

[9] The complex *t*-BuN(H)Sb(μ-N-*t*-Bu)$_2$TeCl$_2$ forms an extended structure involving weak Sb···Cl contacts rather than Te···Cl contacts (33).

© 2002 NRC Canada

Table 6. Selected bond lengths (Å) and bond angles (deg) for **4c**.

Bond lengths (Å)		Bond angles (deg)			
P(1)—N(1)	1.7395(14)	N(1)-P(1)-N(2)	77.37(7)	B(1)-N(2)-P(1)	90.81(11)
P(1)—N(2)	1.7452(14)	N(3)-P(1)-N(1)	105.28(7)	C(20)-N(2)-P(1)	128.08(11)
P(1)—N(3)	1.6544(16)	N(3)-P(1)-N(2)	106.66(7)	C(30)-N(3)-P(1)	129.85(13)
N(1)—B(1)	1.438(2)	B(1)-N(1)-P(1)	90.98(11)	C(30)-N(3)-H	112.0(14)
N(2)—B(1)	1.436(2)	B(1)-N(1)-C(10)	135.11(14)	P(1)-N(3)-H	118.1(14)
B(1)—C(1)	1.570(3)	C(10)-N(1)-P(1)	130.26(11)	N(2)-B(1)-N(1)	98.55(14)
		B(1)-N(2)-C(20)	132.45(14)	N(2)-B(1)-C(1)	131.32(16)
				N(1)-B(1)-C(1)	130.02(16)

Table 7. Selected bond lengths (Å) and bond angles (deg) for **5**.

Bond lengths (Å)		Bond angles (deg)			
P(1)—N(3)	1.6403(12)	N(3)-P(1)-N(1)	109.02(6)	C(30)-N(3)-P(1)	116.16(9)
P(1)—N(1)	1.7661(12)	N(3)-P(1)-N(2)	105.69(6)	C(30)-N(3)-Li(1)*	109.49(11)
P(1)—N(2)	1.8114(12)	N(1)-P(1)-N(2)	75.99(5)	P(1)-N(3)-Li(1)*	128.94(10)
N(1)—B(1)	1.4171(19)	B(1)-N(1)-C(10)	136.94(12)	C(30)-N(3)-Li(1)	136.83(11)
N(2)—B(1)	1.4762(19)	C(20)-N(2)-P(1)	121.40(9)	P(1)-N(3)-Li(1)	90.13(9)
N(2)—Li(1)	2.171(3)	B(1)-N(1)-P(1)	92.11(9)	Li(1)*-N(3)-Li(1)	70.38(12)
N(3)—Li(1)	2.084(3)	B(1)-N(2)-P(1)	88.41(9)	N(1)-B(1)-N(2)	99.13(12)
N(3)—Li(1)*	2.047(3)	C(10)-N(1)-P(1)	127.41(10)	N(1)-B(1)-C(1)	130.33(13)
C(1)—B(1)	1.573(2)	B(1)-N(2)-C(20)	126.64(11)	N(2)-B(1)-C(1)	129.94(13)
		B(1)-N(2)-Li(1)	113.87(11)	N(3)*-Li(1)-N(3)	109.62(12)
		C(20)-N(2)-Li(1)	112.92(11)	N(3)*-Li(1)-N(2)	136.97(14)
		P(1)-N(2)-Li(1)	83.10(8)	N(3)-Li(1)-N(2)	80.60(10)

Fig. 5. ORTEP drawing of $\{Li[PhB(\mu\text{-}N\text{-}t\text{-}Bu)_2PN\text{-}t\text{-}Bu]\}_2$ (**5**) (30% probability ellipsoids). Only the α-carbon atoms of *t*-Bu groups are shown. Starred atoms are related by the symmetry transformation: $-x + 2, -y, -z$.

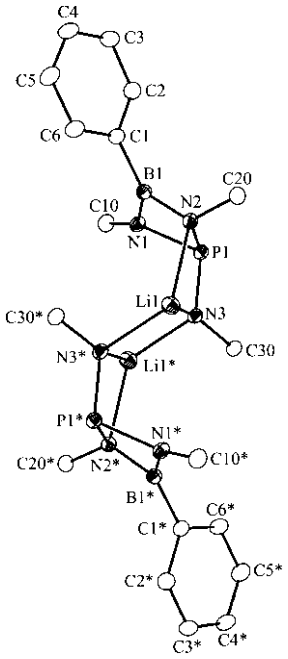

the mean endocyclic P–N bond distance and the geometry at N(3) is planar, suggesting a significant $p\pi$–$p\pi$ interaction between N(3) and P(1).

The reaction of **4c** with one equivalent of *n*-BuLi produced the monolithium derivative $\{Li[Ph(\mu\text{-}N\text{-}t\text{-}Bu)_2PN\text{-}t\text{-}Bu]\}_2$ (**5**), which was shown by X-ray crystallography to be a centrosymmetric dimer (Fig. 5). The monomeric units in **5** are formed by *N*,*N*′-chelation of the $[PhB(\mu\text{-}N\text{-}t\text{-}Bu)_2N\text{-}t\text{-}Bu]^-$ anion to Li^+ through both the exocyclic and one of the endocyclic N atoms. As a result, one of the nitrogen atoms (N1) in the puckered PNBN ring (torsion angle P(1)-N(1)-B(1)-N(2) = 17.58(10)°) is three-coordinate, while the other (N2) is four-coordinate. As indicated in Table 7, this difference is reflected in an asymmetry in the B—N and P—N bond distances (1.4171(19) vs. 1.4762(19) Å and 1.7661(12) vs. 1.8114(12) Å, respectively). The relatively short P(1)—N(3) bond length (1.6403(12) Å) is comparable to the mean value of ~1.65 Å reported for the corresponding P—N bonds in $\{Li[P(N\text{-}t\text{-}Bu)_2]\}_4$ (37). The two monomeric units in **5** are linked by Li–N interactions to give a transoid ladder structure (38) with typical Li–N bond distances. The chelation of the $[PhB(\mu\text{-}N\text{-}t\text{-}Bu)_2PN\text{-}t\text{-}Bu]^-$ anion to Li^+ in **6** does not change the bond angles at the P(III) centre from those observed for **4c**.

The multinuclear (^1H, ^{13}C, ^7Li, ^{11}B, and ^{31}P) NMR data for **5** in THF-d_8 indicated the presence of two components, **5A** and **5B**, in solution in the approximate molar ratio 3:1. The relative intensities of the ^1H and ^{13}C NMR resonances for **5A** and **5B** both indicate C_6H_5, *endo*-*t*-Bu, and *exo*-*t*-Bu

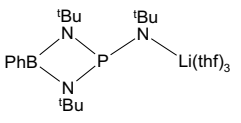

5A

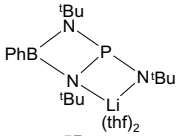

5B

© 2002 NRC Canada

groups in the ratio 1:2:1, consistent with the empirical formula Li[*t*-BuN(μ-N-*t*-Bu)$_2$BPh], in addition to a resonance for a three-coordinate boron atom. Both **5A** and **5B** exhibit singlets in the ^{31}P NMR spectra with chemical shifts of δ 129.9 and 68.1, respectively. It is well established that solvation of Li^+ centres in lithium derivatives of polyimido anions of *p*-block elements may lead to the disruption of polycyclic (cluster) structures or the stabilization of smaller aggregates (39). A pertinent example is the tetramer [Li{P(N-*t*-Bu)$_2$}]$_4$ (40), which forms the solvated dimer [(THF)Li{P(N-*t*-Bu)$_2$}]$_2$ in THF solution (41). Another, more dramatic, demonstration of this effect is the unraveling of the cyclic ladder structure of [Li$_2${C(N-*t*-Bu)$_3$}]$_2$ (42) upon solvation to give the open ladder [(THF)$_3$Li$_2${C(NPh)$_3$}]$_2$ (43). Although the imido (NR) groups are different in these two derivatives, the primary cause of the different structures is clearly the Li^+ centres. For **5**, in the presence of an excess of THF, the most likely solvated complexes are **5A** and **5B**. The former has equivalent endocyclic N-*t*-Bu environments, consistent with the ^{1}H NMR spectrum, while in **5B** this equivalence could arise as a result of exchange of the lithium centre between the two endocyclic nitrogen centres. Such fluxional processes in lithium derivatives of polyimido anions of *p*-block elements have low activation energies (39). The only significant change in the ^{31}P NMR spectrum over the temperature range 183–333 K was an adjustment of the relative amounts of **5A** and **5B** from 1.0:0.26 at 333 K to 1.0:0.65 at 183 K. In the ^{7}Li NMR spectrum, the singlet observed at δ 0.414 at 295 K was resolved into two resonances at δ 0.447 and –0.06 (1.0:0.57) at 233 K. In the ^{31}P NMR spectrum at 233 K the relative intensities of the two components were 1.0:0.61.

The origin of the difference of ~60 ppm in the ^{31}P NMR chemical shifts of **5A** and **5B** is not clear. Unfortunately, the NMR spectra of **5** in the non-coordinating solvent toluene are surprisingly complex and, consequently, do not shed further light on the solution species. The solid-state NMR spectrum of **5** show as a resonance at δ 113.35 with a shoulder at δ 111.28. The observation of a shoulder close to the main resonance is puzzling because **5** has an entrosymmetric structure. This may indicate the presence of a conformational isomer of **5** in the bulk sample that was used in the solid-state NMR experiment. For comparison, the solid-state ^{31}P NMR spectrum of **4c**, which is formed on hydrolysis of **5**, exhibits a singlet at δ 78.9.

In the light of recent work by Stahl et al. (42) on Ni(II) complexes of the mono-anion *cis*-[*t*-BuOP(μ-N-*t*-Bu)$_2$PN-*t*-Bu]$^-$, the ligand behaviour of [PhB(μ-N-*t*-Bu)$_2$PN-*t*-Bu]$^-$ towards transition metals offers the interesting possibility of the involvement of the P(III) centre in the coordination sphere.

Conclusions

Complexes **2**, **4a**, and **4b** are the first examples of boraamidinates-containing element–halide bonds, which provide an opportunity to explore the properties of the boraamidinate ligand via functionalization of the main-group element centre, e.g., in the formation of the monomeric tellurium imide **3** and the chelating P(III) monoanion **5**. An interesting feature of dilithiated boraamidinate complexes, which is not observed for the corresponding amidinates, is the formation of long-lived radicals upon oxidation. Detailed EPR studies will be necessary to characterize these radicals. This propensity for radical formation is likely to lead to interesting chemistry in future investigations of metal–halogen exchange reactions of lithium boraamidinates, especially for those metals which have two (or more) readily accessible oxidation states.

Acknowledgments

We thank the Natural Science and Engineering Research Council of Canada (NSERC) for financial support, Dr. R. McDonald (University of Alberta) for X-ray data collection of **1a** and **1b**, and Dr. M. Parvez for advice in the refinement of the X-ray structures.

References

1. For reviews, see (*a*) F.T. Edelmann. Coord. Chem. Rev. **137**, 403 (1994); (*b*) J. Barker and M. Kilner. Coord. Chem. Rev. **133**, 219 (1994).
2. (*a*) S. Dagorne, I.A. Guzei, M.P. Coles, and R.F. Jordan. J. Am. Chem. Soc. **122**, 274 (2000); (*b*) R. Duchateau, A. Meetsma, and J.H. Teuben. Chem. Commun. 223 (1996).
3. (*a*) E.A.C. Brussee, A. Meetsma, B. Hessen, and J.H. Teuben. Chem. Commun. 497 (2000); (*b*) E.A.C. Brussee, A. Meetsma, B. Hessen, and J.H. Teuben. Organometallics, **17**, 4090 (1998).
4. P. Blais, J.K. Brask, T. Chivers, C. Fedorchuk, and G. Schatte. ACS Symposium Series, in press (2002).
5. H. Heine, D. Fest, D. Stalke, C.D. Hebben, A. Meller, and G.M. Sheldrick. J. Chem. Soc. Chem. Commun. 742 (1990).
6. D. Fest, C.D. Habben, A. Meller, G.M. Sheldrick, D. Stalke, and F. Pauer. Chem. Ber. **123**, 703 (1990).
7. H.-J. Koch, H.W. Roesky, S. Besser, and R. Herbst-Irmer. Chem. Ber. **126**, 571 (1993).
8. C.D. Habben, A. Heine, G.M. Sheldrick, and D. Stalke. Z. Naturforsch. **47b**, 1367 (1992).
9. H. Fuβstetter and H. Nöth. Chem. Ber. **112**, 3672 (1979).
10. D. Gudat, E. Niecke, M. Nieger, and P. Paetzold. Chem. Ber. **121**, 565 (1988).
11. (*a*) C.D. Habben, A. Heine, G.M. Sheldrick, D. Stalke, M. Bühl, and P.v.R. Schleyer. Chem. Ber. **124**, 47 (1991); (*b*) C.D. Habben, R. Herbst-Irmer, and M. Noltemeyer. Z. Naturforsch. **46b**, 625 (1991).
12. W. Luthin, J.-G. Stratmann, G. Elter, A. Meller, A. Heine, and H. Gornitzka. Z. Anorg. Allg. Chem. **621**, 1995 (1995).
13. P. Paetzold, D. Hahnfeld, U. Englert, W. Wojnowski, B. Dreczewski, Z. Pawelec, and L. Walz. Chem. Ber. **125**, 1073 (1992).
14. T. Chivers, X. Gao, and M. Parvez. Angew. Chem. Int. Ed. Engl. **34**, 259 (1995).
15. J.K. Brask, T. Chivers, and G. Schatte. Chem. Commun. 1805 (2000).
16. D.W. Aubrey and M.F. Lappert. J. Chem. Soc. 2927 (1959).
17. N.D.R. Barnett, W. Clegg, L. Horsburgh, D.M. Lindsay, Q.-Y. Liu, F.M. Mackenzie, R.E. Mulvey, and P.G. Williard. Chem. Commun. 2321 (1996).
18. (*a*) SAINT V 5.0. Software for the CCD detector system. Bruker AXS, Inc., Madison, WI. 1998; (*b*) SADABS V. 2.01 (WindowsNT, Service Pack 6). Software for area-detector absorption and other corrections. Bruker AXS, Inc., Madison, WI. 2000; (*c*) HKL DENZO and SCALEPACK V1.96. Z. Otwinowski and W. Minor. *In* Processing of X-ray diffraction

© 2002 NRC Canada

data collected in oscillation mode: Methods in enzymology. Vol. 276. Macromolecular crystallography, Part A. *Edited by* C.W. Carter Jr. and R.M. Sweet. Academic Press, San Diego. 1997. pp. 307–326.
19. (*a*) G.M. Sheldrick. SHELXS-97. Program for the solution of crystal structures. University of Göttingen, Göttingen, Germany. 1997; (*b*) G.M. Sheldrick. SHELXL97–2. Program for the solution of crystal structures. University of Göttingen, Göttingen, Germany. 1997.
20. (*a*) A. Altomare, G. Cascarano, C. Giacovazzo, and A. Guagliardi. SIR-92. A package for crystal structure solution by refinement and direct methods. J. Appl. Crystallogr. **26**, 343 (1993); (*b*) A. Altomare, G. Cascarano, C. Giacovazzo, A. Guagliardi, A.G.G. Moliterni, M.C. Burla, G. Polidori, M. Camalli, and R. Spagna. SIR-97. A package for crystal structure solution and refinement by direct methods. Italy. 1997.
21. B. Eichorn, H. Nöth, and T. Seifert. Eur. J. Inorg. Chem. 2355 (1999).
22. (*a*) D.E. Wigley. Prog. Inorg. Chem. **42**, 239 (1994); (*b*) D.P. Smith, K.D. Allen, M.D. Carducci, and D.E. Wigley. Inorg. Chem. **31**, 1319 (1992).
23. R. Fleischer, S. Freitag, F. Pauer, and D. Stalke. Angew. Chem. Int. Ed. Engl. **35**, 204 (1996).
24. R. Fleischer, S. Freitag, and D. Stalke. J. Chem. Soc. Dalton Trans. 193 (1998).
25. J.K. Brask, T. Chivers, B. McGarvey, G. Schatte, R. Sung, and R.T. Boeré. Inorg. Chem. **37**, 4633 (1998).
26. T. Chivers, G.D. Enright, N. Sandblom, G. Schatte, and M. Parvez. Inorg. Chem. **38**, 5431 (1999).
27. (*a*) N.W. Alcock. Adv. Inorg. Chem. Radiochem. **15**, 1 (1972); (*b*) L. Pauling. The nature of the chemical bond. 3rd ed. Cornell University Press, Ithaca, NY. 1960. Chap. 7. p. 260.
28. H.W. Roesky, J. Münzenburg, R. Bohra, and M. Noltemeyer. J. Organomet. Chem. **418**, 339 (1991).
29. J. Münzenberg, H.W. Roesky, M. Noltemeyer, S. Besser, and R. Herbst-Imer. Z. Naturforsch. **48b**, 199 (1993).
30. H. Folkerts, K. Dehnicke, and J. Magull. Z. Naturforsch. **50b**, 573 (1995).
31. R. Boese, J. Dworak, A. Haas, and M. Pryka. Chem. Ber. **128**, 477 (1995).
32. J. Pietikäinen, R.S. Laitinen, and J. Valkonen. Acta. Chem. Scand. **53**, 963 (1999).
33. T. Chivers and G. Schatte. Inorg. Chem. **41**, 1002 (2002).
34. W. Jacksties, H. Nöth, and W. Storch. Chem. Ber. **118**, 2030 (1985).
35. K.W. Muir. J. Chem. Soc. Dalton Trans. 259 (1975).
36. L. Stahl. Coord. Chem Rev. **210**, 203 (2000), and refs. therein.
37. J.K. Brask, T. Chivers, M.L. Krahn, and M. Parvez. Inorg. Chem. **38**, 290 (1999).
38. A. Downard and T. Chivers. Eur. J. Inorg. Chem. 2193 (2001).
39. J.K. Brask and T. Chivers. Angew. Chem. Int. Ed. Engl. **40**, 3960 (2001).
40. J.K. Brask, T. Chivers, M.L. Krahn, and M. Parvez. Inorg. Chem. **38**, 290 (1999).
41. I. Schranz, L. Stahl, and R.J. Staples. Inorg. Chem. **37**, 1493 (1998).
42. T. Chivers, M. Parvez, and G. Schatte. J. Organomet. Chem. **550**, 213 (1998).
43. P.J. Bailey, A.J. Blake, M. Kryszczuk, S. Parsons, and D. Reed. J. Chem. Soc. Chem. Commun. 1647 (1995).
44. G.R. Lief, C.J. Carrow, L. Stahl, and R.J. Staples. Chem. Commun. 1562 (2001).

© 2002 NRC Canada

Peptide model XXVIII: An exploratory ab initio and density functional study on the side-chain–backbone interaction in *N*-acetyl-L-cysteine-*N*-methylamide and *N*-formyl-L-cysteinamide in their γ_L-backbone conformations

M.A. Zamora, H.A. Baldoni, A.M. Rodriguez, R.D. Enriz, C.P. Sosa, A. Perczel, A. Kucsman, O. Farkas, E. Deretey, J.C. Vank, and I.G. Csizmadia

Abstract: A conformational and electronic study on the energetically preferred conformations (γ_L) of N- and C-protected L-cysteine (P-CONH-CH(CH_2SH)-CONH-Q, where P and Q may be H or Me) was carried out. After restraining the backbone (BB) conformation to its global minimum (γ_L or C_7^{eq}), all nine possible side-chain (SC) conformations were subjected to geometry optimization at the HF/3–21G and the B3LYP/6–31G(d,p) levels of theory. Seven of the nine side-chain conformers were located on the potential-energy surface. All conformers were subjected to an AIM (atoms in molecules) analysis. This study indicates that three of the seven optimized conformers exhibited either or both SC → BB- or BB → SC-type intramolecular hydrogen bonding. Five conformers, however, had distances between a proton and a heteroatom that suggested hydrogen bonding.

Key words: L-cysteine diamides, side-chain potential-energy surface, ab initio and DFT geometry optimization, AIM analysis, intramolecular hydrogen bonding.

Résumé : On a réalisé une étude conformationnelle et électronique des conformations énergétiquement privilégiée (γ_L) de la L-cystéine N- et C-protégée (P-CONH-CH(CH_2SH)-CONH-Q; P et Q peuvent être égaux à H ou à Me). Ainsi, en retreignant la conformation du squelette (BB) à son minimum global (γ_L ou C_7^{eq}), on a soumis les neuf conformations possibles pour la chaîne latérale (SC) à une optimisation de la géométrie aux niveaux HF/3–21G et B3LYP/6–31G(d,p) de la théorie. Sept des neuf conformères de la chaîne latérale se situent sur la surface d'énergie potentielle. Tous les conformères ont été soumis à une analyse par la méthode des atomes dans les molécules (AIM). Cette étude indique que trois des sept conformères optimisés présentent l'une ou l'autre ou les deux types de liaisons intramoléculaires SC → BB ou BB → SC. Toutefois, dans cinq des conformères les distances entre un proton et un hétéroatome suggèrent l'existence d'une liaison hydrogène.

Mots clés : diamides de la L-cystéine, surface d'énergie potentielle de la chaîne latérale, optimisation ab initio et DFT de la géométrie, méthode des atomes dans les molécules (AIM), liaison hydrogène intramoléculaire.

[Traduit par la Rédaction]

Introduction

Cysteine (Cys) is the sulfur analogue of serine (Ser). Both amino acid residues may conveniently be studied computationally in their N- and C-protected forms; Fig. 1 shows *N*-acetyl-L-Cys-*N*-methylamide (**I**) and *N*-formyl-L-Cys-amide (**II**). *N*-Formyl-L-Ser-amide (**III**) has already been studied extensively (1–5) as a continuation of a general investigation including Gly (6, 7), Ala (6–8), Val (9), and Phe (10–12).

In many ways the cysteine residue is similar to serine; one therefore expects the -CH_2-SH moiety of cysteine to be in-

Received 20 March 2001. Published on the NRC Research Press Web site at http://canjchem.nrc.ca on 28 June 2002.

M.A. Zamora, H.A. Baldoni, A.M. Rodriguez, and R.D. Enriz. Department of Chemistry, National University of San Luis, Chacabuco 971, 5700 San Luis, Argentina.
C.P. Sosa. CRAY Inc. 1340 Mendota Heights Rd., Mendota Heights, MN 55120, U.S.A.
A. Perczel,[1] A. Kucsman, and O. Farkas.[2] Institute of Organic Chemistry, Eotvos University, 112 Budapest, PO Box 32, H-1117, Hungary.
E. Deretey, J.C. Vank, and I.G. Csizmadia.[3] Department of Chemistry, University of Toronto, Toronto, ON M5S 3H6, Canada.

[1]Alternative address: Deparment of Biochemistry, University of Oxford, South Parks Road, Oxford OX1 3QU, U.K.
[2]Alternative address: Department of Chemistry, Wayne State University, Detroit, MI 48202, U.S.A.
[3]Corresponding author (e-mail: icsizmad@alchemy.utoronto.ca).

 DOI: 10.1139/V02-076 © 2002 NRC Canada

Fig. 1. γ_L conformations of MeCO-Cys-NHMe (**I**), HCO-Cys-NH_2 (**II**), and HCO-Ser-NH_2 (**III**). The numbering system of the atoms and the torsional angles ω_0, ω_1, ϕ, ψ, χ_1, and χ_2 are shown in this figure.

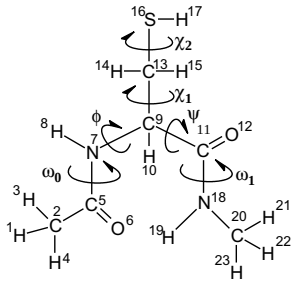

N-acetyl-L-Cys-*N*-methylamide
I

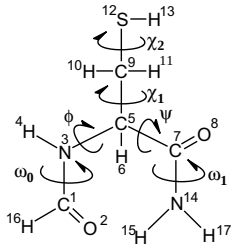

N-formyl-L-Cys-amide
II

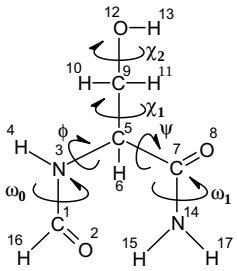

N-formyl-L-Ser-amide
III

volved in intramolecular hydrogen bonding similar to that demonstrated in Fig. 2 for the -CH_2-OH group of serine.

Cysteine, a residue with a polar side chain, is often located on the surface of proteins, and thus is directly involved in various biochemical interactions. Cysteine can mediate structural changes, improve hydration of accessible area, or participate in intermolecular interactions. Thus, cysteine is frequently involved in a wide range of enzymatic reactions including those of cysteine proteases (13–15). In Scheme 1, a simplified mechanism of cysteine protease (HS-E-Im) is shown, where HS symbolizes the mercaptan side chain of a cysteine residue and Im denotes the imidazole moiety in the side chain of a histidine residue. The enzyme is not active at low pH due to protonation at Im, and it is also inactive at high pH due to deprotonation of the SH group. It is only active at neutral pH when internal proton transfer is possible from the SH group to Im.

A schematic mechanism for the hydrolysis of the peptide bond with the catalytic action of cysteine protease is shown in Scheme 2.

In addition to regular cysteine proteases, there are numerous other enzymes that contain free-sulfhydril groups. For example, there is a cysteine-containing enzyme called *transglutaminase*, which does not hydrolyze peptide bonds, but instead transfers an acyl group from one nitrogen to another. This field of study has recently been extensively reviewed (16). Vigorous theoretical investigations of this cysteine-containing pro-enzyme is currently being pursued by other research groups (17).

Fig. 2. A schematic representation of possible intramolecular hydrogen bonds for serine.

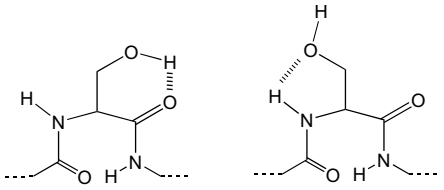

A **B**

Scheme 1.

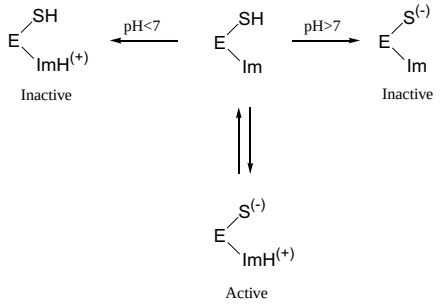

The full conformational space of compound **I** was recently explored by ab initio RHF/3–21G computations (18). On the Ramachandran hypersurface of four independent variables $E = f(\phi, \psi, \chi_1, \chi_2)$ (Fig. 1), 47 conformers were located instead of the expected $3^4 = 81$ stable structures. The relative stabilities of the various conformers were analyzed in terms of side-chain–backbone interactions covering both hydrogen bonding and charge-transfer types. These results indicated that the γ_L-backbone conformation is the preferred form for this compound. In the present report, we have mainly focused our attention on the conformational intricacies of compound **I**, while restricting the backbone conformation to its global minimum (γ_L). A comparative study using different levels of theory of compounds **I–III** was also carried out.

Methods

Conformational analysis

IUPAC-IUB (19) recommended the use of $0° \rightarrow +180°$ in the clockwise direction for rotation and $0° \rightarrow -180°$ for counter-clockwise rotation (Scheme 3). For side-chain torsions, this implied the following range: $-180° \leq \chi_1 \leq 180°$ and $-180° \leq \chi_2 \leq 180°$. On the Ramachandran map, the $-180° \leq \phi \leq 180°$ and $-180° \leq \psi \leq 180°$ cut is indicated by the square drawn in broken lines (Fig. 3).

But for the graphical presentation of the side-chain conformational potential-energy surface (PES), we used the traditional cut ($0° \leq \chi_1 \leq 360°$ and $0° \leq \chi_2 \leq 360°$), similar to that previously suggested by Ramachandran and Sasisekharan (20).

Molecular computations

Initially, the nine side-chain conformations of cysteine in its γ_L-backbone conformation were determined using the topologically probable set of conformers as predicted by multidimensional conformational analysis (MDCA) (21–23).

© 2002 NRC Canada

Scheme 2.

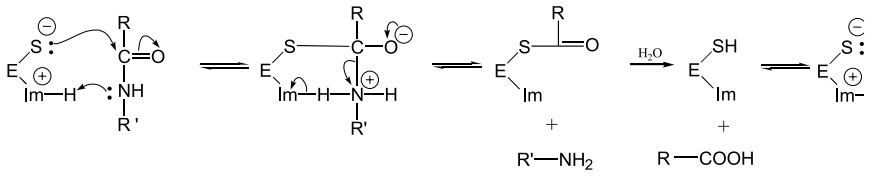

Table 1. Total energy values (Hartree) of the component molecules for isodesmic reactions.

Molecular system	HF/3–21G			B3LYP/6–31G(d,p)		
P-CONH-CH_2-CONH-**Q**	P = Q = H		P = Q = Me	P = Q = H		P = Q = Me
γ_L	–373.6487900		–451.2942433	–377.9165567		–456.5553698
β_L	–373.6477487		–451.2931883	–377.9158533		–456.5536252
CH_3-**R**	R = CH_2-SH	R = CH_2-OH	R = H	R = CH_2-SH	R = CH_2-OH	R = H
	–474.3472547	–153.2226808	–39.976877	–478.0228756	–155.0462074	–40.5238417

Scheme 3.

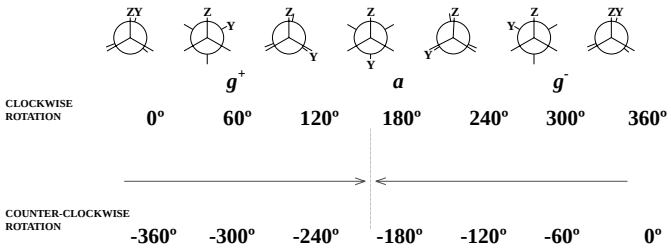

To investigate the side-chain–backbone conformational interaction effects, calculations were performed on compounds **I** and **II** using the Gaussian 94 (24) program at the RHF/3–21G (25) level of theory. This lower level is suitable for the purpose of comparing the present results with those obtained for serine (1, 2), even though the current trend is to rely on larger basis sets at a higher level of theory (8, 26). For this reason, geometry optimizations were also carried out for compounds **I** and **II** at the B3LYP/6–31G(d,p) level of theory.

Stabilization energies

The stabilization energies were calculated with respect to γ_L- as well as to $\beta_L(C_5)$-backbone conformation of N- and C-protected glycine (9, 27) using the following isodesmic (same number of the same type of bonds) reaction, where P and Q may be H (**II**) or CH_3 (**I**) and R = CH_2-SH:

$$\underset{\text{reference conformation } \gamma_L \text{ or } \beta_L}{\text{P-CONH-CH}_2\text{-CONH-Q} + \text{CH}_3\text{-R}} \rightarrow \underset{\text{conformation X}}{\text{P-CONH-CHR-CONH-Q}} + \text{CH}_3\text{-H}$$

The stabilization energy may be calculated as follows:

$$\Delta E_{\text{stabil}} = \{E[\text{P-CONH-CHR-CONH-Q}]_X + E[\text{CH}_3\text{-H}]\} - \{E[\text{P-CONH-CH}_2\text{-CONH-Q}]_{\gamma_L \text{ or } \beta_L} + \text{CH}_3\text{-R}]\}$$

The energy values of the components are summarized in Table 1.

The results of the structure optimizations, namely, geometrical parameters, total energies, relative energies, and stabilization energies, are given in Tables 2–4. The total energies are given in Hartrees, and the relative energies and stabilization energies in kcal mol^{-1} (using the conversion factor: 1 Hartree = 627.5095 kcal mol^{-1}). The numbering system used for *N*-acetyl-L-cysteine-*N*-methyl amide (P = Q = Me) and *N*-formyl-L-cysteinamide (P = Q = H) is shown in Fig. 1.

Fig. 3. Topological representation of the Ramachandran map for an N- and C-protected amino acid P-CONH-CHR-CONH-Q (P and Q may be H or CH_3) showing two full cycles of rotation: $-360° \le \phi \le +360°$; $-360° \le \psi \le +360°$. The central box, denoted by broken line, represents the cut suggested by the IUPAC convention. The four quadrants denoted by solid lines are the conventional cuts. Most peptide residues exhibit nine unique conformations labeled as α_D (α_{LEFT}), ε_D, γ_D (C_7^{ax}), δ_L (β_2), β_L (C_5), δ_D (α'), γ_L (C_7^{eq}), ε_L, and α_L (α_{RIGHT}).

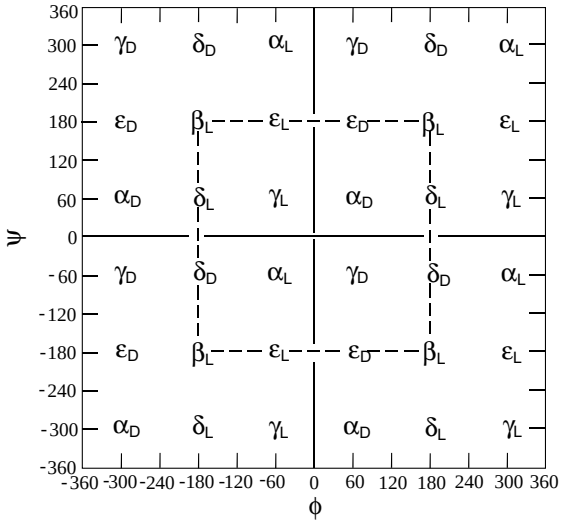

Topological analysis of electron density

The topology of the electron density was analyzed using AIM (atoms in molecules) (28). In this analysis, the gradient $[\nabla\rho(r)]$ and the Laplacian $[\nabla^2\rho(r)]$ play important roles. A critical point of the electron density along the line of two interacting atoms in a molecule is called the bond critical point (BCP), where $\nabla\rho(r) = 0$.

© 2002 NRC Canada

Table 2. Torsional angles and total energy values for compound **I** (CH_3CO-Cys-$NHCH_3$) optimized at HF/3–21G and B3LYP/6–31G(d,p) levels of theory.

Final geometry[a]	ϕ (5–7–9–11)	ψ (7–9–11–18)	χ_1 (7–9–13–16)	χ_2 (9–13–16–17)	ω_0 (2–5–7–9)	ω_1 (9–11–18–20)	Energy (Hartree)	ΔE_{rel} (kcal mol^{-1})	ΔE_{stabil} (γ_L) (kcal mol^{-1})	ΔE_{stabil} (β_L) (kcal mol^{-1})
HF/3–21G										
γ_L (g^+,g^+)	–85.211	64.199	52.657	67.777	–175.164	–179.297	–885.6785541	0.00	–8.74	–9.41
γ_L (g^+,a)	–86.016	63.387	54.989	–123.186	–177.042	–179.075	–885.6716533	4.33	–4.41	–5.07
γ_L (g^+,g^-)	Not found						—	—	—	
γ_L (a,g^+)	–87.218	74.967	–167.496	82.402	–177.482	–177.893	–885.6701841	5.25	–3.49	–4.15
γ_L (a,a)	Not found						—	—	—	
γ_L (a,g^-)	–86.474	69.587	–170.528	–74.251	–175.205	–178.714	–885.6744995	2.54	–6.20	–6.86
γ_L (g^-,g^+)	–87.265	68.555	–68.600	61.474	–176.407	–178.899	–885.6710358	4.72	–4.02	–4.69
γ_L (g^-,a)	–86.515	68.338	–55.821	–169.081	–172.746	–178.742	–885.6726444	3.71	–5.03	–5.70
γ_L (g^-,g^-)	–86.475	69.404	–54.352	–61.657	–172.469	–178.459	–885.6729162	3.54	–5.21	–5.87
B3LYP/6–31G(d,p)										
γ_L (g^+,g^+)	–82.61	66.19	52.84	64.39	–176.59	–178.01	–894.0647503	0.00	–6.49	–7.59
γ_L (g^+,a)	–82.61	66.33	55.53	–121.91	–178.88	–177.92	–894.0595386	3.27	–3.22	–4.32
γ_L (g^+,g^-)	Not found						—	—	—	
γ_L (a,g^+)	–83.87	79.56	–166.63	77.74	179.43	–174.77	–894.0575767	4.50	–1.99	–3.09
γ_L (a,a)	Not found						—	—	—	
γ_L (a,g^-)	–83.81	72.89	–170.93	–70.08	–177.51	–176.64	–894.0608365	2.46	–4.04	–5.13
γ_L (g^-,g^+)	–83.16	71.57	–68.84	54.12	–179.80	–177.38	–894.0583015	4.05	–2.45	–3.54
γ_L (g^-,a)	–84.19	70.68	–55.26	–176.57	–172.56	–176.93	–894.0587452	3.77	–2.72	–3.82
γ_L (g^-,g^-)	–84.47	73.02	–49.36	–58.06	–171.06	–176.27	–894.0597855	3.12	–3.38	–4.47

Note: The calculated relative energies (ΔE_{rel}) and stabilization energies (ΔE_{stabil}) are also shown.
[a]g^+, *gauche* (+60°); *a*, *anti* (180°); g^-, *gauche* (–300°).

© 2002 NRC Canada

Table 3. Torsional angles and total energy values for compound **II** (HCO-Cys-NH_2) optimized at HF/3–21G and B3LYP/6–31G(d,p) levels of theory.

Final geometry	ϕ (1–3–5–7)	ψ (3–5–7–14)	χ_1 (3–5–9–12)	χ_2 (5–9–12–13)	ω_0 (16–1–3–5)	ω_1 (5–7–14–17)	Energy (Hartree)	ΔE_{rel} (kcal mol^{-1})	ΔE_{stabil} (γ_L) (kcal mol^{-1})	ΔE_{stabil} (β_L) (kcal mol^{-1})
HF/3–21G										
γ_L (g^+,g^+)	–83.85	63.13	52.60	68.36	–174.99	–179.46	–808.0328587	0.00	–8.59	–9.24
γ_L (g^+,a)	–84.77	62.40	54.94	–123.34	–176.47	–179.23	–808.0260686	4.26	–4.33	–4.98
γ_L (g^+,g^-)	Not found						—	—	—	
γ_L (a,g^+)	–86.22	73.18	–167.32	83.69	–176.65	–178.01	–808.0244391	5.28	–3.31	–3.96
γ_L (a,a)	Not found						—	—	—	
γ_L (a,g^-)	–85.20	68.21	–169.98	–74.69	–174.83	–178.84	–808.0287635	2.56	–6.02	–6.67
γ_L (g^-,g^+)	–86.04	66.72	–69.12	63.08	–175.93	–179.17	–808.0253109	4.73	–3.85	–4.51
γ_L (g^-,a)	–84.73	66.71	–56.44	–169.94	–173.00	–178.96	–808.0268808	3.75	–4.84	–5.49
γ_L (g^-,g^-)	–84.47	67.84	–54.22	–61.86	–172.74	–178.61	–808.0271721	3.56	–5.02	–5.68
B3LYP/6–31G(d,p)										
γ_L (g^+,g^+)	–80.84	64.98	52.37	65.33	–177.20	–176.96	–815.4257909	0.00	–6.40	–6.84
γ_L (g^+,a)	–81.03	65.19	55.29	–121.44	–179.02	–176.65	–815.4206690	3.21	–3.17	–3.63
γ_L (g^+,g^-)	Not found						—	—	—	
γ_L (a,g^+)	–82.41	78.82	–166.65	78.58	–179.71	–171.45	–815.4186368	4.48	–1.91	–2.35
γ_L (a,a)	Not found						—	—	—	
γ_L (a,g^-)	–82.34	72.25	–170.54	–70.34	–177.42	–174.17	–815.4218597	2.46	–3.93	–4.38
γ_L (g^-,g^+)	–82.05	70.50	–69.32	55.31	–179.63	–175.20	–815.4192734	4.08	–2.31	–2.75
γ_L (g^-,a)	–82.03	70.48	–55.54	–178.87	–173.53	–174.19	–815.4198346	3.73	–2.66	–3.10
γ_L (g^-,g^-)	–82.11	73.25	–48.66	–58.68	–171.11	–172.97	–815.4210135	2.99	–3.40	–3.84

Note: The calculated relative energies (ΔE_{rel}) and stabilization energies (ΔE_{stabil}) are also shown.

© 2002 NRC Canada

Table 4. Torsional angles and total energy values for compound **III** (HCO-Ser-NH_2) optimized at HF/3–21G and B3LYP/6–31G(d,p) levels of theory.

Final geometry	ϕ (1–3–5–7)	ψ (3–5–7–14)	χ_1 (3–5–9–12)	χ_2 (5–9–12–13)	ω_0 (16–1–3–5)	ω_1 (5–7–14–17)	Energy (Hartree)	ΔE_{rel} (kcal mol^{-1})	ΔE_{stabil} (γ_L) (kcal mol^{-1})	ΔE_{stabil} (β_L) (kcal mol^{-1})
HF/3–21G										
γ_L (g^+,g^+)	–83.658	71.421	51.832	69.859	–176.197	–177.549	–486.9195667	0.00	–15.67	–16.32
γ_L (g^+,a)	Not found								—	—
γ_L (g^+,g^-)	Not found								—	—
γ_L (a,g^+)	–86.59	77.84	–170.03	74.00	–177.86	–176.82	–486.8996344	12.50	–3.16	–3.82
γ_L (a,a)	Not found								—	—
γ_L (a,g^-)	–83.397	62.518	179.732	–68.446	–173.778	179.794	–486.9119765	4.76	–10.91	–11.56
γ_L (g^-,g^+)	–85.262	97.114	–65.360	54.082	–177.938	–179.224	–486.9029219	10.44	–5.23	–5.88
γ_L (g^-,a)	–77.091	61.486	–43.944	–178.581	–168.802	179.636	–486.9075817	7.52	–8.15	–8.80
γ_L (g^-,g^-)	–77.250	62.991	–41.004	–75.808	–171.150	–179.957	–486.9076066	7.50	–8.17	–8.82
B3LYP/6–31G(d,p)										
γ_L (g^+,g^+)	–79.84	74.75	54.94	64.77	–178.17	–172.52	–492.4564571	0.00	–11.00	–11.44
γ_L (g^+,a)	Not found							—	—	
γ_L (g^+,g^-)	Not found							—	—	
γ_L (a,g^+)	–82.16	83.06	–167.97	69.62	179.37	–169.79	–492.4408888	9.76	–1.23	–1.68
γ_L (a,a)	Not found							—	—	
γ_L (a,g^-)	–80.61	60.41	–179.44	–64.18	–174.60	179.67	–492.4505714	3.69	–7.31	–7.75
γ_L (g^-,g^+)	–81.48	73.30	–65.61	53.10	177.63	–174.40	–492.4433657	8.21	–2.79	–3.23
γ_L (g^-,a)	–79.43	65.75	–47.87	174.60	–167.23	–175.97	–492.4457011	6.75	–4.25	–4.70
γ_L (g^-,g^-)	–79.22	67.70	–43.63	–69.67	–169.08	–174.94	–492.4463450	6.34	–4.66	–5.10

Note: The calculated relative energies (ΔE_{rel}) and stabilization energies (ΔE_{stabil}) are also shown.

© 2002 NRC Canada

Fig. 4. (*a*) Backbone conformers of all 10122 Cys residues taken from 974 non-homologous proteins (31). Using their backbone-dihedral parameters, all of the above Cys residues were plotted on a [ϕ, ψ] map. (*b*) Locations of calculated ab initio RHF/3–21G MeCO-Cys-NHMe backbone conformers (18) on a [ϕ, ψ] map.

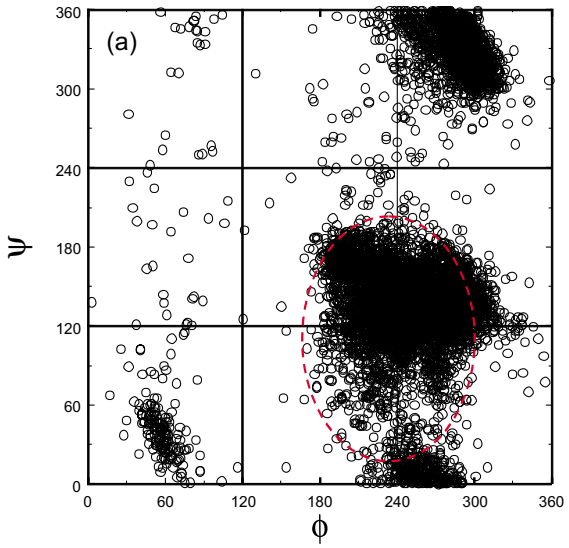

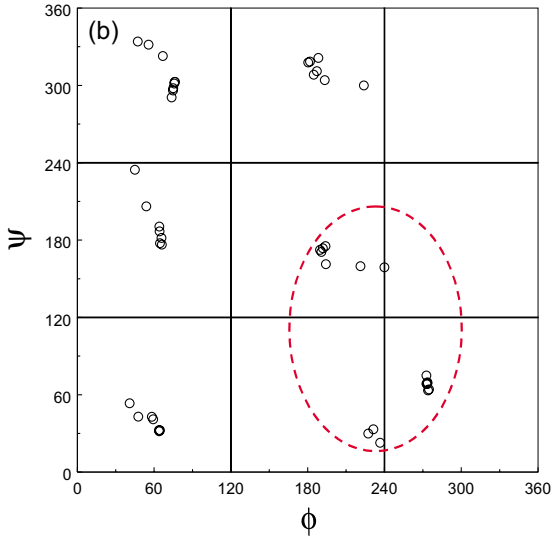

The bond path is made up of a pair of gradient paths, originating at a BCP and terminating at a neighbouring nuclei. The necessary condition for two atoms to be bonded to each other is that their nuclei must be linked by a bond path. The bond path is regarded as "a universal indicator of bonded interaction" (29). The method is widely used for proving the existence of hydrogen bonds (30).

Results and discussion

The comparison of structural parameters from experimental databases (X-ray and NMR) with the ab initio (RHF/3–21G) results is an excellent validation of the computed results. Thus, the comparison of relative energies and the relative probabilities of conformers using a non-homologous database is a possibility for this cross-validation. Let us truncate the backbone of a protein into building units, e.g., amino acid diamides. We will assume that the probability of conformers in proteins depends only on its relative energy. This is a model where several stabilizing factors are neglected, such as inter-residue interactions, long-range effects, and hydration. By acknowledging the limitations of this approach, it is possible to correlate the relative energy of a conformer and the relative probability of the same backbone structure in an ensemble of proteins with known X-ray and NMR structures.

Using a recent (February 2002) X-ray- and NMR-determined protein data set of non-homologous proteins

Fig. 5. The possible nine molecular conformations of MeCO-Cys-NHMe. The two conformations that are crossed over are not minima, the remaining seven were located during HF/3–21G optimization.

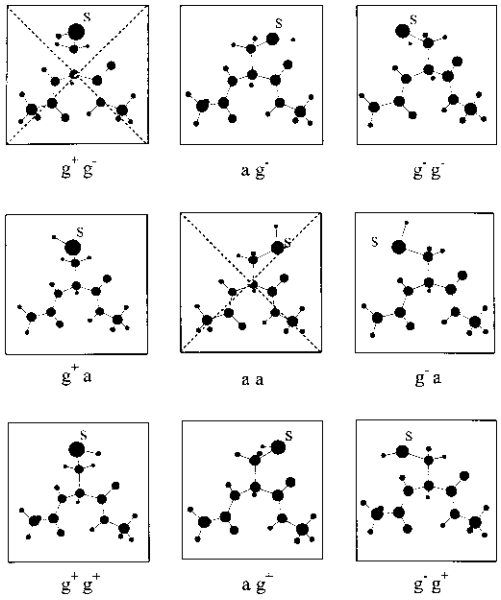

Fig. 6. Relative energies (kcal mol^{-1}) obtained for the different conformations of compounds **I–III**.

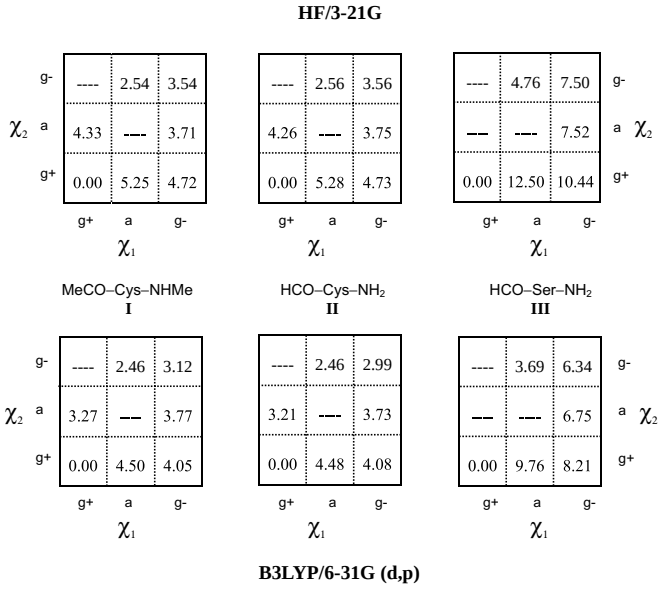

© 2002 NRC Canada

Fig. 7. Correlation of relative energies computed at DFT and HF/3–21G levels of theory for MeCO-Cys-NHMe (top), HCO-Cys-NH_2 (centre), and HCO-Ser-NH_2 (bottom).

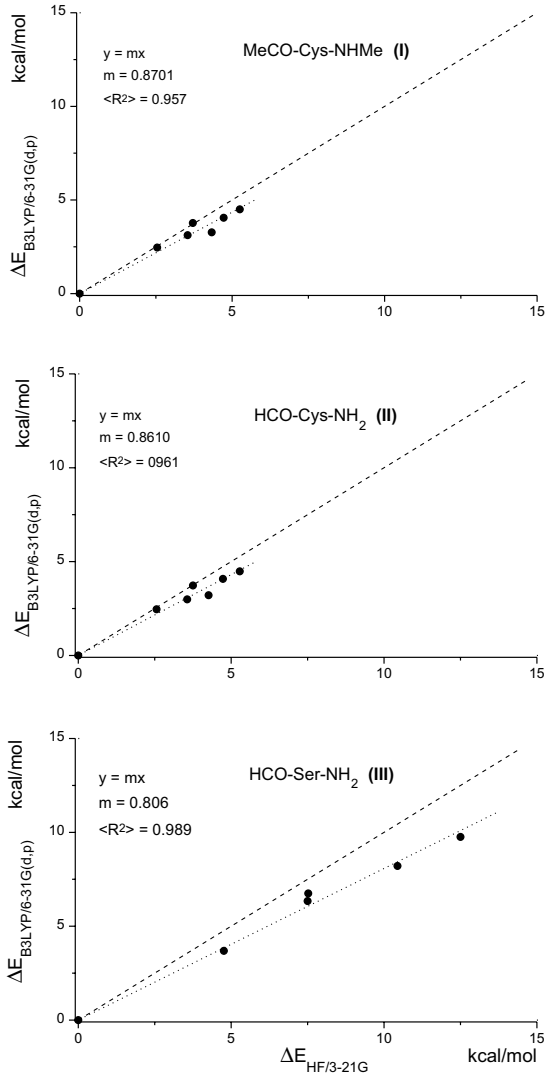

Fig. 8. Correlation of torsional angles computed at DFT and HF/3–21G levels of theory for MeCO-Cys-NHMe (top), HCO-Cys-NH_2 (centre), and HCO-Ser-NH_2 (bottom).

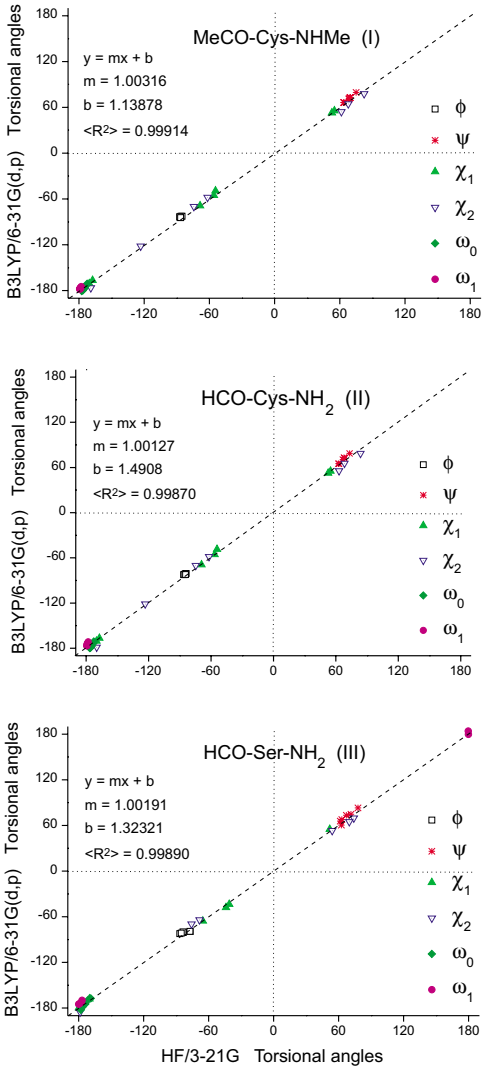

(31), a population-distribution map was generated (Fig. 4*a*). The backbone conformers of 10122 Cys residues, found in a total of 974 proteins, were plotted, showing ϕ vs. ψ values (Fig. 4*a*). The overall appearance of the Ramachandran surface is similar to other previously reported Ramachandran maps (Phe (12) and Ser (32)). Thus Cys shows an "average conformational character."

To perform a comparison between calculated and observed backbone conformers, an additional plot was made with the RHF/3–21G results (Fig. 4*b*). Comparing these data a promising overall similarity emerged. In the highly populated extended β-strand (β_L) and inverse γ-turn (γ_L) region, the location of the RHF/3–21G model structures and the largest probability of experimental- backbone conformers taken from the protein databases are similar (zone denoted with dotted lines in Fig. 4).

It should be noted that the seven γ_L conformers and the seven β_L conformers, together with the three δ_L conformers, are a subgroup formed by the most stable conformers of compound **I**. This low-energy region of the Ramachandran map (often quoted as the β region) is also the most dense area if X-ray- and NMR-determined main-chain probabilities are investigated. Such a correlation permit us to assume that if the diamide model is relevant to the description of main-chain folding of proteins, then the most stable conformers should have the lowest energy.

On the basis of the above results, in the present study we focused our attention on the conformational intricacies of the highly preferred backbone conformation of compounds **I** and **II**, this being the γ_L form.

Conformational study

The nine side-chain conformations, topologically predicted on the basis of MDCA, are depicted for compound **I** in Fig. 5. Two of the structures (g^+g^- and *aa*) are crossed out, since they were not found. On the basis of the $E = f(\chi_1, \chi_2)$ potential-energy surface (PES) generated for HCO-Ser-NH_2 (1), one may anticipate that these minima were eliminated due to a high-energy region or "mountain ridge" formed along the disrotatory diagonal axis. The other seven minima,

© 2002 NRC Canada

Fig. 9. Structures located on the side-chain PES of the γ_L-backbone conformations of N- and C-protected serine and cysteine. The stabilization energies (ΔE_{stabil}, kcal mol^{-1}) exerted by the side chain with respect to the glycine residue in its γ_L conformation are shown in brackets.

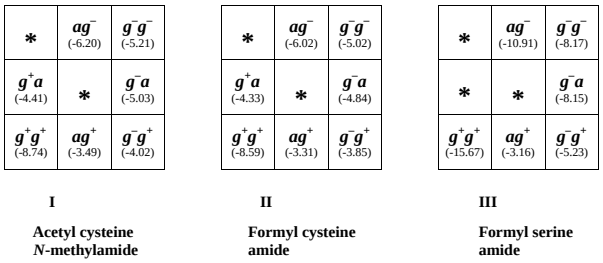

Fig. 10. Spectrum of conformational dependence of the side-chain stabilization energy on the γ_L-backbone conformation of protected Ser and Cys.

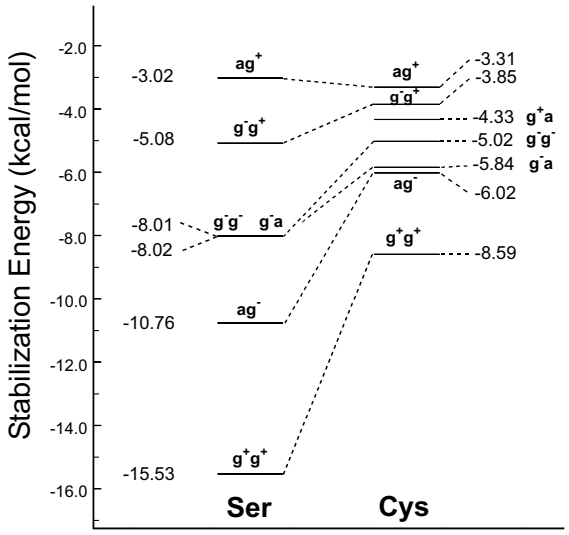

however, were successfully geometry optimized at the HF/3–21G level of theory (Table 2).

The structures of **I** and **II** were geometry optimized at the HF/3–21G level of theory and further optimized at the B3LYP/6–31G(d,p) level of theory (Tables 2 and 3). Their relative energy values are shown in a topological fashion in Fig. 6. For full comparison, HCO-Ser-CONH$_2$ (**III**) conformations were also evaluated at the B3LYP/6–31G(d,p) level of theory (Table 4).

The reliability of the HF/3–21G level of computations can be investigated here since we have results from HF/3–21G and B3LYP/6–31G(d,p) levels. The relative energies (ΔE_{rel}) of compounds **I**–**III**, computed at the two levels of theory, are compared in Fig. 7. Since the global minimum on the relative energy scale is, by definition, always zero, in order for the fitted line to pass over the origin, a $y = mx$ equation was fitted to the data points. While the slopes of the fitted lines are never unity, it is clear that the HF/3–21G results reproduce the trend quite well.

In addition to the relative stabilities, the accuracy of the key torsional angles (in the present case, ϕ, ψ, χ_1, χ_2, ω_0, and ω_1) is of great importance. The correlation of the above torsional angles computed at two levels of theory for compounds **I**–**III** are shown in Fig. 8. The least-square fit was of the type $y = mx + b$. For the cysteine and serine residues, m is not unity nor is b zero. The fitted lines, however, suggest a surprisingly good correlation.

Fig. 11. Relative side-chain stabilization energy values of various amino acids in the γ_L-backbone conformation.

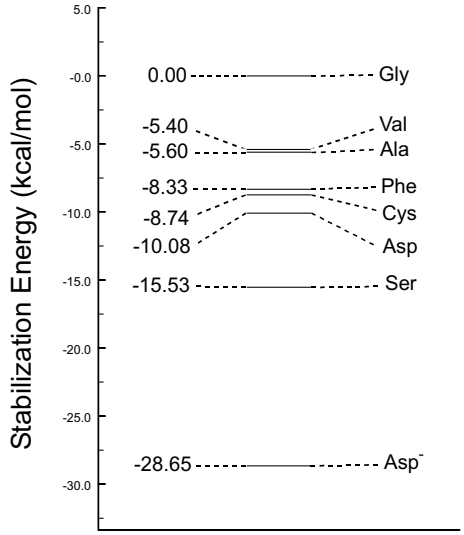

Stabilization energies

Stabilization energies emerging from side-chain interaction with the backbone are traditionally calculated (7, 27) with respect to the global minimum, i.e, the γ_L conformation. It has been noted recently (33), however, that during the *cis*–*trans* isomerization process, the γ_L conformation may disappear for at least some of the amino acids. In other words, the γ_L conformer does not exist as a minimum-energy conformation on some of the *cis*-Ramachandran maps. For this reason, an alternative backbone conformation β_L was selected for calculating the stabilization energy (ΔE_{stabil}). The method of calculation, as outlined in the *Computational methods* section, is the same, but instead of the γ_L conformation of glycine, the β_L conformation is chosen as the reference conformation. Such a new standard may be important in the future, when an ab initio peptide database may include both *cis* and *trans* peptides. Nevertheless, the $\Delta E_{stabil}(\gamma_L)$ values are more practical if we wish to make comparisons with previously reported values.

Figure 9 compares $\Delta E_{stabil}(\gamma_L)$ values for compounds **I**–**III**. It is reassuring to see that the effect of the side-chain stabilization is not affected substantially if we change the protecting group from formyl to acetyl at the nitrogen end and from amide to methylamide at the carboxyl end.

The *N*-acetyl and *N*-methyl amide protecting groups of cysteine **I** are stabilized by the CH$_2$-SH side chain by ~0.16 kcal mol^{-1} more when compared with the same side chain stabilizing the *N*-formyl-cysteinamide (**II**) backbone. There are, however, marked differences when the oxygen is changed to sulfur in the side chain. Undoubtedly, such a change between serine and cysteine, as seen in Fig. 9, is also present in the relative energy values (ΔE_{rel}) presented in Fig. 6. The stabilization energy values are not only numerically different for Ser and Cys but they are also decreased

© 2002 NRC Canada

Fig. 12. Various types of intramolecular interactions in *N*-acetyl-L-cysteine-*N*-methylamide.

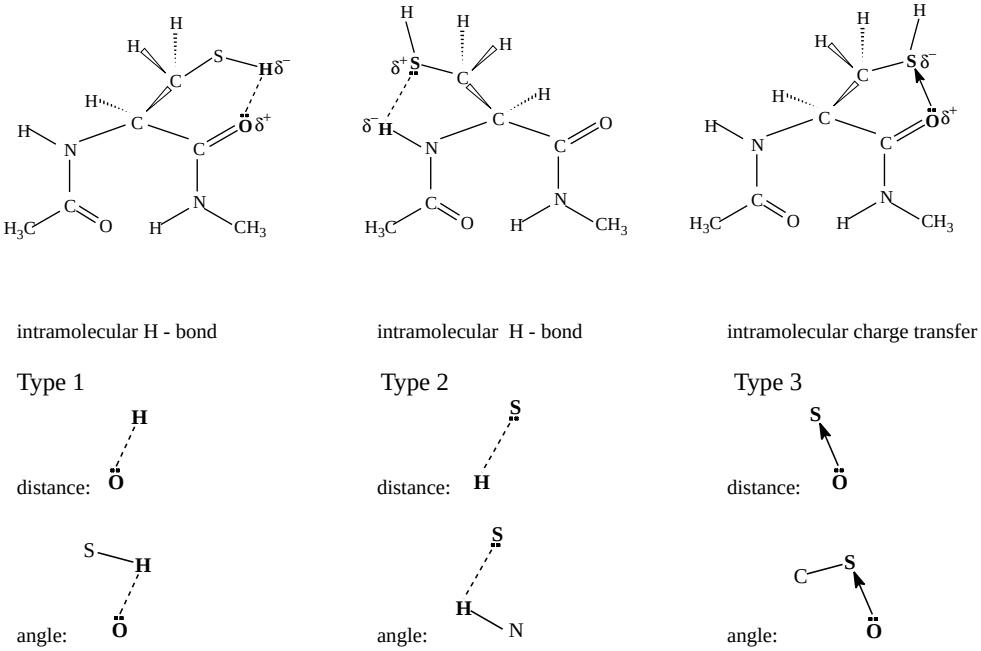

Table 5. Summary of intramolecular interactions in *N*-acetyl-L-cysteine-*N*-methylamide.

Final geometry	Energy (Hartree)	ΔE (kcal mol^{-1})	Type of interaction[a]	Distance (Å)[a,b]	Angle (°)[a]
γ_L (g^+,g^+)	–885.6785541	0.00	2	2.62	112.10
			1	2.30	119.68
γ_L (g^+,a)	–885.6716533	4.33	2	2.63725	111.035
			3	3.08	60.93
γ_L (a,g^-)	–885.6744995	2.54	1	2.43	115.77
γ_L (g^-,a)	–885.6726444	3.71	2	2.94	89.38
γ_L (g^-,g^-)	–885.6729162	3.54	2	2.96	92

[a]Definition is given in Fig. 11.
[b]Maximum threshold values are the sum of van der Waals radii (34, 35). Type 1 (O··H): 1.40 + 1.20 = 2.60 Å; Type 2 (S··H): 1.85 + 1.20 = 3.05 Å; Type 3 (S··O): 1.85 + 1.40 = 3.25 Å.

for Cys and increased for Ser, as seen in Fig. 10. When the global minima are compared, the side chain of Cys is stabilizing the backbone more than that of Phe but less than those of Asp and Ser. Such a "spectrum" of side-chain stabilization is presented in Fig. 11.

The size difference between O and S could play a major role in producing such remarkable energy differences. Additionally, since both make the same kinds of hydrogen bonds it is reasonable to assume that the Ser side chain is more favourably stabilizing than the Cys side chain because hydrogen bonds to and from oxygen atoms are stronger than sulfur atoms. This result is not surprising, since methanol is a liquid and methanethiol is a gas. This is in agreement with the ordering of the g^+g^+, g^+a, and ag^- conformations discussed in the next section.

Intramolecular interactions

The three types of intramolecular interactions, which may occur in the various conformers of cysteine, are shown in Fig. 12. The characteristic distances and angles, as well as the classification of interactions, are summarized in Table 5. Only the g^+a conformer has a heteroatomic distance that is short enough to suggest an O → S charge-transfer interaction.

In agreement with the data presented in Table 6, AIM analysis revealed that extensive side-chain–backbone intramolecular hydrogen-bonding-type interactions exists in three of the seven conformers. These were found to be g^+g^+, g^+a, and ag^-. Taking into account the distances and angles, however, we might consider that five of the seven γ_L conformations are stabilized by hydrogen bonding interactions (Table 5).

The g^+g^+ conformer has the greatest number of hydrogen bonds, so it is not surprising that it emerges as being the global minimum. In addition to the hydrogen bond, which is characteristic of the seven-member ring of the γ_L-backbone conformation, there are two additional hydrogen bonds corresponding to side-chain → backbone (C=O··H-S) and

© 2002 NRC Canada

Table 6. The topological properties of electron-density distribution of For-L-Cys-NH_2 at selected BCPs from B3LYP/6–31G(d,p)//HF/3–21G calculations.

Bond		g^+a	g^+g+	ag^-
O2··H15	ρ_b	0.0225	0.0245	0.0294
	∇^2_b	0.0659	0.0714	0.0679
	ε	0.0102	0.0114	0.0101
	H_b	–0.0041	–0.0047	–0.0037
H13··O8	ρ_b	—	0.0146	0.0117
	∇^2_b	—	0.0483	0.0417
	ε	—	0.2415	0.4547
	H_b	—	0.0065	0.0085
S12··H4	ρ_b	0.0137	0.0139	—
	∇^2_b	0.0488	0.0494	—
	ε	0.7443	0.7259	—
	H_b	0.0113	0.0114	—
Ring				
C5-C7-O8··H13-S12-C9	ρ_b	—	0.0114	0.0106
	∇^2_b	—	0.0484	0.0439
C5-N3-C1-O2··H15-N14-C7	ρ_b	0.0095	0.0097	0.0095
	∇^2_b	0.0502	0.0504	0.0484
C5-C9-S12··H4-N3	ρ_b	0.0134	0.0134	—
	∇^2_b	0.0623	0.0631	—

Note: Covalent bonds are denoted as A–B and hydrogen bonds specified as A··B.

Fig. 13. The contour map of the Laplacian of the electron density for the (g^+g^+) conformation of HCO-Cys-NH_2 calculated at the B3LYP/6–31+G(d,p)//RHF/3–21G level of theory. Bond paths are denoted by lines, bond critical points (BCPs) are denoted by black dots, ring critical points (RCPs) are denoted by open triangles, and the nuclei are denoted by crosses.

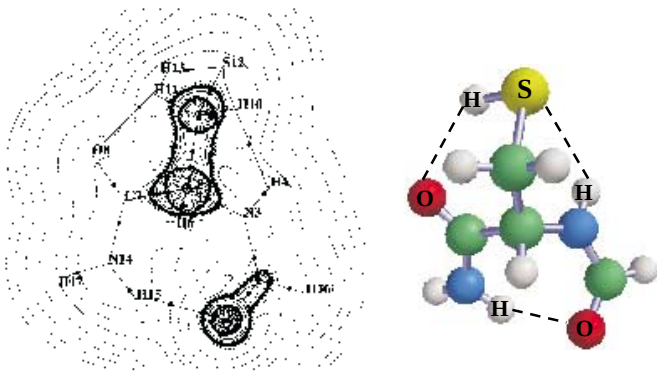

Fig. 14. The contour map of the Laplacian of the electron density for the (g^+a) conformation of HCO-Cys-NH_2 calculated at the B3LYP/6–31+G(d,p)//RHF/3–21G level of theory. Bond paths are denoted by lines, bond critical points (BCPs) are denoted by black dots, ring critical points (RCPs) are denoted by open triangles, and the nuclei are denoted by crosses.

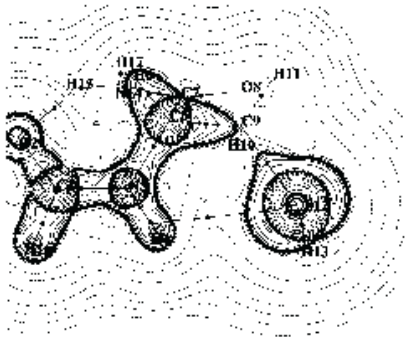

backbone→side-chain (N-H··S-H)-type hydrogen bonding (Fig. 13). The three ring-critical points, associated with the rings formed as the result of intramolecular hydrogen bonding are denoted by open triangles (Δ). The various BCPs are symbolized by solid dots (●).

Beyond the characteristic hydrogen bonding associated with the seven-member ring of the γ_L-backbone conformation, the g^+a conformer also exhibited an N-H··S-H-type hydrogen bonding. In Fig. 14, the ring-critical points are shown by open triangles (Δ) and the various BCPs are symbolized by solid dots (●).

Figure 15 shows the ag^- conformation, featuring a C=O··H-S hydrogen bond in addition to the hydrogen bond associated with the seven-member ring of the γ_L-backbone conformation.

In addition to these side-chain–backbone-type of hydrogen bonds, there exists the backbone—backbone C=O··H-N-type of hydrogen bond, typical in the seven-member ring of the γ_L conformer.

© 2002 NRC Canada

Fig. 15. The contour map of the Laplacian of the electron density for the (ag^-) conformation of HCO-Cys-NH_2 calculated at the B3LYP/6–31+G(d,p)//RHF/3–21G level of theory. Bond paths are denoted by lines, bond critical points (BCPs) are denoted by black dots, ring critical points (RCPs) are denoted by open triangles, and the nuclei are denoted by crosses.

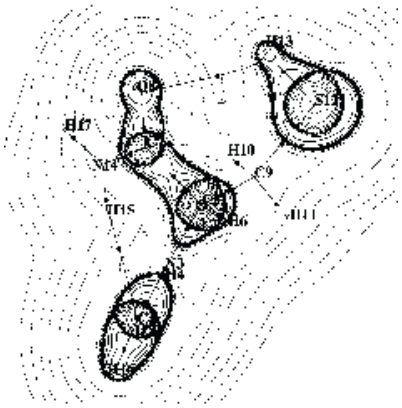

Conclusions

In summary, we found seven different conformations for the side chain of compounds **I** and **II** when the backbone is in γ_L form. These results suggest that the side-chain stabilization is not substantially affected if we change the protecting group from formyl to acetyl at the nitrogen end and from amide to methylamide at the carboxyl end. In contrast, noticeable differences were found when comparing the conformational intricacies of compounds **II** and **III**: only six different conformations were obtained for compound **III** and the order of preference is also different. DFT calculations proved that polar side chains are able to interact with a peptide backbone, eliminating some otherwise legitimate minima through unfavourable backbone and side-chain torsional-angle combinations. The comparative study between compounds **II** and **III** illustrates this point very well. On the basis of our results, we might assume that the strength of hydrogen bonding involved is responsible for the different conformational behavior obtained for these compounds. On the other hand, it is interesting to note that both levels of theory (HF/3–21G and B3LYP/6–31G(d,p)) displayed closely related results indicating that HF/3–21G calculations are satisfactory to use in exploratory conformational studies.

Acknowledgments

We would like to thank Cray Inc. (Eagen, MN) for use of their resources and computer time. We would also like to thank the National Cancer Institute for the use of services at the Frederick Biomedical Supercomputing Center. This work was supported by grants from Universidad Nacional de San Luis (UNSL), and Consejo Nacional de Investigaciones Científicas y Técnicas (CONICET) of Argentina. H.A.B. thanks CONICET for a postdoctoral fellowship. R.D.E. is a carreer researcher of CONICET. I.G.C. would like to thank Domus Hungarica Scientiarium et Atrium for supporting this international research collaboration.

References

1. O. Farkas, A. Perczel, J. Marcoccia, M. Hollosi, and I. Csizmadia. J. Mol. Struct. (Theochem) **331**, 27 (1995).
2. A. Perczel and I. Csizmadia. Int. Rev. Phys. Chem. **14**, 127 (1995).
3. A. Perczel, O. Farkas, and I. Csizmadia. J. Comp. Chem. **17**, 821 (1996).
4. A. Perczel, O. Farkas, and I. Csizmadia. J. Am. Chem. Soc. **118**, 7809 (1996).
5. A. Perczel, O. Farkas, I. Jakli, and I. Csizmadia. J. Mol. Struct. (Theochem) **455**, 315 (1998).
6. A. Perczel, J. Angyan, M. Kajtar, W. Viviani, J.-L. Rivail, J. Marcoccia, and I. Csizmadia. J. Am. Chem. Soc. **113**, 6256 (1991).
7. M. McAllister, A. Perczel, P. Csaszar, W. Viviani, J.-L. Rivail, and I. Csizmadia. J. Mol. Struct. (Theochem) **288**, 161 (1993).
8. G. Endredi, A. Perczel, O. Farkas, M. McAllister, G. Csonka, J. Ladik, and I. Csizmadia. J. Mol. Struct. (Theochem) **391**, 15 (1997).
9. W. Viviani, J.-L Rivail, A. Perczel, and I. Csizmadia. J. Am. Chem. Soc. **115**, 8321 (1993).
10. O. Farkas, M. McAllister, J. Ma, A. Perczel, M. Hollosi, and I. Csizmadia. J. Mol. Struct. (Theochem) **369**, 105 (1996).
11. A. Perczel, O. Farkas, and I. Csizmadia. Can. J. Chem. **75**, 1120 (1997).
12. I. Jakli, A. Perczel, O. Farkas, M. Hollosi, and I. Csizmadia. J. Mol. Struct. (Theochem) **455**, 303 (1998).
13. L. Polgar. FEBS Lett. **47**, 15 (1974).
14. A. Fersht. Enzyme structure and mechanism. 2nd ed. W.H. Freeman, New York. 1984. pp. 413–416.
15. A. Storer and R. Menard. Methods Enzymol. **244**, 486 (1994).
16. L. Muszbek, V. Yee, and Zs. Hevessy. Thromb. Res. **94**, 271 (1999).
17. I. Komároni, L. Kárpáthy, K. Morokuma, and L. Muszbek. 5th World congress of theoretically oriented chemists (WATOC). Book of Abstracts (p.p. 489). Royal Society of Chemistry, London. 1999.
18. M. Zamora, H. Baldoni, J. Bombasaro, M. Mak, A. Perczel, O. Farkas, and R. Enriz. J. Mol. Struct. (Theochem) **540**, 271 (2001).
19. IUPAC-IUB comission on biochemical nomenclature. Biochemistry, **9**, 3471 (1970).
20. I. Ramachandran and V. Sasisekharan. Adv. Protein Chem. **23**, 283 (1968).
21. I. Csizmadia. *In* The chemistry of the thiol group. *Edited by* S. Patai. John Wiley and Sons, New York. 1974.
22. M. Peterson and I. Csizmadia. J. Am. Chem. Soc. **100**, 6911 (1978).
23. M. Peterson and I. Csizmadia. *In* Progress of theoretical organic chemistry. Vol. 3. *Edited by* I.G. Czizmadia. Elsevier, Amsterdam. 1982.
24. Gaussian 94. Revision E.1, E.2, C.3, and D.2. M. Frisch, G. Trucks, H. Schlegel, P.W. Gill, B. Johnson, M. Robb, J. Cheeseman, T. Keith, G. Petersson, J. Montgomery, K. Raghavachari, M. Al-Laham, V. Zakrzewski, J. Ortiz, J. Foresman, J. Cioslowski, B. Stefanov, A. Nanayakkara, M. Challacombe, C. Peng, P. Ayala, W. Chen, M. Wong, J. Andres, E. Replogle, R. Gomperts, R. Martin, D. Fox, J. Binkley, D. Defrees, J. Baker, J. Stewart, M. Head-Gordon, C. Gonzalez, and J. Pople. Gaussian, Inc., Pittsburgh PA. 1995.
25. J. Binkley, J. Pople, and W. Hehre. J. Am. Chem. Soc. **102**, 939 (1980).

© 2002 NRC Canada

26. R. Frey, J. Coffin, S. Newton, M. Ramek, V Cheng, F. Momany, and L. Schafer. J. Am. Chem. Soc. **114**, 5369 (1992).
27. M. McAllister, G. Endredi, W. Viviani, A. Perczel, P. Csaszar, J. Ladik, J-L. Rivail, and I. Csizmadia. Can. J. Chem. **73**, 563 (1995).
28. R. Bader. Atoms in molecules: A quantum theory. Clarendon Press, Oxford. 1990.
29. R. Bader. J. Phys. Chem. A, **102**, 7314 (1998).
30. (*a*) D. Whiterfield and T. Tang. J. Am. Chem. Soc. **115**, 9648 (1993); (*b*) U. Koch and P. Popelier. J. Phys. Chem. **99**, 9747 (1995); (*c*) D. Whitefield, D. Lamba, T. Tangm, and I. Csizmadia. Carbohydrate Res. **286**, 17 (1996); (*d*) J. Platts, S. Howardm, and B. Bracke. J. Am. Chem. Soc. **118**, 2726 (1996); (*e*) D. Fang, P. Fabian, Z. Szekely, X. Fu, T. Tang, and I. Csizmadia. J. Mol. Struct. (Theochem) **427**, 243 (1998); (*f*) P. Popelier. J. Phys. Chem. A, **102**, 1873 (1998).
31. H. Berman, J. Westbrook, Z. Feng, G. Gilliland, T. Bhat, H. Weissig, I. Shindyalov, P. Bourne. The Protein Data Bank. Nucleic Acids Res. **28**, 235 (2000). Last update: 26 Feb. 2002.
32. I. Jákli, A. Perczel, Ö. Farkas, P. Császár, C. Sosa, and I. Csizmadia J. Comp. Chem. **21**, 626 (2000).
33. (*a*) H. Baldoni, L. Torday, A. Rodríguez, G. Zamarbide, R. Enriz, C. Sosa, Ö. Farkas, I. Jákli, A. Perczel, and I. Csizmadia. 5th World congress of theoretically oriented chemists (WATOC). Book of Abstracts (p.p. 212). Royal Society of Chemistry, London, 1999; (*b*) H. Baldoni, G. Zamarbide, R. Enriz, E. Jáuregui, Ö. Farkas, A. Perczel, S. Salpietro, and I. Csizmadia. J. Mol. Struct. (Theochem) **500**, 97 (1998).
34. L. Pauling. The nature of the chemical bond. 3rd ed. Cornell University Press, Ithaca, New York. 1960.
35. J. Emsley. The elements. 3rd ed. Clarendon Press, Oxford. 1998.

© 2002 NRC Canada

Ab initio and DFT conformational analysis of selected flavones: 5,7-dihydroxyflavone (chrysin) and 7,8-dihydroxyflavone

Ken S. Lau, Athena Mantas, Gregory A. Chass, Fernando H. Ferretti, Mario Estrada, Graziela Zamarbide, and Imre G. Csizmadia

Abstract: Ab initio and DFT conformational analysis was performed on the flavone derivatives chrysin (5,7-dihydroxyflavone; 2-phenyl-5,7-dihydroxy-4*H*-1-benzopyran-4-one) and 7,8-dihydroxyflavone (2-phenyl-7,8-dihydroxy-4*H*-1-benzopyran-4-one). The structural features required for optimal stabilization in each molecule were identified. It was discovered that sparsely placed hydroxyl groups, particularly with hydrogen bond-like interactions, resulted in lowering the potential energy minimum for the molecules. It was also noted that one of the factors capable of destroying co-planarity was steric interference between closely placed functional groups across the phenyl and the benzo-γ-pyrane ring. Studies performed on the radical forms of the flavonoids, however, showed that the unpaired electron is confined only to the benzo-γ-pyrane ring, and not delocalized across the phenyl ring.

Key words: flavonoid, flavone, chrysin, ab initio conformational analysis, anti-oxidant, free radical, 5,7-dihydroxyflavone, 7,8-dihydroxyflavone.

Résumé : On a effectué une analyse conformationnelle ab initio et « DFT » sur des dérivés de la flavone: la chrysine (5,7-dihydroxyflavone; 2-phényl-5,7-dihydroxy-4*H*-1-benzopyran-4-one) et la 7,8-dihydroxyflavone (2-phényl-7,8-dihydroxy-4*H*-1-benzopyran-4-one). On a identifié les caractéristiques de la structure qui sont nécessaires pour une stabilisation maximale de chaque molécule. On a découvert que les groupes hydroxyles parsemés, particulièrement ceux avec des interactions de type liaisons hydrogènes, conduisent à des abaissements du minimum de l'énergie potentielle pour les molécules. On a aussi noté que l'interférence stérique entre des groupes fonctionnels situés à proximité l'un de l'autre sur le noyau phényle et le cycle benzo-γ-pyrane est un facteur susceptible de détruire le caractère coplanaire. Toutefois, des études effectuées sur les formes radicalaires des flavonoïdes ont permis de montrer que l'électron célibataire est confiné uniquement sur le cycle benzo-γ-pyrane et qu'il ne se délocalise pas sur le noyau phényle.

Mots clés : flavonoïde, flavone, chrysine, analyse conformationnelle ab initio, antioxydant, radical libre, 5,7-dihydroxyflavone, 7,8-dihydroxyflavone.

[Traduit par la Rédaction]

Introduction

Aging is thought to be associated with various free radical reactions, a series of processes within the body collectively known as "oxidative stress." Generated as by-products of metabolism, free radicals are short-lived, but highly reactive intermediates. Because of the presence of at least one unpaired electron, free radicals will constantly seek to react with other molecules for stabilization. They will react with cellular structures, altering DNA and destroying membranes through lipid peroxidation (1–3). It is proposed that through these processes, age-related degenerative diseases like cancer are induced.

By supplementing a diet with molecules that act as scavengers of these free radicals (anti-oxidants) oxidative damage can be greatly reduced. Anti-oxidants are defined as "any substance that, when present at low concentrations compared with those of an oxidizable substrate, significantly delays or prevents the oxidation of that substrate" (4*a*). They are molecules with the ability to stabilize free radicals and render them harmless. There are various anti-oxidants under study today, some of which include L-ascorbic acid (vitamin C), α-tocopherol (vitamin E), β-carotene, lycopene, and coenzyme Q (4*b*). The molecules of interest in this paper, a class of compounds called flavonoids, also act as anti-oxidants.

Flavonoids are polyphenolic compounds found in many types of plants, occurring mainly as glycosides in fruits, vegetables, nuts, seeds, flowers, and bark (5, 6). The basic structure

Received 16 November 2001. Published on the NRC Research Press Web site at http://canjchem.nrc.ca on 28 June 2002.

K.S. Laua, A. Mantas, G.A. Chass, and I.G. Csizmadia.[1] Department of Chemistry, University of Toronto, Toronto, ON M5S 3H6, Canada.
G.A. Chass and I.G. Csizmadia. Global Institute of Computational Molecular and Materials Science @ Velocet, 210 Dundas Street West, Suite 810, Toronto, ON M5G 2E8, Canada.
F.H. Ferretti, M. Estrada, and G. Zamarbide. Area de Química-Física, Facultad de Química, Bioquímica y Farmacia, Universidad Nacional de San Luis, Chacabuco y Pedernera, 5700 San Luis, Argentina.

[1]Corresponding author (e-mail: icizmad@alchemy.chem.utoronto.ca).

 DOI: 10.1139/V02-113 © 2002 NRC Canada

Fig. 1. The generic structure of flavonoids (above). The structure of flavone, the parent molecule of flavonoids (below).

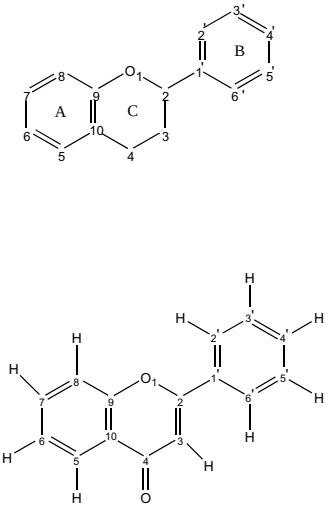

Fig. 2. Suggested radical-scavenging mechanism of chrysin by hydrogen abstraction (19).

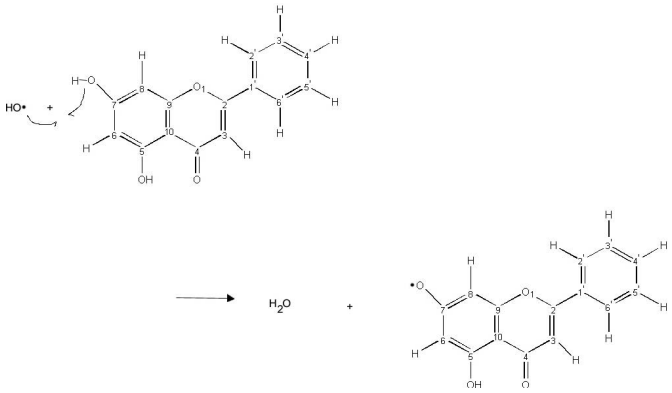

of these compounds resembles that of the parent flavone molecule, which consists of a phenyl group attached to a benzo-γ-pyrane ring (7) (Fig. 1). Because of their anti-aging effects, flavonoids and their derivatives are beginning to receive attention in commercial products, for example, anthocyanidin in ENOCH© grape extract. In 1936, the biological benefits of flavonoids were first introduced by Szent-Gyorgyi (8). These compounds were first thought to reduce arteriole hardening, which is an age-related ailment attributed to free radical oxidations within the body. Furthermore, a subclass of flavonoids called flavonols is the major polyphenolic anti-oxidant found in red wines (9). A statistical analysis performed on the population of France reports that people who consume red wine on a regular basis have a reduced risk of coronary heart diseases (5, 9). It is suggested that flavonols reduce coronary heart disease by preventing oxidation of low-density proteins by free radicals (9).

The exact mechanism of free radical scavenging remains elusive. Previous studies have shown that some structural properties in flavonoids are necessary for anti-oxidant activity. The radical scavenging flavonoids tend to have, on their benzo-γ-pyrane rings, a double bond between the 2,3-carbons, a carbonyl group at carbon 4, and a number of

Fig. 3. The structure of the two molecules used in this study, chrysin and 7,8-dihydroxflavone. The altered numbering system used in this study (above) and the standard IUPAC numbering system (below).

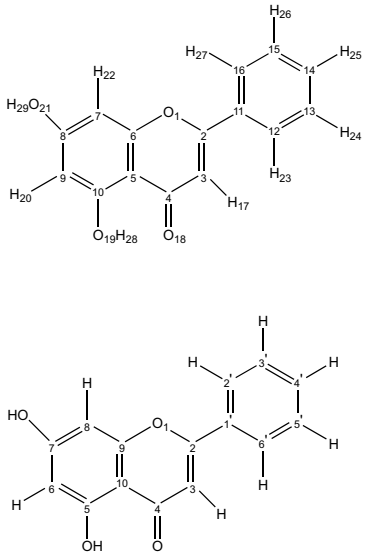

hydroxyl groups distributed among the three rings (5, 6, 9–11). Structural–activity relationships (SAR) of flavonoids are, however, often not consistent with real data. For example, the flavonoid catechin, lacking the C2–C3 double bond and the 4-keto functional group, is a very potent anti-oxidant (12). Furthermore, SARs do not give molecular explanations as to why these structural features are important.

It has been vaguely proposed that a flavonoid molecule neutralizes a free radical in vivo by donating a hydrogen atom to the free radical, forming a flavonoid radical itself (5). Eventually, the flavonoid radical will react with another free radical, thus terminating the reaction (5, 9). Although the exact mechanism remains elusive at this time, there is ample data to support a hydrogen transfer from the molecule to the free radical. In fact, other phenolic anti-oxidants such as quercetin, α-tocopherol, and curcumin are known to use similar mechanisms (13–16).

A recent study by Wright et al. (17) proposes that one of the main properties of a good phenolic anti-oxidant is low bond-dissociation enthalpy (BDE) of the hydrogen being abstracted. The term "chain-breaking anti-oxidant" is introduced because free radicals usually act by a chain-reaction mechanism. It is thought that anti-oxidants can prevent oxidative damage by reacting with free radicals more rapidly and readily than cellular structures do. The lower the BDE of the abstracted hydrogen, the faster it reacts with free radicals, thus preventing the chain reaction with cellular substrates (17). It is important, however, for the anti-oxidant radical to be stable enough, and not initiate any further aggressive reactions.

It has been proposed that the radical scavenging ability of an anti-oxidant is based on three basic properties: (*i*) the inability for the anti-oxidant to undergo auto-oxidation; (*ii*) the lipophilicity of the molecule to localize the main location for anti-oxidant reactions across membranes; and (*iii*) the ability to stabilize a lone electron once it is bound (10–13). It is obvious that flavonoids are mainly lipophilic as seen by their

© 2002 NRC Canada

Fig. 4. Four possible hydroxyl orientations [1]–[4] for chrysin, which may represent four minima on the molecule's potential energy surface. Note the usage of the altered numbering system.

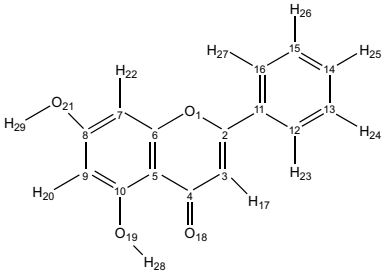

[1]

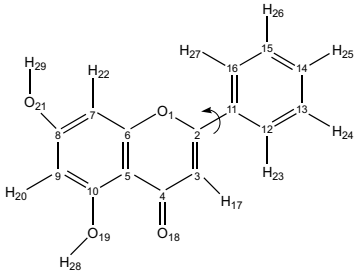

[2]

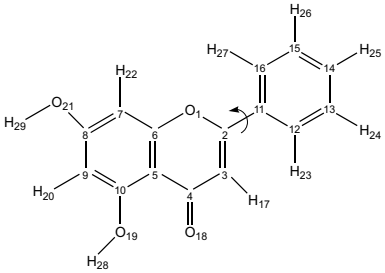

[3]

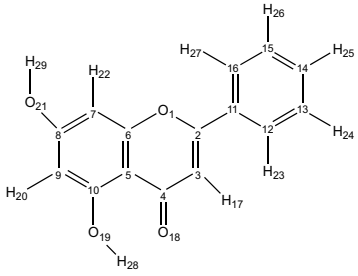

[4]

Fig. 5. Four possible hydroxyl orientations [5]–[8] for 7,8-dihydroxyflavone, which may represent four minima on the molecule's potential energy surface. Note the usage of the altered numbering system.

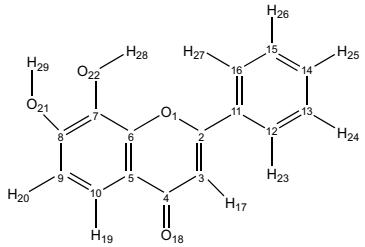

[5]

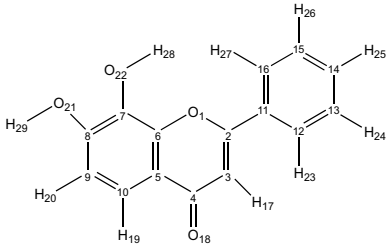

[6]

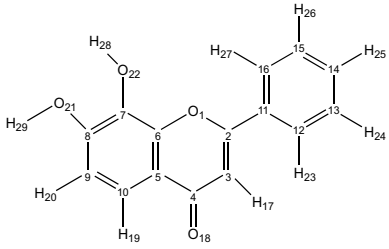

[7]

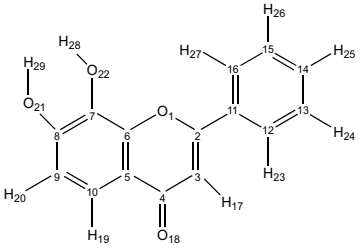

[8]

benzo-γ-pyrane and phenyl structures. Consequently, the overall anti-oxidant properties of flavonoids are determined mostly by the two remaining properties. The optimal geometry required for lone-electron stabilization will be the main focus of this study.

The molecules under study in this paper are chrysin (5,7-dihydroxyflavone; 2-phenyl-5,7-dihydroxy-4*H*-1-benzopyran-4-one) and its structural isomer 7,8-dihydroxyflavone (2-phenyl-7,8-dihydroxy-4*H*-1-benzopyran-4-one) (see Fig. 3). Like its parent molecule flavone, chrysin is a mild anti-oxidant (20). It possesses hydroxyl groups at the 5 and 7 positions on the benzo-γ-pyrane ring, which slightly improves its anti-oxidant activity. A mechanism for free radical scavenging based on hydrogen transfer can be proposed for chrysin (Fig. 2). The degree of conjugation of the system is a good gauge for anti-oxidant strength, since it is important for the stabilization of the unpaired electron.

© 2002 NRC Canada

Fig. 6. Potential energy curve for phenyl-ring rotation of flavone (standard IUPAC numbering) computed at RHF/STO3-G (above) and RHF/3–21G (below) (24).

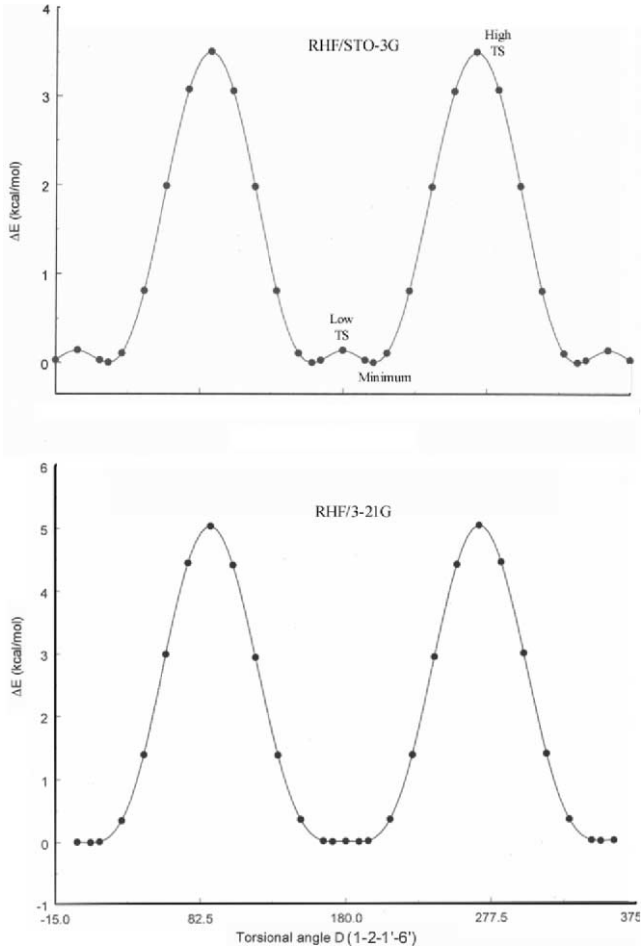

Aside from its radical scavenging ability, chrysin has also been investigated for its inhibition of benzo[*a*]pyrene carcinogenesis based on its activity on cytochrome P450-mediated detoxification (21). Furthermore, chrysin is a dietary supplement for bodybuilding because it is a competitive inhibitor of human aromatase, which actively converts testosterone into estrogen (22, 23). The effect of aromatase inhibition is to increase testosterone levels, which will stimulate muscle growth. The property of chrysin as an aromatase inhibitor can also be used to control breast cancer, because estrogen levels in females play a major role in carcinogenesis. Through mutational studies and computer modeling by Kao et al. (24), it has been suggested that chrysin binds to the active site of aromatase by mimicking the D and C rings of the androgen substrate with its A and C rings. Conformational analysis of these molecules will indicate the most effective conformation for optimal radical scavenging ability and other bioactivities of flavonoids and other polyphenolic compounds.

Computational methodology

The molecules of interest were geometrically optimized with the Gaussian 94 (25) and Guassian 98 (26) program packages. The calculations were initially performed on an Intel Celeron 433-MHz chip with 64 MB of RAM for the low-basis sets, and then on the NIH supercomputers for high-basis sets. Radical computations were also performed on diskless AMD K-7 1.33 GHz CPU, 128 MB PC-clusters at Velocel Communications Inc. (Toronto). The standard IUPAC numbering of flavonoids was altered, as shown in Fig. 3, for the purpose of constructing the input data as Z-matrices. This new numbering system will be referred to for the rest of the paper. For each molecule, four initial assumptions about their hydroxyl (OH) orientations were made and designated as [1]–[4] and [5]–[8], respectively (Figs. 4 and 5). These assumptions were made on the basis of the conjugated electron system of the benzo-γ-pyrane ring forming an essentially planar conformation. Thus, the hydroxyl groups are expected to lie in this plane. The four different orientations may represent four different local minima on the potential energy surface of the one molecule.

Each of the hydroxyl orientations of the three molecules were geometrically optimized using three levels of theory: RHF/3–21G, RHF/6–31G(d), and B3LYP/6–31G(d). The molecules were initially modeled based on a template of flavone, previously optimized at the RHF/3–21G level of theory (25). Furthermore, calculations were performed on the radical forms of a few selected conformations ([1], [6], [7]]) at the UHF/3–21G level of theory to study the free radical scavenging mechanism. In this study, a thermal correction was not applied to the calculations because the energies of the molecules were only used in relative terms.

Frequency calculations were performed after each optimization to ensure that the critical points were indeed minima. A scan of each orientation for each molecule was not performed but it was implied that the energy pattern of the phenyl group's rotation was analogous to that of flavone, whose scan was performed at both the RHF/STO-3G and RHF/3–21G level at 15° intervals (27).

Table 1. Deviation from co-planarity of dihedral angle C12-C11-C2-O1 (α, degrees) computed for chrysin (5,7-dihydroxyflavone) and 7,8-dihydroxyflavone at their minimum energy conformations.

	Optimization		
Compound	RHF/3–21G	RHF/6–31G(d)	B3LYP/6–31G(d)
Chrysin			
[1]	8.46	26.40	18.63
[2]	8.77	27.43	18.72
[3]	0.17	0.28	17.84
[4]	8.78	27.27	19.35
7,8-Dihydroxyflavone			
[5]	25.21	32.64	26.02
[6]	25.07	32.45	25.96
[7]	0.01	0.02	0.02
[8]	25.22	32.64	26.02

Note: There are four equivalent torsional angles that govern minimum energy conformations: (0 + α), (180 – α), (180 + α), and (360 – α).

Results and discussion

The potential energy curve for each orientation is expected to resemble that of flavone (Fig. 6). Because of the

© 2002 NRC Canada

Table 2. Comparisons of minimum energies of dihedral angle C12-C11-C2-O1 rotation computed for chrysin (5,7-dihydroxyflavone) and 7,8-dihydroxyflavone using the lowest energy conformation as the global minimum.

	RHF/3–21G		RHF/6–31G(d)		B3LYP/6–31G(d)	
Compound	Minimum energy E (Hartree)	Relative energy ΔE (kcal mol^{-1})[a]	Minimum energy E (Hartree)	Relative energy ΔE (kcal mol^{-1})[a]	Minimum energy E (Hartree)	Relative energy ΔE (kcal mol^{-1})[a]
Chrysin						
[1]	–868.46	0.00	–873.31	0.00	–878.52	0.00
[2]	–868.43	16.16	–873.29	13.15	–878.50	15.54
[3]	–868.43	17.05	–873.29	14.23	–878.50	16.10
[4]	–868.45	0.84	–873.31	0.60	–878.52	0.59
7,8-Dihydroxyflavone						
[5]	–868.44	0.00	–873.30	0.00	–878.50	0.00
[6]	–868.43	6.88	–873.29	4.62	–878.50	3.91
[7]	–868.43	3.57	–873.29	2.79	–878.50[b]	2.06
[8]	–868.44	0.00	–873.30	0.00	–878.50	0.00

[a] ΔE (kcal mol^{-1}) = 627.51($E_{TS} - E_{min}$) calculated using the lowest minimum energy as E_{min}.
[b] The frequency obtained is small (~19.6 cm^{-1}) and within convergence error. Further calculations were not carried out.

Table 3. Interatomic distances (Å) for atoms sharing hydrogen bond-like interactions computed for chrysin (5,7-dihydroxyflavone) and 7,8-dihydroxyflavone at their minimum energy conformations.

	Optimization		
Compounds	RHF/3–21G	RHF/6–31G(d)	B3LYP/6–31G(d)
Chrysin [1]			
H27—O1	2.30	2.44	2.39
H28—O18	1.75	1.82	1.69
Chrysin [2]			
H27—O1	2.30	2.45	2.40
Chrysin [3]			
H27—O1	2.29	2.33	2.39
Chrysin [4]			
H27—O1	2.30	2.45	2.40
H28—O18	1.76	1.83	1.70
7,8-Dihydroxyflavone [5]			
H27—O1	2.41	2.51	2.46
H28—O1	2.33	2.28	2.25
H29—O22	2.19	2.20	2.17
7,8-Dihydroxyflavone [6]			
H27—O1	2.41	2.50	2.46
H28—O1	2.24	2.24	2.16
7,8-Dihydroxyflavone [7]			
H27—O1	2.25	2.30	2.31
H28—O21	2.16	2.19	2.14
7,8-Dihydroxyflavone [8]			
H27—O1	2.41	2.51	2.46
H28—O1	2.33	2.28	2.25
H29—O22	2.19	2.20	2.17

phenyl group's symmetry, the minima (0 + α), (180 – α), (180 + α), and (360 – α), where α is the deviation from co-planarity, are identical. It is therefore sufficient to geometrically optimize one conformation from the above set of angles.

The torsional angles resulting from phenyl rotation (C12-C11-C2-O1 calculated as deviations from co-planarity (α)) for each hydroxyl orientation of chrysin (5,7-dihydroxyflavone) and 7,8-dihydroxyflavone (as calculated at RHF/3–21G, RHF/6–31G(d), and B3LYP/6–31G(d)) are summarized in Table 1. Aside from chrysin at orientation [3], the geometric data for the compounds seem to be consistent for all three basis sets.

Table 2 compares the relative energies of the orientations in their minimum energy conformations as calculated at RHF/3–21G, RHF/6–31G(d), and B3LYP/6–31G(d). The geometric data of the molecules are summarized graphically in Fig. 7, while the distances (as calculated at RHF/3–21G, RHF/6–31G(d), and B3LYP/6–31G(d)) between pseudo-hydrogen bonded atoms are summarized in Table 3. Table 4 summarizes the geometric conformations of the hydroxyl groups of each conformer in relation to their energies.

The geometric parameters for the two molecules in their different hydroxyl orientations were determined (not shown). Excluding all the C–H, O–H, C3–C4, C4–C5, C2–C11, C2–C3, and C4–O18 bonds, the bond lengths of all conformations fluctuate between 1.37 and 1.40 Å, indicating the strong double-bond characteristics of these bonds (a C—C double bond is typically 1.33 Å in length). For all conformations, the bond connecting the phenyl ring to the benzo-γ-pyrane ring (C2—C11) is in the range of 1.47–1.48 Å. Although this bond has fewer double-bond characteristics, its length is still shorter than a typical C—C single bond (1.54 Å). This data suggests the presence of a π-electron delocalization system in most parts of the molecules, contributing to conjugative stabilization. The conjugation between the phenyl ring and the benzo-γ-pyrane, however, is not as high as that of the rest of the molecule and, therefore, this section of the molecule can be seen as the weakest part of the delocalized system; the easiest portion to become unconjugated.

Trends for stabilization

The disparities in minimum energies are due to the different orientations of the hydroxyl subsituents, which results in different extensions of hydrogen bond-like interactions within the molecule (Table 3). It can easily be shown that the orientations with more hydrogen bond-like interactions

© 2002 NRC Canada

Fig. 7. Geometric conformations of chrysin [1]–[4] (left) and 7,8-dihydroxyflavone [5]–[8] (right).

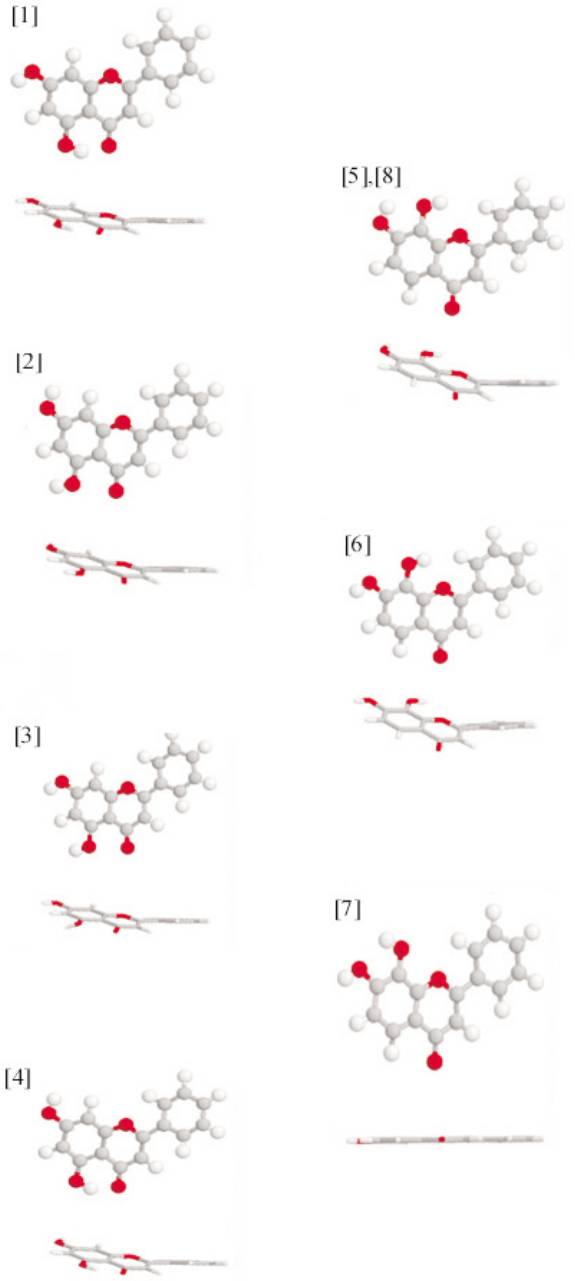

have lower minimum energies than others, and hence, are more stable. For example, for chrysin, orientations [1] and [4] both possess a hydrogen bond-like interaction between O18 and H28 (Table 3), while the other conformers do not have such interactions. Consequently, these two orientations possess lower minimum energies than the others without the hydrogen bond-like interactions (Table 2). The same argument can be made for 7,8-dihydroxyflavone, where orientation [5] proves to be the most stable out of the four orientations (Table 2) because of the two hydrogen bond-like interactions between O1 and H28, and O22 and H29, which result in extra stabilization (Table 3), while other orientations have at most one such hydrogen bond.

Fig. 8*a*. The change of bond lengths from the native form to radical form of chrysin orientation [1]. Hydrogen 29 is abstracted in this case. Note the resonance structure (hence delocalization) available for the radical form.

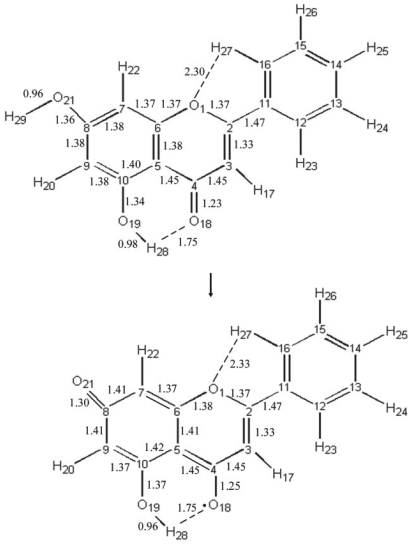

Fig. 8*b*. Spin densities of individual atoms and whole regions of chrysin radical orientation [1].

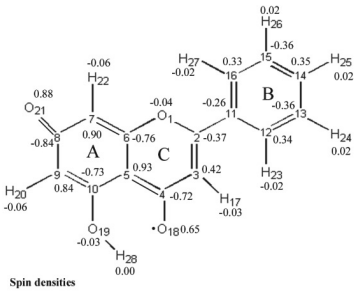

Chrysin (5,7-dihydroxyflavone)

The molecule chrysin gives peculiar results. In particular, there are discrepancies between the optimization results performed at the restricted Hartree–Fock level of theory and the density functional level of theory. This fact is especially emphasized for the phenyl dihedral angle of orientation [3] (Table 1). At the restricted Hartree–Fock level of theory, the molecule with respect to this dihedral angle is essentially coplanar. At the density functional level, the co-planarity disappears, and because the density function method of calculation is more robust, the data from this level of calculation are considered to be more reliable.

Based on the calculations performed at the density functional level, the four hydroxyl orientations of chrysin produce similar results, all having a phenyl torsional angle in the range of 17.8–19.3°. The conjugative stabilization across the phenyl ring does not appear strong, since the deviations from co-planarity of all the orientations are quite high. All the hydroxyl groups, however, remained in plane with the molecule as seen in Table 4, contributing to conjugative stabilization of the benzo-γ-pyrane ring.

© 2002 NRC Canada

Table 4. The optimized dihedral angles of the hydroxyl groups of each conformer, compared with minimum energies.

Chrysin	Level of theory	H28-O19-C10-C5 (°)	H29-O21-C8-C7 (°)	*E* (Hartree)
[1]	RHF/3–21G	–0.07	180.09	–868.46
	RHF/6–31G(d)	–0.08	–179.87	–873.31
	B3LYP/6–31G(d)	–0.13	–179.92	–878.52
[2]	RHF/3–21G	180.03	–0.10	–868.43
	RHF/6–31G(d)	180.06	–0.22	–873.29
	B3LYP/6–31G(d)	–179.95	–0.17	–878.50
[3]	RHF/3–21G	180.00	180.00	–868.43
	RHF/6–31G(d)	180.00	180.00	–873.29
	B3LYP/6–31G(d)	–179.95	–179.91	–878.50
[4]	RHF/3–21G	–0.08	–0.11	–868.45
	RHF/6–31G(d)	–0.06	–0.21	–873.31
	B3LYP/6–31G(d)	–0.11	–0.13	–878.52
7,8-Dihydroxyflavone	Level of theory	H28-O22-C7-C6 (°)	H29-O21-C8-C7 (°)	*E* (Hartree)
[5]	RHF/3–21G	–8.62	–0.34	–868.44
	RHF/6–31G(d)	–13.72	–0.88	–873.30
	B3LYP/6–31G(d)	–6.84	–0.84	–878.50
[6]	RHF/3–21G	–6.82	179.87	–868.43
	RHF/6–31G(d)	–8.23	180.01	–873.29
	B3LYP/6–31G(d)	–4.21	–179.81	–878.50
[7]	RHF/3–21G	–180.01	180.08	–868.43
	RHF/6–31G(d)	180.01	–179.95	–873.29
	B3LYP/6–31G(d)	–179.99	–179.97	–878.50
[8]	RHF/3–21G	–8.66	–0.34	–868.44
	RHF/6–31G(d)	–13.71	–0.88	–873.30
	B3LYP/6–31G(d)	–6.84	–0.84	–878.50

Fig. 9*a*. The change of bond lengths from the native form to radical form of 7,8-dihydroxyflavone orientation [6]. Hydrogen 29 is abstracted in this case. Note the resonance structure (hence delocalization) available for the radical form.

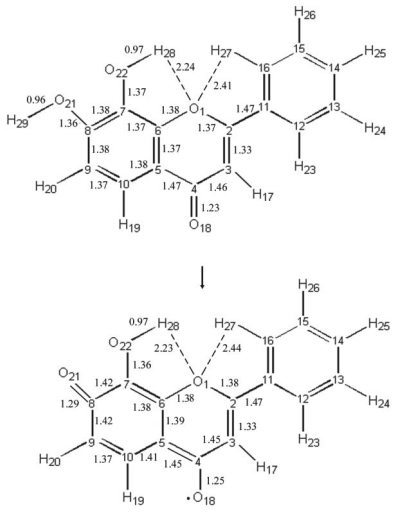

Fig. 9*b*. Spin densities of individual atoms and whole regions of 7,8-dihydroxyflavone radical orientation [6].

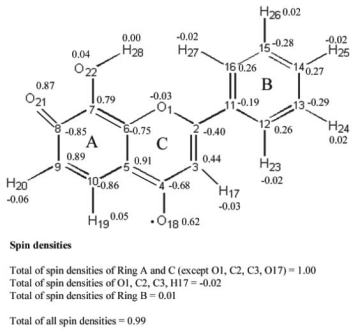

7,8-Dihydroxyflavone

Examining the geometries and energies of each hydroxyl orientation of 7,8-dihydroxyflavone, it is evident that the optimized conformation of orientation [8] has migrated to that of [5]. The migration is the result of excessive steric hindrance between the two hydroxyl groups on C7 and C8 of orientation [8], which causes this orientation to become very unstable and not to exist as a minimum on the potential energy surface. The non-co-planar conformations of orientations [5] and [6] are most likely due to electron cloud repulsion and steric interference between H28 and H27. Additionally, the hydroxyl substituents in these orientations are not in plane with the molecule (Table 4), and although these conformers may have lower minimum energies than orientation [7], the conjugation systems within them are disturbed.

© 2002 NRC Canada

Fig. 10*a*. The change of bond lengths from the native form to radical form of 7,8-dihydroxyflavone orientation [6a]. Hydrogen 29 is abstracted in this case. Note the resonance structure (hence delocalization) available for the radical form.

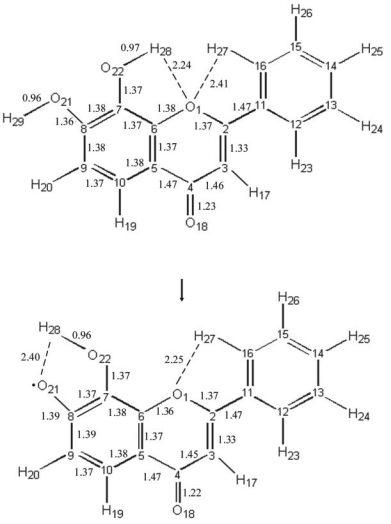

Fig. 10*b*. Spin densities of individual atoms and whole regions of 7,8-dihydroxyflavone radical orientation [6a].

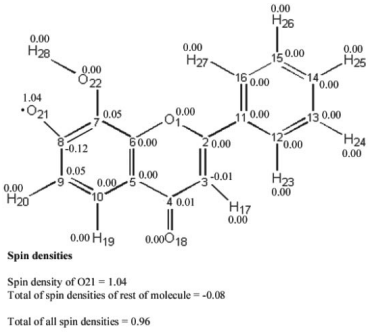

For orientation [7], co-planarity is achieved by three factors: lack of steric hindrance between H28 and H27, conjugative stabilization of the π-electron system, including planar hydroxyl groups (Table 4), and the electronic interaction between O1 and H27 (Table 3), which "locks" the molecule into a planar conformation. Although O1 and H27 are quite far apart (approximately 2.3 Å), and H27 is not highly polarized, some type of dipole-induced dipole interaction may still be established.

Vibrational frequencies

The vibrational frequencies of the molecules at their minimum conformations are performed at B3LYP/6–31G(d) (not shown). The absence of negative frequencies for all molecules except [7] shows that the conformations obtained are indeed minima on their potential energy surfaces. The lone negative frequency obtained for [7] is extremely small (~19.6 cm^{-1}) and is considered to be within convergence error. No further calculation for that molecule was carried out.

Studies on the radical forms of selected conformations

Because the bond dissociation enthalpy of H_2O is one of the strongest of all bonds (119 kcal mol^{-1}), it is obvious that

Fig. 11*a*. The change of bond lengths from the native form to radical form of 7,8-dihydroxyflavone orientation [7]. Hydrogen 28 is abstracted in this case. Note the resonance structure (hence delocalization) available for the radical form.

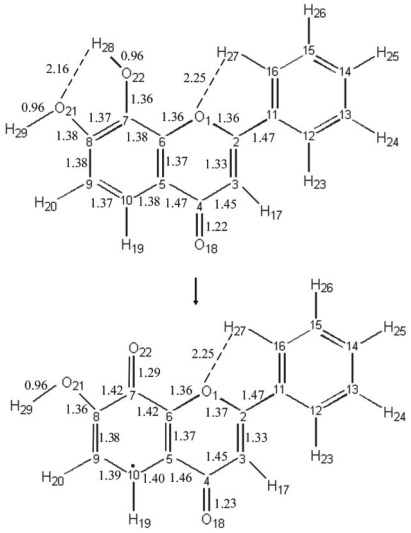

Fig. 11*b*. Spin densities of individual atoms and whole regions of 7,8-radical dihydroxyflavone orientation [7].

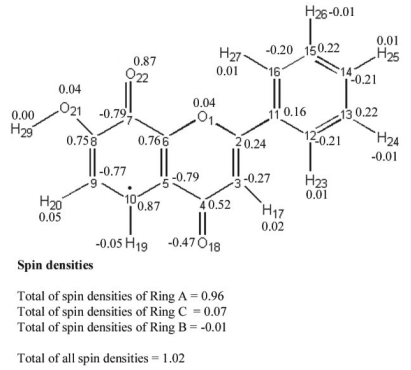

every organic molecule will react exothermically to •OH (17). Hence, the radical forms of the flavonoids are expected to be generated by hydrogen transfer in the presence of •OH:

$$\text{Native flavonoid} + {}^{\bullet}\text{OH} \rightarrow \text{Flavonoid radical} + H_2O$$

The radical forms of conformations [1], [6], and [7] are selected for further calculations because they are the most probable candidates for free radical scavenging by hydrogen transfer. The main determinants for their selections are the availability of a hydrogen atom, either H29 or H28 (on 7,8-dihydroxyflavone only), for abstraction, and the minimal amount of hydrogen bond-like interactions disturbed. For example, H28 of chrysin is not suitable for hydrogen extraction because the molecule attains maximum stabilization when H28 is interacting with O18, thereby making H28 inaccessible. Significant bond lengths and atom-by-atom spin densities resulting from these calculations are shown in Figs. 8–12.

The results obtained for the radical forms of molecules [1] and [6] are similar, since both molecules have H29 extracted from O21. The geometric parameters indicate that the lone

© 2002 NRC Canada

Table 5. The geometric and energetic parameters of the radical forms of selected orientations of the two flavones, chrysin and 7,8-dihydroxyflavone.

Compound	Minimum energy E (Hartree)	Relative energy ΔE (kcal mol^{-1})[a]	Maximum hydrogen bonding	α (°)[b]	Hydroxyl torsional angle (°)
Chrysin					
[1]	–867.87	0.00	Yes	16.81	(5OH) 0.16
7,8-Dihydroxyflavone					
[6]	–867.85	0.00	No	29.02	(8OH) 4.03
[6a]	–867.81	+25.10	Yes	0.03	(8OH) 0.02
[7]	–867.84	0.00	No	0.01	(7OH) 0.02
[7a]	–867.85	–6.28	Yes	0.00	(7OH) 0.02

[a]ΔE (kcal mol^{-1}) = 627.51 ($E_{TS} - E_{min}$) calculated using the lowest minimum energy as E_{min}.
[b]Note that there are four equivalent torsional angles that govern minimum energy conformations: (0 + α), (180 – α), (180 + α), and (360 – α).

Fig. 12*a*. The change of bond lengths from the native form to radical form of 7,8-dihydroxyflavone orientation [7a]. Hydrogen 28 is abstracted in this case. Note the resonance structure (hence delocalization) available for the radical form.

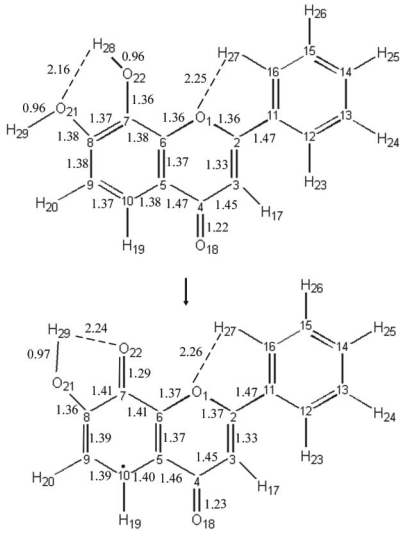

Fig. 12*b*. Spin densities of individual atoms and whole regions of 7,8-radical dihydroxyflavone orientation [7a].

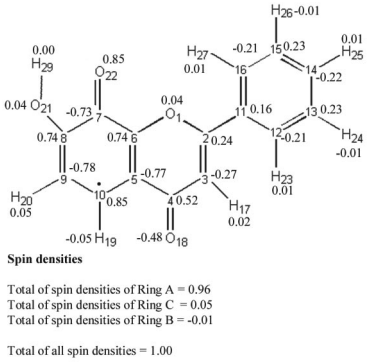

electrons of the radicals may not be localized to O21, and their conformations can adopt *para*-quinoidal structures through resonance (Figs. 8*a*, 9*a*). This conjecture is suggested by the alteration of bond lengths between the native forms of the molecules and their radical forms. The reduction in bond length of O21–C8 in the radical forms indicates that the bond is changing from a pure single bond to one with more double-bond characteristics. Furthermore, bonds O18–C4, C8–C7, C9–C8, C6–C5, and C10-C5 are all lengthened after hydrogen transfer, while bonds C7–C6 and C10–C9 remain unchanged. The significant lengthening of a bond indicates an increase in single-bond characteristics. In the resonance structures of the two molecules, the lone electron can be drawn to reside on O18. From a quantum mechanical standpoint, an electron is not considered to be a particle, but the possibility for electron movement suggests that the lone electron is delocalized across rings A and C. This fact is further reinforced by the spin densities of the molecules (Figs. 8*b*, 9*b*). While combining the spin densities of rings A and C yields a result of nearly 1, ring B has a total spin density of zero (within computational range of accuracy). This result suggests that the lone electron is shared by rings A and C, but not B. The participation of ring B in the delocalization system is therefore negligible. It can also be seen that the spin densities of the atoms in rings A and C are large (>0.5) except for O1, C2, and C3, suggesting the exclusion of these atoms from the delocalization system.

Another possible hydroxyl orientation for the 7,8-dihydroyflavone [6] radical is shown in Fig. 10*a*. This orientation occurs because the rotation barriers for hydroxyl groups in phenolic compounds are low (4 kcal mol^{-1}); the hydrogen atoms on any hydroxyl groups should therefore be free to rotate to their minimum conformations (17) — this hydroxyl orientation is labeled as [6a]. H28 of the hydroxyl group now forms a hydrogen bond with O21, the site where the radical is initially formed. Based on the radical's geometric parameters shown in Fig. 10*a*, a delocalized *para*-quinoidal structure is not observed because the geometry of the radical is nearly the same as its neutral form. The spin densities of radical [6a] also show that most of the charge contributed by the lone electron is localized to O21 (Fig. 10*b*), and not spread throughout the molecule. Furthermore, energy of radical [6a] is higher than that of radical [6] (Table 5; compare rows 2 and 3, column 3). The instability of this conformation suggests that a *para*-quinoidal structure is not formed because delocalization usually leads to stabilization and lower minimum energy. The phenomenon can be explained by the fact that a hydrogen bond formed between H28 and O21 will draw negative charges to O21 to

© 2002 NRC Canada

strengthen that interaction as much as possible. The lone electron will, therefore, stay at O21, which will prevent its movement to other sites. The instability of radical conformation [6a], as opposed to delocalized form [6], will prevent it from being the dominant radical species.

The results from the calculations of the molecule [7] radical are different, because in this case, the hydrogen (H28) is abstracted from O22 instead of O21. Again, the radical can adopt a *para*-quinoidal structure via resonance (Fig. 11*a*), and the geometry of the radical conformation confirms this fact. Bonds C8–C7, C7–C6, C10–C9, and C10–C5 are lengthened, while bonds C9–C8 and C6–C5 remain the same lengths. The longer bond lengths suggest increases in single-bond characteristics, while the shortening of bond O22–C7 suggests an increase in double-bond characteristics in that single bond. Although a slight increase in the bond length (by 0.01 Å) of O18–C4 is observed, it is small enough to be negligible. A delocalized system can be proposed for this radical conformation with the lone electron residing at C10 (Fig. 11*a*), and the spin densities also support the fact that the electron is only delocalized in ring A (Fig. 11*b*). In this particular orientation, rings B and C have small spin densities (<0.5), while ring A has a large spin density adding up to 1 (within computational range of accuracy), signifying that the unpaired electron resides mainly at ring A. The spin densities of C4 and O18 in [7] are much less than those in molecules [1] and [6], suggesting that these atoms in [7] do not participate in the delocalization system as much as those in [1] and [6].

Another possible hydroxyl orientation for the 7,8-dihydroyflavone [7] radical is shown in Fig. 12*a* and is labeled [7a]. The hydrogen of the hydroxyl group H29 now forms a hydrogen bond with O22. Indeed, because of the extra stabilization provided by the hydrogen bond, the minimum energy, compared with conformation [7], is lowered without this hydrogen bond interaction (Table 5; compare rows 4 and 5, column 3). In addition, the delocalized system of the *para*-quinoidal structure is not disturbed; the conformation [7a] therefore represents the most stable conformation for this radical species.

Conclusion

Conjugation contributes to the overall stabilization of the radical complex formed after scavenging. Hydroxyl groups will contribute to conjugative stabilization if placed in a non-sterically hindered way. Stabilization can also be achieved through intramolecular hydrogen bond-like interactions. Dihydroxyflavones, as weak anti-oxidants, possess strong conjugation systems across rings A and C, and perhaps much weaker ones across ring B. This fact is supported by the deviation of the phenyl ring from co-planarity from the rest of the molecule in both the radical and neutral forms. The lone electron of the radical forms of the flavones is also found to be mainly delocalized in rings A and C by spin densities.

Suggestions for further works

As noted by Wright et al. (17), the NDE of a phenolic anti-oxidant would indicate how fast it reacts with a free radical, giving a good indication of its anti-oxidant ability. The NDE of flavonoid anti-oxidants can be determined by calculating the enthalpy of the following reaction and comparing it to the phenol standard:

$$\text{Native flavonoid} \rightarrow \text{Flavonoid radical} + \text{H}^{\bullet}$$

Another logical improvement on this study is to perform the calculations at higher and more reliable levels of theory, especially on the 1-D scans. This improvement applies especially to chrysin at orientation [3], since a discrepancy is detected between the three basis sets. For this molecule, full 1-D scans should be performed at each of the basis sets to show how the energy pattern changes with the level of theory.

Other proven polyphenolic anti-oxidants (not necessarily flavonoids) should also be geometrically analyzed to determine other structural features for radical scavenging abilities. To support the idea of conjugation, the anti-oxidants chosen should possess many possible resonance structures. Furthermore, the molecules should be studied in their hydrated state, since flavonoids usually exist in aqueous environments in the body.

Acknowledgment

The authors are grateful for the use of the supercomputer at the National Cancer Institute of NIH, as well as distributed processing on the PC-unix clusters at Velocel Communications Inc., Toronto, Canada.

References

1. S. Steeken. Chem. Rev. **89**, 503 (1979).
2. K.L. Fong, P.B. McCay, J.L. Poyer, B. B. Keele, and H. Misra. J. Bio. Chem. **248**, 7792 (1973).
3. I.T. Mak and W.B. Weglicki. J. Clin. Invest. **75**, 58 (1985).
4. (*a*) B. Halliwell and J.M.C. Gutteridge. Free Radic. Biol. Med. **18**, 125 (1995). (*b*) L. Ternay, Jr. and V. Sorokin. *In* Oxidants, antioxidants, and free radicals. *Edited by* S.I. Baskin and H. Salem. Taylor & Francis, Washington. 1997. pp 1–60.
5. N.C. Cook and S. Samman. Nutrit. Biochem. **7**, 66 (1996).
6. S.S. Pekkarinen, I.M. Heinonen, and A.I. Hopia. J. Sci. Food Agr. **79**, 499 (1999).
7. L. Vrielynck, J.P. Cornard, J.C. Merlin, and P. Bopp. J. Mol. Str. **297**, 227 (1993).
8. M.E. Shils and R.S. Goodhart. The flavonoids in biology and medicine, a critical review. New York National Vitamin Foundation Inc., New York. 1956.
9. P.T. Gardner, D.B. McPhail, A. Crozier, and G.D. Duthie. J. Sci. Food Agr. **79**, 1011 (1999).
10. J. Terao. *In* Antioxidant food supplements in human health. *Edited by* L. Packer, M. Hiramatsu, and T. Yoshikawa. Academic Press, San Diego. 1999. pp 255–269.
11. C.A. Rice-Evans and N.J. Miller. *In* Flavonoids in health and diseases. *Edited by* C.A. Rice-Evans and L. Packer. Marcel Dekker Inc, New York. 1998. pp 199–219.
12. S.A.B.E. van Acker, A. Bast, and W.J.F. van der Vijgh. *In* Flavonoids in health and diseases. *Edited by* C.A. Rice-Evans and L. Packer. Marcel Dekker Inc, New York. 1998. pp 221–251.
13. S.V. Jovanovic. J. Am. Chem. Soc. **121**, 9677 (1999).
14. S.I. Nagaoka. J. Phys. Chem. **104**, 856 (2000).
15. M.I. de Heer. J. Am. Chem. Soc. **122**, 2355 (2000).

© 2002 NRC Canada

16. S.V. Jovanovic, S. Steenken, M.G. Simic, and Y. Hara. *In* Flavonoids in health and diseases. *Edited by* C.A. Rice-Evans and L. Packer. Marcel Dekker Inc, New York. 1999. pp 137–161.
17. J.S. Wright, E.R. Johnson, and G.A. DiLabio. J. Am. Chem. Soc. **123**, 1173 (2001).
18. S.A.B.E. van Acker, D.J. van den Berg, M.N.J.L. Tromp, D.H. Griffin, W.P. van Bennekom, W.J.F. van der Vijgh, and A. Bast. Free Rad. Bio. Med. **20**, 331 (1996).
19. E. Cadenas. *In* Free radicals, oxidative stress, and antioxidants. *Edited by* T. Ozben, Plenum Press, New York. 1998. pp 237–251.
20. W. Bors, W. Heller, S. Michel, and K. Stettmaier. *In* Flavonoids in the living system. *Edited by* J.A. Manthey and B.S. Buslig. Plenum Press, New York. 1998. pp 409–466.
21. K. Mukai. J. Phys. Chem. **101**, 3746 (1997).
22. D.K. Ho, J.M. Cassady, Y.H. Chae, V.M. Cook, and W.M. Baird. *In* Recent advances of chemistry and molecular biology in cancer research. *Edited by* D. Qianhuan, M. Armour and Z. Qingying. Science Press, Beijing. 1991. pp 65–76.
23. P. Mak, F. Dela Cruz, and S. Chen. Environ. Hea. Pers. **107**, 855 (1999).
24. Y. Kao, C. Zhou, M. Sherman, C.A. Laughton, and S. Chen. Environ. Hea. Pers. **106**, 85 (1998).
25. Gaussian 94, Revision E.2. M.J. Frisch, G.W. Trucks, H.B. Schlegel, P.M.W. Gill, B.G. Johnson, M.A. Robb, J.R. Cheeseman, T. Keith, G.A. Petersson, J.A. Montgomery, K. Raghavachari, M.A. Al-Laham, V.G. Zakrzewski, J.V. Ortiz, J.B. Foresman, J. Cioslowski, B.B. Stefanov, A. Nanayakkara, M. Challacombe, C.Y. Peng, P.Y. Ayala, W. Chen, M.W. Wong, J.L. Andres, E.S. Replogle, R. Gomperts, R.L. Martin, D.J. Fox, J.S. Binkley, D.J. Defrees, J. Baker, J.P. Stewart, M. Head-Gordon, C. Gonzalez, and J.A. Pople. Gaussian, Inc., Pittsburgh, PA. 1995.
26. Gaussian 98, Revision A.9. M.J. Frisch, G.W. Trucks, H.B. Schlegel, G.E. Scuseria, M.A. Robb, J.R. Cheeseman, V.G. Zakrzewski, J.A. Montgomery, Jr., R.E. Stratmann, J.C. Burant, S. Dapprich, J.M. Millam, A.D. Daniels, K.N. Kudin, M.C. Strain, O. Farkas, J. Tomasi, V. Barone, M. Cossi, R. Cammi, B. Mennucci, C. Pomelli, C. Adamo, S. Clifford, J. Ochterski, G.A. Petersson, P.Y. Ayala, Q. Cui, K. Morokuma, D.K. Malick, A.D. Rabuck, K. Raghavachari, J.B. Foresman, J. Cioslowski, J. V. Ortiz, A.G. Baboul, B.B. Stefanov, G. Liu, A. Liashenko, P. Piskorz, I. Komaromi, R. Gomperts, R.L. Martin, D.J. Fox, T. Keith, M.A. Al-Laham, C.Y. Peng, A. Nanayakkara, M. Challacombe, P.M.W. Gill, B. Johnson, W. Chen, M.W. Wong, J.L. Andres, C. Gonzalez, M. Head-Gordon, E.S. Replogle, and J.A. Pople. Gaussian, Inc., Pittsburgh, PA. 1998.
27. A. Mantas, E. Deretey, F.H. Ferretti, M. Estrada, and I.G. Csizmadia. J. Mol. Str. **504**, 77 (2000).

© 2002 NRC Canada

The synthesis of a carbohydrate-like dihydrooxazine and tetrahydrooxazine as putative inhibitors of glycoside hydrolases: A direct synthesis of isofagomine

Wayne M. Best, James M. Macdonald, Brian W. Skelton, Robert V. Stick, D. Matthew G. Tilbrook, and Allan H. White

Abstract: The treatment of benzyl 2,3-*O*-isopropylidene-β-L-xylopyranoside with *N*-hydroxyphthalimide under Mitsunobu conditions, followed by protecting-group interchange, gave benzyl 4-*O*-[(*tert*-butoxycarbonyl)amino]-2,3-*O*-isopropylidene-α-D-arabinoside. Mild acid hydrolysis and catalytic hydrogenolysis afforded 4-*O*-[(*tert*-butoxycarbonyl)amino]-D-arabinose that, upon heating in water, gave the dihydrooxazine [(4*R*,5*S*,6*R*)-5,6-dihydro-4,5-dihydroxy-6-hydroxymethyl-4*H*-1,2-oxazine] as a crystalline solid. A single-crystal structure determination of this solid showed it to exist in the $^5H_6$ conformation. Reduction of the dihydrooxazine gave the tetrahydrooxazine [(4*R*,5*S*,6*R*)-4,5-dihydroxy-6-hydroxymethyl-3,4,5,6-tetrahydro-2*H*-1,2-oxazine]. The dihydrooxazine was an effective inhibitor of two β-glucosidases (K_i = 27 and 35 μM). Benzyl 2,3-*O*-isopropylidene-β-L-xylopyranoside, via the derived imidazylate, was converted into a nitrile that, upon reduction and protecting-group manipulations, gave benzyl 4-*C*-aminomethyl-4-deoxy-α-D-arabinoside. Treatment of this amine with hydrogen and palladium-on-carbon gave isofagomine.

Key words: dihydrooxazine, tetrahydrooxazine, isofagomine, iminosugars, glycosidase inhibitors.

Résumé : Le traitement du 2,3-*O*-isopropylidène-β-L-xylopyranoside de benzyle par du *N*-hydroxyphtalimide dans des conditions de Mitsunobu, suivi d'un échange des groupes protecteurs, conduit à la formation du 4-*O*-[(*tert*-butoxycarbonyl)amino]-2,3-*O*-isopropylidène-α-D-arabinoside de benzyle. Soumis à une hydrolyse acide légère et une hydrogénolyse catalytique, celui-ci fournit alors le 4-*O*-[(*tert*-butoxycarbonyl)amino]-D-arabinose qui, par chauffage dans l'eau, livre la dihydrooxazine [(4*R*,5*S*,6*R*)-5,6-dihydro-4,5-dihydroxy-6-hydroxyméthyl-4*H*-1,2-oxazine] sous la forme de solide cristallin. Une détermination de structure sur un cristal unique montre qu'elle existe dans la conformation $^5H_6$. La réduction de la dihydrooxazine fournit la tétrahydrooxazine [(4*R*,5*S*,6*R*)-4,5-dihydroxy-6-hydroxyméthyl-3,4,5,6-tétrahydro-2*H*-1,2-oxazine]. La dihydrooxazine est un inhibiteur efficace de deux β-glucosidases (K_i = 27 et 35 μM). Le 2,3-*O*-isopropylidène-β-L-xylopyranoside de benzyle, par le biais de l'imidazylate qui en dérive, a été transformé en un nitrile qui, après réduction et des manipulations des groupes protecteurs, fournit le 4-*C*-aminométhyl-4-désoxy-α-D-arabinoside de benzyle. Le traitement de cette amine avec de l'hydrogène et du palladium sur du charbon conduit alors à l'isofagomine.

Mots clés : dihydrooxazine, tétrahydrooxazine, isofagomine, iminosucres, inhibiteurs de glycosidases.

[Traduit par la Rédaction]

Introduction

The making and breaking of the glycosidic linkage are events central to the survival of virtually all organisms. Both processes are mediated by enzymes, generally described as synthases or transferases for the former process and hydrolases for the latter. The study of the mechanism of action of glycoside hydrolases has received much attention in the last half century (1–3).

One way to study the action of an enzyme is to design molecules that will inhibit the normal catalytic process. In this regard, glycoside hydrolases are no exception and there exists a class of inhibitor, generally described as "imino sugars," that encompasses such well-known molecules as swainsonine, castanospermine, nojirimycin, deoxynojirimycin, and fagomine (4, 5). Bols (6) suggested, and subsequently synthesised, an unnatural aza sugar, isofagomine (**1**), which was shown to be a powerful inhibitor of some enzymes that hydrolyze β-D-glycosidic linkages with retention of configuration.

Some years ago, it occurred to us that tetrahydrooxazine **2** might better represent the natural substrate for the enzymes of interest (or, rather, conjugate acid **3** would better represent the transition state commonly implicated in the

Received 29 October 2001. Published on the NRC Research Press Web site at http://canjchem.nrc.ca on 21 June 2002.

Dedicated to the memory of Professor Ray Lemieux.

W.M. Best, J.M. Macdonald, B.W. Skelton, R.V. Stick,[1] D.M.G. Tilbrook, and A.H. White. Department of Chemistry, 35 Stirling Highway, The University of Western Australia, Crawley, WA 6009, Australia.

[1]Corresponding author (e-mail: rvs@chem.uwa.edu.au).

 DOI: 10.1139/V02-060 © 2002 NRC Canada

Scheme 1. P, P′ are protecting groups.

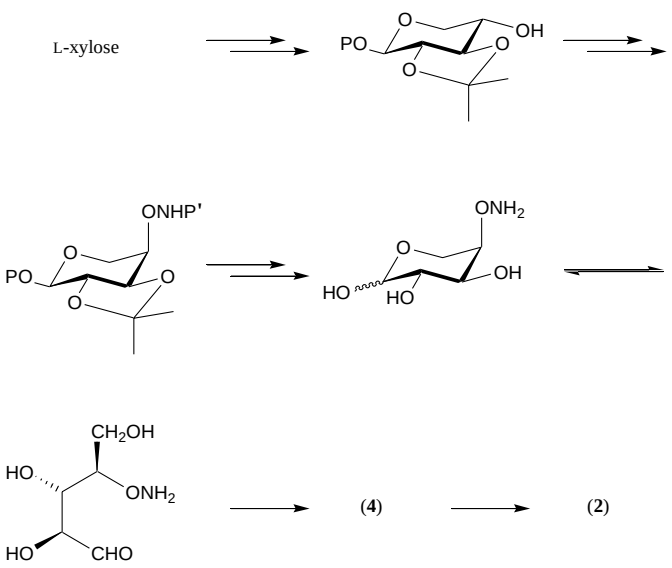

Fig. 1. A single molecule (the asymmetric unit) of **4**, showing 50% probability thermal ellipsoids for the non-hydrogen atoms, hydrogen atoms having arbitrary radii of 0.1 Å.

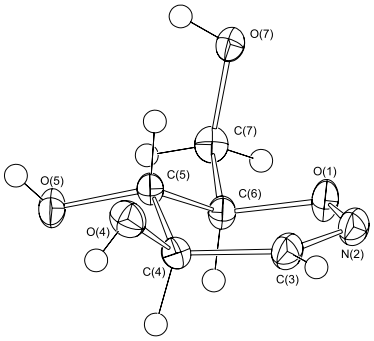

hydrolytic process (1–3)). We thus started a synthetic program that would furnish tetrahydrooxazine **2**, via dihydrooxazine **4**; subsequently, the synthetic route chosen also supplied isofagomine (**1**).

In 1999, during the course of our investigations, Bols and co-workers (7) published a synthesis of the racemic form of **2**, not unexpectedly involving the cycloaddition of a nitroso compound onto a diene. It was always our intention to produce the tetrahydrooxazine as one enantiomer and the success of the process, starting with L-xylose and outlined in Scheme 1, would ultimately depend upon the choice of protecting groups.

Results and discussion

In our initial investigations, D-xylose (in the early stages of our work, it was much cheaper to use this enantiomer) was converted into methyl β-D-xylopyranoside and then to methyl 2,3-*O*-isopropylidene-β-D-xylopyranoside (**5**). *N*-Hydroxyphthalimide (**6**) was seen as a suitable source of the required hydroxylamine residue. Thus, treatment of alcohol **5** with **6** under Mitsunobu conditions gave α-L-arabinoside **7**. Mild acid hydrolysis of **7** then gave diol **8** and a subsequent treatment with phenylhydrazine gave hydroxylamine **9**. Try as we might, hydroxylamine **9** could never be converted into any recognizable product under acidic conditions (there was never any evidence for the formation of the desired product, the enantiomer of the dihydrooxazine (**4**) [*ent*-(**4**)]).

Fig. 2. Unit cell contents, projected down *a*, showing hydrogen bonding.

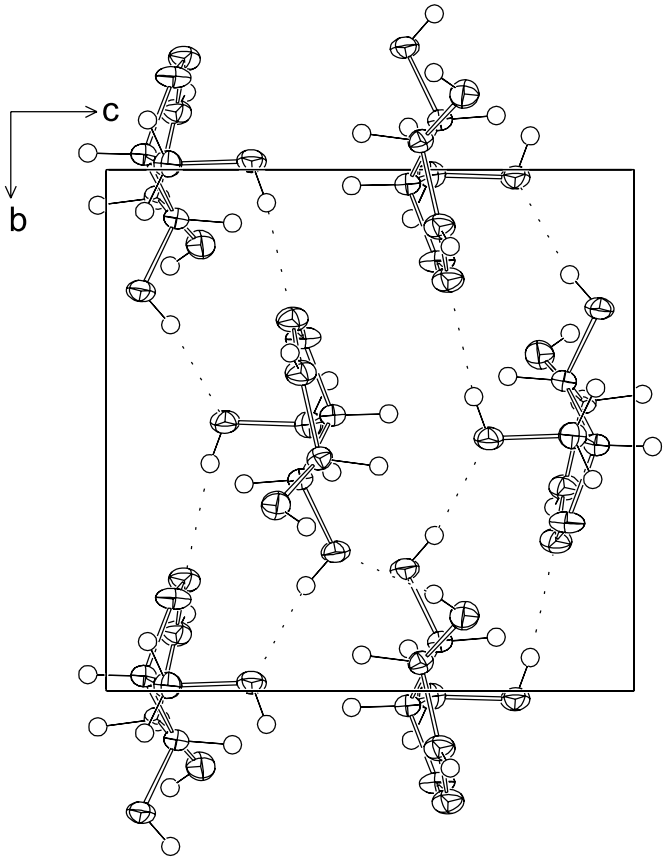

The source of our problem seemed to reside with the choice of a methyl glycoside for the protection of the anomeric centre. The sequence from D-xylose was, therefore, mimicked in both the allyl and 2-trimethylsilylethyl series, resulting in α-L-arabinosides **10** and **11**. But conditions could not be found for the removal of either the allyl or 2-trimethylsilylethyl glycoside with concomitant formation of *ent*-(**4**).

In some desperation, a benzyl glycoside was considered and, subsequently, α-L-arabinoside **12** was synthesized. All attempts at the hydrogenolysis–hydrogenation of **12**, generally over palladium-on-carbon, failed to produce either *ent*-(**4**) or *ent*-(**2**).

Much discussion, heartache, and experimentation were to follow before we hit upon a successful twist for the synthesis of **2** and **4**. L-Xylose was converted into benzyl β-L-xylopyranoside (we now employ trichloroacetimidate methodology for the synthesis of the glycoside, rather than the earlier Koenigs–Knorr approach) and in turn into alcohol **13**. Normal Mitsunobu chemistry gave phthalimide **14**, and

© 2002 NRC Canada

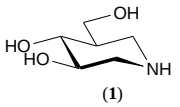

(**1**)

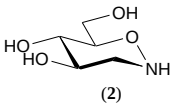

(**2**)

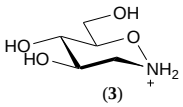

(**3**)

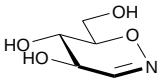

(**4**)

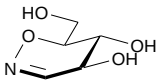

ent-(**4**)

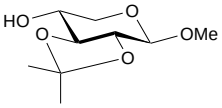

(**5**)

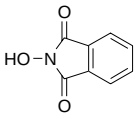

(**6**)

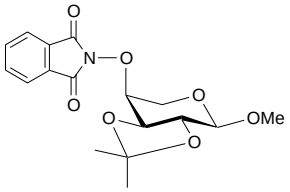

(**7**)

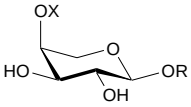

(**8**) X = 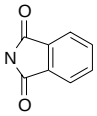 R = Me

(**9**) NH_2 Me

(**10**) NH_2 $CH_2CH{=}CH_2$

(**11**) NH_2 $CH_2CH_2SiMe_3$

(**12**) NH_2 CH_2Ph

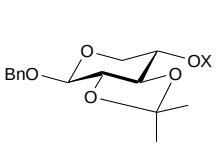

(**13**) X = H

(**20**) SO_2Im

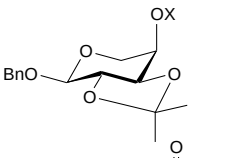

(**14**) X = 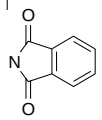

(**15**) NH_2

(**16**) $NHCOOBu^t$

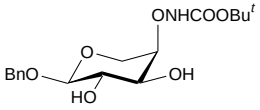

(**17**)

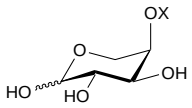

(**18**) X = $NHCOOBu^t$

(**19**) NH_2

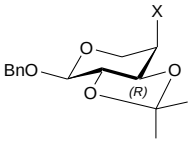

(**21**) X = CN

(**22**) CH_2NH_2

(**23**) $CH_2NHCOOBu^t$

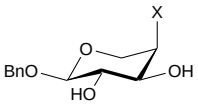

(**24**) X = $CH_2NHCOOBu^t$

(**25**) CH_2NH_2

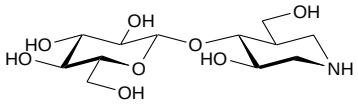

(**26**)

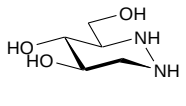

(**27**)

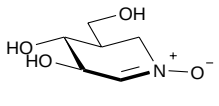

(**28**)

subsequent manipulations gave hydroxylamine **15** and then presumably carbamate **16**. Mild acid hydrolysis of **16** gave diol **17** and subsequent catalytic hydrogenolysis gave hemiacetal **18**. Treatment of **18** in boiling water presumably liberated hydroxylamine **19**, which subsequently formed the desired and crystalline dihydrooxazine **4**! A single-crystal structure determination of **4** (Figs. 1 and 2, Table 1) showed it to exist in the $^5H_6$ conformation.

Dihydrooxazine **4** could be converted into desired tetrahydrooxazine **2** by treatment with sodium cyanoborohydride in acetic acid. Our synthetic material (**2**) shared all of the physical attributes as described by Bols (7), especially in terms of NMR chemical-shift predictions (both ^{1}H and ^{13}C), and possessed a negative value for the specific optical rotation.

Dihydrooxazine **4** acted as an efficient inhibitor of two β-glucosidases isolated from *Aspergillus niger* and *Clostridium saccharolyticium* — **4** had K_i values of 27 and 35 μM, respectively. Bols and co-workers (7) have previously reported an inhibition constant (60 μM) for (±)-(**2**) against almond β-glucosidase.

With the euphoria that comes with the successful conclusion to a long and protracted piece of work, we wondered if our process could be adapted to a synthesis of isofagomine (**1**). (All that was really required was to replace the oxygen of the hydroxylamine by a carbon, and the cyano group seemed a logical choice.) Thus, alcohol **13** was converted into imidazylate **20** (8) and a subsequent treatment with trimethylsilyl cyanide and tetrabutylammonium fluoride gave nitrile **21** (9), a far superior result to our efforts using potassium cyanide in dimethylformamide.

Nitrile **21** was then reduced, presumably to amine **22**, and the product isolated as carbamate **23**. Then, in virtually quantitative yields, mild acid hydrolysis of **23** gave diol **24**, and subsequent treatment with anhydrous acid presumably gave amine **25**. Hydrogenolysis–hydrogenation of **25** over palladium-on-carbon then gave isofagomine (**1**).

We have routinely used the synthesis described here to produce appreciable amounts of isofagomine — the lowest yielding step, the isopropylidenation of benzyl β-L-xylopyranoside, is encountered early on in the sequence and the

© 2002 NRC Canada

Table 1. Molecular non-hydrogen geometries.

Distances (Å)			
O(1)—N(2)	1.405(2)	C(4)—C(5)	1.516(2)
O(1)—C(6)	1.450(2)	C(5)—O(5)	1.418(2)
N(2)—C(3)	1.269(2)	C(5)—C(6)	1.521(2)
C(3)—C(4)	1.506(2)	C(6)—C(7)	1.519(2)
C(4)—O(4)	1.417(2)	C(7)—O(7)	1.425(2)
Angles (°)			
N(2)-O(1)-C(6)	119.3(1)	C(4)-C(5)-C(6)	108.9(1)
O(1)-N(2)-C(3)	119.3(1)	O(5)-C(5)-C(6)	107.8(1)
N(2)-C(3)-C(4)	127.0(1)	O(1)-C(6)-C(5)	111.8(1)
C(3)-C(4)-O(4)	109.1(1)	O(1)-C(6)-C(7)	103.9(1)
C(3)-C(4)-C(5)	109.4(1)	C(5)-C(6)-C(7)	113.8(1)
O(4)-C(4)-C(5)	111.2(1)	C(6)-C(7)-O(7)	111.0(1)
C(4)-C(5)-O(5)	111.3(1)		
Ring torsion angles (°)			
C(6)-O(1)-N(2)-C(3)	–6.9(2)	C(3)-C(4)-C(5)-C(6)	46.0(1)
O(1)-N(2)-C(3)-C(4)	–2.1(2)	C(4)-C(5)-C(6)-O(1)	–55.9(2)
N(2)-C(3)-C(4)-C(5)	–19.3(2)	C(5)-C(6)-O(1)-N(2)	36.7(2)

Note: Hydrogen bonds: OH(4)··O(5) (x – 1/2, 1/2 – y, 2 – z) = 2.747(2), 2.03(2) Å; OH(5)··O(7) (2 – x, y – 1/2, 1.5 – z) = 2.737(2), 1.94(2) Å; OH(7)··N(2) (2 – x, y – 1/2, 1.5 – z) = 2.808(2), 2.05(3) Å.

whole process compares favourably with previously published syntheses (10–16). It is our immediate intention to produce glycosylated versions of isofagomine, such as **26**, and to see if our synthetic sequence can be adopted to produce 1-azafagomine (**27**) (17) and interesting nitrone **28**.

Experimental

General experimental procedures have been given previously (18). HCl in MeOH was generated by the addition of acetyl chloride to anhydrous MeOH.

Structure determination of 4

A full sphere of CCD area-detector diffractometer data was measured (Bruker AXS instrument; (ω–scans, $2\theta_{max}$ = 58°; monochromatic Mo Kα radiation, λ = 0.7107$_3$ Å; T = ~153 K) yielding 6405 total reflections, merging to 939 unique (R_{int} = 0.023), 897 with $F > 4\sigma(F)$ being used in the full matrix least squares refinement (C, N, and O thermal parameter forms anisotropic (x, y, z, U_{iso})$_H$ refined). "Friedel pair" data were not retained distinct, chirality being assigned from the chemistry. Conventional residuals R and R_w (weights: $\sigma^2(F) + 0.0004\,F^2)^{-1}$) on | F | at convergence were 0.028 and 0.039, respectively. Neutral-atom scattering factors were used within the context of the Xtal 3.6 program system (19).

Crystal data

$C_5H_9NO_4$, M = 197.1, orthorhombic, space group $P2_12_12_1$ (D_2^4, No. 19), a = 7.091(1), b = 8.847(1), c = 8.928(1) Å, V = 631.2 Å^3, $D_{calcd.}$ = 1.548 g cm^{-3}, Z = 4, μ_{Mo} = 1.3 cm^{-1} (no correction).

Methyl 2,3-*O*-isopropylidene-4-*O*-(*N*-phthalimido)-α-L-arabinoside (7)

Methyl 2,3-*O*-isopropylidene-β-D-xylopyranoside (20) (**5**) (2.80 g, 13.7 mmol), triphenylphosphine (4.10 g, 15.6 mmol), and *N*-hydroxyphthalimide (**6**) (2.50 g, 15.3 mmol) in THF (20 mL) were cooled (10°C) and treated with diisopropyl azodicarboxylate (3.60 mL, 18.3 mmol) for 3 days at rt. The mixture was then poured into $NaHCO_3$ solution and subjected to normal workup (EtOAc). Flash chromatography (EtOAc–petrol, containing 0.5% Et_3N, 2:3) gave the phthalimide (**7**) (3.10 g, 65%) as a colourless solid; mp 158–160°C; $[\alpha]_D$ +7.8 ($CHCl_3$). ^{1}H NMR (500 MHz, $CDCl_3$) δ: 1.35, 1.40 (2s, CMe_2), 3.57 (s, OMe), 3.64 (dd, $J_{2,3}$ = 9.8, $J_{3,4}$ = 2.4 Hz, H3), 3.66 (dd, $J_{4,5}$ = 1.7, $J_{5,5}$ = 13.6 Hz, H5), 4.30 (dd, $J_{1,2}$ = 7.7 Hz, H2), 4.40 (dd, $J_{4,5}$ = 1.5 Hz, H5), 4.49 (d, H1), 5.04 (m, H4), 7.72–7.73, 7.79–7.81 (2m, 4H, Ar). ^{13}C NMR (125.8 MHz, $CDCl_3$) δ: 26.03, 26.52 (CMe_2), 56.50 (OMe), 65.49 (C5), 72.88, 77.63, 79.64 (C2,3,4), 104.29 (Cl), 111.00 (CMe_2), 123.45, 128.98, 134.42 (6C, Ar), 163.04 (2C, CO).

Methyl 4-*O*-(*N*-phthalimido)-α-L-arabinoside (8)

Phthalimide **7** (1.01 g) in MeOH (40 mL) was treated with hydrochloric acid (0.4 mL of 1 M) for 45 min. The mixture was then concentrated and the residue dissolved in warm $CHCl_3$, filtered and concentrated to give diol **8** (900 mg) as a colourless solid, a portion of which was recrystallized to give colourless needles; mp 205–206°C (EtOH); $[\alpha]_D$ –16.7 ($CHCl_3$). ^{1}H NMR (500 MHz, DMSO-d_6) δ: 3.39 (s, OMe), 3.58 (dd, $J_{4,5}$ = 1.8, $J_{5,5}$ = 12.7 Hz, H5), 3.64 (ddd, $J_{1,2}$ = 6.0, $J_{2,3}$ = 8.5, $J_{2,OH}$ = 4.5 Hz, H2), 3.68 (ddd, $J_{3,4}$ = 3.1, $J_{3,OH}$ = 5.4 Hz, H3), 4.08 (dd, $J_{4,5}$ = 3.8 Hz, H5), 4.11 (d, H1), 4.47–4.51 (m, H4), 4.89 (d, 3-OH), 5.26 (d, 2-OH), 7.86 (s, 4H, Ar). ^{13}C NMR (125.8 MHz, DMSO-d_6) δ: 55.76 (OMe), 61.52 (C5), 70.34, 71.36, 82.86 (C2,3,4), 104.00 (Cl), 123.19, 128.64, 134.71 (6C, Ar), 163.29 (2C, CO). Anal. calcd. for $C_{14}H_{15}NO_7$: C 54.4, H 4.9, N 4.5; found: C 54.4, H 5.0, N 4.5.

Methyl 4-*O*-amino-α-L-arabinoside (9)

Diol **8** (777 mg, 2.50 mmol) in EtOH (15 mL) was treated with phenylhydrazine (0.35 mL, 3.6 mmol) and the mixture stirred (45 min, rt), poured into water, and washed with EtOAc. The aqueous phase was concentrated and the residue triturated with EtOAc (which was discarded) to leave hydroxylamine derivative **9** (357 mg, 79%) as a colourless solid, a portion of which was recrystallized to give colourless needles; mp 144°C (EtOH); $[\alpha]_D$ +32.3 (MeOH). ^{1}H NMR (300 MHz, DMSO-d_6) δ: 3.25 (ddd, $J_{1,2}$ = 6.7, $J_{2,3}$ = 9.0, $J_{2,OH}$ = 4.8 Hz, H2), 3.28 (dd, $J_{4,5}$ = 1.5, $J_{5,5}$ = 12.3 Hz, H5), 3.34 (s, OMe), 3.41–3.46 (m, H3), 3.57–3.60 (m, H4), 3.97 (d, H1), 3.99 (dd, $J_{4,5}$ = 3.0 Hz, H5), 4.79 (br d, $J_{3,OH}$ = 5.4 Hz, 3-OH), 5.00 (br d, 2-OH), 6.00 (br s, NH_2). ^{13}C NMR (75.5 MHz, DMSO-d_6) δ: 55.7 (OMe), 61.5 (C5), 70.6, 71.7, 80.1 (C2,3,4), 104.4 (Cl). Anal. calcd. for $C_6H_{13}NO_5$: C 40.2, H 7.3, N 7.8; found: C 40.4, H 7.2, N 7.9.

Allyl 2,3-*O*-isopropylidene-β-D-xylopyranoside

HCl in MeOH (4 M, 60 μL) was added to allyl β-D-xylopyranoside (21) (2.9 g, 15 mmol) suspended in DMF (13 mL), the mixture cooled (0°C), and 2-methoxypropene (4.0 mL, 42 mmol) added. The mixture was stirred (1 h, rt) and normal work-up ($CHCl_3$) gave a colourless oil. Flash chromatography (EtOAc–petrol, containing 0.5% Et_3N, 1:4) gave allyl 3,4-*O*-isopropylidene-β-D-xyloside as a colourless

© 2002 NRC Canada

syrup (210 mg, 6%). A small sample was distilled (glass T-piece, 0.05 mm Hg, heating block 110–130°C); $[\alpha]_D$ –59 ($CHCl_3$). ^{1}H NMR (500 MHz, $CDCl_3$) δ: 1.46, 1.47 (2s, CMe_2), 3.47–3.54 (m, H3,5), 3.57–3.59 (m, H5), 3.72 (m, H2), 4.11 (tdd, $J_{1',1'}$ = 11.8, $J_{1',2'}$ = 6.4, $J_{1',3'}$ = 1.2 Hz, H1′), 4.17 (dd, $J_{3,4}$ = 9.8, $J_{4,5}$ = 4.3 Hz, H4), 4.29 (d, $J_{1,2}$ = 6.9 Hz, H1), 4.35–4.39 (m, H1′), 5.22–5.25 (m, H3′), 5.31 (dq, $J_{2',3'}$ = 17.1, $J_{3',3'}$ = 1.3 Hz, H3′), 5.89–5.97 (m, H2′). ^{13}C NMR (125.8 MHz, $CDCl_3$) δ: 26.51, 26.73 (C*Me*$_2$), 64.63, 70.88 (C5,1′), 73.06, 73.61, 81.17 (C2,3,4), 103.64 (Cl), 112.44 (*C*Me$_2$), 118.31 (C3′), 133.44 (C2′). Further elution gave allyl 2,3-*O*-isopropylidene-β-D-xylopyranoside (2.7 g, 77%) as a colourless syrup; $[\alpha]_D$ –49 ($CHCl_3$). ^{1}H NMR (500 MHz, C_6D_6) δ: 1.32, 1.36 (2s, CMe_2), 2.40 (d, $J_{4,OH}$ = 2.6 Hz, OH), 3.07 (dd, $J_{4,5}$ = 7.6, $J_{5,5}$ = 11.9 Hz, H5), 3.46–3.53 (m, H2,3), 3.69–3.73 (m, H4), 3.85 (dd, $J_{4,5}$ = 5.3 Hz, H5), 3.92 (tdd, $J_{1',1'}$ = 13.1, $J_{1',2'}$ = 5.7, $J_{1',3'}$ = 1.5 Hz, H1′), 4.24 (tdd, $J_{1',2'}$ = 5.0, $J_{1',3'}$ = 1.6 Hz, H1′), 4.53 (d, $J_{1,2}$ = 6.8 Hz, H1), 4.99 (dq, $J_{2',3'}$ = 10.4, $J_{3',3'}$ = 1.5 Hz, H3′), 5.25 (dq, *J* = 1.7, 17.2 Hz, H3′), 5.81 (dddd, H2′). ^{13}C NMR (125.8 MHz, C_6D_6) δ: 26.76, 26.87 (C*Me*$_2$), 67.49, 69.38 (C5,1′), 69.60 (C4), 77.11, 81.63 (C2,3), 101.44 (C1), 111.19 (*C*Me$_2$), 116.74 (C3′), 134.50 (C2′).

Allyl 2,3-*O*-isopropylidene-4-*O*-(*N*-phthalimido)-α-L-arabinoside

Allyl 2,3-*O*-isopropylidene-β-D-xylopyranoside (2.3 g) was treated with **6** as previously for **5** to give, after flash chromatography (EtOAc–petrol, containing 0.5% Et_3N, 1:4 then 1:2) and trituration with diisopropyl ether, the title phthalimide (2.1 g, 56%) as a colourless solid; mp 148°C; $[\alpha]_D$ +0.5 ($CHCl_3$). ^{1}H NMR (500 MHz, $CDCl_3$) δ: 1.35, 1.41 (2s, CMe_2), 3.63 (dd, $J_{3,4}$ = 2.4, $J_{2,3}$ = 9.9 Hz, H3), 3.66 (dd, $J_{4,5}$ = 1.9, $J_{5,5}$ = 13.6 Hz, H5), 4.19 (tdd, $J_{1',1'}$ = 12.6, $J_{1',2'}$ = 6.4, $J_{1',3'}$ = 1.3 Hz, H1′), 4.34 (dd, $J_{1,2}$ = 7.7 Hz, H2), 4.38–4.42 (m, H5,1′), 4.61 (d, H1), 5.04 (bq, *J* = 1.8 Hz, H4), 5.21 (dq, $J_{2',3'}$ = 10.3 Hz, H3′), 5.34 (dq, $J_{2',3'}$ = 17.2 Hz, H3′), 5.98 (dddd, $J_{1',2'}$ = 5.4 Hz, H2′), 7.71–7.74, 7.79–7.83 (2m, 4H, Ar). ^{13}C NMR (75.5 MHz, $CDCl_3$) δ: 26.02, 26.53 (C*Me*$_2$), 65.41, 69.53 (C5,1′), 72.88, 77.65, 79.59 (C2,3,4), 102.25 (Cl), 110.92 (*C*Me$_2$), 117.94 (C3′), 123.41, 128.96, 134.36 (6C, Ar), 133.66 (C2′), 163.00 (2C, CO).

Allyl 4-*O*-(*N*-phthalimido)-α-L-arabinoside

Allyl 2,3-*O*-isopropylidene-4-*O*-(*N*-phthalimido)-α-L-arabinoside (2.0 g) was treated with hydrochloric acid as previously for **7** to give the title diol (1.9 g) as a colourless solid, a small portion of which was recrystallized to give long, fine, colourless needles; mp 145°C (EtOAc–*i*-Pr_2O); $[\alpha]_D$ –7.3 (MeOH). ^{1}H NMR (500 MHz, $CDCl_3$) δ: 3.69 (dd, $J_{4,5}$ = 1.7, $J_{5,5}$ = 13.0 Hz, H5), 3.78 (dd, $J_{2,3}$ = 9.1, $J_{3,4}$ = 3.4 Hz, H3), 3.90 (dd, $J_{1,2}$ = 6.7 Hz, H2), 4.15 (ddt, $J_{1',1'}$ = 12.7, $J_{1',2'}$ = 6.5, $J_{1',3'}$ = 1.2 Hz, H1′), 4.27–4.29 (m, H4), 4.35 (d, H1), 4.40 (ddt, $J_{1',2'}$ = 5.2, $J_{1',3'}$ = 1.4 Hz, H1′), 4.60 (dd, $J_{4,5}$ = 3.2 Hz, H5), 5.23 (dq, $J_{2',3'}$ = 10.4, $J_{3',3'}$ = 1.4 Hz, H3′), 5.34 (dq, $J_{2',3'}$ = 17.2 Hz, H3′), 5.96 (dddd, H2′), 7.78–7.80, 7.84–7.87 (2m, 4H, Ar). ^{13}C NMR (125.8 MHz, $CDCl_3$) δ: 63.77 (C5), 69.93 (C1′), 71.98, 72.22, 86.77 (C2,3,4), 101.68 (Cl), 118.11 (C3′), 124.01, 128.49, 134.96 (6C, Ar), 133.67 (C2′), 164.02 (2C, CO). Anal. calcd. for $C_{16}H_{17}NO_7 \cdot H_2O$: C 54.4, H 5.4, N 4.0; found: C 54.0, H 5.3, N 4.0.

Allyl 4-*O*-amino-α-L-arabinoside (10)

Allyl 4-*O*-(*N*-phthalimido)-α-L-arabinoside (1.6 g, 4.8 mmol) in $CHCl_3$ (60 mL) was treated with methylhydrazine (0.4 mL, 7.5 mmol) and the mixture stirred (2 h, rt), extracted with water, and the extracts filtered and concentrated. Recrystallization of the residue gave hydroxylamine derivative **10** (620 mg, 63%) as colourless plates; mp 120°C (EtOH); $[\alpha]_D$ +24.5 (MeOH). ^{1}H NMR (500 MHz, DMSO-d_6) δ: 3.24–3.28 (m, H2,5), 3.41–3.44 (m, H3), 3.56–3.57 (m, H4), 3.95–4.00 (m, H5,1′), 4.08 (d, $J_{1,2}$ = 6.8 Hz, H1), 4.17 (tdd, $J_{1',1'}$ = 13.4, $J_{1',2'}$ = 5.0, $J_{1',3'}$ = 1.6 Hz, H1′), 4.77 (d, $J_{3,OH}$ = 5.8 Hz, 3-OH), 4.98 (d, $J_{2,OH}$ = 4.9 Hz, 2-OH), 5.12 (dq, $J_{2',3'}$ = 10.5 Hz, H3′), 5.29 (dq, $J_{2',3'}$ = 17.3 Hz, H3′), 5.83–5.91 (m, H2′), 5.99 (br s, NH_2). ^{13}C NMR (125.8 MHz, DMSO-d_6) δ: 61.60, 68.65 (C5,1′), 70.94, 71.94, 80.15 (C2,3,4), 102.61 (Cl), 116.43 (C3′), 134.97 (C2′). Anal. calcd. for $C_8H_{15}NO_5$: C 46.8, H 7.4, N 6.8; found: C 46.6, H 7.4, N 6.8.

2′-Trimethylsilylethyl β-D-xylopyranoside

HgO (11.5 g, 54.0 mmol), $HgBr_2$ (1.16 g, 3.21 mmol), $CaSO_4$ (36 g), and 2-trimethylsilylethanol (8.0 mL, 56 mmol) in CH_2Cl_2 (75 mL) were stirred (5 min) before tri-*O*-acetyl-α-D-xylopyranosyl bromide (22) (18.3 g, 54.0 mmol) in CH_2Cl_2 (60 mL) was added dropwise. The mixture was stirred (2 days, rt), then filtered through silica with a pad of Celite on top, washing the filter residue with CH_2Cl_2. The combined filtrate and washings were washed with saturated KI solution and brine, then dried, and concentrated to give a yellow oil. Vacuum distillation (Kugelrohr, 30 mm Hg, 170°C) removed the excess 2-trimethylsilylethanol. The residue was dissolved in MeOH (150 mL) and treated with sodium (200 mg). After 2 h, the mixture was neutralized with resin (Dowex-50W, H^+ form), then filtered, washed with MeOH, and the combined filtrate and washings were concentrated to give a pale yellow solid. Recrystallization gave 2′-trimethylsilylethyl β-D-xylopyranoside (6.6 g, 49%) as white flakes; mp 126–128°C (CH_2Cl_2–*i*-Pr_2O); $[\alpha]_D$ –46.9 (MeOH). ^{1}H NMR (300 MHz, $CDCl_3$) δ: 0.02 (s, $SiMe_3$), 0.91–1.11 (m, 2H, H2′), 3.27 (dd, $J_{4,5}$ = 8.9, $J_{5,5}$ = 11.8 Hz, H5), 3.38 (dd, $J_{1,2}$ = 6.9, $J_{2,3}$ = 8.4 Hz, H2), 3.52 (t, *J* = 8.4 Hz, H3), 3.57 (ddd, $J_{1',1'}$ = 11.4, $J_{1',2'}$ = 6.2, 9.8 Hz, H1′), 3.68 (dt, $J_{4,5}$ = 5.0 Hz, H4), 3.93 (ddd, $J_{1',2'}$ = 6.2, 9.7 Hz H1′), 3.95 (dd, H5), 4.29 (d, H1). ^{13}C NMR (75.5 MHz, $CDCl_3$) δ: –1.44 ($SiMe_3$), 18.32 (C2′), 65.26, 67.32 (C5,1′), 69.62, 72.94, 76.04 (C2,3,4), 102.50 (C1). Anal. calcd. for $C_{10}H_{22}O_5Si$: C 48.0, H 8.9; found: C 48.1, H 8.6.

2′-Trimethylsilylethyl 2,3-*O*-isopropylidene-β-D-xylopyranoside

2′-Trimethylsilylethyl β-D-xylopyranoside (1.0 g) was treated with 2-methoxypropene as previously for allyl β-D-xylopyranoside to give a colourless oil (930 mg). Flash chromatography (EtOAc–petrol, containing 0.5% Et_3N, 1:4 then 3:7) gave the title alcohol (580 mg, 50%) as an unstable, colourless oil; $[\alpha]_D$ –43.4 ($CHCl_3$–1% pyridine). ^{1}H NMR (300 MHz, $CDCl_3$) δ: –0.02 (s, $SiMe_3$), 0.91–1.08 (m, 2H, H2′), 1.42, 1.43 (2s, CMe_2), 3.20 (dt, $J_{4,5}$ = 3.3, $J_{5,5}$ = 11.1 Hz, H5), 3.24 (br s, OH), 3.29 (dd, $J_{1,2}$ = 7.6, $J_{2,3}$ = 9.6 Hz, H2), 3.48 (t, $J_{3,4}$ = 9.4 Hz, H3), 3.60 (ddd, $J_{1',1'}$ = 11.3, $J_{1',2'}$ = 6.1, 9.5 Hz, H1′), 3.91 (ddd, $J_{1',2'}$ = 6.1, 9.5 Hz,

© 2002 NRC Canada

H1′), 3.97–4.05 (m, H4,5), 4.60 (d, H1). ^{13}C NMR (75.5 MHz, $CDCl_3$) δ: –1.58 ($SiMe_3$), 18.12 (C2′), 26.47, 26.62 (C*Me*$_2$), 66.73, 67.11 (C5,1′), 68.94, 76.42, 81.04 (C2,3,4), 101.16 (Cl), 111.42 (*C*Me$_2$). Anal. calcd. for $C_{13}H_{26}O_5Si$: C 53.8, H 9.0; found: C 53.9, H 9.0.

2′-Trimethylsilylethyl 2,3-*O*-isopropylidene-4-*O*-(*N*-phthalimido)-α-L-arabinoside

2′-Trimethylsilylethyl 2,3-*O*-isopropylidene-β-D-xylopyranoside (383 mg, 1.30 mmol), triphenylphosphine (420 mg, 1.60 mmol), and **6** (260 mg, 1.60 mmol) in THF (12 mL) were treated with diethyl azodicarboxylate (0.31 mL, 1.6 mmol) for 3 days (rt). Air was bubbled through the mixture (2 h) before it was concentrated and the residue subjected to flash chromatography (EtOAc–petrol, containing 0.5% Et_3N, 1:9 then 1:4) to give the title phthalimide (442 mg, 77%) as an unstable colourless oil. ^{1}H NMR (300 MHz, $CDCl_3$) δ: 0.01 (s, $SiMe_3$), 0.99–1.13 (m, 2H, H2′), 1.34, 1.40 (2s, CMe_2), 3.60–3.73 (m, H3,5,1′), 4.01 (ddd, $J_{1',1'}$ = 10.9, $J_{1',2'}$ = 7.2, 9.4 Hz, H1′), 4.31 (dd, $J_{1,2}$ = 7.4, $J_{2,3}$ = 9.9 Hz, H2), 4.40 (dd, $J_{4,5}$ = 1.6, $J_{5,5}$ = 13.7 Hz, H5), 4.58 (d, H1), 5.03 (dd, $J_{3,4}$ = 3.8 Hz, H4), 7.70–8.81 (m, 4H, Ar). ^{13}C NMR (75.5 MHz, $CDCl_3$) δ: –1.48 ($SiMe_3$), 18.17 (C2′), 26.06, 26.58 (C*Me*$_2$), 65.43, 66.65 (C5,1′), 73.03, 77.74, 79.74 (C2,3,4), 102.93 (Cl), 110.87 (*C*Me$_2$), 123.43, 128.99, 134.36 (6C, Ar), 163.05 (2C, CO).

2′-Trimethylsilylethyl 4-*O*-(*N*-phthalimido)-α-L-arabinoside

2′-Trimethylsilylethyl 2,3-*O*-isopropylidene-4-*O*-(*N*-phthalimido)-α-L-arabinoside (253 mg) in THF (8 mL) was treated with hydrochloric acid (2 mL of 1 M) for 2 days. The mixture was neutralized with resin (Amberlite IRA 400, OH^- form), then filtered, and concentrated to give the title diol (216 mg, 94%) as a colourless crystalline solid; mp 118–120°C; $[\alpha]_D$ –10.7 ($CHCl_3$). ^{1}H NMR (300 MHz, $CDCl_3$) δ: 0.02 (s, $SiMe_3$), 0.92–1.12 (m, 2H, H2′), 2.64 (br s, 2-OH), 3.60 (ddd, $J_{1',1'}$ = 11.3, $J_{1',2'}$ = 6.1, 9.6 Hz, H1′), 3.68 (dd, $J_{4,5}$ = 1.6, $J_{5,5}$ = 13.0 Hz, H5), 3.76 (dd, $J_{2,3}$ = 9.5, $J_{3,4}$ = 3.2 Hz, H3), 3.84 (dd, $J_{1,2}$ = 6.6 Hz, H2), 4.00 (ddd, $J_{1',2'}$ = 6.6, 9.5 Hz, H1′), 4.10 (d, $J_{3,OH}$ = 3.2 Hz, 3-OH), 4.26 (dt, $J_{4,5}$ = 3.0 Hz, H4), 4.29 (d, H1), 4.61 (dd, H5), 7.76–7.87 (m, 4H, Ar). ^{13}C NMR (75.5 MHz, $CDCl_3$) δ: –1.46 ($SiMe_3$), 18.17 (C2′), 63.91, 67.13 (C5,1′), 72.05, 72.30 (C2,3), 86.96 (C4), 102.29 (Cl), 123.96, 128.47, 134.89 (6C, Ar), 163.96 (2C, CO). Anal. calcd. for $C_{18}H_{25}NO_7Si$: C 54.7, H 6.4, N 3.5; found: C 54.7, H 6.4, N 3.5.

2′-Trimethylsilylethyl 4-*O*-amino-α-L-arabinoside (11)

2′-Trimethylsilylethyl 4-*O*-(*N*-phthalimido)-α-L-arabinoside (26 mg) in $CHCl_3$ (3 mL) was treated with methylhydrazine (0.15 mL). After 5 min, TLC showed that no starting material remained and the solution was applied to the top of a small silica-gel column. Elution with $CHCl_3$, then MeCN–$CHCl_3$ (2:3), gave a colourless solid. Recrystallization gave hydroxylamine derivative **11** (16 mg, 92%) as a colourless crystalline solid; mp 140–142°C ($CHCl_3$–petrol); $[\alpha]_D$ +14.2 (MeOH). ^{1}H NMR (300 MHz, $CDCl_3$) δ: 0.17 (s, $SiMe_3$), 0.94–1.12 (m, 2H, H2′), 1.62 (br s, 4H, OH,NH_2), 3.43 (dd, $J_{4,5}$ = 1.2, $J_{5,5}$ = 13.2 Hz, H5), 3.56 (ddd, $J_{1',1'}$ = 11.6, $J_{1',2'}$ = 6.6, 9.6 Hz, H1′), 3.63 (dd, $J_{1,2}$ = 6.8, $J_{2,3}$ = 9.3 Hz, H2), 3.70 (dd, $J_{3,4}$ = 2.4 Hz, H3), 3.91–3.94 (m, H4), 3.97 (ddd, $J_{1',2'}$ = 6.1, 9.5 Hz, H1′), 4.19 (d, H1), 4.24 (dd, $J_{4,5}$ = 2.4 Hz, H5). ^{13}C NMR (75.5 MHz, $CDCl_3$) δ: –1.47 ($SiMe_3$), 18.27 (C2′), 62.86, 67.19 (C5,1′), 72.28, 73.05 (C2,3,4), 102.59 (Cl). Anal. calcd. for $C_{10}H_{23}NO_5Si$: C 45.3, H 8.7, N 5.3; found: C 45.4, H 8.9, N 5.4.

Benzyl 2,3-*O*-isopropylidene-β-D-xylopyranoside

Benzyl β-D-xylopyranoside (23) (7.60 g) was treated as previously for allyl β-D-xylopyranoside to give, after flash chromatography (EtOAc–petrol, containing 0.5% Et_3N, 1:4), benzyl 3,4-*O*-isopropylidene-β-D-xyloside (620 mg, 7%) as a colourless solid, a small portion of which was recrystallized; mp 129–130°C (*i*-Pr_2O; lit. (24) 126°C); $[\alpha]_D$ –79 ($CHCl_3$, lit. (24) –87). ^{1}H NMR (500 MHz, $CDCl_3$) δ: 1.46, 1.47 (2s, CMe_2), 2.52 (br s, OH), 3.49 (dd, $J_{2,3}$ = 9.6, $J_{3,4}$ = 9.0 Hz, H3), 3.54 (t, $J_{4,5} \approx J_{5,5}$ = 10.1 Hz, H5), 3.62 (ddd, $J_{4,5}$ = 4.3, 10.1 Hz, H4), 3.74 (ddd, $J_{1,2}$ = 6.8 Hz, H2), 4.20 (dd, H5), 4.35 (d, H1), 4.59, 4.92 (ABq, *J* = 11.5 Hz, PhCH_2), 7.31–7.37 (m, Ph). ^{13}C NMR (125.8 MHz, $CDCl_3$) δ: 26.54, 26.77 (C*Me*$_2$), 64.72 (C5), 71.80 (Ph*C*H_2), 73.16, 73.66, 81.17 (C2,3,4), 103.67 (Cl), 112.45 (*C*Me$_2$), 128.19, 128.24, 128.58, 136.76 (Ph). Further elution (EtOAc–petrol, containing 0.5% Et_3N, 1:2) gave benzyl 2,3-*O*-isopropylidene-β-D-xylopyranoside (5.26 g, 59%) as a somewhat unstable, colourless syrup; $[\alpha]_D$ –58.0 ($CHCl_3$, lit. (24) –54). ^{1}H NMR (500 MHz, $CDCl_3$) δ: 1.45, 1.46 (2s, CMe_2), 2.22 (d, $J_{4,OH}$ = 3.8 Hz, OH), 3.28 (dd, $J_{4,5}$ = 7.7, $J_{5,5}$ = 11.7 Hz, H5), 3.43 (dd, $J_{1,2}$ = 7.4, $J_{2,3}$ = 9.6 Hz, H2), 3.53 (t, *J* = 9.2 Hz, H3), 4.04–4.08 (m, H4), 4.10 (dd, $J_{4,5}$ = 5.3 Hz, H5), 4.68, 4.89 (ABq, *J* = 11.7 Hz, PhCH_2), 4.74 (d, H1), 7.28–7.39 (m, Ph). ^{13}C NMR (125.8 MHz, $CDCl_3$) δ: 26.58, 26.77 (C*Me*$_2$), 67.26 (C5), 70.44 (Ph*C*H_2), 69.43, 76.56, 81.01 (C2,3,4), 100.77 (Cl), 111.71 (*C*Me$_2$), 127.90, 128.12, 128.43, 136.91 (Ph).

Benzyl 2,3-*O*-isopropylidene-4-*O*-(*N*-phthalimido)-α-L-arabinoside

Benzyl 2,3-*O*-isopropylidene-β-D-xylopyranoside (2.8 g) was treated with **6** as previously for **5** to give after flash chromatography (EtOAc–toluene, containing 0.5% Et_3N, 1:5) an oil. Trituration of this oil with *i*-Pr_2O then gave the title phthalimide (3.4 g, 80%) as a colourless solid, a small portion of which was recrystallized; mp 172–174°C (MeOH); $[\alpha]_D$ –19 ($CDCl_3$). ^{1}H NMR (500 MHz, $CDCl_3$) δ: 1.35, 1.42 (2s, CMe_2), 3.63 (dd, $J_{2,3}$ = 9.9, $J_{3,4}$ = 2.4 Hz, H3), 3.67 (dd, $J_{4,5}$ = 1.9, $J_{5,5}$ = 13.6 Hz, H5), 4.39 (dd, $J_{1,2}$ = 7.7 Hz, H2), 4.43 (dd, $J_{4,5}$ = 1.6 Hz, H5), 4.66 (d, H1), 4.72, 4.97 (ABq, *J* = 11.8 Hz, PhCH_2), 5.05 (m, H4), 7.27–7.43, 7.72–7.75, 7.80–7.83 (3m, 9H, Ar). ^{13}C NMR (125.8 MHz, $CDCl_3$) δ: 26.08, 26.58 (C*Me*$_2$), 65.48 (C5), 70.09 (Ph*C*H_2), 73.00, 77.68, 79.65 (C2,3,4), 102.20 (Cl), 110.97 (*C*Me$_2$), 123.46, 127.76, 128.10, 128.35, 129.02, 134.40, 136.98 (12C, Ar), 163.05 (2C, CO). Anal. calcd. for $C_{23}H_{23}NO_7$: C 64.9, H 5.5, N 3.3; found: C 64.6, H 5.4, N 3.3.

Benzyl 4-*O*-(*N*-phthalimido)-α-L-arabinoside

Benzyl 2,3-*O*-isopropylidene-4-*O*-(*N*-phthalimido)-α-L-arabinoside (2.00 g) was treated with hydrochloric acid as previously for **7** to give the title diol (1.82 g) as a colourless solid, a small portion of which was recrystallized to give colourless micro-needles; mp 183°C (EtOH); $[\alpha]_D$ –20.0

© 2002 NRC Canada

($CHCl_3$). ^{1}H NMR (500 MHz, DMSO-d_6) δ: 3.61 (dd, $J_{4,5}$ = 1.7, $J_{5,5}$ = 12.6 Hz, H5), 3.70–3.75 (m, H2,3), 4.12 (dd, $J_{4,5}$ = 3.8 Hz, H5), 4.32 (d, $J_{1,2}$ = 5.8 Hz, H1), 4.50–4.52 (m, H4), 4.57, 4.80 (ABq, J = 12.2 Hz, PhCH_2), 4.93 (d, J = 5.1 Hz, OH), 5.32 (d, J = 4.4 Hz, OH), 7.28–7.43 (m, Ph), 7.86 (s, 4H, Ar). ^{13}C NMR (125.8 MHz, DMSO-d_6) δ: 61.60 (C5), 69.42 (Ph*C*H_2), 70.48, 71.35, 82.85 (C2,3,4), 102.25 (Cl), 123.21, 127.41, 127.61, 128.18, 128.66, 134.72, 138.01 (12C, Ar), 163.31 (2C, CO). Anal. calcd. for $C_{20}H_{19}NO_7$: C 62.3, H 5.0, N 3.6; found: C 62.5, H 5.2, N 3.8.

Benzyl 4-*O*-amino-α-L-arabinoside (12)

Benzyl 4-*O*-(*N*-phthalimido)-α-L-arabinoside (1.60 g) was treated with methyl hydrazine, as previously for allyl 4-*O*-(*N*-phthalimido)-α-L-arabinoside, to give hydroxylamine derivative **12** (726 mg, 69%) as colourless plates; mp 155–156°C, $[\alpha]_{436}$ −4.0 (MeOH). ^{1}H NMR (500 MHz, DMSO-d_6) δ: 3.31 (dd, $J_{4,5}$ = 1.4, $J_{5,5}$ = 12.3 Hz, H5), 3.34 (ddd, $J_{1,2}$ = 6.7, $J_{2,3}$ = 8.8, $J_{2,OH}$ = 4.8 Hz, H2), 3.46–3.48 (m, H3), 3.60–3.62 (m, H4), 4.03 (dd, $J_{4,5}$ = 3.1 Hz, H5), 4.20 (d, H1), 4.53, 4.75 (ABq, J = 12.2 Hz, PhCH_2), 4.80 (br d, J = 6.2 Hz, 3-OH), 5.05 (d, 2-OH), 6.03 (br s, NH_2), 7.27–7.39 (m, Ph). ^{13}C NMR (125.8 MHz, DMSO-d_6) δ: 61.59 (C5), 69.39 (Ph*C*H_2), 70.98, 71.86, 80.10 (C2,3,4), 102.64 (Cl), 127.33, 127.57, 128.12, 138.10 (Ph). Anal. calcd. for $C_{12}H_{17}NO_5$: C 56.5, H 6.7, N 5.5; found: C 56.2, H 6.7, N 5.4.

Benzyl β-L-xylopyranoside

Tri-*O*-acetyl-L-xylopyranosyl trichloroacetimidate (25) (51.1 g, 120 mmol), benzyl alcohol (38 mL, 0.37 mol), and crushed molecular sieves (3 Å, 15 g) in CH_2Cl_2 (250 mL) were stirred (30 min, 0°C). $Et_2O{\cdot}BF_3$ (1 mL, 7.9 mmol) was added and the reaction was stirred (4 h). Pyridine (120 mL) and acetic anhydride (90 mL) were added and, after 2 h, the reaction was quenched upon the addition of MeOH (70 mL). After 1 h, the mixture was filtered (silica, washing with EtOAc) and the filtrate concentrated. The residue was subjected to normal work up (EtOAc), and rapid silica filtration (EtOAc–petrol, 1:9 then 1:3) afforded a colourless solid (44 g) that was taken up in MeOH and sodium (200 mg) added. After 3 h, the mixture was neutralized with resin (Dowex-50W, H^+ form), then filtered, washed with MeOH, and the combined filtrate and washings concentrated to give a colourless solid. Recrystallization of the solid gave benzyl-β-L-xylopyranoside (26.2 g, 90%) as colourless cubes; mp 112–114°C (EtOAc; lit. (23) 116–117°C).

Benzyl 2,3-*O*-isopropylidene-β-L-xylopyranoside (13)

Compound **13** was prepared as previously for the enantiomer, 60%; $[\alpha]_D$ +65.9 ($CHCl_3$).

Benzyl 2,3-*O*-isopropylidene-4-*O*-(*N*-phthalimido)-α-D-arabinoside (14)

Compound **14** was prepared as previously for the enantiomer, 68%; mp 177.5–179°C (MeOH); $[\alpha]_D$ +18.4 ($CHCl_3$).

Benzyl 4-*O*-amino-2,3-*O*-isopropylidene-α-D-arabinoside (15)

Alcohol **13** (3.23 g, 11.5 mmol), triphenylphosphine (3.93 g, 15.0 mmol), and **6** (2.45 g, 15.0 mmol) in THF (100 mL) were treated with diethyl azodicarboxylate (4.90 mL, 15.0 mmol) for 4 days at rt. The mixture was concentrated and flash chromatography (EtOAc–petrol, containing 0.5% Et_3N, 1:4 then 2:3) gave crude phthalimide **14** (4.62 g) as a pale yellow solid. This solid was dissolved in $CHCl_3$ and treated with $N_2H_4{\cdot}H_2O$ (2 mL, 30 min). The mixture was filtered and the residue washed with $CHCl_3$. The combined filtrate–washings were washed with H_2O and brine, then dried and concentrated to give a pale yellow oil which crystallized. Recrystallization gave hydroxylamine **15** as colourless cubes (1.2 g, 62%); mp 85–87°C (Et_2O–petrol); $[\alpha]_D$ +1.9 ($CHCl_3$). ^{1}H NMR (500 MHz, $CDCl_3$) δ: 1.44, 1.48 (2s, CMe_2), 3.43 (dd, $J_{4,5}$ = 1.5, $J_{5,5}$ = 13.2 Hz, H5), 3.57 (dd, $J_{2,3}$ = 9.8, $J_{3,4}$ = 2.9 Hz, H3), 3.86 (dd, $J_{1,2}$ = 7.7 Hz, H2), 4.18–4.20 (m, H4), 4.32 (dd, $J_{4,5}$ = 1.8 Hz, H5), 4.61 (d, H1), 4.72, 4.97 (ABq, J = 11.8 Hz, PhCH_2), 5.65 (br s, NH_2), 7.27–7.41 (m, Ph). ^{13}C NMR (125.8 MHz, $CDCl_3$) δ: 26.51, 26.58 (C*Me*$_2$), 65.00 (C5), 70.17 (Ph*C*H_2), 73.47, 77.60, 78.36 (C2,3,4), 101.74 (Cl), 110.58 (*C*Me$_2$), 127.77, 128.07, 128.34, 136.94 (Ph). Anal. calcd. for $C_{23}H_{23}NO_7$: C 61.0, H 7.2, N 4.7; found: C 61.2, H 7.1, N 4.6.

Benzyl 4-*O*-[(*tert*-butoxycarbonyl)amino]-α-D-arabinoside (17)

Hydroxylamine **15** (1.12 g, 3.80 mmol) in $CHCl_3$ (70 mL) was treated with triethylamine (1.0 mL) and di-*tert*-butyl dicarbonate (1.24 g, 5.69 mmol). The mixture was heated at reflux overnight and then concentrated. The residue was dissolved in MeOH–$CHCl_3$ (50 mL, 1:1), treated with pyridinium *p*-toluenesulfonate (70 mg) and heated under reflux (1 h), then allowed to cool. The mixture was treated with resin (Amberlite IRA 400, OH^- form), filtered, and then concentrated, co-evaporating with toluene, to afford diol **17** (984 mg, 73%) as a colourless crystalline solid. A small portion was recrystallized to give colourless microcrystals; mp 158–160°C (EtOAc–petrol); $[\alpha]_D$ +5.8, $[\alpha]_{365}$ +35.8 (MeOH). ^{1}H NMR. (500 MHz, $CDCl_3$) δ: 1.46 (s, CMe_3), 3.45 (d, $J_{5,5}$ = 12.5 Hz, H5), 3.67 (dd, $J_{3,4}$ = 3.7, $J_{2,3}$ = 9.2 Hz, H3), 3.71 (dd, $J_{1,2}$ = 6.8 Hz, H2), 4.03–4.05 (m, H4), 4.16 (dd, $J_{4,5}$ = 2.7 Hz, H5), 4.28 (d, H1), 4.59, 4.88 (ABq, J = 11.8 Hz, PhCH_2), 7.26–7.36 (m, Ph). ^{13}C NMR (75.5 MHz, $CDCl_3$) δ: 28.10 (C*Me*$_3$), 63.16 (C5), 70.63 (Ph*C*H_2), 71.96, 72.14 (C2,3), 82.82 (*C*Me$_3$), 83.25 (C4), 101.78 (Cl), 127.85, 128.05, 128.40, 137.02 (Ph), 157.96 (CO). Anal. calcd. for $C_{17}H_{25}NO_7$: C 57.4, H 7.1; found: C 57.5, H 7.1.

4-*O*-[(*tert*-butoxycarbonyl)amino]-D-arabinose (18)

Diol **17** (850 mg), palladium-on-carbon (85 mg of 10%), and hydrochloric acid (0.4 mL of 1 M) in H_2O–THF (1:2, 30 mL) were treated with hydrogen (24 h at 1 atm). The mixture was filtered through Celite, washing with H_2O–THF (1:1). The combined filtrate and washings were neutralized with resin (Amberlite IRA 400, OH^- form), filtered, and then concentrated to give a colourless solid. Flash chromatography (MeOH–$CHCl_3$, 7:93 then 15:85) gave hemiacetal **18** (600 mg, 94%) as a colourless solid; mp 121–123°C; $[\alpha]_D$ +35.2 (MeOH). ^{1}H NMR (500 MHz, MeOH-d_4) δ: 1.50 (s, CMe_3), 3.51 (dd, $J_{1,2}$ = 4.0, $J_{2,3}$ = 8.8 Hz, H2), 3.57–3.65 (m, H3,4), 3.68 (dd, $J_{4,5}$ = 6.6, $J_{5,5}$ = 12.8 Hz, H5), 3.88 (dd,

© 2002 NRC Canada

$J_{4,5}$ = 1.5 Hz, H5), 5.52 (d, H1). ^{13}C NMR (125.8 MHz, MeOH-d_4) δ: 28.37, (C*Me*$_3$), 61.54 (C5), 67.86, 73.96, 80.92, 83.70 (C2,3,4,*C*Me$_3$), 86.62 (C1), 155.85 (CO). FAB-HRMS calcd. for $C_{10}H_{20}NO_7$ (M + 1): 266.1240, found: 266.1251. Anal. calcd. for $C_{10}H_{19}NO_7$: C 45.3, H 7.2; found: C 45.1, H 7.1.

(4*R*,5*S*,6*R*)-5,6-Dihydro-4,5-dihydroxy-6-hydroxymethyl-4*H*-1,2-oxazine (4)

Hemiacetal **18** (130 mg) was heated at reflux in water (7 mL) for 10 min. Freeze drying gave dihydrooxazine **4** (72 mg) as a colourless solid, a portion of which was recrystallized; mp 142–145°C (MeOH–EtOAc–Et_2O); $[\alpha]_D$ = +18.3 (MeOH). ^{1}H NMR (500 MHz, D_2O) δ: 3.80–3.86 (m, H5), 3.89–4.02 (m, 3H, H6,7), 4.29 (dd, $J_{3,4}$ = 1.6, $J_{4,5}$ = 8.3 Hz, H4), 7.29 (d, H3). ^{13}C NMR (125.8 MHz, D_2O) δ: 59.41 (C7), 65.83, 68.40 (C4,5), 80.51 (C6), 151.96 (C3). EI-HRMS calcd. for $C_5H_9NO_4$ (M^+): 147.0532, found: 147.0534. Anal. calcd. for $C_5H_9NO_4$: C 40.8, H 6.2; found: C 41.0, H 6.2.

(4*R*,5*S*,6*R*)-4,5-Dihydroxy-6-hydroxymethyl-3,4,5,6-tetrahydro-2*H*-1,2-oxazine (2)

Dihydrooxazine **4** (140 mg, 0.97 mmol) in AcOH (12 mL) was treated with $NaCNBH_3$ (64 mg, 95%, 0.97 mmol) (40 min, rt). The mixture was concentrated and the residue dissolved in hydrochloric acid (6 mL of 0.05 M) and then applied to a column of cation-exchange resin (Dowex 50W-X2, H^+ form). The column was washed with water, then eluted with hydrochloric acid (3 M). Concentration of the eluate gave a colourless oil that was taken up in MeOH and treated with resin (Amberlite IRA 400, OH^- form). The mixture was filtered and concentrated to give tetrahydrooxazine **2** (160 mg) as a colourless foam, a portion of which was crystallized; mp 149–151°C (MeOH–EtOAc); $[\alpha]_D$ –36.4 (MeOH). ^{1}H NMR (500 MHz, D_2O) δ: 2.92 (dd, $J_{3,3}$ = 13.2, $J_{3,4}$ = 10.7 Hz, H3), 3.28 (dd, $J_{3,4}$ = 5.4 Hz, H3), 3.41 (t, $J_{4,5} \approx J_{5,6}$ = 9.3 Hz, H5), 3.58 (ddd, $J_{6,7}$ = 2.1, 6.2 Hz, H6), 3.67–3.73 (m, H4,7), 3.90 (dd, $J_{7,7}$ = 12.7 Hz, H7). ^{13}C NMR (125.8 MHz, D_2O) δ: 53.26 (C3), 60.54 (C7), 71.05, 71.07 (C4,5), 84.33 (C6) (7). EI-HRMS calcd. for $C_5H_{11}NO_4$ (M^+): 149.0688, found: 149.0692. Anal. calcd. for $C_5H_{11}NO_4$: C 40.3, H 7.4, N 9.4; found: C 40.1, H 7.2, N 9.2.

Benzyl 4-*O*-(imidazyl-1-sulfonyl)-2,3-*O*-isopropylidene-β-L-xyloside (20)

Sodium hydride (60% in mineral oil, 1.0 g, 25 mmol) was added to a chilled mixture of alcohol **13** (5.4 g, 20 mmol) in DMF (30 mL, 0°C) and the mixture stirred (30 min, rt). The mixture was cooled (−40°C) and *N*,*N*′-sulfuryldiimidazole (5.0 g, 25 mmol) in DMF (40 mL) was added dropwise, then the mixture allowed to stir (30 min). MeOH (3 mL) was added and, after a further 30 min, the mixture was allowed to warm to room temperature, then subjected to normal workup (CH_2Cl_2) to give a pale yellow oil. Flash chromatography (EtOAc–petrol, containing 0.5% Et_3N, 1:3 then 1:2) gave imidazole sulfonate **20** (5.75 g, 72%) as a colourless solid. A small portion was recrystallized to give colourless needles; mp 90–92°C (EtOAc–petrol); $[\alpha]_D$ +86.6 ($CHCl_3$). ^{1}H NMR. (300 MHz, $CDCl_3$) δ: 1.30, 1.37 (s, CMe_2), 3.47 (dd, $J_{1,2}$ = 6.9, $J_{2,3}$ = 10.1 Hz, H2), 3.60 (dd, $J_{4,5}$ = 4.7, $J_{5,5}$ = 13.2 Hz, H5), 3.64 (dd, $J_{3,4}$ = 8.2 Hz, H3), 4.17 (dd, $J_{4,5}$ = 5.2 Hz, H5), 4.62, 4.81 (ABq, J = 11.6 Hz, $PhCH_2$), 4.82 (ddd, H4), 4.83 (d, H1), 7.12–7.43 (m, 7H, Ph,Im), 7.97–7.99 (m, Im). ^{13}C NMR (75.5 MHz, $CDCl_3$) δ: 26.29, 26.50 (C*Me*$_2$), 63.40 (C5), 70.27 (Ph*C*H$_2$), 76.43, 76.66, 82.22 (C2,3,4), 99.77 (C1), 113.01 (*C*Me$_2$), 117.80 (2C, Im), 128.05, 128.48, 131.17, 136.52 (Ph), 137.32 (Im). FAB-HRMS calcd. for $C_{18}H_{23}N_2O_7S$ (M + 1): 411.1226, found: 411.1221. Anal. calcd. for $C_{18}H_{22}N_2O_7S$: C 52.7, H 5.4; found: C 53.0, H 5.5.

Benzyl 4-cyano-4-deoxy-2,3-*O*-isopropylidene-α-D-arabinoside (21)

Imidazole sulfonate **20** (4.58 g, 11.2 mmol) was treated with trimethylsilyl cyanide (2.94 mL, 22.3 mmol) in MeCN (100 mL) and the mixture heated under reflux. Tetrabutylammonium fluoride (1.0 M in THF, 17 mmol) was added dropwise over 30 min. After a further 1 h, the mixture was cooled to room temperature, concentrated, and normal work-up (EtOAc) gave a red oil. Flash chromatography (EtOAc–petrol, containing 0.5% Et_3N, 1:5 then 1:3) of the oil gave nitrile **21** as a pale yellow oil (2.61 g, 81%), which crystallized. A small portion was recrystallized to give off-white needles; mp 89–90°C (Et_2O–petrol); $[\alpha]_D$ –21.2 ($CHCl_3$). ^{1}H NMR (300 MHz, $CDCl_3$) δ: 1.47, 1.51 (s, CMe_2), 3.29 (ddd, $J_{3,4}$ = 4.9, $J_{4,5}$ = 1.8, 3.1 Hz, H4), 3.58 (dd, $J_{2,3}$ = 9.4 Hz, H3), 3.64 (dd, $J_{5,5}$ = 12.5 Hz, H5), 3.80 (dd, $J_{1,2}$ = 7.6 Hz, H2), 4.30 (dd, H5), 4.68 (d, H1), 4.69, 4.93 (ABq, J = 11.8 Hz, Ph*C*H$_2$), 7.27–7.42 (m, Ph). ^{13}C NMR (75.5 MHz, $CDCl_3$) δ: 26.39, 26.65 (C*Me*$_2$), 32.82 (C4), 63.66 (C5), 70.38 (Ph*C*H$_2$), 74.53, 76.00 (C2,3), 101.45 (C1), 111.97 (*C*Me$_2$), 116.59 (CN), 120.10, 128.02, 128.48, 136.55 (Ph). FAB-HRMS calcd. for $C_{16}H_{20}NO_4$ (M + 1): 290.1392, found: 290.1398. Anal. calcd. for $C_{16}H_{19}NO_4$: C 66.4, H 6.6; found: C 66.3, H 6.4.

Benzyl 4-{[(*tert*-butoxycarbonyl)amino]methyl}-4-deoxy-2,3-*O*-isopropylidene-α-D-arabinoside (23)

Nitrile **21** (2.0 g, 6.9 mmol) in ether (40 mL) was added dropwise to a mixture of lithium aluminium hydride (730 mg, 17 mmol) in ether (40 mL) and this mixture stirred (1 h). The mixture was quenched with successive additions of H_2O (730 μL), aqueous NaOH (3 M, 730 μL), and H_2O (2.2 mL). The mixture was filtered, washing with ether, and the combined filtrate and washings were concentrated to give an oil (2.5 g). This oil was dissolved in $CHCl_3$ (120 mL) and treated with triethylamine (2 mL) and di-*tert*-butyl dicarbonate (1.7 g, 7.6 mmol). The mixture was heated at reflux overnight, then concentrated to give a colourless solid. Recrystallization gave carbamate **23** as fine needles (1.52 g, 56%); mp 146–148°C (EtOAc–petrol); $[\alpha]_D$ +29.9 ($CHCl_3$). ^{1}H NMR (300 MHz, $CDCl_3$) δ: 1.46 (s, 15H, Me), 2.33–2.43 (m, H4), 3.26–3.49 (m, CH_2N), 3.58 (dd, $J_{4,5}$ = 3.8, $J_{5,5}$ = 12.6 Hz, H5), 3.61–3.69 (m, H2), 3.72 (dd, $J_{2,3}$ = 9.8, $J_{3,4}$ = 5.3 Hz, H3), 3.91 (dd, $J_{4,5}$ = 2.6 Hz, H5), 4.61 (d, $J_{1,2}$ = 7.3 Hz, H1), 4.65, 4.85 (ABq, J = 11.7 Hz, Ph*C*H$_2$), 5.00–5.09 (m, NH), 7.27–7.41 (m, Ph). ^{13}C NMR (75.5 MHz, $CDCl_3$) δ: 26.54, 26.63 (C*Me*$_2$), 28.39 (C*Me*$_3$), 38.08 (CH_2N), 38.99 (C4), 64.93 (C5), 70.10 (Ph*C*H$_2$), 74.43, 77.54 (C2,3), 79.29 (*C*Me$_3$), 101.84 (C1), 110.60

© 2002 NRC Canada

(CMe_2), 127.79, 128.05, 128.37, 137.00 (Ph), 155.89 (CO). FAB-HRMS calcd. for $C_{21}H_{32}NO_6$ (M + 1): 394.2230, found: 394.2247. Anal. calcd. for $C_{21}H_{31}NO_6$: C 64.1, H 7.9; found: C 64.0, H 7.7.

Benzyl 4-{[(*tert*-butoxycarbonyl)amino]methyl}-4-deoxy-α-D-arabinoside (24)

A mixture of carbamate **23** (1.50 g, 3.82 mmol) and pyridinium *p*-toluenesulfonate (80 mg, 310 (mol) in MeOH–$CHCl_3$ (25 mL, 1:1) was heated under reflux (1 h) and allowed to cool. The mixture was treated with resin (Amberlite IRA 400, OH^- form), filtered, and then concentrated, co-evaporating with toluene, to afford diol **24** as a colourless solid (1.30 g). A small portion was recrystallized to give colourless micro-needles; mp 159–162°C (EtOAc–petrol); $[\alpha]_D$ +77.8 ($CHCl_3$). ^{1}H NMR (300 MHz, $CDCl_3$) δ: 1.43 (s, CMe_3), 1.98 (br s, OH), 2.16–2.27 (m, H4), 2.89 (br s, OH), 3.18–3.32 (m, CH_2N), 3.53 (dd, J = 4.0, 11.9 Hz, 1H), 3.68 (dd, J = 3.9, 5.5 Hz, 1H), 3.76–3.87 (m, 2H), 4.53, 4.81 (ABq, J = 11.8 Hz, PhCH_2), 4.59 (d, $J_{1,2}$ = 3.7 Hz, H1), 5.00–5.08 (m, NH), 7.27–7.39 (m, Ph). ^{13}C NMR (75.5 MHz, $CDCl_3$) δ: 28.39 (CMe_3), 37.41 (C4), 38.95 (CH_2N), 60.17 (C5), 69.46, 70.31 (C2,3), 70.04 (PhCH_2), 79.49 (CMe_3), 100.31 (C1), 128.08, 128.55, 136.71 (Ph), 156.34 (CO). FAB-HRMS calcd. for $C_{18}H_{28}NO_6$ (M + 1): 354.1917, found: 354.1924. Anal. calcd. for $C_{18}H_{27}NO_6$: C 61.2, H 7.7; found: C 61.4, H 7.8.

Isofagomine (HCl salt) (1)

Diol **24** (1.3 g) was treated with trifluoroacetic acid (6 mL; 5 min, rt) and the mixture concentrated, co-evaporating with H_2O. The residue was dissolved in MeOH, treated with resin (Amberlite IRA 400, OH^- form), filtered, and then concentrated. MeOH (40 mL), AcOH (1.5 mL), and palladium-on-carbon (150 mg of 10%) were added to the residue and this mixture was treated with hydrogen (overnight, 1 atm). The mixture was filtered through Celite, washing with MeOH, followed by concentration, to give a pale-brown gum (720 mg). This gum was dissolved in hydrochloric acid (4 mL of 1 M) and applied to a cation-exchange column (Dowex 50W-X2, H^+ form). The column was washed with water, then eluted with aqueous NH_3 (1.5 M). The eluate was concentrated and flash chromatography (*i*-PrOH–aqueous NH_3 (7 M), 6:1 then 4:1) gave a colourless oil. This oil was treated with hydrochloric acid (10 mL of 1 M) and concentrated. Freeze drying of the residue gave isofagomine (**1**) (HCl salt) as a colourless gum (660 mg, 96%); $[\alpha]_D$ +16.5 (H_2O). ^{1}H NMR (500 MHz, D_2O) and ^{13}C NMR (125.8 MHz, D_2O) spectral data were in good agreement with those reported previously (12, 14).

A sample of **1** was applied to a cation-exchange column (Dowex 50W-X2, H^+ form). The column was washed with water and then eluted with aqueous NH_3 (1.5 M). The eluate was concentrated to give **1** as the free amine; $[\alpha]_D$ +20.5 (EtOH, lit. (12) +19.6).

Acknowledgments

We thank the Australian Research Council for financial assistance and Dr. Jon Fairweather (working in the laboratory of Professor Marc Claeyssens, Gent, Belgium) for determining the inhibition constants of the dihydrooxazine.

References

1. M.L. Sinnott. Chem. Rev. **90**, 1171 (1990).
2. D.L. Zechel and S.G. Withers. Acc. Chem. Res. **33**, 11 (2000).
3. G. Legler. Adv. Carbohydr. Chem. Biochem. **48**, 319 (1990).
4. B. Ganem. Acc. Chem. Res. **29**, 340 (1996).
5. A. E. Stütz (*Editor*). *In* Nojirimycin and beyond. Wiley-VCH, Weinheim. 1999.
6. M. Bols. Acc. Chem. Res. **31**, 1 (1998).
7. P. Bach and M. Bols. Tetrahedron Lett. **40**, 3461 (1999).
8. S. Hanessian and J.-M. Vatèle. Tetrahedron Lett. **22**, 3579 (1981).
9. E.D. Soli, A.S. Manoso, M.C. Patterson, P. DeShong, D.A. Favor, R. Hirschmann, and A.B. Smith, III. J. Org. Chem. **64**, 3171 (1999).
10. G. Zhao, U.C. Deo, and B. Ganem. Org. Lett. **3**, 201 (2001).
11. G. Pandey and M. Kapur. Tetrahedron Lett. **41**, 8821 (2000).
12. T.M. Jespersen, M. Bols, M.R. Sierks, and T. Skrydstrup. Tetrahedron, **50**, 13449 (1994).
13. S.U. Hansen and M. Bols. J. Chem. Soc. Perkin Trans. 1, 911 (2000).
14. Y. Ichikawa, Y. Igarashi, M. Ichikawa, and Y. Suhara. J. Am. Chem. Soc. **120**, 3007, 5854 (1998).
15. Y.J. Kim, M. Ichikawa, and Y. Ichikawa. J. Org. Chem. **65**, 2599 (2000).
16. J. Andersch and M. Bols. Chem. Eur. J. **7**, 3744 (2001).
17. M. Bols, R.G. Hazell, and I.B. Thomsen. Chem. Eur. J. **3**, 940 (1997).
18. J.C. McAuliffe and R.V. Stick. Aust. J. Chem. **50**, 193 (1997).
19. S.R. Hall, D.J. du Boulay, and R. Olthof-Hazekamp (*Editors*). The Xtal 3.6 system. University of Western Australia, Australia. 2000.
20. J.J. Naleway, C.R.H. Raetz, and L. Anderson. Carbohydr. Res. **179**, 199 (1988).
21. R.F. Helm, J. Ralph, and L. Anderson. J. Org. Chem. **56**, 7015 (1991).
22. L.R. Schroeder, K.M. Counts, and F.C. Haigh. Carbohydr. Res. **37**, 368 (1974).
23. C.K. de Bruyne and G. van der Groen. Carbohydr. Res. **2**, 173 (1966).
24. S. Rio, J.-M. Beau, and J.-C. Jacquinet. Carbohydr. Res. **219**, 71 (1991).
25. M. Mori, Y. Ito, and T. Ogawa. Carbohydr. Res. **195**, 199 (1990).

© 2002 NRC Canada

On expanding the repertoire of glycosynthases: Mutant β-galactosidases forming β-(1,6)-linkages

David L. Jakeman and Stephen G. Withers

Abstract: Oligosaccharide synthesis by enzymatic processes offers the potential for thrusting oligosaccharides to the forefront of pharmaceutical research, in part, due to expedient and scalable reaction protocols. Glycosynthases are an emerging class of mutant enzymes capable of synthesizing glycosidic linkages in high yield. We report a new glycosynthase enzyme generated by a point mutation of *E. coli* β-galactosidase that condenses α-galactosyl fluoride with aryl glucosides forming a β-(1,6) glycosidic linkage. A further point mutation within the enzyme, proximal to the active site, increases the yields significantly.

Key words: glycosyl transfer, glycosynthase, enzymatic oligosaccharide synthesis.

Résumé : La synthèse d'oligosaccharides par des procédés enzymatiques offre la possibilité de projeter les oligosaccharides à l'avant-plan de la recherche pharmaceutique en raison, en partie, au fait que les protocoles de réaction sont relativement simples et qu'il est possible de les réaliser à grande échelle. Les glycosynthases font partie d'une classe d'enzymes mutants en émergence capable de réaliser la synthèse de liens glycosidiques avec des rendements élevés. Dans ce travail, on la préparation d'une nouvelle glycosyntase, obtenue par mutation ponctuelle de la β-galactosidase du *E. coli*, qui permet de condenser le fluorure d'α-galactosyle avec des glucosides d'aryles pour former une liaison β-(1,6) glycosidique. Une autre mutation ponctuelle à l'intérieur de l'enzyme, à proximité du site actif, permet d'augmenter le rendement de façon significative.

Mots clés : transfert d'un glycosyle, glycosynthase, synthèse enzymatique d'un oligosaccharide.

[Traduit par la Rédaction]

Introduction

Oligosaccharides are ubiquitious throughout nature and play a multitude of important roles in biological systems ranging from leukocyte trafficking by glycosaminoglycans (1–3) to the localization of glycoproteins via their glycan moieties (4–9). The diverse roles played by oligosaccharides therefore provide possibilities for the generation of new therapeutics for numerous disease states. Inspired by the possibilities for disease treatment and by the challenges posed by the complex structural architecture of oligosaccharides, chemists have devised and implemented impressive synthetic routes toward these challenging molecules. The very complexity of these compounds, however, hinders development of the efficient and economical syntheses required to produce the quantities of oligosaccharides needed for biological testing. Particularly demanding are the many protecting group manipulations that are needed to ensure control of regio- and stereochemistry. Enzymatic syntheses offer the promise of inherently scalable and shorter routes towards quantities of oligosaccharides because the vital regio- and stereochemical control is governed by the enzyme, thus avoiding laborious protecting group manipulation (10–15).

Glycosynthases (16) are a new class of mutant enzymes for the synthesis of oligosaccharides derived from retaining β-glycoside hydrolases, which cleave glycosides through a double displacement mechanism that proceeds via a covalent glycosyl–enzyme intermediate (Fig. 1*a*). Wild-type β-glycoside hydrolases have been used successfully in the synthesis of glycosides through the coupling of an activated donor sugar to the desired acceptor moiety via a transglycosylation mechanism (Fig. 1*b*). The yields are almost always modest because the product from the transglycosylation reaction is a substrate for hydrolysis (17). These low product yields have been circumvented by using glycosynthases: mutant glycosidases in which the nucleophilic carboxylic acid residue is engineered into a non-nucleophilic residue. The single-point mutation within the enzyme is sufficient to remove all hydrolytic activity yet maintain an active-site architecture appropriate for the condensation of an activated donor sugar (glycosyl fluoride) of the opposite anomeric configuration to that of the natural substrate, with an acceptor sugar. α-Glycosyl fluorides are therefore used with β-glycosynthases, binding into the enlarged active-site pocket generated by the mutation and mimicking the reactive α-glycosyl-enzyme intermediate formed during catalysis by the wild-type enzymes (Fig. 2). Since the report of the initial glycosynthase (AbgGlu358Ala) several glycosynthases have been reported in the literature. These condense various α-hexosyl fluorides onto acceptors with formation of β-(1,3)- or β-(1,4)- glycosidic linkages (18–23). Of particular importance has been the discovery that replacement of the nucleophilic amino

Received 12 December 2001. Published on the NRC Research Press Web site at http://canjchem.nrc.ca on 19 July 2002.

Dedicated to the memory of Professor Raymond U. Lemieux.

D.L. Jakeman and S.G. Withers.[1] Protein Engineering Networks of Centres of Excellence, and Department of Chemistry, 2036 Main Mall, University of British Columbia, Vancouver, BC V6T 1Z1, Canada.

[1]Corresponding author (e-mail: withers@chem.ubc.ca).

 DOI: 10.1139/V02-077 © 2002 NRC Canada

Fig. 1. Mechanisms of the hydrolysis and transglycosylation reactions catalyzed by wild-type LacZ α-galactosidase.

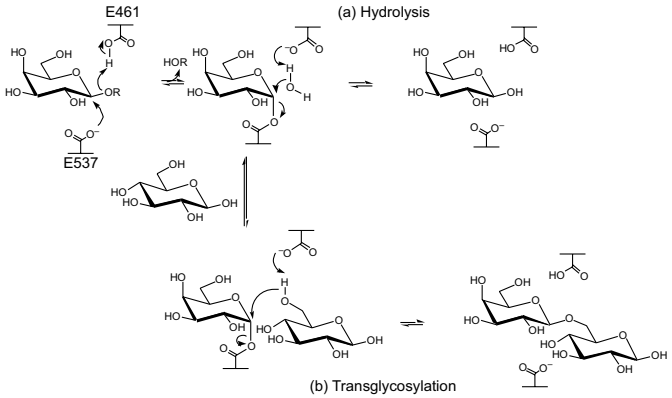

acid with serine rather than alanine leads to more active glycosynthase mutants (19, 23).

In this paper we describe the development of a glycosynthase from glycosyl hydrolase family 2 *Escherichia coli* β-galactosidase (LacZ), which synthesises Gal-β-(1,6)-linkages, a glycosidic linkage hitherto unavailable using known glycosynthases (Fig. 2).

Results and discussion

E. coli LacZ-galactosidase (EC 3.2.1.23) is one of the most commonly used enzymes within molecular biology and was instrumental in determining the operon model of gene regulation. It is responsible for the hydrolysis of lactose (Gal-β-(1,4)-Glc) to provide glucose as a starting point for glycolysis. It also performs transglycosylation reactions between the galactose and glucose moieties from lactose, to form allolactose (Gal-β-(1,6)-Glc), the natural lac-operon inducer. This enzyme is functional as a tetramer of 4 × 116 kDa, thus solution of its 3-D structure represented a considerable "tour de force" of X-ray crystallography (24). Previous work had identified the nucleophilic residue within the active site of LacZ galactosidase as Glu537 by trapping the covalent intermediate through the use of the mechanism-based inactivator, 2,4-dinitrophenyl 2-deoxy-2-fluoro-β-D-galactopyranoside, coupled with electrospray ionization mass spectrometric analysis of HPLC-separated proteolytic digests of the 2-fluorogalactosyl-enzyme intermediate (25).

The stage was therefore set for generation of a glycosynthase from LacZ. To simplify the purification of the enzyme and also allow separation of the mutant from any chromosomally encoded wild-type contaminant, a construct was used that coded a N-terminal His_6-tag fusion. Upon mutation of the nucleophile to serine (Glu537Ser), the mutant protein was over-expressed in *E. coli* strain BL21 λDE3 and isolated by affinity chromatography on a nickel column. Unfortunately, the protein retained significant wild-type activity (1/200) as demonstrated by removal of all activity after incubation of the recombinant protein with sub-stoichiometric amounts of the mechanism-based inactivator. We surmized that this low wild-type activity arose from monomers of the wild-type LacZ galactosidase expressed constitutively from the lac operon associating with the mutant to form active tetrameric units within the cell. These tetrameric units presumably remain associated throughout the affinity purification and, therefore, a small but significant quantity of wild-type LacZ is co-purified with the mutant, despite its lack of an affinity tag. To circumvent wild-type contamination we obtained *E. coli* strain W2244 that has one third of the LacZ gene deleted, and consequently fails to grow on lactose as the sole carbon source (26). The strain was lysogenized with λDE3 phage to introduce the T7 RNA polymerase gene into the W2244 genome as is necessary for expression of genes under control of a T7 promoter. Purification of the gene product from *E. coli* strain W2244 λDE3 resulted in a lower yield of protein than from BL21 λDE3 stocks but, more significantly, wild-type activity was not observed.

Fig. 2. Transglycosylation catalyzed by LacZ glycosynthase mutants.

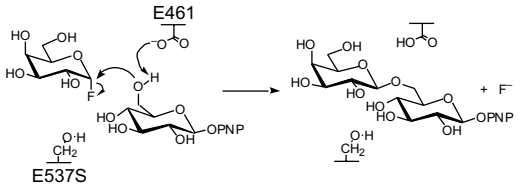

The results of transglycosylation reactions catalyzed by LacZ (Glu537Ser) glycosynthase are summarized in Table 1. Reaction between α-D-galactosyl fluoride (α-GalF) and *para*-nitrophenyl β-D-glucopyranoside (*p*NPGlc) catalyzed by the Glu358Ser mutant resulted in a modest 40% yield of a disaccharide product. To determine the regiochemistry of the linkage, the disaccharide product was acetylated and characterized by NMR. The relative downfield chemical shift of the glucopyranoside ring C-6 in comparison to the other centers, which are acetylated, indicated a β-(1,6)-linkage. The glycosidic linkage formed by the glycosynthase reaction is therefore the same as the linkage formed in the wild-type transglycosylation reaction, consistent with a preferred binding mode for galactose in the aglycone (+1) site in which the 6-hydroxyl of glucose is located close to the anomeric center of the galactosyl enzyme. Comparable yields of product were obtained using a transglycosylation reaction catalyzed by wild-type enzyme to synthesise 3-*O*-methyl allolactose. As with all transglycosylation reactions, product hydrolysis occurred over longer reaction times (27). The glycosynthase reaction yield was significantly greater than that obtained with the wild-type enzyme (40% vs. 10% total of allolactose, lactose and Gal-β-(1,3)-Glc) (28).

The reaction of α-GalF and *p*NP β-cellobioside was also catalyzed by the Glu537Ser mutant enzyme, affording a 63% isolated yield of Gal-β-(1,6)-Glc-β-(1,4)-Glc-*p*NP. While the reaction of α-GalF and phenyl β-D-glucoside afforded a 61% yield of Gal-β-(1,6)-Glc-Ph. Further improvements in yield were therefore sought through additional protein engineering.

Huber and co-workers (29) had reported earlier a single-point mutation (Gly794Asp) that increased the rate of glycosidic-bond cleavage 25-fold relative to the wild-type enzyme, using lactose as substrate. It therefore seemed likely that inclusion of this point mutation within the glycosynthase could improve the performance of this catalyst. The double mutant Glu537Ser/Gly794Asp was therefore generated and the protein was isolated. Two parallel reactions with *p*NP β-cellobioside and α-GalF as the reactants were monitored, one catalyzed by Glu537Ser and the other

© 2002 NRC Canada

Table 1. The reaction of α-D-galactosyl fluoride with various acceptors catalyzed by LacZ Glu537Ser and LacZ Glu537Ser/Gly794Asp.

Product	Isolated product yield %	
	Glu537Ser	Gly794Asp/ Glu537Ser
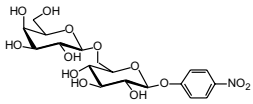	40[a]	70
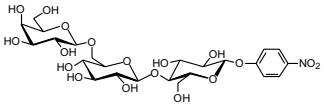	51 (63[a])	80
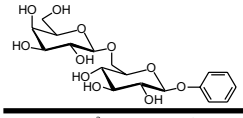	61	85

[a]Reaction performed with an enzyme concentration of 34 μM

catalyzed by Glu537Ser/Gly794Asp. TLC analysis revealed that the double mutant was considerably more active, and upon isolation of the disaccharide product the double mutant gave a higher product yield (80% vs. 51%). With phenyl β-D-glucoside as the acceptor improvements in yield were also observed for the double mutant (85% vs. 61%). The importance of a 794–804 amino-acid residue loop has been shown through recent X-ray crystallographic studies of the structures of LacZ and mutants bound to various substrate, transition-state, and intermediate analogues. Upon the binding of transition-state analogues, this loop was found to move up to 10 Å closer to the active site (30). Figure 3 shows the position of Gly794Asp modeled into the Glu537Gln LacZ-allolactose crystal structure (1jz8.pdb) to minimize steric interactions. This structure confirms that the introduced aspartic acid lies well within the active site and may well interact with the acceptor sugar to facilitate transglycosylation. In addition, since Gly794 resides at one end of this mobile loop, which seems to play a role in catalysis, it is quite possible that the mutation may well affect the preferred conformation of this loop in a way that optimizes turnover.

In conclusion, the existing glycosynthase methodology has been extended to the synthesis of Gal-β-(1,6)-linkages using a serine-nucleophile mutant of LacZ. Improvements in product yield have been obtained by an additional point mutation within the enzyme, which is close to the enzyme active site. Further improvements in the reaction rate should be possible using a combination of random mutagenesis and an appropriate screening protocol similar to that used for selecting improved glycosynthases from *Agrobacterium sp.* glucosidase (18).

Experimental

Enzyme mutagenesis: expression and purification

The plasmid pRSETlacZ was obtained from Invitrogen and codes for a N-terminal His-tagged LacZ gene under the control of a T7 promotor. It was mutated using the Promega GeneEditor in vitro Site-Directed Mutagenesis System as described in the manual with the following oligonucleotide to generate the Glu537Ser mutation: 5′-(P)GATCCTTGCAGTTACGCCCACG-3′ (the mutated codon is underlined). The Gly794Asp mutation was introduced into the wild-type gene using the Promega kit with the following oligonucleotide 5′-(P)AACGACATTGACGTCAGTGAAGCGACC-3′. Both mutants were digested with SacI and AccI restriction endonucleases and run on a 2% agarose gel. The 5000 bp and 800 bp fragments were cut out and purified using a Qiaex II gel extraction kit. The 5000 bp vector backbone from mutant Glu537Ser was ligated with the 800 bp insert encoding Gly794Asp and transformed into XL1-Blue cells to afford the double mutant Glu537Ser/Gly794Asp. Mutations were confirmed by sequence analysis.

Fig. 3. The crystal structure of E537Q LacZ (1jz8.pdb) with allolactose bound in the +1/+2 (shallow) binding site showing the acid–base catalyst (E461), the mutated nucleophile (E537Q), and allolactose bound over W999. The mutation G794D was generated using swisspdbviewer. The loop residues that move during catalysis in the wild-type enzyme are represented as a tube (794–804).

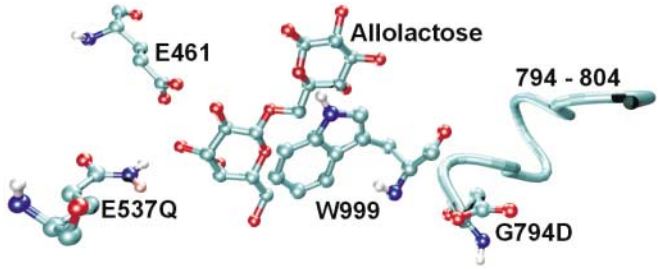

The plasmid coding for Glu537Ser was transformed by electroporation into *E. coli* BL21 λDE3 and induced at OD_{600} = 0.6 with IPTG (0.4 mM final concentration) and allowed to grow for a further four hours. Cells were harvested by centrifugation and passed twice through a French press at 4°C. The mutant, Glu537Ser, was isolated from the supernatant by Ni^{2+} chelation chromatography (His-bind resin, Novagen); yields of 50 mg L^{-1} were obtained. Protein was concentrated using Centricon Plus 20 kDa molecular-weight cut-off membranes.

Strain W2244 (*E. coli* genetic stock centre) was lysogenized with phage λDE3 using the Novagen λDE3 lysogenization protocol. Plasmids coding for Glu537Ser and Glu537Ser/Gly794Asp mutants were transformed into electrocompetent W2244 λDE3 cells. Protein expression and purification in W224 λDE3 was performed exactly as described for strain BL21 λDE3 except that final yields were 5 mg L^{-1}. Protein concentrations were determined by absorbance at 280 nm using the extinction coefficient $E_{280}^{0.1\%}$ = 2.1 cm^{-1}, determined from the amino acid sequence.

Oligosaccharide synthesis and characterization

Enzyme reactions were performed in 200 mM phosphate buffer, pH 7.5, 1 mM $MgCl_2$. Reaction mixtures were monitored by TLC (Kieselgel 60 F_{254} (Merck), ethyl acetate–methanol–water, 7:2:1) and visualized under UV light and by exposure to 10% ammonium molybdate in 2 M H_2SO_4. Reaction mixtures were passed through a 30-kDa ultrafiltration membrane to remove protein, applied to a TosaHaas Amide 80 HPLC column and separated by gradient elution of 80% acetonitrile to 60% acetonitrile. After analysis

© 2002 NRC Canada

and identification by mass spectrometry (ESI), products were acetylated with acetic anhydride–pyridine (1:2) and purified by flash chromatography (ethyl acetate–hexanes) on silica gel (230–400 mesh). ^{1}H and ^{13}C NMR (Bruker Avance, 400 MHz) spectra were internally referenced to the solvent.

4-Nitrophenyl* β-D-*galactopyranosyl-(1,6)*-β-D-*glucopyranoside

4-Nitrophenyl β-D-glucopyranoside (8.7 mg, 29.1 μM) and α-D-galactosyl fluoride (10.6 mg, 58 μM) were dissolved in phosphate buffer (1 mL) containing LacZ E537S (34 μM). After incubation at room temperature for 48 h, with TLC monitoring, the reaction mixture was purified to yield the disaccharide (5.4 mg, 40%).

An identical reaction was performed for the double mutant, with the exception that LacZ E537S G794D (17 μM) was used as catalyst to yield the disaccharide (9.4 mg, 70%). ESI-MS *m*/*z*: 486 $[M + Na]^+$.

4-Nitrophenyl hepta-O-*acetyl* β-D-*galactopyranosyl-(1,6)*-β-D-*glucopyranoside*

^{1}H NMR δ: 1.82, 1.98, 2.02, 2.05, 2.06, 2.08, 2.18 (s, 21H, C*H*$_3$), 3.65 (dd, *J* = 8.1 Hz, 1H, H6), 3.02–3.91 (m, 2H, H5′, H6), 3.96 (ddd, *J* = 8.2, 1.8 Hz, 1H, H5), 4.09 (dd, *J* = 6.4, 11.3 Hz, 1H, H6′), 4.19 (dd, *J* = 6.7, 11.3 Hz, 1H, H6′), 4.48 (d, *J* = 8.0 Hz, 1H, H1′), 4.91–5.00 (m, 2H, H3′, H4), 5.12 (d, *J* = 7.2 Hz, 1H, H2), 5.21 (dd, *J* = 10.5, 8.0 Hz, 1H, H2′), 5.26 (dd, *J* = 9.3, 8.2 Hz, 1H, H3), 5.28 (d, *J* = 7.2 Hz, 1H, H1), 5.39 (d, *J* = 2.6 Hz, 1H, H4′), 7.10 (d, *J* = 7.2 Hz, 2H, Ph), 8.25 (d, *J* = 7.2 Hz, 2H, Ph). ^{13}C NMR δ: 20.5, 20.6, 20.6, 20.6, 61.3, 67.0, 68.3, 68.5, 68.7, 70.7, 70.9, 71.1, 72.5, 73.8, 98.2, 101.2, 116.6, 128.1, 143.2, 161.4, 169.2, 169.6, 170.0, 170.1, 170.3. HRMS (DCI+) *m*/*z*: calcd. for $C_{32}H_{43}N_2O_{20}$ $[M + NH_4]^+$: 775.2409; found: 775.2412.

4-Nitrophenyl* β-D-*galactopyranosyl-(1,6)*-β-D-*glucopyranosyl-(1,4)*-β-D-*glucopyranoside

4-Nitrophenyl β-cellobioside (10.6 mg, 22 μM) and α-D-galactosyl fluoride (18.4 mg, 100 μM) was dissolved in phosphate buffer (1 mL) containing LacZ E537S (17 μM). After incubation at room temperature for 48 h, with TLC monitoring, the reaction mixture was purified to yield the trisaccharide (7.0 mg, 51%).

An identical reaction was performed for the double mutant, with the exception that LacZ E537S G794D (17 μM) was used as catalyst, yielding the trisaccharide (11.0 mg, 80%). ESI-MS *m*/*z*: 648 $[M + Na]^+$.

4-Nitrophenyl deca-O-*acetyl* β-D-*galactopyranosyl-(1,6)*-β-D-*glucopyranosyl-(1,4)*-β-D-*glucopyranoside*

^{1}H NMR δ: 1.54, 1.95, 2.01, 2.02, 2.03, 2.04, 2.08, 2.10, 2.11, (s, 30H, 10 × C*H*$_3$), 3.54–3.59 (m, 1H, H6′), 3.60–3.65 (m, 1H, H5′), 3.83–3.96 (m, 4H, H6′, H5″, H5, H6), 4.05–4.20 (m, 3H, H6, H6″, H6″), 4.5 (d, *J* = 12.4 Hz, 1H, H1′), 4.52 (d, *J* = 12.0 Hz, 1H, H1″), 4.89 (dd, *J* = 8.2, 8.0 Hz, 1H, H2′), 4.93 (dd, *J* = 9.7, 9.7 Hz, 1H, H4′), 5.05 (dd, *J* = 10.4, 3.4 Hz, 1H, H3″), 5.10–5.30 (m, 6H, H3′, H2″, H1–H4), 5.38 (dd, *J* = 3.2, 1 Hz, 1H, H4″), 7.05 (d, *J* = 2.1 Hz, 2H, Ph), 8.20 (d, *J* = 2.1 Hz, 2H, Ph). ^{13}C NMR δ: 20.5, 20.6, 20.6, 20.7, 20.7, 20.8, 61.2, 61.8, 67.1, 67.3, 68.4, 68.6, 70.7, 70.8, 70.8, 71.0, 71.6, 71.8, 73.0, 73.3, 73.3, 73.4, 75.6, 97.9, 100.2, 101.0, 116.6, 125.8, 143.2, 161.2, 169.0, 169.3, 169.4, 169.5, 169.8, 170.0, 170.0, 170.1, 170.2, 170.3. HRMS (DCI+) *m*/*z*: calcd. for $C_{44}H_{59}N_2O_{28}$ $[M + NH_4]^+$: 1063.3269; found: 1063.3254.

Phenyl* β-D-*galactopyranosyl-(1–6)*-β-D-*glucopyranoside* *(31)

Phenyl β-D-glucopyranoside (7.2 mg, 28 μM) and α-D-galactosyl fluoride (18.2 mg, 100 μM) were dissolved in phosphate buffer (1 mL) containing LacZ E537S (17 μM). After incubation at room temperature for 48 h, with TLC monitoring, the reaction mixture was purified to yield the disaccharide (7.1 mg, 61%).

An identical reaction was performed for the double mutant, with the exception that LacZ E537S G794D (17 μM) was used as catalyst to yield the disaccharide (10.0 mg, 85%). ESI-MS *m*/*z*: 441 $[M + Na]^+$.

Acknowledgments

We thank the Protein Engineering Network of Centres of Excellence of Canada, the Natural Sciences and Engineering Research Council of Canada (NSERC), and Neose Technologies Inc. for financial support, and Professor R. E. Huber for advice.

References

1. D.P. Witt and A.D. Lander. Curr. Biol. **4**, 394 (1994).
2. M.E. Mummert, M. Mohamadzadeh, D.I. Mummert, N. Mizumoto, and A. Takashima. J. Exp. Med. **192**, 769 (2000).
3. M.C. Levesque and B.F. Haynes. J. Immunol. **166**, 188 (2001).
4. I. Brockhausen, J. Schutzbach, and W. Kuhns. Acta Anat. **161**, 36 (1998).
5. P. Sears and C.H. Wong. Cell. Mol. Life Sci. **54**, 223 (1998).
6. O. Seitz. ChemBioChem. **1**, 215 (2000).
7. F. Vallee, K. Karaveg, A. Herscovics, K.W. Moremen, and P.L. Howell. J. Biol. Chem. **275**, 41287 (2000).
8. A.R. Walmsley, F.N. Zeng, and N.M. Hooper. Embo J. **20**, 703 (2001).
9. A. Varki. Glycobiology, **3**, 97 (1993).
10. M.M. Palcic. Curr. Opin. Biotechnol. **10**, 616 (1999).
11. K.M. Koeller and C.H. Wong. Nature (London), **409**, 232 (2001).
12. Y. Ichikawa, G.C. Look, and C.H. Wong. Anal. Biochem. **202**, 215 (1992).
13. Y. Ichikawa, G.C. Look, C.H. Wong, and T. Kajimoto. J. Synth. Org. Chem. Jpn. **50**, 441 (1992).
14. S.L. Flitsch. Curr. Opin. Chem. Biol. **4**, 619 (2000).
15. N. Wymer and E.J. Toone. Curr. Opin. Chem. Biol. **4**, 110 (2000).
16. L.F. Mackenzie, Q.P. Wang, R.A.J. Warren, and S.G. Withers. J. Am. Chem. Soc. **120**, 5583 (1998).
17. D.J. Vocadlo and S.G. Withers. *In* Carbohydrates in chemistry and biology Vol. 2. *Edited by* B. Ernst, G.W. Hart, and P. Sinay. Wiley-VCH, Weinheim. 2000. p. 723.
18. C. Mayer, D.L. Jakeman, M. Mah, G. Karjala, L. Gal, R.A.J. Warren, and S.G. Withers. Chem. Biol. **8**, 437 (2001).
19. C. Mayer, D.L. Zechel, S.P. Reid, R.A.J. Warren, and S.G. Withers. FEBS Lett. **466**, 40 (2000).
20. C. Malet and A. Planas. FEBS Lett. **440**, 208 (1998).
21. S. Fort, V. Boyer, L. Greffe, G. Davies, O. Moroz, L. Christiansen, M. Schulein, S. Cottaz, and H. Driguez. J. Am. Chem. Soc. **122**, 5429 (2000).

© 2002 NRC Canada

22. A. Trincone, G. Perugino, M. Rossi, and M. Moracci. Bioorg. Med. Chem. Lett. **10**, 365 (2000).
23. O. Nashiru, D.L. Zechel, D. Stoll, T. Mohammadzadeh, R.A.J. Warren, and S.G. Withers. Angew. Chem. Int. Ed. **40**, 417 (2001).
24. R.H. Jacobson, X.J. Zhang, R.F. DuBose, and B.W. Matthews. Nature, **369**, 761 (1994).
25. J.C. Gebler, R. Aebersold, and S.G. Withers. J. Biol. Chem. **267**, 11126 (1992).
26. A. Cook and J. Lederberg. Genetics, **47**, 1335 (1962).
27. P. Finch and J.H. Yoon. Carbohydr. Res. **303**, 339 (1997).
28. K. Ajisaka, H. Fujimoto, and H. Nishida. Carbohydr. Res. **180**, 35 (1988).
29. M. Martinez-Bilbao, R.E. Holdsworth, L.A. Edwards, and R.E. Huber. J Biol. Chem. **266**, 4979 (1991).
30. D.H. Juers, T.D. Heightman, A. Vasella, J.D. McCarter, L. Mackenzie, S.G. Withers, and B.W. Matthews. Biochemistry, **40**, 14781 (2001).
31. R. Lopéz and A. Fernández-Mayoralas. J. Org. Chem. **59**, 737 (1994).

© 2002 NRC Canada

Potential for using antibiotics combined with a Shiga toxin-absorbing agent for treating 0157:H7 *Escherichia coli* infections

George Mulvey, David J. Rafter, and Glen D. Armstrong

Abstract: Antibiotics are not recommended for treating O157:H7 *Escherichia coli* infections because they may promote Shiga toxin (Stx) release from these bacteria. This could increase the risk of Stx-mediated complications in patients suffering from such infections. Here, we observed increased cell-free Stx in *E. coli* O157:H7 cultures exposed to subinhibitory concentrations of several antibiotics. Synsorb-Pk, an agent with a high affinity for Stx, absorbed Stx activity from the antibiotic-treated cultures. These data suggest certain antibiotics, given in combination with an orally administered Stx-binding agent, may be useful in treating O157:H7 *E. coli* infections.

Key words: Shiga toxin, Synsorb, *Escherichia coli*, O157:H7, antibiotics, therapy.

Résumé : Les antibiotiques ne sont pas recommandés pour le traitement d'infections au *Escherichia coli* 0157:H7 parce que leur utilisation pourrait provoquer la libération de la toxine Shiga (Stx) de ces bactéries et, pour les patients atteints de telles infections, elle pourrait augmenter le risque de complications liées à Stx. Dans ce travail, on a pu observer une augmentation de Stx sans cellule dans des cultures d'*E. coli* 0157:H7 exposées à des concentrations sous-inhibitrices de plusieurs antibiotiques. Le Synsorb-Pk, un agent ayant une grande affinité pour Stx, absorbe l'activité de Stx à partir des cultures traitées par les antibiotiques. Ces données suggèrent que certains antibiotiques, donnés en combinaison en association avec un agent fixant le Stx administré oralement, pourrait s'avérer utile pour traiter des infections au *E. coli* 0157:H7.

Mots clés : toxine Shiga, Synsorb, *Escherichia coli*, 0157:H7, antibiotiques, thérapie.

[Traduit par la Rédaction]

Introduction

Enterohemorrhagic *Escherichia coli* (EHEC) express virulence factors that enable them to colonize in the human intestine, where they cause diarrhea, hemorrhagic colitis, and, occasionally, complications involving the kidneys and, potentially, the central nervous system (1). These EHEC-mediated complications are collectively called the hemolytic-uremic syndrome (HUS). Although numerous *E. coli* serotypes have been isolated from patients with hemorrhagic colitis, the majority of cases in Europe, Japan, and North America involve *E. coli* O157:H7 (1).

The complications associated with EHEC infections are partly cytotoxin-mediated. These EHEC cytotoxins are structurally and functionally related to Shiga toxin (Stx), expressed by *Shigella dysenteriae* type 1 (2). EHEC express functionally related but serologically distinct Stx (2). The first of these, Shiga toxin 1 (Stx1), is virtually identical to the prototypic Stx (3). The second, Stx2, is more distantly related to Stx1 and Stx (2). Variant forms of Stx2 have also been described (2). Regardless of their serological differences, all the Stx's are classic AB_5-type exotoxins composed of an A subunit and a pentamer of five identical B subunits (2). The B pentamer of all Stx's allows them to bind to specific host-cell receptors, the α-Gal-(1,4)-β-Gal disaccharide sequence, which is common to the human P-blood-group antigens (4).

In North America, antibiotics are not recommended for treating EHEC infections because of evidence that these drugs may increase the risk of HUS developing in patients who might otherwise recover from an uncomplicated course of illness (1, 5). In addition, several studies have revealed that subinhibitory doses of antibiotics can increase the amount of Stx released by O157:H7 *E. coli* (6–10).

Previously (11), we described a product, Synsorb-Pk, which is diatomaceous earth (Chromosorb) containing covalently coupled 8-methoxycarbonyloctyl (MCO) α-Gal-(1,4)-β-Gal-(1,4)-β-Glc (Pk-blood group) triglycoside sequences (12). Synsorb-Pk was found to be resistant to digestion in the human GI tract and, because of the attached carbohydrate receptors, effectively bound Stx1 and Stx2 in stools from EHEC-infected children (13). These results suggested that Synsorb-Pk may be helpful in preventing HUS developing

Received 18 November 2001. Published on the NRC Research Press Web site at http://canjchem.nrc.ca on 4 July 2002.

Dedicated to the memory of Professor Raymond U. Lemieux.

G. Mulvey and G.D. Armstrong.[1] Department of Medical Microbiology and Immunology, University of Alberta, Edmonton, AB T6G 2H7, Canada.
D.J. Rafter. Synsorb Biotech Inc., Calgary, AB T2N 3P5, Canada.

[1]Corresponding author (e-mail: glen.armstrong@ualberta.ca).

 DOI: 10.1139/V02-028 © 2002 NRC Canada

in subjects suffering from O157:H7 *E. coli*-mediated colitis, an assumption which is presently being tested in a double-blind placebo-controlled clinical trial (14).

Here, we examined the ability of Synsorb-Pk to remove cell-free Stx from culture supernatants of a clinical O157:H7 *E. coli* isolate exposed to subinhibitory concentrations of several antibiotics. Our objective was to determine the feasibility of using a combination of orally administered Synsorb-Pk and antibiotics for treating patients with EHEC-mediated hemorrhagic colitis. The rationale would be to limit further growth of the bacteria in the intestines of these patients, while concurrently providing a specific absorbent capable of preventing the extra-intestinal dissemination of Stx released from dying organisms.

Methods

For our study, we chose the same antibiotics used by Walterspiel et al. (6). Fosfomycin was included because of the recent Japanese experience with this drug (15–18). Cefixime (Suprax™), Co-trimoxazole (Trimethoprim–Sulfamethoxazole, Bactrim™, 16 mg mL^{-1} and 80 mg mL^{-1} of Trimethoprim and Sulfamethoxazole, respectively), and Ciprofloxacin (Cipro™, i.v.) were from the University of Alberta Hospital Pharmacy (Edmonton, Alberta). The disodium and calcium salts of Fosfomycin, Norfloxacin, and Tetracycline were purchased from Sigma-Aldrich. We used *E. coli* O157:H7 (EEU 396, a University of Alberta Hospital clinical isolate producing Stx 1 and Stx 2) in this study.

With the exception of Tetracycline, all antibiotic stock solutions (1 to 2 mg mL^{-1}) were first prepared using the concentration of antibiotic given on the product label in double-distilled deionized water. Tetracycline was dissolved at a concentration of 2 mg mL^{-1} in 100% ethanol. The antibiotic inhibitory concentrations in EEU 396 *E. coli* O157:H7 were determined using an adaptation of the procedure described in ref. 19. The modification to the procedure, which involved increasing the bacterial-cell density of the cultures, was necessary because the amount of Stx produced by cultures at the recommended cell density (10^5 cfu mL^{-1}) would have been too low to allow us to accurately evaluate the potential beneficial activity of Synsorb-Pk. Serial twofold dilutions of the antibiotic stock solutions were prepared in Mueller-Hinton (MH) broth and each of these diluted antibiotic solutions (30 μL) was transferred to the appropriate wells of a 96-well microtiter plate. In addition, a culture of *E. coli* (EEU 396) was grown overnight, with shaking, in MH broth, and then diluted to an OD of 0.6 (1×10^7 cfu mL^{-1} at 625 nm, in the same medium). This diluted bacterial culture (200 μL) was then mixed with the antibiotics in each of the microtiter plate wells. The microtiter plate was covered with a transparent lid and the OD in each well was automatically recorded every 20 min for a total incubation time of 24 h. The microtiter plate reader was programmed to gently agitate the plates for 10 s before recording the data. The resulting OD vs. time plots were used to determine the minimum growth-inhibiting concentration for each antibiotic.

A control experiment was performed to investigate whether the antibiotics bound to Synsorb-Pk. Synsorb-Pk was added (10 mg mL^{-1}, same concentration used in the Synsorb-Pk Stx binding experiments described below) to each of the antibiotic stock solutions for 24 h. The concentration of antibiotics in the resulting Synsorb-Pk-treated antibiotic solutions was then determined by the modified minimum-bacterial growth-inhibition procedure described above.

Table 1. *Escherichia coli* O157:H7 (strain EEU 396) antibiotic inhibitory concentrations.

Antibiotic	Inhibitory concentration (μg mL^{-1})
Cefixime	0.20
Tetracycline	0.78
Co-trimoxazole	0.10
Fosfomycin (Ca)	12.50
Fosfomycin (DiNa)	12.50
Norfloxacin	0.10
Ciprofloxacin	0.01

To determine the combined effect of antibiotics and Synsorb-Pk on the cell-free Stx concentration in the *E. coli* cultures, bacteria were first grown overnight, with shaking, at 37°C in 200 mL of MH broth. This culture was then diluted to an OD of 0.6 (1×10^7 cfu mL^{-1}) at 625 nm and 50-mL aliquots were proportioned into 125-mL Erlenmeyer flasks. Duplicate flasks were prepared for each of the antibiotics being tested. Antibiotics were added, at one half of their inhibitory concentrations, determined by the procedure described above, to the appropriate groups of flasks and the cultures were incubated for an additional 24 h with shaking at 37°C. Synsorb-Pk (10 mg mL^{-1}, Synsorb Biotech Inc., Calgary, Alberta) was added to one flask in each group and Chromosorb (10 mg mL^{-1}, Chromatographic Specialties Inc.) was added to the second flask of each group at the same time as the antibiotics. A single 24-h-old 50-mL control culture received no antibiotics, Synsorb-Pk, or Chromosorb.

To normalize the various antibiotic-treated cultures for growth-rate-related differences in Stx production, separate aliquots of the single antibiotic-free control culture were diluted with MH medium to the same OD as that of each of the respective antibiotic-treated cultures. The fold increase in cell-free Stx in each of the antibiotic-treated cultures was then calculated relative to the concentration of cell-free toxin in the normalized aliquots of the antibiotic-free cultures.

The amount of cell-free Stx1 and Stx2 in each of the 24-h-old O157:H7 *E. coli* cultures was quantified by the Verocytotoxicity assay described previously (11). Briefly, serial dilutions of the cell-free culture supernatant solutions were added to pre-confluent Vero-cell monolayers in 96-well microtiter plates. These plates were incubated at 37°C in an atmosphere of CO_2–air (5:95) for 48 h. Vero cells remaining attached to the plastic well bottoms were then fixed using 100% methanol and Giemsa stained. The data were recorded using a Spectramax (model 340) microtiter-plate reader set to a wavelength of 620 nm. CD_{50} (the dilution of culture supernatant causing detachment of 50% of the Vero cells from the plastic well bottoms) values were extrapolated from the resulting OD vs. log culture dilution plots. The difference between the CD_{50} values from the Synsorb-Pk-treated and the Chromosorb-treated culture supernatants was used to

© 2002 NRC Canada

Table 2. Synsorb-Pk removes cell-free Stx from antibiotic-treated *E. coli* O157:H7 (EEU 396).

	Percent[a] cell-free Stx removed from cultures by Synsorb-Pk					Antibiotic-induced fold[b] increase in Stx Vero cell CD_{50}				
	Experimental trial					Experimental trial				
Antibiotic	1	2	3	Av	SD[c]	1	2	3	Av	SD[c]
Cefixime	97.2	68.3	98.6	88.0	17.1	2.0	63.0	5.0	23.3	34.4
Tetracycline	96.9	55.0	99.7	83.9	25.0	2.5	112.0	4.3	39.6	62.7
Co-trimoxazole	98.7	40.0	91.1	76.6	31.9	4.0	10.7	3.0	5.9	4.2
Ca^{++} Fosfomycin	98.5	98.0	99.8	98.7	0.9	15.8	2.8	3.4	7.3	7.3
$DiNa^{+}$ Fosfomycin	96.0	94.9	97.5	96.1	1.3	6.3	0.0	5.0	22.7	3.3
Norfloxacin	80.0	82.2	65.6	75.9	9.0	630	87.5	183.2	300.0	289.6
Ciprofloxacin	N.D.[d]	25.0	58.4	41.7	33.4[e]	N.D.	110.0	120.0	115.0	10.0[e]

[a]Calculated according to the formula given in ref. 11

[b]Amount of cell-free Stx in antibiotic-treated cultures causing 50% death of Vero-cell monolayers (CD_{50}) divided by the normalized (see *Methods*) cell-free Stx CD_{50} in an antibiotic-free control culture. The method for determining CD_{50} has been described previously (11).

[c]Standard deviation of the triplicate determinations.

[d]Not done in this trial.

[e]Range of the duplicate determinations.

calculate the percent Synsorb-Pk-mediated reduction in Stx concentration.

Results and discussion

Table 1 lists the antibiotic inhibitory concentrations for *E. coli* O157:H7 (strain EEU 396). As recommended by Walterspiel et al. (6), we used each of these antibiotics at half the respective inhibitory concentrations listed in Table 1 in the 24-h-old cultures to maximize enhanced expression of cell-free Stx by *E. coli*.

It is clear from Table 2 that all the antibiotics increased the amount of cell-free Stx in the EEU 396 culture medium. Moreover, the enhanced production of Stx in Table 2 roughly correlated with the mode of action of the antibiotics tested. For example, Norfloxacin and Ciprofloxacin (both DNA gyrase inhibitors) caused the greatest increases in Stx production. The effect of Fosfomycin, a cell-wall biosynthesis inhibitor, was variable, mediating increases in Stx from 3.3- to 7.3-fold, depending on the ionic form of the drug. Cefixime, another cell-wall biosynthesis inhibitor, mediated a 23-fold increase in Stx production. The combination of Trimethoprim and Sulfamethoxazole (Co-trimoxazole), which acts at the level of dihydrofolate reductase, caused the lowest average (only 5.9-fold) increase in Stx production. Tetracycline, an inhibitor of protein biosynthesis in bacteria, caused an intermediate increase in Stx production. These correlations, however, should be viewed with extreme caution because of the low number of drugs tested in each class and the high degree of variability in the data (Table 2). Nonetheless, regardless of the mode of drug action or the fold of antibiotic-induced increases in Stx, Synsorb-Pk (relative to underivatized Chromosorb) decreased the amount of Stx in the cell-free media in all of the antibiotic-treated cultures (Table 2). This Synsorb-Pk-mediated reduction in antibiotic-induced cell-free Stx ranged from an average of 41.7% for Ciprofloxacin to 98.7% for the calcium form of Fosfomycin.

Our rationale for presenting the data from each of the three experimental trials was to emphasize that we, like others (6, 7, 9, 10), found that the magnitude of the enhancing effect of the various antibiotics on Stx production was quite unpredictable, resulting in the very large standard deviations in Table 2. We attribute this variability to the biological nature of the system and the fact that we performed only a limited number of trials. Nonetheless, we might imagine that this unpredictability, even under strictly controlled laboratory-growth conditions, might be even more acute in the highly variable environments of the intestines of subjects infected by these organisms. Our experimental data, therefore, further emphasize the necessity for exercising prudence when considering the use of any antibiotics for treating patients suffering from an *E. coli* O157:H7 infection in the absence of compounds designed to neutralize Stx.

The reduced cell-free Stx activity in the Synsorb-Pk–antibiotic co-cultures may have resulted if the Synsorb-Pk absorbed the antibiotics, thereby reducing their effective concentrations and preventing an increase in the amount of cell-free Stx in these cultures. The addition of 10 mg mL^{-1} of Synsorb-Pk alone to the antibiotic stock solutions, however, did not alter their effective concentrations as determined by inhibitory concentration measurements. Turbidity measurements confirmed the growth-inhibiting effect of the antibiotics on bacterial growth in cultures containing either Chromosorb or Synsorb-Pk, compared with the antibiotic-free control culture. We therefore feel that the alternative explanation of an indirect Synsorb-Pk effect in our experiments is unlikely.

The observation that the antibiotics listed in Table 2 do not bind to Synsorb-Pk, and are therefore not antagonized by this Stx-absorbing agent, indicates that a combination of antibiotics and orally administered Synsorb-Pk may be effective in reducing the HUS incidence in patients suffering from an EHEC infection. Since clinical trials revealed it is possible to achieve intestinal concentrations of Synsorb-Pk in excess of 10 mg mL^{-1} in *E. coli* O157:H7-infected subjects (14), we speculate that Synsorb-Pk could absorb sufficient amounts of Stx released into the intestinal lumen by the antibiotic-treated bacteria to prevent toxin uptake into the subject's circulatory system. This may allow antibiotics to inhibit the growth of the organisms without increasing the incidence of HUS in these patients. It is also clear from

© 2002 NRC Canada

Table 2 that certain antibiotics, notably the fluoroquinolones, Norfloxacin, and Ciprofloxacin, caused the greatest increase in cell-free Stx in each of the independent trials with these drugs. Further research is needed to determine the precise mechanisms for the variable effect of antibiotics in promoting Stx release from enterohemorrhagic *E. coli* serotypes. In the meantime, our results suggest that should it be deemed clinically necessary to use antibiotics for treating subjects suffering from EHEC-mediated colitis, drugs with a similar mode of action as Norfloxacin and Ciprofloxacin, even in combination with an Stx absorbing agent, should probably be avoided.

Fosfomycin, on the other hand, consistently caused the lowest increases in cell-free Stx in antibiotic-treated *E. coli* O157:H7 cultures and Synsorb-Pk removed virtually all of this released toxin in all three independent trials. In a retrospective study of treatment modalities in Japanese victims of the 1996 O157 EHEC outbreak, 96% received some form of antimicrobial treatment, 84% involving Fosfomycin (20). In another study (16), Fosfomycin significantly reduced the rate of HUS developing in patients, but only if the drug was given within two days of the onset of their illness. Testing in mice further suggests that early application of antibiotics, including Fosfomycin, may attenuate the effects of O157 EHEC infections (21, 22).

Despite the evidence that antibiotics may be useful for treating EHEC-infected patients (16, 20), the data in Table 2 and independent reports of the unpredictable effects of subinhibitory levels of antibiotics on Stx production by different EHEC strains and serotypes (6–10) cannot be disregarded. Nonetheless, the cumulative results imply that a combination of orally administered Synsorb-Pk, or one of the other Stx-binding agents described more recently (23, 24), and possibly Fosfomycin, could be safely used to decrease the incidence of HUS in children suffering from an EHEC infection. Although we cannot say for certain what percent reduction in the amount of Stx would be beneficial in patients receiving antibiotics for an EHEC infection, it can only be assumed that any reduction would probably be beneficial. This assumption will require testing in a relevant EHEC animal-infection model. The study described here limits the number of antibiotics that will need to be tested in such an animal model. We are currently planning to conduct animal studies to further validate proposed combined therapeutic approaches to human *E. coli* O157:H7 infections. Such animal studies will also involve Stx inhibitors, such as Starfish, that have proven to be even more potent than Synsorb-Pk (23).

Acknowledgments

This work was supported by a grant to G.D.A. from the Canadian Bacterial Diseases Network.

References

1. J.P. Nataro and J.B. Kaper. Clin. Microbiol. Rev. **11**, 142 (1998).
2. A.D. O'Brien, V.L. Tesh, A. Donohue-Rolfe, M.P. Jackson, S. Olsnes, K. Sandvig, A.A. Lindberg, and G.T. Keusch. Curr. Top. Microbiol. Immunol. **180**, 65 (1992).
3. S. DeGrandis, J. Ginsberg, M. Toone, S. Climie, J. Friesen, and J. Brunton. J. Bacteriol. **169**, 4313 (1987).
4. C.A. Lingwood. Curr. Opin. Struct. Biol. **2**, 693 (1992).
5. C.S. Wong, S. Jelacic, R.L. Habeeb, S.L. Watkins, and P.I. Tarr. N. Engl. J. Med. **342**, 1930 (2000).
6. J.N. Walterspiel, S. Ashkenazi, A.L. Morrow, and T.G. Cleary. Infection, **20**, 25 (1992).
7. T. Ito, E. Akino, and K. Hiramatsu. J. Jap. Assoc. Infect. Dis. **71**, 130 (1997).
8. K. Izumikawa, Y. Hirakata, T. Yamaguchi, H. Takemura, S. Maesaki, K. Tomono, S. Igimi, M. Kaku, Y. Yamada, S. Kohno, and S. Kamihira. J. Antimicrob. Chemother. **42**, 341 (1998).
9. K. Grif, M.P. Dierich, H. Karch, and F. Allerberger. Eur. J. Clin. Microbiol. Infect. Dis. **17**, 761 (1998).
10. T. Nasu, K. Okamoto, T. Nakanishi, and T. Nishino. Jap. J. Antibio. **52**, 541 (1999).
11. G.D. Armstrong, E. Fodor, and R. Vanmaele. J. Infect. Dis. **164**, 1160 (1991).
12. R.U. Lemieux, D.R. Bundle, and D.A. Baker. J. Am. Chem. Soc. **97**, 4076 (1975).
13. G.D. Armstrong, P.C. Rowe, P. Goodyer, E. Orrbine, T.P. Klassen, G. Wells, A. MacKenzie, H. Lior, C. Blanchard, F. Auclair, B. Thompson, D.J. Rafter, and P.N. McLaine. J. Infect. Dis. **171**, 1042 (1995).
14. G.D. Armstrong, P.N. McLaine, and P.C. Rowe. *In Escherichia coli* O157:H7 and other Shiga toxin-producing *E. coli* strains. *Edited by* J.B. Kaper and A.D. O'Brien. American Society for Microbiology, Washington, D.C. 1998. pp. 374–384.
15. M. Shiomi, M. Togawa, K. Fujita, and R. Murata. Ped. Int. **41**, 228 (1999).
16. K. Ikeda, O. Ida, K. Kimoto, T. Takatorige, N. Nakanishi, and K. Tatara. Clin. Nephrol. **52**, 357 (1999).
17. T. Takeda. Jap. J. Med. Sci. Biol. **51** (Suppl), S124 (1998).
18. T. Takeda, K. Yoshino, E. Adachi, K. Yamagata, H. Uchida, K. Okonogi, and Y. Iizawa. Kan. Zass. **72**, 924 (1998).
19. NCCLS. Antimicrobial susceptability testing. 31–32 ed. NCCLS, Washington, D.C. 1991.
20. M. Yoh, T. Aoki, M. Akao, Y. Sakaue, E. Tsubura, and T. Honda. J. Jap. Assoc. Infect. Dis. **71**, 1144 (1997).
21. T. Kurioka, Y. Yunou, H. Harada, and E. Kita. Eur. J. Clin. Microbiol. Infect. Dis. **18**, 561 (1999).
22. S. Sawamura, K. Tanaka, and Y. Koga. J. Jap. Assoc. Infect. Dis. **73**, 1054 (1999).
23. P.I. Kitov, J.M. Sadowska, G. Mulvey, G.D. Armstrong, H. Ling, N.S. Pannu, R.J. Read, and D.R. Bundle. Nature (London), **403**, 669 (2000).
24. J.C. Paton, T.J. Rogers, R. Morona, and A.W. Paton. Infect. Immun. **69**, 1389 (2001).

© 2002 NRC Canada

Use of the transannular Diels–Alder (TADA) reaction to probe biological receptors: Rational design and synthesis of tricyclic TADA adducts capable of rigidly holding pharmacophore parts

Yves A. Chantigny, Yves L. Dory, András Toró, and Pierre Deslongchamps

Abstract: Transannular Diels–Alder (TADA) adducts constitute a collection of rigid structures, whose conformational diversity is rich. It is possible to design such specifically functionalized molecules capable of binding to known biological targets by molecular modelling MCSS–HOOK (multiple copy simultaneous search). Here we show that such carefully designed compounds can be easily built from small synthons. TADA adducts are very interesting due to their huge conformational diversity, their rigidity (biological interest), and their ease of synthesis (chemical interest).

Key words: tricycles, synthesis, transannular Diels–Alder, macrocyclization, conformation, diversity.

Résumé : Les adduits de la réaction Diels–Alder transannulaire (DATA) constituent une banque de structures rigides dont la diversité conformationnelle est riche. Il est possible de concevoir de telles molécules spécifiques fonctionnalisées capables de se lier à des cibles biologiques connues, par modélisation moléculaire MCSS–HOOK. Nous montrons ici que de tels composés soigneusement sélectionnés peuvent être aisément assemblées à partir de petits synthons. L'intérêt de telles molécules se situe donc à trois niveaux : leur diversité conformationnelle étendue, leur rigidité (intérêt biologique), et leur relative facilité de synthèse (intérêt chimique).

Mots clés : tricycles, synthèse, Diels–Alder transannulaire, macrocyclisation, conformation, diversité.

Introduction

Generating molecular diversity constitutes an important tool for pharmaceutical chemists to discover new drug leads and to study biological targets (1). To date, nature is still one of the most important sources of original structures, although chemists have devised numerous ways to generate the sought-after diversity (2). We too have added milestones to this continuous and general synthetic effort by preparing libraries of macrocycles (3–7). By incorporating a diene and a dienophile within a macrocycle, a transannular Diels–Alder (TADA) reaction can occur (8–10). We have already made a thorough investigation of this reaction and showed that it is a powerful method in organic synthesis. In this work, we want to further demonstrate that the TADA reaction also offers a realistic potential for the creation of molecular diversity and for the synthesis of original structures.

Received 11 December 2001. Published on the NRC Research Press Web site at http://canjchem.nrc.ca on 3 July 2002.

In memory of Professor Raymond U. Lemieux.

Y.A. Chantigny and A. Toró. Laboratoire de synthèse organique, Département de chimie, Institut de pharmacologie de Sherbrooke, Université de Sherbrooke, 3001, 12e avenue Nord, Sherbrooke, QC J1H 5N4, Canada.
Y.L. Dory and P. Deslongchamps.[1] Laboratoire de modélisation moléculaire, Département de chimie, Institut de pharmacologie de Sherbrooke, Université de Sherbrooke, 3001, 12e avenue Nord, Sherbrooke, QC J1H 5N4, Canada.

[1]Corresponding author (e-mail: pierre.deslongchamps@courrier.usherb.ca).

Molecular modelling design of our targets

The TADA macrocyclic precursors can be easily prepared from building blocks, and each of these macrocycles can be divided into four regions (Fig. 1). The reacting part includes two regions: the dienophile, which can be either *cis* (C) or *trans* (T), and the diene, which can be TT, TC, or CT, but not CC since no TADA adducts have ever been obtained from that particular diene geometry (11). The other two regions are the tethers, which define the size and shape of the resulting A and C rings of the TADA adducts. Our previous studies indicated that TADA adducts can reasonably be expected for five- to seven-membered rings for A and C (12). According to these limitations, there are 54 TADA macrocyclic precursors that can be prepared, which yield 144 tricycles after the reaction. The adducts are more numerous than the macrocyclic trienes because each TT diene can give rise to two products and because the enantiomers must also be included. It is obvious that many positions of these 54 bare macrocycles can be substituted so that the diversity expands accordingly. Such huge diversity can, in principle, be exploited in combinatorial libraries.

Another important aspect of the TADA approach resides in the rigidity of the resulting tricyclic frameworks. The 144 tricycles are sufficiently different from each other, so that conformational diversity arises as well. This important aspect can be fruitfully used when carrying out computa-

 DOI: 10.1139/V02-064 © 2002 NRC Canada

Fig. 1. Diversity generated by means of the TADA reaction.

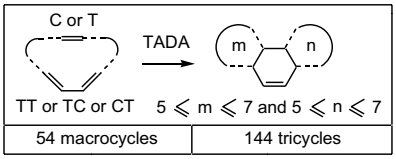

Fig. 2. Use of TADA tricyclic adducts to hold parts pharmacophores.

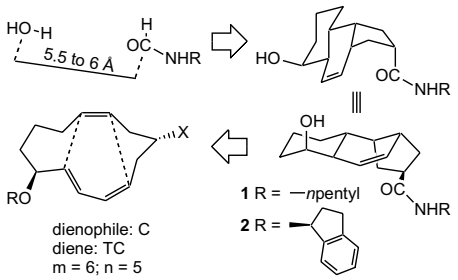

tional drug design, in particular by means of MCSS–HOOK (multiple copy simultaneous search) (13–15). A search on the stain P1/Mahomey of the polyovirus by means of the MCSS method yielded valuable information about the positions, where simple molecules such as water, methanol, amines, and amides, could best interfere with the virus (16). Given the positions and orientations of the suitable functional sites (Fig. 2), HOOK then systematically searched a database of our tricyclic adducts for skeletons that logically connected these binding sites in the presence of the virus. Two structures (**1** and **2**), having a *trans-syn-cis* (TSC) geometry, were obtained as result of that protocol. Both compounds differ only by the nature of their amine moiety; therefore, they can be prepared from the same adequately protected 13-membered tricycle bearing a *cis* (C) dienophile and a *trans–cis* (TC) diene, as previously shown in our model studies (17).

Synthesis

In terms of ease of synthesis, the macrocyclic trienes **21** and **22** (Scheme 1) were identified as being the most suitable TADA precursors. They were prepared in 10 and eight steps, respectively, from the same starting materials **3** and **6** (18, 19). Alcohol **3** was activated as its corresponding mesylate **4**, and subsequently treated with sodium iodide in acetone without purification. Resulting iodide **5** was obtained in 99% yield for the two steps. Upon treatment with *tert*-butyllithium at –78°C, iodide **5** was transformed into its corresponding anion. Addition of aldehyde **6** to the reaction mixture led to alcohol **7** as a mixture of diastereoisomers with a yield of 92%. The alcohol functionality was protected as methoxymethyl ether **8** in 97% yield. The silyl ether was then cleaved with tetrabutyl ammonium fluoride (TBAF) to yield allylic alcohol **9** (95% yield). Allylic chloride **12** was obtained from the preceding alcohol by means of hexachloroacetone (HCA) and triphenylphosphine (Ph_3P) (90%) (20). S_N2 nucleophilic attack of sodium dimethyl malonate onto the allylic iodide (formed in situ by sodium iodide) led to monosubstituted malonate **15** in 71% yield.

Scheme 1.

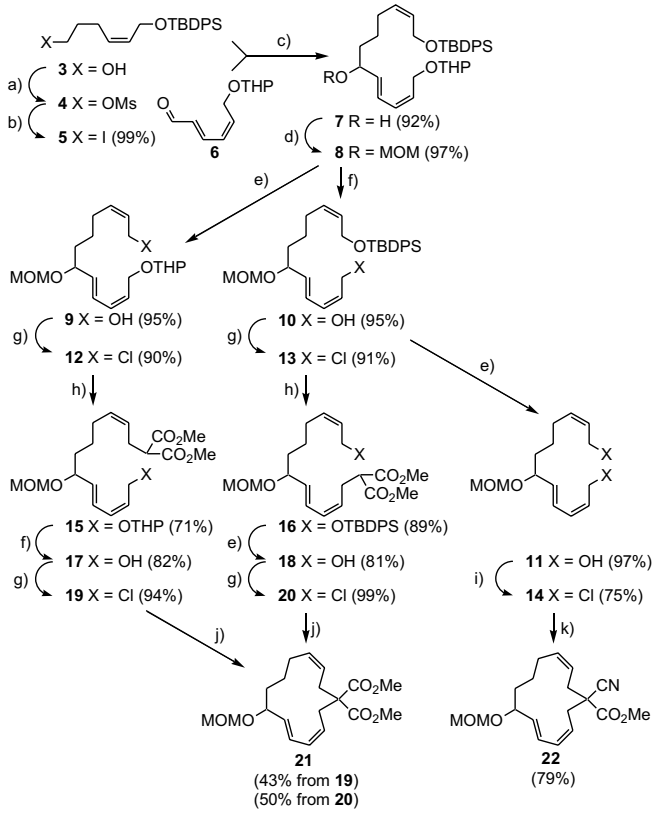

a) MsCl, Et_3N, CH_2Cl_2, 0ºC. b) NaI, acetone, reflux. c) *t*-BuLi, THF, -78ºC. d) KHMDS, MOMCl, THF, 0ºC to 70ºC. e) TBAF, THF, rt. f) PPTS, *i*-PrOH, reflux.g) Ph_3P, HCA, CH_2Cl_2, 0ºC. h) $CH_2(CO_2Me)_2$, NaH, NaI, THF 0ºC to 70ºC. i) Ph_3P, HCA, CH_2Cl_2, -20ºC. j) Cs_2CO_3, CsI, MeCN, 70ºC, slow addition. k) $NCCH_2CO_2Me$, Cs_2CO_3, THF:DMF (2:1), 80ºC, slow addition.

The remaining allylic ether was then cleaved with PPTS to yield alcohol **17** (82%), which was transformed as before into its corresponding allylic chloride **19** (94%). The other macrocyclization precursor (**20**), which would lead to the same macrocycle (**21**), was prepared from the same triether (**8**) by a very similar pathway, with an overall yield of 62% for the five-step sequence. Alternatively, alcohol **10** (obtained from **8** with a yield of 95%) en route to **20**, was transformed into diol **11** by means of TBAF (97% yield). Dichloride **14** was then prepared in 75% yield by means of HCA and Ph_3P as before, but at lower temperature. All three allylic chlorides (**19**, **20**, and **22**) were then subjected to high-dilution macrocyclization conditions. Isomeric chlorides **19** and **20** yielded the same racemic macrocycle (**21**) with similar yields (43 and 50%, respectively) when slowly injected into a mixture of cesium carbonate in acetonitrile. A much better yield of 79% was obtained for the synthesis of macrocycle **22** (mixture of racemic diastereoisomers) when a mixture of methyl cyanoacetate and dichloride **14** in THF was added slowly to a suspension of cesium carbonate in THF and DMF (21). In summary, **21** was obtained from **3**, via **19** and **20**, with overall yields of 18 and 27%, respectively; the yield for **22**, however, was as high as 51%. Consequently, it proved easier to prepare substantial quantities of macrocycle **22** to carry on with the synthesis of **1** and **2**.

Both macrocycles **21** and **22** were heated at 140°C to provoke the TADA reaction (Scheme 2) — the expected TSC

© 2002 NRC Canada

Scheme 2.

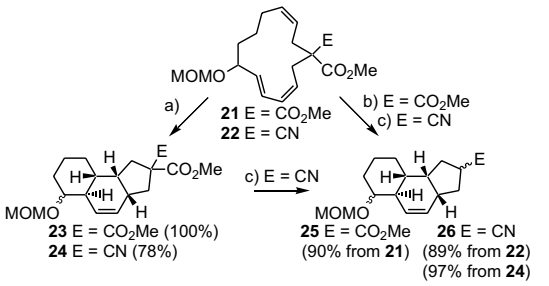

a) xylenes, 140ºC, 4h. b) NaCl, DMSO, 160ºC. c) NaCN, DMSO, 160ºC.

tricycles **23** and **24** were obtained with good yields of 100 and 78%, respectively. Tricycle **23** was produced as a 2:1 mixture (α or β at C4) of two racemic diastereoisomers, whereas **24** was obtained as a mixture of racemic diastereoisomers at C4 and C12. Demethoxycarbonylation of **24** was then performed at 160°C in dimethyl sulfoxide with sodium cyanide (97% yield) (22). Since demethoxycarbonylation occurs at high temperature, we tried successfully to induce both demethoxycarbonylation and TADA together by treating macrocycles **21** and **22** under demethoxycarbonylation conditions. Thus, **21** led to tricycle **25** (90%), when heated at 160°C in DMSO that contained sodium chloride (22); **22** gave **26** in 89% yield when it was treated under identical conditions previously used to prepare **26** from **24**. This confirmed our choice of selecting cyanide **26** (rather than methyl ester **25**) for further work, since it is obtained from **3** with an overall yield of 45%.

All that remained to be done were functional-group manipulations to introduce the amides at the nitrile position and to address the stereochemistry of the amide and the alcohol. To do this, methoxymethyl (MOM) ether **26** was cleaved by means of concentrated HCl to yield alcohol **27** (99% yield) (Scheme 3). Dess–Martin oxidation of this alcohol gave a separable mixture of two racemic ketones **28** (48% yield) and **29** (32% yield). To identify the relative stereochemistry of the nitrile, the major ketone (**28**) was first reduced with a bulky borohydride (lithium triisobutylborohydride) to give exclusively β-OH TSC tricycle **30** (85%) in which the secondary alcohol exists in the axial orientation. The nitrile was then hydrolyzed under basic conditions to corresponding acid **31** (90%), which could undergo iodolactonization to generate lactone **32**. The identities of nitriles **28** and **29** were inferred from that latter experiment, because no lactone can be obtained from the carboxylic acid derived from nitrile **29**. Alcohol **30** was protected as its triisopropyl silyl (TIPS) ether (**33**), with a yield of 99%, by means of TIPS triflate and 2,6-lutidine as a base. Hydrolysis of the nitrile, as before, yielded acid **34** in 83% yield. The acid group was activated as its acid chloride with oxalyl chloride (23). Amylamine was added to the crude acid chloride, and racemic amide-ether **35** was obtained in 80% yield. Alternatively, addition of (*S*)-(+)-1-aminoindane to the acid chloride provided the corresponding amide-ether as an inseparable mixture of racemic diastereoisomers **36** and **37** (73%). Finally, strong acidic conditions (6 N HCl) had to be used to cleave the silyl ethers to afford desired amide-alcohol **1**, together with its enantiomer (81%). The other target (**2**) was prepared in a similar manner from a mixture of **36** and **37**; it could not be separated from its diastereoisomer **38** (yield of 84%).

Scheme 3.

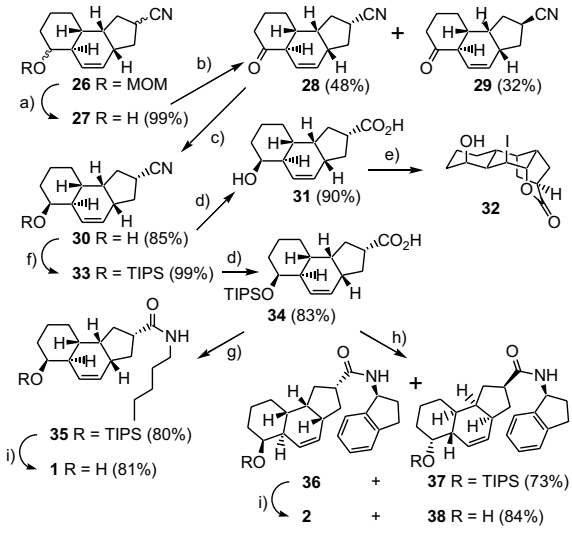

a) 6N HCl, MeOH, rt. b) Dess-Martin, CH_2Cl_2, rt. c) i Li tri-*i*butylborohydride, THF, -78ºC; ii NaOH, H_2O_2, rt. d) NaOH, H_2O_2, MeOH, reflux. e) Na_2CO_3, I_2, H_2O, THF, rt. f) TIPS-triflate, 2,6-lutidine, CH_2Cl_2, rt. g) i $(COCl)_2$, DMF, CH_2Cl_2, rt.; ii amylamine, Et_3N, CH_2Cl_2, rt. h) i $(COCl)_2$, DMF, CH_2Cl_2, rt.; ii (*S*)-(+)-1-aminoindane, Et_3N, CH_2Cl_2, rt. i) 6N HCl, MeOH, reflux

Conclusion

Compounds **1** and **2** proved not to have a significant affinity for the target virus, at least no better than the threshold of the assay, which was set in the sub-micromolar range. Nevertheless, our main goal during this preliminary work was first to demonstrate the chemical utility of TADA adducts for drug design. Thus, TADA tricycles could be used in combinatorial libraries, but the lack of mobility of the tricyclic framework is usually so severe that they should be more useful at the lead optimization stage. Rigidity, however, can be an asset when the shape of the target is precisely known from different theoretical sources (molecular docking or other computational techniques like MCSS–HOOK). In the latter case, rigid skeletons are necessary to hold binding sites (functional groups) uncovered by the theoretical protocol. A collection of reasonably rigid TADA-adduct tricyclic cores can easily provide the diversity necessary to ensure that any combination of two or three binding functional groups can be successfully held in the desired spatial arrangement (within the limits of the span of tricycles). In this work we have proven that, from MCSS–HOOK calculations, adequate tricycles capable of holding binding sites can be selected from a theoretical library of TADA-adduct structures. The resulting chemical targets can be synthesized in a reasonable number of steps, so that the suggested targets can be rapidly tested. In summary, TADA adducts are structurally attractive because their various geometries can cover a large conformational space; they are also chemically attractive because they come from macrocycles easily assembled from smaller pieces.

© 2002 NRC Canada

Experimental

The infrared (IR) spectra were taken on a PerkinElmer 1600 series FT-IR. The NMR spectra were recorded on a Brüker AC 300 instrument. The mass spectra (MS) were obtained on a ZAB-IF spectrometer. Flash chromatography was performed on silica gel Merck 60, 230–400 mesh.

Synthesis

Methanesulfonic acid 6-(*tert*-butyl-diphenyl-silanyloxy)hex-(4Z)-enyl ester (4)

To a solution of alcohol **3** (11.6 g, 32.6 mmol) and triethylamine (6.82 mL, 48.9 mmol) in dichloromethane (150 mL) at 0°C, was added methanesulfonyle chloride (2.78 mL, 35.9 mmol). The mixture was stirred for 1 h and a HCl 1 N solution (100 mL) was added. The mixture was extracted with dichloromethane (3 × 100 mL). The combined organics were dried over $MgSO_4$, filtered, and concentrated under vacuo to yield the crude title compound as an oil (used as is in the next step). IR (cm^{-1}): 3021, 2936, 2859, 1469, 1428, 1356, 1175, 1109, 936, 823, 704, 613. ^1H NMR ($CDCl_3$) δ: 7.70 and 7.40 (2m, 10H, 2 phenyl), 5.65 (m, 1H, C*H*=CHCH$_2$OSi), 5.45 (m, 1H, CH=C*H*CH$_2$OSi), 4.26 (d, *J* = 6.5 Hz, 2H, C*H*$_2$OSi), 4.12 (t, *J* = 7.0 Hz, 2H, C*H*$_2$OMs), 2.92 (s, 3H, SO$_3$C*H*$_3$), 2.00 (q, *J* = 7.0 Hz, 2H, CH$_2$C*H*$_2$CH=CH), 1.71 (quintet, *J* = 6.5 Hz, 2H, C*H*$_2$CH$_2$CH=CH), 1.06 (s, 9H, SiC(C*H*$_3$)$_3$). ^{13}C NMR ($CDCl_3$) δ: 135.4, 133.6, 130.7, 129.6, 128.6, 128.5, 69.0, 60.0, 37.1, 28.7, 26.7, 23.2, 19.0. MS *m/z*: 375 ([M – C_4H_9]$^+$). Exact mass (M – C_4H_9) calcd.: 375.1086; found: 375.1091.

tert-*Butyl-(6-iodo-hex-(2Z)-enyloxy)diphenyl silane (5)*

A solution of crude mesylate **4** (11.6 g, 32.6 mmol) and sodium iodide (48.9 g, 326 mmol) in acetone (250 mL) was heated to reflux for 1.5 h. The cooled mixture was concentrated under vacuo until saturation, diluted with water (150 mL), and extracted with hexanes (3 × 150 mL). The combined organics were washed with brine, dried over $MgSO_4$, filtered on Florisil, and concentrated under vacuo to yield the title compound as an oil (15.14 g, 99% 2 steps). IR (cm^{-1}): 3069, 3017, 2933, 2857, 1467, 1428, 1108, 822, 703, 612, 504. ^1H NMR ($CDCl_3$) δ: 7.70 and 7.40 (2m, 10H, 2 phenyl), 5.65 (m, 1H, C*H*=CHCH$_2$OSi), 5.45 (m, 1H, CH=C*H*CH$_2$OSi), 4.26 (d, *J* = 6.5 Hz, 2H, C*H*$_2$OSi), 3.15 (t, *J* = 7.0 Hz, 2H, C*H*$_2$I), 2.00 (q, *J* = 7.0 Hz, 2H, CH$_2$C*H*$_2$CH=CH), 1.78 (quintet, *J* = 6.5 Hz, 2H, C*H*$_2$CH$_2$I), 1.06 (s, 9H, SiC(C*H*$_3$)$_3$). ^{13}C NMR ($CDCl_3$) δ: 135.5, 133.7, 130.6, 129.6, 128.6, 128.5, 60.2, 33.1, 28.3, 26.8, 19.1, 6.9. MS *m/z*: 407 ([M – C_4H_9]$^+$).

12-(*tert*-Butyl-diphenyl-silanyloxy)-1-(tetrahydropyran-2-yloxy)dodeca-(2Z,4E,10Z)-trien-6-ol (7) (diastereoisomers)

To a solution of *tert*-butyllithium 1.5 M (40 mL, 60 mmol) in ether (100 mL) at –78°C, was added dropwise over 10 min a solution of iodide **5** (14.82 g, 32 mmol) in ether (20 mL). After stirring for 10 min, a solution of aldehyde **6** (5.0 g, 25 mmol) in ether (20 mL) was added dropwise over 10 min. The mixture was allowed to warm to room temperature for 15 min, then cooled to –78°C, and a saturated NH_4Cl solution (40 mL) was added. The mixture was extracted with hexanes (3 × 20 mL). The organics were washed with brine, dried over $MgSO_4$, filtered, and concentrated under vacuo. The residue was purified by flash chromatography (hexanes–ether, 1:1) to yield the title compound as an oil (14.2 g, 92%). IR (cm^{-1}): 3444 (br), 2934, 2858, 1428, 1113, 1077, 1024, 823, 703, 614. ^1H NMR ($CDCl_3$) δ: 7.70 and 7.40 (2m, 10H, 2 phenyl), 6.49 (dd, *J* = 15.0, 11.0 Hz, 1H, CH=C*H*CH=CHCH$_2$), 6.10 (t, *J* = 11.0 Hz, 1H, CH=CHC*H*=CHCH$_2$), 5.72–5.55 (m, 3H, C*H*=CHCH$_2$OSi and C*H*=CHCH=C*H*), 5.39 (m, 1H, CH=C*H*CH$_2$OSi), 4.64 (t, *J* = 4.0 Hz, 1H, OC*H*O), 4.36 (dd, *J* = 6.5 Hz, 1H, C*H*HOTHP), 4.23 (d, *J* = 5.5 Hz, 2H, C*H*$_2$OSi), 4.21–4.08 (m, 2H, CH*H*OTHP and C*H*OH), 3.90 (m, 1H, OC*H*H of THP), 3.52 (m, 1H, OCH*H* of THP), 1.88 (q, *J* = 7.0 Hz, 2H, CH$_2$C*H*$_2$CH=CH), 1.84–1.25 (m, 10H, other CH$_2$), 1.06 (s, 9H, SiC(C*H*$_3$)$_3$). ^{13}C NMR ($CDCl_3$) δ: 135.6, 133.8, 130.7, 129.5, 129.4, 127.6, 97.7, 72.2, 72.1, 62.7, 62.1, 60.2, 36.6, 30.5, 27.3, 26.7, 25.9, 25.2, 19.3, 19.0. MS *m/z*: 552 ([M + NH_4]$^+$), 517 ([M – OH]$^+$). Exact mass ([M + NH_4]$^+$) calcd.: 552.3509; found: 552.3500.

tert-*Butyl-[7-methoxymethoxy-12-(tetrahydropyran-2-yloxy)dodeca-(2Z,8E,10Z)-trienyloxy]diphenyl silane (8) (diastereoisomers)*

To a solution of alcohol **7** (1.294 g, 2.42 mmol) in THF (25 mL) at –78°C, was added a solution of potassium bis(trimethylsilyl) amide 0.5 M (5.81 mL, 2.9 mmol). After 15 min, methyl-methylether chloride (552 μL, 7.26 mmol) was added. After stirring for 2 h, a saturated NH_4Cl solution (30 mL) was added and the mixture was extracted with hexanes (3 × 20 mL). The combined organics were washed with brine, dried over $MgSO_4$, filtered, and concentrated under vacuo. The residue was purified by flash chromatography (hexanes–ether, 3:1) to yield the title compound as an oil (1.35 g, 97%). IR (cm^{-1}): 2940, 2858, 1428, 1113, 1078, 1032, 822, 741, 703, 614, 503. ^1H NMR ($CDCl_3$) δ: 7.70 and 7.40 (2m, 10H, 2 phenyl), 6.44 (dd, *J* = 15.0, 11.0 Hz, 1H, CH=C*H*CH=CHCH$_2$), 6.10 (t, *J* = 11.0 Hz, 1H, CH=CHC*H*=CHCH$_2$), 5.72–5.55 (m, 3H, C*H*=CHCH$_2$OSi and C*H*=CHCH=C*H*), 5.39 (m, 1H, CH=C*H*CH$_2$OSi), 4.65 and 4.48 (2d, *J* = 7.0 Hz, 2 × 1H, OC*H*$_2$O), 4.63 (t, *J*= 4.0 Hz, 1H, OC*H*O), 4.36 (m, 1H, C*H*HOTHP), 4.18 (m, 1H, CH*H*OTHP), 4.23 (d, *J* = 5.5 Hz, 2H, C*H*$_2$OSi), 3.99 (q, *J* = 5.5 Hz, 1H, C*H*OMOM), 3.87 (m, 1H, OC*H*H of THP), 3.52 (m, 1H, OCH*H* of THP), 3.33 (s, 3H, OC*H*$_3$), 1.88 (q, *J* = 7.0 Hz, 2H, CH$_2$C*H*$_2$CH=CH), 1.84–1.25 (m, 10H, other CH$_2$), 1.06 (s, 9H, SiC(C*H*$_3$)$_3$). ^{13}C NMR ($CDCl_3$) δ: 135.5, 135.2, 133.8, 130.5, 130.4, 130.3, 129.5, 129.3, 127.6, 127.5, 127.2, 98.1, 97.8, 93.6, 76.1, 62.9, 62.8, 62.2, 62.1, 60.1, 55.3, 35.1, 30.6, 27.3, 26.7, 25.4, 25.3, 19.5, 19.4, 19.1. MS *m/z*: 596 ([M + NH_4]$^+$), 419 ([M – C_4H_9 – THPO]$^+$). Exact mass ([M + NH_4]$^+$) calcd.: 596.3771; found: 596.3763.

7-Methoxymethoxy-12-(tetrahydropyran-2-yloxy)-dodeca-(2Z,8E,10Z)-trien-1-ol (9) (diastereoisomers)

A solution of methoxymethyl ether **8** (1.3 g, 2.33 mmol) and tetrabutylammonium fluoride (1 M, 4.76 mL, 4.66 mmol) in THF (20 mL) was stirred at –20°C overnight. The mixture was diluted with water (100 mL) and extracted with dichloromethane (3 × 100 mL). The combined organics were dried over $MgSO_4$, filtered, and concentrated under vacuo. The residue was purified by flash chromatography (hexanes–ether, 1:1 to 3:7) to yield the title compound as an oil

© 2002 NRC Canada

(744 mg, 95%). IR (cm^{-1}): 3460, 2941, 2882, 1455, 1387, 1349, 1205, 1120, 1031, 912. ^1H NMR ($CDCl_3$) δ: 6.44 (dd, *J* = 15.0, 11.0 Hz, 1H, CH=CHC*H*=CHCH$_2$), 6.10 (t, *J* = 11.0 Hz, 1H, CH=C*H*CH=CHCH$_2$), 5.68–5.50 (m, 4H, C*H*=C*H* and C*H*=CHCH=C*H*), 4.67 and 4.51 (2d, *J* = 7.0 Hz, 2 × 1H, OCH_2O), 4.65 (t, *J* = 4.0 Hz, 1H, OC*H*O), 4.42–4.20 (m, 2H, CH_2OTHP), 4.18 (d, *J* = 6.5 Hz, 2H, CH_2OH), 4.07 (q, *J* = 5.5 Hz, 1H, C*H*OMOM), 3.87 (m, 1H, OC*H*H of THP), 3.52 (m, 1H, OCH*H* of THP), 3.38 (s, 3H, OCH_3), 2.13 (q, *J* = 7.0 Hz, 2H, CH$_2$CH_2CH=CH), 1.90–1.35 (m, 10H, other CH$_2$). ^{13}C NMR ($CDCl_3$) δ: 134.8, 134.6, 128.9, 128.7, 127.0, 123.53, 123.5, 119.2, 98.7, 95.6, 92.0, 91.8, 91.3, 91.1, 77.9, 60.4, 56.3, 55.9, 26.8, 26.4, 25.0, 23.8, 23.6, 22.0, 19.0.

*12-(***tert***-Butyl-diphenyl-silanyloxy)-6-methoxymethoxy-dodeca-(2***Z***,4***E***,10***Z***)-trien-1-ol (10)***

A solution of silylether **8** (1.57g, 2.72 mmol) and pyridinium *p*-toluenesulfonate (171 mg, 681 μmol) in isopropanol (50 mL) was stirred at reflux for 1 h. The solution was allowed to cool to room temperature and sodium bicarbonate (57.2 g, 681 μmol) was added. The mixture was concentrated under vacuo, water (50 mL) was added, and the mixture extracted with dichloromethane (3 × 50 mL). The combined organics were dried over $MgSO_4$, filtered, and concentrated under vacuo. The residue was purified by flash chromatography (hexanes–ether, 3:1) to yield the title compound as an oil (1.09 g, 81%). IR (cm^{-1}): 3422, 2932, 2858, 1473, 1429, 1149, 1111, 1031, 824, 741, 702. ^1H NMR ($CDCl_3$) δ: 7.70 and 7.40 (2m, 10H, 2 phenyl), 6.42 (dd, *J* = 15.0, 11.0 Hz, 1H, CH=C*H*CH=CHCH$_2$), 6.05 (t, *J* = 11.0 Hz, 1H, CH=CHC*H*=CHCH$_2$), 5.72–5.55 (m, 3H, C*H*=CHCH$_2$OSi and C*H*=CHCH=C*H*), 5.46–5.35 (m, 1H, CH=C*H*CH$_2$OSi), 4.65 and 4.49 (2d, *J* = 7.0 Hz, 2 × 1H, OCH_2O), 4.30 (dd, *J* = 7.0, 1.0 Hz, 2H, CH_2OH), 4.24 (dd, *J* = 6.0, 1.0 Hz, 2H, CH_2OSi), 3.99 (q, *J* = 5.5 Hz, 1H, C*H*OMOM), 3.33 (s, 3H, OCH_3), 1.90 (q, *J* = 7.0 Hz, 2H, CH$_2$CH_2CH=CH), 1.60–1.25 (m, 4H, other CH$_2$), 1.04 (s, 9H, SiC(CH_3)$_3$). ^{13}C NMR ($CDCl_3$) δ: 135.615, 135.527, 135.414, 133.979, 130.536, 130.109, 129.667, 129.527, 129.402, 127.590, 126.916, 93.597, 76.188, 60.176, 58.661, 55.345, 35.045, 27.344, 26.756, 25.308, 19.092. MS *m*/*z*: 512 ([M + NH$_4$]$^+$). Exact mass ([M + NH$_4$]$^+$) calcd.: 512.3196; found: 512.3197.

*6-Methoxymethoxy-dodeca-(2***Z***,4***E***,10***Z***)-triene-1,12-diol (11)***

To a solution of alcohol **10** (1.19 g, 2.41 mmol) in THF (35 mL) at 0°C was added a solution of tetrabutylammonium fluoride (1 M in THF, 4.81 mL, 4.81 mmol). The mixture was allowed to warm to room temperature and stirred for 1.25 h. A saturated NH_4Cl solution (50 mL) was added and the mixture was extracted with dichloromethane (3 × 30 mL). The combined organics were dried over $MgSO_4$, filtered, and concentrated under vacuo. The residue was purified by flash chromatography (ethyl acetate) to yield the title compound as an oil (599 mg, 97%). IR (cm^{-1}): 3372, 2944, 1460, 1440, 1150, 1095, 1029, 855. ^1H NMR ($CDCl_3$) δ: 6.45 (dd, *J* = 15.0, 11.0 Hz, 1H, CH=C*H*CH=CHCH$_2$), 6.06 (t, *J* = 11.0 Hz, 1H, CH=CHC*H*=CHCH$_2$), 5.66–5.45 (m, 4H, C*H*=C*H*, C*H*=CHCH=C*H*), 4.66 and 4.49 (2d, *J* = 7.0 Hz, 2 × 1H, OCH_2O), 4.30 (d, *J* = 7.0 Hz, 2H, CH=CHCH=CHCH_2OH), 4.15 (d, *J* = 6.0 Hz, 2H, CH$_2$CH=CHCH_2OH), 4.05 (q, *J* = 7.0 Hz, 1H, C*H*OMOM), 3.35 (s, 3H, OCH_3), 2.10 (q, *J* = 7.0 Hz, 2H, CH$_2$CH_2CH=CH), 1.70–1.30 (m, 4H, other CH$_2$). ^{13}C NMR ($CDCl_3$) δ: 135.2, 132.4, 130.3, 129.7, 128.8, 127.1, 93.6, 16.2, 58.6, 58.4, 55.4, 64.8, 27.1, 25.2. MS *m*/*z*: 225 ([M – OMe]$^+$), 211 ([M – MOM]$^+$). Exact mass ([M – OMe]$^+$) calcd.: 225.1491; found: 225.1485; ([M – C_2H_5O]$^+$) calcd.: 211.1334; found: 211.1340.

*2-(12-Chloro-6-methoxymethoxy-dodeca-(2***Z***,4***E***,10***Z***)-trienyloxy)-tetrahydro-pyran (12) (diastereoisomers)***

To a solution of alcohol **9** (420 mg, 1.25 mmol) and hexachloroacetone (228 μL, 1.5 mmol) in dichloromethane (10 mL) at 0°C was added triphenylphosphine (492 mg, 1.9 mmol). The mixture was allowed to warm to room temperature and stirred 45 min. The mixture was concentrated under vacuo and purified by flash chromatography (hexanes–ether, 9:1) to yield the title compound as an oil (397 mg, 90%). IR (cm^{-1}): 2942, 1454, 1032. ^1H NMR ($CDCl_3$) δ: 6.44 (dd, *J* = 15.0, 11.0 Hz, 1H, CH=CHC*H*=CHCH$_2$), 6.10 (t, *J* = 11.0 Hz, 1H, CH=C*H*CH=CHCH$_2$), 5.68–5.50 (m, 4H, C*H*=C*H* and C*H*=CHCH=C*H*), 4.67 and 4.51 (2d, *J* = 7.0 Hz, 2 × 1H, OCH_2O), 4.65 (t, *J* = 4.0 Hz, 1H, OC*H*O), 4.42–4.20 (m, 2H, CH_2OTHP), 4.07 (d, *J* = 7.0 Hz, 2H, CH_2Cl), 4.07 (q, *J* = 5.5 Hz, 1H, C*H*OMOM), 3.87 (m, 1H, OC*H*H of THP), 3.52 (m, 1H, OCH*H* of THP), 3.38 (s, 3H, OCH_3), 2.14 (q, *J* = 7.0 Hz, 2H, CH$_2$CH_2CH=CH), 1.90–1.35 (m, 10H, other CH$_2$). ^{13}C NMR ($CDCl_3$) δ: 135.0, 134.9, 130.4, 127.8, 127.4, 125.5, 98.1, 97.9, 93.7, 76.1, 62.9, 62.8, 62.3, 62.2, 55.4, 39.4, 35.0, 30.6, 26.9, 25.4, 25.0, 19.5, 19.4.

tert*-Butyl-(12-chloro-7-methoxymethoxy-dodeca-(2***Z***,8***E***,10***Z***)-trienyloxy)diphenyl silane (13)***

Prepared similar to chloride **12** (91%). IR (cm^{-1}): 3016, 2932, 2858, 1472, 1428, 1149, 1112, 1031, 824, 703, 614. ^1H NMR ($CDCl_3$) δ: 7.70 and 7.40 (2m, 10H, 2 phenyls), 6.43 (dd, *J* = 15.0, 11.5 Hz, 1H, CH=C*H*CH=CHCH$_2$), 6.12 (t, *J* = 11.0 Hz, 1H, CH=CHC*H*=CHCH$_2$), 5.66–5.55 (m, 3H, CH=C*H*CH$_2$OSi and C*H*=CHCH=C*H*), 5.45–5.34 (m, 1H, C*H*=CHCH$_2$OSi), 4.65 and 4.50 (2d, *J* = 7.0 Hz, 2 × 1H, OCH_2O), 4.22 (d, *J* = 6.5 Hz, 2H, CH_2OSi), 4.19 (d, *J* = 8.5 Hz, 2H, CH_2Cl), 4.03 (q, *J* = 5.5 Hz, 1H, C*H*OMOM), 3.34 (s, 3H, OCH_3), 1.89 (q, *J* = 7.0 Hz, 2H, CH$_2$CH_2CH=CH), 1.60–1.24 (m, 4H, other CH$_2$), 1.06 (s, 9H, SiC(CH_3)$_3$). ^{13}C NMR ($CDCl_3$) δ: 137.1, 135.6, 135.5, 134.7, 133.8, 131.8, 130.5, 129.5, 129.4, 127.6, 125.9, 125.6, 93.7, 76.0, 60.1, 55.3, 39.3, 34.9, 27.3, 26.7, 26.5, 25.2, 19.1. MS *m*/*z*: 477 ([M – Cl]$^+$), 455 ([M – C_4H_9]$^+$), 451 ([M – CH_3OCH_2O]$^+$). Exact mass ([M – C_4H_9]$^+$) calcd.: 455.1809; found: 455.1812.

*1,12-Dichloro-6-methoxymethoxy-dodeca-(2***Z***,4***E***,10***Z***)-triene (14)***

To a solution of diol **11** (599 mg, 2.34 mmol) and triphenylphosphine (1.72 g, 6.55 mmol) in dichloromethane (35 mL) at 0°C was added hexachloroacetone (426 μL, 2.81 μmol). The solution was allowed to warm to room temperature and stirred for 20 min. The mixture was concentrated under vacuo and purified by flash chromatography (100% hexanes then 95:5 hexanes–ether) to yield the title compound as an oil (514 mg, 75%). IR (cm^{-1}): 2931, 1453,

© 2002 NRC Canada

1251, 1031, 762. ^{1}H NMR ($CDCl_3$) δ: 6.47 (dd, *J* = 15.0, 11.0 Hz, 1H, CH=C*H*CH=CHCH$_2$), 6.15 (t, *J* = 11.0 Hz, 1H, CH=CHC*H*=CHCH$_2$), 5.7–5.58 (m, 4H, C*H*=C*H* and C*H*=CHCH=C*H*), 4.69 and 4.51 (2d, *J* = 7.0 Hz, 2 × 1H, OCH_2O), 4.20 (dd, *J* = 8.0, 2.5 Hz, 2H, CH=CHCH=CHCH_2Cl), 4.10 (d, *J* = 7.0 Hz, 2H, CH=CHCH_2Cl), 4.15–4.00 (m, 1H, C*H*OMOM), 3.38 (s, 3H, OCH_3), 2.15 (q, *J* = 7.0 Hz, 2H, CH$_2$CH_2CH=CH), 1.70–1.40 (m, 4H, other CH$_2$). ^{13}C NMR ($CDCl_3$) δ: 136.9, 134.7, 131.7, 126.0, 125.7, 125.5, 93.8, 75.8, 55.4, 39.3, 34.9, 26.7, 24.9. MS *m*/*z*: 310 ([M + NH_4]$^+$). Exact mass ([M + NH_4]$^+$) calcd.: 310.1340; found: 310.1333.

2-[7-Methoxymethoxy-12-(tetrahydropyran-2-yloxy)-dodeca-(2Z,8E,10Z)-trienyl]malonic acid dimethyl ester (15) (diastereoisomers)

To a suspension of sodium hydride 60% (200 mg, 5 mmol) in a DMF–THF solution (2:1, 15 mL) at 0°C, was added dropwise dimethylmalonate (640 μL, 5.6 mmol). The mixture was allowed to warm to room temperature and stirred 30 min. This solution was added to a solution of chloride **12** (397 mg, 1.12 mmol) and sodium iodide (168 mg, 1.12 mmol) in THF (10 mL) and heated to 70°C for 2 h. A saturated NH_4Cl solution (40 mL) was added to the cooled mixture and extracted with hexanes (3 × 20 mL). The combined organics were washed with brine, dried over $MgSO_4$, filtered, and concentrated under vacuo. The residue was purified by flash chromatography (hexanes–ether, 9:1) to yield the title compound as an oil (358 mg, 71%). IR (cm^{-1}): 2949, 1738, 1437, 1343, 1272, 1234, 1201, 1150, 1030. ^{1}H NMR ($CDCl_3$) δ: 6.44 (dd, *J* = 15.0, 11.1 Hz, 1H, CH=CH-C*H*=CHCH$_2$), 6.10 (t, *J* = 11.0 Hz, 1H, CH=C*H*HC=CHCH$_2$), 5.65–5.40 (m, 3H, CH=C*H*CH$_2$CH and C*H*=CHCH=C*H*), 5.30 (m, 1H, C*H*=CHCH$_2$CH), 4.67 and 4.51 (2d, *J* = 6.5 Hz, 2 × 1H, OCH_2O), 4.65 (t, *J* = 3.0 Hz, 1H, OC*H*O), 4.42–4.15 (m, 2H, CH_2OTHP), 4.07 (q, *J* = 5.6 Hz, 1H, C*H*OMOM), 3.87 (m, 1H, OC*H*H of THP), 3.52 (m, 1H, OCH*H* of THP), 3.76 (s, 6H, CO$_2$CH_3), 3.40 (t, *J* = 4.0 Hz, 1H, C*H*(CO$_2$Me)$_2$), 3.36 (s, 3H, OCH$_2$OCH_3), 2.64 (t, *J* = 7.5 Hz, 2H, CH_2CH(CO$_2$Me)$_2$), 2.09 (q, *J* = 7.0 Hz, 2H, CH$_2$CH_2CH=CH), 1.90–1.40 (m, 10H, other CH$_2$). ^{13}C NMR ($CDCl_3$) δ: 169.3, 135.1, 132.7, 130.3, 127.6, 127.1, 124.6, 98.0, 97.8, 93.5, 76.1, 62.8, 62.7, 62.2, 62.1, 55.3, 52.4, 51.5, 35.0, 30.5, 26.9, 26.6, 25.3, 25.2, 19.4.

2-[12-(tert-Butyl-diphenyl-silanyloxy)-6-methoxymethoxy-dodeca-(2Z,4E,10Z)-trienyl]malonic acid dimethyl ester (16)

Preparation was similar to malonate **15** (89%). IR (cm^{-1}): 3014, 2953, 2859, 1739, 1429, 1344, 1150, 1033, 824, 703. ^{1}H NMR ($CDCl_3$) δ: 7.66 and 7.40 (2m, 10H, 2 phenyl), 6.43 (dd, *J* = 15.0, 11.0 Hz, 1H, CH=C*H*CH=CHCH$_2$), 6.04 (t, *J* = 11.0 Hz, 1H, CH=CHC*H*=CHCH$_2$), 5.67–5.29 (m, 4H, C*H*=C*H*CH$_2$OSi and C*H*=CHCH=C*H*), 4.66 and 4.49 (2d, *J* = 7.0 Hz, 2 × 1H, OCH_2O), 4.24 (d, *J* = 6.5 Hz, 2H, CH_2OSi), 4.00 (q, *J* = 7.0 Hz, 1H, C*H*OMOM), 3.72 (s, 3H, CO$_2$*Me*), 3.73 (s, 3H, CO$_2$*Me*), 3.42 (t, *J* = 7.5 Hz, 1H, C*H*(CO$_2$Me)$_2$), 3.34 (s, 3H, OCH$_2$OCH_3), 2.77 (dt, *J* = 7.5, 1.0 Hz, 2H, CH_2CH(CO$_2$Me)$_2$), 1.89 (q, *J* = 7.0 Hz, 2H, CH$_2$CH_2CH=CH), 1.60–1.20 (m, 4H, other CH_2), 1.06 (s, 9H, SiC(CH_3)$_3$). ^{13}C NMR ($CDCl_3$) δ: 169.0, 135.5, 135.4, 134.8, 133.7, 130.5, 129.5, 129.4, 129.3, 127.5, 126.9, 126.5, 93.5, 76.1, 60.1, 55.2, 52.3, 51.4, 35.1, 27.3, 27.0, 26.7, 25.3, 19.0. MS *m*/*z*: 551 ([M – C_4H_9]$^+$). Exact mass ([M – C_4H_9]$^+$) calcd.: 551.2465; found: 551.2456.

2-(12-Hydroxy-7-methoxymethoxy-dodeca-(2Z,8E,10Z)-trienyl)malonic acid dimethyl ester (17)

A solution of malonate **15** (693 mg, 1.54 mmol) and pyridinium *p*-toluenesulfonate (77 mg, 0.31 mmol) in methanol (8 mL) was heated to reflux for 3 h. The mixture was cooled to room temperature, sodium bicarbonate (26 mg) was added, and the mixture was concentrated under vacuo. The residue was purified by flash chromatography (hexanes–ether, 1:3) to yield the title compound as an oil (401 mg, 73%). IR (cm^{-1}): 3393, 2932, 1733, 1649, 1628, 1430, 1030. ^{1}H NMR ($CDCl_3$) δ: 6.45 (dd, *J* = 15.0, 11.0 Hz, 1H, CH=CHC*H*=CHCH$_2$), 6.08 (t, *J* = 11.0 Hz, 1H, CH=C*H*CH=CHCH$_2$), 5.68–5.40 (m, 3H, CH=C*H*CH$_2$CH and C*H*=CHCH=C*H*), 5.30 (m, 1H, C*H*=CHCH$_2$CH), 4.67 and 4.51 (2d, *J* = 6.5 Hz, 2 × 1H, OCH_2O), 4.32 (d, *J* = 7.0 Hz, 2H, CH_2OH), 4.07 (q, *J* = 5.5 Hz, 1H, C*H*OMOM), 3.73 (s, 6H, CO$_2$CH_3), 3.40 (t, *J* = 4.0 Hz, 1H, C*H*(CO$_2$Me)$_2$), 3.38 (s, 3H, OCH$_2$OCH_3), 2.64 (t, *J* = 7.5 Hz, 2H, CH_2CH(CO$_2$Me)$_2$), 2.09 (q, *J* = 7.0 Hz, 2H, CH$_2$CH_2CH=CH), 1.70–1.35 (m, 4H, other CH$_2$). ^{13}C NMR ($CDCl_3$) δ: 169.3, 135.0, 132.6, 130.4, 129.3, 127.1, 124.7, 93.4, 76.1, 58.4, 55.3, 52.4, 51.5, 34.9, 26.9, 26.6, 25.4.

2-(12-Hydroxy-6-methoxymethoxy-dodeca-(2Z,4E,10Z)-trienyl)malonic acid dimethyl ester (18)

Compound **18** was prepared similar to alcohol **9** (81%). IR (cm^{-1}): 3448, 3012, 2951, 1738, 1437, 1344, 1275, 1233, 1150, 1096, 1032, 919, 738. ^{1}H NMR ($CDCl_3$) δ: 6.45 (dd, *J* = 15.0, 11.0 Hz, 1H, CH=C*H*CH=CHCH$_2$), 6.06 (t, *J* = 11.0 Hz, 1H, CH=CHC*H*=CHCH$_2$), 5.7–5.48 (m, 3H, CH=C*H*CH$_2$OH and C*H*=CHCH=C*H*), 5.36 (dq, *J* = 11.0, 3.0 Hz, 1H, C*H*=CHCH$_2$OH), 4.68 and 4.52 (2d, *J* = 6.5 Hz, 2 × 1H, OCH_2O), 4.19 (d, *J* = 6.5 Hz, 2H, CH_2OH), 4.07 (q, *J* = 6.5 Hz, 1H, C*H*OMOM), 3.73 (s, 3H, CO$_2$*Me*), 3.72 (s, 3H, CO$_2$*Me*), 3.43 (t, *J* = 7.5 Hz, 1H, C*H*(CO$_2$Me)$_2$), 3.37 (s, 3H, OCH$_2$OCH_3), 2.78 (t, *J* = 7.5 Hz, 2H, CH_2CH(CO$_2$Me)$_2$), 2.12 (q, *J* = 7.0 Hz, 2H, CH$_2$CH_2CH=CH), 1.70–1.40 (m, 4H, other CH$_2$). ^{13}C NMR ($CDCl_3$) δ: 169.1, 134.8, 134.5, 130.4, 127.2, 126.6, 125.4, 93.4, 76.1, 74.5, 55.3, 52.5, 51.3, 39.3, 34.9, 27.0, 26.7, 25.0. MS *m*/*z*: 308 ([M – MOMOH]$^+$), 325 ([M – MOM]$^+$), 338 ([M – CH_3OH]$^+$). Exact mass ([M – CH_3OH]$^+$) calcd.: 338.1729; found: 338.1737.

2-(12-Chloro-7-methoxymethoxy-dodeca-(2Z,8E,10Z)-trienyl)malonic acid dimethyl ester (19)

To a solution of alcohol **17** (294 mg, 80 mmol) and hexachloroacetone (155 μL, 1 mmol) in dichloromethane (10 mL) at 0°C, was added triphenylphosphine (334 mg, 1.28 mmol). After stirring for 1 h at room temperature, the mixture was concentrated under vacuo. The residue was purified by flash chromatography (hexanes–ether, 9:1 to 3:1) to yield the title compound as an oil (288 mg, 94%). IR (cm^{-1}): 2946, 1748, 1735, 1433, 1234, 1145, 1029. ^{1}H NMR ($CDCl_3$) δ: 6.45 (dd, *J* = 15.0, 11.0 Hz, 1H, CH=CHC*H*=CHCH$_2$), 6.08 (t, *J* = 11.0 Hz, 1H, CH=C*H*CH=CHCH$_2$), 5.68–5.40 (m, 3H, CH=C*H*CH$_2$CH and C*H*=CHCH=C*H*), 5.30 (m, 1H, C*H*=CHCH$_2$CH), 4.67 and 4.51 (2d, *J* = 6.5 Hz, 2 × 1H, OCH_2O), 4.20 (dd, *J* = 7.0, 2.0 Hz, 2H,

© 2002 NRC Canada

CH_2Cl), 4.07 (q, *J* = 5.5 Hz, 1H, C*H*OMOM), 3.73 (s, 6H, CO_2CH_3), 3.40 (t, *J* = 4.0 Hz, 1H, C*H*($CO_2Me)_2$), 3.38 (s, 3H, OCH_2OCH_3), 2.64 (t, *J* = 7.5 Hz, 2H, $CH_2CH(CO_2Me)_2$), 2.09 (q, *J* = 7.0 Hz, 2H, CH_2CH_2CH=CH), 1.70–1.35 (m, 4H, other CH_2). ^{13}C NMR ($CDCl_3$) δ: 169.3, 137.0, 132.6, 131.7, 126.9, 126.7, 124.7, 93.7, 76.0, 55.3, 52.4, 51.6, 39.3, 34.9, 26.9, 26.7, 25.1.

2-(12-Chloro-6-methoxymethoxy-dodeca-(2Z,4E,10Z)-trienyl)malonic acid dimethyl ester (20)

Compound **20** was prepared similar to chloride **19** (99 %). IR (cm^{-1}): 3016, 2951, 1754, 1738, 1435, 1345, 1233, 1149, 1031, 666. ^{1}H NMR ($CDCl_3$) δ: 6.46 (dd, *J* = 15.0, 11.0 Hz, 1H, CH=C*H*CH=CHCH$_2$), 6.06 (t, *J* = 11.0 Hz, 1H, CH=CHC*H*=CHCH$_2$), 5.7–5.56 (m, 2H, CH=CHCH=C*H*CH$_2$ and CH=C*H*CH$_2$Cl), 5.53 (dd, *J* = 15.0, 8.0 Hz, 1H, C*H*=CHCH=CHCH$_2$), 5.36 (dq, *J* = 10.5, 3.0 Hz, 1H, C*H*=CHCH$_2$Cl), 4.69 and 4.52 (2d, *J* = 6.5 Hz, 2 × 1H, OCH_2O), 4.09 (d, *J* = 5.0 Hz, 2H, CH_2Cl), 4.05 (m, 1H, C*H*OMOM), 3.73 (s, 3H, CO_2*Me*), 3.72 (s, 3H, CO_2*Me*), 3.43 (t, *J* = 7.5 Hz, 1H, C*H*($CO_2Me)_2$), 3.37 (s, 3H, OCH_2OCH_3), 2.78 (dt, *J* = 7.5, 0.5 Hz, 2H, CH_2CH($CO_2Me)_2$), 2.13 (q, *J* = 7.0 Hz, 2H, CH_2CH_2CH=CH), 1.70–1.30 (m, 4H, other CH_2). ^{13}C NMR ($CDCl_3$) δ: 169.1, 134.8, 134.5, 130.4, 127.2, 126.6, 125.4, 93.4, 76.1, 74.5, 55.3, 52.5, 51.3, 39.3, 39.3, 34.9, 27.0, 26.7, 25.0. MS *m*/*z*: 353 ([M – Cl]$^+$), 358 ([M – CH_3OH]$^+$). Exact mass (M^+) calcd.: 388.1653; found: 388.1647.

7-Methoxymethoxy-cyclotrideca-(3Z,5E,11Z)-triene-1,1-dicarboxylic acid (21)

A solution of chloride **19** (or **20**) (280 mg, 0.72 mmol) in acetonitrile (10 mL) was added over 12 h via a syringe pump, to a solution of cesium carbonate (2.4 g, 7.5 mmol) and cesium iodide (390 mg, 1.5 mmol) in acetonitrile (600 mL) at 70°C (final concentration = 1 mM). Three hours after the final addition, the mixture was cooled to room temperature, filtered on florisil, and concentrated under vacuo. Water (20 mL) was added to the residue and the mixture was extracted with a 1:1 ether–hexanes solution (3 × 20 mL). The combined organics were washed with brine, dried over $MgSO_4$, filtered, and concentrated under vacuo. The residue was purified by flash chromatography (hexanes–ether, 9:1) to yield the final compound as an oil (113 mg, 43%). IR (cm^{-1}): 2951, 1737, 1437, 1208, 1037. ^{1}H NMR ($CDCl_3$) δ: 6.42 (dd, *J* = 15.0, 11.0 Hz, 1H, CH=CHC*H*=CHCH$_2$), 6.21 (t, *J* = 11.0 Hz, 1H, CH=C*H*CH=CHCH$_2$), 5.82 (dd, *J* = 16.0, 5.5, 1H, C*H*=CHCH=CHCH$_2$), 5.45 (m, 1H, C*H*=CHCH$_2$C), 5.10–4.95 (m, 2H, C*H*=CHCH$_2$C and CH=CHCH=C*H*CH$_2$), 4.62 and 4.67 (2d, *J* = 7.0 Hz, 2 × 1H, OCH_2O), 4.13 (m, 1H, C*H*OMOM), 3.75 (s, 6H, CO_2CH_3), 3.38 (s, 3H, OCH_2OCH_3), 2.69 (d, *J* = 8.5 Hz, 2H, CH=CHCH=CHCH_2), 2.51 (d, *J* = 7.0 Hz, 2H, CH=CHCH_2C), 2.20–1.30 (m, 6H, other CH_2). ^{13}C NMR ($CDCl_3$) δ: 171.3, 171.2, 135.6, 135.0, 133.0, 126.5, 124.7, 123.8, 94.4, 76.5, 56.9, 55.3, 52.6, 30.0, 29.2, 29.0, 25.9, 24.8.

1-Cyano-7-methoxymethoxy-cyclotrideca-(3Z,5E,11Z)-trienecarboxylic acid methyl ester (22) (diastereoisomers)

A solution of bischloride **14** (720 mg, 2.25 mmol) and methyl cyanoacetate (298 μL, 3.38 mmol) in THF (20 mL) was added over 10 h using a syringe pump, to a solution of cesium carbonate (11.0 g, 33.8 mmol) in a THF–DMF solution (2:1, 800 mL) at 80°C. The DMF was purged with nitrogen for 1 h before use. One hour after the final addition, the solution was cooled to room temperature, filtered, and concentrated under vacuo. The residue was purified by flash chromatography (hexanes–ether, 8:2) to yield the title compound as an oil (568 mg, 79 %). IR (cm^{-1}): 2934, 2249, 1748, 1440, 1219. ^{1}H NMR ($CDCl_3$) δ: 6.47–6.26 (m, 2H, CH=C*H*C*H*=CHCH$_2$), 5.90 (dt, *J* = 15.0, 6.0 Hz, 1H, CH=CHCH=C*H*CH$_2$), 5.62–5.50 (m, 1H, CH_2CH_2CH=CH), 5.38 (q, *J* = 9.0 Hz, 1H, CH=C*H*CH$_2$C), 5.24 (m, 1H, C*H*=CHCH=CHCH$_2$), 4.62 (m, 2H, OCH_2O), 4.18 (q, *J* = 8.0 Hz, 1H, C*H*OMOM), 3.86 (s, 3H, CO_2CH_3), 3.37 (s, 3H, OCH_2OCH_3), 2.80–2.43 (m, 4H, CH=CHCH_2C), 2.22–1.30 (m, 6H, other CH_2). ^{13}C NMR ($CDCl_3$) δ: 168.7, 137.8, 137.4, 136.7, 134.8, 134.7, 126.8, 126.4, 123.6, 123.1, 122.8, 119.4, 95.1, 77.0, 76.7, 56.0, 54.2, 46.8, 42.9, 46.8, 42.9, 32.1, 31.6, 30.5, 30.2, 29.8, 26.8, 25.2, 24.9. MS *m*/*z*: 319 (M^+). Exact mass (M^+) calcd.: 319.1783; found: 319.1789.

6-Methoxymethoxy-1,3,3a,5a,6,7,8,9,9a,9b-decahydro-cyclopenta[a]naphthalene-2,2-dicarboxylic acid dimethyl ester (23) (diastereoisomers)

A solution of macrocycle **21** (61 mg, 173 μmol) in xylenes (1 mL) was stirred at 140°C for 4 h. The crude was purified by flash chromatography (hexanes–ether, 8:2) to yield the title compound as an oil (61 mg, 100%, OMOM, α:β = 2:1). ^{1}H NMR ($CDCl_3$) δ: 5.83 (d, *J* = 10.0 Hz, 1H, C*H*=CH), 5.48 (dt, *J* = 10.0, 3.0 Hz, 1H, CH=C*H*), 4.77 (d, *J* = 7.0 Hz, 0.66H, OCH_2OMe *alpha*), 4.70 (d, *J* = 7.0 Hz, 0.33H, OCH_2OMe *beta*), 4.63 (d, *J* = 7.0 Hz, 0.66H, OCH_2OMe *alpha*), 4.60 (d, *J* = 7.0 Hz, 0.33H, OCH_2OMe *beta*), 3.90 (m, 0.33H, C*H*OMOM *beta*), 3.72 (s, 3H, CO_2*Me*), 3.68 (s, 3H, CO_2*Me*), 3.39 (s, 2H, OCH_2O*Me*), 3.37 (s, 1H, OCH_2O*Me*), 3.20 (td, *J* = 10.5, 4.5Hz, 0.66H, C*H*OMOM *alpha*), 2.75 (m, 1H, C*H*CH=CH), 2.51 (m, 1H, C*H*CH=CH), 2.30–1.05 (m, 12H, other CH_2 and CH). ^{13}C NMR ($CDCl_3$) δ: 170.0, 129.2, 126.2, 95.6, 79.5, 76.5, 56.0, 53.01, 53.0, 41.9, 41.2, 39.4, 39.2, 33.3, 32.9, 31.0, 30.7, 30.1, 29.7, 24.3.

2-Cyano-6-methoxymethoxy-2,3,3a,5a,6,7,8,9,9a,9b-decahydro-1H-cyclopenta[a]naphthalene-2-carboxylic acid methyl ester (24) (diastereoisomers)

A solution of macrocycle **22** (67 mg, 208 μmol) in xylenes (500 μL) was stirred at 140°C for 8 h. The crude was purified by flash chromatography (hexanes–ether, 8:2) to yield the title compound as an oil (52 mg, 78%). ^{1}H NMR ($CDCl_3$) δ: 5.92 (dd, *J* = 15.0, 6.5 Hz, 1H, C*H*=CH), 5.57 (m, 1H, CH=C*H*), 4.79 (d, *J* = 7.0 Hz, 0.66H, OCH_2OMe *alpha*), 4.71 (d, *J* = 7.0 Hz, 0.33H, OCH_2OMe *beta*), 4.63 (d, *J* = 7.0 Hz, 0.66H, OCH_2OMe *alpha*), 4.60 (d, *J* = 7.0 Hz, 0.33H, OCH_2OMe *beta*), 3.92 (m, 0.33H, C*H*OMOM *beta*), 3.82 (s, 1H, CO_2*Me*), 3.81 (s, 1H, CO_2*Me*), 3.80 (s, 1H, CO_2*Me*), 3.39 (s, 2H, OCH_2O*Me*), 3.38 (s, 1H, OCH_2O*Me*), 3.21 (td, *J* = 10.5, 4.5 Hz, 0.66H, C*H*OMOM *alpha*), 2.93 (m, 1H, C*H*CH=CH), 2.65–1.00 (m, 13H, other CH_2 and CH). ^{13}C NMR ($CDCl_3$) δ: 170.4, 169.4, 169.2, 130.0, 129.9, 129.6, 129.0, 127.5, 126.2, 95.4, 95.0, 79.0, 78.9, 74.9, 55.4, 55.2, 53.6, 53.4, 46.8, 46.6, 42.4, 42.3, 42.1, 41.0, 40.8, 40.7, 40.4, 39.3, 38.8, 38.6, 37.8, 36.4, 36.3,

© 2002 NRC Canada

36.0, 33.5, 32.8, 32.6, 30.8, 30.6, 30.3, 29.7, 24.1, 24.0, 20.7.

*6-Methoxymethoxy-2,3,3a,5a,6,7,8,9,9a,9b-decahydro-1*H-*cyclopenta[a]naphthalene-2-carboxylic acid methyl ester (25) (diastereoisomers)*

A solution of macrocycle **21** (92 mg, 261 μmol), sodium chloride (39 mg, 653 μmol), and water (10 μL) in DMSO (1 mL) was stirred at 160°C for 7 h. Water (10 mL) was added to the cooled solution and the mixture was extracted with a hexanes–ether solution (1:1, 3 × 10 mL). The combined organics were washed with brine, dried over $MgSO_4$, filtered, and concentrated under vacuo to yield the title compound as an oil (66 mg, 90%). ^{1}H NMR (DMSO-d_6) δ: 5.75 (d, *J* = 6.5 Hz, 1H, C*H*=CH), 5.41 (m, 1H, CH=C*H*), 4.71–4.50 (m, 2H, OCH_2O), 3.82 (m, 0.33H, C*H*OMOM, H *alpha*), 3.65 (s, 2H, CO_2*Me*), 3.60 (s, 1H, CO_2*Me*), 3.28 (s, 2H, OCH_2O*Me*), 3.23 (s, 1H, OCH_2O*Me*), 3.10 (m, 0.66H, C*H*OMOM, H *beta*), 2.70 (m, 1H, C*H*CH=CH), 2.53–2.38 (m, 2H, C*H*CH=CH and C*H*CO_2), 2.20–1.00 (m, 12H, other CH_2 and CH).

*6-Methoxymethoxy-2,3,3a,5a,6,7,8,9,9a,9b-decahydro-1*H-*cyclopenta[a]naphthalene-2-carbonitrile (26) (diastereoisomers)*

A solution of macrocycle **22** (1.7 g, 5.43 mmol) and sodium cyanide (293 mg, 6 mmol) in DMSO (25 mL) was stirred at 160°C for 8 h. Water (100 mL) was added to the cooled solution and the mixture was extracted with a hexanes–ether solution (1:1, 3 × 100 mL). The combined organics were washed with brine, dried over $MgSO_4$, filtered, and concentrated under vacuo to yield the title compound as an oil (1.27 g, 89%, OMOM, α:β = 2:1). Alternatively, a solution of tricycle **24** (50 mg, 157 μmol) and sodium cyanide (9.6 mg, 195.6 μmol) in DMSO (500 μL) was stirred at 160°C for 8 h. The mixture was diluted with water (15 mL) and extracted with a hexanes–ether solution (1:1, 3 × 15 mL). The combined organics were washed with brine, dried over $MgSO_4$, filtered, and concentrated under vacuo to yield the title compound as an oil (40 mg, 97%). IR (cm^{-1}): 2927, 2237, 1446, 1149, 1099, 1040. ^{1}H NMR ($CDCl_3$) δ: 5.92–5.88 (m, 1H, C*H*=CH), 5.60–5.42 (m, 1H, CH=C*H*), 4.80–4.57 (m, 2H, OCH_2O), 3.98–3.90 (m, 0.33H, C*H*OMOM, H_{ax}), 3.40 (s, 1H, OCH_2O*Me*), 3.39 (s, 1H, OCH_2O*Me*), 3.36 (s, 0.5H, OCH_2O*Me*), 3.35 (s, 0.5H, OCH_2O*Me*), 3.25–3.10 (m, 0.66H, C*H*OMOM, H_{eq}), 2.90–2.60 (m, 2H, C*H*CH=CHC*H*), 2.9–0.5 (m, 13H, other CH_2 and CH). ^{13}C NMR ($CDCl_3$) δ: 131.3, 131.0, 130.6, 130.1, 129.9, 128.6, 126.2, 123.4, 95.6, 95.1, 79.3, 75.2, 55.5, 55.3, 43.3, 43.2, 41.5, 41.2, 41.0, 40.6, 39.9, 39.6, 39.2, 39.1, 38.6, 36.7, 36.3, 33.7, 32.8, 31.1, 31.0, 30.7, 30.6, 30.3, 29.9, 29.6, 29.5, 27.3, 26.3, 24.3, 24.1, 21.0, 20.8. MS *m*/*z*: 261 (M^+), 246 ([M – CH_3]$^+$), 229 ([M – CH_3OH]$^+$), 216 ([M – MOM]$^+$). Exact mass (M^+) calcd.: 261.1729; found: 261.1733.

*6-Hydroxy-2,3,3a,5a,6,7,8,9,9a,9b-decahydro-1*H-*cyclopenta[a]naphthalene-2-carbonitrile (27) (diastereoisomers)*

A solution of tricycle **26** (1.27 g, 4.85 mol) and HCl 6 N (750 μL) in methanol (125 mL) was heated to reflux for 8 h. The solution was concentrated under vacuo and purified by flash chromatography (hexanes–ether, 40% to 100% ether) to yield the title compound as an oil (1.06 g, 100%). IR (cm^{-1}): 3426, 2928, 2860, 2239, 1449, 1348, 1281, 1059, 1028. ^{1}H NMR ($CDCl_3$) δ: 6.05–5.40 (m, 2H, C*H*=C*H*), 4.10–4.07 (m, 0.33H, C*H*OMOM, H_{ax}), 3.37–3.22 (m, 0.66H, C*H*OMOM, H_{eq}), 2.90–2.60 (m, 2H, C*H*CH=CHC*H*), 2.5–2.3 (m, 1H, C*H*CN), 2.15–1.00 (m, 13H, other CH_2 and CH). ^{13}C NMR ($CDCl_3$) δ: 133.3, 130.8, 130.4, 130.0, 128.4, 128.2, 126.0, 123.5, 73.5, 69.7, 43.3, 43.0, 42.5, 41.4, 41.1, 40.3, 40.0, 39.8, 38.9, 38.7, 36.7, 36.3, 33.0, 32.9, 32.7, 31.2, 31.1, 30.8, 30.7, 30.4, 29.6, 29.2, 26.3, 24.4, 24.3, 20.6, 20.5. MS *m*/*z*: 216 ([M – H]$^+$). Exact mass ([M – H]$^+$) calcd.: 216.1388; found: 216.1392.

*6-Oxo-2,3,3a,5a,6,7,8,9,9a,9b-decahydro-1*H-*cyclopenta[a]naphthalene-2-carbonitrile (28) and (29)*

To a solution of alcohol **27** (145 mg, 671 μmol) in dichloromethane (22 mL) at 0°C, was added Dess–Martin periodinane (370 mg, 872 μmol). The solution was allowed to warm to room temperature and stirred for 30 min. A saturated $NaHCO_3$ solution (30 mL) and sodium thiosulfate (477 mg, 1.92 mmol) were added and stirred 30 min. The mixture was extracted with dichloromethane (3 × 30 mL). The combined organics were dried over $MgSO_4$, filtered, and concentrated under vacuo. The residue was purified by flash chromatography (hexanes–ether, 9:1) to yield two racemic diastereoisomeres as oils (α-nitrile 66 mg and β-nitrile 50 mg, total yield: 80%).

Ketone **28** (α-nitrile). IR (cm^{-1}): 2928, 2850, 2335, 1709, 1450, 1360, 1240, 1145. ^{1}H NMR ($CDCl_3$) δ: 6.03 (d, *J* = 10.0 Hz, 1H, O=CCHC*H*=CH), 5.63 (dt, *J* = 10.0, 2.5 Hz, 1H, CH=C*H*), 2.82–2.70 (m, 3H, C*H*CH=CHC*H* and C*H*CN), 2.48–1.52 (m, 12H, other CH_2 and CH). ^{13}C NMR ($CDCl_3$) δ: 209.95, 131.54, 122.61, 121.91, 47.31, 42.91, 41.87, 41.22, 40.18, 38.31, 36.05, 30.41, 26.50, 26.28. MS *m*/*z*: 215 (M^+). Exact mass (M^+) calcd.: 215.1310; found: 215.1315.

Ketone **29** (β-nitrile). ^{1}H NMR ($CDCl_3$) δ: 6.07 (d, *J* = 10.0 Hz, 1H, O=CCHC*H*=CH), 5.51 (dt, *J* = 10.0, 3.0 Hz, 1H, CH=C*H*), 2.90–2.70 (m, 2H, C*H*CH=CHC*H*), 2.55 (qd, *J* = 9.0, 3.5 Hz, 1H, C*H*CN), 2.49–1.50 (m, 12H, other CH_2 and CH). ^{13}C NMR ($CDCl_3$) δ: 209.84, 130.75, 124.10, 123.0, 46.78, 41.80, 41.14, 39.54, 36.30, 30.22, 29.58, 28.91, 26.34, 26.15.

*6-Hydroxy-2,3,3a,5a,6,7,8,9,9a,9b-decahydro-1*H-*cyclopenta[a]naphthalene-2-carbonitrile (30)*

To a solution of ketone **28** (213 mg, 995 mmol) in THF (15 mL) at –78°C, was added lithium triisobutylborohydride (0.5 M, 2.8 mL, 1.4 mmol). After 3.5 h, NaOH (10%, 2.4 mL, 6 mmol) and H_2O_2 (35%, 583 μL, 6 mmol) were added and the mixture was stirred for 3 h at room temperature. A sodium thiosulfate solution (1 M) was then added and stirred for 30 min. The mixture was extracted with dichloromethane (3 × 50 mL). The combined organic layers were dried over $MgSO_4$, filtered, and concentrated under vacuo. The residue was purified by flash chromatography (100% ether) to yield the title compound as an oil (171 mg, 80%). IR (cm^{-1}): 3312, 2930, 2845, 2232, 1445, 1322, 1064. ^{1}H NMR ($CDCl_3$) δ: 5.63 (dt, *J* = 10.0, 2.5 Hz, 1H, OCHCHCH=C*H*), 5.52 (d, *J* = 10.0 Hz, 1H, OCHCHC*H*=CH), 4.10 (s, 1H, C*H*OH), 2.85–2.65 (m, 2H, C*H*CH=CHC*H*), 2.35 (dt, *J* = 13.5, 9.0 Hz, 1H, C*H*CN), 2.15–1.08

© 2002 NRC Canada

(m, 12H, other CH_2 and C*H*). ^{13}C NMR ($CDCl_3$) δ: 133.2, 128.1, 123.1, 69.7, 43.2, 40.3, 38.9, 36.1, 32.9, 32.7, 31.2, 30.4, 26.2, 20.6. MS *m*/*z*: 217 (M^+). Exact mass (M^+) calcd.: 217.1467; found: 217.1469.

6-Hydroxy-2,3,3a,5a,6,7,8,9,9a,9b-decahydro-1*H*-cyclopenta[a]naphthalene-2-carboxylic acid (31)

To a solution of alcohol **30** (12.5 mg, 58 μmol) in methanol (2 mL) was added an NaOH solution (25%, 416 μL, 2.6 mmol) and a H_2O_2 solution (30%, 600 μL, 12% v/v). The mixture was stirred at 65°C for 24 h and concentrated under vacuo to ~1 mL. The mixture was diluted with water (15 mL), the pH was adjusted to 2 with 1 N HCl, and the mixture extracted with dichloromethane (3 × 15 mL). The combined organics were dried over $MgSO_4$ and concentrated under vacuo. The residue was purified by flash chromatography (acetone–hexanes, 6:1) to yield the title compound as white crystals (12.4 mg, 90%). IR (cm^{-1}): 3400–2300, 3392, 2921, 2851, 1704, 1651, 1463, 1221. ^{1}H NMR (MeOD-d_4) δ: 5.54 (dt, *J* = 10.0, 2.5 Hz, 1H, OCHCHCH=C*H*), 5.42 (d, *J* = 10.0 Hz, 1H, OCHCHC*H*=CH), 3.99 (s, 1H, C*H*OH), 2.8–2.6 (m, 2H, C*H*CH=CHC*H*), 2.25 (dt, *J* = 13.5, 9.0 Hz, 1H, C*H*CO_2H), 2.15–1.12 (m, 12H, other CH_2 and CH).

Iodolactone 32

To a solution of acid **31** (1.5 mg, 3.8 μmol) in THF (0.5 mL) was added one crystal of iodide, one drop of water, and sodium bicarbonate (1 mg, 7.5 μmol). The solution was stirred 3 days at room temperature, then diluted with water (10 mL), and the pH adjusted to 2 with 1 N HCl. The mixture was extracted with dichlorometane (3 × 15 mL). The combined organic layers were dried over $MgSO_4$, filtered, and concentrated under vacuo to yield the title compound as a red oil (2 mg) (excess iodide). IR (cm^{-1}): 3557, 3006, 2956, 2880, 1743, 1601, 1454, 1365, 1244, 1163, 1066, 1002. ^{1}H NMR ($CDCl_3$) δ: 4.68 (t, *J* = 3.5 Hz, 1H, C*H*OC=O), 4.44 (t, *J* = 3.0 Hz, 1H, C*H*I), 4.02 (m, 1H, C*H*OH), 3.05 (q, *J* = 6.5 Hz, 1H, CH_2C*H*CHOC=O), 2.88 (dd, *J* = 7.5, 6.5 Hz, 1H, C*H*CO_2), 2.35–1.12 (m, 13H, other CH and CH_2). ^{13}C NMR ($CDCl_3$) δ: 174.0, 84.5, 69.2, 40.4, 39.8, 35.1, 34.9, 34.5, 34.3, 32.4, 30.8, 30.6, 29.9, 29.7, 18.4. MS *m*/*z*: 362 (M^+), 235 ([M – I]$^+$). Exact mass (M^+) calcd.: 362.0379; found: 362.0387; ([M – I]$^+$) calcd.: 235.1334; found: 235.1339.

6-Triisopropylsilanyloxy-2,3,3a,5a,6,7,8,9,9a,9b-decahydro-1*H*-cyclopenta[a]naphthalene-2-carbonitrile (33)

To a solution of alcohol **30** (55 mg, 254 μmol) and 2,6-lutidine (89 μL, 762 μmol) in dichloromethane (4 mL) at 0°C, was added slowly triisopropylsilane triflate (102 μL, 381 μmol). After 1 h at room temperature, a saturated NH_4Cl solution (30 mL) was added and the mixture extracted with dichloromethane (3 × 30 mL). The combined organics were dried over $MgSO_4$, filtered, and concentrated under vacuo. The residue was purified by flash chromatography (hexanes–ether, 95:5) to give the title compound as an oil (96 mg, 100%). IR (cm^{-1}): 2929, 2237, 1448, 1363, 1278, 1217, 1149, 1097, 1041, 917. ^{1}H NMR ($CDCl_3$) δ: 5.52 (d, *J* = 10.0 Hz, 1H, OCHCHC*H*=CH), 5.44 (dt, *J* = 10.0, 2.5 Hz, 1H, OCHCHCH=C*H*), 4.25 (br s, 1H, C*H*-OTIPS), 2.80–2.66 (m, 2H, C*H*CH=CHC*H*), 2.30 (dt, *J* = 13.5, 9.5 Hz, 2H, C*H*CN), 2.20–1.38 (m, 12H, CH and CH_2), 1.20–0.95 (m, 21H, OTIPS). ^{13}C NMR ($CDCl_3$) δ: 130.6, 130.1, 123.4, 70.8, 43.6, 41.5, 39.0, 36.2, 34.2, 32.6, 31.5, 30.3, 26.2, 20.8, 18.2, 13.3, 12.8, 12.4. MS *m*/*z* : 330 ([M – C_3H_7]$^+$). Exact mass ([M – C_3H_7]$^+$) calcd.: 330.2253; found: 330.2255.

6-Triisopropylsilanyloxy-2,3,3a,5a,6,7,8,9,9a,9b-decahydro-1*H*-cyclopenta[a]naphthalene-2-carboxylic acid (34)

To a solution of silyl ether **33** (67 mg, 180 mmol) in methanol (20 mL) was added NaOH (10%, 3.2 mL) and H_2O_2 (35%, 9 mL). The solution was heated to reflux for 24 h. The cooled solution was concentrated under vacuo to ~10 mL and acidified to pH 2 with HCl (1 N, 25 mL). The solution was extracted with dichloromethane (3 × 30 mL). The combined organics were dried over $MgSO_4$, filtered, and concentrated under vacuo. The residue was purified by flash chromatography (hexanes–ethyl acetate, 6:4) to yield the title compound as an oil (58 mg, 83%). IR (cm^{-1}): 3450–2400, 2929, 2866, 1704, 1463, 1238, 1118, 1066, 882. ^{1}H NMR ($CDCl_3$) δ: 5.53 (d, *J* = 10.0 Hz, 1H, OCHCHC*H*=CH), 5.34 (dt, *J* = 10.0, 2.5 Hz, 1H, OCHCHCH=C*H*), 4.22 (m, 1H, C*H*OTIPS), 2.89–2.60 (m, 2H, C*H*CH=CHC*H*), 2.45–2.15 (m, 1H, C*H*CO_2H), 2.44–0.80 (m, 33H, other CH, CH_2 and CH_3). ^{13}C NMR ($CDCl_3$) δ: 182.3, 131.6, 129.1, 70.9, 43.8, 42.6, 41.5, 38.8, 34.7, 34.3, 32.9, 31.6, 29.7, 28.9, 20.9, 18.3, 18.2, 12.8. MS *m*/*z*: 349 ([M – C_3H_7]$^+$). Exact mass ([M – C_3H_7]$^+$) calcd.: 349.2199; found: 349.2194.

6-Triisopropylsilanyloxy-2,3,3a,5a,6,7,8,9,9a,9b-decahydro-1*H*-cyclopenta[a]naphthalene-2-carboxylic acid pentylamide (35)

To a solution of acid **34** (22 mg, 56 μmol) in dichloromethane (3 mL) at 0°C was added oxalyle chloride (8 μL, 88 μmol) and DMF (1 μL, 11 μmol). The solution was warmed to room temperature. After 1.5 h, triethylamine (9 μL, 67 μmol) and amylamine (13 μL, 112 μmol) were added and stirred 24 h. The mixture was concentrated under vacuo and purified by flash chromatography (hexanes–acetone, 7:3) to yield the title compound as an oil (22 mg, 80%). IR (cm^{-1}): 3300, 2927, 2864, 1643, 1462, 1065. ^{1}H NMR ($CDCl_3$) δ: 5.5–5.3 (m, 3H, C*H*=C*H* and N*H*), 4.22 (br s, 1H, C*H*OTIPS), 3.21 (qd, *J* = 7.0, 1.0 Hz, 2H, CH_2NH), 2.73–2.46 (m, 2H, C*H*CH=CHC*H*), 2.20 (dt, *J* = 13.5, 9.5 Hz, 1H, C*H*CONH) 2.13–0.99 (m, 39H, other CH, CH_2 and CH_3) 0.89 (t, *J* = 7.0 Hz, 3H, CH_2CH_3). ^{13}C NMR and DEPT-135 ($CDCl_3$) δ: 175.6 (s), 132.0 (d), 128.8 (d), 71.0 (d), 45.1 (d), 44.0 (d), 41.5 (d), 39.4 (t), 38.7 (d), 35.6 (t), 34.3 (t), 32.9 (d), 31.6 (t), 29.9 (t), 29.7 (t), 29.3 (t), 29.1 (t), 22.3 (t), 20.9 (t), 18.3 (q), 14.0 (q), 12.8 (d). MS *m*/*z*: 461 (M^+), 418 ([M – C_3H_7]$^+$). Exact mass (M^+) calcd.: 461.3689; found: 461.3680.

6-Triisopropylsilanyloxy-2,3,3a,5a,6,7,8,9,9a,9b-decahydro-1*H*-cyclopenta[a]naphthalene-2-carboxylic acid indan-(1*S*)-ylamide (36) and (37) (diastereoisomers)

Same procedure as for amide **35**, using (*S*)-(+)-1-aminoindane instead of amylamine. The title compound was obtained as an oil (18 mg, 73%) and recovered acid **34** (2 mg). IR (cm^{-1}): 3281, 2936, 2865, 1643, 1539, 1461, 1384, 1243, 1066, 881, 745, 674. ^{1}H NMR ($CDCl_3$) δ: 7.30–7.15 (m, 4H, H-aryl), 5.72–5.33 (m, 3H, C*H*=C*H* and

© 2002 NRC Canada

CON*H*), 4.22 (br s, 1H, C*H*OTIPS), 3.07–0.80 (m, 40H, other CH, CH_2 and CH_3). ^{13}C NMR ($CDCl_3$) δ: 175.4, 143.4, 131.9, 128.9, 127.8, 126.7, 124.7, 123.9, 71.0, 54.5, 45.1, 44.0, 41.5, 38.7, 35.7, 35.5, 34.2, 32.9, 31.6, 30.2, 30.0, 29.8, 20.9, 18.3, 12.8. MS *m*/*z*: 507 (M^+). Exact mass (M^+) calcd.: 507.3532; found: 507.3541.

6-Hydroxy-2,3,3a,5a,6,7,8,9,9a,9b-decahydro-1*H*-cyclopenta[a]naphthalene-2-carboxylic acid pentylamide (1)

A solution of amide **35** (18 mg, 39 μmol) and HCl (6 N, 0.3 mL) in methanol (5 mL) was heated to reflux for 24 h. The cooled solution was concentrated under vacuo and purified by flash chromatography (hexanes–acetone, 7:3) to yield the title compound as an oil (7 mg, 81%). IR (cm^{-1}): 3300, 2927, 2860, 1647, 1548, 1456, 1372, 1249. ^{1}H NMR ($CDCl_3$) δ: 5.66 (dt, *J* = 10.0, 2.5 Hz, 1H, CH=C*H*), 5.49–5.37 (m, 2H, C*H*=CH and CON*H*), 4.06 (br s, 1H, C*H*OH), 3.21 (qd, *J* = 7.0, 1.0 Hz, 2H, CH_2NH), 2.80–2.65 (m, 1H, C*H*CH=CH), 2.63–2.45 (m, 1H, C*H*CH=CH), 2.22 (td, *J* = 13.5 Hz, 1H, C*H*CONH), 2.15–1.00 (m, 18H, other CH and CH_2), 0.89 (t, *J* = 7.0 Hz, 3H, CH_3). ^{13}C NMR ($CDCl_3$) δ: 175.2, 134.8, 126.6, 69.9, 45.0, 43.5, 40.3, 39.5, 38.6, 35.5, 33.3, 32.7, 31.3, 29.8, 29.7, 29.3, 29.1, 22.3, 20.7, 14.0. MS *m*/*z*: 305 (M^+). Exact mass (M^+) calcd.: 305.2355; found: 305.2359.

6-Hydroxy-2,3,3a,5a,6,7,8,9,9a,9b-decahydro-1*H*-cyclopenta[a]naphthalene-2-carboxylic acid indan-(1*S*)-ylamide (2) and (38) (diastereoisomers)

Same procedure as for alcohol **1** but using a mixture of amides **36** and **37** instead of amide **35**. The title compounds were obtained as an oil (18 mg, 84%). IR (cm^{-1}): 3289, 3012, 2930, 2864, 1645, 1538, 1455, 1231, 1056, 988, 909, 732. ^{1}H NMR ($CDCl_3$) δ: 7.30–7.17 (m, 4H, H-aryl), 5.71–5.41 (m, 3H, C*H*=C*H*, CON*H*), 4.08 (br s, 1H, C*H*OH), 3.05–2.50 (m, 5H, CH_2ArC*H*NH and C*H*CH=CHC*H*), 2.25–0.80 (m, 15H, other CH and CH_2). ^{13}C NMR ($CDCl_3$) δ: 175.1, 143.4, 134.8, 134.2, 129.7, 128.0, 126.7, 124.9, 123.9, 70.0, 54.5, 45.0, 43.7, 40.4, 38.7, 35.4, 34.2, 33.6, 33.4, 32.7, 31.3, 30.2, 29.9, 29.7, 20.8. MS *m*/*z*: 351 (M^+). Exact mass (M^+) calcd.: 351.2198; found: 351.2200.

Acknowledgments

This work was supported financially by the Natural Sciences and Engineering Research Council of Canada (NSERC) and by the Fonds pour la Formation de Chercheurs et l'Aide à la Recherche (FCAR). We thank Dr. Diane Joseph-McCarthy from Harvard University for the theoretical design of the target molecules and for running the biological assays.

References

1. Y.C. Martin. J. Comb. Chem. **3**, 231 (2001).
2. E.J. Martin and R.E. Critchlow. J. Comb. Chem. **1**, 32 (1999).
3. M. Ramaseshan, M. Robitaille, J.W. Ellingboe, Y.L. Dory, and P. Deslongchamps. Tetrahedron Lett. **41**, 4737 (2000).
4. M. Ramaseshan, J.W. Ellingboe, Y.L. Dory, and P. Deslongchamps. Tetrahedron Lett. **41**, 4743 (2000).
5. R. Gagnon, Y.L. Dory, and P. Deslongchamps. Tetrahedron Lett. **41**, 4751 (2000).
6. P. Soucy, Y.L. Dory, and P. Deslongchamps. Synlett, **8**, 1123 (2000).
7. M. Ramaseshan, Y.L. Dory, and P. Deslongchamps. J. Comb. Chem. ***2***, 615 (2000).
8. S. Lamothe, A. Ndibwami, and P. Deslongchamps. Tetrahedron Lett. **29**, 1639 (1988).
9. S. Lamothe, A. Ndibwami, and P. Deslongchamps. Tetrahedron Lett. **29**, 1641 (1988).
10. T. Takahashi, K. Shimizu, T. Doi, J. Tsuji, and Y. Fukazawa. J. Am. Chem. Soc. **110**, 2674 (1988).
11. (*a*) P. Deslongchamps. Pure Appl. Chem. **64**, 1831 (1992); (*b*) E. Marsault, A. Toró, P. Nowak, and P. Deslongchamps. Tetrahedron Report, No. 565, **57**, 4243 (2001).
12. Y.L. Dory, P. Soucy, M. Drouin, and P. Deslongchamps. J. Am. Chem. Soc. **117**, 518 (1995).
13. A. Miranker and M. Karplus. Proteins: Structure, Function, and Genetics, **11**, 29 (1991).
14. M.B. Eisen, D.C. Wiley, M. Karplus, and R.E. Hubbard. Proteins: Structure, Function, and Genetics, **19**, 199 (1994).
15. D. Joseph-McCarthy, J.M. Hogle, and M. Karplus. Proteins: Structure, Function, and Genetics, **29**, 32 (1997).
16. A. Caflish, A. Miranker, and M.Karplus. J. Med. Chem. **36**, 2142 (1993).
17. G. Bérubé and P. Deslongchamps. Can. J. Chem. **68**, 404 (1990).
18. N. Hayashi, H. Noguchi, and S. Tsuboi. Tetrahedron, **56**, 7123 (2000).
19. Y.L. Dory, C. Ouellet, S. Berthiaume, A. Favre, and P. Deslongchamps. Bull. Soc. Chim. Fr. **131**, 121 (1994).
20. R. Appel. Angew. Chem. Int. Ed. Engl. **14**, 801 (1975).
21. Y. Chantigny, A. Toró, C.A. Lemelin, and P. Deslongchamps. Tetrahedron Lett. **39**, 7839 (1998).
22. A.P. Krapcho and J.F. Wemaster. J. Org. Chem. **45**, 4105 (1980).
23. G. Martin and M. Martin. Bull. Soc. Chim. Fr. 1637 (1963).

© 2002 NRC Canada

Penicillamine as a ligand in the catalytic asymmetric reduction of ketones

Stephen Hanessian, Eric Jnoff, and Andrew M. Griffin

Abstract: Amino acids derived from D-penicillamine and thiazolidines were studied as ligands for the catalytic asymmetric reduction of ketones with borane. Enantioselectivities up to 83% ee were observed.

Key words: asymmetric reduction, penicillamine, thiazolidine, amino acid.

Résumé : On a étudié le potentiel d'acides aminés dérivés de la D-pénicillamine et de la thiazolidine comme ligands pour la réduction asymétrique catalytique de cétones à l'aide du borane. On a observé des énantiosélectivités allant jusqu'à 83% ee.

Mots clés : réduction asymétrique, pénicillamine, thiazolidine, acide aminé.

[Traduit par la Rédaction]

Introduction

Much effort has focussed on the development of catalysts for the asymmetric reduction of ketones with borane in recent years (for reviews see ref. 1). The best examples to date are the Corey "CBS" oxazaborolidine (2) **1** (Fig. 1), and related precedents reported by Itsuno et al. (3). The Corey catalyst **1**, derived from a functionally biased *S*-prolinol, has been shown to reduce a variety of ketones to the corresponding alcohols in high yields and excellent enantiomeric excesses. The enantioselective reduction of ketones with borane catalyzed by other β-amino alcohols has also been studied by other groups (for recent publications see ref. 4).

We were intrigued by the potential use of readily available, α-amino acids as ligands for the catalytic asymmetric reduction of ketones, rather than the commonly utilized β-amino alcohols. In particular, we were interested in using the relatively inexpensive penicillamine **2**, a trifunctional amino acid, available in both D- and L-form (Fig. 1).

To the best of our knowledge, only three reports of the use of α-amino acids as ligands for the reduction of ketones can be found in the literature. Buono and co-workers (5) reported that *S*-proline is an efficient ligand for the reduction of a variety of aryl and alkyl ketones in the presence of excess borane in refluxing toluene. Enantioselectivities have been reported to range from 81 to >95% in the presence of 10 mol% of *S*-proline. However, a more extensive study by Martens and co-workers (6) has found much lower selectivities with proline as well as a variety of cyclic and bicyclic α-amino acids. In fact, under the conditions reported by Buono and co-workers (5), much lower selectivities ranging from 17 to 30% ee were reported (6). Higher enantioselectivities were obtained with the corresponding amino alcohols (6). In our hands, we could not achieve enantioselectivities higher than 30% in agreement with Martens and co-workers (6). There are only few precedents concerning the use of sulfur-containing amino acids in the asymmetric reduction of ketones (for sulfur-containing amino alcohols see ref. 7). Utilizing cysteine, homocysteine, and derivatives, Xingshu and Rugang (7*e*) reported an ee of 72% for the catalytic reduction of α-bromoacetophenone in presence of thiazolidine **3** at 60°C (Fig. 1). Martens and co-workers (7*a*–7*d*) have obtained moderate to high enantioselectivities with L-methionine and related amino acids.

Fig. 1. Selected ligands for asymmetric reduction of ketones.

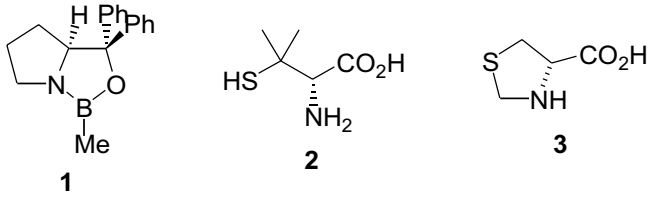

1 **2** **3**

Results and discussion

Following promising results with the reduction of acetophenone in the presence of 10 mol% D-penicillamine **2**, we decided to briefly investigate the functional requirements of representative amino acids. Thus, with D-valine **4**, D-cysteine **5**, and thiazolidine **3** the enantioselectivities were lower than with penicillamine **2**, which was comparable to thiazolidine **6** (Scheme 1). Although enantioselectivities were relatively poor, the yield of phenethyl alcohol was good and all reactions were complete in 10 min at room temperature. It is also interesting to note that the alcohol with the opposite configuration was formed when thiazolidine **6** was used as ligand.

Received 14 June 2001. Published on the NRC Research Press Web site at http://canjchem.nrc.ca on 31 May 2002.

Dedicated to the memory of Raymond Lemieux, a pioneer in carbohydrate chemistry.

S. Hanessian,[1] E. Jnoff, and A.M. Griffin. Department of Chemistry, Université de Montréal, Montréal, QC H3C 3J7, Canada.

[1]Corresponding author (telephone: (514) 343-6738; fax: (514) 343-5728; e-mail: stephen.hanessian@umontreal.ca).

 DOI: 10.1139/V01-174 © 2002 NRC Canada

Scheme 1. Reduction of acetophenone with sulfur-containing amino acids.

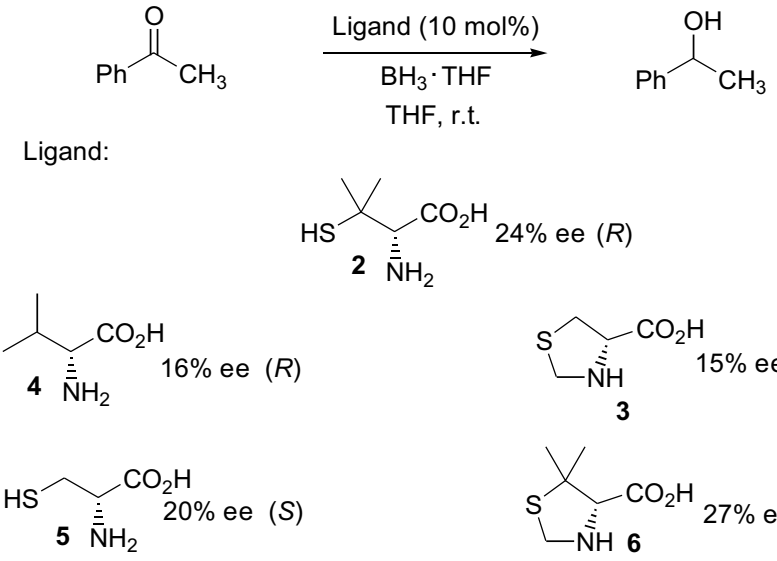

Our initial results using penicillamine **2** as ligand with various ketones and under varying reaction conditions are shown in Table 1. We noticed that when a solution of acetophenone was added to a preformed solution of ligand and borane, an exothermic reaction occurred. We then decided to add the ketone to the reducing mixture at room temperature over a period of 1 h. Under these conditions, the enantioselectivity was increased to 43% with acetophenone, although no enhancement of selectivity was observed for the reduction of α-tetralone and α-bromoacetophenone. Conducting the reactions at 0°C or at room temperature did not change the enantioselectivity significantly. No induction was observed in refluxing toluene (Table 1).

It was apparent that the catalyst derived from penicillamine **2** could only give low to modest enantioselectivities under the reaction conditions employed. We, therefore, turned our attention to the thiazolidine **6**, which was synthesized in one step from penicillamine **2** (8). Addition of acetophenone to the mixture of the borane and catalyst over a period of 1 h gave *S*-phenethyl alcohol with an enantioselectivity of 81% (Table 2). *p*-Substituted acetophenones gave the same level of enantioselectivity. A substantial improvement of enantioselectivity was observed with various tetralones with ee values ranging from 65 to 70% compared to 23% with D-penicillamine. In the case of α-bromoacetophenone, an ee of 74% compared to 16% with D-penicillamine as a catalyst was observed. These results clearly show that thiazolidine **6** is a better ligand than the parent amino acid **2** in these borane reductions of representative ketones. It is also of interest that the sense of induction was reversed.

In view of the well-known precedents utilizing β-amino alcohols as catalysts in borane reductions (1–4), we studied the reduced thiazolidine **7**. Curiously, lower enantioselectivities were observed in the case of acetophenone and α-bromoacetophenone utilizing **7** as catalyst (Table 3, entry 3 vs. 1; entry 7 vs. 5). The use of a basic additive such as *N*,*N*-dimethylaniline has been reported to be beneficial in such reductions (9). Adding 10% of this amine showed no

Table 1. Reduction of ketones using penicillamine **2**.

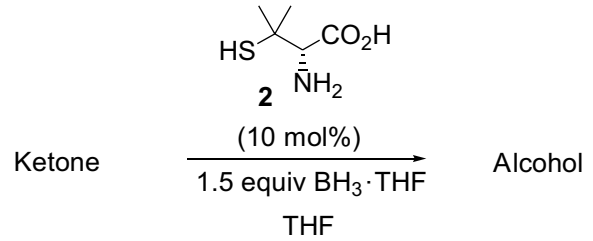

Ketone	Temperature (°C)	Yield (%)	ee (%)[a]	Method
PhCOMe	25	99	24 (*R*)	A
PhCOMe	25	72	43 (*R*)	B
PhCOMe	0	99	31 (*R*)	A
PhCOMe	0	67	38 (*R*)	B
PhCOMe	110	99	0	C
α-Tetralone	25	79	23 (*R*)	A
α-Tetralone	25	50	23 (*R*)	B
$PhCOCH_2Br$	25	53	13 (*S*)	A
$PhCOCH_2Br$	25	70	16 (*S*)	B

Note: Method A. Ketone added in one portion. Method B. Ketone added over 1 h. Method C. Refluxing in toluene.
[a]Determined by HPLC on a chiral column.

enhancement of selectivity when **6** was used as a catalyst (Table 3, entries 1, 2, and 5, 6). However, a substantial improvement of enantioslectivity was observed when the additive was used with the amino alcohol **7** as a catalyst (Table 3, entries 3, 4 and 7, 8).

It is possible that in the presence of the basic additive, the reducing specie is the cyclic oxazaborolidine **9** (Scheme 2) (9). The added base may prevent a second hydride transfer by removing one of the reactive hydrogens from intermediate **8**. As previously mentioned, the additive has an enhancing effect on the enantioselectivity only when **7** is used as a catalyst, but not in the case of **6**. It follows that the effective

© 2002 NRC Canada

Table 2. Reduction of ketones using thiazolidine **6**.

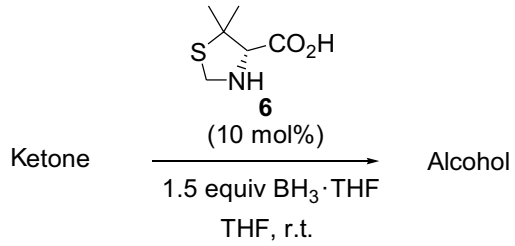

Ketone	Yield (%)[a]	ee (%)[b]
PhCOMe	75	81 (*S*)
p-FC_6H_4COMe	60	80 (*S*)
p-$MeOC_6H_4COMe$	85	59 (*S*)
$PhCOCH_2Br$	72	74 (*R*)
α-Tetralone	71	65 (*S*)
8-Methoxytetralone	83	70 (*S*)

[a]Ketone added over 1 h (see *Experimental*).
[b]Determined by HPLC.

Table 3. Comparison between reduction of ketones with amino acid **6** and amino alcohol **7**.

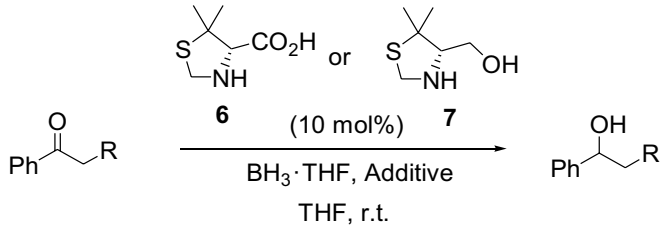

Entry	R	Ligand	Additive (10 mol%)	ee (%)[a]
1	H	**6**	None	81 (*S*)
2	H	**6**	*N*,*N*-Dimethylaniline	81 (*S*)
3	H	**7**	None	54 (*S*)
4	H	**7**	*N*,*N*-Dimethylaniline	83 (*S*)
5	Br	**6**	None	74 (*R*)
6	Br	**6**	*N*,*N*-Dimethylaniline	77 (*R*)
7	Br	**7**	None	54 (*R*)
8	Br	**7**	*N*,*N*-Dimethylaniline	81 (*R*)

[a]Determined by HPLC.

catalyst in the latter case is the oxazaborolidine **9** which is formed directly (Scheme 2).

In conclusion, we have demonstrated that penicillamine **2** and its thiazolidine derivative **6** may be used as a ligand in the catalytic reduction of ketones with borane at room temperature. Up to 81% ee was observed with acetophenone and related ketones in the presence of 10% mol catalyst. Comparable ee values were observed with the corresponding amino alcohol **7**, in the presence of *N*,*N*-dimethylaniline as an additive.

Experimental

[(4*S*)-5,5-Dimethyl-1,3-thiazolidin-4-yl]methanol (7)

To a solution of 0.5 g (3.10 mmol, 1 equiv) of thiazolidine **6** in 10 mL THF were added 15.5 mL (5 equiv) of BH_3·THF (1 M THF). After 1 h stirring at room temperature (r.t.), the mixture was quenched with 2 N HCl. The mixture was diluted with water (10 mL) and the organic phase was extracted with dichloromethane (3 × 10 mL) and dried over $MgSO_4$. Concentration in vacuo, afforded the corresponding oxazaborolidine hydride **8** as a colorless oil. R_f: 0.9 (AcOEt). MS (FAB): 176 ($[M + H]^+$, 7%), 160 ($M^{+\cdot}$-Me$^\cdot$, 100%), 158 ($M^{+\cdot}$-HO$^\cdot$, 24%), 157 ($M^{+\cdot}$-$H_2O^\cdot$, 8%), 146 ($M^{+\cdot}$-[BHOH]$^\cdot$, 25%), 116 (146-$CH_2^\cdot$, 17%). ^{1}H NMR (300 MHz, $CDCl_3$) δ: 4.90–4.75 (br s,1H), 4.31 (dd, 1H, *J* = 11.1 Hz and *J* = 3.3 Hz), 4.15 (dd, 1H, *J* = 12.6 Hz and *J* = 3.0 Hz), 4.02 (t, 1H, *J* = 10.5 Hz), 3.80 (dd, 1H, *J* = 12.6 Hz and *J* = 3.0 Hz), 2.76 (dt, 1H, *J* = 11.1 Hz and *J* = 3.3 Hz), 2.55–2.40 (br s,1H), 1.52 (s, 3H), 1.42 (s, 3H). ^{13}C NMR (75 MHz, $CDCl_3$) δ: 76.1, 57.4, 54.7, 54.4, 29.5, 27.8. This compound was dissolved in 50 mL of MeOH in presence of 1 mL of triethylamine. After 3 h stirring at 70°C, the mixture was concentrated in vacuo, then purified by flash chromatography (AcOEt–MeOH, 95:5), to give 0.31 g of amino alcohol **7**. Yield: 69%. R_f: 0.2 (AcOEt–MeOH 95:5, silica). $[\alpha]_D$: –29.4 (c 0.18., $CHCl_3$). HRMS (EI) *m*/*z* calcd. for $C_6H_{13}NOS$: 148.0796; found: 148.0799. ^{1}H NMR (300 MHz, $CDCl_3$) δ: 4.26 (AB system, 2H, *J* = 9.9 Hz), 3.71 (dd, 1H, *J*= 4.2 Hz and *J* = 10.5 Hz), 3.57 (dd, 1H, *J* = 10.5 Hz and *J* = 9.3 Hz), 2.99 (dd, 1H, *J* = 4.2 Hz and *J* = 9.3 Hz), 2.35–2.10 (br s, 2H), 1.51 (s, 3H), 1.30 (s, 3H). ^{13}C NMR (75 MHz, $CDCl_3$) δ: 73.9, 59.9, 56.5, 52.3, 30.7, 25.7.

Representative reductions

Reduction of ketones in presence of amino acid 6 or amino alcohol 7

To a solution of thiazolidine **6** (8) (30 mg, 0.19 mmol, 0.1 equiv) or amino alcohol **7** (27.9 mg, 0.19 mmol, 0.1 equiv) in 1 mL THF were added 2.8 mL of BH_3·THF (1 M THF, 1.5 equiv) at 0°C. After stirring 10 min, the cooling bath was removed and a solution of ketone (1 equiv) in 1 mL of THF was added over 60 min via a syringe-pump. After 10 min, the mixture was quenched at 0°C by adding 5 mL of 2 N HCl diluted with water (10 mL), the organic phase was extracted with AcOEt (3 × 10 mL), dried over $MgSO_4$, and the product was purified by flash chromatography (AcOEt–hexane). Enantiomeric excesses were measured by HPLC. PhCHOHMe: OB column, λ: 210 nm, flow: 1 mL min^{-1}, hexane–isopropanol 90:10, R_{t1}: 6.44 min (*S*) and R_{t2}: 9.73 min. *p*-$FC_6H_4CHOHMe$: OB column, λ: 210 nm, flow: 1 mL min^{-1}, hexane–isopropanol 98:2, R_{t1}: 17.77 min (*S*) and R_{t2}: 19.89 min. *p*-$MeOC_6H_4CHOHMe$: OB column, λ: 210 nm, flow: 1 mL min^{-1}, hexane–isopropanol 90:10, R_{t1}: 13.54 min (*S*) and R_{t2}: 18.56 min. $PhCHOHCH_2Br$: OB column, λ: 210 nm, flow: 1 mL min^{-1}, hexane–isopropanol 90:10, R_{t1}: 8.02 min and R_{t2}: 10.38 min. (*S*). 8-methoxytetralol: OB column, λ: 210 nm, flow: 1 mL min^{-1}, hexane–isopropanol 90:10, R_{t1}: 6.61 min and R_{t2}: 10.50 min (*S*).

Reduction of ketones in presence of amino alcohol 7 and* N,N-*dimethylaniline

To a solution of amino alcohol **7** (28 mg, 0.19 mmol, 0.1 equiv) and 0.24 mL of *N*,*N*-dimethylaniline in 1 mL

© 2002 NRC Canada

Scheme 2. Effect of an *N*,*N*-dimethylaniline on the reduction of ketones.

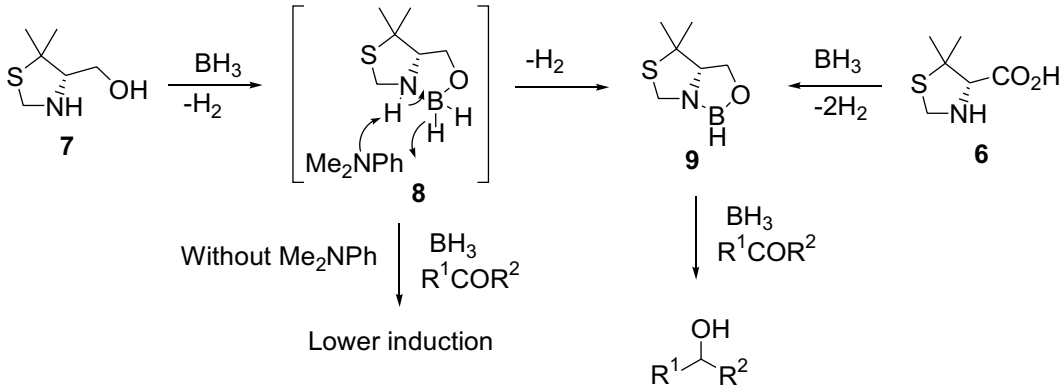

THF was added 1.21 mL of BH_3·THF (1 M THF, 0.65 equiv) at 0°C. After stirring for 2 h at reflux, the mixture was cooled to r.t. and 1.21 mL of BH_3·THF (1 M THF, 0.65 equiv) was added. A solution of ketone (1.9 mmol, 1 equiv) in 1 mL THF was added over 60 min via a syringe-pump. After 10 min, the mixture was quenched at 0°C by adding 5 mL of 2 N HCl. After dilution with water (10 mL), the organic phase was extracted with AcOEt (3 × 10 mL) and dried over $MgSO_4$. The corresponding alcohol was purified by flash chromatography (AcOEt–hexane, 15:85). Enantiomeric excesses were measured by HPLC.

Acknowledgments

We thank the Natural Sciences and Engineering Research Council of Canada (NSERC) for generous financial assistance through the Medicinal Chemistry Chair Program.

References

1. (*a*) S. Itsuno. Org. React. (N.Y.), **52**, 395 (1998); (*b*) V.K. Singh. Synthesis, 605 (1992); (*c*) L. Deloux and M. Srebnik. Chem. Rev. **93**, 763 (1993); (*d*) S. Wallbaum and J. Martens. Tetrahedron: Asymmetry, **3**, 1475 (1992).
2. (*a*) E.J. Corey, R.K. Bakshi, and S.J. Shibata. J. Org. Chem. **53**, 2861 (1988), and refs. cited therein; (*b*) E.J. Corey and C.J. Helal. Angew. Chem. Int. Ed. **37**, 1987 (1998).
3. S. Itsuno, Y. Sakurai, K. Ito, A. Hirao, and S. Nakahama. Bull. Soc. Chem. Jpn. **60**, 395 (1987), and refs. cited therein.
4. (*a*) M. Falorni, C. Collu, and G. Giacomelli. Tetrahedron: Asymmetry, **7**, 2739 (1996); (*b*) M. Masui and T. Shioiri. Synlett, 49 (1996); (*c*) P. Delair, J. Einhorn, and J.L. Luche. Tetrahedron, **51**, 165 (1995).
5. J.M. Brunel, M. Maffei, and G. Buono. Tetrahedron: Asymmetry, **4**, 2255 (1993).
6. T. Mehler, W. Benhen, J. Wilken, and J. Martens. Tetrahedron: Asymmetry, **5**, 185 (1994).
7. (*a*) T. Mehler and J. Martens. Tetrahedron: Asymmetry, **4**, 1983 (1993); (*b*) T. Mehler and J. Martens. Tetrahedron: Asymmetry, **4**, 2299 (1993); (*c*) W. Trentmann, T. Mehler, and J. Martens. Tetrahedron: Asymmetry, **8**, 2033 (1997); (*d*) M. Kossenjans and J. Martens. Tetrahedron: Asymmetry, **9**, 1409 (1998); (*e*) L. Xingshu and X. Rugang. Tetrahedron: Asymmetry, **7**, 2779 (1996).
8. H.E. Howard-Lock, C.J.L. Lock, and P.S. Smalley. Can. J. Chem. **63**, 2411 (1985).
9. (*a*) D. Cai, D. Tschaen, Y.J. Shi, T.R. Verhoeven, R.A. Reamer, and A.W. Douglas. Tetrahedron Lett. **34**, 3243 (1993); (*b*) M. Periasamy, J.V.B. Kanth, and A.S.B. Prasad. Tetrahedron, **50**, 6411 (1994); (*c*) D.M. Tschaen, L. Abramson, D. Cai, R. Desmond, U.H. Dolling, L. Frey, S. Karady, Y.J. Shi, and T.R. Verhoeven. J. Org. Chem. **60**, 4324 (1995); (*d*) M. Falorni, C. Collu, and G. Giacomelli. Tetrahedron: Asymmetry, **7**, 2739 (1996).

© 2002 NRC Canada

Investigation of the reactivity difference between thioglycoside donors with variant aglycon parts

Martina Lahmann and Stefan Oscarson

Abstract: The reactivity of perbenzoylated thioglycosides with various thiol aglycons has been compared and quantified using competitive glycosylation experiments. Methyl 2,3,4-tri-*O*-benzyl-α-D-glucopyranoside was employed as acceptor and DMTST as a promoter. The reactivity was found, as expected, to depend on the electron donating properties of the aglycon. Hence, the most reactive donor, the cyclohexyl thioglycoside, was found to be about three times as reactive as the thioethyl glycoside, which in turn was twice as reactive as the thiomethyl donor. The thiophenyl donor was even less reactive, whereas *p*-halophenyl donors were inert under the glycosylation conditions used — but could be activated using NIS–TfOH as promoter. Furthermore, it was found that galactosyl donors were three to four times more reactive than the corresponding glucosyl derivative. These results allowed the design of an orthogonal coupling between thioglycosides with the same protecting groups (benzoyls) but with different thiol aglycons.

Key words: thioglycosides, orthogonal glycosylations, competititive glycosylations.

Résumé : En se basant sur des expériences de glycosylations compétitives, on a comparé et quantifié la réactivité de thioglycosides perbenzoylés avec diverses thioaglycones. On a utilisé le 2,3,4-tri-*O*-benzyl-α-D-glucopyranoside de méthyle comme accepteur et le DMTST comme promoteur. On a trouvé, tel que prévu, que la réactivité dépend du caractère électrodonneur de l'aglycone. On a donc trouvé que le donneur le plus réactif, le thioglycoside de cyclohexyle, est trois fois plus réactif que le glycoside de thioéthyle qui est lui-même deux fois plus réactif que le donneur thiométhyle. Le donneur thiophényle est encore moins réactif alors que les donneurs *p*-halophényles sont inertes dans les conditions de glycosylation utilisées; ils peuvent toutefois être activés en utilisant le NIS–TfOH comme promoteur. De plus, on a trouvé que les donneurs galactosyles sont de trois à quatre fois plus réactifs que le dérivé glucosyle correspondant. Ces résultats ont permis de mettre au point un couplage orthogonal entre des thioglycosides avec les mêmes groupes protecteurs (benzoyles), mais des thioaglycones différentes.

Mots clés : thioglycosides, glycosylations orthogonales, glycosylations compétitives.

[Traduit par la Rédaction]

Introduction

The reactivity of a glycosyl donor in a glycosylation reaction is dependent on its structure and the reaction conditions. This has enabled orthogonal glycosylations and one-pot synthesis of oligosaccharides using less reactive donors as acceptors. To achieve such glycosylations, various approaches have been used employing the reactivity diversity of, for example, various types of glycosyl donors (1, 2) and differently protected glycosyl donors (3–5). In the latter approach, quantification of the influence of the various protecting schemes on the reactivity was performed using model acceptors and competitive glycosylation studies (4, 5). Additionally, the effect of the promoter and solvent on the reactivity must be considered (6).

Received 10 January 2002. Published on the NRC Research Press Web site at http://canjchem.nrc.ca on 5 July 2002.

Dedicated to the memory of Professor Raymond U. Lemieux.

M. Lahmann and S. Oscarson.[1] Department of Organic Chemistry, Arrhenius Laboratory, Floor 6, Stockholm University, S-106 91 Stockholm, Sweden.

[1]Corresponding author (e-mail: s.oscarson@organ.su.se).

Thioglycoside donors have, apart from being stable substances allowing most protective group manipulations but still easily activated by chemoselective promoters (7–9), an additional advantage — their reactivity can be manipulated by the introduction of different thiol aglycons. A few examples of couplings using this approach have been reported (10–12), but no general study of the reactivity differences has been performed. Here, we describe efforts to quantify the reactivity difference between thioglycoside donors differing only in the aglycon moiety using competitive glycosylation studies. In addition, a sample trisaccharide was synthesized to relate the influence of the leaving group to other preparative conditions.

Results and discussion

As glycosyl donors, perbenzoylated thioglycosides with methyl (13), ethyl (13), phenyl (14), halophenyl (13), tolyl (11), benzyl (13), *n*-butyl (13), *n*-hexyl (15, 16), isopropyl (13), *t*-butyl (17), and cyclohexyl (18) aglycon substituents (Fig. 1) have been prepared and used. As a model acceptor, methyl 2,3,4-tri-*O*-benzyl-α-D-glucopyranoside (**15**) was chosen. Both glucosyl and galactosyl donors were tested. Competitive glycosylations were performed using mainly the ethyl thioglycoside (**Glc-13** or **Gal-13**) as a reference donor

 DOI: 10.1139/V02-101 © 2002 NRC Canada

Fig. 1. Thioglycoside donors employed in the study.

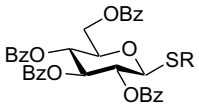

Glc-1 R = *m*-ClPh
2 R = *m*-BrPh
3 R = *p*-BrPh
4 R = *p*-ClPh
5 R = *n*-Bu
6 R = *n*-Hex
7 R = Ph
8 R = Bn
9 R = *i*-Pr
10 R = *t*-Bu
11 R = cHex
12 R = Me
13 R = Et
14 R = Tol

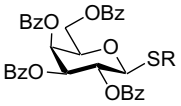

Gal- **6** R = *n*-Hex
7 R = Ph
11 R = cHex
12 R = Me
13 R = Et
14 R = Tol

Scheme 1.

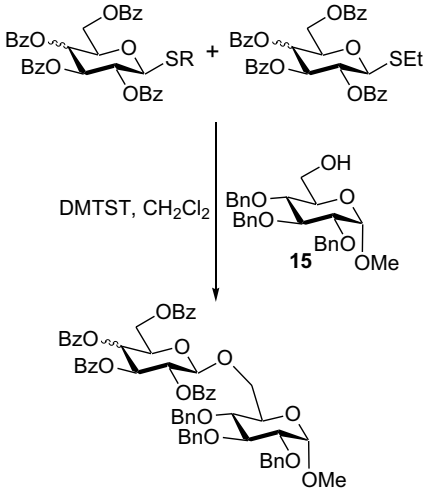

and dimethyl(methylthio)sulfonium trifluoromethylsulfonate (DMTST) (19) as a promoter (Scheme 1). The reaction mixtures were analyzed by HPLC (Fig. 2). Since the product is the same in most reactions, the relative reactivity was estimated by comparing the amounts of non-reacted donors. The results are summarized in Table 1.

As expected, the reactivity is correlated to the electron withdrawing (donating) capacity of the aglycon substituent. Tolyl and phenyl glycosides were slow (Table 1, entries 1–4, 15, 19, and 20), and an even more pronounced difference was observed with halosubstituted phenyl derivatives, which were inert under the conditions used. The latter donors were, however, easily activated by using NIS–AgOTf as the promoter. Of the alkyl glycosides tested, the methyl derivative showed a rather low reactivity (entries 6 and 7), whereas the *n*-butyl and benzyl glycosides were slightly faster (entries 8 and 10). The *n*-hexyl glycoside was comparable to the ethyl glycoside in reactivity (entries 11 and 12), while the branched alkyl glycosides, isopropyl and cyclohexyl, were the most reactive donors. As can be seen, the cyclohexyl derivative is an interesting effective donor (entries 13, 16, and

Fig. 2. HPLC spectra for entry 21 before addition of promoter and 60 min after addition (see *Experimental*).

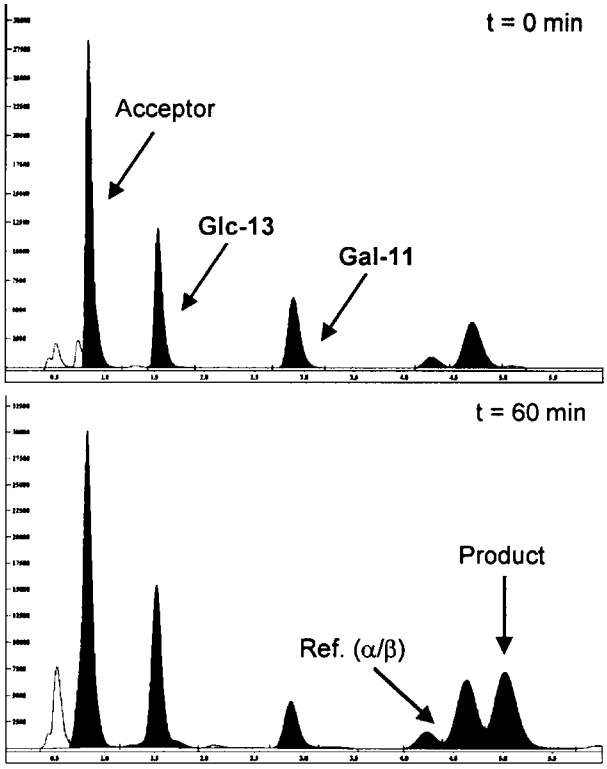

18), but has so far not been widely used (20). The *tert*-butyl glycoside disappeared fastest (entry 22), but mainly gave the decomposition product of the donor and very little of the disaccharide product. In contrast, the perbenzylated *tert*-butyl thioglucoside donor was found to be an excellent donor, as was shown also by Stauch and Boons (21) using IDCP as the promoter.

Competition glycosylations between glucosyl and galactosyl donors showed the galactosides to be more reactive (Table 1, entries 5, 9, 14, 17, and 21 compared with entries 2, 3, 6, 12, and 18, respectively). A good correlation between the different derivatives was obtained, with a reactivity difference of about three to four in favour of the galactoside, which is in good agreement with a result of Wong and co-workers (5).

The reactivity difference between thioglycosides differing only in their thiol aglycons is most often to small to allow efficient orthogonal couplings, especially since the removal of a benzoyl group is activating. Often sugars of different reactivity and protecting group patterns as well as with different thiol aglycons are compared (11). *p*-NO_2-Phenyl thioglycosides have been used as inert acceptors, but to function as donors they have to be activated by conversion of the nitro functionality into an acetamido group, and even then the donor capacity is limited except for neuraminic acid donors (22–25). So far, the only report on orthogonal couplings between thioglycosides varying only in the aglycon functionality to give disaccharide donors was performed using steric effects by Boons et al. (12). Couplings between some of the more reactive (cHex, *i*-Pr, Et) perbenzoylated glycosides donors and less reactive acceptors (Ph, Tol, PhX,

© 2002 NRC Canada

Table 1. Relative reactivity of thioglycosyl donors.

Entry	Donor	Reference donor	Rel. react.[a]
1	Gal-7 (Ph)	Gal-13 (Et)	<0.1
2	Glc-7 (Ph)	Glc-13 (Et)	0.1
3	Glc-14 (Tol)	Glc-13 (Et)	0.1
4	Gal-14 (Tol)	Gal-13 (Et)	0.2
5	Gal-7 (Ph)	Glc-13 (Et)	0.4
6	Glc-12 (Me)	Glc-13 (Et)	0.4
7	Gal-12 (Me)	Gal-13 (Et)	0.5
8	Glc-8 (Bn)	Glc-13 (Et)	0.7
9	Gal-14 (Tol)	Glc-13 (Et)	0.7
10	Glc-5 (*n*-Bu)	Glc-13 (Et)	0.7
11	Gal-6 (*n*-Hex)	Gal-13 (Et)	1.0
12	Glc-6 (*n*-Hex)	Glc-13 (Et)	1.0
13	Glc-9 (*i*-Pr)	Gal-13 (Et)	1.4
14	Gal-12 (Me)	Glc-13 (Et)	1.6
15	Glc-14 (Tol)	Glc-7 (Ph)	1.9
16	Gal-11 (cHex)	Gal-13 (Et)	2.1
17	Gal-6 (*n*-Hex)	Glc-13 (Et)	3.4
18	Glc-11 (*c*-Hex)	Glc-13 (Et)	3.6
19	Glc-12 (Me)	Glc-7 (Ph)	5.8
20	Glc-6 (*n*-Hex)	Glc-7 (Ph)	6.1
21	Gal-11 (cHex)	Glc-13 (Et)	10.3
22	Glc-10 (*t*-Bu)	Glc-13 (Et)	12.5[b]

[a]The reactivity factors were calculated as followed: The peak area of the reference donor (D_{ref}) and the test donor (D_{test}) were normalized to the integral of the reference (R_β) (β-anomer): $D^\circ_{ref} = D_{ref^\circ}/R^\circ_\beta$; $D^\circ_{test} = D_{test^\circ}/R^\circ_\beta$; $D^n_{ref} = D_{ref^n}/R^n_\beta$; and $D^n_{test} = D_{test^n}/R^n_\beta$. From these values the amount of unused donor was calculated, as was the yield of product formed from that particular donor: $Y_{ref} = 1 - D^n_{ref}/D^\circ_{test}$. Resulting in the reactivity of the test donor: $R_{test} = Y_{test}/Y_{ref}$.
[b]Donor decomposes.

4-OH, or 6-OH) were carried out, but were found to be ineffective due to concomitant activation of the supposed acceptor. The combination of employing thiocyclohexyl or thioethyl glycosides as donors and thio *p*-Br-phenyl derivative **16** as acceptor, however, led to efficient product formation (Scheme 2). The amount of promoter (DMTST) had to be reduced compared with standard conditions (1.5 equiv instead of 2–4 equiv), which not only slowed down the couplings but also effectively suppressed activation of the acceptor. The *p*-Br-phenyl group of the obtained disaccharide **17** could then be smoothly activated in a NIS–AgOTf-promoted coupling with model acceptor **15** to produce a trisaccharide **18** (26) in high yield (Scheme 2).

In conclusion, a study of the reactivity of thioglycosides with different aglycon moieties has been performed using competitive glycosylations. The results gave a quantitative estimation of the differences between slow-reacting donors with electron withdrawing aglycons and fast-reacting donors with more electron donating aglycons, as well as the reactivity difference between glucosyl and galactosyl donors. A preparative example of a coupling between an ethyl thioglycoside (donor) and *p*-bromophenyl thioglycoside (acceptor), both carrying benzoyl protecting groups, is also described. Although other factors such as choice of solvent and promoter must be taken into account, these results, in combination with earlier investigations regarding the influence of protecting groups, should be of value for designing efficient orthogonal glycosylations between thioglycosides.

Scheme 2.

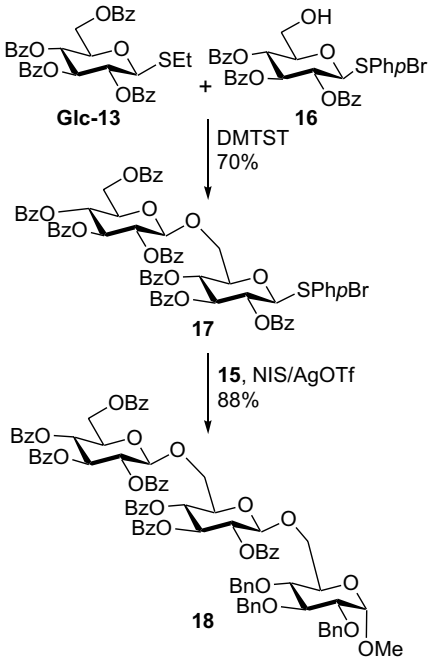

Experimental

All organic solvents were distilled before use. Organic solutions were dried over $MgSO_4$, before concentration, which was performed under reduced pressure at <40°C (bath temperature). NMR spectra were recorded at 300 MHz or 400 MHz (Varian) (^{1}H) or at 75 MHz or 100 MHz (^{13}C), respectively, in $CDCl_3$. For the ^{1}H NMR spectra, TMS was used as internal standard (δ = 0); the ^{13}C NMR spectra were referenced to the chloroform signal (δ = 77.17). Silica gel MERCK 60 (0.040–0.063) was used for flash chromatography. For the competition reactions, several stock solutions were prepared in dry CH_2Cl_2. The HPLC reference was dissolved together with the acceptor. The DMTST solution was left for one day at 4°C to stabilize the solution. The activity of the promoter solution was checked before (and after) each set of competition experiments performing a standard coupling experiment following the coupling procedure for competition experiments but using two equivalents of the reference donor (thioethyl glucoside) instead. All vials and sample tubes were dried and stored in an desiccator before use. For taking aliquots to prepare the reaction mixtures, glass pipettes with fixed volumes (50 μL, 500 μL) were used. The HPLC solvents (CH_3CN–H_2O (83:17), containing 0.1% TFA) were filtered (0.45 μm pores) before use. The reaction mixtures were analyzed on an analytical reversed phase column [column: RP C-18 (Rocket, 33 mm, ID 7 mm, beads size 3 μ, Alltima C18) pH 2.0–7.5] with UV detection (215 nm). During the analysis a low stream of helium was bubbled through the solvents. Once the coupling product was isolated and characterized by proton and carbon NMR. To check for the occurrence of decomposition products, the reactions were followed by TLC (toluene–EtOAc, 3:1; silica-gel F_{254} (E. Merck)) with detection by UV-light and (or) charring with 8% sulphuric acid. MALDI-TOF spectra were

© 2002 NRC Canada

recorded on a Bruker Biflex III with 2′,4′,6′-trihydroxyacetophenone monohydrate (THAP) as the matrix.

Typical preparation of the donors

The peracetylated sugar (2.5 mmol, 1.0 equiv) was dissolved in dry CH_2Cl_2 (2 mL per mmol sugar). Thiol (1.2–1.5 equiv) and $BF_3{\cdot}Et_2O$ (1.5–2 equiv) were successively added. When the reaction was complete (TLC: toluene–EtOAc, 3:1) the reaction mixture was quenched with Et_3N (2.5 equiv), evaporated, and redissolved in CH_2Cl_2, then washed with brine, dried, and concentrated. The crude product was filtered through a plug of silica gel (toluene–EtOAc, 9:1) and after crystallization (95% ethanol or pentane–Et_2O) the β-compounds were obtained. After removal of the acetates with NaOMe, the crude material was benzoylated in pyridine.

Competitive glycosylation experimental procedure

A mixture of the glycoside donor (10 μmol, 1.0 equiv, 1 mmol in CH_2Cl_2), the reference donor (10 μmol, 1.0 equiv, 1 mmol in CH_2Cl_2), the HPLC reference compound (5 μmol, 0.5 equiv, α/β 17:83, 0.5 mmol in CH_2Cl_2), the acceptor (20 μmol, 2.0 equiv, 2 mmol in CH_2Cl_2), and molecular sieves (4 Å) was stirred at room temperature for 30 min. An HPLC sample (5 μL) was taken, centrifuged, and analyzed. DMTST (10 μmol, 1.0 equiv., 1 mmol in CH_2Cl_2) was added and HPLC samples (20 μL) were taken at regular intervals (first set: 30 min, 1 h, 2 h, 4 h, 24 h; second set: 1 h, 3 h), centrifuged, and analyzed. All couplings were carried out as a double experiment at the same time to minimize errors.

4-Bromophenyl 2,3,4-tri-*O*-benzoyl-1-thio-β-D-glucopyranoside (16)

4-Bromophenyl 1-thio-β-D-glucopyranoside (680 mg, 1.92 mmol), dissolved in pyridine (5 mL), was stirred with TBDMSCl (350 mg, 2.3 mmol) and DMAP (cat.) at room temperature over night ($CHCl_3$–MeOH, 9:1). Then benzoyl chloride (2 mL) was added and the mixture was left stirring for additional 2 h (toluene–EtOAc, 6:1). After aqueous work-up, the raw material was purified by silica gel flash-chromatography (pentane–Et_2O, 3:1) to yield 4-bromophenyl 2,3,4-tri-*O*-benzoyl-6-*O*-*tert*-butyldimethylsilyl-1-thio-β-D-glucopyranoside (1.34 g, 1.72 mmol, 90%). ^{1}H NMR δ: 8.3–7.1 (m, 19H), 5.9 (t, *J* = 9.3 Hz, 1H), 5.5 (t, *J* = 9.6 Hz, 1H), 5.4 (t, *J* = 9.9 Hz, 1H), 5.0 (d, *J* = 9.6 Hz, 1H, H-1), 4.0–3.8 (m, 3H), 0.9 (s, 9H, *t-Bu*Si), 0.0 (2s, 6H, Me_2Si). ^{13}C NMR δ: 165.9, 165.1, 165.1 (Ph*C*O), 134.5, 133.8, 133.4, 132.1, 130.3, 129.9, 129.8, 128.5, 128.5, 128.3 (aromatic C), 122.8 (*C*-Br), 85.8 (C-1), 79.7, 74.5, 70.6, 69.1, 62.7, 25.9 (*t-Bu*Si), 18.4 (*t-Bu*Si), –5.2, –5.3 (Me_2Si).

To a cooled (0°C) solution of 4-bromophenyl 2,3,4-tri-*O*-benzoyl-6-*O*-*tert*-butyldimethylsilyl-1-thio-β-D-glucopyranoside (1.28 g, 1.65 mmol) in CH_2Cl_2 (50 mL), was slowly added $BF_3{\cdot}Et_2O$ (520 μL, 4.1 mmol). After 2 h, the reaction mixture was diluted with CH_2Cl_2, washed consecutively with H_2O, $NaHCO_3$, and brine, then dried and concentrated. The crude product was purified by silica gel flash-chromatography (toluene → toluene–EtOAc, 6:1) to yield **16** (0.94 g, 1.42 mmol, 86%). ^{1}H NMR δ: 8.0–7.8 (m, 6H), 7.6–7.1 (m, 13H), 5.9 (t, *J* = 9.6 Hz, 1H), 5.4 (t, *J* = 9.6 Hz, 2H), 5.0 (d, *J* = 9.6 Hz, 1H, H-1), 3.9–3.7 (m, 3H). ^{13}C NMR δ: 166.1, 165.8, 165.1 (Ph*C*O), 135.0, 133.8, 133.5, 133.4, 132.2, 130.0, 129.9, 129.8, 128.6, 128.5, 128.5, 128.4 (aromatic C), 123.1 (*C*-Br), 85.8 (C-1), 79.0, 73.9, 70.5, 69.2, 61.5. MALDI-TOF MS calcd. for $C_{33}H_{27}BrO_8S$: 662.06 [M(^{79}Br)], 664.06 [M(^{81}Br)]; found: 685.05 [M(^{79}Br) + Na]$^+$, 687.06 [M(^{81}Br) + Na]$^+$, 701.03 [M(^{79}Br) + K]$^+$, 703.02 [M(^{81}Br) + K]$^+$.

4-Bromophenyl (2,3,4,6-tetra-*O*-benzoyl-β-D-glucopyranosyl)-(1→6)-2,3,4-tri-*O*-benzoyl-1-thio-β-D-glucopyranoside (17)

A solution of donor **Glc-13** (100 mg, 156 μmol) and acceptor **16** (100 mg, 150 μmol) in dry CH_2Cl_2 (5 mL) was stirred with powdered molecular sieves (4 Å, 200 mg) under argon for 1 h, then DMTST (54 mg, 209 μmol dissolved in 500 μL CH_2Cl_2) was added. The reaction, followed by TLC (toluene–EtOAc, 6:1), was quenched after 4 h by addition of Et_3N (100 μL) and the mixture was diluted with CH_2Cl_2 (20 mL), filtered, and concentrated. The residue was subjected to silica gel column chromatography (pentane–Et_2O, 1:1 followed by toluene–EtOAc, 20:1) to obtain **17** (130 mg, 105 μmol, 70%) as a white solid. ^{1}H NMR δ: 8.0–7.7 (m, 14H), 7.5–6.9 (m, 25H), 5.9 (t, *J* = 9.6 Hz, 1H), 5.8 (t, *J* = 9.4 Hz, 1H), 5.6 (t, *J* = 9.9 Hz, 1H), 5.5 (dd, *J* = 7.7, 9.9 Hz, 1H), 5.3 (t, *J* = 9.6 Hz, 1H), 5.2 (t, *J* = 9.9 Hz, 1H), 4.9 (d, *J* = 7.7 Hz, 1H, H-1′), 4.8 (d, *J* = 9.9 Hz, 1H, H-1), 4.6 (dd, *J* = 3.3, 12.1 Hz, 1H), 4.4 (dd, *J* = 4.4, 12.1 Hz, 1H), 4.0 (m, 3H), 3.9 (dd, *J* = 7.1, 11.5 Hz, 1H). ^{13}C NMR δ: 166.1, 165.9, 165.7, 165.4, 165.2, 165.0 (Ph*C*O), 134.8, 133.6, 133.5, 133.4, 133.3, 132.2, 130.7, 130.0, 129.9, 129.8, 129.6, 129.3, 129.2, 128.9, 128.7, 128.5, 128.4, 128.3, 125.4, 123.0 (aromatic C), 101.5 (C-1′), 85.6 (C-1), 78.2, 74.1, 73.0, 72.5, 71.9, 70.5, 69.6, 68.7, 65.0. MALDI-TOF MS calcd. for $C_{67}H_{53}BrO_{17}S$: 1240.22 [M(^{79}Br)], 1242.42 [M(^{81}Br)]; found: 1263.25 [M(^{79}Br) + Na]$^+$, 1265.25 [M(^{81}Br) + Na]$^+$, 1279.24 [M(^{79}Br) + K]$^+$, 1281.25 [M(^{81}Br) + K]$^+$.

Methyl (2,3,4,6-tetra-*O*-benzoyl-β-D-glucopyranosyl)-(1→6)-(2,3,4-tri-*O*-benzoyl-β-D-glucopyranosyl)-(1→6)-2,3,4-tri-*O*-benzyl-α-D-glucopyranoside (18) (26)

A solution of donor **17** (40 mg, 32 μmol) and acceptor **15** (18 mg, 39 μmol) in dry CH_2Cl_2 (2 mL) was stirred with powdered molecular sieves (4 Å, 100 mg) under argon for 1 h. The mixture was cooled (0°C) and NIS (11 mg, 49 μmol) and AgOTf (cat.) were added. The reaction, followed by TLC (toluene–EtOAc, 6:1), was quenched after 30 min by addition of Et_3N (50 μL), the mixture was then diluted with CH_2Cl_2 (20 mL), filtered, and concentrated. The residue was subjected to silica gel column chromatography (toluene → toluene–EtOAc, 10:1) to yield **18** (42 mg, 28 μmol, 88%). ^{1}H NMR δ: 8.0–7.7 (m, 14H), 7.5–6.9 (m, 36H), 5.8 (t, *J* = 10 Hz, 1H), 5.7 (t, *J* = 10 Hz, 1H), 5.6 (t, *J* = 10 Hz, 1H), 5.4 (m~dd, *J* = 10 Hz, *J* = 8 Hz, 2H), 5.3 (t, *J* = 10 Hz, 1H), 5.0 (d, *J* = 7.8 Hz, 1H,), 4.9 (d, *J* = 11 Hz), 4.7 (d, *J* = 12 Hz, 1H), 4.6 (d, *J* = 11 Hz, 1H), 4.5 (m, 3H), 4.4 (d, *J* = 8 Hz, 1H), 4.3 (m, 2H), 4.1 (d, *J* = 11 Hz, 1H), 4.0 (m, 2H), 3.8 (m, 4H), 3.5–3.3 (m, 4H), 3.3 (s, 3H) ppm. ^{13}C NMR δ: 166.1, 165.8, 165.4, 165.1, 164.9 (Ph*C*O), 139.7–137.5, 133.5–127.4 (aromatic C), 101.5, 100.8 (C-1′, C-1″), 98.2 (C-1), 81.9, 79.8, 75.5, 74.5, 74.4, 73.5, 72.8,

© 2002 NRC Canada

72.4, 72.1, 71.8, 69.7, 69.6, 69.4, 68.6, 67.6, 63.0, 55.4 (O*Me*). MALDI-TOF MS calcd. for $C_{89}H_{80}O_{23}$: 1516.51 $[M]^+$; found: 1539.53 $[M + Na]^+$.

Acknowledgments

We thank Professor Per Garegg for his interest in this research. Financial support from EU (Contract Number ERB FMRX CT96 0025) and from the Swedish Natural Science Research Council are gratefully acknowledged.

References

1. O. Kanie, Y. Ito, and T. Ogawa. J. Am. Chem. Soc. **116**, 12073 (1994).
2. S. Raghavan and D. Kahne. J. Am. Chem. Soc. **11**, 1580 (1993).
3. D.R. Mootoo, P. Konradsson, U. Udodong, and B. Fraser-Reid. J. Am. Chem. Soc. **110**, 5583 (1988).
4. N.L. Douglas, S.V. Ley, U. Lucking, and S.L. Warriner. J. Chem. Soc. Perkin Trans. 1, 51 (1998).
5. Z. Zhang, I.R. Ollman, X.-S. Ye, R. Wischnat, T. Baasov, and C.-H. Wong. J. Am. Chem. Soc. **121**, 734 (1999).
6. M. Lahmann and S. Oscarson. Org. Lett. **2**, 3881 (2000).
7. S. Oscarson. *In* Oligosaccharides in chemistry and biology: A comprehensive handbook. Vol. 1. *Edited by* B. Ernst, G. Hart, and P. Sinaÿ. Wiley-VCH, Weinheim. 2000. p. 93–116.
8. P.J. Garegg. Adv. Carbohydr. Chem. Biochem. **52**, 179 (1997).
9. T. Norberg. *In* Modern methods in carbohydrate synthesis. *Edited by* S.H. Khan and R.A. O'Neill. Harwood Academic Publishers, Amsterdam. 1995. p. 82–106.
10. H.M. Zuurmond, S.C.v.d. Laan, G.A.v.d. Marel, and J.H.v. Boom. Carbohydr. Res. **215**, c1 (1991).
11. A.K. Choudhury, I. Mukherjee, B. Mukhopadhyay, and N. Roy. J. Carbohydr. Chem. **18**, 361 (1999).
12. R. Guertsen, D.S. Holmes, and G.J. Boons. J. Org. Chem. **62**, 8145 (1997).
13. M. Cerny and J. Pacak. Collection Czechoslov. Chem. Commun. **24**, 2566 (1959).
14. R.J. Ferrier and R.H. Furneaux. Carbohydr. Res. **52**, 63 (1976).
15. S. Saito and T. Tsuchiya. Chem. Pharm. Bull. **33**, 503 (1985).
16. S.A. Galema, J.B.F.N. Engberts, and H.A. van Doren. Carbohydr. Res. **303**, 423 (1997).
17. H.B. Wood, B. Coxon, H.W. Diehl, and H.G. Fletcher. J. Org. Chem. **29**, 461 (1964).
18. T. Ogawa and M. Matsui. Carbohydr. Res. **54**, c17 (1977).
19. P. Fügedi and P.J. Garegg. Carbohydr. Res. **149**, c9 (1986).
20. P.J. Garegg, S. Oscarson, and U. Tedebark. J. Carbohydr. Chem. **17**, 587 (1998).
21. T. Stauch and G.J. Boons Synlett, 906 (1996).
22. R. Roy, F.O. Andersson, and M. Letellier Tetrahedron Lett. **33**, 6053 (1992).
23. L.A.J.M. Sliedregt, K. Zegelaarjaarsveld, G.A. van den Marel, and J.H. van Boom. Synlett, 335 (1993).
24. L.A.J.M. Sliedregt, G.A. van den Marel, and J.H. van Boom. Indian Acad. Sci. Chem. Sci. **106**, 1213 (1994).
25. S. Cao, F. Hernández-Matéo, and R. Roy. J. Carbohydr. Chem. **17**, 609 (1998).
26. T. Zhu and G.-J. Boons Tetrahedron Lett. **39**, 2187 (1998).

© 2002 NRC Canada

Anomeric effects of sulfones

Guangwu Chen, Richard W. Franck, Guangli Yang, and Michael Blumenstein

Abstract: The anomeric effect of the sulfone group in tetrahydropyrans has been determined. The value is >2 kcal mol^{-1}, which is larger than the *A*-value of a methyl group but less than the *A*-value of the sulfone in a tetrahydropyran. Hence, in an unsubstituted tetrahydropyranyl sulfone, the equatorial conformer predominates, whereas in a properly substituted methyltetrahydropyranyl sulfone, an axial sulfone is preferred over an axial methyl group.

Key words: sulfone, tetrahydropyran, anomeric effect.

Résumé : On a déterminé l'effet anomère du groupe sulfone dans les tétrahydropyranes. La valeur est supérieure à 2 kcal mol^{-1} et elle est nettement supérieure à la valeur de *A* d'un groupe méthyle, mais elle est inférieure à la valeur de *A* de la sulfone dans un tétrahydropyrane. Il en résulte que dans un tétrahydropyranylsulfone non substituée l'isomère équatorial prédomine alors que dans une méthyltétrahydropyranylsulfone substituée de façon appropriée la sulfone occupera la position axiale de façon préférentielle par rapport à un groupe méthyle axial.

Mots clés : sulfone, tétrahydropyrane, effet anomère.

[Traduit par la Rédaction]

Introduction

The discovery and understanding of the anomeric effect in carbohydrate chemistry begins with Raymond Lemieux and John T. Edward (1). The original arguments rationalized the observation of a diminished equatorial preference of oxygen substituents at the anomeric carbon of carbohydrates in comparison to their equatorial preference in cyclohexanes; similar behavior of other electronegative substituents have since been observed and are included in the rationalization. The sulfone group is an often-prepared and well-known anomeric substituent, used as a starting material for the direct preparation of *C*-glycosides (2), through their lithiation and subsequent desulfonylation (3), via intermediate anomeric lithium (4) and samarium reagents (5) as well as the Ramberg–Bäcklund reaction (6). The sulfone has also been used, rather infrequently, as a leaving group for *O*-glycosylations (7). It was a surprise to us that the anomeric effect of sulfones had not been observed earlier (8). In this paper, experiments that show a large anomeric effect for sulfones are described.

Results and discussion

In our work on applying the Ramberg–Bäcklund reaction to carbohydrate anomeric sulfones, we observed that the α–β ratio of unreacted sulfones **1** and **2** recovered from the basic reaction mixture was not the same as the starting ratio, with the amount of α-isomer enhanced (eq. [1]). This observation could be explained in two ways: (*i*) the β-isomer was reactive whereas the α was not; and (or) (*ii*) the β-isomer was isomerizing to the α-isomer. These two explanations were easily verified. When pure α-isomer **1** was subjected to the Ramberg–Bäcklund conditions, no reaction was observed, consistent with the former explanation; however, when pure β-isomer **2** was subjected to the same conditions, the α-isomer was recovered along with Ramberg–Bäcklund product **3**. These reaction conditions were not an equilibration. The sulfones were, therefore, equilibrated with *t*-BuOK–benzene with no brominating agent present. The equilibrium ratio of β–α achieved in both directions was 57:43. This corresponds to an apparent *A*-value of 0.167 kcal mol^{-1} for the dodecyl sulfone group. Simpler tetrahydropyranyl phenyl sulfones **4**–**7** (eq. [2]) gave similar results (Table 1),

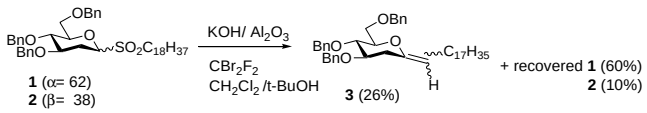

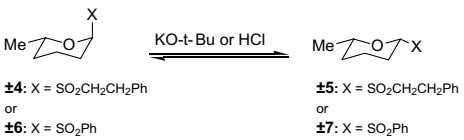

although a different *A*-value was recorded, presumably because of the absence of the electronegative substituents found in **1** and **2**. Tetrahydropyranyl phenethyl sulfones **4** and **5** failed to equilibrate under basic conditions. We assumed that proton exchange was not occurring at the anomeric carbon but at the α′-carbon of the phenethyl group. Thus, we turned to acid-catalyzed equilibration (Table 2). Both the phenyl and phenethyl sulfones gave similar *A*-values,

Received 7 January 2002. Published on the NRC Research Press Web site at http://canjchem.nrc.ca on 8 July 2002.

Dedicated to the memory of Professor Raymond U. Lemieux.

G. Chen, R.W. Franck,[1] G. Yang, and M. Blumenstein. Department of Chemistry, Hunter College, 695 Park Ave., New York City, NY 10021, U.S.A.

[1]Corresponding author (e-mail: rfranck@hunter.cuny.edu).

 DOI: 10.1139/V02-095 © 2002 NRC Canada

Table 1. Sulfone isomerizations via basic conditions.

Entry	Starting material	*T* (°C)	Time	Ratio (*trans*/*cis*)	$\Delta G°$ (kcal mol^{-1})
1	(±)-**6**	85	20 h	1:2.52	−0.658
			5 d	1:2.34	−0.605
2	(±)-**7**	85	20 h	1:5.65[a]	—
			5 d	1:2.52	−0.658
3	(±)-**5**	75	5 d	Only *cis*-isomer[b]	—
4	(±)-**4**/(±)-**5** (1:1.32)	75	5 d	1:1.28[b]	—

[a]No equilibrium obtained.
[b]No obvious isomerization detected.

Table 2. Sulfone isomerizations via acidic conditions.

Entry	Starting material	Conditions	*T* (°C)	Time	Ratio (*trans*/*cis*)	$\Delta G°$ (kcal mol^{-1})
1	(±)-**4**	$CDCl_3$ (0.5 mL)	4	7 w	1:3.84	0.741
2	(±)-**4**/(±)-**5** (1:1.32)	$CDCl_3$ (1 mL), TMSCl (1.5 μL), *t*-BuOH (2 μL)	RT	2 w	1:3.62	0.762
3	(±)-**6**	$CDCl_3$ (0.5 mL)	4	3 w	1:1.27[a]	—
		$CDCl_3$ (1 mL), TMSCl (1.5 μL), *t*-BuOH (2 μL)	RT	2 w	1:3.18	0.685
4	(±)-**6**/(±)-**7** (1:2.52)	$CDCl_3$ (1 mL), TMSCl (12.5 μL), *t*-BuOH (10 μL)	RT	2 d	1:3.15	0.679

[a]No equilibrium obtained.

Scheme 1. Reagents and conditions: (*a*) MMPP, DMF, RT, 70%; (*b*) DiBAL, DCM, –78°C, 111% (raw yield); (*c*) Ac_2O, Et_3N, 4-DMAP, 0°C → RT, 73% (3 steps); (*d*) phenylethanethiol, K-10, benzene, RT, 78%; (*e*) MMPP, THF–H_2O–EtOH (4:4:1), 0°C, 1 h, 95%; (*f*) $NaSO_2Ph$, TFA, DCM, 78%.

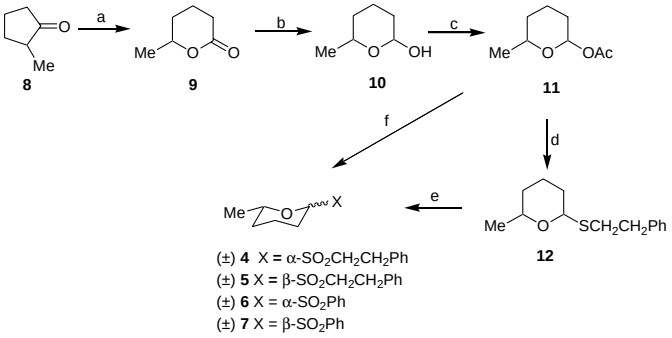

and in the former case, the acid- and base-catalyzed isomer ratios were in good agreement.

The apparent size of the sulfone group was observed by a different method. Thus, *trans*-sulfones **4** and **6** were observed to exist in conformations where the sulfones were axial and the methyls were equatorial. Low-temperature NMR experiments (–110°C) did not succeed in producing spectra that displayed resolved peaks for each of the two possible chair conformers. Only a slight decreased in the $J_{5a,6a}$ value (10.6 Hz) for **6** compared with the value of isomer **7** (11.0 Hz), where the methyl is 100% equatorial, suggests the presence of the flipped-conformer of **6**.

The evaluation of an anomeric effect for a substituent group requires a comparison of the apparent size of the group in an axial position in cyclohexane (where there can be no effect) to its apparent size in tetrahydropyran where an effect may be revealed. The *A*-value for CH_3 in cyclohexane is 1.8 kcal mol^{-1}, while that for SO_2CH_3 is 2.5 kcal mol^{-1} (9). Thus, in cyclohexane, sulfone is larger than methyl by 0.7 kcal mol^{-1}. From the equilibration and conformational

Scheme 2. Reagents and conditions: (*a*) $Ph_3P{\cdot}HBr$, H_2O, ether, 81% (*b*) $CH_3OCH_2CO_2H$, DCC, ether, 87% (*c*) $Yb(OTf)_3$, $C_{18}H_{37}SH$, CH_3CN, 60°C, 89% (*d*) MMPP, 95%.

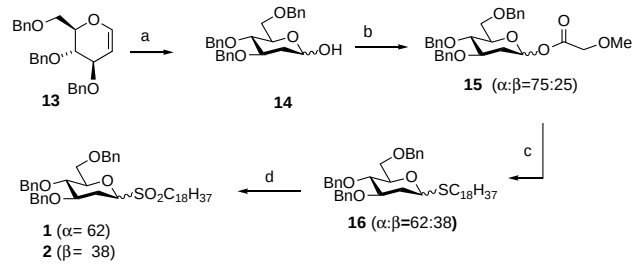

data of the simple methyl tetrahydropyranyl sulfones we have studied, the sulfone appears to be smaller than methyl. We estimate that the apparent *A*-value for the sulfonyl group is 0.7 kcal mol^{-1}. If we assume that the sulfone *A*-value in tetrahydropyran, in the absence of an anomeric effect, should be equal to 2.5 kcal mol^{-1} (the same as the cyclohexane value) then the anomeric effect for the sulfone is $2.5_{predicted} - 0.7_{obsd} = 1.8$ kcal mol^{-1}. It is known, however, that the apparent size of axial groups in tetrahydropyran is larger than in cyclohexanes. We have proposed a correction factor of 1.5 in converting a cyclohexane *A*-value to that for a tetrahydropyran. This factor has been derived by comparison of the *A*-value of CH_3 (1.8) in cyclohexane to that of 2.7 at C-2 in tetrahydropyran (10). Hence the sulfone *A*-value could be as high as $2.5 \times 1.5 = 3.75$ kcal mol^{-1}, which leads to an anomeric effect of $3.75_{predicted} - 0.7_{obsd} = 3.05$ kcal mol^{-1}. In either case, the anomeric effect in favor of an axial sulfone is approximately 70% of the steric effect favoring the equatorial conformer. Hence, in the parent phenylsulfonyl tetrahydropyran itself, the group will appear to be equatorial. This is a different situation from the oxygen anomeric effect, which although a smaller force, overrides an equivalent or somewhat smaller steric effect. It is therefore possible to detect significant amounts of axial anomeric oxygen species in the parent tetrahydropyran under equilibrium

© 2002 NRC Canada

circumstances. Clearly, in the one carbohydrate sulfone we have examined, the anomeric effect is even larger than in the simple cases. Further experiments on a family of carbohydrate sulfones are planned.

Experimental

General methods

^{1}H NMR spectra were recorded on GE QE 300, JEOL FX 400, and Varian 500 spectrometers. Chemical shifts are reported in ppm relative to internal tetramethylsilane (δ = 0.00), chloroform (δ = 7.26), methanol (δ = 3.31), or tetrahydrofuran (δ = 3.58). Coupling constants (*J*) are given in Hertz (Hz). Multiplicities are described by using the following abbreviations: s = singlet; d = doublet; t = triplet; q = quartet; m = multiplet; br = broad. ^{13}C NMR spectra were recorded on GE QE 300 and JEOL FX 400 spectrometers. Chemical shifts are reported in ppm relative to internal standards chloroform (δ = 77.0), acetone (δ = 29.8), or tetrahydrofuran (δ = 67.6). Multiplicities refer to the resonance in the off-resonance spectra and were elucidated using the distortionless enhancement by polarization transfer (DEPT) spectral editing technique, with secondary pulses at 90° and 135°. Coupling constants ($^1J_{C,H}$) are described by using the following abbreviations: s = singlet (due to quaternary carbon); d = doublet (methine); t = triplet (methylene); q = quartet (methyl). Mass spectra were obtained on Agilent Techologies 1100 LC/MSD instrument using electrospray ionization (ESI) mode. Ion mass (*m*/*z*) signals are reported as values in atomic mass units followed, in parentheses, by peak intensities relative to the base peak (100%). Elution of all reactions were monitored by analytical thin layer chromatography (TLC) using silica gel 60 PF^{254} precoated plates (E. Merck), and spots were detected either by UV-absorption or by charring with H_2SO_4–4-methoxybenzaldehyde in methanol or ethanol — R_f values are also given under these conditions. Flash column chromatography was performed using E. Merck silica gel 60 (230–400 mesh). Unless otherwise stated, all commercially available chemicals were used without further purification, but some reagents were dried under vacuum before use. All reactions involving air- and (or) moisture-sensitive reagents were performed under nitrogen atmosphere with dry, freshly distilled solvents using standard syringe–cannula/septa techniques. All solvents were dried by usual methods and stored under nitrogen atmosphere in the dark in well-stoppered bottles. The synthesis of the starting sulfones, illustrated in Schemes 1 and 2, were routine and used known methods.

Oxidation of 2-methylcyclopentanone (8) for synthesis of lactone 9 (11)

To a solution of 2-methylcyclopentanone (8) (3.688 g, 37.6 mmol) in DMF (40 mL) was added MMPP (80%, 35 g, 56.6 mmol, 1.5 equiv). The slightly green suspension was stirred at RT overnight and became a white sticky mixture, whereupon TLC (PE–EE, 1:1) indicated that the oxidation was complete. The mixture was diluted with CH_2Cl_2 (40 mL) and washed with aqueous HCl (2 N, 2 × 30 mL). The combined organic phases were further washed with a saturated solution of $NaHCO_3$ (2 × 30 mL) and water (5 × 30 mL). After drying over Na_2SO_4, the solvent was evaporated under reduced pressure to afford a crude product, which was employed for the next step without further purification. Yield: 3.023 g (26.5 mmol, 70%); R_f = 0.48 (silica gel, PE–EE, 1:1); light yellow oil. ^{1}H NMR (300 MHz, $CDCl_3$) δ: 4.47 (m, 1H, 5-H), 2.67–2.53 (m, 1H, 2-H), 2.52–2.38 (m, 1H, 2-H′), 1.92–1.45 (m, 4H, 2 × 3-H and 2 × 4-H), 1.40 (d, *J* = 6.2 Hz, 3H, 6-H).

6-Methyltetrahydropyran-2-ol (10) (12)

To a stirred solution of lactone **9** (230 mg, 2.0 mmol) in dry CH_2Cl_2 (15 mL) at –78°C was added a solution of *i*-Bu_2AlH in hexane (1.0 M, 4.0 mL, 4.0 mmol, 2.0 equiv). The mixture was allowed to stir for 2 h, at which time TLC indicated that the reduction was clean and complete. The reaction was quenched by careful addition of MeOH (5 mL) and warmed to ambient temperature, whereupon it was treated with a saturated aqueous solution of Rochelle's salt (15 mL) and was allowed to stir for about 2 h until the phases clearly separated. The aqueous phase was extracted with CH_2Cl_2 (3 × 6 mL) and the combined organic phases were dried over Na_2SO_4. Evaporation of the solvents under reduced pressure afforded the crude lactol **10** in a *trans–cis* ratio of 1:1.7. Yield: 258 mg (2.2 mmol, >99%); R_f = 0.60 (silica gel, PE–EE, 1:1); brown yellow oil. ^{1}H NMR (300 MHz, $CDCl_3$) δ: 5.30 (br s, 1H, 2-H of *trans*), 4.72 (dd, *J* = 9.5, 2.2 Hz, 1H, 2-H of *cis*), 3.58 (dqd, *J* = 11.2, 6.2, 2.2 Hz, 1H, 6-H of *trans*), 3.88 (br s, 1H, OH of *cis*), 3.60 (dqd, *J* = 11.2, 6.2, 2.2 Hz, 1H, 6-H of *cis*), 3.25 (br s, 1H, OH of *trans*), 2.00–1.20 (m, 12H, 3 × CH_2 of *cis* and 3 × CH_2 of *trans*), 1.22 (d, *J* = 6.2 Hz, 3H, Me of *cis*), 1.13 (d, *J* = 6.2 Hz, 3H, Me of *trans*).

Acetylation of lactol 10

6-Methyltetrahydropyran-2-ol (**10**) (crude product, ca. 26.5 mmol) was dissolved under nitrogen in $DCM_{abs.}$ (60 mL). To this solution were added triethylamine (5.3 mL, 2 equiv) and acetic anhydride (7.2 mL, 2 equiv). After addition of a catalytic amount of 4-DMAP (64 mg, 0.02 equiv) the mixture was allowed to stir at RT for 1 h, whereupon TLC (PE–EE, 4:1) showed that the acetylation was complete. The mixture was concentrated in controlled vacuo to afford a crude product **11**, which, according to NMR, was so clean that further purification was not necessary. Yield: 4.311 g (27.3 mmol, 73% over 3 steps, *trans–cis* = 1:6.8); R_f = 0.78 (silica gel, PE–EE, 4:1); brown yellow oil with sweet odor. ^{1}H NMR (300 MHz, $CDCl_3$) δ: 6.09 (br s, 1H, 2-H of *trans*), 5.61 (dd, *J* = 9.3, 2.3 Hz, 1H, 2-H of *cis*), 3.90 (dqd, *J* = 11.0, 6.3, 1.8 Hz, 1H, 6-H of *trans*), 3.63 (dqd, *J* = 11.0, 6.0, 2.2 Hz, 1H, 6-H of *cis*), 2.06 (s, 3H, CH_3CO of *cis*), 2.04 (s, 3H, CH_3CO of *trans*), 1.90–1.29 (m, 12H, 3 × CH_2 of *cis* and 3 × CH_2 of *trans*), 1.19 (d, *J* = 5.86 Hz, 3H, Me of *cis*), 1.10 (d, *J* = 6.2 Hz, 3H, Me of *trans*). ^{13}C NMR of *cis*-isomer (75 MHz, $CDCl_3$) δ: 169.1 (s, *C*OCH_3), 94.7 (d, O*C*HOAc), 73.2 (d, *C*HOCHOAc), 31.9, 29.7, 21.7 (3t, 3 × CH_2), 21.5, 21.2 (2q, CO*C*H_3 and CH_3).

Synthesis of thioglycoside 12 (13)

To a solution of lactol acetate **11** (1.824 g, 11.5 mmol) and benzeneethanethiol (1.547 mL, 1.0 equiv) in dry benzene (80 mL) was added montmorillonite K-10 (3 g). The mixture was stirred at RT for 2 h, whereupon TLC (PE–EE,

© 2002 NRC Canada

20:1) showed that the thioglycosylation was complete. After filtration with suction, the solid residue was washed with DCM. The combined filtrates were evaporated in vacuo to afford a crude product, which was purified and partially separated by flash chromatography on silica gel (PE–EE, 20:1). Yield: 2.131 g (9.0 mmol, 78%).

trans-Isomer: R_f = 0.46 (silica gel, PE–EE, 20:1). ^{1}H NMR (300 MHz, $CDCl_3$) δ: 7.35–7.15 (m, 5H, Ph), 5.37 (d, *J* = 5.1 Hz, 1H, 2-H), 4.19 (dqd, *J* = 11.0, 6.2, 2.2 Hz, 1H, 6-H), 2.98–2.75 (m, 4H, CH_2CH_2Ph), 2.00–1.22 (m, 6H, 2 × 3-H, 2 × 4-H, and 2 × 5-H), 1.17 (d, *J* = 6.2 Hz, 3H, Me). ^{13}C NMR (75 MHz, $CDCl_3$) δ: 140.7 (s, Ph-C1), 128.4, 128.2 (2d, Ph-C2,6 and Ph-C3,5), 126.1 (d, Ph-C4), 81.9 (d, O*C*HOCH$_2$CH$_2$Ph), 64.8 (d, *C*HOCHOCH$_2$CH$_2$Ph), 36.7, 33.3, 32.0, 30.3, 19.6 (5t, 5 × CH_2), 21.7 (q, CH_3).

cis-Isomer: R_f = 0.40 (silica gel, PE–EE, 20:1). ^{1}H NMR (300 MHz, $CDCl_3$) δ: 7.30–7.14 (m, 5H, Ph), 4.47 (dd, *J* = 11.0, 2.2 Hz, 1H, 2-H), 3.46 (dqd, *J* = 11.0, 6.2, 1.8 Hz, 1H, 6-H), 3.02–2.84 (m, 4H, CH_2CH_2Ph), 1.92–1.10 (m, 6H, 2 × 3-H, 2 × 4-H, and 2 × 5-H), 1.22 (d, *J* = 6.2 Hz, 3H, Me). ^{13}C NMR (75 MHz, $CDCl_3$) δ: 140.8 (s, Ph-C1), 128.4, 128.3 (2d, Ph-C2,6 and Ph-C3,5), 126.1 (d, Ph-C4), 82.6 (d, O*C*HOCH$_2$CH$_2$Ph), 75.0 (d, *C*HOCHOCH$_2$CH$_2$Ph), 36.8, 32.6, 31.8, 31.5, 24.4 (5t, 5 × CH_2), 22.1 (q, CH_3). ES-MS *m*/*z* (%): 254.2 (100) $[M + NH_4]^+$; 498.2 (25) $[2M + NH_4]^+$; 263.1 (70) $[M + Na]^+$; 503.2 (18) $[2M + Na]^+$.

Oxidation of thioglycoside for syntheses of anomeric sulfones (±)-4 and (±)-5 (14)

The isomeric mixture of thioglycosides (±)-**12** (1.076 g, 4.0 mmol) was dissolved in a mixed solvent (54 mL, THF–H_2O–EtOH, 4:4:1) and to it at 0°C was added MMPP (7.9 g, 2.5 equiv). The mixture was allowed to stir at 0°C for 1 h, at which time TLC (PE–EE, 6:1) indicated the completion of the oxidation. The mixture was neutralized with a saturated solution of $NaHCO_3$ (30 mL). The aqueous phase was extracted with DCM (3 × 20 mL). The combined organic phases were dried over Na_2SO_4. Evaporation of the solvent in vacuo afforded a crude product, which was subsequently purified by flash chromatography (PE–EE, 8:1 to 5:1) to afford the pure title phenylethylsulfone of both (±)-**4** (*trans*) and (±)-**5** (*cis*) in a ratio of 2:3. Yield: 1.16 g (4.32 mmol, 95%). Pure *trans*-sulfide (60 mg, 0.254 mmol) was oxidized according to the same procedure. After work-up and flash chromatography pure *trans*-anomeric sulfone (±)-**4** was obtained (yield: 64 mg, 0.239 mmol, 94%) without observing any isomerization at the anomeric position under the oxidation conditions.

(±)-**4**: R_f = 0.40 (silica gel, PE–EE, 6:1). ^{1}H NMR (300 MHz, $CDCl_3$) δ: 7.42–7.22 (m, 5H, Ph), 4.73 (dd, *J* = 6.2, 2.2 Hz, 1H, 2-H), 4.48 (dqd, *J* = 10.4, 6.2, 2.2 Hz, 1H, 6-H), 3.40–3.12 (2m, 4H, CH_2CH_2Ph), 2.15–1.21 (m, 6H, 2 × 3-H, 2 × 4-H, and 2 × 5-H), 1.23 (d, *J* = 6.2 Hz, 3H, Me). ^{13}C NMR (75 MHz, $CDCl_3$) δ: 140.7 (s, Ph-C1), 128.0, 127.6 (2d, Ph-C2,6 and Ph-C3,5), 126.1 (d, Ph-C4), 86.3 (d, O*C*HSO$_2$CH$_2$CH$_2$Ph), 68.9 (d, *C*HOCHSO$_2$CH$_2$CH$_2$Ph), 50.7 (t, SO$_2$*C*H$_2$CH$_2$Ph), 30.9, 27.2, 20.1, 17.8 (4t, 4 × CH_2), 20.9 (q, CH_3). ES-MS *m*/*z* (%): 286.2 (100) $[M + NH_4]^+$; 554.2 (9) $[2M + NH_4]^+$; 291.1 (38) $[M + Na]^+$; 559.2 (8) $[2M + Na]^+$.

(±)-**5**: R_f = 0.26 (silica gel, PE–EE, 6:1). ^{1}H NMR (300 MHz, $CDCl_3$) δ: 7.45–7.25 (m, 5H, Ph), 4.25 (dd, 1H, *J* = 11.4, 2.2 Hz, 2-H), 3.52–3.42 (m, 2H, 6-H and SO$_2$C*H*H), 3.32 (m, 1H, SO$_2$CH*H*), 3.18 (m, 2H, CH_2Ph), 2.10–1.28 (m, 6H, 2 × 3-H, 2 × 4-H, and 2 × 5-H), 1.26 (d, *J* = 6.3 Hz, 3H, Me). ^{13}C NMR (75 MHz, $CDCl_3$) δ: 140.8 (s, Ph-C1), 128.7, 128.5 (2d, Ph-C2,6 and Ph-C3,5), 126.9 (d, Ph-C4), 90.3 (d, O*C*HSO$_2$CH$_2$CH$_2$Ph), 76.1 (d, *C*HOCHSO$_2$CH$_2$CH$_2$Ph), 50.0 (SO$_2$*C*H$_2$CH$_2$Ph), 27.8 (SO$_2$CH$_2$*C*H$_2$Ph), 32.2, 22.3, 21.9 (3t, 3 × CH_2), 21.8 (q, CH_3). ES-MS *m*/*z* (%): 286.2 (100) $[M + NH_4]^+$; 554.2 (9) $[2M + NH_4]^+$; 559.2 (23) $[2M + Na]^+$; 291.1 (100) $[M + Na]^+$; 559.2 (26) $[2M + Na]^+$.

Preparation of phenylsulfone (±)-6 and (±)-7 (15)

Lactol acetate **11** (50 mg, 0.32 mmol) was dissolved in dry DCM (15 mL) and to it was added sodium benzenesulfinate (109 mg, 0.66 mmol, 2 equiv). After addition of trifluoroacetic acid (0.1 mL, 4 equiv) the mixture was allowed to stir for 4 h at RT, whereupon TLC (PE–EE, 4:1) indicated the completion of the reaction. The mixture was diluted with DCM (15 mL) and then decanted into a saturated solution of $NaHCO_3$ (30 mL). The organic phase was washed once with water (20 mL) and dried over Na_2SO_4. Evaporation of the solvent in vacuo gave a crude product, which was subsequently purified by flash chromatography (PE–EE, 4:1) to afford each pure title phenylsulfone (±)-**6** and (±)-**7** Yield: 59 mg (0.246 mmol, 78%, *trans*-(±)-**6**–*cis*-(±)-**7** = 2:1, separable).

(±)-**6**: R_f = 0.30 (silica gel, PE–EE, 6:1); amorphous solid. ^{1}H NMR (300 MHz, $CDCl_3$) δ: 7.90–7.40 (m, 5H, Ph), 4.38 (dd, *J* = 6.6, 1.5 Hz, 1H, 2-H), 3.45 (dqd, *J* = 10.6, 6.2, 2.3 Hz, 1H, 6-H), 2.10–1.29 (m, 6H, 2 × 3-H, 2 × 4-H, and 2 × 5-H), 1.19 (d, *J* = 6.2 Hz, 3H, Me). ^{13}C NMR (75 MHz, $CDCl_3$) δ: 133.6 (s, Ph-C1), 129.0, 128.6 (2d, Ph-C2,6 and Ph-C3,5), 128.8 (d, Ph-C4), 92.1 (d, O*C*HSO$_2$Ph), 69.6 (d, *C*HOCHSO$_2$Ph), 32.2, 23.6, 18.6 (3t, 3 × CH_2), 21.6 (q, CH_3).

(±)-**7**: amorphous solid; R_f = 0.22 (silica gel, PE–EE, 6:1). ^{1}H NMR (300 MHz, $CDCl_3$) δ: 7.90–7.40 (m, 5H, Ph), 4.73 (dd, *J* = 11.0, 2.2 Hz, 1H, 2-H), 4.60 (dqd, *J* = 11.0, 6.2, 2.2 Hz, 1H, 6-H), 2.20–1.29 (m, 6H, 2 × 3-H, 2 × 4-H, and 2 × 5-H), 1.13 (d, *J* = 6.2 Hz, 3H, Me). ^{13}C NMR (75 MHz, $CDCl_3$) δ: 133.5 (s, Ph-C1), 129.6, 128.7 (2d, Ph-C2,6 and Ph-C3,5), 128.8 (d, Ph-C4), 90.6 (d, O*C*HSO$_2$Ph), 74.5 (d, *C*HOCHSO$_2$Ph), 31.8, 22.5, 21.9 (3t, 3 × CH_2), 21.6 (q, CH_3). ES-MS *m*/*z* (%): 258.2 (100) $[M + NH_4]^+$; 498.2 (25) $[2M + NH_4]^+$; 263.1 (70) $[M + Na]^+$; 503.2 (18) $[2M + Na]^+$.

Isomerization

Initially, isomerization was carried out under basic conditions. Molecules *trans*-(±)-**6** and *cis-(±)-***7** were separately dissolved in dry benzene (2 mL). After addition of *t*-BuOK (10 mg) the solution was isomerized by heating at reflux for 5 days, whereupon the equilibrium was achieved according to the NMR analysis. isomerizations with compounds (±)-**4** and (±)-**5** were done under the similar conditions (*t*-BuOK); however, no isomerization was detected after heating at reflux for 5 days by NMR analysis. (Table 1).

Interestingly, after *trans*-isomer (±)-**4** was stored in $CDCl_3$ in the refrigerator for 3 weeks isomerization was observed,

© 2002 NRC Canada

although equilibrium was not reached. Similarly *trans*-isomer (±)-**6** was isomerized and reached equilibrium after storing in deuterated chloroform in a refrigerator for 7 weeks. Compound (±)-**6** was also stored in THF-d_6 in the refrigerator for 10 weeks; however, according to the NMR analysis, no isomerization was detected.

Acidic isomerization was preformed in NMR tubes at RT by treatment with small amounts of TMSCl and *t*-BuOH. The equilibrium ratios are given in Table 2.

2-Deoxyglucose series

In our synthesis, benzylated thioglycoside **16** was made from benzylated 2-deoxyglucose derivative **15** via the Inanaga–Yb(OTf)$_3$ method (16). Sulfide **16** was oxidized using MMPP to form sulfone **1**,**2** in good yield.

Tri-*O*-benzyl-2-deoxyglucose (14)

To a mixture of **13** (2.083 g, 5 mmol) and THF (15 mL) was added $Ph_3P{\cdot}HBr$ (0.0858 g, 0.25 mmol). The solution was stirred at RT for 10 min, then H_2O was added (0.135 mL, 0.017mol). This mixture was stirred at RT for 3 h. The mixture was treated with saturated $NaHCO_3$ solution (5 mL) and H_2O (10 mL) and extracted with EtOAc (3 × 20 mL). The organic phase was washed by brine, dried over Na_2SO_4, and concentrated. The residue was chromatographed on a column of 100 g silica gel (eluted with 30% EtOAc–petroleum ether) to afford 1.78 g of **14** (81%). ^{1}H NMR ($CDCl_3$, 300 MHz) δ: 7.20–7.30 (m, 15H), 5.41 (d, J = 2.3 Hz, 1H), 4.90 (dd, J = 6.4, 3.0 Hz, 1H), 4.80 (m, 6H), 4.05 (m, 1H), 3.60 (m, 2H), 2.85 (s, 1H, OH), 2.32 (m, 1H), 1.70 (m, 1H).

Tri-*O*-benzyl-2-deoxy-1-*O*-methoxyacetylglucose (15)

To a mixture of 2-deoxyglucose **14** (0.194 mL, 2.53 mmol) and ether (20 mL) was added DCC (0.522 g, 2.53 mmol). The mixture was stirred at RT for 10 min, then methoxyacetic acid (1.10 g, 2.3 mmol) was added, followed by 4-pyrrolidinopyridine (0.034 g, 0.23 mmol). After standing overnight, the solution was filtered to remove the solid phase, and then it was washed with brine (50 mL). The aqueous phase was extracted with ether (3 × 20 mL), dried over Na_2SO_4, and concentrated. The residue was chromatographed on a column of 50 g of silica gel (eluted with 20% EtOAc–petroleum ether) to afford 0.110 g of **15** as a colorless oil (87%, α:β = 3:1). ^{1}H NMR ($CDCl_3$, 300 MHz) δ: 7.20–7.30 (m, 15H), 6.30 (d, J = 2.7 Hz, 1H), 5.77 (dd, J = 10.5, 2.7 Hz, 1H), 4.88 (m, 1H), 4.60 (m, 6H), 3.98 (s, 2H), 3.41 (s, 3H, OMe), 2.35 (m, 1H), 1.85 (m, 1H).

Thioglycoside (16)

A solution of **15** (0.358 g, 0.707 mmol) and octadecyl mercaptan (0.263 g, 0.919 mmol) in dry acetonitrile (10 mL) was warmed to 53°C (bath temp) under nitrogen, and to this mixture was added a solution of Yb(OTf)$_3$ in acetonitrile (5 mmol L^{-1}, 0.71 mL, 0.5 mol%). After stirring for 2 h, the reaction was quenched with saturated $NaHCO_3$ solution (10 mL), and extracted by CH_2Cl_2 (3 × 20 mL). The organic phase was washed by H_2O, dried over Na_2SO_4, and concentrated. The residue was chromatographed on a column of 20 g of silica gel (eluted with 10% EtOAc–petroleum ether) to afford 0.442 g of **16** (89%, α:β = 8:5) as a white solid. Anal. calcd for $C_{45}H_{66}O_4S$: C 76.87, H 9.46, S 4.56; found: C 76.59, H 9.15, S 4.68.

α-Isomer: ^{1}H NMR ($CDCl_3$, 300 MHz) δ: 7.20–7.30 (m, 15H), 4.91–4.53 (m, 6H), 4.52–4.47 (dd, J = 1.5, 11.7 Hz, 1H), 3.78–3.63 (m, 3H), 3.53–3.40 (m, 2H), 2.70 (m, 2H), 2.34 (m, 1H), 1.75 (m, 1H), 1.60 (m, 2H), 1.20 (s, 30H), 0.88 (t, 3H). ^{13}C NMR ($CDCl_3$, 75 MHz) δ: 139.22, 139.15, 138.80, 129.03, 128.94, 128.50, 128.46, 128.35, 128.23, 81.34, 79.31, 78.85, 75.63, 74.17, 72.55, 71.72, 69.72, 36.75, 36.74, 31.79, 30.51, 30.36, 30.16, 30.03, 29.75, 23.51, 14.94.

β-Isomer: ^{1}H NMR ($CDCl_3$, 300 MHz) δ: 7.35–7.21 (m, 15H), 5.45 (d, J = 5.1 Hz, 1H), 4.92–4.49 (m, 6H), 4.19 (m, 1H), 3.95 (m, 1H), 3.83 (dd, J = 3.67, 11.0 Hz, 1H), 3.66 (m, 2H), 2.53 (m, 2H), 2.30 (dd, J = 4.76, 13.19 Hz, 1H), 2.08 (m, 1H), 1.59 (m, 2H), 1.35 (s, 30H), 0.91 (t, 3H).

Sulfone 2

A solution of MMPP (0.227 g, 0.45 mmol) in H_2O (2 mL) was added to a solution of **16** (β-isomer, 0.112 g, 0.159 mmol) in EtOH (2 mL) and THF (2 mL), and the mixture was kept at 55°C for 2 h. The mixture was concentrated to dryness in vacuo. The residue was treated with saturated $NaHCO_3$ solution (10 mL), and extracted with EtOAc (3 × 15 mL), dried over Na_2SO_4, and evaporated to dryness. The residue was purified by chromatography on silica gel (eluted with 25% EtOAc–petroleum ether) to afford pure sulfone **2** (β-isomer) as a white solid 0.11 g (95%). MS calcd. for $C_{45}H_{66}O_6S$: 734; found: 757 ([M + Na]$^+$). When the identical reaction was carried out with the (isomer of **16** as starting material, the α-sulfone **1** was afforded.

α-Isomer: mp 58–60°C. ^{1}H NMR ($CDCl_3$, 300 MHz) δ: 7.20–7.30 (m, 15H), 4.84 (dd, J = 7.0, 3.3 Hz, 1H, H-1), 4.80–4.45 (m, 6H, OCH_2Ph), 4.37 (m, 1H, H-5), 4.20 (m, 1H, H-3), 3.68 (d, J = 3.3 Hz, 2H, H-6), 3.58 (dd, J = 7.2, 9.3 Hz, 1H, H-4), 3.06 (t, 2H), 2.82 (m, 1H, H-2e), 2.06 (m, 1H, H-2a), 1.30 (s, 30H), 0.90 (t, 3H). ^{13}C NMR ($CDCl_3$, 75 MHz) δ: 138.78, 138.71, 138.53, 129.10, 129.02, 128.97, 128.44, 128.37, 128.308, 86.67, 77.53, 76.59, 75.62, 74.76, 74.06, 72.76, 69.73, 50.51, 32.73, 30.50, 30.32, 30.16, 30.08, 29.84, 29.39, 26.31, 23.50, 22.44, 14.93.

β-Isomer: mp 87–88°C. ^{1}H NMR ($CDCl_3$, 300 MHz) δ: 7.34–7.20 (m, 15H), 4.95–4.50 (m, 6H, OCH_2Ph), 4.30 (dd, J = 11.0, 3.0 Hz, 1H, H-1), 3.76–3.51 (m, 5H), 3.60 (t, 2H), 2.65 (m, 1H, H-2e), 1.88 (m, 1H, H-a), 1.27 (s, 30H), 0.88 (t, 3H). ^{13}C NMR ($CDCl_3$, 75 MHz) δ: 137.60, 137.55, 137.32, 128.04, 127.92, 127.60, 127.38, 127.29, 127.19, 127.13, 96.90, 86.78, 79.70, 78.99, 76.78, 74.80, 72.89, 71.02, 68.60, 48.86, 31.47, 29.23, 29.06, 28.89, 28.83, 28.59, 28.15, 27.42, 22.22, 20.75, 13.64.

Isomerization of the α,β isomers of 1 and 2

To a solution of β-sulfone **2** (12 mg, 0.016 mmol) in benzene (1 mL) and *t*-BuOH (0.2 mL) was added *t*-BuOK (10 mg, 0.107 mmol). The reaction mixture was refluxed at 70°C for 24 h. The mixture was diluted by dichloromethane, filtered, and dried in vacuo. The α:β ratio (36:64) was determined by the H-1 peak in ^{1}H NMR.

To a solution of α-sulfone **1** (12 mg, 0.016 mmol) in benzene (1 mL) and *t*-BuOH (0.2 mL) was added *t*-BuOK (10 mg, 0.107 mmol). The reaction mixture was refluxed at

© 2002 NRC Canada

70°C for 24 h. The mixture was diluted by dichloromethane, filtered, and dried in vacuo. The α:β ratio (53:47) was determined by ^{1}H NMR analysis.

To a solution of sulfone **1**,**2** (α:β = 3:1) (20 mg, 0.027 mmol) in THF (5 mL), *t*-BuOH (1 mL), and KOH–Al_2O_3 (20 mg, 50% (by weight), 0.107 mmol) was added crown ether-18 (0.2 equiv). The reaction mixture was heated at reflux (52°C) for one week. The mixture was diluted by dichloromethane, filtered, and dried in vacuo. The α:β ratio (42:58) was determined by the H-1 peak in ^{1}H NMR.

Pure α-sulfone **1** was treated under the above conditions. The α:β ratio (44:56) was determined by ^{1}H NMR.

Acknowledgments

This research was supported by an NIH grant GM60271. The Chemistry Department infrastructure is supported by an NIH RCMI grant RR03037. We thank Martin Olivieri, supported at Hunter College by the Research Corporation Partners in Science Award HS0590, and Dr. J. Edgar Anderson of University College, London for preliminary experiments and data collection in search of compounds that exhibit the sulfone anomeric effect.

References

1. J.T. Edward. *In* The anomeric effect and associated stereoelectronic effects. ACS Symposium Series 539. *Edited by* G.R.J. Thatcher. American Chemical Society, Washington D.C. 1993. pp. 1–5.
2. D.S. Brown, M. Bruno, R.J. Davenport, and S.V. Ley. Tetrahedron, **45**, 4293 (1989).
3. J.-M. Beau and P Sinaÿ. Tetrahedron Lett. **26**, 6193 (1985).
4. (*a*) J.-M. Beau and P Sinaÿ. Tetrahedron Lett. **26**, 6185 (1985); (*b*) J.-M. Beau and P. Sinaÿ. Tetrahedron Lett. **26**, 6189 (1985).
5. O. Jarreton, T. Skrydstrup, J.-F. Espinosa, J. Jiménez-Barbero, and J.-M. Beau. Chem. Eur. J. **5**, 430 (1999), and refs. therein.
6. (*a*) P. Pasetto, X. Chen, C.M. Drain, and R.W. Franck. Chem. Commun. 81, (2001), and refs. therein; (*b*) G. Yang, R.W. Franck, R. Bittman, P. Samadder, and G. Arthur. Org. Lett. **3**, 197 (2001); (*c*) R.J.K. Taylor, F.K. Griffin, and D.E. Paterson. Angew. Chem. Int. Ed. Eng. **38**, 2939 (1999), and refs. therein.
7. D.S. Brown, S.V. Ley, and S. Vile. Tetrahedron Lett. **29**, 4873 (1988).
8. An unusual effect of sulfones in the 5-position of dioxans has been observed, see: E. Juaristi. Introduction to stereochemistry and conformational analysis. John Wiley & Sons, New York. 1991. Chap. 16. p. 273.
9. C. Hackett Bushweller *In* Conformational analysis and stereochemistry of six-membered rings. *Edited by* E. Juaristi. Verlag Chemie, New York. 1995. Chap. 2. p. 25.
10. (*a*) E.L. Eliel, K.D. Hargrave, K.M. Pietrusiewicz, and M. Manoharan. J. Am. Chem. Soc. **104**, 3635 (1982); (*b*) R.W. Franck. Tetrahedron, **39**, 3251 (1983); (*c*) R.W. Franck. *In* Conformational aanalysis and stereochemistry of six-membered rings. *Edited by* E. Juaristi. Verlag Chemie, New York. 1995. Chap. 5. p. 157.
11. P. Brougham, M.S. Cooper, D.A. Cummerson, H. Heaney, and N. Thompson. Synthesis, 1015 (1987).
12. (*a*) D.J. Dixon, S.V. Ley, and E.W. Tate. J. Chem. Soc. Perkin Trans. 1, 2385 (2000); (*b*) V. Ragoussis and V. Theodorou. Synthesis, 84 (1993).
13. (*a*) J.-C. Florrent and C. Monneret. J. Chem. Soc. Chem. Commun. 1171 (1987); (*b*) G.-W. Chen. Ph.D. Thesis, Technical University of Clausthal, Clausthal-Zellenfeld, Germany, 2000. p. 29.
14. P. Belica. Ph.D. Thesis, Graduate School of the City University of New York, New York, 1999.
15. (*a*) A. Fischli and H. Mayer. Helv. Chim. Acta, **58**, 1584 (1975); (*b*) **58**, 1492 (1975).
16. J. Inanaga, Y. Tokoyama, and T. Hanamoto. Tetrahedron Lett. **34**, 2791 **(**1993).

© 2002 NRC Canada

Large-scale preparation of α-D-(1→4)-oligogalacturonic acids from pectic acid

Hong-Ni Fan, Mei-Zheng Liu, and Yuan C. Lee

Abstract: An efficient and inexpensive method for large-scale preparation of α-D-(1→4)-oligogalacturonic acids (oligo-GalA), up to DP 5, from pectic acid is described. Pectic acid was digested with a commercially available pectinase to yield a mixture of oligo-GalA, which was effectively separated by a combination of low-pressure – size-exclusion chromatography based on ion-exchange chromatography to obtain pure oligo-GalA of DP 2–5.

Key words: pectic acid, galacturonic acid, galabiose, galatriose, pectinase.

Résumé : On décrit une méthode efficace et peu coûteuse de préparation à grande échelle des acides α-D-(1→4)-oligogalacturoniques (oligo-GalA), jusqu'à 5 DP, à partir de l'acide pectique. L'acide pectique est soumis à une digestion avec une pectinase commercialement disponible pour conduire à un mélange d'oligo-GalA que l'on peut séparer efficacement par une combinaison de chromatographie d'exclusion de taille à basse pression et de chromatographie d'échange ionique pour obtenir les oligo-GalA de DP allant de 2 à 5.

Mots clés : acide pectique, acide galacturonique, galabiose, galatriose, pectinase.

[Traduit par la Rédaction]

Introduction

Pectic acid, derivable from an abundant plant polymer, pectin, is essentially composed of a repeating unit of α-(1→4)-linked D-galacturonic acid. α-D-(1→4)-Oligogalacturonic acids (oligo-GalA) have been shown to be physiologically active elicitors of plant-defense responses to pathogens (1). On the other hand, galabiose (α-Gal-(1→4)-Gal) has the same anomeric and positional linkages as the repeating unit of pectic acid, differing only by the presence of hydroxymethyl group rather than the carboxyl group at C-6. Galabiose is an important structural unit of some glycolipids, such as Gb3 and Gb4, and is the recognition marker for bacterial toxins (e.g., Shiga toxin and Shiga-like toxins) as well as for certain microbial invasions of human tissues, e.g., uropathogenic *Escherichia coli*, which causes hemorrhagic colitis and hemolytic uremic syndrome (2–6). Synthetic glycoconjugates containing the carbohydrate moiety of Gb_3 (globotriose, α-Gal-(1→4)-β-Gal-(1→4)-Glc) proved to be effective biomimetics for detecting and trapping of certain bacteria toxins and viruses (6–8). Galabiose has been prepared from pectic acid by first obtaining (α-GalA-(1→4)-α-GalA)$_n$ oligomers by partial digestion with pectinase followed by chemical reduction of the carboxylic groups (9–11). There are also some reports describing analysis, separation, and preparation of oligo-GalA with different degrees of polymerization (DP) (9–15). These methods, however, either require non-commercial enzymes, an expensive special ion-exchange resin, or preparative HPLC, and are not suitable for economical large-scale preparation of oligo-GalA. We wanted to prepare large amounts of galabiose and oligosaccharides containing galabiose by an inexpensive procedure, for the purpose of preparing high-affinity inhibitors for some toxins (e.g., Shiga toxin, Shiga-like toxins) and for certain pathogenic bacterial adhesion (16).

In this paper, we describe an efficient large-scale preparation of oligo-GalA (DP 2–5) from pectic acid by partial hydrolysis of pectic acid with a commercially available pectinase and a combination of inexpensive low-pressure column-chromatographic separation methods based on size exclusion and ion exchange.

Received 1 November 2001. Published on the NRC Research Press Web site at http://canjchem.nrc.ca on 5 July 2002.

Dedicated to the memory of Professor Raymond U. Lemieux.

H.-N. Fan, M.-Z. Liu, and Y.C. Lee.[1] Biology Department, 3400 N. Charles St., Johns Hopkins University, Baltimore, MD 21218, U.S.A.

[1]Corresponding author (e-mail: yclee@jhu.edu).

Materials and methods

Materials

Apple pectic acid was obtained from Sigma-Aldrich-Fluka (Milwaukee, WI). Pectinase from *Aspergillus niger* (EC 3.2.1.15), galacturonic acid (GalA), di- and tri-galacturonic acid ($(GalA)_2$ and $(GalA)_3$, respectively), Dowex-50 W × 8 resin (H^+ form, 200 mesh), Dowex-1 × 4 resin (400 mesh), and Sephadex G-25 were from Sigma (St. Louis, MO). Ultrafiltration membranes (YM3, NMWL 3 000) were from Millipore (Bedford, MA).

General methods

Analysis of GalA-oligomers was carried out with high-performance anion-exchange chromatography, HPAEC (17) using a Bio-LC (Dionex, Sunnyvale, CA) with a CarboPac PA-1 column (4.6 × 250 mm) in combination with a pulsed amperometric detector (PAD-2). The detector sensitivity was set at 1 μA. Potential and time settings of the detector were:

 DOI: 10.1139/V02-055 © 2002 NRC Canada

Fig. 1. Time course of hydrolysis of pectic acid with pectinase examined by HPAEC. The number labels mark the DP of the oligogalacturonic acid for the indicated peaks. The time labels on the right of each curve indicate the lengths of hydrolysis, and GalA and $(GalA)_2$ are standards. Equal amounts of the reaction mixture were injected for each run.

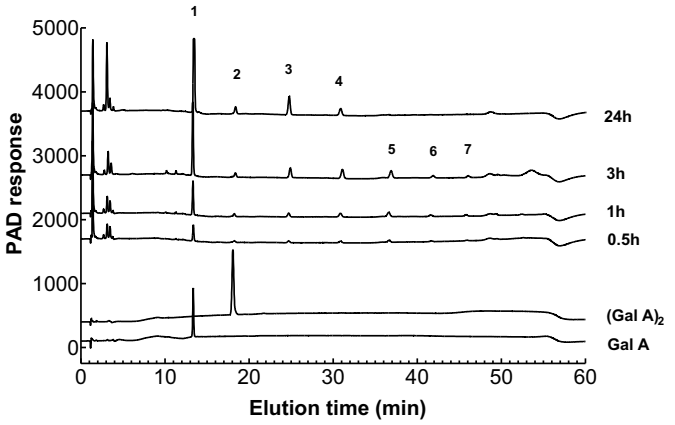

Table 1. Elution gradient (%) of HPAEC for analysis of $(GalA)_n$.

	E2	E3	E4
Time (min)	0.20 M NaOH	Water	0.20 M NaOH/ 1 M NaOAc
0–2	50	48	2
2–9	50	48–30	2–20
9–51	50	30–0	20–50
51–52	50	0–48	50–2
52–62	50	48	2

E_1 = +0.05 V (t_1 = 0.42 s), E_2 = +0.65 V (t_2 = 0.18 s), and E_3 = –0.10 V (t_3 = 0.36 s). Oligo-GalA samples were eluted using the gradients shown in Table 1.

Carbohydrates were determined with a version of the phenol–sulfuric acid method (18). Thin layer chromatography (TLC) was performed on a 0.25-mm layer of silica gel 60 coated on aluminum sheets (E. Merck, Darmstadt, Germany).

Results and discussion

Optimizing conditions for generation of oligo-GalA with DP 1–5 by pectinase digestion

Mixtures of oligo-GalA with different DPs can be obtained by hydrolysis of pectic acid with autoclaving or enzymatic digestion (9–12), but the enzymatic method was found to be the more efficient to degrade pectic acid. For example, depolymerization of pectic acid or pectin (partially esterified pectic acid) with an endopolygalacturonase (19) produces the desired saturated oligo-GalA, while with pectin lyases or pectate lyases, both saturated and unsaturated oligo-GalAs are produced. Unfortunately, such enzymes are not readily available, and thus we chose to use a commercially available pectinase to generate oligo-GalA from pectic acid.

The optimal conditions for generating oligo-GalA (DP 1–5) mixtures were determined by TLC and HPAEC–PAD analysis of the oligosaccharides released in the process of pectinase digestion. During the digestion with 10 or 20 units of pectinase–pectic acid (1.0 g) in 0.1 M acetate buffer, pH 4.0 (see below) at room temperature for 24 h, portions of the digest were removed after 0.5, 1, 3, and 24 h, immediately frozen in a dry-ice acetone bath, and stored frozen. Before analysis, the samples were thawed and heated at 100°C for 10 min to inactivate the pectinase and the precipitate was removed by microcentrifugation. Digestion with 20 units of pectinase–pectic acid (1.0 g) yielded α-(1→4)-oligo-GalA (DP 1–4) as the main products, in which GalA was predominant (Fig. 1). On the other hand, when 10 units of pectinase–pectic acid (1.0 g) were used under the same conditions, a much lower amount of GalA was produced, and the yields of oligo-GalA (DP 2–5) were higher (Fig. 2).

Fig. 2. Elution profiles of pectic acid digested with different amounts of pectinase by HPAEC. A: pectinase (20 units)/pectic acid (1.0 g); B: pectinase (10 units)/pectic acid (1.0 g). The numbers show the DP of the oligogalacturonic acid in the indicated peaks.

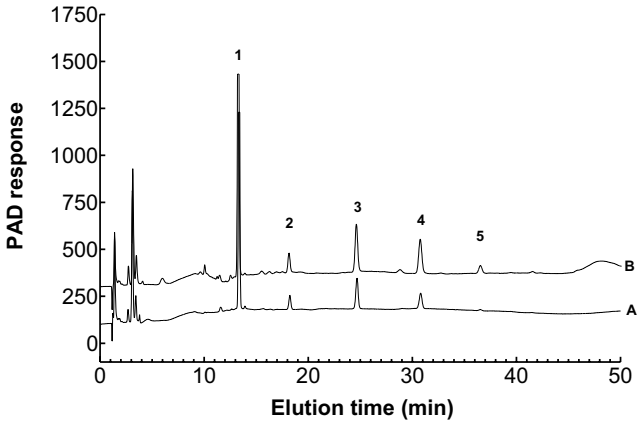

Preparation of oligo-GalA (DP 1–5) mixtures

Pectic acid powder (10.0 g) was suspended in HOAc–NaOAc buffer (each 0.1 M, 500 mL, pH 4.0) and the mixture was incubated at 55°C, sonicated, and stirred until the pectic acid was totally dissolved. The homogeneous but viscous solution was again adjusted to pH 4.0 with 0.1 M NaOAc, and the pectinase (250 μL, ca. 100 units) was added. The solution was gently stirred for 24 h at room temperature; the enzymatic hydrolysis was terminated by heating the mixture at 100°C for 10 min. After cooling, the precipitate and the remaining polymer were removed by ultrafiltration with a stirred cell (200-mL, Millipore, Bedford, MA) using a YM3 membrane. To remove the cations, the filtrate was applied to a column (2.5 × 17.6 cm) of Dowex-50W × 8 resin (H^+ form, 200 mesh) and washed with distilled water (200 mL). The washing was concentrated by rotary evaporation, and the residue was lyophilized to afford 7.68 g of oligo-GalA mixture (76.8% yield).

Size-exclusion chromatography

The oligo-GalA mixture (4.0 g) in HOAc (0.1 M, 20 mL) was applied to a Sephadex G-25 column (5.0 × 218 cm) in 0.1 M HOAc and eluted at a flow rate of 4 mL min^{-1} in 0.1 M HOAc. Fractions (16 mL) were analyzed for carbohydrates by the phenol–H_2SO_4 method (Fig. 3). The

© 2002 NRC Canada

Fig. 3. Elution of oligo-GalA on a Sephadex G-25 column (5.0 × 218 cm). The *y* axis is $A_{480\ nm}$ obtained by the phenol–sulfuric acid method. Approximate positions of the DP of the oligogalacturonic acid are indicated.

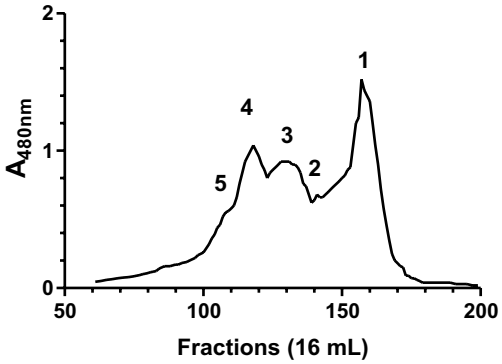

Fig. 4. Separation of oligo-GalA on Dowex-1 × 4 column (2.5 × 46 cm). The column was eluted with a linear gradient generated with 1 L each of 0.4 M and 1.0 M NaOAc (pH 6.0). The numbers indicate the DP of oligo-GalA in the peaks.

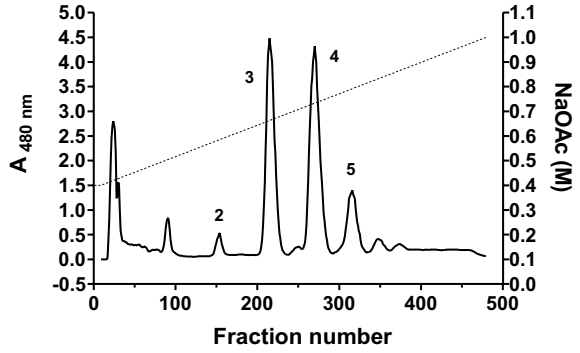

carbohydrate-containing fractions were examined by TLC using silica gel 60 sheets with 1-butanol–formic acid–water (v/v, 4:6:1) as the developing solvent. The R_f values of the oligo-GalA with DPs 1, 2, 3, 4, and 5 were ca. 0.48, 0.35, 0.28, 0.22, and 0.17, respectively. The fractions containing oligo-GalA of DP 2–5 were combined, concentrated by rotary evaporation, and lyophilized to give 2.58 g of product (64.5% yield). Although the Sephadex G-25 column did not fully separate oligo-GalA of DP 2–5, most of the monomer (GalA), which constituted a fairly large proportion of the total digest, could be removed.

Anion-exchange chromatography of oligo-GalA

An example of the anion-exchange chromatography of oligo-GalA is described below. The oligo-GalA mixture (DP 2–5, 1 g) was dissolved in water (10 mL), and the solution was adjusted to pH 12 with 50% aqueous NaOH solution. The mixture was left at room temperature for 1 h and the pH was re-adjusted to 6.0 with 2 M HOAc. The resulting solution was applied to a column (46.5 × 2.5 cm) of Dowex-1 × 4 resin (400 mesh) that had been equilibrated in 0.4 M NaOAc buffer, pH 6.0. The column was washed with 25 mL of the equilibration buffer, and eluted with a linear gradient generated with 1 L each of 0.4 M and 1.0 M NaOAc (pH 6.0). Finally, the column was washed with 1 L of 2.0 M NaOAc (pH 6.0). Fractions were analyzed for carbohydrate

Fig. 5. Identification of each oligo-GalA peak isolated from the Dowex-1 × 4 column (see Fig. 4) with HPAEC.

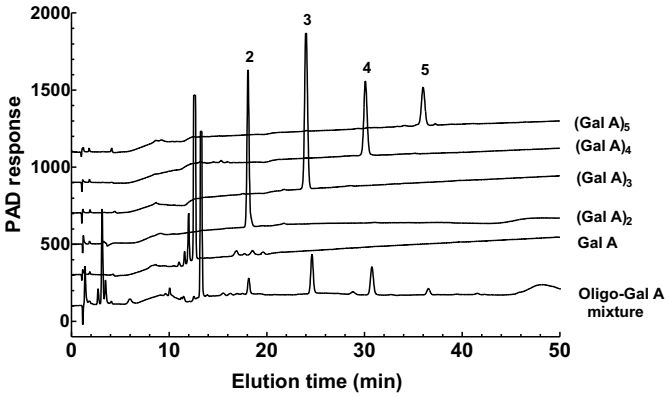

content by the phenol–H_2SO_4 method; the results are shown in Fig. 4. The carbohydrate-containing fractions were analyzed by HPAEC for identification of DP. The purity of each of the isolated peaks is shown in Fig. 5. The individual oligo-GalA peaks were pooled and passed through a column (17.6 × 2.5 cm) of Dowex-50W × 8 resin (H^+ form, 200 mesh) for decationization; the effluent was concentrated by rotary evaporation, followed by lyophilization to give di-, tri-, tetra-, and pentagalacturonic acid ($(GalA)_2$, $(GalA)_3$, $(GalA)_4$, $(GalA)_5$, respectively), with the yields of 1.8, 18.2, 19.9, and 4.9%, respectively.

The alkaline treatment of the oligo-GalA mixture (pH 12 for 1 h) was to open any lactone rings that might have been formed during the gel filtration procedure. Lactonization under acidic condition is often a problem for separation of anionic oligo/polysaccharides with anion-exchange chromatography (20). The separation of oligo-GalA mixture on Dowex 1, a common anion-exchange resin, was excellent (Fig. 4), separating the oligomers better than those reported previously with sophisticated instrumentation (14, 15). Although the column described above has a loading capacity of ~1.0 g of the oligo-GalA mixture, it can be used repeatedly or can be readily scaled up.

Summary

We present here a simple and efficient preparative method of oliogalacturonic acids, up to DP 5, from an inexpensive source, pectic acid. The advantages of our method are the use of an inexpensive commercial enzyme and low-cost chromatographic procedures to yield pure oligo-GalA of DP 2–5 in good overall yield.

Acknowledgment

The authors are grateful to Dr. Reiko T. Lee for carefully reading the manuscript and offering valuable advice.

References

1. C.A. Ryan and E.E. Farmer. Annu. Rev. Plant Physol. Mol. Bio. **42**, 651 (1991).
2. M.A. Karmali, B.T. Steele, M. Petric, and C. Lim. Lancet, **1**, 619 (1983).

© 2002 NRC Canada

3. N. Cimolai, J.E. Carter, B.J. Morrison, and J.D. Anderson. J. Pediatr. **116**, 589 (1990).
4. G.D. Armstrong, E. Fodor, and R. Vanmaele. J. Infect. Dis. **164**, 1160 (1991).
5. L.C.A. Boyd and B., Nephron, **51**, 207 (1989).
6. P.I. Kitov, J.M. Sadowska, G. Mulvey, G.D. Armstrong, H. Ling, N.S. Pannu, R.J. Read, and D.R. Bundle. Nature (London), **403**, 669 (2000).
7. M. Mammen, S.-K. Choi, and G.M. Whitesides. Angew. Chem. Int. Ed. **37**, 2754 (1998).
8. G.D. Armstrong, P.C. Rowe, P. Goodyer, E. Orrbine, T.P. Klassen, G. Ells, A. Mackenzie, H. Lior, C. Blanchard, F. Auclair, B. Thompson, D.J. Rafter, and P.N. McLaine. J. Infect. Dis. **171**, 1042 (1995).
9. J. Ohlsson and G. Magnusson. Carbohydr. Res. **329**, 49 (2000).
10. J. Dahmen, T. Freid, G. Magnusson, G. Noori, and A.-S. Carlstrom. Carbohydr. Res. **129**, 63 (1984).
11. J. Dahmen, T. Freid, G. Magnusson, G. Noori, and A.-S. Carlstrom. Carbohydr. Res. **127**, 15 (1984).
12. M.D. Spiro, K.A. Kates, A.L. Koller, M.A. O'Neill, P. Albersheim, and A.G. Darvill. Carbohydr. Res. **247**, 9 (1993).
13. T.L. Nuederhauser, J. Halling, N.A. Polson, and J.D. Lamb, J. Chromatgraphy A, **804**, 69 (1998).
14. A.T. Hotchkiss, K.B. Hicks, L.W. Doner, and P.L. Irwin. Carbohydr. Res. **215**, 81 (1991).
15. A.T. Hotchkiss, S.L. Lecrinier, and K.B. Hicks. Carbohydr. Res. **334**, 135 (2001).
16. M.-Z. Liu, H.-N. Fan, and Y.C. Lee. Biochimie, **83**, 693 (2001).
17. Y.C. Lee. J. Chromatog. A, **720**, 137 (1996).
18. J.F. McKelvy and Y.C. Lee. Arch. Biochem. Biophys. **132**, 99 (1969).
19. G. Dongowski. J. Chromatography A, **756**, 211 (1996).
20. Y. Zhang and Y.C. Lee. J. Biol. Chem. **274**, 6183 (1999).

© 2002 NRC Canada

Carbohydrate–antibody interactions by NMR for a ^{13}C-labelled disaccharide ligand

Dušan Uhrín, A.V. Krishna Prasad, Jean-Robert Brisson, and David R. Bundle

Abstract: Incorporation of a ^{13}C label into a carbohydrate ligand, methyl 3-*O*-(3,6-dideoxy-α-D-xylohexopyranosyl)-2-*O*-methyl-α-D-mannopyranoside permitted by NMR spectroscopy the study of its binding to the Fab from a monoclonal antibody, Se 155-4. The signals of the free and bound form were observed in the ^{13}C spectrum of the carbohydrate–protein complex. The dissociation rate constants were consequently determined by full lineshape analysis of the ^{13}C spectrum. Comparison with simplified analyses relying only on the linewidth of the ^{1}H and ^{13}C signals of the free ligand were made and the justifications of underlying assumptions used in these analyses were discussed. For ^{1}H NMR, the protein resonances were purged with a ^{13}C filter to observe only the ligand resonances and NOEs between the ligand and the protein.

Key words: carbohydrate, binding, NMR, C-13 label, chemical exchange.

Résumé : L'incorporation d'un marqueur ^{13}C dans un hydrate de carbone servant de ligand, le 3-*O*-(3,6-didésoxy-α-D-xylohexopyranosyl)-2-*O*-méthyl-α-D-mannopyranoside de méthyle a permis d'utiliser la spectroscopie RMN pour étudier sa fixation sur le Fab d'un anticorps monoclonal, Se 155-4. Les signaux des formes libres et liées (conjuguées) ont été observés dans le spectre ^{13}C du complexe glucide–protéine. En se basant sur une analyse complète de la forme des bandes du spectre du ^{13}C, on a par la suite déterminé les constantes de vitesse de la dissociation. On a fait une comparaison avec les analyses n'utilisant que la largeur des bandes des signaux du ^{1}H et du ^{13}C et on discute des hypothèses sous-jacentes utilisées dans ces analyses. Pour la RMN du ^{1}H, les résonances de la protéine ont été purgées à l'aide d'un filtre de ^{13}C afin de n'observer que les résonances du ligand et les eOn entre le ligand et la protéine.

Mots clés : hydrate de carbone, fixation, RMN, marqueur au C-13, échange chimique.

[Traduit par la Rédaction]

Introduction

The realization of the importance of oligosaccharide ligands as potential agonists has highlighted the need for kinetic data of carbohydrate–protein interactions. Here, a synthetically trivial and inexpensive introduction of an isotopic label exploits the observation that replacement of OH by OCH_3 frequently provides oligosaccharide epitopes with virtually unchanged binding strength (1–3). Saccharide sites of this type are ideal candidates for the facile introduction of a $^{13}CH_3O$ group, that yield a singlet resonance well-suited to line-broadening studies in ^{1}H or ^{13}C NMR spectra (4, 5). Incorporation of such a ^{13}C label in methyl 3-*O*-(3,6-dideoxy-α-D-xylohexopyranosyl)-2-*O*-methyl-α-D-mannopyranoside (**1**), was thus used to study binding to the 50 K Dalton Fab from a monoclonal antibody, Se 155-4. From high resolution X-ray (6) structures of Fab–oligosaccharide complexes, the site of methylation at mannose O-2 is solvent exposed and in the native ligand it represents the site of attachment of the third hexose that completes the epitope.

The free and bound signals of the ^{13}C-labelled disaccharide ligand (**1**) were observed in the ^{13}C spectrum permitting full lineshape analysis and determination of dissociation rate constants. Comparison with simplified analyses and more sensitive methods relying only on the linewidth of the ^{1}H and ^{13}C signals of the free ligand were made and the justifications of underlying assumptions used in these analyses were ascertained. For ^{1}H NMR, the protein resonances were purged with a ^{13}C filter to observed only the ligand resonances and NOEs between the ligand and the protein.

Received 9 January 2002. Published on the NRC Research Press Web site at http://canjchem.nrc.ca on 9 July 2002.

Dedicated to the memory of Professor Raymond U. Lemieux who pioneered the applications of the synthesis of carbohydrate for the understanding of protein–carbohydrate interaction by NMR.

A.V.K. Prasad and J.R. Brisson.[1] Institute for Biological Sciences, National Research Council Canada, Ottawa, ON K1A 0R6, Canada.
D.R. Bundle. Department of Chemistry, University of Alberta, Edmonton, AB T6G 2G2, Canada.
D. Uhrín. University of Edinburgh, Department of Chemistry, West Mains Road, Edinburgh EH9 3JJ, U.K.

[1]Corresponding author (e-mail: jean-robert.brisson@nrc.ca).
[2]This is NRC publication no. 42454.

Results

^{13}C lineshape

The ^{13}C spectra of the complex (0.37 mM protein, 1.4 mM sugar) revealed a broader resonance of the bound ligand located 292 ± 2 Hz downfield from the intense OMe signal of the unbound form (Fig. 1). Hence, full lineshape analysis (7) of the bound and free signals was possible and

 DOI: 10.1139/V02-063 © 2002 NRC Canada

Fig. 1. ^{13}C exchange spectra at 150 MHz of the Fab (0.37 mM) and disaccharide (1.4 mM) complex at different temperatures, acquired with 10 000–16 000 scans, 90° pulse, and a recycle delay of 13 s. The simulated spectra using full lineshape analysis are shown as smooth lines.

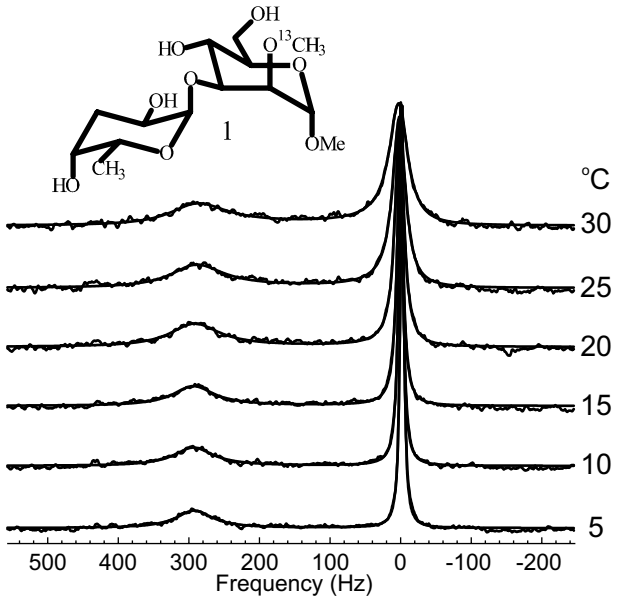

k_{diss} values could be extracted without making any assumptions about the exchange rate (Table 1). The bound form of the sugar could be observed since the bound fraction varied from 0.32 to 0.36 as the temperature increased. The linewidth of the free form increased significantly with temperature (Fig. 1). Since, the fraction bound varied little with temperature, changes in linewidths were due to changes in k_{diss} (7). Values for k_{diss} were also obtained by measuring changes in the linewidth of the free OMe signal at several temperatures, constant protein concentration (0.37 mM), and sugar concentrations from 2.1 to 6.8 mM (fraction of bound sugar from 0.17 to 0.05). Since, the bound fraction was smaller, only the free OMe signal could be detected for reasonable accumulation times. In past studies, since the bound form was not observed, various assumptions had to be made about the exchange regime (4, 5, 8, 9). In our case, since the bound form could be observed ($\Delta\delta = 292 \pm 2$ Hz), the system was in the moderately slow exchange regime (10–13) on the ^{13}C chemical shift time scale ($2\pi\Delta\delta >> k_{diss}$) and the following relation applies (see *Appendix*):

$$[1] \qquad [S_T] = k_{diss}\, n[P_T]/\pi\Delta\Delta\upsilon_{1/2} + n[P_T] - K_D/p_f$$

where $[S_T]$ is the total sugar concentration, $n[P_T]$ is the concentration of protein binding sites, $\Delta\Delta\nu_{1/2} = \Delta\nu_{1/2}^{obs} - \Delta\nu_{1/2}^{free}$ is the contribution of the exchange to the linewidth of the spectral line of the free form, K_D represents the dissociation constant of the sugar–protein complex, and p_f is the molar fraction of the free sugar. Since K_D (1×10^{-5} M) was known from microcalorimetry[3], the last term in eq. [1] can be omitted ($K_D/p_f << n[P_T]$) and k_{diss} determined from the slope of $[S_T]$ vs. $1/\Delta\Delta\nu_{1/2}$ (Fig. 2). The resulting values for k_{diss} were in good agreement with those obtained from the full lineshape analysis (Table 1).

Table 1. Rate (k_{diss} and k_{assoc}) and equilibrium dissociation (K_D) constants at various temperatures for the disaccharide (**1**) binding to Fab Se 155-4.

T (°C)	k_{diss}[a] (s^{-1})	k_{diss}[b] (s^{-1})	k_{diss}[c] (s^{-1})	K_D[d] (M)	k_{assoc}[e] (M^{-1} s^{-1})
5	—[f]	—[f]	7		
10	—[f]	—[f]	16		
15	24	24	27	1.0×10^{-5}	0.3×10^{7}
20	40	39	44	0.6×10^{-5}	0.7×10^{7}
25	46	70	81	1.4×10^{-5}	0.6×10^{7}
30	65	106	123	1.4×10^{-5}	0.9×10^{7}

[a]Equation [1], ^1H detected (±15% estimated error).
[b]Equation [1], ^{13}C detected (±15% estimated error).
[c]Full lineshape analysis, ^{13}C detected (±25% average error).
[d]Titration calorimetry.[3]
[e]$k_{assoc} = k_{diss}{}^c/K_D$.
[f]Values of $\Delta\Delta\upsilon_{1/2}$ are too small for reliable determination of k_{diss}.

Fig. 2. Plot of the total ligand concentration ($[S_T]$) vs. the reciprocal line broadening ($1/\Delta\Delta\nu_{1/2}$) for the free form of the OMe ^{13}C resonance of disaccharide **1** at 15 (●), 20 (■), 25 (▲), and 30°C (▼).

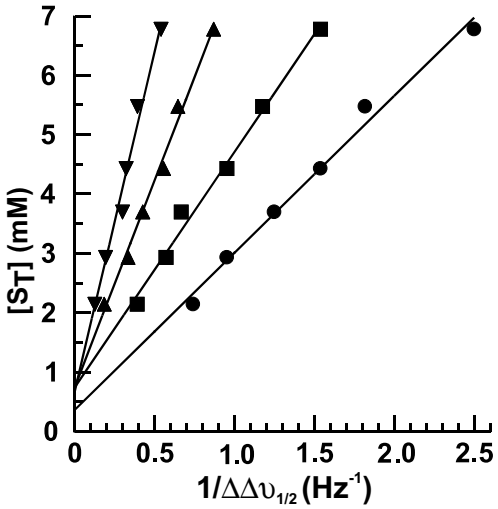

^1H lineshape

The more sensitive method of observing the proton resonances of the sugar by purging the Fab resonances (Fig. 3*a*) with a ^{13}C filter (14, 15) was also used (Fig. 3*b*). The OCH_3 signal of the bound form was not observed for any of the sugar concentrations or temperatures used. Hence, since only the free form was observed, eq. [1] was applied for analysis of its line broadening (Table 1). While there was agreement at lower temperatures (15 and 20°C), values of k_{diss} deviated significantly at higher temperatures (25 and 30°C), indicating that the condition of slow exchange on the chemical shift scale was likely violated and the ^1H resonance of the bound OMe group, although not observed, was much closer to the free OMe signal, ($\Delta\delta \cong 0$). A ^{13}C ω_1-filtered 2D

[3] D.R. Bundle. Private communication. 1994.

© 2002 NRC Canada

Fig. 3. Proton detected spectra at 600 MHz of the Fab (0.37 mM) and disaccharide (2.1 mM) complex at 30°C: (*a*) ^{1}H spectrum, number of scans, NS = 8; (*b*) ^{13}C filtered proton spectrum with 64 transients, and the spin-echo period of the X-filter set to 1.75 ms; (*c*) F1 trace through the ^{13}C- filtered 2D NOE spectrum at the chemical shift of the free OMe resonance. The vertical expansion shows the NOEs from the OMe protons of the saccharide to the aromatic residues of the Fab. The X-filter was set to 3.5 ms and 48 scans were acquired for each of 512 increments. Water was suppressed both during the relaxation (3 s) and NOE mixing intervals (50 ms). The phase-sensitive spectrum was acquired with ^{13}C decoupling during the t_1 and t_2 periods.

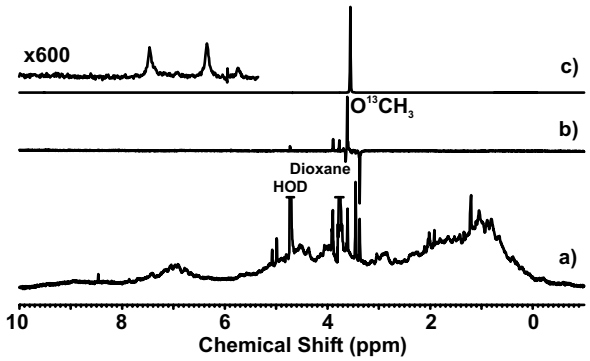

NOESY (16) spectrum was therefore acquired with the intention of locating the chemical shift of OMe protons in the bound form. Only the crosspeaks between the protein and carbohydrate at the F_1 frequency of the free OMe signal were observed (Fig. 3*c*). The intensity of these crosspeaks increased several times with an increase in temperature and thus the exchange rate. Hence, these NOEs were thought to arise through cross relaxation from the protein to the OMe protons in the bound state and then exchange to the free OMe signal (17). Therefore, the chemical shifts of the OMe protons in the bound form could not be determined from this experiment either.

Discussion

The agreement between the k_{diss} values obtained from ^{1}H- and ^{13}C-detected experiments at lower temperatures can be rationalized when considering the following exchange regime for ^{1}H and ^{13}C nuclei. For conditions of: (*i*) fast exchange on the chemical shift scale with $\Delta\delta \cong 0$; (*ii*) slow exchange on the relaxation time scale; and (*iii*) $p_f > 0.7$, a similar linear dependence as eq. [1] had been derived but with the *y*-intercept equal to $-K_D$ (4, 5, 8, 9). When conditions (*ii*) and (*iii*) are satisfied, simulations show that $\Delta\Delta\nu_{1/2}$, is practically independent of $\Delta\delta$, and k_{diss} can be determined from the slope of $[S_T]$ vs. $1/\Delta\Delta\nu_{1/2}$. In our case, at 15 and 20°C, these conditions were satisfied. At lower temperatures, the line broadening changes were too small and difficult to observe. At higher temperatures, condition (*ii*) was violated for protons, which was the source of discrepancy for the k_{diss} values obtained from the ^{1}H linewidths.

For the ^{13}C spectrum, observation of the bound form ($\Delta\delta$ = 292 ± 2 Hz) permitted full lineshape analysis and the determination of dissociation rate constants. In this study, eq. [1] was thus derived for the moderately slow exchange regime to obtain k_{diss} from the linewidth of the free form only. Both type of analyses lead to similar values for k_{diss} (Table 1). In past studies, since the bound form was not observed, $\Delta\delta \cong 0$ had been assumed (4, 5, 8, 9). In our case, if this assumption had been made, the correct values for k_{diss} would still have been determined, since conditions (*ii*) and (*iii*) were met. However, the value of the *y*-intercept would have been wrong, $-K_D$ in the later and $n[P_T]$ in our case (eq. [1]). From Fig. 2, values of 0.7 mM or 0.4 mM were obtained with an error of ±50% taking into account errors of the measurements. This is in agreement with $n = 1$ and $[P_T] = 0.37$ mM.

Hence, the combined use of NMR techniques using a ^{13}C-labelled carbohydrate ligand provided kinetic information to understand the binding of carbohydrate antigens to antibodies. The association rate constants ($k_{assoc} = k_{diss}/K_D$) were also calculated (Table 1) which showed that $k_{assoc} \sim 10^7$ M^{-1} s^{-1} was not diffusion limited, a condition frequently assumed for ligand antibody binding. Under such conditions, it is generally the case that k_{diss} determines the equilibrium constant K_D. Here this is not the case, the variation of K_D with temperature is the product of changes in both the k_{assoc} and k_{diss}.

Experimental

NMR samples were prepared in PBS buffer at pH 7.2 containing 0.02% sodium azide.

Experiments were performed on a 600 MHz (^{1}H) spectrometer using an indirect detection probe for the ^{13}C-filtered experiments and a broadband probe for the ^{13}C experiments. Protein concentrations were 0.13, 0.32, or 0.37 mM. *p*-Dioxane was used as an internal standard. Linewidths, measured at half-height of the ^{13}C or ^{1}H resonance of $O^{13}CH_3$, were corrected for magnetic field inhomogeneity by using the half-width of the *p*-dioxane resonance. Full lineshape analysis of the bound and free form of the ^{13}C resonance of $O^{13}CH_3$ was based on the equations and programs for simulation of lineshapes of an exchanging system for a noncoupled system (7). This permits reliable and efficient iterative total lineshape analyses for multisite exchange systems (18, 19). A simplex minimization method was employed where the chemical shift of the bound and free forms, spin–spin relaxation time of the bound form (T_{2b}), fraction of the ligand bound, and the dissociation rate constant (k_{diss}) were varied. Only the linewidth of the free ligand in the absence of exchange, $\Delta\nu_{1/2}^{free}$ (= $1/\pi T_{2f}$), was fixed.

Acknowledgements

We thank Karol Mikulash for computer programming and full lineshape analysis and Eva Eichler for providing the labelled disaccharide.

References

1. B.W. Sigurskjold, E. Altman, and D.R. Bundle. Eur. J. Biochem. **197**, 239 (1991).
2. B.W. Sigurskjold and D.R. Bundle. J. Biol. Chem. **267**, 8371 (1992).
3. P.V. Nikrad, H. Beierbeck, and R.U. Lemieux. Can. J. Chem. **70**, 241 (1992).

© 2002 NRC Canada

4. K.J. Neurohr, N.M. Young, I.C.P. Smith, and H.H. Mantsch. Biochemistry, **20**, 3499 (1981).
5. K.J. Neurohr, H.H. Mantsch, N.M. Young, and D.R. Bundle. Biochemistry, **21**, 498 (1982).
6. M. Cygler, D.R. Rose, and D.R. Bundle. Science (Washington, D.C.), **253**, 442 (1991).
7. M.L. Martin, J.J. Delpuech, and G.L. Martin. *In* Practical NMR spectrocopy. Heyden, London. 1980.
8. K.A. Kronis and J.P. Carver. Biochemistry, **21**, 3050 (1982).
9. K.A. Kronis and J.P. Carver. Biochemistry, **24**, 826 (1985).
10. J.A. Pople, W.G. Schneider, and H.J. Bernstein. *In* High-resolution nuclear magnetic resonance. McGraw–Hill, New York. 1959.
11. T.J. Swift and R.E. Connick. J. Chem. Phys. **37**, 307 (1962).
12. D.J. Craik and K.A. Higgins. Annu. Rep. NMR Spectrosc. **22**, 61 (1989).
13. E.I. Hyde, B. Birsdall, G.C.K. Roberts, J. Feeney, and A.S.V. Burgen. Biochemistry, **19**, 3746 (1980).
14. M.R. Bendall, D.T. Pegg, D.M. Doddrell, and J. Field. J. Am. Chem. Soc. **103**, 934 (1981).
15. R. Freeman, T.H. Mareci, and G.A. Morris. J. Magn. Reson. **42**, 341 (1981).
16. A. Bax and M.A. Weiss. J. Magn. Reson. **81**, 571 (1987).
17. M.G. Kubinec and D.E. Wemmer. Curr. Opin. Struct. Biol. **2**, 828 (1992).
18. L.W. Reeves and K.N. Shaw. Can. J. Chem. **48**, 3641 (1970).
19. L.W. Reeves and K.N. Shaw. Can. J. Chem. **49**, 3671 (1971).

Appendix A

Determination of the k_{diss} from the linewidth of the free-state signal for slow chemical exchange on the chemical shift scale.

The exchange contribution to the line width of the signal of the free ligand ($\Delta\Delta\upsilon_{1/2}$) is calculated (A1, A2) for slow exchange on the chemical shift scale ($2\pi\Delta\delta >> k_{diss}$) as

$$[A1] \quad \Delta\Delta\upsilon_{1/2} = \Delta\nu_{1/2}^{obs} - 1/\pi T_{2f} = (k_{diss}/\pi)(p_b/p_f)$$

where $\Delta\nu_{1/2}^{obs}$ is the observed half-width, T_{2f} is the spin–spin relaxation time of the ligand in the absence of exchange, p_b and p_f are molar fractions of the bound and free ligands, respectively, and k_{diss} is the dissociation rate constant. By changing the p_b/p_f ratio and measuring the change in the linewidth of the free state, k_{diss} is determined from the slope of the linear dependence of $\Delta\Delta\upsilon_{1/2}$ vs. p_b/p_f. The p_b/p_f ratio, however, is not known unless the dissociation constant (K_D) is determined independently by an alternate method. Approximate solution to this problem has been proposed previously (A3). Equation [A1], derived in this section, offers a more general solution.

In a simple dynamic bimolecular equilibrium, involving a sugar ligand (S) and a protein (P), denoted by S + P $\Leftrightarrow$ SP, the dissociation constant K_D, is given as

$$[A2] \quad K_D = [S][P]/[SP] = ([S_T] - [SP])(n[P_T] - [SP])/[SP]$$

where $[SP]$ is the concentration of the complex, $[S_T]$ and $[P_T]$ are total saccharide and protein concentrations, n is the number of carbohydrate binding sites of the protein. By substituting $[SP] = p_b[S_T]$ and using the identity $p_b + p_f = 1$, K_D can be expressed as:

$$[A3] \quad K_D = [S_T](1 - p_b)(n[P_T] - p_b[S_T])/p_b[S_T] = n[P_T](p_f/p_b) - p_f[S_T]$$

and the total sugar concentration can be written as:

$$[A4] \quad [S_T] = n[P_T]/p_b - K_D/p_f = n[P_T](p_f/p_b) + n[P_T] - K_D/p_f$$

By substituting (p_f/p_b) from [A1] into [A4], eq. [1] is obtained:

$$[1] \quad [S_T] = k_{diss}\, n[P_T]/\pi\Delta\Delta\upsilon_{1/2} + n[P_T] - K_D/p_f$$

When $K_D/p_f << n[P_T]$ a linear dependency of $[S_T]$ on $1/\Delta\Delta\upsilon_{1/2}$ is obtained:

$$[A5] \quad [S_T] = k_{diss}\, n[P_T]/\pi\Delta\Delta\upsilon_{1/2} + n[P_T]$$

Equation [A5] was applied for determination of k_{diss} during the course of this work.

References

A1. J.A. Pople, W.G. Schneider, and H.J. Bernstein. *In* High-resolution nuclear magnetic resonance. McGraw–Hill, New York. 1959.
A2. T.J. Swift and R.E. Connick. J. Chem. Phys. **37**, 307 (1962).
A3. E.I. Hyde, B. Birsdall, G.C.K. Roberts, J. Feeney, and A.S.V. Burgen. Biochemistry, **19**, 3746 (1980).

© 2002 NRC Canada

Sialoside clusters as potential ligands for siglecs (sialoadhesins)

Zhonghong Gan and René Roy

Abstract: Clusters of *O*- and *S*-linked α-sialosides with valencies of two to four were constructed to serve as potential multivalent inhibitors towards sialoadhesins (siglecs). Thus, *O*- and *S*-prop-2-ynyl α-sialosides (**3**, **7**), together with 4-iodophenyl sialoside **5** were prepared from acetochloroneuraminic acid derivative **1** using silver salicylate and propargyl alcohol for **3** and phase-transfer catalysis for **5** and **7**, respectively. Oxidative acetylenic homocoupling of **3** and **7** under Glaser conditions (CuCl, O_2) provided 1,3-diynes **8** and **9** in 83–86% yields. Palladium catalyzed cross-coupling of *O*-prop-2-ynyl sialoside **3** with **5** using $Pd_2(dba)_3$ and PPh_3 gave nonsymmetrical dimer **10** (82%). Alternatively, symmetrical clusters were then prepared as above under Sonogashira cross-coupling conditions with 1,4-diiodobenzene (**11**), 1,3,5-triodobenzene (**14**), and finally 1,2,4,6-tetraiodobenzene (**17**) to provide both *O*- and *S*-linked dimers **12** (93%) and **13** (88%), trimers **15** (81%) and **16** (76%), while only *O*-linked tetramer **18** was prepared in 87% yield. Finally, treatment of the *O*-linked prop-2-ynyl sialoside **3** with Grubbs' metathesis catalyst $Cl_2Ru(PCy_3)_2$=CHPh (**19**) gave, as expected, benzeneannulation regioisomeric trimers **20a**, **20b** in 68% yield.

Key words: siglec, sialoadhesins, sialic acid, Sonogashira, palladium cross-coupling.

Résumé : On a préparé une série d'agrégats d'α-sialosides liés par l'oxygène ou le soufre et de valence allant de deux à quatre qui pourraient éventuellement servir d'inhibiteurs multivalents vis-à-vis des sialoadhésines (siglecs). On a ainsi préparé les α-sialosides de *O*- et de *S*-prop-2-ynyle (**3**, **7**) ainsi que le sialoside de 4-iodophényle (**5**) à partir du dérivé **1** de l'acide acétochloroneuraminique, en utilisant le salicylate d'argent et l'alcool propargylique pour le composé **3** et une catalyse de transfert de phase pour les composés **5** et **7** respectivement. L'homocouplage acétylénique oxydant des composés **3** et **7** dans des conditions de Glazer (CuCl, O_2) a permis d'obtenir les composés **8** et **9** avec des rendements allant de 83 à 86%. Un couplage croisé catalysé par le palladium du sialoside de *O*-prop-2-ynyle **3** avec le composé **5**, à l'aide de $Pd_2(dba)_3$ et de PPh_3, fournit le dimère non symétrique **10** (82%). De façon alternative, des agrégats symétriques ont alors été préparés de la façon mentionnée ci-dessus, en utilisant les conditions de couplage croisé de Sonagashira et du 1,4-diiodobenzène (**11**), du 1,3,5-triiodobenzène (**14**) et finalement du 1,2,4,6-tétraiodobenzène (**17**); on a ainsi obtenu des produits liés par l'oxygène et le soufre dont les dimères **12** (93%) et **13** (88%) et les trimères **15** (81%) et **16** (76%) ainsi que le produit **18** (87%) un tétramère lié uniquement à l'oxygène. Enfin, le traitement du sialoside de prop-2-ynyle lié à l'oxygène, **3**, avec le catalyseur de métathèse de Grubbs, $Cl_2Ru(PCy_3)_2$=CHPh (**19**), conduit, tel que prévu, aux trimères de benzèneannellation régioisomérique **20a**, **20b** avec un rendement de 68%.

Mots clés : siglec, sialoadhésines, acide sialique, Sonogashira, couplage croisé au palladium.

Introduction

Sialic acid is a generic term representing over 40 different structures derived from neuraminic acid, a nine-carbon amino acid sugar (1). The most prevalent member, *N*-acetylneuraminic acid, is usually present as a capping residue on natural glycoproteins and glycolipids. As such, it plays the role of a "terminal elaboration factor" (2) and is thus well-suited in mediating molecular recognition at the cell surface, a property well exploited by several pathogens (1). Conversely, siglecs, a subgroup of immunoglobulin-type animal lectins that mediate cell adhesion and signaling, recognize sialoconjugates. Several siglecs are expressed on cells of the innate immune system and sialoadhesin (or siglec-1) is found on macrophages and has been implicated in lymphocyte adhesion and myeloid cell development (3).

Although siglecs are known to possess only one carbohydrate recognition domain (CRD) (4), multivalent sialosides have been shown to dramatically increase their inhibitory potency towards sialoadhesin (5). Given the importance of multivalent glycoforms in the study of carbohydrate–protein interactions at the molecular level (6) and their potential

Received 9 October 2001. Published on the NRC Research Press Web site at http://canjchem.nrc.ca on 9 July 2002.

Dedicated to the late Raymond U. Lemieux, an outstanding pioneer in carbohydrate chemistry.

Z. Gan and R. Roy.[1] Department of Chemistry, Center for Research in Biopharmaceuticals, University of Ottawa, Ottawa, ON K1N 6N5, Canada.

[1]Corresponding author (e-mail: rroy@science.uottawa.ca).

 DOI: 10.1139/V02-053 © 2002 NRC Canada

Scheme 1.

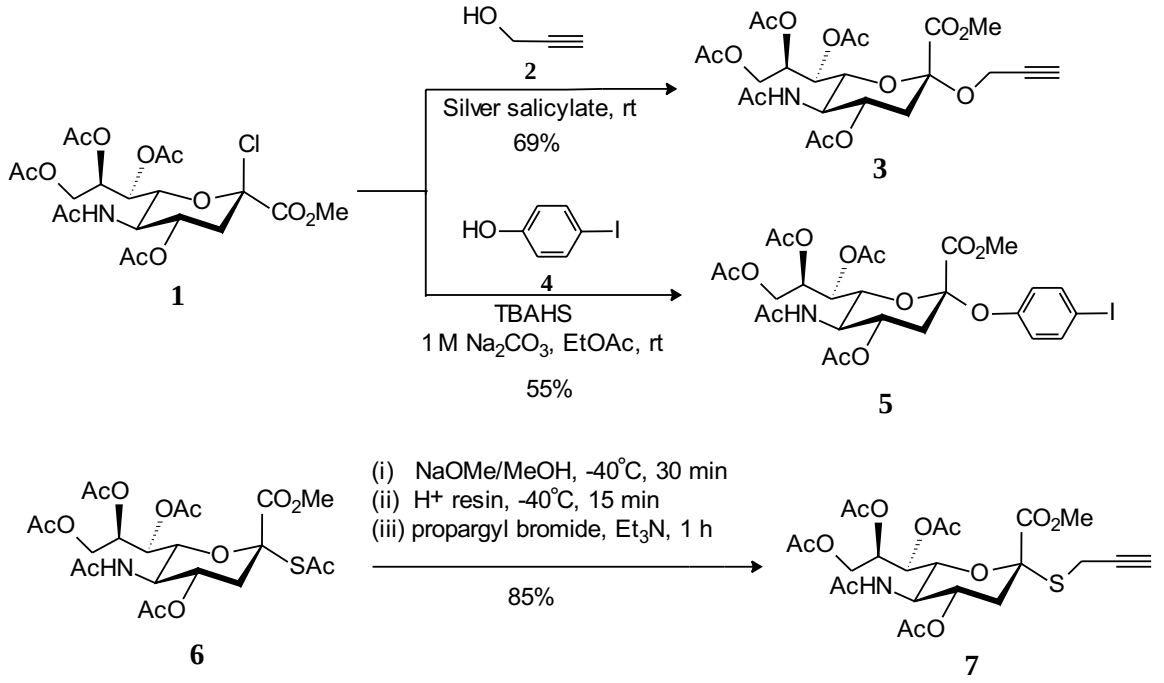

Scheme 2.

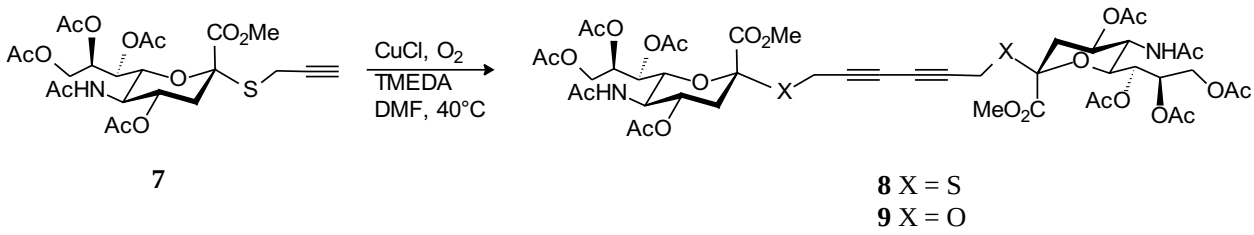

roles in receptor clustering, we propose herein the synthesis of sialic acid clusters using a variety of metal-catalyzed cross-coupling strategies (7).

Results and discussion

The syntheses of the requisite prop-2-ynyl α-sialosides **3**, **5**, and **7** necessary for the palladium-catalyzed homo- and cross-coupling reactions are depicted in Scheme 1. Prop-2-ynyl α-*O*-sialoside **3** was readily accessible from β-acetochloroneuraminic acid **1** using propargyl alcohol in the presence of silver salicylate. The Koenigs–Knorr glycosylation occurred with complete stereocontrol giving rise to the α form as previously observed for analogous cases (8). The pure product can be obtained by recrystalizing the crude sample from ethanol (69%). 4-Iodophenyl α-sialoside **5** was also prepared from **1** using improved phase-transfer catalysis (PTC) conditions developed in our laboratory (9). The synthesis of aryl α-sialosyl derivatives was achieved at room temperature in a two-phase system using ethyl acetate, 1 M sodium carbonate, and tetrabutylammonium hydrogensulfate as phase-transfer catalyst. The reaction was entirely stereoselective and provided **5** in 55% yield. Prop-2-ynyl α-thiosialoside **7** was synthesized from the corresponding thioacetate derivative **6**, itself obtained from **1** under PTC conditions (10). Chemoselective de-*S*-acetylation of **6** under low-temperature Zemplén conditions followed by low-temperature quenching by acidic (H^+) resin generated a sialic acid thiol intermediate (10, 11). The thiol intermediate was then coupled to propargyl bromide to give **7** in 85% yield as previously observed from other glycosyl thioacetates (12) (Scheme 1).

The syntheses of homo-coupling symmetrical diynes can be accomplished by using the Glaser or alternative methods (13). Thus, oxygen was bubbled through a solution of prop-2-ynyl α-sialoside **3**, copper(I) chloride, and TMEDA in DMF at 40°C for 2 h. The desired dimer (**9**) was obtained in 86% yield. The structure of (**9**) was confirmed from its ^{1}H NMR spectrum which did not contain a signal with a chemical shift close to δ 2.24 ppm, the position of the acetylenic proton in the spectrum of the monomer. The mass spectrum of compound (**9**) gave a $M^+ + 1$ peak at 1057.2 Da. This procedure was also successfully applied to prop-2-ynyl α-thiosialoside **7** to afford the corresponding dimer **8** in 83% yield (Scheme 2).

According to our previous studies (14), the use of Sonogashira cross-coupling conditions modified by removal of the copper(I) iodide cocatalyst, can eliminate the formation

© 2002 NRC Canada

Scheme 3.

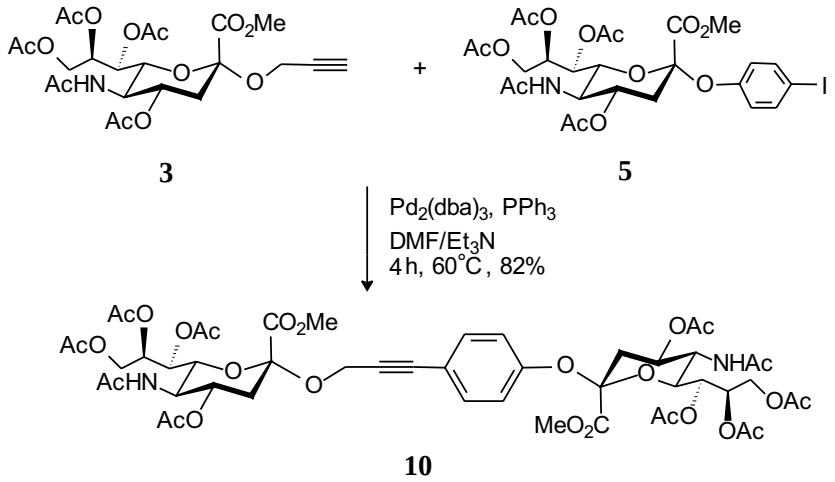

Scheme 4.

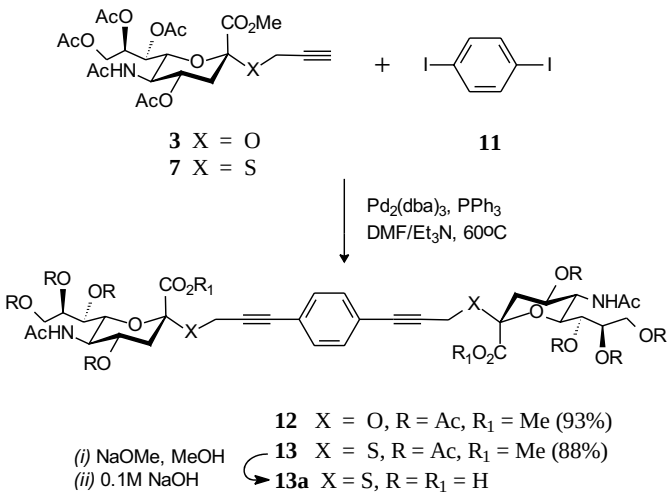

of symmetrical diyne. This new protocol was thus used for the treatment of prop-2-ynyl α-sialoside **3** (1.1 equiv) and 4-iodophenyl *O*-α-sialoside **5** (1 equiv) using tris(dibenzylideneacetone)dipalladium(0) ($Pd_2(dba)_3$) as catalyst at 60°C to afford cross-coupling dimer **10** in 82% yield. As expected, no symmetrical diyne (**9**) was found (Scheme 3).

Similarly, treatment of **3** with 1,4-diiodobenzene (**11**, 1 equiv) under the above reaction conditions provided dimer **12** in 93% yield (Scheme 4). Again, no symmetrical diyne (**9**) was observed. The distinction between the homodimer (**9**) and the crossdimer **12** can be clearly distinguished from two marked differences between their respective ^{13}C NMR spectra. The acetylene peaks of the crossdimer **12** were shifted downfield at δ 86.2 and at 85.6 ppm compared with those of the homodimer (**9**) at δ 74.7 and at 70.1 ppm and the spectra of **12** contained peaks in the aromatic region while those of **9** did not. Previous results showed that thioethers could also undergo cross-coupling with aryl halides under Sonogashira conditions (15). Thus, prop-2-ynyl α-thiosialosides **7** reacted with 1,4-diiodobenzene in the presence of $Pd_2(dba)_3$ at 60°C to afford dimer **13** in 88% yield. Fully protected dimer **13** was sequentially hydrolyzed with NaOMe in methanol followed by 0.1 M NaOH to provide water-soluble **13a**.

Encouraged by the successful synthesis of divalent sialoside derivatives by the Sonogashira reaction, we further expanded this reaction toward the synthesis of larger clusters. As already mentioned, the formation of symmetrical diynes as minor by-products that cause purification problems can be avoided using CuI. However, CuI is a particularly effective co-catalyst which allows the reaction to occur at room temperature. Without CuI, the reaction has to be accomplished at higher temperatures and longer reaction times are required. Since sialic acid trimers and tetramers are easily separated from their corresponding symmetrical diynes, the addition of CuI was employed to help the reactions to occur smoothly and rapidly with more hindered tri- or tetraiodobenzenes.

1,3,5-Triiodobenzene (**14**) was prepared from 1,3,5-tribromobenzene following a known procedure (16). Treatment of 1,3,5-tribromobenzene with KI, I_2, and Ni powder in refluxing DMF afforded 1,3,5-triiodobenzene in 52% yield. Direct polyiodination of benzene with periodic acid and iodine in sulfuric acid at room temperature (rt) provided 1,2,4,6-tetraiodobenzene (**17**) in good yield (73%) (17).

Prop-2-ynyl α-sialoside **3** was treated with 1,3,5-triiodobenzene (**14**) ($Pd_2(dba)_3$, CuI, PPh_3, DMF–Et_3N, rt, 1 h) to give trimer **15** (81%). Trimer **15** was readily separated from a small amount of symmetrical diyne (**9**) as a by-product by silica gel chromatography. Trimer **16** was analogously prepared from prop-2-ynyl α-thiosialoside **7** in 76% yield (Scheme 5).

Treatment of prop-2-ynyl α-sialoside **3** with 1,2,4,6-tetraiodobenzene (**17**) using the above conditions gave *O*-linked tetramer **18** in 87% yield (Scheme 6). Because of the steric hindrance, the reaction with tetraiodobenzene needed longer reaction time for completion (4 h). The structure for **18** was confirmed by its ^1H NMR and ^{13}C NMR spectra and from the molar mass determined by FAB-MS.

Grubbs' catalyst **19** can also be used to catalyze intermolecular cyclotrimerization of three terminal alkynes according to our previous findings (18). Prop-2-ynyl α-sialoside **3** was treated with Grubbs' catalyst **19** in refluxing 1,2-dichloroethane for 24 h. The desired regioisomeric trisubstituted

© 2002 NRC Canada

Scheme 5.

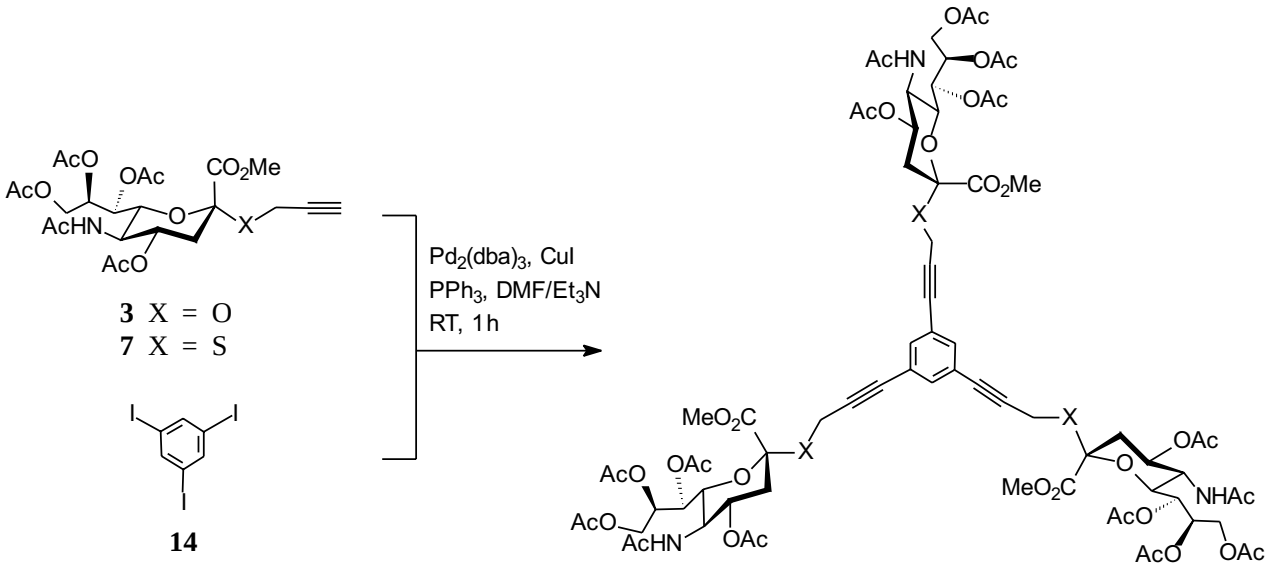

Scheme 6.

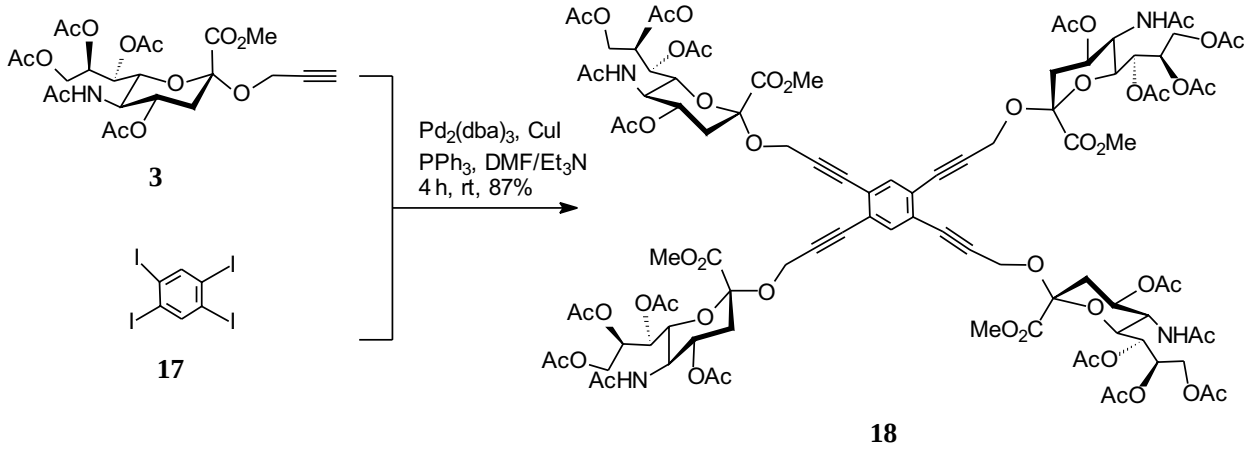

benzene derivatives **20a**, **20b** were isolated as a mixture of 1,2,4-(**20a**) and 1,3,5-(**20b**) regioisomers in 68% yield (Scheme 7). The reaction was found to be highly regioselective in favor of the 1,2,4-regioisomer **20a** over that of **20b** (4.5:1). The regioisomeric structures and the ratio were determined from the ^{1}H NMR spectrum by comparing the data of analogous products reported in the literature (18, 19). The aromatic protons for the 1,2,4-isomer **20a** appeared at δ 7.27 ppm (d, J = 7.8 Hz), 7.23 (s), and 7.19 (d, J = 7.8 Hz) and for the symmetrical 1,3,5-isomer **20b** as a singlet at δ 7.14 ppm. The ^{13}C NMR showed aromatic carbon signals at 136.4, 135.4, 135.0 ppm (quaternary carbons) and 128.7, 127.9, 127.1 ppm (tertiary carbons) for the 1,2,4-isomers and those for 1,3,5-isomer appeared at 137.2 ppm (quaternary carbon) and at 126.4 ppm (tertiary carbon). This novel procedure is therefore complementary to that using dicobalt octacarbonyl [$Co_2(CO)_8$] (19).

Experimental section

General methods

^{1}H and ^{13}C NMR were recorded on a Bruker AMX500 spectrometer at 500 MHz for protons and 125.7 MHz for carbons, respectively. Proton chemical shifts (δ) are given relative to internal chloroform (7.24 ppm) for $CDCl_3$. For carbon spectra, chemical shifts were given relative to $CDCl_3$ (77.0 ppm). Spectral analyses were performed as first-order approximations and were based on correlation spectroscopy (COSY), heteronuclear multiple quantum coherence (HMQC), and one- and two-dimensional distortionless

© 2002 NRC Canada

Scheme 7.

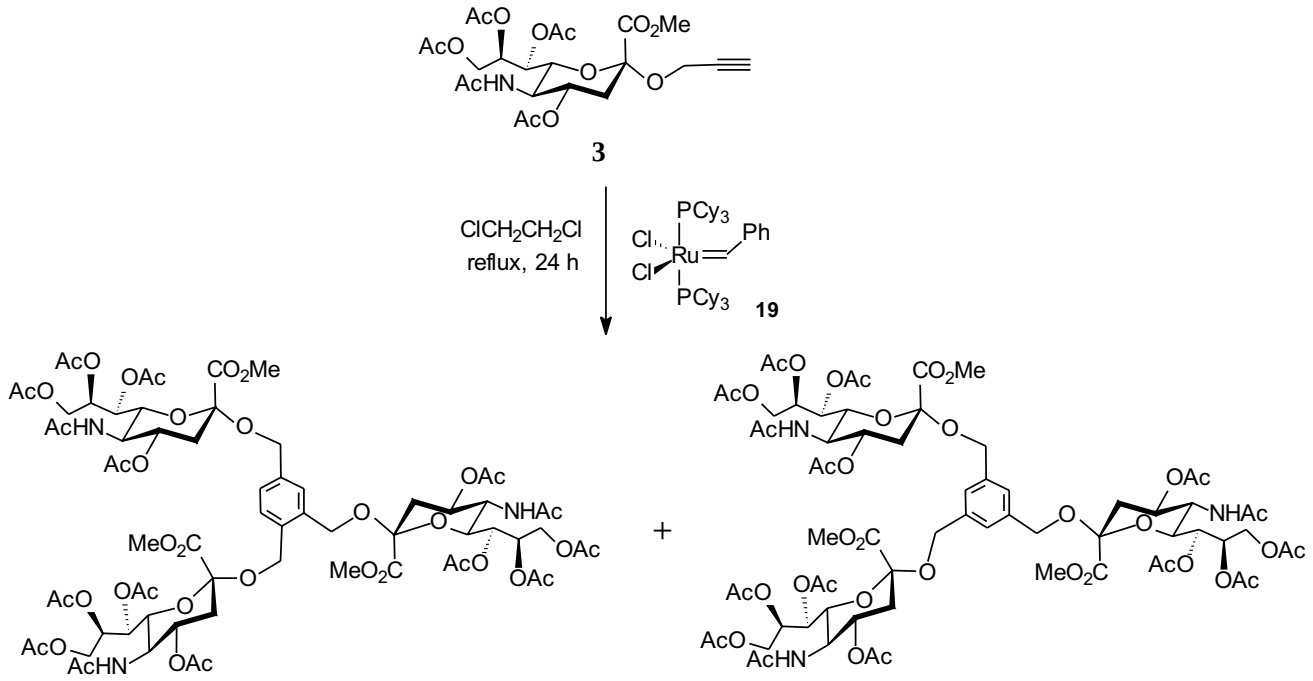

enhancement by polarization transfer (DEPT) experiments. Optical rotations were measured on a PerkinElmer 241 polarimeter. FAB-MS spectra were recorded on a Kratos Concepts IIH with Cs^+ beam and are not high resolution unless stated otherwise. Thin layer chromatography (TLC) was performed using silica gel 60-F_{254} glass plates. Reagents used for developing plates include ceric sulfate (1% w/v) and ammonium sulfate (2.5% w/v) in 10% (v/v) aqueous sulfuric acid, iodine, dilute aqueous potassium permanganate, and UV light. TLC plates were heated to approximately 150°C when necessary. Purifications were performed by gravity or flash chromatography on silica gel 60 (230–400 mesh, E. Merck no. 9385). Solvents were evaporated under reduced pressure using a Büchi rotary evaporator connected to a water aspirator. All chemicals used in the experiments were of reagent grade. Solvents were purified by the published procedures.

*Methyl (prop-2-ynyl 5-acetamido-4,7,8,9-tetra-*O*-acetyl-3,5-dideoxy-*D*-glycero-*α*-*D*-galacto-2-nonulopyranosid) onate (3)*

To a solution of freshly prepared β-acetochloroneuraminic acid **1** (1.18 g, 2.31 mmol) in dry propargyl alcohol (20 mL) containing 4 Å molecular sieves (2 g) was added freshly prepared silver salicylate (0.85 g, 3.47 mmol). The reaction was stirred for 2 h under nitrogen at room temperature in the dark. The slurry was filtered over Celite, washed with dichloromethane, and evaporated to dryness. The residue was dissolved in dichloromethane (30 mL). The organic solution was successively washed with sat. $NaHCO_3$ solution, 5% $Na_2S_2O_3$ solution, and brine. The organic phase was dried over Na_2SO_4 and concentrated under reduced pressure. The crude syrup was crystallized from ethanol to afford pure **3** (840 mg, 69%) as a colorless solid: mp 162–164°C; $[\alpha]_D$ +69.4° (*c* 0.5, CH_3CN). HR-MS calcd. for $C_{23}H_{32}N_1O_{13}(MH^+)$ (*m*/*z*): 530.1874; found: 530.1895. ^{1}H NMR ($CDCl_3$) δ: 5.44 (d, 1H, $J_{5,NH}$ = 9.0 Hz, NH), 5.34 (m, 1H, H-8), 5.25 (dd, 1H, $J_{6,7}$ = 1.3 Hz, $J_{7,8}$ = 8.3 Hz, H-7), 4.80 (m, 1H, H-4), 4.35 (dd, 1H, *J* = 15.7 Hz, -OC*H*$_2$C≡), 4.22 (dd, 1H, $J_{9a,9b}$ = 12.4 Hz, $J_{8,9a}$ = 2.7 Hz, H-9a), 4.10 (dd, 1H, -OC*H*$_2$C≡), 4.04–3.97 (m, 3H, H-5, H-6, H-9b), 3.75 (s, 3H, OCH_3), 2.57 (dd, 1H, $J_{3a,3e}$ = 12.8 Hz, $J_{3e,4}$ = 4.6 Hz, H-3e), 2.39 (dd, 1H, *J* = 2.4 Hz, -C≡C*H*), 2.09, 2.07, 1.98, 1.96, 1.81 (s, 15H, OAcs, NHAc), 1.91 (dd, 1H, $J_{3a,4}$ = 12.5 Hz, H-3a). ^{13}C NMR ($CDCl_3$) δ: 170.8–170.0 (O=Cs), 167.8 (C-1), 98.2 (C-2), 78.9 (-*C*≡CH), 74.4 (-C≡*C*H), 72.6 (C-6), 68.8 (C-4), 68.4 (C-8), 67.2 (C-7), 62.3 (C-9), 52.8 (OCH_3), 52.7 (-O*C*H$_2$C≡), 49.2 (C-5), 37.8 (C-3), 23.0, 21.0, 20.9, 20.7, 20.6 (NHAc, OAcs).

*Methyl (4-iodophenyl 5-acetamido-4,7,8,9-tetra-*O*-acetyl-3,5-dideoxy-*D*-glycero-*α*-*D*-galacto-2-nonulopyranosid) onate (5)*

To a solution of freshly prepared acetochloroneuraminic acid **1** (680 mg, 1.33 mmol) in EtOAc (20 mL) was added a solution of *p*-iodophenol (587 mg, 2.67 mmol) and TBAHS (453 mg, 1.33 mmol) in 1 M Na_2CO_3 (20 mL). The mixture was stirred vigorously for 1 h at room temperature and next diluted with EtOAc (20 mL). The organic phase was separated and washed with brine. The organic phase was dried over Na_2SO_4 and concentrated under reduced pressure. The residue was purified by silica gel column chromatography using CH_2Cl_2–EtOH (30:1, v/v) as eluent to give compound **5** (509 mg, 55%) as a white solid, mp 88–90°C; $[\alpha]_D$ +10.8° (*c* 1.0, $CHCl_3$). FAB-MS calcd. for $C_{26}H_{32}IO_{13}N_1$: 693.45; found: 694.1 ($[M + 1]^+$, 33.9%). ^{1}H NMR ($CDCl_3$) δ: 7.49

© 2002 NRC Canada

(d, 2H, J = 8.8 Hz, aromatic H), 6.76 (d, 2H, aromatic H), 5.58 (bs, 1H, NH), 5.29 (m, 2H, H-7, H-8), 4.87 (m, 1H, H-4), 4.38 (d, 1H, $J_{5,6}$ = 10.8 Hz, H-6), 4.21 (d, 1H, $J_{9a,9b}$ = 12.6 Hz, H-9a), 4.09–4.01 (m, 2H, H-9b, H-5), 3.59 (s, 3H, OCH_3), 2.62 (dd, 1H, $J_{3a,3e}$ = 12.9 Hz, $J_{3e,4}$ = 4.6 Hz, H-3e), 2.14 (dd, 1H, $J_{3a,4}$ = 12.5 Hz, H-3a), 2.08, 2.06, 1.99, 1.97, 1.84 (s, 15 H, OAcs, NHAc). ^{13}C NMR ($CDCl_3$) δ: 170.8–170.0 (O=Cs), 168.0 (C-1), 153.7, 138.2, 121.8, 87.1 (aromatic C), 99.8 (C-2), 73.4 (C-6), 69.1 (C-8), 68.6 (C-4), 67.3 (C-7), 62.0 (C-9), 52.9 (OCH_3), 49.2 (C-5), 38.1 (C-3), 23.0, 20.9, 20.7, 20.6 (NHAc, OAcs).

*Methyl (prop-2-ypnyl 5-acetamido-4,7,8,9-tetra-*O*-acetyl-3,5-dideoxy-2-thio-*D*-glycero-α-*D*-galacto-2-nonulopyranosid) onate (7)*

To a solution of thioacetate sialoside **6** (220 mg, 0.40 mmol) in dry methanol (10 mL), cooled to –40°C, was added a 1 M solution of sodium methoxide (380 μL, 0.38 mmol). The mixture was stirred at –40°C under nitrogen for 30 min. The solution was then neutralized with Amberlite IR-120 H^+ resin at –40°C for 15 min. The solution was filtered. To the filtrate were added prapargyl bromide (80% in toluene, 67 μL, 0.60 mmol) and triethyl amine (112 μL, 0.8 mmol). The solution was stirred at room temperature for 1 h. The solution was poured then into water and exacted by dichloromethane (3 × 10 mL). The combined organic layers were washed with 5% HCl and brine. The organic phase was dried over Na_2SO_4 and concentrated under reduced pressure. The compound **7** (185 mg, 85%) was purified by recrystallization from CH_2Cl_2–hexanes as white solids, mp 186 to 187°C; $[\alpha]_D$ +51° (*c* 0.2, CH_3CN). HR-MS calcd. for $C_{23}H_{32}NO_{12}S$ (MH^+) (*m*/*z*): 546.1645; found: 546.1653. ^{1}H NMR ($CDCl_3$) δ: 5.37 (m, 1H, H-8), 5.31–5.27 (m, 2H, NH, H-7), 4.84 (m, 1H, H-4), 4.25 (dd, 1H, $J_{9a,9b}$ = 12.5 Hz, $J_{8,9a}$ = 2.7 Hz, H-9a), 4.08–3.99 (m, 2H, H-9b, H-5), 3.84 (dd, 1H, $J_{5,6}$ = 10.8 Hz, $J_{6,7}$ = 2.2 Hz, H-6), 3.79 (s, 3H, OCH_3), 3.41, 3.40 (d, 2H, J = 2.6 Hz, -SCH_2C=), 2.69 (dd, 1H, $J_{3a,3e}$ = 12.7 Hz, $J_{3e,4}$ = 4.6 Hz, H-3e), 2.14 (t, 1H, -C≡C*H*), 2.13, 2.09, 2.00, 1.99, 1.83 (s, 15H, OAcs), 1.95 (dd, 1H, $J_{3a,4}$ = 12.3 Hz, H-3a). ^{13}C NMR ($CDCl_3$) δ: 170.8–170.0 (O=Cs), 168.0 (C-1), 82.7 (C-2), 79.5 (-*C*≡CH), 74.2 (C-6), 70.6 (-C≡*C*H), 69.4 (C-4), 68.4 (C-8), 67.2 (C-7), 62.2 (C-9), 53.0 (OCH_3), 49.2 (C-5), 37.4 (C-3), 23.1, 21.1, 20.7, 20.7 (NHAc, OAcs), 16.8 (-S*C*H_2C≡).

General procedure for the homo-coupling of acetylenic thiosugar by Glaser reaction

In a mixture of thiosugar (1 mmol), CuCl (0.3 mmol), and TMEDA (0.6 mmol) in *N*,*N*-dimethylformamide (10 mL) was bubbled O_2 at 40°C for 2 h. Then the brownish green solution was poured into water (100 mL). The mixture was extracted with CH_2Cl_2 (3 × 20 mL). The combined organic phases were washed with brine, dried over Na_2SO_4, and concentrated under vacuum. The residue was purified by silica gel column chromatography.

General procedure for the cross-coupling of acetylenic thiosugar by Sonogashira reaction

To acetylenic thiosugar (1 mmol) and 1,4-diiodobenzene (0.45 mmol) in a degassed solution of DMF and Et_3N (5 mL, 1:1, v/v) were added $Pd_2(dba)_3$ (0.05 mmol) and PPh_3 (0.1 mmol). The solution was stirred at 60°C under nitrogen atmosphere for 2 h. The solution was diluted with CH_2Cl_2 (20 mL), and then washed successively with 5% HCl and brine. The organic phase was dried over Na_2SO_4 and concentrated under vacuum. The residue was purified by silica gel column chromatography.

1,3,5-Triiodobenzene (14)

1,3,5-Tribromobenzene (1.10 g, 3.5 mmol), KI (3.50 g, 21 mmol), Ni powder (2.00 g), I_2 (5.10 g), and DMF (12.5 mL) were added into a 50 mL round-bottomed flask. The flask was evacuated on the vacuum line at 0°C for 15 min. The mixture was refluxed under N_2 for 3 h. After cooling, the solution was poured into a separation funnel. The flask was washed with 3% aq HCl (50 mL) and CH_2Cl_2 (50 mL) until all material, except for Ni powder, was transferred into the separation funnel. The CH_2Cl_2 layer was separated, and the aqueous layer was extracted with CH_2Cl_2. The combined organic phase was washed with distilled water and dried over Na_2SO_4. The solvent was evaporated, leaving a light-brown crude product. This was further purified by sublimation at 60°C overnight. The residue was sublimed at 120–140°C to afford compound **15** (0.83 g, 52%).^{13}C NMR ($CDCl_3$) δ: 144.4, 95.2 (lit. (16) value).

1,2,4,5-Tetraiodobenzene (17)

H_5IO_6 (1.59 g, 6.97 mmol) was dissolved with stirring in conc. H_2SO_4 (25 mL), iodine (5.20 g, 20.5 mmol) was crushed and added to the clear solution. After 30 min of stirring, the dark mixture was placed in an ice bath. Benzene (0.95 g, 12.20 mmol) was then added slowly. The reaction was allowed to stir at room temperature for 2 days. The mixture was poured onto crushed ice. The resulting solid was collected by suction filtration and washed well with methanol to remove iodine. The crude lavender powder was crystallized from 2-methoxyethanol, giving white needles **17** (5.16 g, 73%), mp 253 to 254°C (lit. (17) value mp 253°C). ^{1}H NMR ($CDCl_3$) δ: 7.98 (s, 2H, aromatic H).

General procedure for the homo-coupling of acetylenic sialic acid derivatives (3, 7)

In a mixture of propargyl glycoside (0.2 mmol), CuCl (0.06 mmol), and TMEDA (0.12 mmol) in DMF (5 mL) was bubbled O_2 at 40°C. Then the brownish green solution was poured into water (50 mL). The mixture was extracted with CH_2Cl_2 (3 × 20 mL). The combined organic phases were washed with 5% HCl and brine, dried overNa_2SO_4, and concentrated under vacuum. The residue was purified by silica gel column chromatography CH_2Cl_2–MeOH (20:1, v/v) as eluent.

*1,6-Di-*S*-(methyl 5-acetamido-4,7,8,9-tetra-*O*-acetyl-3,5-dideoxy-*D*-glycero-α-*D*-galacto-2-nonulopyranosylonate)-hex-2,4-di-yne (8)*

Reaction time: 3 h; yield: 83%; mp 131 to 132°C, $[\alpha]_D$ +131.7° (*c* 0.6, $CHCl_3$). FAB-MS calcd.: 1089.12; found: 1089.2 (M^+, 12.2%). ^{1}H NMR ($CDCl_3$) δ: 5.40 (d, 2H, $J_{5,NH}$ = 10.1 Hz, NH), 5.33 (m, 2H, H-8), 5.25 (dd, 2H, $J_{6,7}$ = 2.2 Hz, $J_{7,8}$ = 8.6 Hz, H-7), 4.80 (m, 2H, H-4), 4.20 (dd, 2H, $J_{9a,9b}$ = 12.5 Hz, $J_{8,9a}$ = 2.7 Hz, H-9a), 4.02 (dd, 2H, $J_{8,9b}$ = 5.5 Hz, H-9b), 3.99 (ddd, 2H, $J_{4,5}$ = 10.6 Hz, H-5), 3.83 (dd, 2H, $J_{5,6}$ = 10.8 Hz, H-6), 3.78 (s, 6H, OCH_3), 3.51 (ABq,

© 2002 NRC Canada

2H, J = 16.9 Hz, -SCH_2C≡), 3.38 (ABq, 2H, -SCH_2C≡), 2.65 (dd, 2H, $J_{3a,3e}$ = 12.6 Hz, $J_{3e,4}$ = 4.6 Hz, H-3e), 2.11, 2.07, 1.98, 1.96, 1.81 (s, 30H, OAcs, NHAc), 1.89 (dd, 2H, $J_{3a,4}$ = 12.2 Hz, H-3a). ^{13}C NMR ($CDCl_3$) δ: 170.7–170.0 (O=Cs), 167.9 (C-1), 82.5 (C-2), 74.2 (-SCH_2*C*≡C-), 74.1 (C-6), 69.3 (C-4), 68.2 (C-8), 67.1 (C-7, -SCH_2C≡*C*-), 62.2 (C-9), 53.3 (OCH_3), 49.1 (C-5), 37.4 (C-3), 23.0, 21.1, 20.7, 20.6, 20.6 (NHAc, OAcs), 17.6 (-SCH_2C≡). Anal. calcd. for $C_{46}H_{60}N_2O_{24}S_2$: C 50.73, H 5.55, N 2.57; found: C 50.83, H 5.69, N 2.56.

*1,6-Di-*O*-(methyl 5-acetamido-4,7,8,9-tetra-*O*-acetyl-3,5-dideoxy-*D*-glycero-α-*D*-galacto-2-nonulopyranosylonate)-hex-2,4-di-yne (9)*

Reaction time: 2 h; yield: 86%; mp 118–120°C, $[\alpha]_D$ +23.0° (*c* 1.0, $CHCl_3$). FAB-MS calcd.: 1057.0; found: 1057.2 (M^+, 2.3%). ^{1}H NMR ($CDCl_3$) δ: 5.39–5.31 (m, 4H, NH, H-8), 5.24 (dd, 2H, $J_{6,7}$ = 1.7 Hz, $J_{7,8}$ = 8.6 Hz, H-7), 4.80 (m, 2H, H-4), 4.36 (ABq, 2H, J = 16.2 Hz, -OCH_2C≡), 4.22 (ABq, 2H, -OCH_2C≡), 4.21 (dd, 2H, $J_{9a,9b}$ = 12.4 Hz, $J_{8,9a}$ = 2.7 Hz, H-9a), 4.03–3.98 (m, 6H, H-5, H-6, H-9b), 3.76 (s, 6H, OCH_3), 2.55 (dd, 2H, $J_{3a,3e}$ = 12.8 Hz, $J_{3e,4}$ = 4.6 Hz, H-3e), 2.09, 2.08, 1.98, 1.97, 1.81 (s, 30 H, OAcs, NHAc), 1.88 (dd, 2H, $J_{3a,4}$ = 12.6 Hz, H-3a). ^{13}C NMR ($CDCl_3$) δ: 170.8–169.9 (O=Cs), 167.7 (C-1), 97.9 (C-2), 74.7 (-OCH_2*C*≡C-), 72.6 (C-6), 70.1 (-OCH_2C≡*C*-), 68.8 (C-4), 68.2 (C-8), 67.1 (C-7), 62.3 (C-9), 53.1 (-O*C*H_2C≡), 52.9 (OCH_3), 49.2 (C-5), 37.7 (C-3), 23.0, 21.0, 20.7, 20.7, 20.6 (NHAc, OAcs). Anal. calcd. for $C_{46}H_{60}N_2O_{26}$: C 52.26, H 5.72, N 2.65; found: C 51.92, H 5.75, N 2.65.

*Methyl [4-(methyl 5-acetamido-4,7,8,9-tetra-*O*-acetyl-3,5-dideoxy-*D*-glycero-α-*D*-galacto-2-nonulopyranosyloxyonate prop-2-ynyl) phenyl 5-acetamido-4,7,8,9-tetra-*O*-acetyl-3,5-dideoxy-*D*-glycero-α-*D*-galacto-2-nonulopyranosid] onate (10)*

To a degassed solution of the propargyl sialic acid **3** (58.7 mg, 0.11 mmol) and iodophenyl sialic acid **5** (70 mg, 0.1 mmol) in DMF–Et_3N (4 mL, 1:1) were added $Pd_2(dba)_3$ (5.0 mg, 5.5 μmol) and PPh_3 (5.8 mg, 22 μmol). The mixture was stirred under N_2 at 60°C for 4 h. The solution was poured into water (50 mL). The mixture was extracted with CH_2Cl_2 (3 × 10 mL). The combined organic phases were washed with 5% HCl and brine, dried over Na_2SO_4, and concentrated under vacuum. The residue was purified by silica gel column chromatography using CH_2Cl_2–MeOH (20:1, v/v) as eluent to afford dimer (91 mg, 82%): mp 120 to 121°C, $[\alpha]_D$ +20° (*c* 0.5, $CHCl_3$). ^{1}H NMR ($CDCl_3$) δ: 7.29 (d, 2H, J = 8.6 Hz, aromatic H), 6.93 (d, 2H, aromatic H), 5.47–5.25 (m, 6H, NH, NH′, H-7, H-7′, H-8, H-8′), 4.89 (m, 1H, H-4′), 4.82 (m, 1H, H-4), 4.55 (ABq, 2H, J = 15.6 Hz, -OCH_2C≡), 4.41 (dd, 1H, $J_{5',6'}$ = 10.3 Hz, $J_{6',7'}$ = 1.1 Hz, H-6′), 4.29 (ABq, 2H, -OCH_2C≡), 4.25 (dd, 1H, $J_{9a,9b}$ = 12.4 Hz, $J_{8,9a}$ = 2.8 Hz, H-9a), 4.23 (d, 1H, $J_{9a',9b'}$ = 12.6 Hz, H-9a′), 4.10–4.02 (m, 5H, H-5, H-5′, H-6, H-9b, H-9b′), 3.75 (s, 3H, OCH_3), 3.57 (s, 3H, OCH_3), 2.64 (dd, 1H, $J_{3a',3e'}$ = 12.9 Hz, $J_{3e',4'}$ = 4.6 Hz, H-3e′), 2.60 (dd, 1H, $J_{3a,3e}$ = 12.8 Hz, $J_{3e,4}$ = 4.6 Hz, H-3e), 2.17 (dd, 1 H, $J_{3a',4}$ = 12.6 Hz, H-3a′), 2.12, 2.09, 2.08, 2.07, 2.00, 1.99, 1.99, 1.98, 1.85, 1.83 (s, 30 H, OAcs, NHAcs), 1.96 (dd, 1H, $J_{3a,4}$ = 12.5 Hz, H-3a). ^{13}C NMR ($CDCl_3$) δ: 170.9–169.9 (O=Cs), 168.0 (C-1′), 167.9 (C-1), 154.0, 133.0, 119.4, 117.8 (aromatic C), 99.9 (C-2′), 98.0 (C-2), 85.6 (-OCH_2*C*≡C-), 83.8 (-OCH_2C≡*C*-), 73.4 (C-6′), 72.6 (C-6), 69.1 (C-8′), 68.9 (C-4), 68.6 (C-4′), 68.4 (C-8), 67.3 (C-7′), 67.2 (C-7), 62.3 (C-9), 62.0 (C-9′), 53.6 (-O*C*H_2C≡), 52.9 (OCH_3, OCH_3′), 49.2 (C-5, C-5′), 38.2 (C-3′), 37.9 (C-3), 23.1, 21.0, 20.9, 20.7, 20.6 (NHAcs, Oacs). Anal. calcd. for $C_{49}H_{62}N_2O_{26}$: C 53.75, H 5.71, N 2.56; found: C 53.63, H 5.76, N 2.59.

General procedure for the cross-coupling of acetylenic sialic acid derivatives with 1,4-diiodobenzene (11)

To a degassed solution of the prop-2-ynyl sialosides (**3**, **7**) (0.2 mmol) and 1,4-diiodobenzene (**11**) (30 mg, 91 μmol) in DMF–Et_3N (4 mL, 1:1) were added $Pd_2(dba)_3$ (9.2 mg, 10 μmol) and PPh_3 (10.5 mg, 40 μmol). The mixture was stirred under N_2 at 60°C. The solution was poured into water (50 mL). The mixture was extracted with CH_2Cl_2 (3 × 10 mL). The combined organic phases were washed with 5% HCl and brine, dried over Na_2SO_4, and concentrated under vacuum. The residue was purified by silica gel column chromatography using CH_2Cl_2–MeOH (20:1, v/v) as eluent.

*1,4-Bis-(methyl 5-acetamido-4,7,8,9-tetra-*O*-acetyl-3,5-dideoxy-*D*-glycero-α-*D*-galacto-2-nonulopyranosyloxyonate prop-2-ynyl)benzene (12)*

Reaction time: 2 h; yield: 93%; mp 119–121°C, $[\alpha]_D$ +18.8° (*c* 0.5, $CHCl_3$). FAB-MS calcd.: 1133.09; found: 1133.3 (M^+, 3.6%). ^{1}H NMR ($CDCl_3$) δ: 7.31 (s, 4H, aromatic H), 5.56–5.36 (m, 4H, NH, H-8), 5.27 (dd, 2H, $J_{6,7}$ = 2.0 Hz, $J_{7,8}$ = 8.5 Hz, H-7), 4.83 (m, 2H, H-4), 4.36 (ABq, 2H, J = 15.8 Hz, -OCH_2C≡), 4.33 (ABq, 2H, -OCH_2C≡), 4.25 (dd, 2H, $J_{9a,9b}$ = 12.4 Hz, $J_{8,9a}$ = 2.8 Hz, H-9a), 4.12–4.00 (m, 6H, H-5, H-6, H-9b), 3.74 (s, 6H, OCH_3), 2.60 (dd, 2H, $J_{3a,3e}$ = 12.8 Hz, $J_{3e,4}$ = 4.6 Hz, H-3e), 2.11, 2.08, 1.99, 1.98, 1.83 (s, 30H, OAcs, NHAc), 1.96 (dd, 2H, $J_{3a,4}$ = 12.8 Hz, H-3a). ^{13}C NMR ($CDCl_3$) δ: 170.8–170.0 (O=Cs), 167.9 (C-1), 131.6, 122.6 (aromatic C), 98.1 (C-2), 86.2 (-OCH_2*C*≡C-), 85.6 (-OCH_2C≡*C*-), 72.6 (C-6), 68.8 (C-4), 68.4 (C-8), 67.2 (C-7), 62.3 (C-9), 53.5 (-O*C*H_2C≡), 52.9 (OCH_3), 49.3 (C-5), 37.9 (C-3), 23.1, 21.1, 20.8, 20.7, 20.6 (NHAc, OAcs). Anal. calcd. for $C_{52}H_{64}N_2O_{26}$: C 55.12, H 5.69, N 2.47; found: C 54.82, H 5.75, N 2.49.

*1,4-Bis-(methyl 5-acetamido-4,7,8,9-tetra-*O*-acetyl-3,5-dideoxy-*D*-glycero-α-*D*-galacto-2-nonulopyranosylthioonate prop-2-ynyl)benzene (13)*

Reaction time 3 h; yield: 88%; mp 134–136°C, $[\alpha]_D$ +95° (*c* 0.7, $CHCl_3$). FAB-MS calcd.: 1165.22; found: 1165.2 (M^+, 3.5%). ^{1}H NMR ($CDCl_3$) δ: 7.23 (s, 4H, aromatic H), 5.50 (d, 2H, $J_{5,NH}$ = 9.9 Hz, NH), 5.36 (m, 2H, H-8), 5.26 (dd, 2H, $J_{6,7}$ = 1.6 Hz, $J_{7,8}$ = 8.3 Hz, H-7), 4.81 (m, 2H, H-4), 4.23 (dd, 2H, $J_{9a,9b}$ = 12.4 Hz, $J_{8,9a}$ = 2.4 Hz, H-9a), 4.04–3.98 (m, 4H, H-9b, H-5), 3.83 (dd, 2H, $J_{5,6}$ = 10.7 Hz, H-6), 3.71 (s, 6H, OCH_3), 3.63 (ABq, 2H, J = 16.9 Hz, -SCH_2C≡), 3.58 (ABq, 2H, -SCH_2C≡), 2.67 (dd, 2H, $J_{3a,3e}$ = 12.6 Hz, $J_{3e,4}$ = 4.5 Hz, H-3e), 2.12, 2.05, 1.96, 1.95, 1.81 (s, 30H, OAcs, NHAc), 1.93 (dd, 2H, $J_{3a,4}$ = 12.2 Hz, H-3a). ^{13}C NMR ($CDCl_3$) δ: 170.7–170.0 (O=Cs), 168.0 (C-1), 131.4, 122.8 (aromatic C), 86.6 (C-2), 82.3 (-SCH_2*C*≡C-), 81.8 (-SCH_2C≡*C*-), 74.2 (C-6), 69.4 (C-4), 68.5 (C-8), 67.2 (C-7), 62.2 (C-9), 53.1 (OCH_3), 49.1 (C-5), 37.5 (C-3), 23.0, 21.1, 20.7, 20.7, 20.6 (NHAc, OAcs), 18.0 (-SCH_2C≡).

© 2002 NRC Canada

Anal. calcd. for $C_{52}H_{64}N_2O_{24}S_2$: C 50.73, H 5.55, N 2.57; found: C 50.83, H 5.69, N 2.56.

Fully deprotected divalent sialoside (13a)

To peracetylated sialoside **13** (75 mg, 0.064 mmol) dissolved in MeOH (2 mL) was added 1 M NaOMe in MeOH (1 mL) and the solution was stirred at 25°C. After 4 h, MeOH was removed and 0.1 N NaOH (5 mL) was added. The mixture was stirred at 25°C overnight. The solution was treated with Amberlite IR-120 H^+ resin for 10 min, and filtrered. The filtrate was then freeze-dried to afford compound **13a** in quantitative yield: $[\alpha]_D$ +32.7° (*c* 2.6, H_2O). MS (ES^+) calcd. for $C_{34}H_{44}N_2O_{16}S_2$: 800.86; found: 801.1 ($[M + 1]^+$). ^1H NMR (D_2O) δ: 7.10 (s, 4H, aromatic H), 2.75 (dd, 2H, $J_{3a,3e}$ = 12.4 Hz, $J_{3e,4}$ = 4.5 Hz, H-3e), 1.91 (s, 6H, NHAc), 1.80 (dd, 2H, $J_{3a,4}$ = 12.2 Hz, H-3a). ^{13}C NMR (D_2O) δ: 175.4 (C=O), 170.8 (C-1), 131.3, 122.7 (aromatic C), 88.2 (-SCH$_2$*C*≡C-), 83.4 (C-2), 82.5 (-CH$_2$C≡*C*-), 75.4 (C-6), 71.7 (C-4), 68.8 (C-8), 69.5 (C-7), 63.2 (C-9), 52.1 (C-5), 40.2 (C-3), 22.5 (NHAc), 18.3 (-S*C*H$_2$C≡).

General procedure for the cross-coupling of acetylenic sialic acid derivatives with 1,3,5-triiodobenzene (14)

To a degassed solution of the propargyl sialic acid (0.2 mmol) and 1,3,5-triiodobenzene (**14**) (27.8 mg, 61 μmol) in DMF–Et_3N (4 mL, 1:1) were added $Pd_2(dba)_3$ (9.2 mg, 10 μmol), CuI (3.8 mg, 20 μmol), and PPh_3 (10.5 mg, 40 μmol). The mixture was stirred under N_2 at room temperature for 1 h. The solution was poured into water (50 mL). The mixture was extracted with CH_2Cl_2 (3 × 10 mL). The combined organic phases were washed with 5% HCl and brine, dried over Na_2SO_4, and concentrated under vacuum. The residue was purified by silica gel column chromatography using CH_2Cl_2–MeOH (15:1, v/v) as eluent.

1,3,5-Tris-(methyl 5-acetamido-4,7,8,9-tetra-*O*-acetyl-3,5-dideoxy-D-glycero-α-D-galacto-2-nonulopyranosyloxyonate prop-2-ynyl)benzene (15)

Yield: (81%); mp 129–132°C, $[\alpha]_D$ +16.2° (*c* 0.5, $CHCl_3$). FAB-MS calcd.: 1660.59; found: 1660.5 (M^+, 1.5%). ^1H NMR ($CDCl_3$) δ: 7.37 (s, 3H, aromatic H), 5.40–5.37 (m, 6H, NH, H-8), 5.28 (dd, 3H, $J_{6,7}$ = 1.9 Hz, $J_{7,8}$ = 8.5 Hz, H-7), 4.82 (m, 3H, H-4), 4.53 (ABq, 3H, *J* = 15.9 Hz, -OC*H*$_2$C≡), 4.28 (ABq, 3H, -OC*H*$_2$C≡), 4.24 (dd, 3H, $J_{9a,9b}$ = 12.6 Hz, $J_{8,9a}$ = 2.7 Hz, H-9a), 4.08–4.00 (m, 9H, H-5, H-6, H-9b), 3.74 (s, 9H, OCH_3), 2.60 (dd, 3H, $J_{3a,3e}$ = 12.8 Hz, $J_{3e,4}$ = 4.6 Hz, H-3e), 2.12, 2.09, 1.99, 1.98, 1.83 (s, 45H, OAcs, NHAc), 1.95 (dd, 3H, $J_{3a,4}$ = 12.8 Hz, H-3a). ^{13}C NMR ($CDCl_3$) δ: 171.1–170.0 (O=Cs), 167.8 (C-1), 134.6, 123.2 (aromatic C), 98.1 (C-2), 85.8 (-OCH$_2$*C*≡C-), 84.2 (-OCH$_2$C≡*C*-), 72.6 (C-6), 68.8 (C-4), 68.3 (C-8), 67.2 (C-7), 62.4 (C-9), 53.4 (-O*C*H$_2$C≡), 52.9 (OCH_3), 49.3 (C-5), 37.9 (C-3), 23.1, 21.1, 20.8, 20.7, 20.6 (NHAc, Oacs). Anal. calcd. for $C_{75}H_{93}N_3O_{39}$: C 54.25, H 5.64, N 2.53; found: C 54.55, H 5.63, N 2.50.

1,3,5-Tris-(methyl 5-acetamido-4,7,8,9-tetra-*O*-acetyl-3,5-dideoxy-D-glycero-α-D-galacto-2-nonulopyranosylthioonate prop-2-ynyl)benzene (16)

Yield: (76%); $[\alpha]_D$ +104.7° (*c* 0.3, $CHCl_3$). FAB-MS calcd.: 1708.63; found: 1708.9 (M^+, 2.5%). ^1H NMR ($CDCl_3$) δ: 7.26 (s, 3H, aromatic H), 5.53 (d, 3H, $J_{5,NH}$ = 9.9 Hz, NH), 5.36 (m, 3H, H-8), 5.27 (dd, 3H, $J_{6,7}$ = 2.2 Hz, $J_{7,8}$ = 8.3 Hz, H-7), 4.83 (m, 3H, H-4), 4.24 (dd, 3H, $J_{9a,9b}$ = 12.5 Hz, $J_{8,9a}$ = 2.6 Hz, H-9a), 4.05–3.99 (m, 6H, H-9b, H-5), 3.85 (dd, 3H, $J_{5,6}$ = 10.8 Hz, H-6), 3.72 (s, 9H, OCH_3), 3.59 (s, 6H, -SC*H*$_2$C≡), 2.68 (dd, 3H, $J_{3a,3e}$ = 12.6 Hz, $J_{3e,4}$ = 4.6 Hz, H-3e), 2.13, 2.07, 1.98, 1.97, 1.82 (s, 45H, OAcs, NHAc), 1.93 (dd, 3 H, $J_{3a,4}$ = 12.0 Hz, H-3a). ^{13}C NMR ($CDCl_3$) δ: 170.8–170.0 (O=Cs), 168.0 (C-1), 134.1, 123.5 (aromatic C), 86.3 (C-2), 82.7 (-SCH$_2$*C*≡C-), 81.0 (-SCH$_2$C≡*C*-), 74.2 (C-6), 69.4 (C-4), 68.6 (C-8), 67.2 (C-7), 62.2 (C-9), 53.1 (OCH_3), 49.1 (C-5), 37.5 (C-3), 23.0, 21.1, 20.7, 20.7, (NHAc, OAcs), 17.8 (-S*C*H$_2$C≡). Anal. calcd. for $C_{75}H_{93}N_3O_{36}S_3$: C 52.72, H 5.49, N 2.46; found: C 52.75, H 5.67, N 2.45.

1,2,4,6-Tetrakis-(methyl 5-acetamido-4,7,8,9-tetra-*O*-acetyl-3,5-dideoxy-D-glycero-α-D-galacto-2-nonulopyranosyloxyonate prop-2-ynyl)benzene (18)

To a degassed solution of the prop-2-ynyl sialoside **3** (100 mg, 0.19 mmol) and 1,2,4,5-tetraiodobenzene (**17**) (25 mg, 43 μmol) in DMF–Et_3N (4 mL, 1:1) were added $Pd_2(dba)_3$ (8.6 mg, 9.4 μmol), CuI (3.6 mg, 18.9 μmol), and PPh_3 (9.9 mg, 37.7 μmol). The mixture was stirred under N_2 at room temperature for 4 h. The solution was poured into water (50 mL). The mixture was extracted with CH_2Cl_2 (3 × 10 mL). The combined organic phases were washed with 5% HCl and brine, dried over Na_2SO_4, and concentrated under vacuum. The residue was purified by silica gel column chromatography using CH_2Cl_2–MeOH (10:1, v/v) as eluent to afford tetramer **18** (82 mg, 87%): $[\alpha]_D$ +25.6° (*c* 0.5, $CHCl_3$). FAB-MS calcd.: 2188.08; found: 1696.6 [M^+-$C_{20}H_{28}NO_{13}$ -H, 0.7%). ^1H NMR ($CDCl_3$) δ: 7.44 (s, 2H, aromatic H), 5.47 (d, 4H, $J_{5,NH}$ = 8.4 Hz, NH), 5.37 (m, 4H, H-8), 5.28 (dd, 4H, $J_{6,7}$ = 1.8 Hz, $J_{7,8}$ = 8.4 Hz, H-7), 4.82 (m, 4H, H-4), 4.58 (ABq, 4H, *J* = 16.1 Hz, -OC*H*$_2$C≡), 4.40 (ABq, 4H, -OC*H*$_2$C≡), 4.25 (dd, 4H, $J_{9a,9b}$ = 12.5 Hz, $J_{8,9a}$ = 2.6 Hz, H-9a), 4.07–3.98 (m, 12H, H-5, H-6, H-9b), 3.75 (s, 12H, OCH_3), 2.60 (dd, 4H, $J_{3a,3e}$ = 12.8 Hz, $J_{3e,4}$ = 4.6 Hz, H-3e), 2.12, 2.08, 1.98, 1.97, 1.82 (s, 60 H, OAcs, NHAc), 1.93 (dd, 4H, $J_{3a,4}$ = 12.5 Hz, H-3a). ^{13}C NMR ($CDCl_3$) δ: 170.8–170.0 (O=Cs), 167.8 (C-1), 136.1, 124.8 (aromatic C), 98.1 (C-2), 90.7 (-OCH$_2$*C*≡C-), 83.1 (-OCH$_2$C≡*C*-), 72.5 (C-6), 68.8 (C-4), 68.4 (C-8), 67.1 (C-7), 62.3 (C-9), 53.4 (-O*C*H$_2$C≡), 52.9 (OCH_3), 49.3 (C-5), 37.8 (C-3), 23.0, 21.0, 20.7, 20.7, 20.6 (NHAc, OAcs). Anal. calcd. for $C_{98}H_{122}N_4O_{52}$: C 53.75, H 5.71, N 2.56; found: C 53.46, H 5.67, N 2.50.

1,3,4- and 1,3,5-Tris-(methyl 5-acetamido-4,7,8,9-tetra-*O*-acetyl-3,5-dideoxy-D-glycero-α-D-galacto-2-nonulopyranosyloxyonate methylene)benzene (20a, 20b)

To a solution of the prop-2-ynyl sialoside **3** (100 mg, 0.19 mmol) in dry 1,2-dichloroethane (4 mL) was added ruthenium catalyst **19** (8 mg, 9.7 μmol). The mixture was refluxed under N_2 for 24 h. The solution was evaporated under vacuum. The residue was purified by silica gel column chromatography using CH_2Cl_2–MeOH (10:1, v/v) as eluent to afford two isomers **20a**, **20b** (68 mg, 68%) (1,2,4- and 1,3,5-regioisomers, 9:2). ^1H NMR ($CDCl_3$) δ: 7.27 (d, 1H, *J* = 7.8 Hz, H-Ar), 7.23 (s, 1H, H-Ar), 7.19 (d, 1H, H-Ar), 7.14 (s, 1H, H-Ar for the sym. isomer), 3.69, 355, 3.54 (s, OMe), 3.68 (s, OMe for the syn. isomer), 2.64–2.55 (m, 3H,

© 2002 NRC Canada

H-3e). ^{13}C NMR ($CDCl_3$) δ: 170.9–168.1 (C=Os), 137.2, 126.4 (Ar for sym. Isomer), 136.4, 135.4, 135.0, 128.7, 127.9, 127.1 (Ar), 98.6, 98.3, 98.3 (C-2), 72.5, 72.4, 72.3 (C-6), 69.4 (C-4), 68.5, 68.4 (C-8), 67.3, 67.2 (C-7), 66.5, 64.3, 64.1 (CH_2), 62.3, 62.2, 62.1 (C-9′), 52.6, 52.5, 52.5 (OCH_3), 49.4 (C-5), 38.0, 38.0, 37.9 (C-3), 23.1 (NHAc), 21.1, 20.8, 20.7, 20.7 (Oacs).

Conclusions

In summary, the palladium-catalyzed Sonogashira reaction has been successfully applied for the synthesis of sialic acid clusters of restricted conformational mobility. The procedure is general, high yielding, compatible with the easily removable acetate protecting group, and the sialic acid clusters were isolated in excellent yields. The reactions are applicable to thioglycosides. The choice for these "rigidified" scaffolds is based on the assumption that lesser entropic penalty will be paid upon binding with the siglecs, as previously observed by isothermal titration calorimetry (ITC) for analogous mannoside clusters upon binding to the phytohemagglutinin concanavalin A (20).

Acknowledgment

Support of this work by the Natural Sciences and Engineering Research Council of Canada (NSERC) is gratefully acknowledged.

References

1. S. Kelm and R. Schauer. Int. Rev. Cytol. **175**, 137 (1997).
2. K. Drickamer and M.E. Taylor. Trends Biochem. Sci. **23**, 321 (1998).
3. (*a*) P.R. Crocker and S. Kelm. The siglec family of I-type lectins. *In* Carbohydrates in chemistry and biology. Vol. 4. *Edited by* B. Ernst, G.W. Hart, and P. Sinaÿ. Wiley–VCH, Weinheim. 2000. Chap. 35. p. 579; (*b*) P.R. Crocker and A. Varki. Trends Immunol. **22**, 337 (2001).
4. J.M. Rini and Y. Lobsanov. Curr. Opin. Struct. Biol. **9**, 578 (1999).
5. Y. Hashimoto, M. Suzuki, P.R. Crocker, and A. Suzuki. J. Biochem. (Tokyo), **123**, 468 (1998).
6. (*a*) R. Roy. Curr. Opin. Struct. Biol. **6**, 692 (1996); (*b*) R. Roy. Top. Curr. Chem. **187**, 241 (1997).
7. R. Roy, S.K. Das, R. Dominique, M.C. Trono, F. Hernández-Mateo, and F. Santoyo-González. Pure Appl. Chem. **71**, 565 (1999).
8. R. Roy and C.A. Lafferière. Can. J. Chem. **68**, 2045 (1990).
9. D. Carrière, S.J. Meunier, F.D. Tropper, and R. Roy. J. Mol. Catal. A: Chem. **154**, 9 (2000).
10. R. Roy, D. Zanini, S.J. Meunier, and A. Romanowska. ACS Symp. Ser. **560**, 104 (1994).
11. A. Hasegawa, J. Nakamura, and M. Kiso. J. Carbohydr. Chem. **5**, 11 (1986).
12. Z. Gan and R. Roy. Tetrahedron Lett. **41**, 1155 (2000).
13. (*a*) C. Glaser. Ann. Chem. Pharm. **154**, 137 (1870). For a review and representative examples see: (*b*) P. Siemsen, R.C. Livingston, and F. Diederich. Angew. Chem. Int. Ed. Engl. **39**, 2632 (2000); (*c*) A.S. Hay. J. Org. Chem. **27**, 3320 (1962); (*d*) G. Eglinton and A.R. Galbraith. Chem. Ind. (London), 737 (1956); (*e*) G. Eglinton. J. Chem. Soc. 889 (1959).
14. (*a*) R. Roy, S.K. Das, F. Hernández-Mateo, F. Santoyo-González, and Z. Gan. Synthesis, 1049 (2001); (*b*) B. Liu and R. Roy. J. Chem. Soc. Perkin Trans. 1, 773 (2001).
15. For examples of Glaser and Sonogashira reactions using organosulfur compounds see: (*a*) T.J.J. Müller Tetrahedron Lett. **40**, 6563 (1999); (*b*) M. Fossatelli, A.C.T.H. van der Kerk, S.F. Vasilevsky, and L. Brandsma. Tetrahedron Lett. **33**, 4229 (1992); (*c*) T.X. Nee and G.M. Whitesides. J. Org. Chem. **53**, 2489 (1988); (*d*) U. Fritzsche and S. Hunig. Tetrahedron Lett. **13**, 4831 (1972). For reviews on general palldium cross-couplings, see: (*e*) K. Sonogashira. *In* Comprehensive organic synthesis. Vol. 3. *Edited by* B.M. Trost and I. Fleming. Pergamon Press, New York. 1991. pp. 521–549; (*f*) L. Brandsma, S.F. Vasilevsky, and H.D. VerKruijsse. *In* Application of transition metal catalysts in organic synthesis. Springer, Berlin. 1998. pp. 67–83; (*g*) K. Sonogashira. *In* Metal-catalyzed cross-coupling reactions. *Edited by* F. Diederich and P.J. Stang. Wiley–VCH, Weinheim, Germany. 1998. pp. 203–229.
16. U. Schöberl, T.F. Magnera, R.M. Harrison, F. Fleischer, J.L. Pflug, P.F.H. Schwab, X. Meng, D. Lipiak, B.C. Noll, V.S. Allured, T. Rudaleige, S. Lee, and J. Michl. J. Am. Chem. Soc. **119**, 3907 (1997).
17. D.L. Mattern. J. Org. Chem. **49**, 3051 (1984).
18. S.K. Das and R. Roy. Tetrahedron Lett. **40**, 4015 (1999).
19. R.J. Kauman and R.S. Sidhu. J. Org. Chem. **47**, 4941 (1982).
20. T.K. Dam, R. Roy, S.K. Das, S. Oscarson, and C.F. Brewer. J. Biol. Chem. **275**, 14 223 (2000).

© 2002 NRC Canada

The activation of fibroblast growth factors by heparin: Synthesis and structural study of rationally modified heparin-like oligosaccharides

Rafael Ojeda, Jesús Angulo, Pedro M. Nieto, and Manuel Martín-Lomas

Abstract: Heparin-like hexasaccharide **3** and octasaccharide **4** have been synthesized using a convergent block strategy and their solution conformations have been determined by NMR spectroscopy. Both oligosaccharides contain the basic structural motif of the regular region of heparin but have been constructed as to display negatively charged sulfate groups only on one side of their solution helical structures. This charge distribution along the saccharide chain has been designed to get insight into the proposed mechanism for fibroblast growth factors (FGFs) activation that involves heparin-induced FGF dimerization.

Key words: heparin oligosaccharides, synthesis design, conformational analysis, FGF activation.

Résumé : On a réalisé la synthèse d'un hexasaccharide (**3**) et d'un octasaccharide (**4**) apparenté à l'héparine en faisant appel à une stratégie de synthèse convergente par blocs et on a déterminé leurs conformations en solution à l'aide de la spectroscopie RMN. Les deux oligosaccharides comportent le motif structurel de base de la région régulière de l'héparine, mais leurs structures ont été organisées d'une façon telle qu'elles ne comportent des groupes sulfates chargés négativement que sur un seul côté de leurs structures hélicoïdales en solution. Cette distribution des charges ainsi que la chaîne du saccharide ont été choisies afin d'avoir un aperçu du mécanisme proposé pour l'activation des facteurs de croissance du fibroblaste (FCF) qui implique une dimérisation des FCF induite par l'héparine.

Mots clés : oligosaccharides de l'héparine, modèle de synthèse, analyse conformationnelle, activation des FCF.

[Traduit par la Rédaction]

Introduction

The fibroblast growth factors (FGFs) constitute a family of signaling polypeptides that intervene in a variety of biological processes by stimulating key cellular functions after binding to specific receptor tyrosine kinases at the cell surface (FGFRs) (1). The biological activity of FGFs is tightly regulated by heparin or heparan sulfate glycosaminoglycans (GAGs) (2, 3). Binding of these GAGs to FGFs protects FGFs from degradation (4), however, the precise structural requirements for the GAG chains to regulate the biological activity of the FGFs are not yet well understood at the molecular level. A number of crystal structures of FGF complexes with heparin fragments (5–7), and of FGF-2 (basic FGF) and FGF-1 (acidic FGF) bound to variants of FGFR (8–11) have been determined and several hypotheses on the structure–activity relationship of these complexes have been expressed (12). It is widely accepted that heparin and (or) heparan sulfate would bind to FGFs to cause FGF oligomerization and that these oligomers would interact with FGFRs in the presence of divalent cations giving rise to FGFR dimerization, thus inducing the cellular response (13). According to sedimentation equilibrium experiments, the formation of FGF-2 dimers in the presence of heparin having a *trans* (with two FGF molecules on each side of the polysaccharide chain) or a *cis* (with two FGF molecules on the same side of the polysaccharide chain) configuration has been proposed (14). The existence of both types of dimeric structures has been confirmed by NMR spectroscopy and light scattering (15). The *trans* dimer has also been observed for the FGF-1-heparin complex using X-ray crystallography (7).Whether this type of mechanism, which was originally proposed for FGF-2 (14), would be generally applicable to all the members of the FGF family is still a matter of discussion as the biologically active configuration of the heparin-FGF and the heparin-FGF–FGFR complexes are still open questions (16, 17). The establishment of the molecular basis of the entire biological process and the understanding of the

Received 7 August 2001. Published on the NRC Research Press Web site at http://canjchem.nrc.ca on 19 July 2002.

Dedicated to the memory of Ray Lemieux whose outstanding vision of chemistry and strong personality deeply influenced the early days of the Carbohydrate Group in Seville. We consider ourselves privileged to have been connected to him during the last years of his fruitful life.

R. Ojeda, J. Angulo, P.M. Nieto, and M. Martín-Lomas.[1] Grupo de Carbohidratos. Instituto de Investigaciones Químicas, CSIC, Américo Vespucio s/n, Isla de la Cartuja, 41092 Seville, Spain.

[1]Corresponding author (e-mail: manuel.martin-lomas@iiq.cartuja.csic.es).

 DOI: 10.1139/V02-023 © 2002 NRC Canada

different functions of the FGF family at the molecular level remain, therefore, a difficult problem of chemical and biomedical interest.

One of the difficulties of these investigations resides in the inherent heterogeneity of the GAGs. Heparin and heparan sulfate are primarily constituted by disaccharide repeating units of L-iduronic acid and D-glucosamine linked by $\alpha 1 \rightarrow 4$ glycosidic linkages and typically containing sulfate groups at position 2 of the L-iduronic acid units and positions 2 and 6 of the D-glucosamine units. But these polysaccharides show significant heterogeneity in terms of sulfation pattern, size, and even carbohydrate sequence (18–20). For this reason it is highly desirable to develop effective syntheses of these heparin-like oligosaccharide chains with defined size, sequence, and charge distribution to be used in the interaction studies. In this context, we recently reported a synthetic strategy the effectiveness of which was illustrated by the preparation of hexasaccharide **1** and octasaccharide **2** (21). It has to be mentioned that these oligosaccharides contain L-iduronic acid residues at the reducing end, a sequence which is not available either by enzymatic or chemical degradation of heparin, and that oligosaccharides with the alternative sequence (22–24) and di- and tetrasaccharide sequences containing the above structural motif (25) have previously been synthesized. The overall structures of **1** and **2** in solution (21) resulted in stable right hand helixes with four residues per turn as those reported for natural heparin fragments (26–30). Therefore, **1** and **2** were used as chemically well-defined structural models of naturally occurring heparin-like oligosaccharides to investigate the activation of FGF-1 (21). Both compounds **1** and **2** induced the mitogenic activity of FGF-1 but, as may be expected (31–35), the activating effect of octasaccharide **2** reached a maximum at approximately the same concentration than natural low molecular weight heparin while considerably higher concentrations of **1** were needed to reach an equivalent maximal activation (21). Most interestingly, sedimentation equilibrium analysis results showed that the profile of FGF-1 solutions in the presence of activating concentrations of **2** corresponded to monomeric species thus suggesting that heparin-induced dimerization of FGF-1 in the culture medium surrounding the cell may not be an absolute requirement for FGF-1-induced mitogenesis signaling (21).

The above result prompted us to apply our synthetic strategy to the preparation of hexasaccharide **3** and octasaccharide **4** and to investigate their behavior in FGF-1 activation. We reasoned that, assuming that **3** and **4** would present a solution conformation similar to that shown by **1** and **2**, these structures (**3** and **4**) would display negatively charged sulfate groups only on one side of their right-handed helical structures (Fig. 1). Therefore, if the interaction with the polypeptide is primarily electrostatic in nature, the ability of **3** and **4** to form *trans* dimers with FGF-1would be greatly decreased and, because of their relatively reduced size, both of them would hardly be involved in the formation of *cis* dimers.

In this paper, we report the synthesis of **3** and **4** and present data that indicate that, as expected, their overall solution

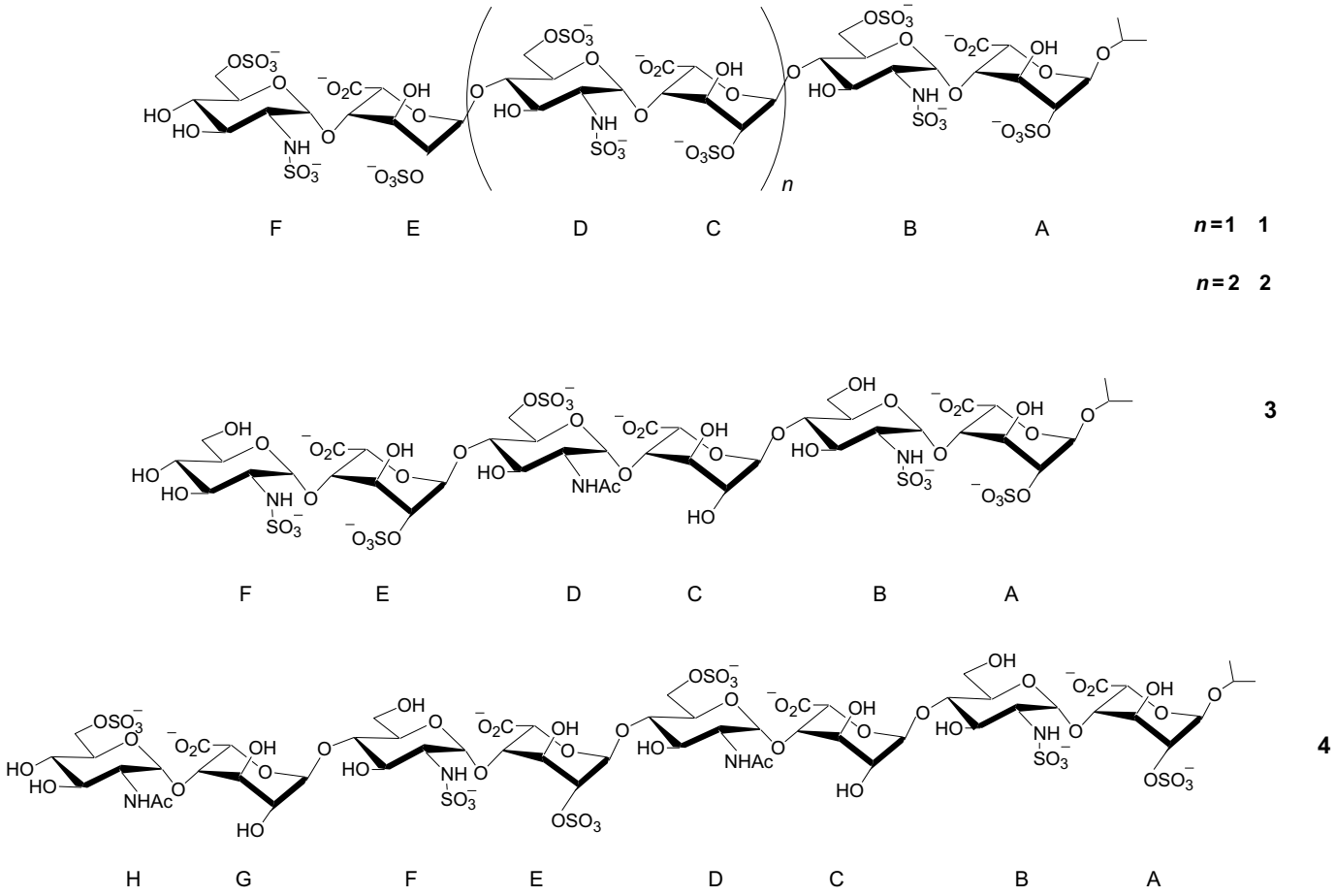

© 2002 NRC Canada

Fig. 1. Crystallographic structure of an FGF-1 *cis*-dimer (protein data bank accession code 1axm) (7) and schematic representation of hexasaccharides **1** and **3**.

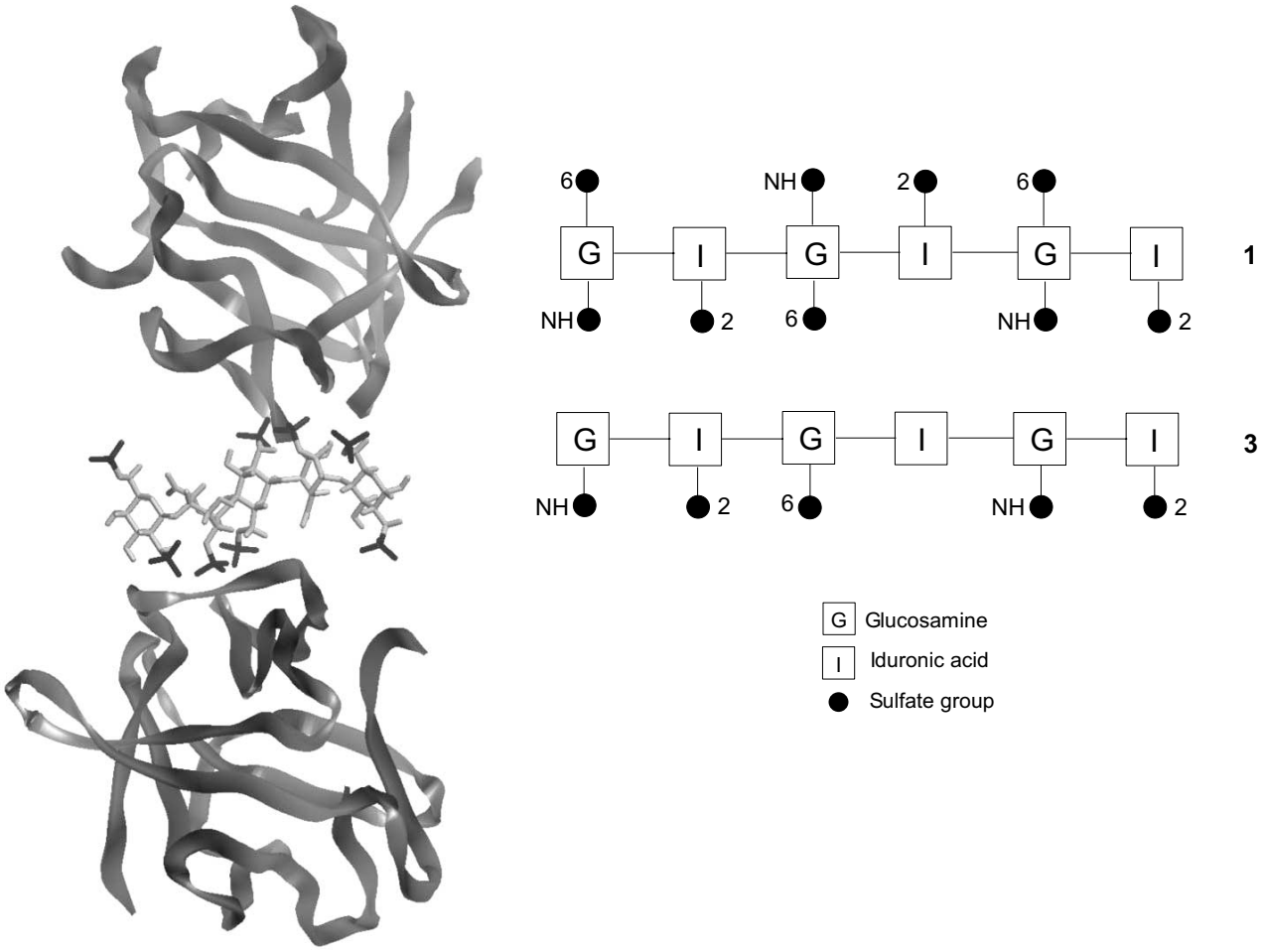

structures are right-handed helixes with four residues per turn. These compounds showed an unexpected biological behavior that will be discussed in detail elsewhere.

Results and discussion

Synthesis

We have reported the synthesis of hexasaccharide **1** and octasaccharide **2** using a convergent $n + 2$ block approach from key disaccharide structures, that may operate as glycosyl donors or as glycosyl acceptors, having protective group patterns that permit formation of the required stereochemistry of the glycosidic linkages and to locate the sulfate groups at the desired positions at a later stage (21). This approach has now proven to be of wide applicability allowing the synthesis of oligosaccharide sequences with different size and sulfation patterns as the target hexasaccharides **3** and **4**. As indicated in Scheme 1 the synthesis of **3** was envisaged from the fully protected hexasaccharide **5** that could be prepared from disaccharide building blocks **6**, **7**, and **8**. These building blocks were obtained from a common disaccharide (**9**) that is readily available from the 2-azido-2-deoxy-D-glucopyranosyl trichloroacetimidate **10** and the iduronic acid glycosyl acceptor **11** (21).

Scheme 2 summarizes the synthesis of the disaccharide building blocks. The nonreducing-end building block **6** was prepared from **9** as already reported (21). This disaccharide (**6**) also provided the reducing-end building block **8** after glycosylation with isopropanol to give **12** (21) followed by regioselective reductive opening of the benzylidene acetal (36). The alternative building block **14** was also prepared from **12** that was transformed into diol **13** (21) and regioselectively acetylated (4% of **13** was recovered). The inner region building block **7** was also prepared from **9** that was transformed into **17** either by selective reduction of the azido group with thioacetic acid (37) to give **15** followed by conventional acetylation or by using the reverse sequence **9** $\rightarrow$ **16** $\rightarrow$ **17**. This latter route was more convenient as acetylation of **15** took place sluggishly most likely as a consequence of hydrogen bonding between the hydroxyl and the acetamido groups.

Glycosylation of low-reactive acceptor **8** with donor **7** afforded tetrasaccharide **19** in 50% yield and unreacted acceptor (46%) (Scheme 3). Compound **19** was deacetylated to give **20** which was benzylated under neutral conditions (38) to yield **21**. Hydrolysis of the benzylidene acetal (39) gave diol **22** that was regioselectively benzoylated (40) to afford tetrasaccharide acceptor **23**.

© 2002 NRC Canada

Scheme 1.

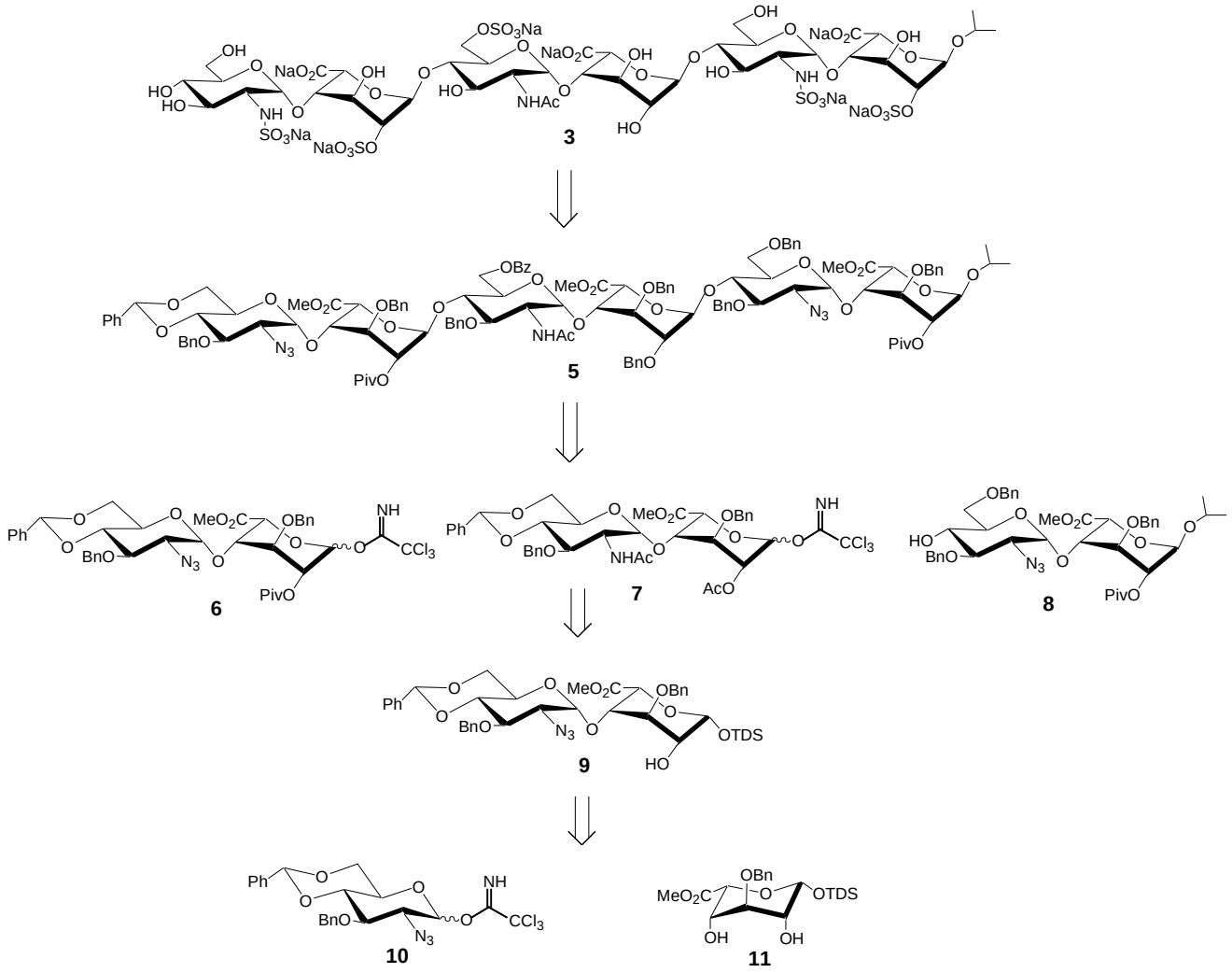

In spite of the moderate yield of the glycosylation reaction, this synthetic route to **23** was more convenient than that using acceptor building block **14** since the deactivating effect of the acetyl group in **14** further complicated the coupling with **7** to give **24** with formation of orthoester and considerable elimination (25% of 2-acetoxyglycal). Compound **24** could be conventionally deacetylated to give **25** that was benzylated to yield **21** (52%).

The coupling of **23** with donor **6** afforded hexasaccharide **5** in 65% yield. The methoxycarbonyl and acyl groups in **5** were removed by treatment with lithium hydroperoxide and then hydroalcoholic potasium hydroxide (41, 42) and the resulting partially protected hexasaccharide **26** was sulfonated and isolated as the sodium salt **27**. Hydrogenolytic cleavage of the benzylidene acetal and benzyl groups and simultaneous reduction of the azido groups in **27** followed by selective *N*-sulfonation yielded compound **3** that was purified using a protocol partially based on the reported purification of synthetic oligosaccharides of the irregular region of heparin (42).

The elongation of the oligosaccharide chain to obtain an octasaccharide (**4**) was performed by adding a new disaccharide building block (**34**) to the nonreducing end of the previously constructed hexasaccharide structure **5**. This building block (**34**) was prepared as indicated in Scheme 4 from the iduronic acid derivative **11** (21, 43) and trichloroacetimidate **29** that was obtained from **28** (21, 44). Coupling of **29** with **11** gave disaccharide **30** that was transformed into trichloroacetimidate **34** following the sequence **30** → **31** → **32** → **33** → **34** as indicated in Scheme 4. Building block acceptor **35** was prepared by regioselective reductive opening of the benzylidene acetal group in **5** (Scheme 5). As expected (21), the glycosylation reaction between **34** with **35** took place in only moderate yield (40%). However, no attempt was made to optimize this reaction since a reasonable amount of octasaccharide **36** was isolated that allowed the subsequent transformations leading to sufficient **4** for structural and biological investigation. The relevance of **4** for these further studies, which was not yet known at this stage, would dictate whether working out some changes in this synthetic strategy may be worthwhile in the near future. The introduction of a needed permanent protecting group at position 2 of the G unit was satisfactorily carried out by selective deacylation using catalytic sodium methoxide in methanol to obtain **37** (80%) followed by benzylation under neutral conditions (38) to afford **38**. The carboxymethyl and *O*-acyl groups were then removed by treatment with lithium hydroperoxide then alcoholic potasium

© 2002 NRC Canada

Scheme 2. Reagents and conditions: (*a*) $NaBH_3CN$, THF, HCl–Et_2O, 92%; (*b*) EtSH, PTSA, CH_2Cl_2, 90%; (*c*) Ac_2O, Py, CH_2Cl_2, –10°C, 85%; (*d*) AcSH, 73–77%; (*e*) Ac_2O, Py, 93–77%; (*f*) $(HF)_n$·Py, THF, –15°C, 78%; (*g*) K_2CO_3, Cl_3CCN, CH_2Cl_2, 94%.

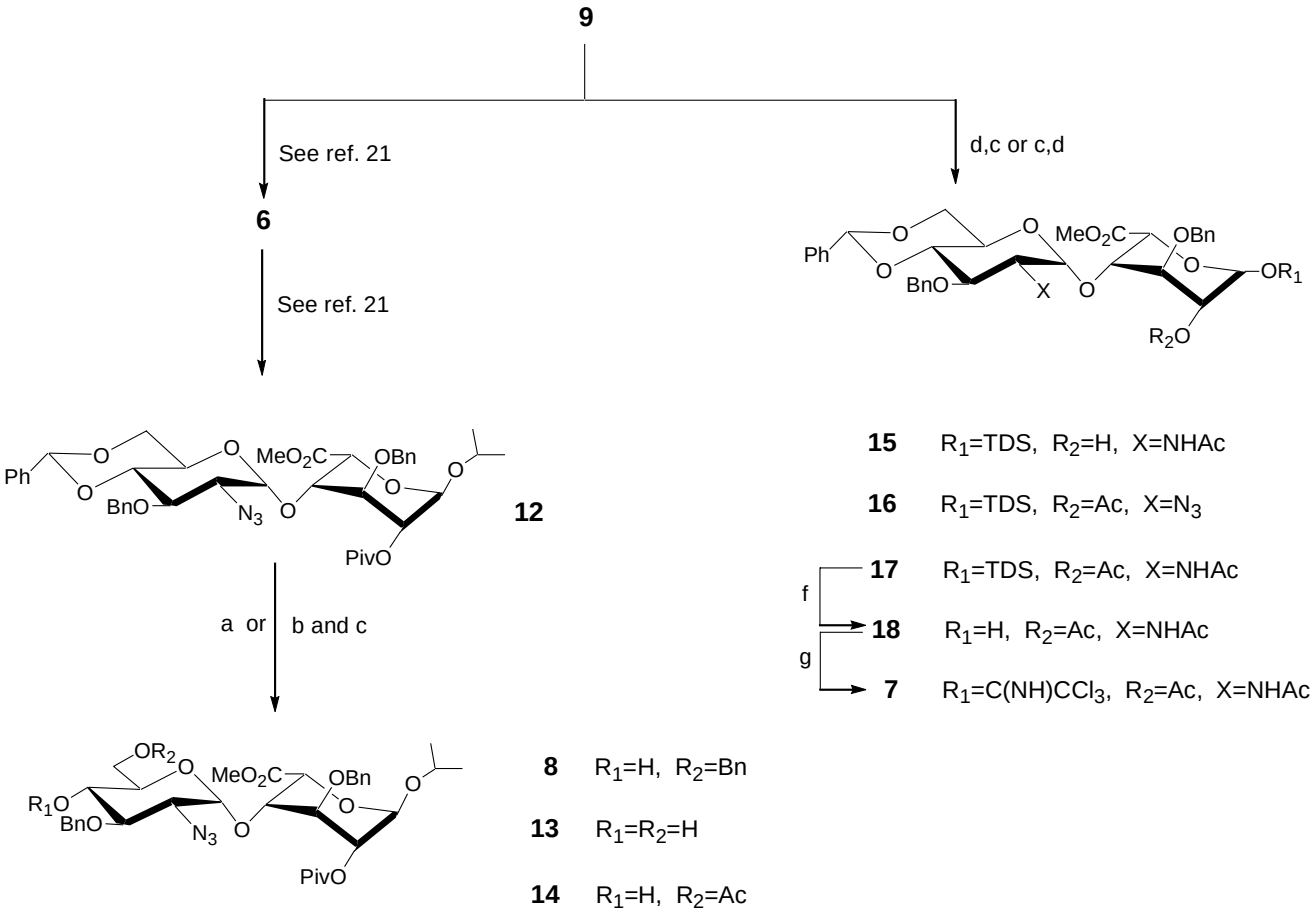

hydroxide to give **39** that was *O*-sulfonated to yield **40**. Hydrogenolytic cleavage of the benzyl groups with concomitant reduction of the azido groups of **40** followed by *N*-sulfonation gave finally octasaccharide **4** that was purified as **3**.

Structural study

The ^1H and ^{13}C NMR spectra of **3** and **4** were fully assigned using conventional 1D and 2D spectroscopy (Table 1). These assignments were carried out by identification of the spin systems of the residues and further connection based on inter-residue NOE. The substitution pattern in **3** and **4** led to a better signal dispersion than that observed in the spectra of hexasaccharide **1** and octasaccharide **2.** The chemical shift values were in agreement with those expected according to reported data for chemicaly modified heparin (45, 46). Three bond coupling constants were obtained from 2D DQF-COSY(47). As expected, the D-glucosaminyl residues showed a single $^4C_1$ conformation and the ω rotamer of the 6-*O*-sulfated units appeared as in **1** (21) as the *gg* conformer. The observed values for the coupling constants of the iduronate residues could be accounted for by the existence of a conformational equilibrium between $^1C_4$ and ^2S_o forms as reported for heparin (Table 2), also confirmed by the H2-H5 NOE (30). Therefore, the lack of the 2-*O*-sulfate group in the C and G units and the further modifications in the neighboring glucosamine residues, absence of 6-*O*-sulfate group in the B and F units and of *N*-sulfate group in the D and H units, do not seem to qualitatively modify the conformational behavior of these iduronate rings with respect to heparin. This result is also in agreement with previous findings that similar structural changes in natural heparin fragments do not influence the inner iduronate ring conformational equilibrium (48).

With regard to the conformation around the glycosidic linkages, the NOEs pattern observed for hexasaccharide **3** was compared to that previously obtained for the parent hexasaccharide **1** (see supplementary data).[2] There were no indications of conformational changes as no major differences were observed and only small intensity variations, which could be attributed to differences in correlation times, were detected. The possibility that the changes in charge distribution in **3** with respect to **1** may partially drive the glycosidic angles towards an *anti*-ψ arrangement could, therefore, be discarded. Furthermore, the exclusive NOEs that should be expected for such *anti*-ψ situations (H1′-H5 for the IdoA–GlcN linkages and H5′-H3 for the GlcN–IdoA ones) could not be observed in NOESY experiments with hexasaccharide **3**.

[2] Supplementary material may be purchased from the Depository of Unpublished Data, Document Delivery, CISTI, National Research Council Canada, Ottawa, ON K1A 0S2, Canada (http://www.nrc.ca/cisti/irm/unpub_e.shtml for information on ordering electronically).

© 2002 NRC Canada

Scheme 3. Reagents and conditions: (*a*) TMSOTf, CH_2Cl_2, 50%; (*b*) MeONa, MeOH, 96%; (*c*) Ag_2O, BnBr, DMF, 88%; (*d*) EtSH, PTSA, CH_2Cl_2, 83%; (*e*) BzCN, Et_3N, CH_3CN, –40°C, 88%; (*f*) TMSOTf, CH_2Cl_2, 65%; (*g*) (*i*) H_2O_2, LiOH aq; (*ii*) KOH aq, MeOH, 98%; (*h*) SO_3·Py, Py, 72%; (*i*) Pd/C, H_2, MeOH–H_2O (9:1); (*j*) SO_3·Py, H_2O, pH = 9.5, 75% from **27**.

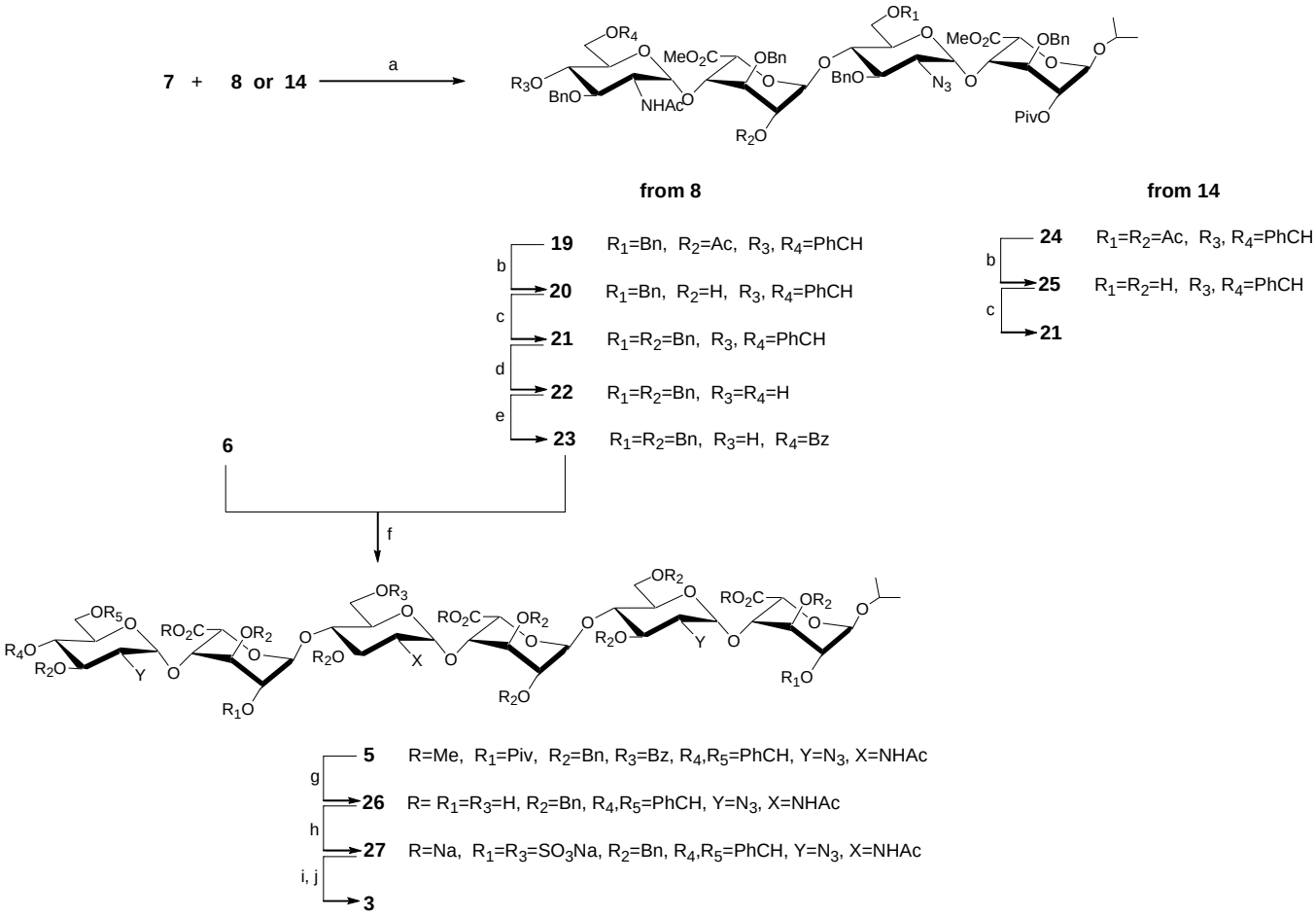

Scheme 4. Reagents and conditions: (*a*) KOH, MeOH; (*b*) BzCl, Py, 96% from **28**; (*c*) $BnNH_2$, Et_2O, 96%; (*d*) DBU, Cl_3CCN, CH_2Cl_2, 87%; (*e*) TMSOTf, CH_2Cl_2, 0°C, 88%; (*f*) Ac_2O, Py, 43% from **29**; (*g*) AcSH, 68%; (*h*) $(FN)_n$·Py, THF, –15°C, 81%; (*i*) K_2CO_3, Cl_3CCN, CH_2Cl_2, 71%.

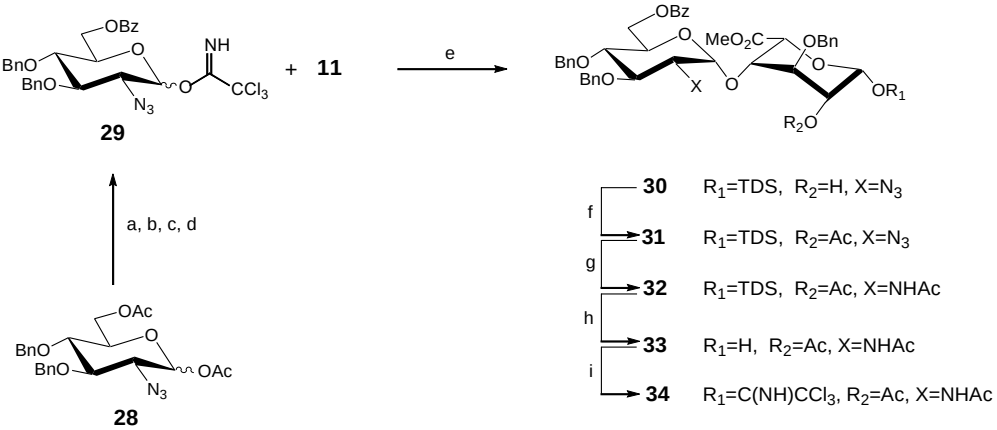

The above qualitative NMR study indicated that the synthetic compounds **3** and **4** present the main structural features of natural heparin oligosaccharides (46). The structural definition of **3** was further improved with a semiquantitative analysis of the NOE data. Heparin fragments larger than five monosaccharide units usually show an anisotropic hydrodynamic behavior with a shape close to a prolate ellipsoid. This feature can be determined through the analysis of σ^{NOE} and (or) the apparent correlation times for the fixed glucosamine interprotonic vectors H1-H2 and H2-H4. As the H1-H2 vector is almost parallel and the H2-H4 almost perpendicular to the main axis of inertia and both distances are

© 2002 NRC Canada

Scheme 5. Reagents and conditions: (*a*) $NaBH_3CN$, THF, HCl–Et_2O, 66%; (*b*) TMSOTf, CH_2Cl_2, 40%; (*c*) MeONa, MeOH–CH_2Cl_2, 80%; (*d*) Ag_2O, BnBr, DMF, 72%; (*e*) (*i*) H_2O_2, LiOH aq; (*ii*) KOH aq, MeOH, 94%; (*h*) SO_3·Py, Py, 64%; (*i*) Pd/C, H_2, MeOH–H_2O (9:1); (*j*) SO_3·Py, H_2O, pH = 9.5, 66% from **40**.

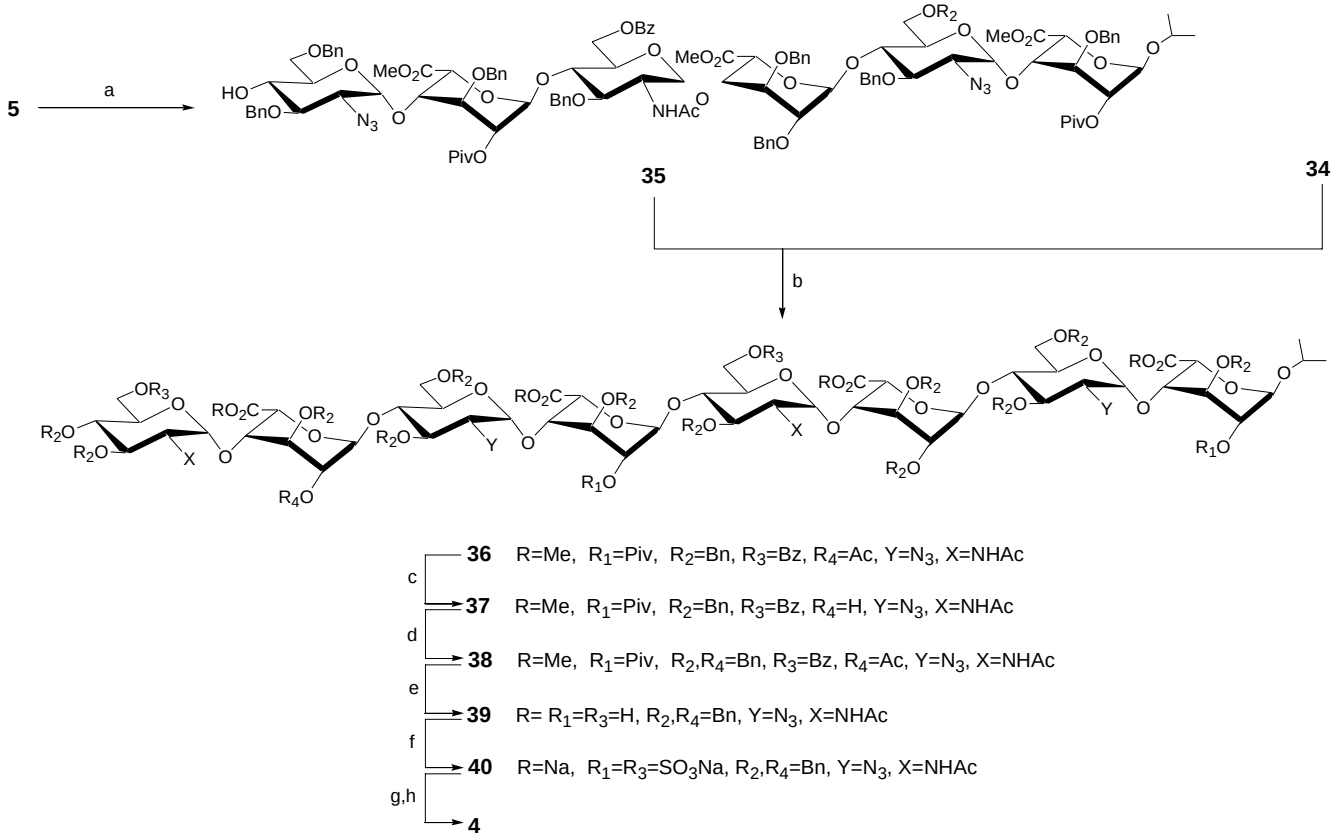

Table 1. Proton and carbon chemical shifts for hexasaccharide **3**.

	A	B	C	D	E	F
H-1	5.22	5.32	4.89	5.15	5.18	5.38
H-2	4.16	3.23	3.66	3.95	4.31	3.18
H-3	4.19	3.64	3.85	3.74	4.19	3.61
H-4	4.00	3.67	4.05	3.76	4.07	3.42
H-5	4.50	3.83	4.74	3.99	4.77	3.80
H-6/H-6′		3.84/3.78		4.37/4.23		3.85/3.76
C-1	99.8	99.7	104.2	97.1	101.9	99.4
C-2	78.6	60.8	72.5	74.1	78.5	60.7
C-3	71.0	72.1	72.2	72.4	71.7	73.8
C-4	78.6	79.7	77.5	78.4	78.4	72.6
C-5	70.8	73.6	72.6	72.0	71.9	74.4
C-6		62.5		69.0		63.0

nearly equal, the observed variation of σ^{NOE} can be attributed to a difference in parallel and perpendicular correlation times. The σ^{NOE} values for **3** were calculated from the NOE growing rate, assuming the isolated spin pairs approximation, by integration of the NOE cross-peaks at several mixing times (200–600 ms) (49). The apparent correlation times for glucosamine vectors H1-H2 and H2-H4, calculated from the σ^{NOE} ratio at 400 and 500 MHz provided a clear indication of this anisotropic tumbling (Table 3) (50). This behavior, which also was previously observed for **1** (21), prevented the accurate calculation of distances from NOE data and a complex full-motion model, which accounts both for internal motions and anisotropy, has to be considered. However, because of the above-mentioned parallel and perpendicular orientation of the H1-H2 and H2-H4 vectors with respect to the main axis of inertia, the known glucosamine H1-H2 and H2-H4 distances can be used as extreme reference values for the estimation of distances from interglycosidic NOEs. The upper and the lower distance limits may be given by considering the parallel and perpendicular correlation times derived from H1-H2 and H2-H4 σ^{NOE}, respectively. The distances thus obtained were in agreement with those expected for a *syn*-Φ disposition of the glycosidic linkages (Table 4) as that reported for heparin and related oligosaccharides.

© 2002 NRC Canada

Table 2. $^3J_{HH}$ observed for iduronate residues of **3**.

	IdoA (**A**)	IdoA (**C**)	IdoA (**E**)	$^1C_4$ (teor.)	^2S_O (teor.)	$^4C_1$ (teor.)
$^3J_{1,2}$	3.0	3.5	3.0	2.9	5.6	8.0
$^3J_{2,3}$	4.9	6.6	5.8	4.0	10.1	10.1
$^3J_{3,4}$	5.4	4.5	4.0	4.0	6.0	9.8
$^3J_{4,5}$	2.9	3.3	2.8	0.8	4.8	3.9

Table 3. σ^{NOE} (500) and σ^{NOE} (400) (s^{-1}) and apparent correlation times (ns) for internal glucosamine NOEs of **3**.

		GlcN (**B**)	GlcN (**D**)	GlcN (**F**)
H1-H2	σ^{NOE} (500)	0.16	0.20	0.13
	σ^{NOE} (400)	0.14	0.19	0.12
	τ_c	1.04	1.37	1.10
H2-H4	σ^{NOE} (500)	0.05	0.09	0.02
	σ^{NOE} (400)	0.03	0.08	0.01
	τ_c	0.60	1.22	0.55

The small differences observed for the H1′-H3:H1′-H4 ratio of the C–D linkage in comparison with those of the A–B and E–F linkages can be attributed to changes of the local flexibility as a consequence of the different substitution pattern.

Finally, a model of hexasaccharide **3** was constructed on the basis of a previous model constructed for **1**. A minimization including TIP3P water and sodium counterions was performed. The system was preequilibrated by several cycles of molecular dynamics with frozen solute coordinates. After minimization of the overall system, the relaxed structure showed the typical helical symmetry of heparin with the five sulfate groups located on one face. The backbone of this structure can be superimposed on the backbone of structure **1** (Fig. 2) This model is in agreement with the key interglycosidic distances calculated from NOE data (Table 4).

Although more detailed structural studies are presently underway, the results presented here clearly indicate that the key three-dimensional elements present in the structure of heparin, helical symmetry and iduronate ring conformational equilibrium, are adequatelly modeled by compounds **3** and **4**.

The induction of the mitogenic activity of FGF-1 by these synthetic compounds (**3** and **4**) in comparison with that promoted by compounds **1** and **2** is now under investigation. Preliminary results indicate that hexasaccharide **3** shows the maximum activating effect. On the other hand, sedimentation equilibrium analysis also shows, in this case, that the profile of FGF-1 solutions in the presence of activating concentrations of **3** and **4** correspond to monomeric species. These results and further studies on the structure–reactivity relationship will be reported in due time.

Experimental

General methods

The ^{1}H NMR spectra were measured at 500 MHz (Bruker DRX-500) with tetramethylsilane or the residual signal of the solvent as the internal standard. The ^{13}C NMR spectra were recorded at 125 MHz. Optical rotations were measured at room temperature in a 1 dm cell on a PerkinElmer 341 polarimeter. Elemental analyses were carried out in a Leco CHNS 932 analyzer. Permeation gel chromatography was performed using Sephadex LH-20 and G-25 (Pharmacia). Ionic exchange chromatography was carried out using Dowex 50WX4 resin (Fluka). Thin-layer chromatography was performed on precoated plates of silica gel (60-F254, E. Merck, Darmstadt) and visualized with H_2SO_4–EtOH (1:9, v/v) or anisaldehyde followed by heating. For column chromatography, silica gel 60 (0.2–0.5 mm, 0.2–0.063 mm, or 0.04–0.015 mm, E. Merck, Darmstadt) and distilled solvents were used. All solvents and reagents were purified and dried according to standard procedures.

Fig. 2. Relaxed structures of hexasaccharides **1** and **3**.

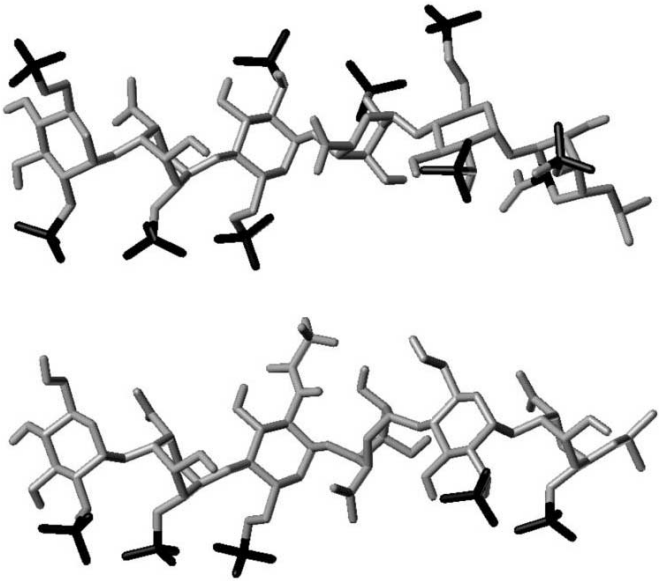

NMR measurements

1D and 2D experiments were recorded in D_2O at 298 K on Bruker DRX-500 and DRX-400 instruments using acetone as the external reference in a 6 mM sample. pH* was adjusted to 7.0. DQF-COSY (51), TOCSY (52), and HMQC (53) experiments were recorded using standard *z*-pulsed field gradient enhanced or selected pulse sequences when possible. Phase-sensitive experiments were performed in all cases using the TPPI (time proportional phase increment) method (54). Data were transformed into phase-sensitive mode after weighting with shifted- square sine-bells functions.

NOESY (55) experiments were carried out at 500 and 400 MHz with mixing times of 250, 300, 325, 350, 400, 500, 550, and 600 ms. The volumes of the cross and diagonal peaks were integrated using standard Bruker software. The normalized cross-peak's volume variation as a function of the mixing time indicated good linearity of the NOE build up curves for the range of mixing times considered. Cross-relaxation rates (σ) were calculated from these

© 2002 NRC Canada

Table 4. Experimental and theoretical interglycosidic distances of hexasaccharide **3**.

Residue	Distance	Minimun	Maximum	Average	Model distance
A	H2—H5	3.26	3.81	3.54	3.96
B	H1—H4(A)	2.22	2.6	2.41	2.39
	H1—H3(A)	2.42	2.83	2.62	2.33
C	H2—H5	2.62	2.97	2.79	3.78
	H1—H4(B)	2.26	2.64	2.45	2.35
	H1—H6(B)	2.42	2.83	2.62	2.31
	H1—H6′(B)	2.22	2.6	2.41	3.90
D	H1—H4(C)	2.37	2.69	2.53	2.57
	H1—H3(C)	2.1	2.38	2.24	2.22
E	H2—H5	2.72	3.08	2.90	4.02
	H1—H4(D)	2.29	2.61	2.45	2.45
	H1—H6(D)	2.16	2.45	2.3	2.42
	H1—H6′(D)	2.85	3.24	3.04	3.84
F	H1—H4(E)	1.82	2.44	2.13	2.51
	H1—H3(E)	1.92	2.57	2.24	2.21

curves assuming the isolated spin pairs approximation at short mixing times by extrapolation to zero time. The apparent correlation times were calculated using the spectral density function of an isotropic rigid molecule, from the ratio σ (500)/σ (400) (56).

Molecular modeling

Molecular modeling was performed using AMBER force field (57) (parameter set "parm91") as integrated in the AMBER 5.0 program (58), modified for carbohydrate molecules by the GLYCAM_93 parameter set (59). Specific parameters for sulfates and sulfamate groups were also included, as described by Huige and Altona (60). The initial structure of the hexasaccharide **3** was built using the ϕ/ψ values found for a minimized structure of the regular heparin-like synthetic hexasaccharide **1** (21). Minimization was carried out using periodic boundary conditions with TIP3P water molecules. Box dimensions were 53 × 50 × 50 Å, large enough to allow for the faces of the box to extend 12 Å beyond the sugar in each direction, reducing in this way the possibility of border effects that could take place if a reorientation of the solute happened during the calculation. It involved the introduction of 3933 water molecules and eight sodium counterions. To enable the cations to solvate appropriately, they were initially located randomly far enough from the solute. The initial water and counterions configuration was subjected to 500 cycles of energy minimization, with the conformation of the sugar frozen. Following this step, a 50 ps volume constant MD simulation was performed, in which only the water molecules were allowed to move. After this preequilibration of the solvent, the next step consisted of 500 cycles of energy minimization of the water molecules, keeping constant the Cartesian coordinates of the solute and counterions. To reach the equilibrium value for the density of the system, the water molecules were subjected to 50 ps pressure constant MD simulation with both the solute and the counterions frozen. Finally, the solvent equilibration procedure involved 500 cycles of steepest descent energy minimization of the water molecules. At this point, the energetic minimum of **3** was obtained using 1500 cycles of conjugated gradient minimization for the whole system.

Methyl (isopropyl 4-*O*-(2-azido-3-*O*-benzyl-2-deoxy-α-D-glucopyranosyl)-3-*O*-benzyl-2-*O*-pivaloyl-α-L-idopyranosyl) uronate (13)

To a solution of **12** (800 mg, 1.02 mmol) in dry CH_2Cl_2 (9 mL), EtSH (374 μL, 5.06 mmol), and catalytic PTSA were added. After stirring for 3 h under an argon atmosphere, the reaction was neutralized with saturated $NaHCO_3$ solution, diluted with CH_2Cl_2 (200 mL), and washed with H_2O (200 mL). The organic layer was dried ($MgSO_4$) and concentrated to dryness. The mixture was purified by flash chromatography (hexane–EtOAc, 1:1) to yield **13** (639 mg, 90%). TLC: 0.14 (hexane–EtOAc, 2:1). $[\alpha]_D^{23}$ –6.6° (*c* 0.6, $CHCl_3$). ^{1}H NMR (500 MHz, $CDCl_3$) δ: 7.37–7.24 (m, 10H, *2 Ph*), 5.18 (d, 1H, *H-1*, $J_{1,2}$ = 4.5 Hz), 5.05 (d, 1H, *H-1′*, $J_{1,2}$ = 3.6 Hz), 4.93 (m, 1H, *H-2*), 4.89 (d, 1H, *1 CH*$_2$Ph, J_{gem} = 11.2 Hz), 4.79–4.69 (m, 4H, *3 CH*$_2$Ph, *H-5*), 4.15 (m, 1H, *H-4*), 3.97–3.91 (m, 2H, *H-3*, *CH*$(CH_3)_2$), 3.80–3.55 (m, 5 H, *H-3′*, *H-4′*, *H-5′*, *H-6′a*, *H-6′b*), 3.75 (s, 3H, COO*CH*$_3$), 3.17 (t, 1H, *H-2′*, $J_{2,1} \approx J_{2,3}$ = 10.7 Hz), 1.22 (s, 9H, C(*CH*$_3$)$_3$), 1.19–1.15 (2d, 6H, CH(*CH*$_3$)$_2$, *J* = 6.2 Hz).

Methyl (isopropyl 4-*O*-(6-*O*-acetyl-2-azido-3-*O*-benzyl-2-deoxy-α-D-glucopyranosyl)-3-*O*-benzyl-2-*O*-pivaloyl-β-L-idopyranosyl) uronate (14)

To a solution of **13** (540 mg, 0.77 mmol) in dry CH_2Cl_2 (12 mL) at –10°C, Py (63 μL, 0.78 mmol) and acetic anhydride (74 μL, 0.78 mmol) were added. After stirring for 24 h, MeOH (1 mL) was added, and was concentrated in vacuo. The crude was purified by flash chromatography (hexane–EtOAc, 2:1) to yield **14** (488 mg, 85%) as well as nonreacting starting material **13** (22 mg, 4%). TLC: 0.33 (hexane–EtOAc, 2:1). $[\alpha]_D^{23}$ –10.1° (*c* 1.0, $CHCl_3$). MALDI-TOF (*m/z*): 766 (M + Na^+), 782 (M + K^+). ^{1}H NMR (500 MHz, $CDCl_3$) δ: 7.37–7.23 (m, 10H, *2 Ph*), 5.18 (d, 1H, *H-1*, $J_{1,2}$ = 4.4 Hz), 5.04 (d, 1H, *H-1′*, $J_{1,2}$ = 3.4 Hz), 4.92 (m, 1H, *H-2*), 4.85 (m, 2H, *2 CH*$_2$Ph), 4.78 (d, 1H, *1 CH*$_2$Ph, J_{gem} = 11.3 Hz), 4.74 (d, 1H, *H-5*, $J_{5,4}$ = 4.0 Hz), 4.69 (d, 1H, *1 CH*$_2$Ph *CH*$_2$Ph, J_{gem} = 11.2 Hz), 4.54 (dd, 1H, *H-6′a*, $J_{6a,6b}$ = 12.5 Hz, $J_{6a,5}$ = 3.5 Hz), 4.13 (m, 2H, *H-4*, *H-6′b*), 3.93 (m, 2H, *H-3*, *CH*$(CH_3)_2$), 3.82 (m, 1H, *H-5′*), 3.76 (s, 3H, COO*CH*$_3$), 3.70 (m, 1H, *H-3′*), 3.40 (m, 1H, *H-4′*), 3.20 (dd, 1H, *H-2′*, $J_{2,1}$ = 3.4 Hz, $J_{2,3}$ = 10.1 Hz), 2.83

© 2002 NRC Canada

(d, 1H, *OH-4*, $J_{OH,4}$ = 3.4 Hz), 2.07 (s 3H, OCO*CH*$_3$), 1.21 (s, 9H, C(*CH*$_3$)$_3$), 1.19 and 1.14 (2 d, 6H, *J* = 6.0 Hz, CH(*CH*$_3$)$_2$). ^{13}C NMR (125 MHz, $CDCl_3$) δ: 177.3, 172.0, 170.0 (*C=O*), 98.4 (*C-1*), 97.2 (*C-1′*), 78.8, 76.0, 75.1, 74.1, 73.1; 71.3, 70.9, 70.7, 70.6, 70.5, 70.1, 62.7, 52.2 (COO*CH*$_3$), 38.8, 27.2 (O*Piv*), 20.8 (OCO*CH*$_3$), 23.3, 21.8 (CH(*CH*$_3$)$_2$). Anal. calcd. for $C_{37}H_{49}N_3O_{13}$ (%): C 59.74, H 6.64, N 5.65; found (%): C 59.74, H 6.52, N 5.57.

Methyl (isopropyl 4-*O*-(2-azido-3,6-di-*O*-benzyl-2-deoxy-α-D-glucopyranosyl)- 3-*O*-benzyl-2-*O*-pivaloyl-β-L-idopyranosyl) uronate (8)

To a solution of **12** (550 mg, 0.696 mmol) in dry THF (20 mL), $NaBH_3CN$ (7 mL of a solution of 1 M $NaBH_3CN$ in THF) was added, and was stirred for 10 h. Afterwards, a solution of 2.5 M HCl in Et_2O was added dropwise until the mixture became acidic. The reaction was neutralized with saturated $NaHCO_3$ solution, diluted with CH_2Cl_2 (25 mL), and washed with H_2O (15 mL). The aqueous layer was extracted with CH_2Cl_2 (2 × 20 mL) and the organic layers were dried ($MgSO_4$) and concentrated in vacuo. The residue was purified by flash chromatography (hexane–EtOAc, 4:1) to yield **8** (505 mg, 92%). TLC: 0.32 (hexane–EtOAc, 4:1). $[\alpha]_D^{23}$ −4.4° (*c* 1.0, CH_2Cl_2). ^{1}H NMR (500 MHz, $CDCl_3$) δ: 7.39–7.24 (m, 15 H, *3 Ph*), 5.21 (d, 1H, *H-1*, $J_{1,2}$ = 4.8 Hz), 5.05 (d, 1H, *H-1′*, $J_{1,2}$ =3.4 Hz), 4.93 (t, 1H, *H-2*, $J_{2,1} \approx J_{2,3}$ = 5.1 Hz), 4.84 (d, 1H, *1* CH_2Ph, J_{gem} = 11.1 Hz), 4.81 (d, 1H, *1* CH_2Ph, J_{gem} = 11.2 Hz), 4.76 (d, 1H, *1* CH_2Ph, J_{gem} = 11.2 Hz), 4.74 (d, 1H, *H-5*, $J_{5,4}$ = 5.0 Hz), 4.70 (d, 1H, *1* CH_2Ph, J_{gem} = 11.1 Hz), 4.57 (d, 1H, *1* CH_2Ph, J_{gem} = 12 Hz), 4.51 (d, 1H, *1* CH_2Ph, J_{gem} = 12 Hz), 4.14 (t, 1H, *H-4*, $J_{4,3} \approx J_{4,5}$ = 5.3 Hz), 3.97 (t, 1H, *H-3*, $J_{3,2} \approx J_{3,4}$ = 5.6 Hz), 3.94 (m, 1 H, *CH*(CH$_3$)$_2$, *J* 6.0 Hz), 3.81 (m, 1H, *H-5′*), 3.72 (s, 3H, COO*CH*$_3$), 3.71–3.67 (m, 3H, *H-3′*, *H-4′*, *H-6′a*), 3.57 (dd, 1H, *H-6′b*, $J_{6b,6a}$ = 10.2 Hz, $J_{6b,5}$ = 4.3 Hz), 3.21 (dd, 1H, *H-2′*, $J_{2,1}$ = 3.4 Hz, $J_{2,3}$ = 9.4 Hz), 2.57 (s, 1H, *OH-4*), 1.21 (s, 9H, C(*CH*$_3$)$_3$), 1.19 and 1.14 (2 d, 6H, *J* = 6.0 Hz, CH(*CH*$_3$)$_2$). ^{13}C NMR (125 MHz, $CDCl_3$) δ: 177.3, 170.0 (*C=O*), 98.2 (*C-1′*), 97.2 (*C-1*), 79.1, 76.2, 74.8, 73.7, 73.6, 72.4, 71.3, 71.0, 70.6, 69.6, 62.6, 52.1 (COO*CH*$_3$), 38.8, 27.2 (O*Piv*), 23.3, 21.8 (CH(*CH*$_3$)$_2$). Anal. calcd. for $C_{42}H_{53}N_3O_{12}$ (%): C 63.70, H 6.75, N 5.30; found (%): C 63.62, H 6.70, N 5.26.

Methyl dimethylthexylsilyl 4-*O*-(2-acetamido-3-*O*-benzyl-4,6-*O*-benzylidene-2-deoxy-α-D-glucopyranosyl)-3-*O*-benzyl-β-L-idopyranuronate (15)

A solution of **9** (255 mg, 0.316 mmol) in thiolacetic acid (2 mL) was stirred for 16 h at room temperature. After concentrating to dryness, the residue was purified by flash chromatography (hexane–EtOAc, 1:1) to yield **15** (639 mg, 90%). TLC: 0.35 (Hexane–EtOAc, 1:1). $[\alpha]_D^{23}$ +59.5° (*c* 1.0, CH_2Cl_2). MALDI-TOF (*m/z*): 845 (M + Na^+), 861 (M + K^+). ^{1}H NMR (500 MHz, $CDCl_3$) δ: 7.45–7.15 (m, 15H, *3 Ph*), 6.82 (d, 1H, *NH*, $J_{NH,2}$ = 9.5 Hz), 5.50 (s, 1H, Ph-*CH*-), 5.00 (s, 1H, *H-1*), 4.83 (d, 1H, *1* CH_2Ph, J_{gem} = 12.1 Hz), 4.64−4.52 (m, 5H, *3* CH_2Ph, *H-1′*, *H-5*), 4.30 (m, 1H, *H-2′*), 4.21 (dd, 1H, *H-6′a*, $J_{6a,5}$ = 4.6 Hz, $J_{6a,6b}$ = 10.1 Hz), 3.94 (s, 1H, *H-4*), 3.82 (s, 3 H, COO*CH*$_3$), 3.74–3.59 (m, 6H, *H-2*, *H-3*, *H-3′*, *H-4′*, *H-5′*, *H-6′b*), 2.63 (s, 1H, *OH-2*), 1.85 (s, 3 H, NHCO*CH*$_3$), 1.64 (m, 1H, *CH*(CH$_3$)$_2$), 0.90–0.88 (m, 12H, CH(*CH*$_3$)$_2$, C(*CH*$_3$)$_2$), 0.26 and 0.19 (2 s, 6H, Si(*CH*$_3$)$_2$). ^{13}C NMR (125 MHz, $CDCl_3$) δ: 170.4, 168.8 (*C=O*), 101.4 (Ph-*CH*-), 98.2 (*C-1*), 93.8 (*C-1′*), 82.8, 74.2, 73.7, 73.4, 72.9, 72.1, 68.7, 68.5, 63.6, 52.6 (*C-2′*), 52.1 (COO*CH*$_3$), 23.0 (NHCO*CH*$_3$), 34.0, 25.1, 20.3, 20.1, 18.6, 18.4, –1.9, –3.6 (O*TDS*). Anal. calcd. for $C_{44}H_{59}NO_{12}Si{\cdot}0.5H_2O$ (%): C 63.59, H 7.28, N 1.68; found (%): C 63.37, H 7.53, N 1.53.

Methyl dimethylthexylsilyl 2-*O*-acetyl-4-*O*-(2-azido-3-*O*-benzyl-4,6-*O*-benzylidene-2-deoxy-α-D-glucopyranosyl)-3-*O*-benzyl-β-L-idopyranuronate (16)

Compound **9** (1 g, 1.24 mmol) was dissolved in Py (10 mL) at 0°C and acetic anhydride (5 mL) was added and was stirred for 48 h. The reaction was diluted with CH_2Cl_2 (250 mL) and washed with 1 N HCl (125 mL). The aqueous layer was extracted with CH_2Cl_2 (2 × 125 mL) and the organic layers were dried ($MgSO_4$) and concentrated in vacuo. The residue was coevaporated with toluene twice and then purified by flash chromatography (hexane–EtOAc, 4:1), to yield **16** (1 g, 93%). TLC: 0.38 (hexane–EtOAc, 4;1). $[\alpha]_D^{23}$ +29.5° (c 1.0, $CHCl_3$). ^{1}H NMR (500 MHz, $CDCl_3$) δ: 7.45–7.24 (m, 15H, *3 Ph*), 5.51 (s, 1H, Ph-*CH*-), 5.07 (b.s., 1H, *H-1*), 4.97 (b. s., 1H, *H-2*), 4.76 (d, 1H, *H-1′*, $J_{1,2}$ = 3.5 Hz), 4.88−4.70 (2 d, 2H, *2* CH_2Ph, J_{gem} = 11.1 Hz), 4.74−4.66 (2 d, 2H, *2* CH_2Ph, J_{gem} = 11.8 Hz), 4.47 (b. s., 1H, *H-5*), 4.30 (dd, 1H, *H-6′a*, $J_{6a,5}$ = 4.9 Hz, $J_{6a,6b}$ = 10.1 Hz), 3.97–3.92 (m, 4H, *H-3′*, *H-4*, *H-5′*, *H-3*), 3.75 (s, 3H, COO*CH*$_3$), 3.64–3.59 (m, 2H, *H-4′*, *H-6′b*), 3.28 (t, 1H, *H-2′*, $J_{2,1} \approx J_{2,3}$ = 9.9 Hz), 2.03 (d, 3H, OCO*CH*$_3$), 1.61 (m, 1H, *CH*(CH$_3$)$_2$), 0.86–0.83 (m, 12H, CH(*CH*$_3$)$_2$, C(*CH*$_3$)$_2$), 0.24 and 0.14 (2s, 6H, Si(*CH*$_3$)$_2$). ^{13}C NMR (125 MHz, $CDCl_3$) δ: 170.7, 168.8 (*C=O*), 137.8–126.1 (*Ph*), 101.6 (Ph-*CH*-), 98.4 (*C-1′*), 93.7 (*C-1*), 82.6, 76.0, 74.8 (*CH*$_2$Ph), 74.3, 73.6, 73.4 (*C-5*), 72.9 (*CH*$_2$Ph), 68.5 (*C-6′*), 67.7, 63.2, 63.1, 52.1 (COO*CH*$_3$), 20.9 (OCO*CH*$_3$), 34.0, 24.8, 20.2, 18.4, –2.0, –3.6 (O*TDS*).

Methyl (dimethylthexylsilyl 4-*O*-(2-acetamido-3-*O*-benzyl-4,6-*O*-benzylidene-2-deoxy-α-D-glucopyranosyl)-2-*O*-acetyl-3-*O*-benzyl-β-L-idopyranosid) uronate (17)

(*a*) A solution of **16** (4.3 g, 5.07 mmol) in thiolacetic acid (55 mL) was stirred for 30 h at room temperature. After concentrating to dryness, the residue was purified by flash chromatography (hexane–EtOAc, 1:1) to yield **17** (3.19 g, 73%).

(*b*) Compound **15** (790 mg, 0.98 mmol) was dissolved in Py (10 mL) at 0°C and acetic anhydride (5 mL) and catalytic DMAP were added and was stirred for 48 h. The reaction was diluted with CH_2Cl_2 (200 mL) and washed with 1 N HCl (100 mL). The aqueous layer was extracted with CH_2Cl_2 (2 × 100 mL) and the organic layers were dried ($MgSO_4$) and concentrated in vacuo. The residue was coevaporated with toluene twice and then purified by flash chromatography (hexane–EtOAc, 1:1) to yield **17** (617 mg, 77%). TLC: 0.39 (hexane–EtOAc, 1:1). $[\alpha]_D^{23}$ +46.3° (*c* 1.0, CH_2Cl_2). MALDI-TOF (*m/z*): 887 (M + Na^+), 903 (M + K^+). ^{1}H NMR (500 MHz, $CDCl_3$) δ: 7.43–7.22 (m, 15H, *3 Ph*), 6.25 (d, 1H, *NH*, $J_{NH,2}$ = 9.6 Hz), 5.52 (s, 1H, Ph-*CH*-), 5.04 (s, 1H, *H-1*), 4.98 (s, 1H, *H-2*), 4.83 (d, 1H, *1* CH_2Ph, J_{gem} = 12.2 Hz), 4.76 (d, 1H, *H-5*, $J_{5,4}$ = 3.6 Hz), 4.67 (d, 1H, *1* CH_2Ph, J_{gem} = 11.8 Hz), 4.60−4.53 (m, 3H, *2* CH_2Ph,

© 2002 NRC Canada

H-1′), 4.29 (m, 1H, *H-2′*), 4.19 (m, 1H, *H-6′a*), 3.87 (s, 1H, *H-4*), 3.85 (s, 1H, *H-3*), 3.74 (s, 3H, COOCH_3), 3.72–3.66 (m, 3H, *H-4′*, *H-5′*, *H-6′b*), 3.52 (m, 1H, *H-3′*), 1.91 (s, 3H, NHCOCH_3), 1.81 (s, 3H, OCOCH_3), 1.58 (m, 1H, *CH*$(CH_3)_2$), 0.83–0.82 (m, 12H, CH$(CH_3)_2$, C$(CH_3)_2$), 0.19 and 0.10 (2s, 6H, Si$(CH_3)_2$). ^{13}C NMR (125 MHz, $CDCl_3$) δ: 170.0, 169.9, 168.4 (*C=O*), 101.4 (Ph-*CH*-), 96.4 (C-1), 93.0 (*C-1′*), 82.4, 76.1, 74.0, 73.3, 73.1, 71.8, 70.3, 68.6, 67.8, 63.4, 52.2 (*C-2′*), 52.0 (COOCH_3), 23.3, 20.9 (OCOCH_3, NHCOCH_3), 33.9, 24.9, 20.1, 19.8, 18.6, 18.4, –1.9, –3.6 (O*TDS*). Anal. calcd. for $C_{46}H_{61}NO_{13}Si$ (%): C 63.94, H 7.11, N 1.62; found (%): C 63.64, H 6.82, N 1.59.

Methyl 4-*O*-(2-acetamido-3-*O*-benzyl-4,6-*O*-benzylidene-2-deoxy-α-D-glucopyranosyl)-2-*O*-acetyl-3-*O*-benzyl-α,β-L-idopyranuronate (18)

To a solution of **17** (2.75 g, 3.18 mmol) at –15°C in dry THF (90 mL) an excess of $(HF)_n$·Py (8.8 mL) was added. The reaction was warmed to 0°C and stirred for 24 h under an argon atmosphere. The mixture was diluted with CH_2Cl_2 (2 × 400 mL) and washed with H_2O (2 × 200 mL) and saturated $NaHCO_3$ solution until neutral pH. The aqueous layer was extracted with CH_2Cl_2 (2 × 200 mL) and the organic layers were dried ($MgSO_4$) and concentrated in vacuo. The residue was purified by flash chromatography (hexane–EtOAc, 1:3) to yield **18** (1.8 g, 78%) as a mixture of α and β anomers. TLC: 0.16 (hexane–EtOAc, 2:3). MALDI-TOF (*m/z*): 774 (M + Na^+), 760 (M + K^+). ^{1}H NMR (500 MHz, $CDCl_3$) δ: 7.44–7.21 (m, 30H, *6 Ph* (α and β)), 5.87 (d, 1H, *NH* (α), $J_{NH,2}$ = 9.0 Hz), 5.71 (d, 1H, *NH* (β), $J_{NH,2}$ = 9.2 Hz), 5.54 (s, 1H, Ph-*CH*- β), 5.53 (s, 1H, Ph-*CH*-α), 5.23 (d, 1H, *H-1* (β), $J_{2,1}$ = 5.7 Hz), 5.16 (s, 1H, *H-1* (α)), 4.91–4.54 (m, 14H, *4* CH_2Ph, *H-1′*, *H-2*, *H-5* (α and β)), 4.27 (m, 2H, *H-2′* (α and β)), 4.23–4.19 (m, 2H, *H-6′a* (α and β)), 3.99–3.91 (m, 5H, *H-4*, *H-3* (α and β), *OH-1* (α)), 3.78 and 3.77 (2s, 6H, COOCH_3 (β and α)), 3.74–3.63 (m, 7H, *H-4′*, *H-5′*, *H-6′b* (α and β), *OH*-1 (β)), 3.53–3.48 (m, 2H, *H-3′* (α and β)), 1.97 (s, 3H, OCOCH_3 (α)), 1.91 (s, 3H, OCOCH_3 (β)), 1.80 (s, 3H, NHCOCH_3 (α)), 1.76 (s, 3H, NHCOCH_3 (β)). ^{13}C NMR (125 MHz, $CDCl_3$) δ: 170.1, 170.0, 169.8, 169.0, 168.6 (*C=O*), 138.3–127.9 (*Ph*), 101.5 (Ph-*CH*-), 97.1 (*C-1′* (α)), 96.7 (*C-1′* (β)), 93.1 (*C-1* (α and β)), 82.4, 75.9, 75.8, 73.5, 73.2, 73.1, 71.4, 71.2, 68.9, 68.6, 67.6, 67.5, 63.6, 63.5, 52.4 (*C-2′* (α and β)), 52.3 (COOCH_3 (α and β)), 23.3, 20.8 (OCOCH_3, NHCOCH_3 (α and β)). Anal. calcd. for $C_{38}H_{43}NO_{13}$·$0.5H_2O$ (%): C 62.45, H 6.07, N 1.92; found (%): C 62.49, H 6.02, N 2.20.

***O*-(Methyl 4-*O*-(2-acetamido-3-*O*-benzyl-4,6-*O*-benzylidene-2-deoxy-α-D-glucopyranosyl)-2-*O*-acetyl-3-*O*-benzyl-α,β-L-idopyranosyluronate) trichloroacetimidate (7)**

To a solution of **18** (620 mg, 0.86 mmol) in dry CH_2Cl_2 (14 mL), Cl_3CCN (1.3 mL, 13.05 mmol) and activated K_2CO_3 (130 mg, 0.95 mmol) were added. After stirring for 1 h the residue was filtered and concentrated to dryness. The residue was purified by flash chromatography (hexane–EtOAc, 1:2) to yield **7** (701 mg, 94%) as a mixture of α and β anomers. TLC (α and β): 0.51 and 0.62 (toluene–EtOAc, 1:2). ^{1}H NMR (500 MHz, $CDCl_3$) δ: 8.73 (s, 1H, O(C=N*H*)CCl_3 α), 8.66 (s, 1H, O(C=N*H*)CCl_3 (β)), 7.44–7.22 (m, 30H, *6 Ph* (α and β)), 6.34 (s, 1H, *H-1* (α)), 6.22 (s, 1H, *H-1* (β)), 5.87 (d, 1H, N*H* (β), $J_{NH,2}$ = 9.3 Hz), 5.72 (d, 1H, N*H* (α), $J_{NH,2}$ = 9.4 Hz), 5.53 (s, 1H, Ph-*CH*-α), 5.52 (s, 1H, Ph-*CH*-β), 5.25 and 5.12 (m, 2 H, *H-2′* (α and β)), 4.98 (s, 1H, *H-5* (α)), 4.87–4.51 (m, 13H, *4* CH_2Ph, *H-1′* (α and β), H-2 (α and β), *H*-5), 4.30 (m, 2H, *H-2′* (α and β)), 4.24–4.17 (m, 2H, *H-6′a* (α and β)), 4.11–4.04 (m, 2H, *H-4* (α), *H-3* (β)), 3.96 (m, 1H, *H-4* (β)), 3.86 (s, 1H, *H-3* (α)), 3.77 (s, 3H, COOCH_3 (α)), 3.76 (s, 3H, COOCH_3 (β)), 3.81–3.64 (m, 6H, *H-4′*, *H-5′*, *H-6′b* (α and β)), 3.52 (m, 2H, *H-3′* (α and β)), 1.94 (s, 3H, OCOCH_3 (α)), 1.92 (s, 3H, OCOCH_3 (β)), 1.81 (s, 3H, NHCOCH_3 (α)), 1.75 (s, 3H, NHCOCH_3 (β)). ^{13}C NMR (125 MHz, $CDCl_3$) δ: 171.1, 170.0, 169.9, 169.7, 169.4, 168.3, 167.6 (*C=O*), 160.5, 160.1 (*C=NH*), 138.4–126.0 (*Ph*), 101.5 (Ph-*CH*-), 97.6 (*C-1′* (β)), 96.2 (*C-1′* (α)), 95.0 (*C-1* (α)), 94.5 (*C-1* (β)), 82.4, 82.3, 76.1, 75.6, 74.1, 73.9, 72.5, 72.2, 72.0, 70.4, 69.9, 69.1, 68.7, 68.6, 66.9, 65.8, 63.7, 63.5, 60.4, 52.5 (*C-2′* (α and β)), 52.3 (COOCH_3 (α and β)), 23.4, 23.2, 21.0, 20.7 (OCOCH_3, NHCOCH_3 (α and β)). Anal. calcd. for $C_{40}H_{43}N_2O_{13}Cl_3$ (%): C 55.47, H 5.00, N 3.23; found (%): C 55.78, H 5.09, N 3.52.

Methyl (isopropyl *O*-(2-acetamido-3-*O*-benzyl-4,6-*O*-benzylidene-2-deoxy-α-D-glucopyranosyl)-(1→4)-*O*-(methyl 2-*O*-acetyl-3-*O*-benzyl-α-L-idopyranosyluronate)-(1→4)-*O*-(6-*O*-acetyl-2-azido-3-*O*-benzyl-2-deoxy-α-D-glucopyranosyl)-(1→4)-3-*O*-benzyl-2-*O*-pivaloyl-α-L-idopyranosyl) uronate (24)

To a solution of **14** (235 mg, 0.32 mmol) and **7** (362 mg, 0.42 mmol) in dry CH_2Cl_2 (0.5 mL) at room temperature, TMSOTf (20 μL of a 0.93 M solution of TMSOTf in dry CH_2Cl_2) was added under an argon atmosphere. After stirring for 7 h 30 min, saturated $NaHCO_3$ solution (2 mL) was added and diluted with CH_2Cl_2 (10 mL). The residue was washed with H_2O (7.5 mL) and then the aqueous layer was extracted with CH_2Cl_2 (2 × 5 mL) and the organic layers were dried ($MgSO_4$) and concentrated in vacuo. The residue was purified by flash chromatography (hexane–EtOAc, 1:2) to yield **24** (150 mg, 33%) and nonreacting acceptor **14** (156 mg, 43%). TLC: 0.24 (hexane–EtOAc, 1:1). $[\alpha]_D^{23}$ +46.3° (*c* 1.0, $CHCl_3$). MALDI-TOF (*m/z*): 1470 (M + Na^+), 1486 (M + K^+). ^{1}H NMR (500 MHz, $CDCl_3$) δ: 7.42–7.22 (m, 25H, *5 Ph*), 6.57 (d, 1H, N*H*, $J_{NH,2}$ = 9.2 Hz), 5.54 (s, 1H, Ph-*CH*-), 5.13 (m, 2H, *H-1a*, *H-1c*), 4.98–4.49 (m, 15H, *H-1b*, *H-1d*, *H-2a*, *H-2c*, *H-5a*, *H-5c*, *H-6b*, *8* CH_2Ph), 4.29 (m, 1H, *H-2d*), 4.17 (m, 1H, *H-6d*), 4.09 (m, 4H, *H-3c*, *H-4a*, *H-4b*, *H-6′b*), 3.93 (m, 3H, *H-3a*, *H-4c*, *CH*$(CH_3)_2$), 3.74 (s, 3H, COOCH_3), 3.60 (s, 3H, COOCH_3), 3.79–3.70 (m, 4H, *H-3b*, *H-4d*, *H-5b*, *H-5d*), 3.65 (dd, 1H, *H-6′d*, $J_{6',6}$ = 9.3 Hz, $J_{6',5}$ = 3.8 Hz), 3.54 (t, 1H, *H-3d*, $J_{3,2} \approx J_{3,4}$ = 9.6 Hz), 3.33 (dd, 1H, *H-2b*, $J_{2,1}$ = 3.2 Hz, $J_{2,3}$ = 10.2 Hz), 2.12 (s, 3H, NHCOCH_3), 2.04 (s, 3H, OCOCH_3), 1.87 (s, 3H, OCOCH_3), 1.21 (s, 9H, C*(*CH_3*)*$_3$), 1.19 and 1.16 (2d, 6H, *J* = 6.5 Hz, CH$(CH_3)_2$). ^{13}C NMR (125 MHz, $CDCl_3$) δ: 177.6, 171.7, 170.3, 170.1, 169.8, 169.0 (*C=O*), 137.7–127.7 (*Ph*), 101.4 (Ph-*CH*-), 98.8 (*C-1c*), 97.2 (*C-1b*), 96.9 (*C-1a*), 96.2 (*C-1d*), 82.4, 78.1, 76.3, 75.9, 75.2, 74.5, 74.0, 73.9, 73.1, 72.9, 72.1, 71.2, 70.1, 69.9, 69.8, 69.5, 68.7, 63.3, 62.9, 61.6, 52.4, 52.2, 51.9, 29.7, 27.2, 23.3, 23.1, 21.7, 21.3, 20.8 (O*Piv*, O*Ac*, NHCOCH_3, O-*i*-Pr). Anal.

© 2002 NRC Canada

calcd. for $C_{75}H_{90}N_4O_{25}\cdot 2.5H_2O$ (%): C 60.35, H 6.41, N 3.75; found: C 60.36, H 6.25, N 3.25.

Methyl (isopropyl *O*-(2-acetamido-3-*O*-benzyl-4,6-*O*-benzylidene-2-deoxy-α-D-glucopyranosyl)-(1→4)-*O*-(methyl 3-*O*-benzyl-α-L-idopyranosyluronate)-(1→4)-*O*-(2-azido-3-*O*-benzyl-2-deoxy-α-D-glucopyranosyl)-(1→4)-3-*O*-benzyl-2-*O*-pivaloyl-α-L-idopyranosyl) uronate (25)

To a solution of **24** (280 mg, 0.19 mmol) in dry MeOH (3 mL), MeONa (90 μL of a 0.43 M solution of MeONa in MeOH) was added and stirred for 24 h. The reaction was diluted with CH_2Cl_2 (10 mL) and washed with saturated NH_4Cl solution (200 mL) and H_2O (5 mL). The organic layer was dried ($MgSO_4$) and concentrated to dryness. The mixture was purified by flash chromatography (hexane–EtOAc, 1:3) to yield **25** (224 mg, 85%). TLC: 0.38 (hexane–EtOAc, 1:2). $[\alpha]_D^{23}$ +20.4° (*c* 1.0, CH_2Cl_2). MALDI-TOF (*m*/*z*): 1386 (M + Na^+), 1402 (M + K^+). ^{1}H NMR (500 MHz, $CDCl_3$) δ: 7.42–7.20 (m, 25H, *5 Ph*), 6.21 (d, 1H, N*H*, $J_{NH,2}$ = 7.7 Hz), 5.50 (s, 1H, Ph-*CH*-), 5.17–5.15 (m, 2 H, *H-1c*, *H-1a*), 5.04 (d, 1H, *H-1b*, $J_{2,1}$ = 3.6 Hz), 4.98 (d, 1H, *H-1d*, $J_{1,2}$ = 3.8 Hz), 4.92 (t, 1H, *H-2a*, $J_{2,1} \approx J_{2,3}$ = 5.1 Hz), 4.86 (d, 1H, *H-5c*, $J_{5,4}$ = 2.5 Hz), 4.77–4.52 (m, 8H, *8* CH_2Ph), 4.72 (d, 1H, *H-5a*, $J_{5,4}$ = 4.6 Hz), 4.18–4.09 (m, 3H, *H-2d*, *H-4a*, *H-6d*), 4.01–3.86 (m, 5H, *H-3a*, *H-3c*, *H-4b*, *H-4c*, *CH*$(CH_3)_2$), 3.69 (s, 3H, COO*CH*$_3$), 3.78–3.65 (m, 8H, *H-2c*, *H-3b*, *H-4d*, *H-5b*, *H-5d*, *H-6′d*, *H-6b*, *H-6′b*), 3.62 (t, 1H, *H-3d*, $J_{3,2} \approx J_{3,4}$ = 9.8 Hz), 3.45 (s, 3H, COO*CH*$_3$), 3.26 (dd, 1H, *H-2b*, $J_{2,1}$ = 3.7 Hz, $J_{2,3}$ = 10.2 Hz), 1.76 (s, 3H, NHCO*CH*$_3$), 1.18 (s, 9H, C(*CH*$_3$)$_3$), 1.19 and 1.17 (2d, 6H, *J* = 6.5 Hz, CH(*CH*$_3$)$_2$). ^{13}C NMR (125 MHz, $CDCl_3$) δ: 177.3, 170.8, 170.0, 169.4 (*C=O*), 138.5–126.1 (*Ph*), 101.5 (Ph-*CH*-), 100.7 (*C-1c*), 98.3 (*C-1b*), 97.3 (*C-1a*), 96.9 (*C-1d*), 82.3, 78.2, 76.3, 75.9, 74.8, 74.3, 74.1, 74.0, 73.6, 73.2, 72.8, 72.5, 72.3, 71.3, 70.9, 68.6, 68.4, 68.1, 63.5, 63.4 (*C-2c*), 61.2, 52.8 (*C-2a*), 52.2, 52.1 (COO*CH*$_3$), 27.2, 23.3, 22.9, 22.8, 21.8, 21.3 (O*Piv*, NHCO*CH*$_3$, O-*i*-Pr). Anal. calcd. for $C_{71}H_{86}N_4O_{23}$ (%): C 62.54, H 6.36, N 4.11; found (%): C 62.45, H 6.51, N 4.12.

Methyl (isopropyl *O*-(2-acetamido-3-*O*-benzyl-4,6-*O*-benzylidene-2-deoxy-α-D-glucopyranosyl)-(1→4)-*O*-(methyl 2-*O*-acetyl-3-*O*-benzyl-α-L-idopyranosyluronate)-(1→4)-*O*-(2-azido-3,6-di-*O*-benzyl-2-deoxy-α-D-glucopyranosyl)-(1→4)-3-*O*-benzyl-2-*O*-pivaloyl-α-L-idopyranosyl) uronate (19)

To a solution of **8** (425 mg, 0.54 mmol) and **7** (600 mg, 0.693 mmol) in dry CH_2Cl_2 (0.5 mL) at room temperature, TMSOTf (8.7 μL, 48 μmol) was added under an argon atmosphere. After stirring for 4 h 30 min, saturated $NaHCO_3$ solution (2 mL) was added and diluted with CH_2Cl_2 (25 mL). The residue was washed with H_2O (20 mL) and then the aqueous layer was extracted with CH_2Cl_2 (2 × 15 mL) and the organic layers were dried ($MgSO_4$) and concentrated in vacuo. The residue was purified by flash chromatography (hexane–EtOAc, 1:1), to yield **19** (401 mg, 50%) and nonreacting acceptor **8** (195 mg, 46%). TLC: 0.33 (hexane–EtOAc, 1:1). $[\alpha]_D^{23}$ +10.0° (*c* 1.0, CH_2Cl_2). ^{1}H NMR (500 MHz, $CDCl_3$) δ: 7.43–7.20 (m, 30H, *6 Ph*), 5.77 (d, 1H, N*H*, $J_{NH,2}$ = 9.5 Hz), 5.52 (s, 1H, Ph-*CH*-), 5.18 (d, 1H, *H-1a*, $J_{1,2}$ = 4.7 Hz), 5.16 (d, 1H, *H-1c*, $J_{1,2}$ = 3.7 Hz), 5.03 (d, 1H, *H-1b*, $J_{1,2}$ = 3.5 Hz), 4.90 (m, 2H, *H-2a*, *H-2c*), 4.84 (d, 1H, *H-1d*, $J_{1,2}$ = 3.1 Hz), 4.81–4.49 (m, 12H, *H-5a*, *H-5c*, *10* CH_2Ph), 4.29 (m, 1H, *H-2d*), 4.15 (dd, 1H, *H-6d* $J_{6,5}$ = 4.4 Hz, $J_{6,6'}$ = 10 Hz), 4.09 (t, 1H, *H-4a*, $J_{4,3} \approx J_{4,5}$ = 5.3 Hz), 4.01 (t, 1H, *H-4b* $J_{4,3} \approx J_{4,5}$ = 9.5 Hz), 3.94–3.91 (m, 3H, *H-3a*, *H-3c*, *CH*$(CH_3)_2$), 3.86 (m, 1H, *H-4c*), 3.80 (d, 1H, *H-5b*, $J_{5,4}$ = 10 Hz), 3.72–3.59 (m, 6H, *H-3b*, *H-6b*, *H-6′b*, *H-4d*, *H-5d*, *H-6′d*), 3.67 (s, 3H, COO*CH*$_3$), 3.50 (t, 1H, *H-3d*, $J_{3,2} \approx J_{3,4}$ = 9.6 Hz), 3.41 (s, 3H, COO*CH*$_3$), 3.30 (dd, 1H, *H-2b*, $J_{2,1}$ = 3.6 Hz, $J_{2,3}$ = 10.3 Hz), 1.83 (s, 3H, OCO*CH*$_3$), 1.63 (s, 3H, NHCO*CH*$_3$), 1.19 (s, 9H, C(*CH*$_3$)$_3$), 1.18 and 1.14 (2d, 6H, *J* = 6.5 Hz, CH(*CH*$_3$)$_2$). ^{13}C NMR (125 MHz, $CDCl_3$) δ: 177.3, 170.1, 169.8, 169.4, 168.8 (*C=O*), 138.4–126.3 (*Ph*), 101.4 (Ph-*CH*-), 98.3 (*C-1b*), 97.6 (*C-1c*), 97.1 (*C-1a*), 82.4, 78.0, 76.3, 74.9, 74.2, 74.1, 73.9, 73.7, 73.6, 73.4, 73.2, 71.6, 71.3, 70.7, 70.4, 70.1, 69.5, 68.7, 67.3, 65.6, 63.7, 62.9, 52.3 (*C-2d*), 52.1, 51.9 (COO*CH*$_3$), 38.8, 27.2, 23.2, 21.8, 20.8 (O*Piv*, NHCO*CH*$_3$, O-*i*-Pr). Anal. calcd. for $C_{80}H_{94}N_4O_{24}$ (%): C 64.24, H 6.33, N 3.75; found (%): C 63.89, H 6.36, N 3.51.

Methyl (isopropyl *O*-(2-acetamido-3-*O*-benzyl-4,6-*O*-benzylidene-2-deoxy-α-D-glucopyranosyl)-(1→4)-*O*-(methyl 3-*O*-benzyl-α-L-idopyranosyluronate)-(1→4)-*O*-(2-azido-3,6-di-*O*-benzyl-2-deoxy-α-D-glucopyranosyl)-(1→4)-3-*O*-benzyl-2-*O*-pivaloyl-α-L-idopyranosyl) uronate (20)

To a solution of **19** (460 mg, 0.307 mmol) in dry MeOH (10 mL), MeONa (73 μL of 1.2 M MeONa in MeOH) was added and stirred for 24 h. The reaction was neutralized with resin (IRA-120 H^+) and filtered. The residue was purified by flash chromatography (hexane–EtOAc, 1:2) to yield **20** (429 mg, 96%). TLC: 0.28 (hexane–EtOAc, 1:1). $[\alpha]_D^{23}$ +14.0° (*c* 1.0, CH_2Cl_2). MALDI-TOF (*m*/*z*): 1475 (M + Na^+), 1491 (M + K^+). ^{1}H NMR (500 MHz, $CDCl_3$) δ: 7.42–7.21 (m, 30H, *6 Ph*), 6.11 (d, 1H, N*H*, $J_{NH,2}$ = 8.2 Hz), 5.50 (s, 1H, Ph-*CH*-), 5.17 (d, 1H, *H-1a*, $J_{1,2}$ = 4.7 Hz), 5.11 (b.s., 1H, *H-1c*), 5.06 (d, 1H, *H-1b*, $J_{1,2}$ = 3.6 Hz), 4.96 (d, 1H, *H-1d*, $J_{1,2}$ = 3.8 Hz), 4.92 (t, 1H, *H-2a*, $J_{2,1} \approx J_{2,3}$ = 5.0 Hz), 4.87 (d, 1H, *H-5c*, $J_{5,4}$ = 2.3 Hz), 4.83 (d, 1H, *1* CH_2Ph, J_{gem} = 12.2 Hz), 4.75 (2d, 2H, *2* CH_2Ph, J_{gem} = 11 Hz), 4.72 (d, 1H, *H-5a*, $J_{5,4}$ = 4.7 Hz), 4.68 (d, 1H, *1* CH_2Ph, J_{gem} = 11 Hz), 4.63 (2d, 2H, *2* CH_2Ph, J_{gem} = 11.5 Hz), 4.56–4.52 (m, 4H, *4* CH_2Ph), 4.18–4.11 (m, 3H, *H-2d*, *H-4a*, *H-6d*), 3.99–3.91 (m, 4H, *H-4b*, *H-3a*, *H-4c*, *CH*$(CH_3)_2$), 3.84 (m, 1H, *H-3c*), 3.72–3.65 (m, 6H, *H-3b*, *H-6b*, *H-6′b*, *H-4d*, *H-5d*, *H-6′d*), 3.63 (s, 3H, COO*CH*$_3$), 3.61–3.55 (m, 3H, *H-2c*, *H-3d*, *H-5b*), 3.46 (m, 1H, *H-3d*), 3.40 (s, 3H, COO*CH*$_3$), 3.30 (dd, 1H, *H-2b*, $J_{2,1}$ = 3.6 Hz, $J_{2,3}$ = 10.3 Hz), 2.60 (d, 1H, *OH-2c*, $J_{OH,2}$ = 4.7 Hz), 1.73 (s, 3H, NHCO*CH*$_3$), 1.19 (s, 9H, C(*CH*$_3$)$_3$), 1.18 and 1.13 (2d, 6H, *J* = 6.5 Hz, CH(*CH*$_3$)$_2$). ^{13}C NMR (125 MHz, $CDCl_3$) δ: 177.3, 170.7, 170.0, 169.3 (*C=O*), 138.4–126.1 (*Ph*), 101.5 (Ph-*CH*-), 100.8 (*C-1c*), 98.3 (*C-1b*), 97.2 (*C-1a*), 96.8 (*C-1d*), 82.3, 78.2, 76.2, 75.2, 75.0, 74.1, 74.0, 73.8, 73.6, 73.2, 72.8, 72.1, 71.4, 71.3, 70.9, 70.4, 69.3, 68.6, 68.3, 68.0, 67.6, 63.4, 63.2, 52.6 (*C-2d*), 52.2, 52.0 (COO*CH*$_3$), 38.8, 29.1, 27.2, 23.3, 22.9, 21.8 (O*Piv*, NHCO*CH*$_3$, O-*i*-Pr). Anal. calcd. for $C_{78}H_{92}N_4O_{23}\cdot H_2O$ (%): C 63.66, H 6.43, N 3.81; found (%): C 63.51, H 6.19, N 4.01.

© 2002 NRC Canada

Methyl (isopropyl *O*-(2-acetamido-3-*O*-benzyl-4,6-*O*-benzylidene-2-deoxy-α-D-glucopyranosyl)-(1→4)-*O*-(methyl 2,3-di-*O*-benzyl-α-L-idopyranosyluronate)-(1→4)-*O*-(2-azido-3,6-di-*O*-benzyl-2-deoxy-α-D-glucopyranosyl)-(1→4)-3-*O*-benzyl-2-*O*-pivaloyl-α-L-idopyranosyl) uronate (21)

(*a*) To a solution of **25** (170 mg, 0.124 mmol), freshly prepared Ag_2O (90 mg, 0.388 mmol) and 4 Å molecular sieves in dry DMF (0.5 mL), freshly distilled benzyl bromide (100 μL, 0.84 mmol) was added. After stirring for 40 h, the solution was filtered through Celite. The residue was purified by flash chromatography (toluene–EtOAc, 5:2) to yield **21** (101 mg, 52%).

(*b*) To a solution of **20** (440 mg, 0.303 mmol) and freshly prepared Ag_2O (161 mg, 0.7 mmol) in dry DMF (0.5 mL), freshly distilled benzyl bromide (100 μL, 0.84 mmol) was added. After stirring for 30 h, the solution was filtered through Celite. The residue was purified by flash chromatography (hexane–EtOAc, 1:1) to yield **21** (411 mg, 88%). TLC: 0.32 (hexane–EtOAc, 1:1). $[\alpha]_D^{23}$ +47.3° (*c* 1.0, $CHCl_3$). MALDI-TOF (*m*/*z*): 1566 ($M + Na^+ + H$), 1581 ($M + K^+$). ^{1}H NMR (500 MHz, $CDCl_3$) δ: 7.44–7.15 (m, 35H, *7 Ph*), 5.92 (d, 1H, N*H*, $J_{NH,2}$ = 9.7 Hz), 5.50 (s, 1H, Ph-*CH*-), 5.29 (d, 1H, *H-1c*, $J_{2,1}$ = 3.7 Hz), 5.16 (d, 1H, *H-1a*, $J_{2,1}$ = 4.6 Hz), 5.04 (d, 1H, *H-1b*, $J_{2,1}$ = 3.6 Hz), 4.91 (t, 1H, *H-2a*, $J_{2,1} \approx J_{2,3}$ = 5.0 Hz), 4.87 (d, 1H, *1* CH_2Ph, J_{gem} = 10.7 Hz), 4.81 (d, 1H, *H-1d*, $J_{2,1}$ = 3.8 Hz), 4.78–4.64 (m, 7H, *H-5c*, *H-5a*, *5* CH_2Ph), 4.57 (d, 1H, *1* CH_2Ph, J_{gem} = 11.9 Hz), 4.52–4.47 (m, 3H, *3* CH_2Ph), 4.43 (d, 1H, *1* CH_2Ph, J_{gem} = 11.9 Hz), 4.42 (d, 1H, *1* CH_2Ph, J_{gem} = 12.1 Hz), 4.31 (m, 1H, *H-2d*), 4.16 (dd, 1H, *H-6d*, $J_{6,5}$ = 4.5 Hz, $J_{6,6'}$ = 10.2 Hz), 4.12 (t, 1H, *H-4a*, $J_{4,3} \approx J_{4,5}$ = 5.2 Hz), 4.04 (t, 1H, *H-4b*, $J_{4,3} \approx J_{4,5}$ = 9.5 Hz), 3.96–3.91 (m, 3H, *H-3a*, *H-4c*, *CH*$(CH_3)_2$), 3.85–3.82 (m, 2H, *H-5b*, *H-3c*), 3.78–3.52 (m, 7H, *H-3b*, *H-3d*, *H-4d*, *H-5d*, *H-6′d*, *H-6b*, *H-6′b*), 3.62 (s, 3H, COO*CH*$_3$), 3.47 (s, 3H, COO*CH*$_3$), 3.44 (t, 1H, *H-2c*, $J_{2,1} \approx J_{2,1}$ = 4.1 Hz), 3.30 (dd, 1H, *H-2b*, $J_{2,1}$ = 3.6 Hz, $J_{2,3}$ = 10.3 Hz), 1.51 (s, 3H, NHCO*CH*$_3$), 1.20 (s, 9H, C(*CH*$_3$)$_3$), 1.19 and 1.14 (2d, 6H, *J* = 6.5 Hz, CH(*CH*$_3$)$_2$). ^{13}C NMR (125 MHz, $CDCl_3$) δ: 177.3, 170.0, 169.1 (*C=O*), 138.6,–126.1 (*Ph*), 101.4 (Ph-*CH*-), 98.7 (*C-1c*), 98.4 (*C-1b*), 98.3 (*C-1d*), 97.2 (*C-1a*), 82.3, 78.1, 76.2, 76.0, 75.8, 74.2, 74.1, 73.7, 73.4, 73.2, 71.8, 71.3, 70.7, 70.3, 69.5, 68.7 (*C-6d*), 67.7, 65.4, 63.6, 63.0 (*C-2b*), 52.2 (*C-2d*), 52.1, 51.9 (COO*CH*$_3$), 29.7, 27.2, 23.3, 22.8, 21.8 (O*Piv*, NHCO*CH*$_3$, O*i*-Pr). Anal. calcd. for $C_{85}H_{98}N_4O_{23}$ (%): C 66.13, H 6.40, N 3.63; found (%): C 65.90, H 6.40, N 3.42.

Methyl (isopropyl *O*-(2-acetamido-3-*O*-benzyl-2-deoxy-α-D-glucopyranosyl)-(1→4)-*O*-(methyl 2,3-di-*O*-benzyl-α-L-idopyranosyluronate)-(1→4)-*O*-(2-azido-3,6-di-*O*-benzyl-2-deoxy-α-D-glucopyranosyl)-(1→4)-3-*O*-benzyl-2-*O*-pivaloyl-α-L-idopyranosyl) uronate (22)

To a solution of **21** (450 mg, 0.291 mmol) in dry CH_2Cl_2 (9 mL), EtSH (108 μL, 1.46 mmol), and catalytic PTSA were added. After stirring for 3 h under an argon atmosphere, the reaction was neutralized with solid $NaHCO_3$, diluted with CH_2Cl_2 (40 mL), and washed with H_2O (40 mL). The organic layer was dried ($MgSO_4$) and concentrated to dryness. The residue was purified by flash chromatography (hexane–EtOAc, 1:3) to yield **22** (351 mg, 83%). TLC: 0.23 (hexane–EtOAc, 1:3). $[\alpha]_D^{23}$ +23.2° (*c* 1.0, CH_2Cl_2). MALDI-TOF (*m*/*z*): 1477 ($M + Na^+$), 1493 ($M + K^+$). ^{1}H NMR (500 MHz, $CDCl_3$) δ: 7.34–7.16 (m, 30H, *6 Ph*), 6.19 (d, 1H, *NH*, $J_{NH,2}$ = 9.6 Hz), 5.29 (d, 1H, *H-1c*, $J_{2,1}$ = 3.1 Hz), 5.16 (d, 1H, *H-1a*, $J_{2,1}$ = 4.5 Hz), 5.04 (d, 1H, *H-1b*, $J_{2,1}$ = 3.5 Hz), 4.91 (t, 1H, *H-2a*, $J_{2,1} \approx J_{2,3}$ = 4.8 Hz), 4.86 (d, 1H, *1* CH_2Ph, J_{gem} = 10.8 Hz), 4.78–4.74 (m, 3H, *H-1d*, *H-5c*, *1* CH_2Ph), 4.73 (d, 1H, *H-5c*, $J_{5,4}$ = 4.5 Hz), 4.69–4.40 (m, 10H, *10* CH_2Ph), 4.22 (m, 1H, *H-2d*), 4.12 (t, 1H, *H-4a*, $J_{4,3} \approx J_{4,5}$ = 5.2 Hz), 4.04 (t, 1H, *H-4b*, $J_{4,3} \approx J_{4,5}$ = 9.5 Hz), 3.94 (t, 1H, *H-3a*, $J_{3,2} \approx J_{3,4}$ = 5.5 Hz), 3.92–3.90 (m, 2H, *H-4c*, *CH*$(CH_3)_2$), 3.85 (m, 1H, *H-5b*), 3.81 (t, 1H, *H-3c*, $J_{3,2} \approx J_{3,4}$ = 4.4 Hz), 3.75 (t, 1H, *H-3b*, $J_{3,2} \approx J_{3,4}$ = 9.8 Hz), 3.72–3.57 (m, 5H, *H-4d*, *H-5d*, *H-6d*, *H-6b*, *H-6′b*), 3.64 (s, 3H, COO*CH*$_3$), 3.46–3.35 (m, 3H, *H-3d*, *H-2c*, *H-6′b*), 3.42 (s, 3H, COO*CH*$_3$), 3.31 (dd, 1H, *H-2b*, $J_{2,1}$ = 3.7 Hz, $J_{2,3}$ = 10.3 Hz), 1.51 (s, 3H, NHCO*CH*$_3$), 1.20 (s, 9H, C(*CH*$_3$)$_3$), 1.18 and 1.14 (2d, 6H, *J* = 6.1 Hz, CH(*CH*$_3$)$_2$). ^{13}C NMR (125 MHz, $CDCl_3$) δ: 177.3, 170.1, 170.0, 169.3 (*C=O*), 138.2–127.6 (*Ph*), 98.7 (*C-1c*), 98.4 (*C-1b*), 97.5 (*C-1d*), 97.3 (*C-1a*), 80.4, 78.2, 76.2, 74.9, 74.2, 74.1, 74.0, 73.9, 73.7, 73.3, 73.2, 72.5, 72.4, 72.2, 71.8, 71.3, 70.7, 70.4, 70.2, 69.2, 63.1, 62.4 (*C-2b*), 52.1, 52.0 (COO*CH*$_3$), 51.8 (*C-2d*), 38.8, 27.2, 23.3, 22.8, 21.8 (O*Piv*, NHCO*CH*$_3$, O-*i*-Pr). Anal. calcd. for $C_{78}H_{94}N_4O_{23}\cdot 0.5H_2O$ (%): C 63.96, H 6.54, N 3.82; found (%): C 63.60, H 6.48, N 3.80.

Methyl (isopropyl *O*-(2-acetamido-6-*O*-benzoyl-3-*O*-benzyl-2-deoxy-α-D-glucopyranosyl)-(1→4)-*O*-(methyl 2,3-di-*O*-benzyl-α-L-idopyranosyluronate)-(1→4)-*O*-(2-azido-3,6-di-*O*-benzyl-2-deoxy-α-D-glucopyranosyl)-(1→4)-3-*O*-benzyl-2-*O*-pivaloyl-α-L-idopyranosyl) uronate (23)

To a solution of **22** (330 mg, 0.227 mmol) in dry CH_3CN (4 mL) at –40°C, BzCN (262 μL of a 0.9 M solution of BzCN in dry CH_3CN) and a few drops of Et_3N were added. After 7 h, MeOH was added and the mixture was allowed to reach room temperature. The solvent was evaporated and the residue was dissolved in MeOH and concentrated to dryness. The residue was purified by flash chromatography (hexane–EtOAc, 1:1) to yield **23** (312 mg, 88%). TLC: 0.29 (hexane–EtOAc, 1:1). $[\alpha]_D^{23}$ +43.2° (*c* 1.0, CH_2Cl_2). MALDI-TOF (*m*/*z*): 1581 ($M + Na^+$), 1597 ($M + K^+$). ^{1}H NMR (500 MHz, $CDCl_3$) δ: 8.03–7.13 (m, 35H, *7 Ph*), 6.16 (d, 1H, *NH*, $J_{NH,2}$ = 9.7 Hz), 5.29 (d, 1H, *H-1c*, $J_{1,2}$ = 3.0 Hz), 5.17 (d, 1H, *H-1a*, $J_{1,2}$ = 4.6 Hz), 5.05 (d, 1H, *H-1b*, $J_{1,2}$ = 3.6 Hz), 4.92 (t, 1H, *H-2a*, $J_{2,1} \approx J_{2,3}$ = 5.0 Hz), 4.84 (d, 1H, *1* CH_2Ph, J_{gem} = 10.5 Hz), 4.83 (s, 1H, *H-1d*), 4.81 (d, 1H, *H-5c*, $J_{5,4}$ = 3.3 Hz), 4.76 (d, 1H, *1* CH_2Ph, J_{gem} = 11.2 Hz), 4.73 (d, 1H, *H-5a*, $J_{5,4}$ = 4.5 Hz), 4.70–4.47 (m, 10H, *H-6d*, *9* CH_2Ph), 4.39 (d, 1H, *1* CH_2Ph, J_{gem} = 12.0 Hz), 4.38 (dd, 1H, *H-6′d*, $J_{6',5}$ = 1.8 Hz, $J_{6',6'}$ = 12.0 Hz), 4.26 (m, 1H, *H-2d*), 4.12 (t, 1H, *H-4a*, $J_{4,3} \approx J_{4,5}$ = 5.2 Hz), 4.04 (t, 1H, *H-4b*, $J_{4,3} \approx J_{4,5}$ = 9.6 Hz), 3.99 (t, 1H, *H-4c*, $J_{4,3} \approx J_{4,5}$ = 3.9 Hz), 3.95 (t, 1H, *H-3a*, $J_{3,2} \approx J_{3,4}$ = 5.4 Hz), 3.93 (m, 1H, *CH*$(CH_3)_2$, *J* = 6.2 Hz), 3.84 (m, 1H, *H-5b*), 3.82 (t, 1H, *H-3c*, $J_{3,2} \approx J_{3,4}$ = 4.3 Hz), 3.74 (t, 1H, *H-3b*, $J_{3,2} \approx J_{3,4}$ = 10.0 Hz), 3.69–3.57 (m, 4H, *H-4d*, *H-5d*, *H-6b*, *H-6′b*), 3.63 (s, 3H, COO*CH*$_3$), 3.43 (s, 3H, COO*CH*$_3$), 3.44–3.40 (m, 2H, *H-3d*, *H-2c*), 3.31 (dd, 1H, *H-2b*, $J_{2,1}$ = 3.6 Hz, $J_{2,3}$ = 10.3 Hz), 1.52 (s, 3H,

© 2002 NRC Canada

NHCOCH_3), 1.20 (s, 9H, C(CH_3)$_3$), 1.19 and 1.14 (2d, 6H, J = 6.1 Hz, CH(CH_3)$_2$). ^{13}C NMR (125 MHz, $CDCl_3$) δ: 177.3, 170.0, 169.2, 166.9 (*C*=*O*), 138.3–127.6 (*Ph*), 98.7 (*C-1c*), 98.4 (*C-1b*), 97.2 (*C-1a*), 97.1 (*C-1d*), 80.2, 78.1, 76.4, 74.9, 74.5, 74.2, 74.1, 73.7, 73.3, 73.2, 73.1, 73.0, 71.9, 71.8, 71.3, 71.0, 70.7, 70.3, 69.7, 69.1, 67.9, 63.1, 63.0, 52.0, 51.9 (COOCH_3, *C-2d*), 38.8, 27.2, 23.3, 22.8, 21.8 (O*Piv*, NHCOCH_3, O-*i*-Pr). Anal. calcd. for $C_{85}H_{98}N_4O_{24}\cdot 0.5H_2O$ (%): C 65.08, H 6.36, N 3.57, found (%): C 64.83, H 6.36, N 3.57.

Methyl (isopropyl *O*-(2-azido-3-*O*-benzyl-4,6-*O*-benzylidene-2-deoxy-α-D-glucopyranosyl)-(1→4)-*O*-(methyl 3-*O*-benzyl-2-*O*-pivaloyl-α-L-idopyranosyluronate)-(1→4)-*O*-(2-acetamido-6-*O*-benzoyl-3-*O*-benzyl-2-deoxy-α-D-glucopyranosyl)-(1→4)-*O*-(methyl 2,3-di-*O*-benzyl-α-L-idopyranosyluronate)-(1→4)-*O*-(2-azido-3,6-di-*O*-benzyl-2-deoxy-α-D-glucopyranosyl)-(1→4)-3-*O*-benzyl-2-*O*-pivaloyl-α-L-idopyranosyl) uronate (5)

To a solution of **23** (90 mg, 57.7 μmol) and **6** (68 mg, 75.7 μmol) in dry CH_2Cl_2 (0.5 mL) at room temperature, TMSOTf (25 μL of a 0.1 M solution of TMSOTf in CH_2Cl_2) was added under an argon atmosphere. After stirring for 2 h 30 min, saturated $NaHCO_3$ solution (1 mL) was added and diluted with CH_2Cl_2 (20 mL). The residue was washed with H_2O (15 mL) and then the aqueous layer was extracted with CH_2Cl_2 (2 × 10 mL) and the organic layers were dried ($MgSO_4$) and concentrated in vacuo. The residue was purified by flash chromatography (hexane–EtOAc, 2:3) to yield **5** (85 mg, 65%) and nonreacting acceptor **23** (27 mg, 30%). TLC: 0.33 (hexane–EtOAc, 3:2). $[\alpha]_D^{23}$ +10.4° (*c* 1.1, CH_2Cl_2). ^{1}H NMR (500 MHz, $CDCl_3$) δ: 8.09–7.13 (m, 50H, *10 Ph*), 5.90 (d, 1H, N*H*, $J_{NH,2}$ = 9.8 Hz), 5.48 (s, 1H, Ph-*CH*-), 5.30 (d, 1H, *H-1c*, $J_{1,2}$ = 3.4 Hz), 5.25 (d, 1H, *H-1e*, $J_{1,2}$ = 3.8 Hz), 5.17 (d, 1H, *H-1a*, $J_{1,2}$ = 4.6 Hz), 5.05 (d, 1H, *H-1b*, $J_{1,2}$ = 3.7 Hz), 4.93–4.90 (m, 3H, *H-2a*, *H-2e*, *H-1f*), 4.85 (d, 1H, *1* CH_2Ph, J_{gem} = 10.9 Hz), 4.83 (d, 1H, *1* CH_2Ph, J_{gem} = 11 Hz), 4.79 (d, 1H, *H-1d*, $J_{1,2}$ = 3.7 Hz), 4.76–4.47 (m, 16H, *H-5a*, *H-5c*, *H-5e*, *H-6d*, *12* CH_2Ph), 4.42 (m, 1H, *H-6′d*), 4.39 (d, 1H, *1* CH_2Ph, J_{gem} = 12 Hz), 4.28 (m, 1H, *H-2d*), 4.27 (d, 1H, *1* CH_2Ph, J_{gem} = 10.9 Hz), 4.19 (dd, 1H, *H-6f*, $J_{6,5}$ = 4.9 Hz, $J_{6,6'}$ = 10.1 Hz), 4.12 (dd, 1H, *H-4a*, $J_{4,3}$ = 4.8 Hz, $J_{4,5}$ = 5.9 Hz), 4.05–3.99 (m, 3H, *H-4b*, *H-4d*, *H-4e*), 3.99–3.90 (m, 4H, *H-3a*, *H-3e*, *H-4c*, *CH*(CH_3)$_2$), 3.88–3.82 (m, 3H, *H-3f*, *H-5b*, *H-5f*), 3.80–3.72 (m, 3H, *H-3c*, *H-3b*, *H-5d*), 3.67 (dd, 1H, *H-6b*, $J_{6,5}$ = 3.0 Hz, $J_{6,6'}$ = 11.7 Hz), 3.63 (s, 3H, COOCH_3), 3.61–3.55 (m, 3H, *H-4f*, *H-6′b*, *H-6′f*), 3.45–3.41 (m, 2H, *H-2c*, *H-3d*), 3.39 (s, 3H, COOCH_3), 3.32 (s, 3H, COOCH_3), 3.32–3.30 (m, 1H, *H-2b*), 3.27 (dd, 1H, *H-2f*, $J_{2,1}$ = 3.8 Hz, $J_{2,3}$ = 10.0 Hz), 1.41 (s, 3H, NHCOCH_3), 1.20 (s, 9H, C(CH_3)$_3$), 1.19 and 1.13 (2d, 6H, J = 6.1 Hz, CH(CH_3)$_2$), 1.11 (s, 9H, C(CH_3)$_3$). ^{13}C NMR (125 MHz, $CDCl_3$) δ: 177.4, 177.3, 170.0, 169.8, 169.3, 169.0, 166.1 (*C*=*O*), 138.4–126.1 (*Ph*), 101.5 (Ph-*CH*-), 99.4 (*C-1f*), 98.7 (*C-1b*, *C-1c*), 98.0 (*C-1e*), 97.2 (*C-1a*, *C-1d*), 82.5, 78.1, 76.3, 76.0, 75.0, 74.9, 74.8, 74.6, 74.5, 74.1, 74.0, 73.7, 73.5, 73.3, 73.2, 71.8, 71.3, 71.1, 70.3, 70.1, 69.9, 69.6, 68.5, 67.8, 63.2, 63.0, 62.9, 62.2, 52.0, 51.9 (COOCH_3), 51.7 (*C-2d*), 38.8, 38.7, 27.2, 27.1, 23.3, 22.8, 21.8 (O*Piv*, NHCOCH_3, O-*i*-Pr). Anal. calcd. for $C_{124}H_{141}N_7O_{35}$ (%): C 65.05, H 6.21, N 4.28; found (%): C 64.85, H 6.18, N 4.23.

Isopropyl *O*-(2-azido-3-*O*-benzyl-4,6-di-*O*-benzylidene-2-deoxy-α-D-glucopyranosyl)-(1→4)-*O*-(3-*O*-benzyl-α-L-idopyranosyluronic acid)-(1→4)-*O*-(2-acetamido-3-*O*-benzyl-2-deoxy-α-D-glucopyranosyl)-(1→4)-*O*-(2,3-di-*O*-benzyl-α-L-idopyranosyluronic acid)-(1→4)-*O*-(2-azido-3,6-di-*O*-benzyl-2-deoxy-α-D-glucopyranosyl)-(1→4)-3-*O*-benzyl-α-L-idopyranosyluronic acid (26)

To a solution of **5** (39 mg, 17.0 μmol) in THF (2 mL) at –5°C, 30% H_2O_2 (0.7 mL) and a 1 M aqueous solution of LiOH (1.1 mL) were added. After stirring for 24 h at room temperature MeOH (1 mL) and a 3 N aqueous solution of KOH (2 mL) were added. After stirring for 24 h more the reaction was neutralized with acidic resin (IRA-120 H^+), filtered, and concentrated. The residue was purified by Sephadex LH-20 (MeOH–CH_2Cl_2, 1:1) to yield **26** (33 mg, 98%). TLC: 0.45 (CH_2Cl_2–MeOH, 8:1). ^{1}H NMR (500 MHz, MeOD) δ: 7.44–7.10 (m, 50 H, *10 Ph*), 5.56 (s, 1H, Ph-*CH*-), 5.37 (b.s., 1H, *H-1c*), 5.05–5.01 (m, 3H, *H-1a*, *H-1b*, *H-1e*), 4.89 (m, 1H, *H-1f*), 4.83 (m, 1H, *H-1d*), 1.48 (m, 3H, NHCOCH_3), 1.17–1.16 (m, 6H, CH(CH_3)$_2$).

Isopropyl *O*-(2-azido-3-*O*-benzyl-4,6-di-*O*-benzylidene-2-deoxy-α-D-glucopyranosyl)-(1→4)-*O*-(3-*O*-benzyl-2-*O*-sulfo-α-L-idopyranosyluronic acid)-(1→4)-*O*-(2-acetamido-3-*O*-benzyl-2-deoxy-6-*O*-sulfo-α-D-glucopyranosyl)-(1→4)-*O*-(2,3-di-*O*-benzyl-α-L-idopyranosyluronic acid)-(1→4)-*O*-(2-azido-3,6-di-*O*-benzyl-2-deoxy-α-D-glucopyranosyl)-(1→4)-3-*O*-benzyl-2-*O*-sulfo-α-L-idopyranosyl)uronic acid hexasodium salt (27)

A mixture of **26** (33 mg, 16.7 μmol) and complex $SO_3\cdot$Py (40 mg, 0.25 mmol) in dry Py (1.5 mL) was stirred under an argon atmosphere. After 24 h, the mixture was cooled and MeOH (1 mL) and CH_2Cl_2 (1 mL) were added. The solution was eluted through a Sephadex LH-20 (MeOH–CH_2Cl_2,1:1). Fractions containing the hexasaccharide were concentrated and passed through a Dowex 50WX4-Na^+ (MeOH–H_2O, 2:1) to yield **27** (28 mg, 72%). TLC: 0.65 (EtOAc–Py–H_2O–AcOH, 8:5:3:1). ^{1}H NMR (500 MHz, MeOD) δ: 7.42–7.10 (m, 50H, 10 *Ph*), 5.56 (s, 1H, Ph-*CH*-), 5.46 (s, 1H, *H-1a* or *e*), 5.32 (s, 1H, *H-1c*), 5.28 (s, 1H, *H-1a* or *e*), 5.15 (d, 1H, *H-1b* or *f*), 5.06 (d, 1H, *H-1b* or *f*), 4.82 (m, 1H, *H-1d*), 1.26 (m, 3H, NHCOCH_3), 1.20 (d, 6H, CH(CH_3)$_2$, J = 6.0 Hz). ^{13}C NMR (125 MHz, MeOD) δ: 101.4 (Ph-*CH*-), 98.8 (*C-1c*), 98.1 (*C-1a* or *e*), 97.5 (*C-1a* or *e*), 96.1 (*C-1b* or *f*), 95.7 (*C-1b* or *f*), 95.5 (*C-1d*).

Isopropyl *O*-(2-deoxy-2-sulfamide-α-D-glucopyranosyl)-(1→4)-*O*-(2-*O*-sulfo-α-L-idopyranosyluronic acid)-(1→4)-*O*-(2-acetamido-2-deoxy-6-*O*-sulfo-α-D-glucopyranosyl)-(1→4)-*O*-(α-L-idopyranosyluronic acid)-(1→4)-*O*-(2-deoxy-2-sulfamide-α-D-glucopyranosyl)-(1→4)-2-*O*-sulfo-α-L-idopyranosyluronic acid octasodium salt (3)

To a solution of **27** (17 mg, 7.24 μmol) in MeOH–H_2O (1.5 mL, 9:1) was hydrogenolyzed in the presence of 10% Pd/C. After 24 h, the suspension was filtered and concentrated to give the desired product which was directly used in the next step without further purification.

© 2002 NRC Canada

The hydrogenolyzed hexasaccharide was dissolved in H_2O (1mL) and the pH of the solution was adjusted to 9.5 with 1 N solution of NaOH. Complex SO_3·Py (24 mg, 10 equiv for each amine group) was added in three portions during 1 h and the pH was maintained at 9.5 by subsequent addition of a 1 N solution of NaOH. A second, third, and fourth portion of complex SO_3·Py were added after 2, 4, and 6 h stirring, respectively. After 24 h, the mixture was neutralized with 0.1 N HCl to pH 7 and then passed through a column of Sephadex G-25 with 0.9% NaCl. The appropriate fractions were pooled and passed through a column of Dowex 50WX4-Na^+ with 0.5 M NaCl and then a column of Sephadex G-25 with H_2O–EtOH (9:1). The fractions which contained the final hexasaccharide were lyophilized to give **3** (9.1 mg, 75% from **27**). Before NMR studies, it was useful to make a last elution on a column of Dowex 50WX4-Na^+ to avoid the formation of calcium salts instead of sodium salts and get a better resolution in the spectra. ^{1}H NMR (500 MHz, D_2O) δ: 5.38 (d, 1H, *H-1f*, $J_{1,2}$ = 3.7 Hz), 5.32 (d, 1H, *H-1b*, $J_{1,2}$ = 3.7 Hz), 5.22 (d, 1H, *H-1a*, $J_{1,2}$ = 3.0 Hz), 5.18 (d, 1H, *H-1e*, $J_{1,2}$ = 3.0 Hz), 5.15 (d, 1H, *H-1d*, $J_{1,2}$ = 4.0 Hz), 4.89 (d, 1H, *H-1c*, $J_{1,2}$ = 3.5 Hz), 1.99 (m, 3H, NHCO*CH*$_3$), 1.17 (d, 3H, CH(*CH*$_3$)$_2$, *J* = 6.2 Hz), 1.16 (d, 3H, CH(*CH*$_3$)$_2$, *J* = 6.2 Hz). ^{13}C NMR (125 MHz, D_2O) δ: 102.9 (*C-1c*), 99.8 (*C-1e*), 97.8 (*C-1a*), 97.6 (*C-1b*), 97.3 (*C-1f*), 94.9 (*C-1d*).

2-Azido-6-*O*-benzoyl-3,4-di-*O*-benzyl-2-deoxy-α,β-D-glucopyranose trichloroacetimidate (29)

To a solution of **28** (1 g, 2.12 mmol) in dry MeOH (8 mL), solid KOH (119 mg, 2.12 mmol) was added, and was stirred for 20 min. The solution was diluted with CH_2Cl_2 (200 mL) and saturated NH_4Cl solution (2 × 100 mL) and H_2O (2 × 100 mL). The organic layer was dried ($MgSO_4$) and concentrated in vacuo. The residue was directly used in the next step without further purification.

To this residue dissolved in Py (10 mL), BzCl (2 mL) was added and stirred at room temperature for 24 h. The reaction was diluted with CH_2Cl_2 (100 mL), washed with H_2O (75 mL) and 1 N HCl solution (75 mL), dried ($MgSO_4$), and concentrated to dryness. The residue was purified by flash chromatography and used in the next step.

To a solution of this residue (1.2 g, 2.04 mmol) in dry Et_2O (10 mL), benzylamine (1.2 mL, 10.9 mmol) was added and was stirred for 4 h. The residue was concentrated to dryness and purified by flash chromatography (hexane–EtOAc, 3:1) and then to a solution of this compound (625 mg, 1.27 mmol) in dry CH_2Cl_2 (7 mL), Cl_3CCN (1.9 mL, 19 mmol) and catalytic DBU were added. After stirring for 1 h the residue was concentrated to dryness. The residue was purified by flash chromatography (hexane–EtOAc (4:1) + 1% Et_3N) to yield **29** (703 mg, 87%) as a mixture of anomers α and β. TLC (α and β): 0.50 and 0.43 (hexane–EtOAc, 3:1). ^{1}H NMR (500 MHz, $CDCl_3$) δ: 8.71 (s, 1H, O(C=*NH*)CCl_3 (α)), 8.69 (s, 1H, O(C=*NH*)CCl_3 (β)), 7.29–7.24 (m, 30H, *3 Ph* (α and β)), 6.42 (d, 1H, *H-1* (α), $J_{1,2}$ = 4.1 Hz), 5.65 (d, 1H, *H-1* (β), $J_{1,2}$ = 8.5 Hz), 4.99–4.84 (m, 6H, *6 CH*$_2$Ph (α and β)), 4.65–4.45 (m, 6H, *2 CH*$_2$Ph (α and β), *H-6a* (α and β), *H-6b* (α and β)), 4.17 (m, 1H, *H-5* α), 4.09 (t, 1H, *H-3* (α), $J_{3,2} \approx J_{3,4}$ = 9.5 Hz), 3.80–3.70 (m, 5H, *H-2* (α and β), *H-4* (α and β), *H-5* (β)), 3.61 (t, 1H, *H-3* (β), $J_{3,2} \approx J_{3,4}$ = 9.0 Hz).

Methyl dimethylthexylsilyl 2-*O*-acetyl-4-*O*-(2-azido-6-*O*-benzoyl-3,4-di-*O*-benzyl-2-deoxy-α-D-glucopyranosyl)-3-*O*-benzyl-β-L-idopyranuronate (31)

To a solution of **11** (600 g, 0.95 mmol) in dry CH_2Cl_2 (20 mL) at 0°C TMSOTf (8.6 μL, 0.048 mmol) was added under an argon atmosphere. A solution of **29** (720 mg, 1.63 mmol) in dry CH_2Cl_2 (30 mL) was added dropwise for 30 min. The reaction was neutralized with saturated $NaHCO_3$ solution and diluted with CH_2Cl_2 (100 mL). The organic layer was washed with H_2O (75 mL), dried ($MgSO_4$), and concentrated in vacuo. The residue was purified by flash chromatography (hexane–EtOAc, 4:1) to yield a mixture of isomers containing **30** which was used directly in the next step.

To a solution of this mixture in Py (10 mL), acetic anhydride (5 mL) was added and was stirred for 24 h. The reaction was diluted with CH_2Cl_2 (100 mL) and washed with H_2O (80 mL) and 1 N HCl solution (80 mL). The organic layer was dried ($MgSO_4$) and concentrated to dryness. The residue was purified by flash chromatography (hexane–EtOAc, 6:1) to yield **31** (391 mg, 43% from **11**). TLC: 0.36 (hexane–EtOAc, 6:1). $[\alpha]_D^{23}$ +76.0° (*c*, 1.0, CH_2Cl_2). ^{1}H NMR (500 MHz, $CDCl_3$) δ: 7.99–7.20 (m, 20H, *4 Ph*), 5.06 (d, 1H, *H-1*, $J_{1,2}$ = 1.5 Hz), 4.99 (b.s., 1H, *H-2*), 4.90 (d, 1H, *H-1′*, $J_{1,2}$ = 3.4 Hz), 4.86 (d, 1H, *1 CH*$_2$Ph, J_{gem} = 11.2 Hz), 4.82 (s, 2H, *2 CH*$_2$Ph), 4.74–4.58 (m, 4H, *3 CH*$_2$Ph, *H-6′a*), 4.47 (d, 1H, *H-5*, $J_{5,4}$ = 1.2 Hz), 4.41 (dd, 1H, *H-6′b*, $J_{6b,5}$ = 2.6 Hz, $J_{6b,6a}$ = 12.3 Hz), 4.22 (m, 1H, *H-5′*), 4.11 (b.s., 1H, *H-4*), 3.99–3.95 (m, 2H, *H-3′*, *H-3*), 3.73 (s, 3H, COO*Me*), 3.70 (m, 1H, *H-4′*), 3.28 (dd, 1H, *H-2′*, $J_{2,1}$ = 3.4 Hz, $J_{2,3}$ = 10.3 Hz), 2.04 (d, 3H, OCO*CH*$_3$), 1.60 (m, 1H, *CH*(CH$_3$)$_2$), 0.86–0.83 (m, 12H, CH(*CH*$_3$)$_2$, C(*CH*$_3$)$_2$), 0.24 and 0.14 (2s, 6H, Si(*CH*$_3$)$_2$). ^{13}C NMR (125 MHz, $CDCl_3$) δ: 170.6, 168.9, 166.1 (*C=O*), 137.8–127.5 (*Ph*), 97.4 (*C-1′*), 93.6 (*C-1*), 80.0 (*C-3′*), 77.9 (*C-4′*), 75.5, 74.9, 74.3, 73.2, 72.9, 72.8, 69.9 (*C-5*), 67.2 (*C-2*), 63.5 (*C-2′*), 62.8 (*C-6*), 52.1 (COO*Me*), 34.1, 24.8, 20.9, 20.2, 19.8 18.6, –2.1, –3.5 (O*TDS*, OCO*CH*$_3$). Anal. calcd. for $C_{51}H_{63}N_3O_{13}Si·0.5H_2O$ (%): C 63.60, H 6.70, N 4.36; found (%): C 63.64, H 6.40, N 4.34.

Methyl dimethylthexylsilyl 4-*O*-(2-acetamido-6-*O*-benzoyl-3,4-di-*O*-benzyl-2-deoxy-α-D-glucopyranosyl)-2-*O*-acetyl-3-*O*-benzyl-β-L-idopyranuronate (32)

A solution of **31** (375 mg, 0.39 mmol) in thiolacetic acid (6 mL) was stirred for 30 h at room temperature. After concentrating to dryness, the residue was purified by flash chromatography (hexane–EtOAc, 1:1) to yield **32** (259 mg, 68%). TLC: 0.45 (hexane–EtOAc, 1:1). $[\alpha]_D^{23}$ +70.5° (*c*, 1.0, CH_2Cl_2). ^{1}H NMR (500 MHz, $CDCl_3$): δ: 8.00–7.18 (m, 20H, *4 Ph*), 6.29 (d, 1H, *NH*, $J_{NH,2}$ = 9.8 Hz), 5.06 (b.s., 1H, *H-1*), 4.98 (b.s., 1H, *H-2*), 4.84–4.77 (m, 2H, *H-1′*, *2 CH*$_2$Ph), 4.84–4.77 (m, 5H, *4 CH*$_2$Ph, *H-5*), 4.48 (d, 1H, *H-6′a*, $J_{6a,6b}$ = 12.1 Hz), 4.40 (dd, 1H, *H-6′b*, $J_{6b,6a}$ = 12.1 Hz, $J_{6b,5}$ = 3.4 Hz), 4.33 (m, 1H, *H-2′*), 3.97 (b.s., 1H, *H-4*), 3.93 (b.s., 1H, *H-3*), 3.85 (m, 1H, *H-5′*), 3.78 (s, 3H, COO*Me*), 3.72 (t, 1H, *H-4′*, $J_{4,3} \approx J_{4,5}$ = 9.1 Hz), 3.58 (t, 1H, *H-3′*, $J_{3,2} \approx J_{3,4}$ = 9.6 Hz), 2.00 (d, 3H, OCO*CH*$_3$), 1.79 (d, 3H,

© 2002 NRC Canada

NHCO*CH*$_3$), 1.59 (m, 1H, *CH*(CH$_3$)$_2$), 0.86–0.82 (m, 12H, CH(*CH*$_3$)$_2$, C(*CH*$_3$)$_2$), 0.21 and 0.12 (2 s, 6H, Si(*CH*$_3$)$_2$). ^{13}C NMR (125 MHz, $CDCl_3$) δ: 170.0, 169.8, 168.5, 166.2 (*C=O*), 138.1–127.8 (*Ph*), 95.3 (*C-1′*), 93.1 (*C-1*), 81.0 (*C-3′*), 77.6 (*C-4′*), 75.4, 74.9, 73.3, 73.0, 71.4, 70.3, 69.5, 67.9 (*C-2*), 63.0 (*C-6′*), 52.3 (COO*Me*), 52.2 (*C-2′*), 34.0, 24.9, 23.4, 20.8, 20.1, 19.8, 18.6, 13.4, –2.0, –3.5 (O*TDS*, OCO*CH*$_3$).

Methyl 4-*O*-(2-acetamido-6-*O*-benzoyl-3,4-di-*O*-benzyl-2-deoxy-α-D-glucopyranosyl)-2-*O*-acetyl-3-*O*-benzyl-β-L-idopyranuronate (33)

To a solution of **32** (220 mg, 3.18 mmol) at –15°C in dry THF (7 mL) an excess of (HF)$_n$·Py (0.7 mL) was added. The reaction was warmed to 0°C and stirred for 24 h under an argon atmosphere. The mixture was diluted with CH_2Cl_2 (2 × 100 mL) and washed with H_2O (2 × 75 mL) and saturated $NaHCO_3$ solution until neutral pH. The aqueous layer was extracted with CH_2Cl_2 (2 × 100 mL) and the organic layers were dried ($MgSO_4$) and concentrated in vacuo. The residue was purified by flash chromatography (CH_2Cl_2–MeOH, 20:1) to yield **33** (153 mg, 81%) as a mixture of anomers α and β. TLC (α and β): 0.41 and 0.29 (hexane–EtOAc, 1:2). ^{1}H NMR (500 MHz, $CDCl_3$) δ: 8.00–7.18 (m, 40H, *4 Ph* (α and β)), 6.51 (d, 1H, *NH* (β), $J_{NH,2}$ = 9.7 Hz), 6.05 (d, 1H, *NH* (α), $J_{NH,2}$ = 9.7 Hz), 5.25 (b.s., 1H, *H-1* (α)), 5.18 (d, 1H, *H-1* (β), $J_{1,2}$ = 3.0 Hz), 4.96 (d, 1H, *H-2* (β), $J_{1,2}$ = 2.6 Hz), 4.93 (b.s., 1H, *H-2* (β)), 4.84–4.75 (m, 11H, *H-1′* (α and β), *H-5* (β), *4 CH*$_2$Ph (α and β)), 4.64–4.38 (m, 17H, *H-5* (α), *H-6a′* (α and β), *H-6b′* (α and β), *8 CH*$_2$Ph (α and β)), 4.37–4.30 (m, 1H, H-2′ (α and β)), 4.07 (m, 1H, *H-3* (β)), 3.99 (m, 2H, *H-3* (α), *H-4* (α)), 3.80 (s, 3H, COO*Me* (α)), 3.79 (s, 3H, COO*Me* (β)), 3.79–3.66 (m, 4H, *H-4′* (α and β), *H-5′* (α and β)), 3.54 (m, 2H, *H-3′* (α and β)), 1.99 (d, 3H, OCO*CH*$_3$ (β)), 1.95 (d, 3H, OCO*CH*$_3$ (α)), 1.81 (d, 3H, NHCO*CH*$_3$ (β)), 1.75 (d, 3H, NHCO*CH*$_3$ (α)). ^{13}C NMR (125 MHz, $CDCl_3$) δ: 170.4, 170.2, 170.1, 169.8, 169.4, 169.2 (*C=O*), 138.9–127.6 (*Ph*), 95.4 (*C-1′* (α)), 94.2 (*C-1′* (β)), 93.1 (*C-1* (α)), 80.7, 77.6, 77.5, 75.3, 74.9, 73.3, 73.2, 72.9, 70.5, 70.4, 69.6, 69.3, 68.3, 67.6, 63.0, 62.9, 60.4, 52.6, 52.5, 52.3, 23.3, 23.2, 20.8, 20.7 (OCO*CH*$_3$ (α and β), NH*CH*$_3$ (α and β)). Anal. calcd. for $C_{45}H_{49}NO_{14}$·0.5H_2O (%): C 64.58, H 6.02, N 1.67, found (%): C 64.63, H 5.94, N 1.67.

***O*-(Methyl 4-*O*-(2-acetamido-6-*O*-benzoyl-3,4-di-*O*-benzyl-2-deoxy-α-D-glucopyranosyl)-2-*O*-acetyl-3-*O*-benzyl-α,β-L-idopyranuronate) trichloroacetimidate (34)**

To a solution of **33** (120 mg, 0.15 mmol) in dry CH_2Cl_2 (1.5 mL), Cl_3CCN (0.22 mL, 2.18 mmol) and activated K_2CO_3 (24 mg, 0.17 mmol) were added. After stirring for 3 h the residue was filtered and concentrated to dryness. The residue was purified by flash chromatography (hexane–EtOAc, 1:2) to yield **34** (100 mg, 71%) as a mixture of anomers α and β. TLC (α and β) 0.37 and 0.20 (hexane–EtOAc, 1:1). ^{1}H NMR (500 MHz, $CDCl_3$) δ: 8.70 (s, 1H, O(C=*NH*)CCl_3 (α)), 8.67 (s, 1H, O(C=*NH*)CCl_3 (β)), 7.99–7.19 (m, 40H, *4 Ph* (α and β)), 6.36 (d, 1H, *H-1* (α)), 6.22 (d, 1H, *H-1* (β), $J_{1,2}$ = 2.3 Hz), 6.20 (d, 1H, *NH* (β), $J_{NH,2}$ = 9.7 Hz), 5.87 (d, 1H, *NH* (α), $J_{NH,2}$ = 9.7 Hz), 5.25 (m, 1H, *H-2* (β)), 4.99 (b.s., 1H, *H-1* (α)), 5.02 (d, 1H, *H-5* (α), $J_{1,2}$ = 2.0 Hz), 4.87–4.85 (m, 2H, *H-1′* (α), *H-1′* (β)), 4.84–4.57 (m, 13H, *H-5* (β), *6 CH*$_2$Ph (α and β)), 4.54–4.36 (m, 6H, *H-2′* (α), *H-2′* (β), *H-6a′* (α), *H-6a′* (β), *H-6b′* (α), *H-6b′* (β)), 4.17–4.15 (m, 2 H, *H-3* (β), *H-4* (α)), 4.03 (m, 1H, *H-4* (β)), 3.92 (m, 1H, *H-3* (α)), 3.80–3.78 (m, 8H, *H-5′* (α), *H-5′* (β), COO*Me* (α and β)), 3.71 (t, 2H, *H-4′* (α), *H-4′* (β), $J_{4,3} \approx J_{4,5}$ = 8.5 Hz), 3.61–3.54 (m, 2H, *H-3′* (α), *H-3′* (β)), 1.98, 1.96, 1.80, 1.76 (m, 12H, OCO*CH*$_3$ (α), OCO*CH*$_3$ (β), NH*CH*$_3$ (α), NH*CH*$_3$ (β)). ^{13}C NMR (125 MHz, $CDCl_3$) δ: 170.1, 169.8, 169.6, 169.3, 168.5, 167.7, 166.4, 166.1 (*C=O*), 160.5, 160.1 (*C*=NH), 138.0–127.6 (*Ph*), 96.3 (*C-1′* (α or β)), 95.0 (*C-1* (α)), 94.8 (*C-1′* (α or β)), 94.5 (*C-1* (β)), 80.9 (*C-3′* (α)), 80.8 (*C-3′* (β)), 77.6 (*C-4′* (β)), 77.5 (*C-4′* (α)), 75.5, 75.4, 75.0, 74.9, 73.9, 73.6, 72.5, 71.3, 70.5, 70.4, 69.1, 69.0, 66.9 (*C-2* (α and β)), 66.7, 62.9 (*C-6′* (α and β)), 52.6, 52.5, 52.4, 52.3 (*C-2′* (α and β), COO*Me*), 23.5, 23.3, 20.7, 20.6 (OCO*CH*$_3$ (α), OCO*CH*$_3$ (β), NH*CH*$_3$ (α), NH*CH*$_3$ (β)).

Methyl (isopropyl *O*-(2-azido-3,6-di-*O*-benzyl-2-deoxy-α-D-glucopyranosyl)-(1→4)-*O*-(methyl 3-*O*-benzyl-2-*O*-pivaloyl-α-L-idopyranosyluronate)-(1→4)-*O*-(2-acetamido-6-*O*-benzoyl-3-*O*-benzyl-2-deoxy-α-D-glucopyranosyl)-(1→4)-*O*-(methyl 2,3-di-*O*-benzyl-α-L-idopyranosyluronate)-(1→4)-*O*-(2-azido-3,6-di-*O*-benzyl-2-deoxy-α-D-glucopyranosyl)-(1→4)-3-*O*-benzyl-2-*O*-pivaloyl-α-L-idopyranosyl) uronate (35)

To a solution of **5** (175 mg, 0.076 mmol) in dry THF (2 mL), $NaBH_3CN$ (1 mL of a solution of 1 M $NaBH_3CN$ in THF) was added, and was stirred for 24 h. Afterwards, a solution of 2.5 M HCl in Et_2O was added dropwise until the mixture became acidic. The reaction was neutralized with saturated $NaHCO_3$ solution (2 mL), diluted with CH_2Cl_2 (10 mL), and washed with H_2O (7 mL). The aqueous layer was extracted with CH_2Cl_2 (2 × 10 mL) and the organic layers were dried ($MgSO_4$) and concentrated in vacuo. The residue was purified by flash chromatography (hexane–EtOAc, 3:2) to yield **35** (115 mg, 66%). TLC: 0.51 (hexane–EtOAc, 1:1). $[\alpha]_D^{23}$ –9.8° (*c* 1.1, CH_2Cl_2). MALDI-TOF (*m/z*): 2311 (M + Na^+ – H), 1486 (M + K^+ – H). ^{1}H NMR (500 MHz, $CDCl_3$) δ: 8.09–7.14 (m, 50H, *10 Ph*), 5.92 (d, 1H, *NH*, $J_{NH,2}$ = 9.7 Hz), 5.31 (d, 1H, *H-1e*, $J_{1,2}$ = 4.6 Hz), 5.28 (d, 1H, *H-1c*, $J_{1,2}$ = 3.4 Hz), 5.17 (d, 1H, *H-1a*, $J_{1,2}$ = 4.5 Hz), 5.05 (d, 1H, *H-1b*, $J_{1,2}$ = 3.5 Hz), 4.97 (d, 1H, *H-1f*, $J_{1,2}$ = 3.4 Hz), 4.95–4.91 (m, 2H, *H-2a*, *H-2e*), 4.85 (d, 1H, *1 CH*$_2$Ph, J_{gem} = 10.9 Hz), 4.82 (d, 1H, *H-1b*, $J_{1,2}$ = 3.3 Hz), 4.76–4.40 (m, 21H, *16 CH*$_2$Ph, *H-5a*, *H-5c*, *H-5e*, *H-6d*, *H-6′d*), 4.33 (d, 1H, *1 CH*$_2$Ph, J_{gem} = 11.3 Hz), 4.29 (m, 1H, *H-2d*), 4.14–4.02 (m, 4H, *H-4a*, *H-4b*, *H-4d*, *H-4e*), 3.96–3.91 (m, 4H, *H-3a*, *H-3e*, *H-4c*, *CH*(CH$_3$)$_2$), 3.85–3.81 (m, 11H, *H-3b*, *H-3c*, *H-3f*, *H-4f*, *H-5b*, *H-5d*, *H-5f*, *H-6b*, *H-6′b*, *H-6f*, *H-6′f*), 3.63 (s, 3H, COO*CH*$_3$), 3.46–3.40 (m, 2H, *H-2c*, *H-3d*), 3.41 (s, 3H, COO*CH*$_3$), 3.32 (s, 3H, COO*CH*$_3$), 3.32–3.30 (m, 1H, *H-2b*), 3.19 (dd, 1H, *H-2f*, $J_{2,1}$ = 3.4 Hz, $J_{2,3}$ = 10.0 Hz), 1.43 (s, 3H, NHCO*CH*$_3$), 1.20 (s, 9H, C(*CH*$_3$)$_3$), 1.16 (s, 9H, C(*CH*$_3$)$_3$), 1.22–1.14 (m, 6H, CH(*CH*$_3$)$_2$). ^{13}C NMR (125 MHz, $CDCl_3$) δ: 177.3, 177.2, 170.0, 169.8, 169.3, 169.2, 166.1 (*C=O*), 138.2–127.2 (*Ph*), 98.9 (*C-1e*), 98.4 (*C-1b*), 98.3 (*C-1f*), 97.8 (*C-1c*), 97.3 (*C-1a*), 97.0 (*C-1d*), 79.3, 78.6, 78.1, 76.3, 75.9, 75.1, 74.9, 74.8, 74.5, 74.2, 74.0, 73.7, 73.6, 73.4, 73.3, 73.2, 72.4, 72.3, 71.8, 71.3, 70.8, 70.6, 70.4, 70.1, 69.5, 69.4, 67.8,

© 2002 NRC Canada

63.0, 62.7, 62.3, 60.4, 51.9 (*C-2d*), 51.7 (COO*CH*$_3$), 51.7 (*C-2d*), 38.8, 27.2, 27.1, 23.3, 22.8, 21.8, 21.0 (O*Piv*, NHCO*CH*$_3$, O-*i*-Pr). Anal. calcd. for $C_{124}H_{143}N_7O_{35}\cdot 1.5H_2O$ (%): C 64.23, H 6.34, N 4.23; found (%): C 64.32, H 6.64, N 4.29.

Methyl (isopropyl *O*-(2-acetamido-6-*O*-benzoyl-3,4-di-*O*-benzyl-2-deoxy-α-D-glucopyranosyl)-(1→4)-*O*-(methyl 2-*O*-acetyl-3-*O*-benzyl-α-L-idopyranosyluronate)-(1→4)-*O*-(2-azido-3,6-di-*O*-benzyl-2-deoxy-α-D-glucopyranosyl)-(1→4)-*O*-(methyl 3-*O*-benzyl-2-*O*-pivaloyl-α-L-idopyranosyluronate)-(1→4)-*O*-(2-acetamido-6-*O*-benzoyl-3-*O*-benzyl -2-deoxy-α-D-glucopyranosyl)-(1→4)-*O*-(methyl 2,3-di-*O*-benzyl-α-L-idopyranosyluronate)-(1→4)-*O*-(2-azido-3,6-di-*O*-benzyl-2-deoxy-α-D-glucopyranosyl)-(1→4)-3-*O*-benzyl-2-*O*-pivaloyl-α-L-idopyranosyl) uronate (36)

To a solution of **35** (130 mg, 56.7 μmol) and **34** (103 mg, 106 μmol) in dry CH_2Cl_2 (0.7 mL) at room temperature, TMSOTf (55 μL of a 0.22 M solution of TMSOTf in CH_2Cl_2) was added under an argon atmosphere. After stirring for 3 h, saturated $NaHCO_3$ solution (0.2 mL) was added and diluted with CH_2Cl_2 (20 mL). The residue was washed with H_2O (15 mL) and then the aqueous layer was extracted with CH_2Cl_2 (2 × 10 mL) and the organic layers were dried ($MgSO_4$) and concentrated in vacuo. The residue was purified by flash chromatography (hexane–EtOAc, 1:2) to yield **36** (60 mg, 40%) and nonreacting acceptor **35** (70 mg, 54%). TLC: 0.40 (hexane–EtOAc, 1:2). $[\alpha]_D^{23}$ +33.3° (*c* 1.0, CH_2Cl_2). MALDI-TOF (*m/z*): 3119 (M + Na^+), 3135 (M + K^+). ^{1}H NMR (500 MHz, $CDCl_3$) δ: 8.08–7.12 (m, 70H, *14 Ph*), 5.99 (d, 1H, *NH h*, $J_{NH,2}$ = 9.6 Hz), 5.90 (d, 1H, *NH d*, $J_{NH,2}$ = 9.4 Hz), 5.31 (d, 1H, *H-1e*, $J_{1,2}$ = 4.8 Hz), 5.29 (d, 1H, *H-1c*, $J_{1,2}$ = 3.1 Hz), 5.17 (d, 1H, *H-1a*, $J_{1,2}$ = 4.2 Hz), 5.12 (d, 1H, *H-1g*, $J_{1,2}$ = 3.2 Hz), 5.04 (d, 1H, *H-1b*, $J_{1,2}$ = 3.0 Hz), 4.96 (d, 1H, *H-1f*, $J_{1,2}$ = 3.2 Hz), 4.83 (m, 1H, *H-1h*), 4.80 (m, 1H, *H-1d*), 4.96–4.90 (m, 2H, *H-2a*, *H-2e*), 4.90–4.23 (m, 33H, *24 CH*$_2$Ph, *H-2g*, *H-5a*, *H-5c*, *H-5e*, *H-5g*, *H-6d*, *H-6′d*, *H-6h*, *H-6′h*), 4.36–4.23 (m, 2H, *H-2d*, *H-2h*), 4.12 (t, 1H, *H-4a*, $J_{4,3} \approx J_{4,5}$ = 5.2 Hz), 4.09–3.86 (m, 10H, *H-3a*, *H-3e*, *H-3g*, *H-4b*, *H-4c*, *H-4d*, *H-4e*, *H-4g*, *H-5h*, *CH*(CH$_3$)$_2$), 3.85–3.64 (m, 10H, *H-3b*, *H-3c*, *H-4f*, *H-4h*, *H-5b*, *H-5d*, *H-6b*, *H-6′b*, *H-6f*, *H-6′f*), 3.62 (s, 3H, COO*CH*$_3$), 3.60–3.49 (m, 3H, *H-3f*, *H-3h*, *H-5f*), 3.46–3.36 (m, 2H, *H-2c*, *H-3d*), 3.41 (s, 6H, *2* COO*CH*$_3$), 3.34–3.21 (m, 2H, *H-2b*, *H-2f*), 3.24 (s, 3H, COO*CH*$_3$), 1.83 (s, 3H, OCO*CH*$_3$), 1.61 (s, 3H, NHCO*CH*$_3$), 1.42 (s, 3H, NHCO*CH*$_3$), 1.20–1.12 (s, 24H, *2* C(*CH*$_3$)$_3$, CH(*CH*$_3$)$_2$). ^{13}C NMR (125 MHz, $CDCl_3$) δ: 177.3, 170.1, 170.0, 169.4, 169.3, 169.2, 168.8, 166.2, 166.1, 166.0 (*C=O*), 138.0–127.2 (*Ph*), 99.2 (*C-1c*), 98.6 (*C-1b*), 98.6 (*C-1f*), 98.1 (*C-1e*), 97.8 (*C-1g*), 97.6 (*C-1a*), 97.5 (*C-1d*), 97.1 (*C-1h*), 80.8, 78.6, 78.0, 77.3, 77.0, 76.8, 75.3, 75.0, 74.8, 74.6, 74.4, 74.2, 74.0, 73.8, 73.7, 73.4, 73.2, 72.4, 71.8, 71.5, 71.3, 70.8, 70.5, 70.4, 69.7, 63.2, 63.0, 62.6, 52.4, 52.0, 51.6, 51.7 (*C-2d*), 38.8, 29.7, 27.2, 27.1, 23.3, 23.1, 22.8, 21.8, 20.7 (O*Piv*, NHCO*CH*$_3$, O-*i*-Pr). Anal. calcd. for $C_{169}H_{192}N_8O_{49}\cdot H_2O$ (%): C 65.07, H 6.20, N 3.59; found (%): C 65.08, H 6.44, N 3.57.

Methyl (isopropyl *O*-(2-acetamido-6-*O*-benzoyl-3,4-di-*O*-benzyl-2-deoxy-α-D-glucopyranosyl)-(1→4)-*O*-(methyl 3-*O*-benzyl-α-L-idopyranosyluronate)-(1→4)-*O*-(2-azido-3,6-di-*O*-benzyl-2-deoxy-α-D-glucopyranosyl)-(1→4)-*O*-(methyl 3-*O*-benzyl-2-*O*-pivaloyl-α-L-idopyranosyluronate)-(1→4)-*O*-(2-acetamido-6-*O*-benzoyl-3-*O*-benzyl-2-deoxy-α-D-glucopyranosyl)-(1→4)-*O*-(methyl 2,3-di-*O*-benzyl-α-L-idopyranosyluronate)-(1→4)-*O*-(2-azido-3,6-di-*O*-benzyl-2-deoxy-α-D-glucopyranosyl)-(1→4)-3-*O*-benzyl-2-*O*-pivaloyl-α-L-idopyranosyl) uronate (37)

To a solution of **19** (460 mg, 0.307 mmol) in dry MeOH and CH_2Cl_2 (1:1, 4 mL), MeONa (56 μL of a 0.178 M solution of MeONa in MeOH) was added and stirred for 40 h. The reaction was neutralized with resin (IRA-120 H^+) and filtered. The residue was purified by flash chromatography (hexane–EtOAc, 1:2) to yield **37** (61 mg, 80%). TLC: 0.45 (hexane–EtOAc, 1:2). $[\alpha]_D^{23}$ +34.2° (*c* 1.0, CH_2Cl_2). ^{1}H NMR (500 MHz, $CDCl_3$) δ: 8.07–7.12 (m, 70H, *14 Ph*), 6.19 (d, 1H, *NH h*, $J_{NH,2}$ = 8.6 Hz), 5.96 (d, 1H, *NH d*, $J_{NH,2}$ = 9.8 Hz), 5.29 (d, 1H, *H-1c*, $J_{1,2}$ = 3.1 Hz), 5.25 (d, 1H, *H-1e*, $J_{1,2}$ = 4.3 Hz), 5.17 (d, 1H, *H-1a*, $J_{1,2}$ = 4.5 Hz), 5.04 (m, 2H, *H-1g*, *H-1b*), 4.98 (d, 1H, *H-1f*, $J_{1,2}$ = 3.3 Hz), 4.94–4.90 (m, 2H, *H-2a*, *H-2e*), 4.86 (d, 1H, *H-1h*, $J_{1,2}$ = 3.1 Hz), 4.79 (m, 1H, *H-1d*), 4.88–4.38 (m, 31H, *23 CH*$_2$Ph, *H-5a*, *H-5c*, *H-5e*, *H-5g*, *H-6d*, *H-6′d*, *H-6h*, *H-6′h*), 4.31–4.26 (m, 2H, *H-2d*, *1 CH*$_2$Ph), 4.19 (m, 1H, *H-2h*), 4.11 (t, 1H, *H-4a*, $J_{4,3} \approx J_{4,5}$ = 5.6 Hz), 4.07–3.91 (m, 9H, *H-3a*, *H-3e*, *H-4b*, *H-4c*, *H-4d*, *H-4e*, *H-4g*, *H-4h*, *CH*(CH$_3$)$_2$), 3.84–3.64 (m, 11H, *H-3b*, *H-3c*, *H-3g*, *H-4f*, *H-5b*, *H-5d*, *H-5h*, *H-6b*, *H-6′b*, *H-6f*, *H-6′f*), 3.61 (s, 3H, COO*CH*$_3$), 3.58–3.52 (m, 4H, *H-2g*, *H-3f*, *H-3h*, *H-5f*), 3.44–3.39 (m, 2H, *H-2c*, *H-3d*), 3.38 (s, 3H, COO*CH*$_3$), 3.33 (s, 3H, COO*CH*$_3$), 3.32–3.27 (m, 2H, *H-2b*, *H-2f*), 3.18 (s, 3H, COO*CH*$_3$), 2.45 (d, 1H, *OH-2g*, $J_{OH,2}$ = 8.3 Hz), 1.65 (s, 3H, NHCO*CH*$_3$), 1.41 (s, 3H, NHCO*CH*$_3$), 1.19–1.13 (s, 24H, *2* C(*CH*$_3$)$_3$, CH(*CH*$_3$)$_2$). ^{13}C NMR (125 MHz, $CDCl_3$) δ: 177.3, 170.5, 170.1, 169.9, 169.2, 166.2 (*C=O*), 138.1–127.1 (*Ph*), 100.9 (*C-1g*), 99.1 (*C-1c*), 98.8 (*C-1b*), 98.7 (*C-1f*), 98.1 (*C-1e*), 97.6 (*C-1a*), 97.4 (*C-1d*), 97.2 (*C-1h*), 80.0, 78.7, 78.2, 78.0, 77.3, 77.1, 76.8, 75.9, 75.3, 74.9, 74.8, 74.6, 74.0, 73.7, 73.5, 73.3, 73.2, 72.8, 71.8, 71.3, 70.6, 70.5, 70.2, 70.1, 69.9, 68.2, 67.7, 63.3, 62.9, 62.6, 52.5, 52.1, 52.0, 51.9, 51.6, 38.8, 29.7, 27.2, 27.1, 23.3, 22.9, 22.8, 21.8 (O*Piv*, NHCO*CH*$_3$, O-*i*-Pr).

Methyl (isopropyl *O*-(2-acetamido-6-*O*-benzoyl-3,4-di-*O*-benzyl-2-deoxy-α-D-glucopyranosyl)-(1→4)-*O*-(methyl 2,3-di-*O*-benzyl-α-L-idopyranosyluronate)-(1→4)-*O*-(2-azido-3,6-di-*O*-benzyl-2-deoxy-α-D-glucopyranosyl)-(1→4)-*O*-(methyl 3-*O*-benzyl-2-*O*-pivaloyl-α-L-idopyranosyluronate)-(1→4)-*O*-(2-acetamido-6-*O*-benzoyl-3-*O*-benzyl-2-deoxy-α-D-glucopyranosyl)-(1→4)-*O*-(methyl 2,3-di-*O*-benzyl-α-L-idopyranosyluronate)-(1→4)-*O*-(2-azido-3,6-di-*O*-benzyl-2-deoxy-α-D-glucopyranosyl)-(1→4)-3-*O*-benzyl-2-*O*-pivaloyl-α-L-idopyranosyl) uronate (38)

To a solution of **37** (55 mg, 0.018 mmol) and freshly prepared Ag_2O (10.2 mg, 0.044 mmol) in dry DMF (0.1 mL), freshly distilled benzyl bromide (24 μL, 0.2 mmol) was added. After stirring for 24 h, the mixture was filtered

© 2002 NRC Canada

through Celite and new Ag_2O (10.2 mg, 0.044 mmol) and benzyl bromide (24 μL, 0.2 mmol) were added. After stirring for 24 h more, the mixture was filtered through Celite and concentrated to dryness. The residue was purified by flash chromatography (hexane–EtOAc, 1:1) to yield **38** (41 mg, 72%). TLC: 0.28 (hexane–EtOAc, 1:1). $[\alpha]_D^{23}$ +30.5° (*c* 1.0, CH_2Cl_2). ^{1}H NMR (500 MHz, $CDCl_3$) δ: 8.07–7.09 (m, 75H, *15 Ph*), 6.05 (d, 1H, *NH d*, $J_{NH,2}$ = 9.8 Hz), 5.88 (d, 1H, *NH h*, $J_{NH,2}$ = 9.5 Hz), 5.30 (d, 1H, *H-1c*, $J_{1,2}$ = 2.8 Hz), 5.27 (d, 1H, *H-1e*, $J_{1,2}$ = 3.7 Hz), 5.24 (d, 1H, *H-1g*, $J_{1,2}$ = 1.1 Hz), 5.17 (m, 1H, *H-1a*, $J_{1,2}$ = 4.5 Hz), 5.05 (m, 1H, *H-1b*, $J_{1,2}$ = 3.2 Hz), 4.97 (d, 1H, *H-1f*, $J_{1,2}$ = 3.2 Hz), 4.95–4.91 (m, 2H, *H-2a*, *H-2e*), 4.86–4.38 (m, 35H, *25 CH*$_2$Ph, *H-1d*, *H-1h*, *H-5a*, *H-5c*, *H-5e*, *H-5g*, *H-6d*, *H-6′d*, *H-6h*, *H-6′h*), 4.36–4.26 (m, 3H, *H-2d*, *H-2h*, *1 CH*$_2$Ph), 4.12 (t, 1H, *H-4a*, $J_{4,3} \approx J_{4,5}$ = 4.8 Hz), 4.10–3.91 (m, 9H, *H-3a*, *H-3e*, *H-4b*, *H-4c*, *H-4e*, *H-4f*, *H-4g*, *H-4h*, *CH*$(CH_3)_2$), 3.85–3.66 (m, 12H, *H-3b*, *H-3c*, *H-3g*, *H-4d*, *H-4f*, *H-5b*, *H-5d*, *H-5f*, *H-5h*, *H-6b*, *H-6f*, *H-6′f*), 3.62 (s, 3H, COO*CH*$_3$), 3.61–3.49 (m, 3H, *H-3d*, *H-3f*, *H-6′b*), 3.45–3.41 (m, 2H, *H-2c*, *H-3h*), 3.44 (s, 3H, COO*CH*$_3$), 3.41 (s, 3H, COO*CH*$_3$), 3.32–3.27 (m, 2H, *H-2b*, *H-2f*), 3.18 (s, 3H, COO*CH*$_3$), 1.49 (s, 3H, NHCO*CH*$_3$), 1.41 (s, 3H, NHCO*CH*$_3$), 1.19–1.13 (m, 24H, *2* C$(CH_3)_3$, CH$(CH_3)_2$). ^{13}C NMR (125 MHz, $CDCl_3$) δ: 177.3, 170.1, 170.1, 169.8, 169.2, 166.2, 166.1 (*C=O*), 138.1–127.1 (*Ph*), 99.1 (*C-1c*), 98.7 (*C-1b*, *C-1f*, *C-1g*), 98.2 (*C-1e*), 97.6 (*C-1a*, *C-1d*), 97.4 (*C-1h*), 78.3, 78.0, 77.3, 77.0, 76.8, 76.3, 75.4, 74.9, 74.5, 74.0, 73.9, 73.7, 73.3, 73.2, 73.1, 73.0, 72.2, 71.8, 71.3, 70.8, 70.3, 70.1, 67.8, 63.2, 62.8, 52.5, 51.9, 51.65, 38.8, 29.7, 27.2, 27.1, 23.3, 22.9, 22.8, 21.8 (O*Piv*, NHCO*CH*$_3$, O-*i*-Pr).

Isopropyl *O*-(2-acetamido-3,4-di-*O*-benzyl-2-deoxy-α-D-glucopyranosyl)-(1→4)-*O*-(2,3-di-*O*-benzyl-α-L-idopyranosyluronic acid)-(1→4)-*O*-(2-azido-3,6-di-*O*-benzyl-2-deoxy-α-D-glucopyranosyl)-(1→4)-*O*-(3-*O*-benzyl-α-L-idopyranosyluronic acid)-(1→4)-*O*-(2-acetamido-3-*O*-benzyl-2-deoxy-α-D-glucopyranosyl)-(1→4)-*O*-(2,3-di-*O*-benzyl-α-L-idopyranosyluronic acid)-(1→4)-*O*-(2-azido-3,6-di-*O*-benzyl-2-deoxy-α-D-glucopyranosyl)-(1→4)-3-*O*-benzyl-α-L-idopyranosyluronic acid (39)

To a solution of **38** (39 mg, 12.4 μmol) in THF (2 mL) at –5°C, H_2O_2 30% (0.7 mL) and a 1 M aqueous solution of LiOH (0.8 mL) were added. After stirring for 24 h at room temperature MeOH (0.8 mL) and a 3 N aqueous solution of KOH (2 mL) were added. After stirring for 24 h more, the reaction was neutralized with acidic resin (IRA-120 H^+), filtered, and concentrated. The residue was purified by Sephadex LH-20 (MeOH–CH_2Cl_2, 1:1) to yield **39** (32 mg, 94%). TLC: 0.47 (CH_2Cl_2–MeOH, 8:1). ^{1}H NMR (500 MHz, CD_3OD) δ: 7.37–7.06 (m, 65H, *13 Ph*), 5.30–5.19 (m, 3H, *H-1b*, *H-1f*, *H-1a* or *e*), 5.06 (s, 1H, *H-1a* or *e*), 5.00 (d, 1H, *H-1c* or *g*, $J_{1,2}$ = 3.4 Hz), 4.98 (d, 1H, *H-1c* or *g*, $J_{1,2}$ = 3.2 Hz), 4.79 (m, 2H, *H-1d*, *H-1h*), 1.61 (s, 6H, *2* NHCO*CH*$_3$), 1.30–1.15 (m, 6H, CH$(CH_3)_2$). ^{13}C NMR (125 MHz, CD_3OD) δ: 99.7 (*C-1a* or *e*), 98.2 (*C-1b* or *f*), 97.6 (*C-1a* or *e*), 97.3 (*C-1b* or *f*), 96.6, 96.4 (*C-1d*, *C-1h*), 95.1 (*C-1c*, *C-1g*).

Isopropyl *O*-(2-acetamido-3,4-di-*O*-benzyl-2-deoxy-6-*O*-sulfo-α-D-glucopyranosyl)-(1→4)-*O*-(2,3-di-*O*-benzyl-α-L-idopyranosyluronic acid)-(1→4)-*O*-(2-azido-3-*O*-benzyl-2-deoxy-α-D-glucopyranosyl)-(1→4)-*O*-(3-*O*-benzyl-2-*O*-sulfo-α-L-idopyranosyluronic acid)-(1→4)-*O*-(2-acetamido-3-*O*-benzyl-2-deoxy-6-*O*-sulfo-α-D-glucopyranosyl)-(1→4)-*O*-(2,3-di-*O*-benzyl-α-L-idopyranosyluronic acid)-(1→4)-*O*-(2-azido-3,6-di-*O*-benzyl-2-deoxy-α-D-glucopyranosyl)-(1→4)-3-*O*-benzyl-2-*O*-sulfo-α-L-idopyranosyluronic acid octasodium salt (40)

A mixture of **39** (32 mg, 11.4 μmol) and complex SO_3·Py (37 mg, 0.23 mmol) in dry Py (1.5 mL) was stirred under an argon atmosphere. After 24 h, the mixture was cooled and MeOH (1 mL) and CH_2Cl_2 (1 mL) were added. The solution was eluted through a Sephadex LH-20 (MeOH–CH_2Cl_2, 1:1). Fractions containing the hexasaccharide were concentrated and passed through a Dowex 50WX4-Na^+ (MeOH–H_2O, 2:1). Finally, the product was purified by reverse phase HPLC to yield **40** (23 mg, 64%). TLC: 0.62 (EtOAc–Py–H_2O–AcOH, 8:5:3:1). ^{1}H NMR (500 MHz, CD_3OD) δ: 7.42–7.00 (m, 65H, *13 Ph*), 5.45–5.15 (5H, *H-1a*, *H-1b*, *H-1e*, *H-1f*, *H-1c* or *g*), 5.05–4.70 (3H, *H-1d*, *H-1h*, *H-1c* or *g*), 1.56 (m, 3H, NHCO*CH*$_3$), 1.46 (m, 3H, NHCO*CH*$_3$), 1.18 (d, 6H, CH*(CH*$_3$*)*$_2$, *J* = 6.0 Hz).

Isopropyl *O*-(2-acetamido-2-deoxy-6-*O*-sulfo-α-D-glucopyranosyl)-(1→4)-*O*-(α-L-idopyranosyluronic acid)-(1→4)-*O*-(2-deoxy-2-sulfamide-α-D-glucopyranosyl)-(1→4)-*O*-(2-*O*-sulfo-α-L-idopyranosyluronic acid)-(1→4)-*O*-(2-acetamido-2-deoxy-6-*O*-sulfo-α-D-glucopyranosyl)-(1→4)-*O*-(α-L-idopyranosyluronic acid)-(1→4)-*O*-(2-deoxy-2-sulfamide-α-D-glucopyranosyl)-(1→4)-2-*O*-sulfo-α-L-idopyranosyluronic acid decasodium salt (4)

To a solution of **40** (23 mg, 7.15 μmol) in MeOH–H_2O (1.5 mL, 9:1) was hydrogenolyzed in the presence of 10% Pd/C. After 24 h, the suspension was filtered and concentrated to give the desired product which was directly used in the next step without further purification.

The hydrogenolyzed hexasaccharide was dissolved in H_2O (1 mL) and the pH of the solution was adjusted to 9.5 with a 1 N solution of NaOH. Complex SO_3·Py (24 mg, 10 equiv for each amine group) was added in three portions over 1 h and the pH was maintained at 9.5 by subsequent addition of a 1 N solution of NaOH. A second, third, and fourth portion of complex SO_3·Py were added after 2, 4, and 6 h stirring, respectively. After 24 h, the mixture was neutralized with a 0.1 N solution of HCl to pH 7 and then chromatographed on a column of Sephadex G-25 with a 0.9% solution of NaCl. The appropriate fractions were pooled and passed through a column of Dowex 50WX4-Na^+ with a 0.5 M solution of NaCl and then a column of Sephadex G-25 with H_2O–EtOH (9:1). The fractions which contained the final hexasaccharide were lyophilized to give **4** (10.4 mg, 66% from **40**). Before NMR studies, it was useful to make a last elution on a column of Dowex 50WX4-Na^+ to avoid the formation of calcium salts instead of sodium salts and get a better resolution in the spectra. ^{1}H NMR (500 MHz, D_2O) δ: 5.38 (d, 1H, *H-1f*, $J_{1,2}$ = 3.3 Hz), 5.30 (d, 1H, *H-1b*, $J_{1,2}$ = 3.3 Hz), 5.23 (d, 1H, *H-1a*, $J_{1,2}$ = 1.8 Hz), 5.19 (d, 1H, *H-1e*, $J_{1,2}$ = 2.7 Hz), 5.16 (d, 1H, *H-1h*, $J_{1,2}$ = 3.8 Hz), 5.14 (d, 1H, *H-1d*, $J_{1,2}$ = 3.3 Hz), 4.88–4.86 (m, 2H, *H-1c*, *H-1g*), 1.99

© 2002 NRC Canada

(m, 3H, NHCOCH_3), 1.98 (m, 3H, NHCOCH_3), 1.18–1.16 (m, 6H, CH(CH_3)$_2$). ^{13}C NMR (125 MHz, MeOD) δ: 101.1 (*C-1c*, *C-1g*), 98.2 (*C-1e*), 97.1 (*C-1b*), 97.0 (*C-1a*), 96.8 (*C-1f*), 94.4 (*C-1d*), 94.3 (*C-1h*).

Acknowledgments

This work was supported by DGES (Grant PB96–0820). R. O. and J. A. thank Fundación Francisco Cobos and Fundación Ramón Areces respectively for fellowships.

References

1. P. Klint and L. Claesson-Welsh. Front. Biosci. **4**, 165, (1999).
2. H.E. Conrad. Heparin-binding Proteins. Academic Press, San Diego. 1998.
3. S. Faham, R.J. Linhardt, and D.C. Rees. Curr. Opin. Struct. Biol. **8**, 578, (1998).
4. M. Klagsbrun. Semin. Cancer Biol. **3**, 81, (1993).
5. D.M. Ornitz, A.B. Herr, M. Nilsson, J. Westman, C.M. Svahn, and K. Waksman. Science (Washington, D.C.), **268**, 432 (1995).
6. S. Faham, R.E. Hileman, J. Fromm, R. Linhardt, and D.C. Rees. Science (Washington, D.C.), **271**, 116 (1996).
7. A.D. DiGabriele, I. Lax, D.I. Chen, C.M. Svahn, M. Jaye, J. Schlessinger, and W.A. Hendrickson. Nature (London), **393**, 812 (1998).
8. A.N. Plotnikov, J. Schlessinger, S.R. Hubbard, and M. Mohammadi. Cell (Cambridge, Mass.), **98**, 641 (1999).
9. D.J. Stauber, A.D. DiGabriele, and W.A. Hendrickson. Proc. Natl. Acad. Sci. U.S.A. **97**, 49 (2000).
10. J. Schlessinger, A.N. Plotnikov, O.A. Ibrahimi, A. Eliseenkova, B.K. Yeh, A. Yayon, R.J. Linhardt, and M. Mohammadi. Mol. Cell **6**, 743 (2000).
11. L. Pellegrini, D.F. Burke, F. Von Dolft, B. Mulloy, and T.I. Blundell. Nature (London), **407**, 1029 (2000).
12. F.Y. Zhou, M. Kan, R.T. Owens, W.L. McKeehan, J.A. Thompson, R.J. Linhardt, and M. Höök. Eur. J. Cell. Biol. **73**, 71 (1997).
13. T. Spivak-Kroizman, M.A. Lemmon, I. Dikic, J.E. Ladbury, D. Pinchasi, J. Huang, M. Jaye, G. Crumley, J. Schlessinger, and I. Lax. Cell (Cambridge, Mass.), **79**, 1015 (1994).
14. A.B. Herr, D.M. Ornitz, R. Sasisekharan, G. Venkataraman, and G. Waksman. J. Biol. Chem. **272**, 16 382 (1997).
15. F.J. Moy, M. Safran, A.P. Seddon, D. Kitchen, P. Bohlen, D. Aviezer, A. Yayon, and R. Powers. Biochemistry, **36**, 4782 (1997).
16. G. Waksman and A.B. Herr. Nat. Struct. Biol. **5**, 527 (1998).
17. G. Venkataraman, R. Raman, V. Sasisekharan, and R. Sasisekharan. Proc. Natl. Acad. Sci. U.S.A. **96**, 3658 (1999).
18. B. Casu. Adv. Carbohydr. Chem. Biochem. **43**, 51 (1985).
19. S.E. Stringer and J.T. Gallagher. Int. J. Biochem. Cell. Biol. **29**, 709 (1997).
20. M. Salmivirta, M.K. Lidholt, and U. Lindahl. FASEB J. **10**, 1270 (1996).
21. J.L. de Paz, J. Angulo, J.M. Lassaletta, P.M. Nieto, M. Redondo-Horcajo, R.M. Lozano, G. Giménez-Gallego, and M. Martín-Lomas. ChemBioChem. **2**, 101 (2001).
22. J. Kovensky, P. Duchaussoy, M. Petitou, and P. Sinaÿ. Tetrahedron: Asymmetry, **7**, 3119 (1996).
23. J. Kovensky, P. Duchaussoy, F. Bono, M. Salmivirta, P. Sizun, J.M. Herbert, M. Petitou, and P. Sinaÿ. Bioorg. Med. Chem. **7**, 1567 (1999).
24. C. Tabeur, J.M. Mallet, F. Bono, J.M. Herbert, M. Petitou, and P. Sinaÿ. Biorg. Med. Chem. **7**, 2003 (1999).
25. (*a*) B. La Ferla, L. Lay, M. Guerini, L. Poletti, L. Panza, and G. Russo. Tetrahedron, **55**, 9867 (1999); (*b*) L. Poletti, M. Fleischer, C. Vogel, M. Guerrini, G. Torri, and L. Lay. Eur. J. Org. Chem. 2727 (2001).
26. B. Mulloy, M.J. Foster, C. Jones, and D.B. Davis. Biochem. J. **293**, 849 (1993).
27. D. Mikhailov, K.H. Mayo, I.R. Vlahov, T. Toida, A. Pervin, and R.L. Linhardt. Biochem. J. **318**, 93 (1996).
28. D. Mikhailov, R.L. Linhardt, and K.H. Mayo. Biochem. J. **328**, 51 (1997).
29. G. Torri, B. Casu, G. Gatti, M. Petitou, J. Choay, J.-C. Jacquinet, and P. Sinaÿ. Biochem. Biophys. Res. Commun. **128**, 138 (1985).
30. B. Casu, J. Choay, D.R. Ferro, G. Gatti, J.-C. Jacquinet, M. Petitou, A. Provasoli, M. Ragazzi, P. Sinaÿ, and G. Torri. Nature (London), **322**, 215 (1986).
31. A. Walker, J.E. Turnbull, and J.T. Gallagher. J. Biol. Chem. **269**, 931 (1994).
32. D.M. Ornitz, A. Yayon, J.G. Flanagan, C.M. Svahn, E. Levi, and P. Leder. Mol. Cell. Biol. **12**, 240 (1992).
33. H. Wang, T. Toida, Y.S. Kim, I. Capila, R.Y. Hileman, M. Bernfield, and R.J. Linhardt. Biochem. Biophys. Res. Commun. **235**, 369 (1997).
34. M. Ishihara, D.J. Tyrell, G.B. Stauber, S. Brown, L.S. Cousens, and R.J. Stack. J. Biol. Chem. **268**, 4675 (1993).
35. D. Avizer, E. Levy, M. Safran, C. Svahn, E. Buddecke, A. Schmidt, G. David, I. Vlodavsky, and A. Yayon. J. Biol. Chem. **269**, 114 (1994).
36. P.J. Garegg, H. Hultberg, and S. Wallin. Carbohydr. Res. **108**, 97 (1982).
37. T. Rosen, I.M. Lico, and D.T.W. Chu. J. Org. Chem. **53**, 1580 (1988).
38. L. Van Hijte and R.D. Little. J. Org. Chem. **50**, 3940 (1985).
39. K.C. Nicolaou, C.A. Veale, C K. Hwang, J. Hutchinson, C.V.C. Prasad, and W.W. Ogilvie. Angew. Chem. Int. Ed. Engl. **30**, 299 (1991).
40. S.A. Abbas and A.H. Haines. Carbohydr. Res. **39**, 358 (1975).
41. L. Rochepeau-Jobron and J.C. Jacquinet. Carbohydr. Res. **305**, 181 (1988).
42. H. Lucas, J.E.M. Basten, T.G. Van Dinther, D.G. Mauleman, S.F. Van Aelst, and C.A.A. van Boeckel. Tetrahedron, **46**, 8207 (1990).
43. R. Ojeda, J.L. de Paz, M. Martín-Lomas, and J.M. Lassaletta. Synlett. **8**, 1316 (1999).
44. D. Tailler, J.C. Jacquinet, A.M. Noirot, and J.M. Beau. J. Chem. Soc. Perkin Trans. 1, 3163 (1992).
45. E.A. Yates, F. Santini, B. De Cristofano, N. Payre, C. Cosentino, M. Guerrini, A. Naggi, G. Torri, and M. Hricovini. Carbohydr. Res. **329**, 239 (2000).
46. B. Mulloy, M.J. Forster, C. Jones, A.F. Drake, E.A. Johnson, and D.B. Davies. Carbohydr. Res. **255**, 1 (1994).
47. D. Jeannerat and G. Bodenhausen. J. Magn. Reson. **141**, 133 (1999).
48. D. Ferro, A. Provasoli, M. Ragazzi, B. Casu, G. Torri, V. Bossennec, B. Perly, P. Sinaÿ, M. Petitou, and J. Choay. Carbohydr. Res. **195**, 157 (1990); C.A.A. van Boeckel, S.F. van Aelst, G.N. Wagenaars, J.-R. Mellema, H. Paulsen, T. Peters, A. Pollex, and V. Sinnwell. Recl. Trav. Chim. Pays–Bas, **106**, 19 (1987).
49. D.A. Cumming and J.P. Carver. Biochemistry, **26**, 6664 (1995).
50. M. Hricovini and G. Torri. Carbohydr. Res. **268**, 159 (1995).
51. A.L. Davis, E.D. Laue, J. Keeler, D. Moskau, and J. Lohman. J. Magn. Reson. **94**, 637 (1991).
52. A. Bax and D.G. Davis. J. Magn. Reson. **65**, 355 (1985).

© 2002 NRC Canada

53. J. Schleucher, M. Schwendinger, M. Sattler, P. Schmidt, O. Schedletzky, S.J. Glaser, O.W. Sorensen, and C. Griesinger. J. Biomol. NMR, **4**, 301 (1994).
54. G. Bodenhausen, R.L. Vold, and R.R. Vold. J. Magn. Reson. **37**, 93 (1980).
55. R. Wagner and S. Berger. J. Magn. Reson. Ser. A, **123**, 119 (1996).
56. D. Neuhaus and M. Williamson. The nuclear Overhauser effect in structural and conformational analysis. VCH, New York. 1989.
57. S.J. Weiner, P.A. Kollman, D.T. Nguyen, and D.A. Case. J. Comp. Chem. **7**, 230 (1986).
58. D.A. Case, D.A. Pearlman, J.W. Caldwell, T.E. Cheatham, III, W.S. Ross, C.L. Simmerling, T.A. Darden, K.M. Merz, R.V. Stanton, A.L. Cheng, J.J. Vincent, M. Crowley, D.M. Ferguson, R.J. Radmer, G.L. Seibel, U.C. Singh, P.K. Weiner, and P.A. Kollman. AMBER 5. University of California, San Francisco. 1997.
59. R.J. Woods, R.A. Dwek, C.J. Edge, and B. Fraser-Reid. J. Phys. Chem. **99**, 3832 (1995).
60. C.J.M. Huige and C. Altona. Comp. Chem. **16**, 56 (1995).

© 2002 NRC Canada

Synthesis of 1,4-anhydro-D-xylitol heteroanalogues of the naturally occurring glycosidase inhibitor salacinol and their evaluation as glycosidase inhibitors

Ahmad Ghavami, Blair D. Johnston, Matthew D. Maddess, Sarah M. Chinapoo, Morten T. Jensen, Birte Svensson, and B. Mario Pinto

Abstract: The syntheses of two 1,4-anhydro-D-xylitol heteroanalogues (**8** and **9**) of the naturally occurring sulfonium ion, salacinol (**3**), containing a sulfur or nitrogen atom in the ring are described. Salacinol (**3**) is one of the active principles in the aqueous extracts of *Salacia reticulata* that are traditionally used in Sri Lanka and India for the treatment of Type 2 diabetes. The synthetic strategy relies on the nucleophilic attack of sulfur or nitrogen analogues of 1,4-anhydro-D-xylitol at the least-hindered carbon of 2,4-*O*-benzylidene-L-erythritol-1,3-cyclic sulfate. The sulfonium ion **8** inhibited barley-α-amylase (AMY1) and porcine pancreatic-α-amylase (PPA), with K_i values of 109 ± 11 and 55 ± 5 μM, respectively. In contrast, the ammonium ion **9** showed no significant inhibition of either AMY1 or PPA. Compounds **8** and **9** also showed no significant inhibition of glucoamylase.

Key Words: glycosidase inhibitors, salacinol analogues, anhydro-D-xylitol heteroanalogues, enzyme inhibition.

Résumé : On décrit les synthèses de deux hétéroanalogues du 1,4-anhydro-D-xylitol (**8** et **9**) qui comportent un atome de soufre ou d'azote dans le cycle de l'ion sulfonium, salacinol (**3**), que l'on retrouve dans la nature. Le salacinol (**3**) est un des principes actifs que l'on retrouve dans la phase d'extraction aqueuse du *Salacia reticulata* utilisée au Sri-Lanka et aux Indes dans le traitement du diabète de type 2. La stratégie de la synthèse repose sur une attaque nucléophile d'analogues soufrés ou azotés du 1,4-anhydro-D-xylitol au niveau du carbone le moins encombré du sulfate 1,3-cyclique du 2,4-*O*-benzylidène-L-érythritol. L'ion sulfonium **8** inhibe l'α-amylase de l'orge (AMY1) et de l'α-amylase du pancréas de porc (PPA) avec des valeurs de K_i de 109 ± 11 et 55 ± 5 μM, respectivement. Par ailleurs, l'ion ammonium **9** ne provoque pas d'inhibition significative de l'AMY1 ou de la PPA. Les composés **8** et **9** n'inhibent pas de façon significative la glucoamylase.

Mots clés : inhibiteurs de glycosidase, analogues du salacinol, hétéroanalogues de l'anhydro-D-xylitol, inhibition enzymatique.

[Traduit par la Rédaction]

Introduction

A program of research to investigate the nature and origin of carbohydrate mimicry is in progress in our laboratory. Thus, we have recently reported the study of the peptide mimicry of carbohydrates recognized by antibodies directed against the Group A *Streptococcus* cell-wall polysaccharide (1) and have recently communicated our results with an antibody directed against the *Shigella flexneri* Y *O*-antigen (2). In the latter study, the crystal structures of the Ab-peptide mimetic and Ab-pentasaccharide complexes were compared. The results indicated that although both ligands engage some common groups on the Ab receptor in H-bonding and hydrophobic interactions, each ligand also displays unique interactions with groups on the protein, lending support to our previous hypothesis that "functional" and not "structural" mimicry might be the mode of mimicry with peptide mimetics (1).

We have also studied the mimicry of carbohydrates by glycomimetics as potential glycosidase inhibitors. Thus, for example, we have described the synthesis and conformational analysis of a sulfonium-ion analogue (**1**) of the glycosidase inhibitor castanospermine (**2**) (3). Our reasoning was inspired by the pioneering work of the late B. Belleau who synthesized sulfonium-ion analogues of the morphinans, levorphanol, and isolevorphanol, and showed that they were agonists or antagonists of morphine for the opiate receptor (*4a–d*). Recently, a new class of glycosidase inhibitor with an intriguing inner-salt sulfonium-sulfate structure was

Received 21 January 2002. Published on the NRC Research Press Web site at http://canjchem.nrc.ca on 19 July 2002.

This work is dedicated, with respect and affection, to the memory of R.U. Lemieux.

A. Ghavami, B.D. Johnston, M.D. Maddess, S.M. Chinapoo, B.M. Pinto.[1] Department of Chemistry, Simon Fraser University, Burnaby, BC V5A 1S6, Canada.
M.T. Jensen and B. Svensson. Department of Chemistry, Carlsberg Laboratory, Gamle Carlsberg Vej 10, DK-2500, Valby, Copenhagen, Denmark.

[1]Corresponding author (e-mail: bpinto@sfu.ca).

 DOI: 10.1139/V02-078 © 2002 NRC Canada

isolated from the roots and stems of the plant *Salacia reticulata*. Extracts of this plant have been traditionally used in the Ayurdevic method of Indian medicine as a treatment

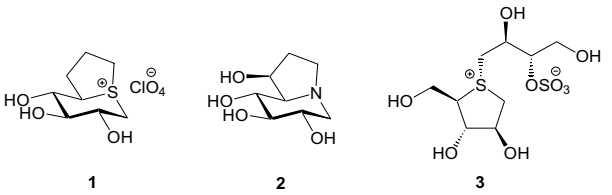

1 **2** **3**

for diabetes. One of the active ingredients of these extracts is the sulfonium salt salacinol (**3**) (5).

We (6) and others (7) have recently reported the synthesis of salacinol (**3**) and its stereoisomers (**4**, **5**), and provided conclusive proof of structure of the natural product. We have also reported the syntheses of the hitherto unknown nitrogen congeners (**6**, **7**) as potential glycosidase inhibitors (8). Enzyme inhibition assays indicated that salacinol (**3**) is a weak (K_i = 1.7 mM) inhibitor of glucoamylase, whereas compounds **6** and **7** inhibit glucoamylase with K_i values in the range about 10-fold higher. The nitrogen analogues **6** and **7** showed no significant inhibitory effect of either barley α-amylase (AMY1) or porcine pancreatic α-amylase (PPA) at concentrations of 5 mM. In contrast, salacinol (**3**) inhib-

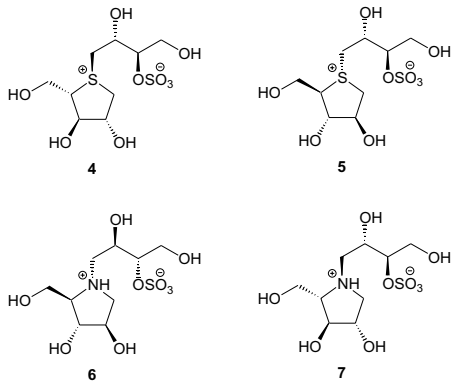

4 **5** **6** **7**

ited AMY1 and PPA in the micromolar range, with K_i values of 15 ± 1 μM and 10 ± 2 μM, respectively (8).

Yuasa and et al. (9) have also investigated the glucosidase inhibitory activities of compounds (**3**) and (**5**) and showed that although salacinol (**3**) is a better inhibitor (IC_{50} = 1.1 μM) of rice α-mannosidase than its diastereomer **5** (IC_{50} = 0.38 mM), the inhibitory activities are comparable for almond α-glucosidase (IC_{50} = 2.1 mM for **3**; 3.6 mM for **5**). In the case of almond β-glucosidase, (**5**) is a better inhibitor than (**3**) ((**3**) showed no activity; IC_{50} = 3.4 mM for (**5**)).

In a recent study, Muraoka et al. (10) showed that salacinol (**3**) inhibits intestinal α-glucosidases: maltase, sucrase, and isomaltase with IC_{50} values of 9.6 μM, 2.5 μM, and 1.8 μM, respectively, whereas compound (**6**) inhibits these enzymes with IC_{50} values of 306 μM, 44 μM, and 136 μM, respectively.

The results described above suggest that the stereochemistry at the different stereogenic centres and the nature of the ring heteroatom in the candidate inhibitors play a significant role in discriminating between different glycosidase

Scheme 1.

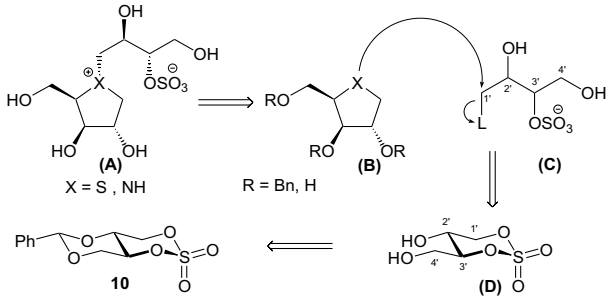

Scheme 2.

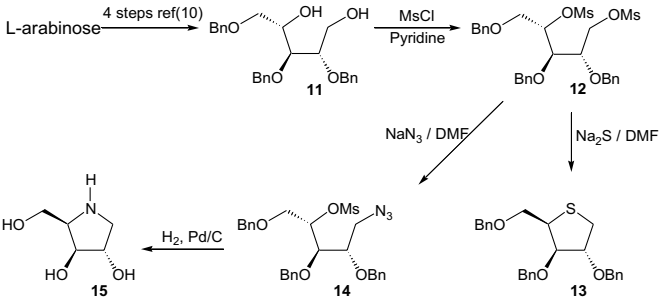

enzymes. Therefore, to probe these structure–function studies further, we now report the syntheses of the thio and iminoxylitol analogues (**8**, **9**) of salacinol (**3**) and their evaluation as glycosidase inhibitors of AMY1, PPA, or glucoamylase.

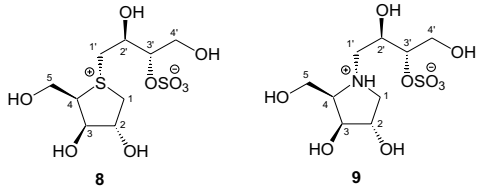

8 **9**

Results and discussion

Retrosynthetic analysis indicated that salacinol (**3**) or its analogues (**A**) could be obtained by alkylation of anhydroalditol derivatives at the ring heteroatom (Scheme 1). As in our previous work (6, 8), the benzylidene acetal **10** of **D** was chosen as the alkylating agent. We envisaged that selective attack of the heteroatom at the least-hindered primary centre would afford the desired sulfonium or ammonium ions.

The cyclic sulfate (**10**) was synthesized in five steps starting from L-glucose (6). The thio- and iminoxylitols (**13**, **15**) were synthesized from L-arabinose. Thus, the diol (**11**) was synthesized from L-arabinose in four steps according to the procedure used by van der Klein et al. (11) to synthesize its enantiomer (Scheme 2). Treatment of the diol (**11**) with methanesulfonyl chloride in pyridine then afforded the dimesylated compound (**12**) (88% yield). Compound (**12**) was used as a key intermediate to synthesize both the thio- and iminoxylitols. Treatment of (**12**) with sodium sulfide in DMF produced compound (**13**) in 95% yield, whereas treatment with sodium azide in DMF followed by

© 2002 NRC Canada

Scheme 3.

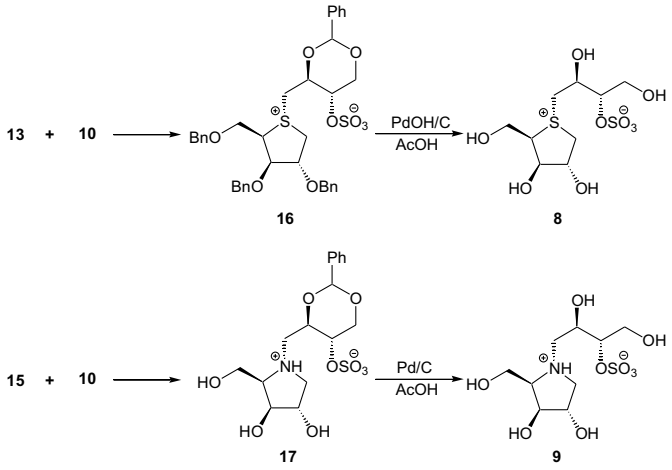

hydrogenolysis afforded the iminoxylitol (**15**) in 55% yield for the two steps (12).

To synthesize the target sulfonium ion **8**, compound **16** was first synthesized by alkylation of 1,4-anhydro-2,3,5-tri-*O*-benzyl-4-thio-D-xylitol (**13**) with the cyclic sulfate **10** (1.2 equiv) in acetone containing K_2CO_3 at 60–70°C in 72% yield. Compound **16** was obtained as the sole coupled product (Scheme 3). The stereochemistry at the stereogenic sulfonium centre in **16** was established by means of a NOESY experiment. Thus, a correlation between H-1′ and H-4, confirmed the trans relationship between the erythritol side chain and C-4 substituent on the anhydroxylitol moiety, which is similar to the stereochemistry at the stereogenic sulfur atom in salacinol (**3**). Deprotection of **16** by hydrogenolysis over a palladium hydroxide catalyst on carbon was problematic because of poisoning of the catalyst but afforded compound **8** in 50% yield.

The corresponding nitrogen congener **17** was synthesized in an analogous manner although, in this case, the increased nucleophilicity of the nitrogen atom did not necessitate benzylation of the hydroxyl groups. Thus, alkylation of 1,4-dideoxy-1,4-imino-D-xylitol (**15**) with the cyclic sulfate **10** (1.2 equiv) in methanol containing K_2CO_3 at 60–70°C afforded compound **17** in 63% yield. The stereochemistry at the stereogenic nitrogen centre in **17** was established by means of a NOESY experiment, as above. In this case, a correlation between H-1′ and H-3, confirmed the trans relationship between the erythritol side chain and the C-3 substituent on the iminoxylitol moiety. Deprotection of **17** by hydrogenolysis over a Pd/C catalyst afforded compound **9** in 83% yield.

Enzyme inhibition assays

Compounds **8** and **9** were tested for their inhibition of three glycosidase enzymes, namely glucoamylase G2, (13, 14) porcine pancreatic α-amylase, and barley α-amylase (15). The effects were compared to those of salacinol (**3**). Glucoamylase G2 was weakly inhibited by salacinol (**3**) (K_i = 1.7 mM) whereas compounds **8** and **9** showed no significant inhibition of glucoamylase. The sulfonium ion **8** inhibited barley α-amylase (AMY1) and porcine pancreatic α-amylase (PPA), with K_i values of 109 ± 11 and 55 ± 5 μM, respectively, as compared to salacinol (**3**), with K_i values of 15 ± 1 and 10 ± 2 μM, respectively. In contrast, the ammonium ion **9** showed no significant inhibition of either AMY1 or PPA (Table 1). It would appear then that analogues **8** and **9** and salacinol (**3**) show discrimination or selectivity for certain glycosidase enzymes, and further testing against a wider panel of enzymes that includes human small intestinal maltase–glucoamylase (16) and human pancreatic α-amylase (17) is planned to map the enzyme selectivity profiles of these compounds.

Table 1. K_i (mM) values of compounds **1** and **3**–**9** against barley α-amylase (AMY1), porcine pancreatic α-amylase (PPA), and glucoamylase.

Compound	AMY1	PPA	Glucoamylase
1	>5	>5	1.32
3	0.015	0.01	1.71
4	>5	>5	2.17
5	>5	>5	1.06
6	>5	>5	>2.5
7	>5	>5	>8
8	0.109	0.052	>5
9	>5	>5	>30

Experimental section

General

Optical rotations were measured at 23°C. ^1H and ^{13}C NMR spectra were recorded at 400.13 and 100.6 MHz. All assignments were confirmed with the aid of two-dimensional ^1H, ^1H (COSYDFTP), or ^1H, ^{13}C (INVBTP) experiments using standard Bruker pulse programs. Column chromatography was performed with Merck Silica gel 60 (230–400 mesh). High resolution mass spectra were measured with liquid secondary ionization fast atom bombardment (LSI-MS (FAB)), run on a Kratos Concept H double focussing mass spectrometer at 10 000 RP, using *meta*-NO_2-benzyl alcohol as the matrix.

Enzyme inhibition assays

The glucoamylase G2 form from *Aspergillus niger* was purified from a commercial enzyme (Novo Nordisk, Bagsvaerd, Denmark) as described (13, 14). The initial rates of glucoamylase G2-catalyzed hydrolysis of maltose was tested with 1 mM maltose as substrate in 0.1 M sodium acetate pH 4.5 at 45°C using an enzyme concentration of 7.0×10^{-8} M and five inhibitor concentrations in the range 1 μm – 5 mM. The effect of the inhibition on rates of substrate hydrolysis were compared for the different compounds. The glucose released was analyzed in aliquots removed at appropriate time intervals using a glucose oxidase assay adapted to microtiter plate reading and using a total reaction volume for the enzyme reaction mixtures of 150 or 300 μL (18). The K_i values were calculated assuming competitive inhibition from $1/v = (1/V_{max}) + [(K_m)/(V_{max}[S]K_i)] \times [I]$, where v is the rate measured in the presence or absence of inhibitor, $[I]$ and $[S]$ the concentrations of inhibitor and substrate, K_m 1.6 mM, and k_{cat} 11.3 s^{-1}, using ENZFITTER (19).

© 2002 NRC Canada

Porcine pancreatic α-amylase (PPA) and bovine serum albumin (BSA) were purchased from Sigma. Amylose EX-1 (DP17; average degree of polymerization 17) was purchased from Hayashibara Chemical Laboratories (Okayama, Japan). Recombinant barley α–amylase isozyme 1 (AMY1) was produced and purified as described (15). An aliquot of the porcine pancreatic α-amylase (PPA) crystalline suspension (in ammonium sulfate) was dialyzed extensively against the assay buffer without BSA. The enzyme concentration was determined by aid of amino acid analysis as determined using an LKB model Alpha Plus amino acid analyzer. The inhibition of AMY1 (3×10^{-9} M) and PPA (9×10^{-9} M) activity towards DP17 amylose was measured at 37°C in 20 mM sodium acetate (pH 5.5, 5 mM $CaCl_2$, 0.005% BSA (for AMY1)) and 20 mM sodium phosphate (pH 6.9, 10 mM NaCl, 0.1 mM $CaCl_2$, 0.005% BSA (for PPA)). Six different final inhibitor concentrations were used in the range 1 μM – 5 mM. The inhibitor was preincubated with enzyme for 5 min at 37°C before addition of substrate. Initial rates were determined by measuring reducing sugar by the copper-bicinchoninate method as described (15, 20). The K_i values were calculated assuming competitive inhibition, as described above for the case of glucoamylase, and a K_m of 0.57 mg mL^{-1} and k_{cat} of 165 s^{-1} for AMY1 and 1 mg mL^{-1} and 1200 s^{-1} for PPA, as determined in the substrate concentration range 0.03–10 mg mL^{-1} using ENZFITTER (19). For the K_i determinations, [S] = 0.7 mg mL^{-1} amylose DP 17 for the AMY1 binding and [S] = 2.5 mg mL^{-1} amylose DP 17 for the PPA binding.

2,3,5-Tri-O-benzyl-L-arabinitol (11)

The diol **11** was synthesized from L-arabinose according to the procedure used by van der Klein et al. (11) to synthesize its enantiomer. $[\alpha]_D^{22}$ –4.6° (*c* 1.0, CH_2Cl_2) (lit. (10) value +6.8° (*c* 1, $CHCl_3$)). ^{1}H NMR (CD_2Cl_2) δ: 7.38–7.25 (15H, m, Ar), 4.65 and 4.61 (2H, 2d, $J_{A,B}$ = 11.4 Hz, C*H*$_2$Ph), 4.60 and 4.57 (2H, 2d, $J_{A,B}$ = 11.2 Hz, C*H*$_2$Ph), 4.55 and 4.51 (2H, 2d, $J_{A,B}$ = 11.9 Hz, C*H*$_2$Ph), 4.00 (1H, dddd, H-4), 3.81–3.74 (3H, m, H-2, H-1a, H-1b), 3.70 (1H, dd, $J_{3,4}$ = 7.0, $J_{2,3}$ = 3.6 Hz, H-3), 3.67 (1H, dd, $J_{5a,5b}$ = 12.2, $J_{4,5a}$ = 3.9 Hz, H-5a), 3.63 (1H, dd, $J_{4,5b}$ = 5.2 Hz, H-5b), 2.90 (1H, d, $J_{OH,4}$ = 5.4 Hz, 4-OH), 2.20 (1H, dd, $J_{OH,1a}$ = 6.1, $J_{OH,1b}$ = 4.6 Hz, 1-OH). ^{13}C NMR (CD_2Cl_2) δ: 138.68, 138.58 ($3C_{ipso}$), 128.76–128.07 ($15C_{Ar}$), 80.08 (C-2), 79.16 (C-3), 74.14, 73.72, 73.15 (3*C*H$_2$Ph), 71.63 (C-5), 70.84 (C-4), 61.82 (C-1).

2,3,5-Tri-O-benzyl-1,4-di-O-methanesulfonyl-L-arabinitol (12)

To a solution of the diol **11** (4.0 g, 9.5 mmol) in pyridine (20 mL) at 0°C was added a solution of methanesulfonyl chloride (1.8 mL, 2.5 equiv) in pyridine (3.0 mL). Stirring was continued at 0°C, and under an N_2 atmosphere until TLC (hexanes–EtOAc, 3:2) showed complete disappearance of the starting material. The solvent was removed under high vacuum, and the residue was dissolved in CH_2Cl_2 (100 mL) and washed with 1 M aq HCl (2 × 30 mL), H_2O (30 mL), and sat. aq $NaHCO_3$ (30 mL), and dried (Na_2SO_4). The solution was concentrated on a rotary evaporator and the product was purified by flash chromatography (hexanes–EtOAc, 3:2) to give **12** as a colourless oil (4.8 g, 88%). $[\alpha]_D^{22}$ +4.1° (*c* 1.5, CH_2Cl_2). ^{1}H NMR (CD_2Cl_2) δ: 7.42–7.20 (15H, m, Ar), 5.01 (1H, ddd, $J_{4,5b}$ = 6.8, $J_{4,5a}$ = $J_{3,4}$ = 3.2 Hz, H-4), 4.72 and 4.59 (2H, 2d, $J_{A,B}$ = 11.1 Hz, C*H*$_2$Ph), 4.65 and 4.61 (2H, 2d, $J_{A,B}$ = 11.0 Hz, C*H*$_2$Ph), 4.53 (2H, s, C*H*$_2$Ph), 4.34–4.29 (2H, m, H-1a, H-1b), 3.96–3.91 (2H, m, H-2, H-3), 3.87 (1H, dd, $J_{5a,5b}$ = 11.3 Hz, H-5a), 3.81 (1H, dd, H-5b), 3.00 (3H, s, OSO_2CH_3), 2.93 (3H, s, OSO_2CH_3). ^{13}C NMR (CD_2Cl_2) δ: 137.95, 137.87, 137.72 ($3C_{ipso}$), 128.84–128.29 ($15C_{Ar}$), 81.52 (C-4), 77.98 (C-2), 77.32 (C-3), 74.75, 73.96, 73.77 (3*C*H$_2$Ph), 6916 (C-5), 68.64 (C-1), 39.04 (OSO_2CH_3), 37.67(OSO_2CH_3). Anal. calcd. for $C_{28}H_{34}O_9S_2$: C 58.12, H 5.92; found: C 58.21, H 6.02.

1,4-Anhydro-2,3,5-tri-O-benzyl-4-thio-D-xylitol (13)

Compound **12** (1.6 g, 2.8 mmol) was dissolved in DMF (10 mL) and $Na_2S \cdot H_2O$ (1.1 g, 1.5 equiv) was added. The mixture was stirred at 100°C until TLC (hexanes–EtOAc, 4:1) showed complete disappearance of the starting material. The solvent was removed under high vacuum, and the residue was dissolved in EtOAc (100 mL) and washed with H_2O (30 mL). The organic phase was dried (Na_2SO_4) and concentrated on a rotary evaporator. The product was purified by flash chromatography (hexanes–EtOAc, 4:1) to give a colourless syrup (1.1 g, 95%). $[\alpha]_D^{22}$ +67° (*c* 1.3, CH_2Cl_2). ^{1}H NMR (CD_2Cl_2) δ: 7.37–7.25 (15H, m, Ar), 4.57–4.47 (6H, m, 3C*H*$_2$Ph), 4.21 (1H, ddd, H-2), 4.13 (1H, dd, $J_{2,3}$ = 3.8, $J_{3,4}$ = 3.5 Hz, H-3), 3.85 (1H, dd, $J_{4,5a}$ = 7.5 Hz, H-5a), 3.80 (1H, ddd, H-4), 3.60 (1H, dd, $J_{5a,5b}$ = 8.2, $J_{4,5b}$ = 5.5 Hz, H-5b), 3.10 (1H, dd, $J_{1a,1b}$ = 11.4, $J_{1a,2}$ = 4.4 Hz, H-1a), 2.85 (1H, dd, $J_{1b,2}$ = 2.1 Hz, H-1b). ^{13}C NMR (CD_2Cl_2) δ: 138.87, 138.56 ($3C_{ipso}$), 128.70–127.86 ($15C_{Ar}$), 83.52 (C-3), 83.47 (C-2), 73.52, 72.95, 71.60 (3*C*H$_2$Ph), 69.85 (C-5), 48.55 (C-4), 33.46 (C-1). Anal. calcd. for $C_{26}H_{28}O_3S$: C 74.25, H 6.71; found: C 74.05, H 6.63.

2,3,5-Tri-O-benzyl-1,4-dideoxy-1,4-[[(2′S,3′S)-2′,4′-O-benzylidene-3′-(sulfooxy)butyl]-episulfoniumylidene]-D-xylitol inner salt (16)

A mixture of the thioxylitol **13** (100 mg, 0.24 mmol) and 2,4-*O*-benzylidene-L-erythritol-1,3-cyclic sulfate (**10**) (80 mg, 1.2 equiv) was dissolved in dry acetone (0.5 mL) and anhyd K_2CO_3 (15 mg) was added. The mixture was stirred in a sealed tube in an oil bath (60–70°C) overnight. The solvent was removed under reduced pressure and column chromatography ($CHCl_3$–MeOH, 10:1 + 0.1% Et_3N) of the crude product gave an amorphous solid (120 mg, 72%). $[\alpha]_D^{22}$ +28° (*c* 0.3, CH_2Cl_2). ^{1}H NMR (CD_2Cl_2) δ: 7.54–7.07 (20H, m, Ar), 5.52 (1H, s, C*H*Ph), 4.60 and 4.49 (2H, 2d, $J_{A,B}$ = 11.7 Hz, C*H*$_2$Ph), 4.57–4.47 (2H, m, H-3′, H-4′ eq), 4.47 and 4.44 (2H, 2d, $J_{A,B}$ = 11.3 Hz, C*H*$_2$Ph), 4.41 (1H, dd, H-1′a), 4.41–4.36 (2H, m, H-2, H-3), 4.27 (1H, ddd, $J_{2',3'}$ = 9.1, $J_{1'a,2'}$ = $J_{1'b,2'}$ = 3.3 Hz, H-2′), 4.09 (1H, ddd, $J_{4,5a}$ = 9.4, $J_{4,5b}$ = 6.0, $J_{3,4}$ = 3.2 Hz, H-4), 4.02 and 3.96 (2H, 2d, $J_{A,B}$ = 11.4 Hz, C*H*$_2$Ph), 3.92 (1H, dd, $J_{1'b,1'a}$ = 13.6 Hz, H-1′b), 3.87 (1H, dd, $J_{1a,1b}$ = 14.4, $J_{1a,2}$ = 3.1 Hz, H-1a), 3.82 (1H, dd, $J_{5a,5b}$ = 9.4 Hz, H-5a), 3.76 (1H, dd, $J_{4'ax,4'eq}$ = $J_{3',4'ax}$ = 12.2 Hz, H-4′ ax), 3.71 (1H, brd, H-1b), 3.67 (1H, dd, H-5b). ^{13}C NMR (CD_2Cl_2) δ: 137.42, 137.17, 136.46 ($4C_{ipso}$), 129.82–126.65 ($20C_{Ar}$), 101.76 (*C*HPh), 82.64 (C-3), 81.74 (C-2), 76.63 (C-2′), 73.92, 73.84, 72.64 (3*C*H$_2$Ph), 69.54 (C-4′), 66.56 (C-4), 66.40 (C-3′), 64.00 (C-5), 51.51 (C-1′),

© 2002 NRC Canada

47.42 (C-1). Anal. calcd. for $C_{37}H_{40}O_9S_2$: C 64.14, H 5.82; found: C 64.45, H 5.85.

1,4-Dideoxy-1,4-[[(2′S,3′S)-2′,4′-dihydroxy-3′-(sulfooxy)butyl]-episulfoniumylidene]-D-xylitol inner salt (8)

The protected compound **16** (150 mg, 0.22 mmol) was dissolved in AcOH–H_2O (4:1, 3 mL) and stirred with palladium hydroxide catalyst on carbon (100 mg) under H_2 (52 psi). After 72 h, the reaction mixture was filtered through a pad of Celite, which was subsequently washed with MeOH. The combined filtrates were concentrated and the residue was purified by column chromatography ($CHCl_3$–MeOH–H_2O, 7:3:1) to give an amorphous solid (36 mg, 50%). $[\alpha]_D^{22}$ +20° (*c* 1.2, MeOH). HR-MS calcd. for $C_9H_{18}O_9S_2$ (M + H): 335.0471; found: 335.0471. ^{1}H NMR (CD_3OD) δ: 4.64–4.59 (1H, m, H-2), 4.55 (1H, dd, $J_{2,3} = J_{3,4}$ = 2.9 Hz, H-3), 4.37 (1H, ddd, H-4), 4.35 (1H, ddd, $J_{1'a,2'}$ = 3.5 Hz, H-2′), 4.25 (1H, ddd, $J_{2',3'}$ = 7.2, $J_{3',4'a} = J_{3',4'b}$ = 3.4 Hz, H-3′), 4.16 (1H, dd, $J_{5a,5b}$ = 11.7, $J_{4,5a}$ = 6.0 Hz, H-5a), 4.07 (1H, dd, $J_{4,5b}$ = 9.0 Hz, H-5b), 3.95 (1H, dd, $J_{1'a,1'b}$ = 13.4 Hz, H-1′ a) 3.93 (1H, dd, H-4′ a), 3.91 (1H, dd, H-1a) 3.88 (1H, dd, $J_{1'b,2'}$ = 8.0 Hz, H-1′ b), 3.81 (1H, dd, $J_{4'b,4'a}$ = 12.1 Hz, H-4′ b), 3.58 (1H, brd, $J_{1b,1a}$ = 13.7 Hz, H-1b). ^{13}C NMR (CD_3OD) δ: 81.05 (C-3′), 79.55 (C-2), 78.56 (C-3), 71.69 (C-4), 67.71 (C-2′), 61.66 (C-4′), 58.92 (C-5), 52.60 (C-1′), 49.26 (C-1).

1′-((1,4-Dideoxy-1,4-imino-D-xylitol)-4-N-ammonium)-2′,4′-O-benzylidene-1′-deoxy-L-erythritol-3′-sulfate (17)

A mixture of 1,4-dideoxy-1,4-imino-D-arabinitol (**15**) (100 mg, 0.74 mmol) and 2,4-*O*-benzylidene-L-erythritol-1,3-cyclic sulfate (**10**) (240 mg, 1.2 equiv) was dissolved in dry MeOH (0.5 mL) and anhyd K_2CO_3 (15 mg) was added. The mixture was stirred in a sealed tube in an oil bath (60–70°C) overnight. The solvent was removed under reduced pressure, and column chromatography (CH_2Cl_2–MeOH, 5:1) of the crude product gave a white solid (191 mg, 63%) that was recrystallized from methanol; mp 202–204°C, $[\alpha]_D^{22}$ +30° (*c* 0.5, H_2O). ^{1}H NMR (D_2O) δ: 7.73–7.58 (5H, m, Ar), 5.93 (1H, s, C*H*Ph), 4.68 (1H, dd, $J_{4'eq,4'ax}$ = 11.0, $J_{3',4'eq}$ = 5.5 Hz, H-4′eq), 4.54 (1H, brt, $J_{2',3'} = J_{1'b,2'}$ = 9.9 Hz, H-2′), 4.50–4.41 (3H, m, H-3, H-3′, H-2), 4.20 (1H, dd, $J_{5a,5b}$ = 12.6, $J_{4,5a}$ = 5.5 Hz, H-5a), 4.18–4.12 (2H, m, H-1′a, H-5b), 4.10 (1H, dd, $J_{3',4'ax}$ = 11.0 Hz, H-4′ax), 4.11–4.01 (2H, m, H-1a, H-4), 3.66 (1H, br dd, $J_{1'b,1'a}$ = 11.6 Hz, H-1′b), 3.56–3.50 (1H, brd, H-1b). ^{13}C NMR (D_2O) δ: 138.50 (C_{ipso}), 132.45 (C_{para}), 131.26 (2C) and 128.62 (2C) (C_{ortho} and C_{meta}), 103.38 (*C*HPh), 78.08 (C-2′), 77.38 (C-3), 76.70 (C-2), 73.31 (C-4), 70.77 (C-4′), 70.41 (C-3′), 63.18 (C-1), 60.01 (C-1′), 59.55 (C-5). Anal. calcd. for $C_{16}H_{22}O_9SN$: C 47.51, H 5.49, N, 3.47; found: C 47.29, H 5.80, N 3.22.

1′-((1,4-Dideoxy-1,4-imino-D-xylitol)-4-N-ammonium)-1′-deoxy-L-erythritol-3′-sulfate (9)

The protected compound **17** (75 mg, 0.18 mmol) was dissolved in AcOH–H_2O (4:1, 5 mL) and stirred with Pd/C (30 mg) under H_2. After 16 h, the reaction mixture was filtered through a pad of Celite, which was subsequently washed with MeOH. The combined filtrates were concentrated and the residue was purified by column chromatography ($CHCl_3$–MeOH–H_2O, 7:3:1) to give an amorphous solid (49 mg, 83%). $[\alpha]_D^{22}$ –5.3° (c 0.8, H_2O). HR-FAB-MS calcd. for $C_9H_{18}O_9SN$ (M + H): 318.0859; found: 318.0859. ^{1}H NMR (D_2O) δ: 4.59–4.40 (4H, m, H-3, H-2, H-2′, H-3′), 4.27–4.17 (2H, m, H-5a, H-5b), 4.18–4.06 (2H, m, H-1a, H-4), 4.11 (1H, dd, $J_{4'a,4'b}$ = 12.6, $J_{3',4'a}$ = 2.0 Hz, H-4′a), 4.02 (1H, dd, $J_{3',4'b}$ = 3.3 Hz, H-4′b), 4.11–3.95 (1H, m, H-1′a), 3.68–3.57 (1H, m, H-1b), 3.57–3.45 (1H, m, H-1′b). ^{13}C NMR (D_2O) δ: 82.52 (C-3′), 77.46 (C-3), 76.56 (C-2′), 73.20 (C-4), 68.42 (C-2), 63.09 (C-1), 62.38 (C-1′), 61.93 (C-4′), 59.38 (C-5).

Acknowledgments

We are grateful to Sidsel Ehlers for technical assistance with the glucoamylase assays. We also thank the Natural Sciences and Engineering Research Council of Canada (NSERC) for financial support and the Michael Smith Foundation for Health Research for a trainee fellowship (to AG).

References

1. S.L. Harris, L. Craig, J.S. Mehroke, M. Rashed, M.B. Zwick, K. Kenar, E.J. Toone, N. Greenspan, F.-I. Auzanneau, J.-R. Marino-Albernas, B.M. Pinto, and J.K. Scott. Proc. Natl. Acad. Sci. U.S.A. **94**, 2434 (1997).
2. B.M. Pinto, J.K. Scott, S.L. Harris, M.A. Johnson, D.R. Bundle, M.C. Chervenak, M.N. Vyas, N.K. Vyas, and F.A. Quiocho. XIX International Carbohydrate Symposium, San Diego, U.S.A., (August 1998), Abstr. CP 132, CO 019; B.M. Pinto. Meeting on anti-idiotypes and mimotopes in vaccine development, Vibo Valentia, Italy, (May 2000); B.M. Pinto. Glycobiology Symposium, Pacifichem 2000 Conference, Honolulu, Hawaii, U.S.A., (December 2000) Abstr. 607.
3. L. Svansson, B.D. Johnston, J-H. Gu, B. Patrick, and B.M. Pinto. J. Am. Chem. Soc. **122**, 10 769 (2000).
4. (*a*) B. Belleau, U. Gulini, B.J. Gour-Salin, and F.R. Ahmed. Can. J. Chem. **63**, 1268 (1985); (*b*) B. Belleau, U. Gulini, R. Camicioli, B.J. Gour-Salin, and G. Sauvé. Can. J. Chem. **64**, 110 (1986); (*c*) S. Lemaire, B. Belleau, and F. Jolicoeur. Adv. Biosci. (Oxford), **75**, 105 (1989); (*d*) F.B. Jolicoeur, D. Ménard, B. Belleau, and S. Lemaire. Int. Narcotics Res. Conf. **89**, 49 (1990).
5. M. Yoshikawa, T. Murakami, H. Shimada, H. Matsuda. J. Yamahara, G. Tanabe, and O. Muraoka. Tetrahedron Lett. **38**, 8367 (1997).
6. A. Ghavami, B.D. Johnston, and B.M. Pinto. J. Org. Chem. **66**, 2312 (2001).
7. H. Yuasa, J. Takada, and H. Hashimoto. Tetrahedron Lett. **41**, 6615 (2000).
8. A. Ghavami, B.D. Johnston, M. Jensen, B. Svensson, and B.M. Pinto. J. Am. Chem. Soc. **123**, 6268 (2001).
9. H. Yuasa, J. Takada, and H. Hashimoto. Bioorg. Med. Chem. Lett. **11**, 1137 (2001).
10. O. Muraoka, S. Ying, K. Yoshikai, Y. Matsuura, E. Yamada, T. Minematsu, G. Tanabe, H. Matsuda, and M. Yoshikawa. Chem. Pharm. Bull. **49**, 1503 (2001).
11. P.A.M. van der Klein, A.E.J. de Nooy, G.A. van der Marel, and J.H. van Boom. Synthesis, 347 (1991).
12. P.A.M. van der Klein, W. Filemon, H.J.G. Broxterman, G.A. van der Marel, and J.H. van Boom. Synth. Commun. **22**, 1763 (1992).

© 2002 NRC Canada

13. B. Svensson, T. Pedersen, I. Svendsen, T. Sakai, and M. Ottesen. Carlsberg Res. Commun. **47**, 55 (1982).
14. B. Stoffer, T.P. Frandsen, P.K. Busk, P. Schneider, I. Svendsen, and B. Svensson. Biochem. J. **292**, 197 (1993).
15. N. Juge, J.S. Andersen, D. Tull, P. Roepstorff, and B. Svensson. Protein Expression Purif. **8**, 204 (1996).
16. B.L. Nichols, J. Eldering, S. Avery, D. Hahn, A. Quaroni, and E. Sterchi. J. Biol. Chem. **273**, 3076 (1998).
17. C. Braun, G.D. Brayer, and S.G. Withers. J. Biol. Chem. **270**, 26 778 (1995).
18. T.P. Frandsen, C. Dupont, J. Lehmbeck, B. Stoffer, M.R. Sierks, R.B. Honzatko, and B.Svensson. Biochemistry, **33**, 13 808 (1994).
19. R.J. Leatherbarrow. Enzfitter, a nonlinear regression data analysis program for IBM PC. Elsevier Science Publishers BV, Amsterdam. 1987.
20. J.D. Fox and J.F. Robyt. Anal. Biochem. **195**, 93 (1991).

© 2002 NRC Canada

Synthesis of conjugates of L-fucose and *ortho*-carborane as potential agents for boron neutron capture therapy

Prakriti Basak and Todd L. Lowary

Abstract: The synthesis of three potential boron neutron capture therapy agents (**6**–**8**) is reported. The compounds synthesized are comprised of *ortho*-carborane covalently attached to L-fucose via C-6. Incorporation of the carborane moiety was achieved either through the reaction of an L-fucose-derived alkyne with decaborane or by the coupling of a 6-amino-L-galactopyranose derivative with carborane carboxylic acid chloride (**18**).

Key words: L-fucose, fucosyltransferase, boron neutron capture therapy, *ortho*-carborane.

Résumé : On a réalisé la synthèse de trois agents (**6**–**8**) pouvant éventuellement être utilisés dans la thérapie par capture de neutrons du bore. Les composés synthétisés comportent de l'*ortho*-carborane lié de façon covalente à du L-fucose par l'intermédiaire de C-6. L'incorporation de la portion carborane a été réalisée par la réaction du décaborane avec un alcyne dérivé du L-fucose ou par le couplage d'un dérivé 6-amino-L-galactopyranose avec le chlorure de l'acide carboxylique du carborane (**18**).

Mots clés : L-fucose, fucosyltransférase, thérapie par capture de neutrons du bore, *ortho*-carborane.

Introduction

The aberrant expression of cell surface oligosaccharides is among the many features that differentiate cancer cells from their healthy counterparts. Although the importance of changes in cell surface glycosylation in disease progression is not completely understood, it has been suggested that these abnormal glycans are involved in the metastasis of various cancers (1–3). The expression of these oligosaccharides is controlled by the activities of cellular glycosyltransferases and glycosidases, and it is known that in many cancerous cells the levels of these enzymes are altered in comparison to non-neoplastic cells (1–3).

In particular, tumor cells often show an increase in fucosylation of cell surface oligosaccharides due to elevated levels of fucosyltransferases (4, 5). These enzymes catalyze the transfer of fucose from guanosine diphosphate β-L-fucose (GDP-Fuc (**1**), Fig. 1) to an oligosaccharide acceptor (e.g., **2**) to give an elongated glycan (e.g., **3**). Given the increased levels of these enzymes in some cancer cells, it should be possible to deliver anti-cancer agents to tumor cells via the attachment of the drug to GDP-Fuc. In this paper we report our initial investigations directed toward the identification of such compounds.

Received 1 August 2001. Published on the NRC Research Press Web site at http://canjchem.nrc.ca on 18 July 2002.

Dedicated to the memory of Professor Raymond U. Lemieux.

P. Basak and T.L. Lowary.[1] Department of Chemistry, 100 West 18th Avenue, The Ohio State University, Columbus, OH 43210, U.S.A.

[1]Corresponding author (e-mail: lowary.2@osu.edu).

The targets chosen were conjugates of L-fucose (**4**, Fig. 2) and *ortho*-carborane (**5**). *Ortho*-carborane, an icosahedral cage compound containing 10 boron atoms and two carbon atoms, is a substrate for boron neutron capture therapy (BNCT) of tumors. Initially developed in the 1950s, BNCT has attracted increasing attention in recent years (6, 7). The physical basis for the treatment is the capture reaction of thermal neutrons by ^{10}B atoms according to one of the two pathways shown in Fig. 3. The high energy particles produced during this reaction are transient species with ionization paths of approximately 10 μm. As a result, a large amount of energy is deposited within a small distance of the capture event. When these reactions occur within living cells, the lethal effect of these particles is limited to the cell itself. Consequently, if a high concentration of boron atoms can be selectively targeted to cancerous tissues, only these cells will be killed upon neutron capture. Carboranes are ideal substrates for BNCT not only because they possess a relatively large number of boron atoms per molecule, but also because there are efficient methods available for their attachment to organic molecules.

Previous reports have described the synthesis of carboranes covalently attached to a variety of biologically relevant organic molecules, including amino acids and peptides (8–10), nucleosides (11), and polyamines (12). Syntheses of glycosylated carboranes have also been carried out (13–18). To date, most of the previously reported glycoconjugates of this type have the carborane group attached to the sugar at the anomeric center. Such a linkage was unsuitable for our purposes and in designing the targets to be synthesized we chose to attach the boron cage to the C-6 methyl group of L-fucose. This choice was made based on previous work by Hindsgaul and co-workers (19, 20), which demonstrated that fucosyltransferases are tolerant of a range of

 DOI: 10.1139/V02-054 © 2002 NRC Canada

Fig. 1. Fucosyltransferase catalyzed reaction.

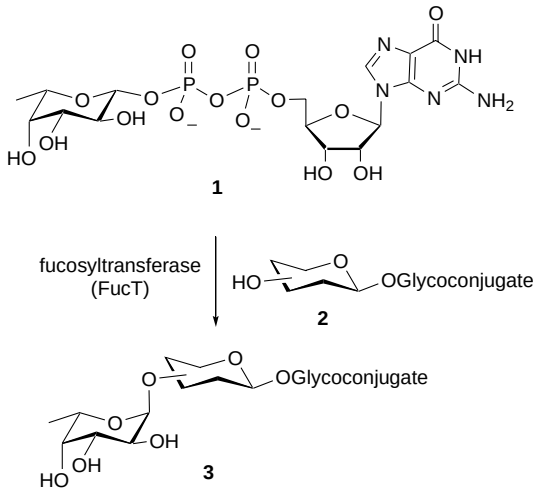

Fig. 2. Target Molecules.

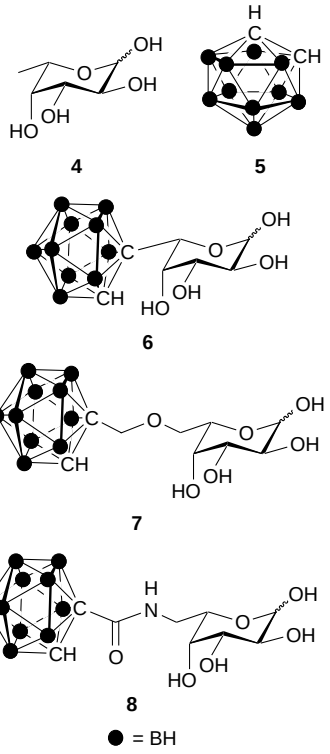

substituents at this position. These investigations showed that GDP-Fuc remains a substrate for fucosyltransferases even when groups as large as a trisaccharide are appended to C-6. We reasoned, therefore, that an *ortho*-carborane group attached at this position would also be tolerated by these enzymes; the volume of the carborane cage is about 50% larger than that of a phenyl group rotating about its C-1-C-4 axis (21). In this paper we describe the synthesis of the *ortho*-carboranyl pyranose[2] derivatives **6**–**8** (Fig. 2), which are precursors to the GDP-Fuc analogs that are expected to be fucosyltransferase substrates.

Fig. 3. Nuclear fission reactions that occur upon capture of a neutron (^{1}n) by a ^{10}B atom.

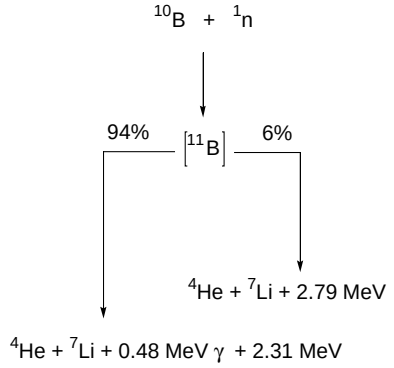

Results and discussion

In designing synthetic routes to **6**–**8**, the choice of protecting groups for the carbohydrate hydroxyls was important. The *ortho*-carborane moiety is base-labile but stable to acid. Although previous syntheses of carboranyl glycosides have employed acetyl protection of the sugar hydroxyl groups, in our hands the use of ester protecting groups gave poor yields of the products upon deprotection. We chose to avoid this problem altogether by using isopropylidene acetals that can be removed in high yield under conditions to which the carborane cage is stable.

The preparation of **6** is shown in Scheme 1. The known alcohol **9** (22) was oxidized with pyridinium chlorochromate to afford aldehyde **10**. Following filtration of the reaction mixture through a pad of silica gel to remove the oxidation reagent, the crude product (obtained in 77% yield) was converted into the dibromo-alkene **11** upon reaction with carbon tetrabromide and triphenylphosphine. The product was obtained in 70% yield. Treatment of **11** with *n*-butyllithium provided alkyne **12** and olefin **13** in 63% and 15% yields, respectively. Incorporation of the *ortho*-carborane moiety into **12** was achieved under standard conditions by reaction with decaborane and acetonitrile in toluene at 80°C, which produced **14** in 58% yield. The presence of the carborane moiety in **14** was demonstrated by the absence of the alkyne hydrogen in the ^{1}H NMR spectrum and the presence of the carborane CH resonance at 4.25 ppm. A broad multiplet from 1.7 to 2.9 ppm, arising from the BH protons, was also present. Furthermore, resonances characteristic of the *ortho*-carborane group were apparent in the ^{11}B NMR spectrum of **14**. Hydrolysis of the acetal protecting groups in **14** was accomplished by reaction with a 9:1 trifluoroacetic acid – water mixture, affording **6** in 91% yield. Inspection of the NMR spectrum of this compound (taken in CD_3OD) showed that all possible ring forms were present, with the pyranose isomers being favored (the α_{pyr}:β_{pyr}:α_{fur}:β_{fur} ratio was 2.9:3.4:1.0:1.2). Presumably, steric congestion between the ring and the relatively bulky *ortho*-carborane moiety destabilizes the pyranose form. Appreciable amounts of the normally minor furanose forms, in which the carborane is further removed from the ring, are therefore populated at equilibrium.

[2] Compound **6** was prepared as a mixture of furanose and pyranose isomers.

© 2002 NRC Canada

Scheme 1. (*a*) PCC, NaOAc, CH_2Cl_2, rt, 77%; (*b*) CBr_4, PPh_3, CH_2Cl_2, 0°C → rt, 70%; (*c*) BuLi, THF, –78 → 0°C, **12**: 63%, **13**: 15%; (*d*) $B_{10}H_{14}$, CH_3CN, 80°C, reflux, 58%; (*e*) TFA:H_2O (9:1), 0°C, 91%.

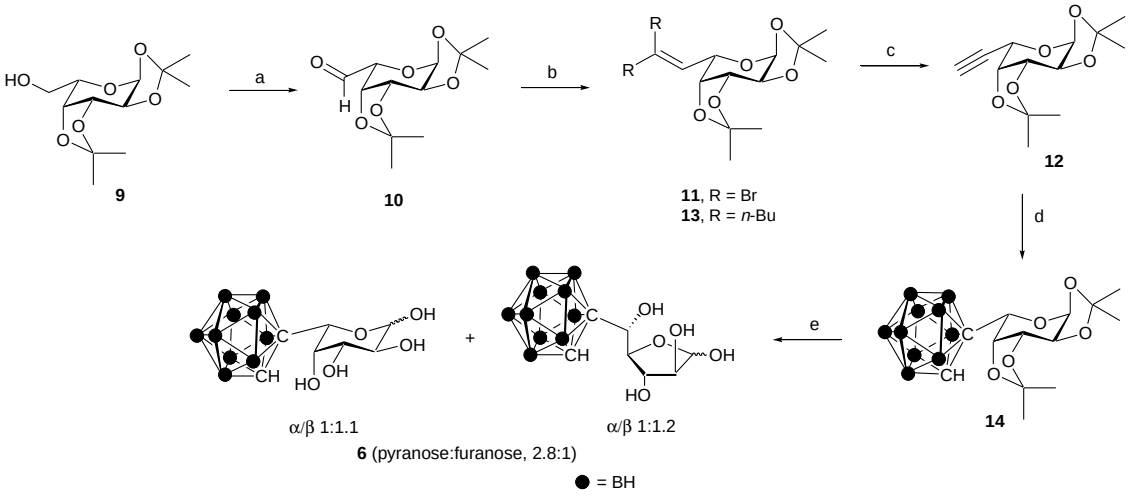

Scheme 2. (*a*) Propargyl bromide, *n*-Bu_4NI, NaH, THF, rt, 70%; (*b*) $B_{10}H_{14}$, CH_3CN, toluene, 80°C, 80%; (*c*) TFA:H_2O (9:1), 0°C, 90%.

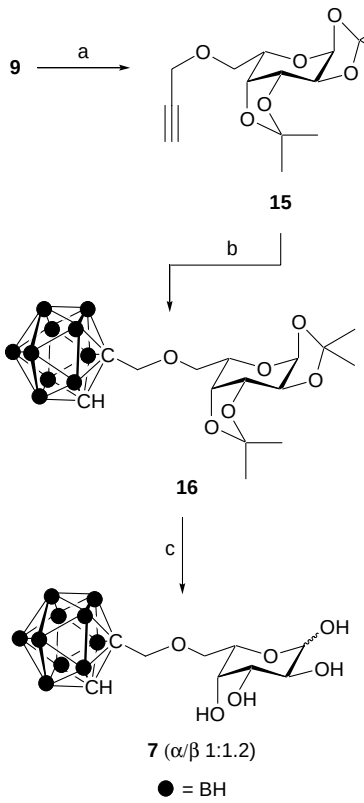

Scheme 3. (*a*) Et_3N, CH_2Cl_2, rt, 92%; (*b*) TFA:H_2O (9:1), 0°C, 93%.

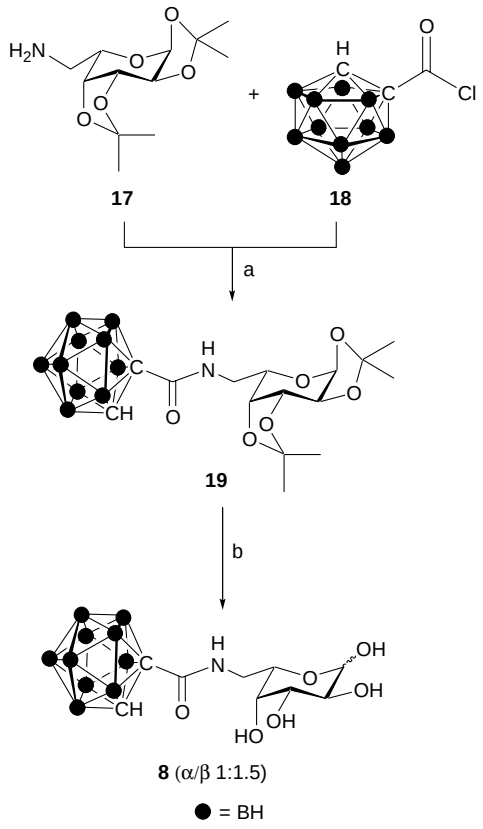

The preparation of **7** and **8** are outlined in Schemes 2 and 3. The synthesis of **7** (Scheme 2) began with alcohol **9** (22), which was alkylated (in 70% yield) with propargyl bromide. The product of this reaction, alkyne **15**, was then reacted with decaborane as was done for the preparation of **14**, to provide **16** in 80% yield. Deprotection by acid hydrolysis proceeded without incident, affording **7** in 90% yield. The preparation of **8** (Scheme 3) began with the known amine **17** (22), which was acylated with **18** (23) in excellent (92%) yield. Cleavage of the protecting groups from the product (**19**) was done as described for the previous two targets providing **8** in 93% yield. In contrast to **6**, both **7** and **8** adopted mostly the pyranose form in CD_3OD, as might be expected in that the carborane moiety is now further away from the carbohydrate ring. Only trace amounts of the furanose forms were detected by ^1H NMR.

© 2002 NRC Canada

Experimental

General Methods

1,2:3,4-Di-*O*-isopropylidene-α-L-galactopyranose (**9**) (22), 6-amino-6-deoxy-1,2:3,4-di-*O*-isopropylidene-α-L-galactopyranose (**17**) (22), and 1,2-dicarba-*ortho*-carboranyl acyl chloride (**18**) (23) were prepared as described previously. Decaborane was purified by sublimation. All reaction solvents were distilled from the appropriate drying agents before use. Reactions were carried out at room temperature under argon unless otherwise indicated. Solvents were evaporated under reduced pressure and below 40°C (bath). Column chromatography was performed on silica gel (43–75 μM). Thin layer chromatography was carried out on Merck silica gel 60 F_{254} plates. Plates were visualized by dipping them either in 10% (w/w) H_2SO_4 in ethanol or 0.5% (w/v) $PdCl_2$ in 10% concentrated HCl–CH_3OH (for boron-containing compounds) and then heating. Melting points are uncorrected. ^{1}H NMR spectra were recorded at 400 or 500 MHz, and chemical shifts are referenced to either TMS (δ: 0.0, $CDCl_3$) or CH_3OD (δ: 4.87, CD_3OD). ^{13}C NMR spectra were recorded at 100 or 125 MHz and ^{13}C chemical shifts are referenced to $CDCl_3$ (77.00, $CDCl_3$), or CD_3OD (49.15, CD_3OD). In the NMR data reported below, the carborane carbons are designated C_1' and C_2', with the former being the attachment site of the carbohydrate. All samples containing boron showed the characteristic spectral features of the *ortho*-carborane moiety in their ^{11}B NMR spectrum. Elemental analyses were performed in-house. Electrospray mass spectra were recorded on samples suspended in THF or CH_3OH.

*1,2:3,4-Di-*O*-isopropylidene-α-L-galacto-hexodialdo-1,5-pyranose (10)*

A suspension of pyridinium chlorochromate (650 mg, 3.0 mmol), sodium acetate (500 mg, 6.0 mmol) and 4 Å molecular sieves (1.33 g) in CH_2Cl_2 (9 mL) was stirred for 1 h. To this mixture was added, drop-wise, a solution of 1,2:3,4-di-*O*-isopropylidene-α-L-galactopyranose (22) (**9**, 264 mg, 1.0 mmol) in dry CH_2Cl_2 (4.5 mL). The reaction mixture was stirred for 2 h before a 1:1 mixture of hexanes and ether (25 mL) was added. The solution was filtered through a bed of silica and the filtrate was concentrated to give the crude aldehyde **10** as an oil (199 mg, 77%), which was carried on to the next step without further purification: ^{1}H NMR ($CDCl_3$) δ: 9.54 (s, 1H, H-6), 5.60 (d, 1H, $J_{1,2}$ = 4.9 Hz, H-1), 4.58 (dd, 1H, $J_{2,3}$ = 2.4 Hz, $J_{3,4}$ = 7.8 Hz, H-3), 4.53 (dd, 1H, $J_{3,4}$ = 7.8 Hz, $J_{4,5}$ = 1.8 Hz, H-4), 4.32 (dd, 1H, $J_{1,2}$ = 4.9 Hz, $J_{2,3}$ = 2.4 Hz, H-2), 4.13 (d, 1H, $J_{4,5}$ = 1.8 Hz, H-5), 1.44, 1.36, 1.28, 1.26 (s, 3H, CH_3). ^{13}C NMR ($CDCl_3$) δ: 199.1 (C=O), 108.0, 109.0 ($C(CH_3)_2$), 95.2 (C-1), 72.7, 70.7, 69.5, 69.4 (C-2, C-3, C-4, C-5), 25.0, 24.8, 23.8, 23.2 (CH_3).

*7,7-Dibromo-6,7-dideoxy-1,2:3,4-di-*O*-isopropylidene-α-L-galacto-hept-6-eno-pyranose (11)*

A solution of triphenylphosphine (1.53 g, 5.9 mmol) and carbon tetrabromide (0.97 g, 2.9 mmol) in dry CH_2Cl_2 (12 mL) was cooled to 0°C. To this solution was added, dropwise, a solution of **10** (190 mg, 0.73 mmol) in dry CH_2Cl_2 (6 mL). The reaction mixture was allowed to warm to room temperature and was stirred for 5 h before water (18 mL) was added. The organic layer was separated and the aqueous layer was extracted with CH_2Cl_2 (2 × 25 mL). The combined organic layers were washed with a saturated aqueous solution of $NaHCO_3$, water, and finally brine. The organic layer was then dried ($MgSO_4$) and concentrated. Chromatography (hexanes–EtOAc, 9:1 → 7:1) of the residue gave alkene **11** as an unstable white solid (210 mg, 70%): $[\alpha]_D^{25}$ + 78.9 (*c* 1.0, $CHCl_3$). R_f = 0.5 (hexanes–EtOAc, 7:1). ESI-MS calcd. for $C_{13}H_{18}Br_2O_5$ (M + Na): 436.9393; found: 436.9375. ^{1}H NMR ($CDCl_3$) δ: 6.63 (d, 1H, $J_{5,6}$ = 8.1 Hz, H-6), 5.52 (d, 1H, $J_{1,2}$ = 5.0 Hz, H-1), 4.63 (dd, 1H, $J_{2,3}$ = 2.5, $J_{3,4}$ = 7.8 Hz, H-3), 4.52 (dd, 1H, $J_{4,5}$ = 2.0 Hz, $J_{5,6}$ = 8.1 Hz, H-5), 4.33 (dd, 1H, $J_{1,2}$ = 5.0 Hz, $J_{2,3}$ = 2.5 Hz, H-2), 4.25 (dd, 1H, $J_{3,4}$ = 7.8 Hz, $J_{4,5}$ = 2.0 Hz, H-4), 1.60, 1.47, 1.34, 1.34 (s, 3H, CH_3). ^{13}C NMR ($CDCl_3$) δ: 135.0 (*C*=CBr_2), 109.4, 110.1 ($C(CH_3)_2$), 96.8 (C-1), 93.0 (C=*C*Br_2), 72.3, 71.2, 70.6, 69.7 (C-2, C-3, C-4, C-5), 26.6, 26.3, 25.4, 24.8 (CH_3).

*6,7-Dideoxy-1,2:3,4-di-*O*-isopropylidene-α-L-galacto-hept-6-ynopyranose (12)*

A solution of **11** (190 mg, 0.46 mmol) in dry THF (2.6 mL) was cooled to –78°C. *n*-BuLi (1.6 M in hexanes, 1.01 mL, 1.62 mmol) was added to the solution dropwise and the mixture was stirred for 1 h at –78°C, then 1 h at 0°C, and finally at room temperature for 3 h. The reaction mixture was treated with a saturated aqueous solution of $NaHCO_3$ (5 mL) and then ether (5 mL) was added. The aqueous and organic layers were separated and then the aqueous layer was extracted with ether (3 × 5 mL). The combined organic layers were washed with water, brine, and then dried ($MgSO_4$), and concentrated. Alkyne **12** was purified by chromatography (hexanes–EtOAc, 7:1 → 5:1) to yield the product as an oil (74 mg, 63%). $[\alpha]_D^{25}$ +126.8 (*c* 0.5, $CHCl_3$). R_f = 0.4 (hexanes–EtOAc, 4:1). ESI-MS calcd. for $C_{13}H_{18}O_5$ (M + Na): 277.1046; found: 277.1069. ^{1}H NMR ($CDCl_3$) δ: 5.49 (d, 1H, $J_{1,2}$ = 5.0 Hz, H-1), 4.56 (dd, 1H, $J_{2,3}$ = 2.5 Hz, $J_{3,4}$ = 7.7 Hz, H-3), 4.54 (dd, 1H, $J_{4,5}$ = 2.0 Hz, $J_{5,7}$ = 2.4 Hz, H-5), 4.25 (dd, 1H, $J_{1,2}$ = 5.0 Hz, $J_{2,3}$ = 2.5 Hz, H-2), 4.22 (dd, 1H, $J_{3,4}$ = 7.7, $J_{4,5}$ = 2.0 Hz, H-4), 2.47 (d, 1H, $J_{5,7}$ = 2.4 Hz, H–7), 1.48, 1.47, 1.32, 1.27 (s, 3H, CH_3). ^{13}C NMR ($CDCl_3$) δ: 110.3, 109.3 ($C(CH_3)_2$), 96.8 (C-1), 79.2 (internal alkyne C), 74.9, 73.0, 71.0, 70.5 (C-2, C-3, C-4, C-5), 60.4 (terminal alkyne C), 26.5, 26.3, 25.2, 24.8 (CH_3).

*7,7-Di-*n*-butyl-6,7-dideoxy-1,2:3,4-di-*O*-isopropylidene-α-L-galacto-hept-6-eno-pyranose (13)*

This compound (25 mg, 15%) was isolated as a by-product in the formation of **12**: $[\alpha]_D^{20}$ +66.7 (*c* 1.0, $CHCl_3$). R_f = 0.4 (hexanes–EtOAc 9:1). ESI-MS calcd. for $C_{21}H_{36}O_5$ (M + Na): 391.2455; found: 391.2428. ^{1}H NMR ($CDCl_3$) δ: 5.56 (d, 1H, $J_{1,2}$ = 5.2 Hz, H-1), 5.43 (d, 1H, $J_{5,6}$ = 8.7 Hz, H-6), 4.59 (dd, 1H, $J_{3,4}$ = 7.9 Hz, $J_{2,3}$ = 2.3 Hz, H-3), 4.51 (dd, 1H, $J_{5,6}$ = 8.7 Hz, $J_{4,5}$ = 1.8 Hz, H-5), 4.30 (dd, 1H, $J_{1,2}$ = 5.2 Hz, $J_{2,3}$ = 2.3 Hz, H-2), 4.12 (dd, 1H, $J_{3,4}$ = 7.9 Hz, $J_{4,5}$ = 1.8 Hz, H-4), 2.12–2.02 (m, 4H), 1.57, 1.49, (s, 3H, $C(CH_3)_2$), 1.46–1.37 (m, 4H, butyl CH_2), 1.35, 1.34 (s, 3H, $C(CH_3)_2$), 1.34–1.29 (m, 8H, butyl CH_2), 0.93–0.87 (m, 6H, butyl CH_3). ^{13}C NMR ($CDCl_3$) δ: 147.3 (C=*C*Bu_2), 119.6 (*C*=CBu_2), 109.4, 108.5 (2 $C(CH_3)_2$), 97.2 (C-1), 74.1, 71.4, 70.7, 64.5 (C-2, C-3, C-4, C-5), 37.2, 31.5, 31.5, 26.5,

© 2002 NRC Canada

26.5, 25.3, 24.8, 23.5, 23.1, 14.6, 14.4 (butyl CH_2 and CH_3 groups, and $C(CH_3)_2$).

*5-(1′,2′-Dicarba-*ortho*-carboranyl)-1,2:3,4-di-*O*-isopropylidene-α-L-arabino-pyranoside (14)*

A solution of **12** (48 mg, 0.19 mmol) and decaborane (58 mg, 0.48 mmol) in dry toluene (5.4 mL) was treated with dry acetonitrile (136 μL) and heated at 60°C until the solution became clear (15 min). The solution was then heated to 80°C and then stirred for 18 h at which point CH_3OH (2 mL) was added. After heating for a further 30 min, the mixture was cooled and concentrated. Chromatography (hexanes–EtOAc, 9:1 → 7:1) gave **14** as a white solid (40 mg, 58%); mp 84 to 85°C. $[\alpha]_D^{17}$ +92.2 (*c* 1.0, $CHCl_3$). R_f = 0.4 (hexanes–EtOAc, 7:1). ESI-MS calcd. for $C_{13}H_{28}B_{10}O_5$ (M + Na): 395.2832; found: 395.2854. ^{1}H NMR ($CDCl_3$) δ: 5.49 (d, 1H, $J_{1,2}$ = 4.8 Hz, H-1), 4.60 (dd, 1H, $J_{2,3}$ = 2.3 Hz, $J_{3,4}$ = 7.9 Hz, Hz, H-3), 4.37 (dd, 1H, $J_{3,4}$ = 7.9 Hz, $J_{4,5}$ = 2.4 Hz, H-4), 4.28–4.26 (m, 3H, carborane CH, H-5, H-2), 2.96–1.77 (br m, 10H, carborane BH), 1.51, 1.44, 1.33, 1.32 (4, 3H, CH_3). ^{13}C NMR ($CDCl_3$) δ: 111.6, 110.8 ($C(CH_3)_2$), 96.8 (C-1), 75.2 (C-1′), 73.1, 72.8 72.3, 69.7, (C-2, C-3, C-4, C-5), 60.1 (C-2′), 27.6, 27.1, 26.2, 25.7 (CH_3).

*5-(1′,2′-Dicarba-*ortho*-carboranyl)-L-arabinose (6)*

Compound **14** (30 mg, 0.07 mmol) was dissolved in trifluoroacetic acid–H_2O (9:1, 1 mL), stirred for 30 min at 0°C and then diluted with water and concentrated. The product was purified by chromatography (CH_2Cl_2–MeOH, 14:1 → 9:1) to afford **6** (20 mg, 91%) as a white solid. Both pyranose and furanose forms were present (ratio α_{pyr}:β_{pyr}:α_{fur}:β_{fur}, 2.9:3.4:1.0:1.2). $[\alpha]_D^{18}$ +1.9 (*c* 1.0, MeOH). ESI-MS calcd. for $C_7H_{20}B_{10}O_5$ (2M + Na): 607.4520; found: 607.4519. Partial ^{1}H NMR (500 MHz, CD_3OD) δ: 5.19 (d, $J_{1,2}$ 4.5 Hz, H-1 (α_{fur})), 5.16 (d, $J_{1,2}$ = 3.9 Hz, H-1 (α_{pyr})), 5.14 (d, $J_{1,2}$ = 2.9 Hz, H-1 (β_{fur})), 4.46 (d, $J_{1,2}$ = 7.4 Hz, H-1 (β_{pyr})). Partial ^{13}C NMR (125 MHz, CD_3OD) δ: 104.2 (C-1 (α_{fur})), 99.8 (C-1 (α_{pyr})), 97.2 (C-1 (β_{fur})), 94.9 (C-1 (β_{pyr})).

*1,2:3,4-Di-*O*-isopropylidene-6-*O*-propynyl-α-L-galactopyranose (15)*

A solution of alcohol **9** (22) (290 mg, 1.13 mmol) in dry THF (3.5 mL) was cooled to 0°C and NaH (60% dispersion in mineral oil, 50 mg, 1.36 mmol) was added. The reaction mixture was stirred at 0°C for 30 min at which point tetrabutylammonium iodide (8 mg, 0.07 mmol) and propargyl bromide (320 mg, 2.83 mmol) were added in succession. The reaction mixture was then allowed to warm to room temperature and was stirred overnight before ice water (0.5 mL) and ether (5 mL) were added. After separating the two layers, the aqueous phase was extracted with ether (3 × 5 mL). The combined organic extracts were dried ($MgSO_4$), concentrated, and the product purified by chromatography (hexanes–EtOAc, 9:1 → 7:1) to afford **15** (240 mg, 70%) as a white solid; mp 61°C. $[\alpha]_D^{25}$ +75.4 (*c* 1.0, $CHCl_3$). R_f = 0.36 (hexanes–EtOAc, 7:1). ESI-MS calcd. for $C_{15}H_{22}O_6$ (M + Na): 321.1309; found: 321.1290. ^{1}H NMR ($CDCl_3$) δ: 5.55 (d, 1H, $J_{1,2}$ = 5.0 Hz, H-1), 4.61 (dd, 1H, $J_{2,3}$ = 2.4 Hz, $J_{3,4}$ = 7.9 Hz, H-3), 4.32 (dd, 1H, $J_{1,2}$ = 5.0 Hz, $J_{2,3}$ = 2.4 Hz, H-2), 4.29–4.21 (m, 3H, H-4, 2 x propargyl CH_2), 4.00 (ddd, 1H, $J_{4,5}$ = 1.7 Hz, $J_{5,6}$ = 7.1 Hz, $J_{5,6'}$ = 5.3 Hz, H-5), 3.78 (dd, 1H, $J_{5,6'}$ = 5.3 Hz, $J_{6,6'}$ = 10.1 Hz, H-6′), 3.67 (dd, 1H, $J_{5,6}$ = 7.1 Hz, $J_{6,6'}$ = 10.1 Hz, H-6), 2.43 (d, 1H, ^3J = 2.4 Hz, alkyne H), 1.55, 1.46, 1.35, 1.33 (s, 3 H, CH_3). ^{13}C NMR ($CDCl_3$) δ: 109.8, 109.0 ($C(CH_3)_2$), 96.8 (C-1), 80.1 (internal alkyne C), 75.0 (propargylic CH_2), 71.6, 71.1, 70.9, 69.1 (C-2, C-3, C-4, C-5), 67.2 (terminal alkyne C), 58.9 (C-6), 26.5, 26.4, 25.5, 24.9 (CH_3).

*6-O-(1′,2′-Dicarba-*ortho*-carboranyl) methyl-1,2:3,4-di-O-isopropylidene-α-L-galactopyranose (16)*

Reaction of decaborane (210 mg, 1.75 mmol), dry acetonitrile (1.25 mL) and propargyl ether **15** (210 mg, 0.7 mmol) in dry toluene (20 mL) as described for the synthesis of **14** (following purification by chromatography (hexanes–EtOAc, 4:1)) gave **16** (230 mg, 80%) as an oil. $[\alpha]_D^{17}$ +74.8 (*c* 0.1, $CHCl_3$). R_f = 0.5 (hexanes–EtOAc, 4:1). ESI-MS calcd. for $C_{15}H_{32}B_{10}O_6$ (M + Na): 439.3094; found: 439.3100. ^{1}H NMR ($CDCl_3$) δ: 5.50 (d, 1H, $J_{1,2}$ = 5.0 Hz, H-1), 4.60 (dd, 1H, $J_{2,3}$ = 2.4 Hz, $J_{3,4}$ = 7.9 Hz, H-3), 4.31 (dd, 1H, $J_{1,2}$ = 5.0 Hz, $J_{2,3}$ = 2.4 Hz, H-2), 4.15 (dd, 1H, $J_{3,4}$ = 7.9 Hz, $J_{4,5}$ = 1.9 Hz, H-4), 4.10 (br s, carborane CH), 3.94–3.89 (m, 3H, H-5, -CH_2OCH_2-carborane), 3.70 (dd, 1H, $J_{5,6'}$ = 4.7 Hz, $J_{6,6'}$ = 10.8 Hz, H-6′), 3.61 (dd, 1H, $J_{5,6}$ = 7.3 Hz, $J_{6,6'}$ = 10.8 Hz, H-6), 2.38–2.00 (br m, 10H, carborane BH), 1.53, 1.43, 1.33, 1.23 (s, 3H, CH_3). ^{13}C NMR ($CDCl_3$) δ: 111.6, 110.8 ($C(CH_3)_2$), 96.8 (C-1), 73.4 (C-1′), 73.0 (-CH_2OCH_2-carborane), 71.4, 71.4, 71.0, 70.8, 67.6 (C-2, C-3, C-4, C-5, C-2′), 58.1 (C-6), 26.4, 26.3, 25.3, 24.7 (CH_3).

*6-O-(1′,2′-Dicarba-*ortho*-carboranyl) methyl-L-galactose (7)*

Compound **16** (30 mg, 0.07 mmol) was deprotected as described for the preparation of **6** using trifluoroacetic acid and water (9:1, 1 mL). The product was purified by chromatography (CH_2Cl_2–CH_3OH, 14:1 → 12:1) to afford **7** (21 mg, 90%) as a white solid. The α_{pyr}:β_{pyr} ratio was 1:1.2 and only trace amounts of the furanose form were detected by NMR. $[\alpha]_D^{17}$ −41.9 (*c* 1.0, MeOH). ESI-MS calcd. for $C_9H_{24}B_{10}O_6$ (M + Na): 359.2468; found 359.2451. Partial ^{1}H NMR (500 MHz, CD_3OD) δ: 5.14 (d, $J_{1,2}$ = 3.5 Hz, H-1 (α_{pyr})) 4.44 (d, $J_{1,2}$ = 6.9 Hz, H-1 (β_{pyr})). Partial ^{13}C NMR (125 MHz, CD_3OD) δ: 99.1 (C-1 (β_{pyr})), 94.6 (C-1 (α_{pyr})).

*6-N-6-Amino-(1′,2′-dicarba-*ortho*-carboranyl carbonyl)-6-deoxy-1,2:3,4-di-*O*-isopropylidene-α-L-galactopyranose (19)*

1′,2′-Dicarba-*ortho*-carboranyl acyl chloride **18** (23) (75 mg, 0.36 mmol) was dissolved in dry CH_2Cl_2 (1.3 mL). Triethylamine (36 mg, 0.36 mmol) was added which produced a slurry. To this was added, dropwise, a solution of **17** (22) (74 mg, 0.29 mmol) in dry CH_2Cl_2 (650 μL). The reaction mixture gradually became clear and, after stirring for 1 h, it was diluted with CH_2Cl_2 (3 mL) and ice water (5 mL) was added. After stirring for 30 min, the two layers were separated and the aqueous layer was extracted with CH_2Cl_2 (2 × 5 mL). The combined organic layers were washed with 0.01 M HCl, a saturated aqueous solution of $NaHCO_3$, water, and brine. The organic layer was then dried ($MgSO_4$), concentrated, and the resulting residue purified by chromatography (hexanes–EtOAc, 5:1) to give **19**, as a white solid (115 mg, 92%); mp 69°C. $[\alpha]_D^{17}$ +16.8 (*c* 1.0, $CHCl_3$). R_f = 0.25 (hexanes–EtOAc, 5:1). ESI-MS calcd. for $C_{15}H_{31}B_{10}O_6$

© 2002 NRC Canada

(M + Na): 452.3047; found: 452.3066. ^{1}H NMR ($CDCl_3$) δ: 6.67 (br t, 1H, $J_{5,NH}$ = 4.6 Hz, NH), 5.51 (d, 1H, $J_{1,2}$ = 4.9 Hz, H-1), 4.61 (dd, 1H, $J_{2,3}$ = 2.4 Hz, $J_{3,4}$ = 7.9 Hz, H-3), 4.31 (dd, 1H, $J_{1,2}$ = 4.9 Hz, $J_{2,3}$ = 2.4 Hz, H-2), 4.28 (br s, carborane CH), 4.19 (dd, 1H, $J_{3,4}$ = 7.9 Hz, $J_{4,5}$ = 1.7 Hz, H-4), 3.86 (ddd, 1H, $J_{4,5}$ = 1.7 Hz, $J_{5,6'}$ = 6.2 Hz, $J_{5,6}$ = 6.1 Hz, H-5), 3.73 (ddd, 1H, $J_{5,6'}$ = 6.2 Hz, $J_{6,6'}$ = 11.3 Hz, $J_{6',NH}$ = 4.6 Hz, H-6′), 3.26 (ddd, 1H, $J_{5,6}$ = 6.1 Hz, $J_{6,6'}$ = 11.3 Hz, $J_{6,NH}$ = 4.6 Hz, H-6), 2.04–1.53 (br m, 10H, carborane BH), 1.48, 1.47, 1.34, 1.34, (s, 3H, CH_3). ^{13}C NMR ($CDCl_3$) δ: 160.1 (C=O), 110.1, 109.3 ($C(CH_3)_2$), 96.6 (C-1), 72.3, 71.2, 71.0, 65.7 (C-2, C-3, C-4, C-5), 60.5 (C-1′), 57.2 (C-2′), 42.2 (C-6), 26.5, 26.3, 25.3, 24.5 (CH_3).

6-N-*6-Amino-(1′,2′-Dicarba*-ortho-*carboranyl carbonyl)-6-deoxy-L-galactose (8)*

Compound **19** (30 mg, 0.07 mmol) was deprotected as described for **6** using trifluoroacetic acid and water (9:1, 1 mL). The product was purified by chromatography (CH_2Cl_2–CH_3OH, 15:1 → 12:1) to afford **8** (22 mg, 93%) as a white solid. The α_{pyr}:β_{pyr} ratio was 1:1.5 and only trace amounts of the furanose form were detected by NMR. $[\alpha]_D^{17}$ –32.9 (*c* 1.0, MeOH). ESI-MS calcd. for $C_9H_{23}B_{10}O_6$ (M + Na): 372.2421; found: 372.2432. Partial ^{1}H NMR (500 MHz, CD_3OD) δ: 5.06 (d, 1H, $J_{1,2}$ = 3.5 Hz, H-1 (α_{pyr})), 4.29 (d, 1H, $J_{1,2}$ = 7.1 Hz, H-1 (β_{pyr})). Partial ^{13}C NMR (125 MHz, CD_3OD) δ: 99.1 (C-1 (β_{pyr})), 94.6 (C-1 (α_{pyr})).

Conclusion

In this paper we have described efficient syntheses of three fucose-*ortho*-carborane derivatives, which can be converted into the corresponding GDP-Fuc analogs in 2 to 3 steps (24, 25). We anticipate, however, that such transformations may not be necessary because **6**–**8** may be substrates for the enzymes involved in the synthesis of **1** via a "salvage pathway" (26). In this pathway, fucose is converted to **1** via fucose 1-phosphate, by the action of two enzymes: L-fucose kinase (27) and GDP-L-fucose pyrophosphorylase (28). In this regard, compounds **7** and **8** may be of more utility than **6**, given the mixture of ring forms present at equilibrium in the latter. The conversion of **6**–**8** into the corresponding GDP analogs is in progress as is the biological evaluation of these compounds.

Acknowledgements

This work was supported by the National Science Foundation (CHE-9875163). We thank Dr. Sheldon G. Shore and Roman Kultyshev for helpful discussions and Douglas M. Krein and Justin B. Houseknecht for technical assistance.

References

1. J.W. Dennis, M. Granovsky, and C.E. Warren. Biochim. Biophys. Acta, **1473**, 21 (1999).
2. J.D. Roberts, J.-L.D. Klein, R. Palmantier, S.T. Dhume, M.D. George, and K. Olden. Cancer Detect. Prev. **22**, 455 (1998).
3. S.-I. Hakomori. Cancer Res. **56**, 5309 (1996).
4. E. Miyoshi, K. Noda, Y. Yamaguchi, S. Inoue, Y. Ikeda, W. Wang, J.H. Ko, N. Uozumi, W. Li, and N. Taniguchi. Biochim. Biophys. Acta, **1473**, 9 (1999).
5. E. Staudacher, F. Altmann, I.B.H. Wilson, and L. März. Biochim. Biophys. Acta, **1473**, 216 (1999).
6. A.H. Soloway, W. Tjarks, B.A. Barnum, F.-G. Rong, R.F. Barth, I.M. Codogni, and J.G. Wilson. Chem. Rev. **98**, 1515 (1998).
7. M.F. Hawthorne. Angew. Chem. Int. Ed. Engl. **32**, 950 (1993).
8. R.R. Kane, R.H. Pak, and M.F. Hawthorne. J. Org. Chem. **58**, 991 (1993).
9. A. Leusch, P.W. Jungblut, and L. Moroder. Synthesis, 305 (1994).
10. O. Leukart, E. Escher, and D. Regoli. Helv. Chim. Acta, **62**, 546 (1979).
11. W. Tjarks. J. Organomet. Chem. **614**, 37 (2000).
12. J. Cai, A.H. Soloway, R.F. Barth, D.M. Adams, J.R. Hariharan, R. Joya, I.M. Wyzlic, and K. Radcliffe. J. Med. Chem. **40**, 3887 (1997).
13. L.F. Tietze and U. Bothe. Chem. Eur. J. **4**, 1179 (1998).
14. L.F. Tietze, U. Bothe, U. Griesbach, M. Nakaichi, T. Hasagawa, H. Nakamura, and Y. Yamamoto. Bioorg. Med. Chem. **9**, 1747 (2001).
15. L.F. Tietze, U. Bothe, U. Griesbach, M. Nakaichi, T. Hasagawa, H. Nakamura, and Y. Yamamoto. ChemBioChem, **2**, 326 (2001).
16. J.L. Maurer, A.J. Serino, and M.F. Hawthorne. Organometallics, **7**, 2519 (1988).
17. L.F. Tietze, U. Bothe, and I. Schuberth. Chem. Eur. J. **6**, 836 (2000).
18. G.B. Giovenzana, L. Lay, D. Monti, G. Palmisano, and L. Panza. Tetrahedron, **55**, 14 123 (1999).
19. G. Srivastava, K.J. Kaur, O. Hindsgaul, and M.M. Palcic. J. Biol. Chem. **267**, 22 356 (1992).
20. C. Hällgren and O. Hindsgaul. J. Carbohydr. Chem. **14**, 453 (1995).
21. A.J. Lunato, J. Wang, J.E. Woollard, A.K.M. Anisuzzaman, W. Ji, F.-G. Rong, S. Ikeda, A.H. Soloway, S. Eriksson, D.H. Ives, T.E. Blue, and W. Tjarks, J. Med. Chem. **42**, 3378 (1999).
22. A.C. Sartorelli and J.A. May. Jr. J. Med. Chem. **22**, 971 (1979).
23. S.B. Kahl, R.A. Kasar, and G.M. Knudsen. Inorg. Chem. **28**, 2936 (1999).
24. T. Uchiyama and O. Hindsgaul. J. Carbohydr. Chem. **17**, 1181 (1998).
25. U.B. Gokhale, O. Hindsgaul, and M.M. Palcic. Can. J. Chem. **68**, 1063 (1990).
26. J.W. Coffey, O.N. Miller, and O.Z. Sellinger. J. Biol. Chem. **239**, 4011 (1964).
27. S.H. Park, I. Pastuszak, R. Drake, and A.D. Elbein. J. Biol. Chem. **273**, 5685 (1998).
28. I. Pastuszak, C. Ketchum, G. Hermanson, E.J. Sjoberg, R. Drake, and A.D. Elbein. J. Biol. Chem. **273**, 30 165 (1998).

© 2002 NRC Canada

The core oligosaccharide component from *Mannheimia (Pasteurella) haemolytica* serotype A1 lipopolysaccharide contains L-*glycero*-D-*manno*- and D-*glycero*-D-*manno*-heptoses: Analysis of the structure and conformation by high-resolution NMR spectroscopy

Jean-Robert Brisson, Ellen Crawford, Dušan Uhrín, Nam Huan Khieu, Malcolm B. Perry, Wayne B. Severn, and James C. Richards

Abstract: Previous studies from our laboratory have indicated that the lipopolysaccharide (LPS) from *Mannheimia haemolytica* serotype A1 contains both L-*glycero*-D-*manno*-heptose and D-*glycero*-D-*manno*-heptose residues. NMR methods making use of 1D ^{1}H selective excitation and 2D (^{1}H, ^{13}C) and (^{1}H, ^{31}P) heteronuclear experiments were used for the structural determination of the major core oligosaccharide components of the deacylated low-molecular-mass LPS obtained following sequential treatment with anhydrous hydrazine and aq KOH. The core oligosaccharide region was found to be composed of a branched octasaccharide linked to the deacylated lipid A moiety via a 3-deoxy-4-phospho-D-*manno*-oct-2-ulosonate residue having the structure,

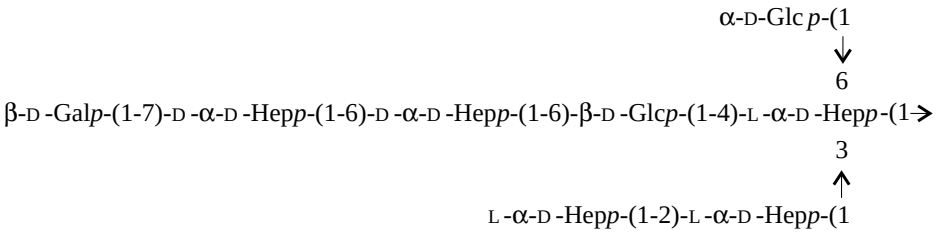

Heterogeneity was found to be present at several linkages. NMR methods were devised to distinguish between the diastereomeric forms of the heptose residues. Synthesized monosaccharides of L-D- and D-D-heptose were used as model compounds for analysis of the ^{1}H and ^{13}C NMR chemical shifts and proton coupling constants. Molecular modeling using a Monte Carlo method for conformational analysis of saccharides was used to determine the conformation of the inner core of the oligosaccharide and to establish the stereochemical relationships between the heptoses.

Key words: LPS, NMR, conformation, oligosaccharide, heptose.

Résumé : Des études antérieures effectuées dans notre laboratoire ont indiqué que le lipopolysaccharide (LPS) obtenu à partir de *Mannheimia haemolytica* sérotype A1 contient des résidus de L-*glycéro*-D-*manno*-heptose ainsi que de D-*glycéro*-D-*manno*-heptose. On a utilisé des méthodes de RMN faisant appel à l'excitation selective du ^{1}H en 1D et à des expériences hétéronucléaires (^{1}H,^{13}C) et (^{1}H,^{31}P) en 2D pour déterminer la structure des composants oligosaccharides principaux du noyau du LPS désacétylé, de faible masse moléculaire, obtenu après un traitement séquentiel avec de l'hydrazine anhydre et du KOH aqueux. On a trouvé que l'oligosaccharide de la région du noyau est formée d'un

Received 10 January 2002. Published on the NRC Research Press Web site at http://canjchem.nrc.ca on 5 August 2002.

Dedicated to the memory of Professor Raymond U. Lemieux who pioneered the applications of NMR spectroscopy for stereochemical and conformational analyses of carbohydrates.

J.-R. Brisson, E. Crawford, N.H. Khieu, M.B. Perry, and J.C. Richards.[1] Institute for Biological Sciences, National Research Council, Ottawa, ON K1A 0R6, Canada.
W.B. Severn. Agricultural Research, Department of Diseases, PO Box 40063, Ward Street, Upper Hutt, New Zealand.
D. Uhrín. University of Edinburgh, Department of Chemistry, West Mains Road, Edinburgh EH9 3JJ, U.K.

[1]Corresponding author (e-mail: jim.richards@nrc.ca).

 DOI: 10.1139/V02-114 © 2002 NRC Canada

oligosaccharide ramifié lié à une portion désacétylée du lipide A par le biais d'un résidu 3-désoxy-4-phospho-D-*manno*-oct-2-ulosonate de structure,

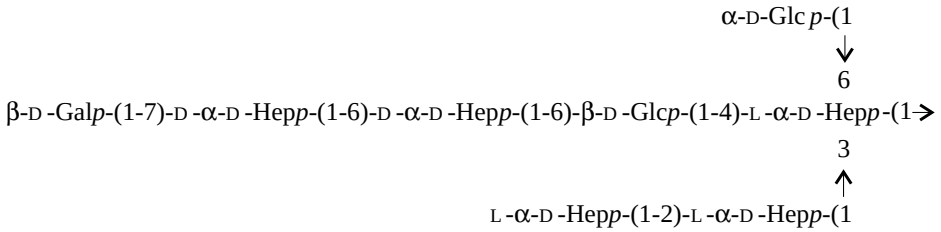

On a observé de l'hétérogénéité à plusieurs points de ramification. On a mis au point des méthodes RMN qui permettent de faire la différence entre les formes diastéréomères des résidus heptoses. On a utilisé des monosaccharides de synthèse de L-D- et D-D-heptoses comme modèles pour l'analyse des déplacements chimiques du ^{1}H et du ^{13}C et des constantes de couplage du proton. On a utilisé la modélisation moléculaire basée sur la méthode de Monte Carlo pour faire l'analyse conformationnelle des saccharides afin déterminer la conformation du noyau de l'oligosaccharide et établir les relations stéréochimiques entre les heptoses.

Mots clés : LPS, RMN, conformation, oligosaccharide, heptose.

[Traduit par la Rédaction]

Introduction

Lipopolysaccharides (LPS) are a complex class of glycolipids that can trigger a cascade of immunological responses in mammals including endotoxic effects and serum antibody production (1). These molecules make up the outer leaflet of the outer membrane of Gram-negative bacteria. LPS has been found to exhibit a common molecular architecture consisting of at least two distinct regions: (*i*) an oligo- or polysaccharide region; and (*ii*) a lipid moiety referred to as lipid A (2). In certain bacteria, the carbohydrate containing region consists of a high-molecular-mass *O*-specific polysaccharide, which is covalently linked to a core oligosaccharide unit (3). Other bacteria, notably *Haemophilus* and *Neisseria s*pp. only produce short-chain LPS, devoid of *O*-polysaccharide chains, in which the carbohydrate region contains mixtures of low-molecular-mass but structurally diverse oligosaccharide components. The saccharide portion of LPS molecules has been found to be linked to the lipid A moieties via the eight-carbon sugar acid, 3-deoxy-D-manno-oct-2-ulosonate (Kdo). The lipid A from several bacterial species has been found (2) to have a relatively conserved structure consisting of a bisphosphorylated β-1,6-linked D-glucosamine (GlcN) disaccharide unit that is substituted by fatty acyl amide and ester groups.

The bacterium *Mannheimia haemolytica* is a new member of the Pasteurellaceae family (4). Originally referred to as *Pasteurella haemolytica*, this group of organisms was classified into two biotypes (designated A and T) which were further subdivided into 17 serotypes (5, 6). This biochemical distinction was based on the ability of the organisms to ferment either arabinose (A-biotype) or trehalose (T-biotype) (7). On the basis of genetic analyses, the *P. haemolytica* biotype T organisms (serotypes T3, T4, T10, and T15) were reclassified as *Pasteurella trehalos* in 1990 (8, 9). More recently the biotype A group of organisms was reclassified into the new genus *Mannheimia* (10). Twelve *M. haemolytica* serotypes are now recognized (A1, A2, A5, A6, A7, A8, A9, A12, A13, A14, A16, and A17). *M. haemolytica* serotype A1 is most frequently associated with bovine pneumonic pasteurellosis (shipping fever), a major cause of sickness and economic loss to the feed lot industry (11, 12). The pathogenesis of diseases caused by *M. haemolytica* in cattle has recently been reviewed (13). Several virulence factors, including a leukotoxin, capsular polysaccharide, and LPS have been identified. *M. haemolytica* LPS has been reported to have a severe damaging effect on bovine endothelial cells (14, 15).

In our laboratory we have undertaken the structural and antigenic characterization of *M. haemolytica* (16, 17) and *P. trehalos* (17–20) LPS to understand the role of these molecules in pathogenesis and protective immunity. Immunochemical studies have revealed that eight of the 12 *M. haemolytica* serotypes can elaborate LPS which contain a common *O*-polysaccharide side chain (17). The structure of the *O*-polysaccharide from serotype A1 is representative and was determined in detail. It consists of a trisaccharide repeating unit having the structure -4)-β-D-Gal*p*-(1–3)-β-D-Gal*p*-(1–3)-β-D-Gal*p*NAc-(1- (16). A detailed structural model for the core oligosaccharide of *M. haemolytica* LPS serotype A1 core oligosaccharide has not been proposed.

Many carbohydrate samples of biological origin are heterogeneous in nature and difficult to separate. To determine their three-dimensional structure, complete NMR assignments are desirable even for heterogeneous products. Only then can conformational analysis (21) be made with the goal of establishing a relationship between three-dimensional structure and biological function (22). Towards this goal, 1D selective NMR methods have been used to determine the structure of mixtures, where the resonances of specific components can be selected to characterize individual components (23–28). 1D selective excitation experiments are analogs of standard 2D and 3D experiments where hard pulses have been replaced by selective pulses. The original phase-cycled experiments (29–42) have more recently been adopted for the use of pulsed-field gradients (43–55). Particularly useful are 1D analogues of 3D experiments (53–55).

© 2002 NRC Canada

Fig. 1. Proton NMR spectrum at 600 MHz of the core oligosaccharide component from *M. haemolytica* serotype A1 LPS in D_2O (300 K, pH 3). The HOD resonance is at 4.756 ppm. Resonances in the anomeric region up from 4.4 ppm are labelled along with the Kdo methylene resonances. The determined structure designated as A1 and nomenclature for the residues are also shown. Heterogeneity due to partial truncation of the backbone oligosaccharide is indicated by dotted arrows at linkage sites. In the text, the minor component for f due to heterogeneity is indicated by f′. Hep_I, Hep_{II}, and Hep_{III} are L-D-heptose while Hep_{IV} and Hep_V are D-D-heptoses. Other residues have the D-configuration.

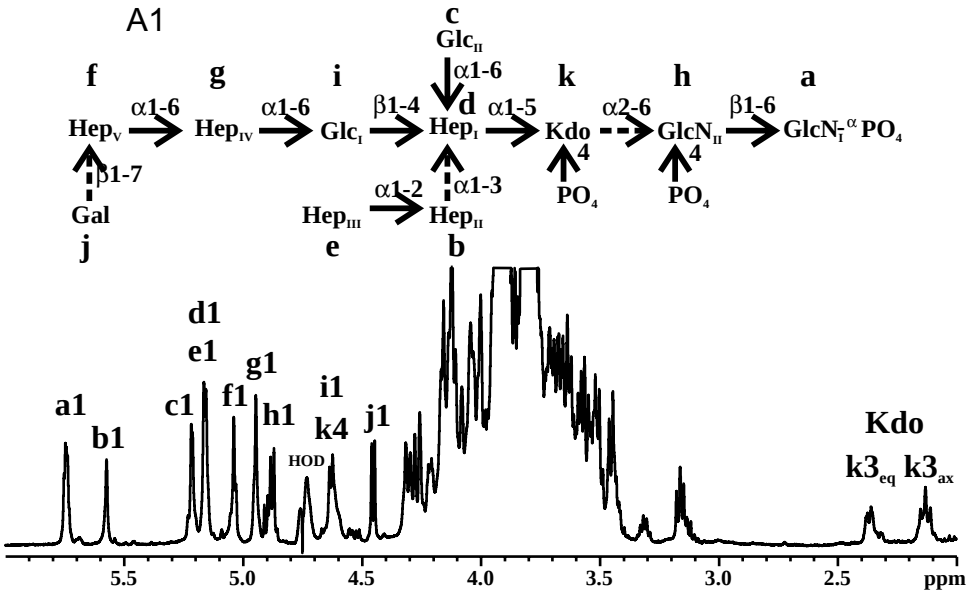

An advantage of 1D selective methods is that the multiplet pattern for each resonance in the 1D selective experiments can be clearly observed due to the same digital resolution as a 1D ^1H spectrum. Also, 1D selective experiments are sometimes preferable to 2D methods for the structural analysis of oligosaccharides as was recently demonstrated in the characterization of some enzymatically synthesized oligosaccharides (56, 57). Also, with selective experiments, incursion in the ring region of carbohydrates is possible. The 1D TOCSY-NOESY permits the isolation of spin systems of interests and the detection of NOEs from proton resonances within the ring allowing NOE constraints to be obtained which cannot be otherwise determined from 2D experiments (58, 59). Recently several reviews have dealt with carbohydrate structural determination by NMR spectroscopy (60–64).

Preliminary studies by chemical, ^1H NMR, and mass spectrometric (MS)-based methods have indicated that the LPS core region of *M. haemolytica* A1 has the composition $Hex_{2-3}Hep_5Kdo$. The Hex_2Hep_5Kdo species is the major core oligosaccharide component in the *O*-chain deficient serotype A8 LPS (17). Analyses of the LPS from these serotypes indicate the core oligosaccharide to contain D-glucose, D-galactose and both L-glycero-D-manno-heptose (L-D-heptose) and D-glycero-D-manno-heptose (D-D-heptose) residues. In the present investigation the structure of the core oligosaccharide of *M. haemolytica* serotype A1 LPS was determined in detail. The sequence, linkage positions, and relative stereochemistries of the heptose-containing oligosaccharide were established by NMR spectroscopic techniques. On the basis of NMR analyses and Monte Carlo calculations a conformational model is now proposed for the core oligosaccharide region of the LPS.

Results and discussion

Our previous analysis of the LPS of *M. haemolytica* serotype A1 revealed Hex_3Hep_5Kdo as the major core oligosaccharide component. This was determined by 1D ^1H NMR and FAB-MS analysis of the oligosaccharide fraction obtained following mild acid hydrolysis (1% HOAc, 100°C, 3 h) of the LPS sample (17). The core oligosaccharide was found to contain D-glucose, D-galactose, L-D-heptose, and D-D-heptose in a molar ratio of 2:1:3:2 in the major fraction as determined by GLC–MS analysis of their alditol acetate and 2-butyl glycoside derivatives. The D-Gal residue was found to be a terminal nonreducing moiety from methylation analysis and was absent in the minor component of the core oligosaccharide fraction, that had the composition of Hex_2Hep_5Kdo. The occurrence of Kdo in the LPS was established by colorimetric analysis.

Treatment of *M. haemolytica* LPS with anhydrous hydrazine followed by strong alkali afforded water-soluble, deacylated LPS oligosaccharides. The deacylated LPS sample was representative of the intact backbone oligosaccharide of the native material containing core and lipid A oligosaccharide moieties. This was confirmed by electrospray ionization ESI-MS which gave molecular ions corresponding to $Hex_3Hep_5Kdo_1HexN_2(H_2PO_3)_3$ as the major oligosaccharide component (see *Experimental section*).

From the proton spectrum (Fig. 1) and HMQC and COSY spectra (Fig. 2), 10 anomeric ^1H NMR resonances were observed, as well as methylene proton resonances. The anomeric resonances were labeled a–j in decreasing order of their ^1H NMR chemical shifts and $k3_{eq}$ and $k3_{ax}$ assigned to the methylene protons of Kdo. The integral for the b1 and de1 and j1 anomeric peaks were 40% less than those for the

© 2002 NRC Canada

Fig. 2. 2D NMR experiments for A1 showing the HMQC spectrum of the anomeric region (*a*), and the COSY (*b*) and NOESY (*c*) spectra of the anomeric and ring region. The arrow indicates the position of the b2 resonance observed near k5.

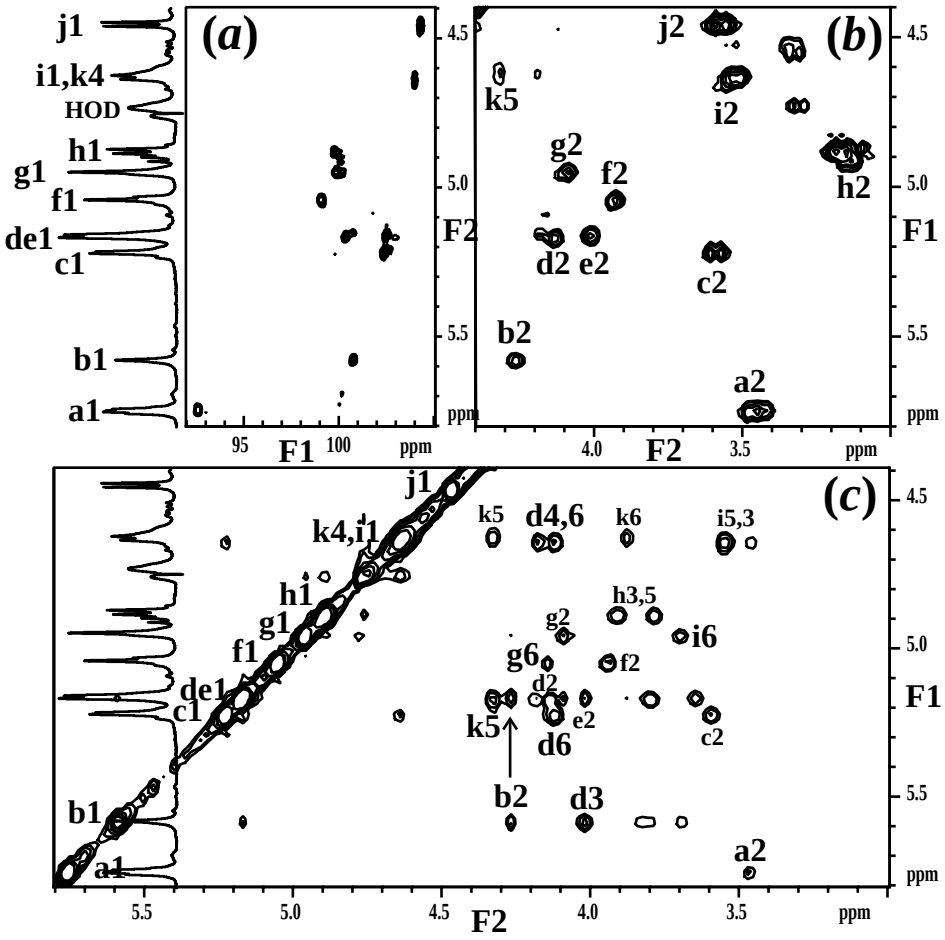

other anomeric resonances confirming heterogeneity in the sample. There was also some heterogeneity at h1 with the appearance of a downfield doublet at 4.91 ppm near h1.

Standard homo- and hetero-nuclear 2D-NMR analyses was undertaken. From the COSY spectrum in Fig. 2, the H-2 resonances could be located. It was realized that for residues **b**, **d**, **e**, **f**, and g, $J_{1,2}$ was small, typical of *manno*-heptoses, and that a 2D-TOCSY could not be used to transfer magnetization from H-1 past H-2. From the HMQC spectrum in Fig. 3, the H-2 of the heptose residues overlapped with other resonances making 2D-TOCSY difficult to analyze for these residues. The 2D-NOESY spectrum also showed an unusually high number of NOEs especially for the b1, de1 resonances. Also, there was overlap of several resonances in the anomeric region. Hence, due to the complexity of the spectra and heterogeneity of the sample, 1D selective methods were used to extract spectral parameters that could not be obtained using standard 2D methods, thus permitting the resolution of the structure and conformational analysis. HMQC-TOCSY and HMBC experiments were also very important in determining the complete assignments, especially for the heptose units. Using this approach, the complete assignment for the ^{1}H and ^{13}C NMR chemical shifts for the major backbone oligosaccharide (A1) was possible (Table 1).

The Kdo-$GlcN_{II}$-$GlcN_{I}$ sequence and partial assignments are known from previous studies (65) and are consistent with the assignments made here. The 1D-TOCSYs for residues **a** and **h** permitted assignment of the resonances and measurement of proton coupling constants (Fig. 4*a*, 4*b*). Location of phosphate groups was confirmed from a ^{31}P HMQC experiment as done previously (65). Assignment of the ^{13}C NMR chemical shifts was then made from HMQC, HMQC-TOCSY, and HMBC spectra. This information led to the definition of residues **a** and **h** as the α-D-GlcN and β-D-GlcN pyranosyl units of the lipid A moiety. Most of the proton, ^{31}P and ^{13}C NMR chemical shifts were similar to those previously reported in a similar structural element (65). In the 1D-TOCSY for h1, the h′5 peak at 3.62 ppm is due to hydrolysis of the Kdo-(2-6)-β-D-$GlcN_{II}$ glycosidic linkage. After several months in solution, the linkage was completely hydrolyzed with h′6 and h′6 appearing at 3.82 and 3.92 ppm, respectively. The sharp anomeric signal at 3.91 ppm was also found to be due to h′1 of this disaccharide.

For Kdo, the H-4 and H-5 resonances were assigned from 1D-TOCSY experiments with selective excitation of H-3_{eq} or H-3_{ax}. The H-4 resonance is shifted downfield due to a phosphate group at C-4, confirmed by a ^{31}P HMQC. A small $J_{5,6} < 1$ Hz impeded the TOCSY transfer past H-5 (Fig. 4*c*). However, a strong NOE is observed between k4 and k6 in Fig. 2*c* in accord with the X-ray structure of Kdo (66). 1D NOESY-TOCSY(k4, k6) was used to complete the assignment

© 2002 NRC Canada

Fig. 3. Selected plots from the heteronuclear ^{1}H-^{13}C 2D NMR spectra of A1. (*a*) In the HMQC spectrum of the ring region some assignments are labelled where possible. (*b*) In the HMQC-TOCSY spectrum, the C7-H7s-C6-H6, C4-H4-C5-H5 TOCSY correlations and those for b2 are labelled. (*c*) In the HMBC spectrum, the H1-C1-O1-C*x* inter-glycosidic correlations are shown for the anomeric proton resonances along with their intra-residue correlations.

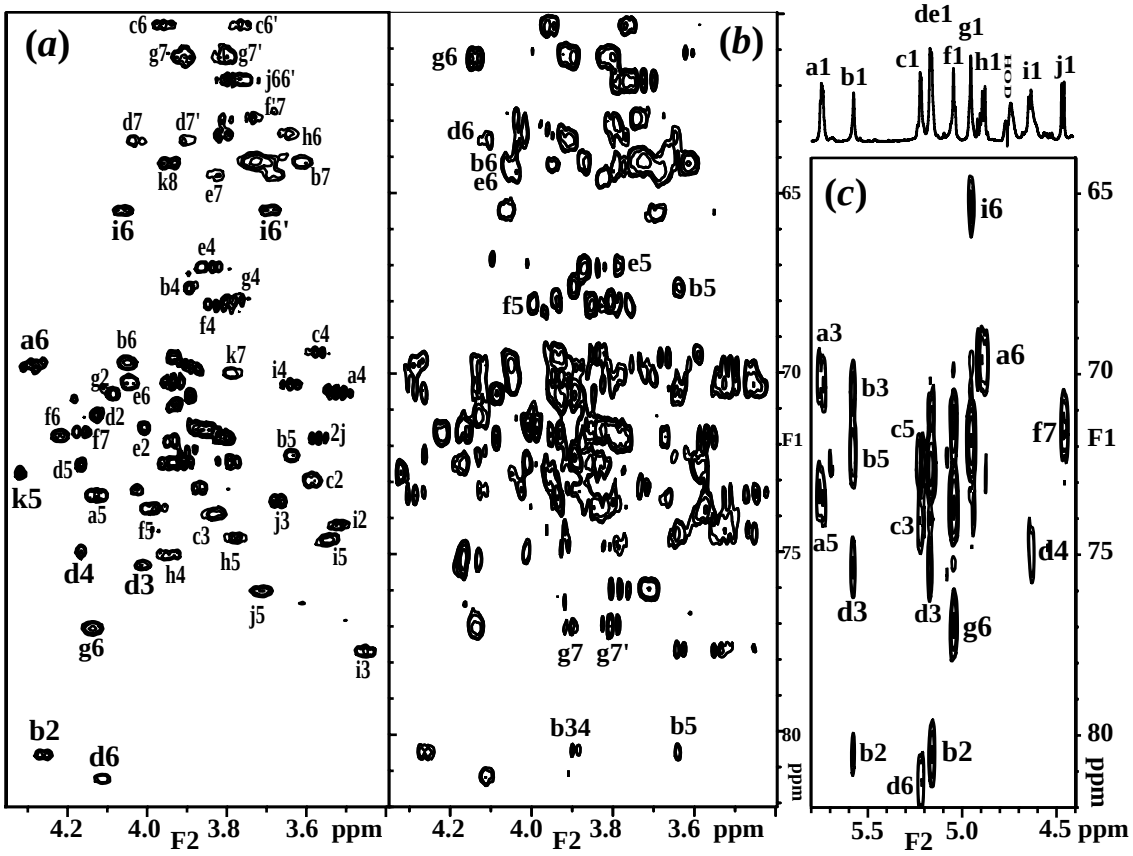

(Fig. 4*d*). As shown later, for the HepI-(1-5)-Kdo linkage, the d1-k7 NOE was also observed, typical of a substitution at C-5 of Kdo (67). Using this NOE, the Kdo resonances detected from the 1D-NOESY-TOCSY (de1, k7) (Fig. 4*e*) had the same chemical shifts and similar multiplet patterns as those found in the previous experiment, thus confirming the Kdo ^{1}H NMR assignments. The ^{13}C NMR assignments for Kdo where then obtained from the HMQC spectrum and confirmed from the HMQC-TOCSY spectrum.

Residue **i** was determined to be 6-substituted β-D-glucose denoted as Glc_I. The anomeric resonance for residue **i** overlapped with the H-4 resonance of Kdo. In the 1D-TOCSY for these two overlapping resonances, it was possible to distinguish the resonances for residue **i** because of the small $J_{5,6}$ coupling constant for Kdo (Fig. 4*c*). All resonances up to H-6s could be detected and coupling constants of the multiplets could be measured. Due to its β-D configuration the i1-i3 and i1-i5 NOE were also observed in the NOESY spectrum (Fig. 2 and Fig. 5*f*). ^{13}C NMR assignments for Glc_I were then obtained from the HMQC spectrum and confirmed with the HMQC-TOCSY spectrum. From a comparison with chemical shifts of terminal glucose (68, 69), a glycosidation down-field shift of 3.7 ppm was observed for the C-6 resonance, indicating its substitution at that position. A substantial shift of –2.2 ppm was also observed for C-5. The rotamer distribution about the C-5—C-6 bond could be determined from the H-5 multiplet observed for the i1-i5 NOE in Fig. 5*f*. It was apparent that both $J_{5,6}$ and $J_{5,6'}$ had small values <2 Hz since the H-5 multiple appeared as a doublet dominated by the large $J_{4,5}$ coupling of 10 Hz. This showed that both H-6 and H-6′ were gauche to H-5 with the O6-C6-C5-O5 = –60° rotamer being preferred in solution.

Residue **c** was determined to be a terminal α-D-glucose denoted as Glc_{II}. From the 1D-TOCSY for c1 (Fig. 4*f*) resonances up to H-5 were detected, indicating that residue **c** was an α-glucose based on the measured proton coupling constants. From the HMQC spectra and comparison with chemical shifts of terminal glucose model compounds (68, 69), all the ^{1}H and ^{13}C NMR assignments could be completed.

The terminal galactose, residue **j**, denoted as Gal, was identified from the 1D-TOCSY of j1 and resonances up to H-4 were observed (Fig. 4*j*). To get past the small $J_{4,5}$ coupling constants and identify H-5, the 1D-TOCSY-NOESY (j1, j4) was done (Fig. 4*h*). From the HMQC spectra and comparison with chemical shifts of terminal galactose model compounds (68, 69), all the ^{1}H and ^{13}C NMR assignments were completed.

To assign the heptose residues, model compounds were synthesized to obtain accurate ^{1}H and ^{13}C NMR chemical shifts and $J_{H,H}$ values. These were crucial in assigning the terminal heptose units by chemical shifts comparisons. Also,

© 2002 NRC Canada

Table 1. NMR chemical shifts (ppm) of the core oligosaccharide component from *Mannheimia* (*Pasteurella) haemolytica* serotype A1 LPS.

Residue	δ_C δ_H	C-1 H-1	C-2 H-2	C-3 H-3 H-3′	C-4 H-4	C-5 H-5	C-6 H-6 H-6′	C-7 H-7 H-7′	C-8 H-8 H-8′
Hep_I		100.3	71.1	75.3	74.9	72.5	81.2	63.5	
D		5.17	4.13	4.01	4.17	4.17	4.11	4.02	
								3.89	
Hep_{II}		100.7	80.5	70.6	67.6	72.2	69.6	64.1	
B		5.57	4.26	3.89	3.90	3.64	4.05	3.70	
								3.60	
Hep_{III}		102.5	71.5	71.5	67.0	72.4	70.2	64.5	
E		5.16	4.01	3.87	3.83	3.78	4.04	3.83	
								3.68	
Hep_{IV}		99.8	70.5	71.7	67.9	71.8	77.0	61.2	
G		4.95	4.08	3.81	3.78	3.94	4.14	3.91	
								3.80	
Hep_V		99.0	70.8	71.5	68.1	73.7	71.7	71.6	
F		5.04	3.93	3.85	3.82	3.99	4.22	4.16	
								3.85	
Hep_V		99.0	70.8	71.5	68.3	73.7	72.8	62.9	
f′		5.04	3.93	3.85	3.77	3.97	4.05	3.79	
								3.73	
Glc_I		104.0	74.2	77.7	70.2	74.6	65.5		
I		4.64	3.51	3.45	3.64	3.54	4.06		
							3.69		
Glc_{II}		102.4	72.9	73.9	69.3	72.4	60.3		
C		5.22	3.58	3.83	3.58	3.95	3.96		
							3.76		
Gal		104.3	71.7	73.5	69.5	76.0	61.8		
J		4.46	3.56	3.67	3.93	3.71	3.80		
							3.76		
$GlcN_I$		92.6	54.8	70.2	70.5	73.4	69.7		
A		5.75	3.45	3.93	3.51	4.13	4.28		
							3.89		
$GlcN_{II}$		99.7	56.3	72.2	75.0	74.6	63.4		
H		4.88	3.17	3.90	3.94	3.78	3.81		
							3.64		
Kdo			99.7	34.5	70.8	72.7	73.2	69.9	64.2
K				2.37	4.61	4.32	3.87	3.78	3.94
				2.13					3.73

Note: Measured at 600 MHz (^1H) in D_2O, 25°C and pH 3 from HMQC and HMBC data with the CH_3 signal of external acetone set at 2.225 ppm for ^1H NMR and 31.07 ppm for ^{13}C NMR. Average error of ±0.2 ppm for δ_C and ±0.02 ppm for δ_H. The minor component for f due to heterogeneity is indicated by f′. The CH_2 spin systems, (H, H′), are in decreasing order of chemical shifts. For Kdo, H-3 and H-3′ are assigned to H-3_{eq} and H-3_{ax}.

upon glycosidation, the ^{13}C NMR resonance of the substituted carbon experiences a substantial down-field glycosidation shift (56, 57). The proton spectra for D-D-heptose and D-L-heptose are shown in Fig. 6. In solution both the α and β forms are present for each compound. Their ^1H NMR spectra were assigned using 1D-TOCSY experiments. To obtain accurate coupling constants and chemical shifts, spin simulations of the proton spectra were done. The simulated spectra are shown in Fig. 6. The simulated spectra reproduced exactly the observed spectra, especially the strong coupling for H-3-H- in D-α-L-heptose (Fig. 6*b*). ^{13}C NMR chemical shifts were assigned using HMQC. The NMR data for the heptose monosaccharides are given in Table 2. The chemical shifts for L-D-heptose are the same as those of D-L-heptose since they are enantiomers of each other.

Residues **b**, **d**, **e**, **f**, and **g** in A1 were identified as heptoses from their narrow anomeric resonance due to the small $J_{1,2}$ coupling and lack of transfer of magnetization beyond H-2 from H-1 in a TOCSY experiment. All the heptoses in A1 had the α-D configuration since the only intra-residue NOE from H-1 was to H-2 (Fig. 2). 1D-TOCSY-TOCSY (H-1, H-2) was used to assign all the heptose residues. The first TOCSY step from H-1 transfers the magnetization to H-2 and further transfer is impeded due to the small $J_{1,2}$ value of 1.8 Hz. However, the second step at H-2 will transfer the magnetization further to higher spins due to the larger $J_{2,3}$ value of 3 Hz. However, for L-D-heptose, transfer of magnetization stops at H-5 due to the small $J_{5,6}$ value of 1.6 Hz. For D-D-heptose, transfer of magnetization is less impeded due to a large $J_{5,6}$ value of 3.2 Hz. However, relaxation

© 2002 NRC Canada

Fig. 4. 1D selective experiments for assignment of the non heptose residues in A1. (*a*) 1D TOCSY (a1, 180 ms); (*b*) 1D TOCSY (h1, 180 ms); (*c*) 1D TOCSY (i1 k4, 180 ms); (*d*) 1D NOESY-TOCSY (i1 k4, 400 ms; k6, 180 ms); (*e*) 1D NOESY-TOCSY (de1, 400 ms; g3 k7, 180 ms); (*f*) 1D TOCSY (c1, 180 ms); (*g*) 1D TOCSY (j1, 180 ms); and (*h*) 1D TOCSY-NOESY (j1, 180 ms; j4, 400 ms). Minor components for f and h due to heterogeneity are indicated by f′ and h′, respectively. The resonance for the first selective step is underlined and the one for second selection step is doubly underlined, where applicable. Selected resonances in the anomeric region are indicated on the left of the spectra.

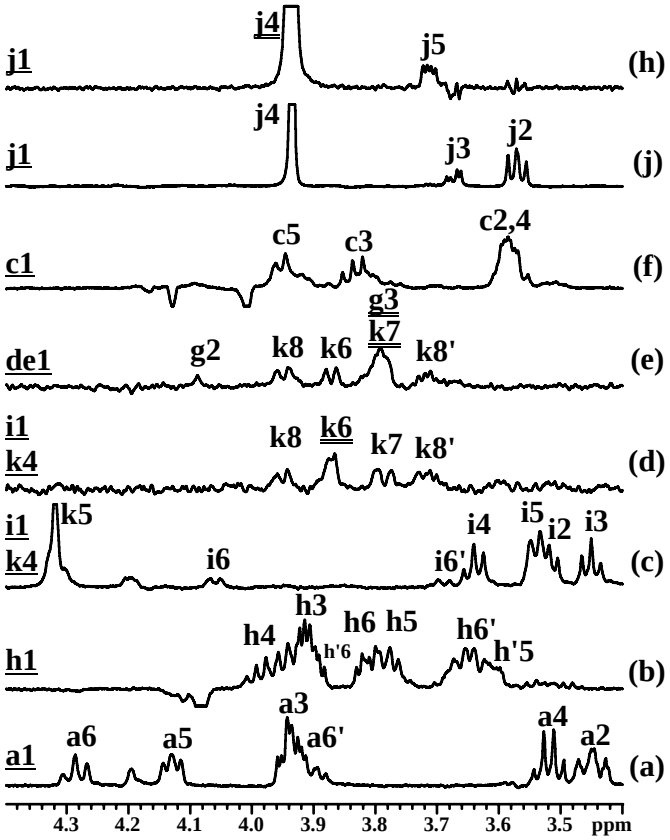

effects can also impede transfer of magnetization and one cannot use a lack of transfer beyond H-5 as proof of L-D-heptose identification.

Residue **b** was determined to be the 2-substituted L-α-D-heptose denoted as Hep_{II}. The 1D-TOCSY-TOCSY (b1, b2) identified resonances at 3.64 ppm and 3.9 ppm (Fig. 7*a*). The multiplet pattern at 3.64 ppm was indicative of a H-5 resonance while those at 3.9 ppm were similar to the strongly coupled H-3 and H-4 resonances observed in the monosaccharide (Fig. 6*b*). To identify H-6 a 1D-TOCSY-NOESY (b2, b5) was done (Fig. 7*b*). In the first TOCSY step for b2, the a6 resonance was also irradiated but the second step only selected the b5 resonance. NOEs from b2 were observed on b3 and b6 along with an inter-residue NOE on d2. Once b6 was located, the HMQC-TOCSY from the C-7-H-7s-C-6-H-6 was used to assign the H-7 and H-7′ resonances (Fig. 3*b*). Assignments for the other resonances were then obtained from the HMQC spectrum and confirmed from the HMQC-TOCSY and HMBC spectra

Fig. 5. 1D selective experiments to detect dipolar interactions in A1. 1D NOESY spectra of the resonances in the anomeric region with a 200 ms mixing time for b1, c1, de1, f1, g1, i1/k4 and a 1D ROESY (f1, 500 ms) for j1 in (*a*)–(*g*), respectively. The selected anomeric resonances and the linkage are indicated on the left of the spectra.

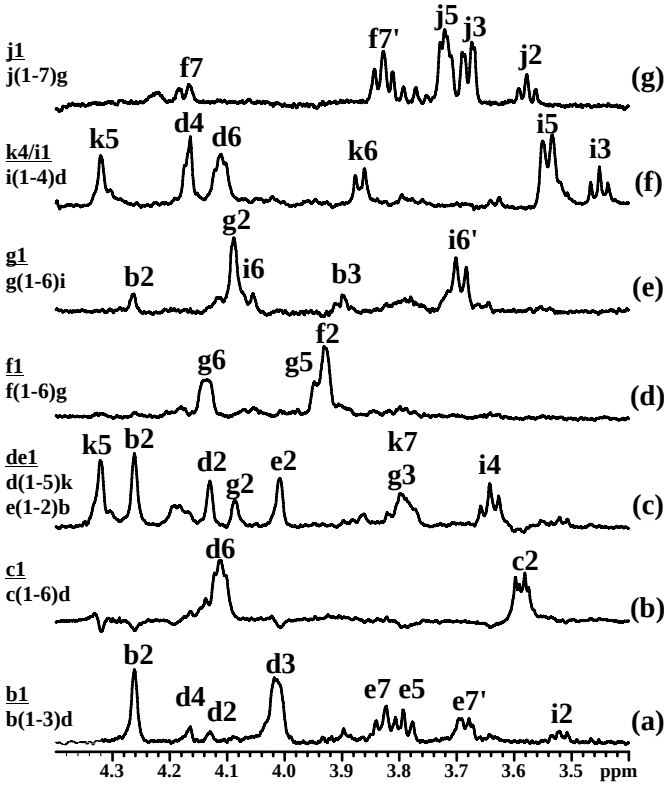

(Fig. 3). Comparison of chemical shifts with those of L-α-D-heptose indicated a 9 ppm down-field shift for C-2 and an up-field shift of –0.8 ppm for C-3 indicative of a substitution at C-2. The C-4 to C-7 chemical shifts were within 0.6 ppm of those of the monosaccharide.

Residue **e** was determined to be a terminal L-α-D-heptose denoted as Hep_{III}. Although the d1 and e1 resonances overlap, this is of no concern since their H-2 resonances did not overlap. The 1D-TOCSY-TOCSY (de1, e2) identified the e3, e4, and e5 spins (Fig. 7*c*). From the b1 NOE in Fig. 5*a*, the e5 resonance was also observed. The high digital resolution of the 1D selective experiments permits accurate matching of resonances between different experiments due to the observation of their multiplet pattern. In Fig. 5*a*, the b1-e7 and b1-e7′ NOEs were also observed. As seen later, these NOEs are due to the close proximity of b1 proton to the e5 and the e7 and e7′ protons. The H-6 resonance was located in the HMQC-TOCSY from C-7-H-7s-C-6-H-6. ^{1}H and ^{13}C NMR assignments were completed with HMQC and HMQC-TOCSY. ^{1}H and ^{13}C NMR chemical shifts of residue **e** were similar to those of L-α-D-heptose.

Residue **d** was identified as a 3,4,6-trisubstituted L-α-D-heptose denoted as Hep_{I}. The 1D-TOCSY-TOCSY (de1, d2) identified a narrow multiplet at 4.17 and a broader one at 4.01 ppm (Fig. 7*d*). The multiplets at 4.01 ppm and 4.17 ppm (d2) were also observed in the 1D-NOESY for b1 (Fig. 5*a*). The resonance at 4.17 ppm was also observed in

© 2002 NRC Canada

Table 2. NMR data for D-L-heptose and D-D heptose monosaccharides.

	δ_C	C-1	C-2	C-3	C-4	C-5	C-6	C-7	
	δ_H	H-1	H-2	H-3	H-4	H-5	H-6	H-7	H-7′
Heptose	$J_{H,H}$	$J_{1,2}$	$J_{2,3}$	$J_{3,4}$	$J_{4,5}$	$J_{5,6}$	$J_{6,7}$	$J_{6,7'}$	$J_{7,7'}$
D-α-L-		95.00[a]	71.45	71.36	67.05	71.81	69.63	63.84	
		5.166	3.914	3.838	3.845	3.749	4.024	3.689	3.652
		1.8	3.1	10.0	9.7	1.6	7.3	5.5	–11.7
D-β-L-		94.74[b]	72.02	74.09	66.69	75.43	69.53	63.57	
		4.866	3.927	3.649	3.788	3.329	3.98	3.713	3.695
		1.0	3.2	10.0	9.8	1.8	7.5	5.8	–11.7
D-α-D-		94.86[a]	71.32	71.38	68.35	73.42	72.72	62.75	
		5.151	3.905	3.812	3.756	3.865	4.018	3.797	3.708
		1.8	3.4	9.4	10.1	3.2	3.3	7.6	–12.0
D-β-D-		94.79[b]	71.84	74.11	68.16	77.22	72.623	62.58	
		4.851	3.921	3.622	3.682	3.423	4.025	3.788	3.725
		1.1	3.3	9.5	9.9	3.3	3.4	7.4	–12.0

Note: Measured at 600 MHz (^{1}H) in D_2O at 25°C from ^{1}H spin simulations and from the ^{13}C spectra (150 MHz) with the CH_3 signal of acetone set at 2.225 ppm for ^{1}H NMR and 31.07 ppm for ^{13}C NMR. δ_C and δ_H are in ppm with an average error of ±0.005 ppm for δ_C and ±0.003 ppm for δ_H. $J_{H,H}$ values are in Hz with an average error of ±0.2 Hz. H-7 and H-7′ are in decreasing g order of chemical shifts.
[a] $J_{C1,H1}$ = 171 ± 1 Hz.
[b] $J_{C1,H1}$ = 160 ± 1 Hz measured from the undecoupled ^{13}C NMR spectrum.

Fig. 6. Proton spectra of heptose monosaccharides. Resolution enhanced spectrum of D-L-heptose at 600 MHz in D_2O, 300 K (*a*) and its simulated spectrum for the α (*b*) and β forms (*c*). Resolution enhanced spectrum of D-D-heptose at 600 MHz in D_2O, 300 K (*d*) and its spin simulated spectra for the α (*e*) and β forms (*f*). The anomerics and H-5β resonances are not shown. Note that strong coupling for the H-3, H-4 and virtual coupling for H-5 resonances are reproduced correctly for (*b*).

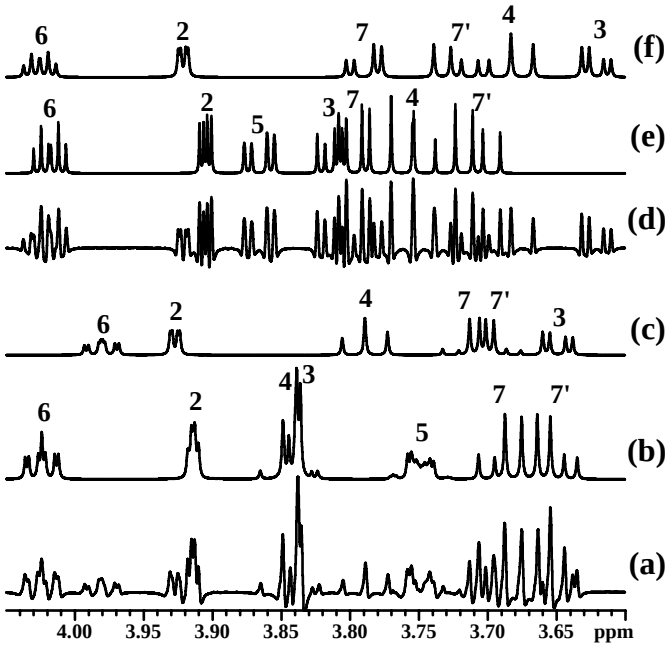

the 1D-NOESY for i1 (Fig. 5*f*). In the HMQC spectrum two narrow crosspeaks at (δc, δh) (74.9, 4.17), (72.5, 4.17) and a broader one at (75.3, 4.01) were identified. HMQC-TOCSY correlations were also observed between these crosspeaks. From a comparison of the ^{13}C NMR chemical shifts with those of the α-D-heptopyranoses in Table 2, it was obvious that the crosspeaks at (74.9, 4.17) and (75.3, 4.01) were subject to a ^{13}C NMR down-field glycosidation shift. Since these three crosspeaks are from d3, d4, or d5, only the d5 crosspeak will not experience a large glycosidation shift since substitutions on heptose cannot occur at C-5. Hence, the crosspeak at (72.5, 4.17) was assigned to (C-5, H-5). The crosspeak at (75.3, 4.01) was assigned to (C-3, H-3) based on the HMBC (d3, d1) and (d3, b1) correlations. The crosspeak at (74.9, 4.01) was thus assigned as (d4, d1), consistent with the observation of the HMBC (d4, i1) correlation and (i1, d4) NOE (Fig. 3 and Fig. 5*f*). The d6 resonance was assigned from the 1D-NOESY from i1, since for the Glc_I-(1-4)-Hep_I linkage, a strong NOE to H-6 is also expected only if residue **d** is L-D-heptose. The d6 resonance was also observed for the 1D-NOESY for c1 (Fig. 5*b*). The H-7 and H-7′ resonances were located from the HMQC-TOCSY (C-7, H-6) crosspeak (Fig. 3) and from 1D-NOESY-TOCSY (i1, d6) (not shown). Comparison of chemical shifts with those of L-α-D-heptose indicated a 3.9, 7.9, and 11.6 ppm down-field glycosidation shift for C-3, C-4, and C-6, respectively.

As shown below, there should be a 4,6-disubstituted L-α-D-heptose (**d′**) present due to heterogeneity on the branching heptose (Fig. 1). From the HMQC and COSY spectra for the anomeric region, no separate signal could be observed either for the H-1 or H-2 due to overlap with other resonances. It is suspected that the proton chemical shifts of d′1 were the same as the one for d1, and that d′2 had a similar chemical shift to e2.

Residue **g** was determined to be a 6-substituted D-α-D-heptose denoted as Hep_{IV}. The 1D-TOCSY-TOCSY (g1, g2) identified the g3, g4, and g5 spins (Fig. 7*e*). The multiplet pattern at 3.94 was indicative of a H-5 resonance. To identify H-6, an 1D-TOCSY-NOESY (g2, g5) was acquired (Fig. 7*f*). NOEs from g2 were observed on g3 and g6 along with a putative inter-residue NOE on i6. Once g6 was located, the HMQC-TOCSY from the C-7-H-7s-C-6-H-6 (Fig. 3*b*) and 1D-NOESY-TOCSY (f1, g6) (Fig. 7*g*) were

© 2002 NRC Canada

Fig. 7. 1D selective experiments for assignment of the heptose residues in A1. (*a*) 1D TOCSY-TOCSY (b1, 75 ms; b2, 75 ms) to detect b3, b4 and b5; (*b*) 1D TOCSY-NOESY (b2, 150 ms; b5, 400 ms) to detect the b5-b6 and b5-b3 NOEs. Note also the strong b5-d2 NOE due to the b(1-3)d linkage; (*c*) 1D TOCSY-TOCSY (de1, 75 ms; e2, 75 ms) to detect e3, e4 and e5; (*d*) 1D TOCSY-TOCSY (de1, 75 ms; d2, 75 ms) to detect d3, d4 and d5; (*e*) 1D TOCSY-TOCSY (g1, 90 ms; g2, 150 ms) to detect g3 to g5; (*f*) 1D TOCSY-NOESY (g2, 150 ms; g5, 400 ms) showing the g5-g6 and g5-g3 NOEs and g5-i6 NOE in accord with the g(1-6)i linkage; (*g*) 1D NOESY-TOCSY (f1, 400 ms; g6 180 ms) to detect the g7 resonances from the f1-g6 interglycosidic NOE in accord with the f(1-6)g linkage; (*h*) 1D TOCSY-TOCSY (f1, 90 ms; f2, 150 ms) for detection of f and f′ resonances up to H-6. Note the clear multiplet pattern for f5 and f′5; (*i*) 1D TOCSY (f6, 40 ms) to detect the f7 resonances only due to the short spin lock time. The resonance for the first selective step is underlined and the one for second selection step is doubly underlined, where applicable. Selected resonances in the anomeric region are indicated on the left of the spectra.

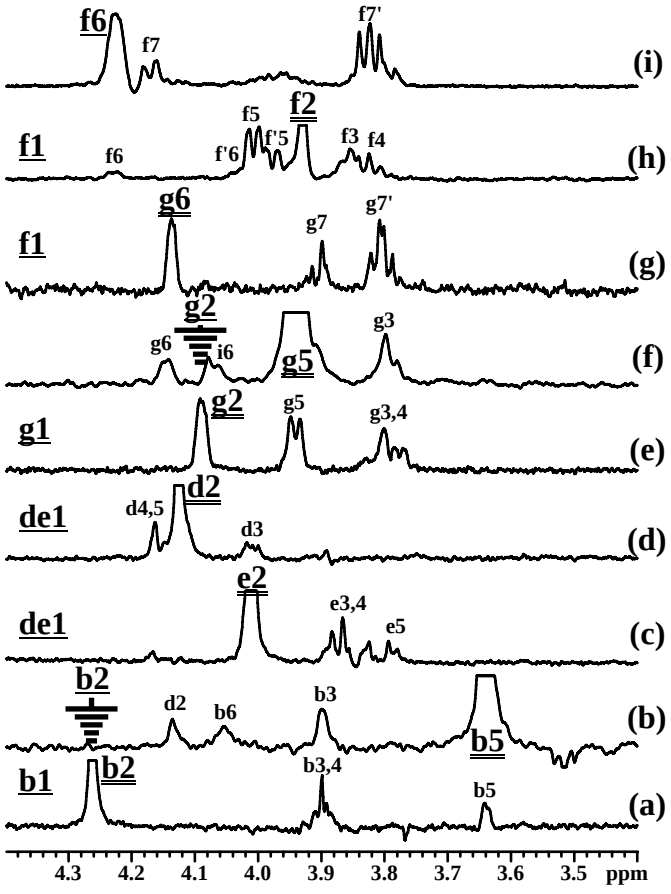

used to assign the H-7 and H-7′ resonances. Assignments for the other resonances were then obtained from the HMQC spectrum and confirmed with the HMQC-TOCSY spectrum (Fig. 3). In the 1D-NOESY (f1), the g6 and g5 resonances were observed (Fig. 5*d*). The NOE f1-g5 NOE can only be possible if residue **g** is a D-D-heptose from molecular modeling studies (see below). Comparison of chemical shifts with those of D-α-D-heptose indicated a 4.3 ppm down-field shift for C-6.

Residue **f** was determined to be a 7-substituted D-α-D-heptose and denoted as Hep_V. The 1D-TOCSY-TOCSY (f1, f2) identified spins up to f6 indicating that residue **f** was a D-D-heptose. The f5 multiplet pattern was quite clear. From a 1D-TOCSY starting on f6, the f7, and f7′ resonances were identified. The ^{13}C NMR assignments were then obtained from the HMQC spectrum and confirmed with the HMQC-TOCSY spectrum. Comparison of chemical shifts with those of α-D-D-heptose indicated a 8.8 ppm down-field shift for C-7. A terminal D-α-D-heptose, denoted **f′**, was only detected due to heterogeneity at this linkage site. As seen in the 1D-TOCSY-TOCSY (f1, f2), the f′5 and f′6 resonance can be detected, along with crosspeaks in the HMQC and HMQC-TOCSY spectra which correspond to those of a terminal D-α-D-heptose similar to those for D-α-D-heptose in Table 2.

The sequence of the core octasaccharide was established from the 1D-NOESY spectrum for the anomeric resonances presented in Fig. 5 and from the HMBC spectrum of the anomeric proton resonances (Fig. 3*c*). Inter-residue NOEs were also observed in 1D-TOCSY-NOESY experiments in Fig. 7*b* and 7*f*. The results are tabulated in Table 3 and the structure shown in Fig. 1. From integration of the anomeric resonances and appearance of new resonances with time, the linkage sites where heterogeneity occurs were determined. The k(2-6)h linkage and the b(1-3)d linkage hydrolyzed over a period of months in solution at pH 3, while the j(1-7)f linkage was stable.

An unusually large number of long-range NOEs were observed spanning up to five sequential residues. For an α-D sugar, the H-1-H-2 intra-residue NOE is expected. For a β-D sugar, the H-1-H-3 and H-1-H-5 intra-residue NOEs are expected. The H-1-C-1-O-1-C-*x*-H-*x* interglycosidic NOEs are expected for (1-*x*) linkage. Inter-residue anomeric NOEs between two linked sugars on the H-*x* ± 1 and H-*x* ± 2 can also occur. Other inter-residue NOEs, not in the vicinity of the glycosidic linkage, are deemed to be long-range NOEs as listed in Table 3.

To explain the large number of long-range NOEs, conformational analysis was done using the Metropolis Monte Carlo (MMC) method to vary the glycosidic linkage angles and sample the multiple conformations of the molecule. Using this method for the inner core oligosaccharide with Kdo at the reducing end, it was found that all the observed long-range NOEs could be explained by the close proximity of the e-b branch to the g-i branch. These long-range NOEs were possible due to restriction of the inner core residues brought about by the three branching points on Hep_I.

A minimum energy conformer obtained from the calculation is shown in Fig. 8. The various interproton distances measured from these coordinates are given in Table 3. As can be observed the occurrence of most NOEs can be explained by the short inter-proton distances. The long-range NOEs for g1-b2 and g1-b3 are not consistent with distances obtained from the molecular model drawn in Fig. 8. Although there is restriction due to the 3,4,6)-Hep_I substitution pattern, there is flexibility about the glycosidic linkage and this must be taken into account. As shown in Fig. 9 for the g1-b2 and g1-b3 distances, multiple conformations having short inter-proton distances are sampled consistent with the observed NOEs. The same situation was applicable for all

© 2002 NRC Canada

Table 3. HMBC and NOE data for A1 and distances from a minimum energy conformer of the core heptasaccharide shown in Fig. 8.

Linkage	HMBC H-1-C-*x*	Intra-residue NOE	*r* (Å)	Inter-residue NOE	*r* (Å)	Long range NOE	*r* (Å)
b(1-3)d	b1-d3	b1-b2	2.6	b1-d3	2.6	b1-e5	3.3
		b5-b3	2.5	b1-d4	3.7	b1-e7	2.9
		b5-b6	2.4	b5-d2	2.3	b1-e7′	2.6
				k3ax-d5	3.2	b1-i2	2.2
c(1-6)d	c1-d6	c1-c2	2.4	c1-d6	2.0	c1-i1	2.4
d(1-5)k		d1-d2	2.6	d1-k5	2.2		
				d1-k7	2.9		
e(1-2)b	e1-b2	e1-e2	2.6	e1-b2	2.1	e1-g2	4.2
				e1-b1	2.8	e1-g3	2.3
						e1-i4	2.0
f(1-6)g[a]	f1-g6	f1-f2	2.6	f1-g6	2.5		
				f1-g5	2.6		
g(1-6)i	g1-i6	g1-g2	2.6	g1-i6	2.6	g1-b2	4.2
		g5-g3	2.6	g1-i6′	2.6	g1-b3	4.9
		g5-g6	2.5	g5-i6	3.0		
i(1-4)d	i1-d4	i1-i3	2.6	i1-d4	2.8	i1-c1	2.4
		i1-i5	2.4	i1-d6	2.1		
j(1-7)f[a]	j1-f7	j1-j2	3.1	j1-f7	2.7		
		j1-j3	2.7	j1-f7′	2.5		
		j1-j5	2.4				

[a]For the j and f residues in the Gal-(1-7)-Hep_V-(1-6)-Hep_{IV} sequence (j-f-g), the average distances from MMC calculations are given.

Fig. 8. Molecular model of a minimum-energy conformer obtained from a MMC calculation of the inner core heptasaccharide of A1. Oxygens are depicted as the larger spheres and hydroxyl protons are removed. Relevant protons are labelled. Note the close proximity of the e-b branch to the g-i branch and the close proximity of the exocyclic chain of residue **e** to the anomeric proton of residue **b** consistent with the long range NOEs observed. Also, note the differences in orientation of the exocyclic chain between L-D heptose (residues **d**, **b**, **e**) and D-D heptose (residue g).

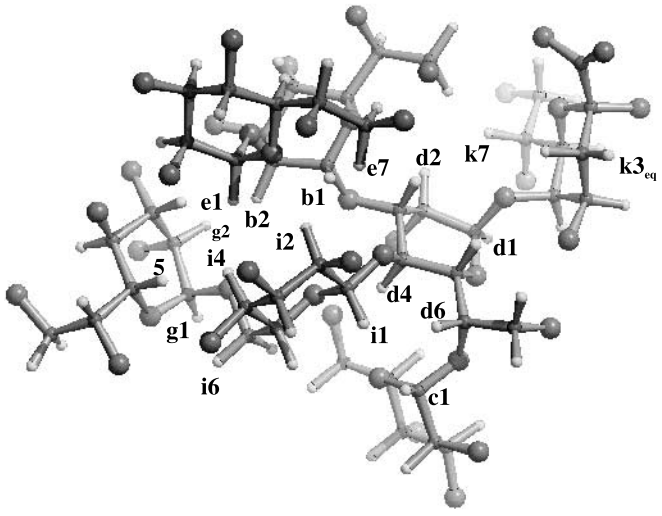

the other long-range and inter-residue NOEs. The long-range NOEs for g1-b2 and g1-b3 and e1-i4 span four residues with mobility about the three glycosidic (ϕ, ψ) angles for a total of 6 df. The long-range NOEs between e1-g2 and e1-g3 that span five residues (e-b-d-i-g) vary even more due to 8 df

Fig. 9. Variation of inter-proton distances (*r*) vs. macro move in a MMC calculation of the inner core heptasaccharide of A1 for b1-e5, b1-e7, e1-i4, e1-g2, g1-b2, g1-b3 in (a)–(g), respectively. Occurrences of interproton distances in the 2–4 Å range are consistent with the observed long range b-e, e-i, and e-g NOEs.

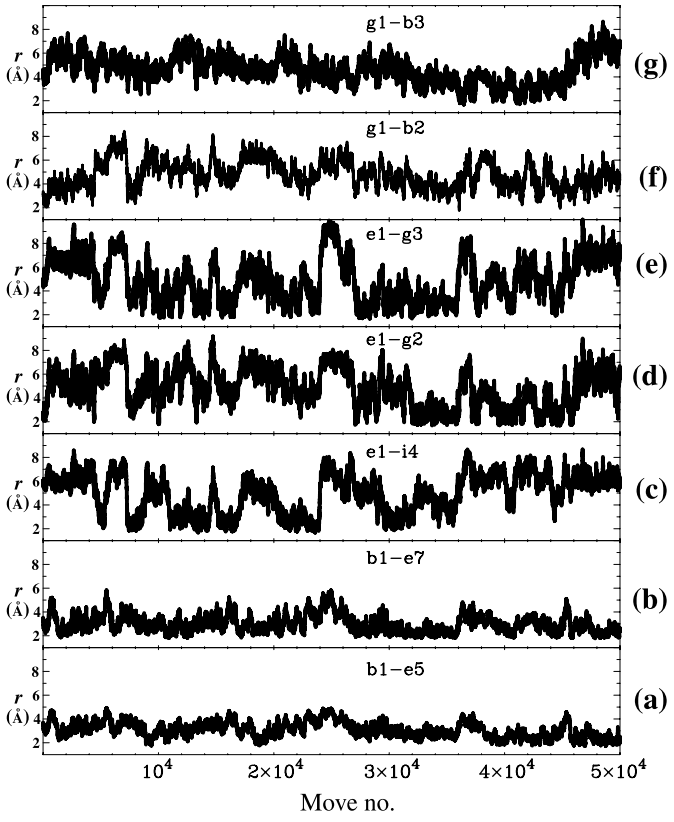

© 2002 NRC Canada

about the glycosidic angles, not counting possible flexibility about the C-5—C-6 bond for the g(1-6)i linkage. The b1-e5, b1-e7, and b1-e7′ are dependent on mobility about the e(1-2)b glycosidic bond and rotation about C-6-C-7 of residue **e**. In all cases, the occurrence of multiple conformations that have short inter-proton distances is consistent with the observed inter-residue and long-range NOEs.

In the present study it was established that the lipid A region of the *M. haemolytica* A1 LPS molecule contains a bis-4,4′-phosphorylated β-1,6 linked D-glucosamine disaccharide moiety. The nature and substitution patterns of the fatty acyl groups attached to this disaccharide have not been reported. The fully acylated LPS molecule makes up the outer most leaflet of the bacterial membrane and is essential for maintaining membrane integrity. The glycose portion of the molecule typically extends out and away from the plane defined by the bacterial membrane. The LPS oligosaccharide portion is important in virulence (70) and is involved in eliciting host immune responses (17). To gain a perspective of the relative sizes and orientation of the core oligosaccharide and membrane-anchoring lipid A regions of this LPS molecule, a molecular model was constructed using the lipid A fatty acid substitution pattern found in a related organism, *Haemophilus influenzae*. This is shown in Fig. 10. The *H. influenzae* lipid A has been reported (71) to have six fatty acyl groups in which the amide group (C-2) and C-3 hydroxyl groups of the reducing glucosamine residue are acylated by 3-hydroxytetradecanoic acid while the C-2′ amide and C-3′ hydroxyl groups of the nonreducing residue are acylated by 3-tetradecanoyloxytetradecanoic acid.[2] As observed in Fig. 10, due to the inner core which provides a fairly rigid structure, the glycose portion projects out from the lipid A moiety which defines the bacterial membrane. More mobility was observed for the terminal residues, especially for the terminal Gal residue. In the NOESY spectrum in Fig. 2, no NOEs for the anomeric resonance were observed consistent with increased mobility of this residue.

The core structures of several LPS have been found to be highly branched (3) and this can result in well-defined conformations for the inner core. In a previous study, the LPS of *Moraxella catharrhalis* was found to adopt an unusual conformation in which a very rare *anti* conformer (72) was observed (73). For a highly branched 3,4,6-trisubstituted D-glucose residue in this LPS molecule, a dihedral angle (C-1′-O-1′-C-4-H-4) near 180° was detected for β-D-Glc*p*-(1–4)-D-Glc*p* linkage to the branched glucose unit.

The results of the present study have provided a detailed picture of the structure of the LPS core oligosaccharide region of *M. haemolytica* serotype A1. We have previously shown that the oligosaccharide region of *M. haemolytica* LPS is immunogenic in mice, sheep, and cattle and that eight of the 12 *M. haemolytica* serotypes (i.e., serotypes A1, A5, A6, A7, A8, A12, A14, and A16) share common core oligosaccharide determinants (17). The core oligosaccharides from serotypes A1 and A8 show almost identical ^{1}H NMR spectra (17) establishing the presence of a common basal structure. Based on the results of the present study it is apparent that the *O*-chain deficient LPS elaborated by *M. haemolytica* serotype A8 lacks the terminal Gal unit in the core oligosaccharide, a residue which possibly provides a site for *O*-chain attachment (16). An understanding of LPS structural differences among *M. haemolytica* serotypes could provide the basis for a vaccine against *M. haemolytica* bovine pasturellosis. Serotype A1 is the principal microorganism responsible for this disease, accounting for 30% of total cattle deaths globally (11). The use of a less virulent serotype or antigens thereof in a vaccine formulation could provide an effective disease management strategy.

Experimental

Preparation of LPS from *M. haemolytica*

Pasteurella (Mannheimia) haemolytica serotype A1 (NRCC 4212) was obtained from the Veterinary Infectious Diseases Organization (VIDO), Saskatoon, SK, Canada. LPS was extracted and purified from fermenter-grown bacteria culture by the hot aqueous phenol method as previously described (16).

Deacylation of LPS to give backbone oligosaccharides

Backbone oligosaccharide was prepared as previously described (74) by modification of the deacylation procedure of Holst et al. (75). Ester-bound fatty acids were removed from the lipid A of the LPS by treatment of a sample (400 mg) with anhydrous hydrazine at ambient temperature (20 mL, 37°C, 30 min). Excess hydrazine was destroyed by addition of acetone (three volumes) to the cooled reaction mixture (0°C). The precipitated *O*-deacylated LPS product was isolated by centrifugation (5000 rpm, 10 min), washed with acetone, and lyophylized from water. Removal of *N*-acyl groups was achieved by heating the *O*-deacylated sample (200 mg) in aq KOH (4 M, 10 mL) at 100°C for 20 h. The reaction mixture was cooled (0°C), neutralized with 4 M HCl, and the precipitated fatty acids removed by centrifugation (12 000 × g, 30 min). The supernatants were filtered in an Amicon concentration cell with a 500-molecular-weight-cutoff membrane (Amicon; YC05) and washed with deionized water until the eluant was free of chloride ions (as determined with aq $AgNO_3$). The dialyzed material was lyophylized to give deacylated LPS (ca. 80 mg). The oligosaccharide was purified by anion-exchange chromatography on DEAE A-25 (74). The backbone oligosaccharide fraction (ca. 50 mg) showed a doubly charged ion at *m*/*z* 1124.8 in the positive ion ESI-MS as the major ion which corresponded to a composition of Hex_3Hep_5 Kdo $HexN_2(H_2PO_3)_3$ (M, 2246.9). MS–MS of the doubly charged ion gave characteristic fragments at *m*/*z* 500 ($HexN_2(H_2PO_3)_2$) and 801 ($KdoHexN_2(H_2\ PO_3)_2$) corresponding to deacylated lipid A and the Kdo-P substituted units, respectively.

D-glycero-L-manno-*Heptose*

The heptose was prepared by the condensation of D-galactose with nitromethane in alkaline methanol (76). The crystalline 1-deoxy-1-nitro-D-*glycero*-L-*manno*-heptitol obtained from the aqueous solution of the deionized products (mp

[2] ES-MS of O-deacylated LPS from *M. heamolytica* serotype A1 is consistant with each glucosamine residue containing an amide-linked 3-hydroxytetradecanoic acid group (data not shown).

© 2002 NRC Canada

Fig. 10. Molecular model of the LPS of *M. haemolytica* A1 constructed using a lipid A having the fatty acyl substitution patterns reported (71) for LPS from *H. influenzae*. The lipid A moiety is colored with the atoms C in black, O in red, and H in white. The sugar moiety is colored with Kdo in gray, heptoses in red or purple, glucose in green, and galactose in blue. The PO_4 groups are yellow. Hydroxyl protons have been removed.

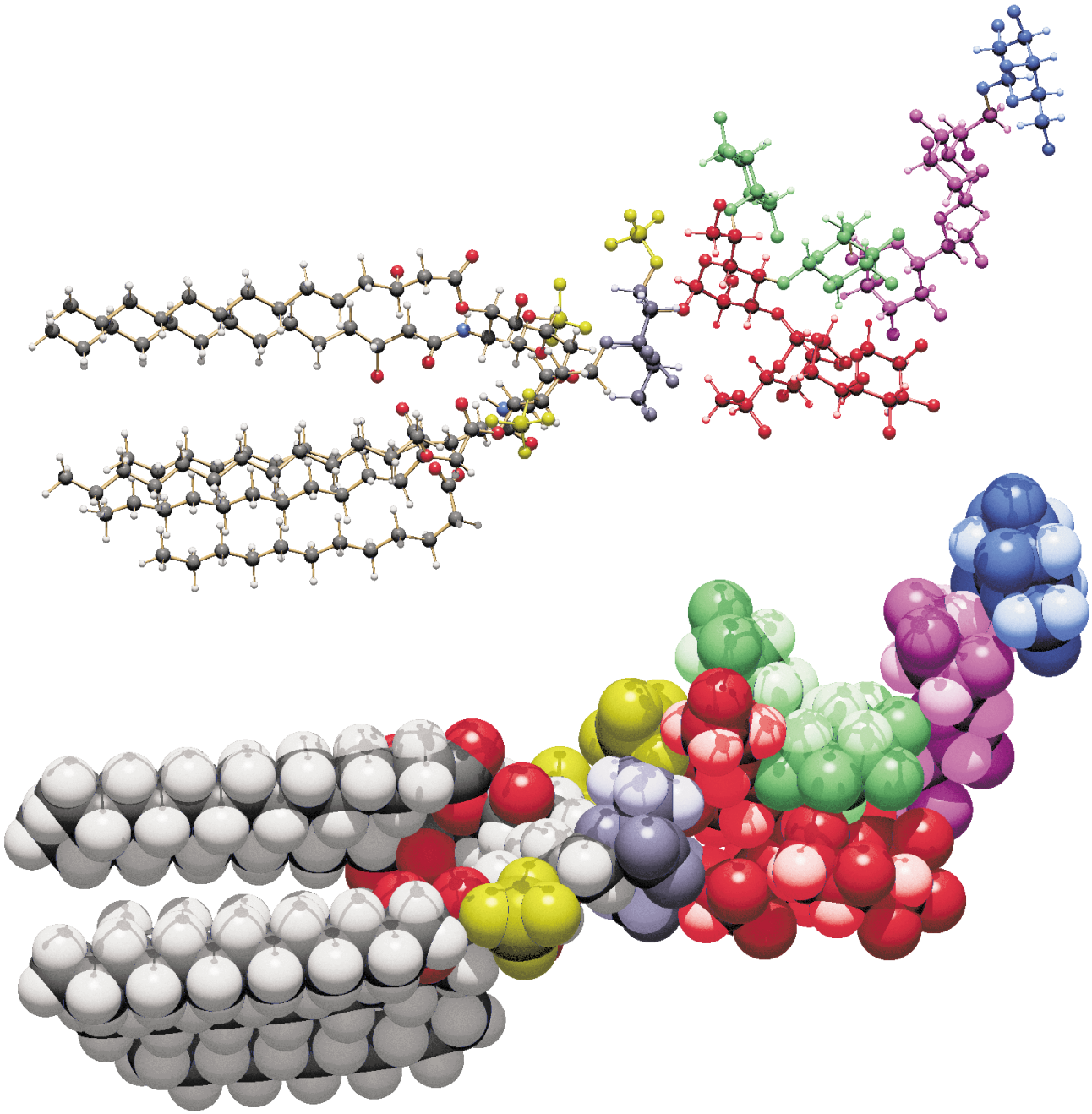

158°C, 21% yield) was converted to its sodium salt. On treatment with dilute sulphuric acid (35°C), followed by deionization with Rexyn 101(H^+) and Amberlite A4(OH^-) ion-exchange resins, the solution was lyophilized to give the heptose as a syrup (80% yield). The product was fractionated by cellulose column chromatography using butan-1-ol–water (1:10 v/v) as the eluant. Fractions containing the heptose were concentrated to dryness under reduced pressure. The D-*glycero*-L-*manno*-heptose having $[\alpha]_D$ –14° (*c* 0.2, water) was pure by paper chromatography and its reduced ($NaBH_4$) and acetylated product on GLC gave a single peak corresponding in retention time with that of authentic hepta-*O*-acetyl-D-*glycero*-L-*manno*-heptitol, establishing its purity.

D-glycero-D-manno-*Heptose*

The heptose was prepared from D-altrose via its condensation with nitromethane to yield 1-deoxy-1-nitro-D-*glycero*-D-*manno*-heptitol (mp 109°C, $[\alpha]_D$ –7.0° (*c* 1.1, EtOH), 27% yield)) whose aqueous sodium salt solution on slow dropwise addition to stirred 20% (v/v) sulfuric acid maintained at 0°C

© 2002 NRC Canada

was converted to D-*glycero*-D-*manno*-heptose (77). The reaction mixture was neutralized with sat. $Ba(OH)_2$ solution, filtered, passed through Rexyn 101(H^+) and Duolite A4(OH^-) ion-exchange resins to remove residual ionic material, and was concentrated to a syrup (92% yield). The heptose product, as indicated by paper chromatography, was contaminated with altrose and unchanged 1-deoxy-1-nitro-D-*glycero*-D-manno-heptitol (ca. 2 to 3%). The product was purified by cellulose column chromatography using butan-1-ol–water (1:10 v/v) as the mobile phase. The D-*glycero*-D-*manno*-mannose had $[\alpha]_D$ +22° (*c* 2, MeOH). A reduced ($NaBH_4$) and acetylated sample on GLC gave a single peak corresponding to authentic hepta-*O*-acetyl-D-*glycero*-D-*manno*-D-heptitol indicating the identity and purity of the synthesized heptose.

Electrospray mass spectrometry

Samples were analyzed on a VG Quattro triple quadrupole mass spectrometer (Micromass, Manchester, U.K.) fitted with an electrospray ion source. Backbone oligosaccharide was dissolved in acetonitrile–water (approx. 1:2 v/v) containing 0.5% acetic acid. Injection volumes were 10 μL and the flow rate was set at 4 mL min^{-1}. The electrospray tip voltage was typically 2.7 kV and the mass spectrometer was scanned from *m*/*z* 50 to 2500 with a scan time of 10 s. For MS–MS experiments, precursor ions were selected using the first quadrupole and fragment ions formed by collisional activation with argon in the RF-only quadrupole cell, were mass analyzed by scanning the third quadrupole. Collision energies were typically 60 ev (laboratory frame of reference).

Nuclear magnetic resonance

NMR spectra were performed on a Bruker AMX 600, AMX 500, or a Varian Inova 600 spectrometer using standard software. All measurements were made at 300 K and at pH 3, containing 10 mg of sample dissolved in 0.6 mL of D_2O. Measurements were done at pH 3 to improve resolution of the proton spectrum as done previously (65). Acetone was used as an internal or external reference at 2.225 ppm for ^1H spectra and 31.07 ppm for ^{13}C spectra. Standard homo- and heteronuclear correlated 2D techniques were used for general assignments of the core oligosaccharide: COSY, TOCSY, NOESY, triple quantum homonuclear correlated experiment, HMQC, HMQC-TOCSY, and HMBC and ^{31}P HMQC (78). Spin simulations for the heptose monosaccharides were performed with standard Varian software. Accurate chemical shifts and coupling constants were obtained from the parameters used to perform the spin simulation and not from the peak listing of the spectra.

Selective 1D-TOCSY, 1D-NOESY, 1D-TOCSY-TOCSY, 1D-TOCSY-NOESY, and 1D-NOESY-TOCSY experiments were performed for complete residue assignment and for determination of inter-residue ^1H-^1H nuclear Overhauser enhancements. The nomenclature used to describe the use of the 1D selective sequences will be 1D EXP (spin, mixing time) and 1D EXP1-EPX2 (spin1, mixing time; spin2, mixing time), where EXP, EXP1, and EXP2 stand for either TOCSY or NOESY. Also, in the figures, the selected resonances are underlined. A doubly underlined resonance means that this resonance was selected as the second selection step. As shown in Fig. 1, all the residues are labeled by letters and the spins are labeled by the atom number, so that a1 refers to the H-1 resonance of residue **a**.

On the AMX spectrometers, selective excitation was achieved by means of half-Gaussian pulses. The mixing time used for a TOCSY depended on the spin system. Usually a range of mixing times (spin lock times) from 30 to 180 ms was used to assign the spin system. The mixing time for a 1D-NOESY depended on the correlation time of the molecule and internal motion about the glycosidic linkage. NOESY mixing times were in the range from 150 to 400 ms. To detect inter-residue NOEs for the terminal Gal residue, a 1D-ROESY experiment was done with a mixing time of 500 ms. For the doubly selective experiments, the selective pulses were kept as short as possible to avoid loss of signal intensity due to relaxation effects. Each part was optimized one at a time. The 1D-TOCSY could be carried out in a matter of minutes. The 1D-NOESY took from minutes to hours depending on the magnitude of the NOE. Some doubly selective experiments took up to 12 h. The 1D-TOCSY-TOCSY and 1D-TOCSY-NOESY were the most efficient. As the sample degraded with time, some experiments were also performed on an Inova 600 spectrometer making use of pulse field gradients.

Molecular modeling

The conformational analysis was done using the Metropolis Monte Carlo method as previously described (79). The PFOS potential was used (80). Minimized coordinates for the monosaccharides were obtained using MM3 (92) available from the Quantum Chemistry Program Exchange (QCPE). The minimum energy conformation for each disaccharide was used as the starting conformation. Starting from the Kdo at the reducing end, calculations were performed for various oligosaccharides up to the complete structure. For the inner core octasaccharide, 5×10^4 macro moves were used with a step length of 5° for the glycosidic linkage and a temperature of 1×10^3 K resulting in an acceptance ratio of 0.36. The molecular model for the inner core octasaccharide was generated using the minimum energy conformer. Distances were extracted from the saved coordinates at each macro move. The complete LPS with lipid A was generated using the lipid A structure (81) and the minimum energy conformer for the Kdo linkage. Molecular drawings were done using Schakal97 from E. Keeler, University of Freiburg, Germany.

Acknowledgements

We thank D.W. Griffith for large-scale production of cells and D. Krajcarski for ESI-MS analyses.

References

1. E.Th. Rietschel, L. Brade, U. Schade, U. Seydel, U. Zähringer, S. Kusmoto, and H. Brade. Bacterial endotoxins: properties and structure of biologically active domains, in surface structures of microorganisms and their interactions with the mammalian host. *In* Proceedings Workshop Conference, Hoechst, Verlag Chemie. *Edited by* E. Schrinner, M.H. Richmond, G. Seibert, and U. Schwarz. Weinheim, Germany. 1988. p. 1.

© 2002 NRC Canada

2. C.R.H. Raetz. Annu. Rev. Biochem. **59**, 129 (1990).
3. O. Holst and H. Brade. Chemical structure of the core region of lipopolysaccharides. *In* Bacterial endotoxic lipopolysaccharides. *Edited by* D.C. Morrison and J.L. Ryan. CRC Press. Boca Raton, Fla. 1992. p. 135.
4. S. Pohl. DNA relatedness among members of *haemophilus, pasteurella* and *actinobacillus. Haemophilus, pasteurella* and *actinobacillus. Edited by* M. Kilian, W. Frederiksen, and E.L. Biberstein. Academic Press. New York. 1981. p. 245.
5. E.L. Biberstein. Biotyping and serotyping of *Pasteurella haemolytica*. *In* Methods in enzymology. *Edited by* T. Bergan and J.R. Norris. Academic Press. New York. 1978. p. 253.
6. M. Younan and L. Fodor. Res. Vet. Sci. **58**, 98 (1995).
7. G.R. Smith. J. Pathol. Bacteriol. **81**, 431 (1961).
8. D.P. Bingham, R. Moore, and A.B. Richards. Am. J. Vet. Res. **51**, 1161 (1990).
9. P.H.A. Sneath and M. Stevens. Nov. Int. J. Syst. Bacteriol. **40**, 148 (1990).
10. O. Angen, M. Quirie, M. Donachie, and M. Bisgaard. Vet. Microbiol. **65**, 283 (1999).
11. D. Griffin. *In* Veterinary clinics of North America: Food animal practice. *Edited by* J. Vestweber and G. St Jean. Philadelphia. 1997. p. 367.
12. W.D.G. Yates. Can. J. Comp. Med. **46**, 225 (1982).
13. A.W. Confer, K.D. Clinkenbeard, and G.L. Murphy. Pathogenesis and virulence of *Pasteurella haemolytica* in cattle: an analysis of current knowledge and future approaches. *In Haemophilus, actinobaccilus* and *pasteurella. Edited by* W. Donachie, F.A. Lainson, and J.C. Hodgson. Plenum Press. New York. 1995. p. 51.
14. M.A. Breider, S. Kumar, and R. Corstvet. Vet. Immuno. Immunopathol. **27**, 337 (1991).
15. D.B. Paulsen, D.A. Mosier, K.D. Clinkenbeard, and A.W. Confer. Am. J. Vet. Res. **50**, 1633 (1989).
16. W.B. Severn and J.C. Richards. Carbohydr. Res. **240**, 277 (1993).
17. R.P. Lacroix, J.R. Duncan, R.P. Jenkins, R.A. Leitch, J.A. Perry, and J.C. Richards. Infect. Immun. **61**, 170 (1993).
18. M.B. Perry and L.A. Babiuk. Can. J. Biochem. Cell Biol. **62**, 108 (1984).
19. R.A. Leitch and J.C. Richards. Can. J. Biochem. Cell Biol. **66**, 1055 (1988).
20. J.C. Richards and R.A. Leitch. Carbohydr. Res. **186**, 275 (1989).
21. R.U. Lemieux and K. Bock. Arch. Biochem. Biophys. **221**, 125 (1983).
22. R.U. Lemieux. Chem. Soc. Rev. **18**, 347 (1989).
23. D.W. Hood, A.D. Cox, M. Gilbert, K. Makepeace, S. Walsh, M.E. Deadman, A. Cody, A. Martin, M. Mansson, E.K. Schweda, J.R. Brisson, J.C. Richards, E.R. Moxon, and W.W. Wakarchuk. Mol. Microbiol. **39**, 341 (2001).
24. E.H. Schweda, J.R. Brisson, G. Alvelius, A. Martin, J.N. Weiser, D.W. Hood, E.R. Moxon, and J.C. Richards. Eur. J. Biochem. **267**, 3902 (2000).
25. I. Sadovskaya, J.R. Brisson, P. Thibault, J.C. Richards, J.S. Lam, and E. Altman. Eur. J. Biochem. **267**, 1640 (2000).
26. J.S. Plested, K. Makepeace, M.P. Jennings, M.A. Gidney, S. Lacelle, J.R. Brisson, A.D. Cox, A. Martin, A.G. Bird, J.C. Tang, J.C. Richards, and E.R. Moxon. Infect. Immun. **67**, 5417 (1999).
27. W.W. Wakarchuk, M. Gilbert, A. Martin, Y. Wu, J.R. Brisson, P. Thibault, and J.C. Richards. Eur. J. Biochem. **254**, 626 (1998).
28. A.D. Cox, M.D. Howard, J.R. Brisson, M. van der Zwan, P. Thibault, M.B. Perry, and T.J. Inzana. Eur. J. Biochem. **253**, 507 (1998).
29. D.G. Davis and A. Bax. J. Am. Chem. Soc. **107**, 9197 (1985).
30. H. Kessler, H. Oschkinat, and C. Griesinger. J. Magn. Reson. **70**, 106 (1986).
31. H. Kessler, U. Anders, G. Gemmecker, and S. Steuernagel. J. Magn. Reson. **85**, 1 (1989).
32. L.D. Hall and T.J. Norwood. J. Magn. Reson. **87**, 331 (1990).
33. J. Friedrich, S. Davies, and R. Freeman. J. Magn. Reson. **80**, 168 (1988).
34. E. Kupce and R. Freeman. J. Magn. Reson. **100**, 208 (1992).
35. X.J. Miao and R. Freeman. J. Magn. Reson. **119**, 145 (1996).
36. R. Bazzo, C.J. Edge, R.A. Dwek, and T.W. Rademacher. J. Magn. Reson. **86**, 199 (1990).
37. D. Boudot, C. Roumestand, F. Toma, and D. Canet. J. Magn. Reson. **90**, 221 (1990).
38. L. Poppe and H. van Halbeek. J. Magn. Reson. **96**, 185 (1992).
39. D. Uhrín, J.R. Brisson, and D.R. Bundle. J. Biomol. NMR, **3**, 367 (1993).
40. S. Holmbeck, P.J. Hajduk, and L. Lerner. J. Magn. Reson. B, **102**, 107 (1993).
41. D. Uhrín, J.R. Brisson, G. Kogan, and H.J. Jennings. J. Magn. Reson. Ser. B, **104**, 289 (1994).
42. K. Zangger and H. Sterk. J. Magn. Reson. **107**, 186 (1995).
43. J. Stonehouse, P. Adell, J. Keeler, and A.J. Shaka. J. Am. Chem. Soc. **116**, 6037 (1994).
44. M.A. Bernstein and L.A. Trimble. Magn. Reson. Chem. **32**, 107 (1994).
45. P. Adell, T. Parella, F. Sanchez-Ferrando, and A. Virgili. J. Magn. Reson. Ser. A, **113**, 124 (1995).
46. C. Dalvit and G. Bovermann. Magn. Reson. Chem. **33**, 156 (1995).
47. T. Facke and S. Berger. J. Magn. Reson. Ser. A, **113**, 257 (1995).
48. C. Dalvit. J. Magn. Reson. **113**, 120 (1995).
49. P. Adell, T. Parella, F. Sanchez-Ferrando, and A. Virgili. J. Magn. Reson. Ser. B, **108**, 77 (1995).
50. T.L. Hwang and A.J. Shaka. J. Magn. Reson. **112**, 275 (1995).
51. K. Stott, J. Stonehouse, J. Keeler, T.L. Hwang, and A.J. Shaka. J. Am. Chem. Soc. **117**, 4199 (1995).
52. G. Xu and J.S. Evans. J. Magn. Reson. Ser. B, **111**, 183 (1996).
53. T. Parella. Magn. Reson. Chem. **34**, 329 (1996).
54. M.J. Gradwell, H. Kogelberg, and T.A. Frankiel. J. Magn. Reson. Ser. B, **124**, 267 (1997).
55. D. Uhrín and P.N. Barlow. J. Magn. Reson. **126**, 148 (1997).
56. W.W. Wakarchuk, D. Watson, F. St Michael, J. Li, Y. Wu, J.R. Brisson, N.M. Young, and M. Gilbert. J. Biol. Chem. **276**, 12 785 (2001).
57. M. Gilbert, J.R. Brisson, M.F. Kawarski, J. Michniewicz, A.M. Cunningham, Y. Wu, N.M. Young, and W.W. Wakarchuk. J. Biol. Chem. **275**, 3896 (2000).
58. J.R. Brisson, S. Uhrinova, R.J. Woods, M. van der Zwan, H.C. Jarrell, L.C. Paoletti, D.L. Kasper, and H.J. Jennings. Biochemistry, **36**, 3278 (1997).
59. K. Scheffler, J.R. Brisson, R. Weisemann, J.L. Magnani, T.C. Wong, B. Ernst, and T. Peters. J. Biomol. NMR, **9**, 423 (1997).
60. J.O. Duus, C.H. Gotfredsen, and K. Bock. Chem. Rev. **100**, 4589 (2000).
61. D. Uhrín and J.R. Brisson. Structure determination of microbial polysaccharides by high resolution NMR spectroscopy. *In* NMR in microbiology: theory and applications. *Edited by* J.N. Barbotin and J.C. Portais. Horizon Scientific Press. Wymondham, U.K. 2000. p. 165.
62. G. Kogan and D. Uhrín. Current NMR methods in the structural elucidation of polysaccharides. *In* New advances in analytical chemistry. *Edited by* Atta-ur-Rahman. Harwood Academic. Amsterdam. 2000. p. 73.

© 2002 NRC Canada

63. D. Uhrín. Concatenation of polarization transfer steps in 1D homonuclear chemical shift correlated experiments. Application to oligo- and polysaccharides. *In* Methods for structure elucidation by high-resolution NMR. *Edited by* Gy. Batta, K.E. Kövér, and C. Szántay, Jr. Elsevier Science B. V. Amsterdam. 1997. p. 51.
64. C. Roumestand, C. Delay, J.A. Gavin, and D. Canet. Magn. Reson. Chem. **37**, 451 (1999).
65. A.D. Cox, J.R. Brisson, V. Varma, and M.B. Perry. Carbohydr. Res. **290**, 43 (1996).
66. G.I. Birnbaum, R. Roy, J.R. Brisson, and H.J. Jennings. J. Carbohydr. Chem. **6**, 17 (1987).
67. E. Altman, J.R. Brisson, and M.B. Perry. Eur. J. Biochem. **170**, 185 (1987).
68. K. Bock and C. Pedersen. Adv. Carbohydr. Chem. Biochem. **41**, 27 (1983).
69. P.-E. Jansson, L. Kenne, and G. Widmalm. Carbohydr. Res. **188**, 169 (1989).
70. M.D. Potter and R.Y. Lo. FEMS Microbiol. Lett. **129**, 75 (1995).
71. I.M. Helander, B. Lindner, H. Brade, K. Altmann, A.A. Lindberg, E.T. Rietschel, and U. Zahringer. Eur. J. Biochem. **177**, 483 (1988).
72. S.A. Wacowich-Sgarbi, C.C. Ling, A. Otter, and D.R. Bundle. J. Am. Chem. Soc. **123**, 4362 (2001).
73. H. Masoud, M.B. Perry, J.R. Brisson, D. Uhrín, and J.C. Richards. Can. J. Chem. **72**, 1466 (1994).
74. W.B. Severn, R.F. Kelly, J.C. Richards, and C. Whitfield. J. Bacteriol. **178**, 1731 (1996).
75. O. Holst, U. Zahringer, H. Brade, and A. Zamojski. Carbohydr. Res. **215**, 323 (1991).
76. J.C. Sowden and D.R. Strobach. J. Am. Chem. Soc. **82**, 954 (1960).
77. R.K. Hulyalkar, J.K.N. Jones, and M.B. Perry. Can. J. Chem. **41**, 1490 (1963).
78. D. Uhrín, J.R. Brisson, L.L. MacLean, J.C. Richards, and M.B. Perry. J. Biomol. NMR, **4**, 615 (1994).
79. T. Peters, B. Meyer, P. Stuike, R. Somorjai, and J.R. Brisson. Carbohydr. Res. **238**, 49 (1993).
80. I. Tvaroska and S. Pérez. Carbohydr. Res. **149**, 389 (1986).
81. Y. Wang and R.I. Hollingsworth. Biochemistry, **35**, 5647 (1996).

© 2002 NRC Canada

New mannotriosides and trimannosides as potential ligands for mannose-specific binding proteins

Richard H. Furneaux, Zbigniew Pakulski, and Peter C. Tyler

Abstract: The α-D-mannopyranosyl and 3,6-di-*O*-(α-D-mannopyranosyl)-α-D-mannopyranosyl neoglycolipids **3**–**6** and the branched and cluster trimannosidic acids **38** and **41** have been made in connection with studies of liposomes as transporters of antigens to dendritic cells.

Key words: mannotrioside, trimannoside, neoglycoconjugate, glycolipid, synthesis.

Résumé : Dans le cadre d'études sur les liposomes comme transporteurs d'antigènes dans des cellules dendritiques, on a préparé les néoglycolipides α-D-mannopyranosyl- et 3,6-di-*O*-(α-D-mannopyranosyl)-α-D-mannopyranosyle (**3**–**6**) ainsi que les acides trimannosidiques ramifié et en agrégat (**38** et **41**).

Mots clés : mannotrioside, trimannoside, néoglycoconjugué, glycolipide, synthèse.

[Traduit par la Rédaction]

Introduction

Terminal α-D-mannopyranosyl units commonly occur in the glycoproteins of pathogenic bacteria, yeasts, viruses, and various parasites and are recognised by receptors of macrophages (1) and dendritic cells (2, 3). Because the branched trisaccharide 3,6-di-*O*-(α-D-mannopyranosyl)-α-D-mannopyranosyl ligand binds with higher affinity to the mannose receptors of human macrophages and dendritic cells than do mono- and linear oligo-mannosyl ligands (4), we began studies of synthetic neoglycoconjugates and liposomes containing this trimer with a view to using the liposomes to transport antigens to dendritic cells.

In the first report of this work (5), we exploited the earlier finding (6, 7) that various α-D-mannopyranosides could be di-*O*-mannosylated concurrently and with some selectivity at O-3 and O-6 by use of tetra-*O*-acetyl-α-D-mannopyranosyl bromide to give the required branched-chain mannotriose derivatives, and we introduced the new tetra-*O*-benzoyl-α-D-mannopyranosyl trichloroacetimidate as glycosylating agent. By its use 8-(methoxycarbonyl)octyl α-D-mannopyranoside was converted to the 3,6-bis-*O*-(2,3,4,6-tetra-*O*-benzoyl-α-D-mannopyranosyl)-mannopyranoside in 55% yield, and the neoglycolipids **1** and **2** (Scheme 1) were made (5). More recently the 3,6-di-*O*-α-D-mannosylation of *p*-nitrophenyl α-D-mannopyranoside in 42% yield by use of tetra-*O*-acetyl-α-D-mannopyranosyl trichloroacetimidate as glycosylating agent has been described (4).

We now report (Scheme 1) the preparation of the neoglycolipids **3**–**6** which differ from analogues **1** and **2** in having four-carbon (compounds **3** and **5**) and six-carbon (compounds **4** and **6**) as opposed to nine-carbon atom spacer groups. Additionally, and with further neoglycolipids in view, the polyoxyethylene glycosides **30** and **34** and the mannotriose-containing acid **38** were made, as well as the alternative cluster type of trimannosyl glycosidic (8) acid **41** (Scheme 2). Considerable effort has gone into the study of this last kind of trimannoside (9).

Results and discussion

The neoglycolipids **3** and **4** (Scheme 1) were made following glycosylations of methyl 4-hydroxybutanoate and methyl 6-hydroxyhexanoate, respectively, by use of tetra-*O*-benzoyl-α-D-mannopyranosyl trichloroacetimidate. The first products **7** and **11** were converted successively to the required neoglycolipids by the previously used processes (5), that is, via the debenzoylated glycosides **8** and **12**, the carboxylic acids **9** and **13** and the *N*-succinimido derivatives **10** and **14**, respectively. The final step involved coupling of the activated acids **10** and **14** with dipalmitoyl-1-α-phosphatidyl ethanolamine (DPPE) to give products **3** and **4**.

Selective bis-(tetra-*O*-benzoyl-α-D-mannosylation) of glycosides **8** and **12**, by use of the glycosylating agent mentioned above, afforded the trisaccharide derivatives **15** and **21** which were isolated following chromatographic separation of their derived diacetates **16** (23% from **8**) and **22** (33% from **12**), respectively. Compounds **16** and **22** were used to prepare the neoglycolipids **5** and **6**, respectively, by the routes used for compounds **3** and **4**, i.e., **16**→**18**→**19**→**20**→**5** and **22**→**24**→**25**→**26**→**6** as also outlined in Scheme 1. The 1→3-, 1→6-linked trisaccharide

Received 30 April 2002. Published on the NRC Research Press Web site at http://canjchem.nrc.ca on 5 August 2002.

Dedicated to the memory of Professor Raymond U. Lemieux.

R.H. Furneaux,[1] Z. Pakulski,[2] and P.C. Tyler. Industrial Research Ltd, PO Box 31–310, Lower Hutt, New Zealand

[1]Corresponding author (e-mail: r.furneaux@irl.cri.nz).
[2]On leave from the Institute of Organic Chemistry, Polish Academy of Sciences, Warsaw, Poland.

 DOI: 10.1139/V02-120 © 2002 NRC Canada

Scheme 1.

Compound	*n*	R^1	R^2	R^3	R^4
7	3	Bz	Bz	Bz	Me
8	3	H	H	H	Me
9	3	H	H	H	H
10	3	H	H	H	Suc
11	5	Bz	Bz	Bz	Me
12	5	H	H	H	Me
13	5	H	H	H	H
14	5	H	H	H	Suc
15	3	H	Man Bz	H	Me
16	3	Ac	Man Bz	Ac	Me
17	3	Ac	Man Bz	Man Bz	Me
18	3	H	Man	H	Me
19	3	H	Man	H	H
20	3	H	Man	H	Suc
21	5	H	Man Bz	H	Me
22	5	Ac	Man Bz	Ac	Me
23	5	Ac	Man Bz	Man Bz	Me
24	5	H	Man	H	Me
25	5	H	Man	H	H
26	5	H	Man	H	Suc

Compound	*n*	R
1	8	H
2	8	Man
3	3	H
4	5	H
5	3	Man
6	5	Man

Man = α–D-mannopyranosyl
Man Bz = tetra-*O*-benzoyl-α-D-mannopyranosyl
Suc = *N*-succinimido

Reagents: i, K_2CO_3, MeOH; ii, NaOH (aq.); iii, *N*-hydroxysuccinimide; DCC; iv, 1,2-hexadecanoyl-sn-glycero-3-phosphoethanolamine, $NaHCO_3$; v, tetra-*O*-benzoyl-D-mannopyranosyl trichloroacetimidate; vi, Ac_2O, Py; vii, NaOMe, MeOH

structures of the products **15** and **21** followed from the ^{1}H NMR characteristics of their diacetates **16** and **22**, the H-2 and H-4 resonances being ca. 1 ppm deshielded with respect to those of H-3, and the $J_{2,3}$ and $J_{3,4}$ coupling constant values being 3.4 and 9.8 Hz, respectively. These data compare closely with those obtained for the corresponding trisaccharide octa-*O*-benzoyl diacetate prepared in the course of making compound **2** (5).

During the isolation of the acetylated trisaccharide derivatives **16** and **22** the (3,4,6-tri-*O*-mannosyl)mannoside by-products **17** and **23**, containing small proportions of other oligosaccharide derivatives, were also obtained. The ^{1}H NMR spectra of monoacetates **17** and **23** showed δ values for the H-2 resonances of the central mannose residues of 5.34 and 5.43, respectively. The less-deshielding acetyl groups are consequently concluded to be substituted at O-2 since, for both of the compounds, the nine protons at the secondary benzoylated ring positions resonated within the range δ 5.79–6.27. The tetrasaccharide by-products are therefore 3,4,6-tris-*O*-(tetra-*O*-benzoyl-mannopyranosyl)-mannopyranosides.

In all the above cases the glycosylation reactions gave no observable orthoester by-products.

En route to alternative types of neoglycolipids the mono- and trisaccharide glycosides **27** and **35** (Scheme 2) were made by standard condensations of tetra-*O*-benzoyl-α-D-mannopyranosyl trichloroacetimidate with the corresponding alcohols whereas, in our hands, the corresponding acetylglycosyl bromide with mercury(II) cyanide was more effective for the preparation of triglycoside **39** from [tris(hydroxymethyl)]methyl-(5-methoxycarbonyl)pentanoamide (8).

From **27** and **35** the acids **30** and **38** were made by standard methods, and from **27** the extended-chain compound **34** was produced via the azide **31**. The dimannosylation of compound **29** gave the 1→3-,1→6-linked trisaccharide derivative **35** in 40% yield, the positions of substitution being determined from the ^{1}H,^{1}H coupling constants of the H-2 and H-4 resonances of the derived diacetate **36**. De-esterification of the substituted triglycoside **39** gave acid **41** via methyl ester **40**.

The biological evaluation of compounds described above will be reported separately.

© 2002 NRC Canada

Scheme 2.

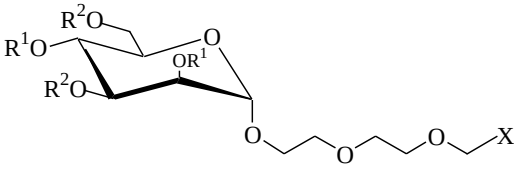

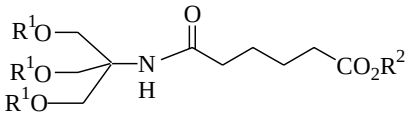

Compound	R^1	R^2	X
27	Bz	Bz	Cl
28	Bz	Bz	CN
29	H	H	CN
30	H	H	CO_2H
31	Bz	Bz	N_3
32	Bz	Bz	NH_2
33	Bz	Bz	$NHCO(CH_2)_4CO_2Me$
34	H	H	$NHCO(CH_2)_4CO_2Me$
35	H	Man Bz	CN
36	Ac	Man Bz	CN
37	H	Man	CN
38	H	Man	CO_2H

Compound	R^1	R^2
39	Man Ac	Me
40	Man	Me
41	Man	H

Man Ac = tetra-*O*-acetyl-α-D-mannopyranosyl.
For other abbreviations see Scheme 1.

Reagents: i, KCN, DMSO; ii, K_2CO_3, MeOH; iii, NaOH (aq.); iv, NaN_3, DMF; v, $NaBH_4$, $NiCl_2$, EtOH; vi, methyl adipate, 2-ethoxy-1-ethoxycarbonyl-1,2-didydroquinoline ; vii, tetra-*O*-benzoyl-D-mannopyranosyl trichloroacetimidate; viii, Ac_2O, Py; ix, NaOMe, MeOH.

Experimental

General methods

All glycosylation reactions were performed under argon in dry CH_2Cl_2. TLC was performed on silica gel HF-254 and column chromatography on silica gel 230–400 mesh (Merck). ^1H NMR spectra were recorded with a Bruker Avance 300 MHz NMR spectrometer equipped with a 5 mm o.d. Quattro nucleus probe or (when indicated) a Varian Unity 500 MHz spectrometer equipped with 5 mm Universe probe. Resonance assignments were by use of DEPT, H,H-COSY, inverse C,H-COSY, and H,H-TOCSY experiments. All spectra were consistent with those expected for the structures assigned to the respective compounds; unresolved resonances and those of substituent groups and carbonyl groups (^{13}C spectra) are frequently not listed. High resolution mass spectra (HR-MS) were measured with a VG70-250S double focussing magnetic sector mass spectrometer or a Mariner 8105 electrospray TOF mass spectrometer. Optical rotations were measured with a PerkinElmer 241 automatic polarimeter. 2-[2-(2-Chloroethoxy)ethoxy]ethanol was purchased from Aldrich.

*3-(Methoxycarbonyl)propyl 2,3,4,6-tetra-*O*-benzoyl-α-D-mannopyranoside (7)*

A solution of 2,3,4,6-tetra-*O*-benzoyl-α-D-mannopyranosyl trichloroacetimidate (5) (4.45 g, 6.0 mmol) and methyl 4-hydroxybutanoate (10) (760 mg, 6.4 mmol) in CH_2Cl_2 (30 mL) was stirred for 30 min at room temperature over molecular sieves (4 Å, 700 mg, finely ground). The solution was cooled in an ice bath and TmsOTf (60 μL) was added. After 20 min the reaction was quenched by addition of Et_3N (0.5 mL), and the solvent was evaporated in vacuo. Column chromatography (hexane–EtOAc, 2:1) gave the title compound **7** (3.60 g, 92%, contaminated with 10% of inseparable methyl 4-hydroxybutanoate): $[\alpha]_D^{20}$ –47 (*c* 1.0, $CHCl_3$, corrected for the impurity). ^1H NMR ($CDCl_3$) δ: 6.10 (t, $J_{3,4}$, $J_{4,5}$ = 10 Hz, 1H, H-4), 5.88 (dd, $J_{2,3}$ = 3.3 Hz, 1H, H-3), 5.69 (dd, $J_{1,2}$ = 1.8 Hz, 1H, H-2), 5.08 (d, 1H, H-1), 4.69 (dd, $J_{5,6}$ = 2.5 Hz, $J_{6,6'}$ = 12.0 Hz, 1H, H-6), 4.50 (dd, $J_{5,6'}$ = 4.4 Hz, 1H, H-6′), 4.42 (m, 1H, H-5), 3.90 (dt, *J* = 9.8, 6.2 Hz, 1H, OC*H*H), 3.73 (s, 3H, Me), 3.61 (dt, *J* = 9.8, 6.3 Hz, 1H, OCH*H*), 2.53 (m, 2H, CH_2), 2.06 (m, 2H, CH_2). ^{13}C NMR ($CDCl_3$) δ: 97.65 (C-1), 70.43, 70.09, 68.93, 67.48 (CH_2), 66.91, 62.87 (CH_2), 51.69 (CH_3), 30.78 (CH_2), 24.73 (CH_2). FAB-HR-MS calcd. for $C_{39}H_{37}O_{12}$ $[M + H]^+$ (*m*/*z*): 697.2285; found: 697.2330.

3-(Methoxycarbonyl)propyl α-D-mannopyranoside (8)

To a solution of compound **7** (3.6 g) in methanol (60 mL) K_2CO_3 (300 mg) was added and the mixture was stirred overnight then neutralized with Amberlyst 15 resin (H^+), filtered and the filtrate was evaporated to dryness. Column chromatography ($CHCl_3$–MeOH, 3:1) of the residue gave

© 2002 NRC Canada

8 (1.03 g, 71% after two debenzoylation treatments): $[\alpha]_D^{20}$ +54.2 (*c* 0.59, MeOH). ^{1}H NMR (CD_3OD) δ: 4.74 (d, $J_{1,2}$ = 1.5 Hz, 1H, H-1), 3.68 (s, Me), 2.44 (t, 2H, CH_2), 1.91 (m, 2H, CH_2). ^{13}C NMR (CD_3OD) δ: 176.03 (C=O), 101.97 (C-1), 75.07, 73.04, 72.56, 69.02, 67.92 (CH_2), 63.33 (CH_2), 52.47 (CH_3), 32.19 (CH_2), 26.40 (CH_2). FAB-HR-MS calcd. for $C_{11}H_{21}O_8$ $[M + H]^+$: 281.1236; found: 281.1243.

3-Carboxypropyl* α-D-*mannopyranoside (9)

NaOH (0.75 mL, 3M aq) was added to a solution of the methyl ester **8** (517 mg, 1.84 mmol) in THF (15 mL) and water (7 mL), The reaction mixture was stirred for 24 h, neutralised with Amberlyst 15 resin (H^+), filtered, concentrated in vacuo and freeze-dried to afford the acid **9** (440 mg, 90%): $[\alpha]_D^{20}$ +46.1 (*c* 0.41, water). ^{1}H NMR (D_2O) δ: 4.78 (d, $J_{1,2}$ = 1.2 Hz, 1H, H-1), 3.46–3.87 (m, 8H), 2.42 (t, 2H, CH_2), 1.86 (m, 2H, CH_2). ^{13}C NMR (D_2O) δ: 178.73 (C=O), 100.11 (C-1), 73.12, 71.00, 70.44, 67.22 (CH_2), 67.15, 61.31 (CH_2), 31.36 (CH_2), 24.55 (CH_2). FAB-HR-MS calcd. for $C_{10}H_{19}O_8$ $[M + H]^+$: 267.1080; found: 267.1084.

3-[Carboxy-2-(1,2-dihexadecanoyl*-sn-*glycero-3-phospho)ethanolamido]propyl* α-D-*mannopyranoside sodium salt (3)

A mixture of acid **9** (119 mg, 0.45 mmol), DCC (248 mg, 1.5 mmol), *N*-hydroxysuccinimide (139 mg, 1.5 mmol) in THF (6.5 mL) – $CHCl_3$ (3 mL) – methanol (6.5 mL) was stirred at room temperature for 24 h. The solvent was removed and column chromatography ($CHCl_3$–MeOH, 4:1) of the residue gave the crude amide **10** (115 mg, 71%). FAB-HR-MS calcd. for $C_{14}H_{12}NO_{10}$ $[M + H]^+$: 364.1244; found: 364.1225.

To a suspension of 1,2-dihexadecanoyl-*sn*-glycero-3-phosphoethanolamine (DPPE, 200 mg, 0.284 mmol) in $CHCl_3$–MeOH (2:1, 6 mL), water (0.4 mL), and $NaHCO_3$ (120 mg, 1.42 mmol) were added, and the mixture was stirred at 30°C for 30 min. A solution of **10** (94 mg, 0.27 mmol) in $CHCl_3$–MeOH (2:1, 6 mL) was added and stirring was continued at 30°C overnight. The solvents were evaporated and column chromatography ($CHCl_3$–MeOH, 3:1) of the residue gave glycolipid **3**, 125 mg (47%): $[\alpha]_D^{20}$ +17.1 (*c* 0.38, $CHCl_3$–MeOH, 3:1). ^{13}C NMR ($CDCl_3$–CD_3OD, 3:1) δ: 174.33, 173.93, 173.61 (C=O), 100.09 (C-1), 72.59, 71.39, 71.15, 70.75, 70.50, 66.55, 66.55 (CH_2), 64.39 (CH_2), 63.80 (CH_2), 62.66 (CH_2), 61.89 (CH_2), 61.18 (CH_2), 60.89 (CH_2), 57.62 (CH_2), 51.60, 40.36 (CH_2), 34.26 (CH_2), 34.11 (CH_2), 31.94 (CH_2), 29.70 (CH_2), 29.36 (CH_2), 29.22 (CH_2), 25.34 (CH_2), 24.94(CH_2), 22.67 (CH_2), 13.96 (CH_3). FAB-HR-MS calcd. for $C_{47}H_{89}NO_{15}P$ $[M]^+$: 938.5970; found: 938.6012.

5-(Methoxycarbonyl)pentyl 2,3,4,6-tetra*-O-*benzoyl*-α-D-*mannopyranoside (11)

Glycosylation of methyl 6-hydroxyhexanoate (11) (0.94 g, 6.4 mmol) was carried out with the glycosylating agent (4.45 g, 6.0 mmol) used in the preparation of compound **7** and gave 5.16 g of crude title compound contaminated with 6-hydroxyhexanoate. A chromatographically purified sample had: ^{1}H NMR ($CDCl_3$) δ: 6.10 (t, $J_{3,4}$, $J_{4,5}$ = 10 Hz, 1H, H-4), 5.92 (dd, $J_{2,3}$ = 3.3 Hz, 1H, H-3), 5.69 (dd, $J_{1,2}$ = 1.8 Hz, 1H, H-2), 5.08 (d, 1H, H-1), 4.69 (dd, $J_{5,6}$ = 2.4 Hz, $J_{6,6'}$ = 12.0 Hz, 1H, H-6), 4.50 (dd, $J_{5,6'}$ = 4.5 Hz, 1H, H-6′), 4.42 (m, 1H, H-5), 3.84 (dt, *J* = 6.6, 6,6, 9.6 Hz, 1H, OC*H*H), 3.68 (s, 3H, CH_3), 3.58 (dt, *J* = 6.6, 6,6, 9.6 Hz, 1H, OCH*H*), 2.36 (t, 2H, CH_2), 1.71 (m, 4H, 2 × CH_2), 1.46 (m, 2H, CH_2). ^{13}C NMR ($CDCl_3$) δ: 98.08 (C-1), 71.02, 70.55, 69.28, 68.83 (CH_2), 67.46, 63.37 (CH_2), 51.87 (CH_3), 34.32 (CH_2), 29.46 (CH_2), 26.08 (CH_2) 25.05 (CH_2). FAB- HR-MS calcd. for $C_{41}H_{41}O_{12}$ $[M + H]^+$: 725.2598; found: 725.2582.

5-(Methoxycarbonyl)pentyl* α-D-*mannopyranoside (12)

Debenzoylation was carried out on compound **11** (5.16 g) as with the ester **7** to give glycoside **12** (1.735 g, 93%, two treatments): $[\alpha]_D^{20}$ +44.1 (*c* 0.76, MeOH). ^{1}H NMR (CD_3OD) δ: 4.74 (d, $J_{1,2}$ = 1.5 Hz, 1H, H-1), 3.84 (dd, $J_{5,6}$ = 2.3 Hz, $J_{6,6'}$ = 11.7 Hz, 1H, H-6), 3.80 (dd, $J_{2,3}$ = 3.2 Hz, 1H, H-2), 3.68–3.77 (m, 3H, H-3, H-6′, OC*H*H), 3.67 (s, 3H, CH_3), 3.62 (t, $J_{3,4}$, $J_{4,5}$ = 9.2 Hz, 1H, H-4), 3.54 (m, 1H, H-5), 3.43 (dt, *J* = 6.6, 6,6, 9.6 Hz, 1H, OCH*H*), 2.35 (t, *J* = 7.4 Hz, 2H, CH_2), 1.64 (m, 4H, 2 × CH_2), 1.44 (m, 2H, CH_2). ^{13}C NMR (CD_3OD) δ: 176.32 (C=O), 101.98 (C-1), 75.02, 73.09, 72.67, 69.08, 68.73(CH_2), 63.36 (CH_2), 52.38 (CH_3), 35.12 (CH_2), 30.62 (CH_2), 27.27 (CH_2), 26.19 (CH_2). FAB-HR-MS calcd. for $C_{13}H_{25}O_8$ $[M + H]^+$: 309.1549; found: 309.1540.

5-Carboxypentyl* α-D-*mannopyranoside (13)

Ester hydrolysis of **12** (785 mg, 2.54 mmol) was carried out as for compound **8** and gave **13** (750 mg, 100%): $[\alpha]_D^{20}$ +53.2 (*c* 0.34, MeOH). ^{1}H NMR (CD_3OD) δ: 4.76 (d, $J_{1,2}$ = 1.5 Hz, 1H, H-1), 3.33–3.89 (m, 8H), 2.28 (t, 2H, CH_2), 1.65 (m, 4H, 2 × CH_2), 1.42 (m, 2H, CH_2). ^{13}C NMR (CD_3OD) δ: 179.48 (C=O), 101.95 (C-1), 74.91, 73.05, 72.65, 69.01, 68.85 (CH_2), 63.17 (CH_2), 36.42 (CH_2), 30.71 (CH_2), 27.43(CH_2), 26.68 (CH_2). FAB-HR-MS calcd. for $C_{12}H_{23}O_8$ $[M + H]^+$: 295.1393; found: 295.1398.

5-(*N*-Succinimidyloxycarbonyl)pentyl* α-D-*mannopyranoside (14)

Amide formation was effected with acid **13** (148 mg, 0.5 mmol) as for analogue **9** and gave amide **14** (170 mg, 89%). ^{13}C NMR (CD_3OD) δ: 101.97 (C-1), 75.00, 73.08, 72.66, 69.09, 68.70 and 63.35 (CH_2), 52.73, 32.55 (CH_2), 30.53 (CH_2), 27.12 (CH_2), 26.92 (CH_2), 25.94 (CH_2). FAB-HR-MS calcd. for $C_{16}H_{26}NO_{10}$ $[M + H]^+$: 392.1557; found: 392.1542.

5-[Carboxy-2-(1,2-dihexadecanoyl*-sn-*glycero-3-phospho)ethanolamido]pentyl* α-D-*mannopyranoside sodium salt (4)

The title glycolipid (170 mg, 87%) was made from amide **14** (77 mg, 0.19 mmol) in like manner to its analogue **3**: $[\alpha]_D^{20}$ +13.1 (*c* 0.58, $CHCl_3$–MeOH, 2:1). ^{13}C NMR ($CDCl_3$–CD_3OD) δ: 101.94, 74.76, 73.12, 72.63, 69.05, 68.82 (CH_2), 63.34 (CH_2), 52.62, 50.11, 35.44 (CH_2), 35.25 (CH_2), 33.51 (CH_2), 31.20 (CH_2), 31.01 (CH_2), 30.92 (CH_2), 30.81 (CH_2), 30.66 (CH_2), 27.22 (CH_2), 26.50 (CH_2), 24.19 (CH_2), 15.09 (CH_3). FAB-HR-MS calcd. for $C_{49}H_{93}NNaO_{15}P$ $[M]^+$: 989.6180; found: 989.6157.

© 2002 NRC Canada

3-(Methoxycarbonyl)propyl 2,4-di-O-acetyl-(2,3,4,6-tetra-O-benzoyl-α-D-mannopyranosyl)-(1→3)-[(2,3,4,6-tetra-O-benzoyl-α-D-mannopyranosyl)-(1→6)]-α-D-mannopyranoside (16) and 3-(methoxycarbonyl)propyl 2-O-acetyl-(2,3,4,6-tetra-O-benzoyl-α-D-mannopyranosyl)-(1→3)-[(2,3,4,6-tetra-O-benzoyl-α-D-mannopyranosyl)-(1→4)]-{[(2,3,4,6-tetra-O-benzoyl-α-D-mannopyranosyl)-(1→6)]}-α-D-mannopyranoside (17)

A solution of glycoside **8** (832 mg, 3.0 mmol) in CH_2Cl_2 (50 mL) was stirred at room temperature over molecular sieves (4 Å, 500 mg, finely ground) for 30 min. The solution was cooled to −40°C and TmsOTf (200 μL) was added, followed by 2,3,4,6-tri-*O*-benzoyl-α-D-mannopyranosyl trichloroacetimidate (4.41 g, 5.95 mmol) in CH_2Cl_2 (30 mL) dropwise over 30 min. The solution was stirred for further 30 min, treated with Et_3N (0.5 mL), and evaporated to dryness. Column chromatography (hexane–EtOAc, 1.5:1, then 1:1) afforded a mixture of trisaccharide (**15**) (FAB-HR-MS calcd. for $C_{79}H_{72}O_{26}Cs$ $[M + Cs]^+$: 1569.3366; found 1569.3367) and tetrasaccharide derivatives (2.863 g). Acetylation of this crude mixture under standard conditions followed by column chromatography (hexane–EtOAc, 1:1) gave the following title compounds.

16:

(1.055 g, 23%): $([\alpha]_D^{20}$ −21.3 (*c* 0.65, $CHCl_3$). ^1H NMR (500 MHz, $CDCl_3$) δ: 6.18 (t, $J_{3'',4''}$, $J_{4'',5''}$ = 10 Hz, 1H, H-4″), 6.13 (t, $J_{3',4'}$, $J_{4',5'}$ = 10 Hz, 1H, H-4′), 5.95 (dd, $J_{2',3'}$ = 3.3 Hz, 1H, H-3′), 5.82 (dd, $J_{2'',3''}$ = 3.2 Hz, 1H, H-3″), 5.75 (dd, 1H, H-2′), 5.53 (dd, 1H, H-2″), 5.44 (m, 2H, H-2,4), 5.37 (d, $J_{1'',2''}$ = 1.7 Hz, 1H, H-1″), 5.16 (d, $J_{1',2'}$ = 1.7 Hz, 1H, H-1′), 4.88 (d, $J_{1,2}$ = 1.7 Hz, 1H, H-1), 4.71 (m, 2H, H-6′a, H-6″a), 4.59 (m, 2H, H-5′, H-5″), 4.52 (m, 2H, H-6′b, H-6″b), 4.37 (dd, $J_{2,3}$ = 3.4 Hz, $J_{3,4}$ = 9.8 Hz, 1H, H-3), 4.02 (m, 2H, H-5,6a), 3.89 (dt, *J* = 6.6, 6,6, 9.6 Hz, 1H, OC*H*H), 3.69 (m, 1H, H-6b), 3.63 (s, 3H, CH_3), 3.57 (dt, *J* = 6.6, 6,6, 9.6 Hz, 1H, OCH*H*), 2.45 (m, 2H, CH_2), 2.32, 2.27 (2s, 2 × 3 H, OAc), 2.00 (m, 2H, CH_2). ^{13}C NMR (125 MHz, $CDCl_3$) δ: 99.46 (C-1″), 97.87 (C-1′), 97.80 (C-1), 75.39 (C-3), 71.39 (C-2), 71.19 (C-2″), 70.86 (C-2′), 70.39 (C-3′), 70.10, 70.07 (C-5, C-5″), 69.78 (C-3″), 69.41 (C-5′), 68.89 (C-4), 67.70 (OCH_2), 67.29 (C-6, C-4′), 66.93 (C-4″), 63.35, 63.02 (C-6′, C-6″), 51.95 (CH_3), 31.19 (CH_2), 25.08 (CH_2), 21.41 (*C*H_3CO), 21.22 (*C*H_3CO). FAB-HR-MS calcd. for $C_{83}H_{76}O_{28}Cs$ $[M + Cs]^+$: 1653.3577; found: 1653.3583.

17:

(1.670 g, 27%, containing small proportions of other oligosaccharide derivatives). ^1H NMR (500 MHz, $CDCl_3$) δ: 6.21 (t, $J_{3'',4''}$, $J_{4'',5''}$ = 10.1 Hz, 1H, H-4″), 6.12, 6.10 (dt, 2H, H-4′, H-4‴), 6.04 (m, 2H, H-2′, H-3′), 5.95 (dd, $J_{2'',3''}$ = 2.7 Hz, 1H, H-3″), 5.91 (dd, $J_{2''',3'''}$ = 3.2 Hz, $J_{3''',4'''}$ = 10.2 Hz, 1H, H-3‴), 5.88 (m, 1H, H-2″), 5.79 (m, 1H, H-2‴), 5.68 (d, $J_{1'',2''}$ = 1.7 Hz, 1H, H-1″), 5.51 (d, $J_{1',2'}$ = 1.5 Hz, 1H, H-1′), 5.34 (dd, $J_{2,3}$ = 3.0 Hz, 1H, H-2), 5.26 (d, $J_{1''',2'''}$ = 1.7 Hz, 1H, H-1‴), 4.83 (d, $J_{1,2}$ = 1.7 Hz, 1H, H-1), 4.43–4.73 (m, 9H, H-5′, 6′a, 6′b, H-5″, 6″a, 6″b, H-5‴, 6‴a, 6‴b), 4.38 (m, 2H, H-3, H-4), 4.23 (dd, $J_{5,6a}$ = 5 Hz, $J_{6a,6b}$ = 12 Hz, 1H, H-6a), 4.18 (dd, $J_{5,6b}$ = 1.5 Hz, 1H, H-6b), 4.00 (m, 1H, H-5), 3.82, 3.48 (2m, 2H, OC$H_2$$CH_2$), 3.58 (s, 3H, CH_3), 2.38 (m, 2H, CH_2), 2.18 (s, 3H, Ac), 1.92 (m, 2H, CH_2). ^{13}C NMR (125 MHz, $CDCl_3$) δ: 100.68 (C-1′), 100.43 (C-1″), 98.53 (C-1‴), 97.14 (C-1), 79.61 (C-3), 76.52 (C-4), 72.29 (C-2), 71.86 (C-2″); 71.66 (C-5), 71.33 (C-2′), 70.78 (C-2‴), 70.48 (C-3‴), 70.27, 70.16, 69.56 (C-5′, C-5″, C-5‴), 69.77, 69.73 (C-3′, C-3″); 68.80 (CH_2), 68.80, 67.25, 67.24 (C-4′, C-4″, C-4‴), 66.97 (C-6), 63.49, 63.08, 62.95 (C-6′, C-6″, C-6‴), 51.95 (CH_3), 31.11 (CH_2), 25.12 (CH_2), 21.38 (*C*H_3CO). FAB-HR-MS calcd. for $C_{115}H_{100}O_{36}Cs$ $[M + Cs]^+$: 2189.5049; found: 2189.5031.

3-(Methoxycarbonyl)propyl (α-D-mannopyranosyl)-(1→3)-[(α-D-mannopyranosyl)-(1→6)]-α-D-mannopyranoside (18)

To a solution of the perester **16** (1.050 g, 0.65 mmol) in MeOH (30 mL) was added NaOMe (8 mmol, 1 M in MeOH), and the mixture was stirred at room temperature for 24 h, taken to pH ~ 5 with Amberlyst 15 (H^+), filtered, and evaporated to dryness to afford the title trisaccharide glycoside **18** (420 mg, 100%): $[\alpha]_D^{20}$ +74.7 (*c* 0.38, H_2O). ^1H NMR (D_2O) δ: 5.07 (d, $J_{1,2}$ = 1.4 Hz, 1H, H-1), 4.86 (d, $J_{1,2}$ = 1.5 Hz, 1H, H-1), 4.77 (d, $J_{1,2}$ = 1.4 Hz, 1H, H-1), 3.43–4.03 (m, 26H), 2.46 (t, 2H, CH_2), 1.93 (m, 2H, CH_2). ^{13}C NMR (D_2O) δ: 177.24 (C=O), 102.77, 100.32, 99.83 (C-1), 79.00, 73.74, 73.11, 71.51, 71.03, 70.81, 70.49, 70.39, 70.08, 67.35 (CH_2), 67.16, 66.12, 65.74 (CH_2), 61.38 (2 × CH_2), 52.65 (CH_3), 31.19 (CH_2) and 24.54 (CH_2). FAB-HR-MS calcd. for $C_{23}H_{41}O_{18}$ $[M + H]^+$: 605.2293; found: 605.2321.

3-Carboxypropyl (α-D-mannopyranosyl)-(1→3)-[(α-D-mannopyranosyl)-(1→6)]-α-D-mannopyranoside (19)

To a solution of glycoside **18** (121 mg, 0.20 mmol) in H_2O (3 mL), NaOH (0.5 mL, 3 M, aq) was added. The reaction mixture was stirred for 2 days, neutralized with Amberlyst 15 resin (H^+), filtered, and freeze-dried to afford the acid **19** (120 mg, 101%): $[\alpha]_D^{20}$ +85.5 (*c* 0.31, MeOH). ^{13}C NMR (CD_3OD) δ: 170.34 (C=O), 104.27, 102.17, 101.81 (C-1), 81.13, 75.32, 74.76, 73.90, 73.06, 72.89, 72.48 (2×CH), 71.81, 69.22, 69.01, 68.17 (CH_2), 67.89, 67.68 (CH_2), 63.29 (2 × CH_2), 32.27 (CH_2), 26.44 (CH_2). FAB-HR-MS calcd. for $C_{22}H_{39}O_{18}$ $[M + H]^+$: 591.2136; found: 591.2159.

3-(N-Succinimidyloxycarbonyl)propyl (α-D-mannopyranosyl)-(1→3)-[(α-D-mannopyranosyl)-(1→6)]-α-D-mannopyranoside (20)

By use of the procedure described for making amide **10**, and using $CHCl_3$ – MeOH – H_2O (5:4:1) as eluent for column chromatography, acid **19** (115 mg, 0.19 mmol) was converted to amide **20** (85 mg, 64%): $[\alpha]_D^{20}$ +87.8 (*c* 0.23, MeOH). ^{13}C NMR ($CDCl_3$) δ: 104.36, 102.28 and 101.81 (C-1, C-1′, C-1″), 81.13, 75.32, 74.76, 73.90, 73.06, 72.89, 72.48, 69.22, 69.01, 67.89, 67.68 (2×CH_2), 63.29 (2×CH_2), 32.27 (CH_2), 30.16, (CH_2), 28.69 (CH_2), 26.17 (CH_2). FAB-HR-MS calcd. for $C_{26}H_{42}NO_{20}$ $[M + H]^+$: 688.2300; found: 688.2317.

3-[Carboxy-2-(1,2-dihexadecanoyl-sn-glycero-3-phospho)ethanolamido]propyl (α-D-mannopyranosyl)-(1→3)-[(α-D-mannopyranosyl)-(1→6)]-α-D-mannopyranoside sodium salt (5)

From amide **20** (83 mg, 0.12 mmol), according to the procedure described for making glycolipid **3**, the analogue **5**

© 2002 NRC Canada

(105 mg, 70%, containing small proportions of 1,2-hexadecanoyl-*sn*-glycero-3-phosphoethanolamine) was obtained following column chromatography with $CHCl_3$–MeOH–H_2O (5:4:1) as eluent: $[\alpha]_D^{20}$ +26.4 (*c* 0.25, $CHCl_3$–MeOH, 3:1). ^{13}C NMR ($CDCl_3$) δ: 106.47, 104.85 and 104.04 (C-1, C-1′, C-1″), 83.33, 77.55, 76.92, 75.90, 75.30, 75.00, 74.65, 71.32, 71.10, 70.17, 69.78, 68.63, 68.04, 66.85, 66.01, 65.27, 44.72, 38.48, 38.33, 36.92, 36.15, 33.93, 33.58, 33.40, 29.53, 29.14, 26.88 and 18.17. FAB-HR-MS calcd. for $C_{59}H_{110}NNaO_{25}P$ $[M]^+$: 1286.7002; found: 1286.6958.

5-(Methoxycarbonyl)pentyl 2,4-di-O-acetyl-(2,3,4,6-tetra-O-benzoyl-α-D-mannopyranosyl)-(1→3)-[(2,3,4,6-tetra-O-benzoyl-α-D-mannopyranosyl)-(1→6)]-α-D-mannopyranoside (22) and 5-(methoxycarbonyl)pentyl 2-O-acetyl-(2,3,4,6-tetra-O-benzoyl-α-D-mannopyranosyl)-(1→3)-[(2,3,4,6-tetra-O-benzoyl-α-D-mannopyranosyl)-(1→4)]-{[(2,3,4,6-tetra-O-benzoyl-α-D-mannopyranosyl)-(1→6)]}-α-D-mannopyranoside (23)

A solution of glycoside **12** (917 mg, 2.97 mmol) in CH_2Cl_2 (50 mL) was mannosylated as for the analogue **8**, and column chromatography (hexane–EtOAc, 1.5:1, then 1:1) afforded two main fractions (692 mg) and (2.73 g) (in order of elution), both as mixtures of products mainly containing trisaccharide derivative **21** and a tetrasaccharide analogue. Acetylation of the second fraction under standard conditions followed by column chromatography (hexane–EtOAc, 1:1) gave the trisaccharide glycoside perester **22** and **23**. The latter contained small proportions of impurities — probably tri- and tetra-saccharide isomers of the main products.

22:

(1.543 g, 33% from **12**): $[\alpha]_D^{20}$ –17.7 (*c* 0.52, $CHCl_3$). ^1H NMR (500 MHz, $CDCl_3$) δ: 6.18 (t, $J_{3'',4''}$, $J_{4'',5''}$ = 10.0 Hz, 1H, H-4″), 6.12 (t, $J_{3',4'}$, $J_{4',5'}$ = 10.0 Hz, 1H, H-4′), 5.94 (dd, $J_{2',3'}$ = 3.4 Hz, 1H, H-3′), 5.81 (dd, $J_{2'',3''}$ = 3.2 Hz, 1H, H-3″), 5.74 (dd, $J_{1',2'}$ = 1.7 Hz, 1H, H-2′), 5.52 (dd, $J_{1'',2''}$ = 1.7 Hz, 1H, H-2″), 5.43 (m, 2H, H-2,4), 5.37 (d, 1H, H-1″), 5.16 (d, 1H, H-1′), 4.87 (d, $J_{1,2}$ = 1.5 Hz, 1H, H-1), 4.71 (dd, $J_{5',6'a}$ = 2.3 Hz, $J_{6'a,6'b}$ = 12.1 Hz, 1H, H-6′a), 4.68 (dd, $J_{5'',6''a}$ = 2.3 Hz, $J_{6''a,6''b}$ = 12.3 Hz, 1H, H-6″a), 4.58 (m, 2H, H-5′, H-5″), 4.53 (dd, $J_{5'',6''b}$ = 3.7 Hz, 1H, H-6″b), 4.51 (dd, $J_{5',6'b}$ = 3.8 Hz, 1H, H-6′b), 4.38 (dd, $J_{2,3}$ = 3.4, $J_{3,4}$ = 9.8 Hz, 1H, H-3), 4.01 (m, 2H, H-5,6a), 3.84 (dt, *J* = 6.6, 6,6, 9.6 Hz, 1H, OC*H*H), 3.69 (m, 1H, H-6b), 3.59 (s, 3H, CH_3), 3.50 (dt, *J* = 6.6, 6,6, 9.6 Hz, 1H, OCH*H*), 2.29 (m, 8H, CH_2, 2 × Ac), 1.66 (m, 4H, 2 × CH_2), 1.42 (m, 2H, CH_2). ^{13}C NMR (125 MHz, $CDCl_3$) δ: 99.36 (C-1″), 97.71, 97.67 (C-1, C-1′), 75.44 (C-3), 71.41 (C-2), 71.10 (C-2″), 70.74 (C-2′), 70.30 (C-3′), 69.95 (C-5, C-5″), 69.71 (C-3″), 69.26 (C-5′), 68.78 (C-4), 68.33 (CH_2), 67.24, 67.21 (C-4′, C-6), 66.82 (C-4″), 63.25 (C-6′), 62.92 (C-6″), 51.65 CH_3), 34.18 (CH_2), 29.29 (CH_2), 26.04 (CH_2), 24.99 (CH_2), 21.35 (*C*H_3CO), 21.13 (*C*H_3CO). FAB-HR-MS calcd. for $C_{85}H_{80}O_{28}Cs$ $[M + Cs]^+$: 1681.3890; found: 1681.3899.

23:

(1.033 g, 17% from **12**). ^1H NMR (500 MHz, $CDCl_3$) δ: 6.27 (t, $J_{3'',4''}$, $J_{4'',5''}$ = 10.1 Hz, 1H, H-4″), 6.17 (2t, 2H, H-4′, H-4‴), 6.12 (m, 2H, H-2′, H-3′), 6.07 (dd, 1H, $J_{2'',3''}$ = 2.9 Hz, H-3″), 5.99 (dd, $J_{2''',3'''}$ = 3.4 Hz, $J_{3''',4'''}$ = 10.0 Hz, 1H, H-3‴), 5.96 (m, 1H, H-2″), 5.86 (dd, 1H, $J_{1''',2'''}$ = 1.7 Hz, H-2‴), 5.76 (d, $J_{1'',2''}$ = 1.7 Hz, 1H, H-1″), 5.59 (d, $J_{1',2'}$ = 1.5 Hz, 1H, H-1′), 5.43 (dd, $J_{2,3}$ = 2.9 Hz, 1H, H-2), 5.35 (d, 1H, H-1‴), 4.90 (d, $J_{1,2}$ = 1.7 Hz, 1H, H-1), 4.52–4.82 (m, 9H, H-5′, 6′a, 6′b, H-5″, 6″a, 6″b, H-5‴, 6‴a, 6‴b), 4.50 (dd, 1H, H-3), 4.42 (t, *J* = 9.8 Hz, 1H, H-4), 4.31 (dd, $J_{5,6a}$ = 5.0 Hz, $J_{6a,6b}$ = 11.8 Hz, 1H, H-6a), 4.17 (dd, $J_{5,6b}$ = 1.5 Hz, 1H, H-6b), 4.07 (m, 1H, H-5), 3.81, 3.47 (2m, 2H, CH_2), 3.61 (s, 3H, CH_3), 2.34 (m, 2H, CH_2), 2.27 (s, 3H, Ac), 1.69 (m, 4H, 2 × CH_2), 1.45 (m, 2H, CH_2). ^{13}C NMR (125 MHz, $CDCl_3$) δ: 100.68 (C-1′), 100.46 (C-1″), 98.53 (C-1‴), 97.10 (C-1), 79.77 (C-3), 76.57 (C-4), 72.45 (C-2), 71.89 (C-2″), 71.57 (C-5), 71.37 (C-2′), 70.76 (C-2‴), 70.51 (C-3‴), 70.30, 70.26, 69.79, 69.76 and 69.53 (C-3′, C-3″, C-5′, C-5″, C-5‴), 68.65 (CH_2), 67.84, 67.44, 67.28 (C-4′, C-4″, C-4‴), 67.02 (C-6), 63.52, 63.10, 62.97 (C-6′, C-6″, C-6‴), 51.77 (CH_3), 34.33 (CH_2), 29.49 (CH_2), 26.12 (CH_2), 25.14 (CH_2), 21.43 (*C*H_3CO). FAB-HR-MS calcd. for $C_{117}H_{104}O_{36}Cs$ $[M + Cs]^+$: 2217.5362; found: 2217.5339.

5-(Methoxycarbonyl)pentyl (α-D-mannopyranosyl)-(1→3)-[(α-D-mannopyranosyl)-(1→6)]-α-D-mannopyranoside (24)

To a solution of diacetate **22** (1.502 g, 0.97 mmol) in MeOH (30 mL) was added NaOMe (X M in MeOH, 12 mL) and the mixture was stirred at room temperature for 24 h, neutralized to pH ~ 5 with Amberlyst 15 (H^+), filtered, and evaporated to dryness to afford the de-esterified glycoside **24** (575 mg, 94%): $[\alpha]_D^{20}$ +79.7 (*c* 0.33, H_2O). ^1H NMR (D_2O) δ: 5.09 (d, $J_{1,2}$ = 1.4 Hz, 1H, H-1′), 4.88 (d, $J_{1,2}$ = 1.4 Hz, 1H, H-1″), 4.80 (d, $J_{1,2}$ = 1.4 Hz, 1H, H-1), 3.67 (s, 3H, CH_3), 3.50–4.07 (m, 7H, H-2,3,4,5,6, OC$H_2$$CH_2$), 2.39 (t, *J* = 7.4 Hz, 2H, CH_2), 1.61 (m, 4H, 2 × CH_2), 1.37 (m, 2H, CH_2). ^{13}C NMR (D_2O) δ: 177.98, 102.76, 100.29, 99.82 (C-1, C-1′, C-1″), 79.00, 73.74, 73.12, 71.51, 71.06, 70.79, 70.42, 70.41, 70.13, 68.24 (CH_2), 67.18, 67.17, 66.21, 65.79 (CH_2), 61.39 (2 CH_2), 52.53 (CH_3), 34.02 (CH_2), 28.54 (CH_2), 25.40 (CH_2), 24.40 (CH_2). FAB-HR-MS calcd. for $C_{25}H_{45}O_{18}$ $[M + H]^+$: 633.2606; found: 633.2630.

5-Carboxypentyl (α-D-mannopyranosyl)-(1→3)-[(α-D-mannopyranosyl)-(1→6)]-α-D-mannopyranoside (25)

Acid **25** (774 mg, 96%) was obtained from methyl ester **24** (821 mg, 1.30 mmol) by use of the procedure applied to make analogue **9**: $[\alpha]_D^{20}$ +87.3 (*c* 0.75, H_2O). ^{13}C NMR (D_2O) δ: 179.56 (C=O), 102.71, 100.26, 99.78 (C-1, C′-1, C″-1), 79.00, 73.68, 73.06, 71.47, 71.05, 70.79, 70.47, 70.40, 70.13, 68.20 (CH_2), 67.14, 66.20, 65.77 (CH_2), 61.37 (2 CH_2), 34.37 (CH_2), 28.57 (CH_2), 25.41 (CH_2), 24.51 (CH_2). FAB-HR-MS calcd. for $C_{24}H_{43}O_{18}$ $[M + H]^+$: 619.2449; found: 619.2468.

5-[Carboxy-2-(1,2-dihexadecanoyl-sn-glycero-3-phospho)ethanolamido]pentyl (α-D-mannopyranosyl)-(1→3)-[(α-D-mannopyranosyl)-(1→6)]-α-D-mannopyranoside sodium salt (6)

Fom acid **25** (125 mg, 0.202 mmol), following the procedure described to make amide **14**, crude succinimidyl derivative (**26**) was obtained, and was used without further purification, following the method described for making the glycolipid **5**. The sodium salt **6** (132 mg, 50% from acid **25**)

© 2002 NRC Canada

was isolated after column chromatography on silica gel with $CHCl_3$–MeOH–H_2O (5:4:1) as eluent: $[\alpha]_D^{20}$ +37.0 (*c* 0.6, $CHCl_3$–MeOH, 2:1). ^{13}C NMR ($CDCl_3$–CD_3OD) δ: 102.71, 100.26 and 99.78 (C-1, C-1′, C-1″), 79.00, 73.68, 73.06, 71.47, 71.05, 70.79, 70.47, 68.20, 67.14, 66.20, 63.87 (CH_2), 63.35 (CH_2), 62.38 (CH_2), 61.35 (CH_2), 40.03 (CH_2), 35.84 (CH_2), 33.93 (CH_2), 33.78 (CH_2), 33.42 (CH_2), 31.67 (CH_2), 29.40 (CH_2), 29.08 (CH_2), 28.86 (CH_2), 25.69 (CH_2), 25.25 (CH_2), 24.65 (CH_2), 22.36 (CH_2), 13.41 (CH_3). FAB-HR-MS calcd. for $C_{61}H_{113}NNa_2O_{25}P$ $[M + Na]^+$: 1336.7135; found: 1336.7076.

2-[2-(2-Chloroethoxy)ethoxy]ethyl 2,3,4,6-tetra-O-*benzoyl*-α-D-*mannopyranoside (27)*

2-[2-(2-Chloroethoxy)ethoxy]ethanol (1.00 g, 5.95 mmol) was glycosylated according to the procedure described for making glycoside **7**, to give product **27** (4.07 g, 91%): $[\alpha]_D^{20}$ −48.2 (*c* 0.57, $CHCl_3$). ^1H NMR ($CDCl_3$) δ: 6.11 (t, $J_{3,4}$, $J_{4,5}$ = 10.1 Hz, 1H, H-4), 5.94 (dd, $J_{2,3}$ = 3.3 Hz, 1H, H-3), 5.73 (dd, $J_{1,2}$ = 1.8 Hz, 1H, H-2), 5.16 (d, 1H, H-1), 4.70 (m, 1H, H-6), 4.50 (m, 2H, H-5,6′), 4.00–3.61 (m, 12H, spacer protons). ^{13}C NMR ($CDCl_3$) δ: 98.22 (C-1), 71.83 (CH_2), 71.20 (CH_2), 71.14 (CH_2), 70.90, 70.61 (CH_2), 70.47, 69.25, 68.05 (CH_2), 67.39, 63.27 (CH_2), 43.18 (CH_2). FAB-HR-MS calcd. for $C_{40}H_{40}ClO_{12}$ $[M + H]^+$: 747.2208; found: 747.2184.

2-[2-(2-Cyanoethoxy)ethoxy]ethyl 2,3,4,6-tetra-O-*benzoyl*-α-D-*mannopyranoside (28)*

A mixture of chloro-compound **27** (3.98 g, 5.33 mmol), potassium cyanide (3.26 g 50 mmol), and DMSO (40 mL) was stirred under argon at 65°C for 22 h. Water (100 mL) was added, and the mixture was extracted with EtOAc (4 × 50 mL). The combined organic extracts were washed with H_2O (20 mL), dried (Na_2SO_4), and evaporated to dryness. Column chromatography (hexane–EtOAc, 1:1) of the residue gave the nitrile **28** (2.77 g, 70%): $[\alpha]_D^{20}$ –37.2 (*c* 0.78, $CHCl_3$). IR (film) (cm^{-1}): 2253. ^1H NMR ($CDCl_3$) δ: 6.11 (t, $J_{3,4}$, $J_{4,5}$ = 10.1 Hz, 1H, H-4), 5.93 (dd, $J_{2,3}$ = 3.3 Hz, 1H, H-3), 5.72 (dd, $J_{1,2}$ = 1.8 Hz, 1H, H-2), 5.16 (d, 1H, H-1), 4.70 (m, 1H, H-6), 4.50 (m, 2H, H-5,6′), 4.00–3.70 (m, 12H, spacer H), 2.63 (t, *J* = 6.4 Hz, 2H, C*H*$_2$CN). ^{13}C NMR ($CDCl_3$) δ: 118.34 (CN), 98.23 (C-1), 71.19 (2 × CH_2), 70.88, 70.64 (CH_2), 70.47, 69.28, 68.02 (CH_2), 67.39, 66.44 (CH_2), 63.26 (CH_2), 19.28 (CH_2). FAB-HR-MS calcd. for $C_{41}H_{40}NO_{12}$ $[M + H]^+$: 738.2550; found: 738.2573.

2-[2-(2-Cyanoethoxy)ethoxy]ethyl α-D-*mannopyranoside (29)*

De-esterification of tetrabenzoate **28** (320 mg, 0.43 mmol), following the procedure described for making glycoside **8**, gave glycoside **29** (128 mg, 92%): $[\alpha]_D^{20}$ +47.0 (*c* 0.61, MeOH). IR (film) (cm^{-1}): 2252.; ^{13}C NMR (CD_3OD) δ: 120.16 (CN), 102.13 (C-1), 74.99, 72.99, 72.51, 72.02 (CH_2), 71.95 (CH_2), 71.85 (CH_2), 69.03, 68.18 (CH_2), 67.51 (CH_2), 63.35 (CH_2), 19.66 (CH_2). FAB-HR-MS calcd. for $C_{13}H_{24}NO_8$ $[M + H]^+$: 322.1502; found: 322.1500.

*2-[2-(2-*α-D-*Carboxyethoxy)ethoxy]ethyl* α-D-*mannopyranoside (30)*

A mixture of nitrile **29** (79 mg, 0.24 mmol) in NaOH (1 mL, 3 M) was stirred at room temperature for 24 h, neutralized with Amberlyst 15 (H^+) resin, filtered, and freeze-dried to afford acid **30** (81 mg, 100%): $[\alpha]_D^{20}$ +38.0 (*c* 0.41, H_2O). ^{13}C NMR (D_2O) δ: 176.89 (C=O), 100.37 (C-1), 73.16, 72.14 (CH_2), 70.92, 70.37, 69.98 (CH_2), 67.18, 66.87 (CH_2), 61.35 (CH_2), 60.81 (CH_2) 57.80 (CH_2), 37.34 (CH_2). FAB-HR-MS calcd. for $C_{13}H_{25}O_{10}$ $[M + H]^+$: 341.1448; found: 341.1449.

2-[2-(2-Azidoethoxy)ethoxy]ethyl 2,3,4,6-tetra-O-*benzoyl*-α-D-*mannopyranoside (31)*

A mixture of chloro-compound **27** (2.785 g, 3.72 mmol), sodium azide (2.6 g 40 mmol), and DMF (40 mL) was stirred under argon at 65°C for 19 h. Water (60 mL) was added, and the mixture was extracted with EtOAc (3 × 30 mL). The combined organic extracts were washed with water (10 mL), dried (Na_2SO_4), and evaporated to dryness. Column chromatography (hexane–EtOAc, 1:1) of the residue gave of azide **31** (2.655 g, 95%): $[\alpha]_D^{20}$ –43.7 (*c* 0.6, $CHCl_3$). IR (film) (cm^{-1}): 2105. ^1H NMR ($CDCl_3$) δ: 6.11 (t, $J_{3,4}$, $J_{4,5}$ = 10.0 Hz, 1H, H-4), 5.95 (dd, $J_{2,3}$ = 3.3 Hz, 1H, H-3), 5.73 (dd, $J_{1,2}$ = 1.8 Hz, 1H, H-2), 5.16 (d, 1H, H-1), 4.70 (m, 1H, H-6), 4.50 (m, 2H, H-5,6′), 4.0–3.6 (m, 10H, spacer H), 3.38 (t, *J* = 5.0 Hz, 2H, CH_2N_3). ^{13}C NMR ($CDCl_3$) δ: 98.23 (C-1), 71.28 (CH_2), 71.15 (CH_2), 70.90, 70.63 (CH_2), 70.50, 69.25, 68.06 (CH_2), 67.40, 63.26 (CH_2), 51.10 (CH_2), 14.57 (CH_2). FAB-HR-MS calcd. for $C_{40}H_{39}N_3O_{12}Cs$ $[M + Cs]^+$: 886.1588; found: 886.1538.

2-{2-[2-(5-Methoxycarbonylpentanoylamino)ethoxy]ethoxy}ethyl α-D-*mannopyranoside (34)*

To a solution of azide **31** (1.30 g, 1.72 mmol) in EtOH (25 mL), $NaBH_4$ (325 mg, 8.5 mmol) was added followed by a solution of $NiCl_2$ in EtOH (1.5 mL, 0.2 M), and the mixture was stirred at room temperature for 45 min, filtered through a pad of silica gel (thickness ~ 5 cm) and washed with $CHCl_3$–MeOH (2:1). The filtrate and washings were taken to dryness and purified by column chromatography ($CHCl_3$–MeOH, 3:1) to give the amine **32** (660 mg, 53%). ^{13}C NMR (CD_3OD) δ: 99.53 (C-1), 72.15, 71.99 (CH_2), 71.90, 71.64 (CH_2), 71.49 (CH_2), 70.50, 68.91 (CH_2), 68.41, 68.33 (CH_2), 64.00 (CH_2), 41.05 (CH_2). A solution of amine **32** (200 mg, 0.27 mmol), monomethyl adipate (48 mg, 0.3 mmol), and 2-ethoxy-1-ethoxycarbonyl-1,2-dihydroquinoline (12) (74 mg, 0.3 mmol) in EtOH (10 mL) was heated under reflux for 3 h and taken to dryness in vacuo. Column chromatography ($CHCl_3$–MeOH, 50:1) of the residue gave amide **33** (244 mg, 100%). ^{13}C NMR ($CDCl_3$) δ: 98.23 (C-1), 71.04, 70.90 (CH_2), 70.72 (CH_2), 70.55, 70.49 (CH_2), 70.33 (CH_2), 69.28, 68.06 (CH_2), 67.35, 63.26 (CH_2), 51.84 (CH_3), 39.75 (CH_2), 36.51 (CH_2), 34.11 (CH_2), 25.46 (CH_2), 24.81 (CH_2). A mixture of amide **33** (1.615 g, 18.6 mmol) and K_2CO_3 (200 mg) in MeOH (20 mL) was stirred overnight, neutralized with Amberlyst 15 (H^+), filtered, and taken to dryness in vacuo. Column chromatography ($CHCl_3$–MeOH, 3:1) of the residue gave the de-esterified glycoside **34** (530 mg, 63%): $[\alpha]_D^{20}$ +32.1 (*c* 0.57, MeOH). ^{13}C NMR (CD_3OD) δ: 102.17 (C-1), 75.03, 73.01, 72.54, 72.02 (CH_2), 71.82 (CH_2), 71.71 (CH_2), 71.06 (CH_2), 69.07, 68.13 (CH_2), 63.40 (CH_2), 52.43 (CH_3), 40.79 (CH_2), 37.00 (CH_2), 34.86 (CH_2), 26.77 (CH_2), 25.91 (CH_2). FAB-

© 2002 NRC Canada

HR-MS calcd. for $C_{19}H_{36}NO_{11}$ $[M + H]^+$: 454.2288; found: 454.2326.

2-[2-(2-Cyanoethoxy)ethoxy]ethyl (2,3,4,6-tetra-O-benzoyl-α-D-mannopyranosyl)-(1→3)-[(2,3,4,6-tetra-O-benzoyl-α-D-mannopyranosyl)-(1→6)]-α-D-mannopyranoside (35)

Glycoside **29** (580 mg, 1.8 mmol) and 2,3,4,6-tetra-*O*-benzoyl α-D-mannopyranosyl trichloroacetimidate (2.667 g, 3.6 mmol) were treated according to the procedure described for making compound **21**, and gave mixed products (1.585 g). Column chromatography (hexane–EtOAc, 1:1) afforded the title trisaccharide derivative **35** (1.070 g, 40%): $[\alpha]_D^{20}$ –24.4 (*c* 0.36, $CHCl_3$). IR (film) (cm^{-1}): 2252.; ^1H NMR ($CDCl_3$) δ: 6.12 (t, J = 10 Hz, 2H, H-4′, H-4″), 6.00 (m, 2H, H-3′, H-3″), 5.86 (dd, $J_{1',2'}$ = 1.7 Hz, $J_{2',3'}$ = 3.0 Hz, 1H, H-2′), 5.79 (dd, $J_{1'',2''}$ = 1.7 Hz, $J_{2'',3''}$ = 3.2 Hz, 1H, H-2″), 5.44 (d, 1H, H-1″), 5.33 (d, 1H, H-1′), 4.83 (d, 1H, H-1), 3.90–4.95 (m, 12H), 3.60–3.72 (m, 10H, spacer H), 2.58 (t, J = 6.4 Hz, 2H, CH_2CN). ^{13}C NMR ($CDCl_3$) δ: 118.05 (CN), 100.07, 99.75, 97.62 (C-1,1′,1″), 82.54, 71.41, 70.73, 70.56, 70.22, 69.49, 68.91, 67.50, 66.98, 66.87, 65.90, 63.26, 62.96 (CH_2), 18.85 (*C*H_2CN); (other CH_2 carbon resonances not identified). FAB-HR-MS calcd. for $C_{81}H_{76}NO_{26}$ $[M + H]^+$: 1478.4656; found: 1478.4629.

2-[2-(2-Cyanoethoxy)ethoxy]ethyl (α-D-mannopyranosyl)-(1→3)-[(α-D-mannopyranosyl)-(1→6)]-α-D-mannopyranoside (37)

Standard acetylation of an analytical sample of the trisaccharide derivative **35** yielded 2-[2-(2-cyanoethoxy)ethoxy]ethyl 2,4-di-*O*-acetyl-(2,3,4,6-tetra-*O*-benzoyl-α-D-mannopyranosyl)-(1→3)-[(2,3,4,6-tetra-*O*-benzoyl-α-D-mannopyranosyl)-(1→6)]-α-D-mannopyranoside (**36**): $[\alpha]_D^{20}$ –20.2 (*c* 0.54, $CHCl_3$). IR (film) (cm^{-1}): 2252. ^1H NMR (500 MHz, $CDCl_3$) δ: 6.19 (t, $J_{3'',4''}$, $J_{4'',5''}$ = 10.1 Hz, 1H, H-4″), 6.12 (t, $J_{3',4'}$, $J_{4',5'}$ = 10.1 Hz, 1H, H-4′), 5.92 (dd, $J_{2',3'}$ = 3.3 Hz, 1H, H-3′), 5.81 (dd, $J_{2'',3''}$ = 3.3 Hz, 1H, H-3″), 5.73 (dd, $J_{1',2'}$ = 1.7 Hz, 1H, H-2′), 5.51 (dd, $J_{1'',2''}$ = 1.7 Hz, 1H, H-2″), 5.47 (dd, $J_{2,1}$ = 1.7 Hz, $J_{2,3}$ = 3.4 Hz, 1H, H-2), 5.43 (t, $J_{3,4}$, $J_{4,5}$ = 10.0 Hz, 1H, H-4), 5.36 (d, 1H, H-1″), 5.17 (d, 1H, H-1′), 4.94 (d, 1H, H-1), 4.69–4.75 (m, 2H, H-6′a, H-6″a), 4.55–4.63 (m, 2H, H-5′, H-5″), 4.49 (m, 2H, H-6′b, H-6″b), 4.40 (dd, 1H, H-3), 4.10 (m, 1H, H-5), 4.01 (dd, $J_{5,6}$ = 6.8 Hz, $J_{6a,6b}$ = 10.7 Hz, 1H, H-6a), 3.60–3.73 (m, 11H, H-6b and spacer H), 2.55 (t, J = 6.5 Hz, 2H, CH_2CN). ^{13}C NMR (125 MHz, $CDCl_3$) δ: 99.40 (C-1″), 97.87 (C-1), 97.73 (C-1′), 75.33 (C-3), 71.17 (C-2), 71.08 (C-2″, spacer CH_2), 70.90 (spacer CH_2), 70.73 (C-2′), 70.49 (C-3′, CH_2), 70.02 (C-5″), 69.85 (C-5), 69.77 (C-3″), 69.38 (C-5′), 68.90 (C-4), 67.43, 67.30 (C-6, spacer CH_2), 67.24 (C-4′), 66.87 (C-4″), 66.31 (spacer CH_2), 63.29 (C-6′), 62.91 (C-6″), 21.42 (Ac), 21.21 (Ac), 19.16 (*C*H_2CN).

A mixture of perester **35** (895 mg, 0.605 mmol) and K_2CO_3 (250 mg) in MeOH (30 mL) was stirred at room temperature for 22 h, neutralized to pH ~ 5 with Amberlyst 15 (H^+), filtered, and evaporated to dryness to afford title compound **37** (230 mg, 59%): $[\alpha]_D^{20}$ +73.9 (*c* 0.41, H_2O). ^{13}C NMR (D_2O) δ: 120.35 (CN), 102.78, 100.58 and 99.85 (C-1,1′,1″) 79.01, 73.74, 73.11, 71.49, 71.04, 70.81, 70.50, 70.38, 70.09 (CH_2), 69.97 (2 × CH_2), 67.17 (CH, CH_2), 66.10, 65.79 (2 × CH_2), 61.40 (2 × CH_2), 18.52 (*C*H_2CN). FAB-HR-MS calcd. for $C_{25}H_{44}NO_{18}$ $[M + H]^+$: 646.2558; found: 646.2560.

2-[2-(2-Carboxyethoxy)ethoxy]ethyl (α-D-mannopyranosyl)-(1→3)-[(α-D-mannopyranosyl)-(1→6)]-α-D-mannopyranoside (38)

Hydrolysis of the nitrile **37** (90 mg) was carried out in sodium hydroxide solution (2 mL, 3 M, aq) over 2 days at 20°C. Water (5 mL) was added and the base was neutralized to pH ~ 5 with Amberlyst resin (H^+). Evaporation of the solvent gave the title acid (95 mg, 102%): $[[\alpha]_D^{20}$ +70.0 (*c* 0.43, H_2O). ^{13}C NMR (D_2O) δ: 105.31, 103.12, 102.38 (C-1, C-1′, C-1″), 81.50, 76,29, 75.66, 74.70 (CH_2), 74.03, 73.57, 73.34, 72.93, 72.53 (2 CH_2), 69.70 (CH_2), 68.65, 68.24 (CH_2), 63.95 (2CH_2), 63.37 (CH_2), 37.92 (CH_2). FAB-HR-MS calcd. for $C_{25}H_{45}O_{20}$ $[M^+]$: 665.2504; found: 665.2508.

N-*[Tris-(2,3,4,6-tetra-O-acetyl-α-D-mannopyranosyloxymethyl)]methyl-(5-methoxycarbonyl)pentanoamide (39)*

A mixture of tetra-*O*-acetyl-α-D-mannopyranosyl bromide (3.69 g, 8.97 mmol), *N*-[tris(hydroxymethyl)]methyl-(5-methoxycarbonyl)pentanoamide (8) (590 mg, 2.24 mmol) and $HgCN_2$ (2.3 g, 9.1 mmol) in CH_3NO_2–toluene (1:1 v/v, 60 mL) was heated at 60°C for 3.5 h. The mixture was evaporated in vacuo to a syrup, dissolved in $CHCl_3$ (150 mL), and the organic layer was washed with NaCl solution (3 × 60 mL, sat., aq), H_2O (50 mL), dried (Na_2SO_4), and evaporated to dryness. Column chromatography ($CHCl_3$–MeOH, 30:1) of the residue gave the title compound (1.555 g, 55%): $[\alpha]_D^{20}$ +30.7 (*c* 0.88, $CHCl_3$). ^1H NMR ($CDCl_3$) δ: 5.33–5.17 (m, 9H, H-2,3,4), 4.85 (d, $J_{1,2}$ = 1.3 Hz, 3H, H-1), 4.34 (dd, $J_{5,5}$ = 4.9 Hz, $J_{6,6'}$ = 12.3 Hz, 3H, H-6), 4.13 (m, $J_{5,6'}$ = 2.4 Hz, H-6′, 6H, OC*H*HCN), 3.96 (m, 3H, H-5), 3.73 (d, $^2J_{H,H}$ = 10.1 Hz, 3H, OCH*H*CN), 3.66 (s, 3H, CH_3), 2.35 (m, 2H, CH_2), 2.11 (m, 2H, CH_2), 1.71 (m, 4H, CH_2), 2.14, 2.12, 2.04, 1.98 (4s, 36H, Ac). ^{13}C NMR ($CDCl_3$) δ: 103.06 (C-1), 73.84, 73.7, 71.11 (CH_2), 70.52, 66.78 (CH_2), 63.74 (C), 56.19 (CH_3), 41.25 (CH_2), 38.15 (CH_2), 29.72 (CH_2), 28.81 (CH_2), 25.31 (*C*H_3CO). FAB-HR-MS calcd. for $C_{53}H_{76}NO_{33}$ $[M + H]^+$: 1254.4300; found: 1254.4381.

N-*[Tris-(α-D-mannopyranosyloxymethyl)]methyl-(5-methoxycarbonyl)pentanoamide (40)*

To a solution of perester **39** (2.45 g, 1.95 mmol) in methanol (30 mL) was added NaOMe (2 drops, X M in MeOH) and the mixture was stirred at room temperature overnight. Removal of the solvent afforded the triglycoside **40** (1.47 g, 100%): $[\alpha]_D^{20}$ +45.4 (*c* 2.52, MeOH). ^{13}C NMR (CD_3OD) δ: 176.48 and 176.33 (C=O), 102.77 (C-1), 75.24, 73.16, 72.39, 69.22, 67.30 (CH_2), 63.22 (CH_2), 61.03 (C), 50.29 (CH_3), 37.60 (CH_2), 34.85 (CH_2), 26.92 (CH_2), 25.91 (CH_2). FAB-HR-MS calcd. for $C_{29}H_{52}NO_{21}$ $[M + H]^+$: 750.3032; found: 750.3067.

N-*[Tris-(α-D-mannopyranosyloxymethyl)]methyl-5-carboxypentanoamide (41)*

To a solution of methyl ester **40** (1.47 g, 1.95 mmol) in THF (30 mL) and H_2O (15 mL), sodium hydroxide (1.3 mL, 3 M aq) was added. The mixture was stirred for 48 h, neutralized with Amberlyst 15 resin (H^+), filtered, evaporated in vacuo, and freeze-dried to afford acid **41** (1.45 g, 100%):

© 2002 NRC Canada

$[\alpha]_D^{20}$ +42.7 (*c* 0.66, H_2O). ^{13}C NMR (D_2O) δ: 180.43 and 177.00 (C=O), 100.77 (C-1), 73.42, 71.10, 70.37, 67.16, 65.87 (CH_2), 61.25 (CH_2), 59.81 (C), 36.52 (CH_2), 35.00 (CH_2), 25.55 (CH_2), 24.61 (CH_2). FAB-HR-MS calcd. for $C_{28}H_{50}NO_{21}$ $[M + H]^+$: 736.2875; found: 736.2829.

Acknowledgements

We thank the New Zealand Foundation for Research, Science & Technology for funding, Dr H. Wong for NMR spectroscopy, HortResearch, Palmerston North, New Zealand for mass spectral analyses, and Prof. R.J. Ferrier for assistance in the preparation of this manuscript.

References

1. R.A.B. Ezekowitz and P.D. Stahl. J. Cell. Sci. Suppl. **9**, 121 (1998).
2. F. Sallusto, M. Cella, C. Danieli, and A. Lanzavecchia. J. Exp. Med. **182**, 389 (1995).
3. W. Jiang, W.J. Swiggard, C. Heufler, M. Peng, A. Mirza, R.M. Steinman, and M.C. Nussenzweig. Nature (London), **375**, 151 (1995).
4. H. Tanaka, Y. Nishida, and K. Kobayashi. J. Carbohydr. Chem. **19**, 413 (2000).
5. B. Becker, R.H. Furneaux, F. Reck, and O.A. Zubkov. Carbohydr. Res. **315**, 148 (1999).
6. K.J. Kaur and O. Hindsgaul. Glycoconjugate J. **8**, 90 (1991).
7. R. Roy, D. Page, S. Figueroa-Perez, and V. Verez-Bencomo. Glycoconjugate J. **15**, 251 (1998).
8. Y.C. Lee. Carbohydr. Res. **67**, 509 (1978).
9. T.K. Lindhorst, S. Kötter, U. Krallman-Wenzel, and S. Ehlers. J. Chem. Soc. Perkin Trans. 1, 823 (2001).
10. C.D. Reeve, D.H.G. Crout, K. Cooper, and M.J. Fray. Tetrahedron: Asymmetry, **3**, 785 (1992).
11. E. Bosone, P. Farina, G. Guazzi, S. Innocenti, V. Marotta, and U. Valcavi. Synthesis, 942 (1983).
12. B. Belleau and G. Malek. J. Am. Chem. Soc. **90**, 1651 (1968).

© 2002 NRC Canada

Synthesis and in vitro evaluation of substituted aryl- and hetarylmethyl phosphonate and phosphate — UMP derivatives as potential glucosyltransferase inhibitors

Asish K. Bhattacharya, Florian Stolz, Jürgen Kurzeck, Wolfgang Rüger, and Richard R. Schmidt

Abstract: The enzyme β(1→4)-glucosyltransferase (BGT) catalyses the transfer of glucose from uridine diphosphoglucose (UDP-Glc) to 5-hydroxymethylcytosine (5-HMC) bases in double-stranded DNA. Potential inhibitors of BGT were developed by structure-based design and synthesized. The designed inhibitors **1**–**6** provide conformational mimicry of the transition state in glucosyltransfer reactions. The key synthetic steps involve a Michaelis–Arbuzov reaction followed by coupling with uridine-5′-morpholidophosphate as activated UMP derivative. The compounds were tested for in vitro inhibitory activity against BGT and the inhibition kinetics were examined. Three of the designed molecules were found to be potential inhibitors of BGT having IC_{50} values in the micromolar (μM) range. Useful structure–activity relationships were established which provide guidelines for the design of future generations of inhibitors of BGT.

Key words: β-glucosyltransferase, transition state, enzyme inhibitors, structure-based design, synthesis.

Résumé : La transférase de β(1→4)-glucosyle (BGT) est un enzyme qui catalyse le transfert du glucose de l'uridine diphosphoglucose (UDP-Glc) aux bases 5-hydroxyméthylcytosines (5-HMC) de l'ADN à doubles brins. En se basant sur la structure, on a développé et réalisé la synthèse d'inhibiteurs potentiels de la BGT. Les inhibiteurs proposés (**1**–**6**) fournissent une imitation conformationnelle de l'état de transition des réactions de transfert du glucosyle. Les étapes de synthèse clés implique une réaction de Michaelis–Arbuzov, suivie d'un couplage avec un 5′-morpholinophosphate d'uridine sous la forme de dérivé activé UMP. L'activité inhibitrice des composés contre le BGT a été vérifiée in vitro et on a étudié la cinétique de l'inhibition. On a trouvé que trois des molécules synthétisées sont des inhibiteurs potentiels du BGT, avec des valeurs de IC_{50} au niveau micromolaire (μM). On a établi des relations structure–activité intéressantes; elles fournissent des indications générales pour le développement des futures générations d'inhibiteurs de BGT.

Mots clés : transférase de β-glucosyle, état de transition, inhibiteurs d'enzyme, développement sur la base de la structure, synthèse.

[Traduit par la Rédaction]

Introduction

The biosynthesis of complex carbohydrates, oligosaccharides, and other glycosylated cellular metabolites is of major importance, since these molecules are directly involved in numerous biological and cellular processes (1). The role of glycobiology ranges from storage of photosynthetic products, cell–cell recognition and adhesion, as well as glycosylation of proteins (2–6). Thus, in glycobiology, one of the central questions raised is understanding the fundamental basis of the incredibly diverse set of glycan structures observed in nature (7). What we do know is that there are a myriad of glycosyltransferases, each with its sugar specific donor and with acceptor and linkage specificity, which are responsible for the biosynthesis of these remarkably complex structures. From a medicinal chemist's standpoint, the study of these glycosyltransferases has begun to throw new light onto these areas ranging from bacterial toxicity to mammalian development. Moreover, the role played by glycosyltransferases in the etiology of disease, as well as their potential role as therapeutic targets, are also now being appreciated (8). Despite tremendous progress made in this

Received 4 December 2001. Published on the NRC Research Press Web site at http://canjchem.nrc.ca on 7 August 2002.

We dedicate this paper to the memory of Professor Raymond U. Lemieux.

A.K. Bhattacharya, F. Stolz, and R.R. Schmidt.[1] Fachbereich Chemie, Universität Konstanz, Fach M725, D-78457, Konstanz, Germany.
J. Kurzeck and Wolfgang Rüger. Arbeitsgruppe Molekulare Genetik, Fakultät für Biologie, Ruhr Universität, D-44780 Bochum, Germany.

[1]Corresponding author (e-mail: Richard.Schmidt@uni-konstanz.de).

 DOI: 10.1139/V02-119 © 2002 NRC Canada

field, the molecular basis of many processes are still uncertain (9). The glycosyltransferases of the Leloir pathway are key catalysts for the synthesis of oligosaccharides and glycoconjugates in vivo (10–14).

β(1→4)-Glucosyltransferase (BGT) is an enzyme encoded by a number of bacteriophages belonging to the T-even group. It catalyses the transfer of glucose from uridine diphosphoglucose (UDP-Glc) to 5-hydroxymethylcytosine (5-HMC) bases in double-stranded DNA (15). Glucosylation protects the infecting viral DNA from host restriction enzymes (16). In addition to its protective role, the glucosylation has also been implicated in the control of phage-specific gene expression by influencing transcripton in vivo and in vitro (17). Another example of DNA modification by glucosylation has been found in *Trypanosoma brucei* (18) where glucosylation is believed to be involved in regulating the expression of variant surface glycoproteins, used by the parasite for protection from immune recognition (19). BGT is one of two enzymes involved in the glucosylation of T4 phage DNA. In contrast to its counterpart α-glucosyltransferase (AGT), which forms α-glycosidic linkages, BGT catalyses the formation of β-glycosidic linkages, between the Glc and the modified 5-HMC base. Recognition specificity resides in the opposite base, namely G, therefore T4 BGT also glucosylates 5-HMU.[2] Regarding this glucosylation of 5-HMU, it does not take place if A or C or even an abasic site face 5-HMU on the opposite DNA strand. Thus, recognition specificity must reside in the hydroxymethyl group and the opposing G (20, 21). Inhibition or modulation of this transfer reaction provides an excellent opportunity for intervention of oligosaccharide biosynthesis and to obtain a more complete understanding of the structure–activity relationship of oligosaccharides on a molecular basis (22). This endeavour is also an interesting excursion to the basis of carbohydrate–protein recognition, which has gained seminal contributions by the late Professor Lemieux (23).

Earlier, we had reported (24) the synthesis of a transition state based analog of galactosyltransferase which exhibited high-inhibition properties towards galactosyltransferases. Encouraged by this, we have recently reported (25) transition-state-based analogs of sialyltransferases which showed very high affinity towards the enzyme in the nanomolar range. However, the aryl analogs mimicking the sugar of CMP-Neu5Ac turned out to be potent inhibitors exhibiting very high binding affinity to α(2→6)-sialyltransferase (26). Herein we describe the design, synthesis, and in vitro inhibiting activities of inhibitors **1**–**6** (27) (Fig. 1), in order to derive requirements for the structure–activity relationship of glucosyltransferases as well as to ascertain essential substituents on aryl and hetaryl moieties.

For the synthesis of sugar mimetics **1**–**4** the appropriate phosphonates **15**–**18** had to be synthesized first. We based our approach essentially on the Michaelis–Arbuzov reaction of bromides **11**–**14** with tris-(trimethylsilyl) phosphite to generate the corresponding phosphonates **15**–**18**. The required benzyl bromide derivatives **11** and **12** (28) were prepared from their corresponding methyl precursors **7** and **8**, respectively, by treating them with *N*-bromosuccinimide

Fig. 1. Structures of designed inhibitors **1**–**6**.

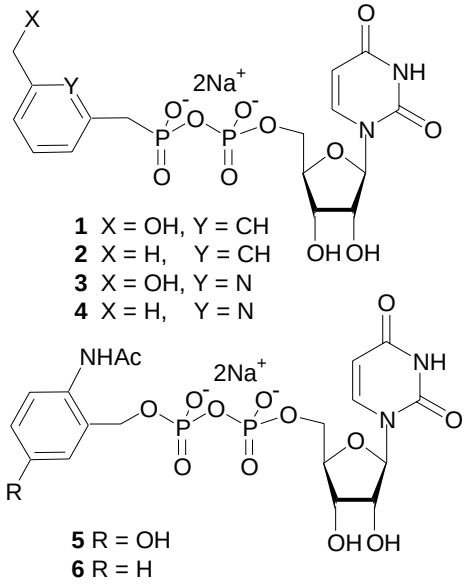

(NBS) in the presence of catalytic amounts of dibenzoyl peroxide (DBP) in refluxing carbon tetrachloride (Scheme 1). The bromides **11** and **12** on Michaelis–Arbuzov reaction with tris-(trimethylsilyl) phosphite in toluene at 95°C for 4 h furnished the respective bis-trimethylsilylphosphonates **15** and **16** based on the ^{1}H NMR spectra in quantitative yield. The bis-trimethylsilylphosphonates are highly labile to moisture and had to be stored under argon. They were used in the next step without further purification. The deprotection of the TMS groups and subsequent preparation of sodium salts were carried out in one pot by treating the phosphonates **15** and **16** with sodium methanolate in methanol at 0°C for 30 min, which after usual work up furnished disodium salts **19** and **20**. They were transformed into their corresponding bis-triethylammonium salts **23** and **24** by ion exchange (Amberlite IR-120, $HNEt_3^+$ form).

The synthesis of mimetics **1**–**6** was performed following a recent procedure (29*a*) which is an improved variant of the Moffat–Khorana phosphomorpholidate coupling method (29*b*). The phosphonophosphates or diphosphates were isolated in 42–52% yield. The ^{1}H NMR and ^{13}C NMR spectra showed the expected signals and total assignment could be performed by 2D NMR experiments. The ^{31}P NMR spectra also showed the characteristic signals associated with the phosphorous atom. Reaction of bis-triethylammonium salts **23** and **24** with uridine-5′-morpholidophosphate as activated UMP derivative in the presence of 1*H*-tetrazole in pyridine for 3 days at room temperature afforded **1** and **2** as white powders, respectively, after isolation and purification by HPLC, ion exchange (Amberlite IR-120 (Na^+ form)), and lyophilization.

In similar fashion, synthesis of **3** and **4** were also carried out (Scheme 1). Treatment of **9** (30) with NBS in the presence of catalytic amounts of α,α′-azo-isobutyronitrile (AIBN) in CCl_4 and irradiation of the reaction mixture for 8 h with a Hg lamp furnished **13** whereas bromide **14** (31, 32) was

[2] A manuscript based on the latest results of recognition specifity of BGT is in preparation by J. Kurzeck and W. Rüger.

© 2002 NRC Canada

Scheme 1. Reagents and conditions: (*i*) NBS, cat. DBP, CCl_4, reflux, 4 h, 40–45% (for **7** and **8**); (*ii*) NBS, cat. AIBN, CCl_4, Hg lamp, 8h, 45% (for **9**); (*iii*) CBr_4, PPh_3, NEt_3, CH_2Cl_2, 0°C, 1 h, 42% (for **10**); (*iv*) $P(OTMS)_3$, toluene, 95°C, 3.5–4 h, quant.; (*v*) 0.2 M NaOMe–MeOH, 0°C, 30 min, Amberlite IR-120 (H^+ form); (*vi*) Amberlite IR-120 ($HNEt_3^+$ form), 80–90% (two steps); (*vii*) UMP-morpholidate, 1*H*-tetrazole, py, 3 days, rt, RP-18; (*viii*) Amberlite IR-120 (Na^+ form), 42–52% (two steps).

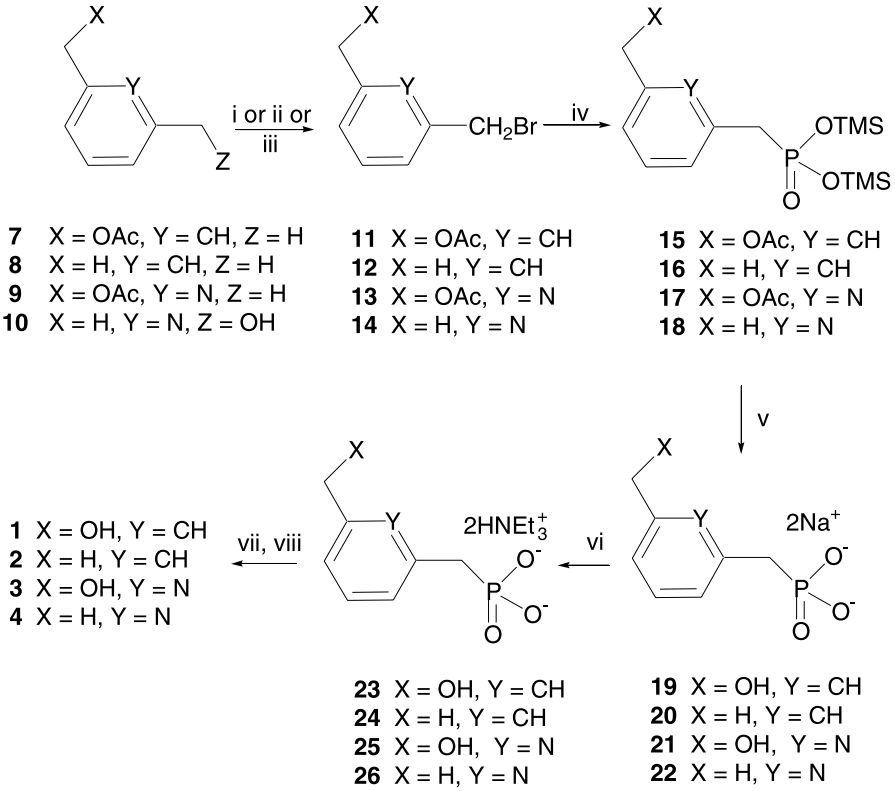

7 X = OAc, Y = CH, Z = H
8 X = H, Y = CH, Z = H
9 X = OAc, Y = N, Z = H
10 X = H, Y = N, Z = OH

11 X = OAc, Y = CH
12 X = H, Y = CH
13 X = OAc, Y = N
14 X = H, Y = N

15 X = OAc, Y = CH
16 X = H, Y = CH
17 X = OAc, Y = N
18 X = H, Y = N

1 X = OH, Y = CH
2 X = H, Y = CH
3 X = OH, Y = N
4 X = H, Y = N

23 X = OH, Y = CH
24 X = H, Y = CH
25 X = OH, Y = N
26 X = H, Y = N

19 X = OH, Y = CH
20 X = H, Y = CH
21 X = OH, Y = N
22 X = H, Y = N

prepared by treatment of **10** with CBr_4–Ph_3P–Et_3N in CH_2Cl_2 at 0°C. Subsequent reactions of bromides **13** and **14** with tris-trimethylsilyl phosphite furnished the corresponding phosphonates **17** and **18** which were transformed into their bis-triethylammonium salts **25** and **26** in the usual way. Their reaction with uridine-5′-morpholidophosphate in presence of 1*H*-tetrazole (29) in pyridine for 3 days at room temperature furnished **3** and **4** as white powders, respectively, after isolation and purification by HPLC, ion exchange (Amberlite IR-120 (Na^+ form)) and lyophilization.

The synthesis of compounds **5** and **6** were accomplished as delineated in Scheme 2. The required alcohol **28** was prepared from the readily available aldehyde **27** (33) in 60% yield by treating the latter with $NaBH_4$ in KH_2PO_4 buffer (34) in dry methanol (Scheme 3). The allyl protected phosphates **30** and **31** were synthesized in an one-pot reaction. The alcohols **28** and **29** (35) were coupled with bis(allyloxy)(diisopropylamino)phosphine in dry dichloromethane–acetonitrile (1:1) activated by 1*H*-tetrazole and then the resulting phosphites were oxidized with *tert*-butylhydroperoxide to phosphates **30** and **31** in 76 and 51% yield, respectively. The deprotection of allyl protecting groups were carried out by treating the allylesters **30** and **31** with dimedone in THF at room temperature catalyzed by tetrakis-(triphenylphosphine)-palladium. The bis-triethylammonium salts **32** and **33** were obtained after flash chromatography ($CHCl_3$–MeOH–H_2O, 6:4:1 + 1% Et_3N) in 64 and 72% yield, respectively.

Finally, compounds **5** and **6** were synthesized by the reaction of bis-triethylammonium salts **32** and **33** with uridine-5′-morpholidophosphate as activated UMP derivative in pyridine catalyzed by 1*H*-tetrazole (29) for 3 days at room temperature. Isolation and purification by HPLC followed by ion exchange [Amberlite IR-120 (Na^+ form)] and lyophilization afforded **5** and **6** as white powders in 43 and 45% yield, respectively.

Biological results

The compounds synthesized were tested for in vitro inhibitory activity with β(1→4)-glucosyltransferase which was isolated as previously reported (36). The biological studies reveal a strong structure–activity relationship for the binding of inhibitors **1**–**6** to BGT. The IC_{50} values (concentration of inhibitor at which 50% activity of the enzyme is observed) of inhibitors **1**–**6** were determined and are listed in Table 1. Inhibitor **2** showed an IC_{50} value of 1.9×10^{-3} M whereas compound **1** showed very little inhibition thereby indicating that the potential inhibitor from the substituted aryl group should be lipophilic. However, to our surprise compounds **3** and **4** were totally inactive. Acetamidobenzyl derivative **6** showed an IC_{50} value of 9.6×10^{-5} M ($K_i = 3.2 \times 10^{-5}$ M) whereas the *para*-hydroxy-substituted derivative **5** showed an IC_{50} value of 7.8×10^{-4} M. Thus, **6** exhibits an affinity to the enzyme which is comparable to the natural substrate (UDP-Glc: $K_M = 3.6 \times 10^{-5}$ M). X-ray studies with some of

© 2002 NRC Canada

Scheme 2. Reagents and conditions: (*i*) (*i*-Pr_2N)P(OAll)2, 1*H*-tetrazol, CH_2Cl_2–CH_3CN (1:1), rt, 2.5 h; (*ii*) *t*-BuOOH, 0°C, 1.5 h, 76% (for **30**), 51% (for **31**); (*iii*) dimedone, $Pd(PPh_3)_4$, THF, Et_3N, rt, 1.5 h, 64% (for **32**), 72% (for **33**); (*iv*) UMP-morpholidate, 1*H*-tetrazol, py, rt, 3 days, RP-18; (*v*) Amberlite IR-120 (Na^+ form), 43% (for **5**), 45% (for **6**).

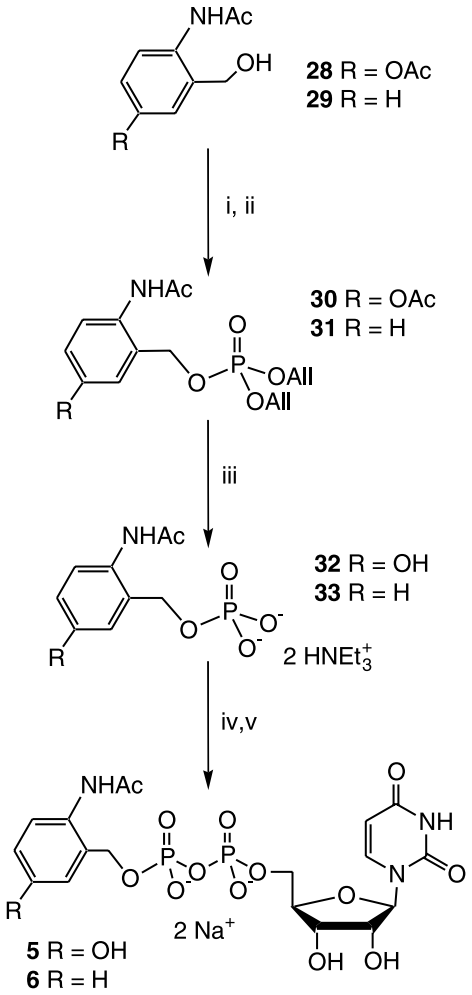

these compounds bound to BGT will be reported in due course.

In conclusion, our inhibition studies clearly indicate that: (*i*) phosphates **5** and **6** are better inhibitors than phosphonates **1**–**4** in general; (*ii*) acetamido functionality on the aryl residue greatly enhances the inhibition property; (*iii*) in phosphonates, methyl substitution shows some activity; and (*iv*) substituted pyridyl phosphonates **3** and **4** are not active at all. Our studies have also revealed that benzene rings are accepted by this glucosyltransferase (and presumably by carbohydrate processing enzymes in general) as mimics of carbohydrate residues. Thus, useful structure–activity relationships and further guidelines for the design of future generations of inhibitors of BGT are provided.

Experimental section

Solvents were purified according to the standard procedures. NMR measurements were recorded at 22°C on a Bruker AC250 Cryospec or Bruker DRX 600 spectrometers.

Scheme 3. Reagents and conditions: (*i*) $NaBH_4$, KH_2PO_4, MeOH, 30 min, rt, 60%.

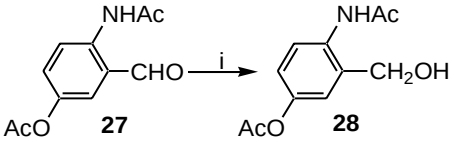

Table 1. IC_{50} values of transition-state analogues **1**–**6**.[a]

Inhibitor	IC_{50} (M)	K_i (competitive) (M)
1	$>5 \times 10^{-3}$	
2	$1.9\ (\pm 0.1) \times 10^{-3}$	
3	$>1 \times 10^{-2}$	
4	$>1 \times 10^{-2}$	
5	$7.8\ (\pm 0.3) \times 10^{-4}$	
6	$9.6\ (\pm 0.4) \times 10^{-5}$	$3.2\ (\pm 0.1) \times 10^{-5}$[b]
UDP	$1.8\ (\pm 0.1) \times 10^{-3}$	

[a]For details, see the *Experimental section.*
[b]K_M of UDP-Glc: 3.6×10^{-5} M.

Tetramethylsilane (TMS) or the resonance of the deuterated solvent was used as an internal standard; solvents: $CDCl_3$ (δ = 7.24), D_2O (δ = 4.63), [D_6]DMSO (δ = 2.49). For ^{31}P NMR, phosphoric acid was used as an external standard; ^{31}P NMR spectra were broadband ^1H-decoupled. MALDI-mass spectra were recorded on a Kratos Kompact Maldi 1 and 2,5-dihydroxybenzoic acid (DHB) or 6-aza-2-thiothymine (ATT) were used as matrices. FAB mass spectra were measured on a Finnigan MAT312/AMD 5000 spectrometer. Thin layer chromatography (TLC) was performed on Merck silica gel plastic plates $60F_{254}$ or Merck glass plates RP-18; compounds were visualized by treatment with a solution of $(NH_4)_6Mo_7O_{24}{\cdot}4H_2O$ (20 g) and $Ce(SO_4)_2$ (0.4 g) in 10% sulfuric acid (400 mL). Flash chromatography was performed on J.T. Baker silica gel 60 (0.040–0.063 mm) at a pressure of 0.3 bar. MPLC was performed at a pressure of 5–10 bar; column: silica gel LiChroprep Si 60 (Merck, 15–25 μm, 28 × 2.5 cm). Preparative HPLC separations were performed on an Autochrom system with a Shimadzu LC8A preparative pump and a Rainin Dynamax UV 1 detector at 260 nm. The column used was a Lichrosorb RP-18, 7 μm, 250 × 16 mm (Knauer, Germany). Mixtures of acetonitrile and 0.05 M triethylammonium bicarbonate (TEAB) (pH 7.0 to 7.2) were used as the mobile phase.

2-Acetoxymethyl-6-methylpyridine (9)

2-Acetoxymethyl-6-methylpyridine (**9**) was synthesized following a procedure by Baker et al. (32). The NMR data were in good agreement with the reported data (30).

General procedure for the synthesis of compounds (11) and (12)

To a solution of **7** or **8** (6–9 mmol) in carbon tetrachloride (CCl_4) (20–60 mL), *N*-bromo succinamide (NBS) (1 equiv) and a catalytic amount of dibenzoyl peroxide (DBP) were added and refluxed for 4 h. Evaporation of the solvent and chromatography (MPLC or flash) of the residue afforded compounds **11** or **12**, respectively.

© 2002 NRC Canada

3-Bromomethylbenzyl acetate (11)

Treatment of 3-methylbenzyl acetate **7** (1.0 g, 6.1 mmol) according to the general procedure afforded **11** (620 mg, 42%) as a colorless oil after MPLC (toluene). R_f = 0.67 (petroleum ether–ethyl acetate, 19:1). ^{1}H NMR (250 MHz, $CDCl_3$) δ: 2.11 (s, 3H, COCH_3), 4.49 (s, 2H, Ar-CH_2Br), 5.10 (s, 2H, Ar-CH_2OAc), 7.34–7.38 (m, 4H, Ar-*H*). MS (EI) (*m*/*z*): 242 (M^+). Anal. calcd. for $C_{10}H_{11}BrO_2$ (243.01): C 49.43, H 4.56; found: C 49.23, H 4.50.

3-Methylbenzyl bromide (12)

Treatment of *m*-xylene **8** (1.0 g, 9.4 mmol) according to the general procedure afforded **12** (780 mg, 45%) as a colorless oil after flash chromatography (petroleum ether–ethyl acetate, 19:1). R_f = 0.60 (petroleum ether–ethyl acetate, 19:1). The physical data were in agreement with the reported (28) data.

2-Acetoxymethyl-6-bromomethylpyridine (13)

A mixture of **9** (1.0 g, 6.0 mmol), NBS (1.1 g, 6.1 mmol) and α,α′-azo-isobutyronitrile (AIBN) (100 mg, 0.61 mmol) in CCl_4 (65 mL) was irradiated with a Hg lamp for 8 h. Flash chromatography (petroleum ether–ethyl acetate, 7:3) afforded **13** (660 mg, 45%) as a colorless oil. R_f = 0.44 (petroleum ether–ethyl acetate, 3:2). ^{1}H NMR (250 MHz, $CDCl_3$) δ: 2.17 (s, 3H, COCH_3), 4.55 (s, 2H, Ar-CH_2Br), 5.23 (s, 2H, Ar-CH_2OAc), 7.28 (d, $J_{3,4}$ = 7.6 Hz, 1H, H-3), 7.40 (d, $J_{5,4}$ = 7.6 Hz, 1H, H-5), 7.72 (dd, $J_{4,3}$ = $J_{4,5}$ = 7.6 Hz, 1H, H-4). MS (EI) (*m*/*z*): 243 (M^+). Anal. calcd. for $C_9H_{10}NO_2Br$ (244.1): C 44.44, H 4.12, N 5.76; found: C 44.34, H 4.18, N 5.66.

2-Bromomethyl-6-methylpyridine (14)

To a stirred solution of 2-(hydroxymethyl)-6-methylpyridine (1.0 g, 8.1 mmol) in dry CH_2Cl_2 (80 mL) at 0°C, carbon tetrabromide (CBr_4) (3.2 g, 9.8 mmol), triphenyl phosphine (PPh_3) (2.6 g, 9.8 mmol), and triethylamine (Et_3N) (1.1 mL, 820 mg, 8.1 mmol) were added successively. After 1 h when the reaction was complete (TLC), the reaction mixture was dried in vacuo and purified by flash chromatography (*n*-pentane–diethyl ether, 9:1) to afford **14** (630 mg, 42%) as a colorless oil. The physical data were in full agreement with the reported data (32). R_f = 0.29 (*n*-pentane–diethyl ether, 4:1). ^{1}H NMR (250 MHz, $CDCl_3$) δ: 2.56 (s, 3H, CH_3), 4.52 (s, 2H, Ar-CH_2Br), 7.07 (d, $J_{3,4}$ = 7.7 Hz, 1H, H-3), 7.25 (d, $J_{5,4}$ = 7.7 Hz, 1H, H-5), 7.58 (dd, $J_{4,3}$ = $J_{4,5}$ = 7.7 Hz, 1H, H-4). MS (EI) (*m*/*z*): 185 (M^+), 106 $(M - Br)^+$. Anal. calcd. for C_7H_8NBr (186.1): C 45.51, H 4.32, N 7.57; found: C 45.36, H 4.34, N 7.48.

General procedure for the synthesis of phosphonates (15–18)

A mixture of **11**, **12**, **13**, or **14** (1 mmol) and tris-(trimethylsilyl) phosphite (2 mmol) in dry toluene (2 mL) was heated under argon to 95°C for 4 h to afford **15**, **16**, **17**, or **18**, respectively, in a quantitative reaction (^{1}H NMR). The formed trimethylsilyl bromide was distilled off under slightly reduced pressure. The mixture was concentrated in vacuo and excess tris-(trimethylsilyl) phosphite was removed under high vacuum (0.01 mbar). The residue to be kept under argon was used as such in the next step without further purification.

Bis-(trimethylsilyl) 3-(acetoxymethyl)benzylphosphonate (15)

A mixture of **11** (160 mg, 0.67 mmol) and tris-(trimethylsilyl) phosphite (420 μL, 2.0 mmol) in dry toluene (2 mL) was treated as described in the general procedure to afford **15** as a colorless oil which was used in the next step without further purification. ^{1}H NMR (600 MHz, $CDCl_3$) δ: 0.27 (d, J = 1.2 Hz, 18H, 6CH_3), 2.08 (s, 3H, COCH_3), 3.06 (d, J = 22.3 Hz, 2H, Ar-CH_2P), 5.07 (s, 2H, Ar-CH_2OAc), 7.22–7.43 (m, 4H, Ar-*H*). ^{13}C NMR (150.8 MHz, $CDCl_3$) δ: 0.9, 1.0 (6C, 6CH_3), 21.0 (1C, COCH_3), 35.5 (d, $J_{C,P}$ = 156.1 Hz, 1C, Ar-CH_2P), 66.1 (1C, Ar-CH_2OAc), 126.6, 128.6, 129.7, 130.0, 132.6, 136.1 (6C, Ar), 170.8 (1C, COCH$_3$). ^{31}P NMR (243 MHz, $CDCl_3$) δ: 21.81. MS (EI) (*m*/*z*): 388 (M^+) for $C_{16}H_{29}O_5PSi_2$ (388.5).

Bis-(trimethylsilyl) 3-methylbenzylphosphonate (16)

A mixture of **12** (195 mg, 1.06 mmol) and tris-(trimethylsilyl) phosphite (600 μL, 2 mmol) in dry toluene (2 mL) was treated as described in the general procedure above to afford **16** as a colorless oil. ^{1}H NMR (600 MHz, $CDCl_3$) δ: 0.30 (d, J = 1.2 Hz, 18H, 6CH_3Si), 2.31 (s, 3H, CH_3), 3.02 (d, J = 22.1 Hz, 2H, Ar-CH_2P), 7.01–7.30 (m, 4H, Ar-*H*). ^{31}P NMR (243 MHz, $CDCl_3$) δ: 22.18. MS (EI) (*m*/*z*): 330 (M^+) for $C_{14}H_{27}O_3PSi_2$ (330.5).

Bis-(trimethylsilyl) 2-[6-(acetoxymethyl)pyridyl]methylphosphonate (17)

A mixture of **13** (360 mg, 1.50 mmol) and tris-(trimethylsilyl) phosphite (950 μL, 3.0 mmol) in dry toluene (2 mL) was treated as described in the general procedure above to afford **17** as a colorless oil. ^{1}H NMR (600 MHz, $CDCl_3$) δ: 0.31 (d, J = 1.2 Hz, 18H, 6CH_3Si), 2.12 (s, 3H, COCH_3), 3.31 (d, J = 22.7 Hz, 2H, Ar-CH_2P), 5.15 (s, 2H, Ar-CH_2OAc), 7.20 (d, $J_{3,4}$ = 7.7 Hz, 1H, H-3), 7.31 (d, $J_{5,4}$ = 7.7 Hz, 1H, H-5), 7.62 (dd, $J_{4,3}$ = $J_{4,5}$ = 7.7 Hz, 1H, H-4). ^{31}P NMR (243 MHz, $CDCl_3$) δ: 12.61. FAB-MS (positive mode, matrix: $CHCl_3$–NBA–NaI) (*m*/*z*): 390 $(M + H)^+$, 412 $(M + Na)^+$ for $C_{15}H_{28}NO_5PSi_2$ (389.5).

Bis-(trimethylsilyl) 2-(6-methylpyridyl)methylphosphonate (18)

A mixture of **14** (360 mg, 1.50 mmol) and tris-(trimethylsilyl) phosphite (950 μL, 3.0 mmol) in dry toluene (2 mL) was treated as described in the general procedure above to afford **18** as a colorless oil. ^{1}H NMR (600 MHz, $CDCl_3$) δ: 0.32 (d, J = 1.2 Hz, 18H, 6CH_3Si), 2.46 (s, 3H, CH_3), 3.24 (d, J = 22.7 Hz, 2H, Ar-CH_2P), 6.95 (d, $J_{3,4}$ = 7.6 Hz, 1H, H-3), 7.12 (d, $J_{5,4}$ = 7.6 Hz, 1H, H-5), 7.45 (dd, $J_{4,3}$ = $J_{4,5}$ = 7.6 Hz, 1H, H-4). MS (EI) (*m*/*z*): 331 (M^+) for $C_{13}H_{26}NO_3PSi_2$ (331.5).

General procedure for the synthesis of disodium salts (19–22)

The crude phosphonate (≅0.35g) was disolved in dry CH_2Cl_2 (3 mL) under argon and the solution added dropwise through a syringe to a sodium methoxide solution (30 mL, 0.2 M) at 0°C. After 30 min, small amounts of Amberlite IR-120 (H^+ form) were added to the solution with stirring till the solution became neutral (pH paper). The solution was

© 2002 NRC Canada

filtered and the resin was washed once with MeOH (5 mL) and added to the filtrate. The filtrate was evaporated and coevaporated with water to furnish a solid. Finally, the solid obtained was lyophilized with water to afford the disodium salt as a white powder.

Disodium 3-(hydroxymethyl)benzylphosphonate (19)

The phosphonate **15** (270 mg, crude material) was disolved in dry CH_2Cl_2 (3 mL) under argon and was treated with sodium methoxide solution (30 mL, 0.2 M) at 0°C as per the general procedure described above to yield **19** as a white powder (166 mg, 98%). ^{1}H NMR (600 MHz, $CDCl_3$) δ: 2.72 (d, J = 19.7 Hz, 2H, Ar-CH_2P), 4.46 (s, 2H, Ar-CH_2OH), 7.04–7.18 (m, 4H, Ar-*H*). ^{13}C NMR (151 MHz, D_2O) δ: 36.2 (d, $J_{C,P}$ = 127 Hz, 1C, Ar-*C*H_2P), 63.6 (1C, Ar-*C*H_2OH), 123.8, 127.9, 128.2, 128.5, 138.0, 139.2 (6C, Ar). ^{31}P NMR (243 MHz, D_2O) δ: 19.01. FAB-MS (negative mode, matrix: DMSO–H_2O–glycerol, 1:1:1) (*m*/*z*): 201 [M – 2Na^+ + H^+]$^-$ for $C_8H_9O_4PNa_2$ (246.1).

Disodium 3-methylbenzylphosphonate (20)

The phosphonate **16** (374 mg, crude material) was dissolved in dry CH_2Cl_2 (3 mL) under argon and was treated with sodium methoxide solution (30 mL, 0.2 M) at 0°C as per the general procedure described above to yield **20** as a white powder (250 mg, 96%). ^{1}H NMR (600 MHz, $CDCl_3$) δ: 2.17 (s, 3H, CH_3) 2.67 (d, J = 19.8 Hz, 2H, Ar-CH_2P), 6.97 (d, $J_{4,5}$ = 7.8 Hz, 1H, H-4), 7.05 (d, $J_{5,6}$ = 7.8 Hz, 1H, H-6), 7.10 (s, 1H, H-2), 7.13 (dd, $J_{5,4}$ = $J_{5,6}$ = 7.8 Hz, 1H, H-5). ^{31}P NMR (243 MHz, D_2O) δ: 19.02. FAB-MS (negative mode, matrix: H_2O–glycerol, 1:1) (*m*/*z*): 185 [M – 2Na^+ + H^+]$^-$ for $C_8H_9O_3PNa_2$ (230.1).

Disodium 2-[6-(hydroxymethyl)pyridyl]methylphosphonate (21)

The phosphonate **17** (580 mg, crude material) was dissolved in dry CH_2Cl_2 (3 mL) under argon and was treated with sodium methoxide solution (30 mL, 0.2 M) at 0°C as per the general procedure described above to yield **21** as a white powder (320 mg, 86%). ^{1}H NMR (250 MHz, $CDCl_3$) δ: 2.97 (d, J = 20.7 Hz, 2H, Ar-CH_2P), 4.96 (s, 2H, Ar-CH_2OH), 7.12 (d, $J_{3,4}$ = 7.8 Hz, 1H, H-3), 7.18 (d, $J_{5,4}$ = 7.8 Hz, 1H, H-5), 7.59 (dd, $J_{4,3}$ = $J_{4,5}$ = 7.8 Hz, 1H, H-4). FAB-MS (positive mode, matrix: H_2O – CH_3CN – 0.1% TFA, 1:1:1) (*m*/*z*): 248 [M + 2Na^+ + H]$^+$ for $C_7H_8NO_4PNa_2$ (247.1).

Disodium 2-(6-methylpyridyl)methylphosphonate (22)

The crude phosphonate **18** (1.11 g) was dissolved in dry CH_2Cl_2 (3 mL) under argon and was treated with sodium methoxide solution (30 mL, 0.2 M) at 0°C as per the general procedure described above to yield **22** as a white powder (693 mg, 90%). ^{1}H NMR (250 MHz, $CDCl_3$) δ: 2.41 (s, 3H, CH_3), 2.95 (d, J = 19.6 Hz, 2H, Ar-CH_2P), 7.15 (d, $J_{3,4}$ = 7.8 Hz, 1H, H-3), 7.28 (d, $J_{5,4}$ = 7.8 Hz, 1H, H-5), 7.74 (dd, $J_{4,3}$ = $J_{4,5}$ = 7.8 Hz, 1H, H-4). FAB-MS (negative mode, matrix: H_2O–glycerol, 1:1) (*m*/*z*): 186 [M – 2Na^+ + H^+]$^-$, 208 [M + Na^+]$^-$ for $C_7H_8NO_3PNa_2$ (231.1).

General procedure for the synthesis of bis-triethylammonium salts (23–26)

The disodium salts of **19**, **20**, **21**, or **22** were dissolved in H_2O and passed through a column (10 × 2.5 cm) containing Amberlite IR-120 ($HNEt_3^+$-form). The column was washed thoroughly with H_2O and all the fractions collected were lyophilized to afford **23**, **24**, **25**, or **26** as a colorless oil.

Bis-triethylammonium 3-(hydroxymethyl)benzylphosphonate (23)

The disodium salt **19** (250 mg, 1.02 mmol) was treated as per the general procedure described above to furnish **23** as a colorless oil (380 mg, 92%). ^{1}H NMR (600 MHz, D_2O) δ: 1.19 (t, J = 7.3 Hz, 18H, NCH$_2$CH_3), 2.96 (d, J = 20.6 Hz, 2H, Ar-CH_2P), (q, J = 7.3 Hz, 12H, NCH_2CH$_3$), 4.54 (s, 2H, Ar-CH_2OH), 7.11 (m, 2H, H-4, H-6), 7.17 (s, 1H, H-2), 7.19 (dd, $J_{5,4}$ = $J_{5,6}$ = 7.6 Hz, 1H, H-5). ^{13}C NMR (151 MHz, D_2O) δ: 7.7 (1C, NCH$_2$CH$_3$), 35.1 (d, $J_{C,P}$ = 128 Hz, 1C, Ar-*C*H_2P), 46.2 (1C, NCH$_2$CH$_3$), 63.4 (1C, Ar-*C*H_2OH), 124.7, 128.1, 128.2, 128.4, 135.0, 139.7 (6C, Ar). ^{31}P NMR (243 MHz, D_2O) δ: 19.49 Hz. FAB-MS (negative mode, matrix: MeOH–glycerol, 1:1) (*m*/*z*): 201 [M – 2$HNEt_3^+$ + H^+]$^-$ for $C_{20}H_{41}N_2O_4P$ (404.5).

Bis-triethylammonium 3-methylbenzylphosphonate (24)

The disodium salt **20** (100 mg, 0.43 mmol) was treated as per the general procedure described above to furnish **24** as a colorless oil (156 mg, 92%). ^{1}H NMR (600 MHz, D_2O) δ: 1.09 (t, J = 7.3 Hz, 18H, NCH$_2$CH_3), 2.14 (s, 3H, CH_3), 2.82 (d, J = 20.7 Hz, 2H, Ar-CH_2P), 3.01 (q, J = 7.3 Hz, 12H, NCH_2CH$_3$), 6.80–7.12 (m, 4H, Ar-*H*). FAB-MS (negative mode, matrix: MeOH–glycerol, 1:1) (*m*/*z*): 185 [M – 2$HNEt_3^+$ + H^+]$^-$ for $C_{20}H_{41}N_2O_3P$ (388.5).

Bis-triethylammonium 2-[6-(hydroxymethyl)pyridyl]methylphosphonate (25)

The disodium salt **21** (320 mg, 1.30 mmol) was treated as per the general procedure described above to furnish **25** as a colorless oil (478 mg, 92%). ^{1}H NMR (250 MHz, D_2O) δ: 1.06 (t, J = 7.3 Hz, 18H, NCH$_2$CH_3), 2.95 (q, J = 7.3 Hz, 12H, NCH_2CH$_3$), 3.09 (d, J = 21.7 Hz, 2H, Ar-CH_2P), 5.04 (s, 2H, Ar-CH_2OH), 7.31 (m, 2H, H-3, H-5), 7.79 (dd, $J_{4,3}$ = $J_{4,5}$ = 7.7 Hz, 1H, H-4). FAB-MS (positive mode, matrix: H_2O – CH_3CN – 0.1% TFA (1:1:1), glycerol) (*m*/*z*): 248 [M – $HNEt_3^+$ + 2Na^+ + H^+]$^+$ for $C_{19}H_{40}N_3O_4P$ (405.5).

Bis-triethylammonium 2-(6-methylpyridyl)methylphosphonate (26)

The disodium salt **22** (428 mg, 1.85 mmol) was treated as per the general procedure described above to furnish **23** as a colorless oil (605 mg, 84%). ^{1}H NMR (250 MHz, D_2O) δ: 1.09 (t, J = 7.3 Hz, 18H, NCH$_2$CH_3), 2.56 (s, 3H, CH_3), 3.02 (q, J = 7.3 Hz, 12H, NCH_2CH$_3$), 3.24 (d, J = 20.8 Hz, 2H, Ar-CH_2P), 7.59 (d, $J_{3,4}$ = 7.9 Hz, 1H, H-3), 7.62 (d, $J_{5,4}$ = 7.9 Hz, 1H, H-5), 8.23 (dd, $J_{4,3}$ = $J_{4,5}$ = 7.9 Hz, 1H, H-4). ^{31}P NMR (243 MHz, D_2O) δ: 13.80 Hz. FAB-MS (positive mode, matrix: CH_3CN – 0.1% TFA (1:1), glycerol) (*m*/*z*): 188 [M – 2NEt_3^+ + H^+]$^-$ for $C_{19}H_{40}N_3O_3P$ (389.5).

General procedure for the synthesis of (1–6)

A mixture of **23**, **24**, **25**, **26**, **31**, or **32** (0.13–0.25 mmol) and 4-morpholine-*N*,*N*′-dicyclohexylcarboxamidinium uridine 5′-monophosphomorpholidate (0.17–0.27 mmol) was evaporated with dry pyridine (3 × 1.5 mL). To this mixture, vacuum-dried 1*H*-tetrazole (0.29–1.10 mmol) and dry pyridine (1 mL) were added under argon and the solution was stirred

© 2002 NRC Canada

at room temperature (rt) for 3 days. The reaction mixture was evaporated and coevaporated with water (2 × 1 mL). The residue was purified by preparative HPLC (0.05 M triethylammonium hydrogencarbonate buffer + 4–8% MeCN, flow rate: 10–18 mL min^{-1}). The fractions containing product were pooled and evaporated. The residue was dissolved in water (2 mL) and passed through a column (2.5 × 12 cm) of Amberlite IR-120 (Na^+ form). The column was washed with water (50 mL) and the collected fractions were evaporated. The residue thus obtained was dissolved in a few drops of water and then precipitated with EtOH (5 mL). The suspended solution was centrifuged and the supernatant was carefully decanted to afford a white solid which was dissolved in water and lyophilized. After lyophilization, **1**, **2**, **3**, **4**, **5**, or **6** was obtained as a white powder in 42–52% yield.

Disodium uridine 5′-phosphono [3-(hydroxymethyl)benzyl]phosphate (1)

A mixture of **23** (86 mg, 0.21 mmol) and 4-morpholine-*N*,*N*′-dicyclohexylcarboxamidinium uridine 5′-monophosphomorpholidate (187 mg, 0.27 mmol) and 1*H*-tetrazole (32 mg, 0.46 mmol) in dry pyridine (1 mL) was treated as per the general procedure described above. After 3 days, the product was purified by HPLC (0.05 M triethylammonium hydrogencarbonate buffer + 6% MeCN, flow rate: 18 mL min^{-1}, t_R 14.0 min). Compound **1** was obtained as a white powder (62 mg, 52%) after ion exchange and precipitation. ^{1}H NMR (600 MHz, D_2O) δ: 3.10 (d, J = 21.4 Hz, H 2H, -1a″, H-1b″), 3.96 (m, 1H, H-5a′), 4.02 (m, 1H, H-5b′), 4.12 (m, 2H, H-3′, H-4′), 4.20 (dd, $J_{2',3'} = J_{2',1'}$ = 4.9 Hz, 1H, H-2′), 4.53 (s, 2H, -CH_2OH), 5.77 (d, $J_{5,6}$ = 8.0 Hz, 1H, H-5), 5.86 (d, $J_{1',2'}$ = 4.9 Hz, 1H, H-1′), 7.14–7.25 (m, 4H, H-3″, H-5″, H-6″, H-7″), 7.75 (d, $J_{6,5}$ = 8.0 Hz, 1H, H-6). ^{13}C NMR (151 MHz, D_2O, assignment by HMQC) δ: 35.06 (d, $J_{C,P}$ = 133.5 Hz, 1C, C-1″), 63.4 (1C, Ar-CH_2OH), 64.0 (1C, C-5′), 68.9 (1C, C-3′), 73.2 (1C, C-2′), 82.4 (1C, C-4′), 88.1 (1C, C-1′), 102.2 (1C, C-5), 124.7, 128.2, 128.3, 128.6, 134.4, 139.7 (6C, Ar), 140.6 (1C, C-6). ^{31}P NMR (243 MHz, D_2O) δ: –9.95 (d, J = 27.6 Hz, $P(O)O_3$), 15.04 (d, J = 27.6 MHz, $CP(O)O_2$). MS (MALDI, negative mode, matrix: ATT, H_2O) (*m*/*z*): 507.5 $[M - 2Na^+ + H^+]^-$ for $C_{17}H_{20}N_2O_{12}P_2Na_2$ (552.28).

Disodium uridine 5′-phosphono (3-methylbenzyl)phosphate (2)

A mixture of **24** (50 mg, 0.13 mmol) and 4-morpholine-*N*,*N*′-dicyclohexylcarboxamidinium uridine 5′-monophosphomorpholidate (116 mg, 0.17 mmol) and 1*H*-tetrazole (20 mg, 0.29 mmol) in dry pyridine (1 mL) was treated as per the general procedure described above. After 3 days, the product was purified by HPLC (0.05 M triethylammonium hydrogencarbonate buffer + 8% MeCN, flow rate: 18 mL min^{-1}, t_R 27.8 min). Compound **2** was obtained as a white powder (29 mg, 42%) after ion exchange and precipitation. ^{1}H NMR (600 MHz, D_2O) δ: 2.22 (s, 3H, CH_3), 3.05 (d, J = 21.4 MHz, 2H, H-1a″, H-1b″), 3.95 (m, 1H, H-5a′), 4.04 (m, 1H, H-5b′), 4.11 (m, 2H, H-3′, H-4′), 4.21 (dd, $J_{2',3'} = J_{2',1'}$ = 4.9 Hz, 1H, H-2′), 5.78 (d, 1H, $J_{5,6}$ = 8.1 Hz, H-5), 5.85 (d, $J_{1',2'}$ = 4.9 Hz, 1H, H-1′), 6.99–7.14 (m, 4H, H-3″, H-5″, H-6″, H-7″), 7.78 (d, $J_{6,5}$ = 8.1 Hz, 1H, H-6). ^{13}C NMR (151 MHz, D_2O) δ: 19.89 (1C, *C*H_3), 35.0 (d, $J_{C,P}$ = 135 Hz, 1C, C-1″), 63.9 (1C, C-5′), 68.8 (1C, C-3′), 73.2 (1C, C-2′), 82.5 (1C, C-4′), 8.0 (1C, C-1′), 102.0 (1C, C-5), 126.2, 127.8, 129.91, 129.95, 133.9, 137.8 (6C, Ar), 140.9 (1C, C-6), 151.3, 165.8 (2C, C-2, C-4). ^{31}P NMR (243 MHz, D_2O) δ: –10.3 (d, J = 27.7 Hz, $P(O)O_3$), 15.1 (d, J = 27.7 MHz, $CP(O)O_2$). MS (MALDI, negative mode, matrix: ATT, H_2O) (*m*/*z*): 491.6 $[M - 2Na^+ + H^+]^-$ for $C_{17}H_{20}N_2O_{11}P_2Na_2$ (536.28).

Disodium uridine 5′-phosphono {2-[6-(hydroxymethyl)pyridyl]methyl}phosphate (3)

A mixture of **25** (100 mg, 0.25 mmol) and 4-morpholine-*N*,*N*′-dicyclohexylcarboxamidinium uridine 5′-monophosphomorpholidate (227 mg, 0.33 mmol) and 1*H*-tetrazole (45 mg, 0.56 mmol) in dry pyridine (1 mL) was treated as per the general procedure described above. After 3 days, the product was purified by HPLC (0.05 M triethylammonium hydrogencarbonate buffer + 5% MeCN, flow rate: 10 mL min^{-1}, t_R 29.5 min). Compound **3** was obtained as a white powder (59 mg, 42%) after ion-exchange and precipitation. ^{1}H NMR (600 MHz, D_2O) δ: 3.28 (d, J = 21.8 Hz, 2H, H-1a″, H-1b″), 3.98 (m, 1H, H-5a′), 4.03 (m, 1H, H-5b′), 4.11 (m, 1H, H-4′), 4.13 (dd, $J_{3'',2''} = J_{3'',4''}$ = 4.9 Hz, 1H, H-3′), 4.20 (dd, $J_{2',3'} = J_{2',1'}$ = 5.0 Hz, 1H, H-2′), 4.59 (s, 2H, Ar-CH_2OH), 5.74 (d, $J_{5,6}$ = 7.8 Hz, 1H, H-5), 5.87 (d, 1H, $J_{1',2'}$ = 5.0 Hz, H-1′), 7.24 (d, $J_{5'',6''}$ = 7.6 Hz, 1H, H-5″), 7.30 (d, $J_{7'',6''}$ = 7.6 Hz, 1H, H-7″), 7.67 (dd, $J_{6'',5''} = J_{6'',7''}$ = 7.6 Hz, 1H, H-6″), 7.72 (d, $J_{6,5}$ = 7.8 Hz, 1H, H-6). ^{31}P NMR (243 MHz, D_2O) δ: –10.00 (d, J = 27.6 Hz, $P(O)O_3$), 12.20 (d, J = 27.6 MHz, $CP(O)O_2$). FAB-MS (positive mode, matrix: H_2O – CH_3CN – 0.1% TFA (1:1:1), glycerol) (*m*/*z*): 532 $[M - Na^+ + 2H^+]^+$ for $C_{16}H_{19}N_3O_{12}P_2Na_2$ (553.27).

Disodium uridine 5′-phosphono [2-(6-methylpyridyl)methyl]phosphate (4)

A mixture of **26** (70 mg, 0.18 mmol) and 4-morpholine-*N*,*N*′-dicyclohexylcarboxamidinium uridine 5′-monophosphomorpholidate (124 mg, 0.18 mmol) and 1*H*-tetrazole (22 mg, 0.31 mmol) in dry pyridine (1 mL) was treated as per the general procedure described above. After 3 days, the product was purified by HPLC (0.05 M triethylammonium hydrogencarbonate buffer + 4% MeCN, flow rate: 10 mL min^{-1}, t_R 14.13 min). Compound **4** was obtained as a white powder (58.5 mg, 42%) after ion exchange and precipitation. ^{1}H NMR (600 MHz, D_2O) δ: 2.46 (s, 3H, CH_3), 3.00 (d, J = 19.6 MHz, 2H, H-1a″, H-1b″), 4.06 (m, 1H, H-5a′), 4.13 (m, 2H, H-5b′, H-4′), 4.21 (m, 2H, H-3′, H-2′), 5.80 (d, $J_{5,6}$ = 8.1 Hz, 1H, H-5), 5.82 (d, $J_{1',2}$ = 4.2 Hz, 1H, H-1′), 7.20 (d, $J_{5'',6''}$ = 7.7 Hz, 1H, H-5″), 7.33 (d, 1H, $J_{7'',6''}$ = 7.8 Hz, H-7″), 7.79 (m, 2H, H-6″, H-6). ^{31}P NMR (243 MHz, D_2O) δ: –9.63 (bd, $P(O)O_3$), 17.14 (bd, $CP(O)O_2$). FAB-MS (positive mode, matrix: H_2O – CH_3CN – 0.1% TFA (1:1:1), glycerol) (*m*/*z*): 516 $[M - Na^+ + 2H^+]^+$ for $C_{16}H_{19}N_3O_{11}P_2Na_2$ (537.27).

2-Acetamido-5-acetoxy-benzaldehyde (27)

2-Acetamido-5-acetoxy-benzaldehyde (**27**) was synthesized as previously described (33).

© 2002 NRC Canada

4-Acetamido-3-hydroxymethylphenyl acetate (28)

To a solution of **27** (220 mg, 1.0 mmol) in dry methanol (25 mL), potassium dihydrogen phosphate (1.36 g, 10 mmol) was added. The reaction mixture was cooled to 0°C and then $NaBH_4$ (94 mg, 2.5 mmol) was added under argon and further stirred for 30 min. Then cold water (20 mL) was poured into the reaction mixture and the solution was acidified to pH 5 with 5% HCl solution. The methanol was distilled off and the aqueous phase was extracted with CH_2Cl_2 (5 × 80 mL). The organic phase was washed with water and dried over $MgSO_4$. Evaporation and flash chromatography (toluene–acetone, 3:1) afforded **28** (130 mg, 60%) as a white solid. R_f = 0.45 (toluene–acetone, 1:1), mp 140–142°C. ^{1}H NMR (250 MHz, [D_6]DMSO) δ: 2.03 (s, 3H, NHCOCH_3), 2.25 (s, 3H, OCOCH_3), 4.45 (d, J = 5.6 Hz, C 2H, H_2-Ar), 5.31 (t, J = 5.7 Hz, 1H, CH_2OH, exchanged with D_2O), 6.95 (dd, $J_{2,6}$ = 2.7 Hz, $J_{5,6}$ = 8.6 Hz, 1H, H-6), 7.15 (d, $J_{2,6}$ = 2.7 Hz, 1H, H-2), 7.41 (d, $J_{5,6}$ = 8.6 Hz, 1H, H-5), 9.29 (s, 1H, NH). Anal. calcd. for $C_{11}H_{13}NO_4$ (223.2): C 59.19, H 5.87; found: C 58.90; H 5.71.

(2-Acetamido-5-acetoxy-benzyl) diallyl phosphate (30)

To a solution of **28** (160 mg, 0.717 mmol) in a mixture of dry CH_2Cl_2 and dry MeCN (each 10 mL) under argon, vacuum-dried 1*H*-tetrazole (135 mg, 1.94 mmol) was added at room temperature. Bis(allyloxy)(diisopropylamino)phosphine (250 μL, 0.95 mmol) was added dropwise to the reaction mixture through a syringe under argon. After stirring at room temperature for 2.5 h, the reaction mixture was cooled to 0°C and 5.5 M *t*-BuOOH solution in Nonan (195 μL, 1.07 mmol) was added dropwise and after completion of the addition, the reaction mixture was further stirred for 1.5 h at room temperature. After completion of the reaction (TLC), $Na_2S_2O_3$ solution (50 mL) was poured into the reaction mixture. The organic phase was washed successively with NaCl solution, $NaHCO_3$ solution, and once again with NaCl solution (each 50 mL). The aqueous solution was extracted with CH_2Cl_2 (2 × 25 mL) and added to the organic phase. The pooled organic phase was dried ($MgSO_4$) and evaporated to dryness. The residue after flash chromatography (toluene–acetone, 4:1) afforded **30** as a colorless oil (210 mg, 76%). R_f = 0.52 (toluene–acetone, 1:1). ^{1}H NMR (250 MHz, $CDCl_3$) δ: 2.24 (s, 3H, NHCOCH_3), 2.30 (s, 3H,OCOCH_3), 4.49 (m, 4H, CH_2=CH-CH_2), 5.03 (d, J = 11.2 Hz, 2H, CH_2Ph), 5.22–5.37 (m, 4H, CH_2=CH-CH_2), 5.81–5.95 (m, 2H, CH_2=CH-CH_2), 7.12 (d, $J_{6,4}$ = 1.8 Hz, 1H, H-6), 7.14 (dd, $J_{4,3}$ = 9.5 Hz, $J_{4,6}$ = 1.8 Hz, 1H, H-4), 8.03 (d, $J_{3,4}$ = 9.5 Hz, 1H, H-3), 9.16 (bs, 1H, NH). MS (MALDI, positive mode, matrix: DHB, THF): 406.5 [M + Na]$^+$. Anal. calcd. for $C_{17}H_{22}NO_7P$ (383.3): C 53.27, H 5.78, N 3.65; found: C 53.16, H 5.87, N 3.45.

Bis-triethylammonium (2-acetamido-5-hydroxy)benzyl phosphate (32)

To a solution of **30** (180 mg, 0.47 mmol) in dry THF (6 mL), dimedone (330 mg, 2.35 mmol) and tetrakis-(triphenylphosphine)-palladium (100 mg, 0.087 mmol) was added and stirred at room temperature protected from light. After 1.5 h when the TLC showed no starting material, Et_3N (0.25 mL) was added and further stirred for 20 min at room temperature. The reaction mixture was evaporated and the residue was purified over flash chromatography ($CHCl_3$–MeOH–H_2O, 6:4:1 + 1% Et_3N) and afforded a mixture of **32** and 5-*O*-acetylated product which was dissolved in MeOH (50 mL). To this solution, Et_3N (4 mL) was added and stirred at 45°C for 20 h. The reaction mixture was evaporated in vacuum and lyophilized in water. After lyophilization, compound **32** was obtained as a colorless oil (140 mg, 64%). R_f = 0.3 ($CHCl_3$–MeOH–H_2O, 6:4:1). ^{1}H NMR (250 MHz, D_2O) δ: 1.08 (t, J = 7.4 Hz, 18H, NCH_2CH_3), 2.01 (s, 3H, COCH_3), 3.00 (q, J = 7.4 Hz, 12H, NCH_2CH$_3$), 4.59 (d, J = 6.4 Hz, 2H, CH_2Ar), 6.67 (dd, $J_{4,3}$ = 8.6 Hz, $J_{4,6}$ = 2.9 Hz, 1H, H-4), 6.87 (d, $J_{6,4}$ = 2.9 Hz, 1H, H-6), 7.04 (d, $J_{3,4}$ = 8.6 Hz, 1H, H-3). MS (MALDI, positive mode, matrix: DHB) (*m*/*z*): 284 [M – 2HEt$_3$N$^+$ + 2H$^+$ + Na$^+$]$^+$ for $C_{21}H_{41}N_3O_6P$ (463.5).

Disodium (2-acetamido-5-hydroxy)benzyl-uridine-5′-diphosphate (5)

A mixture of **32** (32 mg, 0.069 mmol) and 4-morpholine-*N*,*N*′-dicyclohexylcarboxamidinium uridine 5′-monophosphomorpholidate (106 mg, 0.15 mmol) and 1*H*-tetrazole (24 mg, 0.34 mmol) in dry pyridine (1 mL) was treated as per the general procedure described above. After 3 days, the product was purified by HPLC (0.05 M triethylammonium hydrogencarbonate buffer + 5% MeCN, flow rate: 16 mL min^{-1}, t_R 8.5 min). Compound **5** was obtained as a white powder (18.3 mg, 43%) after ion exchange and precipitation. ^{1}H NMR (250 MHz, D_2O) δ: 2.00 (s, 3H, COCH_3), 3.95–4.02 (m, 5H, H-2′, H-3′, H-4′, H-5a′, H-5b′), 4.69 (d, 2H, CH_2Ar), 5.56 (d, J = 8.1 Hz, 1H, 5-H), 5.66 (d, J = 2.9 Hz, 1H, H-1′), 6.61 (dd, $J_{4,3}$ = 8.6 Hz, $J_{4,6}$ = 2.8 Hz, 1H, H-4′′), 6.80 (d, $J_{6,4}$ = 2.8 Hz, 1H, H-6′′), 6.93 (d, $J_{3,4}$ = 8.6 Hz, 1H, H-3′′), 7.62 (d, J = 8.1 Hz, 1H, H-6). ^{31}P NMR (243 MHz, D_2O) δ: –12.2 (bd, 2P). MS (MALDI, negative mode, matrix: ATT, H_2O) (*m*/*z*): 566 [M – 2Na$^+$ + H$^+$]$^-$ for $C_{18}H_{21}N_3O_{14}P_2$ Na$_2$ (611.4).

2-Acetamidobenzyl alcohol (29)

2-Acetamidobenzyl alcohol (**29**) was synthesized from 2-aminobenzyl alcohol by following the procedure reported by Söderbaum and Widman (35*a*) in 95% yield. All the physical data were in agreement with the reported (35*b*) data.

2-Acetamidobenzyl diallyl phosphate (31)

To a solution of **29** (190 mg, 1.15 mmol) in a mixture of dry CH_2Cl_2 and dry MeCN (each 12.5 mL) under argon, vacuum dried 1*H*-tetrazole (220 mg, 3.14 mmol) was added at room temperature. Bis(allyloxy)(diisopropylamino)phosphine (557 μL, 2.18 mmol) was added dropwise to the reaction mixture through a syringe under argon. After stirring for 2.5 h at rt, the reaction mixture was cooled to 0°C, and 5.5 M *t*-BuOOH solution in Nonan (400 μL, 2.2 mmol) was added dropwise and on completion of the addition, the reaction mixture was further stirred for 1.5 h at rt. After completion of the reaction (TLC), $Na_2S_2O_3$ solution (50 mL) was poured into the reaction mixture. The organic phase was washed successively with NaCl solution, $NaHCO_3$ solution, and once again with NaCl solution (each 50 mL). The aqueous solution was extracted with CH_2Cl_2 (2 × 25 mL) and added to the organic phase. The pooled organic phase was

© 2002 NRC Canada

dried ($MgSO_4$) and evaporated to dryness. The residue after flash chromatography (toluene–acetone, 3:1) afforded **31** as a colorless oil (190 mg, 51%). R_f = 0.5 (toluene–acetone, 1:1). ^{1}H NMR (250 MHz, $CDCl_3$) δ: 2.24 (s, 3H, COCH_3), 4.48 (m, 4H, CH_2=CH-CH_2), 5.07 (d, J = 11.0 Hz, 2H, CH_2-Ar), 5.22–5.35 (m, 4H, CH_2=CH-CH_2), 5.80–5.96 (m, 2H, CH_2=CH-CH_2), 7.14 (dd, $J_{5,6}$ = 7.5 Hz, $J_{5,4}$ = 7.4 Hz, 1H, H-5), 7.34 (d, $J_{6,5}$ = 7.5 Hz, 1H, H-6), 7.41 (dd, $J_{4,3}$ = 7.5 Hz, $J_{4,5}$ = 7.4 Hz, 1H, H-4), 8.01 (d, $J_{3,4}$ = 7.5 Hz, 1H, H-3), 9.16 (bs, 1H, NH). MS (MALDI, positive mode, matrix: DHB, THF) (*m*/z): 348.5 $[M + Na^+]^+$, 364.6 $[M + K^+]^+$. Anal. calcd. for $C_{15}H_{20}NO_5P$ (325.3): C 55.38, H 6.20; found: C 55.11, H 6.27.

Bis-triethylammonium-2-acetamidobenzyl phosphate (33)

To a solution of **31** (130 mg, 0.40 mmol) in dry THF (6 mL), dimedone (320 mg, 2.28 mmol) was added and stirred at room temperature protected from light. After 1.5 h when the TLC showed no starting material, Et_3N (0.15 mL) was added and further stirred for 15 min at room temperature. The reaction mixture was evaporated and the residue was purified over flash chromatography ($CHCl_3$–MeOH–H_2O, 6:4:1 + 1% Et_3N). The product obtained after flash chromatography was lyophilized with water to afford **33** as a colorless powder (128 mg, 72%). R_f 0.37 ($CHCl_3$–MeOH–H_2O, 6:4:1). ^{1}H NMR (250 MHz, [D_6]DMSO) δ: 1.09 (t, J = 7.3 Hz, 18H, NCH_2CH_3), 2.07 (s, 3H, COCH_3), 2.89 (q, J = 7.3 Hz, 12H, NCH_2CH_3), 4.64 (d, J = 9.0 Hz, 2H, CH_2Ar), 6.99 (dd, $J_{5,4}$ = $J_{5,6}$ = 8.0 Hz, 1H, H-5), 7.24–7.27 (m, 2H, H-4, H-6), 8.00 (d, J = 8.0 Hz, 1H, H-3), 11.26 (bs, 1H, NH). ^{1}H NMR (250 MHz, D_2O) δ: 1.09 (t, J = 7.3 Hz, 18H, NCH_2CH_3), 2.04 (s, 3H, COCH_3), 3.01 (q, J = 7.3 Hz, 12H, NCH_2CH_3), 4.73 (d, overlapping with D_2O peak, CH_2Ar), 7.19–7.25 (m, 3H, H-4, H-5, H-6), 7.37 (d, J = 7.3 Hz, 1H, H-3). MS (MALDI, positive-mode, matrix: DHB, H_2O) (*m*/*z*): 268.6 $[M - 2HNEt_3^+ + 2H^+ + Na^+]^+$, 284.5 $[M - 2HNEt_3^+ + 2H^+ + K^+]^+$ for $C_{21}H_{41}N_3O_5P$ (447.53).

Disodium (2-acetamidobenzyl)-uridine-5′-diphosphate (6)

A mixture of **33** (100 mg, 0.22 mmol) and 4-morpholine-*N*,*N*′-dicyclohexylcarboxamidinium uridine 5′-monophosphomorpholidate (160 mg, 0.23 mmol) and 1*H*-tetrazole (77 mg, 1.1 mmol) in dry pyridine (1 mL) was treated as per the general procedure described above. After 3 days, the product was purified by HPLC (0.05 M triethylammonium hydrogencarbonate buffer + 5% MeCN, flow rate: 16 mL min^{-1}, t_R 14.0 min). Compound **6** was obtained as a white powder (57.8 mg, 45%) after ion exchange and precipitation. ^{1}H NMR (250 MHz, D_2O) δ: 2.04 (s, 3H, COCH_3), 3.90–4.01 (m, 5 H, H-2′, H-3′, H-4′, H-5a′, H-5b′), 4.74 (d, J = 4.4 Hz, 2H, CH_2Ar), 5.58 (d, J = 8.0 Hz, 1H, H-5), 5.66 (d, J = 3.2 Hz, 1H, H-1′), 7.12–7.19 (m, 3 H, H-4″, H-5″, H-6″), 7.32 (d, J = 6.9 Hz, 1H, H-3″), 7.63 (d, J = 8.0 Hz, 1H, H-6). ^{13}C-NMR (151 MHz, D_2O) δ: 22.3 ($COCH_3$), 64.5 (1C, C-5′), 64.5 (1C, Ar-CH_2), 69.2, 73.8, 83.0 (3C, C-2′, C-3′, C-4′), 88.6 (1C, C-1′), 102.4 (1C, C-5), 126.7–134.4 (6C, C-1″, C-2″, C-3″, C-4″, C-5″, C-6″), 141.4 (1C, C-6), 151.5, 166.0 (2C, C-2, C-4), 173.9 (1C, COCH$_3$). ^{31}P NMR (243 MHz, D_2O) δ: –12.5 (bd, 2P). FAB-MS (negative mode, matrix: glycerin + NBA, DMSO) (*m*/*z*): 594 $[M - H^+]^-$, 572 $[M - Na^+]^-$, 550 $[M - 2Na^+ + H^+]^-$ for $C_{18}H_{21}N_3O_{13}P_2Na_2$ (595.4).

Inhibition studies of β-glucosyltransferase of phage T4

The activity of β-glucosyltransferase was monitored by the transfer of ^{14}C-glucose from the substrate ^{14}C-UDPGlc to 5-hydroxymethylcytosine (HMC) of unglucosylated T4*DNA. T4*DNA was obtained from progeny phage propagating in a UDPGlc$^-$ *Escherichia coli* K host strain (W4597). The reaction mixture used to determine the IC_{50} in the inhibition studies, contained 100 mM Tris–HCl, pH 7.9, 9 μg of T4*DNA, 25 mM $MgC1_2$, 200 μM UDPGlc (Sigma), 5 μL of ^{14}C-UDPGlc (NEN, 330 mCi mmol^{-1} or 1.85 MBq, delivered in a total volume of 2 mL), 0.5 μg BGT and different inhibitors, with concentrations varying between 0.5 and 2.5 mM in a total assay volume of 100 μL. After 15 min of incubation at 30°C, the reaction mixtures were transferred onto DEAE filter disks (Whatman DE81). The filters were washed three times with 5 mL of a buffer containing 0.5 M NaH_2PO_4, pH 7.0, dried and counted in a Beckman scintillation counter, model LS 6000 TA.

K_m and V_{max} values were determined in essentially the same buffer and reaction volume, however, the concentrations of the substrate mixture varied between 1.6 and 200 μM and the inhibitors were added at constant concentrations of 0.5, 1, and 2 mM, respectively. The different substrate concentrations were obtained by the appropriate dilution of a mix containing UDPGlc and ^{14}C-UDPGlc in a ratio of 27.5:1. Radioactivity transferred from the substrate to the T4*DNA, again was measured as described above.

Acknowledgments

This work was supported by the Deutsche Forschungsgemeinschaft and the Fonds der Chemischen Industrie. A.K.B. is grateful to the *Deutscher Akademischer Austauschdienst* (DAAD) for a research fellowship. We are grateful to Ms. Anke Friemel and Mr. Klaus Hägele, Fachbereich Chemie, Universität Konstanz, Konstanz for recording NMR (600 MHz) and FAB-MS, respectively.

References

1. A.C. Weymouth-Wilson. Nat. Prod. Rep. **14**, 91 (1997).
2. A. Varki. Glycobiology, **3**, 97 (1993).
3. R.A. Dwek. Chem. Rev. **96**, 683 (1996).
4. S. Kornfeld and R. Kornfeld. Annu. Rev. Biochem. **54**, 631 (1985).
5. J.C. Paulson and K.J. Colley. J. Biol. Chem. **264**, 17 615 (1989).
6. J.W. Dennis, M. Granovsky, and C.E. Warren. BioEssays, **21**, 412 (1999).
7. (*a*) R.R. Schmidt. *In* Strategis for the chemical synthesis of glycoconjugates in glycosciences: Status and perspectives. *Edited by* H.-J. Gabius and S. Gabius. Chapman and Hall, Weinheim. 1997. pp. 31–53; (*b*) R.R. Schmidt. Pure Appl. Chem. **70**, 397 (1998), and refs. cited therein.
8. For recent reviews on glycosyltransferases see (*a*) D. Kapitonov and R.K. Yu. Glycobiology, **9**, 961 (1999); (*b*) C. Breton and A. Imberty. Curr. Opin. Struct. Biol. **9**, 563 (1999); (*c*) J M. Rini and N. Sharon. Curr. Opin. Struct. Biol. **10**, 507 (2000); (*d*) U.M. Ünligil and J.M. Rini. Curr. Opin. Struct. Biol. **10**, 510 (2000).

© 2002 NRC Canada

9. C. Schaub, B. Müller, and R.R. Schmidt. Glycoconjugate J. **15**, 345 (1998).
10. (*a*) L.F. Leloir. Science (Washington, D.C.), **172**, 1299 (1971); (*b*) L.F. Leloir, R. Caputto, C. E. Cardini, and A.C. Paladini. J. Biol. Chem. **184**, 333 (1950).
11. (*a*) B. Müller, T.J. Martin, C. Schaub, and R.R. Schmidt. Tetrahedron Lett. **39**, 509 (1998); (*b*) T.J. Martin and R.R. Schmidt. Tetrahedron Lett. **34**, 1765 (1993); (*c*) R.R. Schmidt, B. Wegmann, and K.-H. Jung. Liebigs Ann. Chem. 121 (1991).
12. (*a*) R. Schmidt. XIVth Int. Carbohydr. Sympl. PL 8, Stockholm (Sweden), Aug. 1988; (*b*) R.R. Schmidt, H. Gaden, and H. Jatzke. Tetrahedron Lett. **31**, 327 (1990); (*c*) R.R. Schmidt. *In* Carbohydrates — Synthetic methods and application in medicinal chemistry. *Edited by* H. Ogura, A. Hasegawa, and T. Suami. Kodoanasha Scientific Ltd., Tokyo. 1992. pp. 68–88.
13. (*a*) M.M. Palcic, L.D. Heerze, O.P. Srivastava, and O. Hindsgaul. J. Biol. Chem. **264**, 17 174 (1989); (*b*) D. Noort, G.A. van der Marel, A. van der Gen, G.J. Mulder, and J.H. van Boom. Recl. Trav. Chim. Pays–Bas, **110**, 53 (1991), and refs. cited therein.
14. H. Sun, J. Yang, K.E. Amaral, and B.A. Horenstein. Tetrahedron Lett. **42**, 2451 (2001), and references. cited therein.
15. (*a*) E. Volkin. J. Am. Chem. Soc. **76**, 5892 (1954); (*b*) M. Jesaitis. Nature (London), **178**, 637 (1956); (*c*) J. Josse and A. Kornberg. J. Biol. Chem. **237**, 1968 (1962).
16. H.R. Revel. *In* DNA modification: Glucosylation in bacteriophage T4. *Edited by* C.K. Mathews, E.M. Kutter, G. Mosig, and P.B. Berget. ASM Publications, Washington, D.C. 1983. pp. 156–165.
17. (*a*) G.S. Cox and T.W. Conway. J. Virol. **12**, 1279 (1973); (*b*) K. Dharmalingam and E.B. Goldberg. Virology, **96**, 393 (1979); (*c*) W. Rüger. Eur. J. Biochem. **88**, 109 (1978).
18. J.H. Gommers-Ampt, F. Vanleeuwen, A.L.J. DeBeer, J.F.G. Vliegenthart, M. Dizdaroglu, J.A. Kowlak, P.F. Crain, and P. Borst. Cell (Cambridge, Mass.), **75**, 1129 (1993).
19. P. Borst and A.H. Fairlamb. Annu. Rev. Microbiol. **52**, 745 (1998).
20. S. Morera, A. Imberty, U. Aschke-Sonnenborn, W. Rüger, and P.S. Freemont. J. Mol. Biol. **292**, 717 (1999).
21. A. Vrielink, W. Rüger, H.P.C. Driessen, and P.S. Freemont. EMBO J. **13**, 3413 (1994).
22. F. Amann, C. Schaub, B. Müller, and R.R. Schmidt. Chem. Eur. J. **6**, 1106 (1998).
23. R.U. Lemieux. Acc. Chem. Res. **29**, 373 (1994), and refs. cited therein.
24. (*a*) K. Frische. Ph.D Dissertation, Universität Konstanz, Konstanz, Germany, 1992; (*b*) R.R. Schmidt and K. Frische. Bioorg. Med. Chem. Lett. **3**, 1747 (1993); (*c*) K. Frische and R.R. Schmidt. Liebigs Ann. Chem. 325 (1994).
25. C. Schaub, B. Müller, and R.R. Schmidt. Eur. J. Org. Chem. 1745, (2000), and refs. cited therein.
26. B. Müller, C. Schaub, and R.R. Schmidt. Angew. Chem. **110**, 3021 (1998); Angew. Chem. Int. Ed. **37**, 2893 (1998).
27. A.K. Bhattacharya, F. Stolz, and R.R. Schmidt. Tetrahedron Lett. **42**, 5393 (2001).
28. (*a*) W.H. Hunter and D.E. Edgar. J. Am. Chem. Soc. **54**, 2025 (1932); (*b*) C. Venkatachalapathy and K. Pitchumani. Tetrahedron, **53**, 2581 (1997).
29. (*a*) V. Wittmann and C.H. Wong. J. Org. Chem. **62**, 2144 (1997); (*b*) J.G. Moffat and H.G. Khorana. J. Am. Chem. Soc. **83**, 649 (1961).
30. G. Jones, D.J. Mouat, and D.J. Tonkinson. J. Chem. Soc. Perkin Trans. 1, 2719, (1985).
31. R.A. Barnes and H.M. Fales. J. Am. Chem. Soc. **75**, 3830 (1953).
32. W. Baker, K.M. Buggle, J.F.W. McOmie, and D.A.M. Watkins. J. Chem. Soc. 3594, (1958).
33. T. Doppler, H. Schmid, and H.-J. Hansen. Helv. Chim. Acta, **62**, 271 (1979).
34. N. Danbresse, C. Francesch, F. Mhamdi, and C. Rolando. Synthesis, 369, (1994).
35. (*a*) H.G. Söderbaum and O. Widman. Chem. Ber. **22**, 1666 (1889); (*b*) S.A. Glover, K.M. Jones, I.R. McNee, and C. Rowbottom. J. Chem. Soc. Perkin Trans. 2, 1367 (1996).
36. J. Tomaschewski, H. Gram, J.W. Crabb, and W. Rüger. Nucleic Acids Res. **13**, 7551 (1985) and refs. cited therein.

© 2002 NRC Canada

Glycodendrimers based on cellobiosyl-derived monomers[1]

Stacey A. Kalovidouris, W. Bruce Turnbull, and J. Fraser Stoddart

Abstract: Reductive amination of suitably functionalized trisaccharide monomers, based on cellobiosylgalacto residues, has made it possible to construct high-molecular-weight glycodendrons and glycodendrimers for the display of large bioactive oligosaccharides and proteins in a well-defined manner.

Key words: cellobiose, glycodendrimers, reductive amination, trisaccharide monomers.

Résumé : L'amination réductrice de trisaccharides monomères fonctionnalisés de façon appropriée et attachés à de résidus cellobiosylgalactose permet de construire des glycodendrons et des glycodendrimères de masses moléculaires élevées grâce auxquels on peut présenter de grosses molécules d'oligosaccharides et de protéines bioréactifs d'une façon bien définie.

Mots clés : cellobiose, glycodendrimères, amination réductrice, trisaccharides monomères.

Introduction

The incorporation of carbohydrates into dendritic structures continues to be pursued vigorously by a growing number of research groups (1). The driving force behind glycodendrimer research has been the desire to mimic Nature's use of multivalency (2) to enhance both the avidity and selectivity of interactions between oligosaccharide ligands and their corresponding protein receptors. There is a growing appreciation (3) that the structure of the underlying dendritic scaffold is as important to achieving efficient multivalent interactions as presenting multiple copies of the ligand. Thus, developing novel dendritic structures for this purpose may be considered to be a worthy pursuit. We (4, 5) and others (6) have identified that, in addition to the bioactive ligands, oligosaccharides show great potential as building blocks for multivalent and dendritic scaffolds. In this sense, carbohydrates can provide (7) vast diversity in constitution, configuration and conformation in addition to lending themselves well as multifunctional building blocks for constructing branched structures. Small changes in constitution can provide large differences in biological activities, e.g., in the highly selective recognition (8) of α-2,3- and α-2,6-linked sialosides by Siglecs 1 and 2, respectively. But perhaps the most subtle, yet profound, of possible structural changes results from the inversion of configuration at a single carbon atom such as in the repeating unit of the common (1→4)-linked polymers of glucose — i.e., amylose and cellulose (9). The α(1→4)-linkages in amylose promote the adoption of a helical structure by the polymer, in which intramolecular hydrogen bonding between primary and secondary hydroxy groups on adjacent turns of the helix, leads to the formation of channels capable of supramolecular complexation. In contrast, the β(1→4)-linkages of cellulose lead to a more extended structure promoting intermolecular hydrogen bonding between polymer strands and insoluble crystalline fibers. In addition to the changes in overall shape, the spacial distributions of substituent groups (e.g., C-6 hydroxymethyl groups) on the polymers are also different. Whereas, in amylose, all of the primary hydroxy functions point away from the same side of the polymer chain — reminiscent of the primary face of cyclodextrins — the same groups in cellulose are directed in opposing directions from adjacent sugar residues. The graphical representations of maltosyl and cellobiosyl residues shown in Fig. 1 illustrate the background behind our motivation to be able to compare

Received 6 December 2001. Published on the NRC Research Press Web site at http://canjchem.nrc.ca on 15 August 2002.

It was Ray Lemieux who provided intellectual leadership in the field of carbohydrate chemistry during the second half of the 20th century. His contribution to our fundamental knowledge of the nature of the carbohydrates was profound, all-encompassing, and far-reaching. During the last decade or so, our basic understanding of the mechanisms by which carbohydrates are bound by proteins has advanced enormously. These advances were only possible because of the seminal work done by Lemieux in the 1980s. We dedicate this paper to the memory of Ray.

S.A. Kalovidouris, W.B. Turnbull,[2] and J.F. Stoddart.[3] Department of Chemistry and Biochemistry, University of California, Los Angeles, 405 Hilgard Avenue, Los Angeles, CA 90095–1569, U.S.A.

[1]The paper is Part 10 in a series on Synthetic carbohydrate dendrimers.
[2]Present address: Astbury Centre for Structural Molecular Biology, School of Biochemistry and Molecular Biology, University of Leeds, Leeds LS2 9JT, U.K.
[3]Corresponding author (e-mail: stoddart@chem.ucla.edu).

 DOI: 10.1139/V02-116 © 2002 NRC Canada

Scheme 1. (*a*) TMSOTf, CH_2Cl_2, 4 Å MS (75%); (*b*) NaOMe, MeOH; TBDMSCl, C_5H_5N; Ac_2O, C_5H_5N (50% over three steps); (*c*) Br_2, PPh_3, CH_2Cl_2 (96%); (*d*) NHMeBn (57%); (*e*) NaOMe, MeOH (90%); H_2, $Pd(OH)_2$ on C, MeOH (quant.); (*f*) NaOMe, MeOH (90%); TFA, H_2O (9:1) (80%); (*g*) $NaCNBH_3$, MeOH, AcOH (94%).

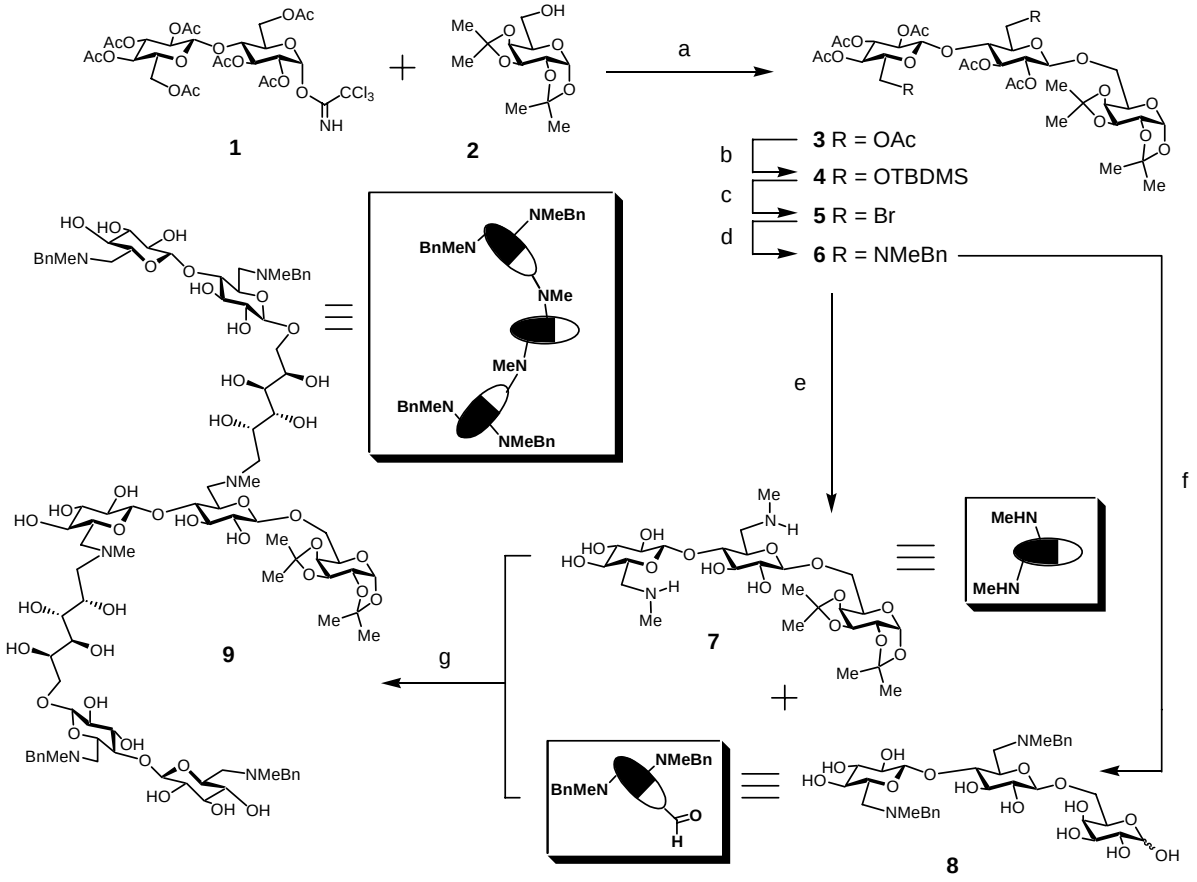

and contrast glycodendrons and glycodendrimers incorporating these two diastereoisomerically related residues.

Recently, we have outlined (5) an approach for the synthesis of dendritic oligosaccharides via reductive amination of a reducing sugar, using a trisaccharide bearing two methylamino groups. Our first choice was to use a maltosylgalactose repeating unit that incorporates the α(1→4)-linkage (associated with amylose) between the branching points of resulting dendrons. Here, we describe the synthesis of analogous compounds that incorporate the corresponding β(1→4)-linkage of cellobiose in a first step toward the general development of oligosaccharide-based dendrimers that exhibit broad structural diversity derived from their constituent building blocks.

Fig. 1. A graphical representation of maltosyl and cellobiosyl residues.

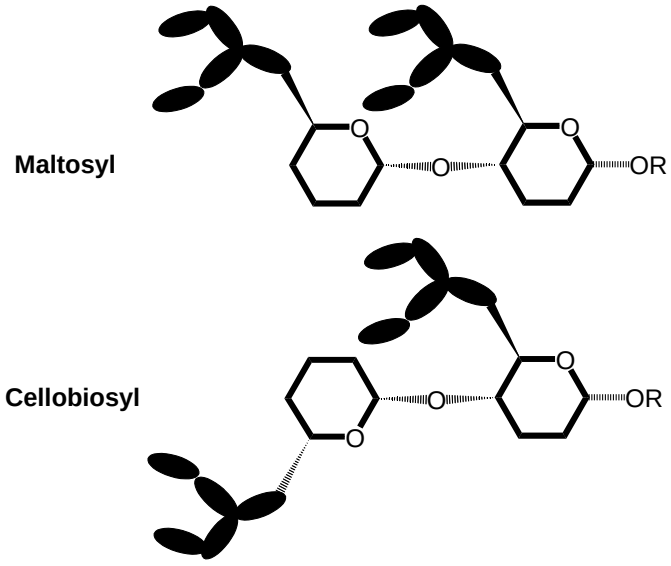

Results and discussion

Synthesis of the AB_2 monomers and the dendron

The synthesis of the first-generation cellobiosylgalacto-based dendron **9** is outlined in Scheme 1. Starting from the known (10) peracetylated α-cellobiosyl-trichloroacetimidate **1** as the glycosyl donor and 1,2:3,4-di-*O*-isopropylidene-α-D-galactopyranose (**2**) as the glycosyl acceptor, the protected trisaccharide **3** was obtained in 75% yield using TMSOTf as the promoter. With the ultimate objective being that of introducing protected secondary amino functions at the primary positions of the two glucopyranosyl residues, the *O*-acetyl protecting groups were removed using Zemplén conditions. Thereafter, the two primary hydroxyl groups were protected

© 2002 NRC Canada

Scheme 2. (*a*) $ClCO_2Et$, C_6H_6, H_2O, KOH (40%); (*b*) $LiAlH_4$, THF (56%).

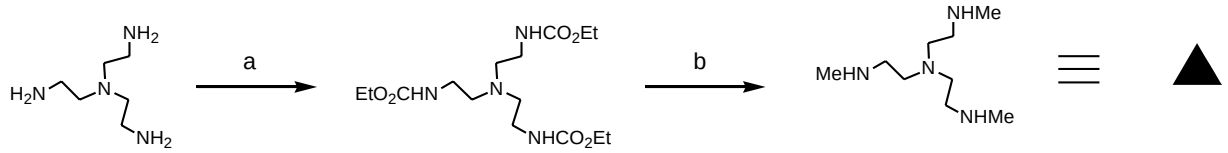

11 **12** **13**

Fig. 2. DEPT 135 spectrum (CD_3OD, 125 MHz) of dendron **9**.

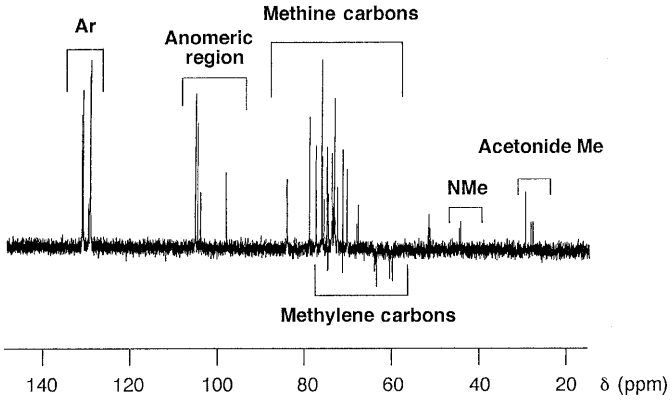

Fig. 3. ES-MS spectrum of dendron **9**.

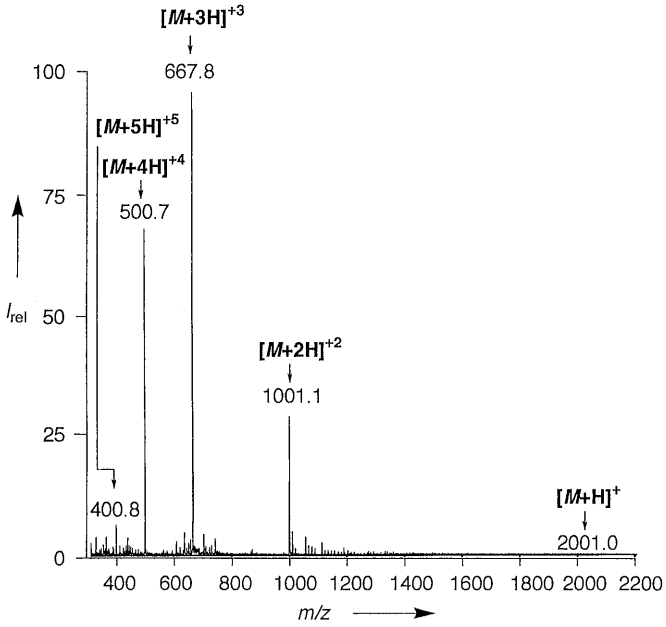

as their TBDMS ethers before the secondary ones were reacetylated to afford the fully protected trisaccharide **4**. The last three steps were performed in an overall yield of 50%. The bis-silyl ether was then converted directly into the dibromide **5** in 96% yield with triphenylphosphine and bromine. When **5** was heated with neat benzylmethylamine, the fully protected trisaccharide (**6**) was obtained in 57% yield. One of the required AB_2 monomers, namely the trisaccharide (**7**), carrying two secondary amino functions, was isolated quantitatively following hydrogenolysis of **6** in the presence of Pearlman's catalyst. The other AB_2 monomer (**8**) was obtained in 80% yield following removal of the cyclic acetals in **6** by TFA-catalyzed hydrolysis. The two AB_2 monomers (**7** and **8**) were coupled by reductive amination to give the first-generation dendron (**9**) in 94% yield. DEPT-135 ^{13}C NMR and ES-MS spectra are presented in Figs. 2 and 3, respectively. Of the 11 different methylene carbon atoms present in the dendron, seven can be identified as negative peaks in the ^{13}C NMR spectrum. The ES-MS reveals peaks at 2001.0, 1001.1, 667.8, 500.7, and 400.8 for the $[M + H]^+$, $[M + 2H]^{2+}$, $[M + 3H]^{3+}$, $[M + 4H]^{4+}$, and $[M + 5H]^{5+}$ ions obtained from the dendron (**9**).

Synthesis of the core

The synthesis of the tris[2-(methylamino)ethyl]amine-based core (**13**) is depicted in Scheme 2. A published procedure (11) was followed to obtain **13** in two steps, starting from tris(2-aminoethyl)amine (**11**). In the first step, the triscarbamate (**12**) was prepared by reacting **11** with ethylchloroformate under basic conditions. In the second step, **12** was reduced with lithium aluminum hydride to afford the tris[2-(methylamino)ethyl]amine core (**13**).

Synthesis of the glycodendrimers

The syntheses of the zero-generation glycodendrimer (**14**) and the first-generation glycodendrimer (**16**) are summarized in Scheme 3. The graphical representations of molecular structures employed in this scheme are defined in Schemes 1 and 2. The zero-generation glycodendrimer (**14**) was isolated in 69% yield following coupling by reductive amination of the AB_2 monomer (**8**) with the tris[2-(methylamino)ethyl]amine core (**13**). This glycodendrimer was easily soluble in water. However, upon its acetylation (Scheme 4), the resulting peracetylated derivative (**15**) was soluble in polar organic solvents, e.g., methanol and dimethylformamide, but not in chlorinated solvents, e.g., dichloromethane and chloroform. The MALDI-TOF mass spectrum (Fig. 4) of **15** exhibited an $[M + H]^+$ peak at *m*/*z* 3407 with an isotope distribution that matches well with that of the calculated one. Employing reductive amination once again to couple the dendron (**10**) with the tris[2-(methylamino)ethyl]amine core (**13**) results in the formation of the first-generation glycodendrimer (**16**) in 56% yield. This glycodendrimer (**16**) and its peracetylated derivative (**17**) (see Scheme 5) exhibit solubility characteristics similar to those already described for the zero-generation counterparts **14** and **15**. The MALDI-TOF mass spectrum (Fig. 5) of **17** exhibited an $[M + H]^+$ peak at *m*/*z* 9078 along with fragmentation peaks at *m*/*z* 8062, 7159, 6227, 5153, 4305, 3017, and 1987. These fragmentations

© 2002 NRC Canada

Scheme 3. (*a*) $NaCNBH_3$, AcOH, MeOH (94%); (*b*) $NaCNBH_3$, AcOH, MeOH (69%); (*c*) TFA, H_2O (9:1) (80%); (*d*) $NaCNBH_3$, AcOH, MeOH (56%).

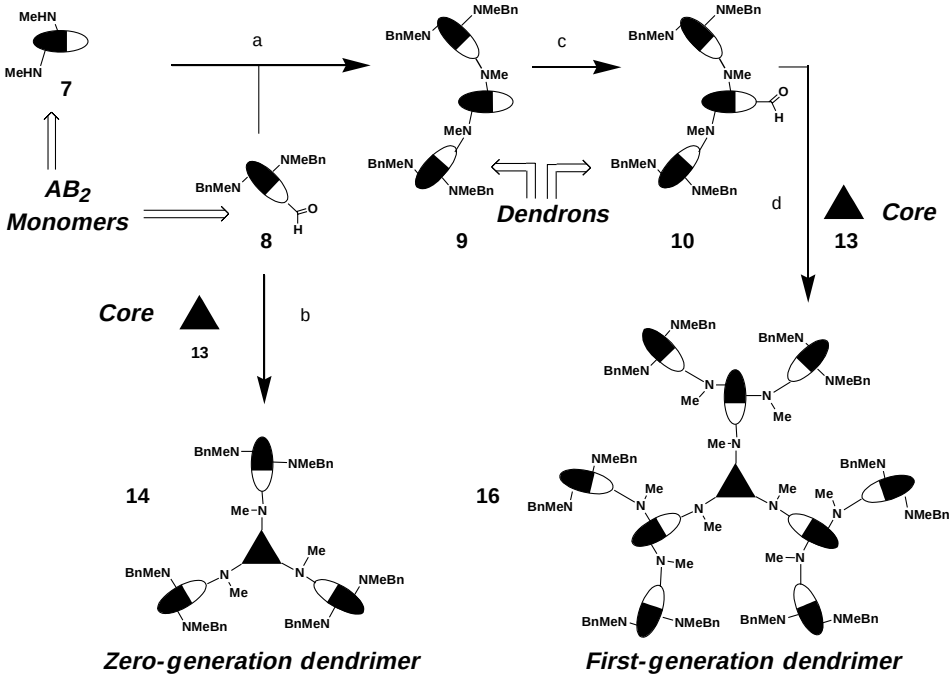

Scheme 4. (*a*) Ac_2O, C_5H_5N, DMAP (45%).

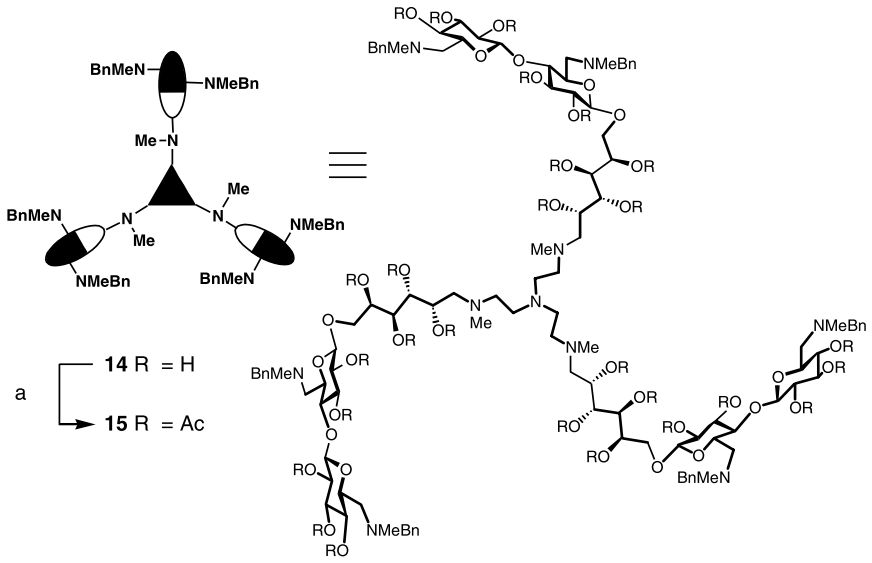

result from cleavages of glycosyl linkages and β-elimination on the amine linkages at the positions indicated by open arrows in Fig. 5. These types of cleavages in oligosaccharide derivatives are well precedented in the literature (12).

Experimental section

General methods

Chemicals were purchased from Aldrich and were used as received except for sodium cyanoborohydride (Aldrich), which was purified by the published procedure (13). Reactions were carried out under a dry argon atmosphere and the solvents were dried prior to use according to literature procedures (14). Thin-layer chromatography (TLC) was carried out on aluminum sheets precoated with silica gel 60F (Merck 5554). The plates were inspected by UV light and developed either with iodine vapor or by treatment with 5% H_2SO_4 in EtOH, followed by heating. Column chromatography was carried out using silica gel 60F (Silicycle). Preparative reversed phase chromatography was performed on fully endcapped C-18, or on C-8 silica gel 100 (230–400 mesh, Fluka), and gel permeation chromatography (GPC) was performed using a 25 × 900 mm column of Sephadex LH20 resin (Sigma), eluting with MeOH. Analytical reversed

© 2002 NRC Canada

Scheme 5. (*a*) Ac_2O, C_5H_5N, DMAP (33%).

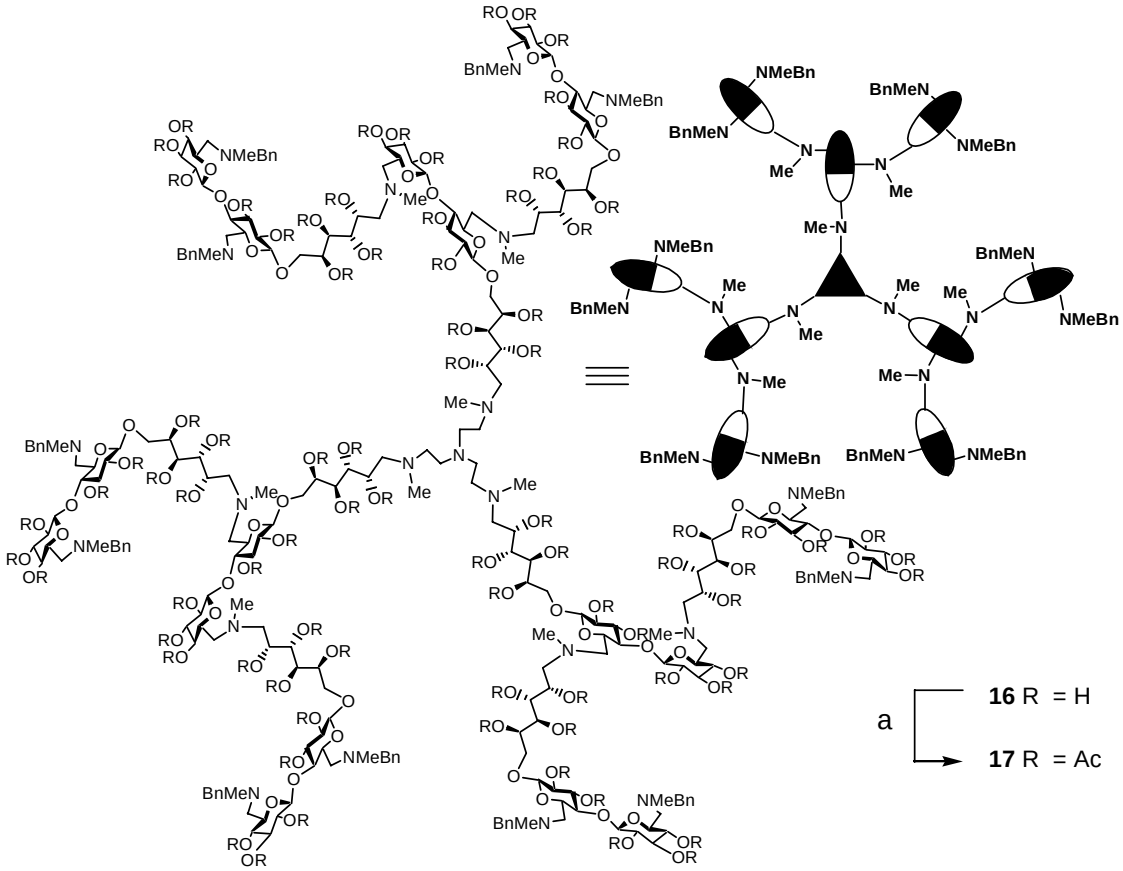

Fig. 4. MALDI-TOF mass spectrum of a zero-generation dendrimer **15**.

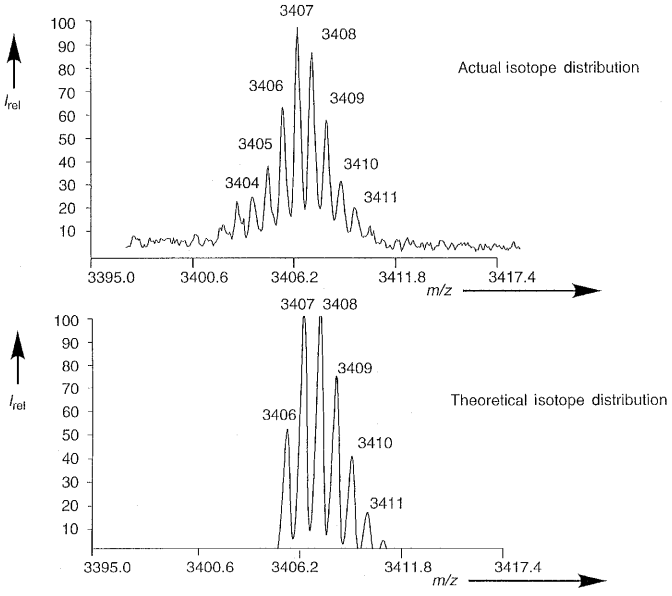

phase HPLC was conducted using a Hypersil 5 μm BDS C-18 silica column (ThermoQuest, 4.6 × 250 mm) under isocratic elution (MeOH–H_2O–TFA, 65:35:0.0001) with UV detection using a Dynamax PDA-2 diode array detector. Matrix-assisted laser desorption ionization time-of-flight mass spectra (MALDI-TOF-MS) and fast atom bombardment mass spectra (FAB-MS) were performed on either Perceptive Biosystems Voyager RP (MALDI) or VG SAB-SE (FAB) mass spectrometers. Electrospray mass spectrometry (ES-MS) was recorded on a Sciex API IIIR triple quadrupole electrospray mass spectrometer using H_2O–MeCN–HCOOH (50:50:0.1) as the mobile phase. ^1H and ^{13}C NMR spectra were recorded using Bruker ARX400, ARX500, and Advance 500 spectrometers with the residual solvent or TMS as the internal standard. The chemical shifts are expressed on the δ scale in parts per million (ppm). The following abbreviations are used to explain the observed multiplicities: s (singlet), d (doublet), dd (doublet of doublets), t (triplet), m (multiplet), br (broad).

*2,3,4,6-Tetra-*O*-acetyl-*β*-D-glucopyranosyl-(1→4)-2,3,6-tri-*O*-acetyl-*β*-D-glucopyranosyl-(1→6)-1,2:3,4-di-*O*-isopropylidene-*α*-D-galactopyranose (3)*

The glycosyl donor **1** (13.4 g, 17 mmol) and the glycosyl acceptor **2** (6.7 g, 26 mmol) were stirred with powdered 4 Å molecular sieves (13.0 g) in CH_2Cl_2 (250 mL) for 2 h under an argon atmosphere. The mixture was then cooled to 0°C and trimethylsilyl trifluoromethanesulfonate (610 μL, 3.4 mmol) was added and stirring was continued at 0°C for 30 min. The reaction was then quenched by the addition of Et_3N (0.47 mL, 3.4 mmol). The solution was filtered through Celite and the filtrate was concentrated. Column chromatography (SiO_2, CH_2Cl_2:EtOAc (8:2)) gave **3** (11 g, 75%) as a solid foam. $[\alpha]_D^{20}$ –11.6 (*c* = 1 in $CHCl_3$). HR-MS (FAB)

© 2002 NRC Canada

Fig. 5. MALDI-TOF mass spectrum of a first-generation dendrimer **17**.

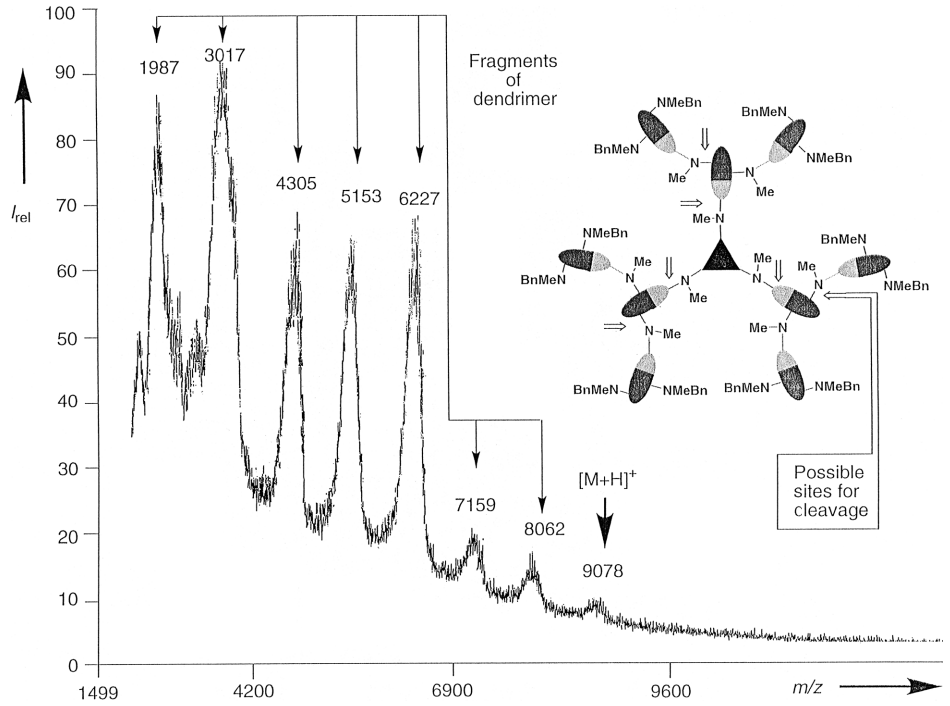

calcd. for $C_{38}H_{54}O_{23}Na$ (M + Na): 901.2954; found: 901.2976. ^{1}H NMR ($CDCl_3$, 400 MHz) δ: 1.36, 1.42, 1.43, 1.53 (4 × s, 12H, 2 × CMe_2), 1.91, 1.94, 1.96, 1.98, 2.02, 2.06 (7 × s, 21H, 7 × Ac), 3.57–3.59 (m, 1H, H-5b), 3.59–3.61 (m, 2H, H-6a, H-5c), 3.68 (t, J = 9.3 Hz, 1H, H-4b), 3.80–3.85 (m, 1H, H-5a), 3.91 (dd, $J_{5,6}$ = 3.8 Hz, $J_{6,6'}$ = 11.4 Hz, 1H, H-6a′), 3.98 (br d, $J_{6,6'}$ = 12.5 Hz, 1H, H-6c), 4.04 (dd, $J_{5,6}$ = 5.0 Hz, $J_{6,6'}$ = 12.1 Hz, 1H, H-6b), 4.10 (d, J = 7.84 Hz, 1H, H-4a), 4.22 (m, 1H, H-2a), 4.28 (dd, $J_{5,6}$ = 4.6 Hz, $J_{6,6'}$ = 12.5 Hz, 1H, H-6c′), 4.42–4.47 (m, 2H, H-1c, H-6b′), 4.55 (m, 2H, H-1b, H-3a), 4.82–4.87 (m, 2H, H-2c, H-2b), 4.99–5.14 (m, 3H, H-4c, H-3c, H-3b), 5.42 (d, $J_{1,2}$ = 4.9 Hz, 1H, H-1a). ^{13}C NMR ($CDCl_3$, 100 MHz) δ: 20.6 (3C), 20.7, 20.8, 20.9, 21.0, 24.4, 25.0, 25.9, 26.0, 59.1, 59.2, 60.0, 60.3, 68.4, 68.5, 68.6, 68.7, 69.0, 69.3, 69.5, 69.8 (2C), 70.0 (2C), 72.0 (2C), 75.0, 95.0, 101.0 (2C), 169.4, 169.8, 169.9, 170.1, 170.4, 170.5, 170.6.

*2,3,4-Tri-*O*-acetyl-6-*O*-tert-butyldimethylsilyl-*β*-D-glucopyranosyl-(1→4)-2,3-di-*O*-acetyl-6-*O*-tert-butyldimethylsilyl-*β*-D-glucopyranosyl-(1→6)-1,2:3,4-di-*O*-isopropylidene-*α*-D-galactopyranose (4)*

The acetyl protecting groups in **3** were removed under standard Zemplén conditions (NaOMe–MeOH) and then *tert*-butyldimethylsilyl chloride (3 g, 20 mmol) was added to a stirred solution of the deacetylated trisaccharide **3** (3 g, 5.1 mmol) in C_5H_5N (15 mL) at 0°C. After 1 h, additional *tert*-butyldimethylsilyl chloride (1 g, 6.6 mmol) was added, and stirring was continued at room temperature overnight before quenching the reaction with MeOH. The mixture was concentrated and redissolved in CH_2Cl_2 and washed with 1 M HCl, sat. $NaHCO_3$, and H_2O, before drying over anhyd Na_2SO_4, and concentrating to an oil. This oil was treated with Ac_2O (20 mL) and C_5H_5N (20 mL) and the solution was left to stir at room temperature overnight. Following concentration and coevaporation with PhMe, the mixture was dissolved in EtOAc (500 mL) and washed consecutively with 1 M HCl, sat. $NaHCO_3$, and sat. NaCl solutions, before drying (Na_2SO_4), and concentrating to a foam. Column chromatography (SiO_2, CH_2Cl_2:EtOAc (9:1)) gave **4** (2.69 g, 50%) as a foamy semisolid. $[\alpha]_D^{20}$ –17.9 (c = 1 in $CHCl_3$). HR-MS (FAB) calcd. for $C_{46}H_{78}O_{21}Si_2Na$ (M + Na): 1045.4472; found: 1045.4501. ^{1}H NMR ($CDCl_3$, 400 MHz) δ: 0.00, 0.01, 0.08, 0.09 (4 × s, 12H, 4 × SiMe), 0.80, 0.91 (2 × s, 18H, 2 × $SiCMe_3$), 1.30 (s, 6H, CMe_2), 1.40, 1.49 (2 × s, 6H, CMe_2), 1.96, 1.99, 2.03, 2.04, 2.07 (5 × s, 15H, 5 × Ac), 3.28 (m, 1H, H-5b), 3.43–3.44 (m, 1H, H-5c), 3.61 (m, 1H, H-6a′), 3.67–3.73 (m, 2H, H-6c, H-6c′), 3.87 (m, 4H, H-4b, H-5a, H-6b, H-6b′), 3.96 (dd, $J_{5,6}$ = 4.1 Hz, $J_{6,6'}$ = 11.2 Hz, 1H, H-6a), 4.16 (br d, J = 7.9 Hz, 1H, H-4a), 4.27 (m, 1H, H-2a), 4.49 (d, J = 8.0 Hz, 1H, H-1b), 4.56 (dd, $J_{2,3}$ = 2.0 Hz, $J_{3,4}$ = 7.9 Hz, 1H, H-3a), 4.66 (d, $J_{1,2}$ = 8.0 Hz, 1H, H-1c), 4.80–4.85 (m, 2H, H-2b, H-2c), 4.98 (t, $J_{3,4} \approx J_{4,5}$ = 9.5 Hz, 1H, H-4c), 5.02–5.15 (m, 2H, H-3b, H-3c), 5.50 (d, $J_{1,2}$ = 4.9 Hz, 1H, H-1a). ^{13}C NMR ($CDCl_3$, 100 MHz) δ: –5.5, –5.4, –5.3, –4.9, 18.4, 18.6, 20.6, 20.7, 20.8, 20.9, 21.0, 24.4, 25.0, 25.8 26.9, 26.0 (3C), 26.1 (3C), 60.4, 63.0, 67.5, 68.3, 68.5, 70.1, 70.4, 70.5, 70.6, 70.7, 71.0, 71.1, 72.1, 75.1, 75.3, 94.9, 100.2, 100.6, 108.6, 109.3, 169.2, 169.9, 170.2, 170.3, 170.4.

*2,3,4-Tri-*O*-acetyl-6-bromo-6-deoxy-*β*-D-glucopyranosyl-(1→4)-2,3-di-*O*-acetyl-6-bromo-6-deoxy-*β*-D-glucopyranosyl-(1→6)-1,2:3,4-di-*O*-isopropylidene-*α*-D-galactopyranose (5)*

Bromine (0.234 mL, 4.6 mmol) was added with stirring at 0°C to a solution of bis-silylether **4** (1.9 g, 1.9 mmol), PPh_3 (1.25 g, 25.5 mmol), and CH_2Cl_2 (15 mL). The orange precipitate, which formed immediately, dissolved after stirring for 19 h at room temperature, to give a clear brown solution.

© 2002 NRC Canada

This solution was diluted with CH_2Cl_2 (100 mL) and was washed with sat. $NaHCO_3$ followed by H_2O, before drying (Na_2SO_4), filtering, and concentrating. Column chromatography (SiO_2, CH_2Cl_2:EtOAc (9:1)) gave **5** (1.6 g, 96%) as a foamy semisolid. $[\alpha]_D^{20}$ –22.9 (c = 1 in $CHCl_3$). HR-MS (FAB) calcd. for $C_{34}H_{48}Br_2O_{19}Na$ (M + Na): 943.1038; found: 943.1036. ^{1}H NMR ($CDCl_3$, 500 MHz) δ: 1.32, 1.43, 1.49, 1.59 (4 × s, 12H, 2 × CMe_2), 1.99, 2.04, 2.05, 2.06, 2.08 (5 × s, 15H, 5 × Ac), 3.32–3.36 (m, 1H, H-5b), 3.48 (dd, $J_{5,6}$ = 2.6 Hz, $J_{6,6'}$ = 8.8 Hz, 1H, H-6b), 3.56–3.60 (m, 1H, H-5c), 3.66–3.76 (m, 1H, H-6c), 3.85 (t, J = 9.2 Hz, 1H, H-4b), 3.91–3.93 (m, 1H, H-5a), 4.00 (dd, $J_{5,6}$ = 3.5 Hz, $J_{6,6}$ = 7.8 Hz, 1H, H-6a), 4.18 (dd, $J_{3,4}$ = 6.27 Hz, $J_{4,5}$ = 1.63 Hz, 1H, H-4a), 4.27–4.29 (m, 1H, H-2a), 4.57 (d, J = 7.9 Hz, 1H, H-3a), 4.58 (d, J = 7.9 Hz, 1H, H-3c), 4.9–5.3 (m, 4H, H-3b, H-3c, H-4c, H-2c), 5.48 (d, J = 4.9 Hz, 1H, H-1a). ^{13}C NMR ($CDCl_3$, 125 MHz) δ: 20.7, 20.8 (3C), 21.1, 24.5, 25.2, 26.1 (2C), 30.4, 31.7, 67.9, 69.4, 70.5, 70.7, 70.8, 71.4, 71.6, 71.8, 71.9, 72.9, 73.4 (2C), 76.9, 96.3, 99.9, 101.1, 108.8, 109.5, 169.0, 169.4, 169.9, 170.0, 170.4.

***2,3,4-Tri*-O-*acetyl*-6-N-*benzyl*-6-*deoxy*-6-*methylamino*-β-D-*glucopyranosyl*-(1→4)-2,3-*di*-O-*acetyl*-6-N-*benzyl*-6-*deoxy*-6-*methylamino*-β-D-*glucopyranosyl*-(1→6)-1,2:3,4-*di*-O-*isopropylidene*-α-D-*galactopyranose* (6)**

The dibromide **5** (0.4 g, 0.4 mmol) and *N*-benzylmethylamine (0.28 mL) were stirred together at 80°C overnight. The next day, the reaction mixture was concentrated, redissolved in C_5H_5N (2 mL) and Ac_2O (2 mL), and left to stir at room temperature overnight. The brown solution was coevaporated with PhMe before the resulting oily liquid was diluted in CH_2Cl_2 and washed consecutively with 1 M HCl, sat. $NaHCO_3$ and H_2O, dried (Na_2SO_4), filtered, and concentrated to an oil. Column chromatography (SiO_2, hexanes–EtOAc (6:4 to 1:1)) gave **6** (0.2 g, 57%) as an amorphous tan foam. $[\alpha]_D^{20}$ –15.8 (c = 1 in $CHCl_3$). HR-MS (MALDI-TOF) calcd. for $C_{50}H_{68}N_2O_{19}$ (M + H): 1001.4494; found: 1001.4480. ^{1}H NMR ($CDCl_3$, 500 MHz) δ: 1.29, 1.31, 1.40, 1.49 (4 × s, 12H, 2 × CMe_2), 1.80, 1.94, 1.97, 1.99, 2.01 (5 × s, 15H, 5 × Ac), 2.23, 2.36 (2 × br s, 6H, 2 × NMe), 2.42–2.58 (m, 2H, H-6c, H-6c′), 2.75–2.85 (m, 2H, H-6b, H-6b′), 3.40–3.68 (m, 6H, H-5b, H-5c, H-6a′, 3 × PhC*H*), 3.86–4.00 (m, 4H, H-4b, H-5a, H-6a, PhC*H*), 4.15 (dd, $J_{3,4}$ = 6.5 Hz, $J_{4,5}$ = 1.4 Hz, 1H; H-4a), 4.28 (m, 1H, H-2a), 4.50 (d, J = 7.65 Hz, 1H, H-1b), 4.56 (dd, $J_{3,4}$ = 2.25 Hz, $J_{3,2}$ = 5.6 Hz, 1H, H-3a), 4.79–4.90 (m, 4H, H-2b, H-2c, H-4c, H-1c), 5.01 (t, $J_{2,3} \approx J_{3,4}$ = 8.9 Hz, 1H, H-3c), 5.16 (t, $J_{2,3} \approx J_{3,4}$ = 9.5 Hz, 1H, H-3b), 5.48 (d, $J_{1,2}$ = 4.9 Hz, 1H, H-1a), 7.25–7.36 (m, 10H, Ar-H). ^{13}C NMR ($CDCl_3$, 125 MHz) δ: 20.4, 20.5, 20.6, 20.7, 21.0, 24.2, 24.9, 25.5, 25.9, 42.8, 43.5, 56.5, 57.3, 62.3, 62.8, 67.5, 68.7, 70.3, 70.5, 71.4, 71.8, 72.3, 73.2 (3C), 75.6, 76.7, 76.9, 96.1, 99.3, 101.2, 108.5, 109.2, 125.0 (2C), 126.9 (4C), 128.3 (4C), 128.9 (2C), 169.5, 169.8, 169.9, 170.1, 170.4.

***6-Deoxy*-6-*methylamino*-β-D-*glucopyranosyl*-(1→4)-6-*deoxy*-6-*methylamino*-β-D-*glucopyranosyl*-(1→6)-1,2:3,4-*di*-O-*isopropylidene*-α-D-*galactopyranose* (7)**

To a methanolic (5 mL of MeOH) solution of the pentaacetate **6** (1 g, 1 mmol), NaOMe (1mL, 0.5 M in MeOH, 0.5 mmol) was added and the mixture was left to stir at room temperature overnight. The solution was then neutralized with Amberlite IR-120 (H^+ form) ion exchange resin, filtered, and concentrated. A solution of this deacetylated product (0.6 g, 0.76 mmol) in MeOH (50 mL) was treated with 10% $Pd(OH)_2$/C (300 mg) under H_2 for 2 h. The solution was filtered through a bed of Celite and the filtrate was concentrated to give **7** (460 mg, 90%) as an amorphous solid upon freeze-drying from H_2O. $[\alpha]_D^{20}$ –17.9 (c = 1 in $CHCl_3$). ES-MS (M + H): 611.4. ^{1}H NMR (CD_3OD, 500 MHz) δ: 1.33, 1.34, 1.40, 1.52 (4 × s, 12H, 2 × CMe_2), 2.44, 2.46 (2 × br s, 6H, 2 × NMe), 2.61 (dd, $J_{5,6}$ = 8.3 Hz, $J_{6,6'}$ = 12.7 Hz, 1H, H-6c), 2.65 (dd, $J_{5,6}$ = 7.8 Hz, $J_{6,6'}$ = 12.6 Hz, 1H, H-6b), 2.95 (dd, $J_{5,6}$ = 2.8 Hz, $J_{6,6'}$ = 12.7 Hz, 1H, H-6c′), 3.13 (dd, $J_{5,6}$ = 2.8 Hz, $J_{6,6'}$ = 12.6 Hz, 1H, H-6b′), 3.15 (t, $J_{3,4} \approx J_{4,5}$ = 9.2 Hz, 1H, H-4c), 3.18–3.26 (m, 2H, H-2b, H-2c), 3.31–3.42 (m, 3H, H-3c, H-4b, H-5c), 3.44–3.54 (m, 2H, H-3b, H-5b), 3.65 (dd, $J_{5,6}$ = 8.2 Hz, $J_{6,6'}$ = 11.4 Hz, 1H, H-6a), 4.01–4.05 (m, 2H, H-5a, H-6a), 4.28 (dd $J_{3,4}$ = 8.0 Hz, $J_{4,5}$ = 1.5 Hz, H-4a), 4.30 (d, $J_{1,2}$ = 7.8 Hz, 1H, H-1b), 4.34 (d, $J_{1,2}$ = 7.9 Hz, 1H, H-1c), 4.36 (dd, $J_{1,2}$ = 5.0 Hz, $J_{2,3}$ = 2.4 Hz, H-2a), 4.62 (dd, $J_{2,3}$ = 2.4 Hz, $J_{3,4}$ = 8.0 Hz, 1H, H-3a), 5.51 (d, $J_{1,2}$ = 4.9 Hz, 1H, H-1a). ^{13}C NMR (CD_3OD, 125 MHz) δ: 24.6, 25.1, 26.3 (2C), 36.1 (2C), 53.1, 53.5, 66.8, 68.9, 69.8, 71.9, 72.4, 73.5, 74.4, 74.7, 74.8, 75.0, 75.5, 77.8, 82.9, 97.7, 104.4, 104.8, 110.0, 110.4.

***6*-N-*Benzylmethylamino*-6-*deoxy*-β-D-*glucopyranosyl*-(1→4)-6-N-*benzylmethylamino*-6-*deoxy*-β-D-*glucopyranosyl*-(1→6)-D-*galactose* (8)**

The diacetonide **6** (620 mg, 785 μmol) was dissolved in 90% aq TFA (5 mL) and was allowed to stir at room temperature for 10 min before coevaporation with MeOH three times. Column chromatography (C-8 reversed phase silica, H_2O to MeOH) gave **8** (445 mg, 80%) as an amorphous solid after freeze-drying from H_2O. $[\alpha]_D^{20}$ 0 (c = 1 in H_2O). ES-MS (m/z): 711.5 $[M + H]^+$. Selected ^{1}H NMR data (CD_3OD, 500 MHz) δ: 2.26 (2 × s, 6H, 2 × NMe), 2.61 (dd, $J_{5,6}$ = 7.9 Hz, $J_{6,6'}$ = 13.0 Hz, 1H, H-6c), 2.73 (dd, $J_{5,6}$ = 7.5 Hz, $J_{6,6'}$ = 13.5 Hz, 1H, H-6b), 2.78 (dd, $J_{5,6}$ = 3.5 Hz, $J_{6,6'}$ = 13.0 Hz, 1H, H-6c′), 3.10 (br d, $J_{6,6'}$ = 13.5 Hz, 1H, H-6b′), 3.14 (t, $J_{3,4} \approx J_{4,5}$ = 9.2 Hz, 1H, H-4c), 3.21 (t, $J_{1,2} \approx J_{2,3}$ = 8.0 Hz, 1H, H-2c), 3.26 (dd, $J_{1,2}$ = 8.0 Hz, $J_{2,3}$ = 9.0 Hz, 1H, H-2b), 3.34 (t, $J_{3,4} \approx J_{4,5}$ = 9.0 Hz, 1H, H-3c), 4.32–4.45 (m, ca. 2.5H, β-anomerics), 5.14 (d, $J_{1,2}$ = 3.4 Hz, ca. 0.5H, H-1a (α)), 7.25–7.39 (m, 10H, 2 × C_6H_5).

***6,6′*-N,N′-*bis*[6,6′-*bis*-N-*benzylmethylamino*-6,6′-*dideoxy*-β-*cellobiosyl*-(1→6)-D-*galactit*-1-*yl*]-6,6′-*dideoxy*-6,6′-*dimethylamino*-β-*cellobiosyl*-(1→6)-1,2:3,4-*di*-O-*isopropylidene*-α-D-*galactopyranose* (9)**

Acetic acid (10 μL, 200 μmol) was added to a solution of the reducing sugar **8** (211 mg, 300 μmol), the bismethylamine **7** (70 mg, 114 μmol), and sodium cyanoborohydride (49 mg, 740 μmol) in MeOH (1 mL). The reaction mixture was stirred and heated under reflux for 8 h. Since HPLC analysis indicated that the reaction had gone to completion, the mixture was allowed to cool to room temperature, diluted with H_2O (3 mL), and purified by preparative reversed phase chromatography (15 g C-18 reversed phase, MeOH–H_2O–TFA (0:100:0.0001 to 100:0:0.0001)) to afford

© 2002 NRC Canada

pure **9** (216 mg, 94%). $[\alpha]_D^{20}$ –6.7 (*c* = 1 in H_2O). ES-MS (*m*/*z*): 2001.0 $[M + H]^+$, 1001.1 $[M + 2H]^{+2}$, 667.8 $[M + 3H]^{+2}$, 500.7 $[M + 4H]^{+4}$, 400.8 $[M + 5H]^{+5}$. Selected ^{1}H NMR data (CD_3OD, 500 MHz) δ: 1.30, 1.33, 1.38, 1.50 (4 × s, 12H, 2 × CMe_2), 2.70 (br s, 12H, 4 × N*Me*Bn), 2.88 (br s, 3H, NMe), 2.98 (br s, 3H, NMe), 3.13 (t, $J_{3,4} \approx J_{4,5}$ = 9.1 Hz, 2H, H-4f, H-4i), 3.17 (t, $J_{3,4} \approx J_{4,5}$ = 9.0 Hz, 1H, H-4c), 3.37 (t, $J_{2,3} \approx J_{3,4}$ = 9.1 Hz, 3H, H-3c, H-3f, H-3i), 3.44 (t, $J_{3,4} \approx J_{4,5}$ = 9.0 Hz, 3H, H-4b, H-4e, H-4f), 4.36 (m, 1H, H-2a), 4.40–4.49 (m, 6H, H-1b, H-1c, H-1e, H-1f, H-1h, H-1i), 4.62 (dd, $J_{2,3}$ = 2.2 Hz, $J_{3,4}$ = 7.9 Hz, 1H, H-3a), 5.51 (d, $J_{1,2}$ = 4.9 Hz, 1H, H-1a), 7.42–7.50 (m, 20H, 4 × C_6H_5). Selected ^{13}C/DEPT135/HMQC NMR data (CD_3OD, 125 MHz) δ: 24.6 (C*Me*$_2$), 25.1 (C*Me*$_2$), 26.4 (2C, C*Me*$_2$), 41.8 (2C, N*Me*Bn), 42.1 (2C, N*Me*Bn), 42.8 (NMe), 43.4 (NMe), 58.1, 58.8 (2 × 3C, C-6b, C-6c, C-6e, C-6f, C-6h, C-6i), 61.9 (2C, 2 × *C*H_2Ph), 62.2 (2C, C-1d, C-1g), 62.4 (2C, 2 × *C*H_2Ph), 69.9 (C-6a), 73.3, 73.4 (C-6d, C-6g), 76.1 (C-3b), 76.3 (C-3e, C-3h), 77.8 (3C, C-3c, C-3f, C-3i), 83.0, 83.1, 83.2 (C-4b, C-4e, C-4h), 97.7 (C-1a), 103.8, 104.5 (2C), 105.0 (2C), 105.1 (C-1b, C-1c, C-1e, C-1f, C-1h, C-1i), 110.1, 110.5 (2 × *C*Me_2), 130.1 (4 × C-Ar), 130.2 (2 × C-Ar), 130.3 (2 × C-Ar), 130.4 (2 × C-Ar), 130.6 (2 × C-Ar), 131.8 (4 × C-Ar), 132.1 (2 × C-Ar), 132.2 (2 × C-Ar) 162.9 (2 × C-Ar), 163.2 (2 × C-Ar).

6,6′*-N,N′-*bis*[*6,6′-bis*-N-*benzylmethylamino-6,6′-dideoxy*-β-*cellobiosyl-(1→6)-D-galactit-1-yl]-6,6′-dideoxy-6,6′-dimethylamino*-β-*cellobiosyl-(1→6)-D-galactose (10)

The diacetonide **9** (120 mg, 60 μmol) was dissolved in 90% aq TFA (5 mL) and was allowed to stir at room temperature for 10 min before coevaporation with MeOH three times. Column chromatography (C-8 reversed phase silica, H_2O to MeOH) gave **10** (90 mg, 80%) as an amorphous solid after freeze-drying from H_2O. $[\alpha]_D^{20}$ –1 (*c* = 1 in H_2O). ES-MS (*m*/*z*): 1920.3 $[M + H]^+$, 961.2 $[M + 2H]^{+2}$, 641.1 $[M + 3H]^{+3}$, 480.9 $[M + 4H]^{+4}$. Selected ^{1}H NMR data (CD_3OD, 500 MHz) δ: 4.37–4.39 (br m, ca. 6.5H, anomerics), 5.06 (br s, ca. 0.5 H, H-1a (α)), 7.36–7.46 (m, 20H, C_6H_5).

Tris(2-{*N*-[6-N-*benzylmethylamino-6-deoxy*-β-D-*glucopyranosyl-(1→4)-6*-N-*benzylmethylamino-6-deoxy*-β-D-*glucopyranosyl-(1→6)-D-galactit-1-yl]methylamino}ethyl)amine (14)

Acetic acid (2.28 μL, 45 μmol) was added to a solution of the reducing sugar **8** (50 mg, 70 μmol), tris[2-(methylamino)ethyl]amine (**13**) (11) (3 mg, 19 μmol), and sodium cyanoborohydride (43 mg, 682 μmol) in MeOH (1000 μL). The reaction mixture was stirred and heated under reflux for 6 h. When HPLC analysis indicated that the reaction had gone to completion, the mixture was allowed to cool to room temperature, diluted with H_2O (2 mL), and purified by preparative reversed phase chromatography (15 g C-18 reversed phase, MeOH–H_2O–TFA (0:100:0.0001 to 100:0:0.0001)) to afford **14** (30 mg, 69%). $[\alpha]_D^{20}$ –48 (*c* = 1 in H_2O). LR-FAB (*m*/*z*): 2288.4 $[M + H]^+$. Selected ^{1}H NMR (CD_3OD, 500 MHz) δ: 2.77, 2.90 (2 × 3C, N*Me*Bn), 4.36–4.40 (m, 6H, anomerics), 7.39–7.46 (m, 30H, C_6H_5). Selected ^{13}C NMR data (CD_3OD, 125 MHz) δ: 64.9 (C-6a), 104.5, 105.1 (C-1b, C-1c).

Tris(2-{*N*-methyl[2,3,4-tri-O-acetyl-6-N-benzylmethylamino-6-deoxy*-β-D-*glucopyranosyl-(1→4)-2,3-di-O-acetyl-6-N-benzylmethylamino-6-deoxy*-β-D-*glucopyranosyl-(1→6)-2,3,4,5-tetra-O-acetyl-D-galactit-1-yl]amino}ethyl)amine (15)

The zero-generation dendrimer **14** (30 mg) was dissolved in a solution of DMAP (2 mg) in Ac_2O (4 mL) and C_5H_5N (4 mL) and the mixture was left to stir at room temperature for 36 h and then concentrated by coevaporation with PhMe before diluting with EtOAc and washing with 1 M HCl, sat. $NaHCO_3$ and sat. NaCl solutions, drying (Na_2SO_4), and concentrating to an oil. GPC ($CHCl_3$:MeOH, 3:1) gave **15** (20 mg, 45%) as an oil. $[\alpha]_D^{20}$ –40 (*c* = 1 in MeOH). MALDI-TOF (*m*/*z*): 3407 $[M + H]^+$, 3429 $[M + Na]^+$, 3446 $[M + K]^+$. ^{1}H NMR (DMF-d_7, 500 MHz) δ: 1.92, 1.96, 2.02, 2.05, 2.06, 2.07, 2.11, 2.12, 2.27 (9 × s, 81H, 27 × COMe), 2.4–2.6 (m, 18H, H-6), 2.74 (br s, 9H, 3 × NMe), 2.74 (br s, 9H, 3 × NMe), 2.92 (br s, 18 H, 6 × NMe), 3.91–3.96 (m, 18H, NCH_2Ph), 4.28 (dd, 3H, *J* = 4.4 Hz, *J* = 7.41 Hz, H-4), 4.78 (dd, 3H, *J* = 7.8 Hz, *J* = 9.4 Hz, H-3), 4.86–4.90 (m, 3H, H-5), 5.06 (d, 3H, *J* = 7.9 Hz, H-1), 5.16 (t, 3H, *J* = 9.0 Hz, H-2), 5.22 (d, 3H, 9.0 Hz, H-1), 5.27–5.45 (m, 24H), 7.27–7.43 (m, 30H, C_6H_5). DEPT-135 ^{13}C NMR (DMF-d_7, 125 MHz) δ: 20.2, 20.4, 20.5, 20.6, 20.7, 21.0, 42.4, 42.9, (57.2), (58.2), (62.3), (67.8), 68.3, 68.7, 69.4, 71.1, 71.8, 72.2, 72.5, 73.1, 73.5, 74.7, 77.2, 100.0, 100.5, 127.3, 128.7, 129.2, 129.3.

Tris[2-(*N*-{6,6′-N,N′-*bis*[6,6′-*bis*-N-*benzylmethylamino-6,6′-dideoxy*-β-*cellobiosyl-(1→6)-D-galactit-1-yl]-6,6′-dideoxy-6,6′-dimethylamino*-β-*cellobiosyl-(1→6)-D-galactit-1-yl}methylamino)ethyl]amine (16)

Acetic acid (2.28 μL, 45 μmol) was added to a solution of the reducing sugar **10** (90 mg, 47 μmol), tris[2-(methylamino)ethyl]amine **13** (2 mg, 12 μmol), and sodium cyanoborohydride (10 mg, 121 μmol) in MeOH (1 mL). The reaction mixture was stirred and heated under reflux for 6 h. When HPLC analysis indicated that the reaction had gone to completion, the mixture was allowed to cool to room temperature, diluted with H_2O (2 mL), and purified by preparative reversed phase chromatography (15 g C-18 reversed phase, MeOH–H_2O–TFA (0:100:0.0001 to 100:0:0.0001)) to afford **16** (60 mg, 56%). $[\alpha]_D^{20}$ –27 (*c* = 1 in H_2O). MALDI-TOF (*m*/*z*): 5926.1 $[M + Na]^+$. Selected ^{1}H NMR (CD_3OD, 500 MHz): δ: 4.32–4.43 (m, 18H, anomerics), 7.40–7.50 (m, 60H, C_6H_5).

Tris[2-(*N*-methyl{2,2′,3,3′,4′-penta-O-acetyl-6,6′-dideoxy-6,6′-di-N-methyl-6,6′-bis[2,2′,3,3′,4′-penta-O-acetyl-6,6′-bis*-N-*benzylmethylamino-6,6′-dideoxy*-β-*cellobiosyl-(1→6)-2,3,4,5-tetra-O-acetyl-D-galactit-1-yl]amino*-β-*cellobiosyl-(1→6)-2,3,4,5-tetra-O-acetyl-D-galactit-1-yl}amino)ethyl]amine (17)

The first-generation dendrimer **16** (35 mg, 15 μmol) was dissolved in a solution of DMAP (2 mg) in Ac_2O (4 mL) and C_5H_5N (4 mL) and was left to stir at room temperature for 36 h and then concentrated by coevaporation with PhMe before diluting with EtOAc and washing with 1 M HCl, sat. $NaHCO_3$ and sat. NaCl solutions, drying (Na_2SO_4), and concentrating to an oil. GPC ($CHCl_3$:MeOH, 3:1) gave **17** (18 mg, 33%) as an oil. $[\alpha]_D^{20}$ –19 (*c* = 1 in H_2O). MALDI-TOF (*m*/*z*): 9078 $[M + H]^+$. ^{1}H NMR (DMF-d_7, 500 MHz,

© 2002 NRC Canada

350 K) δ: 1.34, 1.41, 1.96, 1.99, 2.02, 2.03, 2.06, 2.07, 2.09, 2.14, 2.16, 2.19, 2.21 (13 × s, 243H, 81 × COMe), 2.4–2.6 (m, 18H, H-6), 2.74 (br s, 9H, 3 × NMe), 2.77–2.81 (br s, 27H, 9 × NMe), 2.87–2.93 (br s, 36H, 12 × NMe), 3.91 (m, 36H, NCH_2Ph), 4.51–4.85 (m, 41H), 5.12–5.38 (m, 41H), 5.51–5.70 (m, 41H), 7.51–7.59 and 7.89 (m, 60H, C_6H_5). DEPT-135 ^{13}C NMR (DMF-d_7, 125 MHz, 300 K) δ: 20.3, 20.4, 20.5, 20.6, 20.8, 21.1, 47.5, 47.8, (57.0), (57.3), 64.6, (62.0), (67.7), 68.2, 68.3, 68.6, 70.1, 71.7, 73.1, 73.4, 74.5, 76.0, 81.1, 97.2, 102.8, 103.4, 128.9, 128.9, 129.7, 129.8, 130.9, 131.2.

Conclusion

The research we have reported in this short paper has established that we can not only synthesize glycodendrons containing cellobiosylgalacto residues but we can also attach these glycodendrons to a trivalent core. These glycodendrons and glycodendrimers add further diversity to the carbohydrate scaffolds we are currently constructing to display large bioactive oligosaccharides (15) and proteins (16) in a predetermined and reasonably precise way on the peripheries of such glycodendrons and glycodendrimers.

Acknowledgements

We thank UCLA for generous financial assistance. The material based upon the use of the Bruker Advance 500 and the ZAB-SE spectrometers is supported by the National Science Foundation under equipment grant no. CHE-9974928 and CHE-9808175. The MALDI-TOF data were acquired in the Mass Spectrometry Facility at UC Riverside by Ron New. WBT is the recipient of a Wellcome Trust International Prize Travelling Research Fellowship.

References

1. (*a*) T. Lindhorst. Top. Curr. Chem. **218**, 201 (2002); (*b*) W.B. Turnbull and J.F. Stoddart. Rev. Mol. Biotechnol. **90**, 231 (2002).
2. R.T. Lee and Y.C. Lee (*Editors*). *In* Neoglycoconjugates: Preparation and applications. Academic Press, San Diego. 1994.
3. I. Vrasidas, N.J. de Mol, R.M.J. Liskamp, and R.J. Pieters. Eur. J. Org. Chem. 4685 (2001).
4. (*a*) B. Colonna, V.R. Harding, S.A. Nepogodiev, F.M. Raymo, N. Spencer, and J.F. Stoddart. Chem. Eur. J. **4**, 1244 (1998); (*b*) P.R. Ashton, S.E. Boyd, C.L. Brown, N. Jayaraman, S.A. Nepogodiev, and J.F. Stoddart. Chem. Eur. J. **2**, 1115 (1997).
5. (*a*) W.B. Turnbull, S.A. Kalovidouris, and J.F. Stoddart. Chem. Eur. J. **8**, 2988 (2002); (*b*) W.B. Turnbull, A.R. Pease, and J.F. Stoddart. ChemBioChem. **1**, 70 (2000).
6. (*a*) K. Sadalapure and T.K. Lindhorst. Angew. Chem. Int. Ed. **39**, 2010 (2000); (*b*) H. Sashiwa, Y. Makimura, Y. Shigemasa, and R. Roy. J. Chem. Soc. Chem. Commun. 909 (2000); (*c*) S. Sabesan, J.O. Duus, S. Neira, P. Domaille, S. Kelm, J.C. Paulson, and K. Bock. J. Am. Chem. Soc. **114**, 8363 (1992).
7. R.A. Laine. Glycobiology, **4**, 759 (1994).
8. G. Reuter and H.-J. Gabius. Biol. Chem. Hoppe–Seyler, **377**, 325 (1996).
9. (*a*) P.M. Collins and R.J. Ferrier. *In* Monosaccharides. John Wiley and Sons, New York. 1995; (*b*) B. Bernet and A. Vasella. Helv. Chim. Acta, **83**, 2055 (2000).
10. F.J. Urban, B.S. Moore, and R. Breitenbach. Tetrahedron Lett. **31**, 4421 (1990).
11. H. Schmidt, C. Lensink, S.K. Xi, and J.G. Verkade. Z. Anorg. Allg. Chem. 75 (1989).
12. (*a*) T. Yamagaki and H. Nakanishi. Anal. Sci. **17**, 83 (2001); (*b*) D.J. Harvey, A.P. Hunter, R.H. Bateman, J. Brown, and G. Critchley. Int. J. Mass Spectrom. 131 (1999); (*c*) T. Yamagaki. Trends Glycosci. Glycotechnol. **11**, 227 (1999); (*d*) Y. Liu and D.E. Clemmer. Anal. Chem. **69**, 2504 (1997); (*e*) K.K. Mock, M. Davey, and J.S. Cottrell. Biochem. Biophys. Res. Commun. **177**, 644 (1991); (*f*) B. Domon and C.E. Costello. Glycoconjugate J. **5**, 397 (1988).
13. C.F. Lane. Synthesis, 135 (1975).
14. D.D. Perrin and W.L.F. Armarego. *In* Purification of laboratory chemicals. 3rd ed. Pergamon Press, Oxford. 1988.
15. (*a*) J.R. Allen and S.J. Danishefsky. J. Am. Chem. Soc. **121**, 10 875 (1999); (*b*) E.C. Rodriguez, L.A. Marcaurelle, and C.R. Bertozzi. J. Org. Chem. **63**, 7134 (1998). (*c*) P.P. Deshpande and S.J. Danishefsky. Nature (London), **387**, 164 (1997).
16. R.C. Werlen, M. Lankinen, R.E. Offord, P.A. Schubiger, A. Smith, and K. Rose. Cancer Res. **56**, 809 (1996).

© 2002 NRC Canada

The reactions of 3-alkylindoles with cyclopropanes: An unusual rearrangement leading to 2,3-disubstitution

Dylan B. England, Tom K. Woo, and Michael A. Kerr

Abstract: Indoles that bear an alkyl substituent in the 3-position, when treated with cyclopropanediesters, typically undergo a [3 + 2]-annulation reaction in a kinetically controlled process (**1**→**4**). If the reaction is performed at elevated temperatures for a longer period of time, a rearrangement of the putative intermediate **3** occurs in which the alkylating species undergoes a migration to the 2-position followed by loss of a proton to reform the benzopyrrole ring. The yields range from 78 to 10%. If a 3-allylindole is used in combination with a cyclopropanediester, which is further substituted with an alkenyl moiety, the product is an effective ring closing metathesis substrate and can be converted to the 1,3,3*a*,4,5,6-hexahydro-1*H*-pyrido[3,2,1-*jk*]carbazole system. A mechanistic discussion of the rearrangement process is presented.

Key words: indole, cyclopropanediester, Lewis acid, ytterbium triflate, rearrangement.

Résumé : Les indoles porteurs d'un substituant alkyle en position 3, traités par des cyclopropanediesters, conduisent généralement à une réaction d'annellation [3 + 2] par un processus sous contrôle cinétique. Si on effectue la réaction à température élevée, pour une période prolongée, il se produit un réarrangement de l'intermédiaire putatif (**3**) au cours duquel l'espèce qui provoque l'alkylation subit une migration vers la position 2 qui est suivie d'une perte d'un proton pour reformer un noyau benzopyrrole. Les rendements varient de 78 à 10%. Si l'on utilise un 3-allylindole en combinaison avec un cyclopropanediester substitué par une portion alcényle, le produit est un substrat résultant d'une réaction effective de métathèse conduisant à une formation de cycle; ce substrat peut être transformé en un système 1,3,3*a*,4,5,6-hexahydro-1*H*-pyrido[3,2,1-*jk*]carbazole. On présente une discussion du mécanisme du processus de réarrangement.

Mots clés : indole, cyclopropanediester, acide de Lewis, triflate d'ytterbium, réarrangement.

[Traduit par la Rédaction]

Introduction

The importance of the indole moiety in biological and medicinal chemistry is unarguably significant. An enormous fraction of the bioactive alkaloids known are based on the indole nucleus (1). Medicinal chemists have repeatedly turned to indole-based compounds for inspiration and indeed many indole-containing compounds are marketed as therapeutic agents (2). It should come as no surprise, then, that there continues to be considerable emphasis on new methods for the formation and the elaboration of the benzopyrrole ring system (3). Such methods add to the toolbox of the synthetic chemist and aid in the chemical synthesis of indole alkaloids (4).

Received 2 August 2001. Published on the NRC Research Press Web site at http://canjchem.nrc.ca on 13 August 2002.

This paper is dedicated to the memory of Professor Raymond U. Lemieux.

D.B. England, T.K. Woo, and M.A. Kerr.[1] Department of Chemistry, The University of Western Ontario, London, ON N6A 5B7, Canada.

[1]Corresponding author (e-mail: makerr@uwo.ca).

For some time now, our research group has been interested in the elaboration of the indole nucleus for the purposes of natural products synthesis. In particular we have focussed on new ways to take advantage of the natural nucleophilic character of indoles. We have found, for example, that lanthanide triflates (in particular ytterbium triflate) are effective in promoting the nucleophilic addition of indoles to electron-deficient olefins (5) and cyclopropanes (6, 7). In addition, we (5*a*, 6) and others (8) have reported that high pressures are effective in further amplifying the nucleophilic behaviour of indoles. In our more recent work (6) we have shown that indoles with no substituents are efficiently alkylated with cyclopropanediesters producing 2-carboalkoxy-4-indolyl butanoate esters **5** (Scheme 1). Indoles which bear substitution at the 3-position, upon treatment with the cyclopropanediester, yield the cyclopentannulation product **4** (7). It was noted, that if the reactions (**1**→**4**) of substrates where where R^2 = H was performed under high-temperature conditions, a by-product **6** (a formal 2-alkylation) was formed in small amounts (<5%) and in some cases (R^4 = Ph) in significant amounts.

Driven by curiosity, we subjected one example (Scheme 2) to forcing conditions (refluxing acetonitrile, 4 days) and were able to produce **8** as the sole identifiable product in 76% yield. By comparison, if the reaction was

 DOI: 10.1139/V02-125 © 2002 NRC Canada

Scheme 1.

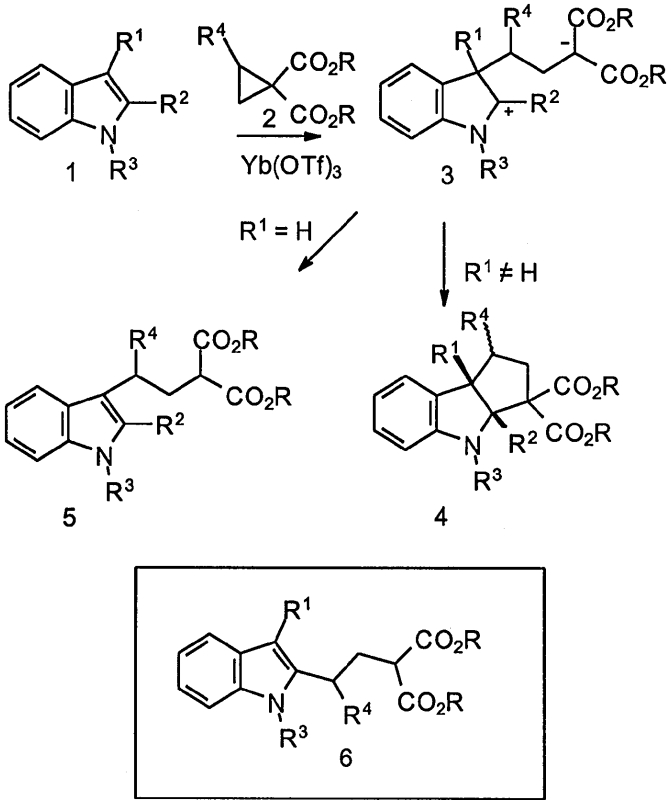

Scheme 2.

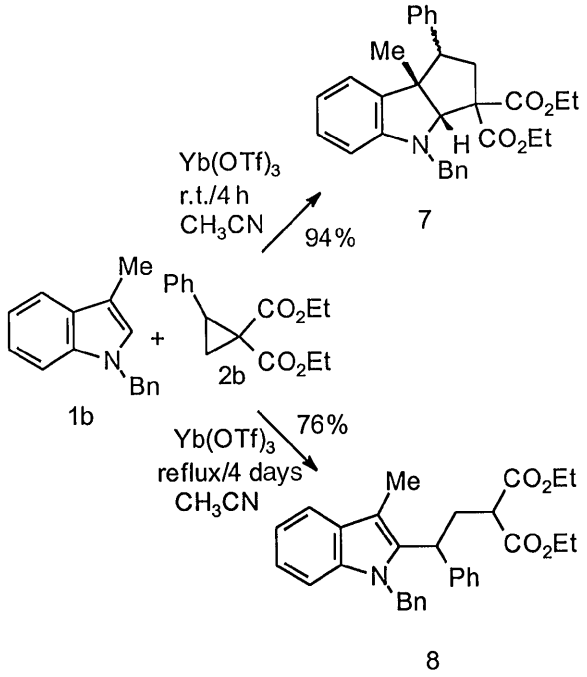

performed under milder conditions (rt, 4 h), the annulation product **7** was formed in 94% yield. Herein we detail a mechanistic picture which explains the formation of the 2-alkylated indoles and the factors which favour its formation over cyclopentannulation. In some select cases the process is synthetically useful and products can be intermediates for the synthesis of more complex indole systems.

Results and discussion

Indoles which bear a substituent at the 3-position often undergo further electrophilic substitution at the 2-position (9) (Scheme 3). While appearing as a direct electrophilic attack, it is widely accepted that substitution at the 2-position of 3-substituted indoles such as **9** proceeds via further 3-alkylation to form intermediate **11** followed by a rearrangement to **12** and subsequent loss of a proton to form **10**. Naidoo and co-workers (10) suggest that the direct formation of the cationic intermediate **12** would be a higher energy process than via intermediate **11.**

A mechanistic scenario for our observations, which illustrates the rearrangement, is shown in Fig. 1. Intuitive relative energies were born out by density functional theory calculations at the B3LYP level of theory[2] on **I** through **V** using R^1 = R^2 = Me and R^3 = H. In a first step common to the formation of both products, the indole may react with the cyclopropanediester to produce intermediate immonium ion **II,** which can suffer two fates. In a kinetic process, ring closure

Scheme 3.

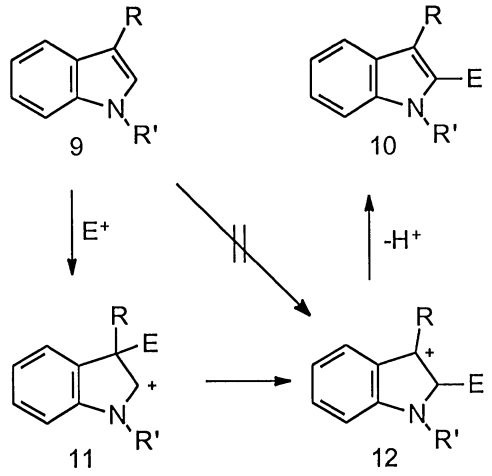

of the malonic enolate can occur to produce cyclopentannulation product **IV**. Alternatively **II** may rearrange to produce the 3° benzyllic carbocation **III**. Transfer of a proton in **III** yields the thermodynamic product **V**. Although the potential energy surfaces linking the structures in Fig. 1 were not studied in detail, the geometry optimization of **II** often led to the formation of **IV**. This suggests that a small energetic barrier for the rearrangement process (**II**–**IV**) exists. Similarly, geometry optimization of **III** often lead directly to **V**, again suggesting a small barrier for this process. It is interesting that the heating of compounds of type **IV** for extended periods of time leads to the formation of **V** as well as a small amount of the starting indole, illustrating the reversibility of the annulation.

[2] Energies refer to those resulting from a global geometry optimization protocol. For a description of the theoretical methods employed see the *Experimental* section.

© 2002 NRC Canada

Fig. 1. Putative mechanistic scenario for the formation and rearrangement of **IV** and **V**. Energies shown are relative to *I*, calculated at the B3LYP/6-31G** level of theory using $R^1 = R^2 = Me$ and $R^3 = H$. Relative energies include zero-point vibrational energy corrections.

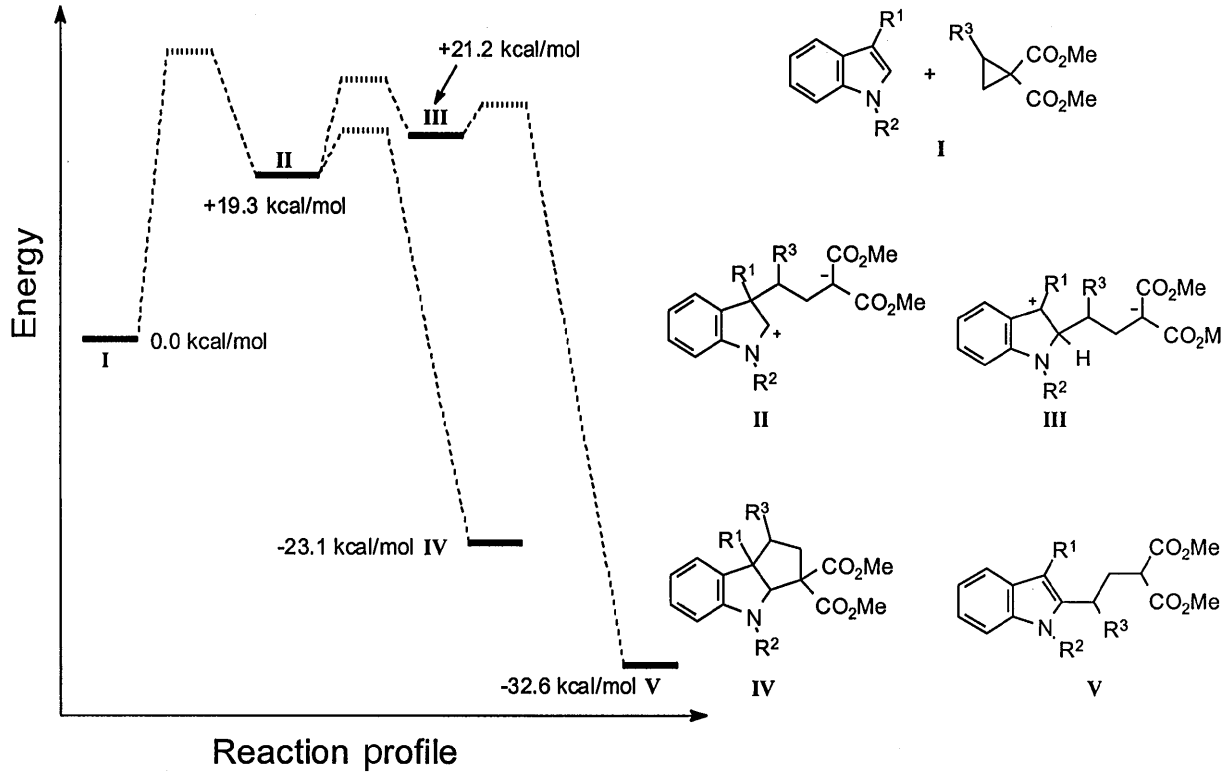

Table 1.

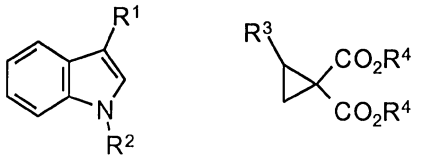

	R^1	R^2		R^3	R^4
1a	Me	Me	2a	$CH=CH_2$	Me
1b	Me	Bn	2b	Ph	Et
1c	$CH_2CH=CH_2$	Bn	2c	CH=CHPh	Me

To probe the synthetic utility of the rearrangement, a series of indoles (11) and cyclopropanes (12) were prepared according to literature procedures (Table 1). In general the reactions of the indoles with the cyclopropanes were performed in refluxing acetonitrile. The results are shown in Table 2. In most cases the annulation product was formed first and soon disappeared (by TLC) to yield the product resulting from 2-alkylation. Phenyl cyclopropane **2b**, upon reaction with **1a** gave **13** in quite acceptable yield (78%). Other cyclopropanes were less well behaved, undergoing rearrangements in yields that would be of questionable synthetic utility. Our interest in having a vinylcyclopropane **2a** undergo this reaction stemmed from our desire to have a pendant double bond in the product that could be a useful handle for further functionalization (vide infra). To exploit the beneficial effects of the phenyl group while retaining this exploitable functionality, we employed the styrenyl cyclopropane **2c**. In the reaction with 1,3-dimethylindole, **14** was produced in acceptable yield, while the product of the reaction with 3-allyl-1-benzylindole produced **18** in 31% yield. A variety of reaction conditions were explored to optimize the yields. Alternative Lewis acid catalysts, solvents, times, and temperatures offered no improvement in the yields of the alkylation products.

In all reactions involving cyclopropane **2a** and **2c**, a significant amount of compound **24** was formed (Scheme 4). This observed product likely originates from what could be described as a vinylogous Wagner–Meerwein rearrangement of the intermediate immonium ion (**19** or **20**) to **21** or **22** which occurs in competition with the predicted rearrangement.

Compounds such as **17** and **18** were prepared with an eye towards ring closing metathesis (RCM) (13). Treatment of **17** or **18** with the commercially available Grubb's catalyst (13) **28**, resulted in the formation of the dihydrocarbazole **25** in 85 and 96% yield, respectively (Scheme 5). Hydrogenation of the double bond gave the tetrahydrocarbazole **26**. Treatment of **25** with a metallic palladium catalyst in the presence of oxygen yielded the carbazole **27** in 67% yield.

In summary we have detailed an interesting rearrangement reaction which results in the 2-alkylation of 3-substituted indoles. The products may be further elaborated by ring closing metathesis to yield tetrahydrocarbazoles which may be of synthetic utility for the preparation of a large variety of indole alkaloids. Efforts are underway to improve the

© 2002 NRC Canada

Table 2.

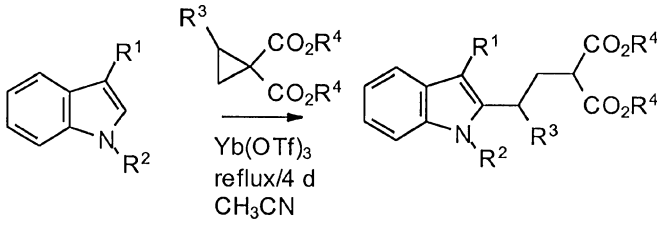

Indole	Cyclopropane	Product (yield)	
1a	2b	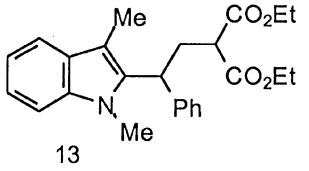 13	(78%)
1a	2c	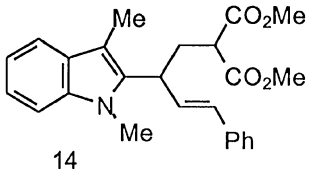 14	(44%)
1a	2a	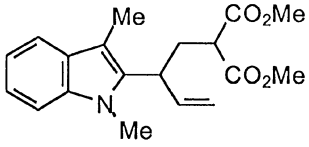 15	(22%)
1b	2a	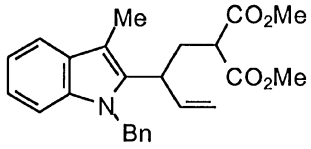 16	(16%)
1c	2a	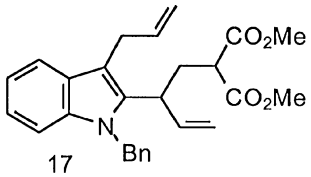 17	(18%)
1c	2c	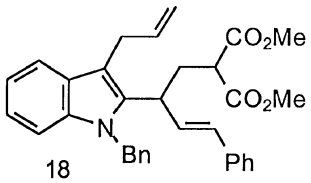 18	(27%)

efficiency of the rearrangement protocol so that it may be of general utility. Results of our efforts will be reported in due course.

Experimental

General considerations (energy calculations)

Due to the conformational variability of the structures of interest, the following global optimization protocol was utilized to estimate relative energies. To generate a large

Scheme 4.

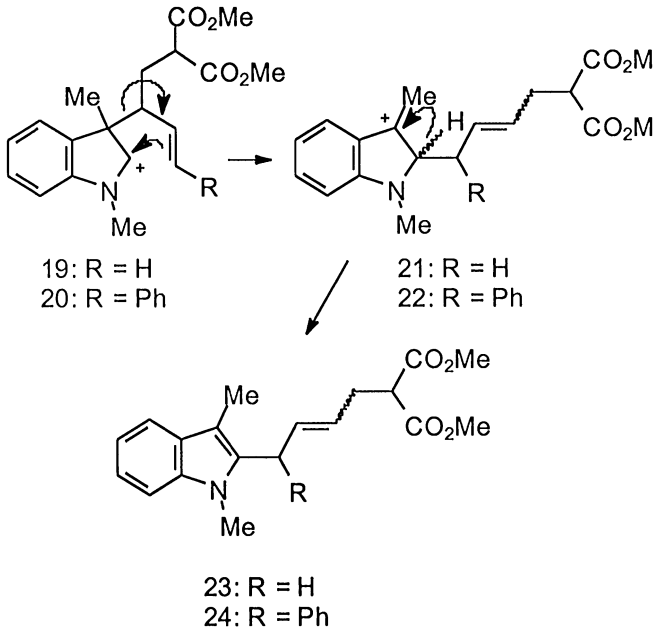

Scheme 5.

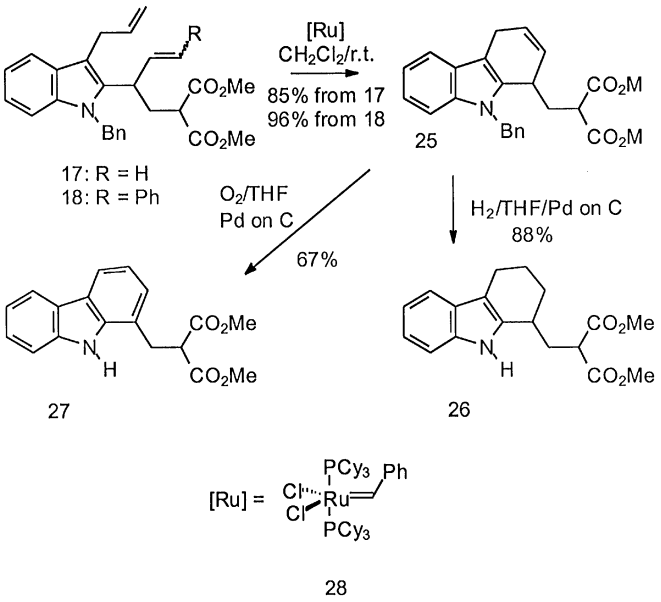

number of conformations that might lead to a global minimum, a high-temperature molecular dynamics simulation was performed for each of **II**–**V** using the SYBYL molecular mechanics force field. Partial atomic charges for the SYBYL calculations were obtained using the Merz–Singh–Kollman (17) electrostatic potential charge fitting procedure as implemented in the Gaussian 98 suite of programs (19) from a fully optimized structure at the B3LYP/6-31G** level (15, 16). For the purpose of generating the point charges for the SYBYL calculations, an arbitrary conformation was utilized. Using the SYBYL potential, a 10 ns molecular dynamics simulation was performed with a time step of 1 fs where the temperature was approximately maintained at 1300 K by velocity rescaling every 50 000 time steps.

© 2002 NRC Canada

Two hundred structures were generated from this MD simulation by sampling every 50 ps. These 200 structures were then fully optimized at the PM3 (18) semi-empirical level with the Gaussian 98 package. The five lowest energy structures were then fully optimized at the B3LYP/6-31G** level with Gaussian 98. The geometry optimization of some complexes often resulted in the formation of another. Consequently, we report on the lowest energy structures consistent with structures **II** through **V**. For each of the lowest energy structures, harmonic vibrational frequency analysis at the B3LYP/6-31G** level was performed with no constraints for the purpose of estimating the zero-point vibrational energy. The relative energies reported in Fig. 1 are zero-point energy corrected. It is important to note that the high-temperature molecular dynamics was used only to generate structures for the global optimization protocol and that the relative energies are approprate to the zero K limit. Furthermore, the calculations have been performed on the gas-phase molecules such that that solvation effects have been neglected.

General considerations (preparative chemistry)

All reactions were performed in anhydrous acetonitrile either as purchased from VWR (DriSolv) or distilled from CaH_2. $Yb(OTf)_3$ was used as the hydrate as purchased from Aldrich. TLC analysis was performed on E. Merck glass plates precoated with silica gel 60 F254. Flash column chromatography (FCC) was performed on silica gel purchased from Silicycle. ^{1}H NMR spectra were recorded at 400 or 600 MHz. ^{13}C NMR spectra were recorded at 100 or 125 MHz. Mass spectra (EI) were recorded using an ionizing voltage of 70 eV.

General procedure for the Yb(OTf)3-catalyzed 2-alkylation of indoles with cyclopropanediesters

The indole (2 equiv), cyclopropane (1 equiv), and $Yb(OTf)_3$ (5 mol%) were charged into a dry flask equipped with a stirring bar. Acetonitrile was added via syringe and the mixture stirred under argon for the indicated time at reflux. The solvent was removed in vacuo and the residue purified by FCC on silica using mixtures of EtOAc–hexanes.

Diethyl 2-[2-(1,3-dimethyl-1H-indol-2-yl)-2-phenyl ethyl] malonate (13)

The general procedure above was followed using indole **1a** (0.290 g, 2.0 mmol), cyclopropane **2b** (0.262 g, 1.0 mmol), and $Yb(OTf)_3$ (0.031 g, 0.05 mmol) in 3 mL acetonitrile. The mixture was refluxed for 1.5 days to give, after purification, 318 mg of **13** (78%) as an oil. IR (thin film on NaCl plates υ) (cm^{-1}): 1747, 1730, 1601, 1472, 1447. ^{1}H NMR ($CDCl_3$) δ: 7.57 (d, *J* = 8.1 Hz, 1H), 7.31–7.17 (m, 7H), 7.13–7.09 (m, 1H), 4.59–4.55 (m, 1H), 4.26–4.16 (m, 2H), 4.03–3.95 (m, 1H), 3.91–3.85 (m, 1H), 3.41 (s, 3H), 3.31–3.28 (m, 1H), 3.02–2.94 (m, 1H), 2.81–2.74 (m, 1H), 2.33 (s, 3H), 1.26 (t, *J* = 7.2 Hz, 3H), 1.13 (t, *J* = 7.2 Hz, 3H). ^{13}C NMR ($CDCl_3$) δ: 169.3, 169.2, 141.4, 137.1, 135.0, 128.5, 128.3, 127.3, 126.5, 121.3, 118.7, 118.4, 109.3, 108.7, 61.5, 61.5, 50.2, 38.7, 31.6, 30.5, 14.0, 13.9, 9.3. EI-HR-MS for $C_{25}H_{29}NO_4$ calcd.: 407.2097; found: 407.2097.

Dimethyl 2-[(3E)-2-(1,3-dimethyl-1H-indol-2-yl)-4-phenyl-3-butenyl] malonate (14)

The general procedure above was followed using indole **1a** (0.290 g, 2.0 mmol), cyclopropane **2c** (0.260 g, 1.0 mmol), and $Yb(OTf)_3$ (0.031 g, 0.05 mmol) in 3 mL acetonitrile. The mixture was refluxed for 6 h to give, after purification, 178 mg of **14** (44%) as an oil. IR (thin film on NaCl plates υ) (cm^{-1}): 1751, 1734, 1472, 1435. ^{1}H NMR ($CDCl_3$) δ: 7.54 (d, *J* = 7.8 Hz, 1H), 7.34–7.18 (m, 7H), 7.11 (dt, *J* = 6.9, 1.2 Hz, 1H), 6.44 (dd, *J* = 16.2, 4.7 Hz, 1H), 6.37 (dd, *J* = 16.2, 4.7 Hz, 1H), 4.06 (ddd, *J* = 8.8, 4.9, 4.9 Hz, 1H), 3.72 (s, 3H), 3.69 (s, 3H), 3.51 (s, 3H), 3.32 (dd, *J* = 8.2, 6.0 Hz, 1H), 2.71–2.55 (m, 2H), 2.30 (s, 3H). ^{13}C NMR ($CDCl_3$) δ: 169.7, 169.5, 137.1, 136.8, 134.3, 130.7, 129.9, 128.6, 128.3, 127.7, 127.5, 126.2, 121.3, 118.8, 118.3, 108.8, 52.7, 52.6, 49.8, 37.2, 32.4, 30.7, 9.3. EI-HR-MS for $C_{25}H_{27}NO_4$ calcd.: 405.1940; found: 405.1933.

Dimethyl 2-[2-(1,3-dimethyl-1H-indol-2-yl)-3-butenyl] malonate (15)

The general procedure above was followed using indole **1a** (0.290 g, 2.0 mmol), cyclopropane **2a** (0.184 g, 1.0 mmol), and $Yb(OTf)_3$ (0.031 g, 0.05 mmol) in 3 mL acetonitrile. The mixture was refluxed for 1.5 days to give, after purification, 72 mg of **15** (22%) as an oil. IR (thin film on NaCl plates υ) (cm^{-1}): 1751, 1734, 1472, 1434. ^{1}H NMR ($CDCl_3$) δ: 7.51 (d, *J* = 7.9 Hz, 1H), 7.25 (d, *J* = 7.9 Hz, 1H), 7.19 (t, *J* = 7.9 Hz, 1H), 7.09 (t, *J* = 7.9 Hz, 1H), 6.06 (ddd, *J* = 17.2, 10.2, 5.4 Hz, 1H), 5.17 (dd, *J* = 10.4, 1.2 Hz, 1H), 5.07 (dd, *J* = 17.2, 1.2 Hz, 1H), 3.91–3.85 (m, 1H), 3.72 (s, 3H), 3.65 (s, 3H), 3.49 (s, 3H), 3.27 (t, *J* = 8.3, 6.2 Hz, 1H), 2.60–2.46 (m, 2H), 2.25 (s, 3H). ^{13}C NMR ($CDCl_3$) δ: 169.6, 169.5, 138.1, 137.1, 134.2, 128.3, 121.2, 118.7, 118.2, 115.7, 108.7, 108.5, 52.6, 52.5, 49.7, 37.8, 31.7, 30.6, 9.1. EI-HR-MS for $C_{19}H_{23}NO_4$ calcd.: 329.1627; found: 329.1628.

Dimethyl 2-[2-(1-benzyl-3-methyl-1H-indol-2-yl)-3-butenyl] malonate (16)

The general procedure above was followed using indole **1b** (0.442 g, 2.0 mmol), cyclopropane **2a** (0.184 g, 1.0 mmol), and $Yb(OTf)_3$ (0.031 g, 0.05 mmol) in 3 mL acetonitrile. The mixture was refluxed for 1.5 days to give, after purification, 73 mg of **16** (18%) as an oil. IR (thin film on NaCl plates υ) (cm^{-1}): 1751, 1734, 1636, 1466, 1453. ^{1}H NMR ($CDCl_3$) δ: 7.57–7.55 (m, 1H), 7.26–7.09 (m, 6H), 6.93 (d, *J* = 7.4 Hz, 2H), 5.94 (ddd, *J* = 17.2. 10.3, 5.9 Hz, 1H), 5.33 (AB, 2H), 5.03 (d, *J* = 10.3 Hz, 1H), 4.87 (d, *J* = 17.2 Hz, 1H), 3.76–3.71 (m, 1H), 3.68 (s, 3H), 3.51 (s, 3H), 3.27 (dd, *J* = 8.4, 6.0 Hz, 1H), 2.50–2.42 (m, 1H), 2.37–2.27 (m, 1H), 2.31 (s, 3H). ^{13}C NMR ($CDCl_3$) δ: 169.6, 169.4, 138.1, 137.6, 136.8, 134.5, 128.8, 128.6, 127.0, 125.8, 121.6, 119.1, 118.2, 115.8, 109.4, 108.8, 52.6, 52.4, 49.4, 46.8, 38.1, 31.8, 9.4. EI-HR-MS for $C_{25}H_{27}NO_4$ calcd.: 405.1940; found: 405.1937.

Dimethyl 2-[2-(3-allyl-1-benzyl-1H-indol-2-yl)-3-butenyl] malonate (17)

The general procedure above was followed using indole **1c** (0.247 g, 1.0 mmol), cyclopropane **2a** (0.184 g,

© 2002 NRC Canada

1.0 mmol), and $Yb(OTf)_3$ (0.031 g, 0.05 mmol) in 3 mL acetonitrile. The mixture was refluxed for 1.5 days to give, after purification, 69 mg of **17** (16%) as an oil. IR (thin film on NaCl plates υ) (cm^{-1}): 1751, 1734, 1636, 1465, 1453, 1435. ^1H NMR ($CDCl_3$) δ: 7.59 (d, *J* = 6.8 Hz, 1H), 7.27–7.08 (m, 6H), 6.93 (d, *J* = 7.2 Hz, 2H), 6.05–5.90 (m, 2H), 5.38 (AB, 2H), 5.11–5.01 (m, 3H), 4.91 (d, *J* = 17.5 Hz, 1H), 3.79–3.73 (m, 1H), 3.70 (s, 3H), 3.53 (s, 3H), 3.59–3.49 (m, 2H), 3.28 (dd, *J* = 8.5, 6.0 Hz, 1H), 2.53–2.42 (m, 1H), 2.32–2.25 (m, 1H). ^{13}C NMR ($CDCl_3$) δ: 169.6, 169.3, 137.9, 137.9, 137.3, 137.1, 135.2, 128.6, 128.1, 127.0, 125.8, 121.7, 119.2, 118.8, 116.0, 114.8, 111.0, 109.6, 52.6, 52.4, 49.4, 47.0, 37.9, 32.0, 29. EI-HR-MS for $C_{27}H_{29}NO_4$ calcd.: 431.2097; found: 431.2101.

*Dimethyl 2-[(3**E**)-2-(3-allyl-1-benzyl-1**H**-indol-2-yl)-4-phenyl-3-butenyl] malonate (18)*

The general procedure above was followed using indole **1c** (0.400 g, 1.6 mmol), cyclopropane **2c** (0.443 g, 1.7 mmol), and $Yb(OTf)_3$ (0.050 g, 0.08 mmol) in 7 mL acetonitrile. The mixture was refluxed for 1 day to give, after purification, 255 mg of **18** (31%) as an oil. IR (thin film on NaCl plates υ) (cm^{-1}): 1750, 1734, 1495, 1466, 1453. ^1H NMR ($CDCl_3$) δ: = 7.59 (d, *J* = 7.2 Hz, 1H), 7.28–7.04 (m, 11H), 6.93 (d, *J* = 7.7Hz, 2H), 6.26 (dd, *J* = 15.7, 6.4 Hz, 1H), 6.10 (d, *J* = 15.7 Hz, 1H), 6.06–5.97 (m, 1H), 5.42 (AB, 2H), 5.10–5.02 (m, 2H), 3.95–3.90 (m, 1H), 3.68 (s, 3H), 3.66–3.49 (m, 2H), 3.55 (s, 3H), 3.32 (dd, *J* = 8.5, 6.0 Hz, 1H), 2.58–2.50 (m, 1H), 2.40–2.33 (m, 1H). ^{13}C NMR ($CDCl_3$) δ: 169.6, 169.3, 137.9, 137.3, 137.1, 136.7, 135.6, 131.1, 129.5, 128.7, 128.4, 127.4, 127.1, 126.1, 125.9, 121.7, 119.3, 118.8, 115.0, 111.0, 109.7, 109.5, 52.7, 52.5, 49.5, 47.1, 37.6, 32.8, 29.2. EI-HR-MS for $C_{33}H_{33}NO_4$ calcd.: 507.2410; found: 507.2413.

*Dimethyl 2-[(9-benzyl-4,9-dihydro-1**H**-carbazole-1-yl)methyl]malonate (25)*

Indole **18** (0.255 mg, 0.50 mmol) and Grubbs' catalyst **28** (21 mg, 0.025 mmol) were charged into a dry flask equipped with a stirring bar. Dichloromethane was added via syringe and the mixture stirred under argon at room temperature for 4 h. The mixture was then concentrated in vacuo and purified by column chromatography (EtOAc–hexanes as the eluent) to yield 0.195 g (96%) of **25** as a an oil. IR (thin film on NaCl plates υ) (cm^{-1}): 1751, 1733, 1466, 1453, 1435. ^1H NMR ($CDCl_3$) δ: 7.52 (d, *J* = 8.2 Hz, 1H), 7.26–7.07 (m, 6H), 6.95 (d, *J* = 7.8 Hz, 2H), 6.17–6.15 (m, 1H), 5.77–5.73 (m, 1H), 5.45 (d, *J* = 17.2 Hz, 1H), 5.32 (d, *J* = 17.2 Hz, 1H), 3.68 (s, 3H), 3.68–3.63 (m, 2H), 3.48–3.44 (m, 1H), 3.36 (t, *J* = 7.0 Hz, 1H), 3.14 (s, 3H), 2.47 (ddd, *J* = 12.9, 6.6, 6.6 Hz, 1H), 2.36 (ddd, *J* = 14.1, 7.0, 3.3 Hz, 1H). ^{13}C NMR ($CDCl_3$) δ: 170.2, 169.2, 138.1, 137.2, 133.3, 128.7, 127.5, 127.1, 126.6, 126.5, 125.9, 121.6, 119.1, 118.1, 109.6, 109.3, 52.6, 52.2, 47.5, 46.7, 34.0, 32.0, 23.7. EI-HR-MS for $C_{25}H_{25}NO_4$ calcd.: 403.1784; found: 403.1787.

*Dimethyl 2-[(9-benzyl-2,3,4,9-tetrahydro-1**H**-carbazole-1-yl)methyl]malonate (26)*

Dihydrocarbazole **25** (0.089 g, 0.22 mmol) was dissolved in dry THF in a flask equipped with a stirring bar. 10% Pd/C (5 wt%) was added quickly and the flask was purged with H_2 gas. The mixture was then stirred under a balloon of H_2 at ambient temperature for 3 h. The reaction mixture was then filtered over a pad of Celite, rinsed with THF, and subjected to flash chromatography on silica gel (EtOAc–hexanes as the eluent) to yield 0.079 g (88%) of **26** as an oil. IR (thin film on NaCl plates υ) (cm^{-1}): 1750, 1734, 1480, 1453, 1435. ^1H NMR ($CDCl_3$) δ: 7.51 (d, *J* = 8.3 Hz, 1H), 7.27–7.06 (m, 6H), 6.91 (d, *J* = 7.9 Hz, 2H), 5.43 (s, 2H), 3.69 (s, 6H), 3.56 (dd, *J* = 11.3, 3.8 Hz, 1H), 2.88–2.83 (m, 1H), 2.77–2.65 (m, 2H), 2.35 (ddd, *J* = 13.5, 11.4, 1.6 Hz, 1H), 2.06 (ddd, *J* = 15.2, 11.7, 1.6 Hz, 1H); 1.93–1.78 (m, 4H). ^{13}C NMR ($CDCl_3$) δ: 169.7, 169.6, 138.4, 137.4, 137.0, 128.5, 127.2, 126.9, 125.8, 121.3, 118.9, 118.0, 110.1, 109.6, 52.7, 52.6, 49.5, 45.9, 32.3, 29.5, 25.8, 20.9, 18.1. EI-HR-MS for $C_{25}H_{27}NO_4$ calcd.: 405.1940; found: 405.1954.

Acknowledgements

We wish to thank the Natural Sciences and Engineering Research Council (NSERC), The Ontario Ministry of Science and Technology, and MedMira Laboratories for funding. We also wish to thank SHARCNET, The Canadian Foundation for Innovation, and the Ontario Innovation Trust for the support of computing resources. D.B.E. is the recipient of an Ontario Graduate Scholarship.

References

1. (*a*) G.W. Gribble. Comprehensive heterocyclic chemistry. Vol. 2. 2nd ed. Pergammon Press, New York. 1996. pp. 203–257; (*b*) V. Snieckus. The alkaloids. Vol. 11. Academic Press, New York. 1968. Chap. 1.
2. G.W. Gribble. Comprehensive heterocyclic chemistry. Vol. 2. 2nd ed. Pergammon Press, New York. 1996. pp. 211–213.
3. (*a*) G.W. Gribble. J. Chem. Soc. Perkin. Trans. 1, 1045 (2000); (*b*) R.J. Sundberg. Indoles. Academic Press, San Diego. 1996; (*c*) R.K. Brown. Heterocyclic compounds. Vol. 25. Wiley, New York. 1972. Pt. 1. Chap. 2.
4. (*a*) A. Rahman and A. Basha. Indole alkaloids. Harwood Academic Publishers, Amsterdam. 1998; (*b*) J.E. Saxton. Heterocyclic compounds. Vol. 25. Wiley, New York. 1994. Suppl. to Pt. 4; (*c*) J.E. Saxton. Heterocyclic Compounds. Vol. 25. Pt 4. Wiley, New York. 1983.
5. (*a*) P.E. Harrington and M.A. Kerr. Can. J. Chem. **76**, 1256 (1998); (*b*) M.A. Kerr and P.E. Harrington. Synlett. 1047 (1996).
6. P.E. Harrington and M.A. Kerr. Tetrahedron Lett. 5949 (1997).
7. (*a*) D.B. England, T.D.O. Kuss, R.G. Keddy, and M.A. Kerr. J. Org. Chem. **66**, 4704 (2001); (*b*) M.A. Kerr and R. Keddy. Tetrahedron Lett. 5671 (1999).
8. H. Kotsuki, K. Hayashida, T. Shimanouchi, H. Nishizawa. J. Org. Chem. **61**, 984 (1996); H. Kotsuki, M. Teraguchi, N. Shimomoto, and M. Ochi. Tetrahedron Lett. **37**, 3727 (1996); H. Kotsuki, M. Nishiuchi, S. Kobayashi, and H. Nishizawa. J. Org. Chem. **55**, 2969 (1990); K. Matsumoto, S. Nakamura, and R.M. Acheson. Heterocycles, **14,** 1959 (1980); H. Kotsuki, Y. Mori, H. Nishizawa, M. Ochi, and K. Matsuoka. Heterocycles, **19**, 1915 (1982).
9. R.J. Sundberg. The chemistry of indoles. Academic Press, New York. 1970. pp. 78–83.
10. A.H. Jackson, B. Naidoo, and P. Smith. Tetrahedron, **24**, 6119 (1969).
11. Indole **1c** was prepared by reaction of the corresponding 3-lithio derivative with allyl bromide. See: M. Amat, S.

© 2002 NRC Canada

Sathyanarayana, S. Hadida, and J. Bosch. Heterocycles, **43**, 1713 (1996).
12. **2a**: R.W. Kierstead, R.P. Linstead, and B.C.L. Weedon. J. Chem. Soc. 3610 (1952). Literature preparation of cyclopropanes **2b** and **2c**: E.J. Corey and M. Chaykovsky. J. Am. Chem. Soc. **87**, 1353 (1965).
13. For an brief review of olefin metathesis with many good references see: T.M. Trnka and R.H. Grubbs. Acc. Chem. Res. **34**, 18 (2001).
14. T.-S. Kam, K.-M. Sim, and T.-M. Lim. Tetrahedron Lett. **40**, 5409 (1999).
15. A.D. Becke. J. Chem. Phys. **98**, 5648 (1993).
16. C. Lee, W. Yang, and R.G. Parr. Phys. Rev. B: Condens. Matter, **37**, 785 (1988).
17. B.H. Besler, K.M. Merz, Jr., and P. Kollman. J. Comput. Chem. **11**, 431 (1990).
18. J.J.P. Stewart. J. Comput. Chem. **10**, 209 (1989).
19. M.J. Frisch, G.W. Trucks, H.B. Schlegel, G.E. Scuseria, M.A. Robb, J.R. Cheeseman, V.G. Zakrzewski, J.A. Montgomery, R.E. Stratmann, J.C. Burant, S. Dapprich, J.M. Millam, A.D. Daniels, K.N. Kudin, M.C. Strain, O. Farkas, J. Tomasi, V. Barone, M. Cossie, R. Cammi, B. Mennucci, C. Pomelli, C. Adamo, S. Clifford, J. Ochterski, G.A. Petersson, P.Y. Ayala, Q. Cui, K. Morokuma, D.K. Malick, A.D. Rabuck, K. Raghavachari, J.B. Foresman, J. Cioslowski, J.V. Ortiz, A.G. Baboul, B.B. Stefanov, G. Liu, A. Liashenko, P. Piskorz, I. Komoaromi, R. Gomperts, R.L. Martin, D.J. Fox, T. Keith, M.A. Al-Laham, C.Y. Peng, A. Nanayakkara, M. Challacombe, P.M.W. Gill, B. Johnson, W. Chen, M.W. Wong, J.L. Andres, C. Gonzalez, M. Head-Gordon, E.S. Replogle, and J.A. Pople. Gaussian 98 ver. A. 9. Gaussian, Inc. Pittsburg, PA. 1998.

© 2002 NRC Canada

Towards high affinity carbohydrate-binding proteins: Directed evolution of murine galectin-3

Joseph J. Lundquist, Brendan M. Kiburz, Jeffrey K. Wu, Kenneth D. Gibbs, Jr., and Eric J. Toone

Abstract: Towards a better understanding of the molecular basis of affinity, a directed evolution of murine galectin-3 (G3) was initiated to produce mutants with improved affinity for lactose and *N*-acetyllactosamine relative to the wild-type protein. A series of *N*-terminal truncations were developed to facilitate incorporation of the 35 kDa protein into a phage-display construct. Analysis of the various assemblies revealed that all such deletions produced protein unsuitable for use in directed evolution studies. Following fusion of the full-length galectin to p3 of filamentous phage, three libraries were constructed and biopanned for increased affinity for lactose. The first two libraries, of 1×10^5 and 1×10^6 members, respectively, were assembled through a combination of error-prone PCR and DNA shuffling. A third library was constructed using a modified staggered extension protocol (StEP), but contained only 10 members. Mutants were also engineered site-specifically to test the role of key residues in or near the binding pocket. Analysis of the mutants by ITC identified one mutation (R158G) that produces a twofold increase in affinity for lactose and another that results in a sixfold increase in affinity for *N*-acetyllactosamine. Solid-phase binding analysis of phage for nonexpressing proteins indicated that two other mutants demonstrated increased binding to β-methyllactose relative to the wild-type protein. Together these studies validate the evolutionary approach and set the stage for the development of novel carbohydrate-binding proteins.

Key words: phage display, directed evolution, galectin, thermodynamics, carbohydrates.

Résumé : Dans le but de mieux comprendre les bases moléculaires de son affinité, on a initié une évolution dirigée de la murine-galectine-3 (G3) afin de produire des mutants ayant une meilleure affinité que la protéine naturelle pour le lactose et la *N*-acétyllactosamine. On a développé une série de produits tronqués au niveau *N*-terminal qui permettent de mieux incorporer la protéine de 35 kDa dans un assemblage présentant le phage. Une analyse de divers types d'assemblage a permis de découvrir que de tels tronquaqes conduisent à une protéine qui n'est pas appropriée pour un usage dans des études d'évolution dirigée. À la suite d'une fusion de la galectine complète à un p de 3 à un phage filamenteux, on a préparé trois banques et dont on a évalué d'un point de vue biologique le degré d'affinité pour le lactose. Les deux premières banques qui comprennent respectivement 1×10^5 et 1×10^6 membres ont été assemblées par le biais d'une combinaison PCR et de réarrangement d'ADN qui est sujette à erreur. La troisième bibliothèque a été obtenue en faisant appel à un protocole d'extension décalé modifié (« StEP »), mais elle ne comportait que 10 membres. On a aussi préparé des mutants à spécification de site pour évaluer le rôle des résidus clés dans ou près de la poche de fixation. L'analyse des mutants par ITC a permis d'identifier une mutation (R158G) qui permet de doubler l'affinité pour le lactose et une autre qui multiplie par six cette affinité pour la *N*-acétyllactosamine. Une analyse de la fixation du phage en phase solide pour des protéines qui ne donnent pas d'expression indique que deux autres mutants possèdent un pouvoir de fixation accru pour le β-méthyllactose par rapport à la protéine naturelle. Ces études considérées ensemble permettent de valider l'approche évolutionnaire et de mettre tout en place le développement de nouvelles protéines pouvant se lier à des hydrates de carbone.

Mots clés : mise en évidence du phage, évolution dirigée, galectine, thermodynamique, hydrates de carbone.

[Traduit par la Rédaction]

Introduction

Protein-carbohydrate interactions play important roles in myriad biological events. Bacterial infections, fertilization, host entry by viruses, and inflammatory responses are all mediated by specific interactions between carbohydrate-binding proteins and their cognate cell-surface carbohydrate receptors (1–12). Although protein–carbohydrate interactions

Received 14 December 2001. Published on the NRC Research Press Web site at http://canjchem.nrc.ca on 13 August 2002.

Dedicated to the memory of Professor Raymond U. Lemieux.

J.J. Lundquist, B.M. Kiburz, J.K. Wu, K.D. Gibbs, Jr., and E.J. Toone.[1] Departments of Biochemistry and Chemistry, Duke University, Durham, NC 22708, U.S.A.

[1]Corresponding author: (e-mail: toone@chem.duke.edu).

 DOI: 10.1139/V02-086 © 2002 NRC Canada

are vital to many biological events, they are uniformly weak: dissociation constants range from millimolar to micromolar (13).

The molecular basis of affinity and specificity in aqueous association phenomena in general is poorly understood. Although structural data reveal favorable interactions, such as hydrogen bonds and salt bridges, they offer no understanding of the extent to which these interactions stabilize the bound complex. Water is a unique medium, both in bulk and in detail, that provides energetically favorable contacts with a wide range of solutes. Under such conditions, a binding event is necessarily a cycle during which energetically favorable contacts between solute and solvent are lost and replaced by a corresponding set of interactions between solutes. A better understanding of the energetic consequences of these cycles is prerequisite to the rational construction of molecular motifs with a priori predictable properties.

Considering the complexity of association phenomena in general, it is not surprising that the basis for the weak affinity of protein–carbohydrate interactions is unclear. On one hand, the structure of carbohydrates might mandate that binding cycles cannot provide a favorable energetic increment greater than about 6 kcal mol^{-1}. On the other hand, the observed affinities may simply reflect the requirements for biological activity, where dissociation is frequently as important as binding. The long-term goals of our research are to understand the molecular basis of affinity in aqueous solution and the maximum affinity with which a carbohydrate can be bound by a protein. Considerable effort has been expended towards the synthesis of carbohydrates with enhanced binding behavior relative to native epitopes; with few exceptions, these studies have universally failed to yield high-affinity ligands (14–35). Work towards modification of the protein partner has shown some promise (36–40). Here, we present initial results on the enhancement of lectin affinity through random protein modification.

We selected murine galectin-3 (G3), a 35-kDa monomeric member of the galectin family of proteins that bind β-galactosides, for directed evolution (41–45). The function of galectin-3 is not fully understood, although it appears to posses a number of interesting attributes that include pre-mRNA splicing and anti-apoptotic signaling (46–48). The expression of various galectins also correlates with a number of cancer states (49–51). The protein is found in the cytosol and nucleus of several cell types in a temporally regulated fashion depending on developmental phase (52). In some cases the protein is secreted into extracellular spaces through a non-classical pathway (52).

Galectin-3 is a chimeric galectin, characterized by an *N*-terminal domain connected to a *C*-terminal domain through a short linker. The *N*-terminal region consists of a 12-amino-acid cell-directing sequence that includes a phosphorylation site followed by a series of glycine- and proline-rich repeats that vary in number and composition (53–57). The *C*-terminal domain consists of the canonical galectin fold, comprising 12 β-sheets, and contains the carbohydrate-binding site. No crystal structure is available for murine galectin-3, although a structure has been determined for the *C*-terminal domain of the human homolog with which the murine galectin shares greater than 90% sequence identity (58, 59).

Using murine galectin-3 as our starting point, we have engineered and isolated truncated forms of the protein and tested their utility for phage display. We have also incorporated the full-length protein into filamentous phage. Concurrently, a new expression system was developed to facilitate expression. This new system also greatly reduces the time necessary for protein purification. Following these preliminary studies, random mutations were introduced into the protein via a combination of error-prone PCR and DNA shuffling techniques. Increased affinity mutants were selected from these libraries by biopanning. These mutants, as well as chimeric proteins and site-directed mutants, were analyzed for ligand binding by isothermal titration calorimetry. Several galectin-3 mutants could not be expressed; the binding of those mutants was tested by a phage-based binding assay. Here we report the prelimary results of these studies.

Experimental

General

Ampicilin, tetracycline, kanamycin, lactose, β-methyllactose, and *N*-acetyllactosamine were purchased from Sigma. Restriction enzymes *Bam*HI, *Bgl*II, *Sph*I, *Eco*RI, and *Sfi*I, as well as Deep Vent DNA polymerase were obtained from New England Biolabs. T4 ligase and dNTPs were obtained from Boehringer–Mannheim. Plasmid prCBP35s was obtained from Dr. J. L.Wang, Department of Biochemistry, Michigan State University. Plasmid fUSE5 and *Escherrichia coli* strain K91 were obtained from Dr. G. P. Smith, Division of Biological Science, University of Missouri. K91 starved cells were prepared by the procedure of Pratt and co-workers (60). Protein concentrations were determined by the method of Edelhoch (61). Unless stated otherwise, all transformations are carried out by chemical transformation.

Assembly of truncated G3

Using plasmid prCBP35s as a template, polymerase chain reaction (PCR) amplification was carried out with the appropriate *N*-terminal primer (Table 1) and a reverse primer (5′-CGG TAT TTA GTA GCC ATG TTG-3′) that corresponds to a randomly selected downstream sequence. Thirty PCR cycles were conducted (94°C for 30 s, 50°C for 30 s, and 74°C for 60 s). The amplified section was digested with *Eco*RI and ligated into the vector pIN-III-*Omp*A1. The final plasmid was transformed into XL-10 Gold cells (Stratagene). Isolated DNA was analyzed for insert orientation by repeating the PCR; clones containing the correct orientation were sequenced for verification of the coding frame.

Expression and isolation of the G3 and truncations

Plasmids containing insert corresponding to either wild-type or truncated G3 were transformed into BL21 Codon Plus RP cells (Stratagene). A starter culture was prepared from a single colony transferred into 5 mL Luria broth supplemented with 100 μg mL^{-1} ampicilin and incubated at 37°C overnight. Terrific broth (1 L) supplemented with 100 μg mL^{-1} of ampicilin was inoculated with the starter culture and allowed to grow at room temperature for 2 h before the addition of isopropyl-1-thio-β-galactopyranoside (IPTG) to a final concentration of 50 μM. The culture was incubated with shaking (300 rpm) for 20 h at room temperature. Cells were

© 2002 NRC Canada

Table 1. PCR primers.

Primer	Sequence (5′→3′)
pINSeq	AAT TCA CAC AGG AAA CAG CTA TGA
d50	GCT GAA TTC GGG GCC TAC CCA GGA CAG GCT
d91	GCT GAA TTC CAA CCT GCC CCT GGA GCC TTC
d96	GCT GAA TTC GCC TTC CCA GGG CAA CCT GGG
d101	GCT GAA TTC CCT GGG GCA CCT GGG GCC TAC
d116	GCT GAA TTC GCT GCT GGC CCT TAT GGT GTC
G3rev	CGG TAT TTA GTA GCC ATG TTG
PDfor	TTG GCC GAC GTG GCC GAA TTC CGA GAC AGC TTT
PDrev	CGG GCC CCA GAC GCC CCG ATC ATG GCG TGG TTA GCG CT
EcoG3	TCG GGA TCC GCG AGA CAG CTT TTC GCT
BamG3	GGC TAA GAA TTC GAT CAT GGC GTG GTT AGC
S251Af	GAA ATC AGC CAA CTG GGG ATC GCT CGT GAC ATA ACC CTC AGC GCT
S251Ar	AGC GCT GAG GGT TAT GTC ACG AGC GAT CCC CAG TTG GCT GAT TTC
W195Ff	ACG AAG CAG GAC AAT AAC TTC GGA AAG GAA GAA AGA CAG
W195Fr	CTG TCT TTC TTC CTT TCC GAA GTT ATT GTC CTG CTT CGA

harvested by centrifugation (5000 × *g*, 15 min) and the cell-pellet was resuspended in 25 mL of 1 M tris buffer (pH 7.0) containing 10 mM β-mercaptoethanol, 1 mM phenylmethylsulfonyl fluoride (PMSF), 10 μg mL^{-1} soybean trypsin inhibitor, 0.5 μg mL^{-1} leupeptin, and 5 trypsin inhibition units (TIU) L^{-1} aprotinin and stored at 4°C. After 4 h, the resultant mixure was centrifuged (18 000 × *g*, 30 min) and the supernatant was fractionated at 65% ammonium sulfate. The crude protein precipitate collected by centrifugation (12 000 × *g*, 20 min), resuspended in 75 mM tris buffer containing 75 mM NaCl, 2 mM EDTA, 1 mM β-mercaptoethanol, 1 mM PMSF at pH 7.5 and applied to a lactosylsepharose column (approx. 25 mL resin) pre-equilibrated in the same buffer. The resin was washed with 20 column volumes of loading buffer then eluted with five column volumes of buffer supplemented with 0.3 M lactose. Fractions were checked for purity by SDS-PAGE under denaturing conditions and positive fractions were concentrated using a YM-3 filter in an Amicon stirred cell.

Construction of plasmid for pET expression

Using the appropriate template (prCBP35s for wild-type, phage plasmid from biopanning, or assembled insert for chimeric constructs), 30 PCR cycles (94°C for 30 s, 53°C for 30 s, and 74°C for 60 s) were carried out with the primers EcoG3 and BamG3 (Table 1). The amplified section was digested with *Eco*RI (4 h at 37°C) and purified with a Qiagen PCR purification kit. The purified DNA was digested with *Bam*HI (4 h at 37°C) and purified by extraction from a 1% agarose gel using a Qiagen gel extraction kit. Ligation into a similarly prepared pET28b vector gave the final plasmid that was transformed into XL-10 Gold cells (Stratagene). Plasmids from resultant colonies were isolated and analyzed for insert by PCR. Colonies that tested positive were sequenced for verification of the coding frame.

Expression and isolation of His-tagged G3 and mutants

Plasmids containing insert for either wild-type or mutant G3 were transformed into BL21 Codon Plus RP cells (Stratagene). A starter culture was prepared by transfer of a single colony into 5 mL Luria broth supplemented with 50 μg mL^{-1} kanamycin and incubated at 37°C overnight. Terrific broth (TB, 1 L) supplemented with 50 μg mL^{-1} of kanamycin was inoculated with starter culture and allowed to grow at 37°C for 3 h before adding IPTG to a final concentration of 1 mM. The resultant culture was incubated with shaking (300 rpm) for 3.5 h. Cells were harvested by centrifugation (5000 × *g*, 15 min) and the cell-pellet was subjected to partial disruption by a freeze–thaw cycle. The cell-pellet was resuspended in binding buffer (5 mM imidazole, 0.5 M NaCl, 20 mM tris, pH 7.9) and sonicated using a Fisher Model 550 probe sonicator (three 2-min pulses at power level 4). Lysed cells were centrifuged (23 000 × *g*, 30 min) and the supernatant was applied to a column containing 7 mL His Bind resin pre-equilibrated according to the manufacturer's instructions. The column was washed with six column volumes of binding buffer followed by 10 column volumes of wash buffer (25 mM imidazole, 0.5 M NaCl, 20 mM tris, pH 7.9). Protein was eluted with six column volumes of elution buffer (0.5 M imidazole, 0.5 M NaCl, 20 mM tris, pH 7.9). Fractions containing the desired protein were pooled and concentrated using an Amicon stirred cell fitted with a YM-3 filter.

Site-directed mutagenesis of G3

Using plasmid prCBP35s as a template, PCR (30 cycles of 94°C for 30 s, 45°C for 30 s, and 68°C for 17 min) was carried out with primers W195Ffor and W195Frev (Table 1) and *Pfu*Turbo polymerase (Strategene). The reaction mixture was digested with *Dpn*I, purified with a Qiagen PCR purification kit, and transformed into XL-10 Gold cells (Stratagene). Plasmids from the resultant colonies were isolated and sequenced. Plasmids containing the W195F mutation were transformed into BL21-Codon Plus cells and protein was expressed as described above. This protocol was repeated using primers S251Afor and S251Arev to provide the S251A mutant.

Construction of plasmid for phage display of G3 (pf5G3)

PCR (30 cycles of 94°C for 30 s, 53°C for 30 s, and 74°C for 60 s) was carried out from prCBP35s with the primers

© 2002 NRC Canada

PDfor and PDrev (Table 1). The amplified section was digested with *Sfi*I (4 h at 37°C) and purified with a Qiagen PCR purification kit (Qiagen). Ligation into similarly prepared fUSE5 vector gave the complete plasmid (pf5G3) that was transformed into DH10B MAX competent cells (Gibco) and plated on to LB/agar media supplemented with tetracycline (40 μg mL^{-1}). Plasmids from the resultant colonies were isolated and analyzed for insert by PCR. Colonies that tested positive by PCR were sequenced for verification of the coding frame.

Test for infectious phage

A single colony of the transformed DH10B MAX cells was used to inoculate a 5 mL aliquot of Luria broth (LB) supplemented with tetracycline (40 μg mL^{-1}). Growth proceeded for 12 h at 37°C prior to centrifugation (2 × 10 000 *g*, 30 min). Starved K91 *E. coli* cells (10 μL) were mixed with 10 μL of phage-containing supernatant and the medium was incubated for 10 min at 25°C. Luria broth was added and the infection was incubated at 37°C for 1 h prior to plating on LB/agar plates containing tetracycline (40 μg mL^{-1}) and kanamycin (100 μg mL^{-1}). The presence of colonies indicates the presence of infectious phage in the original growth medium.

Phage assay for lactose binding

A modified microtiter plate displaying either β-lactose (Calbiochem) or an *N*-acetyl cap was washed with PBS (2×) and blocked with 1% BSA in PBS (100 μL) for 2 h at room temperature. The plate was washed (3×) with PBS containing 0.05% v/v Tween-20 (PBST), then 100 μL phage solution (a dilution of medium in PBS that produced 10 colony forming units per μL) was added to the plate prior to incubation for 2 h at 37°C. The plate was washed with PBST (3×). Lactose (0.3 M in PBS) was added and the plates were incubated for 1 h at 37°C. Lactose solutions were transferred to a sterile microtiter plate and an infection was carried out as above. The number of colonies obtained from the lactose and control plates were then compared.

Library construction and isolation

PCR (45 cycles of 94°C for 30 s, 52°C for 30 s, and 74°C for 120 s) was carried out on prCBP35s with Taq polymerase and the primers PDfor and PDrev (Table 1). Amplification was conducted in buffer supplemented to final concentrations of 6.8 mM $MgCl_2$, 400 μM dITP, 200 μM dCTP, 200 μM dTTP, 80 μM dGTP, and 20 μM dATP. The generated insert library was purified with a Qiagen PCR purification kit and digested with deoxyribonuclease I (0.24 U mL^{-1} reaction) in a buffer of 33 mM tris, 0.67 mM $MgCl_2$, pH 7.4. The digestion proceeded at 25°C for 10 min before being heated to 94°C for 15 min. The DNA fragments were purified with a MERmaid spin kit (Bio101). Reassembly of the DNA fragments was accomplished by PCR using Taq polymerase in the supplied buffer but without additional primers (45 cycles of incubation at 94°C for 30 s, 50°C for 30 s, and 74°C for 30 s). The reassembled material was purified with a Qiagen PCR purification kit and subject to PCR amplification (30 cycles of incubation at 94°C for 30 s, 50°C for 30 s, and 68°C for 60 s) using PDfor and PDrev primers. Amplified DNA was purified using a Qiagen PCR purification kit and subject to digestion with *Sfi*I (4 h at 37°C) followed by a second purification. Ligation into similarly prepared fUSE5 vector resulted in plasmid that was purified as before and eluted with MilliQ Ultrapure water. The ligated material was electroporated into DH10B MAX electrocompetent cells (Gibco) using a MicroPulse electroporator (BioRad) with 0.2 cm cuvettes at 2.7 kV (5.2 ms decay). Cultures of electroporated cells were prepared in 5 mL LB broth supplemented with tetracycline and incubated for 1 h at 37°C. After incubation, the cultures were used to inoculate 1 L of TB supplemented with tetracycline (40 μg mL^{-1}). A 0.5 mL aliquot was removed from the medium for the estimation of electroporation efficiency by determining the number of transformants yielded; the remaining broth was incubated with shaking for 24 h. The electroporation efficiency provided an estimate of the library size.

After 24 h, phage-containing media was isolated by centrifugation (8000 × *g*, 15 min) and the supernatant was mixed with 0.15 volumes of PEG–NaCl (16.7% PEG 8000 in 3.3 M NaCl) by gentle inversion (100×). The phage were allowed to precipitate over 16 h at 4°C. The solution was centrifuged (8000 × *g*, 20 min) and the pellets were resuspended in a total volume of 30 mL PBS. This solution was centrifuged (20 000 × *g*, 15 min) to remove insoluble material. The supernatant was transferred to another centrifuge tube, 0.167 volumes of PEG–NaCl was added, and, after mixing by several inversions, the solution was centrifuged (20 000 × *g*, 15 min). The phage pellet was resuspended in 15 mL PBS and cleared of insoluble material as before. The supernatant was then transferred to another centrifuge tube containing 0.25 volumes of PEG–NaCl, mixed and centrifuged (20 000 × *g*, 10 min). The phage pellet was resuspended in 4 mL PBS and shaken at 25°C for 1 h before being cleared of insoluble material. The resultant solution containing the purified phage library was used as a stock; 1:10 – 1:100 dilutions were used for biopanning assays.

Error-prone modification of staggered extension protocol

StEP (64) (90 cycles of incubation at 94°C for 30 s and 50°C for 5 s) was conducted on prCBP35s using the primers PDfor and PDrev (Table 1). Taq polymerase was used in the supplied reaction buffer supplemented to final concentrations of 6.8 mM $MgCl_2$, 400 μM dITP, 200 μM dCTP, 200 μM dTTP, 80 μM dGTP, and 20 μM dATP. The amplified material was purified using a Qiagen PCR purification kit, digested with *Sfi*I, and utilized as a library of inserts.

Biopanning of G3 displaying phage

Diluted phage library (100 μL) was added to two wells of a β-lactose displaying microtiter plate (Calbiochem). The plate was incubated with gentle shaking for 1 h at 25°C then washed with PBST supplemented with 200 mM lactose (15×). The elution solution (50 μL; 100 μM glycine, 1 mg mL^{-1} BSA, 300 mM lactose, pH 2.2) was added to the wells and the plate was allowed to incubate at 25°C for 1 h with gentle shaking. Lactose solutions were subsequently transferred to wells in a sterile microtiter plate containing 10 μL neutralization solution (1 M tris, pH 9.1). After a 5 min incubation, 10 μL of K91 starved cells were added, initiating transfection as above. Plasmids from individual

© 2002 NRC Canada

colonies were isolated and sequenced to determine the position and nature of mutations.

Solid-phase analysis of binding

Prior to each assay, the concentration of phage required to give a maximum of 10–100 colonies upon binding to lactose-displaying plates in the absence of inhibitor was determined. A series of wells on a microtiter plate were blocked overnight with 1% BSA in PBS. After blocking, the wells were washed three times with assay buffer (10 mM tris, 1 mM EDTA, 1 mM β-mercaptoethanol, pH 8.5) and 40 μL of serial fourfold dilutions of β-methyllactose were added to each well followed by 10 μL of galectin-displaying phage. After incubating for 1 h at 25°C, the solutions were transferred to a series of wells on a lactose plate and allowed to incubate with gentle shaking at 25°C for another hour. The wells were washed three times with assay buffer containing 0.05% (v/v) Tween-20 before 50 μL elution buffer (100 μM glycine, 1 mg mL^{-1} BSA, 300 mM lactose, pH 2.2) was added. The plates were incubated with gentle shaking at 25°C for 1 h, then elution solution was transferred to a series of wells on a sterile microtiter plate containing 10 μL of neutralization solution (1 M tris, pH 9.1). After 5 min, 10 μL of K91 starved cells were added, initiating infection as described above. Using the number of colonies obtained in the absence of inhibitor as 0% inhibition, the colony number was plotted as a function of inhibitor concentration and the IC_{50} was determined from the best-fit sigmoidal curve (Origin 2.9).

Assembly of chimeric protein inserts

Inserts corresponding to mutant and wild-type galectin-3 were obtained by PCR as before. Following amplification, the inserts were digested with *Sph*I, producing fragments corresponding to the *N*- and *C*-terminal halves of the protein separated at amino acid 143. The fragments were separated on a 1.3% agarose gel and extracted using a Qiagen Gel extraction kit. The chimeric inserts were assembled by ligating one half of the wild-type insert to the complementary half of the mutant insert under standard conditions. The resultant product was amplified by PCR as described above, purified with a Qiagen PCR purification kit, and sequenced before further use as a template for the assembly of the chimeric plasmid.

Isothermal titration microcalorimetry for galectin-3

Calorimetric experiments were carried out on a MicroCal Omega isothermal titration microcalorimeter; details on the instrument and mathematical analyses are described elsewhere (63, 64). The reaction cell (volume = 1.3678 mL) contained a solution of 0.12–0.05 mM galectin-3 in buffer (10 mM tris, 1 mM EDTA, 1 mM β-mercaptoethanol). A series of 30 injections of carbohydrate solution (2–10 mM) were made. The volume of each injection was 8 μL, the duration of injection was 8 s, and the time between injections was 3 min. The data from the resulting injections were integrated to generate a titration curve. A non-linear least-squares fit of the data was used to determine the binding constant (K), the enthalpy of binding (ΔH), and the stoichiometry of binding (n).

Table 2. Galectin-3 truncations from this study.

Protein	Size (kDa)	Size of bacterial pellet from 1 L TB growth[a]	Lactose affinity
Full-length	30.0	+	Yes
d50	25.1	+	Yes
d91	20.4	+	Yes
d96	20.9	—	No
d101	20.4	–	Yes
d116	19.0	+	No

[a](—) Represents a pellet size of less than 1 g, (–) a pellet of ~3 g, (+) a pellet of ~7 g.

Results and discussion

Truncation of galectin-3

We initially sought to produce a truncated version of galectin-3; such a protein was attractive for two reasons. First, the size of the native protein is close to the size limit for stable incorporation into p3 of filamentous phage. Although phage can typically tolerate inserts of approximately 30–35 kDa, larger inserts hamper both assembly and infectivity of the phage (65–68). Second, the library size required for complete examination of single mutants grows exponentially with the number of residues in the protein (69, 70). Since the *N*-terminal domain of galectin-3 does not appear to participate in carbohydrate binding, mutations in this region increase the library size through mutation of residues that are presumably uninvolved in binding. By eliminating this domain, even partially, the number of neutral mutations is reduced.

Initial truncation of galectin-3 was attempted at position 116. The selection of this position was based on Wang et al.'s (53) observation that a post-translational digest at position 118 produced protein that retained lactose-binding activity. It was reported in the same paper that a recombinant construct beginning at position 145 failed to produce active protein. A new restriction site was introduced upstream of the DNA corresponding to position 116 in the protein. Digestion of the PCR product with *Eco*RI followed by ligation into the plasmid pIN-III-*Omp*A2 and transformation into *E. coli* provided the appropriate DNA. All attempts at isolating protein from this construct were unsuccessful. A series of truncations were next designed at positions 50, 91, 96, and 101 in the *N*-terminus of galectin-3 (referred to as d50, d91, d96, and d101, respectively). Using the established protocols developed for d116, assembly of the corresponding plasmids was readily accomplished allowing the production of d50, d91, d96, and d101. Table 2 details the various proteins and expression characteristics.

Deletion mutant d101 was initially utilized for study. Although the bacteria grew sluggishly, a small amount (<1 mg) of purified d101 was isolated from 2 L of growth. Attempts to optimize growth conditions failed to improve protein yields, and our attention turned to d96. This construct was apparently toxic, and cells failed to grow following induction. Both d91 and d50 yielded protein expression at roughly the same level as full-length galectin-3. Both proteins aggregate at concentrations above 20 μM, a level too dilute for calorimetry experiments. Based on these data, we chose to

© 2002 NRC Canada

Fig. 1. (*a*) Graphical representation of protein folding and ligand binding (90). Possible sequences are represented on the *x* and *y* axes with the overall free energy of folding or binding represented by the *z*-axis. Both methods are successful along path A. (*b*) Cross-section of energy funnel across path B. Exhaustive sequence search can only be carried out in a small region (depicted in yellow) and results in trapping the search in the energy minimum. (*c*) Cross-section of energy funnel across path B. Random sampling along the path depicted in orange will find members outside the local minimum, allowing global minimum to be eventually discovered.

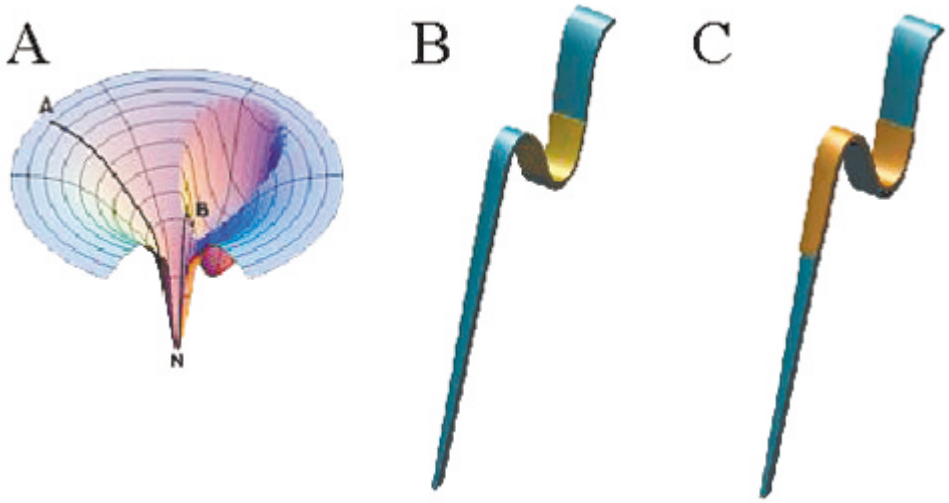

proceed with directed evolution studies using full-length galectin-3.

Phage display of murine galectin-3

The primary goal of this research is to prepare high affinity mutants of galectin-3 to better understand the structural basis of affinity. We propose to generate these mutants randomly through a directed evolution approach. Relative affinity is usefully assayed by a phage display and biopanning approach; accordingly, we next set out to present G3 on the surface of filamentous phage. The insert for galectin-3 was readily cloned from pET28b and inserted between *Sfi*I sites in the phage display vector fUSE5, allowing display of G3 as the *N*-terminal fusion to the phage protein p3. As G3 is close to the size limit for proteins stably displayed on p3, several tests were undertaken to ensure active protein was present on the phage surface. The phage construct was electroporated into DH10B cells for phage production, and isolated phage were tested for the ability to infect cells and bind lactose.

Phage were initially tested for infectivity since large proteins fused to p3 are known to inhibit infection efficiency (66). Phage mixed with K91 starved cells under standard conditions yielded lawns when plated on LB/agar supplemented with kanamycin and tetracycline indicating that phage were infectious. For a qualitative determination of lactose affinity, dilute phage were incubated for 1 h in microtiter plates capped with either *N*-acetyl (control) groups or lactose. After washing, the phage were eluted and infections carried out. No colonies were generated from capped wells, while lactose-displaying wells gave approximately 200 colonies. We thus conclude that galectin-3 displayed as a p3 fusion retains lactose affinity, enabling a biopanning selection strategy.

Directed evolution of galectin-3

With methods for selection established, construction of libraries could now proceed. Two conceptual strategies for library generation were contemplated: an exhaustive search of a small area of sequence space or a partial search of a much larger area of sequence space (Fig. 1). In the former case, a mutagenesis technique is utilized to prepare all possible single, double, or triple mutants. In the latter case, mutagenesis techniques are used that produce a large number of multiple mutants separated widely in sequence space. The appropriate choice between these two approaches requires knowledge of the "shape" of the energy landscape between wild-type and optimum proteins. In addition, assumptions are necessarily made regarding the uniqueness of both the optimum protein and the path along the landscape toward the optimum. Local minima too deep for escape by a small number of mutations are the bane of in vitro and, presumably, in vivo evolutionary expeditions.

In the first strategy, a library of inserts designed to vary two to three random positions within the protein is prepared. For a 200-amino-acid protein, varying three positions results in a library of less than 1×10^9. A library size of 1×10^{10} provides every possible double and triple mutant to be analyzed at 95% confidence, and is near the limit of that available with phage display (65, 69). However, if a local energy minimum for ligand binding is realized by a mutation at a small number of positions, these mutations will dominate the selection. Subsequent rounds of mutation will fail to achieve further enhancement in binding, since the space searched is too small to escape the minimum. In the second case, a library of inserts containing three to six positions varied randomly is constructed, but not all such mutants are generated simultaneously since the total number is prohibitive. This library samples a larger nonrelated population and thus avoids problems of a dominant local energy minimum by allowing access to mutants that are sufficiently different to escape the local minimum. Previous work by Arnold and co-workers (71) regarding the directed evolution of subtilisin indicated that a saturation approach may prove beneficial in selecting particularly active enzymes, and we chose to follow this suggestion.

© 2002 NRC Canada

Fig. 2. Ribbon diagrams based on human galectin-3 (PDB accession 1A3K) highlighting residues changed in the mutants based in the mouse homologue. Images were created with MOLSCRIPT and rendered with RASTER3D (91, 92).

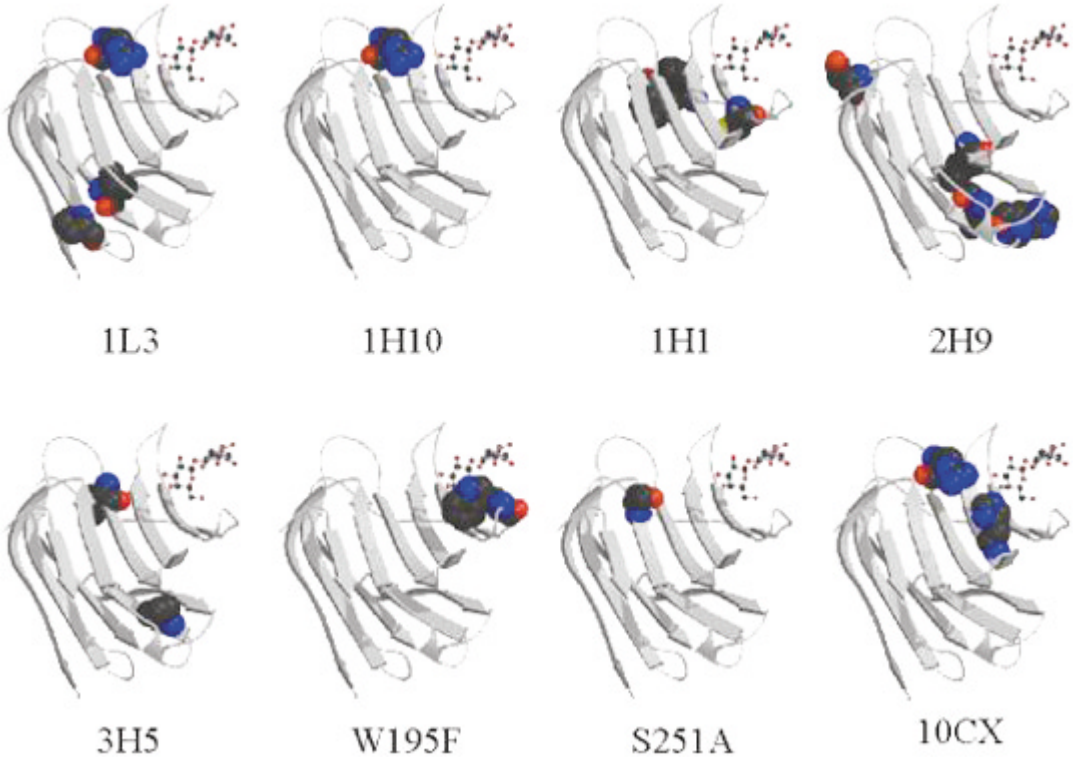

Libraries of random mutants can be constructed using error-prone PCR and DNA shuffling as a source of diversity (72–78). In many respects, error-prone PCR replicates the evolutionary process of asexual organisms and, as such, is potentially limited in the same manner as these organisms. Specifically, the "Muller's ratchet" phenomenon ultimately limits both the degree and rate of evolution of such species (79). In theory, shuffling obviates these limitations by introducing the essential element of sexual reproduction: the production of unique hybrid genes as a random combination of related parental sequences. To maximize the mutational frequency, both techniques were used here in series. Starting with DNA corresponding to native galectin-3, a set of mutants was generated via error-prone PCR and then shuffled. The resultant library was digested with *Sfi*I and ligated into fUSE5 vector prior to electroporation into DH10B cells. After growth for 24 h, the phage were isolated and purified. This procedure was utilized to create two libraries of 1×10^5 and 1×10^6 members, respectively.

A third library was created using a modification of the staggered extension process (StEP) developed by Arnold and co-workers (62). In this protocol, PCR is carried out on mutagenized DNA under conditions where the temperature is rapidly cycled between the annealing and denaturing temperatures. During the heating phase, the reaction briefly passes through the extension temperature, allowing a short extension before the complex is disrupted. By repeating this cycle numerous times, mutations from multiple parental genes are incorporated into the final hybrid. We attempted modification of this protocol by utilizing native DNA and error-prone PCR conditions; we thus imagined the process might introduce and shuffle mutations simultaneously allowing rapid creation of a large, diverse library. Although the process produced DNA that was successfully incorporated into phage, sequencing of random phage from the library indicated that the final library size was less than 10. The failure to generate a large library is likely due to the nature of the random mutant introduction. Presumably the short extension time, in conjunction with the low efficiency of misincorporation under error-prone PCR conditions, provides few mutants.

Table 3. Mutants isolated from various libraries.

Protein name	Deletions and (or) mutations
WTG3	Wild-type murine galectin-3
1L3	Δ92–96, P137L, R158G,V216A
1H1	Δ84–92, C187R, F204L, F206S
1H10	Δ92–96, R158G
2H9	Δ52–69, P84S, Y109H, F163L, H222R, K224E, L255P
3H5	I159T, F223S
3L1	L145P, R182G
3L2	A47T, S110G M149T, I214M, E219D, S251G

All three libraries were selected for high-affinity mutants by biopanning against lactose. Briefly, purified phage were incubated in wells on a lactose-displaying microtiter plate for 1 h at room temperature. After incubation, plates were washed with PBST supplemented with 200 mM lactose (0–3 times for low stringency selection, 15 times for high stringency), then an acidic (pH 2.2) elution buffer containing 0.3 M lactose was added. After 1 h, the solution was neutralized and K91 *E. coli* were infected with the isolated phage.

© 2002 NRC Canada

Table 4. Chimeric proteins and site-directed mutants.

Protein name	Deletions and (or) mutations
Chimeric proteins	
10NWC	Δ92–96
WN10C	R158G
10N1C	Δ92–96, C187R, F204L, F206S
1NWC	Δ84–92
WN1C	C187R, F204L, F206S
2NWC	Δ52–69, P84S. Y109H
WN2C	P84S, Y109H, F163L, H222R, K224E, L255P
Other	
10CX	R158G, H172Y
W195F	W195F
S251A	S251A

Plasmids were isolated from the resultant colonies and sequenced were to determine the nature of the mutations present (Table 3).

Following sequence identification, high-stringency library members were cloned and ligated into pET28b for protein production and isolation. The low stringency library member from the first library (1L3) was also inserted into pET28b to determine the difference in affinity required to produce high and low stringency "hits". Figure 2 shows mutated residues obtained by this selection strategy and the position of the mutations in the structure of the human homolog.

Assembly of chimeric proteins and site-directed mutants

Analysis of the sequences isolated in the first and second libraries revealed an unusual pattern: all mutants demonstrated some form of deletion in the *N*-terminal domain. Because this domain is not involved in carbohydrate binding, it was of interest to determine the relative contributions of *N*-terminal and *C*-terminal mutations to carbohydrate binding. Toward this goal, chimeric proteins were prepared by digesting wild-type G3 and mutants with *Sph*I, separating the two domains at position 143. Following agarose gel purification, the domains were recombined and amplified via PCR to form wild-type/mutant chimeras (Table 4). During the course of chimeric protein assembly, an additional spontaneous mutation within the binding site (H172Y) was created and analyzed. In addition, site-directed mutants were initially assembled as a possible line of investigation failing directed evolution. These mutants would better establish the roles of residues at the periphery of and within the binding site (W195F, S251A). As progress towards evolved proteins was realized, engineering of further site-directed mutants was abandoned as unlikely to result in enhanced binding. As before, the various inserts were cloned into pET28b for protein expression.

Expression and analysis of galectin-3 proteins

Following transformation of the various plasmids into BL21(DE3)-RP Codon Plus cells, expression was carried out under standard conditions. Unfortunately, expression was not realized with 1H1, 2H9, 3H5, any of their *C*-terminal chimeras, or S251A. Decreased growth temperature coupled with increased incubation times failed to improve expression. No inclusion bodies were detected, suggesting either digestion of misfolded protein or lack of expression as a source of the problem. Use of an *E. coli* strain that supplements all rare codons in galectin-3 also failed to produce protein, indicating that rare codon usage is not the source of the observed phenomena. All other proteins were stable at concentrations required for calorimetry. In calorimetry buffer (10 mM tris, 1 mM EDTA, 1 mM β-mercaptoethanol, pH 8.5), 1H10 was soluble at 0.5 mM, an almost fivefold increase in maximum solubility over wild-type protein. Isothermal titration microcalorimetry was carried out with all soluble mutants against βMeLac and LacNAc. A representative titration is shown in Fig. 3; data are summarized in Table 5.

Fig. 3. Representative example of isothermal titration calorimetry data. Thirty injections of *N*-acetyllactosamine (1.6 mM) were made into 0.1 mM 1H10 mutant in 10 mM tris, 1 mM EDTA, 1 mM β-mercaptoethanol, pH 8.5. Raw data for the titration (upper panel) is integrated with the individual points (■) and the best-fit curve (–) displayed (bottom panel).

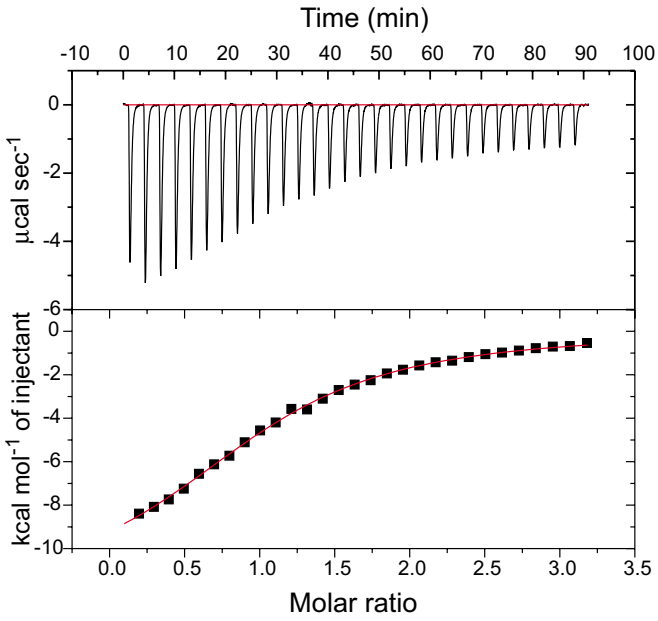

Data from Table 5 both validate the biopanning selection and provide initial information regarding the role of various residues for ligand binding in the protein. High-stringency mutant 1H10 binds β-methyllactose with greater affinity than does low stringency mutant 1L3, validating the biopanning selection strategy. Interestingly, 1L3 binds β-MeLac with *lower* affinity than wild-type. Since no phage displaying the wild-type protein were recovered in the low stringency wash, this observation suggests that no wild-type is present in the library. In addition, the increased solubility of 1H10 allowed calorimetric evaluation of monosaccharide binding, a process not feasible with wild-type protein. While no enhancements of greater than threefold are observed in the first three libraries, this is not surprising since they are all first-generation libraries. Frequently, first-generation directed evolution libraries appear to have modest gains (approximately two- to 10-fold) in activity (80–82).

The chimeric proteins also provide insight into the contributions of specific mutations to overall affinities. First, the increased affinity of 1H10 is also observed in WN10C — the *C*-terminal half of 1H10 — suggesting that the majority

© 2002 NRC Canada

Table 5. Calorimetry results for galectin-3 and mutants.

Protein[a]	Compound	K (M^{-1})	n	ΔG^b	$-T\Delta S^b$	ΔH^b
WT	βMeGal	<8 000				
WT	βMeGlc	<8 000				
WT	βMeLac	18 000	1	–5.8 ± 0.4	0.1 ± 0.9	–5.9 ± 0.8
WT	LacNAc	12 000	1	–5.6 ± 0.3	2.6 ± 0.9	–8.2 ± 0.9
WT	Cellobiose	<8 000				
1L3	βMeLac	12 000	1	–5.4 ± 0.7	5.2 ± 2.8	–10.6 ± 2.8
1L3	LacNAc	23 000	1	–5.8 ± 0.3	5.6 ± 1.1	–11.4 ± 1.1
1H10	βMeGal	4 000	1	–4.8 ± 0.7	–4.1 ± 0.7	–0.7 ± 0.1
1H10	βMeGlc	<2 000				
1H10	βMeLac	33 000	1	–6.0 ± 0.4	0.7 ± 0.5	–6.7 ± 0.3
1H10	LacNAc	25 000	1	–5.9 ± 0.3	5.1 ± 0.4	–11.0 ± 0.3
10NWC	βMeLac	21 000	1	–5.8 ± 0.3	1.8 ± 0.85	–7.6 ± 0.8
10NWC	LacNAc	30 000	1	–6.0 ± 0.3	5.8 ± 0.6	–11.8 ± 0.6
1NWC	βMeLac	21 000	1	–5.8 ± 0.5	0.6 ± 0.7	–6.4 ± 0.5
1NWC	LacNAc	29 000	1	–6.0 ± 0.5	3.7 ± 1.1	–9.7 ± 1.0
2NWC	βMeLac	18 000	1	–5.8 ± 1.0	–2.3 ± 1.0	–3.5 ± 0.3
2NWC	LacNAc	73 000	1	–6.5 ± 0.5	–0.4 ± 0.64	–6.1 ± 0.4
WN10C	βMeLac	29 000	1	–6.0 ± 0.4	0.5 ± 0.6	–6.5 ± 0.5
WN10C	LacNAc	26 000	1	–5.9 ± 0.4	7.6 ± 0.9	–13.5 ± 0.8
W195F	βMeLac	<8 000				
W195F	LacNAc	<8 000				
10CX	βMeLac	<10 000				
10CX	LacNAc	<10 000				

[a]In 10 mM tris, 1 mM EDTA, 1 mM BME, at pH 8.5.
[b]In kcal mol^{-1}.

of the increase in affinity of 1H10 arises from the R158G mutation. The observed increase in affinity might arise from an increased flexibility of the binding site as the arginine side chain by the C_α proton of glycine. All *N*-terminal deletions and mutations produced no significant change in binding β-methyllactose. On the other hand, all *N*-terminal deletions and mutations resulted in at least some increase in affinity for *N*-acteyllactosamine, with a sixfold increase observed for 2NWC. The deletions might alter the flexibility of this domain, in turn allowing more favorable interactions between the protein and the *N*-acetyl moiety. NMR and modeling studies suggest that the *N*-terminal domain, while largely unstructured, may interact with the binding site (83, 84). The *N*-terminal domain of galectin-3 is also known to modulate galectin dimerization (85–88), a process that could be coupled to ligand binding. Because thermodynamic parameters are state functions, a change in *any* contributing process leads to changes in the overall measured parameters. If deletions in the *N*-terminal domain shift the monomer and dimer equilibrium, an alteration in *apparent affinity* is observed. Previous studies have failed to observe dimer by either gel filtration or analytical ultracentrifugation, implying that the dimerization interaction is weak (83, 84, 89). In the absence of additional data, it is difficult to discern which of these factors contribute to the observed phenomena.

Site-directed mutations in or near the binding site provide little useful information regarding binding. The mutation at the periphery of the binding pocket (S251A) failed to express. No significant formation of inclusion bodies was detected, and we assume that the protein failed to fold. Mutation of the key tryptophan (W195F) residue resulted in a protein that was readily expressed, but yielded calorimetric traces with either β-methyllactose or *N*-acetyllactosamine identical to control titrations, indicating a complete lack of binding activity. This tryptophan indole is located directly beneath the galactose moiety in crystal structure and provides a hydrophobic interaction with the apolar carbohydrate face (59). The spontaneous mutant 10CX is modified at position 172, replacing a histidine that donates a hydrogen bond to the axial O-4 of the galactose moiety with tyrosine (59). This residue is also located directly above tryptophan 195 and may preorganize the protein for ligand binding. 10CX is also interesting in that it contains the positive mutation R158G, a residue proximal to position 172. As with W195F, this mutant fails to bind either β-methyllactose or *N*-acetyllactosamine. Presumably, the favorable impact of the R158G mutation is more than offset by the tyrosine at 172 that prevents either hydrogen bonding or interaction of the tryptophan residue with the apolar face of the carbohydrate ligand.

Table 6. Solid-phase quantification of phage binding.

Protein displayed	IC_{50} (μM) of βMeLac
WT	20
H1	30
2H9	10
3H5	<8

Because protein could not be isolated for several high-stringency mutants, quantification of the relative binding affinity was determined by a solid-phase plate-binding assay. This assay is similar to a typical ELISA, but utilizes phage infectivity to quantify the extent of binding (Table 6).

© 2002 NRC Canada

All mutant phage show IC_{50} values against β-methyllactose equivalent to, or better than, wild-type protein. One mutant, 3H5, demonstrated a greater than threefold increase in inhibitory activity despite arising from a small library. This observation suggests that many galectin-3 mutations increase affinity for lactose ligands; additional mutants will presumably not be difficult to discover. Continued progress toward higher-affinity galectins is quite likely, although the ultimate extent of available enhancement is unclear. Bundle and coworkers (40) isolated mutant anti-serogroup B *O*-polysaccharide antibodies by biopanning serogroup B lipopolysaccharide. While ELISA analysis of mutants selected from the relatively small (1×10^6) library showed IC_{50} values of approximately 20 nM, ITC demonstrated that the mutants had association constants similar to wild-type (~1×10^5 M^{-1}). This result implies that either the number of mutants that produce increased affinity are few or that $1 \times 10^5 - 1 \times 10^6$ M^{-1} represents a fundamental limit in binding constant for this protein scaffold. Arguing against this latter conclusion, Marvin and Hellinga (36) recently modified maltose-binding protein (MBP) from *E. coli*, introducing a number of natural and unnatural side chains at position 324. These studies produced a mutant with an apparent binding constant of 1.2×10^8 M^{-1}, suggesting that enhancements well beyond 1×10^6 M^{-1} can be realized for other protein–carbohydrate interactions.

The dose-dependent response behavior of phage binding to β-methyllactose indicates that galectin-3 fused to p3 behaves similarly to the native protein. Directed evolution can result in the discovery of phage that have affinity for the solid support of the microtiter plate rather than the ligand of interest resulting in false positive hits. From the phage-binding assay, we can eliminate the possibility of protein affinity for the support as a confounding issue. The question remains as to the source of the protein expression difficulty. Protein fused to p3 is apparently folded and competent; the data indicate that fusion of the mutant protein to p3 allows stabilization. In the absence of the p3 fusion, the mutant protein might fail to fold properly, resulting in protein digestion.

Conclusions

Several conclusions arise from this work. First and foremost, galectin-3 can be displayed on the surface of filamentous phage and used in a biopanning selection strategy. The biopanning assay has been validated by a number of different means, and has been used for the discovery of mutants with increased binding affinity. Second and of equal importance to our long-term goals, the number of mutations available for galectin-3 that result in the increased affinity for ligands must be large since even small libraries contain adventitious mutations. Based on this observation, we are confident that further mutations will result in higher affinity carbohydrate-binding proteins. Finally, modification of the *N*-terminal domain of galectin-3 clearly affects expression of the protein and its affinity for ligands. We are continuing our efforts in this area, and the results will be reported in due course.

Acknowledgements

We are grateful to Dr. John L. Wang for his gift of the plasmid prCBP35s and to Dr. George Smith for the generous gift of the fUSE5 vector and *E. coli* strain K91 as well as documents necessary for the development of the phage display system. J.J.L. acknowledges support from the National Institute of Health Biological Chemistry Training Program (T32GM08858). This work was supported by the National Institutes of Health (GM57179).

References

1. L. Warren. Bound carbohydrates in nature. Cambridge University Press, Cambridge. 1994.
2. G.R. Vasta, M. Quesenberry, H. Ahmed, and N. O'Leary. Dev. Comp. Immunol. **23**, 401 (1999).
3. A. Varki. J. Clin. Invest. **99**, 158 (1997).
4. S.J. York, L.S. Arneson, W.T. Gregory, N.M. Dahms, and S. Kornfeld. J. Biol. Chem. **274**, 1164 (1999).
5. D.C. Wiley and J.J. Skehel. Ann. Rev. Biochem. **56**, 365 (1987).
6. B.D. Shur. Curr. Opin. Cell Biol. **5**, 854 (1993).
7. M.G. Rossmann. Protein Sci. **3**, 1712 (1994).
8. F. Quignon, F. Thomas, C. Gantzer, A. Huyard, and L. Schwartzbrod. Water Res. **32**, 1222 (1998).
9. J.B. Lowe and P.A. Ward. J. Clin. Invest. **99**, 822 (1997).
10. P.P. Firpo, I. Axberg, M. Scheibel, and E.A. Clark. AIDS Res. Hum. Retroviruses, **8**, 357 (1992).
11. S.F. Dellert and M.B. Cohen. Gastroenterol. Clin. North Am. **23**, 637 (1994).
12. L.H. Bookbinder, A. Cheng, and J.D. Bleil. Science (Washington, D.C.), **269**, 86 (1995).
13. E.J. Toone. Curr. Opin. Struct. Biol. **4**, 719 (1994).
14. H. Beierbeck, L.T.J. Delbaere, M. Vandonselaar, and R.U. Lemieux. Can. J. Chem. **72**, 463 (1994).
15. R. Cromer, U. Spohr, D.P. Khare, J. Lependu, and R.U. Lemieux. Can. J. Chem. **70**, 1511 (1992).
16. M.H. Du, U. Spohr, and R.U. Lemieux. Glycoconjugate J. **11**, 443 (1994).
17. O. Hindsgaul, D.P. Khare, M. Bach, and R.U. Lemieux. Can. J. Chem. **63**, 2653 (1985).
18. R.U. Lemieux, F.F.Z. Georges, and Z. Smiatacz. Heterocycles, **13**, 169 (1979).
19. R.U. Lemieux, S.Z. Abbas, and B.Y. Chung. Can. J. Chem. **60**, 58 (1982).
20. R.U. Lemieux, S.Z. Abbas, M.H. Burzynska, and R.M. Ratcliffe. Can. J. Chem. **60**, 63 (1982).
21. R.U. Lemieux, A.P. Venot, U. Spohr, P. Bird, G. Mandal, N. Morishima, O. Hindsgaul, and D.R. Bundle. Can. J. Chem. **63**, 2664 (1985).
22. R.U. Lemieux, R. Cromer, and U. Spohr. Can. J. Chem. **66**, 3083 (1988).
23. R.U. Lemieux, R. Szweda, E. Paszkiewiczhnatiw, and U. Spohr. Carbohydr. Res. **205**, C12 (1990).
24. R.U. Lemieux, M.-H. Du, and U. Spohr. J. Am. Chem. Soc. **116**, 9803 (1994).
25. R.U. Lemieux, M.-H. Du, U. Spohr, S. Acharya, and A. Surolia. Can. J. Chem. **72**, 158 (1994).
26. R.U. Lemieux. Acc. Chem. Res. **29**, 373 (1996).
27. R.U. Lemieux, C.C. Ling, N. Sharon, and H. Streicher. Isr. J. Chem. **40**, 167 (2000).
28. P.V. Nikrad, J.R. Pearlstone, M.R. Carpenter, R.U. Lemieux, and L.B. Smillie. Biochem. J. **272**, 343 (1990).

© 2002 NRC Canada

29. P.V. Nikrad, H. Beierbeck, and R.U. Lemieux. Can. J. Chem. **70**, 241 (1992).
30. E. Petrakova, U. Spohr, and R.U. Lemieux. Can. J. Chem. **70**, 233 (1992).
31. S. Sabesan and R.U. Lemieux. Can. J. Chem. **62**, 644 (1984).
32. U. Spohr, O. Hindsgaul, and R.U. Lemieux. Can. J. Chem. **63**, 2644 (1985).
33. U. Spohr, N. Morishima, O. Hindsgaul, and R.U. Lemieux. Can. J. Chem. **63**, 2659 (1985).
34. U. Spohr and R.U. Lemieux. Carbohydr. Res. **174**, 211 (1988).
35. U. Spohr, E. Paszkiewiczhnatiw, N. Morishima, and R.U. Lemieux. Can. J. Chem. **70**, 254 (1992).
36. J.S. Marvin and H.W. Hellinga. Nat. Struct. Biol. **8**, 795 (2001).
37. R.M. Revelle, D. Scott, and P.J. Beck. J. Biol. Chem. **271**, 16 160 (1996).
38. E.T. Jordan and I.J. Goldstein. Eur. J. Biochem. **230**, 958 (1995).
39. M. Cho and R.D. Cummings. Biochemistry, **35**, 13 081 (1996).
40. S.J. Deng, C.R. MacKenzie, J. Sadowska, J. Michniewicz, M. Young, D.R. Bundle, and S.A. Narang. J. Biol. Chem. **269**, 9533 (1994).
41. H. Leffler and S.H. Barondes. J. Biol. Chem. **261**, 1011 (1986).
42. K. Kasai and J. Hirabayashi. J. Biochem. **119**, 1 (1996).
43. R.C. Hughes. Biochem. Soc. Trans. **25**, 1194 (1995).
44. N.L. Perillo, M.E. Marcus, and L.G. Baum. J. Mol. Med. (Berlin), **76**, 402 (1998).
45. G.A. Rabinovich. Cell Death Differ. **6**, 711 (1999).
46. S.F. Dagher, J.L. Wang, and R.J. Patterson. Proc. Natl. Acad. Sci. U.S.A. **92**, 1213 (1995).
47. R.-Y. Yang, K.K. Hsu, and F.-T. Liu. Proc. Natl. Acad. Sci. U.S.A. **93**, 6737 (1996).
48. J. Kopitz, C. von Reitzenstein, S. Andre, H. Kaltner, J. Uhl, V. Ehemann, M. Cantz, and H.-J. Gabius. J. Biol. Chem. **276**, 35 917 (2001).
49. F. Orlandi, E. Saggiorato, G. Pivano, B. Puligheddu, A. Termine, S. Cappia, P. DeGiuli, and A. Angeli. Cancer Res. **58**, 3015 (1998).
50. X.C. Xu, A.K. el-Nagger, and R. Lotan. Am. J. Pathol. **147**, 814 (1995).
51. Y. Honjo, P. Nangia-Makker, H. Inohara, and A. Raz. Clin. Cancer Res. **7**, 661 (2001).
52. R.C. Hughes. Biochem. Biophys. Acta, **1473**, 172 (1999).
53. N. Agrwal, Q. Sun, S.Y. Wang, and J.L. Wang. J. Biol. Chem. **268**, 14 932 (1993).
54. J.M. Rini and Y.D. Lobsanov. Curr. Opin. Struct. Biol. **9**, 578 (1999).
55. J.M. Rini. Annu. Rev. Biophys. Biomol. Struct. **24**, 551 (1995).
56. R.C. Hughes. Biochimie, **83**, 667 (2001).
57. H.C. Gong, Y. Honjo, P. Nangia-Makker, V. Hogan, N. Mazurak, R.S. Bresalier, and A. Raz. Cancer Res. **59**, 6239 (1999).
58. M.W. Robertson, K. Aldbrandt, D. Keller, and F.-T. Liu. Biochemistry, **29**, 8093 (1990).
59. J. Seetharaman, A. Kanigsberg, R. Slaaby, H. Leffler, S.H. Barondes, and J.M. Rini. J. Biol. Chem. **273**, 13 047 (1998).
60. W.O. Salivar, H. Tzagoloff, and D. Pratt. Virology, **24**, 359 (1964).
61. H. Edelhoch. Biochemistry, **6**, 1948 (1967).
62. H. Zhao, L. Giver, Z. Shao, J.A. Affholter, and F.A. Arnold. Nat. Biotechnol. **16**, 258 (1998).
63. E. Freire, O.L. Mayorga, and M. Straume. Anal. Chem. **62**, A950 (1990).
64. T. Wiseman, S. Williston, J.F. Brandts, and L.N. Lin. Anal. Biochem. **179**, 131 (1989).
65. S.S. Sidhu, H.B. Lowman, B.C. Cunningham, and J.A. Wells. Methods Enzymol. **328**, 333 (2000).
66. G.P. Smith and V.A. Petrenko. Chem. Rev. **97**, 391 (1997).
67. D.A. Marvin. Curr. Opin. Struct. Biol. **8**, 150 (1998).
68. H.B. Lowman. Annu. Rev. Biophys. Biomol. Struct. **26**, 401 (1997).
69. O. Kuchner and F.H. Arnold. Trends Biotechnol. **15**, 523 (1997).
70. T. Clackson and J.A. Wells. Trends Biotechnol. **12**, 173 (1994).
71. K. Miyazaki and F.H. Arnold. J. Mol. Evol. **49**, 716 (1999).
72. M.H. Dai, Y.M. Zhu, W.H. Jiang, and G.P. Zhao. Prog. Biochem. Biophys. **27**, 360 (2000).
73. W.P.C. Stemmer. Nature (London), **370**, 389 (1994).
74. W.P.C. Stemmer. Proc. Natl. Acad. Sci. U.S.A. **91**, 10 747 (1994).
75. D.W. Leung, E. Chen, and D.V. Goeddel. Technique. **1**, 11 (1989).
76. S. Harayama. Trends Biotechnol. **16**, 76 (1998).
77. R.C. Cadwell and G.F. Joyce. PCR Methods Appl. **2**, 28 (1992).
78. N. Wymer, L.V. Buchanan, D. Henderson, N. Mehta, C.H. Botting, L. Pocivavsek, C.A. Fierke, E.J. Toone, and J.H. Naismith. Structure (London), **9**, 1 (2001).
79. H.J. Muller. Mutat. Res. **1**, 2 (1964).
80.. P.L. Wintrode, K. Miyazaki, and F.H. Arnold. J. Biol. Chem. **275**, 31 635 (2000).
81. J.C. Moore and F.H. Arnold. Nat. Biotechnol. **14**, 458 (1996).
82. K. Miyazaki, P.L. Wintrode, R.A. Grayling, D.N. Rubingh, and F.A. Arnold. J. Mol. Biol. **297**, 1015 (2000).
83. E.A.M. Barboni, S. Bawumia, K. Henrick, and R.C. Hughes. Glycobiology, **10**, 1201 (2000).
84. B. Birdsall, J. Feeny, I.D.J. Burdett, S. Bawumia, E.A.M. Barboni, and R.C. Hughes. Biochemistry, **40**, 4859 (2001).
85. R.-Y. Yang, P.N. Hill, D.K. Hsu, and F.-T. Liu. Biochemistry, **37**, 4086 (1998).
86. B. Mehul, S. Bawumia, S.R. Martin, and R.C. Hughes. J. Biol. Chem. **269**, 18 250 (1994).
87. B. Mehul, S. Bawumia, and R.C. Hughes. FEBS Lett. **360**, 160 (1995).
88. D.K. Hsu, R.I. Zuberi, and F.T. Liu. J. Biol. Chem. **267**, 14 167 (1992).
89. S.M. Massa, D.N.W. Cooper, H. Leffler, and S.H. Barondes. Biochemistry, **32**, 260 (1993).
90. H.S. Chan and K.A. Dill. Proteins, **30**, 2 (1998).
91. P.J. Kraulis. J. Appl. Crystallogr. **24**, 946 (1991).
92. E.A. Merritt and D.J. Bacon. Methods Enzymol. **277**, 505 (1997).

© 2002 NRC Canada

Examination of the structural basis for O(H) blood group specificity by *Ulex europaeus* Lectin I

Gerald F. Audette, Douglas J.H. Olson, Andrew R.S. Ross, J. Wilson Quail, and Louis T.J. Delbaere

Abstract: The structural basis for carbohydrate specificity of the first lectin from *Ulex europaeus* (UE-I) is reported. UE-I is a dimeric metalloglycoprotein that binds the H-type 2 human blood group determinant (α-L-Fucα(1→2)-β-D-Galβ(1→4)-β-D-GlcNAcα-), the blood group determinant present on the surface of O-type erythrocytes. The structural characteristics of UE-I involved in carbohydrate recognition have been examined using mass spectrometry (MS) and X-ray diffraction analysis. MS analysis allowed for discrimination between the different primary structures reported for UE-I. To examine the binding of the H-type 2 blood group determinant by UE-I, the methyl glycosides of the fucose monosaccharide (α-L-Fuc-OMe), known to exhibit primary binding specificity, and the H-type 2 trisaccharide (H-type 2-OMe) were, in two separate experiments, co-crystallized into the binding site of UE-I. The UE-I:α-L-Fuc-OMe complex crystallizes in the monoclinic space group $P2_1$, with unit cell dimensions a = 71.81, b = 69.00, and c = 119.02 Å, and β = 106.76°. Two UE-I dimers are observed to be present within the asymmetric unit, and the model has been refined to a R-value and R_{Free} of 0.202 and 0.289, respectively, to 2.3 Å resolution. The preliminary model of the UE-I:H-type 2-OMe complex has been refined at 3.0 Å resolution. The UE-I:H-type 2-OMe complex crystallizes in the orthorhombic space group $C222_1$, with unit cell dimensions a = 88.80, b = 164.75, and c = 77.42 Å, and a single UE-I dimer is present within the asymmetric unit. The carbohydrate recognition domain of UE-I has been identified to be comprised of residues Glu44, Thr86, Asp87, Arg102, Ala103, Gly104, Gly105, Tyr106, Ile129, Val133, Asn134, Trp136, Tyr219, and Arg222. Several critical protein–carbohydrate interactions have been identified, including the role of the hydrophobic interaction between the Thr86 side chain and C-5-CH_3 of the α-L-Fuc-OMe. The role of these interactions in carbohydrate recognition–binding by UE-I, as well as differences between the observed and previously modeled complexes, are discussed.

Key words: *Ulex europaeus* lectin I, H-type 2 human blood group determinant, protein–carbohydrate interactions, X-ray crystallography, chemical mapping.

Résumé : On a établi les bases structurales de la spécificité de l'hydrate de carbone de la première lectine provenant d'Ulex europaeus (EU-I). EU-I est une métalloglycoprotéine dimère qui se lie au déterminant du groupe sanguin humain H de type-2 (α-L-Fucα(1→2)-β-D-Galβ(1→4)-β-D-GlcNAcα-), le déterminant du groupe sanguin présent à la surface des érythrocytes de type-O. Les caractéristiques structurales de UE-I impliquées dans la reconnaissance du carbohydrate ont été examinées en faisant appel à la spectrométrie de masse (SM) et à la diffraction des rayons X. L'analyse par SM a permis de distinguer entre les différentes structures primaires proposées pour UE-I. Afin d'étudier le site de fixation du déterminant du groupe sanguin humain H de type-2 par UE-I, on a procédé à deux expériences séparées au cours desquelles on a procédé à la cocristallisation dans le site de fixation de UE-I des glycosides de méthyle d'une part du monosaccharide du fucose (α-L-Fuc-OMe), reconnu pour présenter une spécificité pour le site de fixation primaire, et d'autre part du trisaccharide H de type-2 (H de type-2-OMe). Le complexe UE-I:α-L-Fuc-OMe cristallise dans le groupe d'espace $P2_1$ avec a = 71,81, b = 69,00 et c = 119,02 Å et β = 106,76°. On a observé la présence de deux dimères de UE-I dans l'unité asymétrique et on a affiné le modèle jusqu'à des valeurs de R et R_{libre} de 0,0202 et 0,289 respectivement à une résolution de 2,3 Å. Le modèle préliminaire du complexe UE-I:H-type-2-OMe a été affiné jusqu'à une résolution de 3,0 Å. Ce complexe cristallise dans le groupe orthorhombique $C222_1$, avec a =

Received 10 September 2001. Published on the NRC Research Press Web site at http://canjchem.nrc.ca on 13 August 2002.

Dedicated to Professor R.U. Lemieux in memory of his friendship, his many valuable discussions, and scientific contributions.

G.F. Audette,[1] A.R.S. Ross,[2] and L.T.J. Delbaere.[3] Department of Biochemistry, University of Saskatchewan, 107 Wiggins Road, Saskatoon, SK S7N 5E5, Canada.
D.J.H. Olson. Plant Biotechnology Institute, National Research Council Canada, 110 Gymnasium Place, Saskatoon, SK S7N 0W9, Canada.
J.W. Quail. Department of Chemistry, University of Saskatchewan, 110 Science Place, Saskatoon, SK S7N 5C9, Canada.

[1]Current address: Department of Medical Microbiology & Immunology, 1–15 Medical Sciences Building, University of Alberta, Edmonton, AB T6G 2H7, Canada.
[2]Current address: Plant Biotechnology Institute, National Research Council Canada, 110 Gymnasium Place, Saskatoon, SK S7N 0W9, Canada.
[3]Corresponding author (e-mail: louis.delbaere@usask.ca).

 DOI: 10.1139/V02-134 © 2002 NRC Canada

88,80, *b* = 164,75 et *c* = 77,42 Å et on n'observe la présence que d'un seul dimère UE-I dans l'unité asymétrique. On a établi que le domaine de reconnaissance du carbohydrate du UE-I comprend les résidus Glu44, Thr86, Asp87, Arg102, Ala103, Gly104, Gly105, Tyr106, Ile129, Val133, Asn134, Trp136, Tyr219 et Arg222. On a identifié plusieurs interactions protéine–carbohydrate critiques, y compris le rôle de l'interaction hydrophobe entre la chaîne latérale du Thr86 et le C-5-CH_3 du α-L-Fuc-OMe. On discute du rôle de ces interactions dans la reconnaissance/fixation du carbohydrate par UE-I ainsi que des différences entre les complexes modélisés antérieurement et les complexes observés.

Mots clés : lectine I d'*Ulex europaeus*, déterminant du groupe sanguin humain H de type-2, interactions protéine–carbohydrate, diffraction des rayons X, carte chimique.

[Traduit par la Rédaction]

Introduction

Protein–carbohydrate interactions are involved in a wide range of important biological processes. These processes include, but are not limited to, cellular infection by invading microorganisms, the subsequent cellular defense and immune response to the invading pathogen, fertilization, leukocyte trafficking and infiltration, and cancer metastasis (1–3). The lectins are a class of proteins that exhibit a polyvalent affinity for carbohydrates; this polyvalency arises from the association of monomeric subunits into mainly dimeric and tetrameric molecules (3). A wide variety of different lectins are present in living cells and tissues. Their carbohydrate specificity is akin to antigenic recognition by antibodies (4) and enzymatic substrate specificity (5), yet lectins are neither products of the immune system nor do they exhibit enzyme-like catalytic properties. The role of lectins appears limited to specific cross-linking interactions, which allow lectins to serve as recognition molecules for various biological events (1, 2).

Extracts from the seeds of *Ulex europaeus* (common gorse), a leguminous shrub native of Western Europe, have been shown to agglutinate type O erythrocytes (6); the first lectin present in these extracts, *U. europaeus* lectin I (UE-I), was the agglutinating agent, with a carbohydrate specificity for α-L-fucose (7). The classical ABO blood-group in humans was initially identified by Landsteiner (8) at the turn of the 20th century. Landsteiner identified three classes of blood, based upon the agglutination of erythrocytes from one individual when mixed with the serum of another. He labeled these blood-groups in terms of antigenic substances as groups A and B, based on this agglutinating activity. The third group, O, was thus labeled for its lack of agglutinating activity (9). The ABO blood group determinants were subsequently identified as being carbohydrate in nature (10). The O blood group determinant, identified as the H-type 2 trisaccharide (α-L-Fucα(1→2)-β-D-Galβ(1→4)-β-D-GlcNAcα-) (Fig. 1*a*), was also the precursor of the A and B blood group determinants, which are tetrasaccharides (10). It is this trisaccharide that is recognized by UE-I. Though classified as an α-L-fucose-specific legume lectin, UE-I binds α-L-fucose with an affinity that is approximately 100-fold less than the binding of the complete H-type 2 determinant (11).

In the absence of crystallographic information, a method has been developed to probe the interactions between protein and carbohydrate. This method, known as chemical mapping (12), was developed based on the interactions between the Lewis b blood group determinant and the fourth lectin from *Griffonia simplicifolia* (GS-IV) observed in the crystal structure (13). The chemical mapping method employs the generation of monodeoxy and mono-*O*-methyl derivatives of the carbohydrate to generate a chemical map of the carbohydrate epitope, which is recognized by the protein. Application of this method to the binding of the H-type 2 blood group determinant by UE-I has been reported (11, 14–16). These inhibition studies into the binding of the H-type 2 determinant by UE-I have revealed several key interactions between protein and carbohydrate (Table 1) (16), and allowed for the generation of the chemical map for the epitope of the H-type 2 trisaccharide recognized by UE-I (Fig. 1*a*).

Fig. 1. The human H-type 2 blood group determinant. (*a*) The β-methyl glycoside of the H-type 2 trisaccharide (α-L-Fucα(1→2)-β-D-Galβ(1→4)-β-D-GlcNAcα-) (H-type 2-OMe). Structural units *a*, *b*, and *c* are β-D-GlcNAc-OMe, β-D-Gal, and α-L-Fuc, respectively. (*b*) The methyl glycoside of α-L-fucose (α-L-Fuc-OMe) shown in a perspective representation with atomic numbering for clarity.

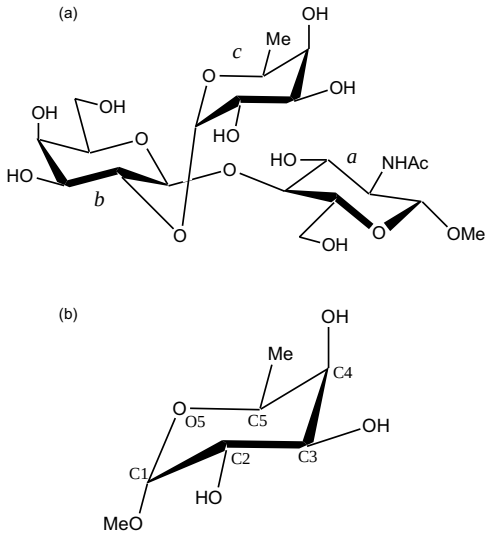

The lectins from leguminous plants have contributed significantly to our understanding of the structural nature of carbohydrate specificity exhibited by proteins (17–20) — the majority of knowledge about lectins and their interactions with carbohydrate is from crystallographic analysis of the Glc/Man, Gal/GalNAc and complex specific legume lectins (20). Very little structural information is available regarding the carbohydrate specificity of the α-L-fucose-specific lectins, though the structure of the native UE-I has been recently reported to 2.2 Å resolution (21). This study revealed

© 2002 NRC Canada

Fig. 2. MALDI-TOF MS spectra of trypsin-digested UE-I. Several peaks were found to correspond to peptide fragments of an in silico digestion of UE-I, and are indicated in the spectra and in Table 2. The horizontal axis represents the observed *m*/*z* ratios for the UE-I peptide fragments, and the vertical axes represent the percent relative intensity (left) and measured peak height of the most intense or base peak (right). The peak at *m*/*z* 1889.01 confirmed the presence of Thr in the X86-Asp87 *cis*-peptide, and the peak at *m*/*z* 2097.13 allowed for discrimination between the Konami et al. (22) and Audette et al. (21) primary structures of the UE-I peptide Glu204–Arg222. The peak at *m*/*z* 842.51 is due to the autolysis of trypsin.

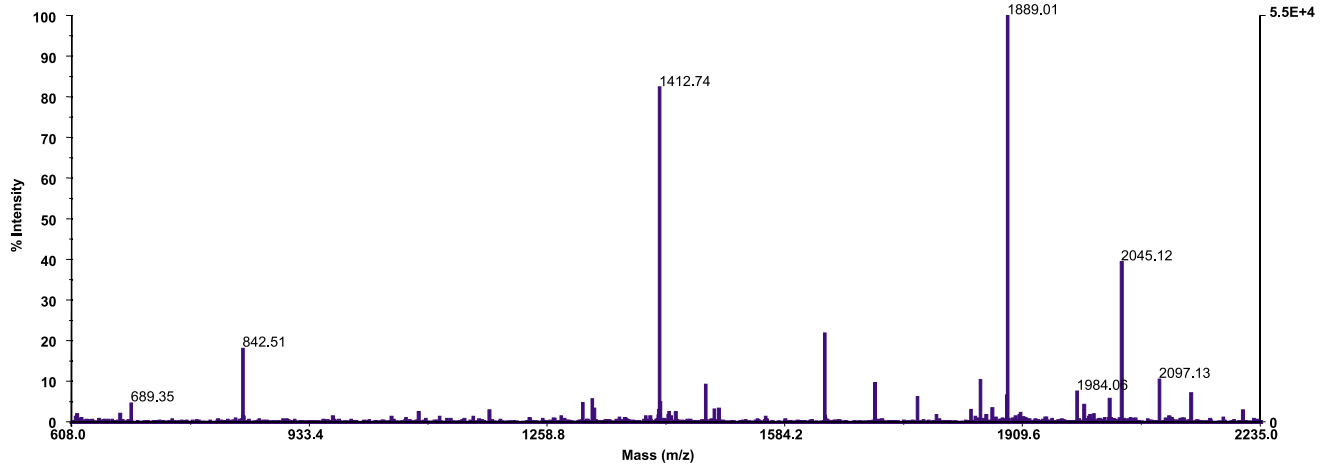

Table 1. Chemical mapping of the epitopes of H-type 2-OMe recognized by UE-I.

	Relative potencies[b]	
Position altered[a]	Monodeoxy	Mono-*O*-methyl
3a	46	40
6a	250	150
3b	3	70
4b	37	44
6b	60	45
2c	0.6	Inactive
3c	0.11	Inactive
4c	Inactive	Inactive
5c (*nor*)[14]	3	—

Note: For source, see ref. 16.
[a]Structural unit designations are as described in Fig. 1*a*.
[b]By radioimmunoassay, setting the potency of H-type 2-OMe at 100 (11).

several differences between other legume lectins, and included the modeling of the β-methyl glycoside of the H-type 2 trisaccharide (H-type 2-OMe) within the carbohydrate binding site to predict the interactions between protein and carbohydrate in correlation with the available chemical mapping data (21).

The present study examines the structural nature of the recognition of the H-type 2 blood group determinant by UE-I through mass spectrometry and X-ray diffraction analysis of the complex of UE-I and the methyl glycoside of α-L-fucose (α-L-Fuc-OMe; Fig. 1*b*) at 2.3 Å resolution. Also, a preliminary analysis of a low resolution structure of the UE-I:H-type 2-OMe complex allows for the identification of the interactions between protein and carbohydrate at the periphery of the binding site, which confer extended carbohydrate specificity to the lectin. The interactions observed between protein and carbohydrate are in correlation with the observed chemical mapping data; however, these observed interactions differ from those predicted in the previous modeling studies. The observed interactions, carbohydrate specificity of UE-I, and differences from the modeling studies are discussed.

Results and discussion

Mass spectrometry

Electrospray ionization mass spectrometric (ESI-MS) analysis of UE-I indicates that the molecular weights of the two monomeric UE-I subunits are 30 049.0 and 31 243.0 Da (data not shown). These values correlate well with observations made during SDS-PAGE analysis of UE-I, in which the dimer separates as two distinct bands of approximately 30 kDa molecular weight (data not shown). It was noted, however, that the molecular weight of the UE-I monomer, based on the primary structure observed in the electron density is 26 606 Da (21). This apparent difference in molecular weight between UE-I monomers may be attributed to differential glycosylation states of each subunit.

Examination of the crystal structure of the native UE-I (21) revealed several differences between the reported primary structure of UE-I (22) and that observed in the electron density. To verify the crystallographically observed amino acid sequence of UE-I (21) vs. that of the published primary structure (22), matrix-assisted laser desorption/ionization-time of flight mass spectrometric (MALDI-TOF MS) analysis was performed on a tryptic digest of UE-I. Both the upper and lower bands of SDS-PAGE separated UE-I were subjected to identical digestion and MALDI-TOF MS protocols; a representative mass spectrum is shown in Fig. 2. The *m*/*z* ratios for each peptide peak were compared with those predicted for a theoretical (in silico) tryptic digest. Peaks at *m*/*z* 842.51, 1045.56, 2211.10, and 2383.93 can be attributed to autolysis of trypsin, and were thus excluded from analysis.

Several peaks were found to correspond to those predicted from the theoretical digest (Table 2). Of particular interest was the peak observed at *m*/*z* 2097.13. This peak corresponds to the residues between Glu204 and Arg222, and allowed for discrimination between the differing primary

© 2002 NRC Canada

Table 2. MALDI-TOF analysis of trypsinized UE-I.

$[M + H]^+$ (*m/z*)		Residue range
Predicted	Observed	
689.36	689.35	Ser152–Arg157
1412.71	1412.74	Val37–Arg50
1888.98	1889.01	Ala84–Arg101
2045.08	2045.12	Ala84–Arg102
1984.00	1984.06	Tyr162–Lys179
2097.07	2097.13	Glu204–Arg222
2140.10	2140.17	Arg161–Lys179

sequences. Within this region, a Gly → Ser change was required to account for the electron density observed at residue 217 (21). The corresponding $[M + H]^+$ ion for this region (with the Gly → Ser change) has a predicted *m*/*z* of 2097.07, which matches closely the observed MS peak. The peptide fragment with a Gly at position 217 would have an *m*/*z* of 2067.03; no corresponding peak was observed in the mass spectrum.

No other peaks were observed that would correspond to peptides containing expected differences in the UE-I sequence. It is possible that glycosylation of the protein may prevent correlation between observed and predicted *m*/*z* values for glycosylated peptides. Also, non-specific cleavage by trypsin may result in peptide fragments that will not correlate with an in silico trypsin digest of the target protein. Nevertheless, the available MS data suggests that the primary structure determined via X-ray analysis (21) is indeed correct. This, together with the fact that Asn116 was not observed in the structure of native UE-I, indicates that continuous numbering of UE-I residues can be applied throughout the sequence (Ser1–Ser242). For native UE-I (21), however, discontinuous residue numbering (Ser1–Cys115 and Asp117–Ser243) was retained to coincide with the published amino acid sequence of Konami and co-workers (22).

Quality of the crystallographic models of the UE-I–carbohydrate complexes

The final model of the UE-I:α-L-Fuc-OMe complex consists of two UE-I dimers within the asymmetric unit, related by non-crystallographic symmetry (NCS). The structure was refined to 2.3 Å resolution (diffraction data summarized in Table 3). The final model consists of 240 amino acid residues in three of the four UE-I monomers; the fourth UE-I monomer contains 239 amino acid residues. No electron density was observed for the final two C-terminal residues in UE-I subunits A, B, and C, nor for the final three C-terminal residues for UE-I subunit D. Four calcium and four manganese ions are present in the model (one Ca^{2+} and one Mn^{2+} per subunit). There are four bound α-L-Fuc-OMe molecules in the final model, with one α-L-Fuc-OMe molecule located in the predicted carbohydrate recognition domain (CRD) of each UE-I monomer. Electron density was observed at Asn23 and Asn111 of all UE-I monomers, which correspond to *N*-linked oligosaccharide at these positions; however, the observed density was not sufficiently resolved to allow for modeling of the *N*-linked carbohydrate. There are 266 solvent (water) molecules present in the final model, and a single MPD molecule was observed adjacent to Cys60 of the third UE-I monomer.

The stereochemical quality of the final model was analyzed using the program PROCHECK (23). A total of 80.6% of the amino acid residues are within the most favored regions of the Ramachandran plot (24); 18.7% of the residues are located in the additional allowed regions, and six residues (0.7%) are located in generously allowed regions. The mean coordinate error from Luzzatti plot analysis (25) is 0.15 Å. The final refinement statistics are summarized in Table 3.

The model of the UE-I:H-type 2-OMe complex consists of a single UE-I dimer within the asymmetric unit refined to 3.0 Å resolution (Table 3). The model consists of 240 amino acid residues in both UE-I subunits, two calcium and two manganese ions (one Ca^{2+} and Mn^{2+} per subunit), and a single bound H-type 2-OMe is present in the final model, located in the predicted CRD of the UE-I subunit A. Electron density was observed at Asn23 and Asn111 of both UE-I monomers, which correspond to *N*-linked oligosaccharide at these positions; however, the observed density was not sufficiently resolved to allow for modeling of the *N*-linked carbohydrate. Because of the resolution of the data, no solvent (water) molecules were included in the model. The stereochemical quality of the model was analyzed using the program PROCHECK (23). A total of 68.4% of the amino acid residues are within the most favored regions of the Ramachandran plot (24); 27.8% of the residues are located in the additional allowed regions, and the remaining residues (3.8%) are located in generously allowed regions. The mean coordinate error from Luzzatti plot analysis (25) is 0.20 Å; refinement statistics are summarized in Table 3.

Overall structure of UE-I

The tertiary and quaternary structure of UE-I have been discussed previously (21). Both the UE-I:α-L-Fuc-OMe and UE-I:H-type 2-OMe complexes of UE-I exhibit a similar overall structure to that of the native protein (Fig. 3). A comparison between the UE-I molecules indicates only slight differences; the average root mean square differences (rmsd) between C^α atoms of the native UE-I and the first and second dimers of the UE-I:α-L-Fuc-OMe complex are 0.63 and 0.68 Å, respectively. The average rmsd between the native UE-I and the UE-I:H-type 2-OMe complex is 0.96 Å, and between the UE-I:H-type 2-OMe complex and the first and second dimers of the UE-I:α-L-Fuc-OMe complex are 0.93 and 0.87 Å, respectively.

Examination of the monomeric subunits of UE-I in both complexes also indicate that differences between subunits are minimal. In the UE-I:α-L-Fuc-OMe complex, the overall average rmsd between C^α atoms is 0.46 Å. The B-factors are also similar between the UE-I subunits, with average B-factors (main-chain/side-chain) of 20.4 $Å^2$/20.5 $Å^2$, 22.6 $Å^2$/22.2 $Å^2$, 22.1 $Å^2$/22.3$Å^2$, and 19.4 $Å^2$/19.8 $Å^2$ for UE-I subunits A–D, respectively. Side chains of several residues were observed to have little electron density: Lys83 of subunit A, Asn40 of subunit B, Thr240 of subunit C, and Asn39, Lys83, and Asn239 of subunit D. These residues were replaced with alanines during refinement. In the UE-I:H-type 2-OMe complex, the average rmsd between C^α atoms of subunit A and B is 0.20 Å, and the average B-factors

© 2002 NRC Canada

Table 3. Data collection and refinement statistics for the UE-I complexes.

	α-L-Fuc-OMe	H-Type 2-OMe
Diffraction data		
Resolution range (Å)	40–2.30	40–3.00
(Last shell) (Å)	(2.32–2.30)	(3.03–3.00)
No. unique reflections	44 883 (944)	9 793 (244)
Completeness (%)	87.9 (76.8)	89.1 (77.7)
Mean $I/\sigma(I)$	14.93 (2.62)	11.29 (2.47)
R_{Symm}[a]	0.075 (0.457)	0.157 (0.489)
Crystal mosaicity (°)	1.49	1.61
Refinement statistics		
Diffraction agreement		
Resolution range (Å)	40–2.30	30–3.0
R-value[b]	0.202	0.284
R_{Free}[c]	0.289	0.421
No. of unique reflections	28,417	8,376
Quality of structure		
Model parameters		
Total protein non-H atoms	7449	3738
Solvent molecules	266	—
B-factor model	Individual isotropic	Individual isotropic
Mean B-factors (Å^2)[d]		
Main-chain	21.0	19.4
Side-chain	21.2	19.2
Bound carbohydrate	27.8	20.5
Solvent molecules	23.2	—
rmsd from stereochemical ideality		
Bonds (Å)	0.01	0.01
Angles (°)	1.67	1.99
Dihedrals (°)	26.14	26.01
Impropers (°)	1.30	1.55

[a] $R_{Symm} = \Sigma_j|I_j - \langle I\rangle|/\Sigma_j I_j$ where j is a set of observations of equivalent reflections and $\langle I\rangle$ is the average intensity of the reflection.
[b] *R*-value = $\Sigma_{hkl}|F_o - F_c|/\Sigma_{hkl}|F_o|$. All data, final refinement cycle.
[c] Randomly chosen test set of 5% of unique reflections (1419 reflections).
[d] Mean B-factors are averaged over both UE-I dimers in the UE-I:α-L-Fuc-OMe complex, and over both monomeric subunits of the UE-I:H-type 2-OMe complex.

are (main-chain/side-chain) 19.1 Å^2/17.9 Å^2 and 19.7 Å^2/20.4 Å^2 for subunits A and B, respectively. In all subunits of both UE-I complexes no electron density was observed for residues 241 and 242, sequenced as Asn and Ser by Konami and co-workers (22).

The carbohydrate binding site of UE-I

Carbohydrate specificity in the legume lectins is based upon the monosaccharide that exhibits the highest binding affinity, even though monosaccharide binding is weaker than the binding of the complete oligosaccharide, which the lectin recognizes (20). Examination of the native UE-I identified the UE-I CRD as a small depression at the surface of the lectin (22), comprised of residues Glu44, Thr86, Asp87, Gly104-Gly105, Ile129, Val133, Asn134, Trp136, Tyr219, and Arg222 (21). A molecule of α-L-Fuc-OMe was observed in the CRD of each UE-I subunit (Fig. 4*a*). Each α-L-Fuc-OMe molecule fit the observed electron density well; the average B-factor for the four α-L-Fuc-OMe molecules is 27.8 Å^2. The α-L-Fuc-OMe molecules make several hydrophilic and hydrophobic interactions with UE-I, which are summarized in Table 4 and illustrated in Fig. 4*b*. Of particular interest is the hydrophobic interaction between C6 of the bound α-L-Fuc-OMe and $C^{\gamma 2}$ of Thr86, with an average interatomic distance of 3.4 Å. This interaction likely plays a significant role in the carbohydrate specificity of UE-I, and will be discussed in greater detail in the following section. A stacking interaction, as is commonly observed in the carbohydrate complexes of legume lectins (20), is provided by Tyr219 to the hydrophobic back face of the bound α-L-Fuc-OMe. Also, the residues involved in carbohydrate binding by UE-I must be updated to include Arg102, due to an observed hydrogen bond between the N^{H2} and O2 of α-L-Fuc-OMe, as well as Ala103 and Tyr106, which make van der Waals contacts. Indeed, it was observed that the Arg102 side chain moved an average of 1.1 Å (measured via the C^{ζ} atom of the side chain) towards the carbohydrate upon binding to make the observed hydrogen bond with the O2 of α-L-Fuc-OMe (Fig. 5). Arg222 also exhibited movement towards the CRD upon carbohydrate binding, with an average movement of 0.7 Å (measured via the C^{ζ} atom of the side chain); no other residues of the CRD exhibited appreciable movement upon carbohydrate binding (Fig. 5). The UE-I CRD is, therefore, comprised of Glu44, Thr86, Asp87, Arg102, Ala103,

© 2002 NRC Canada

Fig. 3. The UE-I dimer. Shown above is the ribbon representation of the superposition of the C^{α} trace of the various UE-I dimers. The first and second UE-I dimer of the UE-I:α-L-Fuc-OMe complex are shown in gray and green, respectively, the native UE-I (21) is in cyan, and the UE-I:H-type 2-OMe complex is in magenta. Figures 3 through 5 were produced using the program SETOR (53).

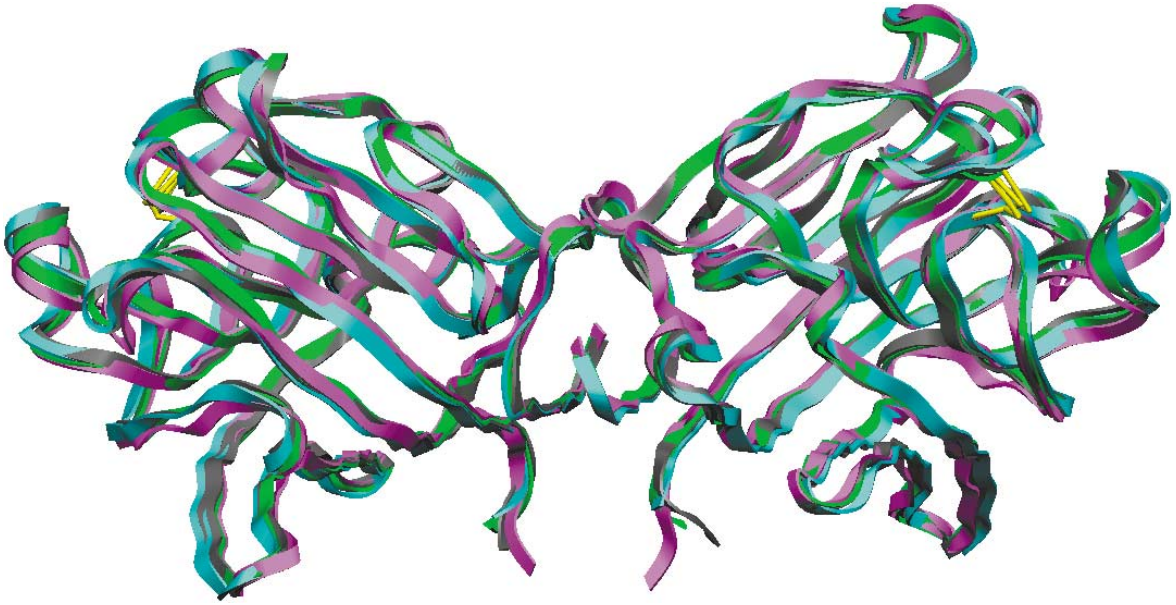

Gly104, Gly105, Tyr106, Ile129, Val133, Asn134, Trp136, Tyr219, and Arg222.

A single H-type 2-OMe molecule was found in the UE-I:H-type 2-OMe CRD, and is present in the CRD of subunit A; the electron density in the CRD of subunit B was insufficiently resolved to allow for modeling of the bound carbohydrate. The galactose and *N*-acetylglucosamine moieties of the H-type 2-OMe fit the observed electron density, however, the fucose moiety of the trisaccharide was not as well resolved. It is thought that the fucose moiety of the bound H-type 2-OMe will indeed appear as is observed in the UE-I:α-L-Fuc-OMe complex due to similar positions of the C1, O1, and C7 atoms of α-L-Fuc-OMe and the C1*c*, O2*b*, and C2*b* atoms of H-type 2-OMe (structural unit designations as in Fig. 1*a*); this shall be confirmed upon examination of the UE-I:H-type 2-OMe complex at higher resolution.

Carbohydrate specificity of UE-I

The development of methodologies for complex oligosaccharide synthesis have greatly aided the study of protein–carbohydrate interactions (26); these methodologies are particularly useful when crystallographic data of the complex is unavailable. Indeed, the identification of the effects of slight structural changes to the carbohydrate on the efficacy of binding allows for the prediction of the chemical map of the carbohydrate epitope (12).

The chemical mapping method was applied to the systematic investigation of the interaction between UE-I and the H-type 2 blood group determinant (15), which resulted in the generation of a chemical map of the H-type 2 epitope (Fig. 1) (16). Several conclusions were made upon examination of the results of inhibition studies into the binding of H-type 2-OMe by UE-I (Table 1). In particular, when both deoxygenation and *O*-methylation of hydroxyl groups of the epitope abolish binding, these hydroxyls are identified as being deep within the CRD making critical hydrogen bonds with the protein. When deoxygenation significantly decreases but *O*-methylation exhibits little effect on binding, these hydroxyl groups are interpreted as being closer to the periphery of the binding site. Finally, when neither deoxygenation nor *O*-methylation significantly affect binding, these groups are identified as remaining in the aqueous phase upon complexation.

The observed interactions that occur between UE-I and the bound carbohydrate in the UE-I:α-L-Fuc-OMe complex correlate well with the observed chemical mapping data. In particular, O2, O3, and O4 of α-L-Fuc-OMe make several hydrogen bonds to residues of the UE-I CRD (Fig. 4*b*, Table 4). These interactions occur deep within the CRD. For example, O4 of the α-L-Fuc-OMe was observed to make hydrogen bonds with Asp87 $O^{\delta 2}$ (2.8 Å), Gly105 N (3.0 Å), and Asn134 $N^{\delta 2}$ (3.0 Å). Both Asp87 and Gly105 are located at the bottom of the UE-I CRD, and Asn134 is located close to the bottom of the CRD (Fig. 4*b*). Deoxygenation of the group would result in removal of the hydrogen bonding capacity of that group, while *O*-methylation would prevent interaction through steric interference between the carbohydrate and protein. Disruption of one or all of these interactions would prevent stabilization of the fucose moiety within the CRD as observed in inhibition studies (Table 1) (14).

The presence of a Thr at the X86–Asp87 position is a unique feature of the α-L-Fuc-specific legume lectins; the residue at this position is generally Ala (20). Chemical mapping of the H-type 2-OMe indicated that alteration of the C-5-CH_3 group of the fucose moiety results in significantly reduced binding (Table 1). The authors noted, however, that the effect of replacing this group with a hydrogen atom may have an effect on the conformational preference of the carbohydrate (14). The examination of the UE-I:α-L-Fuc-OMe complex reveals that the C-5-CH_3 group of the α-L-Fuc-OMe makes a significant hydrophobic interaction with $C^{\gamma 2}$ of the Thr86 side-chain as well as several van der Waals

© 2002 NRC Canada

Fig. 4. The bound carbohydrate within the UE-I CRD. (*a*) The bound α-L-Fuc-OMe. Shown is the α-L-Fuc-OMe found in the CRD of the UE-I subunit A of the UE-I:α-L-Fuc-OMe complex in the electron density from an $\boldsymbol{F}_o$-$\boldsymbol{F}_c$ omit electron density map of the final refined structure contoured at the 1σ contour level. The α-L-Fuc-OMe is coloured according to standard element colours (as per SETOR; 53), and the electron density is shown in blue. (*b*) Stereographic representation of the bound α-L-Fuc-OMe within the CRD of the first UE-I subunit in the UE-I:α-L-Fuc-OMe complex. Backbone atoms are in gray, side-chains are in standard colours, and bound carbohydrate is in green. Interactions between the bound α-L-Fuc-OMe and UE-I are listed in Table 4, and hydrogen bonds between the protein and carbohydrate are highlighted.

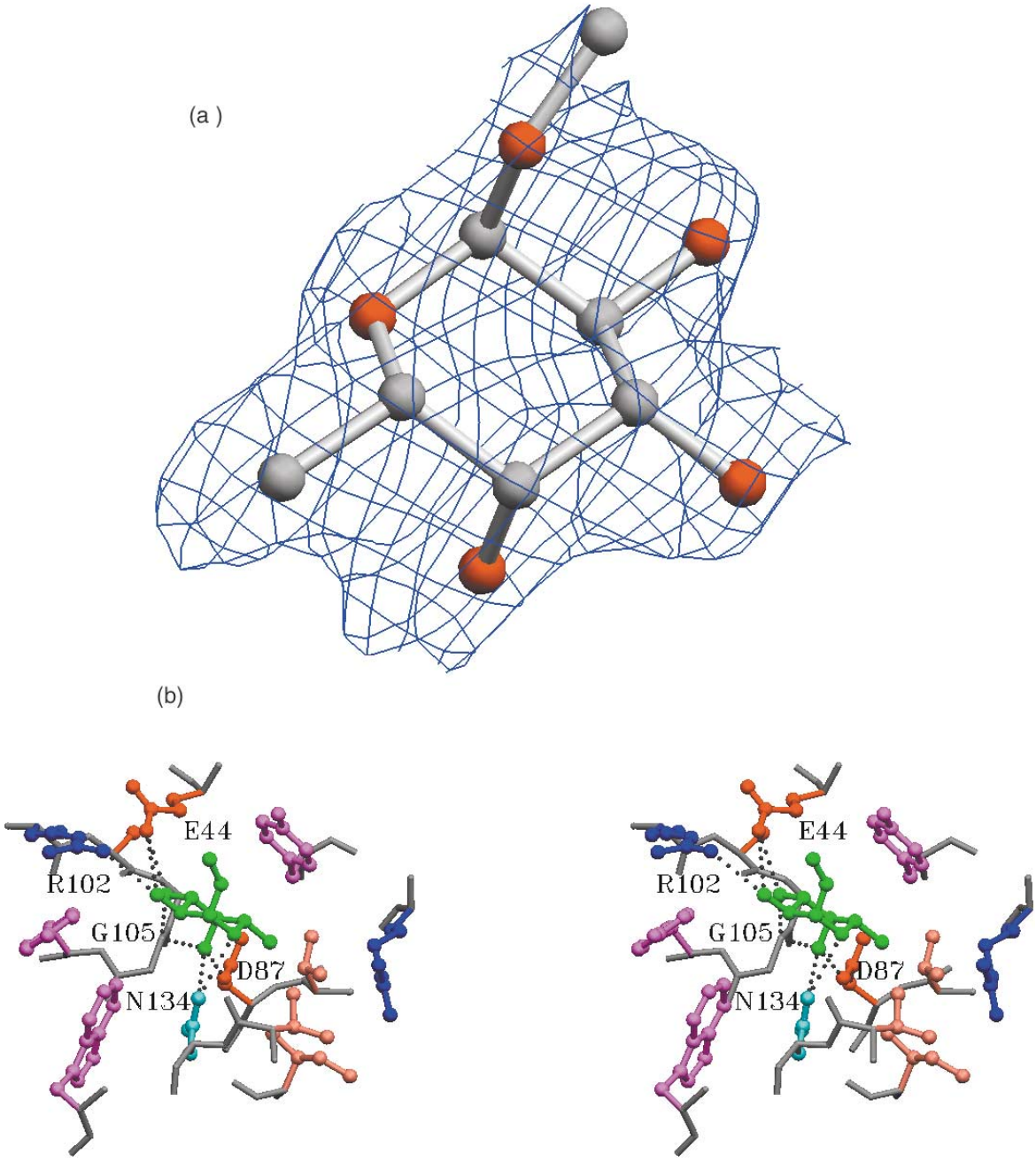

contacts with hydrophobic residues of the UE-I CRD (Table 4; Fig. 4*b*). These hydrophobic interactions provide stability to the UE-I:α-L-Fuc-OMe complex, and arise from the orientation of the α-L-fucose within the UE-I CRD, in which the hydroxyl groups of the fucose moiety make the most favorable hydrogen bonds with the protein. Thus, disruption of this interaction through replacement with a hydrogen atom (14) would result in significantly reduced binding, as observed in the decreased potency of the congener during inhibition studies (Table 1) (16).

While carbohydrate specificity of the legume lectins is classified based upon which monosaccharide exhibits greatest binding affinity (20), the true specificity for the lectins is for oligomeric structures; this extended specificity arises from interactions between protein and carbohydrate at the periphery of the CRD. Two possible interactions were

© 2002 NRC Canada

Fig. 5. Comparison of the CRD observed in the native UE-I (21) and in the UE-I:α-L-Fuc-OMe complex. Shown is the stereo view of the superposition of the CRD from subunit A of the native UE-I onto the CRD observed from subunit A of the UE-I:α-L-Fuc-OMe complex. The Arg102 side chain was observed to move an average of 1.1 Å towards the carbohydrate upon binding to hydrogen bond with O2 of the α-L-Fuc-OMe molecule. Arg222 was also observed to move towards the CRD upon carbohydrate binding (0.7 Å); however, no other residues exhibited appreciable movement towards the CRD upon binding the α-L-Fuc-OMe. Main chain atoms are in gray, side chain atoms of the native UE-I are in green, side chain atoms of UE-I in the complex are in magenta, and the bound α-L-Fuc-OMe molecule (represented in ball and stick form) is in cyan.

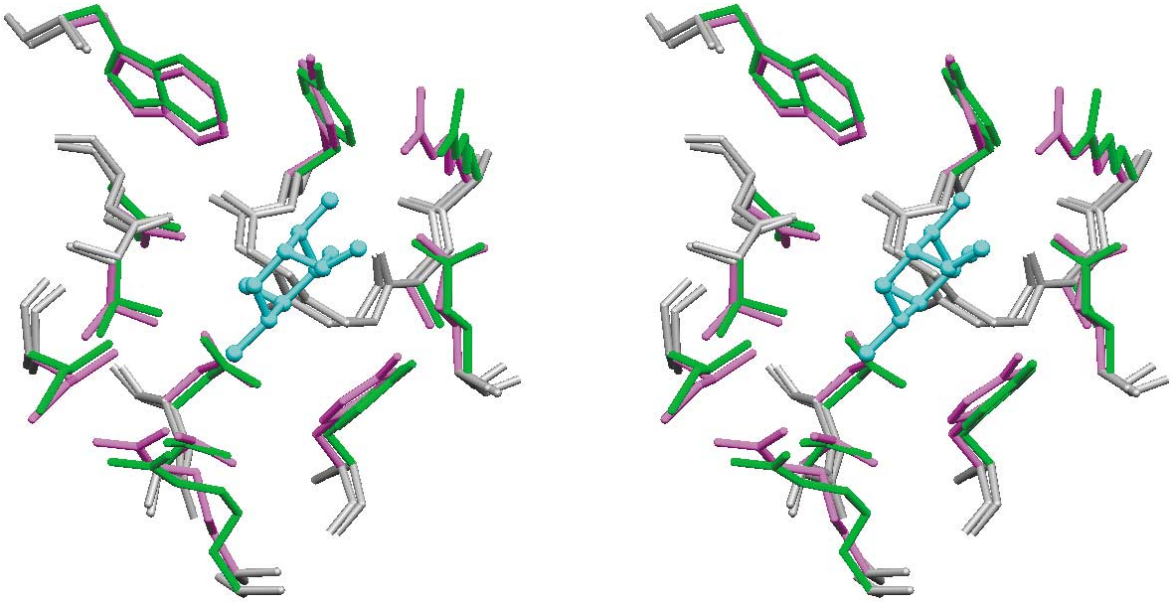

Table 4. Interactions between the bound α-L-Fuc-OMe and UE-I.

α-L-Fuc-OMe	UE-I	Distance (Å)[a]
Hydrogen bonds		
O2	Glu44-$O^{\delta1/\varepsilon2}$	3.5
	Arg102-N^{H2}	3.6
O3	Glu44-$O^{\varepsilon2}$	2.8
	Gly105-N	2.9
O4	Asp87-$O^{\delta2}$	2.8
	Gly105-N	3.0
	Asn134-$N^{\delta2}$	3.0
O5	Asn134-$N^{\delta2}$	3.4
van der Waals contacts[b]		
C1	Val133, Asn134	
C2	Glu44, Tyr106, Asn134	
C3	Glu44, Gly105, Tyr219	
C4	Asp87, Gly105, Asn134, Tyr219	
C5	V133, N134, Y219	
C6	T86, D87, I129, V133, Y219	
C7	Tyr219	
O1	Tyr219	
O2	Glu44, Arg102, Tyr106	
O3	Glu44, Ala103, Gly104, Gly105	
O4	Asp87, Gly104, Gly105, Asn134	
O5	Val133, Asn134	

[a]Hydrogen bond distances are averaged over all four bound α-L-Fuc-OMe molecules.

[b]van der Waals contacts were identified through visual inspection with a maximum distance of 4.0 Å.

observed between UE-I and the H-type 2-OMe — hydrogen bonds between O3 of Gal and Arg102 N^{H2} (3.1 Å) and between O6 of GlcNAc and N^{H1} of Arg222 (2.8 Å). Both interactions correlate with the chemical mapping data (Table 1); both interactions are located at the periphery of the binding site, and disruption of these interactions would result in a slight decrease in binding of the trisaccharide by the protein.

The presence of calcium and manganese ions in the legume lectin has been proposed to induce electron delocalization in the binding site and thus increase the strength of the hydrogen bonds between protein and bound carbohydrate (27). Asn134 both hydrogen bonds to O4 of the α-L-Fuc-OMe through $N^{\delta2}$ (3.0 Å) as well as coordinates the Ca^{2+} through $O^{\delta2}$. Thus, it is likely that the proposed electron delocalization occurs, which results in increasing the strength of the hydrogen bonds between protein and carbohydrate upon complexation.

Finally, an ordered water structure has been identified as playing a role in carbohydrate binding by legume lectins (20, 28–32). The identification of the high entropy barrier to binding of H-type 2-OMe by UE-I ($T\Delta S$ = –20.5 kcal mol^{-1}), as well as a high enthalpy of binding (–29 kcal mol^{-1}), led to the inference that an ordered water structure played a role in H-type 2-OMe binding by UE-I, and to the coining of the term "hydraphobic effect" (33) to describe this role of water in the binding of hydrophilic surfaces in the presence of large molar excesses of water as is found on the surface of proteins. No ordered water molecules were observed in the CRD of UE-I in either UE-I:carbohydrate complex. Indeed, the α-L-Fuc-OMe fits snugly within the UE-I CRD, making

© 2002 NRC Canada

numerous hydrophobic and hydrophilic interactions (Table 4; Fig. 4*b*). It can therefore be inferred that the role of ordered water molecules in carbohydrate binding is in the coordination of calcium and manganese ions, which results in stabilization of the protein–carbohydrate complex through the above noted electron delocalization of binding site residues. It is unlikely that ordered water molecules are present within the CRD after formation of the protein–carbohydrate complex, and the observed entropic and enthalpic effects are due, at least in part, to release of water from the CRD upon carbohydrate binding.

Comparison of modeling and crystallographic studies

The modeling of the H-type 2-OMe in the CRD of the native UE-I (21) predicted several interactions between protein and carbohydrate, which would correlate with the observed chemical mapping data (Table 1). The interactions observed between UE-I and the α-L-Fuc-OMe in the UE-I:α-L-Fuc-OMe complex (Fig. 4*b*; Table 4), and those between UE-I and the bound H-type 2-OMe in the UE-I:H-type 2-OMe complex, also correlate with the chemical mapping data. The observed interactions do not, however, correspond with those predicted from the modeling studies.

The differences between modeled and crystallographically observed binding of the H-type 2 epitope may be understood as follows. During the modeling studies, the roles of Thr86 and Arg102 in carbohydrate binding were not initially apparent. Also, an ordered water structure was thought to play a role in carbohydrate binding; this was found to not be the case upon examination of the CRD in the UE-I:α-L-Fuc-OMe complex (Fig. 4*b*). Finally, the starting orientation of the H-type 2-OMe during modeling was based upon the overlap of the carbohydrate on to the R-MPD observed within the CRD (21). These factors resulted in the minimization of a complex (21) that correlated well with the chemical mapping data but does not correlate with the bound carbohydrate observed in the CRD of UE-I.

Materials and methods

Protein and carbohydrate sources

UE-I was purchased from EY Laboratories (San Mateo, CA, U.S.A., lot No's 141216H0529–30, 150604H0808–30, and 150902J0514–30) in pure form; no further purification was performed. Both α-L-Fuc-OMe and H-type 2-OMe were prepared according to previously reported procedures (14, 16, 34) and provided by Professor R.U. Lemieux (University of Alberta, deceased) in pure form; no further purification was performed.

Mass spectrometric analysis of UE-I

Molecular mass analysis of the two monomeric UE-I subunits was performed by ESI-MS using a Quattro LC triple-quadrupole mass spectrometer (Micromass, Manchester, U.K.) operating in the positive ion mode. An aqueous solution of UE-I (2 μL at 9.4 μM) was introduced by flow injection at 15 μL min^{-1}, using water–acetonitrile (50:50) as the carrier. Electrospray conditions were as follows: capillary 3.78 V; cone 25 V; source temperature 85°C. The first quadrupole was scanned in the *m*/*z* range 600–2000 at 3.95 s per scan. Scans corresponding to the sample elution profile were combined and processed using the MaxEnt software algorithm (MassLynx, version 3.5, Micromass) to obtain molecular weight information for the two UE-I subunits.

Information on the primary structure of UE-I was obtained by MALDI-TOF MS analysis of tryptic digests from SDS-PAGE separated subunits. Approximately 2.5 μg protein were applied to each of three separate lanes on a 12% SDS-PAGE gel in the presence of β-mercaptoethanol as described by Laemmli (35). The separate UE-I bands were excised from the gel, cut into 1 mm squares, and placed in 1.5 mL microcentrifuge tubes for destaining, reduction, alkylation, and tryptic digestion.

Digestion and MS analysis of the SDS-PAGE purified subunits were performed at the National Research Council's Plant Biotechnology Institute in Saskatoon. Tryptic digestion of the excised bands proceeded according to reported protocols (36), after which the peptides were resuspended in 10 μL of 0.1% TFA and desalted by solid-phase extraction using disposable pipette tips ($ZipTip_{C18}$, Millipore) according to the manufacturer's instructions. Peptides were eluted in 1–2 μL of 0.1% TFA/75% acetonitrile directly onto a MALDI target plate. An equal volume of matrix solution (5 mg mL^{-1} α-cyano-4-hydrocinnamic acid in 0.1% TFA/50% acetonitrile) was applied to the sample and allowed to dry. A 1:1 mixture of matrix and mass calibrant was also placed beside the sample for close external calibration. MALDI-TOF MS analysis was performed on a Voyager-DE STR (Applied Biosystems, Framingham, MA) operating in the positive ion, delayed extraction, and reflectron modes and using the following parameters: accelerating voltage 20 000 V; grid voltage 72.5%; guide wire voltage 0.001%; delay 100 ns; laser power 2290. Spectra were obtained by combining 400 scans and applying mass calibration, baseline correction, noise filtering, and de-isotoping procedures using the spectrometer software (Data Explorer v. 4.0, Applied Biosystems).

Crystallization UE-I:carbohydrate complexes

Crystallization of the carbohydrate complexes of UE-I proceeded as follows. The UE-I complexes were produced by adding α-L-Fuc-OMe or H-type 2-OMe to UE-I with a final protein concentration of 10 mg mL^{-1} and carbohydrate concentrations of 0.34 or 0.64 mg mL^{-1} for α-L-Fuc-OMe or H-type 2-OMe, respectively, in 0.1 M sodium cacodylate buffer (pH 7.0), 0.1 mM calcium chloride, and 0.1 mM manganese chloride. These solutions were allowed to stand for at least 1 h on ice prior to crystallization. Crystals were grown by the vapour diffusion method from 4 μL drops containing 5 mg mL^{-1} UE-I:α-L-Fuc-OMe or UE-I:H-type 2-OMe complex, 0.05 M sodium cacodylate buffer (pH 4.0), 0.05 M sodium acetate buffer (pH 4.0), 5 mM calcium chloride, 5 mM manganese chloride, 25–30% (v/v) R,S-MPD, and 0.5% (v/v) PEG 550 MME ether were equilibrated over 1 mL reservoirs containing 0.1 M sodium acetate buffer (pH 4.0), 10 mM calcium chloride, 10 mM manganese chloride, 50–60% (v/v) R,S-MPD and 1% (v/v) PEG 550 MME at 287 or 293 K. These crystallization conditions are similar to those previously reported for the native UE-I (21, 37).

Crystals of both complexes took over 6 months to appear. Crystals of the UE-I:α-L-Fuc-OMe were generally clear plates of average dimensions 0.35 × 0.15 × 0.10 mm that were not suitable for X-ray diffraction analysis due to

© 2002 NRC Canada

disordered stacking of the plates during crystal growth. A single clear, rod-like crystal of α-L-Fuc-OMe complex suitable for X-ray diffraction analysis was, however, produced. The UE-I:α-L-Fuc-OMe complex crystallized in the monoclinic space group $P2_1$, with unit cell dimensions a = 71.81, b = 69.00, and c = 119.02 Å, and β = 106.76°. Two UE-I dimers are present within the asymmetric unit, with a Matthews coefficient (38) of 2.67 $Å^3$ Da^{-1} and an estimated 53.6% (v/v) solvent content. Crystals of the UE-I:H-type 2-OMe complex were generally clear plates of average dimensions 0.30 × 0.15 × 0.10 mm. The UE-I:H-type 2-OMe complex crystallizes in the orthorhombic space group $C222_1$, with unit cell dimensions a = 88.89, b = 164.75, and c = 77.42 Å. A single UE-I dimer is present within the asymmetric unit, with a Matthews coefficient (38) of 2.66 $Å^3$ Da^{-1} and an estimated 52.7% (v/v) solvent content. Crystals of both UE-I complexes were flash cooled for X-ray diffraction analysis in 0.35-mm cryoloops (Hampton Research, Laguna Niguel, CA) by direct immersion in liquid nitrogen. The crystals were then stored in liquid nitrogen prior to X-ray diffraction analysis.

Data collection of the UE-I:α-L-Fuc-OMe complex

X-ray diffraction data of the UE-I:α-L-Fuc-OMe complex were collected by Dr. M. Becker at beamline X12-C of the National Synchrotron Light Source (NSLS) at Brookhaven National Laboratory (Upton, NY) under the remote access (courier based) data collection program.[4] Data were collected in 180 images from a single crystal at 100 K on a Brandeis 1.2 CCD detector (39), using a wavelength of 1.0 Å, an exposure time of 50 s, and a 1° rotation per image. The diffraction data were indexed using the OneButton interface (40) for DENZO and scaled using the SCALEPACK software package (41). Diffraction data were collected to 2.00 Å resolution, however, the data were truncated to 2.30 Å resolution as it was observed that the mean $I/\sigma(I)$ of the data dropped below 2.0 at resolutions above 2.30 Å. A summary of the data collection statistics is shown in Table 3.

Structure solution and model refinement of the UE-I:α-L-Fuc-OMe complex

The molecular replacement method was used to solve the structure of the UE-I:α-L-Fuc-OMe complex using the program AMoRe of the CCP4 software package (42, 43). The search model was the native UE-I dimer (protein only; PDB accession code 1FX5) (21). To determine the initial positions of the two molecules within the asymmetric unit, the top six peaks from the rotation search were used in the translation search. The top peak from the initial translation search was interpreted as the first UE-I dimer, and was then fixed. With the first UE-I dimer fixed, the translation search was repeated to determine the position of the second UE-I dimer with respect to the first. After obtaining the initial coordinates for both molecules, rigid body refinement in AMoRe resulted in a correlation coefficient and R-value of 0.762 and 0.415, respectively.

The molecular replacement solution was subjected to an initial rigid-body, positional, and B-factor refinement followed by the generation of an electron density map using the X-PLOR software package (44, 45). It was observed that the two UE-I:α-L-Fuc-OMe complex molecules within the asymmetric unit were related by non-crystallographic symmetry (NCS) rotation and translation operations. During the initial rounds of structure refinement, the backbone atoms of both the UE-I:α-L-Fuc-OMe complex molecules were, therefore, restrained by the NCS operations. The R-value at the end of this initial round of refinement was 0.288 at 2.5 Å resolution.

Upon examination of the initial $2\boldsymbol{F}_o - \boldsymbol{F}_c$ electron density map using TURBO-FRODO (46), electron density was observed to correspond to a bound α-L-Fuc-OMe within the binding site of each UE-I subunit. The α-L-Fuc-OMe was placed into the electron density using coordinates obtained from hard sphere exo-anomeric (HSEA) calculations (47). Also, electron density was observed that would represent a calcium ion and a manganese ion in each UE-I monomer, known to be present adjacent to the binding sites of legume lectins (20); these ions were placed in the electron density during model building. Electron density was also observed near Cys60 of the third UE-I monomer, which would represent a molecule of the crystallization precipitant, R-MPD. Finally, electron density was observed at residues Asn23 and Asn111 of the UE-I monomers, which would correspond to *N*-linked oligosaccharide. This electron density was not sufficiently resolved, however, to allow for modeling of the *N*-linked carbohydrate.

Rounds of model building were followed by simulated annealing refinement, B-factor refinement, and new σ_A weighted (48, 49) electron density map generation using X-PLOR. Of the 44 883 unique reflections, 5% of the reflections were randomly selected to evaluate R_{Free} (50, 51); a total of 1419 reflections were chosen for the R_{Free} test set. All cycles of structure refinement, with exception of the final cycle, used a working set consisting of 95% of the unique reflections and a test set consisting of the 5% randomly chosen reflections. The final cycle of refinement used all data. The simulated annealing refinements consisted of a prepstage of 160 cycles of minimization followed by a slow-cooling stage starting at 3000 K and decreasing to 300 K in steps of 50 K and a time step of 0.5 fs (1 fs = 10^{-15} s). Slow-cooling was followed by 120 cycles of conjugate gradient minimization and 40 cycles of B-factor refinement. Engh and Huber (52) bond and angle parameters and a bulk solvent correction were employed throughout refinement; weighting was obtained from the CHECK procedure in X-PLOR. Water molecules were placed into the structure manually using a difference ($\boldsymbol{F}_o - \boldsymbol{F}_c$) electron density map. Upon refinement, some water molecules developed large B-factors (>40 $Å^2$). These were removed from the structure and new water molecules added as they were located in subsequent difference maps.

The space group of the UE-I:α-L-Fuc-OMe complex was determined to be $P2_1$, with two UE-I dimers within the

[4] Diffraction data for the UE-I:α-L-Fuc-OMe complex were collected at the single-crystal diffraction facility at beamline X12-C of the National Synchrotron Light Source at Brookhaven National Laboratory. This facility is supported by the United States Department of Energy Offices of Health and Environmental Research and of Basic Energy Sciences under prime contract DE-AC02–98CH10886, by the National Science Foundation, and by National Institutes of Health Grant 1P41 RR12408–01A1.

© 2002 NRC Canada

asymmetric unit. The two UE-I:α-L-Fuc-OMe complex molecules within the asymmetric unit were related by non-crystallographic symmetry (NCS) rotation and translation operations. The NCS rotation angle between the two molecules is 179.18°, and the NCS rotation axis is almost parallel to the *b*-axis. This relation between UE-I dimers is such that the crystal exhibits pseudo-C centering, which results in the intensities of the $h + k$ odd reflections being weak in comparison to the $h + k$ even reflections. This distribution of reflection intensities results in a large number of the reflections which are weak. It is known that pseudo-centering of a crystal, with this large number of weak reflections, results in abnormally high R and R_{Free} values. For this reason, the refinement of the UE-I:α-L-Fuc-OMe complex employed a low amplitude cut-off. The final R-value and R_{Free} of the UE-I:α-L-Fuc-OMe complex are 0.202 and 0.289, respectively.

Data collection of the UE-I:H-type 2-OMe complex

X-ray diffraction data for the UE-I:H-Type 2-OMe complex were collected at BioCARS beamline 14-BM-D of the Advanced Photon Source (APS) at Argonne National Laboratory (Argonne, IL).[5] Data were collected in 179 images from a single crystal at 100 K on a ADSC Quantum 4 CCD detector (Area Detector Systems Corporation, Poway, CA), using a wavelength of 1.00 Å, an exposure time of 15 s, a 1° rotation per image, and a crystal-to-detector distance of 168.5 mm. The diffraction data were indexed and scaled using the DENZO/SCALEPACK software package (41). A summary of the data collection statistics is shown in Table 3.

Structure solution and model refinement of the UE-I:H-type 2-OMe complex

The molecular replacement method was used to solve the structure of the UE-I:H-type 2-OMe complex using the program AMoRe of the CCP4 software suite (42, 43). The search model was the native UE-I dimer (PDB accession code 1FX5) (21). To determine the initial position of the UE-I dimer within the asymmetric unit, the top five peaks from the rotation search were used in the translation search. Rigid body refinement in AMoRe of the initial coordinates for the UE-I dimer resulted in a correlation coefficient and R-value of 0.561 and 0.447, respectively.

Upon examination of the initial $2\boldsymbol{F}_o - \boldsymbol{F}_c$ electron density map using TURBO-FRODO (46), density was observed to correspond to a bound H-Type 2-OMe within CRD of the first UE-I subunit. The electron density was not sufficiently resolved at this stage, however, to allow for fitting of the H-Type 2-OMe within the carbohydrate binding site. Also, electron density was observed that would represent a calcium and a manganese ion in each UE-I monomer, and electron density was observed at residues Asn23 and Asn111 of the UE-I monomers, which would correspond to *N*-linked oligosaccharide. The calcium and manganese ions and bound H-Type 2-OMe were added to the model in a similar fashion as that described for the UE-I:α-L-Fuc-OMe complex during subsequent rounds of model building; electron density was insufficiently resolved to allow for addition of *N*-linked oligosaccharide.

Refinement was performed as described for the UE-I:α-L-Fuc-OMe complex. During refinement, 5% of the unique reflections (493) were randomly chosen to evaluate R_{Free}, and the backbone atoms of the UE-I subunits were restrained by the NCS operators by which the subunits were related. The final R-value and R_{Free} of the structure are 0.284 and 0.421, respectively. At the resolution of the crystallographic data for the UE-I:H-Type 2-OMe complex (30–3.0 Å), it was not possible to locate solvent (water) molecules.

Protein data bank accession numbers

The coordinates and structure amplitudes for the UE-I:α-L-Fuc-OMe complex have been deposited in the RCSB Protein Data Bank (accession codes RCSB014305 and 1JXN). The coordinates and structure factor amplitudes for the UE-I:H-type 2-OMe complex have not been deposited in the PDB due to the low resolution of the crystallographic data; deposition shall be done upon refinement of the model against higher resolution diffraction data.

Acknowledgments

The authors wish to express their gratitude to Professor R.U. Lemieux, who provided both the carbohydrates for this study and insightful discussions prior to his death. The authors also wish to thank Dr. L. Prasad for helpful discussions, and Dr. M. Becker (NSLS) and Mr. G. Navrotsky (BioCARS) for their assistance during data collection. G.F.A. gratefully acknowledges financial assistance from the Colleges of Graduate Studies and Medicine from the University of Saskatchewan. This work was supported by a Canadian Institutes for Health Research operating grant to L.T.J.D. (MT-10162) and a Natural Sciences and Engineering Research Council of Canada (NSERC) operating grant to J.W.Q.

References

1. N. Sharon and H. Lis. Science (Washington, D.C.), **246**, 227 (1989).
2. N. Sharon and H. Lis. Essays Biochem. **30**, 59 (1995.).
3. N. Sharon and H. Lis. Chem. Rev. **98**, 637 (1998).
4. R.U. Lemieux, R. Cromer, and U. Spohr. Can. J. Chem. **66**, 3083 (1988).
5. R.U. Lemieux, U. Spohr, M. Bach, D.R. Cameron, T.P. Frandsen, B.B. Stoffer, B. Svensson, and M.M. Palcic. Can. J. Chem. **74**, 319 (1996).
6. W.C. Boyd and E. Shapleigh. Blood, **9**, 1195 (1954).
7. I. Matsumoto and T. Osawa. Biochim. Biophys. Acta, **194**, 180 (1969).
8. K. Landsteiner. Wien. Klin. Wschr. **14**, 1132 (1901).
9. K. Landsteiner. Biochem. Z. **104**, 280 (1920).

[5] Diffraction data for the UE-I:H-type 2-OMe complex were collected at beamline 14BM-D of the BioCARS Sector 14 at the Advanced Photon Source. Use of the Advanced Photon Source was supported by the United States Department of Energy, Basic Energy Sciences, Office of Science, under Contract No. W-31–109-Eng-38. Use of the BioCARS Sector 14 was supported by the National Institutes of Health, National Center for Research Resources, under grant number RR07707.

© 2002 NRC Canada

10. W.M. Watkins. *In* Glycoproteins. Their composition, structure and function. *Edited by* A. Gottschalk. Elsevier, Amsterdam. 1972. pp. 830–891.
11. O. Hindsgaul, D.P. Khare, M. Bach, and R.U. Lemieux. Can. J. Chem. **63**, 2653 (1985).
12. P.V. Nikrad, H. Beiberbeck, and R.U. Lemieux. Can. J. Chem. **70**, 241 (1992).
13. L.T.J. Delbaere, M. Vandonselaar, L. Prasad, J.W. Quail, K.S. Wilson, and Z. Dauter. J. Mol. Biol. **230**, 950 (1993).
14. O. Hindsgaul, T. Norberg, J. Le Pendu, and R.U. Lemieux. Carbohydr. Res. **109**, 109 (1982).
15. U. Spohr, E. Paszkiewicz-Hnatiw, N. Morishima, and R.U. Lemieux. Can. J. Chem. **70**, 254 (1992).
16. M. Du, U. Sphor, and R.U. Lemieux. Glycoconjugate J. **11**, 443 (1994).
17. N.K. Vyas. Curr. Opin. Struct. Biol. **1**, 732 (1991).
18. N.M. Young and R.P. Oomen. J. Mol. Biol. **228**, 924 (1992).
19. V. Sharma and A. Surolia. J. Mol. Biol. **267**, 433 (1997).
20. R. Loris, T. Hamelryck, J. Bouckaert, and L. Wyns. Biochim. Biophys. Acta, **1383**, 9 (1998).
21. G.F. Audette, M. Vandonselaar, and L.T.J. Delbaere. J. Mol. Biol. **304**, 423 (2000).
22. Y. Konami, K. Yamamoto, and T. Osawa. J. Biochem. **109**, 650 (1991).
23. R.A. Laskowski, M.W. MacArthur, D.S. Moss, and J.M. Thornton. J. Appl. Cryst. **26**, 283 (1993).
24. C. Ramakrishnan and G.N. Ramachandran. Biophys. J. **5**, 909 (1965).
25. V. Luzzatti. Acta Cryst. **A5**, 802 (1952).
26. R.U. Lemieux. Chem. Soc. Rev. **7**, 423 (1978).
27. L.T.J. Delbaere, M. Vandonselaar, L. Prasad, J.W. Quail, J.R. Pearlstone, M.R. Carpenter, L.B. Smillie, P.V. Nikrad, U. Spohr, and R.U. Lemieux. Can. J. Chem. **68**, 1116 (1990).
28. Y. Bourne, P. Rouge, and C. Cambillau. J. Biol. Chem. **265**, 18161 (1990).
29. R. Loris, P.P.G. Stas, and L. Wyns. J. Biol. Chem. **269**, 26722 (1994).
30. R. Ravishankar, K. Suguna, A. Surolia, and M. Vijayan. Acta Crystallog. Sect. D, **55**, 1375 (1999).
31. M. Vijayan and N. Chandra. Curr Opin. Struct. Biol. **9**, 707 (1999).
32. J. Habash, J. Raftery, R. Nuttall, H.J. Price, C. Wilkinson, A.J. Kalb, and J.R. Helliwell. Acta Crystallog. Sect. D, **56**, 541 (2000).
33. R.U. Lemieux. Acc. Chem. Res. **29**, 373 (1996).
34. M. Dejter-Juszynski and H.M. Flowers. Carbohydr. Res. **41**, 308 (1975).
35. L. Laemmli. Nature (London), **227**, 680 (1970).
36. O.N. Jensen, M. Wilm, A. Shevchenko, and M. Mann. *In* 2-D proteome analysis protocols. *Edited by* A.J. Link. Humana Press, Totowa, NJ. 1999. pp. 513–530.
37. M. Vandonselaar and L.T.J. Delbaere. J. Mol. Biol. **243**, 345 (1994).
38. B.W. Matthews. J. Mol. Biol. **33**, 491 (1968).
39. W.C. Phillips, M. Stanton, A. Stewart, H. Qian, C. Ingersoll, and R.M. Sweet. J. Appl. Crystallog. **33**, 243 (2000).
40. R.M. Sweet and J.M. Skinner. *In* Proceedings from the macromolecular crystallography computing school. *Edited by* P.E. Bourne and K. Watenpaugh. Western Washington University, WA, U.S.A. August 17–22, 1996.
41. Z. Otwinowski and W. Minor. Methods Enzymol. **276**, 307 (1997).
42. CCP4. The SERC (U.K.) collaborative computing project No. 4: A suite of programs for protein crystallography. Acta Crystallog. Sect. D, **50**, 760 (1994).
43. J. Navaza. AMoRe: an automated package for molecular replacement. Acta Crystallog. Sect. A, **50**, 157 (1994).
44. A.T. Brünger, J. Kuriyan, and M. Karplus. Science (Washington, D.C.), **235**, 458 (1987).
45. A.T. Brünger. X-PLOR. Version 3.1. A system for X-ray crystallography and NMR. Yale University Press, New Haven and London. 1993.
46. A. Roussel and C. Cambillau. TURBO-FRODO. Biographics, Marseilles, France. 1992.
47. R.U. Lemieux, K. Bock, L.T.J. Delbaere, S. Koto, and V.S. Rao. Can. J. Chem. **58**, 631 (1980).
48. R.J. Read. Acta Crystallog. Sect. A, **42**, 140 (1986).
49. R.J. Read. Acta Crystallog. Sect. A, **46**, 900 (1990).
50. A.T. Brünger. Nature (London), **355**, 472 (1992).
51. A.T. Brünger. Acta Crystallog. Sect. D, **49**, 24 (1993).
52. R.A. Engh and R. Huber. Acta Crystallog. Sect. A, **47**, 392 (1991).
53. S.V. Evans. J. Mol. Graph. **11**, 134 (1993).

© 2002 NRC Canada

^{1}H NMR studies on the solution conformation of contulakin-G and analogues

Lill Kindahl, Corine Sandström, A. Grey Craig, Thomas Norberg, and Lennart Kenne

Abstract: The conformation of contulakin-G, a bioactive 16 amino acid *O*-linked glycopeptide (ZSEEGGSNAT*KKPYIL) with the disaccharide β-D-Gal(1→3)α-D-GalNAc attached to the threonine residue in position 10, has been investigated by ^{1}H NMR spectroscopy. The ^{1}H NMR data for the non-glycosylated peptide and for two glycopeptide analogues, one with the monosaccharide α-D-GalNAc at Thr^{10} and one with the disaccharide β-D-Gal(1→3)α-D-GalNAc at Ser^7, all of lower bioactivity than contulakin-G, have also been collected. The chemical shifts, NOEs, temperature coefficients of amide protons, and $^3J_{NH,\alpha H}$-values suggest that all four compounds exist mainly in random coil conformations. Some transient populations of folded conformations are also present in the glycopeptides and turns, probably induced by the sugars, are present in the peptide chain around the site of glycosylation. In the two peptides *O*-glycosylated at Thr^{10}, the rotation of α-D-GalNAc around the linkage between the sugar and the peptide is restricted. There is evidence for a hydrogen bond between the amide proton of α-D-GalNAc and the peptide chain that could contribute to this torsional rigidity. An intramolecular hydrogen bond between the carbohydrate and the peptide chain does not exist in the peptide *O*-glycosylated at the Ser^7 residue.

Key words: conformation, contulakin-G, NMR, *O*-linked glycopeptide.

Résumé : Faisant appel à la RMN du ^{1}H, on a étudié la conformation de la contulakine-G, un glycopeptide (ZSEEGGSNAT*KKPYIL) bioactif comportant seize acides aminés *O*-liés au disaccharide β-D-Gal(1→3)α-D-GalNAc attaché à un résidu de thréonine en position 10. On a aussi recueille les données de RMN du ^{1}H pour le peptide non-glycosylé et pour deux glycopeptides analogues, l'un comportant le monosaccharide α-D-GalNAc au niveau Thr^{10} et l'autre comportant le disaccharide β-D-Gal(1→3)α-D-GalNAc au niveau Ser^7 dont la bioactivité est toujours inférieure à celle de la contulakine-G. Les déplacements chimiques, les effets Overhauser nucléaires, les coefficients de température des protons de l'amide et les valeurs de $^3J_{NH,\alpha H}$ suggèrent que les quatre composés existent principalement dans des conformations en spirales aléatoires. Dans les glycoprotéines, il existe aussi des populations transitoires de conformations repliées et, dans la chaîne peptidique autour du site de glycosylation, il existe aussi des inversions qui sont probablement induites par les sucres. Dans les deux peptides *O*-glycosylés au niveau Thr^{10}, la rotation du α-D-GalNAc autour de la liaison entre le sucre et le peptide est restreinte. Il y a des indications à l'effet qu'une liaison hydrogène entre le proton de l'amide du α-D-GalNAc et la chaîne peptidique pourrait contribuer à cette rigidité conformationnelle. Il n'existe pas de liaison hydrogène intramoléculaire entre l'hydrate de carbone et la chaîne peptidique du peptide *O*-glycosylé au niveau du résidu Ser^7.

Mots clés : conformation, contulakine-G, RMN, glycopeptide *O*-lié.

[Traduit par la Rédaction]

Introduction

Contulakin-G is a *Conus* venom peptide initially isolated and purified from the marine snail *Conus geographus* based on its ability to induce sluggishness in mice. Contulakin-G was found (1) to be a 16 amino acid *O*-linked glycopeptide with the sequence ZSEEGGSNAT*KKPYIL, where the *N*-terminus was blocked with a pyroglutamic acid residue (Z) and the disaccharide β-D-Gal(1→3)α-D-GalNAc(1→ was attached to the threonine residue in position 10 (see Scheme 1).

There is significant sequence identity between the carboxy-terminus of contulakin-G and members of the neurotensin family of neurotransmitters. Although the binding affinity of contulakin-G for cloned neurotensin receptors in vitro proved to be significantly lower than neurotensin, contulakin-G was shown to be a neurotensin receptor agonist at physiologically relevant concentrations (1). Recently, contulakin-G was shown to be an extremely potent broad spectrum analgesic in a number of models of acute pain when administered intrathecally. When compared with the non-glycosylated contulakin-G and with neurotensin, which is known to be an analgesic, contulakin-G was two orders of

Received 14 November 2001. Published on the NRC Research Press Web site at http://canjchem.nrc.ca on 17 August 2002.

Dedicated to the memory of Professor Raymond U. Lemieux.

L. Kindahl, C. Sandström,[1] T. Norberg, and L. Kenne. Department of Chemistry, Swedish University of Agricultural Sciences, P.O. Box 7015, SE-750 07 Uppsala, Sweden.
A.G. Craig. The Clayton Foundation Laboratories for Peptide Biology, The Salk Institute, La Jolla, CA 92037.

[1]Corresponding author (e-mail: corine.sandstrom@kemi.slu.se).

 DOI: 10.1139/V02-115 © 2002 NRC Canada

Scheme 1. Structure of contulakin-G (**2**) and the non-glycosylated (**1**) and glycosylated (**3** and **4**) analogues.

pGlu[1]-Ser-Glu-Glu-Gly[5]-Gly-Ser-Asn-Ala-Thr[10]-Lys-Lys-Pro-Tyr-Ile[15]-Leu-OH (**1**)

pGlu[1]-Ser-Glu-Glu-Gly[5]-Gly-Ser-Asn-Ala-Thr[10]-Lys-Lys-Pro-Tyr-Ile[15]-Leu-OH (**2**)

β-D-Gal*p*-(1→3)-α-D-Gal*p*NAc-(1

pGlu[1]-Ser-Glu-Glu-Gly[5]-Gly-Ser-Asn-Ala-Thr[10]-Lys-Lys-Pro-Tyr-Ile[15]-Leu-OH (**3**)

α-D-Gal*p*NAc-(1

pGlu[1]-Ser-Glu-Glu-Gly[5]-Gly-Ser[7]-Asn-Ala-Thr[10]-Lys-Lys-Pro-Tyr-Ile[15]-Leu-OH (**4**)

β-D-Gal*p*-(1→3)-α-D-Gal*p*NAc-(1

pGlu = pyroglutamic acid:

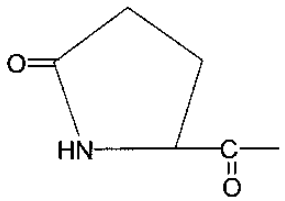

magnitude more potent in vivo (2). Furthermore, the behavioural toxicity of contulakin-G appears to be much lower than neurotensin, giving contulakin-G a considerably more favourable therapeutic index than neurotensin. In recognition of these properties, contulakin-G has entered preclinical trials for short-term management of post-operative pain (3).

The mechanism by which the sugar residues affect the biological activity is not yet understood but several possibilities exist to explain the significantly increased potency of glycosylated contulakin-G. It might be due to an alternative mode of action, or to a modulation of the kinetics of the interaction between ligand and receptor. It might also be due to an enhanced supply of the substance to the site of action due to inhibition of proteolytic degradation by the glycan. The enhanced supply can also be a consequence of more desirable pharmacokinetic profile and enhanced uptake through the blood brain barrier (4). Also, glycosylation may alter the conformation of the peptide, or the binding to the receptor in a way which is favourable for activity. Previous NMR studies on *O*-linked glycopeptides have suggested that one consequence of *O*-glycosylation in small peptides is to limit the number of conformations available to an otherwise flexible peptide (5–12). In most cases, the peptide backbone tends to bend away from the sugar residue. In addition, evidence for a hydrogen bond between the sugar and the glycosylated threonine residue that helps in forming a glyco-turn has been obtained (13–15). However, a recent study has also shown that glycosylation is not always turn-inducing, but can in some cases result in local straightening of the peptide backbone (16). Thus, the effect of glycosylation on conformation appears to depend on the nature of the sugar, and on the amino acid residues at and around the glycosylation site.

In this paper, as a first step towards understanding the effect of glycosylation on the biological activity of contulakin-G, we have carried out an NMR study on the solution conformation of contulakin-G (**2**), its unglycosylated counterpart (**1**), and two analogues, one with the monosaccharide α-D-GalNAc at Thr[10] (**3**), and one with the disaccharide β-D-Gal(1→3)α-D-GalNAc at Ser[7] (**4**) (Scheme 1). The potency of **1**–**4** has been determined using the tail flick assay of antinociception (17). The data showed that shifting the position of the glycosylation from residue 10 to 7, and reducing the size of the glycan decrease the activity compared with the native contulakin-G (17). In relative terms, **2** is the most potent, **3** is more potent than **4**, which has approximately the same potency as **1** (17). Thus, one of the primary goals of this work was to compare the conformations of glycosylated and non-glycosylated versions of contulakin-G to investigate if differences in conformation could be correlated to the observed differences in biological activity.

Experimental

Sample preparation

The synthesis of the non-glycosylated form of contulakin-G (**1**) and of contulakin-G (**2**) has been previously described

© 2002 NRC Canada

(1). The synthesis of **3** and **4** was performed in a similar fashion as described in (1). The full experimental details will be reported elsewhere.

The samples were prepared by dissolving ~1 mg of (glyco)peptide in 50 μL 99.98% D_2O, H_2O–D_2O (95:5), or a buffer containing H_2O–D_2O (95:5), 100 mM sodium chloride, 13.5 mM sodium acetate, pH 5.6. The solutions were then transferred into 1.7- or 2.1-mm NMR capillaries. NMR spectra were also recorded in trifluoroethanol (TFE)–H_2O (1:1).

NMR spectroscopy

All NMR experiments were performed on a Bruker DRX-600 spectrometer equipped with a 2.5-mm microprobe. The NMR spectra unless specified were recorded at 5, 15, or 25°C. The temperature coefficients were calculated for the amide protons in H_2O–D_2O and H_2O–TFE solutions using ^{1}H NMR chemical shift data measured by variation of the temperature from 5 to 45°C in steps of 5°C. The two-dimensional NMR spectra were recorded in the phase-sensitive mode using the TPPI method (18). For experiments in D_2O, the residual HDO peak was suppressed by pre-irradiation at low decoupler power. For experiments in 95% H_2O – 5% D_2O, the WATERGATE pulse sequence (19) was used for water suppression. The DQF-COSY and TOCSY spectra were typically acquired with 4K data points in t_2 and 512 points in t_1 and a repetition delay of 1.5 s. In TOCSY, mixing times of 60 and 100 ms were used. NOESY and ROESY spectra were recorded with mixing times (τ_m) from 100 to 600 ms for NOESY and 100 to 300 ms for ROESY. 256 Spectra of 4K data points were acquired and a repetition delay of 2.5 s was used. The ^{1}H NMR chemical shifts were measured relative to the resonance of the methyl signal of acetone (δ 2.225) added as an internal reference.

Results and discussion

Assignment of ^{1}H NMR resonances

The assignment of the proton resonances of **1**–**4** was done from a combination of two-dimensional DQF-COSY, TOCSY, and NOESY experiments, and the chemical shifts are given in Tables 1 and 2.

^{1}H NMR chemical shifts

The ^{1}H NMR chemical shifts, measured for the amino acid residues in the glycosylated peptides **2**–**4**, are similar to those in the corresponding non-glycosylated peptide **1**, with the exception of signals from NH and αH protons of the residues at and around the glycosylation sites (Table 1, Fig. 1). Thus, the NH and αH signals of Thr^{10} in **2** and **3** show large downfield shifts upon glycosylation at Thr^{10}. Also, the αH signal of the preceding residue, Ala^9, shows a large downfield shift, whereas the αH signal of the second residue from the glycosylation site (αH Lys^{12}) shows a large upfield shift. In a similar way, the NH and αH signals of Ser^7 in **4** are deshielded upon glycosylation. Small effects are also seen on the chemical shifts of Asn^8 and Ala^9 signals. Apart from the effect of glycosylation, the ^{1}H NMR chemical shifts for the signals of αH from the amino acids in the peptide **1** and the glycosylated peptides **2**–**4** are similar to those reported for peptides with random coil conformations (20).

NOEs in the peptide chain

NOEs (Fig. 2) observed in NOESY and ROESY spectra recorded at several mixing times identified the presence of some transient secondary structures. Sequential $d_{NN}(i,i+1)$ NOEs in flexible peptides are representative of folded conformations in terms of turn or helical structures with d_{NN} = 2.3–3.4 Å (21–23). In an extended conformation, the average d_{NN} is 4.5 Å, while the $d_{\alpha N}(i,i+1)$ is ~ 2.2 Å (21–23). In the non-glycosylated peptide **1**, sequential $d_{\alpha N}(i,i+1)$ NOEs, characteristic of extended backbone conformations were observed along the whole peptide chain. In addition, a $d_{NN}(i,i+1)$ NOE was also observed between Asn^8 and Ala^9 and between Ile^{15} and Leu^{16} (Fig. 3*a*).

In contulakin-G, **2**, the sequential $d_{\alpha N}(i,i+1)$ NOE pattern characteristic of extended conformations was also observed along the whole peptide chain. Additional sequential $d_{NN}(i,i + 1)$ NOEs were observed for Ser^7/Asn^8, Asn^8/Ala^9 and Ala^9/Thr^{10} (Fig. 3*b*). A $d_{NN}(i,i + 1)$ NOE was also found between Tyr^{14} and Ile^{15} and between Ile^{15} and Leu^{16}. These $d_{NN}(i,i + 1)$ NOEs are indicative of local structures in terms of folded conformations, but the sites of local structure most likely occur in a subpopulation of the predominantly disordered solution ensemble of conformers. The existence of the proline residue at position 13 led us to probe for β-turn structures. The NOEs that are diagnostic of turns (where Pro = i + 1) include $d_{NN}(i + 2,i + 3)$, $d_{\alpha N}(i,i + 2)$, and either $d_{\alpha N}(i + 1,i + 2)$ for type II or $d_{\delta N}(i + 1,i + 2)$ for type I turns. We observed cross-peaks at $d_{NN}(Tyr^{14}, Ile^{15})$ and $d_{\alpha N}(Pro^{13}, Tyr^{14})$, but no cross-peaks at $d_{\alpha N}(Lys^{12}, Tyr^{14})$ or $d_{\delta N}(Lys^{12}, Tyr^{14})$ were found.

In the glycopeptide monoglycosylated at Thr^{10} (**3**) the sequential $d_{\alpha N}(i,i + 1)$ NOE pattern characteristic of extended conformations was also observed along the whole peptide chain. Sequential $d_{NN}(i,i + 1)$ NOEs were found from Gly^5 to Thr^{10}. Isolated $d_{NN}(i,i + 1)$ NOEs were also found between Ser^2 and Glu^3 and between Tyr^{14} and Ile^{15}. In **4**, where the disaccharide is attached at Ser^7, sequential $d_{\alpha N}(i,i + 1)$ NOEs were found along the whole peptide chain, with the exception for the $d_{\alpha N}(i,i + 1)$ NOE between Lys^{11} and Lys^{12}. $d_{NN}(i,i + 1)$ NOEs were observed for Gly^5/Gly^6, Ser^7/Asn^8, Asn^8/Ala^9, Thr^{10}/Lys^{11}, and Tyr^{14}/Ile^{15}. The presence of local structures in **1**–**4** was supported by the observation of weak $d_{\alpha N}(i,i + 2)$ NOEs (Fig 2).

Sugar-peptide NOEs

Five NOEs between the Thr^{10} and Lys^{11} residues and the directly attached α-D-GalNAc residue were observed for **2** and **3**: NH(Thr^{10})-NH(α-D-GalNAc), NH(Lys^{11})-H-1(α-D-GalNAc), NH(Thr^{10})-H-3(α-D-GalNAc), H-β(Thr^{10})-H-1(α-D-GalNAc), H-γ(Thr^{10})-H-1(α-D-GalNAc) (Fig. 4). The fact that the NOEs from the peptide are to only one side of the sugar indicates a relatively persistent interaction between the peptide and the sugar, and a restricted rotation of the sugar around the sugar–peptide linkage. This restricted rotation is also supported by the small $^3J_{\alpha,\beta}$-value (1.5 Hz in **2** and 2 Hz in **3**) measured for the Thr^{10} residue. Such a small value indicates a preference for an orthogonal orientation between the Thr^{10} α- and β-protons (14). If the α-D-GalNAc residue was undergoing motion relative to the peptide backbone through rotation around the C(α)—C(β) bond of Thr^{10}, a value of ~5 Hz, as measured in the non-glycosylated peptide (**1**) would be expected. In **4**, three NOEs were found

© 2002 NRC Canada

Table 1. ^{1}H NMR chemical shifts (ppm) of **1**–**4** at 25°C in H_2O–D_2O (95:5), pH 5.6.

Residue	Compd	NH	αH	βH	Others
pGlu[1]	**1**	7.94	4.40	2.10	γ-CH_2 2.43, 2.54
	2	7.90	4.41	1.99	γ-CH_2 2.41, 2.56
	3		4.42	2.11	γ-CH_2 2.44, 2.56
	4		4.42	2.11	γ-CH_2 2.43, 2.55
Ser[2]	**1**	8.46	4.48	3.88	
	2	8.46	4.48	3.89	
	3	8.46	4.49	3.89	
	4	8.47	4.49	3.89	
Glu[3]	**1**	8.56	4.43	1.98	γ-CH_2 2.47, 2.14
	2	8.58	4.43	1.99	γ-CH_2 2.47, 2.15
	3	8.61	4.41	1.99	γ-CH_2 2.14, 2.44
	4	8.62	4.41	1.97	γ-CH_2 2.14, 2.43
Glu[4]	**1**	8.43	4.39	1.98	γ-CH_2 2.47, 2.14
	2	8.44	4.38	1.99	γ-CH_2 2.47, 2.15
	3	8.45	4.37	1.98	γ-CH_2 2.14, 2.43
	4	8.45	4.38	1.97	γ-CH_2 2.14, 2.44
Gly[5]	**1**	8.47	3.99		
	2	8.47	3.99		
	3	8.46	3.99		
	4	8.47	3.99		
Gly[6]	**1**	8.29	4.01		
	2	8.29	4.02		
	3	8.29	4.02		
	4	8.25	4.04		
Ser[7]	**1**	8.33	4.46	3.88	
	2	8.33	4.46	3.89	
	3	8.34	4.44	3.92, 3.86	
	4	8.49	4.65	4.00, 3.79	
Asn[8]	**1**	8.52	4.72	2.85, 2.77	γ-NH_2 6.93, 7.60
	2	8.48	4.75	2.85, 2.77	γ-NH_2 6.91, 7.57
	3	8.48	4.73	2.86, 2.78	γ-NH_2 6.92, 7.59
	4	8.63	4.72	2.86, 2.76	γ-NH_2 6.94, 7.59
Ala[9]	**1**	8.18	4.29	1.40	
	2	8.10	4.49	1.41	
	3	8.09	4.45	1.41	
	4	8.35	4.39	1.42	
Thr[10]	**1**	8.06	4.29	4.20	γ-CH_3 1.20
	2	8.55	4.52	4.33	γ-CH_3 1.30
	3	8.29	4.53	4.31	γ-CH_3 1.28
	4	8.10	4.29	4.19	γ-CH_3 1.21
Lys[11]	**1**	8.23	4.33	1.80	γ-CH_2 1.39, δ-CH_2 1.65, ε-CH_2 2.97
	2	8.45	4.38	1.81	γ-CH_2 1.47, δ-CH_2 1.47, ε-CH_2 2.99
	3	8.35	4.36	1.69	γ-CH_2 1.43, δ-CH_2 1.68, ε-CH_2 3.00
	4	8.30	4.34	1.69	γ-CH_2 1.43 δ-CH_2 1.68, ε-CH_2 3.01
Lys[12]	**1**	8.32	4.57	1.76	γ-CH_2 1.43, δ-CH_2 1.67, ε-CH_2 3.00
	2	8.35	4.45	1.78	γ-CH_2 1.48, δ-CH_2 1.74, ε-CH_2 3.03
	3	8.37	4.46	1.71	γ-CH_2 1.43, δ-CH_2 1.72, ε-CH_2 3.03
	4	8.34	4.56	1.69	γ-CH_2 1.43 δ-CH_2 1.68, ε-CH_2 3.01
Pro[13]	**1**		4.38	1.81, 2.24	γ-CH_2 2.00, δ-CH_2 3.79, 3.61
	2		4.39	1.84, 2.25	γ-CH_2 2.01, δ-CH_2 3.84, 3.62
	3		4.39	1.82, 2.25	γ-CH_2 2.01, δ-CH_2 3.83, 3.62
	4		4.39	1.79, 2.22	γ-CH_2 1.99, δ-CH_2 3.79, 3.62
Tyr[14]	**1**	8.12	4.58	3.00	^{2,6}H 7.12, 6.83
	2	8.17	4.57	3.00	^{2,6}H 7.13, 6.84
	3	8.13	4.58	3.00	^{2,6}H 6.84, 7.13
	4	8.08	4.59	3.01	^{2,6}H 6.84, 7.12

© 2002 NRC Canada

Table 1 (*concluded*).

Residue	Compd	NH	αH	βH	Others
Ile[15]	**1**	7.93	4.14	1.77	γ-CH_2 1.39, 1.10, γ-CH_3 0.88, δ-CH_3 0.83
	2	7.93	4.14	1.78	γ-CH_2 1.40, 1.11, γ-CH_3 0.88, δ-CH_3 0.83
	3	7.92	4.13	1.79	γ-CH_2 1.40, 1.12, γ-CH_3 0.93, δ-CH_3 0.83
	4	7.93	4.14	1.80	γ-CH_2 1.40, 1.11, γ-CH_3 0.88, δ-CH_3 0.83
Leu[16]	**1**	8.24	4.30	1.65	γ-CH_3 1.64, δ-CH_3 0.94, 0.88
	2	8.13	4.26	1.62	γ-CH_3 1.63, δ-CH_3 0.94, 0.89
	3	7.98	4.22	1.60	γ-CH_3 1.60, δ-CH_3 0.94, 0.88
	4	7.97	4.22	1.61	γ-CH_3 1.61, δ-CH_3 0.94, 0.89

Table 2. ^{1}H NMR chemical shifts (ppm) for the sugar signals in **2**–**4** at 25°C in H_2O–D_2O (95:5), pH 5.6.

	Compd	H-1	H-2	H-3	H-4	H-5	H-6	NH	NAc
β-D-Gal*p*	**2**	4.45	3.54	3.60	3.91	3.61	3.73, 3.70		
	4	4.50	3.52	3.63	3.92	n.d.	n.d.		
α-D-Gal*p*NAc	**2**	4.88	4.23	4.03	4.21	4.05	~3.6, ~3.7	7.66	2.02
	3	4.88	4.01	3.91	3.90	4.02	3.76	7.63	2.03
	4	4.91	4.36	3.95	4.23	4.03	3.75	8.19	2.04

Note: n.d., not determined due to spectral overlap.

Table 3. $^3J_{NH,\alpha H}$ vicinal coupling constants (Hz) and NH temperature coefficients (dδ/dT, ppb/°C) for the NH protons in **1** and **2** in H_2O–D_2O (95:5), pH 5.6.

Residue	$^3J_{NH,\alpha H}$				dδ/dT			
	1	**2**	**3**	**4**	**1**	**2**	**3**	**4**
pGlu[1]	<1	<1	—	—	7.5	13.4	—	—
Ser[2]	6.6	6.2	6.6	6.7	[a]	[a]	9.7	9.5
Glu[3]	7.0	7.0	7.0	7.1	9.3	15.2	9.4	8.1
Glu[4]	7.0	7.0	7.4	6.6	8.7	9.1	9.0	9.2
Gly[5]	11.4[b]	11.5[b]	11.7[b]	11.9[b]	8.2	7.2	7.6	8.1
Gly[6]	11.5[b]	11.7[b]	11.7[b]	11.7[b]	7.5	6.9	9.9	8.9
Ser[7]	6.6	6.8	6.2	6.4	11.0	7.8	9.0	8.8
Asn[8]	7.3	7.5	7.0	6.2	7.7	7.9	7.8	9.2
Ala[9]	5.9	5.9	5.7	6.0	6.0	6.7	6.5	8.6
Thr[10]	7.5	8.6	9.0	7.5	8.6	8.4	8.5	9.3
Lys[11]	7.3	7.2	7.5	6.8	10.1	10.8	9.8	10.6
Lys[12]	7.0	6.2	6.1	6.0	10.2	9.9	10.2	11.6
Pro[13]	—	—	—	—	—	—	—	—
Tyr[14]	7.1	7.3	7.1	7.5	13.2	13	13.9	13.6
Ile[15]	8.6	8.8	8.4	8.8	9.9	8.3	9.5	9.6
Leu[16]	7.3	7.1	7.3	7.3	9.1	8.8	9.2	9.2
NHGal*p*NAc	—	10.1	9.5	9.7	—	5.8	5.7	11.1

[a]Not calculated because of spectral overlap; the chemical shifts could not be measured accurately in the all temperature ranges.
[b]$^3J_{NH,\alpha H} + {}^3J_{NH,\alpha' H}$.

between the peptide chain and the sugars, namely NH(Ser[7])-NH(α-D-GalNAc), H-β(Ser[7])-H1(α-D-GalNAc), and Hβ′(Ser[7])-H1(α-D-GalNAc). The αH signal of Ser[7] appears in the NMR spectrum as a triplet of 9.9 Hz ($^3J_{\alpha H,\beta H} + {}^3J_{\alpha H,\beta' H}$), as in the non-glycosylated peptide (**1**) suggesting a free rotation of the sugar around the sugar–peptide linkage.

$^3J_{NH,\alpha H}$ Values

The $^3J_{NH,\alpha H}$ values for each amino acid in the peptide chain are similar in the non-glycosylated **1** and glycosylated peptides **2**–**4**. The $^3J_{NH,\alpha H}$ values are in the range 5.7–9.0 Hz in **1**–**4**, (Table 3) suggesting random coil or extended conformations. It is sometimes difficult to distinguish between random and extended structures since they can give similar chemical shifts and J values. Extended conformations are identified by both sequential $d_{\alpha N}(i,i+1)$ NOEs and backbone $^3J_{NH,\alpha H}$ values > 8 Hz on a stretch of sequential residues. Thus, the existence of sequential $d_{\alpha N}(i,i+1)$ NOEs along the peptide chain would indicate extended conformations. However, most $^3J_{NH,\alpha H}$ values are lower than 8 Hz. An increase in the $^3J_{NH,\alpha H}$ value from 7.5 to 8.6 Hz can be observed for Thr[10] in **2** and **3** compared to **1** and **4**. This

© 2002 NRC Canada

Fig. 1. Chemical shift differences (Δδ, ppm) between the glycosylated **2**–**4** and non-glycosylated **1** peptides shown for (*a*) amide protons and; (*b*) α-protons.

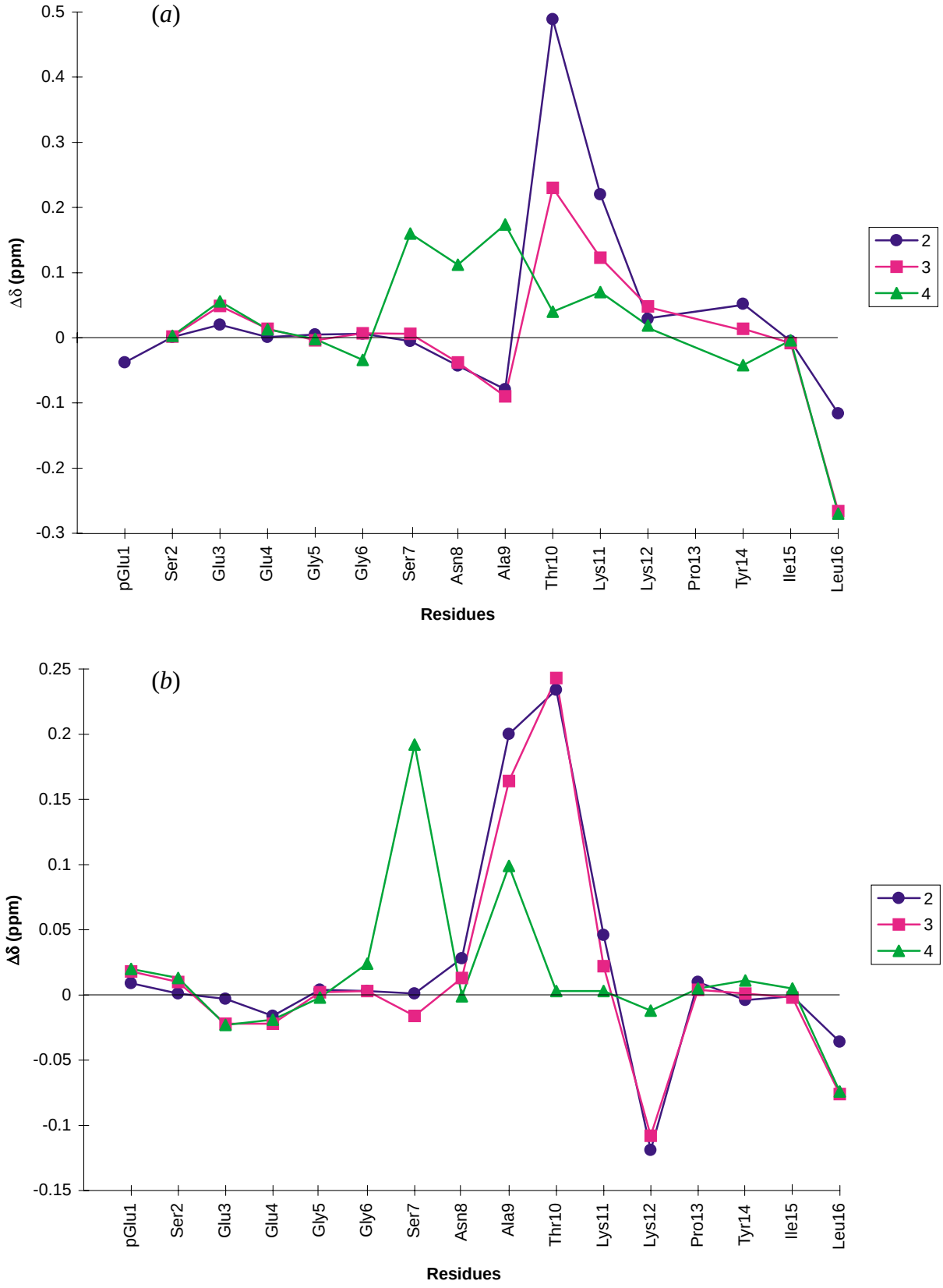

© 2002 NRC Canada

Fig. 2. Intra- and inter-residue NOEs involving the backbone NH protons in **1**–**4**. A line indicates the presence of a NOE; no distinction is made between strong, medium, and weak NOEs. (*a*) **1**, NOESY, 25°C, mixing time 300 ms; (*b*) **2**, NOESY, 25°C, mixing time 300 ms; (*c*) **3**, NOESY, 5°C, mixing time 300 ms; (*d*) **4**, NOESY, 5°C, mixing time 300 ms.

larger value of $^3J_{NH,\alpha H}$ in **2** and **3** is in agreement with the existence of some populations of ordered secondary structures (18). The $^3J_{NH,H2}$ of 10.1 Hz measured for GalNAc demonstrates a *trans* orientation of NH and C(2)H.

Temperature coefficients for the NH protons

The extent to which an amide proton is exposed to the solvent is reflected in the dependence of its chemical shift on temperature (22, 24). Thus, signals from exposed amides shift more than those from an ordered structure. The temperature dependence of NH chemical shifts is a useful way to detect the presence of hydrogen bonds. Signals from NH involved in hydrogen bonds show less temperature dependence ($d\delta/dT < -6$ ppb/°C) than those from NH protons exposed to the solvent. The temperature coefficients ($d\delta/dT$) for the NH proton signals from **1**–**4** were measured in H_2O–D_2O (95:5) solution from a series of one-dimensional spectra recorded between 5° and 45°C (Table 3). The signals from NH protons in the peptide chain show $d\delta/dT$ above –6.0 ppb/°C confirming than the peptide chain in **1**–**4** adopts mainly extended conformations. Of particular interest is the low value of the temperature coefficient of NH of

© 2002 NRC Canada

Fig. 3. The NH–NH region of the 2D NOESY spectra of the (glyco)peptides **1**–**4** in H_2O–D_2O (95:5) recorded at 600 MHz. (*a*) **1**, ROESY, 25°C, mixing time 200 ms; (*b*) **2**, NOESY, 25°C, mixing time 300 ms; (*c*) **3**, NOESY, 5°C, mixing time 300 ms; (*d*) **4**, NOESY, 5°C, mixing time 300 ms.

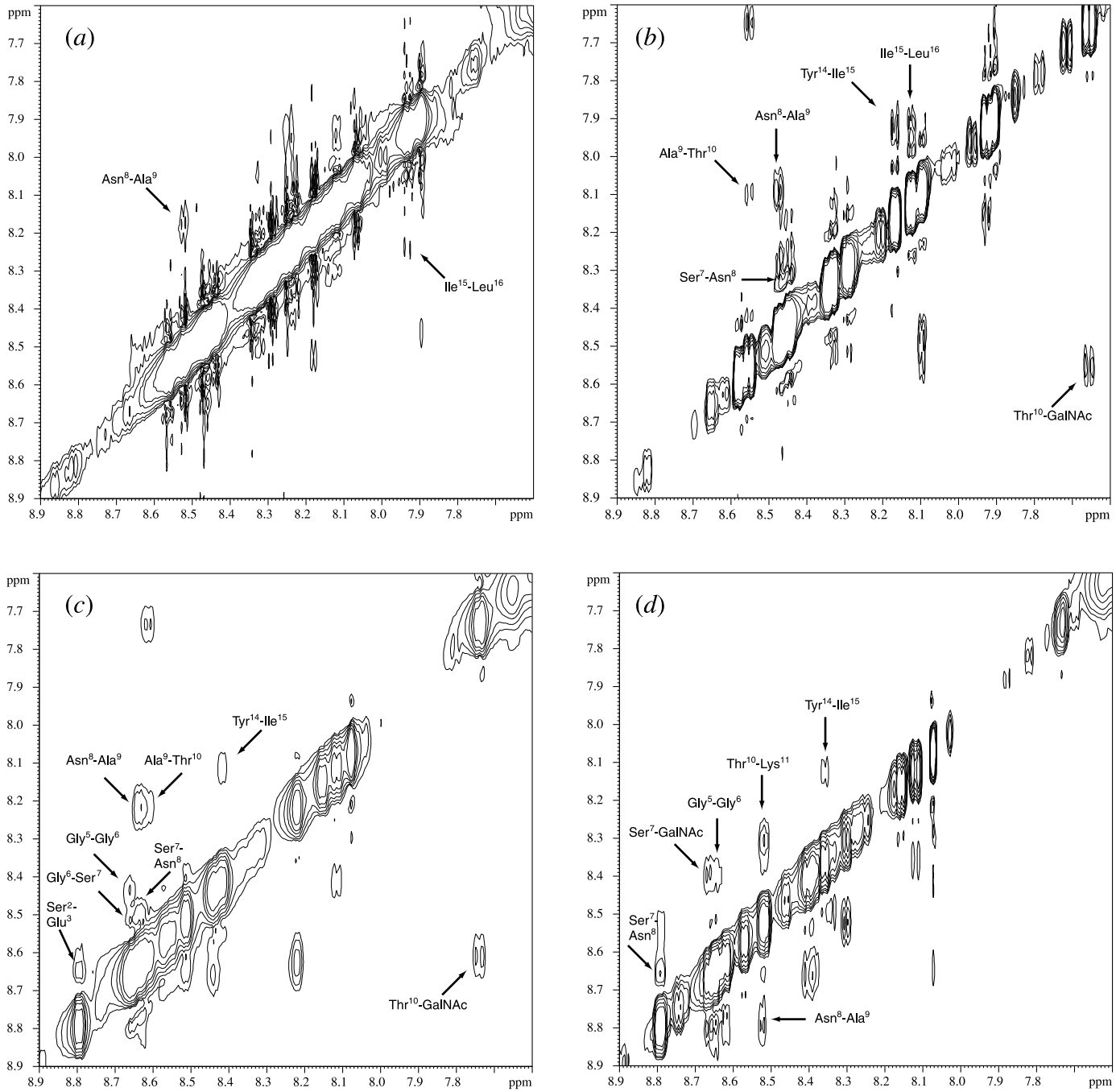

α-D-GalNAc in **2** and **3** (–5.8 and –5.7 ppb/°C, respectively, in water solution). These values indicate that the torsional rigidity between the sugar and the peptide, suggested by the NOEs and by the value of the $^3J_{\alpha,\beta}$ (Thr^{10}) coupling constant (vide infra), may be enforced by a hydrogen bond interaction between NH of α-D-GalNAc and Thr^{10}. In contrast, the large value for the temperature coefficient of NH of α-D-GalNAc in **4** (–11.1 ppb/°C) indicates that this proton is not protected from exchange with the solvent through hydrogen bond formation.

Studies in TFE–H_2O

Since a large number of NMR studies on peptides (16, 25) have shown that the use of TFE as a solvent can induce helix formation in some peptides, NMR spectra were also recorded in 50% TFE – 50% H_2O. When the peptides **1**–**4** were ana-

© 2002 NRC Canada

Fig. 4. Schematic representation of interresidual NOEs observed at the junction between the peptide and the saccharides in **2**–**4**.

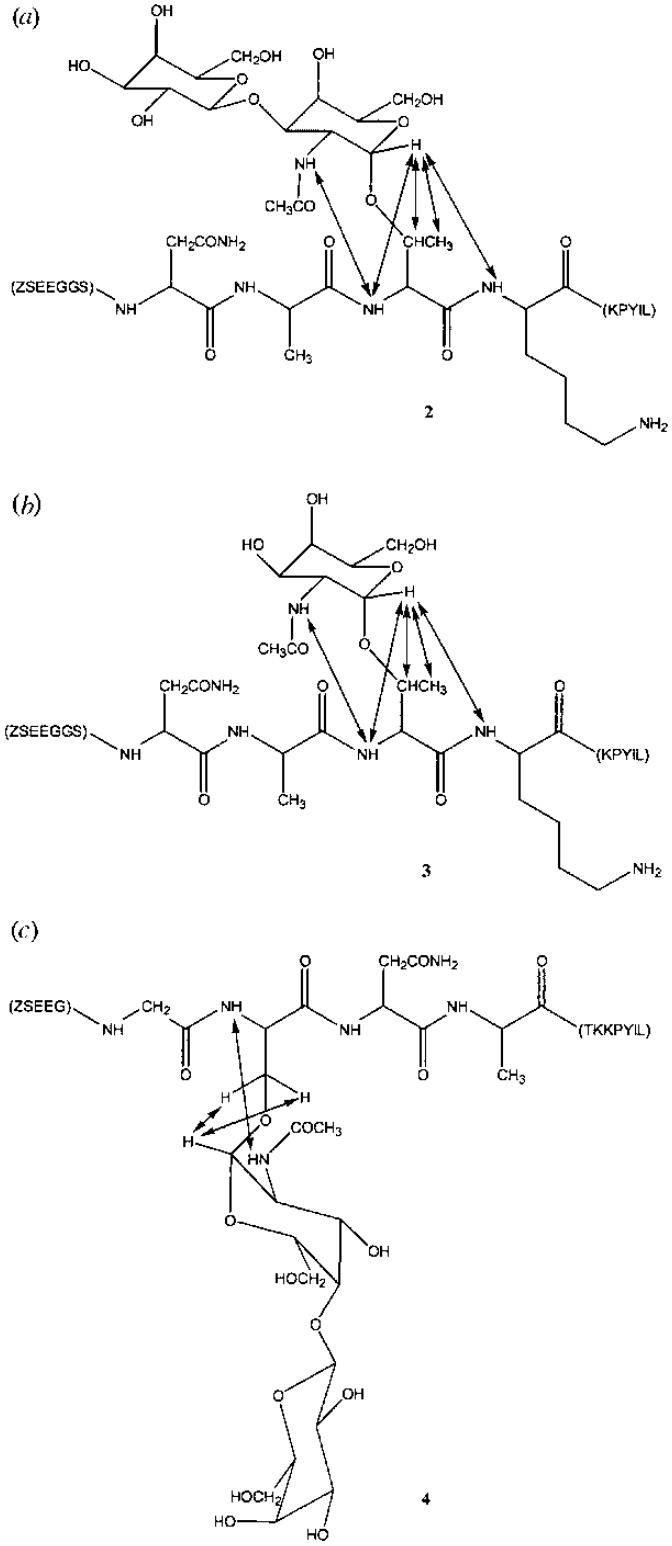

lysed in TFE–H_2O solutions, similar ^1H NMR chemical shifts of the amino acids in the glycosylated and non-glycosylated peptides were observed, except for the residues at the junction site. The shifts due to glycosylation were, however, not as large as in water. The $^3J_{NH,\alpha H}$ values were very similar to those measured in water. The temperature coefficients ($d\delta/dT$) were slightly smaller than those obtained for the compounds in water. Most of the NH protons in the peptide chain had $d\delta/dT$ values above –6.0 ppb/°C, with the exception of Ala^9 in **1**, **2**, and **3**, and of Thr^{10} and Ile^{15} in **1** and **2**. As in water, the $d_{\alpha N}(i,i+1)$ NOEs characteristic of extended conformations were observed all along the peptide chains in the glycosylated and non-glycosylated peptides. The $d_{NN}(i,i+1)$ NOEs present in water were also present in TFE–H_2O, but additional $d_{NN}(i,i+1)$ NOEs were also found. The hydrogen bond interaction between Thr^{10} and α-D-GalNAc found for **2** and **3** in water is also present in TFE–H_2O solution.

Conclusion

This NMR study shows that the four analogues mainly exist in random coil conformations. Interestingly, in the glycosylated peptides, some transient populations of folded conformation are also present. In **2** and **3**, which are *O*-glycosylated at the Thr^{10} residue, the rotation of the α-D-GalNAc residue around the bond between the sugar and the peptide is restricted. An intramolecular hydrogen bond between the amide proton of α-D-GalNAc and probably the carbonyl oxygen of the *O*-linked Thr^{10} residue, stabilises the structure. In peptide **4**, *O*-glycosylated at Ser^7, there is no hydrogen bond between the sugar residue and the peptide chain. Since **2** and **3**, which are *O*-glycosylated at the Thr^{10} residue, are more active than the non-glycosylated peptide **1** and the peptide *O*-glycosylated at Ser^7 (**4**), it is possible that the stabilization of conformation by hydrogen bonding to the sugar could be a key factor for the biological activity. It should be noted that in an NMR study of human salivary mucin derived *O*-linked glycopeptides, a hydrogen bond was also found in threonine-glycosylated peptides, but not in serine-glycosylated peptides (15).

The presence of sequential NH–NH NOEs from Ser^7 to Thr^{10} in **2**, from Gly^5 to Thr^{10} in **3**, and from Ser^7 to Ala^9 in **4** indicates that the glycopeptides have a folded structure in these regions. In contulakin-G (**2**), NH–NH NOEs from Tyr^{14} to Leu^{16} suggest that an additional turn is also formed at the *C*-terminal end of the peptide chain. This shows that glycosylation leads not only to local changes in conformations at the junction site, but also induces long distance conformational changes. In **3** and **4**, only the NH–NH Tyr^{14}–Ile^{15} NOE was observed. Since the six *C*-terminal amino acids of contulakin-G are similar to several members of the neurotensin class of peptides, it might be that the terminal turn at the Tyr^{14}–Leu^{16} residues, which exists only in contulakin-G, the most active of the four analogues, and which is induced by glycosylation at Thr^{10} with the disaccharide, is an additional conformational feature important for the biological activity.

Acknowledgements

This work was supported by grants from the Swedish Natural Science Research Council and the National Institute of Health (Grant GM48677).

© 2002 NRC Canada

References

1. A.G. Craig, T. Norberg, D. Griffin, C. Hoeger, M. Akhtar, K. Schmidt, W. Low, J. Dykert, E. Richelson, V. Navarro, J. Mazella, M. Watkins, D. Hillyard, L. Imperial, L.J. Cruz, and B.M. Olivera. J. Biol. Chem. **274**, 13 752 (1999).
2. J.D. Wagstaff, R.T. Layer, A.G. Craig, B.M. Olivera, and R.T. McCabe. *In* Proceedings of the 29th Annual Meeting of the Society for Neuroscience, **25**, 1944 (1999).
3. R.M. Jones and G. Bulaj. Curr. Opin. Drug Discov. Develop. **3**, 141 (2000).
4. R. Polt and M.M. Palian. Drugs of the Future, **26**, 561 (2001).
5. D.H. Live, R.A. Kumar, X. Beebe, and S.J. Danishefsky. Proc. Natl. Acad. Sci. U.S.A. **93**, 12 759 (1996).
6. X.L. Huang, M.C. Smith, J.A. Berzofsky, and J.J. Barchi. FEBS Lett. **393**, 280 (1996).
7. X.L. Huang, J.J. Barchi, E.D.T. Lung, P.P. Roller, P.L. Nara, J. Muschik, and R.R. Garrity. Biochemistry, **36**, 10 846 (1997).
8. S.E. O'Connor and B. Imperiali. Chem. Biol. **5**, 427 (1998).
9. A.H. Andreotti and D. Kahne. J. Am. Chem. Soc. **115**, 3352 (1993).
10. K.W. Rickert and B. Imperiali. Chem. Biol. **2**, 751 (1995).
11. R. Liang, A.H. Andreotti, and D. Kahne. J. Am. Chem. Soc. **117**, 10 395 (1995).
12. L. Kirnarsky, O. Prakash, S.M. Vogen, M. Nomoto, M.A. Hollingsworth, and S. Sherman. Biochemistry, **39**, 12 076 (2001).
13. N.J. Maeji, Y. Inoue, and R. Chujo. Int. J. Peptide Res. **29**, 699 (1987).
14. Y. Mimura, Y.Yamamoto, Y. Inoue, and R. Chujo. Int. J. Biol. Macromol. **14**, 242 (1992).
15. G.A. Naganagowda, T.L. Gururaja, J. Satyanarayana, and M.J. Levine. J. Peptide Res. **54**, 290 (1999).
16. A.M. McManus, L. Otvos, Jr., R. Hoffmann, and D.J. Craik. Biochemistry, **38**, 705 (1999).
17. A.G. Craig et al. Manuscript in preparation.
18. D. Marion and K. Wuthrich. Biochem. Biophys. Res. Commun. **113**, 967 (1983).
19. M. Piotto, V. Saudek, and V. Sklenár. J. Biomol. NMR, **2**, 661 (1992).
20. G. Merutka, H.J. Dyson, and P.E. Wright. J. Biomol. NMR, **5**, 14 (1995).
21. K. Wüthrich. *In* NMR of proteins and nucleic acids. John Wiley & Sons, New York. 1986. pp. 169–171.
22. H.J. Dyson, M. Rance, R.A. Houghten, R.A. Lerner, and P.E. Wright. J. Mol. Biol. **201**, 161 (1988).
23. H.J. Dyson and P.E. Wright. Annu. Rev. Biophys. Chem. **20**, 519 (1991).
24. G.R. Zimmermann, P. Legault, M.E. Selsted, and A. Pardi. Biochemistry, **34**, 13 663 (1995).
25. M. Buck. Q. Rev. Biophys. **31**, 297 (1998).

© 2002 NRC Canada

An effective strategy for structural elucidation of oligosaccharides through NMR spectroscopy combined with peracetylation using doubly ^{13}C-labeled acetyl groups

Brad Bendiak, Tammy T. Fang, and David N.M. Jones

Abstract: The use of NMR spectroscopy for the elucidation of larger carbohydrate structures isolated from natural sources is principally limited by severe overlap of ^{1}H signals, poor sensitivity when experiments involve ^{13}C nuclei, and difficulties in conclusively establishing linkage positions. Peracetylation of oligosaccharides with doubly ^{13}C-labeled acetyl groups provides several major advantages for their structural elucidation when combined with specifically tailored NMR pulse sequences. The 2.5–4.7 Hz *J*-coupling constants between acetyl carbonyl-^{13}C nuclei and protons of the sugar ring at the sites of acetylation enables these sites to be readily assigned. By inference, glycosidic linkage positions on monosaccharides can be unambiguously determined. *This can be used in lieu of permethylation* analysis, yet does not require degradation of oligosaccharides. Spectral dispersion in the directly detected (^{1}H) dimension is increased ~2.6–2.7-fold due to the downfield shifting of sugar-ring protons at the positions of acetylation. Peracetylation also introduces three new frequency dimensions for NMR studies, namely the ^{13}CO, ^{13}C^{Me}, and ^{1}H^{Me} frequencies of the acetyl groups. These frequencies can be correlated to sugar protons, either independently or in combination, in alternative 2-, 3-, or 4-D experiments. The use of Hartmann–Hahn coherence transfer combined with zero-quantum dephasing periods permits purely absorptive in-phase multiplets to be extracted and enables accurate scalar couplings between ring protons to be measured, even in multidimensional experiments. Results are illustrated on a nonasaccharide-alditol derived from *N*-linked glycoproteins and on some smaller structures containing sialic acids and *N*-acetylhexosamines. Methods for small-scale sample acetylation using the superacylation catalyst, 4-dimethylaminopyridine, are described. A brief historical perspective pertinent to the fundamental contributions of Dr. R.U. Lemieux to the field of carbohydrate NMR is also presented.

Key words: NMR, oligosaccharides, peracetylation, doubly ^{13}C-labeled acetyl groups, tailored pulse sequences, heteronuclear Hartmann–Hahn.

Résumé : L'utilisation de la spectroscopie RMN pour l'élucidation des structures de grosses molécules d'hydrates de carbone isolées de sources naturelles est limitée principalement par les importants recouvrements des signaux du ^{1}H, de la faible sensibilité des expériences impliquant le noyau ^{13}C et par les difficultés à établir de façon concluante les positions de liaisons. Le peracétylation des oligosaccharides par des groupes acétyles doublement marqués au ^{13}C apporte de nombreux avantages importants à l'élucidation de leur structure, surtout lorsqu'on combine cette technique à la RMN avec des séquences pulsées sur mesure. La constante de couplage, *J*, de 2,5 à 4,7 Hz entre les noyaux de ^{13}C du groupe carbonyle des acétyles et les protons du cycle du sucre aux points d'acétylation permet d'assigner facilement ces sites. Par déduction, les positions des liaisons glycosidiques sur les monosaccharides peuvent être déterminées facilement. À cette fin, *on peut utiliser cette technique à la place de l'analyse par perméthylation* et elle ne requière pas de dégradation des oligosaccharides. La dispersion spectrale dans la dimension directement détectée (^{1}H) est augmentée par un facteur de 2,6 à 2,7 en raison d'un déplacement vers les bas champs des protons du cycle du sucre aux positions d'acétylation. La peracétylation introduit aussi trois nouvelles dimensions de fréquence pour les études RMN, soit les fréquences ^{13}CO, ^{13}C^{Me} et ^{1}H^{Me} des groupes acétyles. On peut établir des corrélations entre ces fréquences et les protons du sucre, de façon indépendante ou en combinaison, dans des expériences alternatives en 2-D, 3-D ou 4-D. L'utilisation de transfert de cohérence de Hartmann–Hahn, combiné aux périodes de déphasage à quantum zéro, permet d'extraire des multiplets en phase strictement absorbants et de mesurer des couplages scalaires précis

Received 14 January 2002. Published on the NRC Research Press Web site at http://canjchem.nrc.ca on 21 August 2002.

In memory of Raymond Lemieux, teacher and advisor (B.B.).

B. Bendiak[1] and T.T. Fang. Department of Cellular and Stuctural Biology, University of Colorado Health Sciences Center, 4200 east ninth avenue, Denver, CO 80262, U.S.A.
D.N.M. Jones. Department of Pharmacology, University of Colorado Health Sciences Center, 4200 east ninth avenue, Denver, CO 80262, U.S.A.

[1]Corresponding author (e-mail: brad.bendiak@uchsc.edu).

 DOI: 10.1139/V02-132 © 2002 NRC Canada

entre les protons du cycle, même dans des expériences multidimensionnelles. Les résultats sont illustrés à l'aide d'un alditol non saccharide dérivé de glycoprotéines *N*-liées et de quelques structures plus petites contenant des acides sialiques et des *N*-acétylhexosamines. On décrit les méthodes utilisées pour l'acétylation de petits échantillons en faisant appel au catalyseur de superacétylation, la 4-diméthylaminopyridine. On présente aussi une brève perspective historique aux contributions fondamentales du M.R.U. Lemieux au domaine de la RMN des carbohydrates. On propose aussi un tour d'horizon historique permettant de mettre en contexte les contributions fondamentales de M.R.U. Lemieux au secteur de l'IRM des glucides.

Mots clés : RMN, oligosaccharides, peracétylation, groupes acétyles doublement marqués au ^{13}C, séquences pulsées sur mesure, Hartmann–Hahn hétéronucléaire.

[Traduit par la Rédaction]

Introduction

Historical perspective and Dr. R.U. Lemieux

It is fitting in an article dedicated to the memory of Dr. Raymond Lemieux that NMR spectroscopy of carbohydrates is at least one research topic. It is now taken for granted that measurement of ^1H–^1H J couplings provides important dihedral angle information for structural determination of molecules by NMR, according to the Karplus (1) approximation of 1963 ($J_{H,H'} = A + B \cos \phi + C \cos 2\phi$), where for sp^3-hybridized carbons, A, B, and C are numerical constants and ϕ represents the three-bond dihedral angle. Less well known is that this equation was a modified equation related to a wavefunction that, in 1959, Karplus showed could be fitted approximately by two curves, $8.5 \cos^2\phi - 0.28$ (Hz) where $0° \leq \phi \leq 90°$, and $9.5 \cos^2\phi - 0.28$ (Hz) where $90° \leq \phi \leq 180°$ (2). Even less well appreciated is that in the 1959 paper, the only experimental NMR evidence that Karplus cited to verify the theoretical relationship (Table 1 of that article) was a publication by Lemieux et al. (3), who had presented the 40 MHz ^1H NMR spectra of various six-membered ring compounds in 1956 and 1957 (4, 5) and 1958 (3, 6, 7). In the 1957 paper, Lemieux et al. reported their discovery that spin–spin coupling constants would likely be useful for determination of configuration of organic molecules (in general) because, they stated "It was also observed that configuration has an effect on spin-coupling constants as well as on chemical shift. Analysis of the spectra for the acetyl derivatives of glucose, galactose, xylose, and arabinose showed that the spin coupling between hydrogens on neighboring carbon atoms is 2 to 3 times greater when both the hydrogens are in axial orientation than when one or both of the hydrogens are in equatorial orientation." In their 1958 papers (3, 6, 7), they examined additional peracetylated monosaccharides having different anomeric configurations, including a series of chlorinated cyclohexanes, isomeric trichloromethyltrioxanes, and other cyclohexane derivatives. A crucial and very convincing demonstration of the relationship between ^1H–^1H J couplings and configuration was presented for two isomers of 1,3-dimethoxy-2-acetoxycyclohexane, where the ring proton signal at the acetoxy position resonated well downfield (6). Even at 40 MHz, the multiplet pattern of the ring proton having the acetoxy substitution was clearly observable and showed two large couplings when the proton was located diaxially with respect to both vicinal protons (a triplet) and one large and one small coupling when one vicinal proton was diaxially positioned and one located equatorially (a quartet, Fig. 2 of ref. 6). These papers were not only the first reports of carbohydrate NMR spectra, they were the seminal papers that experimentally established a relationship between spin–spin couplings and the three-bond dihedral angle. In a somewhat prophetic statement in one 1958 paper (7), Dr. Lemieux commented that "an almost endless number of such applications of high-resolution nuclear magnetic resonance spectroscopy can be envisaged for gaining information on the immediate environment of atoms in organic molecules."

It is safe to say that the NMR tapestry contributed to by so many investigators since that statement shows no sign of becoming threadbare. The past 10–15 years alone have seen major improvements in coherence transfer–selection methods, the widespread adoption of pulsed-field gradients, the extensive development of adiabatic pulses, and the development of methods for subspectral accumulation and (or) editing. Although Dr. Lemieux could not have foreseen many of these important developments, it is a tribute to his instinct that NMR would evolve explosively. Finally, of course, his many important contributions to synthetic carbohydrate chemistry and control of anomeric configuration were crucial to the success it now enjoys, which will no doubt be the topic of many contributions to this volume.

Introduction proper

Complex carbohydrates represent an extremely variable repertoire of molecules, and have been the target of NMR studies directed along two general lines, primary structural elucidation and conformation and (or) dynamics (8–12). In isolated oligosaccharides from any source, there may be hundreds of monomers or potential monomers having alternate stereo- or regiochemistries that need to be identified. This includes various amino sugars (13–15), deoxy sugars (14, 16, 17), branched-chain sugars (14, 18), uronic acids (14, 15), and unusual sugars having more than six carbons or more than one modification, or the presence of both types of enantiomers in the same oligosaccharide (15, 19). In addition, the vast majority of oligosaccharides are still isolated from natural sources having a natural abundance of ^{13}C. In some cases, as in carbohydrates generated by bacterial or cell cultures, incorporation of ^{13}C into the sugar backbone can be achieved, which is important for conformational and (or) dynamic studies using NMR spectroscopy (20–24). However, this is simply not possible for carbohydrates isolated from most multicellular organisms.

Traditionally, permethylation analysis (25–28) has played a very important role in the structural determination of oligosaccharides. The success of this method is based on the

© 2002 NRC Canada

logic that all free hydroxyl groups are converted to a derivative (a methyl ether) that permits the positions of the formerly free hydroxyl groups to be identified. These methods rely on depolymerization, either solvolytic (25) or reductive (28), to generate methylated monomers. After further appropriate reduction and (or) acetylation, monosaccharide derivatives are produced that can be compared, both by GC retention time and electron-impact mass spectra, to those of standards, thereby enabling glycosidic linkage positions to be inferred.

NMR spectroscopy of oligosaccharides peracetylated with doubly ^{13}C-labeled acetyl groups provides the same information given by permethylation analysis, and is based on precisely the same logic — that all free hydroxyl groups are converted to a derivative (in this case, an acetyl ester), which permits the positions of the formerly free hydroxyl groups to be identified. In this case, however, the information is extracted by identifying a ^{13}C–^{1}H three-bond *J* coupling between the acetyl carbonyl carbon and the ring proton at the position of acetylation.

We have now measured approximately 650 such couplings in 40 different oligosaccharides, with the observation that these $^{3}J_{C,H}$ coupling constants range from 2.5–4.7 Hz (based on initial observations of this range, see ref. 29). All four-bond couplings between acetyl carbonyl carbons and ring protons at adjacent positions on the sugar ring are small and within linewidth (less than 0.5–1 Hz). Sites that are not acetylated do not show these $^{3}J_{C,H}$ couplings. These include the anomeric position, the position of cyclization, and the *position of a glycosidic linkage*. In addition, sites having other pre-existing substituents, such as phosphate monoesters, would not be acetylated. Three major advantages of peracetylation–NMR over classical permethylation analysis are first, that depolymerization is not required — the data is derived from intact oligosaccharides. Second, a series of standards are not necessary to compare GC retention times for determination of stereochemistry. Third, acetyl groups are both easy to remove to recover the initial oligosaccharide (30, 31) or can be easily replaced with methyl ethers under permethylation conditions, if so desired, for permethylation or other mass spectral analyses.

In this report, methods are described that are specialized for primary structural elucidation of oligosaccharides. They focus on the specific advantages provided through peracetylation of oligosaccharides with doubly ^{13}C-labeled acetyl groups. An explicit NMR strategy is outlined that describes new pulse sequences tailored to the benefits of the introduced acetyl groups. The key advantages provided by these methods are (*i*) they permit glycosidic linkage positions of monosaccharides within larger carbohydrates to be unambiguously assigned. (*ii*) They result in a marked increase in spectral resolution, both in the directly detected (^{1}H) dimension and three indirectly detected dimensions provided by the acetyl-group nuclear frequencies. The increased spectral dispersion in the directly detected dimension results in far fewer strong couplings between protons. These advantages are unique to ^{13}C-acetylation and are not available to underivatized oligosaccharides ^{13}C-labeled in the sugar backbone. (*iii*) They make it possible to resolve purely absorptive in-phase multiplets that permit accurate measurement of ^{1}H–^{1}H *J*-coupling constants and enable stereochemistries of individual sugars in oligosaccharides to be determined. (*iv*) They take advantage of the fact that ^{13}CO, $^{13}C^{Me}$, and $^{1}H^{Me}$ frequencies fall within narrow isolated spectral ranges. Selective excitation and decoupling pulses can be applied to eliminate the effects of *J*-coupling so that the signals approach their natural linewidths in the indirect dimensions.

While experiments are illustrated using a few oligosaccharides derived from glycoproteins to demonstrate important advantages, this strategy is entirely general and its potential application to carbohydrates from all sources is emphasized.

Results and discussion

Strategy for elucidation of carbohydrate structures using ^{13}C-acetylation and tailored pulse sequences

A flow chart is shown (Fig. 1) outlining the basic strategy behind the use of doubly ^{13}C-labeled acetyl groups for structural determination of oligosaccharides. The approach involves (*i*) initial assignment and accurate measurement of ring proton scalar couplings. This defines each spin system and enables sugar stereochemistries to be confidently determined. (*ii*) Unambiguous identification of substitution sites on each sugar ring, as revealed by assignment of *O*-acetyl positions. (*iii*) Determination of which specific sugars are linked to each other, as established by interresidue correlations.

Assignment of signals and measurement of ^{1}H–^{1}H *J* couplings of monosaccharide spin systems

Gradient COSY (gCOSY) and carbonyl ^{13}C-decoupled gCOSY

^{1}H–^{1}H Gradient COSY experiments are now routine, and the additional spectral dispersion induced by acetylation of an oligosaccharide results in many more resolved cross-peaks as compared with the same spectrum of the underivatized structure recorded in D_2O. The experiment is performed both with and without ^{13}CO decoupling during the evolution time and free induction decay. Comparison of these two spectra reveals the sites of acetylation based on the additional acetyl-^{13}CO/sugar-^{1}H couplings observed in the multiplet patterns. A standard ^{13}CO-decoupled gCOSY of the typical *N*-linked "biantennary" oligosaccharide-alditol (**1**, Scheme 1) containing nine sugars in D_2O-saturated $CDCl_3$ is shown in Fig. 2A. Figure 2B shows an expansion of the fully ^{13}CO-decoupled gCOSY spectrum and Fig. 2C shows the same region without ^{13}CO decoupling. In the fully ^{13}CO-decoupled experiment the cross-peak multiplet patterns are determined solely by ^{1}H–^{1}H couplings. The presence of a ^{13}CO–$^{1}H^{sugar}$ coupling within this multiplet in the non-decoupled spectrum identifies this ^{1}H as a site of acetylation. The magnitude of these ^{13}CO–$^{1}H^{sugar}$ couplings as measured in other experiments ranges from 2.5–4.7 Hz. This is a sensitive experiment as it is homonuclear and noise is minimized through the use of gradients (32). Collection of a larger number of increments (1000–2000) provides good resolution in F_1, which is useful if multiplets partially overlap. Where there is significant overlap of two or more cross-peaks, additional experiments are required to obtain complete assignments.

© 2002 NRC Canada

Fig. 1. Flow chart showing of the strategy for structural elucidation of oligosaccharides peracetylated with doubly ^{13}C-labeled acetyl groups. Tailored pulse sequences were designed for (A) definition of individual spin systems, (B) identification of linkage substitutions via assignment of all acetylation sites, and (C) identification of specific interresidue connectivities.

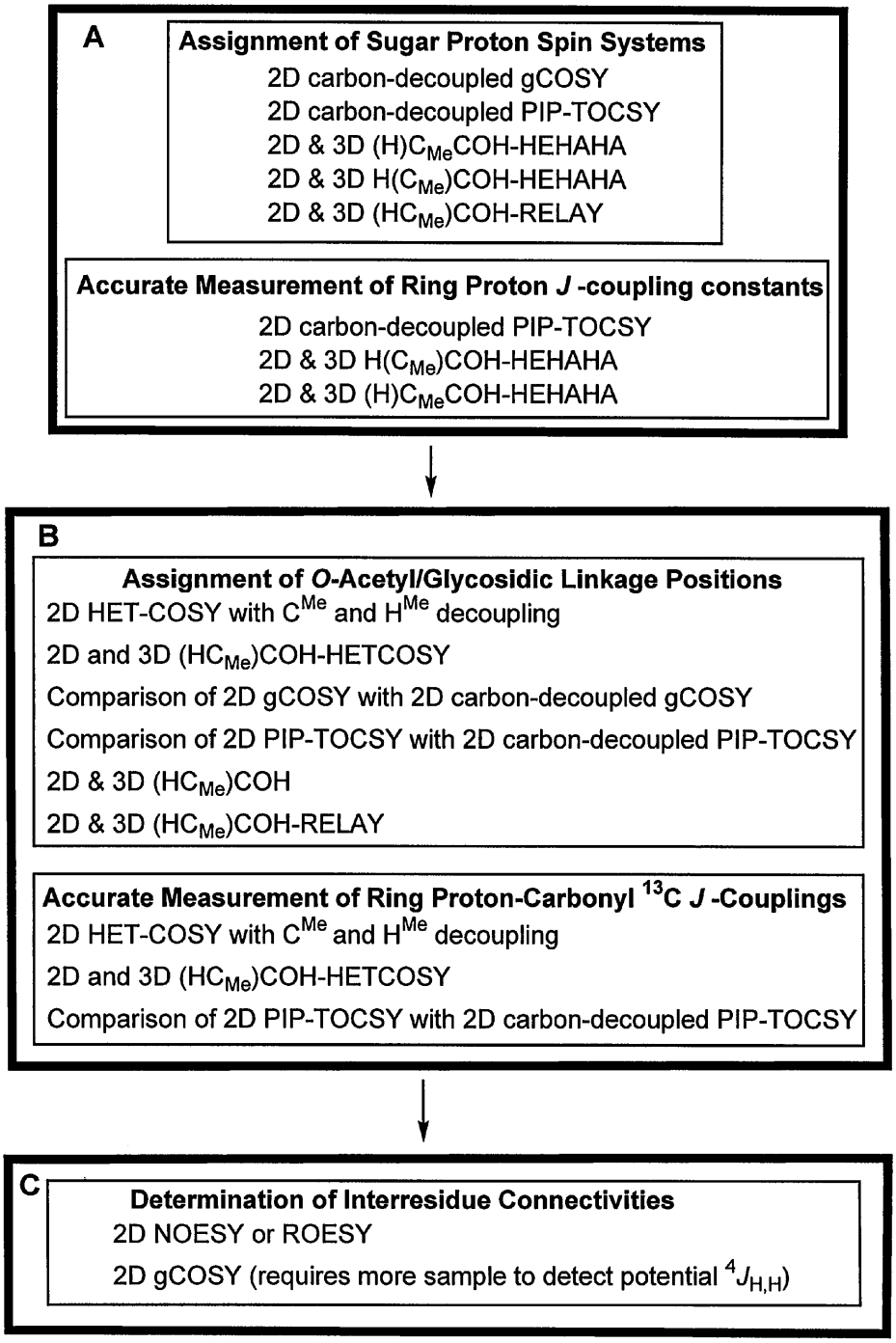

Measurement of scalar couplings directly from COSY-type cross-peaks is not generally applicable for many combinations of coupling constants due to overlap and interference of in-phase and antiphase components. Although homonuclear E.COSY or P.E.COSY methods (33, 34) have been described for measuring such coupling constants, specific difficulties in certain situations have been pointed out for these (35, 36) and their more selective variants, STRIPE or SUPERSTRIPE COSY (37). Recently, Delaglio et al. (38) have developed an interactive computer program that enables coupling constants to be determined in regular COSY spectra by amplitude-constrained multiplet evaluation (ACME). We have found, however, that ^1H–^1H *J*-couplings can be measured directly and accurately from pure-absorption in-phase multiplets in "pure in-phase" TOCSY (PIP-TOCSY) experiments and in novel NMR experiments designed to correlate acetyl nuclear frequencies to ring proton frequencies, as described below.

© 2002 NRC Canada

Fig. 2. (A and B) Carbonyl-decoupled gCOSY spectra of structure **1** (Scheme 1, where acetyl groups shown in bold type are doubly ^{13}C-labeled). This spectrum was accumulated with elimination of the GlcNAc N-H:H-2 couplings by deuterium exchange using D_2O layered on the $CDCl_3$ (27°C). Detailed NMR parameters were previously described (29). The boxed multiplet in (A), assigned to the H-3/H-4 cross peak of GlcNAc2, is shown expanded in (B), with the H-3 frequency along the horizontal axis. (C) The same region of the spectrum of the same compound run under identical conditions, except that the carbonyl frequencies were not decoupled. The additional coupling of a 3-*O*-acetyl ^{13}CO nucleus is clearly observed along the horizontal axis, but the 4-position is substituted with a β-Man, hence shows no additional splitting of the multiplet pattern along the vertical axis.

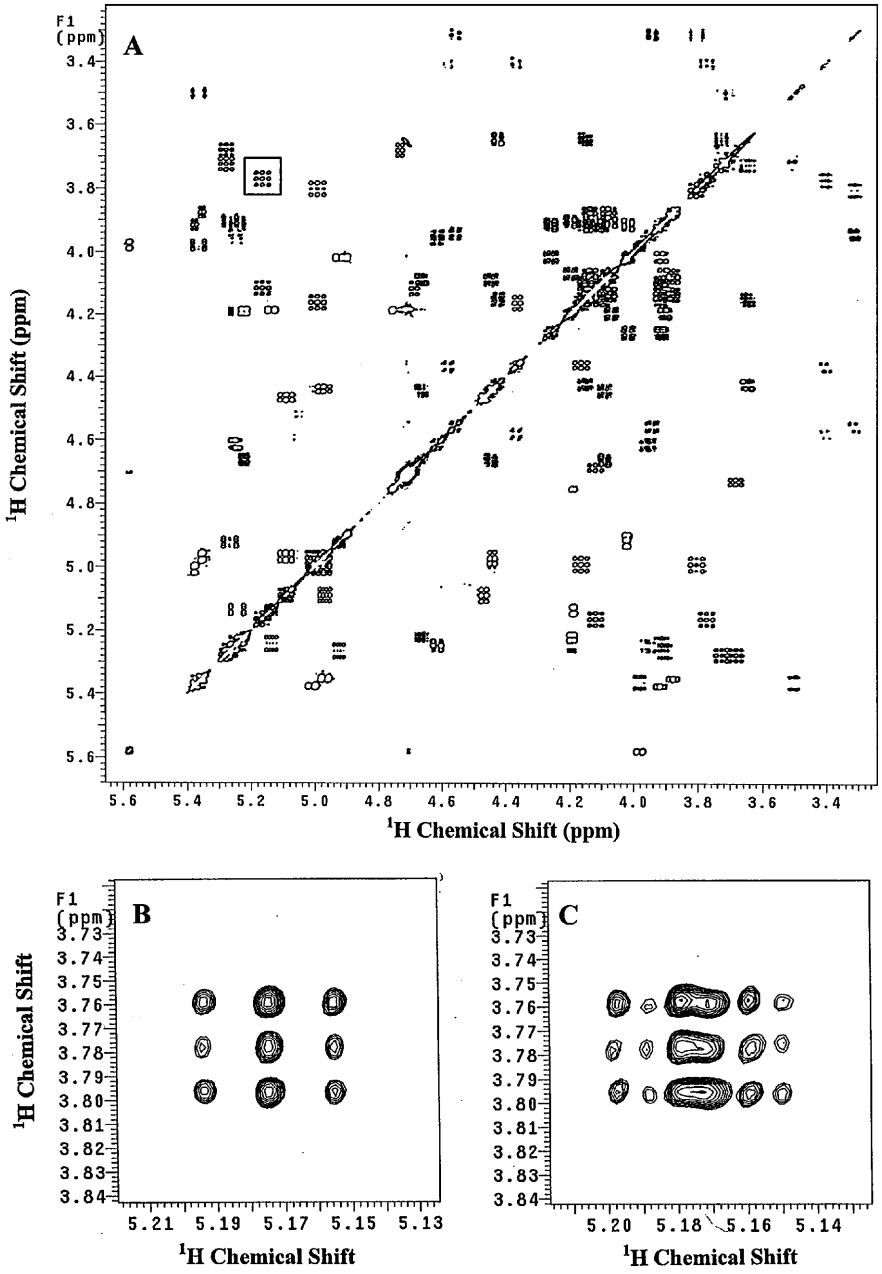

Carbonyl ^{13}C-decoupled pure in-phase TOCSY (PIP-TOCSY)

The accurate measurement of ring proton *J*-coupling constants in carbohydrates is crucial to define the stereochemistry of each monosaccharide. TOCSY experiments are attractive for this purpose because they connect complete individual spin systems and coherence transfer occurs in-phase (39–41). However, zero-quantum coherences of the type $I_yS_x - I_xS_y$ develop during Hartmann–Hahn mixing periods that, if not suppressed, can result in phase distortions of cross-peak multiplets. Methods to suppress zero-quantum coherences have been discussed in some detail (39–41). One effective solution to this problem are the zero-quantum dephasing schemes of Davis et al. (39), which use a spin-lock pulse applied during application of a B_0 gradient. This eliminates the effects of zero-quantum coherences in a single accumulation, which is in contrast to *z*-filters that require repetitions with varying delays. These schemes yield near perfect multiplet patterns in the directly detected dimension.

The basic PIP-TOCSY pulse sequence is shown in Fig. 3A. Although Davis et al. (39) applied dephasing

© 2002 NRC Canada

Scheme 1.

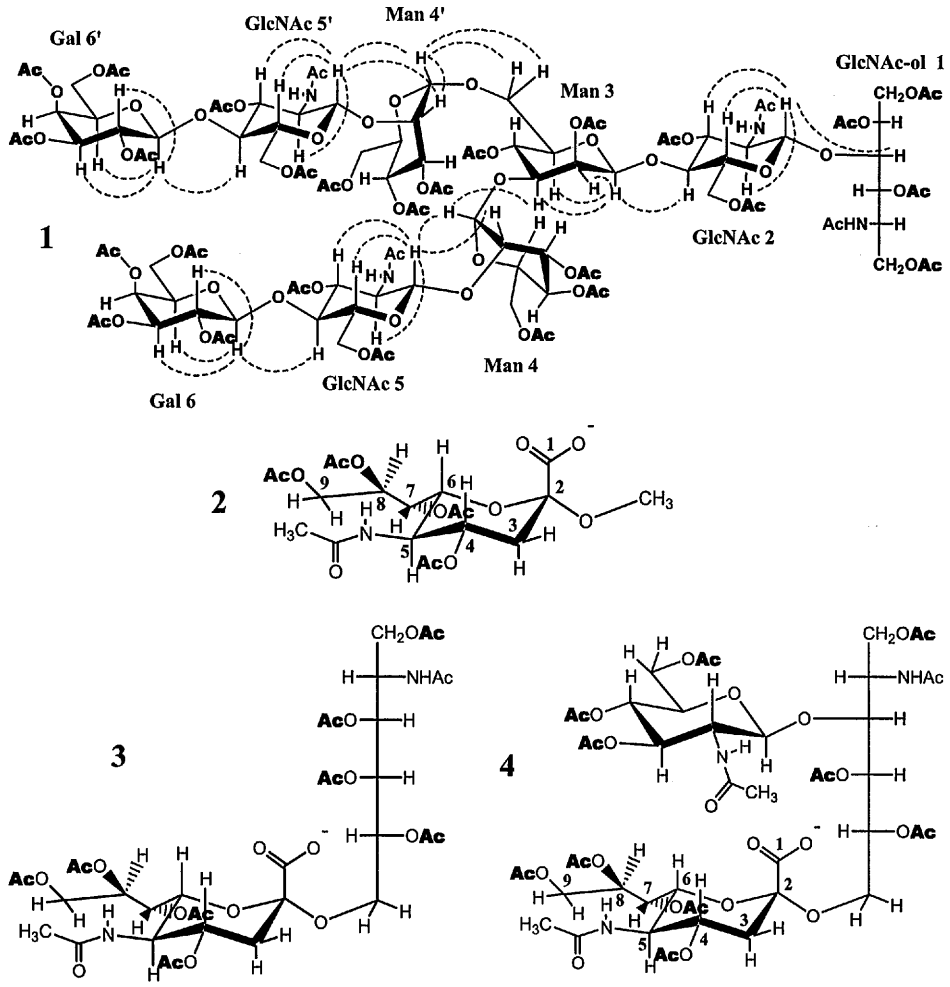

periods before and after the TOCSY mixing period, practically we have found that a single dephasing scheme applied after the mixing period is sufficient to suppress zero-quantum coherences in almost all cross-peaks except those very near the diagonal, where the difference in the frequency offset is small (~15–30 Hz). A PIP-TOCSY spectrum of ^{13}C-acetylated oligosaccharide **1** is shown in Fig. 4A, recorded using the pulse sequence of Fig. 3A where ^{13}CO was decoupled during t_1 and t_2. A trace of the boxed multiplet in Fig. 4A taken parallel to the F_2 axis is shown in Fig. 4B, and the same multiplet is shown in Fig. 4C without ^{13}CO-decoupling in the t_2 dimension. The positions of acetylation again are immediately assignable based on the additional splitting seen in the spectrum without ^{13}C decoupling during t_2. Multiplets are pure-absorption in-phase and the decoupled spectrum yields accurate values of ^{1}H–^{1}H coupling constants. A key point is that the experiment usually yields a series of multiplet patterns at different F_1 frequencies that can be used for additional measurements of the same ^{1}H–^{1}H *J* couplings. This is particularly important if overlap in some regions of the spectrum is an issue. The limits of peak resolution are approximately 1.5–2.0 Hz. The experiment is sensitive as it is homonuclear. Another point worthy of mention is that the GlcNAc amide N–H protons resonate downfield (~5.8 to 7.0 ppm) and couple (8.0–9.6 Hz) to H-2 protons, enabling these spin systems to be straightforwardly identified (Fig. 4A).

(H)C$_{Me}$COH-HEHAHA and H(C$_{Me}$)COH-HEHAHA

Homonuclear 2-D ^{1}H–^{1}H experiments are normally insufficient to adequately resolve all cross-peaks in larger oligosaccharide structures. To extend NMR studies to larger carbohydrates, additional methods to reduce spectral overlap are required. The introduction of ^{13}C-labeled acetyl groups provide additional frequency dimensions that can be used to improve overall spectral dispersion. The frequencies of the ^{13}CO, ^{13}C^{Me}, and ^{1}H^{Me} nuclei are well separated from each other and other signals in the spectrum and can be independently manipulated through selective excitation and (or) decoupling schemes. The (H)C$_{Me}$COH-HEHAHA and H(C$_{Me}$)COH-HEHAHA experiments were designed to correlate sugar-ring ^{1}H frequencies with the acetyl ^{13}CO, ^{13}C^{Me}, and ^{1}H^{Me} frequencies to provide increased spectral dispersion. At the same time these experiments were designed to retain the pure-absorption in-phase nature of the cross-peak multiplets so that accurate sugar ^{1}H–^{1}H *J* couplings could be measured in a single experiment

Correlation of the acetyl ^{13}C and ^{1}H frequencies with the sugar-ring protons is made by coherence transfer from magnetization originating on acetyl ^{1}H^{Me}, rather than an out-and-back

© 2002 NRC Canada

Fig. 3. Pulse sequences used to record (A) the PIP-TOCSY and carbon-decoupled PIP-TOCSY; (B) the H^{Me}, C^{Me}-decoupled HET-COSY; (C) the $HC_{Me}COH$-HEHAHA; and (D) the $HC_{Me}COH$-HETCOSY. In all sequences wide solid bars represent hard 180° pulses and narrow bars represent hard 90° pulses. Shaped 180° pulses are represented as solid filled curves and shaped 90° pulses are represented as gray shaded curves. (A) Homonuclear Hartmann–Hahn mixing uses a DIPSI-3 matching period (76) with a field strength of 4.03 kHz for 35.7 ms. The spin-lock pulse (SLx) was applied for periods of 30–60 ms (usually 60 ms) at the same time as the trapezoidally shaped gradient pulse (gz-trap) (39). This gradient had a maximum strength of 4 G cm^{-1} and the period used to ramp the gradient up to its maximum field strength (and subsequently back down to zero) was 25% of the total gradient duration (30–60 ms). Experiments were conducted with or without GARP (77) decoupling of ^{13}CO frequencies during the direct detection period. (B) The selective 90° pulse acting on ^{13}CO was applied for 600 μs with an e-burp-2 profile (78). The selective 180° pulses (*a*) applied at the $^{13}C^{Me}$ and $^{1}H^{Me}$ frequencies during the middle of the evolution time were seduce–1 180° pulses (79) applied for 250 μs on $^{13}C^{Me}$ (phase modulated by 150 ppm) and 1.4 ms on $^{1}H^{Me}$ (phase modulated by 1.52 ppm). In (C), the pulse sequence was identical to the $(H)C_{Me}COH$-HEHAHA pulse sequence (43) except that an additional incremented evolution time was included within the initial $^{1}H^{Me}$–$^{13}C^{Me}$ INEPT transfer. The $^{13}C^{Me}$ nuclei were inverted using a hyperbolic secant pulse (*d*) and quadratic phase errors were refocused by applying the same pulse at (*e*) but the direction of the frequency sweep was reversed (80–82). In (D), the first part of the pulse sequence is identical to that of (C) up to the time of the broken line marked with a *. The final portion containing the t_3 period was identical to the evolution time period and pulses described in (B). For (B–D), selective ^{13}C 90° pulses acting on *z* magnetization were applied for 600 μs with an e-burp-2 profile (78) and selective ^{13}C 90° pulses acting on transverse magnetization were applied for 600 μs as a Q5 Gaussian pulse (83). Pulse (*b*) was a hyperbolic secant pulse (80, 81), and (*c*) a hyperbolic secant pulse to refocus the quadratic shift, with durations and phase modulations as previously described (43). Gradient strengths and durations were also as previously described (43).

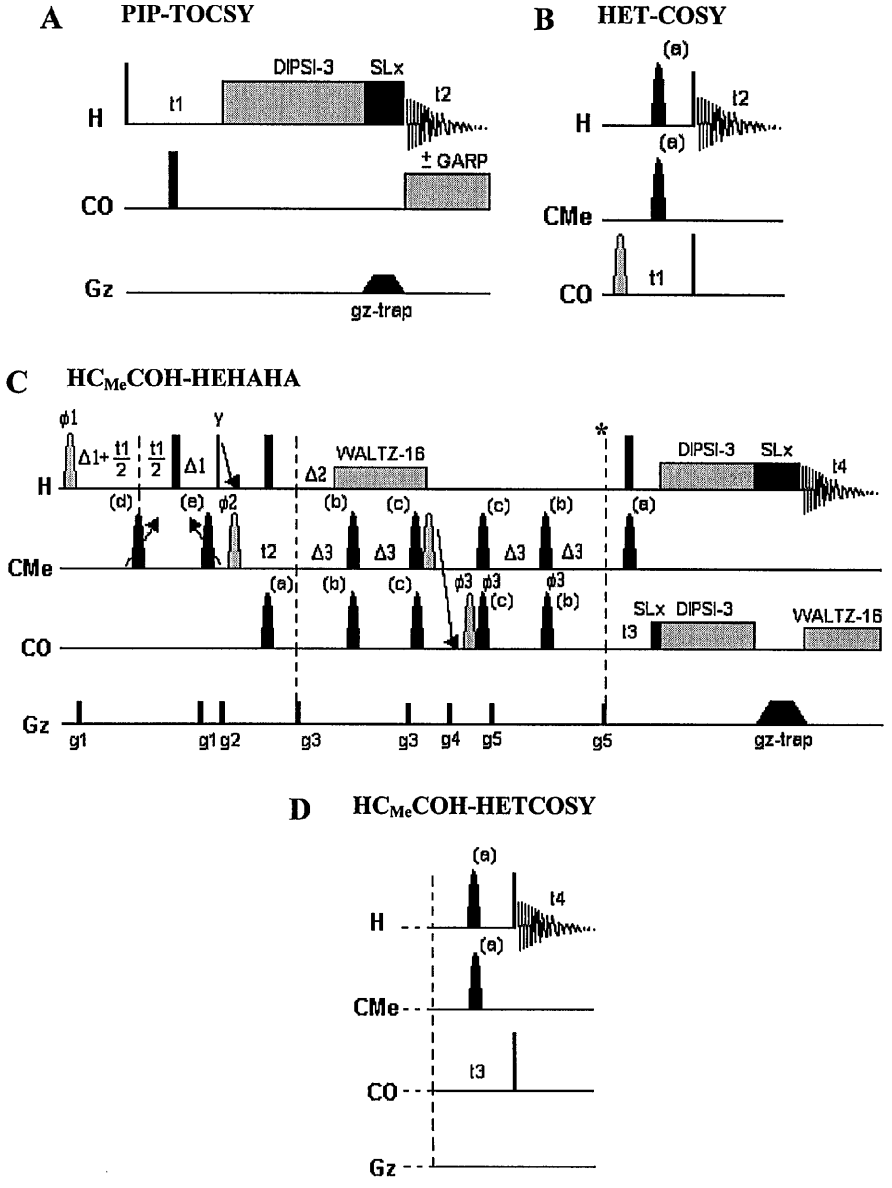

© 2002 NRC Canada

Fig. 4. (A) A PIP-TOCSY spectrum of peracetylated oligosaccharide **1** having doubly ^{13}C-labeled acetyl groups. The spectrum (A) was accumulated with inclusion of the GARP decoupling scheme (77) to decouple ^{13}CO frequencies in the directly detected dimension. It was accumulated in H_2O-saturated $CDCl_3$ at 27°C. The magnetization transferred from GlcNAc N-H signals to other ring protons is readily observable along both frequency axes (the N-H diagonal peaks are indicated). A trace through the boxed multiplet in (A) is shown in (B), representing the sugar backbone H-3 multiplet of GlcNAc5′. The same multiplet is shown in (C) in an otherwise identical spectrum accumulated without ^{13}CO decoupling during the detection period.

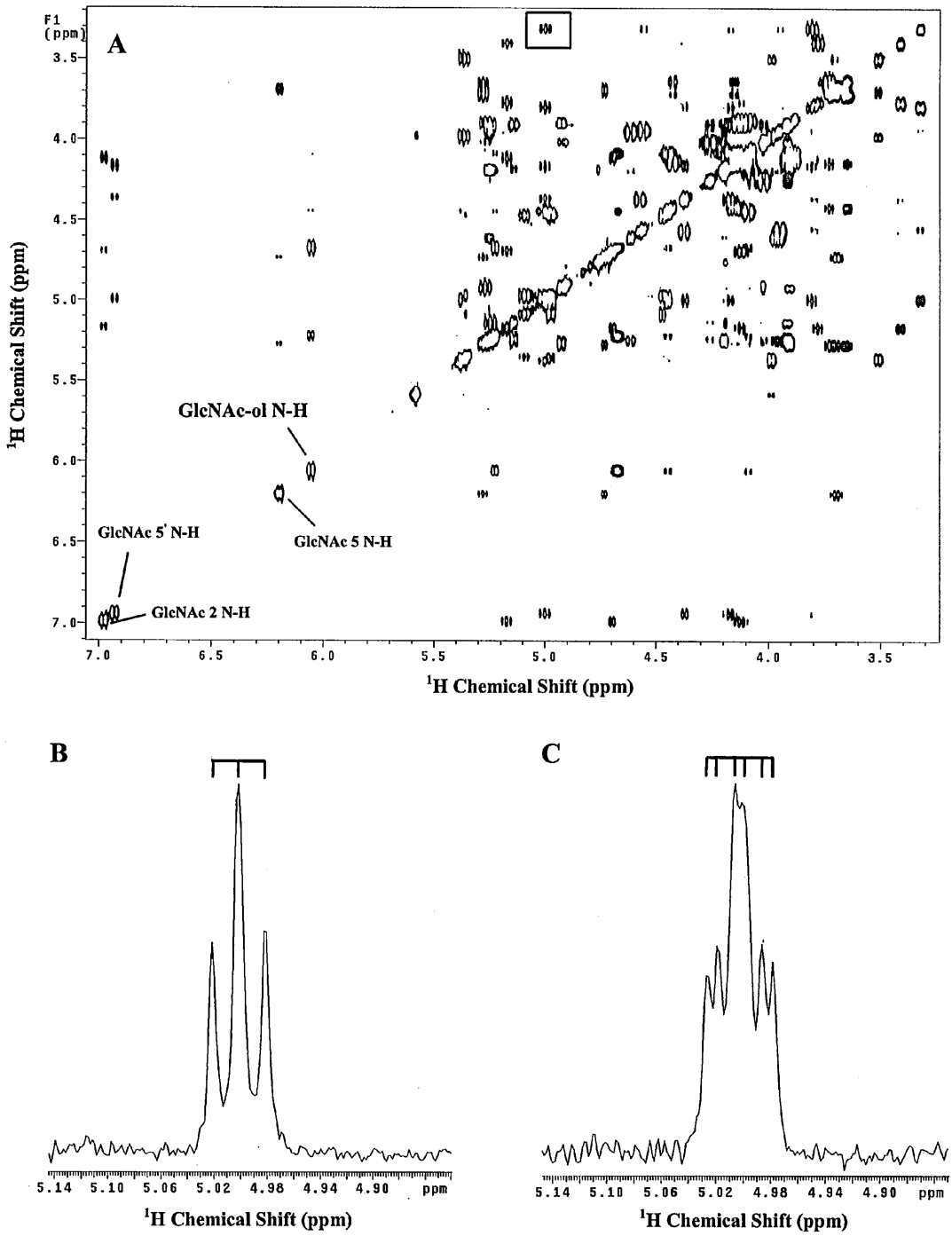

approach starting with magnetization on the sugar-ring protons. The one-bond ^{1}H–^{13}C and ^{13}C–^{13}C couplings within the acetyl spin system are large, and INEPT-type transfers (42) permit efficient coherence transfer through the acetyl system to the acetyl ^{13}CO (43). This results in a significant time saving (total time 16 ms) as compared with an HMBC-type transfer from a sugar-ring proton to an acetyl ^{13}CO (about 125 ms). In addition, each step in the direct INEPT transfer through the acetyl system is dependent on a single *J* coupling, and not a range of *J* couplings so coherence transfer can be optimized and arranged so that it occurs pure in-phase to the acetyl ^{13}CO. Subsequent coherence transfer

© 2002 NRC Canada

Figs. 5A,B. Correlations of sugar-ring proton frequencies to acetyl group ^{13}CO (A), $^{13}C^{Me}$ (B), and $^{1}H^{Me}$ (C) frequencies using the $HC_{Me}COH$-HEHAHA pulse sequence of Fig. 3C. Spectra were all acquired using peracetylated oligosaccharide **1** having doubly ^{13}C-labeled acetyl groups. The pure-absorption in-phase nature of the multiplets is shown in panel (D), which represents a trace taken parallel to the ^{1}H axis at the arrow shown in panel (A). These multiplets arise from protons of the Gal6 residue that correlate to the acetyl ^{13}CO at the 2-position of the sugar. Spectra were all recorded in D_2O-saturated $CDCl_3$ at 27°C.

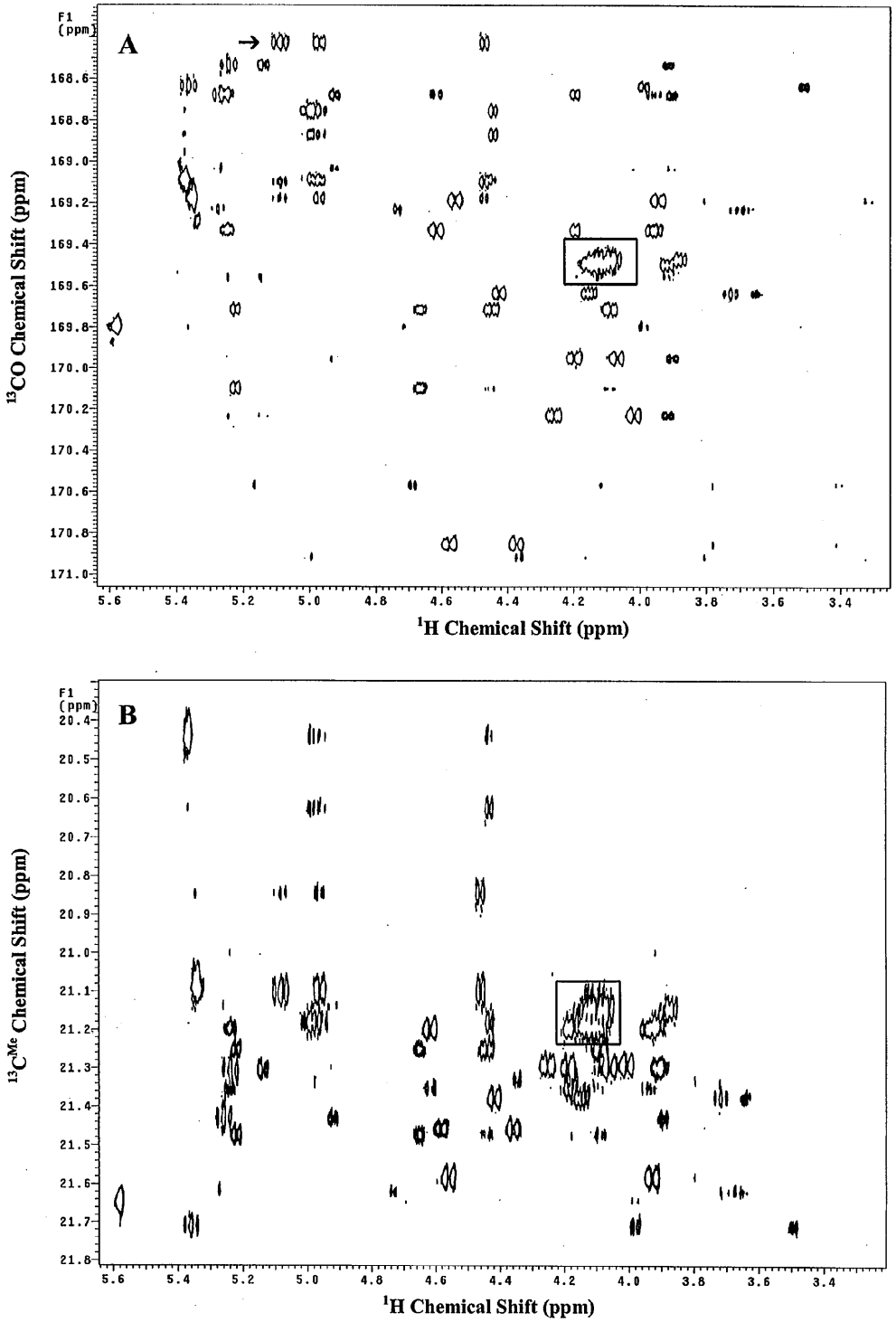

from the ^{13}CO to the sugar-ring protons may be achieved through different methods but in-phase transfer is best achieved through the use of heteronuclear Hartmann–Hahn matching (HEHAHA, 44–46). The HEHAHA transfer step to a sugar proton is accompanied by homonuclear Hartmann–Hahn (HOHAHA) transfer of magnetization within the sugar spin system (44–46). This is unavoidable but is advantageous as additional sugar–proton correlations are observed to a single ^{13}CO frequency (43). When combined with suppression of zero-quantum effects as described

© 2002 NRC Canada

Figs. 5C,D.

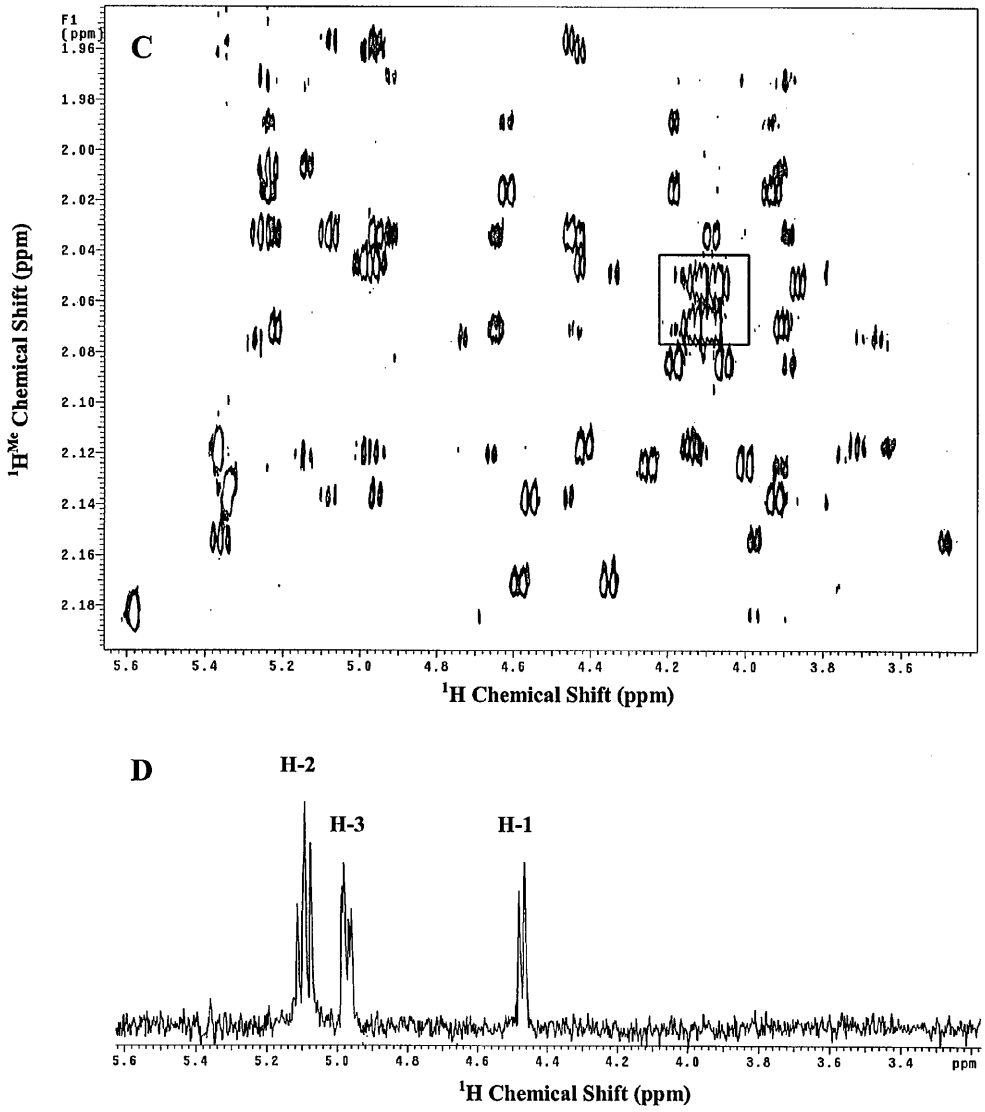

above (39) these experiments result in cross-peak multiplet patterns that are in-phase and purely absorptive. From these multiplets, scalar couplings between ring protons can be accurately measured and used to define sugar stereochemistries (43). The pulse sequence shown in Fig. 3C can be used to establish correlations from the sugar protons to any combination of the acetyl-group nuclei in 3-D or 4-D experiments at the investigator's discretion.

Shown in Figs. 5A–C are 2-D spectra of peracetylated nonasaccharide-alditol **1**, where sugar protons were separately correlated to the ^{13}CO, $^{13}C^{Me}$, and $^1H^{Me}$ frequencies of the acetyl groups using the $HC_{Me}COH$-HEHAHA pulse sequence of Fig. 3C. The $(H)C_{Me}COH$-HEHAHA pulse sequence correlating $^{13}C^{Me}$, ^{13}CO, and $^1H^{ring}$ was described earlier (43). The more general pulse sequence (Fig. 3C) also achieves correlations to $^1H^{Me}$ frequencies by including an incremented evolution period in the first $^1H^{Me}$–$^{13}C^{Me}$ transfer step. For oligosaccharide **1**, this particular correlation (Fig. 5C) was useful for resolution of some sugar-proton signals that did not resolve with correlation to either the ^{13}CO or $^{13}C^{Me}$ frequencies (boxed in Figs. 5A–C). In the oligosaccharides we have examined to date, the different acetyl-group frequencies appear to correlate randomly to sugar-ring protons. Hence, for any given oligosaccharide, it is difficult to predict which correlations to the ^{13}CO, $^{13}C^{Me}$, or $^1H^{Me}$ frequencies will provide the best spectral dispersion for a 2-D experiment. In practice, performing all three 2-D variants first is useful and consumes less NMR time than 3-D experiments (Figs. 5A–C). A 1-D trace at the F_1 frequency shown with the arrow in Fig. 5A is presented in Fig. 5D. From a series of similar traces at different F_1 frequencies and from different 2-D subspectra, many of the ^1H–^1H J couplings can be extracted. So far, in combination with PIP-TOCSY experiments, these 2-D spectra have resulted in assignments and measurements of almost all ^1H–^1H J coupling constants for oligosaccharides that we have examined containing up to 15 sugars.

Taken together, the above correlations provide a powerful combination for assignment of sugar-proton frequencies, for resolution of cross-peaks in multiple dimensions, and for

© 2002 NRC Canada

Table 1. Chemical shifts (ppm) and coupling constants ($J_{H,H}$) for the peracetylated oligosaccharide-alditol **1** having doubly ^{13}C-labeled acetyl groups.

	Gal 6	Gal 6′	GlcNAc 5	GlcNAc 5′	Man 4	Man 4′	Man 3	GlcNAc2	GlcNAc-ol
Chemical shift									
H-1a	—	—	—	—	—	—	—	—	4.450
H-1b	—	—	—	—	—	—	—	—	4.091
H-1	4.476	4.450	4.734	4.374	4.907	4.762	4.715	4.699	—
H-2	5.095	4.981	3.699	4.171	4.026	4.194	5.582	4.122	4.673
H-3	4.976	5.017	5.281	5.001	4.929	5.142	3.990	5.172	5.228
H-4	5.360	5.383	3.730	3.810	5.272	5.250	5.368	3.783	4.198
H-5	3.882	3.921	3.650	3.325	3.906	3.918	3.513	3.415	5.253
H-6a	4.139	4.155	4.429	4.558	4.201	4.262	3.731	4.575	4.618
H-6b	4.083	4.104	4.155	3.951	4.071	4.020	3.682	4.377	3.960
H-N	—	—	6.202	6.934	—	—	—	6.983	6.059
Coupling constants (Hz)									
$J_{1a,1b}$	—	—	—	—	—	—	—	—	–12.1
$J_{1a,2}$	—	—	—	—	—	—	—	—	2.8
$J_{1b,2}$	—	—	—	—	—	—	—	—	2.5
$J_{1,2}$	7.9	7.5	7.5	8.4	<2.0	<2.0	<1.5	8.3	—
$J_{2,3}$	10.5	10.6	9.8	10.6	3.5	3.3	3.3	10.5	8.2
$J_{3,4}$	3.5	3.3	8.0	9.6	9.2	9.2	9.3	9.0	~2.2
$J_{4,5}$	<2.0	<2.0	9.9	9.0	10.5	10.6	9.5	9.5	7.1
$J_{5,6a}$	6.7	8.1	~2.3	<1.5	3.5	4.6	2.7	~2.2	2.4
$J_{5,6b}$	7.5	6.1	5.3	~2.2	<2.0	<2.0	<1.5	<1.5	7.5
$J_{6a,6b}$	–11.7	–11.4	–12.2	–12.2	–12.4	–12.4	–13.1	–12.2	–12.3
$J_{NH,H-2}$	—	—	8.0	9.5	—	—	—	9.5	9.2

Note: Data were extracted from spectra accumulated in H_2O-saturated $CDCl_3$ at 27°C, relative to internal TMS. Chemical shifts were primarily determined from traces of purely absorptive in-phase multiplets in the directly detected dimension of 2-D PIP-TOCSY or HC_{Me}COH-HEHAHA experiments. All multiplets were first-order, except for a minor second-order effect observed for Gal6′ H-2 and H-3 signals.

measurement of ^1H–^1H *J* couplings. As an example, the complete assignment of the chemical shifts and coupling constants of nonasaccharide-alditol **1** is presented in Table 1.

Assignment of *O*-acetyl and glycosidic linkage positions

Both the gCOSY and PIP-TOCSY experiments described above can be used to identify the sites of acetylation in cases where cross-peak multiplets are well resolved. In larger oligosaccharides, however, spectral overlap occurs and the detail in cross-peak multiplets that indicates the presence of an additional ^{13}CO–$^1H^{ring}$ coupling may be obscured. In these instances additional experiments are required to establish sites of acetylation.

We have used two different methods to correlate the acetyl ^{13}CO frequencies with the sugar protons *directly at the site of acetylation*. The first was heteronuclear COSY (HET-COSY) with detection of ^1H signal and the second was $H(C_{Me})COH$ (43). Figure 6 shows the HET-COSY spectrum of nonasaccharide-alditol **1** recorded with the pulse sequence shown in Fig. 3B, where the $^{13}C^{Me}$ and $^1H^{Me}$ were decoupled during t_1. All three-bond correlations between ^{13}CO and $^1H^{ring}$ were observable and permitted measurement of the $^3J_{C,H}$ for ring protons based on the single splitting along the ^{13}C axis. For the exocyclic methylene protons (-CH_2OAc), ^{13}CO is coupled to two protons resulting in two splittings along the ^{13}C dimension, and which often results in cancellation in the middle of the multiplet along that axis. These are easily discernable from the cross-peak multiplets of ring (-CH(OAc)-) protons for two reasons. First, two proton frequencies correlate to a single ^{13}C frequency, which are both seen in traces at specific ^{13}C (F_1) frequencies (Fig. 6). Second, the chemical shifts of acetylated exocyclic (-CH_2OAc) sugar protons are found from 3.8 to 4.7 ppm, always upfield of acetylated sugar-ring (-CH(OAc)-) protons, which occur in the region from 4.8 to 5.8 ppm (Fig. 6).

The HET-COSY correlation (Fig. 3B) begins with the intrinsic magnetization of the ^{13}CO nuclei. We have also examined another related pulse sequence shown in Fig. 3D termed (HC_{Me})COH-HETCOSY, where the magnetization originates in $^1H^{Me}$ protons and is transferred to ^{13}CO nuclei through two INEPT steps via the $^{13}C^{Me}$ nuclei. This pulse sequence resulted in comparable cross-peak intensities (^{13}CO-sugar ^1H cross-peaks) to those observed for the direct pulse on ^{13}CO nuclei of the pulse sequence shown in Fig. 3B. The (HC_{Me})COH-HETCOSY experiment will, however, be important for measuring these coupling constants in larger oligosaccharides, where spectral resolution in additional dimensions is necessary. The implementation of incremented evolution times in both INEPT transfers is straightforward, as shown in Fig. 3C.

The $H(C_{Me})$COH pulse sequence (43) may be used to observe ^{13}CO–$^1H^{sugar}$ correlations with higher sensitivity than the HET-COSY. This experiment completely collapses multiplets in the indirect dimension and results in better resolution and sensitivity than the HET-COSY-based experiment. The cross-peaks in this spectrum are more complex and are not pure in-phase. The intensity of the cross-peaks are dependent both on ^{13}CO–$^1H^{ring}$ and $^1H^{ring}$–$^1H^{ring}$ coupling constants. Consequently, it may be necessary to acquire a series of spectra with different delays in the final

© 2002 NRC Canada

Fig. 6. Direct sugar-^{1}H/acetyl-^{13}CO couplings as revealed by the $^{13}C^{Me}$, $^{1}H^{Me}$-decoupled HET-COSY spectrum (pulse sequence of Fig. 3B). The spectrum was accumulated using peracetylated oligosaccharide **1** having doubly ^{13}C-labeled acetyl groups. Cross-peaks of all correlations are indicated. This spectrum was recorded in H_2O-saturated $CDCl_3$ at 27°C.

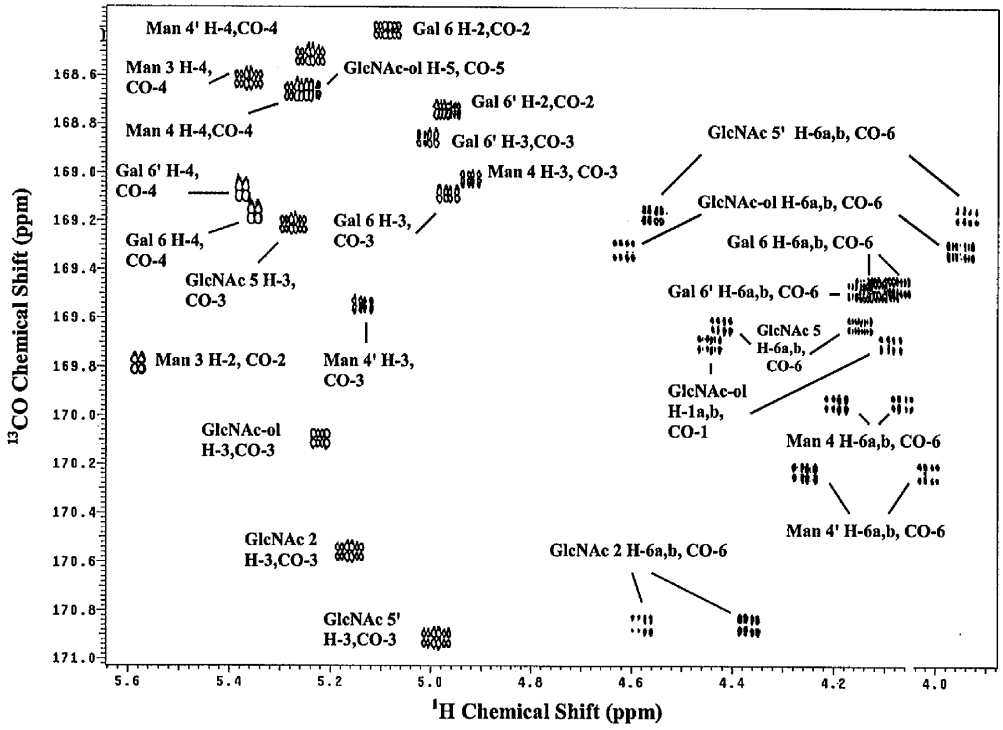

INEPT period to observe all of the correlations (43). From a practical perspective, if enough material is available to perform the HET-COSY-type experiment in a reasonable time period (8–10 h) it provides all the ^{13}CO-sugar ^{1}H correlations and enables measurement of their couplings in one experiment. If some of the cross-peaks (usually the ^{13}CO-6/H-6 cross-peaks) prove more difficult to observe in a reasonable time period, they will be observable using the H(C_{Me})COH pulse sequence (discussed in detail in ref. 43). Again, if necessary, additional dimensions can be added in the H(C_{Me})COH experiment (ie., during the $^{1}H^{Me}$–$^{13}C^{Me}$ or $^{13}C^{Me}$–^{13}CO transfers) as shown in Fig. 3C.

The above experiments result in correlations that reveal all the sites of acetylation. By inference, the positions of glycosidic linkages can be assigned, as they can never be acetylated. The positions of glycosidic substitutions are readily distinguished because the H-1 signal shows only one $^{3}J_{H,H}$ coupling (to H-2), the H-5 (of hexopyranosides) shows three $^{3}J_{H,H}$ couplings (to H-4, H-6a, and H-6b), and a glycosidic substitution site shows just two $^{2\text{ or }3}J_{H,H}$ couplings, enabling a glycosidic linkage position to be unambiguously determined.

For all oligosaccharides that we have so far examined, a combination of gCOSY, PIP-TOCSY, (H)C_{Me}COH-HEHAHA, and H(C_{Me})COH-HEHAHA pulse sequences have proven adequate to assign all sugar-ring protons and measure all their ^{1}H–^{1}H *J* couplings. The HET-COSY and H(C_{Me})COH experiments have enabled all acetylated positions to be assigned. An additional experiment, the H(C_{Me})COH-RELAY (described in ref. 43) may be used to correlate acetyl ^{13}CO to sugar ^{1}H frequencies both at the site of acetylation and to additional protons immediately adjacent to those sites. This experiment may prove useful for larger oligosaccharides as an independent method to establish sugar-proton assignments or to confirm them.

Interresidue adjacencies via NOESY and ROESY experiments, and occasional scalar couplings

NOESY and ROESY correlation experiments (47–50) can be used to establish interresidue adjacencies after the positions of glycosidic linkages have been unambiguously established using through-bond correlations between acetyl ^{13}CO and sugar protons. These experiments were actually demonstrated some time ago in peracetylated structures examined without ^{13}C in the acetyl groups (51, 52). Nonasaccharide-alditol **1** yielded reasonably strong NOESY cross-peaks. A number of cross-peaks from the anomeric protons were assignable in this structure and the interproton NOE interactions are shown in Scheme 1. These assignments permitted monosaccharide adjacencies to be established, which, along with the through-bond assignments of the linkage sites via acetylation positions, enabled the overall structure to be deduced *from first principles.* Based on observations so far, assignment of 2-D NOESY or ROESY cross-peaks is the most difficult aspect of overall structural assignment. The use of ROESY is required for structures where $\omega\tau_c$ approaches 1, where ω is the angular Larmor frequency and τ_c is the motional correlation time. For acetylated oligosaccharides this is in the range of 4–6 sugars. To improve resolution in additional dimensions, we are currently developing methods to correlate acetyl ^{13}C nuclei to ring protons prior to the NOESY transfer step.

As was highlighted by Otter and Bundle (53), four- or five-bond *interresidue* ^{1}H–^{1}H *J* couplings may be observed

© 2002 NRC Canada

Fig. 7. A gradient COSY spectrum (^{13}CO-decoupled) of doubly ^{13}C-labeled, peracetylated 2-acetamido-2-deoxy-6-*O*-α-(5-*N*-acetylneuraminyl)-D-galactitol (**3**). Spectra were recorded in water-saturated $CDCl_3$. Individual cross-peaks of the *N*-acetylneuraminic acid residue are indicated.

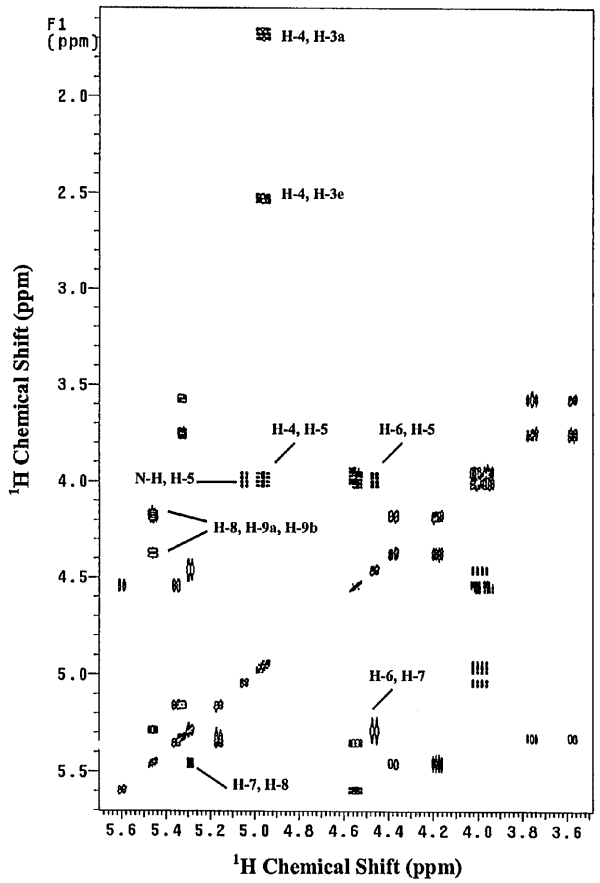

between residues across glycosidic linkages in COSY experiments. We have also observed these correlations, which are much less intense than $^{2\text{ or }3}J_{H,H}$. The ability to observe these long-range couplings depends on whether enough sample is available for the signals to be detected above the noise in the time selected to run the experiment. If observed, they provide corroborative information to NOESY or ROESY data.

Results with sialylated oligosaccharides

Oligosaccharides having *N*-acetylneuraminic acid are straightforward to peracetylate with minor modifications of the method. The basic pattern of the acetylated NeuNAc spin system and some salient points for assigning and measuring ^{1}H–^{1}H *J* couplings can be illustrated with a few examples of smaller structures (**2**–**4**). The protons on the acetylated positions 4, 7, and 8 are found downfield with respect to those on the acetylated position 9, *N*-acetylated position 5, and cyclization position 6. The amide proton overlaps approximately with the downfield *O*-acetylated protons. The H-3e/H-3a protons are both found well upfield, between 1.5–2.7 ppm. A ^{13}CO-decoupled gCOSY experiment with doubly ^{13}C-labeled *O*-peracetylated structure **2**, as its deuterated triethylammonium salt, permitted full assignment of the spin system. The ^{1}H–^{1}H *J* couplings (Hz) were extracted from a 1-D spectrum and are as follows: $J_{3e,3a}$ = –12.0; $J_{3a,4}$ = 11.9; $J_{3e,4}$ = 4.6; $J_{4,5}$ = 10.3; $J_{NH,5}$ = 10.2; $J_{5,6}$ = 10.6; $J_{6,7}$ = 2.2; $J_{7,8}$ = 7.3; $J_{8,9a}$ = 2.9; $J_{8,9b}$ = 6.4; $J_{9a,9b}$ = –12.3. These coupling constants were similar for sialic acids in all oligosaccharides we have examined so far. For example, a ^{13}CO-decoupled gCOSY spectrum of disaccharide-alditol **3** (Fig. 7) shows minor chemical shift differences from **2**, but the sialic acid coupling networks are straightforward to clarify starting with the H-3a/H-3e signals. Using trisaccharide-alditol **4**, the ^{13}CO-decoupled PIP-TOCSY spectrum (Fig. 8A) reveals the three independent spin systems. Traces taken at the arrows shown in Fig. 8A reveal the crucial couplings of all the ring protons for the sialic acid and β-GlcNAc residue (Figs. 8B and C). Magnetization starting from H-4 of the sialic acid proceeds to H-3a, H-3e, H-5, N-H, and H-6 (Fig. 8B). The pure in-phase nature of all these multiplets permitted accurate measurement of ^{1}H–^{1}H *J* couplings and an immediate identification of the sialic acid spin system. Similarly, magnetization starting from N-H of the β-GlcNAc residue proceeded to H-2, H-1, H-3, and H-4 of the sugar ring, and the measurable coupling constants of these multiplets enabled an unambiguous determination of the stereochemistry of this residue within the larger molecule. In a similar manner, the pure-absorption in-phase correlations of sugar-ring protons to acetyl ^{13}CO, $^{13}C^{Me}$, or $^1H^{Me}$ frequencies observed in $HC_{Me}COH$-HEHAHA experiments enabled sugar ^{1}H–^{1}H *J* couplings to be measured directly (spectra not shown).

Comparisons with other derivatives or correlations to sugar hydroxyl protons

As was indicated earlier (29), in theory, any functional group having magnetically susceptible nuclei could be used to identify the positions of free hydroxyl groups, which includes the protons of hydroxyl groups themselves (54–56) prior to derivatization. In consideration of derivatives in general, one key issue is whether the majority of oligosaccharides can actually be fully derivatized. We have examined acetylation, methylation, and trimethylsilylation as potential derivatives for NMR studies as they are the most commonly used to fully derivatize carbohydrate structures.

The protons of hydroxyl groups in underivatized oligosaccharides correlate to sugar-ring protons in predominantly H_2O solutions (54–56) or in polar aprotic solvents such as deuterated dimethylsulfoxide or *N*,*N*-dimethylformamide. Three major advantages of peracetylation are evident over direct correlation of sugar-ring protons to hydroxyl protons. First, spectral dispersion of the sugar-ring protons is not significantly altered in H_2O–co-solvent mixtures or in polar aprotic solvents, and hence these protons are still crowded within a 1.0 ppm region. Second, there are difficulties in limiting fast exchange of hydroxyl protons in water to the point where reasonably narrow linewidths can be observed. This requires the use of co-solvents that permit temperatures to be lowered below 0°C and the careful deionization of solutions (56). These lower temperatures also affect motional correlation times and broaden linewidths by other mechanisms. In polar organic solvents, very dry conditions are important. For example, we have examined the use of *N*,*N*-dimethylformamide-d_7 (Isotec) well dried over molecular sieves (Sigma, product M-0133, 1/16 inch pellets). Exchange was negligible in the complete absence of water and measurable

© 2002 NRC Canada

Fig. 8. (A) A PIP-TOCSY spectrum of peracetylated oligosaccharide **4** having doubly ^{13}C-labeled acetyl groups, derived from bovine submaxillary mucin. The spectrum was performed with GARP decoupling in the directly detected dimension, in water-saturated $CDCl_3$ at 27°C. Traces parallel to the F_2 (horizontal axis) are shown, representing signals at the F_1 frequencies pointed out with the large, open arrow (in B), and the smaller arrow (in C). The trace in (B) reveals part of the spin system of the *N*-acetylneuraminic acid. Magnetization derived from H-4 is transferred through the spin system from the H-3's to H-6 and these correlations were observable as purely absorptive in-phase multiplets. Similarly, the trace in (C) shows the coupling network of the β-GlcNAc residue. Magnetization derived from the N-H proton is transfered from H-1 to H-4. These traces enabled all sugar-ring ^1H–^1H *J*-coupling constants to be measured for these monosaccharides.

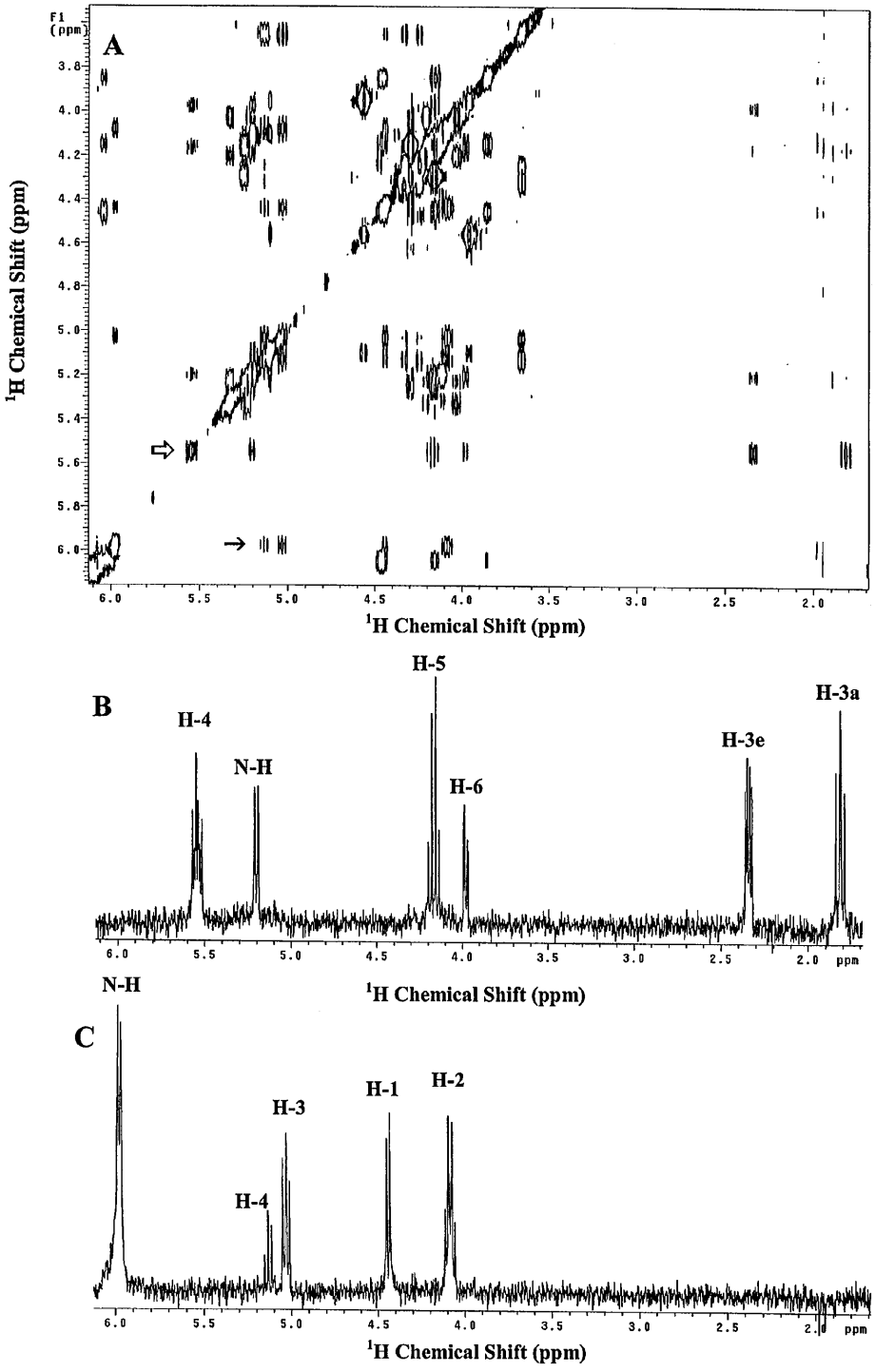

sugar-^{1}H/hydroxyl-^{1}H coupling constants can be extracted *at room temperature*. The hydroxyl proton signals resonate downfield of sugar-ring protons as well-resolved doublets of narrow linewidth (data not shown). Third, unlike acetylation,

© 2002 NRC Canada

where three independent frequencies may be correlated, hydroxyl protons permit only one additional frequency domain to be correlated to ring protons.

The use of methylated derivatives also proved to have specific drawbacks. Most importantly, permethylation does not result in any appreciable downfield shifting of sugar-ring proton signals, so overlap of these multiplets is essentially the same for derivatized sugars as for the underivatized structures. Added to this difficulty, methyl proton signals almost completely overlap with the sugar-ring proton multiplets, which prevents any selective excitation or decoupling of methyl proton frequencies. Pulses on the methyl carbon result in the vast majority of coherence transfer to methyl protons through the large $^1J_{C,H}$ coupling, which cannot be selectively decoupled. With peracetylation, the availability of three different frequency domains that can be independently manipulated using selective decoupling and (or) excitation pulses is far superior for multidimensional experiments.

We also attempted trimethylsilylation of smaller di- and trisaccharide-alditols, based on a report by Uhrin et al. (57) that correlated ^{29}Si to sugar protons at the site of trimethylsilylation. In reactive reagents for derivatization such as trimethylsilyl chloride, ^{29}Si is, however, commercially limited to natural abundance (5.1%). Also, trimethylsilylation does not induce an appreciable downfield shift of protons at trimethylsilylated positions (see ref. 57 and preliminary experiments, not shown). TMS ethers, being prone to hydrolysis, are also less stable than acetyl groups — rendering further chromatography of such derivatives essentially impossible, should minor initial oligosaccharide contaminants be present in the sample. Hence, we suggest that for the purposes of structural elucidation of oligosaccharides, the use of doubly ^{13}C-labeled acetyl esters have several important advantages over the use of either methyl or trimethylsilyl ethers, or over the use of protonated hydroxyl groups themselves.

Practical aspects of peracetylation and sample preparation for NMR

The use of the superacylation catalyst 4-dimethylaminopyridine in a pyridine–acetic anhydride solution markedly accelerates acylation and all solvent components can be almost entirely removed by volatilization. Additional partitioning between chloroform and a deuterated triethylammonium sulfate solution completely eliminates the catalyst and additional washes of the chloroform phase results in essentially pure peracetylated product. There are two crucial issues in the acylation process worthy of note. First, any salts in a sample prior to drying can result in poor solubility in the pyridine–acetic anhydride solution. Both sonication and prior concentration in vacuo in the presence of glycerol can help to alleviate this problem, but the best solution for neutral oligosaccharides is to ensure they are free of salt by passage through small well-washed columns (in Pasteur pipettes having a glass wool plug) of Dowex AG50W-X8 (H^+ form, 100–200 mesh) and AG1-X8 (OAc^- form, 100–200 mesh) prior to concentration. Second, sialylated oligosaccharides must be converted to triethylammonium or tripropylammonium salts, as described in the *Experimental* section. It is crucial to observe full solubility of the sample prior to heating. We have found the described conditions are required to completely acetylate without the need for chromatography. NMR is the best tool to check for completion of acetylation, where any minor components will be evident and where the heteronuclear COSY experiment permits a count of the acetyl ^{13}CO/sugar ^{1}H correlations. It should be noted that these acetylation conditions were determined for oligosaccharides containing fewer than ~20 monomers, and should be applicable to a majority of structures in this size range. Methods were designed for volatility of solvents and other components to permit immediate analysis by NMR. For large polysaccharides, a number of other acylation methods have been reported, especially in the peracylation of cellulose, which is of commercial importance (reviewed in ref. 58). The conditions reported are especially effective in initial solubilization of larger polymers, and may be applicable if solubilization in the system reported herein is ineffective.

Regarding NMR spectroscopy, the chemical shifts of the samples in $CDCl_3$ alone are not reproducible. The addition of water or D_2O to saturate the solvent has significant effects on chemical shifts and is mandatory for reproducible results. Presumably by saturating the $CDCl_3$ phase, hydrogen-bonding and other (electrostatic) dipole–dipole interactions are limited within and between molecules. Relative to internal tetramethylsilane, chemical shifts are reproducible to within ±0.002 ppm whether obtained from 1-D experiments or from traces in the directly detected dimension of 2-D or 3-D experiments where purely absorptive in-phase multiplets are recorded with the same Hz per point ratio as 1-D experiments. Depending on the experiments that need to be performed to extract all pertinent data, approximately 35–250 nmol of sample is required, and can take from about 1 to 4 days of NMR time to complete.

Conclusions

Major advantages to peracetylation with doubly ^{13}C-labeled acetyl groups

Compared to the typical acquisition of NMR data of oligosaccharides in D_2O, any one of the advantages below would be an important reason to peracetylate with doubly ^{13}C-labeled acetyl groups. Together, they provide a powerful justification for use of this strategy for carbohydrate structural elucidation. The combined acetylation–NMR approach provides new tools for the extraction of detailed structural information of larger oligosaccharides.

(*i*) Enables linkage sites to be determined — The ability to assign the sites of acetyl-group substitution is based on the 2.5–4.7 Hz through-bond coupling ($^3J_{C,H}$) observed between acetyl ^{13}CO carbons and ring protons at the positions of acetylation (29, 43). The position of a glycosidic linkage can therefore be unambiguously assigned. With underivatized structures in D_2O, this information cannot be sensitively obtained. Observation of through-bond ^{13}C–^{1}H couplings across glycosidic linkages is very insensitive in natural abundance structures. The strongest interresidue ^{1}H–^{1}H NOE's may not be between two protons directly across the glycosidic linkage (59), and the same conclusion was reached for long-range interresidue correlations sometimes seen in gCOSY experiments (53).

© 2002 NRC Canada

(*ii*) Increased spectral dispersion in the sugar ^{1}H dimensions — Underivatized oligosaccharides in D_2O display a spectral range for ring protons between ~3.2 and 4.2 ppm and anomeric signals from ~4.4 to 5.4 ppm. Hence, six out of seven signals for a typical hexose reside in a range of 1.0 ppm, resulting in severe overlap and frequent strong coupling effects. In peracetylated structures, sugar-ring proton signals range from ~3.2 to 5.8 ppm, approximately 2.6–2.7-fold greater than in D_2O. This is almost a sevenfold increase in the area where cross-peaks are found in ^{1}H–^{1}H correlated experiments, an enormous advantage for solving larger structures. In addition, far fewer strong couplings occur. These are both important advantages over biosynthetic ^{13}C labeling of the sugar backbone, where ^{1}H dispersion is unchanged.

(*iii*) Markedly improves the ability to prove stereochemistry of monosaccharides within oligosaccharides, through combined use of indirect dimensions and pure in-phase coherence transfer — Based on the orientation of hydroxyl groups with respect to the sugar ring, each monosaccharide has its own characteristic pattern of *J*-couplings. Measurement of ring ^{1}H–^{1}H *J* values by extraction of purely absorptive in-phase multiplets (39) is crucial for delineation of individual spin systems. Resolution of ring proton multiplets is markedly improved through their correlation to the ^{13}CO, $^{13}C^{Me}$, or $^{1}H^{Me}$ dimensions. From these multiplets, $J_{1,2}$, $J_{2,3}$, $J_{3,4}$, and $J_{4,5}$ may be accurately measured, which defines the stereochemistry, anomeric configuration, and ring form of an individual sugar. For pyranosides, the ring conformations are relatively rigid and appear essentially the same after acetylation. We have not yet examined oligosaccharides containing furanosides, but expect that acetylated furanosides will be more flexible, and that more information regarding the *J*-coupling patterns of acetylated furanosides with specific substitutions will need to be amassed from model structures prior to confident identification of their stereochemistries in unknown molecules.

(*iv*) Greatly increases sensitivity in experiments using ^{13}C frequencies — Experiments designed to correlate acetyl ^{13}C frequencies with sugar-ring protons, or that compare ^{13}C–^{1}H coupled multiplets vs. carbon-decoupled spectra, can be performed at ~90-fold greater sensitivity than any natural abundance spectra. This would simply not be possible without the introduction of the ^{13}C acetyl groups. These advantages apply to oligosaccharides isolated from virtually any source, and are not limited to oligosaccharides prepared by biosynthetic ^{13}C-labeling of sugar backbone carbons.

(*v*) Provides flexibility in the type of NMR experiments that are possible — The widely separated frequencies of the ^{13}CO, $^{13}C^{Me}$, and $^{1}H^{Me}$ nuclei permit independent manipulation through band-selective excitation and (or) decoupling schemes. This provides a powerful means for controlling magnetization transfers and for elimination of unwanted couplings during evolution or direct-detection periods, thereby simplifying cross-peak multiplet structures in the different dimensions as desired.

(*vi*) Amide protons in HexNAc residues resonate downfield — The NH protons of HexNAc residues resonate well downfield in water-saturated $CDCl_3$ (5.9–7.0 ppm), and these protons selectively identify HexNAc spin systems via pure in-phase homonuclear Hartmann–Hahn transfer. In D_2O, these protons are quickly exchanged in underivatized structures, although it is possible to correlate them in predominantly H_2O solutions (60).

(*vii*) Advantages over other functional groups we have examined — These were pointed out in the *Results and discussion* section; major advantages of acetylation over methylation or trimethylsilyation were evident, as well as over the use of hydroxyl protons themselves.

Information not obtained by these methods

Regarding information that cannot be extracted with these methods, the determination of specific enantiomers (D or L forms) of monosaccharides within oligosaccharides is currently not possible. Also, unambiguous identification of inorganic substituents having magnetically susceptible nuclei at low natural abundance is not possible, although a substitution site would be evident. The presence of non-protonated carbons, as occurs in uronic acids, or novel branched-chain monosaccharides, for example, would also warrant use of additional methods. In these cases, degradation to monosaccharides (61, 62) or mass spectrometry (63, 64) would be either advantageous or necessary. Mass spectrometry of intact oligosaccharides should always be performed as it provides a completely independent vantage for structural evaluation. We use it routinely because it readily reveals any substituents, such as sulfates, unobservable by NMR, and because it provides important confirmatory information regarding branch patterns and potentially linkage positions when cross-ring cleavages occur. Although peracetylated oligosaccharides can be examined by mass spectrometry, direct losses of ketenes are abundant and permethylated structures yield more detailed structural information. Prior peracetylation is however fully compatible with latter permethylation, as acetylation of carbohydrate structures increases their initial solubility in dimethylsulfoxide during the permethylation procedure. The acetates are rapidly cleaved and the sites are then available for methylation.

The strategy reported here of combining tailored NMR pulse sequences with ^{13}C-acetylation of oligosaccharides provides a great deal more structural information than can be garnered by other NMR methods. The advantages so outweigh conventional NMR spectroscopy of underivatized structures in D_2O that for the purposes of primary structural elucidation we currently peracetylate routinely. It is interesting to note that back at a time when 40 MHz was considered a "high-field" instrument, the very first spectra of carbohydrates happened to be obtained from sugar peracetates, which showed just enough resolution to decipher details of their fine structure. In what appears to be the very first report of carbohydrate NMR, Lemieux and Kullnig (5) stated that "The proton resonance spectra of a variety of fully acetylated sugars and sugar alcohols were determined in chloroform solution in order to gain an appreciation of the possible use of this new physical method in the field of carbohydrate chemistry. Well-resolved signals were produced by the various kinds of hydrogen atoms found in these compounds, except for the C_5-hydrogen of a hexopyranose acetate, in which case the band is overlapped with that of the C_6-methylene hydrogens."

With the current benefits enjoyed at markedly higher field strength instruments, much larger structures should be possible

© 2002 NRC Canada

to elucidate as ^{13}C-labeled peracetates. Regarding the size of oligosaccharides that might be examined by these new methods, reports from the literature indicate that peracetylated polysaccharides, such as cellulose acetate having >100 monomers (65), display very narrow linewidths when examined in $CDCl_3$ at 50°C, a somewhat higher temperature than reported here. This suggests that some polysaccharides, although very high in molecular weight, have internal mobilities about glycosidic bonds that will render them amenable to these procedures. The often-used approach to polysaccharide elucidation, by internal site-selective cleavage to substructures and fractionation by some means, should enable their structures to be solved by these techniques where such subunits are less than ~20 monomers in size. The upper size limits of oligosaccharides to which these methods may be applicable could be significantly larger at higher temperatures.

Experimental

Oligosaccharides were isolated from bovine fibrin, fetuin, and submaxillary mucin (66–71), and those presented in detail here were illustrative of 40 peracetylated oligosaccharides studied to date having doubly ^{13}C-labeled acetates. All were examined after borohydride reduction (72) to avoid anomeric mixtures at the reducing end. 2-*O*-Methyl-α-D-5-*N*-acetylneuraminic acid was from Sigma.

Peracetylation

Peracetylation was carried out using the superacylation catalyst 4-dimethylaminopyridine, which has been reported to catalyze acylation reactions approximately 10^5 times faster than pyridine alone (73). A dried oligosaccharide (between ~100 μg to 2 mg, in a 1.5 mL vial with Teflon cap) was dissolved in a solution (175 μL) containing 4-dimethylaminopyridine (25 mM, Aldrich, 99+%) in pyridine (99.9+%, HPLC grade, Sigma-Aldrich). To the solution was added acetic anhydride (25 μL, 1,1′,2,2′-$^{13}C_4$, Isotec or Cambridge Isotopes), the vial capped under argon or nitrogen, and the sample heated at 50°C for 5 h. For larger structures, full dissolution accompanied gentle warming, which was carried out at 30–35°C usually up to about 1 h, with occasional brief (about 5 s) sonication periods in a sonication bath being necessary for some oligosaccharides prior to heating to 50°C for 5 h. It was important to observe complete solubilization of the sample prior to heating. Occasional sonication at lower temperatures must be continued for as long as necessary for dissolution. The sample was then concentrated to dryness on a Speed-Vac concentrator (~3–4 h). Most of the 4-dimethylaminopyridine is volatilized under good vaccuum (<50 milliTorr) and residual quantities were subsequently extracted. The product was taken up in 1 mL chloroform and extracted 3 times with 0.5 mL of a solution containing 0.1 M triethylammonium sulfate, pH 6.5 (prepared from triethylammonium-d_{15}, Cambridge Isotopes or Isotec, and dilute sulfuric acid), then 3 times with 0.5 mL water. The chloroform phase was concentrated as above, and the sample was again concentrated in $CDCl_3$ prior to being taken up in 0.7–1.0 mL $CDCl_3$ for NMR, with a trace of tetramethylsilane added as an internal standard. For samples of less than 100 μg, the sample was initially concentrated from 100 μL water containing 1% glycerol, which dried the material in a glycerol phase. This prevented losses due to sticking on glass, and enabled rapid dissolution of structures in the pyridine — superacylation catalyst — acetic anhydride phase. The peracetylated glycerol was volatile, and was completely removed by concentration twice from $CHCl_3$ under vacuum. Sialylated oligosaccharide-alditols were converted to their triethylammonium salts prior to acetylation by inclusion of 10 mM triethylammonium acetate, pH 7, as a buffer during their chromatography on Sephadex G-10 or G-15 columns (used for final desalting after HPLC with NaCl gradients). Sialylated oligosaccharides were peracetylated much more readily as such, rather than as Na^+ salts, due to increased solubility during acetylation. Tripropylamine salts may also be used; they ultimately are replaced during extraction with deuterated triethylammonium sulfate. With small sialylated structures (fully *O*-acetylated structures **2** and **3**) some of the product entered the water phases and needed to be back-extracted in chloroform for further recovery. With larger structures, this was not an issue. After peracetylation, all sialylated molecules were exposed to water during the chloroform–water extraction procedure to ensure hydrolysis of any potential mixed anhydride at the carboxyl group.

Where samples contained a minor oligosaccharide contaminant prior to peracetylation, reversed-phase HPLC was performed to separate products according to Hall and Patrick (74) on a column of Spherisorb ODS-2, 3 μm bead size (Alltech). Peracetylated oligosaccharides are very sensitive to UV detection at 200 nm using acetonitrile–water to elute. With sialylated oligosaccharides, inclusion of 1 mM triethylammonium acetate in the eluent was used as a volatile ion-pairing reagent, which markedly improved retention times.

Sample preparation for NMR spectroscopy

Samples were prepared for NMR experiments by adding water (or D_2O, 10–50 μL) directly to the sample in $CDCl_3$ in a 5-mm NMR tube (Wilmad), which floated on and saturated the $CDCl_3$. Exchangeable protons can be replaced by deuterium or back again with impunity by layering water or D_2O (about 0.3 mL) over the organic phase, allowing time to equilibrate, carefully removing it with an elongated pipette and repeating this twice to fully exchange. In 5-mm tubes, enough $CDCl_3$ was added so that the water was at least 1 cm above the receiver coil. Samples were not mixed, just layered with water; small water droplets stick on the sides of the NMR tube in the area of the coil if mixed thoroughly. The addition of water or D_2O is absolutely necessary to obtain reproducible chemical shifts in $CDCl_3$. In 3-mm tubes having a magnetic susceptibility matched to chloroform, with a glass insert to minimize sample volume to the region of the coil (Shigemi Co.), the sample was dissolved in 200 μL $CDCl_3$, the insert set in position, and water (20 μL) layered on top by adding it down the side of the insert. To prevent evaporation of the solvent, the sample can be effectively sealed using a heat-shrinkable plastic tubing at the top of the tube (product 278–1627B, Radio Shack) and a hot air blower.

NMR spectroscopy

NMR spectroscopy was carried out on a Varian Inova instrument equipped with *z*-axis gradients at a ^1H frequency of

© 2002 NRC Canada

500 MHz. For all samples, experiments were carried out at 27°C, with some samples also recorded at 35°C to compare linewidths. Either a Varian 5-mm or Nalorac 3-mm triple resonance probe was used. The spectrometer was configured with pulse shaping capability on both ^{1}H and ^{13}C transmitter channels and on the gradient channel. Shaped pulse waveforms were generated using the Varian software "Pbox" and verified in the program "Pulsetool," then checked experimentally. Gradient waveforms were generated from in-house programs. Data were either processed with VNMR (Varian) or Felix (MSI Inc.). A mild composite sinebell–Gaussian window function (75) was applied in all dimensions prior to Fourier transformation. Details of specific pulse sequences are indicated in the legend of Fig. 3 and in ref. 43.

Acknowledgments

Funding is gratefully acknowledged from the Mizutani Foundation for Glycosciences, the University of Colorado Health Sciences Center, an NCI supplement to the University of Colorado Cancer Center Core grant NIH5-P30-CA46934–10, and for instrumentation, the Howard Hughes Medical Institute. We also thank Shigemi Co. for discussions concerning use and sealing of microsample tubes containing chloroform.

References

1. M. Karplus. J. Am. Chem. Soc. **85**, 2870 (1963).
2. M. Karplus. J. Chem. Phys. **30**, 11 (1959).
3. R.U. Lemieux, R.K. Kullnig, and R.Y. Moir. J. Am. Chem. Soc. **80**, 2237 (1958).
4. R.U. Lemieux, R.K. Kullnig, H.J. Bernstein, and W.G. Schneider. J. Am. Chem. Soc. **79**, 1005 (1957).
5. R.U. Lemieux and R.K. Kullnig. Abstracts of papers, 130th meeting of the American Chemical Society, Atlantic City, N.J. Sept 16–21. 1956. Abstract p. 10-D.
6. R.U. Lemieux, R.K. Kullnig, H.J. Bernstein, and W.G. Schneider. J. Am. Chem. Soc. **80**, 6098 (1958).
7. R.U. Lemieux. Trans. Roy. Soc. Can. **32**, 31 (1958).
8. J.F.G. Vliegenthart, L. Dorland, and H. van Halbeek. Adv. Carbohydr. Chem. Biochem. **41**, 209 (1983).
9. J.P. Carver and A.A. Grey. Biochemistry, **20**, 6607 (1981).
10. T.A.W. Koerner, J.H. Prestegard, and R.K. Yu. Methods Enzymol. **138**, 38 (1987).
11. T. Peters and M. Pinto. Curr. Opin. Struc. Biol. **6**, 710 (1996).
12. C.A. Bush, M. Martin-Pastor, and A. Imberty. Ann. Rev. Biophys. Biomol. Struc. **28**, 269 (1999).
13. D. Horton. *In* The amino sugars. The chemistry and biology of compounds containing amino sugars. Vol. 1A. *Edited by* R.W. Jeanloz. Academic Press, New York. 1969. pp. 1–211.
14. B. Lindberg. Adv. Carbohydr. Chem. Biochem. **48**, 279 (1990).
15. D.R. Lide. CRC handbook of chemistry and physics. 74th ed. CRC Press, Boca Raton, Florida. 1993. pp. 7-22 to 7-27.
16. R.F. Butterworth and S. Hanessian. Adv. Carbohydr. Chem. Biochem. **26**, 279 (1971).
17. N.K. Kochetkov and G.P. Smirnova. Adv. Carbohydr. Chem. Biochem. **44**, 287 (1986).
18. J. Yoshimura. Adv. Carbohydr. Chem. Biochem. **42**, 69 (1984).
19. H. Bretting, G. Jacobs, I. Benecke, W.A. Konig, and J. Thiem. Carbohydr. Res. **139**, 225 (1985).
20. P. Dais. Adv. Carbohydr. Chem. Biochem. **51**, 63 (1995).
21. M. Martin-Pastor and C.A. Bush. Biopolymers, **54**, 235 (2000).
22. B. Bose-Basu, J. Zajicek, G. Bondo, S. Zhao, M. Kubsch, I. Carmichael, and A.S. Serianni. J. Magn. Res. **144**, 207 (2000).
23. J. Chung, J.R. Tolman, K.P. Howard, and J.H. Prestegard. J. Magn. Reson. Ser. B, **102**, 137 (1993).
24. R. Harris, T.J. Rutherford, M.J. Milton, and S.W. Homans. J. Biomol. NMR, **9**, 547 (1997).
25. B. Lindberg and J. Lonngren. Methods Enzymol. **50**, 3 (1978).
26. S. Hakomori. J. Biochem. **55**, 205 (1964).
27. I. Ciucanu and F. Kerek. Carbohydr. Res. **131**, 209 (1984).
28. G.R. Gray. Methods Enzymol. **193**, 573 (1990).
29. B. Bendiak. Carbohydr. Res. **315**, 206 (1999).
30. J. Herzig, A. Nudelman, H.E. Gottlieb, and B. Fischer. J. Org. Chem. **51**, 727 (1986).
31. J. Eberling, P. Braun, D. Kowalczyk, M. Schultz, and H. Kunz. J. Org. Chem. **61**, 2638 (1996).
32. R. Hurd. J. Magn. Reson. **87**, 422 (1990).
33. C. Griesinger, O.W. Sorensen, and R.R. Ernst. J. Magn. Reson. **75**, 474 (1987).
34. L. Mueller. J. Magn. Reson. **72**, 191 (1987).
35. T.J. Norwood. J. Magn. Reson. Ser. A, **114**, 92 (1995).
36. L. Zhu, B.R. Reid, and G.P. Drobny. J. Magn. Reson. Ser. A, **115**, 206 (1995).
37. J. Yang, K. McAteer, L.A.P. Silks, R. Wu, N.G. Isern, C.J. Unkefer, and M.A. Kennedy. J. Magn. Reson. **146**, 260 (2000).
38. F. Delaglio, Z. Wu, and A. Bax. J. Magn. Reson. **149**, 276 (2001).
39. A.L. Davis, G. Estcourt, J. Keeler, E.D. Laue, and J.J. Titman. J. Magn. Reson. Ser. A, **105**, 167 (1993).
40. J.J. Titman, A.L. Davis, E.D. Laue, and J. Keeler. J. Magn. Reson. **89**, 176 (1990).
41. S.J. Glaser and J.J. Quant. Adv. Magn. Opt. Reson. **19**, 59, (1996).
42. G.A. Morris and R. Freeman. J. Am. Chem. Soc. **101**, 760 (1979).
43. D.N.M. Jones and B. Bendiak. J. Biomol. NMR, **15**, 157 (1999).
44. E.R.P. Zuiderweg. J. Magn. Reson. **89**, 533 (1990).
45. L.R. Brown and B.C. Sanctuary. J. Magn. Reson. **91**, 413 (1991).
46. M. Ernst, C. Griesinger, R.R. Ernst, and W. Bermel. Mol. Phys. **74**, 219 (1991).
47. J. Jeener, B.H. Meier, P. Bachmann, and R.R. Ernst. J. Chem. Phys. **71**, 4546 (1979).
48. S. Macura and R.R. Ernst. Mol. Phys. **41**, 95 (1980).
49. A.A. Bothner-By, R.L. Stephens, J. Lee, C.D. Warren, and R.W. Jeanloz. J. Am. Chem. Soc. **106**, 811 (1984).
50. A. Bax and D.G. Davis. J. Magn. Reson. **63**, 207 (1985).
51. J. Dabrowski, A. Ejchart, R. Bruntz, and H. Egge. FEBS Lett. **246**, 229 (1989).
52. S. Gasa, M. Nakamura, A. Makita, M. Ikura, and K. Hikichi. Eur. J. Biochem. **155**, 603 (1986).
53. A. Otter and D.R. Bundle. J. Magn. Reson. Ser. B, **109**, 194 (1995).
54. M.C.R. Symons, J.A. Benbow, and J.M. Harvey. Carbohydr. Res. **83**, 9 (1980).
55. L. Poppe and H. van Halbeek. J. Am. Chem. Soc. **113**, 363 (1991).
56. C. Sandstrom, H. Baumann, and L. Kenne. J. Chem. Soc. Perkin Trans. 2, 809 (1998).
57. D. Uhrin, S. Uhrinova, E. Eichler, and J.-R. Brisson. J. Magn. Reson. Ser. A, **115**, 119 (1995).
58. T. Heinze and W.G. Glasser. *In* Cellulose derivatives: modification, characterization and nanostructures. ACS symposium

© 2002 NRC Canada

series 688. *Edited by* T. Heinze and W.G. Glasser. 1998. pp. 2–18.
59. C.A. Bush, Z.-Y. Yan, and B.N.N. Rao. J. Am. Chem. Soc. **108**, 6168 (1986).
60. K. Hard, B.A. Spronk, C.H. Hokke, J.P. Kamerling, and J.F.G. Vliegenthart. FEBS Lett. **287**, 108 (1991).
61. K. Leontin and J. Lonngren. Meth. Carbohydr. Chem. **9**, 87 (1993).
62. S. Oshima, J. Kumanotani, and C. Watanabe. J. Chromatog. **259**, 159 (1983).
63. V.N. Reinhold, B.B. Reinhold, and C.E. Costello. Anal. Chem. **67**, 1772 (1995).
64. A. Dell, A.J. Reason, K.-H. Khoo, M. Panico, R.A. McDowell, and H.R. Morris. Meth. Enzymol. **230**, 108 (1994).
65. V.S. Rao, F. Sauriol, A.S. Perlin, and M.T. Phan Viet. Can. J. Chem. **63**, 2507 (1984).
66. B. Bendiak and D.A. Cumming. Carbohydr. Res. **144**, 1 (1985).
67. B. Bendiak, J. Orr, I. Brockhausen, G. Vella, and C. Phoebe. Anal. Biochem. **175**, 96 (1988).
68. B. Bendiak, M. Harris-Brandts, S.W. Michnick, J.P. Carver, and D.A. Cumming. Biochemistry, **28**, 6491 (1989).
69. D.A. Cumming, C.G. Hellerqvist, M. Harris-Brandts, S.W. Michnick, J.P. Carver, and B. Bendiak. Biochemistry, **28**, 6500 (1989).
70. S. Martensson, S.B. Levery, T.T. Fang, and B. Bendiak. Eur. J. Biochem. **258**, 603 (1998).
71. W.G. Chai, E.F. Hounsell, G.C. Cashmore, J.R. Rosankiewicz, J. Feeney, and A.M. Lawson. Eur. J. Biochem. **207**, 973 (1992).
72. M.L. Wolfrom and A. Thompson. Meth. Carbohydr. Chem. **2**, 65 (1963).
73. E. Scriven. J. Chem. Soc. Rev. **12**, 129 (1983).
74. N.A. Hall and A.D. Patrick. Anal. Biochem. **178**, (1989).
75. R.R. Ernst, G. Bodenhausen, and A. Wokaun. Principles of nuclear magnetic resonance in one and two dimensions. Clarendon Press, Oxford. 1987.
76. A.J. Shaka, C.J. Lee, and A. Pines. J. Magn. Reson. **77**, 274 (1988).
77. A.J. Shaka, P.B. Barker, and R. Freeman. J. Magn. Reson. **64**, 547 (1985).
78. H. Geen and R. Freeman. J. Magn. Reson. **93**, 93 (1991).
79. M.A. McCoy and L. Mueller. J. Magn. Reson. Ser. A, **101**, 122 (1993).
80. M.S. Silver, R.I. Joseph, and D.I. Hoult. J. Magn. Reson. **59**, 347 (1984).
81. J. Baum, R. Tycko, and A. Pines. Phys. Rev. **A32**, 3435 (1985).
82. E. Kupce and R. Freeman. J. Magn. Reson. **127**, 36 (1997).
83. L. Emsley and G. Bodenhausen. J. Magn. Reson. **97**, 135 (1992).

© 2002 NRC Canada

A strategy for the one-pot synthesis of sialylated oligosaccharides

Zhiyuan Zhang, Kenichi Niikura, Xue-Fei Huang, and Chi-Huey Wong

Abstract: A new strategy has been developed for the synthesis of branched sialylated oligosaccharides using one-pot technology. Sialyl donors are in general too weak in reactivity to be used as the first glycosyl donors in the one-pot synthesis. When sialic acid is linked to a different sugar such as galactose, the reactivity is, however, significantly enhanced and can be tuned to enable the one-pot synthesis. A combination of NIS–TfOH–AgOTf was used for activation of the thioglycosides to improve the glycosylation yield when a hindered acceptor was used, as illustrated in the one-pot assembly of sialylated hexasaccharide.

Key words: one-pot synthesis, sialyl oligosaccharides, new activation.

Résumé : Faisant appel à une technologie monotope, on a développé une nouvelle stratégie pour réaliser la synthèse d'oligosaccharides sialylés ramifiés. La réactivité des donneurs sialyles est généralement trop faible pour les utiliser comme premiers donneurs de glycosyle dans une synthèse monotope. Lorsque l'acide sialique est lié à divers sucres, comme le galactose, la réactivité est toutefois considérablement augmentée et elle peut être ajustée pour utilisation dans une synthèse monotope. Lorsque des accepteurs stériquement empêchés ont été utilisés, on a fait appel à une combinaison de NIS–TfOH–AgOTf pour l'activation des thioglycosides afin d'augmenter le rendement de la glycosylation; cette technique est illustrée par la synthèse monotope d'un hexasaccharide sialylé.

Mots clés : synthèse monotope, saccharides sialylés, nouvelle activation.

[Traduit par la Rédaction]

Introduction

Sialylated oligosaccharides are attractive targets for synthesis as most cancer cells carry sialylated oligosaccharides as unique markers on their surface (1). However, synthesis of sialylated oligosaccharides remains a major problem (2), mainly due to the low yield and low stereoselectivity in the sialylation step. Strategically, the difficult sialylation should be conducted at the early stage to maximize the overall yield and stereoselectivity. Sialic acid is, however, often found at the nonreducing end of oligosaccharides, and most methods developed for oligosaccharide synthesis start from the reducing end to the nonreducing end. The strategy based on Danishefsky et al.'s (3) glycal assembly, via epoxide intermediates, starts from the nonreducing end, but it is not applicable to sialic acid, as undesirable β-selectivity occurs.

Alternatively, fragment coupling using sialyl oligosaccharides as glycosylation reagents may minimize the problems. Another approach is based on the one-pot strategy (4), where an oligosaccharide is assembled rapidly from the nonreducing end to the reducing end by sequential addition of building blocks, with the most reactive one being added first. However, sialic acid thioglycosides (even a per-*O*-benzylated thioglycoside) are much less reactive and less influenced by the protecting group than the other thioglycosides (5). We have found that the major effect on the anomeric reactivity of sialic acid is from the carboxyl, not from the side-chain protecting groups. The reactivity difference between per-*O*-benzylated and per-*O*-acetylated sialosides is less than 100, compared to ~1×10^5 for the corresponding thioglycosides of the other sugars (5). Reduction of the carboxyl group does increase the reactivity by >1×10^4, but the α-selectivity is completely diminished and gives mainly the undesirable β-glycoside product (5). To tackle this problem, we decided to use sialylated disaccharides as building blocks in the one-pot synthesis, as the reactivity of a disaccharide or trisaccharide glycosyl donor is mainly determined by the reducing end unit (4*d*). Here we report the representative one-pot synthesis of a protected sialyl Lewis X hexasaccharide (1) to illustrate this strategy.

Received 4 December 2001. Published on the NRC Research Press Web site at http://cjc.nrc.ca on 20 August 2002.

Dedicated to the memory of Professor Raymond U. Lemieux.

Z. Zhang, K. Niikura, X.-F. Huang, and C.-H. Wong.[1] Department of Chemistry and the Skaggs Institute for Chemical Biology, The Scripps Research Institute, 10550 North Torrey Pines Road, La Jolla, CA 92037, U.S.A.

[1]Corresponding author (e-mail: wong@scripps.edu).

Experimental and results and discussion

As shown in Fig. 1, the target molecule could be assembled from the sialylated disaccharide **2**, the thiofucoside **4**, the 2-*N*-Phth glucoside **3**, and the lactoside **5**. This strategy is based on the following analysis: when a 2-*O*-acylated glycosyl donor couples with a 2-*N*-phthalimido protected 3,4-diol glucosyl acceptor (i.e., **2** + **3**), it is expected to give a 1,4-β linked product (5). This would allow the one-pot strategy to proceed through a fucosylation with **4** after the

 DOI: 10.1139/V02-131 © 2002 NRC Canada

Fig. 1. Retro-synthetic analysis for the one-pot assembly of protected sialyl Lewis X hexasaccharide.

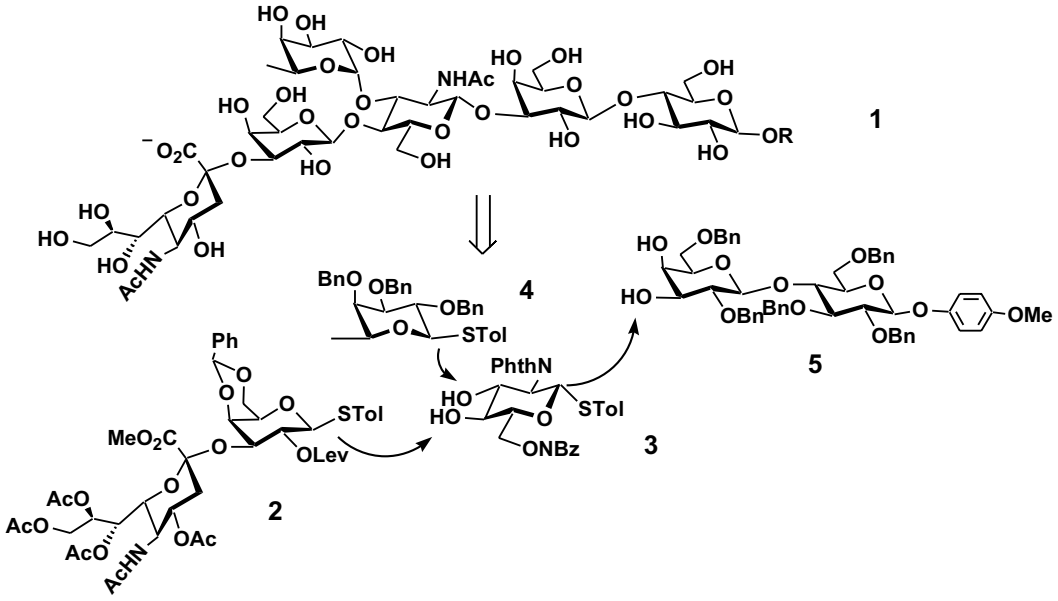

first step, followed by coupling with the final acceptor lactoside **5**.

We expect that the 2,3-linked disaccharide **2** would have a similar reactivity as the methylphenyl 2,3-di-*O*-benzoyl-4,6-*O*-benzylidene-1-thio-β-D-galactopyranoside (RRV = 285), and would be at least 10 times more reactive than 6-*O*-nitrobenzoyl-2-*N*-phthalimido β-glucoside **3**. Compound **2** was synthesized from phosphite **6** (7) and thiogalactoside **7** followed by acylation. The desired α-product **8** was isolated in 21% yield, and the lactonized product **9** was the major side product (8% yield). Protection of the 2-OH group using levulinic acid gave the desired product **2** in 86% yield.

To reduce the reactivity of the 2-*N*-Phth glucoside, a nitrobenzoyl group was selected as the 6-*O* protecting group. Monobenzoylation of the 2-*N*-phthalimido glucoside **3** was first tried with *p*-NO_2BzCl–DMAP–pyridine in THF. This reaction mainly gave two products, the 3,6-di-*p*-nitrobenzoylated compound **10** (35% yield), and 6-*O*-NBz **3** (53% yield), which were difficult to purify. However, pure compound **3** was easily obtained in 83% yield when we treated compound **10** with $(Bu_2Sn)_2O$ followed by *p*-nitrobenzoyl chloride.

The last component, lactoside acceptor **5**, was prepared (in 74% overall yield) from the free lactoside **11** (Fig. 2) through three steps and a single purification. An improved procedure, using DMF as the cosolvent together with α,α-dimethoxypropane under H_2SO_4 treatment, gave a good yield of isopropylidene lactoside. The crude product was subjected to further benzylation and TFA treatment to give the diol **5** after final purification.

Before we started the assembly, we measured the reactivities of compound **2** and compound **3**, using the HPLC method developed in this group. Compound **2** (RRV = 1308) was found to be 23 times more reactive than compound **3** (RRV = 57). To make sure that the glycosylation and the regio- and stereoselectivities would work as predicted during the one-pot synthesis, we tried a one-pot synthesis (Fig. 3) of the protected Lewis X trisaccharide **14**, and the product was isolated in more than 85% yield.

Encouraged by this result, we then conducted the assembly of the four components **2**–**5** in a one-pot procedure. Our experience suggests that exclusively dry conditions are the key to a successful glycosylation step, and these conditions are even more important in the one-pot procedure as more reagents and substrates are added to the reaction flask. The relative amounts of building blocks used is also one of the important factors. Normally, the use of less equivalents of the acceptor at each step can have many advantages. First, it increases the selectivity; for example, if the concentration ratio of the donor and the acceptor in the beginning is 1.5, the ratio would roughly be ~2.0 in the middle of the reaction, and much higher near the end. Second, the excess amount of donor can still be activated, even though all of the acceptor is consumed and trapped by the released succinimide to form the glycosyl succinimide. When the last acceptor is an *O*-linked glycoside, using an excess of the acceptor will increase the yield. Through several attempts at the synthesis of the SLe X hexasaccharide, we found that the optimal ratio of building blocks (**2**:**3**:**4**:**5**) is 1.3:1:1.5:2.

We first tried the one-pot assembly using NIS–TfOH as the promoter. TLC analysis showed a good result in the first step (coupling **2** with **3**); however, almost no reaction was observed in the second step, probably due to the steric hindrance at 3-OH after the 4-OH position was glycosylated to the disaccharide **2**. In addition, most of the thiofucoside **4** was converted to its succinimide derivative.

To reduce the amount of the succinimide, we have developed a new procedure (Fig. 4) using NIS–TfOH–AgOTf. In this reaction the side product TolS-I is generated, as shown in Scheme 1. In the presence of AgOTf, it reacts with TolS-I to generate another more powerful promoter, TolS-OTf (8), which can further activate the donor. In this manner, 0.5 equiv of NIS, together with 0.5 equiv of AgOTf, activate 1 equiv of the donor. As an extended application of this reaction, we used 1.5 equiv of compound **2** and 1.5 equiv of NIS in the first step (Fig. 4). The resultant mixture ideally is composed of about 1 equiv of trisaccharide product, 0.5 equiv of succinimide derivative of compound **2**, and

© 2002 NRC Canada

Fig. 2. Preparation of building blocks. (*a*) TMSOTf, MS AW-300, CH_2CI_2–CH_3CN; (*b*) Levilunic acid, EDC, DMAP, CH_2CI_2; (*c*) $(Bu_3Sn)_2O$, *o*-NBzCl, 82%; (*d*) CMA, α,α-dimethoxy isopropane; (*e*) NaH, BnCl, DMF; (*f*) TFA–CH_2Cl_2, overall 82% yield.

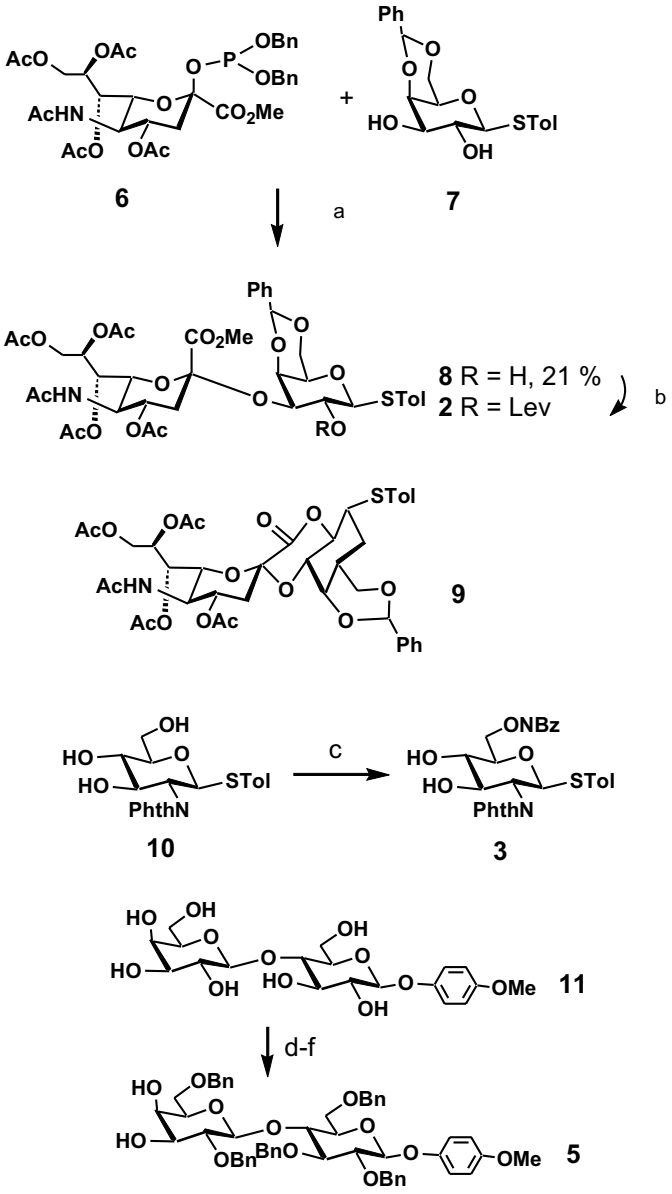

Fig. 3. One-pot synthesis of a protected Lewis X trisaccharide.

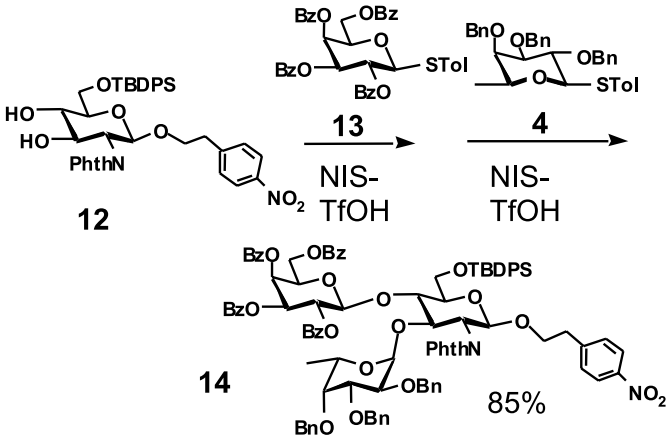

Fig. 4. One-pot synthesis of sialyl Lewis X hexasaccharide.

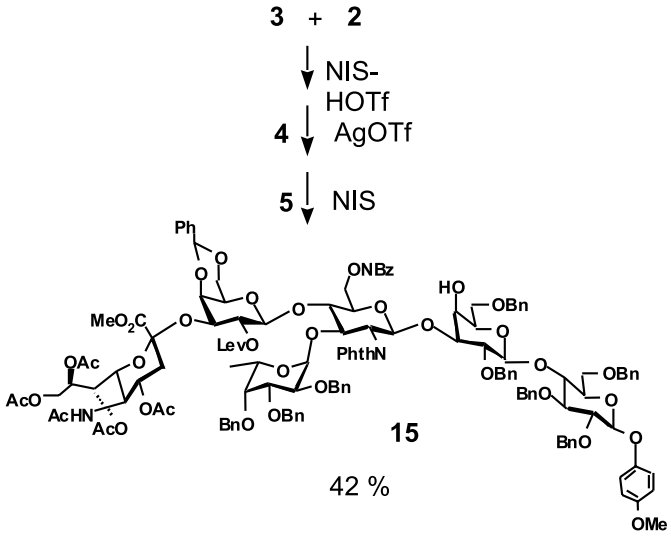

Scheme 1. Proposed mechanisms of NIS–TfOH and AgOTf activation of thioglycosides.

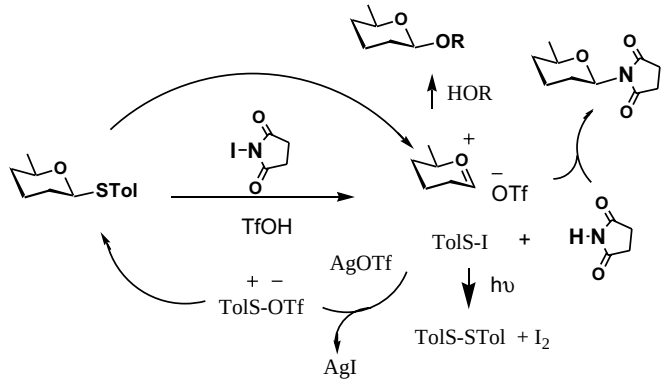

1.5 equiv amount of ToS-I. Therefore, addition of AgOTf after adding thiofucoside **4** in the second step would generate an adequate amount of TolS-OTf (8) to activate the trisaccharide and to give the tetrasaccharide. In the last step we used NIS for the coupling, as the lactoside diol **5** (2.5 equiv) is much more reactive than succinimide, and less hindered. By using this one-pot procedure, we were able to isolate the final hexasaccharide **15** in 42% yield after flash chromatography.[2]

In summary, we have successfully developed a one-pot synthesis of sialyl oligosaccharide using a sialylated disaccharide and other building blocks in combination with regioselective glycosylation. We have also developed a new method using NIS–TfOH–AgOTf for activation of thioglycosides. Further application of the one-pot strategy in

[2] Supplementary material may be purchased from the Depository of Unpublished Data, Document Delivery, CISTI, National Research Council Canada, Ottawa, ON K1A 0S2, Canada (http://www.nrc.ca/cisti/irm/unpub_e.shtml).

© 2002 NRC Canada

the syntheses of more complicated and highly branched natural oligosaccharides is in progress.

Acknowledgements

This research was supported by the U.S. Department of Health and Human Services National Institutes of Health (NIH) and the Skaggs Chemical Biology Program.

References

1. (*a*) T. Feizi. Nature (London), **314**, 53 (1985); (*b*) P.O. Livingston. Curr. Opin. Immunol. **4**, 624 (1992); (*c*) S. Hakomori and Y. Zhang. Chem. Biol. **4**, 97 (1997).
2. G.-J. Boons and A.V. Demchenko. Chem. Rev. **100**, 4539 (2000).
3. S.J. Danishefsky, K.F. McClure, J.T. Randolph, and R.B. Ruggeri. Science (Washington, D.C.), **260**, 4 (1993).
4. (*a*) S. Raghavan and D. Kahne. J. Am. Chem. Soc. **115**, 1580 (1993); (*b*) H. Yamada, T. Harada, and T. Takahashi. J. Am. Chem. Soc. **116**, 7919 **(**1994**)**; (*c*) S.V. Ley and H.W.M. Priepke. Angew. Chem. Int. Ed. Engl. 33, 2292 (1994); (*d*) Z. Zhang, I.R. Ollmann, X.-S. Ye, R. Wischnat, T. Baasov, and C.-H. Wong. J. Am. Chem. Soc. **121**, 734 (1999); (*e*) F. Burkhart, Z. Zhang, S. Wacowich-Sgarbi, and C.-H. Wong. Angew. Chem. Int. Ed. Engl. **40**, 1274 (2001).
5. X.-S. Ye, X.-F. Huang, and C. H. Wong. Chem. Commun. **11**, 974 (2001).
6. U. Ellervik and G. Magnusson. J. Org. Chem. **63**, 9314 (1998).
7. M.M. Sim, H. Kondo, and C.H. Wong. J. Am. Chem. Soc. **115**, 2260 (1993).
8. V. Martichonok and G.M. Whitesides. J. Org. Chem. **61**, 1702 (1996).

© 2002 NRC Canada

Serological and conformational properties of *E. coli* K92 capsular polysaccharide and its *N*-propionylated derivative both illustrate that induced antibody does not recognize extended epitopes of polysialic acid: Implications for a comprehensive conjugate vaccine against groups B and C *N. meningitidis*

Robert A. Pon, Nam Huan Khieu, Qing-Ling Yang, Jean-Robert Brisson, and Harold J. Jennings

Abstract: The capsular polysaccharide of *E. coli* K92 (K92P) contains elements in common with the capsular polysaccharides of both groups B and C *N. meningitidis*, and may therefore form the basis of a bivalent vaccine. In an attempt to augment the cross-protective immune response to group B meningococci, the *N*-acetyl groups of the K92P were replaced by *N*-propionyl groups (NPrK92P) and conjugated to protein. This strategy had previously been applied with success to the poorly immunogenic capsular polysaccharide of group B meningococcus (GBMP), and the bactericidal epitope was found to be exclusively mimicked by extended helical segments of the NPrGBMP. The NPrK92P-conjugate, in relation to a K92P-conjugate, failed to enhance the response to GBMP but did generate a measurable response to NPrGBMP, but only at the expense of a greatly reduced GCMP response. Despite the presence of an immune response to NPrGBMP, the anti-NPrK92 serum was not bactericidal. Competitive inhibition studies with NPrGBMP oligosaccharides suggested the NPrK92 antibodies could not cross-react with the protective epitope on group B meningococci, as defined by extended helical segments of the NPrGBMP, but only recognized short non-bactericidal NPrGBMP epitopes. This hypothesis was supported from the conformational and molecular dynamics studies of the K92P, which demonstrated a lack of extended conformations that resemble the GBMP extended epitope. Indeed, the conformational properties of the K92P more closely resembled those of the GCMP, thereby explaining the observed moderate cross-protection of the K92P antiserum towards group C meningococci. Thus, on the basis of these results, it can be concluded that K92P, regardless of *N*-propionyl modification, will not serve as an effective single vaccine component against both groups B and C meningococci.

Key words: conjugate vaccine, *Neisseria meningitidis*, polysialic acid, NMR, molecular dynamics.

Résumé : Le polysaccharide capsulaire du *E. coli* K92 (K92P) comprend des éléments communs avec les polysaccharides capsulaires des *N. meningitidis* des groupes B et C et il pourrait donc être à la base d'un vaccin bivalent. Dans un essai d'augmenter la réponse immunitaire à protection croisée par rapport au méningocoque du groupe B, on a remplacé les groupes *N*-acétyles du K92P par des groupes *N*-propionyles (NPrK92P) et on les a conjugués à une protéine. On avait utilisé antérieurement cette stratégie avec succès avec le polysaccharide capsulaire peu immunogène du méningocoque du groupe B (GBMP) et on a trouvé que l'épitope bactéricide n'est répliqué que par des segments hélicoïdaux étendus du NPrGBMP. Par rapport à un conjugué à K92P, le conjugué au NPrK92P n'augmente pas la réponse au GBMP; il provoque toutefois une réponse mesurable au NPrGBMP, mais la réponse au GCMP est toutefois grandement réduite. Malgré la présence d'une réponse immunitaire au NPrGBMP, le sérum anti-NPrK92 n'est pas bactéricide. Des études d'inhibitions compétitives avec des oligosaccharides NPrGBMP suggèrent que les anticorps NPrK92 ne peuvent pas réagir de façon croisée avec l'épitope protecteur des méningocoques du groupe B, tels que définis par des segments hélicoïdaux étendus de NPrGBMP; ils ne reconnaissent que de courtes chaînes d'épitopes

Received 10 January 2002. Published on the NRC Research Press Web site at http://canjchem.nrc.ca on 21 August 2002.

Dedicated to the memory of Professor Raymond U. Lemieux.

R.A. Pon, N.H. Khieu, Q.-L. Yang, J.-R. Brisson, and H.J. Jennings.[1] Institute of Biological Sciences,[2] National Research Council of Canada, 100 Sussex Drive, Ottawa, ON K1A 0R6, Canada.

[1]Corresponding author (e-mail: harry.jennings@nrc.ca).
[2]NRCC document No. 42447.

 DOI: 10.1139/V02-141 © 2002 NRC Canada

NPrGBMP non-bactéricides. Cette hypothèse est confirmée par des études de dynamiques moléculaire et conformationnelle du K92P qui ont démontré l'absence de conformations étendues qui pourraient ressembler à l'épitope étendu du GBMP. Les propriétés conformationnelles du K92P ressemblent en fait beaucoup plus à celles du GCMP; ceci expliquerait la protection croisée modérée observée du sérum K92P vis-à-vis des méningocoques du groupe C. Sur la base de ces résultats, on peut donc conclure que le K92P, même avec une modification *N*-propionyle, ne pourra pas servir de composant unique d'un vaccin efficace contre les méningocoques des groupes B et C.

Mots clés : vaccin conjugué, *Neisseria meningitidis*, acide polysialique, RMN, dynamique moléculaire.

[Traduit par la Rédaction]

Introduction

The *E. coli* K92 polysaccharide (K92P) is composed of alternating α(2,8)- and α(2,9)-linked sialic acid units (1). These structural elements are also respective components of the group B and group C meningococcal polysaccharides (GBMP and GCMP, respectively) (2, 3). Because of the poor immunogenicity of the group B polysaccharide (4), a protein conjugate of the K92 polysaccharide was evaluated as a possible alternate vaccine against disease caused by both group B and group C meningococci (5). Substantial antibody levels to GCMP were generated in mice; however, the response to the GBMP remained poor, despite an observed increase in GBMP-antibody titre relative to the homologous antiserum from a comparable GBMP conjugate. Similar results were noted from studies conducted in non-human primates that compared different group B meningococcal vaccine constructs, although the effect was lower and resulted in no observable GBM bactericidal activity (6, 7).

In previous studies, we had shown that the immunogenicity of the GBMP could be greatly improved by a simple chemical modification, in which its *N*-acetyl groups were replaced by *N*-propionyl (NPr) groups prior to its conjugation to protein (8). In addition, this antibody was found to be bactericidal against all group B meningococci (9–11), and the epitope responsible for bactericidal activity was exclusively associated with extended helical segments of the NPrGBMP (12–15). This demonstrates the great potential of this type of synthetic vaccine for group B meningococcal prophylaxis, especially when one considers that there is still no fully efficacious vaccine available (16). Using the same strategy, we hoped to enhance bactericidal activity against group B meningococci induced by a conjugate of the NPrK92 polysaccharide, while at the same time maintaining an adequate immune response to the GCMP.

Numerous studies have characterized the unique requirement for >10 contiguous sialic acid residues for binding to GBMP specific antibody (17–19), as opposed to the classical binding size of three to four carbohydrate residues (20). We have employed NMR and molecular dynamic studies to characterize the intrinsic properties of the GBMP, which gives rise to this unique binding behaviour (14, 15, 21). It was proposed that the GBMP-specific antibody only recognized polysialic acids capable of forming extended helical epitopes, which are highly dependent on the spatial distribution of the negative charge and the reduced mobility between interchain residues (14, 15). Furthermore, X-ray crystallography and thermodynamic studies were entirely consistent with this hypothesis (13).

Using this approach, this study demonstrates that the conformational properties of the K92 polysaccharide or its *N*-propionylated derivative are more similar to GCMP as opposed to GBMP, which therefore precludes their use in a comprehensive vaccine towards both groups B and C meningococci.

Results

Antiserum to K92P cross reacts with GCMP but not to GBMP

Conjugate vaccines comprising the capsular polysaccharide of *E. coli* K92 (alternating α(2,8)- and α(2,9)-*N*-acetyl neuraminic acid (NeuAc) residues) were proposed to function as a comprehensive vaccine towards both group B and group C meningococcus (α(2-8) and α(2-9)NeuAc homopolymers, respectively) (Fig. 1) (5). To test this hypothesis, T-independent GBM, GCM, and K92 polysaccharides were converted to T-dependent antigens by covalently coupling them to tetanus toxoid (TT). We have also previously demonstrated that the poor immunogenicity of GBMP-conjugate vaccines can be enhanced by chemically modifying the *N*-acetyl functionalities to their propionylated homologs (8). This not only enhances its immunogenicity, but propionylated GBMP (NPrGBMP) was also found to mimic a unique bacterial epitope found on the surface of GBM, and NPrGBMP-specific antisera possessed both bactericidal and protective activity in mice (11, 12). In an attempt to enhance the potential functional component of K92 antisera to GBM, vaccine constructs were also generated with modified NPrK92 polysaccharide (Fig. 1). Direct-binding ELISA analysis on antisera to the various vaccine constructs revealed strong recognition of their homologous polysaccharide antigens, with the exception of the poor reactivity to GBMP by GBMP–TT antiserum, as previously observed (Fig. 2). Cross reactivity of the individual antisera was then assessed by ELISA using both native and modified GBM, GCM, and K92 polysaccharide – HSA conjugates (Fig. 2). K92 antiserum cross reacted modestly with GCMP–HSA (~fivefold less than native K92–HSA) but noticeably did not react to any great extent with GBMP–HSA. GCMP antiserum conversely cross-reacted strongly with K92–HSA, but again failed to recognize GBMP–HSA. These results suggest there is a shared epitope between K92P and GCMP that is not present within the GBMP.

Similar cross-reactivity studies were performed to assess the impact of *N*-propionylation of K92, employed in an attempt to enhance any potential GBM specific activity arising from a K92 conjugate vaccine (Fig. 2). Consistent with prior observations, NPrGBMP–TT resulted in a strong antibody

© 2002 NRC Canada

Fig. 1. Structures of the *N*-propionyl modified- and native-capsular polysaccharides of *E. coli* K92 and groups B and C *N. meningitidis*.

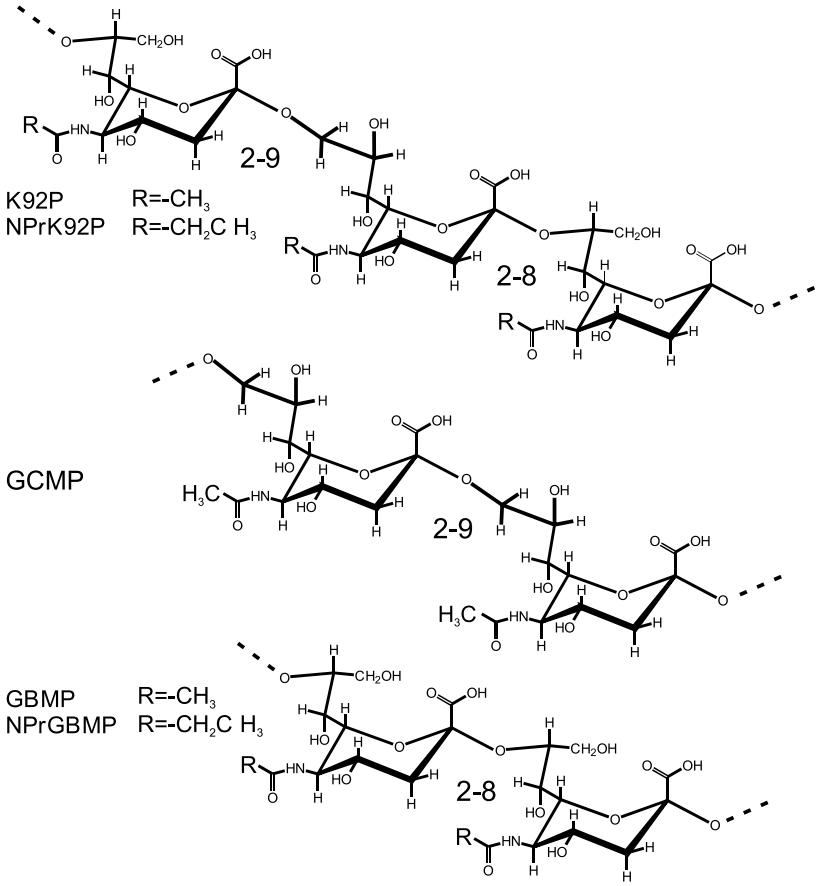

Fig. 2. Reactivity profiles of native and NPr-modified K92P, GBMP, and GCMP-TT conjugate vaccines determined by direct-binding ELISA. The 96-well plate was coated with HSA conjugates of each respective polysaccharide and the mean ELISA titer was determined to evaluate both the homologous and cross-reactivity profiles of the individual conjugate vaccine antisera. ELISA titers are represented by the total IgG response and were calculated from the OD × dilution^{-1} averaged over three points on the curve.

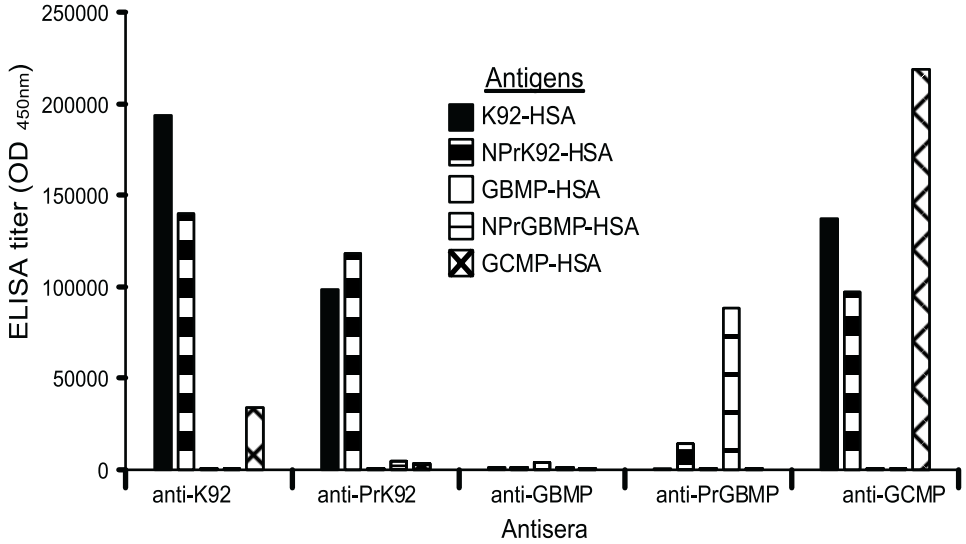

response to its homologous antigen compared with GBMP–TT sera to native GBMP (88 400 vs. 3 750 titre, respectively). Also similar to previous results, the NPrGBMP–TT antiserum was highly specific for NPrGBMP and showed only very low cross reactivity with native GBMP (<1% cross reactivity). The NPrGBMP–TT antiserum, however, was able to weakly recognize NPrK92P (14 567 vs. 88 400 titre for NPrK92P vs. NPrGBMP, respectively). In contrast, the NPrK92–TT antiserum only recognized, in addition to its homologous antigen, the native form of K92 and cross

© 2002 NRC Canada

Table 1. Bactericidal activity of *N*-acetyl and *N*-propionyl K-92 antisera towards *N. meningitidis* group B and C.

	Bactericidal titer[a] — pooled mice sera		Bactericidal titer — individual mouse serum			
			GCM		GBM	
Antiserum	GCM	GBM	No. of mice with bact. activity[b]	Bact. activity–range	No. of mice with bact. activity	Bact. activity–range
N-Acetyl K-92	>900	—[c]	8/10	900–>900	2/10	60
N-Propionyl K-92	—	—	2/10	>900	0/10	—

[a]Reciprocal dilution of antiserum required for 50% killing of either GCM 6OE C11 or GBM 80–165.
[b]Number of mice whose serum yields greater than 50% killing of GCM or GBM
[c]Signifies below level of 50% kill.

Fig. 3. Antibodies elicited by NPrK92P–TT are maximally inhibited by NeuPr oligosacchrides with degrees of polymerization >4. Binding of NPrK92P antiserum to NPrGBMP–HSA was competitively inhibited by NeuPr oligosaccharides of increasing size and assessed using ELISA.

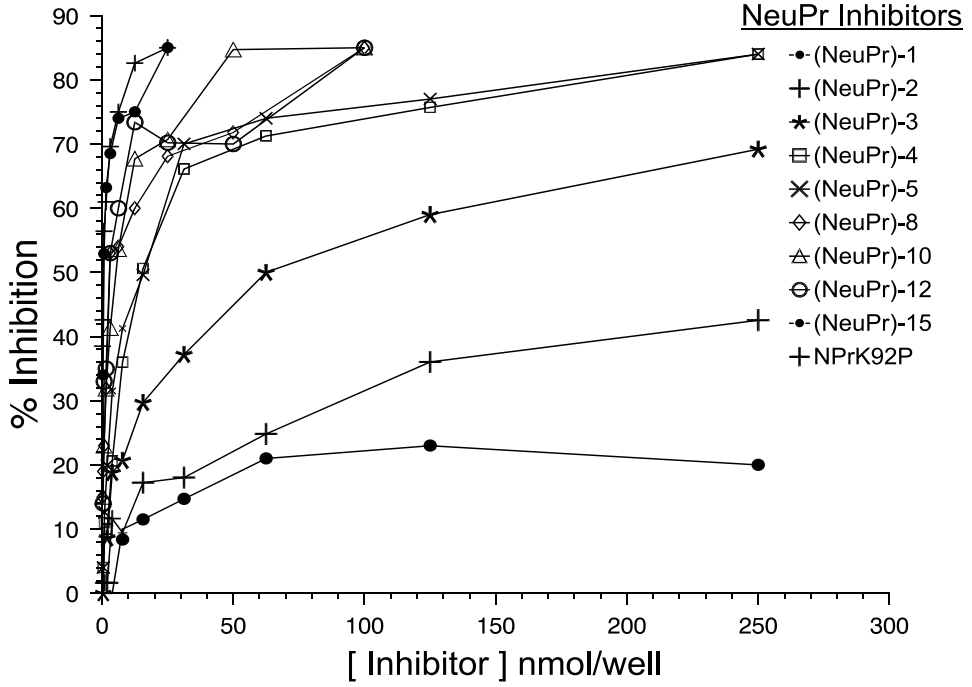

reacted poorly with NPrGBMP–, GBMP–, and GCMP–HSA conjugates. This suggests that the propionyl group modification of K92P will not be an effective strategy for increased protection against GBM, since there is poor reactivity to the putative GBM epitope that is mimicked by NPrGBMP. Similarly, the poor cross reactivity observed towards GCMP suggests that the modification will also result in decreased activity towards GCM.

K92 antiserum can kill GCM but not GBM

To determine whether the K92– or NPrK92–TT conjugate vaccines generate effector activity towards GCM and (or) GBM, their bactericidal activities were evaluated (Table 1). It was evident that both individual mouse- and pooled-K92 antisera generated significant bactericidal activity against GCM ($Titre_{Bactericidal} > 900$), while only marginal GBM bactericidal activity (2 out of 10 individual mice) was observed ($Titre_{Bactericidal} \approx 60$). In contrast, individual NPrK92–TT antisera elicited GCM bactericidal activity in only 2 out of 10 mice ($Titre_{Bactericidal} > 900$); again no GBM bactericidal activity was observed. These results are entirely consistent with our ELISA findings where the K92 antiserum was cross reactive with only GCMP, and the NPrK92 antiserum was poorly cross reactive to all (GCMP, GBMP, and NPrGBMP, Fig. 2).

Antibodies to NPrK92 are inhibited by small oligosaccharide fragments of NPrGBMP

Inhibition binding studies using oligosaccharides with increasing degrees of polymerization have proven to be extremely useful in probing the epitope size requirements for antibody to polysaccharide antigens (17, 19). To probe the size requirements of K92-specific antibodies for the α(2,8) polysialic acid component, a series of (-8NeuPrα2-) oligosaccharides were used to competitively inhibit the binding of NPrK92 antiserum to NPrGBMP capsular polysaccharide (Fig. 3). From this analysis, it was evident that significant inhibition occurred with a (-8NeuPrα2-) tetrasaccharide fragment — this inhibition was only minimally enhanced with oligosaccharides of increasing size. This result contrasts the inhibition binding behaviour of NPrGBMP antiserum, where the majority of NPrGBMP-specific antibodies, which

© 2002 NRC Canada

Fig. 4. ^{13}C NMR resonances of atoms involved in the glycosidic linkages for increasing repeat units (RU) of K92P oligosaccharides.

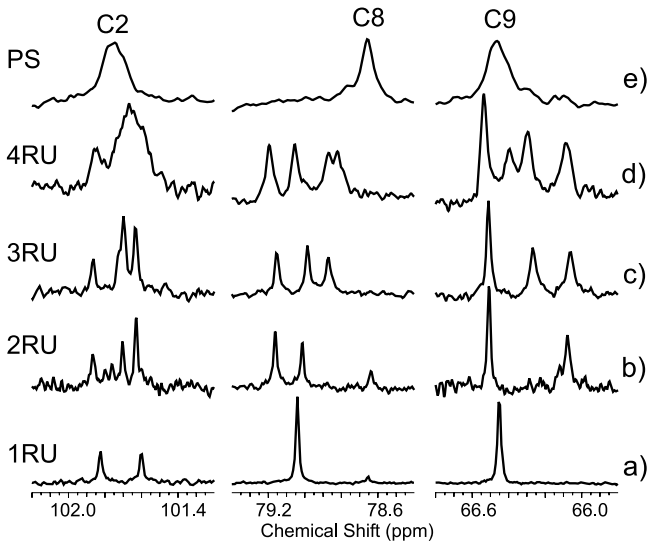

recognize an extended epitope of α(2,8) polysialic acid, were characterized by progressive inhibition with (-8NeuPrα2-) oligosaccharides up to n = 16 (12). Taken together these results suggest that the observed NPrGBMP cross reactivity generated from NPrK92–TT immunization was directed towards short epitopes of NPrGBMP and not towards extended epitopes, which were previously shown to be a prerequisite for GBM bactericidal activity and protection in a passive mouse model.

NMR and conformational analysis

NMR studies were performed on oligosaccharides derived from GBMP, GCMP, and K92P to probe their conformational properties. Proton vicinal coupling constant measurements, which are dependent on the H-C-C-H torsion angles, were used to estimate the flexibility of the exocyclic chains. Flexibility of (2,8)-linked NeuAc is primarily due to rotation around the glycosidic bond, while for the (2,9)-linked NeuAc, there is an additional degree of freedom about the C8–C9 bond. The GCMP $J_{H,H}$ coupling constants ($J_{6,7}$ = 1 Hz, $J_{7,8}$ = 10 Hz, $J_{8,9}$ = 2 Hz, and $J_{8,9'}$ = 6 Hz) indicated that the ω7 is near 60°, ω8 near 180°, and that the CH_2OH group is not restricted to one rotamer (22). For K92P, the determination of the $J_{H,H}$ coupling constants for both the trisaccharide and polysaccharide was complicated by the ^1H NMR spectral overlap. It was expected however that the (2,8)- and the (2,9)-linkages present in K92P would behave similarly to their linkage counterparts within GBMP and GCMP, respectively. Thus, all these polysaccharides exist in solution as random coils because of their high degree of flexibility about both their glycosidic and exocyclic bonds.

^{13}C NMR chemical shift differences surrounding the glycosidic bonds within oligo-repeat units of increasing size have been interpreted to reflect the conformational distribution of the various residues, with a coalescence of signals occurring when conformational equilibrium is established (21). No differences in chemical shifts were found for the C2 and C9 atoms surrounding the (2,9)-glycosidic bond in both a GCMP trisaccharide and the polysaccharide itself, indicating similar flexibility. Chemical shift differences for C8 and C9 atoms surrounding both the (2,8)- and (2,9)-linkages, were observed in K92 oligo-repeat units up to n = 4–5 (Fig. 4). Both of these observations are in contrast with the chemical shift behaviour for GBMP oligosaccharides of increasing size, where coalescence of the signals occurred only at high degrees of polymerization (n = 6). This indicated that both GCMP and K92 exhibited increased mobility around their internal linkages relative to GBMP, despite the fact that they all existed as random coils in solution.

The potential energy (PE) maps were calculated for the dimers of GBMP and GCMP (Figs. 5*a* and 5*d*). The PE surface for the dimer indicated that the conformational mobility of the sialic acids, with respect to (ϕ, φ), would be flexible since there is an extensive, relatively flat potential region. The aqueous MD results (Figs. 5*b* and 5*e*) also indicated considerable flexibility in the region of lowest energy of the PE map. The (2,8)-linkage was moderately rigid as compared with the (2,9)-linkage. In our case, the (2,8)-linkage showed more flexibility than in a previous study (23). For the (2,8)-linkage the ω7 and ω8 values were also consistent with the ω7 and ω8 rotamers being gauche (60°), as found by NMR studies (15). The extended conformation of the bound epitope for α(2,8)-linked polysialic acid with ϕ = 166°, φ = 137°, ω7 = 55°, and ω8 = 70° (13) is readily accessible in the PE surface (Fig. 4*a*), although at higher energy than the global minimum (15). Comparison of the PE and MD maps, suggests that although the presence in solution of such a conformer is not highly favored dynamically, it is still accessible to antibody binding. The aqueous MD simulation of the (2,9)-linked tetra sialic acid revealed an even more extensive dynamics region consistent with its PE map (Fig. 5*e*). The aqueous MD simulation for $(K92P)_4$ showed that the extensive mobility also apply to all the central (2,8)- and (2,9)-linkages.

For extended epitopes (GBMP), the spatial organization of the PS becomes important. As Perez and Vergelati (24) noted in their study of polysaccharide conformations, the spatial organization of the PS can de defined by consecutive fragments that can have well-defined helical parameters. For GBMP, various helical structures are probable (Fig. 5*g*). The postulated helical epitope for GBMP (13) has six residues per turn (n = 6) with ρ = 60° and λ = 0.8. Because GCMP has greater flexibility, a wider range of helical parameters are possible (Fig. 5*h*) — although mostly for short helices with n = 2 (ρ = 180°). Extended helices are not favored and similar conformations to that of the GBMP helix cannot be found. Similarly, extended helices for K92 are not favored. As previously shown for GBMP, its conformational properties are not affected by replacing the NAc group with an NPr group (14). Similarly, molecular modeling of the NPrGCMP and NPrK92P tetrasaccharide showed no effect on their conformation.

Discussion

In previous studies (5–7), which had the goal of using K92 as a bivalent vaccine against disease caused by groups B and C meningococci, it was ascertained that, while the conjugated form of K92P gave a strong cross-reactive immune response to GCMP, the response to GBMP was marginal

© 2002 NRC Canada

Fig. 5. (ϕ, ψ) Solid contour map with the relative PE scale for $(GBMP)_2$ in (*a*) from white (low energy) to black (high energy). Aqueous MD simulation for $(GBMP)_2$ in (*b*) and the central (2,8)-linkage for $(K92P)_4$ in (*c*). (φ, ψ) Solid contour map for $(GCMP)_2$ in (*d*). Aqueous MD simulation for $(GCMP)_2$ in (*e*) and the central (2,9)-linkage for $(K92P)_4$ in (*f*). Polar (ρ, λ) distribution of helical parameters for GBMP in (*g*), GCMP in (*h*), and K92P in (*i*) where $\rho = 360°/n$, *n* being the number of residues per turn, and λ is the degree of maximum elongation (0 to 1).

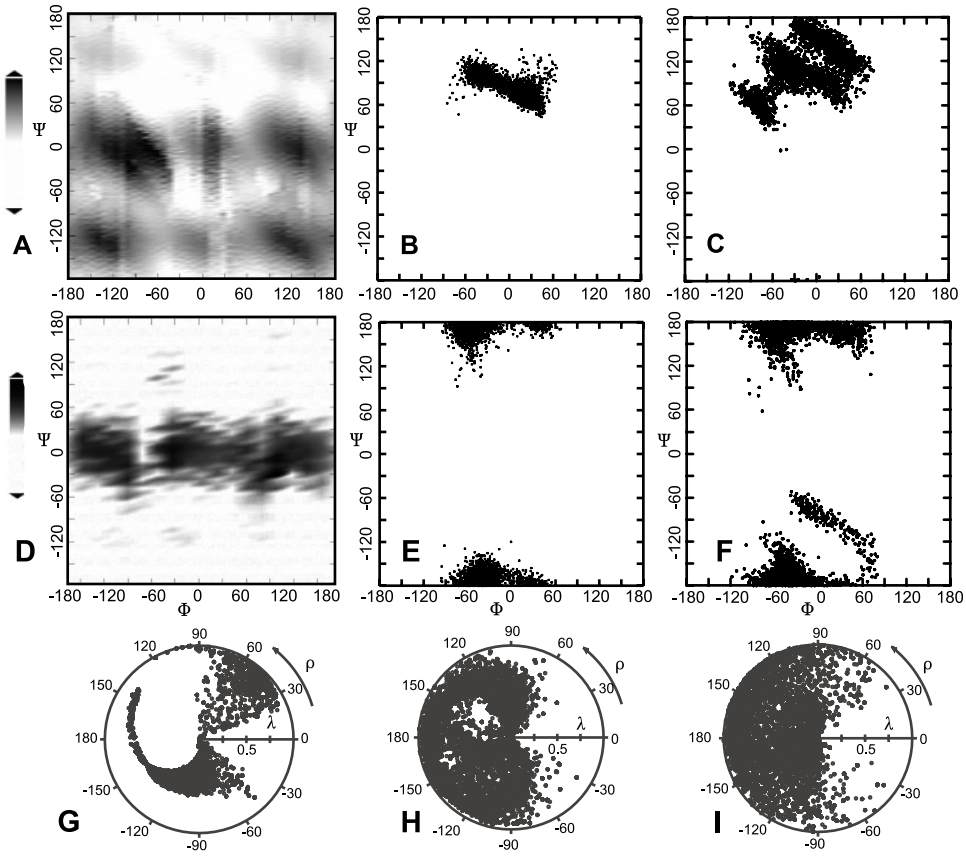

by comparison. It was also concluded from these studies that the K92P conjugate was superior to the GBMP conjugate in terms of inducing GBMP-specific antibodies (5). Our control studies generally confirm these results, with the exception that our GBMP conjugate was able to raise more GBMP-specific antibody relative to our K92P-conjugate antiserum, consistent with the results found in a study done on monkeys (6). The titre difference was marginal, however, and indeed the K92P-conjugate induced antiserum possessed low levels of GBM bactericidal activity; this despite having lower quantities of a specific antibody relative to the GBMP-conjugate antiserum. This failure of the K92P conjugate to raise significant levels of GBMP cross-reactive antibody therefore precludes its usefulness as a vaccine candidate to group B meningococcus, as evidenced by its poor bactericidal response to GBM. To preserve the concept of using K92 as a bivalent vaccine against groups B and C meningococci, it was imperative that the immune response to the group B component be enhanced. To achieve this, we converted the native K92 polysaccharide into its *N*-propionylated derivative followed by its conjugation to protein; a strategy proven successful in rendering the GBMP more immunogenic (8).

The results of the experiments were not encouraging on two fronts. Firstly, we observed that by chemically modifying K92P, its ability to generate cross-reactive antibody to the GCMP was considerably reduced in comparison to the native K92P conjugate and, furthermore, this antibody possessed reduced bactericidal activity against group C meningococci. It must therefore be concluded that *N*-propionylation of K92P resulted in a conjugate with diminished protective properties against group C meningococci when compared with K92–TT. This finding is consistent with our previous studies investigating the effect of *N*-propionylating GCMP, where virtually all the bactericidal activity resided within the smaller GCMP specific antibody fraction, while the larger fraction that was specific to NPrGCMP, was completely unable to kill GCM (unpublished results). Secondly, the most important factor that mitigates against the use of an NPrK92 conjugate as a bivalent vaccine against groups B and C meningococci, is its failure to sufficiently augment antibody levels, or the protective properties of these antibodies, to either GBMP or NPrGBMP.

We can explain the above observations in terms of the epitopic specificities of the NPrK92 antiserum. Our serological evidence suggests that NPrK92P cannot adopt the extended helical conformation of NPrGBMP (12–15), which is essential for the induction of bactericidal antibodies against group B meningococci (9–12). It is not likely that the effect of *N*-propionylation was responsible for our serological observations, since we have previously shown with the GBMP that *N*-acyl modifications marginally impact

© 2002 NRC Canada

its conformational properties (14). Furthermore, since the negative charge distribution and inter-residue mobilities within NPrK92P and K92P remained consistent, it was expected that conformationally, they would behave similarly. Our NMR and molecular dynamics studies support the notion that both the native K92P and NPrK92P should have similar serological behaviour, since in both cases extended helices are not favoured, and indeed similar conformations to that of the GBMP helix were not found. In other words, both the K92 and NPrK92 polysaccharides are unable to mimic the extended helical epitope found in the GBMP, which is characterized by 8–10 contiguous α(2,8)-linked sialic acids. Consequently, K92P or NPrK92P conjugates are unable to elicit an antibody capable of recognizing these epitopes on the surface of group B meningococci, which is critical to invoke a bactericidal response (12). Illustrating this concept, it was possible to generate a small amount of NPrGBMP cross-reactive antibody with the NPrK92P conjugate; however, there was no associated GBM bactericidal activity. Inhibition of antibody binding to NPrGBMP, clearly demonstrated that complete inhibition was achieved using relatively short (-8NeuPrα2-) oligosaccharides (n = 4 or 5), signifying the NPrK92 antibodies were capable of recognizing short epitopes of GBMP, most probably by only recognizing the conformational features present in the terminal residues. Furthermore, it has been well established that such epitopes are not bactericidal against group B meningococci (12).

It is interesting to note that K92P, and to a lesser extent NPrK92P, share common bactericidal epitopes with GCMP. Given the similar chemical shift behaviour of GCMP and K92P oligosaccharides, together with the low probability that these polysaccharides can adopt extended helical conformations, it is likely that the epitopes giving rise to GCMP cross-reactive antibody are short. This is consistent with our previous studies that show that GCMP-conjugate induced antibodies are generated to short conventional epitopes (17).

Experimental

General

E. coli Ec432 (O73:K92:H34) (K92), *N. meningitidis* strains 80–165 (B:2b:P1.Ham) (GBM), and 60EC11 (L3) (GCM) were obtained from the Population and Public Health Branch (Ottawa, Canada). *E. coli* K92 capsular polysaccharide (K92P) was prepared and purified essentially as described (25), using Davis supplemented minimal medium. GBMP-, NPrGBMP-, GCMP-, and NPrGCMP-tetanus toxoid conjugates were prepared as described (12).

K92P modification, oligosaccharide generation, and conjugate vaccine formation

N-Propionylation of K92P was carried out in a similar manner to that reported for NPrGBMP (12). Briefly, K92P (100 mg) was *N*-deacetylated using 2 M NaOH (10 mL) containing $NaBH_4$ (100 mg) for 6.5 h at 110°C. The *N*-deacetylated product was then treated with propionic anhydride (10 equiv) at a constant pH (9.5) using autotitration with 2 M NaOH. Following exhaustive dialysis and lyophilization, complete derivitization was confirmed by ^{1}H NMR spectroscopy.

High molecular weight K92P and NPrK92P were depolymerized by $NaIO_4$ treatment resulting in the oxidative cleavage of the susceptible C7–C8 vicinal diol of the α(2,9)-*N*-acetyl neuraminic acid (NeuAc) residues. Briefly, high molecular weight polysaccharide (100 mg; 0.16 mmol repeat unit) in phosphate buffer (0.2 M, pH 7.5) was treated in stages with a 0.5 M $NaIO_4$ solution (200 μL final) with monitoring by size-exclusion (SEC) HPLC (Superose-12; Amersham Pharmacia, Baie D'Urfe, Canada). The depolymerized polysaccharide was size fractionated on a BioGel A.5 column (1.6 × 100 cm; Bio-Rad, Hercules, Ca), collecting 10 kD fragments as previously described (12). K92, NPrK92, and GCM oligosaccharides were generated in a similar manner from their respective high molecular weight polysaccharides (100 mg; 0.16 mmol repeat unit) using more extensive $NaIO_4$ treatment (0.25 equiv) and SEC-HPLC monitoring (Superdex-75; Amersham Pharmacia). Pure oligosaccharides were isolated by anion exchange chromatography as described (17). For NMR analysis, oligosaccharide terminal aldehydes were first reduced with $NaBH_4$ (100 equiv)

NPrK92P and K92P protein conjugates were prepared by incubating the respective 10 kD oxidized fragment (15 mg) with either tetanus toxoid monomer (TTm; 5 mg; Statenserum Institut, Copenhagen, Denmark) or human serum albumin (HSA; 7.5 mg; Sigma, St. Louis, MI) and $NaBH_3CN$ (10 mg) in phosphate buffer (0.1 M; pH 8.1) for 5 days. K92-protein conjugates were purified from starting materials by SEC chromatography (BioGel A.5). Sugar-to-protein analysis (26) revealed a 33.3 and 36.1% (wt/wt) NeuAc incorporation within the K92– and NPrK92–TT conjugates, respectively.

Mouse immunizations

Groups of ten mice per vaccine (female CFI; 6–8 weeks; Charles River, St. Constant, Canada) were immunized intraperitonealy with NPrK92P–, K92P–, GBMP–, NPrGBMP–, and GCMP–TT conjugate vaccines (2 μg NeuAc/0.2 mL/mouse) emulsified in RIBIs complete adjuvant (RIBI ImmunoChem, Hamilton, MT). The mice were boosted with equivalent vaccine doses on day 21 and day 35, followed by exsanguination and harvesting of blood 10 days later.

Serological analysis by ELISA

Microtitre plates (96-well; Corning, Corning, NY) were all coated at 4°C for 1 h with HSA-polysaccharide conjugate (1 μg/well). Following plate washing with 0.5% Tween-20 in PBS (3 times) and blocking (1% BSA in PBS), serial dilutions of antisera in 3% BSA were performed. Incubation (rt, 1 h) was followed by washing (2 times) and the addition of a 1:2000 dilution in 3% BSA of a peroxidase labeled goat anti-mouse IgG (H + L) antibody (Cedarlane, Hornby, Ont.). The reaction was stopped after 15 min with 1 M H_3PO_4 (50 μL), and the plates were read at 450 nm using a BioTek multiscan ELISA reader (Fisher Scientific, Ottawa, ON).

Competitive-inhibition assays with (-8NeuPrα2-) oligosaccharides were performed by first incubating graded amounts of oligosaccharides at an optimal dilution of antiserum (OD_{450} = 1) in 3% BSA for 1 h at 4°C. Oligosaccharide–antibody mixtures were then transferred to a 96-well plate

© 2002 NRC Canada

pre-absorbed with the HSA-coating antigen of interest and treated as described above.

Bactericidal assays

GBM 80–165 and GCM 60EC11 were grown overnight on Chocolate agar plates (QueLab, Montreal, Que.) at 37°C/5% CO_2, followed by re-inoculation of a second plate and incubating for a further 5 h. Dilutions of antiserum in HBSS containing 1% casein hydrozylate were performed in a 96-well plate, to which were added 30 μL of a 1:20 000 dilution (2 500 CFU/well) of either a freshly isolated suspension of GBM or GCM (OD_{490} = 0.29). Freshly thawed baby-rabbit complement (20 μL, Cedarlane) was immediately added to each well, followed by incubation at 37°C with shaking for 1 h. The contents of each well were mixed before plating onto Chocolate agar (20 μL/plate) and CFUs were enumerated following overnight incubation. The % killing was calculated relative to HBSS controls according to the following equation: $\%kill = (CFU_{control} - CFU_{treated})/CFU_{control} \times 100$.

NMR spectroscopy and molecular modeling

Capsular polysaccharides and oligosaccharides were prepared at concentrations of 5–10 mg in 0.5 mL 99.9% D_2O, pH 7, Na^+ salt. Experiments were performed on a 600 MHz (^1H) NMR spectrometer. ^{13}C NMR chemical shifts are referenced to internal acetone (CH_3) set at 31.07 ppm.

Potential energy (PE) calculations for the $(GBMP)_2$ and $(GCMP)_2$ disaccharides was performed by energy minimization (BFGS method) of a set of geometries under the torsional angle restraints of Φ (*b*O6-*b*C2-*b*O2-*a*C8) and Ψ (*b*C2-*b*O2-*a*C8-*a*C7) for αNeuAc(2,8)αNeuAc (*b*-*a*), or Φ (*b*O6-*b*C2-*b*O2-*a*C9) and Ψ (*b*C2-*b*O2-*a*C9-*a*C8) for αNeuAc(2,9)αNeuAc (*b*-*a*) using 8° increments constrained by a harmonic force constant of 200 kcal rad^{-2} and a dielectric constant of 80. Torsional maps were generated using Discover-3 and Analysis modules of the INSIGHTII software package (Accelrys). Helical parameters were calculated as previously described (27).

Molecular dynamic (MD) simulations for the $(GBMP)_2$ and $(GCMP)_2$ disaccharides were performed with AMBER 5.0 software package on a SGI computer (Indigo 2 Solid Impact R10000 195 MHz). The GLYCAM_93 parameter set (27) and its structural database were used to generate the initial conformation for sialic acids and prepare them for MD simulation with the SANDER module. In addition, different starting values for the glycosidic torsional angles were applied in separate dynamics runs, while the initial values chosen for ω7 (O6-C6-C7-O7) and ω8 (O7-C7-C8-O8) were 55° and 70°, respectively. The Na^+ counter ion was initially placed 3 Å from the carboxylate oxygen atom. TIP-3P water molecules were used in MD with periodic boundary conditions, and the box sizes set to extend 12 Å beyond the sugar. Energy minimization (500 cycles using steepest descent method) was performed first to configure water and the Na^+ counter ion, followed by 50 ps MD with minimization for water only. All the atoms in the system were then subjected to 500-cycle steepest descent energy minimization before being heated to 300 K for 100 ps. A 3000 ps MD run was finally performed at a constant temperature of 300 K and with a dielectric constant of unity. The Verlet algorithm with a 2 fs time step was applied for the simulation where bond lengths involving hydrogen atoms were constrained via the SHAKE algorithm. The Maxwell distribution at 5 K was used to generate initial atomic velocities. MD simulation was similarly performed for $(K92P)_4$, $(-9NeuAc\alpha2,8NeuAc\alpha2-)_4$.

Compound data

GCMP

^1H NMR (600 MHz, D_2O) δ: 1.72 ($H3_a$), 2.75 ($H3_e$), 3.67 (H4), 3.85 (H5), 3.72 (H6), 3.59 (H7), 3.99 (H8), 3.68 (H9), 3.85 (H9′), 2.05 (NAc). $J_{3a,3e}$ = –12.5, $J_{3a,4}$ = 12.1, $J_{3e,4}$ = 4.7, $J_{4,5}$ = 9.5, $J_{5,6}$ = 11.0, $J_{6,7}$ = 1.0, $J_{7,8}$ = 10.0, $J_{8,9}$ = 2.2, $J_{8,9'}$ = 5.6, $J_{9,9'}$ = –10.0 Hz. ^{13}C NMR (150 MHz, D_2O) δ: 174.4 (C1), 101.1 (C2), 40.9 (C3), 69.3 (C4), 52.6 (C5), 73.0 (C6), 69.0 (C7), 71.0 (C8), 66.1 (C9), 22.9 (CH_3), 175.7 (C=O).

K92P (-9NeuAcα2,8NeuAcα2-) (b-a)

^1H NMR (600 MHz, D_2O) δ: 1.68 ($aH3_a$), 2.66 ($aH3_e$), 3.57 (aH4), 3.82 (aH5), 3.80 (aH6), 3.84 (aH7), 4.15 (aH8), 4.14 (aH9), 3.67 (aH9′), 2.07 (aNAc), 1.77 ($bH3_a$), 2.76 ($bH3_e$), 3.64 (bH4), 3.84 (bH5), 3.60 (bH6), 3.61 (bH7), 3.92 (bH8), 3.78 (bH9), 3.65 (bH9′), 2.03 (bNAc). ^{13}C NMR (150 MHz, D_2O) δ: 174.5 (aC1), 101.7 (aC2), 41.0 (aC3), 68.8 (aC4), 53.4 (aC5), 74.1 (aC6), 70.1 (aC7), 78.7 (aC8), 62.2 (aC9), 23.3 (aCH_3), 175.8 (aC=O), 174.0 (bC1), 101.7 (bC2), 40.7 (bC3), 69.8 (bC4), 52.5 (bC5), 73.3 (bC6), 68.8 (bC7), 71.4 (bC8), 66.5 (bC9), 23.0 (bCH_3), 175.6 (bC=O).

References

1. W. Egan, T.Y. Liu, D. Dorow, J.S. Cohen, J.D. Robbins, E.C. Gotschlich, and J.B. Robbins. Biochemistry, **16**, 3687 (1977).
2. A.K. Bhattacharjee, H.J. Jennings, C.P. Kenny, A. Martin, and I.C. Smith. J. Biol. Chem. **250**, 1926 (1975).
3. H.J. Jennings, A.K. Bhattacharjee, D.R. Bundle, C.P. Kenny, A. Martin, and I.C. Smith. J. Infect. Dis. **136**, S78 (1977).
4. F.A. Wyle, M.S. Artenstein, B.L. Brandt, D.L. Tramont, D.L. Kasper, S.L. Altieri, S.L. Berman, and J.M. Luengo. J. Infect. Dis. **126**, 514 (1972).
5. S.J. Devi, J.B. Robbins, and R. Schneerson. Proc. Natl. Acad. Sci. U.S.A. **88**, 7175 (1991).
6. S.J. Devi, W.D. Zollinger, P.J. Snoy, J.Y. Tai, P. Costantini, F. Norelli, R. Rappuoli, and C.E. Frasch. Infect. Immun. **65**, 1045 (1997).
7. W.D. Zollinger, E.E. Moran, S.J. Devi, and C.E. Frasch. Infect. Immun. **65**, 1053 (1997).
8. H.J. Jennings, R. Roy, and A. Gamian. J. Immunol. **137**, 1708 (1986).
9. F.E. Ashton, J.A. Ryan, F. Michon, and H.J. Jennings. Microb. Pathog. **6**, 455 (1989).
10. H.J. Jennings, A. Gamian, F. Michon, and F.E. Ashton. J. Immunol. **142**, 3585 (1989).
11. H.J. Jennings, A. Gamian, and F.E. Ashton. J. Exp. Med. **165**, 1207 (1987).
12. R.A. Pon, M. Lussier, Q.L. Yang, and H.J. Jennings. J. Exp. Med. **185**, 1929 (1997).
13. S.V. Evans, B.W. Sigurskjold, H.J. Jennings, J.R. Brisson, R. To, W.C. Tse, E. Altman, M. Frosch, C. Weisgerber, H.D. Kratzin, S. Klebert, M. Vaesen, D. Bitter-Suermann, D.R. Rose, N.M. Young, and D.R. Bundle. Biochemistry, **34**, 6737 (1995).

© 2002 NRC Canada

14. H. Baumann, J.R. Brisson, F. Michon, R. Pon, and H.J. Jennings. Biochemistry, **32**, 4007 (1993).
15. J.R. Brisson, H. Baumann, A. Imberty, S. Perez, and H.J. Jennings. Biochemistry, **31**, 4996 (1992).
16. H.J. Jennings and R.A. Pon. Polysaccharides and glycoconjugates as human vaccines. *In* Polysaccharides in medicinal applications. *Edited by* S. Dumitriu. Marcel Dekker, New York. 1994. p. 443.
17. H.J. Jennings, R. Roy, and F. Michon. J. Immunol. **134**, 2651 (1985).
18. J. Finne and P.H. Makela. J. Biol. Chem. **260**, 1265 (1985).
19. E.A. Kabat, J. Liao, E.F. Osserman, A. Gamian, F. Michon, and H.J. Jennings. J. Exp. Med. **168**, 699 (1988).
20. J. Cisar, E.A. Kabat, M.M. Dorner, and J. Liao. J. Exp. Med. **142**, 435 (1975).
21. F. Michon, J.R. Brisson, and H.J. Jennings. Biochemistry, **26**, 8399 (1987).
22. K. Bock and J.O. Duus. J. Carbohydr. Chem. **13**, 513 (1994).
23. R.M. Venable, F. Bizik, T.J. Henderson, and W. Egan. J. Mol. Struct. (Theochem) **395**, 375 (1997).
24. S. Perez and C. Vergelati. Biopolymers, **24**, 1809 (1985).
25. D.R. Bundle, H.J. Jennings, and C.P. Kenny. J. Biol. Chem. **249**, 4797 (1974).
26. L. Svennerholm. Biochim. Biophys. Acta, **24**, 604 (1957).
27. J.R. Brisson, S. Uhrinova, R.J. Woods, M. van der Zwan, H.C. Jarrell, L.C. Paoletti, D.L. Kasper, and H.J. Jennings. Biochemistry, **36**, 3278 (1997).

© 2002 NRC Canada

Anchimeric assistance in hexosaminidases

Brian L. Mark and Michael N.G. James

Abstract: Configuration retaining glycosidases catalyse the hydrolysis of glycosidic bonds via a double displacement mechanism, typically involving two key active site carboxyl groups (Glu or Asp). One of the enzymic carboxyl groups functions as a general acid–base catalyst, the other acts as a nucleophile. Alternatively, configuration-retaining hexosaminidases from the sequence-related glycosidase families 18, 20, and 56 lack a suitably positioned enzymic nucleophile; instead, they use the carbonyl oxygen atom of the neighbouring C2-acetamido group of the substrate. The carbonyl oxygen atom of the 2-acetamido group provides anchimeric assistance to the enzyme catalyzed reaction by acting as an intramolecular nucleophile, attacking the anomeric center and forming a cyclized oxazolinium ion intermediate that is stereochemically equivalent to the glycosyl–enzyme intermediate formed in the "normal" double displacement mechanism. Although there is little sequence similarity between families 18, 20, and 56 hexosaminidases, X-ray crystallographic studies demonstrate that they have evolved similar catalytic domains and active site architectures that are designed to distort the bound substrate so that the C2-acetamido group can become appropriately positioned to participate in catalysis. The substrate distortion allows for a substrate-assisted catalytic reaction that displays all the general characteristics of the classic double-displacement mechanism including the formation of a covalent intermediate.

Key words: glycoside hydrolase, hexosaminidase, glycosidase, substrate-assisted catalysis, anchimeric assistance.

Résumé : Les glycosidases qui maintiennent la configuration catalysent l'hydrolyse des liaisons glycosidiques par le biais d'un mécanisme de double déplacement qui implique d'une façon typique deux groupes carboxyles de sites actifs clés (Glu ou Asp). L'un des groupes carboxyles enzymatiques agit comme un catalyseur acide–base général alors que l'autre agit comme nucléophile. De façon alternative, les hexosaminidases qui maintiennent la configuration et qui proviennent des familles de glycosidases à séquences apparentées 18, 20 et 56 ne comportent pas de nucléophile enzymatique bien orienté; elles utilisent plutôt l'oxygène du carbonyle du groupe acétamido en C2 du substrat. L'atome d'oxygène du carbonyle du groupe acétamido en C2 fournit l'assistance anchimérique à la réaction catalysée par l'enzyme en agissant comme un nucléophile intramoléculaire qui attaque le centre anomère et qui forme un ion oxazolinium cyclique intermédiaire qui est l'équivalent stéréochimique de l'intermédiaire glycosyle-enzyme qui se forme dans le mécanisme de double déplacement "normal". Même si la similarité de séquence est faible entre les familles 18, 20 et 56 des hexosaminidases, des études de diffraction des rayons X montrent qu'elles ont développé des domaines catalytiques semblables et que les architectures des sites actifs sont façonnées de manière à déformer le substrat lié de façon à ce que le groupe acétamido en C2 puisse se positionner correctement pour participer à la catalyse. La distorsion du substrat permet de réaliser une réaction catalytique assistée par le substrat qui présente toutes les caractéristiques générales du mécanisme classique de double déplacement, y compris la formation d'un intermédiaire covalent.

Mots clés : hydrolase de glycoside, hexosaminidase, glycosidase, catalysée assistée par le substrat, assistance anchimérique.

[Traduit par la Rédaction]

Received 27 November 2001. Published on the NRC Research Press Web site at http://canjchem.nrc.ca on 24 August 2002.

Dedicated to the memory of Professor Raymond U. Lemieux.

B.L. Mark and M.N.G. James.[1,2] Canadian Institutes of Health Research Group in Protein Structure and Function, Department of Biochemistry, 4–74 Medical Sciences Building, University of Alberta, Edmonton, AB T6G 2H7, Canada.

[1]Corresponding author (e-mail: michael.james@ualberta.ca).

[2]Dedicatory note by Michael James: Conformations of pyranose rings were a fascination for Ray Lemieux. Ray foresaw the need for X-ray crystallographic studies of carbohydrates and was one of the major movers to establish X-ray crystallography at the University of Alberta. I had the pleasure, as a post-doctoral fellow with David Hall, to collaborate with Ray on the structures of monosaccharides, some of which exhibited unusual pyranose ring conformations. These early structures of compounds synthesized by A. Richard Morgan when he was a Ph.D. student with Ray, led the way to the reverse anomeric effect. Our present review is centered on enzymes that distort pyranose rings into conformations that allow for anchimeric assistance by 2-deoxy-2-*N*-acetamido groups in hydrolytic reactions. Certainly, the structures that are discussed in our review would have been of great interest to Ray as enzymes that have evolved to carry out reactions on the carbohydrates that were so dear to Ray's heart. It was a great pleasure and inspiration to have been associated with Ray at the time I was formulating my own research program in enzyme structure and function.

 DOI: 10.1139/V02-130 © 2002 NRC Canada

Introduction

It has been well documented in physical organic chemistry that a chemical reaction can be accelerated by the intramolecular participation of a functional group on the reactant (1). The functional group acts as an intramolecular catalyst, providing what is referred to as anchimeric assistance to the catalytic mechanism of the reaction. Having a catalyst attached to the reactant such that it is not stereochemically nor structurally hindered from accessing the reactive centre, not only increases the effective concentration of the catalyst at the site of chemical reactivity, but also it provides an entropic advantage by reducing at least one aspect of the reaction mechanism from what would typically be a bimolecular to a unimolecular event (reviewed in ref. 2). Many biological substrates have functional groups possessing the required characteristics that could allow for their participation in enzyme catalysis via anchimeric assistance (substrate-assisted catalysis). Indeed, much evidence has been provided for the involvement of such functional groups in the mechanisms of natural and engineered enzymes including GTPases, type II restriction endonucleases, serine proteinases, and glycoside hydrolases (glycosidases) (3). Of particular interest to the authors of this review is the role of anchimeric assistance in glycosidases that catalyze the hydrolysis of β(1→4) linked glycosidic bonds between C2 *N*-acetylated hexosamine residues (*N*-acetylhexosamine) and other sugars. Neighbouring C2-acetamido group participation has been well documented in the acid-catalyzed hydrolysis of *N*-acetylglucosaminides in solution (4), and a number of glycosidases have evolved to incorporate C2-acetamido group participation into their catalytic mechanisms. Enzymes that hydrolyze *N*-acetylhexosamine-containing substrates are generally referred to as hexosaminidases and they have received much attention over the last 50 years. Recently, structural and biochemical research endeavors have provided new insights into the catalytic mechanisms of hexosaminidases and the role of anchimeric assistance.

The hexosaminidases

The term hexosaminidase is usually reserved for enzymes that catalyze the removal of *N*-acetylhexosamine residues from the non-reducing end of oligosaccharides and glycoconjugates; however, it may also be used in a generic sense to refer to all glycosidases that hydrolyze glycosidic bonds between an *N*-acetylhexosamine residue and an adjacent sugar. Thus, the term hexosaminidase also includes chitinases, chitobiases, hyaluronidases, and lysozymes (for an extensive review of the glycosidases, see ref. 5). Chitinases hydolyze chitin, the β(1→4) linked polymer of *N*-acetylglucosamine (NAG), either randomly within the polymer chain (*endo*-acting) or at the ends of the polymer (*exo*-acting). Chitobiases hydrolyze the glycosidic linkage within chitobiose (di-β(1→4)-NAG) and have also been shown to hydrolyze tri- and tetra-β(1→4)-NAG as well (6). Hyaluronidases are *endo-N*-acetylhexosaminidases that hydrolyze the β(1→4) glycosidic linkage between NAG and glucuronic acid (GlcA) within the glycosaminoglycan hyaluronic acid (HA) (7). Lysozymes hydrolyze the peptidoglycan cell wall of Gram-positive bacteria, which are composed of crosslinked oligosaccharides of alternating β(1→4) linked NAG and *N*-acetylmuramic acid (NAM) residues. Hen egg white (HEW) lysozyme, the exemplary member of the hexosaminidases and glycosidases in general, was the first enzyme to have its three-dimensional structure determined using X-ray crystallographic methods. This early crystallographic work on HEW lysozyme provided the first insights into enzyme catalysis at the molecular level (8, 9).

Glycosidases have been classified into families based on primary amino acid sequence similarities. There are currently more than 70 sequence-related families, of which at least 30 contain members that have had their three-dimensional structures determined (10–12). Although the individual sequence-related families may contain enzymes with distinct substrate specificites, structural studies have shown that within many of these families, the protein fold is highly conserved. Thus, once the three-dimensional structure has been determined for at least one of the proteins within a family, comparative molecular modeling techniques can be used to predict the molecular structure of other family members (for examples, see refs. 13 and 14). The URL http://afmb.cnrs-mrs.fr/~cazy/CAZY/index.html contains a frequently updated database of the sequence-related glycosidase families. Moreover, glycosidases exist in one of two possible mechanistic groups: those that catalyze bond hydrolysis with net retention of anomeric configuration and those that invert the anomeric configuration (15, 16). It has been found that this mechanistic distinction is conserved within each sequence-related family — all members of an individual family catalyze reactions with the same stereochemical outcome (17).

Biochemical and structural studies of the hexosaminidases from families 18, 20, and 56 demonstrate that these enzymes use an anchimeric-assistance mechanism involving neighboring C2-acetamido group participation. Family 18 consists of chitinases and *endo*-β-*N*-acetylhexosaminidases; whereas, family 20 contains chitobiases and β-hexosaminidases, including the human β-hexosaminidase isoforms A and B. Human β-hexosaminidase isoform A is a heterodimer of subunits α (encoded by *HEXA*) and β (encoded by *HEXB*), while isoform B is a homodimer of β subunits. Inborn errors in *HEXA* and *HEXB* result in Tay-Sachs and Sandhoff disease, respectively (18). These serious genetic diseases have made the human β-hexosaminidase isoforms, and family 20 enzymes in general, the focus of much biomedical research. Family 56 contains hyaluronidases and recently discovered mutations in *HYAL1*, a human gene encoding a serum hyaluronidase, have been shown to be linked to a disorder known as mucopolysaccharidosis IX (19). Although the hexosaminidases from families 18, 20, and 56 share very little overall sequence identity, they have similar $(\beta/\alpha)_8$ catalytic domains (Fig. 1), and a number of their catalytic residues are identical (20, 21). The glycosidases within these families carry out glycosidic bond hydrolysis with net retention of anomeric configuration (6, 21–25) and, interestingly, the active site residues that are identical among these three families, give rise to common structural features that are involved in optimizing the C2-acetamido group participation in a double-displacement mechanism described below.

© 2002 NRC Canada

General glycosidase mechanisms

For the vast majority of glycosidases, there are two key active site carboxyl groups (Glu or Asp) that are intimately involved in the catalytic mechanisms of both inverting and retaining glycosidases (26, 27). Inverting glycosidases use a single displacement mechanism for which the two carboxyl groups are typically spaced 10.5 Å apart, thereby allowing for a substrate molecule and a water molecule to bind between them (15, 16, 27). One of the carboxyl groups promotes general acid-catalyzed cleavage of the glycosidic bond, whereas the other acts as a general base, catalyzing the nucleophilic attack of a water at the anomeric centre in a single nucleophilic reaction that occurs via an oxocarbenium ion-like transition state (16, 26, 28, 29). The result of this reaction is a hemiacetal product with inverted anomeric stereochemistry (Fig. 2A).

Retaining glycosidases use a double displacement mechanism for which the two carboxyl groups are spaced 5.5 Å apart, on average, and allow only for a substrate molecule to fit between them (15, 16, 27). One carboxyl group promotes general acid-catalyzed cleavage of the glycosidic bond, whereas the other acts as a nucleophile, directly attacking the anomeric centre and forming a covalent glycosyl–enzyme intermediate. After departure of the leaving group, the intermediate, which has an inverted anomeric centre relative to the substrate, undergoes general base catalyzed nucleophilic attack by an incoming water molecule to yield a product with retained anomeric stereochemistry (Fig. 2B, upper pathway) (26). Both steps of the double displacement mechanism proceed through transition states with substantial oxocarbenium ion character (16, 28, 29).

Alternatively, the configuration-retaining hexosaminidases from families 18, 20, and 56 lack an apparent enzymic nucleophile needed to form the glycosyl–enzyme intermediate in the first step of the double-displacement mechanism. Instead, the C2-acetamido group of the substrate participates in the reaction and assumes the role of the missing nucleophile (Fig. 2B, lower pathway) (13, 20, 21, 26). A number of equivalent catalytic residues within the active sites of families 18, 20, and 56 glycosidases result in common structural features that appropriately distort the bound substrate so that the carbonyl oxygen atom of the C2-acetamido group can become positioned for nucleophilic attack at the anomeric centre. In keeping with the geometrical considerations of the general retaining mechanism, this substrate distortion creates an average distance of 5.4 Å between the C2-acetamido group oxygen atom of the substrate and the carboxyl oxygens of the enzymic general acid–base catalytic residue. In the first step of the mechanism, the enzymic carboxyl group promotes general acid-catalyzed cleavage of the glycosidic bond, while a concerted nucleophilic attack by the C2-acetamido group oxygen results in an enzyme-stabilized oxazolinium-ion intermediate (30, 31). After departure of the leaving group, the cyclized intermediate undergoes base-catalyzed nucleophilic attack by an incoming water molecule at the anomeric centre to yield a product with retained stereochemistry. As for the "normal" double displacement mechanism, both steps of the reaction are believed to pass through oxocarbenium ion-like transition states (30). Another example of a glycosidase lacking a suitably disposed nucleophile in its active site is soluble lytic transglycosylase (32), and suggests that anchimeric assistance may be used by glycosidases from other sequence-related families.

Fig. 1. Ribbon diagrams of representative three-dimensional glycosidase structures from the sequence-related families 18 (A), 20 (B), and 56 (C). Although there is little sequence identity amoung the three families, they all have similar $(\beta/\alpha)_8$ barrel catalytic domains, shown here with α-helices and loops in light blue and β-strands in purple. (A) Family 18 Chitinase B from *Serratia marcescens* (36). (B) Family 20 β-hexosaminidase from *Streptomyces plicatus* (30). (C) Family 56 hyaluronidase from bee venom (21). The catalytic domains of family 18 and 20 glycosidases contain a typical eight-stranded β-barrel; however, the β-barrel of the bee venom hyaluronidase is incomplete and only contains seven β-strands. The ribbon diagrams were drawn with MOLMOL (55) and rendered with PovRay™ (Hallam Oaks Pty. Ltd).

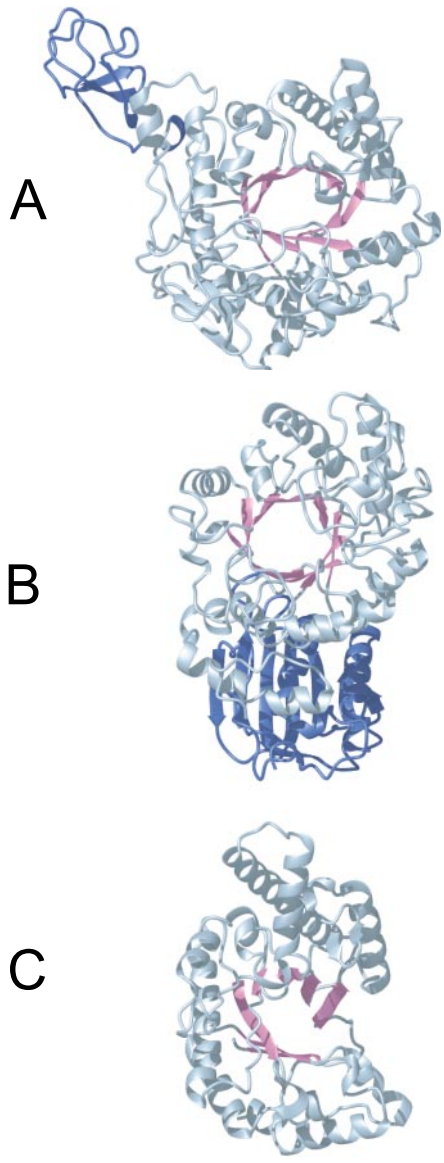

© 2002 NRC Canada

Fig. 2. Proposed catalytic mechanisms for inverting (A) and retaining glycosidases (B). Hydroxyl groups and C6 have been removed from the sugar ring for clarity and, ignoring the C2-acetamido group, the mechanisms shown in panels (A) and (B) (upper pathway) can be used to describe the catalytic mechanisms of inverting and retaining glycosidases in general. The mechanism shown in panel (B), lower pathway, involves anchimeric assistance from the C2-acetamido group, and the carboxylate illustrated beneath the cyclic intermediate is not positioned to act as a nucleophile. Instead, this carboxylate represents an enzymic residue, common amoung families 18, 20, and 56 glycosidases, and is responsible for stabilizing the positive charge that develops on the acetamido nitrogen, N2, upon cyclization (see Fig. 4B and related text). No attempt has been made to indicate the true position of this enzymic residue. Crystallographic evidence has demonstrated that the Michaelis complexes of β-retaining glycosidases, using either the upper or lower pathway in panel (B), contain a distorted substrate such that the glycosidic bond and leaving group (*R*) adopt a pseudo-axial position (13, 34, 35). Molecular modeling studies suggest that the Michaelis complex of inverting glycosidases may also contain a similarly distorted substrate (40, 41). Convincing structural evidence is lacking for the conformation of product bound in the –1 subsite. However, there is some evidence to suggest that the conformation of the pyranose ring of the product bound in the –1 subsite of β-retaining glycosidases is not a relaxed $^4C_1$ chair and is instead slightly distorted towards a higher energy half-chair-like structure (35, 38). A high-energy conformation for bound product may indeed prompt its expulsion from the active site. Figure drawn with CS CHEMDRAW STD. (CambridgeSoft Corp., Cambridge, Mass, U.S.A.).

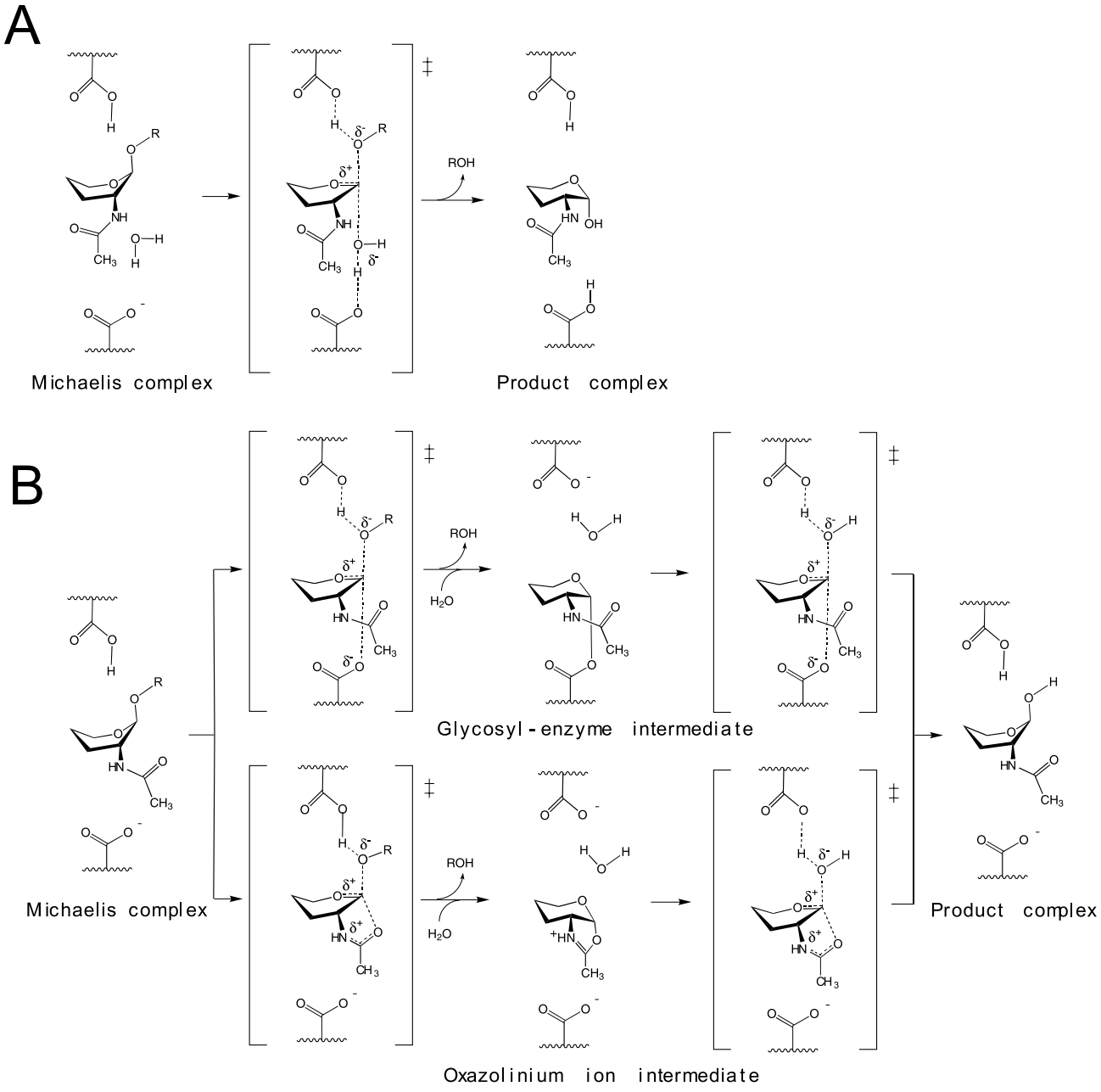

© 2002 NRC Canada

Substrate distortion

According to the currently accepted *–n* to *+n* nomenclature for glycosidase sugar-binding subsites (33) (where *n* is an integer and *–n* signifies the non-reducing end and *+n* the reducing end of the bound oligosaccharide), the scissile glycosidic bond of the substrate spans subsites –1 and +1. Crystallographically determined structures of complexes between intact substrates and retaining β-glycosidases demonstrate significant distortions in the pyranoside ring of the sugar bound in the –1 subsite prior to bond cleavage (Fig. 3) (13, 34–36). Distortion in the pyranoside ring bound in the –1 subsite was first proposed for HEW lysozyme in the late 1960's (37), and most recently supported by a high-resolution structure determination of the complex of HEW lysozyme with NAM–NAG–NAM bound as a product (38). Although the product complex between HEW lysozyme and NAM–NAG–NAM suggested a sofa conformation for the pyranose ring of the NAM residue bound in the –1 subsite, the true extent of substrate distortion was not revealed, however, until structures of retaining β-glycosidases were determined in complex with intact substrates spanning the active site, indicating that substrate interactions at the +1 subsite contribute significantly to pyranoside ring distortion in the –1 subsite (39).

The first three-dimensional structure of an intact substrate spanning the active site of a glycosidase was determined crystallographically — it was a complex between a family 20 chitobiase from *Serratia marcescens* and its natural substrate chitobiose (13). Although it is unclear why the chitobiose was not cleaved by the chitobiase crystals, the non-reducing and reducing NAG residues of the intact chitobiose molecule were located in the –1 and +1 subsites, respectively. The pyranoside ring of the sugar bound in subsite –1 was found to be distorted from the standard $^4C_1$ chair conformation into a skew-boat conformation such that the scissile bond and leaving group were held in a pseudo-axial orientation by the enzyme (Fig. 3). Representative hexosaminidases of both *endo*- and *exo*-acting enzymes from families 18 and 20, respectively, demonstrate this mode of substrate distortion in their respective Michaelis complexes (Figs. 4A and B) (13, 36). The three-dimensional structure of a Michaelis complex for a family 56 glycosidase has not been determined thus far; however, the structure of a family 56 hyaluronidase from bee venom has been solved in complex with a hyaluronic acid tetramer bound product (21). The substrate distortions seen in the Michaelis complexes for the family 18 and 20 glycosidases are nearly identical to those observed in the crystallographically determined Michaelis complexes of retaining cellulases from families 5 and 7 (34, 35). It has been postulated that similar substrate distortion also occurs in the enzyme-substrate complexes of inverting β-glycosidases (40, 41). Together, these findings suggest that a distorted pseudo-axial position for the glycosidic linkage and leaving group may indeed be a general mechanistic requirement for retaining and inverting β-glycosidases. Indeed, distortion of the pyranoside ring in the –1 site from a $^4C_1$ chair towards a boat conformation helps to satisfy the requirements of stereoelectronic theory. A boat conformation orients a lone pair of electrons on the ring oxygen (O5) antiperiplanar with respect to the scissile bond and leaving group. This

Fig. 3. Stereographic representation of a superposition of the small molecule crystal structure of unbound chitobiose (green carbon atoms) (56) and chitobiose bound to a family 20 *Serratia marcescens* chitobiase as a Michaelis complex (gray carbon atoms) (13). For both molecules, nitrogen atoms are shown in blue and oxygens in red. As previously demonstrated by Tews et al. (13), a superposition of these two structures shows that the non-reducing sugar of chitobiose, bound to the –1 subsite of the *S. marcescens* chitobiase, is distorted from a $^4C_1$ chair (as observed for the unbound chitobiose (green)), into a skew-boat conformation. The pyranoside ring distortion brings the leaving group and scissile bond into a pseudo-axial position and moves the anomeric carbon atom to a position slightly above the plane of the sugar ring. The skew-boat conformation allows the C2-acetamido group of the non-reducing sugar bound in the –1 subsite group to rotate approximately 156° about the C2–N2 bond so that the carbonyl oxygen atom O7 is positioned underneath the α-face of the sugar ring and into position for nucleophilic attack at the anomeric centre. All superpositions were carried out using the program O (57) and molecular diagrams were drawn with MOLSCRIPT (58) and rendered with the RASTER 3D (59).

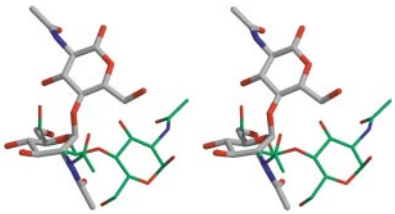

conformational arrangement maximizes electron donation from O5 to the antibonding orbital at the electron deficient anomeric center and thus accommodates much of the positive charge that develops at the anomeric center during the transition states (42, 43). The pseudo-axial orientation of the leaving group also places the oxygen atom of the glycosidic bond in an appropriate position for lateral protonation by the enzymic general acid catalyst (39).

In addition to the pyranoside ring distortion, the glycosidases from families 18, 20, and 56 have evolved remarkable active site architectures that position the C2-acetamido group of the NAG reside bound in the –1 subsite so that the carbonyl oxygen of this functional group can provide anchimeric assistance to the catalytic reaction. Although families 18, 20, and 56 share little sequence homology, the –1 subsite of the enzymes belonging to these families contain a homologous hydrophobic pocket that orients the C2-acetamido group into an appropriate position for nucleophilic attack at the anomeric centre (Fig. 4A) (13, 20, 21, 36). For the enzymes within each family, there exist an Asp and Tyr located in analogous positions on either side of the pocket (Fig. 4B). The Asp residue is positioned so that it can form a short hydrogen-bonding interaction with nitrogen atom (N2) of the C2-acetamido group; whereas, the position of the Tyr residue allows for it to form a hydrogen bond with the carbonyl oxygen atom (O7) of the C2-acetamido group (13, 21, 30, 36). These hydrogen bonds not only help to steer and lock the C2-acetamido group into position for nucleophilic attack, they also enhance the polarization of the amide beyond its naturally occurring dipole moment,

© 2002 NRC Canada

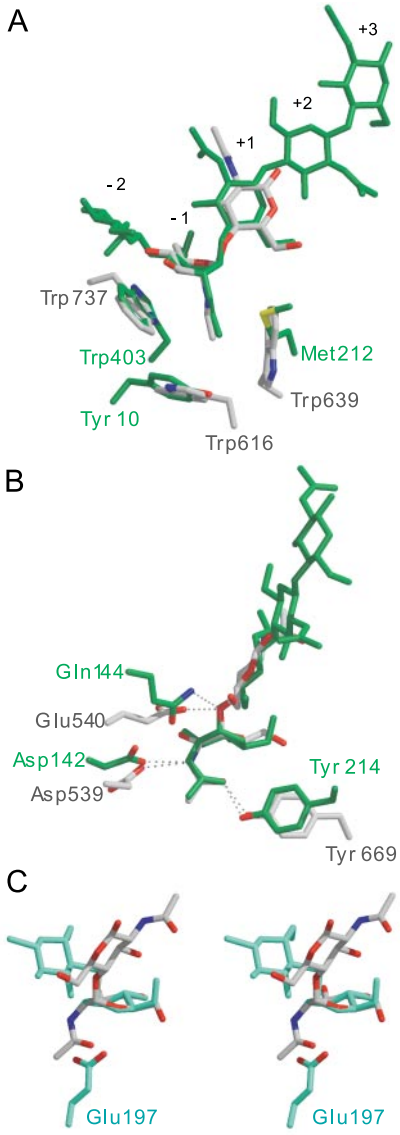

Fig. 4. Superpositions of crystallographic Michaelis complexes determined for representative family 18 and 20 glycosidases (A and B) (13, 36) and a family 7 β-retaining endoglucanase I from *Fusarium oxysporum* (C) (34). (A) Superposition of a family 20 chitobiase (gray carbon atoms) (13) and family 18 *endo*-chitinase (ChiB) (all atoms are green) from *S. marcescens* (36). The occupied sugar-binding subsites –2 to +3 have been labeled. The superposition demonstrates that *endo*- and *exo*-acting glycosidases from families 18 and 20, respectively, distort the pyranoside ring of the sugar bound in the –1 subsite from a $^4C_1$ chair into a skew boat prior to bond cleavage. This distortion results in a pseudo-axial orientation of the scissile glycosidic bond and leaving group. Both glycosidases have an analogus hydrophobic pocket as part of their –1 sugar binding subsites. This pocket helps to position the carbonyl oxygen of the C2-acetamido group underneath the α-face of the sugar and into an appropriate position for catalysis. A similar distorted position for the C2-acetamido group is observed for the NAG residue bound in the –1 subsite of the bee venom hyaluronidase product complex (21). (B) Rotated 90° relative to panel (A), this diagram of the superposition between the family 18 chitinase and family 20 chitobiase shows analogous hydrophilic residues that interact with the bound substrate. The general acid–base residue Glu540 from the family 20 chitobiase and the analogus family 18 chitinase residue Gln144 (mutated from a Glu in the wild-type enzyme), are equally situated to interact with the pseudo-axially positioned glycosidic oxygen atom of the substrate. The residues Asp539 and Tyr669 from the family 20 chitobiase and Asp142 and Tyr214 from the family 18 chitinase, form equivalent hydrogen-bonding interactions with the C2-acetamido nitrogen N2 and carbonyl oxygen O7, respectively. These hydrogen-bonding interactions not only appear to lock the C2-acetamido group into a catalytically favorable position, they may also polarize the amide and increase the nucleophilicity of O7. Recently, a crystallographic complex between a mutated form of the family 20 chitobiase (Asp539Ala) and chitobiose demonstrated that in the absence of the Asp539 carboxylate, the carbonyl oxygen of the C2-acetamido group does not become positioned underneath the α-face of the pyranoside ring as shown here, but instead occupies the space where the missing Asp caboxyl group is normally located (60). This complex supports the conjecture that Asp539 and the equivalent Asp in other family 18 and 20 glycosidases is important for positioning the C2-acetamido group into a catalytically competent position. (C) Superposition of the *F. oxysporum* endoglucanase I from family 7 (34) and the family 20 chitobiase from *S. marcescens* (13). The crystallographic Michaelis complex between endoglucanase I and a non-hydrolyzable substrate (shown in light green) demonstrated that substrate distortion occurs in an analogous manner to that observed for family 18 and 20 glycosidases, where the sugar bound to subsite –1 is distorted into a skew-boat and the scissile bond and leaving group are in a pseudo-axial position (34). Moreover, as previously demonstrated by Sulzenbacher et al. (34), the superposition of these two Michaelis complexes reveals that the carboxylate of the enzymic nucleophile, Glu197, of endoglucanase I superposes almost perfectly with the C2-acetamido group oxygen of the non-reducing sugar of chitobiose bound to the family 20 chitobiase. The remarkable spatial equivalence of the two functional groups within the active sites of these glycosidases clearly indicates that the C2-acetamido group oxygen is suitably positioned to act in place of an enzymic nucleophile in the catalytic mechanism of family 18 and 20 glycosidases.

thereby causing a further increase in charge density on the carbonyl oxygen and increasing its nucleophilicity. Kinetic studies with substrate analogues and inhibitors have provided biochemical support for the structural findings that implicate C2-acetamido group participation in the catalytic mechanism of the glycosidases from families 18, 20, and 56 (6, 7, 22, 31, 44, 45).

Interestingly, it can be been shown that the nucleophilic oxygen atom of Glu197 of the family 7 β-retaining endoglucanase I from *Fusarium oxysporum* (which uses the catalytic mechanism described in Fig. 2B, upper pathway) essentially overlaps the position of the C2-acetamido carbonyl oxygen of chitobiose bound to the family 20 chitobiase from *Serratia marcescens* when the two structures are superimposed (Fig. 4C) (34). Thus, anchimeric assistance by the neighboring C2-acetamido group of the substrate not only replaces the need for a second enzymic carboxylate, but also the stereochemistry of the nucleophilic attack is conserved between retaining β-glycosidases that use either an enzymic or substrate-based nucleophile.

© 2002 NRC Canada

Fig. 5. Crystallographic complex of the 1-*N*-azasugar GalNAc-isofagomine (IFG, brown carbon atoms) bound in –1 sugar-binding subsite of a β-*N*-acetylhexosaminidase from *Streptomyces plicatus* (gray carbon atoms) (46). For both the enzyme and azasugar inhibitor, oxygen atoms are shown in red and nitrogen atoms in blue. The conformation of GalNAc-isofagomine is distorted from a $^4C_1$ chair toward a half-chair. The endocyclic nitrogen atom N1 is displaced 0.4 Å below the least-squares plane defined by atoms C2, C3, C5, and C9 (C9 replaces the endocyclic oxygen atom O5 of pyranose rings); whereas, atom C4 is displaced 0.7 Å above this plane. N1 is assumed to be protonated when bound to the enzyme; the axial proton forms a 2.7 Å intramolecular hydrogen bond with the C2-acetamido group oxygen O7 (dashed magenta line), whereas the equatorial proton forms a novel 2.8 Å hydrogen bond with the carboxyl group of the general acid–base residue Glu314. The intramolecular hydrogen bond between N1 and O7 of GalNAc-isofagomine is analogus to the strong electrostatic interaction demonstrated to occur between N1 of a xylobiose-derived 1-*N*-azasugar inhibitor and the enzymic nucleophile of Cex, a family 10 β-retaining glycosidase from *Cellulomonas fimi* (46, 47).

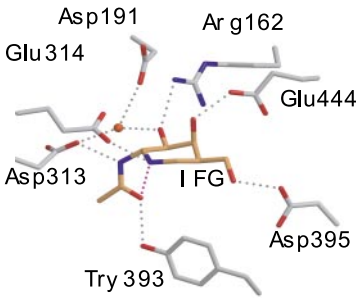

A family 20 β-hexosaminidase from *Streptomyces plicatus* was recently shown to be strongly inhibited by a C2 *N*-acetylated 1-*N*-azasugar, GalNAc-isofagomine (K_i = 2.7 μM) (Fig. 5) (46). 1-*N*-Azasugar inhibitors are thought to derive most of their binding energy from a strong electrostatic interaction between the protonated endocyclic nitrogen at the "anomeric" centre of the inhibitor and the negatively charged enzymic nucleophile of a retaining β-glycosidase (47). It was therefore surprising to find that a 1-*N*-azasugar could also act as a potent competitive inhibitor of a glycosidase lacking an enzymic nucleophile. The crystallographically determined complex between *S. plicatus* β-hexosaminidase and GalNAc-isofagomine provided an explanation for the effective binding of this inhibitor to the enzyme. The complex demonstrated that the binding mode of the inhibitor allowed for a novel 2.8 Å hydrogen-bonding interaction to occur between the endocyclic ring nitrogen of the inhibitor and the carboxyl group of the enzymic general acid–base catalytic residue Glu314. An equivalent hydrogen-bonding interaction is not observed in the recent crystallographically determined complex between a xylobiose-derived 1-*N*-azasugar inhibitor and Cex, a family 10 β-retaining glycosidase from *Cellulomonas fimi* (47). Cex instead contains an enzymic nucleophile to which the endocyclic ring nitrogen of the xylobiose-derived 1-*N*-azasugar was found to closely interact. The lack of such an electrostatic interaction between the *S. plicatus* β-hexosaminidase and GalNAc-isofagomine appears to allow for the inhibitor to bind so that the endocyclic ring nitrogen can instead form a compensatory hydrogen-bonding interaction with the general acid–base catalytic residue. This alternative hydrogen bond seems to explain the unexpected potency of GalNAc-isofagomine towards the β-hexosaminidase and may form the basis for a new series of pharmacological agents that inhibit family 20 glycosidases.

Intermediate structure

The oxazolinium ion intermediate formed by C2-acetamido group participation in the catalytic mechanism of families 18, 20, and 56 glycosidases is too hydrolytically unstable for use in crystallographic studies. A relatively stable analogue, NAG-thiazoline, was synthesized and shown to be a potent competitive inhibitor of jack bean β-hexosaminidase (K_i = 280 nM) (31). Furthermore, it was shown that a precursor substrate of NAG-thiazoline, 4-methylumbelliferyl-2-deoxy-2-thioacetamido-β-glucoside, could be converted into NAG-thiazoline by jack bean β-hexosaminidase, leading to time dependent loss of enzyme activity and thereby providing direct biochemical support for anchimeric assistance and the formation of a covalent, cyclized intermediate by the enzyme.

Recently, an X-ray crystal structure of NAG-thiazoline in complex with the family 20 β-hexosaminidase from *S. plicatus* was determined (Fig. 6) (30).[3] The structure of the complex indicates that after the reaction has progressed through the first transition state to the cyclized intermediate (Fig. 2B, lower pathway), the sugar ring (bound in the –1 subsite) relaxes from the skew-boat conformation, as observed in the Michaelis complex of the related chitobiase from *S. marcescens* (13), to what could best be described as a $^4C_1$ chair conformation (Fig. 7). Taken together, the crystal structures of the Michaelis complex from the family 20 chitobiase, and the intermediate analogue bound to the family 20 β-hexosaminidase, reveals that the anomeric carbon

[3] Crystallographic data for the protein structures discussed in this review are available from the Protein Data Bank (URL: http://www.rcsb.org/pdb/) under the following PDB identifiers: *S. marcescens* chitobiase in complex with chitobiose, 1QBB; Mutant *S. marcescens* chitobiase (D539A) in complex with chitobiose, 1C7S; *S. plicatus* β-hexosaminidase in complex with the intermediate analouge NAG-thiazoline, 1HP5; *S. plicatus* β-hexosaminidase in complex with GalNAc-isofagomine, 1JAK; Mutant *S. marcescens* ChiB (E144Q) in complex with penta-NAG, 1E6N; *S. marcescens* ChiB in complex with allosamidin, 1E6R; Mutant *S. marcescens* ChiA (E315Q) in complex with octa-NAG, 1EHN; Mutant *S. marcescens* ChiA (D313A) in complex with octa-NAG, 1EIB; Mutant *S. marcescens* ChiA (Y390F) in complex with hexa-NAG, 1FFR; *F. oxysporum* endoglucanse 1 in complex with thio-DP5 (methyl-*S*-β-D-glucopyranosyl-(1→4)-*S*-4-thio-β-D-glucopyranosyl-(1→4)-*S*-4-thio-β-D-glucopyranosyl-(1→4)-*S*-4-thio-β-D-glucopyranosyl-(1→4)-*S*-4-thio-α-D-glucopyranoside), 1OVW; NAG-(1→4)-2-deoxy-2-fluoro-β-D-glucopyranosyl·HEW lysozyme covalent intermediate complex, 1H6M; Hevamine in complex with allosamidin, 1LLO; Bee venom hyaluronidase in complex with hyaluronic acid tetramer, IFCV. Crystallographic data for the structure of chitobiose is available from the Cambridge Crystallographic Data Centre (URL: http://www.ccdc.cam.ac.uk/) under the refcode ACHITM10.

© 2002 NRC Canada

Fig. 6. Crystallographic complex between the oxazolinium ion intermediate analogue NAG-thiazoline (NGT) and a family 20 β-*N*-acetylhexosaminidase from *Streptomyces plicatus* (30). The conformation of the pyranose ring of NAG-thiazoline approaches that of a relaxed $^4C_1$ chair and is held within the –1 subsite of the enzyme (gray carbon atoms) by an extensive hydrogen bonding network (dashed lines). Site directed mutagenesis studies confirm that the bidentate hydrogen-bonding interaction occurring between O3 and O4 of NAG-thiazoline and the conserved family 20 residue Arg162, appears to be particularly important for binding substrate and stabilizing transition states that occur along the reaction corrdinate (13, 14, 61). Glu314 acts as the general acid–base residue for this β-hexosaminidase and does not interact with the intermediate analogue. The thiazoline ring of the cyclic intermediate analogue forms the same hydrogen-bonding interactions as observed for the C2-acetamido group in the Michaelis complexes of related family 18 and 20 glycosidases (Fig. 4B). In particular, the short hydrogen bond formed between Asp313 and the C2-acetamido group nitrogen N2 is understood to balance the positive charge that develops on this nitrogen atom upon cyclization to form the oxazolinium ion intermediate (Fig. 2B, lower pathway). Asp313 is conserved among family 20 glycosidases and has an equivalent residue in family 18 glycosidases, indicating that the charge stabilization provided by this residue is a common mechanistic feature of both glycosidase families.

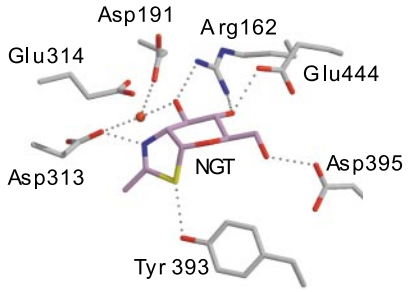

atom (C1) experiences the greatest nuclear motion along the reaction coordinate. Initially, atom C1 is above the plane of the sugar ring and then, as the covalent bond to the glycosidic oxygen breaks, the anomeric center (C1) moves approximately 0.9 Å to a position below the plane of the sugar ring, where it forms a new covalent bond with the C2-acetamido group oxygen atom, resulting in an oxazolinium ion intermediate (Fig. 2B, lower pathway). The nuclear motion proposed for the anchimeric assistance mechanism of family 20 glycosidases is in agreement with the recently proposed theory of electrophilic migration of the anomeric center along the reaction coordinate of HEW lysozyme and retaining β-glycosidases in general (48).

The pyranoside ring conformation of the cyclic intermediate analogue NAG-thiazoline bound to the *S. plicatus* β-hexosaminidase is strikingly similar to that observed for the recently determined glycosyl–enzyme intermediate structure of HEW lysozyme (Fig. 8) (48) and other retaining β-glycosidases that use an enzymic nucleophile (35, 49, 50). The "textbook" mechanism of HEW lysozyme originally proposed by Phillips (9), suggested a dissociative S_N1-type reaction mechanism involving a long-lived oxocarbenium ion intermediate that was stabilized by the enzyme through

Fig. 7. Stereographic representation of a superposition of the *S. plicatus* β-hexosaminidase–NAG-thiazoline intermediate complex (coloured as in Fig. 6) (30) and the *S. marcescens* chitobiase–chitobiose Michaelis complex (atoms and labels shown in green) (13). Both family 20 glycosidases contain three conserved Trp residues that help to position the C2-acetamido group and stabilize the oxazolinium ion intermediate as indicated by the NAG-thiazoline analogue. The superposition clearly demonstrates that upon cleavage of the scissile glycosidic bond and nucleophilic attack by the C2-acetamido oxygen, the pyranose ring of the sugar bound in the –1 subsite relaxes from a skew-boat conformation as observed for chitobiose (CBS) towards a relaxed $^4C_1$ chair as seen for NAG-thiazoline (NGT). This conformational change requires very little movement by any atoms other than the migration of the anomeric centre from above the β-face to below the α-face of the sugar ring (30).

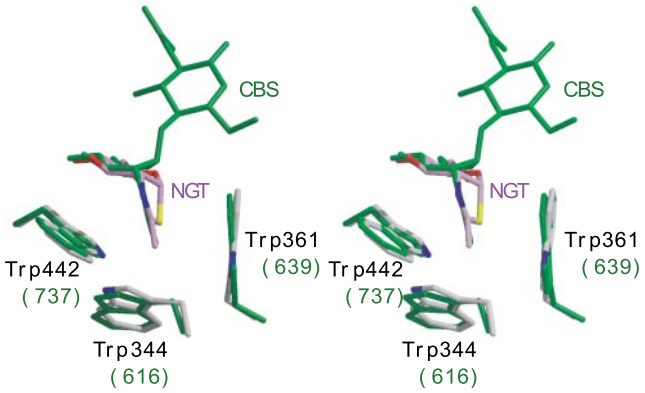

electrostatic interactions, primarily with the carboxylate of Asp52. Vocadlo et al. (48) have recently trapped and solved the crystal structure of a glycosyl–enzyme intermediate form of HEW lysozyme (Fig. 8), demonstrating, however, that this enzyme proceeds via a covalent intermediate during catalysis and uses instead the S_N2-type double-displacement mechanism described in the upper pathway of Fig. 2B. This finding now places HEW lysozyme in the general class of retaining glycosidases and strengthens the general configuration-retaining mechanism that includes substrate distortion, electrophilic migration of the anomeric carbon atom during catalysis, and the formation of a covalent intermediate.

Previously, an Asp52Ala mutant of HEW lysozyme was found to retain appreciable activity against substrates that were believed to have no functional groups that could compensate for the missing Asp carboxylate (51). Thus, it was assumed that Asp52 was not essential to the catalytic mechanism of HEW lysozyme. The authors did not consider, however, that the residual activity could have been a result of C2-acetamido group participation. It is possible that the C2-acetamido group of the sugar bound in the –1 subsite during catalysis might have compensated for the missing carboxyl group on the mutant enzyme. It could occupy the position of the missing Asp52 carboxylate in a conformation similar to that observed for the Michaelis complexes of the family 18 and 20 glycosidases. This conformation may then result in the formation of an oxazoline intermediate as opposed to the glycosyl–enzyme intermediate observed by Vocadlo et al. (48).

© 2002 NRC Canada

Fig. 8. Comparison of the enzyme bound conformation of NAG-thiazoline (NGT) (30) and the covalent NAG-(1→4)-2-deoxy-2-fluoro-β-D-glucopyranosy-HEW lysozyme intermediate structure (only the sugar bound in the –1 subsite is shown (G2F)) (48). The comparison clearly demonstrates that the sugar ring bound in the –1 subsite of both the *S. plicatus* β-hexosaminidase and HEW lysozyme intermediate complexes, adopts a conformation best described as a $^4C_1$ chair regardless of whether the nucleophile is provided by the substrate or by the enzyme.

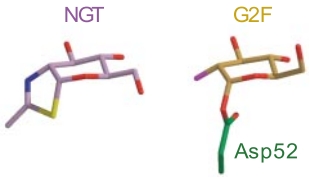

There is convincing crystallographic evidence for the formation of an oxazolinium ion intermediate on the catalytic pathway of family 18 glycosidases. The potent family 18 chitinase inhibitor, allosamidin, is a natural pseudo-trisaccharide with an aminocyclitol derivative at its "non-reducing" end that mimics the stereochemical characteristics of the oxazolinium ion intermediate (52). The structure of this inhibitor has been determined in complex with the chitinase–lysozyme hevamine (22), and Chitinase B (ChiB) from *S. marcescens* (36). A superposition of the *S. plicatus* β-hexosaminidase–NAG-thiazoline and hevamine–allosamidin complexes demonstrates that the oxazoline-like structure of allosamidin not only occupies the same location as the thiazoline ring of NAG-thiazoline, but also it forms the same hydrogen-bonding interactions with equivalent Asp and Tyr residues (Fig. 9). A similar observation is found when the *S. marcescens* ChiB–allosamidin and NAG-thiazoline–β-hexosaminidase complexes are superimposed. Although the structure of a complex between a family 56 hyaluronidase and a cyclic intermedate analogue has not been determined, it has recently been demonstrated that a GlcA-β(1→3)-NAG oxazoline derivative can be used as an "activated" substrate monomer for the artificial synthesis of hyaluronic acid by either bovine or ovine testicular hyaluronidase (7).

Finally, a well-ordered water molecule can be observed approximately 3.3–3.4 Å from C1 of the allosamizoline ring when in complex with either hevamine or ChiB from *S. marcescens* (36). This water molecule is hydrogen-bonded to the respective general acid–base residue of each enzyme (ChiB Glu 144, hevamine Glu 127) and is in roughly the same position as the glycosidic oxygen atom prior to cleavage (36). If an oxazolinium ion intermediate were to be bound in the position of the allosamizoline ring in these complexes, this water molecule would be perfectly poised for base-catalyzed nucleophilic attack at the anomeric center of the intermediate, completing the catalytic cycle and producing a product with retained anomeric stereochemistry (36). Support for these findings in family 18 glycosidases is provided by the family 20 *S. plicatus* β-hexosaminidase in complex with NAG-thiazoline (30). In this complex, one of the hydroxyl groups of a glycerol molecule, bound in the +1 subsite, is hydrogen-bonded to the general acid–base residue Glu314 and is positioned 3.5 Å above the β-face of the intermediate analogue. This hydroxyl group occupies a position

Fig. 9. Superposition of the *S. plicatus* β-hexosaminidase–NAG-thiazoline complex (30) and family 18 hevamine–allosamidin complex (22). The oxazoline-like moiety of the naturally occurring chitinase inhibitor allosamidin and the thiazoline ring of NAG-thiazoline occupy the same relative position within the active site of each enzyme. The striking similarity of the active site architecture and hydrogen-bonding interactions responsible for binding the oxazoline-like moieties of allosamidin to hevamine and NAG-thiazoline to *S. plicatus* β-hexosamnindase, provides convincing evidence for the formation of a cyclic intermediate in the reaction pathways of both family 18 and 20 glycosidases.

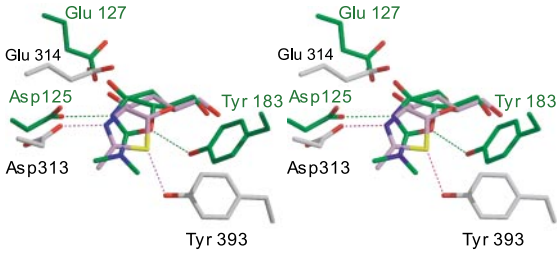

analogous to that of the water molecule observed in the complexes between allosamidin and the family 18 glycosidases discussed above, and is indeed well situated to attack C1 of an oxazolinium ion intermediate.

In light of the recent structural and biochemical findings for family 18 and 20 glycosidases and for HEW lysozyme, an alternative mechanism recently proposed on the basis of structural studies of a family 18 Chitinase A (ChiA) from *Serratia marcescens* seems unlikely (53). A series of S. *marcescens* ChiA structures containing various active site mutations were solved in complex with octa- or hexa-*N*-acetylglucosamine. Based primarily on the electron density ascribed to a hexa-*N*-acetylglucosamine molecule bound in the active site of a ChiA mutant (Tyr390Phe, ChiA Tyr390 is equivalent to the Tyr residues shown in Figs. 4B, 5, 6, and 9), it was concluded that the C2-acetamido group of the sugar bound in the –1 subsite of the enzyme was inappropriately positioned to form an oxazolinium ion intermediate (53). Instead, it was suggested that the carbonyl oxygen atom of the acetamido group assisted in stabilizing a long-lived oxocarbenium ion intermediate through electrostatic interactions in an S_N1-type mechanism. However, there is now a substantial amount of evidence refuting a glycosidase mechanism involving a long-lived oxocarbenium ion intermediate (5, 48), and the electron density for the sugar bound in the –1 subsite of this complex is ambiguous. Thus, mechanistic conclusions based on the structure of this complex are suspect, and C2-acetamido group participation that results in the formation of a cyclized oxazolinium ion intermediate in the catalytic mechanism of *S. marcescens* ChiA should not be ruled out based on these findings alone.

Conclusions

There is a substantial amount of evidence demonstrating that anchimeric assistance is a common mechanistic feature of the glycosidases belonging to families 18, 20, and 56. Future structural and functional investigations may demonstrate anchimeric assistance to be an integral mechanistic component of glycosidases in other sequence-related families.

© 2002 NRC Canada

Substrate-assisted catalysis may have indeed occurred during the evolutionary history of many enzymes. It has been suggested for the serine proteinases at least, that the spontaneous formation of the classic triad of catalytic residues (Ser-His-Asp) would have been a highly unlikely evolutionary event. Alternatively, it was proposed that the serine proteinases once contained only a catalytic diad (Ser and Asp) and operated via an anchimeric assistance mechanism whereby the His residue of the catalytic triad was provided by the substrate (54). It was only later in evolutionary history that these proteinases incorporated within their active sites a suitably positioned His residue that could take over from the substrate, thereby dramatically broadening substrate specificity (54). We may be observing a similar evolutionary path for the glycosidases from families 18, 20, and 56; however, it is also possible that existing evolutionary pressures demand that these enzymes maintain an active site architecture and catalytic mechanism that is dependent and specific for the presence of the C2-acetamido group. Regardless of the evolutionary fate of the family 18, 20, and 56 glycosidases, these enzymes presently have an active site structure that carries out a catalytic mechanism displaying all the general characteristics of the double-displacement mechanism first proposed by Koshland (26). They provide unique support for the general mechanism of retaining β-glycosidases that includes substrate distortion, formation of a covalent intermediate, and electrophilic migration of C1 along the reaction coordinate.

Acknowledgments

We thank D.J. Vocadlo for critical reading of the manuscript and J.C. Parrish for help with preparing figures. Research funding is provided to M.N.G.J. and B.L.M. by the Canadian Institutes for Health Research (CIHR). B.L.M. is supported by studentships from the CIHR, the Alberta Heritage Foundation for Medical Research, and the University of Alberta.

References

1. W.P. Jencks. *In* Catalysis in chemistry and enzymology. McGraw-Hill, Inc., New York. 1969.
2. A. Fersht. Structure and mechanism in protein science: A guide to enzyme catalysis and protein folding. W.H. Freeman Publishing, New York. 1998.
3. W. Dall'Acqua and P. Carter. Protein Sci. **9**, 1 (2000).
4. D. Piszkiewicz and T.C. Bruice. J. Am. Chem. Soc. **90**, 2156 (1968).
5. G.J. Davies, M.L. Sinnott, and S.G. Withers. *In* Comprehensive biological catalysis. *Edited by* M.L. Sinnott. Academic Press Ltd., New York. 1998. p. 119.
6. S. Drouillard, S. Armand, G.J. Davies, C.E. Vorgias, and B. Henrissat. Biochem. J. **328**, 945 (1997).
7. S. Kobayashi, H. Morii, R. Itoh, S. Kimura, and M. Ohmae. J. Am. Chem. Soc. **123**, 11825 (2001).
8. C.C. Blake, D.F. Koenig, G.A. Mair, A.C. North, D.C. Phillips, and V.R. Sarma. Nature (London), **206**, 757 (1965).
9. D.C. Phillips. Sci. Am. **215**, 78 (1966).
10. B. Henrissat. Biochem. J. **280**, 309 (1991).
11. B. Henrissat and A. Bairoch. Biochem. J. **293**, 781 (1993).
12. B. Henrissat and A. Bairoch. Biochem. J. **316**, 695 (1996).
13. I. Tews, A. Perrakis, A. Oppenheim, Z. Dauter, K.S. Wilson, and C.E. Vorgias. Nat. Struct. Biol. **3**, 638 (1996).
14. B.L. Mark, G.A. Wasney, T.J. Salo, A.R. Khan, Z. Cao, P.W. Robbins, M.N. James, and B.L. Triggs-Raine. J. Biol. Chem. **273**, 19618 (1998).
15. M.L. Sinnott. Chem. Rev. **90**, 1171 (1990).
16. J.D. McCarter and S.G. Withers. Curr. Opin. Struct. Biol. **4**, 885 (1994).
17. B. Henrissat and G. Davies. Curr. Opin. Struct. Biol. **7**, 637 (1997).
18. R.A. Gravel, J.T.R. Clark, M.M. Kaback, D. Mahuran, K. Sandhoff, and K. Suzuki. *In* The Metabolic basis of inherited disease. 7th ed. McGraw-Hill Inc., New York. 1995.
19. B. Triggs-Raine, T.J. Salo, H. Zhang, B.A. Wicklow, and M.R. Natowicz. Proc. Natl. Acad. Sci. U.S.A. **96**, 6296 (1999).
20. I. Tews, A.C. Terwisscha van Scheltinga, A. Perrakis, K.S. Wilson, and B.W. Dijkstra. J. Am. Chem. Soc. **119**, 7954 (1997).
21. Z. Markovic-Housley, G. Miglierini, L. Soldatova, P.J. Rizkallah, U. Muller, and T. Schirmer. Structure Fold. Des. **8**, 1025 (2000).
22. A.C. Terwisscha van Scheltinga, S. Armand, K.H. Kalk, A. Isogai, B. Henrissat, and B.W. Dijkstra. Biochemistry, **34**, 15619 (1995).
23. S. Armand, H. Tomita, A. Heyraud, C. Gey, T. Watanabe, and B. Henrissat. FEBS Lett. **343**, 177 (1994).
24. B. Iseli, S. Armand, T. Boller, J.M. Neuhaus, and B. Henrissat. FEBS. Lett. **382**, 186 (1996).
25. E.C. Lai and S.G. Withers. Biochemistry, **33**, 14743 (1994).
26. D.E. Koshland. Biol. Rev. **28**, 416 (1953).
27. G. Davies and B. Henrissat. Structure, **3**, 853 (1995).
28. J.D. McCarter, M.J. Adam, and S.G. Withers. Biochem. J. **286**, 721 (1992).
29. M.N. Namchuk and S.G. Withers. Biochemistry, **34**, 16194 (1995).
30. B.L. Mark, D.J. Vocadlo, S. Knapp, B.L. Triggs-Raine, S.G. Withers, and M.N.G. James. J. Biol. Chem. **276**, 10330 (2001).
31. S. Knapp, D. Vocadlo, Z. Gao, B. Kirk, J. Lou, and S.G. Withers. J. Am. Chem. Soc. **118**, 6804 (1996).
32. A.M. Thunnissen, H.J. Rozeboom, K.H. Kalk, and B.W. Dijkstra. Biochemistry, **34**, 12729 (1995).
33. G.J. Davies, K.S. Wilson, and B. Henrissat. Biochem. J. **321**, 557 (1997).
34. G. Sulzenbacher, H. Driguez, B. Henrissat, M. Schulein, and G.J. Davies. Biochemistry, **35**, 15280 (1996).
35. G.J. Davies, L. Mackenzie, A. Varrot, M. Dauter, A.M. Brzozowski, M. Schulein, and S.G. Withers. Biochemistry, **37**, 11707 (1998).
36. D.M. van Aalten, D. Komander, B. Synstad, S. Gaseidnes, M.G. Peter, and V.G. Eijsink. Proc. Natl. Acad. Sci. U.S.A. **98**, 8979 (2001).
37. T. Imoto, L.N. Johnson, A.C.T. North, D.C. Phillips, and J.A. Rupley. *In* The enzymes. Vol. 7. *Edited by* P. Boyer. Academic Press Ltd., New York. 1972. p. 665.
38. N.C. Strynadka and M.N. James. J. Mol. Biol. **220**, 401 (1991).
39. D.L. Zechel and S.G. Withers. Acc. Chem. Res. **33**, 11 (2000).
40. A. Varrot, M. Schulein, and G.J. Davies. Biochemistry, **38**, 8884 (1999).
41. T.T. Teeri, A. Koivula, M. Linder, G. Wohlfahrt, C. Divne, and T.A. Jones. Biochem. Soc. Trans. **26**, 173 (1998).
42. P. Deslongchamps. Stereoelectronic effects in organic chemistry. Pergamon Press, New York. 1983.
43. A.J. Kirby. Acc. Chem. Res. **17**, 305 (1984).
44. G. Legler and R. Bollhagen. Carbohydr. Res. **233**, 113 (1992).
45. C.S. Jones and D.J. Kosman. J. Biol. Chem. **255**, 11861 (1980).

© 2002 NRC Canada

46. B.L. Mark, D.J. Vocadlo, D. Zhao, S. Knapp, S.G. Withers, and M.N.G. James. J. Biol. Chem. **276**, 42131 (2001).
47. V. Notenboom, S.J. Williams, R. Hoos, S.G. Withers, and D.R. Rose. Biochemistry, **39**, 11553 (2000).
48. D.J. Vocadlo, G.J. Davies, R. Laine, and S.G. Withers. Nature (London), **412**, 835 (2001).
49. V. Notenboom, C. Birsan, M. Nitz, D.R. Rose, R.A.J. Warren, and S.G. Withers. Nat. Struct. Biol. **5**, 812 (1998).
50. A. White, D. Tull, K. Johns, S.G. Withers, and D.R. Rose. Nat. Struct. Biol. **3**, 149 (1996).
51. I. Matsumura and J.F. Kirsch. Biochemistry, **35**, 1881 (1996).
52. S. Sakuda, A. Isogai, S. Matsumoto, and A. Suzuki. Tetrahedron, **27**, 2475 (1986).
53. Y. Papanikolau, G. Prag, G. Tavlas, C.E. Vorgias, A.B. Oppenheim, and K. Petratos. Biochemistry, **40**, 11338 (2001).
54. P. Carter and J.A. Wells. Science (Washington, D.C.), **237**, 394 (1987).
55. R. Koradi, M. Billeter, and K. Wuthrich. J. Mol. Graphics. **14**, 51 (1996).
56. F. Mo and L.H. Jensen. Acta. Crystallogr. Sect. B, **34**, 1562 (1978).
57. T.A. Jones, J.Y. Zou, S.W. Cowan, and M. Kjeldgaard. Acta. Crystallogr. Sect. A, **47**, 110 (1991).
58. P.J. Kraulis. J. App. Crystallogr. **24**, 946 (1991).
59. E.A. Merritt and D.J. Bacon. Methods Enzymol. **277**, 505 (1997).
60. G. Prag, Y. Papanikolau, G. Tavlas, C.E. Vorgias, K. Petratos, and A.B. Oppenheim. J. Mol. Biol. **300**, 611 (2000).
61. Y. Hou, D. Vocadlo, S. Withers, and D. Mahuran. Biochemistry, **39**, 6219 (2000).

© 2002 NRC Canada

Reciprocal donor acceptor selectivity (RDAS): A new concept for "matching" donors with acceptors

Bert Fraser-Reid, J. Cristobal Lopez, K.V. Radhakrishnan, Mateusz Mach, Urs Schlueter, Ana Gomez, and Clara Uriel

Abstract: Lemieux's extensive work on replacement reactions at the anomeric center helped to establish the fact that the O-2-protecting group of a donor exerts powerful control over stereoselectivity in glycoside coupling reactions. This manuscript shows that the O-2-protecting group of a donor also exerts powerful, indeed sometimes total, control over regioselectivity in glycosidation of diols. The latter acceptors also exhibit preferences over the donor, thereby providing evidence for the concept of reciprocal donor acceptor selectivity (RDAS). The latter concept is put to the test by simultaneously presenting an acceptor diol with equivalent amounts of two donors, in the hope of achieving double differential glycosidation leading to one-pot assembly of a trisaccharide. When the pair of donors did *not* conform to RDAS principles the reaction did not proceed beyond a dissacharide. However, when the pair was RDAS sanctioned, a *single* trisaccharide (out of four possibilities) was obtained.

Key words: regiocontrolled glycosidation, armed and disarmed donors, di- and trioxolenium ions, oxocarbenium ion.

Résumé : Les nombreux travaux de Lemieux sur les réactions de remplacement au niveau du centre anomérique on permis d'établir le fait que le groupe protecteur en position O-2 d'un donneur exerce un contrôle important sur le stéréosélectivité des réactions de couplage des glycosides. Les résultats présentés dans ce travail montrent que le groupe protecteur en position O-2 exerce aussi un contrôle important, et quelquefois total, sur la régiosélectivité de la glycosidation des diols. Ces accepteurs présentent aussi des préférences par rapport au donneur et ceci correspond à des indications en faveur du concept d'une sélectivité réciproque donneur accepteur (SRDA). On a évalué ce dernier concept en présentant un diol accepteur à des quantités équivalentes de deux donneurs, en espérant obtenir une glycosidation doublement différentielle qui conduirait à un assemblage monotope d'un trisaccharide. Dans les cas où la paire de donneurs n'est pas conforme au concept de SRDA, la réaction ne procède pas au-delà du disaccharide. Toutefois, lorsque la paire était conforme au concept de SRDA, on n'obtient qu'un seul trisaccharide (parmi les quatre possibilités).

Mots clés : glycosidation, donneurs armés et désarmés, ions di- et trioxolénium, ion oxocarbénium.

[Traduit par la Rédaction]

Introduction

By the time Lemieux began his studies on "Replacement reactions at the anomeric center" (1), Isbell's elegant rationalization for the stereoselectivity observed in reactions of "acetyl glycoside halides" had been recognized as a monumental mechanistic breakthrough (2) (Scheme 1*a*), which was to give rise to the concept of neighboring group participation in organic chemistry (3). Thus Isbell's work showed that an O-2 acyl protecting group would foster 1,2-*trans* glycoside synthesis (**1**→**3**) a process in which a dioxolenium ion (**2**) was subsequently (4) implicated (Scheme 1*a*). The corollary of this insight was that a nonparticipating group would enhance the chances of obtaining the corresponding 1,2-*cis* stereoisomer (5).

However, enhance did not mean ensure, as was already evident to Lemieux from repeated failures to conquer sucrose using fully benzylated donors, which had led instead to excellent syntheses of "β-sucrose" (6). In this context, Lemieux's historic breakthrough utilizing Briggl's anhydride as a donor (7) (Scheme 1*b*) was seemingly contra-intuitive since epoxide cleavage should (and usually did) proceed from the β-face. However, prior investigations had given evidence of O-6 involvement (Scheme 1*b*) when "large" nucleophilic acceptors were used (8). In addition to being another type of "neighboring group participation", Lemieux's synthesis demonstrated the importance of "matching" donor with acceptor, although the concept had not been explicitly stated as such (see below).

Received 13 February 2002. Published on the NRC Research Press Web site at http://canjchem.nrc.ca on 28 August 2002.

Dedicated to the memory, teachings, and wisdom of Ray Lemieux, our Doktorvater/vater.

B. Fraser-Reid,[1] K.V. Radhakrishnan, M. Mach, and U. Schlueter. Natural Products and Glycotechnology Research Institute Inc. (NPG), 4118 Swarthmore Road, Durham, NC 27706, U.S.A.
J.C. Lopez, A. Gomez, and C. Uriel. Instituto de Quimica Organica General (CSIC), Juan de la Cierva 3, Madrid 28006, Spain.

[1]Corresponding author (e-mail: dglucose@aol.com).

 DOI: 10.1139/V02-137 © 2002 NRC Canada

Scheme 1.

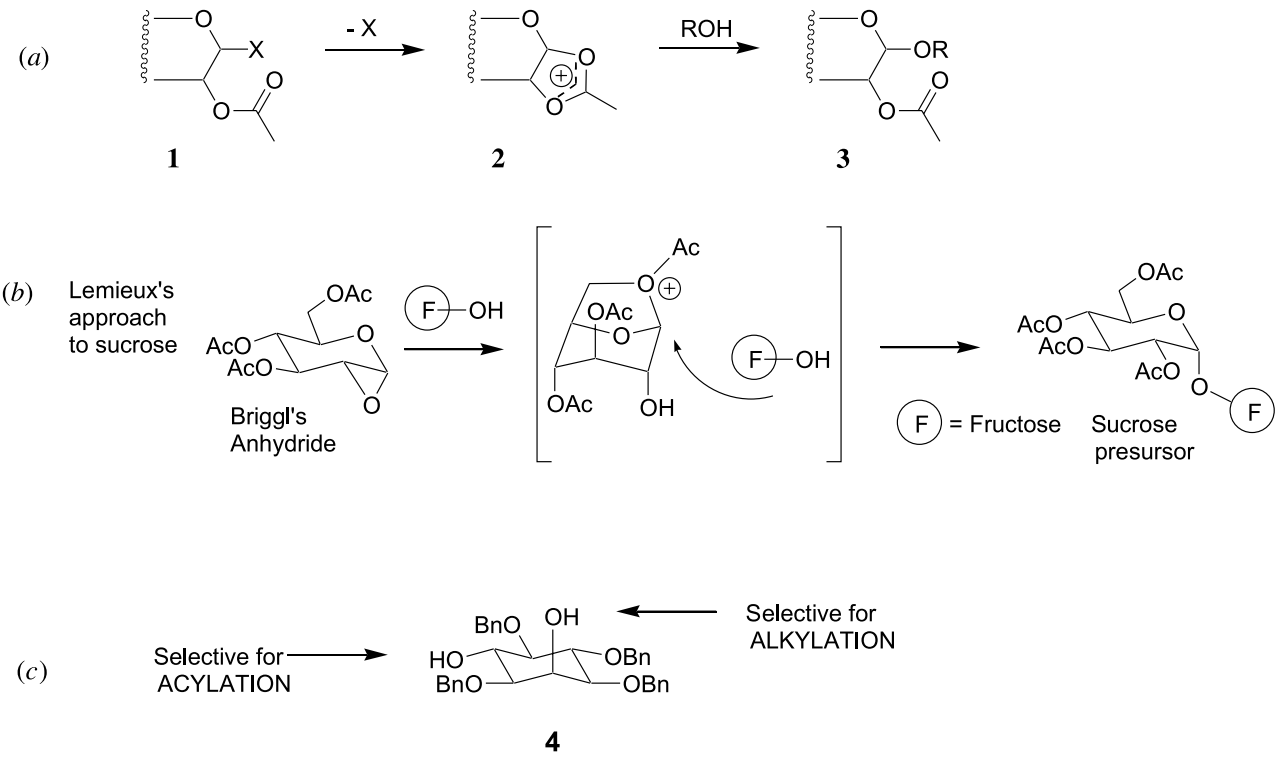

Following Isbell's lead, the O-2 protecting group has been justifiably established as an implement for anomeric stereocontrol — as is apparent from various textbooks dealing with carbohydrate synthesis (9). Nevertheless, recent reports (10) from our laboratory suggest that an O-2 protecting group can also provide a ready, low-tech implement for achieving regio control in glycosidation of polyhydroxylic acceptors.

These observations have profound importance for matching donor with acceptor, a concept, which has long been championed by Paulsen et al. (11). However, that matching modality is not to be confused with the subsequent, and now common usage of the term for "double stereodifferentiation" as introduced by Masamune et al. (12) in connection with the coupling of two enantiopure partners. In this regard, Masamune's usage is ably demonstrated by Spijker and VanBoeckel's example (13) showing that a given acceptor gave better yields with a D donor than its L enantiomer. On the other hand, Paulsen's matching concept has also demonstrated in VanBoeckel's collaboration with Petitou (14) on heparin analogs, in which prodigious preliminary experimentation served to reveal the best "match" for each linkage of the oligosaccharide array.

Results

Our interest in this question of regioselectivity emanated from the observation reported in 1998 (15) that the *myo*-inositol diol **4**, underwent acylation at C-6-OH exclusively, but alkylation primarily at C-2-OH, when a unimolar amount of the pertinent reagent was used (Scheme 1*c*). These differences in regioselectivity could not be rationalized by imputing "more or less" reactivity to either the OH or to the alkylation and (or) acylation reagent in question. For example, the (presumably) "more reactive" equatorial C-6-OH was rejected by the more reactive benzylating agent.

We were interested to see if the regioselectivity shown for **4** in Scheme 1*c* could be extended to glycosidation reactions. For this experiment, Lemieux's procedure (16) allowed ready preparation of orthoesters such as **5** (17) (Scheme 2). Acid-catalyzed rearrangement gave the disarmed 2-*O*-acyl donor (NPG_{AC}) **6**, which was transformed by two routine reactions into the armed (18) counterpart **7**. Compounds **8**–**10** were obtained similarly. Thus, a variety of *n*-pentenyl donors, armed and disarmed (18) to different extents, were available which could be made to react under similar conditions on a level playing field, so that valid comparisons could be drawn.

When diol **4** was treated with 1 equiv of the *manno* NPG_{AC} **6a**, the only compound obtained was the pseudo disaccharide **11a** (Scheme 3*a* and Table 1, entry *i*). The NPOE **5a** followed similar regioselectivity giving **11a** exclusively — indeed in the better yield of 73% (Table 1, entry *ii*). By contrast, the armed counterpart **7a**, gave a mixture of regioisomers **11b** and **12b** in a 1:3 ratio (Table 1, entry *iii*).

In all of these studies (above and below), assignment of the regiosomeric structures was readily accomplished by acylating the material in question, and determining the couplings of the newly downshifted proton (these are shown in the *Experimental* section). For example in **11a**, acetylation gave rise to a double doublet at 5.84 ppm (J = 2.8 and 2.4 Hz) readily assignable to the inositol's H-2. By contrast the benzoate of **12** gave rise to a double doublet at 5.76 ppm (J = 9.6 and 10 Hz) as required by the inositol's H-6.

The trends in Scheme 3*a* for inositol **4** prompted us to examine the comparable mannoside diol **13**. The results were

© 2002 NRC Canada

Scheme 2.

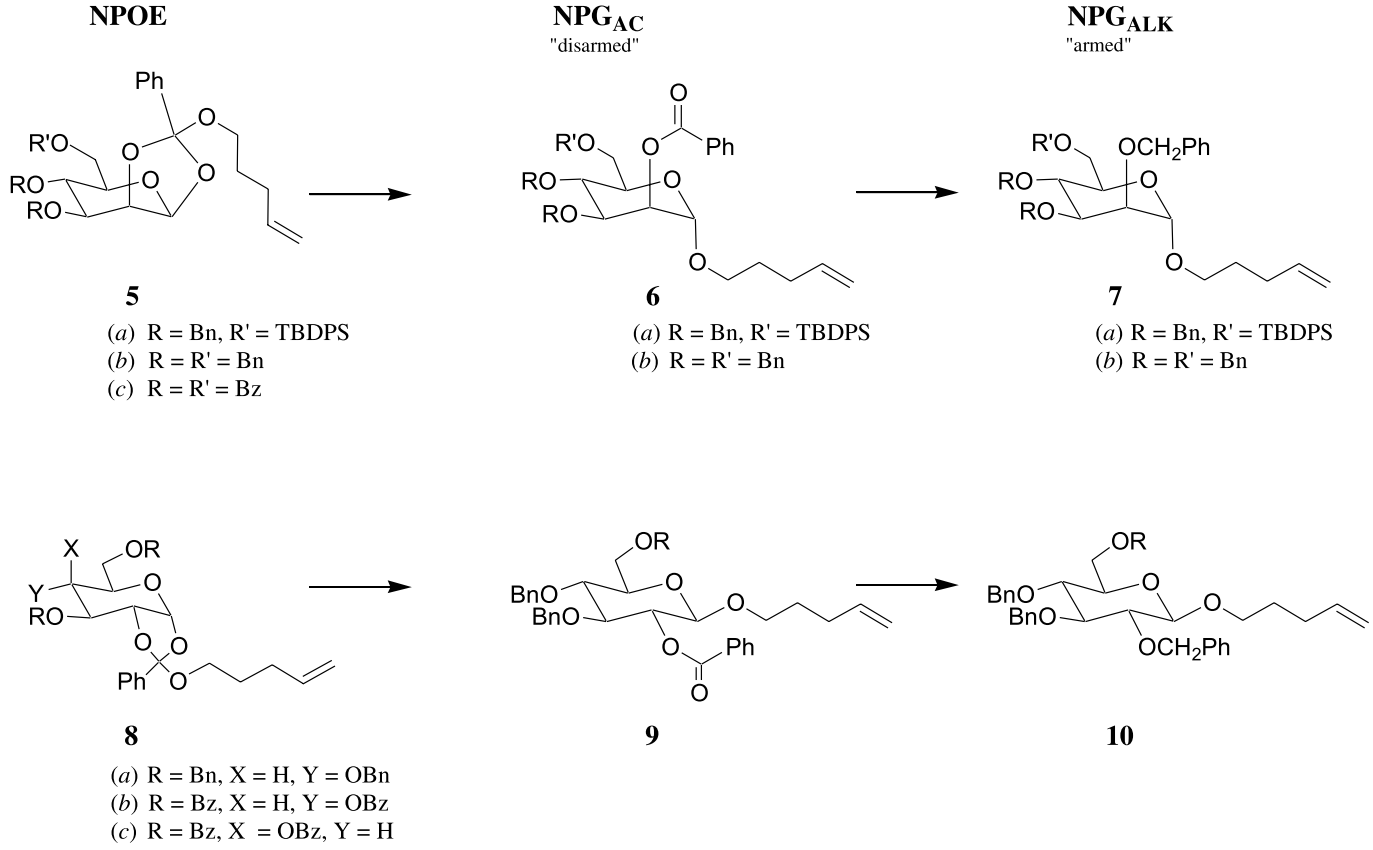

even more striking in that both the NPOE **5b** and the armed NPG$_{ALK}$ **7b**, reacted to give respectively, **14** only, and **15** mainly.

That these remarkable regioselectivities were not confined to *manno*-NPOEs was established by showing that the *gluco*- and *galacto*-NPOEs **8b** and **8c**, were also regioselective for the C-6-OH of **4** (Scheme 3*c*) giving disaccharides **16a** and **16b** in 76% and 73% yields, respectively.

The results in Scheme 3*a* and 3*b* (Table 1, entries *i–v*) challenged our assumptions about which hydroxyl group of compounds **4** and **13** would (should!) be the more reactive. Thus, if the accepted wisdom correlating reactivity and orientation were applied, the equatorial-OH of each should have been glycosylated more readily by the armed donor **7**, than by the disarmed counterpart **5**.

We therefore decided to examine the merits of a steric hindrance-based rationalization by employing altroside **17** (Scheme 4), the two hydroxyl groups of which present an unequivocal choice of steric environments. We found, as indicated in Scheme 4, that the armed donor **7b** showed little discrimination between the two sites of **17**, although the unencumbered C-2-OH should have been a clear favorite. Instead, the C-2-mannosylation product **19** was minor, whereas the C-3-regioisomer **18a** was major in a 1:2 ratio) (Table 1, entry *vi*).

On the other hand, the very hindered C-3-OH was selected exclusively by NPOEs **5b** and **5c**, to give **18b** and **18c**, respectively, reaching quantitative proportions (92%) with the NPOE **5c**. (Table 1, entries *vii* and *viii*).

The anomeric glucosides **20** and **23** were logical choices since the relative reactivities of the hydroxyl groups have been frequently tested with respect to acylating and alkylating reagents (19). According to the results of some earlier glycosidation studies (20, 21), there would seem to be very little difference in reactivity between the C-2- and C-3-OH groups. To leverage these slight differences, the reactions were begun at –78°C and allowed to warm to room temperature gradually. Under these non-forcing conditions, the donors tended to decompose, and so substantial amounts of the acceptor diols were recovered. Nevertheless, the reactivities were clearly discernible as shown in Scheme 5. Thus, the α-diol **20**, reacted with the *manno*-NPOE to give **21a** and **22a** in a 7.4:1 ratio. Similarly, the *gluco*-NPG$_{AC}$ donor **9**, gave overwhelming preferences for the C-2-OH producing **21b** and **22b** in a 7.6:1 ratio. On the other hand, with the "armed donors" NPG **7b** and **10**, the regioselectivities were unremarkable, sending out mixed messages about their preferences. Thus, C-3-OH was favored in the former giving mainly **22c** (22) with armed **7b**, but C-2-OH was favored (slightly) with the armed donor, the latter **10** giving mainly **21d** (22) (Table 1, entries *xii* and *xiii*).

Comparison of the "same" reaction in entries *x* and *xi* of Table 1 is instructive. The yield at the higher temperature is nearly twice as high as at the lower temperature, but with a 50% sacrifice in regioselectively.

For the β-anomer **23**, the regioselectivities were less pronounced; however, NPOE **5b** and NPG$_{AC}$ **9** were consistent in their preference for C-2-OH (Table 1, entries *xiv* and *xv*),

© 2002 NRC Canada

Scheme 3.

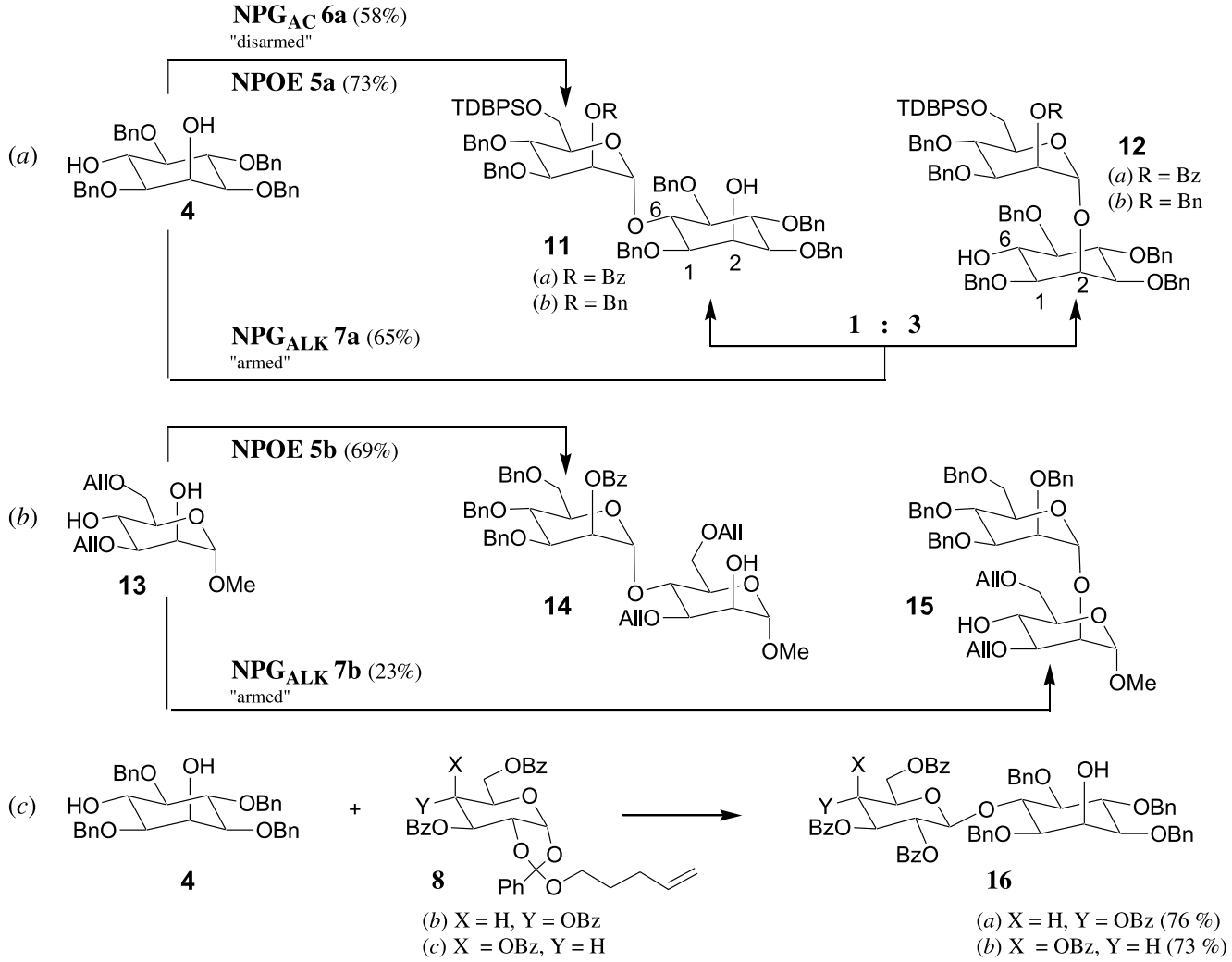

whereas NPG$_{ALK}$ **7b** and **10**, again sent mixed messages in their preferences for C-2-OH and (or) C-3-OH (Table 1, entries *xvi* and *xvii*).

Discussion

The concept of reciprocal donor acceptor selectivity (RDAS)

The data above provide a new angle to the donor–acceptor matching principle adumbrated by Paulsen and co-workers (5, 11). The regioselectivities observed in Schemes 3–5 clearly cannot be accommodated by traditional explanations based on reactivity and (or) steric hindrance.

This conclusion is dramatically exemplified in the results of altroside **17** (Scheme 4 and Table 1, entries *vi–viii*) where the exclusive preference of the C-3-OH for NPOEs **5b** and **5c**, a remarkable 92% in the case of the latter, must be regarded as surprising. But even more surprising is the fact that the unencumbered C-2-OH of **17** underwent no detectable coupling with NPOE **5b** or **5c**.

Thus, the results in Scheme 4 implied that the donor as well as the acceptor were expressing strong independent selectivities. The formation of **18** and **19** therefore reveal the interplay of reciprocal donor acceptor selectivity (RDAS).

Although the concept of RDAS emanated from regioselective preferences observed in a series of diols (see Table 1), the concept also has profound implications for glycosidic coupling, *even where the acceptor has only one hydroxyl group*. Unfortunately, gathering pertinent literature examples is problematic because (*i*) reactions that fail, or proceed in unflattering yields, are rarely reported; (*ii*) forcing conditions may have been used to eke out the coveted success, instead of going-with-the-flow; (*iii*) yields may have been enhanced by changing reagents and (or) conditions, thereby vitiating the ability to draw comparisons.

Fortunately, reports from van Boom's laboratory provide a vivid example of RDAS (23, 24) in which failure and success related to a specific target, similar reactants and conditions having been maintained. Thus, in attempting to prepare the trisaccharide **27** (Scheme 6), the 2-*O*-benzoyl thioglycoside donor **26**, reacted with disaccharide **11**, to provide only a 10% yield of the desired target material (23). However, when the same donor (**26**) was exposed to disaccharide **12**, the target was produced in the excellent yield of 84% (24). The results clearly indicated that the disarmed donor

© 2002 NRC Canada

Table 1. Regioselective glycosidation of acceptor diols.

Entry	Substrate	Donor	Reaction	Glycosidation sites (products)	Overall yields %
(*i*)	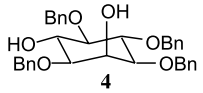 **4**	NPG_{AC} **6a**	A	O6 only (**11a**)	58
(*ii*)		NPOE **5a**	A	O6 only (**11a**)	73
(*iii*)		NPG_{ALK} **7a**	A	O2/O6 (3:1) (**12** / **11b**)	65
(*iv*)	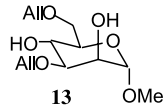 **13**	NPOE **5b**	A	O4 only (**14**)	69
(*v*)		NPG_{ALK} **7b**	A	O2 mainly (**15**)	23
(*vi*)	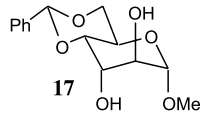 **17**	NPG_{ALK} **7b**	C	O3/O2 (2:1) (**18a** / **19**)	37
(*vii*)		NPOE **5b**	B	O3 only (**18b**)	52
(*viii*)		NPOE **5c**	B	O3 only (**18c**)	92
(*ix*)	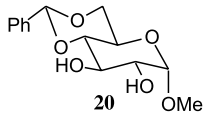 **20**	NPOE **5b**	D	O2/O3 (7.4:1) (**21a** / **22a**)	42
(*x*)		NPG_{AC} **9**	D	O2/O3 (7.6:1) (**21b** / **22b**)	25
(*xi*)		NPG_{AC} **9**	D (0 °C)	O2/O3 (3:1) (**21b** / **22b**)	42
(*xii*)		NPG_{ALK} **7b**	D	O2/O3 (1:3) (**21c** / **22c**)	36
(*xiii*)		NPG_{ALK} **10**	D	O2/O3 (1.5:1) (**21d** / **22d**)	53
(*xiv*)	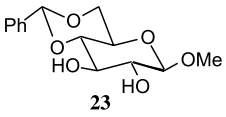 **23**	NPOE **5b**	D	O2/O3 (3.5:1) (**24a** / **25a**)	36
(*xv*)		NPG_{AC} **9**	D	O2/O3 (1.8:1) (**24b** / **25b**)	11
(*xvi*)		NPG_{ALK} **7b**	D	O2/O3 (1:2.9) (**24c** / **25c**)	35
(*xvii*)		NPG_{ALK} **10**	D	O2/O3 (1.2:1) (**24d** / **25d**)	51

Scheme 4.

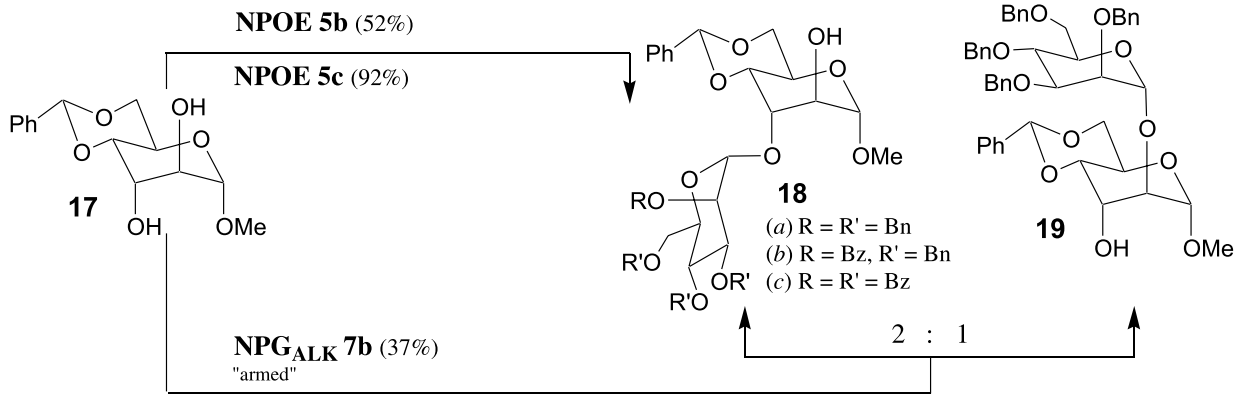

26, was "matched" with the C-6-OH of **12**, but not the C-2-OH of **11**.

The concept of RDAS suggests that one-pot, target-oriented, double glycosidations should be possible *when appropriate partners are employed*. A case in our laboratory involving non-reciprocal donors is seen in Scheme 7*a*. Thus, treatment of the diol acceptor **4**, with 2 equiv of donor **7a** stopped at disaccharide stage **12b**. Difficulty in proceeding to trisaccharide **28** was evident from the fact, that subsequent treatment of disaccharide **12b** with 3 equiv of the armed donor (**7a**) afforded only a 14% yield of **28a** (25).

Note that our poor result (25) coincides with van Boom's 10% yield in Scheme 6*a* confirming that these are couplings not RDAS sanctioned.

© 2002 NRC Canada

Scheme 5.

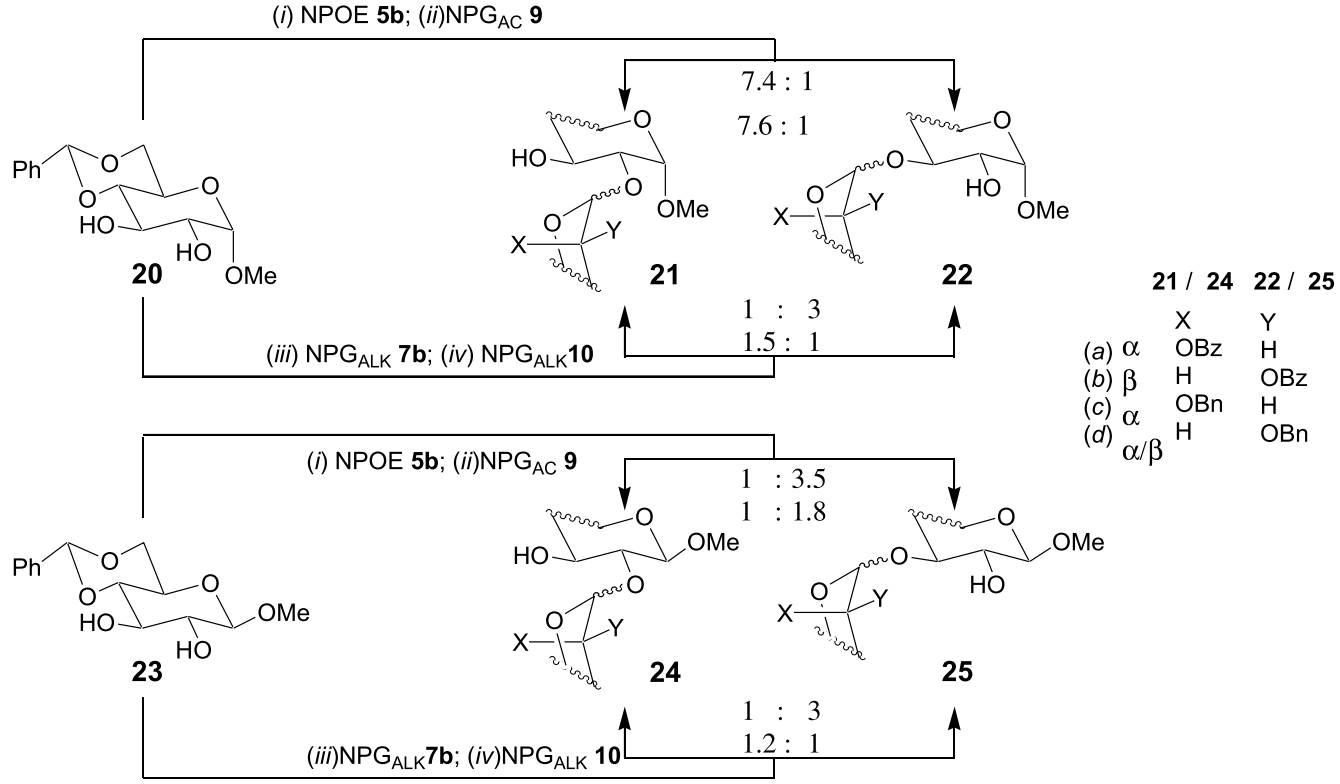

Scheme 6.

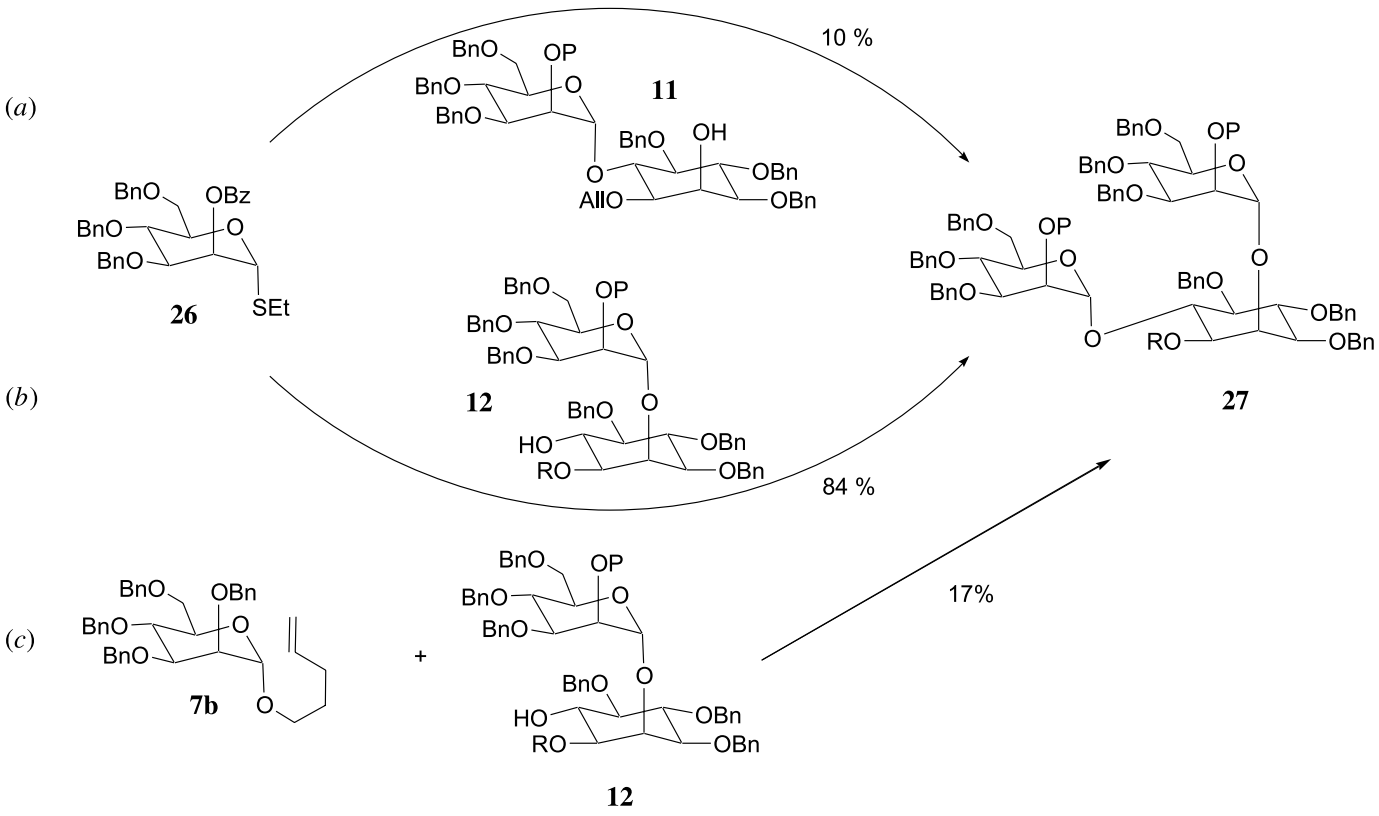

© 2002 NRC Canada

Scheme 7.

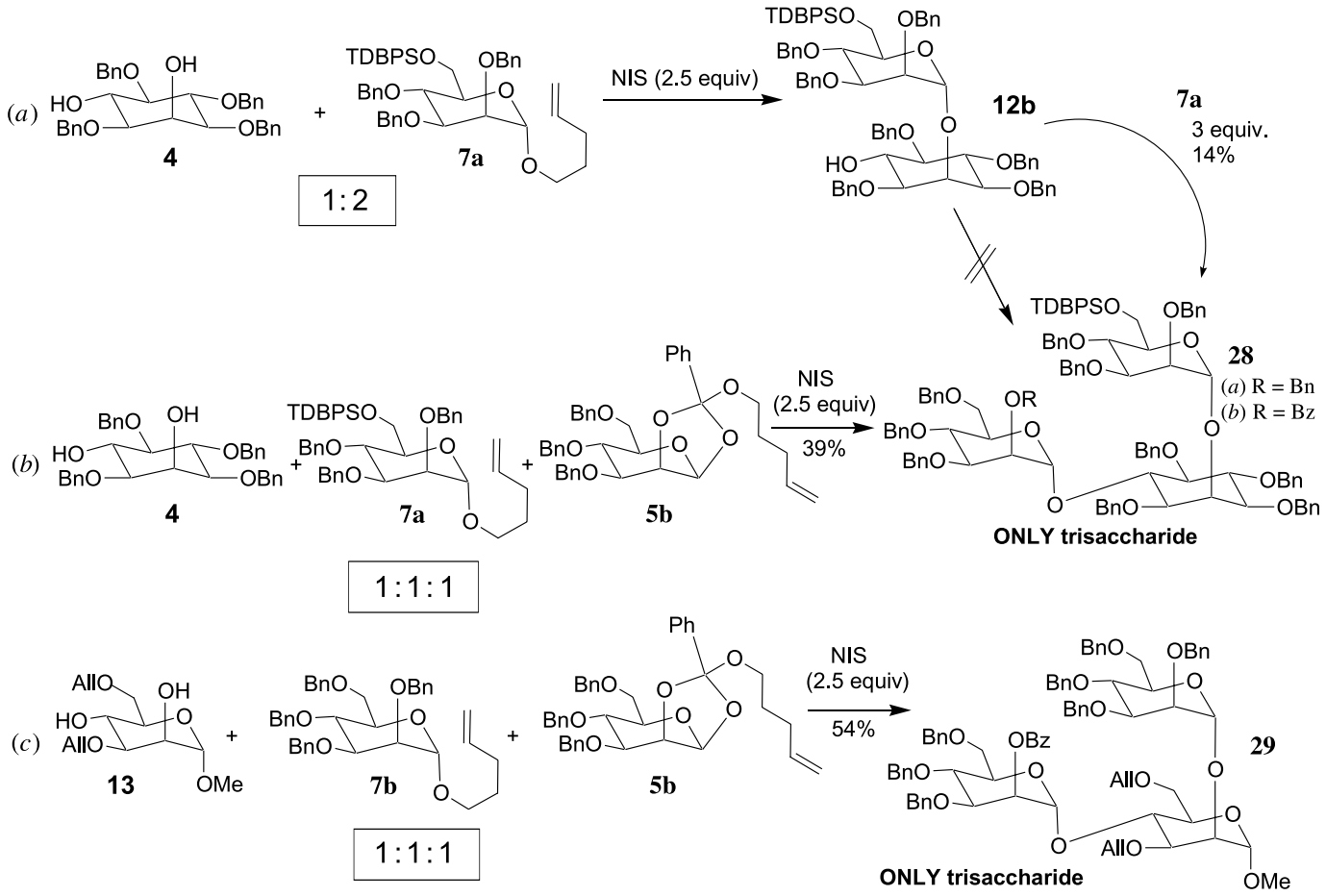

By contrast a 1:1:1 mixture of the diol **4** + NPOE **5b** + NPG_{ALK} **7a** in the presence of 2.5 equiv of the promoter gave the trisaccharide **28b** in unoptimized yield of 39% (Scheme 7*b*). Similarly diol **13** + donors **5b** and **7b** gave trisaccharide **29** in 54% yield. Clearly, in both cases, each of the donors had gone to its RDAS-sanctioned site.

Rationalization

A rationalization of the basis for RDAS obviously requires analysis of both the donor and acceptor. With respect to donors, an examination of Table 1 shows that the NPOE–NPG_{AC} group displays similar preferences qualitatively, and is generally more discriminating than NPG_{ALK}. Are these choices related to the donor's reactivity? This question prompted us to determine the relative reactivities of donors **5b**, **6b**, and **7b**. We have recently shown that oxidative hydrolysis provides a ready method for comparing relative reactivities of any two *n*-pentenyl glycosyl donors (26). Using this method, the ranking of the donors was found to be **5b** > **7b** > **6b**. These observations show that the regioselectivities are not dependent on the relative reactivities of the donors, since the most and least reactive donors, NPOE **5b** and NPG_{AC} **6b**, respectively, showed regioselectivity for the same hydroxyl (C-6-OH) of the diol **4**. *Thus, RDAS is not based on donor reactivity.*

As shown in Scheme 8, NPOE and NPG_{AC} are able to produce the same intermediate complex where the charge is distributed over two (dioxolenium) and three (trioxolenium) oxygens, **30** and **31**, respectively. The charge in this complex may be described as "diffuse" in contrast to that on the armed oxocarbenium ion **32** where the charge is more "compact". Experiments and theoretical studies are underway to determine whether the diffuse–compact dichotomy is valid, and the results will be described in due course.

Analysis of factors which have an impact on the diols' selectivities is more difficult. But as shown for Scheme 4 in the *Discussion* section, *RDAS is not based on steric hindrance* of the acceptor's OH.

The most thorough investigation of glycosidation of polyhydroxylic acceptors has been undertaken by Vasella in connection with his scholarly development of the chemistry of glycosylidene carbenes (**33**) as glycosyl donors (27) (Scheme 9). These donors are unique in that they proceed to the critical oxocarbenium ion intermediate (**34**) by bond formation to a proton, whereas "classical donors" (**35**) achieve the same objective by bond cleavage (sooner or later!), usually electrophile induced, of the anomeric leaving group. For **33**, the more acidic OH group should therefore be the preferred glycosidation site. In turn, hydrogen bonding within the diol **28** can be a determining influence on the acidity of the OH concerned.

The results obtained by us thus far, do not provide any insight into the implications of OH-acidity and (or) hydrogen bonding. The role of such factors await future study.

© 2002 NRC Canada

Scheme 8.

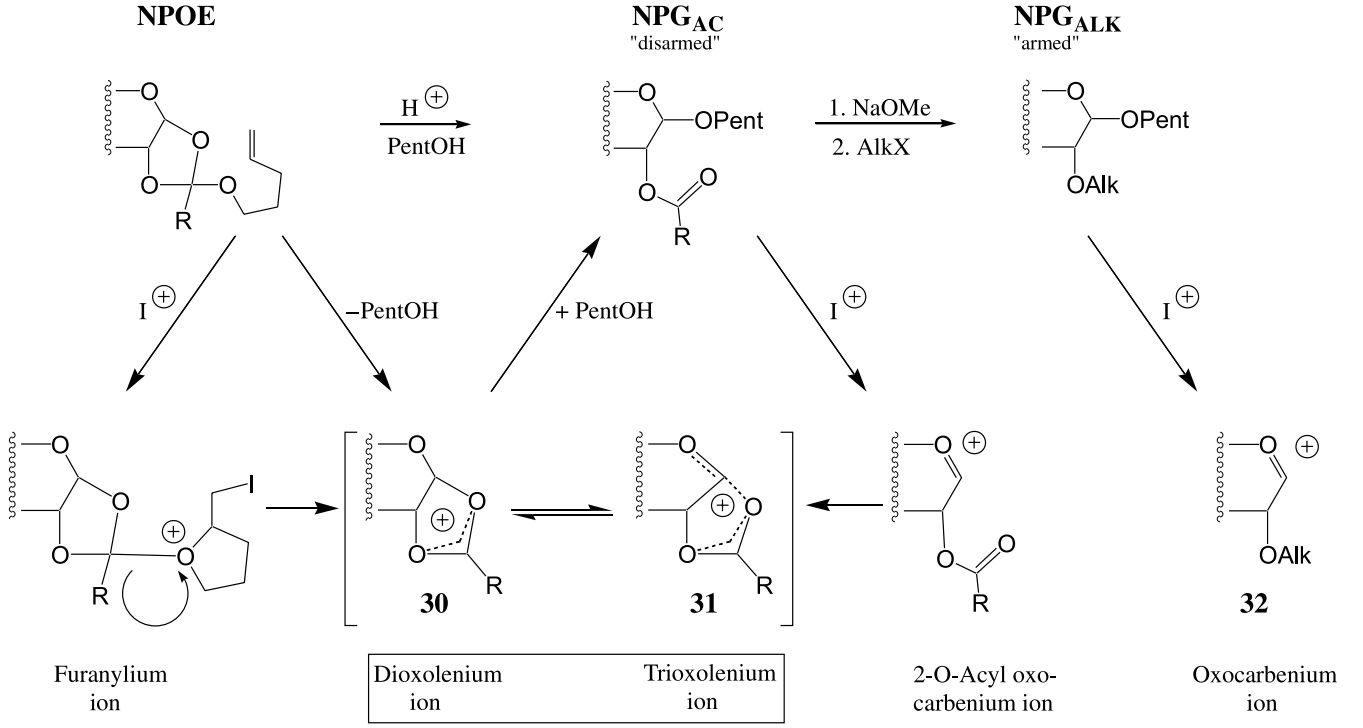

Experimental

General procedures

All NMR spectra were recorded on a GE 300 or a Varian 400 MHz NMR spectrometer and chemical shifts are reported relative to internal TMS. Chemical ionization (CI) mass spectroscopy was done on a Hewlett–Packard 5988A GC–MS using 1% ammonia in methane as the reagent gas, with a source temperature of 100°C, at 1 torr (1 torr = 133.322 Pa). High-resolution mass spectra (HR-MS) and fast atom bombardment (FAB) analyses were recorded with a JEOL JMS-SX 102A mass spectrometer operating at 10 K resolution, using a dithiothreitol–dithioerythritol or *m*-nitrobenzyl alcohol as the matrix with xenon as the fast atom. Elemental analyses were conducted at Atlantic microlab, Norcross, GA. All reactions were conducted under an argon atmosphere. Thin layer chromatography (TLC), was done on plates (Riedel-de Haen, coated with silicagel 60F 254) and were detected by UV or by spraying or dipping in ammonium molybdate solution and subsequent heating.

The regioisomers were separated by flash chromatography, evaporated to dryness, and weighed to obtain the ratios reported in Schemes 3–5 and Table 1. Flash column chromatography was performed on silica gel (spectrum SIL 58, 230 –400 mesh, grade 60) using mixtures of hexane and ethyl acetate as eluants. Dichloromethane and toluene were distilled from CaH_2. *N*-Iodosuccinimide was purchased from Aldrich and recrystallized from hot CH_2Cl_2.

Glycosidation conditions

(*a*) The diol (~0.092 mmol) and glycosyl donor (~0.119 mmol) were dissolved in a small quantity of toluene, azeotroped to dryness, and then dissolved in CH_2Cl_2 (2 mL) at 0°C under an argon atmosphere. *N*-Iodosuccinimide (0.1219 mmol) was added to the solution, and after stirring for 3 min, TDBMSOTf (0.027 mmol) was added. The reaction was quenched after 20 min with 10% aqueous sodium thiosulfate and saturated aqueous sodium bicarbonate, extracted with CH_2Cl_2, and worked up in the usual way. After work up the mixture was separated by flash chromatography to give the disaccharide products.

(*b*) To a solution of the diol (0.208 mmol) and the glycosyl donor (0.16 mmol) in anhyd CH_2Cl_2 (3 mL) were added molecular sieves 5 Å (100 mg) and NIS (73 mg, 0.32 mmol) at –30°C. After stirring for 5 min, $BF_3{\cdot}OEt_2$ (6 μL, 0.048 mmol) was added. The reaction was quenched after 15 min and processed as in part (*a*).

(*c*) To a solution of diol (0.208 mmol) and glycosyl donor (0.16 mmol) in anhyd CH_2Cl_2 (3 mL) were added molecular sieves 5 Å (97 mg) and NIS (73 mg, 0.32 mmol) at –30°C. After stirring for 5 min, $BF_3{\cdot}OEt_2$ (6 μL, 0.048 mmol) was added. The mixture was allowed to warm to 0°C. After 40 min the reaction was quenched and processed as in part (*a*).

(*d*) The diol (0.177 mmol, 50 mg) and the glycosyl donor (0.177 mmol) were dissolved in a small quantity of a dichloromethane–toluene mixture, azeotroped to dryness, and then dried under vacuum for ~30 min. The residue was taken up in dry dichloromethane (2 mL for α-acceptor, 10 mL for β-acceptor) and molecular sieves (4 Å) were added. The reaction mixture was kept under an argon atmosphere at –78°C (acetone – dry ice) and 68 mg (0.266 mmol, 1.5 equiv) of *N*-iodosuccinimide were added. After 3 min stirring, 10 μL (0.05 mmol, 0.3 equiv) of TBDMSOTf were added. After 15 min at –78°C the reaction mixture was allowed to warm up to room temperature. The reaction was quenched after 45 min with 10% aqueous sodium thiosulphate and saturated aqueous sodium bicarbonate solution,

© 2002 NRC Canada

Scheme 9.

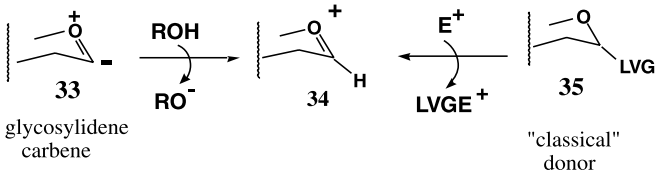

extracted with dichloromethane, dried with sodium sulfate, and purified by column chromatography using silica gel (hexanes – ethyl acetate, 4:1 → 1:1).

Identification of regioisomers

The ^{1}H NMR spectra of the chromatographically pure reaction product, before and after acylation, were examined for new signals in the 6.0–5.4 ppm region. The coupling contant(s) of the new proton gave unequivocal information about its proton's environment. In the ^{1}H NMR data listed below, the "new" signal upon acylation is shown in italics.

*1,3,4,5-Tetra-*O*-benzyl-6-*O*-(2-*O*-benzoyl-3,4-di-*O*-benzyl-6-*O*-[*tert*-butyldiphenylsilyl]-α-D-mannopyranosyl)-D-myo-inositol (11a)*

(*a*) The diol **4** and the NPG_{AC} donor **6a** were reacted under conditions (*a*). Standard work up and flash column chromatography (EtOAc–hexanes, 1:4) afforded **11a** (65 mg, 58%) as a colorless paste.

(*b*) The diol **4** and glycosyl donor **5a** were reacted under conditions (*a*) for 20 min. Standard work up, and flash column chromatography of the crude residue (EtOAc–hexanes, 1:4) afforded **11a** (80 mg, 73%) as a colorless paste. ^{1}H NMR (400 MHz, $CDCl_3$) δ: 8.12–6.84 (m, 45H, Ar-H), 5.78 (dd, *J* = 1.6 Hz, 2 Hz, 1H), 5.60 (d, *J* = 1.6 Hz, 1H, H-1), 4.90–4.55 (m, 12H, $BnCH_2$), 4.22 (dd, *J* = 9.6, 10 Hz, 1H), 4.17–4.12 (m, 2H), 4.05 (dd, *J* = 3.2, 10 Hz, 1H), 3.98–3.91 (m, 2H), 3.58–3.48 (m, 2H), 3.37 (dd, *J* = 2.8, 3.2 Hz, 1H), 3.34 (dd, *J* = 3.2, 3.2 Hz, 1H), 3.27 (dd, *J* = 9.6, 9.2 Hz, 1H), 2.36 (br s, 1H, OH), 1.06 (s, 9H). ^{13}C NMR (100 MHz, $CDCl_3$) δ: 165.74 (C=O Ph), 139.09, 138.53, 138.25, 137.86, 137.16, 135.93, 135.64, 133.78, 133.31, 132.94, 130.00, 129.36, 128.57, 128.46, 128.39, 128.27, 128.22, 128.03, 127.96, 127.88, 127.55, 127.49, 127.09, 98.26 (C-1), 81.34, 81.06, 80.61, 79.50, 78.41, 75.81, 75.51, 74.93, 74.92, 74.08, 72.63, 72.10, 71.47, 69.31, 66.44, 62.39, 26.84, 19.31. Acetylation of **11a** gave a colorless paste. ^{1}H NMR (400 MHz, $CDCl_3$) δ: 8.12–6.83 (m, 45H, Ar-H), 5.84 (dd, *J* = 2.8, 2.4 Hz, 1H), 5.80 (dd, *J* = 1.6, 2 Hz, 1H), 5.60 (d, *J* = 1.2 Hz, 1H, H-1) 4.01–4.47 (m, 12H, $BnCH_2$,s), 4.14 (dd, *J* = 9.6, 10 Hz, 1H), 4.07–3.96 (m, 3H), 3.83 (dd, *J* = 9.6, 9.6 Hz, 1H), 3.61–3.52 (m, 2H), 3.46 (dd, *J* = 3.2, 3.2 Hz, 1H), 3.44 (dd, *J* = 2.8, 3.2 Hz, 1H), 3.31 (dd, *J* = 9.6, 9.6 Hz, 1H), 2.10 (s, 3H), 1.05 (s, 9H). ^{13}C NMR (100 MHz, $CDCl_3$) δ: 170.39 ($OCOCH_3$), 165.97 (OCOPh), 139.08, 138.49, 138.17, 137.65, 137.52, 136.82, 135.94, 135.66, 133.65, 133.36, 132.95, 130.01, 129.41, 129.29, 128.86, 128.48, 128.42, 128.22, 128.12, 128.02, 127.83, 127.60, 127.57, 127.43, 127.22, 127.12, 97.99 (C-1), 81.68, 81.08, 78.72, 78.32, 78.12, 75.99, 75.76, 75.03, 74.66, 74.06, 72.17, 71.86, 71.42, 69.05, 65.93, 62.55, 26.83, 21.03, 19.27. FAB-MS *m*/*z*: 1265.56 $[M - 1]^+$. Anal. calcd. for $C_{79}H_{82}O_{13}Si$: C 74.86, H 6.52; found: C 74.66, H 6.59.

*1,3,4,5-Tetra-*O*-benzyl-2-*O*-(2,3,4-tri-*O*-benzyl-6-*O*-[tert-butyldiphenylsilyl]-α-D-mannopyranosyl)-D-myo-inositol (12b) and 1,3,4,5-tetra-*O*-benzyl-6-*O*-(2,3,4-tri-*O*-benzyl-6-*O*-[tert-butyldiphenylsilyl]-α-D-mannopyranosyl)-D-myo-inositol (11b)*

The diol **4** and glycosyl donor **7a** were reacted under the general glycosidation conditions. The crude residue obtained after work up on purification by flash column chromatography (EtOAc–hexanes, 1:4) afforded **12b** (49 mg, 49%) and **11b** (15 mg, 16%). Acetylation of **11b** gave a colorless paste: ^{1}H NMR (400 MHz, $CDCl_3$) δ: 7.71–6.88 (m, Ar), 5.84 (dd, *J* = 2.8, 2.4 Hz, 1H), 5.49 (d, *J* = 1.2 Hz, 1H) 4.91–4.32 (m, 14H), 4.18 (dd, *J* = 10, 10 Hz, 1H), 4.06 (dd, *J* = 10 Hz, 9.6 Hz, 1H), 3.92–3.76 (m, 4H), 3.59–3.57 (m, 2H), 3.44 (dd, *J* = 10 Hz, 2.8 Hz, 1H), 3.37 (dd, *J* = 9.6, 2.4 Hz, 1H), 3.28 (dd, *J* = 9.6, 9.6 Hz, 1H), 2.12 (s, 3H), 0.99 (s, 9H). FAB-MS *m*/*z*: 1251.56 $[M - 1]^+$. Data for **12**: ^{1}H NMR (400 MHz, $CDCl_3$) δ: 7.75–6.92 (m, 45H, Ar), 5.35 (d, *J* = 1.2 Hz, 1H, H-1), 4.95–4.41 (m, 14H, Bn), 4.37 (t, *J* = 2.4 Hz, 1H), 4.26 (dd, *J* = 10, 9.6 Hz, 1H), 3.98–3.85 (m, 3H), 3.79–3.71 (m, 3H), 3.57 (d, *J* = 11.2 Hz, 1H), 3.32–3.25 (m, 2H), 3.19–3.16 (dd, *J* = 9.6, 2 Hz, 1H), 2.39 (br s, 1H, OH), 1.02 (s, 9H, *t*-Bu). ^{13}C NMR δ: 138.99, 138.67, 138.57, 137.73, 137.43, 136.096, 135.64, 133.91, 133.61, 129.42, 129.36, 128.62, 128.47, 128.347, 128.29, 128.22, 128.18, 128.13, 128.06, 128.02, 127.96, 127.74, 127.56, 127.47, 127.36, 127.33, 127.17, 127.11, 127.06, 98.00 (C-1), 83.22, 80.85, 80.47, 79.38, 79.15, 75.78, 75.61, 75.21, 74.43, 72.90, 72.71, 72.16, 72.10, 70.08, 62.70, 26.80, 19.33. FAB-MS *m*/*z*: 1209.6 $[M - 1]^+$. Benzoylation under standard conditions afforded a colorless paste: ^{1}H NMR (400 MHz, $CDCl_3$) δ: 8.17–6.95 (m, Ar), 5.76 (dd, *J* = 9.6, 10 Hz, 1H), 5.40 (br s, 1H), 4.99–4.41 (m, 15H), 4.27 (dd, *J* = 10, 10 Hz, 1H), 4.02–3.86 (m, 4H), 4.27 (dd, *J* = 11.2, 2.8 Hz, 1H), 3.60–3.51 (m, 2H), 3.42 (dd, *J* = 10, 2 Hz, 1H), 3.30 (dd, *J* = 10, 2.3 Hz, 1H), 1.03 (s, 9H). FAB-MS *m*/*z*: 1312.45 $[M - 1]^+$, 1354.40 $[M + K]^+$, 1447.42 $[M + Cs]^+$.

*Methyl-3,6-di-*O*-allyl-4-*O*-(2-*O*-benzoyl-3,4,6-tri-*O*-benzyl-α-D-mannopyranosyl)-α-D-mannopyranoside (14)*

The diol **13** and glycosyl donor **5b** were reacted under conditions (*a*). The crude residue on flash column chromatography (EtOAc–hexanes, 1:3) afforded **14** (69%) as a colorless paste. ^{1}H NMR (400 MHz, $CDCl_3$) δ: 8.07–7.19 (m, 20H, Ar-H), 6.04–5.85 (m, 2H), 5.67 (dd, *J* = 2, 2.8 Hz, 1H), 5.42 (d, *J* = 1.6 Hz, 1H, H-1), 5.33–5.09 (m, 4H), 4.89–4.73 (m, 4H), 4.59–4.52 (m, 3H), 4.14–3.88 (m, 10H), 3.78–3.63 (m, 5H), 3.39 (s, 3H), 2.42 (s, 1H, OH). ^{13}C NMR (100 MHz, $CDCl_3$) δ: 165.48, (OCOPh), 138.45, 138.04, 134.83, 134.02, 133.01, 129.92, 128.31, 128.27, 127.91, 127.56, 127.50, 118.33, 116.83, 99.98 (C-1), 99.51 (C-1′), 79.72, 78.15, 75.21, 74.15, 73.50, 73.13, 72.60, 72.44, 71.53, 70.46, 70.19, 69.33, 69.08, 67.54, 54.99. FAB-MS *m*/*z*: 809.3 $[M - 1]^+$, 811.3 $[M + 1]^+$. Acetylation of **14** afforded the acetate as a colorless paste: ^{1}H NMR (400 MHz, $CDCl_3$) δ: 8.00–7.13 (m, 20H, Ar-H), 5.92–5.81 (m, 2H), 5.65 (dd, *J* = 2.4, 2.8 Hz, 1H), 5.38 (d, *J* = 2 Hz,

© 2002 NRC Canada

1H, H-1), 5.21 (d, *J* = 1.2 Hz, 1H) 5.19 (dd, *J* = 2, 3.2 Hz, 1H), 5.17 (d, *J* = 1.6 Hz, 1H), 5.08–5.05 (m, 2H), 4.82–4.64 (m, 4H), 4.52–4.47 (m, 3H), 4.06–3.62 (m, 14H), 3.32 (s, 3H), 2.02 (s, 3H).

Methyl-3,6-di-O-allyl-2-O-(2,3,4,6-tetra-O-benzyl-α-D-mannopyranosyl)-α-D-mannopyranoside (15)

The diol **13** and glycosyl donor **7b** were reacted under conditions (*a*) for 3 min. Standard work up followed by flash column chromatography (EtOAc–hexanes, 1:3) afforded **15** (23%) as a colorless paste. ^{1}H NMR (400 MHz, $CDCl_3$) δ: 7.35–7.15 (m, 20H, Ar-H), 5.95–5.81 (m, 2H), 5.30–5.11 (m, 4H), 5.09 (br s, 1H, H-1), 4.88–4.46 (m, 12H), 4.10–3.35 (m, 21H), 3.24 (s, 3H). FAB-MS *m*/*z*: 795 $[M - 1]^+$. Benzoylation afforded the corresponding benzoate: ^{1}H NMR (300 MHz, $CDCl_3$) δ: 8.13–8.04 (d, 2H, Ar-H), 7.64–7.14 (m, 23H, Ar-H), 5.85–5.06 (m, 2H), 5.36 (dd, *J* = 9.6, 9.3 Hz, 1H), 5.19 (br s, 1H), 5.15–4.99 (m, 4H), 4.91–4.80 (m, 2H), 4.72–4.46 (m, 7H), 4.07–3.85 (m, 11H), 3.74 (br s, 2H), 3.55 (br s, 2H), 3.29 (s, 3H). ^{13}C NMR (100 MHz, $CDCl_3$) δ: 172.25 (OCOPH), 138.60, 138.59, 138.58, 134.72, 134.64, 134.00, 133.30, 130.41, 129.92, 129.48, 128.69, 128.61, 128.55, 128.21, 128.11, 127.93, 127.70, 127.63, 117.45, 117.03, 100.01 (C-1), 100.20 (C-1), 79.64, 75.14, 75.08, 74.73, 74.46, 73.46, 72.69, 72.62, 72.37, 72.08, 71.59, 70.45, 70.15, 69.76, 55.11.

Methyl-4,6-O-benzylidene-3-O-(2-O-benzoyl-3,4,6-tri-O-benzyl-α-D-mannopyranosyl)-α-D-altropyranoside (18b)

The altroside diol **17** and the NPOE glycosyl donor **5b**, were allowed to react under conditions (*b*) for 15 min. After work up the crude material was purified by flash chromatography (hexane– EtOAc, 3:2) to give the 3-*O*-mannosylated derivative of **18b** in 52% yield. ^{1}H NMR (300 MHz, $CDCl_3$) δ: 8.09–7.06, (m, 25H), 5.60 (m, 1H), 5.55 (s, 1H), 5.14 (d, *J* = 1.8 Hz, 1H), 4.87 (d, *J* = 10.9 Hz, 1H), 4.81 (d, *J* = 11.2 Hz, 1H), 4.63 (d, *J* = 12.4 Hz, 1H), 4.61 (br s, 1H), 4.58 (d, *J* = 12.1 Hz, 1H), 4.49 (d, *J* = 10.9 Hz, 1H), 4.33 (m, 10H), 3.77 (m. 1H), 3.62 (dd, *J* = 11.0, 3.7 Hz, 1H), 3.43 (dd, *J* = 11.0, 1.6 Hz, 1H), 3.40 (s, 3H). ^{13}C NMR (75 MHz, $CDCl_3$) δ: 165.88 (OC(O)Ph), 138.81, 138.42, 137.98, 137.42, 133.10, 129.96, 129.88, 128.94, 128.37, 128.26, 128.21, 128.13, 127.85, 127.59, 127.46, 127.36, 127.32, 126.34, 102.33 (PhCH), 101.83 (C-1), 95.57 (C-1′), 77.88, 74.92, 74.72, 74.31, 72.92, 71.93, 71.63, 71.08, 69.42, 69.29, 68.61, 67.93, 58.67, 55.57. API-ES *m*/*z*: 837 $[M + NH_4]^+$.

Methyl-4,6-O-benzylidene-3-O and 2-O (2,3,4,6-tetra-O-benzyl-α-D-mannopyranosyl)-α-D-altropyranosides (18a and 19)

To a solution of diol **17** and glycosyl donor **7b** were reacted under conditions (*a*). After stirring for 5 min, $BF_3{\cdot}OEt_2$ (6 mL, 0.048 mmol) was added. The mixture was allowed to warm to 0°C. After 90 min the reaction was quenched and after work up the crude residue was purified by flash column chromatography (hexane–EtOAc, 7:3) to give the *O*-3 and *O*-2 mannosylated products **18a** and **19** in 2:1 ratio in 37% combined yield. Data for *O*-3 product **18a**: ^{1}H NMR (300 MHz, $CDCl_3$) δ: 7.56–7.01 (m, 25H), 5.54 (s, 1H), 5.00 (d, *J* = 1.8 Hz, 1H), 4.92–4.44 (m, 9H), 4.30–3.43 (m, 12H), 3.30 (s, 3H). ^{13}C NMR (75 MHz, $CDCl_3$) δ: 139.05, 138.88, 138.48, 137.62, 132.11, 128.80, 128.26, 128.11, 127.83, 127.68, 127.48, 127.25, 126.36, 125.99, 102.25 (PhCH), 101.79 (C-1), 95.00 (C-1′), 79.65, 77.42, 75.08, 74.78, 74.67, 72.76, 72.50, 71.22, 70.33, 69.96, 69.34, 69.15, 67.32, 58.76, 55.31. Data for **19**: ^{1}H NMR (200 MHz, $CDCl_3$) δ: 7.57–7.18 (m, 25H), 5.63 (s, 1H), 4.98 (d, *J* = 2.1 Hz, 1H), 4.92–4.50 (m, 9H), 4.33 (dd, *J* = 10.1, 4.8 Hz, 1H), 4.12 (dd, *J* = 10.1, 4.9 Hz, 1H), 3.98–3.69 (m, 10H), 3.29 (s, 3H). ^{13}C NMR (75 MHz, $CDCl_3$) δ: 138.41, 138.31, 138.11, 137.42, 129.06, 128.37, 128.24, 128.07, 127.79, 127.48, 126.27, 102.25 (PhCH), 100.35 (C-1), 99.51 (C-1′), 79.41, 76.76, 76.68, 75.50, 75.12, 73.39, 72.93, 72.68, 72.46, 69.57, 69.25, 67.68, 58.07, 55.50. API-ES *m*/*z*: 828 $[M + Na]^+$.

Methyl-4,6-O-benzylidene-3-O-(2,3,4,6-tetra-O-benzoyl-α-D-mannopyranosyl)-α-D-altropyranoside (18c)

A solution of diol **17** and glycosyl donor **5c** were reacted under conditions (*b*) for 15 min. After work up the crude residue was purified by flash chromatography (hexane–EtOAc, 4:1) to give the *O*-3 mannosylated product **18c** in 92% yield. ^{1}H NMR (300 MHz, $CDCl_3$) δ: 8.10–7.18 (m, 25H), 6.12 (t, *J* = 10.1 Hz, 1H), 5.93 (dd, *J* = 10.1, 3.3 Hz, 1H), 5.73 (dd, *J* = 3.2, 1.8 Hz, H1), 5.65 (s, 1H), 5.25 (d, *J* = 1.6 Hz, 1H), 4.79 (dt, *J* = 10.1, 2.6 Hz, 1H), 4.70 (s, 1H), 4.55–4.28 (m, 4H), 4.11 (dd, *J* = 9.5, 3.2 Hz, 1H), 3.98 (dd, *J* = 12.5, 3.2 Hz, 1H), 3.84 (t, *J* = 10.2 Hz, 1H), 3.51 (s, 3H). ^{13}C NMR (75 MHz, $CDCl_3$) δ: 166.13 (OC(O)Ph), 165.52 (OC(O)Ph), 165.35 (×2) (OC(O)Ph), 137.65, 133.36, 133.32, 133.03, 132.87, 130.01, 129.76, 129.70, 129.35, 129.26, 129.11, 128.52, 128.35, 128.25, 128.21, 126.14, 102.28 (PhCH), 101.79 (C-1), 95.63 (C-1′), 74.82, 73.09, 70.63, 70.32, 69.33, 68.58, 68.39, 66.46, 62.01, 58.78, 55.51. API-ES *m*/*z*: 883 $[M + Na]^+$.

Methyl-4,6-O-benzylidene-2 and 3-O-(3,4,6-tri-O-benzyl-2-O-benzoyl-α-D-mannopyranosyl)-α-D-glucopyranoside (21a and 22a)

The diol **20** and donor **5b** reacted under conditions (*d*) to give **21a** and **22a** in a 7.4:1 ratio.

*For **21a***

R_f = 0.31 (hexanes–EtOAc, 2:1). ^{1}H NMR (300 MHz, $CDCl_3$) δ: 8.03 (d, 2H), 7.16–7.56 (m, 23H), 5.72 (dd, 1H), 5.60 (s, 1H), 5.47 (d, 1H), 4.86–6.94 (m, 3H), 4.74 (d, 1H), 4.73 (d, 1H), 4.53 (d, 1H), 4.52 (d, 1H), 4.49 (d, 1H), 4.36 (dd, 1H), 4.30 (dd, 1H), 3.99–4.09 (m, 3H), 3.71–3.90 (m, 4H), 3.38 (s, 3H), 2.03 (s, 3H). LR-FAB-MS *m*/*z*: 817 $[M - H]^+$.

*For **22a***

R_f = 0.48 (hexanes–EtOAc, 2:1). ^{1}H NMR (300 MHz, $CDCl_3$) δ: 8.07 (d, 2H), 7.15–7.60 (m, 23H), 5.64 (dd, 1H), 5.56 (s, 1H), 5.10 (d, 1H), 4.83–4.87 (m, 2H), 4.80 (d, 1H), 4.71 (d, 1H), 4.60 (d, 1H), 4.54 (d, 1H), 4.52 (d, 1H), 4.29 (dd, 1H), 4.15–4.24 (m, 2H), 4.03–4.11 (m, 2H), 3.86 (dd, 1H), 3.69–3.82 (m, 5H), 3.47 (dd, 1H), 3.43 (s, 3H), 3.20 (d, 1H). LR-FAB-MS *m*/*z*: : 941 $[M + Na]^+$, 817 $[M - H]^+$.

Methyl-4,6-O-benzylidene-2 and 2-O-(3,4,6-tri-O-benzyl-2-O-benzoyl-β-D-mannopyranosyl)-α-D-glucopyranoside (21b and 22b)

(*a*) The diol **20** and donor **9** reacted under conditions (*d*) to give **21b** and **22b** in a 7.6:1 ratio in 25% overall yield.

© 2002 NRC Canada

*For **21b***

^{1}H NMR (300 MHz, $CDCl_3$) δ: 8.01–7.98 (m, 2H), 7.57–7.52 (m, 1H), 7.44–7.10 (m, 22H), 5.45 (t, *J* = 9.6 Hz, 1H, H-3), 5.41 (s, 1H, PhCH), 5.29 (dd, *J* = 8.1, 9.6 Hz, 1H, H-2′), 5.01 (d, *J* = 3.6 Hz, 1H, H-1), 4.82–4.51 (m, 7H), 4.25 (dd, *J* = 5.1, 10.2 Hz, 1H, H-6_a), 3.92–3.81 (m, 2H), 3.74–3.56 (m, 6H), 3.45 (dd, *J* = 9.0, 9.6 Hz, 1H), 3.38 (s, 3H, OCH_3), 1.41 (s, 3H, $OC(O)CH_3$). FAB$^+$-MS *m*/*z* (%): 859 ([M – H]$^+$, 100), 883 ([M + Na]$^+$, 21).

*For **22b***

^{1}H NMR (300 MHz, $CDCl_3$) δ: 7.98–7.95 (m, 2H), 7.59–7.54 (m, 1H), 7.45–7.08 (m, 22H), 5.44 (s, 1H, PhCH), 5.22 (dd, *J* = 7.8, 8.1 Hz, 1H, H-2′), 4.84–4.47 (m, 9H), 4.26–4.20 (m, 2H), 3.81–3.67 (m, 5H), 3.53–3.52 (m, 2H), 3.32–3.29 (m, 1H), 3.29 (s, 3H, OCH_3), 1.80 (s, 3H, $OC(O)CH_3$). FAB$^+$-MS *m*/*z* (%): 859 ([M – H]$^+$, 100).

(*b*) When the reaction was carried out at 0°C instead of –78°C, the ratio of **21b** to **22b** was 3:1 and the overall yield was 42%.

Methyl-4,6-O-benzylidene-2 and 3-O-(2–3,4,6-tetra-O-benzyl-α-D-mannopyranosyl)-α-D-glucopyranoside (21c and 22c)

The diol **20** and donor **7b** reacted under conditions (*d*) to give **21c** and **22c** in a 1:3 ratio and 30% yield.

*For **21c***

R_f = 0.23 (hexanes–EtOAc, 4:1). ^{1}H NMR (300 MHz, $CDCl_3$) δ: 7.05–7.50 (m, 25H), 5.53 (s, 1H), 5.41 (d, 1H), 4.92 (d, 1H), 4.88 (d, 1H), 4.78 (dd, 1H), 4.68 (d, 1H), 4.48–4.58 (m, 4H), 4.38 (d, 1H), 4.35 (d, 1H), 4.29 (dd, 1H), 3.92–4.01 (m, 3H), 3.88 (ddd, 1H), 3.72–3.82 (m, 4H), 3.62 (dd, 1H), 3.33–3.40 (m, 1H), 3.38 (s, 3H), 2.02 (s, 3H). LR-FAB-MS *m*/*z*: 803 [M – H]$^+$.

*For **22c***

R_f = 0.28 (hexanes–EtOAc, 4:1). ^{1}H NMR (300 MHz, $CDCl_3$) δ: 7.10–7.65 (m, 25H), 5.67 (dd, 1H), 5.46 (s, 1H), 4.78–4.89 (m, 5H), 6.66 (d, 1H), 6.65 (d, 1H), 4.61 (d, 1H), 4.54 (d, 1H), 6.69 (d, 1H), 4.26 (dd, 1H), 3.67–3.96 (m, 8H), 3.50 (dd, 1H), 3.33 (s, 3H), 3.28–3.38 (m, 2H), 1.98 (s, 3H). LR-FAB-MS *m*/*z*: 827 [M + Na]$^+$, 803 [M – H]$^+$.

Methyl-4,6-O-benzylidene-2 and 3-O-(2–3,4,6-tetra-O-benzyl-α/β-D-glucopyranosyl-α-D-glucopyranoside (21d and 22d)

The diol **20** and donor **10** were reacted under conditions (*d*) to give **21d** and **22d** in an 1.2:1 ratio.

*For **21d** (α-anomer)*

Selected ^{1}H NMR (300 MHz, $CDCl_3$) peaks δ: 5.61 (t, *J* = 9.6 Hz, 1H), 5.46 (s, 1H, PhCH), 2.00 (s, 3H, $OC(O)CH_3$). Lit. (28) δ value: 5.62 (t, *J* = 9.7 Hz, 1H, H-3), 5.47 (s, 1H), 2.01 (s, 3H).

*For **21d** (β-anomer)*

Selected ^{1}H NMR (300 MHz, $CDCl_3$) peaks δ: 5.65 (t, *J* = 9.6 Hz, 1H), 5.47 (s, 1H, PhCH), 1.76 (s, 3H, $OC(O)CH_3$). Lit. (28) δ value: 5.65 (t, *J* = 9.8 Hz, 1H, H-3), 5.48 (s, 1H), 1.78 (s, 3H).

*For **22d** (α -anomer)*

Selected ^{1}H NMR (300 MHz, $CDCl_3$) peaks δ: 5.58 (d, *J* = 3.0 Hz, 1H), 5.46 (s, 1H, PhCH), 2.02 (s, 3H, $OC(O)CH_3$). Lit. (28) δ value: 5.58 (d, *J* = 3.5 Hz, 1H, H-1′), 5.46 (s, 1H), 2.03 (s, 3H).

*For **22d** (β-anomer)*

Selected ^{1}H NMR (300 MHz, $CDCl_3$) peaks δ: 5.50 (s, 1H, PhCH), 1.94 (s, 3H, $OC(O)CH_3$). Lit. (28) δ value: 5.51 (s, 1H), 1.96 (s, 3H).

Methyl-4,6-O-benzylidene-2 and 3-O-(3,4,6-tri-O-benzyl-2-O-benzoyl-α-D-mannopyranosyl)-β-D-glucopyranoside (24a and 25a)

The diol **23** and donor **5b** were reacted under conditions (*d*) to give **24a** and **25a** in a 3.5:1 ratio and 36% overall yield.

*For **24a***

^{1}H NMR (300 MHz, $CDCl_3$) δ: 8.07 (d, 2H), 7.17–7.56 (m, 23), 5.65 (dd, 1H), 5.52 (s, 1H), 5.32 (dd, 1H), 5.30 (d, 1H), 4.84 (d, 1H), 4.81 (d, 1H), 4.72 (d, 1H), 5.59 (d, 1H), 4.54 (d, 1H), 4.53 (d, 1H), 4.37 (d, 1H), 6.33 (dd, 1H), 4.24 (dd, 1H), 4.00–4.12 (m, 2H), 3.74–3.87 (m, 5H), 3.56 (s, 3H), 3.44 (ddd, 1H), 2.01 (s, 3H). LR-FAB-MS *m*/*z*: 817 [M – H]$^+$.

*For **25a***

R_f = 0.32 (hexanes–EtOAc, 2:1). ^{1}H NMR (300 MHz, $CDCl_3$) δ: 8.06 (d, 2H), 7.17–7.58 (m, 23H), 5.75 (dd, 1H), 5.58 (s, 1H), 5.38 (d, 1H), 4.85 (d, 1H), 4.78 (d, 1H), 4.56 (d, 1H), 4.54 (d, 1H), 4.53 (d, 1H), 4.37 (dd, 1H), 4.28 (d, 1H), 4.05–4.16 (m, 2H), 3.84–3.93 (m, 3H), 3.79 (dd, 1H), 3.66 (dd, 1H), 3.57 (s, 3H), 3.38–3.51 (m, 2H), 2.85 (d, 1H). LR-FAB-MS *m*/*z*: 817 [M – H]$^+$.

Methyl-4,6-O-benzylidene-2 and 3-O-(3,4,6-tri-O-benzyl-2-O-benzoyl-β-D-mannopyranosyl)-β-D-glucopyranoside (24b and 25b)

The diol **23** and donor **9** reacted under conditions (*d*) to give an 1.8:1 mixture (11% overall yield) of **29b** and **25b**.

*For **24b***

^{1}H NMR (300 MHz, $CDCl_3$) δ: 8.02–7.99 (m, 2H), 7.59–7.09 (m, 23H) 5.38 (s, 1H, PhCH), 5.24 (dd, *J* = 8.1, 9.7 Hz, 1H, H-2′), 5.17 (dd, *J* = 7.8, 9.3 Hz, 1H, H-3), 4.94–4.55 (m, 7H), 4.29 (dd, *J* = 5.1, 10.5 Hz, 1H, H-6_a), 3.81–3.42 (m, 10H), 3.48 (s, 3H, OCH_3), 1.77 (s, 3H, $OC(O)CH_3$).

*For **25b***

^{1}H NMR (300 MHz, $CDCl_3$) δ: 7.99–7.97 (m, 2H), 7.73–7.69 (m, 1H), 7.46–7.09 (m, 22H), 5.40 (s, 1H, PhCH), 5.20 (dd, *J* = 8.1, 8.7 Hz, 1H, H-2′), 4.97 (dd, *J* = 7.8, 9.0 Hz, 1H, H-2), 4.82–4.20 (m, 9H), 3.95 (dd, *J* = 8.7, 9.0 Hz, 1H), 3.83–3.57 (m, 5H), 3.50 (br d, *J* = 3.6 Hz, 2H), 3.37 (s, 3H, OCH_3), 3.32–3.28 (m, 1H), 2.17 (s, 3H, $OC(O)CH_3$).

Methyl-4,6-O-benzylidene-2 and 3-O-(2–3,4,6-tetra-O-benzyl-α-D-mannopyranosyl)-β-D-glucopyranoside (24c and 25c)

The diol **23** and donor **7b** reacted under conditions (*d*) to give **24c** and **25c** in an 1:3 ratio (35% overall yield).

© 2002 NRC Canada

*For **25c***

R_f = 0.31 (hexanes–EtOAc, 2:1). ^{1}H NMR (300 MHz, $CDCl_3$) δ: 7.08–7.68 (m, 25H), 5.51 (s, 1H), 5.44 (d, 1H), 4.96 (dd, 1H), 4.86 (d, 1H), 4.63 (d, 1H), 4.53 (s, 2H), 4.48–4.57 (m, 3H), 4.44 (d, 1H), 4.38 (d, 1H), 4.36 (dd, 1H), 4.09 (dd, 1H), 3.64–3.93 (m, 8H), 3.49 (s, 3H), 3.44 (dd, 1H), 2.04 (s, 3H). LR-FAB-MS *m*/*z*: 803 $[M - H]^+$.

*For **24c***

R_f = 0.31 (hexanes–EtOAc, 2:1). ^{1}H NMR (300 MHz, $CDCl_3$) δ: 7.13–7.43 (m, 25H), 5.45 (s, 1H), 5.34 (d, 1H), 5.24 (dd, 1H), 4.88 (d, 1H), 4.73 (s, 2H), 4.66 (d, 1H), 4.60 (d, 1H), 4.59 (d, 1H), 4.57 (d, 1H), 4.51 (d, 1H), 4.34 (dd, 1H), 4.33 (d, 1H), 3.99 (dd, 1H), 3.68–3.81 (m, 7H), 3.54 (dd, 1H), 3.46 (dd, 1H), 3.41 (s, 3H), 2.01 (s, 3H). LR-FAB-MS *m*/*z*: 827 $[M + Na]^+$, 803 $[M - H]^+$.

Methyl-4,6-O-benzylidene-2 and 3-O-(2–3,4,6-tetra-O-benzyl-α/β-D-glucopyranosyl)-β-D-glucopyranoside (24d and 25d)

The diol **23** and donor **10** were reacted under conditions (*d*) to give **24d** and **25d** in an 1.2:1 ratio (51% overall yield).

*For **24d** (α-anomer)*

Selected ^{1}H NMR (300 MHz, $CDCl_3$) peaks δ: 5.54 (d, *J* = 3.6 Hz, 1H), 5.46 (s, 1H, PhCH), 2.00 (s, 3H, $OC(O)CH_3$). Lit. (28) δ value: 5.55 (d, *J* = 3.5 Hz, 1H, H-1′), 5.47 (s, 1H), 2.01 (s, 3H).

*For **24d** (β-anomer)*

Selected ^{1}H NMR (300 MHz, $CDCl_3$) peaks δ: 5.48 (s, 1H, PhCH), 1.93 (s, 3H, $OC(O)CH_3$). Lit. (28) δ value: 5.49 (s, 1H), 1.94 (s, 3H).

*For **25d** (α-anomer)*

Selected ^{1}H NMR (300 MHz, $CDCl_3$) peaks δ: 5.57 (d, *J* = 3.6 Hz, 1H), 3.50 (s, 3H, OCH_3), 2.02 (s, 3H, $OC(O)CH_3$). Lit. (28) δ value: 5.58 (d, *J* = 3.4 Hz, 1H, H-1′), 3.51 (s, 3H), 2.03 (s, 3H).

*For **25d** (β-anomer)*

Selected ^{1}H NMR (300 MHz, $CDCl_3$) peaks δ: 3.49 (s, 3H, OCH_3), 3.21 (m, 1H), 1.92 (s, 3H, $OC(O)CH_3$). Lit. (28) δ value: 3.49 (s, 3H), 3.22 (ddd, *J* = 2.3, 4.9, 9.2 Hz, 1H, H-5′), 2.03 (s, 3H).

1,3,4,5-Tetra-O-benzyl-2-O-(2,3,4-tri-O-benzyl-6-O-[tert-butyldiphenylsilyl]-α-D-mannopyranosyl-6-O-(2-O-benzoyl-2,4,6-tri-O-benzyl-α-D-mannopyranosyl)-D-myo-inositol (28)

The diol **4** (50 mg, 0.092 mmol) and glycosyl donors **5b** (90 mg. 0.12 mmol) and **7a** (75 mg, 0.12 mmol) were taken up together in a small quantity of toluene and azeotroped to remove traces of water. The mixture was dissolved in CH_2Cl_2 (3 mL) at 0°C under an argon atmosphere. *N*-Iodosuccinimide (54 mg, 0.24 mmol) was added to the solution. After stirring for 3 min, TBDMSOTf (12 μL, 0.054 mmol) was added. The reaction was quenched after 1 h with 10% aqueous sodium thiosulphate and saturated sodium bicarbonate, and extracted with CH_2Cl_2. The organic layer was removed under reduced pressure. The crude residue on flash column chromatography (EtOAc–hexanes, 1:4) afforded the pseudo-trisaccharide **28** (62 mg, 0.036 mmol, 39%) as the only trisaccharide along with **11a** (40 mg, 0.037 mmol, 40%). Note: To confirm the regioselectivity, the pseudo-disaccharide **11a** was coupled with **7a** which afforded the same pseudo-trisaccharide **28**. ^{1}H NMR (400 MHz, $CDCl_3$) δ: 8.10–6.94 (m, 65H, Ar-H), 5.83–5.81 (dd, *J* = 2.4, 2 Hz, 1H), 5.626–5.621 (d, *J* = 2 Hz, 1H, H-1), 5.35 (s, 1H, H-1), 4.97–4.36 (m, 20H), 4.29–3.99 (m, 7H), 3.93–3.90 (dd, *J* = 2.8, 9.6 Hz, 1H), 3.85–3.59 (m, 4H), 3.48–3.26 (m, 5H), 1.03 (s, 9H). FAB-MS *m*/*z*: 1745.76 $[M - 1]^+$. Anal. calcd. for $C_{111}H_{114}O_{17}Si$: C 76.26, H 6.57; found: C 76.00, H 6.71.

Methyl-3,6-di-O-allyl-1-O-methyl-2-O-(2,3,4,6-tetra-O-benzyl-α-D-mannopyranosyl)-4-O-(2-O-benzoyl-3,4,6-tri-O-benzyl-α-D-mannopyranosyl)-α-D-manno-pyranoside (29)

The diol **13** (27.4 mg, 0.1 mmol) and glycosyl donors **5b** (68.42 mg, 0.11 mmol) and **7b** (66.88 mg, 0.11 mmol) were taken up together in a small quantity of toluene and azeotroped to remove traces of water. The mixture was dissolved in CH_2Cl_2 (3 mL) at 0°C under an argon atmosphere. *N*-Iodosuccinimide (58.5 mg, 0.26 mmol) was added to the solution. After stirring for 3 min, TBDMSOTf (13.78 μL, 0.06 mmol) was added. The reaction mixture was quenched after 1 h with 10% aqueous sodium thiosulphate and saturated sodium bicarbonate, and extracted with CH_2Cl_2. The organic layer was removed under reduced pressure. The crude residue on flash column chromatography (EtOAc–hexanes, 1:4) afforded the trisaccharide **29** (45 mg, 0.034 mmol, 54%) as the major product, along with the disaccharide **14** (20 mg, 0.025 mmol, 39%). Unreacted acceptor **13** (10 mg, 0.03 mmol) was recovered. Note: Regioselectivity was confirmed by coupling disaccharide **14** with **7b** affording the same trisaccharide **29** in 36% isolated yield. ^{1}H NMR (400 MHz, $CDCl_3$) δ: 8.09–8.06 (d, 2H, Ar-H), 7.58–7.06 (m, 38H, Ar-H), 5.94–5.84 (m, 2H), 5.70 (br s, 1H), 5.39 (br s, 1H), 5.26–4.99 (m, 5H), 4.95–4.46 (m, 15H), 4.12–3.61 (m, 21H), 3.24 (s, 3H). ^{13}C NMR (100 MHz, $CDCl_3$) δ: 165.31 (OCOPh), 138.59, 138.53, 138.45, 138.39, 138.27, 138.07, 135.01, 134.01, 134.32, 133.04, 130.03, 129.96, 129.92, 128.39, 128.30, 128.28, 128.24, 128.19, 128.04, 127.98, 127.96, 127.83, 127.81, 127.69, 127.59, 127.48, 117.68, 116.41, 99.81 (C-1), 99.68 (C-1), 97.80 (C-1), 79.82, 79.43, 78.32, 75.26, 74.91, 74.76, 74.16, 74.00, 73.49, 73.36, 73.24, 72.56, 72.32, 72.27, 72.15, 71.55, 70.84, 70.70, 69.74, 69.48, 69.03, 54.81. Anal. calcd. for $C_{80}H_{86}O_{17}$: C 72.82, H 6.57; found: C 72.90, H 6.66.

Acknowledgements

BFR is grateful to the Human Frontier Science Program Organization and Synthon Chiragenics of Monmouth Junction, NJ, U.S.A. for partial support of this work. C.U. thanks the Comunidad Autónoma de Madrid for a postdoctoral fellowship. Funding from the Dirección General de Investigación Científica y Técnica (grant: PPQ2000-1330).

References

1. R.U. Lemieux. Adv. Carbohydr. Chem. **9**, 1 (1954).
2. H.S. Isbell. Annu. Rev. Biochem. **9**, 65 (1940); H.L. Frush and H.S. Isbell. J. Res. Natl. Bur. Stand. (U.S.), **27**, 413 (1941).
3. B. Capon and S.P. McManus. Neighboring group participation. Plenum Press, New York. 1976.

© 2002 NRC Canada

4. For a convenient summary see: A.F. Bochkov and G.E. Zaikov. Chemistry of the *O*-glycosidic bond. Pergamon Press, Oxford, U.K. 1979. Chap. 2.
5. H. Paulsen. Angew. Chem. Int. Ed. Engl. **21**, 152 (1982).
6. A. Pictet and H. Vogel. Helv. Chim. Acta, **11**, 436 (1928), and subsequent papers; J.C. Irvine, J.W.H. Oldham, and A.F. Skinner. J. Am. Chem. Soc. **51**, 1279 (1929); H.H. Schlubach and B. Middelhoff. Ann. **550**, 1344 (1942); W.W. Binkley and M.L. Wolfrom. J. Am. Chem. Soc. **68**, 2171 (1946); A. Klemer and B. Dietzel. Tetrahedron Lett. 275 (1970); R.K. Ness and H.G. Fletcher, Jr. Carbohydr. Res. **17**, 465 (1971).
7. R.U. Lemieux and G. Huber. J. Am. Chem. Soc. **78**, 4117 (1956).
8. R.U. Lemieux. Can. J. Chem. **31**, 949 (1953); R.U. Lemieux and G. Huber. Can. J. Chem. **33**, 128 (1955).
9. See for example: P. Collins and R. Ferrier. Monosaccharides: Their chemistry and their roles in natural products. John Wiley and Sons, Chichester, U.K. 1995. Chap. 3; T.K. Lindhorst. Essentials of carbohydrate chemistry and biochemistry. Wiley–VCH, Weinheim. 2000; H. Paulsen. *In* Modern methods in carbohydrate synthesis. *Edited by* S.H. Khan and R.A. O'Neill. Barwood Academic Publishers, London, U.K. 1996; W.W. Pigman and R.M. Goepp, Jr. Chemistry of the carbohydrates. Academic Press, New York. 1948. p. 159; G.-J. Boons. Tetrahedron, **52**, 1995 (1996); A.F. Bochkov and G.E. Zaikov. Chemistry of the *O*-glycosidic bond. Pergamon Press, Oxford. 1979. Chap. 2 and Chap. 3.
10. G. Anilkumar, L.G. Nair, and B. Fraser-Reid. Org. Lett. **2**, 2587 (2000); B. Fraser-Reid, J.C. Lopez, K.V. Radhakrishnan, M. Mach, U. Schlueter, A.M. Gomez, and C. Uriel. J. Am. Chem. Soc. **124**, 3198 (2002).
11. H. Paulsen, M. Paal, D. Hadamczyk, and K.-M. Steiger. Carbohydr. Res. **133**, 71 (1984), C1-C5; H. Paulsen and O. Lockhoff. Chem. Ber. **114**, 3079 (1981); H. Paulsen, D. Hadamczyk, W. Kutschker, and A. Bunsch. Liebigs. Ann. Chem. 129 (1985).
12. S. Masamune, W. Choy, J.S. Petersen, and L.R. Sita. Angew. Chem. Int. Ed. Engl. **23**, 1 (1985).
13. N.M. Spijker and C.A.A. van Boeckel. Angew. Chem. **103**, 179 (1990); Angew Chem. Int. Ed. Engl. **30**, 180 (1991).
14. C.A.A. van Boeckel and M. Petitou. Angew Chem. **105**, 1741 (1993); Angew Chem. Int. Ed. Engl. **32**, 1671 (1993).
15. G. Anilkumar, Z.J. Jia, R. Kraehmer, and B. Fraser-Reid. J. Chem. Soc. Perkin Trans. 1, 3591 (1999).
16. R. Lemieux, T. Takeda, and B.Y. Chung. ACS Symp. Ser. 39 (1976).
17. C. Roberts, R. Madsen, and B. Fraser-Reid. J. Am. Chem. Soc. **117**, 1546 (1995); J.G. Allen and B. Fraser-Reid. J. Am. Chem. Soc. **121**, 468 (1999); C. Roberts, C.L. May, and B. Fraser-Reid. Carbohydr. Lett. **1**, 89 (1994).
18. D.R. Mootoo, P. Konradsson, U. Udodong, and B. Fraser-Reid. J. Am. Chem. Soc. **110**, 5583 (1988).
19. A.H. Haines. Adv. Carbohydr. Chem. Biochem. **33**, 11 (1976); J. Stanek, Jr. Top. Curr. Chem. **154**, 209 (1990); A.C. Richardson and J.M. Williams. Tetrahedron, **23**, 1641 (1967); R.C. Chalk, D.H. Ball, and L. Long, Jr. J. Org. Chem. **31**, 1509 (1966); A.K. Mitra, D.H. Ball, and L. Long, Jr. J. Org. Chem. **27**, 160 (1962); H.M. Flowers. Carbohydr. Res. **100**, 418 (1982); H.M. Flowers. Carbohydr. Res. **39**, 245 (1975).
20. (*a*) P.R. Muddasani, B. Bernet, and A. Vasella. Helv. Chim. Acta. **77**, 334 (1994); (*b*) P.R. Muddasani, E. Bozo, B. Bernet, and A. Vasella. Helv. Chim Acta, **77**, 257 (1994).
21. (*a*) K. Takeo. Carbohydr. Res. **77**, 131 (1979); (*b*) S. Hanessian and J. Banoub. Carbohydr. Res. **53**, C13 (1977); (*c*) B. Coxon and H.G. Fletcher. J. Org. Chem. **26**, 2892 (1961).
22. These compounds were identified by comparing their NMR data with those published in the following: P.R. Muddasani, E. Bozo, B. Bernet, and A. Vasella. Helv. Chem. Acta. **77**, 257 (1994).
23. G.H. Veeneman, S.H. Van Leeuwen, H. Zurmond, and J.H. van Boom. J. Carbohydr. Chem. **9**, 783 (1990).
24. C.J.J. Elie, R. Verduyn, C.E. Dreff, D.M. Brounts, G.A. van der Marel, and J.H. van Boom. Tetrahedron, **46**, 8243 (1990).
25. G. Anilkumar, M. Gilbert, and B. Fraser-Reid. Tetrahedron, **56**, 1993 (2000).
26. B.G. Wilson and B. Fraser-Reid. J. Org. Chem. **60**, 317 (1995).
27. For excellent summaries of his work, see (*a*) A. Vasella. Bioorganic chemistry carbohydrates. *Edited by* S.M. Hecht. Oxford University Press, New York. 1999. Chap. 2; (*b*) A. Vasella. A new approach to the synthesis of glycosides. Pure Appl. Chem. **65**, 731 (1994).
28. B. Bernet and A. Vasella. Helv. Chim. Acta. **83**, 995 (2000).

© 2002 NRC Canada

Stochastic conformational search on the Lewis X (Le^x) trisaccharide and three Le^x analogues

France-Isabelle Auzanneau, Elizabeth Sourial, Jonathan M. Schmidt, and Miklos Feher

Abstract: Biased stochastic conformational searches using the MMFF94 force field and the Born continuum solvation model were applied to the molecular modeling of the Lewis X (Le^x) trisaccharide (β-D-Gal-(1,4)-[α-L-Fuc-(1,3)]-β-D-GlcNAc-OH) and three Le^x analogues, in which each of the three sugar units was replaced by another sugar residue, i.e., *N*-acetyl-glucosamine by glucose, galactose by glucose, and fucose by rhamnose. The stochastic search accurately identified a lowest energy conformation of the Le^x determinant that corresponds to the reported conformations of Le^x deduced experimentally in the solid state by X-ray crystallography and in solution by NMR measurements. In this conformation stacking exists between the galactosyl and fucosyl residues. Five new local minima for the Le^x trisaccharide were found within 3 kcal mol^{-1} of the global minimum using the stochastic search and metric scaling. Modeling studies of the analogues showed that the stacking observed in the Le^x trisaccharide was maintained when either galactosyl or *N*-acetylglucosamine were replaced by glucosyl residues. In contrast, substitution of the fucose residue by rhamnose led to two conformers in which stacking of the galactose and rhamnose residues was no longer maintained. These results indicate that the substitution of the non-reducing end galactosyl or *N*-acetyl-glucosaminyl residues by a glucose unit in the dimeric Lewis X ($dimLe^x$) tumour associated antigen could help in the development of a vaccine that cross-reacts with $dimLe^x$ but no longer displays Le^x associated three-dimensional epitopes also presented by non-cancerous cells. In contrast, an analogue in which the fucosyl residue is replaced by rhamnose does not constitute a good vaccine candidate, since our results indicate that this substitution will induce an important conformational change that is likely to abolish cross-reactivity with the natural $dimLe^x$ tumor associated antigen.

Key words: molecular modeling, stochastic, conformational analysis, Lewis X, oligosaccharide.

Résumé : On a fait des recherches conformationnelles stochastiques biaisées en utilisant le champ de force MMFF94 et modèle de solvatation continue de Born. On a appliqué la modélisation moléculaire au trisaccharide Lewis X (Le^x) (β-D-Gal-(1,4)-[α-L-Fuc-(1,3)]-β-D-GlcNAc-OH) et à trois analogues Le^x dans lesquels chacune des trois unités de sucre a été remplacée par un autre résidu de sucre, par exemple la *N*-acétyl-glucosamine par du glucose, le galactose par du glucose et le fucose par du rhamnose. Les recherches stochastiques ont permis d'identifier correctement une conformation d'énergie minimale du déterminant Le^x qui correspond aux conformations rapportées expérimentalement pour Le^x en se basant sur la diffraction des rayons X à l'état solide et sur des mesures de RMN en solution. Dans cette conformation, il existe un empilement entre les résidus galactosyle et fucosyle. En se basant sur l'étude stochastique et sur une mise à l'échelle métrique, on a identifié cinq nouveaux minima locaux pour le trisaccharide Le^x; ils se trouvent en deçà de 3 kcal mol^{-1} du minimum global. Les études de modélisation des analogues ont montré que l'empilement observé dans le trisaccharide Le^x sont maintenues quand on remplace le galactosyle ou la *N*-acétylglucosamine par des résidus glucosyles. Toutefois, la substitution du résidu de fucose par du rhamnose conduit à deux conformères dans lesquels l'empilement des résidus galactose et rhamnose n'est plus maintenu. Ces résultats indiquent que la substitution par une unité glucose des résidus galactosyle et *N*-acétylglucosaminyle dans portion non réductrice de la molécule d'antigène Lewis X dimère ($dimLe^x$) associée à la tumeur, pourrait aider au développement d'un vaccin donnant lieu à une réaction croisée avec le $dimLe^x$ sans toutefois présenter les épitopes tridimensionnels associés au Le^x qui sont aussi présents dans les cellules non cancéreuses. Toutefois, un analogue dans lequel le résidu fucosyle a été remplacé par un rhamnose n'est pas un bon candidat à un vaccin puisque nos résultats indiquent que cette substitution induira un changement conformationnel important qui empêchera la réactivité croisée avec l'antigène $dimLe^x$ naturel associé à la tumeur.

Mots clés : modélisation moléculaire, stochastique, analyse conformationnelle, Lewis X, oligosaccharide.

[Traduit par la Rédaction]

Received 10 May 2002. Published on the NRC Research Press Web site at http://canjchem.nrc.ca on 29 August 2002.

This paper is dedicated to Professor Raymond U. Lemieux.

F.-I. Auzanneau.[1] Department of Chemistry and Biochemistry, University of Guelph, Guelph, ON N1G 2W1, Canada.
E. Sourial,[2] **J.M. Schmidt, and M. Feher.**[1] SignalGene Inc., 2–33 Laird Road, Guelph, ON N1G 4P7, Canada.

[1]Corresponding authors (e-mail for F.I.A.: auzanneau@chembio.uoguelph.ca; e-mail for M.F.: miklos.feher@signalgene.com).
[2]Present address: Chemical Computing Group Inc., Suite 910, 1010 Sherbrooke Street West, Montreal, QC H3A 2R7, Canada.

 DOI: 10.1139/V02-163 © 2002 NRC Canada

Fig. 1. The tumour associated carbohydrate antigen dimeric Lewis X (dimLe^x).

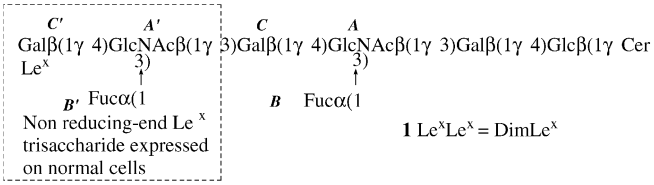

Introduction

Aberrant glycosylation in human cancer was first indirectly suggested in the mid-sixties when several papers reported the accumulation of fucose-containing glycolipids in adenocarcinomas (1, 2). Tumour associated carbohydrates antigens (TACAs) can be involved in specific immune responses, during which antibodies recognizing specific carbohydrate epitopes are produced. Extensive work has been performed on glycoconjugates displaying TACAs as potential vaccines against cancer and the approach was shown to be very promising (3–8). Monoclonal antibodies raised against the tumour associated hexasaccharide dimeric Le^x **1** (Fig. 1, dimLe^x) were shown to recognize internal epitopes of dimLe^x displayed by colorectal tumour tissues (9–13). If used as a vaccine, however, the dimLe^x hexasaccharide is also likely to trigger the production of antibodies binding to the non-reducing trisaccharide Le^x (Fig. 1) also largely expressed in normal tissues and cells (14). To avoid such autoimmune reactions, our research program is aimed at discovering analogues of the dimLe^x hexasaccharide that would retain the internal epitopes present on the surface of colorectal cancer cells but no longer possess the epitopes associated with the Le^x trisaccharide ***A′(B′)C′***. Thus, we are investigating the possibility of using analogues of hexasaccharide **1** in which one of the sugar units ***A′***, ***B′***, or ***C′*** defining the Le^x epitope is replaced by other sugar residue (Fig. 2), i.e., *N*-acetylglucosamine by glucose (**2**), galactose by glucose (**3**), and fucose by rhamnose (**4**). It is reasonable to expect that the conformational changes induced by any of these substitutions will affect the cross-reactivity between the analogues and the natural antigen. In fact, if the conformations of hexasaccharides **2**–**4** are drastically different from that of **1** it is likely that these analogues will not maintain the wanted cross-reactivity with dimLe^x. In contrast, if the conformations of hexasaccharides **2**–**4** are similar to that of **1** they could retain a tumor-associated cross-reactivity with the natural dimeric antigen while losing cross-reactivity with the Le^x determinant. Predicting such conformational changes will allow significant savings to our synthetic efforts. If the conformations of hexasaccharides **2**–**4** are similar to that of **1**, the conformation of the non-reducing trisaccharide ***A′***(***B′***)***C′*** in these analogues must also be similar to that of the Le^x residue ***A′***(***B′***)***C′*** in dimLe^x **1**. Conversely, it seems reasonable to expect that any drastic conformational change imposed to the terminal trisaccharide ***A′***(***B′***)***C′*** by these substitutions will induce a large conformational change in the corresponding hexasaccharide. Thus, the computationally less demanding conformational study of trisaccharide analogues **7**–**9** is sufficient to obtain a good insight into the conformational changes imposed by these substitutions to the hexasaccharides **2**–**4**. To assess if analogues **7**–**9** (Fig. 3) would maintain a Le^x-like conformation while presenting different electrostatic topographies to anti-Le^x antibodies, we applied biased stochastic conformational searches using the Molecular Operating Environment program suite (15). In this stochastic search method all bonds including ring and side-group bonds are allowed to rotate randomly and simultaneously to generate new molecular conformations that are energetically evaluated. Thus, this search method attempts to map the whole conformational space without any driving force, as is the case in some other conformational search methods, such as MMC calculations. The energies were calculated using the MMFF94 force field (16) and applying the Born continuum solvation model (17–19), which has been shown (20) to be efficient for the modeling of carbohydrates.

Fig. 2. Analogues of dimLe^x as potential targets for vaccine development.

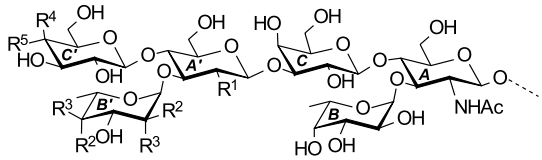

2 R^1 = OH, R^2 = R^4 = OH, R^3 = R^5 = H
3 R^1 = NHAc, R^2 = R^5 = OH, R^3 = R^4 = H
4 R^1 = NHAc, R^2 = R^5 = H, R^3 = R^4 = OH

To assess the validity of our results on the analogues, we first applied the stochastic search method to the molecular modeling of the Le^x determinant, for which a large amount of both computational and experimental data is available in the literature. In fact, the lowest energy conformation of the Le^x trisaccharide methyl glycoside (**6**) was first calculated in the pioneering work of Lemieux and co-workers (21) who developed the Hard Sphere ExoAnomeric (HSEA) modeling method (22). Since these early calculations, other molecular mechanics force field methods have been applied to the modeling of this trisaccharide (23–25). Moreover, in a thorough study, Csonka et al. (26) used ab initio calculations (HF/6–31G(d)) to validate the results obtained in the molecular modeling of trisaccharides **5** and **6** using the MM2*–SUMM conformational search method. In addition to being calculated by these various methods, the conformation of the Le^x trisaccharide was also experimentally determined both by NMR measurements (23, 25) for its solution state and X-ray crystallography (27) for its solid state. Thus, because the conformational manifold of the Le^x trisaccharide has been well established computationally and experimentally, it was used as a test case to evaluate the stochastic search method and force field used in our study before applying it to analogues **7**–**9**.

Computational methods

All calculations in this work were performed using the fully programmable Molecular Operating Environment program suite (15). Conformational searches were performed with the stochastic search method, as implemented in MOE (15). The procedure is similar to the RIPS method (28). In stochastic searches new molecular conformations are generated by random

© 2002 NRC Canada

Fig. 3. Le^x (**5**), Le^x β-methyl glycoside (**6**), and analogues of Le^x (**7**–**9**) modeled.

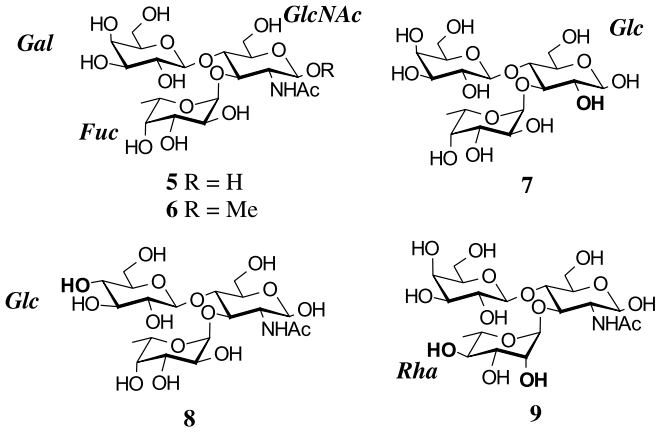

rotation of bonds (including ring bonds) instead of only Cartesian coordinate perturbation. In the calculations a bias of ~30° was selected, which means that dihedral angles were rotated by random angle with a sum-of-gaussians distribution with peaks at multiples of 30°. To make the search even more efficient, a simultaneous Cartesian perturbation of 0.4 Å was also applied. The structures were subsequently optimized using the Merck force field (MMFF94, ref. 16) and employing the Born continuum solvation model (17–19) as implemented in MOE. Each resulting conformation was checked to determine if it had already been generated by comparing all atom positions using a predefined root-mean-square (RMS) tolerance (0.1 Å in this work). The hydrogens were included in establishing the RMS tolerance because of the importance of hydrogen bonding among these carbohydrates: molecules with identical heavy atom positions but different hydrogen positions may substantially differ in energy. The procedure was terminated when the number of failures to find new conformations exceeded 10 000 in a row, a stringent criterion. Conformations with energies over 10 kcal mol^{-1} above the respective minima were rejected. In the process, 1034 conformations were obtained for the Le^x trisaccharide **5**, whereas the number of conformers for analogues **7**–**9** were 442, 268, and 472, respectively. During the entire process, the absolute configuration of each molecule was preserved.

To identify conformations with similar properties, conformer generation was followed by a clustering process. This conformer clustering was based on the metric scaling procedure (29), an efficient technique to project high dimensional conformational space to two dimensions. In metric scaling the distances between points representing different conformers are equal to the RMS distance between the corresponding conformers themselves, provided all eigenvalues in the process are positive. This was satisfied in all examples. The metric scaling technique allows the visual inspection of differences between clusters, which makes it simple to determine the optimum number of clusters. Only heavy atoms were involved in the metric scaling.

The minimum energy geometry of selected conformers of Le^x (**5**) were also calculated using the AM1 and PM3 semi-empirical calculations, without considering the effects of solvation. At termination of the optimizations, the average gradient was less than 0.0001 kcal $Å^{-1}$ mol^{-1}. Electrostatic potential surfaces were calculated from the Gasteiger charges of the surface atoms.

Fig. 4. (A) Overlay of the lowest energy conformation calculated for Le^x with the crystal structure reported by Perez et al. (27). (B) Overlay of the local minimum found for **5** 8.3 kcal mol^{-1} above the global minimum (Table 2, entry 1) with the local minimum reported by Peters and co-workers (25) (Table 2, entry 2).

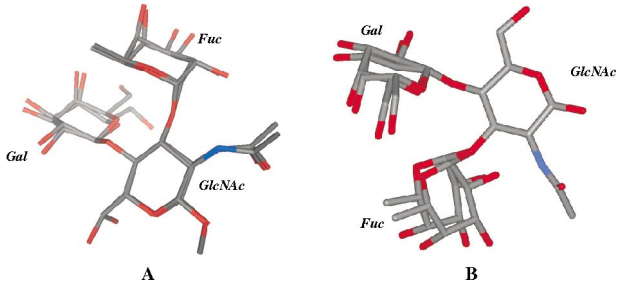

Results

A large number of crystal structures and semi-empirical calculations have revealed that pyranose rings adopt well-defined geometries and exist in their regular unstrained chair conformations: $^4C_1$ for D-GlcNAc, D-Glc, and D-Gal or $^1C_4$ for L-Fuc and L-Rha (30). Since the flexibility of these rings is limited, the global shape of oligosaccharides depends mainly on the rotation of the individual sugar residues around the glycosidic linkages. The relative orientations of the carbohydrate units in an oligosaccharide are usually expressed in terms of the torsional angles of the glycosidic linkages Φ and Ψ, which are defined here as Φ = O5-C1-O-C′*x* and Ψ = C1-O-C′*x*-C′(*x* + 1) for the (1 → *x*) linkages. The angles measured for the global minimum found by the stochastic search are given in Table 1 (entry 1). Table 1 (entries 2–6) also gives the Φ/Ψ torsional angles for the minimum energy conformations previously found by various conformational search methods (21, 23–25) and further supported by the ab initio calculations of Csonka et al. (entry 7, ref. 26). As can be seen from these results the global minimum found by the stochastic search is in complete agreement with those calculated by the various computational methods. Table 1, entries 8 and 9, as well as Fig. 4A show that the closely related conformations of the Le^x trisaccharide in the solid state found by X-ray crystallography (27) are in full agreement with the global minimum obtained by the stochastic search (entry 1). Finally, the solution conformations deduced experimentally by NMR measurements (NOEs and non-selective T_1) reported by Miller et al. (23) and more recently by Peters and co-workers (25) are given in Table 1, entries 10 and 5, respectively. Again, these conformations are in very good agreement with the global minimum found by the stochastic search (Table 1, entry 1). As described in Table 2 (entry 1) and illustrated in Fig. 4B, the stochastic search also found a local minimum 8.3 kcal mol^{-1} above the global minimum that corresponds to a local minimum found by Metropolis Monte Carlo simulations 7.3 kcal mol^{-1} (see Table 2, entry 2) above the global minimum.

Because it allows random rotation of all bonds, the stochastic search is a powerful method for locating additional conformational minima that were not necessarily found

© 2002 NRC Canada

Table 1. Torsional angles[a] measured for the lowest energy conformations of the Le^x determinant found computationally (entries 1–7), and experimentally by X-ray crystallography (entries 8 and 9) and NMR measurements (entries 5 and 10).

		Galβ(1–4)GlcNAc		Fucα(1–3)GlcNAc	
Entry	Method	Φ^1 (°)	Ψ^1 (°)	Φ^2 (°)	Ψ^2 (°)
1	Stochastic search[b]	–68	–107	–62	146
2	HSEA[c]	–65	–110	–65	145
3	CHARMm[d]	–57	–118	–45	144
4	CICADA[e]	–75	–104	–81	151
5	MMC[f]	–68	–110	–72	146
6	SUMM[g]	–70	–106	–78	147
7	Ab initio HF/6–31G(d)[h]	–73	–105	–79	137
8	X-ray (1)[i]	–80	–105	–72	139
9	X-ray (2)[i]	–70	–108	–77	139
10	SIMNOE[j]	–55	–120	–45	145

[a]Torsional angles at the glycosidic linkages are defined as Φ = O5-C1-O-C′x and Ψ = C1-O-C′x-C′(x + 1) for the (1 → x) linkages.
[b]Global minimum found by the stochastic search in this work (see text for details).
[c]Lowest energy conformation calculated by HSEA (21).
[d]Lowest energy conformation found (23) with CHARMm using the force field developed for carbohydrates by Rasmussen et al.
[e]Conformation found (24) by the CICADA method using the MM3 force field and a large dielectric constant to simulate a water environment.
[f]Lowest energy conformation found in Metropolis Monte Carlo simulations (25) using the GEGOP program (HSEA force field) and supported by experimental NOE measurements.
[g]Conformation found by the SUMM search using the MM2* (26) force field in vacuum.
[h]Vacuum calculation using the ab initio HF/6–31G(d) method (26).
[i]Crystal structures of Le^x(OMe) **6** (27).
[j]Conformation supported experimentally by NOEs and non-selective T_1 NMR measurements (23).

Table 2. Torsional angles[a] for a local minimum found by the stochastic search 8.3 kcal mol^{-1} (entry 1) above the global minimum and two local minima found by Metropolis Monte Carlo simulations (entries 2 and 3, ref. 25).

			Galβ(1–4)GlcNAc		Fucα(1–3)GlcNAc	
Entry	Method	Rel. energy (kcal mol^{-1})	Φ^1 (°)	Ψ^1 (°)	Φ^2 (°)	Ψ^2 (°)
1	Stochastic search	8.3	–61	–104	–157	103
2	MMC	7.3	–53	–103	–145	92
3	MMC	8.3	–80	–97	–113	125

[a]Torsional angles at the glycosidic linkages are defined as in Table 1.

using other search methods. In fact, the stochastic search on **5** lead to 1034 conformations in a 10 kcal mol^{-1} window above the global minimum. Nineteen conformations were found within 3 kcal mol^{-1} of the lowest energy conformation. Five of these conformations presented twisted or inverted chairs and were discarded. The torsional angles Φ and Ψ angles were defined in MOE for each glycosidic linkage and automatically measured for the remaining 12 conformers. Based on these angles the conformations were found to fall into six main clusters (**A**–**F**) listed in Table 3. The overlays of the conformers belonging to the same cluster (**A**, **C**, and **D**) are represented in Fig. 5. These overlays show that conformations that belong to the same cluster but have different energies differ essentially in the orientation of the CH_2OH or *N*-acetyl groups. These results can be related to the work of Csonka et al. (26). In their study the conformations found by MM2*–SUMM within 1 kcal mol^{-1} of the global minima for trisaccharides **5** and **6** were also evaluated at the ab initio (HF/6–31G(d)) level. These results based on a higher level of calculations also point towards an important energy contribution defined by the orientation of the side chains and hydroxyl groups to the total energy of conformations having the same Φ and Ψ angles. As can be seen in Fig. 6, metric scaling on heavy atoms (29) allowed the simple identification and distinction of the six clusters, **A**–**F**.

Based on the *N*-acetylglucosamine ring we rigidly aligned the local minima best representing each of the conformational families (**A**–**F**) found by the stochastic search. The results presented in Fig. 7 show that these conformers differ from each other mostly in the orientation of the galactose residue represented in blue and to a lesser extent in the orientation of the fucosyl residue represented in red. Thus, our results seem to be in contrast with previous studies in which it was concluded from molecular dynamics (23) and ab initio calculations (26) that the Le^x trisaccharide was fairly rigid around the glycosidic linkages. However, it was also shown by Csonka et al. (26) that there was no obvious correlation between the MM2* energies calculated for the reducing trisaccharide **5** and the methyl glycoside analogue **6**. Thus, to assess whether the conformations found by the stochastic search for reducing analogue **5** could be reasonably expected for glycoside **6** used in most other calculations, we performed semi-empirical geometry optimizations of selected conformations of hemiacetal **5** and methyl glycoside **6**. Calculations at the PM3 and AM1 levels suggest that conformer **B** is about 3–3.5 kcal mol^{-1} more energetic

© 2002 NRC Canada

Table 3. Torsional angles[a] for conformations of Le^x (**5**) found by the stochastic search within 3 kcal mol^{-1} of the global minimum.

			Galβ(1–4)GlcNAc		Fucα(1–3)GlcNAc	
Entry	Conformer	Rel. energy (kcal mol^{-1})	Φ^1 (°)	Ψ^1 (°)	Φ^2 (°)	Ψ^2 (°)
1	**A**	0	–68	–107	–62	146
2	**A**	1.2	–77	–102	–70	144
3	**A**	2.6	–74	–102	–71	146
4	**B**	1.4	–71	60	–100	98
5	**C**	1.7	–56	77	–71	161
6	**C**	2.7	–57	75	–68	167
7	**C**	2.9	–56	76	–70	162
8	**D**	1.8	–144	–137	–54	167
9	**D**	1.8	–143	–140	–54	170
10	**D**	2.0	–150	–134	–53	162
11	**E**	2.7	47	–106	–62	157
12	**F**	2.8	–149	–142	–156	102

[a]Torsional angles at the glycosidic linkages are defined as in Table 1.

Fig. 5. Cluster A: overlay of the three conformations listed in Table 3, entries 1–3. Cluster C: overlay of the three conformations listed in Table 3, entries 5–7. Cluster D: overlay of the three conformations listed in Table 3, entries 8–10.

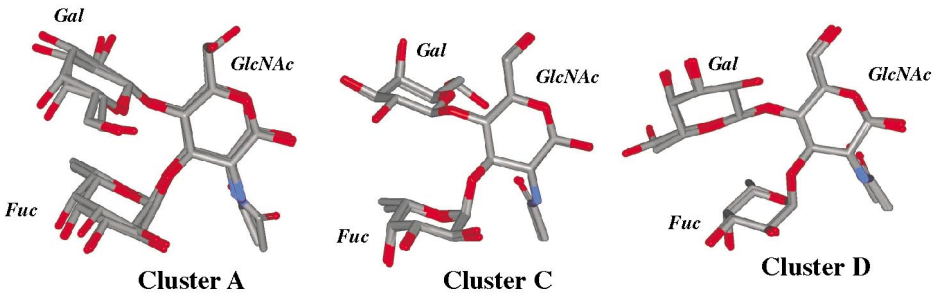

Fig. 6. Analysis of the conformational manifold of Le^x within 3 kcal mol^{-1} of the global minimum by metric scaling on heavy atoms (29). Six clusters (**A**–**F**; circles) can be visually identified and distinguished from one another.

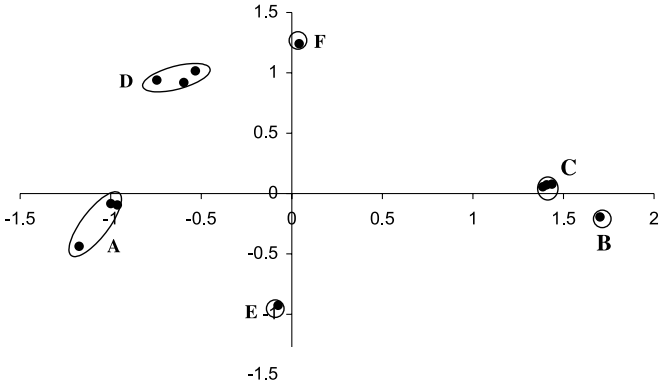

Fig. 7. Rigid alignment based on the *N*-acetylglucosamine ring of the local minima best representing each of the conformational families **A**–**F** found by the stochastic search (Table 3, entries 1, 4, 5, 8, 11, and 12). The galactose and fucose residues are shown in blue and red, respectively. These views are related to each other through a 90° rotation around a vertical axis.

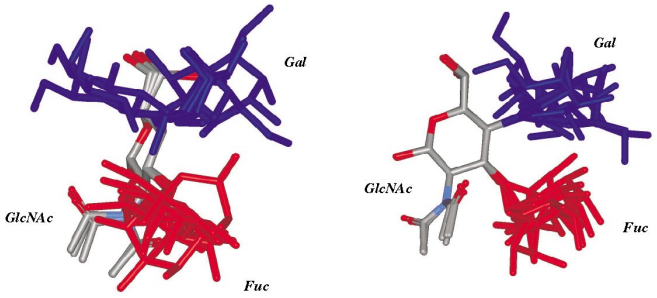

than conformer **A** and that methyl glycoside conformer **B** remains about 2.5–3 kcal mol^{-1} more energetic than conformer **A** (see Table 4). These calculations confirmed that the new families of conformers identified by the stochastic search are indeed likely to be in the 5 kcal mol^{-1} window from the global minimum. Nevertheless, accounting for the relative energy of conformers remains an important issue in conformational analysis. In fact, Csonka et al. (26) showed that while the MM2* method provided small energy differences for the first 11 rotamers of trisaccharide **5** (1 kcal mol^{-1}), ab initio calculations (HF/6–31G(d)) on the same rotamers yielded more than 4.5 kcal mol^{-1} in energy difference. It is also known that there are great differences in relative energies of conformers when calculated with different force fields (20) and that the energies calculated for individual conformations are often highly inaccurate. Thus, the extent

© 2002 NRC Canada

Table 4. Semi-empirical calculations on Le^x (**5**) and Le^x β-methyl glycoside (**6**) for the conformations **A** and **B** found by the stochastic search (see Table 3, entries 1 and 4).

Conformer (compound)	PM3 Relative energy (kcal mol^{-1})	AM1 Relative energy (kcal mol^{-1})
A (**5**)	0	0
B (**5**)	3.0	3.7
A (**6**)	0	0
B (**6**)	3.0	2.3

Table 5. Torsional angles for conformations found by the stochastic search within 3 kcal mol^{-1} of the global minima for analogues **7**–**9**.

Entry	Analogue (conformer)	Rel. energy (kcal mol^{-1})	Φ^1 (°)	Ψ^1 (°)	Φ^2 (°)	Ψ^2 (°)
1	**7**[a] **(A)**	0	–72	–105	–73	146
2	**7**[a] **(C)**	2.0	–69	65	–58	170
3	**7**[a] **(E)**	2.1	47	–109	–63	157
4	**8**[b] **(A)**	0	–70	–108	–59	151
5	**9**[c] **(H)**	0	–50	82	–102	150
6	**9**[c] **(I)**	2.4	–76	–106	–161	96

[a]Torsional angles are defined as in Table 1 with Φ^1/Ψ^1 and Φ^2/Ψ^2 corresponding to the β-Gal-(1,4)-Glc and α-Fuc-(1,3)-Glc glycosidic linkages, respectively.
[b]Torsional angles are defined as in Table 1 with Φ^1/Ψ^1 and Φ^2/Ψ^2 corresponding to the β-Glc-(1,4)-GlcNAc and α-Fuc-(1,3)-GlcNAc glycosidic linkages, respectively.
[c]Torsional angles are defined as in Table 1 with Φ^1/Ψ^1 and Φ^2/Ψ^2 corresponding to the β-Gal-(1,4)-GlcNAc and α-Rha-(1,3)-GlcNAc glycosidic linkages, respectively.

with which these new conformational families are indeed populated in solution is uncertain. So far the NMR measurements reported for the Le^x determinant (23, 25) did not point towards a close contact (2.1–2.3 Å) between $H\text{-}1^G$ and $H\text{-}3^{GN}$, which should be observed for the conformations **B** and **C**. It is to be borne in mind that although a powerful method to support highly populated conformations, multiple conformations can, however, only be observed by NMR if the conformational change is fast. In fact, the local minimum found by Peters and co-workers (25) 7.3 kcal mol^{-1} above the global minimum that should have given a NOE signal corresponding to a 2 Å contact between $H\text{-}6^F$ and NAc^{GN} could not be experimentally observed. In contrast, a second local minimum found in the same study 8.3 kcal mol^{-1} above the global minimum was supported by NMR data (25).

Even though the additional conformational families that were described above have not, so far, been supported by experimental evidence, it is clear that the stochastic search method applied to the modeling of trisaccharide **5** reliably identified the lowest energy conformation generally found computationally and supported experimentally for the Le^x determinant. Thus, this search method was applied to the modeling of trisaccharides **7**–**9** to obtain an accurate description of the lowest energy conformations of these analogues. Stochastic conformational searches of analogues **7**–**9** (Fig. 3) led to fewer conformers than that obtained for the Le^x trisaccharide. In fact, in a 3 kcal mol^{-1} window from the global minima, three conformational families were found for analogue **7**, one for analogue **8**, and two for analogue **9**. When defined by the Φ, Ψ torsional angles, as reported in Table 5, the lowest energy conformations obtained for analogues **7** and **8** (entries 1 and 4, respectively) are similar to that obtained for the Le^x trisaccharide reported in Table 3, entry 1. Thus replacing the *N*-acetylglucosaminyl or galactosyl residues by glucose did not result in a large conformational change in the trisaccharide. In addition, the other two conformational families identified for analogue **7** (**C** and **E**, Table 5, entries 2 and 3) were also found in the Le^x conformational search. In contrast, substitution of the fucosyl by a rhamnosyl residue as in analogue **9** resulted in a dramatic change in the conformation of the trisaccharide. As reported in Table 5 (entries 5 and 6), two new conformational families (**H** and **I**) were identified. When comparing the global minimum obtained for **9** (**H**) with that calculated for Le^x (**A**), the rhamnosyl residue ($\Phi^2 = –102°$, $\Psi^2 = 150°$) assumes essentially the same orientation as the fucosyl residue ($\Phi^2 = –62°$, $\Psi^2 = 146°$), while the galactosyl residue occupies a drastically different orientation shown by the value of the Ψ torsional angle (Ψ^1 (**A**) = –107°, Ψ^1 (**H**) = 82°). In contrast, when comparing the local minimum **I** given in Table 5 (entry 6) with the Le^x global minimum **A**, we observe that the galactosyl residues assume the same orientation ($\Phi^1 = –76°$, $\Psi^1 = –106°$ vs. $\Phi^1 = –68°$, $\Psi^1 = –107°$), while the rhamnosyl residue in **I** assumes a different orientation from the fucosyl residue in **A** ($\Phi^2 = –161°$, $\Psi^2 = 96°$ vs. $\Phi^2 = –62°$, $\Psi^2 = –146°$). Interestingly, this conformation is very similar to the conformer found 8.3 kcal mol^{-1} above the global minimum in Le^x and described in Table 2 (entry 1). Thus, as shown in Fig. 8, the stacking that exists between the galactosyl and fucosyl residues in the Le^x trisaccharide is maintained when either galactosyl or *N*-acetylglucosamine are replaced by glucosyl residues but is abolished when the fucosyl residue is replaced by a rhamnosyl residue. Non-stacked rotamers were also identified by Csonka and Sosa (31) in their ab initio conformational study of Lewis X analogues **10** and **11** shown in Fig. 9. The global minima found for these two analogues had the usual stacked conformation between the galactose and fucose residues. Non-stacked rotamers of low energy were frequent, however, amongst the

© 2002 NRC Canada

Fig. 8. Electrostatic potential map for the global minimum of (A) the Le^x trisaccharide; (B) analogue **7**; (C) analogue **8**; (D) analogue **9**.

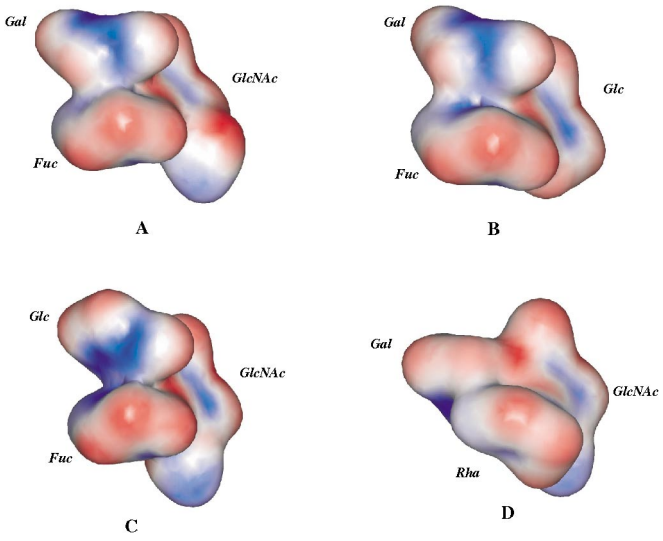

rotamers of the 1,2-ethandiol analogue **10**, while one such rotamer was found 2.3 kcal mol^{-1} above the global minimum for analogue **11**. Thus, the study by Csonka and Sosa (31) shows that while an increased flexibility around the ethanediol linker in analogue **10** allows access to non-stacked conformations, stacking between the galactosyl and fucosyl residues constitute a stabilizing force since the stacked conformation remains the lowest energy one. In our results, the absence of stacked conformations for analogue **9** likely results from the loss of this stabilizing force.

Conclusions

The stochastic conformational search was used successfully to model the Le^x trisaccharide since it accurately identified a lowest energy conformation of the Le^x determinant in agreement with previous computational studies (21–26). This global minimum fits the conformation of Le^x deduced experimentally in the solid state by X-ray crystallography (27) and in solution by NMR measurements (23, 25).

Through the random rotation of all bonds, which was typically repeated a few hundred thousand times for each molecule, the stochastic search is a highly efficient method for mapping all conformational minima. The twelve conformers found for Le^x within 3 kcal mol^{-1} of the global minimum were efficiently clustered using metric scaling (29) on heavy atoms permitting the visual identification of six major conformational families, five of which were previously unknown. Although these new conformational families are not yet supported by the experimental data collected so far for Le^x, they were shown to be energetically reasonable. It has been shown (19) that the active conformations of Le^x that bound to isolectin A from *Lotus tetragonolus* and to *Aleuria Aurantia* were radically different from the assumed rigid global minimum of Le^x. Interestingly, one of these conformations was not supported experimentally (25) in the unbound state. The identification of these new conformational families using the stochastic search could, therefore, constitute an important finding to help the discovery of new active conformations of the Le^x determinant.

Fig. 9. Lewis X analogues studied by Csonka and Sosa (31) using ab initio calculations with HF/6–31G(d).

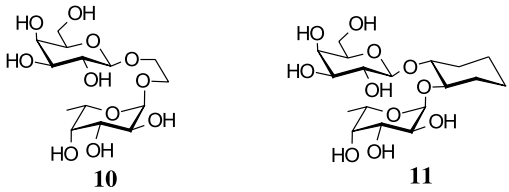

Studies of oligosaccharides binding to biological receptors require a good knowledge of the conformations that oligosaccharide in question can adopt. In contrast, it is reasonable to expect that most antibodies generated during an immune response induced against an oligosaccharide (like any of analogues **1**–**4**) will target its most populated conformations in the unbound state. Thus, to save on unnecessary synthetic efforts, our research required that the stochastic search used here accurately model the lowest energy conformers of the Le^x determinant and its analogues. Since it gave a reliable description of the lowest energy conformation of the Le^x trisaccharide, which is supported experimentally, we can use the global minima found for analogues **7**–**9** by the stochastic search to gain insight on the conformational differences between these analogues and the Le^x determinant. Substituting the galactose or *N*-acetylglucosamine residues by glucose did not alter the overall conformation of the global minimum. In contrast, substitution of the fucose residue by rhamnose led to different global and local minima in which stacking of the galactose and rhamnose residues was no longer observed as is the case for the galactose and fucose residues in Le^x. It is interesting to note that one of the conformations obtained for analogue **9** is in fact very similar to the conformations assumed by Le^x in its bound form to isolectin A from *Lotus tetragonolus* and to *Aleuria Aurantia* agglutinin and shown in Table 2, entries 2 and 3 (25).

The electrostatic potential surfaces of Le^x and the three analogues studied here are displayed in Fig. 8. These results indicate that the subtle changes that result from the substitution of the galactose or *N*-acetylglucosamine residues by a glucose unit could be sufficient to abolish the cross-reactivity of hexasaccharides **2** and **3** with the Le^x determinants displayed on normal cells. These substitutions, however, do not induce a drastic conformational change that would also surely abolish cross-reactivity based on common internal epitopes between these analogues and the cancer associated dimLe^x antigen. In contrast, the large conformational change imposed by replacing the fucosyl residue by a rhamnosyl unit in trisaccharide **9** will likely be reflected in the conformation of hexasaccharide **4**. Thus, we can expect that analogue **4** will also loose major internal epitopes displayed by the tumour associated hexasaccharide dimLe^x and, therefore, will not be cross-reactive with this antigen. We conclude from this study that only hexasaccharide **2** and **3** constitute interesting candidates to develop dimLe^x-based anti-cancer vaccines.

© 2002 NRC Canada

Acknowledgments

The authors would like to thank Dr. Anne Imberty (CERMAV, Grenoble, France) and her colleagues for providing the Le^x crystal structure coordinates.

References

1. S. Hakomori and R.W. Jeanloz. J. Biol. Chem. **239**, 3606 (1964).
2. S. Hakomori, J. Koscielak, K.J. Bloch, and R.W. Jeanloz. J. Immunol. **98**, 31 (1967).
3. S.J. Danishefsky and J.R. Allen. Angew. Chem. Int. Ed. **39**, 837 (2000).
4. Z.G. Wang, L.J. Williams, X.-F. Zhang, A. Zatorski, V. Kudryashov, G. Ragupathi, M. Spassova, W. Bornmann, S.F. Slovin, H.I. Scher, P.O. Livingston, K.O. Lloyd, and S.J. Danishefsky. Proc. Natl. Acad. Sci. U.S.A. **97**, 2719 (2000).
5. S.F. Slovin, G. Ragupathi, S. Alduri, G. Ungers, K. Terry, S. Kim, M. Spassova, W.G. Bornmann, M. Fazzari, L. Dantis, K. Olkiewicz, K.O. Lloyd, P.O. Livingston, S.J. Danishefsky, and H.I. Scher. Proc. Natl. Acad. Sci. U.S.A. **96**, 5710 (1999).
6. T. Toyokuni and A.K. Singhal. Chem. Soc. Rev. 231 (1995).
7. C.A. King and F.K. Stevenson. Chem. Ind. **7**, 266 (1997).
8. P.O. Livingston, G.J. Ritter, H.F. Oettegen, and L.J. Old. U.S.A. Patent 5, 102, 663 (1992).
9. Y. Fukushi, S.-I. Hakomori, E. Nudelman, and N. Cochran. J. Biol. Chem. **259**, 4681 (1984).
10. Y. Fukushi, S.-I. Hakomori, and T. Shepard. J. Exp. Med. **159**, 506 (1984).
11. Y. Fukushi, R. Kannagi, S.-I. Hakomori, T. Shepard, B.G. Kulander, and J.W. Singer. Cancer Res. **45**, 3711 (1985).
12. S.H. Itzkowitz, M. Yuan, Y. Fukushi, A. Palekar, P.C. Phelps, A.M. Shamsuddin, B.T. Trump, S.-I. Hakomori, and Y.S. Kim, Cancer Res. **46**, 2627 (1986).
13. H. Nakasaki, T. Mitomi, T. Noto, K. Ogoshi, H. Hanaue, Y. Tanaka, H. Makuuchi, H. Clausen, and S.-I. Hakomori. Cancer Res. **49**, 3662 (1989).
14. S. Zhang, H.S. Zhang, C. Cordon-Cardo, V.E. Reuter, A.K. Singhal, K.O. Lloyd, and P.O. Livingston. Int. J. Cancer, **73**, 50 (1997).
15. Molecular operating environment. Version 2001.01. Chemical Computing Group Inc., Montreal, Canada.
16. T.A. Halgren. J. Comp. Chem. **17**, 490 (1996).
17. W.C. Still, A. Tempczyk, R.C. Hawley, and T. Hendrickson. J. Am. Chem. Soc. **112**, 6127 (1990).
18. D. Qiu, P.S. Shenkin, F.P. Hollinger, and W.C. Still. J. Phys. Chem. A, **101**, 3005 (1997).
19. M. Schaefer and M.A. Karplus. J. Phys. Chem. **100**, 1578 (1996).
20. S. Pérez, A. Imberty, S.B. Engelsen, G. Gruza, K. Mazeau, J. Jimenez-Barbero, A. Poveda, J.-F. Espinosa, B.P. van Eyck, G. Johnson, A.D. French, M.L.C.E. Kouwijzer, P.D.J. Grootenuis, A. Bernardi, L. Raimondi, H. Senderowitz, V. Durier, G. Vergoten, and K. Rasmussen. Carbohydr. Res. **314**, 141 (1998).
21. H. Thogersen, R.U. Lemieux, K. Bock, and B. Meyer. Can. J. Chem. **60**, 44 (1982).
22. R.U. Lemieux, K. Bock, L.T.J. Delbaere, S. Koto, and V.S.R. Rao. Can. J. Chem. **58**, 631 (1980).
23. K.E. Miller, C. Mukhopadhyay, P. Cagas, and A. Bush. Biochemistry, **31**, 6703 (1992).
24. A. Imberty, E. Mikros, J. Koca, R. Mollicone, R. Oriol, and S. Pérez. Glycoconj. J. **12**, 331 (1995).
25. T. Haselhorst, T. Weimar, and T. Peters. J. Am. Chem. Soc. **123**, 10 705 (2001).
26. G.I. Csonka, C.P. Sosa, and I.G. Csizmadia. J. Phys. Chem. **104**, 3381 (2000).
27. S. Pérez, N. Mouhous-Riou, N.E. Nifant'ev, Y.E. Tsvetkov, B. Bachet, and A. Imberty. Glycobiol. **6**, 537 (1996).
28. D.M. Ferguson and D.J. Raber. J. Am. Chem. Soc. **111**, 4371 (1989).
29. M. Feher and J.M. Schmidt. J. Chem. Inf. Comp. Sci. **41**, 346 (2001).
30. A. Imberty and S. Pérez. Chem. Rev. **100**, 4567 (2000).
31. G.I. Csonka and C.P. Sosa. J. Phys. Chem. **104**, 7113 (2000).

© 2002 NRC Canada

Thermodynamic binding studies of cell surface carbohydrate epitopes to galectins-1, -3, and -7: Evidence for differential binding specificities

Nisar Ahmad, Hans-J. Gabius, Herbert Kaltner, Sabine André, Ichiro Kuwabara, Fu-Tong Liu, Stefan Oscarson, Thomas Norberg, and C. Fred Brewer

Abstract: Binding of a series of sialylated and non-sialylated cell surface carbohydrates to bovine heart galectin-1, recombinant murine galectin-3, and recombinant human galectin-7 was investigated by isothermal titration microcalorimetry (ITC) and hemagglutination inhibition measurements. Galectin-7 shows nearly equal affinities for lactose and Galβ(1–4)GlcNAc (LacNAc-II). Galectin-7, however, displays six- and 11-fold weaker affinity for LacNAc-II compared with galectins-1 and -3, respectively. The affinity of galectin-7 for LacNAc-II containing oligosaccharides is also weaker than the other two galectins. ITC measurements show that all three galectins bind to di- and trimeric oligomers of LacNAc-II, which are epitopes found in poly-*N*-acetyllactosamine chains of glycoprotein receptors, with affinity constants similar to that of LacNAc-II. The binding valencies of the di- and trimeric LacNAc-II oligomers were observed to be one from ITC measurements, indicating formation of 1:1 complexes with all three galectins. Thus, galectins-1, -3, and -7 all possess binding sites that primarily accommodate one LacNAc-II moiety per monomer of protein. Sialylated oligosaccharides show different specificities for the three galectins. While 2,3-sialyl LacNAc-II binds to all three galectins, 2,6-sialyl LacNAc-II fails to bind to any of the galectins; 2,6-sialylated diLacNAc binds well to galectin-3 and galectin-7, but only weakly to galectin-1. Similar results are obtained with 2,6-sialyl lacto-*N*-neo-tetraose, which has a reducing end lactose moiety. Thus, unlike galectin-1, which predominantly recognizes non-reducing terminal LacNAc-II residues in oligosaccharides, galectins-3 and -7 recognize both non-reducing terminal LacNAc-II residues as well as internal LacNAc-II and lactose residues in sialylated and non-sialylated oligosaccharides.

Key words: isothermal titration microcalorimetry, galectins, binding specificities, lectins, carbohydrates.

Résumé : Faisant appel à des titrages microcalorimétriques isothermes (TMI) et à des mesures d'inhibition de l'hémagglutination, on a étudié la fixation d'une série d'hydrates de carbones de surfaces cellulaires sialylées et non sialylées à la galectine-1 cardiaque bovine, à la galectine-3 de la murine recombinante et à la galectine-7 humaine recombinante. La galectine-7 présente des affinités pratiquement égales pour le lactose et la Galβ(1-4)GlcNAc (LacNAc-II). Toutefois, la galectine-7 présente des affinités pour le LacNAc-II qui sont respectivement six et onze fois plus faibles que celles des galectines-1 et -3. L'affinité de la galectine-7 pour les oligosaccharides contenant du LacNAc-II est aussi plus faible que celle des deux autres galectines. Des mesures de TMI montrent que les trois galectines se lient aux oligomères di- et trimères du LacNAc-II, des épitopes que l'on retrouve dans les chaînes de poly-*N*-acétyllactosamine des récepteurs glycoprotéiniques; les constantes d'affinité sont semblables à celles observées avec le LacNAc-II. Sur la base des TMI, on a déterminé les valences des liaisons des oligomères di- et trimères du LacNAc-II et elles indiquent qu'il y a formation de complexes 1:1 avec chacune des trois galectines. Les galectines-1, -3 et -7 possèdent toutes des sites de fixation qui accommodant en première approximation une portion de LacNAc-II par monomère de protéine. Les oligosaccharides sialylés présentent des spécificités différentes pour les trois galectines. Alors que la 2,3-sialyle LacNAc-II se fixe aux trois galectines, le 2,6-disialyle diLacNAc se fixe bien à la galectine-3 et à la galectine-7, elle ne se fixe que faiblement à la galectine-1. On a obtenu des résultats semblables avec le 2,6-sialyl lacto-*N*-néo-tétraose qui comporte un lactose avec une partie réductrice. Donc, contrairement à la galectine-1 qui reconnaît de façon prédominante les oligosaccharides portant des résidus LacNAc-II avec une extrémité non réductrice,

Received 28 March 2002. Published on the NRC Research Press Web site at http://canjchem.nrc.ca on 28 August 2002.

Dedicated to the memory of Professor Raymond U. Lemieux.

N. Ahmad and C.F. Brewer.[1] Departments of Molecular Pharmacology, and Microbiology and Immunology, Albert Einstein College of Medicine, Bronx, NY 10461, U.S.A.
H.-J. Gabius, H. Kaltner, and S. Andre. Institut für Physiologische Chemie, Ludwig-Maximilians Universität München, 80539 München, Germany.
I. Kuwabara and F.-T. Liu. Department of Dermatology, University of California, Davis, CA 95817, U.S.A.
S. Oscarson. Department of Organic Chemistry, Stockholm University, S-106 91, Stockholm, Sweden.
T. Norberg. Department of Chemistry, Swedish University of Agricultural Sciences, S-750 07, Uppsala, Sweden.

[1]Corresponding author (e-mail: brewer@aecom.yu.edu).

 DOI: 10.1139/V02-162 © 2002 NRC Canada

la galectine-3 et la galectine-7 reconnaissent les deux résidus LacNAc-II avec une extrémité non réductrice ainsi que les résidus lactose et LacNAc-II internes des oligosaccharides sialylés et non sialylés.

Mots clés : calorimétrie à titration isotherme, galectines, spécificités des liaisons, lectines, glucides.

[Traduit par la Rédaction]

Introduction

Galectins are a family of Ca^{2+}-independent animal lectins defined by common consensus sequences and structures, with specificities for β-Gal and LacNAc-II (Fig. 1) residues in oligosaccharides (1–3). Since they are also expressed in nematodes and porifera, they are of ancient origin with conservation of their structure for more than a billion years (2, 4). Fourteen members of the family have currently been identified in mammals and designated galectins-1–14, and more are likely to be found since homologies have already been reported in the literature (4–6). Indeed, there may be a galectin superfamily with some members not possessing lectin-like properties, similar to the situation with C-type lectins (7, 8). For mammalian galectins-1–14, progress has been made in determining some of their biological activities which include roles in the regulation of inflammation, and modulators of cell adhesion, cell proliferation, and cell death (8, 9).

The structures of the mammalian galectins can be identified as prototypes (galectins-1, -2, -5, -7, -10, and probably -11, -13, and -14) that exist as monomers or homodimers consisting of one carbohydrate-recognition domain (CRD); a chimera type (galectin-3) that contains a non-lectin *N*-terminal short sequence segment followed by 8–129 amino acid long collagen-like repeats connected to the C-terminal of about 140 amino acids; and a tandem-repeat type (galectins-4, -6, -8, and -9) composed of two CRD domains in a single polypeptide chain connected by a linker peptide (1–3). The X-ray crystal structures of galectin-1 (10, 11), galectin-2 (12), galectin-7 (13), galectin-10 (14), and CRD domain of galectin-3 (15) have been reported (6). Studies of the carbohydrate binding specificities of the galectins have been largely restricted to galectin-1 (16, 17) and galectin-3 (17–19), with conflicting data reported for galectin-10, the Charcoat–Leyden crystal protein (14, 20). These studies generally show specificities of the galectins for LacNAc-II residues, with higher affinities reported for some naturally occurring oligosaccharides. Indeed, there is evidence that the galectins recognize polylactosamine chains with high affinity (cf. 21, 22), and that these chains are receptor sites on the surface of cells (cf. 23). However, thermodynamic data for mammalian galectins binding to LacNAc-II oligomers and sialyl LacNAc-II oligomers has not been reported.

Considerable insight has been gained on the biological properties of specific galectins. Galectin-1 has been implicated in various biological processes in multicellular organisms including inflammation, development, mRNA splicing, differentiation, and cell adhesion (1–3). Galectin-1 has also recently been demonstrated to play a role in the immune system by mediating apoptosis of activated T cells with CD7 as target (24). Galectin-3 has also been shown to exhibit roles in regulating inflammation, cell growth, and cell adhesion (3, 25). Galectin-3, unlike galectin-1, possesses anti-apoptotic

Fig. 1. Structures of carbohydrates.

Lactose - Galβ(1-4)Glc~OH

Methyl β-Lactose - Galβ(1-4)Glcβ(1-)OCH_3

LacNAc-I - Galβ(1-3)GlcNAc~OH

LacNAc-II - Galβ(1-4)GlcNAc~OH

Methyl β-LacNAc-I - Galβ(1-3)GlcNAcβ(1-)OCH_3

Methyl β-LacNAc-II - Galβ(1-4)GlcNAcβ(1-)OCH_3

ThiodiGal - Galβ(1-1)βGal

DiLacNAc - Galβ(1-4)GlcNAcβ(1-3)Galβ(1-4)GlcNAc~OH

TriLacNAc - Galβ(1-4)GlcNAcβ(1-3)Galβ(1-4)GlcNAcβ(1-3)Galβ(1-4)GlcNAc~OH

Lacto-N-tetraose - Galβ(1-3)GlcNAcβ(1-3)Galβ(1-4)Glc~OH

Lacto-N-neo-tetraose - Galβ(1-4)GlcNAcβ(1-3)Galβ(1-4)Glc~OH

2,3-Sialyl LacNAc - Neu5Acα(2-3)Galβ(1-4)GlcNAc~OH

2,6-Sialyl LacNAc - Neu5Acα(2-6)Galβ(1-4)GlcNAc~OH

2,6-Sialyl DiLacNAc - Neu5Acα(2-6)Galβ(1-4)GlcNAcβ(1-3)Galβ(1-4)GlcNAc~OH

2,6-Sialyl Lacto-N-neo-tetraose - Neu5Acα(2-6)Galβ(1-4)GlcNAcβ(1-3)Galβ(1-4)Glc~OH

"Trisaccharide" - GlcNAcβ(1-3)Galβ(1-4)Glc~OH

effects in various cells, and its expression has been shown to correlate with the metastatic potentials of certain cancers (26). Galectin-7 is reported to be marker for stratified epithelia (27). It has been shown that the galectin-7 gene is a transcriptional target of the tumor suppressor protein p53 and may play a role in the proapoptotic function of p53 (28). Concerning malignant cells, expression of galectin-7 is elevated in chemically induced rat mammary carcinomas (29), and its mRNA could be detected frequently in human breast and colon cancer cell lines (30). Galectin-7 thus appears to be another member of the galectin family with regulatory activity for cell survival. Diversification within the galectin family intimates that functional aspects will not simply be redundant. Besides the different CRD presentation in tandem-repeat prototype vs. chimera-type galectins, the carbohydrate binding properties might differ. Hence determining the fine carbohydrate binding specificities of these galectins is important in understanding their biological functions.

In the present report, we report hemagglutination inhibition data and thermodynamic data obtained by isothermal titration microcalorimetry (ITC) for binding of bovine heart galectin-1, recombinant murine galectin-3, and recombinant human galectin-7 to LacNAc-I and -II and related cell surface carbohydrate epitopes including di- and trimeric oligomers of LacNAc-II, and sialylated analogs of LacNAc-II and diLacNAc. The results demonstrate important differences in the binding specificities of the three galectins.

© 2002 NRC Canada

Experimental

Materials

Bovine heart was purchased from Pel-Freez Biologicals. Fetuin, cyanogen bromide, LacNAc-II, lactose, methyl β-lactoside, galactose, methyl β-galactopyranoside, dithiogalactopyranoside (ThiodiGal), lacto-*N*-tetraose, lacto-*N*-neotetraose, 2,3-sialyl LacNAc, 2,6-sialyl LacNAc, and 2,6-sialyl-lacto-*N*-neo-tetraose (Fig. 1) were obtained from Sigma Chemical Co. LacNAc-I and methyl β-LacNAc-I were obtained from Toronto Research Chemicals. Methyl β-LacNAc-II, DiLacNac, TriLacNAc, "trisaccharide," and 2,6-sialyl DiLacNAc (Fig. 1) were chemically and (or) enzymatically synthesized and will be reported elsewhere. All other reagents were of analytical grade.

Purification and expression of the proteins

Fetuin was desialylated and purified as previously described (31). Asialofetuin-Sepharose was prepared by following a published procedure (32). Bovine heart lectin (BHL) (galectin-1) was purified using the procedure for the isolation of calf spleen galectin-1 (31). SDS-PAGE of the affinity purified lectin was found to contain one additional band. Affinity purified lectin was fractionated into two clear peaks (I and II) by gel chromatography using a Sephadex G-50 column in the presence of 0.05 mM lactose. The 2nd peak corresponded to BHL and was found to be pure by SDS-PAGE. Fractions containing the 2nd peak were pooled, extensively dialyzed against PBS containing 10 mM β-mercaptoethanol, and then stored at 4°C.

Murine galectin-3 and human galectin-7 were purified after recombinant expression, using the plasmid prCBP35, kindly provided by J.L. Wang (East Lansing, MI) and *E. coli* JA221 cells (33) or pQE60-hGal-7 (establishment of a NcoI cleavage site required to switch from Ser^2 to Ala^2 in the protein sequence) and *E. coli* M15{pREP4} cells. Both proteins showed single bands by SDS-PAGE.

Monomeric lectin concentrations were determined spectrophotometrically at 280 nm using the specific extinction coefficients of the three proteins ($E^{1\%}_{1cm}$). $E^{1\%}_{1cm}$ values of 5.4, 6.1, and 5.5 were used for BHL, galectin-3, and galectin-7, respectively, as determined from ITC experiments. Molecular masses of the galectins were determined by MALDI and electrospray ionization mass spectrometry and were found to be 14 500 Da for galectin-1, 27 500 Da for galectin-3, and 14 600 Da for galectin-7. The carbohydrate concentration was measured by the phenol–sulfuric acid method (34, 35).

Hemagglutination inhibition assays

Hemagglutination assays were performed by serial dilution technique (36). Rabbit erythrocytes (3% (v/v)) were prepared in 20 mM sodium phosphate buffer containing 0.15 M NaCl, pH 7.2, whereas the sugar and protein solutions were prepared in 20 mM sodium phosphate buffer containing 0.15 M NaCl and 10 mM β-mercaptoethanol, pH 7.2. The final concentration of β-mercaptoethanol in the assay was 5 mM.

Isothermal titration microcalorimetry

Isothermal titration calorimetry (ITC) experiments were performed using an MCS Microcalorimeter from Microcal Inc. (Northampton, MA). A typical titration profile is shown in Fig. 2. Protein and carbohydrate samples were prepared in 20 mM sodium phosphate buffer containing 0.15 M NaCl and 10 mM β-mercaptoethanol, pH 7.2. The protein solution (2.5 mL) was taken in a syringe and loaded into the ITC sample cell (cell volume = 1.34 mL). Reducing agents in the buffer were found to increase the time for the baseline stabilization, which varied from 3–6 h. The effect of DTT on baseline stabilization was greater than β-mercaptoethanol. Degassing of protein solutions and using fresh buffers (maximum 12 h storage time) was found to decrease the time for baseline stabilization from 4 to 1 h. After the baseline had stabilized, 4-μL injections of the carbohydrate solution were added from the computer-controlled 100-μL rotating syringe (400 rpm) into the protein solution; exothermic heat changes accompanying the additions were recorded. The time period between the two consecutive injections was fixed at 4 min to allow the exothermic peak to return to the baseline. Control experiments were carried out by making identical injections into the cell-containing buffer with no protein. The experimental data were fitted using software ORIGIN TM Version 2.9 supplied by Microcal, with ΔH (enthalpy change in kcal mol^{-1}), K_a (association constant in M^{-1}), and n (number

Fig. 2. ITC profile of galectin-3 (69 μM) titrated with 2,6-sialyl DiLacNAc (6.0 mM) in pH 7.2 buffer at 300 K.

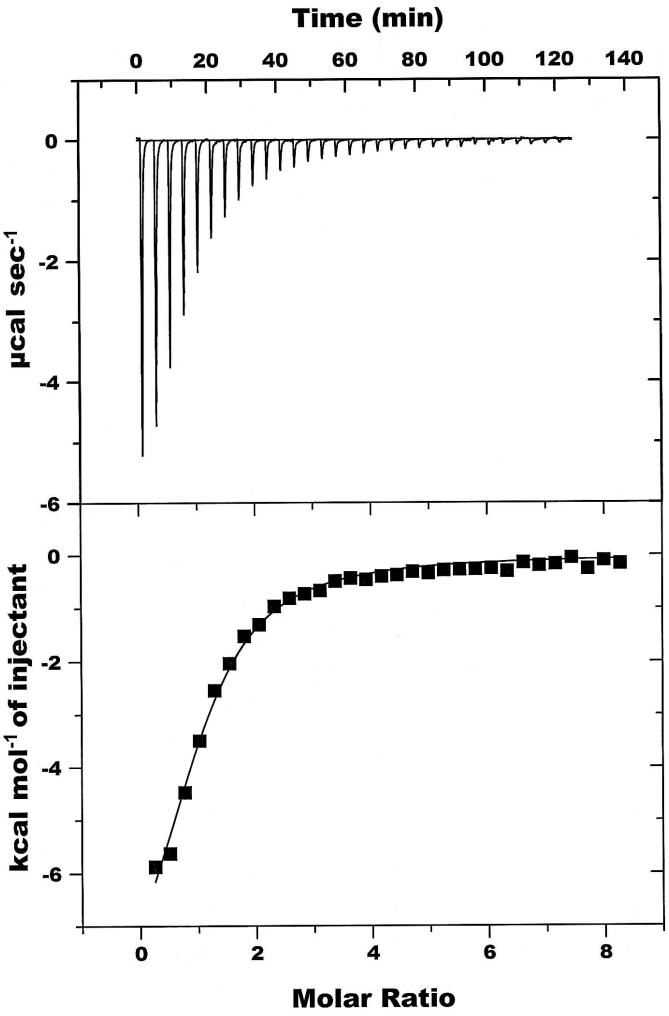

© 2002 NRC Canada

of binding sites per monomer) as adjustable parameters. The value of unitless constant c ($c = K_a M_t n$, where M_t is the initial protein concentration, K_a is the association constant in M^{-1}, and n is the number of binding sites per monomer of protein), is of great importance since it determines the shape of the binding isotherm (37). All the experiments were performed with c values of $1 < c < 200$. The instrument was calibrated using the calibration kit containing ribonuclease A (RNase A) and cytidine 2′-monophosphate supplied by the manufacturer. Thermodynamic parameters were calculated by using the standard equation, $\Delta G = \Delta H - T\Delta S = -RT \ln K_a$, where ΔG, ΔH, and ΔS are the changes in the free energy, enthalpy, and entropy of binding, respectively. T is the absolute temperature in kelvin, and R = 1.98 cal mol^{-1} K^{-1}. Different batches of recombinant murine galectin-3 were found to contain varying amounts of inactive molecules, with n values less than 1.0 (the lowest value of n was 0.6). These galectin-3 samples were purified by passage over an ASF-Sepharose affinity column until the n value was close to 1.0, using LacNAc-II as the titrating sugar in ITC measurements. Galectin-3 samples were tested with LacNAc-II before and after an ITC experiment with a new saccharide.

Results and discussion

Table 1 shows ITC thermodynamic data at two temperatures (287 and 300 K) for the binding of bovine heart galectin-1, murine recombinant galectin-3, and human recombinant galectin-7 to the carbohydrates in the present study. Table 2 shows hemagglutination inhibition data at room temperature for the three galectins. The most immediate conclusion from the data in both tables is that galectin-7 possesses weaker affinity for carbohydrates presenting LacNAc-II as the primary binding epitope, relative to the other two galectins. For example, ITC data in Table 1 show that the K_a value for galectin-7 binding LacNAc-II is nearly sixfold lower than the corresponding value for galectin-1, and nearly 11-fold weaker than that of galectin-3. Interestingly, the enthalpy of binding (ΔH) for galectin-7 to LacNAc-II (–11.8 kcal mol^{-1}) is greater than that of galectin-1 (–9.2 kcal mol^{-1}) and galectin-3 (–7.5 kcal mol^{-1}). Conversely, the entropy of binding ($-T\Delta S$) for galectin-7 to LacNAc-II is more unfavorable (7.4 kcal mol^{-1}) than that of galectin-1 (3.7 kcal mol^{-1}) and galectin-3 (1.6 kcal mol^{-1}). Because of the weaker affinity of galectin-7 for carbohydrates, most of the ITC binding data for galectin-7 was obtained at 287 K and compared with similar data for galectins-1 and -3 at the same temperature.

Thermodynamics of binding of disaccharides to galectins-1 and -3

The thermodynamics of binding of bovine heart galectin-1 and recombinant murine galectin-3 to simple disaccharides are shown in Table 1. The disaccharide LacNAc exists as two isomers in nature (LacNAc-I and -II), which differ in their linkage between Gal and GlcNAc. LacNAc-I possesses a β(1–3) linkage and LacNAc-II possesses a β(1–4) linkage. Previous studies of the binding of human galectin-1 (17) and rat galectin-3 (38) to an asialofetuin-Sepharose column showed similar inhibitory activities for LacNAc-I and LacNAc-II. ITC data at 300 K in Table 1 reveals that there is little difference in the K_a values of bovine heart galectin-1 for LacNAc-I (0.90×10^4 M^{-1}) vs. LacNAc-II (1.1×10^4 M^{-1}); the enthalpies of binding (ΔH) are –7.9 and –9.2 kcal mol^{-1}, respectively. Likewise, murine galectin-3 shows little difference in its K_a values for LacNAc-I (0.82×10^4 M^{-1}) vs. LacNAc-II (1.9×10^4 M^{-1}), with ΔH values of –6.4 and –7.5 kcal mol^{-1}, respectively. These results thus demonstrate similar affinities of both galectins for type I and II isomers of LacNAc. These results agree with those of Schwarz et al. (39) for bovine spleen galectin-1, and Surolia and co-workers (21) for recombinant human galectin-3.

Galectin-1 from a number of sources (40–42) has previously been shown to bind to β-thiodigalactopyranoside (ThiodiGal) with affinities comparable to LacNAc-II. Galectin-3 from human (17) and rat lung (38) has also been shown to bind to ThiodiGal. ITC data in Table 1 shows that bovine heart galectin-1 and recombinant murine galectin-3 bind to ThiodiGal at 300 K with nearly the same K_a values as LacNAc-II (factor of two difference for galectin-1). The enthalpies of binding ($-\Delta H$) of galectin-1 to the two disaccharides are similar, as are the $-\Delta H$ values for galectin-3 binding the two sugars. Thus, bovine spleen galectin-1 and recombinant murine galectin-3 share similar binding thermodynamics to ThiodiGal. These results are similar to those recently reported by Surolia and co-workers (21) for recombinant human galectin-3.

Binding of LacNAc-II oligomers to galectins-1 and -3

The thermodynamics of binding at 300 K of bovine heart galectin-1 and murine galectin-3 to dimeric (DiLacNAc) and trimeric (TriLacNAc) oligomers of LacNAc-II are shown in Table 1. Galectin-1 possesses K_a values of 0.74×10^4 and 2.2×10^4 M^{-1} for Di- and TriLacNAc, respectively, as compared with 1.1×10^4 M^{-1} for LacNAc-II. Hence, the K_a values for Di- and TriLacNAc are similar to that of LacNAc-II. The ΔH values for the three carbohydrates are also similar: –9.2 kcal mol^{-1} for LacNAc-II; –11.4 kcal mol^{-1} for DiLacNAc; and –10.1 kcal mol^{-1} for TriLacNAc. Furthermore, the n values for all three carbohydrates, the number of binding sites per monomer of protein, are all close to one, suggesting that all three oligosaccharides bind to the same site in the protein. The n values are also an indication of the valencies of the carbohydrates (43). Thus, all three oligosaccharides are monovalent, even though Di- and TriLacNAc have two and three LacNAc-II residues, respectively. Hemagglutination inhibition data with Di- and TriLacNAc also shows similar affinities of galectin-1 for all three carbohydrates (Table 2).

These results suggest that galectin-1 possesses a binding site that recognizes primarily one LacNAc residue, even when binding oligomers of LacNAc-II. ^{13}C NMR studies by Pierce and co-workers (44) of the binding of a C2S galectin-1 mutant from Chinese hamster ovary cells to specifically labeled oligomers of LacNAc-II also concluded that galectin-1 bound primarily to the non-reducing terminal LacNAc-II residues of the oligomers. The X-ray crystal structure of bovine spleen galectin-1 in complex with LacNAc-II also shows only one mole of the disaccharide bound to the protein (11).

Lacto-*N*-tetraose, which has the structure Galβ(1–3)GlcNAcβ-(1–3)Galβ(1-4)Glc, has previously been shown to bind well

© 2002 NRC Canada

Table 1. Thermodynamic binding parameters of bovine heart galectin-1, murine recombinant galectin-3, and human recombinant galectin-7 with carbohydrates.

Sugars	K_a[a] ($M^{-1}\times10^{-4}$)	$-\Delta H$[b] (kcal mol^{-1})	$-\Delta G$[c] (kcal mol^{-1})	$-T\Delta S$[d] (kcal mol^{-1})	n[e] (sites/monomer)
Bovine heart galectin-1					
Temp = 300 K					
LacNAc-I	0.90	7.9	5.4	2.5	0.97
LacNAc-II	1.1	9.2	5.5	3.7	1.01
ThiodiGal	1.8	9.8	5.8	4.0	1.04
DiLacNAc	0.74	11.4	5.3	6.1	0.94
TriLacNAc	2.2	10.1	5.9	4.2	0.94
Lacto-*N*-tetraose	1.0	9.7	5.5	4.2	0.94
Temp = 287 K					
Lactose	0.61	9.7	5.0	4.7	0.94
LacNAc-II	2.4	8.7	5.7	3.0	0.99
2,3-Sialyl LacNAc	2.3	8.5	5.7	2.8	1.08
Galectin-3					
Temp = 300 K					
LacNAc-I	0.82	6.4	5.3	1.1	0.92
LacNAc-II	1.9	7.5	5.9	1.6	1.01
ThiodiGal	0.98	7.8	5.5	2.3	1.08
DiLacNAc	3.5	8.8	6.2	2.6	1.07
TriLacNAc	6.3	9.8	6.6	3.2	0.92
2,6-Sialyl-DiLacNAc	3.2	9.7	6.2	3.5	0.98
Lacto-*N*-tetraose	2.6	5.0	6.1	1.1	0.95
Temp = 287 K					
LacNAc-II	3.7	9.7	6.0	3.7	0.95
2,3-Sialyl LacNAc	3.3	8.3	5.9	2.4	0.96
2,6-Sialyl lacto-*N*-neotetraose	2.1	6.4	5.6	0.8	1.05
2,6-Sialyl-DiLacNac	4.8	10.1	6.1	4.0	0.94
Trisaccharide[f]	0.88	7.7	5.2	2.5	0.96
Galectin-7					
Temp = 300 K					
Lactose	0.22	10.6	4.6	6.0	1.03
LacNAc-II	0.17	11.8	4.4	7.4	0.99
Temp = 287 K					
ThiodiGal	0.40	10.0	4.7	5.3	1.08
Lactose	0.49	10.5	4.8	5.7	1.02
LacNAc-II	0.63	11.3	5.0	6.3	1.07
DiLacNac	0.74	12.3	5.1	7.2	1.08
TriLacNAc	0.65	11.4	5.0	6.4	1.07

[a]Errors in K_a range from 1–7%.
[b]Errors in ΔH are 1–4%.
[c]Errors in ΔG are less than 2%.
[d]Errors in $T\Delta S$ are 1–7%.
[e]Errors in n are less than 4%.
[f]GlcNAcβ (1-3)Galβ (1-4)Glc.

to human galectin-1 (17). Lacto-*N*-tetraose possesses both a non-reducing terminal LacNAc-I moiety and a non-reducing terminal lactose moiety. Hemagglutination inhibition data demonstrate that bovine heart galectin-1 binds to lacto-*N*-tetraose as well as LacNAc-II (Table 2). ITC analysis shows a K_a value of 1.0×10^4 M^{-1} for galectin-1 binding to lacto-*N*-tetraose (Table 1), which is similar to that of LacNAc-II and DiLacNAc (Table 1). In addition, although there are two potential binding moieties in lacto-*N*-tetraose, the non-reducing terminal LacNAc-I moiety and the reducing internal lactose moiety, the n value for the tetrasaccharide is close to one. These results also support the conclusion that the CRD of bovine heart galectin-1 accommodates only one LacNAc or lactose residue in the above carbohydrates. Similar data were obtained for lacto-*N*-neo-tetraose by hemagglutination inhibition data (Table 2).

Table 1 shows the ITC thermodynamic data of galectin-3 binding to Di- and TriLacNAc. The K_a values for binding LacNAc-II, Di-, and TriLacNAc are 1.9×10^4, 3.5×10^4, and 6.3×10^4 M^{-1}, respectively; the ΔH values are –7.5,

© 2002 NRC Canada

Table 2. Relative inhibitory potencies of different sugars for bovine heart galectin-1 and recombinant murine galectin-3 mediated hemagglutination of rabbit erythrocytes.

Saccharide	Galectin-1[a]	Galectin-3[a]
Lactose	0.2 (2.2)	0.2 (2.2)
LacNAc-I	0.8 (0.51)	0.8 (0.51)
LacNAc-II	1.0 (0.41)	1.0 (0.41)
DiLacNAc	0.7 (0.58)	1.4 (0.29)
TriLacNAc	1.2 (0.35)	2.3 (0.17)
Lacto-*N*-tetraose	1.1 (0.37)	0.6 (0.70)
Lacto-*N*-neo-tetraose	1.2 (0.70)	0.6 (0.70)
2,3-Sialyl LacNAc	0.6 (0.70)	0.6 (0.70)
2,6-Sialyl LacNAc	NI[b] (4.8)	NI[b] (4.8)
2,6 Sialyl DiLacNAc	0.1 (0.39)	1.2 (0.34)
2,6-Sialyl-lacto-*N*-neo-tetraose	0.1 (0.39)	1.6 (0.25)
"Trisaccharide"[c]	NI[b] (3.1)	0.4 (1.0)

[a]With respect to LacNAc-II. The concentration (mM) of sugar required for inhibition is shown in parenthesis.
[b]NI = not inhibitory.
[c]GlcNAcβ (1-3)Galβ (1-4)Glc~OH.

Table 3. Relative inhibitory potencies of different sugars for recombinant human galectin-7 mediated hemagglutination of rabbit erythrocytes.

Saccharides	Relative inhibitory potency[a]
Galactose	0.02 (66)
Methyl β-galactopyranoside	0.02 (86)
Lactose	0.9 (1.8)
Methyl β-lactoside	0.8 (2.0)
LacNAc-I	1.6 (1.0)
Methyl β-LacNAc-I	2.3 (0.7)
LacNAc-II	1.0 (1.6)
Methyl β-LacNAc-II	0.5 (3.3)
ThiodiGal	0.5 (3.5)
Trisaccharide[b]	0.7 (2.3)
DiLacNAc	0.7 (2.3)
TriLacNAc	1.4 (1.2)
Lacto-*N*-tetraose	1.2 (1.4)
Lacto-*N*-neo-tetraose	1.5 (1.1)
2,3-Sialyl LacNAc	0.3 (5.0)
2,6-Sialyl LacNAc	NI[c] (7.2)
2,6-Sialyl lacto-*N*-neo-tetraose	2.1 (0.8)
2,6-Sialyl DiLacNAc	1.2 (1.4)

[a]With respect to LacNAc-II. The concentration (mM) of sugar required for inhibition is shown in parenthesis.
[b]GlcNAcβ (1-3)Galβ (1-4)Glc~OH.
[c]NI = not inhibitory.

–8.8, and –9.8 kcal mol^{-1}, respectively. Hence there is a factor of three increase in the affinity of galectin-3 from LacNAc-II to TriLacNAc, and a 2.3 kcal mol^{-1} increase in $-\Delta H$ values. Hemagglutination inhibition data also support the ITC data for the relative affinities of all three carbohydrates for galectin-3 (Table 2). The *n* values for galectin-3 binding to Di- and TriLacNAc are also close to one (Table 1), as for LacNAc-II, suggesting that all three oligosaccharides bind to the same site in the protein. The X-ray crystal structure of the CRD domain of human galectin-3 (C-terminal end of galectin-3) also shows one lactose molecule bound per monomer of the protein (15). The *n* values of one for Di- and TriLacNAc also indicate that these oligomers are monovalent in binding to galectin-3, even though they possess two and three LacNAc residues, respectively.

Table 1 shows that galectin-3 binds lacto-*N*-tetraose with a K_a value between that of LacNAc-II and DiLacNAc. Interestingly, the ΔH for lacto-*N*-tetraose binding to galectin-3 is much lower (–5.0 kcal mol^{-1}) relative to that of LacNAc-II (–7.5 kcal mol^{-1}) and Di- and TriLacNAc. The *n* value of one for galectin-3 binding lacto-*N*-tetraose indicates that the tetrasaccharide binds to one site in the protein, as observed for the other carbohydrates in Table 1. Similar data were obtained for lacto-*N*-neo-tetraose by hemagglutination inhibition data (Table 2).

Binding of sialylated LacNAc-II analogs

Galectin-1 from a number of sources is known to bind 2,3-sialyl lactose as well as lactose (17, 38, 45). Hemagglutination inhibition data in Table 2 shows that galectin-1 from bovine heart binds to 2,3-sialyl LacNAc as well as to LacNAc-II. Table 1 shows that the K_a value at 287 K for galectin-1 binding to 2,3-sialyl LacNAc (2.3×10^4 M^{-1}) is nearly the same as that for LacNAc-II (2.4×10^4 M^{-1}). Table 1 also shows that the $-\Delta H$ values for galectin-1 binding to the two oligosaccharides (–8.5 and –8.7 kcal mol^{-1}, respectively) are also similar. Galectin-1 from a number of sources is known not to bind to 2,6-sialyl lactose (17, 38). Hemagglutination inhibition data in Table 2 confirm that bovine heart galectin-1 does not bind to 2,6-sialyl LacNAc.

Galectin-3 from rat lung has been shown to bind threefold more weakly to 2,3-sialyl lactose than to lactose (38). Human galectin-3 exhibits nearly the same relative affinities for the two oligosaccharides in the inhibition assay (17). Table 2 presents hemagglutination inhibition data indicating that murine galectin-3 binds 2,3-sialyl LacNAc as well as LacNAc-II. Lack of precipitation of a neogylcoprotein with this sugar epitope (18) is thus not due to insufficient binding. ITC data in Table 1 indicate that the K_a value of 3.3×10^4 M^{-1} for 2,3-sialyl LacNAc at 287 K compared with LacNAc-II (3.7×10^4 M^{-1}) at that temperature for galectin-3. The ΔH values are –8.3 and –9.7 kcal mol^{-1}, respectively, for 2,3-sialyl LacNAc and LacNAc-II indicating that substitution of the non-reducing end Gal unit is tolerated.

Hemagglutination inhibition data in Table 2 shows that murine galectin-3 does not bind to 2,6-sialyl LacNAc, as has been previously demonstrated for this protein from human (17) and rat lung (38).

Since neither galectin-1 nor galectin-3 binds 2,6-sialyl LacNAc, 2,6-sialyl DiLacNAc was synthesized to determine if either galectin could bind to the internal (reducing end) LacNAc-II residue. While hemagglutination inhibition data in Table 2 show that galectin-1 binds 12-fold more weakly to 2,6-sialyl DiLacNAc than to LacNAc-II, galectin-3 binds 2,6-sialyl DiLacNAc as well as LacNAc-II. ITC data in Table 1 confirm these observations by showing that galectin-3 possesses nearly the same K_a value for 2,6-sialyl DiLacNAc (3.2×10^4 M^{-1}) as for LacNAc-II (1.9×10^4 M^{-1}). These results indicate binding of galectin-3 but not galectin-1 to the reducing LacNAc residue of 2,6-sialyl DiLacNAc.

© 2002 NRC Canada

Similar results for galectin-3 binding to 2,6-sialyl lacto-*N*-neo-tetraose were obtained. 2,6-Sialyl lacto-*N*-neo-tetraose differs from 2,6-sialyl DiLacNAc in having a type I LacNAc moiety at the non-reducing end of the molecule and a lactose moiety at the reducing end of the molecule. Hemagglutination inhibition data in Table 2 shows that galectin-3 binds 2,6-sialyl lacto-*N*-neo-tetraose nearly as well as LacNAc-II, and 16-fold better than galectin-1. ITC data obtained at 287 K shows that the K_a value for 2,6-sialyl lacto-*N*-neo-tetraose of galectin-3 is twofold less than for LacNAc-II. These results demonstrate that galectin-3 recognizes the internal lactose moiety in 2,6-sialyl lacto-*N*-neo-tetraose.

The trisaccharide GlcNAcβ(1–3)Galβ(1–4)Glc, which is present in 2,6-sialyl lacto-*N*-neo-tetraose and lacto-*N*-tetraose, was synthesized to further test the ability of galectin-3, but not galectin-1, to bind to "internal" lactose residues in oligosaccharides. Table 2 shows hemagglutination inhibition data that indicates that galectin-1 does not bind to the trisaccharide. Table 2, however, demonstrates that galectin-3 binds to the trisaccharide nearly as well as to lactose. ITC results at 287 K in Table 1 show that galectin-3 possesses a K_a value ~fourfold less than LacNAc-II, and only ~twofold less than 2,6-sialyl-lacto-*N*-neo-tetraose, which has a reducing end lactose moiety. The ΔH value for galectin-3 binding to the trisaccharide is –7.7 vs. –6.4 kcal mol^{-1} for 2,6-sialyl-lacto-*N*-neo-tetraose. These findings support the conclusion that galectin-3, but not galectin-1, can bind well to internal LacNAc or lactose residues in the above oligosaccharides.

The X-ray crystal structure of the CRD domain of human galectin-3 (15) shows differences in the amino acids near the binding site of the lectin with respect to galectin-1. Specifically, Ser29 in galectin-1 is replaced by Arg144 in galectin-3, and Leu31 in galectin-1 is replaced by Ala146 in galectin-3, and further modeling with the CRD of hamster galectin-3 implicated Arg 139, Glu 230, and Ser 232 as relevant for a putative extended binding site (46). These differences may account for the differences in specificities between galectin-3 and galectin-1.

Galectin-7 binding to carbohydrates

As previously mentioned, the ITC data at 300 K in Table 1 shows that galectin-7 possesses a K_a of 0.17×10^4 M^{-1} for LacNAc-II, which is nearly sixfold lower than that for galectin-1 (1.1×10^4 M^{-1}) and nearly 11-fold weaker than that of galectin-3 (1.9×10^4 M^{-1}). The ΔH value for galectin-7 binding LacNAc-II (–11.8 kcal mol^{-1}) is greater than that of galectin-1 (–9.2 kcal mol^{-1}) and galectin-3 (–7.5 kcal mol^{-1}). Conversely, $T\Delta S$ of galectin-3 binding LacNAc-II is more unfavorable (–7.4 kcal mol^{-1}) than that of galectin-1 (–3.7 kcal mol^{-1}) and galectin-3 (–1.6 kcal mol^{-1}). Hence, galectin-7 has a lower K_a for LacNAc-II than galectin-1 and galectin-3 because of its unfavorable binding entropy.

Galectin-1 from human (17), rat lung (38), bovine spleen (47), and the homologue of avain liver (42) all show four- to fivefold increases in affinity for LacNAc-II relative to lactose. Similarly, galectin-3 from rat and human lung (17, 38) both bind LacNAc-II with higher affinity than lactose. Bovine heart galectin-1 in the present study also binds LacNAc-II with ~fourfold higher affinity than lactose (Table 1), as does murine galectin-3 (Table 2). ITC data in Table 1 shows that galectin-7 at 300 K binds lactose with nearly the same K_a ($0.22 \times 10\,4$ M^{-1}) as LacNAc-II (0.17×10^4 M^{-1}). The same relative results are obtained at 287 K (Table 1). Table 1 shows that at 287 K bovine heart galectin-1 has a K_a for lactose of 0.61×10^4 M^{-1}, which is similar to the K_a of galectin-7 (0.49×10^4 M^{-1}) for lactose. Thus, galectin-7 binds lactose with nearly the same affinity as galectin-1. Based on the crystallographic data (11, 14) the extent of polar interaction of the *N*-acetyl part of the GlcNAc moiety in human galectin-7 is reduced to one with Arg53, whereas in bovine heart galectin this group makes contact with Arg48, Arg73, and Glu71. These results indicate a difference in specificity for lactose and LacNAc between galectin-7 and galectins-1 and -3. Similar data were obtained by hemagglutination inhibition measurements (Table 3).

ITC data in Table 1 at 287 K show that there is little difference in the specificity of galectin-7 binding to ThiodiGal as compared with lactose and LacNAc-II, and that their $-\Delta H$ values are similar for all three disaccharides. These results are similar to those for galectin-1 and galectin-3 in Table 1.

Table 1 shows the thermodynamics of binding Di- and TriLacNAc to galectin-7 at 287 K. There are little differences in the K_a values of LacNAc-II (0.64×10^4 M^{-1}), Di- (0.74×10^4 M^{-1}), and TriLacNAc (0.65×10^4 M^{-1}). The same is true for the ΔH values for all three carbohydrates. Hemagglutination inhibition data also support these findings (Table 3). The value of n for all three carbohydrates is also close to one, indicating that they are likely to bind to the same site in galectin-7, and that all three oligosaccharides are univalent. These results indicate that galectin-7 recognizes one predominant LacNAc-II moiety in binding to LacNAc-II oligomers, as observed for galectins-1 and -3. The X-ray crystal structure of human galectin-7 also shows one molecule of LacNAc-II in the B monomer of the protein (14), in agreement with these findings, while access to the A monomer is blocked in soaking experiments by crystal packing contacts.

Hemagglutination inhibition data in Table 3 demonstrates that galectin-7 binds to 2,3-sialyl LacNAc but not to 2,6-sialyl LacNAc. These findings are similar to those for galectins-1 and -3. The hemagglutination inhibition data also shows that galectin-7 binds to 2,6-sialyl DiLacNAc nearly as well as LacNAc-II. These results indicate that galectin-7 can recognize the internal (reducing end) LacNAc-II moiety of 2,6-sialyl DiLacNAc, as can galectin-3. Data in Table 3 also reveals that galectin-7 binds to 2,6-sialyl lacto-*N*-neotetraose slightly better than LacNAc-II. Binding of galectin-7 to lacto-*N*-tetraose and lacto-neo-*N*-tetraose are also similar to that of LacNAc-II (Table 3). Galectin-7 can also recognize the trisaccharide moiety, GlcNAcβ(1–3)Galβ(1–4)Glc~OH, which is present in lacto-*N*-tetraose and lacto-neo-*N*-tetraose. These results indicate that galectin-7, like galectin-3 but not galectin-1, can recognize internal LacNAc or lactose residues in the above carbohydrates. The X-ray crystal structure of human galectin-7 shows conservation of the carbohydrate binding residues of galectin-1, however there are significant changes in the binding pocket due to shortening of a loop structure in the region (14). These differences may relate to the observed differences in specificity of galectin-7 relative to galectins-1 and -3.

© 2002 NRC Canada

Table 3 also provides relative binding data for various mono- and oligosaccharides to galectin-7. The results indicate that galectin-7 is specific for lactose and LacNAc determinants.

Summary

The results of ITC and hemagglutination inhibition measurements demonstrate that galectin-7 possesses six- to 11-fold weaker affinities for carbohydrates with LacNAc as part of binding epitopes than galectins-1 and -3, respectively. Galectin-7 binds lactose and LacNAc-II with nearly the same affinity as is lactose for galectins-1 and -3. Galectin-7 thus differs in its fine carbohydrate binding specificity from galectins-1 and -3 in this regard. The present findings also show that galectin-1 is limited to binding primarily the non-reducing terminal LacNAc residues of oligosaccharides, while galectins-3 and -7 bind to non-reducing terminal LacNAc residues as well as internal LacNAc (and lactose) residues of oligosaccharides. These differences in the specificities of the three galectins may be related to their different biological activities and will be helpful to design head-groups of glycoclusters with improved target galectin selectivity (48, 49).

Acknowledgments

This work was supported by the National Cancer Institute (Grant No. CA-16054); the Department of Health, Education, and Welfare and Core Grant P30 CA-13330 from the same agency (C.F.B.); and a grant from the Wilhelm Sander-Stiftung (Munich; H.-J.G). The NMR facility at AECOM was supported by Instrumentation Grant I-S10-RR02309 from the National Institute of Health and DMB-8413723 from the National Science Foundation.

References

1. S.H. Barondes, D.N.W. Cooper, M.A. Gitt, and H. Leffler. J. Biol. Chem. **269**, 20 807 (1994).
2. K.-i. Kasai and J. Hirabayashi. J. Biochem. **119**, 1 (1996).
3. H.-J. Gabius. Eur. J. Biochem. **243**, 543 (1997).
4. D.N.W. Cooper and S.H. Barondes. Glycobiology, **9**, 979 (1999).
5. J. Hirabayashi, Y. Arata, and K. Kasai. Trends Glycosci. Glycotechnol. **9**, 113 (1997).
6. R.-Y. Yang, D.K. Hsu, L. Yu, J. Ni, and F.-T. Liu. J. Biol. Chem. **276**, 20 252 (2001).
7. K. Drickamer. Curr. Opin. Struct. Biol. **9**, 585 (1999).
8. H.-J. Gabius. Naturwissenschaften, **87**, 108 (2000).
9. H. Kaltner and B. Stierstorfer. Acta. Anat. (Basel), **161**, 162 (1998).
10. Y. Bourne, B. Bolgiano, D.-I. Liao, G. Strecker, P. Cantau, O. Herzberg, T. Feizi, and C. Cambillau. Nat. Struct. Biol. **1**, 863 (1994).
11. D.-I. Liao, G. Kapadia, H. Ahmed, G.R. Vatsa, and O. Herzberg. Proc. Natl. Acad. Sci. U.S.A. **91**, 1428 (1994).
12. T.D. Lobsanov, M.A. Gitt, H. Leffler, S.H. Barondes, and J.M. Rini. J. Biol. Chem. **268**, 27 034 (1993).
13. D.D. Leonidas, E.H. Vatzaki, H. Vorum, J.E. Celis, P. Madsen, and K.R. Acharya. Biochemistry, **37**, 12 930 (1998).
14. D.D. Leonidas, B.L. Elbert, Z. Zhou, H. Leffler, S.J. Ackerman, and K.R. Acharya. Structure, **3**, 1379 (1995).
15. J. Seetharaman, A. Kanigsberg, R. Slaaby, H. Leffler, S.H. Barondes, and J.M. Rini. J. Biol. Chem. **273**, 13 047 (1998).
16. R.T. Lee, Y. Ichikawa, H.J. Allen, and Y.C. Lee. J. Biol. Chem. **265**, 7864 (1990).
17. C.P. Sparrow, H. Leffler, and S.H. Barondes. J. Biol. Chem. **262**, 7383 (1987).
18. R.N. Knibbs, N. Agrawal, J.L. Wang, and I.J. Goldstein. J. Biol. Chem. **268**, 14 940 (1993).
19. S. Sato and R.C. Hughes. J. Biol. Chem. **267**, 6983 (1992).
20. G.J. Swaminathan, D.D. Leonidas, M.P. Savage, S.J. Ackerman, and K.R. Acharya. Biochemistry, **38**, 13 837 (1999).
21. K. Bachhawat-Sikder, C.J. Thomas, and A. Surolia. FEBS Lett. **500**, 75 (2001).
22. M. Cho and R.D. Cummings. Trends Glycosci. Glycotechnol. **9**, 47 (1997).
23. K.E. Pace, C. Lee, P.L. Stewart, and L.G. Baum. J. Immunol. **163**, 3801 (1999).
24. K.E. Pace, H.P. Hahn, M. Pang, J.T. Nguyen, and L.G. Baum. J. Immunol. **165**, 2331 (2000).
25. F.T. Liu. Clin. Immunol. **97**, 79 (2000).
26. P. Nangia-Makker, S. Akahani, R. Bresalier and A. Raz. *In* Lectins and pathology. *Edited by* M. Caron and A.-P. Sève. Harwood Academic Publications, Amsterdam. 2000.
27. T. Magnaldo, D. Fowlis, and M. Darmon. Differentiation, **63**, 159 (1997).
28. K. Polyak, Y. Xia, J.L. Zweler, K.W. Kinzler, and B. Vogelstein. Nature (London), **389**, 300 (1997).
29. J. Lu, H. Pei, M. Kaeck, and H.J. Thompson. Mol. Carcinog. **20**, 204 (1997).
30. H. Lahm, S. André, A. Hoeflich, J.R. Fischer, B. Sordat, H. Kaltner, E. Wolf, and H.-J. Gabius. J. Cancer Res. Clin. Oncol. **127**, 375 (2001).
31. D. Gupta and C.F. Brewer. Biochemistry, **33**, 5526 (1994).
32. I. Parikh, S. March, and P. Cuatercasas. Methods Enzymol. **34**, 77 (1974).
33. N. Agrwal, Q. Sun, S.-Y. Wang, and J.L Wang. J. Biol. Chem. **268**, 14 932 (1993).
34. M. Dubois, K.A. Gilles, J.K. Hamilton, P.A. Rebers, and F. Smith. Anal. Chem. **28**, 350 (1956).
35. S.K. Saha and C.F. Brewer. Carbohydr. Res. **254**, 157 (1994).
36. T. Osawa and I. Matsumoto. Methods Enzymol. **28B**, 323 (1972).
37. T. Wiseman, S. Williston, J.F. Brandt, and L.-N. Lin. Anal. Biochem. **179**, 131 (1989).
38. H. Leffler and S.H. Barondes. J. Biol. Chem. **261**, 10 119 (1986).
39. F.P. Schwarz, H. Ahmed, M.A. Bianchet, L.M. Amzel, and G.R. Vasta. Biochemistry, **37**, 5867 (1998).
40. R. Ramkumar, A. Surolia, and S.K. Podder. Biochem. J. **308**, 237 (1995).
41. D. Gupta, M. Cho, R.D. Cummings, and C.F. Brewer. Biochemistry, **35**, 15 236 (1996).
42. S. Bharadwaj, H. Kaltner, E.Y. Korchagina, N.V. Bovin, H.-J. Gabius, and A. Surolia. Biochim. Biophys. Acta, **1472**, 191 (1999).
43. T.K. Dam, R. Roy, S.K. Das, S. Oscarson, and C.F. Brewer. J. Biol. Chem. **275**, 14 223 (2000).
44. S.D. Virgilio, J. Glushka, K. Moremen, and M. Pierce. Glycobiology, **9**, 353 (1999).
45. H. Ahmed, H.J. Allen, A. Sharma, and K.L. Matta. Biochemistry, **29**, 5315 (1990).
46. K. Henrick, S. Bawumia, E.A.M. Barboni, B. Mehul, and R.C. Hughes. Glycobiology, **8**, 45 (1998).
47. H. Ahmed, N.E. Fink, J. Pohl, and G.R. Vasta. J. Biochem. **120**, 1007 (1996).

© 2002 NRC Canada

48. S. André, P.J.C. Ortega, M.A. Perez, R. Roy, and H.-J. Gabius. Glycobiology, **9**, 1253 (1999).

49. N. Yamazaki, S. Kojima, N.V. Bovin, S. André, S. Gabius, and H.-J. Gabius. Adv. Drug Deliv. Rev. **43**, 225 (2000).

© 2002 NRC Canada

Synthesis of a polyphosphorylated GPI-anchor core structure

Martina Lahmann, Per J. Garegg, Peter Konradsson, and Stefan Oscarson

Abstract: Using a linear assembly approach a highly differentially protected derivative of the common GPI-anchor core structure (α-D-Man-(1→6)-α-D-Man-(1→2)-α-D-Man-(1→4)-α-D-GlcNH$_2$-(1→6)-D-*myo*-inositol) has been synthesized. All mannose donors were prepared from a common thioglycoside precursor (**1**), and coupled to GlcN$_3$-*myo*-inositol acceptor **5** in a linear five-step glycosylation–deprotection sequence in 49% overall yield, to give the key intermediate **10**, with orthogonal temporary protecting groups at the 6″, 2″, 6′, and 2 positions of the trimannoside motif and at the 1 and 2 positions of the inositol part. Consecutive removal of the temporary protecting groups in the trimannoside moiety followed by phosphorylation, gave a tetraphosphate derivative in 60% overall yield. Removal of a camphor acetal afforded a 1,2-inositol diol, which was converted to a 1,2-cyclic phosphate using commercial methyl dichlorophosphate (→**17**, 95%). One-step deprotection using sodium in liquid ammonia afforded the target polyphosphorylated core structure **18** (60%), which will be tested for metabolic insulin action.

Key words: glycophosphatidylinositols, linear synthesis, glycosylations, inositolphosphoglycans, IPG.

Résumé : Faisant appel à une approche d'assemblage linéaire, on a réalisé la synthèse d'un dérivé, portant des groupes protecteurs fortement diversifiés, de la structure ancrée fondamentale du GPI, le α-D-Man-(1→6)-α-D-Man-(1→2)-α-D-Man-(1→4)-GlcNH$_2$-(1→6)-D-*myo*-inositol. Tous les groupes mannoses donneurs ont été préparés à partir d'un thioglycoside précurseur commun, **1**, et ils ont été couplés à un GlcN$_3$-*myo*-inositol accepteur, **5**, dans une séquence en cinq étapes de glycosylation-déprotection, avec un rendement global de 49%, pour conduire à l'intermédiaire clé **10** portant des groupes protecteurs orthogonaux temporaires dans les positions 6″, 2″, 6′ et 2 du motif trimannoside et dans les positions 1 et 2 de la portion inositol. Les éliminations consécutives des groupes protecteurs temporaires de la portion mannoside, suivies d'une phosphorylation, on conduit au dérivé tétraphosphate, avec un rendement global de 60%, à partir duquel on a enlevé un acétal du camphre pour obtenir un diol 1,2-inositol qui a été transformé en un phosphate 1,2-cyclique à l'aide de dichlorophosphate de méthyle commercial (→**17**, 95%). Une déprotection en une étape à l'aide de sodium dans l'ammoniac liquide fournit le structure fondamentale phosphorylée recherchée, **18**, avec un rendement de 60% qui a été évaluée pour son action d'insuline métabolique.

Mots clés : glycophosphatidylinositols, synthèse linéaire, glycosylations, inositolphosphoglycanes, IPG.

[Traduit par la Rédaction]

Introduction

Ever since the discovery of a new way to anchor proteins to cell membranes through glycosylphosphatidylinositol structures (GPI-anchors, see refs. 1–3), these anchor structures have been of a main research interest, both analytically, synthetically, and biologically. Isolation and analysis have shown that these structures are present in almost all species, and that their structure is not only partly conserved but also species specific (2, 3). All GPI-anchors found and characterized so far contain a common pseudo-pentasaccharide backbone, α-D-Man-(1→6)-α-D-Man-(1→2)-α-D-Man-(1→4)-α-D-GlcNH$_2$-(1→6)-D-*myo*-inositol, but the substitution pattern varies between species (Fig. 1). Apart from functioning as protein anchors, a number of functions have been suggested for the GPI-structures (2, 3), such as they have been implicated as second messengers to insulin (4–6) and polyphosphorylated derivatives have been shown to give an insulin-type effect and have been considered as drug candidates towards diabetes (7).

The novelty and complexity of these structures in combination with the interest to investigate more in detail their biological functions have resulted in a number of syntheses of parts of the backbone, the complete backbone, and also the backbone with various substituents (8–10). The latter syntheses have generally been directed towards a species specific target molecule not allowing too much variation in the substitution pattern. Recently, Ley and co-workers (10) presented a synthesis of the backbone with orthogonal temporary protecting groups at relevant positions allowing the continued synthesis of a variant of species specific GPI-anchor structures. Another feature of their synthesis is that the orthogonal and one-pot glycosylations are used in the

Received 28 August 2001. Published on the NRC Research Press Web site at http://canjchem.nrc.ca on 29 August 2002.

Dedicated to the memory of Professor Raymond U. Lemieux.

M. Lahmann, P.J. Garegg, and S. Oscarson.[1] Department of Organic Chemistry, Arrhenius Laboratory, Stockholm University, S-106 91 Stockholm, Sweden.
P. Konradsson. Department of Chemistry/IFM, Linköping University, S-581 83 Linköping, Sweden.

[1]Corresponding author (e-mail: s.oscarson@organ.su.se).

 DOI: 10.1139/V02-160 © 2002 NRC Canada

Fig. 1. Schematic structure of GPI anchors.

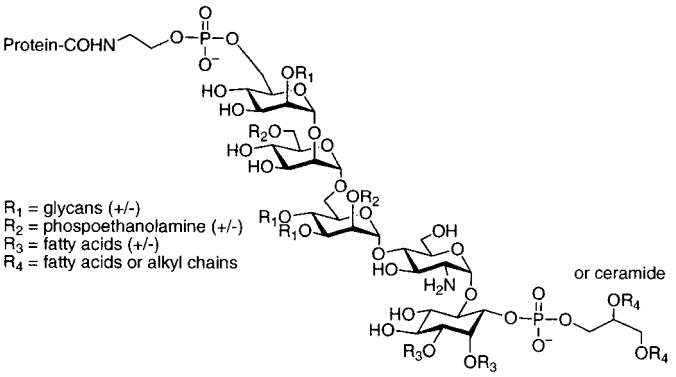

build-up of the target structures, utilizing the different reactivity of both the uniquely protected donors and the variety of donors. Although conceptually elegant, such an approach requires considerable fine-tuning of the reactivity to be successful. We herein describe a synthesis, using a linear synthetic approach, of a similar highly and differentially protected backbone structure that, will allow for the syntheses of most types of species-specific structures from the same intermediate. Furthermore, the temporary protecting groups were sequentially removed and the resulting hydroxyl derivatives were phosphorylated and deprotected to give a polyphosphorylated structure, which will be investigated for insulin activity.

Results and discussions

The linear approach can have considerable advantages, especially since the target structure is a rather small molecule containing no repeating units (at least no larger than a monosaccharide). Only monosaccharide donors have to be prepared and all mannose donors can be prepared from a common precursor. The protecting-group strategy can be planned to be optimal (selective and complete) in terms of protection and deprotection, since almost no considerations have to be taken to the reactivity or stereochemical influence of the protecting-group pattern in the various mannose donors. In the coupling reactions, self condensation and transglycosylation reactions, often found side reactions in orthogonal glycosylations, are not possible, which results in excellent glycosylation yields.

As donors we chose thioglycosides (11, 12). All the three different mannose donors could be obtained in a few high-yielding steps from the same precursor: ethyl 3,4-di-*O*-benzyl-1-thio-α-D-mannopyranoside (13) (**1**) (Scheme 1). Regioselective silylation at the primary position followed by benzoylation or *p*-methoxybenzylation gave donors **2** (80%) and **3** (85%), respectively. Subsequent desilylation and allylation afforded mannose donor **4** (64% overall yield). With these donors in hand the pseudo-pentasaccharide could then be assembled through three efficient glycosylations all promoted by DMTST in diethyl ether to ensure α-selectivity (Scheme 2). Acceptor **5** (14) and donor **2** were coupled to give pseudo-trisaccharide **6** in 98% yield. Removal of the TBDMS-protecting group afforded acceptor **7** (85%), which was condensed with donor **3** to yield the tetrasaccharide **8** in quantitative yield. Removal of the *p*-methoxybenzyl group

Scheme 1. Reagents and conditions: (*a*) TBDMSCl, pyridine; (*b*) BzCl, pyridine; (*c*) TBDPSCl, pyridine; (*d*) MBnCl, NaH, 0°C; (*e*) TBAF, THF; (*f*) AllBr, NaH, DMF, 0°C.

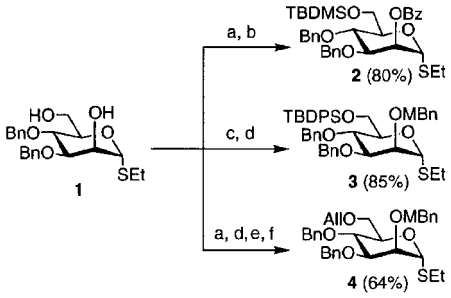

by DDQ treatment (→ **9**, 72%) and subsequent glycosylation with thioglycoside **4** gave the target intermediate **10** in 84% yield and a 49% overall yield over the five steps. The α-configuration of all glycosidic linkages was proven by the $^1J_{C,H}$ coupling constants of the anomeric carbons, which all were above 168 Hz.

In compound **10** all the functionalities are now in place to allow continued syntheses of many different GPI anchor structures. To prove the orthogonality of the temporary protecting groups, the groups were removed one by one in sequence to produce a tetraol (Scheme 3). The allyl group was removed under neutral conditions using an iridium catalyst followed by hydrolysis of the obtained vinyl ether with NIS–H_2O (15) (→ **11**, 98%). Removal of the *p*-methoxybenzyl protecting group was accomplished by DDQ treatment to give diol **12** (84%). The benzoate was removed using Zemplén conditions (→ **13**, 85%) and finally the silyl group was cleaved by TBAF treatment to give the tetraol **14** (86%) in an overall deprotection yield of 60%.

As mentioned, GPI structures have been suggested as insulin second messengers (4, 5). A key structure is believed to be a 1,2-cyclic phosphate on the insulin moiety obtained through enzymatic cleavage of the native glycerol fragment (6). Additional phosphorylation has been shown to enhance the biological activity (7). Accordingly, the tetraol was phosphorylated using the amidite approach (16) to give benzyl protected 6‴,2‴,6″,2′-tetraphosphate derivative **15** in quantitative yield, which was subsequently processed to give the corresponding 1,2-cyclic phosphate **17** (Scheme 4). Acidic hydrolysis of the campher acetal (→ **16**, 46%) followed by treatment with commercial methyl dichlorophosphate afforded **17** in 95% yield after work-up. Catalytic hydrogenolysis to remove benzyl protecting group is often troublesome with phosphate-containing compounds; however, as found earlier (17, 18), Birch-type reaction conditions smoothly removed all benzyl groups without any indication (NMR, MALDI-TOF MS) of phosphate migration or hydrolysis or opening of the cyclic phosphate. Concomitantly, the azido function was reduced, in a one-pot reaction, to yield target structure **18** in 60% yield.

Conclusion

In summary, a most effective linear synthesis of a highly differentially protected backbone structure of GPI anchors has been performed. The temporary protecting groups can be removed in an orthogonal fashion to allow synthesis of

© 2002 NRC Canada

Scheme 2. Reagents and conditions: (*a*) DMTST, Et_2O, MS (4 Å); (*b*) TBAF, THF; (*c*) DDQ, CH_2Cl_2–H_2O.

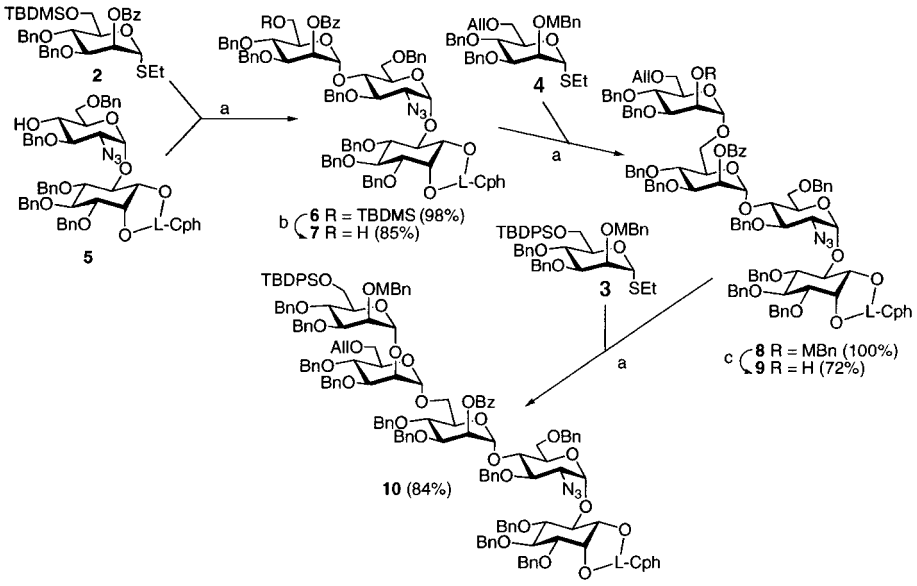

Scheme 3. Reagents and conditions: (*a*) (*i*) Pd/C, iridium catalyst, H_2, (*ii*) NIS, H_2O; (*b*) DDQ, CH_2Cl_2–H_2O; (*c*) NaOMe, MeOH; (*d*) TBAF, THF.

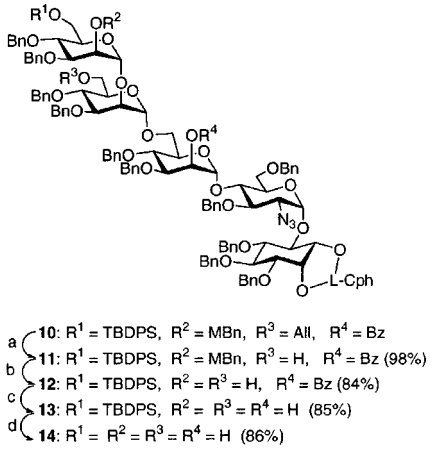

various substituted anchor structures. The partly deprotected structures can be polyphosphorylated and deprotected using Birch-type reaction conditions in high yields, to give synthetic phosphoinositolglycans.

Experimental

All organic solvents were distilled before use, except Et_2O, which was stored over Na. Organic solutions were dried over $MgSO_4$ before concentration, which was performed under reduced pressure at <40°C (bath temperature). NMR spectra were recorded at 270 (JEOL), 300, 400, or 600 MHz (Varian) (^{1}H), or at 67.5, 75, or 100 MHz (^{13}C), unless otherwise stated, in $CDCl_3$. For ^{1}H NMR spectra, TMS was used as internal standard (δ = 0). ^{13}C NMR spectra were referred to the chloroform signal (δ = 77.17). ^{31}P NMR spectra were standardized by using an external H_3PO_4 sample (δ = 0). TLC was performed on silica gel 60 F_{254} (Merck) plates with detection by UV-light and (or) charring with 8% sulfuric acid. Column chromatography was performed on silica gel (Matrix Silica Si 60A, 35–70m, Amicon). MALDI-TOF spectra were recorded on a Bruker Biflex III using PEG 1500 as calibration reference.

Ethyl 2-*O*-benzoyl-3,4-di-*O*-benzyl-6-*O*-*tert*-butyldimethylsilyl-1-thio-α-D-mannopyranoside (2)

TBDMSCl (325 mg, 2.16 mmol) and a catalytic amount of DMAP were added to a solution of ethyl 3,4-di-*O*-benzyl-1-thio-α-D-mannopyranoside (13) (**1**, 550 mg, 1.36 mmol) in pyridine (2 mL). The reaction mixture was stirred at room temperature for about 3 h when benzoyl chloride (1 mL) was added and stirring was continued for an additional 45 min. For work up, the mixture was diluted with toluene, washed with water and brine, dried ($MgSO_4$), and concentrated. To remove the main part of pyridine, co-evaporation with toluene was performed twice before applying the residue to flash chromatography (light petroleum (bp 40–65°C) – Et_2O, 5:1) to give **2** (680 mg, 1.09 mmol, 80%). $[\alpha]_D$ +39 (*c* 1.0, $CHCl_3$). ^{1}H NMR ($CDCl_3$) δ: 0.06 (s, 6H, Me_2Si), 0.92 (s, 9H, *t-Bu*Si), 1.30 (m, 3H, *Me*CH_2S), 2.65 (m, 2H, SCH_2), 3.80–4.10 (m, 5H), 4.54, 4.65, 4.76, 4.92 (4 × d, 4 × 1H, PhCH_2), 5.38 (s, 1H, H-1), 5.68 (br s, 1H, H-2) 7.18–8.12 (m, 13H), 8.12 (m, 2H). ^{13}C NMR ($CDCl_3$) δ: – 4.9 (Me_2Si), 15.1 (*Me*CH_2S), 18.5 (*t-Bu*Si), 25.6 (SCH_2), 26.1 (*t-Bu*Si), 62.4, 71.2, 71.8, 73.2, 74.6, 75.3, 78.9 (C2–C6, CH_2Ph), 82.5 (C1), 127.8–138.8 (aromatic C), 165.9 (Ph*C*O). Anal. calcd. for $C_{35}H_{46}O_6SSi$: C 67.49, H 7.44; found: C 67.38, H 7.56.

Ethyl 3,4-di-*O*-benzyl-6-*O*-*tert*-butyldiphenylsilyl-2-*O*-*p*-methoxybenzyl-1-thio-α-D-mannopyranoside (3)

TBDPSCl (1.3 mL, 4.9 mmol) and a catalytic amount of DMAP were added to a solution of **1** (1.35 g, 3.34 mmol) in pyridine (10 mL). The reaction mixture was stirred at room temperature for about 24 h, then diluted with toluene and washed with brine and water, dried ($MgSO_4$), and filtered. The filtrate was concentrated and the pyridine co-evaporated with toluene. The crude product was purified by flash-chromatography (toluene–EtOAc, 3:1) to give ethyl 3,4-di-*O*-benzyl-6-*O*-*tert*-butyldiphenylsilyl-1-thio-α-D-manno-

© 2002 NRC Canada

Scheme 4. Reagents and conditions: (*a*) (*i*) DBDIPPA, tetrazole, (*ii*) MCPBA; (*b*) TFA; (*c*) (*i*) $MeOPOCl_2$, pyridine, (*ii*) HCl; (*d*) Na, NH_3 (l).

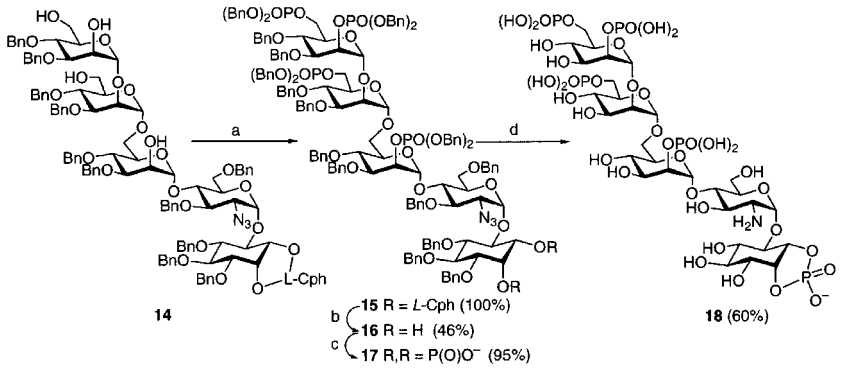

pyranoside (1.98 g, 3.08 mmol, 92%). $[\alpha]_D$ +70 (*c* 1.0, CH_2Cl_2). ^{13}C NMR ($CDCl_3$) δ: 14.8 (*Me*CH_2S), 19.4 (*t-Bu*Si), 24.6 (S*CH*$_2$), 26.7, 26.9 (*t-Bu*Si), 63.2 (C6), 70.1, 72.3, 72.9, 74.7, 75.3, 80.7, (C2–C5, *CH*$_2$Ph), 82.8 (C1), 127.7–136.0 (aromatic C). A solution of this derivative (1.47 g, 2.29 mmol) in dry DMF (20 mL) was cooled to 0°C. NaH (190 mg, ~60% dispersed in oil) was added and the mixture was stirred for 30 min. Freshly prepared *p*-methoxybenzyl bromide (1.0 mL), dissolved in DMF (10 mL), was added dropwise. After 3 h the reaction was quenched by addition of MeOH (1 mL), diluted with toluene, washed with water and brine, dried ($MgSO_4$), and concentrated. Purification by flash chromatography (toluene–EtOAc, 18:1) gave **3** (1.60 g, 2.10 mmol, 92%). $[\alpha]_D$ +41 (*c* 1.0, $CHCl_3$). ^1H NMR ($CDCl_3$) δ: 1.06 (s, 9H, *t-Bu*Si), 1.22 (m, 3H, *Me*CH_2S), 2.56 (m, 2H, S*CH*$_2$), 3.68–4.10 (m, 8H), 4.46–4.76 (m, 5H, Ar*CH*$_2$), 4.92 (d, 1H, Ar*CH*$_2$), 5.38 (s, 1H, H-1), 5.68 (br s, 1H, H-2), 6.74–7.80 (m, 24H). ^{13}C NMR ($CDCl_3$) δ: 15.0 (*Me*CH_2S), 19.4 (*t-Bu*Si), 25.1 (S*CH*$_2$), 26.9 (*t-Bu*Si), 55.4 (*Me*OBn), 63.4 (C6), 71.8, 72.3, 73.5, 75.1, 75.3, 76.5, 80.6, 81.4 (C1–C5, *CH*$_2$Ph, MBn), 113.9 (MBn), 127.7–138.7 (aromatic C), 159.2 (MBn). Anal. calcd. for $C_{46}H_{54}O_6SSi$: C 72.40, H 7.13; found: C 72.27, H 7.28.

Ethyl 6-*O*-allyl-3,4-di-*O*-benzyl-2-*O*-*p*-methoxybenzyl-1-thio-α-D-mannopyranoside (4)

TBDMSCl (920 mg, 6.1 mmol) and a catalytic amount of DMAP were added to a solution of **1** (1.6 g, 4.0 mmol) in pyridine (10 mL). The reaction mixture was stirred at room temperature for about 3 h and then diluted with toluene, washed with water and dried over $MgSO_4$. After filtration, the mixture was concentrated and co-evaporated from toluene. Subsequent purification by flash-chromatography (toluene–EtOAc, 9:1) of the crude product afforded ethyl 3,4-di-*O*-benzyl-6-*O*-*tert*-butyldimethylsilyl-1-thio-α-D-mannopyranoside (1.7 g, 3.3 mmol, 83%) as a colourless syrup. A solution of this derivative (1.00 g, 1.93 mmol) in dry DMF (20 mL) was cooled to 0°C. NaH (120 mg, ~60% dispersed in oil) was added and the mixture was stirred for 30 min. Freshly prepared *p*-methoxybenzyl bromide (750 μL) dissolved in DMF (10 mL) was added dropwise. After 30 min the reaction was quenched by addition of MeOH (1 mL), diluted with toluene and washed with water and brine. Drying ($MgSO_4$), filtration, and evaporation gave a residue, which was purified by flash chromatography (toluene → toluene–EtOAc, 18:1) to yield ethyl 3,4-di-*O*-benzyl-2-O-*p*-methoxybenzyl-6-*O*-*tert*-butyldimethylsilyl-1-thio-α-D-mannopyranoside (1.16 g, 1.82 mmol, 94%). $[\alpha]_D$ +25 (*c* 1.0, CH_2Cl_2). ^{13}C NMR ($CDCl_3$) δ: 15.0 (*Me*CH_2S), 18.5 (*t-Bu*Si), 25.0 (S*CH*$_2$), 26.1 (*t-Bu*Si), 55.4 (*Me*OBn), 62.9 (C6), 71.6, 72.2, 73.6, 75.3, 76.1, 77.4, 80.5, 81.4 (C1–C5, *CH*$_2$Ph, MBn), 113.9 (MBn), 127.7–130.4, 138.7, 138.9 (aromatic C), 159.3 (MBn). This compound (1.10 g, 1.72 mmol) dissolved in a TBAF–THF solution (3.6 mL, 1 M) was stirred at room temperature overnight. After concentration, the residue was applied to flash chromatography (toluene → toluene–EtOAc, 12:1 → toluene–EtOAc, 3:1) to obtain ethyl 3,4-di-*O*-benzyl-2-*O*-*p*-methoxybenzyl-1-thio-α-D-mannopyranoside (780 mg, 1.49 mmol, 87%). ^{13}C NMR ($CDCl_3$) δ: 15.0 (*Me*CH_2S), 25.5 (S*CH*$_2$), 55.4 (*Me*OBn), 62.5 (C6), 72.1, 72.2, 72.5, 75.2, 76.2, 80.5, 82.4 (C1–C5, *CH*$_2$Ph, MBn), 114.0 (MBn), 127.8–129.7, 138.4, 138.4 (aromatic C), 159.2 (MBn). This compound (780 mg, 1.49 mmol) was dissolved in dry DMF (5 mL) and cooled to 0°C. NaH (120 mg, ~60% dispersed in oil) and allyl bromide (300 μL, 3.55 mmol) were added and the reaction mixture was allowed to reach room temperature. After 2 h the reaction was quenched by addition of MeOH (1 mL). The mixture was diluted with toluene, washed with water, dried ($MgSO_4$), and concentrated. Purification by flash chromatography (toluene–EtOAc, 12:1) gave **4** (792 mg, 1.40 mmol, 94%). $[\alpha]_D$ +57 (*c* 1.0, CH_2Cl_2). ^1H NMR ($CDCl_3$) δ: 1.24 (m, 3H, *Me*CH_2S), 2.58 (m, 2H, S*CH*$_2$), 3.60–3.84 (m, 7H), 3.90–4.18 (m, 4H), 4.48–4.74 (m, 6H), 4.92 (d, 1H, Ar*CH*$_2$), 5.14 (m, 1H), 5.26 (m, 1H), 5.36 (s, 1H, H-1), 5.94 (m, 1H), 6.80–6.84 (m, 2H), 7.16–7.40 (m, 12H). ^{13}C NMR ($CDCl_3$) δ: 15.2 (*Me*CH_2S), 25.5 (S*CH*$_2$), 55.4 (*Me*OBn), 69.4 (C6), 71.6, 71.9, 72.0, 72.5, 75.2, 75.3, 75.8, 80.4, 81.9 (C1–C5, *CH*$_2$Ph, MBn, allyl), 113.8 (MBn), 116.8 (allyl), 127.86–130.2 (aromatic C), 134.9 (allyl), 138.4, 138.7 (aromatic C), 159.2 (MBn). Anal. calcd. for $C_{33}H_{40}O_6S$: C 70.18, H 7.14; found: C 69.88, H 7.08.

(2-*O*-Benzoyl-3,4-di-*O*-benzyl-6-*O*-*tert*-butyldimethylsilyl-α-D-mannopyranosyl)-(1→4)-(2-azido-3,6-di-*O*-benzyl-2-deoxy-α-D-glucopyranosyl)-(1→6)-3,4,5-tri-*O*-benzyl-1,2-*O*-(L-1,7,7-trimethyl[2.2.1]bicyclohept-6-yliden)-D-*myo*-inositol (6)

A solution of **5** (14) (46 mg, 48 μmol) and **2** (30 mg, 48 μmol) in dry Et_2O (10 mL) was stirred with powdered

© 2002 NRC Canada

molecular sieves (4 Å) under argon for 1 h when DMTST (41 mg, 158 μmol) was added. The reaction, followed by TLC (toluene–EtOAc, 12:1), was quenched after 3.5 h by addition of Et_3N (100 μL), and then the mixture was diluted with Et_2O (20 mL), filtered through Celite, and concentrated. The residue was subjected to silica gel column chromatography (toluene–EtOAc, 12:1) to obtain **6** (71 mg, 47 μmol, 98%). $[\alpha]_D$ +42 (*c* 1.0, CH_2Cl_2). ^{1}H NMR ($CDCl_3$) δ: 0.02 (s, 6H, *Me*$_2$Si), 0.74–2.10 (m, 27H, *t-Bu*Si, Cph), 3.24–4.98 (m, 29H), 5.50 (s, 1H), 5.61 (d, *J* = 1 Hz, 1H) 5.66 (s, 1H), 7.00–7.66 (m, 38H), 8.06 (d, 2H). ^{13}C NMR ($CDCl_3$) δ: –4.9 (*Me*$_2$Si), 10.1, 20.7, 20.9 (Cph), 26.2 (*t-Bu*Si), 27.2, 30.1, 44.9, 45.3, 48.2, 51.8 (Cph), 61.8, 63.4, 68.6–76.7, 78.3–80.8 ($C^{ino}1$–$C^{ino}6$, C2–C6, C2′–C6′, CH_2Bn), 95.7 (C1) 99.3 (C1′), 118.1 (Cph-acetal), 127.5–139.1 (aromatic C), 165.4 (Ph*C*O). Anal. calcd. for $C_{90}H_{105}N_3O_{16}Si$: C 71.45, H 7.00; found: C 71.28, H 6.84.

(6-*O*-Allyl-3,4-di-*O*-benzyl-2-*O*-*p*-methoxybenzyl-α-D-mannopyranosyl)-(1→6)-(2-*O*-benzoyl-3,4-di-*O*-benzyl-α-D-mannopyranosyl)-(1→4)-(2-azido-3,6-di-*O*-benzyl-2-deoxy-α-D-glucopyranosyl)-(1→6)-3,4,5-tri-*O*-benzyl-1,2-*O*-(L-1,7,7-trimethyl[2.2.1]bicyclo-hept-6-yliden)-D-*myo*-inositol (8)

TBAF (55 μL, 1 M solution in THF) was added to a solution of **6** (71 mg, 47 μmol) in freshly distilled THF (5mL). After 6 h additional TBAF (55 μL) was added and after 24 h 30 μL more. Although the reaction was not complete (as monitored by TLC (toluene–EtOAc, 12:1) after 48 h the mixture was diluted with toluene, washed with water, dried ($MgSO_4$), and concentrated. The residue was applied onto a silica gel column and eluted (toluene–EtOAc, 15:1) to give 2-*O*-benzoyl-3,4-di-*O*-benzyl-α-D-mannopyranosyl)-(1→4)-(2-azido-3,6-di-*O*-benzyl-2-deoxy-α-D-glucopyranosyl)-(1→6)-3,4,5-tri-*O*-benzyl-1,2-*O*-(L-1,7,7-trimethyl[2.2.1]bicycloheptt-6-yliden)-D-*myo*-inositol (**7**, 56 mg, 40 μmol, 85%). $[\alpha]_D$ +35 (*c* 1.0, CH_2Cl_2). ^{13}C NMR ($CDCl_3$) δ: 10.2, 20.7, 20.9 (Cph), 27.2, 30.1, 45.0, 45.3, 48.2, 51.8 (Cph), 62.0, 63.6, 68.1–76.9, 78.3–80.7 ($C^{ino}1$–$C^{ino}6$, C2–C6, C2′–C6′, CH_2Bn), 95.6 (C1) 99.1 (C1′), 118.1 (Cph-acetal), 127.5–138.4 (aromatic C), 165.2 (Ph*C*O). A solution of **4** (28 mg, 50 μmol) and **7** (75 mg, 54 μmol) in dry Et_2O (10 mL) was stirred with powdered molecular sieves (4 Å) under argon for 1 h, when DMTST (40 mg, 155 μmol) was added. The reaction, monitored by TLC (light petroleum (bp 40–60°C) – Et_2O, 1:1), was quenched after 1.5 h by addition of Et_3N (100 μL) and stirred for a further 20 min. The mixture was diluted with Et_2O (20 mL), filtered through Celite, and concentrated. The residue was subjected to silica gel column chromatography (toluene–EtOAc, 12:1) to obtain **8** (95 mg, 50 μmol, quant.). $[\alpha]_D$ +41 (*c* 1.0, CH_2Cl_2). ^{1}H NMR ($CDCl_3$) δ: 0.78–1.96 (m, 16H, Cph), 3.30–5.20 (m, 52H), 5.50 (s, 1H), 5.61 (d, *J* = 1 Hz, 1H) 5.66 (s, 1H), 5.81 (m, 1H), 6.78 (d, 2H), 7.00–7.45 (m, 48H), 8.00 (d, 2H). ^{13}C NMR ($CDCl_3$) δ: 10.0 (Cph), 20.6, 20.9, 27.2, 30.0, 45.0, 45.4, 48.2, 51.8 (Cph), 55.4 (*MeO*Bn), 63.6–80.8 ($C^{ino}1$–$C^{ino}6$, C2–C6, C2′–C6′, C2″–C6″, CH_2Bn, MBn, allyl), 95.6 (C1), 98.4 (C1″), 99.1 (C1′), 113.7 (MBn), 116.7 (allyl), 118.2 (Cph-acetal), 125.3–138.7 (aromatic C, allyl), 159.0 (MBn), 165.4 (Ph*C*O). Anal. calcd. for $C_{115}H_{125}N_3O_{22}$: C 72.65, H 6.63; found: C 72.38, H 6.60.

(3,4-Di-*O*-benzyl-6-*O*-*tert*-butyldiphenylsilyl-2-*O*-*p*-methoxybenzyl-α-D-mannopyranosyl)-(1→2)-(6-*O*-allyl-3,4-di-*O*-benzyl-α-D-mannopyranosyl)-(1→6)-(2-*O*-benzoyl-3,4-di-*O*-benzyl-α-D-mannopyranosyl)-(1→4)-(2-azido-3,6-di-*O*-benzyl-2-deoxy-α-D-glucopyranosyl)-(1→6)-3,4,5-tri-*O*-benzyl-1,2-*O*-(L-1,7,7-trimethyl[2.2.1]bicycloheptt-6-yliden)-D-*myo*-inositol (10)

DDQ (17 mg, 75 μmol) was added to a solution of **8** (90 mg, 47 μmol) in water saturated CH_2Cl_2 (5% H_2O, 5 mL) and stirred overnight at room temperature. The mixture was diluted with CH_2Cl_2 (15 mL), washed with water and $Na_2S_2O_3$ (10% aq), dried ($MgSO_4$), and concentrated. The crude product was purified by flash chromatography (toluene–EtOAc, 6:1) to give 60 mg (34 μmol, 72%) of (6-*O*-allyl-3,4-di-*O*-benzyl-α-D-mannopyranosyl)-(1→6)-(2-*O*-benzoyl-3,4-di-*O*-benzyl-α-D-mannopyranosyl)-(1→4)-(2-azido-3,6-di-*O*-benzyl-2-deoxy-α-D-glucopyranosyl)-(1→6)-3,4,5-tri-*O*-benzyl-1,2-*O*-(L-1,7,7-trimethyl[2.2.1]bicycloheptt-6-yliden)-D-*myo*-inositol (**9**). $[\alpha]_D$ +51 (*c* 1.0, CH_2Cl_2). ^{13}C NMR ($CDCl_3$) δ: 10.0, 20.6, 20.9, 27.2, 30.0, 45.0, 45.3, 48.2, 51.8 (Cph), 63.4–80.8 ($C^{ino}1$–$C^{ino}6$, C2–C6, C2′–C6′, C2″–C6″, CH_2Bn, allyl), 95.6 (C1), 98.4 (C1″), 99.1 (C1′), 116.9 (allyl), 118.2 (Cph-acetal), 125.3–138.7 (aromatic C, allyl), 165.3 (Ph*C*O). A solution of **9** (300 mg, 168 μmol) and **3** (130 mg, 170 μmol) in dry Et_2O (80 mL) was stirred with powdered molecular sieves (4 Å) under argon for 1 h. Then DMTST (150 mg, 0.58 mmol) was added. The reaction, monitored by TLC (light petroleum (bp 40–60°C) – Et_2O, 1:1), was quenched after 45 min by addition of Et_3N (500 μL) and stirred for another 20 min. The mixture was diluted with Et_2O (20 mL), filtered through Celite, and concentrated. The residue was subjected to silica gel column chromatography (toluene–EtOAc, 12:1) to obtain 350 mg (141 μmol, 84%) of **10**. $[\alpha]_D$ +21 (*c* 1.0, CH_2Cl_2). ^{1}H NMR ($CDCl_3$) δ: 0.78–1.96 (m, 25H, *t-Bu*Si, Cph), 3.30–5.20 (m, 61H), 5.28 (d, *J* = 2 Hz, 1H), 5.50 (s, *J* = 2 Hz, 1H), 5.58 (d, *J* = 4 Hz, 1H), 5.63 (m, 1H), 5.71 (m, 1H), 6.78 (d, 2H), 7.00–8.00 (m, 72H). ^{13}C NMR ($CDCl_3$) δ: 10.0 (Cph), 19.6 (*t-Bu*Si), 20.6, 20.9, 21.7 (Cph), 27.2 (*t-Bu*Si, Cph), 30.0, 45.0, 45.3, 48.2, 51.8 (Cph), 55.3 (*MeO*Bn), 63.4–80.8 ($C^{ino}1$–$C^{ino}6$, C2–C6, C2′–C6′, C2″–C6″, C2‴-C6‴, CH_2Bn, MBn, allyl), 95.5 (C1), 98.7 (C1″), 98.8 (C1‴), 99.2 (C1′), 113.6 (MBn), 116.3 (allyl), 118.2 (Cph-acetal), 125.4–139.0 (aromatic C, allyl), 158.9 (MBn), 165.3 (Ph*C*O). Anal. calcd. for $C_{151}H_{165}N_3O_{27}Si$: C 73.07, H 6.70; found: C 72.93, H 6.75.

(3,4-Di-*O*-benzyl-6-*O*-*tert*-butyldiphenylsilyl-α-D-mannopyranosyl)-(1→2)-(3,4-di-*O*-benzyl-α-D-mannopyranosyl)-(1→6)-(2-*O*-benzoyl-3,4-di-*O*-benzyl-α-D-mannopyranosyl)-(1→4)-(2-azido-3,6-di-*O*-benzyl-2-deoxy-α-D-glucopyranosyl)-(1→6)-3,4,5-tri-*O*-benzyl-1,2-*O*-(L-1,7,7-trimethyl[2.2.1]bicyclohept-6-yliden)-D-*myo*-inositol (12)

Compound **10** (700 mg, 282 μmol) was dissolved in freshly distilled THF (10 mL) and stirred 10 min with a catalytic amount of Pd/C. The filtered solution was degassed and set under argon. After addition of 1,5-cyclooctadienebis(methyldiphenylphosphine)iridium(I)·PF_6 (27 mg, 32 μmol), the solution was saturated with hydrogen until the intensive red colour of the mixture had disappeared (approx. after 20 min). The solution was stirred for 1 h under argon at

© 2002 NRC Canada

room temperature, then NIS (420 mg, 1.87 mmol) and H_2O (1.75 mL) were added. After 2.5 h the reaction mixture was diluted with EtOAc, washed consecutively with 10% aqueous $Na_2S_2O_3$, $NaHCO_3$, dried ($MgSO_4$), and concentrated. The crude product was purified by flash chromatography (toluene–EtOAc, 12:1) to give (3,4-di-*O*-benzyl-6-*O*-*tert*-butyldiphenylsilyl-2-*O*-*p*-methoxybenzyl-α-D-mannopyranosyl)-(1→2)-(3,4-di-*O*-benzyl-α-D-mannopyranosyl)-(1→6)-(2-*O*-benzoyl-3,4-di-*O*-benzyl-α-D-mannopyranosyl)-(1→4)-(2-azido-3,6-di-*O*-benzyl-2-deoxy-α-D-glucopyranosyl)-(1→6)-3,4,5-tri-*O*-benzyl-1,2-*O*-(L-1,7,7-trimethyl[2.2.1]bicycloheptyliden)-D-*myo*-inositol (**11**, 674 mg, 276 μmol, 98%). $[\alpha]_D$ +30 (*c* 1.0, CH_2Cl_2). ^{13}C NMR ($CDCl_3$) δ: 10.0 (Cph), 19.6 (*t-Bu*Si), 20.6, 20.9 (Cph), 27.2 (*t-Bu*Si), 30.0, 45.0, 45.3, 48.2, 51.8 (Cph), 55.4 (*MeO*Bn), 61.9–80.8 ($C^{ino}1$–$C^{ino}6$, C2–C6, C2′–C6′, C2″–C6″, C2‴–C6‴ CH_2Bn, MBn), 95.5 (C1), 98.7 (C1″), 98.8 (C1‴), 99.1 (C1′), 113.6 (MBn), 118.2 (Cph-acetal), 125.4–138.7 (aromatic C), 158.9 (MBn), 165.3 (Ph*C*O). DDQ (80 mg, 350 μmol) dissolved in CH_2Cl_2 (2 mL) was added to an ice cooled solution of **11** (650 mg, 266 μmol) in water saturated CH_2Cl_2 (5% H_2O, 25 mL) and stirred for 4 h, an additional 30 mg of DDQ in portions of 10 mg were added until the conversion was complete. The mixture was diluted with CH_2Cl_2 (100 mL); washed with water, $Na_2S_2O_3$ (10% aq), and $NaHCO_3$; dried ($MgSO_4$); and concentrated. The crude product was purified by flash chromatography (toluene–EtOAc, 12:1) to give **12** (520 mg, 224 μmol, 84%). $[\alpha]_D$ +28 (*c* 1.0, CH_2Cl_2). ^1H NMR ($CDCl_3$) δ: 0.80–1.96 (m, 25H, *t-Bu*Si, Cph), 3.30–4.90 (m, 52H), 5.19 (s, 1H), 5.52 (s, 1H), 5.59 (d, *J* = 3 Hz, 1H), 5.63 (m, 1H), 7.00–8.00 (m, 70H). ^{13}C NMR ($CDCl_3$) δ: 10.0 (Cph), 19.5 (*t-Bu*Si), 20.6, 20.9 (Cph), 27.1 (*t-Bu*Si), 30.1, 45.0, 45.3, 48.2, 51.8 (Cph), 61.9–80.8 ($C^{ino}1$–$C^{ino}6$, C2–C6, C2′–C6′, C2″–C6″, C2‴–C6‴, CH_2Bn), 95.5 (C1), 98.7 (C1″), 99.1 (C1′), 100.9 (C1‴), 118.2 (Cph-acetal), 125.4–138.7 (aromatic C), 165.3 (Ph*C*O).

(3,4-Di-*O*-benzyl-α-D-mannopyranosyl)-(1→2)-(3,4-di-*O*-benzyl-α-D-mannopyranosyl)-(1→6)-(3,4-di-*O*-benzyl-α-D-mannopyranosyl)-(1→4)-(2-azido-3,6-di-*O*-benzyl-2-deoxy-α-D-glucopyranosyl)-(1→6)-3,4,5-tri-*O*-benzyl-1,2-*O*-(L-1,7,7-trimethyl[2.2.1]bicyclohept-6-yliden)-D-*myo*-inositol (14)

Compound **12** (490 mg, 211 μmol) was deacetylated under Zemplén conditions. To speed up the reaction, the mixture was warmed to 45°C. After 3 days the reaction mixture was neutralized with H^+ ion exchange resin, filtered, and concentrated. The residue was purified by flash-chromatography (toluene–EtOAc, 6:1→3:1) to obtain (3,4-di-*O*-benzyl-6-*O*-*tert*-butyldiphenylsilyl-α-D-mannopyranosyl)-(1→2)-(3,4-di-*O*-benzyl-α-D-mannopyranosyl)-(1→6)-(3,4-di-*O*-benzyl-α-D-mannopyranosyl)-(1→4)-(2-azido-3,6-di-*O*-benzyl-2-deoxy-α-D-glucopyranosyl)-(1→6)-3,4,5-tri-*O*-benzyl-1,2-*O*-(L-1,7,7-trimethyl[2.2.1]bicyclohept-6-yliden)–D-*myo*-inositol (**13**, 400 mg, 180 μmol, 85%). $[\alpha]_D$ +40 (*c* 1.0, CH_2Cl_2). ^{13}C NMR ($CDCl_3$) δ: 10.0 (Cph), 19.6 (*t-Bu*Si), 20.6, 20.9 (Cph), 27.1 (*t-Bu*Si), 30.1, 45.0, 45.3, 48.2, 51.8 (Cph), 62.0–80.6 ($C^{ino}1$–$C^{ino}6$, C2–C6, C2′–C6′, C2″–C6″, C2‴–C6‴, CH_2Bn), 95.4 ($J_{C1,H1}$ = 173 Hz, C1), 99.1 ($J_{C1,H1}$ = 168 Hz, C1′), 100.2, 101.4 ($J_{C1,H1}$ = 176, 169 Hz, C1″, C1‴), 118.2 (Cph-acetal), 127.2–138.5 (aromatic C). Compound **13** (350 mg, 157 μmol) was dissolved in THF (10 mL) and TBAF (200 μL, 1 M in THF) was added. The mixture was stirred at room temperature overnight, then concentrated, and purified by flash chromatography (toluene–EtOAc, 3:1→2:1) to give 267 mg (135 μmol, 86%) of **14**. $[\alpha]_D$ +50 (*c* 1.0, CH_2Cl_2). ^1H NMR ($CDCl_3$) δ: 0.80–2.04 (m, 16H, Cph), 3.34–4.90 (m, 52H), 5.03 (s, 1H), 5.06 (s, 1H), 5.28 (s, 1H), 5.58 (d, *J* = 2 Hz, 1H), 7.00–7.40 (m, 55H). ^{13}C NMR ($CDCl_3$) δ: 10.1, 20.7, 20.9, 27.3, 30.1, 45.0, 45.4, 48.2, 51.8 (Cph), 62.0–81.0 ($C^{ino}1$–$C^{ino}6$, C2–C6, C2′–C6′, C2″–C6″, C2‴–C6‴, CH_2Bn), 95.5 (C1), 99.5 (C1′), 100.8, 101.2 (C1″, C1‴), 118.2 (Cph-acetal), 127.5–128.6 and 137.5–138.6 (aromatic C). Anal. calcd. for $C_{117}H_{131}N_3O_{25}$: C 71.00, H 6.67; found: C 70.85, H 6.65.

(2,6-Di-[ammoniumphosphate]-α-D-mannopyranosyl)-(1→2)-(6-[ammoniumphosphate]-α-D-mannopyranosyl)-(1→6)-(2-[ammoniumphosphate]-α-D-mannopyranosyl)-(1→4)-(2-amino-2-deoxy-α-D-glucopyranosyl)-(1→6)-D-*myo*-inositol 1,2-cyclic phosphate ammonium salt (18)

1*H*-Tetrazole (115 mg, 1.64 mmol) was added to a solution of **14** (230 mg, 116 μmol) and dibenzyl diisopropylphosphoramidite (225 μL, 700 μmol) in CH_2Cl_2 (3.5 mL). After 20 min the reaction mixture was cooled to 0°C and 70% *m*-chloroperbenzoic acid (230 mg) was added. The mixture was stirred an additional 15 min and then diluted with CH_2Cl_2 and washed with $Na_2S_2O_3$ (10% aq), $NaHCO_3$ and, water. After drying ($MgSO_4$), filtration, and concentration, the crude product was subjected to flash chromatography (toluene → toluene–EtOAc, 20 → 25%) to yield (3,4-di-*O*-benzyl-2,6-bis-*O*-dibenzyloxyphosphoryl-α-D-mannopyranosyl)-(1→2)-(3,4-di-*O*-benzyl-6-*O*-dibenzyloxyphosphoryl-α-D-mannopyranosyl)-(1→6)-(3,4-di-*O*-benzyl-2-*O*-dibenzyloxyphosphoryl-α-D-mannopyranosyl)-(1→4)-(2-azido-3,6-di-*O*-benzyl-2-deoxy-α-D-glucopyranosyl)-(1→6)-3,4,5-tri-*O*-benzyl-1,2-*O*-(L-1,7,7-trimethyl[2.2.1]bicyclohept-6-yliden)-D-*myo*-inositol (**15**, 364 mg, 116 μmol, quant.). $[\alpha]_D$ +23 (*c* 1.0, CH_2Cl_2). ^{13}C NMR ($CDCl_3$) δ: 10.2, 20.8, 21.0, 27.4, 30.2, 45.2, 45.5, 48.3, 51.9 (Cph), 63.3–80.8 ($C^{ino}1$–$C^{ino}6$, C2–C6, C2′–C6′, C2″–C6″, C2‴–C6‴, CH_2Bn), 95.5 (C1), 98.9 (C1′), 99.4, 99.9 (C1″, C1‴), 118.3 (Cph-acetal), 127.2–138.6 (aromatic C). ^{31}P NMR ($CDCl_3$) δ: 4 signals between –0.5 and +0.5. TFA (1 mL) was added at 0°C to a solution of **15** (300 mg, 100 μmol) in CH_2Cl_2 (10 mL). The mixture was stirred for 18 h (room temperature), quenched by the addition of Et_3N (1 mL), and concentrated. The residue was purified by flash chromatography (toluene–EtOAc, 2:1) to give (3,4-di-*O*-benzyl-2,6-bis-*O*-dibenzyloxyphosphoryl-α-D-mannopyranosyl)-(1→2)-(3,4-di-*O*-benzyl-6-*O*-dibenzyloxyphosphoryl-α-D-mannopyranosyl)-(1→6)-(3,4-di-*O*-benzyl-2-*O*-dibenzyloxyphosphoryl-α-D-mannopyranosyl)-(1→4)-(2-azido-3,6-di-*O*-benzyl-2-deoxy-α-D-glucopyranosyl)-(1→6)-3,4,5-tri-*O*-benzyl-D-*myo*-inositol (**16**, 132 mg, 46 μmol, 46%). $[\alpha]_D$ +32 (*c* 1.0, CH_2Cl_2). ^{13}C NMR ($CDCl_3$) δ: 53.6, 64.2, 66.3–81.7 ($C^{ino}1$–$C^{ino}6$, C2–C6, C2′–C6′, C2″–C6″, C2‴–C6‴, CH_2Bn), 98.2, 98.7 (C1, C1″), 98.9, 99.0, 99.7, 99.7 (C1′, C1‴), 127.2–128.7, 135.6–137.8, 137.9–138.5 (aromatic C). ^{31}P NMR ($CDCl_3$) δ: 4 signals between –0.5 and +0.5. Methyl dichlorophosphate (50 μL, 50 mmol) was dissolved in dry pyridine (1 mL) at 15°C (water bath). The mixture was stirred for 20 min, after which a solution of **16**

© 2002 NRC Canada

(48 mg, 16.6 μmol) in dry pyridine (500 μL) was added. After 2 h the starting material was consumed (TLC: $CHCl_3$–MeOH, 9:1) and the reaction was quenched by addition of $NaHCO_3$. The mixture was transferred into a 100-mL round bottom flask (using approx. 10 mL pyridine) and concentrated. The residue was dissolved and partitioned between $CHCl_3$ (60 mL) and water (10 mL). HCl (1 M, aq.) was added until the solution was pH 1 (4 mL). The aqueous phase was extracted with $CHCl_3$, and the combined organic phases were dried ($MgSO_4$) and concentrated. After co-evaporation two times from EtOH, the crude product (3,4-di-*O*-benzyl-2,6-bis-*O*-dibenzyloxyphosphoryl-α-D-mannopyranosyl)-(1→2)-(3,4-di-*O*-benzyl-6-*O*-dibenzyloxy-phosphoryl-α-D-mannopyranosyl)-(1→6)-(3,4-di-*O*-benzyl-2-*O*-dibenzyloxyphosphoryl-α-D-mannopyranosyl)-(1→4)-(2-azido-3,6-di-*O*-benzyl-2-deoxy-α-D-glucopyranosyl)-(1→6)-3,4,5-tri-*O*-benzyl-D-*myo*-inositol 1,2-cyclic phosphate (**17**, 48 mg, 95%) was obtained, which was immediately used for the next reaction step. Raw material **17** dissolved in dry THF (2 mL) was dropped into liquid ammonia (20 mL). A catalytic amount of sodium was added to the white emulsion, which turned rapidly into a deep blue solution. After 2 min, NH_4Cl (s) was carefully added until the solution turned white again. The liquid ammonia was allowed to evaporate. The dry residue was dissolved in water (20 mL), and washed once with Et_2O (10 mL). After concentration, the crude product was purified by size exclusion chromatography (G15, eluent water containing 1% n-BuOH) to give, after freeze-drying, **18** (12 mg, 10 μmol, 60%). ^{1}H NMR (D_2O) δ: 3.38–4.60 (m, 31H), 5.14 (s, 1H), 5.25 (s, 1H), 5.49 (1H). ^{13}C NMR (D_2O) δ: 55.1, 60.9, 64.8, 64.9, 67.2, 67.3, 70.3–73.3, 74.8, 75.0, 76.6, 77.8, 79.5, 80.2, 82.2 ($C^{ino}1$–$C^{ino}6$, C2–C6, C2′–C6′, C2″–C6″, C2‴–C6‴), 96.8 (C1), 99.4 (C1″), 100.5, 101.5 (C1′, C1‴). ^{31}P NMR (D_2O) δ: 0.3, 0.9 ($PO(OH)_2$), 15.8 (cyclic phosphate). MALDI-TOF MS: 1209.2 $[M + H]^+$, 1227.2 $[M + H + NH_4]^+$, 1231.2 $[M + Na]^+$.

Acknowledgments

Financial support from EU (Contract Number ERB FMRX CT96 0025) and from the Swedish Natural Science Research Council are gratefully acknowledged.

References

1. M.A.J. Ferguson, S.W. Homans, R.A. Dwek, and T.W. Rademacher. Science (Washington, D.C.), **239**, 753 (1988).
2. M.J. McConville and M.A.J. Ferguson. Biochem. J. **294**, 305 (1993).
3. R.N. Cole and G.W. Hart. *In* Glycoproteins II. *Edited by* J. Montreuil, J.F.G. Vliegenthart, and H. Schachter. Elsevier, Amsterdam. 1997. pp. 69–88.
4. S. Alemany, J.M. Mato, and P. Strålfors. Nature (London), **330**, 77 (1987).
5. P. Strålfors. Nature (London), **335**, 554 (1988).
6. R. Plourde, M. d'Aarcao, and A.R. Saltiel. J. Org. Chem. **57**, 2606 (1992).
7. W. Frick, A. Bauer, J. Bauer, S. Wied, and G. Müller. Biochem. **37**, 13 421 (1998).
8. R. Madsen, U.E. Udodong, C. Roberts, D.R. Mootoo, P. Konradssson, and B. Fraser-Reid. J. Am. Chem. Soc. **117**, 1554 (1995).
9. T.G. Mayer and R.R. Schmidt. Eur. J. Org. Chem. **3**, 1153 (1999).
10. D.K. Baeschlin, L.G. Green, M.G. Hahn, B. Hinzen, S.J. Ince, and S.V. Ley. Tetrahedron: Asymmetry, **11**, 173 (2000).
11. S. Oscarson. *In* Carbohydrates in chemistry and biology: A comprehensive handbook. *Edited by* B. Ernst, G. Hart, and P. Sinaÿ. Wiley-VCH, Weinheim. 2000.
12. P.J. Garegg. Adv. Carbohydr. Chem. Biochem. **52**, 179 (1997).
13. R. Verduyn, J.J.A. Belien, C.M. Freef-Tromp, G.A. van der Marel, and J.H. van Boom. Tetrahedron Lett. **32**, 6637 (1991).
14. J. Lindberg, L. Öberg, P.J. Garegg, and P. Konradsson. Tetrahedron, **58**, 1387 (2002).
15. T. Nukada, H. Lucas, P. Konradsson, and C.A.A. van Boeckel. Synlett, 365 (1991).
16. K.-L. Yu and B. Fraser-Reid. Tetrahedron Lett. **29**, 979 (1988).
17. K. Ruda, J. Lindberg, P.J. Garegg, S. Oscarson, and P. Konradsson. Tetrahedron, **56**, 3969 (2000).
18. K. Ruda, J. Lindberg, P.J. Garegg, S. Oscarson, and P. Konradsson. J. Am. Chem. Soc. **122**, 11 067 (2000).

© 2002 NRC Canada

Oligosaccharide recognition by antibodies: Synthesis and evaluation of talose oligosaccharide analogues

T.L. Lowary, E. Eichler, and D.R. Bundle

Abstract: A series of monosaccharide **(4**–**6)**, disaccharide **(3**, **7**–**12),** and trisaccharide (**13**–**15)** analogs of the native ligand **2,** which fills the binding site of monoclonal antibody Se 155.4, have been synthesized and their bioactivity measured by solid- and solution-phase assays. The syntheses of disaccharide analogs sought to replace galactose by various alkyl groups at the O-2 position of mannose. The activity of one of these O-2 alkyl analogs was 75% of that observed for the trisaccharide and points to only weak net bonding between the solvent exposed galactose residue and the antibody binding site. The synthesis of talose analogs **13** and **14**, where the mannose or galactose residues of **2** were replaced by talose produced ligands with activities from one-third to one-half of that seen for the native ligand **2**. These activity changes did not exhibit discernable correlations with the ability of talose to disrupt water of solvation.

Key words: abequose, 3,6-dideoxy-D-*xylo*-hexose, talose disaccharide and trisaccharide, antibody oligosaccharide interactions, molecular recognition of carbohydrates, water in antibody complexes, *Salmonella* LPS, monoclonal antibody Se 155.4, bacterial *O*-antigen.

Résumé : On a réalisé la synthèse d'une série de monosaccharides (**4**–**6**), de disaccharides (**3, 7**–**12**) et de trisaccharides (**13**–**15**), des analogues du ligand naturel **2** qui remplit le site de liaison de l'anticorps monoclonal Se 155.4 et on a mesuré leur bioactivité par des essais en phase solide ainsi qu'en solution. Dans les synthèses des analogues de la série des disaccharides, on a tenté de remplacer le galactose par divers groupes alkyles en position O-2 du mannose. L'activité de l'un de ces analogues O-2 alkylés est égale à 75% de celle observée pour le trisaccharide et elle suggère qu'il n'existe qu'une faible liaison nette entre le résidu de galactose exposé au solvant et le site de liaison de l'anticorps. Les synthèses des analogues **13** et **14** dans lesquels les résidus de mannose ou de galactose du composé **2** ont été remplacés par du talose conduisent à des ligands dont les activités varient entre un tiers et une demie de celle observée avec le ligand **2** naturel. Ces changements d'activité ne donnent pas lieu à des corrélations qui pourraient avoir une corrélation avec l'habilité du talose à désorganiser l'eau de solvatation.

Mots clés : abéquose, 3,6-didésoxy-D-*xylo*-hexose, disaccharide et trisaccharide du talose, interactions anticorps-oligosaccharide, reconnaissance moléculaire des hydrates de carbone, eau dans des complexes d'anticorps, *Salmonella* LPS, anticorps monoclonal Se 155.4, *O*-antigène bactérien.

[Traduit par la Rédaction]

Introduction

The binding of carbohydrates by proteins is a biologically significant event, known to play a critical role in a diverse number of physiological processes such as viral (1, 2) and bacterial (3–5) infection and inflammation arising from cell adhesion (6–9). Consequently, in recent years interest in developing oligosaccharide-based therapeutics that inhibit carbohydrate–protein recognition has increased (3, 10, 11). However, to realize the potential of carbohydrate-based drugs, the milli- to micromolar K_ds characteristic of sugar–protein interactions must be improved (enhanced). This in turn requires a deeper appreciation of the origins of the free energy of binding. A significant body of three-dimensional structural data has been accumulated for oligosaccharide–protein complexes (12, 13). Despite supporting studies by NMR and thermodynamic measurements, the relative importance of competing processes that contribute to ΔG remains a subject of controversy (14, 15). Recent work suggests that solvation effects may make a far greater contribution to ΔG then was previously realized (16, 17). Possibly linked to the role of water is the observation by Lemieux that modification of functional groups located at or near the periphery of oligosaccharide–protein complexes can result in large swings in the enthalpy and entropy of binding, while the free energy changes by only small values. This observation led to

Received 4 December 2001. Published on the NRC Research Press Web site at http://canjchem.nrc.ca on 28 August 2002.

We dedicate this paper to the memory of Professor Raymond U. Lemieux.

T.L. Lowary. Department of Chemistry, The Ohio State University, 100 W 18th Avenue, Columbus, OH 43210, U.S.A.
E. Eichler. Institute for Biological Sciences, National Research Council Canada, Ottawa, ON K1A 0R6, Canada.
D.R. Bundle.[1] Department of Chemistry, University of Alberta, Edmonton, AB T6G 2G2, Canada.

[1]Corresponding author (dave.bundle@ualberta.ca).

 DOI: 10.1139/V02-118 © 2002 NRC Canada

Fig. 1. (*a*) Bound conformation I (20) with a direct Abe O-2 to Man O-2 H-bond; (*b*) bound conformation II (21) with a water mediated Abe O-2 to Man O-2 H-bond. Note also the different H-bonding between the antibody and the galactose residue.

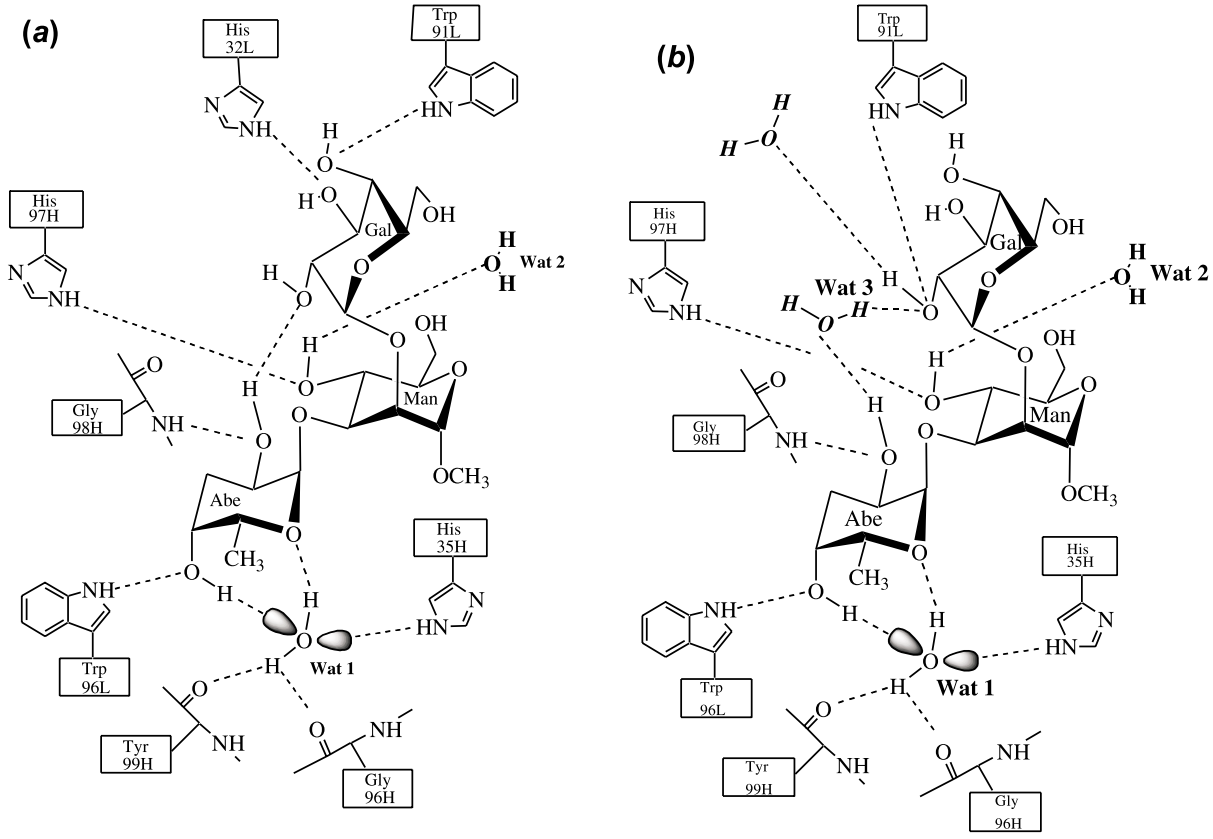

the proposal (18) (so far not realized) that significant gains in free energy might be achieved by concentrating on modification of groups in these positions. Here we focus on the synthesis of a carbohydrate epitope that should significantly disrupt structure of solvent, at least about the unbound carbohydrate ligand.

For this purpose we chose as a model system the monoclonal antibody Se 155.4 which recognizes a bacterial lipopolysaccharide antigen via the Gal[Abe]Man trisaccharide epitope (**2**). It is part of the tetrasaccharide α-D-Gal*p*-(1→2)[α-D-[Abe*p*-(1→3)]-α-D-Man*p*-(1→4)-α-L-Rha*p* (**1**) that comprises the repeating unit of the *O*-polysaccharide component of LPS (19). The structural (20, 21) and energetic (22–24) aspects of antigen binding to Se 155.4 have been well characterized, and an efficient *Escherichia coli* expression system has permitted extensive binding site mutagenesis (25) and antibody engineering studies (26, 27).

Functional group replacements of hydroxyl groups of the mannose (Man) and galactose (Gal) residues are reported here together with modification of the abequose (Abe) residue. The structural changes of the epitope are designed to probe the relative importance of hydrogen groups that are accessible to solvent water. The abequose C-2 hydroxyl group accepts a hydrogen bond from Gly 98 and donates a hydrogen bond to the Gal C-2 hydroxyl either directly (Fig. 1*a*) or via a water molecule (Fig. 1*b*). At the monosaccharide level, this was probed by methylation (**5**) or inversion of configuration (**6**) (Fig. 2). The relative importance of hydrogen bonds to the Man O-4 and Gal O-2 centres in trisaccharide **2** were investigated by synthesis of oligosaccharides in which a mannose or galactose residue is replaced by the corresponding talopyranoside: disaccharides **11** and **12** and trisaccharides **13** and **14** (Fig. 2). An additional rationale for investigating the activity of talopyranose containing structures derives from the observation that talose, more than other hexoses, disrupts the structure of water of solvation (28–31). Recently, the importance of solvent effects on protein binding of amphiphilic ligands has received attention (15, 32) and has been shown to make a large contribution to ΔG via enthalpic and entropic terms (16). Further information about the importance of the galactosyl residue in **2** was provided by the replacement of this moiety with small alkyl chains in compounds **7**–**10** (Fig. 2).

The results also raise questions about the strength of hydrogen bonds between protein and solvent exposed ligand-OH groups, the existence of which is based on the proximity and geometry of heavy atoms observed in high resolution crystal structures (20, 21). Two such hydrogen bonds involve the Gal O-3 and Gal O-4 atoms. Replacement of these hydroxyl groups by -OMe and -Cl, as in compound **15**, should abolish the hydrogen bond donor capability of the functionalities (33).

Results and discussion

Synthesis of methyl 2-*O*-methyl-3,6-dideoxy-α-D-*xylo*-hexopyranoside (5)

Treatment of methyl 3,6-dideoxy-α-D-*xylo*-hexopyranoside (**4**) (34) with barium oxide and a limiting amount of methyl iodide provided, in 45% yield, the 2-*O*-methyl derivative **5**.

© 2002 NRC Canada

Fig. 2. Tetrasaccharide repeating unit of the *Salmonella* LPS (**1**) and the native trisaccharide epitope (**2**). Synthetic targets **3**–**15**.

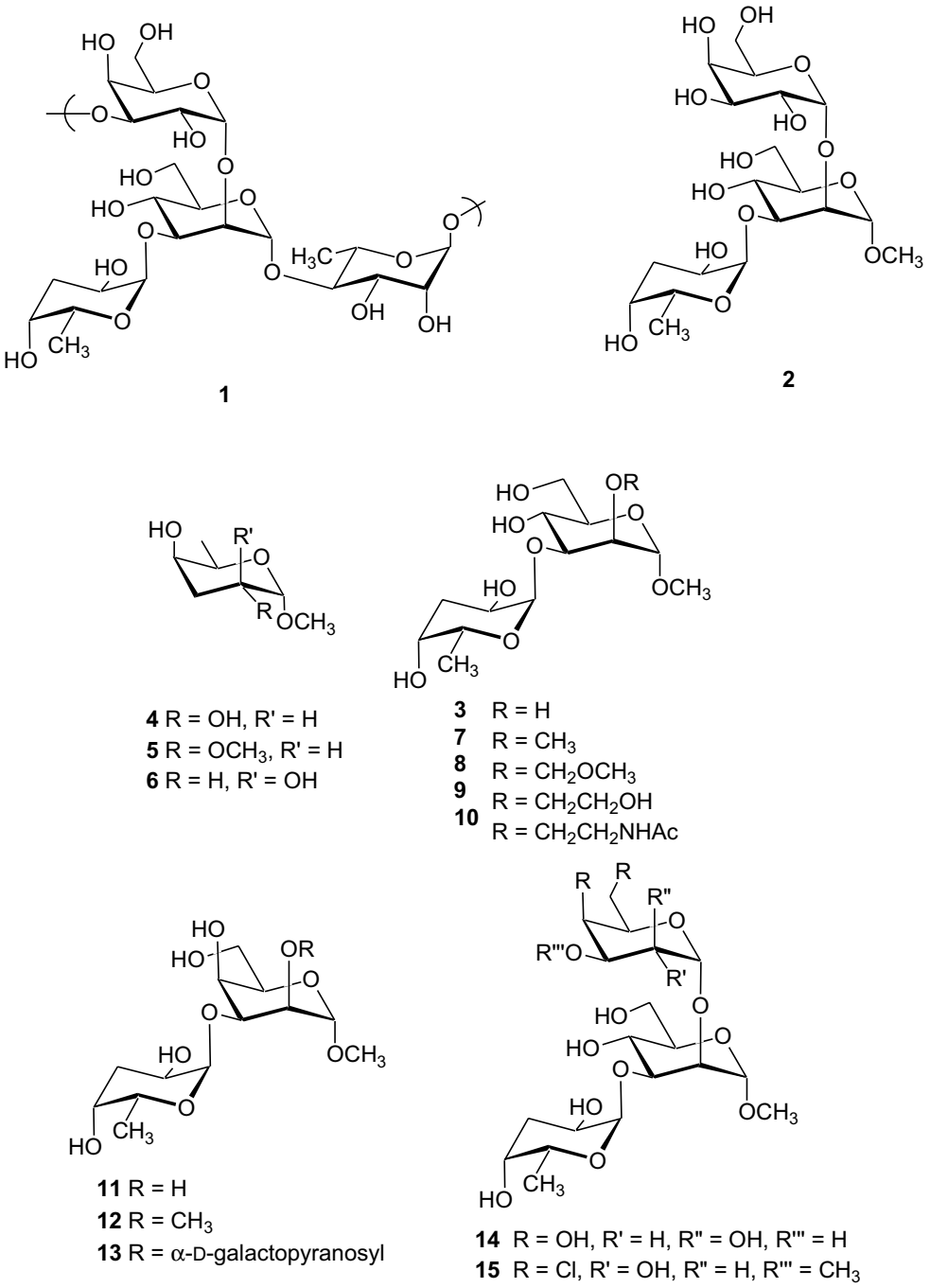

The regiochemistry of methylation was established by comparing the ^{1}H NMR chemical shifts of product **5** with those of starting material **4** (Scheme 1).

Synthesis of methyl 3,6-dideoxy-α-D-*lyxo*-hexopyranoside (6)

Treatment of methyl 3,6-dideoxy-D-*arabino*-hexopyranoside (**16**) (35) with *tert*-butyldiphenylsilyl chloride in pyridine with catalysis by DMAP resulted in the formation of the silyl ether **17** in 80% yield. Silylation of this alcohol proved to be extremely sluggish, possibly owing to steric hindrance resulting from the size of the silyl protecting group. Consequently, attempts were made to prepare the less bulky *tert*-butyldimethylsilyl ether. However, protection with this group was equally slow and this approach was therefore abandoned. It was hoped that a large protecting group on O-2 would facilitate the stereoselectivity of a later reduction (see below) and for this reason the use of smaller protecting groups was not investigated.

Subsequent treatment of **17** with sodium methoxide to remove the benzoate ester provided alcohol **18** in 94% yield (Scheme 1). The stereochemistry at C-4 was then inverted, first by oxidation with pyridinium chlorochromate and then by reduction with sodium borohydride, to provide, in 76% yield over the two steps, the 3,6-dideoxy-D-*lyxo*-hexopyranoside derivative **19**. The reduction was not, however,

© 2002 NRC Canada

Scheme 1. (*a*) CH_3I, BaO, $Ba(OH)_2$, DMF; (*b*) TBDPSCI, pyridine, DMAP; (*c*) $NaOCH_3$, CH_3OH; (*d*) PCC, CH_2Cl_2, then $NaBH_4$, CH_3OH; (*e*) TBAF, THF.

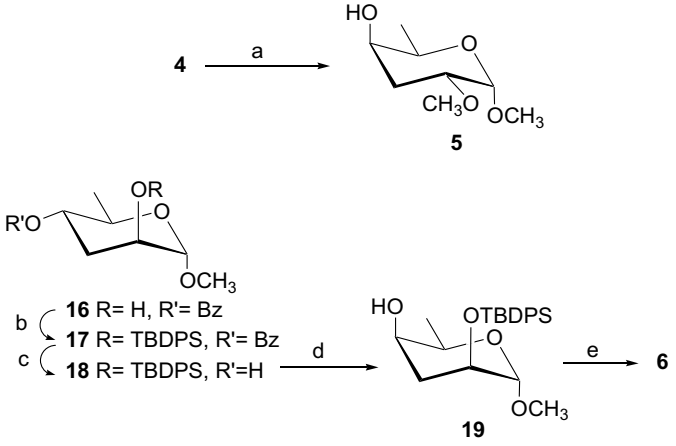

completely stereoselective and thus a small amount (16%) of methyl-3,6-dideoxy-D-*arabino*-hexopyranoside (**18**) was also obtained. Removal of the silyl ether in **19** with tetrabutylammonium fluoride provided the desired product **6** in 95% yield. Interestingly, compound **6** is a volatile liquid; attempts to dry the compound while heating under vacuum resulted in complete evaporation overnight.

Synthesis of 2-*O*-alkylated disaccharides (Scheme 2) (7–10)

Methylation of the previously reported (36) disaccharide **20** provided methyl ether **21** in 87% yield. Hydrogenation of the benzyl protecting groups provided the deprotected disaccharide **7** (66%).

The 2-methoxymethyl derivative **8** could be prepared after prolonged reaction of disaccharide alcohol **20** with chloromethyl methyl ether. The MOM-protected disaccharide **22** was obtained in 80% yield and then converted to the target compound **8** by hydrogenation (88% yield).

Protection of **20** as a 2-*O*-allyl ether was achieved by reaction with allyl bromide to give **23** (92%). Ozonolysis of the allyl double bond and reductive work-up with sodium borohydride gave, in 70% yield, the 2′-hydroxyethyl ether disaccharide **24**. A portion of this alcohol was then deprotected (H_2, Pd/C) to give disaccharide **9** (74%). The remainder of alcohol **24** was converted to the phthlamido derivative **25** under Mitsunobu conditions (37) in 91% yield. Removal of the phthalimide group with hydrazine acetate and acetylation of the resulting amino group gave the protected *N*-acetyl disaccharide **26**. After deprotection, the disaccharide **10** was obtained in 62% yield from **25**.

Synthesis of talopyranosyl-containing disaccharides (Scheme 3) (11, 12)

Preparation of the two disaccharides containing talopyranosyl residues began with the known mannoside **27** (38), which was subjected to an oxidation–reduction protocol to provide the talopyranoside alcohol **28** in 85% yield. The benzoate ester was removed by transesterification (92%) and the resulting diol protected as benzyl ethers (97%) to give **30**. Hydrolysis of the isopropylidene acetal from **30** gave methyl 4,6-di-*O*-benzyl-talopyranoside (**31**) in 91% yield. Transient protection of the diol as an orthobenzoate was achieved by reaction of **31** with trimethylorthobenzoate and was followed immediately by treatment with acid to afford the 2-*O*-benzoate **32** (81%). Glycosylation of **32** with the abequose thioglycoside **33** (39) provided the fully protected disaccharide **34** in 83% yield. Treatment of **34** with sodium methoxide gave the disaccharide alcohol **35** in 96% yield. A portion of this alcohol was hydrogenated to provide disaccharide **11** (84%). Methylation of the remainder of **35**

Scheme 2. (*a*) CH_3I, NaH, DMF; (*b*) MOMCl, Hunig's base, acetone; (*c*) AllBr, NaH, DMF; (*d*) O_3, CH_2Cl_2–CH_3OH, then $NaBH_4$; (*e*) $(Ph_3)_3P$, DEAD, phthalimide, THF; (*f*) H_2NNH_2–HOAc, CH_3OH, then Ac_2O, pyridine; (*g*) H_2, 10% Pd/C, HOAc.

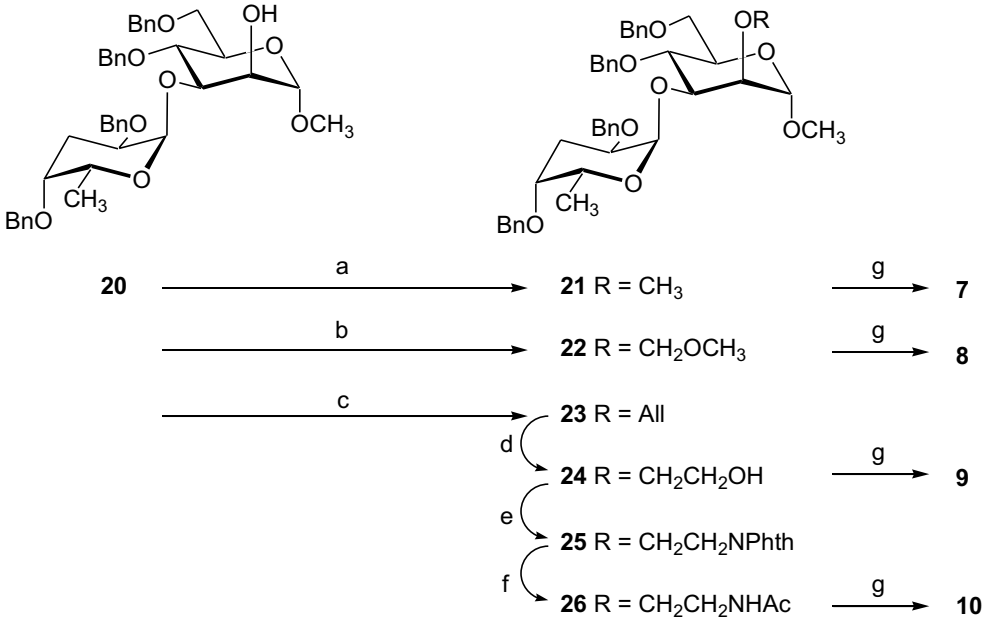

© 2002 NRC Canada

Scheme 3. (*a*) PCC, CH_2Cl_2, then $NaBH_4$, CH_3OH; (*b*) $NaOCH_3$, CH_3OH; (*c*) BnBr, NaH, DMF; (*d*) 80% HOAc–H_2O; (*e*) $PhC(OCH_3)_3$, *p*-TsOH, CH_2Cl_2, then 80% HOAc–H_2O; (*f*) **33**, NIS, AgOTf, CH_2Cl_2; (*g*) CH_3I, NaH, DMF; (*h*) H_2, 10% Pd/C, HOAc.

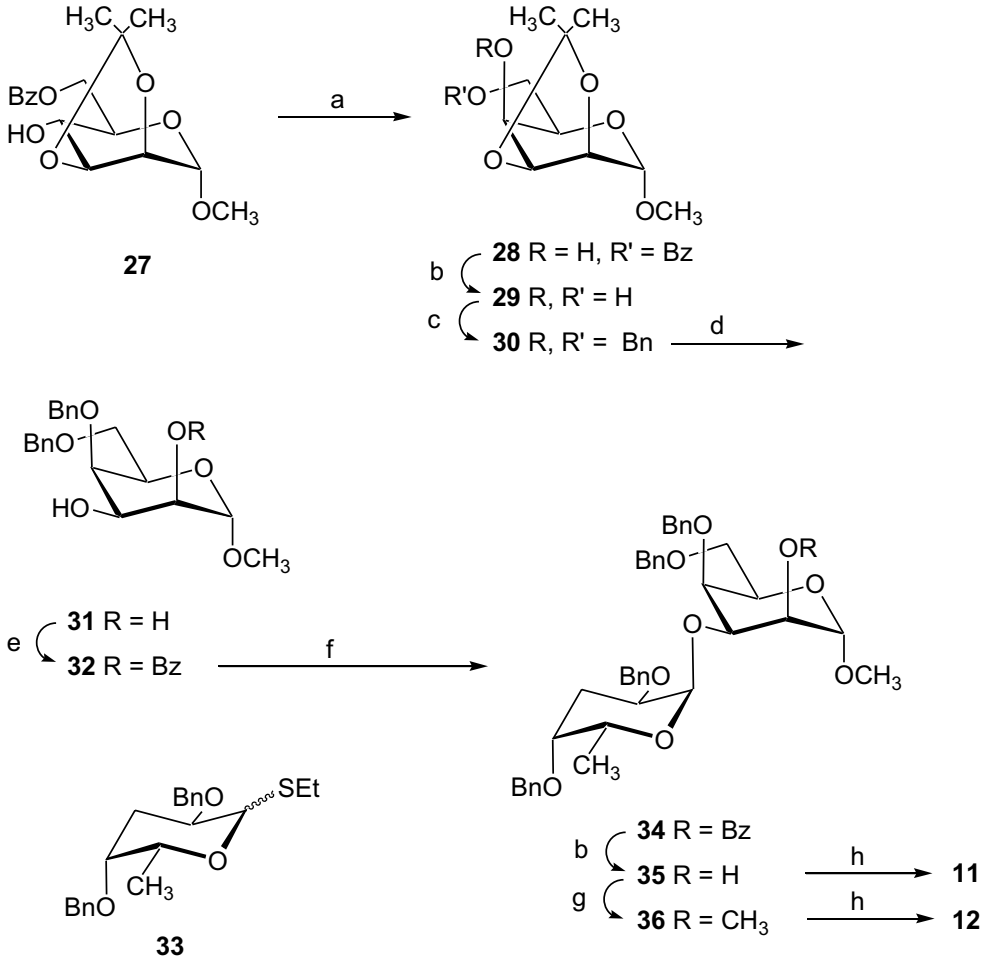

Scheme 4. (*a*) **35**, NIS, AgOTf, CH_2Cl_2; (*b*) H_2, 10% Pd/C, HOAc.

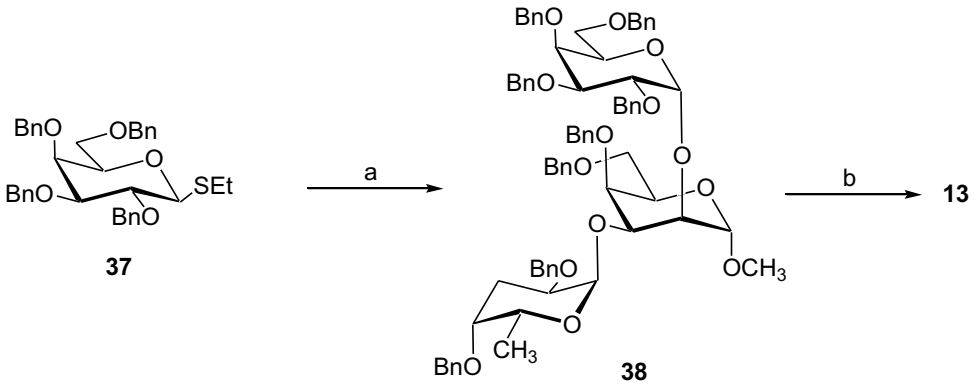

gave the 2-*O*-methyl disaccharide **36** (90%), which was deprotected by hydrogenation to disaccharide **12** in 78% yield.

Synthesis of talopyranosyl-containing trisaccharides (13, 14)

Alcohol **35** was glycosylated with the galactose thioglycoside **37** (40) to provide the trisaccharide **38** in modest (35%) yield. The desired product, **13**, was obtained in 86% yield upon hydrogenation (Scheme 4).

The synthesis of trisaccharide **14** required first the preparation of a suitable talopyranosyl donor that could be coupled to disaccharide alcohol **20**. To this end, the acetal protected methyl talopyranoside **29** was converted to methyl α-D-talopyranoside (**39**) by acid hydrolysis (Scheme 5). Acetylation then gave **40** in 76% yield (from **29**). Acetolysis provided the peracetate **41** (41) (95%), which in turn was

© 2002 NRC Canada

Scheme 5. (*a*) 95% TFA–H_2O; (*b*) Ac_2O, pyridine; (*c*) Ac_2O, H_2SO_4; (*d*) 48% HBr–HOAc, Ac_2O; (*e*) EtSH, $BF_3{\cdot}OEt_2$, CH_2Cl_2.

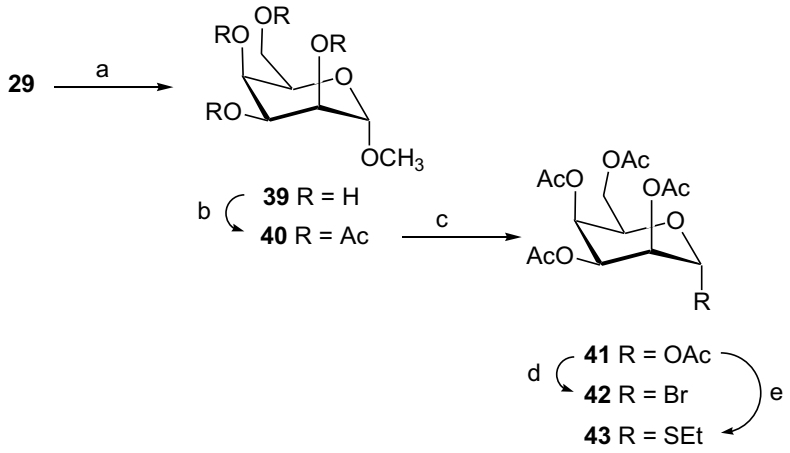

Scheme 6. (*a*) **20**, AgOTf, collidine, CH_2Cl_2.

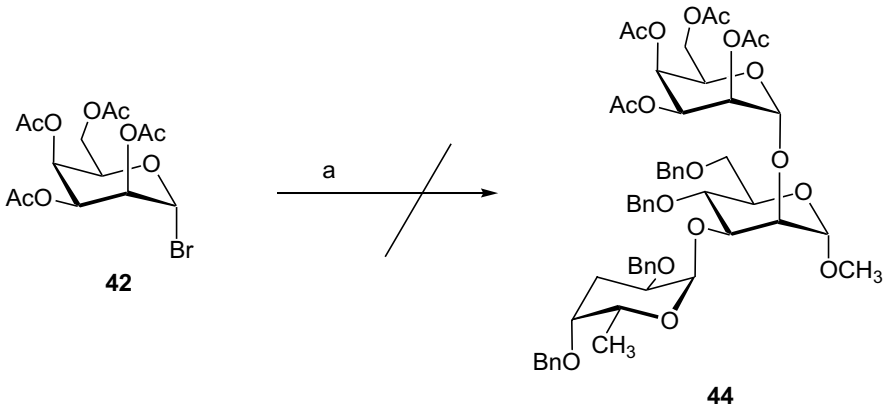

converted to the unstable talosyl-bromide **42** in quantitative yield. Unfortunately, when the disaccharide acceptor **20** was treated with an excess of bromide **42**, no trisaccharide product **44** could be isolated (Scheme 6). Decomposition of the bromide upon addition of the promoter (AgOTf) was virtually instantaneous. In hopes of circumventing this problem, attempts were made to prepare the more stable thioglycoside donor **43** from the peracetate using ethanethiol and boron trifluoride etherate. These attempts failed as well; despite prolonged reaction times and elevated temperatures, only small amounts (<10%) of **43** could be obtained. Therefore, another route to a more stable talopyranose donor was investigated.

Acetonation of galactoside **45** (42) with dimethoxypropane provided, in 66% yield, **46** (Scheme 7). Regioselective protection of this acetonide as a 6-*O*-silyl ether (**47**) could be achieved in 85% yield. Oxidation of the C-2 hydroxyl group under Swern conditions and subsequent reduction with sodium borohydride gave, in 85% yield, an anomeric mixture of thioglycosides **48** with the talo-configuration. Presumably the basic conditions of the oxidation resulted in the anomerization of the product ketone. Removal of the isopropylidene and silyl protecting groups was achieved by acid hydrolysis to give ethyl 1-thio-talopyranoside (**49**) which was immediately acetylated to give thioglycoside **43** in 89% yield. Either anomer of **43** could be used in the ensuing glycosylation reaction. When the acceptor **20** was treated with the glycosyl donor **43**, trisaccharide **44** was obtained in 47% yield. Final deprotection of **44** by transesterification and hydrogenation afforded the desired trisaccharide **14** (87%) (Scheme 7).

Synthesis of the dichlorogalactosyl containing trisaccharide (15) (Scheme 8)

Synthesis of the galactose thioglycoside donor **55** required for the preparation of trisaccharide **15**, began with the treatment of 3-*O*-methyl glucose (**50**) (43) with sulfuryl chloride. The dichlorinated galactosyl chloride **51** was obtained as a mixture of anomers (1:1.7 (α:β), total yield 65%). Conversion to the methyl glycoside and concurrent removal of the chlorosulfate group gave **52** as an anomeric mixture of methyl glycosides (1.7:1 (α:β), total yield 67%). Proceeding only with the α-anomer, the hydroxyl group in glycoside **52** was protected as a benzyl ether (71%) and then **53** was subjected to acetolysis affording **54** in an 80% yield. Reaction of acetate **54** with ethanethiol gave the desired thioglycoside **55** (42%). Finally, glycosylation of disaccharide alcohol **20** with **55** provided the trisaccharide **56** (73%). The target trisaccharide **15** was obtained in 66% yield upon hydrogenation.

Talopyranosides in the $^4C_1$ conformation experience a strong destabilizing interaction between axial hydroxyl groups at C-2 and C-4. However, adoption of the $^1C_4$ chair is not likely, since an even stronger destabilizing interaction

© 2002 NRC Canada

Scheme 7. (*a*) $(CH_3)_2C(OCH_3)_2$, *p*-TsOH, CH_3CN, then CH_3OH, HOAc; (*b*) TBDMSCI, DMAP, pyridine; (*c*) $(CO)_2Cl_2$, DMSO, Et_3N, then $NaBH_4$, CH_3OH; (*d*) 80% HOAc–H_2O; (*e*) Ac_2O, pyridine; (*f*) **20**, NIS, AgOTf, CH_2Cl_2; (*g*) $NaOCH_3$, CH_3OH, then H_2, 10% Pd/C, HOAc.

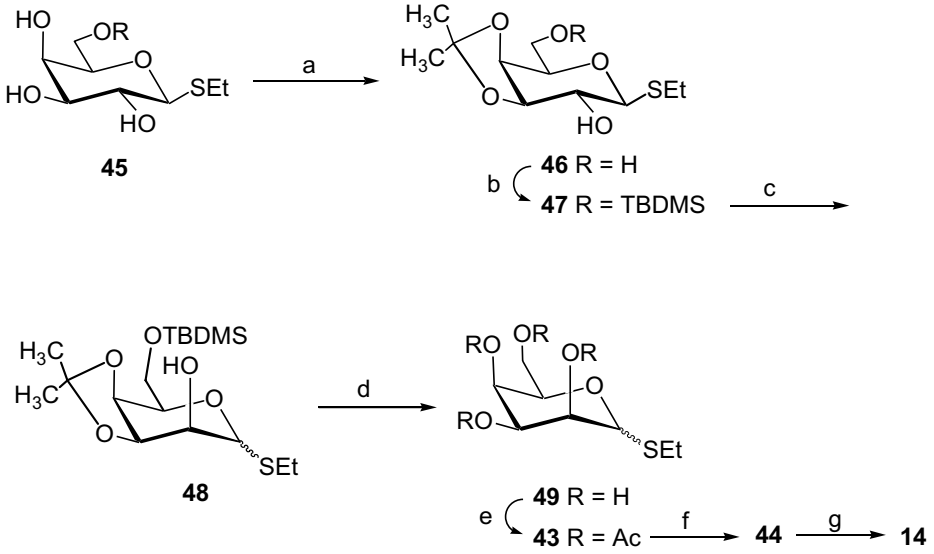

Scheme 8. (*a*) $SOCl_2$, pyridine, $CHCl_3$; (*b*) I_2, CH_3OH, then $NaOCH_3$, CH_3OH; (*c*) anomer separation; (*d*) BnBr, NaH, DMF; (*e*) Ac_2O, HOAc, H_2SO_4; (*f*) EtSH, $BF_3{\cdot}OEt_2$, CH_2Cl_2; (*g*) **20**, NIS, AgOTf, CH_2Cl_2; (*h*) H_2, 10% Pd/C, HOAc.

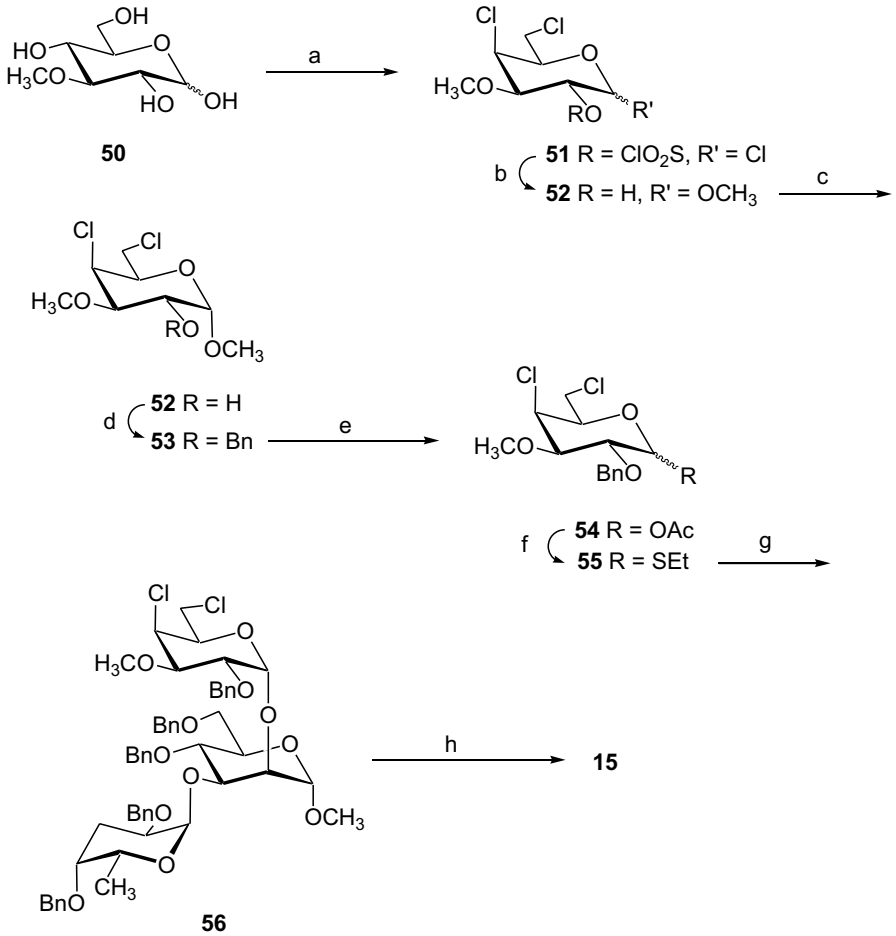

then arises between axial substituents at C-3 and C-6. Distortion of the $^4C_1$ chair to skew conformations could occur and it is likely that such conformations could be readily sampled. Coupling constants (^3J) for the $^4C_1$ chair are expected

© 2002 NRC Canada

Fig. 3. Solid-phase inhibition assays for selected compounds. Trisaccharide **15** (△), trisaccharide **13** (□), disaccharide **7** (▼), disaccharide **10** (●).

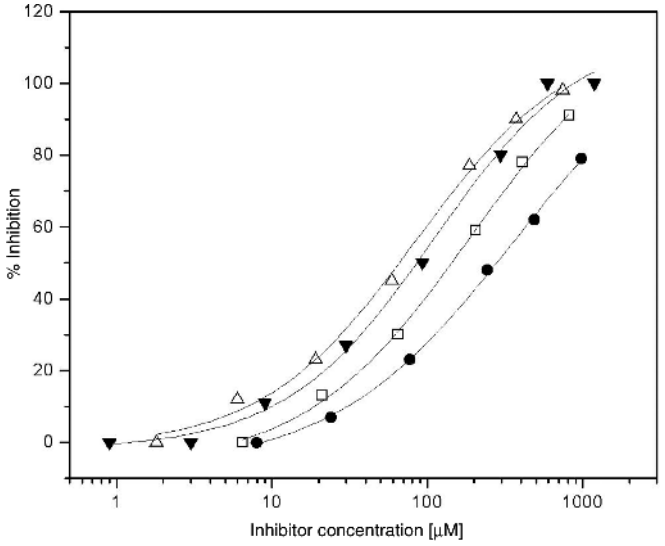

to be small since there are no vicinal diaxial hydrogens. Flattening of the ring or skewing would lead to high ^3J values as neighbouring protons change from ~60° toward 0°. Observed values, especially for $J_{2,3}$ and $J_{3,4}$ show no clear trend toward such larger coupling constants. In several instances these coupling constants are lower than the expected 3–5 Hz for equatorial–axial hydrogens. A complete analysis of this conformational issue is beyond the scope of this paper, but there is no strong evidence to suggest that the α-talopyranosides reported here adopted conformations that deviate significantly from the $^4C_1$ chair.

The activity of the synthetic mono- (**4**–**6**), di- (**3**,**7**–**12**) and trisaccharides (**13**–**15**) as inhibitors of antibody binding were initially evaluated in a previously described solid-phase binding assay (24, 44). In brief, affinity purified Se 155.4 antibody is absorbed onto microtitre plates and the binding of biotinylated *O*-polysaccharide antigen to the solid-phase antibody is measured in the presence and absence of inhibitors. The data for representative oligosaccharides are shown (Fig. 3). The association constants were determined by titration microcalorimetry (Table 1) for all compounds except **6** and **15**[2]. Data for compounds **3**–**5** and **8** are taken from ref. 24 and were determined at an earlier date and on different equipment. Disaccharide **7** (^{13}C labeled in the 2-*O*-methyl group) has been used to derive kinetic data for ligand antibody interactions and to observe ligand–protein NOEs (45).

A detailed analysis of the full calorimetry data will be reported together with molecular modeling[2]. However, several points emerge from the data (Table 1). The relatively high activities of 2-*O*-alkylated disaccharides **7** and **9** are consistent with earlier interpretations that in solution any hydrogen bonds between the galactose residue and the antibody site are very weak and of little net benefit. For disaccharide analogs substitution of mannose by talose results in a five- to 10-fold loss of binding energy, which correlates with the important hydrogen bond from a histidine residue to Man O-4 (Fig. 1). When talose is substituted for mannose and galactose in trisaccharides **13** and **14** a two- to threefold loss of binding occurs. As will be reported elsewhere, modeling of the antibody complex with each of these trisaccharides shows that the hydrogen bonding patterns of Fig. 1 can be maintained with only small movements about the glycosidic linkages. It is also apparent that initial hopes that the talose analogs would provide readily discernable trends to correlate with solvent reorganization about the ligand antibody complex have not been realized.

Table 1. Association constants and relative inhibitory power of the mono-, di-, and trisaccharides **3**–**15**.

Compound	$K_a \times 10^5$ (M^{-1})[a]	Relative inhibitory power[b]
2	2.1	100
3	0.24[c]	11
4	0.015[c]	0.7
5	0.019[c]	0.9
6	–ve	Inactive
7	1.43	68
8	0.69[c]	32
9	1.58	75
10	0.55	26
11	0.05	2
12	0.14	6
13	0.70	33
14	1.17	55
15	~1.5–1.8[d]	71–85

[a]Determined by calorimetry; the standard deviation for duplicate measurements of *K* was never greater than ±2%.
[b]Inhibition potency of **2** set as 100.
[c]Taken from ref. 24 and determined by calorimetry.
[d]Value taken from solid-phase immunoassay; estimated from the IC_{50} (44) determined with an accuracy of ±5%.

Experimental

Optical rotations were measured with a PerkinElmer 241 polarimeter at 22 ± 2°C. Analytical TLC was performed on Silica Gel 60-F_{254} (E. Merck, Darmstadt) with detection by quenching of fluorescence and (or) by charring with sulfuric acid. Iatrobeads refers to a beaded silica gel 6RS-8060 manufactured by Iatron Laboratories (Tokyo). All commercial reagents were used as supplied and chromatography solvents were distilled prior to use. Column chromatography was performed on Silica Gel 60 (40–60 μM, E. Merck, Darmstadt). Millex-GV (0.22 μM) filter units were from Millipore (Mississauga, ON). ^1H NMR were recorded at 360 MHz (Bruker AM-360) or at 500 MHz (Varian Unity 500) with either internal $CHCl_3$ (δ: 7.24, $CDCl_3$) or internal acetone (δ: 2.225, D_2O). ^{13}C NMR were recorded either at 75.5 MHz (Bruker AM-300) or 125.7 MHz (Varian Unity 500) with internal $CHCl_3$ (δ: 77.00, $CDCl_3$) or internal acetone (δ: 37.01, D_2O). ^1H NMR data are reported as though they were first order. Proton and carbon resonances for **7** and **9**–**15** were assigned using ^1H-^1H and ^1H-^{13}C correlation 4 carried out at room temperature. Organic solutions were

[2]M. Warwas and D.R. Bundle. Unpublished results.

© 2002 NRC Canada

dried prior to concentration under vacuum at <40°C (bath). Microanalyses were carried out by the analytical services at this department and all samples, except **6**, submitted for elemental analyses were dried overnight under vacuum with phosphorus pentoxide at 56°C (refluxing acetone). Compound **6** was dried at room temperature. High resolution mass spectra (HR-MS) of **6** were recorded on a Kratos MS-50 instrument using electron-impact ionization. For other compounds, FAB-HR-MS were recorded on samples suspended in Cleland's matrix using a Kratos MS-50B instrument with xenon as the bombarding gas. Inhibition assays were performed in 96 well microtiter plates as previously described (24), and inhibition curves were drawn using the software package Origin 5.0 (OriginLab, Northampton, MA). Titration microcalorimetry was performed as previously described (22, 24).

Methyl 2-*O*-methyl-3,6-dideoxy-α-D-*xylo*-hexopyranoside (5)

To a stirred suspension of **4** (33) (350 mg, 2.16 mmol), barium oxide (1.32 g, 8.64 mmol), and barium hydroxide octahydrate (350 mg, 1.08 mmol) in DMF (10 mL) was added methyl iodide (151 μL, 2.38 mmol). The reaction was stirred for 4 h, diluted with CH_2Cl_2, and filtered through Celite. The filtrate was concentrated under reduced pressure, diluted with CH_2Cl_2, and washed successively with saturated solutions of $KHCO_3$ and NaCl. After drying ($MgSO_4$) and evaporation of the solvent, the product was chromatographed (hexane–EtOAc, 1:1) to provide **5** (170 mg, 45%) as an oil. $[\alpha]_D$ +118.7 (*c* 1.7, $CHCl_3$). R_f = 0.40 (hexane–EtOAc, 1:3). The regiochemistry of methylation was established by ^{1}H decoupling experiments. ^{1}H NMR ($CDCl_3$) δ: 4.69 (d, $J_{1,2}$ = 3.0 Hz, 1H, H-1), 3.83 (q, $J_{5,6}$ = 6.5 Hz, 1H, H-5), 3.67 (br. s, 1H, H-4), 3.57 (ddd, $J_{2,3eq}$ = 5.0 Hz, $J_{2,3ax}$ = 12.0 Hz, 1H, H-2), 3.35 (s, 3H, OCH_3), 3.29 (s, 3H, OCH_3), 2.01 (ddd, $J_{3ax,3eq}$ = 13.0 Hz, $J_{2,3eq}$ = 5.0 Hz, $J_{3eq,4}$ = 3.0 Hz, H-3eq), 1.86 (ddd, $J_{3ax,4}$ = 3.0 Hz, 1H, H-3ax), 1.11 (d, $J_{5,6}$ = 6.5 Hz, 3H, H-6). Anal. calcd. for $C_8H_{16}O_4$ (176.21): C 54.53, H 9.15; found: C 54.10, H 9.29.

Methyl 4-*O*-benzoyl-2-*O*-*tert*-butyldiphenylsilyl-3,6-dideoxy-α-D-*arabino*-hexopyranoside (17)

Alcohol **16** (34) (1.0 g, 3.76 mmol) was dissolved in pyridine (25 mL) and then DMAP (500 mg) was added followed by *tert*-butyldiphenylsilyl chloride (2.0 mL, 7.9 mmol). The reaction was heated to 60°C and stirred for 6 days and then the solution cooled and partitioned between water and CH_2Cl_2. The organic layer was then washed in succession with 0.5 N HCl, water, and a saturated solution of NaCl, and then dried (Na_2SO_4). After evaporation, chromatography (pentane–ethyl acetate, 9:1) gave the product **17** (1.50 g, 80%) as an oil. $[\alpha]_D$ +83.2 (*c* 0.9, $CHCl_3$). R_f = 0.53 (pentane–ethyl acetate, 9:1). ^{1}H NMR ($CDCl_3$) δ: 7.30-8.05 (m, 15H, Ph), 5.32 (ddd, $J_{3ax,4}$ = 13.0 Hz, $J_{3eq,4}$ = 4.5 Hz, $J_{4,5}$ = 10.0 Hz, 1H, H-4), 4.39 (br. s, 1H, H-1), 3.90–3.98 (m, 2H, H-2, H-5), 3.28 (s, 3H, OCH_3), 2.20 (dt, $J_{3ax,3eq}$ = 12.5 Hz, $J_{2,3eq}$ = 4.5 Hz, H-3eq), 1.86 (ddd, $J_{3ax,4}$ = 13.0 Hz, $J_{2,3ax}$ = 3.0 Hz, 1H, H-3ax), 1.33 (d, $J_{5,6}$ = 6.5 Hz, 3H, H-6), 1.17 (s, 9H, C(CH_3)$_3$). ^{13}C NMR ($CDCl_3$) δ: 165.57 (C=O), 100.20 (C-1), 54.74 (OCH_3), 32.45 (C-3), 26.98 (C(CH_3)$_3$), 19.26 (*C*(CH$_3$)$_3$), 18.07 (C-6). Anal. calcd. for $C_{30}H_{36}O_5Si$ (504.70): C 71.39, H 7.19; found: C 71.59, H 7.31.

Methyl 2-*O*-*tert*-butyldiphenylsilyl-3,6-dideoxy-α-D-*arabino*-hexopyranoside (18)

Benzoate **17** (950 mg, 1.88 mmol) was dissolved in CH_3OH (50 mL) and a small piece of sodium was added. After stirring for 36 h, the reaction was quenched by adding acetic acid until the pH was neutral. The solvent was evaporated and then the residue chromatographed (pentane–ethyl acetate, 6:1) to give the product **18** (710 mg, 94%) as an oil. $[\alpha]_D$ +19.1 (*c* 0.8, $CHCl_3$). R_f = 0.20 (pentane–ethyl acetate, 6:1). ^{1}H NMR ($CDCl_3$) δ: 7.20–7.70 (m, 10H, Ph), 4.30 (br. s, 1H, H-1), 3.88–3.92 (m, 1H, H-2), 3.73–3.84 (m, 1H, H-4), 3.49–3.58 (m, 1H, H-5), 3.21 (s, 3H, OCH_3), 1.93 (ddt, $J_{2,3eq}$ = 3.5 Hz, $J_{1,3eq}$ = 1.0 Hz, H-3eq), 1.64 (ddd, $J_{3ax,3eq}$ = 13.0 Hz, $J_{3ax,4}$ = 11.5 Hz, $J_{2,3ax}$ = 2.5 Hz, 1H, H-3ax), 1.39 (d, $J_{4,4\text{-OH}}$ = 6.0 Hz, 1H,), 1.34 (d, $J_{5,6}$ = 6.5 Hz, 3H, H-6), 1.10 (s, 9H, C(CH_3)$_3$). ^{13}C NMR ($CDCl_3$) δ: 99.96 (C-1), 54.55 (OCH_3), 35.70 (C-3), 26.98 (C(CH_3)$_3$), 19.25 (*C*(CH$_3$)$_3$), 17.93 (C-6). Anal. calcd. for $C_{23}H_{32}O_4Si$ (400.59): C 68.96, H 8.05; found: C 68.60, H 7.85.

Methyl 3,6-dideoxy-2-*O*-*tert*-butyldiphenylsilyl-α-D-*lyxo*-hexopyranoside (19)

Compound **18** (674 mg, 1.61 mmol) was dissolved in CH_2Cl_2 (30 mL) and stirred with crushed 4 Å molecular sieves (500 mg) for 15 min. Pyridinium chlorochromate (1.74 g, 8.05 mmol) was added and the reaction stirred for 4 h at which point there was a complete conversion to the ketone (R_f = 0.89, pentane–ethyl acetate, 4:1). The reaction was filtered through Celite and washed with water and a saturated solution of NaCl and then dried (Na_2SO_4). After evaporation of the organic layer, the resulting residue was dried for 1 h under vacuum. The black solid was then dissolved in CH_3OH (50 mL) and $NaBH_4$ (100 mg, 2.66 mmol) added. After stirring for 10 min, the reaction was quenched by adding acetic acid until the pH was neutral. The solvent was evaporated and then the residue chromatographed (pentane–ethyl acetate, 9:1) to give the product **19** (488 mg, 76%) and some starting material **18** (108 mg, 16%) as oils. $[\alpha]_D$ –4.0 (*c* 0.9, $CHCl_3$). R_f = 0.67 (pentane–ethyl acetate, 9:1). ^{1}H NMR ($CDCl_3$) δ: 7.25–7.75 (m, 10H, Ph), 4.30 (br. s, 1H, H-1), 3.84 (dq, $J_{4,5}$ = 1.0 Hz, $J_{5,6}$ = 6.5 Hz, 1H, H-5), 3.74–3.80 (m, 2H, H-2, 4-OH), 3.45–3.52 (m, 1H, H-4), 3.16 (s, 3H, OCH_3), 2.07 (ddd, $J_{3ax,3eq}$ = 14.5 Hz, $J_{2,3ax}$ = 4.5 Hz, $J_{3ax,4}$ = 1.5 Hz, 1H, H-3ax), 1.89 (dt, $J_{2,3eq}$ = 3.0 Hz, H-3eq), 1.30 (d, $J_{5,6}$ = 6.5 Hz, 3H, H-6), 1.12 (s, 9H, C(CH_3)$_3$). ^{13}C NMR ($CDCl_3$) δ: 100.35 (C-1), 54.76 (OCH_3), 31.71 (C-3), 26.93 (C(CH_3)$_3$), 19.01 (*C*(CH$_3$)$_3$), 17.09 (C-6). Anal. calcd. for $C_{23}H_{32}O_4Si$ (400.59): C 68.96, H 8.05; found: C 68.91, H 8.27.

Methyl 3,6-dideoxy-α-D-*lyxo*-hexopyranoside (6)

Silyl ether **19** (450 mg, 1.12 mmol) was dissolved in THF (7.5 mL) and then tetrabutyl ammonium flouride (2.5 mL of a 1 M solution in THF, 2.24 mmol) was added. The reaction was stirred for 30 min and then evaporated. Chromatography of the residue (pentane–ethyl acetate, 1:1) gave the product **6** (172 mg, 95%) as an oil. $[\alpha]_D$ +46.4 (*c* 0.9, H_2O). R_f = 0.34

© 2002 NRC Canada

(pentane–ethyl acetate, 1:1). ^{1}H NMR (D_2O) δ: 4.658 (br. s, 1H, H-1), 4.025 (dq, $J_{4,5}$ = 2.0 Hz, $J_{5,6}$ = 7.0 Hz, 1H, H-5), 3.72–3.74 (m, 1H, H-2), 3.72–3.70 (m, 1H, H-4), 3.420 (s, 3H, OCH_3), 2.036 (ddd, $J_{3ax,3eq}$ = 14.0 Hz, $J_{2,3a} \approx J_{3a,4}$ = 3.5 Hz, 1H, H-3ax), 1.960 (dddd, $J_{2,3eq}$ = 3.5 Hz, $J_{1,3eq}$ = 1.0 Hz, H-3eq), 1.224 (d, $J_{5,6}$ = 7.0 Hz, 3H, H-6). ^{13}C NMR (D_2O) δ: 101.463 (C-1), 68.155 (C-5), 67.868 (C-4), 66.256 (C-2), 55.614 (OCH_3), 31.523 (C-3), 16.379 (C-6). Anal. calcd. for $C_7H_{14}O_4$ (162.19): C 51.84, H 8.70; found: C 51.97, H 8.90. HRMS calcd.: 162.0892; found: 162.0886.

Methyl 3-*O*-(2,4-di-*O*-benzyl-3,6-dideoxy-α-D-*xylo*-hexopyranosyl)-2-*O*-methyl-4,6-di-*O*-benzyl-α-D-mannopyranoside (21)

Sodium hydride (20 mg, 0.42 mmol, 50% dispersion in oil) was washed twice with petroleum ether under an N_2 atmosphere. The solvent was decanted and the solid suspended in DMF (4 mL). Methyl 3-*O*-(2,4-di-*O*-benzyl-3,6-dideoxy-α-D-*xylo*-hexopyranosyl)-4,6-di-*O*-benzyl-α-D-mannopyranoside (35) (**20**, 102 mg, 0.15 mmol) was then added as a solid and the reaction mixture was cooled to 0°C, and methyl iodide (20 μL, 0.3 mmol) added. After 1 h the reaction was quenched by the addition of methanol and the solvent evaporated. The resulting residue was then taken up in CH_2Cl_2 and washed succesively with water, 1 N HCl, water, $NaHCO_3$, and a saturated solution of NaCl. After drying ($MgSO_4$) and evaporation of the solvent the product was purified by chromatography (hexane–EtOAc, 3:1) to give **21** (91 mg, 87%) as an amorphous solid. $[\alpha]_D$ +64.7 (*c* 0.7, $CHCl_3$). R_f = 0.45, (hexane–EtOAc, 3:1). ^{1}H NMR ($CDCl_3$) δ: 7.10–7.30 (m, 20H, Ph), 5.13 (s, 1H, H-1′), 5.14 (d, ^2J = 12.0 Hz, 1H, PhCH_2), 4.86 (br. s, 1H, H-1), 4.62, 4.57, 4.54, 4.49, 4.45, 4.41, 4.38 (7d, ^2J = 12.0 Hz, 7H, PhCH_2), 4.18 (dd, $J_{5',6'}$ = 6.5 Hz, 1H, H-5′), 4.11 (dd, $J_{2,3}$ = 3.0 Hz, $J_{3,4}$ = 9.5 Hz, 1H, H-3), 3.32–3.90 (m, 2H, H-2′, H-4), 3.77–3.80 (m, 1H, H-5), 3.69–3.75 (m, 2H, H-6a, H-6b), 3.64 (br. s, 1H, H-2), 3.49 (s, 3H, OCH_3), 3.48 (br. s, 1H, H-4′), 3.41 (s, 3H, OCH_3), 1.99–2.14 (m, 2H, H-3′eq, H-3′ax), 1.22 (d, $J_{5'6'}$ = 6.6 Hz, 3H, H-6′). ^{13}C NMR ($CDCl_3$) δ: 99.26 (C-1′), 97.36 (C-1). Anal. calcd. for $C_{42}H_{50}O_9$ (698.86): C 72.18, H 7.21; found: C 72.35, H 7.27.

Methyl 3-*O*-(3,6-dideoxy-α-D-*xylo*-hexopyranosyl)-2-*O*-methyl-α-D-mannopyranoside (7)

Disaccharide **21** (77 mg, 0.11 mmol) was dissolved in acetic acid (4 mL) and then 10% Pd/C (70 mg) was added and the reaction was stirred under an atmosphere of H_2 for 3 h. The reaction was filtered through Celite and the filtrate evaporated, coevaporating twice with toluene. Chromatography (water) on Biogel P-2 gave **7** (24.5 mg, 66%) as an amorphous white solid after lyophilization. $[\alpha]_D$ +38.1 (*c* 0.5, H_2O). ^{1}H NMR (D_2O) δ: 5.059 (d, $J_{1',2'}$ = 4.0 Hz, 1H, H-1′), 4.972 (d, $J_{1,2}$ = 1.5 Hz, 1H, H-1), 4.070 (dq, $J_{4',5'}$ = 1.0 Hz, $J_{5',6'}$ = 6.5 Hz, 1H, H-5′), 3.999 (ddd, $J_{2',3'eq}$ = 6.0 Hz, $J_{2',3'ax}$ = 12.0 Hz, 1H, H-2′), 3.87–3.91 (m, 3H, H-3, H-6a, H-4′), 3.72–3.76 (m, 2H, H-4, H-6b), 3.697 (dd, $J_{2,3}$ = 3.5 Hz, 1H, H-2), 3.650 (ddd, $J_{4,5}$ = 9.5 Hz, $J_{5,6a}$ = 2.0 Hz, $J_{5,6b}$ = 6.0 Hz, 1H, H-5), 3.477 (s, 3H, ether OCH_3), 3.434 (s, 3H, aglycon OCH_3), 1.95–2.06 (m, 2H, H-3′ax, H-3′eq), 1.193 (d, $J_{5',6'}$ = 6.5 Hz, 3H, H-6′). ^{13}C NMR (D_2O) δ: 101.452 (C-1′, $^1J_{C,H}$ = 169.6 Hz), 97.887 (C-1, $^1J_{C,H}$ = 170.7 Hz), 80.435 (C-2), 79.308 (C-3), 73.405 (C-5), 69.142 (C-4′), 67.759 (C-5′), 67.094 (C-4), 64.359 (C-2′), 61.682 (C-6), 58.819 (ether OCH_3), 55.724 (aglycon OCH_3), 33.755 (C-3′), 16.357 (C-6′). Anal. calcd. for $C_{14}H_{26}O_9$ (338.36): C 49.70, H 7.74; found: C 49.34, H 7.76.

Methyl 3-*O*-(2,4-di-*O*-benzyl-3,6-dideoxy-α-D-*xylo*-hexopyranosyl-2-*O*-methoxymethyl-4,6-di-*O*-benzyl-α-D-mannopyranoside (22)

To a stirred solution of alcohol **20** (35) (68 mg, 0.1 mmol) in acetone (4 mL) was added ethyldiisopropylamine (40 μL, 0.21 mmol) and chloromethyl methyl ether (20 μL, 0.22 mmol). The reaction was stirred at room temperature for 1 h and then heated at 60°C for 48 h during which time ethyldiisopropylamine (40 μL, 0.21 mmol) and chloromethyl methyl ether (20 μL, 0.22 mmol) were added twice. The reaction was cooled, the solvent evaporated, and the crude material taken up in CH_2Cl_2, and washed succesively with water, 1 N HCl, water, $NaHCO_3$, and a saturated solution of NaCl. The organic layer was dried ($MgSO_4$) and the solvent evaporated to provide a residue that was chromatographed (hexane–EtOAc, 3:1) to give the product **22** (57.3 mg, 80%) as an oil. $[\alpha]_D$ +87.1 (*c* 0.9, $CHCl_3$). R_f = 0.35 (hexane–EtOAc, 3:1). ^{1}H NMR ($CDCl_3$) δ: 7.10–7.30 (m, 20H, Ph), 5.23 (d, $J_{1',2'}$ = 3.0 Hz, 1H, H-1′), 5.12 (d, ^2J = 12.0 Hz, 1H, PhCH_2), 4.89 (d, ^2J = 7.0 Hz, 1H, OCH_2O), 4.87 (br. s, 1H, H-1), 4.78 (d, ^2J = 7.0 Hz, 1H, OCH_2O), 4.65, 4.56, 4.54, 4.49, 4.47, 4.37, 4.36 (d, ^2J = 12.0 Hz, 7H, PhCH_2), 4.25 (dd, $J_{2,3}$ = 3.0 Hz, $J_{3,4}$ = 9.5 Hz, 1H, H-3), 4.08 (q, $J_{5',6'}$ = 6.5 Hz, 1H), 3.96 (t, $J_{3,4}$, $J_{4,5}$ = 9.5 Hz, 1H, H-4), 3.93 (br. s, 1H, H-2), 3.86 (ddd, $J_{2',3'eq}$ = 5.0 Hz, $J_{2',3'ax}$ = 12.0 Hz, 1H, H-2′), 3.81–3.72 (m, 3H, H-5, H-6a, H-6b), 3.40–3.45 (m, 7H, H-4′, 2 × OCH_3), 1.91–2.11 (m, 2H, H-3′eq, H-3′ax), 1.20 (d, $J_{5',6'}$ = 6.5 Hz, 3H, H-6′). ^{13}C NMR ($CDCl_3$) δ: 99.86 (OCH_2O), 98.83 (C-1′), 97.25 (C-1). Anal. calcd. for $C_{43}H_{52}O_{10}$ (728.88): C 70.86, H 7.19; found: C 70.88, H 7.26.

Methyl 3-*O*-(3,6-dideoxy-α-D-*xylo*-hexopyranosyl-2-*O*-methoxymethyl-α-D-mannopyranoside (8)

Glycoside **22** (39 mg, 0.05 mmol) was dissolved in ethanol (4 mL), and then 10% Pd/C (40 mg) was added and the reaction stirred under an atmosphere of H_2 for 24 h. At this point the reaction was still not complete and therefore additional 10% Pd/C (40 mg) and acetic acid (0.5 mL) were added. After 3 h the reaction was finished and the solution was filtered through Celite and the filtrate evaporated, coevaporating twice with toluene. Chromatography (water) on Biogel P-2 gave **8** (17.5 mg, 88%) as an amorphous white solid after lyophilization. $[\alpha]_D$ +27.7 (*c* 0.6, H_2O). ^{1}H NMR (D_2O) δ: 5.12 (d, $J_{1',2'}$ = 3.5 Hz, 1H, H-1′), 4.91 (br. s, 1H, H-1), 4.80–4.86 (m, 2H, 2 × OCH_2O), 4.06–4.00 (m, 2H, H-2′, H-5′), 3.95–3.99 (m, 2H, H-2, H-3), 3.88–3.93 (m, 2H, H-6a, H-4′), 3.84 (t, $J_{3,4} \approx J_{4,5}$ = 10.0 Hz, H-4), 3.77 (dd, $J_{6a,6b}$ = 12.5 Hz, $J_{5,6b}$ = 6.0 Hz, 1H, H-5), 3.64–3.69 (m, 1H, H-4), 3.43 (s, 3H, OCH_3), 3.45 (s, 3H, OCH_3), 1.97–2.02 (m, 2H, H-3′eq, H-3′ax), 1.18 (d, $J_{5',6'}$ = 6.5 Hz, 3H, H-6′). ^{13}C NMR (D_2O) δ: 101.00 (C-1′), 99.83 (C-1), 97.28

© 2002 NRC Canada

(OCH_2O). Anal. calcd. for $C_{15}H_{28}O_{10}$ (368.86): C 48.91, H 7.66; found: C 48.70, H 7.53.

Methyl 2-*O*-allyl-4,6-di-*O*-benzyl-3-*O*-(2,4-di-*O*-benzyl-3,6-dideoxy-α-D-*xylo*-hexopyranosyl)-α-D-mannopyranoside (23)

Disaccharide alcohol **20** (35) (500 mg, 0.73 mmol) was dissolved in DMF (20 mL) and then sodium hydride (76 mg, 2.5 mmol) was added and the reaction was stirred for 10 min. Allyl bromide (200 μL, 2.35 mmol) was then added and the solution stirred for 2 h. Methanol was added to quench the excess base and then the reaction was diluted with EtOAc and washed with water and a saturated solution of NaCl. After drying (Na_2SO_4), and solvent evaporation, the product was purified by chromatography (pentane–EtOAc, 3:1) to give **23** (488 mg, 92%) as an oil. $[\alpha]_D$ +64.3 (*c* 0.9, $CHCl_3$). R_f = 0.65 (pentane–EtOAc, 3:1). ^{1}H NMR ($CDCl_3$) δ: 7.10–7.40 (m, 20H, Ph), 5.95 (dddd, $^3J_{trans}$ = 17.0 Hz, $^3J_{cis}$ = 10.5 Hz, ^3J = 5.5 Hz, 1H, OCH_2CH=CH_2), 5.33 (dddd, ^2J = 1.5 Hz, 1H, OCH_2CH=CH_2), 5.12–5.19 (m, 2H, H-1′, 1 × OCH_2CH=CH_2), 5.11 (d, ^2J = 11.5 Hz, 1H, PhCH_2), 4.81 (d, $J_{1,2}$ = 1.5 Hz, 1H, H-1), 4.64, 4.54, 4.52, 4.47, 4.37, 4.36 (d, ^2J = 12.0 Hz, 7H, PhCH_2), 4.08–4.24 (m, 4H, 2 × OCH_2CH=CH_2, H-5′, H-3), 3.93 (t, $J_{3,4} \approx J_{4,5}$ = 9.0 Hz, 1H, H-4), 3.70–3.87 (m, 5H, H-2, H-5, H-6a, H-6b, H-2′), 3.43 (br. s, 1H, H-4′), 3.37 (s, 3H, OCH_3), 2.12 (dt, $J_{3'eq,3'ax}$ = 13.0 Hz, $J_{2',3'eq}$, $J_{3'eq,4'}$ = 3.5 Hz, 1H, H-3′eq), 1.96 (dt, $J_{2',3'ax}$ = 13.0 Hz, $J_{3'ax,4'}$ = 2.5 Hz, 1H, H-3′ax), 1.18 (d, $J_{5',6'}$ = 6.5 Hz, H 1H, H-6′). ^{13}C NMR ($CDCl_3$) δ: 135.12 (OCH_2CH=CH_2), 116.50 (OCH_2CH=CH_2), 99.98 (C-1′), 98.25 (C-1), 69.42 (OCH_2CH=CH_2), 66.58 (C-6), 54.76 (OCH_3), 27.52 (C-3′), 16.56 (C-6′). Anal. calcd. for $C_{44}H_{52}O_9$ (724.89): C 72.90, H 7.23; found: C 72.95, H 7.43.

Methyl 4,6-di-*O*-benzyl-3-*O*-(2,4-di-*O*-benzyl-3,6-dideoxy-α-D-*xylo*-hexopyranosyl)-2-*O*-(2′-hydroxyethyl)-α-D-mannopyranoside (24)

A solution of **23** (500 mg, 0.73 mmol) in 1:1 CH_2Cl_2:CH_3OH (20 mL) was cooled to –78°C and O_3 was bubbled through the solution until a blue color persisted. Then $NaBH_4$ (100 mg) was added and the reaction was allowed to come to room temperature. The solution was then neutralized with acetic acid, diluted with CH_2Cl_2 and washed with water. The organic layer was dried (Na_2SO_4), evaporated, and chromatographed (pentane–EtOAc, 1:1) to give **24** (278 mg, 70%) as an oil. $[\alpha]_D$ +65.4 (*c* 1.1, $CHCl_3$). R_f = 0.41 (pentane–EtOAc, 1:1). ^{1}H NMR ($CDCl_3$) δ: 7.00–7.40 (m, 20H, Ph), 5.25 (d, $J_{1',2'}$ = 3.5 Hz, 1H, H-1′), 5.03 (d, ^2J = 11.5 Hz, 1H, PhCH_2), 4.81 (d, $J_{1,2}$ = 1.5 Hz, 1H, H-1), 4.33–4.65 (m, 7H, 7 × PhCH_2), 4.21 (dd, $J_{2,3}$ = 3.5 Hz, $J_{3,4}$ = 9.5 Hz, 1H, H-3), 4.07 (dq, $J_{4',5'}$ = 1.0 Hz, $J_{5',6'}$ = 6.5 Hz, 1H, H-5′), 3.99 (t, $J_{3,4} \approx J_{4,5}$ = 9.5 Hz, 1H, H-4), 3.59–3.87 (m, 9H, H-2, H-5, H-6a, H-6b, H-2′, 2 × OCH_2CH_2OH, 2 × OCH_2CH_2OH), 3.46 (br. s, 1H, H-4′), 3.38 (s, 3H, OCH_3), 3.03 (t, ^2J = 6.0 Hz, 1H, OH), 2.13 (dt, $J_{3'eq,3'ax}$ = 13.0 Hz, $J_{2',3'eq} \approx J_{3'eq,4'}$ = 3.5 Hz, 1H, H-3′eq), 1.92 (dt, $J_{2',3'ax}$ = 13.0 Hz, $J_{3'ax,4'}$ = 2.5 Hz, 1H, H-3′ax), 1.19 (d, $J_{5',6'}$ = 6.5 Hz, 1H, H-6′). ^{13}C NMR ($CDCl_3$) δ: 98.63 (C-1′), 98.18 (C-1), 70.52 (OCH_2CH_2OH), 68.88 (C-6), 61.61 (OCH_2CH_2OH), 54.80 (OCH_3), 27.17 (C-3′), 16.53 (C-6′). Anal. calcd. for $C_{43}H_{52}O_{10}$ (728.88): C 70.86, H 7.19; found: C 70.74, H 6.71.

Methyl 2-*O*-(2′-hydroxyethyl)-3-*O*-(3,6-dideoxy-α-D-*xylo*-hexopyranosyl)-α-D-mannopyranoside (9)

Alcohol **24** (100 mg, 0.13 mmol) was dissolved in acetic acid (5 mL) and 10% Pd/C (50 mg) added and the reaction stirred overnight under a flow of H_2. The catalyst was filtered, the solvent evaporated and the product was purified by chromatography on Iatrobeads (CH_2Cl_2–CH_3OH, 4:1). The product obtained was then redissolved in water, filtered through a 0.22 μM filter and lyophilized to give **9** (35 mg, 74%), as an amorphous white solid. $[\alpha]_D$ +73.4 (*c* 0.6, H_2O). R_f = 0.21 (CH_2Cl_2–CH_3OH, 4:1). ^{1}H NMR (D_2O) δ: 5.105 (d, $J_{1',2'}$ = 3.5 Hz, 1H, H-1′), 4.941 (d, $J_{1,2}$ = 1.5 Hz, 1H, H-1), 4.070 (q, $J_{5',6'}$ = 6.5 Hz, 1H, H-5′), 4.106 (ddd, $J_{1',2'}$ = 3.5 Hz, $J_{2',3'eq}$ = 7.0 Hz, $J_{2',3'ax}$ = 11.0 Hz, 1H, H-2′), 3.926 (dd, $J_{2,3}$ = 3.0 Hz, $J_{3,4}$ = 9.5 Hz, 1H, H-3), 3.87–3.91 (m, 2H, H-6a, H-4′), 3.860 (t, $J_{4,5}$ = 9.5 Hz, 1H, H-4), 3.70–3.83 (m, 6H, H-2, H-6b, 2 × CH_2CH_2OH, 2 × CH_2CH_2OH), 3.656 (ddd, $J_{4,5}$ = 9.5 Hz, $J_{5,6a}$ = 2.5 Hz, $J_{5,6b}$ = 6.0 Hz, 1H, H-5), 3.432 (s, 3H, OCH_3), 1.98–2.05 (m, 2H, H-3′ax, H-3′eq), 1.182 (d, $J_{5',6'}$ = 6.5 Hz, 3H, H-6′). ^{13}C NMR (D_2O) δ: 101.238 (C-1′, $^1J_{C,H}$ = 170.4 Hz), 98.906 (C-1, $^1J_{C,H}$ = 170.0 Hz), 79.425 (C-2), 78.799 (C-3), 73.485 (OCH_2CH_2OH), 73.064 (C-5), 69.126 (C-4′), 67.759 (C-5′), 67.258 (C-4), 64.301 (C-2′), 61.591 (OCH_2CH_2OH), 61.529 (C-6), 55.666 (OCH_3), 33.764 (C-3′), 16.306 (C-6′). HR-FABMS calcd. for $C_{15}H_{28}O_{10}$ $[M + Na]^+$: 391.1580; found: 391.1595.

Methyl 4,6-di-*O*-benzyl-3-*O*-(2,4-di-*O*-benzyl-3,6-dideoxy-α-D-*xylo*-hexopyranosyl)-2-*O*-(2′-phthlamidoethyl)-α-D-mannopyranoside (25)

Compound **24** (300 mg, 0.41 mmol) was dissolved in THF (5 mL) and triphenylphosphine (215 mg, 0.82 mmol) and phthalimide (91 mg, 0.62 mmol) were added followed by diethylazodicarboxylate (141 μL, 0.82 mmol). The reaction was stirred overnight and evaporated. Chromatography (toluene–EtOAc, 9:1) provided **25** (320 mg, 91%) as an oil. $[\alpha]_D$ +57.6 (*c* 1.4, $CHCl_3$). R_f = 0.38 (toluene–EtOAc, 9:1). ^{1}H NMR ($CDCl_3$) δ: 7.00–7.80 (m, 24H, Ph), 5.09 (d, $J_{1',2'}$ = 3.5 Hz, 1H, H-1′), 4.99 (d, ^2J = 11.5 Hz, 1H, PhCH_2), 4.75 (d, $J_{1,2}$ = 1.5 Hz, 1H, H-1), 4.28–4.53 (m, 7H, 7 × PhCH_2), 4.06 (dd, $J_{2,3}$ = 2.5 Hz, $J_{3,4}$ = 8.5 Hz, 1H, H-3), 3.88–4.02 (m, 9H, H-2, H-4, H-5, H-6a, H-6b, H-2′, H-5′, 2 × OCH_2CH_2NPhth), 3.63 (dd, ^2J = 10.5 Hz, J_{vic} = 1.5 Hz, 1H, CH_2NPhth), 3.33 (s, 3H, OCH_3), 3.20 (br. s, 1H, H-4′), 1.94 (dt, $J_{3'eq,3'ax}$ = 13.0 Hz, $J_{2',3'eq}$, $J_{3'eq,4'}$ = 3.5 Hz, 1H, H-3′eq), 1.67 (dt, $J_{2',3'ax}$ = 13.0 Hz, $J_{3'ax,4'}$ = 2.5 Hz, 1H, H-3′ax), 1.15 (d, $J_{5',6'}$ = 6.5 Hz, 1H, H-6′). ^{13}C NMR ($CDCl_3$) δ: 167.85 (C=O), 99.06 (C-1′), 97.71 (C-1), 69.48 (OCH_2CH_2NPhth), 66.50 (C-6), 54.67 (OCH_3), 37.79 (OCH_2CH_2NPhth), 27.29 (C-3′), 16.46 (C-6′). Anal. calcd. for $C_{51}H_{52}NO_{11}$ (854.98): C 71.65, H 6.13, N 1.64; found: C 71.50, H 6.44, N 1.63.

Methyl 2-*O*-(2′-acetamidoethyl)-4,6-di-*O*-benzyl-3-*O*-(2,4-di-*O*-benzyl-3,6-dideoxy-α-D-*xylo*-hexopyranosyl)-α-D-mannopyranoside (26)

Phthalimide **25** (300 mg, 0.34 mmol) was dissolved in methanol (15 mL) and hydrazine acetate (805 mg,

© 2002 NRC Canada

10.2 mmol) was added. The reaction was heated at reflux for 3 h and then more hydrazine acetate (805 mg, 10.2 mmol) was added. After refluxing for another 20 h the solution was cooled and the solvent evaporated. Pyridine (20 mL) was added followed by acetic anhydride (10 mL), and the reaction stirred overnight. The mixture was then diluted with EtOAc and washed with 0.5 N HCl, water, and brine. Evaporation of the solvent followed by chromatography (pentane–EtOAc, 3:1) provided **26** which was characterized only by ^{1}H NMR and then immediately carried through to the next reaction. ^{1}H NMR ($CDCl_3$) δ: 7.10–7.40 (m, 20H, Ph), 6.55 (br. s, 1H, N*H*), 5.24 (d, $J_{1',2'}$ = 3.5 Hz, 1H, H-1′), 5.07 (d, ^2J = 11.5 Hz, 1H, PhCH_2), 4.74 (d, $J_{1,2}$ = 1.5 Hz, 1H, H-1), 4.34–4.64 (m, 7H, 7 × PhCH_2), 4.19 (dd, $J_{2,3}$ = 3.0 Hz, $J_{3,4}$ = 9.5 Hz, 1H, H-3), 4.01–4.09 (m, 2H, H-4, H-5′) 3.85 (dt, $J_{2',3'eq}$ = 3.5 Hz, $J_{2',3'ax}$ = 13.0 Hz, 1H, H-2′), 3.58–3.79 (m, 8H, H-2, H-5, ^2JH-6a, H-6b, 2 × OCH_2CH_2NHAc, 2 × OCH$_2$CH_2NHAc), 3.46 (br. s, 1H, H-4′), 3.37 (s, 3H, OCH_3), 2.12 (dt, $J_{3'eq,3'ax}$ = 13.0 Hz, $J_{3'eq,4'}$ = 3.5 Hz, 1H, H-3′eq), 1.83–1.93 (m, 4H, NHCOCH_3, H-3′ax), 1.19 (d, $J_{5',6'}$ = 6.5 Hz, 1H, H6′).

Methyl 2-*O*-(2′-acetamidoethyl)-3-*O*-(3,6-dideoxy-α-D-*xylo*-hexopyranosyl)-α-D-mannopyranoside (10)

The protected *N*-acetyl disaccharide **26** (from above) was dissolved in acetic acid (5 mL) and 10% Pd/C (200 mg) added and the reaction stirred overnight under a flow of H_2. The catalyst was then filtered away and the solvent evaporated. Purified by chromatography on Iatrobeads (CH_2Cl_2–CH_3OH, 4:1) gave a product that was then redissolved in water, filtered through a 0.22 μM filter and lyophilized to give **10** (85 mg, 62% from **25**), as an amorphous white solid. $[\alpha]_D$ +76.4 (*c* 0.6, H_2O). R_f = 0.29 (CH_2Cl_2–CH_3OH, 4:1). ^{1}H NMR (D_2O) δ: 5.094 (d, $J_{1',2'}$ = 4.0 Hz, 1H, H-1′), 4.899 (d, $J_{1,2}$ = 1.5 Hz, 1H, H-1), 4.021 (ddd, $J_{2',3'eq}$ = 6.0 Hz, $J_{2',3'ax}$ = 11.5 Hz, 1H, H-2′), 4.006 (q, $J_{5',6'}$ = 7.0 Hz, 1H, H-5′), 3.912 (dd, $J_{2,3}$ = 3.5 Hz, $J_{3,4}$ = 10.0 Hz, 1H, H-3), 3.86–3.91 (m, 2H, H-6a, H-4′), 3.835 (t, $J_{4,5}$ = 10.0 Hz, 1H, H-4), 3.74–3.80 (m, 3H, H-2, H-6b, CH_2CH$_2$NHAc), 3.67–3.72 (m, 1H, CH_2CH$_2$NHAc), 3.648 (ddd, $J_{5,6a}$ = 2.5 Hz, $J_{5,6b}$ = 6.5 Hz, 1H, H-5), 3.426 (s, 3H, OCH_3), 3.33–3.42 (m, 2H, 2 × CH$_2$CH_2NHAc), 1.94–2.01 (m, 5H, H-3′ax, H-3′eq, NHCOCH_3), 1.174 (d, $J_{5',6'}$ = 7.0 Hz, 3H, H-6′). ^{13}C NMR (D_2O) δ: 174.986 (C=O), 101.297 (C-1′, $^1J_{C,H}$ = 169.9 Hz), 98.892 (C-1, $^1J_{C,H}$ = 170.7 Hz), 79.090 (C-3), 78.005 (C-2), 73.566 (C-5), 69.995 (O*C*H$_2$CH$_2$NHAc), 69.116 (C-4′), 67.841 (C-5′), 67.334 (C-4), 64.294 (C-2′), 61.669 (C-6), 55.712 (O*C*H$_3$), 40.305 (OCH$_2$*C*H$_2$NHAc), 33.853 (C-3′), 22.756 (NHCO*C*H$_3$), 16.346 (C-6′). HR-FABMS calcd. for $C_{17}H_{31}NO_{10}Na$ [M + Na]$^+$: 432.1846; found: 432.1847.

Methyl 6-*O*-benzoyl-2,3-*O*-isopropylidene-α-D-talopyranoside (28)

The known mannoside **27** (37) (3.0 g, 8.88 mmol) was dissolved in CH_2Cl_2 (70 mL) and stirred with crushed 4 Å molecular sieves (10 g) for 15 min. Pyridinium chlorochromate (9.6 g, 44.37 mmol) was added and the reaction stirred for 4 h at which point there was a complete conversion to the ketone (R_f = 0.51, hexane–EtOAc, 2:1). The reaction was filtered through Celite and then washed with water and a saturated solution of NaCl. After drying (Na_2SO_4) and evaporation of the organic layer, the resulting residue was dried for 1 h under vacuum. The black solid was dissolved in CH_3OH (50 mL) and $NaBH_4$ (336 mg, 8.88 mmol) added. After stirring for 10 min, the reaction was quenched by adding acetic acid until the pH was neutral. The solvent was evaporated and then the residue chromatographed (hexane–EtOAc, 1:1) to give the product **28** (2.54 g, 85%) as a crystalline solid; mp 111 to 112°C. $[\alpha]_D$ +39.1 (*c* 1.0, $CHCl_3$). R_f = 0.40 (hexane–EtOAc, 2:1). ^{1}H NMR ($CDCl_3$) δ: 7.30–8.10 (m, 5H, Ph), 5.01 (s, 1H, H-1), 4.53–4.67 (m, 2H, H-6a, H-6b), 4.24 (t, $J_{5,6a}$, $J_{5,6b}$ = 5.0 Hz, H-5), 4.03–4.10 (m, 2H, H-2, H-3), 3.84 (t, $J_{3,4}$, $J_{4,4\text{-OH}}$ = 6.0 Hz, H-4), 3.42 (s, 3H, OCH_3), 2.41 (d, 1H, 4-OH), 1.59, 1.39 (s, 3H, C(CH_3)$_2$). ^{13}C NMR ($CDCl_3$) δ: 166.36 (C=O), 109.62 (O_2C(CH$_3$)$_2$), 98.50 (C-1), 66.43 (C-6), 55.19 (O*C*H$_3$), 25.90, 25.17 (O_2C(*C*H$_3$)$_2$). Anal. calcd. for $C_{17}H_{22}O_7$ (338.36): C 60.35, H 6.55; found: C 60.35, H 6.65.

Methyl 2,3-*O*-isopropylidene-α-D-talopyranoside (29)

Benzoate **28** (10.0 g, 29.58 mmol) was dissolved in CH_3OH (125 mL) and $NaOCH_3$ (200 mg) was added. After stirring overnight, the solution was neutralized with Amberlite IR-120 (H+) resin, filtered and evaporated. Chromatography (hexane–EtOAc, 1:1) gave **29** (6.37 g, 92%) as a white foam. $[\alpha]_D$ +42.2 (*c* 1.5, $CHCl_3$). R_f = 0.18 (hexane–EtOAc, 1:1). ^{1}H NMR ($CDCl_3$) δ: 4.99 (s, $J_{1,2}$ = 1.0 Hz, 1H, H-1), 4.26 (dd, $J_{3,4}$ = 6.5 Hz, 1H, H-3), 4.07 (dd, $J_{2,3}$ = 5.0 Hz, 1H, H-2), 4.00 (ddd, $J_{5,6a}$ = 4.0 Hz, $J_{6a,6b}$ = 12.5 Hz, $J_{6a,6\text{-OH}}$ = 7.5 Hz, 1H, H-6a), 3.78–3.88 (m, 3H, H-4, H-5, H-6b), 3.44 (s, 3H, OCH_3), 2.50 (d, $J_{4,4\text{-OH}}$ = 5.5 Hz, 1H, 4-OH), 2.26–2.32 (m, 1H, 6-OH), 1.57, 1.39 (s, 3H, C(CH_3)$_2$). ^{13}C NMR ($CDCl_3$) δ: 109.63 (O_2C(CH$_3$)$_2$), 98.72 (C-1), 62.82 (C-6), 55.36 (O*C*H$_3$), 25.90, 25.08 (O_2C(*C*H$_3$)$_2$). Anal. calcd. for $C_{10}H_{18}O_6$ (234.25): C 51.27, H 7.74; found: C 51.21, H 7.69.

Methyl 4,6-di-*O*-benzyl-2,3-*O*-isopropylidene-α-D-talopyranoside (30)

Diol **29** (850 mg, 3.62 mmol) was dissolved in DMF (50 mL) and cooled to 0°C. Sodium hydride (400 mg, 80% dispersion in oil, 13.3 mmol) was added and the mixture stirred for 15 min. To this solution was added benzyl bromide (1.5 mL, 12.6 mmol) and the reaction stirred overnight while being allowed to warm to room temperature. The reaction was then quenched with CH_3OH and the solution partitioned between water with CH_2Cl_2. The organic layer was washed with water and a saturated solution of NaCl, and then dried (Na_2SO_4), and evaporated. Chromatography (pentane–EtOAc, 6:1) gave **30** (1.45 g, 97%) as an oil. $[\alpha]_D$ +1.1 (*c* 0.9, $CHCl_3$). R_f = 0.42 (pentane–EtOAc, 6:1). ^{1}H NMR ($CDCl_3$) δ: 7.25–7.35 (m, 10H, Ph), 4.88 (s, $J_{1,2}$ = 2.0 Hz, 1H, H-1), 4.85, 4.52, 4.49, 4.43 (4d, ^2J = 11.5 Hz, 8H, PhCH_2), 4.36 (dd, $J_{3,4}$ = 7.0 Hz, 1H, H-3), 4.06 (dd, $J_{2,3}$ = 4.5 Hz, 1H, H-2), 3.96 (ddd, $J_{4,5}$ = 3.0 Hz, $J_{5,6a}$ = 4.0 Hz, $J_{5,6b}$ = 5.5 Hz, 1H, H-5), 3.81 (dd, $J_{4,5}$ = 3.0 Hz, 1H, H-4), 3.71 (dd, $J_{5,6a}$ = 7.0 Hz, $J_{6a,6b}$ = 10.0 Hz, 1H, H-6a), 3.55 (dd, $J_{5,6b}$ = 5.5 Hz, 1H, H-6b), 3.42 (s, 3H, OCH_3), 1.52, 1.36 (s, 3H, C(CH_3)$_2$). ^{13}C NMR ($CDCl_3$) δ: 110.06 (O_2C(CH$_3$)$_2$), 98.93 (C-1), 74.41, 73.40 (PhCH_2), 69.75 (C-6), 55.56 (O*C*H$_3$), 26.18, 25.37 (O_2C(*C*H$_3$)$_2$). Anal.

© 2002 NRC Canada

calcd. for $C_{24}H_{30}O_6$ (414.50): C 69.54, H 7.30; found: C 69.56, H 7.44.

Methyl 4,6-di-*O*-benzyl-α-D-talopyranoside (31)

Taloside **30** (1.40g, 3.37 mmol) was dissolved in 80% acetic acid (25 mL) and heated at 80°C for 30 min. The solution was cooled and evaporated leaving an oily residue that was chromatographed (pentane–EtOAc, 1:1) to provide the product **31** (1.15 g, 91%) as an oil that crystallized upon standing; mp 64–66°C. $[\alpha]_D$ +37.0 (*c* 0.8, $CHCl_3$). R_f = 0.33 (pentane–EtOAc, 1:1). ^{1}H NMR ($CDCl_3$) δ: 7.20–7.40 (m, 10H, Ph), 4.78 (s, $J_{1,2}$ = 1.5 Hz, 1H, H-1), 4.74, 4.62, 4.58, 4.48 (4d, ^2J = 11.5 Hz, 4H, PhCH_2), 3.96 (t, $J_{5,6a}$, $J_{5,6b}$ = 7.0 Hz, 1H, H-5), 3.91 (dd, $J_{2,3}$ = 3.5 Hz, 1H, H-2), 3.82 (dt, $J_{3,4}$ = 3.5 Hz, $J_{3,3\text{-OH}}$ = 10.0 Hz, 1H, H-3), 3.60–3.71 (m, 3H, H-4, H-6, H-6), 3.37 (s, 3H, OCH_3), 3.36 (s, 1H, 2-OH), 2.72 (d, 1H, 3-OH). ^{13}C NMR ($CDCl_3$) δ: 102.09 (C-1), 76.16, 73.57 (PhCH_2), 68.79 (C-6), 55.19 (OCH_3). Anal. calcd. for $C_{21}H_{36}O_6$ (374.44): C 67.36, H 7.00; found: C 69.43, H 7.07.

Methyl 2-*O*-benzoyl-4,6-di-*O*-benzyl-α-D-talopyranoside (32)

Compound **31** (500 mg, 1.34 mmol) was dissolved in CH_2Cl_2 (10 mL) and triethylorthoformate (2.3 mL, 13.4 mmol) was added followed by *p*-TsOH (20 mg). The reaction was complete after stirring for 5 h as indicated by the appearance of a new TLC spot (R_f = 0.55, pentane–EtOAc, 3:1). The acid was neutralized with triethylamine and the solvent evaporated. The residue was redissolved immediately in 80% acetic acid (25 mL), stirred for 30 min, and evaporated. Chromatography (pentane–EtOAc, 3:1) of the resulting oil provided the product **32** (520 mg, 81%) as an oil. ^{1}H NMR ($CDCl_3$) δ: 7.10–7.90 (m, 15H, Ph), 5.12 (ddd, $J_{2,3}$ = 4.5 Hz, $J_{2,4}$ = 0.5 Hz, 1H, H-2), 4.87 (d, $J_{1,2}$ = 1.0 Hz, 1H, H-1), 4.76, 4.66, 4.63, 4.48 (4d, ^2J = 11.5 Hz, 4H, PhCH_2), 4.08–4.16 (m, 2H, H-3, H-5), 3.91–3.96 (m, 2H, H-4, H-6a), 3.75 (dd, $J_{5,6a}$ = 6.0 Hz, $J_{6a,6b}$ = 9.5 Hz, 1H, H-6a), 3.41 (s, 3H, OCH_3), 2.72 (d, $J_{3,3\text{-OH}}$ = 10.0 Hz, 1H, 3-OH).

Methyl 2-*O*-benzoyl-4,6-di-*O*-benzyl-3-*O*-(2,4-di-*O*-benzyl-3,6-dideoxy-α-D-*xylo*-hexopyranosyl)-α-D-talopyranoside (34)

Alcohol **32** (500 mg, 1.04 mmol) and donor **33** (38) (506 mg, 1.36 mmol) were dried with crushed 4 Å molecular sieves over P_2O_5 under vacuum overnight. The solids were suspended in CH_2Cl_2 (40 mL) and cooled to –40°C. *N*-Iodosuccinimide (310 mg, 1.36 mmol) and silver triflate (30 mg, 0.12 mmol) were then added. After 15 min, the reaction turned dark red and the reaction was allowed to proceed for another 15 min at which point it was quenched with triethylamine. After diluting with CH_2Cl_2 the solution was washed in succession with a saturated solution of sodium thiosulfate, water, a saturated solution of NaCl, and then dried (Na_2SO_4). Evaporation of the solvents and chromatography (pentane–EtOAc, 6:1) gave the product **34** (680 mg, 83%) as an oil. $[\alpha]_D$ +16.2 (*c* 0.9, $CHCl_3$). R_f = 0.38 (pentane–EtOAc, 6:1). ^{1}H NMR ($CDCl_3$) δ: 7.05–8.00 (m, 25H, Ph), 5.35 (m, 1H, H-2), 5.18 (d, ^2J = 12.0 Hz, 1H, PhCH_2), 4.89 (d, $J_{1,2}$ = 1.0 Hz, 1H, H-1), 4.50–4.64 (m, 6H, PhCH_2), 4.41 (d, ^2J = 12.0 Hz, 1H, PhCH_2), 4.16 (t, $J_{2,3} \approx J_{3,4}$ = 3.5 Hz, 1H, H-3), 4.09 (dt, $J_{4,5}$ = 1.0 Hz, $J_{5,6b}$ = 6.0 Hz, 1H, H-5), 3.90–3.98 (m, 2H, H-4, H-2′), 3.86 (dd, $J_{5,6a}$ = 6.0 Hz, $J_{6a,6b}$ = 9.5 Hz, 1H, H-6a), 3.78 (dd, $J_{5,6b}$ = 6.0 Hz, 1H, H-6b), 3.42 (s, 3H, OCH_3), 3.35 (br. s, 1H, H-4′), 2.11 (dt, $J_{2,3e'} \approx J_{3e',4}$ = 3.5 Hz, $J_{3'eq,3'ax}$ = 13.0 Hz, 1H, H-3′eq), 1.82 (dt, $J_{3'ax,4}$ = 13.0 Hz, $J_{2',3'ax}$ = 2.5 Hz, 1H, H-3′ax), 1.08 (d, $J_{5'6'}$ = 6.5 Hz, 3H, H-6′). ^{13}C NMR ($CDCl_3$) δ: 166.31 (C=O), 98.96 (C-1), 97.70 (C-1′), 74.38, 73.33, 71.07, 70.79 (PhCH_2), 69.24 (C-6), 54.86 (OCH_3), 27.42 (C-3′), 16.03 (C-6′). Anal. calcd. for $C_{48}H_{52}O_{10}$ (788.94): C 73.08, H 6.64; found: C 72.82, H 6.68.

Methyl 4,6-di-*O*-benzyl-3-*O*-(2,4-di-*O*-benzyl-3,6-dideoxy-α-D-*xylo*-hexopyranosyl)-α-D-talopyranoside (35)

The protected disaccharide **34** (560 mg, 0.71 mmol) was dissolved in CH_3OH (50 mL) and a small piece of sodium was added. The reaction was stirred overnight and then neutralized with Amberlite IR-120 (H+) resin. After filtration of the resin and evaporation of the CH_3OH the product was purified by chromatography (pentane–EtOAc, 3:1) to give the product **35** (466 mg, 96%) as an oil. $[\alpha]_D$ +42.0 (*c* 1.0, $CHCl_3$). R_f = 0.30 (pentane–EtOAc, 3:1). ^{1}H NMR ($CDCl_3$) δ: 7.20–7.40 (m, 20H, Ph), 5.05–5.10 (m, 2H, H-1′, PhCH_2), 4.76 (br. s, 1H, H-1), 4.37–4.66 (m, 5H, PhCH_2), 4.33 (q, $J_{5'6'}$ = 6.5 Hz, 1H, H-5′), 4.25 (d, ^2J = 12.0 Hz, 1H, PhCH_2), 3.81–3.97 (m, 5H, H-4, H-2, H-3, H-5, H-2′), 3.55–3.63 (m, 2H, H-6a, H-6b), 3.50 (br. s, 1H, H-4), 3.37 (s, 3H, OCH_3), 2.22 (dt, $J_{2,3'eq} \approx J_{3'eq,4}$ = 3.5 Hz, $J_{3'eq,3'ax}$ = 13.0 Hz, 1H, H-3′eq), 2.02 (dt, $J_{3'ax,4}$ = 13.0 Hz, $J_{2',3'ax}$ = 2.5 Hz, 1H, H-3′ax), 1.20 (d, $J_{5'6'}$ = 6.5 Hz, 3H, H-6′). ^{13}C NMR ($CDCl_3$) δ: 102.72 (C-1), 98.59 (C-1′), 75.13, 73.50, 71.43, 71.05 (PhCH_2), 69.08 (C-6), 55.12 (OCH_3), 28.03 (C-3′), 16.53 (C-6′). Anal. calcd. for $C_{41}H_{48}O_9$ (684.83): C 71.91, H 7.07; found: C 71.76, H 7.23.

Methyl 3-*O*-(3,6-dideoxy-α-D-*xylo*-hexopyranosyl)-α-D-talopyranoside (11)

To a solution of **35** (120 mg, 0.18 mmol) in acetic acid (5 mL) was added 10% Pd/C (100 mg) and the reaction was stirred overnight under a flow of H_2. After filtration of the catalyst and evaporation of the solvent the residue was subjected to chromatography (CH_2Cl_2–CH_3OH, 4:1) on Iatrobeads. The product obtained was then redissolved in water, filtered through a 0.22 μM filter and lyophilized to give the product **11** (49 mg, 84%) as an amorphous white solid. R_f = 0.27 (CH_2Cl_2–CH_3OH, 4:1). $[\alpha]_D$ +161.0 (*c* 0.6, H_2O). ^{1}H NMR (D_2O) δ: 5.066 (d, $J_{1',2'}$ = 3.5 Hz, 1H, H-1′), 4.882 (d, $J_{1,2}$ = 1.5 Hz, 1H, H-1), 4.130 (dd, $J_{3,4}$ = 1.5 Hz, 1H, H-3), 4.096 (dq, $J_{4',5'}$ = 0.5 Hz, 1H, H-5′), 4.041 (ddd, $J_{2',3'ax}$ = 13.0 Hz, $J_{2',3'eq}$ = 5.0 Hz, 1H, H-2′), 3.967 (ddd, $J_{2,3}$ = 3.0 Hz, $J_{2,4}$ = 1.5 Hz, 1H, H-2), 3.87–3.93 (m, 3H, H-4, H-5, H-4′), 3.858 (dd, $J_{5,6a}$ = 8.0 Hz, $J_{6a,6b}$ = 12.0 Hz, 1H, H-6a), 3.793 (dd, $J_{5,6b}$ = 4.5 Hz, 1H, H-6b), 3.438 (s, 3H, OCH_3), 2.099 (dt, $J_{2',3'ax}$ = 13.0 Hz, $J_{3'ax,3'eq}$ = 13.0 Hz, $J_{3'ax,4'}$ = 3.0 Hz, 1H, H-3′ax), 1.999 (dt, $J_{2',3'eq}$ = 5.0 Hz, $J_{3'eq,4'}$ = 5.0 Hz, 1H, H-H-3′eq), 1.158 (d, $J_{5',6'}$ = 7.0 Hz, 3H, H-6′). ^{13}C NMR (D_2O) δ: 102.146 (C-1, $^1J_{C,H}$ = 171.6 Hz), 97.263 (C-1′, $^1J_{C,H}$ = 168.4 Hz), 72.159 (C-5), 71.79 (C-4), 70.697 (C-2), 69.211 (C-4′), 67.718 (C-5′), 67.590 (C-3), 64.044 (C-2′), 62.316 (C-6), 55.663 (OCH_3), 33.696 (C-3′), 16.156

© 2002 NRC Canada

(C-6′). HR-FAB-MS calcd. for $C_{13}H_{24}O_9Na$ $[M + Na]^+$: 347.1318; found: 347.1320.

Methyl 4,6-di-*O*-benzyl-3-*O*-(2,4-di-*O*-benzyl-3,6-dideoxy-α-D-*xylo*-hexopyranosyl)-2-*O*-methyl-α-D-talopyranoside (36)

Alcohol **35** (136 mg, 0.20 mmol) was dissolved in DMF (5 mL) and cooled to 0°C. Sodium hydride (18.0 mg, 80% dispersion in oil, 0.6 mmol) was added and the mixture stirred for 10 min. To this solution was added methyl iodide (20 μL, 0.60 mmol) and the reaction stirred overnight while being allowed to warm to room temperature. Upon quenching the reaction with CH_3OH, the solution was partitioned between water with CH_2Cl_2. The organic layer was then washed with water, a saturated solution of NaCl, dried (Na_2SO_4), and evaporated. Chromatography (pentane–EtOAc, 3:1) gave **36** (124 mg, 90%) as an oil. $[\alpha]_D$ +49.5 (*c* 1.0, $CHCl_3$). R_f = 0.25 (pentane–EtOAc, 3:1). ^{1}H NMR ($CDCl_3$) δ: 7.15–7.40 (m, 20H, Ph), 5.09 (d, $J_{1',2'}$ = 3.5 Hz, 1H, H-1′), 4.92 (d, ^2J = 12.0 Hz, 1H, PhCH_2), 4.83 (d, $J_{1,2}$ = 2.0 Hz, 1H, H-1), 4.68, 4.63 (d, ^2J = 12.0 Hz, 1H, PhCH_2), 4.31–4.58 (m, 6H, PhCH_2), 4.23 (q, 1H, H-5′), 3.75–4.10 (m, 5H, H-3, H-4, H-5, H-6a, H-2′), 3.58 (dd, $J_{6a,6b}$ = 10.5 Hz, $J_{5,6b}$ = 5.0 Hz, 1H, H-6b), 3.53 (s, 3H, OCH_3), 3.48 (br. s, 1H, H-4′), 3.38–3.45 (m, 4H, OCH_3, H-2), 2.18 (dt, $J_{2,3'eq} \approx J_{3'eq,4}$ = 3.5 Hz, $J_{3'eq,3'ax}$ = 13.0 Hz, 1H, H-3′eq), 1.92 (dt, $J_{3'ax,4}$ = 13.0 Hz, $J_{2',3'ax}$ = 2.5 Hz, 1H, H-3′ax), 1.23 (d, $J_{5'6'}$ = 6.5 Hz, 3H, H-6′). ^{13}C NMR ($CDCl_3$) δ: 98.31 (C-1), 98.07 (C-1′), 73.90, 73.39, 71.28, 70.95 (PhCH_2), 69.30 (C-6), 59.19 (OCH_3), 55.18 (OCH_3), 27.73 (C-3′), 16.66 (C-6′). Anal. calcd. for $C_{42}H_{50}O_9$ (698.86): C 72.19, H 7.21; found: C 71.73, H 7.40.

Methyl 3-*O*-(3,6-dideoxy-α-D-*xylo*-hexopyranosyl)-2-*O*-methyl-α-D-talopyranoside (12)

Methyl ether **36** (118 mg, 0.17 mmol) was dissolved in acetic acid (5 mL) and then 10% Pd/C (100 mg) was added. The reaction was stirred overnight under a flow of H_2. After filtration of the catalyst and evaporation of the solvent the residue was subjected to chromatography (CH_2Cl_2–CH_3OH, 9:1) on Iatrobeads. The product obtained was then redissolved in water, filtered through a 0.22 μM filter and lyophilized to give the product **12** (45 mg, 78%) as an amorphous white solid. R_f = 0.55 (CH_2Cl_2–CH_3OH, 4:1). $[\alpha]_D$ +143.4 (*c* 0.5, H_2O). ^{1}H NMR (D_2O) δ: 5.045 (d, $J_{1,2}$ = 1.5 Hz, 1H, H-1), 5.021 (d, $J_{1',2'}$ = 4.0 Hz, 1H, H-1′), 4.069 (dq, $J_{4',5'}$ = 1.5 Hz, $J_{5',6'}$ = 7.0 Hz, 1H, H-5′), 4.035 (dd, $J_{3,4}$ = 3.0 Hz, $J_{4,5}$ = 1.0 Hz, 1H, H-4), 4.015 (ddd, $J_{1',2'}$ = 4.0 Hz, $J_{2',3'ax}$ = 13.0 Hz, $J_{2',3'eq}$ = 5.0 Hz, 1H, H-2′), 3.957 (t, $J_{2,3}$ = 3.0 Hz, $J_{3,4}$ = 3.0 Hz, 1H, H-3), 3.86–3.90 (m, 2H, 4–5, H-4′), 3.825 (dd, $J_{5,6a}$ = 8.0 Hz, $J_{6a,6b}$ = 11.5 Hz, 1H, H-6a), 3.752 (dd, $J_{5,6b}$ = 4.0 Hz, $J_{6a,6b}$ = 11.5 Hz, 1H, H-6b), 3.486 (s, 3H, aglycon OCH_3), 3.441 (ether OCH_3), 2.088 (dt, $J_{2',3'ax}$ = 13.0 Hz, $J_{3'ax,3'eq}$ = 13.0 Hz, $J_{3'ax,4'}$ = 3.0 Hz, 1H, H-3′ax), 1.998 (ddd, $J_{2',3'eq}$ = 5.0 Hz, $J_{3'ax,3'eq}$ = 13.0 Hz, $J_{3'eq,4'}$ = 4.0 Hz, 1H, H-3′eq), 1.184 (d, $J_{5',6'}$ = 7.0 Hz, 3H, H-6′). ^{13}C NMR (D_2O) δ: 98.530 (C-1, $^1J_{C,H}$ = 170.7 Hz), 97.895 (C-1′, $^1J_{C,H}$ = 168.6 Hz), 79.796 (C-2), 72.525 (C-3), 72.324 (C-5), 69.217 (C-4′), 67.773 (C-5′), 67.309 (C-4), 64.056 (C-2′), 62.264 (C-6), 59.319 (ether OCH_3), 55.675 (aglycon OCH_3), 33.715 (C-3′), 16.260 (C-6′). HR-FAB-MS calcd for $C_{14}H_{26}O_9Na$ $[M + Na]^+$: 361.1475; found: 361.1480.

Methyl 4,6-di-*O*-benzyl-3-*O*-(2,4-di-*O*-benzyl-3,6-dideoxy-α-D-*xylo*-hexopyranosyl)-2-*O*-(2,3,4,6-tetra-*O*-benzyl-α-D-galactopyranosyl)-α-D-talopyranoside (38)

Disaccharide **35** (170 mg, 0.25 mmol) and thioglycoside **37** (39) (297 mg, 0.51 mmol) were dried with crushed 4 Å molecular sieves (500 mg) over P_2O_5 under vacuum overnight. The solids were suspended in CH_2Cl_2 (10 mL) and cooled to 0°C. *N*-Iodosuccinimide (124 mg, 0.55 mmol) and silver triflate (14 mg, 0.055 mmol) were then added. After stirring for 40 min and warming to room temperature, the reaction was quenched with triethylamine. Dilution with CH_2Cl_2 was followed by washing with a saturated solution of sodium thiosulfate, water, and a saturated solution of NaCl. After drying (Na_2SO_4) and evaporation of the solvent, chromatography (toluene–EtOAc, 9:1) gave the product **38** (106 mg, 35%) as an oil. $[\alpha]_D$ +58.8 (*c* 0.9, $CHCl_3$). R_f = 0.31 (toluene–EtOAc, 9:1). ^{1}H NMR ($CDCl_3$) δ: 7.10–7.40 (m, 40H, Ph), 5.38 (d, ^2J = 12.0 Hz, 1H, PhCH_2), 5.16 (d, $J_{1,2}$ = 2.0 Hz, 1H, H-1), 5.06 (d, $J_{1',2'}$ = 3.5 Hz, 1H, H-1′), 5.02 (d, $J_{1'',2''}$ = 3.5 Hz, 1H, H-1″), 4.83, 4.80 (d, ^2J = 12.0 Hz, 1H, PhCH_2), 4.40–4.65 (m, 13H, PhCH_2), 4.23 (d, ^2J = 12.0 Hz, 1H, PhCH_2), 3.54–4.15 (m, 14H, H-3, H-4, H-5, H-6a, H-6b, H-2′, H-5′, H-2″, H-3″, H-4″, H-5″, H-6a″, H-6b″), 3.26 (s, 3H, OCH_3), 2.63 (br. s, 1H, H-4′), 1.90 (dt, $J_{2',3'eq}$, $J_{3'eq,4'}$ = 3.5 Hz, $J_{3'eq,3'ax}$ = 13.0 Hz, 1H, H-3′eq), 1.77 (dt, $J_{3'ax,4}$ = 13.0 Hz, $J_{2',3ax}$ = 2.5 Hz, 1H, H-3′ax), 1.06 (d, $J_{5'6'}$ = 6.5 Hz, 3H, H-6′). ^{13}C NMR ($CDCl_3$) δ: 100.26 (C-1″), 99.93 (C-1), 99.01 (C-1′), 69.20 (C-6), 66.41 (C-1″), 54.91 (OCH_3), 27.75 (C-3′), 16.46 (C-6′). Anal. calcd. for $C_{75}H_{82}O_{14}$ (1207.47): C 74.60, H 6.84; found: C 74.81, H 7.29.

Methyl 3-*O*-(3,6-dideoxy-α-D-*xylo*-hexopyranosyl)-2-*O*-(α-D-galactopyranosyl)-α-D-talopyranoside (13)

The protected trisaccharide **38** (78 mg, 0.06 mmol) was dissolved in acetic acid (5 mL) and then 10% Pd/C (100 mg) was added. The reaction was stirred overnight under a flow of H_2. After filtration of the catalyst and evaporation of the solvent, the residue was subjected to chromatography (CH_2Cl_2–CH_3OH–water, 65:35:5) on Iatrobeads. The product obtained was then redissolved in water, filtered through a 0.22 μM filter and lyophilized to give **13** (26 mg, 86%) as an amorphous white solid. $[\alpha]_D$ +176.8 (*c* 0.5, H_2O). R_f = 0.58 (CH_2Cl_2–CH_3OH–water, 65:35:5). ^{1}H NMR (D_2O) δ: 5.304 (d, $J_{1',2'}$ = 3.5 Hz, 1H, H-1′), 5.060 (d, $J_{1'',2''}$ = 4.0 Hz, 1H, H-1″), 5.056 (s, 1H, H-1), 4.01–4.15 (m, 6H, H-2, H-3, H-4, H-2′, H-5′, H-5″), 3.980 (d, $J_{3'',4''}$ = 3.5 Hz, 1H, H-4″), 3.919 (dd, $J_{3'',4''}$ = 3.5 Hz, 1H, H-3″), 3.85–3.90 (m, 3H, H-5, H-6a, H-4′), 3.826 (dd, $J_{2'',3''}$ = 10.0 Hz, 1H, H-2″), 3.750 (d, $J_{5'',6''}$ = 6.0 Hz, 1H, H-6″), 3.428 (s, 3H, OCH_3), 2.00–2.02 (m, 2H, H-3′ax, H-3′eq), 1.176 (d, $J_{5',6'}$ = 6.5 Hz, 3H, H-6′). ^{13}C NMR (D_2O) δ: 101.618 (C-1″, $^1J_{C,H}$ = 173.7 Hz), 100.858 (C-1, $^1J_{C,H}$ = 174.2 Hz), 95.856 (C-1′, $^1J_{C,H}$ = 169.9 Hz), 79.936 (C-2), 72.422 (C-5″), 72.052 (C-5), 70.944 (C-3), 70.136 (C-4″), 70.038 (C-3″), 69.260 (C-2″), 69.171 (C-4′), 67.911 (C-5), 66.372 (C-4), 63.992 (C-2′), 62.240 (2 C, C-6, C-6″), 55.626 (OCH_3), 33.896

© 2002 NRC Canada

(C-3′), 16.186 (C-6′). HR-FAB-MS calcd. for $C_{19}H_{31}O_{14}Na$ $[M + Na]^+$: 509.1846; found: 509.1833.

Methyl 2,3,4,6-tetra-*O*-acetyl-α-D-talopyranoside (40)

Acetal **29** (6.10 g, 26.07 mmol) was dissolved in trifluoroacetic acid:water (9:1, 50 mL), stirred overnight, and then evaporated to a thick oil. The residue was then dissolved in pyridine (50 mL), cooled to 0°C, and acetic anhydride (20 mL) added. After stirring overnight while warming to room temperature the reaction was quenched by adding CH_3OH and the solution evaporated. Chromatography (hexane–EtOAc, 3:1) gave **40** (7.17 g, 76%) as a an oil. $[\alpha]_D$ +64.7 (*c* 0.9, $CHCl_3$). R_f = 0.34 (hexane–EtOAc, 2:1). ^{1}H NMR ($CDCl_3$) δ: 5.31 (br. d, $J_{3,4}$ = 3.5 Hz, 1H, H-4), 5.28 (t, $J_{2,3}$ = 3.5 Hz, 1H, H-3), 5.08 (dt, $J_{2,4}$ = 1.5 Hz, $J_{2,3}$ = 3.5 Hz, 1H, H-2), 4.79 (d, $J_{1,2}$ = 1.5 Hz, 1H, H-1), 4.04–4.16 (m, 3H, H-5, H-6a, H-6b), 3.40 (s, 3H, OCH_3), 2.12, 2.13, 2.05, 1.98 (s, 3 H, OCOCH_3). ^{13}C NMR ($CDCl_3$) δ: 170.75, 170.50, 170.19, 170.01 (*C*=O), 99.33 (C-1), 62.10 (C-6), 55.30 (O*C*H_3), 20.89, 20.67, 20.58 (OCO *C*H_3). Anal. calcd. for $C_{15}H_{22}O_{10}$ (362.34): C 49.72, H 6.12; found: C 49.23, H 6.21.

1,2,3,4,6-Penta-*O*-acetyl-α-D-talopyranose (41)

Methyl glycoside **40** (5.5 g, 15.2 mmol) was dissolved in acetic anhydride (120 mL) and the solution cooled to 0°C. H_2SO_4 (400 μL) was added dropwise from a microsyringe and the reaction allowed to continue for 2 h at 0°C. The reaction was quenched by adding CH_2Cl_2 and then a solution of $NaHCO_3$ and stirring for 20 min. The reaction was diluted with more CH_2Cl_2 and then washed with $NaHCO_3$, water, and a saturated solution of NaCl. After drying (Na_2SO_4) and evaporation of the solvent, the product **41** (5.6 g, 95%) was obtained as a white crystalline solid; mp 103–105°C (lit. (40) value mp +104 to 105°C). $[\alpha]_D$ +68.8 (*c* 1.3, $CHCl_3$) (lit. (40) value $[\alpha]_D$ +68° (*c* 0.6)). R_f = 0.28 (hexane–EtOAc, 2:1). ^{1}H NMR ($CDCl_3$) δ: 6.12 (d, $J_{1,2}$ = 2.0 Hz, 1H, H-1), 5.34 (br. d, $J_{3,4}$ = 3.5 Hz, 1H, H-4), 5.29 (t, $J_{2,3}$ = 3.5 Hz, 1H, H-3), 5.08 (ddd, $J_{2,4}$ = 1.0 Hz, 1H, H-2), 4.30 (dt, $J_{4,5}$ = 1.5, 7.0 Hz, 1H, H-5), 4.18 (dd, $J_{6a,6b}$ = 11.0 Hz, $J_{5,6a}$ = 7.0 Hz, 1H, H-6a), 4.12 (dd, $J_{5,6b}$ = 7.0 Hz, 1H, H-6b), 2.13 (s, 6H, 2 × OCOCH_3), 2.12, 2.02, 1.99 (s, 3H, OCOCH_3). ^{13}C NMR ($CDCl_3$) δ: 170.37, 170.07, 169.64, 169.65, 168.02 (*C*=O) 91.14 (C-1), 61.41 (C-6), 20.82, 20.72, 20.60, 20.52 (OCO*C*H_3). Anal. calcd. for $C_{16}H_{22}O_{11}$ (390.35): C 49.23, H 5.68; found: C 49.26, H 5.63.

2,3,4,6-Tetra-*O*-acetyl-α-D-talopyranosyl bromide (42)

The peracetate **41** (500 mg, 1.28 mmol) was stirred with 45% HBr in acetic acid (10 mL) and acetic anhydride (1 mL) for 2 h. The solution was then evaporated to provide, in quantitative yield as determined by ^{1}H NMR, **42** as a yellow oil. Attempts to purify the product by flash chromatography resulted in complete decomposition of the bromide. ^{1}H NMR ($CDCl_3$) δ: 6.41 (s, 1H, H-1), 5.70 (t, $J_{2,3}$ = 3.5 Hz, 1H, H-3), 5.53 (br. d, $J_{3,4}$ = 3.5 Hz, 1H, H-4), 5.42 (d, $J_{2,3}$ = 3.5 Hz, 1H, H-2), 4.49 (br. t, $J_{5,6a}$, $J_{5,6b}$ = 6.0 Hz, 1H, H-5), 4.26 (dd, $J_{6a,6b}$ = 10.5 Hz, 1H, H-6a), 4.20 (dd, $J_{5,6b}$ = 6.5 Hz, 1H, H-6b), 2.03, 2.00, 1.90, 1.85 (s, 3H, OCOCH_3).

Ethyl 3,4-*O*-isopropylidene-1-thio-β-D-galactopyranoside (46)

The deprotected thioglycoside **45** (41) (285 mg, 1.28 mol) was suspended in dry CH_3CN (5 mL) and dimethoxypropane (785 μL, 6.40 mmol) was added followed by *p*-TsOH (15 mg). After 10 min the solid was dissolved and the reaction was allowed to proceed for 2 h. Water (1 mL) was added and the reaction stirred for 30 min before being neutralized with triethylamine and evaporated. Chromatography (EtOAc) gave the product **46** (222 mg, 66%) as a white crystalline solid; mp 88–91°C. $[\alpha]_D$ +13.9 (*c* 0.9, $CHCl_3$). R_f = 0.55 (EtOAc). ^{1}H NMR ($CDCl_3$) δ: 4.21 (dd, $J_{4,5}$ = 2.0 Hz, 1H, H-4), 4.27 (d, $J_{1,2}$ = 10.0 Hz, 1H, H-1), 4.09 (dd, $J_{3,4}$ = 5.5 Hz, 1H, H-3), 3.76–4.01 (m, 3H, H-6a, H-6b, H-5), 3.56 (ddd, $J_{2,3}$ = 7.0 Hz, $J_{2,2\text{-OH}}$ = 2.0 Hz, 1H, H-2), 2.70–2.80 (m, 2H, SCH_2CH$_3$), 2.45 (d, 1H, 2-OH), 2.10 (dd, $J_{6a,6\text{-OH}}$ = 4.0 Hz, $J_{6b,6\text{-OH}}$ = 9.5 Hz, 1H), 1.51, 1.35 (s, 3H, (CH_3)$_2$CO$_2$), 1.32 (t, ^3J = 6.5 Hz, 1H, SCH$_2$CH_3). ^{13}C NMR ($CDCl_3$) δ: 110.18 ((CH$_3$)$_2$*C*O$_2$), 85.23 (C-1), 62.25 (C-6), 28.03, 26.21 ((*C*H$_3$)$_2$CO$_2$), 24.30 (S*C*H$_2$CH$_3$), 15.18 (SCH$_2$*C*H$_3$). Anal. calcd. for $C_{11}H_{20}O_5S$ (264.34): C 49.98, H 7.63, S 12.13; found: C 50.16, H 7.96, S 12.04.

Ethyl 3,4-*O*-isopropylidene-6-*O*-*tert*-butyldimethylsilyl-1-thio-β-D-galactopyranoside (47)

Diol **46** (600 mg, 2.26 mole) was dissolved in dry pyridine (30 mL) and then *tert*-butyldimethylsilyl chloride (408 mg, 2.71 mmol) was added followed by DMAP (15 mg). The reaction was stirred overnight and then diluted with CH_2Cl_2 and washed successively with 0.5 N HCl, water, and a saturated solution of NaCl. After drying (Na_2SO_4), the organic layer was evaporated. Chromatogaphy (hexane–EtOAc, 2:1) gave the product **47** (700 mg, 85%) as an oil. $[\alpha]_D$ –5.1 (*c* 0.9, $CHCl_3$). R_f = 0.68 (hexane–EtOAc, 2:1). ^{1}H NMR ($CDCl_3$) δ: 4.25 (dd, $J_{3,4}$ = 5.5 Hz, $J_{4,5}$ = 2.5 Hz, 1H, H-4), 4.24 (d, $J_{1,2}$ = 10.0 Hz, 1H, H-1), 4.04 (dd, $J_{2,3}$ = 7.0 Hz, 1H, H-3), 3.78–3.89 (m, 3H, H-6a, H-6b, H-5), 3.55 (ddd, $J_{2,2\text{-OH}}$ = 2.0 Hz, 1H, H-2) 2.65–2.80 (m, 2H, SCH_2CH$_3$), 2.37 (d, $J_{2,2\text{-OH}}$ = 2.0 Hz, 1H, 2-OH), 1.53, 1.35 (s, 3H, (CH_3)$_2$CO$_2$), 1.32 (t, ^3J = 6.5 Hz, 1H, SCH$_2$CH_3), 0.90 (s, 9H, SiC(CH_3)$_3$), 0.08 (s, 6H, Si(CH_3)$_2$). ^{13}C NMR ($CDCl_3$) δ: 109.97 ((CH$_3$)$_2$*C*O$_2$), 85.58 (C-1), 62.10 (C-6), 28.28, 26.29 ((*C*H$_3$)$_2$CO$_2$), 25.82 (SiC(*C*H$_3$)$_3$), 24.46 (S*C*H$_2$CH$_3$), 18.26 (Si*C*(CH$_3$)$_3$), 15.39 (SCH$_2$*C*H$_3$), –5.34, –5.50 (Si(*C*H$_3$)$_2$). Anal. calcd. for $C_{17}H_{34}O_5SSi$ (378.60): C 53.93, H 9.05, S 8.47; found: C 54.06, H 8.95, S 8.52.

Ethyl 3,4-*O*-isopropylidene-6-*O*-*tert*-butyldimethylsilyl-1-thio-β-D-talopyranoside (48)

Oxalyl chloride (220 μL, 1.98 mmol) was dissolved in CH_2Cl_2 (10 mL) and cooled to –78°C. To this solution was added dropwise DMSO (310 μL, 4.36 mmol) in CH_2Cl_2 (10 mL). When the solution had stirred for 30 min, **47** (500 mg, 1.32 mmol) dissolved in CH_2Cl_2 (10 mL) was added dropwise over 10 min. After stirring for another 20 min and warming to –60°C, triethylamine (1.2 mL, 8.85 mmol) was added and the reaction brought to room temperature. After 40 min, water was added and the layers separated. The organic layer was washed with water, a saturated solution of NaCl, and then dried (Na_2SO_4). Evaporation of the solvent provided a residue that was immediately

© 2002 NRC Canada

dissolved in methanol (50 mL) and then $NaBH_4$ (100 mg, 2.64 mmol) was added. After stirring for 20 min, the reaction was quenched with acetic acid and the solvent evaporated. TLC indicated a mixture of two easily separable products (R_f = 0.66 and 0.61 (hexane–EtOAc, 2:1)), which were later shown to be an anomeric mixture of talopyranosides. The residue was coevaporated with CH_3OH (3 × 50 mL) and the residue chromatographed (hexane–EtOAc, 3:1). The two products **48** were isolated as oils, the β-glycoside (343 mg, 69% yield) and the α-glycoside (81 mg, 16% yield). Only the β-glycoside was fully characterized. $[\alpha]_D$ –34.6 (*c* 0.7, $CHCl_3$). ^{1}H NMR ($CDCl_3$) δ: 4.52 (d, $J_{1,2}$ = 1.5 Hz, 1H, H-1), 4.16–4.22 (m, 2H, H-3, H-4), 3.76–3.94 (m, 4H, H-5, H-6a, H-6b, H-2), 2.65–2.76 (m, 2H, SCH_2CH_3), 2.42 (d, $J_{2,2\text{-OH}}$ = 8.5 Hz, 1H, 2-OH), 1.58, 1.36 (s, 3H, $(CH_3)_2CO_2$), 1.30 (t, ^3J = 6.5 Hz, 1H, SCH_2CH_3), 0.84 (s, 9H, $SiC(CH_3)_3$), 0.08 (s, 6H, $Si(CH_3)_2$). ^{13}C NMR ($CDCl_3$) δ: 109.80 ($(CH_3)_2CO_2$), 84.42 (C-1), 62.13 (C-6), 25.81 ($SiC(CH_3)_3$), 25.74 ($(CH_3)_2CO_2$), 25.71 (SCH_2CH_3), 25.49 ($(CH_3)_2CO_2$), 18.25 ($SiC(CH_3)_3$), 15.24 (SCH_2CH_3), –5.36, –5.50 ($Si(CH_3)_2$). Anal. calcd. for $C_{17}H_{34}O_5SSi$ (378.60): C 53.93, H 9.05, S 8.47; found: C 53.97, H 9.02, S 8.48.

Ethyl 2,3,4,6-tetra-*O*-acetyl-1-thio-β-D-talopyranoside (43)

Acetal **48** (279 mg, 0.74 mmol) was dissolved in 80% acetic acid (35 mL) and the solution heated for 1 h at 80°C. The solution was cooled, the solvent evaporated and the residue immediately dissolved in pyridine (20 mL). Following the addition of acetic anhydride (5 mL) and DMAP, the reaction was stirred overnight before being quenched by cooling to 0°C and adding CH_3OH. The mixture was then diluted with CH_2Cl_2 and washed with 0.5 N HCl, water, and a saturated solution of NaCl. After drying (Na_2SO_4) and evaporation, chromatography (hexane–EtOAc, 2:1) gave the product **43** (258 mg, 89%) as an oil. $[\alpha]_D$ –53.8 (*c* 1.0, $CHCl_3$). R_f = 0.33 (hexane–EtOAc, 2:1). ^{1}H NMR ($CDCl_3$) δ: 5.37 (dd, $J_{3,4}$ = 3.5 Hz, $J_{4,5}$ = 1.5 Hz, 1H, H-4), 5.27 (dd, $J_{2,3}$ = 3.5 Hz, 1H, H-2), 5.08 (t, 1H, H-3), 4.76 (d, $J_{1,2}$ = 1.0 Hz, 1H, H-1), 4.21 (dd, $J_{5,6a}$ = 7.0 Hz, $J_{6a,6b}$ = 11.5 Hz, 1H, H-6a), 4.15 (dd, $J_{5,6b}$ = 7.0 Hz, 1H, H-6b), 3.92 (dt, $J_{4,5}$ = 1.5 Hz, 1H, H-5), 2.73 (q, ^3J = 6.5 Hz, 2H, SCH_2CH_3), 2.13, 2.09, 2.01, 1.94 (s, 3H, $OCOCH_3$), 1.28 (t, 1H, ^3J = 6.5 Hz, SCH_2CH_3). ^{13}C NMR ($CDCl_3$) δ: 170.37, 170.15, 170.03, 169.52 (C=O), 83.24 (C-1), 61.81 (C-6), 25.75 (SCH_2CH_3), 20.61, 20.53, 20.47, 20.35 ($OCOCH_3$), 14.96 (SCH_2CH_3). Anal. calcd. for $C_{10}H_{18}O_5S$ (392.42): C 48.97, H 6.16, S 8.17; found: C 49.18, H 6.09, S 8.22.

Methyl 2-*O*-(2,3,4,6-tetra-*O*-acetyl-α-D-talopyranosyl)-3-*O*-(2,4-di-*O*-benzyl-3,6-dideoxy-α-D-*xylo*-hexopyranosyl)-4,6-di-*O*-benzyl-α-D-mannopyranoside (44)

Talose donor **43** (114 mg, 0.292 mmol) and disaccharide **20** (35) (50 mg, 0.73 mmol) were dried with crushed 4 Å molecular sieves (300 mg) under vacuum with P_2O_5. The solids were suspended in CH_2Cl_2 (5 mL) and the solution cooled to 0°C. Upon stirring for 30 min, *N*-iodosuccinimide (65 mg, 0.292 mmol) and silver triflate (7.5 mg, 0.029 mmol) were added. The reaction was quenched with triethylamine after 1 h and the reaction mixture diluted with CH_2Cl_2, filtered, and then the organic layer washed with a saturated solution of sodium thiosulfate, water and a saturated solution of NaCl. After drying (Na_2SO_4) and evaporation of the solvent, the product was purified by chromatography (hexane–EtOAc, 1:1) to give **44** (35 mg, 47%) as an oil. $[\alpha]_D$ +69.1 (*c* 1.1, $CHCl_3$). R_f = 0.54 (hexane–EtOAc, 1:1). ^{1}H NMR ($CDCl_3$) δ: 7.10–7.50 (m, 20H, Ph), 5.27 (t, $J_{2'',3''}$, $J_{3'',4''}$ = 3.5 Hz, 1H, H-3″), 5.24 (br. s, 1H, H-2″), 5.17 (br. s, 1H, H-4″), 5.11 (br. s, 1H, H-1′), 5.06 (d, J_{gem} = 11.5 Hz, 1H, $PhCH_2$), 5.05 (s, 1H, H-1″), 4.93 (d, $J_{1,2}$ = 2.0 Hz, 1H, H-1), 4.34–4.60 (m, 7H, 7 × $PhCH_2$, H-5′), 4.20 (dd, $J_{5'',6a''}$ = 6.0 Hz, $J_{6a'',6b''}$ = 11.5 Hz, 1H, H-6a″), 4.15 (dd, $J_{2,3}$ = 2.5 Hz, $J_{3,4}$ = 9.5 Hz, 1H, H-3), 4.04 (dd, $J_{5'',6b''}$ = 7.0 Hz, 1H, H-6b″), 3.93–4.00 (m, 2H, H-4, H-2), 3.88 (dd, $J_{5'',6a''}$ = 6.0 Hz, 1H, H-5″), 3.81 (dt, $J_{2',3'eq}$ = 3.5 Hz, $J_{2',3'ax}$ = 12.5 Hz, 1H, H-2′), 3.70–3.76 (m, 1H, H-5), 3.60–3.69 (m, 2H, H-6a, H-6b), 3.54 (br. s, 1H, H-4′), 3.37 (s, 3H, OCH_3), 1.90–2.15 (m, 14H, 12 × $OCOCH_3$, H-3′ax, H-3′eq), 1.12 (d, $J_{5',6'}$ = 6.5 Hz, 1H, H-6′). ^{13}C NMR ($CDCl_3$) δ: 170.48, 170.10, 169.78, 169.32 (C=O), 100.35 (C-1), 99.78 (C-1″), 99.00 (C-1′), 74.69 ($PhCH_2$), 73.20 ($PhCH_2$), 71.43, 70.81 ($PhCH_2$), 69.21 (C-6), 62.58 (C-6″), 54.96 (OCH_3), 27.56 (C-3′), 20.89, 20.74, 20.69 ($OCOCH_3$), 16.47 (C-6′). Anal. calcd. for $C_{55}H_{66}O_{18}$ (1015.12): C 65.08, H 6.55; found: C 64.54, H 6.40.

Methyl 2-*O*-(α-D-talopyranosyl)-3-*O*-(3,6-dideoxy-α-D-*xylo*-hexopyranosyl)-α-D-mannopyranoside (14)

Trisaccharide **44** (51 mg, 0.05 mmol) was dissolved in CH_3OH (5 mL) and then $NaOCH_3$ (15 mg) was added. The reaction was stirred overnight and neutralized with Amberlite IR-120 (H+) resin. The solution was filtered, the filtrate evaporated and the residue immediately redissolved in acetic acid (10 mL). 10% Pd/C (30 mg) was added, and the reaction was stirred under a flow of H_2 overnight. The catalyst was filtered off and the solvent evaporated to yield a yellow residue. The colored impurities were removed by redissolution in water and filtration through a C-18 reverse-phase cartridge. The filtrate was evaporated and then passed through a Biogel P-2 column using water as the eluant. Concentration of the product by evaporation, filtration through a 0.22 μM filter and lyophilization gave the product **14** (21.2 mg, 87%) as an amorphous white solid. $[\alpha]_D$ +99.0 (*c* 0.7, H_2O). ^{1}H NMR (D_2O) δ: 5.205 (s, 1H, H-1″), 5.097 (d, $J_{1',2'}$ = 3.5 Hz, 1H, H-1′), 5.028 (d, $J_{1,2}$ = 2.0 Hz, 1H, H-1), 4.101 (dd, $J_{2,3}$ = 3.0 Hz, 1H, H-2), 4.01–4.07 (m, 3H, H-2′, H-5′, H-5″), 3.983 (dd, $J_{3,4}$ = 10.0 Hz, 1H, H-3), 3.91–3.97 (m, 3H, H-2″, H-3″, H-4″), 3.88–3.97 (m, 2H, H-6a, H-4′), 3.871 (t, $J_{4,5}$ = 10.0 Hz, 1H, H-4), 3.820 (dd, $J_{5,6'a}$ = 8.0 Hz, $J_{6''a,6''b}$ = 12.0 Hz, 1H, H-6″a), 3.74–3.79 (m, 2H, H-6b, H-6″b), 3.653 (ddd, $J_{5,6a}$ = 2.0 Hz, $J_{5,6b}$ = 6.0 Hz, 1H, H-5), 3.438 (s, 3H, OCH_3), 1.90–2.04 (m, 2H, H-3′ax, H-3′eq), 1.194 (d, $J_{5',6'}$ = 6.5 Hz, 3H, H-6′). ^{13}C NMR (D_2O) δ: 103.273 (C-1″, $^1J_{C,H}$ = 172.2 Hz), 101.15 (C-1′, $^1J_{C,H}$ = 170.8 Hz), 100.916 (C-1, $^1J_{C,H}$ = 174.5 Hz), 79.868 (C-3), 78.453 (C-2), 73.539 (C-5), 72.950 (C-5″), 71.085 (C-4″), 70.481 (C-2″), 69.037 (C-4′), 68.021 (C-5′), 67.404 (C-4), 65.976 (C-3″), 64.245 (C-2′), 62.426 (C-6″), 61.629 (C-6), 55.681 (OCH_3), 33.776 (C-3′), 16.324 (C-6′). Anal. calcd. for $C_{19}H_{34}O_{14}$-H_2O (504.29): C 45.24, H 7.19;

© 2002 NRC Canada

found: C 45.48, H 7.11. HR-FAB-MS calcd. for $C_{19}H_{31}O_{14}Na$ $[M + Na]^+$: 509.1846; found: 509.1843.

4,6-Dichloro-2-*O*-chlorosulfo-4,6-dideoxy-3-*O*-methyl-α/β-D-galactopyranosyl chloride (51)

3-*O*-Methyl-α-D-glucopyranose (42) (**50**, 194 mg, 1.0 mmol) was dissolved in pyridine (1 mL) and $CHCl_3$ (5 mL) and the flask purged with N_2. The solution was cooled to –78°C and sulfuryl chloride (0.5 mL, 6.25 mmol) was added slowly and then the bath was removed and the reaction was stirred for 24 h. The reaction was then diluted with $CHCl_3$ and washed successively with 1 N H_2SO_4, water, 1 N $KHCO_3$, water, and a saturated solution of NaCl. The organic phase was then dried ($MgSO_4$), evaporated and chromatographed (hexane–EtOAc, 4:1) to provide **51** as two separable anomers. The α-anomer (70 mg, 20%) was obtained as a liquid and the β-anomer (120 mg, 35%) as an amorphous solid. α-Anomer: $[\alpha]_D$ +180.8 (*c* 0.4, $CHCl_3$). R_f = 0.75 (hexane–EtOAc, 3:1). ^{1}H NMR ($CDCl_3$) δ: 6.36 (d, $J_{1,2}$ = 4.0 Hz, 1H, H-1), 5.13 (dd, $J_{2,3}$ = 10.0 Hz, 1H, H-2), 4.76 (br. d, $J_{3,4}$ = 2.5 Hz, 1H, H-4), 4.46 (dd, $J_{5,6a}$ = 8.5 Hz, $J_{5,6b}$ = 5.5 Hz, 1H, H-5), 3.98 (dd, 1H, H-3), 3.74 (dd, $J_{6a,6b}$ = 11.0 Hz, 1H, H-6a), 3.66 (dd, 1H, H-6′), 3.51 (s, 3H, OCH_3). ^{13}C NMR ($CDCl_3$) δ: 89.58, (C-1, $^1J_{C,H}$ = 186.0 Hz). Anal. calcd. for $C_7H_{10}Cl_4O_5S$ (352.03): C 23.88, H 2.86, S 9.11; found: C 24.20, H 2.83, S 9.29. β-Anomer: $[\alpha]_D$ +55.4 (*c* 0.9, CHCl3). R_f = 0.40 (hexane–EtOAc, 3:1). ^{1}H NMR ($CDCl_3$) δ: 5.28 (d, $J_{1,2}$ = 8.5 Hz, 1H, H-1), 5.10 (dd, $J_{2,3}$ = 9.5 Hz, 1H, H-2), 4.73 (dd, $J_{4,5}$ = 1.0 Hz, 1H, H-4), 3.93 (dd, $J_{5,6a}$ = 7.5 Hz, $J_{5,6b}$ = 6.0 Hz, 1H, H-5), 3.78 (m, 2H, H-6a, H-6b), 3.65 (dd, 1H, $J_{3,4}$ = 3.5 Hz, H-3), 3.54 (s, 3H, OCH_3). ^{13}C NMR ($CDCl_3$) δ: 86.62 (C-1, $^1J_{C,H}$ = 174.0 Hz). Anal. calcd. for $C_7H_{10}Cl_4O_5S$ (352.03): C 23.88, H 2.86, S 9.11; found: C 24.41, H 2.91, S 9.45.

Methyl 4,6-dichloro-4,6-dideoxy-3-*O*-methyl-α/β-D-galactopyranoside (52)

Glycosyl chloride **51** (150 mg, 0.43 mmol) was dissolved in CH_3OH (5 mL), a few crystals of I_2 were added, and the reaction stirred for 48 h. Water (200 μL) was added and the reaction stirred for an additional 4 h. The solvent was then evaporated, coevaporating twice with toluene. The residue was then dissolved in 1 M $NaOCH_3$ (300 μL) and stirred overnight at which point the reaction pH had become slightly acidic. The solvent was evaporated and chromatographed (1:1 hexane–EtOAc) to give **52** as two separable anomers. Both the α-anomer (44 mg, 42%) and β-anomer (26 mg, 25%) were obtained as amorphous solids. α-Anomer: $[\alpha]_D$ +192.8 (*c* 0.7, $CHCl_3$). R_f = 0.25 (hexane–EtOAc, 1:1). ^{1}H NMR ($CDCl_3$) δ: 4.83 (d, $J_{1,2}$ = 3.5 Hz, 1H, H-1), 4.56 (d, $J_{3,4}$ = 2.5 Hz, 1H, H-4), 4.09 (br. t, $J_{5,6a}$, $J_{5,6b}$ = 6.5 Hz, 1H, H-5), 3.97 (dd, $J_{2,3}$ = 9.5 Hz, 1H, H-2), 3.66–3.68 (m, 2H, H-6a, H-6b), 3.60 (dd, 1H, H-3), 3.47 (s, 3H, OCH_3), 3.36 (s, 3H, OCH_3). ^{13}C NMR ($CDCl_3$) δ: 99.41 (C-1). Anal. calcd. for $C_8H_{14}O_4Cl_2$ (247.10): C 39.89, H 5.71; found: C 39.32, H 5.75. β-Anomer: $[\alpha]_D$ +32.8 (*c* 0.4, $CHCl_3$). R_f = 0.20, (hexane–EtOAc, 1:1). ^{1}H NMR ($CDCl_3$) δ: 4.56 (d, $J_{3,4}$ = 3.5 Hz, 1H, H-4), 4.24 (d, $J_{1,2}$ = 7.5 Hz, 1H, H-1), 3.69–3.80 (m, 4H, H-5, H-2, H-6a, H-6b), 3.55 (s, 3H, OCH_3), 3.48 (s, 3H, OCH_3), 3.39 (dd, $J_{2,3}$ = 9.5 Hz, 1H, H-3). ^{13}C NMR ($CDCl_3$) δ: 104.25 (C-1). Anal. calcd. for $C_8H_{14}O_4Cl_2$ (247.10): C 39.89, H 5.71; found: C 39.12, H 5.85.

Methyl 2-*O*-benzyl-4,6-dichloro-4,6-dideoxy-3-*O*-methyl-α-D-galactopyranoside (53)

To a stirred suspension of **52** (49 mg, 0.2 mmol) and powdered NaOH (12 mg, 0.3 mmol) in DMF (3 mL) was added benzyl bromide (31 μL, 0.26 mmol). The reaction was instantaneous and was immediately quenched with CH_3OH. The reaction was diluted with toluene and washed with water and then a saturated solution of NaCl. After drying ($MgSO_4$) and solvent evaporation, the product was titrated with hexane to give **53** (48 mg, 71%) as an amorphous white solid. $[\alpha]_D$ +83.3 (*c* 0.7, $CHCl_3$). R_f = 0.60 (hexane–EtOAc, 3:1). ^{1}H NMR ($CDCl_3$) δ: 7.14–7.25 (m, 5H, Ph), 4.74, 4.50 (d, ^2J = 12.0 Hz, 1H, PhCH_2), 4.48 (d, $J_{1,2}$ = 4.0 Hz, 1H, H-1), 4.46 (br. s, 1H, H-4), 3.98 (br. t, $J_{5,6a}$, $J_{5,6b}$ = 6.5 Hz, 1H, H-5), 3.69 (m, 2H, H-2, H-3), 3.52 (m, 2H, H-6a, H-6b), 3.41 (s, 3H, OCH_3), 3.28 (s, 3H, OCH_3). ^{13}C NMR ($CDCl_3$) δ: 98.9 (C-1). Anal. calcd. for $C_{15}H_{20}Cl_2O_4$ (337.23): C 53.43, H 5.98; found: C 53.58, H 5.87.

1-*O*-Acetyl-2-*O*-benzyl-4,6-dichloro-4,6-dideoxy-α/β-D-galactopyranose (54)

Methyl glycoside **53** (250 mg, 0.75 mmol) was dissolved in acetic anhydride:HOAc:H_2SO_4 (50:20:0.5, 10 mL) and stirred at 0°C for 1 h and then at room temperature for 30 min. The reaction was quenched by pouring the solution into an ice cold $KHCO_3$ solution and then the product was extracted with CH_2Cl_2. The organic layer was washed with water and a saturated solution of NaCl and then dried ($MgSO_4$) and evaporated. Chromatography (hexane–EtOAc, 6:1) of the residue afforded **53** as two separable anomers. Both the α-anomer (185 mg, 68%) and the β-anomer (34 mg, 12%) were obtained as solids. α-Anomer: $[\alpha]_D$ +156.3 (*c* 0.5, $CHCl_3$). R_f = 0.35 (hexane–EtOAc, 4:1). ^{1}H NMR ($CDCl_3$) δ: 7.25–7.35 (m, 5H, Ph), 6.22 (d, $J_{1,2}$ = 4.0 Hz, 1H, H-1), 4.69 (d, ^2J = 11.5 Hz, 1H, PhCH_2), 4.66 (d, $J_{3,4}$ = 3.5 Hz, 1H, H-4), 4.60 (d, ^2J = 11.5 Hz, 1H, PhCH_2), 4.14 (ddd, $J_{5,6a}$ = 8.5 Hz, $J_{5,6b}$ = 5.5 Hz, $J_{4,5}$ = 0.5 Hz, 1H, H-5), 3.90 (dd, $J_{2,3}$ = 10.0 Hz, 1H, H-2), 3.76 (dd, 1H, H-3), 3.64 (dd, $J_{6a,6b}$ = 11.0 Hz, 1H, H-6a), 3.55 (dd, 1H, H-6b), 3.50 (s, 3H, OCH_3), 2.15 (s, 3H, OCOCH_3). ^{13}C NMR ($CDCl_3$) δ: 90.22 (C-1). Anal. calcd. for $C_{16}H_{20}Cl_2O_5$ (365.24): C 52.62, H 5.52; found: C 52.86, H 5.60. β-Anomer: $[\alpha]_D$ +25.5 (*c* 0.5, $CHCl_3$). R_f = 0.5 (hexane–EtOAc, 4:1). ^{1}H NMR ($CDCl_3$) δ: 7.26–7.33 (m, 5H, Ph), 5.56 (d, $J_{1,2}$ = 8.0 Hz, 1H, H-1), 4.83, 4.66 (d, ^2J = 11.5 Hz, 1H, PhCH_2), 4.60 (d, $J_{3,4}$ = 3.5 Hz, 1H, H-4), 3.87 (ddd, $J_{4,5}$ = 0.5 Hz, $J_{5,6a}$ = 8.0 Hz, $J_{5,6b}$ = 5.5 Hz, 1H, H-5), 3.71–3.76 (m, 2H, H-2, H-6a), 3.66 (d, $J_{6a,6b}$ = 11.0 Hz, 1H, H-6b), 3.50–3.64 (m, 4H, H-3, OCH_3), 2.01 (s, 3H, OCOCH_3). ^{13}C NMR ($CDCl_3$) δ: 93.87 (C-1). Anal. calcd. for $C_{16}H_{20}Cl_2O_5$ (365.24): C 52.62, H 5.52; found: C 52.89, H 5.50.

Ethyl 2-*O*-benzyl-4,6-dichloro-4,6-dideoxy-3-*O*-methyl-1-thio-α-D-galactopyranoside (55)

Compound **54** (40 mg, 0.11 mmol) was dissolved in CH_2Cl_2 (3 mL) and crushed 4 Å molecular sieves (40 mg) were added. Ethanethiol (50 μL, 0.65 mmol) and boron trifluoride etherate (50 μL, 0.4 mmol) were added and the

© 2002 NRC Canada

reaction stirred for 6 h. At this point additional ethanethiol (50 μL, 0.65 mmol) and boron trifluoride etherate (50 μL, 0.4 mmol) were added and the reaction was stirred overnight. The reaction was quenched by the addition of triethylamine (110 μL, 0.8 mmol), and the mixture filtered through Celite and evaporated. Chromatography (hexane–EtOAc, 6:1) of the residue gave **55** (4 mg, 10% and 13 mg, 32%) as an α/β mixture, both as solids. α-Anomer: $[\alpha]_D$ +205.7 (*c* 0.5, $CHCl_3$). R_f = 0.55 (hexane–EtOAc, 6:1). ^{1}H NMR ($CDCl_3$) δ: 7.24–7.37 (m, 5H, Ph), 5.28 (d, $J_{1,2}$ = 5.5 Hz, 1H, H-1), 4.71, 4.66 (d, ^2J = 12.0 Hz, 1H, PhC*H*$_2$), 4.57 (d, $J_{3,4}$ = 2.5 Hz, 1H, H-4), 4.54 (d, $J_{5,6}$ = 6.5 Hz, 1H, H-5), 4.06 (dd, $J_{2,3}$ = 9.5 Hz, 1H, H-2), 3.68–3.59 (m, 3H, H-3, H-6a, H-6b), 3.48 (s, 3H, OC*H*$_3$), 2.50–2.62 (m, 2H, SC*H*$_2$CH$_3$), 1.26 (d, 3H, ^3J = 7.5 Hz, SCH$_2$C*H*$_3$). ^{13}C NMR ($CDCl_3$) δ: 83.56 (C-1). Anal. calcd. for $C_{16}H_{22}Cl_2O_3S$ (367.32): C 52.32, H 6.04, S 8.73; found: C 52.12, H 6.22, S 8.56.

Methyl 2-*O*-(2-*O*-benzyl-4,6-dichloro-4,6-dideoxy-3-*O*-methyl-α-D-galactopyranosyl)-3-*O*-(2,4-di-*O*-benzyl-3,6-dideoxy-α-D-*xylo*-hexopyranosyl)-4,6-di-*O*-benzyl-α-D-mannopyranoside (56)

Thioglycoside donor **55** (22 mg, 0.06 mmol) and alcohol **20** (35) (38 mg, 0.06 mmol) were dissolved in CH_2Cl_2 (10 mL) and the flask purged with N_2. Crushed 4 Å molecular sieves (300 mg) were added and the mixture stirred for 2 h. *N*-Iodosuccinimide (31 mg, 13.8 mmol) was added followed by the dropwise addition of a previously prepared 0.13 M solution of TfOH in CH_2Cl_2. After adding 100 μL of this solution, the reaction was complete. Triethylamine (100 μL) was added and the suspension diluted with CH_2Cl_2 and filtered through Celite. The filtrate was washed successively with a saturated solution of $NaHCO_3$, 10% sodium thiosulfate, water, and a saturated solution of NaCl. After drying ($MgSO_4$) and evaporation of the solvent, the residue was chromatographed (hexane–EtOAc, 9:1) to provide **56** (39 mg, 73%) as a thick syrup. $[\alpha]_D$ +107.3 (*c* 0.9, $CHCl_3$). R_f = 0.40 (hexane–EtOAc, 9:1). ^{1}H NMR ($CDCl_3$) δ: 5.45 (d, $J_{1'',2''}$ = 2.0 Hz, 1H, H-1″), 5.21 (d, $J_{1',2'}$ = 3.0 Hz, 1H, H-1′), 5.02, 4.92 (d, ^2J = 11.5 Hz, 1H, PhC*H*$_2$), 4.89 (br. s, $J_{1,2}$ = 1.5 Hz, 1H, H-1), 4.78, 4.64, 4.50 (d, ^2J = 11.5 Hz, 3H, PhC*H*$_2$), 4.49 (br. s, 1H, H-4″), 4.20–4.29 (m, 7H, H-5″, H-3, 5 × PhC*H*$_2$), 4.11–4.17 (m, 1H, H-4), 4.04 (br. s, 1H, H-2), 4.03–4.08 (m, 1H, H-5′), 3.90 (m, 2H, H-2″, H-3″), 3.78 (m, 3H, H-2′, H-5, H-6a), 3.60–4.70 (m, 3H, H-6b, H-6″a, H-6″b), 3.44 (s, 3H, OC*H*$_3$), 3.40 (s, 3H, OC*H*$_3$), 3.05 (s, 1H, H-4′), 1.95–1.96 (dt, $J_{2',3'eq}$, $J_{3'eq,4'}$ = 3.5 Hz, $J_{3'eq,3'ax}$ = 13.0 Hz, 1H, H-3′eq), 1.73 (ddd, $J_{3'ax,4'}$ = 12.5 Hz, $J_{2',3'ax}$ = 2.0 Hz, 1H, H-3′ax), 1.15 (d, $J_{5',6'}$ = 6.5 Hz, 3H, H-6′). ^{13}C NMR ($CDCl_3$) δ: 99.38 (C-1), 98.95 (C-1′), 97.67 (C-1″). Anal. calcd. for $C_{55}H_{64}Cl_2O_{12}$ (990.02): C 66.73, H 6.52; found: C 66.91, H 6.70.

Methyl 2-*O*-(4,6-dichloro-4,6-dideoxy-3-*O*-methyl-α-D-galactopyranosyl)-3-*O*-(3,6-dideoxy-α-D-*xylo*-hexopyranosyl)-α-D-mannopyranoside (15)

Trisaccharide **56** (39 mg, 0.04 mmol) was dissolved in acetic acid (10 mL) and 10% Pd/C (40 mg) added. The reaction was stirred under an atmosphere of H_2 for 4 h and then was filtered through Celite and the filtrate evaporated. Chromatography (water) on Bio-Gel P-2 gave, after lyophilization, **15** (14 mg, 66%) as a foam. $[\alpha]_D$ +146.6 (*c* 0.5, H_2O). ^{1}H NMR (D_2O) δ: 5.332 (d, $J_{1'',2''}$ = 3.5 Hz, 1H, H-1″), 5.112 (d, $J_{1',2'}$ = 3.5 Hz, 1H, H-1′), 5.052 (d, $J_{1,2}$ = 2.0 Hz, 1H, H-1), 4.855 (dd, $J_{3'',4''}$ = 3.0 Hz, $J_{4'',5''}$ = 1.0 Hz, 1H, H-4″), 4.415 (ddd, $J_{5'',6''a}$ = 5.0 Hz, $J_{5'',6''b}$ = 6.5 Hz, 1H, H-5″), 4.106 (t, $J_{2,3}$ = 2.0 Hz, 1H, H-2), 4.072 (dq, $J_{4',5'}$ = 1.0 Hz, 1H, H-5′), 3.99–4.06 (m, 2H, H-2′, H-3), 3.979 (t, $J_{3,4} \approx J_{4,5}$ = 9.5 Hz, 1H, H-4), 3.948 (dd, 3.5, $J_{2'',3''}$ = 10.0 Hz, 1H, H-2″), 3.86–3.92 (m, 3H, H-6a, H-4′, H-3″), 3.76–3.85 (m, 3H, H-6b, H-6″a, H-6″b), 3.674 (ddd, $J_{5,6a}$ = 2.0 Hz, $J_{5,6b}$ = 5.5 Hz, 1H, H-5), 3.473 (s, 3H, OC*H*$_3$), 3.434 (s, 3H, OC*H*$_3$), 1.90–2.02 (m, 2H, H-3′eq, H-3′ax), 1.183 (d, $J_{5',6'}$ = 6.5 Hz, 3H, H-6′). ^{13}C NMR (D_2O) δ: 101.110 (C-1′, $^1J_{C,H}$ = 171.2 Hz), 100.799 (C-1″, $^1J_{C,H}$ = 173.3 Hz), 100.356 (C-1, $^1J_{C,H}$ = 173.2 Hz), 77.206 (C-3), 77.920 (C-2), 77.767 (C-3″), 73.796 (C-5), 70.952 (C-5″), 69.108 (C-4′), 68.156 (C-2″), 67.738 (C-5′), 67.460 (C-4), 64.160 (C-2′), 61.423 (C-6), 59.945 (C-4″), 57.174 (OCH_3), 55.712 (OCH_3), 44.489 (C-6″), 33.733 (C-3′), 16.251 (C-6′). Anal. calcd. for $C_{20}H_{34}Cl_2O_{12}$ (539.39): C 44.54, H 6.35; found: C 44.49, H, 6.55.

Acknowledgements

This work was supported by the Natural Sciences and Engineering Research Council of Canada (NSERC). T. L. L. was the recipient of a post-doctoral fellowship from the Alberta Heritage Foundation for Medical Research. The authors thank Dr. Albin Otter for carrying out the high-field NMR spectral analysis of the final compounds and Joanna Sadowska for invaluable technical assistance.

References

1. R.A. Gruters, J.J. Neefjes, M. Tersmette, R.E.Y. de Goede, A. Tulp, G. Huisman, F. Miedema, and L. Ploegh. Nature (London), **330**, 74 (1987).
2. D.C. Wiley and J.J. Skehel. Annu. Rev. Biochem. **56**, 365 (1987).
3. M. Aronson, O. Medalia, L. Schori, D. Mirelman, N. Sharon, and I.J. Ofek. J. Infect. Dis. **139**, 329 (1979).
4. H.C. Krivan, D.D. Roberts, and V. Ginsburg. Proc. Natl. Acad. Sci. U.S.A. **85**, 6157 (1988).
5. K.-A. Karlsson. Annu. Rev. Biochem. **58**, 309 (1989).
6. M.L. Philips, E. Nudelman, F.C.A. Gaeta, M. Perez, A.K. Singhal, S.-I. Hakomori, and J.C. Paulson. Science (Washington, D. C.), 250, 1130 (1990).
7. M. Tiemeyer, S.J. Sweidler, M. Ishihara, M. Moreland, H. Schweingruber, P. Hirtzer, and B.K. Brandley. Proc. Natl. Acad. Sci. U.S.A. **88**, 1138 (1991).
8. L.A. Lasky. Science (Washington, D. C.), **258**, 964 (1992).
9. I. Ofek and N. Sharon. Infect. Immun. **56**, 539 (1988).
10. K.-A. Karlsson, M.A. Milh, and J. Ångström. *In* Molecular recognition in host–parasite interactions. *Edited by* T.K. Korhonen. Plenum Press, New York. 1992. p. 115.
11. A. Varki. Glycobiology, **3**, 97 (1993).
12. D.R. Bundle and N.M. Young. Curr. Opin. Struct. Biol. **2**, 666 (1992).
13. E.J. Toone. Curr. Opin. Struct. Biol. **4**, 719 (1994).
14. J.P. Carver. Pure Appl. Chem. **65**, 763 (1993).

© 2002 NRC Canada

15. R.U. Lemieux, L.T.J. Delbaere, H. Beierbeck, and U. Spohr. Ciba Found. Symp. No. 158, Host-Guest Molecular Interactions: From Chemistry to Biology, London, U.K., Wiley, Chichester. 1991. p. 231.
16. M.C. Chervenak and E.J. Toone. J. Am. Chem. Soc. **116**, 10 533 (1994).
17. R.U. Lemieux. Acc. Chem. Res. **29**, 373 (1996).
18. R.U. Lemieux, M.-H. Du, and U. Spohr. J. Am. Chem. Soc. **116**, 9803 (1994).
19. D.R. Bundle. Top. Curr. Chem. **154**, 1 (1990).
20. M. Cygler, D.R. Rose, and D.R. Bundle. Science (Washington, D. C.), **253**, 442 (1991).
21. A. Zdanov, Y. Li, D.R. Bundle, S.-J. Deng, C.R. MacKenzie, S.A. Narang, N.M. Young, and M. Cygler. Proc. Natl. Acad. Sci. U.S.A. **91**, 6423 (1994).
22. B.W. Sigurskjold, E. Altman, and D.R. Bundle. Eur. J. Biochem. **197**, 239 (1991).
23. B. Sigurskjold and D.R. Bundle. J. Biol. Chem. **267**, 8371 (1992).
24. D.R. Bundle, E. Eichler, M.A.J. Gidney, M. Meldal, A. Ragauskas, B.W. Sigurskjold, B. Sinnott, D.C. Watson, M. Yaguchi, and N.M. Young. Biochemistry, **33**, 5172 (1994).
25. D.A. Brummell, V.P. Sharma, N.N. Anand, D. Bilous, G. Dubuc, J. Michniewicz, C.R. MacKenzie, J. Sadowska, B.W. Sigurskjold, B. Sinnott, N.M. Young, D.R. Bundle, and S.A. Narang. Biochemistry, **32**, 1180 (1993).
26. S.-J. Deng, C.R. MacKenzie, J. Sadowska, J. Michniewicz, N.M. Young, D.R. Bundle, and S.A. Narang. J. Biol. Chem. **269**, 9533 (1994).
27. S.-J. Deng, C.R. MacKenzie, T. Hirama, R. Brousseau, T. Lowary, N.M. Young, D.R. Bundle, and S.A. Narang. Proc. Natl. Acad. Sci. U.S.A. **92**, 4992 (1995).
28. S.A. Galema, M.J. Blandamer, and J.B.F.N.J. Engberts. J. Am. Chem. Soc. **112**, 9665 (1990).
29. S.A. Galema, M.J. Blandamer, and J.B.F.N.J. Engberts. J. Org. Chem. **57**, 1995 (1992).
30. S.A. Galema and H. Høiland. J. Phys. Chem. **95**, 5321 (1991).
31. S.A. Galema, E. Howard, J.B.F.N. Engberts, and J.R. Grigera. Carbohydr. Res. **265**, 215 (1994).
32. R.U. Lemieux, M.-H. Du, and U. Spohr. J. Am. Chem. Soc. **116**, 9803 (1994).
33. K.A. Watson, E.P. Mitchell, L.N. Johnson, J.C. Son, C.J.F. Bichard, M.G. Orchard, G.W.J. Fleet, N.G. Oikonomakos, D.D. Leonidas, M. Kontou, and A. Papageorgioui. Biochemistry, **33**, 5745 (1994).
34. H.H. Baer and D.J. Astles. Carbohydr. Res. **126**, 343 (1984).
35. G. Ekborg, P.J. Garegg, and G. Gotthammar. Acta Chem. Scand. Ser. B, **B29**, 765 (1975).
36. D.R. Bundle and E. Eichler. Bioorg. Med. Chem. **2**, 1221 (1994).
37. O. Mitsunobu. Synthesis, 1 (1981).
38. M.E. Evans and F.W. Parrish. Carbohydr. Res. **54**, 105 (1977).
39. T.L. Lowary, E. Eichler, and D.R. Bundle. J. Org. Chem. **60**, 7316 (1995).
40. A.K. Sarkar, A.K. Ray, and N. Roy. Carbohydr. Res. **190**, 181 (1989).
41. H. Paulsen. Methods Carbohydr. Chem. **6**, 142 (1972).
42. R.U. Lemieux. Can. J. Chem. **29**, 1079 (1951).
43. J.C. Irvine and T.P. Hogg. J. Chem. Soc. Trans. **105**, 1386 (1914).
44. P.J. Meikle and D.R. Bundle. Glycoconjugate J. **7**, 207 (1990).
45. D. Uhrín, A.V.K. Prasad, J.-R. Brisson, and D.R. Bundle. Can. J. Chem. **80**, 904 (2002).

© 2002 NRC Canada

Synthesis of three *Salmonella* epitopes for biosensor studies of carbohydrate–antibody interactions

Henry N. Yu, Chang-Chun Ling, and David R. Bundle

Abstract: Disaccharides **1**–**3** corresponding to the antigenic determinants of *Salmonella* serotypes A, B, and D_1 were synthesized in a form suited for use in biosensors. The disaccharide determinants each contain a unique 3,6-dideoxyhexose, namely abequose (3,6-dideoxy-D-*xylo*-hexose), paratose (3,6-dideoxy-D-*ribo*hexose), and tyvelose (3,6-dideoxy-D-*arabino*-hexose), are α-linked to the 3-position of D-mannopyranose. The disaccharides were further derivatized with a linear aglycon that has a terminal amino group, and can be readily coupled to pertinent chains carrying a terminal thiol for the construction of self-assembled monolayers (SAMs). Efficient routes that employed a single 3,6-dideoxygenation step were developed for the synthesis of paratoside **15** and tyveloside **22**.

Key words: *Salmonella O*-antigens, lipopolysaccharide, abequose, paratose, tyvelose, 3,6-dideoxyhexose, deoxygenation, glycoside tethers, immobilization via pentenyl glycosides.

Résumé : On a synthétisé des formes appropriées à un usage comme biosenseurs des disaccharides **1**–**3**, qui correspondent aux déterminants antigéniques de la *Salmonella* de sérotypes A, B et D_1. Les déterminants disaccharides comportent chacun un 3,6-didésoxyhexose unique, soit l'abéquose (3,6-didésoxy-D-*xylo*-hexose), le paratose (3,6-didésoxy-D-*ribo*-hexose) et le tyvelose (3,6-didésoxy-D-*arabino*-hexose), ainsi qu'une liaison α à la position 3 du D-mannopyranose. On en a ensuite préparé des dérivés à l'aide d'une aglycone linéaire portant un groupe amino terminal; ces dérivés peuvent facilement être couplés à des chaînes appropriées portant une fonction thiol terminale pour la construction de monocouches autoassemblées (MAA). On a développé des voies efficaces de synthèse du paratoside **15** et du tyveloside **22** qui font appel à une réaction permettant d'effectuer une 3,6-didéoxygénation en une seule étape.

Mots clés : *O*-antigènes de la *Salmonella*, lipopolysaccharide, abéquose, paratose, tyvelose, 3,6-didésoyxhexose, désoxygénation, téthères glycosidiques, immobilisation via des glycosides de pentényle.

[Traduit par la Rédaction]

Introduction

Structural and thermodynamic studies of carbohydrate–protein interactions have played a fundamental role in the development of an understanding of the features of a variety of carbohydrate-based biological recognition systems (1). Although a few examples of carefully designed carbohydrate clusters, such as the decameric *Escherichia coli* toxin inhibitor, Starfish (2), have demonstrated extraordinary association constants, carbohydrates generally exhibit association constants for proteins in the millimolar to micromolar range. Since carbohydrates are normally devoid of convenient spectroscopic reporter groups, convenient methods for the accurate and rapid measurement of these relatively weak interactions (affinity) are limited. Traditionally, solid-phase enzyme immunoassays (EIA) have been employed to give an indirect estimate of the association constant (K_a) (3). Titration microcalorimetry provides a very accurate measure of K_a as well as a complete thermodynamic description, enthalpy (ΔH), and entropy (ΔS) for reactions in solution. However, the drawback of this method is the requirement for large amounts of protein sample, typically 10–25 mg of relatively pure protein per measurement (3, 17). Surface plasmon resonance (SPR) has emerged as an alternative since it was first reported in the early 1990s (4, 18). This extremely sensitive technique is able to provide a value of K_a from on and off rates (5). Whitesides and co-workers were the first to use alkanethiolates to form self-assembled monolayers (SAMs) on gold surfaces for SPR analysis (6). This technique represents several advantages over other coating methods: (*i*) monolayers prepared from alkanethiols terminated in oligo(ethylene glycol) groups are inert to the nonspecific adsorption of protein (7, 8); (*ii*) linkers with defined length can be easily tailored chemically before attachment to the gold surface; and (*iii*) ligands are presented in a homogenous environment where their density can be easily

Received 4 December 2001. Published on the NRC Research Press Web site at http://canjchem.nrc.ca on 28 August 2002.

We dedicate this paper to the memory of Professor Raymond U. Lemieux.

H.N. Yu, C.-C. Ling, and D.R. Bundle.[1] Department of Chemistry, University of Alberta, Edmonton, AB T6G 2G2, Canada.

[1]Corresponding author (e-mail: dave.bundle@ualberta.ca).

 DOI: 10.1139/V02-121 © 2002 NRC Canada

Fig. 1. Three disaccharide antigenic determinants of *Salmonella* serogroups B (**1**), A (**2**), and D_1 (**3**) derivatized for conjugation to biosensors.

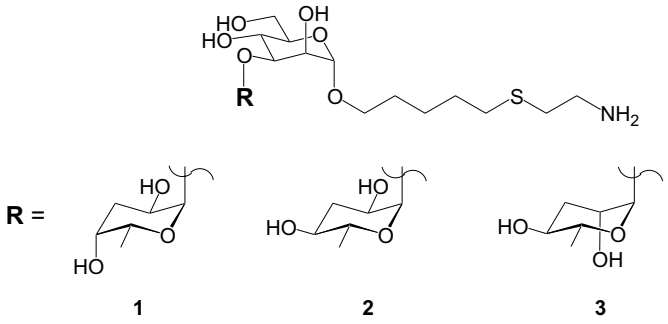

Scheme 1. (*a*) (*i*) Bu_2SnO, toluene, reflux; (*ii*) *p*-MBnCl, Bu_2NBr, toluene, 60°C; (*b*) BnBr, NaH, DMF; (*c*) CAN, $CH_3CN–H_2O$.

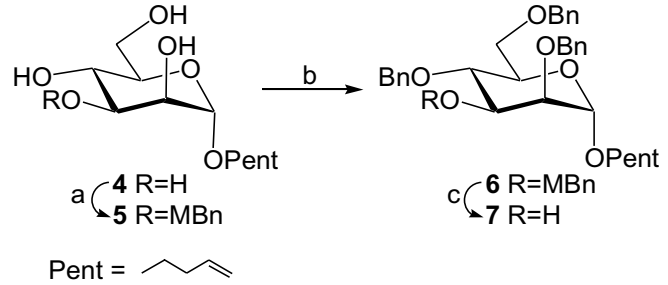

controlled. Experiments varying the linker length and carbohydrate density have been reported recently to probe the multivalency effect (9–11).

We report here the synthesis of three functionalized disaccharides (**1**–**3**), which are readily available for coupling to a pertinent chain carrying a terminal thiol. The functionalized disaccharide glycosides can then be conjugated to a gold surface to form SAMs for SPR or other biosensor analysis (12) (Fig. 1). These disaccharides are located in the *O*-antigen segment of the lipopolysaccharide component of the *Salmonella* cell wall (13). The 3,6-dideoxyhexoses function as the principal structural elements, antigenic determinants, or epitopes recognized by antibodies. Following cases of *Salmonella* food poisoning patient sera contains antibodies specific for the LPS *O*-antigen of the infecting bacterium. In the case of infection by *Salmonella* of serotypes A, B, and D_1, the antibodies bind and recognize disaccharides with terminal paratose, abequose, and tyvelose residues (14). The structural (15) and thermodynamic aspects (16, 17) of the abequose trisaccharide binding to monoclonal antibody Se155-4 have been well characterized by our group. SPR or other biosensor analysis using SAMs would provide a highly sensitive method to secure sensitive, rapid, and accurate measurement of association constants to complement our recent SPR analysis of antibody binding sites using a BSA-*O*-polysaccharide conjugates as the stationary phase (18).

Results and discussion

The 4-pentenyl group was introduced by Fraser-Reid's group (19) as a versatile and temporary protecting group for the anomeric position of sugars. It can be activated to conduct glycosylation under the promotion of *N*-iodosuccinimide. Fraser-Reid et al. (19, 20) have also developed an armed–disarmed strategy to synthesize oligosaccharides using this group. The group has appeal due to its linear structure and its terminal double bond that can be further derivatized to extend the linear chain, while remaining consistent with orthogonal protection strategies for the introduction of other functional groups during elaboration of oligosaccharides. In the context of the target disaccharides **1**–**3**, glycosyl acceptor **7** was identified as convenient synthon. As shown in Scheme 1, compound **7** was synthesized from 4-pentenyl α-D-mannopyranoside **4** (19). The 3-position was selectively protected as the *p*-methoxybenzyl ether under di-*n*-butyltin oxide activation (→**5**, 60%). The remaining hydroxyl groups were benzylated (→**6**, 76%). After removal of the *p*-methoxybenzyl group with ceric ammonium nitrate, the desired acceptor **7** was obtained in good yield (72%).

Scheme 2. (*a*) EtSH, $BF_3·Et_2O$, CH_2Cl_2; (*b*) (*i*) NaOMe, MeOH; (*ii*) BnBr, NaH, DMF.

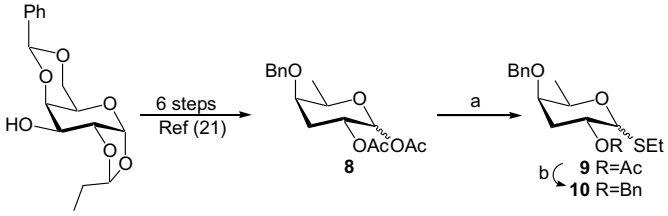

We next turned our attention to methods for the rapid and convenient synthesis of the abequose, paratose, and tyvelose donors **10**, **16**, and **23**, respectively. As all the three 3,6-dideoxyhexose units adopt the α-configuration, we employed a nonparticipating benzyl ether group to protect the 2-position. Our recent published synthetic route to abequose allowed us to prepare the rare hexose in large quantity (Scheme 2) (21). The desired thioabequoside **10** was prepared from diacetate **8** (21). The anomeric *O*-acetate was first transformed to the thioethyl glycoside using a conventional method to afford the thioglycoside **9** as an anomeric mixture (α/β (1:3), 95%). The 2-*O*-acetyl group was then replaced with a benzyl group by first transesterifying the acetate, followed by benzylation of the intermediate alcohol to give **10** (22) in 92% overall yield for these two transformations.

The paratose methyl glycoside **12** was prepared from a known dibromide **11** (Scheme 3) (23). In the literature the dibromo-dideoxy hexose was reduced by catalytic hydrogenation in 85% yield. Barton–McCombie radical deoxygenation conditions (24) converted **11** into diol **12** in near quantitative yield (98%). After acetylation (→**13**) (25), this glycoside was subjected to acetolysis to yield the tri-*O*-acetate **14**, in 94% yield. Glycosidation with ethanethiol afforded thioglycoside **15** (75%, α/β (1:3)). The benzylated thioglycoside was finally prepared by a conventional two-step transformation sequence (→**16**, 78%).

We have published a method to synthesize a tyvelose donor from methyl α-glucopyranoside via an eight-step reaction sequence (26). A more concise synthesis of this dideoxyhexose was desired and we chose to exploit selectively benzoylated mannose derivatives to achieve this objective in four steps. It is known that when mannopyranosides are treated with excess trimethyl orthobenzoate in the presence

© 2002 NRC Canada

Scheme 3. (*a*) Bu_3SnH, AlBN, toluene, reflux; (*b*) Ac_2O, pyridine; (*c*) Ac_2O, H_2SO_4 (cat.); (*d*) EtSH, $BF_3{\cdot}Et_2O$, CH_2Cl_2; (*e*) (*i*) NaOMe, MeOH; (*ii*) BnBr, NaH, DMF.

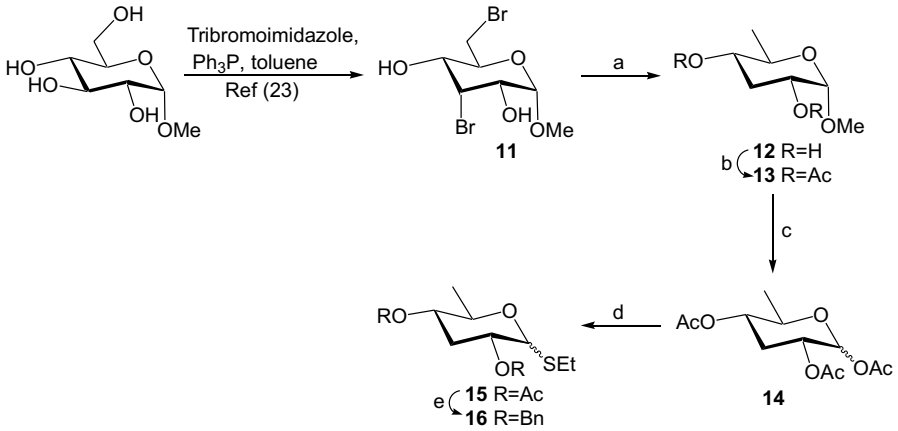

Scheme 4. (*a*) NaOMe, MeOH; then Etl; (*b*) (*i*) $PhC(OMe)_3$, CSA, $CHCl_3$; (*ii*) 90% AcOH – H_2O; (*c*) 1,1′-thiocarbonyldiimidazole, toluene, reflux; (*d*) Bu_3SnH, AlBN, toluene, reflux; (*e*) (*i*) NaOMe, MeOH; (*ii*) NaH, BnBr, DMF.

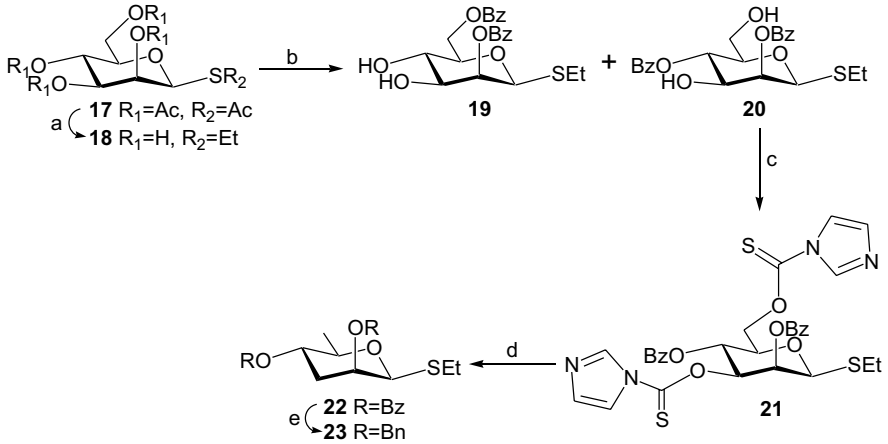

of acid followed by hydrolysis, two dibenzoylated compounds are obtained as the major products; one is the 2,4-di-*O*-benzoate, and the other is the corresponding 2,6-isomer (27, 28). Ethyl 1-thio-β-D-mannopyranoside **18** was prepared in 96% yield from 2,3,4,6-tetra-*O*-acetyl-1-*S*-acetyl-1-thio-β-D-mannopyranose (**17**) following our published methodology (28) (Scheme 4). Treatment of the β-thiomannoside **18** with excess trimethyl orthobenzoate in the presence of camphorsulphonic acid followed by opening of the intermediate orthoesters with 90% acetic acid – water afforded the undesired 2,6-dibenzoylated product **19** (43%) and the desired 2,4-dibenzoylated product **20** (44% yield). After activating the OH-3 and OH-6 groups in **20** using imidazolylthiocarbonyl groups (→**21**, 76%), the tyveloside **22** was obtained in 45% yield using Barton radical deoxygenation conditions with tri-*n*-butyltin hydride as reducing agent in boiling toluene. Attempts to increase the yield by varying reaction conditions failed. To rule out the possibility that the thioethyl group might be complicating the radical reaction, the *O*-methyl glycoside analogue of compound **22**, methyl 2,4-di-*O*-benzoyl-3,6-di-*O*-(imidazolylthiocarbonyl)-α-D-mannopyranoside, was synthesized and subjected to the same deoxygenation condition (data not reported) and a similar yield was obtained. A comparable yield was reported in the literature when the authors attempted to deoxygenate a 3,6-anhydro-galactopyranosyl derivative bearing two phenoxythiocarbonyl groups at the 2,4-positions (29). Normally, having a participating group at the O-2 position, donor **22** should be suitable for the preparation of α-tyveloside. However, in our acceptor, we have a 4-pentenyl group at the anomeric centre; preliminary studies demonstrated that when MeOTf was used to activate **22** for the glycosylation of **7**, orthoester was formed; when NIS–TfOH was used, the 4-pentenyl group was decomposed by the reagent. We thus decided to prepare the corresponding benzylated donor **23**, thereby allowing us to use MeOTf as activating reagent (30) and avoid the formation of orthoester. The benzoyl groups of **22** were replaced by benzyl groups as before to afford the tyvelose donor **23** in excellent yield (95%).

With all three 3,6-dideoxyhexose donors (**10**, **16**, and **23**) and the mannopyranosyl acceptor **7** in hand, glycosylations were carried out (Scheme 5). Coupling of **10** with **7** under activation by methyl triflate and 2,6-di-*tert*-butyl-4-methylpyridine in Et_2O afforded disaccharide **24** (82%), with excellent anomeric selectivity (α/β, 40:1). Compound **16** was glycosidated by **7** in a similar fashion to give **25** in good yield, but poor stereoselectivity (80%, α/β (3:2)).

© 2002 NRC Canada

Scheme 5. (*a*) MeOTf, DTBMP, Et_2O, 0°C; (*b*) Na, NH_3 (liquid), MeOH, –78°C; (*c*) $HSCH_2CH_2NH_3^+Cl^-$, MeOH, UV light (254 nm).

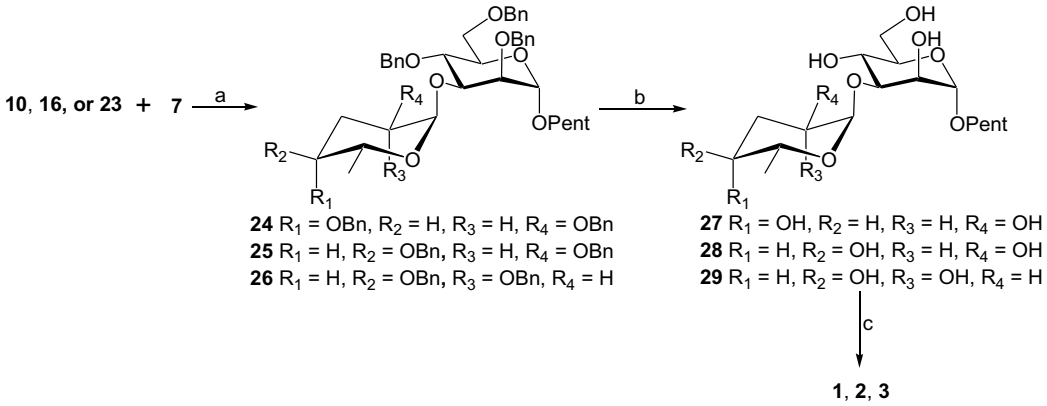

Disaccharide **26** was obtained in the same fashion (70%) with excellent stereoselectivity; no β-isomer was detected. Debenzylation for all three disaccharides was smoothly carried out by Birch reduction with preservation of the terminal double bond of the 4-pentenyl group provided that the reaction temperature was kept at –78°C. Reverse-phase HPLC allowed complete separation of the anomeric isomers (→**27** (100%), →**28** (47%α + 33%β), →**29** (84%)). The anomeric configuration of the protected and deprotected disaccharide products were confirmed by measurement of the one-bond heteronuclear coupling constant $^1J_{C1,H1}$ (31), since the $^3J_{1,2}$ homonuclear coupling constants would not distinguish the α- and β-tyvelose anomers.

The elongation and functionalization of the aglycon was achieved through photoaddition of cysteamine hydrochloride (32) to the terminal double bond to afford the desired target disaccharides **1** (90%), **2** (71%), and **3** (94%).

In summary, three immunodominant disaccharide epitopes present in the *O*-antigens of *Salmonella* LPS were synthesized as their 4-pentenyl glycosides and were functionalized for incorporation into SAMs. SPR studies with these compounds are in progress and will be reported in due course.

Experimental

Optical rotations were measured with a PerkinElmer 241 polarimeter at 22 ± 2°C. Analytical TLC was performed on Silica Gel 60-F_{254} (E. Merck, Darmstadt) with detection by quenching of fluorescence and (or) by charring with sulfuric acid. All commercial reagents were used as supplied and chromatography solvents were distilled prior to use. Column chromatography was performed on Silica Gel 60 (40–60 μM, E. Merck, Darmstadt). ^{1}H NMR spectra were recorded on 300 MHz (Varian), 400 MHz (Varian), 500 MHz (Varian), or 600 MHz (Varian) spectrometers. The first-order proton chemical shifts (δ_H) were referenced to either residual $CHCl_3$ (δ_H 7.24, $CDCl_3$) or internal acetone (δ_H 2.225, D_2O). HMQC-NMR spectra were recorded on Varian Unity 300, 400, 500, or 600 MHz NMR spectrometers. The ^{13}C chemical shifts (δ_C) were referenced to internal $CDCl_3$ (δ_C 77.00, $CDCl_3$). Organic solutions were dried prior to concentration under vacuum at <40°C (bath). Reverse-phase chromatography was performed on a Waters 600 HPLC system, using a Beckman semipreparative C-18 column (10 × 250 mm, 5 μ), and the products were detected with a Waters 2487 UV detector or a Waters 2410 refractive index monitor. Microanalyses and electrospray mass spectra were performed by the analytical services of this department.

4-Pentenyl 3-*O*-*p*-methoxybenzyl-α-D-mannopyranoside (5)

To a solution of 4-pentenyl α-D-mannopyranoside **4** (19) (6.86 g, 27.6 mmol) in anhydrous toluene (120 mL), was added di-*n*-butyltin oxide (7.56 g, 29.8 mmol); the mixture was refluxed with azeotropic removal of water for 6 h using a Dean–Stark tube. The reaction was cooled to 60°C, tetra-*n*-butylammonium bromide (9.79 g, 30.1 mmol) and 4-methoxybenzyl chloride (4.13 mL, 30.4 mmol) were added, and the reaction was stirred for 16 h at the same temperature. The mixture was concentrated and the residue was purified by column chromatography on silica gel (MeOH–EtOAc, 19:1 v/v), to give compound **5** (6.1 g, yield 60%). $[\alpha]_D^{22}$ +18.5 (*c* 2.6, $CHCl_3$). ^{1}H NMR ($CDCl_3$, 300 MHz) δ: 7.28–6.84 (m, 4H, MBn), 5.76 (ddt, *J* = 6.5, 10.2, 16.9 Hz, 1H, C*H*=CH_2), 4.96 (m, 2H, CH=CH_2), 4.77 (d, *J* = 1.1 Hz, 1H, H-1), 4.54 (d, *J* = 11.2 Hz, 1H, MBn), 4.49 (d, 1H, MBn), 4.00–3.30 (m, 8H, H-2 + H-3 + H-4 + H-5 + H-6 + OCH_2CH_2), 2.05 (m, 2H, CH_2CH=CH_2), 1.61 (m, 2H, OCH_2=CH_2). HR-ES-MS calcd. for $C_{19}H_{28}O_7Na^+$: 391.173273; found: 391.172706.

4-Pentenyl 2,4,6-tri-*O*-benzyl-3-*O*-*p*-methoxybenzyl-α-D-mannopyranoside (6)

To an ice-cooled solution of compound **5** (6.0 g, 16.3 mmol) in DMF (100 mL) under argon, was added sodium hydride (95%, 2.47 g, 97.8 mmol), and the mixture was stirred for 0.5 h. Benzyl bromide (8.7 mL, 72.9 mmol) was added dropwise and the reaction was continued for 6 h at room temperature. The reaction was cooled to 0°C and quenched with MeOH (10 mL). The mixture was concentrated and the resulting residue was partitioned between EtOAc (500 mL) and 5% aq NaCl solution (2 × 300 mL). The organic phase was dried over anhyd Na_2SO_4 and concentrated. Compound **6** (7.9 g, yield 76%) was obtained by column chromatography on silica gel (hexane–EtOAc, 19:1 v/v). $[\alpha]_D^{22}$ +33.2 (*c* 3.8, $CDCl_3$). ^{1}H NMR ($CDCl_3$, 600 MHz) δ: 7.36–6.83 (m, 19H, 3 × Bn + MBn), 5.76 (tdd, *J* = 6.6, 10.1, 16.9 Hz, 1H, C*H*=CH_2), 4.95 (m, 2H, CH=CH_2), 4.85 (d, *J* = 10.8 Hz, 1H, Bn), 4.81 (d, *J* = 1.9 Hz, 1H, H-1), 4.74 (d, *J* = 12.5 Hz, 1H, Bn), 4.69 (d, 1H, Bn), 4.63 (d, *J* = 12.1 Hz, 1H, Bn),

© 2002 NRC Canada

4.54 (d, *J* = 8.1 Hz, 2H, MBn), 4.52 (d, 1H, Bn), 4.88 (d, 1H, Bn), 3.93 ("t", *J* = 9.3 Hz, 1H, H-4), 3.87 (dd, *J* = 3.1 Hz, 1H, H-3), 3.78–3.70 (m, 4H, H-6 + H-5 + H-2), 3.65 (td, *J* = 6.6, 9.7 Hz, 1H, OC*H*$_2$CH$_2$), 3.34 (td, 1H, OC*H*$_2$CH$_2$), 2.04 (m, 2H, C*H*$_2$CH=CH$_2$), 1.60 (m, 2H, OCH$_2$C*H*$_2$). ^{13}C NMR (600 MHz, $CDCl_3$, from HMQC) δ: 137.8 (*C*H=CH$_2$), 129.2–127.2 (3 × Bn + MBn), 113.8 (MBn), 114.7 (CH=*C*H$_2$), 96.8 (C-1, $J_{C1,H1}$ = 165.1 Hz), 79.7 (C-3), 74.9 (Bn), 74.9 (C-4), 74.7 (C-2), 73.2 (Bn), 72.4 (Bn), 71.8 (C-5), 71.7 (MBn), 69.2 (C-6), 66.8 (O*C*H$_2$), 30.2 (*C*H$_2$CH=CH$_2$), 28.3 (OCH$_2$*C*H$_2$). HR-ES-MS calcd. for $C_{40}H_{46}O_7Na^+$: 661.314124; found: 661.314477. Anal. calcd. for $C_{40}H_{46}O_7$: C 75.21, H 7.26; found: C 75.11, H 7.49.

4-Pentenyl 2,4,6-tri-*O*-benzyl-α-D-mannopyranoside (7)

Compound **6** (5.45 g, 8.53 mmol) and ceric ammonium nitrate (11.7 g, 21.3 mmol) were stirred in a mixture of acetonitrile (100 mL) and water (10 mL). After 45 min, the mixture was concentrated. The residue was dissolved in dichloromethane (250 mL) and the organic solution was washed with water (100 mL), 5% brine (100 mL), and dried over Na_2SO_4. After concentration, the residue was purified by column chromatography on silica gel (hexane–EtOAc, 8:1 v/v) to give compound **7** (3.2 g, yield 72%). $[\alpha]_D^{22}$ +16.2 (*c* 3.7, $CHCl_3$), (lit. (33) value $[\alpha]_D^{22}$ +21). ^{1}H NMR ($CDCl_3$, 600 MHz) δ: 7.36–7.21 (m, 15H, 3 × Bn), 5.76 (tdd, *J* = 6.6, 10.2, 17.0 Hz, 1H, C*H*=CH$_2$), 4.95 (m, 2H, CH=C*H*$_2$), 4.89 (d, *J* = 1.7 Hz, 1H, H-1), 4.83 (d, *J* = 11.0 Hz, 1H, Bn), 4.73 (d, *J* = 11.9 Hz, 1H, Bn), 4.65 (d, *J* = 12.1 Hz, 1H, Bn), 4.55 (d, 1H, Bn), 4.53 (d, 1H, Bn), 4.51 (d, 1H, Bn), 3.97 (ddd, *J* = 3.7, 9.0, 9.0 Hz, 1H, H-3), 3.77–3.66 (m, 6H, H-5 + H-6 + H-2 + OC*Ha*HbCH_2 + H-4), 3.37 (td, *J* = 6.4, 9.7 Hz, 1H, OCHa*Hb*CH_2), 2.28 (d, 1H, 3-OH), 2.06 (m, 2H, C*H*$_2$CH=CH$_2$), 1.62 (m, 2H, OCH$_2$C*H*$_2$). HR-ES-MS calcd. for $C_{32}H_{38}O_6Na^+$: 541.256609; found: 541.256245. Anal. calcd. for $C_{32}H_{38}O_6$: C 74.11, H 7.39; found: C 74.12, H 7.56.

Ethyl 2-*O*-acetyl-4-*O*-benzyl-3,6-dideoxy-1-thio-α-D-*xylo*-hexopyranoside (9α) and ethyl 2-*O*-acetyl-4-*O*-benzyl-3,6-dideoxy-1-thio-β-D-*xylo*-hexopyranoside (9β)

A mixture of 1,2-di-*O*-acetyl-4-*O*-benzyl-3,6-dideoxy-α,β-D-*xylo*-hexopyranose **8** (α/β (1:3), 99 mg, 0.31 mmol), ethanethiol (34 μL, 0.41 mmol) and 4 Å molecular sieves in anhyd CH_2Cl_2 (3 mL) was cooled to 0°C under argon, and $BF_3{\cdot}Et_2O$ (59 μL, 0.47 mmol) was added dropwise. The mixture was stirred at room temperature for 30 min and quenched with Et_3N (1 mL). The solvent was evaporated and the residue was purified by silica gel (hexane–EtOAc, 9:1 v/v), to give the α-anomer **9**α (23 mg, yield 23%) and β-anomer **9**β (72 mg, yield 72%). Data for **9**α: $[\alpha]_D^{22}$ +141.6 (*c* 3.1, $CHCl_3$). ^{1}H NMR ($CDCl_3$, 300 MHz) δ: 7.37–7.25 (m, 5H, Bn), 5.54 (d, *J* = 5.0 Hz, 1H, H-1), 5.29 (d′t′, *J* = 12.2 Hz, 1H, H-2), 4.71 (d, *J* = 12.0 Hz, 1H, Bn), 4.44 (d, 1H, Bn), 4.23 (dq, *J* = 1.8, 6.5 Hz, 1H, H-5), 3.47 (m, 1H, H-4), 2.55 (m, 2H, CH_2), 2.19 (ddd, *J* = 1.4, 13.4 Hz, 1H, H-3a), 2.05 (s, 3H, OAc), 1.81 (ddd, *J* = 2.7 Hz, 1H, H-3b), 1.25 (t, *J* = 7.4 Hz, 3H, CH_3), 1.20 (d, 3H, H-6). HR-ES-MS calcd. for $C_{17}H_{24}O_4SNa^+$: 347.129301; found: 374.129515. Anal. calcd. for $C_{17}H_{24}O_4S$: C 62.93, H 7.46; found: C 63.23, H 7.72. Data for **9**β: $[\alpha]_D^{22}$ –77.8 (*c* 4.1, $CHCl_3$). ^{1}H NMR ($CDCl_3$, 600 MHz) δ: 7.35–7.25 (m, 5H, Bn), 5.07 (ddd, *J* = 5.0, 9.9, 11.4 Hz, 1H, H-2), 4.73 (d, *J* = 12.3 Hz, 1H, Bn), 4.44 (d, 1H, Bn), 4.43 (d, 1H, H-1), 3.62 (dq, *J* = 1.5, 6.4 Hz, 1H, H-5), 3.41 (m, 1H, H-4), 2.69 (m, 2H, CH_2), 2.56 (ddd, *J* = 3.3, 13.6 Hz, 1H, H-3a), 2.05 (s, 3H, OAc), 1.50 (ddd, *J* = 2.8 Hz, 1H, H-3b), 1.25 (d, 3H, H-6), 1.24 (d, *J* = 7.5 Hz, 3H, CH_3). ^{13}C NMR ($CDCl_3$, 600 MHz) δ: 120.8 (Bn), 84.4 (C-1), 76.5 (C-5), 74.2 (C-4), 70.7 (Bn), 66.4 (C-2), 32.9 (C-3), 23.1 (CH_2), 20.8 (OAc), 16.8 (C-6), 6.2 (CH_3). HR-ES-MS calcd. for $C_{17}H_{24}O_4SNa^+$: 347.129301; found: 374.129420. Anal. calcd. for $C_{17}H_{24}O_4S$: C 62.93, H 7.46; found: C 63.45, H 7.68. As both α and β anomers are equally reactive in glycosylation reactions, **9**α and **9**β were not separated.

Ethyl 2,4-di-*O*-benzyl-3,6-dideoxy-1-thio-α,β-D-*xylo*-hexopyranoside (10)

To a solution of compound **9**α,β (α/β (1:3), 200 mg, 0.62 mmol) in dry MeOH (20 mL) was added a catalytic amount of MeONa. The mixture was stirred overnight at room temperature. After neutralization with DOWEX 50W (H^+) resin, the organic solution was concentrated, and the resulting residue was dissolved in anhyd DMF (10 mL) at 0°C; NaH (60% in mineral oil, 244 mg, 6.1 mmol) was then added. After 5 min, benzyl bromide (0.37 mL, 3.1 mmol) was added dropwise, and the reaction was continued for 2 h at room temperature. The reaction was quenched with MeOH (1 mL) and the mixture was diluted with EtOAc (100 mL), washed with 5% brine (2 × 50 mL), dried over Na_2SO_4, and concentrated. The pure **10** (α/β (1:3), 211 mg, yield 92%) was obtained after chromatography on silica gel (toluene–EtOAc, 19:1 v/v). Physical data were identical to the literature (22).

Methyl 3,6-dideoxy-α-D-*ribo*-hexopyranoside (12)

To a refluxing solution of 3,6-dibromosugar **11** (23) (2.55 g, 8.0 mmol) in dry toluene (150 mL) was added dropwise a solution of tri-*n*-butyltin hydride (6.5 mL, 24.2 mmol) and azobis(cyclohexylcarbonitrile) (0.2 g, 818 μmol) in dry toluene (50 mL) under argon. After 1 h, the mixture was concentrated. The residue was purified by column chromatography on silica gel (toluene–EtOAc, 1:9 v/v) to give compound **12** (1.27 g, 98%). Physical data were identical to the literature (23).

1,2,4-Tri-*O*-acetyl-3,6-dideoxy-α,β-D-*ribo*-hexopyranose (14)

To a mixture of compound **13** () (1.20 g, 4.88 mmol) in acetic anhydride (35 mL) was added a solution of conc. H_2SO_4 (95%, 90 μL). After 1 h, the reaction was quenched with sat. $NaHCO_3$ solution (50 mL) and extracted with dichloromethane (300 mL). The organic layer was washed with H_2O (200 mL) and dried over Na_2SO_4. The solvent was evaporated and the residue was purified by silica gel (hexane–EtOAc, 4:1 v/v), to give compound **14** (α/β (4:1), 1.14 mg, yield 85%). ^{1}H NMR ($CDCl_3$, 300 MHz) for α-anomer δ: 6.15 (d, *J* = 3.4 Hz, 1H, H-1), 4.97 (ddd, *J* = 5.0, 12.5 Hz, 1H, H-2), 4.60 (ddd, *J* = 4.8, 9.8, 11.4 Hz, 1H, H-4), 3.84 (dq, *J* = 6.1 Hz, 1H, H-5), 2.28 (d′t′, *J* = 12.2 Hz, H-3a), 2.14 (s, 3H, OAc), 2.05 (s, 3H, OAc), 1.95 (s, 3H, OAc), 1.88 (d′t′, 1H, H-3b), 1.15 (d, 3H, H-6); β-anomer δ: 5.65 (d, *J* = 8.2 Hz, 1H, H-1), 4.97 (ddd, *J* = 5.2, 11.4 Hz, 1H, H-2), 4.60 (ddd, *J* = 4.8, 9., 11.0 Hz, 1H,

© 2002 NRC Canada

H-4), 3.67 (dq, *J* = 6.1 Hz, 1H, H-5), 2.57 (d′t′, *J* = 12.3 Hz, H-3a), 2.09 (s, 3H, OAc), 2.04 (s, 3H, OAc), 2.01 (s, 3H, OAc), 1.59 (d′t′, 1H, H-3b), 1.21 (d, 3H, H-6). HR-ES-MS calcd. for $C_{12}H_{18}O_7Na^+$: 297.09447; found: 297.09491. Anal. calcd. for $C_{12}H_{18}O_7$: C 52.55, H 6.62; found: C 52.39, H 6.49.

Ethyl 2,4-di-*O*-acetyl-3,6-dideoxy-1-thio-α,β-D-*ribo*-hexopyranoside (15)

A mixture of **14** (890 mg, 3.24 mmol) and ethanethiol (360 μL, 4.86 mmol) in anhydrous CH_2Cl_2 (20 mL) was cooled to 0°C under argon, $BF_3{\cdot}Et_2O$ (617 μL, 4.86 mmol) was added dropwise, and the mixture was stirred at room temperature for 18 h. The reaction was quenched with Et_3N (1 mL) and the solvent was evaporated. The residue was purified by silica gel chromatography (hexane–EtOAc, 9:1 v/v) to yield compound **15** as an inseparable α/β mixture (α/β (1:3), 671 mg, yield 75%). ^{1}H NMR ($CDCl_3$, 300 MHz) for β-anomer δ: 4.83 (ddd, *J* = 5.0, 9.8, 11.2 Hz, 1H, H-2), 4.55 (ddd, *J* = 4.7, 9.5, 11.5 Hz, 1H, H-4), 4.36 (d, 1H, H-1), 3.45 (dq, *J* = 6.2 Hz, 1H, H-5), 2.65 (m, 2H, SCH_2), 2.52 (d′t′, *J* = 9.4 Hz, H-3a), 2.04 (s, 3H, OAc), 2.02 (s, 3H, OAc), 1.52 (d′t′, 1H, H-3b), 1.23 (t, *J* = 7.5 Hz, 3H, CH_2CH_3), 1.20 (d, 3H, H-6); α-anomer δ: 5.48 (d, *J* = 5.2 Hz, 1H, H-1), 4.97 (d′t′, *J* = 5.0, 12.3 Hz, 1H, H-2), 4.55 (ddd, *J* = 4.8, 9.7, 11.0 Hz, 1H, H-4), 4.11 (dq, *J* = 6.2 Hz, 1H, H-5), 2.54 (m, 2H, SCH_2), 2.20 (d′t′, *J* = 11.8 Hz, H-3a), 2.02 (s, 6H, 2 × OAc), 1.80 (d′t′, 1H, H-3b), 1.24 (t, *J* = 7.4 Hz, 3H, CH_2CH_3), 1.14 (d, 3H, H-6). HR-ES-MS calcd. for $C_{12}H_{20}O_5SNa^+$: 299.092916; found: 299.093086. Anal. calcd. for $C_{12}H_{20}O_5S$: C 52.15, H 7.29; found: C 52.44, H 7.42.

Ethyl 2,4-di-*O*-benzyl-3,6-dideoxy-1-thio-α,β-D-*ribo*-hexopyranoside (16)

To a solution of compound **15** (α/β (1:3), 253 mg, 0.92 mmol) in anhyd MeOH (4.5 mL) was added a catalytic amount of NaOMe, and the reaction was continued for 2 h at room temperature. The mixture was neutralized with DOWEX 50W (H^+) resin and the organic solvent was evaporated. The residue was dissolved in anhyd DMF (9 mL) at 0°C under argon, NaH (60% in mineral oil, 368 mg, 9.2 mmol) was added, and the mixture was stirred for 5 min. Benzyl bromide (1.08 mL, 9.08 mmol) was added dropwise, and the reaction was stirred for 2 h at room temperature. MeOH (1 mL) was added to quench the reaction and the mixture was diluted with EtOAc (100 mL). The organic solution was washed with 5% brine (2 × 50 mL), dried over Na_2SO_4 and concentrated. The pure compound **16** (α/β (1:3), 266 mg, yield 78%) was obtained by chromatography on silica gel (toluene–EtOAc, 19:1 v/v). ^{1}H NMR ($CDCl_3$, 600 MHz) for β-anomer δ: 7.36–7.26 (m, 10H, 2 × Bn), 4.68 (d, *J* = 11.5 Hz, 1H, Bn), 4.59 (d, *J* = 11.5 Hz, 1H, Bn), 4.49 (d, 1H, Bn), 4.43 (d, Bn), 4.41 (d, *J* = 9.3 Hz, 1H, H-1), 3.35 (dq, *J* = 6.0, 9.0 Hz, 1H, H-5), 3.28 (ddd, *J* = 9.3, 11.2 Hz, 1H, H-2), 3.08 (overlapped, 1H, H-4), 2.71 (overlapped, 2H, SCH_2), 2.60 (m, 1H, H-3a), 1.48 (d′t′, *J* = 11.2 Hz, H-3b), 1.29 (overlapped, 3H, CH_2CH_3), 1.28 (d, 3H, H-6); α-anomer δ: 7.36–7.26 (m, 10H, 2 × Bn), 5.33 (d, *J* = 5.0 Hz, 1H, H-1), 4.65 (d, *J* = 10.6 Hz, 1H, Bn), 4.61 (d, *J* = 11.5 Hz, 1H, Bn), 4.49 (d, 1H, Bn), 4.42 (d, 1H, Bn), 4.06 (dq, *J* = 6.0 Hz, 9.2 Hz, 1H, H-5), 3.73 (d′t′, *J* = 4.6, 12.0 Hz, 1H, H-2), 3.05 (overlapped, 1H, H-4), 2.71 (overlapped, 2H, SCH_2), 2.30 (m, 1H, H-3a), 1.74 (d′t′, *J* = 11.7 Hz, H-3b), 1.29 (overlapped, 3H, CH_2CH_3), 1.22 (d, 3H, H-6). HR-ES-MS calcd. for $C_{22}H_{28}O_3SNa^+$: 395.165687; found: 395.165698. Anal. calcd. for $C_{22}H_{28}O_3S$: C 70.93, H 7.58; found: C 70.80, H 7.60.

Ethyl 1-thio-β-D-mannopyranoside (18)

To a solution of 2,3,4,6-tetra-*O*-acetyl-1-*S*-acetyl-1-thio-β-D-mannopyranose **17** (28) (4.6 g, 11.3 mmole) in dry MeOH (50 mL) under argon, was added a solution of NaOMe–MeOH (21 mL, 3.5 M), and the mixture was stirred for 2 h. Ethyl iodide (2 mL, 25.0 mmol) was added dropwise and the reaction was continued under argon for 2 h at room temperature. The mixture was neutralized with Dowex 50W (H^+) resin and concentrated. Compound **18** (2.43 g, 96%) was obtained by reverse-phase chromatography using a gradient of MeOH–H_2O as eluent (0 → 20%). $[\alpha]_D^{22}$ –93.3 (*c* 7.3, MeOH). ^{1}H NMR (D_2O, 600 MHz) δ: 4.88 (s, 1H, H-1), 4.04 (d, *J* = 3.5 Hz, 1H, H-2), 3.91 (dd, *J* = 12.3 Hz, 1H, H-6a), 3.73 (dd, 1H, H-6b), 3.67 (dd, *J* = 9.5 Hz, 1H, H-3), 3.60 ("t", *J* = 9.7 Hz, 1H, H-4), 3.43 (ddd, *J* = 2.4, 6.0 Hz, 1H, H-5), 2.76 (m, 2H, CH_2), 1.38 (t, *J* = 7.3 Hz, 3H, CH_3). ^{13}C NMR (D_2O, 600 MHz, from HMQC) δ: 84.6 (C-1, $J_{C1,H1}$ = 154.3 Hz), 81.1 (C-5), 74.8 (C-3), 73.2 (C-2), 67.5 (C-4), 62.1 (C-6). HR-ES-MS calcd. for $C_8H_{16}O_5SNa^+$: 247.06107; found: 247.06091. Anal. calcd. for $C_8H_{16}O_5S$: C 42.84, H 7.19; found: C 42.81, H 7.19.

Ethyl *2,6*-di-*O*-benzoyl-1-thio-β-D-mannopyranoside (19) and ethyl 2,4-di-*O*-benzoyl-1-thio-β-D-mannopyranoside (20)

A suspension of compound **18** (1.2 g, 1.02 mmol), trimethyl orthobenzoate (3.8 mL, 5.3 mmol), and a catalytic amount of camphor sulfonic acid in $CHCl_3$ (250 mL) was evaporated down to 10 mL; this solution became almost clear. TLC showed that there was still unreacted starting material. $CHCl_3$ (150 mL) was added to the solution again, and the solution was again evaporated to a 10 mL volume. This process was repeated until TLC indicated the complete conversion of starting material. Triethylamine (3 mL) was added, and the mixture of intermediate orthoesters was concentrated to a syrup. The syrup was treated with 90% acetic acid – H_2O (50 mL) for 30 min at 20°C, and the solution was concentrated. After column chromatography on silica gel (EtOAc–toluene, 20 → 50%) compound **20** (1.02 g, 44%) and compound **19** (0.99 g, 43%) were obtained. Data for **20**: $[\alpha]_D^{22}$ –93.6 (*c* 2.8, $CHCl_3$). ^{1}H NMR ($CDCl_3$, 400 MHz) δ: 8.13–7.43 (m, 10H, Bz), 5.76 (d, *J* = 3.7 Hz, 1H, H-2), 5.39 ("t", *J* = 9.7 Hz, 1H, H-4), 4.92 (s, 1H, H-1), 4.19 (dd, *J* = 9.8 Hz, 1H, H-3), 3.85 (dd, *J* = 2.3, 12.2 Hz, 1H, H-6a), 3.78 (dd, *J* = 5.3, 12.2 Hz, 1H, H-6b), 3.73 (ddd, 1H, H-5), 2.76 (q, *J* = 7.5 Hz, 2H, CH_2), 1.29 (t, 3H, CH_3). HR-ES-MS calcd. for $C_{22}H_{24}O_7SNa^+$: 455.114045; found: 455.114338. Anal. calcd. for $C_{22}H_{24}O_7S$: C 61.10, H 5.59; found: C 61.11, H 5.43. Data for **19**: $[\alpha]_D^{22}$ –78.5 (*c* 9.3, $CHCl_3$). ^{1}H NMR ($CDCl_3$, 600 MHz) δ: 8.12–7.30 (m, 10H, Bz), 5.64 (dd, *J* = 0.92, 3.3 Hz, 1H, H-2), 4.86 (d, 1H, H-1), 4.80 (dd, *J* = 4.6, 12.1 Hz, 1H, H-6a), 4.62 (dd,

© 2002 NRC Canada

J = 2.2 Hz, 1H, H-6b), 3.93 (d′t′, *J* = 3.5, 9.3 Hz, 1H, H-3), 3.83 (d′t′, *J* = 3.3, 9.5 Hz, 1H, H-4), 3.67 (ddd, 1H, H-5), 2.96 (d, 1H, 4-OH), 2.73 (m, 2H, CH_2), 2.65 (d, 1H, 3-OH), 1.28 (t, *J* = 7.5 Hz, 3H, CH_3). HR-ES-MS calcd. for $C_{22}H_{24}O_7SNa^+$: 455.114045; found: 455.114045. Anal. calcd. for $C_{22}H_{24}O_7S$: C 61.10, H 5.59; found: C 61.42, H, 5.57.

Ethyl 2,4-di-O-benzoyl-3,6-di-O-(imidazolylthiocarbonyl)-1-thio-β-D-mannopyranoside (21)

A mixture of compound **20** (230 mg, 0.53 mmol) and 1,1′-thiocarbonyldimidazole (368 mg, 2.07 mmol) in anhydrous toluene (4.0 mL) was refluxed for 4 h. The solvent was removed under reduced pressure and the residue was purified by column chromatography on silica gel (toluene–EtOAc, 1:1 v/v) to afford **21** (264 mg, 76%). $[\alpha]_D^{22}$ –83.9 (*c* 1.3, $CHCl_3$). ^{1}H NMR ($CDCl_3$, 400 MHz) δ: 8.40–6.83 (m, 16H, Bz + Im), 6.14 (dd, *J* = 3.4, 9.9 Hz, 1H, H-3), 6.11 (d, 1H, H-2), 5.99 (“t”, *J* = 9.9 Hz, 1H, H-4), 5.12 (s, 1H, H-1), 5.10 (dd, *J* = 2.5, 12.1 Hz, 1H, H-6a), 4.79 (dd, *J* = 5.1 Hz, 1H, H-6b), 4.31 (ddd, 1H, H-5), 2.80 (q, *J* = 7.5 Hz, 2H, CH_2), 1.31 (t, 3H, CH_3). HR-ES-MS calcd. for $C_{30}H_{29}N_4O_7S_3^+$: 653.119840; found: 653.119769. Anal. calcd. for $C_{30}H_{28}N_4O_7S_3$: C 55.20, H 4.32, N 8.58; found: C 55.33, H 4.23, N 8.41.

Ethyl 2,4-di-*O*-benzoyl–3,6-dideoxy-1-thio-β-D-*arabino*-hexopyranoside (22)

To a refluxing solution of compound **21** (700 mg, 1.07 mmol) in dry toluene (8.0 mL) was added dropwise a solution of tri-*n*-butyltin hydride (0.8 mL, 3.0 mmol) and azobis(cyclohexylcarbonitrile) (90 mg, 368 μmol) in dry toluene (5.0 mL) under argon. After 6 h, the mixture was concentrated. Chromatography of the resulting residue on silica gel (toluene–EtOAc, 19:1 v/v) gave compound **22** (195 mg, 45%). Physical data were similar to those in the literature (33).

Ethyl 2,4-di-*O*-benzyl–3,6-dideoxy-1-thio-β-D-*arabino*-hexopyranoside (23)

To a solution of compound **21** (195 mg, 0.49 mmol) in dry MeOH (5 mL) was added a catalytic amount of MeONa. The mixture was stirred overnight at room temperature. After neutralization with DOWEX 50W (H^+) resin, the reaction was concentrated. The residue was dissolved in anhyd DMF (9 mL) at 0°C under argon and NaH (60% in mineral oil, 180 mg, 4.5 mmol) was then added. After 5 min, benzyl bromide (0.53 mL, 4.5 mmol) was added dropwise, and the reaction was continued for 2 h at room temperature. MeOH (1 mL) was added to quench the reaction, and the mixture was diluted with EtOAc (100 mL), washed with 5% brine (2 × 50 mL), dried over Na_2SO_4 and concentrated. Pure **23** (172 mg, yield 95%) was obtained by chromatography on silica gel (toluene–EtOAc, 9:1 v/v). $[\alpha]_D^{22}$ –10.0 (*c* 1.3, $CHCl_3$). ^{1}H NMR ($CDCl_3$, 600 MHz) δ: 7.35–7.25 (m, 10H, Bn), 4.58 (s, 1H, H-1), 4.56 (overlapped, 2H, Bn), 4.49 (d, *J* = 11.5 Hz, 1H, Bn), 4.44 (d, 1H, Bn), 3.71 (m, 1H, H-2), 3.45 (ddd, *J* = 4.4, 9.2, 11.2 Hz, 1H, H-4), 3.37 (qd, *J* = 6.1 Hz, 1H, H-5), 2.67 (q, *J* = 7.3 Hz, 2H, CH_2), 2.38 (d′t′, *J* = 3.7 Hz, 13.6 Hz, 1H, H-3a), 1.39 (ddd, *J* = 2.8 Hz, 1H, H-3b), 13.3 (d, 3H, H-6), 1.26 (t, *J* = 7.5 Hz, 1H, CH_3). HR-ES-MS calcd. for $C_{22}H_{28}O_3Na^+$: 395.165687; found: 395.165827. Anal. calcd. for $C_{22}H_{28}O_3S$: C 70.93, H 7.58; found: C 70.78, H 7.45.

4-Pentenyl 2,4-di-*O*-benzyl-3,6-dideoxy-α-D-*xylo*-hexopyranosyl-(1→3)-2,4,6-tri-*O*-benzyl-α-D-mannopyranoside (24α) and 4-pentenyl 2,4-di-*O*-benzyl-3,6-dideoxy-β-D-*xylo*-hexopyranosyl-(1→3)-2,4,6-tri-*O*-benzyl-α-D-mannopyranoside (24β)

To a mixture of **10** (1.18 g, 3.17 mmol), **7** (1.13 g, 2.17 mmol), 2,6-di-*tert*-butyl-4-methylpyridine (0.87 g, 4.24 mmol), and 4 Å molecular sieves in anhyd Et_2O (20 mL) at 0°C under argon, methyl trifluoromethanesulfonate (737 μL, 6.51 mmol) was added dropwise. The mixture was stirred at room temperature for 6 h and then quenched with Et_3N (3 mL). The molecular sieves were removed by filtration and the solvent was evaporated. The resulting residue was purified by column chromatography on silica gel (hexane–EtOAc, 24:1 v/v), to give the α-anomer **24**α (1.45 g, yield 80%) and β-anomer **24**β (34 mg, yield 2%). Data for **24**α: $[\alpha]_D^{22}$ +38.8 (*c* 4.0, $CHCl_3$). ^{1}H NMR ($CDCl_3$, 600 MHz) δ: 7.34–7.12 (m, 25H, 5 × Bn), 5.78 (tdd, *J* = 6.6, 10.1, 16.9 Hz, 1H, C*H*=CH_2), 5.14 (d, *J* = 3.3 Hz, 1H, H-1′), 5.07 (d, *J* = 11.4 Hz, 1H, Bn), 4.95 (m, 2H, CH=CH_2), 4.89 (d, *J* = 1.8 Hz, 1H, H-1), 4.73 (d, *J* = 12.1 Hz, 1H, Bn), 4.60 (d, *J* = 12.1 Hz, 2H, Bn), 4.49 (d, 1H, Bn), 4.48 (d, *J* = 12.1 Hz, 1H, Bn), 4.44 (d, 1H, Bn), 4.43 (d, *J* = 12.5 Hz, 1H, Bn), 4.35 (d, 1H, Bn), 4.30 (d, 1H, Bn), 4.15 (dd, *J* = 9.3 Hz, 1H, H-3), 3.97 (“t”, *J* = 9.5 Hz, 1H, H-4), 3.84 (m, 1H, H-5′), 3.80–3.76 (m, 2H, H-2′ + H-5), 3.75 (dd, *J* = 3.1 Hz, 1H, H-2), 3.71 (m, 2H, H-6), 3.67 (m, 1H, OC*Ha*HbCH_2), 3.38 (td, *J* = 6.4, 9.5 Hz, 1H, OCHa*Hb*CH_2), 3.26 (br s, 1H, H-4′), 2.10–2.03 (m, 3H, CH_2CH=CH_2 + H-3′a), 1.88 (d′t′, *J* = 2.6, 12.8 Hz, 1H, H-3′b), 1.65 (tt, *J* = 7.0, 7.0 Hz, 2H, OCH_2CH_2), 1.04 (d, *J* = 6.6 Hz, 3H, H-6′). ^{13}C NMR ($CDCl_3$, 600 MHz, from HMQC) δ: 138.0 (*C*H=CH_2), 128.2–126.9 (5 × Bn), 114.6 (CH=*C*H_2), 98.8 (C-1, $J_{C1,H1}$ = 169.3 Hz), 97.0 (C-1′, $J_{C1',H1'}$ = 169.3 Hz), 78.4 (C-3), 77.9 (C-2), 75.5 (C-4′), 74.8 (C-4), 74.3 (Bn), 73.2 (2 × Bn), 71.9 (C-5), 71.6 (Bn), 70.9–70.7 (2 × Bn), 70.7 (C-2′), 69.3 (C-6), 66.9 (O*C*H_2), 66.3 (C-5′), 30.2 (*C*H_2CH=CH_2), 28.5 (OCH_2*C*H_2), 27.1 (C-3′), 16.4 (C-6′). HR-ES-MS calcd. for $C_{52}H_{60}O_9Na^+$: 851.413504; found: 851.413319. Anal. calcd. for $C_{52}H_{60}O_9$: C 75.34, H 7.29; found: C 74.98, H 7.41. Data for **24**β: $[\alpha]_D^{22}$ +21.4 (*c* 2.8, $CHCl_3$). ^{1}H NMR ($CDCl_3$, 600 MHz) δ: 7.34–7.15 (m, 25H, 5 × Bn), 5.75 (tdd, *J* = 6.6, 10.3, 17.0 Hz, 1H, C*H*=CH_2), 5.00 (d, *J* = 10.4 Hz, 1H, Bn), 4.93 (m, 2H, CH=CH_2), 4.81 (d, *J* = 2.2 Hz, 1H, H-1), 4.77 (d, *J* = 12.1 Hz, 1H, Bn), 4.73 (d, *J* = 12.1 Hz, 2H, Bn), 4.66 (d, 1H, Bn), 4.64 (d, *J* = 11.7 Hz, 1H, Bn), 4.58–4.53 (m, 5H, H-1′ + 3 × Bn), 4.42 (d, 1H, Bn), 4.38 (d, *J* = 12.1 Hz, 1H, Bn), 4.32 (dd, *J* = 3.1, 8.6 Hz, 1H, H-3), 3.92 (“t”, *J* = 9.0 Hz, 1H, H-4), 3.79–3.70 (m, 4H, H-2 + H-5 + H-6), 3.63 (m, 2H, OC*Ha*HbCH_2 + H-2′), 3.58 (dq, *J* = 1.5, 6.4 Hz, 1H, H-5′), 3.36 (m, 1H, H-4′), 3.34 (td, *J* = 6.6, 9.9 Hz, 1H, OCHa*Hb*CH_2), 2.36 (ddd, *J* = 3.1, 4.8, 13.7 Hz, 1H, H-3′a), 2.03 (m, 2H, CH_2CH=CH_2), 1.60 (tt, *J* = 6.8, 7.3 Hz, 2H, OCH_2CH_2)), 1.48 (ddd, *J* = 2.8, 11.5 Hz, 1H, H-3′b), 1.19 (d, 3H, H-6′). HR-ES-MS calcd. for $C_{52}H_{60}O_9Na^+$: 851.413504; found: 851.413576. Anal. calcd. for $C_{52}H_{60}O_9$: C 75.34, H 7.29; found: C 74.89, H 7.44.

© 2002 NRC Canada

4-Pentenyl 2,4-di-*O*-benzyl-3,6-dideoxy-α,β-D-*ribo*-hexopyranosyl-(1→3)-2,4,6-tri-*O*-benzyl-α-D-mannopyranoside (25)

To a mixture of **16** (94 mg, 0.25 mmol), **7** (196 mg, 0.38 mmol), 2,6-di-*tert*-butyl-4-methylpyridine (103 mg, 0.50 mmol) in anhyd Et_2O (5 mL) at 0°C under argon, methyl trifluoromethanesulfonate (87 μL, 0.77 mmol) was added dropwise. The mixture was stirred at room temperature for 7.5 h and then quenched with Et_3N (1 mL). The mixture was concentrated and the resulting residue was purified by column chromatography on silica gel (toluene–EtOAc, 49:1 v/v) to give compound **25** as an inseparable mixture of anomers (α/β (3:2), 167 mg, yield 80%). ^{1}H NMR ($CDCl_3$, 600 MHz) for α-isomer δ: 7.42–7.12 (m, 25H, 5 × Bn), 5.77 (m, 1H, C*H*=CH_2), 5.11 (d, *J* = 3.3 Hz, 1H, H-1′), 5.04 (d, *J* = 11.5 Hz, 1H, Bn), 4.97 (m, 2H, CH=C*H*$_2$), 4.93 (d, *J* = 11.0 Hz, 1H, Bn), 4.86 (d, *J* = 2.0 Hz, 1H, H-1), 4.76 (d, *J* = 12.2 Hz, 1H, Bn), 4.65–4.58 (overlapped, 3H, 3 × Bn), 4.51–4.42 (overlapped, 3H, 4 × Bn), 4.18 (dd, *J* = 3.1, 9.5 Hz, 1H, H-3), 4.00 ("t", *J* = 9.7 Hz, 1H, H-4), 3.84 (dq, *J* = 6.2, 9.1 Hz, 1H, H-5′), 3.80–3.64 (m, 4H, H-2 + H-5 + H-6a + OC*Ha*HbCH$_2$), 3.43 (d′t′, *J* = 3.3, 11.7 Hz, 1H, H-2′), 3.36 (m, 2H, H-6b + OCHa*Hb*CH$_2$), 3.04 (ddd, *J* = 4.4, 11.2 Hz, 1H, H-4′), 2.31 (d′t′, *J* = 11.5 Hz, 1H, H-3′a), 2.06 (m, 2H, C*H*$_2$CH=CH$_2$), 1.92 (d′t′, 1H, H-3′b), 1.63 (m, 2H, OCH$_2$C*H*$_2$), 1.17 (d, 3H, H-6′). Selected data for β-anomer δ: 4.82 (d, *J* = 2.2 Hz, 1H, H-1), 4.54 (d, *J* = 7.5 Hz, 1H, H-1′), 4.29 (dd, *J* = 3.1, 8.6 Hz, 1H, H-3), 3.94 ("t", *J* = 9.0 Hz, 1H, H-4), 3.80–3.64 (m, 4H, H-2 + H-5 + H-6a + OC*Ha*HbCH$_2$), 3.38–3.34 (m, 3H, H-5′ + H-6b + OCHa*Hb*CH$_2$), 3.28 (ddd, *J* = 5.0, 11.9 Hz, 1H, H-2′), 3.08 (ddd, *J* = 4.4, 9.0, 11.0 Hz, 1H, H-4′), 2.50 (d′t′, *J* = 12.5 Hz, 1H, H-3′a), 2.06 (m, 2H, C*H*$_2$CH=CH$_2$), 1.63 (m, 2H, OCH$_2$C*H*$_2$), 1.50 (d′t′, 1H, H-3′b), 1.24 (d, *J* = 6.1 Hz, 3H, H-6′). HR-ES-MS calcd. for $C_{52}H_{60}O_9Na^+$: 851.413504; found: 851.412747. Anal. calcd. for $C_{52}H_{60}O_9$: C 75.34, H 7.28; found: C 75.30, H 7.30.

4-Pentenyl 2,4-di-*O*-benzyl-3,6-dideoxy-α-D-*arabino*-hexopyranosyl-(1→3)-2,4,6-tri-*O*-benzyl-α-D-mannopyranoside (26)

To a mixture of **23** (50 mg, 0.13 mmol), **7** (77 mg, 0.15 mmol), 2,6-di-*tert*-butyl-4-methylpyridine (55 mg, 0.27 mmol), and 4 Å molecular sieves in anhyd Et_2O (2 mL) at 0°C under argon, methyl trifluoromethanesulfonate (46 μL, 0.41 mmol) was added dropwise. The mixture was stirred at room temperature for 2 h and then quenched with Et_3N (1 mL). The mixture was concentrated and the resulting residue was purified by column chromatography on silica gel (toluene–EtOAc, 49:1 v/v) to give compound **26** (78 mg, yield 70%). $[\alpha]_D^{22}$ +40.0 (*c* 1.5, $CHCl_3$). ^{1}H NMR ($CDCl_3$, 600 MHz) δ: 7.40–7.12 (m, 25H, 5 × Bn), 5.70 (m, 1H, C*H*=CH_2), 5.06 (s, 1H, H-1′), 4.95 (m, 2H, CH=C*H*$_2$), 4.82 (s, 1H, H-1), 4.76 (d, *J* = 11.9 Hz, 1H, Bn), 4.70 (d, *J* = 12.3 Hz, 1H, Bn), 4.66 (d, 1H, Bn), 4.64 (d, *J* = 12.6 Hz, 1H, Bn), 4.56 (d, *J* = 11.5 Hz, 1H, Bn), 4.50 (d, 1H, Bn), 4.48 (d, 1H, Bn), 4.46 (d, 1H, Bn), 4.34 (d, *J* = 12.1 Hz, 1H, Bn), 4.23 (d, 1H, Bn), 4.18 (dd, *J* = 2.8, 9.7 Hz, 1H, H-3), 3.76 ("t", *J* = 9.7 Hz, 1H, H-4), 3.86 (m, 1H, H-5′), 3.76–3.70 (m, 3H, H-2 + H-5 + H-6a), 3.66 (m, 2H, H-6b + OC*Ha*HbCH$_2$), 3.61 (m, 1H, H-2′), 3.45 (m, 1H, H-4′), 3.36 (ddd, *J* = 3.1, 7.3 Hz, 12.8 Hz, 2H, OCHa*Hb*CH$_2$), 2.21 (m, 1H, H-3′a), 2.07 (m, 2H, C*H*$_2$CH=CH$_2$), 1.92 (d′t′, *J* = 1.5, 11.5 Hz, 1H, H-3′b), 1.63 (m, 2H, OCH$_2$C*H*$_2$), 1.25 (d, *J* = 7.0 Hz, 3H, H-6′). ^{13}C NMR (600 MHz, $CDCl_3$, from HMQC) δ: 138.1 (*C*H=CH$_2$), 128.2–126.2 (5 × Bn), 114.8 (CH=*C*H$_2$), 98.6 (C-1′, $J_{C1',H1'}$ = 167.9 Hz), 97.6 (C-1, $J_{C1,H1}$ = 167.3 Hz), 77.9 (C-5), 77.4 (C-3), 75.6 (C-2′), 75.3 (C-4′), 75.2 (C-4), 74.4 (Bn), 73.2 (Bn), 72.4 (Bn), 71.6 (C-2), 70.8 (Bn), 70.6 (Bn), 69.0 (C-6), 68.4 (C-5′), 66.8 (O*C*H$_2$), 30.0 (*C*H$_2$CH=CH$_2$), 29.2 (C-3′), 28.4 (OCH$_2$*C*H$_2$), 17.8 (C-6′). HR-ES-MS calcd. for $C_{52}H_{60}O_9Na^+$: 851.413504; found: 851.413354. Anal. calcd. for $C_{52}H_{60}O_9$: C 75.34, H 7.28; found: C 74.94, H 7.29.

4-Pentenyl 3,6-dideoxy-α-D-*xylo*-hexopyranosyl-(1→3)-α-D-mannopyranoside (27)

Redistilled liquid ammonia (50 mL) was collected in a flask with the help of a dry ice – acetone condenser, sodium (83 mg) was added, a dark blue solution was obtained and the mixture was cooled to –78°C. A solution of compound **24**α (200 mg, 0.24 mmol) and anhyd MeOH (52 μL, 1.29 mmol) in anhyd THF (20 mL) was added dropwise to a blue mixture during the course of 1 h. After another 1.5 h, the reaction was then quenched with MeOH (2 mL), the ammonia was evaporated to dryness. The residue was dissolved in MeOH and the mixture was neutralized to pH 7 by addition of 25% AcOH in H_2O. After concentration, the residue was purified by reverse-phase chromatography using a gradient of MeOH–H_2O (0 → 50%) as eluent to afford **27** (91 mg, 100%). $[\alpha]_D^{22}$ +70.0 (*c* 1.2, H_2O). ^{1}H NMR (D_2O, 600 MHz) δ: 5.92 (tdd, *J* = 6.6, 10.3, 17.0 Hz, 1H, C*H*=CH$_2$), 5.10 (d, *J* = 3.7 Hz, 1H, H-1′), 5.10 (overlapped, 1H, CH=C*Ha*Hb), 5.03 (m, 1H, CH=CHa*Hb*), 4.85 (d, *J* = 1.7 Hz, 1H, H-1), 4.12 (dq, *J* = 1.3, 6.6 Hz, 1H, H-5′), 4.05 (dd, *J* = 1.8 Hz, 3.1 Hz, 1H, H-2), 4.01 (d′t′, *J* = 4.0, 12.5 Hz, 1H, H-2′), 3.90–3.87 (m, 3H, H-3 + H-6a + H-4′), 3.84 ("t", *J* = 9.7 Hz, 1H, H-4), 3.77 (m, 2H, OC*Ha*HbCH$_2$ + H-6b), 3.70 (ddd, *J* = 2.2, 5.7, 9.5 Hz, 1H, H-5), 3.56 (d′t′, *J* = 6.1, 12.1 Hz, 1H, OCHa*Hb*CH$_2$), 2.16 (m, 2H, C*H*$_2$CH=CH$_2$), 2.06 (d′t′, *J* = 2.9, 13.0 Hz, 1H, H-3′a), 1.98 (d′t′, *J* = 4.6 Hz, 1H, H-3′b) 1.74 (m, 2H, OCH$_2$C*H*$_2$), 1.16 (d, 3H, H-6′). ^{13}C NMR (D_2O, 600 MHz, from HMQC) δ: 138.7 (*C*H=CH$_2$), 116.7 (CH=*C*H$_2$), 101.2 (C-1′, $J_{C1',H1'}$ = 169.8 Hz), 100.3 (C-1, $J_{C1,H1}$ = 171.9 Hz), 79.2 (C-3), 74.0 (C-5), 71.2 (C-2), 69.0 (C-4′), 68.1 (OCH$_2$), 65.5 (C-5′), 66.3 (C-4), 65.0 (C-2′), 61.9 (C-6), 33.4 (C-3′), 30.2 (*C*H$_2$CH=CH$_2$), 28.6 (OCH$_2$*C*H$_2$), 16.0 (C-6′). HR-ES-MS calcd. for $C_{17}H_{30}O_9Na^+$: 401.178753; found: 401.178537.

4-Pentenyl 3,6-dideoxy-α-D-*ribo*-hexopyranosyl-(1→3)-α-D-mannopyranoside (28α) and 4-pentenyl 3,6-dideoxy-β-D-*ribo*-hexopyranosyl-(1→3)-α-D-mannopyranoside (28β)

Compound **25** (74 mg, 89.3 μmol) was deprotected as described for **24**α to afford **28**α (16 mg, yield 47%) and **28**β (11 mg, yield 33%). Data for **28**α: $[\alpha]_D^{22}$ +86.0 (*c* 1.0, H_2O). ^{1}H NMR (CD_3OD, 600 MHz) δ: 5.84 (ddt, *J* = 6.8, 10.3, 17.0 Hz, 1H, C*H*=CH$_2$), 5.02 (m, 1H, CH=C*Ha*Hb), 4.97 (d, *J* = 3.7 Hz, 1H, H-1′), 4.95 (m, 1H, CH=CHa*Hb*), 4.72 (d, *J* = 1.7 Hz, 1H, H-1), 3.94 (dd, *J* = 4.1 Hz, 1H, H-2), 3.83 ("t", *J* = 9.5 Hz, 1H, H-4), 3.80 (m, 2H, H-6a + H-3), 3.77–3.70 (m, 3H, OC*Ha*HbCH$_2$ + H-5′ + H-6b), 3.63 (d′t′,

© 2002 NRC Canada

J = 4.0, 12.1 Hz, 1H, H-2′), 3.56 (ddd, J = 2.4, 5.7 Hz, 1H, H-5), 3.44 (dd, J = 6.4, 9.7 Hz, 1H, OCHa*Hb*CH_2), 2.27 (ddd, J = 4.6, 9.3, 11.4 Hz, 1H, H-4′), 2.15 (m, 2H, C*H*$_2$CH=CH_2), 1.92 (d′t′, J = 11.4 Hz, 1H, H-3′a), 1.81 (d′t′, 1H, H-3′b), 1.69 (m, 2H, OCH_2C*H*$_2$), 1.18 (d, J = 6.2 Hz, 3H, H-6′). ^{13}C NMR (CD_3OD, 600 MHz, from HMQC) δ: 139.3 (*C*H=CH_2), 115.1 (CH=*C*H$_2$), 101.4 (C-1′, $J_{C1',H1'}$ = 168.3 Hz), 101.0 (C-1, $J_{C1,H1}$ = 170.8 Hz), 80.6 (C-3), 74.5 (C-5), 71.9 (C-2), 71.5 (C-4′), 70.1 (C-5′), 69.0 (C-2′), 67.7 (O*C*H$_2$), 67.4 (C-4), 62.5 (C-6), 37.0 (C-3′), 31.2 (*C*H$_2$CH=CH_2), 29.6 (OCH_2*C*H$_2$), 17.6 (C-6′). HR-ES-MS calcd. for $C_{17}H_{30}O_9Na^+$: 401.178753; found: 401.178571. Data for **28**β: $[\alpha]_D^{22}$ –114.8 (*c* 3.1, H_2O). ^{1}H NMR (CD_3OD, 600 MHz) δ: 5.84 (ddt, J = 6.6, 10.3, 17.0 Hz, 1H, C*H*=CH_2), 5.02 (m, 1H, CH=C*Ha*Hb), 4.95 (m, 1H, CH=CHa*Hb*), 4.78 (d, J = 1.7 Hz, 1H, H-1), 4.29 (d, J = 7.7 Hz, 1H, H-1′), 3.93 (dd, J = 3.3 Hz, 1H, H-2), 3.82 (dd, J = 2.4, 11.9 Hz, 1H, H-6a), 3.75 (m, 2H, OC*Ha*HbCH_2 + H-3), 3.69 (dd, J = 5.9 Hz, 1H, H-6b), 3.67 (“t”, J = 9.5 Hz, 1H, H-4), 3.55 (ddd, 1H, H-5), 3.45 (m, 2H, H-2′ + OCHa*Hb*CH_2), 3.35 (dq, J = 6.2, 9.3 Hz, 1H, H-5′), 3.24 (ddd, J = 4.6, 9.2, 11.2 Hz, 1H, H-4′), 2.27 (d′t′, J = 4.8, 12.1 Hz, 1H, H-3′a), 2.14 (m, 2H, *C*H$_2$CH=CH_2), 1.69 (m, 2H, OCH_2C*H*$_2$), 1.46 (d′t′, J = 11.7 Hz, 1H, H-3′b), 1.26 (d, J = 6.2 Hz, 3H, H-6′). HR-ES-MS calcd. for $C_{17}H_{30}O_9Na^+$: 401.178753; found: 401.179064.

4-Pentenyl 3,6-dideoxy-α-D-arabino-hexopyranosyl-(1→3)-α-D-mannopyranoside (29)

Compound **26** (60 mg, 72 μmol) was converted to **29** (23 mg, 84%) in the same manner as **24**α. $[\alpha]_D^{22}$ –47.2 (*c* 1.8, H_2O). ^{1}H NMR (D_2O, 600 MHz) δ: 5.94 (tdd, J = 6.6, 10.3, 16.9 Hz, 1H, C*H*=CH_2), 5.11 (m, 1H, CH=C*Ha*Hb), 5.04 (m, 1H, CH=CHa*Hb*), 4.90 (s, 1H, H-1′), 4.85 (s, 1H, H-1), 4.08 (m, 1H, H-2′), 4.05 (m, 1H, H-2), 3.89 (m, 2H, H-3 + H-6a), 3.82 (qd, J = 6.2, 9.5 Hz, 1H, H-5′), 3.78 (“t”, J = 9.5 Hz, 1H, H-4), 3.77 (m, 2H, H-6b + OC*Ha*HbCH_2), 3.70 (ddd, J = 2.2, 5.9, 9.3 Hz, 1H, H-5), 3.63 (ddd, J = 4.6, 11.2 Hz, 1H, H-4′), 3.57 (dt, J = 6.0, 9.9 Hz, 1H, OCHa*Hb*CH_2), 2.18 (m, 2H, C*H*$_2$CH=CH_2), 2.06 (d′t′, J = 4.0, 13.6 Hz, 1H, H-3′a), 1.90 (ddd, J = 2.9 Hz, 1H, H-3′b), 1.75 (m, 2H, OCH_2C*H*$_2$), 1.28 (d, 3H, H-6′). ^{13}C NMR (600 MHz, D_2O, from HMQC) δ: 138.2 (*C*H=CH_2), 115.7 (CH=*C*H$_2$), 102.1 (C-1′, $J_{C1',H1'}$ = 170.7 Hz), 100.5 (C-1, $J_{C1,H1}$ = 170.7 Hz), 78.5 (C-3), 73.7 (C-5), 70.9 (C-5′), 70.8 (C-2), 68.2 (O*C*H$_2$ + C-2′), 67.6 (C-4′), 66.9 (C-4), 61.6 (C-6), 34.1 (C-3′), 30.4 (*C*H$_2$CH=CH_2), 28.5 (OCH_2*C*H$_2$), 17.4 (C-6′). HR-ES-MS calcd. for $C_{17}H_{30}O_9Na^+$: 401.178753; found: 401.178261.

5-(2-Aminoethylthio)pentyl 3,6-dideoxy-α-D-*xylo*-hexopyranosyl-(1→3)-α-D-mannopyranoside, hydrochloride salt (1)

Compound **27** (10 mg, 26.4 μmol) and 2-aminoethanethiol hydrochloride (15 mg, 0.13 mmol) were dissolved in anhyd degassed MeOH (1 mL). The solution was stirred under argon for 48 h with irradiation by UV light of 254 nm wavelength. The solvent was evaporated and the resulting residue was purified by reverse-phase HPLC to give **1** (11.7 mg, 90%). $[\alpha]_D^{22}$ –127.2 (*c* 1.8, H_2O). ^{1}H NMR (D_2O, 600 MHz) δ: 5.10 (d, J = 3.7 Hz, 1H, H-1′), 4.85 (d, J = 1.7 Hz, 1H, H-1), 4.12 (dq, J = 1.3, 6.6 Hz, 1H, H-5′), 4.05 (dd, J = 3.1 Hz, 1H, H-2), 4.01 (ddd, J = 4.8, 12.5 Hz, 1H, H-2′), 3.90–3.87 (m, 2H, H-4′ + H-3), 3.83 (“t”, J = 9.7 Hz, 1H, H-4), 3.79–3.73 (m, 3H, OC*Ha*HbCH_2 + H-6), 3.69 (ddd, J = 2.2, 5.9 Hz, 1H, H-5), 3.56 (td, J = 5.9, 9.9 Hz, 1H, OCHa*Hb*CH_2), 2.84 (t, J = 6.4 Hz, 2H, SCH_2), 2.69 (t, J = 6.7 Hz, 2H, $CH_2NH_3^+Cl^-$), 2.60 (t, J = 7.3 Hz, 2H, CH_2S), 2.06 (d′t′, J = 2.9, 13.2 Hz, 1H, H-3′a), 1.98 (d′t′, J = 4.2 Hz, 1H, H-3′b), 1.68–1.61 (m, 4H, OCH_2CH_2 + CH_2CH_2S), 1.48 (m, 2H, $OCH_2CH_2CH_2$), 1.16 (d, 3H, H-6′). ^{13}C NMR (CD_3OD, 600 MHz, from HMQC) δ: 102.2 (C-1′, $J_{C1',H1'}$ = 167.3 Hz), 101.2 (C-1, $J_{C1,H1}$ = 164.6 Hz), 81.1 (C-3), 74.5 (C-5), 72.0 (C-2), 69.8 (C-4′), 68.5 (O*C*H$_2$), 67.6 (C-5′), 66.7 (C-4), 65.0 (C-2′), 62.7 (C-6), 41.2 (S*C*H$_2$), 36.0 (C-3′), 34.8 (SCH_2*C*H$_2$), 32.0 (*C*H$_2$S), 30.1 (OCH_2*C*H$_2$ + *C*H$_2$CH$_2$S), 26.2 (OCH_2CH_2*C*H$_2$), 16.7 (C-6′). HR-ES-MS calcd. for $C_{19}H_{38}NO_9SNa^+$: 456.226729; found: 456.227016.

5-(2-Aminoethanethio)pentyl 3,6-dideoxy-α-D-*ribo*-hexopyranosyl-(1→3)-α-D-manno-pyranoside (hydrochloride salt) (2)

As described for **1**, **28**α (13 mg, 34.4 μmol) was converted to **2** (12 mg, 71%). $[\alpha]_D^{22}$ –171.8 (*c* 1.1, H_2O). ^{1}H NMR (D_2O, 600 MHz) δ: 5.05 (d, J = 3.7 Hz, 1H, H-1′), 4.88 (d, J = 1.8 Hz, 1H, H-1), 4.05 (dd, J = 3.1 Hz, 1H, H-2), 3.88 (m, 2H, H-3 + H-6a), 3.83 (“t”, J = 9.5 Hz, 1H, H-4), 3.81 (ddd, J = 4.8, 12.3 Hz, 1H, H-2′), 3.78–3.71 (m, 3H, H-6b + OC*Ha*HbCH_2 + H-5′), 3.67 (ddd, J = 2.2, 6.0 Hz, 1H, H-5), 3.56 (td, J = 6.1, 9.9 Hz, 1H, OCHa*Hb*CH_2), 3.37 (ddd, J = 4.6, 9.5, 11.4 Hz, 1H, H-4′), 3.21 (t, J = 6.8 Hz, 2H, SCH_2), 2.84 (t, J = 6.8 Hz, 2H, C*H*$_2$NH$_3^+$Cl$^-$), 2.62 (t, J = 7.3 Hz, 2H, CH_2S), 2.13 (d′t′, J = 11.5 Hz, 1H, H-3′a), 1.78 (d′t′, 1H, H-3′b), 1.64 (m, 4H, OCH_2CH_2 + CH_2CH_2S), 1.48 (m, 2H, $OCH_2CH_2CH_2$), 1.22 (d, J = 6.2 Hz, 3H, H-6′). ^{13}C NMR (D_2O, 600 MHz, from HMQC) δ: 100.2 (C-1′, $J_{C1',H1'}$ = 168.0 Hz), 100.1 (C-1, $J_{C1,H1}$ = 168.4 Hz), 79.2 (C-3), 73.6 (C-5), 70.9 (C-2), 70.4 (C-4′), 69.8 (C-5′), 68.3 (O*C*H$_2$), 67.8 (C-2′), 66.7 (C-4), 61.6 (C-6), 39.0 (S*C*H$_2$), 35.0 (C-3′), 30.3 (*C*H$_2$S), 28.8 *C*H$_2$NH$_3^+$Cl$^-$), 28.7 (OCH_2*C*H$_2$ + *C*H$_2$CH$_2$S), 25.2 (OCH_2CH_2*C*H$_2$), 17.1 (C-6′). HR-ES-MS calcd. for $C_{19}H_{38}NO_9S^+$: 456.226729; found: 456.226642.

5-(2-Aminoethylthio)pentyl 3,6-dideoxy-α-D-*arabino*-hexopyranosyl-(1→3)-α-D-manno-pyranoside, acetic acid salt (3)

As described for **1**, **29** (20 mg, 53 μmol) was converted to **3** and isolated as the acetate salt form after purification by reverse-phase HPLC using a gradient of MeOH–H_2O (containing 0.3% acetic acid), (25.5 mg, 94%). $[\alpha]_D^{22}$ +54 (*c* 2.1, H_2O). ^{1}H NMR (D_2O, 600 MHz) δ: 4.88 (s, 1H, H-1′), 4.84 (d, J = 1.7 Hz, 1H, H-1), 4.06 (dd, J = 3.1, 4.7 Hz, 1H, H-2′), 4.03 (dd, J = 3.2 Hz, 1H, H-2), 3.88 (dd, J = 2.3, 12.3 Hz, 1H, H-6a), 3.87 (dd, J = 9.6 Hz, 1H, H-3), 3.78 (m, 3H, H-5′ + H-6b + OC*Ha*HbCH_2), 3.75 (“t”, J = 9.6 Hz, 1H, H-4), 3.67 (ddd, J = 6.0 Hz, 1H, H-5), 3.61 (ddd, J = 4.5, 9.3, 11.4 Hz, 1H, H-4′), 3.56 (td, J = 6.1, 9.9 Hz, 1H, OCHa*Hb*CH_2), 3.21 (t, J = 6.7 Hz, 2H, SCH_2), 2.85 (t, J = 6.6 Hz, 2H, C*H*$_2$NH$_3^+$OAc$^-$), 2.62 (t, J = 7.3 Hz, 2H, CH_2S), 2.04 (d′t′, J = 13.6 Hz, 1H, H-3′a), 1.94 (s, 3H, OAc), 1.87 (ddd, J = 14.0 Hz, 1H, H-3′b), 1.64 (m, 4H, OCH_2CH_2 +

© 2002 NRC Canada

CH_2CH_2S), 1.48 (m, 2H, $OCH_2CH_2CH_2$), 1.26 (d, J = 6.4 Hz, 3H, H-6′). ^{13}C NMR (D_2O, 600 MHz, from HMQC) δ: 101.9 (C-1′, $J_{C1',H1'}$ = 171.4 Hz), 100.4 (C-1, $J_{C1,H1}$ = 168.9 Hz), 78.9 (C-3), 73.8 (C-5), 71.0 (C-5′), 70.7 (C-2), 68.6 (OCH_2), 68.1 (C-2′), 67.9 (C-4′), 66.8 (C-4), 61.6 (C-6), 39.0 (SCH_2), 34.0 (C-3′), 31.5 (CH_2S), 28.8 $CH_2NH_3^+OAc^-$ + OCH_2CH_2 + CH_2CH_2S), 26.0 ($OCH_2CH_2CH_2$), 23.0 (OAc^-), 17.0 (C-6′). HR-ES-MS calcd. for $C_{19}H_{38}NO_9S^+$: 456.226729; found: 456.227209.

References

1. A. Varki. Glycobiology, **3**, 97 (1993).
2. P.I. Kitov, J.M. Sadowska, G. Mulvey, G.D. Armstrong, H. Ling, N.S. Pannu, R.J. Read, and D.R. Bundle. Nature (London), **403**, 669 (2000).
3. D.R. Bundle. Recognition of carbohydrate antigens by antibody binding sites. *In* Carbohydrates. *Edited by* S. Hecht. Oxford University Press Inc., Oxford. 1995. pp. 370–440.
4. U. Jönsson, L. Fägerstam, B. Ivarssson, B. Johnsson, R. Karlsson, K. Lundh, S. Löfås, B. Persson, H. Roos, I. Rönnberg, S. Sjölander, E. Stenberg, R. Ståhlberg, C. Urbaniczky, H. Östlin, and M. Malmqvist. BioTechniques, **11**, 620 (1991).
5. W.M. Mullett, E.P.C. Lai, and J.M. Yeung. Methods — A Companion to Methods Enzymol. **22**, 77 (2000).
6. M. Mrksich. Chem. Soc. Rev. **29**, 267 (2000), and refs. therein.
7. K.L. Prime and G.M. Whitesides. J. Am. Chem. Soc. **115**, 10 714 (1993).
8. M. Mrksich, G.S. Sigal, and G.M. Whitesides. Langmuir, **11**, 4383 (1995).
9. N. Horan, L. Yan, H. Isobe, G.M. Whitesides, and D. Kahne. Proc. Natl. Acad. Sci. U.S.A. **96**, 11 782 (1999).
10. D.A. Mann, M. Kanai, D.J. Maly, and L.L. Kiessling. J. Am. Chem. Soc. **120**, 10 575 (1998).
11. B.T. Houseman and M. Mrksich. Angew. Chem. Int. Ed. **38**, 782 (1999).
12. P.I. Kitov, C. Railton, and D.R. Bundle. Carbohydr. Res. **307**, 361 (1998).
13. D.R. Bundle. Top. Curr. Chem. **154**, 1 (1990), and refs. therein.
14. A.A. Lindberg, R. Wollin, G. Gruse, and S.B. Svenson. Am. Chem. Soc. Symp. Ser. **231**, 83 (1983)
15. A. Zdanov, Y. Li, D.R. Bundle, S.-J. Deng, C.R. Mackenzie, S.A. Narang, N.M. Young, and M. Cygler. Biochemistry, **33**, 5172 (1994).
16. B.W. Sigurskjold and D.R. Bundle. J. Biol. Chem. **267**, 8371 (1992).
17. B.W. Sigurskjold, E. Altman, and D.R. Bundle. Eur. J. Biochem. **197**, 239 (1991).
18. C.R. Mackenzie, T. Hirama, S.-J. Deng, D.R. Bundle, S.A. Narang, and N.M. Young. J. Biol. Chem. **271**, 1527 (1995).
19. B. Fraser-Reid, U.E. Udodong, A. Wu, H. Ottosson, J.R. Merritt, C.S. Ral, C. Roberts, and R. Madsen. Synlett, 927 (1992), and refs. therein.
20. D.R. Mootoo, P. Konradsson, U. Udodong, and B. Fraser-Reid. J. Am. Chem. Soc. **110**, 5583 (1988).
21. H.N. Yu, P. Zhang, C.-C. Ling, and D.R. Bundle. Tetrahedron: Asymmetry, **11**, 465 (2000).
22. T.L. Lowary, E. Eichler, and D.R. Bundle. J. Org. Chem. **60**, 7316 (1995).
23. B. Classon, P.J. Garegg, and B. Samuelsson. Can. J. Chem. **59**, 339 (1981).
24. D.H.R. Barton and S.W. McCombie. J. Chem. Soc. Perkin Trans. 1, 1574 (1975).
25. G. Ekborg and S. Svensson. Acta Chem. Scand. **27**, 1437 (1973).
26. M.A. Probert, J. Zhang, and D.R. Bundle. Carbohydr. Res. **296**, 149 (1996).
27. S. Oscarson and A. Tiden. Carbohydr. Res. **247**, 323 (1993).
28. H.N. Yu, C.-C. Ling, and D.R. Bundle. J. Chem. Soc. Perkin Trans. 1, 832 (2001).
29. C.J. France, I.M. McFarlane, C.G. Newton, P. Pitchen, and D.H.R. Barton. Tetrahedron, **47**, 6381 (1991).
30. A.V. Demchenko and G.-J. Boons. J. Org. Chem. **66**, 2547 (2001).
31. K. Bock and C. Pedersen. J. Chem. Soc. Perkin Trans. 2, 293 (1974).
32. R.T. Lee and Y.C. Lee. Carbohydr. Res. **37**, 193 (1974).
33. R.K. Jain, X.-G. Liu, S.R. Oruganti, E.V. Chandrasekaran, and K.L. Matta. Carbohydr. Res. **271**, 185 (1995).

© 2002 NRC Canada

Synthesis of disaccharide congeners of the *Trichinella spiralis* glycan and binding site mapping of two monoclonal antibodies

Ping Zhang, Judith Appleton, Chang-Chun Ling, and David R. Bundle

Abstract: The tetrasaccharide epitope, β-D-Tyv*p*(1→3)β-D-GalNAc*p*(1→4)[α-L-Fuc*p*(1→3)]β-D-GlcNAc*p* (**1**) is the major constituent of the *N*-glycan expressed on the cell surface of the parasite *Trichinella spiralis*. Two monoclonal antibodies (Mabs 9D4 and 18H1) that protect rats against infection by *T. spiralis* bind the terminal disaccharide epitope β-D-Tyv*p*(1→3)β-D-GalNAc*p* conjugated to BSA. The syntheses of disaccharide congeners containing mono-deoxy, mono-methyl, as well as modifications to replace the acetamido group are reported. These target disaccharides were assayed for binding to the protective MAbs. For each antibody different clusters of three hydroxyl groups, that include C-2 and C-4 of tyvelose and for 18H1, the GalNAc acetamido group, provide the key polar interactions with the antibody binding sites. Mapping of the sites by functional group replacement revealed a similar pattern of recognition for the dideoxyhexose by the two MAbs while each recognizes distinct surfaces of the GalNAc residue. Consequently although both antibodies bury the 4-OH of tyvelose, the principal contact surface occurs on opposite sides of the 3,6-dideoxyhexose.

Key words: β-tyveloside, 3,6-dideoxy-D-*arabino*-hexose, *Trichinella* carbohydrate antigen, antibody mapping, *Trichinella spiralis*, *N*-glycans, molecular recognition of carbohydrates, antigen topology, functional group replacement.

Résumé : Le tétrasaccharide épitope, β-D-Tyv*p*(1→3)β-D-GalNAc*p*(1→4)[α-L-Fuc*p*(1→3)]β-D-GlcNAc*p* (**1**) est un constituant majeur du *N*-glucane extrait de la surface de la cellule du parasite *Trichinella spiralis*. Deux anticorps monoclonaux (Mabs 9D4 et 18H1) qui protègent les rats contre les infections par le *T. spiralis* se lient au disaccharide terminal épitope β-D-Tyv*p*(1→3)β-D-GalNAc*p* conjugué au BSA. On rapporte les synthèses de congénères du disaccharide comportant des modifications de type monodésoxy- ou monométhyle ainsi que le remplacement du groupe acétamido. On a évalué les capacités de ces disaccharides à se lier aux MAbs protecteurs. Pour chacun des anticorps, différents ensembles de trois groupes hydroxyles incluant les C-2 et C-4 du tyvelose ainsi que le groupe acétamido GalNAc du 18H1 fournissent les interactions polaires clés avec les sites de liaison de l'anticorps. Une carte des sites obtenue par le remplacement des groupes fonctionnels a permis de réaliser qu'un patron semblable existe pour la reconnaissance du didésoxyhexose par les deux MAbs alors que chacun d'eux reconnaît des surfaces distinctes du résidu GalNAc. En conséquence, même si les deux anticorps ensevelissent le 4-OH du tyvelose, le principal contact de surface se produit sur les faces opposées du 3,6-didésoxyhexose.

Mots clés : β-tyveloside, 3,6-didésoxy-D-*arabino*-hexose, hydrate de carbone antigène du *Trichinella*, carte de l'anticorps, *Trichinella spiralis*, *N*-glycanes, reconnaissance moléculaire des hydrates de carbone, topologie des antigènes, remplacement d'un groupe fonctionnel.

[Traduit par la Rédaction]

Introduction

The causative agent of trichinosis a parasitic nematode, *Trichinella spiralis*, has an exceptionally large host range and is endemic in many carnivorous animals. The parasite establishes itself in the intestinal epithelia of the host animal, following consumption of infected tissue and causes acute muscle pain, fatigue, fever, and in severe cases, death (1). During invasion, *T. spiralis* secretes an array of glycoproteins that are key to successful colonization of the intestine by the parasite. Antibodies against the glycan portion of the glycoproteins can prevent parasitic invasion and cause expulsion of the *T. spiralis* larvae from the intestine (2, 3). Here the syntheses of congeners of the native, terminal disaccharide β-D-Tyv*p*(1→3)β-D-GalNAc*p* are reported. The inhibitory activities of these ligands are used to define the precise specificity and topology of the epitope's contact surface with the binding sites of two protective rat

Received 4 December 2001. Published on the NRC Research Press Web site at http://canjchem.nrc.ca on 4 September 2002.

We dedicate this paper to the memory of Professor Raymond U. Lemieux.

P. Zhang, C.-C. Ling, and D.R. Bundle.[1] Department of Chemistry, The University of Alberta, Edmonton, AB T6G 2G2, Canada.
J. Appleton. James A. Baker Institute, College of Veterinary Medicine, Cornell University, Ithaca, NY 14853, U.S.A.

[1]Corresponding author (e-mail: dave.bundle@ualberta.ca).

 DOI: 10.1139/V02-117 © 2002 NRC Canada

monoclonal antibodies (MAbs) produced from lymphocytes of rats infected with *T. spiralis*.

In common with many other nematodes (4), *Trichinella* secretes and displays on its cuticle a large number of proteins that display a rich repertoire of *N*-linked glycans (5, 6). Complex-type *N*-glycans in eukaryotes are characterized by the presence of variable numbers of antennae (usually two, three, or four, called bi-, tri-, and tetraantennary, respectively). In mammals the antennae stubs are usually elongated by the addition of β-Gal to give β-Gal(1→4)GlcNAc or "LacNAc". In a restricted number of mammalian glycoproteins, β-GalNAc is added to the GlcNAc stubs in place of β-Gal and thus they have β-GalNAc(1→4)GlcNAc or "LacdiNAc" antennae. Both types of antennae are found in vertebrates but LacdiNAc is the preferred antennae building block in many helminths including *Trichinella* (5, 6). The L1 stage of *T. spiralis* modifies LacdiNAc with phosphorylcholine moieties or by substitution with 3,6-dideoxy-D-*arabino*-hexose (D-tyvelose), a sugar normally confined to the cell wall lipopolysaccharide (LPS) of gram-negative bacteria. Both modifications create highly immunogenic epitopes.

Trichinella spiralis faces an aggressive immune response from its animal host, but avoids extinction by changing its expression of antigenic molecules as it changes life stages (7, 8) and by residing in intracellular habitats (9, 10). Antibody responses induced by L1 stage larvae in the intestine and in the muscle are largely directed at *N*-glycans unique to this stage (11–14). Glycans capped by tyvelose are the target of protective immunity against *T. spiralis* and antibodies specific for one of these glycans protect rats against reinfection with *T. spiralis* (3, 15, 16). The structure of the antennae of the protective antigen is shown (**1**, Fig. 1). The most striking and unusual feature is the presence of tyvelose as its β-pyranoside form rather than the α-anomer, which previously was the only naturally occurring form to have been observed in bacterial LPS antigens of pathogenic *Salmonella* (17).

Some monoclonal tyvelose-specific antibodies that bind the *T. spiralis* glycan provide protection to passively immunized rats (3, 5). Antibody 9D4 has high protective efficacy in rats and exhibits high affinity for tetrasaccharide **1**. Another tyvelose specific antibody 18H1, also shows poor protective efficacy (3, 15). It fails to cause expulsion of larvae from the intestines of rats, even though it exhibits most of the inhibitory effects shown by antibody 9D4.

No structural details of these antibody binding sites are available, although preliminary crystallographic data has been collected for MAb 9D4, and both antibody Fv regions have been partially sequenced (18). The 3,6-dideoxy arabinohexose was inferred to be linked to the *N*-glycans via the rare β-linkage based on binding studies with di- (16, 19), tri- (20, 21), and tetrasaccharides (22, 23). MAb 9D4 showed the highest affinity for tetrasaccharide **1**, while trisaccharide **2** had five times weaker affinity than the tetrasaccharide, and three times higher affinity than the disaccharide **3** (Table 1) (21, 24). This indicates the binding site of this antibody has contacts to all four sugars of the tetrasaccharide **1**, while the majority of its binding energy is focused around the dideoxyhexose containing disaccharide, an observation that has been found for other antibodies recognizing glycans containing dideoxyhexoses (25). MAb 18H1 unexpectedly recognized the trisaccharide **2** with an affinity comparable to that of the tetrasaccharide **1** and recognized the disaccharide **3** with six times higher affinity. This data is clearly inconsistent with earlier rationalization of the poor protective efficacy of MAb 18H1 that hypothesized it had been raised against a non-fucosylated linear arm of the glycan (16), and that the linear trisaccharide **2** was the preferred epitope. This would require that trisaccharide **2** be bound more tightly than the branched tetrasaccharide **1**. Consistent with the mapping data from the three different sized ligands (**1**–**3**), MAb 9D4 shows a higher affinity for its complementary ligand **1** than 18H1 shows for its smaller and complementary disaccharide epitope **3** (Table 1).

Fig. 1. The structure of the terminal tetrasaccharide **1** of the *N*-glycan expressed by the L1 stage larvae of the *T. spiralis* parasite, and its component terminal trisaccharide **2** and disaccharide **3**.

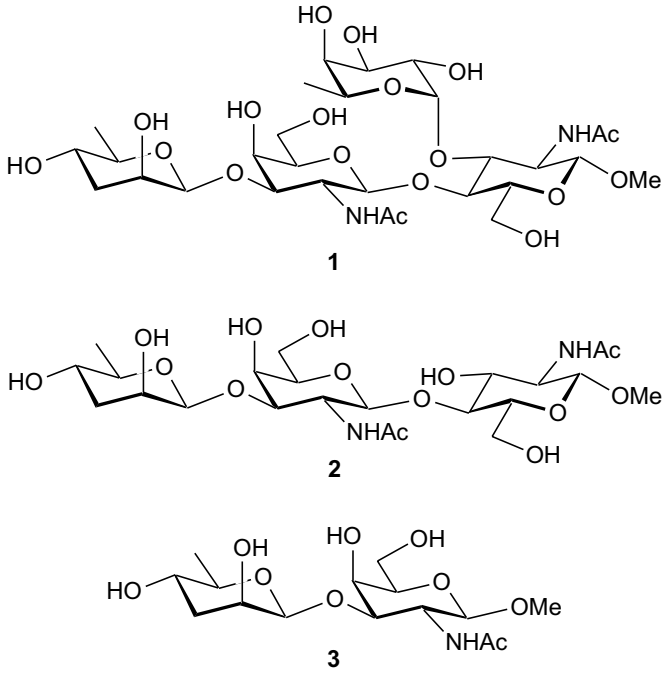

Chemical mapping by functional group replacement has proven to be a very successful tool to acquire information about carbohydrate-binding sites of antibodies (26–30), enzymes (31, 32), and lectins (26, 33). The strategy as devised by Lemieux and co-workers (34) involves the use of monodeoxy and mono-*O*-methyl congeners to identify the most important polar contacts between the carbohydrate epitope and protein. When the binding data of the modified epitopes with protein are combined with computer-assisted modeling, an overall picture of the binding site emerges, and the carbohydrate surface located in the site vs. that exposed to solvent water as well as the complementary interacting surfaces can be identified.

Results and discussion

The methyl glycoside of β-D-Tyv*p*(1→3)β-D-GalNAc*p* **3**, together with 11 other synthetic targets (Fig. 2) are used in this chemical mapping study. Disaccharides **4** and **5** are used to probe the importance of the 2-acetamido-2-deoxy group for binding, while analogs **6**–**8** contain modifications to probe the 4-position of GalNAc and disaccharides **9** and **10**,

© 2002 NRC Canada

Fig. 2. The structures of the synthetic disaccharide congeners **4**–**14** of the native disaccharide **3**.

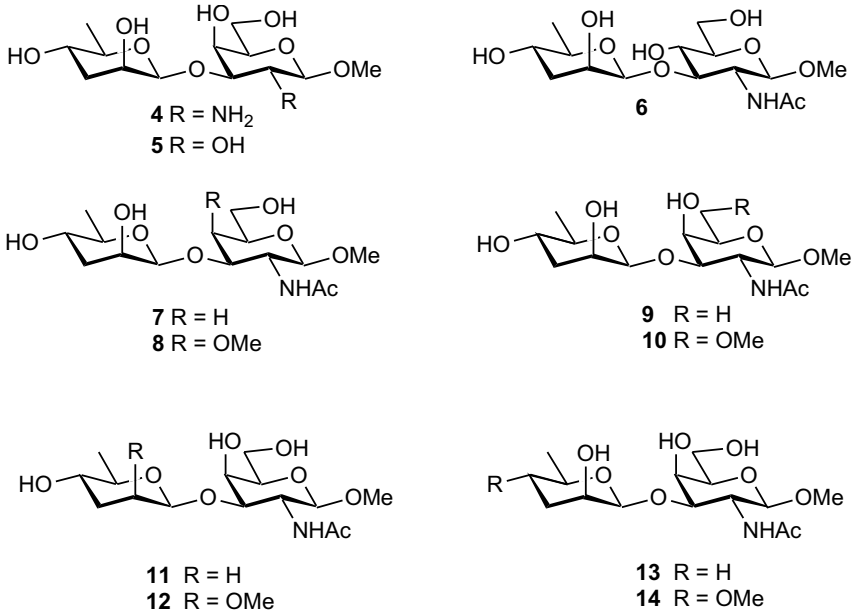

Table 1. Epitope size of the *Trichinella spiralis* glycan recognized by MAbs 9D4 and 18H1.

Oligosaccharide	IC_{50} (μM)[a]		Relative inhibitory power[b]	
inhibitor	9D4	18H1	9D4	18H1
Tetrasaccharide **1**	15	>500	100	< 9
Trisaccharide **2**	58	~480	26	~19
Disaccharide **3**	178	93	8	100

[a]Calculated from 50% inhibition data with an estimated accuracy of ~ ±5%.
[b]Inhibition potency of **1** or **3** set as 100.

the 6-position of GalNAc. Modifications were made to the tyvelose residue to investigate the contributions of the hydroxyl groups at the C-2′ and C-4′ positions. Compounds **11** and **12** are 2′-monodeoxy and 2′-*O*-monomethyl congeners while compounds **13** and **14** are 4′-monodeoxy and 4′-*O*-monomethyl analogues.

Initially, disaccharides **5** and **6** were prepared from an easily accessible tyvelose donor **15** (22) (Scheme 1), using insoluble silver zeolite as promoter. When reacting with galactosyl acceptor **16** (35) or glucosamine acceptor **17**, the disaccharides **18** and **19** were obtained in only poor yields (→**18** (15%), →**19** (26%)). These are typical and representative yields in the preparation of β-mannopyranosides using insoluble silver salt and halides as donors. Both the disaccharides **18** and **19** were deprotected by hydrogenation to give targeted compounds **5** (89%) and **6** (97%).

In our synthesis of several targets, differentiation between the hydroxyl group OH-4′ and OH-2′ of the tyvelose residue was essential. Obviously the donor **15** was not satisfactory since both positions are protected by benzyl groups. Even though the synthetic scheme seems short, the fact that the glycosylations proceeded in low yields also prevented us from obtaining final products in reasonable amounts, especially when an extended reaction sequence was involved. This necessitated an alternative route for creation of the β-tyveloside linkage.

Use of a 3,6-dideoxy-D-ribohexopyranose (paratose) derivative as a precursor of the target tyvelosides became the strategy of choice, since the anomeric β-linkage is easily introduced by exploiting a C-2 participating group. The C-2 hydroxyl group can be inverted to its C-2 epimer through an oxidation–reduction sequence (36, 37). It was reported that by carefully choosing the reducing agent, the axial OH-2 epimer could be obtained in high yield. Recently, we published a new methodology to allow the preparation of 3,6-dideoxy-D-hexopyranoses (abequose and paratose) on a large scale and in high yields (38); furthermore, this methodology permits the facile introduction of different protecting groups at the C-2 and C-4 positions. For this purpose we employed a previously prepared paratose thioglycoside **20** as starting material (38).

Since benzoyl and pivaloyl protecting groups are superior participating groups when compared to the corresponding acetate ester, we converted **20** to the 2-OH derivative **21** and then prepared the corresponding benzoylated and pivaloylated donors **22** and **23** (Scheme 2). In our preliminary investigation, it was found that **22** and **23** gave similar yields when reacted with 2-azido galactosyl acceptor **24** (39). Due to the relative ease with which the benzoate group can be removed, the benzoylated donor **22** was used for all glycosylations. Using *N*-iodosuccinimide – triflic acid as the activation conditions, the disaccharide **25** was obtained in 83% yield. After removal of benzoate (→**26**, 94%), the 2′-hydroxyl group was oxidized to the corresponding ketone **27** by DMSO–Ac_2O. The intermediate ketone **27** was not isolated but immediately reduced. When excess L-selectride was used as the reducing reagent, the corresponding β-tyveloside was obtained in excellent stereoselectivity (→**28**, 92%), no paratose derivative was detected by NMR,

© 2002 NRC Canada

Scheme 1. (*a*) Silver zeolite – MS 4 Å – CH_2Cl_2; (*b*) H_2–$Pd(OH)_2$/C–MeOH.

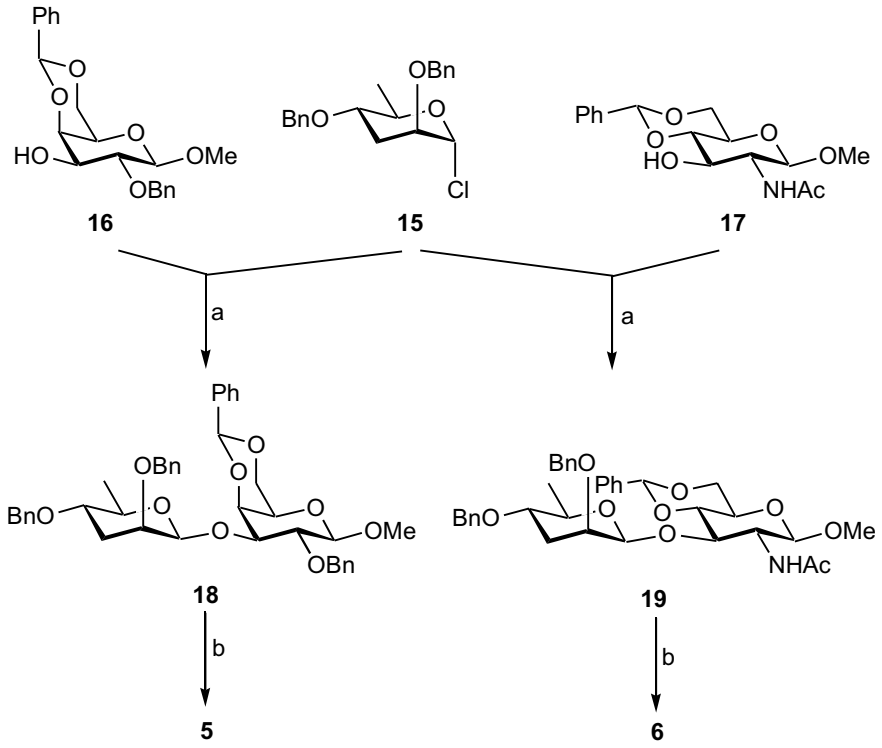

Scheme 2. (*a*) MeONa–MeOH; (*b*) BzCl–Py–CH_2Cl_2; (*c*) PivCl–Py–CH_2Cl_2; (*d*) NIS – TfOH – MS 4 Å – CH_2Cl_2; (*e*) DMSO–Ac_2O; (*f*) L-selectride–THF; (*g*) Na–NH_3 (liq.); (*h*) Ac_2O–MeOH; (*i*) H_2–$Pd(OH)_2$–MeOH; (*j*) (*i*) Bu_2SnO–MeOH, (*ii*) MeI–CsF–DMF.

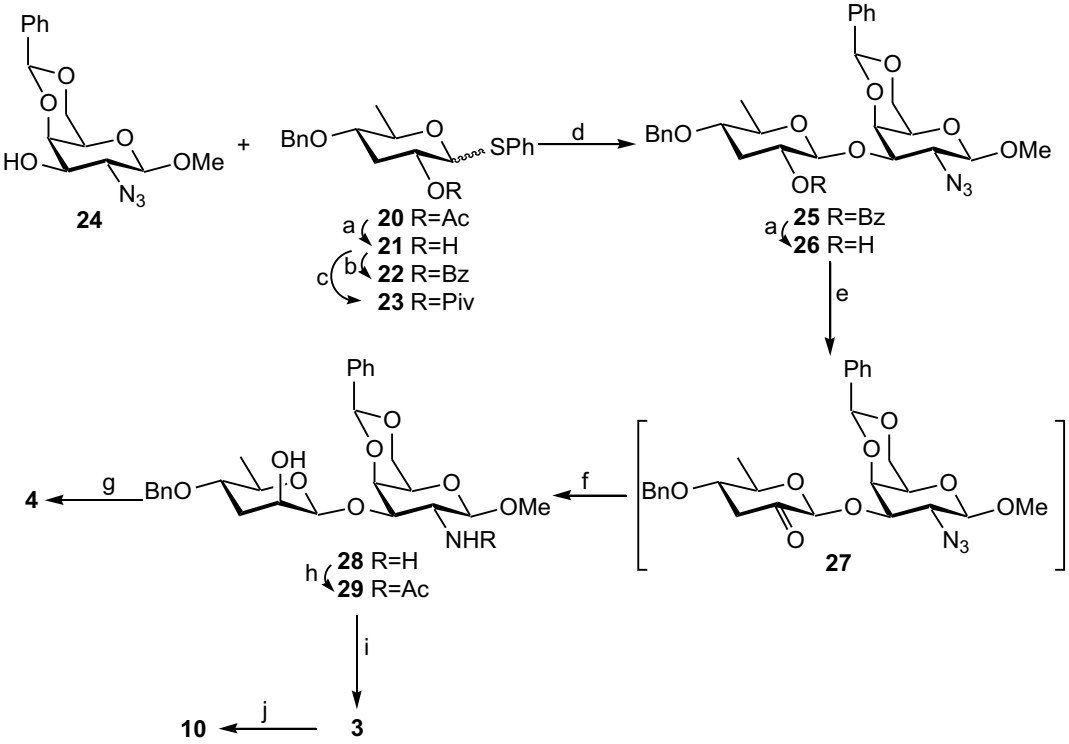

and the 2-azido group was simultaneously reduced to the amine. The amino disaccharide **4** (90%) was obtained from **28** following removal of benzyl and benzylidene groups by Birch reduction. The fully protected 2-amino disaccharide **28** was acetylated using acetic anhydride in methanol (→**29**, 93%), and the protecting groups were successfully removed by hydrogenation to afford the native disaccharide **3** (88%). When compound **3** was subjected to a dibutyltin-oxide-assisted

© 2002 NRC Canada

Scheme 3. (*a*) MeI–NaH–DMF; (*b*) H_2–$Pd(OH)_2$/C–MeOH; (*c*) Im_2CS–toluene, 90°C; (*d*) *n*-Bu_3SnH–AIBN–toluene, reflux.

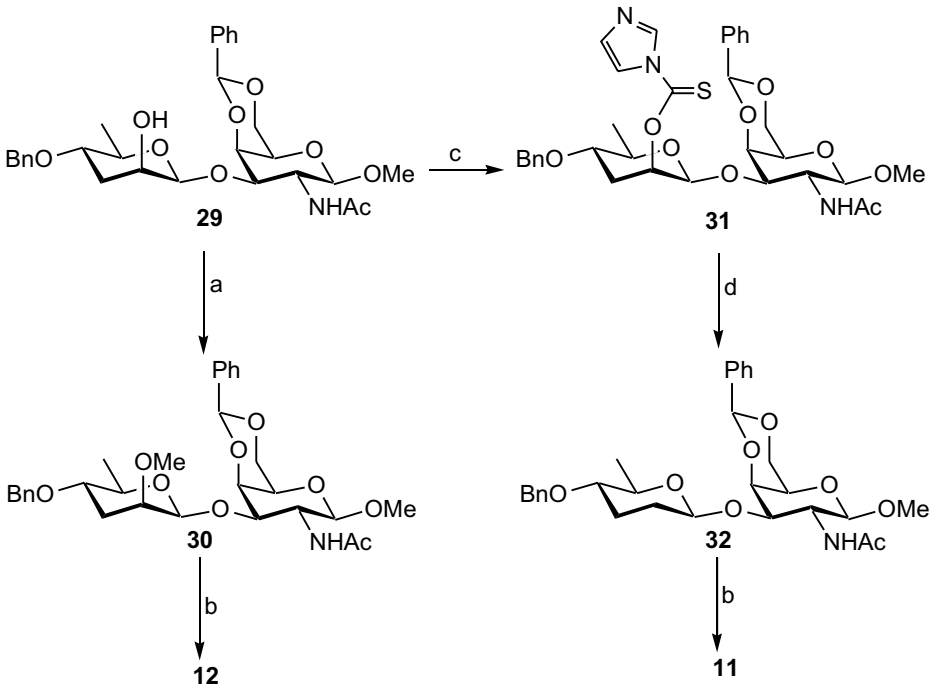

Scheme 4. (*a*) BzCl–Py–CH_2Cl_2; (*b*) NH_4HCO_2–Pd/C–MeOH, reflux; (*c*) Im_2CS–toluene, 90°C; (*d*) *n*-Bu_3SnH–AIBN–toluene, reflux; (*e*) (*i*) MeONa–MeOH, (*ii*) H_2–$Pd(OH)_2$/C–MeOH.

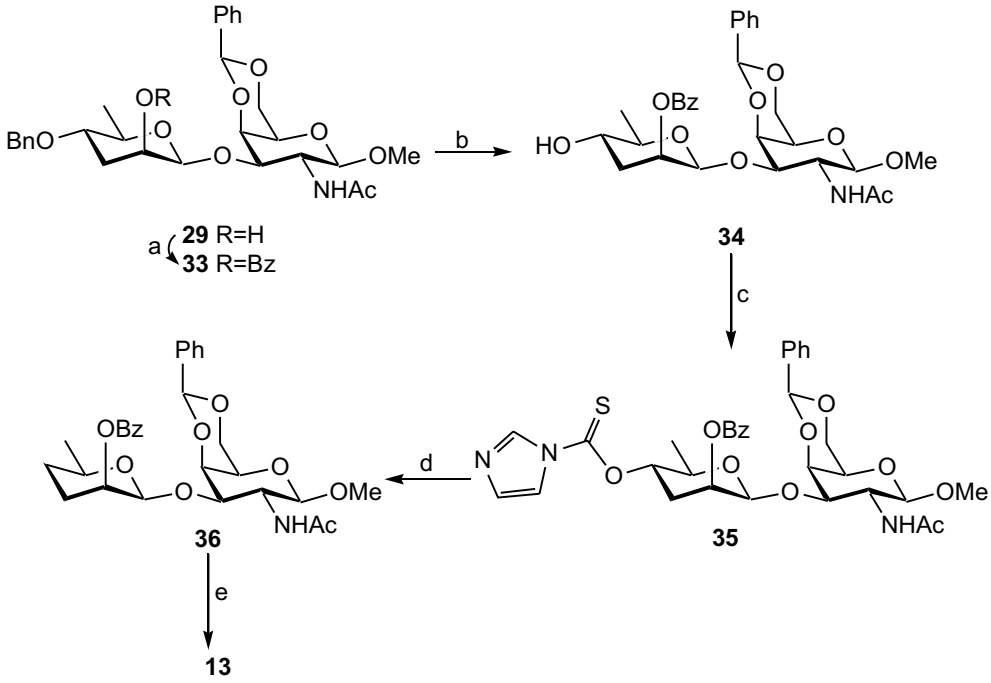

methylation, the corresponding 6-*O*-methyl ether derivative **10** was obtained in moderate yield (44%).

With compound **29** in hand, the 2′-hydroxyl group was methylated using sodium hydride (Scheme 3) and a controlled amount of methyl iodide as reagent, the methylated derivative **30** was obtained (37%). The poor yield reflected incomplete methylation which results from the conditions employed which are designed to avoid *N*-methylation. The benzyl and benzylidene were removed by hydrogenation to give the 2′-OMe disaccharide **12** (93% yield). To prepare the corresponding 2′-deoxgenated disaccharide **11**, **29** was transformed to **31** (98%) by reaction with 1,1′-thiocarbonyldiimidazole, and 2′-deoxygenation was realized after subjecting **31** to reaction with tributyltin hydride (→**32**, 95%) (40). After hydrogenation, the desired 2′-deoxy compound **11** was obtained in excellent yield (95%).

The 4′-deoxygenated disaccharide **13** was prepared from disaccharide **29** (Scheme 4). Benzoylation of **29** gave **33**

© 2002 NRC Canada

Scheme 5. (*a*) NH_4HCO_2–Pd/C–MeOH, reflux; (*b*) Bz_2O–Py–DMAP; (*c*) H_2–$Pd(OH)_2$/C–MeOH; (*d*) TsCl–Py; (*e*) LiBr–KI–DMF, 100°C; (*f*) *n*-Bu_3SnH–AIBN–toluene, reflux; (*g*) NaOMe–MeOH.

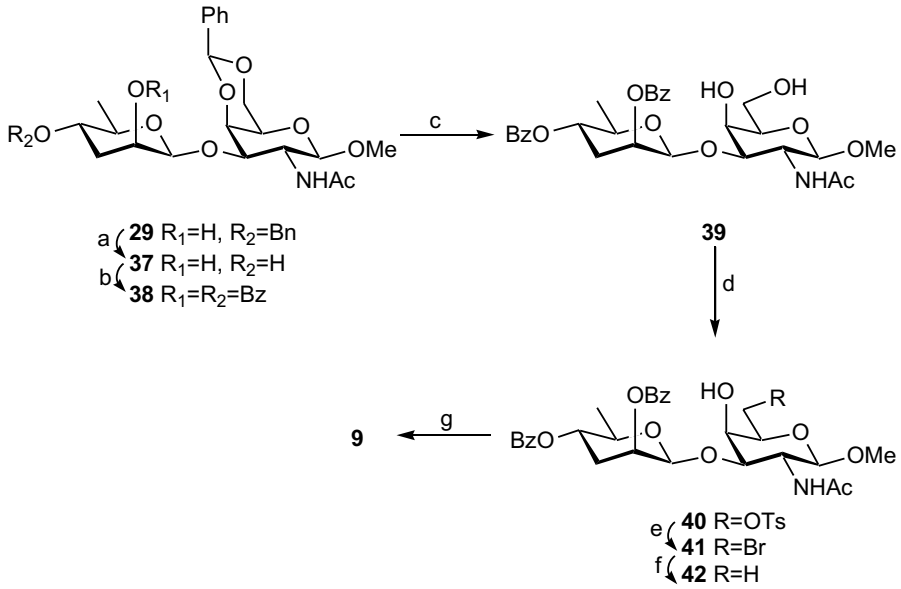

Scheme 6. (*a*) MeI–NaH–DMF; (*b*) 10% H_2SO_4 – THF, 65°C; (*c*) BzCl–Py–CH_2Cl_2; (*d*) Me_3SiSPh – TMSOTf – MS 4 Å – CH_2Cl_2; (*e*) NIS – TfOH – MS 4 Å – CH_2Cl_2; (*f*) MeONa–MeOH; (*g*) DMSO–Ac_2O; (*h*) L-selectride–THF; (*i*) H_2–$Pd(OH)_2$/C–MeOH.

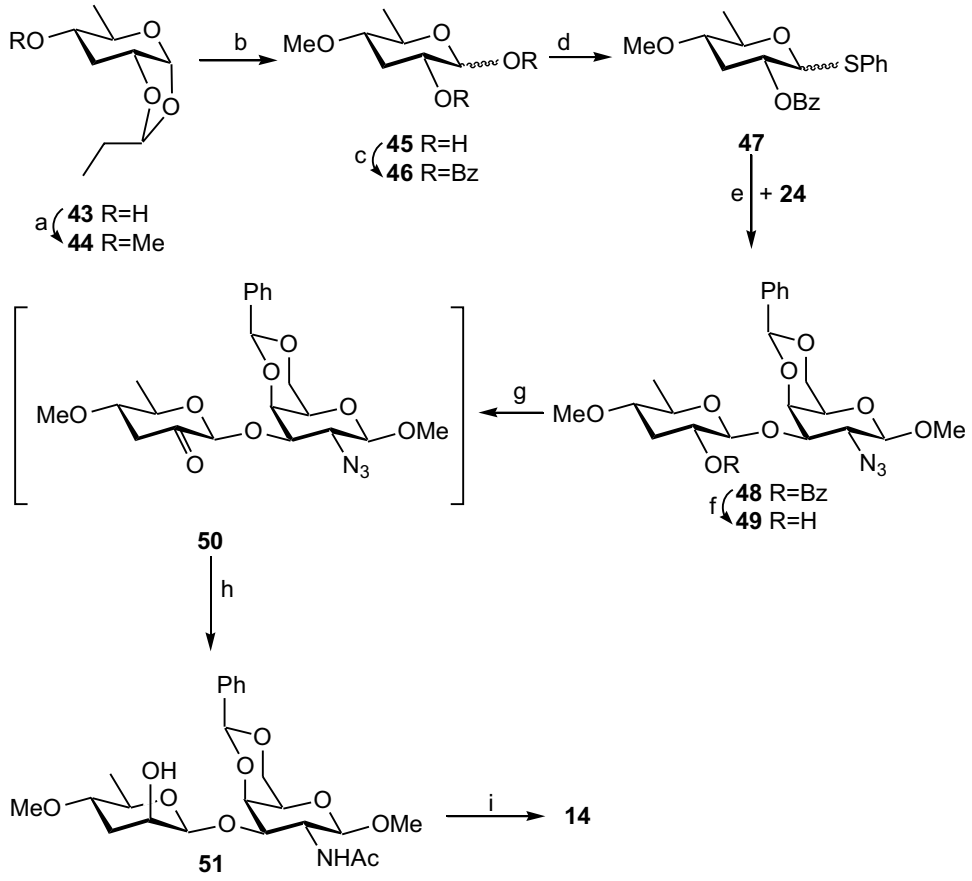

(87%), and the 4′-benzyl group was selectively removed by transfer hydrogenation in the presence of the benzylidene acetal using ammonium formate – Pd-C conditions (→**34**, 78%). The 4′-OH was deoxygenated via a similar sequence to that described for the synthesis of compound **32**, (→**35** (92%), →**36** (83%)), and the final disaccharide **13** was obtained after removing the protecting groups by Zemplen transesterification and hydrogenation (→**13**, 88%).

© 2002 NRC Canada

Scheme 7. (*a*) $(Bu_3Sn)_2O$–BzCl–toluene; (*b*) MeOTf–DTBMP–CH_2Cl_2, reflux; (*c*) NaOMe–MeOH; (*d*) *t*-$BuMe_2SiCl$–Py; (*e*) NIS – TfOH – MS 4 Å – CH_2Cl_2; (*f*) DMSO–Ac_2O; (*g*) (*i*) L-selectride–THF, (*ii*) Ac_2O–MeOH; (*h*) (*i*) H_2–$Pd(OH)_2$/C–MeOH, (*ii*) TBAF–THF.

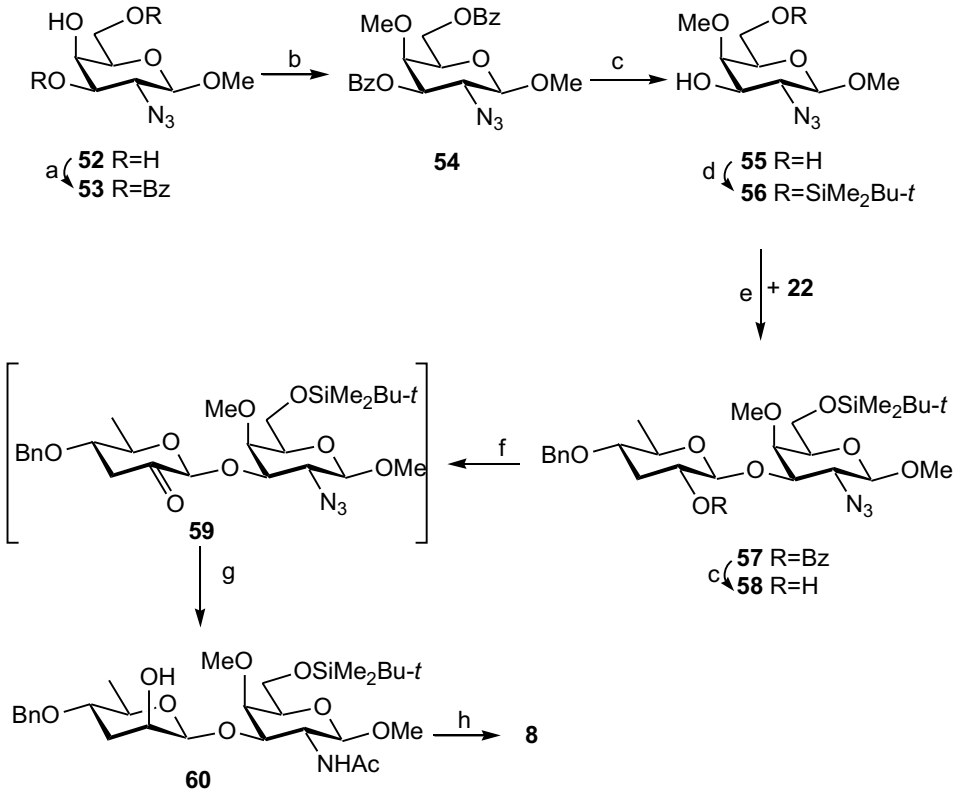

Scheme 8. (*a*) BzCl–Py–CH_2Cl_2; (*b*) $NaBH_3CN$ – HCl – MS 4 Å –THF; (*c*) Im_2CS–toluene, 90°C; (*d*) *n*-Bu_3SnH–AIBN–toluene, reflux; (*e*) MeONa–MeOH; (*f*) NIS – TfOH – MS 4 Å – CH_2Cl_2; (*g*) DMSO–Ac_2O; (*h*) L-selectride–THF; (*i*) Na–NH_3.

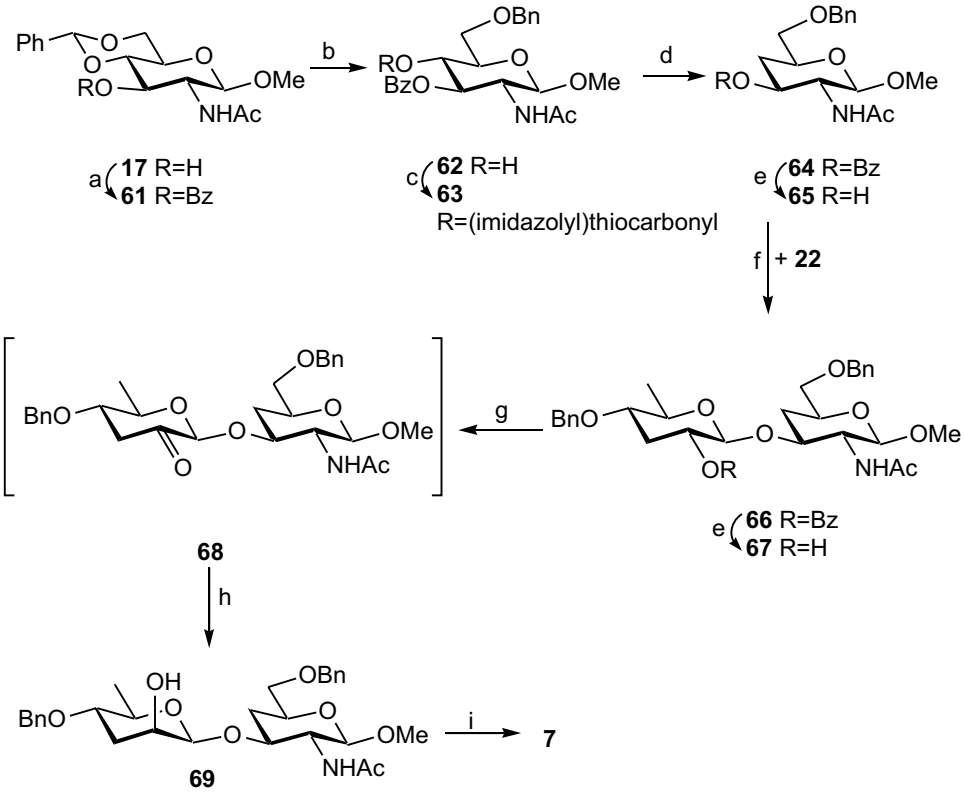

© 2002 NRC Canada

The synthesis of 6-deoxyGalNAc disaccharide **9** also started from compound **29** (Scheme 5). The benzyl ether was removed selectively in the presence of the benzylidene acetal in a manner similar to the conversion of **33** to **34** to give **37** (79%), together with **3** (11%) resulting from loss of the benzylidene acetal. The diol **37** was benzoylated (→**38**, 89%), and the acetal was removed under standard hydrogenation conditions using palladium hydroxide on charcoal as catalyst (→**39**, 89%). The 6-OH was reduced through a sequence of tosylation (→**40**), displacement by bromide to give **41**, and reduction using tributyltin hydride (→**42**). The intermediates **40**–**42** were not isolated, and after transesterification of the 2′,4′-dibenzoate **42**, the targeted compound **9** was obtained in moderate yield (49% from **39**).

Initially it was planned to obtain the 4′-OMe disaccharide **14** by methylation of intermediate **34**. However, when **34** was methylated using methyl triflate and 2,6-di-*tert*-butyl-4-methylpyridine, no methylated product was isolated. It was then decided to use a 4-*O*-methylated paratose donor **47** as starting material (Scheme 6). The paratose thioglycoside **47** was obtained in several transformation steps. Thus, starting from compound **43** (38), the 4-OH was methylated (→**44**, 92%), and the 1,2-propylidene acetal was hydrolyzed and the diol **45** benzoylated (→**46**, 96%). The anomeric benzoate was converted to the mixture of anomeric thioglycosides **47** (89%) using $PhSSiMe_3$–TMSOTf as reagents. Disaccharide **48** was obtained in good yield (78%) after coupling **47** with acceptor **24** using *N*-iodosuccinimide – triflic acid as promoter. After removing the 2′-benzoate (→**49**, 94%), the 4′-*O*-methylated disaccharide **10** was obtained by oxidation to the keto compound **50** followed by reduction and deprotection (→**51** (76%), →**14** (94%)).

To prepare the 4-*O*-monomethylated disaccharide **8**, we decided to use compound **56** as an acceptor (Scheme 7). Compound **56** has a methyl group preinstalled at the 4-position, and was prepared starting from 2-azido galactopyranosyl derivative **52** (39). Thus, by heating a solution of triol **52** with bis(tributyltin)oxide, the 3,6-positions were benzoylated to give **53** in very good yield (86%) and selectivity. The 4-OH was methylated (→**54**, 94%) using methyl triflate as reagent in the presence of the bulky base, 2,6-di-*tert*-butyl-4-methylpyridine. The benzoates were removed (→**55**, 97%) and the primary hydroxyl group was selectively silylated using *tert*-butyldimethylsily chloride as reagent to give the acceptor **56** (84%). Glycosylation of **56** with donor **22** afforded the disaccharide **57** in 71% yield. After removing the 2′-*O*-benzoate (→**58**, 98%), the 2′-equatorial hydroxyl group was inverted to the corresponding 2′-axial configuration by an oxidation–reduction sequence as describe above (→**60**, 76%), and the disaccharide **8** (88%) was obtained following deprotection.

The synthesis of 4-mono-deoxygenated disaccharide **7** (Scheme 8) started with glucosamine alcohol **17**. The 3-hydroxyl group was protected as a benzoate (→**61**, 96%), and the 4,6-*O*-benzylidene acetal was regioselectively opened to afford the alcohol **62** in excellent yield (95%). The 4-OH position was deoxygenated through a two-step Barton–McCombie deoxygenation reaction (40) as describe above (→**63** (94%), →**64** (88%)). After removing the 3-*O*-benzoate (→**65**, 94%), the acceptor **65** was glycosylated by donor **22** to produce the disaccharide **66** in moderate yield (54%).

Fig. 3. Representative inhibition curves obtained with the monoclonal antibody 9D4 and the following disaccharides: disaccharide **10** (6-*O*-methyl GalNAc congener) (●), disaccharide **4** (2-amino GalNAc congener) (■), native disaccharide **3** (▼), disaccharide **5** (2-hydroxy GalNAc congener) (▲). Microtiter plates were coated with [β-D-Tyv(1→3)β-D-GalNAc]$_8$-BSA glycoconjugate and diluted monoclonal antibody solutions containing increasing amounts of inhibitor were added to the plate. Bound antibody was detected by a species-specific antibody–horseradish peroxidase conjugate and percentage inhibitions are expressed relative to wells that contained no inhibitor. Each point is the average of three values and the standard deviation on each point was ±5% or better.

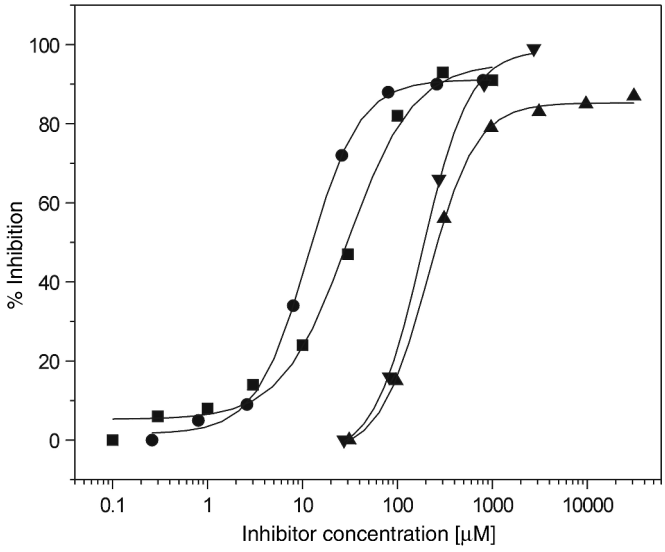

Compound **66** was debenzoylated to give the alcohol **67** (91%). Oxidation gave the keto derivative **68**, which was reduced to give **69.** The protecting groups were finally removed by Birch reduction to afford the pure 4-deoxy-disaccharide **7** (overall 23% yield from **67**).

We have described the synthesis of a comprehensive set of disaccharide congeners **4**–**14** (Fig. 2) related to the *T. spiralis* epitope β-D-Tyv*p*(1→3)β-D-GalNAc*p* (**3**). The congeners are modified at each position bearing a hydroxyl or acetamido group. The ability of these disaccharides to inhibit binding of the monoclonal antibodies 9D4 and 18H1 to a β-D-Tyv*p*(1→3)β-D-GalNAc*p* BSA glyconconjugate (16) was assayed in a solid-phase ELISA format. Briefly the disaccharide conjugate was coated on ELISA plates and incubated with antibody in the presence of increasing amounts of inhibitor. Bound antibody was detected by a goat anti-rat IgG antibody and percentage inhibition was calculated relative to wells that contained no inhibitor. The structure activity data was used to infer a topological map of the epitope surface for each antibody binding site. The quality of the inhibition data obtained in this work is illustrated in Fig. 3 and the inhibitory activities for compounds **1**–**14** with both monoclonal antibodies 9D4 and 18H1 are recorded in Tables 1–3.

In designing the set of congeners we followed the approach pioneered by Lemieux and co-workers (34) for detecting intermolecular hydrogen bonds present in a protein–oligosaccharide complex. The inhibitory power of mono-deoxy and mono-*O*-methyl congeners identifies hydroxyl

© 2002 NRC Canada

Table 2. Inhibitory activities of disaccharides **3**–**14** with the IgG MAb 9D4.

Compound	IC_{50} (μM)[a]	Relative inhibitory power[b]
3	178	100
4	30	588
5	220	90
6	–ve	0
7	199	89
8	–ve	0
9	239	75
10	10	1780
11	190	94
12	20	890
13	–ve	0
14	–ve	0

[a]Calculated from 50% inhibition data with an estimated accuracy of ~ ±5%.
[b]Inhibition potency of **3** set as 100.

Table 3. Inhibitory activities of disaccharides **3**–**14** with the IgG MAb 18H1.

Compound	IC_{50} (μM)[a]	Relative inhibitory power[b]
3	93	100
4	–ve	0
5	–ve	0
6	60	150
7	68	137
8	127	75
9	112	80
10	45	200
11	370	25
12	18	500
13	–ve	0
14	–ve	0

[a]Calculated from 50% inhibition data with an estimated accuracy of ~ ±5%.
[b]Inhibition potency of **3** set as 100.

groups that are buried and involved in key polar interactions with the protein, as well as those hydroxyl groups exposed to solvent water. Hydroxyl groups that are positioned around the periphery of the complex may also be identified from the relative inhibitory power of monodeoxy and mono-*O*-methyl congeners thus providing a detailed topology of the interacting surface. Inactive monodeoxy and mono-*O*-methyl congeners pinpoint hydroxyl groups that are buried and involved in key polar interactions. When these modifications are made to solvent exposed hydroxyl groups only minor changes are registered in their binding activity. However, when mono-*O*-methylation or monodeoxygenation replaces hydroxyl groups that lie at the periphery of the protein–oligosaccharide complex large swings in activity for either one or both of the derivatives can be observed. Frequently the changes may result in enhanced binding energy. In general, binding at the periphery is indicated when the deoxy congener is active but the mono-*O*-methyl compound is inactive (41). However, if a hydroxyl at the periphery is an acceptor of a hydrogen bond the *O*-methyl derivative may be even more active than the deoxy congener (42, 43).

At first appearance the recognition of the dideoxyhexose residue by both antibodies is similar. The C-4 hydroxyl group is buried in the binding site and makes essential polar contacts. The hydroxyl group at C-2 appears to make much weaker polar contacts perhaps via a hydrogen bond either from the protein or via a water molecule. Mono-*O*-methyl disaccharide **12** is five to eight times more active than **3** with each antibody, whereas, with the antibody 9D4, the deoxy compound is almost as active as the native disaccharide **3**, while with 18H1 the same compound is fourfold less active. In both cases this suggests that this hydroxyl group resides close to the periphery of the binding site. When interacting with 18H1 **12** may either accept a hydrogen bond or the methyl group can make favourable contacts with the protein, and (or) displace a water molecule.

It is immediately obvious that the two monoclonal antibodies recognize the GalNAc residue via completely different surfaces. The 2-acetamido group is of major importance for MAb 18H1, since disaccharides modified at C-2 (**4** and **5**) are inactive. The C-4 hydroxyl group is clearly not involved in protein contacts since the C-4 epimer **6** is more active than **3**, and the 4-deoxy and mono-*O*-methyl disaccharides **7** and **8** have activities close to that of **3**. The C-6 hydroxyl must reside close to the periphery of the binding site since the methyl ether **10** is twice as active as **3**.

The recognition of GalNAc by MAb 9D4 is quite distinct. The acetamido group is not important to binding, since Gal may substitute for GalNAc without impact, and in fact the free amino disaccharide **5** is almost six times more active than **3**. Steric changes at C-4 are prohibitive since the C-4 epimer **6** is inactive, as is the mono-*O*-methyl disaccharide **8**. However, the 4-deoxy disaccharide **7** is almost unchanged compared to **3.** The 6-deoxy disaccharide **9** is only slightly less active than **3**, while the methyl ether **10** is 18 times more active than **3**. This suggests that both C-4 and C-6 hydroxyl group reside at the edge of the binding site and the C-6 *O*-methyl group is able to make a productive interaction at the periphery of the binding site via van der Waal contacts or by replacing a water molecule.

These data (Table 3) may be integrated with the initial inhibition data for tetra, tri, and disaccharides **1**–**3** (Table 1) and lead to the conclusion that the poorly protective MAb 18H1 only interacts with the terminal disaccharide of the *T. spiralis N*-glycan chains. There are no antibody contacts with the proximal branching fucose residue, since the underside of the Tyv and GalNAc residues contact the binding site leaving Tyv O-2 at the periphery and the major polar contacts being O-4 (Tyv) and the 2-acetamido group of GalNAc. This is consistent with the noninvolvement of GalNAc 4-OH. The key polar groups and those at the periphery of the binding site are shown in the stereo plots as CPK plots and as a Connolly surface (44) (Fig. 4).

While the recognition of Tyv by MAb 9D4 initially appeared to be similar to that by 18H1, the most deeply buried surface of the Tyv likely extends around the opposite face involving the C-6 methyl group and ring oxygen atoms. For 9D4 the involvement of its binding site with the GalNAc residue is almost the exact opposite of the situation with 18H1, and must involve the top face of the GalNAc residue. Whereas, the acetamido group can be replaced by OH without significant loss of binding, both O-4 and O-6 are close to the periphery of the site, and since the fucose residue is adjacent to these groups and protrudes from this upper face,

© 2002 NRC Canada

Fig. 4. Stereo drawings of the epitopes recognized by antibodies 9D4 and 18H1. Functional groups shown in red make crucial hydrogen bonds with the binding sites. Groups shown in pink are involved in contacts at the periphery of the binding site. Groups shaded blue are also located at the periphery. (*a*) Space-filling model showing the epitope residues Tyv O-4 and O-2 and GalNAc O-4 that create the contact surface for the 9D4 epitope. (*b*) Connolly surface of the 9D4 epitope. (*c*) Space-filling model showing the epitope residues Tyv O-4 and O-2 and GalNAc acetamido groups that create the contact surface for the 18H1 epitope. (*d*) Connolly surface of the 18H1 epitope.

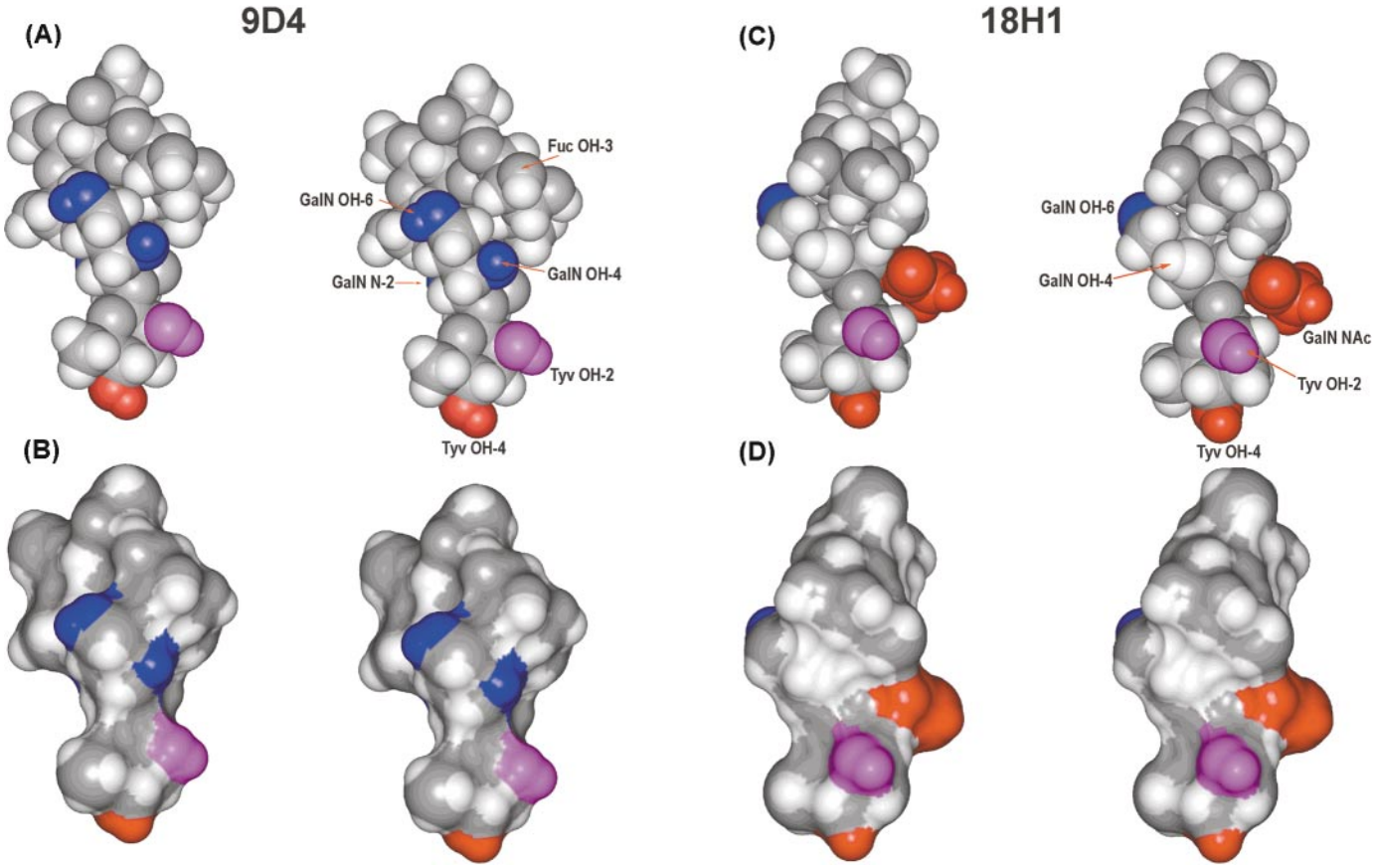

its involvement in binding together with a minor contribution from the GlcNAc residue are readily appreciated (Fig. 4, Tables 1 and 2).

Investigation of a number of antibody binding sites by functional group replacement studies has shown that a small number of hydroxyl groups, and where appropriate, acetamido groups provide from two to four key polar contacts. Without these complex formation does not occur. The binding of *T. spiralis N*-glycans to antibody 18H1 conforms to this pattern, where O-4 of tyvelose and the acetamido group of GalNAc are involved in crucial polar interactions and to a lesser extent O-2 of tyvelose. Monoclonal 9D4 is quite different and its recognition of the disaccharide involves only one key polar contact, which is again O-4 of tyvelose. The tyvelose residue is recognized from the opposite face, which would require its 6-deoxy group to be buried and involved in hydrophobic contacts. Involvement of GalNAc O-4 and O-6 at the periphery is consistent with this, as is the ability to modify the acetamido function without penalty. The complete recognition surface of the carbohydrate epitope for 9D4 must extend to include the GlcNAc and Fuc residues since both trisaccharide **2** and tetrasaccharide **1** are more active inhibitors than the disaccharide **3** (Table 1). One or both of these residues may provide additional polar contacts. At this stage we would infer that this is most likely to be O-2 or O-3 of fucose.

The superior protective ability of MAb 9D4 correlates with the higher affinity for its larger tetrasaccharide target epitope, which is about 20 times the affinity of the poorly protective MAb 18H1 for its smaller disaccharide target epitope (Table 1) (21, 24). Although the key recognition element in both cases is the terminal disaccharide, the surface of the oligosaccharide epitope that is buried determines the degree to which the buried surface area can be extended. For MAb 9D4 the inclusion of the fucose residue can be contrasted with the restriction of MAb 18H1 to contacts that do not extend beyond the terminal disaccharide and involve polar contacts with O-4 and O-2 (Tyv) and NHAc (GalNAc) and possible non-polar interactions with this group. It appears that the additional specificity element and larger surface area of interaction lead to tighter binding and that this is essential for full bioactivity.

Experimental

General methods

Optical rotations were measured with a PerkinElmer 241 polarimeter for samples in a 10-cm cell at 22 ± 2°C and $[\alpha]_D$

© 2002 NRC Canada

values are given in units of 10^{-1} deg cm^2 g^{-1}. Analytical TLC was performed on plates of Silica Gel 60-F_{254} (Merck, Darmstadt) with detection by quenching of fluorescence and (or) by charring with 5% sulfuric acid in water. All commercial reagents were used as supplied and chromatography solvents were distilled prior to use. Column chromatography was performed on Silica Gel 60 (Silicycle, Quebec, Canada). ^{1}H NMR spectra were recorded on Varian Unity 300, 500, or 600 MHz. The first-order proton chemical shifts δ_H are referenced to either residual $CHCl_3$ (δ_H 7.24, $CDCl_3$) or residual CD_2HOD (δ_H 3.30, CD_3OD), or internal acetone (δ_H 2.225, D_2O). First order coupling constants are given in Hz. HMQC-NMR spectra were recorded on Varian spectrometers operating at 300, 500, or 600 MHz. The ^{13}C chemical shifts (δ_C) are referenced to internal $CDCl_3$ (δ_C 77.00, $CDCl_3$). Organic solutions were dried prior to concentration under vacuum at <40°C (bath). Final compounds were purified by reverse-phase chromatography performed on a Waters 600 HPLC system, using a Beckman semipreparative C-18 column (10 × 250 mm, 5 μ), and the products were detected with a Waters 2487 UV detector or a Waters 2410 refractive index monitor. Microanalyses and electrospray mass spectra were performed by the analytical services of this department. Reaction yields were not optimized.

Enzyme immunoassay

Inhibition assays were performed in triplicate in 96 well microtiter plates with the previously described rat monoclonal antibodies 18H1 (IgG_1) and 9D4 (IgG_{2c}) (3). Microtiter plates were incubated for 18 h at 4°C with a solution of [β-D-Tyv(1→3)β-D-GalNAc]$_8$-BSA glycoconjugate (100 μL/well) dissolved in 0.01 M phosphate-buffered saline solution at a concentration of 1 μg mL^{-1} (16). The plate was washed with PBST (5×) and blocked for 1 h at room temperature by incubation with 2% BSA in PBS (100 μL). After the plate had been washed with PBST (3×), antibody solution with or without inhibitor was added (100 μL) to the plate incubated for 18 h at room temperature. Monoclonal antibody 18H1 was used from ascites fluid at a final dilution of 5×10^{-5} and 9D4 at a dilution of 1.5×10^{-3}. The plate was washed with PBST (5×), and goat anti-rat IgG antibody conjugated to horse radish peroxidase (Kirkegaard and Perry Lab, Mandel, Guelph, ON) solution (100 μL) diluted (1:5000) in PBS was incubated for 1 h at room temperature. The plate was washed with PBST (5×), 3,3′,5,5′-tetramethylbenzidine (TMB, 100 μL) was added, and after 2 min the colour reaction was stopped by the addition of 1 M phosphoric acid (100 μL). Absorbance was read at 450 nm and percent inhibition was calculated using wells containing no inhibitor as the reference point. Triplicate samples typically exhibited OD values with a standard deviation of ±5% or better. Wells with OD values outside this error range were discarded and eliminated from the data analysis. Inhibition curves were drawn using the software package Origin 5.0 (OriginLab, Northampton, MA), and the IC_{50} value was computed by the software.

Methyl 2-*O*-benzyl-4,6-*O*-benzylidene-3-*O*-(2,4-di-*O*-benzyl-3,6-dideoxy-β-D-*arabino*-hexopyranosyl)-β-D-galactopyranoside (18)

A mixture of acceptor **16** (35) (105 mg, 0.28 mmol), silver zeolite (300 mg), and 4 Å molecular sieves (300 mg) in anhyd CH_2Cl_2 (3 mL) was stirred for 30 min at room temperature, and cooled to −40°C. A solution of tyvelosyl chloride **15** (125 mg, 0.36 mmol, prepared by reacting the corresponding hemi-acetal with oxalyl chloride (22)) in anhyd CH_2Cl_2 (2.5 mL) was added dropwise and the mixture was slowly warmed to room temperature and stirred for 24 h. The mixture was filtered off, and the filtrate was concentrated. The disaccharide **18** was obtained by chromatography on silica gel using 15% EtOAc – toluene as eluent (29 mg, 15%), $[\alpha]_D$ + 27.3 (*c* 2.1, $CHCl_3$). ^{1}H NMR ($CDCl_3$) δ: 7.51–7.58 (m, 2H, Ar), 7.10–7.36 (m, 18H, Ar), 5.56 (s, 1H, PhCH), 4.83 (d, 1H, *J* = 11.2 Hz, Bn), 4.77 (d, 1H, *J* = 13.2 Hz, Bn), 4.75 ("s", 1H, H-1′), 4.68 (d, 1H, *J* = 13.2 Hz, Bn), 4.55 (d, 1H, *J* = 11.5 Hz, Bn), 4.27–4.37 (m, 4H, H-1, H-6a, H-4, Bn), 4.06 (dd, 1H, *J* = 1.6, 12.3 Hz, H-6b), 3.76–3.84 (m, 2H, H-2, H-3), 3.57 (s, 3H, OMe), 3.28–3.52 (m, 4H, H-5, H2′, H-4′, H-5′), 2.23 (d′t′, 1H, *J* = 4.0, 13.4 Hz, H-3e′), 1.31 (d, 3H, *J* = 6.1 Hz, H-6′), 1.18 (m, 1H, H-3a′). Anal. calcd. for $C_{41}H_{46}O_9$: C 72.12, H 6.79; found: C 72.19, H 6.49.

Methyl 3-*O*-(3,6-dideoxy-β-D-*arabino*-hexopyranosyl)-β-D-galactopyranoside (5)

A mixture of disaccharide **18** (26 mg, 0.038 mmol) and 10% $Pd(OH)_2$ on charcoal (20 mg) in MeOH (10 mL) was hydrogenated overnight. The catalyst was filtered and the filtrate was concentrated, and the residue was purified by reverse phase HPLC using H_2O–MeOH (linear gradient 0 → 20%) as eluent to afford **5** (11 mg, 89%), $[\alpha]_D$ –21.2 (*c* 0.6, MeOH). ^{1}H NMR (CD_3OD) δ: 4.76 (d, 1H, *J* = 1.1 Hz, H-1′), 4.16 (m, 1H, H-1, high order), 4.03 (m, 1H, H-4), 3.96 (m, 1H, H-2′), 3.69–3.79 (m 2H, H-6a, H-6b), 3.59–3.61 (m, 2H, H-2, H-3), 3.45–3.57 (m, 6H, H-5, H-4′, OMe, H-4), 3.30 (dq, 1H, *J* = 6.1, 9.3 Hz, H-5′), 2.14 (ddd, 1H, *J* = 3.3, 4.6, 13.6 Hz, H-3e′), 1.55 (ddd, 1H, *J* = 2.9, 11.4, 13.6 Hz, H-3a′), 1.27 (d, 3H, *J* = 6.1 Hz, H-6′). HR-ES-MS *m/e* calcd. for $C_{13}H_{24}O_9$ (MNa^+): 347.13180; found: 347.131922.

Methyl 2-acetamido-3-*O*-(2,4-di-*O*-benzyl-3,6-dideoxy-β-D-*arabino*-hexopyranosyl)-4,6-*O*-benzylidene-2-deoxy-β-D-glucopyranoside (19)

A mixture of acceptor **17** (45) (88 mg, 0.27 mmol), silver zeolite (300 mg), and 4 Å molecular sieves (400 mg) in anhyd CH_2Cl_2 (3 mL) was stirred for 30 min at room temperature, and cooled to −40°C. A solution of tyvelosyl chloride **15** (173 mg, 0.50 mmol, prepared by reacting the corresponding hemi-acetal with oxalyl chloride (22)) in anhyd CH_2Cl_2 (2.5 mL) was added dropwise and the mixture was slowly warmed to room temperature and stirred for 24 h. The mixture was filtered off, and the filtrate was concentrated. The disaccharide **19** was obtained by chromatography on silica gel using 35% EtOAc – toluene as eluent (44 mg, 26%), $[\alpha]_D$ –0.8 (*c* 1.7, $CHCl_3$). ^{1}H NMR ($CDCl_3$) δ: 7.47–7.52 (m, 2H, Ar), 7.23–7.37 (m, 13H, Ar), 5.52 (s, 1H, PhCH), 5.45 (d, 1H, *J* = 7.1Hz, NH), 4.86 (d, 1H, *J* = 8.2 Hz, H-1), 4.70 (d, 1H, *J* = 1.2 Hz, H-1′), 4.64 (d, 1H, *J* = 12.5 Hz, Bn), 4.58 (d, 1H, *J* = 12.5 Hz, Bn), 4.38–4.50 (m, 3H, 2 × Bn, H-3), 4.32 (dd, 1H, *J* = 4.9, 10.4 Hz, H-6a), 3.76 (t, 1H, *J* = 10.2 Hz, H-4), 3.65 (t, 1H, *J* = 9.2 Hz, H-6b), 3.59 (m, 1H, H-2′), 3.47 (s, 3H, OMe), 3.36–3.53 (m, 3H, H-5, H-4′, H-5′), 3.13 (m, 1H, H-2), 2.27 (ddd, 1H,

© 2002 NRC Canada

J = 4.5, 4.5, 13.5 Hz, H-3e′), 1.74 (s, 3H, Ac), 1.43 (br m, 1H, H-3a′), 1.20 (d, 3H, *J* = 5.7 Hz, H-6′). Anal. calcd. for $C_{36}H_{43}O_9N$: C 68.23, H 6.84, N 2.21; found: C 68.01, H 6.81, N 2.19.

Methyl 2-acetamido-3-*O*-(3,6-dideoxy-β-D-*arabino*-hexopyranosyl)-2-deoxy-β-D-glucopyranoside (6)

Disaccharide **19** (40 mg, 0.063 mmol) was deprotected in a similar fashion as compound **5** and compound **6** (22.4 mg, 97%) was purified by reverse-phase HPLC using H_2O–MeOH (linear gradient $0 \rightarrow 20\%$) as eluent. $[\alpha]_D$ –29.7 (*c* 0.7, MeOH). ^{1}H NMR (D_2O) δ: 4.63 (d, 1H, *J* = 0.9 Hz, H-1′), 4.50 (d, 1H, *J* = 8.6 Hz, H-1), 3.94 (dd, 1H, *J* = 2.3, 13.0 Hz, H-6a), 3.90 (m, 1H, H-2′), 3.80 (dd, 1H, *J* = 6.8, 10.4 Hz, H-2), 3.77 (dd, 1H, *J* = 5.5, 13.0 Hz, H-6b), 3.70 (dd, 1H, *J* = 9.0, 10.8 Hz, H-3), 3.57 (m, 1H, H-4′), 3.53 ("t", 1H, 10.8 Hz, H-4), 3.52 (s, 3H, OMe), 3.46–3.52 (m, 2H, H-5, H-5′), 2.19 (ddd, 1H, *J* = 3.7, 4.6, 13.9 Hz, H-3e′), 2.04 (s, 3H, Ac), 1.68 (ddd, 1H, *J* = 3.1, 11.5, 14.3 Hz, H-3a′), 1.29 (d, 3H, *J* = 6.2 Hz, H-6′). HR-ES-MS *m*/*e* calcd. for $C_{15}H_{27}O_9N$ (MNa^+): 388.15835; found: 388.158837.

Phenyl 4-*O*-benzyl-3,6-dideoxy-1-thio-α,β-D-ribo-hexopyranoside (21)

Thioglycoside **20** (38) (α/β: 37:73, 3.50 g, 9.40 mmol) was transesterified in anhyd MeOH with a catalytic amount of NaOMe. After 3 h, the mixture was neutralized with Amberlite IR-120 (H^+), and evaporated to dryness to give alcohol **21** (α/β: 37:73, 3.10 g, quantitative). ^{1}H NMR ($CDCl_3$) for β-anomer δ: 7.25–7.53 (m, 10H, Ar), 4.61 (d, 1H, *J* = 11.7 Hz, Bn), 4.46 (d, 1H, *J* = 11.7 Hz, Bn), 4.45 (d, 1H, *J* = 9.5 Hz, H-1), 3.40–3.49 (m, 2H, H-2, H-5), 3.15 (ddd, 1H, *J* = 4.4, 8.8,10.8 Hz, H-4), 2.63 (d′t′, 1H, *J* = 4.6, 12.3 Hz, H-3e), 1.49 (d′t′, 1H, *J* = 11.4, 11.4 Hz, H-3a), 1.34 (d, 1H, *J* = 6.3 Hz, H-6); α-anomer δ: 7.25–7.51 (m, 10H, Ar), 5.40 (d, 1H, *J* = 4.6 Hz, H-1), 4.64 (d, 1H, *J* = 11.5 Hz, Bn), 4.50 (d, 1H, *J* = 11.5 Hz, Bn), 4.12 (dq, 1H, *J* = 6.1, 9.2 Hz, H-5), 3.93 (d′t′, 1H, *J* = 4.6, 9.0, 11.5 Hz, H-2), 3.16 (m, 1H, H-4), 2.40 (dd′t′, 1H, *J* = 0.7, 4.2, 12.3 Hz, H-3e), 1.57 (d′t′, 1H, 11.7, 11.7 Hz, H-3a), 1.30 (d, 3H, *J* = 6.1 Hz, H-6). Anal. calcd. for $C_{19}H_{22}O_3S$: C 69.06, H 6.71; found: C 68.73, H 6.77.

Phenyl 2-*O*-benzoyl-4-*O*-benzyl-3,6-dideoxy-1-thio-α,β-D-ribo-hexopyranoside (22)

Benzoyl chloride (2.4 mL, 20.5 mmol) was added dropwise to an ice-cold solution of alcohol **21** (2.80 g, 8.47 mmol) in a mixture of anhyd CH_2Cl_2 (60 mL) and anhydrous pyridine (30 mL), and the mixture was stirred for 3 h. Methanol (2 mL) was added to quench the reaction, and the mixture was concentrated to dryness. The residue was dissolved in EtOAc (150 mL), and the organic solution was washed with 2 M HCl (1 × 50 mL), sat. $NaHCO_3$ (1 × 50 mL), and saturated brine (1 × 50mL), dried and evaporated. Chromatography on silica gel using 5% EtOAc – hexane as eluent gave the donor **22** as an inseparable mixture of anomers (α/β: 37:73, 3.39 g, 92% yield). ^{1}H NMR ($CDCl_3$) for β-anomer δ: 8.05 (m, 2 H, Bz), 7.57 (m, 1H, Bz), 7.42–7.49 (m, 4H, Ar), 7.20–7.37 (m, 8H, Ar), 4.91 (ddd, 1H, *J* = 4.9, 9.9, 10.9 Hz, H-2), 4.82 (d, 1H, *J* = 9.9 Hz, H-1), 4.62 (d, 1H, *J* = 11.5 Hz, Bn), 4.46 (d, 1H, *J* = 11.5 Hz, Bn), 3.52 (dq, 1H, *J* = 6.1, 9.0 Hz, H-5), 3.27 (ddd, 1H, *J* = 4.5, 9.0, 10.9 Hz, H-4), 2.84 (d′t′, 1H, *J* = 4.6, 11.9 Hz, H-3e), 1.66 (d′t′, 1H, *J* = 11.1, 11.1 Hz, H-3a), 1.39 (d, 1H, *J* = 6.1 Hz, H-6); α-anomer δ: 8.08 (m, 1H, Bz), 7.57 (m, 1H, Bz), 7.42–7.49 (m, 4H, Ar), 7.20–7.37 (m, 8H, Ar), 5.76 (d, 1H, *J* = 5.0 Hz, H-1), 5.29 (d′t′, 1H, *J* = 5.1, 10.1 Hz, H-2), 4.68 (d, 1H, *J* = 11.6 Hz, Bn), 4.51 (d, 1H, *J* = 11.6 Hz, Bn), 4.28 (dq, 1H, *J* = 6.1, 9.2 Hz, H-5), 3.30 (ddd, 1H, *J* = 4.6, 7.1, 11.0 Hz, H-4), 2.54 (dd′t′, 1H, *J* = 1.2, 4.6, 11.8 Hz, H-3e), 2.00 (d′t′, 1H, 12.0, 12.0 Hz, H-3a), 1.29 (d, 3H, *J* = 6.2 Hz, H-6). Anal. calcd. for $C_{26}H_{26}O_4S$: C 71.86, H 6.03; found: C 71.95, H 6.16.

Phenyl 4-*O*-benzyl-3,6-dideoxy-2-*O*-pivaloyl-1-thio-α,β-D-ribo-hexopyranoside (23)

The alcohol **21** (80 mg, 0.24 mmol) was reacted with pivaloyl chloride (89.4 μL, 0.73 mmol) in a similar fashion to afford the pivaloyl donor **23** (α/β: 37:73, 92 mg, 92%). ^{1}H NMR ($CDCl_3$) for β-anomer δ: 7.21–7.48 (m, 10H, Ar), 4.64–4.73 (m, 2H, H-1, H-2), 4.61 (d, 1H, *J* = 11.4 Hz, Bn), 4.43 (d, 1H, *J* = 11.4 Hz, Bn), 3.44 (dq, 1H, *J* = 6.1, 9.0 Hz, H-5), 3.20 (ddd, 1H, *J* = 4.5, 9.1, 10.9 Hz, H-4), 2.65 (d′t′, 1H, *J* = 4.5, 12.1 Hz, H-3e), 1.50 (m, 1H, H-3a), 1.34 (d, 1H, *J* = 6.1 Hz, H-6), 1.23 (s, 9H, Piv); α-anomer δ: 7.21–7.48 (m, 10H, Ar), 5.65 (d, 1H, *J* = 5.2 Hz, H-1), 4.96 (d′t′, 1H, *J* = 5.1, 10.1 Hz, H-2), 4.67 (d, 1H, *J* = 11.5 Hz, Bn), 4.48 (d, 1H, *J* = 11.5 Hz, Bn), 4.22 (dq, 1H, *J* = 6.1, 9.2 Hz, H-5), 3.23 (m, 1H, m, H-4), 2.36 (dd′t′, 1H, *J* = 1.2, 4.6, 12.0 Hz, H-3e), 1.84 (d′t′, 1H, *J* = 12.1, 12.1 Hz, H-3a), 1.26 (d, 3H, *J* = 6.2 Hz, H-6), 1.25 (s, 9H, Piv). Anal. calcd. for $C_{24}H_{30}O_4S$: C 69.53, H 7.29; found: C 69.33, H 7.52.

Methyl 2-azido-3-*O*-(2-*O*-benzoyl-4-*O*-benzyl-3,6-dideoxy-β-D-ribo-hexopyranosyl)-4,6-*O*-benzylidene-2-deoxy-β-D-galactopyranoside (25)

A mixture of donor **22** (α/β: 37:73, 807 mg, 1.86 mmol), acceptor **24** (39) (519 mg, 1.70 mmol), and 4 Å molecular sieves (1.5 g) in anhyd CH_2Cl_2 (16 mL) was cooled to –60°C, and NIS (796 mg, 3.70 mmol) was added. After stirring for 1 h, TfOH (31 μL) was added dropwise, the reaction was continued for 3 h and warmed to –30°C. Et_3N (1.0 mL) was added to quench the reaction. The insoluble material was filtered off and washed with CH_2Cl_2. The organic solution was washed with a 1:1 mixture of aq $Na_2S_2O_3$ (10%) and $NaHCO_3$ (sat.) (1 × 50 mL), dried and concentrated. Disaccharide **25** was obtained by chromatography on silica gel using 5% EtOAc – toluene as eluent (891 mg, 83% yield), $[\alpha]_D$ –14.9 (*c* 0.8, $CHCl_3$). ^{1}H NMR ($CDCl_3$) δ: 8.08 (m, 2H, Bz), 7.56 (m, 1H, Bz), 7.20–7.51 (m, 12H, Ar), 5.52 (s, 1H, PhCH), 4.87–4.95 (m, 2H, H-1′, H-2′), 4.63 (d, 1H, *J* = 11.4 Hz, Bn), 4.45 (d, 1H, *J* = 11.4 Hz, Bn), 4.31 (dd, 1H, *J* = 1.5, 12.4 Hz, H-6a), 4.21–4.25 (m, 2H, H-1, H-4), 3.78 (dd, 1H, *J* = 8.0, 10.6 Hz, H-2), 3.50–3.59 (m, 5H, OMe, H-3, H-5′), 3.40 (m, 1H, H-5), 3.30 (ddd, 1H, *J* = 4.5, 9.1, 10.9 Hz, H-4′), 2.85 (d′t′, 1H, *J* = 4.5, 12.1 Hz, H-3e′), 1.59 (d′t′, 1H, *J* = 11.1, 11.1 Hz, H-3a′), 1.34 (d, 3H, *J* = 6.1 Hz, H-6′). Anal. calcd. for $C_{34}H_{37}O_9N_3$: C 64.65, H 5.90, N 6.65; found: C 64.47, H 5.61, N 6.29.

Methyl 2-azido-3-*O*-(4-*O*-benzyl-3,6-dideoxy-β-D-ribo-hexopyranosyl)-4,6-*O*-benzylidene-2-deoxy-β-D-galactopyranoside (26)

Disaccharide **25** (550 mg, 0.811 mmol) was dissolved in anhyd MeOH (5 mL), and a solution of NaOMe in MeOH

© 2002 NRC Canada

(100 μL) was added. After 2 h, the solution was neutralized with Amberlite IR-120 (H^+) resin and filtered. The filtrate was concentrated and the disaccharide **26** was obtained by chromatography on silica gel using 20% EtOAc–toluene as eluent (432 mg, 94% yield), $[\alpha]_D$ +39.0 (*c* 0.5, $CHCl_3$). ^1H NMR ($CDCl_3$) δ: 7.53 (m, 2H, Ph), 7.26–7.38 (m, 8H, Ar), 5.53 (s, 1H, PhCH), 4.62 (d, 1H, *J* = 11.6 Hz, Bn), 4.45 (d, 1H, *J* = 11.6 Hz, Bn), 4.44 (d, 1H, *J* = 7.3 Hz, H-1′), 4.32 (dd, 1H, *J* = 1.6, 12.4 Hz, H-6a), 4.25 (dd, 1H, *J* = 0.5, 3.6 Hz, H-4), 4.22 (d, 1H, *J* = 8.0 Hz, H-1), 4.05 (dd, 1H, *J* = 1.7, 12.4 Hz, H-6b), 3.86 (dd, 1H, *J* = 8.0, 10.6 Hz, H-2), 3.58 (s, 2H, OMe), 3.42–2.56 (m, 3H, H-3, H-2′, H-5′), 3.40 (m, 1H, H-5), 3.30 (ddd, 1H, *J* = 4.4, 8.8, 10.9 Hz, H-4′), 2.50 (d′t′, 1H, *J* = 4.7, 12.3 Hz, H-3e′), 1.44 (d′t′, 1H, *J* = 11.7, 11.7 Hz, H-3a′), 1.29 (d, 3H, *J* = 6.2 Hz, H-6′). Anal. calcd. for $C_{27}H_{33}O_8N_3$: C 61.64, H 6.30, N 7.96; found: C 61.88, H 6.34, N 7.88.

Methyl 2-amino-3-*O*-(4-*O*-benzyl-3,6-dideoxy-β-D-*arabino*-hexopyranosyl)-4,6-*O*-benzylidene-2-deoxy-β-D-galactopyranoside (28)

The alcohol **26** (289 mg, 0.548 mmol) was dissolved in a mixture of anhyd DMSO (4 mL) and Ac_2O (2 mL) at 0°C. The reaction was left at ambient temperature overnight. After removing the solvents under reduced pressure, the mixture was filtered through a thin bed of silica gel using 40% EtOAc–hexane as eluent to give the intermediate ketone **27** (235 mg, 82% yield) which was divided in two parts for the preparation of both compound **28** and **29**.

A portion of **27** (40 mg, 0.076 mmol) was dissolved in anhyd THF (3 mL) at 0°C, a solution of L-selectride in THF (1.0 M, 300 μL, 0.3 mmol) was added dropwise and the reaction was continued for 1 h. Water (1 mL) was added and the reaction mixture was concentrated. The syrupy mixture was dissolved in CH_2Cl_2 (50 mL), washed with a 10% aqueous solution of $Na_2S_2O_3$ (20 mL) and saturated brine (20 mL), dried and concentrated. The mixture was purified by chromatography on silica gel using 5% MeOH–CH_2Cl_2 as eluent to afford the amine **28** (35 mg, 92% yield), $[\alpha]_D$ +40.2 (*c* 1.5, $CHCl_3$). ^1H NMR ($CDCl_3$) δ: 7.49 (m, 2H, Ar), 7.22–7.36 (m, 8H, Ar), 5.53 (s, 1H, PhCH), 4.76 (d, 1H, *J* = 1.0 Hz, H-1′), 4.59 (d, 1H, *J* = 11.5 Hz, Bn), 4.44 (d, 1H, *J* = 11.5 Hz, Bn), 4.31 (dd, 1H, *J* = 1.4, 12.4 Hz, H-6a), 4.25 ("d", 1H, *J* = 3.1 Hz, H-4), 4.12 (d, 1H, *J* = 7.8 Hz, H-1), 4.05 (dd, 1H, *J* = 1.7, 12.4 Hz, H-6b), 3.94 (m, 1H, H-2′), 3.65 (dd, 1H, *J* = 3.9, 10.5 Hz, H-3), 3.53 (s, 3H, OMe), 3.48 (m, 2H, H-4′ +H-5′), 3.41 (m, 1H, H-5), 3.26 (dd, 1H, *J* = 7.9, 10.4 Hz, H-2), 2.43 (d′t′, 1H, *J* = 3.9, 13.7 Hz, H-3e′), 1.52 (m, 1H, H-3a′), 1.32 (d, 3H, *J* = 5.7 Hz, H-6′). HR-ES-MS *m*/*e* calcd. for $C_{27}H_{35}O_8N$ (MH^+): 502.24409; found: 502.244418.

Methyl 2-amino-3-*O*-(3,6-dideoxy-β-D-arabino-hexopyranosyl)-2-deoxy-β-D-galactopyranoside (4)

With the help of a dry ice – acetone condenser, liquid ammonia (25 mL) was collected in a flask containing the amine **28** (35 mg, 0.07 mmol). A small piece of sodium (100 mg) was added, and reaction was continued for 4 h. During this time, the reaction mixture remained dark blue. The condenser was removed and MeOH (0.5 mL) was added. The colour of the reaction mixture turned white and the ammonia was allowed to evaporate. After the evaporation of NH_3, the residue was purified by reverse-phase chromatography using a gradient of H_2O–MeOH (0 → 30%) as eluent to yield compound **4** (20.5 mg, 90% yield), $[\alpha]_D$ –7.1 (*c* 0.2, MeOH). ^1H NMR (D_2O) δ: 4.84 (d, 1H, *J* = 0.7 Hz, H-1′), 4.60 (d, 1H, *J* = 8.6 Hz, H-1), 4.28 ("d", 1H, *J* = 2.9 Hz, H-4), 4.10 (m, 1H, H-2′), 4.03 (dd, 1H, *J* = 2.9, 10.8 Hz, H-3), 3.84 (dd, 1H, *J* = 7.9, 11.7 Hz, H-6a), 3.78 (dd, 1H, *J* = 4.2, 11.7 Hz, H-6b), 3.76 (m, 1H, H-5), 3.61 (s, 3H, OMe), 3.58 (ddd, 1H, *J* = 4.8, 9.34, 11.5 Hz, H-4′), 3.48 (dq, 1H, *J* = 6.0, 9.3 Hz, H-5′), 3.32 (dd, 1H, *J* = 8.6, 10.6 Hz, H-2), 2.20 (ddd, 1H, *J* = 3.5, 4.6, 13.9 Hz, H-3e′), 1.69 (ddd, 1H, *J* = 2.9, 11.5, 14.1 Hz, H-3e′), 1.28 (d, 3H, *J* = 6.1 Hz, H-6′). HR-ES-MS *m*/*e* calcd. for $C_{13}H_{25}O_8N$ (MNa^+): 346.14779; found: 346.148284.

Methyl 2-acetamido-3-*O*-(4-*O*-benzyl-3,6-dideoxy-β-D-*arabino*-hexopyranosyl)-4,6-*O*-benzylidene-2-deoxy-β-D-galactopyranoside (29)

The intermediate ketone **27** (106 mg, 0.2 mmol) was dissolved in anhyd THF (3 mL) at 0°C, a solution of L-selectride in THF (1.0 M, 1.5 mL, 1.5 mmol) was added dropwise, and the reaction was continued at 0°C for 1 h. Water (0.3 mL) was added, after 10 min, Ac_2O (2 mL) was added dropwise, the reaction was continued for 30 min. After concentration, the mixture was dissolved in CH_2Cl_2 (100 mL), the organic solution was washed with a 10% aqueous solution of $Na_2S_2O_3$ (1 × 50 mL) and saturated brine (50 mL), dried, and evaporated. The mixture was purified by chromatography on silica gel using 2.5% MeOH–CH_2Cl_2 as eluent to afford compound **29** (102 mg, 93% yield), $[\alpha]_D$ +56.5 (*c* 0.6, $CHCl_3$). ^1H NMR ($CDCl_3$) δ: 7.46–7.52 (m, 2H, Ar), 7.22–7.36 (m, 8H, Ar), 5.95 (d, 1H, *J* = 7.0 Hz, NH), 5.52 (s, 1H, PhCH), 5.02 (d, 1H, *J* = 8.2 Hz, H-1), 4.73 (dd, 1H, *J* = 3.4, 11.1 Hz, H-3), 4.57 (d, 1H, *J* ~ 1 Hz, H-1′), 4.56 (d, 1H, *J* = 11.5 Hz, Bn), 4.42 (d, 1H, *J* = 11.5 Hz, Bn), 4.26–4.36 (m, 2H, H-6a, H-4), 4.04 (dd, 1H, *J* = 1.6, 12.4 Hz, H-6b), 3.83 (br m, 1H, H-2′), 3.51 (br, 4H, OMe, H-5), 3.38–3.50 (m, 3H, H-2, H-4′, H-5′), 2.33–2.39 (m, 2H, H-3e′, OH-2′), 1.85 (s, 3H, Ac), 1.38 (m, 1H, H-3a′), 1.30 (d, 3H, *J* = 5.6 Hz, H-6′). HR-ES-MS *m*/*e* calcd. for $C_{29}H_{37}O_9N$ (MNa^+): 566.23660; found: 566.236763.

Methyl 2-acetamido-3-*O*-(3,6-dideoxy-β-D-*arabino*-hexopyranosyl)-2-deoxy-β-D-galactopyranoside (3)

Compound **29** (25 mg, 0.046 mmol) was deprotected in a similar fashion as compound **5** and disaccharide **3** (14.7 mg, 88% yield) was purified by reverse-phase HPLC using a gradient of H_2O–MeOH (0 → 30%) as eluent, $[\alpha]_D$ –32.4 (*c* 0.5, MeOH). ^1H NMR (D_2O) δ: 4.68 (d, 1H, *J* = 0.7 Hz, H-1′), 4.44 (d, 1H, *J* = 8.6 Hz, H-1), 4.12 ("d", 1H, *J* = 3.1 Hz, H-4), 4.01 (dd, 1H, *J* = 8.6, 10.8 Hz, H-2), 3.89 (m, 1H, H-2′), 3.89 (dd, 1H, *J* = 3.1, 10.8 Hz, H-3), 3.82 (dd, 1H, *J* = 7.9, 11.7 Hz, H-6a), 3.77 (dd, 1H, *J* = 4.2, 11.7 Hz, H-6b), 3.70 (m, 1H, H-5), 3.55 (ddd, 1H, *J* = 4.8, 9.3, 11.4 Hz, H-4′), 3.52 (s, 3H, OMe), 3.43 (dq, 1H, *J* = 6.2, 9.5 Hz, H-5′), 2.17 (ddd, 1H, *J* = 3.5, 4.8, 14.1 Hz, H-3e′), 2.02 (s, 3H, Ac), 1.65 (ddd, 1H, *J* = 3.1, 11.5, 14.3 Hz, H-3a′), 1.27 (d, 3H, *J* = 6.2 Hz, H-6′). HR-ES-MS *m*/*e* calcd. for $C_{15}H_{27}O_9N$ (MNa^+): 388.15835; found: 388.158854.

© 2002 NRC Canada

Methyl 2-acetamido-3-*O*-(3,6-dideoxy-β-D-*arabino*-hexopyranosyl)-2-deoxy-6-*O*-methyl-β-D-galactopyranoside (10)

A mixture of tetraol **3** (31.6 mg, 0.0865 mmol) and dibutyltin oxide (26 mg, 0.104 mmol) in anhydrous methanol (4 mL) was refluxed for 2 h. The mixture was concentrated and coevaporated with toluene (2 × 15 mL), and dried under high vacuum. The mixture was dissolved in anhyd DMF (2 mL). CsF (40 mg, 0.259 mmol) and MeI (16 μL, 0.259 mmol) were added, and the reaction was heated to 50°C overnight. The solution was concentrated under reduced pressure and the desired 6-*O*-methyl disaccharide **10** was obtained by reverse-phase HPLC using a gradient of H_2O–MeOH (0 → 20%) as eluent (14.5 mg, 44% yield), $[\alpha]_D$ –34.8 (*c* 0.3, MeOH). Starting material **3** (18 mg) was also recovered. ^{1}H NMR (D_2O) δ: 4.68 ("s", 1H, H-1′), 4.45 (d, 1H, *J* = 8.6 Hz, H-1), 4.10 ("d", 1H, *J* = 3.2 Hz, H-4), 4.01 (dd, 1H, *J* = 8.6, 10.8 Hz, H-2), 3.89 (m, 1H, H-2′), 3.87 (dd, 1H, *J* = 3.1, 10.8 Hz, H-3), 3.83 (m, 1H, H-5), 3.72 (dd, 1H, *J* = 7.7, 10.8 Hz, H-6a), 3.68 (dd, 1H, *J* = 4.0, 11.0 Hz, H-6b), 3.55 (ddd, 1H, *J* = 4.6, 9.2, 11.4 Hz, H-4′), 3.52 (s, 3H, OMe), 3.44 (dq, 1H, *J* = 6.0, 9.3 Hz, H-5′), 3.42 (s, 3H, OMe), 2.17 (ddd, 1H, *J* = 3.7, 4.6, 13.9 Hz, H-3e′), 2.03 (s, 3H, Ac), 1.65 (ddd, 1H, *J* = 3.1, 11.5, 14.3 Hz, H-3a′), 1.28 (d, 3H, *J* = 6.2 Hz, H-6′). HR-ES-MS *m/e* calcd. for $C_{16}H_{29}O_9N$ (MNa^+): 402.17400; found: 402.174490.

Methyl 2-acetamido-3-*O*-(4-*O*-benzyl-3,6-dideoxy-2-*O*-methyl-β-D-*arabino*-hexopyranosyl)-4,6-*O*-benzylidene-2-deoxy-β-D-galactopyranoside (30)

Alcohol **29** (42 mg, 0.077 mmol) was dissolved in anhyd DMF (1 mL) at 0°C, NaH (9 mg, 0.38 mmol) was added, and the mixture was stirred for 15 min. MeI (5.2 μL, 0.085 mmol) was added, and the reaction was continued for another 1 h. Methanol (100 μL) was added, and the mixture was concentrated. Chromatography on silica gel using 5% MeOH–CH_2Cl_2, gave the desired disaccharide **30** (16 mg, 37% yield), $[\alpha]_D$ +42.6 (*c* 0.5, $CHCl_3$). ^{1}H NMR ($CDCl_3$) δ: 7.44–7.53 (m, 2H, Ar), 7.21–7.33 (m, 8H, Ar), 5.78 (d, 1H, *J* = 6.4 Hz, NH), 5.55 (s, 1H, PhCH), 5.02 (d, 1H, *J* = 8.2 Hz, H-1), 4.67 (br d, 1H, *J* ~ 1 Hz, H-1′), 4.59 (dd, 1H, *J* = 3.3, 11.1 Hz, H-3), 4.55 (d, 1H, *J* = 11.6 Hz, Bn), 4.44 (d, 1H, *J* = 11.6 Hz, Bn), 4.34 (d, 1H, *J* = 3.1 Hz, H-4), 4.30 (dd, 1H, *J* ~ 1, 12.4 Hz, H-6a), 4.06 (dd, 1H, *J* = 1.4, 12.3 Hz, H-6b), 3.35–3.58 (m, 5H, H-5′, H-2′, H-4′ H-2, H-5), 3.50 (s, 3H, OMe), 3.40 (s, 3H, OMe), 2.35 (ddd, 1H, *J* = 4.4, 4.4, 13.5 Hz, H-3e′), 1.93 (s, 3H, Ac), 1.43 (dd, 1H, *J* = 3.0, 10.3, 13.3 Hz, H-3a′), 1.31 (d, 3H, H-6′). Anal. calcd. for $C_{30}H_{39}O_9N$: C 64.62, H 7.05, N 2.51; found: C 64.32, H 7.15, N 2.59.

Methyl 2-acetamido-3-*O*-(3,6-dideoxy-2-*O*-methyl-β-D-*arabino*-hexopyranosyl)-2-deoxy-β-D-galactopyranoside (12)

Disaccharide **30** (16 mg) was deprotected in a similar fashion as compound **5** and disaccharide **12** (10.1 mg, 93% yield) was obtained by flash chromatography on reverse-phase silica gel followed by reverse-phase HPLC using a gradient of H_2O–MeOH (0 → 30%) as eluent. $[\alpha]_D$ –36.5 (*c* 0.2, MeOH). ^{1}H NMR (D_2O) δ: 4.73 ("s", 1H, H-1′), 4.44 (d, 1H, *J* = 8.6 Hz, H-1), 4.13 ("d", 1H, *J* = 3.1 Hz, H-4), 4.01 (dd, 1H, *J* = 8.6, 10.8 Hz, H-2), 3.83 (dd, 1H, *J* = 7.9, 12.1 Hz, H-6a), 3.81 (dd, 1H, *J* = 3.1, 10.8 Hz, H-3), 3.77 (dd, 1H, *J* = 4.2, 11.7 Hz, H-6b), 3.70 (m, 1H, H-5), 3.56 (m, 1H, H-2′), 3.52 (s, 3H, OMe), 3.42–3.48 (m, 2H, H-4′, H-5′), 3.41 (s, 3H, OMe), 2.37 (d′t′, 1H, *J* = 3.7, 14.1 Hz, H-3e′), 2.03 (s, 3H, Ac), 1.54 (ddd, 1H, *J* = 2.8, 11.2, 14.1 Hz, H-3a′), 1.26 (d, 3H, *J* = 5.7 Hz, H-6′). HR-ES-MS *m/e* calcd. for $C_{16}H_{29}O_9N$ (MNa^+): 402.17400; found: 402.174693.

Methyl 2-acetamido-3-*O*-(4-*O*-benzyl-3,6-dideoxy-2-*O*-imidazoylthiocarbonyl-β-D-*arabino*-hexopyranosyl)-4,6-*O*-benzylidene-2-deoxy-β-D-galactopyranoside (31)

To a solution of disaccharide **29** (30 mg, 0.055 mmol) in anhydrous toluene (2.5 mL), was added 1,1′-thiocarbonyldiimidazole (27 mg, 0.15 mmol), and the mixture was heated to 90°C for 17 h. After cooling, the mixture was concentrated, and disaccharide **31** was obtained following chromatography on silica gel using 2% MeOH–CH_2Cl_2 as eluent (35.3 mg, 98% yield), $[\alpha]_D$ +21.5 (*c* 0.3, $CHCl_3$). ^{1}H NMR ($CDCl_3$) δ: 8.31 (s, 1H, imidazole), 7.20–7.44 (m, 11H, Ar), 6.71 (s, 1H, imidazole), 5.88 (d, 1H, *J* = 6.5 Hz, NH), 5.66 (m, 1H, H-2′), 5.51 (s, 1H, PhCH), 4.95 (d, 1H, *J* = 8.2 Hz, H-1), 4.87 ("s", 1H, H-1′), 4.75 (dd, 1H, *J* = 3.4, 11.1 Hz, H-3), 4.54 (d, 1H, *J* = 11.5 Hz, Bn), 4.42 (d, 1H, *J* = 11.5 Hz, Bn), 4.33 ("d", 1H, *J* = 3.3 Hz, H-4), 4.30 (dd, 1H, *J* = 1.2, 12.5 Hz, H-6a), 4.05 (dd, 1H, *J* = 1.4, 12.4 Hz, H-6b), 3.58 (m, 1H, H-5′), 3.50 (m, 4H, H-5, OMe), 3.40 (m, 1H, H-2), 3.25 (m, 1H, H-4), 2.63 (ddd, 1H, *J* = 3.9, 3.9, 14.5 Hz, H-3e′), 1.95 (s, 3H, Ac), 1.70 (ddd, 1H, *J* = 3.0, 11.1, 14.1 Hz, H-3a′), 1.34 (d, 3H, *J* = 6.1 Hz, H-6′). Anal. calcd. for $C_{33}H_{39}O_9N_3S$: C 60.63, H 6.01, N 6.43; found: C 60.37, H 6.13, N 6.34.

Methyl 2-acetamido-3-*O*-(4-*O*-benzyl-2,3,6-trideoxy-β-D-erythro-hexopyranosyl)-4,6-*O*-benzylidene-2-deoxy-β-D-galactopyranoside (32)

To a refluxing solution of disaccharide **31** (35.3 mg, 0.054 mmol) in anhydrous toluene (2 mL) was added dropwise a solution of tributyltin hydride (45 μL, 0.16 mmol) in toluene (0.75 mL), and a catalytic amount of AIBN (~2 mg) was added, the reaction was refluxed for 8 h. After concentration, the mixture was chromatographed on silica gel using 2% MeOH–CH_2Cl_2 as eluent to give disaccharide **32** (27 mg, 95% yield), $[\alpha]_D$ +68.9 (*c* 0.6, $CHCl_3$). ^{1}H NMR ($CDCl_3$) δ: 7.46–7.52 (m, 2H, Ar), 7.20–7.38 (m, 8H, Ar), 5.85 (br, 1H, NH), 5.53 (s, 1H, PhCH), 5.06 (d, 1H, *J* = 8.2 Hz, H-1), 4.56–4.67 (m, 3H, H-3, Bn, H-1′), 4.43 (d, 1H, Bn), 4.33 (d, 1H, *J* = 3.2 Hz, H-4), 4.29 (dd, 1H, *J* ~ 1, 12.5 Hz, H-6a), 4.05 (dd, 1H, *J* = 1.4, 12.5 Hz, H-6b), 3.50 (m, 4H, OMe, H-5), 3.34–3.46 (m, 2H, H-2, H-5′), 3.04 (m, 1H, H-4′), 2.15 (m, 1H, H-3e′), 1.89 (s, 3H, Ac), 1.84 (m, 1H, H-3a′), 1.30–1.62 (m, 2H, H-2a′, H-2b′), 1.27 (d, 3H, *J* = 6.1 Hz, H-6′). Anal. calcd. for $C_{29}H_{37}O_8N$: C 66.02, H 7.07, N 2.66; found: C 66.38, H 7.30, N 2.68.

Methyl 2-acetamido-3-*O*-(2,3,6-trideoxy-β-D-erythro-hexopyranosyl)-2-deoxy-β-D-galactopyranoside (11)

Compound **32** (25 mg, 0.047 mmol) was deprotected in a similar fashion as compound **5** and disaccharide **11** (15.7 mg, 95% yield) was obtained by reverse-phase HPLC using a gradient of H_2O–MeOH (0 → 30%) as eluent. $[\alpha]_D$ –29.0 (*c* 0.2, MeOH). ^{1}H NMR (D_2O) δ: 4.69 (dd, 1H, *J* =

© 2002 NRC Canada

2.0, 9.5 Hz, H-1′), 4.44 (d, 1H, *J* = 8.6 Hz, H-1), 4.09 ("d", 1H, *J* = 3.3 Hz, H-4), 3.98 (dd, 1H, *J* = 8.8, 10.8 Hz, H-2), 3.83 (dd, 1H, *J* = 3.1, 10.8 Hz, H-3), 3.82 (dd, 1H, *J* = 8.1, 11.2 Hz, H-6a), 3.76 (dd, 1H, *J* = 4.4, 11.9 Hz, H-6b), 3.69 (m, 1H, H-5), 3.52 (s, 3H, OMe), 3.42 (dq, 1H, *J* = 6.2, 9.2 Hz, H-5′), 3.27 (m, 1H, H-4′), 2.04 (m, 1H, H-3e′), 2.03 (s, 3H, Ac), 1.84 (m, 1H, H-2e′), 1.45–1.59 (m, 2H, H-2a′, H-3a′), 1.26 (d, 3H, *J* = 6.2 Hz, H-6′). HR-ES-MS *m*/*e* calcd. for $C_{15}H_{27}O_8N$ (MNa^+): 372.16344; found: 372.163591.

Methyl 2-acetamido-3-*O*-(2-*O*-benzoyl-4-*O*-benzyl-3,6-dideoxy-β-D-*arabino*-hexopyranosyl)-4,6-*O*-benzylidene-2-deoxy-β-D-galactopyranoside (33)

Disaccharide **29** (50 mg, 0.092 mmol) was dissolved in a 1:1 mixture of pyridine–CH_2Cl_2 (3 mL) at –30°C, benzoyl chloride (12 μL, 0.101 mmol) was added and the reaction was stirred at ambient temperature for 7 h. TLC revealed that the starting material was not completely consumed. The reaction mixture was cooled to –30°C and more benzoyl chloride (8 μL, 0.068 mmol) was added. The reaction was allowed to warm to –10°C over 30 min, at which point TLC showed the starting material to be completely transformed. Methanol (200 μL) was added, and the mixture was concentrated under reduced pressure. Chromatography on silica gel using 2% MeOH–CH_2Cl_2 as eluent gave compound **33** (52 mg, 87% yield), $[\alpha]_D$ +44.3 (*c* 0.7, $CHCl_3$). ^{1}H NMR ($CDCl_3$) δ: 7.98 (m, 2H, Bz), 7.46 (m, 1H, Bz), 7.08–7.36 (m, 7H, Ar), 5.88 (d, 1H, *J* = 6.8 Hz, NH), 5.51 (s, 1H, PhCH), 5.34 (m, 1H, H-2′), 5.05 (d, 1H, *J* = 8.2 Hz, H-1), 4.81 (s, 1H, H-1′), 4.68 (dd, 1H, *J* = 3.4, 11.1 Hz, H-3), 4.55 (d, 1H, *J* = 11.5 Hz, Bn), 4.41 (d, 1H, *J* = 11.5 Hz, Bn), 4.33 (d, 1H, *J* = 3.1 Hz, H-4), 4.29 (dd, 1H, *J* = 1.2, 12.3 Hz, H-6a), 4.04 (dd, 1H, *J* = 1.6, 12.3 Hz, H-6b), 3.57 (m, 1H, H-5′), 3.48 (s, 1H, H-5′), 3.47 (s, 4H, OMe, H-5), 3.31–3.46 (m, 2H, H-4′, H-2), 2.46 (d′t′, 1H, *J* = 4.0,, 14.0 Hz, H-3e′), 1.95 (s, 3H, Ac), 1.70 (ddd, 1H, 3.2, 11.2, 14.1 Hz, H-3a′), 1.36 (d, 1H, *J* = 6.1 Hz, H-6′). Anal. calcd. for $C_{36}H_{41}O_{10}N$: C 66.76, H 6.38, N 2.16; found: C 66.38, H 6.28, N 2.05.

Methyl 2-acetamido-3-*O*-(2-*O*-benzoyl-3,6-dideoxy-β-D-*arabino*-hexopyranosyl)-4,6-*O*-benzylidene-2-deoxy-β-D-galactopyranoside (34)

A mixture of disaccharide **33** (52 mg, 0.08 mmol), HCO_2NH_4 (25 mg, 0.40 mmol) and 5% Pd-C (34 mg) in MeOH (10 mL) was heated to reflux for 1 h. The catalyst was filtered off and the filtrate was concentrated. Disaccharide **34** was obtained by chromatography on silica gel using 2% MeOH – CH_2Cl_2 as eluent (35.2 mg, 78% yield), $[\alpha]_D$ +32.6 (*c* 0.5, $CHCl_3$). ^{1}H NMR ($CDCl_3$) δ: 7.98 (m, 2H, Bz), 7.45 (m, 1H, Bz), 7.07–7.34 (m, 7H, Ar), 6.08 (d, 1H, *J* = 7.1 Hz, NH), 5.50 (s, 1H, PhCH), 5.31 (m, 1H, H-2′), 5.00 (d, 1H, *J* = 8.2 Hz, H-1), 4.78 ("s", 1H, H-1′), 4.65 (dd, 1H, *J* = 3.3, 11.1 Hz, H-3), 4.10 (d, 1H, *J* = 3.3 Hz, H-4), 4.27 (dd, 1H, *J* ~ 1.0, 12.3 Hz, H-6a), 4.02 (dd, 1H, *J* = 1.3, 12.3 Hz, H-6b), 3.61 (m, 1H, H-4′), 3.46 (s, 4H, OMe, H-5), 3.34–3.45 (m, 2H, H-5′, H-2), 2.29 (d′t′, 1H, *J* = 5.1, 14.0 Hz, H-3e′), 1.96 (s, 3H, Ac), 1.66 (ddd, 1H, 3.2, 11.2, 14.1 Hz, H-3a′), 1.34 (d, 1H, *J* = 6.1 Hz, H-6′). Anal. calcd. for $C_{29}H_{35}O_{10}N$: C 62.47, H 6.33, N 2.51; found: C 62.26, H 6.34, N 2.33.

Methyl 2-acetamido-3-*O*-(2-*O*-benzoyl-3,6-dideoxy-4-*O*-imidazoylthiocarbonyl-β-D-*arabino*-hexopyranosyl)-4,6-*O*-benzylidene-2-deoxy-β-D-galactopyranoside (35)

To a solution of disaccharide **34** (30 mg, 0.055 mmol) in anhydrous toluene (3 mL), was added 1,1′-thiocarbonyldiimidazole (35 mg, 0.18 mmol), and the mixture was heated to reflux for 8 h. After cooling, the mixture was concentrated, and the disaccharide **35** was obtained by chromatography on silica gel using 2.5 → 5% MeOH – CH_2Cl_2 as eluent (32.9 mg, 92% yield), $[\alpha]_D$ +5.2 (*c* 0.5, $CHCl_3$). ^{1}H NMR ($CDCl_3$) δ: 8.29 (t, 1H, *J* = 0.8 Hz, imidazole), 8.03 (m, 2H, Bz), 7.56 (t, 1H, 1.6 Hz, imidazole), 7.51 (m, 1H, Bz), 7.13–7.38 (m, 7H, Ar), 7.03 (dd, 1H, *J* = 0.8, 1.6 Hz, imidazole), 6.00 (d, 1H, *J* = 7.1 Hz, NH), 5.56 (m, 1H, H-4′), 5.53 (s, 1H, PhCH), 5.43 (m, 1H, H-2′), 4.96 (d, 1H, *J* = 1.5 Hz, H-1′), 4.93 (d, 1H, *J* = 8.2 Hz, H-1), 4.69 (dd, 1H, *J* = 3.4, 11.2 Hz, H-3), 4.27–4.36 (m, 2H, H-4, H-6a), 4.06 (dd, 1H, *J* = 1.6, 12.4 Hz, H-6b), 3.94 (dq, 1H, *J* = 6.1, 9.0 Hz, H-5′), 3.53 (m, 1H, H-2), 3.49 (m, 1H, H-5), 3.48 (s, 3H, OMe), 2.67 (d′t′, 1H, *J* = 4.5, 13.8 Hz, H-3e′), 1.93 (s, 3H, Ac), 1.84 (ddd, 1H, 3.4, 10.5, 13.8 Hz, H-3a′), 1.37 (d, 1H, *J* = 6.2 Hz, H-6′). Anal. calcd. for $C_{33}H_{37}O_{10}N_3S$: C 59.36, H 5.59, N 6.29; found: C 59.01, H 5.33, N 6.24.

Methyl 2-acetamido-3-*O*-(2-*O*-benzoyl-3,4,6-trideoxy-β-D-threo-hexopyranosyl)-4,6-*O*-benzylidene-2-deoxy-β-D-galactopyranoside (36)

To a refluxing solution of disaccharide **35** (32.9 mg, 0.061 mmol) in anhydrous toluene (2 mL) was added dropwise a solution of tributyltin hydride (41 μL, 0.15 mmol) in toluene (0.75 mL), and a catalytic amount of AIBN (~2 mg) was added, the reaction was continued to reflux for 3 h. After concentration, the mixture was chromatographed on silica gel using 2% MeOH – CH_2Cl_2 as eluent to give disaccharide **36** (22 mg, 83% yield), $[\alpha]_D$ +36.2 (*c* 0.6, $CHCl_3$). ^{1}H NMR ($CDCl_3$) δ: 8.01 (m, 2H, Bz), 7.46 (m, 1H, Bz), 7.09–7.36 (m, 7H, Ar), 5.85 (d, 1H, *J* = 6.9 Hz, NH), 5.53 (s, 1H, PhCH), 5.16 (m, 1H, H-2′), 5.03 (d, 1H, *J* = 8.2 Hz, H-1), 4.71 (d, 1H, *J* = 1.1 Hz, H-1′), 4.63 (dd, 1H, *J* = 3.4, 11.2 Hz, H-3), 4.35 (d, 1H, *J* = 3.3 Hz, H-4), 4.29 (dd, 1H, *J* = 1.5, 12.3 Hz, H-6a), 4.04 (dd, 1H, *J* = 1.4, 12.3 Hz, H-6b), 3.64 (m, 1H, H-5′), 3.47 (m, 4H, H-5+ OMe), 3.41 (m, 1H, H-2), 2.07 (m, 1H, H-3e′), 1.96 (s, 3H, Ac), 1.72 (m, 1H, H-3a′), 1.30–1.68 (m, 2H, H-4a′, H4e′), 1.27 (d, 3H, *J* = 6.2 Hz, H-6′). Anal. calcd. for $C_{29}H_{35}O_9N$: C 64.31, H 6.51, N 2.59; found: C 64.00, H 6.42, N 2.56.

Methyl 2-acetamido-3-*O*-(3,4,6-trideoxy-β-D-threo-hexopyranosyl)-2-deoxy-β-D-galactopyranoside (13)

Compound **36** (22 mg, 0.0406 mmol) was dissolved in anhyd MeOH (3 mL), and a solution of NaOMe in MeOH (1.5 M, 400 μL) was added. After 1 h, the mixture was neutralized with Amberlite IR-120 (H^+), the solution was filtered and evaporated to dryness. The residue was hydrogenated in a similar fashion as compound **5** and disaccharide **13** (12.5 mg, 88% yield) was purified by reverse-phase HPLC using a gradient of H_2O–MeOH (0 → 30%) as eluent. $[\alpha]_D$ –34 (*c* 0.5, MeOH). ^{1}H NMR (D_2O) δ: 4.60 (d, 1H, *J* = 0.9 Hz, H-1′), 4.45 (d, 1H, *J* = 8.6 Hz, H-1), 4.12 ("d", 1H, *J* = 3.1 Hz, H-4), 4.02 (dd, 1H, *J* = 8.6,

© 2002 NRC Canada

10.8 Hz, H-2), 3.87 (dd, 1H, *J* = 3.3, 10.8 Hz, H-3), 3.83 (dd, 1H, *J* = 7.9, 11.9 Hz, H-6a), 3.78 (dd, 1H, *J* = 4.2, 11.7 Hz, H-6b), 3.69–3.72 (m, 3H, H-2′, H-5′, H-5), 3.52 (s, 3H, OMe), 2.03 (s, 3H, Ac), 1.89 (m, 1H, H-3e′), 1.75 (m, 1H, H-3a′), 1.42–1.47 (m, 2H, H-4e′, H-4a′), 1.21 (d, 3H, *J* = 6.2 Hz, H-6′). HR-ES-MS *m*/*e* calcd. for $C_{15}H_{27}O_8N$ (MNa^+): 372.16344; found: 372.164136.

Methyl 2-acetamido-3-*O*-(3,6-dideoxy-β-D-arabino-hexopyranosyl)-4,6-*O*-benzylidene-2-deoxy-β-D-galactopyranoside (37)

To a solution of disaccharide **29** (243 mg, 0.45 mmol) in MeOH (35 mL), was added 10% Pd-C (250 mg) and HCO_2NH_4 (243 mg, 3.86 mmol), and the mixture was heated to reflux for 1 h. The catalyst was filtered off, and the filtrate was concentrated. The syrupy mixture was purified by chromatography on silica gel using 10% → 20% MeOH – CH_2Cl_2 as eluent to give first disaccharide **37** (160 mg, 79% yield) and then disaccharide **1** (18 mg, 11% yield), $[\alpha]_D$ +30.3 (*c* 0.4, MeOH). ^{1}H NMR ($CDCl_3$) δ: 7.48 (m, 2H, Ph), 7.29–7.35 (m, 3H, Ph), 5.81 (br, 1H, NH), 5.53 (s, 1H, PhCH), 5.01 (d, 1H, *J* = 8.3 Hz, H-1), 4.77 (dd, 1H, *J* = 3.2, 11.1 Hz, H-3), 4.60 ("s", 1H, H-1′), 4.32 ("d", 1H, *J* = 3.2 Hz, H-4), 4.30 (dd, 1H, *J* = 1.0, 12.2 Hz, H-6a), 4.06 (dd, 1H, *J* = 1.1, 12.2 Hz, H-6b), 3.82 (m, 1H, H-2′), 3.65 (ddd, 1H, *J* = 4.4, 9.2, 10.8 Hz, H-4′), 3.51 (s, 4H, OMe, H-5), 3.44 (m, 1H, H-2), 3.30 (dq, 1H, *J* = 6.1, 9.0 Hz, H-5′), 2.24 (d′t′, 1H, *J* = 3.8, 14.1, H-3e′), 1.44 (ddd, 1H, *J* = 2.9, 11.0, 13.7 Hz, H-3a′), 1.31 (d, 3H, *J* = 6.1 Hz, H-6′). Anal. calcd. for $C_{22}H_{31}O_9N$: C 58.27, H 6.89, N 3.09; found: C 57.84, H 6.90, N 3.08.

Methyl 2-acetamido-3-*O*-(2,4-di-*O*-benzoyl-3,6-dideoxy-β-D-*arabino*-hexopyranosyl)-4,6-*O*-benzylidene-2-deoxy-β-D-galactopyranoside (38)

Benzoic anhydride (112 mg, 0.534 mmol) and DMAP (10 mg, 0.0818 mmol) were added to diol **37** (80.9 mg, 0.178 mmol) was dissolved in anhydrous pyridine (3 mL). After stirring for 18 h at ambient temperature, H_2O (0.5 mL) was added to destroy the excess anhydride, and the mixture was concentrated to dryness. Dibenzoate **38** was obtained by chromatography on silica gel using 3% MeOH – CH_2Cl_2 as eluent (105 mg, 89% yield), $[\alpha]_D$ +25.2 (*c* 0.8, $CHCl_3$). ^{1}H NMR ($CDCl_3$) δ: 8.03 (m, 2H, Bz), 7.98 (m, 2H, Bz), 7.12–7.60 (m, 11H, Ar), 5.78 (d, 1H, *J* = 7.0 Hz, NH), 5.54 (s, 1H, PhCH), 5.43 (m, 1H, H-2′), 5.08 (m, 1H, H-4′), 4.99 (d, 1H, *J* = 8.3 Hz, H-1), 4.91 (d, 1H, *J* = 1.3 Hz, H-1′), 4.70 (dd, 1H, *J* = 3.4, 11.2 Hz, H-3), 4.36 (d, 1H, *J* = 3.3 Hz, H-4), 4.30 (dd, 1H, *J* = 1.3, 12.4 Hz, H-6a), 4.06 (dd, 1H, *J* = 1.6, 12.4 Hz, H-6b), 3.81 (dq, 1H, *J* = 6.2, 9.0 Hz, H-5′), 3.49 (m, 1H, H-5), 3.48 (s, 3H, OMe), 3.47 (m, 1H, H-2), 2.54 (d′t′, 1H, *J* = 4.4, 13.9 Hz, H-3e′), 1.97 (s, 3H, Ac), 1.85 (ddd, 1H, *J* = 3.3, 10.5, 13.9 Hz, H-3a′),1.35 (d, 3H, *J* = 6.1 Hz, H-6′). Anal. calcd. for $C_{36}H_{39}O_{11}N$: C 65.35, H 5.94, N 2.12; found: C 65.55, H 5.93, N 1.95.

Methyl 2-acetamido-3-*O*-(2,4-di-*O*-benzoyl-3,6-dideoxy-β-D-*arabino*-hexopyranosyl)-2-deoxy-β-D-galactopyranoside (39)

A solution of compound **38** (52 mg, 0.078 mmol) in MeOH (30 mL) was hydrogenated over 10% $Pd(OH)_2$ for 18 h. The catalyst was filtered off and the filtrate was concentrated. Diol **39** was purified by chromatography on silica gel using 5% MeOH – CH_2Cl_2 as eluent (40 mg, 89% yield), $[\alpha]_D$ –48.1 (*c* 0.3, $CHCl_3$). ^{1}H NMR ($CDCl_3$) δ: 8.05 (m, 2H, Bz), 7.98 (m, 2H, Bz), 7.53–7.61 (m, 2H, Bz), 7.40–7.49 (m, 4H, Bz), 5.94 (br, 1H, NH), 5.46 (m, 1H, H-2′), 5.10 (m, 1H, H-4′), 5.03 (d, 1H, *J* = 8.2 Hz, H-1), 4.86 (br s, 1H, H-1′), 4.62 (dd, 1H, *J* = 3.1, 10.6 Hz, H-3), 4.10 (d, 1H, *J* = 2.5 Hz, H-4), 3.94 (dd, 1H, *J* = 6.5, 11.6 Hz, H-6a), 3.75–3.88 (m, 2H, H-6b, H-5′), 3.62 (m, 1H, H-5), 3.47 (s, 3H, OMe), 3.05 (m, 1H, H-2), 2.55 (d′t′, 1H, *J* = 3.7, 14.1 Hz, H-3e′), 2.03 (s, 3H, Ac), 1.92 (ddd, 1H, *J* = 3.2, 10.5, 14.1 Hz, H-3a′),1.34 (d, 3H, *J* = 6.1 Hz, H-6′). Anal. calcd. for $C_{29}H_{35}O_{11}N$: C 60.72, H 6.15, N 2.44; found: C 60.38, H 6.05, N 2.66.

Methyl 2-acetamido-3-O-(3,6-dideoxy-β-D-arabino-hexopyranosyl)-2,6-dideoxy-β-D-galactopyranoside (9)

Tolunesulfonyl chloride (12.5 mg, 0.066 mmol) was added to a solution of compound **39** (34.7 mg, 0.06 mmol) in anhydrous pyridine (2 mL), and the reaction was stirred at room temperature for 3 h. Water (0.3 mL) was added to quench the reaction. The mixture was diluted with EtOAc (50 mL), washed with brine (1 × 25 mL), dried and concentrated. Lithium bromide (34.2 mg, 0.39 mmol) and KI (6 mg, 0.036 mmol) were added to a solution of the residue in DMF (1.5 mL), and the resulting solution was heated to 100°C for 1 h. The reaction mixture was diluted with EtOAc (75 mL), washed with brine (sat., 2 × 25 mL), dried and evaporated. Tributyltin hydride (330 μL, 0.12 mmol) and AIBN (5 mg, 0.03 mmol) were added to a refluxing solution of bromide **41** (25 mg, 0.04 mmol) in anhydrous toluene (2 mL). After 1 h, the reaction was cooled to room temperature and concentrated. The syrupy mixture was dissolved in anhyd MeOH (5 mL), and a solution of MeONa in MeOH (1.5 M, 50 μL) was added. After stirring for 1 h, the reaction was neutralized with Amberlite IR-120 (H^+) resin, filtered and concentrated. Disaccharide **9** was obtained by reverse-phase HPLC using a gradient of H_2O–MeOH (0 → 30%) as eluent (10.5 mg, 49% yield), $[\alpha]_D$ –38.4 (*c* 0.5, MeOH). ^{1}H NMR (D_2O) δ: 4.68 (d, 1H, *J* = 0.9 Hz, H-1′), 4.42 (d, 1H, *J* = 8.6 Hz, H-1), 3.97 (dd, 1H, *J* = 8.6, 10.8 Hz, H-2), 3.94 ("d", 1H, *J* = 3.1 Hz, H-4), 3.89 (m, 1H, H-2′), 3.86 (dd, 1H, *J* = 3.1, 10.8 Hz, H-3), 3.80 (dq, 1H, *J* = 0.7, 6.6 Hz, H-5), 3.55 (ddd, 1H, *J* = 4.8, 9.3, 11.5 Hz, H-4′), 3.49 (s, 3H, OMe), 3.43 (dq, 1H, *J* = 6.1, 9.3 Hz, H-5′), 2.17 (ddd, 1H, *J* = 3.5, 4.8, 14.1 Hz, H-3e′), 2.02 (s, 3H, Ac), 1.65 (ddd, 1H, *J* = 2.9, 11.5, 14.3 Hz, H-3e′), 1.29 (d, 3H, *J* = 6.4 Hz, H-6), 1.27 (d, 3H, *J* = 6.0 Hz, H-6′). HR-ES-MS *m*/*e* calcd. for $C_{15}H_{27}O_8N$ (MNa^+): 372.16344; found: 372.163372.

3,6-Dideoxy-4-*O*-methyl-1,2-*O*-propylidene-α-D-ribo-hexopyranose (44)

Sodium hydride (60% in mineral oil, 218 mg, 5.445 mmol) was added to a solution of compound **43** (38) (205 mg, 1.089 mmol) in anhyd DMF, followed after 10 min by MeI (136 μL, 2.178 mmol), and the reaction was stirred at ambient temperature for 2 h. MeOH (0.5 mL) was added to quench the reaction, and the reaction mixture was diluted with EtOAc (75 mL), washed with brine (sat., 2 × 30 mL),

© 2002 NRC Canada

dried and evaporated. The compound **44** was obtained by chromatography on silica gel using 20% EtOAc – hexane as eluent (201 mg, 92% yield), $[\alpha]_D$ +44.6 (*c* 0.5, $CHCl_3$). ^1H NMR ($CDCl_3$) δ: 5.30 (d, 1H, *J* = 5.2 Hz, H-1), 4.73 (t, 1H, *J* = 4.9 Hz, CH_3CH_2CH), 4.01 (m, 1H, H-2), 3.80 (dq, 1H, *J* = 6.1, 9.3 Hz, H-5), 3.31 (s, 3H, OMe), 3.08 (m, 1H, H-4), 2.17 (ddd, 1H, *J* = 1.7, 2.6, 15.5 Hz, H-3e), 1.86 (ddd, 1H, *J* = 3.6, 7.6, 15.9 Hz, H-3a), 1.77 (m, 2H, CH_3CH_2), 1.23 (d, 3H, *J* = 6.3 Hz, H-6), 0.98 (t, 3H, *J* = 7.6 hz, CH_3CH_2). Anal. calcd. for $C_{10}H_{18}O_4$: C 59.39, H 8.97; found: C 59.63, H 8.88.

1,2-Di-*O*-benzoyl-3,6-dideoxy-4-*O*-methyl-α,β-D-ribo-hexopyranose (46)

The 1,2-*O*-propylidene derivative **44** (112 mg, 0.55 mmol) was dissolved in THF (5 mL), and a 10% aqueous solution of H_2SO_4 (1 mL) was added, and the reaction was stirred at 65°C for 2 h. The mixture was diluted with CH_2Cl_2 (100 mL), washed with aq $NaHCO_3$ (sat., 2 × 30 mL), dried, and evaporated to afford the crude diol **45** that was used directly to the next step. Benzoyl chloride (314.9 μL, 1.21 mmol) was added to an ice-cold solution of the crude diol **45** in a mixture of anhyd CH_2Cl_2 (1 mL) and pyridine (0.5 mL), and the reaction was continued for 1 h. Methanol (0.5 mL) was added to quench the reaction. The reaction mixture was diluted with CH_2Cl_2 (50 mL), the solution extracted with H_2O, then dried, and evaporated. Dibenzoate **46** was obtained as a α,β-mixture by chromatography on silica gel using 10% EtOAc – hexane as eluent (α/β: 1:1, 197 mg, 96% yield). ^1H NMR (CD_3OD) for α-anomer δ: 8.10 (m, 2H, Bz), 7.90 (m, 2 H, Bz), 7.30–7.63 (m, 3H, Bz), 6.52 (d, 1H, *J* = 3.3 Hz, H-1), 5.27 (m, 1H, H-2), 3.89 (dq, 1H, *J* = 6.4, 9.3 Hz, H-5), 3.43 (s, 3H, OMe), 3.17 (m, 1H, H-4), 2.66 (dd′t′, 1H, *J* = 0.9, 4.4, 11.4 Hz, H-3e), 2.05 (d′t′, 11.5, 11.5 Hz, H-3a), 1.29 (d, 3H, *J* = 6.1 Hz, H-6); β-anomer δ: 8.02 (m, 2H, Bz), 7.96 (m, 2 H, Bz), 7.30–7.63 (m, 3H, Bz), 6.06 (d, 1H, *J* = 8.2 Hz, H-1), 5.24 (m, 1H, H-2), 3.67 (dq, 1H, *J* = 6.1, 9.0 Hz, H-5), 3.40 (s, 3H, OMe), 3.12 (m, 1H, H-4), 2.83 (d′t′, 1H, *J* = 4.9, 12.1 Hz, H-3e), 1.66 (d′t′, 11.9, 11.9 Hz, H-3a), 1.35 (d, 3H, *J* = 6.1 Hz, H-6). Anal. calcd. for $C_{21}H_{22}O_6$: C 68.10, H 5.99; found: C 68.43, H 5.95.

Phenyl 2-*O*-benzoyl-3,6-dideoxy-4-*O*-methyl-1-thio-α,β-D-ribo-hexopyranoside (47)

A solution of **46** (185 mg, 0.50 mmol) in anhydrous toluene (3 mL) was stirred with molecular sieves 4 Å (400 mg) for 30 min at 0°C. Me_3SiSPh (244 μL, 1.25 mmol) was added, followed by TMSOTf (97 μL, 0.5 mmol). Reaction was continued at room temperature overnight. Triethylamine (0.5 mL) was added, and the insoluble material was filtered off. After evaporation, the thioglycoside **47** was obtained by chromatography of the residue on silica gel using 5% EtOAc – hexane as eluent (α/β 4:6, 160 mg, 89%). ^1H NMR ($CDCl_3$) for α-anomer δ: 8.09 (m, 2H, Bz), 7.57 (m, 1H, Bz), 7.45 (m, 2H, Bz), 7.17–7.28 (m, 5H, Ph), 5.75 (d, 1H, *J* = 5.1 Hz, H-1), 5.29 (d′t′, 1H, *J* = 5.1, 12.4 Hz, H-2), 4.18 (dq, 1H, *J* = 6.2, 9.2 Hz, H-5), 3.40 (s, 3H, OMe), 3.07 (ddd, 1H, *J* = 4.5, 9.3, 10.9 Hz, H-4), 2.52 (dd′t′, 1H, *J* = 0.7, 4.5, 11.9 Hz, H-3e), 1.87 (d′t′, 1H, *J* = 12.1, 12.1 Hz, H-3a), 1.26 (d, 3H, *J* = 6.2 Hz, H-6); β-anomer δ: 8.04 (m, 2H, Bz), 7.57 (m, 1H, Bz), 7.46 (m, 2H, Bz), 7.26 (m, 5H, Ph), 4.90 (d′t′, 1H, *J* = 4.8, 9.9 Hz, H-21), 4.80 (d, 1H, *J* = 9.9 Hz, H-1), 3.42 (dq, 1H, *J* = 6.2, 9.2 Hz, H-5), 3.36 (s, 3H, OMe), 3.02 (m, 1H, H-4), 2.82 (d′t′, 1H, *J* = 4.5, 12.0 Hz, H-3e), 1.53 (d′t′, 1H, *J* = 12.1, 12.1 Hz, H-3a), 1.36 (d, 3H, *J* = 6.2 Hz, H-6). Anal. calcd. for $C_{20}H_{22}O_4S$: C 67.02, H 6.19; found: C 67.34, H 6.16.

Methyl 2-azido-3-*O*-(2-*O*-benzoyl-3,6-dideoxy-4-*O*-methyl-β-D-ribo-hexopyranosyl)-4,6-*O*-benzylidene-2-deoxy-β-D-galactopyranoside (48)

A mixture containing thioglycoside **47** (140 mg, 0.40 mmol), alcohol **24** (39) (95 mg, 0.31 mmol) and 4 Å molecular sieves (500 mg) in CH_2Cl_2 was stirred for 30 min and *N*-iodosuccinimide (146 mg, 0.62 mmol) was added. After the reaction mixture had been cooled to –60°C, TfOH (6 μL, 0.067 mmol) was added, and the reaction was continued for 3 h. Triethylamine (0.5 mL) was added to quench the reaction, and disaccharide **48** was obtained in a similar fashion to that described above (134.7 mg, 78% yield), $[\alpha]_D$ –14.7 (*c* 0.8, $CHCl_3$). ^1H NMR ($CDCl_3$) δ: 8.02–8.08 (m, 2 H, Bz), 7.20–7.57 (m, 8H, Ar), 5.50 (s, 1H, PhCH), 4.82–4.96 (m, 2H, H-1′ + H-2′), 4.30 (dd, 1H, *J* = 1.6, 12.4 Hz, H-6a), 4.23 (br d, 1H, *J* = 3.1 Hz, H-4), 4.21 (d, 1H, *J* = 8.0 Hz, H-1), 4.04 (dd, 1H, *J* = 1.6, 12.4 Hz, H-6b), 3.77 (dd, 1H, *J* = 8.0, 10.6 Hz, H-2), 3.55 (s, 3H, OMe), 3.51 (dd, 1H, *J* = 3.5, 10.6 Hz, H-3), 3.43 (dq, 1H, *J* = 6.1, 9.0 Hz, H-5′), 3.39 (m, 1H, H-5), 3.35 (s, 3H, OMe), 3.04 (ddd, 1H, *J* = 4.5, 9.0, 10.8 Hz, H-4′), 2.79 (d′t′,1H, *J* = 4.4, 12.1 Hz, H-3e′), 1.45 (d′t′, 1H, *J* = ~11.5, 11.5 Hz, H-3a′), 1.31 (d, 3H, *J* = 6.1 Hz, H-6′). Anal. calcd. for $C_{28}H_{33}O_9N_3$: C 60.53, H 5.99, N 7.56; found: C 60.64, H 6.00, N 7.32.

Methyl 2-azido-3-*O*-(3,6-dideoxy-4-*O*-methyl-β-D-ribo-hexopyranosyl)-4,6-*O*-benzylidene-2-deoxy-β-D-galactopyranoside (49)

Compound **48** (140 mg, 0.25 mmol) was transesterified as described above to give the disaccharide **49** (107 mg, 94% yield), $[\alpha]_D$ +22.7 (*c* 1.1, $CHCl_3$). ^1H NMR ($CDCl_3$) δ: 7.51 (m, 2H, Ph), 7.31–7.38 (m, 3H, Ph), 5.52 (s, 1H, PhCH), 4.43 (d, 1H, *J* = 7.3 Hz, H-1′), 4.31 (dd, 1H, *J* = 1.5, 12.4 Hz, H-6a), 4.24 ("d", 1H, *J* = 3.4 Hz, H-4), 4.22 (d, 1H, *J* = 8.0 Hz, H-1), 4.04 (dd, 1H, *J* = 1.7, 12.4 Hz, H-6b), 3.85 (dd, 1H, *J* = 8.1, 10.5 Hz, H-2), 3.58 (s, 3H, OMe), 3.53 (dd, 1H, *J* = 3.5, 10.6 Hz, H-3), 3.52 (dq, 1H, *J* = 6.1, 9.0 Hz, H-2′), 3.32–3.42 (m, 5H, H-5, H-5′, OMe), 3.35 (s, 3H, OMe), 2.92 (ddd, 1H, *J* = 4.4, 8.8, 10.9 Hz, H-4′), 2.49 (d′t′, 1H, *J* = 4.7, 12.3 Hz, H-3e′), 1.36 (d′t′, 1H, *J* ~ 11.5, 11.5 Hz, H-3a′), 1.28 (d, 3H, *J* = 6.1 Hz, H-6′). Anal. calcd. for $C_{21}H_{29}O_8N_3$: C 55.87, H 6.48, N 9.31; found: C 55.81, H 6.36, N 9.40.

Methyl 2- acetamido-3-*O*-(3,6-dideoxy-4-*O*-methyl-β-D-*arabino*-hexopyranosyl)-4,6-*O*-benzylidene-2-deoxy-β-D-galactopyranoside (51)

The disaccharide **49** (96.3 mg, 0.21 mmol) was oxidized by a mixture of Ac_2O (1 mL) and anhydrous DMSO (2 mL) at room temperature for 18 h to give the intermediate ketone **50**, after purification by column chromatography on silica gel using 50% EtOAc – hexane as eluent. Ketone **50** (66.2 mg, 0.147 mmol) was dissolved in anhyd THF

© 2002 NRC Canada

(2.5 mL) at 0°C, a solution of L-selectride in THF (1 M, 500 μL, 0.50 mmol) was added, and the reaction was continued for 1 h. Water (0.5 mL) was added to quench the reaction, and Ac_2O (0.5 mL) was added. After stirring for 30 min, the reaction mixture was concentrated to dryness. Disaccharide **51** was obtained by chromatography on silica gel using 5% MeOH – CH_2Cl_2 as eluent (52.6 mg, 76% yield), $[\alpha]_D$ +28.3 (*c* 0.7, $CHCl_3$). ^{1}H NMR (CD_3OD) δ: 7.45–7.51 (m, 2 H, Ph), 7.28–7.35 (m, 3H, Ph), 5.97 (d, 1H, *J* = 4.6 Hz, NH), 5.51 (s, 1H, PhCH), 5.01 (d, 1H, *J* = 8.2 Hz, H-1), 4.73 (dd, 1H, *J* = 3.4, 11.3 Hz, H-3), 4.56 (br "s", 1H, H-1′), 4.26–4.36 (m, 2H, H-6a, H-4), 4.04 (dd, 1H, *J* = 1.5, 12.4 Hz, H-6b), 3.81 (m, 1H, H-2′), 3.28–3.56 (m, 9H, 2 × OMe, H-5, H-2, H-5′), 3.18 (m, 1H, H-4′), 2.32 (d′t′, 1H, *J* = 4.1, 13.6 Hz, H-3e′), 1.84 (s, 3H, Ac), 1.22–1.34 (m, 4H, H-6′, H3a′). Anal. calcd. for $C_{23}H_{33}O_9N$: C 59.09, H 7.12, N 3.00; found: C 59.19, H 7.11, N 2.99.

Methyl 2-acetamido-3-*O*-(3,6-dideoxy-4-*O*-methyl-β-D-*arabino*-hexopyranosyl)-2-deoxy-β-D-galactopyranoside (14)

Compound **51** (42 mg, 0.09 mmol) was hydrogenated in a similar fashion as compound **5** and disaccharide **14** (32 mg, 94% yield) was obtained by reverse-phase HPLC using a gradient of H_2O–MeOH (0 → 30%) as eluent. $[\alpha]_D$ –24.5 (*c* 0.4, MeOH). ^{1}H NMR (D_2O) δ: 4.69 ("s", 1H, H-1′), 4.44 (d, 1H, *J* = 8.6 Hz, H-1), 4.12 ("d", 1H, *J* = 3.1 Hz, H-4), 4.01 (dd, 1H, *J* = 8.2, 10.6 Hz, H-2), 3.91 (m, 1H, H-2′), 3.86 (dd, 1H, *J* = 3.3, 10.8 Hz, H-3), 3.82 (dd, 1H, *J* = 7.9, 11.9 Hz, H-6a), 3.77 (dd, 1H, *J* = 4.2, 11.7 Hz, H-6b), 3.70 (m, 1H, H-5), 3.52 (s, 3H, OMe), 3.49 (dq, 1H, *J* = 6.2, 9.2 Hz, H-5′), 3.39 (s, 3H, OMe), 3.25 (ddd, 1H, *J* = 4.6, 9.3, 11.2 Hz, H-4′), 2.38 (d′t′, 1H, *J* = 4.2, 13.9 Hz, H-3e′), 2.02 (s, 3H, Ac), 1.54 (ddd, 1H, *J* = 2.9, 11.4, 14.1 Hz, H-3a′), 1.29 (d, 3H, *J* = 6.2 Hz, H-6′). HR-ES-MS *m*/*e* calcd. for $C_{16}H_{29}O_9N$ (MNa^+): 402.17400; found: 402.173637.

Methyl 2-azido-3,6-di-*O*-benzoyl-2-deoxy-β-D-galactopyranoside (53)

A solution of triol **52** (39) (860 mg, 3.9 mmol) and bis(tributyltin)oxide in anhydrous toluene (60 mL) was refluxed for 4.5 h with azeotropic removal of water. The solution was cooled to room temperature, and BzCl (1.0 mL, 8.97 mmol) was added. After stirring for 2.5 h, the mixture was diluted with EtOAc (75 mL), washed with brine (1 × 30 mL), dried and evaporated. Dibenzoate **53** was obtained by chromatography on silica gel using 15% EtOAc – hexane as eluent (1.46 g, 86% yield), $[\alpha]_D$ +29.8 (*c* 0.5, $CHCl_3$). ^{1}H NMR ($CDCl_3$) δ: 8.08 (m, 2H, Bz), 8.01 (m, 2H, Bz), 7.53–7.63 (m, 2H, Bz), 7.39–7.49 (m, 4H, Bz), 4.98 (dd, 1H, *J* = 3.2, 10.8 Hz, H-3), 4.66 (dd, 1H, *J* = 6.8, 11.4 Hz, H-6a), 4.51 (dd, 1H, *J* = 6.2, 11.3 Hz, H-6b), 4.34 (d, 1H, *J* = 8.0 Hz, H-1), 4.20 ("d", 1H, *J* = 2.7 Hz, H-4), 3.93 (dd, 1H, *J* = 8.0, 10.8 Hz, H-2), 3.91 (m, 1H, H-5), 3.61 (s, 3H, OMe), 2.53 (br s, 1H, OH-4). Anal. calcd. for $C_{21}H_{21}O_7N_3$: C 59.01, H 4.95, N 9.83; found: C 58.75, H 4.85, N 9.60.

Methyl 2-azido-3,6-di-*O*-benzoyl-2-deoxy-4-*O*-methyl-β-D-galactopyranoside (54)

A solution of dibenzoate **53** (416 mg, 0.973 mmol), MeOTf (330 μL, 2.91 mmol), and 2,6-di-*tert*-butyl-4-methylpyridine in anhyd CH_2Cl_2 (15 mL) was refluxed for 4 h. The mixture was diluted with EtOAc (75 mL), washed with H_2O (1 × 30 mL), dried and evaporated to dryness. The protected glycoside **54** was obtained by chromatography on silica gel using 15% EtOAc – hexane as eluent (401 mg, 94% yield), $[\alpha]_D$ –15.4 (*c* 0.6, $CHCl_3$). ^{1}H NMR ($CDCl_3$) δ: 8.11 (m, 2H, Bz), 8.02 (m, 2H, Bz), 7.53–7.64 (m, 2H, Bz), 7.40–7.52 (m, 4H, Bz), 5.00 (dd, 1H, *J* = 2.9, 10.8 Hz, H-3), 4.58 (dd, 1H, *J* = 6.4, 11.1 Hz, H-6a), 4.49 (dd, 1H, *J* = 6.8, 11.1 Hz, H-6b), 4.31 (d, 1H, *J* = 8.0 Hz, H-1), 3.82 (dd, 1H, *J* = 8.1, 10.7 Hz, H-2), 3.91 (m, 1H, H-5), 3.82 (br d, 1H, *J* = 2.9 Hz, H-4), 3.59 (s, 3H, OMe), 3.50 (s, 3H, OMe). Anal. calcd. for $C_{22}H_{23}O_7N_3$: C 59.86, H 5.25, N 9.52; found: C 59.83, H 5.31, N 9.28.

Methyl 2-azido-2-deoxy-4-*O*-methyl-β-D-galactopyranoside (55)

Dibenzoate **54** (350 mg, 0.79 mmol) was debenzoylated as described above to give the selectively methylated monosaccharide **55** (179 mg, 97% yield), $[\alpha]_D$ –12.2 (*c* 0.7, $CHCl_3$). ^{1}H NMR ($CDCl_3$) δ: 4.15 (m, 1H, H-1, high order), 3.94 (dd, 1H, *J* = 7.4, 11.2 Hz, H-6a), 3.94 (dd, 1H, *J* = 7.4, 11.2 Hz, H-6a), 3.77 (dd, 1H, *J* = 4.9, 11.2Hz, H-6b), 3.56 (s, 3H, OMe), 3.55 (s, 3H, OMe), 3.45–3.51 (m, 4H, H-2, H-3, H-4, H-5). Anal. calcd. for $C_8H_{15}O_5N_3$: C 41.20, H 6.48, N 18.02; found: C 41.53, H 6.53, N 18.33.

Methyl 2-azido-6-*O*-tert-butyldimethylsilyl-2-deoxy-4-*O*-methyl-β-D-galactopyranoside (56)

Diol **55** (108 mg, 0.46 mmol) was dissolved in anhydrous pyridine (4 mL), *t*-$BuMe_2SiCl$ (98 mg, 0.65 mmol) was added, and the reaction was stirred at ambient temperature for 3 h. Water (0.3 mL) was added and the mixture was concentrated. The syrup was chromatographed on silica gel using 15% EtOAc – hexane as eluent to yield **56** (135.1 mg, 84% yield), $[\alpha]_D$ –5.0 (*c* 0.6, $CHCl_3$). ^{1}H NMR ($CDCl_3$) δ: 4.11 (m, 1H, H-1, high order), 3.79 (dd, 1H, *J* = 8.6, 9.6 Hz, H-6a), 3.73 (dd, 1H, *J* = 5.6, 9.8 Hz, H-6a), 3.61 (br, 1H, H-4), 3.59 (s, 3H, OMe), 3.52 (s, 3H, OMe), 3.37–3.47 (m, 3H, H-2, H-3, H-5), 0.88 (s, 9H, *tert*-BuSi), 0.06 (s, 6H, $SiMe_2$). Anal. calcd. for $C_{14}H_{29}O_5N_3Si$: C 48.39, H 8.41, N 12.09; found: C 48.70, H 8.59, N 11.73.

Methyl 2-azido-3-*O*-(2-*O*-benzoyl-4-*O*-benzyl-3,6-dideoxy-β-D-ribo-hexopyranosyl)-6-*O*-*tert*-butyldimethylsilyl-2-deoxy-4-*O*-methyl-β-D-galactopyranoside (57)

A solution of acceptor **56** (40 mg, 0.115 mmol), thioglycoside **22** (55 mg, 0.127 mmol), and 4 Å molecular sieves (500 mg) in anhyd CH_2Cl_2 (3 mL) was stirred for 1 h, cooled to –40°C and NIS (54 mg, 0.23 mmol) and TfOH (4 μL) were added. After 1 h, the reaction was quenched with Et_3N. The mixture was diluted with EtOAc (75 mL), filtered, washed with a 10% aqueous solution of $Na_2S_2O_3$, dried and evaporated. Disaccharide **57** was obtained by chromatography on silica gel using 8% EtOAc – hexane as eluent (55 mg, 71%), $[\alpha]_D$ –3.4 (*c* 0.6, $CHCl_3$). ^{1}H NMR ($CDCl_3$) δ: 8.07 (m, 2H, Bz), 7.53 (m, 1H, Bz), 7.42 (m, 2H, Bz), 7.24–7.38 (m, 5H, Bn), 4.90 (m, 1H, H-2′), 4.77 (d, 1H, *J* = 7.9 Hz, H-1′), 4.63 (d, 1H, *J* = 11.5 Hz, Bn), 4.45 (d, 1H, *J* = 11.5 Hz, Bn), 4.10 (d, 1H, *J* = 7.9 Hz, H-1), 3.73–3.83 (m, 2H, H-6a, H-4), 3.66 (dd, 1H, *J* = 5.3, 9.4 Hz, H-6b), 3.45–3.63 (m, 8H, 2 × OMe, H-5′, H-2), 3.35–3.45 (m, 2H, H-3, H-5), 3.26 (m, 1H, H-4′), 2.80 (d′t′, 1H, *J* = 4.8, 12.0 Hz,

© 2002 NRC Canada

H-3e′), 1.60 (d′t′, 1H, *J* = 11.5, 11.5 Hz, H-3a′), 1.30 (d, 3H, *J* = 6.1 Hz, H-6′), 0.88 (s, 9H, *t*-BuSi), 0.06 (s, 6H, Me_2Si). Anal. calcd. for $C_{34}H_{49}O_9N_3Si$: C 60.78, H 7.35, N 6.25; found: C 60.57, H 7.17, N 5.83.

Methyl 2-azido-3-*O*-(4-*O*-benzyl-3,6-dideoxy-β-D-*ribo*-hexopyranosyl)-6-*O*-*tert*-butyldimethylsilyl-2-deoxy-4-*O*-methyl-β-D-galactopyranoside (58)

A solution of **57** (50 mg, 0.0744 mmol) in anhyd MeOH (5 mL) at 0°C was de-acylated by addition of a solution of NaOMe in MeOH (1.5 M, 200 μL). After stirring for 5 h at 0°C, the mixture was neutralized with Amberlite IR-120 (H^+) resin and evaporated. The residue was chromatographed on silica gel using 15% EtOAc – hexane as eluent to give **58** (41.5 mg, 98% yield), $[\alpha]_D$ –11.6 (*c* 0.7, $CHCl_3$). ^1H NMR ($CDCl_3$) δ: 7.25–7.36 (m, 5H, Bn), 4.63 (d, 1H, *J* = 11.6 Hz, Bn), 4.45 (d, 1H, *J* = 11.6 Hz, Bn), 4.35 (d, 1H, *J* = 7.5 Hz, H-1′), 4.11 (d, 1H, *J* = 7.9 Hz, H-1), 3.74–3.82 (m, 2H, H-6a, H-4), 3.65–3.73 (m, 2H, H-3, H-6b), 3.54 (s, 3H, OMe), 3.36–3.53 (m, 7H, OMe, H-2′, H-5′, H-2, H-5), 3.13 (m, 1H, H-4′), 2.53 (d′t′, 1H, *J* = 4.7, 12.2 Hz, H-3e′), 1.47 (d′t′, 1H, *J* = 11.8, 11.8 Hz, H-3a′), 1.33 (d, 3H, *J* = 6.1 Hz, H-6′), 0.87 (s, 9H, *t*-BuSi), 0.05 (s, 6H, Me_2Si). Anal. calcd. for $C_{27}H_{45}O_8N_3Si$: C 57.12, H 7.99, N 7.40; found: C 57.00, H 7.83, N 7.45.

Methyl 2-acetamido-3-*O*-(4-*O*-benzyl-3,6-dideoxy-β-D-*arabino*-hexopyranosyl)-6-*O*-*tert*-butyldimethylsilyl-2-deoxy-4-*O*-methyl-β-D-galactopyranoside (60)

Alcohol **58** (55 mg, 0.097 mmol) was oxidized using DMSO (2 mL) and Ac_2O (1 mL) as described above. The intermediate ketone **59** was reduced using a solution of L-selectride in THF (1.0 M, 200 μL) and acetylated using Ac_2O as described above to give the disaccharide **60** (43 mg, 76% yield), $[\alpha]_D$ +4.0 (*c* 0.6, $CHCl_3$). ^1H NMR ($CDCl_3$) δ: 7.22–7.36 (m, 5H, Bn), 6.05 (d, 1H, *J* = 6.9 Hz, NH), 4.85 (d, 1H, *J* = 8.2 Hz, H-1), 4.54–4.66 (m, 3H, H-3, H-1′, Bn), 4.43 (d, 1H, *J* = 11.5 Hz, Bn), 3.91 (br d, 1H, *J* = 2.7 Hz, H-4), 3.87 (m, 1H, H-2′), 3.62–3.80 (m, 2H, H-6a, H-6b), 3.37–3.60 (m, 9H, 2 × OMe, H-5, H-4′, H-5′), 3.25 (m, 1H, H-2), 2.85 (br s, 1H, OH-2′), 2.41 (d′t′, 1H, *J* = 3.1, 13.6 Hz, H-3e′), 1.49 (m, 1H, H-3a′), 1.28 (d, 3H, *J* = 5.2 Hz, H-6′), 0.88 (s, 9H, *t*-BuSi), 0.05 (s, 6H, Me_2Si). Anal. calcd. for $C_{29}H_{49}O_9NSi$: C 59.66, H 8.46, N 2.40; found: C 59.96, H 8.78, N 2.27.

Methyl 2-acetamido-3-*O*-(3,6-dideoxy-β-D-arabino-hexopyranosyl)-2-deoxy-4-*O*-methyl-β-D-galactopyranoside (8)

Compound **60** (35 mg, 0.06 mmol) was hydrogenated in a similar fashion as compound **5**. After evaporation, the residue was dissolved in anhyd THF (2 mL), a solution of TBAF in THF (1.0 M, 50 μL) was added and reaction was continued for 5 h. After concentration, disaccharide **8** was obtained by reverse-phase HPLC using a gradient of H_2O–MeOH (0 → 30%) as eluent (20 mg, 88% yield), $[\alpha]_D$ –47.6 (*c* 0.2, MeOH). ^1H NMR (D_2O) δ: 4.62 (d, 1H, *J* = 0.6 Hz, H-1′), 4.41 (d, 1H, *J* = 8.6 Hz, H-1), 3.97 (dd, 1H, *J* = 8.4, 10.8 Hz, H-2), 3.87 (dd, 1H, *J* = 3.1, 11.0 Hz, H-3), 3.86 (m, 2H, H-2′, H-3), 3.82 ("d", 1H, J = 3.1 Hz, H-4), 3.77–3.81 (m, 2H, H-6a, H-6b), 3.67 (m, 1H, H-5), 3.55 (m, 1H, H-4′), 3.50 (s, 3H, OMe), 3.42 (dq, 1H, *J* = 6.2, 9.2 Hz, H-5′), 2.17 (ddd, 1H, *J* = 3.5, 4.8, 13.9 Hz, H-3e′), 2.02 (s, 3H, Ac), 1.65 (ddd, 1H, *J* = 3.1, 11.7, 14.3 Hz, H-3a′), 1.29 (d, 3H, *J* = 6.2 Hz, H-6′). HR-ES-MS *m*/*e* calcd. for $C_{16}H_{29}O_9N$ (MH^+): 402.17400; found: 402.174200.

Methyl 2-acetamido-3-*O*-benzoyl-4,6-*O*-benzylidene-2-deoxy-β-D-glucopyranoside (61)

Benzoyl chloride (646 μL, 5.57 mmol) was added dropwise to an ice-cold solution of alcohol **17** (45) (1.5 g, 4.6 mmol) in a mixture of anhyd CH_2Cl_2 (10 mL) and pyridine (8 mL), and the mixture was stirred at room temperature for 5 h. Methanol (1 mL) was added, the mixture was concentrated and dissolved in CH_2Cl_2 (100 mL), washed with 5% $NaHCO_3$ (2 × 50 mL), saturated brine (1 × 50 mL), dried and evaporated. The benzoylated acetal **61** was obtained by chromatography on silica gel using 5% MeOH–CH_2Cl_2 as eluent (1.90 g, 96%), $[\alpha]_D$ –99.2 (*c* 0.8, $CHCl_3$). ^1H NMR ($CDCl_3$) δ: 8.03 (m, 2H, Bz), 7.56 (m, 1H, Bz), 7.43 (m, 2H, Bz), 7.40 (m, 2H, Ph), 7.26–7.32 (m, 3H, Ph), 6.05 (d, 1H, *J* = 9.5 Hz, NH), 5.58 (t, 1H, *J* = 9.8 Hz, H-3), 5.53 (s, 1H, PhCH), 4.47 (d, 1H, *J* = 8.4 Hz, H-1), 4.37 (dd, 1H, *J* = 5.0, 10.5 Hz, H-6a), 4.32 (d′t′, 1H, *J* = 10.0 Hz, 10.0 Hz, H-2), 3.86 (t, 1H, *J* = 9.4 Hz, H-4), 3.83 (t, 1H, *J* = 10.3 Hz, H-6b), 3.67 (m, 1H, H-5), 3.42 (s, 3H, OMe), 1.89 (s, 3H, Ac). Anal. calcd. for $C_{23}H_{25}O_7N$: C 64.63, H 5.90, N 3.28; found: C 64.56, H 5.88, N 3.21.

Methyl 2-acetamido-3-*O*-benzoyl-6-*O*-benzyl-2-deoxy-β-D-glucopyranoside (62)

To a mixture containing compound **61** (1.0 g, 2.34 mmol), $NaBH_3CN$ (1.8 g, 28 mmol), and 4 Å molecular sieves (1.5 g) in anhyd THF (20 mL), was added a trace amount of methyl orange (~1 mg). A saturated solution of HCl in anhydrous ether (30 mL) was added dropwise until the color of the reaction became slightly pink. The reaction was continued for 2 h, the mixture was diluted with EtOAc (50 mL), and filtered. After concentration, the residue was dissolved in EtOAc (120 mL), and the solution was washed with 2 M HCl (2 × 50 mL), 10% $NaHCO_3$ aqueous solution (2 × 50 mL), dried, and evaporated. The alcohol **62** was obtained by chromatography on silica gel using 7.5% MeOH – CH_2Cl_2 as eluent (950 mg, 95%), $[\alpha]_D$ –13.2 (*c* 0.3, $CHCl_3$). ^1H NMR ($CDCl_3$) δ: 8.03 (m, 2H, Bz), 7.57 (m, 1H, Bz), 7.44 (m, 2H, Bz), 7.40 (m, 2H, Ph), 7.25–7.36 (m, 5H, Ph), 5.56 (d, 1H, *J* = 9.2 Hz, NH), 5.27 (dd, 1H, *J* = 9.0, 10.7 Hz, H-3), 4.64 (d, 1H, *J* = 11.9 Hz, Bn), 4.58 (d, 1H, *J* = 11.9 Hz, Bn), 4.48 (d, 1H, *J* = 8.3 Hz, H-1), 4.11 (d′t′, 1H, *J* = 8.8, 10.7 Hz, H-2), 3.90 (t, 1H, *J* = 9.3 Hz, H-4), 3.86 (dd, 1H, *J* = 4.9, 10.3 Hz, H-6a), 3.83 (dd, 1H, *J* = 4.8, 10.3 Hz, H-6b), 3.62 (m, 1H, H-5), 3.50 (s, 3H, OMe), 1.86 (s, 3H, Ac). Anal. calcd. for $C_{23}H_{27}O_7N$: C 64.32, H 6.34, N 3.26; found: C 64.16, H 6.12, N 3.01.

Methyl 2-acetamido-3-*O*-benzoyl-6-*O*-benzyl-2-deoxy-4-imidazoylthiocarbonyl-β-D-glucopyranoside (63)

1,1′-Thiocarbonyldiimidazole (538 mg, 2.72 mmol) was added to a solution of compound **62** (585 mg, 1.36 mmol) in anhydrous toluene (10 mL) and the mixture was heated to 90°C overnight. The solution was diluted with EtOAc (75 mL), washed with brine (1 × 25 mL), dried and concentrated to dryness to give **63** (691 mg, 94%), $[\alpha]_D$ –21.0 (*c*

© 2002 NRC Canada

0.8, $CHCl_3$). ^1H NMR ($CDCl_3$) δ: 8.13 (s, 1H, imidazole), 7.90 (m, 2H, Bz), 7.62 (s, 1H, imidazole), 7.51 (m, 1H, Bz), 7.17–7.40 (m, 7H, Ar), 7.02 (s, 1H, imidazole), 6.08 (t, 1H, *J* = 9.5 Hz, H-4), 5.86 (d, 1H, *J* = 8.8 Hz, NH), 5.78 (t, 1H, *J* = 10.5 Hz, H-3), 4.76 (d, 1H, *J* = 8.4 Hz, H-1), 4.46 (s, 2H, Bn), 4.08 (m, 1H, H-2), 3.96 (m, 1H, H-5), 3.71 (dd, 1H, *J* = 3.8, 10.6 Hz, H-6a), 3.65 (dd, 1H, *J* = 5.0, 10,8 Hz, H-6b), 3.54 (s, 3H, OMe), 1.86 (s, 3H, Ac), Anal. calcd. for $C_{27}H_{29}O_7N_3S$: C 60.10, H 5.42, N 7.79; found: C 60.21, H 5.33, N 7.72.

Methyl 2-acetamido-3-*O*-benzoyl-6-*O*-benzyl-2,4-dideoxy-β-D-xylo-hexopyranoside (64)

A solution of **63** (321.4 mg, 0.60 mmol) in anhydrous toluene (15 mL) was heated to reflux, a solution of tributyltin hydride (535 μL, 1.93 mmol) in anhydrous toluene (5 mL) and a catalytic amount of AIBN (~10 mg) were added. After 4 h, the deoxygenation was complete. Compound **64** was obtained by chromatography on silica gel using 3% MeOH – CH_2Cl_2 as eluent (217 mg, 88% yield), $[\alpha]_D$ –8.2 (*c* 0.7, $CHCl_3$). ^1H NMR ($CDCl_3$) δ: 7.99 (m, 2H, Bz), 7.54 (m 1H, Bz), 7.41 (m, 2H, Bz), 7.24–7.35 (m, 5H, Bn), 5.42 (br, 1H, NH), 4.57 (s, 2H, Bn), 4.43 (d, 1H *J* = 8.4 Hz, H-1), 4.02 (d′t′, 1H, *J* = 8.9, 10.3 Hz, H-2), 3.80 (m, 1H, H-5), 3.63 (dd, 1H, *J* = 5.7, 10.2 Hz, H-6a), 3.54 (dd, 1H, *J* = 4.6, 10.2 Hz, H-6b), 3.50 (s, 3H, Ome), 2.22 (ddd, 1H, *J* = 1.8, 5.1, 12.6 Hz, H-4e), 1.87 (s, 3H, Ac), 1.72 (d′t′, 1H, *J* = 11.5, 11.5 Hz, H-3a). Anal. calcd. for $C_{23}H_{27}O_6N$: C 66.81, H 6.58, N 3.39; found: C 66.59, H 6.41, N 3.02.

Methyl 2-acetamido-6-*O*-benzyl-2,4-dideoxy-β-D-xylo-hexopyranoside (65)

A solution of NaOMe in MeOH (1.5 M, 200 μL) was added to a solution of compound **64** (400 mg, 0.967 mmol) in anhyd MeOH (50 mL), and the reaction was stirred at room temperature for 2 h. After neutralization with Amberlite IR-120 (H^+), the organic solution was evaporated, and the acceptor **65** was obtained by chromatography on silica gel using 5% MeOH – CH_2Cl_2 as eluent (280 mg, 94% yield), $[\alpha]_D$ –63.3 (*c* 0.5, $CHCl_3$). ^1H NMR ($CDCl_3$) δ: 7.23–7.34 (m, 5H, Bn), 6.08 (d, 1H, *J* = 4.6 Hz, NH), 4.57 (d, 1H, *J* = 12.1 Hz, Bn), 4.52 (d, 1H, *J* = 12.1 Hz, Bn), 4.21 (d, 1H, *J* = 8.1 Hz, H-1), 3.77 (m, 1H, H-3), 3.65 (m, 1H, H-5), 3.58 (dd, 1H, *J* = 6.0, 10.3 Hz, H-6a), 3.51 (dd, 1H, *J* = 4.3, 10.2 Hz, H-6b), 3.48 (s, 3H, OMe), 3.30 (m, 1H, H-2), 2.05 (m, 1H, H-4e), 2.02 (s, 3H, Ac), 1.46 (d′t′, 1H, *J* = 11.6, 11.6 Hz, H-4a). Anal. calcd. for $C_{16}H_{23}O_5N$: C 62.12, H 7.49, N 4.53; found: C 61.87, H 7.37, N 4.29.

Methyl 2-acetamido-3-*O*-(2-*O*-benzoyl-4-*O*-benzyl-3,6-dideoxy-β-D-ribo-hexopyranosyl)-6-*O*-benzyl-2,4-dideoxy-β-D-xylo-hexopyranoside (66)

N-Iodosuccinimide (125 mg, 0.52 mmol) was added to a mixture of donor **22** (230 mg, 0.52 mmol), acceptor **65** (82 mg, 0.26 mmol), and 4 Å molecular sieves (350 mg) in anhyd CH_2Cl_2 (5 mL) The reaction was cooled to –60°C, and TfOH (5.0 μL) was added. After 3 h, the reaction was neutralized with Et_3N (0.5 mL), diluted with EtOAc (75 mL), and filtered. The organic solution was washed with a 10% aqueous solution of $Na_2S_2O_3$ (1 × 30 mL), and the mixture was purified by repeated chromatography on silica gel using 5% MeOH – CH_2Cl_2 to afford the disaccharide **66** (91 mg, 54% yield) in pure form, $[\alpha]_D$ +38.2 (*c* 0.5, $CHCl_3$). ^1H NMR (CDCl3) δ: 8.10 (m, 2H, Bz), 7.57 (m, 1H, Bz), 7.44 (m, 2H, Bz), 7.25–7.33 (m, 10H, Bn), 5.41 (d, 1H, *J* = 6.7 Hz, NH), 4.96 (m, 1H, H-2′), 4.90 (d, 1H, *J* = 8.2 Hz, H-1), 4.64 (d, 1H, *J* = 7.6 Hz, H-1′), 4.61 (d, 1H, *J* = 11.5 Hz, Bn), 4.57 (d, 1H, *J* = 12.1 Hz, Bn), 4.53 (d, 1H, *J* = 12.1 Hz, Bn), 4.46 (m, 1H, H-3), 4.45 (d, 1H, *J* = 11.7 Hz, Bn), 3.72 (m, 1H, H-5), 3.56 (dd, 1H, *J* = 5.9, 10.1 Hz, H-6a), 3.45–3.55 (m, 2H, H-5′, H-6b), 3.43 (s, 3H, OMe), 3.24 (m, 1H, H-4′), 2.76 (m, 1H, H-2), 2.65 (d′t′, 1H, *J* = 4.9, 12.0 Hz, H-3e′), 2.24 (m, 1H, H-4e), 1.62 (d′t′, 1H, *J* = 11.7, 11.7 Hz, H-3a′), 1.56 (s, 3H, Ac), 1.50 (d′t′, 1H, *J* = 11.6, 11.6 Hz, H-4a), 1.30 (d, 3H, *J* = 6.1 Hz, H-6′). HR-ES-MS *m*/*e* calcd. for $C_{36}H_{43}O_9N$ (MNa^+): 656.28355; found: 656.283345.

Methyl 2-acetamido-3-*O*-(4-*O*-benzyl-3,6-dideoxy-β-D-ribo-hexopyranosyl)-6-*O*-benzyl-2,4-dideoxy-β-D-xylo-hexopyranoside (67)

Disaccharide **66** (70 mg, 0.11 mmol) was dissolved in anhyd MeOH (15 mL), and a solution of NaOMe in MeOH (1.5 M, 200 μL) was added, the reaction was stirred at room temperature overnight. After neutralization with Amberlite IR-120 (H^+), the mixture was concentrated to dryness. The alcohol **67** was obtained (53 mg, 91% yield) by chromatography on silica gel using 7.5% MeOH – CH_2Cl_2 as eluent, $[\alpha]_D$ +3.3 (*c* 0.6, $CHCl_3$). ^1H NMR (CDCl3) δ: 7.22–7.34 (m, 10H, Bn), 5.58 (d, 1H, *J* = 7.9 Hz, NH), 4.57 (d, 1H, *J* = 11.3 Hz, Bn), 4.56 (d, 1H, *J* = 12.1 Hz, Bn), 4.53 (d, 1H, *J* = 12.1 Hz, Bn), 4.43 (d, 1H, *J* = 9.3 Hz, H-1), 4.41 (d, 1H, *J* = 11.8 Hz, Bn), 4.21 (d, 1H, *J* = 7.5 Hz, H-1′), 3.88 (m, 1H, H-3), 3.68 (m, 1H, H-5), 3.59 (dd, 1H, *J* = 6.0 Hz, 10.1 Hz, H-6a), 3.45–3.55 (m, 5H, H-2, H-6b, OMe), 3.34–3.42 (m, 2H, H-2′, H-5′), 3.10 (m, 1H, H-4′), 2.46 (d′t′, 1H, *J* = 4.6, 12.2 Hz, H-3e′), 2.19 (ddd, 1H, *J* = 1.8, 5.2, 13.4 Hz, H-4e), 1.99 (s, 3H, Ac), 1.57 (d′t′, 1H, *J* = 11.5, 11.4 Hz, H-4a), 1.38 (d′t′, 1H, *J* = 11.6, 11.6 Hz, H-3a′), 1.25 (d, 3H, *J* = 6.1 Hz, H-6′). HR-ES-MS *m*/*e* calcd. for $C_{29}H_{39}O_8N$ (MNa^+): 552.25734; found: 552.257502.

Methyl 2-acetamido-3-*O*-(3,6-dideoxy-β-D-*arabino*-hexopyranosyl)-2,4-dideoxy-β-D-xylo-hexopyranoside (7)

A solution of alcohol **67** (25 mg, 0.047 mmol) in anhyd DMSO (2 mL) and Ac_2O (1 mL) was stirred at 0°C for 30 min, and the reaction was left at room temperature overnight. After evaporation, the residue was partitioned in a mixture of EtOAc – 10% aqueous NaCl solution, and the organic solution was evaporated and dissolved in anhyd THF (3 mL) at 0°C. A solution of L-selectride in THF (1.0 M, 200 μL, 0.20 mmol) was added and the reaction was left at 0°C for 1 h. Water (0.3 mL) was added and the mixture was diluted with EtOAc (50 mL), washed with $Na_2S_2O_3$, brine, dried and concentrated to give crude **69**. Liquid ammonia (25 mL) was collected in a flask containing compound **69** (15 mg, 0.028 mmol) equipped with a dry ice condenser. Sodium (50 mg, 0.97 mmol) was added to this solution, and reaction was continued for 4 h. Methanol (0.5 mL) was added, and the condenser was removed to allow ammonia to evaporate. The residue was dissolved in H_2O (3 mL), and neutralized with a saturated aqueous solution of NH_4Cl and

© 2002 NRC Canada

evaporated. The desired disaccharide **7** was obtained by reverse-phase HPLC using a gradient of H_2O–MeOH (0 → 30%) as eluent (4.0 mg, 23%), $[\alpha]_D$ –55.5 (*c* 0.4, MeOH). ^1H NMR (D_2O) δ: 4.67 ("s", 1H, H-1′), 4.40 (d, 1H, *J* = 8.6 Hz, H-1), 3.89 (ddd, 1H, *J* = 5.1, 10.6, 10.6 Hz, H-3), 3.84 (m, 1H, H-2′), 3.63–3.72 (m, 3H, H-5, H-6a, H-6b), 3.62 (dd, 1H, *J* = 8.6, 10.1 Hz, H-2), 3.56 (ddd, 1H, *J* = 4.6, 9.3, 11.4 Hz, H-4′), 3.51 (s, 3H, OMe), 3.43 (dq, 1H, *J* = 6.1, 9.3 Hz, H-5′), 2.13–2.18 (m, 2H, H-3e′, H-4e), 2.02 (s, 3H, Ac), 1.64 (ddd, 1H, *J* = 3.1, 11.5, 14.3 Hz, H-3a′), 1.50 (d′t′, 1H, *J* = 11.5, 11.5 Hz, H-4a), 1.27 (d, 3H, *J* = 6.2 Hz, H-6′). HR-ES-MS *m/e* calcd. for $C_{15}H_{27}O_8N$ (MNa^+): 372.16344; found: 372.163817.

Acknowledgements

We thank Mrs. Joanna Sadowska for invaluable technical support. Financial support was provided by research grants to D.R. Bundle from the Natural Sciences and Engineering Research Council of Canada (NSERC) and the University of Alberta. Work in the laboratory of J.A. Appleton was supported by a grant from the National Institutes of Health (AI14490).

References

1. W.C. Campbell. *Trichella* and *Trichinosis*. Plenum Press, New York. 1983.
2. J.A. Appleton and D.D. McGregor. Science (Washington, D.C.), **226**, 70 (1984).
3. J.A. Appleton, L.R. Schain, and D.D. McGregor. Immunology, **65**, 487 (1988).
4. S.M. Haslam, H.R. Morris, and A. Dell. Trends Parasitol. **17**, 231 (2001).
5. N. Wisnewski, M. McNeil, R.B. Grieve, and D.L. Wassom. Mol. Biochem. Parasitol. **1**, 25 (1993).
6. A.J. Reason, L.A. Ellis, J.A. Appleton, N. Wisnewski, R.B. Grieve, M. McNeil, D.L. Wassom, H.R. Morris, and A. Dell. Glycobiology, **4**, 593 (1994).
7. M. Philipp, P.M. Taylor, R.M.E. Parkhouse, and B.M. Ogilvie. J. Exp. Med. **154**, 210 (1981).
8. M. Jungery and B.M. Ogilvie. J. Immunol. **129**, 839 (1982).
9. K.A. Wright. J. Parasitol. **65**, 441 (1979).
10. D.P. Jasmer. Parasitol. Today, **11**, 185 (1995).
11. E.Y. Denkers, D.L. Wassom, C.J. Krco, and C.E. Hayes. J. Immunol. **144**, 3152 (1990).
12. E.Y. Denkers, D.L. Wassom, and C.E. Hayes. Mol. Biochem. Parasitol. **41**, 241 (1990).
13. M.G. Ortega-Pierres, L. Yepez-Mulia, W. Homan, H.R. Gamble, P.L. Pim, Y. Takahashi, D.L. Wassom, and J.A. Appleton. Parasite Immunol. **18**, 273 (1996).
14. P.J. Peters, L.F. Gagliardo, E.A. Sabin, A.B. Betchen, K. Ghosh, J.B. Oblak, and J.A. Appleton. Infect. Immun. **67**, 4661 (1999).
15. L.A. Ellis, A.J. Reason, H.R. Morris, A. Dell, R. Iglesias, F.M. Ubeira, and J.A. Appleton. Glycobiology, **4**, 585 (1994).
16. L.A. Ellis, C.S. McVay, M.A. Probert, J. Zhang, D.R. Bundle, and J.A. Appleton. Glycobiology, **7**, 383 (1997).
17. O. Lüderitz. Angew. Chem. Intl. Ed. Engl. **9**, 649 (1970).
18. Y. Zheng, M.Sc. Thesis, University of Alberta, 1998.
19. M.A. Probert, J. Zhang, and D.R. Bundle. Carbohydr. Res. **296**, 149 (1996).
20. M. Nitz and D.R. Bundle. J. Org. Chem. **65**, 3064 (2000).
21. M. Nitz. Ph.D. Thesis, University of Alberta, 2001.
22. M.A. Probert, J. Zhang, and D.R. Bundle. Carbohydr. Res. **296**, 149 (1996).
23. J. Zhang, A. Otter, and D.R. Bundle. Bioorg. Med. Chem. **4**, 1989 (1996).
24. J.A. Appleton, A. Dell, M. Nitz, and D.R. Bundle. Trends in Glycoscience and Glycotechnology, **13**, 481 (2002).
25. D.R. Bundle, E. Eichler, M.A.J. Gidney, M. Meldal, A. Ragauskas, B.W. Sigurskjold, B. Sinnott, D.C. Watson, M. Yaguchi, and N.M. Young. Biochemistry, **33**, 5172 (1994).
26. R.U. Lemieux. Chem. Soc. Rev. **18**, 347 (1989).
27. D.R. Bundle. Pure Appl. Chem. **61**, 1171 (1989).
28. C.P.J. Glaudemans. Chem. Rev. **91**, 25 (1991).
29. F.-I. Auzanneau, H.R. Hanna, and D.R. Bundle. Carbohydr. Res. **240**, 161 (1993).
30. F.-I. Auzanneau and D.R. Bundle. Carbohydr. Res. **247**, 195 (1993).
31. K. Bock and B.W. Sigurskjold. *In* Studies in natural products chemistry. Vol. 7. *Edited by* Atta-ur-Rahman. Elsevier, Amsterdam. 1990. p. 29.
32. P. Street, C.R. Armstrong, and S.G. Withers. Biochemistry, **25**, 6021 (1986).
33. R.U. Lemieux, C.-C. Ling, N. Sharon, and H. Streicher. Isr. J. Chem. **40**, 167 (2000).
34. P.V. Nikrad, H. Beierbeck, and R.U. Lemieux. Can. J. Chem. **70**, 241 (1992).
35. J. Kihlberg, T. Frejd, K. Jansson, and G. Magnusson. Carbohydr. Res. **152**, 113 (1986).
36. J.J. Gridley and H.M.I. Osborn. J. Chem. Soc. Perkin Trans. 1, 1471 (2000), and refs. therein.
37. F.W. Lichtenthaler, U. Klares, Z. Szurmai, and B. Werner. Carbohydr. Res. **305**, 293 (1998).
38. H.N. Yu, P. Zhang, C.-C. Ling, and D.R. Bundle. Tetrahedron: Assymetry, **11**, 465 (2000).
39. A. Marra, X. Dong, M. Petitou, and P. Sinay. Carbohydr. Res. **195**, 39 (1989).
40. D.H.R. Barton and S.W. McCombie. J. Chem. Soc. Perkin Trans. 1, 1574 (1975).
41. R.U. Lemieux. Complex carbohydrates in Drug Research. *In* The Alfred Benzon symposium no. 36. *Edited by* K. Bock and H. Clausen. Munksgaard, Copenhagen. 1994. p. 188.
42. M.-H. Du, U. Spohr, and R.U. Lemieux. Glycoconjugate J. **11**, 443 (1994).
43. R.U. Lemieux. Acc. Chem. Res. **29**, 373 (1996).
44. M.L. Connolly. Science (Washington, D.C.), **221**, 709 (1983).
45. S. Sabesan and J.C. Paulson. J. Am. Chem. Soc. **108**, 2068 (1986).

© 2002 NRC Canada

Characterization of some mesogenic alkyl 1-thioglycosides

B. Henrissat, G.K. Hamer, M.G. Taylor, and R.H. Marchessault

Abstract: A series of dodecyl 1-thio-β-D-glycosides has been synthesized and characterized (DSC, NMR, CP MAS, X-ray diffraction) as possible new marking materials with liquid-crystalline properties. These compounds undergo solid to liquid crystal phase transitions at various temperatures, which depend on the nature of the carbohydrate part of the structure. Their liquid-crystalline phases show extreme shear thinning behaviour.

Key words: liquid crystal, powder X-ray diffraction, phase transition, thioglycoside, solid-state NMR, marking material

Résumé : On a effectué la synthèse et on a caractérisé (DSC, RMN, CP MAS, diffraction des rayons X) une série de 1-thio-β-D-glycosides de dodécyle, de nouveaux marqueurs potentiels ayant des propriétés de cristaux liquides. Ces composés subissent des transitions de solide à cristal liquide à diverses températures qui dépendent de la nature de la portion hydrate de carbone de la structure. Leurs phases cristal liquide présentent un comportement extrême de fluidisation par cisaillement.

Mots clés : cristal liquide, diffraction de rayons X par des poudres, transition de phase, thioglycoside, RMN à l'état solide, marqueur.

[Traduit par la Rédaction]

Introduction

Alkyl glycosides have been shown to be thermotropic mesogens when the alkyl chain ranges from heptyl upwards (1). Because of the great variety of possible carbohydrates, alkyl chain length, type of linkage and its position of attachment to the sugar molecule, it has been predicted that several million carbohydrate liquid crystals could be obtained (2). A few of these amphiphilic carbohydrates have found biochemical applications as non-ionic detergents for membrane protein extraction (3). As part of a research program concerned with the evaluation of their liquid-crystalline phase as potential materials with advanced properties, we report here synthesis and the characterization of some dodecyl 1-thioglycosides.

Experimental

General methods

Solutions were evaporated below 45°C under diminished pressure. TLC was performed on silica gel F254 (Aldrich), eluent was ethyl acetate – hexane (1:2, v/v) and detection was done with 5% sulfuric acid in ethanol followed by heating. The ^{1}H and ^{13}C NMR spectra were recorded at 250 and 62.5 MHz, respectively, on a Bruker AM 250 spectrometer. Chemical shifts are given with respect to external tetramethylsilane. Differential scanning calorimetry was carried out with a PerkinElmer DSC-2C calorimeter on 12 mg samples sealed in aluminum capsules. The heating and cooling rates were 20°C min^{-1}. Powder X-ray diagrams were obtained in a Warhus flat-film camera by using Ni-filtered Cu Kα radiation on the sample loaded in 0.5-mm capillary tubes.

Solid-state ^{13}C NMR

High resolution ^{13}C NMR spectra were acquired at 50.3 MHz with a Bruker CXP 200 instrument. Cross-polarization (CP) was performed with Hartmann–Hahn matched radio-frequency fields of about 60 Hz. Spectra were collected with a 1 ms contact time and 6 s recycle delay over a sweep width of 10 kHz. Magic-angle spinning (MAS) at about 2.5 kHz was achieved in a probe from Doty Scientific. A small chip of linear polyethylene (NBS Standard Reference Material 1475) was added to the samples to provide a chemical shift reference at 32.9 ppm (4) with respect to tetramethylsilane. The spectrum of the liquid-crystalline phase was not recorded because cross-polarization was ineffective due to high molecular mobility. Furthermore, the

Received 4 December 2001. Published on the NRC Research Press Web site at http://canjchem.nrc.ca on 4 September 2002.

Dedicated to the memory of Professor Raymond U. Lemieux.

B. Henrissat,[1] G.K. Hamer,[2] M.G. Taylor and R.H. Marchessault.[3,4] Xerox Research Centre of Canada, 2660 Speakman Drive, Mississauga, ON L5K 2L1, Canada.

[1]Present address: AFMB-CNRS, 31 Chemin Joseph Aiguier, 13402, Marseille CEDEX 20, France.
[2]Present address: Unit 1 2280 South Milway, Mississauga, ON L5L 2P4, Canada.
[3]Present address: Department of Chemistry, McGill University, 3420 University St., Montreal, QC H3A 2A7, Canada.
[4]Corresponding author (e-mail: Robert.marchessault@mcgill.ca).

 DOI: 10.1139/V02-157 © 2002 NRC Canada

Table 1. ^{1}H NMR data for ring protons of 1-thio-β-D-glycosides **4**, **9**, **14**, and **15**.

Compound	Chemical shifts (ppm) and coupling constants (Hz)						
	H-1	H-2	H-3	H-4	H-5	H-6a	H-6b
4	4.48 d ($J_{1,2}$ = 10.0)	5.23 t ($J_{2,3}$ = 10.0)	5.09 t ($J_{3,4}$ = 10.0)	5.03 t ($J_{4,5}$ = 10.0)	3.71 m ($J_{5,6a}$ = 5.0)	4.25 dd ($J_{6a,6b}$ = 12.0)	4.14 dd ($J_{5,6b}$ = 2.5)
9	4.48 d ($J_{1,2}$ = 10.0)	5.24 t ($J_{2,3}$ = 10.0)	5.05 dd ($J_{3,4}$ = 4.0)	5.43 dd ($J_{4,5}$ = 1.0)	3.93 dt ($J_{5,6a}$ = 8.0)		
	H-1	H-2	H-3	H-4	H-5a	H-5b	
14	4.51 d ($J_{1,2}$ = 10.0)	5.28 t ($J_{2,3}$ = 10.0)	4.97 t ($J_{3,4}$ = 10.0)	4.95 m ($J_{4,5a}$ = 10.0)	4.23 dd ($J_{5a,5b}$ = 13.0)	3.38 dd ($J_{4,5b}$ = 6.0)	
15	4.24 d ($J_{1,2}$ = 10.0)	3.04 t ($J_{2,3}$ = 10.0)	3.18 t ($J_{3,4}$ = 10.0)	3.34 m ($J_{4,5a}$ = 10.0)	3.78 dd ($J_{5a,5b}$ = 12.0)	3.08 dd ($J_{4,5b}$ = 6.0)	

Notes: For each compound: 1st line, chemical shift; 2nd line, multiplicity; 3rd line, coupling constant (in parenthesis). d= doublet; t = triplet; dd = doublet of doublets; m = multiplet.

sample flowed under the rapid spinning conditions, leading to imbalance in the rotor and to magic angle spinning instabilities.

Syntheses

Syntheses of the 2-thiopseudourea derivatives **2**, **7**, and **12** from the corresponding glycosyl bromides **1**, **6**, and **11** were done as previously described (5). *S*-alkylation was adapted from a classical procedure (6). In a typical experiment, the 2-thiopseudourea derivative (40 g) and potassium carbonate (70 g) in water (60 mL) are stirred with dichloromethane at room temperature, the extract is concentrated, and the residue is alkylated with an appropriate alkyl halide (75 mL). De-*O*-acetylation was effected with sodium methoxide in methanol.

Results and discussion

Tetra-*O*-acetyl-α-D-glucopyranosyl bromide (7) **1** was converted into 2-*S*-(tetra-*O*-acetyl-β-D-glucopyranosyl)-2-thiopseudourea hydrobromide **2** according to standard procedures (5). 2,3,4,6-Tetra-*O*-acetyl-1-thio-β-D-glucopyranose **3** was generated from **2** and was *S*-alkylated in situ with 1-bromododecane in the presence of potassium carbonate (6). Treatment of the resulting dodecyl 2,3,4,6-tetra-*O*-acetyl-1-thio-β-D-glucopyranoside **4** with a catalytic amount of sodium methoxide gave the expected dodecyl 1-thio-β-D-glucopyranoside **5**. An identical synthetic route was followed for the synthesis of dodecyl 1-thio-β-D-galacto- **10** and -xylo-pyranoside **15** starting, respectively, from tetra-*O*-acetyl-α-D-galactopyranosyl bromide (8) **6** and tri-*O*-acetyl-α-D-xylopyranosyl bromide (9) **11**.

^{1}H NMR (e.g., Table 1) has been used to characterize the stereochemistry of the synthetic intermediates **4**, **9**, and **14** as well as of the final products **5**, **10**, and **15**. The anomeric β configuration is unambiguously confirmed by the large coupling constants $J_{H\text{-}1,H\text{-}2}$ of about 10 Hz (Table 1).

The three dodecyl 1-thioglycosides **5**, **10**, and **15** have been examined under polarized light with an optical microscope equipped with a heating stage. Upon heating, all samples undergo melting to a birefringent liquid characteristic of a liquid-crystalline phase. When further heating is applied, they change to isotropic fluids and loose their birefringence. Upon cooling, the reverse succession of events is observed, i.e., the appearance of a liquid-crystalline phase and then, at lower temperatures, crystallization to a solid. The melting behavior of **5**, **10**, and **15** was examined by differential scanning calorimetry. A typical thermogram is shown in Fig. 1. The transition temperatures of the three dodecyl 1-thioglycosides **5**, **10**, and **15** are reported in Table 2. It is interesting to note that the crystal – liquid crystal transitions (K2-LC) occur at significantly higher temperatures on heating than on cooling. Also, while 1-thio-glycosides **10** and **15** both exhibit crystal-to-crystal transitions (K1-K2), glycoside **5** does not. It is possible that such a transition also occurs for the latter compound, but at a temperature lower than ambient.

A solid-state ^{13}C NMR study was done with dodecyl 1-thio-β-D-xylopyranoside **15** because the two transitions of

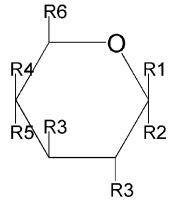

1. R^1 = H; R^2 = Br; R^3 = R^5 = OAc; R^4 = H; R^6 = CH_2OAc
2. R^1 = S-C(=NH)-NH_2·HBr; R^2 = H; R^3 = R^5 = OAc; R^4 = H; R^6 = CH_2OAc
3. R^1 = SH; R^2 = H; R^3 = R^5 = OAc; R^4 = H; R^6 = CH_2OAc
4. R^1 = S-$(CH_2)_{11}$-CH_3; R^2 = H; R^3 = R^5 = OAc; R^4 = H; R^6 = CH_2OAc
5. R^1 = S$(CH_2)_{11}$-CH_3; R^2 = H; R^3 = R^5 = OH; R^4 = H; R^6 = CH_2OH
6. R^1 = H; R^2 = Br; R^3 = R^4 = OAc; R^5 = H; R^6 = CH_2OAc
7. R^1 = S-C(=NH)-NH_2·HBr; R^2 = H; R^3 = R^4 = OAc; R^5 = H; R^6 = CH_2OAc
8. R^1 =SH; R^2 = H; R^3 = R^4 = OAc; R^5 = H; R^6 = CH_2OAc
9. R^1 =S-$(CH_2)_{11}$-CH_3; R^2 = H; R^3 = R^4 = OAc; R^5 = H; R^6 = CH_2OAc
10. R^1 = S-$(CH_2)_{11}$-CH_3; R^2 = H; R^3 = R^4 = OH; R^5 = H; R^6 = CH_2OH
11. R^1 =H; R^2 = Br; R^3 = R^5 = OAc; R^4 = R^6 = H
12. R^1 = S-C(=NH)-NH_2·HBr; R^2 = H; R^3 = R^5 = OAc; R^4 = R^6 = H
13. R^1 = SH; R^2 = H; R^3 = R^5 = OAc; R^4 = R^6 = H
14. R^1 = S-$(CH_2)_{11}$-CH_3; R^2 = H; R^3 = R^5 = OAc; R^4 = R^6 = H
15. R^1 = S-$(CH_2)_{11}$-CH_3; R^2 = H; R^3 = R^5 = OH; R^4 = R^6 = H

© 2002 NRC Canada

Fig. 1. Differential scanning calorimetry thermogram of dodecyl 1-thio-β-D-xylopyranoside **15**. The top and bottom curves correspond to the heating and cooling cycles, respectively. (Endo) and (Exo) indicate *endo*- and *exo*-thermal transitions, respectively.

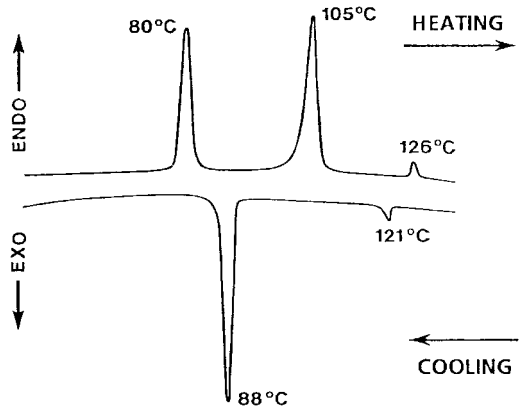

Fig. 2. Solid-state ^{13}C NMR spectra of dodecyl 1-thio-β-D-xylopyranoside **15** at 25°C (K1 form) (A) and 90°C (K2 form) (B).

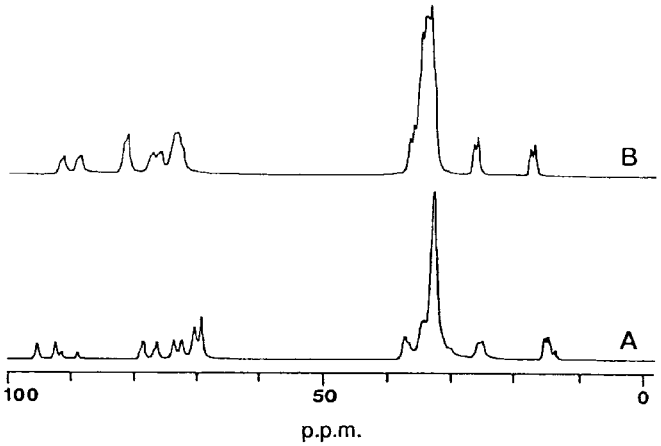

Table 2. Transition temperatures derived from differential scanning calorimetry.

		Transitions (°C)[a]		
Compound	Conditions	K1↔K2	K2↔LC	LC↔ISO
5	Heating	—	60	164
	Cooling	—	—	158
10	Heating	88	115	171
	Cooling	—	50–60	171
15	Heating	80	105	126
	Cooling	—	88	121

[a]K1↔K2: crystal-to-crystal transition; K2↔LC: crystal-to-liquid crystal transition (melting point); LC↔ISO: liquid crystal-to-isotropic liquid transition (clearing point).

interest (K-K2 and K2-LC) occur at temperatures (80 and 105°C, respectively) compatible with the heating stage of our spectrometer. Figures 2A and 2B show the solid-state spectra recorded at 25 and 90°C, i.e., under and above the K1-K2 transition. In both forms, there are indications of multiple resonance for individual chemically equivalent carbons. This effect is more pronounced in the spectrum of the K1 form, where obvious splittings are observed for many resonances, especially for the terminal methyl group at 15 ppm and for the sugar C-1 carbon at 90 ppm. Specific resonance assignments are difficult since the peak positions change dramatically in the two forms. The peaks in the 87–95 ppm region can, however, be assigned with confidence to the C-1 carbon of the sugar ring. By analogy with the solution NMR spectrum, the remaining peaks can probably be assigned in order of decreasing chemical shift: C-3, C-2, C-4, C-5.

In the K1 form, the resonance assigned to C-1 of compound **15** clearly consists of four lines between 88 and 95 ppm with relative intensities of about 2:2:1:1. A similar situation is noted for the peaks at 77 and 79 ppm, each of which has a shoulder. Application of resolution enhancement shows four lines in this region with relative intensities of about 1:2:1:2. These observations indicate that there are four magnetically non-equivalent environments for the sugar ring in this crystal form. It is interesting to note that the X-ray crystal structure of octyl 1-thio-β-D-xylopyranoside (a lower homologue of compound **15** but with a shorter alkyl chain) shows a disordered structure where the carbohydrate moiety has two orientations with equal occupancy (10). The solid-state NMR results here show that a disordered structure could also be valid for dodecyl 1-thio-β-D-xylopyranoside **15**. A mixture of crystal polymorphs could also explain the peak multiplicity observed for **15**; however, in such a case the differential scanning calorimetry thermogram would show a more complex melting profile. The spectrum of the higher temperature form (K2), although of lower definition, also shows peak multiplicity, indicating at least two non-equivalent environments in the crystal (Fig. 2B).

The cooling behavior of the 1-thio-glycoside **15** was also investigated by solid-state NMR. Although it was not possible to record the spectrum of the material in the liquid crystal form, it was, however, heated in the spectrometer for one hour at 110°C and then cooled to 27°C. The differential scanning calorimetry data (Fig. 1 and Table 2) indicated that on cooling from the liquid-crystalline phase, **15** underwent only one transition to the intermediate crystal form (K2). Figure 3A shows the spectrum of the sugar-ring carbons obtained immediately after cooling the material. This spectrum clearly corresponds to the K2 form as seen by comparison with the spectrum obtained at 90°C (Fig. 3B). The sample was allowed to equilibrate at room temperature for 24 h before another spectrum was acquired at 27°C. In this case (Fig. 3C), it is seen that the material has returned to the K1 form by comparison with the original room temperature spectrum (Fig. 3D). It is interesting to note that the same number of lines is observed as in the original spectrum (Fig. 2A), but that there are differences in the relative intensities. These intensity variations may originate from a non-isotropic orientation of the crystals during the thermal transitions, which occurred under high-speed magic angle spinning conditions in the magnetic field of the NMR spectrometer.

Powder X-ray diffraction diagrams of **15** were recorded to characterize its crystal-to-crystal transition at 80°C and to further identify the crystalline form obtained after standing 24 h at room temperature. Table 3 lists the main *d* spacings

© 2002 NRC Canada

Fig. 3. Solid-state ^{13}C NMR spectra of the carbohydrate part of dodecyl 1-thio-β-D-xylopyranoside **15** after different heat treatments. (A) Spectrum obtained at 27°C immediately after 1 h of treatment at 110°C; (B) spectrum of the K2 form obtained at 90°C; (C) same as (A) but after 24 h at room temperature; (D) spectrum of the K1 form (never heated).

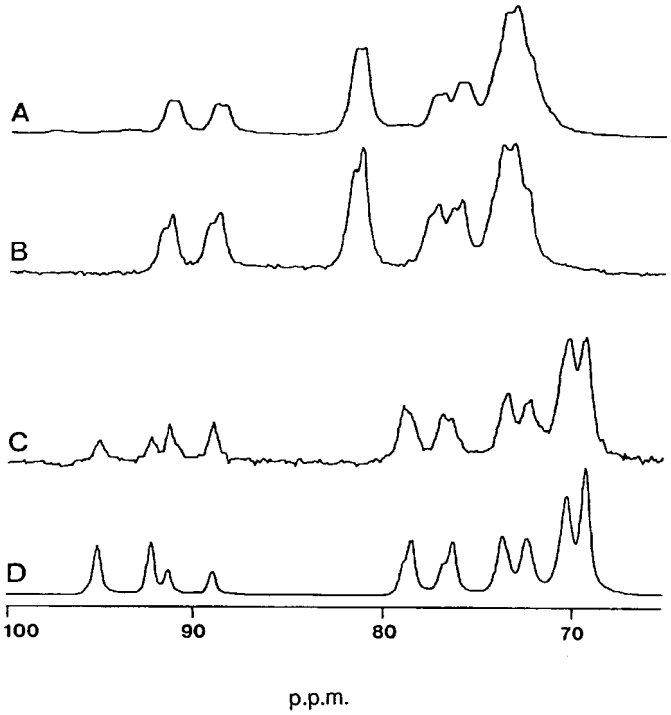

measured for compound **15** at room temperature (A), immediately after heating two hours at 90°C (B), and 24 h later (C). One clearly observes different *d* spacings after heating above the transition temperature. After 24 h standing at room temperature, the material returns to its low temperature polymorph.

Conclusions

This work covers part of an extensive program at Xerox Corporation on marking materials. The subject herein is described as hot-melt inks suitable for ink jet printing. A set of examples in a United States patent (11) makes use of the research described herein. The carbohydrate chemistry leading to synthesis of these liquid-crystalline materials is outlined schematically in the above referenced patent and their characterization was inspired by published data. However, while this work was in progress a related study by van Doren et al. (12) appeared, which reminded us of how Jeffrey (2) pioneered the field of carbohydrate mesogens. His basic crystal-line-packing model, for liquid-crystalline alkyl 1-glycosides, which can be applied to the compounds in this study, is a hydrogen-bonded layer of carbohydrate moieties with the alkyl chains pointing outwards in parallel arrangement (2). The latter are the first to melt, while the hydrogen-bonded layers resist the thermal motion up to a higher temperature. Jeffrey (2) predicted a staggering potential for easily available liquid-crystalline compounds from carbohydrate molecules.

Table 3. X-ray *d* spacings (Å) observed for dodecyl 1-thio-β-D-xylopranoside **15**.

Conditions[a]		
A	B	C
12.70	15.60	12.65
7.35	7.68	7.33
6.54	5.43	6.56
4.77	4.60	4.75
4.02	4.36	4.00
	4.20	
	4.10	

[a](A) sample room temperature; (B) same as (A) but after 2 h at 90°C; (C) same as (B) but after 24 h at room temperature.

Acknowledgment

Dr. Arthur Perlin kindly reviewed the manuscript and provided helpful comments.

References

1. G.A. Jeffrey and S. Bhattacharjee. Carbohydr. Res. **115**, 53 (1983).
2. G.A. Jeffrey. Acc. Chem. Res. **19**, 168 (1986).
3. For example see: C. Baron and T.E. Thompson. Biochim. Biophys. Acta, **283**, 276 (1975); S.L. Wagner and R.D. Gray. Biochemistry, **24**, 3809 (1985); J. Cordoba, M.D. Reboiras, and M.N. Jones. Int. J. Biol. Macromol. **10**, 270 (1988).
4. D.L. VanderHart. J. Chem. Phys. **84**, 1196 (1986).
5. D. Horton. Methods Carbohydr. Chem. **2**, 433 (1963).
6. M. Cerny and J. Pacak. Chem. Listy, **52**, 2090 (1958).
7. R. U. Lemieux. Methods Carbohydr. Chem. **2**, 221 (1963).
8. J. Conchie and G.A. Levy. Methods Carbohydr. Chem. **2**, 335 (1963).
9. F. Weygand. Methods Carbohydr. Chem. **1**, 182 (1962).
10. S. Bhattacharjee and G.A. Jeffrey. Mol. Cryst. Liq. Cryst. **101**, 247 (1983).
11. W.M. Schwarz, R.H. Marchessault, L. Alexandru, and B. Henrissat. U.S. Patent 5 006 170 (1991).
12. H.A. van Doren, R. van der Geerst, R.H. Kellogg, and H. Wynberg. Carbohyd. Res. **194**, 71 (1989).

© 2002 NRC Canada

Type I interferon structures: Possible scaffolds for the interferon-alpha receptor complex

Tattanahalli L. Nagabhushan, Paul Reichert, Mark R. Walter, and Nicholas J. Murgolo

Abstract: The structures of several type I interferons (IFNs) are known. We review the structural information known for IFN alphas and compare them to other interferons and cytokines. We also review the structural information known or proposed for IFN–cell receptor complexes. However, the structure of the IFN – cell receptor – IFN receptor2 (IFNAR2) and IFN receptor1 (IFNAR1) complex has not yet been determined. This paper describes a structural model of human IFN-IFNAR2/IFNAR1 complex using human IFN-α_{2b} dimer as the ligand. Both the structures of recombinant human IFN-α_{2b} and IFN-β were determined by X-ray crystallography as zinc-mediated dimers. Our proposed model was generated using human IFN-α_{2b} dimer docked with IFNAR2/IFNAR1. We compare our model with the receptor complex models proposed for IFN-β and IFN-γ to contrast similarities and differences. The mutual binding sites of human IFN-α_{2b} and IFNAR2/IFNAR1 complex are consistent with available mutagenesis studies.

Key words: three dimensional structure, antiviral activity, receptor, interferon.

Résumé : On connaît les structures de plusieurs interférons (IFN) de type I. On passe en revue les informations structurales connues pour les IFN alpha et on les compare à celles connues pour d'autres interférons et cytokines. On passe aussi en revue les informations structurales connues ou proposées pour les complexes IFN–cellule réceptrice. Toutefois, les structures du complexe INF – cellule réceptrice – IFN récepteur 2 (IFNAR2) et IFN récepteur 1 (IFNAR 1) n'a pas encore été déterminée. Dans ce travail, utilisant le dimère interféron humain-α_{2b} comme ligand, on décrit un modèle structural du complexe humain IFN-IFNAR2/IFNAR1. Faisant appel à la diffraction des rayons X sur des dimères reliés au zinc, on a déterminé les structures des recombinants humains humain-α_{2b} ainsi que IFN-β. Notre modèle proposé a été généré en utilisant le dimère humain IFN-α_{2b} arrimé au IFNAR2/IFNAR1. On a comparé notre modèle avec les modèles du complexe récepteur proposés pour IFN-β et IFN-γ pour mettre en relief les similarités et les différences. Les sites de fixation mutuels du dimère humain IFN-α_{2b} et du IFNAR2/IFNAR1 sont en accord avec les études disponibles de mutagénèse.

Mots clés : structure tridimensionnelle, activité antivirale, récepteur, interféron.

[Traduit par la Rédaction]

Introduction

General

The diverse and multiple biological properties of interferons (IFNs) have driven the need for an understanding of their activity at the molecular level. In 1957, Issacs and Lindenmann (1) discovered IFNs as antiviral agents. IFNs are a family of structurally and functionally related proteins that exhibit antiviral and antiproliferative effects on various cell types. They have been shown to exhibit various potent immunomodulatory effects including regulation of natural killer cell activity and modulation of major histocompatability antigen expression as well as antiproliferative activity against malignant cells (1–5).

Classification of interferons

IFNs were historically classified according to the cells of origin (i.e., leukocyte, fibroblast, and immune IFN). More modern designations are based on immunogenic properties and gene sequences. The major classes of IFNs are IFN-α, -β, -τ, and -ω, which are also designated type I (acid stable), and IFN-γ designated type II (acid labile). The IFN-α gene family is known to consist of at least 14 distinct human members that encode 12 different proteins (6). Sequencing

Received 14 December 2001. Published on the NRC Research Press Web site at http://canjchem.nrc.ca on 30 August 2002.

Dedicated to the memory of Professor Raymond U. Lemieux.

T.L. Nagabhushan.[1] Schering Plough Research Institute, Discovery Research, Kenilworth, NJ 07033, U.S.A.
P. Reichert. Schering-Plough Research Institute, Department of Structural Chemistry, Kenilworth, NJ 07033, U.S.A.
M.R. Walter. Center for Biophysical Sciences and Engineering, Department of Microbiology, University of Alabama at Birmingham, Birmingham, AL 35294, U.S.A.
N.J. Murgolo.[1] Schering-Plough Research Institute, Department of Bioinformatics, Kenilworth, NJ 07033, U.S.A.

[1]Corresponding authors (e-mail for T.L.N.: tattanahan@aol.com; e-mail for N.J.M.: nicholas.murgolo@spcorp.com).

 DOI: 10.1139/V02-158 © 2002 NRC Canada

of mammalian genomes has led to identification of additional classes including limitin (7) and IFN-κ (8). A number of synthetic and hybrid genes have been expressed to produce unnatural proteins including consensus IFN (9). Consensus IFN is a synthetic IFN-α designed by assembling each of the most frequently observed amino acids in several IFN-α subtypes (9). The human IFN-α species are particularly homologous in amino acid sequence (about 78%) and generally display a high level of species specificity in their biological activities. Primary amino acid comparisons of the IFN-α subtypes with human IFN-β and IFN-γ reveal sequence identities of about 30% and 10%, respectively, (10). The type I IFN-α family contains proteins of 166 amino acid residues except for IFN-α_2, which has 165 residues, and IFN-ω with 172 residues. All the IFN-α subtypes contain two disulfide bridges with Cys1–Cys99 and Cys29–Cys138, except IFN-α_2, which lacks position 44 and forms the disulfide bridges with Cys1–98 and Cys29–Cys138 and for IFN-α_8, which forms the first disulfide bridge with Cys1–Cys100. IFN-β has only one disulfide bridge at Cys31–Cys141 (11). The most biophysical information has been reported for recombinant *E. coli* derived human α- and β-interferon. The homogeneity of human recombinant IFN-α_{2b} has been analyzed using various physio–chemical methods developed to analyze the quality of interferon preparations including gel electrophoresis, reverse phase HPLC, NMR, various mass spectral methods, and circular dichroism (12).

IFN-α and IFN-β interact with two receptor components on cell surfaces, interferon alpha receptor 1 (IFNAR1) and interferon alpha receptor 2 (IFNAR2), which belong to the class II cytokine receptor superfamily (13). Both subunits of the receptor are required for selective ligand recognition and the receptors recognize distinct ligand epitopes (14). IFNAR1 contains four extracellular Ig-like domains, while IFNAR2 contains two extracellular Ig-like domains. Sequence similarity to tissue factor and IFN-γ receptors (both of which contain two Ig-like extracellular domains) suggest IFNAR1 and IFNAR2 will adopt similar folds. The availability of high-resolution structures of these receptors has facilitated homology modeling of IFNAR1 and IFNAR2. Such models are useful for mapping ligand and antibody epitopes.

Structural information on IFN-α, -β, and -γ and interleukin-10

IFN-α

Although crystallization of human recombinant IFN-α_{2a} was first reported in 1982 (15), high quality crystals of the zinc-mediated non-covalent dimer of human recombinant IFN-α_{2b} were not reported until 1996 (16). The crystallographic asymmetric unit contains three non-covalent dimers of the IFN-α_{2b} monomer shown in complimentary orientations in Fig. 1. The zinc-binding site is formed from adjacent glutamic acid residues (Glu41 and Glu42) located on the 3_{10} helix at the C-terminal end of the AB loop of each monomer. The overall fold of IFN-α_{2b} is similar to the previously determined structure of murine recombinant IFN-β (17). Each monomer of IFN-α_{2b} is composed of five α-helices, labeled A–E, linked by one overhand connection (AB loop) and three short segments (BC, CD, and DE loops). The topology of IFN-α_{2b} resembles the classical up-up-down-down four helix bundle motif: helices A, B, C, and E comprise the

Fig. 1. Molecular structure of IFN-α_{2b}. (A) Ribbon diagram; (B) dimer. (A) Helices A–E are in cyan, A–B loop 3_{10} helices are in magenta. (B) Independent monomers are in cyan and green; zinc is indicated by a yellow sphere.

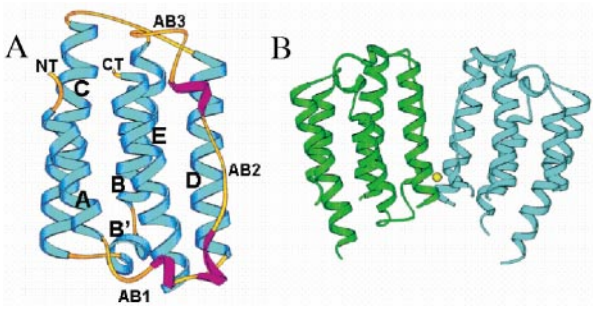

helix bundle (Fig. 1). IFN-α_{2b} is distinguished from the classical topology by helix D (consisting of 20 residues) that replaces the second extended overhand loop (CD loop) observed in class 1 long chain cytokines (18).

Multidimensional heteronuclear NMR spectroscopy was used to determine the solution structure of recombinant human IFN-α_{2a} at pH 3.5 at 2–2.2 mM protein concentration (19). The lower pH was required for structure determination because unspecific aggregation at higher pH led to low-quality solution ^{1}H NMR spectra with broad resonance lines. As observed for the crystal structure of IFN-α_{2b}, IFN-α_{2a} consists of five α-helices, four of which are arranged to form a left handed helix bundle with an up-up-down-down topology and two overhead connections. Among the structurally related four helical bundle cytokines, the structure of IFN-α_{2a} is most similar to that of IFN-α_{2b}, murine IFN-β, and human IFN-β. The crystal structure of ovine IFN-τ (20) is similar to the crystal structures of IFN-α_{2b}, human IFN-β, and murine IFN-β and the NMR solution structure of IFN-α_{2a}.

IFN-β

To date, X-ray crystallographic structures have been determined for murine *E. coli* derived IFN-β (17) and CHO cell derived glycosylated human IFN-β (21). The overall topology of both murine and human recombinant IFN-β monomeric structures is most similar to IFN-α_{2b}. Interestingly, human IFN-β and IFN-α_{2b} both crystallize as zinc-mediated dimers (Fig. 2B). However, the human IFN-β zinc-mediated dimer forms a different dimer interface compared with the IFN-α_{2b} crystal structure. The dimer interface of human IFN-β contains a zinc atom that is coordinated by histidine residues from adjacent monomers. A water molecule completes the tetrahedral zinc coordination between His121 (helix D) and Glu43 (AB loop) of one monomer and Gln94 (AB loop) and His97 (helix C) of the complimentary monomer. Dimerization has been observed for other helical cytokines and in some cases has been correlated with receptor activity (18). The biological significance of dimer formation of human IFN-β and IFN-α_{2b} is unclear.

IFN-γ

In 1991, the first human interferon structure determined was of recombinant human *E. coli* derived IFN-γ (22) (Fig. 2C). Human IFN-γ is a homodimer in solution and crystallizes with two dimers related by non-crystallographic twofold axis in the asymmetric unit. The protein was primarily

© 2002 NRC Canada

Fig. 2. Comparison of dimer structures of (A) IFN-α_{2b}; (B) IFN-β; (C) IFN-γ; and (D) IL-10. Each independent monomer is either in cyan or green. For IFN-α_{2b} and IFN-β the coordinate zinc is indicated by a yellow sphere.

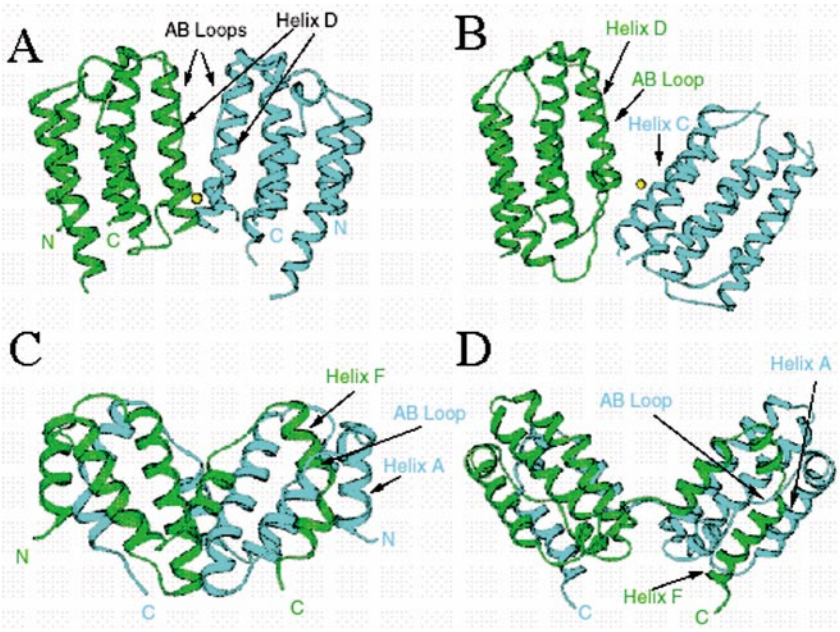

α-helical with six helices in each subunit. Subsequently, the recombinant rabbit IFN-γ structure was reported to be topologically identical to human IFN-γ (23). Both structures were predominantly α-helical with extensive interdigiation of the α-helical segments of the two polypeptide chains. The high resolution structure (2 Å) of bovine IFN-γ reported in 2000 was most similar in overall topology to the human IFN-γ (3.5 Å) (24). The structure of a biologically active single chain mutant of human IFN-γ was reported in 2000 (25). The single-chain mutant was derived by linking the two peptide chains of the IFN-γ dimer by a seven-residue linker and changing His111 in the first chain to an aspartic acid residue.

Interleukin-10

Interleukin-10 (IL-10) is a cytokine that inhibits production of pro-inflammatory cytokines including IFN-γ and TNF-α. Physiochemical studies on recombinant human IL-10 indicate that human IL-10 is predominately a non-covalent dimer at neutral pH with two disulfide bridges (26). The crystal structure of recombinant human CHO cell derived IL-10 is a dimer composed of identical polypeptide chains related by a twofold axis (27) (Fig. 2D). Each IL-10 monomer consists of six α-helices. The main-chain folds resemble IFN-γ in which the structural integrity of each domain is dependent on the intertwining of helices from each peptide chain. IL-10 and IFN-γ structures have comparable overall topology (v shape), interdomain angle (129° in both structures), and five amino acid sequences conserved in all amino acid sequences in the core. The high resolution crystal structure of refolded *E. coli* derived human IL-10 (28) has overall topology most similar to the recombinant CHO cell derived IL-10.

Dimer interactions

IFN-α_{2b}, human IFN-β, IL-10, and IFN-γ have dimeric units in their crystal structures (Figs. 2A–D). Both IFN-α_{2b} and human IFN-β crystallized as zinc-mediated dimers; however, IL-10 and IFN-γ crystallize as non-covalent intercalated dimers. All of these cytokines bind to class 2 cytokine receptors. The dimeric form of IL-10 and IFN-γ are important for optimal receptor activation, whereas there is no evidence that IFN-α or IFN-β dimers are important for activating their receptors.

IFN-α_{2b} zinc-mediated dimer is most similar to human IFN-β at the monomer level in the overall topology, folds, and elements of secondary structure. The major structural differences of the main chain reside in the exposed loops. Differences include (*i*) helix B in IFN-α_{2b} is kinked, which is absent in human IFN-β; (*ii*) helix E in IFN-α_{2b} is rotated around its axis relative to the orientation in human IFN-β; (*iii*) and human IFN-β is glycosylated at a single site Asn80 at the end of helix C, whereas IFN-α_{2b} is non-glycosylated. All the alpha interferons except for one species are glycosylated. Glycoslation does not interfere with dimer formation in human IFN-β.

IL-10 and human IFN-β display the best overall structural identity with each other; however, they do not share any significant sequence homology. While each domain of IL-10 resembles the long chain monomeric cytokines, the dimer fold of IL-10 (Fig. 2D) is most like IFN-γ (Fig. 2C). The two notable differences in the dimers are the size (length of helices) and orientation of the domains. In IL-10 the helix bundles are perpendicular to one another, while in IFN-γ the domains are oriented at an angle of about 60°. The domains of IL-10 are constrained to exhibit the 90° interdomain angle due to the conformations of the crossover connections that are formed. Analysis of interactions in the core of IL-10 and IFN-γ shows a close structural correspondence of a five residue cluster (IFN-γ motif). IL-10 and IFN-γ both contain similar flexible regions.

Members of the type I IFN family have homology to each other, bind to the same cell surface receptors (type II), and have overlapping function (6, 29–31). This review is specific

© 2002 NRC Canada

Fig. 3. Molecular structure of IFN-γ and its soluble high-affinity receptor. The ligand dimer is colored as in Fig. 2; IFN-γR1 molecules are in yellow and magenta.

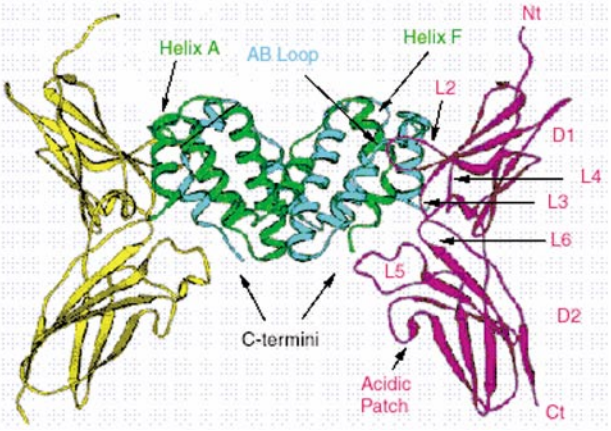

to interferon and interferon-like structures. Several broad reviews on type I and type II cytokines are available (32).

Currently, crystal structures are not available for any type I interferon receptor complex. Here we review structural features on the related IFN-γ and IL-10 receptor complexes. Based on this analysis, we propose a model for the interferon/interferon-receptor complex.

Comparison of the structures of IFN-γ and IL-10 receptor complexes

The crystal structure of IFN-γ bound to its high affinity receptor (IFN-γR1) was first completed in 1995 (33). The complex contains two IFN-γR1s that bind the identical twofold related surfaces of IFN-γ to form a 2:1 IFN-γR1/IFN-γ complex (Fig. 3). Formation of this complex on the cell surface requires that the twofold of IFN-γ be approximately parallel to the cell membrane. Although IFN-γ oligomerizes two IFN-γR1s, the receptors do not interact with one another and are separated by ~100 Å, where they are predicted to enter the cell membrane.

The α-helical core of IFN-γ bound to IFN-γR1 is essentially identical to the previously determined crystal structure of unbound IFN-γ; however, significant structural differences are observed for the AB loop of IFN-γ, which makes extensive contacts with IFN-γR1. These contacts result in well-ordered AB loops that contain one turn of 3_{10} helix. In contrast, the AB loops in the crystal structure of unbound IFN-γ exhibit highly variable conformations. The conformational flexibility of this region is also supported by NMR studies. Although the mobility of the AB loop is influenced by IFN-γR1 binding, the positively charged C-terminal tail of IFN-γ remains flexible and is not observed in the structure of the complex (22, 33, 34).

Although it is not observed in the structure, this region of IFN-γ is likely involved in receptor binding. It has been demonstrated to affect receptor recognition and heparin sulfate binding by BIAcore (35). Antibodies raised against this region of IFN-γ block STAT1 alpha nuclear translocation, a requirement for biological activity (36). Mutation or deletion of the C-terminus affects receptor binding, dsRNA cleavage, and antiviral activity (37, 38). Peptides corresponding to the C-terminus compete with IFN-γ for receptor binding (39).

The extracellular fragment of IFN-γR1 folds into two domains to form a narrow rod-like molecule with overall dimensions of 75 × 25 × 15 Å. The N-terminal (D1) and C-terminal (D2) domains are connected by a short linker that adopts one turn of an α-helix. Unique to IFN-γR1, D1 and D2 are linked by a disulfide bond between Cys108 in the helical linker and Cys153 in D2. Approximately 1090 Å of surface area is buried in the D1–D2 interface that consists mostly of hydrophobic residues. The interdomain angle between D1 and D2 is approximately 120°. The IFN-γ binding site is located in a crevice between D1 and D2.

The domains of IFN-γR1 are structurally similar to fibronectin type III domains (FBNIII). D1 adopts a FNBIII β-sandwich fold that is characterized by two β-sheets comprised of β-strands A, B, and E and G, F, C, and C′. Although D1 of IFN-γR1 adopts a standard FBNIII topology, D2 contains an additional three residue β-strand (strand D) that is linked to β-strand E by a buried disulfide bond between Cys181 and Cys186. β-Strand D forms part of the A, B, and E β-sheet, and with the exception of Cys181, its residues display five solvent accessible glutamic and aspartic acid residues on the receptor surface. The BC loop contributes an additional five acidic residues that combine with β-strand D to form an acidic patch near the domain interface (Fig. 3). This patch has been hypothesized to form a transient binding site for the basic C-terminal tail of IFN-γ.

The structure of IFN-γR1 provided the first opportunity to compare the three-dimensional structures of class 1 and class 2 cytokine receptors as defined by Bazan (31). Comparison of IFN-γR1 with growth hormone receptor (GHR), the prototypical class 1 cytokine, revealed IFN-γR1 and GHR exhibit different domain angles of 120° and 90°, respectively. The functional consequence of the different domain angles is that GHR displays six ligand binding loops compared with five for IFN-γR1. Thus, the AB loop from D1 participates in growth hormone binding in the GHR but is buried in the domain interface in IFN-γR1.

Residues of IFN-γ in the binding interface are located on two discontinuous polypeptide segments. The first is comprised of helix A, the AB loop, and helix B, while the second contains helix F. IFN-γ is oriented with its N- and C-termini near the D1–D2 interface with the AB loop interacting with the L2 loop on D1. A total of 960 $Å^2$ of accessible surface is buried in each binding interface. The aromatic receptor residues Tyr52 loop 2 (144 $Å^2$), Trp210 loop 6 (95 $Å^2$), and Trp85 loop 3 (75 $Å^2$), contribute almost one third of the total buried surface area. Tyr52 and Trp85 form a large protruding surface that makes extensive contacts with the AB loop, His111, and Glu112 of IFN-γ. Of the eleven hydrogen bonds and salt bridges identified in the interface, five involve mainchain atoms of the AB loop. Near the end terminus of the molecule, IFN-γ residues Val5 N termini, Ile114 helix F, and Ala118 helix F, pack against Trp210 loop 6 and Val209 loop 6 of the receptor. In 2000, the crystal structure of the complex of human IFN-γ with the soluble glycosylated extracellular part of IFN-γRα revealed the presence of a third receptor molecule not directly associated with the IFN-γ dimer (40).

© 2002 NRC Canada

Fig. 4. Molecular structure of IL-10/sIL-l0R1 (A) 1:2 and (B) 2:4 complexes. In plate (A) IL-10 monomers in cyan and green, while the sIL-10R1 molecules are in yellow and magenta. In plate (B) IL-10 monomers are in yellow, blue, cyan, and magenta, and sIL-10R1 molecules are in cyan and green.

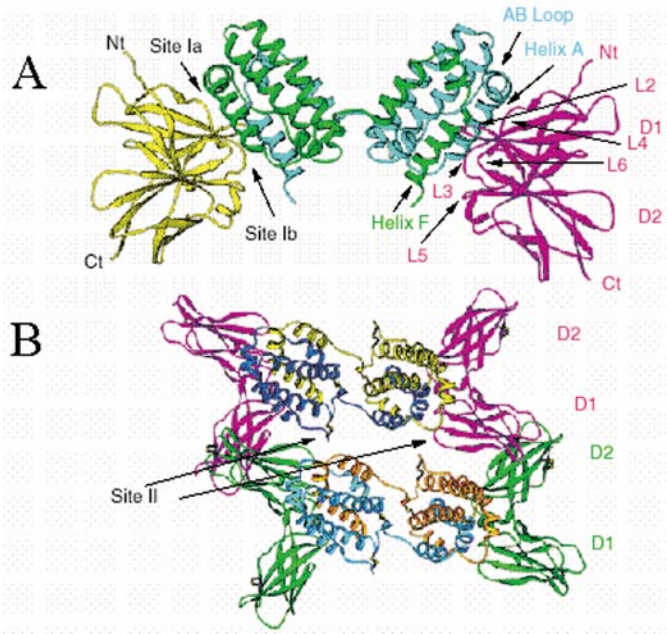

The IL-10/IL-10R1 complex

The crystal structure of the IL-10/IL-10R1 complex shares many similarities with the IFN-γ/IFN-γR1 complex (41). Like IFN-γ, IL-10 uses the same surfaces comprised of helix A, AB loop, and helix F to bind two IL-10R1s and form a 1:2 IL-10/IL-10R1 complex (Fig. 4). Despite differences in the domain orientations of IL-10 and IFN-γ, the separation between the C-terminal ends of the twofold related IL-10R1s is very similar to the IFN-γ/IFN-γR1 complex (~110 Å vs. 100 Å).

Comparison of bound and unbound IL-10 reveals a conserved α-helical core that does not change its structure upon receptor binding. As observed for IFN-γ, the AB loop of unbound IL-10 is flexible but adopts a rigid conformation due to several contacts with IL-10R1 in the receptor complex. Despite receptor binding the N-terminal ten and C-terminal two residues are not observed in the IL-10/IL-10R1 complex and are assumed to be flexible.

IL-10R1 folds into two FBN-III domains to form an L-shaped molecule. The individual domains of IL-10R1 and IFN-γR1 are structurally similar. Comparison of D1 and D2 domains results in root-mean-square deviations of 1.2 Å (81 Cα atoms) and 1.6 Å (71 Cα atoms), respectively. Despite similar domain structures, IL-10R1 and IFN-γR1 exhibit markedly different interdomain angles of 90° and 120°, respectively. Despite the different domain angles, IL-10R1 and IFN-γR1 still use the same five loops (L2–L6) to bind their respective ligands; however, the positions of the L2–L3 D1 loops change relative to the L5–L6 loops on D2. For IL-10R1, these loops are separated by ~20 Å, while in IFN-γR1 the distance is only 12 Å. These differences allow IFN-γR1 to bind the short A and F helices in IFN-γ, while IL-10R1 is more suited to bind to the longer A and F helices of IL-10.

As a result, IL-10R1 contacts IL-10 at two distinct surfaces labeled Ia and Ib. Site Ia occurs where the A–B loop crosses helix F, while site Ib is located near the N-terminus of helix A and the C-terminus of helix F. Receptor binding loops L2–L4 interact exclusively with site Ia, while loops L5 and L6 in D2 interact with site Ib. As previously observed for IFN-γR1, IL-10R1 residue Tyr43 located on loop 2 buries the most surface area of any residue (~105 $Å^2$) into a shallow cavity created by helix F and the AB loop.

Unique to the IL-10 system, IL-10 and sIL-10R1 form a complex consisting of two IL-10 dimers and four IL-10R1 molecules in solution. A 2:4 complex is also formed in the IL-10/IL-10R1 crystals by two adjacent 1:2 complexes that separated by unit cell translation of 46 Å and offset an additional ~21 Å in a direction approximately perpendicular to the unit cell translation (Fig. 4). Contacts in the interface (site II) between the complexes are formed between IL-10R1 D1 from one complex with IL-10 and IL-10R1 D2 of the adjacent complex. The location of the L2 loop in the site II as well as the site I interface suggests that assembly of the 2:4 is dependent on the initial formation of the site I interface (e.g., 1:2 complex). Sequence similarities between IL-10R1 and IL-10R2 suggest both receptors may bind such that IL-10R2 may bind to the IL-10R1 binding site. This 2:4 complex provides a model for how IL-10R1 and IL-10R2 may associate to form a biologically active IL-10/IL-10R1/IL-10R2 complex.

Molecular models for IFN/IFN receptor complexes

IFNAR1 and IFNAR2 are members of the class 2 cytokine receptor family (31) permitting modeling of their extracellular domains from the crystal structure of human IFN-γ receptor 1 (33, 40) or tissue factor (42). Several prior models of IFNAR1 and IFNAR2 based upon IFN-γ receptor 1 and tissue factor have been presented (37–41).

Homology models were constructed for human IFNAR2 and IFNAR1 based on the crystal structure of IFN-γ receptor 1 (33). Models were constructed for the two extracellular domains of IFNAR2 (residues 1–202), extracellular domains 1–2 of IFNAR1 (residues 1–202), and extracellular domains 3–4 of IFNAR1 (residues 203–407). The alignment of IFNAR1 domains and IFN-γ receptor 1 was previously described by Cutrone and Langer (43). IFNAR2, IFNAR1 domain 1–2, and IFNAR1 domain 3–4 models were constructed by the Segment Match Modeling Approach (44) and refined with the Encad program as implemented in the Look (Molecular Applications Group, formerly of Palo Alto, CA) program. The models were further refined by molecular mechanics minimization with the InsightII/Discover program (Accelrys, San Diego, CA).

The molecular model of IFNAR2 was docked manually with the InsightII program to the zinc dimer crystal structure of IFN-$α_{2b}$ (16) using the site and orientation previously suggested from mutational analysis (45–48). Prior mutational analysis suggested key IFN-$α_{2b}$–IFNAR2 interactions are D35–K50, R144–E79, R149–E79, S152–H78, R144–M48, and R22–Y45. Based on our docked orientation the last interaction is likely indirect.

© 2002 NRC Canada

Fig. 5. The IFN-α_{2b}/IFNAR1/IFNAR2 complex. IFN-α_{2b} is shown in cyan, IFNAR1 in green, and IFNAR2 in red.

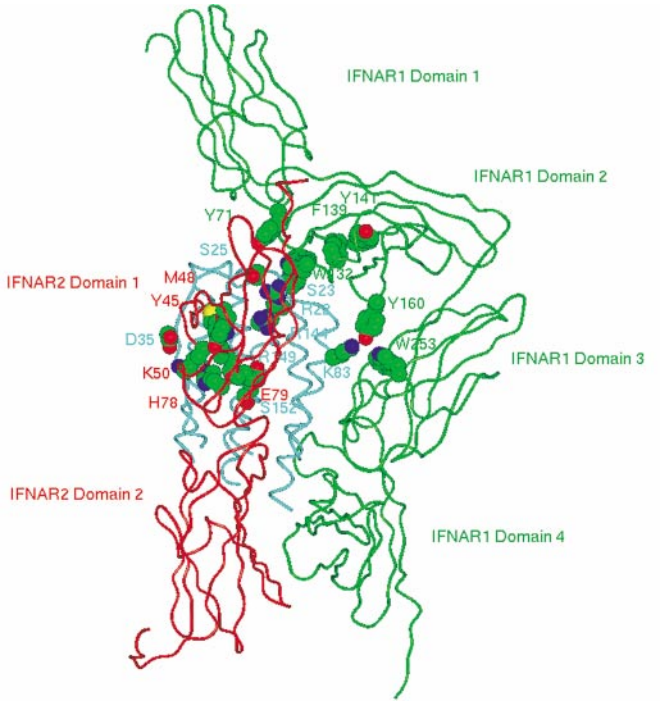

Fig. 6. The IFN-α_{2b}/IFNAR1/IFNAR2 dimer model. Coloring as in Fig. 5; zinc is indicated by a yellow sphere.

The molecular models of the IFNAR1 domain 1–2 and domain 3–4 were first docked to the IFN-α_{2b} crystal structure independently and were later annealed to form a peptide bond between domains 2 and 3 with residues mapped by mutagenesis as forming the IFNAR1 binding site on the same side of the model as suggested from prior modeling (43). Mapping of bovine IFNAR1 binding residues in that work demonstrated the importance of IFNAR1 domains 2 and 3 (49). Domain 2 residues mapped by loss of binding mutations included W132, F139, Y141, and Y160, while a single domain 1 residue Y71 and a single domain 3 residue W253 appeared important as well. Of residues previously noted to form the IFNAR1/IFN-α recognition site, Y71, W132, and Y160 of the first two domains appear to form an available surface for docking, with F139 and Y141 propping up these positions. Prior IFN-α chimers and mutations suggest the IFNAR1 recognizes IFN-α AB loop residues 16–28 as well as K83 and Y90 (50). Given the expected similar orientation of IFNAR1 and IFNAR2 transmembrane segments, we oriented the IFNAR1 domain 1–2 model along the AB loop and the domain 3–4 model against IFN-α K83 and Y90. Specific interactions could be formed in docking between IFN-α_{2b}–IFNAR1 S23 and S25–Y71, R22–W132, K83–Y160, and K83–W253. The resulting annealed IFNAR1 model contain an approximately perpendicular angle between domains 2 and 3. The resulting IFN-α_{2b} zinc dimer IFNAR1/IFNAR2 complex model was subject to further refinement by molecular mechanics minimization with InsightII/Discover.

The docked orientation of the IFN-α_{2b}/IFNAR1/IFNAR2 complex is presented in Fig. 5. IFNAR1 and IFNAR2 do not have a significant contact region excepting the N-terminus of IFNAR2. The association of IFNAR1 and IFNAR2 does not require IFN-α_{2b} dimer formation in this orientation. Chimeric constructs using the extracellular domain of the EPO receptor and transmembrane and intracellular regions of IFNAR1 demonstrate receptor dimerization is required for induction of effector genes (51). A similar construct with the extracellular domain of IFN-γR1 and transmembrane and intracellular regions of IFNAR2 shows receptor dimerization is sufficient to induce biological activity (52). Thus, ligand dimerization, perhaps mediated by zinc, may permit a complex to form with two molecules of IFNAR1 and IFNAR2. These receptors could recognize identical sites on the dimer in a manner analogous to IFN-γR1 (33).

IFNAR2 dimerization may be a requirement for antiviral activity. Both IFNAR2 and IFNAR1 are subject to alternative splicing, producing soluble-receptor isoforms. Differential regulation of IFNAR2 isoform expression has been recently suggested as a means of modulating type I IFN responses (53). While the intracellular domain of IFNAR2 is required for signal transduction, interaction of its soluble isoform, containing only the extracellular domain, with its membrane anchored isoform is sufficient to confer antiviral activity even in the absence of type I IFN (54). The nature of this interaction is unclear as direct contact between IFNAR2 extracellular domains is not seen in our proposed model (see Fig. 6).

Although, it is perceived that IFN-α_2 exists as a monomer at physiologically relevant concentrations, local concentration at the receptor or receptor mediated association may obligate dimer formation. NMR and dynamic light-scattering studies have shown IFN-α_2 exists in a oligomeric rather than monomeric state at neutral pH (19, 55). Since IFN-γ and

© 2002 NRC Canada

IL-10 activate their respective receptors as dimers, we used the dimer of IFN-α_{2b} to generate symmetrical counterparts for IFNAR1 and IFNAR2 on the IFN-α_{2b} dimer. This orientation is shown in Fig. 6. From this model, it is evident IFN-α_{2b} dimers could recognize two copies of IFNAR1 and IFNAR2.

IFN-β can form a dimer with zinc as well, although the monomer orientation differs from IFNA2 (56). The IFNAR1/IFNAR2 complex also appears to recognize IFN-β at a different location on the ligand framework (56).

Conclusion

The proposed IFN-α_{2b}/IFNAR1/IFNAR2 model of a dimer ligand binding to a pair of receptors on each of the chains of the ligand is consistent with the model proposed for the binding of cytokines to class 2 receptors.

Acknowledgments

We thank Gideon Schrieber for providing Proofs of the IFN-α_{2b}/IFNAR2 complex paper prior to publication. We thank Patricia Weber and Johanthan Greene for help in the preparation of this manuscript.

References

1. A. Issacs and J. Lindenmann. Proc. Roy. Soc. London Ser. B, **147**, 258 (1957).
2. L.M. Pfeffer, C.A. Dinarello, R.B. Herberman, B.R.G. Williams, E.C. Borden, R. Bordens, M.R. Walter, T.L. Nagabhushan, P.P. Trotta, and S. Petska. Cancer Research, **58**, 2489 (1998).
3. S. Baron, S.K. Tyring, W.R. Fleishmann, D.H. Niesel, G.R. Klimpel, J. Stanton, and T.K. Hughes. JAMA, **266**, 1375 (1991).
4. T.L. Nagabhushan and A. Giaquinto. *In* Regulatory practice for biopharmaceutical production. *Edited by* A.S. Lubiniecki and S.A. Vargo. John Wiley & Sons, New York. 1995. p. 221.
5. E. Jaeckel, M. Cornberg, H. Wedemeyer, T. Santantonio, J. Mayer, M. Zankel, G. Pastore, M. Dietrich, C. Trautwein, and M.P. Manns. New England J. Med. **345**, 1452 (2001).
6. S. Petska, J.A. Langer, K.C. Zoon, and C.E. Samuel. Ann Rev Biochem. **56**, 727 (1987).
7. K. Oritani, K.L. Medina, Y. Tomiyama, J. Ishikawa, Y. Okajima, M. Ogawa, T. Yokota, K. Aoyama, I. Takahashi, P.W. Kincade, and Y. Matsuzawa. Nat. Med. **6**, 659 (2000).
8. D.W. LaFleur, B. Nardelli, T. Tsareva, D. Mather, P. Feng, M. Semenuk, K. Taylor, M. Buergin, D. Chinchilla, V. Roshke, G. Chen, S.M. Ruben, P.M. Pitha, T.A. Coleman, and P.A. Moore. J. Biol. Chem. **276**, 39 765 (2001).
9. K.Y. Alton, Y. Stabinsky, R. Richards, B. Ferguson, L. Goldstein, B. Altrock, L. Miller, and N. Stebbing. *In* The biology of the interferon system 1983. *Edited by* E. De Maeyer and H. Schellekens. Elseiver Science Publishing Co., Amsterdam, Holland. 1983. p. 119.
10. M.R. Walter, R. Bordens, T.L. Nagabhushan, B.R.G. Williams, R.B. Herberam. C.A. Dinarello, E.C. Borden, P.P. Trotta, S. Petska, and L.M. Pfeffer. Cancer Biother. Radiopharm. **13**, 143 (1998).
11. G.C. Viscomi. Biotherapy, **10**, 59 (1997).
12. T.L. Nagabhushan, H. Surprenant, H.V. Le, R. Kosecki, A. Levine, P. Reichert, B. Sharma, H. Tsai, P. Trotta, J. Bausch, C. Foster, S. Gruber, J. Hoogerheide, and S. Mercorelli. *In* Interferon: Research, clinical application and regulatory consideration. *Edited by* K.C. Zoon, P.D. Noguchi, and T.-Y. Liu. Elisevier Science Publishing Co., New York. 1984. p. 79.
13. K. Oritani, P.W. Kincade, C. Zhang, Y. Tomiyama, and Y. Matsuzawa. Cytokine & Growth Factor Reviews, **12**, 337 (2001).
14. K.E. Mogensen, M. Lewerenz, J. Reboul, G. Lutfalla, and G. Uze. J. Interferon Cytokine Res. **19**, 1069 (1999).
15. D.L. Miller, H. Kung, and S. Petska. Science (Washington, D.C.), **215**, 689 (1982).
16. R. Radhardrishnan, L.J. Walter, A. Hruza, P. Reichert, P.P. Trotta, T.L. Nagabhushan, and M.R. Walter. Structure, **4**, 1453 (1996).
17. T. Senda, T. Shimazu, S. Matsuda, G. Kawano, H. Shimizu, K.T. Nakamura, and Y. Mitsui. EMBO J. **11**, 3193 (1992).
18. S. Sprang and J.F. Bazan. Curr. Opin. Struc. Biol. **3**, 815 (1993).
19. W. Klaus, B. Gsell, A.M. Labhardt, B. Wipf, and H. Senn. J. Mol. Biol. **274**, 661 (1997).
20. R. Radhakrishnan, L.J. Walter, P.S. Subramaniam, H.M. Johnson, and M.R. Walter. J. Mol. Biol. **286**, 151 (1999).
21. M. Karpusas, M. Nolte, C.B. Benton, W. Meier, W.N. Lipscomb, and S. Goelz. Proc. Natl. Acad. Sci. U.S.A. **94**, 11 813 (1997).
22. S.E. Ealick, W.J. Cook, S. Vijay-Kumar, M. Carson, T.L. Nagabhushan, P.P. Trotta, and C.E. Bugg. Science (Washington, D.C.), **252**, 698 (1991).
23. C.T. Samudz, L.E. Burton, and J.R. Rubin. J. Biol. Chem. **266**, 21 791 (1991).
24. M. Randal and A.A. Kossiakoff. Acta Crystallogr. Sect. D, **56**, 14 (2000).
25. A. Landar, B. Curry, M.H. Parker, R. DiGiacomo, S.R. Indelicato, T.L. Nagabhushan, G. Rizzi, and M.R. Walter. J. Mol. Biol. **299**, 169 (2000).
26. R. Syto, N.J. Murgolo, E.H. Braswell, P. Mui, E. Huang, and W.T. Windsor. Biochemistry, **37**, 16 943 (1998).
27. M.R. Walter and T.L. Nagabhushan. Biochemistry, **34**, 12 118 (1995).
28. A. Zdanov, C. Schalk-Hihi, A. Gustchina, M. Tsang, J. Weatherbee, and A. Wloadawer. Structure, **3**, 591 (1995).
29. E. De Maeyer and J. DeMaeyer-Guignard. Intern. Rev. Immunol. **17**, 53 (1998).
30. K. Oritani, P.W. Kincade, C. Zhang, Y. Tomiyama, and Y. Matsuzawa. Cytokine & Growth Factor Reviews, **12**, 337 (2001).
31. F. Bazan. Proc. Natl. Acad. Sci. U.S.A. **87**, 6934 (1990).
32. D.A. Rozwarski, A.M. Groneborn, G.M. Clore, J.F. Bazan, A. Bohm, A. Wlodawer, M. Hatada, and P.A. Karplus. Structure, **2**, 159 (1994).
33. M.R. Walter, W.T. Windsor, T.L. Nagabhushan, D.J. Lundell, C.A. Lunn, P.J. Zavodny, and S.K. Narula. Nature (London), **376**, 230 (1995).
34. M. Randal and A.A. Kossiakoff. Structure, **9**, 155 (2001).
35. R. Sadir, E. Forest, and H. Lortat-Jacob. J. Biol. Chem. **273**, 10 919 (1998).
36. P.S. Subramanian, J. Larkin, 3rd, M.G. Mujtaba, M.R. Walter, and H.M. Johnson. J. Cell. Sci. **113**, 2771 (2000).
37. D.L. Lundell and S.K. Narula. Pharmacol. Ther. **64**, 1 (1994).
38. C.H. Shein and M. Haugg. Biochem. J. **307**, 123 (1994).
39. N.D. Griggs, M.D. Jarpe, J.L. Pace, C.W. Russell, and H.M. Johnson. J. Immunol. **149**, 517 (1992).
40. D.J. Thiel, M.H.I. Du, R.L. Walter, A. D'Arcy, C. Chene, M. Fountoulakis, G. Garotta, F.K. Winkler, and S.E. Ealick. Structure, **8**, 927 (2000).
41. K. Josephson, N.J. Logsdon, and M.R. Walter. Immunity, **14**, 35 (2001).

© 2002 NRC Canada

42. Y.A. Muller, M.H. Ultsch, and A.M. de Vos. J. Mol. Biol. **256**, 306 (1992).
43. E.C. Cutrone and J.A. Langer. J. Biol. Chem. **276**, 17 140 (2001).
44. M. Levitt. J. Mol. Biol. **226**, 507 (1992).
45. L.C. Roisman, J. Piehler, J.Y. Trosset, H.A. Scheraga, and G. Schreiber. J. Interferon Cytokine Res. **21 Suppl. 1**, S64 (2001).
46. L.C. Roisman, J. Piehler, J.-Y. Trosset, H.A. Scheraga, and G. Schreiber. Proc. Natl. Acad. Sci. U.S.A. **98**, 13 231 (2001).
47. J. Piehler, L.C. Roisman, and G. Schreiber. J. Biol. Chem. **275**, 40 425 (2000).
48. Chuntharapai, V. Gibbs, J. Lu, A. Ow, S. Marsters, A. Ashkenazi, A. De Vos, and K.J. Kim. J. Immunol. **163**, 766 (1999).
49. J. Lu, A. Chuntharapai, J. Beck, S. Bass, A. Ow, A.M. De Vos, V. Gibbs, and K.J. Kim. J. Immunol. **160**, 1782 (1998).
50. G. Uze, G. Lutfalla, and K.E. Mogensen. J. Interferon Cytokine Res. **15**, 3 (1995).
51. E. Pattyn, X. Van Ostade, L. Schauvliege, A. Verhee, M. Kalai, J. Vanderckhove, and J. Tavernier. J. Biol. Chem. **274**, 34 838 (1999).
52. S.V. Kotenko, L.S. Izotova, O.V. Mirochnitchenko, C. Lee, and S. Pestka. Proc. Natl. Acad. Sci. U.S.A. **96**, 5007 (1999).
53. M.P. Hardy, P.J. Herzog, and C.M. Owczarnek. Biochem. J. **365**, 355 (2002).
54. C.S. Han, Y. Chen, T. Ezashi, and R.M. Roberts. Proc. Natl. Acad. Sci. U.S.A. **98**, 6138 (2001).
55. Y.S. Wang, S. Youngster, J. Bausch, R. Zhang, C. McNemar, and D.F. Wyss. Biochemistry, **39**, 10 634 (2000).
56. M. Karpusas, A. Whitty, L. Runkel, and P. Hochman. Cell Mol. Life Sci. **54**, 1203 (1998).

© 2002 NRC Canada

Novel substrates for efficient enzymatic transglycosylation by *Bacillus circulans*

Shiro Komba and Yukishige Ito

Abstract: To develop transglycosylation for efficient preparation of *N*-acetyllactosamine (Galβ(1→4)GlcNAc, LacNAc), β-galactosidase mediated transglycosylation using novel substrates *Bacillus Circulans* was explored. To make transglycosylation entropically favorable over hydrolysis, donor (lactose or galactose) and acceptor (*N*-acetylglucosamine, GlcNAc) components were connected to a single molecule. For that purpose, 1,2- and 1,3-benzenedimethanol and 2-hydroxy-5-nitro- and 5-hydroxy-2-nitro-benzyl alcohol were screened as linkers and enzymatic transglycosylation was examined under several conditions. In the case of 2-hydroxy-5-nitro-benzyl connected substrate **40**, an indication of the occurrence of intramolecular transglycosylation was observed, and the desired product (**58**) was obtained in 26% isolated yield. The same reaction in the presence of CMP sialic acid and α-(2→6)-sialyltransferase gave sialyl LacNAc **87** in one pot in 39% isolated yield. Additionally, the effect of the *C*-2 substituent of the acceptor component was briefly examined using substrates containing NHAlloc (**72**), NHTroc (**73**), and N_3 (**74**) groups. Although the occurrence of intramolecular transglycosylation was not clear in these cases, disaccharides **81**–**83** were obtained in reasonable yields.

Key words: galactosidase, intramolecular transglycosylation, *N*-acetyllactosamine, sialyltransferase.

Résumé : Faisant appel à de nouveaux substrats *Bacillus circulan*, on a étudié la réaction de transglycolisation catalysée par une β-galactosidase dans le but de développer une méthode de transglycosylation permettant de préparer la *N*-acétyllactosamine (Galβ(1→4)GlcNAc, LacNAc) d'une façon efficace. Afin de rendre la réaction de transglycosylation entropiquement favorable et de la rendre plus favorable que l'hydrolyse, on a relié les blocs donneur (lactose ou galactose) et accepteur (*N*-acétylglucosamine, GlcNAc) dans une seule molécule. À cette fin, on a utilisé les benzène-1,2- et 1,3-diméthanols ainsi que les alcools 2-hydroxy-5-nitro et 5-hydroxy-2-nitrobenzyliques comme connecteurs et on a étudié les réactions de transglycosylation sous plusieurs conditions. Dans le cas du substrat **40**, faisant appel à l'alcool 2-hydroxy-5-nitrobenzylique comme connecteur, on a observé des indications à l'effet de l'existence d'une réaction de transglycosylation intramoléculaire et on a obtenu le produit désiré, **58**, avec un rendement de 26% de produit isolé. La même réaction effectuée en présence de CMP de l'acide sialique et d'α-(2→6)-sialyltransférase dans une réaction monotope conduit à la formation de la LacNAc sialyée, **87**, avec un rendement de 39% en produit isolé. De plus, on a fait une brève étude de l'effet du substituant en *C*-2 du composant accepteur en utilisant des substrats portant des groupes NHAlloc (**72**), NHTroc (**73**) et N_3 (**74**). Même si les possibilités de réactions de transglycosylation intramoléculaire ne sont pas claires dans ces cas, on a obtenu les disaccharides **81**–**83** avec des rendements raisonnables.

Mots clés : galactosidase, transglycosylation intramoléculaire, *N*-acétyllactosamine, sialyltransférase.

[Traduit par la Rédaction]

Introduction

N-Acetyllactosamine (LacNAc) is a widespread component of glycoproteins (1), glycolipids (2), and glycosaminoglycans (3). It is particularly important as a core structure of ligands for cell adhesion molecules, for instance selectin (4) and CD22 (5). It was first isolated from porcine gastric mucin as a growth factor for *Lactobacillus bifidus var. pennysylvanicus* by Tomarelli et al. (6). A number of chemical approaches toward LacNAc have been reported (7–11). Most typically, it can be prepared from lactose (Lac) via lactal using azidonitration, developed by Wong and Lemieux (12) and Lemieux and Ratcliff (13), as the key transformation.

On the other hand, Wong et al. (14) developed a highly efficient LacNAc producing system, by using β-(1→4)-galactosyltransferase (EC 2.4.1.90), in combination with multiple enzymes for UDP–galactose recycling. This landmark achievement opened the way for glycosyltransferase catalyzed preparative scale oligosaccharide synthesis (15). Limitations in terms of the cost, availability, and stability of the enzymes and sugar nucleotides are still not negligible, however.

Received 3 December 2001. Published on the NRC Research Press Web site at http://canjchem.nrc.ca on 4 September 2002.

Dedicated to the memory of late Professor Ray Lemieux in recognition of his greatest contribution to carbohydrate chemistry.

S. Komba and Y. Ito.[1] The Institute of Physical and Chemical Research (RIKEN), 2–1 Hirosawa, Wako-shi, Saitama 351–0198, Japan.

[1]Corresponding author (e-mail: yukito@postman.riken.go.jp).

 DOI: 10.1139/V02-156 © 2002 NRC Canada

Scheme 1.

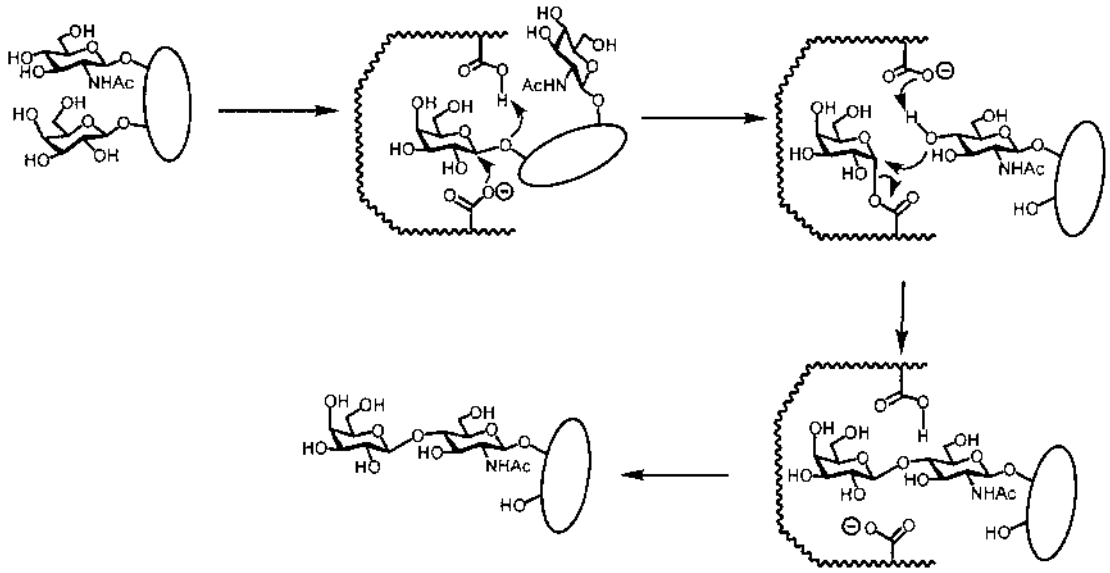

The glycosidase-based approach is attractive due to the following reasons: (*i*) an inexpensive (e.g., lactose) or easily obtainable (e.g., aryl β-D-galactoside) donor can be used; (*ii*) compared with glycosyltransferases, this group of enzymes are much more stable, easier to handle, and generally cheaper. Zilliken et al. (16) reported the first enzymatic synthesis of LacNAc from lactose and *N*-acetylglucosamine (GlcNAc) in the presence of extracts from *Lactobacillus bifidus*, although the yield was low from the standpoint of practical use. More recently, quite extensive studies on the use of β-D-galactosidase (EC 3.2.1.23) from *Bacillus circulans* have been reported by several groups (17–22).

Although these pioneering works clearly revealed the potential of galactosidase as a valuable tool for the synthesis of biologically relevant oligosaccharides, attainable yields have not been satisfactory. In most cases, a large excess of either glycosyl donor (e.g., lactose) or acceptor (*N*-acetylglucosamine) was used in order that the transglycosylation can compete with hydrolysis. It would be extremely difficult to suppress the hydrolysis to an extent that transglycosylation using an equimolar amount of glycosyl donor–acceptor can be achieved in a synthetically useful efficiency. One potential solution would be to perform the glycosyl transfer in an intramolecular manner by connecting the donor and acceptor components together into a single molecule (Scheme 1). Transglycosylation may be favorable over hydrolysis on the condition that the donor and acceptor portions of the substrate fit simultaneously into the binding pocket of the enzyme. In this paper, the first success in finding the substrate that, in part, fulfills these demands, is reported (23).

Results and discussion

As a tether to connect donor and acceptor components, our initial attention was focused on (**2**) 1,2-(*ortho*)-, and (**3**) 1,3-(*meta*)-benzenedimethanol, and substrates **9** and **10** were designed. These substrates were synthesized in a straightforward manner as depicted in Scheme 2. Although rather forcing conditions (75°C, 12 h) were required, the reactions of **2** and **3** with oxazoline **1** (24) selectively gave **4** and **5** in 59 and 74% yield, respectively, without noticeable contamination with diglycosylated products. Subsequent glycosylation with lactosyl trichloroacetimidate **6** (25) was effected in the presence of TMSOTf to afford **7** and **8** in 75 and 79% yield, respectively. Finally, *O*-acyl protecting groups were removed by sodium methoxide, and the designed substrates **9** and **10** were obtained in quantitative yield. These compounds were then examined as substrates for enzymatic transglycosylation using β-galactosidase from *B. circulans*, and the courses of the reactions were monitored by analytical HPLC (Fig. 1). Based on MALDI-TOF-MS and NMR analysis, peaks assignable as the desired products **15** and **16** (MALDI-MS *m*/*z*: ([M + Na]$^+$, 688) were identified, and their structures were rigorously confirmed by NMR analysis of corresponding acetates **17** and **18**. The yields of transglycosylated products **15** and **16** were rather low (~5%), however. While hydrolysis toward **11** and **12** was the overwhelmingly major pathway, it was noteworthy that the formation of bis-disaccharides **13** and **14** was dominant over **15** and **16** throughout the reaction.[2] Since the formation of **13** and **14** is possible only by intermolecular pathway, it is most probable that the intramolecular pathway made only a minor contribution, if any, to the formation of **15** and **16** (Scheme 3). Their formation would most likely be a result of sequential intermolecular transglycosylation and deglycosylation (i.e., (**9**, **10**)→(**13**, **14**)→(**15**, **16**)). This conclusion was supported by the extremely similar profiles of the *ortho* (**9**) and *meta* (**10**) isomers.

The above negative results obtained by **9** and **10** implied that the topological relationship of Gal and GlcNAc residues

[2] In addition, products that, based on MALDI-TOF mass, are assignable as multiply galactosylated, were detected. Their structures were not rigorously confirmed, however (see Figs. 1–5).

© 2002 NRC Canada

Scheme 2.

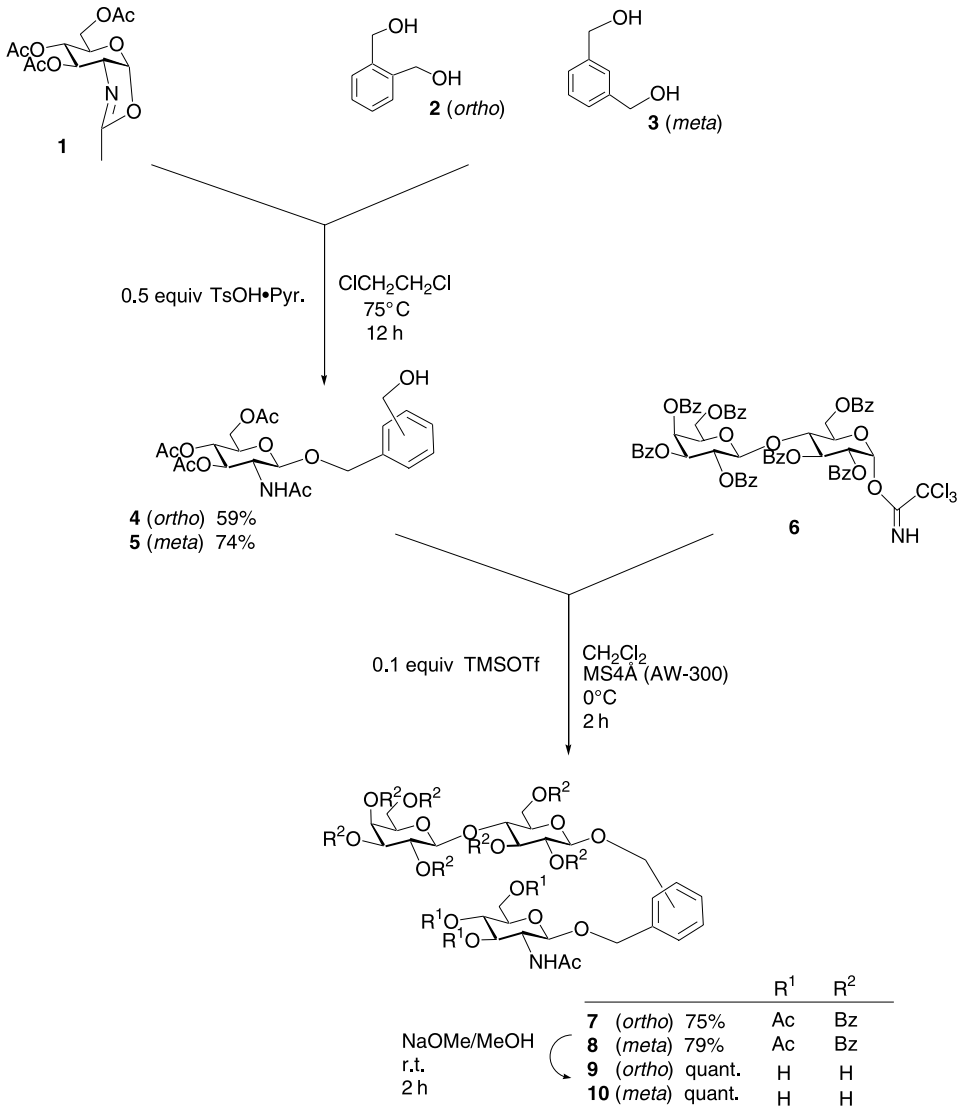

of these compounds does not fit the binding pocket of β-galactosidase. We therefore decided to attenuate the distance between these residues by changing the linker. To that end, 2-hydroxy-5-nitrobenzyl (*ortho*) (**20**) and 5-hydroxy-2-nitrobenzyl (*meta*) alcohol (**21**) were chosen, which each have one less methylene unit compared with **2** and **3**. Because they are unsymmetrical diols, regioisomers can be produced simply by changing the order of glycosylation (i.e., **36**–**37** and **38**–**39**). Additional diversity of the substrate can be generated by incorporating the galactose residue, instead of lactose, directly on the phenolic oxygen (i.e., **40** and **41**). In the latter case, the substrates can be viewed as derivatives of *p*-nitrophenyl galactoside, a well explored reactive donor for enzymatic transglycosylation.

Preparation of these substrates was achieved in a concise and divergent manner as depicted in Scheme 4. It commenced with a $BF_3{\cdot}OEt_2$-mediated chemoselective glycosylation of the primary hydroxy groups of **20** and **21**, with either lactosyl (**19**) (26) or glucosaminyl (**24**) (27) acetate to give **22** and **23** or **25** and **26**, respectively, in 67–85% yield. For the glycosylation of the unreactive phenolic hydroxy group, trichloroacetimidates **27** (28), **30** (25), and **33** (25) gave highly satisfactory results. To our surprise, addition of molecular sieves (MS), a common practise in glycosylation to ensure anhydrous conditions, deteriorated the efficiency of these particular reactions. Namely, when **22** and **23** were reacted with **27** in the presence of MS AW-300, the yields of **28** and **29** were less than 40%, while the same products were obtained in excellent yields in their absence. Reactions of **25** and **26** with **30** and **31** were likewise performed to give **31**, **32**, **34**, and **35** in 85–97% yield. Somewhat unexpectedly, in the case of the preparation of **34**, a significant amount of the corresponding α-isomer was also synthesized (α:β = 1:3.3). The obtained products were then subjected to deprotection, uneventfully, to give **36**–**41**.

These compounds were examined as substrates for transglycosylation in a similar manner as that described for **15** and **16**. Namely, each substrate (8 mM) was incubated with *B. circulans* β-galactosidase in 50 mM acetate buffer (pH 5.0), and the reactions were followed by analytical HPLC (Fig. 2).

In the case of substrates carrying lactose as a donor component (**36**–**39**), severe peak overlaps retarded the interpretation

© 2002 NRC Canada

Fig. 1. Time course of β-galactosidase catalyzed reactions: (*a*) compound **9** (8 mM) was incubated with 0.5 U of β-galactosidase in 2.5 mL of acetate buffer (50 mM, pH 5.0) at 36°C; (*b*) compound **10** (8 mM) was incubated with 1.2 U of β-galactosidase under identical conditions as (*a*). Aliquots of the mixture were analyzed by HPLC. Peaks were assigned as follows based on MALDI-TOF-MS analysis: ■ starting material (**9** and **10**); ○ GlcNAcGlc (**11** and **12**); ● LacNAcGlc (**15** and **16**); □ LacNAcLac (**13** and **14**); ◆ GalLacNAcLac.

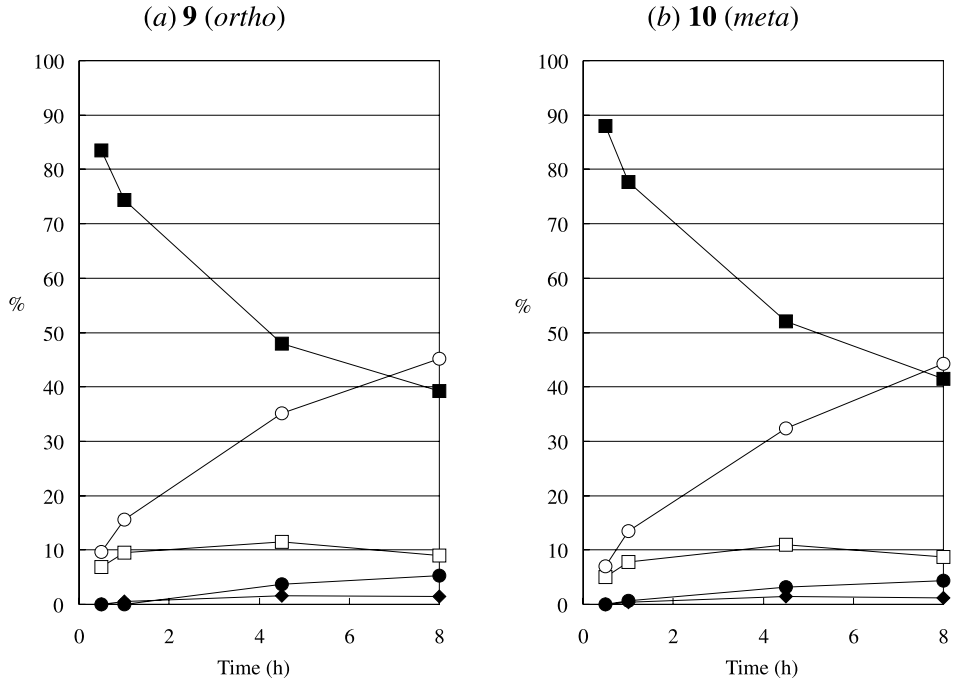

Scheme 3.

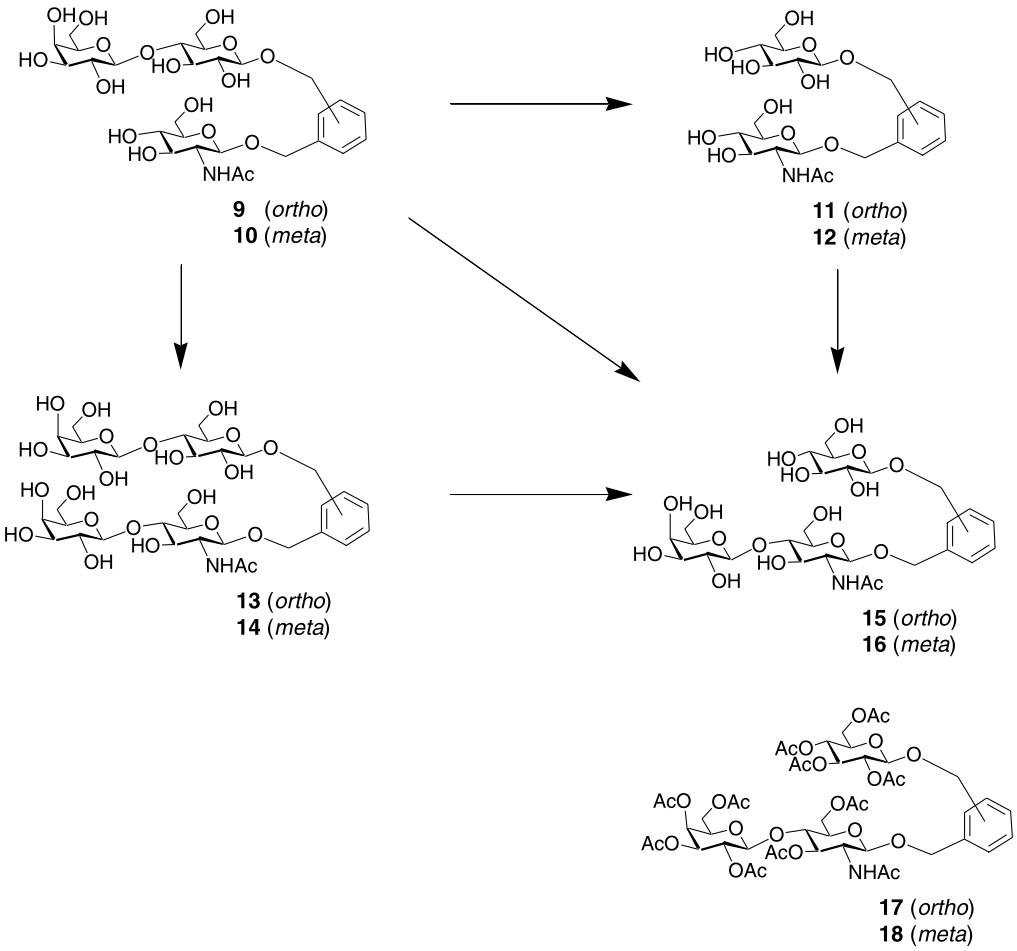

© 2002 NRC Canada

Scheme 4. Reagents and conditions: (*a*) 2 equiv $BF_3{\cdot}OEt_2$ in CH_2Cl_2 at rt for 1 h; (*b*) 0.5 equiv $BF_3{\cdot}OEt_2$ in CH_2Cl_2 at rt for 1 h; (*c*) (*i*) 75 equiv NH_2NH_2 in EtOH at 90°C for 3 h, (*ii*) Ac_2O in MeOH at rt for 8 h.

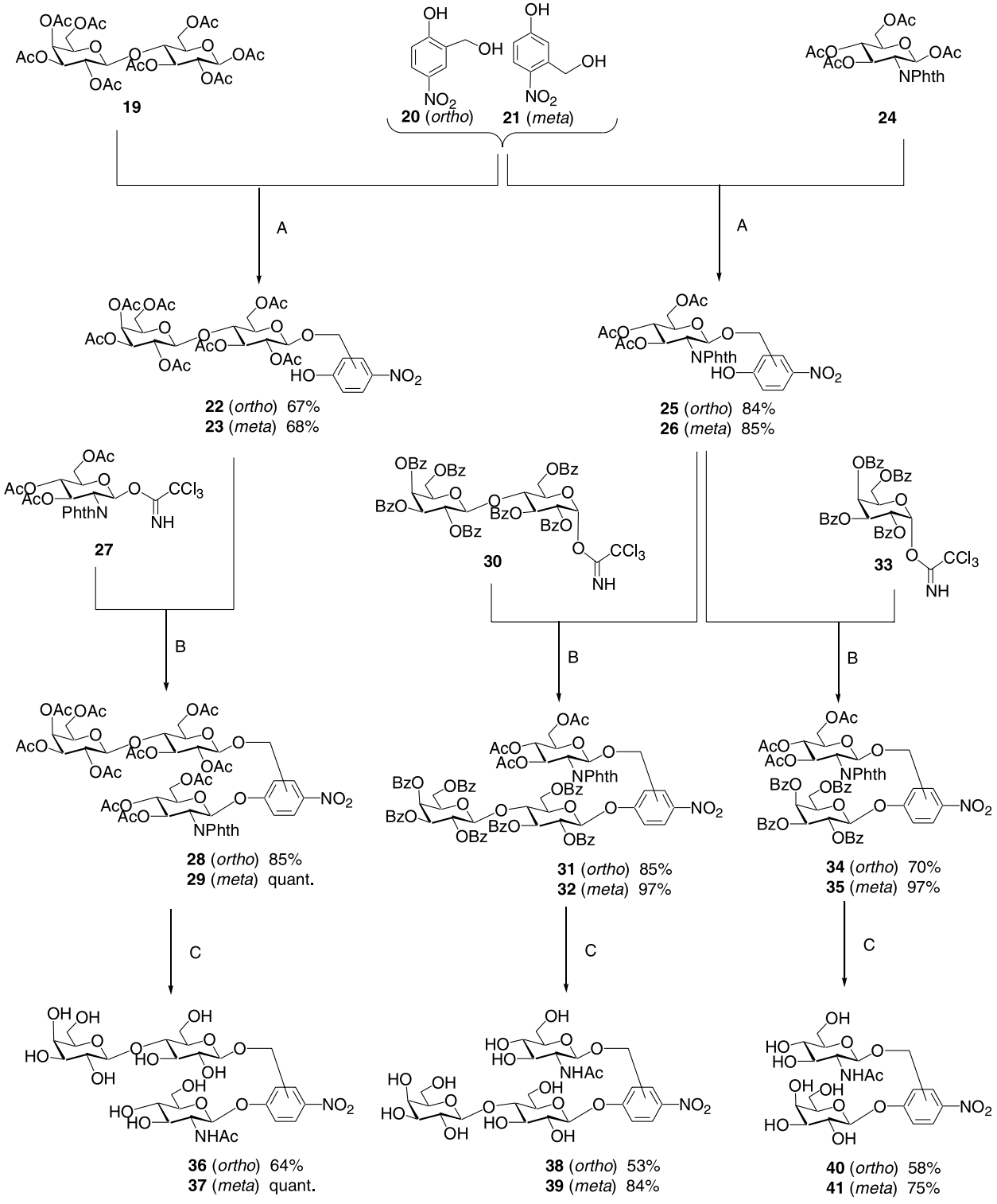

of the HPLC profiles. To enhance the peak assignments, aliquots of the mixtures were treated with β-*N*-acetylglucosaminidase from Jack beans (Sigma Co., Ltd.). After this treatment, galactosylated products, including the desired products (**54**–**57**) and bis-disaccharides (**48**–**51**), were readily distinguished from substrates and hydrolyzed products (**42**–**45**) by their resistance. In any event, no indication of intramolecular glycosyl transfer was obtained from these substrates; that is, at the early stage of incubation, the formation of **48**, **49**, **50**, and **51** was dominant over **54**, **55**,

© 2002 NRC Canada

Fig. 2. Time course of β-galactosidase catalyzed reactions using substrates derived from the nitro-containing linker (Scheme 4). (*a*) Compound **36** (8 mM) was incubated with 0.34 U of β-galactosidase in 1.8 mL of acetate buffer (50 mM, pH 5.0) at 36°C; (*b*) compound **37** (8 mM) was incubated with 0.34 U of β-galactosidase, under identical conditions as (*a*) aliquots of the mixture were analyzed by HPLC. Peaks were assigned as follows based on MALDI-TOF-MS analysis: ■ starting material (**36** and **37**); ○ GlcNAcGlc (**42** and **43**); ● LacNAcGlc (**54** and **55**); □ LacNAcLac (**48** and **49**); × GlcNAcGalLac (regioisomer of **48** and **49**, structure not confirmed); ◆ $GlcNAcGal_2Lac$ (structure not confirmed); (*c*) compound **38** (8 mM) was incubated with 0.34 U of β-galactosidase in 1.8 mL of acetate buffer (50 mM, pH 5.0) at 36°C; (*d*) compound **39** (8 mM) was incubated with 0.10 U of β-galactosidase, under identical conditions as (*c*). Aliquots of the mixture were analyzed by HPLC. Peaks were assigned as follows based on MALDI-TOF-MS analysis: ■ starting material (**38** and **39**); ○ GlcNAcGlc (**44** and **45**); ● LacNAcGlc (**56** and **57**); □ LacNAcLac (**50** and **51**); × GlcNAcGalLac (regioisomer of **50** and **51**, structure not confirmed); ◆ $GlcNAcGal_2Lac$ (structure not confirmed).; (*e*) compound **40** (8 mM) was incubated with 0.13 U of β-galactosidase in 0.70 mL of acetate buffer (50 m M, pH 5.0) at 36°C; (*f*) compound **41** (8 mM) was incubated with 0.44 U of β-galactosidase under idential conditions as in (*e*). Aliquots of the mixture were analyzed by HPLC. Peaks were assigned as follows based on MALDI-TOF-MS analysis: ■ starting material (**40** and **41**); ○ GlcNAc (**46** and **47**); ● LacNAc (**58** and **59**); □ LacNAcGal (**52** and **53**); × $Gal_2GlcNAc$ (regioisomer of **52** and **53**, structure not confirmed); ◆ $Gal_3GlcNAc$ (structure not confirmed).

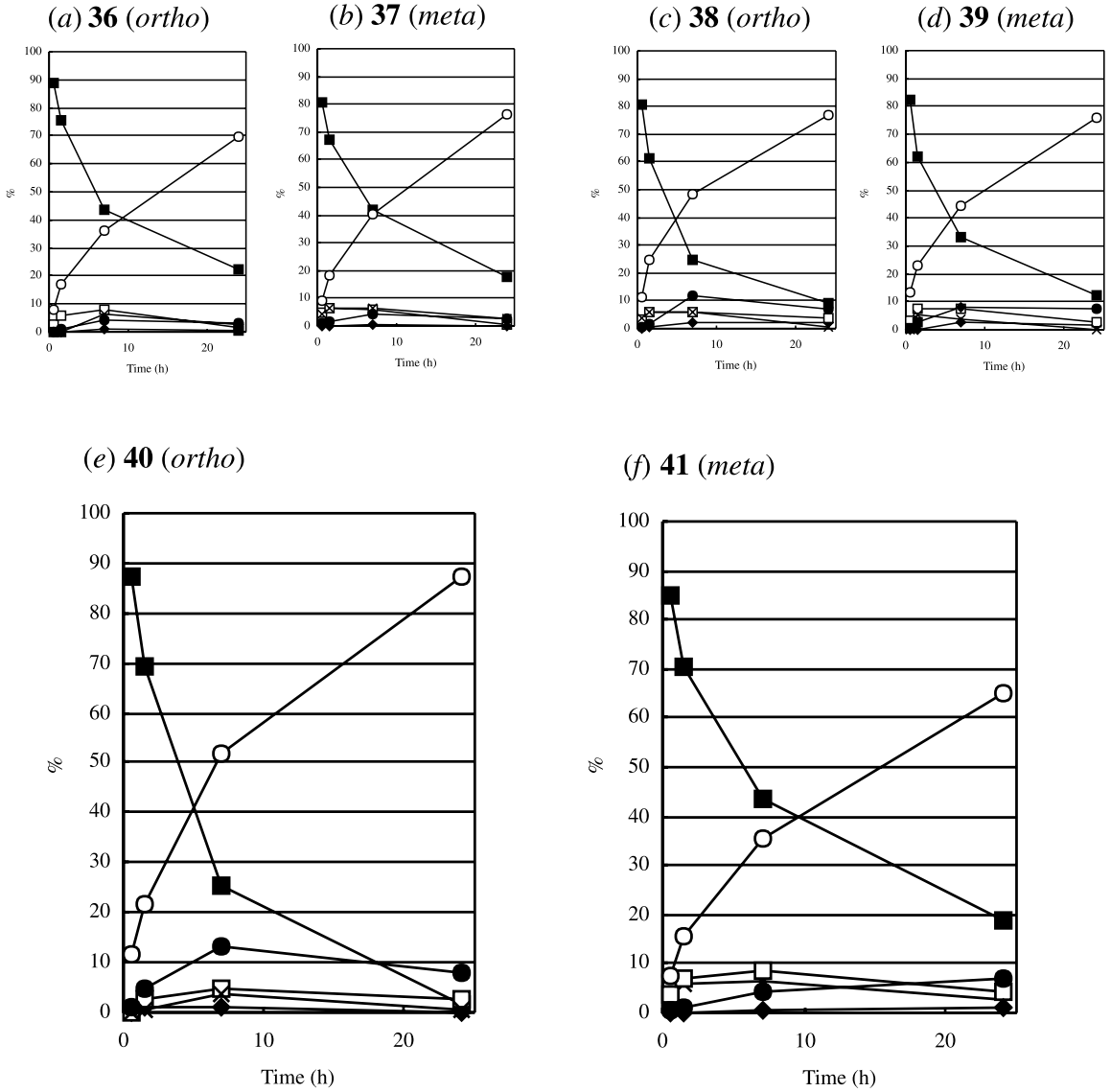

56, and **57**.[2] Nevertheless, it was observed that a significant amount of the transglycosylated product (**56**) was formed from *ortho* substrate **38**.

On the other hand, the profile of substrate **40** was markedly different. In this particular case, the formation of the LacNAc derivative (closed circle) was dominant over that of **52** even at the early stage of incubation ([**40**] > [**46**]).[2] Since the rates of intermolecular glycosyl transfer are likely to be similar between **40** and **46** ($k_1 \approx k_2$), it was inferred that the intramolecular pathway is functional ($k_3 > k_1, k_2$) (Scheme 5). By contrast, when starting from the *meta* oriented substrate **41**, it was found that the transglycosylation was far less efficient.

© 2002 NRC Canada

Scheme 5.

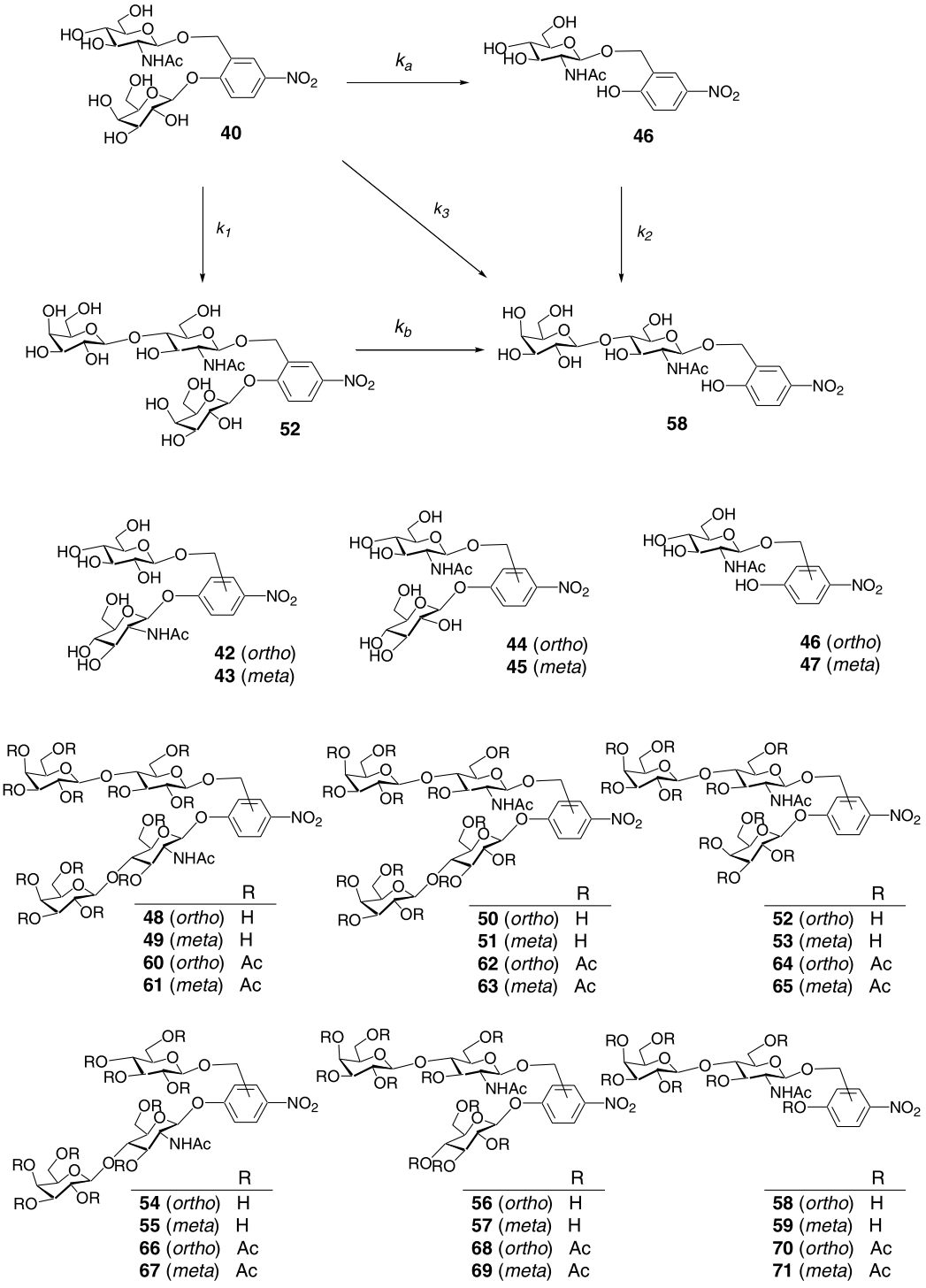

The formation of intermolecularly glycosylated product **53** preceded that of **59**, which means that the direct pathway was insignificant.

Using the preferred substrate **40**, the effects of substrate concentration (i.e., Table 1, entries 1–4), organic solvents (entries 6–12), and buffer pH (entry 5) were briefly examined. Contrary to several precedents on enzymatic transglycosylation (17, 20, 21), the beneficial effect of organic solvent was not observed (entries 6–12). A preparative scale reaction was performed at 20 mM concentration in acetate buffer (entry 3). Thus, using 50 mg (94 μmol) of compound **40**, incubation with β-galactosidase (430 mU) for 3 h afforded 26% yield (13.1 mg) of **58**, the structure of which was rigorously confirmed by NMR analysis of the corresponding acetate **70**. Subsequently, the effect of the glucosamine *C*-2 substituent was examined. Considering the potential synthetic utility of the expected products, three types of substrates were prepared, namely *N*-allyloxycarbonyl (Alloc) protected **72**,

© 2002 NRC Canada

Fig. 3. Time course of β-galactosidase catalyzed reactions using *C*-2 modified substrates (Scheme 7); (*a*) compound **72** (20 mM) was incubated with 86 mU of β-galactosidase in 86.5 μL of acetate buffer (50 mM, pH 5.0) at 36°C; (*b*) compound **73** (20 mM) was incubated with 86 mU of β-galactosidase under identical conditions as (*a*); (*c*) compound **74** (10 mM) was incubated with 172 mU of β-galactosidase under identical conditions as (*a*). Aliquots of the mixture were analyzed by HPLC. Peaks were assigned as follows based on MALDI-TOF-MS analysis: ■ starting material (**72** and **73** and **74**); ○ GlcNR (**75** and **76** and **77**); ● LacNR (**81** and **82** and **83**); □ LacNRGal (**78** and **79** and **80**); × Gal_2GlcNR (regioisomer of **78** and **79** and **80**, structure not confirmed); ◆ Gal_3GlcNR (structure not confirmed).

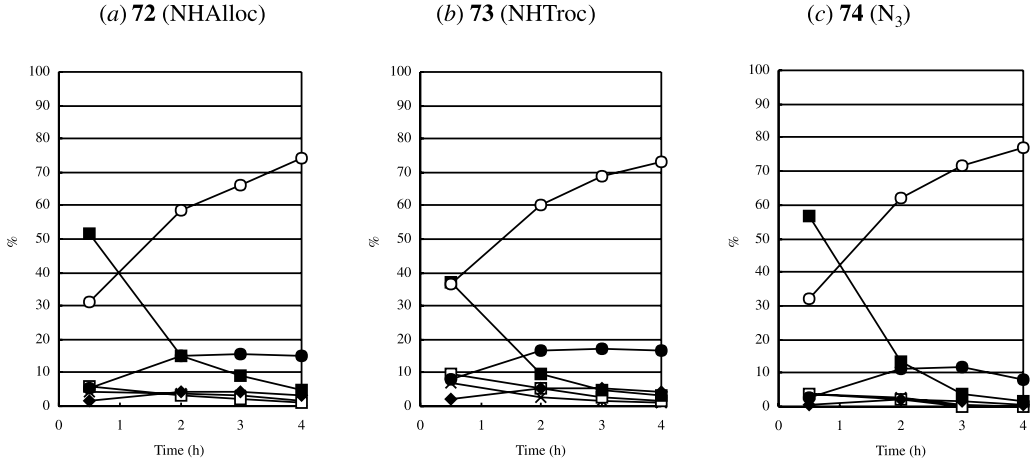

Table 1. Effects of solvent and substrate concentration.

Entry	**40** (mM)	Enzyme (mU)	Solvent (mL)[a]	Time (h)	Yield (%)
1	0.8	43	A (2.3)	48	4[b]
2	8	86	A (0.23)	8	15[b]
3	20	430	A (4.7)	3	26[c]
4	20	430	A (4.7)	4	18[b]
5	20	86	B (0.09)	4.5	15[c]
6	8	130	C (0.23)	24	7[b]
7	8	130	C (0.23)	72	14[b]
8	8	130	C (0.23)	96	14[b]
9	8	130	D (0.23)	24	2[b]
10	8	43	E (0.23)	8	10[b]
11	8	43	E (0.23)	24	13[b]
12	8	43	E (0.23)	72	1[b]

[a](A) 50 mM acetate buffer, pH 5.0; (B) 200 mM HEPES, pH 7.5; (C) 50% acetonitrile in A; (D) 60% triethyl phosphate in A; (E) 20% 2-ethoxyethyl ether in A.
[b]Based on HPLC relative peak integrations, quantified at 245 nm.
[c]Isolated yield.

N-trichloroethoxycarbonyl (Troc) protected **73**, and *C*-2 azide **74**. To synthesize these substrates, compound **34** was used as the common intermediate. Thus, **34** was treated with hydrazine hydrate in EtOH to remove *N*-phthalimido and *O*-acyl groups. The resultant amine was treated with either allyl chloroformate – $NaHCO_3$, trichloroethyl chloroformate – $NaHCO_3$, or TfN_3–Cu_2SO_4–K_2CO_3 (29), to afford **72**, **73**, and **74** in 64, 80, and 53% yield, respectively (Scheme 6).

Enzymatic transglycosylations were examined under conditions optimized for **40** (20 mM substrates in 50 mM acetate buffer, pH 5.0, Fig. 3 (Scheme 7). In these cases, the dominancy of intramolecular transglycosylation was not as clear as **40**, because the formation of the expected products (**81**–**83**) was slightly behind the initial formation of intermolecularly transferred products (**78**–**80**);[2] nonetheless, carbamate-protected lactosamine derivatives **81** and **82** were formed with an efficiency comparable with **58**. These products were quite resistant to galactosidase mediated hydrolysis. Preparative scale reactions using **72** (17.3 μmol), **73** (15 μmol), and **74** (9.6 μmol) were performed, in the same manner as described for **40**, to give **81**, **82**, and **83** in 21, 21, and 11%, respectively (Scheme 8), the structures of which were rigorously confirmed by NMR analysis of the corresponding acetates (**84**, **85**, and **86**). Since *N*-Alloc- (30) and *N*-Troc-protected derivatives (31) and *C*-2 azide (13, 32) are useful as glycosyl donors for the β- and α-selective glycosylation of 2-amino sugars, respectively, this procedure may be useful for the chemoenzymatic synthesis of complex oligosaccharides.

We then turned our attention to the synthesis of sialyl LacNAc by using galactosidase mediated transglycosylation, in combination with sialyltransferase. Since it is obvious that the LacNAc product **58** is susceptible to further digestion by β-galactosidase (to provide **46**), its yield under standard conditions does not reflect the relative rates of intramolecular transglycosylation and hydrolysis (i.e., k_3 vs. k_a). In fact, the yield of **58** (26%) dropped to 18% after 4 h incubation (Table 1, entries 3 and 4). To minimize the extent of post-transglycosylation hydrolysis, and to gain a more accurate estimation of the efficiency of transglycosylation, α-(2→6)-sialyltransferase (rat, recombinant, *Spodoptera frugiperda*) (Calbiochem Co., Ltd.) (33, 34) and CMP sialic acid were added to the system to trap **58** as a galactosidase resistant product **87** (Scheme 9, Figs. 4 and 5). As expected, smooth formation of sialyl-α-(2→6)-LacNAc **87** (□) was observed, and its amount did not decrease after prolonged incubation. In a preparative scale run, substrate **40** was used (25 mg, 47 μmol), incubated in 200 mM HEPES buffer (2.4 mL, pH 7.5) in the presence of β-galactosidase (100 mU), α-(2→6)-sialyltransferase (60 mU), and CMP-sialic acid (30 mg,

© 2002 NRC Canada

Scheme 6.

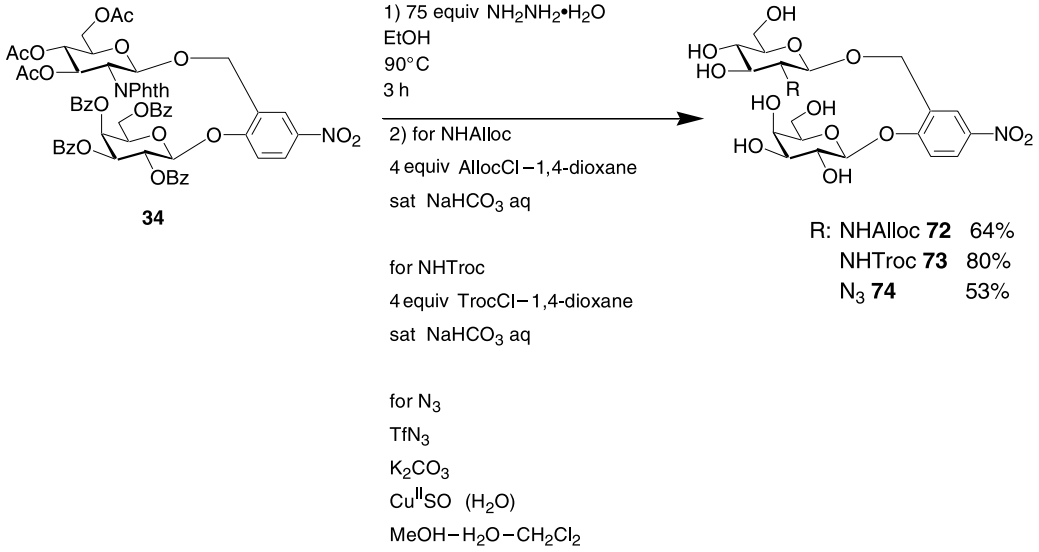

Scheme 7.

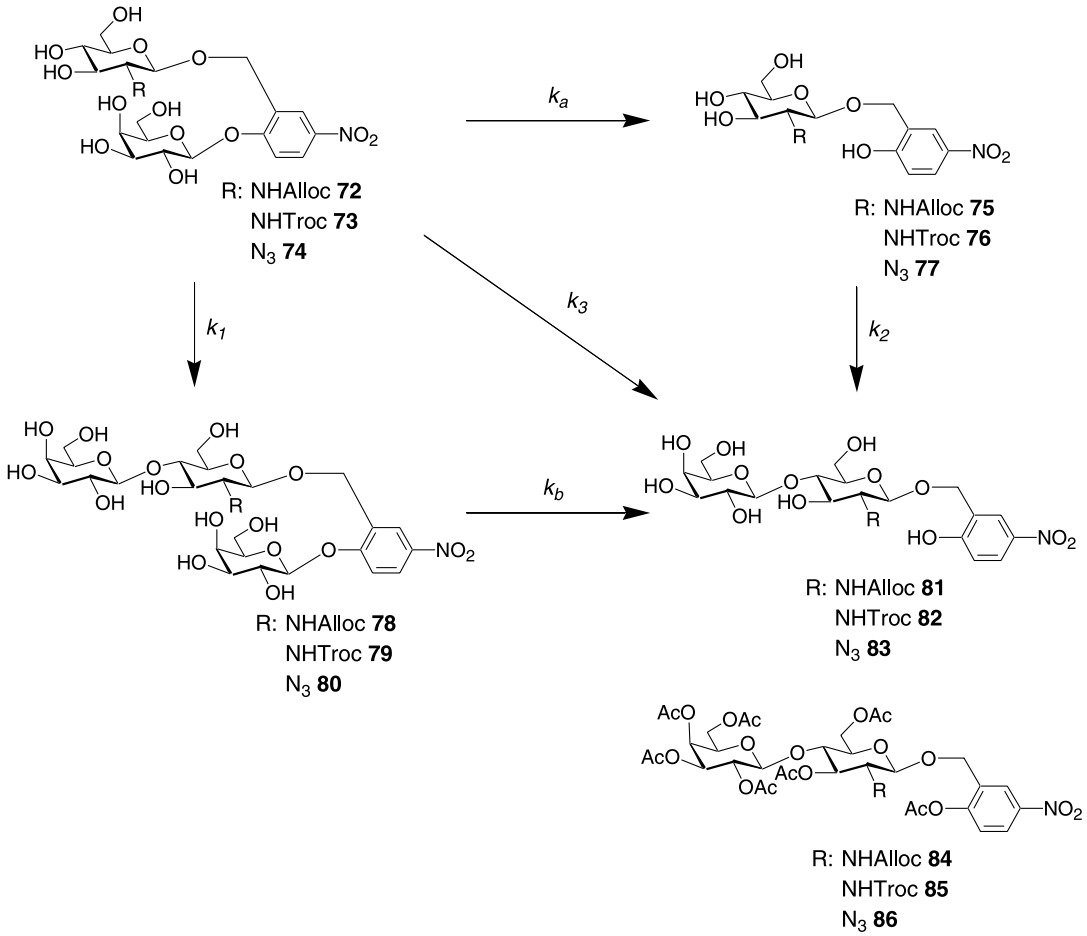

46 μmol). After 17 h, successive purification by Sephadex LH-20 and preparative HPLC afforded sialyl-α-(2→6)-LacNAc **87** in 39% yield (15.4 mg).

In conclusion, a novel method for the preparation of LacNAc and sialyl LacNAc was developed using β-galactosidase mediated intramolecular transglycosylation,

© 2002 NRC Canada

Scheme 8.

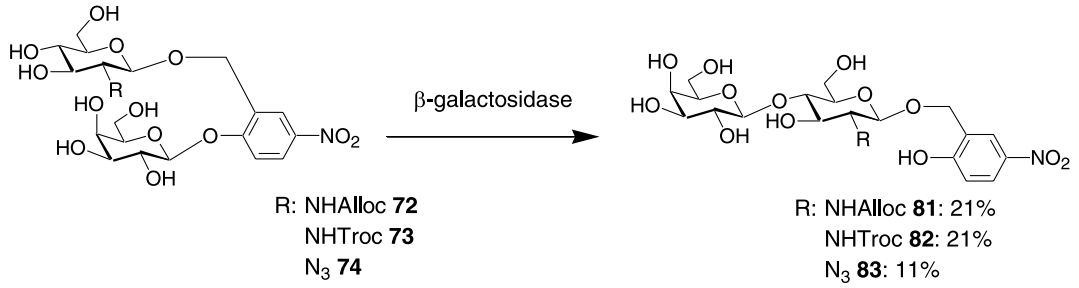

Scheme 9.

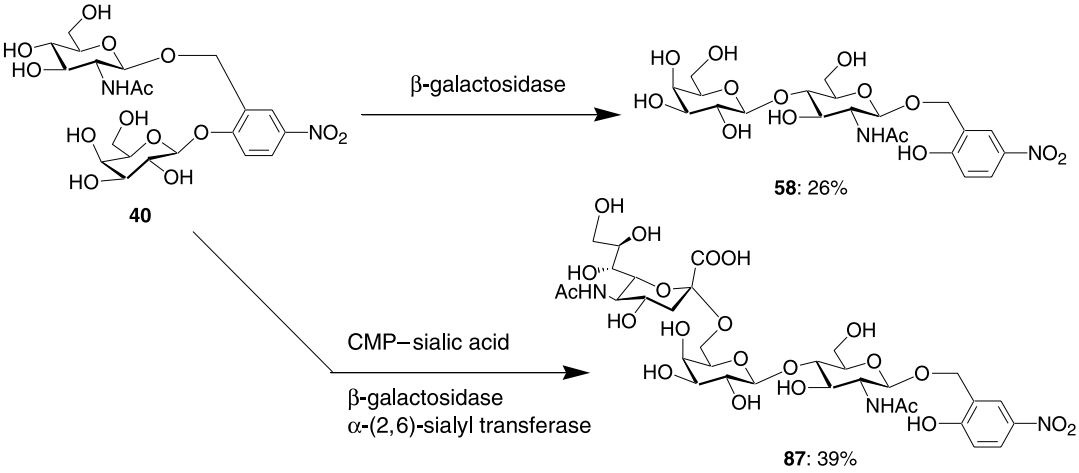

using substrates that have glycosyl donor and aglycon portions connected by a tether.

Experimental[3]

General methods

Column chromatography was performed on Silica Gel 60N (spherical, neutral) (Kanto chemical Co., Inc.). Preparative reverse-phase HPLC was performed on a Waters HPLC system (Millennium[32] operation system), using a Mightysil RP-18 GP 250–20 (5 μm) (Kanto chemical Co., Inc.), with a flow rate of 10 mL min^{-1}, and detected at 256 nm with a photodiode array detector (Waters 996). The solvent systems were: (*a*) TFA–water (1:1000) and (*b*) TFA–acetonitrile–water (1:900:100). Analytical reverse phase HPLC separations were performed on a Waters HPLC system, using a Mightysil RP-18 GP 250–3.0 (5 μm) (Kanto chemical Co., Inc.), with a flow rate of 0.6 mL min^{-1}, and detected at 256 nm with the same detector as above, using the same solvent system as above. MALDI-TOF-MS was performed in the positive ion mode on a Kompact MALDI IV tDE (Shimadzu Co., Ltd.), using a matrix of 2,5-dihydroxybenzoic acid or α-cyano-4-hydroxycinnamic acid, and an angiotensin I (MW = 1296.5) as a standard. FAB-MS was performed in the positive ion mode on a JMS-HX110 (JEOL), using a matrix mixture of glycerol and 3-nitrobenzyl alcohol. Optical rotations were measured with a DIP-370 digital polarimeter (Japan spectroscopic Co., Ltd.) at 22°C. ^{1}H NMR spectra were recorded at 400 MHz (JEOL JNM-AL400), or at 500 MHz (JEOL JNM-ECP500), in $CDCl_3$ (internal Me_4Si, δ: 0.00), DMSO-d_6, CD_3OD, or D_2O. ^{13}C NMR spectra were recorded at 100 or 125 MHz, respectively, on the same instruments in $CDCl_3$, DMSO-d_6, CD_3OD, or D_2O (internal MeOH, δ: 49.0). β-Galactosidase from *Bacillus circulans* was purchased from Daiwa Kasei K.K. (Japan). α-(2→6)-Sialyltransferase from rat, recombinant, *Spodoptera frugiperda* was purchased from Calbiochem Co., Ltd. β-*N*-Acetylglucosaminidase from Jack beans was purchased from Sigma Co., Ltd. All solvents and reagents were reagent grade and were used without further purification.

Enzymatic transglycosylation: typical procedure 1

A solution of substrate **9** (13.7 mg, 20.5 μmol, 8 mM) in 50 mM sodium acetate buffer (2.5 mL, pH 5.0) was incubated with β-D-galactosidase (0.5 U) at 36°C. After 30 min, 1 h, 4.5 h, and 8 h, aliquots of the reaction mixture were taken (ca. 200 μL) and terminated by heating at 95°C for 10 min. Each of them was separated by HPLC, first using 90% solvent A and 10% solvent B for 10 min, then the linear gradient 10–100% solvent B for 170 min. The eluted peaks were detected 254 nm UV absorption and the

[3] Experimental details for preparation of substrates were provided as Supplementary Material. Supplementary data may be purchased from the Depository of Unpublished Data, Document Delivery, CISTI, National Research Council Canada, Ottawa, ON K1A 0S2, Canada (http://www.nrc.ca/cisti/irm/unpub_e.shtml for information on ordering electronically).

© 2002 NRC Canada

Fig. 4. HPLC profiles of β-galactosidase – α-sialyltransferase reaction of **40**: (*a*) 1.5 h, (*b*) 6.5 h. Retention times of starting material (**40**), $Gal_2GlcNAc$ (**52**), NeuAcGalGlcNAc (**87**), and GlcNAc (**46**) are 17.87, 18.34, 22.25, and 22.53 min, respectively.

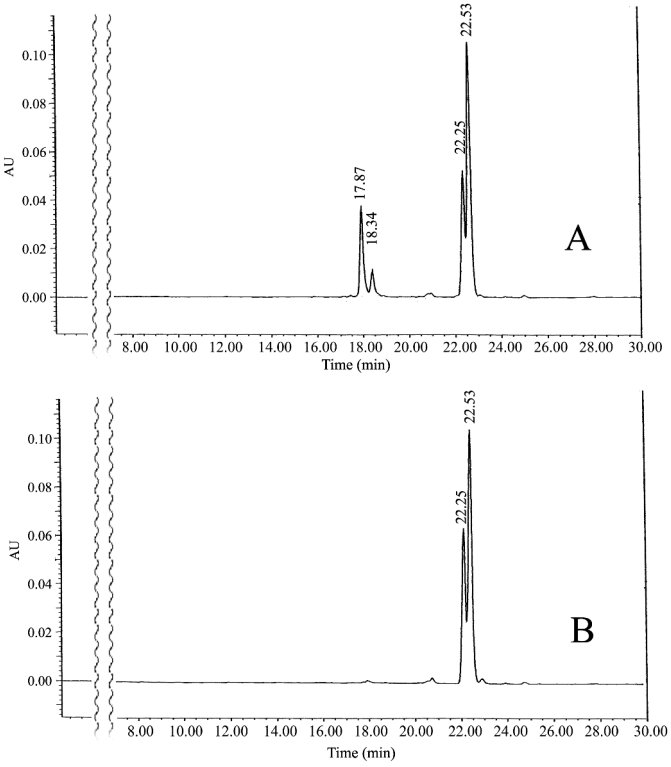

composition was calculated by integral curves. The fractions containing products were analyzed by MALDI-TOF-MS and each product was acetylated for extensive ^1H NMR analysis.

Enzymatic transglycosylation: typical procedure 2

A solution of substrate **36** (10 mg, 14.3 μmol, 8 mM) in 50 mM sodium acetate buffer (1.8 mL, pH 5.0) was added to β-D-galactosidase (0.34 U) and incubated at 36°C. After 30 min, 1.5 h, 7 h, and 24 h, aliquots of the reaction mixture were taken and terminated by heating at 95°C for 10 min, and part of them were analyzed by analytical HPLC, first using 100% solvent A for 5 min, then the linear gradient 0–30% solvent B for 30 min.

Residual aliquots (180 μL) were treated with β-*N*-acetylglucosaminidase (62.5 mU) at 36°C for 2 days, then the reaction mixtures were terminated by heating at 95°C for 10 min. Each of them was analyzed by HPLC, 90% solvent A and 10% solvent B as isocratic mode. The eluted peaks were detected at 254 nm using UV absorption and the composition was calculated by integral curves.

Combined transglycosylation–sialylation: preparation of compound 87

To a solution of **40** (25 mg, 46.7 μmol, 20 mM) and CMP-Neu5Ac (30.8 mg, 46.7 μmol) in 200 mM HEPES buffer (2.3 mL, pH 7.5) containing 20 mM $MgCl_2$, 5.3 mM $MnCl_2$, and 20 mM KCl, was added α-(2→6)-sialyltransferase (60 mU), followed by β-D-galactosidase (2.2 U). The mixture was incubated at 36°C for 18 h, and terminated by heating at 95°C for 10 min. After concentration, the mixture was roughly purified by Sephadex LH-20 gel filtration column chromatography (H_2O). Fractions containing **87** were concentrated and the mixture was purified by preparative HPLC, first using 100% solvent A for 5 min, then the linear gradient 0–30% solvent B for 30 min to give sialylated compound **87** (15.4 mg, 39%), together with hydrolyzed compound **46** (10.8 mg, 61%). Compound **87**: ^1H NMR (500 MHz, D_2O and MeOH) δ: 8.06 (d, 1H, $J_{Ph4,Ph5}$ = 3.2 Hz, Ph6), 8.01 (dd, 1H, $J_{Ph3,Ph4}$ = 9.2 Hz, $J_{Ph4,Ph6}$ = 3.2, Ph4), 6.49 (d, 1H, $J_{Ph3,Ph4}$ = 9.2 Hz, Ph3), 4.75 (d, 1H, J_{gem} = 12.8 Hz, PhCH),

Fig. 5. Time course of β-galactosidase – α-sialyltransferase reaction of **40**. Compound **40** (20 mM) was incubated with 86 mU of β-galactosidase and α-(2→6)-sialyltransferase (2.4 mU) in 95 μL of HEPES (200 mM, pH 7.5), 20 mM $MgCl_2$, 5.3 mM $MnCl_2$, 20 mM KCl, and CMP-sialic acid (20 mM), at 36°C. Peaks were assigned as follows based on MALDI-TOF-MS analysis: ◆ starting material (**40**); × GlcNAc (**46**); □ NeuAcGalGlcNAc (**87**); ■ $Gal_2GlcNAc$ (**52**).

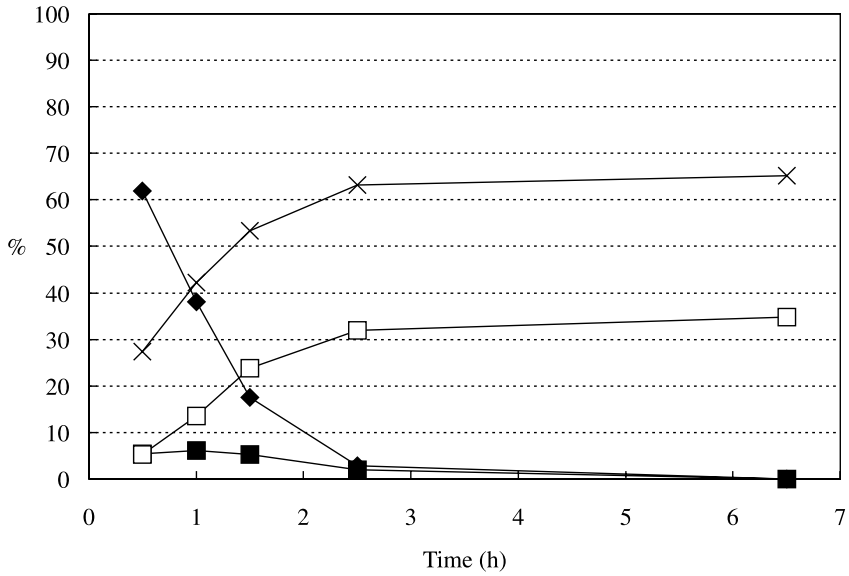

© 2002 NRC Canada

4.63 (d, 1H, J_{gem} = 13.3 Hz, PhCH′), 4.57 (d, 1H, $J_{1,2}$ = 8.2 Hz, H-1Gal), 4.40 (d, 1H, $J_{1,2}$ = 7.8 Hz, H-1GlcN), 2.64 (dd, 1H, $J_{3eq,4}$ = 4.1 Hz, J_{gem} = 11.9 Hz, H-3eq sialic acid), 2.00 and 1.95 (2s, 6H, 2NAc), 1.66 (dd, 1H, $J_{3ax,4}$ = J_{gem} = 11.9 Hz, H-3ax sialic acid). ^{13}C NMR (150 MHz, D_2O, NaOD, and MeOH) δ: 176.4 (C_{Ph2}), 175.1 (C_{NAc}=O GlcN), 174.8 (C_{NAc}=O sialic acid), 173.7 (C-1 sialic acid), 133.1 (C_{Ph5}), 127.6 (C_{Ph4}-H), 127.2 (C_{Ph6}-H), 126.5 (C_{Ph1}), 119.6 (C_{Ph3}-H), 103.8 (C-1 Gal), 100.5 (C-1 GlcN), 100.4 (C-2 sialic acid), 80.2 (C-4 GlcN), 74.8 (C-5 GlcN), 74.0 (C-5 Gal), 73.1 (C-3 Gal), 72.7 (C-3 GlcN), 72.7 (C-6 sialic acid), 71.9 (C-8 sialic acid), 70.8 (C-2 Gal), 68.9 (C-4 Gal), 68.6 (C-7 sialic acid), 68.4 (C-4 sialic acid), 67.0 (C_{Bn}-H_2), 63.6 (C-6 Gal), 62.8 (C-9 sialic acid), 60.7 (C-6 GlcN), 55.4 (C-2 GlcN), 52.2 (C-5 sialic acid), 40.5 (C-3 sialic acid), 22.3 and 22.2 ($2C_{NAc}$-H_3). MALDI-MS *m/z*: 848 ($[M + Na]^+$).

Acknowledgments

This work was supported by the Special Postdoctoral Researchers Program at RIKEN. We thank Dr. H. Koshino and his staff for NMR measurements and Ms. A. Takahashi for technical assistance.

References

1. M. Fukuda. Biochim. Biophys. Acta, **780**, 119 (1985).
2. T. Feize, H.C. Gooi, R.A. Childs, J.K. Pickard, K. Uemura, L.M. Koomes, S.J. Thorpe, and E.F. Hounsell. Biochim. Soc. Trans, **12**, 591 (1984).
3. R.V. Iozzo and A.D. Murdoch. FASEB J. **10**, 598 (1996).
4. R.K. Jain, B.G. Huang, E.V. Chandrasekaran, and K.L. Matta. Chem. Commun. 23 (1997).
5. T.M. Wrodnigg and A.E. Stutz. Angew. Chem. Int. Ed. **38**, 827 (1999).
6. R.J. Tomarelli, J.B. Hassinen, E.R. Eckhardt, R.H. Clark, and F.W. Bernhart. Arch. Biochem. Biophys. **48**, 225 (1954).
7. A.A. Sherman, O.N. Yudina, A.S. Shashkov, V.M. Menshov, and N.E. Nifant'ev. Carbohydr. Res. **330**, 445 (2001).
8. S. Figueroa-Perez and V. Verez-Bencomo. Carbohydr. Res. **317**, 29 (1999).
9. E. Lattova and L. Petrus. Carbohydr. Res. **235**, 289 (1992).
10. T. Ogawa and S. Nakabayashi. Carbohydr. Res. **97**, 81 (1981).
11. J. Alais and A. Veyrieres. Carbohydr. Res. **207**, 11 (1990).
12. T.C. Wong and R.U. Lemieux. Can. J. Chem. **62**, 1207 (1984).
13. R.U. Lemieux and R.M. Ratcliffe. Can. J. Chem. **57**, 1244 (1979).
14. C.H. Wong, S.L. Haynie, and G.M. Whitesides. J. Org. Chem. **47**, 5416 (1982).
15. C.H. Wong, R.L. Halcomb, Y. Ichikawa, and T. Kajimoto. Angew. Chem. Int. Ed. Engl. **34**, 412 (1995).
16. F. Zilliken, P.N. Smith, C.S. Rose, and P. György. J. Biol. Chem. **217**, 79 (1955).
17. (*a*) K. Sakai, R. Katsumi, H. Ohi, T. Usui, and Y. Ishido. J. Carbohydr. Chem. **11**, 553 (1992); (*b*) T. Usui, S. Morimoto, Y. Hayakawa, M. Kawaguchi, T. Murata, Y. Matahira, and Y. Nishida. Carbohydr. Res. **285**, 29 (1996).
18. E. Farkas and J. Thiem. Eur. J. Org. Chem. 3073 (1999).
19. (*a*) S. Takayama, M. Shimazaki, L. Qiao, and C.H. Wong. Bioorg. Med. Chem. Lett. **6**, 1123 (1996); (*b*) T. Kitamura, S. Takayama, H. Huang, and C.H. Wong. Angew. Chem. Int. Ed. Engl. **35**, 2348 (1996).
20. J.H. Yoon and J.S. Rhee. Carbohydr. Res. **327**, 377 (2000).
21. K. Priya and D. Loganathan. Tetrahedron, **55**, 1119 (1999).
22. J. Fang, W. Xie, J. Li, and P.G. Wang. Tetrahedron Lett. **39**, 919 (1998).
23. A part of this work was published in a preliminary form: S. Komba and Y. Ito. Tetrahedron Lett. **42**, 8501 (2001).
24. C. Auge and A. Veyrierés. Carbohydr. Res. **46**, 293 (1976).
25. R.R. Schmidt and J. Michel. Angew. Chem. Int. Ed. Engl. **19**, 731 (1980).
26. C.S. Hudson and J.M. Johnson. J. Am. Chem. Soc. **37**, 1270 (1915).
27. A. Medgyes, E. Farkas, A. Liptak, and V. Pozsgay. Tetrahedron, **53**, 4159 (1997).
28. G. Grundler and R.R. Schmidt. Carbohydr. Res. **135**, 203 (1985).
29. (*a*) J.T. Lundquist, IV and J.C. Pelletier. Org. Lett. **3**, 781 (2001); (*b*) P.B. Alper, S.H. Hung, and C.H. Wong. Tetrahedron Lett. **37**, 6029 (1996).
30. A. Vargas-Berenguel, M. Meldal, H. Paulsen, and K. Bock. J. Chem. Soc. Perkin Trans. 1, 2615 (1994).
31. (*a*) J. Rademann, A. Geyer, and R.R. Schmidt. Angew. Chem. Int. Ed. Engl. **37**, 1241 (1998); (*b*) N. Sawada, M. Ito, H. Ishida, and M. Kiso. Tetrahedron Lett. **42**, 1745 (2001).
32. W. Kinzy and R.R. Schmidt. Justus Liebigs Ann. Chem. 1537 (1985).
33. For the previous work on the combined use of β-galactosidase and sialyltransferase. G.F. Herrmann, Y. Ichikawa, C. Wandrey, F.C.A. Gaeta, J.C. Paulson, and C.H. Wong. Tetrahedron Lett. **34**, 3091 (1993).
34. (*a*) J. Weinstein, U. de Sausa-e-Silva, and J.C. Paulson. J. Biol. Chem. **257**, 13 835 (1982); (*b*) M.A. Williams, H. Kitagawa, A.K. Datta, J.C. Paulson, and J.C. Jamieson. Glycoconjugate J. **12**, 755 (1995); (*c*) K.B. Wlasichuk, M.A. Kashem, P.V. Nikrad, P. Bird, C. Jiang, and A.P. Venot. J. Biol. Chem. **268**, 13 971 (1993).

© 2002 NRC Canada

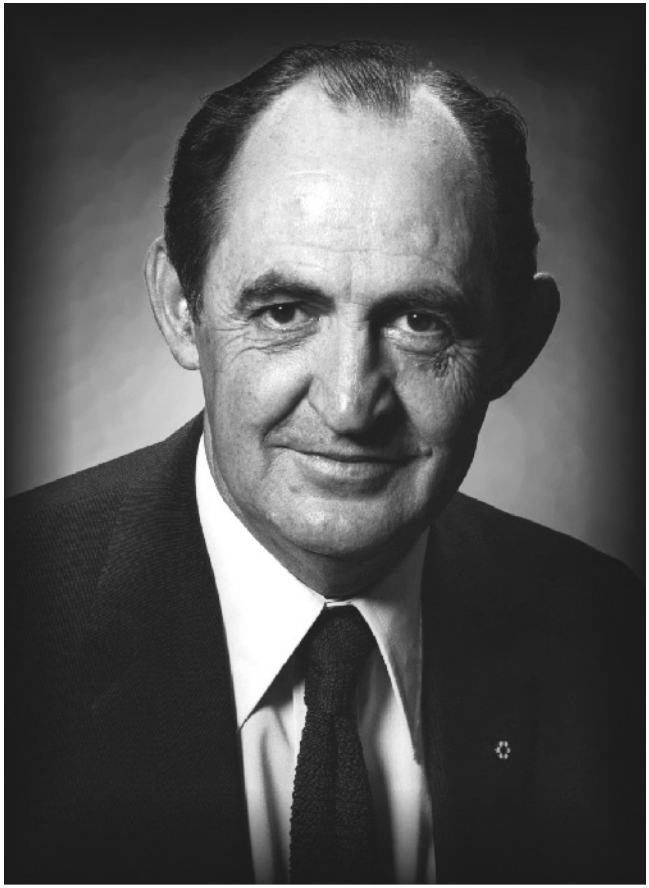

Professor Raymond U. Lemieux

© 2002 NRC Canada

Professor Raymond U. Lemieux

The following excerpt from David Bundle's excellent biography of Ray Lemieux for an upcoming volume of *Advances in Carbohydrate Chemistry and Biochemistry*, says it all: "His work was a dominating factor in converting this field from an academic specialization to one of great practical importance in chemistry, biology and medicine. He provided the area….with….[so many]….conceptual and experimental tools….[that it] shows a very rare and special degree of insight into chemical problems." In a nomination letter for an award (that Ray incredulously did not receive), this writer noted that Ray "entered an area where the practices relied on….in-house expertise and trade secrets. He rebelled at the notion that these vagaries had to be accepted as…."the strange world of carbohydrate chemistry"….[for]….such a view relegated the matter to the realm of magic." Lemieux's attempts to transform the "magic"….into…."science" provided spin-off materials that are so well blended into the fabric of chemistry that their origins are undetectable — and frequently unattributed.

Foremost among these is the use of NMR for structure elucidation. The writer once listened as Ray recalled the 1957 realization that the low-field signals with large and small spacings in the 40 MHz spectra were from the anomeric α and β protons, which led to the immediate epiphany that organic structure proof would thereafter be forever changed. Indeed, a young theoretical chemist who had listened to one of Lemieux's lectures about these observations returned to Harvard and the result was the Karplus equation.

But there is more to this landmark event that also provides another glimpse into Ray's modus operandi — the seemingly arrogant advice that "you never learn much by talking to people who are doing the same thing you are". Appropos, the major co-authors on the 1957 paper were NRC physical chemists, for in those days NMR was the playground of physicists. This cunning, prospector's intuition was to propel Ray into "molecular recognition" long before that sobriquet had been coined, and thence into the nettlesome world of immunology, and as his final triumph, a postulate about the source of binding energy between proteins and carbohydrate epitopes.

In his Wolf Prize address in 1999, Ray expressed satisfaction at accomplishing what he had set out to. If so he must have been aware of Yogi Berra's famous advice, "when you come to a fork in the road, take it," for his perennial concern with the anomeric centre brought him into 1950s conflict with the giants of organic chemistry. After all, he had the temerity to suggest that the thermodynamically stable anomers of glucose had the aglycon in the axial orientation, not equatorial as Barton's fledgling comformational analysis demanded.

Indeed, therein lay the impetus for the landmark NMR study that was to prove him right, and thence provide fodder for the anomeric effect, a phenomenon that has now returned to enrich its physical organic chemistry roots.

Professor Raymond U. Lemieux

L'extrait qui suit, tiré de la superbe biographie de Ray Lemieux, signée par David Bundle et destinée à une prochaine parution de *Advances in Carbohydrate Chemistry and Biochemistry*, est on ne peut plus éloquente : « Ses travaux ont significativement contribué à transformer ce secteur de facture résolument théorique en un domaine de forte incidence pratique pour la chimie, la biologie et la médecine. Il a livré au secteur une pléiade d'outils conceptuels et expérimentaux... qui reflètent une profonde compréhension des problèmes chimiques. » Dans une lettre de mise en candidature de Ray (pour un prix que Ray n'a pas remporté, à l'étonnement général), l'auteur écrivait que « Ray a abordé la profession à une époque où les pratiques étaient jalousement gardées. Or, il n'était pas prêt à accepter cet obscurantisme de la chimie des glucides, qui ne faisait que cultiver le mystère entourant la matière ». Ce désir de Lemieux de lever le voile du mystère grâce à la science a révélé des principes aujourd'hui si fondamentaux pour la chimie que leur origine est souvent passée sous silence, voire oubliée.

Le recours à la RMN pour déterminer la structure des matériaux est une pratique qui offre un bon exemple. En effet, l'auteur se souvient avoir écouté Ray lui raconter comment ce dernier a conclu, en 1957, que les signaux de champ à faible intensité ponctués de longues et de courtes chutes caractéristiques du spectre de 40 MHz avaient pour origine les protons anomériques α et β, et comment il a alors compris que cette découverte allait à jamais changer la façon de déterminer les structures organiques. De fait, un jeune chimiste théoricien d'alors, inspiré par un exposé de Lemieux au cours duquel ce dernier partageait ses conclusions, est retourné à Harvard et a formulé la fameuse équation de Karplus.

Si ces circonstances sont en soi marquantes, elles ont aussi frayé les voies à une vision, parfois qualifiée d'arrogante, que Ray allait épouser : « On apprend bien peu en se contentant de ne discuter qu'avec ses confrères. » Il importe de mentionner que les principaux coauteurs de l'article de 1957 étaient des physicochimistes du CNRC puisque, à cette époque, la RMN était le joujou des physiciens. Son audacieuse intuition allait faire de Ray une véritable tête d'affiche de la « reconnaissance des molécules » et de l'épineux domaine de l'immunologie et allait lui inspirer son postulat sur la source de l'énergie de liaison entre les protéines et les épitopes glucidiques, dernière note triomphale de sa carrière.

Dans le discours qu'il a prononcé lorsqu'on lui a remis le prix Wolf en 1999, Ray s'est dit satisfait de son parcours professionnel. Qu'il l'ait su ou non, il vivait au diapason du fameux aphorisme de Yogi Berra : « Quand on arrive à un embranchement, il ne faut pas hésiter à le prendre. » À preuve, son insatiable intérêt pour le centre anomérique a hérissé, en 1950, les grands de la chimie organique d'alors. Rien de surprenant : n'avait-il pas osé avancer que les anomères du glucose stables du point de vue de la thermodynamique portaient l'aglicone en position axiale plutôt qu'équatoriale, contrairement à ce que dictait la nouvelle analyse conformationnelle de Barton?

De fait, c'est à cette témérité que l'on doit la publication du rapport phare sur la RMN qui a prouvé la justesse de l'instinct de Ray et qui a mis en lumière l'effet anomérique, phénomène qui a ensuite largement été mis à profit dans le secteur de la chimie organique physique.

© 2002 NRC Canada

Ray's birth on June 16, 1920 to a homesteading family at Lac la Biche, behind God's back in Northern Alberta, is hardly the beginning for such a storied career, but it does exemplify the nexus between education and social mobility. Fortunately, his oldest sister and surrogate mother — for the real one died when he was seven — was "going with" a physics undergrad at the University of Alberta, and this culminated in Ray coming under the tutelage of Ruben Sandin, U of A's legendary mentor of young chemists. Rube sent him to Clifford Purves at McGill's Pulp and Paper Institute, where he was introduced to the vagaries of carbohydrate chemistry.

Purves sent Ray to Ohio State, where Melvin Wolfrom was engrossed in structure elucidation of streptomycin. He was thus introduced to the emerging "amino sugar" antibiotics that challenged penicillin's pre-eminence, and brought him into competition with the Umezawa brothers of Japan. Indeed the α-glucosaminide motif of these antibiotics may have been the well-spring of the elegant methodologies for anomeric stereocontrol that poured forth from his lab in the 1960–1970s.

Two side issues at Ohio State deserve mention, the more important of which will conclude this tribute. The less important is that Ray, in Wolfrom's lab, correlated the absolute stereochemistries of sugars and amino acids. In so doing he completed a bridge that led Emil Fischer to his "lock and key" theory, because enzyme action on anomeric sugars provided the impetus for the theory. Ray's tribute to Fischer is worthwhile reading.

No biography of Ray would be complete without mention of his visceral commitment to Canada. His valiant attempts in the 1960s at start-up companies to capitalize upon results from academic labs was two generations too soon, and they foundered even with the help of his wealthy industrialist brother. And while he greatly admired, probably even envied, the U.S.A.'s caution-be-damned attitude, the idea of going south was completely anathema to him. He preferred to light a candle rather than curse the dark, and the candle that shone most brightly was Chembiomed, which commercialized the immunoabsorbents that were leveraged from the chemical synthesis, and monumental molecular recognition studies of the blood group oligosaccharides.

Not surprisingly, Ray's elevation to Canada's highest civilian accolade, Companion of the Order of Canada in 1996, was a crowning adornment that went well with the King Faisal International Prize and the Albert Einstein World Award that preceeded it. The celebrated Wolf Prize for Chemistry was to follow it three years later — one year before his death.

Finally, the second "side issue" from Ohio State transcends all of the above, for Ray clearly shared the sentiments of Jacqueline Kennedy-Onassis: "It doesn't matter how successful you are if you mess up with your children." It was at Ohio State that Ray met a physical chemistry graduate student who was to become his wife. Jeannie's remarkable sense of humour must surely have been the perfect foil to harness Ray's boundless energy.

Si la naissance de Ray, le 16 juin 1920, dans une famille pionnière de Lac la Biche, dans le nord de l'Alberta, est un début bien humble pour celui qui allait devenir un si grand homme, elle témoigne de l'intime relation entre l'instruction et la mobilité sociale. En effet, la soeur aînée de Ray, qui jouait aussi le rôle de mère de famille puisque la mère de Ray est décédée lorsque celui n'avait que sept ans, était inscrite au baccalauréat en physique à l'Université de l'Alberta. Dans son sillage, Ray a gagné les rangs de cette université et a eu la chance d'être supervisé par Ruben Sandin, réputé pour l'encadrement qu'il offrait à ses disciples. Ruben a ensuite confié Ray à Clifford Purves, à l'Institut de pâtes et papiers de McGill, ce qui a constitué son introduction au mystérieux monde de la chimie des glucides.

Ensuite, Purves a cru bon de recommander Ray à Melvin Wolfrom, qui s'appliquait alors à élucider la structure de la streptomycine, à l'Université d'état de l'Ohio. Ray a ainsi abordé l'étude de ce nouvel antibiotique aminosucre susceptible de détrôner la pénicilline et, ce faisant, est entré dans l'arène avec les frères Umezawa du Japon. De fait, il y a fort à parier que le motif structural de l'α-glucosaminide de ces antibiotiques est au coeur des élégantes méthodologies de stéréocontrôle anomérique enfantées par le laboratoire de Ray au cours des années 1960 et 1970.

Deux autres réalisations à l'Université de l'état de l'Ohio sont dignes de mention ici, la plus marquante étant réservée à la fin du présent article. La première est l'établissement par Ray, dans le laboratoire de Wolfrom, de la corrélation de la stéréochimie absolue des glucides et des acides aminés. Ses efforts ont donné le coup d'envoi à la théorie « de la clé et de la serrure » d'Emil Fischer, inspirée par l'idée de l'action des enzymes sur les glucides anomériques. L'hommage flatteur que Ray rend à Fischer mérite lecture.

Nul ne peut parler de Ray sans souligner son affection pour le Canada. Ses vaillants efforts, au cours des années 1960, pour mettre sur pied des entreprises susceptible de tirer profit des résultats des laboratoires de recherche étaient trop visionnaires pour l'époque (Après tout, on parle d'un avant-gardisme de deux générations!) et se sont soldés par l'échec, malgré l'appui financier du frère de Ray, un industriel fortuné. Et bien que Ray ait admiré, peut-être envié, la vision de mépris du danger cultivée aux États-Unis, il n'a jamais voulu emporter ses pénates chez nos voisins du Sud. Il préférait allumer une bougie plutôt que maudire l'obscurité. Et sa bougie la plus brillante a été Chemibiomed, société qui a commercialisé les immunoadsorbants ayant découlé de la synthèse chimique et d'études de reconnaissances moléculaires marquantes des oligosides des groupes sanguins.

Il n'y a donc rien eu de surprenant à ce que Ray reçoive en 1996 le plus éminent honneur civil du Canada, soit le titre de Compagnon de l'Ordre du Canada, joyau qui allait s'ajouter au prix international King Faisal et au prix mondial Albert Einstein dont on l'avait déjà décoré. Trois ans plus tard, un an avant son décès, il allait aussi recevoir le prix Wolf, particulièrement convoité dans le domaine de la chimie.

La seconde « réalisation » que Ray attribuait à l'Université de l'état de l'Ohio dominait toutes les autres à ses yeux. En effet, Ray partageait l'opinion de Jacqueline Kennedy-Onassis, soit que le succès professionnel ne compte pour rien si sa famille est mise à mal. C'est donc à l'Université de l'état de l'Ohio que Ray a fait la connaissance d'une étudiante en chimie, Jeannie, qui allait devenir son épouse. Le fin sens de l'humour de Jeannie

© 2002 NRC Canada

Their five daughters and one son were his pride and joy, and he rejoiced in their impressive accomplishments ranging from the university professoriat to the Canadian national soccer team. How remarkable that in his ACS-sponsored autobiography *How Sweet it Was*, he cited his family as his proudest achievement.

Bert O. Fraser-Reid

s'est sans nul doute avéré le complément idéal à l'ardent caractère de Ray. Ray éprouvait une vive fierté pour ses cinq filles et pour son fils et s'enorgueillissait de leurs admirables réalisations, depuis l'enseignement universitaire jusqu'à la participation à l'équipe nationale canadienne de soccer. De fait, dans son autobiographie intitulée « *How sweet it was* », Ray affirmait que sa famille était de loin sa plus enviable réussite.

Bert O. Fraser-Reid

© 2002 NRC Canada

Thermolysis of a spiro-fused oxadiazoline: The carbonyl ylide–cyclic carbene–diradical sequence

Nadine Merkley and John Warkentin

Abstract: Thermolysis of spiro-fused oxadiazoline **1** in benzene led to loss of N_2 to form a carbonyl ylide intermediate. Most of the ylide fragmented to acetone and 4-phenyl-1,3-dioxane-2-ylidene, which could be trapped with *tert*-butyl alcohol. In the absence of the trapping agent, the major pathway followed by the carbene was fragmentation to a diradical, 5-phenyl-2-oxa-1-oxo-1,5-pentanediyl. The latter diradical coupled to α-phenyl-γ-butyrolactone and decarboxylated to afford cyclopropylbenzene. Other products from the reaction were those of *apparent* insertion of the carbene into a C–H bond of the benzene solvent and into a C–H bond of acetone. Such reactions appear to be without precedent — alternative, non-carbene mechanisms are proposed.

Key words: dioxacarbene, carbonyl ylide, cyclopropylbenzene, diradical, lactone, oxadiazoline.

Résumé : La thermolyse de l'oxadiazoline à fusion spiro, **1**, dans le benzène, conduit à une perte d'azote et à la formation d'un intermédiaire carbonyl-ylure. L'ylure se fragmente principalement en acétone et en 4-phényl-1,3-dioxane-2-ylidène que l'on peut piéger avec de l'alcool *tert*-butylique. En absence de piège, la voie réactionnelle principale suivie par le carbène en est une de fragmentation en biradical, le 5-phényl-2-oxa-1-oxopentane-1,5-diyle. Ce dernier radical peut se coupler à l'α-phényl-γ-butyrolactone et il se décarboxyle pour former du cyclopropylbenzène. Parmi les autres produits de la réaction, on a observé ceux résultant de l'insertion *apparente* du carbène dans une liaison C–H du benzène agissant comme solvant et dans une liaison C–H de l'acétone. De telles réactions ne semblent pas avoir été observées antérieurement et on propose des mécanismes alternatifs n'impliquant pas de carbène.

Mots clés : dioxacarbène, carbonyl-ylure, cyclopropylbenzène, biradical, lactone, oxadiazoline.

[Traduit par la Rédaction]

Introduction

Thermolysis of oxadiazolines (**1**) is now a well-established method for the generation of alkoxy- or dialkoxycarbenes (1). Fragmentation of alkoxy- or dialkoxycarbenes to radicals was reported many years ago, primarily for gas phase conditions (2), and computations for model systems followed (3). Such fragmentations of dialkoxycarbenes to radical pairs, in solution under relatively mild conditions, have recently been studied experimentally (4) and modeled (without solvation) with smaller analogues (3). Fragmentation of cyclic oxy- or dioxycarbenes to corresponding diradicals appears to be limited to a theoretical study by Borden and Hoo (5).

We now report the synthesis and thermolysis of oxadiazoline **1** in benzene at 110°C. The thermolysis occurs through a number of intermediates that are formed sequentially including a carbonyl ylide (**2**), a carbene (**3**), and diradicals **4** and **5** (Scheme 1).

Methods

Oxadiazoline **1** was synthesized by means of the sequence of reactions shown in Scheme 2. Ring opening of **6** was selective, leading primarily to **7**, which was saponified to **8**. The hydrazinolysis of **9** was also selective, affording primarily **10**, which crystallized from solution during the reaction. Oxidation of **11** with $Pb(OAc)_4$ led to a mixture of **1** and **12**. The intramolecular acid catalyzed substitution, leading from **12** to **1** to complete the cyclization, was modeled after intermolecular analogues (6).

A sample of **1** in benzene-d_6, in a sealed tube, was heated at 110°C for 72 h before an ^{1}H NMR spectrum of the crude mixture of products was acquired. The solvent and volatile products were then evaporated and the residue was chromatographed on SiO_2.

Results and discussion

Evidence for an ylide intermediate (**2**) came from the finding that a minor product was ketone **15** (Scheme 3). The yield of that product was not affected by inclusion of acetone (1.1 M) in the benzene solution of **1**, indicating that it could not have arisen from insertion of **3** into a C–H bond of acetone. Moreover, it could not have arisen from *any* reaction of free acetone.

We suggest that **15** arose from **2** through **13**, which came from a 1,4-sigmatropic H-shift in **2**. Such rearrangements of carbonyl ylides are known (7). Apparently, a fully concerted

Received 2 April 2002. Published on the NRC Research Press Web site at http://canjchem.nrc.ca on 16 August 2002.

N. Merkley and J. Warkentin.[1] Department of Chemistry, McMaster University, 1280 Main St. W., Hamilton, ON L8S 4M1, Canada.

[1]Corresponding author (e-mail: warkent@mcmaster.ca).

 DOI: 10.1139/V02-126 © 2002 NRC Canada

Scheme 1.

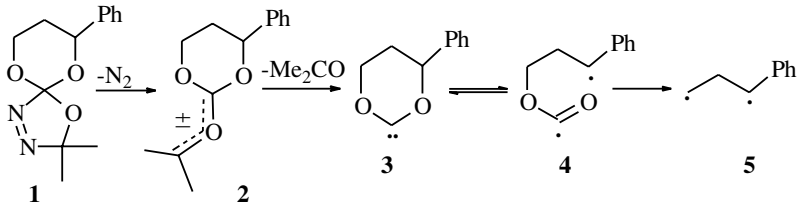

Scheme 2.

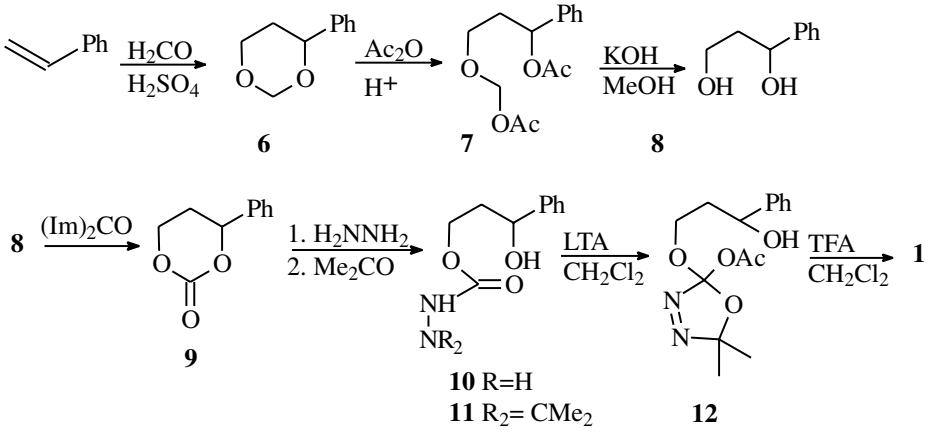

Scheme 3.

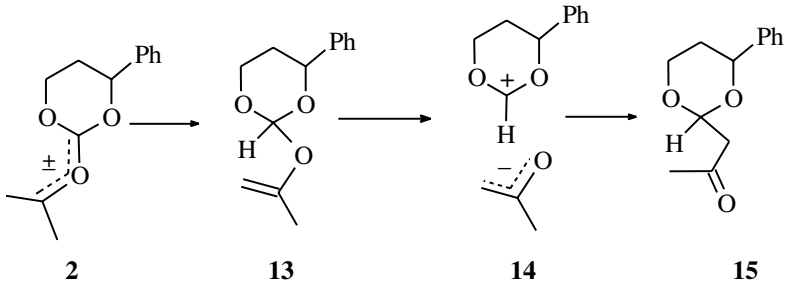

Scheme 4.

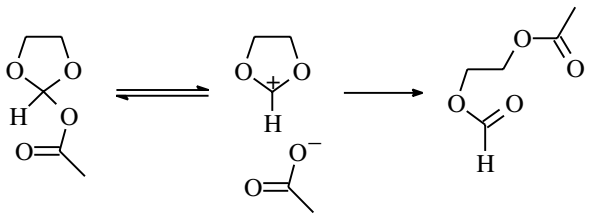

fragmentation of the oxadiazoline, to the carbene, N_2, and acetone, as suggested by Smith (8) on the basis of computation, is not general. Rearrangement of **13** to **15** is unprecedented, to the best of our knowledge, but it is reasonable, given that both fragments of ion pair **14** that are proposed for the rearrangement are stabilized. A good model system is the 2-acetoxy acetal **16**, thermolysis of which at 120°C affords the mixed diester **18** in 68% yield (9). The reaction can be understood in terms of reversible formation of an ion pair and nucleophilic substitution at carbon (Scheme 4). Return of the ion pair to **16** presumably scrambles the oxygen atoms of the acetoxy group whereas the enolate fragment in Scheme 3 would bond to carbon to form **15** irreversibly.

The formation of diastereomers **19** from thermolysis of **1** in benzene containing *tert*-butyl alcohol is evidence for carbene **3**, whereas the formation of lactone **20** and cyclopropylbenzene (**21**) in the absence of *tert*-butyl alcohol indicates that **3** fragments to diradical **4** (Scheme 5). There is analogy for the fragmentation of **3** to diradical **4** in the fragmentation of cinnamyloxy(methoxy)carbene to cinnamyl and methoxycarbonyl radicals and of benzyloxy(methoxy)carbene to benzyl and methoxycarbonyl radicals (4).

Cyclopropylbenzene (**21**) is an expected product from **5**, which is an intermediate from decarboxylation of **4**. We were unable to detect (by GC, with authentic samples for reference) either 1- or 3-propenylbenzene, which might also have arisen from **5** by means of intra- or intermolecular H-transfer. Reversal of **4** to **3** is speculative but, because **4** must be born with the geometry shown and because the barrier to radical coupling cannot be large, the reversal step (**4a**→**3**) is a probable, albeit invisible, reaction.

© 2002 NRC Canada

Scheme 5.

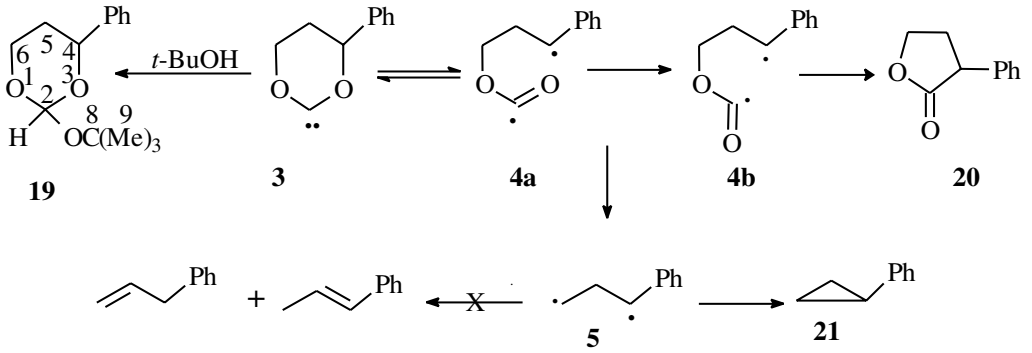

Scheme 6.

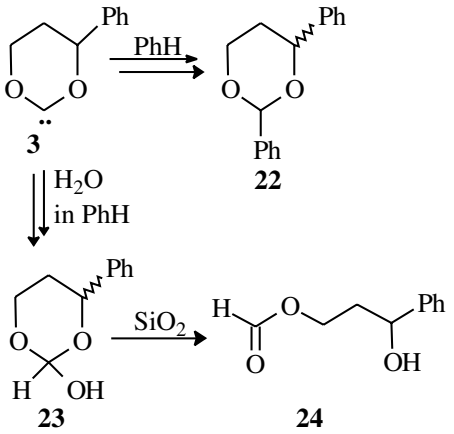

Scheme 7.

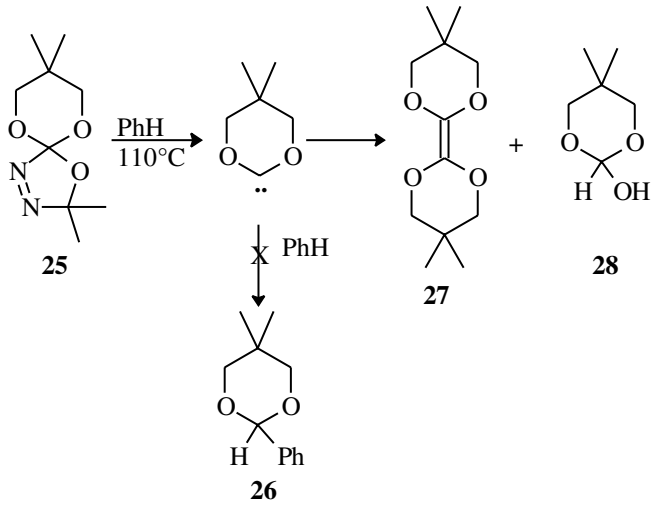

The formation of **20** and **21** in roughly equal amounts means that the rate constants for cyclization and decarboxylation of **4** at 110°C are very similar. The rate constant for decarboxylation was estimated as follows. From the Arrhenius equation of Newcomb (10) we obtained the rate constant k_H at 110°C for the reaction of RCH_2OCO radicals with $HSnBu_3$ ($k_H = 1.77 \times 10^6$ M^{-1} s^{-1}). The ratio k_H/k_{CO2} was available from the product ratio RCH_3:RCH_2OCHO = 38:25 for the reaction of RCH_2OCO radicals with $HSnBu_3$ (average concentration 0.025 M) in toluene at 110°C (11). Thus, the rate constant for decarboxylation came to $k_{CO2} \sim 6.8 \times 10^4$ s^{-1}, and the upper limit of the rate constant for cyclization of **4**, to form **20**, could be set at about 1×10^5 s^{-1}. That estimated rate constant is smaller than might have been expected, given that the process is an intramolecular coupling of a diradical to a five-membered ring. The reason for the small rate constant must lie in the fact that the initial conformation **4a** is the wrong one for coupling to **20**. Rotation into conformation **4b**, over a barrier of about 9 kcal mol^{-1}, is required (12) before lactone **20** can form. Such a barrier could limit the rate of coupling considerably, because the conformations **4a** and **4b** are only two of many conformations of the diradical. Rotations about the other single bonds of **4a** have barriers (13) smaller than 4 kcal mol^{-1} and therefore other conformations of the diradical will be populated before conformation **4b** is reached. Moreover, when **4b** is reached it will have only about a one-in-four chance of being in the singlet state (14). With these features in consideration, the relatively slow coupling of **4** to lactone **20** becomes understandable.

Additional products, not shown in the previous Schemes, were diastereomeric 2,4-diphenyl-1,3-dioxanes (**22**) (12) and diastereomeric hemiorthoformates (4-phenyl-1,3-dioxan-2-ols) (**23**). The latter products are readily accounted for in terms of capture of carbene **3** by adventitious water. Hemiorthoformates (**23**) were thermally stable, but an attempt at isolation by chromatography on silica led to 1-phenyl-1,3-propanediol-3-formate (**24**) (Scheme 6).

We were surprised to find **22** (12%, 6:1 ratio of diastereomers), because dialkoxycarbenes have never been shown to insert into a C–H bond of benzene. In fact, the more nucleophilic imidazolidene-2-ylidene does not appear to react with toluene, although products from apparent insertions into the acidic C–H bonds of acetylene and of a sulphone had been observed (15*a*). 1,3,4-Triphenyl-4,5-dihydro-1*H*-1,2,4-triazole-5-ylidene undergoes many reactions but not insertion into C–H bonds (15*b*). A possible reason for the apparently higher reactivity of **3**, relative to that of acyclic dialkoxycarbenes, was thought to be the enforced 0°, 0° conformation. For allyloxyhydroxycarbene, the 0°, 0° conformation was calculated to be 11.7 kcal mol^{-1} higher in energy than the most stable (180°, 180°) conformation (3*c*). A reduction of the stability of the carbene, as a result of raising the energy of the ground state, would reduce the barrier to insertion if the transition state for insertion were affected less, or not at all, by the conformational restriction. This attractive explanation was abandoned when it was found that

© 2002 NRC Canada

Scheme 8.

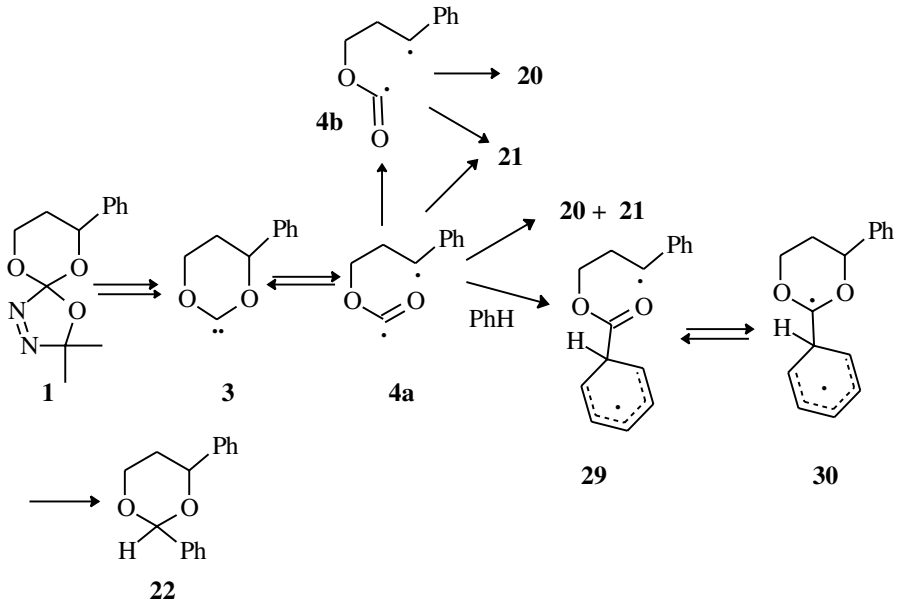

Scheme 9.

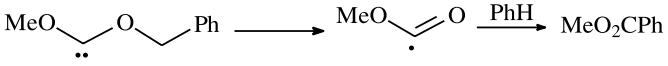

Scheme 10.

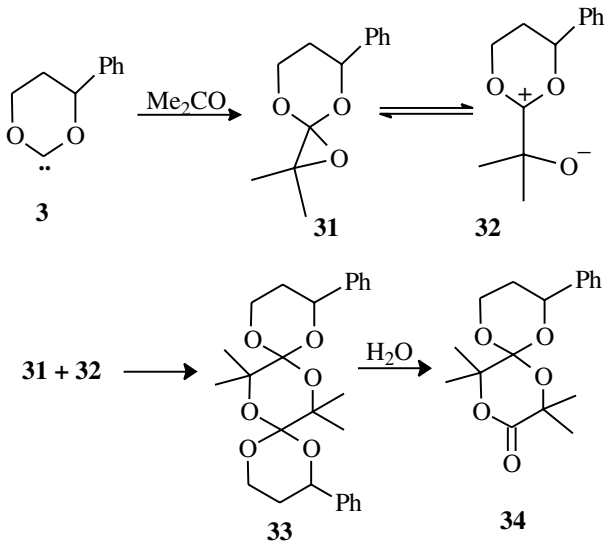

thermolysis of **25** in benzene (16) gave the carbene dimer **27** (20%) and 5,5-dimethyl-1,3-dioxan-2-ol (**28**, 21%), the latter being the result of reaction of the carbene with adventitious water (Scheme 7). There were additional products, but **26** could not be detected. With the results in Scheme 7, it is hard to ascribe **22** (Scheme 6) to insertion of **3** into benzene.

The only alternative mechanism that we could conceive of is radical substitution on benzene through the sequence of Scheme 8. Both intra- and intermolecular additions of acyl radicals to double bonds are known (17), as is radical aromatic substitution (18), and relatively slow closure of **4** (above) could permit aromatic substitution, via **29** and **30**, to

Scheme 11.

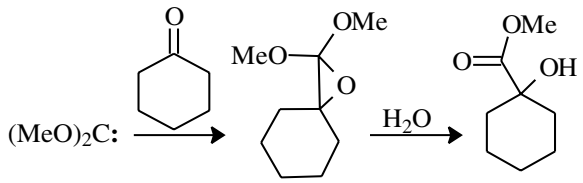

compete. The carbene from **25** does not fragment to a radical pair and attack on benzene was therefore not observed.

Having estimated the rate constant for decarboxylation and coupling, we were able to estimate the rate constant for attack on benzene by **4a** and (or) **4b** as follows. Knowing that the rates of coupling and decarboxylation are about twice as large as that of attack on benzene (from yields of the products) we could set $k_{CO_2} = 2k_{benzene}$[benzene]. The concentration of benzene is about 10 M and k_{CO_2} has an upper limit of 1×10^5 s^{-1} (above). Thus $k_{benzene}$ would not need to have a value greater than about 5×10^4 M^{-1} s^{-1} for aromatic substitution to compete. Aromatic substitution occurred when methoxycarbonyl radicals, generated in benzene by thermolysis of methyl azodicarboxylate at 130°C, gave methyl benzoate in 13% yield (19). Support for the postulate that aromatic substitution with **4** occurred also came from the discovery of methyl benzoate (3%) in the product mixture formed when benzyloxy(methoxy)carbene was generated in benzene (Scheme 9). We had not recognized that minor product previously (4*b*).

The cyclization step, **29→30**, is a 6-endo process for which there are now many examples, although we were unable to find a very close analogue (20). Subsequent formation of diastereomers **22** by a radical mechanism is not surprising, because kinetic control could apply in the migration step that forms the new C–H bond. There is ample precedent for the postulated H-migration in **30**. Analogous migrations from C-2 of 1,3-diyls are well known (21) although mono-radicals do not rearrange in that way. Synthesis

© 2002 NRC Canada

Scheme 12.

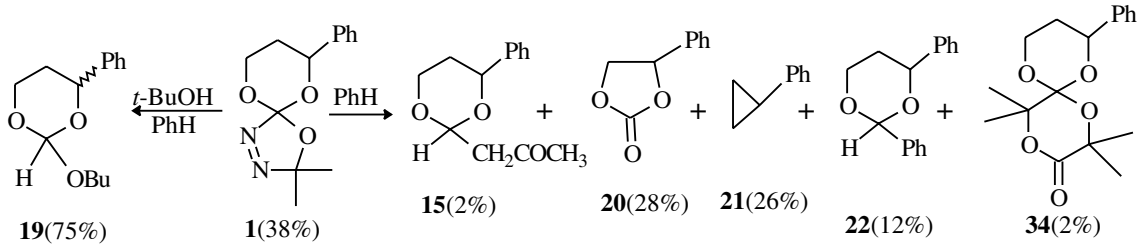

of authentic **22** by acid-catalyzed reaction of 1-phenyl-1,3-propanediol with benzaldehyde gave only one diastereomer, which we assume was the more stable *cis*-isomer, formed under thermodynamic control.

Spiro-fused ester **34** was also obtained, in 2% yield. The structure is not in doubt, but the source of it is not known. Addition of acetone (initial concentration 1.1 M) before thermolysis raised the yield of **34** to 28%! We have not developed an attractive explanation for its formation. A partial solution to the problem involves attack of the carbene (**3**) on acetone to afford **32**, which, like **2**, should be equilibrated with the oxirane **31** (Scheme 10). The postulated reaction of the carbene with acetone is in keeping with the observation that dimethoxycarbene reacts with cyclohexanone to afford an oxirane (22). Coupling of two units of **32** is unlikely, because **32** is a reactive intermediate that must be formed very slowly from **1**. However, a reaction between **31** and **32** is plausible, given that **31** is expected to be quite polar. Only two 2,2-dialkoxyoxiranes have been reported to date (22, 23) and they are sensitive materials that hydrolyse readily, as shown for one of them in Scheme 11. A bimolecular reaction between **31** and **32** would be expected to lead to **33**, and partial hydrolysis of **33** after the reaction tube was opened would yield the observed **34** (Scheme 10). Water in the added acetone cannot be a major contributor because the acetone was dried carefully and because the yield of hemiorthoformate (**23**) did not rise as a result of adding acetone to the benzene solvent prior to thermolysis.

In summary, the thermolysis chemistry of oxadiazoline **1** is exceptionally rich. It loses N_2 to form carbonyl ylide **2** that undergoes 1,4-sigmatropic rearrangement to afford **15** via **13**. The major fate of **2** is fragmentation to carbene **3** that can be trapped efficiently in a bimolecular reaction with *tert*-butyl alcohol. If **3** is not intercepted, it undergoes ring opening to diradical **4,** which undergoes three reactions at comparable rates. The diradical attacks benzene through a sequence of unprecedented reactions that lead to substitution product **22**. Diyl **4** also cyclizes to lactone **20** and it decarboxylates to afford phenylcyclopropane via cyclization of diyl **5**. Finally, the formation of **34** suggests that oxirane **31** is an undetected intermediate from the reaction of **3** with acetone. The products, accounted for individually above, are listed in Scheme 12.

Experimental

General

NMR spectra were collected with Bruker AV-300 or AV-500 NMR spectrometers, with samples in $CDCl_3$. The chemical shifts, in ppm, are referenced to the ^1H signal from residual $CHCl_3$ at 7.26 ppm or to the ^{13}C signal at 77.0 ppm. The coupling constants of the first-order multiplets are in Hz. Chemical shift assignments are based on analysis of ^1H–^1H COSY, ^1H–^{13}C HSQC, and ^1H–^{13}C HMBC spectra. Connectivities of the atoms were determined with the aid of both ^1H–^{13}C HMBC and ^1H–^{13}C HSQC 2-D NMR experiments. Assignments of signals to axial (ax) and equatorial (eq) ^1H atoms are based on good analogy (24).

4-Phenyl-1,3-dioxane (6) (25)

Styrene (100 g, 0.96 mol) was dissolved in 200 mL (2.5 mol) of 37% formaldehyde. Concentrated H_2SO_4 (8.0 mL, 0.14 mol) was added, the round-bottom flask was fitted with a reflux condenser, and the mixture was refluxed for 7 h. After cooling, the solution was washed twice with 160 mL of benzene and the combined benzene layers were washed twice with 250 mL of water. Most of the benzene was removed by distillation (80°C) at atmospheric pressure. The pressure was then reduced to 2 mm Hg (1 mm Hg = 133.322 Pa), and 4-phenyl-1,3-dioxane was collected as a clear oil (83.9 g, 0.51 mol, 57%), boiling between 96 and 130°C. ^1H NMR (200 MHz, $CDCl_3$) δ: 1.71 (m, 1H), 2.10 (ddd, ^3J = 4.9 Hz, ^3J = 12.2 Hz, ^3J = 12.4 Hz, ^2J = 12.4 Hz, 1H), 3.87 (ddd, ^3J = 2.5 Hz, ^3J = 11.8 Hz, ^2J = 11.8 Hz, 1H), 4.19 (dd, ^3J = 4.8 Hz, ^2J = 11.4 Hz, 1H), 4.64 (dd, ^3J = 2.5 Hz, ^2J = 11.2 Hz, 1H), 4.89 (d, ^2J = 6.3 Hz, 1H), 5.22 (d, ^2J = 6.3 Hz, 1H), 7.26–7.39 (m, 5H).

1,5-Diacetoxy-5-phenyl-2-oxapentane (7) (26)

Concentrated HCl (1 mL) was added to 4-phenyl-1,3-dioxane (**6**) (80 g, 0.49 mol) dissolved in acetic anhydride (138 mL, 1.46 mol) and the solution was heated to 80°C for 20 h. The solution was cooled, neutralized with 10% NaOH to pH 7 (as determined with universal litmus paper), and then washed twice with ether (50 mL). The ether layer was dried with magnesium sulfate. After vacuum filtration the ether was removed with a rotary evaporator leaving **7** (108.4 g, 0.41 mol, 83%) as an orange oil. ^1H NMR (500 MHz, $CDCl_3$) δ: 1.87 (s, 3H), 1.90–1.96 (m, 1H), 1.99 (s, 3H), 2.05–2.12 (m, 1H), 4.01–4.06 (m, 1H), 4.13–4.18 (m, 1H), 4.65 (m, 1H), 5.01 (d, ^3J = 2.6 Hz, 1H), 5.28 (d, ^3J = 2.6 Hz, 1H), 7.24–7.32 (m, 5H). ^{13}C NMR (125 MHz, $CDCl_3$) δ: 20.49, 20.60, 36.70, 60.80, 78.01, 86.81, 126.36, 127.82, 128.35, 140.81, 170.17, 170.58. EI-MS *m/z*: 206 (1), 177 (4), 163 (3), 146 (17), 133 (6), 117 (29), 107 (25), 91 (6), 77 (8), 43 (100). CI-MS (NH_3) *m/z*: 284 ($[M + NH_4]^+$, 28), 177 (100), 146 (17), 117 (95), 75 (4).

1-Phenyl-1,3-propanediol (8) (27)

To a solution of **7** (15.62 g, 0.058 mol) in 10 mL of ether was slowly added a saturated solution of KOH in methanol

© 2002 NRC Canada

(30 mL). The solution was stirred for 3 h before it was neutralized with 5% HCl. The aqueous–methanol layer was extracted twice with 30 mL of ether. Evaporation of most of the ether and subsequent distillation of the residue gave 1-phenyl-1,3-propanediol (4.7 g, 0.031 mol, 54%), boiling at 119°C, 0.5 mm Hg (1 mm Hg = 133.322 Pa) (lit. (28) value bp 117 to 118°C at 0.25 mm Hg). ^{1}H NMR (200 MHz, CD_3OD) δ: 1.68–1.91 (m, 2H), 3.62–3.41 (m, 2H), 4.83 (dd, ^3J = 2.6 Hz, ^3J = 5.4 Hz, 1H), 7.22–7.52 (m, 5H). ^{13}C NMR (50 MHz, CD_3OD) δ: 42.71, 65.50, 75.92, 126.73, 128.20, 129.40, 146.33. ^{1}H NMR (200 MHz, $CDCl_3$) δ: 1.86 (m, 2H), 3.76 (m, 2H), 4.83 (dd, ^3J = 4.7 Hz, ^3J = 7.9 Hz, 1H), 7.22–7.52 (m, 5H). ^{13}C NMR (50 MHz, $CDCl_3$) δ: 40.34, 60.44, 73.08, 125.55, 127.25, 128.25, 144.19. EI-MS *m/z*: 152 ([M]$^+$, 14), 133 (9), 105 (50), 107 (100), 91 (16), 79 (78), 51 (23), 43 (16). CI-MS (NH_3) *m/z*: 170 ([M + NH_4]$^+$, 21), 152 (100), 135 (56), 117 (86), 91 (16).

4-Phenyl-1,3-dioxan-2-one (9) (29)

1,1′-Carbonyldiimidazole (3.51 g, 0.022 mol) in 100 mL of dichloromethane was added dropwise (ca. 1 h) to a solution of **8** (3.0 g, 0.02 mol) and pyridine (4.4 mL, 0.054 mol) in 180 mL of dichloromethane. After stirring overnight the solution was washed three times with 5% HCl (250 mL), and once each with water (250 mL) and brine (250 mL). The dichloromethane layer was dried with $MgSO_4$ and, after filtration, the solvent was removed with a rotary evaporator to leave **9** as white crystals (2.49 g, 0.014 mol, 70%) after recrystallization from hot ethanol; mp 53–54°C. ^{1}H NMR (300 MHz, $CDCl_3$) δ: 2.20–2.38 (m, 2H), 4.46–4.51 (m, 2H), 5.51 (dd, ^3J = 3.8 Hz, ^3J = 9.6 Hz, 1H), 7.26–7.44 (m, 5H). ^{13}C NMR (75 MHz, $CDCl_3$) δ: 29.42, 66.87, 80.15, 125.67, 127.83, 129.0 137.90, 148.77 (C=O). EI-MS *m/z*: 178 ([M]$^+$, 12), 117 (82), 104 (100), 91 (11), 77 (51), 56 (48), 51 (36). CI-MS (NH_3) *m/z*: 196 ([M + NH_4]$^+$, 100), 179 ([M + H]$^+$, 30), 134 (9), 117 (89), 104 (8). HR-MS calcd. for $C_{10}H_{10}O_3$: 178.0629; found: 178.0657.

Synthesis of 10 by hydrazinolysis of 9

Hydrazine monohydrate (7.1 mL, 0.15 mol) was added, with stirring, to 4-phenyl-1,3-dioxan-2-one (**9**) (3.96 g, 0.022 mol) in 70 mL of dichloromethane under nitrogen. In about 2 h a white precipitate had formed. The heterogeneous mixture was filtered leaving the product as white crystals (3.63 g, 0.017 mol, 77%). ^{1}H NMR (200 MHz, CD_3OD) δ: 1.92 (m, 2H), 4.00–4.12 (m, 2H), 4.66 (m, 1H), 7.17–7.26 (m, 5H). ^{13}C NMR (50 MHz, CD_3OD) δ: 39.50, 63.39, 71.73, 126.93, 128.38, 129.38, 145.96, 160.69 (C=O). EI-MS *m/z*: 211 ([M + H]$^+$, 1), 192 (7), 134 (9), 118 (11), 117 (100), 91 (11), 79 (16), 57 (11), 43 (12). CI-MS (NH_3) *m/z*: 211 ([M + H]$^+$, 3), 193 (100), 152 (13), 135 (8), 117 (100), 105 (8), 76 (11), 69 (19), 43 (52).

3-Isopropylidene carbazic acid 3-hydroxy-3-phenylpropyl ester (11)

To a solution of **10** (1.10 g, 5.23 mmol) in dichloromethane (10 mL) was added 1 mL of acetone. After the **10** had dissolved, Na_2SO_4 (0.24 g, 1.4 mmol) was added, and the mixture was stirred for 2 h. The Na_2SO_4 was removed by filtration and the solvent was removed with a rotary evaporator. Compound **11** was obtained as a white solid (0.78 g, 3.1 mmol, 60%); mp 109–110°C. ^{1}H NMR (300 MHz, $CDCl_3$) δ: 1.82 (s, 3H), 2.03 (s, 3H), 2.07–2.11 (m, 2H), 4.24–4.27 (m, 1H), 4.45–4.53 (m, 1H), 4.81 (dd, ^3J = 4.2 Hz, ^3J = 4.5 Hz, 1H), 7.27–7.38 (m, 5H). ^{13}C NMR (75 MHz, $CDCl_3$) δ: 16.24, 25.49, 38.62, 63.30, 71.36, 125.89, 127.69, 128.64, 144.10, 151.37, 154.45. EI-MS *m/z*: 251 ([M + H]$^+$, 1), 144 (15), 117 (100), 91 (17), 72 (38), 56 (31), 43 (38). CI-MS (NH_3) *m/z*: 251 ([M + H]$^+$, 29), 233 (23), 193 (48), 117 (100), 99 (12), 72 (19). HR-MS calcd. for $C_{13}H_{19}N_2O_3$: 251.1395; found: 251.1382.

3,4-Diaza-2,2-dimethyl-7-phenyl-1,6,10-trioxaspiro[5.4]dec-3-ene (1)

To an ice-cooled solution of lead(IV) acetate (4.43 g, 0.010 mol) in dichloromethane (25 mL) under nitrogen was added, dropwise, over a period of 1 h, a solution of **11** (1 g, 0.004 mol) in dichloromethane (5 mL). After addition, stirring was continued for 2 days. The solution was filtered through Celite, washed four times with 25 mL of 5% $NaHCO_3$ solution and dried over Na_2SO_4. ^{1}H NMR spectroscopy of an aliquot indicated that the product was probably a mixture of **1** and **12**. The solvent was evaporated and the residue was dissolved in dichloromethane (20 mL) before trifluoroacetic acid (0.01 mL) was added. After 90 min the cyclization of **12** to **1**, monitored with TLC, was complete. The solution was washed with aqueous NaOH and dried over $MgSO_4$. Evaporation of the solvent and radial chromatography of the residue (Chromatotron, 10% EtOAc – hexanes) gave **1**, a white solid, as a mixture of two diastereomers in 1:1 ratio (0.38 g, 1.5 mmol, 38%). ^{1}H NMR (composite spectrum, 300 MHz, $CDCl_3$) δ: 1.48 (s, 3H), 1.52 (s, 3H), 1.53 (s, 6H), 1.90–2.03 (m, 2H), 2.18–2.39 (m, 2H), 4.23–4.31 (m, 2H), 4.35 (ddd, ^3J = 3.5 Hz, ^3J = 11.3 Hz, ^2J = 11.3 Hz, 1H) 4.81 (ddd, ^3J = 2.8 Hz, ^3J = 11.8 Hz, ^2J = 11.9 Hz, 1H), 5.24 (dd, ^3J = 3.1 Hz, ^3J = 11.6 Hz, 1H), 5.73 (dd, ^3J = 2.7 Hz, ^3J = 11.6 Hz, 1H), 7.23–7.40 (m, 10H). ^{13}C NMR (composite spectrum, 75 MHz, $CDCl_3$) δ: 24.49, 24.64, 31.74, 31.92, 63.02, 65.16, 74.62, 77.09, 119.81, 120.44, 125.92, 128.18, 128.54, 140.21 (analogous, but not spirocyclic, oxadiazolines typically have a C-5 signal at δ 118.7–119.4 and a C-2 signal at δ 136.7–137.9) (30). EI-MS *m/z*: 162 ([M–N_2–Me_2CO]$^+$, 1), 116 (72), 117 (100), 104 (12), 91 (19), 65 (3), 43 (19).

Thermolysis of 1 in the presence of *tert*-butyl alcohol

A solution of oxadiazoline **1** (27.4 mg, 0.11 mmol) and *tert*-butyl alcohol (82.2 mg, 1.1 mmol) in 2 mL of benzene was flame sealed into an NMR tube. The tube was heated for 72 h at 110°C with a constant-temperature oil bath. Two diastereomers of 2-*tert*-butoxy-4-phenyl-1,3-dioxane (**19**) (75% combined yield) were obtained in a ratio of 3:1, as determined by integration of clean singlets at δ 5.64 and 6.03. The crude sample was not purified but the signals corresponding to the major diastereomer could be assigned. Some integrations are approximate, because of partial overlap with signals from the minor diastereomer.

^{1}H NMR (major diastereomer, 500 MHz, C_6D_6) δ: 1.59 (s, 9H, CH_3), 1.48–1.73 (dm, 1H, H5-eq), 1.96 (ddd, ^3J = 5.0 Hz, ^3J = 12.6 Hz, ^3J = 12.4 Hz, ^2J = 12.4 Hz, 1H, H5-ax), 3.36–3.50 (m, 1H, H6-ax), 3.57 (dd, ^3J = 1.4 Hz, ^3J = 4.0 Hz, ^2J = 11.0 Hz, 1H, H6-eq), 5.32 (dd, ^3J =

© 2002 NRC Canada

2.4 Hz, ^3J = 11.7 Hz, 1H, H4-ax), 6.03 (s, 1H), 7.03–7.37 (m, 5H). ^{13}C NMR (125 MHz, C_6D_6) δ: 28.74 (C9), 33.77 (C5), 58.32 (C6), 69.44 (C4), 77.13 (C8), 105.21 (C2), 125.91, 128.08, 128.32, 142.90. EI-MS *m/z*: 152 (6), 134 (31), 107 (100), 79 (84), 59 (14), 51 (30). CI-MS (NH_3) *m/z*: 196 (8), 179 (8), 152 (24), 134 (17), 117 (100), 105 (19).

Thermolysis of 1 in benzene

Oxadiazoline **1** (0.1515 g, 0.61 mmol), and the internal standard 1,4-dimethoxybenzene (0.0205 g, 0.148 mmol) were dissolved in 6 mL of benzene and sealed into a thermolysis tube after three cycles of freeze-pump-thaw degassing. The tube was then kept in an oil bath at 110°C for 72 h. The crude mixture of products was injected into the GC–FID to determine the product yields. The peak areas were corrected for the detector response and products were identified by coinjection of authentic compounds. The remainder of the mixture was freed from solvent and the residue was separated by radial chromatography (Chromatotron, 100% hexanes) to afford the following products.

*Cyclopropylbenzene (**21**) (31)*

26%. ^{1}H NMR (200 MHz, $CDCl_3$) δ: 0.85 (m, 2H), 1.11 (m, 2H), 2.02 (m, 1H), 7.19–7.43 (m, 5H). EI-MS *m/z*: 118 ($[M]^+$, 54), 117 (100), 115 (48), 91 (74), 77 (22).

*4-Phenyl-1,3-dioxan-2-one (**9**) (29)*

5%.

*α-Phenyl-γ-butyrolactone (**20**) (32, 33)*

28%. ^{1}H NMR (300 MHz, $CDCl_3$) δ: 2.40 (dddd, ^3J = 8.2, 9.2, 10.1 Hz, ^2J = 12.6 Hz, 1H), 2.71 (dddd, ^3J = 3.4, 6.8, 9.1 Hz, ^2J = 12.6 Hz, 1H), 3.80 (dd, ^3J = 9.7 Hz, ^3J = 9.9 Hz, 1H), 4.34 (ddd, ^3J = 6.7, 9.1 Hz, ^2J = 9.1 Hz, 1H), 4.46 (ddd, ^3J = 3.4, 8.2 Hz, ^2J = 9.1 Hz, 1H), 7.27–7.40 (m, 5H). ^{13}C NMR (75 MHz, $CDCl_3$) δ: 31.62, 45.54, 66.56, 127.71, 127.98, 129.00, 136.79, 177.43. EI-MS *m/z*: 162 ($[M]^+$, 22), 117 (100), 103 (16), 91 (48), 77 (24), 63 (14), 51 (15). HR-MS calcd. for $C_{10}H_{10}O_2$: 162.0681; found: 162.0675.

*4-Phenyl-1,3-dioxan-2-ol (**23**)*

19% (not isolable, structure assignment tentative, diastereomer ratio not known). EI-MS *m/z*: 163 ($[M - OH]^+$, 1), 133 (2), 117 (100), 105 (30), 91 (20), 77 (39).

*1-Phenyl-1,3-propanediol-3-formate (**24**) (34)*

^{1}H NMR (300 MHz, $CDCl_3$) δ: 2.02–2.19 (m, 2H), 4.23 (ddd, ^3J = 5.9 Hz, ^3J = 5.7 Hz, ^3J = 5.7 Hz, ^2J = 11.3 Hz, 1H), 4.43 (ddd, ^3J = 5.9 Hz, ^3J = 5.7 Hz, ^3J = 5.7 Hz, ^2J = 11.3 Hz, 1H), 4.83 (dd, ^3J = 5 Hz, ^3J = 7.6 Hz, 1H), 7.35–7.36 (m, 5H), 8.08 (s, 1H). ^{13}C NMR (75 MHz, $CDCl_3$) δ: 37.93, 61.27, 71.31, 125.85, 128.04, 128.80, 143.90, 161.22. EI-MS *m/z*: 180 ($[M]^+$, 3), 163 (4), 152 (7), 134 (52), 107 (96), 91 (20), 79 (100), 51 (21), 43 (17). HR-MS calcd. for $C_{10}H_{12}O_3$: 180.0786; found: 180.0778.

*1-(4-Phenyl-1,3-dioxan-2-yl)-2-propanone (**15**)*

2%. Apparently only one diastereomer was isolated. ^{1}H NMR (500 MHz, $CDCl_3$) δ: 1.70 (ddd, ^3J = 2.5 Hz, ^3J = 3.5 Hz, ^2J = –13.4 Hz, 1H, H5-eq), 1.99 (dddd, ^3J = 4.6 Hz, ^2J = –13.3 Hz, ^3J = 11.9 Hz, ^3J = 11.9 Hz, 1H, H5-ax), 2.22 (s, 3H), 2.84 (d, ^3J = 5.1 Hz, 2H), 3.94 (ddd, ^3J = 2.6 Hz, ^3J = 11.7 Hz, ^2J = –11.9 Hz, 1H, H6-ax), 4.20 (ddd, ^3J = 1.3 Hz, ^3J = 4.9 Hz, ^2J = –11.5 Hz, 1H, H6-eq), 4.72 (dd, ^3J = 2.5 Hz, ^3J = 11.4 Hz, 1H, H4-ax), 5.17 (t, ^3J = 5.1 Hz, 1H, H2), 7.28–7.4 (m, 5H). ^{13}C NMR (125 MHz, $CDCl_3$) δ: 31.51, 33.17, 49.33, 67.02, 78.93, 99.06, 125.95, 127.98, 128.61, 141.49, 205.21. CI-MS (NH_3) *m/z*: 238 ($[M + NH_4]^+$, 25), 221 ($[M + H]^+$, 58), 187 (31), 152 (30), 135 (44), 117 (100), 91 (14), 78 (10), 43 (14).

*8,8,11,11-Tetramethyl-2-phenyl-1,5,7,10-tetraoxa-9-oxospiro[5.5]undecane (**34**)*

2%. Connectivity determined by means of ROESY 2-D NMR spectroscopy. IR (NaBr, neat) (cm^{-1}): 1739. ^{1}H NMR (500 MHz, C_6D_6) δ: 1.15 (dddd, ^3J = 1.5, 2.6, 2.6 Hz, ^2J = 13.4 Hz, 1H, H3-eq), 1.48 (s, 3H, H11′), 1.50 (s, 3H, H11″), 1.53 (s, 3H, H8′), 1.56 (s, 3H, H8″), 1.62 (dddd, ^3J = 4.9, 11.7, 12.9 Hz, ^2J = 13.1 Hz, 1H, H3-ax), 3.41 (ddd, ^3J = 1.6, 4.9 Hz, ^2J = 11.1 Hz, 1H, H4-eq), 3.97 (ddd, ^3J = 2.5, 12.8 Hz, ^2J = 11.1 Hz, 1H, H4-ax), 5.00 (dd, ^3J = 2.7, 11.7 Hz, 1H, H10-ax), 7.08–7.12 (m, 5H). ^{13}C NMR (125 MHz, C_6D_6) δ: 24.07 (C11′), 24.20 (C11′), 28.58 (C8′), 28.72 (C8′), 32.47 (C3), 60.34 (C4), 71.65 (C2), 76.74 (C11), 84.16 (C8), 109.07 (C6), 128.85, 128.39, 128.15, 141.42, 171.06 (C=O). EI-MS *m/z*: 204 (4), 179 (4), 117 (100), 104 (18), 70 (70), 43 (37). CI-MS (NH_3) *m/z*: 307 ($[M + H]^+$, 18), 134 (18), 117 (100), 70 (32). The yield of this product rose to 28% in an experiment in which the starting solvent was 1.1 M in acetone.

*2,4-Diphenyl-1,3-dioxane (**22**)*

12%. Diastereomers in 6:1 ratio (by NMR, after chromatography, which failed to separate them and may have altered the initial diastereomer ratio). ^{1}H NMR (major diastereomer, 500 MHz, $CDCl_3$) δ: 1.81 (ddd, ^3J = 2.5, 4.0 Hz, ^2J = 13.4 Hz, 1H, H5-eq), 2.14 (dddd, ^3J = 4.9, 12.2, 11.9 Hz, ^2J = 13.4 Hz, 1H, H5-ax), 4.14 (ddd, ^3J = 2.5, 11.9 Hz, ^2J = 11.9 Hz, 1H, H6-ax), 4.37 (ddd, ^3J = 1.3, 4.9 Hz, ^2J = 11.5 Hz, 1H, H6-eq), 4.92 (dd, ^3J = 2.6, 11.4 Hz, H4-ax), 5.73 (s, 1H, H2-ax), 7.28–7.58 (m, 10H). ^{13}C NMR (125 MHz, $CDCl_3$) δ: 33.63 (C5), 67.48 (C6), 79.29 (C4), 101.79 (C2), 126.03, 126.38, 127.89, 128.38, 128.59, 128.95, 131.04, 138.88, 141.86. EI-MS *m/z*: 239 ($[M - H]^+$, 1), 134 (7), 117 (61), 105 (100), 78 (35), 77 (82), 51 (32). CI-MS (NH_3) *m/z*: 241 ($[M + H]^+$, 24), 152 (16), 134 (40), 117 (100), 91 (24). The minor diastereomer was inferred from the presence of a singlet at 5.23 ppm, upfield from that of the major diastereomer by 0.55 ppm. In the two diastereomers formed from trapping of the carbene with *tert*-butyl alcohol the minor diastereomer gave rise to a singlet 0.39 ppm upfield from the signal for the orthoformyl H of the major diastereomer.

Thermolysis of 1 in the presence of added acetone

A solution of oxadiazoline **1** (0.1684 g, 0.679 mmol) and acetone (0.5 mL) in benzene (5.5 mL) was sealed into a thermolysis tube after three cycles of freeze–pump–thaw degassing. The tube was kept in an oil bath at 110°C for 72 h. After thermolysis the internal standard, 1,4-dimethoxybenzene (6.8 mg, 0.1218 mmol), was added and the crude solution was injected into the GC–FID for determination of product yields. Detector response factors were applied to obtain the corrected yields below.

© 2002 NRC Canada

Cyclopropylbenzene (**21**) (4%), α-phenyl-γ-butyrolactone (**20**) (5%), 2-hydroxy-4-phenyl-1,3-dioxane (**23**) (21%), 1-(4-phenyl-1,3-dioxan-2-yl)-2-propanone (**15**) (2%), 8,8,11,11-tetramethyl-2-phenyl-1,5,7,10-tetraoxa-9-oxospiro[5.5]undecane (**34**) (28%), 2,4-diphenyl-1,3-dioxane (diastereomers) (**22**) (13%), 4-phenyl-1,3-dioxan-2-one (**9**) (7%).

Synthesis of *cis*-2,4-diphenyl-1,3-dioxane

The procedure was modeled after one (35) for making an analogue. To 1-phenyl-1,3-propanediol (5 g, 0.032 mol) and benzaldehyde (3.4 g, 0.036 mol) in dichloromethane (50 mL) was added *p*-toluenesulfonic acid (0.5 g, 2.9 mmol). The solution was stirred overnight before it was washed with 10 mL of $NaHCO_3$ and dried over Na_2SO_4. The residue obtained upon removal of the solvent was purified by means of column chromatography (10% EtOAc – hexanes) yielding **22** (5.65 g, 73%). The *cis* configuration was assigned on the basis of the known preference for the C-2 phenyl group to be in the equatorial position (36). ^{1}H NMR (200 MHz, $CDCl_3$) δ: 1.83 (m, 1H, H5-eq), 2.18 (dddd, ^3J = 4.9, 12.2, 12.2 Hz, ^2J = 12.3 Hz, 1H, H5-ax), 4.16 (ddd, ^3J = 2.3, 11.8 Hz, ^2J = 11.8 Hz, 1H, H6-ax), 4.40 (ddd, ^3J = 1.0, 4.5 Hz, ^2J = 11.4 Hz, 1H, H6-eq), 4.98 (dd, ^3J = 2.4, 11.2 Hz, 1H, H4-ax), 5.73 (s, 1H, H2), 7.33–7.66 (m, 10H).

3,4-Diaza-2,2,8,8-tetramethyl-1,6,10-trioxaspiro[5.4]dec-3-ene (25)

The synthesis and properties of **25** have been described (16).

5,5-Dimethyl-1,3-dioxan-2-ol (28)

Unstable material, isolated in 21% yield by preparative GC (OV-17, 6′ × 1/4″, He at 40 mL min^{-1}) and tentatively identified as **28**. ^{1}H NMR (200 MHz, C_6D_6) δ: 1.02 (s, 3H), 1.76 (s, 3H), 3.13 (d, ^2J = 10.6 Hz, 2H), 3.81 (d, ^2J = 10.6 Hz, 2H), 5.97 (s, 1H).

Carbene dimer (27)

Yield 20%, isolated by preparative GC (conditions above). ^{1}H NMR (300 MHz, C_6D_6) δ: 0.067 (s, 12H), 3.43 (s, 8H). ^{13}C NMR (75 MHz, C_6D_6) δ: 21.86, 30.95, 78.36, 136.69. EI-MS *m/z*: 229 ([M + H]$^+$, 4), 191 (8), 161 (13), 132 (32), 115 (92), 69 (100), 56 (78). HR-MS calcd. for $C_{12}H_{21}O_4$ [M + H]$^+$: 229.1439; found: 229.1453.

Acknowledgements

The authors are grateful for an operating grant from the Natural Sciences and Engineering Research Council of Canada (NSERC), from which this work was financed. Helpful discussions with Professor R.A. Bell and the assistance of Dr. D. Hughes with the acquisition and interpretation of NMR spectra are also gratefully acknowledged.

References

1. J. Warkentin. J. Chem. Soc. Perkin Trans. 1, 2161 (2000).
2. (*a*) R.J. Crawford and R. Raap. Proc. Chem. Soc. London, 370 (1963); (*b*) R.W. Hoffmann. Angew. Chem. Int. Ed. Engl. **10**, 529 (1971); (*c*) R.W. Hoffmann, R. Hirsch, R. Fleming, and M.T. Reetz. Chem. Ber. **105**, 3532 (1972); (*d*) P.C. Oele and R. Louw. Tetrahedron Lett. 4941 (1972); (*e*) A.M. Foster and W.C. Agosta. J. Am. Chem. Soc. **95**, 608 (1973); (*f*) G.B. Merrill and H. Schechter. Tetrahedron Lett. 4527 (1975); (*g*) W.T. Borden, P.W. Concannon, and D.L. Phillips. Tetrahedron Lett. 3161 (1973); (*h*) W.T. Borden and L.H. Hoo. J. Am. Chem. Soc. **100**, 6274 (1978); (*i*) J.M. Cummins, T.A. Porter, and M. Jones, Jr. J. Am. Chem. Soc. **120**, 6473 (1998).
3. (*a*) D. Feller, W.T. Borden, and E.R. Davidson. J. Comput. Chem. **1**, 158 (1980); (*b*) D.L. Reid, J. Hernandez-Trujillo, and J. Warkentin. J. Phys. Chem. A, **104**, 3398 (2000); (*c*) D.L. Reid and J. Warkentin. J. Chem. Soc. Perkin Trans. 2, 1980 (2000).
4. (*a*) P.C. Venneri and J. Warkentin. J. Am. Chem. Soc. **120**, 11 182 (1998); (*b*) N. Merkley, M. El-Saidi, and J. Warkentin. Can. J. Chem. **78**, 356 (2000).
5. W.T. Borden and L.H. Hoo. J. Am. Chem. Soc. **100**, 6274 (1978).
6. K. Kassam, D.L. Pole, M. El-Saidi, and J. Warkentin. J. Am. Chem. Soc. **116**, 1161 (1994).
7. (*a*) A.P. Hitchcock, S. Zweep, T. Steel, M. Békhazi, and J. Warkentin. Can. J. Chem. **60**, 2914 (1982); (*b*) A.C. Lottes, J.A. Landgrebe, and K. Larsen. Tetrahedron Lett. **30**, 4089 (1989); (*c*) M.W. Majchrzak and J. Warkentin. Can. J. Chem. **67**, 1753 (1989); (*d*) T. Golz, S. Hammes and F.-G. Klärner. Chem. Ber. **126**, 485 (1993).
8. W.B. Smith. J. Org. Chem. **60**, 7456 (1995).
9. A.P.M. van der Veek and F.H. van Putten. Tetrahedron Lett. 3951 (1970).
10. P.A. Simakov, F.N. Martinez, J.H. Horner, and M. Newcomb. J. Org. Chem. **63**, 1226 (1998).
11. J. Pfenniger, C. Heuberger, and W. Graf. Helv. Chim. Acta, **63**, 2328 (1980).
12. A preliminary communication has been published. N. Merkley, D.L.Reid, and J. Warkentin. Tetrahedron Lett. **43**, 1927 (2002).
13. J.P. Lowe. *In* Progress in physical organic chemistry. Vol. 6. *Edited by* A. Streitwieser, Jr. and R.W. Taft. Interscience Publishers, New York. 1968.
14. L. Salem and C. Rowland. Angew. Chem. Int. Ed. Engl. **11**, 92 (1972).
15. (*a*) A.J. Arduengo, III, J.C. Calabrese, F. Davidson, H.V.R. Dias, J.R. Goerlich, R. Krafczyk, W.J. Marshall, M. Tamm, and R. Schmutzler. Helv. Chim. Acta, **82**, 2348 (1999); (*b*) D. Enders, K. Breuer, J. Runsink, and J.R. Teles. Liebigs Ann. 2019 (1996).
16. N. Merkley and J. Warkentin. Arkivoc [online], **2**, 7 (2001). (OT-243C). Available from http://www.arkat-usa.org/ark/journal/volume2/part3/tee/001/.
17. D.L. Boger and R.J. Mathvink. J. Am. Chem. Soc. **112**, 4003 (1990).
18. C. Chatgilialoglu, D. Crich, M. Komatsu, and I. Ryu. Chem. Rev. **99**, 1921 (1999).
19. M. Fiorentino, L. Testafarri, M. Tiecco, and L. Troisi. J. Org. Chem. **41**, 173 (1976).
20. (*a*) M. Breithor, L. Herndon, and H.M.R. Hoffmann. Tetrahedron, **53**, 8401 (1997); (*b*) P. Double and G. Pattenden. J. Chem. Soc. Perkin Trans. 1, 2005 (1998); (*c*) E.W. Della, C. Kostakis, and P.A. Smith. Org. Lett. **1**, 363 (1999); (*d*) S. Handa and G. Pattenden. J. Chem. Soc. Perkin Trans. 1, 843 (1999); (*e*) I. Ryu, S. Ogura, S. Minakata, and M. Komatsu. Tetrahedron Lett. **40**, 1515 (1999).
21. J.E. Baldwin and R. Shukla. J. Phys. Chem. A, **103**, 7821 (1999).
22. M. Dawid, P.C. Venneri, and J. Warkentin. Can. J. Chem. **79**, 110 (2001).

© 2002 NRC Canada

23. M.S. Newman and E. Kilbourn. J. Org. Chem. **35**, 3186 (1970).
24. (*a*) R.J. Abraham and P. Loftus. *In* Proton and carbon-13 NMR spectroscopy: an integrated approach. Heydon, London. 1979. pp. 44–46; (*b*) H. Booth. *In* Application of ^{1}H NMR spectroscopy to the conformational analysis of cyclic compounds. Prog. NMR spectroscopy. Vol 5. *Edited by* J.W. Emsley, J. Feeney, and L.H. Sutcliffe. Pergamon Press, New York. 1969. pp. 149–381; (*c*) F.A. Bovey. *In* Nuclear magnetic resonance spectroscopy. 2nd ed. Academic Press, New York. 1988; (*d*) R.K. Harris. *In* Nuclear magnetic resonance spectroscopy. Pitman Publishing Inc., Marshfield, Mass. 1983. p. 223.
25. (*a*) R.L. Shriner and P.R. Ruby. *In* Org. Synth. Coll. Vol. IV. *Edited by* N. Rabjohn. John Wiley & Sons, New York. 1960. p. 786; (*b*) J. Delmau, J.-C. Duplan, and M. Davidson. Tetrahedron, **23,** 4371 (1967).
26. H. Moe and B.B. Corson. J. Org. Chem. **24**, 1768 (1959).
27. T. Sakomoto, Y. Kondo, and H. Yamanaka. Tetrahedron Lett. **33**, 6845 (1992).
28. H.C. Brown and S. Kim. J. Org. Chem. **49**, 1064 (1984).
29. M. Fujiwara, A. Baba, and H. Matsuda, J. Heterocycl. Chem. **26**, 1659 (1989).
30. M. El-Saidi, K. Kassam, D.L. Pole, T. Tadey, and J. Warkentin. J. Am. Chem. Soc. **114**, 8751 (1992).
31. C. Galli. Magn. Reson. Chem. **27**, 214 (1989).
32. Y. Ishii, T. Yoshida, K. Yamawaki, and M. Ogawa. J. Org. Chem. **53**, 5549 (1998).
33. S. Karlsson, A. Hallberg, and S. Gronowitz. J. Organomet. Chem. **403**, 133 (1991).
34. O. Meresz, K.P. Leung, and A.S. Denes. Tetrahedron Lett. 2797 (1972).
35. V.V. Chistyakov and L.N. Pospelova. Dokl. Akad. Nauk SSSR, **296**, 496 (1987).
36. E. Eliel, W.F. Bailey, K.B. Wiberg, H. Connon, and F.W. Nader. Liebigs Ann. Chem. 2240 (1976).

© 2002 NRC Canada

Synthesis, structure, and electrochemistry of cobalt(III) complexes with bis(benzoylacetone)-ethylenediimine Schiff base

Mehdi Amirnasr, Rasoul Vafazadeh, and Amir H. Mahmoudkhani

Abstract: A series of complexes of the type *trans*-$[Co((BA)_2en)(amine)_2]ClO_4$ — where $(BA)_2en$ is the bis(benzoylacetone)ethylenediimine dianion and the amines are morpholine (mrpln) **1**, aniline (aniln) **2**, benzylamine (bzlan) **3**, piperidine (pprdn) **4**, *p*-toluidine (*p*-toldn) **5**, and pyrrolidine (prldn) **6** — has been synthesized and characterized by elemental analysis, UV–vis, ^1H NMR, and ^{13}C NMR spectroscopy. The crystal and molecular structure of *trans*-$[Co((BA)_2en)(mrpln)_2]ClO_4$ (**1**) has been determined by X-ray crystallography. The electrochemical reduction of these complexes at a glassy-carbon electrode, in the potential range of 0.5 to –2.0 V (vs. Ag/AgCl), in acetonitrile solution, indicates that the first reduction potential of Co(III/II) is irreversible, which is accompanied by the dissociation of the axial amine–cobalt bonds. This potential is dependent on the pK_a of the axial amines. The second reduction potential of Co(II/I) shows reversible behavior and is also independent of the axial amine pK_a. These results indicate the loss of the axial amines in the first redox process and the involvement of a four-coordinate species in the second redox step.

Key words: Schiff base, cobalt(III), axial amine, electrochemical properties, crystal structure.

Résumé : On a synthétisé une série de complexes du type *trans*-$[Co(BA)_2en)(amine)_2]ClO_4$ dans lesquels $(BA)_2en$ = dianion bis(benzoylacétone)éthylènediimine et amine = morpholine (mrpln) **1**; aniline (aniln) **2**; benzylamine (bzlan) **3**; pipéridine (pprdn) **4**; *p*-toluidine (*p*-toldn) **5** et pyrrolidine (prldn) **6** et on les a caractérisés par analyse élémentaire et spectroscopies UV–vis et RMN du ^1H et du ^{13}C. On a étudié les structures cristallines et moléculaires du *trans*-$[Co(BA)_2en)(mrpln)_2]ClO_4$ (**1**) par diffraction des rayons X. La réduction électrochimique de ces complexes au niveau d'une électrode de carbone vitreux, à un potentiel allant de 0,5 à –2,0 V (vs. Ag/AgCl), en solution dans l'acétonitrile, indique que le premier potentiel de réduction de Co(III/II) est irréversible et qu'il est accompagné d'une dissociation des liaisons amine–cobalt axiales. Ce potentiel varie avec le pK_a des amines axiales. Le deuxième potentiel de réduction de Co(II/I) met en évidence un comportement réversible et il est aussi indépendant du pK_a de l'amine axiale. Ces résultats indiquent que la perte des amines axiales se produit dans le premier processus redox et que les quatre espèces coordinées sont impliquées dans la deuxième étape.

Mots clés : base de Schiff, cobalt(III), amine axiale, propriétés électrochimiques, structure cristalline.

[Traduit par la Rédaction]

Introduction

The chemistry of transition-metal complexes with Schiff base ligands continues to be the subject of growing interest (1–3). Many of these compounds are relevant to the biochemistry of vitamins, enzymes, and coenzymes (4–6). The remarkable chemical similarity between cobalamines and cobaloximes is now well recognized to be a consequence of the fortuitous near-identicality of the effective coordinating strengths of these chemically unrelated ligand systems. The conjugated tetradentate ligands are chelating agents that coordinate to the four equatorial positions of square pyramidal or octahedral structures of metal centers. The resulting compounds are known to serve as models for the natural Corrine ring complexes, and thus for vitamin B_{12} and its co-enzyme (6–11). The properties of the model complexes are strongly dependent on the nature of the axial ligands. The mutual interdependence of the properties of the two axial ligands can be assessed by structural, spectroscopic, thermodynamic, and kinetic methods (7, 8, 12–17). Limited comparisons of properties determined by many of these methods suggest that cobalamines and various models have the same type of dependence on the *trans*-ligands.

In this paper we report the synthesis of *trans*-$[Co((BA)_2en)(amine)_2]ClO_4$ complexes with primary and secondary amines as axial ligands, where the amines are morpholine (mrpln) **1**, aniline (aniln) **2**, benzylamine (bzlan) **3**, piperidine (pprdn) **4,** *p*-toluidine (*p*-toldn) **5**, and

Received 2 March 2002. Published on the NRC Research Press Web site at http://canjchem.nrc.ca on 21 August 2002.

M. Amirnasr.[1] Department of Chemistry, Isfahan University of Technology, Isfahan 84156–83111, Iran.
R. Vafazadeh. Department of Chemistry, Tarbiat Modarres University, PO Box 14155-4838 Tehran, Iran.
A.H. Mahmoudkhani. Department of Chemistry, Göteborg University, SE-412 96 Göteborg, Sweden.

[1]Corresponding author (e-mail: amirnasr@cc.iut.ac.ir).

 DOI: 10.1139/V02-122 © 2002 NRC Canada

Fig. 1. *trans*-[Co((BA)$_2$en)(X)$_2$]ClO$_4$ (X = amine) complexes.

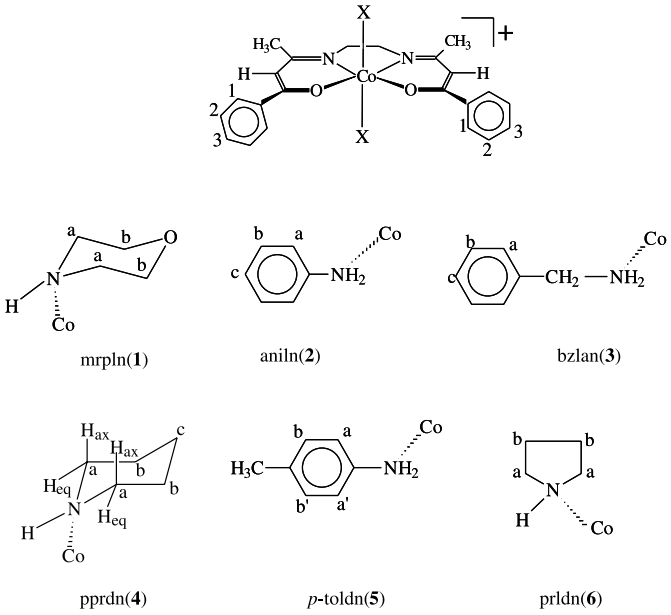

pyrrolidine (prldn) **6** (Fig. 1). These cobalt(III) Schiff base complexes are among the few reported cases containing neutral *N*-donor axial ligands (18, 19).

Experimental

Caution! Transition-metal complex perchlorate salts are known to be hazardous and must be treated with care, especially in the presence of organic solvents.

Materials

Bis(benzoylacetone)ethylendiimine $H_2(BA)_2$en was prepared as described in the literature (20). $Co(OH)_2$ was freshly prepared prior to each synthesis by adding an aqueous solution of NaOH to a solution of $Co(NO_3)_2 \cdot 6H_2O$ in water (with a molar ratio of 2:1), filtering the precipitate immediately, and washing it with acetone. Bis(benzoylacetone)ethylendiiminocobalt(II) ([Co((BA)$_2$en)]) was synthesized by the method of McCarty et al. (20).

Piperidine (Aldrich), benzylamine, morpholine, pyrrolidine, and aniline (Merck) were distilled under reduced pressure. All other chemicals were commercial reagent grade and used as received from Aldrich and Merck.

Physical measurements

Electronic absorption spectra were measured by a Shimadzu UV-240 spectrophotometer. ^{1}H and ^{13}C NMR spectra were obtained on a Bruker Avance DRX500 (500 MHz) NMR spectrometer in CD_3OD solvent. Proton chemical shifts are reported in parts per million (ppm) relative to an internal Me_4Si standard. All measurements were made at 20°C. Elemental analyses were performed using a Heraeus CHN-O-RAPID elemental analyzer. The IR spectra were recorded on a Shimadzu 435 spectrophotometer using the KBr pellet technique.

Cyclic voltammetry studies were carried out by using an EG&G Princeton Applied Research Model 384B. An Ag/AgCl electrode containing 3 M NaCl served as the reference electrode, a Pt wire as the counter electrode, and a glassy-carbon electrode as the working electrode. Cyclic voltammetric measurements were performed in acetonitrile with 50 mM tetra-*n*-butylammonium percholorate (TBAP) as the supporting electrolyte, under nitrogen atmosphere.

Synthesis of *trans*-[diaminebis(benzoylacetone)ethylenediiminatocobalt(III)] perchlorate complexes (*trans*-[Co((BA)$_2$en)(amine)$_2$]ClO$_4$) (1–6)

The appropriate amine (30 mmol) was added to a stirring suspension of 10 mmol (4.05 g) of the [Co((BA)$_2$en)] complex in 150 mL acetone and air was bubbled slowly through the reaction mixture for 4 h. To the resulting clear brown solution was added 15 mmol (1.84 g) of solid $NaClO_4$ and the solution was stirred for an additional period of 1 h. The resulting solution was left overnight to give a brown precipitate. The solid product was filtered off and recrystallized from an acetone–ethanol (2:1 v/v) mixture. The brown crystals were isolated by filtration, washed with cold ethanol and then dried in vacuum.

1: Yield 78%. Anal. calcd. for $C_{30}H_{40}ClN_4O_8Co$: C 53.06, H 5.94, N 8.25; found: C 53.10, H 5.80, N 8.20.

2: Yield 55%. Anal. calcd. for $C_{34}H_{36}ClN_4O_6Co$: C 59.09, H 5.25, N 8.11; found: C 58.80, H 5.25, N 8.10.

3: Yield 69%. Anal. calcd. for $C_{36}H_{40}ClN_4O_6Co$: C 60.13, H 5.61, N 7.79; found: C 59.60, H 5.90, N 7.45.

4: Yield 67%. Anal. calcd. for $C_{32}H_{44}ClN_4O_6Co$: C 56.93, H 6.57, N 8.30; found: C 56.72, H 6.50, N 8.50.

5: Yield 66%. Anal. calcd. for $C_{36}H_{40}ClN_4O_6Co$: C 60.03, H 5.61, N 7.79; found: C 60.00, H 5.80, N 7.80.

6: Yield 57%. Anal. calcd. for $C_{30}H_{40}ClN_4O_6Co$: C 55.69, H 6.23, N 8.66; found: C 55.57, H 6.30, N 8.45.

X-ray crystallography

Brown crystals of *trans*-[Co((BA)$_2$en)(mrpln)$_2$]ClO$_4$ suitable for X-ray crystallography were obtained by slow evaporation of its solution in acetone–ethanol (1:1 v/v) at room temperature. Data were collected on a Siemens SMART CCD diffractometer using graphite-monochromated Mo Kα (λ = 0.71073 Å) radiation. A full sphere of the reciprocal lattice was scanned by 0.3° steps in ω with a crystal-to-detector distance of 3.97 cm. The preliminary orientation matrix was obtained from the first frames using SMART (21). The frames were integrated using the preliminary orientation matrix, which was updated every 100 frames. Final cell parameters were obtained by refinement on the positions of reflections with $I > 10\sigma(I)$, after integration of all the frames using SAINT (21). The data were empirically corrected for absorption and other effects using SADABS (22). The structure was solved by direct methods and refined by the full-matrix least-squares method on F^2 data using SHELXTL (23). All non-H atoms were refined anisotropically, except oxygen atoms of the perchlorate ion, which were found to be disordered over two positions with site occupancy factors of 0.71 and 0.29. They were refined isotropically with the restrain bond distances of 1.42 Å. The H atoms were constrained to idealized geometries and refined isotropically.

© 2002 NRC Canada

Table 1. Crystallographic and refinement data for complex **1**.

Crystal	1
Empirical formula	$C_{30}H_{40}ClCoN_4O_8$
Formula weight	679.04
Crystal system, space group	Monoclinic, $P2_1/c$ (No.14)
a (Å)	19.6710(4)
b (Å)	9.6186(1)
c (Å)	18.9893(3)
β (°)	118.546(1)
V (Å^3)	3156.14(9)
T (K)	297(2)
Z, ρ (calcd.) (g cm^{-3})	4, 1.429
Crystal dimensions (mm)	0.35 × 0.25 × 0.20
μ (mm^{-1})	0.684
F(000)	1424
Index ranges	$-24 \le h \le 21$
	$-12 \le k \le 12$
	$-23 \le l \le 23$
Reflections collected	27231
Independent reflections	6452
R_{int} (int.)	0.029
Reflections observed [$I > 2\sigma(I)$]	5423
Data/restraints/parameters	6452/8/390
Goodness-of-fit on F^2	1.021
R_1, wR_2 for observed reflections[a]	0.054, 0.162
R_1, wR_2 for all data	0.065, 0.176
Weighting scheme (x/y)[b]	0.1064/3.4596
Largest res. peak and hole (e Å^{-3})	1.256 and –1.156

[a] $R_1 = \Sigma||F_o| - |F_c|| / \Sigma|F_o|$. $wR_2 = \{\Sigma[w(F_o^2 - F_c^2)^2] / \Sigma[w(F_o^2)^2]\}^{1/2}$.
[b] $w = 1/[\sigma^2(F_o^2) + (xP)^2 + yP]$. $P = (F_o^2 + 2F_c^2)/3$.

The crystallographic and refinement data are summarized in Table 1.[2]

Results and discussion

Synthesis

H_2(BA)en was prepared by the condensation of benzoylacetone with ethylenediamine as reported in the literature (20). This compound was further characterized by IR, UV–vis, ^{1}H, and ^{13}C NMR spectroscopy. Six Co(III) complexes (**1**–**6**) were prepared by air oxidation of [Co^{II}((BA)$_2$en)] in the presence of the appropriate amine (Fig. 1). A slow stream of air was passed through a stirring suspension of [Co^{II}((BA)$_2$en)] in acetone, to which was added excess amine. The air oxidation was continued for a period of 4 h, during which time the solution changed from red to brown. Dark brown crystals of these complexes were obtained in good yield (55–78%). All complexes reported here are diamagnetic, as expected for a low-spin d^6-configuration.

Fig. 2. ORTEP diagram of the cation of complex **1** showing the atom-labeling scheme. Displacement ellipsoids are shown at the 20% probability level (H atoms and the ClO_4 group are not shown for clarity).

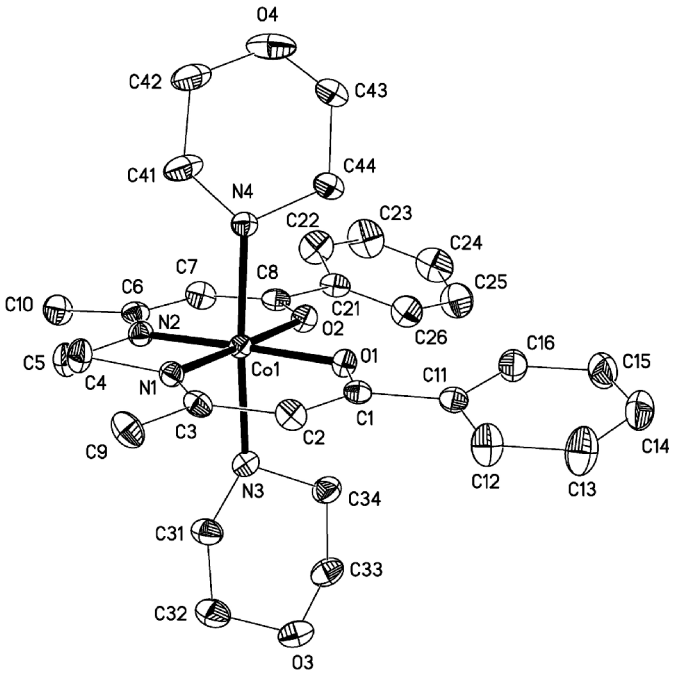

Structure of the cobalt(III) complex with morpholine

The molecular structure of the *trans*-[Co((BA)$_2$en)(mrpln)$_2$]ClO_4 complex is shown in Fig. 2. Selected bond lengths and angles are listed in Table 2. The octahedral coordination of Co(III) is slightly distorted, the (BA)$_2$en Schiff base ligand (ONNO ligand) coordinates the cobalt ion in four equatorial positions, and the two amine molecules occupy the two axial positions of the octahedral complex. The Co—O and Co—N bond distances of the (BA)$_2$en ligand in the equatorial plane are symmetric within the limits of experimental error. The Co—O(1) and Co—O(2) bond lengths are 1.893(2) and 1.900(2) Å, respectively, and compare well with the Co—O distances found in *trans*-[Co(acacen)(piperidine)$_2$]NCS (1.894(2), 1.900(2) Å) and *trans*-[Co(3-Cl-acacen)(NH$_3$)$_2$]BPh_4 (1.881(4) Å) (18, 19). The Co—N(1) and Co—N(2) bond lengths are 1.899(3) and 1.905(3) Å, respectively, which is in good agreement with the Co—N distances found in *trans*-[Co(acacen)(piperidine)$_2$]NCS (1.899(2), 1.905(2) Å) and *trans*-[Co(3-Cl-acacen)(NH$_3$)$_2$]BPh_4 (1.8918(9) Å) (18, 19).

The average cobalt—nitrogen bonds in the axial positions (Co—N$_{av}$ = 2.04 Å) compare well with the Co—N distances found in cobalt–amine (e.g., [Co(NH$_3$)$_6$]Cl_3, Co—N = 1.963 Å) (24) and cobalt–amine complexes of different derivatives of acacen (2.042 Å (18) and 1.960 Å (19)). The Co—N$_{eq}$ are shorter than Co—N$_{ax}$ by approximately 0.133 to 0.149 Å due to the presence of π-backbonding in Co—N$_{imine}$ of the

[2] Crystallographic data (excluding structure factors) for structure **1** may be purchased from the Depository of Unpublished Data, Document Delivery, CISTI, National Research Council Canada, Ottawa, ON K1A 0S2, Canada (http://www.nrc.ca/cisti/irm/unpub_e.shtml for information on ordering electronically). CCDC 172735 contains the supplementary data for this paper. These data can be obtained, free of charge, via www.ccdc.cam.ac.uk/conts/retrieving.html (or from the Cambridge Crystallographic Data Centre, 12 Union Road, Cambridge CB2 1EZ, U.K.; fax: +44 1223 336033; or deposit@ccdc.cam.ac.uk).

© 2002 NRC Canada

Table 2. Selected bond lengths (Å) and angles (°) for **1**.

Bond lengths (Å)	
Co1—O1	1.893(2)
Co1—O2	1.900(2)
Co1—N1	1.899(3)
Co1—N2	1.905(3)
Co1—N3	2.042(3)
Co1—N4	2.038(3)
Bond angles (°)	
O1-Co1-O2	86.10(9)
O1-Co1-N1	93.89(10)
O2-Co1-N1	178.75(11)
O1-Co1-N2	178.40(11)
O2-Co1-N2	94.26(11)
N1-Co1-N2	85.87(11)
O1-Co1-N4	87.41(10)
O2-Co1-N4	89.84(10)
N1-Co1-N4	88.91(11)
N2-Co1-N4	94.15(11)
O1-Co1-N3	89.64(10)
O2-Co1-N4	87.20(10)
N1-Co1-N3	94.04(10)
N2-Co1-N3	88.82(11)
N4-Co1-N3	175.96(10)

Table 3. Selected torsion angles (°) for **1**.

ϕ_1 (N1-C3-C2-C1)	3.2(5)
ϕ_2 (O1-C1-C2-C3)	3.6(5)
ϕ_3 (N2-C6-C7-C8)	3.8(5)
ϕ_4 (O2-C8-C7-C6)	–3.0(6)
ϕ_5 (N1-C4-C5-N2)	–31.7(4)
ϕ_6 (O1-C1-C11-C16)	7.6(4)
ϕ_7 (O2-C8-C21-C26)	18.7(4)

Fig. 3. Deviation (Å) of atoms from the basal skeleton for complex **1**.

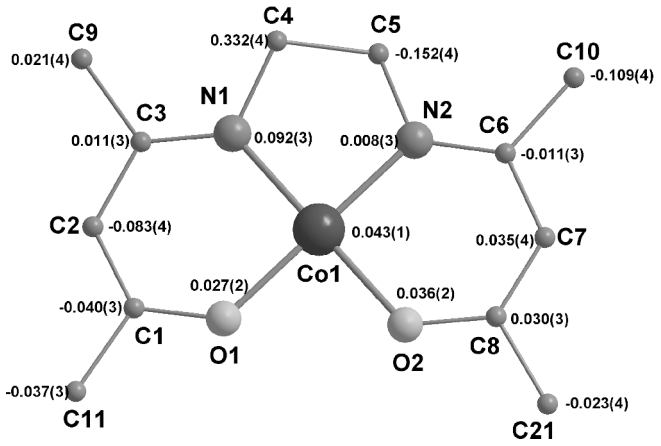

equatorial ligand. Those differences are 0.135 to 0.145 Å and 0.059 to 0.068 Å in *trans*-[Co(acacen)(piperidine)$_2$]NCS and *trans*-[Co(3-Cl-(acacen)(NH$_3$)$_2$]BPh$_4$, respectively.

All angles around the Co center deviate significantly from 90° indicating a rectangular distortion. The ligand-cobalt-ligand bond angles in the equatorial plane consist of two that are larger than 90° (O(1)-Co-N(1) (93.89(10)°), O(2)-Co-N(2) (94.26(11)°)) and two smaller angles (O(1)-Co-O(2) (86.10(9)°)) and N(1)-Co-N(2) (85.87(11)°)) (see Table 2) that are close to the corresponding values in *trans*-[Co(acacen)(piperidine)$_2$]NCS (94.1(1)°, 95.2(1)°, 84.6(1)°, 86.2(1)°) (18) and *trans*-[Co(3-Cl-acacen)(NH$_3$)$_2$]BPh$_4$ (94.06(14)°, 94.06(14)°, 84.3(3)°, 87.58(5)°) (19).

The diagonal angles of 178.75(11)° and 178.40(11)° are indicative of a slight tetrahedral distortion of the basal coordination of Co(III), which in the case of perfect planarity have values of 180°. This distortion is also reflected by the torsion angles of ~3° in the six-membered rings of basal coordination (see Table 3) and the angle between the best least-squares planes (Co1-O1-C1-C2-C3-N1) and (Co1-O2-C8-C7-C6-N2) being 3.36(10)°. Deviations of atoms from the least-squares plane (χ^2 = 3379) defined by the main basal skeleton are illustrated in Fig. 3.

The (N-)H atoms of the morpholine axial ligands are involved in hydrogen bonds with the oxygen atoms of the perchlorate anions, forming chains along the *c* axis. This behavior has also been seen in the IR spectrum of the compound (vide infra). The geometry of these hydrogen bonds is given in Table 4.

Spectral studies

The octahedral geometry of complex **1** is evident from the X-ray structural analysis (Fig. 2). An octahedral *trans*-structure for the other complexes (**2**–**6**) can be inferred based on the similarity of the ^{1}H and ^{13}C NMR spectra of these complexes with those of complex **1**. The signal appearing at ~6 ppm in the ^{1}H NMR spectrum **1** is assigned to the two =C*H* groups (Table 5) and indicates that the equatorial coordination sites are occupied by the (BA)$_2$en ligand, leading to the magnetically equivalent =C*H* protons (25). The methyl protons adjacent to the nitrogen (C*H*$_3$(N)) appear as a singlet at 2.4 to 2.6 ppm and the four ethylenediamine protons give a multiplet at ~3.31 ppm. The aromatic protons of the phenyl rings in the Schiff base ligand appear as a complex multiplet at ~7.4 to 8.2 ppm. The axially coordinated amine (N*H*) proton(s) appear at ~3.29 to 4.13 ppm (depending on the type of amine). The chemical shifts of the aromatic and aliphatic protons of the axial amines are listed in Table 5.

In the ^{13}C NMR spectrum a signal appears at 22.37 to 22.66 ppm due to the methyl carbon of the equatorial ligand NC(*C*H$_3$). The two signals at ~170 and ~175 ppm are assigned to (O*C*)Ph and (N*C*)CH$_3$, respectively (25). The ethylene carbons appear at 52.70 to 53.61 ppm and the signal at 93.67 to 94.30 ppm corresponds to -H*C*= groups in different complexes. The ^{13}C NMR signals of the axial amines are shown in Table 6. The signals at 45.64 and 20.04 ppm correspond to Ph-*C*H$_2$-NH$_2$ and H$_2$N-C$_6$H$_4$-*C*H$_3$, respectively, in the benzylamine and *p*-toluidine complexes. Other signals, corresponding to the aromatic carbons of benzylamine, *p*-toluidine, and aniline as axial ligands, appear in a narrow range close to the aromatic carbons of the Schiff base (Table 6).

The IR spectrum of the ligand exhibits a strong band at 1540 cm^{-1} due to ν C=N (26, 27). This band in the IR spectra of the complexes is shifted to a lower frequency by ~30 cm^{-1} and appears at 1508 cm^{-1}. The fairly broad band of medium intensity appearing at 1278 cm^{-1}, which corresponds

© 2002 NRC Canada

Table 4. The intermolecular hydrogen bonding geometry for **1**.

D—H···A	*d*(D—H) (Å)	*d*(H···A) (Å)	*d*(D···A) (Å)	< (DHA) (°)
N3—H3···O11	0.91	2.51	3.333(7)	151
N4—H4···O12[a]	0.91	2.53	3.362(8)	153

[a]Symmetry code: *x*, –*y* + 1/2, *z* – 1/2.

Table 5. ^{1}H NMR data for *trans*-[Co((BA)$_2$en)(X)$_2$]ClO$_4$ complexes[a,b].

X	CH_3	$(CH_2)_2$	=CH	H_1	$H_{2,3}$	NH	Other peaks
mrpln (**1**)	2.56 (6H, s)	3.31 (4H, m)	6.05 (2H, s)	8.18, 8.26 (4H, dd) (J = 2–4)	7.51 (6H, m)	3.68 (2H, br t) (J = 4.5)	2.31 (8H, m, NCH_2) 3.45 (8H, m, OCH_2)
aniln (**2**)	2.31 (6H, s)	3.31 (4H, m)	5.80 (2H, s)	8.00 (4H, dd) (J_o = 1.7, J_m = 7.8)	7.42–7.48 (6H, m)	3.59 (4H, br s)	6.76 (2H, br d, H_a) (J = 7.5) 6.98 (4H, t, H_b) (J = 7.8) 7.10 (4H, t, H_c) (J = 7.4)
bzlan (**3**)	2.46 (6H, s)	3.31 (4H, m)	5.99 (2H, s)	8.19 (4H, dd) (J_o = 2.0, J_m = 6.9)	7.50 (6H, m)	3.29 (4H, br s)	7.04 (2H, br d, H_a) (J = 7.5) 7.14–7.19 (6H, m, $H_{b,c}$) 3.75 (4H, s, -CH_2-)[c]
pprdn (**4**)	2.53 (6H, s)	3.31 (4H, m)	6.01 (2H, s)	8.12 (4H, dd) (J_o = 1.7, J_m = 7.8)	7.50 (6H, m)	4.11 (2H, s)	2.01 (4H, br t, NCH_{ax}) (J = 12.1) 2.55 (4H, br t, NCH_{eq}) (J = 7.1) 1.31–1.55 (12H, br m, $CH_2CH_2CH_2$)
p-toldn (**5**)	2.31 (6H, s)	3.31 (4H, m)	5.81 (2H, s)	7.98 (4H, dd) (J_o = 1.5, J_m = 7.8)	7.42–7.48 (6H, m)	3.54 (4H, br s)	6.65 (4H, d, H_a) (J = 8.3) 6.80 (4H, d, H_b) (J = 8.0) 2.10 (6H, s, CH_3)[d]
prldn (**6**)	2.47 (6H, s)	3.31 (4H, m)	5.96 (2H, s)	8.19 (4H, dd) (J_o = 2.3, J_m = 6.6)	7.48 (6H, m)	3.90 (2H, br s)	1.50 (8H, m, H_b) 2.25, 2.47 (8H, m, H_a)
H_2(BA)$_2$en	2.21 (6H, s)	3.78 (4H, m)	5.82 (2H, s)	7.95 (4H, dd) (J_o = 1.8, J_m = 7.9)	7.44–7.51 (6H, m)	—	—

[a]In ppm relative Me_4Si.
[b]s = singlet, t = triplet, m = multiplet, dd = doublet of doublet.
[c]Ph-CH_2-NH_2
[d]H_2N-C_6H_4-CH_3.

Table 6. ^{13}C NMR data for *trans*-[Co((BA)$_2$en)(amine)$_2$]ClO$_4$ (**1**–**6**) complexes[a,b].

X	*C*CH_3	*C*H_3	=*C*H-	(*C*H_2)$_2$	*C*Ph	Ph	axial ligand
mrpln (**1**)	173.65	22.76	94.14	53.19	172.92	127.03 (C(3)), 128.55 (C(2)), 130.54 (C(1))	49.89 (C(a)), 66.63 (C(b))
aniln (**2**)	172.95	22.57	93.89	52.77	171.74	122.86, 125.05, 127.33, 128.09, 128.70, 129.97	
bzlan (**3**)	172.90	22.43	94.30	53.26	171.59	126.91, 127.81, 128.46, 128.54, 128.77, 130.31, 45.64[c]	
pprdn (**4**)	173.12	22.42	94.16	53.03	172.34	126.93 C(3)), 128.60 (C(2)), 130.60 (C(1))	23.86 (C(c)), 27.28 (C(b)), 50.22 (C(a))
p-toldn (**5**)	172.90	22.53	93.93	52.70	171.54	127.30, 127.96, 129.24, 129.92, 135.24, 20.06[d]	
prldn (**6**)	173.39	22.52	93.67	53.60	171.63	126.78 (C(3)), 128.45 (C(2)), 130.29 (C(1))	23.44 (C(b)), 48.60 (C(a))

[a]In ppm relative Me_4Si.
[b]The signals due to the aromatic carbons of the equatorial and axial ligands have similar chemical shift.
[c]Ph-CH_2-NH_2.
[d]H_2N-C_6H_4-CH_3.

© 2002 NRC Canada

Table 7. Electronic absorption data of *trans*-[Co((BA)$_2$en)(amine)$_2$]ClO$_4$ (**1**–**6**) complexes in acetonitrile solution.

X	λ_{LF} (nm) (ε, M^{-1} cm^{-1})	$\lambda_{\pi \rightarrow \pi^*}$ (nm) (ε, M^{-1} cm^{-1})[a]	$\lambda_{\pi \rightarrow \pi^*}$ (nm) (ε, M^{-1} cm^{-1})[b]
mrpln (**1**)	455(720) Sh	377(11 100)	—
aniln (**2**)	500(820) Sh	372(11 800)	315(9900) Sh
bzlan (**3**)	455(570) Sh	378(10 200)	305(8660)
pprdn (**4**)	450(575) Sh	372(11 500)	—
p-toldn (**5**)	495(810) Sh	370(12 000)	—
prldn (**6**)	445(555) Sh	382(9850)	313(9400)
H$_2$(BA)$_2$en	—	350(32 000)	242(19 500)

[a] $\pi \rightarrow \pi^*$ Transitions azomethine chromophore.
[b] $\pi \rightarrow \pi^*$ Transition involves the imine C=N group.

Fig. 4. Cyclic voltammogram of the *trans*-[Co((BA)$_2$en)(X)$_2$]ClO$_4$ in acetonitrile at 293 K. Scan rate: 100 mV s^{-1}. (*a*) X = prldn, $c = 4 \times 10^{-3}$ M; (*b*) X = bzlan, $c = 8 \times 10^{-3}$ M.

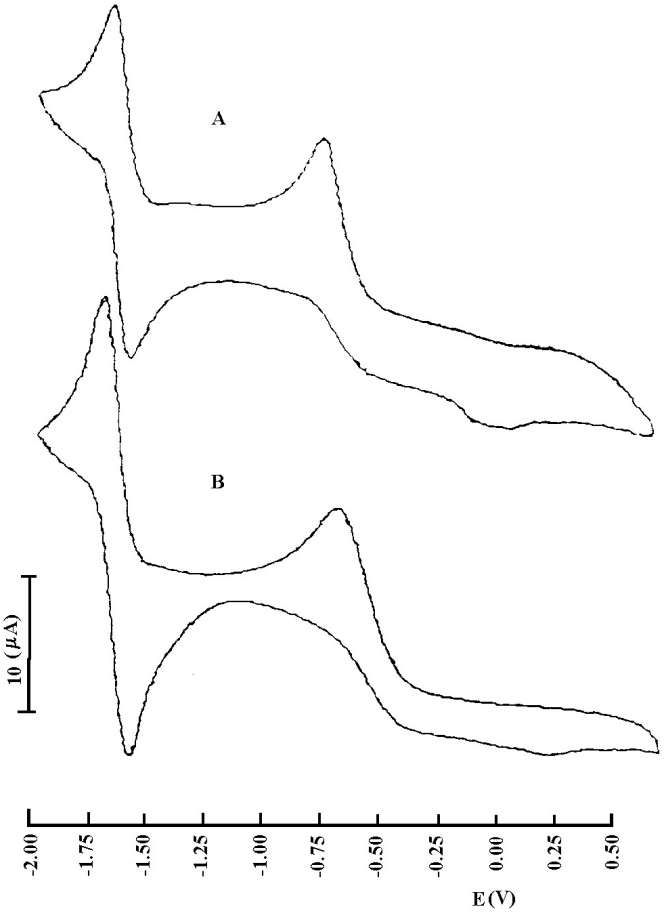

to the intramolecular hydrogen bonding in the free ligand (27), is absent in the complexes. The bands corresponding to the axial amine N—H stretching vibrations appear in the range of 3200–3300 cm^{-1}. These bands, as expected, are shifted to lower frequencies by ~150 cm^{-1} relative to the uncoordinated amines, and are broadened due to the formation of hydrogen bonds with the oxygen atoms of the perchlorate anions.

The absorption spectrum of the H$_2$(BA)$_2$en ligand exhibits two bands in the regions of 350 nm ($\varepsilon \approx 3400$ M^{-1} cm^{-1}) and 243 nm ($\varepsilon \approx 19000$ M^{-1} cm^{-1}) (28). The band at lower energy ($\lambda = 350$ nm) involves a $\pi \rightarrow \pi^*$ transition, which includes the π orbital functions of the azomethine chromophore. This $\pi \rightarrow \pi^*$ transition involves molecular orbitals that originate from the C=N group. The other band ($\lambda = 243$ nm) arises from $\pi \rightarrow \pi^*$ transitions involving the phenyl rings. However, no $n \rightarrow \pi^*$ band is observed in the H$_2$(BA)$_2$en spectrum (19).

The first $\pi \rightarrow \pi^*$ transitions in *trans*-[Co((BA)$_2$en)(amine)$_2$]ClO$_4$ complexes are red-shifted approximately 20 nm relative to that of the free ligand (Table 7). In contrast to the cobalt(III)–acacen complexes, the $\pi \rightarrow \pi^*$ transitions in **1**–**6** are more intense, because of the extended conjugate system (19). The nature of the axial ligand (amine) does not show any significant influence on the position of this band.

Electrochemistry

The cyclic voltammograms (CV) of *trans*-[Co((BA)$_2$en)(X)$_2$]ClO$_4$ complexes ((*a*) X = prldn, $c = 4 \times 10^{-3}$ M; (*b*) X = bzlan, $c = 8 \times 10^{-3}$ M), in the potential range between 0.70 and –2.00 V (vs. Ag/AgCl) in acetonitrile solution, and with 50 mM tetra-*n*-butylammonium perchlorate (TBAP) as the supporting electrolyte at a glassy carbon electrode, are shown in Fig. 4.

E1ectrochemistry in the absence of amines

A scan in the negative direction in the absence of a coordinating amine ligand indicates that the first irreversible reduction wave at ca. 0.75 V is due to the following process (eq. [1]) (9, 19):

[1] *trans*-[Co^{III}((BA)$_2$en)]$^+$ + 2X $\rightarrow$ *trans*-[Co^{III}((BA)$_2$en)(X)$_2$]$^+$

Since the electron is added to the antibonding d_{z^2} orbital the reduction of the Co(III) complex is accompanied by the loss of its axial ligands in the absence of coordinating ligands and in weakly coordinating solvents (19).

The second wave at –1.69 V has the peak potential difference of ca. 70 mV with the same anodic (i_{pa}) and cathodic (i_{pc}) peak currents. This is an indication of the following reversible one-electron-transfer process (eq. [2]):

[2] *trans*-[Co^{II}((BA)$_2$en)] + e$^-$ $\rightarrow$ *trans*-[Co^{I}((BA)$_2$en)]$^-$

When the direction of scanning is reversed and carried out in the positive region, at much higher potentials between 0.2 and –0.2 V, the Co(II) complex is reoxidized to the octahedral Co(III) complex *trans*-[Co^{III}((BA)$_2$en)(X)$_2$]$^+$, i.e. the (*trans*-[Co^{II}((BA)$_2$en)] $\leftrightarrow$ *trans*-[Co^{III}((BA)$_2$en)]$^+$ + e$^-$) electron

© 2002 NRC Canada

Table 8. Reduction potentials for the *trans*-$[Co((BA)_2en)(X)_2]ClO_4$ complexes in acetonitrile solution and pK_b of the amines.[a]

$[Co((BA)_2en)(X)_2]^+$ X	E_{pc} (III → II)[b] (mV)	$E_{1/2}$ (II →I)[c] (mV)	pK_b[d]
pyrrolidine	–810	–1690	2.73
piperidine	–790	–1695	2.88
benzylamine	–740	–1685	4.67
morpholine	–700	–1690	5.60
para-toluidine	–580	–1690	8.92
aniline	–520	–1685	9.30

[a]Potentials are vs. Ag/AgCl in 3 M NaCl, T = 298 K, $c = 4 \times 10^{-3}$ M. Scan rate: 100 mV s^{-1}.
[b]Cathodic peak potential for the process $[Co^{III}((BA)_2en)(X)_2]^+ + e^- \rightarrow [Co^{II}((BA)_2en)] + 2X$.
[c]Formal potential for the reversible process $[Co^{II}((BA)_2en)] + e^- \leftrightarrow [Co^{II}((BA)_2en)]^-$.
[d]References 28 and 29.

transfer process is followed by the following chemical reaction (eq. [3]):

[3] *trans*-$[Co^{III}((BA)_2en)]^+ + 2X \rightarrow$ *trans*-$[Co^{III}((BA)_2en)(X)_2]^+$

The reduction potential data of the cobalt complexes are summarized in Table 8. The results show that the nature of the axial ligand (amine) has a strong influence on the anodic peak potentials (i_{pa}) for the first reduction process $Co^{III} + e^- \rightarrow Co^{II}$ (differing by almost 290 mV), which is related to the basicity strength of the respective amine. The electron affinity of cobalt(III) in the complexes increases with increasing pK_b (decreasing basicity strength) of the axial ligand; therefore, the corresponding reduction potentials shift to more negative values. In fact, there is a linear relation between the pK_b of the axial amine ligand (29, 30) and the first cathodic potential (E_{pc}) of the complexes. These results are in accord with those obtained for similar Co(III) complexes reported in the literature (9, 19).

The second reduction potential corresponding to Co(II/I) was not influenced by the basicity strength of the axial amine, which indicates the absence of the axial ligands and the involvement of a four-coordinate square-planar species in this redox process.

Electrochemistry in the presence of the amines

The Co(III/II) couple dependence on exact axial ligation shows chemical reversibility, but has a much slower rate of electron transfer than the Co(II/I) couple (9). In an attempt to achieve reversible electrochemical behavior of *trans*-$[Co((BA)_2en)(pprdn)_2]ClO_4$ (**4**) the cyclic voltammetry (CV) was carried out in the presence of excess piperidine (pprdn). The cyclic voltammogram of the *trans*-$[Co((BA)_2en)(pprdn)_2]ClO_4$ complex in the presence of excess pprdn is shown in Fig. 5. In the absence of additional pprdn in the solution, the first reduction process of Co(III/II) is irreversible. Upon addition of excess piperidine, the oxidation wave of Co(II) is shifted towards more negative potentials (by almost 400 mV). By increasing the piperidine concentration (to an [amine]:[complex] ratio of ~100:1), the Co(III/II) redox couple becomes quasireversible, with ΔE_p = 110 mV and a value of 0.9 for the ratio of anodic to cathodic peak currents (i_{pa}/i_{pc}). In contrast to Co(III/II), the redox potential of the Co(II/I) couple is not significantly changed by the addition of excess amine to the solution.

Fig. 5. Changes in the cyclic voltammogram of the *trans*-$[Co((BA)_2en)(pprdn)_2]ClO_4$ complex at different piperidine concentration ratios: (*a*) 0, (*b*) 10, (*c*) 50, (*d*) 100.

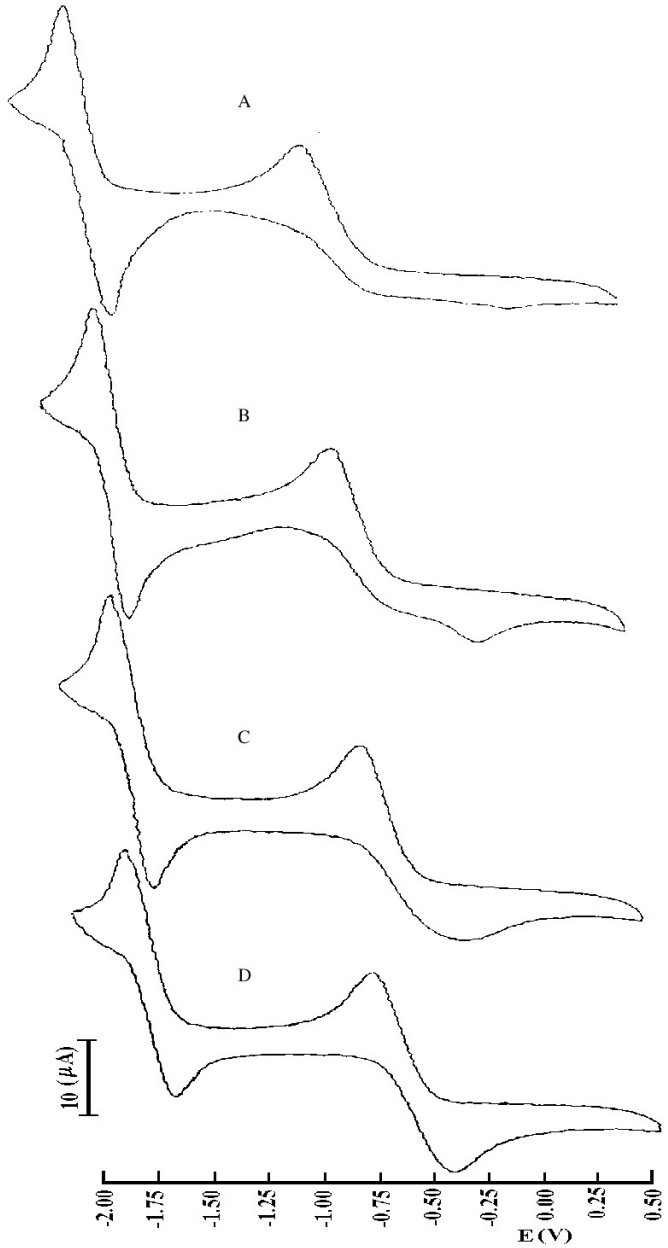

© 2002 NRC Canada

Conclusion

The combination of spectral, structural, and electrochemical measurements we have described has illustrated the main features of the coordination and redox chemistry of the trans-[Co((BA)$_2$en)(amine)$_2$]ClO_4 complexes. The coordination geometry around the Co(III) center in **1**–**6** is a distorted octahedron of N_2O_2 + N_2. Electrochemical studies have revealed that the first reduction process Co(III/II) is irreversible and strongly influenced by the nature of the axial amines. A 290 mV change in the Co(III)/Co(II) cathodic peak is observed when the axial ligands are changed from pyrrolidine to aniline. This process becomes quasi-reversible upon the addition of excess amine. The Co(II)/Co(I) couple is reversible and insensitive to moderate concentrations of axial ligands.

The observed trends in the electrochemical behavior and reactivity of these complexes are along the same line as those reported for closely related Schiff base cobalt complexes, with potential biological applications.

Acknowledgments

The authors are grateful to the Isfahan University of Technology and Tarbiat Modarres University Research Council for partial support of this work. We also thank Dr. A. Salimy for his assistance in the electrochemical measurements and Mr. Bijanzadeh for obtaining the ^1H and ^{13}C NMR spectra. We wish to thank the Division of Inorganic Chemistry, Department of Chemistry, Göteborg University for providing X-ray structure determination facilities.

References

1. M.M. Aly. J. Coord. Chem. **43**, 89 (1998).
2. X.R. Bu, C.J. Jackson, D.V. Derveer, X.Z. You, Q.J. Meng, and R.X. Wang. Polyhedron, **16**, 2991 (1997).
3. H.Y. Liu, B. Schaebert, and R.H. Holm. J. Am. Chem. Soc. **113**, 9529 (1991).
4. E.V. Rybak-Akimova, W. Otto, P. Deardorf, R. Roesner, and D.H. Busch. Inorg. Chem. **36**, 2746 (1997).
5. N.W. Alcock and D.H. Busch. Chem. Rev. **94**, 585 (1994).
6. J.P. Glusker, T. Wagner, C.E. Afshar, H.L. Carrel, U. Englert, and H.P.C. Hogenkamp. Inorg. Chem. **38**, 1785 (1999).
7. M.P. Jensen and J. Halpern. J. Am. Chem. Soc. **121**, 2182 (1999).
8. L.G. Marzilli, R. Cini, and S.J. Moore. Inorg. Chem. **37**, 6890 (1998).
9. L.G. Marzilli and A. Gerli. Inorg. Chem. **31**, 1152 (1992).
10. C. Huilan, H. Deyan, Y. Hong, T. Wenxia, J. Chen, P. Zheng, and C. Chen. Inorg. Chem. **35**, 1502 (1996).
11. J.M. Pratt. Chem. Soc. Rev. **14**, 161 (1985).
12. L. Randaccio, N.B. Pahor, and E. Zangrando. Chem. Soc. Rev. **18**, 225 (1989).
13. M. Amirnasr and R. Vafazadeh. Int. J. Chem. Kinet. **34**, 387 (2002).
14. L.G. Marzilli, S.M. Polson, R. Cini, and C. Pifferi. Inorg. Chem. **36**, 314 (1997).
15. L.G. Marzilli, M.F. Summers, E. Zangrando, N.B. Pahor, and L. Randaccio. J. Am. Chem. Soc. **108**, 4830 (1986).
16. B.P. Hay and R.G. Finke. J. Am. Chem. Soc. **109**, 8012 (1987).
17. B.P. Hay and R.G. Finke. J. Am. Chem. Soc. **108**, 4820 (1986).
18. M. Amirnasr and R. Vafazadeh. Scientia Iranica, **4**, 35 (1997).
19. A. Böttcher, T. Takeuchi, K.I. Hardcastle, T.J. Meade, and H.B. Gray. Inorg. Chem. **36**, 2498 (1997).
20. P.J. McCarty, R.J. Hovey, K. Ueno, and A.E. Martell. J. Am. Chem. Soc. **77**, 5820 (1955).
21. SMART and SAINT: Area detector control and integration software. Siemens Analytical X-ray Instruments Inc., Madison, Wisconsin, U.S.A. 1995.
22. G.M. Sheldrick. SADABS: Program for empirical absorption correction of area detectors. University of Göttingen, Germany. 1996.
23. SHELXTL Version 5.10. Bruker AXS Inc., Madison, Wisconsin, U.S.A. 1997.
24. G.J. Kruger and E.C. Reynhardt. Acta Crystallogr. Sect. B: Struct. Crystallogr. Cryst. Chem. **34**, 915 (1978).
25. F.L. Lindoy and H.W. Louie. Inorg. Chem. **20**, 4186 (1981).
26. K. Ueno and A.E. Martel. J. Phys. Chem. **60**, 1270 (1956).
27. N. Yamazaki and Y. Hohokabe. Bull. Chem. Soc. Jpn. **44**, 63 (1971).
28. D.F. Averill and R.F. Broman. Inorg. Chem. **17**, 3389 (1978).
29. D.D. Perrin. Dissociation constants of organic bases in aqueous solution. Butterworths, London. 1972.
30. CRC handbook of chemistry and physics. 79th ed. *Edited by* D.R. Lide. CRC Press, Boca Raton, Florida, U.S.A. 1998.

© 2002 NRC Canada

Thermal oscillations in the bromate – oxalic acid – $MnSO_4$ – H_2SO_4 – acetone system: A calorimetric study

Sudeshna Biswas, Kallol Mukherjee, Dulal Chandra Mukherjee, and Satya Priya Moulik

Abstract: The oscillatory reaction of potassium bromate, oxalic acid, and $MnSO_4$ in the presence of acetone in aq H_2SO_4 solutions has been studied calorimetrically at different concentrations of substrates. Acetone and oxalic acid have been found to accelerate the reaction by increasing the oscillation frequency. On the other hand, $MnSO_4$ has a retarding effect; the frequency of oscillation decreases systematically with increasing concentration of $MnSO_4$. Potassium bromate shows mixed behavior in this respect. The total heat evolved during the reaction per mol of oxalic acid consumed has been evaluated, which can be used to calculate the concentrations of the various reactants at different stages of the reaction. The effects of different electrolytes (KCl, NaCl, $BaCl_2$, $CaCl_2$, $SrCl_2$, NaBr, NaI, KNO_3, $NaNO_3$, and $Ca(NO_3)_2$) and solvents (dimethylformamide, 1,4-dioxane, acetonitrile, and tetrahydrofuran) on the extents of oscillation and the enthalpy change for the process have been also examined.

Key words: Belousov–Zhabotinsky reaction, oscillatory reaction, oxalic acid, calorimetry, acetone.

Résumé : Faisant appel à la calorimétrie et opérant à diverses concentrations de substrat, on a étudié la réaction oscillatoire du bromate de potassium, avec l'acide oxalique et le $MnSO_4$, en présence d'acétone, en solutions aqueuses de H_2SO_4. On a observé que l'acétone et l'acide oxalique accélèrent la réaction en augmentant la fréquence d'oscillation. D'autre part, le $MnSO_4$ ralentit la réaction; la fréquence de l'oscillation diminue de façon systématique avec une augmentation de la concentration du $MnSO_4$. De ce point de vue, le comportement du bromate de potassium est mixte. On a évalué la chaleur totale dégagée au cours de la réaction, par mol d'acide oxalique et on peut utiliser cette valeur pour calculer les concentrations des divers réactifs à différents stages de la réaction. On a aussi examiné les effets de divers électrolytes (KCl, NaCl, $BaCl_2$, $SrCl_2$, NaBr, NaI, KNO_3, $NaNO_3$ et $Ca(NO_3)_2$) ainsi que celles de divers solvants (diméthylformamide, 1,4-dioxane, acétonitrile et tétrahydrofurane) sur l'oscillation et le changement d'enthalpie pour ce processus.

Mots clés : réaction de Belousov–Zhabotinsky, réaction oscillatoire, acide oxalique, calorimétrie, l'acétone.

[Traduit par la Rédaction]

Introduction

Studies of the Belousov–Zhabotinsky (B-Z) oscillatory chemical reaction (1) have been the subject of growing importance and interest. The fundamental chemistry of the B-Z system has been clarified by the FKN (Field, Körös, and Noyes) mechanism (2) and by mathematical models (3–5). The methodologies that have been liberally employed so far for studying the B-Z reaction are based on potentiometric and spectrophotometric measurements. The results of calorimetric measurements (6, 7) are also being used to understand the oscillatory phenomena with the objective of getting straightforward information about the thermochemical behavior of the system.

Noszticzius and Bódiss (8) have studied the B-Z reaction with oxalic acid in place of malonic acid, and others (9–13) have studied the reaction in the presence of acetone (a bromine scavenger). This complex oscillatory system has been monitored by voltage oscillations as well as by absorbance oscillations. But so far, this system has not been studied by following temperature oscillations. In our earlier communications, (6, 14, 15) we have reported calorimetrically measured temperature oscillations of the bromate – gallic acid – sulfuric acid B-Z system as a function of bromate concentration, with and without ferroin as a catalyst, in the presence of mixed solvents and electrolytes. As studies of the temperature oscillation of the B-Z reaction involving oxalic acid as the organic substrate are not very common in the literature, we have undertaken an investigation of the thermochemical behavior of the bromate – oxalic acid – $MnSO_4$ – H_2SO_4 – acetone B-Z oscillatory system. As solvents (14, 16, 17) and added electrolytes (15, 17–19) are found to have marked effects on the B-Z system, we have also investigated their

Received 5 September 2001. Published on the NRC Research Press Web site at http://canjchem.nrc.ca on 30 August 2002.

S. Biswas, K. Mukherjee,[1] D.C. Mukherjee,[2] and S.P. Moulik.[3] Centre for Surface Science, Department of Chemistry, Jadavpur University, Calcutta-700032, India.

[1]Present address: Department of Chemistry, A.P.C. College, West Bengal, India.
[2]Present address: Department of Chemistry, Calcutta University, Calcutta-700009, India.
[3]Corresponding author (e-mail: cssju@yahoo.co.uk).

 DOI: 10.1139/V02-146 © 2002 NRC Canada

Fig. 1. Oscillatory thermogram of the bromate – oxalic acid – acetone – H_2SO_4 – $MnSO_4$ system at 303 K. [$KBrO_3$] = 0.14 mol dm^{-3}, [OA] = 0.0625 mol dm^{-3}, [H_2SO_4] = 1.25 equiv dm^{-3}, [$MnSO_4$] = 0.0013 mol dm^{-3}, [AC] = 0.5 mol dm^{-3}.

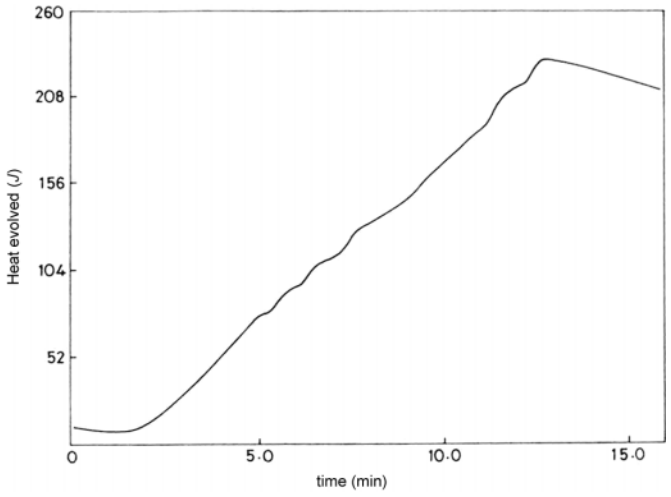

Fig. 2. Oscillatory thermogram of the bromate – oxalic acid – acetone – H_2SO_4 – $MnSO_4$ system at 303 K. [$KBrO_3$] = 0.14 mol dm^{-3}, [H_2SO_4] = 1.25 equiv dm^{-3}, [$MnSO_4$] = 0.0013 mol dm^{-3}, [AC] = 1.0 mol dm^{-3}. (*a*) [OA] = 0.05 mol dm^{-3}, (*b*) [OA] = 0.04 mol dm^{-3}.

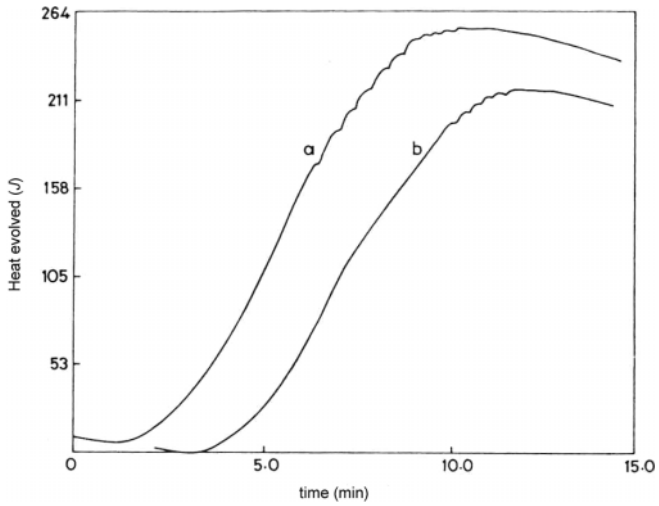

effects on the oscillatory process, and have attempted to rationalize the results.

Experimental section

Materials

Potassium bromate, sulfuric acid, oxalic acid (OA), acetone (AC), manganous sulfate, and tetrahydrofuran (THF) were products of Merck (Germany). The electrolytes used in this study were A.R. grade products of Merck (India). The solvents dimethylformamide (DMF), acetonitrile (ACN), and 1,4-dioxane (DX) were A.R. grade products of S.D. Fine Chemicals (India). Doubly distilled conductivity water was used in all preparations.

Method

The reaction was studied in a TRONAC 458 isoperibol titration calorimeter at 303 K. A solution (18 mL) with a composition of 0.155 mol dm^{-3} $KBrO_3$, 1.1 mol dm^{-3} acetone, and 1.25 equiv dm^{-3} H_2SO_4 were loaded into the reaction vessel of the calorimeter. A mixture (2 mL) of 0.625 mol dm^{-3} oxalic acid and 0.013 mol dm^{-3} manganous sulfate in H_2SO_4 was added from a burette into the reaction vessel. The change in heat during the oscillations was recorded with a Houston Omniscribe stripchart recorder. The heat produced during the reaction was evaluated from the peak height and slope values of the produced thermograms (Figs. 1 and 2) following the procedure described earlier (6). The effect of concentration of a component on the oscillatory reaction was studied by changing its concentration at constant concentrations of the other components.

Results and discussion

The oscillatory reaction process

The BrO_3^-–$MnSO_4$–H_2SO_4–OA–AC mixed-substrate B-Z system is a complex one. The overall reaction is (8):

[1] $HBrO_3 + 2(COOH)_2 + CH_3COCH_3 \rightarrow 4CO_2 + 3H_2O + BrCH_2COCH_3$

Br_2 inhibits the process whereas CO_2 does not. CH_3COCH_3 scavenges Br_2 and the oscillation persists longer in the presence of CH_3COCH_3 (10).

$HBrO_2$ is a vital component for the deceleration and acceleration of the oscillatory process (8).

The following reaction steps for the mechanism have been proposed (20):

[2] $BrO_3^- + Br^- + 2H^+ \rightleftharpoons HBrO_2 + HOBr$

[3] $Br^- + HBrO_2 + H^+ \rightleftharpoons 2HOBr$

[4] $Br^- + HOBr + H^+ \rightleftharpoons Br_2 + H_2O$

[5] $BrO_3^- + HBrO_2 + H^+ \rightleftharpoons 2BrO_2\bullet + H_2O$

[6] $Mn^{2+} + BrO_2\bullet + H^+ \rightleftharpoons Mn^{3+} + HBrO_2$

[7] $BrO_2\bullet + (COOH)_2 \rightarrow HBrO_2 + CO_2 + HCO_2\bullet$

[8] $HOBr + (COOH)_2 \rightarrow H_2O + CO_2 + HCO_2\bullet + Br\bullet$

The Br_2 is removed from the system by the following reactions:

[9] $Br\bullet + CH_3COCH_3 \rightarrow Br^- + CH_3COCH_2\bullet + H^+$

[10] $CH_3COCH_2\bullet + Br_2 \rightarrow BrCH_2COCH_3 + Br\bullet$

[11] $CH_3COCH_2\bullet + CH_3COCH_2\bullet \rightarrow CH_3COCH_2CH_2COCH_3$

[12] $CH_3COCH_3 + H^+ \rightleftharpoons CH_2{=}COHCH_3 + H^+$

[13] $CH_2{=}COHCH_3 + Br_2 \rightarrow BrCH_2COCH_3 + H^+ + Br^-$

© 2002 NRC Canada

Table 1. Effect of varying acetone concentration on the bromate – oxalic acid – $MnSO_4$ – H_2SO_4 – acetone system at 303 K.

[AC] (mol dm^{-3})	n	ΔH_R (kJ mol^{-1})
0.2	—	22
0.3	1	30
0.4	2	130
0.5	5	167
0.6	6	181
0.7	7	200
0.8	7	214
0.9	10	233
1.0	11	278

Note: $[H_2SO_4]$ = 1.25 equiv dm^{-3}, $[MnSO_4]$ = 0.0013 mol dm^{-3}, [OA] = 0.0625 mol dm^{-3}, $[KBrO_3]$ = 0.14 mol dm^{-3}. ΔH_R is expressed per mol of OA.

Table 2. Effect of varying oxalic acid concentration.

[OA] (mol dm^{-3})	n	ΔH_R (kJ mol^{-1})
0.03	—	280
0.04	5	266
0.05	10	251
0.06	11	278
0.07	11	273
0.08	15	253
0.09	15	283
0.1	15	241

Note: $[H_2SO_4]$ = 1.25 equiv dm^{-3}, $[MnSO_4]$ = 0.0013 mol dm^{-3}, [AC] = 1.0 mol dm^{-3}, $[KBrO_3]$ = 0.14 mol dm^{-3}. ΔH_R is expressed per mol of OA.

General thermal behavior of the oscillatory process

Addition of mixed solutions of $MnSO_4$ and oxalic acid from the burette into the potassium bromate solution in the calorimeter vessel released a large amount of initial heat for several minutes, which was estimated by a previously reported procedure (6). After that, regular (also irregular) oscillations of the released heat were observed. A large induction period before the beginning of oscillations was reported by Guedes and Faria (10). The release of appreciable initial heat was also observed in the bromate – gallic acid – H_2SO_4 – ferroin system studied by us (14, 15). The results are exemplified in Figs. 1 and 2. The number of oscillation (n) and the enthalpy of reaction expressed in kJ mol^{-1} (ΔH_R) were evaluated. This ΔH_R includes the initial heat and the heat released in the oscillatory regime, and is expressed per mol of oxalic acid based on the consideration that all the other reaction components are in excess compared to oxalic acid, so that at the end of the reaction, all the oxalic acid is consumed. From the ΔH_R values, the consumption of a component during the different stages of the reaction can be estimated. In this calculation, ΔH_R at a certain stage becomes proportional to the oxalic acid consumed and is thus related to the consumption of other reacting species, acetone and bromoacetone by way of the necessary mass balance equations. It is observed from the results given in Tables 1–6 that the ΔH_R values have shown a direct correlation only with the acetone concentration ([AC]); the other components, oxalic acid, salts, and mixed solvents have not shown an observable correlation. The oscillations also are found to increase with the concentration of acetone and not with the concentrations of the other components. This reflects the clear Br_2 scavenging effect of acetone; the ΔH_R–[AC] profile has been found to be fairly linear. The same physical quantities of n and ΔH_R were also estimated at different concentrations of the reagents (OA, AC, $MnSO_4$, and $KBrO_3$), salts (chlorides of K, Na, Ba, Sr, and Ca; nitrates of K, Na, and Ca; NaBr and NaI), and solvents (DX, ACN, THF, and DMF).

Effect of substrate concentration

The oscillatory process was examined as a function of the concentration of each of AC, OA, $MnSO_4$, and $KBrO_3$ at fixed concentrations of the other components.

With increasing acetone concentration, the number of oscillations increased. No oscillation was observed at 0.2 mol dm^{-3} acetone concentration calorimetrically, though Wittmann et al. (9) reported oscillations from potentiometric studies below 0.21 mol dm^{-3} of acetone. At 0.3 mol dm^{-3}, only a single oscillation was observed. At 0.4 mol dm^{-3} acetone, there was a lag period of 8 min between two oscillations. This lag period was reduced to 3 min at 0.5 mol dm^{-3} acetone (Fig. 1). Above 0.5 mol dm^{-3} acetone, no such distinct halt was observed. Wittmann et al. (9) also potentiometrically observed a pause of oscillation in the OA–AC mixed-substrate B-Z system, at 0.21 to 1.4 mol dm^{-3} acetone (Table 1).

With increasing OA concentration, the number of oscillation increased. Oscillation was not observed below 0.04 mol dm^{-3} OA. At 0.05 mol dm^{-3} and 0.04 mol dm^{-3} OA, a combination of high- and low-amplitude oscillations was observed. At 0.04 mol dm^{-3} OA, three high-amplitude initial oscillations were followed by two low-amplitude oscillations. At 0.05 mol dm^{-3} OA, six high-amplitude oscillations were followed by four low-amplitude oscillations. This type of mixed high- and low-amplitude oscillations was also reported by Guedes and Faria (10) from spectrophotometric studies. In the present study, mixed high- and low-amplitude oscillations were not observed at >0.05 mol dm^{-3} OA (see Fig. 2 and Table 2).

With increasing $MnSO_4$ concentration, the number of oscillation decreased. We could not increase the indicator concentration above 0.0015 mol dm^{-3} due to the Br_2 liberation in acid solution. Interestingly, no oscillation was observed in the absence of $MnSO_4$ or in the presence of ferroin indicator. (Table 3).

With increasing $KBrO_3$ concentration, the number of oscillations decreased. Also, >0.22 mol dm^{-3} $KBrO_3$ could not be used here because of the Br_2 liberation in acid solution (Table 4).

Though with increasing concentration of substrate the rates of chemical reactions generally increase, the opposite effect may be explained due to complex formation of the added reactants in the activated state, thereby inhibiting the formation of products. Increased concentrations of $KBrO_3$ and Mn^{2+} lead to increased formation of $HBrO_2$ and HOBr through rxns. [2]–[6] and that causes the increase in the bromine concentration. As the acetone concentration is kept fixed in those experiments, some unscavenged Br_2 may be present to inhibit the process. In this complex chemical reaction, understanding of the inhibition by the substrate may require information on the different activated states, which at present is not known. OA, on the other hand, offered an activating effect in the reaction up to a certain concentration

© 2002 NRC Canada

Table 3. Effect of varying $MnSO_4$ concentration.

$[MnSO_4]$ (mol dm^{-3})	n	ΔH_R (kJ mol^{-1})
0.0011	13	277
0.0012	12	261
0.0013	11	278
0.0014	9	235
0.0015	8	231

Note: $[H_2SO_4]$ = 1.25 equiv dm^{-3}, [OA] = 0.0625 mol dm^{-3}, [AC] = 1.0 mol dm^{-3}, $[KBrO_3]$ = 0.14 mol dm^{-3}. ΔH_R is expressed per mol of OA.

Table 4. Effect of varying $KBrO_3$ concentration.

$[KBrO_3]$ (mol dm^{-3})	n	ΔH_R (kJ mol^{-1})
0.06	10	222
0.10	11	232
0.14	11	278
0.18	6	249
0.22	3	274

Note: $[H_2SO_4]$ = 1.25 equiv dm^{-3}, [OA] = 0.0625 mol dm^{-3}, [AC] = 1.0 mol dm^{-3}, $[MnSO_4]$ = 0.0013 mol dm^{-3}. ΔH_R is expressed per mol of OA.

above, which n did not change. Such a saturation point was reached at ~0.08 mol dm^{-3} of OA. AC produced a good activating effect on the reaction by its bromine scavenging ability (10, 20). The presence of Br_2 inhibits oscillations, as has been pointed by other authors (8–11, 20). Acetone reacts with bromine to produce bromoacetone (eq. [13]) and consequently reduces the Br_2 concentration. All the results discussed above are presented in Tables 1–4.

Effect of mixed solvents

DX and ACN showed similar inhibitory effects on the OA–$KBrO_3$–AC–$MnSO_4$ system. In both the cases, the number (n) of oscillations decreased with increasing volume fraction of the organic component. In the case of DX, the oscillation ceased at 20 volume% DX, and for ACN at 15%. For THF, n also decreased and the decrease was very rapid compared to DX and ACN. Addition of very small amounts of THF increased n by almost a factor of two relative to the aqueous medium. With increasing volume fraction of THF, n decreased sharply and the oscillatory behavior ended at 3% THF. DMF showed completely different behavior. The number of oscillations (n) initially increased from 0.5 to 4% DMF, then started decreasing from 5 to 10% DMF. Higher percentages of DMF could not be used due to the liberation of Br_2.

Lalitha and Ramaswamy (16) have studied the bromate – gallic acid – ferroin system at a fixed composition (20 volume%) of the organic solvents (DX, THF, ACN, and DMF) in water. For these systems, n increased in the order DMF > THF > ACN > DX. In this study, we have used variable compositions, thereby obtaining variable n values. A comparison of the results at a fixed composition (1 volume% organic solvents) gives the order THF > DMF > DX ≈ ACN. This sequence fails, however, at higher proportions of the organic solvents.

It is considered by Lalitha and Ramaswamy (16) and Jha et al. (17) that the bromination of the active methylene compound is an important factor for an oscillatory reaction (where malonic acid or related organic substrates are used), and it occurs through the electrophilic substitution by bromonium ion (Br^+). As a result of poor solvation of this Br^+ in mixed solvent media, it performs faster bromination, thereby decreasing the frequency of oscillation. But this generalization is not possible for the present system where the organic substrate is oxalic acid with no active methylene group. The solvents can react with very reactive intermediates of the B-Z system (like bromine dioxide, bromous acid, hypobromous acid, etc.). How these and other factors affect the course of the reaction is difficult to assess and decipher. The results are presented in Table 5.

Table 5. Effect of mixed solvents.

Solvent (volume%)	n	ΔH_R (kJ mol^{-1})
Water	11	278
DX (0.5)	11	261
DX (1)	10	256
DX (2)	10	248
DX (4)	9	235
DX (5)	8	243
DX (10)	6	246
DX (15)	3	251
DX (17)	1	236
DX (20)	—	208
THF (0.5)	21	261
THF (1)	18	217
THF (2)	11	200
THF (2.5)	6	181
THF (3)	—	121
ACN (0.5)	10	252
ACN (1)	10	254
ACN (2)	9	269
ACN (4)	8	252
ACN (5)	7	241
ACN (10)	5	235
ACN (12)	3	223
ACN (13.5)	1	228
ACN (15)	—	218
DMF (0.5)	11	258
DMF (1)	12	244
DMF (2)	12	227
DMF (3)	13	248
DMF (4)	16	247
DMF (5)	15	238
DMF (7.5)	14	224
DMF (10)	12	222

Note: $[H_2SO_4]$ = 1.25 equiv dm^{-3}, [OA] = 0.0625 mol dm^{-3}, [AC] = 1.0 mol dm^{-3}, $[MnSO_4]$ = 0.0013 mol dm^{-3}, $[KBrO_3]$ = 0.14 mol dm^{-3}. ΔH_R is expressed per mol of OA.

Effect of added electrolytes

Jacobs and Epstein (18) have studied the effect of chloride on the oscillations in the bromate – cerium – malonic acid system. The effect of chloride on the above-mentioned system under a variety of conditions has been reported and a mechanism has been proposed. The chloride inhibition mechanism involves the oxidation of chloride to chlorous acid which reduces Ce(IV) to Ce(III), preventing oscillation. The oscillations resume when the chlorous acid has been

© 2002 NRC Canada

Table 6. Effect of added electrolytes.

Electrolyte	n	ΔH_R (kJ mol^{-1})
Chlorides and nitrates[a]		
KCl	10	253
NaCl	11	256
$BaCl_2$	10	242
$SrCl_2$	10	250
$CaCl_2$	11	266
KNO_3	11	259
$NaNO_3$	11	268
$Ca(NO_3)_2$	11	265
[NaBr] (equiv dm^{-3})		
1×10^{-7}	11	271
1×10^{-6}	10	266
1×10^{-5}	10	263
1×10^{-4}	10	256
[NaI] (equiv dm^{-3})		
1×10^{-7}	10	254
1×10^{-6}	10	254
1×10^{-5}	10	257

Note: $[H_2SO_4]$ = 1.25 equiv dm^{-3}, [OA] = 0.0625 mol dm^{-3}, [AC] = 1.0 mol dm^{-3}, $[MnSO_4]$ = 0.0013 mol dm^{-3}, $[KBrO_3]$ = 0.14 mol dm^{-3}. ΔH_R is expressed per mol of OA.
[a]At 1×10^{-5} equiv dm^{-3}.

completely oxidized to chlorate. The inhibitory effect of iodide ion on the B-Z system (19) and bromide ion on the Briggs–Rauscher (21) reaction have also been studied. Nitrate, sulfate, and perchlorate salts have been shown (18) not to affect the malonic acid – bromate – Ce^{3+}(catalyst) – H_2SO_4 B-Z reaction. However, Jha et al. (17) observed inhibitory effects on this B-Z reaction at high $NaNO_3$ concentrations. We also observed inhibitory effects of chloride and nitrate salts on the bromate – gallic acid – H_2SO_4 – ferroin oscillatory process (15).

In the present study, experiments were performed with five chloride salts (KCl, NaCl, $BaCl_2$, $SrCl_2$, and $CaCl_2$). Inhibition was almost insignificant; the n values remained unaltered up to electrolyte concentrations of about 1×10^{-2} equiv dm^{-3}. The oscillatory process was also not inhibited by KNO_3, $NaNO_3$, and $Ca(NO_3)_2$ up to 1×10^{-2} equiv dm^{-3}. With NaBr and NaI, a slight inhibition was observed with increasing concentration of the electrolyte from 1×10^{-7} to 1×10^{-2} equiv dm^{-3}.

The effects of added electrolytes up to 1×10^{-5} equiv dm^{-3} on n are presented in Table 6. We studied this effect up to electrolyte concentrations of 1×10^{-2} equiv dm^{-3}. As the values of n remain more or less the same with increasing electrolyte concentration beyond 1×10^{-5} equiv dm^{-3}, the results for this concentration range are not shown in the table.

This insignificant inhibitory effect of the above-mentioned electrolytes is in sharp contrast to other oscillatory reaction processes (15, 18) where distinct reduction of n was observed, even with electrolyte concentrations as low as 1×10^{-7} equiv dm^{-3}. In our previous work (15), we reported inhibitory effects of chloride and nitrate salts on the bromate – gallic acid – H_2SO_4 – ferroin reaction, studied by both calorimetry and potentiometry. A probable mechanism of the inhibitory effects of the chloride ion on the bromate – gallic acid – H_2SO_4 – ferroin reaction was presented (15), but an explanation of the effect of nitrate salts could not be proposed. For the present system, calorimetric studies have not shown any significant inhibition and it may be assumed that potentiometric observation should give the same result. Why chloride and nitrate ions do not contribute to the process by way of interaction with $HBrO_2$ and $\bullet BrO_2$, which are vital products (15), requires further examination.

Conclusions

Increasing the concentration of different components of the oscillatory system individually, keeping others constant, has marked effects on n. $KBrO_3$ and $MnSO_4$ have shown decreasing effects on n, whereas acetone has shown an increasing effect. Oxalic acid has produced a hyperbolic saturation effect.

ΔH_R values for the overall heat evolved in the oscillatory reaction per mol of oxalic acid consumed has been found to be linearly related with the acetone concentration. Based on ΔH_R, the consumption of the reacting components at different stages of oscillation can be estimated.

THF, ACN, and DX have retarding effects on n. A maximum for n has been observed for DMF.

Electrolytes have practically no effect on the oscillatory process.

Acknowledgements

Sudeshna Biswas thanks Jadavpur University for laboratories to pursue the work in the Centre for Surface Science, Department of Chemistry. We thank Dr. R.S. Banerjee of the Department of Chemistry, Calcutta University for useful information.

References

1. A.M. Zhabotinsky. Biofizika, **9**, 306 (1964).
2. R.J. Field, E. Körös, and R.M. Noyes. J. Am. Chem. Soc. **94**, 8649 (1972).
3. A.M. Zhabotinsky, F. Buchholtz, A.B. Kiyatkin, and I.R. Epstein. J. Phys. Chem. **97**, 7578 (1993).
4. A.B. Rovinsky and A.M. Zhabotinsky. J. Phys. Chem. **88**, 6081 (1984).
5. A.B. Rovinsky. J. Phys. Chem. **88**, 4 (1984).
6. K. Mukherjee, S.P. Moulik, and D.C. Mukherjee. Int. J. Chem. Kinet. **27**, 561 (1995).
7. D. Janjic, P. Stroot, and U. Burger. Helv. Chem. Acta, **57**, 266 (1974).
8. Z. Noszticzius and J. Bódiss. J. Am. Chem. Soc. **101**, 3177 (1979).
9. M. Wittmann, P. Stirling, and J. Bódiss. Chem. Phys. Lett. **141**, 241 (1987).
10. M.C. Guedes and R.B. Faria. J. Phys. Chem. **102**, 1973 (1998).
11. P. Ševčík and L. Adamčíková. Coll. Czech. Chem. Commun. **50**, 799 (1985).
12. Z. Noszticzius. Magy. Kem. Foly. **85**, 330 (1979).
13. H.R. Weigt. Z. Chem. **30**, 260 (1990).
14. S. Biswas, K. Mukherjee, S.N. Basu, D.C. Mukherjee, and S.P. Moulik. Z. Phys. Chem. (Muenchen), **215**, 575 (2001).

© 2002 NRC Canada

15. S. Biswas, K. Mukherjee, D.C. Mukherjee, and S.P. Moulik. Indian J. Chem. Sect. A: Inorg. Bio-inorg. Phys. Theor. Anal. **39A**, 912 (2000).
16. P.V. Lalitha and R. Ramaswamy. Int. J. Chem. Kinet. **25**, 457 (1993).
17. P.N. Jha, B.N. Prasad, and R.K. Prasad. J. Indian Chem. Soc. **65**, 177 (1988).
18. S.S. Jacobs and I.R. Epstein. J. Am. Chem. Soc. **98**, 1721 (1976).
19. R.J. Kaner and I.R. Epstein. J. Am. Chem. Soc. **100**, 4073 (1978).
20. R.J. Field and P.M. Boyd. J. Phys. Chem. **89**, 3707 (1985).
21. R. Cervellati and B. Mongiorgi. Int. J. Chem. Kinet. **30**, 641 (1998).

© 2002 NRC Canada

Cyclodextrin-, UV-, and high pH-induced fluorescence enhancement of the pesticide azinphos-methyl: Applications to its trace analysis

Brian D. Wagner, Adam C. Sherren, and Matthew A. Rankin

Abstract: Various methods for the enhancement of the fluorescence of the pesticide azinphos-methyl are reported. The addition of hydroxypropyl-β-cyclodextrin was found to moderately enhance the fluorescence by a factor of three, presumably via inclusion of the pesticide into the cyclodextrin cavity. This complexation was found to occur with an association constant of 690 ± 140 M^{-1}. This enhancement was found to be too low to be useful in a fluorescence-based analytical method for this pesticide. Exposure of azinphos-methyl to UV light was also found to result in enhanced fluorescence, with much larger enhancement than in the case of addition of cyclodextrins. This enhancement was presumed to occur via photolysis of azinphos-methyl to a more fluorescent photoproduct. However, the difficulty of providing a constant UV dosage prevents its useful application as a fluorescence-based analytical method. Finally, it was found that base hydrolysis of azinphos-methyl resulted in a very large fluorescence enhancement. Although this enhancement was previously reported in the literature, it was found that contrary to the published reports, the hydrolysis occurred rapidly at room temperature, with no need for carrying out the reaction at increased temperature. Fluorescence enhancements of a factor of 300 were obtained by simply adding the appropriate amount of an aqueous NaOH solution to the aqueous azinphos-methyl sample. This procedure was used as the basis of a simple fluorescence-based analytical method for azinphos-methyl in water, with excellent linear calibration curves obtained down to concentrations of 5 ppb.

Key words: fluorescence spectroscopy, pesticides, azinphos-methyl, fluorescence enhancement, host–guest inclusion.

Résumé : On a développé diverses méthodes permettant de rehausser la fluorescence du pesticide « azinphos-méthyle ». On a trouvé que l'addition d'hydroxypropyl-β-cyclodextrine augmente la fluorescence par un facteur de trois, probablement par l'inclusion du pesticide dans la cavité de la cyclodextrine. On a observé que la complexation se fait avec une constante d'association de 690 ± 140 M^{-1}. On a trouvé que cette augmentation est trop faible pour être utile dans une méthode analytique de ce pesticide faisant appel à la fluorescence. On a observé que l'exposition du pesticide à de la lumière UV provoque aussi une augmentation de la fluorescence qui est beaucoup plus grande que celle observée avec les cyclodextrines. On a fait l'hypothèse que ceci résulte d'une photolyse de l'« azinphos-méthyle » en un photoproduit plus fluorescent. Toutefois, la difficulté de fournir un dosage constant d'UV rend difficile son application à une méthode analytique de ce pesticide faisant appel à la fluorescence. Enfin, on a trouvé que l'hydrolyse de l'« azinphos-méthyle » par une base conduit à une très importante augmentation de la fluorescence. Même si cette élévation a été rapportée dans la littérature antérieurement, on a trouvé que contrairement à ce qui avait alors été rapporté l'hydrolyse de produit rapidement à la température ambiante, sans qu'il soit nécessaire d'augmenter la température de la réaction. On a obtenu des facteurs d'augmentation de la fluorescence de l'ordre de 300 en ajoutant simplement la quantité appropriée d'une solution aqueuse de NaOH à un échantillon d'« azinphos-méthyle ». On a utilisé cette méthode comme base d'une méthode faisant appel à la fluorescence qui permet de faire simplement l'analyse de l'« azinphos-méthyle » dans l'eau, avec d'excellentes courbes de calibration linéaires jusqu'à des concentrations aussi faibles que 5 ppb.

Mots clés : spectroscopie de fluorescence, pesticides, « azinphos-méthyle », augmentation de la fluorescence, inclusion hôte–invité.

[Traduit par la Rédaction]

Introduction

Prince Edward Island (PEI) has a very high proportion of cultivated land. In 1998, there were a total of 404 000 acres of land used for agriculture (1), representing 29% of the total land area of the province. As a consequence, PEI has one of the highest uses of pesticides per total land area in Canada. In 1998, a total of 886 218 kg of pesticides were purchased on PEI, including herbicides, insecticides, and fungicides (1). The use of pesticides in agricultural applications has led to a great deal of controversy and debate on the

Received 22 April 2002. Published on the NRC Research Press Web site at http://canjchem.nrc.ca on 30 August 2002.

B.D. Wagner,[1] A.C. Sherren, and M.A. Rankin.
Department of Chemistry, University of Prince Edward Island, Charlottetown, PEI C1A 4P3, Canada.

[1]Corresponding author (e-mail: bwagner@upei.ca).

 DOI: 10.1139/V02-133 © 2002 NRC Canada

Fig. 1. The structures of: (*a*) AZM, and (*b*) HP-β-CD (R = H or $CH_2CHOHCH_3$).

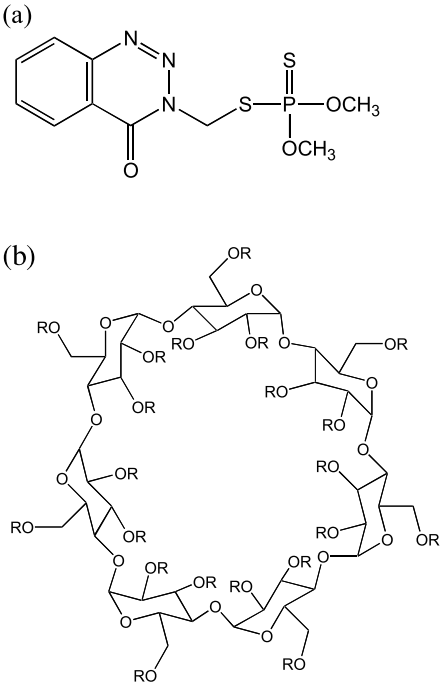

environmental impact of this high pesticide usage, including its impact on human health, drinking water, and ecosystems. Although most of these issues remain unresolved, one easily identifiable negative consequence of pesticide use in this province is the recent epidemic of fish kills in PEI rivers and streams. These incidents have occurred every summer since 1994 (with the exception of 1997), with nine fish kills reported in 1999 alone.[2] Each of these incidents involve the deaths of at least hundreds of fish. Pesticides have been identified as the cause of many of these fish kills; water samples collected from affected areas have shown levels of various pesticides well above the toxic level for fish.[2,3] Many of these incidents occur after heavy rains, which in combination with long-sloping fields and lack of significant buffer zones between cultivated fields and natural waterways, results in large run-offs of pesticide-laden water into rivers and streams.[2,3]

One pesticide which has been identified in the river water samples taken after most of these fish kill incidents is azinphos-methyl (AZM), the structure of which is shown in Fig. 1*a*. AZM is an organophosphorus insecticide, with a relatively long persistence for this type of pesticide (2, 3). It is a highly efficient insecticide and acaricide, and works as both a contact insecticide and a stomach poison (2, 3). It is also highly toxic to nontarget species, with an oral LD_{50} of 4.4–16 mg kg^{-1} for male rats (3). It is a potentially significant contaminant in natural waters, owing to its solubility of 30 ppm (2), and its extremely high toxicity to aquatic organisms. For example, it has a 96 h LC_{50} of 3 ppb for rainbow trout (3). By comparison, in one of the fish-kill incidents studied, which occurred in August 2000, the water sampled after the incident was found to contain AZM at the level of 73.2 ppb[3], well above the toxic threshold. AZM is classed as a Group C pesticide on PEI, with annual sales between 1000 and 9999 kg (compared to Group A pesticides with annual sales over 50 000 kg) (1). Although AZM is not one of the most heavily used pesticides on PEI, its importance in fish kills is a result of its high toxicity to aquatic organisms and its relatively high solubility. In a report entitled *Relative ranking of acute pesticide risks to fish*, published by the PEI Department of Technology and Environment (4), AZM has a rating description of EH (Extremely hazardous), the highest risk ranking. It should be noted that AZM is used not only on PEI, but throughout Canada, for example as an insecticide in apple orchards. The Canadian Environmental Quality Guideline for AZM in water is 20 ppb.

The current method for determination of AZM in natural waters on PEI involves extraction into CCl_4, followed by HPLC. This method has three major disadvantages: the use of an environmentally harmful chlorinated solvent, the relatively high cost of analysis, and the fact that the analysis must be performed in a laboratory. There would be a great advantage to a technique which could be done on-site. Fluorescence has found significant application as the basis for the analysis of other pesticides (5, 6). Furthermore, the recent development of portable, hand-held fluorimeters provides the potential for the development of a fluorescent-based analytical field technique. However, AZM is only weakly fluorescent in aqueous solution. Thus, to use a fluorescence-based analytical technique, sensitive in the ppb region in which AZM can have an environmental impact in natural waters, it is necessary to include some method for enhancing its natural fluorescence. Fluorescence enhancement by cyclodextrins has been previously applied to other pesticides (7–9); this method might also be useful for AZM. There have also been reports of fluorescence enhancement of other pesticides upon exposure to UV radiation, via photolysis to a more fluorescent photoproduct (10–12), as well as a report of decreased fluorescence from a number of aromatic pesticides upon UV irradiation (13). In terms of AZM itself, the only reports of its fluorescence enhancement have been upon base hydrolysis, involving the heating of AZM solutions at high pH and at 85°C for 10 min (14), or at 90°C for 30 min (15). This requirement of heating the solutions at high temperature severely limits the applicability of this fluorescence enhancement method as a field technique.

In this paper we describe three methods by which the weak natural fluorescence of AZM can be enhanced: addition of modified β-cyclodextrins, UV exposure, and high pH (with no heating). Furthermore, we show that the measurement of AZM fluorescence at high pH provides a sensitive and accurate quantitative analytical method with no need for prior heating of the sample, and propose its use in the trace analysis of this pesticide in natural waters, and as the basis for a fluorescence-based field analysis method for AZM.

Experimental

AZM, β-CD, and HP-β-CD were obtained from Aldrich Chemical Company. HP-β-CD is available with various degrees of substitution; the highest substitution available was

[2] Sharrat, S. Deadly combination seen as main reason for fish kills. *The Guardian*. (Charlottetown, PEI). September 18, 1999.
[3] Pesticides blamed for recent fish kills. *The Guardian*. (Charlottetown, PEI). September 1, 2000.

© 2002 NRC Canada

used, namely 1.8 (an average of 1.8 hydroxyls out of the 3 per monomer unit were substituted). All compounds were used as received. Tests of the water content of the CDs showed values of 11.8 and 3.3% for β-CD and HP-β-CD, respectively (based on mass loss after heating for 4 h in a vacuum oven at 180°C). The CDs were not dried before use, however the calculated CD concentrations were corrected using the determined water content values.

Solutions for fluorescence studies were prepared using nanopure distilled and deionized water. Unless otherwise indicated, the concentration of the AZM solutions was 7.6×10^{-6} M; this concentration was chosen as the lowest that would still give a reasonably measurable absorbance at the excitation wavelength used for the fluorescence measurements (see below) and a well-defined fluorescence spectrum. It should be noted that this concentration corresponds to 2.43 ppm, a value much higher than that found for AZM in natural water samples. Nevertheless, this concentration was deemed to be best for these tests of AZM fluorescence enhancement, as it is essential to be able to accurately measure the fluorescence spectrum of AZM in water at neutral pH in the absence of any added cyclodextrin or other treatment for use as a reference. Solutions for studies of the pH dependence of AZM fluorescence were prepared using appropriate aqueous buffer solutions. Solutions for the analysis studies at pH 12 were prepared by adding 0.20 mL of 0.10 M aq NaOH solution to 1.8 mL of the AZM test solution in a fluorescence cuvette, shaking thoroughly, and letting stand for 5 min before measuring the fluorescence spectrum.

Absorption spectra were measured on a Cary 50 Bio UV–vis spectrophotometer. Fluorescence spectra were obtained on a Photon Technology International LS-100 luminescence spectrometer using 1×1 cm^2 quartz fluorescence cells, with an excitation wavelength of 320 nm. This excitation wavelength was chosen as the longest wavelength at which AZM shows a significant absorption band. Excitation at lower wavelengths would be slightly absorbed by added cyclodextrins at high concentrations, and would also be more likely to be absorbed by other species present in natural water samples. The 7.6×10^{-6} M AZM solutions had an absorbance of 0.04 at this wavelength. All spectra were obtained at 21 ± 2°C. Solutions were not oxygen-purged, as preliminary investigations showed a negligible effect of purging on the observed fluorescence intensity (<5%). All fluorescence spectra were baseline corrected by subtraction of the spectrum of a water blank; this procedure also served to remove a water Raman scattering band at ca. 360 nm, which was significant in spectra with low intensity. Fluorescence enhancements (F/F_o) were determined as the ratio of the integrated area under the corrected fluorescence spectrum (I_F vs. wavenumber) of treated AZM (added CD, UV-exposed, or high pH) relative to that of untreated AZM solution.

Results and discussion

Fluorescence enhancement by hydroxypropyl β-cyclodextrin

The fluorescence enhancement of guest molecules upon inclusion into cyclodextrins has been well documented (16). Cyclodextrins (CDs) are cyclic oligosaccharides of glucopyranose (17); a general structure of β-cyclodextrin (the oligomer containing seven glucopyranose units) is shown in Fig. 1*b*, with R = H in the case of the parent β-cyclodextrin. CDs are highly soluble in aqueous solution. More importantly, they have a truncated cone structure in aqueous solution, with a well-defined internal cavity (17). Hydrophobic guest molecules can become included within the relatively less polar CD cavity, forming a supramolecular host–guest inclusion complex. The fluorescence of CD-included guest molecules is often significantly enhanced relative to the fluorescence of the free guest in aqueous solution. This can be the result of a number of factors, the most important being the effect of the decreased polarity of the environment of the guest within the CD cavity, but also including hindrance of rotational motion within the guest molecule, and protection from external quencher species.

Cyclodextrins can be chemically modified, by replacing some or all of the hydroxyl hydrogens by other groups (18). Such chemically modified CDs often have improved properties over their unmodified parents, for example improved solubility, and greater abilities to enhance fluorescence. Recent work in our laboratory has been focused on the enhancement of guest fluorescence by alkyl- and hydroxyalkyl-substituted CDs; we have shown that hydroxypropyl-β-cyclodextrin (HP-β-CD, R = $CH_2CHOHCH_3$ in Fig. 1*b*) in particular provides significantly larger fluorescence enhancement of polarity-sensitive fluorescent probes (in this case anilinonaphthalene sulfonates) than does β-CD itself (19, 20). We proposed this enhancement to be a result of the hydroxypropyl substituents on the rims providing an extended nonpolar cavity, which can therefore bind hydrophobic guests more strongly, as well as providing an even less polar cavity relative to aqueous solution.

In this work, the ability of HP-β-CD to significantly enhance the fluorescence of AZM was investigated, with the goal of using any observed significantly CD-enhanced fluorescence in a trace analysis scheme. Figure 2 shows the fluorescence spectrum of 7.6×10^{-6} M AZM in the absence (*a*) and presence (*b*) of 10 mM HP-β-CD. As can be seen from this figure, significant fluorescence enhancement was observed, with a value of F/F_o of 2.7 in this case, and an

Fig. 2. The fluorescence spectrum of AZM in: (*a*) the absence, and (*b*) the presence of 10 mM HP-β-CD.

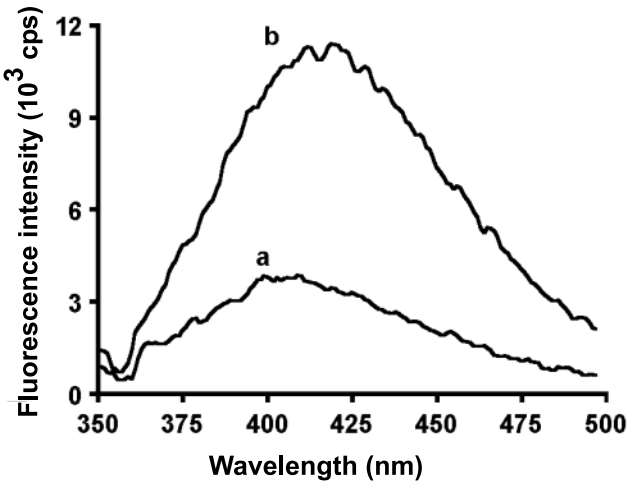

© 2002 NRC Canada

Fig. 3. The fluorescence enhancement F/F_o of M AZM as a function of HP-β-CD concentration. The solid line shows the fit of the experimental data to eq. [1], with F_{max}/F_o = 2.98 and K = 687 M^{-1}. The inset shows the reciprocal–reciprocal plot with a linear fit.

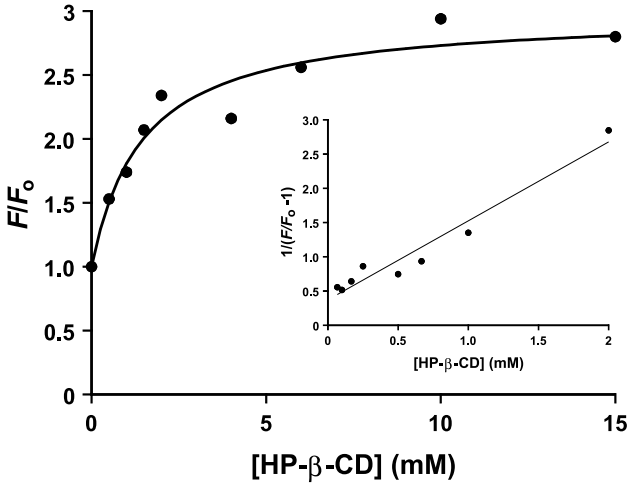

accompanying small red-shift of ca. 15 nm. This result suggests that AZM has become included in the HP-β-CD cavity. Similar studies were also performed using unmodified β-CD: fluorescence enhancement of AZM was also observed, but at lower values, with F/F_o ranging from 1.2 to 1.6. These results confirm our expectation that modified HP-β-CD would provide better enhancement results than the parent β-CD.

The association constant K for the formation of the host–guest inclusion complex from the free host and guest molecules can be obtained by measuring the fluorescence enhancement F/F_o as a function of host concentration, using the equation (21, 22)

$$[1] \qquad F/F_o = 1 + (F_{max}/F_o - 1)\,\frac{[CD]_o K}{1 + [CD]_o K}$$

where F_{max}/F_o is the fluorescence enhancement when all of the guests have been included. Equation [1] assumes that only 1:1 host–guest inclusion complexes are formed. This assumption can be tested using the double-reciprocal plot (or Benesi–Hildebrand plot (23)) of $1/(F/F_o - 1)$ vs. $1/[CD]$; this plot will be linear if only 1:1 complexes form, but will be nonlinear if higher-order complexes form. The double-reciprocal plot, shown as an inset in Fig. 3, is linear, indicating that higher-order complexes are not involved. The fit of the data in Fig. 3 to eq. [1] using the non-linear least-squares method yielded a value of K = 690 ± 140 M^{-1}, and F_{max}/F_o = 2.98 ± 0.30. In terms of reported values of K for other guests in HP-β-CD, this is a moderate to low value.

The maximum enhancement of a factor of 3.0 obtained with HP-β-CD is much too small to be useful for a trace analysis method for AZM in the ppb region. We estimate that significant fluorescence signals could be measured down to ca. 500 ppb at best using this enhanced fluorescence; this is well above the low ppb region required for natural water samples. Furthermore, as can be seen from Fig. 3, there was a fair degree of scatter in the measured values of F/F_o; this scatter is also noticeable in the double-reciprocal plot. Although decent values of F/F_o were obtainable by averaging a number of trials (from 3–5 trials at each CD concentration), this variability was not observed in such experiments performed in our lab with other guests (19, 20). This variability would also limit the applicability of this method in a trace analysis scheme.

Fig. 4. The fluorescence spectrum of AZM recorded immediately upon insertion into the fluorimeter (*a*), and (*b*) after 80 minutes and (*c*) 120 minutes in the fluorimeter.

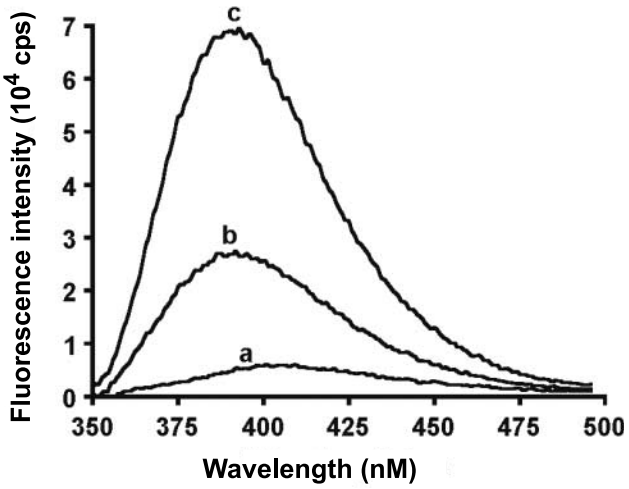

Fluorescence enhancement by UV exposure

It was observed that if the measurement of the fluorescence spectrum of an AZM solution was repeated (i.e. using the same solution in the cuvette), then the subsequently measured fluorescence intensity was larger than that initially measured. It was further noted that the longer the solution was left in the fluorimeter (continuously exposed to the 320 nm excitation light), the larger the fluorescence intensity measurement. This result is illustrated in Fig. 4, which shows the fluorescence spectrum of a single sample of AZM that was left sitting in the fluorimeter sample holder, measured initially and after 80 and 120 min. This figure indicates that a very large enhancement of the AZM fluorescence occurs upon extended absorption of the UV excitation light, much larger than that obtained in the presence of HP-β-CD (as shown in Fig. 2), with a significant blue-shifting of the emission spectrum by ca. 20 nm. These observations were consistent and reproducible. Figure 5 shows a plot of the UV-induced fluorescence enhancement F/F_o (integrated fluorescence intensity relative to that measured initially) of another AZM solution under constant illumination by the fluorimeter excitation lamp at 320 nm, measured over the course of just over 7 hours. As can be seen, the AZM fluorescence intensity was found to increase steadily (except for a spike at 20 min), then level off after ca. 5 hours. This was followed by a slow but continual decrease in intensity. The maximum fluorescence enhancement of 13.1 is significantly larger than the maximum fluorescence enhancement of 3.0 obtained by adding HP-β-CD.

We propose that AZM is photolyzed by UV light, generating a more fluorescent unidentified photoproduct with a blue-shifted spectrum. This hypothesis agrees with the literature reports of UV-induced fluorescence enhancement of

© 2002 NRC Canada

Fig. 5. The integrated fluorescence intensity of AZM as a function of time of exposure to the UV excitation light in the fluorimeter.

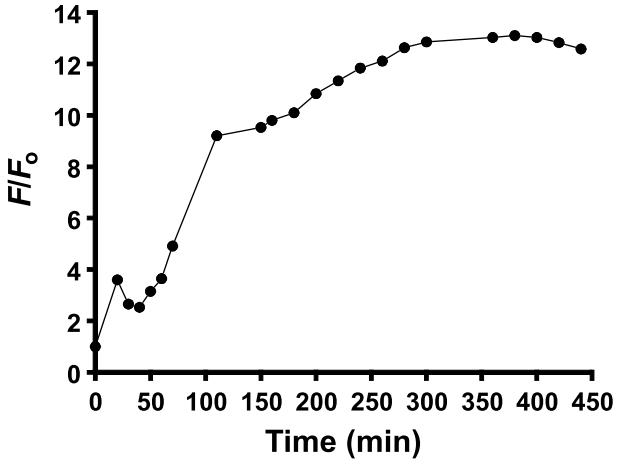

Fig. 6. The peak fluorescence intensity of AZM as a function of pH.

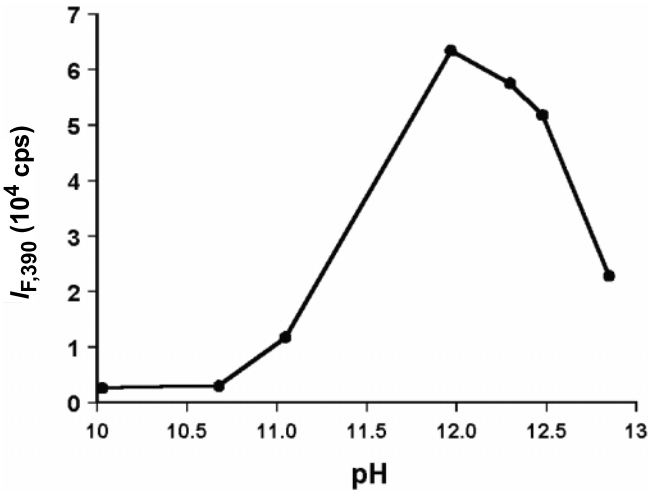

other pesticides (10–12) that also invoke the photochemical formation of a more fluorescent product as the explanation for the observed fluorescence enhancement. The eventual decrease in fluorescence after prolonged UV exposure suggests that this more fluorescent photoproduct is itself subsequently photolyzed. This subsequent photolyzation is also suggested by attempts to enhance the fluorescence of AZM solutions using a hand-held UV lamp. In all cases, no fluorescence was measurable from these solutions, even after short exposures. This lack of fluorescence must be a result of complete photolysis of the AZM to non-fluorescent photoproducts upon exposure to this relatively high intensity UV source. Such complete photolysis clearly takes much longer to occur upon exposure to the much weaker and more monochromatic UV light from the fluorimeter excitation lamp.

The values of the fluorescence enhancements of AZM observed by UV exposure are much larger than those observed by cyclodextrin inclusion, and would potentially be useful in a trace analysis technique for AZM. However, an accurate fluorescence method based on UV-irradiation would require every sample and standard solution to be exposed to exactly the same amount of UV irradiation. This uniformity would be very difficult for a number of reasons, including lamp stability and water transparency (in the case of natural water samples), and would especially be difficult in a field application. Furthermore, the fluorescence signal is actually destroyed if the AZM solution is exposed to too high an amount of UV. For these reasons, application of this observed UV-induced fluorescence enhancement of AZM is considered to be impractical, and was not pursued. However, we do plan to undertake photochemical product and laser flash photolysis studies, to identify the structure of the more fluorescent photoproduct of AZM, as well as the final non-fluorescent photoproducts.

Fluorescence enhancement at high pH

As a final attempt to obtain analytically useful fluorescence enhancement of AZM, the effect of increasing the pH to basic conditions was investigated. This attempt was mainly motivated by the literature reports of significantly enhanced AZM fluorescence at high pH after heating of the AZM solutions at high temperatures (14, 15). This enhanced fluorescence was proposed to be the result of base hydrolysis of AZM to the much more fluorescent compound anthranilic acid, a reaction which was reported to be too slow to be useful at room temperature (14). Our goal was to see whether heating of the samples is in fact required for base hydrolysis and its associated fluorescence enhancement to occur.

Figure 6 shows a plot of the peak fluorescence intensity (at 390 nm) of AZM as a function of pH at room temperature using various buffered solutions. This figure clearly shows a dramatic increase in fluorescence as pH is increased to basic conditions. However, this increased fluorescence begins to decline if the pH is too high. The optimum pH for enhanced AZM fluorescence is shown to be ca. pH 12. Figure 7 shows the fluorescence spectrum of AZM in pure water at neutral pH and at pH 12. In this case (and for all subsequent measurements at pH 12), the solutions were prepared by adding NaOH solution to obtain $[OH^-] = 0.0100$ M (an identical volume of pure water was added to the neutral pH solution), giving pH = 12, with the expected pH confirmed using a pH meter. This method of pH adjustment is more convenient than using a buffer solution, and more importantly can be applied directly to natural water samples. This figure indicates the dramatic fluorescence increase that can be obtained by simply adding the appropriate amount of NaOH to an AZM solution at room temperature. This result is contrary to the literature report described above, which claims that the hydrolysis of AZM is too slow to be useful at room temperature. It is not clear why a different result was obtained in the present study. A comparison of the two spectra in Fig. 7 gives a fluorescence enhancement F/F_o of 300. The emission at pH 12 is also slightly blue-shifted with respect to that at pH 7, by ca. 12 nm. This is a much larger enhancement than was obtained by either CD addition or UV exposure. More importantly, this enhancement is large enough to be potentially useful as the basis for a fluorescence trace analysis method for AZM, as it should result in significant and easily measurable fluorescence signals from AZM, even in the low ppb range.

© 2002 NRC Canada

Fig. 7. The fluorescence spectrum of AZM at: (*a*) pH = 7.0, and (*b*) pH = 12.0.

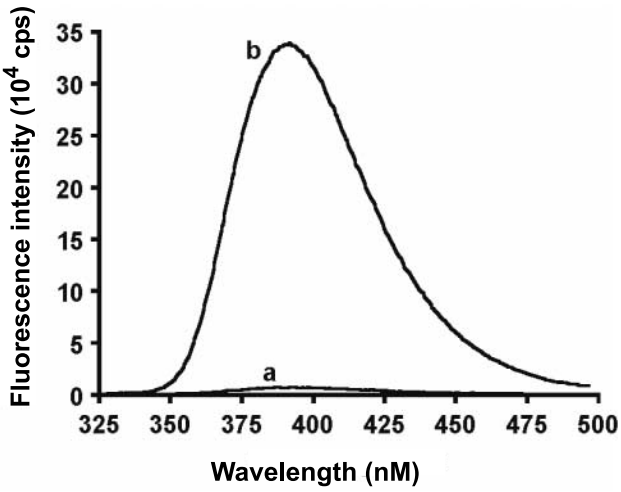

To test the usefulness of this NaOH-hydrolyzed AZM technique, calibration plots of peak fluorescence intensity (I_F at 390 nm) as a function of AZM concentration in the ppb range were constructed. Solutions were carefully prepared using the protocol described in the experimental section. Typical results are shown in Fig. 8 for the 100–500 ppb and 5–100 ppb ranges. Analysis of these calibration plots using linear regression gave the following results:

[2] 100–500 ppb plot: I_F = 596.5 cps/ppb × [AZM] + 5447 cps, r = 0.9997

[3] 5–100 ppb plot: I_F = 616.1 cps/ppb × [AZM] + 2786 cps, r = 0.998

The excellent linearity in these plots throughout the 5 to 500 ppb range shows that this method of fluorescence enhancement could be used to determine AZM concentrations in this range, and thus is potentially useful as the basis for a fluorescence trace analysis method for AZM in natural waters. For example, the concentration of 73.2 ppb reported in a river water sample after a particular fish kill incident could easily and accurately be determined using the calibration plot shown in Fig. 8*b*.

It should be noted that we chose a standard waiting time of 5 min for the solution to hydrolyze before measurement of the fluorescence spectrum, mainly for experimental convenience. Some further fluorescence signal increase was observed past this time, with the intensity leveling off after approximately 30 min. Calibration curves with higher signals were obtained when samples were allowed to hydrolyze for 30 min before the spectrum was measured; however, we did not feel that the higher signals obtained warranted the greatly increased waiting time in the experiment, especially considering the excellent results obtained with the shorter waiting time.

We are currently investigating the application of this NaOH-induced fluorescence enhancement method to the development of a trace analysis method for AZM determination in natural waters. This application will present an additional potential complication, namely unknown fluorescence background signals, which could vary from sample to sample with natural water samples. Thus, comprehensive studies of the fluorescence signal measured from "clean" (i.e. AZM-free) natural water samples must be undertaken first, to see if such background fluorescence of waters from PEI streams will be significant compared to the signals obtained from enhanced AZM fluorescence. It should be noted that there have been numerous reports in the literature of fluorescence detection of various pollutants, including pesticides, in natural waters, in which background fluorescence was found to be insignificant (7–12).

Fig. 8. Calibration curves for the peak intensity of AZM as a function of concentration upon addition of NaOH over two different AZM concentration ranges: (*a*) 100–500 ppb, and (*b*) 5–100 ppb. The solid line is the linear fit of the data, with parameters given in the text.

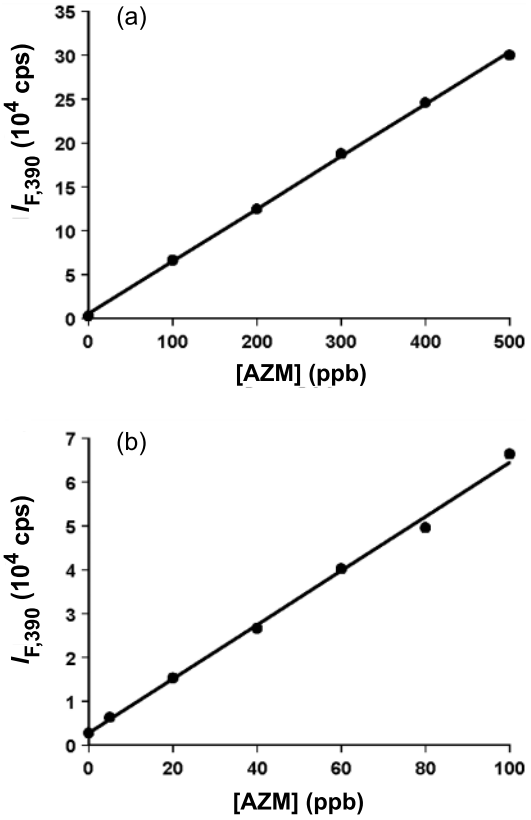

Conclusions

AZM fluorescence is moderately enhanced by the addition of hydroxypropyl-β-cyclodextrin, by a factor of ca. three. However, this enhancement is far too small to be applicable to a fluorescence-based analytical method. AZM fluorescence was found to be more significantly enhanced by exposure to UV radiation (320 nm), presumably by photolysis to a more fluorescent product. However, difficulties in exposing samples to equal UV dosage, especially in the field, would be expected to severely limit the practicality of this enhancement method. Finally, an extremely large AZM fluorescence enhancement of a factor of 300 was obtained at an increased pH of 12.0. This method did not require heating of

© 2002 NRC Canada

the solution as was previously reported in the literature; in fact, the large enhancement could be obtained simply by adding a specific amount of NaOH solution to the sample, mixing, and measuring the fluorescence spectrum. This method was shown to produce calibration curves with excellent linearity, even in the range of 5–100 ppb, the concentration range in which AZM has been shown to exist in natural waters during and just after fish kill incidents. The next phases in this project will involve the application of this high pH-enhanced fluorescence to natural water samples, followed by investigations into the use of a portable fluorimeter for the development of a fluorescence-based field technique for this pesticide. Although the additional complication of unknown levels of background fluorescence from the chemically complicated natural water samples will be present, fluorescence-based techniques for other pesticides have been successfully applied to river water samples.

Acknowledgments

Financial support was provided by the Natural Sciences and Engineering Research Council of Canada (NSERC) and a University Summer Research Assistantship for MAR.

References

1. Pesticide Regulatory Program. Department of Agriculture and Forestry, Government of Prince Edward Island, Canada. 1998 Pesticide Sales Report. July 1999.
2. K.A. Hassall. The biochemistry and use of pesticides. 2nd ed. MacMillan Press, London. 1990.
3. The pesticide management education program at Cornell University. http://pmep.cce.cornell.edu/ [cited March 2002].
4. Department of Technology and Environment, Government of Prince Edward Island, Canada. Relative ranking of acute pesticide risks to fish. December 1999.
5. J.-J. Aaron. Anal. Proc. **30**, 72 (1993).
6. A. Coly and J.-J. Aaron. Talanta, **46**, 815 (1998).
7. J.C. Márquez, M. Hernández, and F. García Sánchez. Analyst (Cambridge U.K.), **115**, 1003 (1990).
8. S. Pandero, A. Gómez-Hens, and D. Pérez-Bendito. Talanta, **40**, 225 (1993).
9. A. Coly and J.-J. Aaron. Anal. Chim. Acta, **360**, 129 (1998).
10. S. Traore and J.J. Aaron. Anal. Lett. **20**, 1995 (1987).
11. C.J. Miles and H.A. Moye. Anal. Chem. **60**, 220 (1988).
12. B.M. Patel, H.A. Moye, and R. Weinberger. Talanta, **38**, 913 (1991).
13. A. Coly and J.-J. Aaron. Analyst (Cambridge U.K.), **119**, 1205 (1994).
14. F. García Sánchez and A. Aguilar Gallardo. Analyst (Cambridge U.K.), **117**, 195 (1992).
15. J.L. Vilchez-Quero, J. Rohand, R. Avidad-Castañeda, A. Navalón, and L.F. Capitán-Vallvey. Fresenius. J. Anal. Chem. **350**, 626 (1994).
16. S. Li and W.C. Purdy. Chem. Rev. **92**, 1457 (1992).
17. J. Szelti. Chem. Rev. **98**, 1743 (1998).
18. A.B. Kahn, P. Forgo, K.J. Stine, and V.T. D'Souza. Chem. Rev. **98**, 1977 (1998).
19. B.D. Wagner and P.J. MacDonald. J. Photochem. Photobiol. A, **114**, 151 (1998).
20. B.D. Wagner and S.J. Fitzpatrick. J. Inclusion Phenom. Macrocyclic Chem. **38**, 467 (2000).
21. A. Muñoz de la Peña, F. Salinas, M.J. Gómez, M.I. Acedo, and M. Sánchez Peña. J. Inclusion Phenom. Mol. Recognit. Chem. **15**, 131 (1993).
22. C.N. Sanramé, R.H. de Rossi, and G.A. Argüello. J. Phys. Chem. **100**, 8151 (1996).
23. H.A. Benesi and H. Hildebrand. J. Am. Chem. Soc. **71**, 2703 (1949).

© 2002 NRC Canada

Synthesis and reactivity of palladium and platinum diimine complexes containing boronate esters

Arienne S. King, Liliya G. Nikolcheva, Christopher R. Graves, Anna Kaminski, Christopher M. Vogels, Robert H.E. Hudson, Robert J. Ireland, Stephen J. Duffy, and Stephen A. Westcott

Abstract: Condensation of α-diketones (2,3-butanedione, benzil, and acenaphthenequinone) with 3-$H_2NC_6H_4Bpin$ (pin = 1,2-$O_2C_2Me_4$) gave the corresponding boron-containing α-diimines. The addition of these ligands to $[MCl_2(coe)]_2$ (coe = *cis*-cyclooctene, M = Pd or Pt) gave complexes of the type *cis*-MCl_2(α-diimine) in moderate to high yields. The platinum complexes have been examined for their ability to bind to DNA using enzyme digest studies. These complexes were found to bind to single-stranded DNA as well as, or better than, the non-boron containing controls, and showed binding similar to that of cisplatin (*cis*-$PtCl_2(NH_3)_2$).

Key words: boronate esters, diazabutadienes, DNA-binding, platinum.

Résumé : La condensation d'α-dicétones (butane-2,3-dione, benzile, et acénaphtènequinone) avec le 3-$H_2NC_6H_4Bpin$ (pin = 1,2-$O_2C_2Me_4$) conduit à la formation d'α-diimines contenant du bore. L'addition de ces ligands au $[MCl_2(coe)]_2$ (coe = *cis*-cyclooctène; M = Pd, Pt) fournit des complexes du type *cis*-MCl_2(α-diimine) avec des rendements allant de modérés à élevés. Faisant appel à des études de digestion d'enzymes, on a évalué la capacité de ces complexes du platine à se fixer sur l'ADN. Vis-à-vis de l'ADN à brin unique, ces complexes se fixent aussi bien, ou mieux, que les contrôles ne contenant pas de bore et leur taux de fixation est semblable à celui du cisplatine, *cis*-$PtCl_2(NH_3)_2$.

Mots clés : esters de l'acide boronique, diazabutadiènes, fixation de l'ADN, platine.

[Traduit par la Rédaction]

Introduction

Interest in compounds containing boronic acids $[RB(OH)_2]$ or boronate esters $[RB(OR')_2]$ arises from their remarkable versatility in organic synthesis (1) as well as from their potent biological activities (2–11). As part of our ongoing program generating novel boron compounds (12), we decided to examine the synthesis and reactivity of a series of α-diimines containing boronate esters.

1,4-Diazabutadienes (α-diimines) have both been used extensively as ligands for transition metals, owing to their ease of preparation and ability to fine-tune both steric and electronic properties (13). The resulting coordination complexes have been utilized in organic synthesis and catalysis (13–20) and as luminescence labels for the detection and photochemical cleavage of DNA (21). Diazabutadienes have also been used in dehalosilylation – ring-closure reactions of $SbCl_3$ and $BiCl_3$ to give the corresponding 1,2,5-pnictadiazoles (22). Some of the unique chemical and physical properties observed for metal diimine complexes have been attributed to the relatively strong π-acceptor ability of the diazabutadiene ligands, resulting from an energetically low-lying LUMO (23). Although fluorinated α-diimines have recently been prepared (24), to the best of our knowledge no such systems containing boronate esters have been reported. Diimines containing these electron-withdrawing groups would be expected to possess low lying LUMOs, and consequently, be strong π-acceptors. The results of our initial investigations into preparing these compounds, and the corresponding palladium and platinum complexes, are presented herein.

Received 7 June 2002. Published on the NRC Research Press Web site at http://canjchem.nrc.ca on 30 August 2002.

A.S. King, **L.G. Nikolcheva**, **C.R. Graves**, **C.M. Vogels**, **S.J. Duffy, and S.A. Westcott.**[1] Department of Chemistry, Mount Allison University, Sackville, NB E4L 1G8, Canada. **R.J. Ireland.** Department of Biology and Biochemistry, Mount Allison University, Sackville, NB E4L 1G7, Canada. **A. Kaminski and R.H.E. Hudson**. Department of Chemistry, The University of Western Ontario, London, ON N6A 5B7, Canada.

[1]Corresponding author (e-mail: swestcott@mta.ca).

Experimental

The reagents and solvents used were obtained from Aldrich Chemicals. NMR spectra were recorded on a JEOL JNM-GSX270 FT-NMR spectrometer. ^{1}H NMR chemical shifts are reported in ppm and referenced to residual protons in deuterated solvent at 270 MHz. ^{11}B NMR chemical shifts are referenced to external $F_3B{\cdot}OEt_2$ at 87 MHz. ^{13}C NMR chemical shifts are referenced to solvent carbon resonances as internal standards at 68 MHz. Multiplicities are reported as (s) singlet, (d) doublet, (t) triplet, (q) quartet, (m) multiplet, (br) broad, and (ov) overlapping. Infrared spectra were obtained using a Mattson Genesis II FT-IR spectrometer, and are reported in cm^{-1}. Melting points were measured (uncorrected) with a Mel-Temp apparatus. Microanalyses for C, H, and N were carried out at Desert Analytics (Tucson,

 DOI: 10.1139/V02-145 © 2002 NRC Canada

AZ) and CMA (Vancouver, BC). All reactions were carried out in ambient conditions and the products were found to be stable indefinitely under those circumstances. Polymerization experiments were done by Dr. Marc Kristen (Basell Polyolefin GmbH).[2]

Synthesis

1,4-Bis[3-(4,4,5,5-tetramethyl-1,3,2-dioxaborolan-2-yl)-phenyl]-2,3-dimethyl-1,4-diaza-1,3-butadiene (1a)

An EtOH solution (5 mL) of 3-$H_2NC_6H_4$Bpin (3-APBpin (pin = 1,2-$O_2C_2Me_4$)) (1.67 g, 7.62 mmol) was added dropwise to 2,3-butanedione (0.30 g, 3.48 mmol) in EtOH (3 mL). Following the addition of formic acid (1 drop), the reaction was heated at reflux (4 h) and then stored at 0°C, whereupon a beige precipitate formed, which was collected by suction filtration and washed with hexane (3 × 10 mL). Yield: 1.10 g (65%); mp 225–227°C. IR (Nujol) (cm^{-1}): 2937, 2912, 2856, 1637, 1599, 1570, 1483, 1464, 1417, 1358, 1321, 1265, 1201, 1140, 1076, 966, 901, 881, 849, 804, 779, 714, 706, 671. ^{1}H NMR ($CDCl_3$) δ: 7.54 (d, *J* = 8 Hz, 2H, Ar), 7.36 (ov dd, *J* = 8 Hz, 2H, Ar), 7.22 (br s, 2H, Ar), 6.85 (br d, *J* = 8 Hz, 2H, Ar), 2.11 (s, 6H, N=C(CH_3)), 1.34 (s, 24H, BO_2(CH_3)$_4$). ^{13}C NMR δ: 168.3, 150.5, 130.2, 130 (br, C-B), 128.5, 124.9, 121.6, 83.9, 25.0, 15.5. ^{11}B NMR δ: 31 (br).

1,4-Bis[3-(4,4,5,5-tetramethyl-1,3,2-dioxaborolan-2-yl)-phenyl]-2,3-diphenyl-1,4-diaza-1,3-butadiene (1b)

A CH_2Cl_2 solution (10 mL) of 3-APBpin (1.17 g, 5.35 mmol) was added dropwise to benzil (0.50 g, 2.38 mmol) in methylene chloride (10 mL). Activated molecular sieves (10 g) were added and the reaction was heated at reflux for 24 h. The molecular sieves were removed by suction filtration and washed with CH_2Cl_2 (3 × 10 mL). Removal of the solvent under vacuum gave an oil that was triturated with cold Et_2O (10 mL) to afford a yellow solid. Yield: 0.87 g (60%); mp 224°C. IR (Nujol) (cm^{-1}): 2915, 2856, 1620, 1461, 1376, 1315, 1268, 1142, 1071, 965, 899, 853, 785, 697. ^{1}H NMR ($CDCl_3$) δ: 7.88 (br d, *J* = 8 Hz, 4H, Ar), 7.46–7.35 (ov m, 8H, Ar), 7.06 (ov dd, *J* = 8 Hz, 2H, Ar), 6.97 (br s, 2H, Ar), 6.56 (br d, *J* = 8 Hz, 2H, Ar), 1.26 (s, 12H, BO_2(CH_3)$_4$), 1.22 (s, 12H, BO_2(CH_3)$_4$). ^{13}C NMR δ: 164.4, 148.8, 138.0, 131.0, 130.9, 130 (br, C-B), 128.7, 128.4, 127.8, 126.7, 122.9, 83.6, 24.9, 24.8. ^{11}B NMR δ: 31 (br).

1,4-Bis[3-(4,4,5,5-tetramethyl-1,3,2-dioxaborolan-2-yl)-phenyl]-2,3-acenaphthene-1,4-diaza-1,3-butadiene (1c)

A CH_2Cl_2 solution (10 mL) of 3-APBpin (1.20 g, 5.49 mmol) was added dropwise to acenaphthenequinone (0.50 g, 2.74 mmol) in CH_2Cl_2 (10 mL), in the presence of activated molecular sieves (10 g). The reaction was allowed to proceed at room temperature for 12 days, at which point the sieves were removed by suction filtration and the solution was washed with CH_2Cl_2 (3 × 10 mL). Removal of the solvent under vacuum gave an oily mixture that was triturated with Et_2O (3 × 5 mL) to afford an orange solid. Yield: 1.11 g (70%); mp 245°C. IR (Nujol) (cm^{-1}): 2974, 2882, 2843, 1666, 1644, 1594, 1568, 1461, 1415, 1359, 1315, 1271, 1231, 1143, 1098, 1072, 1045, 964, 943, 871, 850, 783, 703. ^{1}H NMR ($CDCl_3$) δ: 7.85 (d, *J* = 8 Hz, 2H, Ar), 7.69 (d, *J* = 8 Hz, 2H, Ar), 7.55 (s, 2H, Ar), 7.46 (ov dd, *J* = 8 Hz, 2H, Ar), 7.33 (ov dd, *J* = 8 Hz, 2H, Ar), 7.20 (br d, *J* = 8 Hz, 2H, Ar), 6.78 (d, *J* = 8 Hz, 2H, Ar), 1.33 (s, 24H, BO_2(CH_3)$_4$). ^{13}C NMR δ: 161.2, 151.4, 141.8, 131.2, 130.7, 130 (br, C-B), 128.8 (2C), 128.7, 127.7, 124.3, 124.1, 121.2, 83.9, 25.0. ^{11}B NMR δ: 30 (br).

(1,4-Bis[3-(4,4,5,5-tetramethyl-1,3,2-dioxaborolan-2-yl)-phenyl]-2,3-dimethyl-1,4-diaza-1,3-butadiene)dichloropalladium(II) (2a)

To a stirred CH_2Cl_2 solution (10 mL) of [$PdCl_2$(coe)]$_2$ (0.10 g, 0.17 mmol), **1a** (0.18 g, 0.37 mmol) in CH_2Cl_2 (5 mL) was added dropwise. The reaction was allowed to proceed for 18 h, at which point the solvent was removed under vacuum to afford an orange solid, which was then triturated with Et_2O (3 × 10 mL). Yield: 0.19 g (84%); mp 200–202°C (decomp.). IR (Nujol) (cm^{-1}): 2943, 2904, 2870, 1603, 1462, 1427, 1358, 1311, 1269, 1140, 1076, 964, 858, 704. ^{1}H NMR ($CDCl_3$) δ: 7.76 (br d, *J* = 8 Hz, 2H, Ar), 7.54 (br ov m, 2H, Ar), 7.38 (br ov m, 4H, Ar), 2.13 (br s, 6H, N=C(CH_3)), 1.34 (s, 24H, BO_2(CH_3)$_4$). ^{13}C NMR δ: 179.6, 145.0, 134.4, 129.8 (br, C-B), 128.9, 128.3, 126.1, 84.2, 25.1, 21.2. ^{11}B NMR δ: 31 (br). Anal. calcd. for $PdCl_2C_{28}H_{38}N_2B_2O_4$: C 50.51, H 5.77, N 4.21; found: C 49.94, H 5.87, N 4.16.

(1,4-Bis[3-(4,4,5,5-tetramethyl-1,3,2-dioxaborolan-2-yl)-phenyl]-2,3-diphenyl-1,4-diaza-1,3-butadiene)dichloropalladium(II) (2b)

A CH_2Cl_2 solution (5 mL) of **1b** (0.12 g, 0.20 mmol) was added dropwise to a stirred solution of [$PdCl_2$(coe)]$_2$ (0.05 g, 0.09 mmol) in CH_2Cl_2 (10 mL). The reaction was allowed to proceed for 6 h, at which point the solvent was removed under vacuum to afford an orange solid. The solid was triturated with Et_2O (3 × 10 mL). Yield: 0.11 g (77%); mp 214–216°C (decomp.). IR (Nujol) (cm^{-1}): 2937, 2868, 1601, 1462, 1423, 1377, 1358, 1319, 1271, 1142, 1074, 999, 852, 723, 700, 561. ^{1}H NMR ($CDCl_3$) δ: 7.52 (br d, *J* = 8 Hz, 4H, Ar), 7.38 (br d, *J* = 8 Hz, 2H, Ar), 7.08–6.92 (br ov m, 12H, Ar), 1.29 (s, 24H, BO_2(CH_3)$_4$). ^{13}C NMR δ: 178.6, 145.4, 134.0, 132.2, 130.3, 130 (br, C-B), 129.9, 128.7, 127.9, 127.6, 127.3, 84.0, 25.0. ^{11}B NMR δ: 31 (br). Anal. calcd. for $PdCl_2C_{38}H_{42}N_2B_2O_4$: C 57.78, H 5.37, N 3.55; found: C 56.94, H 5.31, N 3.49.

(1,4-Bis[3-(4,4,5,5-tetramethyl-1,3,2-dioxaborolan-2-yl)-phenyl]-2,3-acenaphthene-1,4-diaza-1,3-butadiene)dichloropalladium(II) (2c)

A CH_2Cl_2 solution (5 mL) of **1c** (0.11 g, 0.19 mmol) was added dropwise to a stirred solution of [$PdCl_2$(coe)]$_2$ (0.05 g, 0.09 mmol) in CH_2Cl_2 (10 mL). The reaction was allowed to proceed for 6 h, whereupon removal of the solvent under vacuum afforded an orange solid, which was triturated with Et_2O (3 × 5 mL). Yield: 0.11 g (80%); mp 338°C (decomp.). IR (Nujol) (cm^{-1}): 2967, 2945, 2894, 2871, 2847, 1599, 1579, 1461, 1376, 1359, 1141, 971, 735, 701. ^{1}H NMR

[2] Supplementary material may be purchased from the Depository of Unpublished Data, Document Delivery, CISTI, National Research Council Canada, Ottawa, ON K1A 0S2, Canada (http://www.nrc.ca/cisti/irm/unpub_e.shtml).

© 2002 NRC Canada

($CDCl_3$) δ: 8.09 (d, *J* = 8 Hz, 2H, Ar), 7.93 (d, *J* = 8 Hz, 2H, Ar), 7.78 (br s, 2H, Ar), 7.59 (ov dd, *J* = 8 Hz, 2H, Ar), 7.49–7.43 (ov m, 4H, Ar), 6.73 (d, *J* = 8 Hz, 2H, Ar), 1.33 (s, 24H, $BO_2(CH_3)_4$). ^{13}C NMR (in DMF) δ: 177.4, 147.9, 146.1, 135.0, 133.0, 132.2, 131.0 (br, C-B), 129.7, 129.5, 129.1, 126.7, 126.1, 126.0, 84.9, 25.2. ^{11}B NMR δ: 29 (br). Anal. calcd. for $PdCl_2C_{36}H_{38}N_2B_2O_4$: C 56.76, H 5.04, N 3.68; found: C 56.94, H 5.08, N 3.90.

(1,4-Bis[3-(4,4,5,5-tetramethyl-1,3,2-dioxaborolan-2-yl)-phenyl]-2,3-dimethyl-1,4-diaza-1,3-butadiene)dichloroplatinum(II) (3a)

A CH_2Cl_2 solution (5 mL) of **1a** (0.14 g, 0.29 mmol) was added dropwise to a stirred solution of $[PtCl_2(coe)]_2$ (0.10 g, 0.13 mmol) in CH_2Cl_2 (10 mL). The reaction was allowed to proceed for 18 h, at which point the solvent was removed under vacuum to give an oily solid. The mixture was triturated with Et_2O (4 × 5 mL) to afford an orange solid. Yield: 0.15 g (76%); mp 204°C (decomp.). IR (Nujol) (cm^{-1}): 2943, 2908, 2870, 1603, 1462, 1377, 1358, 1313, 1269, 1213, 1142, 1076, 964, 858, 806, 704, 677. ^1H NMR ($CDCl_3$) δ: 7.78 (br d, *J* = 8 Hz, 2H, Ar), 7.56–7.31 (br ov m, 6H, Ar), 1.76 (s, 6H, N=C(CH_3)), 1.33 (s, 24H, $BO_2(CH_3)_4$). ^{13}C NMR δ: 178.1, 145.1, 134.6, 130 (br, C-B), 128.4, 128.1, 126.5, 84.2, 25.1, 21.0. ^{11}B NMR δ: 31 (br). Anal. calcd. for $PtCl_2C_{28}H_{38}N_2B_2O_4$: C 44.58, H 5.09, N 3.71; found: C 44.78, H 5.38, N 3.63.

(1,4-Bis[3-(4,4,5,5-tetramethyl-1,3,2-dioxaborolan-2-yl)-phenyl]-2,3-diphenyl-1,4-diaza-1,3-butadiene)dichloroplatinum(II) (3b)

A CH_2Cl_2 solution (5 mL) of **1b** (0.20 g, 0.33 mmol) was added dropwise to a stirred solution of $[PtCl_2(coe)]_2$ (0.12 g, 0.16 mmol) in CH_2Cl_2 (10 mL). The reaction was allowed to proceed for 4 h, at which point the solvent was removed under vacuum to afford an oil, which was triturated with Et_2O (3 × 5 mL) and hexane (4 × 5 mL) to afford a red solid. Yield: 0.17 g (60%); mp 278°C (decomp.). IR (Nujol) (cm^{-1}): 2945, 2902, 2872, 1603, 1462, 1377, 1358, 1325, 1271, 1144, 1076, 964, 854, 700, 567. ^1H NMR ($CDCl_3$) δ: 7.56 (br d, *J* = 8 Hz, 4H, Ar), 7.41 (br ov m, 4H, Ar), 7.07–6.81 (br ov m, 10H, Ar), 1.29 (s, 24H, $BO_2(CH_3)_4$). ^{13}C NMR δ: 178.3, 145.7, 134.1, 132.9, 131.3, 130 (br, C-B), 129.5, 128.1, 127.8 (2C), 127.2, 84.0, 25.0. ^{11}B NMR δ: 31 (br). Anal. calcd. for $PtCl_2C_{38}H_{42}N_2B_2O_4$: C 51.95, H 4.83, N 3.19; found: C 51.57, H 4.61, N 3.22.

(1,4-Bis[3-(4,4,5,5-tetramethyl-1,3,2-dioxaborolan-2-yl)-phenyl]-2,3-acenaphthene-1,4-diaza-1,3-butadiene)dichloroplatinum(II) (3c)

A CH_2Cl_2 solution (5 mL) of **1c** (0.16 g, 0.27 mmol) was added dropwise to a stirred solution of $[PtCl_2(coe)]_2$ (0.10 g, 0.13 mmol) in CH_2Cl_2 (10 mL). The reaction was allowed to proceed for 4 h, at which point the solvent was removed under vacuum. The resultant oily solid was triturated with Et_2O (3 × 10 mL) to afford a red solid. Yield: 0.17 g (77%); mp 350°C (decomp.). IR (Nujol) (cm^{-1}): 2924, 2855, 1600, 1420, 1358, 1303, 1210, 1145, 967, 856, 777, 703. ^1H NMR ($CDCl_3$) δ: 8.24 (d, *J* = 8 Hz, 2H, Ar), 7.96 (d, *J* = 8 Hz, 2H, Ar), 7.88 (br s, 2H, Ar), 7.67–7.57 (ov m, 4H, Ar), 7.40 (ov dd, *J* = 8 Hz, 2H, Ar), 6.89 (br d, *J* = 8 Hz, 2H, Ar), 1.33 (s, 24H, $BO_2(CH_3)_4$). ^{13}C NMR δ: 175.6, 147.2, 144.5, 135.6, 132.2, 131.0, 130 (br, *C*-B), 129.7, 129.1, 128.8, 126.3, 126.1, 124.5, 84.2, 25.0. ^{11}B NMR δ: 30 (br). Anal. calcd. for $PtCl_2C_{36}H_{38}N_2B_2O_4$: C 50.84, H 4.51, N 3.29; found: C 50.44, H 4.69, N 3.40.

Nuclease digest studies

Binding of the platinum complexes to DNA was investigated using enzymatic degradation of the DNA to nucleosides. Nucleosides were detected using reverse-phase HPLC. The sequence of the model 20-mer DNA strand used in this study (eq. [1]) has two predominant cisplatin-binding-sites: TGGT on one strand and AGGA on the complementary strand. Both the single and the double DNA strands were incubated with each platinum complex, in a 1:3 DNA:Pt molar ratio, for 24 h, in the dark. Samples (2.0 nmol of single-stranded and 1.0 nmol of double-stranded DNA) were digested in series with DNAse I (Amersham Biosciences) (36 U, 4 h), nuclease P1 (Sigma) (10 U, 18 h), and alkaline phosphatase (Promega) (20 U, 4 h), at 37°C, to convert the DNA strand into mononucleosides. The samples were heated to 90°C for 2 min, centrifuged at 10 000 g for 30 s, and then the protein pellet was discarded. The nucleoside composition in each sample was analyzed at 254 nm on a C_{18} column, using a Pro-Star RP-HPLC (Varian). The isocratic solvent system used was Et_3NH–OAc (93%, 20 mM, pH 6.5) and CH_3CN (7%, 1 mL min^{-1}). The areas under the nucleoside peaks were integrated and the G:C ratio analyzed and compared with ANOVA, followed by post-hoc multiple comparisons with Bonferonni's adjustment.

[1] 5′ T C T C C T T C **T G G T** C T C T T C T C 3′
3′ A G **A G G A** A G A C C A G A G A A G A G 5′

Equation [1] illustrates the sequence of the DNA 20-mer used in the binding studies. Possible platinum binding sites are shown in bold type.

Results and discussion

Diimines

Protection of the boronic acid groups in commercially available 3-aminophenylboronic acid (3-$H_2NC_6H_4B(OH)_2$), by transesterification with pinacol ($HOCMe_2CMe_2OH$) to prevent unwanted formation of anhydrides (25), gave quantitative formation of aminoboronate ester 3-$H_2NC_6H_4$Bpin (3-APBpin (pin = $O_2C_2Me_4$)) (12). Unfortunately, the addition of 3-APBpin to glyoxal gave complex product distributions, as evidenced by ^1H NMR spectroscopy, and isolation of the corresponding boron-containing diazabutadiene proved unsuccessful. This result is not surprising as previous studies have shown that glyoxal reacts with electron-deficient amines, such as 3-nitroaniline, to give high yields of 1,2-dihydroxy-1,2-diamino compounds (26). Conversely, we found that reactions of 3-APBpin proceeded smoothly with substituted α-diketones, 2,3-butanedione, benzil, and acenaphthenequinone, to give the corresponding boron-containing α-diimines (**1a**–**1c**) in moderate yields (Fig. 1). All diazabutadienes were characterized by multinuclear NMR spectroscopy. A peak at ca. δ 30 ppm in the ^{11}B NMR spectra is indicative of a three-coordinate boron atom, which suggests that no appreciable intermolecular interaction

© 2002 NRC Canada

Fig. 1. α-Diimines derived from 3-APBpin.

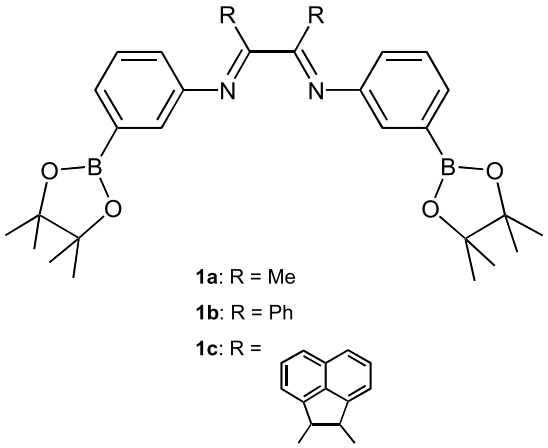

occurs with the basic imine functionality in solution (27). Although one boron resonance is observed for **1b**, it is interesting to note that two separate peaks are observed for the Bpin methyl groups in the ^{1}H NMR spectra, presumably arising from the perpendicular phenyl groups in the backbone. It is plausible that restricted rotation about the B–C bond causes this loss of symmetry.

Palladium complexes

To examine the potential of these electron withdrawing diimines to act as ligands, we have prepared palladium complexes **2a**–**2c** by the addition of **1a**–**1c** to organic-soluble $[PdCl_2(coe)]_2$ (28, Fig. 2). Indeed, complexes **2a**–**2c** were prepared in high yield and characterized using a number of physical methods, including multinuclear NMR spectroscopy. The boron atom appears to maintain its three-coordinate geometry in solution, as evidenced by a peak at 30 ppm in the ^{11}B NMR spectra. Coincidentally, only one peak is observed for the Bpin methyl groups in the ^{1}H NMR spectra for **2b**.

Electrophilic 1,4-diazabutadiene palladium complexes have found extensive application as catalysts in the polymerization of alkynes (29) and alkenes (14, 30–34). Unfortunately, attempts to catalyze the polymerization of ethylene using complexes **2a**–**2c** proved unsuccessful. Although the addition of electron-withdrawing boronate ester groups should enhance polymerization activities, previous studies have shown that palladium diimine complexes also require bulky substituents in the ortho- position of the *N*-aryl group to be effective catalysts. Indeed, complexes lacking this steric requirement are known to give oligomerization products (14). It appears that the boronate ester groups in **2a**–**2c** are too far removed from the metal center to provide the steric requirement needed for polymerization. Future studies will, therefore, concentrate on designing analogous diimine catalysts derived from 2-APBpin (35).

Platinum complexes

Cisplatin (*cis*-$PtCl_2(NH_3)_2$) is one of the most effective chemotherapeutic agents currently used for the treatment of ovarian, bladder, and testicular cancer (36–44). The drug has to be administered intravenously, however, and has dose-limiting side effects such as severe renal toxicity, neurotoxicity, and emesis, arising, in part, from the low solubility of cisplatin in water. These problems, along with the fact that cancer cells treated with cisplatin acquire resistance to the drug, have resulted in considerable research focussed on the development of a more effective platinum drug that can be administered orally and with reduced side effects. Cisplatin acts by making intra- and interstrand cross-links with DNA, which result in a halt of replication and lead to programmed cell death. Structural analogues of cisplatin, however, react with DNA in a way similar to the parent drug and therefore cause similar biological effects (36). In fact, to be considered for clinical evaluation, a new platinum drug should have an activity different from that of cisplatin and thereby eliminate multi-factorial drug resistance. Therefore, it is highly unlikely that future platinum drug candidates will adhere to the classical structure-activity relationships for cisplatin analogues. Toward this objective, we have prepared platinum complexes (**3a**–**3c**) containing α-diimines by addition to $[PtCl_2(coe)]_2$ (45, Fig. 2). The use of bidentate ligands prevents trans labilization and undesired displacement of the ligands by sulfur and nitrogen donors in biomolecules, interactions that are believed to be responsible for the adverse side effects associated with cisplatin (42).

Interactions of platinum complexes with DNA

As the efficacy of platinum-based anticancer drugs is believed to arise from the coordination of the metal to DNA (43), we decided to examine the binding potential of plati-

Fig. 2. Preparation of metal complexes.

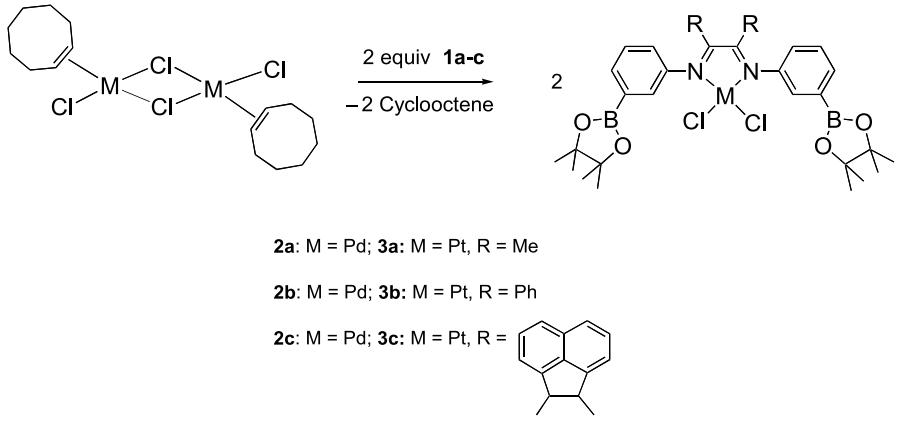

© 2002 NRC Canada

Fig. 3. The G:C ratio from the nuclease digests of single-stranded 20-mer DNA. Values are mean ±95%CI (n = 10). Complex **4c** is not significantly different from the non-platinum control at $p > 0.05$.

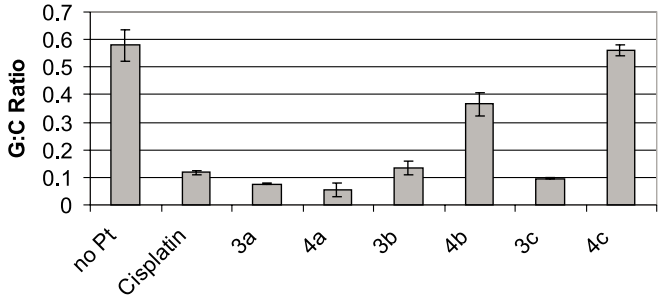

Fig. 4. The G:C ratio from the nuclease digests of double-stranded 20-mer DNA. Values are mean ±95%CI (n = 10). Complexes **3b**, **4b**, and **4c** are not significantly different from the non-platinum control at $p > 0.05$.

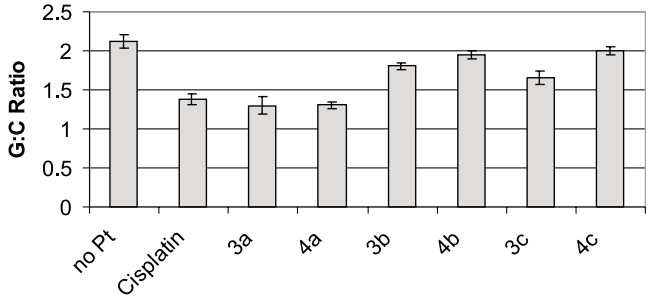

num complexes **3a**–**3c** using a 20-bp strand (46). This DNA model contains one preferential binding site (a TGGT motif) in the single strand and a second binding site (AGGA) on the complementary strand. The degree of platinated DNA can be quantified by enzymatically degrading the DNA strand and separating the mononucleosides and Pt-containing dinucleotides using reverse-phase HPLC (47–49). Platinum binding will result in the formation of *cis*-[Pt(diimine){d(GpG)}], and the amount of free guanosine can, therefore, be negatively correlated to the degree of platinated DNA. Cytosine can be used as an internal standard because its concentration is not affected by platinated DNA (50–52).

As expected, the nuclease digest results showed that treatment with cisplatin significantly decreased the G:C ratio (compared to the unplatinated control) in both single-stranded (Fig. 3) and double-stranded DNA (Fig. 4), and confirmed that cisplatin binds well to both types of DNA. The binding affinity for single-stranded DNA was also found to decrease as the size of the backbone of the non-boron diimine compounds (**4a**–**4c**, 14) increased. This result was also evident in the double-stranded samples. It is possible that the larger, more sterically-hindered backbones of **4b** and **4c** do not fit into the binding site and are therefore excluded from the major groove of double-stranded DNA. Remarkably, the boron-containing compounds (**3a**–**3c**) bound to single-stranded DNA as well as, or better than, the non-boron controls, and exhibited binding capabilities not significantly different from those of cisplatin. Binding among the boron complexes could not be correlated with the size of the backbone. These results suggest that the boronate ester may indeed contribute to the increased affinity of these compounds to bind to single-stranded DNA. Compound **3b** showed significant binding to single-, but not to double-stranded DNA; presumably, the flexibility of the DNA single-strand was sufficient to allow access to the binding site, but the complex could not fit into the major groove of the helix in the double-stranded DNA. This binding difference may provide higher selectivity in rapidly dividing cancer cells, where the DNA is replicated at a higher rate, and, as a result, is more often in the single-stranded form. Achieving significant binding to single-, but not to double-stranded DNA, might provide a solution to the problems associated with current platinum therapies. Future work in this area will examine the cytotoxicities of compounds **3a**–**3c**, and relate these findings to binding studies in an effort to design more potent and less toxic platinum complexes for the treatment of cancer.

Conclusion

α-Diimines, derived from the condensation of substituted α-diketones and aminoboronate ester 3-$H_2NC_6H_4$Bpin (pin = $O_2C_2Me_4$), have been prepared in moderate yield and used as ligands for palladium and platinum. The platinum complexes have been studied for their ability to bind to DNA. The boron-containing complexes bound to single-stranded DNA as well as, or better than, the non-boron containing controls, and showed binding not significantly different from that of cisplatin.

Acknowledgements

Thanks are gratefully extended to the Research Corporation (Cottrell College Science Award), Natural Sciences and Engineering Council of Canada (NSERC), Canada Research Chairs program (CRC), the University of Western Ontario, and Mount Allison University for financial support. We also thank Dan Durant (MAU) for expert technical assistance, Dr. Marc Ö. Kristen (Basell Polyolefine GmbH) for conducting polymerization studies, and anonymous reviewers for helpful comments.

References

1. N. Miyaura and A. Suzuki. Chem. Rev. **95**, 2457 (1995).
2. C. Morin. Tetrahedron, **50**, 12 521 (1994).
3. G.S. Weston, J. Blázquez, F. Baquero, and B.K. Shoichet. J. Med. Chem. **41**, 4577 (1998).
4. V.S. Stoll, B.T. Eger, R.C. Hynes, V. Martichonok, J.B. Jones, and E.F. Pai. Biochemistry, **37**, 451 (1998).
5. J. Adams, M. Behnke, S. Chen, A.A. Cruickshank, L.R. Dick, L. Grenier, J.M. Klunder, Y. Ma, L. Plamondon, and R.L. Stein. Bioorg. Med. Chem. Lett. **8**, 333 (1998).
6. C. Gao, B.J. Lavey, C.L. Lo, A. Datta, P. Wentworth Jr., and K.D. Janda. J. Am. Chem. Soc. **120**, 2211 (1998).
7. W. Han, J.C. Pelletier, L.J. Mersinger, C.A. Kettner, and C.N. Hodge. Org. Lett. **1**, 1875 (1999).
8. J.D. Cox, N.N. Kim, A.M. Traish, and D.W. Christianson. Nat. Struct. Biol. **6**, 1043 (1999).

© 2002 NRC Canada

9. T. Pandey and R.V. Singh. Main Group Met. Chem. **23**, 345 (2000).
10. T. Pandey and R.V. Singh. Synth. React. Inorg. Met. Org. Chem. **30**, 855 (2000), and refs. therein.
11. T. Pandey and R.V. Singh. Met. Based Drugs, **7**, 7 (2000).
12. C.M. Vogels, L.G. Nikolcheva, D.W. Norman, H.A. Spinney, A. Decken, M.O. Baerlocher, F.J. Baerlocher, and S.A. Westcott. Can. J. Chem. **79**, 1115 (2001).
13. G. Van Koten and K. Vrieze. Adv. Organomet. Chem. **21**, 151 (1982).
14. S.D. Ittel, L.K. Johnson, and M. Brookhart. Chem. Rev. **100**, 1169 (2000).
15. C. Carfagna, G. Gatti, D. Martini, and C. Pettinari. Organometallics, **20**, 2175 (2001).
16. M. Schmid, R. Eberhardt, M. Klinga, M. Leskelä, and B. Rieger. Organometallics, **20**, 2321 (2001).
17. D.J. Tempel, L.K. Johnson, R.L. Huff, P.S. White, and M. Brookhart. J. Am. Chem. Soc. **122**, 6686 (2000).
18. D.M. Haddleton, A.J. Clark, D.J. Duncalf, A.M. Heming, D. Kukulj, and A.J. Shooter. J. Chem. Soc. Dalton Trans. 381 (1998).
19. S. Mecking, L.K. Johnson, L. Wang, and M. Brookhart. J. Am. Chem. Soc. **120**, 888 (1998).
20. R. van Asselt, E. Rijnberg, and C.J. Elsevier. Organometallics, **13**, 706 (1994).
21. A.H. Krotz, L.Y. Kuo, and J.K. Barton. Inorg. Chem. **32**, 5963 (1993).
22. B.N. Diel, P.J. Deardorff, and C.M. Zelenski. Heteroat. Chem. **10**, 423 (1999).
23. W. Friederichsen and A. Böttcher. Heterocycles, **16**, 1009 (1981).
24. B.N. Diel, P.J. Deardorff, and C.M. Zelenski. Tetrahedron Lett. **40**, 8523 (1999).
25. V. Martichonok and J.B. Jones. J. Am. Chem. Soc. **118**, 950 (1996).
26. J.M. Kliegman and R.K. Barnes. J. Org. Chem. **35**, 3140 (1970).
27. H. Nöth and B. Wrackmeyer. Nuclear magnetic resonance spectroscopy of boron compounds. Springer-Verlag, Berlin. 1978.
28. C.M. Vogels, H.L. Wellwood, T.L. Hennigar, K. Biradha, M.J. Zaworotko, and S.A. Westcott. Can. J. Chem. **77**, 1196 (1999).
29. H. Yoshida, E. Shirakawa, Y. Nakao, Y. Honda, and T. Hiyama. Bull. Chem. Soc. Jpn. **74**, 637 (2001).
30. R. van Asselt, C.J. Elsevier, W.J.J. Smeets, A.L. Spek, and R. Benedix. Recl. Trav. Chim. Pays–Bas, **113**, 88 (1994).
31. F.A. Hicks and M. Brookhart. Organometallics, **20**, 3217 (2001).
32. S.J. McLain, J. Feldman, E.F. McCord, K.H. Gardner, M.F. Teasley, E.B. Coughlin, K.J. Sweetman, L.K. Johnson, and M. Brookhart. Macromolecules, **31**, 6705 (1998).
33. T.R. Younkin, E.F. Connor, J.I. Henderson, S.K. Friedrich, R.H. Grubbs, and D.A. Bansleben. Science (Washington, D.C.), **287**, 460 (2000).
34. K. Onitsuka, M. Segawa, and S. Takahashi. Organometallics, **17**, 4335 (1998)
35. O. Baudoin, D. Guenard, and F. Gueritte. J. Org. Chem. **65**, 9268 (2000).
36. E.R. Jamieson and S.J. Lippard. Chem. Rev. **99**, 2467 (1999).
37. J. Reedijk. Chem. Rev. **99**, 2499 (1999).
38. E. Wong and C.M. Giandomenico. Chem. Rev. **99**, 2451 (1999).
39. H. Rauter, R.D. Domencio, E. Menta, A. Oliva, Y. Qu, and N. Farrell. Inorg. Chem. **36**, 3919 (1997).
40. S.U. Dunham and S.J. Lippard. J. Am. Chem. Soc. **117**, 10 702 (1995).
41. N. Poklar, D.S. Pilch, S.J. Lippard, E.A. Redding, S.U. Dunham, and K.J. Breslauer. Proc. Natl. Acad. Sci. U.S.A. **93**, 7606 (1996).
42. E.T. Martins, H. Baruah, J. Kramarczyk, G. Saluta, C.S. Day, G.L. Kucera, and U. Bierbach. J. Med. Chem. **44**, 4492 (2001), and refs. therein.
43. S.T. Sullivan, J.S. Saad, F.P. Fanizzi, and L.G. Marzilli. J. Am. Chem. Soc. **124**, 1558 (2002).
44. Y. Qu, J.A. Fitzgerald, H. Rauter, and N. Farrell. Inorg. Chem. **40**, 6324 (2001).
45. M.P. Shaver, C.M. Vogels, A.I. Wallbank, T.L. Hennigar, K. Biradha, M.J. Zaworotko, and S.A. Westcott. Can. J. Chem. **78**, 568 (2000).
46. J.A. Rice, D.M. Crothers, A.L. Pinto, and S.J. Lippard. Proc. Natl. Acad. Sci. U.S.A. **85**, 4159 (1988).
47. A. Eastman. Biochemistry, **22**, 3927 (1983).
48. A.M.J. Fichtinger-Schepman, J.L. van der Veer, J.H.J. den Hartog, P.H.M. Lohman, and J. Reedijk. Biochemistry, **24**, 707 (1985).
49. M. Sharma, R. Jain, E. Ionescu, and H.K. Slocum. Anal. Biochem. **228**, 307 (1995).
50. B. Lippert. Cisplatin: Chemistry and biochemistry of a leading anticancer drug. Wiley-VCH, Zürich. 1999.
51. J. Reedijk. Chem. Commun., 801 (1996).
52. T.W. Hambley. J. Chem. Soc. Dalton Trans. 2711 (2001).

© 2002 NRC Canada

Attempt to approach the role of phenolic phenylpropenol structures in the photoyellowing of softwood mechanical pulps

Brigitte Ruffin, Stéphane Grelier, Aziz Nourmamode, and Alain Castellan

Abstract: Three biphenyl (**I**, **II**, **III**) compounds and a benzylarylether (**IV**) compound were synthesized to detect and quantify the presence of phenolic phenylpropenols in unbleached, peroxide-bleached, or sodium borohydride-reduced mechanical softwood pulps. The methodology used is based on a gas chromatography – mass spectrometry search of the prepared compounds in the residue obtained after ethylation, thioacidolysis, and desulfurization of the pulps. Detection of biphenyl **I** ($\approx 4 \times 10^{-6}$ mol g^{-1}) in unbleached and $NaBH_4$-reduced pulps is indicative of the presence of phenolic coniferaldehyde units in these pulps. Traces of biphenyl **II**, found in the peroxide-bleached pulp, probably came from ferulic acid units formed by oxidation of coniferaldehyde by H_2O_2. No biphenyl ether **III** or benzylaryl ether **IV** were detected in the three pulps. This result indicates that phenolic phenylpropenol units are not present in softwood mechanical pulps and do not contribute to the fast part of their photoyellowing.

Key words: mechanical pulp, photoyellowing, phenol, coniferyl alcohol, biphenyl.

Résumé : Trois biphenyls (**I**, **II**, **III**) et un éther benzylaryle (**IV**) ont été synthétisés afin de détecter et quantifier la présence de structures phénylpropénol dans des pâtes mécaniques de bois tendre non-blanchie, blanchie avec du peroxyde d'hydrogène ou réduite avec du borohydrure de sodium. La méthodologie utilisée est basée sur une recherche, par chromatographie – spectrométrie de masse, des composés préparés dans le résidu obtenu après éthylation, thioacidolyse et désulfuration des pâtes. La détection du biphényl **I** ($\approx 4 \times 10^{-6}$ mol g^{-1}) dans la pâte non-blanchie et dans celle réduite par $NaBH_4$ indique la présence de motifs coniféraldéhyde phénolique dans ces pâtes. Les traces du biphényl **II**, trouvées dans la pâte blanchie avec H_2O_2, proviennent vraisemblablement de structures acide férulique formées par oxydation par H_2O_2 d'unités coniféraldéhyde. L'absence de détection du biphényl **III** ou de l'éther benzylaryle dans les trois pâtes indique que les unités phénylpropénol phénolique ne sont pas présentes dans les pâtes mécaniques de bois tendre et ne contribue pas à la phase rapide de leur photojaunissement.

Mots clés : pâte à papier, lignine, photojaunissement, phénols, alcool conifférylique.

Introduction

High-yield pulps are obtained by the mechanical refining of wood. This defibration of lignocellulosic material might induce some chemical modification and new chemical structures might be formed. Phenylcoumaran and β-1 units are turned into stilbenes (1–3), β-*O*-4 entities are converted into *para*-hydroxybenzaldehydes (4), and coniferyl alcohols create α,β-unsaturated groups (5). Acidic treatment generates stilbenes (6) and phenylcoumarones, which are very sensitive to UV light (7, 8).

Comparison of the fluorescence emission between stone-ground wood pulp and native wood (*abies* (fir)) (9) leads to the conclusion that pulp and wood behave similarly. Reduction of the material with sodium borohydride enhanced the fluorescence due to coniferyl alcohol and biphenyl units. It was observed that when paper and wood were subject to photobleaching of the fluorescent chromophores, the materials exhibited a photochromic effect (10). The borohydride-reduced woods performed differently in the photobleaching experiment from their paper counterpart. These subtle differences were attributed to stilbene chromophores formed by mechanochemistry present in paper and not in the wood (10). Nevertheless, studies on the effect of mechanical refining on the formation of photoactive chromophores in black spruce chips casts doubt on this effect (11).

When lignin-rich pulps are bleached with alkaline hydrogen peroxide, β-1 units are transformed into stilbenes (12), and α-carbonyl phenols and coniferaldehydes are converted into methoxyhydroquinones (13, 14). All these chromophores are considered to have a key role in the photoyellowing of bleached lignin-rich pulps (15). Lee and Sumimoto (16) considered that *para*-hydroxybenzoquinone derivatives, including stilbene-, biphenyl-, or diphenylether-conjugated structures, were the major ones responsible for color reversion of pulps. However, recent studies on light-induced brightness loss of pulps, which were targeted on the role of stilbene phenols formed from β-1 units (17) and stilbenes (including hydroquinone moieties formed from β-5 units (18)), indicate a minor role of these structural elements.

According to model studies (8, 19), phenolic coniferyl alcohol units were found to be very light-sensitive and might

Received 19 March 2002. Published on the NRC Research Press Web site at http://canjchem.nrc.ca on 30 August 2002.

B. Ruffin, S. Grelier, A. Nourmamode, and A. Castellan.[1] Laboratoire de Chimie des Substances Végétales, Université Bordeaux 1, 351 cours de la Liberation, F-33405 Talence, France.

[1]Corresponding author (e-mail: a.castellan@ipin.u-bordeaux.fr).

 DOI: 10.1139/V02-123 © 2002 NRC Canada

Fig. 1. Compounds obtained by thioacidolysis followed by desulfurization (Raney nickel) of coniferyl alcohol and coniferaldehyde (22, 24).

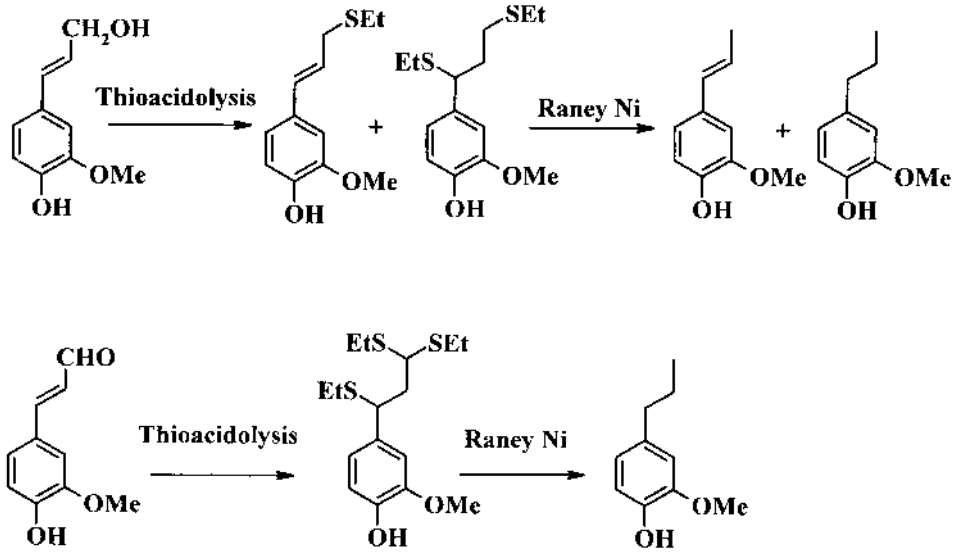

participate in the photoyellowing of bleached high-yield pulps. In our continuous effort to determine structures at the origin of the fast photoyellowing of lignocellulosic materials (17 to 18, 20 to 21), we present in this paper an attempt to detect, in pulp, the phenolic phenylpropenol moiety included in biphenyl or diarylether structures. The methodology used was thioacidolysis, followed by desulfurization with Raney nickel, GC–MS analysis, and comparison of the data with those from authentic samples synthesized for the purpose.

Results and discussion

General

During irradiation of thermomechanical pulps, Pan et al. (22) observed the formation of coniferyl aldehydes and the disappearance of coniferyl alcohols. Moreover, fluorescence studies on milled wood lignin (MWL) have revealed a great reactivity of coniferyl alcohol structures under irradiation (23); in particular, they are turned into coniferyl aldehydes and other structures that emit at 500 nm. It was observed that coniferyl aldehydes deactivate the emission at 400 nm caused by biphenyl structures. Based on this observation, we decided to attempt to detect and quantify phenolic phenylpropenols in high yield pulps and follow their evolution under UV–vis irradiation.

A widespread method for analysis and quantitative determination of lignin units is thioacidolysis; this method is a depolymerization of lignin by ethanethiol in the presence of $BF_3{\cdot}Et_2O$, followed by gas chromatography separation and mass spectrometry analysis of the products (24). For analysis of lignin-condensed structures by thioacidolysis, a desulfurization step with Raney nickel is necessary, because condensed structures are too heavy to be analyzed by GC. However, reductive treatment leads to the formation of a propyl chain for both coniferyl alcohol and coniferyl aldehyde (Fig. 1) (24).

To differentiate phenolic coniferyl alcohol elements from non-phenolic coniferyl alcohol units, the pulp was ethylated. In this study, we looked for coniferyl alcohol structures included in the lignin macrostructure as biphenyl elements, such as structures **A** and **B**, and diarylether units, such as structure **C** (Fig. 2). Biphenyl structures were found to exist in high proportion in lignin in the form of dibenzodioxocin (25).

By thioacidolysis followed by desulfurization, structure **A** should lead to compounds **I–III** (Fig. 2). The same treatment applied on structure **B** should give compounds **I** and **III**. The syntheses of the biphenyl model compounds **I–III** and the diarylether model **IV** (representative of structure **C**) (Fig. 2) were completed. Compound **V**, isomer of **III**, was not considered because it is not formed from structure **B**, and unit **A** is accounted for by dimers **I–III**. The investigation was made on three pulps: unbleached mechanical softwood pulp (MSP) (mainly from spruce), hydrogen peroxide bleached MSP, and sodium borohydride reduced MSP (vide infra).

Synthesis of compounds

Synthesis of compound **I** is described in Fig. 3. The key step in this synthesis is the monoprotection of one of the two phenoxyl groups of the biphenyl. Eugenol is converted into the dehydrodimer by oxidative coupling with potassium ferricyanide. The compound obtained is then hydrogenated and monoethylated by treatment with diethylsulfate with sodium hydroxide, thanks to the different acidity between the two phenolic groups (26).

Compound **II** could not be obtained by isomerization of the corresponding isomer at high temperature (unlike isoeugenol, which is obtained from eugenol by treatment with sodium hydroxide in diethylene glycol (27)). Other attempts with different solvents (DMSO, THF) or bases (*t*-BuOK) were conducted without success. Compound **II** was prepared according to the route described in Fig. 4. GC–MS analysis of compound **II** revealed the presence of four propene chain isomers in the relative ratio 36:30:19:15. According to their relative stability, the highest and lowest figures could be assigned to *E*,*E* and *Z*,*Z* isomers.

Compound **III** was synthesized according to the scheme described in Fig. 5. The key step for this synthesis is the Kharasch reaction between a Grignard reagent and an aryl halide (28, 29).

© 2002 NRC Canada

Fig. 2. Phenolic phenylpropenol units present in softwood pulp and structures resulting from thioacidolysis and desulfurization treatments.

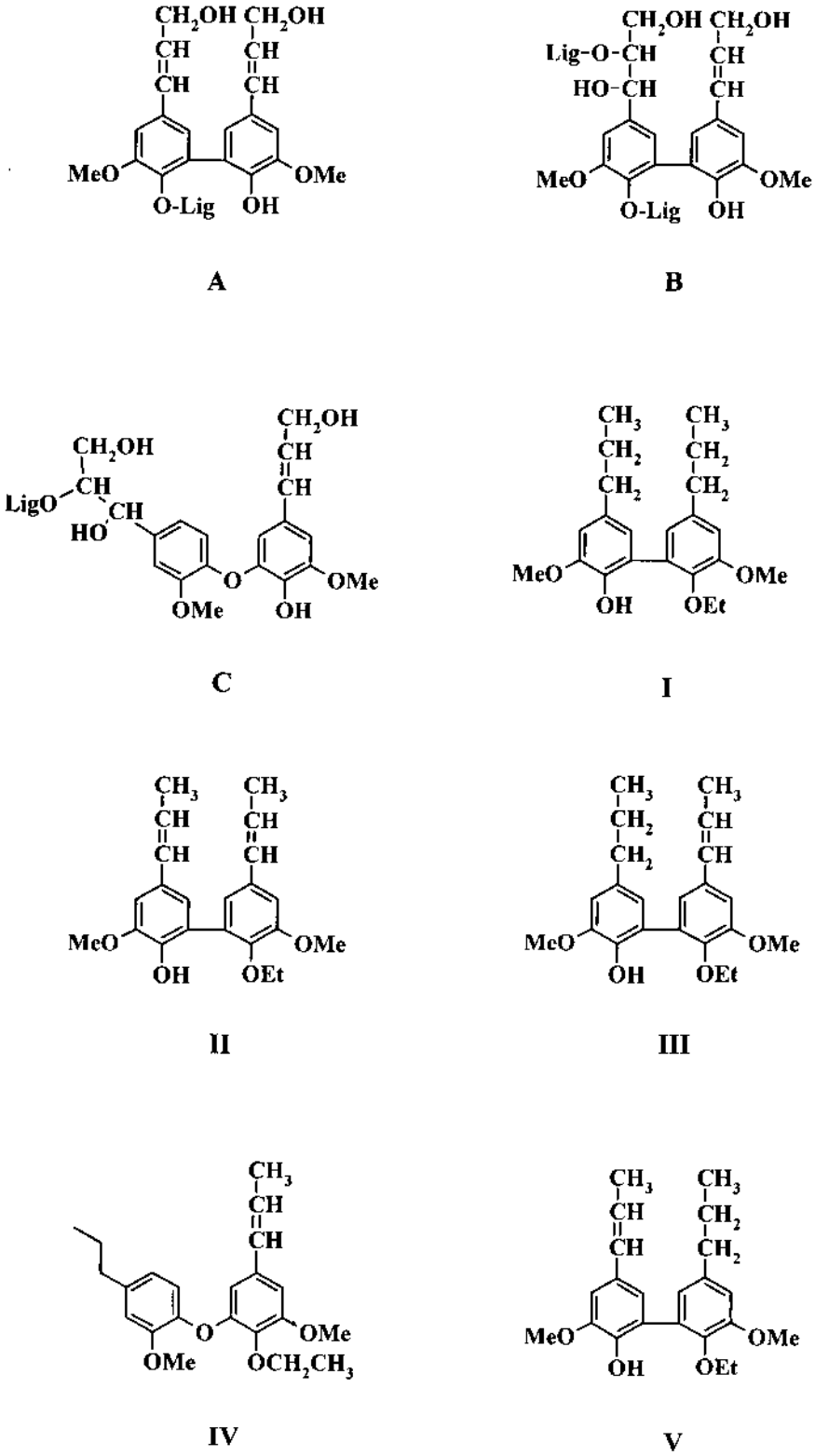

Compound **IV** was obtained by the reaction sequence described in Fig. 6. The yield (3.5%) is very low because the main product formed by this procedure was compound **2**. The latter is formed by oxidative coupling of compound **10** in the presence of Cu^{2+} (30).

Analysis of the pulps

To characterize only phenolic coniferyl alcohol structures, the pulp was treated with diethylsulfate in alkaline medium — this is a very efficient reaction to etherify phenols. Then the pulps were thioacidolysed and desulfurized. GC–MS

© 2002 NRC Canada

Fig. 3. Synthetic scheme of compound **I**.

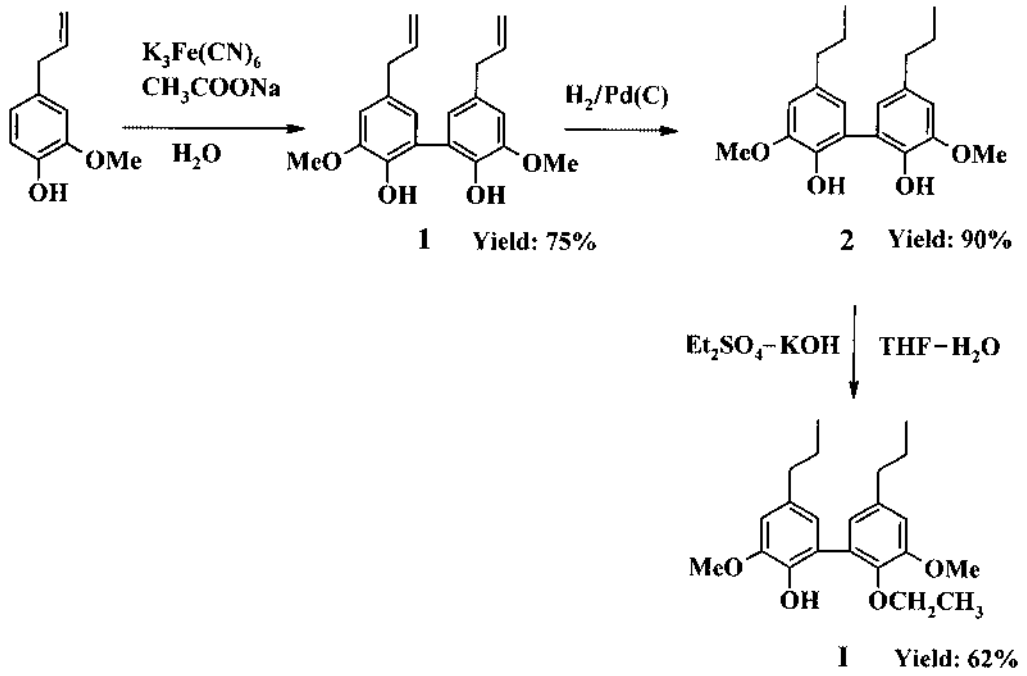

Fig. 4. Synthetic scheme of compound **II**.

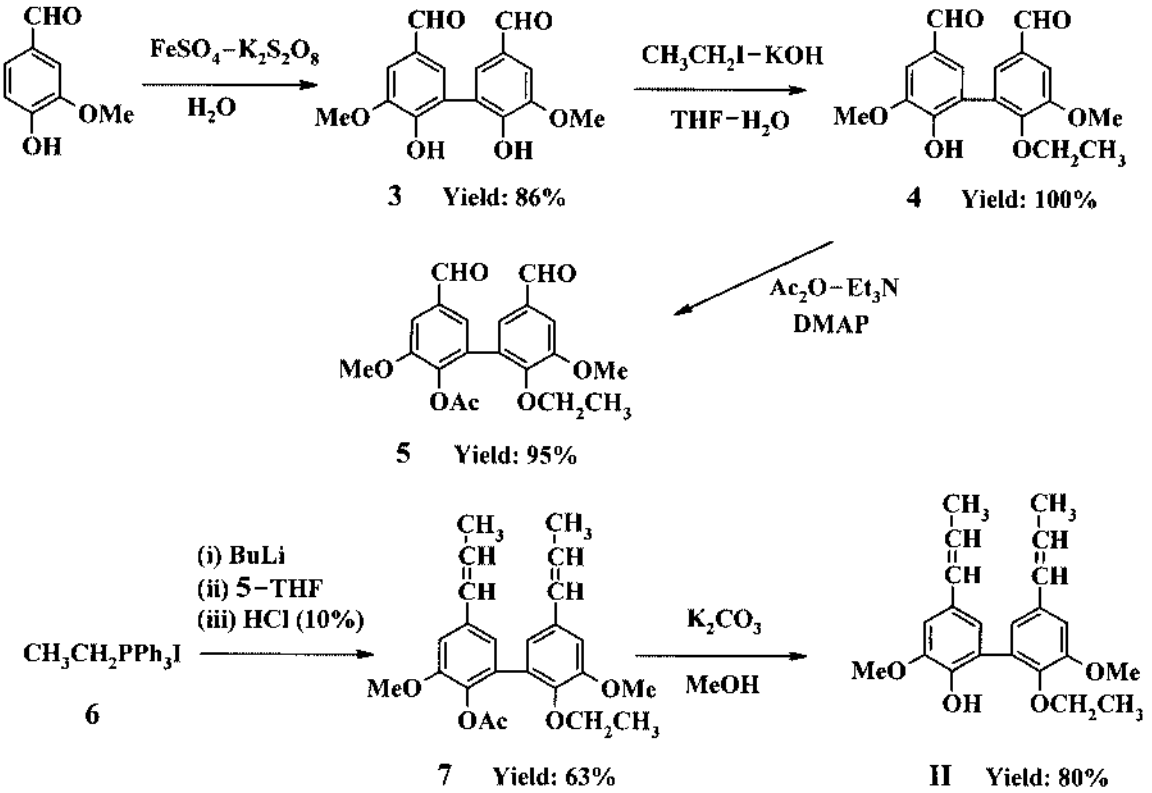

analyses are reported in Table 1 for unbleached and H_2O_2- and $NaBH_4$-treated pulps.

Among the four studied compounds, only compound **I** was found in unbleached and reduced pulps, in minute quantity ($\approx 4 \times 10^{-6}$ mol g^{-1}), which represents an order of magnitude higher than that found for stilbene phenols in peroxide bleached pulps (17). In peroxide bleached pulp, compound **I** was not detected. It is likely that compound **I** is not formed from phenylpropenol units but from phenylpropenal ones, these structures being degraded by hydrogen peroxide.

© 2002 NRC Canada

Fig. 5. Synthetic scheme of compound **III**.

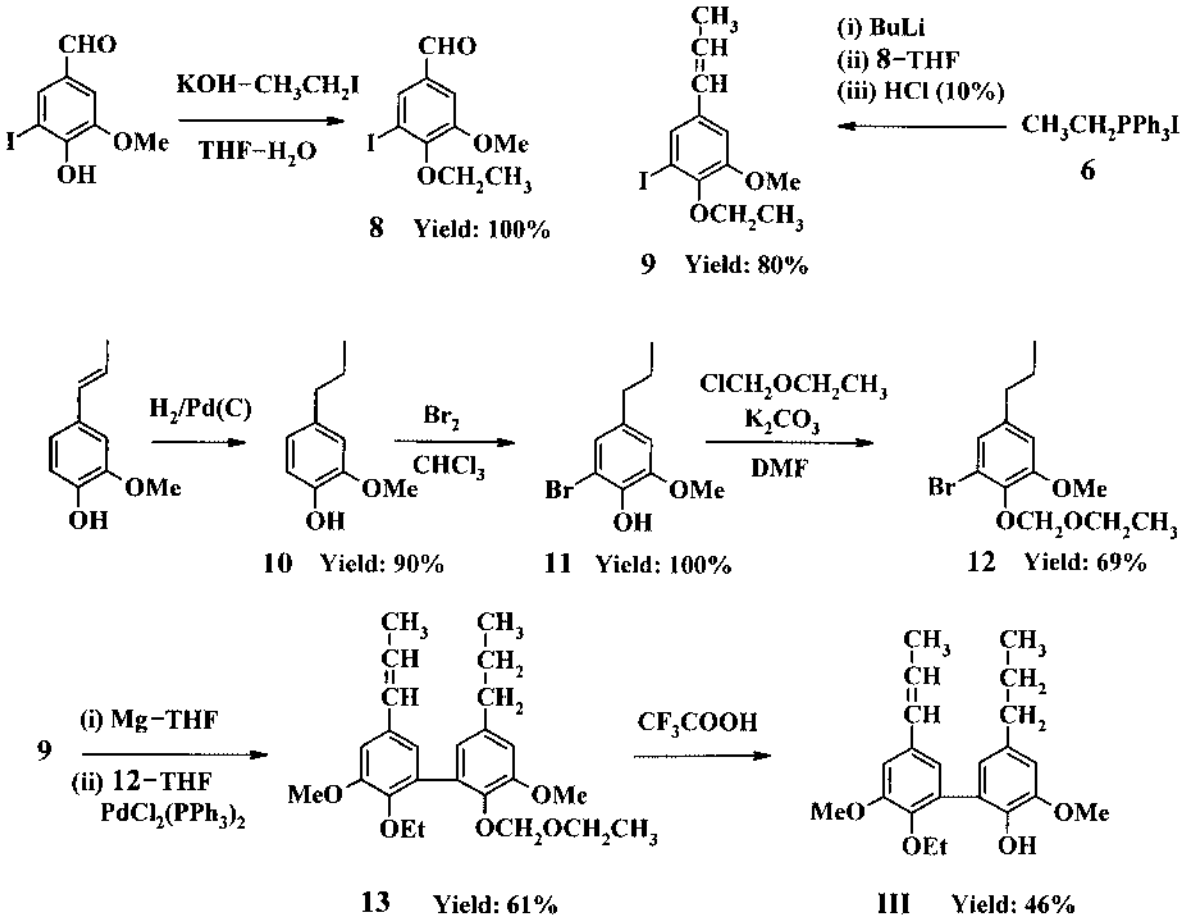

Fig. 6. Synthetic scheme of compound **IV**.

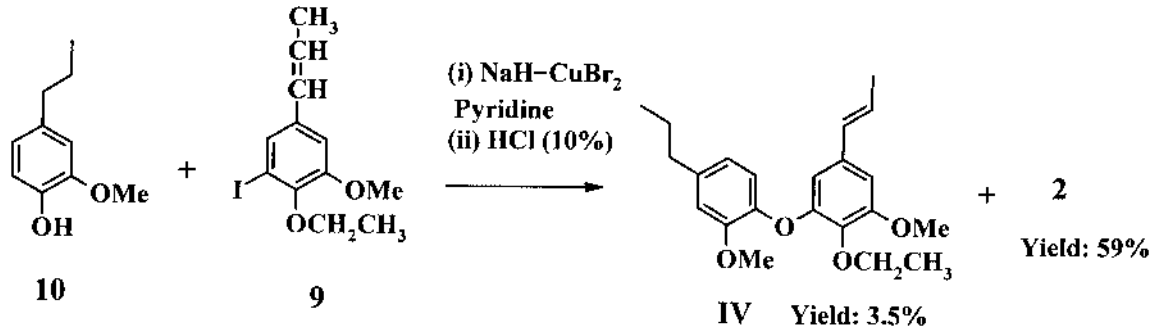

Traces of compound **II** were detected only for peroxide treated pulp in the form of two isomers, *E,E* and *Z,E* or *E,Z*. These isomers might be formed from cinnamic acid structures generated by the action of hydrogen peroxide on coniferaldehyde units. The lack of detection of compounds **III** and **IV** would indicate a very low content of phenolic coniferyl alcohol units or an inefficient ethylation of phenols, which is improbable considering the detection of compound **I** and the large excess of diethylsulfate used to treat pulps.

The lack of detection of compounds **III** and **IV** indicates that phenolic phenylpropenol units are not present in large amounts in bleached softwood mechanical pulps and therefore do not contribute to their fast photoyellowing.

Experimental

General

Melting points were measured with a Mettler FP62 heating block. NMR spectra were recorded on a Bruker DPX200 (^{1}H, ^{13}C) spectrometer (reference Me_4Si, solvent $CDCl_3$). The IR and UV absorption spectra were performed on PerkinElmer Paragon 1000 PC and Hitachi U-3300 spectrometers, respectively. Mass spectra were obtained using a VG Micromass Autospec Q instrument incorporating an electron ionization source (70 eV).

The usual chemicals were obtained from Aldrich, and they were used without further purification. The synthesized compounds were purified by column chromatography on

© 2002 NRC Canada

Table 1. Detection and quantification by GC–MS of compounds **I**, **II**, **III**, and **IV** in softwood mechanical pulps after thioacidolysis and desulfurization.

Pulp and (or) compounds (1×10^{-6} mol g^{-1})	I	II	III	IV
Untreated pulp	3.7	n.d.	n.d.	n.d.
H_2O_2-bleached pulp	—	Trace of two isomers	n.d.	n.d.
$NaBH_4$-reduced pulp	4.5	n.d.	n.d.	n.d.

Note: n.d. = not detected

silica gel 60 (70−200 mesh) using the appropriate eluents. The solid products were crystallized after chromatography.

Analysis of the compounds was performed by gas chromatography (GC) with a flame ionization detector (Shimadzu GC 14A equipped with a CR4A Chromatopac data analyzer) or GC (Hewlett-Packard 5890 chromatograph) interfaced with a mass spectrometer (VG Micromass Autospec Q). The GC analyses were made using capillary columns (J and W Scientific) (30 m × 0.25 mm; film thickness, 0.25 μm; stationary phase DB-5MS). The injector port temperature was set at 280°C and the detector port temperature at 300°C (Shimadzu GC 14A). The transfer line between the GC apparatus and the mass spectrometer source was fixed at 220°C. The oven temperature program (GC) started at 180°C (1 min), then rose between 180 and 300°C with a gradient of 4°C min^{-1}, and finally was set to 300°C (30 min).

Chemical treatment of pulp

Bleaching of pulp with hydrogen peroxide

Mechanical pulp, mainly from spruce (0.5 g), kindly given by Dr. Petit-Conil (Centre Technique du Papier, Grenoble, France), was treated with hydrogen peroxide (30%, 0.5 mL) and sodium hydroxide (10 mg in 50 mL of water) in a plastic bag. After being heated at 50°C for 4 h, the pulp was washed with distilled water, diluted hydrochloric acid (5%), and water to bring the pH near 5. The pulp was filtered and keep at 4°C before etherification with diethylsulfate.

Reduction of pulp with $NaBH_4$

Mechanical pulp mainly from spruce (0.5 g) was reacted with sodium borohydride (0.5 g in 20 mL of water). After being stirred at room temperature for 2 days, the pulp was washed with hydrochloric acid (5%) and water to bring the pH near 5. The pulp was filtered and kept at 4°C before etherification with diethylsulfate.

Ethylation of pulps

The defiberized pulps (3 g) in suspension in water (100 mL) were treated under magnetic stirring and a nitrogen atmosphere with 5 mL of 10% sodium hydroxide solution. The mixtures were heated at 40°C for 15 min and then diethylsulfate (2 mL) was added. The stirring was continued for 1 h and then the alternating addition of sodium hydroxide and diethylsulfate was repeated. This cycle was repeated once more. Then the pulp was successively washed with dilute hydrochloric acid (5%) and distilled water (to pH ≈ 5), and filtered. The pulp was first dried in an oven at 40°C and then over P_2O_5 under vacuum before thioacidolysis treatment.

Thioacidolysis and Raney nickel treatment of pulps

Thioacidolysis and desulfurization experiments were performed according to a procedure described by Lapierre et al. (24, 31). Pulp (50 mg), treated with 10 mL of thioacidolysis solution (10 mL EtSH + 2.4 mL $BF_3{\cdot}Et_2O$ + 80 mL dioxan), was heated at 100°C for 4 h under magnetic stirring. After hydrolysis with diluted $NaHCO_3$ solution until pH 3 to 4, the reaction mixture was extracted with dichloromethane. To the dichloromethane solution, docosane was added as an internal standard for quantitative measurements. The organic phase was washed with water, dried over magnesium sulfate, and evaporated under vacuum. The solid residue was dissolved in 0.5 mL of dichloromethane and reacted with 2 mL of aqueous Raney nickel solution (50%) in 10 mL of methanol for 4 h at 80°C. After cooling, the resulting mixture was hydrolyzed with hydrochloric acid (10%) and extracted with dichloromethane. The organic phase, after washing with water, was dried over magnesium sulfate and evaporated to 0.5 mL. The organic phase was silylated with BSTFA (50 μL) in the presence of pyridine (10 μL) at room temperature for 30 min.

Syntheses

Synthesis of compound I

*5,5′-Diallyl-2,2′-dihydroxy-3,3′-dimethoxybiphenyl (dihydrodiisoeugenol) (**1**)*

A solution of eugenol (5.0 g, 30.5 mmol) and sodium acetate (9.0 g, 110.0 mmol) in water (200 mL) was treated, dropwise, with a solution of potassium ferricyanide (20.0 g, 60.8 mmol) in water (200 mL). After being stirred at room temperature for 3 h, the reaction mixture was filtered and the solid product was purified by crystallization in CH_2Cl_2 – petroleum ether (PET), affording the expected biphenyl **1** as beige crystals (3.8 g), yield 75%; mp 107°C (lit. (32) value mp +106°C). ^{1}H NMR ($CDCl_3$) δ: 3.40 (d, 4H, CH_2), 3.84 (s, 6H, OCH_3), 5.17 (d, 4H, $=CH_2$), 6.0 (m, 4H, CH), 6.9–7.0 (m, 4H, ArH). ^{13}C NMR ($CDCl_3$) δ: 40.0 (CH_2), 56.1 (OCH_3), 110.7 (CH Ar), 115.7 ($=CH_2$), 123.1 (CH Ar), 124.3 (C Ar), 131.9 (C Ar), 137.7 (=CH), 140.9 (C Ar), 147.2 (C Ar).

*2,2′-Dihydroxy-3,3′-dimethoxy-5,5′-di-*n*-propylbiphenyl (**2**)*

Hydrogenation of compound **1** (2.0 g, 6.1 mmol) in methanol (75 mL) containing 0.2 g of carbon palladium (10%) was accomplished by treating the mixture under hydrogen pressure (180 bar) for 24 h at room temperature. The mixture, after filtration, afforded a beige solid (1.8 g, 90%); mp 152°C (lit. (33) value mp +152°C). IR (KBr) (cm^{-1}): 850, 1050, 1145, 1230, 1260, 1375, 1425, 2920, 2945, 3300. ^{1}H NMR ($CDCl_3$) δ: 0.95 (t, 6H, CH_3), 1.63 (m, 4H, CH_2), 2.55 (t, 4H, CH_2), 3.91 (s, 6H, OCH_3), 6.03 (s, 2H, OH), 6.7

© 2002 NRC Canada

(m, 4H, ArH). ^{13}C NMR ($CDCl_3$) δ: 13.9 (CH_3), 24.8 (CH_2), 37.9 (CH_2), 56.1 (OCH_3), 110.6 (CH Ar), 122.9 (CH Ar), 124.4 (C Ar), 134.7 (C Ar), 140.5 (C Ar), 147.1 (C Ar).

2-Hydroxy-2′-ethoxy-3,3′-dimethoxy-5,5′-di-n-*propylbiphenyl (**I**)*

A solution of compound **2** (600 mg, 1.82 mmol) in THF (50 mL) was treated with a solution of potassium hydroxide (102 mg, 1.82 mmol) and diethylsulfate (0.5 mL, 4.0 mmol). After being stirred at 70°C for 12 h, the solution was reacted with a solution of hydrochloric acid (10%). The aqueous layer was extracted with CH_2Cl_2. The combined organic layers were washed with water, dried over $MgSO_4$, filtered, and concentrated. The product was purified by chromatography on silica gel (eluent Et_2O–PET, 60:40) affording the expected compound **I** (400 mg, 62%) as a pale yellow oil. IR (NaCl) (cm^{-1}): 840, 1050, 1140, 1230, 1460, 1580, 2870, 2930, 2960. ^{1}H NMR ($CDCl_3$) δ: 0.84 (t, 3H, CH_3), 0.86 (t, 3H, CH_3), 1.02 (t, 3H, CH_3), 1.55 (m, 4H, 2×CH_2), 2.46 (t, 2H, CH_2), 2.48 (t, 2H, CH_2) 3.74 (q, 2H, OCH_2), 3.78 (s, 3H, OCH_3), 3.80 (s, 3H, OCH_3), 6.6–6.7 (m, 4H, ArH), 6.72 (s, 1H, OH). ^{13}C NMR ($CDCl_3$) δ: 13.8 (CH_3), 14.0 (CH_3), 15.3 (CH_3), 24.6 (CH_2), 24.8 (CH_2), 37.8 (CH_2), 38.0 (CH_2), 55.9 (OCH_3), 56.1 (OCH_3), 69.9 (OCH_2), 111.2 (CH Ar), 111.7 (CH Ar), 122.9 (CH Ar), 123.4 (CH Ar), 128.2 (C Ar), 132.6 (C Ar), 134.3 (C Ar), 139.2 (C Ar), 141.2 (C Ar), 142.4 (C Ar), 148.5 (C Ar), 152.6 (C Ar). MS (TMS derivative): 430 ($[M]^+$,100%), 401 (10%), 387 (14%), 357 (9%), 73 (31%).

Synthesis of compound II

*4,4′-Diformyl-2,2′-dihydroxy-3,3′-dimethoxybiphenyl (**3**)*

Vanillin (5.0 g, 33 mmol) in hot water (200 mL) was treated by ferrous sulfate (200 mg, 0.7 mmol) and potassium persulfate (5.0 g, 20 mmol) at 100°C for 2 h. The resulting product was filtered and dried in an oven, affording the expected compound **3** (4.3 g, 86%); mp 304°C (lit. (34) value mp +305°C). IR (KBr) (cm^{-1}): 750, 850, 1050, 1150, 1260, 1420, 1460, 1590, 1680, 3260. ^{1}H NMR (DMSO) δ: 3.98 (s, 6H, OCH_3), 7.4 (s, 4H, ArH), 9.85 (s, 2H, CHO). ^{13}C NMR (DMSO) δ: 56.0 (OCH_3), 109.0 (CH Ar), 124.5 (CH Ar), 127.9 (C Ar), 128.2 (C Ar), 148.1 (C Ar), 150.3 (C Ar), 191.1 (CHO).

*2-Ethoxy-4,4′-diformyl-2′-hydroxy-3,3′-dimethoxybiphenyl (**4**)*

Dehydrodivanillin **3** (3.0 g, 9.9 mmol) in THF (100 mL) was treated with a solution of potassium hydroxide (0.6 g, 10.0 mmol) in water (10 mL) and iodoethane (3.2 g, 20.5 mmol). After being refluxed for 6 h, the mixture was reacted with a solution of hydrochloric acid (10%). The aqueous layer was extracted with CH_2Cl_2. The combined organic layers were washed with water, dried over $MgSO_4$, filtered, and concentrated, affording the expected compound **4** (3.3 g, 100%) as a pale yellow solid; mp 195°C. IR (KBr) (cm^{-1}): 740, 890, 1040, 1150, 1180, 1260, 1420, 1580, 1700, 3250. ^{1}H NMR ($CDCl_3$) δ: 1.11 (t, 3H, CH_3), 3.98 (s, 3H, OCH_3), 4.01 (q, 2H, OCH_2), 4.06 (s, 3H, OCH_3), 6.59 (s, 1H, OH), 7.4–7.5 (m, 4H, ArH), 9.86 (s, 1H, CHO), 9.92 (s, 1H, CHO).

*2-Ethoxy-4,4′-diformyl-2′-acetoxy-3,3′-dimethoxybiphenyl (**5**)*

A solution of **4** (3.3 g, 9.9 mmol) in CH_2Cl_2 (50 mL) was treated with triethylamine (5 mL, 36.1 mmol), acetic anhydride (1.4 mL, 12.6 mmol), and traces of 4-dimethylaminopyridine (DMAP). After being refluxed for 20 h, the mixture was reacted with water. The aqueous layer was extracted with CH_2Cl_2. The combined organic layers were washed with water, dried over $MgSO_4$, filtered, and concentrated, affording the expected compound **5** (3.5 g), yield 95%, as a pale yellow solid; mp 127°C. IR (KBr) (cm^{-1}): 740, 890, 1040, 1130, 1180, 1270, 1380, 1576, 1700, 1765. ^{1}H NMR ($CDCl_3$) δ: 1.08 (t, 3H, CH_3), 2.10 (s, 3H, OAc), 3.92 (q, 2H, OCH_2), 3.94 (s, 3H, OCH_3), 3.95 (s, 3H, OCH_3), 7.2–7.5 (m, 4H, ArH), 9.87 (s, 1H, CHO), 9.95 (s, 1H, CHO).

*Ethyltriphenylphosphonium iodide (**6**)*

A solution of iodoethane (3.0 g, 19.1 mmol) in toluene (50 mL) was treated with triphenylphosphine (6.0 g, 23.0 mmol) at 80°C for 3 h. The resulting white product was filtered and dried, affording the expected salt **6** (6.8 g), yield 84%; mp 168°C (lit. (35) value mp +168 to 169°C).

*2-Ethoxy-4,4′-diformyl-2′-acetoxy-3,3′-dipropenylbiphenyl (**7**)*

An *n*-butyl lithium solution in *n*-hexane (2.5 mol L^{-1}, 5.2 mmol) was added to a solution of the phosphonium salt **6** (2.1 g, 5 mmol) in anhyd THF (30 mL) under an N_2 atmosphere and the mixture was stirred at –70°C for 15 min. The resulting red solution was treated with a solution of aldehyde **5** (0.9 g, 2.4 mmol) in anhyd THF (20 mL). After being stirred at room temperature for 2 h, the mixture was reacted with a solution of hydrochloric acid (10%). The aqueous layer was extracted with CH_2Cl_2. The combined organic layers were washed with water, dried over $MgSO_4$, filtered, and concentrated. The product was purified by chromatography on silica gel (eluent CH_2Cl_2) affording the expected compound **7** (0.6 g, 63%) as a yellow solid; mp 127°C. IR (KBr) (cm^{-1}): 760, 790, 960, 1050, 1140, 1460, 1580, 1700, 1770, 2950. ^{1}H NMR ($CDCl_3$) δ: 1.1 (t, 3H, CH_3), 1.6 (2d, 6H, CH_3), 2.0 (s, 3H, OAc), 3.9 (m, 8H, 2 × OCH_3 and OCH_2), 5.5–6.0 (m, 4H, CH=CH), 6.8 (m, 4H, ArH). ^{13}C NMR ($CDCl_3$) δ: 15.4 (CH_3), 20.4 (Ac), 56.0 (OCH_3), 56.3 (OCH_3), 69.6 (OCH_2), 109.7 (CH Ar), 110.1 (CH Ar), 127.1 (CH Ar), 127.4 (CH Ar), 130.7 (C Ar), 132,0 (C Ar), 132.5 (C Ar), 134.3 (C Ar), 190.8 (CHO), 191.0 (CHO).

*2-Ethoxy-4,4′-diformyl-2′-hydroxy-3,3′-dipropenylbiphenyl (**II**)*

A solution of **7** (600 g, 1.52 mmol) in methanol (50 mL) was treated with potassium carbonate (250 mg, 1.81 mmol). After being stirred at room temperature for 4 h, the mixture was reacted with a solution of hydrochloric acid (10%). The aqueous layer was extracted with CH_2Cl_2. The combined organic layers were washed with water, dried over $MgSO_4$, filtered, and concentrated. The product was purified by chromatography on silica gel (eluent CH_2Cl_2–Et_2O, 98:2) affording the expected compound **II** (450 mg, 80%) as a pale yellow oil; mp 127°C. ^{1}H NMR ($CDCl_3$) δ: 1.1 (t, 3H, CH_3), 1.8 (d, 3H, CH_3), 1.9 (d, 3H, CH_3), 3.9 (m, 8H, 2 × OCH_3 and OCH_2), 5.6–7.0 (m, 8H, ArH, and CH=CH). Four stereoisomers displaying the same mass spectrum were identified by GC–MS (retention time: 18.8 (30%), 19.7 (36%),

© 2002 NRC Canada

20.0 (15%), and 21.0 min (19%)). MS (TMS derivative): 426 ([M]$^+$, 100%), 383 (12%), 73 (35%).

Synthesis of compound III

*4-Ethoxy-5-iodo-3-methoxybenzaldehyde (**8**)*

5-Iodovanillin (3.0 g, 10.8 mmol) in THF (75 mL) was treated with a solution of potassium hydroxide (1.0 g, 17.8 mmol) in water (10 mL) and iodoethane (4.0 g, 25.6 mmol). After being refluxed for 6 h, the mixture was reacted with water. The aqueous layer was extracted with CH_2Cl_2. The combined organic layers were washed with a solution of hydrochloric acid (10%), dried over $MgSO_4$, filtered, and concentrated, affording the expected compound **8** (3.3 g, 100%) as white crystals; mp 42°C. IR (KBr) (cm^{-1}): 590, 670, 790, 1040, 1150, 1270, 1390, 1460, 1560, 1580, 1690, 2970. ^{1}H NMR ($CDCl_3$) δ: 1.25 (t, 3H, CH_3), 3.83 (s, 3H, OCH_3), 4.05 (q, 2H, OCH_2), 7.23 (d, 1H, ArH), 7.77 (d, 1H, ArH), 9.81 (s, 1H, CHO). ^{13}C NMR ($CDCl_3$) δ: 15.7 (CH_3), 56.2 (OCH_2), 69.5 (OCH_3), 110.0 (CH Ar), 118.3 (C-I), 128.6 (CH Ar), 132.8 (C Ar), 151.0 (C Ar), 154.2 (C Ar), 169.9 (CHO).

*2-Ethoxy-1-iodo-3-methoxy-5-propenylbenzene (**9**)*

An *n*-butyl lithium solution in *n*-hexane (2.5 mol L^{-1}, 10.0 mmol) was added to a solution of the phosphonium salt **6** (4.2 g, 10.0 mmol) in anhyd THF (50 mL) under N_2 atmosphere and the mixture was stirred at –70°C for 15 min. The resulting red solution was treated with a solution of aldehyde **8** (3.0 g, 9.8 mmol) in anhyd THF (40 mL). After being stirred at room temperature for 2 h, the mixture was reacted with a solution of hydrochloric acid (10%). The aqueous layer was extracted with CH_2Cl_2. The combined organic layers were washed with water, dried over $MgSO_4$, filtered, and concentrated. The product was purified by chromatography on silica gel (eluent CH_2Cl_2) affording the expected compound **9** (2.5 g), yield 80%, as a pale yellow solid; mp 33°C. IR (KBr) (cm^{-1}): 780, 870, 960, 1050, 1140, 1230, 1250, 1510, 2950. ^{1}H NMR ($CDCl_3$) δ: 1.44 (t, 3H, CH_2-CH_3), 1.87 (2 × dd, 3H, CH-CH_3), 3.85 (s, 3H, OCH_3), 4.04 (q, 2H, OCH_2), 6.0–6.4 (m, 2H, CH=CH), 6.79 (d, 1H, ArH, J = 1.72 Hz), 6.81 (d, 1H, ArH, J = 1.72 Hz). ^{13}C NMR ($CDCl_3$) δ: 14.8 (CH_3), 18.4 (CH-CH_3), 55.8 (OCH_2), 64.3 (OCH_3), 108.8 (CH Ar), 112.7 (CH=), 118.7 (C-I), 123.7 (CH), 130.6 (CH), 131.1 (C Ar), 148.2 (C Ar), 149.5 (C Ar).

*2-Methoxy-4-*n*-propylphenol (**10**)*

Hydrogenation of eugenol (3.0 g, 18.3 mmol) in methanol (75 mL) containing 0.3 g of carbon palladium (10%) was accomplished by treating the mixture under hydrogen pressure (80 bar) for 24 h at 40°C. The mixture, after filtration, afforded compound **10** (2.7 g, 90%) as a green oil. IR (NaCl) (cm^{-1}): 795, 820, 1030, 1120, 1150, 1270, 1430, 1460, 1500, 1600, 2870, 2930, 2960, 3500. ^{1}H NMR ($CDCl_3$) δ: 0.7 (t, 3H, CH_3), 2.25 (t, 2H, CH_2), 2.85 (t, 2H, CH_2), 3.45 (s, 3H, OCH_3), 5.3 (s, 1H, OH), 6.2–6.7 (m, 3H, ArH).

*2-Bromo-6-methoxy-4-*n*-propylphenol (**11**)*

A solution of bromine (0.7 mL, 13.6 mmol) in $CHCl_3$ (60 mL) was added dropwise to a solution of **10** (2.0 g, 12.0 mmol) in $CHCl_3$ (100 mL) at 0°C. Once the addition was completed, the mixture was stirred at room temperature for 2 h. The solvent was removed and compound **11** (3.0 g, 100%) was obtained as a beige solid; mp 83°C (lit. (36) value mp +82.5 to 83.5°C). IR (KBr) (cm^{-1}): 820, 860, 960, 1040, 1150, 1200, 1270, 1500, 1590, 2870, 2930, 2950, 3420. ^{1}H NMR ($CDCl_3$) δ: 0.96 (t, 3H, CH_3), 1.60 (q, 2H, CH_2), 2.60 (t, 2H, CH_2), 3.85 (s, 3H, OCH_3), 6.66 (s, 1H, ArH), 7.08 (s, 1H, ArH). ^{13}C NMR ($CDCl_3$) δ: 13.8 (CH_3), 23.5 (CH_2), 37.9 (CH_2), 56.1 (OCH_3), 112.2 (CH Ar), 114.6 (C-Br), 118.4 (CH Ar), 133.3 (C Ar), 144.3 (C Ar), 145.9 (C Ar).

*1-Bromo-2-ethoxymethoxy-3-methoxy-5-propylbenzene (**12**)*

A solution of **11** (2.9 g, 11.8 mmol) in DMF (120 mL) was treated with potassium carbonate (9.0 g, 65.2 mmol) and chloromethylethylether (3.4 mL, 36.6 mmol). After being stirred at 80°C for 18 h, the mixture was reacted with a solution of hydrochloric acid (10%). The aqueous layer was extracted with CH_2Cl_2. The combined organic layers were washed with water, dried over $MgSO_4$, filtered, and concentrated. The product was purified by chromatography on silica gel (eluent CH_2Cl_2) affording the expected compound **12** (2.5 g, 69%) as a green oil. IR (NaCl) (cm^{-1}): 850, 950, 1160, 1250, 1460, 1500, 2870, 2930, 2960. ^{1}H NMR ($CDCl_3$) δ: 0.92 (t, 3H, CH_3), 1.15 (t, 3H, CH_3), 1.8 (m, 2H, CH_2), 2.8 (m, 2H, CH_2), 3.78 (q, 2H, OCH_2), 3.85 (s, 3H, OCH_3) 5.24 (s, 2H, OCH_2O), 6.8–7.0 (m, 2H, ArH).

*2′-Ethoxy-2-ethoxymethoxy-3,3′-dimethoxy-5′-propenyl-5-propylbiphenyl (**13**)*

Magnesium (0.2 g, 5.0 mmol) and two crystals of iodine in anhyd THF (5 mL) under an N_2 atmosphere were treated with a solution of **9** (1.0 g, 3.1 mmol) in anhyd THF (30 mL). After being stirred at 70°C for 6 h, the mixture was transferred dropwise into a second flask charged with palladium (II) bis-(triphenylphosphine) dichloride (0.2 mg, 0.28 mmol), compound **12** (0.95 g, 3.1 mmol), and 20 mL of anhyd THF. After being stirred at 70°C for 8 h, the mixture was reacted with a solution of hydrochloric acid (10%). The aqueous layer was extracted with CH_2Cl_2. The combined organic layers were washed with water, dried over $MgSO_4$, filtered, and concentrated. The product was purified by chromatography on silica gel (eluent CH_2Cl_2), affording the expected compound **13** (800 mg, 61%) as an orange oil. ^{1}H NMR ($CDCl_3$) δ: 0.94 (t, 3H, CH_3), 1.12 (t, 3H, CH_3), 1.35 (m, 3H, CH_3), 1.47 (m, 2H, CH_2), 1.72 (2d, 3H, CH_3-CH=), 3.79 (t, 2H, OCH_2), 3.87 (s, 3H, OCH_3), 3.89 (s, 3H, OCH_3), 4.15 (s, 2H, OCH_2), 5.22 (s, 2H, OCH_2O), 5.8–6.2 (m, 2H, CH=CH), 6.4–6.8 (m, 4H, ArH).

*2′-Ethoxy-2-hydroxy-3,3′-dimethoxy-5′-propenyl-5-propylbiphenyl (**III**)*

A solution of **13** (500 mg, 1.2 mmol) in CH_2Cl_2 (30 mL) was treated with trifluoroacetic acid (0.09 mL, 1.2 mmol). After being stirred at room temperature for 4 h, the mixture was reacted with water. The aqueous layer was extracted with CH_2Cl_2. The combined organic layers were washed with water, dried over $MgSO_4$, filtered, and concentrated to afford the expected compound **III** (*Z* isomer, 200 mg, 46%) as a yellow oil. IR (NaCl) (cm^{-1}): 960, 1050, 1230, 1250, 1500, 2950, 3600. ^{1}H NMR ($CDCl_3$) δ: 0.92 (t, 3H, CH_3), 1.35 (m, 3H, CH_3), 1.49 (m, 2H, CH_2), 1.75 (2d 3H, CH_3-CH=), 2.64 (m, 2H, CH_2), 3.88 (s, 3H, OCH_3), 3.91 (s, 3H, OCH_3), 4.21 (s, 2H, OCH_2O), 5.8–6.2, m, CH=CH), 6.4–6.8

© 2002 NRC Canada

(m, 4H, ArH). ^{13}C NMR ($CDCl_3$) δ: 13.8 (CH_3), 14.5 (CH_3), 17.7 (CH_3), 24.2 (CH_2), 37.5 (CH_2), 55.2 (OCH_3), 56.6 (OCH_3), 64.8 (OCH_2), 112.1 (CH), 117.0 (CH), 120.0 (CH), 121.5 (CH), 124.1 (CH), 126.8 (CH), 128.3 (C Ar), 130.5 (C Ar), 130.8 (C Ar), 131.4 (C Ar), 144.3 (C Ar), 145.9 (C Ar), 147.2 (C Ar), 149.1 (C Ar). MS (TMS derivative): 428 ([M]$^+$,100%), 399 (10%), 385 (15%), 73 (32%).

*2-Ethoxy-3,2′-dimethoxy-5-propenyl-4′-propyldiarylether (**IV**)*

A solution of **10** (560 mg, 3.4 mmol) in pyridine (15 mL) was treated with sodium hydride (90 mg, 3.7 mmol) and copper bromide (490 mg, 3.4 mmol). Then compound **9** (550 mg, 1.7 mmol) was added. After being stirred at 125°C for 18 h, the mixture was reacted with a solution of hydrochloric acid (10%). The aqueous layer was extracted with CH_2Cl_2. The combined organic layers were washed with water, dried over $MgSO_4$, filtered, and concentrated. The products were purified by chromatography on silica gel (eluent CH_2Cl_2) affording **2** (360 mg, 59%) as white crystals; mp 152°C (lit. (33) value mp +152°C), and compound **IV** (20 mg, 3.5%) as a pale oil. IR (NaCl) (cm^{-1}): 790, 1040, 1210, 1260, 1420, 1460, 1500, 1590, 2870, 2930, 2960. ^{1}H NMR ($CDCl_3$) δ: 0.95 (t, 3H, CH_3), 1.27 (t, 3H, CH_3), 1.62, 1.80, 2.56, 3.80, 3.82 (s, 3H, OCH_3), 3.86 (s, 3H, OCH_3), 4.10 (q, 2H, OCH_2), 6.0 to 6.8 (m, 8H, ArH, and CH=CH). ^{13}C NMR ($CDCl_3$) δ: 13.8 (CH_3), 15.4 (CH_3), 18.2 (CH_3), 24.7 (CH_2), 29.7 (CH_2), 37.8 (OCH_2), 55.8 (OCH_3), 55.9 (OCH_3), 104.3 (CH Ar), 109.0 (CH Ar), 112.9 (CH Ar), 119.2 (CH Ar), 120.6 (CH Ar), 125.1 (CH Ar), 130.5 (CH Ar), 133.3 (C Ar), 138.6 (C Ar), 139.5 (C Ar), 143.7 (C Ar), 148.1 (C Ar), 150.3 (C Ar), 153.9 (C Ar). MS: 356 ([M]$^+$,100%), 327 (20%), 296 (34%), 150 (31%).

Conclusion

Three biphenyl dimers (**I**–**III**) and one benzylaryl ether (**IV**) were synthesized to show the presence and the importance of phenolic coniferyl alcohol structures in the photoyellowing of high-yield pulps. The dimer **I**, incorporating two propyl chains, was detected in unbleached and sodium borohydride-reduced high-yield pulps in small amounts (≈4 × 10^{-6} mol g^{-1}). It is probably formed by thioacidolysis and Raney nickel treatments from phenolic biphenyl bearing coniferyl aldehyde moieties. Biphenyl **II**, which includes two propenyl chains, was detected in small amounts in peroxide bleached high-yield pulps, in the form of two stereoisomers. Biphenyl **II** probably comes from a ferulic-acid-type structure obtained from an oxidized propenal chain. No arylether **IV** or biphenyl **III** compounds were detected. This result probably indicates that phenolic phenylpropenol units are not present in softwood mechanical pulps, so they do not contribute to the photoyellowing process. A similar conclusion was obtained by us, on the involvement of stilbene phenol leucochromophores (17), and recently confirmed by Johansson et al. (37). After this study and others, the molecular origins of the fast photoyellowing of high-yield pulps remains to be established.

References

1. D.Y. Lee, M. Matsuoka, and M. Sumimoto. Holzforschung, **44**, 415 (1990).
2. D.Y. Lee, M. Matsuoka, and M. Sumimoto. Proceedings: Int. Symp. Wood Pulping Chem. 5th, Raleigh, NC, U.S.A. 21 (1989).
3. Z. Wu, M. Matsuoka, D.Y. Lee, and M. Sumimoto. Mokuzai Gakkaishi, **37**, 164 (1991).
4. D.Y. Lee and M. Sumimoto. Holzforschung, **44**, 347 (1990).
5. D.Y. Lee, S. Tachibana, and M. Sumimoto. Cellulose Chem. Technol. **22**, 201 (1988).
6. S. Li and K. Lundquist. Holzforschung, **53**, 39 (1999)
7. A. Castellan, N. Colombo, A. Nourmamode, J. Zhu, D. Lachenal, R.S. Davidson, and L. Dunn. J. Wood Chem. Technol. **10**, 461 (1990).
8. C. Noutary, P. Fornier de Violet, J. Vercauteren, and A. Castellan. (*a*) Res. Chem. Intermed. **21**, 223 (1995); (*b*) Res. Chem. Intermed. **21**, 247 (1995).
9. A. Castellan, H. Choudhury, R.S. Davidson, and S. Grelier. J. Photochem. Photobiol. A, **81**, 117 (1994).
10. A. Castellan, H. Choudhury, R.S. Davidson, and S. Grelier. J. Photochem. Photobiol. A, **81**, 123 (1994).
11. J.H. Zhu, C. Archer, F. MacNab, M.P. Andrews, G. Kubes, and D.G. Gray. J. Pulp Pap. Sci. **23**, J305 (1997).
12. (*a*) A.J. Nonni and C.W. Dence. Holzforschung, **42**, 37 (1988); (*b*) W.J. Leigh, T.J. Lewis, V. Lin, and J.A. Postigo. Can. J. Chem. **74**, 263 (1996).
13. S. Omori and C.W. Dence. Wood Sci. Technol. **15**, 113 (1981).
14. G. Gellerstedt and R. Agnemo. Acta Chem. Scand. **B34**, 275 (1980).
15. C. Heitner. ACS Symp. Ser. **531**, 1 (1993).
16. D.Y. Lee and M. Sumimoto. Holzforschung, **45** (supplement), 15 (1991).
17. B. Ruffin, A. Castellan, S. Grelier, A. Nourmamode, S. Riela, and V. Trichet. J. Appl. Polym. Sci. **18**, 333 (1998).
18. B. Ruffin and A. Castellan. Can. J. Chem. **78**, 73 (2000).
19. C. Jaeger, A. Nourmamode, and A. Castellan. Holzforschung, **47**, 375 (1993).
20. S. Bearnais-Barbry, R. Bonneau, and A. Castellan. J. Phys. Chem. A, **103**, 11 136 (1999).
21. S. Bearnais-Barbry, R. Bonneau, and A. Castellan. Photochem. Photobiol. **74**, 542 (2001).
22. X. Pan, D. Lachenal, C. Lapierre, and B. Monties. Proceedings: Int. Symp. Wood Pulping Chem. 6th, Melbourne, Australia, **1**, 451 (1991).
23. A. Castellan, A. Nourmamode, C. Noutary, C. Belin, and P. Fornier de Violet. J. Wood Chem. Technol. **12**, 19 (1992).
24. C. Lapierre, B. Pollet, and B. Monties. Phytochemistry, **30**, 659 (1991).
25. P. Karhunen, J. Mikkola, A. Pajunen, and G. Brunow. Nord. Pulp Pap. Res. J. **14**, 123 (1999).
26. G. Aulin-Erdtman. Sven. Papperstidn. **56**, 91 (1953).
27. G.M. Lampman, J. Andrews, W. Bratz, O. Hanssen, K. Kelley, D. Perry, and A. Ridgeway. J. Chem. Educ. **54**, 776 (1977).
28. M.S. Kharasch and E.K. Fields. J. Am. Chem. Soc. **63**, 2316 (1941).
29. S.P. Stanforth. Tetrahedron, **54**, 263 (1998).
30. D.L. Boger and D. Yohannes. Tetrahedron, **30**, 2053 (1989).
31. C. Lapierre, B. Pollet, and B. Monties. Holzforschung, **45**, 61 (1991).
32. H.A. Jones and H.L. Haller. J. Am. Chem. Soc. **62**, 2558 (1940).
33. J.F. Rabek, J. Sanetra, and B. Ranby. Macromolecules, **19**, 1674 (1986).
34. K. Elbs and H. Lerch. J. Prakt. Chem. **93**, 1 (1916).
35. W.A. Henderson and S.A. Buckler. J. Am. Chem. Soc. **82**, 5794 (1960).
36. K. Freudenberg and K.C. Renner. Chem. Ber. **98**, 1879 (1965).
37. M. Johansson, L. Zhang, and G. Gellerstedt. Nord. Pulp Pap. Res. J. **17**, 5 (2002).

© 2002 NRC Canada

Electrochemical oxidation of 6-propionyl-2-(*N*,*N*-dimethylamino)naphthalene (prodan) in acetonitrile on Pt electrodes: Reversible dimerization of prodan radical cations

Marcela Beatriz Moressi, María Alicia Zón, and Héctor Fernández

Abstract: The electrooxidation of 6-propionyl-2-(*N*,*N*-dimethylamino)naphthalene (prodan) has been investigated for the first time. It has been performed on both conventional size platinum electrodes and platinum ultramicroelectrodes in acetonitrile by cyclic voltammetry with convolution analysis and controlled-potential electrolysis. The voltammetric responses at room temperature are similar to those corresponding to a kinetically controlled anodic electron-transfer process. Cyclic voltammetry measurements were also carried out at different concentrations of prodan and at different temperatures. Chemical transformation of the radical monocation formed after the electrochemical oxidation of prodan, as deduced from reverse controlled potential bulk electrolysis and cyclic voltammetry measurements, gives evidence for the reversible dimerization of prodan radical cations. Both diagnostic criteria and digital simulation confirm that radical–radical coupling is the reversible chemical reaction coupled to the initial electron transfer step, to give the corresponding dimeric dication. The kinetic and thermodynamic parameters for the first electron transfer reaction and the dimerization process were estimated from digital simulation at 293 K. Values of 8.0×10^6 M^{-1} and 3.2×10^5 M^{-1} s^{-1} were determined for the dimerization reaction equilibrium constant and the dimer formation rate constant, respectively. The diffusion coefficient of prodan was determined from both limiting currents from convoluted cyclic voltammograms as well as limiting currents on ultramicroelectrodes. For such cases where the electron number exchanged in the electrode process is unknown, a method derived from the combination of data previously indicated is also proposed to obtain the diffusion coefficient of the electroactive species.

Key words: prodan, cyclic voltammetry, reaction mechanism, reversible dimerization, electron transfer reactions, radical cation.

Résumé : On a étudié l'électrooxydation du 6-propionyl-2-(*N*,*N*-diméthylamino)naphtalène (prodan). Ces études ont été réalisées sur des électrodes de platine de taille conventionnelle ainsi que sur des ultramicroélectrodes de platine, dans l'acétonitrile, en faisant appel à la voltampérométrie cyclique avec analyse de convolution et un potentiel d'électrolyse contrôlé. Les réponses voltampérométriques à la température ambiante sont semblables à celles d'un processus de transfert d'électron anodique sous contrôle cinétique. On a aussi effectué des mesures de voltampérométrie cyclique à diverses concentrations de prodan et à diverses températures. Des mesures de voltampérométrie cyclique et d'électrolyse globale inverse sous potentiel contrôlé suggèrent que la transformation chimique du monocation radicalaire qui se forme après l'oxydation électrochimique du prodan conduit à une dimérisation réversible des cations radicaux du prodan. Des critères diagnostiques et une simulation digitale permettent de confirmer que le couplage radical–radical est la réaction chimique réversible couplée à l'étape initiale de transfert d'électron et qu'elle conduit au dication dimère correspondant. Les paramètres cinétiques et thermodynamiques pour la réaction de transfert du premier électron et pour le processus de dimérisation ont été évalués à partir de la simulation digitale à 293 K. On a déterminé des valeurs de $8{,}0 \times 10^6$ M^{-1} et $3{,}2 \times 10^5$ M^{-1} s^{-1} respectivement pour la constante d'équilibre de la réaction de dimérisation et pour la constante de vitesse de formation du dimère. On a déterminé le coefficient de diffusion du prodan à partir des courants limites tant des voltampérogrammes cycliques convulés que des courants limites sur les ultramicroélectrodes. Pour obtenir le coefficient de diffusion des espèces électroactives dans les cas où on ne connaît pas le nombre d'électrons qui sont échangés au cours du processus à l'électrode, on propose aussi une méthode suggérée antérieurement et dérivée de la combinaison de données.

Mots clés : prodan, voltampérométrie cyclique, mécanisme réactionnel, dimérisation réversible, réactions de transfert d'électron, cation radical.

[Traduit par la Rédaction]

Received 10 December 2001. Published on the NRC Research Press Web site at http://canjchem.nrc.ca on 11 September 2002.

M.B. Moressi, M.A. Zón, and H. Fernández.[1] Departamento de Química y Física, Universidad Nacional de Río Cuarto, Agencia Postal No. 3 – (5800)-Río Cuarto, Córdoba, Argentina.

[1]Corresponding author (e-mail: hfernandez@exa.unrc.edu.ar).

 DOI: 10.1139/V02-112 © 2002 NRC Canada

Introduction

6-Propionyl-2-(*N*,*N*-dimethylamino)naphthalene (prodan) was introduced by Weber et al. (1) as a sensitive fluorescent probe for the electrostatic character of its environment. It has both an electron donor and an electron acceptor substituent in its molecular structure (see Fig. 1).

Prodan has a ground-state dipole moment between 2 and 2.5 D. Due to its large excited-state dipole moment (18–20 D), the maximum emission energy of prodan is highly dependent upon solvent polarity and its ability to hydrogen bond with protic solvents. The extension of its preferential solvation in binary solvent mixtures, where one component is capable of hydrogen bonding, was studied by fluorescence spectroscopy (2).

Prodan has been used in protein and more recently in lipid research (3–5). When this molecule is incorporated to membranes, its fluorescence spectra are sensitive to the physical state of the surrounding phospholipids. It is mainly located at the membrane surface (3), although FT-IR measurements indicate some degree of penetration into the interior lipid bilayer (6). Excited-state relaxation of prodan is sensitive to the nature of the linkage (ester or ether) between the phospholipid hydrocarbon tails and the glycerol backbone (7).

AM1 semiempirical calculations performed on the ground state of prodan predicted that this molecule has a planar conformation (8), in agreement with the X-ray crystal structure data. These theoretical calculations also allowed for estimations of the rotational barriers (0.03 kcal mol^{-1} for the propionyl and 0.33 kcal mol^{-1} for the amino group) and of the heat of formation (ΔE_f = 6.74 kcal mol^{-1}) (8).

As far as we know, no electrochemical study has been performed on this substrate. In this work, we discuss the results from the electrochemical oxidation of prodan in 0.1 M $NaClO_4$ + acetonitrile (ACN) on conventional-size platinum-disk electrodes (CSE) as well as platinum-disk ultramicroelectrodes (UME) by using cyclic voltammetry (CV) and controlled-potential bulk electrolysis.

Experimental

Reagents

Prodan was obtained from Molecular Probes and used as received. ACN (Sintorgan, HPLC grade) was dried over molecular sieves (3 Å) for 48 h prior to use and then used without further purification. $NaClO_4$ (Koch Light A.R.) was purified as previously reported (9). Stock solutions of prodan were prepared in ACN. Working solutions were prepared daily by adding aliquots of stock solutions to the 0.1 M $NaClO_4$ + ACN reaction medium, and protected from light. Prodan concentration was in the 0.05–6 × 10^{-3} M range. Sigma Chemical Co supplied analytical grade ferrocene.

Apparatus and experimental measurements

Cyclic voltammetry and large-scale electrolysis were performed with an EG&G Princenton Applied Research (PAR) potenciostat–galvanostat Model 273, equipped with Model PAR270 electrochemical-analysis software. The scan rate (v) was in the range of 0.010–100 V s^{-1}. Universal Programmer PARC model 175 was used with PAR 273 for high-sweep-rate experiments, and voltammograms were recorded in a Tektronic 7633 storaged oscilloscope.

Fig. 1. Chemical structure of 6-propionyl-2-(*N*,*N*-dimethylamino)naphthalene (prodan).

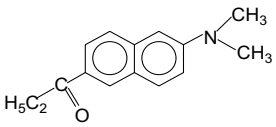

Electrochemical measurements were performed in a two-compartment Pyrex cell (10). Working electrodes were a Pt disk CSE or inlaid Pt disk UME. Pt UME were constructed in our laboratory as previously described (11). Before each measurement, the working electrodes were pretreated as reported elsewhere (11, 12). The electrochemical area of Pt CSE (A = 0.126 cm^2) as well as the Pt UME radii were calculated as previously reported (11, 12). The UME radii were in the range from 5 to 30 μm. The counter electrode was a platinum foil of large area (approx 2 cm^2). The reference electrode was an aqueous saturated calomel electrode (SCE) fitted with a fine-glass Luggin capillary containing a bridge solution identical to that of the sample being measured. Bulk-electrolysis cell and the corresponding electrodes were of the type described elsewhere (13). Positive-feedback techniques were employed in all experiments to compensate for solution resistance. All solutions were purged with solvent-saturated pure nitrogen. For most of the experiments, the working temperature was 293 ± 0.1 K, although it was changed in the 293–318 K range for some experiments to get more information about of the electrode-reaction mechanism. Fitting of experimental voltammograms was carried out through the BAS DigiSim® software, although simulations on UME were performed through POLAR 4.1 software (14). Calculations for chemical structures of probable reaction products were made through HyperChem® software.

Results and discussion

Cyclic voltammetry at CSE

Cyclic voltammograms of prodan at 293 K, and prodan bulk concentrations (c^*_{Pr}) in the order of 10^{-3} M are shown in Figs. 2*a* and 2*b*. An irreversible oxidation peak was observed on the anodic sweep at ~0.700 V. On the reverse sweep, a reduction peak appeared at ~0 V. An increase of the sweep rate from 0.025 to 100 V s^{-1} did not bring about any significant change in this picture. Typical voltammetric data for the anodic peak at different c^*_{Pr} in the 0.025–1.5 V s^{-1} range are tabulated in Table 1. Plots of the oxidation peak current ($I_{p,a}$) vs. $v^{1/2}$ were concave. $I_{p,a}/v^{1/2}c^*_{Pr}$ plots decrease with $v^{1/2}$ (Fig. 3), indicating that reaction(s) coupled to the initial electron transfer is (are) present (15). The anodic peak potential ($E_{p,a}$) was shifted in the anodic direction with an increase in the scan rate, while it was shifted in the cathodic direction as the c^*_{Pr} increases. Slopes of 0.021 ± 0.001 V/decade and −0.019 ± 0.001 V/decade were calculated from $E_{p,a}$ vs. log v and $E_{p,a}$ vs. log c^*_{Pr} plots, respectively. These findings are in good agreement with theoretical behaviour expected for electro-dimerization reactions through radical–radical coupling ("DIM1", see Scheme 1), where the coupling reaction is the rate determining step (RDS), i.e.:

© 2002 NRC Canada

Fig. 2. (*a*) Experimental and (*b*) simulated cyclic voltammograms of prodan in 0.1 M $NaClO_4$ + ACN. Working electrode: Pt disk (A = 0.126 cm^2). Reference electrode: ECS. v = 0.050 V s^{-1}. c^*_{Pr} = (*a*) 5.4 × 10^{-3} M and (*b*) 2.8 × 10^{-3} M. (*c*) Convoluted cyclic voltammograms: (1) c^*_{Pr} = 2.8 × 10^{-3} M, v = 0.200 V s^{-1}; (2) c^*_{Pr} = 5.4 × 10^{-3} M, v = 0.050 V s^{-1} (T = 293 K).

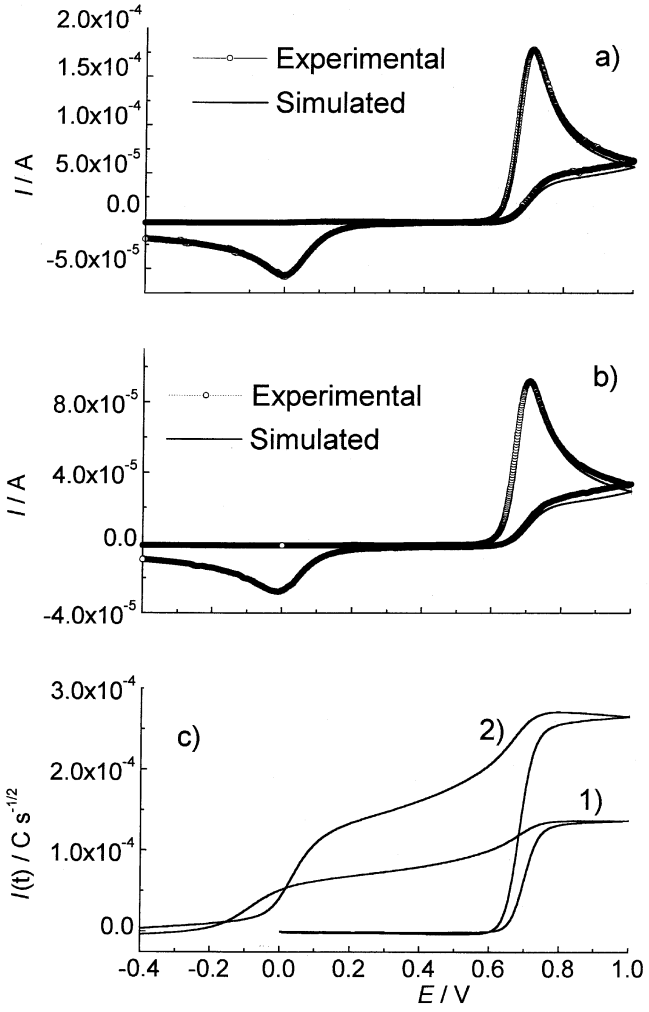

$\partial E_p/\partial \log v$ = 0.0197 V/decade and $\partial E_p/\partial \log c^*$ = −0.0197 V/decade at 25°C (16–18). Another dimerization mechanism ("DIM2", see Scheme 2) involving the radical cation – neutral substrate coupling was disregarded since the experimental data do not fit the parameters of diagnostic criteria for both limiting cases of the DIM2 mechanism, i.e., $\partial E_p/\partial \log v$ = 0.0296 V/decade and $\partial E_p/\partial \log c^*$ = –0.0296 V/decade or $\partial E_p/\partial \log v$ = 0.0197 V/decade and $\partial E_p/\partial \log c^*$ = −0.0394 V/decade at 25°C depending on the relative rate constants of chemical reactions involved in DIM2 mechanism (Scheme 2) (18). Because of the dependence of the peak potential on the scan rate one cannot distinguish between the two mechanisms. On the other hand, the variation of peak potential with log c^* is significantly different for the radical–radical coupling mechanism (DIM1, Scheme 1) and both limiting cases of the radical–substrate coupling mechanism (DIM2, Scheme 2) (18).

Fig. 3. Dependence of $I_{p,a}/v^{1/2}c^*_{Pr}$ on sweep rate at different concentrations. c^*_{Pr}: (●) 0.66 mM; (◆) 1.01 mM; (▼) 2.80 mM; (▲) 5.4 mM. The solid line is the simulated curve for Scheme 3 with the parameters shown in Table 2.

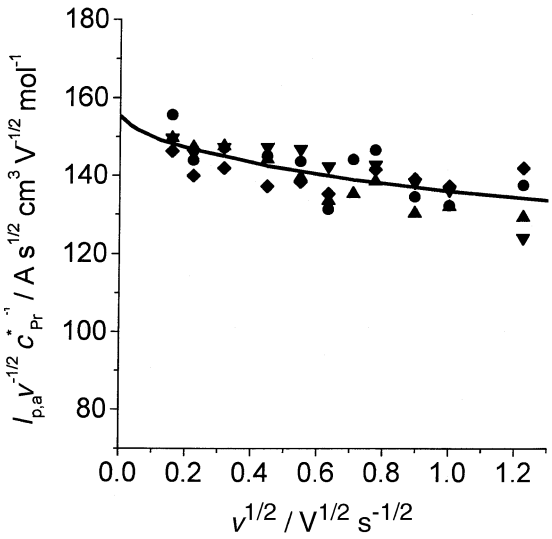

Scheme 1.

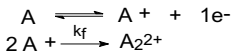

Scheme 2.

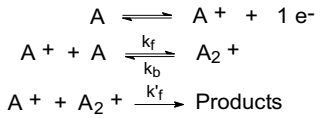

The reactivity of the radical ion has been largely studied (18–20), including the competitive radical–radical and radical–substrate coupling dimerization mechanisms by digital simulation (18). The applicability of the configuration mixing (CM) model to estimate energy barriers for these reactions has been also discussed (18).

Since reactants, transition states, and products for the two competitive mechanisms differ by only a single electron, steric factors should be the same for both pathways and it would be expected that the competition between the two mechanisms to be governed principally by electronic factors. On the basis of the CM model, it is possible to predict that radical–radical coupling dimerization (DIM1) will not have an electronic barrier, while that for radical–substrate coupling dimerization (DIM2) it will be significant. Moreover, the CM model predicts that DIM1 dimerization mechanism is ~7 kcal mol^{-1} thermodynamically more favourable than DIM2 dimerization mechanism (18).

Additionally, no complementary peak for the reduction peak is displayed on a third scan from cyclic voltammograms registered in the potential range from −0.4 to 1 V by using two consecutive cycles.

Convoluted cyclic voltammograms after subtraction of the background currents are shown in Fig. 2*c*. It can be observed that the convoluted current ($\bar{I}$(t)) value returns to zero after cyclic scan is complete. This behaviour indicates that the

© 2002 NRC Canada

Table 1. Voltammetric data for the anodic oxidation peak of prodan in ACN + 0.1 M $NaClO_4$ reaction medium for some of the c^*_{Pr} studied.

$c^*_{Pr} \times 10^3$ (M)	v (V s^{-1})	$E_{p,a}$ (V)	$I_{p,a}$ (μA)	$I_{p,a}/v^{1/2}c^*_{Pr}$ (A $s^{1/2}$ cm^3 $V^{-1/2}$ mol^{-1})	$c^*_{Pr} \times 10^3$ (M)	v (V s^{-1})	$E_{p,a}$ (V)	$I_{p,a}$ (μA)	$I_{p,a}/v^{1/2}c^*_{Pr}$ (A $s^{1/2}$ cm^3 $V^{-1/2}$ mol^{-1})
0.66	0.025	0.716	16.25	155.7	1.01	0.025	0.710	23.42	146.4
	0.050	0.721	21.25	144.0		0.050	0.715	30.77	140.0
	0.100	0.729	30.72	147.2		0.100	0.723	40.74	142.0
	0.200	0.735	42.82	145.1		0.200	0.729	62.13	137.3
	0.300	0.739	51.96	143.7		0.300	0.731	76.70	138.4
	0.400	0.742	54.86	131.4		0.400	0.735	86.70	135.4
	0.500	0.744	67.31	144.2		0.600	0.737	111.00	141.6
	0.600	0.746	74.96	146.6		0.800	0.739	126.00	139.2
	0.800	0.748	79.45	134.6		1	0.742	139.00	137.3
	1	0.750	87.34	132.3		1.5	0.746	176.00	142.0
	1.5	0.754	104.21	129.0					
2.8	0.025	0.703	66.32	149.8	5.4	0.025	0.698	127.86	149.7
	0.050	0.708	91.34	145.9		0.050	0.704	177.86	147.3
	0.100	0716	130.48	147.4		0.100	0.713	252.0	147.6
	0.200	0.721	184.64	147.4		0.200	0.717	348.3	144.2
	0.300	0.726	225.23	146.9		0.300	0.721	412.56	139.5
	0.400	0.729	252.23	142.4		0.400	0.723	456.02	133.5
	0.600	0.733	309.76	142.8		0.500	0.725	516.67	135.3
	0.800	0.738	346.13	138.3		0.600	0.728	579.17	138.5
	1	0.741	381.58	136.3		0.800	0.730	629.17	130.3
	1.5	0.740	425.71	124.1		1	0.732	712.14	132.0
						1.5	0.735	822.5	124.4

product of the oxidation reaction is entirely converted back to the substrate (21). The advantages of the convolution technique in the treatment of experimental data from cyclic voltammograms are well known (15, 22). Similar to the pure diffusion control model, the mathematical expression for the limiting convolution current ($\bar{I}_L$) for electrodimerization reactions through radical–radical coupling under pure kinetic control is expressed as (22),

$$[1] \qquad \bar{I}_L = nFAD^{1/2}c^* \qquad \text{(1)}$$

where n is the number of electrons exchanged per molecule of the electrolyzed substrate, F is the Faraday constant, A is the electrode area, and D is the diffusion coefficient of the electroactive species. Limiting convolution currents can be used to determine the diffusion coefficient of prodan if $n = 1$ (from controlled-potential bulk electrolysis, see below). An average value of $\bar{D}$ ($(2.03 \pm 0.05) \times 10^{-5}$ cm^2 s^{-1}) was calculated for prodan at 293 K from the data extracted from convoluted voltammograms, similar to those shown in Fig. 2*c*. The plots of E vs. log $[(\bar{I}_L - \bar{I}(t))/I^{2/3}]$ were linear, with an average slope of 0.064 ± 0.002 V/decade, close to that theoretically predicted for a consecutive dimerization coupled to a reversible monoelectronic-transfer reaction, i.e., 0.0591 V/decade at 25°C (22).

To obtain more information about the overall reaction mechanism, additional experiments were performed by variation of temperature at lower concentrations and scan rates than those indicated previously. Marked changes were observed in voltammetric responses when concentration was decreased and temperature was increased (Fig. 4). At a low concentration and low scan rate ($c^*_{Pr} = 5 \times 10^{-5}$ M, v = 0.020 V s^{-1}), a new cathodic peak starts to appear in the potential range from 0.5 to 0.8 V as the temperature is increased (see Figs. 4*a*–*c*). This electrochemical signal can be assigned to the reduction of the radical monocation generated during the anodic scan. The cathodic peak observed in the potential range of 0.2 to −0.4 V at room temperature is poorly defined under these experimental conditions; however, a new complementary cathodic peak (0.5−0.8 V) was better defined at the lowest concentration and the highest temperature studied, i.e., 5.0×10^{-5} M and 318 K, respectively. This behaviour can be clearly inferred from cyclic voltammograms shown in Fig. 5, despite the fact that they are poorly defined at that low concentration of prodan.

A detailed evaluation of changes observed in cyclic voltammograms by variation of concentration, scan rate, and temperature led us to conclude that formation of the radical cations was followed by a reversible dimerization of the species producing a dimeric dication (Scheme 3). Dimeric dications can then be reduced during the cathodic scan (in one or two electrochemical steps) to give the neutral dimer, which can dissociate to regenerate the starting reactant. This process would give rise to a cathodic peak located at about 0 V. Further support to this mechanism is given below.

It is well known that the enthalpy of organic radical coupling reactions is negative (23). Although the contribution of reaction entropy for dimerization reactions can not be neglected, the reaction enthalpy would have a greater contribution than the reaction entropy on the Gibbs free energy. This can be inferred from experimental results obtained by Smie and Heinze (24) for the reversible dimerization of the radical cations formed through the anodic oxidation of diphenylpolyenes. Similar findings have also been recently reported for dimer dication formation through a reversible

© 2002 NRC Canada

Fig. 4. Cyclic voltammograms of prodan in 0.1 M $NaClO_4$ + ACN obtained at different temperatures. c^*_{Pr} = 5.0 × 10^{-5} M, v = 0.020 V s^{-1}, T = (*a*) 293 K; (*b*) 304 K; and (*c*) 318 K.

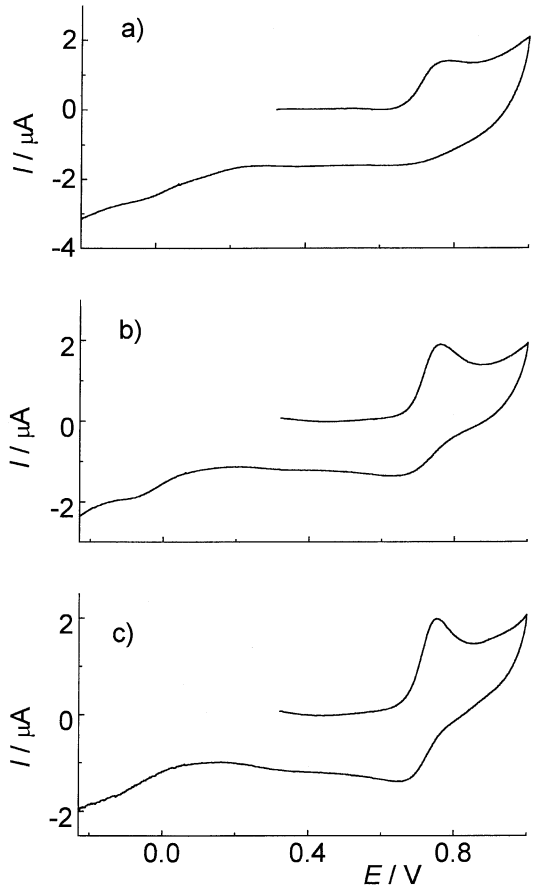

Scheme 3.

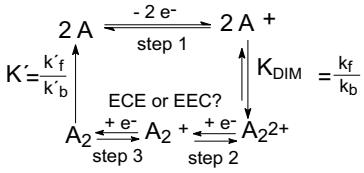

radical cation – radical cation dimerization with 3,3′,5,5′-tetramethyl-2,2′-bithiophene as the starting molecule (25). Thus, taking into account the voltammetric results obtained by changing temperature, which appear very similar to those found for systems mentioned above (24, 25), it is proposed that the dimerization equilibrium established between radical cations of prodan and the formed dimeric dication is shifted towards the radical monocation as the temperature is increased. Additionally, the dependence of voltammetric responses with concentration is another clear indication that the initial charge-transfer reaction is followed by a reversible second-order reaction, assumed to be a dimerization process. Thus, at higher temperatures and lower concentrations of the starting reactant, the follow-up chemical reaction attains a thermodynamic equilibrium. Although the electrogenerated radical cation undergoes fast dimerization in the time scale of the experiment, the dimeric product is dissociated into radical cations, which are reduced to the neutral species on the voltammetric reverse scan. At higher concentrations and lower temperatures, the overall electrochemical process is kinetically controlled and the dimerization reaction dominates (25). Under these conditions, cyclic voltammograms show only the cathodic peak in the potential range from 0.2 to −0.4 V, which can be ascribed to the reduction of the dimeric product.

Fig. 5. Cyclic voltammograms of prodan in 0.1 M $NaClO_4$ + ACN obtained at different prodan concentrations. T = 318 K, v = 0.100 V s^{-1}, c^*_{Pr} = (*a*) 5.0 × 10^{-5} M and (*b*) 1.0 × 10^{-4} M.

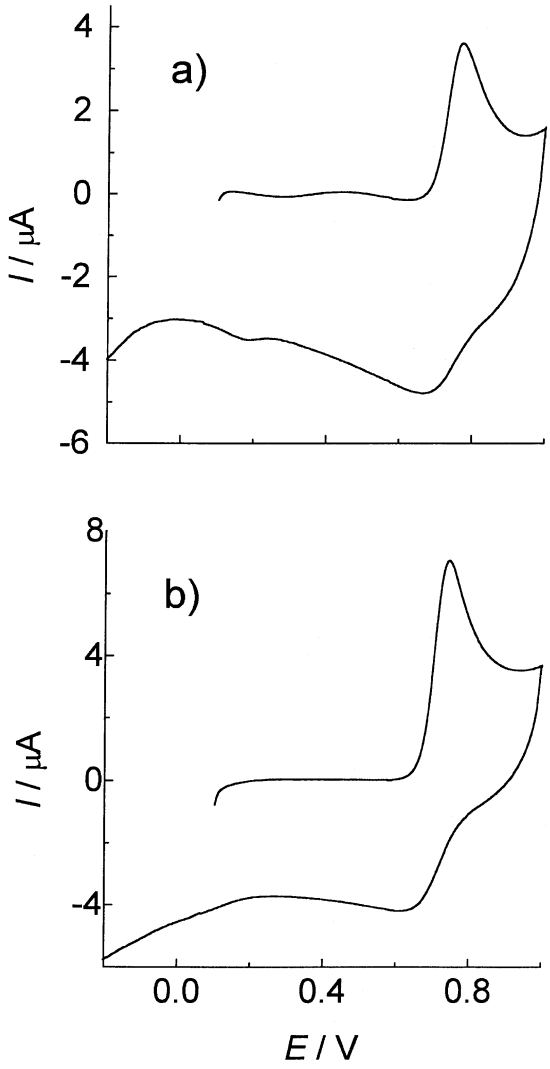

Simulation and fitting of cyclic voltammograms

The cyclic voltammograms (Scheme 3) at different sweep rates and concentrations of the reactant were generated by digital simulation to obtain parameters for diagnostic criteria. Thus, we found $\partial E_p/\partial \log v$ = (0.0223 ± 0.0003) V/decade and $\partial E_p/\partial \log c^*$ = –(0.0192 ± 0.0002) V/decade. Agreement between simulated and theoretical (see above) $\partial E_p/\partial \log c^*$ values is excellent, but the $\partial E_p/\partial \log v$ values differ by ~13%. This difference may be a consequence of additional steps that follow the dimer formation. Regardless, the difference is small enough to consider that the DIM1

© 2002 NRC Canada

Table 2. Formal potential and heterogeneous kinetic parameters for the main electron transfer reaction (Scheme 3, step 1) as well as equilibrium constant and forward and backward rate constants for the dimerization reaction obtained from the best fitting according to Scheme 3 at 293 K.

$E_f^\circ(1)$ (V)	$k_f^\circ(1)$ (cm s^{-1})	$(1 - \alpha)_1$	K_{DIM} (M^{-1})	k_f (s^{-1} M^{-1})	k_b (s^{-1})
0.740	0.19	0.5	8.0×10^6	3.2×10^5	0.04

mechanism still governs the dimer formation in Scheme 3. Experimental values (already shown above) agree very well with values calculated from the simulation for Scheme 3. Figure 3 also shows the variation in $I_{p,a}/v^{1/2}c^*$ with $v^{1/2}$ calculated from the simulation and the parameters of the best fitting (see below). As it can be observed, agreement with experimental values is also very good.

Experimental cyclic voltammograms were also fitted by digital simulation. The best fitting curves (solid lines in Figs. 2*a* and 2*b*) at different concentrations and scan rates were obtained when the Scheme 3 was used as the reaction mechanism model, i.e., considering a radical–radical coupling (DIM1). Simulations of cyclic voltammograms were also performed at other scan rates than those shown in Figs. 2*a* and 2*b*, i.e., 0.075, 0.100, and 0.2 V s^{-1} at the same concentrations indicated in the figures. The DIM2 mechanism gave a poorer fitting than the DIM1 mechanism, which is in good agreement with results of experimental data and diagnostic criteria (see above). It can be seen in Fig. 2 that the fits using the DIM1 mechanism were very good. The small differences found at the end of the anodic scan and the beginning of the reverse cathodic scan for the experimental and simulated curves might be explained by considering the difficulty in obtaining the faradaic currents properly corrected for by the background currents in that potential region.

The quantitative analysis results of the fitting of experimental cyclic voltammograms are gathered in Table 2. $E_f^\circ(1)$, $k_f^\circ(1)$, and $(1 - \alpha)_1$ are the formal potential, the formal heterogeneous rate constant, and the anodic transfer coefficient, respectively, for the main anodic charge-transfer reaction (Scheme 3, step 1). K_{DIM}, k_f, and k_b are the equilibrium constant and the forward and backward rate constants, respectively, for the dimerization reaction.

The low value for the dimer dissociation rate constant ($k_b = 0.04$ s^{-1}) explains that under normal experimental conditions the overall reaction is kinetically controlled even at low scan rates. In the voltammetric reverse scan the signal for the successive reduction of the dimeric product is, therefore, particularly strong.

The thermodynamic and kinetic parameters for reactions other than the dimerization reaction in Scheme 3 can also be obtained from the fitting procedure, although they are probably not meaningful, because it was assumed that the concentration of prodan dimer in solution is very low, if detectable at all. It has also not been possible to distinguish by digital simulation whether the reduction of the dimeric dication follows an EEC or an ECE reaction mechanism. The values of these thermodynamic and kinetic parameters were, however, used to generate theoretical cyclic voltammograms to establish diagnostic criteria, as was previously indicated.

Through simulation techniques, Evans et al. (26) generated working curves for the mechanism shown in Scheme 1. There, $(E_p - E_f^\circ)$ for the anodic peak and cathodic–anodic peak current ratio were correlated to a kinetic parameter (Ψ_k) defined as $\Psi_k = Kc^*[a/(k_f c^* + k_b)]^{1/2}$, where a is the scan rate parameter (Fv/RT); the other parameters have been previously defined. For very large Ψ_k, Evans et al. (26) have shown that dimerization does not occur for any Kc^* value and the peak moves 28.5 mV in the positive direction of E_f°. As Ψ_k decreases, a transition to a pure kinetics region occurs, where essentially irreversible dimerization occurs. The peak potential moves 39.4 mV in the negative direction per decade decrease in Ψ_k until a transition occurs to the equilibrated dimerization, i.e., the pure diffusion region (27). In this region, $E_{p,a}$ again becomes independent of Ψ_k but is negative of E_f° to an extent dependent on Kc^*. This fact reflects the thermodynamic effect of the reversible dimerization following electron transfer (26). Thus, with the experimental $E_{p,a}$ at different concentrations of prodan and different sweep rates and kinetic parameters and $E_f^\circ = 0.740$ V (calculated from the best fitting, see Table 2), values for $(E_p - E_f^\circ)$ and Ψ_k were obtained. From interpolation in the $(E_p - E_f^\circ)$ vs. log Ψ_k plot (Fig. 1 in ref. 26), a $7 \times 10^6 - 2 \times 10^7$ M^{-1} range was established for K_{DIM}. The value of $K_{DIM} = 8.0 \times 10^6$ M^{-1} obtained from our best fitting of experimental data (Table 2) agrees well with values calculated from the Evans et al. plot. On the other hand, from the cathodic and anodic peak current ratio as function of log Ψ_k (Fig. 3 in ref. 26), the experimental log Ψ_k interval matches the range corresponding to a pure chemical-reaction kinetic-control region, with a reversible dimerization behaviour (defined as KP_r in ref. 26). These are complementary results, which allow us to infer that Scheme 3 proposed for the anodic oxidation of prodan is highly probable to be the correct one.

Controlled-potential bulk electrolysis

Bulk electrolysis were carried out at a potential ~0.1 V more positive than the anodic peak potential. The result found for the number of electrons exchanged per molecule of electrolyzed substrate from three replicated measurements, expressed as mean ± standard deviation, was $n = 1.00 \pm 0.25$. Cyclic voltammograms taken after 30 min of electrolysis by employing three consecutive hemicycles showed a pronounced diminution of the oxidation peak of prodan during the first anodic hemicycle (compare Figs. 6*a* and 6*b* (*i*)) as well as an increase in the reduction peak current during the second cathodic hemicycle. Also, an increase in the oxidation peak current during the third anodic consecutive hemicycle was observed (Fig. 6*b* (*ii*)), clearly showing that the original substrate is recovered after the cathodic scan. No new peaks were found on the second hemicycle (the cathodic hemicycle). Moreover, reverse controlled-potential bulk electrolysis performed at −0.2 V allowed the recovery of the cyclic voltammogram of prodan obtained from fresh solutions (compare Figs. 6*c* and 6*a*). On the other hand, the average cathodic charge (Q_c) obtained after performing the

© 2002 NRC Canada

Fig. 6. Cyclic voltammograms recorded: (*a*) before the electrolysis; (*b*) after 30 min of electrolysis by employing three consecutive hemicycles, where (*i*) and (*ii*) represent the first and the second anodic hemicycles, respectively; and (*c*) after performing the reverse electrolysis for 30 min (see text). $c^*_{Pr} = 1.76 \times 10^{-3}$ M, $v = 0.050$ V s^{-1}, $T = 293$ K.

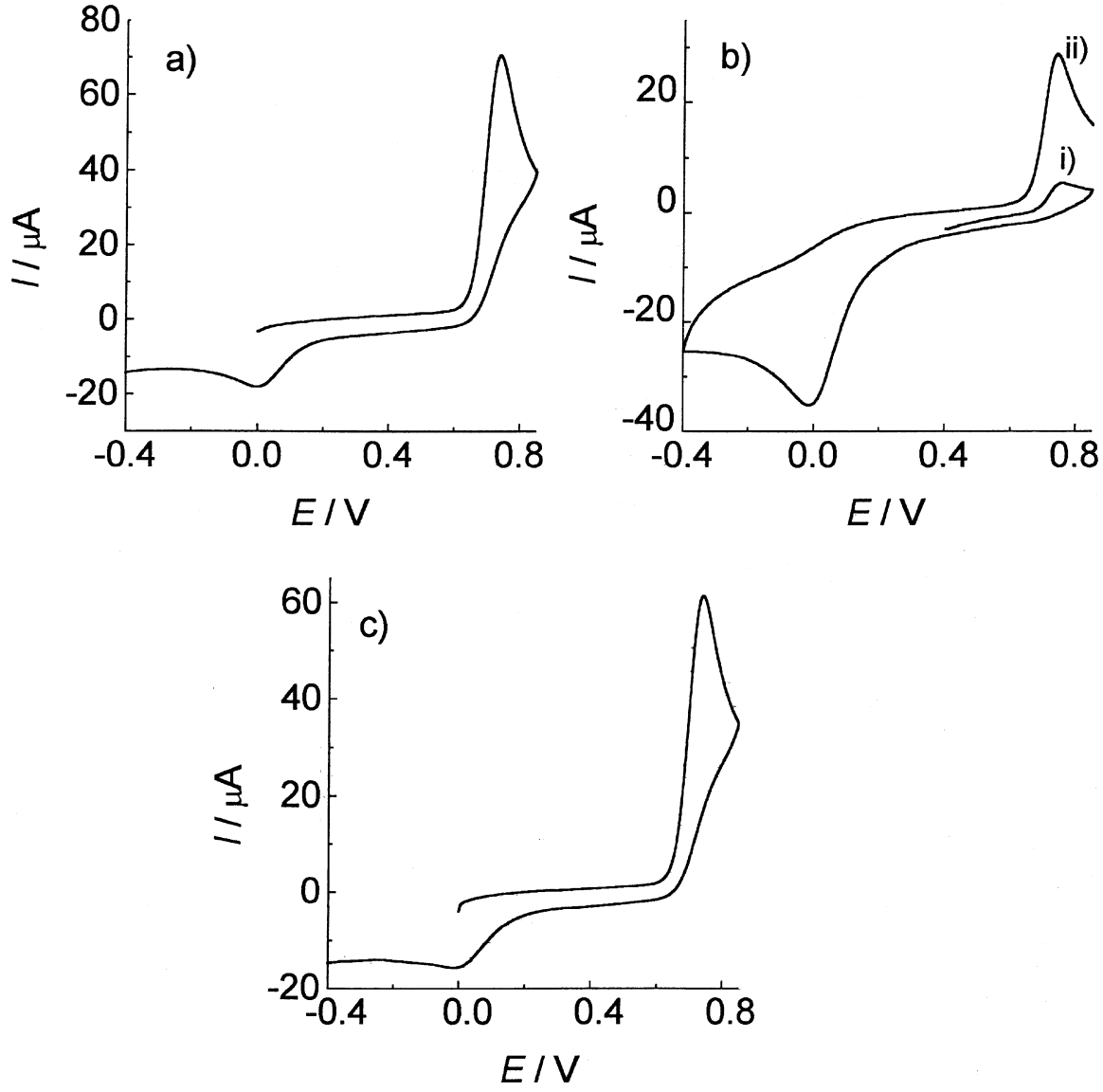

reverse electrolysis for 30 min ($Q_c = 791 \pm 6$ μC) was very close to that measured during the anodic electrolysis, i.e., the anodic charge ($Q_a = 777 \pm 5$ μC). The original colourless of prodan + 0.1 M $NaClO_4$ + ACN solutions was retrieved after carrying out the reverse controlled-potential bulk electrolysis.

The dissociation of the reduced dimer (A_2 in Scheme 3) occurs extensively on reverse preparative-electrolysis time scale, from which the starting material can be regenerated. This would clearly explain the experimental results previously discussed for anodic and cathodic (reverse) controlled-potential bulk electrolysis.

The UV–vis absorption spectra (28) obtained before and after the anodic electrolysis showed a few changes in the shape of the bands. The increase in absorbance (*a*) at λ = 346 nm is responsible for the apparition of a light yellow colour in the electrolyzed solutions — this colour disappears after the reverse electrolysis. These results indicate little or no increase in conjugation of the dimeric molecule (A_2 in Scheme 3) with respect to that of prodan.

Cyclic voltammetry at UME

Typical quasi-steady-state voltammograms obtained at Pt UME at low sweep rates are shown in Fig. 7. Under these conditions, quasi-steady-state responses are due to convergent diffusion predominating over planar diffusion (29–32). An expression for the diffusion-limited quasi-steady-state current (I_L) for a UME was derived by Saito (33),

© 2002 NRC Canada

Fig. 7. Quasi-steady-state cyclic voltammograms of prodan in 0.1 M $NaClO_4$ + ACN. Working electrodes: Pt disk UME: r = (*a*) 11 μm; (*b*) 18.3 μm; and (*c*) 26.5 μm. Reference electrode: ECS. $c^*_{Pr} = 5.6 \times 10^{-4}$ M, $v = 0.010$ V s^{-1}, $T = 293$ K.

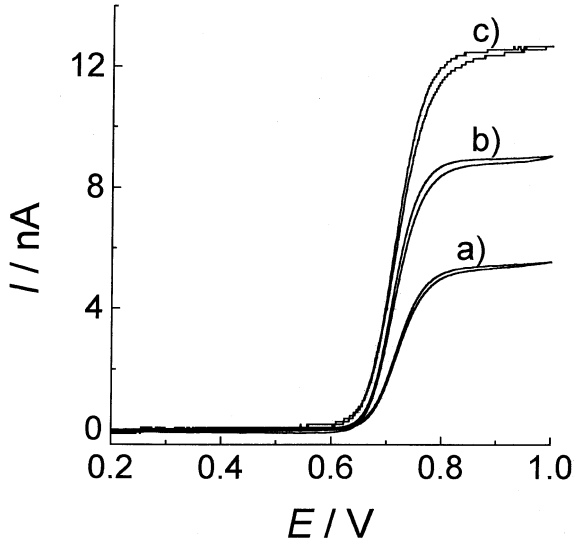

$$[2] \qquad I_L = 4nFc^*Dr$$

where r is the UME radius; the other terms have been previously defined.

As stated elsewhere (30), the use of UME of convenient radius can mask coupled chemical reactions and, thus, the resulting current-potential curves do not differ from those obtained from a pure charge-transfer reaction. To assess this statement, and with the purpose of checking if eq. [2] corresponds also to the limiting current for the reaction mechanism shown in Scheme 3, digital simulations for UME were performed using POLAR 4.1 software. As far as we know, POLAR 4.1 is the only commercial program for the simulation of reaction mechanisms at UME. Linear sweeps at different dimerization rate constant in the 0.04–3.2 × 10^8 M^{-1} range for a given UME radius ($r = 11 \times 10^{-4}$ cm) and $c^* = 5.4 \times 10^{-3}$ M were, therefore, generated with POLAR 4.1. The other parameters for simulation were obtained from the fitting procedure carried out on Pt CSE cyclic voltammograms. It was found that $E_{1/2}$ is independent on k_f up to k_f = ~0.1, but for k_f values higher than ~3.2 M^{-1} s^{-1}, $E_{1/2}$ is linear with log k_f with a slope of –0.0131 V/decade. I_L is independent of k_f within 0.1% accuracy but varies linearly with UME radius and c^* for a given D. These results suggest that eq. [2] could also represent the limiting current for a mechanism of the type here proposed. Thus, the diffusion coefficient of prodan can be also calculated from eq. [2] when $n = 1$ (from controlled-potential bulk electrolysis) for a solution of prodan at $c^*_{Pr} = 5.6 \times 10^{-4}$ M and UME's of three different radii, i.e., 11.0 × 10^{-4}, 18.3 × 10^{-4}, and 25.6 × 10^{-4} cm. The corresponding limiting currents were: 5.31, 8.88, and 12.5 nA, respectively, (see Fig. 7). An average value for the diffusion coefficient of $\bar{D}$ = (2.22 ± 0.03) × 10^{-5} cm^2 s^{-1} was calculated.

For such cases where the electron number exchanged in the electrochemical reaction is unknown, we propose here an alternative method for the determination of the diffusion coefficient of the electroactive species that is independent of the exchanged electron number in the electrode process. It is based in the combination of convolution limiting currents on CSE and limiting currents on UME data through the ratio of $\bar{I}_L$ (eq. [1]) and I_L (eq. [2]),

$$[3] \qquad D = (AI_Lc^*_{con}/4rc^*_{UME}\bar{I}_L)^2$$

where c^*_{con} and c^*_{UME} are the reactant concentration for convolution and UME experiments, respectively.

An average value of $\bar{D}_{Pr}$ of (2.37 ± 0.06) × 10^{-5} cm^2 s^{-1} was calculated from a set of $\bar{I}_L$ and I_L for different prodan concentrations and different UME radii.

It seems reasonable to calculate a most probable value for the diffusion coefficient of prodan under the experimental conditions as an average of the values found from convoluted and UME voltammetry, i.e., $\overline{\bar{D}}_{Pr}$ = (2.2 ± 0.1) × 10^{-5} cm^2 s^{-1}.

Alternatively, another method based on the use of an internal standard was employed in quasi-steady-state CV UME measurements as another way to check the exchanged electron number in the electrode process. It is well known that ferrocene (Fc) undergoes an uncomplicated monoelectronic electrooxidation ($n_{Fc} = 1$) to its corresponding monocation. A diffusion coefficient value for Fc (D_{Fc}) in 0.1 M $NaClO_4$ + ACN reaction medium was previously determined in our laboratory, i.e., $D_{Fc} = 2.32 \times 10^{-5}$ cm^2 s^{-1} (11). Thus, taking into account the corresponding limiting currents (eq. [2]) for prodan- and Fc-redox couples at the same UME, one obtains

$$[4] \qquad \frac{n_{Pr}}{n_{Fc}}\frac{D_{Pr}}{D_{Fc}} = \frac{I_{L,Pr}}{c^*_{Pr}}\frac{c^*_{Fc}}{I_{L,Fc}}$$

where the symbols Pr and Fc represent to prodan and ferrocene compounds, respectively. An average value of 0.95 ± 0.01 was calculated for the right term of eq. [4]. From this result, and by using $D_{Pr}/D_{Fc} = 0.948$, it was determined that $n_{Pr} = 1.00$, which is in excellent agreement with the n value previously determined from controlled-potential bulk electrolysis measurements.

Analysis of the I vs. E characteristics obtained from digital simulation on UME using the reaction mechanism shown in Scheme 3 and employing parameters obtained from the best fitting of Pt CSE cyclic voltammograms renders values of $\partial E/\partial \log [(I_L - I)/I] = 0.055 \pm 0.008$ V/decade ($n = 1$) and $E_{3/4} - E_{1/4} = 0.060$ V at 293 K. Experimental E vs. log $[(I_L - I)/I]$ plots were linear, with slopes of 0.053 ± 0.002 V/decade, in reasonable agreement with the simulated value.

Moreover, a positive shift in the half-wave potential ($E_{1/2}$) of quasi-steady-state voltammograms was experimentally observed as the UME radius was decreased (see Fig. 7), with a slope of about 0.008 V/decade. Results for $E_{1/2}$ vs. UME radius from simulation experiments give an exponential decay-type plot. Nevertheless, in the narrow interval of the experimental radius variation, a near-linear variation of $E_{1/2}$ with r can be assumed from simulated data. From it, a slope of about −0.012 V/decade was calculated in the 11–26.5 μm radii interval. Thus, the experimental slope value is relatively close to that obtained by simulation. Shifts in $E_{1/2}$ on UME are reported to be a consequence of heterogeneous kinetics (34). Thus, for the narrow-radius interval worked in

© 2002 NRC Canada

Fig. 8. Structure of 6-propionyl-2-(*N*,*N*-dimethylamino)naphthalene dimer dication according to AM1 calculations when the σ bond was formed between C8–C8. C—C Distance = 1.546 Å.

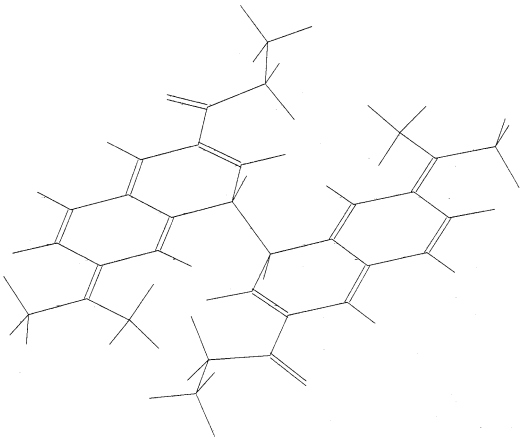

this paper, no definitive conclusion can be drawn about $E_{1/2}$ shifts.

Reactivity of prodan radical cations

Results for the electrooxidation of prodan found in this work for the 0.1 M $NaClO_4$ + ACN reaction medium suggest that the formation of radical cations in the first redox step is followed by a reversible dimerization to produce the corresponding dimeric dication (DIM1 mechanism, Scheme 3). These results also show that the coupling between the radical cations and neutral species can be ruled out (16, 18, 27). Besides, reversible dimerization reactions have been previously invoked in a number of electrochemical reaction schemes (26, 35–37).

The reactivity of prodan radical cations might be explained by considering that the radical cation generated in the initial step of the electrochemical oxidation would have a low stability, because the propionyl group present in the prodan structure is an electron withdrawing substituent. On the other hand, it has been generally found that electron donating substituents tend to stabilize radical cations (38, 39). Furthermore, in the absence of severe steric effects, the radical ion reactivity is dominated by the degree of coupling between charge and radical centres (19). Decoupling of these functions, charge, and radical centres is expected to enhance the reactivity of one or both of the centres. Substitution with heteroatom substituents at different positions of radical cations is expected to decouple the charge and radical centres. For example, dimerization rates of arene radical cations were observed to be greatly enhanced by methoxy and *N*,*N*-dimethylamino substituents, which separate the charge and radical centres (19). Thus, the dimerization of prodan radical cations would be favoured by the presence of *N*,*N*-dimethylamino group in its molecular structure (see Fig. 1). According to the different resonance structures of the prodan radical cation, the possible radical centres would be at carbons 1, 3, and 8 and the oxygen atom of carbonyl group. Taking into account steric factors, the radical centres at C8 and oxygen appear as the most reactive sites. From the analysis given above, prodan radical cations should have low stability and great capability for dimerization. This hypothesis is verified from experimental results, i.e., the coupling rate

Fig. 9. Structure of 6-propionyl-2-(*N*,*N*-dimethylamino)naphthalene dimer dication according to AM1 calculations when the σ bond was formed between oxygen atoms of the carbonyl groups. O—O Distance = 1.323 Å.

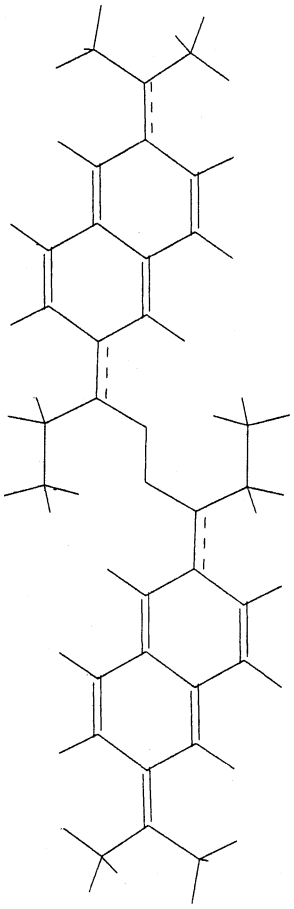

constant (k_f) of prodan radical cations is very high and the dissociation rate constant (k_b) is very low (see Table 2). This helps to explain why the complementary cathodic peak at about 0.5–0.8 V is poorly defined, even at high temperatures and low concentrations. The fact that the radical–radical coupling dimerization mechanism is favoured over the competitive radical–substrate dimerization mechanism can be explained by considering that the low stabilization of the radical cations does not allow sufficient time for diffusion of these species from the electrode surface to the solution, where collisions with parent molecules would be more likely. A covalent interaction between the two cationic species can be explained by taking into account the very low rate constant for the cleavage of the dimeric dication, despite the strong continued coulombic repulsion. This interpretation has been already given by Heinze and co-workers (25) for the reversible formation of bithiophene radical cations. Thus, taking into account the results published for oligoenes (24), thiantrenes, and bithiophenes (25), and those shown for prodan in this report, we propose that a σ bond is formed in the dimeric prodan structure. The dimer structure is still unknown. From AM1 calculations done by assuming a σ bond between the two radical cations in C8—C8 position as well as between the oxygen atoms of the carbonyl groups, the

© 2002 NRC Canada

dimerization coupling through O—O renders the most stable structure, according to the heat of formation of these species in the gas phase, i.e., $\Delta H^{2+}_{f,Pr}$ (C—C) = +615.2 kcal mol^{-1}; $\Delta H^{2+}_{f,Pr}$ (O—O) = +468.7 kcal mol^{-1}. The dimer structures obtained from AM1 calculation are shown in Figs. 8 and 9. To establish the most probable structure of the dication in solution, however, the solvation energies (not known) for these species must be considered as well as the isolation of the dimer should be performed. Further studies are in progress in this way.

Conclusions

The electrochemical oxidation of prodan in the 0.1 M $NaClO_4$ + ACN reaction medium is reported for the first time. Experimental results allow us to infer that the formation of radical cations in the initial electron transfer reaction is followed by a reversible dimerization of these species to produce the corresponding dimeric dication (DIM1 mechanism, Scheme 3). Additionally, both the digital simulation of cyclic voltammograms and the diagnostic criteria also show that the coupling between the radical cations and neutral species can be ruled out.

Acknowledgments

Financial support from Consejo Nacional de Investigaciones Científicas y Técnicas (CONICET) and Secretaría de Ciencia y Técnica (SECyT) from the Universidad Nacional de Río Cuarto is gratefully acknowledged. M.B. Moressi thanks CONICET for the postdoctoral fellowship. The authors thank Professor L.E. Sereno for use of DIGISIM simulation software. We are indebted to Lilia Fernández for language assistance.

References

1. G. Weber and F.J. Farris. Biochemistry, **18**, 3075 (1979).
2. W.P. Zurawsky and S.F. Scarlatta. J. Phys. Chem. **96**, 6012 (1992).
3. P.L.-G. Chong. Biochemistry, **27**, 399 (1988).
4. T. Parasassi, E.K. Krasnowska, L. Bagatolli, and E. Gratton. J. Fluoresc. **8**, 365 (1998).
5. E.A. Lissi, E.B. Abuin, M.A. Rubio, and A. Ceron. Langmuir, **16**, 178 (2000).
6. P.L.-G. Chong, S. Capes, and P.T.T. Wong. Biochemistry, **28**, 8358 (1989).
7. A. Sommer, F. Paltauf, and A. Hermetter. Biochemistry, **29**, 11 134 (1990).
8. P. Ilich and F.G. Prendergast. J. Phys. Chem. **93**, 4441 (1989).
9. H. Fernández. Ph.D. thesis. Universidad Nacional de Río Cuarto, Argentina. 1978.
10. H. Fernández and L. Sereno. An. Asoc. Quim. Arg. **74**, 421 (1986).
11. M.A. Zón, M.B. Moressi, L.E. Sereno, and H. Fernández. Bol. Soc. Chil. Quím. **39**, 139 (1994).
12. M.A. Zón, H. Fernández, L. Sereno, and J.J. Silber. Electrochim. Acta, **32**, 71 (1987).
13. A.H. Arévalo, H. Fernández, J.J. Silber, and L. Sereno. Electrochim. Acta, **35**, 741 (1990).
14. POLAR 4.1 for Windows. Electrochemical simulation and data analysis. Pty Ltd., Kingsford, Sydney, Australia.
15. A.J. Bard and L.R. Faulkner. *In* Electrochemical methods. Fundamentals and applications. J. Wiley & Sons, New York. 1980.
16. J.M. Savéant and E. Vianello. Electrochim. Acta, **12**, 1545 (1967).
17. L. Nadjo and J.M. Savéant. J. Electroanal. Chem. **44**, 327 (1973).
18. V.D. Parker. Acta Chem. Scand. **52**, 154 (1998).
19. V.D. Parker. Acta Chem. Scand. **52**, 145 (1998), and refs. cited therein.
20. F. Effenberger, W.-D. Stohrer, K.-E. Mack, F. Reisinger, W. Seufert, H.A. Kramer, R. Foll, and E. Vogelmann. J. Am. Chem. Soc. **112**, 4849 (1990).
21. F.E. Woodard, R.D. Goodin, and P.J. Kinlen. Anal. Chem. **56**, 1920 (1984).
22. J.C. Imbeaux and J.M. Saveant. J. Electroanal. Chem. **44**, 169 (1973).
23. L.G. Wade, Jr. *In* Química orgánica. 2nd ed. Prentice-Hall Hispanoamericana, S.A. 1993.
24. A. Smie and J. Heinze, Angew. Chem. Int. Ed. Engl. **36**, 363 (1997).
25. P. Tschuncky, J. Heinze, A. Smie, G. Engelmann, and G. Koβmehl, J. Electroanal. Chem. **433**, 223 (1997).
26. D.H. Evans, P.J. Jimenez, and M. Kelly. J. Electroanal. Chem. **163**, 145 (1984).
27. C.P. Andrieux, L. Nadjo, and J.M. Savéant. J. Electroanal. Chem. **26**, 147 (1970).
28. R.P. Haugland. *In* Handbook of fluorescent probes and research chemicals. 5th ed. Molecular Probes, Inc., Eugene. 1992–1994.
29. K.B. Oldham, C.G. Zoski, A.M Bond, and D.A. Sweigart. J. Electroanal. Chem. **248**, 467 (1988).
30. Edited by M.I. Montenegro, M.A. Queirós, and J.L. Dachbach. Microelectrodes: theory and applications, NATO ASI Series. Vol. 197. Klumer Academic Publishers, Dordrech. 1990.
31. Y. Zhang, C.D. Baer, C. Camaioni-Neto, P. O'Brien, and D.A. Sweigart. Inorg. Chem. **30**, 1682 (1991).
32. K.B. Oldham and J.C. Myland. *In* Fundamentals of electrochemical science. Academic Press, Inc., San Diego, California. 1994.
33. Y. Saito. Rev. Polarogr. **15**, 177 (1968).
34. M. Fleischmann, S. Pons, D. Rolinson, and P.P. Schmidt. *In* Ultramicroelectrodes. Datatech Systems, Inc., Morganton, U.S.A. 1987.
35. C.Th. Pederson, V.D. Parker, and O. Hammerich. Acta Chem. Scand. B, **30**, 478 (1976).
36. O. Hammerich and V.D. Parker. Acta Chem. Scand. B, **35**, 341 (1981).
37. P. Margaretha and V.D. Parker. Acta Chem. Scand. B, **36**, 260 (1982).
38. R.F. Nelson and R.N. Adams. J. Am Chem. Soc. **90**, 3925 (1968).
39. S.C. Creason, J. Wheeler, and R.F. Nelson. J. Org. Chem. **37**, 4440 (1972).

© 2002 NRC Canada

Crystal structure and spectral considerations of 5-methyl-2-nitraminopyridine *N*-oxide

A. Szemik-Hojniak, T. Głowiak, I. Deperasińska, and A. Puszko

Abstract: The crystal structure of 5-methyl-2-nitraminopyridine *N*-oxide (5M) has been determined and its electronic absorption spectra in the solution have been investigated. In the solid, two monomeric proton-transferred (PT) units of 5M are perpendicularly located in the crystal lattice. They are connected by two intermolecular hydrogen bonds of different strength (O-H···N 2.647(3) and 2.695(3) Å). In the gas phase the same relative arrangement of both 5M (PT) monomers has been found. As results from semiempirical PM3-CI calculations (12–14), the prototropic amino (H) ↔ imino (PT) equilibrium may occur in the solution. Assignment of experimental absorption bands to the calculated transition energies of both forms of 5M reveals that hydrogen bonded 5M (PT) dimers are dominant in cyclohexane while imino (PT) monomers seem to prevail in acetonitrile solution. The different character of electronic transitions and different relative arrangement of both monomers in amino (H) than in imino (PT) dimers are responsible for very low oscillator strengths and dipole moments of the former.

Key words: crystal structure, methylated nitraminopyridine *N*-oxides, semiempirical PM3-CI computations, intermolecular hydrogen bonding.

Résumé : La structure cristalline de *N*-oxyde de la 5-méthyl-2-nitraminopyridine (5M) a été déterminée et son spectre d'absorption électronique étudié. En phase solide, deux unités monomères avec un proton transféré 5M (PT) sont localisées perpendiculairement dans une cellule cristalline. Elles sont liées par deux liaisons hydrogènes O-H···N intermoléculaires et asymétriques, 2,647(3) et 2,695(3) Å. En phase gazeuse, le même arrangement des deux monomères a été observé. Les calculs semi-empirique PM3-CI (12–14) indiquent que l'équilibre prototropique amino (H) ↔ imino (PT) peut exister en solution. L'identification des bandes d'absorption expérimentale aux énergies de transition calculées des formes amino et imino de 5M montre que des dimères 5M (PT) liés par des liaisons hydrogènes sont majoritaires dans le cyclohexane alors que dans l'acétonitrile l'équilibre des deux formes se déplace en faveur du monomère imino (PT). Le caractère différent des transitions électroniques et les différents arrangements relatifs des monomères dans les amino (H) et imino (PT) dimères sont à l'origine des très faibles forces oscillatoires et de des moments dipolaires de la forme amino (H).

Mots clés : structure cristalline, *N*-oxydes de méthyl-nitraminopyridines, calculs semi-empiriques PM3-CI, liaison hydrogène intermoléculaire.

[Traduit par la Rédaction]

1. Introduction

Crystallographic structures and absorption spectra of several nitraminopyridine *N*-oxides (NAPNO) have been published recently (1–3). These compounds belong to a wide class of pyridine *N*-oxide derivatives known as antifungal drugs (4, 5) and those that crystallize as non-centrosymmetric crystals may display a nonlinear second-order response (6). Among the NAPNO series, till now, only one non-centrosymmetric compound has been found, i.e., the 3-nitraminopyridine *N*-oxide (1). Others (1, 2) had been shown to be centrosymmetric.

NAPNO dimers (1–3) are linked through N-H···O or O-H···N hydrogen bonds and therefore may be also treated as model compounds for planar and nearly planar, hydrogen bonded nucleobase dimers (7). Contrary to earlier recognized CT (charge transferred) derivatives of pyridine (8), pyridine *N*-oxides (9), and methyl-aminopyridine *N*-oxides (10), in the NAPNO series due to the proximity of the amino and the nitro group in one complexed nitramino (-NH-NO_2) function, a substantial distortion of electron density across the molecule takes place. This in turn affects not only the *push–pull* properties of the *N*-oxide group (1, 2, 8–11) but also decreases the electron accepting abilities of the nitro group itself (1, 2).

In previously published nitraminopyridine *N*-oxide compounds, the nitramino group was attached to the carbon atom in an ortho (2NAPNO), meta (3NAPNO), or para (4NAPNO) (1, 3) position with respect to the NO group. The second substituent in the 2NAPNO molecule (the methyl group)

Received 18 April 2002. Published on the NRC Research Press Web site at http://canjchem.nrc.ca on 11 September 2002.

A. Szemik-Hojniak[1] **and T. Głowiak**. Faculty of Chemistry, University of Wroclaw, Joliot-Curie 14 st, 50-383 Wroclaw, Poland.
I. Deperasińska. Institute of Physics, Pol. Acad. of Sciences, Al. Lotników 32/46, 02-668 Warsaw, Poland.
A. Puszko. Institute of Chemical and Food Technology, University of Economics, 53-345 Wrocław, Poland.

[1]Corresponding author (e-mail: anias@wchuwr.chem.uni.wroc.pl).

 DOI: 10.1139/V02-142 © 2002 NRC Canada

Table 1. Summary of data collection and processing parameters for 5M.

5M	
Formula	$C_6H_7N_3O_3$
Colour	Light brown
Molecular mass	169.15
Space group	*C*2/*c*
Temperature (K)	293 (2)
Cell volume (Å^3)	2927.9 (10)
Crystal system	Monoclinic
Cell constants (25)	$19.4 < 2\theta < 36.5$
a (Å)	29.984(6)
b (Å)	7.406(2)
c (Å)	13.584(3)
α	90.00
β (°)	103.92 (3)
γ	90.00
Formula units/unit cell	16
D_{calc} (mg m^{-3})	1.535 (1)
D_{exp} (mg m^{-3})	1.54
Absorption coefficient (mm^{-1})	1.079
Difractometer/scan	Kuma KM4/ω – 2θ
Radiation (Å) (graph. monochromated)	1.54180
Max crystal dimensions (mm)	0.15 × 0.20 × 0.30
No. of standard ref. and int.	3 (100 ref.)
Standards decay (%)	<3.5
2θ Range (°)	160
Range of *h*, *k*, *l*	0/38, 0/8, –17/16
Reflections measured/independ.	3045/3001 (R_{int} = 0.0181)
Reflections observed ($I > 2\sigma(I)$)	1993
Corrections applied	Lorentz and polarization effects
Computer programs	SHELXS 97 (16), SHELXL 97 (17)
Structure solution	Direct methods
Treatment of hydrogens atoms	Refined parameters: *x*, *y*, *z*, U_{iso}
No. of parameters varied	228
GOF	1.126
$R_1 = \Sigma(\|F_o\| - \|F_c\|)/\Sigma(\|F_o\|)$	0.0524
$wR_2=\{\Sigma[wF_o^2 - F_o^2)^2]/\Sigma[w(F_o^2)^2]\}^{1/2}$	0.1556
R_1/R_2 Indices (all data)	0.0808/0.1857
Extinction coefficient	0.00120 (17)
Function minimized	$\Sigma w(\Delta F^2)^2$
Largest feature final diff. map (e A^{-3})	0.249 and – 0.214

was in position 3 (3M) (2) or in position 4 (4M) (2). In this work, being a continuation of our earlier study on methylated-2-nitramino pyridine *N*-oxides (2), the compound with the methyl group in position 5 of 2NAPNO, i.e., 5-methyl-2-nitraminopyridine *N*-oxide, henceforth called 5M, will be thoroughly discussed. In section 2, experimental details of X-ray analysis and PM3-CI computations are described while section 3A and B is devoted to the structure consideration. In particular we noticed that crystalline 5M proton-transferred (PT) dimers consist of two mutually perpendicular monomers with the amino hydrogen being at the NO group. Identical orthogonality of monomeric planes has also been found in the PM3-optimized 5M (PT) dimer (12–14). Contrary to that, a parallel arrangement of both monomers was stated in complementary calculated amino (H) dimers. In section 4, experimental absorption electronic bands of 5M in nonpolar and polar aprotic solvents are assigned to the calculated ones and the reasons for very small oscillator strength and dipole moment values observed in amino (H) dimers are analysed. This analysis is given within the framework of the results of the semi-empirical PM3-CI calculations. Conclusions are presented in section 5.

2. Experimental details and calculations

The title compound was obtained in accordance with the procedures described elsewhere (15). Crystals were grown from a methanol–water (1:1) solution. All X-ray measurements were performed on the KUMA KM-4 diffractometer with graphite-monochromated Cu K_α radiation at room temperature. The stability of the crystal was monitored by the measurement of three standards every 100 reflections. The data were corrected for Lorentz and polarization effects. No absorption correction was applied. Experimental details are given in Table 1.

© 2002 NRC Canada

Table 2. Final atomic coordinates ($\times 10^{-4}$) and equivalent thermal parameters with ESDs in parentheses for 5M.

	x	*y*	*z*	*U*(eq)
O(11)	4200(1)	310(3)	584(2)	66(1)
O(12)	2972(1)	–3180(4)	555(2)	82(1)
O(13)	3490(1)	–5192(4)	1086(3)	109(1)
N(11)	4405(1)	–1341(3)	846(2)	52(1)
N(12)	3681(1)	–2392(3)	675(2)	54(1)
N(13)	3380(1)	–3667(4)	776(2)	66(1)
C(11)	4137(1)	–2806(4)	858(2)	50(1)
C(12)	4376(1)	–4462(5)	1048(2)	59(1)
C(13)	4844(1)	–4497(5)	1194(2)	64(1)
C(14)	5105(1)	–2956(5)	1174(2)	60(1)
C(15)	4864(1)	–1373(5)	995(2)	58(1)
C(16)	5619(1)	–2967(8)	1355(3)	77(1)
O(21)	3226(1)	773(3)	359(2)	60(1)
O(22)	4532(1)	1699(4)	2769(2)	89(1)
O(23)	4041(1)	2558(5)	3596(2)	106(1)
N(21)	3062(1)	950(3)	1215(2)	50(1)
N(22)	3813(1)	1171(3)	2077(2)	56(1)
N(23)	4133(1)	1817(4)	2861(2)	64(1)
C(21)	3364(1)	1218(4)	2123(2)	52(1)
C(22)	3162(1)	1415(5)	2948(2)	62(1)
C(23)	2697(1)	1412(5)	2810(3)	66(1)
C(24)	2401(1)	1229(4)	1856(3)	62(1)
C(25)	2603(1)	947(4)	1069(3)	57(1)
C(26)	1886(1)	1290(7)	1679(4)	80(1)

Note: *U*(eq) is defined as one-third of the trace of the orthogonalized U_{ij} tensor.

The structure was solved by direct methods with SHELXS-97 (16) and refined by full-matrix least-square methods using SHELXL-97 (17) with anisotropic thermal parameters for non-H atoms. At intermediate stages of the refinement, the difference maps showed all H atoms. In the final cycles of the refinement parameters for H-1 and H-2 with isotropic thermal parameters were included. All other atoms were placed by geometry using a riding model and assigned thermal parameters equal to 1.2 times the U_{eq} of the attached C for aromatic H atoms and 1.5 times the U_{eq} of the attached C for methyl H atoms. Scattering factors were taken from *International tables for X-ray crystallography* (18). Final atomic parameters for 5M are presented in Table 2.

The UV absorption spectra in the solution were recorded on CARY-1 UV–vis spectrometer at 298 K. All solvents used were of spectral grade. The quantum-mechanical, semiempirical PM3 method (12–14) was used for calculations. Full geometry optimization was performed for a monomer and a dimer of 5M in its molecular (H) and (PT) form. The energies of the electronic excited states were determined by means of the configuration interaction (CI) with 257 singly excited configurations between 16 HOMO and 8 LUMO orbitals taken into account.

3. Structure considerations

A. Crystal structure

The final crystal structure with atom numbering of 5M, and the projection of the unit cell of 5M along the *y* axis are presented in Figs. 1(*a*) and 1(*b*), respectively. The bond length and valence angles for 5M are displayed in Table 3.

Table 3. Bond lengths (Å) and angles (°) for molecules A and B of 5M with ESDs in parentheses.

A		B	
Bond lengths (Å)			
O(11)—N(11)	1.376(3)	O(21)—N(21)	1.376(3)
O(12)—N(13)	1.241(3)	O(22)—N(23)	1.237(3)
O(13)—N(13)	1.222(4)	O(23)—N(23)	1.227(4)
N(11)—C(15)	1.342(4)	N(21)—C(25)	1.340(4)
N(11)—C(11)	1.352(4)	N(21)—C(21)	1.358(4)
N(12)—N(13)	1.336(3)	N(22)—N(23)	1.338(3)
N(12)—C(11)	1.364(4)	N(22)—C(21)	1.362(4)
C(11)—C(12)	1.413(4)	C(21)—C(22)	1.405(4)
C(12)—C(13)	1.367(5)	C(22)—C(23)	1.361(5)
C(12)—H(3)	0.94(3)	C(23)—C(24)	1.390(5)
C(13)—C(14)	1.388(5)	C(24)—C(25)	1.366(4)
C(13)—H(4)	0.87(3)	C(24)—C(26)	1.506(5)
C(14)—C(15)	1.367(4)		
C(14)—C(16)	1.504(5)		
Bond angles (°)			
C(15)-N(11)-C(11)	125.0(3)	C(25)-N(21)-C(21)	124.9(3)
C(15)-N(11)-O(11)	115.6(2)	C(25)-N(21)-O(21)	116.0(2)
C(11)-N(11)-O(11)	119.1(2)	C(21)-N(21)-O(21)	119.0(2)
N(13)-N(12)-C(11)	119.6(2)	N(23)-N(22)-C(21)	118.8(2)
O(13)-N(13)-O(12)	121.3(3)	O(23)-N(23)-O(22)	121.7(3)
O(13)-N(13)-N(12)	123.8(3)	O(23)-N(23)-N(22)	123.3(3)
O(12)-N(13)-N(12)	114.9(3)	O(22)-N(23)-N(22)	114.9(3)
N(11)-C(11)-N(12)	112.9(2)	N(21)-C(21)-N(22)	114.0(2)
N(11)-C(11)-C(12)	114.9(3)	N(21)-C(21)-C(22)	114.7(3)
N(12)-C(11)-C(12)	132.2(3)	N(22)-C(21)-C(22)	131.3(3)
C(13)-C(12)-C(11)	120.1(3)	C(23)-C(22)-C(21)	121.0(3)
C(12)-C(13)-C(14)	123.0(3)	C(22)-C(23)-C(24)	122.1(3)
C(15)-C(14)-C(13)	115.6(3)	C(25)-C(24)-C(23)	116.1(3)
C(15)-C(14)-C(16)	120.8(4)	C(25)-C(24)-C(26)	120.8(3)
C(13)-C(14)-C(16)	123.6(4)	C(23)-C(24)-C(26)	123.1(3)
N(11)-C(15)-C(14)	121.4(3)	N(21)-C(25)-C(24)	121.1(3)
N(11)-O(11)-H(1)	105(3)	N(21)-O(21)-H(2)	102(3)

5M crystallizes in the centrosymmetric *C*2/*c* space group and, like earlier investigated non-methylated 2NAPNO (1) or methylated 4M (2), occurs in its (PT) form, i.e. with the amino proton being transferred to the NO group. Simultaneously, a bare nitrogen of the amino group becomes a hydrogen bond acceptor of the proton originating from the -NOH group of an adjacent 5M (PT) molecule. Hence, two different molecules A and B form a cyclic dimer with two different, intermolecular, asymmetric and linear hydrogen bonds; O(11)-H(1)···N(22) = 2.647(3) Å and O(21)-H(2)···N(12) = 2.695(3) Å. The corresponding two O-H-N angles are 180(4)° and 174(4)°, respectively. The two monomers of 5M dimer are perpendicularly located each with respect to another as illustrated in Fig. 1(*b*).

The methyl group substituted in the *meta* position in 5M or in the *para* position in 4M (2) relative to the NO group does not affect the electronic conjugation of the functional groups with the π system of the aromatic ring. Only a substantial steric hindrance due to the *ortho effect* was found in 3M (2) with the methyl group adjacent to nitramino group.

© 2002 NRC Canada

Fig. 1. (*a*) The numbering scheme of two symmetry independent molecules of 5M. The broken lines represent the hydrogen bonds in the crystal. The ellipsoids correspond to 30% probability of contours of atomic displacement; (*b*) view of the structure along the [010] direction.

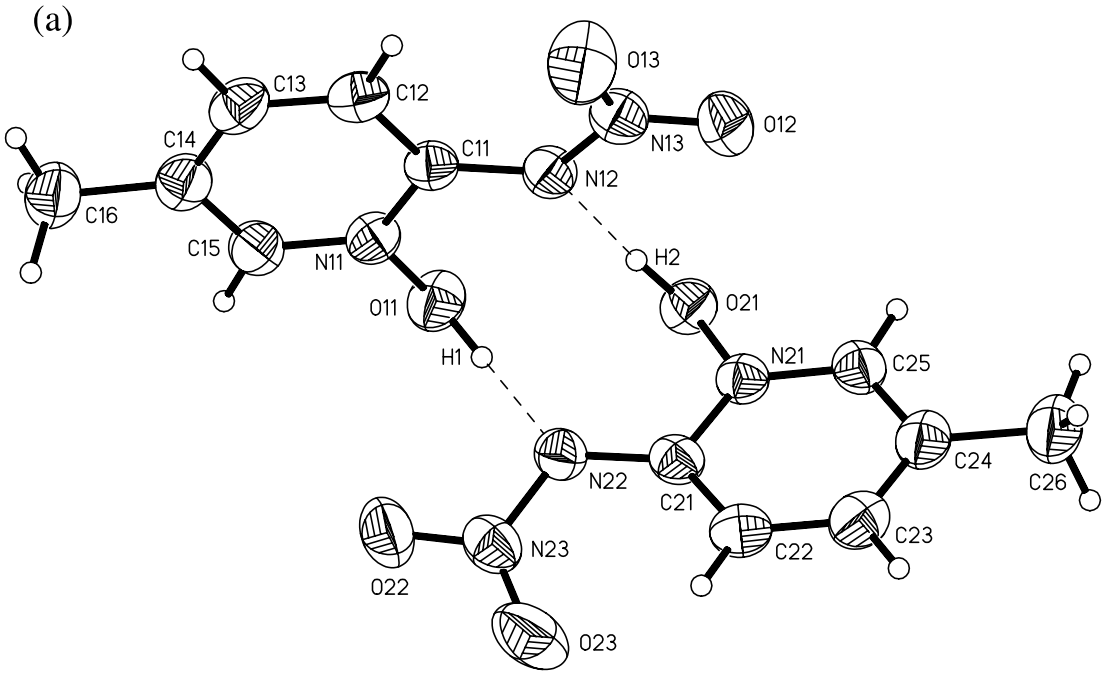

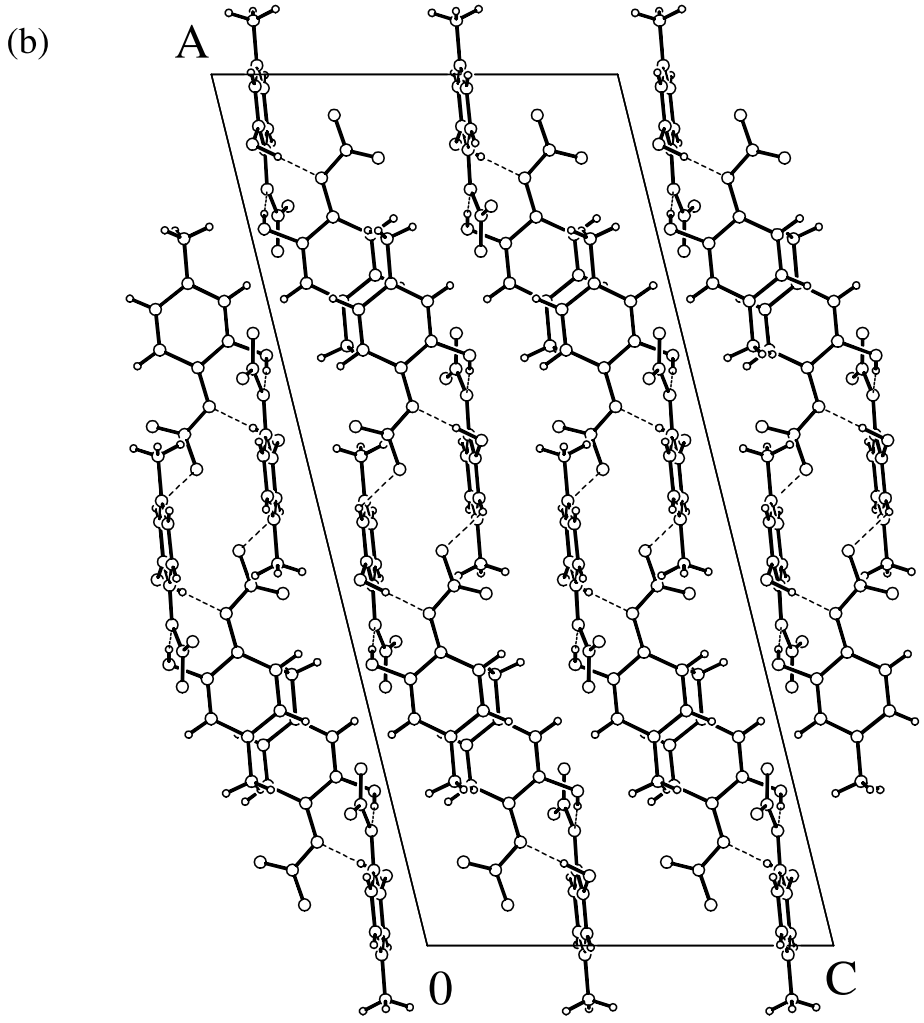

© 2002 NRC Canada

Table 4. Comparison of X-ray data of 5M with those of 4M (PT) (**2**) and 2NAPNO (PT) (**1**) structures.

Compound	5M	4M (PT)	2NAPNO (PT)
Displacement of the NO group (°)	(A) –174.0(2)	(A) 175.1(3)	(A) –176.2(2)
	(B) 176.2(2)	(B) 173.3(3)	(B) –174.7(2)
d (N—O)$_{NO}$ (Å)	(A) 1.376(3)	(A) 1.377(4)	(A) 1.383(3)
	(B) 1.374(3)	(B) 1.373(4)	(B) 1.375(2)
Displacement of $N_{(amino)}$ atom (°)	(A) 178.8(2)	(A) –175.6(3)	(A) 177.3(3)
	(B) –179.9(3)	(B) 178.7(4)	(B) 175.8 (2)
d (C_{ar}—N_{amino}) (Å)	(A) 1.360(3)	(A) 1.367(4)	(A) 1.368(3)
	(B) 1.354(3)	(B) 1.356(4)	(B) 1.364(3)
Displacement of the NO_2 group (°)	(A) –172.2(2)	(A) –178.9(3)	(A) –168.7(2)
	(B) 164.7(2)	(B) –170.8(3)	(B) –169.2(2)
d (N_{amino}—N_{nitro}) (Å)	(A) 1.334(3)	(A) 1.337(4)	(A) 1.349(3)
	(B) 1.332(3)	(B) 1.349(4)	(B) 1.347(3)
d (C_{ar}—N_{NO}) (Å)	(A) 1.355(3)	(A) 1.362(4)	(A) 1.367(3)
	(B) 1.358(4)	(B) 1.359(4)	(B) 1.361(3)

There, displacement of the whole NO_2 group is larger than in 5M and 4M (2). This is demonstrated in Table 4.

An average value of the appropriate dihedral angle in 5M, 4M (2), and 3M (2) is 168.45(2)°, –174.8(3)°, and –70.8(3)°, respectively. This angle in 5M is rather like that in non-methylated 2NAPNO (168.8(2)°) (1).

The appearance of the molecular (H) or (PT) form of the NAPNO series depends on the different arrangement of two monomers in the crystal lattice and on the degree of electronic conjugation of all functional groups with the π system of the pyridine ring. A perpendicular arrangement of both monomers in dimer predicts the (PT) form while a mutually parallel arrangement, the (H) form. It follows that an average displacement of the nitro group and of the amino nitrogen atom as well as an average C_{ar}—N_{amino} distance is usually slightly smaller in the (PT) form (2). On the other hand, displacement of the NO group from the ring plane and an average N—O bond length are slightly larger in (PT) than in (H) form.

As viewed in Fig. 1, both molecules of the 5M dimer are perpendicularly orientated, as for instance those in 4M (PT) dimer (2). Others with the parameters mentioned above also point at a (PT) form of 5M. For example, the average C_{ar}—N_{amino} distance in 5M (1.357(3) Å) is similar to that in 4M (PT) (1.361(4) Å), but significantly shorter than that in 3M (H) (1.401(2) Å). Also, the N—O distance in 5M (1.375(3) Å) is similiar to the N—O distance in 4M (PT) (1.375(4) Å) (2), while a substantially shorter value was found in 3M (H) (1.316(2) Å) (2).

In methylated derivatives of 4-nitropyridine *N*-oxide such as 3-methyl-4-nitropyridine *N*-oxide (9), 3,5-dimethyl-4-nitropyridine *N*-oxide (19), and 2,3-dimethyl-4-nitropyridine *N*-oxide (20), the average C_{ar}—C_{methyl} distance is about 1.50 Å. In methylated nitraminopyridine *N*-oxides, similar values of 1.502(4) Å in 5M and 1.495(6) Å in 4M (2) were found.

Fig. 2. (*a*) Atom numeration in 5M (H); and (*b*) in 5M (PT) (structures used in PM3 optimization).

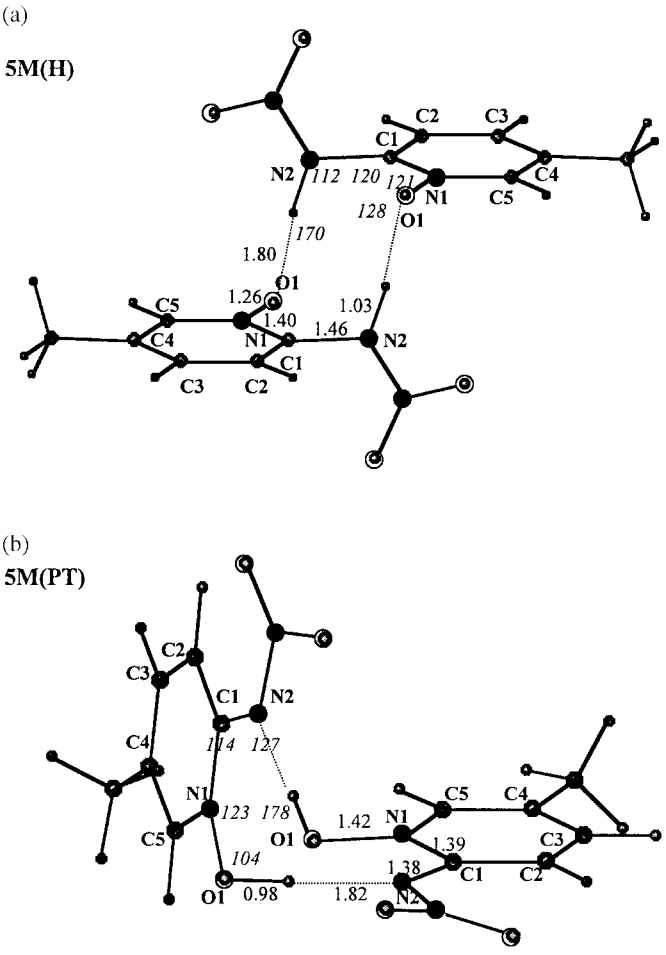

B. Molecular geometries

PM3-optimized structures of the 5M monomer and dimer both in (PT) and in its complementary (H) form were used in theoretical absorption spectra calculations. More appropriate names of imino (PT) and amino (H) species are proposed for the gas and the liquid phase, in place of the (PT) and (H) forms, respectively, used for the solid state. Geometrical parameters of optimized molecules are consistent with experimental crystallographic data and some are given in Fig. 2.

Experimental, averaged N···H and H—O bond lengths are 1.69(4) and 0.98(4) Å, respectively, while the corresponding calculated values are 1.82 and 0.98 Å, respectively. Also the

© 2002 NRC Canada

Fig. 3. The difference of charge distribution between the dimer and monomer of 5M vs. particular atoms of the 5M-amino (H) and 5M-imino (PT) form.

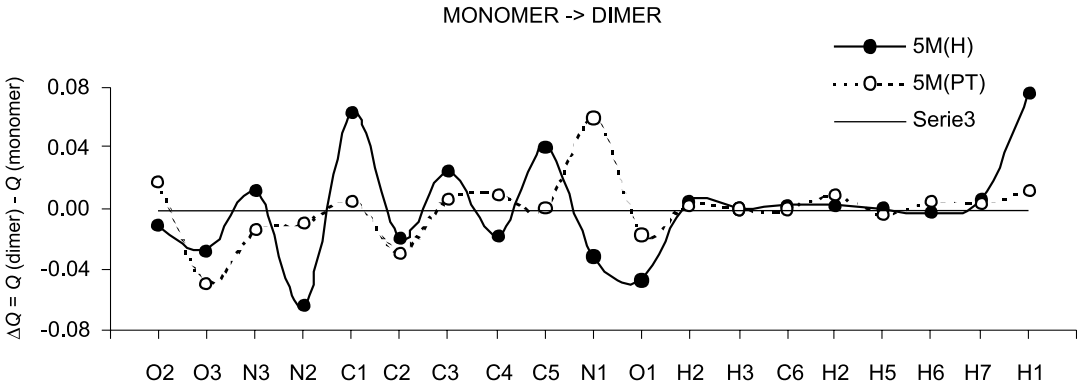

theoretical value (104.5°), ascribed to the NOH valence angle agrees with the experimentally obtained value of 103.5(2)°.

A relative arrangement of both optimized 5M (PT) monomers (Fig. 2(*b*)), shows the same orthogonality of planes as that found in the crystalline 5M (Fig.1(*b*)), 2NAPNO (PT) (1), and 4M (PT) dimers (2). In the same way, the planes of the calculated complementary 5M (H) monomers in the amino (H) dimer are observed to be parallel (Fig. 2(*a*)).

Results from total energy difference (3.58 kcal mol^{-1}) between amino (H) and imino (PT) species of 5M, show that the latter is more stable in the gas phase. Also the binding energy (E_B), calculated as the energy difference between the energy of dimer (E_D) and the sum of the energies of the two corresponding monomers (E_M), i.e., $E_B = E_D - 2E_M$, shows a better stability of the (PT) species (8.14 kcal mol^{-1}) than the amino (H) species (7.54 kcal mol^{-1}). Nonetheless, in the amino (H) ↔ imino (PT) prototropic equilibria in solution both species may occur. In a polar solvent, a larger dipole moment of the imino (PT) monomer (8.41 D), in comparison to the 5M (H) monomer (6.36 D), may shift the equilibrium in the direction of the imino (PT) species. On the other hand, almost dipole-less dimers (0.84 D for the 5M (PT) dimer and 0.01D for the 5M (H) dimer) point to the hydrogen-bonded dimeric structures that may be encountered in the non-polar solvents.

A distortion of the charge distributions found in NAPNO molecules (1, 2), as caused by the proximity of substituents with different mesomeric effects, brings about both structural and spectral consequences. The usual electron- and hydrogen-bond-accepting properties of the nitro group (20), are strongly weakened at the expense of the NO group (1, 2) and the intermolecular hydrogen bond is weakened at the expense of the NO group. Intermolecular hydrogen bonding occurs between the nitrogen (N(12) (or N(22))) and the protonated -N(21)-O(21)-H(2) (or N(11)-O(11)-H(1)) group of the neighboring 5M (PT) molecule instead of an intramolecular hydrogen bond with the nitro group. This is due to the slightly smaller negative charges on the oxygen atoms of the nitro group (O(12) (–0.671 e) and O(13) (–0.593 e)) than that on the amino nitrogen atom N(12) (–0.708 e) in the imino 5M (PT) monomer.

On dimerization, some changes in charge distribution are observed in both types of dimers, which are energetically stabilized in comparison to their monomeric units. These changes, as differences of charge distribution between dimer and monomer of the 5M (H) and 5M (PT) species vs. particular atoms are presented in Fig. 3.

Atoms N(13) (N(23)), N(12) (N(22)), and N(11) (N(21)) are those of the nitro, amino, and nitroxo groups, respectively, whereas oxygen atoms O(12, 13) (O(22, 23)) and O(11) (O(21)) belong to the NO_2 and to the NO group, respectively. Atoms C(11)-C(15) (C(21)-C(25)) are those of the pyridine ring and atom C(16) (C(26)) is from the methyl group. As seen in Fig. 3, changes of atomic charges due to complexation occur to the same extent both on the hydrogen bonding components as well as on the ring atoms. Electron density increases on the amino nitrogen atom N(12) (N(22)) being (–0.708 e) and (–0.718 e) in the 5M (PT) form of the monomer and dimer, respectively, and (–0.270 e) and (–0.334 e) in the 5M (H) form of the monomer and dimer, respectively.

The strongest effect of charge redistribution on dimerization can be noted with respect to the ring atoms C(11) (C(21)) and N(11) (N(21)) where atomic charges (with hydrogens summed into heavy atoms) for the monomer and dimer are 0.079 and 0.083, respectively, for the former and 0.436 and 0.496, respectively, for the latter. These changes are connected more with the cyclic shifts of the charge within the ring itself than with its migration from a particular functional group into the ring or vice versa. Spectral consequences of the variable charge distribution in 5M may be easily followed when HOMO and LUMO orbitals of both forms, as depicted in the molecular energy level diagram shown in Table 5.

Values included in Table 5 show the contributions of atomic orbitals of 5M (H) or 5M (PT) species of dimer into HOMO and LUMO orbitals. Charge distribution in HOMO and LUMO orbitals was calculated in the form of the sum of squares of three components, i.e. the N_2O_2 fragment (nitramino group), the pyridine ring (R), and the oxygen atom of the NO group (O). Summation has been extended over the factors of the *s*, p_x, p_y, and p_z orbitals of a given atom.

In both cases, as seen in Table 5, dimer orbitals form pairs of orbitals of a similar energy, being symmetric and antisymmetric combinations of monomer orbitals localized to the same extent on both units of dimer.

The HOMO orbitals of the 5M (H) dimer are mostly localized on the ring, with the exception of orbitals numbered 63 and 64, which are partially localized also on the O_{NO} atom. On the other hand, inspection of LUMO orbitals

© 2002 NRC Canada

Table 5. The molecular orbitals energy diagram for 5M(H) and 5M(PT) and characteristics of localization of HOMO (61–64) and LUMO (65–70) orbitals.

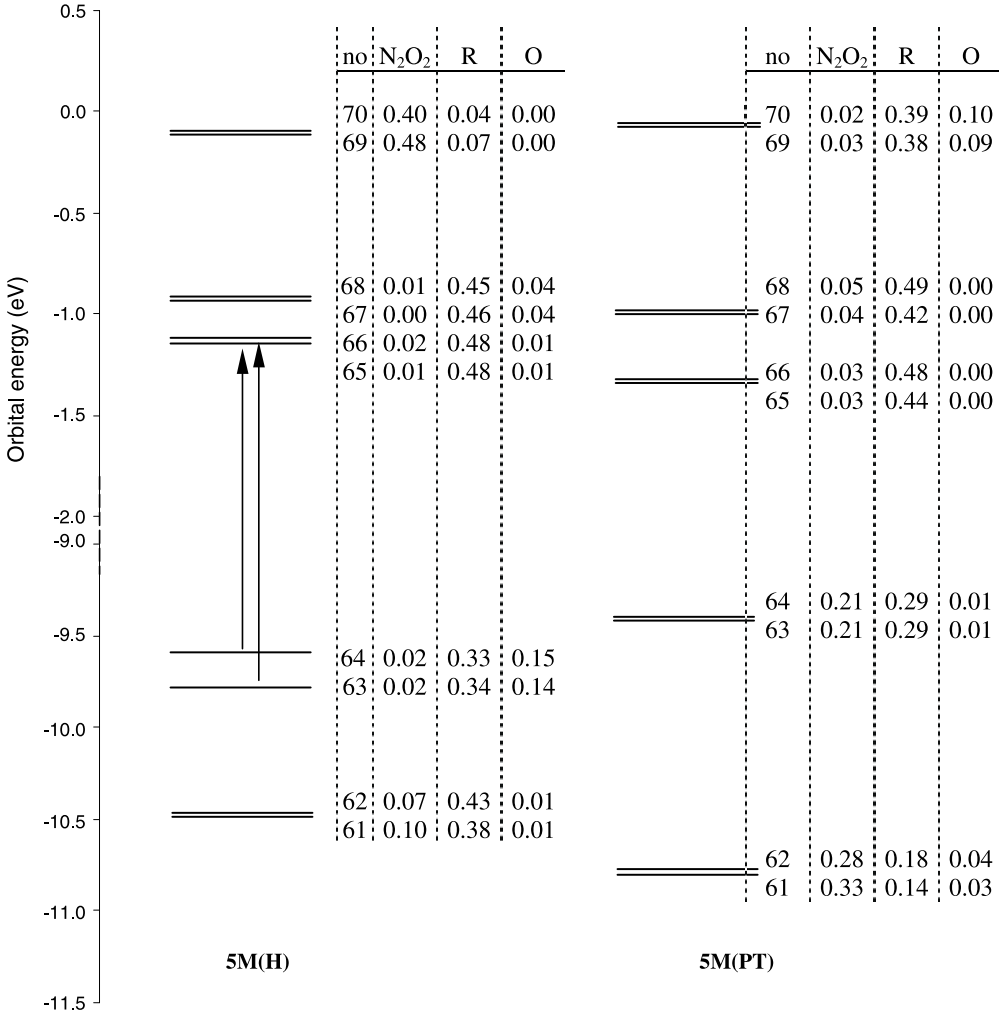

Note: As an example: electronic configurations (64 → 65 and 63 → 66) have composed the $S_0 \rightarrow S_1$ transition in 5M (H) (see Table 6 and text for definition of N_2O_2, R, and O values).

shows that the first four orbitals of both 5M forms are practically localized on the ring while only orbitals numbered 69 and 70 of 5M (H) dimer are localized on the N_2O_2 fragment involving, in this case, the amino (-NH) nitrogen.

The HOMO orbitals of the 5M (PT) dimer have a mixed character being partly localized on the ring and partly on the N_2O_2 fragment involving the imino nitrogen atom (see orbitals numbered 61 and 62 in Table 5).

Such differences in the character of particular molecular orbitals of both forms of 5M can lead to changes in acid–base properties of the mentioned atoms and to a cooperative excited-state double-proton transfer (ESDPT) process in 5M dimers. ESDPT was also found in dimers of 7-azaindoles (7AI) (21, 22), 1-azacarbazoles (23), and in the 2-pyridone dimer (7) which are linked by two intermolecular N-H···N and N-H···O hydrogen bonds, respectively.

4. Experimental and calculated electronic spectra

The PM3-CI results of transition energy, oscillator strength, and dipole moment calculations for each transition of 5M (H) and 5M (PT) monomers and dimers are illustrated in Table 6.

Experimental absorption spectra of 5M in cyclohexane and in acetonitrile are demonstrated in Fig. 4 and Table 7.

In Fig. 4, the spectra are presented together with calculated and then Gaussian-diffused (half-width 1000 cm^{-1}) spectra in pure amino (H) and imino (PT) forms as well as in the 1:1 (H:PT) hypothetical mixture of both species (50% of amino and 50% of imino form (2)). One may diffuse the calculated spectra because each of the experimental bands is the envelope of several electronic transitions — each of them with their own Franck–Condon (FC) structure (24). In the solution, due to molecular properties, temperature, and interactions with solvent, each FC line is broadened and observed bands are diffused. It is difficult to differentiate the role of particular factors and for these reasons, in the first approximation, we simulate the spectrum as envelopes of Gaussian contours corresponding to the calculated electronic transitions. Their heights correspond to the calculated oscillator strengths. The value of 1000 cm^{-1} is taken as the width of each contour. Such a value leads to relatively good fits and it does not exceed the width of diffused bands of single

© 2002 NRC Canada

Table 6. Transition energies, oscillator strengths, and dipole moment values for monomers and dimers of the 5M (H) and 5M (PT) forms; PM3-CI computations.

5M (H)						5M(PT)					
Monomer			Dimer			Monomer			Dimer		
E_{tr} (cm^{-1})	f	μ (D)	E_{tr} (cm^{-1})	f	μ (D)	E_{tr} (cm^{-1})	f	μ (D)	E_{tr} (cm^{-1})	f	μ (D)
28 535	0.071	4.942	29 160	0.000	0.001	27 451	0.193	6.245	27 308	0.048	1.314
			29 308	0.072	0.001				28 573	0.240	1.168
32 463	0.073	5.508	32 154	0.000	0.001	29 160	0.005	6.893	30 399	0.016	1.641
			32 588	0.156	0.002				30 590	0.514	1.622
35 223	0.007	7.952	35 605	0.000	0.033	30 039	0.254	7.299	32 780	0.018	1.721
			35 616	0.003	0.031				32 812	0.004	1.713
35 529	0.000	5.807	35 825	0.000	0.003	34 878	0.001	2.773	37 021	0.001	1.134
			35 899	0.026	0.002				37 034	0.000	1.125
37 097	0.016	4.328	38 290	0.000	0.145	41 564	0.473	8.115	41 100	0.003	1.375
			38 306	0.024	0.146				41 436	0.703	1.319
38 213	0.057	6.667	39 534	0.045	0.005	42 998	0.000	10.684	42 030	0.071	1.987
			39 557	0.000	0.003				42 037	0.002	1.993
40 966	0.008	10.627	41 818	0.091	0.103	44 251	0.138	5.589	43 446	0.000	5.590
			41 874	0.000	0.102				43 453	0.002	5.592
43 869	0.701	6.338	42 953	0.000	0.002	45 981	0.000	3.011	44 190	0.100	1.156
			42 982	2.086	0.003				44 404	0.217	0.834
44 818	0.690	5.324	43 452	0.139	0.004	47 036	0.000	5.068	45 398	0.015	0.494
			43 799	0.000	0.005				45 405	0.047	0.427
45 595	0.316	4.079	45 180	0.763	0.018	47 811	0.028	3.146	46 341	0.011	1.414
			45 317	0.000	0.015				46 380	0.006	1.401
47 188	0.032	6.339	46 836	0.376	0.003	48 287	0.408	7.211	47 296	0.788	2.077
			47 090	0.000	0.002				48 133	0.000	3.462
48 964	0.182	3.297	47 983	0.000	0.365	49 903	0.003	1.244	48 155	0.007	3.441

Table 7. Experimental electronic absorption spectra of 5M in two solvents (λ^{A}_{max}(nm, cm^{-1}) and I_A (absorption intensity)).

Solvent	λ^{A}_{max} (nm, cm^{-1})	I_A
Cyclohexane	336.1, 29 753	0.06
	298.1, 33 545	0.15
	260.6, 38 372	0.32
	229.2, 43 630	0.32
Acetonitrile	414.0, 24 154	0.02
	337.8, 29 603	0.13
	281.5, 35 523	0.16
	262.8, 38 051	0.19
	222.1, 45 024	0.35
	198.6, 50 352	0.48

electronic transitions of hydrocarbons in more polar solvent (25). The simulated spectra may facilitate identification of the types of species present in the solution, so they may be treated as the reference spectra.

On the basis of calculated transition energies and oscillator strengths of the monomers and dimers (Table 6) of both forms, some differences between their spectra may be formulated as follows: (*i*) the first absorption band of the dimer (at about 29 000cm^{-1}) should be blue-shifted and of a higher intensity than that of the corresponding monomer; (*ii*) the spectra of (PT) and (H) forms differ both in the maxima positions and in intensity distributions. The first absorption band of the (PT) form (at about 28 000 cm^{-1}) is slightly red-shifted and has a higher intensity than that of the (H) form. In the higher wavenumber region of the (PT) spectrum, two distinct bands of a medium intensity are expected, compared to a single band of a higher intensity in the (H) form.

Absorption bands of the electronic spectra of 5M dimers, similarly to those of 3M and 4M (2), are built upon a large number of electronic transitions. Also, as previously demonstrated (1, 2), in the region of the first absorption band, i.e., between 25 000 and 35 000 cm^{-1}, the values of the oscillator strength of imino (PT) form are significantly higher than those of the amino (H) form. The transitions, building up the first absorption band, are more precisely described in Table 8.

Table 8 shows that differences between the spectra of the (H) and the (PT) forms have their source in the different character of electronic transitions. Thus, the first absorption band of the amino (H) species (between 29 000 and 33 000 cm^{-1}) is built upon the (R, O) → R transitions (R means the pyridine ring; and O is the oxygen atom of the NO group), i.e., the transition from the highest two HOMO orbitals (nos. 63, 64) to the first four lower lying LUMO orbitals (nos. 65–68). The parallel nature of both planes in the amino (H) dimer leads in some transitions to zero oscillator strengths as well as to a zero dipole moment, despite that each of the two components has a non-zero value.

In the case of (PT) form, the (N_2O_2, R) → R transitions (N_2O_2 is the nitramino fragment involving the amino nitrogen atom and the nitro group), i.e., from the above-mentioned HOMO orbitals (nos. 63, 64) into the six LUMO orbitals

© 2002 NRC Canada

Table 8. Some first electronic transitions together with the indicated character of transition in monomeric units of the 5M (H) and 5M (PT) dimers; PM3-CI calculations.

5M (H)				5M (PT)			
E_{tr} (cm^{-1})	f	Description of transition	Character of transition	E_{tr} (cm^{-1})	f	Description of transition	Character of transition
29 160	0.000	64 —> 65 0.40	(R,O) → R	27 308	0.048	64 —> 66 –0.46	(N_2O_2,R) → R
		63 —> 66 –0.40	(R,O) → R			63 —> 65 0.46	(N_2O_2,R) → R
29 308	0.072	64 —> 66 0.37	(R,O) → R	28 573	0.240	64 —> 65 –0.45	(N_2O_2,R) → R
		63 —> 65 –0.37	(R,O) → R			63 —> 66 0.45	(N_2O_2,R) → R
32 154	0.000	64 —> 67 0.36	(R,O) → R	30 399	0.016	64 —> 68 –0.43	(N_2O_2,R) → R
		63 —> 68 –0.36	(R,O) → R			63 —> 67 –0.43	(N_2O_2,R) → R
32 588	0.156	64 —> 68 –0.36	(R,O) → R	30 590	0.514	64 —> 67 0.44	(N_2O_2,R) → R
		63 —> 67 0.36	(R,O) → R			63 —> 68 0.44	(N_2O_2,R) → R
				32 780	0.018	64 —> 69 0.48	(N_2O_2,R) → (R,O)
						63 —> 70 –0.48	(N_2O_2,R) → (R,O)
				32 812	0.004	64 —> 70 0.48	(N_2O_2,R) → (R,O)
						63 —> 69 –0.48	(N_2O_2,R) → (R,O)

Fig. 4. Experimental electronic absorption spectra of 5M in cyclohexane (CH), and in acetonitrile (AN) solution. For comparison purposes, also the calculated (PM3-CI) electronic absorption spectra of pure amino (H) and imino (PT) form as well as that of 1:1 (H:PT) hypothetical mixture of 5M are demonstrated. They were simulated as the envelope of Gaussian contours corresponding to the calculated electronic transition. Their heights correspond to the calculated oscillator strengths. The value of 1000 cm^{-1} is taken as the width of each contour (see text for details).

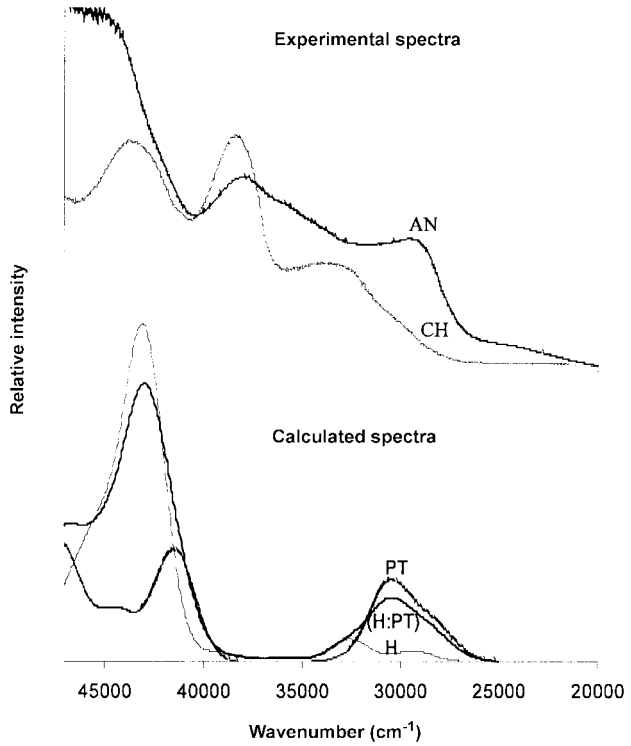

(nos. 65–68, as well as to the highest two orbitals (nos. 69 and 70)) are dominant. A perpendicular arrangement of both monomeric units in the (PT) dimer, results in slightly larger values of oscillator strengths and dipole moment than in the (H) species.

Assignment of calculated transition energies (Table 6 and Fig. 4) to experimental absorption bands (Table 7), shows that: (*i*) in cyclohexane, the first two experimental bands at 29 753 cm^{-1} (shoulder 336 nm, I_A = 0.06) and at 33 545 cm^{-1} (298 nm, I_A = 0.15) may correspond to the first two calculated transitions of the 5M (PT) dimer which are at about 28 000 cm^{-1} (shoulder 28 573 cm^{-1}, f = 0.240) and at 30 590 cm^{-1} (maximum, f = 0.514), respectively. This allows a supposition that the hydrogen bonded and weakly polar imino 5M (PT) dimers may prevail in the non-polar solvent. This may be corroborated further by the presence of an experimental middle wavenumber region band at 38 372 cm^{-1} (260.6 nm, I_A = 0.33). The latter is seen in the theoretical absorption spectrum of a pure 5M (PT) form (Fig. 4) in the region between 35 000 and 42 000 cm^{-1} (41 436 cm^{-1}, f = 0.703). The last experimental band observed at 43 630 cm^{-1} (I_A = 0.32) might be ascribed to theoretical band of the 5M (PT) dimer at 44 404 cm^{-1} (f = 0.217); (*ii*) in acetonitrile, the region between 20 000 and 35 000 cm^{-1} of the experimental spectrum of 5M (Table 7), resembles rather more the calculated spectrum of a 1:1 (H:PT) hypothetical mixture (Fig. 4) than that of a pure (H) or (PT) form. In so strong a polar solvent, the intermolecular hydrogen-bonded network between 5M monomers may undergo a partial breaking and both types of polar monomers, theoretically, may appear in the solution. However, due to the significantly larger dipole moment of the imino (PT) monomer, the imino (PT) species may be the dominant one. In such a case, the experimental spectrum results from the overlapping bands of monomers and dimers and has a complicated character in comparison to the calculated one.

The first three experimental bands at 24 151 cm^{-1} (414 nm, I_A = 0.02), 29 603 cm^{-1} (337.8 nm, I_A = 0.13), and 38 051 cm^{-1} (262.8 nm, I_A = 0.19) may be assigned to the first three transition energies of the 5M (PT) monomer (Table 6). These are at 27 451 cm^{-1} (f = 0.198), at 30 039 cm^{-1} (f = 0.254), and at 41 564 cm^{-1} (f = 0.473), respectively. Experimental evidence pointing to the presence of amino 5M (H) monomers is reflected by the shoulder at 35 523 cm^{-1} (281.5 nm, I_A = 0.16) and the band at 45 021 cm^{-1} (222.1 nm, I_A = 0.35). Their theoretical transition energies, as calculated for the monomer of pure (H) form (Table 6),

© 2002 NRC Canada

are at 37 097 cm^{-1} (f = 0.016) and at 45 595 cm^{-1} (f = 0.316), respectively.

A small red shift of the experimental bands in acetonitrile solution, in comparison to calculated transition energies in the gas phase, results from dipole–dipole interactions that take place in the solution.

5. Conclusions

X-ray analysis and the results of PM3-CI calculations have been used to investigate the crystal structure and the spectral properties of 5M. The former shows that in the solid, the (PT) dimer is formed of two perpendicular monomeric units linked through two of different length, intermolecular O-H···N hydrogen bonds. The same orthogonality of both monomers was found in PM3-optimized imino 5M (PT) dimer.

From the results of PM3-CI computations it was concluded that the prototropic amino (H) – imino (PT) equilibria might be present in the solution.

Change in the acid–base properties of hydrogen bonding components caused by the charge redistribution on HOMO–LUMO transitions, seems to be a "driving force" for a possible excited-state-double-proton transfer (ESDPT) to occur in both types of 5M dimers.

Zero or nearly zero values of oscillator strength and dipole moment of the amino (H) dimer, in comparison to slightly larger although still small ones of the imino (PT) dimer, are due to the different character of electronic transitions and different relative arrangements of the two monomers in both dimers.

Assignment of experimental absorption bands to the calculated transition energies of both 5M species reveals that hydrogen-bonded dimers dominate in cyclohexane, whereas a shift in prototropic equilibrium in the direction of the monomeric imino (PT) form seems to prevail in acetonitrile solution.

References

1. A. Szemik-Hojniak, T. Głowiak, A. Puszko, and Z. Talik. J. Mol. Struct. **449**, 77 (1998).
2. A. Szemik-Hojniak, T. Głowiak, I. Deperasiñska, and A. Puszko. J. Mol. Struct. **597**, 279 (2001).
3. J. Michalski, J. Hanuza, M. Mączka, Z. Talik, and T. Głowiak, A. Szemik-Hojniak, and J.H. Van der Maas. J. Mol. Struct. **596**, 109 (2001).
4. K. Fukui, A. Imamura, and C. Nagata. Bull. Chem. Soc. Jpn. **33**, 122 (1960).
5. I.T. Okabayashi. J. Ferment. Technol. **31**, 373 (1953).
6. J. Zyss, D.S. Chemla, and J.F. Nicoud. J. Chem. Phys. **74**, 4800 (1981).
7. A. Müller, F. Talbot, and S. Leutwyler. J. Chem. Phys. **112**, 3717 (2000).
8. G. Favini, A. Gamba, and I.R. Bellobono. Spectrochim. Acta Part A, **23A**, 89 (1967).
9. F. Baert, P. Schweiss, G. Heger, and M. More. J. Mol. Struct. **178**, 29 (1988).
10. H. Nakai, T. Saito, and M. Yamakawa. Acta Crystallogr. Sect. C: Cryst. Struct. Commun. **C44**, 533 (1988).
11. A. Puszko, L. Wasylina, and Z. Pawełka. Monatsh. Chem. **127**, 601 (1996).
12. J.J. Stewart. J. Comput. Chem. **10**, 209 (1989).
13. HyperChem. Computation chemistry. Publication HC50-00-03-00. Printed in Canada. Hypercube Inc. 1996.
14. M.J.S. Dewar, E.G. Zoebish, E.F. Healy, and J.P. Stewart. J. Am. Chem. Soc. **107**, 3902 (1985).
15. T. Talik and Z. Talik. Pr. Nauk. Akad. Ekonomicznej. **199**, 145 (1982).
16. G.M. Sheldrick. SHELXS-97. Program for the solution of crystal structures. University of Göttingen, Germany. 1997.
17. G.M. Sheldrick. SHELXL-97. Program for the refinement of crystal structures. University of Göttingen, Germany. 1997.
18. International tables for X-ray crystallography. Vol. 4. Kynoch Press, Birmingham. 1974.
19. M. Shiro, M. Yamakawa, and T. Kubota. Acta Crystollogr. Sect. B: Struct. Crystallogr. Cryst. Chem. **B33**, 1549 (1977).
20. M. Yamakawa, T. Kubota, and K. Ezumi, Y. Mizuno. Spectrochim. Acta, **30**, 2103 (1974).
21. H. Bulska and A. Chodkowska. J. Am. Chem. Soc. **102**, 3259 (1980).
22. H. Bulska, A. Grabowska, B. Pakuła, J. Sepioł, J. Waluk, and U.P. Wild. J. Lumin. **29**, 65 (1984).
23. J. Waluk, A. Grabowska, B. Pakuła and J. Sepioł. J. Phys. Chem. **88**, 1160 (1984).
24. B. Henry and W. Siebrand. *In* Organic molecular photophysics. Vol. 1. Wiley, London. 1973. pp.196–210.
25. I.B. Berlman. Handbook of fluorescence spectra of aromatic molecules. Academic Press, New York. 1965.

© 2002 NRC Canada

Synthesis and solid-state molecular structures of bis- and mono-nitrosobenzene complexes of ruthenium porphyrins

Jonghyuk Lee, Brendan Twamley, and George B. Richter-Addo

Abstract: Bis-nitrosobenzene complexes of the form (por)Ru(PhNO)$_2$ (por = TPP, TTP; TPP = tetraphenylporphyrinato dianion, TTP = tetratolylporphyrinato dianion) have been prepared in good yields from the reaction of the (por)Ru(CO) precursor with excess PhNO in dichloromethane. The IR spectra of the complexes (as KBr pellets) displayed new bands at ~1348 cm^{-1}, due to υ_{NO}. The solid-state molecular structure of (TPP)Ru(PhNO)$_2$ was determined by single-crystal X-ray diffraction, and revealed that the PhNO ligands are bound to the Ru center via the *N*-binding mode. Reactions of the (por)Ru(PhNO)$_2$ complexes with excess 1-methylimidazole gave the mono-nitrosobenzene complexes (por)Ru(PhNO)(1-MeIm). The IR spectra revealed a lowering of υ_{NO} in these mononitrosobenzene derivatives by ~27 cm^{-1}, a feature consistent with the replacement of one π-acid PhNO ligand with the more basic 1-MeIm ligand. The solid-state molecular structure of (TPP)Ru(PhNO)(1-MeIm) reveals, in addition to the *N*-binding of the PhNO ligand, an essentially parallel arrangement of the C-N-O (of PhNO) and imidazole planes; this is in contrast with the (TPP)Ru(PhNO)$_2$ complex, in which the C-N-O planes (of PhNO) are essentially perpendicular.

Key words: nitroso, X-ray, ruthenium, porphyrin, imidazole.

Résumé : La réaction du précurseur (por)Ru(CO) avec un excès de PhNO, dans le dichlorométhane, permet de préparer les complexes du bis-nitrosobenzène, de la forme (por)Ru(PhNO)$_2$ (por = TPP, TTP; TPP = dianion tétraphénylporphyrinato, TTP = dianion tétratolylporphyrinato), avec de bons rendements. Les spectres IR des complexes (sous la forme de pastilles de KBr) présentent de nouvelles bandes aux environ de 1348 cm^{-1} dues à υ_{NO}. Faisant appel à la diffraction des rayons X sur un cristal unique, on a déterminé la structure moléculaire à l'état solide du (TPP)Ru(PhNO)$_2$; elle révèle que les ligands PhNO sont liés au centre Ru par le biais d'un mode de fixation par l'azote. Les réactions des complexes (por)Ru(PhNO)$_2$ avec un excès de 1-méthylimidazole conduisent à la formation de complexes mononitrosobenzène (por)Ru(PhNO)(1-MeIm). Le spectre IR de ces dérivés mononitrosobenzène met en évidence un abaissement d'environ 27 cm^{-1} de la υ_{NO}, une caractéristique en accord avec le remplacement d'un ligand PhNO π-acide par le ligand plus basique 1-MeIm. La structure moléculaire à l'état solide du (TPP)Ru(PhNO)(1-MeIm) met en évidence la fixation par l'azote du ligand PhNO ainsi qu'un arrangement essentiellement parallèle des plans C-N-O (du PhNO) et de l'imidazole; cette observation est en opposition à ce qui est observé avec le complexe (TPP)Ru(PhNO)$_2$ dans lequel les plans C-N-O (du PhNO) sont essentiellement perpendiculaires.

Mots clés : nitroso, diffraction des rayons X, ruthénium, porphyrine, imidazole.

[Traduit par la Rédaction]

Introduction

The binding of nitrosobenzene and related RNO compounds (R = alkyl, aryl) to the metal centers in heme biomolecules is a naturally occurring phenomenon, and evidence for RNO binding to the heme site has been established for hemoglobin, myoglobin, cytochrome P450, guanylyl cyclase, NO synthase, and other heme biomolecules; a comprehensive discussion of this subject area has been presented in a recent review (1). For example, various amine-containing drugs can be metabolized by cytochrome P450, resulting in RNO formation and binding to the heme, and the tight binding of the RNO group can inhibit the enzymatic activity.

Much of our understanding of RNO binding to the heme site in heme-containing biomolecules still comes from studies of RNO binding to synthetic metalloporphyrins. Mansuy et al. (2) reported, in 1983, that *i*-PrNO binds to ferrous porphyrins via the *N*-binding mode. Several years ago, we reported the first X-ray structural study of the binding of nitrosoarenes to ferrous and ferric porphyrins, and showed that the nature of binding (*N*-bound vs. *O*-bound) depended on the formal oxidation state of the metal (3). Since then, other structural reports have also been published on RNO binding to metalloporphyrins of Fe (4), Mn (5), Co (6), Ru (6), and Os (7).

Received 1 June 2002. Published on the NRC Research Press Web site at http://canjchem.nrc.ca on 13 September 2002.

J. Lee and G.B. Richter-Addo.[1] Department of Chemistry and Biochemistry, University of Oklahoma, 620 Parrington Oval, Norman, OK 73019, U.S.A.
B. Twamley. X-ray Structural Laboratory, University Research Office, 109 Morrill Hall, University of Idaho, Moscow, ID 83844–3010, U.S.A.

[1]Corresponding author (e-mail: grichteraddo@ou.edu).

 DOI: 10.1139/V02-155 © 2002 NRC Canada

We are particularly interested in RNO binding to Ru(II) porphyrins, since the latter species serve as good models for low-spin d^6 systems similar to low-spin ferrous heme. In this report, we present and describe the successful syntheses of bis-nitrosobenzene complexes of Ru(II) tetraarylporphyrins — namely (por)Ru(PhNO)$_2$ — and their ready conversion by reaction with 1-methylimidazole to the axially unsymmetrical (por)Ru(PhNO)(1-MeIm) derivatives. In particular, we examine the electronic and structural consequences of PhNO binding, and discuss the effect of the axial imidazole ligand on the orientation of the trans PhNO ligand.

Experimental section

All reactions were performed under an atmosphere of prepurified nitrogen, using standard Schlenk glassware, and (or) in an Innovative Technology Labmaster 100 dry box. Solutions for spectral studies were also prepared under a nitrogen atmosphere. Solvents were distilled from the appropriate drying agents under nitrogen, just prior to use (CH_2Cl_2 (CaH_2), hexane (CaH_2)).

Chemicals

(TPP)Ru(CO) and (TTP)Ru(CO) were prepared by published procedures (8). The samples were converted, in moist air, to (por)Ru(CO)$(H_2O)_x$ ($x \leq 1$) species (por = TPP, TTP) (9). PhNO (97%) and 1-methylimidazole (1-MeIm, 99+%) were purchased from Aldrich Chemical Co. and used as received. Chloroform-*d* (99.8%) was obtained from Cambridge Isotope Laboratories.

Instrumentation

Infrared spectra were recorded on a Bio-Rad FT-155 FT-IR spectrometer. Proton NMR spectra were obtained on a Varian 400 MHz spectrometer and the signals referenced to the residual signal of the employed solvent. All coupling constants are in Hz. FAB mass spectra were obtained on a VG-ZAB-E mass spectrometer. UV–vis spectra were recorded on a Hewlett-Packard model 8453 diode array instrument. Wavelengths are reported with ε values, or as % intensities for the samples whose yields were too small for accurate concentration measurements.

Preparation of (por)Ru(PhNO)$_2$ compounds (por = TPP, TTP)

(TPP)Ru(CO) (0.100 g, 0.135 mmol) and excess PhNO (0.040 g, 0.362 mmol) were dissolved in CH_2Cl_2 (20 mL). The reaction mixture was stirred at room temperature for 30 min, during which time it turned from red to brown. The solvent was removed in vacuo. The residue was redissolved in CH_2Cl_2 (10 mL), and the product solution was transferred to the top of a neutral alumina column (2 × 20 cm), and eluted with CH_2Cl_2 in air. The brown product was collected and dried in vacuo. The residue was dissolved in CH_2Cl_2 (10 mL). Slow evaporation of the solvent in air gave crystalline (TPP)Ru(PhNO)$_2$ (0.086 g, 0.093 mmol, 69% isolated yield). UV–vis (5.18×10^{-6} M in CH_2Cl_2) λ (nm) (ε (mM^{-1}, cm^{-1})): 307 (37), 411 (184), 525 (17). IR (KBr pellet) (cm^{-1}): υ_{NO} 1348 (s) (overlapping with the porphyrin band); also 3055 (vw), 3024 (vw), 1597 (m), 1587 (vw), 1529 (w), 1487 (w), 1454 (w), 1441 (w), 1306 (m), 1208 (w), 1177 (w), 1157 (vw), 1072 (m), 1010 (vs), 859 (m), 833 (w), 794 (m), 754 (s), 737 (vw), 714 (w), 702 (s), 665 (w), 528 (vw). ^{1}H NMR ($CDCl_3$) δ: 8.54 (s, 8H, pyrrole-H of TPP), 8.12 (m, 8H, *o*-H of TPP), 7.71 (m, 12H, *m*/*p*-H of TPP), 6.46 (br t, 2H, *p*-H of PhNO), 5.99 (br t, 4H, *m*-H of PhNO), 2.41 (br d, *J* = 6.8 Hz, 4H, *o*-H of PhNO). LR-FAB-MS *m*/*z* (%): 851 ([(TPP)Ru(NO)(PhNO)]$^+$, 26), 821 ([(TPP)Ru(PhNO)]$^+$, 19), 714 ([(TPP)Ru]$^+$, 100).

The (TTP)Ru(PhNO)$_2$ compound was prepared similarly from (TTP)Ru(CO) and excess PhNO. The brown product was obtained in 75% isolated yield. UV–vis (CH_2Cl_2) λ (nm): 310 (18), 413 (100), 525 (9). IR (KBr pellet) (cm^{-1}): υ_{NO} 1346 (s) (overlapping with the porphyrin band); also 3022 (vw), 2921 (vw), 1586 (vw), 1529 (w), 1454 (w), 1305 (m), 1212 (w), 1181 (m), 1108 (w), 1072 (m), 1010 (vs), 858 (m), 798 (s), 766 (m), 716 (m), 691 (m), 669 (w), 643 (vw), 524 (m). ^{1}H NMR ($CDCl_3$) δ: 8.54 (s, 8H, pyrrole-H of TTP), 7.99 (d, *J* = 8 Hz, 8H, *o*-H of TTP), 7.50 (d, *J* = 8 Hz, 8H, *m*-H of TTP), 6.43 (br, 2H, *p*-H of PhNO), 5.95 (br, 4H, *m*-H of PhNO), 2.67 (s, 12H, C*H*$_3$ of TTP), 2.38 (br, 4H, *o*-H of PhNO). LR-FAB-MS *m*/*z* (%): 907 ([(TTP)Ru(NO)(PhNO)]$^+$, 32), 877 ([(TTP)Ru(PhNO)]$^+$, 15), 770 ([(TTP)Ru]$^+$, 100).

Preparation of (por)Ru(PhNO)(1-MeIm) compounds (por = TPP, TTP)

To a CH_2Cl_2 (10 mL) solution of (TPP)Ru(PhNO)$_2$ (0.020 g, 0.021 mmol) was added 2 equiv of 1-MeIm. This mixture was stirred at room temperature for 30 min, during which time it turned from brown to red-purple. The solvent was removed in vacuo. An ^{1}H NMR spectrum of the residue in $CDCl_3$ showed the quantitative formation of (TPP)Ru(PhNO)(1-MeIm), together with the presence of some unreacted 1-MeIm. Spectroscopically pure (TPP)Ru(PhNO)(1-MeIm) was obtained in 80% yield by recrystallization of the residue from a CH_2Cl_2–hexane solution (1:3) at –20°C. UV–vis (3.19×10^{-6} M in CH_2Cl_2) λ (nm) (ε (mM^{-1}, cm^{-1})): 307 (42), 413 (257), 533 (24). IR (KBr pellet) (cm^{-1}): υ_{NO} 1322 (s); also 3127 (vw), 3052 (w), 3022 (w), 1596 (m), 1529 (m), 1482 (w), 1440 (m), 1348 (m), 1303 (m sh), 1237 (w), 1207 (w), 1177 (w), 1157 (w), 1109 (w), 1072 (m), 1008 (vs), 949 (vw), 924 (vw), 888 (vw), 833 (vw), 815 (vw), 793 (m), 752 (s), 701 (s), 665 (w), 615 (w), 527 (w). ^{1}H NMR ($CDCl_3$) δ: 8.37 (s, 8H, pyrrole-H of TPP), 8.05 (m, 8H, *o*-H of TPP), 7.64 (m, 12H, *m*/*p*-H of TPP), 6.39 (tt, *J* = 7.2, 1.2 Hz, 1H, *p*-H of PhNO), 5.96 (m, 2H, *m*-H of PhNO), 4.74 (dd (apparent t), *J* = 1.2, 1.2 Hz, 1H of 1-MeIm), 2.64 (m, 2H, *o*-H of PhNO), 2.18 (s, 3H, C*H*$_3$ of 1-MeIm), 1.58 (br dd (apparent br t), 1H of 1-MeIm), 1.22 (dd (apparent t), *J* = 1.2, 1.2 Hz, 1H of 1-MeIm). LR-FAB-MS *m*/*z* (%): 903 ([(TPP)Ru(PhNO)(1-MeIm)]$^+$, 18), 822 ([(TPP)Ru(PhNO) + H]$^+$, 19), 796 ([(TPP)Ru(1-MeIm)]$^+$, 51), 714 ([(TPP)Ru]$^+$, 100).

The (TTP)Ru(PhNO)(1-MeIm) compound was obtained similarly in 57% isolated yield after recrystallization from a CH_2Cl_2–hexane solution (1:5) at –20°C. UV–vis (CH_2Cl_2) λ (nm): 310 (8), 414 (100), 533 (4). IR (KBr pellet) (cm^{-1}): υ_{NO} 1321 (s); also 3127 (vw), 3020 (w), 2953 (vw), 2921 (w), 2869 (vw), 1530 (m), 1506 (w), 1449 (w), 1348 (m), 1287 (w), 1237 (w), 1212 (w), 1181 (m), 1108 (m), 1092 (w), 1071 (m), 1007 (vs), 947 (vw), 886 (w), 847 (vw), 798

© 2002 NRC Canada

Table 1. Crystal data and structure refinement.

Compound	$(TPP)Ru(PhNO)_2$	$(TPP)Ru(PhNO)(1\text{-MeIm})\cdot 0.25CH_2Cl_2$
Empirical formula	$C_{56}H_{38}N_6O_2Ru$	$C_{54.25}H_{39.5}N_7O_1Cl_{0.5}Ru$
Formula weight	927.99	924.22
T (K)	203(2)	202(2)
Crystal system	Triclinic	Monoclinic
Space group	$P\bar{1}$	$P2(1)/c$
a (Å), α (°)	11.3020(14), 82.49(2)	13.246(2), 90
b (Å), β (°)	11.4637(14), 77.93(2)	22.622(4), 123.36(1)
c (Å), γ (°)	18.207(2), 73.26(2)	17.608(2), 90
V (Å^3), Z	2202.8(5), 2	4406.9(11), 4
$D_{calcd.}$ (g cm^{-3})	1.399	1.393
Absorption coefficient (μ) (mm^{-1})	0.408	0.435
F(000)	952	1898
Crystal size (mm)	0.35 × 0.15 × 0.15	0.21 × 0.18 × 0.08
θ range for data collection (°)	1.15–27.61	1.84–25.00
Completeness to θ (%)	98.6 (27.61°)	99.9 (25.00°)
Index ranges	$-14 \le h \le 14$, $-14 \le k \le 14$, $-23 \le l \le 23$	$-15 \le h \le 15$, $-18 \le k \le 26$, $-20 \le l \le 16$
Reflections collected	23 276	31 193
Independent reflections	10 077 (R_{int} = 0.0467)	7753 (R_{int} = 0.0776)
Absorption correction	Empirical	Empirical
Max and min transmission	0.9414 and 0.8705	0.9660 and 0.9141
Data/restraints/parameters	10 077/0/586	7753/6/576
Goodness-of-fit on F^2	1.016	1.126
Final R indices [$I > 2\sigma(I)$]	R_1 = 0.0447, wR_2 = 0.0882	R_1 = 0.0754, wR_2 = 0.1483
R indices (all data)	R_1 = 0.0767, wR_2 = 0.0971	R_1 = 0.1170, wR_2 = 0.1623
Largest diff. peak and hole (e Å^{-3})	0.470 and −0.370	1.325 and −1.241

(s), 764 (w), 716 (m), 694 (m), 667 (vw), 644 (vw), 524 (m). ^{1}H NMR ($CDCl_3$) δ: 8.38 (s, 8H, pyrrole-H of TTP), 7.95 (dd, J = 7.6, 1.6 Hz, 4H, *o*-H of TTP), 7.89 (dd, J = 7.6, 1.6 Hz, 4H, *o′*-H of TTP), 7.47 (br d, J = 7.6 Hz, 4H, *m*-H of TTP), 7.42 (br d, J = 7.6 Hz, 4H, *m′*-H of TTP), 6.36 (br t, J = 8 Hz, 1H, *p*-H of PhNO), 5.93 (br t, J = 8 Hz, 2H, *m*-H of PhNO), 4.71 (br dd (apparent br t), 1H of 1-MeIm), 2.65 (s, 12H, CH_3 of TTP), 2.62 (br d, J = 8 Hz, 2H, *o*-H of PhNO), 2.16 (s, 3H, CH_3 of 1-MeIm), 1.56 (br, 1H of 1-MeIm), 1.20 (br dd (apparent br t), 1H of 1-MeIm). LR-FAB-MS *m*/*z* (%): 959 ([(TTP)Ru(PhNO)(1-MeIm)]$^+$, 23), 877 ([(TTP)Ru(PhNO)]$^+$, 20), 852 ([(TTP)Ru(1-MeIm)]$^+$, 48), 770 ([(TTP)Ru]$^+$, 100).

X-ray crystallographic studies

Crystals were removed from the flasks and covered with a layer of hydrocarbon oil. Suitable crystals were selected, attached to a glass fiber and placed in the low-temperature nitrogen stream. Data were collected at low temperature using a Siemens (Bruker) SMART 1K instrument (Mo Kα radiation, λ = 0.71073 Å) equipped with a Siemens (Bruker) LT-2A low-temperature device. Data were measured using ω scans of 0.3° per frame for 30 s, and a full sphere of data was collected. The first 50 frames were recollected at the end of data collection to monitor for decay. Cell parameters were retrieved using SMART (10) software and refined using SAINTPlus (11) on all observed reflections. Data reduction and correction for *Lp* and decay was performed using the SAINTPlus software. Absorption corrections were applied using SADABS (12). The structures were solved by direct methods and refined by the least-squares method on F^2 using the SHELXTL v.5.10 program package (13). The structure was solved in the respective space groups by analyses of systematic absences. All non-hydrogen atoms were refined anisotropically. Hydrogen atoms were placed in their geometrically generated positions and refined using a riding model. No decomposition was observed during data collection. Details of the data collection and refinement are given in Table 1. Further details are provided in the Supporting information.[2] Displacement ellipsoids in Figs. 1 and 2 were drawn at the 50% probability level.

(TPP)Ru(PhNO)$_2$ (1)

Purple needles of the compound were grown by recrystallization from a CH_2Cl_2–hexane (1:10) mixture left for 1 week at –20°C. A total of 2132 frames were collected with a final resolution of 0.77 Å.

(TPP)Ru(PhNO)(1-MeIm)·(0.25CH$_2$Cl$_2$) (2)

Suitable crystals for X-ray crystallography were grown from a CH_2Cl_2–hexane solution (1:3) left for 2 weeks at

[2] Supplementary data may be purchased from the Depository of Unpublished Data, Document Delivery, CISTI, National Research Council Canada, Ottawa, ON K1A 0S2, Canada (http://www.nrc.ca/cisti/irm/unpub_e.shtml for information on ordering electronically). CCDC 190593 and 190594 contain the supplementary data for this paper. These data can be obtained, free of charge, via www.ccdc.cam.ac.uk/conts/retrieving.html (or from the Cambridge Crystallographic Data Centre, 12 Union Road, Cambridge, U.K.; fax +44 1223 336033; or deposit@ccdc.cam.ac.uk).

© 2002 NRC Canada

Fig. 1. Molecular structure of (TPP)Ru(PhNO)$_2$. Hydrogen atoms have been omitted for clarity.

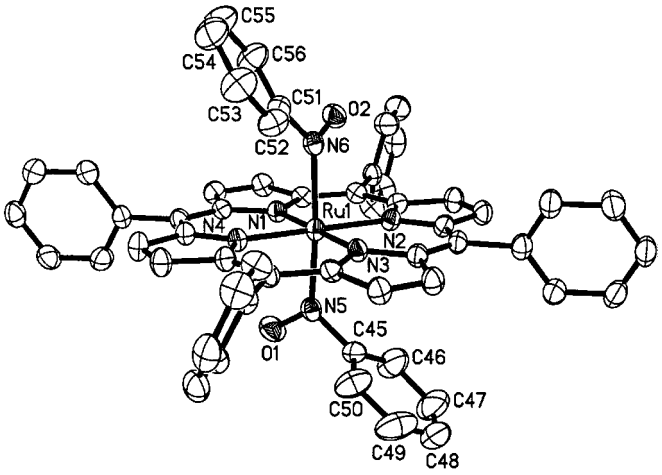

–20°C. A total of 1471 frames were collected with a final resolution of 0.84 Å.

Results and discussion

Synthesis of the bis-nitrosobenzene complexes

James and co-workers (14) previously reported the synthesis of (OEP)Ru(PhNO)$_2$ from the reaction of (OEP)Ru(CO) with excess PhNO in dichloromethane. Using similar methodology, we successfully synthesized and reported the related compound (OEP)Ru(ONC$_6$H$_4$NMe$_2$)$_2$ (6). We have now extended this synthetic methodology to the preparation of bis-nitrosobenzene complexes of *tetraaryl*porphyrin complexes of Ru.

The reaction of excess PhNO with the (por)Ru(CO) compounds (por = TPP, TTP) generates, after work-up, the bis-nitrosobenzene complexes (por)Ru(PhNO)$_2$ in 69% (TPP) and 75% (TTP) isolated yields (eq. [1]).

[1] (por)Ru(CO) + excess PhNO $\rightarrow$ (por)Ru(PhNO)$_2$ + CO

These brown bis-nitrosobenzene complexes are moderately air-stable in solution and can be stored in air in the solid state for several months without noticeable decomposition. They are soluble in CH_2Cl_2 and toluene, but are insoluble in hexane. We were not able to detect the proposed intermediate (por)Ru(CO)(PhNO) compounds by IR spectroscopy, and this differs from the case of the previously reported (and similar) reaction of (OEP)Ru(CO) with *N*,*N*-dimethyl-*p*-nitrosoaniline to give (OEP)Ru(ONC$_6$H$_4$NMe$_2$)$_2$ via a detectable intermediate, (OEP)Ru(CO)(ONC$_6$H$_4$NMe$_2$) (6).

The IR spectra of the new (por)Ru(PhNO)$_2$ complexes (as KBr pellets) show new bands at ~1348 cm^{-1} assignable to υ_{NO}. The marked drop in υ_{NO} from free PhNO at 1506 cm^{-1} is consistent with the view that the π^* orbitals of the PhNO ligands withdraw electron density from the "(por)Ru" fragment in the (por)Ru(PhNO)$_2$ complexes (1). Further evidence of the PhNO ligands behaving as π-acids comes from the X-ray crystal structure of (TPP)Ru(PhNO)$_2$ (see later).

Fig. 2. Molecular structure of (TPP)Ru(PhNO)(1-MeIm). Hydrogen atoms have been omitted for clarity.

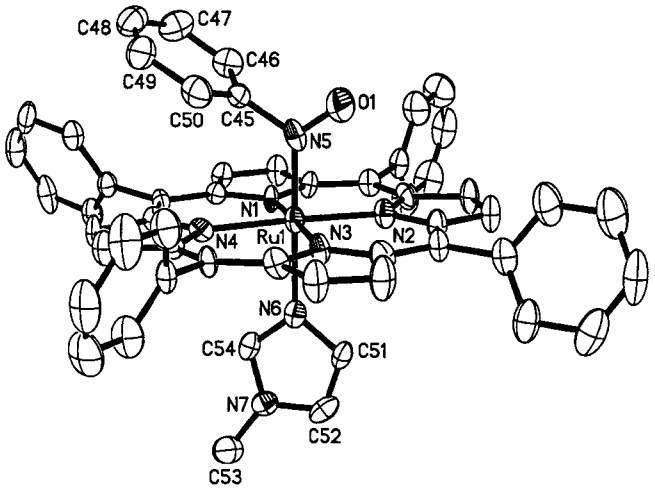

The ^{1}H NMR spectra of the (por)Ru(PhNO)$_2$ complexes in $CDCl_3$ show, as expected, peaks for both the porphyrin macrocycle and the PhNO ligands in these diamagnetic, and formally d^6, Ru(II) complexes. For example, the pyrrole-protons of the porphyrin macrocycle are at 8.54 ppm for both the (por)Ru(PhNO)$_2$ complexes (por = TPP, TTP). The *o*- and *m*-protons of the tetraaryl groups in (TTP)Ru(PhNO)$_2$ are resolved, and are at 7.99 and 7.50 ppm, respectively.

Synthesis of the mono-nitrosobenzene complexes

Many heme-containing biomolecules contain histidine as the axial proximal ligand. Thus, we were interested in synthesizing the axially unsymmetrical (por)Ru(PhNO)(1-MeIm) complexes to examine their spectroscopic properties and to determine the effect of the axial imidazole ligand on the binding of PhNO in these complexes.

The mono-nitrosobenzene complexes, (por)Ru(PhNO)(1-MeIm) (por = TPP, TTP), are readily prepared in 80% (for TPP) and 57% (for TTP) isolated yields, from the reaction of the precursor, (por)Ru(PhNO)$_2$, with an excess of 1-MeIm (eq. [2]).

[2] (por)Ru(PhNO)$_2$ + 1-MeIm $\rightarrow$ (por)Ru(PhNO)(1-MeIm) + PhNO

The ^{1}H NMR spectra of the crude product mixtures in $CDCl_3$ (after a 30 min reaction time in CH_2Cl_2 at room temperature, followed by solvent removal in vacuo, and redissolution of the product in $CDCl_3$) showed the presence of the desired mono-nitrosobenzene complexes and unreacted organic 1-MeIm as the only H-containing species. Despite the use of an excess of 1-MeIm in these reactions, the formation of the mono-nitrosobenzene complexes as the only Ru-containing products indicates that only one PhNO ligand in the (por)Ru(PhNO)$_2$ complexes is susceptible to substitution reaction under our reaction conditions. Interestingly, a similar observation has been made by James and co-workers (14) who reported that (OEP)Ru(PhNO)$_2$ reacts with 2 equiv of pyridine at room temperature to generate the mono-substituted product (OEP)Ru(PhNO)(py) within 10 min. We have also obtained ^{1}H NMR spectroscopic

© 2002 NRC Canada

evidence for the formation of (OEP)Os(PhNO)(1-MeIm) from the reaction of the previously reported $(OEP)Os(PhNO)_2$ with an excess of 1-MeIm.[3] These red-purple mono-nitrosobenzene complexes of Ru are moderately air-stable, showing no signs of decomposition in air after 1 month in the solid state and at least 8 h in solution. As with their bis-nitrosobenzene precursors, they are soluble in CH_2Cl_2 and toluene, but are insoluble in hexane.

The IR spectra of the (por)Ru(PhNO)(1-MeIm) complexes show bands at ~1321 cm^{-1} assignable to υ_{NO}. These bands are shifted by ~27 cm^{-1} to lower wavenumbers relative to the bis-nitrosobenzene precursors (υ_{NO} 1348 cm^{-1} (TPP) or 1346 cm^{-1} (TTP)). This shifting of υ_{NO} to lower wavenumbers is consistent with the replacement of one of the π-acid PhNO ligands (in the bis-nitrosobenzene precursor) with the more basic 1-MeIm ligand, which results in more Ru→N(O)Ph back-donation in the mono-nitrosobenzene complexes. The ^1H NMR spectra of the mono-nitrosobenzene complexes in $CDCl_3$ also reveal, in addition to porphyrin signals, peaks due to both the coordinated PhNO and 1-MeIm ligands. The chemical shifts of the $\delta_{pyrrole}$ protons of the mono-nitrosobenzene complexes (8.37–8.38 ppm) are slightly upfield shifted relative to those of the bis-nitrosobenzene complexes (8.54 ppm), indicative of a slight increase in electron-density of the porphyrin macrocycles in the mono-nitrosobenzene complexes relative to the bis-nitrosobenzene complexes. Importantly, the ^1H NMR spectrum of (TTP)Ru(PhNO)(1-MeIm) reveals that the *ortho*-protons of the *meso*-aryl substituent on the porphyrin rings are not equivalent, and the *meta*-protons are also nonequivalent; this is a common feature for *p*-substituted tetraphenylporphyrin complexes of the form (por)M(X)(Y) containing different ligands on each face of the porphyrin plane (15, 16). The ^1H NMR spectral peak patterns for the coordinated 1-MeIm ligands are assigned according to Leyden and Cox (17).

X-ray crystallographic characterization

The molecular structures of $(TPP)Ru(PhNO)_2$ and (TPP)Ru(PhNO)(1-MeIm) are shown in Figs. 1 and 2, respectively. Selected bond lengths, angles, and axial ligand orientations are shown in Fig. 3.

As can be seen in Figs. 1 and 2, the nitrosobenzene ligands are attached to the formally Ru(II) centers via an η^1-N bonding mode. The Ru—N(por) distances for $(TPP)Ru(PhNO)_2$ fall in the range of 2.047(2)–2.060(2) Å. Perpendicular atom displacements of the atoms in the porphyrin skeleton from the 24-atom mean porphyrin plane are shown in the middle of Fig. 3(*a*). The porphyrin macrocycle of $(TPP)Ru(PhNO)_2$ exhibits a *saddle* distortion, and the Ru atom resides in the plane of the porphyrin (a calculated displacement from the 24-atom mean porphyrin plane of only 0.03 Å).

The axial Ru—N (of PhNO) bond lengths in $(TPP)Ru(PhNO)_2$ are 1.953(2) and 2.049(2) Å, and the N—O bond lengths are 1.243(3) and 1.248(3) Å. The sum of angles around the nitroso nitrogens are ~360°, indicative of the planarity around the nitroso N-atoms. The axial N-Ru-N bond angle is 171.67(9)°, and this deviates only slightly from strict linearity. The axial ligand orientations in $(TPP)Ru(PhNO)_2$ are shown in Fig. 3(*a*). The PhNO ligands in $(TPP)Ru(PhNO)_2$ are oriented perpendicular to each other, and their C-NO groups essentially bisect the porphyrin nitrogens.

The molecular structure of (TPP)Ru(PhNO)(1-MeIm) was also obtained and shown in Figs. 2 and 3(*b*). As with $(TPP)Ru(PhNO)_2$, the nitrosobenzene ligand in (TPP)Ru(PhNO)(1-MeIm) is bound to the Ru(II) center via an η^1-N bonding mode. The Ru—N(por) distances are in the 2.039(4) Å to 2.062(5) Å range. Perpendicular atom displacements of the atoms in the porphyrin skeleton from the 24-atom mean porphyrin plane are shown in the middle of Fig. 3(*b*), and unlike $(TPP)Ru(PhNO)_2$, the porphyrin macrocycle of (TPP)Ru(PhNO)(1-MeIm) exhibits a *ruffled* distortion. The axial Ru—N(PhNO) and O—N(Ph) bond lengths are 1.884(6) Å and 1.267(7) Å, respectively. The axial ligand orientations in (TPP)Ru(PhNO)(1-MeIm) are also shown in Fig. 3(*b*). Interestingly, and unlike in the case of $(TPP)Ru(PhNO)_2$, the PhNO and 1-MeIm ligands in (TPP)Ru(PhNO)(1-MeIm) are oriented essentially parallel to each other, and their C-NO (for PhNO) and C-N-C (for 1-MeIm) groups essentially bisect the porphyrin nitrogens.

There are several notes of interest regarding the molecular structures of $(TPP)Ru(PhNO)_2$ and (TPP)Ru(PhNO)(1-MeIm). For example, the axial Ru—N(PhNO) bond length (1.953(2) to 2.049(2) Å) in $(TPP)Ru(PhNO)_2$ is longer than the related axial Ru—N(PhNO) distance of 1.884(6) Å seen in (TPP)Ru(PhNO)(1-MeIm), and this observation is suggestive of *decreased* Ru→N(O)Ph back-bonding in $(TPP)Ru(PhNO)_2$ relative to that in (TPP)Ru(PhNO)(1-MeIm). This view is consistent with the IR and ^1H NMR spectroscopic results discussed in the previous section. The O—N(Ph) bond lengths are not significantly different within these bis- and mono-nitrosobenzene complexes.

The most chemically interesting features of the structures of these (TPP)Ru(PhNO)-containing complexes are the axial ligand orientations. Indeed, the examination of the axial ligand orientations in heme model complexes is of importance due partly to the fact that the axial ligand orientations are affected by the electronic structure of the metal center. We have previously reported the single-crystal X-ray structure of the $(TPP)Fe(PhNO)_2$ complex containing two axial π-acidic PhNO ligands, and proposed that the presence of two axial π-acid ligands results in the perpendicular orientation of the axial ligands, and that this orientation maximizes the π-back-bonding from the HOMOs of the low-spin (TPP)Fe(II) fragment (namely the filled d_{xz} and d_{yz} orbitals) into the empty π* orbitals of the axial PhNO ligands (3). We have observed similar perpendicular axial ArNO ligand orientations in $(por)Os(ArNO)_2$ complexes (7). Indeed, and as expected, the PhNO ligands in $(TPP)Ru(PhNO)_2$ are oriented perpendicular to each other, indicating that the PhNO ligands act as π-acids in this complex.

[3] Data for (OEP)Os(PhNO)(1-MeIm). ^1H NMR ($CDCl_3$) δ: 9.18 (s, 4H, *meso*-H of OEP), 6.17 (br tt, 1H, *p*-H of PhNO), 5.74 (m, 2H, *m*-H of PhNO), 4.61 (dd (apparent t), *J* = 1.2, 1.2 Hz, 1H of 1-MeIm), 3.75 (m, 16H, CH_2CH_3 of OEP), 2.99 (m, 2H, *o*-H of PhNO), 2.08 (s, 3H, CH_3 of 1-MeIm), 1.75 (t, *J* = 8 Hz, 24H, CH_2CH_3 of OEP), 1.33 (br, 1H of 1-MeIm), 1.05 (dd (apparent t), *J* = 1.2, 1.2 Hz, 1H of 1-MeIm).

© 2002 NRC Canada

Fig. 3. Structural data for (*a*) (TPP)Ru(PhNO)$_2$ and (*b*) (TPP)Ru(PhNO)(1-MeIm). Selected bond lengths and angles are shown at the top. Perpendicular atom displacements from the 24-atom porphyrin plane (in 0.01 Å units) are shown at the middle. Also shown are the two axial ligand orientations at the middle and the bottom: α is the torsion angle involving O-N-Ru-N(por), and β is the torsion angle involving O-N-Ru-N(por) (for (TPP)Ru(PhNO)$_2$) or C-N-Ru-N(por) (for (TPP)Ru(PhNO)(1-MeIm)). The solid dot represents the nitroso oxygen atom, and the solid line represents the O-N-C unit of the PhNO ligand situated above the porphyrin plane. The dashed line represents the O-N-C unit of the second PhNO ligand situated below the porphyrin plane (for (TPP)Ru(PhNO)$_2$), or the C-N-C unit of the 1-MeIm ligand (for (TPP)Ru(PhNO)(1-MeIm)) situated below the porphyrin plane.

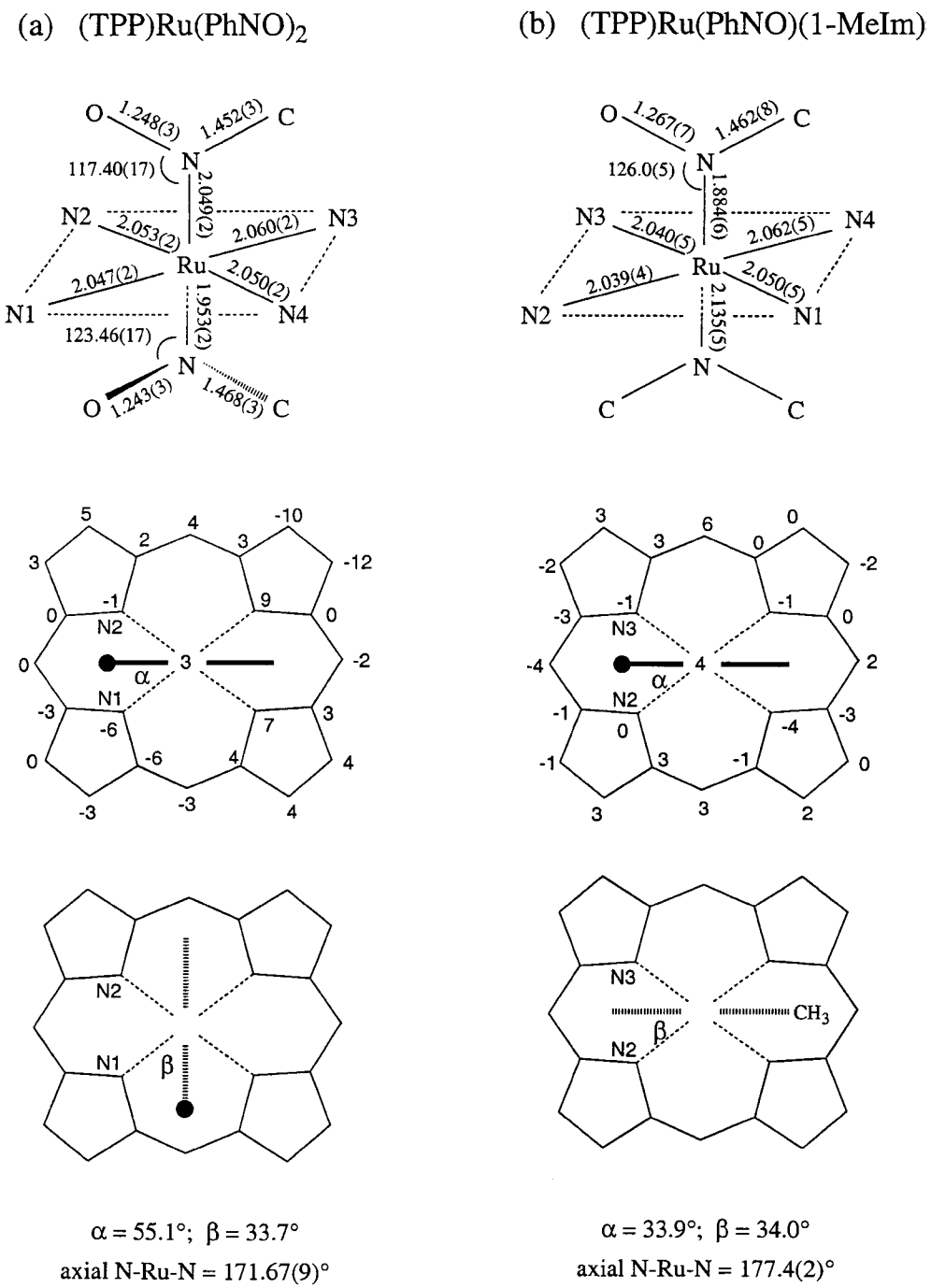

α = 55.1°; β = 33.7°
axial N-Ru-N = 171.67(9)°

α = 33.9°; β = 34.0°
axial N-Ru-N = 177.4(2)°

The axial ligand orientation observed for the solid-state structure of (TPP)Ru(PhNO)(1-MeIm) (Fig. 3(*b*)) provides an interesting comparison with that seen for (TPP)Ru(PhNO)$_2$ (Fig. 3(*a*)). Thus, the PhNO and 1-MeIm ligands in (TPP)Ru(PhNO)(1-MeIm) are nearly parallel to each other. This axial ligand orientation, observed for (TPP)Ru(PhNO)(1-MeIm), suggests that the 1-MeIm ligand could act as a π donor in this case. Indeed, the parallel orientation seen for (TPP)Ru(PhNO)(1-MeIm) might be expected to maximize the π-back-bonding from one of two filled d_π

© 2002 NRC Canada

orbitals of Ru(II) into the empty π^* orbital of the PhNO ligand.

Conclusion

We have successfully obtained isolable bis-nitrosobenzene and mono-nitrosobenzene complexes of ruthenium tetraarylporphyrins. The comparative spectroscopic and single-crystal X-ray crystallographic information obtained from this work reveals differences in the π-acidic and basic character of the PhNO and 1-MeIm ligands when situated *trans* to PhNO. This result is of great interest to model heme chemistry involving nitroso-based ligands, and poses additional questions that need to be addressed. For example, how important is axial ligand orientation for the dissociation of *trans* ligands? Such questions form the focus of future studies in this area.

Acknowledgements

We are grateful to the National Science Foundation (CHE-0076640) for support of this work.

References

1. J. Lee, L. Chen, A.H. West, and G.B. Richter-Addo. Chem. Rev. **102**, 1019 (2002).
2. D. Mansuy, P. Battioni, J.-C. Chottard, C. Riche, and A. Chiaroni. J. Am. Chem. Soc. **105**, 455 (1983).
3. L.-S. Wang, L. Chen, M.A. Khan, and G.B. Richter-Addo. Chem. Commun. 323 (1996).
4. N. Godbout, L.K. Sanders, R. Salzmann, R.H. Havlin, M. Wojdelski, and E. Oldfield. J. Am. Chem. Soc. **121**, 3829 (1999).
5. S.J. Fox, L. Chen, M.A. Khan, and G.B. Richter-Addo. Inorg. Chem. **36**, 6465 (1997).
6. L. Chen, J.B. Fox, Jr., G.-B. Yi, M.A. Khan, and G.B. Richter-Addo. J. Porphyrins Phthalocyanines, **5**, 702 (2001).
7. L. Chen, M.A. Khan, G.B. Richter-Addo, V.G. Young, Jr., and D.R. Powell. Inorg. Chem. **37**, 4689 (1998).
8. D.P. Rillema, J.K. Nagle, L.F. Barringer, Jr., and T.J. Meyer. J. Am. Chem. Soc. **103**, 56 (1981).
9. L.V. Andreasen, I.M. Lorkovic, G.B. Richter-Addo, and P.C. Ford. Nitric Oxide, **6**, 228 (2002).
10. SMART: Bruker molecular analysis research tool. Madison, WI, U.S.A. 1997–1998.
11. SAINTPlus: Data reduction and correction program. Madison, WI, U.S.A. 1999.
12. G.M. Sheldrick. SADABS: An empirical absorption correction program. Madison, WI, U.S.A. 1999.
13. G.M. Sheldrick, SHELXTL: Structure determination software suite. Madison, WI, U.S.A. 1998.
14. C. Crotti, C. Sishta, A. Pacheco, and B.R. James. Inorg. Chim. Acta **141**, 13 (1988).
15. S.S. Eaton and G.R. Eaton. J. Am. Chem. Soc. **99**, 6594 (1977).
16. S.S. Eaton and G.R. Eaton. J. Am. Chem. Soc. **97**, 3660 (1975).
17. D.E. Leyden and R.H. Cox. Analytical applications of NMR. John Wiley & Sons, New York. 1977. p. 186.

© 2002 NRC Canada

Potentiometric study of equilibrium acidities of some carbon acids in acetonitrile

M. Stanczyk-Dunaj, W. Galezowski, and A. Jarczewski

Abstract: The pK_a values for 30 C-acids of the type $CH{\cdot}R^1{\cdot}R^2{\cdot}R^3$ — where the R^1, R^2, and R^3 substituents are H, alkyl, and aryl, and the most common electron withdrawing groups used in studies of proton-transfer reaction — are given herein. The pK_a values have been measured potentiometrically in acetonitrile, using a glass electrode. These values were determined in a buffer solution consisting of a C-acid and its tetrabutylammonium salt, at constant ionic strength (0.001 M), at 25°C. The measurements were done under nitrogen, to prevent oxidation of the anion. The influence of water within the sample of the tetrabutylammonium hydroxide base was negligible. The lowest pK_a value of 19.1 was found for bis(4-nitrophenyl)cyanomethane, while the largest pK_as that could be measured were limited by the basicity of the hydroxide ion, and did not exceed 28. A satisfactory agreement between spectrophotometric and potentiometric acidities was achieved.

Key words: C-acids, pK_a values, acetonitrile, potentiometry, proton transfer.

Résumé : On a mesuré les valeurs de pK_a de 30 C-acides du type $CH{\cdot}R^1{\cdot}R^2{\cdot}R^3$ dans lesquels les substituants R^1, R^2 et R^3 sont des H, alkyle, aryle et la plupart des groupes électroaffinitaires utilisés dans l'étude de la réaction de transfert de proton. Les valeurs de pK_a ont été mesurées potentiométriquement, dans l'acétonitrile, à l'aide d'une électrode de verre. Ces valeurs ont été déterminées dans une solution tampon formée d'un C-acide et de son sel de tétrabutylammonium, à force ionique constante de 0,001 M, à 25°C. Les mesures ont été faites sous atmosphère d'azote, pour éviter l'oxydation de l'anion. L'influence de l'eau contenue dans l'échantillon de la base, hydroxyde de tétrabutylammonium, est négligeable. La valeur la plus faible de pK_a est associée au bis(4-nitrophényl)cyanométhane alors que les valeurs les plus élevées étaient limitées par la basicité de l'ion hydroxyde et ne dépassaient pas 28. On a observé une corrélation satisfaisante entre les acidités spectrophotométriques et potentiométriques.

Mots clés : C-acides, valeurs de pK_a, acétonitrile, potentiométrie, transfert de proton.

[Traduit par la Rédaction]

Introduction

The pK_a values for C-acids of different structure and strength are crucial for studying proton-transfer reactions and the formation of hydrogen-bonded complexes in acetonitrile. They are essential for determining Brønsted parameters (1, 2) and the symmetry of the transition state (3–6), which are two of the major factors influencing deuterium kinetic isotope effects. Obviously, any discussion of the symmetry of the hydrogen bonds in the complexes formed with C-acids and strong organic bases in acetonitrile requires precise pK_a values (7, 8). Acetonitrile appears to be the most commonly used solvent in kinetic and equilibrium experiments of proton-transfer reactions.

A survey of spectrophotometric pK_a values for C-acids in acetonitrile has already been published (9). The aim of this paper is to measure the pK_a values for a set of 30 C-acids of the type $CH{\cdot}R^1{\cdot}R^2{\cdot}R^3$, where R^1, R^2, and R^3 are H, alkyl, aryl, and the most common electron withdrawing groups that activate C-acids, such as nitro, cyano, alkylsulfonyl, and carboxyalkyl (Table 1), all in acetonitrile, using the potentiometric method (10). The measurements were performed using buffer solutions of the appropriate C-acid and its tetrabutylammonium salt, at a constant ionic strength (0.001 M), at 25°C.

The spectrophotometric results reported in the previous paper (9) were measured in buffer solutions composed of a strong amine base of known potentiometric pK_a value, and its perchlorate or picrate salt. This way, the pK_a values for 11 of the C-acids most commonly used in kinetic and equilibrium experiments of proton-transfer reactions were found. This method is impractical, however, when (*i*) the absorption band of the salt of the C-acid is buried under the absorption of the amine base, which is in large excess compared with the C-acid; (*ii*) some amine bases tend to homoconjugate with their cations (11, 12), which causes undesirable complications; and (*iii*) spectrophotometric pK_a values for C-acids could show some scatter due to various errors in the pK_as of the amine bases. A comparison between the spectrophotometric and potentiometric pK_a values for C-acids is, therefore, of interest.

Since a water solution of tetrabutylammonium hydroxide was used to prepare the measuring buffer solutions, water

Received 24 January 2002. Published on the NRC Research Press Web site at http://canjchem.nrc.ca on 17 September 2002.

M. Stanczyk-Dunaj, W. Galezowski, and A. Jarczewski.[1]
Faculty of Chemistry, A. Mickiewicz University, Grunwaldzka 6, 60–780 Poznañ, Poland.

[1]Corresponding author (e-mail: arnold@amu.edu.pl).

 DOI: 10.1139/V02-164 © 2002 NRC Canada

present in the system could have a significant effect on our results. Thus, some experiments concerning this effect were made.

Results and discussion

In the kinetic and equilibrium experiments, a number of strong C-acids of differring structure were tested (13) (Table 1). In previous kinetic and equilibrium experiments, uncomplicated C-acids, such as **3**, were used (14). At that time, the large primary deuterium kinetic isotope effect (KIE) values were attributed to three factors: steric hindrance of the reacting base (15, 16), symmetry of the transition state (9, 13, 17), and polarity of the solvent used (13, 18, 19). To find the factors influencing the values of KIE, the series of C-acids with increasing R substituent bulk, and hence increasing steric hindrance, were synthesized and used (2, 13, 16, 19, 20). Then, most kinetic experiments used strong C-acids with different steric hindrances in the vicinity of the reaction center.

The ionization process is multistep, leading from the carbon acid, via a carbanion or carbanion-like structure, to exocyclic nitronate, cyanate or other forms of anions stabilized by resonance provided for the appropriate electron withdrawing groups present in the molecule (21–24).

We have already found that the products of the proton-transfer reaction of a relatively strong carbon acid with a strong amine base in acetonitrile are mostly dissociated into free ions. Some ion association was observed for alkanenitronates, especially upon addition of cations that act as hydrogen bond donors (25). In this work, the use of tetrabutylammonium salts and moderate concentrations minimized ion association.

The pK_a values were calculated using eq. [1],

$$[1] \qquad pK_a = pH + \log [AH] - \log [A^-] - \log f$$

and activity coefficients were calculated from the Debye-Hückel equation (eq. [2]) (1).

$$[2] \qquad -\log f = 1.51\ \mu^{1/2};\ \mu = 1 \times 10^{-3}\ M$$

The buffers were made by combining a solution of a C-acid (0.002 M) in acetonitrile and a very small volume of 40% tetrabutylammonium hydroxide solution at a 2:1 molar ratio. This way, the concentrations of [AH] (0.001 M) and [A^-] (0.001 M), and the ionic strength (0.001 M), were kept constant. The concentration of water (neglecting the content within the acetonitrile solvent) in the measuring buffers was 0.0224 M.

The strength of the OH^- base determines the limits of the pK_a values that can be measured by this method. Triphenylmethane, for instance, does not react with OH^- in acetonitrile, which could be anticipated taking into account the pK_a of 30.6 (26) for this C-acid in DMSO, and the typical ΔpK_a between acetonitrile and DMSO.

In acetonitrile, the pH of a 0.001 M solution of Bu_4NOH is approximately 30.2. Thus the hydroxide ion is by several pK units more basic in this solvent than is tetramethylguanidine (pK_a = 23.3) (27) or DBU (pK_a = 23.9) (10), while in water these bases are of comparable strength. The pK_a values for C-acids **1**–**30** are collected in Table 1.

Fig. 1. Hammet relationship for 4-X-phenyl(4-nitrophenyl)cyanomethanes in acetonitrile at 25°C. The σ values are the same as in ref. 10.

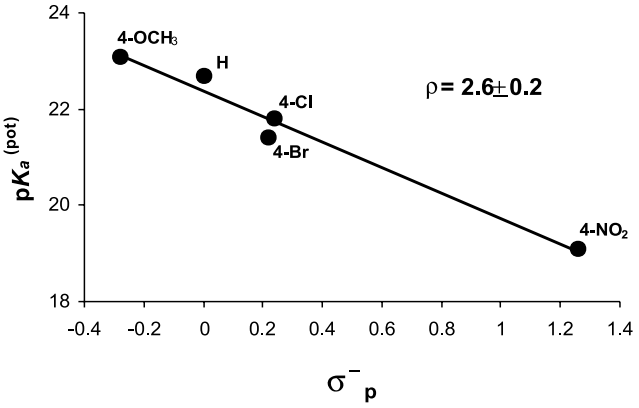

The strongest C-acid in this set appears to be bis(4-nitrophenyl)cyanomethane (**15**, pK_a = 19.1). Acetonitrile solutions of this C-acid in contact with traces of ground glass easily turn blue when a stopper is tightly fit to a measuring flask containing a solution of this acid. Acidities measured in this work are limited by the basicity of the hydroxide ion and do not exceed pK_a = 28. Ionization of considerably weaker C-acids could not be studied using bases much stronger than OH^- in acetonitrile anyway, because of the decomposition of the solvent (28). Acetonitrile is a C-acid itself, and its pK_a in MeCN can be estimated (p$K_a \approx 43$) from its pK_a in DMSO (p$K_a \approx 31.3$) (29) and $\Delta pK_a^{(MeCN-DMSO)}$. This estimate agrees with Schwesinger's assumption that the pK_a for MeCN is ca. 44 (28). More importantly, even carefully dried acetonitrile contains some water that will react with very strong bases, making the results of these experiments with dilute solutions dubious.

The pattern of the change in pK_a with varying substituents is trivial, except for the pK_a of 4-nitrophenyl[bis(ethylsulfonyl)]methane, which is greater than for the 4-cyanophenyl derivative. A Hammet relationship for the series of 4-X-phenyl(4-nitrophenyl)cyanomethanes gave $\rho = 2.6 \pm 0.2$ (Fig. 1), which shows the considerable sensitivity of the substituent on the phenyl ring to acidity levels. As expected, the replacement of the nitro- group by a cyano- group on the aliphatic carbon greatly reduced the acidity of 4-nitrophenylnitromethane (**3**) (pK_a = 20.4) by about 4.8 pK_a units, to 25.2 for 4-nitrobenzylcyanide (**10**). The influence of steric hindrance on the pK_a values — caused by the bulk of alkyl substituents in the vicinity of the reaction center — is clearly visible for the following group of carbon acids: 4-nitrophenylnitromethane (**3**) (pK_a = 20.4), 1-(4-nitrophenyl)-1-nitroethane (**4**) (pK_a = 23.2), 1-(4-nitrophenyl)-1-nitropropane (**5**) (pK_a = 23.6), 2-methyl-1-(4-nitrophenyl)-1-nitropropane (**6**) (pK_a = 25.7), and 2,2-dimethyl-1-(4-nitrophenyl)-1-nitropropane. (**7**) (pK_a = 26.2). In the series of 2,6-dialkyl-4-nitrophenylphenylcyanomethanes, the increase in pK_a with increasing steric hindrance is modest when the methyl groups are replaced with *i*-propyl groups, while all dialkyl derivatives are considerably weaker acids than the parent 4-nitrophenyl-phenylcyanomethane.

In the last column of Table 1, references to relevant kinetic studies of some C-acids are given. For comparison,

© 2002 NRC Canada

Table 1. Potentiometric pK_a values for C-acid derivatives of methane CH·R^1·R^2·R^3 in acetonitrile at 25°C.

C-acid	R^1	R^2	R^3	pK_a [a]	pK_a [b]	Relevant kinetic studies refs.
1	NO_2	Phenyl	Methyl	25.4_1		
2	NO_2	Phenyl	Ethyl	26.1_0		
3	NO_2	4-Nitrophenyl	H	20.3_9	20.7 (9); 20.6 (6)	13, 14, 21, 58
4	NO_2	4-Nitrophenyl	Methyl	23.2_4		25, 59
5	NO_2	4-Nitrophenyl	Ethyl	23.5_7	23.9 (9)	20, 25, 58
6	NO_2	4-Nitrophenyl	*i*-Propyl	25.7_3	25.9 (25)	17, 20, 25, 58
7	NO_2	4-Nitrophenyl	*t*-Butyl	24.3_5		
8	CN	CN	H	22.4_5		
9	CN	Phenyl	Phenyl	28.2_3		
10	CN	4-Nitrophenyl	H	25.2_5	25.4 (25)	17, 44
11	CN	4-Nitrophenyl	Phenyl	22.7_2	22.7 (1)	15, 33, 46
12	CN	2,6-Dimethyl-4-nitrophenyl	Phenyl	25.7_8		54
13	CN	2,6-Diethyl-4-nitrophenyl	Phenyl	25.9_4		
14	CN	2,6-Di-*i*-propyl-4-nitrophenyl	Phenyl	26.1_9		
15	CN	4-Nitrophenyl	4-Nitrophenyl	19.0_7	19.0 (9)	44, 45, 61
16	CN	4-Nitrophenyl	4-Chlorophenyl	21.8_3		45
17	CN	4-Nitrophenyl	4-Bromophenyl	21.3_8	21.3 (9)	45
18	CN	4-Nitrophenyl	4-Methoxyphenyl	23.1_1	23.1 (9)	45
19	4-Nitrophenyl	4-Nitrophenyl	H	26.0_5		62
20	4-Nitrophenyl	4-Nitrophenyl	4-Nitrophenyl	25.1_9		
21	2,4,6-Trinitrophenyl	H	H	23.2_2	23.2 (9)	49, 50, 63
22	2,4,6-Trinitrophenyl	Methyl	Methyl	25.8_0		46
23	C_2H_5-SO_2	C_2H_5-SO_2	Phenyl	24.2_3		64, 65
24	C_2H_5-SO_2	C_2H_5-SO_2	4-Chlorophenyl	23.4_3		62, 64, 65
25	C_2H_5-SO_2	C_2H_5-SO_2	4-Cyanophenyl	22.3_4		62, 64, 65
26	C_2H_5-SO_2	C_2H_5-SO_2	4-Nitrophenyl	22.8_8		64, 65
27	COO-*t*-Bu	COO-*t*-Bu	Methyl	27.6_0		
28	COOEt	COOEt	2,4-Dinitrophenyl	22.2_3		31
29	$COCH_3$	$COCH_3$	H	24.4_9		
30		9-Cyanofluorene		20.8_0	20.8 (9)	

[a]In this work, standard deviations are typically less than 0.1.
[b]Spectrophotometric pK_a refs. are given in parentheses.

ten pK_as measured by the spectrophotometric method (9, 30) are given in the sixth column of Table 1. In each case satisfactory agreement was achieved. The largest differences, not exceeding 0.3 pK_a units, were found for **3**, **5**, and **6**, while for some C-acids the fit was perfect. The good correspondence of spectrophotometric and potentiometric pK_as is shown in Fig. 2.

There were two possibilities to distort the pK_a values: the consecutive oxidation reaction of an anion A^- (31, 32), and the influence of water brought to the system by the addition of tetrabutylammonium hydroxide base. This base is commercially available as a concentrated water solution (see *Experimental*). Then, too, the addition of the base to a C-acid solution in acetonitrile to make the buffer added some amount of water, in addition to water already present in even thoroughly-dried solvent, and that formed in the proton-transfer reaction. One could expect that the basicity of OH^- might be strongly dependent on the amount of water present in the medium. The response of the electrode to the concentration of water added to a tetrabutylammonium hydroxide

Fig. 2. The relation between spectrophotometric and potentiometric pK_as for various C-acids in acetonitrile at 25°C. The numbers denote C-acids according to Table 1.

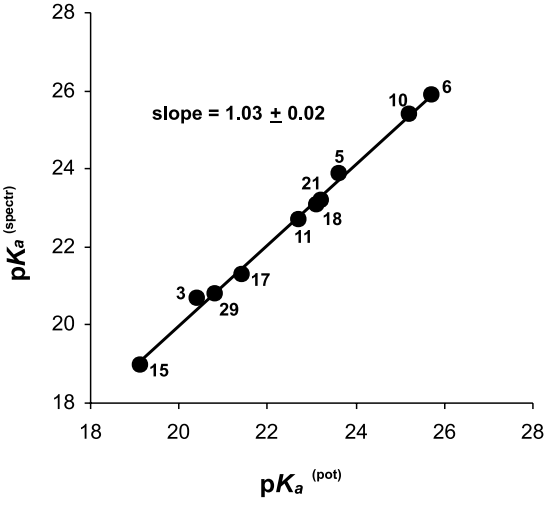

© 2002 NRC Canada

Table 2. Effect of water on potentiometric measurements in acetonitrile.

	E (mV)	
$[H_2O]$ (mol dm^{-3})	Tetrabutylammonium hydroxide (1×10^{-3} M)	**3** (1×10^{-3} M) and its tetrabutylammonium salt (1×10^{-3} M)
0.0214	–1186.0	–590.7
0.0429	–1189.8	–590.1
0.0858	–1188.7	–592.7
0.1716	–1183.5	–593.1
0.2145	–1183.6	–593.4
2.145	–804.3	–570.9

Table 3. Equilibrium acidities of various C-acids in acetonitrile and DMSO.

C-Acids	pK_a^{MeCN}	pK_a^{DMSO}	$\Delta pK_a^{(MeCN-DMSO)}$
4-Nitrophenylnitromethane (**3**)	20.3_9	8.62 (34)	11.7_7
Malononitrile (**8**)	22.4_0	11.03 (35), 11.4 (36)	11.4, 11.0
4-Nitrobenzylcyanide (**10**)	25.2	12.03[a] (37), 12.3 (38)	13.2_2, 12.9
Bis(4-nitrophenyl)cyanomethane (**15**)	26.0_5	14.94[b] (39)	11.1_1
Tri(4-nitrophenyl)methane (**20**)	25.1_9	12.84[c] (40)	12.3_5
2,4,6-Trinitrotoluene (**21**)	23.2_2	10.5[b] (39)	12.7
2,4-Pentanedione (**29**)	24.9_9	13.4 (41)	11.6
9-Cyanofluorene (**30**)	20.8_0	8.01[a] (42)	12.7_9

[a]10% H_2O.
[b]50% H_2O.
[c]20% H_2O.

solution (0.001 M) in acetonitrile or in the measuring buffers was weak for water concentrations in the range up to 0.2 M, however, as shown in Table 2. The concentration of water in the measuring solutions was 0.0224 M because of water content in the added base and water produced in the proton-transfer reaction. An important argument for the weak dependence of pK_a on water content in the ranges below 0.01 M lies in the virtually-equal results obtained by potentiometric and spectrophotometric methods (9). In the latter, the concentration of water was determined by the quality of the solvent and amine base. The content of 0.001% of water in acetonitrile makes approximately 0.00044 M solution.

Usually, alkanenitronates are reasonably stable in dilute solutions with a large excess of amine base, which is normally the case in spectrophotometric measurements. They become labile, however, in relatively concentrated solutions of buffers consisting of the alkanenitronate salts and nitroalkanes used in our potentiometric study. Then, as we already know, the anions derived from some cyano-group-activated C-acids, and those forming double-hydrogen-bonded complexes as products, are particularly sensitive to the trace amounts of oxygen present in the measuring system (17, 31, 32). All the measurements were therefore carried out under nitrogen. This made most of the anions of the C-acids stable for at least one hour. Benzyl cyanide, however, with an expected pK_a of 32 based on its pK_a in DMSO (pK_a^{DMSO} = 21.91) (33), decomposed in a 0.002 M hydroxide solution (even under anaerobic conditions) and is therefore not present in Table 1.

An approximately constant shift between the pK_a values measured in acetonitrile and in DMSO, $\Delta pK_a^{(MeCN-DMSO)}$, holds up for the results obtained in the present study (Table 3). Based on limited data, it seems that the pK_a shift for C-acids between DMSO and acetonitrile is 12 ± 1. Thus, this shift is larger for C-acids than for amine cations (with a range between 6–10) and phenols, or carboxylic acids (with a range between 10–12), and similar to that for indicators such as phenolphthalein or phenol red (27).

Experimental

The syntheses of C-acids have been completed as described elsewhere: 1-nitro-1-phenylethane (**1**) and bis(4-nitrophenyl)methane (**19**) (9, 43), 1-nitro-1-phenylpropane (**2**) (9, 43), 4-nitrophenylnitromethane (**3**) (14), 1-(4-nitrophenyl)-1-nitroethane (**4**) (20), 1-(4-nitrophenyl)-1-nitropropane (**5**) (20), 2-methyl-1-(4-nitrophenyl)-1-nitropropane (**6**) (20), benzylcyanide (Aldrich), malononitrile (**8**) (Fluka, purified by sublimation before use), diphenylcyanomethane (**9**) (Aldrich, sublimed before use), 4-nitrobenzylcyanide (**10**) (Fluka) (17), 4-nitrophenylphenylcyanomethane (**11**) (44, 45), bis(4-nitrophenyl)cyanomethane (**15**) (30, 44), 4-chlorophenyl(4-nitrophenyl)cyanomethane (**16**) (46), 4-bromophenyl(4-nitrophenyl)cyanomethane (**17**) (45), 4-methoxyphenyl(4-nitrophenyl)cyanomethane (**18**) (45), bis(4-nitrophenyl)methane (**19**) (47), tri(4-nitrophenyl)methane (**20**) (48), 2,4,6-trinitrotoluene (**21**) (49, 50, 51), 2,4,6-trinitrocumene (**22**) (46), phenyl[bis(ethylsulfonyl)]methane (**23**) (52), 4-chlorophenyl[bis(ethylsulfonyl)]methane (**24**) (52), 4-cyanophenyl[bis(ethylsulfonyl)]methane (**25**) (52), 4-nitrophenyl[bis(ethylsulfonyl)]methane (**26**) (53), di-*tert*-butyl-2-methylmalonate (**27**) (53), diethyl-(2,4-dinitrophenyl)malonate (**28**) (31), 2,4-pentanedione (**29**) (Adrich), 9-cyanofluorene (**30**) (9), (2,6-dimethyl-4-nitrophenyl)phenylcyanomethane (**12**). (2,6-Diethyl-4-nitrophenyl)phenylcyano-

© 2002 NRC Canada

methane (**13**) and (2,6-di-*i*-propyl-4-nitrophenyl)phenylcyanomethane (**14**) were obtained from a modified procedure by Leffek and Pruszynski (54); details will be described elsewhere (55). 2,2-Dimethyl-1-(4-nitrophenyl)-1-nitropropane (**7**) was prepared as described for **6** (20) (a major byproduct in this synthesis was p-(2,2-dimethyl-1-chloropropyl)nitrobenzene, which was very resistant to acidic or basic hydrolysis). Phenyl[bis(ethylsulfonyl)]methane **23**, 4-chlorophenyl[bis-(ethylsulfonyl)]methane (**24**), 4-cyanophenyl[bis(ethylsulfonyl)]methane (**25**), and 4-nitrophenyl[bis(ethylsulfonyl)]methane (**26**) were prepared according to Aiken et al. (64, 65).

Acetonitrile (Romil, spectro grade) was fractionally distilled over CaH_2 and carefully handled to prevent atmospheric contamination. Tetrabutylammonium hydroxide (40%), an aqueous concentrated solution, was purchased from Aldrich. A sample of this product was titrated with standardized HCl.

The IR, NMR, and MS spectra and melting points of these compounds are in agreement with those given in the references. The commercial products were purified before use to meet their specific physical properties.

The measurements of C-acid pK_as (**1**–**30**) were performed in an H-type cell equipped with a thermostated water jacket, to maintain a constant temperature (25 ± 0.1°C). The potentiometric cell and the procedure used have been described, in detail, by Leffek et al. (10).

The side arm of an external reference half-cell was dipped into a tetraethylammonium perchlorate solution (0.1 M). The reference electrode was a flowing junction, Ag/AgNO3 (0.01 M) in acetonitrile (half-cell). The middle compartment was closed on both sides with fine porosity sintered glass, and was filled with 0.1 M tetraethylammonium perchlorate in acetonitrile. The large compartment holding the glass electrode was filled with the buffer (acetonitrile) solution, and prepared with C-acid (0.002 M), and its tetrabutylammonium hydroxide (0.001 M) at constant ionic strength (0.001 M). Tetrabutylammonium hydroxide had been chosen because it eliminates homoconjugation, which is a distracting factor for many amine bases in acetonitrile (56). The middle and glass electrode compartments were equipped with taps, providing easy drainage after each set of measurements. When not in use, the glass electrode was kept in pure acetonitrile. The storage of the glass electrode in acetonitrile ensured the reliability and reproducibility of the measurements. The new electrode was conditioned in acetonitrile at least 2 days before use.

The calibration of the glass electrode (CORNING, Ag/AgCl category No. 476026) was accomplished with a series of buffer solutions, composed of tetraethylammonium picrate (0.002 M) and picric acid in the range of 0.0001 M to 0.007 M (7 buffers), according to the methods published by Leffek et al. (10) and Coetzee and Padmanabhan (57). The measurements were carried out using an Elmetron CX 721 multifunction computer meter.

The solutions and the measuring cell compartments were protected against oxygen, CO_2, and atmospheric moisture. Then the pK_a measurements were carried out in the following manner: into the measuring compartment, 10 mL of the appropriate C-acid (0.002 M) in acetonitrile was placed. This solution was purged with pure N_2 saturated with acetonitrile vapors, using a stainless steel injection needle to remove O_2 and repel eventual access of atmospheric CO_2 and moisture during equilibration. Then 6.5 μL of 40% tetrabutylammonium hydroxide (to make a 0.001 M solution of the salt) was added using a Hamilton microsyringe, with continuous bubbling of nitrogen. The needle was removed and the cell was tightly closed. Each pK_a value given in Table 1 is an average of three separate measurements. The pK_a values have been measured in 10 and 20 min intervals to assure equilibration of the system, and also to be sure that side effects are negligible. The readings were converted to pH, then the pK_a values were obtained from eq. [1]. The standard deviations were not larger than 0.1 pK_a unit.

Acknowledgments

The authors are grateful for financial support from the Polish Committee of Sciences (grant 7T 09A 074 21).

References

1. A.J. Kresge. Can. J. Chem. **52**, 1897 (1974).
2. W. Galezowski, I. Grzeskowiak, and A. Jarczewski. Can. J. Chem. **77**, 1042 (1999).
3. F.W. Westheimer. Chem. Rev. **61**, 265 (1961).
4. R.P. Bell, W.H. Sachs, and R.L. Tranter. Trans. Faraday Soc. **67**, 1995 (1971).
5. E.F. Caldin and V. Gold (*Editors*). Proton-transfer reactions. Chapman and Hall, London. 1975.
6. J.R. Gandler and C.F. Bernasconi. J. Am. Chem. Soc. **114**, 631 (1992).
7. G. Zundel. *In* The hydrogen bond: recent development in theory and experiments. Vol. 2. *Edited by* P. Schuster, G. Zundel, and C. Sandorfy. North Holland Pub. Co., Amsterdam. 1976.
8. W. Galezowski, A. Jarczewski, M. Stanczyk, B. Brzezinski, F. Bartl, and G. Zundel. J. Chem. Soc. Faraday Trans. **93**, 2515 (1997).
9. W. Galezowski, M. Stanczyk, and A. Jarczewski. Can. J. Chem. **75**, 285 (1997).
10. K.T. Leffek, P. Pruszynski, and K. Thanapaalasingham. Can. J. Chem. **67**, 590 (1989).
11. I.M. Kolthoff and M.K. Chantooni. J. Am. Chem. Soc. **97**, 1376 (1975).
12. I.F. Coetzee and G.R. Padmanabhan. J. Am. Chem. Soc. **20**, 5005 (1965).
13. A. Jarczewski. Wiad. Chem. **54**, 203 (2000).
14. E.F. Caldin, A. Jarczewski, and K.T. Leffek. Trans. Faraday Soc. **67**, 110 (1971).
15. E.S. Lewis and L.H. Funderburk. J. Am. Chem. Soc. **89**, 2322 (1967).
16. W. Galezowski, I. Grzeskowiak, and A. Jarczewski. J. Chem. Soc. Perkin Trans. 2, 1607 (1998).
17. P. Pruszynski and A. Jarczewski. J. Chem. Soc. Perkin Trans. 2, 1117 (1986).
18. E.F. Caldin and S. Mateo. J. Chem. Soc. Faraday Trans. 1, **72**, 112 (1976).
19. W. Galezowski and A. Jarczewski. Can. J. Chem. **68**, 2242 (1990).
20. W. Galezowski and A. Jarczewski. J. Chem. Soc. Perkin Trans. 2, 1647 (1989).
21. G. Moutiers, V. Thuet, and F. Terrier. J. Chem. Soc. Perkin Trans. 2, 1479 (1997).
22. R.A. McClelland and S. Steenken. Can. J. Chem. **65**, 353 (1987).

© 2002 NRC Canada

23. C.F. Bernasconi, D.V.A. Kliner, A.S. Mullin, and J.X. Ni. J. Org. Chem. **53**, 3442 (1988).
24. F. Terrier, H.-Q. Xie, and P.G. Farrell. J. Org. Chem. **55**, 2610 (1990).
25. W. Galezowski, M. Stanczyk, I. Grzeskowiak, and A. Jarczewski. J. Chem. Soc. Perkin Trans. 2, 2647 (1996).
26. F.G. Bordwell, J.F. Bares, J.E. Bartmess, G.J. McCollum, M. Van Der Puy, N.R. Vanier, and W.S. Matthews. J. Org. Chem. **42**, 321 (1977).
27. I.M. Kolthoff, M.K. Chantooni, and S. Bhowmik. J. Am. Chem. Soc. **90**, 23 (1968).
28. R. Schwesinger. Angew. Chem. Int. Ed. Engl. **26**, 1164 (1987).
29. W.S. Matthews, J.E. Bares, J.E. Bartmess, F.G. Bordwell, J.F. Cornforth, G.E. Drucker, Z. Margolin, R.J. McCallum, and N.R. Vanier. J. Am. Chem. Soc. **97**, 7006 (1975).
30. W. Galezowski and A. Jarczewski. Can. J. Chem. **70**, 935 (1992).
31. K.T. Leffek and A.E. Matinopoulos-Scordou. J. Chem. Soc. Perkin Trans. 2, 1099 (1979).
32. I. Grzeskowiak, W. Galezowski, and A. Jarczewski. Can. J. Chem. **79**, 1128 (2001).
33. K. Bowden and S.I.J. Hirani. J. Chem. Soc. Perkin Trans. 2, 1889 (1990).
34. J.R. Keeffe, J. Morey, C.A. Palmer, and L.C. Lee. J. Am. Chem. Soc. **101**, 1295 (1979).
35. C.D. Ritchie and R.E. Uschold. J. Am. Chem. Soc. **90**, 2821 (1968).
36. F.G. Bordwell, N.R. Vanier, W.S. Matthews, J.B. Hendrickson, and P.I. Skipper. J. Am. Chem. Soc. **97**, 7160 (1975).
37. C.F. Bernasconi and J.X. Ni. J. Am. Chem. Soc. **115**, 5060 (1993).
38. E.A. Walters. J. Phys. Chem. **81**, 21 (1977).
39. F. Terrier, H.Q. Xie, and P.G. Farrell. J. Org. Chem. **55**, 2610 (1990).
40. F. Terrier, T. Boubaker, L. Xiao, and P.G. Farrell. J. Org. Chem. **57**, 3924 (1992).
41. C.D. Ritchie. *In* Solute–solvent interactions. *Edited by* J.F. Coetzee and C.D. Ritchie. Marcel Dekker, New York. 1969. p. 219.
42. C.F. Barnasconi and F. Terrier. J. Am. Chem. Soc. **109**, 7115 (1987).
43. W. Galezowski. Ph.D. Thesis. A. Mickiewicz University, Poznañ, Poland, 1988.
44. A. Jarczewski and P. Pruszynski. Pol. J. Chem. **58**, 1175 (1984).
45. M. Hojatti and K. T. Leffek. Can. J. Chem. **62**, 2653 (1984).
46. M.K. Biswas, A. Jarczewski, and K.T. Leffek. Can. J. Chem. **65**, 1007 (1987).
47. A. Jarczewski and K.T. Leffek. Can. J. Chem. **50**, 24 (1972).
48. J.D. Margerum, L.J. Miller, E. Saito, M.S. Brown, H.S. Mosher, and R. Hardwick. J. Phys. Chem. **66**, 2434 (1962).
49. P. Pruszynski and A. Jarczewski. Ann. Soc. Chim. Pol. **51**, 2171 (1977).
50. N. Sugimoto and M. Sasaki. J. Chem. Soc. Faraday Trans. 1, **81**, 1441 (1985).
51. A. Jarczewski and P. Pruszynski. Can. J. Chem. **57**, 669 (1979).
52. M.W. Cronyn. J. Am. Chem. Soc. **47**, 1225 (1952).
53. W.H. Puterbaugh, F.W. Swamer, and C.R. Hauser. J. Am. Chem. Soc. **74**, 3438 (1952).
54. K.T. Leffek and P.P. Pruszynski. Can. J. Chem. **66**, 1454 (1988).
55. K. Minksztym and A. Jarczewski. Submitted.
56. I.M. Kolthoff and M.K. Chantooni. J. Am. Chem. Soc. **90**, 3005 (1967).
57. J.F. Coetzee and G.R. Padmanabhan. J. Phys. Chem. **66**, 1708 (1962).
58. E.F. Caldin and S. Mateo. J. Chem. Soc. Faraday Trans. 1, **71**, 1876 (1975).
59. A. Jarczewski, G. Schroeder, P. Pruszynski, and K.T. Leffek. Can. J. Chem. **64**, 1021 (1986).
60. A. Jarczewski, P. Pruszynski, and K.T. Leffek. Can. J. Chem. **61**, 2029 (1983).
61. P. Pruszynski and K.T. Leffek. Can. J. Chem. **69**, 205 (1991).
62. A. Jarczewski, P. Pruszynski, and K.T. Leffek, Can. J. Chem. **53**, 1176 (1975).
63. E.F. Caldin and G. Long. Proc. R. Soc. London Ser. A, **226**, 263 (1955).
64. F. Aiken, B.G. Cox, and P.E. Sørensen. J. Chem. Soc. Perkin Trans. 2, 783 (1993).
65. A. Jarczewski and I. Binkowska. Pol. J. Chem. **75**, 1895 (2001).

© 2002 NRC Canada

A ^{19}F nuclear magnetic resonance study of the conjugate Brønsted–Lewis superacid HSO_3F–SbF_5. Part II.

Jobst Kühn-Velten, Matthias Bodenbinder, Raimund Bröchler, Gerhard Hägele, and Friedhelm Aubke

Abstract: Solutions of SbF_5 in HSO_3F with x_{SbF_5} = 0.012 to 0.405 are studied by 500 MHz ^{1}H NMR (299 K) and 471 MHz ^{19}F NMR (213–250 K), using NMR tubes fitted with fluoropolymer lining. The initial process during dissolution is the fast solvolysis of monomeric SbF_5 in HSO_3F according to $SbF_5 + nHSO_3F \rightarrow SbF_{5-n}(SO_3F)_n + n$HF ($n$ = 1, 2). All HF formed during solvolysis will no longer be removed by reaction with glass, but will remain in the superacid system. Besides participation in the fast formation of various fluoro-fluorosulfato anions $[SbF_{6-n}(SO_3F)_n]^-$ (n = 0, 1, 2) and acidium ions $[H_2X]^+_{(solv.)}$ (X= F, SO_3F), HF is involved in slow-exchange reactions of the type $[SbF_{6-n}(SO_3F)_n]^-_{(solv.)} + HF \rightarrow [SbF_{7-n}(SO_3F)_{n-1}]^-_{(solv.)} + HSO_3F$ (n = 1, 2) detected because of a delay of 3 months between sample preparation and measurements and confirmed by repeating theses measurements after a further 3 months. There are three notable differences to our earlier study, affecting concentrations of the fluoro-fluorosulfato antimonate anions observed: (*i*) in dilute solutions $[SbF_6]^-$ is formed in high concentrations (34.7–76.1%), with $[Sb_2F_{11}]^-$ now clearly detected at intermediate to high SbF_5 concentrations (up to 5.8%); (*ii*) bis-fluorosulfato anions (*cis*-, *trans*-$[SbF_4(SO_3F)_2]^-$) are found in much lower concentrations only, which decrease further with time, while tris-fluorosulfato anions ($[SbF_3(SO_3F)_3]^-$) are now no longer observed; (*iii*) these reduced concentrations of poly-fluorosulfato anions in dilute solutions are responsible for the formation of fewer μ-SO_3F-oligomers at lower concentrations, when more SbF_5 is added. As a consequence, the HSO_3F–SbF_5 magic acid system is now less complex than found previously and only seven anionic species are clearly observed.

Key words: superacids, antimony(V) fluoroanions, ^{1}H NMR, ^{19}F NMR, solvolysis.

Résumé : Faisant appel à la RMN du ^{1}H à 500 MHz (299 K) et à celle du ^{19}F à 471 MHz (213 à 250 K), on a étudié des solutions de SbF_5 dans du HSO_3F, avec x_{SbF_5} = 0,012 à 0,405 dans des tubes RMN recouverts d'un fluoropolymère. Le processus initial de la dissolution est une solvolyse rapide du SbF_5 monomère dans du HSO_3F suivant l'équation: $SbF_5 + nHSO_3F \rightarrow SbF_{5-n}(SO_3F)_n + n$HF ($n$ = 1, 2). Tout le HF qui se forme au cours de la solvolyse demeure dans le système superacide duquel il n'est pas éliminé. En plus de sa participation dans la formation rapide de divers anions fluoro-fluorosulfato $[SbF_{6-n}(SO_3F)_n]^-$ (n = 0, 1, 2) et d'ions acidium $[H_2X]^+_{(solv.)}$ (X = F, SO_3F), le HF est impliqué dans les réactions lentes d'échanges du type: $[SbF_{6-n}(SO_3F)_n]^-_{(solv.)} + HF \rightarrow [SbF_{7-n}(SO_3F)_{n-1}]^-_{(solv.)} + HSO_3F$ (n = 1, 2) que l'on a détectées en raison d'un délai de trois mois entre la préparation de l'échantillon et les mesures; celles-ci ont été confirmées en répétant ces mesures après un nouveau délai de trois mois. Il y a trois différences notables par rapport à notre étude antérieure, celles affectant les concentrations observées des anions fluoro-fluorosulfato antimoniates: (*i*) en solutions diluées, l'anion $[SbF_6]^-$ se forme à des concentrations élevées (34,7 à 76,1%) alors que l'anion $[Sb_2F_{11}]^-$ peut maintenant être détecté à des concentrations de SbF_5 allant d'intermédiaires à élevées (jusqu'à 5,8%); (*ii*) on n'observe que des concentrations beaucoup plus faibles des anions bis-fluorosulfato (*cis*-, *trans*-$[SbF_4(SO_3F)_2]^-$) et elles diminuent avec le temps alors que l'on n'observe plus la présence des anions ($[SbF_3(SO_3F)_3]^-$); (*iii*) lorsqu'on ajoute du SbF_5, ces concentrations réduites des anions poly-fluorosulfato en solutions diluées sont responsables pour la formation de moins d'oligomères μ-SO_3F à faibles concentrations. En conséquence, le système de l'acide magique HSO_3F–SbF_5 est maintenant moins complexe que ce que l'on croyait auparavant et on n'observe que sept espèces anioniques.

Mots clés : superacides, fluoroanions de l'antimoine(V), RMN du ^{1}H, RMN du ^{19}F, solvolyse.

[Traduit par la Rédaction]

Received 31 January 2002. Published on the NRC Research Press Web site at http://canjchem.nrc.ca on 26 September 2002.

Dedicated to Professor Hans Bürger on the occasion of his 65th birthday.

J. Kühn-Velten and G. Hägele.[1] Anorganische Chemie und Strukturchemie, Heinrich-Heine-Universität Düsseldorf, Universitätsstr. 1, D-40225 Düsseldorf, Germany.
M. Bodenbinder, R. Bröchler, and F. Aubke.[2] Department of Chemistry, The University of British Columbia, Vancouver, BC V6T 1Z1, Canada.

[1]Corresponding author (e-mail: haegele@uni-duesseldorf.de).
[2]Corresponding author (e-mail: aubke@chem.ubc.ca).

 DOI: 10.1139/V02-139 © 2002 NRC Canada

Introduction

In the quest for strongly electrophilic or superelectrophilic (1) cations, conjugate Brønsted–Lewis superacids (2, 3) like HF–SbF_5 and HSO_3F–SbF_5 play an important role as reaction media and solvents. Examples of their applications range from the generation of the large family of carbocations (4) to more recent studies of the formation of superelectrophilic metal carbonyl cations (5), which are exclusively generated in superacids. Many of their salts and derivatives have recently been structurally characterized by single crystal X-ray diffraction and vibrational spectroscopy (5).

The conjugate superacid HF–SbF_5 (2, 3) appears to display higher Brønsted acidities at high SbF_5 concentrations (6, 7) and possesses a somewhat greater versatility in synthetic applications (5). This is on account of the smaller number and simpler composition of counteranions such as $[SbF_6]^-$, $[Sb_2F_{11}]^-$, $[Sb_3F_{16}]^-$, which are reportedly present (8) in solution.

On the other hand, magic acid HSO_3F–SbF_5 has found wider applications on account of practical considerations (2, 4). HSO_3F is at ambient temperatures compatible with glass (9) and can be purchased and purified easily (9). In contrast, anhyd HF (10) can only be handled safely in metal or fluoropolymer materials and is, on account of its high volatility, a considerable health hazard. It is also difficult to remove traces of H_2O from technical grade hydrogen fluoride, which requires the addition of reactive fluorides like BiF_5 or SbF_5. This is in contrast to the reported purification of HSO_3F (9) by distillation, which converts traces of H_2O into HF and H_2SO_4.

Both HF (11) and HSO_3F (2, 3) have, in spite of earlier claims (2), identical Hammett $-H_0$ values (12). This would suggest, that conjugate superacids with comparable concentrations of SbF_5 would be expected to show similar Brønsted acidities. But this is reportedly not the case (6, 7). In spite of its lower Brønsted acidity, magic acid has been the preferred medium for the generation of a large number of stable carbocations (1, 2, 4).

To understand more fully the composition and speciation in magic acid, we have recently reinvestigated the magic acid system at variable SbF_5 concentrations by modern NMR methods (13). As in all earlier studies (2, 14–16), all measurements are made in glass. Based on results which are described in detail (13), the following conclusions are reached: (*i*) the HSO_3F–SbF_5 system is more complex than previously (2, 14–16) assumed and 13 different anions are unambiguously identified; (*ii*) at low concentrations of SbF_5, monomeric anionic species of the type $[SbF_{6-n}(SO_3F)_n]^-$ (n = 1–3) dominate. At high concentrations of SbF_5, increasing amounts of oligomers are formed; (*iii*) μ-F bridges in oligomeric anions are found only in $[Sb_2F_{11}]^-$. In all other instances, the SO_3F group functions as a bridging group in oligomeric anions; (*iv*) there is strong evidence presented for the formation of $[H_3O]^+$ in magic acid. This evidence comes from ^1H NMR spectra of HSO_3F–SbF_5 at variable concentrations (13) and more convincingly from the isolation of $[H_3O][Sb_2F_{11}]$ from HSO_3F–SbF_5 and its subsequent structural characterization by single crystal X-ray diffraction (17); (*v*) the presence in the oxonium salt (17) of $[Sb_2F_{11}]^-$ as counteranion, which is barely detectable in the ^{19}F NMR spectrum of HSO_3F–SbF_5 solutions (13), points to slow exchange equilibria, which have so far not been described nor investigated; (*vi*) the formation of $[SbF_6]^-$ is not explainable by SO_3 elimination as proposed by Olah and co-workers (3, 4) or solely by ligand redistribution as suggested by Dean and Gillespie (15). A convincing rationale for its formation is still outstanding.

To account for the presence of $[H_3O]^+$, it was proposed (13), that initial fast solvolysis of monomeric SbF_5 in HSO_3F occurs, according to eq. [1]:

$$[1] \qquad n\mathrm{HSO_3F} + \mathrm{SbF_5} \rightarrow \mathrm{SbF_{5-n}(SO_3F)_n} + n\mathrm{HF}\ (n = 1, 2)$$

Some or most of the HF formed in this manner, will react with glass to form H_2O (in addition to SiF_4), which will then be protonated to $[H_3O]^+$ and hence acts as a base in the superacid. Consequently the in situ formation of the base H_2O will reduce the overall acidity of magic acid, relative to that of HF–SbF_5 (18). Consistent with these observations, there are two types of cations observed in the system: the acidium ion $[H_2SO_3F]^+$ and the oxonium ion $[H_3O]^+$. The concentrations of both are found to increase with increasing SbF_5 concentration as monitored by ^1H NMR (13).

The acidium ion is formed immediately in a fast reaction according to eq. [2] as an example:

$$[2] \qquad 2\mathrm{HSO_3F} + \mathrm{SbF_4(SO_3F)} \rightarrow [\mathrm{H_2SO_3F}]^+_{(\mathrm{solv.})} + [\mathrm{SbF_4(SO_3F)_2}]^-_{(\mathrm{solv.})}$$

This equation describes a Lewis acid promoted self-dissociation of HSO_3F (9).

We have now reinvestigated the magic acid system HSO_3F–SbF_5 with four important modifications to the previous study (13): (*i*) to avoid formation of $[H_3O]^+$ in substantial concentrations, measurements were conducted in NMR tubes with fluoropolymer lining; (*ii*) instead of a 200 MHz spectrometer (13) a 500 MHz spectrometer was employed, to achieve a higher separation of signals; (*iii*) we limited measurements to systems with x_{SbF_5} up to 0.4, to pay more attention to solutions with low and intermediate concentrations of SbF_5; and (*iv*) for each sample, ^{19}F NMR measurements in the Sb–F region were repeated after about 3 months, to detect any changes caused by suspected slow, previously (14–16) unreported equilibria.

In our earlier study (13), mainly broad, poorly resolved spectra for mol fractions x_{SbF_5} above 0.6 were observed. We, therefore, reduced the number of samples from nine to five. A number of oligomeric μ-SO_3F bridged fluoro-fluorosulfato anions, identified previously (13) for solutions with high SbF_5 concentrations only, appeared either in negligible concentrations or not at all. They were, therefore, not discussed in the present study.

Due to the collaborative nature of this study, the samples were prepared at UBC (Vancouver) and the spectra were recorded at the Heinrich-Heine-Universität (Düsseldorf). This caused a delay of 2–4 months between sample preparation and the first acquisition of NMR data. Hence the exact composition of the various samples immediately after mixing of SbF_5 and HSO_3F is unknown, but is assumed to be similar, than found previously (13), as will be discussed below. This procedure and repeated measurements after a further 3 months

© 2002 NRC Canada

Table 1. Composition of samples 1–5 made up from HSO_3F and SbF_5.

Sample	x_{SbF_5} [a]	$n(HSO_3F)$ [b] (mmol)	$n(SbF_5)$ [b] (mmol)	c_{rel} (HSO_3F) [c] (mol %)	c_{rel} (SbF_5) [c] (mol %)
1	0.012	109.70	1.28	98.85	1.15
2	0.064	100.01	6.87	93.57	6.43
3	0.100	92.06	10.19	90.03	9.97
4	0.202	86.38	21.80	79.85	20.15
5	0.405	78.43	53.43	59.48	40.52

[a] x_{SbF_5} (mol fraction).
[b] Amounts (mmol).
[c] c_{rel} (relative concentrations (mol %)).

have allowed the detection of a slow SO_3F- vs. F exchange reaction which has been suspected (17), but has never been clearly demonstrated (14–16) before.

As in our earlier study (13), we have again avoided the use of diluents like SO_2ClF or SO_2F_2, which have been used by others (14–16) in studies of the HSO_3F–SbF_5 system, to reduce the viscosity of the system and to permit the recording of spectra at low temperatures (14–16). While there are practical considerations (1, 2, 4), which favor the use of diluents like SO_2ClF, SO_2F_2, and SO_2 in synthesis because they will facilitate the dissolution of hydrocarbon precursors for the generation of carbocations in superacids (4), in a study of this nature, diluents alter the nature of the solvent–solute interaction in HSO_3F–SbF_5 as will be discussed below.

The solutions with x_{SbF_5} up to 0.202 (samples 1–4) were measured at 213 ± 1 K. To investigate the temperature dependency of the product distribution, samples 1–5 were also measured at 233 ± 1 K up to 250 K in dependence of antimony pentafluoride concentration, as can be seen in Table 1.

To detect the nature and direction of slow reactions, involving equilibria of anions $[SbF_{6-n}(SO_3F)_n]^-_{(solv.)}$ (n = 1, 2) initially formed and anhyd HF generated in situ (see eq. [1]) or HSO_3F, a number of measurements were repeated after 3–6 months and in one case after 4 years.

In slow exchanges, several types of reactions involving octahedral anions may be anticipated: (*i*) a homotopic ligand exchange (*a*) -F vs. -F (-F = fluoro ligand) or (*b*) $-SO_3F$ vs. $-SO_3F$; or (*ii*) a heterotopic ligand exchange (*a*) -F vs. $-SO_3F$ or (*b*) $-SO_3F$ vs. -F, which in an acidic medium may be viewed as equilibrium reactions of the type:

$$[3] \qquad HSO_3F + [SbF_{6-n}(SO_3F)_n]^- \rightleftharpoons HF + [SbF_{5-n}(SO_3F)_{n+1}]^-$$

Processes of type (*i*) do not change the composition of the complex anions under investigation and will not be detected by NMR. They might be studied by isotopic labeling. In either case of processes of the type (*ii*), the nature of the anionic solute will change, which is detectable by NMR. These exchange reactions, involving octahedrally coordinated anions are expected to be slow.

Experimental

Preparation of NMR samples

The procedures for purification of fluorosulfuric acid (HSO_3F) (9) and antimony(V) fluoride (SbF_5) were identical to those reported previously (13). Also identical were the methods used to prepare the samples by mixing the components inside a dry box (13) (Vacuum Atmosphere Corporation Dry-Lab model DI 001-SG filled with dry N_2 and equipped with an HE493-Dry Train) by magnetic stirring in fluoroplastic containers. The compositions of the five samples were established by weighing inside the dry box, using a Mettler top loading balance. The NMR tubes of 5 mm o.d. were fitted with linings of FEP (copolymer of tetrafluoroethylene and hexafluoropropylene (DuPont de Nemours). Linings of 4.1 mm o.d. and 3.5 mm i.d. were made from the commercially available material (BEMU Inc., Krefeld) by Professor H.J. Frohn, University of Duisburg, who has pioneered this technique. The NMR tubes were fitted with Teflon stopcocks and sealed subsequently inside the dry box by epoxy resin. The concentrations of the five samples prepared, are listed in Table 1.

NMR spectroscopy

NMR spectra were recorded using a DRX Avance 500 NMR spectrometer (Bruker Analytische Meßtechnik GmbH, Karlsruhe), operating at 500 MHz and 471 MHz, respectively, for ^1H and ^{19}F NMR. Neither spinning nor internal lock compounds were used. The magnetic field was locked to D_2O and after replacing the lock sample, NMR spectra were recorded from mixtures of SbF_5 and HSO_3F. The DRX Avance 500 magnet was found to be very stable. The field drift was less than 0.01 ppm h^{-1}. Hence, NMR measurements without the use of a lock were judged to be sufficiently accurate. Specific acquisition and processing parameters for NMR spectra are listed in Table 2. All FIDs were zero filled, which led to an increase of data points in the real spectrum by a factor of two. Prior to Fourier transformation, line-broadening factors (LB) were applied to FIDs, as shown in Table 2 and in individual spectra. Phase and baseline corrections were done manually, to achieve optimal conditions for the recording of precision NMR spectra. All spectra were evaluated with a 1D-WinNMR 5.1 version 960901 (Bruker Franzen Analytik GmbH., Bremen), to extract accurate data for frequencies, intensities, and linewidths. Proton chemical shifts were referenced vs. external (ext.) TMS, while ext. CF_3COOH in D_2O was used (with δ_F = –76.04 ppm vs. $CFCl_3$) for the determination of fluorine chemical shifts. Fluorine NMR spectra showed dynamic NMR line shapes. Suitable temperatures were chosen and maintained to obtain good resolution as listed with individual spectra. Individual species found in magic acid mixtures via ^{19}F NMR were identified using standard F,F-COSY techniques and assignments described in the preceding paper.

© 2002 NRC Canada

Table 2. Spectroscopic acquisition parameters.

Spectrum	Sample no.	x_{SbF_5}	t^a (days)	T^b (K)	TD^c (k)	NS^d	LB^e (Hz)	SW^f (ppm)	SW^g (Hz)	SF^h (MHz)
H	1	0.012	69	299	64	64	0	6.01	3 005	500.135
H	2	0.064	69	299	16	64	0	6.01	3 005	500.135
H	3	0.100	69	299	32	64	0	6.01	3 005	500.135
H	4	0.202	69	299	32	64	0	6.01	3 005	500.135
H	5	0.405	69	299	32	64	0	6.01	3 005	500.135
F (FSO)	1	0.012	123	213	64	256	0	88.54	41 667	470.614
F (FSO)	2	0.064	123	213	64	256	0	88.54	41 667	470.614
F (FSO)	3	0.100	123	213	64	256	1	88.54	41 667	470.614
F (FSO)	4	0.202	123	243	64	256	1	88.54	41 667	470.614
F (FSO)	4	0.202	123	213	64	256	1	88.54	41 667	470.614
F (FSO)	5	0.405	54	250	64	64	2	19.97	9 398	470.612
F (FSO)	5	0.405	54	233	64	64	2	19.97	9 398	470.612
F (SbF)	1	0.012	123	213	128	256	4	212.53	100 000	470.531
F (SbF)	1	0.012	233	213	128	128	4	90.05	42 373	470.536
F (SbF)	2	0.064	123	213	128	256	4	212.53	100 000	470.531
F (SbF)	2	0.064	233	213	128	128	4	90.05	42 373	470.536
F (SbF)	3	0.100	123	213	128	256	4	212.53	100 000	470.531
F (SbF)	3	0.100	233	233	128	128	4	90.05	42 373	470.536
F (SbF)	3	0.100	1442	233	128	256	4	90.05	42 373	470.541
F (SbF)	3	0.100	1442	213	128	256	4	90.05	42 373	470.541
F (SbF)	4	0.202	123	243	128	256	4	212.53	100 000	470.531
F (SbF)	4	0.202	123	213	128	256	4	212.53	100 000	470.531
F (SbF)	4	0.202	233	233	128	128	4	90.05	42 373	470.536
F (SbF)	5	0.405	54	250	128	256	4	64.99	30 581	470.537
F (SbF)	5	0.405	54	233	128	256	4	79.90	37 594	470.537
F (SbF)	5	0.405	233	233	128	128	4	90.05	42 373	470.536

[a]*t*: Age of sample (days).
[b]*T*: abs. temperature (K).
[c]File size (k) (Bruker standard).
[d]Number of scans (Bruker standard).
[e]Line broadening (Hz) (Bruker standard).
[f]Sweep width (Hz) (Bruker standard).
[g]Sweep width (ppm) (Bruker standard).
[h]Frequency (MHz) (Bruker standard).

The relevant data for COSY acquisition are: *TD* = 4096, *NS* = 8, *SW* = 70.14 ppm, *SWH* = 33 003 Hz.

Results

Discussion of typical NMR spectra — Results and observations

^{1}H NMR spectra

The results of the ^{1}H NMR spectra are listed in Table 3 and are compared to earlier results (13). A typical 500 MHz ^{1}H NMR spectrum for sample 2 x_{SbF_5} = 0.06 is shown in Fig. 1.

For samples 1–5 the dominant ^{1}H-signal is due to the acidium ions ($[H_2X]^+$, X = F, SO_3F). The second, weak resonance is, in agreement with earlier observations (13, 14), attributed to $[H_3O]^+$. Only minute amounts of $[H_3O]^+$ were observed, when using fluoropolymer linings, while considerable quantities were formed in glass NMR tubes (13). The difference in chemical shifts $\Delta_\delta = \delta_H$ (acidium ion) – δ_H ($[H_3O]^+$) increased with increasing values for x_{SbF_5} following a linear relation: $\Delta_\delta = 4.74x_{SbF_5} + 0.11$ with a correlation coefficient of 0.999.

^{19}F NMR Spectra

FSO_3 region:

^{19}F NMR (471 MHz) spectra of samples 1–5 were clearly divided into two separate regions, indicative for SO_3F and the Sb(V)F containing moieties. While most of the Sb(V)F species of type $[SbF_{6-n}(SO_3F)_n]^-$ and oligomers discussed in this paper are identified by their F-F coupling patterns, spectra in the fluorosulfato region are singlets. Long range couplings of type F-S-O-Sb-F were not resolved. These would allow structurally significant correlations. Demanding and costly experiments using ^{17}O or ^{33}S isotopes would be required, for a deeper, comprehensive analysis of magic acid anions in the F-SO_3 region.

In spite of these limitations, trends in chemical shifts and relative intensities of resonances may be used to correlate some of the observed SO_3F resonances and to assign these to species, identified unambiguously in the Sb-F- region as discussed below. For example, Fig. 2 shows that unequivocal evidence is obtained for $[SbF_5(SO_3F)]^-$ (B1), $[(SbF_5)_2$-μ-$SO_3F]^-$ (E), and the solvent HSO_3F. As in our previous study (13), the notation for species present in magic acids is adopted from ref. 16 and shown in Scheme 1 together with the NMR spin assignment. Assignments based solely on

© 2002 NRC Canada

Table 3. Results from 500 MHz ^{1}H NMR studies.

Sample	Proton NMR parameters					
	x_{SbF_5}	Method	δ_H (ppm)[c] acidium ion	δ_H (ppm)[c] $[H_3O]^+$	$\Delta\delta$ (ppm)[d]	Integral ratio[e]
	0.01	[a]	9.455			100:(<0.1)
1	0.012	[b]	9.684	9.502	0.182	100:(<0.1)
	0.05	[a]	9.513	9.050	0.463	100:2.48
2	0.064	[b]	9.787	9.379	0.408	100:2.02
	0.10	[a]	9.582	9.255	0.327	100:3.65
3	0.100	[b]	9.840	9.292	0.548	100:2.91
	0.20	[a]	9.758	8.964	0.794	100:11.02
4	0.202	[b]	10.114	9.069	1.045	100:1.93
	0.36	[a]	10.064	8.663	1.401	100:31.68
5	0.405	[b]	10.583	8.515	2.068	100:4.39
	0.49	[a]	10.244	8.263	1.981	100:53.26

Note: Integral ratio acidium ion$^+$: H_3O^+. $\Delta\delta = \delta_H$ (acidium ion$^+$) – δ_H ($[H_3O]^+$).
[a]See ref. 13.
[b]Present work.
[c]Chemical shift (ppm).
[d]Difference $\Delta\delta = \delta_H$ (acidium ion) – δ_H ($[H_3O]^+$).
[e]Normalized integral ratio = integral (acidium ion)/integral ($[H_3O]^+$).

Fig. 1. ^{1}H NMR (500 MHz) spectrum of sample 2: x_{SbF_5} = 0.064, t = 69 days, T = 299 K, LB = 0 Hz. Peak at δ_H = 9.8 ppm (acidium ion). Peak at δ_H = 9.38 ppm ($[H_3O]^+$). Insert: y-axis expanded; x-axis (δ_H [ppm] vs. ext. TMS).

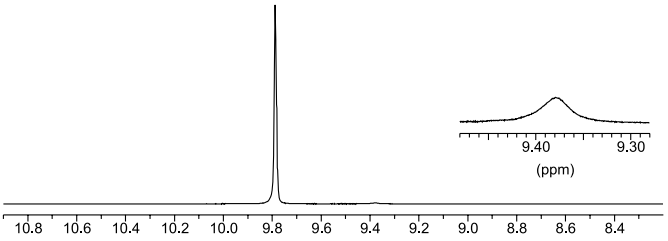

Fig. 2. ^{19}F NMR spectrum (471 MHz) in the HSO_3F region of sample 3: x_{SbF_5} = 0.100, t = 123 days, T = 213 K, LB = 1 Hz.: from left to right: peak 1: δ_F = 41.60 ppm, $[SbF_5(SO_3F)]^-$ (B1); peak 2: δ_F = 40.99 ppm, $[(SbF_5)_2$-μ-$SO_3F]^-$ (E); peak 3: δ_F = 40.33 ppm, HSO_3F (A). x-axis: δ_F [ppm] vs. $CFCl_3$ calc. (see text).

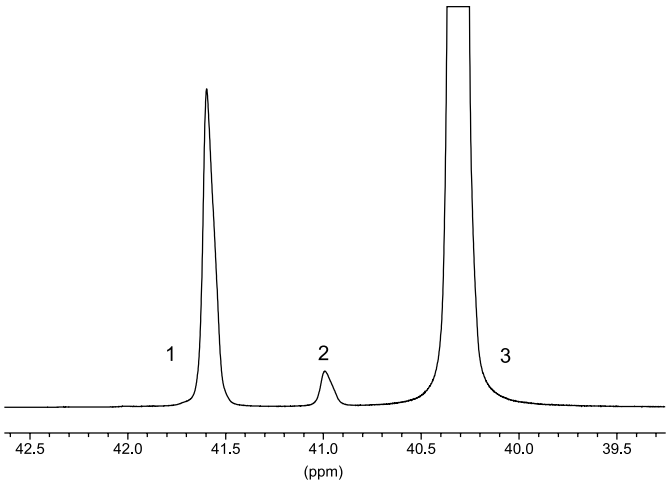

chemical shifts in the SO_3F-region are in general not possible, since as discussed above, spin–spin coupling data are not available in the F-SO_3 region. Numerical results for the -SO_3F region are listed in Table 4.

Since proton transfer is rapid on the NMR time scale, the dominant peak, assigned to HSO_3F, represents in principle the dynamically averaged chemical shift $<\delta_F>$ (19) originating from three specific contributions of δ_i following:

$$[4] \qquad <\delta_F> = \sum_{i=0}^{2} x_i \cdot \delta_i$$

where x_i stands for the mol fractions and δ_i for the specific chemical shifts of $H_i[SO_3F]^{i-1}$ (i = 0–2). Since the autoprotolytic constant K_{id} of HSO_3F is small, as discussed above, the apparent NMR signal will be dominated by the solvent formally described as $H_i[SO_3F]^{i-1}$ (i = 1). Hence ion specific chemical shifts δ_i (i = 0 or i = 2) are not extractable from this averaged signal.

F-Sb(V) region:

As discussed in our preceding paper (13), this region is most informative on account of the observation of F-F coupling, giving rise to multiplet structures. ^{19}F NMR (471 MHz) studies of the Sb(V)F regions lead to the spectra shown in Fig. 3, with the corresponding data listed in Tables 5(*a*), 5(*b*), and 6. Species identified well above the 1% level are shown in Table 7 and Scheme 1.

We wish to direct attention to the strong solvent effects, recognizable in Fig. 3, where from the bottom to top five spectra are shown with increasing SbF_5 concentration (samples 1–5). Species are identified by similarities of spectral structures (multiplet structures), not by the absolute values of their chemical shifts. It is useful to note, that $^2J_{FF}$ in -SbF_5 units is found to be around 100 Hz, while -SbF_4- units show significantly different values of around 120 Hz.

Obviously, where chemical shifts for individual species are influenced by solvent effects, they are less significant than coupling constants. Hence no attempt is made, to

© 2002 NRC Canada

Scheme 1. Species present in magic acid samples 15: B1, F, Z, E, G, J, I. Spin assignment used for NMR spectroscopic discussions.

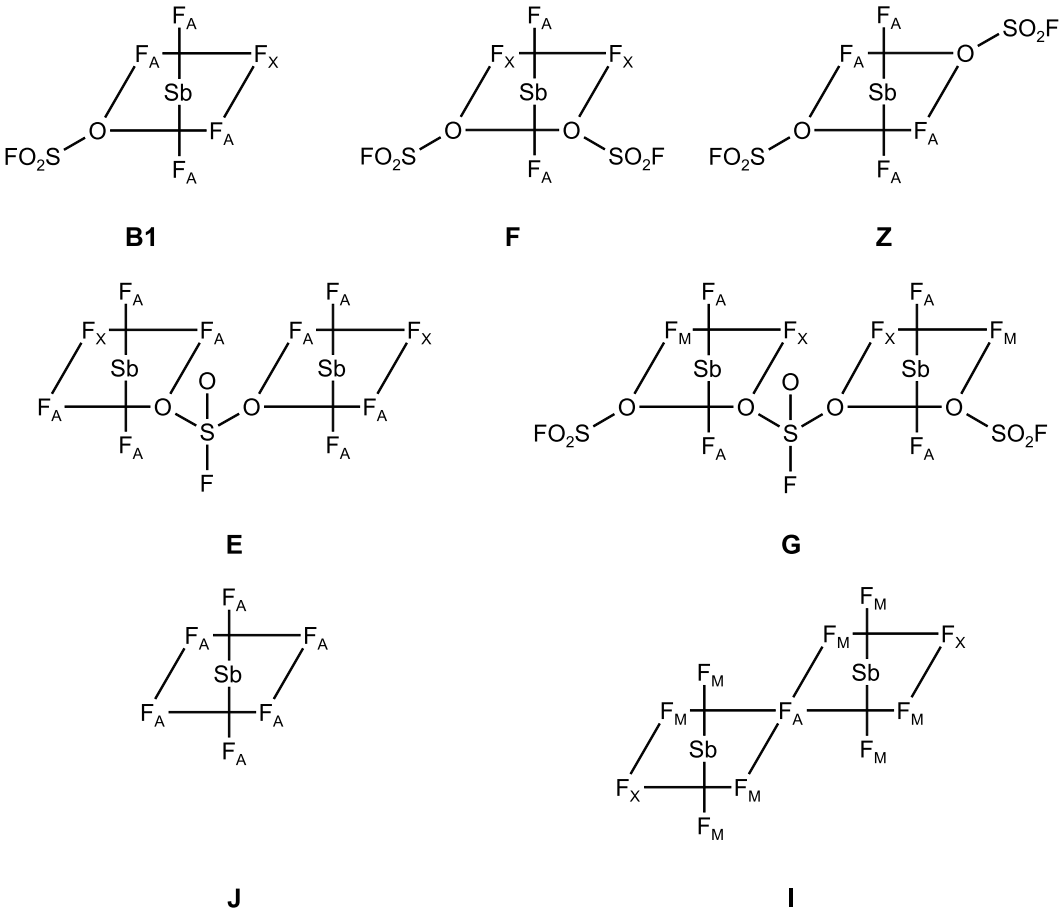

Fig. 3. Comparison of 471 MHz ^{19}F NMR spectra of samples 1–5. From lower to upper trace: x_{SbF_5} for: 1 (0.012), 2 (0.064), 3 (0.100), 4 (0.202), 5 (0.405). *x*-axis: δ_F (ppm) vs. $CFCl_3$ calcd. (see text).

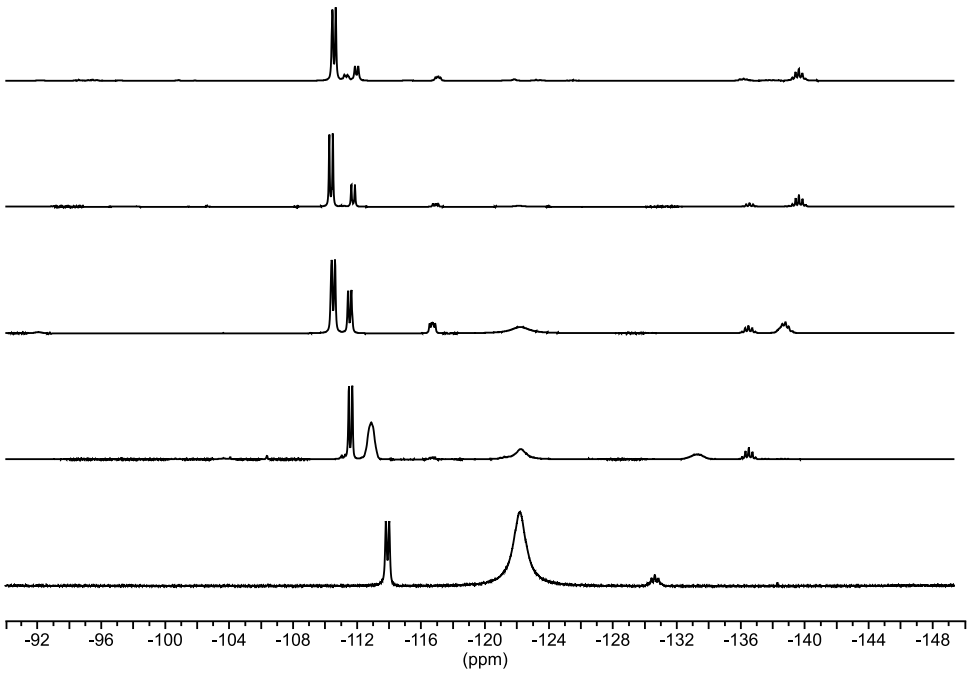

correct δ_F data by the susceptibility of the samples. This striking solvent effect is thought to be due to a variation in concentrations of HSO_3F and HF, generated during solvolysis, with the HF concentration obviously decreasing

© 2002 NRC Canada

Table 4. Results from 470 MHz ^{19}F NMR studies (HSO_3F region).

Species	Chemical shifts and molar ratio of main species from the HSO_3F region					
	δ (ppm)	Δδ (ppm)	Integral	Ratio Sb/F	Δδ (ppm)	Ratio
Sample 1 (x_{SbF_5} = 0.012, t = 123 days, T = 213 K, x_a = 0.01)						
A + n.i.s.	40.46	0	147.96		0	330.07
n.i.s.	39.32	–1.14	1.00		1.49	1.00
Sample 2 (x_{SbF_5} = 0.064, t = 123 days, T = 213 K, x_a = 0.05)						
B1	41.51	1.13	4.05	4.97	1.08	3.86
E + n.i.s.	41.06	0.68	1.00	1.00	0.94	1.00
A	40.38	0	84.13		0	214.79
Sample 3 x_{SbF_5} = 0.100, t = 123 days, T = 213 K, x_a = 0.10)						
B1 + n.i.s.	41.60	1.27	7.25	8.14	1.19	3.89
E	40.99	0.66	1.00	1.00	0.90	1.00
A	40.33	0	79.14		0	105.84
Sample 4 (x_{SbF_5} = 0.202, t = 123 days, T = 213 K, x_a = 0.19)						
B1	41.51	1.31	7.18	7.47	1.32	2.50
E	40.86	0.66	1.00	1.00	1.75	1.00
A	40.20	0	30.16		0	8.92
Sample 4 (x_{SbF_5} = 0.202, t = 123 days, T = 243 K, x_a = 0.19)						
B1	41.36	1.15	7.59	8.28	1.32	2.50
E	40.84	0.63	1.00	1.00	1.75	1.00
A + n.i.s.	40.21	0	32.01		0	8.92
Sample 5 (x_{SbF_5} = 0.405, t = 54 days, T = 233 K, x_a = 0.36)						
B1	41.83	1.17	9.67	10.90	1.30	1.87
E	41.24	0.58	1.00	1.00	0.71	1.00
A	40.66	0	8.47		0	4.26
Sample 5 (x_{SbF_5} = 0.405, t = 54 days, T = 250 K, x_a = 0.49)						
B1	41.78	1.10	9.10	n.int.	1.40	3.70
E	41.32	0.64	1.00	n.int.	0.76	1.00
A	40.68	0	8.28			2.73

Note: A (HSO_3F), n.i.s. (not identified species in very low concentrations), $\Delta\delta = \delta_F(\text{species}) - \delta_F(HSO_3F)$, x_a (mol fraction x_{SbF_5} given in ref. 13) n.int. (not integrated).

in the order of samples 1–5. Alternatively, the increased concentration of antimony containing species can contribute to an altered susceptibility of the samples. A more conclusive theory for topospecific chemical shifts δ_F in Sb(V)F species is not available at this time.

In our series, the chemical shifts δ_F of species E are nearly constant and not strongly dependent on x_{SbF_5}, while B1 shows a more complex behavior. A larger ratio for B1:E is found for measurements using fluoropolymer linings, compared to previous studies with conventional high precision glass NMR tubes (13). At $x_{SbF_5} > 0.2$ the ratio HSO_3F:B1 is larger for the series using fluoropolymer linings. As an example for the analytical procedures used, the ^{19}F NMR and the F,F-COSY spectra of sample 3 (x_{SbF_5} = 0.100) are shown in Figs. 4 and 5.

Discussion and general observations

As is apparent from Fig. 1 and Table 3, there are a number of fundamental differences to the spectra obtained by us previously on the HSO_3F–SbF_5 system without the use of fluoropolymer linings (13): (*i*) in the ^1H NMR spectra, the characteristic resonance at ~9.0 ppm is of very low intensity and barely detectable. The minute amount of $[H_3O]^+$ found in the present study appears to be due to trace impurities of HF (see Table 3) present in both the solvent (HSO_3F) and the solute (SbF_5), which are both handled in glass during their purification; (*ii*) *in the ^{19}F NMR spectra*, a resonance, previously found at ~–162 ppm and attributed to $SiF_{4(solv.)}$ or $[SiF_6]^{2-}$, is now absent; (*iii*) *in the S-F region* at ~45–40 ppm and *in the Sb-F region* of –90 to –140 ppm, fewer resonances are observed and the spectra are much simpler under those conditions (13); (*iv*) resonances, attributed to tris- and bis-substituted fluorosulfato-fluoro antimonate anions, are either absent or only seen at low concentrations of SbF_5. The polyfluorosulfato-antimonate anions are seen as monomeric building blocks for fluorosulfato bridged oligomers; (*v*) conversely, the $[SbF_6]^-$ anion found previously at concentrations of ~1%, is clearly detected and is now the dominant species in dilute solutions (sample 1), where it is present at 34.7%, which increased to 76.1% after 3 months. This increase by 41.4% is entirely at the expense of the fluorosulfato anions B1, F, and Z, whose combined concentrations decrease by a total of 41.5% over 3 months. Also the $[Sb_2F_{11}]^-$ anion is directly observed in samples 2–5. This has not been possible previously (13), even though the reported isolation and structural characterization of $[H_3O][Sb_2F_{11}]$ from magic acid (17) has provided evidence

© 2002 NRC Canada

Table 5. Results from 470 MHz ^{19}F NMR studies (region of fluoroantimonate systems).

(*a*) Assignment of species from FF-COSY data (fluoroantimonate systems).*

Species	δ_A (ppm)	J (Hz)	Habitus	δ_M (ppm)	J (Hz)	Habitus	δ_X (ppm)	J (Hz)	Habitus
Sample 1 (x_{SbF_5} = 0.012, t = 233 days, T = 213 K)									
B1	–113.91	100	d				–130.64	99	q
Sample 2 (x_{SbF_5} = 0.064, t = 233 days, T = 213 K)									
I	–92.12	58	n_p	–116.72	100/60	dd	–138.77	102	q
G	–100.65	122	t	–117.61	125/109	dt	–126.60	109	$(dt)_p$
F	–103.65	115	t				–121.23	120	t
n.id.	–111.16	102	d_x				–134.41	102	q_p
n.id.	–111.09	102	d_x				–137.54	100	q_x
B1	–111.60	101	d				–136.52	100	q
E	–112.89	n.det.	broad				–133.29	n.det.	broad
Sample 3 (x_{SbF_5} = 0.100, t = 233 days, T = 233 K)									
I	–92.07	57	n	–116.72	98/60	dd	–137.92	102	q_p
B1	–110.52	99	d				–138.81	97	q_p
E	–111.55	100	d				–136.50	100	q
Sample 4 (x_{SbF_5} = 0.202, t = 233 days, T = 233 K)									
I	–92.26	59	n	–116.92	100/59	dd	–139.02	101	q_{px}
n.id.	–97.24	125	2 t_{px}				–123.04	n.det.	m
n.id.	–98.09	126	t_{tan}				–122.04	n.det.	m
B1	–110.38	99	d				–139.66	99	q
n.id.	–111.06	100	d_x				–138.27	100	q_x
E	–111.76	101	d				–136.57	101	q
Sample 5 (x_{SbF_5} = 0.405, t = 233 days, T = 233 K)									
I	–92.12	56	n_p	–116.97	96/60	dd	–139.14	n.det.	q_p
F	–94.50	128	t				–123.11	126	t
G	–95.36	127	t, broad	–121.19	128/105	$(dt)_p$	–125.42	118/104	dt
n.id.	–96.99	n.det.	t_{px}				–123.34	n.det.	t_p
B1	–110.47	99	d				–139.55	98	q
n.id.	–111.24	n.det.	2 d_x				–137.64	n.det.	2 q_{px}
E	–111.88	100	d				–136.09	99	q

(*b*) Chemical shifts δ [ppm] of singlet generating species.

Sample	x_{SbF_5}	t (days)	T (K)	Z (A_4) δ_F (ppm)	J (A_6) δ_F (ppm)
1	0.012	123	213	–106.83	–122.65
1	0.012	233	213	–106.45	–122.19
2	0.064	123	213		–122.63
2	0.064	233	213	106.37	–122.25
3	0.100	123	213		–122.63
3	0.100	233	233		–122.21
4	0.202	123	213		–122.53
4	0.202	123	243		–122.36
4	0.202	233	233		–122.10
5	0.405	54	233		–121.46
5	0.405	233	233		–121.75

*d (doublet), t (triplet), q (quintet), n (nonet), m (multiplet), index$_p$ (partially obscured), index$_x$ (overlapping), n.id. (not identified), n.det. (not determined).

for its presence in solution. The formation of $[Sb_2F_{11}]^-$ and possibly higher μ-F oligomers is attributed to the equilibria of the type:

$$[5] \qquad SbF_5 + [SbF_6]^- \underset{HF}{\overset{SbF_5}{\rightleftharpoons}} [Sb_2F_{11}]^-$$

Interestingly at x_{SbF_5} = 0.405, the concentration of $[Sb_2F_{11}]^-$ is higher than that of $[SbF_6]^-$ (see Tables 5 and 6); (*vi*) at high SbF5 concentrations (samples 4 and 5, x_{SbF_5} = 0.202 and 0.405, respectively), SbF_5 appears to be involved in formation of oligomeric species E, G, and I as well as other not identified oligomeric species (see Table 6). Consequently, solvolysis is now less likely (eq. [1]), HF formation

© 2002 NRC Canada

Table 6. Results from 470 MHz ^{19}F NMR studies.

				Composition (%) of samples 1–5							
				Monomers				Oligomers			
Sample	x_{SbF_5}	t (days)	T (K)	F A_2X_2	Z A_4	J A_6	B1 A_4X	E 2 A_4X	G A_2MX	I $A[M_4X]_2$	Others div.
1	0.012	123	213	4.8	2.0	34.7	58.6				
1	0.012	233	213	0.3	0.2	76.1	23.4				
2	0.064	123	213	n.int.		6.5	71.6	14.1	0.7	1.3	5.8
2	0.064	233	213	3.6		20.8	41.6	28.1	1.4	0.9	3.6
3	0.100	123	213			8.2	79.0	9.7	n.int.	3.1	
3	0.100	233	233			20.3	58.7	15.1	n.int.	5.8	
4	0.202	123	213			1.0	79.2	10.6		1.0	8.2
4	0.202	123	243			1.5	81.1	9.8		1.5	6.1
4	0.202	233	233			2.8	76.3	12.4		2.8	5.6
5	0.405	54	233	n.int.		0.9	67.6	6.2	3.1	3.4	18.7
5	0.405	233	233	2.1		1.0	61.4	8.0	4.1	2.9	205

Note: Others (other species, see ref. 13), div. (several spin systems), n.int. (not integrated).

Table 7. A comparison of monomeric fluoro-fluorosulfato anions found previously (13) and now in dilute solutions.

	Solution x_{SbF_5} = 0.001	Solution x_{SbF_5} = 0.012	Solution x_{SbF_5} = 0.012
Species	Previous results (13) (mol %)	Present results (t = 123 days) (mol %)	Present results (t = 223 days) (mol %)
$[SbF_6]^-$	2	34.7	76.1
$[SbF_5(SO_3F)]^-$	15	58.6	23.4
cis-$[SbF_4(SO_3F)_2]^-$	48	4.8	0.3
trans-$[SbF_4(SO_3F)_2]^-$	21	2.0	0.2
mer-$[SbF_3(SO_3F)_3]^-$	14	n.o.	n.o.

Note: n.o. (not observed).

Fig. 4. (*a*) ^{19}F NMR spectrum (471 MHz) of the Sb-F region from sample 3: x_{SbF_5} = 0.100, t = 123 days, T = 213 K, LB = 4 Hz. x-Axis: δ_F (ppm) vs. $CFCl_3$ calcd. (see text); (*b*) ^{19}F NMR spectrum (471 MHz) of the Sb-F region from sample 3: x_{SbF_5} = 0.100, t = 233 days, T = 233 K, LB = 4 Hz. x-axis: δ_F (ppm) vs. $CFCl_3$ calcd. (see text).

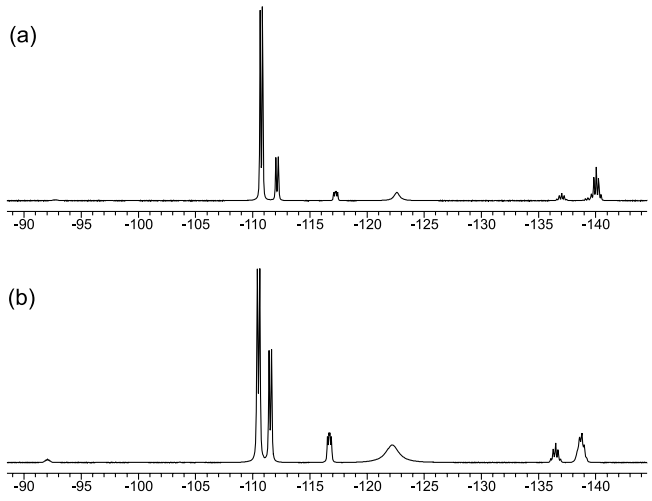

is suppressed, and monomeric $[SbF_5(SO_3F)]^-$ (B1) is now the dominant anion, whose concentration is reduced only insignificantly by conversion to E, due to complexation; (*vii*) fluorosulfato bridged oligomeric anions have at comparable concentrations much lower abundances then reported previously (13); (*viii*) the total number of species which are clearly identified at significant levels and analyzed is reduced from 13 (13) to about seven.

The latter is in part due to the smaller concentration range chosen for this study compared to the previous one (13), where many oligomeric species are only observed and analyzed at high SbF_5 concentrations. We have chosen in this study to forgo any detailed identification of these oligomers, with the exception of $[Sb_2F_{11}]^-$ and its fluorosulfato analogue $[(SbF_5)_2\text{-}\mu\text{-}SO_3F]^-$ and to concentrate on monomeric anions. A further reason for the low abundance of μ-SO_3F oligomers is the above noted absence of tris- and low concentrations of bis-fluorosulfato anions, as discussed above and illustrated by eq. [6]. Both are viewed as "building blocks" for μ-SO_3F bridged oligomers.

$$[6] \qquad [SbF_5(SO_3F)]^- + SbF_5 \rightleftharpoons [(SbF_5)_2\text{-}\mu\text{-}SO_3F]^-$$

An important feature is our failure now and previously (13) to detect any μ-F bridged oligomers, which also contain terminal -OSO_2F-groups, as had been found previously (2, 14–16). There are two reasons for these earlier claims: (*i*) some earlier studies (14–16) date back to the period of 1969–1978 and involve the early applications of NMR methods to superacids, with assignments occasionally very tentative and multiplets frequently unresolved; and (*ii*) earlier

© 2002 NRC Canada

Fig. 5. $^{19}F,^{19}F$ -COSY spectrum (471 MHz) of the Sb-F region from sample 3: x_{SbF_5} = 0.100. t = 233 days, T = 233 K. x-axis: δ_F (ppm) vs. $CFCl_3$ calcd. (see text).

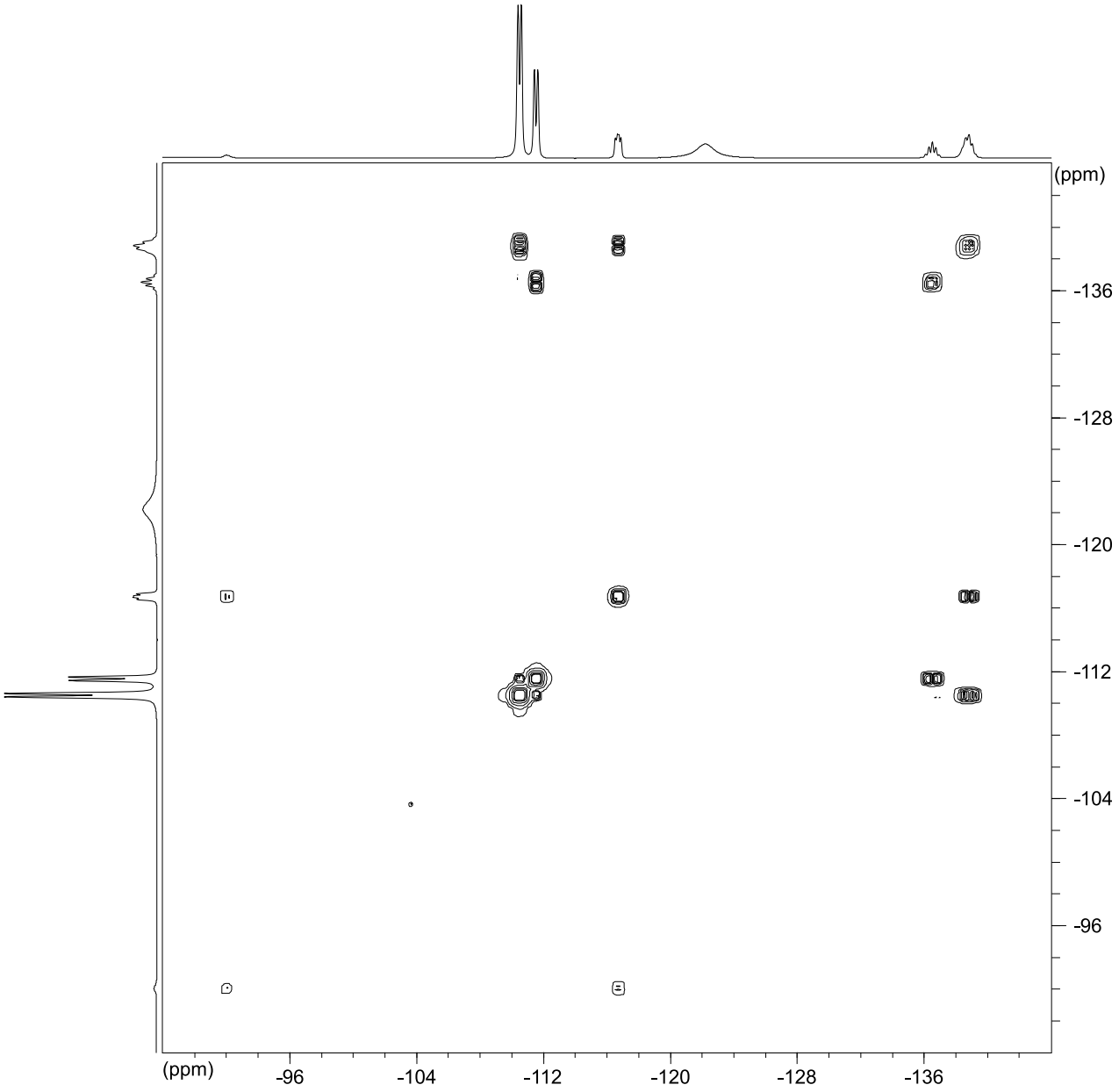

studies have used diluents like SO_2ClF (16), SO_2F_2, or SO_2 (14) to avoid viscosity broadening and allow measurements at lower temperatures and at higher SbF_5 concentrations.

These diluents have, in our opinion, two effects on the protonic super acid: (*i*) they interrupt the hydrogen bonding in the superacids and exert a structure breaking effect; and (*ii*) the ionizing and solvolyzing ability of the superacid is significantly reduced. This is best illustrated by the observation of oligomeric μ-F bridged species in studies involving diluents. The use of diluents is in essence the addition of substantial amounts of an aprotic solvent to a protonic Brønsted acid. This results in formation of a mixed solvent system.

Hence, earlier studies (16) on solutions of HSO_3X (X = F, CF_3) and SbF_5 in SO_2ClF (16) are strictly not comparable to our studies of the binary system HSO_3F and SbF_5 reported here and previously (13). The same limitation must be applied to a very recent study of the HF–SbF_5 system in SO_2ClF (8(*b*)) and to measurements of the Brønsted acidities by NMR methods (6, 7).

The acidity rankings by Sommer et al. (6, 7) based on measurements in SO_2FCl are called into question.

In summary it is conceivable, that the *cis*-F bridged chain structures found in liquid SbF_5, are partly retained in the mixed solvent system HSO_3F–SO_2ClF, allowing reactions of oligomeric $(SbF_5)_n$ (n = 2, 3, 4) with the bases SO_3F^- (16) or F^- (19) to give F bridged oligomers with terminal $^-OSO_2F$ (16) groups. It is our observation, that in strongly solvolyzing and ionizing HSO_3F (9), oligomeric $(SbF_5)_n$ (n = 2, 3, 4) is broken up into monomeric species, even at high

© 2002 NRC Canada

Scheme 2. Concerted reactions in magic acids made up from HSO_3F and SbF_5.

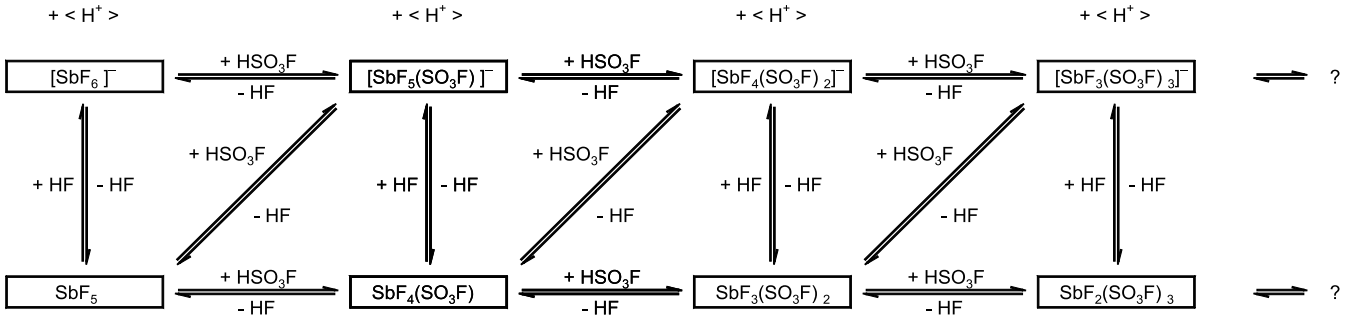

SbF_5 concentrations, and F bridged oligomers were not found in our study, with the exception of $[Sb_2F_{11}]^-$.

A summary of the proposed reactions

A very simple route to the main constituent of the magic acid system, the anion $[SbF_5(SO_3F)]^-$, is the direct reaction between monomeric SbF_5 and the self-ionization ion SO_3F^- according to:

$$[7] \quad SbF_{5\ (solv.)} + SO_3F^-_{(solv.)} \rightleftharpoons [(SbF_5(SO_3F)]^-_{(solv.)}$$

is probably incorrect for the simple reason that in HSO_3F the self-ionization constant of $K_{id} = 3.8 \times 10^{-8}$ (9) implies a very low concentration of SO_3F^- at 25°C.

A more likely formation reaction of the anion $[SbF_5(SO_3F)]^-$ is:

$$[8] \quad 2HSO_3F + SbF_{5\ (solv.)} \rightleftharpoons [(H_2SO_3F)]^+_{(solv.)} + [SbF_5(SO_3F)]^-_{(solv.)}$$

A probable first step in the formation of magic acids is the one-step fast solvolysis of SbF_5:

$$[9] \quad SbF_5 + HSO_3F \rightleftharpoons [SbF_4(SO_3F)] + HF$$

which is in our opinion the main source of HF as is discussed in this study. Due to the fluoropolymer lining inside the NMR tubes, HF formed via eq. [9] is no longer converted to $[H_3O]^+$ by a scavenger reaction with glass (from NMR tubes), as observed previously (13). Consequently HF can now get involved in anion formation in three ways.

Reaction with the Lewis acid SbF_5

$$[10] \quad 2HF + SbF_{5\ (solv.)} \rightleftharpoons [H_2F]^+_{(solv.)} + [SbF_6]^-_{(solv.)}$$

is expected to be fast. This will explain in part the high initial concentrations of $[SbF_6]^-$ at low x_{SbF_5} (0.012 and 0.064).

Reaction with a Lewis acid such as $SbF_4(SO_3F)$

$$[11] \quad 2HF + SbF_4(SO_3F)_{(solv.)} \rightleftharpoons [H_2F]^+_{(solv.)} + [SbF_5(SO_3F)]^-_{(solv.)}$$

is expected to be again a fast process. The analogous reactions in HSO_3F will result in an increase in the SO_3F contents of the anion. This was indeed observed in our earlier studies (13).

Slow -F vs. -SO_3F exchange

$$[12] \quad HF + [SbF_4(SO_3F)_2]^-_{(solv.)} \rightleftharpoons HSO_3F + [SbF_5(SO_3F)]^-_{(solv.)}$$

and

$$[13] \quad HF + [SbF_5(SO_3F)]^-_{(solv.)} \rightleftharpoons HSO_3F + [SbF_6]^-_{(solv.)}$$

Equation [13] explains the observed increase in $[SbF_6]^-$ with time in samples 1 and 2, noted in diluted solutions. It is clearly seen in Tables 5 and 6, that in samples 1–3, initially formed $[SbF_5(SO_3F)]^-$ is with time partly converted to $[SbF_6]^-$ and in samples 2 and 3 with increasing SbF_5 concentrations to $[(SbF_5)_2\text{-}\mu\text{-}SO_3F]^-$ (E). This is consistent with our experimental findings, where the species formed may be classified according to concentrations observed as shown in Table 7 and Scheme 1.

Conclusion

A system of concerted, slow reactions leads to equilibria in magic acids made up from HSO_3F and SbF_5 as shown in Scheme 2.

Solvolysis takes place in a horizontal direction, while vertical and diagonal directions indicate the addition of HSO_3F and HF, respectively, to Lewis acids of type $SbF_{5-i}(SO_3F)_i$. Complex anions of type $[SbF_{6-j}(SO_3F)_j]^-$ were formed, which were counterbalanced by $<H^+>$ symbolizing the acidium ions $H_2SO_3F^+$ and H_2F^+. Our present study unequivocally confirms the formation of species with $j = 0$–2 in relevant concentrations of >1 mol %. The main products (>5%) were $[SbF_6]^-$ and $[SbF_5(SO_3F)]^-$ while *cis*- and *trans*-$[SbF_4(SO_3F)_2]^-$ are formed in the 1–5% range.

None of the free Lewis acids $SbF_{5-i}(SO_3F)_i$ were detected in the ^{19}F NMR spectra. This indicates the high reactivity of such species to form the complex anions described above. Secondary addition products may be formed from the Lewis acids $SbF_{5-i}(SO_3F)_i$ and the complex anions $[SbF_{6-j}(SO_3F)_j]^-$ leading to oligomeric species as described formally by:

© 2002 NRC Canada

[14] $$a\mathrm{SbF}_{5-i}(\mathrm{SO_3F})_i + b[\mathrm{SbF}_{6-j}(\mathrm{SO_3F})_j]^- \rightleftharpoons [\mathrm{SbF}_{a(5-i)+b(6-j)}(\mathrm{SO_3F})_{ai+bj}]^-$$

Obviously, depending on a and b, several stereoisomers of such anions may exist, e.g., having μ-F- (in case of $[Sb_2F_{11}]^-$ only) and μ-O-S(O)(F)-O- bridges between or different location patterns for the -F and -SO_3F substituents attached to the octahedral skeletons of the antimony units (13). While a larger number of such anions were observed by NMR studies in glass NMR tubes (13) only a few and only simple species ($[Sb_2F_{11}]^-$, $[Sb_2F_{10}(SO_3F)]^-$, and $[Sb_2F_8(SO_3F)_3]^-$), all defined by $a = b = 1$, were visible above the 1% level when using fluoropolymer linings.

In the beginning phase of our studies we had considerable problems in understanding the spectrum of sample 1: high concentration of $[SbF_6]^-$, low concentration of $[SbF_5(SO_3F)]^-$, almost no $[SbF_4(SO_3F)_2]^-$, which indicates an excess of HF/F^- in this system. There appears to be more fluoride than would be formed according to Scheme 2 (magic acid equilibria). Consequently, traces of HF must originate from the materials used. Technical grade SbF_5 and HSO_3F have been carefully purified by established distillation methods (9(*b*)). However, even after purification the presence of trace amounts of HF in SbF_5 and (or) HSO_3F can not be ruled out. We do not expect that excess HF originates in considerable quantities as a result of an auto-dissociation of HSO_3F following (9):

[15] $$\mathrm{HSO_3F} \rightleftharpoons \mathrm{HF} + \mathrm{SO_3}$$

since the corresponding self-dissociation constant K_{sd}^{25} is as low as 3×10^{-7}. To support this assumption by experimental evidence we have studied a comparative series of magic acids derived from triflic acid CF_3SO_3H, where the formation of HF by an auto-dissociation analogue to eq. [15] is virtually impossible. Results of this investigations will be published as Part III in a separate consecutive paper of this series.

In summary, we view the distribution of monomeric anions found previously (13) at high dilutions to be representative of the nature and concentration of superacid anions formed in the absence of HF. All measurements in this concentration range made in the present study are affected by HF, causing a slow fluoro-fluorosulfato exchange because of the delay of 3 months between preparation and the initial measurements as discussed above. This is best shown in Table 7.

A necessary conclusion needs to be reached: the avoidance of H_2O formation by interaction of HF with glass and subsequent protonation to $[H_3O]^+$, demonstrated here, implies that magic acid (HSO_3F–SbF_5), when contained in fluoroplastic containers, must exhibit higher Brønsted acidities, than when used in glass. It will be difficult however to measure these acidities at high SbF_5 concentration, by reliable H_0 determinations (12). The use of indicator bases as practiced by Gillespie and Peel (20, 21) beyond the $-H_0$ value of 24 appears to be experimentally very challenging as discussed previously (22, 23). The use of H_2O as indicator proposed by Gold et al. (24, 25) appears to be unsound (22, 23). NMR methods by Sommer et al. (6, 7), cited here, involving solutions in diluents are problematic as well as discussed by us here and previously (13). It is hoped, that a new imaginative approach may be found, to allow H_0 measurement at these high acidities to confirm our conclusions.

Acknowledgement

Financial support by Fonds der Chemischen Industrie (FCI) (GH), Natural Sciences and Engineering Research Council of Canada (NSERC), (FA), North Atlantic Treaty Organization (NATO), (collaborative research grant to GH, FA), Alexander von Humboldt Stiftung (AvH), (research prize to FA, PDF to RB), and Deutsche Forschungsgemeinschaft (DFG) (PDF to MB) are gratefully acknowledged. Professor H.J. Frohn is thanked for supplying the fluoropolymer linings. Thanks are due to M. Puhl and C. Uhlemann (Heinrich-Heine-Universität, Düsseldorf) for technical assistance. In addition we wish to thank Professor R.C. Thompson (UBC) for helpful discussions.

References

1. G.A. Olah. Angew. Chem. Int. Ed. Engl. **32**, 767 (1993).
2. G.A. Olah, G.K.S. Prakash, and J. Sommer. Superacids. Wiley, New York. 1985, and refs. therein.
3. T.A. O'Donnell. Superacids and acidic melts as inorganic chemical reaction media. VCH, Weinheim. 1993.
4. G.A. Olah and P. von R. Schleyer (*Editors*). Carbonium ions. Vols. 1–5. Wiley Interscience, New York. 1968, 1970, 1972, 1973, 1976.
5. (*a*) H. Willner and F. Aubke. Angew. Chem. Int. Ed. Engl. **109**, 2506 (1997); (*b*) H. Willner and F. Aubke. *In* Inorganic chemistry highlights. *Edited by* G. Meyer, D. Naumann, and L. Wesemann. Wiley-VCH, Weinheim, Germany. 2002. pp. 195–212.
6. J. Sommer, P. Canivet, S. Schwartz, and P. Rimmelin. J. Am. Chem. Soc. **100**, 2576 (1978).
7. J. Sommer, P. Canivet, S. Schwartz, and P. Rimmelin. Nouv. J. Chim. **5**, 45 (1981).
8. (*a*) J. Bacon, P.A.W. Dean, and R.J. Gillespie. Can. J. Chem. **48**, 3413 (1970); (*b*) J.-C. Culman, M. Fauconet, R. Jost, and J. Sommer. New J. Chem. **23**, 863 (1999).
9. (*a*) R.C. Thompson. *In* Inorganic sulphur chemistry. *Edited by* G. Nickless. Elsevier, Amsterdam. 1968. p. 587; (*b*) R.C. Thompson, J. Barr, R.J. Gillespie, J.B. Milne, and R.A. Rothenbury. Inorg. Chem. **4**, 1641 (1965); (*c*) R.J. Gillespie, J.B. Milne, and R.C. Thompson. Inorg. Chem. **5**, 468 (1966).
10. M.F.A. Dove and A.F. Clifford. *In* Chemistry in non-aqueous ionizing solvents. *Edited by* J. Jander, H. Spandau, and C.C. Addison. Vieweg, Braunschweig/Wiesbaden. 1971, and refs. therein.
11. R.J. Gillespie and J. Liang. J. Am. Chem. Soc. **110**, 6037 (1988).
12. L.P. Hammett and A.J. Deyrup. J. Am. Chem. Soc. **54**, 2721 (1932).
13. D. Zhang, M. Heubes, G. Hägele, and F. Aubke. Can. J. Chem. **77**, 1869 (1999).
14. A. Commeyras and G.A. Olah. J. Am. Chem. Soc. **91**, 2929 (1969).
15. P.A.W. Dean and R.J. Gillespie. J. Am. Chem. Soc. **91**, 7264 (1969).
16. D. Brunel, A. Germain, and A. Commeyras. Nouv. J. Chim. **2**, 275 (1978).

© 2002 NRC Canada

17. D. Zhang, S.J. Rettig, J. Trotter, and F. Aubke. Inorg. Chem. **35**, 6113 (1996).
18. P.L. Fabré, J. Devynk, and B. Tremillon. Chem. Rev. **82**, 591 (1982).
19. (*a*) G. Hägele. *In* Phosphorus-^{31}P-NMR spectral properties in compound characterization and structural analysis. *Edited by* L. D. Quin und J. G. Verkade. VCH, Weinheim, Germany. 1994. pp. 395–409; (*b*) G. Hägele and U. Holzgrabe. *In* NMR spectroscopy in drug development and analysis. U. Holzgrabe, I. Wawer and B. Diehl (*Editors-in chief*). Wiley-VCH GmbH., Weinheim. 1999. pp. 61–76; (*c*) G. Hägele, Z. Szakács, J. Ollig, S. Hermens, and C. Pfaff. Heteroat. Chem. **11**, 562 (2000).
20. R.J. Gillespie and P.E. Peel. J. Am. Chem. Soc. **95**, 5173 (1973).
21. R.J. Gillespie and P.E. Peel. Adv. Phys. Org. Chem. **9**, 1 (1972).
22. D. Tonti, R. Jost, and J. Sommer. J. Chem. Soc. Perkin Trans. 2, 1793 (1986).
23. R. Jost and J. Sommer. Rev. Chem. Intermed. **9**, 171 (1988).
24. V. Gold, K. Laali, K.P. Morris, and L.Z. Zdunek. J. Chem. Soc. Chem. Commun. 769 (1981).
25. V. Gold, K. Laali, K.P. Morris, and L.Z. Zdunek. J. Chem. Soc. Perkin Trans. 2, 859 (1985).

© 2002 NRC Canada

Ligand scrambling reactions of cyano(thione)gold(I) complexes and determination of their equilibrium constants

Saeed Ahmad, Anvarhusein A. Isab, and Herman P. Perzanowski

Abstract: Ligand scrambling reactions in cyano(thione)gold(I) complexes ([>C=S-Au-CN]) to form $[Au(>C=S)_2]^+$ and $[Au(CN)_2]^-$ species have been investigated for a series of thiones in DMSO using ^{13}C and ^{15}N NMR spectroscopy. Rapid approach to equilibrium occurred and resulted in distinct signals for the [>C=S-Au-CN] and $[Au(CN)_2]^-$ complexes, both in ^{13}C and ^{15}N NMR. Equilibrium constants (K_{eq}) were determined for scrambling of all the complexes by integrating the CN resonances in the ^{13}C NMR recorded at 298 K. The influence of various factors (initial concentration, ionic strength, temperature, and solvent polarity) on the K_{eq} value was examined for a representative complex (ImtAuCN (Imt = Imidazolidine-2-thione)).

Key words: cyanogold(I) complexes, thiones, ligand scrambling, NMR, K_{eq}.

Résumé : Faisant appel à la spectroscopie RMN du ^{13}C et du ^{15}N et opérant dans le DMSO avec une série de thiones, on a étudié les réactions de brouillage de complexes cyan(thione)or(I) ([>C=S-Au-CN]) qui conduisent à la formation des espèces $[Au(>(C=S)_2]^+$ et $[Au(CN)_2]^-$. Il y a une approche rapide de l'équilibre et l'apparition de signaux distincts pour les complexes de [>C=S-Au-CN] et $[Au(CN)_2]^-$ tant en RMN du ^{13}C que celle du ^{15}N. On a déterminé les constantes d'équilibre ($K_{éq}$) pour le brouillage de chacun des complexes en intégrant les résonances du CN dans les spectres RMN du ^{13}C enregistrés à 298 K. Utilisant le complexe ImtAuCN (Imt= imidazoline-2-thione) comme exemple, on a examiné l'influence de divers facteurs (concentration initiale, force ionique, température et polarité du solvant) sur les valeurs de $K_{éq}$.

Mots clés : complexes cyanoor(I), thiones, brouillage de ligands, RMN, $K_{éq}$.

[Traduit par la Rédaction]

Introduction

It has been suggested that gold drugs (used for the treatment of rheumatoid arthritis (1, 2)) and their metabolites react in vivo with cyanide to form the intermediates $[RS\text{-}Au\text{-}CN]^-$ and [Et_3P-Au-CN], which undergo disproportionation generating $[Au(CN)_2]^-$ that is readily taken up by red blood cells (RBCs) (3–8). The cyanide is produced in the body by oxidation of SCN^- in polymorphonuclear leukocytes (3, 4). Although the concentration of cyanide in RBCs is very low (0.3 to 1 μM) (9), the very large formation constant of $[Au(CN)_2]^-$ ($\log \beta = 36$) (10) favors its formation. The level of $[Au(CN)_2]^-$ is higher for smokers than for nonsmokers because of inhalation of HCN from tobacco smoke (6, 11). Several studies describe the formation of $[Au(CN)_2]^-$ by disproportionation of L-Au-CN complexes in solution (12–18) according to the following equilibrium:

$$[1] \qquad 2\text{L-Au-CN} \rightleftarrows [AuL_2]^+ + [Au(CN)_2]^-$$

Received 7 January 2002. Published on the NRC Research Press Web site at http://canjchem.nrc.ca on 7 October 2002.

S. Ahmad, A.A. Isab,[1] and H.P. Perzanowski. Department of Chemistry, King Fahd University of Petroleum and Minerals, Dhahran 31261, Saudi Arabia.

[1]Corresponding author (e-mail: aisab@kfupm.edu.sa).

Cyano(ergothione)gold(I) is the only cyano(thione)gold(I) complex known to exhibit such a scrambling reaction in solution (18). However, cyano(*N*,*N*′-dimethylthiourea)gold(I) exists as an ionic complex ($[AuL_2]^+[Au(CN)_2]^-$) in the solid state (19). Cyano(thione)gold(I) complexes may be useful as models for the cyano intermediates of gold drugs ($[RS\text{-}Au\text{-}CN]^-$). Therefore, in the present study we carried out an investigation of scrambling reactions of various cyano(thione)gold(I) complexes. We were also able to measure the equilibrium constants (K_{eq}) for the scrambling of the complexes by integration of CN resonances in the ^{13}C NMR. Because of the possible biological implications of these reactions (3–6), the effects of several extrinsic factors on K_{eq} were systematically examined for one of the complexes (Imt-Au-CN). The external influences examined are the initial concentrations, ionic strength of the medium, temperature and the polarity of the solvent. The dependence of K_{eq} on initial concentration was studied in DMSO-d_6, while the effects of temperature and ionic strength were examined in methanol-d_4.

The structures of the thiones used in this study are described in Scheme 1.

Experimental

Chemicals

AuCN, using 99% ^{13}C- and ^{15}N-labeled KCN, was prepared according to the published procedure (13).

 DOI: 10.1139/V02-165 © 2002 NRC Canada

Scheme 1. (*a*) *N*,*N*′-Dimethylthiourea (DmTu); (*b*) R = H, imidazolidine-2-thione (Imt); (*c*) R = CH_3, *N*-methylimidazolidine-2-thione (MeImt); (*d*) R = C_2H_5, *N*-ethylimidazolidine-2-thione (EtImt); (*e*) R = C_3H_7, *N*-propylimidazolidine-2-thione (PrImt), (*f*) R = *i*-C_3H_7, *N*-(*i*-propyl)imidazolidine-2-thione (*i*-PrImt); (*g*) 1,3-diazinane-2-thione (Diaz); (*h*) 1,3-diazipane-2-thione (Diap).

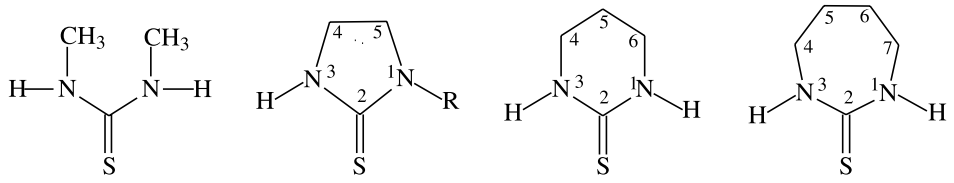

(a) (b-f) (g) (h)

Table 1. Elemental analyses of the [>C=S-Au-CN] complexes.

	Found (calcd.) (%)			
Complex	C	H	N	S
DmTuAuCN	15.18 (14.68)	2.44 (2.46)	13.26 (12.85)	9.24 (9.80)
MeImtAuCN	17.37 (17.70)	2.31 (2.38)	11.38 (12.39)	10.54 (9.45)
DiapAuCN	19.58 (20.40)	2.73 (2.85)	11.19 (11.90)	8.42 (9.08)

N,*N*′-Dimethylthiourea, CD_3OD, and DMSO-d_6 were obtained from Fluka Chemical Co. All the thiones were synthesized according to the procedure described in the literature (by the addition of CS_2 to diamines in ether and then heating the resulting adduct at 100°C for 2 to 3 h, followed by its crystallization in methanol) (20, 21). In all ligands except DmTu and Diap, C-2 contains 5% labeled carbon-13.

Preparation of complexes

All [>C=S-Au-CN] complexes were prepared according to the published procedure, by refluxing an equimolar amount of the thione and AuCN in methanol and then crystallizing in methanol (22). The complexes of DmTu, Diaz, and Diap ligands could not be crystallized in methanol, instead sticky materials were obtained which were separated by addition of diethyl ether. The elemental analysis for five of the eight complexes is already reported (22) and for the remaining three complexes, it is given in Table 1.

^{1}H, ^{13}C, and ^{15}N NMR measurements

^{1}H NMR spectra were obtained on a Jeol JNM-LA 500 NMR spectrometer operating at a frequency of 500.00 MHz. ^{13}C NMR spectra were obtained at the frequency of 125.65 MHz with ^{1}H broadband decoupling at 298 K. The spectral conditions were: 32 000 data points, 0.967 s acquisition time, 1.00 or 30.00 s pulse delay, and 45° pulse angle. ^{13}C NMR chemical shifts relative to TMS were assigned according to the reference given in the literature (23).

The ^{15}N NMR spectrum was recorded at 50.55 MHz using $NH_4{}^{15}NO_3$ as the external reference, which lies at 375.11 ppm relative to pure CH_3NO_2 (380.2 ppm) (24). The spectral conditions for ^{15}N were: 32 000 data points, 0.721 s acquisition time, 2.50 s delay time, 60° pulse angle, and approx. 5000–10 000 scans.

T_1 values for the ^{13}C nuclei were measured only for the complex Imt-Au-CN using the inversion recovery method. The average values obtained were: 5.5 s for $[Au(CN)_2]^-$, 3.9 s for the CN carbon of Imt-Au-CN, and 5.0 s for the >C=S carbon of Imt-Au-CN. Based on these T_1 values, a delay time of 30.0 s was used to record the ^{13}C NMR spectra of all the complexes so that the spectra could be integrated quantitatively.

Results and discussion

The ligand scrambling reactions of the cyano(thione)gold(I) complexes in DMSO were investigated by ^{13}C and ^{15}N NMR spectroscopy. The ^{1}H NMR chemical shifts of N-H protons and ^{13}C NMR chemical shifts of all the ligands and their gold(I) complexes are given in Table 2.

In ^{1}H NMR, the N-H signal was broadened upon coordination and a down-field shift of almost 1.0 ppm was observed in the N-H proton of all the ligands. The appearance of the N-H signal in the ^{1}H NMR spectra of all ligands after complexation shows that the ligands were coordinating in the thione form in solution.

In ^{13}C NMR, no significant change in the chemical shifts of the ligands upon complexation was observed except in the C-2 resonance (Table 1). A shift of 8–10 ppm in C-2 resonance indicates that in all the complexes gold(I) is bonded to thione ligands through the sulfur atom only (22, 23). Typical ^{13}C and ^{15}N NMR spectra for a representative complex (Imt-Au-^{13}C^{15}N) are shown in Fig. 1.

The ^{13}C and ^{15}N NMR shifts of CN^- and coupling constants ($^1J_{C\text{-}N}$) of the [>C=S-Au-CN] complexes are given in Table 3.

In the CN region of the ^{13}C NMR spectrum, two intense resonances were observed for all the complexes (Fig. 1(*b*)). One CN resonance at 149.6 ppm is characteristic of $[Au(CN)_2]^-$ (13, 14), while the other resonance corresponds to the [>C=S-Au-CN] complexes. These two resonances demonstrate that [>C=S-Au-CN] type complexes undergo the same type of ligand scrambling reaction as given by eq. [1], i.e.,

$$[2] \qquad 2[>C{=}S\text{-}Au\text{-}CN] \rightleftarrows [Au(>C{=}S)_2]^+ + [Au(CN)_2]^-$$

The $[Au(CN)_2]^-$ resonance appeared as a triplet (or a broad singlet) with an average coupling constant of 5.9 Hz.

© 2002 NRC Canada

Table 2. ^{1}H and ^{13}C NMR chemical shifts of thiones and their cyanogold(I) complexes in DMSO-d_6.

Species	N-H	C-2	C-4	C-5	C-6	N-C1	N-C2
DmTu	7.38	182.64	—	—	—	30.66	—
DmTuAu^{13}C^{15}N	8.63	172.70	—	—	—	32.12	—
	8.46[a]					29.96[a]	
Imt	7.98	183.44	43.97	43.97	—	—	—
		185.14	45.71	45.71[b]			
ImtAu^{13}C^{15}N	9.30	174.64	45.05	45.05	—	—	—
		178.08	46.30	46.30[b]			
$[Au(Imt)_2]^+$	—	177.32	46.39	46.39[b]	—	—	—
MeImt	8.02	182.90	40.60	50.18	—	33.39	—
MeImtAu^{13}C^{15}N	9.12	174.08	41.88	51.61	—	33.91	—
EtImt	7.99	182.05	40.68	47.03	—	40.41	11.80
EtImtAu^{13}C^{15}N	9.18	173.22	41.92	48.61	—	41.63	11.96
PrImt	7.99	182.55	40.79	47.70	—	47.38	19.86, 11.00[c]
PrImtAu^{13}C^{15}N	9.17	173.68	41.93	49.12	—	48.28	19.84, 10.88[c]
i-Pr-Imt	7.96	181.44	40.85	42.02	—	45.64	18.92
i-Pr-ImtAu^{13}C^{15}N	9.10	172.90	41.84	43.63	—	47.96	19.24
Diaz	7.81	175.62	39.76	19.19	39.76	—	—
DiazAu^{13}C^{15}N	8.98	166.67	[d]	18.16	[d]	—	—
Diap	7.76	187.91	44.76	27.12	27.12	—	—
DiapAu^{13}C^{15}N	8.84	[e]	44.62	25.83	25.83	—	—

[a]Resonances due to inequivalent CH_3 groups.
[b]Resonances in methanol.
[c]N-C3.
[d]Overlapped with DMSO.
[e]Not observed.

Table 3. ^{13}C and ^{15}N NMR chemical shifts of CN, coupling constants and K_{eq} of cyanogold(I) complexes in DMSO.

Species	$\delta^{13}C$ (ppm)	$\delta^{15}N$ (ppm)	$^{1}J_{C\text{-}N}$ (Hz)	K_{eq} (±esd)
DmTuAu^{13}C^{15}N	144.22	281.22	9.3	0.98 ± 0.03
ImtAu^{13}C^{15}N	144.40	281.18	9.3	0.630 ± 0.005
	147.02	262.23	10.3	0.45[a] ± 0.01
MeImtAu^{13}C^{15}N	143.64	281.18	9.0	0.56 ± 0.02
EtImtAu^{13}C^{15}N	143.62	281.36	10.4	0.62 ± 0.01
PrImtAu^{13}C^{15}N	143.60	281.38	9.3	0.59 ± 0.01
i-Pr-ImtAu^{13}C^{15}N	143.81	280.99	[b]	0.55 ± 0.01
DiazAu^{13}C^{15}N	144.75	281.12	8.2	0.91 ± 0.01
DiapAu^{13}C^{15}N	144.69	281.10	[b]	0.96 ± 0.01
ErSAu^{13}C^{15}N (18)[a]	146.98	261.98	8.3	1.08
Ph_3PAuCN (13, 14)[a]	156.2	—	6.4	0.112
Me_3PAuCN (13, 14)[a]	158.3	267.35	6.8	0.37
Et_3PAuCN (13, 14)[a]	160.4	265.54	6.5	0.24
(*i*-Pr)$_3$PAuCN (13, 14)[a]	160.9	264.61	6.2	0.29
Cy_3PAuCN (13, 14)[a]	160.29	264.35	5.5	0.49

[a]Values in methanol.
[b]Not observed.

The triplet appearance of the $[Au(CN)_2]^-$ resonance occurred because the ^{13}C-^{15}N in $[Au(CN)_2]^-$ follows the AA′XX′ spin system as described in the previous studies (14, 15, 18). The ^{13}C-^{15}N resonance due to [>C=S-Au-$^{13}C^{15}N$] complexes is a doublet with the $^{1}J_{C\text{-}N}$ values given in Table 3. In the ^{13}C NMR of Imt-Au-CN in methanol, the $[Au(CN)_2]^-$ resonance was observed at 152.41 ppm. Separate resonances for thione ligands in [>C=S-Au-CN] and $[Au(>C=S)_2]^+$ species were typically not observed either due to their rapid exchange or because the chemical shifts of the two species are overlapped so that they could not be resolved. However, we were able to observe these for one of the complexes (Imt-Au-CN) at 240 K in methanol (Fig. 1(*c*)). The >C=S and C-4/5 resonances of Imt-Au-CN and $[Au(>C=S)_2]^+$ which were observed as average resonances at 298 K, were clearly separated into two peaks at 240 K (Fig. 1(*c*)). Thus, we were able to detect both species ($[Au(>C=S)_2]^+$ and $[Au(CN)_2]^-$) formed as a result of the scrambling of Imt-Au-CN. The analogous species in the scrambling of R_3P-Au-CN complexes ($[Au(R_3P)_2]^+$) was detected at room temperature by ^{31}P NMR (13, 14). For the DmTu-Au-CN complex, two resonances for methyl carbons of DmTu were detected

© 2002 NRC Canada

Fig. 1. (*a*) 125.65 MHz ^{13}C NMR spectrum of Imt in DMSO-d_6; (*b*) ^{13}C NMR spectrum of Imt-Au-$^{13}C^{15}N$ at 298 K in DMSO-d_6; (*c*) ^{13}C NMR spectrum of Imt-Au-$^{13}C^{15}N$ at 240 K in methanol (C-2 of the thione is enriched to 2% and C′ are the resonances corresponding to $[Au(Imt)_2]^+$); (*d*) 50.55 MHz ^{15}N NMR spectrum of Imt-Au-$^{13}C^{15}N$ in DMSO-d_6.

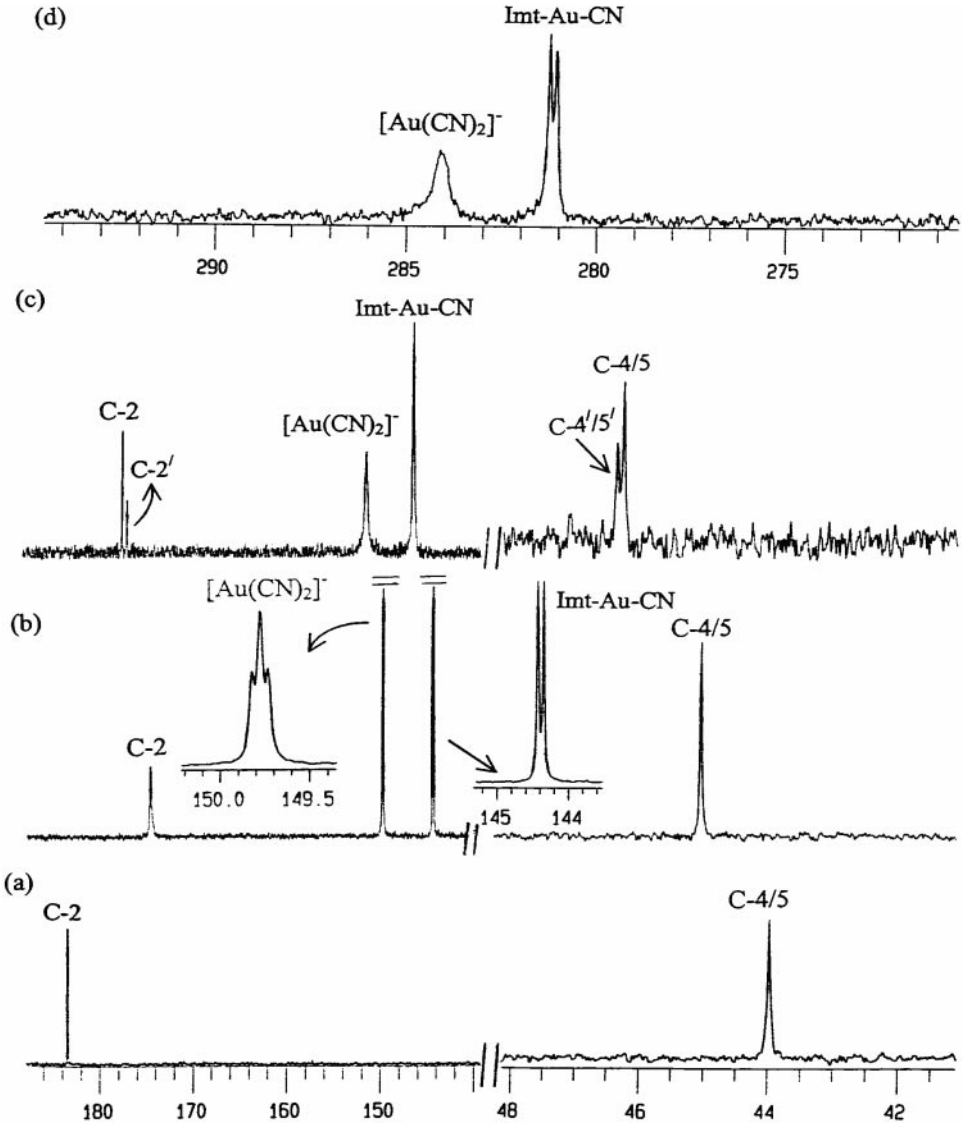

showing that the methyl groups are inequivalent. These two resonances for methyl carbons could not be due to the [DmTu-Au-CN] and $[Au(DmTu)_2]^+$ species, since we also observed two resonances for methyl carbons in the reaction of DmTu with $AgNO_3$. Two resonances were also observed for N-H (and CH_3) protons in ^1H NMR (Table 2). The crystal structure of DmTu-Au-CN demonstrates that both N-H hydrogen atoms of DmTu are involved in hydrogen bonding to the nitrogen of cyanide (19). Thus the two methyl groups and N-H protons would be inequivalent and behave differently in NMR.

Dimethyl sulfoxide is believed to interact weakly with AuCN, since in the ^{13}C NMR of a mixture of AuCN and DMSO, two CN resonances corresponding to $[Au(CN)_2]^-$ and DMSO–AuCN (135.03 ppm, $^1J_{C\text{-}N}$ = 10.1 Hz) species were observed. However, the CN resonance due to DMSO–AuCN was not observed in any of the thione complexes.

The results of the ^{15}N NMR studies are consistent with the ^{13}C NMR data. The ^{15}N NMR also showed two resonances for the CN^- nitrogen corresponding to equilibrium (2) (Fig. 1(*d*)). The resonance at 284.1 ppm was a triplet (or a broad singlet) of $[Au(CN)_2]^-$ with an average coupling constant of 5.9 Hz. The other resonance was a doublet due to ^{13}C-^{15}N coupling in the >C=S-Au-$^{13}C^{15}N$ complexes (Table 3). When a ^{15}N NMR of Imt-Au-CN was taken in methanol, a significant shift in these resonances was observed. The $[Au(CN)_2]^-$ resonance was observed at 264.7 ppm and the Imt-Au-CN resonance at 262.2 ppm.

Equilibrium constants (K_{eq}) were measured for the >C=S-Au-CN complexes at 298 K using a 0.025 M solution of each complex in DMSO-d_6. The K_{eq} values were calculated from the relative intensities of the ^{13}C-^{15}N resonances of [>C=S-Au$^{13}C^{15}N$] and $[Au(^{13}C^{15}N)_2]^-$ in the ^{13}C NMR, which gave the relative concentrations of all three species

© 2002 NRC Canada

Fig. 2. K_{eq} vs. [Imt-Au-$^{13}C^{15}N$]$_0$ at 298 K for concentrations ranging from 0.0125 to 0.10 M in DMSO-d_6.

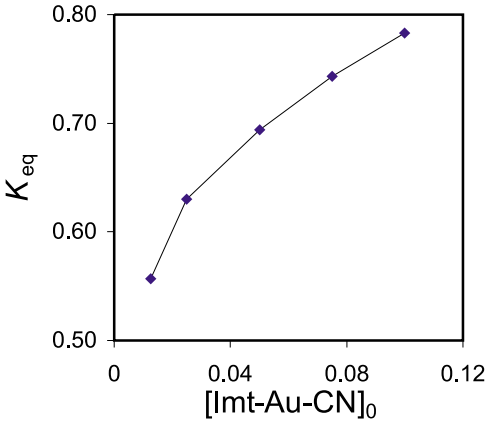

Fig. 3. K_{eq} vs. [NH_4NO_3] for 0.05 M Imt-Au-$^{13}C^{15}N$ at 298 K in methanol (NH_4NO_3 concentrations ranging from 0.2 to 1.0 M).

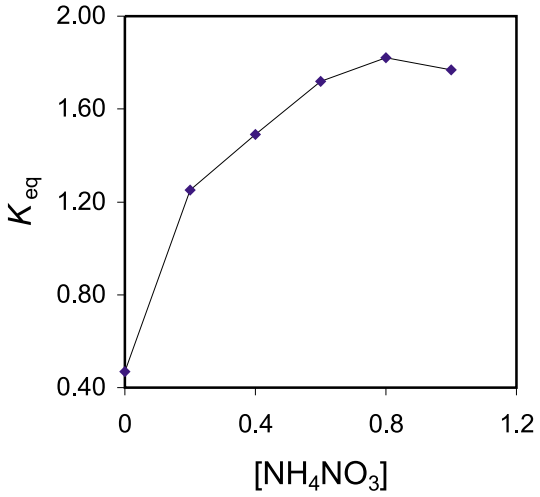

because of the stoichiometric relationship (I[Au($^{13}C^{15}N)_2]^-$ = I[Au (>C=S)$_2]^+$):

$$K_{eq} = \frac{(I[\mathrm{Au}(^{13}\mathrm{C}^{15}\mathrm{N})_2]^-)(I[\mathrm{Au}(>\mathrm{C}{=}\mathrm{S})_2]^+)}{(I[>\mathrm{C}{=}\mathrm{S}\text{-}\mathrm{Au}^{13}\mathrm{C}^{15}\mathrm{N}])^2}$$

Each K_{eq} is the result of five to six measurements. The average K_{eq} values thus found for the complexes are listed in Table 3 and for comparison, K_{eq} values of some known cyanogold(I) complexes are also given. The intensity of the CN resonances was found to be unchanged when spectra were taken after 1 week showing that the scrambling equilibrium was achieved rapidly for these complexes.

The effect of several factors on the magnitude of K_{eq} was examined for a representative complex (Imt-Au-CN). The first extrinsic factor examined was the initial concentration of the complex [Imt-Au-CN]$_o$. Initial concentrations ranging from 0.0125 to 0.10 M in DMSO-d_6 were used. A plot of K_{eq} vs. [Imt-Au-CN]$_o$ shows that K_{eq} value increases consistently with increasing [Imt-Au-CN]$_o$ (Fig. 2). An increase in [Imt-Au-CN]$_o$ generates more [Au(Imt)$_2]^+$ and [Au(CN)$_2]^-$ which in turn increases ionic strength resulting in the larger K_{eq} values (13).

Fig. 4. K_{eq} vs. temperature for 0.05 M Imt-Au-$^{13}C^{15}N$ in methanol for the temperature range 240–320 K.

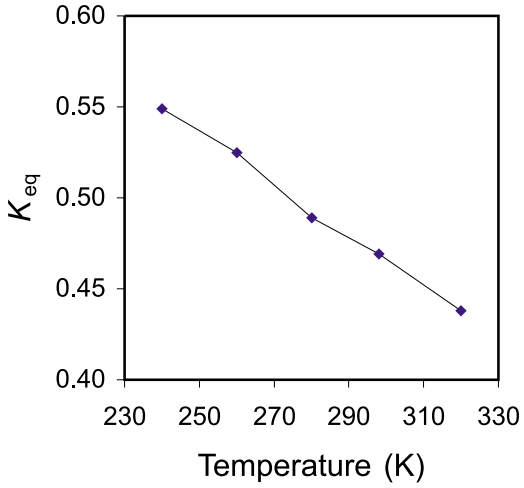

The second external influence examined was the ionic strength of the solution. NH_4NO_3 (a salt having component ions with a low affinity for gold(I)) (13) was used to control the ionic strength of the solution. ^{13}C NMR spectra were acquired for 0.05 M [Imt-Au-CN] in CD_3OD with NH_4NO_3 at concentrations ranging from 0.20 to 1.0 M. Figure 3 shows a plot of K_{eq} vs. the concentration of NH_4NO_3. The K_{eq} value increases with NH_4NO_3 concentration up to 0.80 M. Since ionic complexes are generated by the scrambling process, an increase in ionic strength leads to an increase in the activity coefficients for [Au(Imt)$_2]^+$ and [Au(CN)$_2]^-$ with a subsequent increase in K_{eq}. A decrease in K_{eq} at [NH_4NO_3] greater than 1.0 M is perhaps due to ion pairing. This result is consistent with that reported for Et_3PAuCN (13). The increase in K_{eq} observed by increasing ionic strength is more than that observed by changing concentration.

To examine the effect of temperature on K_{eq}, the ^{13}C NMR spectra were obtained at the temperatures of 240, 260, 280, 298, and 320 K in CD_3OD. When K_{eq} values are plotted against temperature, an inverse correlation was observed (Fig. 4). The K_{eq} value decreased with increasing temperature indicating that the scrambling reaction is exothermic in the forward direction (eq. [2]) according to the van't Hoff equation ($\ln K = -\Delta H°/RT + C$). $\Delta H°$ for this reaction can be obtained if ln K is plotted vs. $1/T$ in the above equation. Such a plot is shown in Fig. 5 and the $\Delta H°$ value obtained from this plot is –1.81 kJ mol $^{-1}$.

Polarity of the solvent should also have a significant effect on K_{eq} because the increased solvation of the ionic species generated as a result of the scrambling process should ultimately result in larger K_{eq} values. The K_{eq} values obtained in different solvents using a 0.025 M solution of the complex are shown in Table 4. The K_{eq} values are consistent with the polarity of the solvent except methanol. Methanol being a protic solvent solvates the anion (25) ([Au(CN)$_2]^-$) (which is more stable) strongly and thus would result in a larger K_{eq}.

Besides external factors, it was observed in the scrambling reactions of cyanogold (I) complexes of phosphines, that K_{eq} is also affected by the intrinsic factors, which are electronic and steric (13). Among the intrinsic factors, the basicity of the phosphine was found to be the most important which

© 2002 NRC Canada

Fig. 5. A plot of ln K vs. $1/T$ for Imt-Au-$^{13}C^{15}N$ in methanol.

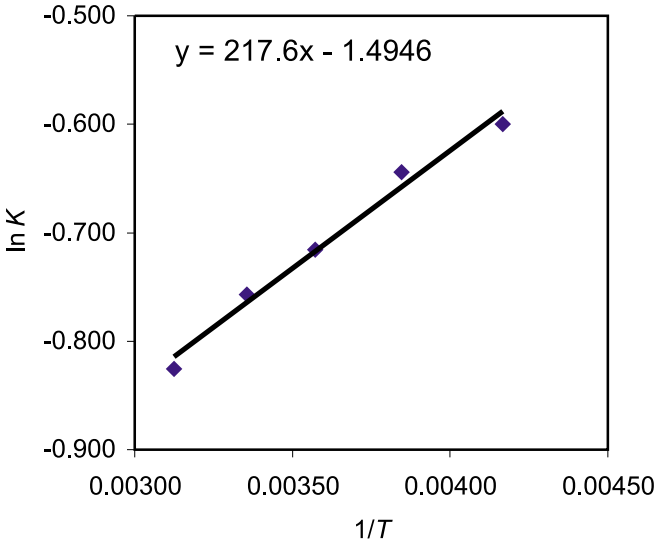

Table 4. K_{eq} values for the scrambling of Imt-Au-$^{13}C^{15}N$ in different solvents at 298 K.

Solvent	μ (debye)[a]	K_{eq}
DMSO	3.9	0.63
Acetonitrile	3.44	0.34
Methanol	2.87	0.45
Acetone	2.69	0.19

[a]Values taken from ref. 25.

affects K_{eq}. An increase in K_{eq} was observed with an increase in basicity of the phosphine (13). However, the π accepting ability of the phosphines may be an additional factor in the stability of R_3PAuCN complexes, which would result in a lower K_{eq} value. As shown in Table 3, the K_{eq} values for the cyanogold(I) complexes of thiones are comparatively larger than for the complexes of phosphines. The larger K_{eq} values indicate that the thiones are more basic towards Au(I) but weaker π acceptors compared to the phosphines. The smaller Au—P bond length and greater Au—CN distance in R_3PAuCN complexes (26) compared to the Au—S and Au—CN distances in [>C=S-AuCN] complexes (19) also support this conclusion. For example, the Au—P bond length in Me_3PAuCN was found to be 2.275 Å (26), while in ImtAuCN, the Au—S distance was 2.294 Å (19). The corresponding Au—CN distances were 2.04 and 1.966 Å, respectively. The smaller Au—CN distance in [>C=S-AuCN] is due to greater donation of electron density by the thione.

In the scrambling reactions of cyano(phosphine)gold(I) complexes (13, 14), it was observed that with increasing basicity of phosphines, the δ (^{13}C) for CN also increased due to the increased π bond character in the Au—C bond, while the δ (^{15}N) was decreased. However, in the present study, $\delta^{13}C$ and $\delta^{15}N$ for CN and the coupling constants ($^1J_{C\text{-}N}$) in all the complexes are very close showing that the difference in their basicity is smaller. Table 3 shows the highest value of $\delta^{13}C$ for the CN resonance of Diaz–AuCN indicating that it is the most basic, while the PrImt–AuCN with the lowest $\delta^{13}C$ is the least basic among the thiones.

The present study concludes that cyano(thione)gold(I) complexes undergo a similar kind of scrambling process in solution as observed for cyano(phosphine)gold(I) complexes. However, the $[Au(>C=S)_2]^+$ species formed by the scrambling of >C=S-Au-CN complexes could only be detected at lower temperatures. The scrambling equilibrium is dependent on such factors as the initial concentration of the complex, ionic strength of the solution, temperature and polarity of the solvent, with polarity of the solvent showing a major influence on K_{eq}.

Acknowledgement

This research was supported by the KFUPM Research Committee under project no. CY/NMR-STUDIES/214.

References

1. C.F. Shaw, III. Chem. Rev. **99**, 2589 (1999).
2. S.L. Best and P.J. Sadler. Gold Bull. **29**, 87 (1996).
3. G.G. Graham and M.M. Dale. Biochem. Pharm. **39**, 1697 (1990).
4. G.G. Graham and A.J. Kettle. Biochem. Pharm. **56**, 307 (1998).
5. G.G. Graham, J.R. Bales, M.C. Gtootveld, and P.J. Sadler. J. Inorg. Biochem. **25**, 163 (1985).
6. A.A. Isab, A.L. Hormann, M.T. Coffer, and C.F. Shaw, III. J. Am. Chem. Soc. **110**, 3278 (1988).
7. A.J. Canunumalla, S. Schraa, A.A. Isab, C.F. Shaw, III, E. Gleichman, L. Dunemann, and M. Turfeld. J. Biol. Inorg. Chem. **3**, 9 (1998).
8. A.J. Canumalla, N. Al-Zamil, M. Philips, A.A. Isab, and C.F. Shaw, III. J. Inorg. Biochem. **85**, 67 (2001).
9. Y. Zhang, E.V. Hess, K.G. Pyrhuber, J.G. Dorsey, K. Tepperman, and R.C. Elder. Inorg. Chim. Acta, **229**, 271 (1995).
10. R.D. Hancock, N.P. Finnkelstein, and A. Avers. J. Inorg. Nucl. Chem. **34**, 3747 (1972).
11. D. Lewis, H.A. Apell, C.J. McNeil, M.S. Iqbal, D.H. Brown, and W.E. Smith. Ann. Rheum. Dis. **42**, 566 (1983).
12. A.L. Hormann, C.F. Shaw, III, D.W. Bennett, and W.M. Reiff. Inorg. Chem. **25**, 3953 (1986).
13. A.L. Hormann and C.F. Shaw, III. Inorg. Chem. **29**, 4683 (1990).
14. A.A. Isab, M.S. Hussain, M.N. Akhtar, M.I.M. Wazeer, and A.R. Al-Arfaj. Polyhedron, **18**, 1401 (1999).
15. S. Ahmad, A.A. Isab, M.N. Akhtar, A.R. Al-Arfaj, and M.S. Hussain. J. Coord. Chem. **51**, 225 (2000).
16. S. Ahmad, A.A. Isab, H.P. Perzanowski, M.S. Hussain, and M.N. Akhtar. Transition Met. Chem. **27**, 177 (2002).
17. G. Lewis and C.F. Shaw, III. Inorg. Chem. **25**, 58 (1986).
18. S. Ahmad and A.A. Isab. Inorg. Chem. Commun. **4**, 362 (2001).
19. F.B. Stocker and D. Britton. Acta Crystallogr. Sect. C: Cryst. Struct. Commun. **C56**, 798 (2000).
20. G.D. Thorn. Can. J. Chem. **33**, 1278 (1955).
21. L. Maier. Helv. Chim. Acta, **53**, 1417 (1970).
22. A.A. Isab and M.S. Hussain. J. Coord. Chem. **15**, 125 (1986).
23. A.A. Isab. Polyhedron, **8**, 2823 (1989), and refs. therein.
24. M.N. Akhtar, A.A. Isab, A.R. Al-Arfaj, and M.S. Hussain. Polyhedron, **16**, 125 (1997), and refs. therein.
25. T.H. Lowry and K.S. Richardson. *In* Mechanism and theory in organic chemistry. Harper and Row Publishers, New York. 1981. p. 162.
26. S. Ahrland, B. Aurivillius, K. Dreish, B. Noren, and A. Oskarsson. Acta Chem. Scand. **46**, 262 (1992), and refs. therein.

© 2002 NRC Canada

Alkoxide-functionalized cyclopentadienyl complexes of yttrium containing a two-carbon tether

Roland A.L. Gendron, David J. Berg, and Tosha Barclay

Abstract: The ligand $C_5H_4(CH_2CH_2CAr^F{}_2OH)$ (**3**) (Ar^F = 3,5-$C_6H_3(CF_3)_2$) was prepared in two steps, from the iodo ester $ICH_2CH_2CO_2Me$ by way of the cyclopentadienyl ester $C_5H_5CH_2CH_2CO_2Me$ (**2**), in 55% overall yield. Thermal reaction of **3** with $\{Y[N(SiMe_3)_2]_2(THF)_2(\mu\text{-}Cl)\}_2$ afforded the neutral chloride complex $\{\eta^5{:}\eta^1\text{-}C_5H_4[CH_2CH_2C(O)(3,5\text{-}C_6H_3(CF_3)_2)_2]\}YCl\{THF\}_n$ (**5a**: n = 2, **5b**: n = 1). Metathesis reactions of **5** with 1 equiv of $NaN(SiMe_3)_2$, LiO-2,6-*t*-$Bu_2C_6H_3$, and $LiCH(SiMe_3)_2$ afforded $\{\eta^5{:}\eta^1\text{-}C_5H_4[CH_2CH_2C(O)(3,5\text{-}C_6H_3(CF_3)_2)_2]\}Y\{N(SiMe_3)_2\}\{THF\}_n$ (**6**), $\{\eta^5{:}\eta^1\text{-}C_5H_4[CH_2CH_2C(O)(3,5\text{-}C_6H_3(CF_3)_2)_2]\}Y\{O\text{-}2,6\text{-}t\text{-}Bu_2C_6H_3\}\{THF\}_n$ (**7**), and $\{\eta^5{:}\eta^1\text{-}C_5H_4[CH_2CH_2C(O)(3,5\text{-}C_6H_3(CF_3)_2)_2]\}Y\{CH(SiMe_3)_2\}\{THF\}_n$ (**8**), respectively, (**a**: n = 2, **b**: n = 1). Exposure of the *bis*(THF) solvates to reduced pressure resulted in desolvation to the *mono*(THF) adducts for **5**–**8**. The solid state structure of **6b** was established by X-ray crystallography. In addition, formation of a spirocyclic ether ($C_4H_6CH_2CH_2C(O)(3,5\text{-}C_6H_3(CF_3)_2)_2$ **4**), obtained by the intramolecular cyclization of ligand **3**, was confirmed by X-ray crystallography.

Key words: yttrium, organometallic, cyclopentadienyl, X-ray, alkoxide, chelate, alkyl, hybrid ligand, NMR, cyclization.

Résumé : On a préparé le ligand $C_5H_4(CH_2CH_2CAr^F{}_2OH)$ (**3**) (Ar^F = 3,5-$C_6H_3(CF_3)_2$) en deux étapes à partir de l'ester iodé $ICH_2CH_2CO_2Me$, par le biais de l'ester cyclopentadiényle, $C_5H_5CH_2CH_2CO_2Me$ (**2**), avec un rendement global de 55%. La réaction thermique du composé **3** avec $\{Y[N(SiMe_3)_2]_2(THF)_2(\mu\text{-}Cl)\}_2$ conduit à la formation du complexe chloré neutre $\{\eta^5{:}\eta^1\text{-}C_5H_4[CH_2CH_2C(O)(3,5\text{-}C_6H_3(CF_3)_2)]\}YCl\{THF\}_n$ (**5a**: n = 2, **5b**: n = 1). Les réactions de métathèse des composés **5** avec un équivalent de $NaN(SiMe_3)_2$, LiO-2,6-*t*-$Bu_2C_6H_3$ et $LiCH(SiMe_3)_2$ conduisent respectivement au $\{\eta^5{:}\eta^1\text{-}C_5H_4[CH_2CH_2C(O)(3,5\text{-}C_6H_3(CF_3)_2)]\}Y\{N(SiMe_3)_2\}\{THF\}_n$ (**6**), $\{\eta^5{:}\eta^1\text{-}C_5H_4[CH_2CH_2C(O)(3,5\text{-}C_6H_3(CF_3)_2)]\}Y\{O\text{-}2,6\text{-}t\text{-}Bu_2C_6H_3\}\{THF\}_n$ (**7**) et $\{\eta^5{:}\eta^1\text{-}C_5H_4[CH_2CH_2C(O)(3,5\text{-}C_6H_3(CF_3)_2)]\}Y\{CH(SiMe_3)_2\}\{THF\}_n$ (**8**) (**a**: n = 2, **b**: n = 1). Si l'on soumet les produits *bis*(THF) solvatés **5**–**8** à une pression réduite, il en résulte une désolvatation conduisant aux adduits *mono*(THF). On a déterminé la structure du composé **6b** par diffraction des rayons X. De plus on a confirmé par diffraction des rayons X que la cyclisation intramoléculaire du ligand **3** conduit à la formation d'un éther spirocyclique, $C_4H_6CH_2CH_2(CO)(3,5\text{-}C_6H_5(CF_3)_2)_2$ (**4**).

Mots clés : yttrium, organométallique, cyclopentadiényle, rayons X, alcoolate, chélate, alkyle, ligand hybride, RMN, cyclisation.

[Traduit par la Rédaction]

Introduction

The development of *hybrid* ligands that contain both Cp and a pendant anionic group has been an important trend in organometallic chemistry of the lanthanides and group 4 elements during the past decade (1–3). The introduction of new Cp-alkoxide and Cp-amide mixed ligands has been especially successful because these ligands form metal complexes with coordination spheres that are more open than the corresponding *bis*(cyclopentadienyl) systems. Group 4 complexes containing these ligands have been extensively studied and have been widely applied to olefin polymerization chemistry (3). It is particularly surprising, then, that Cp-alkoxides have not been widely investigated as ligands in yttrium or lanthanide chemistry (2(*c*), 4, 5).[2] Ligands of this type developed for use in group 4 chemistry, however, are often poorly suited to group 3 and lanthanide chemistry because they do not possess sufficient steric bulk to satisfy the coordination sphere of the larger metals. In particular, many of the existing ligands bear no substituents on the alkoxide carbon.

In earlier work, we reported the preparation of a Cp-alkoxide ligand (**1**) with a single carbon bridge between the Cp unit and the alkoxide carbon (6). The preparation of simple

Received 5 July 2002. Published on the NRC Research Press Web site at http://canjchem.nrc.ca on 7 October 2002.

R.A.L. Gendron and D.J. Berg.[1] Department of Chemistry, University of Victoria, P.O. Box 3060, Victoria, BC V8W 3V6, Canada.
T. Barclay. Department of Chemistry, North Harris College, 2700 W. W. Thorne Drive, Houston, TX 77073, U.S.A.

[1]Corresponding author (e-mail: djberg@uvic.ca).

[2]Cyclopentadienyl ligands bearing *neutral* pendant donors are well known in yttrium and lanthanide chemistry. Literature prior to 1994 has been reviewed (5*a*). Several complexes of this type have been reported more recently (5(*b*)–5(*l*)).

 DOI: 10.1139/V02-174 © 2002 NRC Canada

yttrium complexes of the type (CpO)YX (CpO = **1**; X = Cl, Cp, $N(SiMe_3)_2$, 2,6-*t*-$Bu_2C_6H_3O$, $CH(SiMe_3)_2$) was generally complicated by the tenacious retention of additional anionic groups to form "*ate*" complexes of the type $(CpO)YX_2^-$, suggesting that ligand **1** lacks sufficient steric bulk to stabilize the neutral (CpO)YX species. Indeed, one of the most persistent problems encountered in previous work was rapid redistribution of the anionic *mono*(ligand) "ate" complexes to the *bis*(ligand) species $(CpO)_2Y^-$, clearly demonstrating the small effective size of **1**.

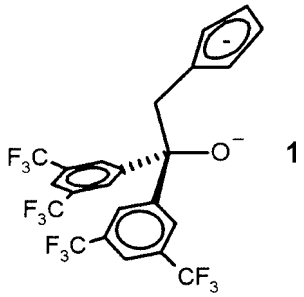

1

To *close down* the coordination sphere somewhat, **1** can be modified by adding bulk at the Cp or by extending the length of the tether by one carbon (7, 8). So far, our attempts to modify the ligand by using a substituted Cp (C_5Me_4, fluorenyl, indenyl) have not met with success, primarily because chelate coordination of the substituted Cp group does not occur (bridging interactions predominate, leading to insoluble materials). While work is still continuing in that direction, the second option may prove to be a better choice. This is a particularly attractive option because we have observed a tendency for ligand cleavage to occur between the alkoxide carbon and the lone CH_2 group in **1** (6). Presumably, addition of another CH_2 between the alkoxide and the Cp ring will help stabilize the ligand by removing any resonance effects involved in the ligand cleavage mechanism.

A two-atom backbone has been applied in organolanthanide chemistry for several neutral pendant donors (9) and one recently reported pendant alkoxide donor (10). The latter was found to stabilize larger iodide complexes, but no hydrocarbyl chemistry was reported. In the related yttrium hydride ($[Y(\eta^5:\eta^1\text{-}C_5Me_4SiMe_2NCMe_3)(\mu\text{-}H)(THF)]_2$) (4(*e*)), extension of the backbone by a single carbon, to give $[Y(\eta^5:\eta^1\text{-}C_5Me_4CH_2SiMe_2NCMe_3)(\mu\text{-}H)(THF)]_2$ (11), showed distinct changes in geometry and reactivity. The observed bite angles opened from 97.8(2)° and 97.4(2)° to 104.9(2)° and 104.3(2)°, respectively, and catalytic activity toward hydrosilation of styrene was higher in the yttrium complex with the longer "-CH_2SiMe_2-" link ($PhSiH_3$: 100% conversion, 1 h, vs. 80% conversion, 7 h) (11). This effect has been ascribed to an increased contribution of monomer in the monomer–dimer equilibrium for complexes containing the ligand with an extended backbone. VT-NMR studies on the monomer–dimer dissociation kinetics of $(Cp^*_2YH)_2$ indicated that the terminal hydride Cp^*_2YH is much more active toward olefin insertion than the dimeric form (12). This finding supports the theory of a dissociative mechanism as the rate-determining step in olefin insertion and, consequently, polymerization. Bulky ligands can only enhance dimer dissociation (i.e., backbone extension), so reactivity should increase with larger ligand size; however, excessive bulk leads to oversaturation of the metal and inhibits the approach of the inserting species. The solution is to use a synthesis that allows the adjustment of bulk in small increments, so as to approach, but not overshoot, the desired ligand size. The extension of the backbone by sequential addition of CH_2 units seems the most logical approach. In this contribution we report the synthesis of a new Cp-alkoxide ligand with an extended two-carbon backbone between the Cp and alkoxide carbons and the formation of several neutral yttrium complexes derived from it.

Experimental

General procedures

All manipulations were carried out under an argon atmosphere, with the rigorous exclusion of oxygen and water, using standard glovebox (Braun MB150-GII) or Schlenk techniques. Tetrahydrofuran (THF), hexane, and toluene were dried by distillation from sodium benzophenone ketyl under argon immediately prior to use. 3,5-*Bis*(trifluoromethyl)bromobenzene and methyl 3-chloropropionate were purchased commercially (Aldrich) and used as received. $Li[3,5\text{-}C_6H_3(CF_3)_2]$ was prepared from *n*-butyl lithium and $3,5\text{-}C_6H_3(CF_3)_2Br$ in hexane at –78°C. The precipitated fluorinated aryl lithium salt was washed with cold hexane and redissolved in diethyl ether before use. Care must be taken to keep $Li[3,5\text{-}C_6H_3(CF_3)_2]$ cold during all operations, since it is unstable above –20°C. The iodo ester ($ICH_2CH_2CO_2CH_3$) was prepared using conventional halogen exchange between methyl 3-chloropropionate and NaI in acetone (13). Yttrium tris(2,6-di-*t*-butylphenoxide) (14) and $\{Y[N(SiMe_3)_2]_2(THF)_2(\mu\text{-}Cl)\}_2$ (6) were prepared according to literature procedures.

^1H (360 MHz), ^{13}C (90.55 MHz), ^{19}F (338.86 MHz), and ^{29}Si (71.54 MHz) NMR were recorded on a Bruker AMX-360 MHz spectrometer. All deuterated solvents were dried over activated 4 Å molecular sieves, and spectra were recorded using 5 mm tubes fitted with a Teflon valve (Brunfeldt) at room temperature unless otherwise specified. ^1H and ^{13}C NMR spectra were referenced to residual solvent resonances. ^{19}F NMR spectra were referenced to external CCl_3F, and ^{29}Si NMR spectra were referenced to external TMS. Melting points were recorded using a Büchi melting point apparatus and are not corrected. Canadian Microanalytical (Delta, B.C) performed elemental analyses. Despite the use of co-oxidants such as V_2O_5 and PbO_2, the analytical data for most metal complexes were consistently 1 to 2% low in carbon. This may be due to metal carbide formation. Mass spectra were recorded on a Kratos Concept H spectrometer using chemical ionization (methane), electron impact (70 eV), or liquid secondary ion mass spectroscopy (LSIMS).

Methyl 3-cyclopentadienylpropionate (2)

To a dry 500 mL Schlenk flask was added $ICH_2CH_2C(O)OCH_3$ (1.61 g, 7.5 mmol), 10 mL diethyl ether, and a Teflon-coated stir-bar. The light yellow solution was stirred under argon and cooled to –78°C. In a separate 100 mL Schlenk flask, sodium cyclopentadienide (0.660 g, 7.5 mmol) was dissolved in 10 mL THF and added slowly via canula. The mixture was allowed to reach room temperature and stirred overnight under argon. The resulting white suspension was quenched with 1 M NH_4Cl (100 mL), and

© 2002 NRC Canada

the organic phase was extracted with 3 × 20 mL of diethyl ether and dried over anhyd $MgSO_4$. Removal of the solvent gave a mixture of the 1-alkylCp (**2a**) and 2-alkylCp (**2b**) isomers as yellow liquids in a 1.2:1 ratio. The 5-alkyl isomer was not observed. Yield: 0.751 g (66%). Major isomer **2a** (1-alkylCp): ^{1}H NMR (*d*-chloroform) δ: 6.40 (m, 1H, Cp-*H*3), 6.26 (dq, 1H, Cp-*H*4, *J* = 5.1, 1.5 Hz), 6.03 (m, 1H, Cp-*H*2), 3.67 (s, 3H, C(O)OCH_3)), 2.95 (dd, 2H, Cp-*H*5), 2.72 (t, 2H, CH_2C(O)OCH$_3$, $^3J_{HH}$ = 8.1 Hz), 2.57 (m, 2H, CH_2CH$_2$C(O)OCH$_3$, *J* = 8.1 Hz). ^{13}C NMR δ: 173.69 (*C*(O)OCH$_3$), 145.29 (Cp-*C*1), 134.12 (Cp-*C*3), 131.04 (Cp-*C*4), 126.90 (Cp-*C*2), 41.35 (C(O)O*C*H$_3$), 41.34 (Cp-*C*5), 33.98 (CpCH$_2$*C*H$_2$C(O)), 25.09 (Cp*C*H$_2$CH$_2$C(O)). Minor isomer **2b** (2-alkylCp): ^{1}H NMR (*d*-chloroform) δ: 6.41 (m, 1H, Cp-*H*3, overlaps **2a**), 6.39 (dq,1H, Cp-*H*4, *J* = 5.1, 1.5 Hz), 6.17 (m, 1H, Cp-*H*1), 3.67 (s, 3H, C(O)OCH_3)), 2.89 (dd, 2H, Cp-*H*5), 2.72 (t, 2H, CH_2C(O)OCH$_3$, overlaps **2a**, $^3J_{HH}$ = 8.1 Hz), 2.57 (m, 2H, CH_2CH$_2$C(O)OCH$_3$, overlaps **2a**, *J* = 8.1 Hz). ^{13}C NMR δ: 173.69 (*C*(O)OCH$_3$, overlaps **2a**), 147.47 (Cp-*C*2), 132.32 (Cp-*C*1), 132.13 (Cp-*C*4, overlaps **2a**), 129.67 (Cp-*C*3), 43.28 (C(O)O*C*H$_3$), 41.34 (Cp-*C*5), 33.98 (CpCH$_2$*C*H$_2$C(O), overlaps **2a**), 25.88 (Cp*C*H$_2$CH$_2$C(O)).

3-Cyclopentadienyl-1,1-di(3,5-bis(trifluoromethyl)phenyl)propanol (3)

A 5 mL ethereal solution of **2** (1.76 g, 11.6 mmol) was added dropwise to a cold solution of Li[3,5-$C_6H_3(CF_3)_2$] (37.1 mmol) in 30 mL of diethyl ether (–78°C) with vigorous stirring. The resulting deep red solution was stirred for an additional 30 min at –78°C before quenching with 100 mL of aqueous NH_4Cl (1 M). The organic phase was extracted with 3 × 20 mL diethyl ether and dried over anhyd $MgSO_4$. Filtration and removal of solvent under vacuum afforded **3** as a yellow oil that contained the 1-alkyl and 2-alkyl isomers in a 1.2:1 ratio. The product was further dried for 1 day over 4 Å molecular sieves and stored as a 0.46 M toluene solution to avoid intermolecular Diels-Alder dimerization. Yield: 5.02 g (79%). Major isomer **3a** (1-alkylCp): ^{1}H NMR (d_6-benzene) δ: 7.79 (s, 4H, *o*-arylC*H*), 7.59 (s, 2H, *p*-arylC*H*), 6.16 (m, 1H, Cp-*H*3), 6.17 (dq, 1H, Cp-*H*4, *J* = 5.2, 1.4 Hz), 5.69 (m, 1H, Cp-*H*2), 2.67 (m, 2H, Cp-*H*5), 2.00 (m, 2H, CpCH$_2$CH_2CO), 1.92 (m, 2H, CpCH_2CH$_2$CO), 1.45 (s, 1H, CO*H*). ^{13}C NMR δ: 147.77 (*ipso*-aryl*C*), 146.98 (Cp-*C*1), 135.04 (Cp-*C*3), 132.15 (q, aryl*C*CF$_3$, $^2J_{CF}$ = 34 Hz), 131.84 (Cp-*C*4), 131.56 (Cp-*C*2), 125.88 (*o*-aryl*C*), 125.82 (q, *C*F$_3$, $^1J_{CF}$ = 236 Hz), 125.87 (*p*-aryl*C*, overlaps *o*-aryl*C*), 65.65 (*C*OH), 43.19 (Cp-*C*5), 41.37 (CH$_2$*C*H$_2$CO), 24.57 (*C*H$_2$CH$_2$CO). ^{19}F NMR δ: –63.09 (C*F*$_3$). Minor isomer **3b** (2-alkylCp): ^{1}H NMR (d_6-benzene) δ: 7.79 (s, 4H, *o*-arylC*H*, overlaps **3a**), 7.59 (s, 2H, *p*-arylC*H*, overlaps **3a**), 6.25 (m, 1H, Cp-*H*3, overlaps **3a**), 6.34 (dq, 1H, Cp-*H*4, *J* = 5.3, 1.5 Hz), 5.91 (m, 1H, Cp-*H*1), 2.44 (q, 2H, Cp-*H*5), 2.00 (m, 2H, CpCH$_2$CH_2CO, overlaps **3a**), 1.92 (m, 2H, CpCH_2CH$_2$CO, overlaps **3a**), 1.37 (s, 1H, CO*H*). ^{13}C NMR δ: 148.83 (*ipso*-aryl*C*), 146.98 (Cp-*C*2, overlaps **3a**), 133.60 (Cp-*C*1), 132.14 (q, *C*CF$_3$, $^2J_{CF}$ = 34 Hz, overlaps **3a**), 131.80 (Cp-*C*4), 131.56 (Cp-*C*3, overlaps **3a**), 125.88 (*o*-aryl*C*), 125.82 (q, *C*F$_3$, $^1J_{CF}$ = 236 Hz, overlaps **3a**), 125.87 (*p*-aryl*C*, overlaps *o*-aryl*C*), 65.65 (*C*OH, overlaps **3a**), 41.08 (Cp-*C*5), 40.26 (CH$_2$*C*H$_2$CO), 24.57 (*C*H$_2$CH$_2$CO, overlaps **3a**). ^{19}F NMR δ: –63.09 (C*F*$_3$, **3a** and **3b**). LSI-MS *m/z* (%): 548 ([M]$^+$, 22), 530 ([M$^+$ – H$_2$O], 60), 240 ($C_6H_3(CF_3)_2CO$, 100), 213 ($C_6H_3(CF_3)_2C$, 50).

$C_4H_6CH_2CH_2C(O)(3,5\text{-}C_6H_3(CF_3)_2)_2$ (4)

A 10 mL toluene solution of **3** (1.02 g) became turbid after storage for 3 days at room temperature. Removal of toluene and recrystallization from hexane at room temperature produced long colorless prisms of the intramolecularly cyclized product **4**. Monitoring this reaction by ^{1}H NMR showed that cyclization was detectable after 2 days and essentially complete after 3 days for a dilute solution (0.03 M) in d_6-benzene at 22°C. Cyclization can be minimized by storage of dilute solutions of **3** in toluene at –30°C. Yield: 0.66 g (60%). ^{1}H NMR (d_6-benzene) δ: 7.94 (s, 2H, *o*-arylCH_a), 7.91 (s, 2H, *o*-arylCH_b), 7.57 (s, 2H, *p*-arylC$H_{a,b}$), 5.61 (m, 1H, C2-*H*, *J* = 5.5, 2.4 Hz), 5.38 (m, 1H, C3-*H*, *J* = 5.5, 2.4 Hz), 2.20 (m, 1H, C4-H_a, *J* = 5.5 Hz), 1.93 (t, 2H, C1-CH$_2$CH_2CO, $^3J_{HH}$ = 6.6 Hz), 1.92 (m, 1H, C4-H_b), 1.92 (m, 1H, C5-H_a), 1.47 (m, 1H, C5-H_b, *J* = 2.4 Hz), 1.33 (t, 2H, C1-CH_2CH$_2$CO, $^3J_{HH}$ = 6.6 Hz). ^{13}C NMR δ: 149.51 (*ipso*-arylC_a), 149.44 (*ipso*-arylC_b), 134.74 (*C*1), 134.17 (*C*2), 132.20 (q, *C*CF$_3$, $^2J_{CF}$ = 33 Hz), 125.83 (*o*-aryl*C*), 125.20 (q, *C*F$_3$, $^1J_{CF}$ = 273 Hz), 121.48 (*p*-aryl*C*), 97.03 (*C*OH), 86.127 (*C*3), 39.63 (CH$_2$*C*H$_2$CO), 37.57 (*C*4), 36.48 (*C*5), 30.89 (*C*H$_2$CH$_2$CO). ^{19}F NMR δ: –62.85 (C$F_{3a,b}$). EI-MS *m/z* (%): 548 ([M]$^+$, 100), 455 ([M$^+$ – F], 42), 241 (3,5-$C_6H_3(CF_3)_2CO$, 40).

$\{\eta^5\text{:}\eta^1\text{-}C_5H_4[CH_2CH_2C(O)(3,5\text{-}C_6H_3(CF_3)_2)_2]\}YCl\{THF\}_n$ (5a: *n* = 2, 5b: *n* = 1)

A 60 mL thick-walled Schlenk flask with a Teflon stopcock was charged with Y[N(SiMe$_3$)$_2$]$_3$ (0.352 g, 0.618 mmol), YCl_3 (0.060 g, 0.309 mmol), and 10 mL THF under an argon atmosphere. The flask was sealed and stirred at 80°C for 2 h. The colourless solution of {Y[N(SiMe$_3$)$_2$]$_2$(THF)$_2$(μ-Cl)}$_2$, formed in situ, was then cooled to –20°C and a 10 mL toluene solution of **3** (0.508 g, 0.927 mmol) was added slowly via syringe. The solution was once again sealed and heated at 80°C for 2 h, becoming more yellow in colour. Solvent was then removed in vacuo, and the off-white solid recrystallized from hot toluene in the glovebox, yielding the chloride (**5**) as small white nodules. Yield: 0.549 g (80%); mp 189 to 190°C. ^{1}H NMR (d_6-benzene – d_8-THF, 5:1) δ: 8.18 (s, 4H, *o*-aryl*H*), 7.67 (s, 2H, *p*-aryl*H*), 6.28 (br s, 2H, Cp*H*), 5.87 (br s, 2H, Cp*H*), 3.55 (m, 8H, α-THF *H*), 2.54 (br s, 2H, CH$_2$CH_2CO), 2.45 (br s, 2H, CH_2CH$_2$CO), 1.43 (m, 8H, β-THF *H*). ^{13}C NMR δ: 154.39 (*ipso*-aryl*C*), 131.30 (q, *C*CF$_3$, $^2J_{CF}$ = 32 Hz), 127.13 (*o*-aryl*C*), 126.30 (Cp-*C*1), 124.00 (q, *C*F$_3$, $^1J_{CF}$ = 283 Hz), 120.35 (*p*-aryl*C*), 111.01 (Cp*C*), 110.45 (Cp*C*), 79.49 (*C*OY), 67.48 (α-THF *C*), 42.55 (CH$_2$*C*H$_2$CO), 25.63 (*C*H$_2$CH$_2$CO), 24.57 (β-THF *C*). ^{19}F NMR δ: –62.58 (C*F*$_3$). Anal. calcd for (*mono*(THF) adduct **5b**) $C_{28}H_{22}ClF_{12}O_2Y$ (%): C 45.26, H 2.98; found: C 43.98, H 3.24.

$\{\eta^5\text{:}\eta^1\text{-}C_5H_4[CH_2CH_2C(O)(3,5\text{-}C_6H_3(CF_3)_2)_2]\}Y\{N(SiMe_3)_2\}\{THF\}_n$ (6a: *n* = 2, 6b: *n* = 1)

An Erlenmeyer flask was charged with **5** (0.122 g, 0.160 mmol) and 20 mL of toluene in the glovebox. To the rapidly stirred sticky suspension was added a 10 mL toluene

© 2002 NRC Canada

solution of $NaN(SiMe_3)_2$ (0.030 g, 0.16 mmol). The suspension was stirred at 70°C for 2 h, during which time the solids became white and free-flowing. Filtration through Celite on a glass frit and removal of solvent in vacuo gave the product as a crude yellow solid. Recrystallization of this solid from a toluene–hexane mixture gave pure **6** as a white powder. Yield: 0.090 g (65%); mp 135 to 136°C. **6a** (*bis*(THF) adduct): ^{1}H NMR (d_6-benzene) δ: 7.88 (s, 4H, *o*-aryl*H*), 7.63 (s, 2H, *p*-aryl*H*), 6.24 (t, 2H, Cp*H*, $^3J_{HH}$ = 2.5 Hz), 5.82 (t, 2H, Cp*H*, $^3J_{HH}$ = 2.5 Hz), 3.58 (m, 8H, α-THF *H*), 2.32 (br s, 4H, CH_2CH_2CO, CH_2CH_2CO), 1.27 (m, 8H, β-THF *H*), 0.09 (s, 18H, SiMe_3). ^{13}C NMR δ: 153.40 (*ipso*-aryl*C*), 131.17 (q, CCF_3, $^2J_{CF}$ = 33 Hz), 129.73 (Cp-*C*1), 126.28 (*o*-aryl*C*), 123.90 (q, CF_3, $^1J_{CF}$ = 273 Hz), 120.23 (*p*-aryl*C*), 110.91 (Cp*C*), 110.82 (Cp*C*), 78.89 (*C*OY), 70.46 (α-THF *C*), 43.04 (CH_2CH_2CO), 24.85 (β-THF *C*), 23.40 (CH_2CH_2CO), 4.50 (SiMe_3). ^{19}F NMR δ: –62.54 (CF_3). ^{29}Si NMR δ: –10.22 (*Si*Me_3).

Exposure of **6a** to vacuum for extended periods of time resulted in the loss of one THF molecule to give **6b**. The NMR data for **6b** were essentially identical to those for **6a**, with the exception that the THF resonances integrated to only 4H each rather than 8H. Anal. calcd for (**6b**) $C_{34}H_{40}F_{12}NO_2Si_2Y$ (%): C 47.06, H 4.65, N 1.61; found: C 46.12, H 4.55, N 1.55.

{η^5:η^1-C_5H_4[CH_2CH_2C(O)(3,5-$C_6H_3(CF_3)_2)_2$]}Y{O-2,6-*t*-$Bu_2C_6H_3$}{THF}$_n$ (7a: *n* = 2, 7b: *n* = 1)

Crude **7** was isolated as a white solid using a procedure analogous to **6** (0.300 g, 0.368 mmol), starting from **5** and Li(O-2,6-*t*-$Bu_2C_6H_3$) (0.088 g, 0.368 mmol). Repeated recrystallization from hexane at –30°C produced **7a** as small colourless crystals. Exposure to vacuum overnight produced the *mono*(THF) adduct (**7b**) with the same NMR data, suggesting fast exchange of the remaining THF. Yield: 0.271 g (75%); mp 110 to 111°C. ^{1}H NMR (d_6-benzene) δ: 7.80 (s, 4H, *o*-aryl*H*), 7.61 (s, 2H, *p*-aryl*H*), 7.32 (d, 2H, *m*-phenoxide *H*, $^3J_{HH}$ = 8.1 Hz), 6.83 (t, 1H, *p*-phenoxide *H*, $^3J_{HH}$ = 8.1 Hz), 6.22 (t, 2H, Cp*H*, $^3J_{HH}$ = 2.9 Hz), 5.82 (t, 2H, Cp*H*, $^3J_{HH}$ = 2.9 Hz), 3.34 (m, 8H, α-THF *H*), 2.52 (br t, 2H, CH_2CH_2CO), 2.37 (t, 2H, CH_2CH_2CO, $^3J_{HH}$ = 5.1 Hz), 1.47 (s, 18H, CMe_3), 1.08 (m, 8H, β-THF *H*). ^{13}C NMR δ: 162.22 (d, *ipso*-phenoxide *C*, $^2J_{YC}$ = 5.0 Hz), 154.24 (*ipso*-aryl*C*), 137.60 (*o*-phenoxide *C*), 131.64 (q, CCF_3, $^2J_{CF}$ = 32 Hz), 129.25 (Cp-*C*1), 126.62 (*m*-phenoxide *C*), 125.47 (*o*-aryl*C*), 123.71 (q, CF_3, $^1J_{CF}$ = 273 Hz), 121.82 (*p*-aryl*C*), 116.95 (*p*-phenoxide *C*), 111.42 (Cp*C*), 110.97 (Cp*C*), 79.18 (d, *C*OY, $^2J_{YC}$ = 3.8 Hz), 71.60 (α-THF *C*), 42.58 (CH_2CH_2CO), 34.89 (CMe_3), 31.22 (CMe_3), 24.80 (β-THF *C*), 23.96 (CH_2CH_2CO). ^{19}F NMR δ: –62.47 (CF_3). Anal. calcd for (*mono*(THF) adduct **7b**) $C_{42}H_{43}F_{12}O_3Y$ (%): C 55.27, H 4.75; found: C 54.03, H 4.90.

{η^5:η^1-C_5H_4[CH_2CH_2C(O)(3,5-$C_6H_3(CF_3)_2)_2$]}Y{CH-$(SiMe_3)_2$}{THF}$_n$ (8a: *n* = 2, 8b: *n* = 1)

Crude **8a** was isolated as a white solid using a procedure analogous to that used for **6**, starting from **5** (0.100 g, 0.122 mmol) and $LiCH(SiMe_3)_2$ (0.0203 g, 0.122 mmol). Repeated recrystallization from hexane at –30°C produced **8a** as a white microcrystalline solid. Exposure to vacuum overnight produced the *mono*(THF) adduct (**8b**). In solution, **8b** shows fluxional behavior, as evidenced by broadened resonances observed in the ^{1}H NMR spectrum. These broadened lines sharpen at higher temperatures (+80°C). Yield: 0.069 g (60%); mp 102 to 103°C. ^{1}H NMR (d_6-benzene) δ: 7.90 (br s, 4H, *o*-aryl*H*), 7.63 (br s, 2H, *p*-aryl*H*), 6.20 (br m, 2H, Cp*H*), 5.79 (br s, 2H, Cp*H*), 3.35 (m, 8H, α-THF *H*), 2.25 (br s, 2H, CH_2CH_2CO), 2.24 (br s, 2H, CH_2CH_2CO, overlaps preceding CH_2), 1.11 (m, 8H, β-THF *H*), 0.15 (s, 18H, SiMe_3), –1.11 (d, 1H, C*H*$(SiMe_3)_2$, $^2J_{YH}$ = 4.3 Hz). ^{13}C NMR δ: 152.81 (*ipso*-aryl*C*), 131.26 (q, CCF_3, $^2J_{CF}$ = 33 Hz), 126.20 (*o*-aryl*C*), 123.63 (q, CF_3, $^1J_{CF}$ = 273 Hz), 120.39 (*p*-aryl*C*), 111.39 (Cp*C*), 111.39 (overlapping Cp*C*), 78.92 (*C*OY, $^2J_{YC}$ = 3.7 Hz), 70.78 (α-THF *C*), 43.77 (CH_2CH_2CO), 24.50 (β-THF *C*), 23.27 (CH_2CH_2CO), 32.37 (d, *C*H$(SiMe_3)_2$, $^1J_{CY}$ = 39 Hz), 25.07 (β-THF *C*), 4.54 (SiMe_3). ^{19}F NMR δ: –62.53. ^{29}Si NMR δ: –7.56 (*Si*Me_3, $^2J_{YSi}$ = 1.6 Hz). Anal. calcd for (*mono*(THF) adduct **8b**) $C_{35}H_{41}F_{12}O_2Si_2Y$ (%): C 48.49, H 4.77; found: C 45.88, H 4.43.

X-ray crystallography

Crystals of **4** and **6b** were isolated from hexane and a toluene–hexane mixture, respectively. The crystals were placed in mineral oil under an atmosphere of argon and sealed in a glass capillary. Data were collected on a Siemens Smart 1000 (**4**) or a Nonius CAD 4F diffractometer (**6b**) equipped with graphite monochromated Mo Kα or Cu Kα radiation at 293 K, respectively. Structure solutions were carried out using teXsan98 (15) and refinement was done on *F*. Refinement of **4** was plagued by severe disorder problems and was only sufficient to establish the connectivity of the molecule.[3]

The data for **6b** were corrected for Lorentz and polarization effects, and a correction for secondary extinction was applied (coefficient = $2.91(4) \times 10^{-6}$). An empirical absorption correction was applied (absorption range: 0.92 – 1.00). Refinement proceeded normally although, as usual, rotational disorder of the CF_3 groups was observed. This was modeled successfully by allowing the six 0.5 occupancy fluorine atoms and the carbon of each CF_3 group to refine isotropically. The weak data set obtained for this crystal prevented anisotropic refinement of these atoms owing to the low data-to-parameter ratio. Hydrogen atoms were included in idealized positions and were not refined. The final Fourier difference maps showed maximum and minimum peaks of +0.66 and –0.52 e Å^{-3}, respectively, all in the vicinity of the disordered CF_3 groups. Thermal ellipsoid plots were drawn with ORTEP3 (16).

Results

Since the epoxide ring-opening route used to prepare **1** could not be used to prepare Cp-alkoxides with an extended

[3] Supplementary data may be purchased from the Depository of Unpublished Data, Document Delivery, CISTI, National Research Council Canada, Ottawa, ON K1A 0S2, Canada (http://www.nrc.ca/cisti/irm/unpub_e.shtml for information on ordering electronically). CCDC contains the supplementary data for this paper. These data can be obtained, free of charge, via www.ccdc.cam.ac.uk/conts/retrieving.html (or from the Cambridge Crystallographic Data Centre, 12 Union Road, Cambridge, U.K.; fax +44 1223 336033; or deposit@ccdc.cam.ac.uk).

© 2002 NRC Canada

Scheme 1. (*a*) NaCp, THF–Et_2O, –78°C; (*b*) NaI, acetone, 24 h; (*c*) 3.2 equiv Li(3,5-$C_6H_3(CF_3)_2$), THF–Et_2O, –78°C.

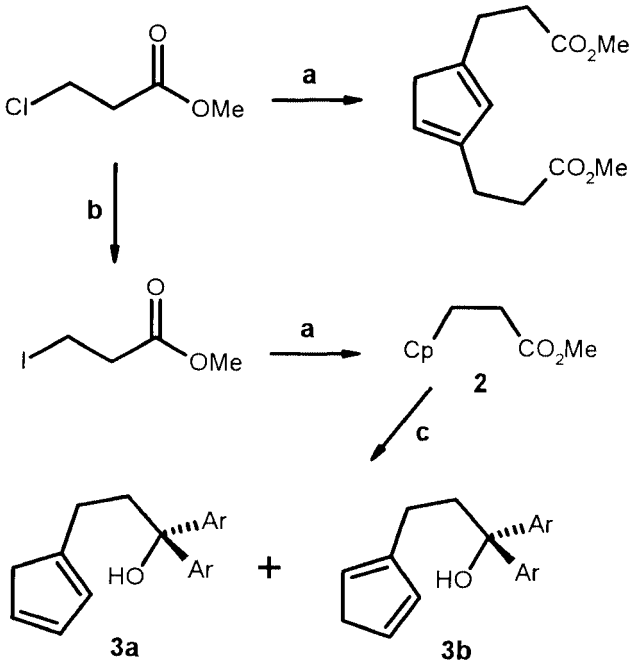

backbone, a new ligand synthesis was developed (Scheme 1). Although the three-step synthesis gives an overall yield of 55%, highly specific conditions are required in each step to achieve these results. The use of the iodo-ester and sodium cyclopentadienide appears to be critical in obtaining the desired cyclopentadienyl ester (**2**). We found that if the commercially available chloroester or the bromoester was not converted to the iodide, the diester $C_5H_4(CH_2CH_2C(O)OMe)_2$ was produced as the major product, rather than **2**. This was observed regardless of the addition rate or reaction temperatures. Similar disubstituted products have been observed by Peters (17) when RC(O)Cl was treated with NaCp. Selective substitution at the CH_2I group occurred with NaCp; use of LiCp resulted in a mixture of products. The crude ester was distilled under static vacuum (ca. 1 torr (1 torr = 133.322 Pa)) to give **2** as a yellow liquid containing a 1.2:1 mixture of the 1-alkyl and 2-alkyl isomers. The two fluorinated phenyl groups were incorporated at the ester carbon by the addition of 3,5-*bis*(trifluoromethyl)phenyl lithium to **2**. Three equiv of the lithium salt must be used because deprotonation of the cyclopentadienyl group occurs readily. Following hydrolysis of the reaction mixture, **3** was isolated as a pure yellow oil, again containing the 1-alkyl and 2-alkyl substituted isomers in 1.2:1 ratio.

The protonated ligand **3** must be stored at –30°C as a dilute toluene solution (<0.5 M) to avoid irreversible transformation products. As a neat oil, **3** undergoes the expected Diels-Alder cyclization in a period of about 1 week at room temperature. Even in dilute solution (0.5 M), however, the 2-alkyl substituted isomer (**3b**) undergoes alcohol addition across one double bond of the diene in Markovnikov fashion, to give the spirocyclic ether **4** (eq. [1]). The identity of **4** was initially determined by ^{13}C DEPT, which identified four inequivalent CH_2 carbons, and ^1H-^1H COSY experiments,

Fig. 1. ORTEP3 (16) plot for **4** (30% probability, fluorine atoms omitted for clarity).

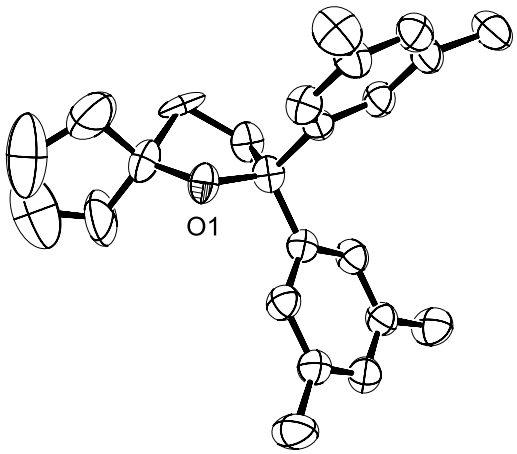

which established connectivity of all protons observed in the ^1H NMR. The structure of **4** was unequivocally established by an X-ray diffraction study, although the quality of the X-ray data was only sufficient to establish connectivity (Fig. 1). This result was unexpected since tertiary alcohols are generally inactive to alkene addition. Some intramolecular additions of primary or secondary alcohols have been observed, but in the presence of palladium or rhenium compounds (18). The electron withdrawing properties of the *meta*-CF_3 groups of the phenyls presumably promote the cyclization of **3**, which occurs spontaneously at room temperature. The Diels-Alder reaction is competitive with the intramolecular cyclization only at higher concentrations (>0.5 M) of ligand.

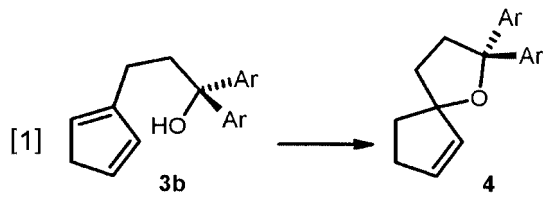

On a smaller scale, the cleanest and most straightforward way to access yttrium complexes containing the deprotonated form of ligand **3** is to prepare the chloride complex (CpO)YCl(THF)$_n$ (**5a**: n = 2; **5b**: n = 1, HCpOH = **3**) from **3** and $[Y\{N(SiMe_3)_2\}_2(THF)(\mu\text{-}Cl)]_2$, where the latter is prepared in situ from YCl_3 and $Y[N(SiMe_3)_2]_3$ in THF (Scheme 2). Reactions under 1 mmol in scale afford **5** in high yield (70–80%), but larger scale reactions generate oily by-products that must be separated by recrystallization from toluene–hexane mixtures. In general, all yttrium complexes containing the Cp-alkoxide derived from **3** exhibit lower melting points and much higher solubilities in hydrocarbons than their analogues derived from **1** (6). These observations suggest that intermolecular packing interactions or weak bridging interactions have been disrupted by the addition of another CH_2 unit in the ligand backbone.

Reaction of **5** with 1 equiv of $NaN(SiMe_3)_2$ initially forms a silyamide complex as the *bis*(THF) adduct (**6a**) (Scheme 2), which readily loses one coordinated THF to give the *mono*(THF) adduct (**6b**) under vacuum. NMR data

© 2002 NRC Canada

Scheme 2. (*a*) THF, 80°C, 2 h; (*b*) $NaN(SiMe_3)_2$, toluene, 70°C, 2 h; (*c*) $Li(O\text{-}2,6\text{-}C_6H_3(t\text{-}Bu)_2)$, toluene, 20°C, 2 h; (*d*) $LiCH(SiMe_3)_2$, toluene, 20°C, 2 h.

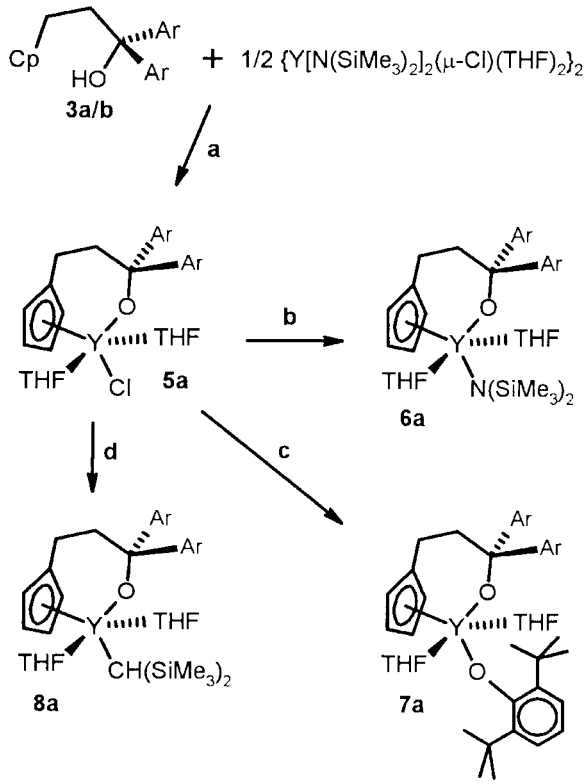

supports mirror plane symmetry for the *bis*(THF) complex (**6a**). Chemical shifts are essentially unchanged between the *bis* and *mono*(THF) adducts, suggesting that exchange of coordinated THF is rapid at room temperature. The two methylene carbons of the backbone show distinct resonances in the ^{13}C NMR, but their respective proton resonances are coincidental and show a broad singlet of integration 4 at δ = 2.32 ppm in the ^1H NMR.

X-ray quality crystals of **6b** were obtained through slow evaporation of a hexane solution of the *bis*(THF) adduct **6a**. The solid-state structure of **6b** is shown in Fig. 2, crystallographic data are summarized in Table 1, and selected bond distances and angles are presented in Table 2. The geometry at yttrium is best described as pseudo-tetrahedral with a single THF occupying the fourth coordination site. The formal coordination number at yttrium is 6, reduced from the 7-coordinate environment found in $\{\eta^5\text{:}\eta^1\text{-}C_5H_4[CH_2C(O)(3,5\text{-}C_6H_3(CF_3)_2)_2]\}Y\{O\text{-}2,6\text{-}t\text{-}Bu_2C_6H_3\}\{THF\}_2$ (6). The bite angle of the Cp^{cent}-Y-O (105.3(9)°) unit in **6b** is opened significantly compared with the phenoxide above Cp^{cent}-Y-O (93.77(13)°) or $\{\eta^5\text{:}\eta^1\text{-}C_5H_4[CH_2C(O)(3,5\text{-}C_6H_3(CF_3)_2)_2]\}_2Y^-\ Li^+\{THF\}_2$ Cp^{cent}-Y-O (95.69(13)°), as expected for the increased backbone chain length. This change is more dramatic than that seen in the analogous amido systems $[Y(\eta^5\text{:}\eta^1\text{-}C_5Me_4SiMe_2NCMe_3)(\mu\text{-}H)(THF)]_2$ (4(*e*)) and $[Y(\eta^5\text{:}\eta^1\text{-}C_5Me_4CH_2SiMe_2NCMe_3)(\mu\text{-}H)(THF)]_2$ (11), where the change in bite angle was only 7.0°. The average Y—Cp^{cent} distance is 2.339(14) Å, slightly shorter than that in $\{\eta^5\text{:}\eta^1\text{-}C_5H_4[CH_2C(O)(3,5\text{-}C_6H_3(CF_3)_2)_2]\}Y\{O\text{-}2,6\text{-}t\text{-}Bu_2C_6H_3\}\{THF\}_2$ (Y—Cp^{cent} = 2.400(5) Å) as a consequence of the reduced coordination number (CN) of **6b** (Y^{3+}: 1.04 Å, CN 6; 1.10 Å, CN 7). The yttrium nitrogen bond length Y(1)—N(1) of 2.207(8) Å of the *bis*(trimethylsilyl)amido group is comparable to that found in the homoleptic silylamide $Y[N(SiMe_3)_2]_3$ (Y—N 2.224(6) Å) (19).

Fig. 2. ORTEP3 (16) plot for **6b** (40% probability, fluorine atoms omitted for clarity).

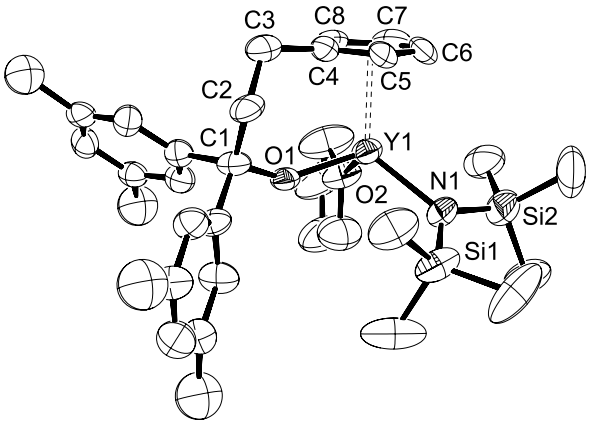

Table 1. Crystallographic data for **6b**.

	6b
Empirical formula	$C_{34}H_{40}F_{12}NO_2Si_2Y$
Formula weight	867.75
Crystal system	Monoclinic
Space group	$P2_1/a$ (No. 14)
a (Å)	10.3467(7)
b (Å)	33.260(3)
c (Å)	12.603(2)
β (°)	108.118(10)
V (Å^3)	4122.1(8)
Z	4
$D_{calcd.}$ (g cm^{-3})	1.40
Absorption coefficient (μ) (cm^{-1})	33.1
Radiation, λ (Å)	Cu Kα, 1.5418
T (K)	293
$2\theta_{max}$ (°)	100.0
Reflections collected	4570
Independent reflections	4330
R^a, $R_w{}^b$	0.074, 0.040

$^aR = \Sigma(|F_o|\text{-}|F_c|)/\Sigma|F_o|$.
$^bR_w = [\Sigma w(|F_o|\text{-}|F_c|^2)/\Sigma w(|F_o|)^2]^{1/2}$.

The phenoxide **7a** was formed cleanly from the reaction of **5** with 1 equiv of $LiO\text{-}2,6\text{-}t\text{-}Bu_2C_6H_3$ (Scheme 2) as the *bis*(THF) adduct, according to ^1H NMR spectroscopy. Coupling to ^{89}Y was observed in the ^{13}C NMR for both the *ipso*-phenoxide ($^2J_{YC}$ = 5.0 Hz) and the ligand YO*C* ($^2J_{YC}$ = 3.8 Hz) carbons. Elemental analysis supports facile loss of THF, as only the *mono*(THF) adduct (**7b**) was observed after exposure to vacuum.

Replacement of the phenoxide with more reactive hydrocarbyls was not successful by metathesis with $LiCH(SiMe_3)_2$ or $LiCH_2SiMe_3$, as the complex would not eliminate lithium phenoxide. Reaction of **5** with 1 equiv of

© 2002 NRC Canada

Table 2. Selected bond distances (Å) and angles (°) for **6b**.

Bond distances			
Y1—O1	2.060(6)	Y1—O2	2.299(7)
Y1—N1	2.207(8)	Y1—C4	2.627(11)
Y1—C5	2.610(10)	Y1—C6	2.603(11)
Y1—C7	2.629(12)	Y1—C8	2.640(11)
Y1—Cp^{cent} [a]	2.339(14)		
Bond angles			
Cp^{cent}-Y1-O1	105.3(9)	Cp^{cent}-Y1-O2	114.0(5)
Cp^{cent}-Y1-N1	122.5(9)	O1-Y1-O2	92.8(3)
O1-Y1-N1	113.3(3)	O2-Y1-N1	104.8(3)
Y1-O1-C1	145.1(6)	Y1-N1-Si1	119.6(4)
Y1-N1-Si2	118.4(5)	Si1-N1-Si2	121.9(5)

[a] Cp^{cent} represents the centroid of the C5 ring (C4-C8).

$LiCH(SiMe_3)_2$, however, readily forms the alkyl complex **8a** (Scheme 2) as a *bis*(THF) adduct, which again loses THF under vacuum to give a *mono*(THF) adduct (**8b**). Complex **8b** was produced in good yield, and both elemental analysis and NMR confirmed the degree of THF solvation. The Cp region of the ^{1}H NMR spectrum of **8b** is broadened somewhat at room temperature, but it sharpens to a pair of multiplets at 80°C, consistent with mirror plane symmetry. Amazingly, no noticeable decomposition of the alkyl complex was observed with repeated heating during the VT analysis. This is an interesting observation, since alkyl complexes of lanthanides are usually thermally unstable. Yttrium coupling was again observed for the alkoxy carbon of the ligand ($^2J_{YC}$ = 3.7 Hz) in the ^{13}C NMR of **8b**.

Discussion

Changing the length of the tether connecting the Cp and alkoxide functionality in the CpO ligand system has profound effects on the type of lanthanide complexes obtained. Extension of the chain by just one CH_2 unit (going from ligands based on **1** (6) to those based on **3**) completely avoids the problems associated with formation of anionic "ate" complexes. In fact, despite repeated attempts, we could not prepare the *bis*(ligand) "ate" complex $(CpO)_2Y^-$ Li^+ for the CpO ligand containing a two-carbon tether, whereas we had great difficulty *avoiding* this complex for the one-carbon tether ligand **1**. The neutral complexes (**5**–**8**) obtained here with the two-carbon tether show no tendency to undergo ligand redistribution reactions.

Despite the success in obtaining neutral, monomeric yttrium complexes, however, silylamide **6b** is not an active catalyst for ε-caprolactone polymerization, and the alkyl **8b** shows very modest oligomerization activity only. Complex **8b** shows no activity as an olefin polymerization catalyst. The reasons for this are not entirely clear, although the presence of coordinated THF may be expected to decrease activity. Related $(CpO)ZrCl_2$ complexes show very high ethylene polymerization activity for complexes containing the shorter tether (ligand **1**) (20),[4] so it seems unlikely that the perfluorophenyl substituted alkoxide is itself detrimental to insertion. Studies to examine the effects of longer chain tethers and replacement of the CF_3 substituents with CH_3 groups are continuing. We hope that these studies will clarify the reasons for the low insertion activity observed here. In addition, we are also investigating the use of complexes like **5** and **7** as Lewis acid catalysts.

Acknowledgements

We thank Mrs. C. Greenwood for assistance in recording the NMR spectra and Dr. David McGillivray for obtaining the mass spectra. This research was supported by the Natural Sciences and Engineering Research Council of Canada (NSERC) and a University of Victoria Internal Research Grant (to D.J.B.).

References

1. Leading references can be found in: (*a*) R. Vollmerhaus, M. Rahim, R. Tomaszewski, S. Xin, N.J. Taylor, and S. Collins. Organometallics, **19**, 2161 (2000); (*b*) A. Martin, R. Uhrhammer, T. G. Gardner, R.F. Jordan, and R.D. Rogers. Organometallics, **17**, 382 (1998); (*c*) A.K. Hughes, A. Meetsma, and J.H. Teuben. Organometallics, **12**, 1936 (1993). (*d*) L. Lee, D.J. Berg, F.W.B. Einstein, and R.J. Batchelor. Organometallics, **16**, 1819 (1997).
2. For leading references see: (*a*) J. Okuda. Comments Inorg. Chem. **16**, 185 (1994); (*b*) J. Okuda and T. Eberle. *In* Metallocenes: synthesis, reactivity, application. Vol. 1. *Edited by* A. Togni and R.A. Halterman. Wiley-VCH, New York. 1998. Chap 7; (*c*) K.C. Hultzsch, P. Voth, P. Beckerle, T.P. Spaniol, and J. Okuda. Organometallics, **19**, 228 (2000).
3. (*a*) P.J. Shapiro, W.D. Cotter, W.P. Schaefer, J.E. Labinger, and J.E. Bercaw. J. Am. Chem. Soc. **116**, 4623 (1994); (*b*) W.A. Herrmann and M.J.A. Moraweitz. J. Organomet. Chem. **482**, 1 (1994); (*c*) W.A. Herrmann, W. Baratta, and M.J.A. Moraweitz. J. Organomet. Chem. **497**, C4 (1995); (*d*) W.A. Herrmann, M.J.A. Moraweitz, and W. Baratta. J. Organomet. Chem. **506**, 357 (1996); (*e*) P.-J. Sinnema, L. van der Veen, A.L. Spek, N. Veldman, and J.H. Teuben. Organometallics, **16**, 4245 (1997), and refs. therein.
4. (*a*) Y. Mu, W.E. Piers, M.-A. MacDonald, and M.J. Zaworotko. Can. J. Chem. **73**, 2233 (1995); (*b*) K.C. Hultzsch, T.P. Spaniol, and J. Okuda. Organometallics, **16**, 4845 (1997); (*c*) K.C. Hultzsch and J. Okuda. Macromol. Rapid Commun. **18**, 809 (1997); (*d*) K.C. Hultzsch, T.P. Spaniol, and J. Okuda. Organometallics, **17**, 485 (1998); (*e*) K.C. Hultzsch, T.P. Spaniol, and J. Okuda. Angew. Chem. Int. Ed. Engl. **38**, 227 (1999).
5. (*a*) F.T. Edelmann, *In* Comprehensive Organometallic Chemistry II; *Edited by* M.F. Lappert. Pergamon, London, 1995, Vol. 4, Chapter 2. (*b*) G. Molander, H. Schumann, E.C.E. Rosenthal, and J. Demtschuk. Organometallics, **15**, 3817 (1996); (*c*) C. Qian, C. Zhu, Y. Lin, and Y. Xing. J. Organomet. Chem. **507**, 41 (1996); (*d*) C. Qian, B. Wang, D. Deng, J. Sun, F. E. Hahn, J. Chen, and P. Zhang. J. Chem. Soc. Dalton Trans. 955 (1996); (*e*) A.A. Trifonov, P. van de Weghe, J. Collin, A. Domingos, and I. Santos. J. Organomet. Chem. **527**, 225 (1997); (*f*) H. Schumann, F. Erbstein, R. Weimann, and J. Demtschuk. J. Organomet. Chem. **536**, 541 (1997);

[4] $(CpO)ZrCl_2$, 1000 equiv MAO, 50°C, 3 atm ethylene: 4500 kg polyethylene [mol Zr]$^{-1}$ h^{-1} (M_w = 7.5 × 10^5 amu, M_w/M_n = 3.5) for CpO = $C_5H_4(CH_2)C(O)(3,5\text{-}C_6H_3(CF_3)_2)$; 80 kg polyethylene [mol Zr]$^{-1}$ h^{-1} for CpO = $C_5H_4(CH_2CH_2)C(O)(3,5\text{-}C_6H_3(CF_3)_2)$.

© 2002 NRC Canada

(*g*) H. Schumann, E.C.E. Rosenthal, J. Demtschuk, and G. Molander. Organometallics, **17**, 5324 (1998); (*h*) C. Qian, G. Zou, and J. Sun. J. Chem. Soc. Dalton Trans. 1607 (1998); (*i*) M.N. Bochkarev, I.L. Fedushkin, V.I. Nevodchikov, A.V. Protchenko, H. Schumann, and F. Girgsdies. Inorg. Chim. Acta **280**, 138 (1998); (*j*) H. Schumann, F. Erbstein, D.F. Karasiuk, I.L. Fedushkin, J. Demtschuk, and F. Girgsdies. Z. Anorg. Allg. Chem. **625**, 781 (1999); (*k*) C. Qian, G. Zou, and J. Sun. J. Chem. Soc. Dalton Trans. 519 (1999); (*l*) Q. Liu, J. Huang, Y. Qian, and A.C.S. Chan. Polyhedron **18**, 2345 (1999).

6. R.A.L. Gendron, D. J. Berg, P. Shao, and T. Barclay. Organometallics, **20**, 4279 (2001).
7. K.N. Harrison and T.J. Marks, J. Am. Chem. Soc. **114**, 9220 (1992).
8. (*a*) C.M. Fendrick, L.D. Schertz, V.W. Day, and T.J. Marks. Organometallics, **7**, 1828 (1988); (*b*) H. Schumann, L. Esser, J. Loebel, A. Dietrich, D. van der Helm, and X. Ji. Organometallics, **10**, 2585 (1991).
9. (*a*) C. Qian and G. Zou. J. Chem. Soc. Dalton Trans. 1599 (1994); (*b*) C. Qian, Z. Xie, and Y. Huang. J. Organomet. Chem. **323**, 285 (1987); (*c*) C. Qian, Z. Xie, and Y. Huang. J. Organomet. Chem. **398**, 251 (1990); (*d*) C. Qian, Z. Xie, and Y. Huang. J. Organomet. Chem. **412**, 61 (1991); (*e*) G. Paolucci, R.D. D'Ippolito, C. Ye, C. Qian, J. Graper, and R.D. Fischer. J. Organomet. Chem. **471**, 97 (1994); (*f*) C. Qian, G. Zou, and L. Gao. J. Organomet. Chem. **525**, 23 (1996); (*g*) C. Qian, G. Zou, J. Sun, and Y. Chen. Organometallics, **20**, 3106 (2001); (*h*) C. Qian and D. Zhu. J. Organomet. Chem. **445**, 79 (1993).
10. A. Trifonov, F. Ferri, and J. Collin. J. Organomet. Chem. **582**, 211 (1999).
11. A. Trifonov, T.P. Spaniol, and J. Okuda. Organometallics, **20**, 4869 (2001).
12. C.P. Casey, J.A. Tunge, T.U. Lee, and D.W. Carpenetti. Organometallics, **21**, 389 (2002).
13. S. Kulstad and L.A. Malmstein. Acta Chem. Scand. Ser. B, **33B**, 469 (1979).
14. P.B. Hitchcock, M.F. Lappert, and A. Singh. J. Chem. Soc. Chem. Comm. 1499 (1983).
15. Molecular Structure Corporation. 1998. teXsan for Windows [computer program. Version 1.05. The Woodlands, Texas.
16. L.J. Farrugia. J. Appl. Crystallogr. **30**, 565 (1997).
17. D. Peters. J. Chem. Soc. 1757 (1957).
18. J. March and M.B. Smith. Advanced Organic Chemistry. 5th ed. Wiley-Interscience Publications, John Wiley and Sons, New York. 2000. p. 996.
19. M. Westerhausen, M. Hartmann, A. Pfitzner, and W. Schwarz. Z. Anorg. Allg. Chem. **621**, 837 (1995).
20. R.A.L. Gendron. M.Sc. Thesis, University of Victoria, Victoria, British Columbia, Canada. 2002.

© 2002 NRC Canada

Reactions of 1,3-dipolar aldazines and ketazines with the dipolarophile dimethyl acetylenedicarboxylate

Abdullah El-Alali and Ahmed S. Al-Kamali

Abstract: The prepared aldazines (aldehyde azines) and ketazines (ketone azines) were allowed to react with 2 mol of the acetylene derivative. The first products formed were pentalene azine derivatives, which in some cases underwent skeletal rearrangment into acyclic tetraene azines. The latter underwent, in the case of some aldazine products, further skeletal rearrangment into *N*-allyl pyrazoles. The occurence of these rearrangments is dependant on the nature of the aldehydes or ketones used.

Key words: dimethyl acetylenedicarboxylate (DMAD), aldazines, ketazines, *N*-allyl pyrazoles.

Résumé : On a fait réagir des aldazines (azines d'aldéhydes) et des cétazines (azines de cétones) avec deux molécules de dérivés acétyléniques. Les premiers produits formés sont des dérivés azines du pentalène qui, dans quelques cas, subissent des réarrangements du squelette conduisant à des azines tétraènes acycliques. Dans certains cas, ces dernières subissent d'autres réarrangements du squelette avec formation de *N*-allylpyrazoles. La formation de ces produits de réarrangements dépend de la nature des aldéhydes ou des cétones utilisées.

Mots clés : acétylènedicarboxylate de diméthyle « DMAD », aldazines, cétazines, *N*-allylpyrazoles.

[Traduit par la Rédaction]

Introduction

The 1,3-dipolar aldazines or ketazines are actually 1,3-heterodienes and have double 1,3-dipolar sites (Scheme 1).

These acyclic 1,3-heterodienes adopt the s-trans conformation due to steric interactions of the alkyl or aryl substituents. This conformation does not undergo the [4 + 2]-cycloadditions known as the Diels–Alder reactions (1, 2). The above mentioned heterodienes **1** (Scheme 1), reacted with 2 equiv of dipolarophiles, such as dimethyl acetylenedicarboxylate **2**, in [2 + 3]-cycloaddition (3–5) reactions and gave, in this case, the pentalene azines **3** (Scheme 2).

Only two aldazines out of 10 and three ketazines out of six stayed in the bicyclic azine **3** as the final products. The formation of the acyclic teraene azines **4**, as the final product of three ketazines, after their conversion with the acetylene derivative **2**, can only happen through skeletal rearrangment (5) of the bicyclic form **3** as depicted in Scheme 3. The *N*-allyl pyrazoles **7** as final products of the eight aldazines are formed through further skeletal rearrangment of the acyclic form **4**, leading to a zwitterion **5** and then to the intermediates **6**. The latter tautomerizes in the final stage to the *N*-allyl pyrazoles **7**, as shown in the slightly modified mechanism in the literature (5) (Scheme 3).

Scheme 1.

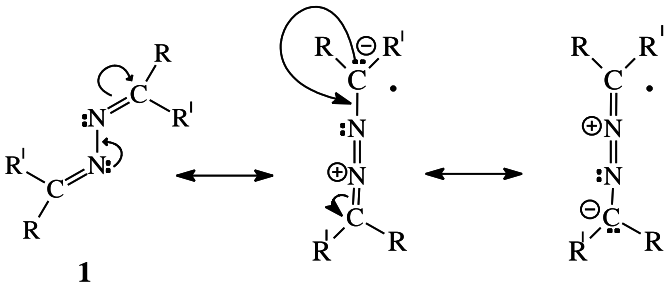

1

Scheme 2.

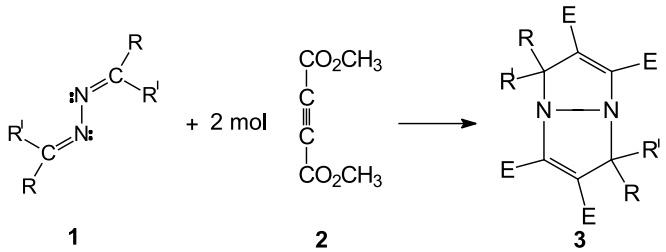

1 **2** **3**

R = alkyl or aryl R^1 = H, CH_3 or alkyl E = CO_2CH_3

Characterization of all products was achieved by using ^{1}H NMR, ^{13}C NMR, FT IR spectroscopy and elemental analysis.

Investigation of the skeletal rearrangment taking place in some cases is in progress. The observed reactions in the

Received 11 October 2001. Published on the NRC Research Press Web site at http://canjchem.nrc.ca on 7 October 2002.

A. El-Alali[1] and A.S. Al-Kamali. Department of Chemistry, Mutah University, P.O. Box 7. Al-Karak-H.K. of Jordan.

[1]Corresponding author (e-mail: elalali@mutah.edu.jo).

 DOI: 10.1139/V02-169 © 2002 NRC Canada

Scheme 3.

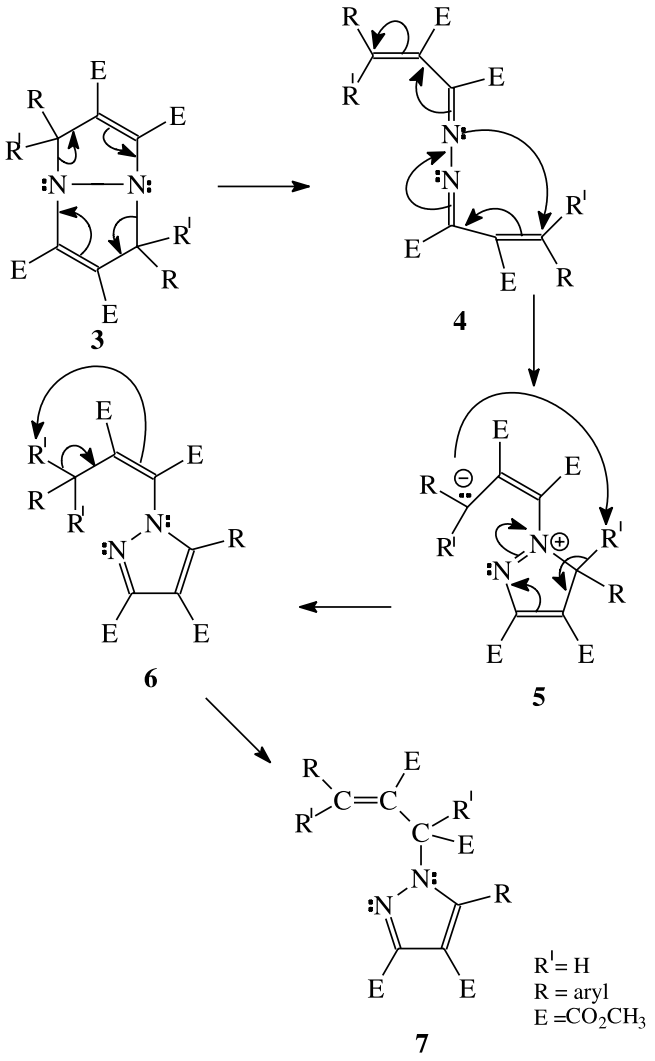

Table 1. The aldehydes and aldazines.

No. of aldehyde	R	No. of the aldazines	Reference
8	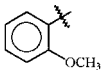	18	11
9	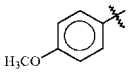	19	11
10	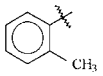	20	12
11		21	12
12	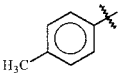	22	12
13		23	–
14		24	13
15		25	13
16	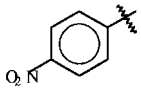	26	13
17	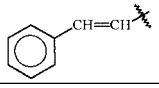	27	13

Table 2. Physical and analytical data.

Aldazine	mp (°C) (Colour)	Yield (%)	IR-KBr imine λ (cm^{-1})	Time of reflux	^{1}H NMR δ (ppm)
23	135–137, Yellow	81	1617	2 h	7.3–8.2 (m, 8H, aromatic), 9.1 (s, 2H, imine)

literature (3–5) and in this work do not give a clear explanation. Also the formation of *N*-allyl pyrazoles is highly interesting. Similar compounds in the literature possess biological activities such as antipyritic (6), antitumor (7), herbicidal (8), and antibiotic (9, 10). The bioassay of these compounds will be investigated later.

Results and discussion

Preparation of the aldazines and ketazines (Scheme 4 and Tables 1–4)

From Table 1, one can predict that only aromatic aldazines were prepared (11–13) and the 2-chlorobenzaldehyde **23** was not reported. All other reported aldazines were prepared in modified procedures. The characterization of the aldazine **23** is depicted in Table 2.

The aromatic ketazines **32–35** (Table 3), were also prepared by modified procedures. Only the ketazine **35** is reported (14). In the case of the ketazines, a few drops of glacial acetic acid were added to the reaction mixture which were not necessary for the preparation of aldazines, due to their high reactivity.

The characterization of the ketazines **32–34** is shown in Table 4.

The two available alicyclic ketones **36** and **38** were allowed to react with hydrazine monohydrate and gave the desired ketazines **37** and **39** (Scheme 5).

Preparation of the bicyclic azines (Scheme 6)

As depicted in Scheme 6, only the two aldazines (2-chlorobenzaldehyde azine **23** and 4-nitrobenzaldehyde azine **26**) stayed in the final product as the bicyclic forms **40** and

© 2002 NRC Canada

Scheme 4.

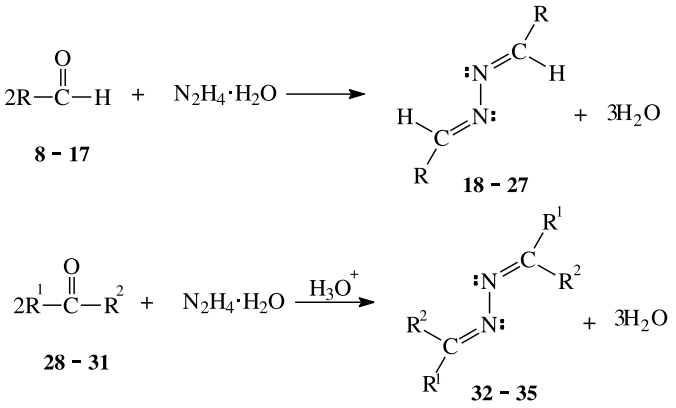

Table 3. The ketones and ketazines.

No. of the ketone	R^1	R^2	No. of the ketazines	Reference
28	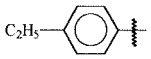	CH_3	32	–
29		CH_3	33	–
30		CH_3	34	–
31	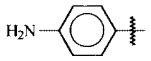	CH_3	35	14

Table 4. Physical and analytical data.

No. of the ketazine	mp (°C) (Colour)	Yield (%)	R-KBr imine λ (cm^{-1})	Time of reflux	^{1}H NMR δ (ppm)
32	106–108, Orange	87	1601	20 h	1.25 (t, 6H, J = 1.0 Hz, CH_3), 2.3 (s, 6H, CH_3-imine), 2.7 (9, 4H, J = 1.0 Hz, CH_2), 7.2–7.9 (2d, 8H, J = 0.5 Hz, aromatic)
33	88–90, Orange	98	1605	40 h	2.7 (s, 6H, CH_3), 6.5–7.2 (m, 6H, aromatic)
34	95–96, Orange	86	1590	20 h	2.35 (s, 6H, CH_3), 7.1–7.5 (m, 6H, aromatic)

Scheme 5.

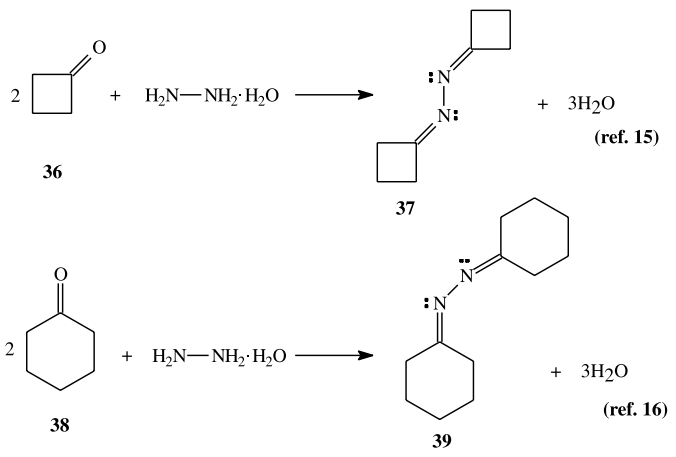

41, respectively. The 2-acetylthiophene azine **33** is the only aromatic ketone azine that formed the bicyclic diazine **42**. It could be, that from the above mentioned compounds, the electron-withdrawing chloro- and nitro- groups, and in the case of the thiophene moiety, the nature of the aromatic ring, why they stayed in the bicyclic form. The two acyclic ketone azines **37** and **39** were chosen because of this observation. These acyclic ketone azines gave the spiro bicyclic azines **43** and **44** (Table 5).

The physical and analytical data are shown in Table 6. Elemental analysis for the products **41, 42**, and **44** was not measured, instead, mass spectrometric data were measured in addition to the spectroscopic data (Table 7).

In the IR spectra, the imine stretching vibration is absent. Moreover, the spiro compounds **43** and **44** represent a good method for preparation of such spiro molecules.

Preparation of the acyclic tetraene azines (Scheme 7)

The acyclic tetraene azines **45–47** are symmetrical molecules as in the case of the bicyclic azines, but the stretching vibrations of the imine groups are present in the FT IR spectra at 1612.61, 1636.14, and 1674 cm^{-1} (17, 18). The chemical shift of the carbon of this imine group at 158 ppm is present, which is absent in the bicyclic spectra (Tables 8–10).

As shown in Table 8, the aryl groups carry in the compounds **45** and **47**, ethyl and amino groups in the para position, which are electron-donating groups. In compound **46**, the furan ring is an electron-rich molecule, and as a preliminary observation, these electron-donating groups could be the reason behind the ring-opening of the bicyclic forms, leading to the stable and highly conjugated acyclic forms. The elemental analysis for compounds **46** and **47** was not conducted, but mass spectrometric data are available (Tables 9 and 10).

Preparation of the *N*-allyl pyrazoles (Scheme 8)

The *N*-allyl pyrazoles **48–55** (Scheme 8) were formed by the reaction of the aldazines **18**, **19**, **20**, **21**, **22**, **24**, **25**, and **27** with 2 equiv of DMAD **2.** The reactions with phenylacetylene, diphenylacetylene, and methyl propiolate were unsuccessful. This could be due to the electron-poor LUMO of the DMAD **2**, which can react with the electron-rich HOMO of the 1,3-dipolar compounds. The nature of the aryl groups, yield, and time of reflux are given (Table 11).

© 2002 NRC Canada

Scheme 6.

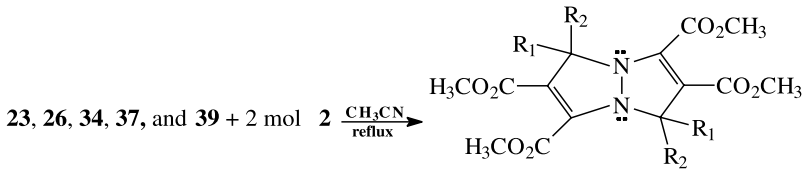

40–44

Table 5. The bicyclic azines.

No. of the azine	No. of the bicyclic azine	R^1	R^2	Yield (%)	Time of reflux
23	40	H	2-Chlorophenyl	65	4 days
26	41	H	4-Nitrophenyl	77	2 days
34	42	CH_3	2-Thiophenyl	70	12 days
37	43	Spiro cyclobutane moiety		75	12 h
39	44	Spiro cyclohexane moiety		68	24 h

Table 6. Physical and analytical data.

No. of the bicyclic azine	mp (°C) (colour)	Molecular formula and weight (g mol^{-1})	Elemental analysis calcd. and (or) found (%)		
			C	H	N
40	176 to 177	$C_{26}H_{22}N_2O_8Cl_2$	55.62	3.95	4.99
	White	561.37	55.48	4.05	5.08
41	Yellow	$C_{26}H_{22}N_4O_{12}$	Not measured		
	Oil	582.47			
42	Amber	$C_{24}H_{24}N_2O_8S_2$	Not measured		
	Oil	532.57			
43	Yellow	$C_{20}H_{24}N_2O_8$	57.13	5.75	6.66
	Oil	420.41	58.01	5.85	6.87
44	Yellow	$C_{24}H_{32}N_2O_8$	Not measured		
	Oil	476.52			

Table 7. Spectroscopic and spectrometric data.

No. of the product	IR (cm^{-1}) (carbonyl)	^1H NMR δ (ppm)	^{13}C NMR δ (ppm)	MS (M^+) base-peak and other fragments
40	1728.75	3.5–4.0 (4s, 12H, CH_3-ester), 5.7 (s, 2H, allylic-H), 7.1–7.5 (m, 8H, aromatic)	51–53 (2 peaks, CH_3-ester), 63 (allylic-C), 125–155 (8 peaks-sp^2 carbons), 163–168 (2 peaks, CO-ester)	—
41	1740.33	3.6–3.8 (4s, 12H, CH_3-ester), 6.4 (s, 2H, allylic-H), 8.3–8.5 (2d, 8H, J = 0.5 Hz, aromatic)	50–53 (2 peaks, CH_3-ester), 62 (1 peak, allylic-C), 124–135 (6 peaks, sp^2-C), 162–168 (2 peaks, CO-ester)	582, 260 (100%), 352, 323, 291, 202
42	1736.47	2.35 (s, 6H, CH_3), 3.6–4.0 (4s, 12H, CH_3-esters), 6.3–7.5 (3m, 6H, aromatic)	29 (1 peak, allylic-CH_3), 52–53 (2 peaks, CH3-ester), 63 (1 peak, allylic-C), 130–156 (6 peaks, sp^2-C), 165–168 (2 peaks, CO-ester)	532, 416 (100%), 472, 430, 408, 274
43	1736.57	1.9–2.0 (m, 12H, cyclobutane ring), 3.7–3.8 (2s, 12H, CH_3-ester)	15–18 (3 peaks, cyclobutane), 51–52 (2 peaks, CH_3-ester), 133–135 (2 peaks, sp^2-C), 162–168 (2 peaks, CO-ester)	—
44	1732.19	1.9–2.0 (m, 20H, cyclohexane ring), 3.7–3.9 (2s, 12H, CH_3-ester)	16–19 (4 peaks, cyclohexane), 52–53 (2 peaks, CH_3-ester), 133–135 (2 peaks, sp^2-C), 163–168 (2 peaks, CO-ester)	476, 153 (100%), 318, 205, 175

© 2002 NRC Canada

Scheme 7.

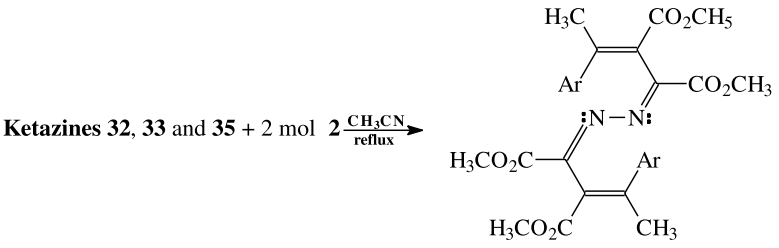

45–47

Table 8. The acyclic azines.

No. of the ketazine	No. of the acyclic azine	Ar	Yield (%)	Time of reflux
32	45	4-Ethylphenyl	78	60 h
33	46	4-Furfuryl	73	5 days
35	47	4-Aminophenyl	75	60 h

Table 9. Physical and analytical data.

No. of the acyclic azine	mp (°C) (colour)	Molecular formula and weight (g mol^{-1})	Elemental analysis calcd. and (or) found (%)		
			C	H	N
45	Amber	$C_{32}H_{36}N_2O_8$	66.65	6.29	4.86
	Oil	476.63	65.98	6.72	4.89
46	Amber	$C_{24}H_{24}N_2O_{10}$	—		
	Oil	500.45			
47	153–155	$C_{28}H_{30}N_4O_8$	—		
	Yellow	550.55			

Table 10. Spectroscopic and spectrometric data.

No. of the product	IR (cm^{-1}) (carbonyl and (or) imine)	^{1}H NMR δ (ppm)	^{13}C NMR δ (ppm)	MS (M^+), base-peak and other fragments
45	1732.61	1612.99	1.6 (t, 6H, CH_3-ethyl, J = 0.5Hz), 2.3 (s, 6H, CH_3), 2.6 (q, 4H, CH_2, J = 0.5 Hz), 3.8–3.9 (2s, 12H, OCH_3), 7.3–7.7 (2m, 8H)	15–20 (2 peaks, ethyl), 51–52 (2 peaks, OCH_3), 115–145 (6 peaks, sp^2-C), 157 (1 peak, C = N), 163–166 (2 peaks, CO-ester)
46	1721.03, 1636.14	2.3 (s, 6H, CH_3), 3.7–3.8 (s, 12H, OCH_3), 6.5–7.5 (3m, 6H, aromatic)	29 (1 peaks, CH_3), 51–52 (2 peaks, OCH_3), 100–144 (6 peaks, sp^2-C), 156 (1 peak, C = N), 162–165 (2 peaks, CO-ester)	500, 216 (100%), 366, 250, 203, 149, 123
47	1740.33, 1674.73	2.3 (s, 6H, CH_3), 3.7 (s, 12H, OCH_3), 5.5 (s, 4H, NH_2), 6.8–7.9 (2d, 8H, J = 0.5 Hz, aromatic)	15 (1 peak, CH_3), 51–53 (2 peaks, OCH_3), 95–148 (6 peaks, sp^2-C), 158 (1 peak, C = N), 164–169 (2 peaks, CO-ester)	550, 275 (100%), 260, 245, 216, 157, 149

Scheme 8.

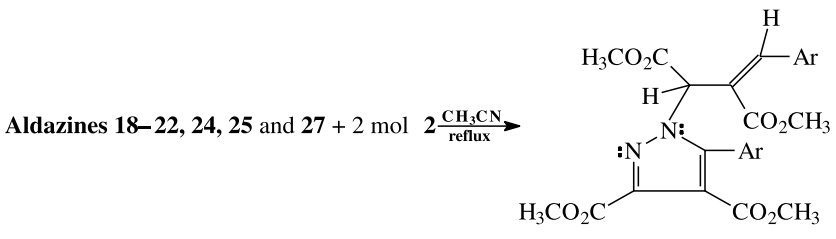

48–55

© 2002 NRC Canada

Table 11. The *N*-allyl pyrazoles.

No. of product	Ar	Yield %	Time of reflux
48	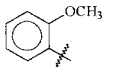	78	50 h
49	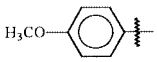	88	85 h
50		85	6 days
51	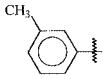	73	9 days
52	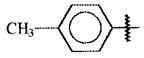	87	6 days
53		65	6 days
54		73	61 h
55	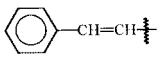	70	58 h

The physical and analytical data are given (Table 12), and the spectroscopic and spectrometric data are shown in Table 13. The formation of these products was identified mainly by NMR. The unsymmetrical shape was recognized by the number of carbon peaks in the ^{13}C NMR, where almost all carbon peaks were present. The four peaks of the ester carbonyls were apparent between 162–169 ppm and the peak of the allylic carbon atoms appeared between 58–64 ppm. In the ^{1}H NMR spectra, one observed four singlets between 3.8 to 4.0 ppm for the methyl groups of the esters. Moreover, the allylic protons in all compounds were observed as singlets between 5.9 to 7.2 ppm, whereas the vinylic protons appeared as singlets between 8.0 to 8.4 ppm. In the FT IR spectroscopy, the carbon double bonds and imine vibrations between 1600–1660 cm^{-1} were present as broad peaks and could not be singly specified. Vibrations of the carbonyl groups of the esters were present between 1724.89–1744.19 cm^{-1}.

Experimental

Materials and equipment

o-, *m*-, and *p*-Toluylaldehydes and *p*-methoxybenzaldehyde were purchased from Fluka Co. Cinnamaldehyde was purchased from the Gainland Chemical Co. Cyclobutanone was purchased from the Aldrich Co. Dimethyl acetylenedicarboxylate, 2-acetylfuran, 4-amino acetophenone, and 1-naphthalenecarboxaldehyde were purchased from the Merck Co. Hydrazine hydrate (51%) was purchased from Janssen-Chimica. The cyclohexanone was purchased from May and Baker Ltd. 2-Acetyl thiophene (19) and 4-ethyl acetophenone (20) were prepared following literature procedures. The solvents acetonitrile, methanol, ethanol, toluene, and *n*-hexane were dried and distilled over calcium hydride. Diethyl ether and THF were dried over sodium and benzophenone. All dried solvents were kept over activated molecular sieves. The liquid aldehydes and ketones were distilled prior to their use.

Analytical and preparative thin-layer chromatography (TLC) were performed on silica gel plates precoated with silica gel GF_{254} from theLaboratory Rasoyan Co.

Uncorrected melting points were obtained on an electrothermal melting point apparatus. Infrared spectra were recorded as KBr-disc or liquid films on a Matsson 5000 FT IR spectrophotometer. ^{1}H and ^{13}C NMR spectra were recorded with a Bruker AC-200 MHz in a solution of $CDCl_3$ and with TMS as an internal reference.

Electron impact (EI) mass spectra were recorded using a Finnigan MAT731 spectrophotometer at 70 eV. Elemental analyses were determined by M.H.W. Laboratories in Arizona, U.S.A.

The aldazines (18–27)

General procedure A (modified):

The aldehyde (2.1 mol) was added slowly to the cooled mixture of 1.0 mol hydrazine hydrate dissolved in ethanol or methanol. The mixture was heated over a steam bath for 1.0 h, then refluxed for several hours. The time of reflux depended on the nature of the aldehyde used. The reaction was followed by TLC. The solvent was removed in vacuo and the residue was recrystallized either from ethanol or methanol.

*2,2′-Dimethoxybenzaldazine (**18**):*

It was prepared following the modified procedure A. 2-Methoxybenzaldehyde (5.0 g, 0.041 mol) and 0.64 g (0.02 mol) of hydrazine were used. The reaction time was 3.0 h, mp 143 to 144°C, yellow needles, and 95% yield.

*4,4′-Dimethoxybenzaldazine (**19**):*

Procedure A was used; mp 167 to 168°C and with 91% yield.

*2,2′-Dimethylbenzaldazine (**20**):*

Procedure A was used. The reaction time was only 10 min at room temperature. The yellow solid was washed with ice water, and crystallized from ethanol; mp 68–70°C and with 85% yield.

*3,3′-Dimethylbenzaldazine (**21**):*

Procedure A was used; mp 106–108°C and with 82% yield.

*4,4′-Dimethylbenzaldazine (**22**):*

It was prepared following known procedure (12); mp 157–159°C and with 90% yield.

*2,2′-Dichlorobenzaldazine (**23**):*

Procedure A was used. Details are depicted in Table 2 in the text.

© 2002 NRC Canada

Table 12. Physical and analytical data of *N*-allyl pyrazoles.

No. of the *N*-allyl pyrazoles	mp (°C) (colour)	Molecular formula and weight (g mol^{-1})	Elemental analysis calcd. and (or) found (%)		
			C	H	N
48	168–170	$C_{28}H_{28}N_2O_{10}$	60.86	5.11	5.07
	Yellow	552.52	61.08	4.89	5.09
49	Yellow	$C_{28}H_{28}N_2O_{10}$	60.86	5.11	5.07
	Oil	552.52	60.66	5.13	4.87
50	Amber	$C_{28}H_{28}N_2O_8$	64.61	5.42	5.38
	Oil	520.52	64.40	5.53	5.26
51	138–140	$C_{28}H_{28}N_2O_8$	64.61	5.42	5.38
	White	520.52	64.80	5.51	5.54
52	134–136	$C_{28}H_{28}N_2O_8$	64.61	5.42	5.38
	White	520.52	64.72	5.51	5.39
53	Amber	$C_{30}H_{32}N_2O_8$	68.91	4.76	4.73
	Oil	548.58	67.81	5.47	4.24
54	Amber	$C_{34}H_{28}N_2O_8$	55.93	4.27	5.93
	Oil	592.58	56.75	4.74	4.52
55	Yellow	$C_{30}H_{28}N_2O_8$	—	—	—
	Oil	544.54			

Table 13. Spectroscopic and spectrometric data.

No. of the product	IR (cm^{-1}) (carbonyl and (or) imine)	^{1}H NMR δ (ppm)	^{13}C NMR δ (ppm)	MS (M^+), base-peak and other fragments
48	1724.89	3.6 (s, 6H, OCH_3-rings), 3.6–3.9 (4s, 12H, OCH_3-esters), 6.0 (s, 1H, allylic-H), 6.7–7.5 (m, 8H, aromatic), 8.05 (s, 1H, vinylic-H)	52–53 (6 peaks, OCH_3), 61 (1 peak, allylic-C), 111–158 (17 peaks, sp^2-C), 163–168 (4 peaks, CO-ester)	552, 289 (100%), 263, 230, 204, 171, 145
49	1725.40	3.5–3.7 (2s, 6H, OCH_3-rings), 3.6–3.9 (4s, 12H, OCH_3-ester), 6.0 (s, 1H, allylic), 6.8–7.4 (m, 8H, aromatic), 8.0 (s, 1H, vinylic)	51–58 (6 peaks, OCH_3), 61 (1 peak, allylic), 115–160 (13 peaks, sp^2-C), 163–169 (4 peaks, CO-ester)	—
50	1728.75	2.2–2.3 (2s, 6H, CH_3-rings), 3.5–4.0 (4s, 12H, OCH_3-ester), 5.9 (s, 1H, allylic), 6.8–7.3 (m, 8H, aromatic), 8.0 (s, 1H, vinylic)	22–23 (2 peaks, CH_3-rings), 51–54 (4 peaks, OCH_3), 58 (1 peak, allylic), 114–158 (17 peaks, sp^2-C), 162–168 (4 peaks, CO-ester)	550, 273 (100%), 247, 214, 188, 129
51	1732.19	2.1–2.2 (2s, 6H, CH_3-rings), 3.5–4.0 (4s, 12H, OCH_3-ester), 6.1 (s, 1H, allylic), 6.8–7.5 (m, 8H, aromatic), 8.1 (s, 1H, vinylic)	22–23 (2 peaks, CH_3-rings), 50–53 (4 peaks, OCH_3), 59 (1 peak, allylic), 114–159 (17 peaks, sp^2-C), 163–169 (4 peaks, CO-ester)	—
52	1728.75	2.1–2.3 (2s, 6H, CH_3-rings), 3.5–3.9 (4s, 12H, OCH3-ester), 5.9 (s, 1H, allylic), 6.9–7.2 (m, 8H, aromatic), 8.0 (s, 1H, vinylic)	22–23 (2 peaks, CH_3-ring), 51–54 (4 peaks, OCH3), 59 (1 peak, allylic), 114–148 (13 peaks, sp^2-C), 162–168 (4 peaks, CO-ester)	—
53	1726.73	3.5–4.0 (4s, 12H, OCH_3-ester), 5.7 (s, 1H, allylic), 6.8–8.0 (m, 14H, aromatic), 8.4 (s, 1H, vinylic)	51–53 (4 peaks, OCH_3), 63 (1 peak, allylic-C), 115–162 (25 peaks, sp^2-C), 166–168 (4 peaks, CO-ester)	—
54	1734.12	3.7–3.9 (4s, 12H, OCH_3-ester), 6.0 (s, 1H, allylic), 6.5–7.7 (m, 6H, aromatic), 8.0 (s, 1H, vinylic)	51–53 (4 peaks, OCH_3), 63 (1 peak, allylic), 130–158 (13 peaks, sp^2-C), 164–168 (4 peaks, CO-ester)	—
55	1744.19	3.9–4.0 (4s, 12H, OCH_3-ester), 7.2 (S, 1H, allylic), 7.5–8.1 (m, 14H, vinyl benzene), 8.3 (s, 1H, vinylic)	51–54 (4 peaks, OCH_3), 62 (1 peak, allylic-C), 114–159 (17 peaks, sp^2-C), 162–167 (4 peaks, CO-ester)	544, 259 (100%), 417, 402, 232, 183.

© 2002 NRC Canada

*1,1′-Naphthaldazine (**24**):*

Procedure A was used. The reaction time was 10 min at room temperature. The solid product was crystallized from ethanol with a few drops of hydrochloric acid; mp 155–157°C and with 86% yield.

*2,2′-Furfuralazine (**25**):*

Procedure A was used. The reaction time took 20 h under reflux. The residue was extracted with ether, dried over $MgSO_4$, and after removal of ether, a brown solid was obtained; mp 111 to 112°C and with 88% yield.

*4,4′-Dinitrobenzaldazine (**26**):*

Precedure A was used. The reaction time was 10 min at room temperature. The solid residue was crystallized in pyridine; m., 296 to 297°C and with 89% yield.

*Cinnamaldazine (**27**):*

Preparation and crystallization carried out as for compound **24**; mp 173 to 174°C and with 86% yield.

The acyclic ketazines (32–35)

General procedure B (modified procedure):

2.1 mol of ketone was added slowly to 1.0 mol of hydrazine hydrate with a few drops of glacial acetic acid dissolved in methanol or ethanol. The reaction mixture was then refluxed for 20–40 h depending on the nature of the ketone. The solid residue was extracted with ether and washed successfully with 10% $NaHCO_3$. The ether layer was dried over $MgSO_4$ and the solvent was removed in vacuo. The solid products were crystallized from ethanol.

*4.4′-Diethylacetophenone azine (**32**):*

Procedure B was used. Details in Table 4. Recrystallization was achieved from petroleum ether.

*2,2′-Diacetylfuran azine (**33**):*

Procedure B was used. Details in Table 4.

*2,2′-Diacetylthiophene azine (**34**):*

Precedure B was used. For details, see Table 4. Recrystallization as for compound **32**.

*4,4′-Diaminoacetophenone azine (**35**):*

Procedure B was used. Details in Table 4.

The alicyclic ketazines 37 and 39

*Cyclobutanone azine (**37**):*

It was prepared using a modified procedure to that reported in the literature (15).

A mixture of 1.17 g (17 mmol) of the cyclobutanone and 0.54 g (8 mmol) of the hydrazine hydrate in 40 mL of toluene and 10 mL of ethanol was refluxed for 4 h, then strirred at room temperature overnight. After removal of the solvents, the residue was extracted with 100 mL of ether and dried over $MgSO_4$. The ether layer was cooled in a dry ice bath. After a few hours, white crystals precipitated and were separated by suction filteration; mp 68 to 69°C and with 83% yield.

*Cyclohexanone azine (**39**):*

Procedure B was used without an acid catalyst. Another preparation was also elaborated following the reported procedure (16) as follows: a mixture of 16.5 g (0.17 mmol) of cyclohexanone, 4.0 g (0.08 mmol) of hydrazine hydrate, and 25 g (0.3 mole) of sodium acetate were dissolved in 100 mL of H_2O and 100 mL of ethanol. The reaction mixture was heated for 4 h over a water bath. Five times its weight of $ZnCl_2$ (82.5 g) was added to the reaction mixture and heated at 130°C. A complex compound precipitated ($C_{12}H_{20}N_2.HCl{\cdot}ZnCl_2$). The melting point was 271 to 272°C and it decomposed with ammonia gas and gave the oily product **39** in 75% yield.

The preparation of the products:

General procedure C (modified)

A mixture of 1.0 mol azine and 3.0 mol of DMAD was dissolved in dry acetonitrile and heated under reflux for a period of time (see Tables 5–13). After removal of the solvent in vacuo, the excess DMAD was removed under reduced pressure (0.5 mmHg (1 mmHg = 133.322 Pa), 50°C). The residual amber oil was redissolved in methanol, and scratched with a glass rod for a few hours. The formed solid was crystallized from methanol, and the liquid products were purified by TLC plates or column chromatography.

*The bicycle azines (**40**–**44**):*

*1,5-Bis(2′-chlorophenyl)-2,3,6,7-tetrakis(carbomethoxy)-1,5-dihydro-pyrazolo[1,2-a]pyrazole (**40**):*

Procedure C was used. Details in Tables 5–7.

*1,5-Bis(4′-nitrophenyl)-2,3,6,7-tetrakis(carbomethoxy)-1,5-dihydropyrazolo[1,2-a]pyrazole (**41**):*

Procedure C was used The oily product was separated on TLC plates (50% EtOAc in hexane). See details in Tables 5–7.

*1,5-Bis(2′-thiophenyl)-2,3,6,7-tetrakis(carbomethoxy)-1,5-dimethylpyrazolo[1,2-a]pyrazole (**42**):*

Procedure C was used. The oily product was separated on TLC plates (30% EtOAc in hexane). See Tables 5, 6, and 7.

*1,5-Bis(spirocyclobutane)-2,3,6,7-tetrakis(carbomethoxy) dihydropy-razolo[1,2-a]pyrazole (**43**):*

Procedure C was used. The oily product was separated on TLC plates (30% EtOAc in hexane). See details in Tables 5–7.

*1,5-Bis(spirocyclohexane)-2,3,6,7-tetrakis(carbomethoxy)dihydropy-razolo[1,2-a]pyrazole (**44**):*

Procedure C was used. Separation on TLC (30% MeOH in hexane). Details in Tables 5–7.

*The acyclic azines (**45**–**47**):*

All these compounds were prepared following procedure C, and their data are depicted in Tables 8–10.

*Methyl-2-oxo-3-carbomethoxy-4-methyl-4-(4′-ethylphenyl)-but-3-enoate azine (**45**):*

Separation on a TLC plate (30% EtOAc in hexane).

*Methyl-2-oxo-3-carbomethoxy-4-methyl-4-(2′-furfuryl)-but-3-enoate azine (**46**):*

Separation on a TLC plate (20% EtOAc in hexane).

© 2002 NRC Canada

*Methyl-2-oxo-3-carbomethoxy-4-methyl-4-(4'-aminophenyl)-but-3-enoate azine (**47**):*

Separation was achieved by recrystallization from methanol.

The N*-allylphyrazoles (**48**–**55**):*

All these products were prepared following procedure C. The data are depicted in Tables 11–13.

*Methyl-2-[3',4'-dicarbomethoxy-5-(2''-methoxylphenyl)-1'-pyrazolyl]-3-carbo-methoxy-4-(2''-methoxyphenyl)but-3-enoate (**48**):*

Separated by crystallization from methanol.

*Methyl-2-[3',4'-dicarbomethoxy-5'-(4''-methoxyphenyl)-1'-pyrazoly-l]-3-carbo-methoxy-4-(4''-methoxyphenyl)-but-3-enoate (**49**):*

Separated on a TLC plate (50% EtOAc in hexane).

*Methyl-2-[3',4'-dicarbomethoxy-5'-(2''-methylphenyl)-1'-pyrazolyl]-3-carbo-methoxy-4-(2''-methylphenyl)-but-3-enoate (**50**):*

Separation procedure used was the same as in compound **49**.

*Methyl-2-[3',4'-dicarbomethoxy-5'-(4''-methylphenyl)-1'-pyrazolyl]-3-carbo-methoxy-4-(3''-methylphenyl)-but-3-enoate (**51**):*

Separated by crystallization from methanol.

*Methyl-2-[3',4'-dicarbomethoxy-5'-(4''-methylphenyl)-1'-pyrazolyl]-3-carbo-methoxy-4-(4''-methylphenyl)-but-3-enoate (**52**):*

Separated by crystallization from methanol.

Methyl-2-[3',4'-dicarbomethoxy-5'-(1''naphthalyl)-1'-pyrazolyl]-3-carbo-methoxy-4-(1''-naphthalyl)-but-3-enoate (53):

Separated on TLC plates using (ether:dichloromethane, 0.5:9.5).

*Methyl-2-[3',4'-dicarbomethoxy-5'-(2''-furyl)-1'-pyrazolyl]-3-carbom-ethoxy-4-(2''-furyl)-but-3-enoate (**54**):*

Separation procedure used was the same as in compound **49**.

*Methyl-2-[3',4'-dicarbomethoxy-5'-styryl-1'-pyrazolyl]-3-carbometh-oxy-4-styryl-but-3-enoate (**55**):*

Separated on TLC plates (30% EtOAc in hexane).

Conclusion

The transformations in this work delivered three types of products namely, the bicyclic azines, the acyclic azines, and the *N*-allyl pyrazoles. Investigation of the rearrangements is now going on in our research laboratory to develop an explanation. Furthermore, the bicyclic azines (the pentalene derivatives) are compounds of interest to many researchers. The acyclic tetraene azines could undergo thermal or photochemical cyclization to become interesting compounds. As mentioned before, the *N*-allyl pyrazoles are promising compounds and could possess biological activities.

References

1. D.L. Boger. Chem. Rev. **86**, 781 (1986).
2. J. Sauer and R. Sustmann. Angew. Chem. Int. Ed. Engl. **19**, 779 (1980).
3. K. Burger, W. Thenn, R. Rauh, and H. Schickaneder. Angew. Chem. Int. Ed. Engl. **13**, 477 (1974).
4. K. Burger, H. Schickaneder, and W. Thenn. Tetrahedron Lett. 1125 (1975).
5. S. Evans, R.C. Gearhart, L.J. Guggenberger, and E.E. Schweizer. J. Org. Chem. **42**, 452 (1977).
6. M.H. Elnagdi. Tetrahedron, **30**, 2791 (1974).
7. M.H.D.M. Fleita and M.R.H. Elmoghayar. Tetrahedron, **31**, 63 (1975).
8. B.W. Doming. U.S. Patent 3 833 582, 1974; Chem. Abstr. **81**, 152 270 (1974).
9. D.A. Carson and K.P. Chang. Biochem. Biophys. Res. Commun. **100**, 1377 (1981).
10. H. Umer Zawa and T. Takeuchi. Jpn. Patent 7 213 718, 1972; Chem. Abstr. **77**, 124 794 (1972).
11. L N. Ferguson and T.C. Goodwin. J. Am. Chem. Soc. **71**, 633 (1949).
12. H.E. Zimmerman and S. Somasekhara. J. Am. Chem. Soc. **82**, 5865 (1960).
13. E.R. Blout and R.M. Gofstein. J. Am. Chem. Soc. **67**, 13 (1945).
14. E R. Blout, V.W. Eager, and R.M. Gofstein. J. Am. Chem. Soc. **68**, 1983 (1946).
15. C.G. Overberger, H. Biletch, A.B. Finestone, J. Liker, and J. Herbert. J. Am. Chem. Soc. **75**, 2078 (1953).
16. W.H. Perkin and S.G. Plant. J. Chem. Soc. **125**, 1508 (1924); Chem. Abstr. **18**, 2162 (1924).
17. V.M. Kolb, A.C. Kuffel, H.O. Spiwek, and T.E. Janota. J. Org. Chem. **54**, 2771 (1989).
18. D.H.R. Barton, R.E. O'Brien, and S. Sternhell. J. Chem. Soc. 470 (1962).
19. H.D. Hartough and A.I. Kosak. J. Am. Chem. Soc. **69**, 1012 (1947).
20. R.Q. Brewster, C.A. Vanderwerf, and W.E. McEwen. Unitized experiments in organic chemistry. 4th ed. Wadsworth Publishing Co., Belmont, California, U.S.A. 1977.

© 2002 NRC Canada

Structural and conformational studies of 5-(1*H*-pyrrol-2-ylmethylene)-substituted imidazolidine-2,4-diones and thiazolidine-2,4-diones

Alfonso de Dios, Maria Luz de la Puente, Alfonso Rivera-Sagredo, and Juan Felix Espinosa

Abstract: Some imidazolidine-2,4-dione (hydantoin) and thiazolidine-2,4-dione (TZD) derivatives with a 1*H*-pyrrol-2-ylmethylene substituent at the 5-position (**1**–**8**) have been synthesized via an aldol condensation reaction. A mixture of *Z*- and *E*- stereoisomers was obtained, as confirmed by HPLC and NMR studies. Assignment of the stereochemistry was achieved through chemical shift knowledge, NOE, and $^3J_{H,C}$ data. The conformation of the molecules depends on the configuration at the double bond. While the (NH,C *cis*) form is the most stable conformer for the *E*-isomer, the (NH,C *trans*) form is the preferred conformer for the *Z*-isomer. The temperature coefficients of the NH pyrrole protons reveal the existence of an intramolecular hydrogen bond for the *E*-isomers.

Key words: hydantoin, TZD, NMR spectroscopy, conformational analysis, temperature coefficient.

Résumé : Faisant appel à une réaction de condensation aldolique, on a réalisé la synthèse de dérivés de l'imidazolidine-2,4-dione (hydrantoïne) et de la thiazolidine-2,4-dione (TZD) portant un substituant 1*H*-pyrrol-2-ylméthylène en position 5 (**1**–**8**). La formation de mélanges de stéréoisomères *Z*- et *E*- a été confirmée par des études de CLHP et de RMN. L'attribution de la stéréochimie a été réalisée sur la base de connaissances chimiques et de données relatives aux valeurs $^3J_{H,C}$ et d'effet Overhauser nucléaire. La conformation des molécules dépend de la configuration de la double liaison. Alors que le forme NH,C *cis* correspond à la conformation la plus stable de l'isomère *E*, la forme NH,C *trans* correspond à la conformation la plus stable de l'isomère *Z*. Les coefficients de température des protons NH du pyrrole mettent en évidence l'existence d'une liaison hydrogène intramoléculaire pour les isomères *E*.

Mots clés : hydantoïne, TZD, spectroscopie RMN, analyse conformationnelle, coefficient de température.

[Traduit par la Rédaction]

Introduction

Imidazolidine-2,4-dione (hydantoin) (1) and thiazolidine-2,4-dione (TZD) (2) derivatives are good examples of compounds that exhibit a wide range of interesting biological properties. The hydantoin scaffold is a common feature present in orally active fibrinogen (1(*a*)) and angiotensin II (1(*b*)) receptor antagonists, anticonvulsant sodium channels (1(*c*)), and muscarinic receptor ligands (1(*d*)). The synthesis of combinatorial libraries of hydantoins for biological screening (1(*e*)) is a clear indication of their pharmaceutical relevance. On the other hand, some TZD derivatives that show high affinity for peroxisome proliferator-activated receptor γ (PPARγ) are very well known hypoglycemic drugs (2(*a*)).

As these two scaffolds are usually responsible for key interactions in the receptor binding sites, Structure-activity relationship studies (SAR) techniques have been employed to correlate biological activity with differences in steric and electrostatic parameters (1(*c*)). In this context, structural and conformational analysis of the aforementioned derivatives may be a very powerful tool to understanding possible binding modes, thus facilitating SAR studies.

As part of a medicinal chemistry project developed in our laboratories, we have synthesized several hydantoin and TZD derivatives (**1**–**8**, Fig. 1). *E*- and *Z*- isomers were isolated by preparative HPLC and their configuration assigned by NMR spectroscopy. The conformational preferences were investigated to gain insight into the influence of the geometry on the pharmacological properties of the compounds.

Received 16 May 2002. Published on the NRC Research Press Web site at http://canjchem.nrc.ca on 11 October 2002.

A. de Dios, M.L. de la Puente, A. Rivera-Sagredo, and J.F. Espinosa.[1] Centro de Investigación Lilly, Avenida de la Industria 30, 28 108 Alcobendas, Madrid, Spain.

[1]Corresponding author (e-mail: Espinosa_Juan_F@lilly.com).

Results and discussion

Synthesis

Aldol condensations of commercially available or easily accessible starting materials with pyrrole-2-carboxaldehyde and using standard thermodynamic control conditions were carried out (3). An excess of aldehyde, a catalytic amount of amine base in THF, and long refluxing times were employed to afford mixtures of *E*–*Z* compounds (Scheme 1). Attempts to isolate the stereoisomers by silica gel chromatography were unsuccessful; thus purification was performed by HPLC.

An efficient system capable of baseline resolving the two *E*–*Z* isomers was developed. A series of parameters (composition of the mobile phase, column packing, and additives)

 DOI: 10.1139/V02-175 © 2002 NRC Canada

Scheme 1. Preparation of compounds **1**–**8**.

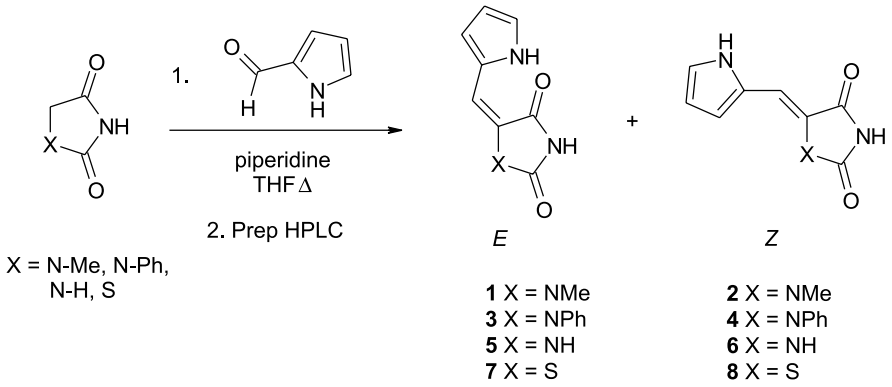

Fig. 1. Structure of compounds **1**–**8** showing the atomic numbering.

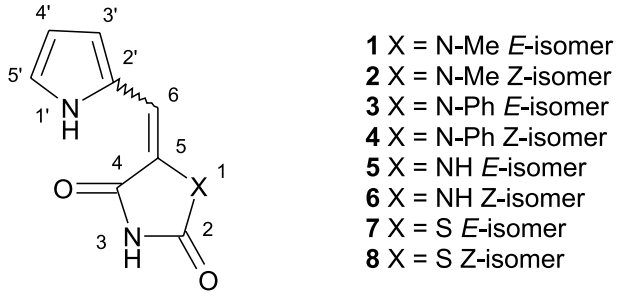

Fig. 2. Preferred configuration for 3-(1*H*-pyrrol-2-ylmethylene)-substituted indolin-2-ones (see also: ref. (3)).

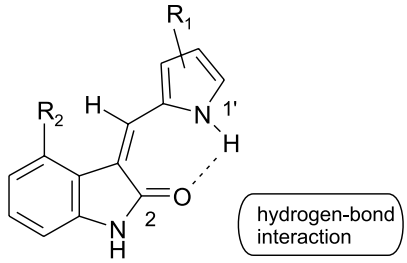

were tested to find suitable conditions for isolation of both isomers. Reverse phase chromatography using a gradient of water–acetonitrile and trifluoroacetic acid as additives and a variety of stationary phases, including C8–C18 and phenyl series, allowed the separation of the stereoisomers. For hydantoin derivatives, the major component of the *E*–*Z* mixture eluted earlier than the minor one. In contrast, for the TZD mixture the major component eluted in second place, which suggested a change of stereoselectivity relative to the hydantoin series.

As the reaction was carried out under thermodynamic control conditions, we envisioned that internal hydrogen bond formation between the C4 carbonyl group and the NH1′ of the pyrrole ring should favour the formation of the corresponding *E* isomer. In fact, the predominance of this configuration had been reported (100% of population based on NOE data) for related 3-(1*H*-pyrrol-2-ylmethylene)-indolin-2-ones (Fig. 2). The authors postulated an intramolecular hydrogen, located between the C-2 carbonyl oxygen atom of the indolin-2-one ring and the proton on the N1′ of pyrrole, to explain this selectivity. They did not, however, provide any experimental evidence to support its existence. In our experiments, analytical studies detected the presence of both stereoisomers and showed different isomer ratios for each case. Integration of the ^{1}H NMR spectra of the mixtures confirmed the change in stereoselectivity inferred from HPLC data. While the reaction progressed with high selectivity for the N-methyl (**1**, **2**) and the N-phenyl (**3**, **4**) hydantoins (93:7 and 86:14 *E*:*Z* mixture ratios, respectively), no significant selectivity was found for the NH hydantoins (**5**, **6**) (44:56, *E*:*Z*). Unexpectedly, the opposite selectivity was found for the TZDs (**7**, **8**), and the *Z*-isomer was the major product of the reaction (11:89, *E*:*Z*). The configurational assignment is described in detail in the following section.

Hydrogen bond formation alone, therefore, can not explain the observed stereoselectivity, and other factors have to be considered. Our data indicates that steric hindrance is more important than intramolecular hydrogen bonding in determining the stereoselectivity of the reaction. Steric interferences between the pyrrole ring and the N-substituent are present for the *Z*-isomers **2** and **4**, which favour the formation of the *E*-isomers **1** and **3** with high selectivity. However, the absence of steric hindrance for the *Z*-isomer **6** increases the proportion of this isomer. Moreover, the isomeric ratio obtained for TZD further supports the minor role of hydrogen bonding. For this latter compound, the *Z*-isomer **8** does not exhibit steric interferences and is the major product of the reaction.

Stereochemistry assignment

The first step was the assignment of all the proton and carbon resonances on the basis of ^{1}H, ^{13}C, correlation spectroscopy (COSY), heteronuclear single-quantum correlation (HSQC), and heteronuclear multiple-bond correlation (HMBC) experiments recorded in DMSO. The NH proton of the pyrrole ring was distinguished from the NH proton of the hydantoin moiety through its coupling to the pyrrole protons, as observed in a COSY experiment. The configuration at the double bond was determined through one-dimensional NOE spectroscopy (1D-NOESY) experiments. Inversion of the methyl protons in **1** produced a nuclear Overhauser effect (NOE) to the olefinic proton H6, whereas no NOEs to the pyrrole protons were detected, indicating that the methyl group and the olefinic proton are on the same side of the

© 2002 NRC Canada

Fig. 3. Summary of the relevant NOEs observed for each conformer of hydantoins **1** and **2**. Solid and dotted arrows represent strong and weak NOEs respectively. The detected hydrogen bond is also shown.

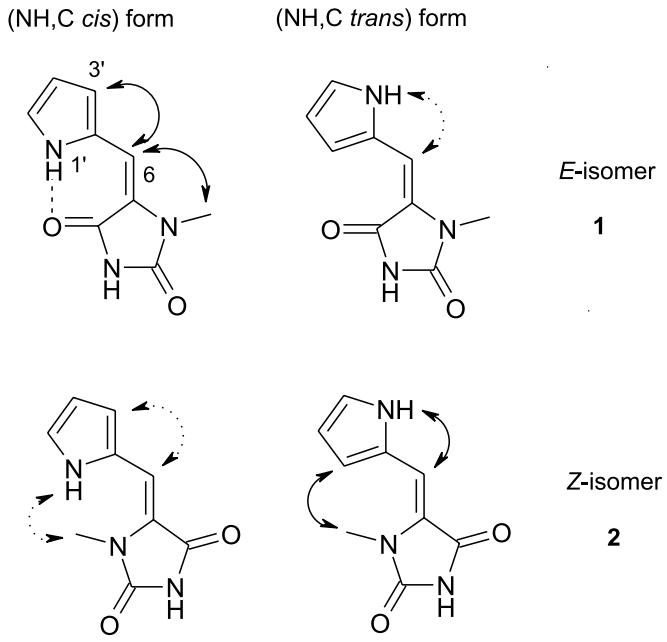

molecule (Fig. 3). On the other hand, NOEs between the methyl protons and the pyrrole protons were observed for **2**. These results reveal that **1** is the *E*-isomer and **2** is the *Z*-isomer. Analogously, NOEs between H6 and the *ortho* protons of the N-phenyl ring, and between H6 and NH1, were observed for **3** and **5**, respectively, corresponding to the *E*-isomer. By contrast, NOEs between the pyrrole protons and the *ortho* protons of the N-phenyl ring, and between the pyrrole protons and the NH proton, were detected for **4** and **6**, respectively, which is consistent with the Z-isomers.

We have found a correlation between the *Z–E* configuration of the compounds and the chemical shifts of H6 and H1′ (Table 1). In this regard, the pyrrole H1′ appears at high frequency in the *E*-isomer relative to the *Z*-isomer, whereas the olefinic proton exhibits the opposite behaviour. This relationship may be attributed to the influence of the carbonyl group of the hydantoin ring. While the NH-pyrrole (H1′) is deshielded by the carbonyl in the *E*-isomer, the olefinic proton (H6) is deshielded in the *Z*-isomer, and the corresponding proton signals move to higher shifts.

Unfortunately, NOE analysis cannot be utilized for the elucidation of the stereochemistry of compounds **7** and **8**. Although Prabhakar et al. (2(*b*)) have proposed to use IR data for the configurational assignment of TZD analogues, we have been able to determine the stereochemistry by NMR data, using the relationship between configuration and chemical shift derived for compounds **1**–**6**. Thus, the comparison of H1′ and H6 chemical shifts of **7** and **8** (Table 1) suggest that the compounds correspond to the *E*- and the *Z*-isomer, respectively. This empirical assignment can be confirmed through three-bond ^{1}H-^{13}C coupling constants. It is well known that these couplings present a Karplus-type dependence on the dihedral bond that can be used for identification of configurational isomers (4). The magnitude of the

Table 1. H6 and H1′ chemical shifts and (H6/H3′):(H6/H1′) NOE intensity ratios determined for compounds **1**–**8**.

Compound	Configuration	$\delta_{H1'}$	δ_{H6}	NOE ratio (H6/H3′):(H6/H1′)
1	*E*	11.99	6.47	7:1
2	Z	11.23	6.52	1:8
3	*E*	12.01	6.07	4:1
4	*Z*	11.22	6.72	1:11
5	*E*	11.93	6.32	5:1
6	*Z*	11.18	6.41	1:3
7	*E*	12.16	7.25	—
8	*Z*	11.67	7.66	1:10

Note: — indicates data not measured.

coupling from the olefinic proton (H6) to the carbonyl carbon (C4) across the double bond should indicate the relative disposition, which is higher for the *trans* arrangement (*E*-isomer). The validity of this prediction was verified for hydantoins **1**–**6**, whose stereochemistry was elucidated through NOE analysis as outlined above. $^{3}J_{C,H}$ spin-spin coupling constants were measured from gated ^{1}H-decoupling ^{13}C NMR spectra. C4 appeared as a doublet for the N-methyl and N-phenyl derivatives (**1**–**4**), and as a triplet for the N-H derivatives (**5** and **6**) because the carbon was also coupled to NH1. This extra coupling was removed by acquiring a ^{13}C spectrum with selective NH1 decoupling, resulting in a doublet from which the coupling of interest could be measured. The $^{3}J_{H6,C4}$ value for compounds **1**, **3**, and **5** (*E*-isomers) is 10.2 Hz in all the cases, whereas compounds **2**, **4**, and **6** (*Z*-isomers) present a lower value (5.9 Hz), consistent with NOE-based assignments. This relevant H,C coupling constant was also determined for **8**. The experimental value for this compound is 5.9 Hz, which indicates the *Z*-configuration at the double bond, in agreement with the stereochemistry deduced from chemical shift data.

Conformational analysis

The conformation of these derivatives depends on rotation around the C2′—C6 bond, which determines the relative orientation of the pyrrole and the hydantoin or TZD rings. The compounds can adopt the (NH,C *cis*) form or the (NH,C *trans*) form, as shown in Fig. 3 for **1** and **2**. The conformational analysis of 2-substituted pyrroles has attracted special attention in the literature. In particular, 2-formyl pyrrole has been extensively studied through several methods (5). The less polar (NH,O *cis*) form, stabilized by a hydrogen bond, was determined to be the most stable conformer through dipolar moment measurements (5(*a*)), IR data (5(*b*)), and NMR spectroscopy (5(*c*)). Particularly, coupling constant analysis showed that the (NH,O *cis*) conformer was 95% populated in solution (5(*c*)). This conformational preference was rationalized through molecular orbital calculations (6). Analogously, the conformation of 2-substituted imine derivatives has also been studied through dipolar moment measurements and five-bond H,H couplings (7). These studies demonstrated the preponderance of the (NH,N *cis*) conformer in solution, which was also proposed to be stabilized by a hydrogen bond. In contrast, divergent conclusions have been reported for 2-vinyl pyrroles, and the major conformation in solution remains unclear (8). In our

© 2002 NRC Canada

case, we predict the (NH,C *cis*) form to be the major conformer in solution for the *E*-isomers, allowing the pyrrole-NH and the carbonyl oxygen to form an intramolecular hydrogen bond; however, a preferred conformation cannot be anticipated for the *Z*-isomers.

The major conformation in solution was determined for the hydantoins **1**–**6** through 1D-NOESY experiments in DMSO. The H6/H3′ and the H6/H1′ NOEs are exclusive for the (NH,C *cis*) and the (NH,C *trans*) forms, respectively (Fig. 3). For **1**, **3**, and **5** (*E*-isomers), the H6/H3′ NOE is much stronger than the H6/H1′ NOE, indicating that the (NH,C *cis*) form is the preferred conformer in solution. The (H6/H3′):(H6/H1′) NOE intensity ratios, which account for the relative conformer populations, suggest that the N-methyl hydantoin displays the highest population of the (NH,C *cis*) conformer (Table 1). Interestingly, for hydantoins **2** and **4** (*Z*-isomers), the NOE intensities are interchanged and the H6/H1′ NOE is now much stronger than the H6/H3′ NOE. This finding reflects the existence of a conformational change around the C2′—C6 bond, and the (NH,C *trans*) form becomes the major conformer in solution for both compounds. This conclusion is reinforced by the observation of strong NOEs between H3′ and the methyl protons for **2**, and between H3′ and the phenyl protons for **4**. It is interesting to note that, for **4**, the predominance of this conformer can also be deduced from chemical shift data. Some of the pyrrole protons in this compound present anomalous, low δ_H values due to the shielding produced by the phenyl ring. While H3′ presents the lowest chemical shift (4.51 ppm), H1′ has a typical value (11.22 ppm), which reveals the proximity of H3′ to the phenyl ring, showing the predominance of the (NH,C *trans*) form. For the *Z*-isomer **6**, the H6/H1′ NOE is also stronger than the H6/H3′ NOE (Table 1), which indicates that the (NH,C *trans*) form is the major conformer in solution, although its population decreases relative to **2** and **4**.

As the pyrrole-NH and the carbonyl oxygen are located on the same side in the preferred conformer of the *E*-isomers, an internal hydrogen bonding may exist for this configuration, as proposed by Sun et al. (3) for the indolin-2-one series (Fig. 2). The exchangeable protons involved in hydrogen bonds tend to appear at higher shifts owing to the effect of the oxygen atom (9). Indeed, the chemical shifts of the pyrrole-NH in compounds **1**, **3**, and **5** are higher than the values in compounds **2**, **4**, and **6** (Table 1), which suggests the presence of an intramolecular hydrogen bond. This prediction has been demonstrated experimentally by studying the change of $\delta_{H1'}$ with temperature, expressed by the chemical shift temperature coefficient (9). As temperature changes affect the mobility of solvent molecules, the chemical shifts of exchangeable protons that are involved in intermolecular hydrogen bonds with the solvent have larger chemical shift temperature-dependence than the intramolecularly hydrogen bonded protons, which have little interaction with the solvent. The temperature coefficient of H1′ was determined for hydantoins **1**–**6**. The experimental values measured for **1**, **3**, and **5** (–1.0, –1.1, and –1.1 ppb K^{-1}, respectively) are much smaller than those obtained for **2**, **4**, and **6** (−4.4, −6.9, and −4.1 ppb K^{-1}, respectively). The comparison between sets of values confirms the presence of an intramolecular hydrogen bond for the *E*-isomers.

Similar investigations were performed for TZDs in DMSO. The temperature coefficients of H1′ for the *E*-isomer (**7**) and for the *Z*-isomer (**8**) are –1.2 and –4.4 ppb, respectively. These values indicate the presence of a hydrogen bond in **7**, which implies that the (NH,C *cis*) form is the preferred conformer for the *E*-isomer. Moreover, 1D-NOESY experiments were carried out for compound **8** (Fig. 2*b*). H6 inversion produces a strong NOE to H1′ and a weak NOE to H3′ (intensity ratio 10:1), demonstrating the predominance of the (NH,C *trans*) for the *Z*-isomer. The results point out that the conformational preferences for TZDs are similar to those found for hydantoins, and swapping the nitrogen atom for a sulfur atom at the 1-position does not change the conformational behaviour of the molecules.

The predominance of the (NH,C *cis*) form over the (NH,C *trans*) form for the *E*-isomers can be interpreted in terms of an intramolecular hydrogen bond that stabilizes this conformation. Nevertheless, there is no clear explanation for the preference of the (NH,C *trans*) form for the *Z*-isomers. As the pyrrole-NH is more accessible to the solvent in this latter conformer, we suggest that this orientation may facilitate the formation of intermolecular hydrogen bonds with solvent molecules.

Experimental section

Starting materials (1-methyl hydantoin (**9**), hydantoin (**10**), and thiazolidine-2,4-dione (**11**)) and reagents were commercially available (Aldrich Co.). 1-Phenyl hydantoin (**12**) was prepared according to the procedure reported by Casagrande et al. (10) as follows: N-phenyl glycine (3.02 g, 20 mmol) was suspended in 90 mL of water and 0.1 mL of glacial acetic acid. The mixture was stirred and heated at 60°C for 30 min. A solution of potassium cyanate (1.62 g, 20 mmol) in 10 mL of water was slowly added and the solution heated for 1.5 h. Then, 2.5 mL of concentrated HCl (35%) was added dropwise and the reaction was heated at 90°C for 16 h. After cooling the solution at room temperature, a precipitate was formed. The solid was filtered off, rinsed with water, dried under high vacuum, and triturated thoroughly to yield 1.75 g of pure product (49% yield). ES-MS: 175.0 ($[M^+ - H]$).

General procedure for the synthesis of imidazolidine-2,4-diones (1–6) and thiazolidine-2,4-diones (7–8)

To a suspension of the starting material (**9**–**12**, 1 equiv) in THF (10 mL), pyrrole 2-carboxaldehyde (2 equiv) was added in one portion. A catalytic amount of piperidine (0.1 equiv) was added, and the mixture stirred and heated at reflux for 5–16 h. Then, the reaction was cooled down to room temperature and the solvent evaporated in vacuo. The residue was diluted with EtOAc and sequentially washed with 5% aqueous HCl, water, and brine. After drying over Na_2SO_4 and evaporating the solvents in vacuo, the crude product was prepurified by silica gel chromatography to remove the excess of starting aldehyde and to afford pure *E*–*Z* mixtures. These mixtures were then subjected to preparative HPLC, as detailed in the text.

© 2002 NRC Canada

1-Methyl-5-(1H-pyrrol-2-ylmethylene)-imidazolidine-2,4-dione:* E-*isomer (1) and* Z-*isomer (2)

Obtained as a 93:7 *E–Z* mixture, with 65% overall yield after purification of the crude product using hexane–acetone (6:1). **1**: ^{1}H NMR (DMSO): 11.99 (s, 1H, NH1′), 11.45 (s, 1H, NH3), 7.08 (m, 1H, H5′), 6.58 (m, 1H, H3′), 6.47 (s, 1H, H6), 6.20 (m, 1H, H4′), 3.07 (s, 3H, Me). ^{13}C NMR (DMSO): 164.6 (C4), 152.7 (C2), 126.6 (C2′), 123.9 (C5), 122.0 (C5′), 116.0 (C3′), 110.0 (C4′), 107.9 (C6), 25.7 (Me). **2**: ^{1}H NMR (DMSO): 11.23 (s, 1H, NH1′), 11.20 (s, 1H, NH3), 6.96 (m, 1H, H5′), 6.52 (s, 1H, H6), 6.46 (m, 1H, H3′), 6.17 (m, 1H, H4′), 3.20 (s, 3H, Me). ^{13}C NMR (DMSO): 164.5 (C4), 155.3 (C2), 125.5 (C5), 123.8 (C2′), 121.3 (C5′), 112.4 (C3′), 110.0 (C4′), 102.3 (C6), 29.3 (Me). **1**, **2**: ESI+-MS: 192.1 ($[M + H]^+$).

1-Phenyl-5-(1H-pyrrol-2-ylmethylene)-imidazolidine-2,4-dione:* E-*isomer (3) and* Z-*isomer (4)

Obtained as an 86:14 *E–Z* mixture, with 60% overall yield after purification of the crude product using hexane–EtOAc (2:1). **3**: ^{1}H NMR (DMSO): 12.01 (s, 1H, NH1′), 11.73 (s, 1H, NH3), 7.57 (t, 2H, *m*-protons phenyl), 7.49 (t, 1H, *p*-proton phenyl), 7.42 (d, 2H, *o*-protons phenyl), 7.09 (m, 1H, H5′), 6.54 (m, 1H, H3′), 6.16 (m, 1H, H4′), 6.07 (s, 1H, H6). ^{13}C NMR (DMSO): 164.3 (C4), 152.1 (C2), 133.0, 129.6, 128.6, 128.5, 126.0 (C2′), 124.8 (C5), 122.6 (C5′), 116.6 (C3′), 110.2 (C4′), 108.2 (C6). **4**: ^{1}H NMR (DMSO): 11.46 (s, 1H, NH3), 11.22 (s, 1H, NH1′), 7.36–7.43 (m, 3H, *m*- and *p*-protons phenyl), 7.29 (d, 2H, *o*-protons phenyl) 6.83 (m, 1H, H5′), 6.72 (s, 1H, H6), 5.77 (m, 1H, H4′), 4.51 (m, 1H, H3′). ^{13}C NMR (DMSO): 164.7 (C4), 154.2 (C2), 124.1 (C2′), 134.6, 128.8, 128.5, 127.4, 123.3 (C5′), 116.6 (C5), 113.4 (C3′), 110.2 (C4′), 103.4 (C6). **3**, **4**: ESI+-MS: 254.1 ($[M + H]^+$).

5-(1H-Pyrrol-2-ylmethylene)-imidazolidine-2,4-dione:* E-*isomer (5) and* Z-*isomer (6)

Obtained as a 44:56 *E–Z* mixture, with 55% overall yield after purification of the crude product using hexane–EtOAc (1:3). **5**: ^{1}H NMR (DMSO): 11.93 (s, 1H, NH1′), 11.24 (s, 1H, NH3), 10.12 (s, 1H, NH1), 7.05 (m, 1H, H5′), 6.52 (m, 1H, H3′), 6.32 (s, 1H, H6), 6.17 (m, 1H, H4′). ^{13}C NMR (DMSO): 165.3 (C4), 153.2 (C2), 126.7 (C2′), 122.8 (C5), 121.6 (C5′), 115.2 (C3′), 109.7 (C4′), 107.6 (C6). **6**: ^{1}H NMR (DMSO): 11.18 (s, 1H, NH1′), 10.98 (s, 1H, NH3), 10.04 (s, 1H, NH1), 6.98 (m, 1H, H5′), 6.80 (m, 1H, H3′), 6.41 (s, 1H, H6), 6.19 (m, 1H, H4′). ^{13}C NMR (DMSO): 165.4 (C4), 155.0 (C2), 125.5 (C2′), 122.1 (C5), 121.6 (C5′), 112.3 (C3′), 110.5 (C4′), 100.9 (C6). **5**, **6**: ESI+-MS: 178.0 ($[M + H]^+$).

5-(1H-Pyrrol-2-ylmethylene)-thiazolidine-2,4-dione:* E-*isomer (7) and* Z-*isomer (8)

Obtained as an 11:89 *E–Z* mixture, with 75% overall yield after purification of the crude product using hexane–EtOAc (5:1–1:1). **7**: ^{1}H NMR (DMSO): 12.25 (s, 1H, NH3), 12.16 (s, 1H, NH1′), 7.27 (m, 1H, H5′), 7.25 (s, 1H, H6), 6.73 (m, 1H, H3′), 6.29 (m, 1H, H4′). **8**: ^{1}H NMR (DMSO): 12.25 (s, 1H, NH3), 11.67 (s, 1H, NH1′), 7.66 (s, 1H, H6), 7.20 (m, 1H, H5′), 6.47 (m, 1H, H3′), 6.35 (m, 1H, H4′). ^{13}C NMR (DMSO): 167.8 (C2), 167.2 (C4), 126.9 (C2′), 124.3 (C5′), 122.2 (C6), 115.1 (C5), 113.5 (C3′), 111.9 (C4′). **7**, **8**: ESI+-MS: 195.0 ($[M + H]^+$).

Analytical HPLC

The chromatographic system consisted of an HP 1100 liquid chromatograph (Hewlett-Packard, Germany) coupled in series with an HP photodiode array detector (PAD), an evaporation light scattering detector (Polymer Labs, U.K), and an HP single quadrupole mass-selective detector (MSD) with an installed electrospray ionization (ESI) source. Process control and data handling were carried out using HP ChemStation software. The chromatographic studies were performed using Spherisorb C8/C18 and Spherisorb P (Waters, U.S.A.) reverse phase columns (250 × 4.6 mm I.D., 5 μm particle size) protected by a pre-column filter filled with the corresponding stationary phases. The mobile phase consisted of water–TFA (0.05%, solvent A) and acetonitrile–TFA (0.05%, solvent B). Elution was carried out using a linear gradient, starting from 30% solvent B to 100% solvent B over 15 min. This gradient was followed by a 5 min isocratic elution with 100% B before going back to the initial solvent mixture in 5 min. An interval of 10 min was allowed between subsequent runs. When the phenyl package was the selected stationary phase, the gradient elution went from 5 to 65% B over 15 min, while the rest of the chromatographic parameters were kept as described above. All runs were performed at room temperature at a flow rate of 1 mL min^{-1}. The eluent was monitored by PDA detector and the absorbance spectra (210–400 nm) were recorded continuously during the course of each run.

Preparative HPLC

Reverse-phase purification was carried out using a Waters Delta Prep^{TM} 4000 liquid chromatograph (Waters, U.S.A.) controlled through the Millenium 32 software package. Purifications were conducted with a 250 × 2 cm Spherisorb C18 column, using the same eluents as in analytical HPLC but at a flow rate of 10 mL min^{-1}. All isomers so obtained were examined for purity by analytical HPLC.

NMR experiments

NMR spectra of **1**–**8** were acquired on a Bruker Avance 500 spectrometer in DMSO at 30°C with an inverse probe. Proton spectra were also recorded at 70°C. Proton and carbon chemical shifts were referenced to the residual solvent signals at 2.50 and 39.5 ppm, respectively. Different types of carbon experiments were performed: standard ^{13}C NMR spectra with proton broadband decoupling, the gated ^{1}H-decoupling version that yields proton-coupled spectra, and ^{13}C spectra with ^{1}H single frequency decoupling. One-dimensional spectra were acquired using 32K data points, which were zero-filled to 64K data points previous to Fourier transformation. Absolute value COSY, phase-sensitive HSQC, and HMBC spectra were acquired using gradient-selection techniques (gs-COSY, gs-HSQC, and gs-HMBC). Acquisition data matrices were defined by 1K × 256 points in t_2 and t_1, respectively. The 2D data matrices were multiplied by appropriate window functions and zero-filled to 1K × 512 matrices prior to Fourier transformation. 1D-NOESY experiments were carried out with the selective 1D double-pulse field gradient spin echo module (11) using a mixing time of 400 ms.

© 2002 NRC Canada

2D-NOESY experiments were also performed with the same mixing time and with 2K × 256 matrices. Data were processed using the XWINNMR Bruker program on a Silicon Graphics computer.

Conclusions

This report describes the synthesis, stereochemical assignment, and conformational studies of a number of 5-(1*H*-pyrrol-2-ylmethylene)-substituted imidazolidine-2,4-diones and thiazolidine-2,4-diones that may exhibit inhibitory activity against a wide range of receptors. We have demonstrated that, regardless of the type of ring (hydantoin or TZD) or the N-substitution for the hydantoin derivatives, the (NH,C *cis*) form is the most stable conformer for the *E*-isomer and the (NH,C *trans*) form is the most stable conformer for the *Z*-isomer. The conformation around the C2′—C6 bond is therefore controlled by the configuration at the double bond.

We have shown that the *E*-isomer has the pyrrole-NH involved in an internal hydrogen bond with the carbonyl oxygen of the hydantoin or TZD rings, whereas such interaction is absent in the *Z*-isomer, leaving both groups available to establish intermolecular hydrogen bonds with the protein receptor. On the other hand, the pyrrole-NH in the *E*-isomer may form simultaneous hydrogen bonds with two donor atoms: the carbonyl oxygen of the ligand and a second electronegative atom of the receptor. These three-centre hydrogen bonds are common in the crystal structures of protein complexes (12). Thus, the knowledge of the conformational preferences and the spatial relationship between the hydrogen bond donors (NH) and the acceptors (C=O) for these compounds constitutes useful information for developing structure–activity relationships.

References

1. (*a*) H.U. Stilz, W. Guba, B. Jablonka, M. Just, O. Klingler, W. König, V. Wehner, and G. Zoller. J. Med. Chem. **44**, 1158 (2001); (*b*) J.J. Edmunds, S. Klutchko, J.M. Hamby, A.M. Bunker, C.J.C. Connolly, R.T. Winters, J. Quin III, I. Sircar, J.C. Hodges, R.L. Panek, J.A. Keiser, and A.M. Doherty. J. Med. Chem. **38**, 3759 (1995); (*c*) M.L. Brown, C.C. Zha, C.C. Van Dyke, G.B. Brown, and W.J. Brouillette. J. Med. Chem. **42**, 1537 (1999), and refs. cited therein; (*d*) R.L. Hudkins, D.L. DeHaven-Hudkins, and P. Doukas. Bioorg. Med. Chem. Lett. **7**, 979 (1997); (*e*) S.H. DeWitt and A.W. Czarnik. Acc. Chem. Res. **29**, 114 (1996).
2. (*a*) M. Oguchi, K. Wada, H. Honma, A. Tanaka, T. Kaneko, S. Sakakibara, J. Ohsumi, N. Serizawa, T. Fujiwara, H. Horikoshi, and T. Fujita. J. Med. Chem. **43**, 3052 (2000), and refs. cited therein; (*b*) C. Prabhakar, G. Madhusudhan, K. Sahadev, Ch. Maheedhara Reddy, M.R. Sarma, G. Om. Reddy, R. Chakrabarti, C. Seshagiri Rao, T. Dileep Kumar, and R. Rajagopalan. Bioorg. Med. Chem. Lett. **8**, 2725 (1998).
3. L. Sun, N. Tran, F. Tang, H. App, P. Hirth, G. McMahon, and C. Tang. J. Med. Chem. **41**, 2588 (1998).
4. T.D.W. Claridge. High-resolution NMR techniques in organic chemistry. Vol. 19. Pergamon, New York. 1999. Chap 4. p. 123.
5. (*a*) A. Marinangelli. Ann. Chim. (Rome), **44**, 219 (1954); (*b*) R.A. Jones and A.G. Moritz. Spectrochim. Acta, **21**, 295 (1965); (*c*) M. Farnier and T. Drakenberg. J. Chem. Soc. Perkin Trans. 2, 333 (1975).
6. (*a*) H. Lumbroso and G.C. Papalardo. J. Chem. Phys. **3**, 71 (1974); (*b*) I.G. John, G.L.D. Ritchie, and L. Radom. J. Chem. Soc. Perkin Trans. 2, 1601 (1977); (*c*) W.M.F. Fabian. J. Comput. Chem. **9**, 369 (1988).
7. B. Oussaid, C. Hubert, L. Moeini, B. Garrigues, and J.-P. Fayet. Can. J. Chem. **71**, 623 (1993).
8. (*a*) K. Jao, A.L. Hinde, and L. Radom. Nouv. J. Chim. **3**, 473 (1979); (*b*) J. Kao and L. Radom. J. Am. Chem. Soc. **101**, 311 (1979).
9. G. Scheler, U. Haubenreisser, and H. Rosenberger. J. Magn. Reson. **44**, 134 (1981).
10. Casagrande et al. U.S. Patent 4 579 861, 1986.
11. K. Stott, J. Stonehouse, J. Keeler, T.-L Hwang, and A. J. Shaka. J. Am. Chem. Soc. **117**, 4199 (1995).
12. G.A. Jeffrey and W. Saenger. Hydrogen Bonding in Biological Structures. Springer-Verlag, New York. 1994. Chap 2. p. 20.

© 2002 NRC Canada

Synthesis of heteronuclear bifunctional Lewis acids by transmetalation of 1,8-bis(trimethylstannyl)naphthalene with BCl_3

Marcus Schulte and François P. Gabbaï

Abstract: Reaction of 1,8-bis(trimethylstannyl)naphthalene (**1**) with an excess of BCl_3 at –78°, followed by warming to 0°C, results in the exclusive formation of the novel bifunctional Lewis acid 1-(chlorodimethylstannyl)-8-(dichloroboryl)naphthalene (**2**), a compound in which a boryl and a stannyl moiety coexist at the *peri*-positions of a naphthalene core. At elevated temperature compound **2** undergoes a chloride–methyl exchange, which affords 1-(dichloromethylstannyl)-8-(chloromethylboryl)naphthalene (**3**). Compounds **2** and **3** have been characterized by multi-nuclear NMR spectroscopy. The single crystal X-ray analysis for compound **3** reveals a sterically crowded structure with an essentially trigonal planar boron center, and a tin center pentacoordinated in a [4+1]-fashion. Upon exposure to traces of water, compound **3** is converted into the borinic acid derivative 1-(dichloromethylstannyl)-8-(hydroxymethylboryl)naphthalene (**4**), which has been characterized by multi-nuclear NMR spectroscopy and single crystal X-ray analysis.

Key words: multidentate Lewis acids, organoboranes, organostannanes.

Résume : La réaction du 1,8-bis(trimethylstannyl)naphthalene (**1**), et du BCl_3 a –78°C suivie d'une élévation de la température a 0°C mène à la formation de l'acide de Lewis bifonctionnel 1-(chlorodimethylstannyl)-8-(dichloroboryl)naphthalene (**2**). Ce nouveau composé, **2**, possède un groupement boryle ainsi qu'un groupement stannyle liés aux positions *peri* du noyau aromatique. Sous l'effet de la température, ce composé s'isomérise pour produire le 1-(dichloromethylstannyl)-8-(chloromethylboryl)naphthalene (**3**). Les composés **2** et **3** ont été caractérisés par RMN multinucléaire. La structure du composé **3**, qui a été déterminé par diffraction des rayons X sur monocristal, révèle l'existence d'un encombrement stérique important. Dans cette structure, l'atome de bore est trivalent et adopte une géométrie de coordination triangulaire et plane. L'atome d'étain est lié à quatre ligands et forme une interaction longue avec un atome de chlore provenant du bore. Le composé **3** s'hydrolyse pour former le 1-(dichloromethylstannyl)-8-(hydroxymethylboryl)naphthalene (**4**), un acide borinique qui a été caractérisés par RMN multinucléaire et par diffraction des rayons X sur monocristal.

Mot clés : acides de Lewis multidentates, organoboranes, organostannanes.

Introduction

Organostannanes have often been used as starting material for the vinylation, arylation, and alkylation of boron halides (1). In these reactions, carbon—boron bond formation is accompanied by elimination of a triorganotin halide species. Application of this synthetic strategy to the case of polydentate boranes has also been visited (2–5). For example, 1,2-(diboryl)benzenes are readily prepared by reactions of the corresponding distannanes with boron halide reagents (3–5). With the emergent use of boron polydentate Lewis acids in material science (6), molecular recognition (7–11), and catalysis (5, 12–15), the discovery of new synthetic routes to such species is fully warranted. As part of our ongoing efforts in this direction, we have studied the potential of 1,8-bis(trimethylstannyl)naphthalene (**1**) (16) to serve as a precursor to *peri*-borylated naphthalene derivatives. While this synthetic approach has been used for the preparation of gallium and indium *peri*-substituted naphthalene derivatives (17–19), we note that the *peri*-borylated derivatives (8, 20, 21) have been typically synthesized by the metathesis reaction of 1,8-dilithionaphthalene with boron halides or alkoxides.

Received 13 June 2002. Published on the NRC Research Press Web site at http://canjchem.nrc.ca on 13 October 2002.

M. Schulte and F.P. Gabbaï.[1] Department of Chemistry, Texas A&M University, College Station, TX 77843-3255, U.S.A.

[1]Corresponding author (e-mail: gabbai@mail.chem.tamu.edu).

Results and discussion

The reaction of **1** with an excess of BCl_3 in CH_2Cl_2 at –78°C followed by warming to 0°C affords 1-(chlorodimethylstannyl)-8-(dichloroboryl)naphthalene (**2**) as a pale green oil (Scheme 1). Thus, despite the presence of an excess of BCl_3, only one of the stannyl groups of the starting material is replaced by a boryl moiety. This contrasts with the rapid formation of 1,2-bis(dichloroboryl)benzene in the reaction of 1,2-bis(trimethylstannyl)benzene with BCl_3 (3, 5). We note, however, that the reaction of 1,1′-bis(trimethylstannyl)ferrocene with BCl_3 results in the substitution of only one stannyl group, as observed in the case of **1** (22). The ^{11}B NMR spectrum of **2** displays a broad signal at

 DOI: 10.1139/V02-177 © 2002 NRC Canada

Scheme 1. Synthesis of the 1-stannyl-8-borylnaphthalenes **2**, **3**, and **4**.

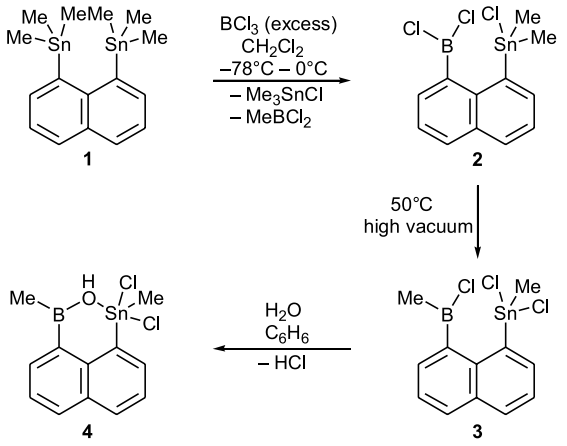

δ 52.0 in the expected range for aryldichloroboranes. The ^{119}Sn NMR spectrum shows a signal at δ 140.0 indicating the formation of a chlorodimethylstannyl moiety at the aromatic core (23). Compound **2** is rather unstable and undergoes a rearrangement reaction when exposed to elevated temperatures. Upon heating to 50°C for 6 h in high vacuum, ligand exchange occurs leading to the formation of 1-(dichloromethylstannyl)-8-(chloromethylboryl)naphthalene (**3**) (Scheme 1). Recrystallization from toluene–pentane at –40°C affords **3** in the form of beige single crystals. The ^{11}B NMR spectrum of **3** displays a broad signal at δ 64.6. The ^{119}Sn NMR spectrum shows a signal at δ –8.3 indicating the formation of a dichloromethylstannyl moiety at the aromatic core (23). The identity of **3** is confirmed by the detection in the ^{1}H NMR spectrum of two equally intense singlets that correspond to the B-Me and Sn-Me groups, the latter displaying the expected tin satellites. Upon exposure to traces of water, compound **3** is converted into a borinic acid derivative 1-(dichloromethylstannyl)-8-(hydroxymethylboryl)naphthalene (**4**) (Scheme 1), which has been characterized by multi-nuclear NMR spectroscopy and single crystal X-ray analysis as well. While most NMR spectroscopic features are analogous to those of **3**, the resonance of the ^{119}Sn dichloromethylstannyl in **4** (δ –90.3) is shifted upfield, which likely reflects the coordination of an additional ligand at tin (24).

The structures of **3** and **4** have been confirmed by X-ray analysis (Figs. 1 and 2). Both compounds crystallize in the monoclinic space group $P2_1$ with two molecules in the unit cell. In addition to the naphthalene backbone, a methyl group, and two chloride anions that constitute the four primary ligands, the coordination sphere of the tin center of these derivatives also contains a bridging chloride (**3**) or hydroxide (**4**) ligand originating from the neighboring boryl moiety. The resulting intramolecular Sn···Cl(3) contact of 3.177(2) Å in **3** is long but remains within the sum of the van der Waals radii of these two elements. As a result, the coordination geometry of the tin atom in **3** is best described as monocapped tetrahedral ((4+1) coordination). In **4**, the bridging hydroxide forms a relatively short intramolecular

Fig. 1. ORTEP view of 1-(dichloromethylstannyl)-8-(chloromethylboryl)naphthalene (**3**) in the crystal, showing 50% probability ellipsoids and the atom numbering scheme. Selected bond lengths (Å) and angles (°): Sn—C(01) 2.117(6), Sn—C(1) 2.136(5), Sn—Cl(1) 2.370(2), Sn—Cl(2) 2.354(1), Sn···Cl(3) 3.177(2), B—C(02) 1.545(8), B—C(8) 1.546(9), B—Cl(3) 1.834(7), B···Cl(2) 3.069(7), C(01)-Sn-C(1) 131.2(2), C(01)-Sn-Cl(1) 102.6(2), C(01)-Sn-Cl(2) 110.3(2), C(01)-Sn···Cl(3) 76.5(2), C(1)-Sn-Cl(1) 101.1(2), C(1)-Sn-Cl(2) 106.8(1), C(1)-Sn···Cl(3) 77.2(2), Cl(1)-Sn-Cl(2) 99.82(6), Cl(1)-Sn···Cl(3) 176.24(4), Cl(2)-Sn···Cl(3) 83.91(5), C(02)-B-C(8) 128.4(5), C(02)-B-Cl(3) 115.7(5), C(02)-B···Cl(2) 88.5(4), C(8)-B-Cl(3) 114.7(4), C(8)-B···Cl(2) 96.4(4), Cl(3)-B···Cl(2) 96.5(3), Sn-Cl(2)···B 77.3(1), B-Cl(3)···Sn 81.7(2), Sn-C(1)-C(9) 127.7(4), B-C(8)-C(9) 129.5(5).

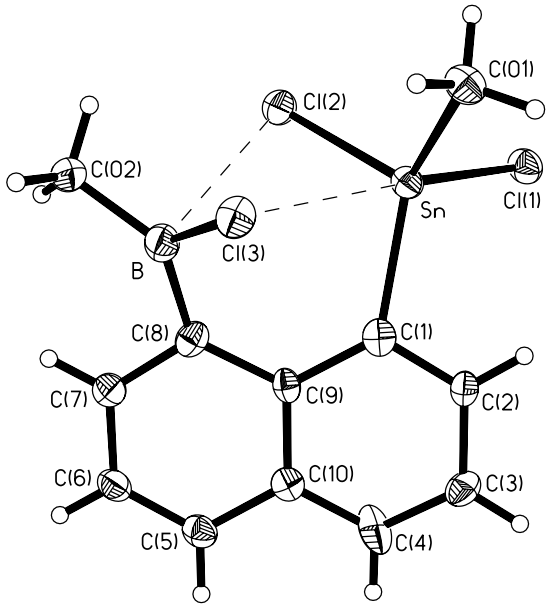

Sn···O contact of 2.370(3) Å, which confirms the participation of the hydroxide in the coordination sphere of the tin atom. Thus, and as confirmed by the difference between the three equatorial angles and the three axial angles involving Cl(1) ($\Delta\Sigma(\Theta)$) (25),[2] the coordination geometry of the tin atoms in **4** ($\Delta\Sigma(\Theta)$ = 71.9°) is closer to a trigonal bipyramid than in **3** ($\Delta\Sigma(\Theta)$ = 44.8°). The coordination geometry of the boron center is essentially trigonal planar (Σ_{angles} = 358.8° (**3**), 359.9° (**4**)). The slight deviation observed in the coordination geometry of the boron center in **3** can be correlated to the presence of a weak intramolecular B···Cl(2) contact of 3.069(7) Å. The structure of **3** and **4** presents a number of features characteristic of sterically hindered *peri*-substituted naphthalene derivatives (26). The Sn-C(1)-C(9) (127.7(4)° (**3**), 125.1(3)° (**4**)) and B-C(8)-C(9) (129.5(5)° (**3**), 127.2(3)° (**4**)) angles substantially deviate from the ideal value of 120°. The core of the naphthalene backbone is slightly twisted as reflected by the dihedral angles of 5.6° (**3**) and 4.2° (**4**) formed between the planes defined by C(1)-C(8)-C(9) and C(4)-C(5)-C(10). The stannyl and boryl moieties are displaced above and below the plane of the naphthalene

[2] $\Delta\Sigma(\Theta) = \Sigma\Theta_{eq} - \Sigma\Theta_{ax}$ has been used to quantify the distortion of a tetrahedral tin center ($\Delta\Sigma(\Theta) = 0°$) toward a trigonal bipyramidal geometry ($\Delta\Sigma(\Theta) = 90°$). The equatorial and axial angles are those involving the coordinated ligand that sits *trans* from the approaching ligand.

© 2002 NRC Canada

Fig. 2. ORTEP view of 1-(dichloromethylstannyl)-8-(hydroxymethylboryl)naphthalene (**4**) in the crystal, showing 50% probability ellipsoids and the atom numbering scheme. Selected bond lengths (Å) and angles (°): Sn—C(01) 2.120(4), Sn—C(1) 2.119(4), Sn—Cl(1) 2.474(1), Sn—Cl(2) 2.366(1), Sn···O 2.370(3), B—C(02) 1.560(6), B—C(8) 1.564(6), B—O 1.391(5), B···Cl(2) 3.288(5), C(01)-Sn-C(1) 134.3(2), C(01)-Sn-Cl(1) 95.8(1), C(01)-Sn-Cl(2) 111.1(1), C(01)-Sn···O 86.9(1), C(1)-Sn-Cl(1) 97.7(1), C(1)-Sn-Cl(2) 111.8(1), C(1)-Sn···O 84.2(1), Cl(1)-Sn-Cl(2) 91.83(4), Cl(1)-Sn···O 173.91(8), Cl(2)-Sn···O 82.11(8), C(02)-B-C(8) 124.3(4), C(02)-B-O 118.8(4), C(02)-B···Cl(2) 100.6(3), C(8)-B-O 116.8(4), C(8)-B···Cl(2) 101.6(3), O-B···Cl(2) 70.4(2), Sn-Cl(2)···B 66.70(9), B-O···Sn 114.2(3), Sn-C(1)-C(9) 125.1(3), B-C(8)-C(9) 127.

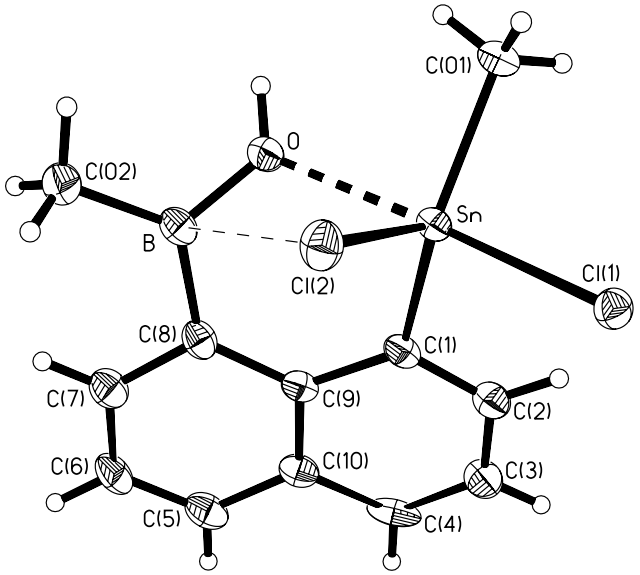

backbone by 0.376 and 0.553 Å, respectively in **3** and by 0.237 and 0.384 Å, respectively in **4**.

Experimental section

General methods

All experiments were carried out under a dry inert atmosphere of N_2 using standard Schlenk technique or a glove box (Unilab, M. Braun). The solvents were purified by distillation from appropriate drying agents under N_2. Boron trichloride was purchased from Aldrich and used without further purification. 1,8-Bis(trimethylstannyl)naphthalene was prepared according to a published procedure (16). The microanalyses were performed by Atlantic Microlab, Norcross, GA. The melting points were measured on samples in sealed capillaries and are uncorrected.

NMR spectroscopy

NMR spectra were recorded on a Varian Unity Inova 400 FT NMR spectrometer (399.67 MHz for ^{1}H, 128.23 MHz for ^{11}B, 100.50 MHz for ^{13}C, 149.04 MHz for ^{119}Sn) by using internal deuterium lock. Chemical shifts (δ) are given in ppm, and are referenced against external Me_4Si (^{1}H, ^{13}C), $BF_3{\cdot}Et_2O$ (^{11}B), and Me_4Sn (^{119}Sn).

Crystallography

Crystals of 1-(dichloromethylstannyl)-8-(chloromethylboryl)naphthalene (**3**) were grown from a toluene–pentane solution at −40°C, and of 1-(dichloromethylstannyl)-8-(hydroxymethyl)naphthalene (**4**) from a chloroform–pentane solution at room temperature, respectively. Owing to the reactive nature of the compounds, the crystals were handled under a blanket of dry mineral oil during mounting. The crystals selected for data collection were mounted on a glass fiber with apiezon grease, and rapidly transferred into the cold N_2 stream of the low-temperature accessory. Intensity data for the crystals were collected on a Siemens SMART CCD diffractometer at 110(2) K, using graphite monochromated Mo Kα radiation (λ = 0.71073 Å), and 0.3°-wide ω-scans with a crystal to detector distance of 5.0 cm. The structures were solved by direct method (27) and refined by full-matrix least-squares against F^2 (28). Crystallographic data are given in Table 1.[3]

1-(Chlorodimethylstannyl)-8-(dichloroboryl)naphthalene (2)

A solution of 1,8-bis(trimethylstannyl)naphthalene (**1**) (1.00 g, 2.20 mmol) in CH_2Cl_2 (10 mL) was cooled to –78°C and BCl_3 (2.50 g, 21.3 mmol) was added by Schlenk to Schlenk condensation. The reaction mixture was kept at –78°C for 60 min, warmed to 0°C, and all volatiles were removed in high vacuum to give **2** (829 mg, 2.12 mmol, 96%) as a pale green oil. Compound **2** was used in the next step without further purification. ^{1}H NMR (C_6D_6) δ: 0.36 (s, 6H, $^2J(^{117,119}\text{Sn-}^1\text{H})$ = 66, 69 Hz, CH_3), 7.04 (dd, 1H, $^3J(^1\text{H-}^1\text{H})$ = 7 + 8 Hz, H-3 or H-6), 7.22 (dd, 1H, $^3J(^1\text{H-}^1\text{H})$ = 8 Hz, $^4J(^1\text{H-}^1\text{H})$ = 1 Hz, H_{arom}), 7.27 (dd, 1H, $^3J(^1\text{H-}^1\text{H})$ = 8 Hz, $^4J(^1\text{H-}^1\text{H})$ = 1 Hz, H_{arom}), 7.44 (dd, 1H, $^3J(^1\text{H-}^1\text{H})$ = 7 + 8 Hz, H-3 or H-6), 8.03 (dd, 1H, $^3J(^1\text{H-}^1\text{H})$ = 7 Hz, $^4J(^1\text{H-}^1\text{H})$ = 1 Hz, H_{arom}), 8.65 (dd, 1H, $^3J(^1\text{H-}^1\text{H})$ = 7 Hz, $^4J(^1\text{H-}^1\text{H})$ = 1 Hz, H_{arom}). ^{13}C NMR (C_6D_6) δ: 5.1 ($^1J(^{117,119}\text{Sn-}^{13}\text{C})$ = 461, 483 Hz, CH_3), 124.9, 126.1, 126.3, 129.2, 133.9, 134.7, 134.8, 135.4, 137.8, 139.3 (all C_{arom}). ^{11}B NMR (C_6D_6) δ: 52.0. ^{119}Sn NMR (C_6D_6) δ: 140.0. No elemental analysis on account of the low stability of the compound.

1-(Dichloromethylstannyl)-8-(chloromethylboryl)naphthalene (3)

A sample of **2** (500 mg, 1.28 mmol) was heated to 50°C under a vacuum of 10^{-3} torr (1 torr = 133.322 Pa) for 8 h and the residue re-crystallized from a toluene–pentane mixture (1:1) to give **3** (419 mg, 1.07 mmol, 84%) as a beige solid; mp 110°C (decomposition (dec.)). ^{1}H NMR (C_6D_6) δ: 1.10 (s, 3H, $^2J(^{117,119}\text{Sn-}^1\text{H})$ = 73, 77 Hz, $SnCH_3$), 1.38 (s, 3H, BCH_3), 6.99 (dd, 1H, $^3J(^1\text{H-}^1\text{H})$ = 7 + 8 Hz, H-3 or H-6), 7.11 (dd, 1H, $^3J(^1\text{H-}^1\text{H})$ = 7 + 8 Hz, H-3 or H-6), 7.43

[3] Supplementary data may be purchased from the Depository of Unpublished Data, Document Delivery, CISTI, National Research Council Canada, Ottawa, ON K1A 0S2, Canada (http://www.nrc.ca/cisti/irm/unpub_e.shtml for information on ordering electronically). Crystallographic data have also been deposited at the CCDC, and copies can be obtained on request, by quoting the publication citation and the deposition numbers 185099–185100. These data can be obtained, free of charge, via www.ccdc.cam.ac.uk/conts/retrieving.html (or from the Cambridge Crystallographic Data Centre, 12 Union Road, Cambridge, U.K.; fax +44 1223 336033; or deposit@ccdc.cam.ac.uk).

© 2002 NRC Canada

Table 1. Crystallographic data for **3** and **4**.

	3	**4**
Empirical formula	$C_{12}H_{12}Cl_3SnB$	$C_{12}H_{13}Cl_2OSnB$
Formula weight (g mol^{-1})	392.07	373.62
Crystal system	Monoclinic	Monoclinic
Crystal size (mm)	0.30 × 0.11 × 0.04	0.36 × 0.22 × 0.15
Space group	$P2_1$	$P2_1/n$
a (Å)	6.5448(8)	6.3170(5)
b (Å)	9.512(1)	10.2364(8)
c (Å)	11.319(1)	10.9679(8)
β (°)	101.824(2)	104.362(1)
V (Å^3)	689.7(1)	687.06(9)
Z	2	2
D_{calcd} (mg m^{-3})	1.888	1.806
μ (mm^{-1})	2.406	2.227
F(000)	380	364
θ range (°)	1.84 to 28.82	1.92 to 28.57
Index ranges	$-8 \le h \le 8$	$-8 \le h \le 8$
	$-12 \le k \le 8$	$-12 \le k \le 12$
	$-15 \le l \le 14$	$-7 \le l \le 14$
Reflections measured	4304	5347
Completeness to θ_{max}	89.3	88.1
Independent reflections, R_{int}	2433, 0.0294	2879, 0.0586
Parameters	154	154
GoF (F^2)	0.94	1.079
R_1 (F) [$I > 2\sigma(I)$]	0.0337	0.0300
wR_2 (F) [$I > 2\sigma(I)$]	0.0891	0.0827
Largest diff. peak and hole (e Å^{-3})	1.705 and –0.764	0.807 and –1.439

(dd, 1H, $^3J(^1H\text{-}^1H)$ = 8 Hz, $^4J(^1H\text{-}^1H)$ = 1 Hz, H_{arom}), 7.49 (dd, 1H, $^3J(^1H\text{-}^1H)$ = 8 Hz, $^4J(^1H\text{-}^1H)$ = 1 Hz, H_{arom}), 7.58 (dd, 1H, $^3J(^1H\text{-}^1H)$ = 7 Hz, $^4J(^1H\text{-}^1H)$ = 1 Hz, H_{arom}), 7.94 (dd, 1H, $^3J(^{117,119}Sn\text{-}^1H)$ = 95, 99 Hz, $^3J(^1H\text{-}^1H)$ = 7 Hz, $^4J(^1H\text{-}^1H)$ = 1 Hz, H-2). ^{13}C NMR (C_6D_6) δ: 10.5 ($^1J(^{117,119}Sn\text{-}^{13}C)$ = 535, 560 Hz, $SnCH_3$), 14.1 (BCH_3), 124.8 (C_{arom}), 126.00 ($J(^{117,119}Sn\text{-}^{13}C)$ = 90, 94 Hz, C_{arom}), 132.8 ($J(^{117,119}Sn\text{-}^{13}C)$ = 19 Hz, C_{arom}), 134.9 ($J(^{117,119}Sn\text{-}^{13}C)$ = 22 Hz, C_{arom}), 135.7 ($J(^{117,119}Sn\text{-}^{13}C)$ = 14 Hz, C_{arom}), 136.2 (C_{arom}), 137.8 ($J(^{117,119}Sn\text{-}^{13}C)$ = 53 Hz, C_{arom}), 138.3 (C_{arom}), 140.2 (C_{arom}), 142.00 ($^1J(^{117,119}Sn\text{-}^{13}C)$ = 763, 798 Hz, C-1). ^{11}B NMR (C_6D_6)) δ: 64.6. ^{119}Sn NMR (C_6D_6) δ: –8.3. Elemental anal. calcd. (%) for $C_{12}H_{12}Cl_3SnB$ (392.07): C 36.76, H 3.08; found: C 37.38, H 3.17.

1-(Dichloromethylstannyl)-8-(hydroxymethylboryl)naphthalene (4)

To a solution of **3** (200 mg, 0.510 mmol) in benzene (10 mL) was added water (9.10 μL, 0.510 mmol) and the mixture stirred for 15 min. The solvent was evaporated in vacuo and the residue re-crystallized from $CHCl_3$–pentane (1:1) to give **4** (101 mg, 0.270 mmol, 53%) as a colorless solid; mp 139–140°C. ^1H NMR (C_6D_6) δ: 0.53 (s, 3H, BCH_3), 0.93 (s, 3H, $^2J(^{117,119}Sn\text{-}^1H)$ = 76, 80 Hz, $SnCH_3$), 5.55 (s, 1H, OH), 7.13 (dd, 1H, $^3J(^1H\text{-}^1H)$ = 7 + 8 Hz, H-3 or H-6), 7.21 (dd, 1H, $^3J(^1H\text{-}^1H)$ = 7 + 8 Hz, H-3 or H-6), 7.50 (dd, 1H, $^3J(^1H\text{-}^1H)$ = 8 Hz, $^4J(^1H\text{-}^1H)$ = 1 Hz, H_{arom}), 7.58 (dd, 1H, $^3J(^1H\text{-}^1H)$ = 8 Hz, $^4J(^1H\text{-}^1H)$ = 1 Hz, H_{arom}), 7.75 (dd, 1H, $^3J(^1H\text{-}^1H)$ = 7 Hz, $^4J(^1H\text{-}^1H)$ = 1 Hz, H_{arom}), 8.61 (dd, 1H, $^3J(^1H\text{-}^1H)$ = 7 Hz, $^4J(^1H\text{-}^1H)$ = 1 Hz, H_{arom}). ^{13}C NMR (C_6D_6) δ: 14.3 ($^1J(^{117,119}Sn\text{-}^{13}C)$ = 562, 588 Hz, $SnCH_3$), 22.7 (BCH_3), 125.00, 125.8, 127.6, 128.6, 132.7, 134.9, 138.9, 140.0 (all C_{arom}, only 8 signals detected). ^{11}B NMR (C_6D_6) δ: 51.0. ^{119}Sn NMR (C_6D_6) δ: –90.3. Elemental anal. calcd. (%) for $C_{12}H_{13}OCl_2SnB$ (373.62): C 38.57, H 3.51; found: C 38.44, H 3.48.

Conclusion

The reaction of **1** with boron trichloride results in the substitution of only one of the stannyl moieties of the starting material. Although an analogous partial transmetalation reaction is observed in the reaction of **1** with $GaCl_3$, these results come in marked contrast with those obtained in the reaction of 1,2-bis(trimethylstannyl)-benzene with boron trichloride (3). In the latter case, the reactions have been shown to result in a complete transmetalation of the stannyl moieties and formation of 1,2-diborylated benzene derivatives. Finally, compounds **1** and **2** constitute notable examples of heteronuclear bifunctional Lewis acids (2), whose acceptor properties should lie between those of the corresponding boron (3–15) and tin polydentate systems (23, 29).

Acknowledgements

We thank the Alexander von Humboldt Stiftung (grant to M.S.), the Robert A. Welch Foundation (grant A-1423), and the National Science Foundation (NSF) (grant CAREER CHE-0094264) for generous financial support. The purchase of a CCD X-ray diffractometer was made possible by a grant from the NSF (CHE-98 07975).

© 2002 NRC Canada

References

1. (*a*) H. Nöth and H. Vahrenkamp. J. Organomet. Chem. **11**, 399 (1968); (*b*) H. Nöth and P. Fritz. Z. Anorg. Allg. Chem. **322**, 297 (1963); (*c*) J.E. Burch, W. Gerrard, M. Howarth, and E.F. Mooney. J. Chem. Soc. 4916 (1960).
2. F. Jäkle, A.J. Lough, and I. Manners. Chem. Commun. 453 (1999).
3. D. Kaufmann. Chem. Ber. **120**, 901 (1987).
4. J.J. Eisch and B.W. Kotowicz. Eur. J. Inorg. Chem. 761 (1998).
5. M.V. Metz, D.J. Schwartz, C.L. Stern, P.N. Nickias, and T.J. Marks. Angew. Chem. Int. Ed. Engl. **39**, 1312 (2000).
6. M. Fontani, F. Peters, W. Scherer, W. Wachter, M. Wagner, and P. Zanello. Eur. J. Inorg. Chem. 1453 (1998).
7. (*a*) D.F. Schriver and M.J. Biallas. J. Am. Chem. Soc. **89**, 1078 (1967); (*b*) D.J. Saturnino, M. Yamauchi, W.R. Clayton, R.W. Nelson, and S.G. Shore. J. Am. Chem. Soc. **97**, 6063 (1975).
8. (*a*) H.E. Katz. J. Org. Chem. **50**, 5027 (1985); (*b*) H.E. Katz. Organometallics, **6**, 1134 (1987).
9. M. Reilly and T. Oh. Tetrahedron Lett. **35**, 217 (1995).
10. H.E. Katz. J. Org. Chem. **54**, 2179 (1989).
11. (*a*) K. Nozaki, M. Yoshida, and H. Takaya. Bull. Chem. Soc. Jpn. **69**, 2043 (1996); (*b*) K. Nozaki, T. Tsutsumi, and H. Takaya. J. Org. Chem. **60**, 6668 (1995).
12. E.Y.-X. Chen and T.J. Marks. Chem. Rev. **100**, 1391 (2000).
13. (*a*) V.C. Williams, W.E. Piers, W. Clegg, M.R.J. Elsegood, S. Collins, and T.B. Marder. J. Am. Chem. Soc. **121**, 3244 (1999); (*b*) V.C. Williams, C. Dai, Z. Li, S. Collins, W.E. Piers, W. Clegg, M.R.J. Elsegood, and T.B. Marder. Angew. Chem. Int. Ed. Engl. **38**, 3695 (1999); (*c*) W.E. Piers, G.J. Irvine, and V.C. Williams. Eur. J. Inorg. Chem. 2131 (2000); (*d*) V.C. Williams, G.J. Irvine, W.E. Piers, Z. Li, S. Collins, W. Clegg, M.R.J. Elsegood, and T.B. Marder. Organometallics, **19**, 1619 (2000); (*e*) L.D. Henderson, W.E. Piers, G.J. Irvine, and R. McDonald. Organometallics, **21**, 340 (2002).
14. M. Reiley and T. Oh. Tetrahedron Lett. **36**, 221 (1995).
15. B. Schilling, V. Kaiser, and D. Kaufmann. Chem. Ber. **130**, 923 (1997).
16. D. Seyferth and S.C. Vick. J. Organomet. Chem. **141**, 173 (1977).
17. J.D. Hoefelmeyer, M. Schulte, and F.P. Gabbaï. Inorg. Chem. **40**, 3833 (2001).
18. (*a*) M. Tschinkl, J.D. Hoefelmeyer, T.M. Cocker, R.E. Bachman, and F.P. Gabbaï. Organometallics, **19**, 1826 (2000); (*b*) J.D. Hoefelmeyer, D. Brode, and F.P. Gabbaï. Organometallics, **20**, 5653 (2001).
19. M. Schulte and F.P. Gabbaï. Chem. Eur. J. **8**, 3802 (2002).
20. (*a*) J.D. Hoefelmeyer and F.P. Gabbaï. J. Am. Chem. Soc. **122**, 9054 (2000); (*b*) J.D. Hoefelmeyer and F.P. Gabbaï. Organometallics, **21**, 982 (2002).
21. A. Hergel, H. Pritzkow, and W. Siebert. Angew. Chem. Int. Ed. Engl. **33**, 1247 (1994).
22. J.A. Gamboa, A. Sundararaman, L. Kakalis, A.J. Lough, and F. Jäkle. Organometallics, **21**, 4169 (2002).
23. R. Altmann, K. Jurkschat, M. Schürmann, D. Dakternieks, and A. Duthie. Organometallics, **17**, 5858 (1998).
24. A.G. Davies. Organotin chemistry. VCH, Weinheim. 1997. Chap 2.
25. U. Kolb, M. Beuter, and M. Dräger, Inorg. Chem. **33**, 4522 (1994).
26. (*a*) J.F. Blount, F. Cozzi, J.R. Damewood Jr, L.D. Iroff, U. Sjostrand, and K. Mislow. J. Am. Chem. Soc. **102**, 99 (1980); (*b*) R. Schröck, K. Angermaier, A. Sladek, and H. Schmidbaur. Organometallics, **13**, 3399 (1994).
27. G. Sheldrick. 1986. SHELXS-86 Program for crystal structure solution [computer program]. Institut für Anorganische Chemie, Universität Göttingen. Göttingen, Germany.
28. G. Sheldrick. 1997. SHELXL-97 Program for crystal structure refinement [computer program]. Institut für Anorganische Chemie, Universität, Göttingen. Göttingen, Germany.
29. M. Schulte, M. Schürmann, and K. Jurkschat. Chem. Eur. J. **7**, 347 (2001), and refs. cited therein.

© 2002 NRC Canada

The antimicrobial nalidixic acid as a probe for molecular recognition of α- and β-cyclodextrins

I.S. Shehatta, M.S. Ibrahim, and M.R. Sultan

Abstract: The inclusion of the antibacterial drug nalidixic acid (NAL) in α- and β-cyclodextrin (CD) cavities was studied using UV–vis absorption and voltammetric methods. It was corroborated that the UV absorption bands of NAL are intensified in the presence of α- and β-CDs. A pronounced decrease in the peak currents of NAL was also noticed upon the addition of α- and β-CDs. From the changes in the peak currents, it was concluded that NAL forms 1:1 inclusion complexes with the various hosts, which is also revealed in the phase solubility profile of the NAL–β-CD system, as a representative example. From voltammetric data, the logarithm of the binding constants were calculated to be 2.60 and 3.20 for α- and β-CDs, respectively. The magnitude of the formation constants, as well as the Gibbs free energies for NAL with α- and β-CDs, shows that NAL is bound more strongly to β-CD, with a more apolar cavity, than to α-CD. These observations suggest that hydrophobic interaction is the most important recognition element in the binding process. All orientations of entering NAL into the cavity have been considered herein, with the purpose of characterizing the inclusion complex of NAL with CD. Combining the experimental results and molecular modeling and energy calculations on the inclusion complexes yielded a more detailed picture of the solution structure of the complex formed between NAL and either α-CD or β-CD. It was inferred that the inclusion process can occur through the 2-methylpyridine side. An additional hydrogen bond was also found to be formed between the carboxyl group of NAL, which remains outside the β-CD cavity, and the secondary hydroxyl group of β-CD. This hydrogen bond should, therefore, be operating as an important second recognition element in the NAL–β-CD system.

Key words: cyclodextrins, host–guest association, inclusion complexes, nalidixic acid, solubility, voltammetry.

Résumé : Faisant appel à des méthodes voltampérométrique ainsi que de spectroscopie UV–vis, on a étudié l'inclusion de l'acide nalidixique (NAL), un antibactérien, dans des cavités de α- et β-cyclodextrines (CD). Il a été corroboré que l'intensité des bandes d'absorption UV du NAL est augmentée en présence des α- et β-CD. On a aussi noté une diminution sensible dans les courants de pic du NAL lors de l'addition des α- et β-CD. Sur la base des changements dans les courants de pic, on en conclut que le NAL forme des complexes d'inclusion 1:1 avec les divers hôtes; comme exemple représentatif, ceci se révèle à partir du profil de solubilité de phase du système NAL–β-CD. Utilisant les données voltampérométriques, on a aussi calculé que les valeurs du logarithme des constantes de fixation sont respectivement de 2,60 et 3,20 pour les α- et β-CD. L'amplitude des constantes de formation ainsi que des énergies libres de Gibbs pour NAL avec les α- et β-CD démontent que, par opposition à l'α-CD, le NAL est lié plus fortement à la β-CD qui comporte une cavité apolaire. Ces observations suggèrent que l'interaction hydrophobe constitue l'élément de reconnaissance le plus important du processus de fixation. Dans le but de caractériser le complexe d'inclusion du NAL avec la CD, on a considéré toutes les orientations du NAL au moment de son entrée dans la cavité. Une combinaison des résultats expérimentaux avec la modélisation moléculaire et les calculs d'énergie des complexes d'inclusion permettent d'obtenir une vue plus détaillée de la structure en solution du complexe qui se forme entre le NAL et l'α-CD ou la β-CD. On en déduit que le processus d'inclusion peut se produire par le côté de la 2-méthylpyridine. On a aussi trouvé qu'une liaison hydrogène se forme entre le groupe carboxyle du NAL, qui demeure à l'extérieur de la cavité de la β-CD, et groupe l'hydroxyle secondaire de la β-CD. On en conclut que la liaison hydrogène doit jouer un rôle de reconnaissance secondaire important dans le cas du système NAL–β-CD.

Mots clés : cyclodextrines, association hôte–invité, complexes d'inclusion, acide nalidixique, solubilité, voltampérométrie.

[Traduit par la Rédaction]

Received 18 March 2002. Published on the NRC Research Press Web site at http://canjchem.nrc.ca on 17 October 2002.

I.S. Shehatta,[1, 2] M.S. Ibrahim,[3] and M.R. Sultan. Chemistry Department, Faculty of Science, United Arab Emirates University, Al-Ain 17551, UAE.

[1]Corresponding author: (e-mail: ishehatta@yahoo.com).
[2]Address for correspondence: Chemistry Department, Faculty of Science, Mansoura University, Mansoura, Egypt.
[3]Address for correspondence: Chemistry Department, Faculty of Science, Assiut University, Assiut 71516, Egypt.

 DOI: 10.1139/V02-124 © 2002 NRC Canada

Introduction

Nalidixic acid is the first analogue of a class of the most important and impressive antimicrobial drugs called fluoroquinolones. This group of drugs inhibits the activity of bacterial DNA gyrase, an enzyme that controls the supercoiling of DNA by converting relaxed, covalently closed, circular DNA to a superhelical form by an energy-dependent strand breakage and resealing process (1). NAL has been extensively used as an antibacterial agent in the treatment of urinary tract infection and is effective against a variety of gram-negative pathogens (2, 3).

NAL is poorly soluble in water and its bioavailability is thus limited. Among the various approaches to improve the solubility and bioavailability of poorly soluble drugs are the use of cyclodextrin inclusion complexes, which have often proven to be successful (4, 5).

Cyclodextrins are cyclic oligosaccharides of α-D-glucose units, linked by α-1,4 bonds, and produced by enzymatic degradation of starch. They have doughnut shapes and a relatively hydrophobic cavity. These are among the most important and widely studied examples of host molecules that are able to form inclusion complexes with a variety of guests. Generally, the inclusion complex involves total or partial spatial entrapment of guest molecules in the cavity of the host molecule, without the formation of any covalent bonds. The stability of the complexes is primarily determined by how closely the guest and the lipophilic cone-like cavity are matched in size and shape. A perfect fit of the guest into the CD cavity enhances the host–guest interactions and leads to an increase in the value of the association constant.

Studies (6–9) regarding the interaction of NAL with cyclodextrins are surprisingly contradictory. α-CD has been reported to enhance the solubility of NAL (6); however, conflicting reports (7, 8) have concluded that an inclusion complex was not formed between NAL and β-CD. This lack of formation was attributed either to the NAL molecule being too large to be able to enter the β-CD cavity, or because of steric hindrance, although the average cavity diameter of β-CD is larger than α-CD. Two different association constant (*K*) values were also reported (7, 9) for the binding of NAL with γ-CD. Moreover, the data reported in literature were based upon UV, IR, X-ray, fluorescence, solubility, dissolution, and thermal methods (6–9). Electrochemical techniques have not been used to study the interaction of NAL with interesting hosts. In recent years, electrochemical investigations of substrate–cyclodextrin interactions (10–13) have provided a useful complement to the previously mentioned methods.

These considerations prompted us to study the interaction of NAL with α- and β-CDs using three independent techniques, namely solubility, spectroscopy, and voltammetry. In a continuation of our previous work (13–16), the aim of the present study was to improve the solubility of NAL in aqueous solution, and thereby to improve its bioavailabiliy. This goal was attained via the formation of an inclusion complex with β-CD. From that formation, the effects of β-CD concentration on the solubility of NAL in aqueous solution was determined. The association constants for the complexes formed between NAL and α-CD or β-CD were also calculated using voltammetric techniques. Moreover, the work was extended to an analysis of the influence of the CD cavity size on the complexation process with NAL, as well as to the driving forces for this process. Finally, molecular modeling and energy calculations were carried out to visualize the type of site interaction, and thus to elucidate the geometry of the inclusion complex.

Experimental

Materials

Nalidixic acid, α-CD, and β-CD were purchased from Sigma and were used as received. Stock solutions of α-CD and β-CD were prepared by dissolving the desired weights in water. Stock solutions of NAL were prepared by dissolving an appropriate amount of the drug in methanol. The supporting electrolytes (reagent grade, Merck, Darmstadt) were phosphate, Britton-Robinson (BR), and acetate buffers prepared in the usual way. The ionic strength was maintained constant (0.5 M) by adding $NaNO_3$. Double-distilled water was used to prepare the solutions. Methanol was the solvent of choice due to: (*i*) its ability to dissolve NAL appreciably; (*ii*) its structural similarity to water among other solvents; and (*iii*) its low affinity for binding with CD (17), which renders it a poor competitor with NAL for CD.

Apparatus

The solubility experiments were performed at constant temperature (25 ± 0.5°C) in a shaking water bath (Precision Scientific Group, Chicago, IL). The pH measurements were made using an ORION pH-meter, model M64 (ORION Research, Boston MA), accurate to ±0.05 pH unit. All spectrophotometric measurements were conducted using a Shimadzu UV-2101 PC UV–vis scanning spectrophotometer (Shimadzu, Kyoto, Japan), using matched quartz cuvettes of 1.0 cm path length. Differential pulse stripping voltammetry (DPSV) and cyclic voltammetry (CV) were carried out using a PAR Model 264A polarographic analyzer – stripping voltammeter, in conjunction with a PAR Model 303A HMDE and *x-y* recorder model RE0151. The area of the HMDE was 1.2×10^{-2} cm^2. The three-electrode system was completed by an Ag/AgCl (sat. KCl) reference electrode and a Pt-wire auxiliary electrode. A PAR Model 305 stirrer was also used for DPSV.

Methods

Solubility measurements

The solubilization of NAL in water and aqueous β-CD solution was carried out according to the method of Higuchi and Connors (18). An excess amount of NAL was added into the aqueous solutions containing increasing amount of β-CD solution (0 to 5×10^{-3} M). The mixture was shaken in a water bath (2 h, 310 K) and then agitated further at room temperature (70 h, 25 ± 0.5°C) until the equilibrium state was reached. The resulting suspension was filtered through filter paper (0.45 μm). The concentration of NAL in the filtrate was assayed spectrophotometrically at 257 nm; there was no interference from CD at this wavelength. The concentration of NAL was also determined potentiometrically. Each solubility was determined in triplicate.

© 2002 NRC Canada

Spectrophotometric measurements

Complex formation between NAL and α-CD or β-CD was also studied using the spectral shift of NAL upon the addition of various hosts. The concentration of NAL in these studies was 5×10^{-5} M, while the cyclodextrin concentrations were varied up to 12 mM.

Voltammetric measurements

For voltammetric measurements, the test solution was placed in a polarographic cell (volume ≈15 mL) and deoxygenated by bubbling nitrogen for 15 min. In the case of DPSV, the accumulation was performed on the HMDE, and the solution was stirred at the accumulation potential of $E_{acc} = -0.4$ V for 30 s. The voltammetric response was obtained using a pulse repetition time of 0.2 s, within an amplitude of 100 mV, and a scan rate of 20 mV s^{-1} (or 100 mV s^{-1} for CV, unless otherwise stated). While preconcentration was done in the stirred solutions, a quiescent period of 15 s was allowed before the potential scan was started. Typical CV peak potentials were reproducible to better than ±5 mV and DPSV peak potentials to ±2 mV. The concentration of NAL and the total volume of solution (10 mL) were kept constant, and the CD concentration varied, while carrying out the electrochemical procedures. All experiments were carried out at ambient temperature (25.0 ± 0.5°C).

Molecular modeling and computational details

Molecular modeling and energy calculations were carried out on PCMODEL version 6.0 (Serena software). The starting geometry of α-CD or β-CD was generated by connecting two D-glycopyranose monomers (taken from the library) via an α-(1→4) glycosidic linkage, and then conjugated to determine the energy minimized conformation. This conjugation was continued by adding another D-glucopyranose moiety each time, until six or seven such molecules were arranged symmetrically to get a well-shaped structure having energy minimized conformations for α-CD and β-CD, respectively. Finally, the cavity dimensions (depth, diameter of the wider and narrower rims) were calculated and compared with the reported values. Similarly, the geometry of NAL was built from scratch using library molecular fragments to determine energy minimized conformation. The dimensions of the drug molecule were also calculated. All possible topologies for the entry of the guest (NAL) into the cavity of the host (α-CD or β-CD) were generated. The portion of NAL and the extent of its penetration in the CD cavity were also observed on the computer monitor on the entire *x*, *y*, and *z* axes. This molecular modeling can tell us what portion of the guest can penetrate and be retained inside the CD cavity if its length is more than the depth of the host cavity. Moreover, from what direction (wider or narrower rim of CD) the drug enters could also be visualized.

Results and discussion

To study the association of NAL with CDs, changes in the physicochemical properties of the drug (such as solubility, absorbance, and electrochemical behaviour) were followed, as a function of cyclodextrin concentration, by fixing the pH of the 5% v/v methanol–water solution.

Fig. 1. Phase solubility diagram of NAL in phosphate buffer (pH = 5), in the presence of different β-CD concentrations.

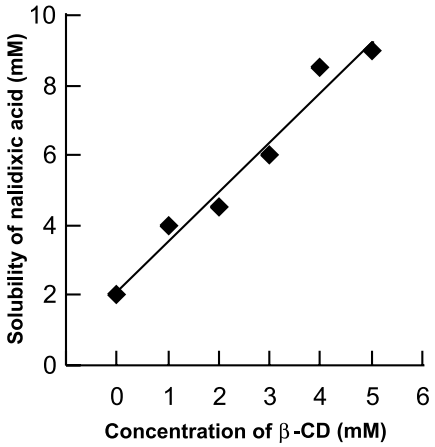

Solubility studies

Figure 1 shows the phase solubility diagram of NAL in aqueous solution in the presence of different concentrations of β-CD. The solubility of NAL increased in an approximately linear manner as a function of the β-CD concentration. This result would lead to the conclusion that a soluble complex having 1:1 stoichiometry was formed with β-CD, i.e. an A_L-type solubility diagram according to Higuchi and Connors (18). It was also assumed that a complex with a 1:1 stoichiometry was formed because the straight line had a slope less than unity (19). In aqueous solutions of the NAL–β-CD complex, the free drug molecules are in equilibrium with the drug molecules entrapped within the cavity. Thus, on increasing the concentration of β-CD, more NAL molecules will transfer from the aqueous solution to the hydrophobic cavity of β-CD. One can therefore expect that more NAL will dissolve in water in the presence of β-CD than will dissolve in the absence of it, and consequently, the solubility of NAL increases with increasing concentration of β-CD.

The apparent stability constant (log $K = 3$) of the formed complex was calculated from the solubility diagram according to eq. [1],

$$[1] \qquad K = \text{slope}/S_o\ (1 - \text{slope})$$

using the slope of the phase solubility diagram and the determined NAL solubility value in water for S_o. The obtained solubility value of NAL (S_o) in aqueous solution is in fair agreement with the literature values (20, 21).

The Gibbs free energies of transfer of NAL from aqueous solution to the cavity of β-CD (Table 1) have been calculated from the following equation,

$$[2] \qquad \Delta G^{\circ}_{trans} = -RT \ln (S/S_o)$$

where S and S_o are the solubilities of NAL in the presence and absence of β-CD. As can be seen from Table 1, the ΔG°_{trans} values are negative, and increase negatively with increasing β-CD concentration. This result indicates that the transfer process is spontaneous, and supports the view that β-CD is a more favourable environment than water for NAL. Moreover, the interaction between NAL and β-CD increases with increasing β-CD content.

© 2002 NRC Canada

Table 1. Values of the standard Gibbs energy of transfer of nalidixic acid, from aqueous solution to the hydrophobic cavity of β-CD, at 298.2 K.

[β-CD] (10^3, M)	$-\Delta G^{\circ}_{trans}$ (kJ mol^{-1})
1	1.72
2	2.01
3	2.72
4	3.59
5	3.73

Spectroscopic studies

Complex formation between NAL and CDs was studied using the spectral shift method in 5% v/v methanol–water at pH = 5 (phosphate buffer). The absorption spectra of 5×10^{-5} M NAL in the phosphate buffer exhibited three distinct absorption bands at 218, 257, and 323 nm. Some important changes in the absorption spectra of NAL at 257 nm (Fig. 2) were observed upon the addition of α- and β-CD. As can be seen in Fig. 2, for both the NAL–α-CD and NAL–β-CD systems, the addition of the host molecule results in an increase in the absorbance intensity, but does not cause a shift in λ_{max}. Similar behaviour was observed for a hepatoprotectant drug thioctic acid – β-CD system (22), as well as for anthracene–, phenothiazine–, and thianthren–β-CD systems (12). As α-CD or β-CD shows no absorption above 220 nm, we can reasonably attribute these variations primarily to the formation of the inclusion complexes of the NAL–CD systems. These changes in the absorbance values are believed to result from changes in the solvent micro-environment upon inclusion of the solute. The changes observed in molar absorbance values may result from the loss of hydrogen-bonding that accompanies the transfer of the guest molecule from the solution to the cyclodextrin cavity. This hypothesis is reasonable based on the fact that there are no proton-donating groups inside the cavity of the cyclodextrin molecule.

However, the maximum change in absorbance ($\Delta A_{max} \approx 0.2$) was so small that the association constant K_{CD-NAL} could not be accurately determined by fitting the experimental data to the well-known UV-binding isotherm (23). This feature indicates that UV spectroscopy is not sensitive enough to be useful in the study of the CD–NAL system, or any other system, where the presence of CD does not result in a clear change in the spectroscopic properties of the drug. Similar conclusions have been obtained for the β-CD – thioctic acid system (22), as well as for other CD–substrate systems (24, 25).

Voltammetric studies

The nature of the electrochemical process of NAL in the absence and presence of various host molecules was investigated by cyclic voltammetry (CV). The cyclic voltammogram of free NAL (1.9×10^{-5} M) in the phosphate buffer is illustrated in Fig. 3 (curve 1), which shows two reduction processes, the first process (P_1) being reversible, followed by an irreversible process (P_2). The main process (P_2) was found to be the more concentration-sensitive peak, and was therefore assigned to the reduction of the carbonyl group (on C-4) to the 4-hydroxy product (26). The reduction peak P_1 has been reported previously for similar compounds (27), and was attributed to the reduction of Hg(II), which is bound

Fig. 2. UV–vis spectra of 5.0×10^{-5} M NAL in phosphate buffer (pH = 5, 5% methanol), in the absence (1), and presence of (*a*): (2) 1 mM, (3) 5 mM, and (4) 6 mM β-CD; and (*b*): (2) 2 mM, (3) 10 mM, and (4) 12 mM α-CD.

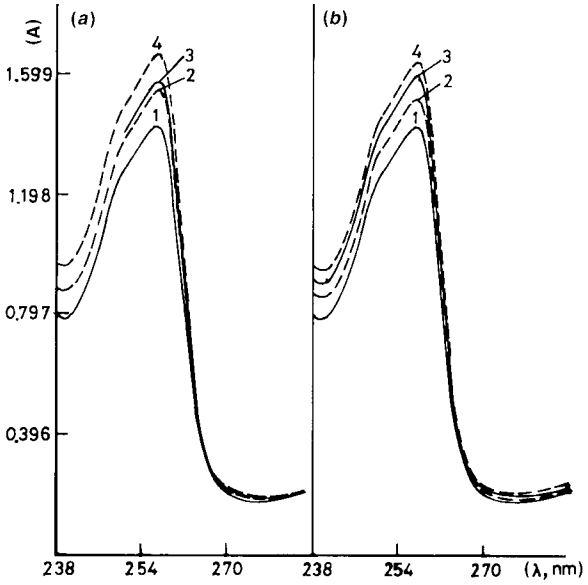

to the adsorbed Hg(II)–NAL film through the heterocyclic nitrogen atom N-8. We were interested in the most sensitive signal (P_2) for the following studies, and for the titrations with cyclodextrins. The cyclic voltammograms of NAL in the absence and the presence of α-CD, as a representative example, were recorded as a function of potential, in the phosphate buffer of varying pH (from pH 2 to pH 7), to elucidate the optimum pH for studying the interaction of NAL with different hosts (Fig. 3(*a*)–3(*c*)). In the presence of the host molecule, the peak potentials, as well as the peak currents of NAL are modified. As shown in Fig. 3, the peak currents (P_2) decreased to ca. 53%, 70%, and 43% (curve 2) of those recorded in the absence of α-CD (curve 1) for pH 2, 5, and 7, respectively. This behaviour suggests that the neutral NAL species (pK_a = 6.00) interact more strongly with cyclodextrins. On the other hand, the broadening of the CV peak (P_1) in the absence of α-CD (Fig. 3, curve 1), and its appearance as a needle-like peak in the presence of α-CD (Fig. 3, curve 2), is probably due to the morphology of the adsorbed film on the HMDE surface. As shown previously (28), the broad peak reflects a flat orientation of the adsorbed NAL species at the electrode surface; however, the needle-like peak points to a vertical orientation of the adsorbed NAL–α-CD complex. These results indicate that the complexation of the NAL molecules enhances the stacking interactions, and hence would be expected to facilitate the formation of a perpendicularly stacked layer of NAL–α-CD complexes on the electrode surface.

The effect of buffer constituents on the binding affinity of NAL to CDs was also studied at pH 5, in the presence of several supporting buffer electrolytes (e.g., acetate, phosphate, and BR buffers). The best results, with respect to shape and reproducibility, as well as to the enhancement of host–guest interactions, were obtained using the phosphate buffer solution; hence, the phosphate buffer (pH 5) was considered optimum, and was used throughout the present work.

© 2002 NRC Canada

Fig. 3. Cyclic voltammograms for 1.9×10^{-5} M NAL solution in the absence (1), and in the presence of 5×10^{-3} M α-CD (2) at: (*a*) pH 2, (*b*) pH 5, and (*c*) pH 7 phosphate buffer (5% methanol), at HMDE, scan rate 100 mV s^{-1}.

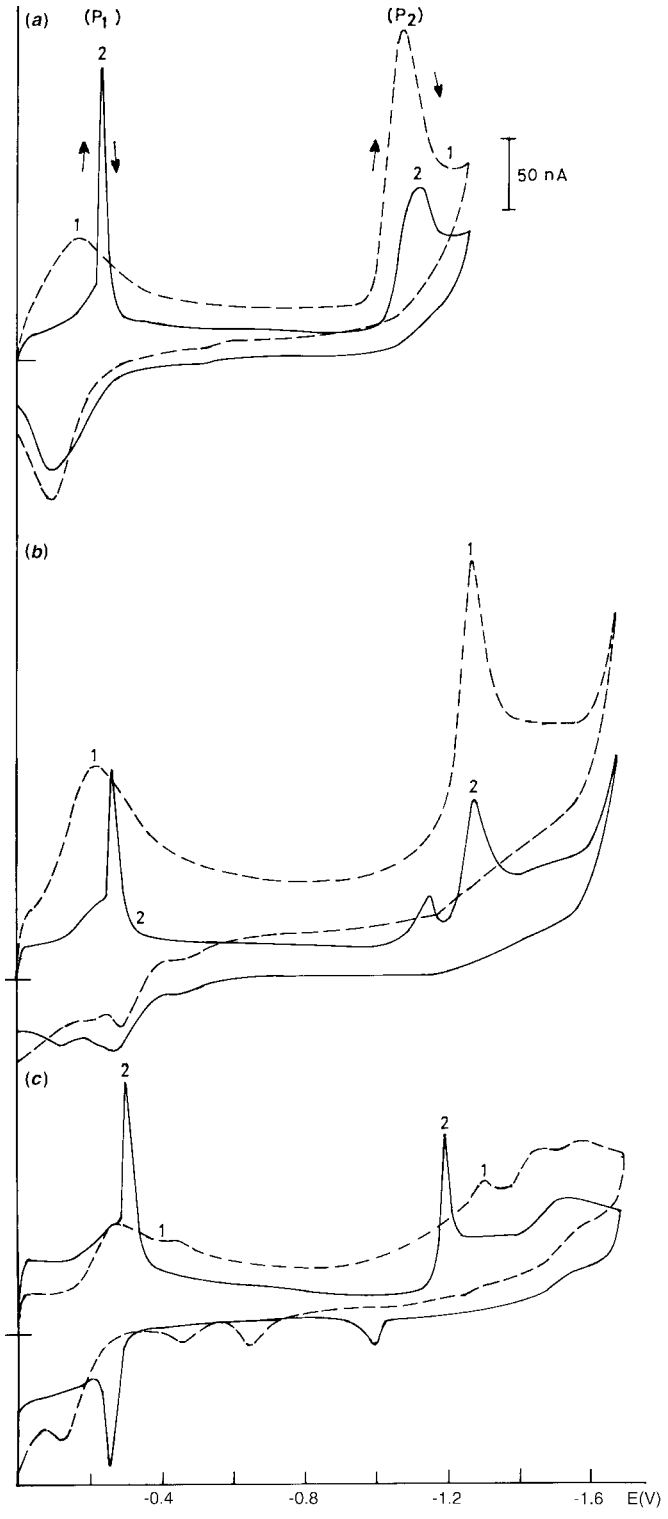

The effect of scan rate (ν) on the NAL process (P_2) at the HMDE, in both the absence and the presence of host molecules, was examined. Experimental plots of i_p vs. $\nu^{1/2}$ for NAL, NAL–α-CD, and NAL–β-CD adducts showed linear dependence on the square root of the scan rate, indicating diffusional mass-transport of the electroactive species to the HMDE surface (29). By linear regression of the data, the following relations were obtained

[3] $$i_p \text{ (nA)} = 13.6 + 10.4\ \nu^{1/2} \quad (R = 0.987)$$

$$i_p \text{ (nA)} = -6.25 + 6.43\ \nu^{1/2} \quad (R = 0.999)$$

$$i_p \text{ (nA)} = -3.81 + 5.70\ \nu^{1/2} \quad (R = 0.998)$$

for NAL, NAL–β-CD, and NAL–α-CD, respectively. The slopes of the linear $i_p - \nu^{1/2}$ plots diminished markedly in the presence of β-CD and α-CD, to about 55% and 44% of their respective values in the absence of host molecule. In terms of these results, the decrease of the peak currents in the presence of various host molecules can be attributed to the decrease in the apparent diffusion coefficients of NAL–host adducts. From an analysis of these slopes, the diffusion coefficient (D_f) of free NAL was found to be 9.95×10^{-6} cm^2 s^{-1}, whereas $D_b = 1.98 \times 10^{-6}$ and 1.56×10^{-6} cm^2 s^{-1} were measured for the bound NAL in the presence of 1.7×10^{-3} M β-CD and 1.9×10^{-3} M α-CD, respectively. These values are in good agreement with those previously reported for the reduction of other species due to association with DNA (30) or with micellar assembles (31, 32). In principle, the formation of a substrate–micelle aggregate is expected to increase the effective radius of the substrate by a factor of about four, which explains the observed changes in diffusion coefficients (31). The peak current could also be reduced if the host molecule caused an increase in the viscosity of the solution resulting in a decrease in the diffusion coefficient, but no change in solution viscosity could be detected over the concentration range used for the host molecules. Therefore, the decrease of the peak current (detected upon the addition of the host) is obviously due to the lower diffusion coefficient of the bulky inclusion complexes, compared to that of free NAL.

Further evidence for the strong interaction of NAL with the asymmetric environment of the CD cavity was obtained from DPSV. The recorded DPS voltammograms of 5×10^{-6} M NAL in the phosphate buffer (pH 5) exhibited two cathodic peaks, at potentials −0.190 and −1.125 V, corresponding to peaks P_1 and P_2 obtained by CV. In the presence of different concentrations of β-CD or α-CD, the solution of NAL yielded electrochemical behaviour similar to solutions of the free guest, but the cathodic peak (P_2) potentials, as well as the peak currents, were considerably influenced (Fig. 4): the cathodic peak potentials were slightly shifted to the more negative potentials. This result reveals that NAL is more difficult to reduce in the presence of β-CD or α-CD — as a result of the NAL entering the hydrophobic cavity — with lower polarity relative to the bulk solution. Also, the peak current is diminished due to the decrease of the diffusion coefficients of the host–guest associates compared to that of the free guest, as discussed above.

The decrease in peak current (P_2) enables us to calculate the formation constant of the complexes formed between NAL and the studied host molecules. The *K* values could therefore be calculated from the following equation (as explained in our previous work (13)),

© 2002 NRC Canada

Fig. 4. Differential pulse stripping voltammograms for 5.0×10^{-6} M NAL in phosphate buffer (pH = 5, 5% methanol), at HMDE, in the absence (1), and presence of (2) 9.9×10^{-5} M, (3) 1.96×10^{-4} M, (4) 3.85×10^{-4} M, (5) 6.66×10^{-4} M, and (6) 8.25×10^{-4} M β-CD. Scan rate 20 mV s^{-1}, accumulation time 30 s, E_{acc} = –0.4 V, and pulse amplitude 100 mV.

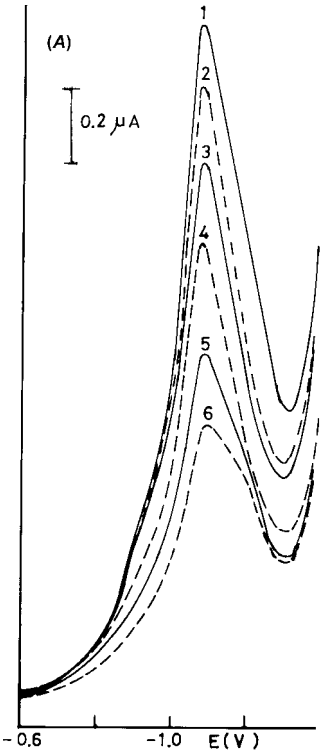

$$[4] \qquad \frac{i_o}{i_o - i} = \frac{1}{1 - C} + \frac{1}{K(1 - C)[H]}$$

where i_o and i are the peak currents of free NAL and NAL in the presence of CDs, [H] is the concentration of CDs, and C is the proportionality constant. According to this equation, on plotting $(i_o/(i_o - i))$ vs. 1/[H], the ratio of the intercept to the slope gives the value of K. The plots in all NAL–guest systems are linear with good correlation coefficients ($R \geq 0.99$), indicating that 1:1 complexes are formed in all cases. The K values obtained by this approach, as well as the formation constant of NAL with γ-CD previously reported (7, 9), are shown in Table 2. There is fair agreement, within experimental error, between the K values of NAL–β-CD obtained from both voltammetric and solubility techniques.

Table 2. The formation constant and standard Gibbs free energy of the binding of nalidixic acid with cyclodextrins, in 5% v/v methanol phosphate buffer (pH = 5), at 298.2 K.

Host	log K	$-\Delta G^\circ$ (kJ mol^{-1})
α-CD	2.60	14.8
β-CD	3.20	18.3
γ-CD	2.45,[a] 1.27[b]	

[a]Reference 7, using the spectrofluorimetric method.
[b]Reference 9(*a*), using the solubility method.

Binding mode and mechanism of the inclusion complex

Valero et al. (33) have calculated the dielectric constant of the cyclodextrin cavities from the spectral dependence of the solvent polarity. They found that the cyclodextrin cavities of α-CD, β-CD, and γ-CD have lower polarity than bulk water, and that the β-CD interior is the most hydrophobic of the three cavities studied. This finding indicates that the microenvironment of a substrate in β-CD is more hydrophobic than the corresponding value for α-CD or γ-CD. This difference could lead to a tighter filling of β-CD (i.e. a greater penetration of the drug into the β-CD cavity), and consequently a greater hindrance of the entry of water molecules. This hypothesis is consistent with the trend of K values of NAL (Table 2). The binding constants listed in Table 2 indicate that the interaction of NAL–β-CD is particularly strong because of the snug fit of NAL into the β-CD cavity, but the binding of NAL to α-CD (with its smaller cavity) and to γ-CD (with its larger cavity) is poorer. This result highlights the importance of the size–fit relationship between the host and the guest in determining the strength of binding. The remarkable enhancement in the association constant with the decreasing dielectric constant of the CD cavity suggests, therefore, that the major contributing factor is the hydrophobic interaction.

The change in standard Gibbs free energy (ΔG°) for the binding of NAL with the CDs was calculated from the well-known relationship:

$$[5] \qquad \Delta G^\circ = -RT \ln K$$

These values were found to be negative (Table 2), revealing that the binding process is favourable. Consequently, the transfer of NAL from an aqueous solution to the CD cavity is spontaneous. Moreover, the change in Gibbs free energy corresponding to the association process is close to, or even of the same order of magnitude as that calculated above, possibly indicating similar inclusion structures for NAL in both the α-CD and β-CD cavities.

To elucidate the structure of the inclusion complex and the group responsible for the inclusion into CD, it is informative to consider the binding constants of smaller, nondrug molecules formed by groups contained in NAL. The K value (158.5) of the pyridine–α-CD complex was therefore taken from literature (34) for comparison.

NAL can enter the CD cavity in three different ways:

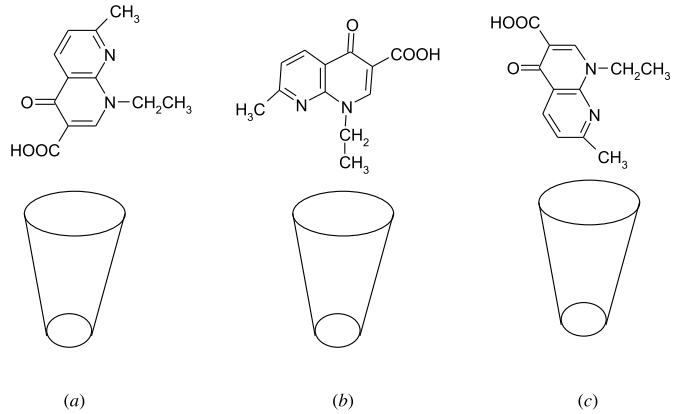

© 2002 NRC Canada

Fig. 5. Energy-minimized structure for the NAL–α-CD complex.

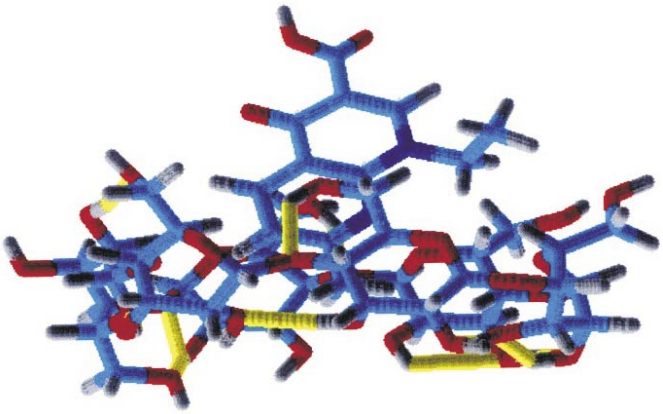

Orientation (*a*) may not be very likely because highly hydrophilic groups are included in the relatively hydrophobic cavity. Moreover, these groups (C=O and –COOH) are more stabilized by water molecules (through hydrogen bonding) than by CD.

If it is supposed that the complexation is due to the inclusion of the ethyl group at N-1 into the cavity of α-CD (orientation (*b*)), then the expected free energy change should be about 6 kJ mol^{-1}. This value is attributable to the change in free energy for each methylene group included in α-CD, ~3 kJ mol^{-1} at 298.15 K (14–16). However, we obtained 14.88 kJ mol^{-1} for the NAL–α-CD complex, which indicates that this topology for the entry of NAL into the α-CD cavity is also excluded. The smaller cavity of α-CD binds more tightly with a linear alkyl group than that of β-CD (14–16); however, the absorption spectra and the voltammetric studies, as well as the *K* values, show that the binding affinity of NAL to β-CD is better than to α-CD. Orientation (*b*) is therefore not the favourable one.

NAL is thus expected to take orientation (*c*) when complexing with CDs. The size of the 2-methylpyridine group seems to fit the cavity size of CD. It was reported (34) that the logarithm of the binding constant of pyridine with α-CD, at 298.15 K, is log K = 2.20, which is slightly smaller than that obtained for the NAL–α-CD complex. The inclusion of NAL into the cavity therefore proceeds in such a way that the methyl pyridine side penetrates the cavity. The inclusion process in NAL can thus occur through the 2-methylpyridine side, leaving the carboxyl group outside the hydrophilic cavity, protruding into water. This orientation leads to the formation of hydrogen bonds between the carboxyl group and the hydroxyl groups of β-CD, resulting in an enhancement of the stability of the NAL–β-CD complex. The release of originally incorporated water molecules from the CD cavity is another important factor that can also contribute to the stabilization of the NAL–CD complex. The high-enthalpy water molecules released can form hydrogen bonds with the bulk water molecules.

To test the reliability of these hypotheses, we carried out calculations on all possible complexes of NAL with α-CD or β-CD, taking into account the different modes of inclusion. The more favourable interaction energy was obtained for topology (*c*), where the energy was found to decrease by ≈ 176 and 226 kJ for α-CD and β-CD, respectively. This result reveals that NAL–β-CD is more stable than NAL–α-CD. The energy-minimized conformation of the NAL–α-CD structure, as a representative example, is shown in Fig. 5. This figure shows that the drug enters through the wider rim and penetrates through the axis of the CD cavity along its depth. It was observed that the maximum width of the NAL molecule (5.02 Å) was less than the diameter of β-CD (≈7 Å) (35), facilitating the penetration of the molecule into the β-CD cavity, but the length of the NAL molecule (7.88 Å) was more than the cavity depth (≈7 Å) (35). The protruding carboxylic group thus forms hydrogen bonds with the secondary OH group located on the larger rim of the β-cyclodextrin. The proposed structural formula of the NAL–β-CD inclusion complex is given in Fig. 6(*a*). On the other hand, as the width of NAL is larger than the diameter of α-CD (4.5 Å) (35), NAL should not be able to fully penetrate into α-CD. In other words, only part of the NAL molecule can be accommodated into the α-CD cavity, leaving the rest of the molecule protruding into water (Fig. 6(*b*)). This explains why the orientation of adsorbed NAL changes in the presence of α-CD, as discussed before in the section on cyclic voltammetry. In the case of γ-CD (diameter 8.5 Å), the NAL molecule is loosely packed into this large cavity, leading to weak interactions, and consequently, a small *K* value (Table 2).

Fig. 6. Proposed structural formula of nalidixic acid complexes with (*a*) β-CD and (*b*) α-CD.

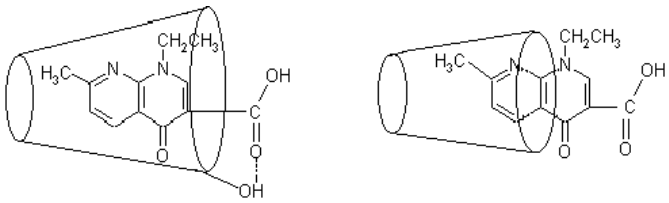

Finally, the voltammetric study showed that the binding affinity of NAL is much higher at pH 5 than at the other pH values. This result indicates that the CD cavities have a preferential affinity for the neutral acid form than for the ionized ones. This preference can be explained as follows: NAL (pK_a = 6.00) at pH 5 is primarily in the neutral form, whereas at pH 2 and pH 7, NAL is in the cationic and anionic forms, respectively. At pH 2, NAL interacts with H^+ through N-8, forming the NAL cation, and this hinders full penetration into the cavity. At pH 7, NAL exists as the anionic carboxylate. The requirement for solvation of the charged carboxylate group by water may thus prohibit the 2-methyl group from fully penetrating the CD cavity, whereas deeper penetration may be possible with the neutral carboxylic acid group.

References

1. N. Rosenstiel and D. Adam. Drugs, **47**, 872 (1994).
2. R. Gleckman, S. Alvarez, D.W. Joubert, and S.J. Matthews. Am. J. Hosp. Pharm. **36**, 1071 (1979).
3. H. Ogata, N. Aoyagi, K. Kaniwa, T. Shibazaki, A. Ejima, N. Takasugi, E. Mafune, T. Hayashi, and K. Suwa. Int. J. Clin. Pharmacol. Ther. Toxicol. **22**, 175 (1984).

© 2002 NRC Canada

4. A.B. Bareza, J. Rohonezy, N. Rozlosnik, T. Gilany, B. Szabo, G. Lovas, T. Braun, J. Samu, and L. Bareza, J. Chem. Soc. Perkin Trans. 2, 191 (2001).
5. T. Loftsson, H. Guomundsdottir, J.F. Sigurjonsdottir, H.H. Sigurosson, S.D. Sigfusson, M. Masson, and E. Stefansson. Int. J. Pharm. **212**, 29 (2001).
6. K. Kimura, T. Endo, H. Nagase, H. Ueda, K. Tomono, S. Kobayashi, and T. Nagai. S.T.P. Pharma Sci. **10**, 409 (2000).
7. I. Duran-Meras, A.M. de la Pena, F. Salinas, and I.R. Caceres. Analyst, **119**, 1215 (1994).
8. I. Duran-Meras, A.M. de la Pena, F. Salinas, and I.R. Caceres. Appl. Spectrosc. **51**, 684 (1997).
9. (*a*) N. Celebi, O. Shirakura, N. Mizushima, Y. Machida, and T. Nagai. Doga TU, J. Med. Pharm. **11**, 216 (1987); (*b*) N. Celebi and T. Nagai. S.T.P. Pharma. **3**, 868 (1987).
10. G.-C. Zhao, J.-J. Zhu, J.-J. Zhang, and H.-Y. Chen. Anal. Chim. Acta, **394**, 337 (1999).
11. T. Matsue, D.H. Evans, T. Osa, and N. Kobayashi. J. Am. Chem. Soc. **107**, 3411 (1985).
12. X.-J. Dang, M.-Y. Nie, J. Tong, and H.-L. Li. J. Electroanal. Chem. **448**, 61 (1998).
13. I.S. Shehatta and M.S. Ibrahim. Can. J. Chem. **79**, 1431 (2001).
14. I. Shehatta. React. Funct. Polym. **28**, 183 (1996).
15. D. Hallen, A. Schn, I. Shehatta, and I. Wadsö. J. Chem. Soc. Faraday Trans. **88**, 2859 (1992).
16. M. Bastos, L.-E. Briggner, I. Shehatta, and I. Wadsö. J. Chem. Thermodyn. **22**, 1181 (1990).
17. A. Mounoz de la Pena, T.T. Ndou, J.B. Zung, K.L. Greene, D.H. Live, and I.M. Warner. J. Am. Chem. Soc. **113**, 1572 (1991).
18. T. Higuchi and K.A. Connors. Adv. Anal. Chem. Instrum. **4**, 117 (1965).
19. D.I. Tose, C. Martin, M.M. Goni, and M.C. Martinez-Ohaniz. Drug Dev. Ind. Pharm. **24**, 301 (1998).
20. D.L. Ross and C.M. Riley. Int. J. Pharm. **63**, 237 (1990).
21. R. Staroscik and J. Sulkowska. Acta Pol. Pharm. **28**, 601 (1971).
22. E. Juquera and E. Aicart. J. Pharm. Sci. **88**, 626 (1999).
23. K.A. Connors. Binding constants: The measurement of molecular complex stability. John Wiley & Sons, New York. 1987.
24. K. Kano, Y. Tamiya, and S. Hashimoto. J. Inclusion Phenom. **13**, 287 (1992).
25. M. Cotta-Ramusino, L. Rufini, and C. Mustazza. J. Inclusion Phenom. **15**, 359 (1993).
26. R. Starosak, I. Prachowska, and J. Sulkowska. Pharmazie, **29**, 387 (1974).
27. M.S. Ibrahim. Fresenius J. Anal. Chem. **367**, 189 (2000).
28. M.S. Ibrahim. Electrochim. Acta, **40**, 1913 (1995).
29. A.J. Bard and L.R. Faulkner. Electrochemical methods. John Wiley & Sons, New York. 1980.
30. M.T. Carter, M. Rodriguez, and A.J. Bard. J. Am. Chem. Soc. **111**, 8901 (1989).
31. A.E. Kaifer and A.J. Bard. J. Phys. Chem. **89**, 4876 (1985).
32. G.L. McIntire, D.M. Chiappardi, R.L. Casselberry, and H.N. Blount. J. Phys. Chem. **86**, 2632 (1982).
33. M. Valero, L.J. Rodríguez, and M.M. Velázquez. Il Farmaco, **51**, 525 (1996).
34. E.A. Lewise and L.D. Hansen. J. Chem. Soc. Perkin Trans. 2, 2081 (1973).
35. M.L. Bender and M. Komiyama. Cyclodextrin chemistry. Springer-Verlag, Berlin. 1978, and refs. therein.

© 2002 NRC Canada

Studies of a benzoporphyrin derivative with Pluronics

N. Hioka, R.K. Chowdhary, N. Chansarkar, D. Delmarre, E. Sternberg, and D. Dolphin

Abstract: The synthetic route for the benzoporphyrin derivatives produces two regioisomers in equimolar quantities (ring A and B isomers). A derivative of the A-ring product, BPD-MA (benzoporphyrin-derivative monoacid ring A, verteporfin), has recently been approved in North America and Europe for the treatment of age-related macular degeneration. The B-ring isomers, contrary to the A-ring isomers, exhibit high aggregation in many formulations, which results in inadequate drug delivery for clinical uses. To avoid aggregation, a non-ionic surfactant polymer such as a Pluronic — poly(ethylene oxide)-poly(propylene oxide)-poly(ethylene oxide) — may be used as a formulation excipient. The triblock polymer investigated here is designated P123 (or poloxamer 403). When used to formulate a monoacid benzoporphyrin B-ring derivative (**2**), a critical micelle concentration of P123 in water occurred at approximately 0.015 to 0.03%. The apparent pK_a of compound **2** was dependent on its concentration in P123, and decreased as the molar ratio (P123:**2**) increased. High concentrations of P123 and neutral pH were found to be the best conditions to maintain the drug in its monomeric form. Kinetic studies suggest that the aggregate of **2** contains several molecules, and is formed by a catalyzed self-assembly process. Samples with 1 mg mL^{-1} of drug, at pH = 7.4, and 4.8% of Pluronic showed satisfactory capacity to load and keep monomers stable. This formulation has potential PDT applications.

Key words: Pluronic, poloxamers, block copolymers, photosensitizing drug, photodynamic therapy (PDT), formulation, micelles.

Résumé : La voie de synthèse des dérivés de la benzoporphyrine conduit à deux régioisomères en quantités équimolaires (isomères des cycles A et B). Un dérivé du produit du cycle A, BPD-MA, (le dérivé monoacide du cycle A de la benzoporphyrine, la vertéporfine) a récemment été approuvé en Amérique du Nord et en Europe pour le traitement de la dégénérescence maculaire associée à l'âge. Les isomères du cycle B, contrairement aux isomères du cycle A, présentent des niveaux d'agrégation élevés dans plusieurs formulations qui les rendent impropres à la dissémination du médicament pour les utilisations cliniques. On peut d'éviter l'agrégation en utilisant comme additif de formulation un agent de surface polymère, non ionique, tel qu'un Pluronique — poly(oxyde d'éthylène)-poly(oxyde de propylène)-poly(oxyde d'éthylène). Le polymère à trois blocs étudié ici est désigné P123 (ou poloxamère 403). Lorsqu'on l'utilise dans la formulation d'un dérivé monoacide du cycle B de la benzoporphyrine (**2**), on observe une concentration micellaire critique de P123 dans l'eau aux environs de 0,015 à 0,03%. Le pK_a apparent du composé **2** dépend de sa concentration dans P123 et il diminue avec une augmentation du rapport molaire (P123:**2**). On a trouvé que des concentrations élevées de P123 et un pH neutre correspondent aux conditions optimales pour maintenir le médicament dans sa forme monomère. Des études cinétiques suggèrent que l'agrégat de **2** contient plusieurs molécules et qu'il se forme par un processus d'autoassemblage autocatalysé. Des échantillons de 1 mg mL^{-1} de médicament, à un pH = 7,4 et une concentration de 4,8% de pluronique présentent une capacité satisfaisante à dissoudre et à maintenir les monomères stables. Cette formulation a du potentiel dans les applications de thérapie photodynamique (TPD).

Mots clés: Pluronique, poloxamères, copolymères à blocs, médicament photosensibilisant, thérapie photodynamique (TPD), formulation, micelles.

[Traduit par la Rédaction]

Introduction

Photodynamic therapy (PDT) is an approved treatment against cancer and age related macular degeneration, and has been shown to be efficient against psoriasis, arthritis and other diseases (1, 2). The first officially approved drug for PDT was Photofrin®, which exhibited some side effects such as prolonged skin photosensitivity, a long waiting time be-

Received 26 June 2002. Published on the NRC Research Press Web site at http://canjchem.nrc.ca on 17 October 2002.

N. Hioka. Departamento de Quimica, Universidade Estadual de Maringa, Brazil.
R.K. Chowdhary, N. Chansarkar, D. Delmarre, E. Sternberg, and D. Dolphin.[1] Department of Chemistry, University of British Columbia, 2036 Main Mall, Vancouver, BC V6T 1Z1, Canada.

[1]Corresponding author (e-mail address: ddolphin@qltinc.com).

 DOI: 10.1139/V02-167 © 2002 NRC Canada

tween intravenous injection and photo activation (2 days), and limited light penetration through tissue (1) of the 630 nm light used to activate it. The photoactive component of the liposomal formulated verteporfin (recently approved for the treatment of age-related macular degeneration) is a benzoporphyrin derivative monoacid ring A (BPD-MA, **1**). The synthetic route to this type of molecule provides, in equimolar quantities, two reduced porphyrin rings (A and B, which are ring regioisomers). Both sets of regioisomers show similar ability to accumulate selectively and be retained by abnormal or hyperproliferative cells, such as cancerous tissue (3–5). Both classes exhibit a tendency to form aggregates (6, 7), following the typical behavior of many porphyrin and chlorin compounds (8). The A-ring compounds exhibit less tendency to aggregate, however, and can be used in liposomal formulations (5, 9). In contrast, the B-ring derivatives exhibit high aggregation behavior, resulting in nonhomogeneous solutions and diminution of singlet oxygen formation (6), which is suggested as one of the most significant species involved in cell death (1, 10).

To avoid aggregation and to improve drug concentration in target tissues, the formulation of the drug is especially important. We have investigated the use of Pluronic (poloxamers), water-soluble triblock copolymers containing ethylene oxide units (PEO = the hydrophilic regions) at the extremities and propylene oxide units (PPO = the hydrophobic section) in the middle (often denoted PEO-PPO-PEO or $(EO)_m(PO)_n(EO)_m$). Because of their synthetic versatility, a number of copolymers are commercially available for distinct uses in different areas, which include drug solubilization and controlled release (11–13). Many of them are believed to form micelles with the terminal PEO sections hydrated at the surface and the PPO section in the hydrophobic core (12, 14).

The basis of this work was the investigation of drug formulations for PDT using Pluronic P123 and a benzoporphyrin B-ring derivative (**2**). P123 (or poloxamer number 403) has a molecular weight of 5750 with 30% of hydrophile PEO (m = 21 and n = 67).

Materials and methods

Reagents

Pluronic P123 (paste) was supplied by BASF, U.S.A. The photosensitizing drugs (BPD-MA **1** and **2**) were synthesized using standard procedures (15). 1,6-Diphenyl-1,3,5-hexatriene (DPH, Sigma) was used as received. The ionic strength was maintained by adding KCl (0.1 mol L^{-1}). Buffers (0.01 mol L^{-1}) were potassium phosphate (pH range 6.2–8.5) and potassium phthalate (pH range 3.9–6.1). All solvents were analytical grade.

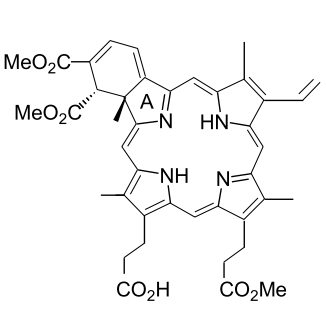

1

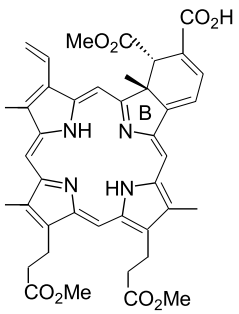

2

Procedures

The aggregation process was monitored by UV–vis spectroscopy (Hewlett-Packard 8452 A and Cary-50). The spectra of **2** were obtained using cells with path length 0.01 cm (cylindrical-shaped) for concentrated solutions (approximately 1×10^{-3} mol L^{-1}) and 1.0 cm for dilute solutions (approximately 1×10^{-5} mol L^{-1}). The term molar ratio refers to the ratio [P123]:[**2**] using molar concentrations. For the stock preparation, P123 (paste, 2 g) was dissolved in 100 mL of water and mixed (Mixer Thermolyne, type 16700) for 2 to 3 h. All Pluronic concentrations are presented by percentage of weight of polymer per water volume (w/v). All stock solutions of **2** (prepared in dimethyl sulfoxide (DMSO)) and DPH (prepared in methanol) were protected from light and were refrigerated.

Critical micelle concentration (cmc)

The cmc determination (duplicate) was performed for Pluronic P123 by a solubilization method (13) using DPH as a probe, and by a method based on dye monomer–aggregate equilibration (16) using **2** as the probe. All Pluronic solutions were kept in a water bath for at least 4 h, to achieve thermal and mechanical equilibrium. A stock solution of DPH was prepared at 1.1×10^{-3} mol L^{-1}, and aliquots of 3.0 μL (microsyringe) were added to each 2.0 mL of Pluronic solution. For **2**, 4.0 μL from a stock solution (3×10^{-3} mol L^{-1} in DMSO) was added to each 2.0 mL of P123 solution, and mixed for 15 s (mixer). The solutions were kept in the dark (1 h for DPH and 30 min for **2**), before the visible or fluorescence (Aminco-Bowman Series 2) spectra were recorded.

Effect of pH

Solutions of **2** (1.14×10^{-5} mol L^{-1}) at different pH and in several fixed concentrations of P123 were investigated ([P123] from 0 to 0.16% w/v). The ionic strength was kept constant (0.1 mol L^{-1} KCl), and phosphate and phthalate potassium buffers (0.01 mol L^{-1}) were used. P123 solutions (2.25 mL) were previously prepared with KCl and KOH (to set the initial pH to approximately 7.3) and kept at least 4 h at 25°C. 14 μL of **2** (stock, $c = 2.05 \times 10^{-3}$ mol L^{-1} in DMSO) were added to the sample and mixed (using the mixer for 15 s). After 1 to 2 min, 0.25 mL (micropipette) of the buffer solutions, at the desired pH, were added, and the behaviour of monomer and aggregate equilibrium was monitored with respect to time. For 0, 0.04, and 0.06% P123, experiments were performed in duplicate. To investigate the effect of [**2**] on the pH dependence of aggregation, 0.06% of P123 was used with different concentrations of **2**.

Kinetic investigation of the aggregation process

The same procedures used to investigate the effect of pH on **2**–P123 solutions were used to study the aggregation behaviour with respect to time. Only the kinetics of acid-pH solutions were followed, because at neutral or alkaline pH the aggregation processes were too slow. The monomer and aggregate peaks were monitored simultaneously.

© 2002 NRC Canada

Fig. 1. Visible spectra of **2** in DMSO. Monomer and aggregate ([**2**] = 1.1 × 10^{-5} mol L^{-1} in DMSO–water).

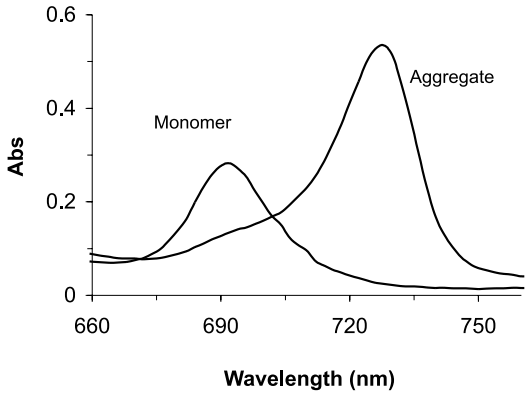

Micellar size determination using laser light scattering

The micelle size was measured by laser light scattering (submicron particle sizer model 370, NICOMP, Santa Barbara, CA). Solutions with 1 mg of **2** and 10% of P123 (pH = 7.4) were analyzed. Solutions at low concentrations of **2** (3.5 × 10^{-6} mol L^{-1}) and Pluronic (0.06 and 0.2%), with pH = 7.4, were also examined.

Formulations

Solutions with different P123 concentrations were prepared by a thin film method. Compound **2** and P123 were codissolved in methylene dichloride; after solvent evaporation via rotary evaporation, the thin film produced was hydrated with an aqueous potassium phosphate solution. Samples were lyophilized and rehydrated using 1 mL of pure water, leading to final solutions composed of [buffer] = 0.01 mol L^{-1}, pH 7.4, [**2**] = 1.4 × 10^{-3} mol L^{-1} (1 mg mL^{-1}), and P123 concentrations as presented in Table 1. After the solution was well mixed, visible spectra were obtained with respect to time.

Aliquots of the solutions prepared as described in Table 1 were frozen immediately after rehydration, and were used to check the stability of the diluted samples. These solutions were defrosted and aliquots of 40 μL were added to 2.0 mL (1:50 dilution) of pure water and buffer solution (pH = 7.4, c = 0.01 mol L^{-1}). The stability of their monomeric species was followed with respect to time.

Results and discussion

For **2** in DMSO (or other organic solvents), the most intense Q-band appeared at 692 nm (ε = 32 000 M^{-1} cm^{-1}), corresponding to the monomeric species, while the aggregate peak showed a red-shifted band with a more intense peak at 715 to 738 nm (see Fig. 1). The wavelength of the aggregate peak was dependent on solution conditions. Samples exhibiting aggregation peaks usually precipitated with time.

For **2** in Pluronic solutions, the monomer peak had a molar absorptivity (ε) around 27 000 M^{-1} cm^{-1}, while the aggregate peak intensity was higher (approximately 50 000 M^{-1} cm^{-1}).

Table 1. Sample preparation with [**2**] = 1.4 × 10^{-3} mol L^{-1} (1 mg mL^{-1}), pH = 7.4.

Sample	P123 (mg)	[P123] (%, w/v)	Molar ratio [P123]:[**2**]
0	16.9	1.7	2
1	26.8	2.7	3
2	47.7	4.8	6
3	75.6	7.6	9
4	100.8	10.1	13
5	125.8	12.6	16
6	154.3	15.4	19
7	199.7	20.0	25

Fig. 2. Absorbance at 356 nm as a function of P123 concentration ([DPH] = 1.6 × 10^{-6} mol L^{-1}, pH = 7.25, [phosphate] = 0.01 mol L^{-1}, 30°C).

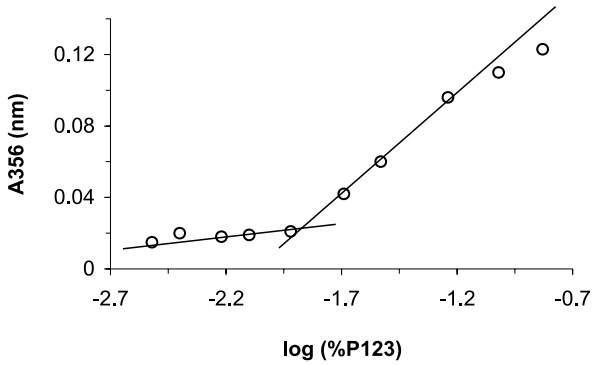

Critical micelle concentration of P123

DPH in methanol exhibits an absorption peak at 356 nm and an emission peak at 428 nm (excitation at 356 nm). DPH is insoluble in water (or low P123 concentration). As the P123 concentration increased, the absorbance and fluorescence intensity also increased. A plot of absorbance at 356 nm (or fluorescence intensity at 428 nm) vs. log (%P123) produced two straight lines whose intercept gave the cmc (see Fig. 2 as an example) (13).

Cmc determination using **2** (soluble in water at low concentration) as a probe is based upon a monomer ⇄ aggregation equilibrium (16). Compound **2** in aqueous solutions, at low P123 concentration, exhibited an aggregation band. At higher P123 concentration, this band decreased, while the monomer peak at 692 nm increased. This aggregation behavior of **2** enabled the determination of the P123 cmc. The absorption ratio of the aggregate and monomer peaks as a function of log (%P123) is shown in Fig. 3. The cmc value was obtained from the intercept.

Table 2 presents cmc values obtained from experiments with DPH and **2** under different conditions.

The cited cmc value for P123 at 25°C (13) is 0.03%, which agrees with our results using both probes (0.028% and 0.029% for DPH and **2**, respectively). At 30°C and pH 7.3, the value found with both compounds (0.020%) demonstrated again the agreement between these two methods. The values obtained with **2** at different buffer concentrations (0.01 and 0.1 mol L^{-1}) are in accordance with the literature, which predicts that the cmc decreases with salt

© 2002 NRC Canada

Fig. 3. Effect of P123 concentration on monomer–aggregate equilibrium (25°C) ([**2**] = 6×10^{-6} mol L^{-1}).

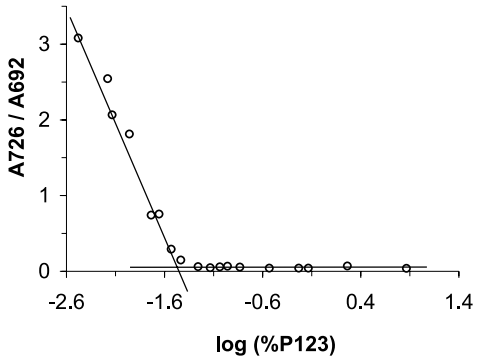

Fig. 4. Effect of pH on monomer–aggregate equilibrium ([**2**] = 1.14×10^{-5} mol L^{-1}, [P123] = 0.04%, [KCl] = 0.1 mol L^{-1}, [buffer] = 0.01 mol L^{-1}) (25°C). Experimental points were obtained at 90 min after buffer addition.

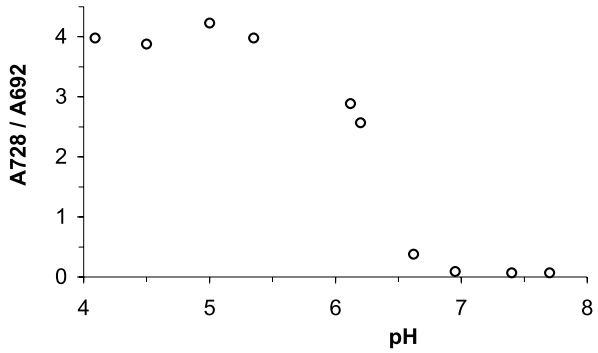

addition (13, 17). These experiments with **2** clearly demonstrated that the micelles of P123 stabilize it in the monomeric form.

Effect of pH on stability

Solutions of **2** in P123 at low pH showed a red-shifted peak corresponding to aggregates. All samples were, therefore, initially prepared at neutral pH (without buffer). At low pH, after buffer addition, a decrease of the 692 nm peak and a simultaneous increase in the aggregate band with respect to time was observed. At neutral or higher pH, aggregation was diminished (but not completely avoided), probably resulting from the negative–negative charge repulsion of the carboxylate group on **2**. The ratio between the aggregate and monomer peaks at an arbitrarily fixed time was taken as a parameter to estimate the magnitude of the effect. An example is presented in Fig. 4.

The extent of the aggregation process with pH (Fig. 4) permits an estimate of the pK_a value of **2** at that Pluronic concentration. This method cannot directly measure pK_a, however, since protonation is followed by aggregation. The pK_a value did not change with time of analysis. For the example presented in Fig. 4, the measured pK_a was 6.4. For solutions without Pluronic, **2** exhibits only one peak around 718 nm, which decreases with time at lower pH. To estimate these pK_as, absorbance as a function of pH was used. Measurements of these apparent pK_a values, obtained using this indirect technique at different P123 concentrations, are shown in Table 3.

Table 2. Average cmc values of P123 using DPH and **2**.

Probe	Temp (°C)	Phosphate (mol L^{-1})	pH	cmc
DPH	25	—	—	0.028
DPH	30	0.01	7.3	0.020
2	25	—	—	0.029
2	30	0.01	7.3	0.020
2	30	0.1	7.3	0.015

Table 3. Apparent pK_a for **2** and the maximum wavelength of the aggregate band at different P123 concentrations (25°C).

[P123] (%, w/v)	Molar ratio [P123]:[**2**]	pK_a (±0.1)	λ_{max} (nm)
0.0	0	6.8	718
0.02	3	6.6	728
0.04	6	6.4	728
0.05	8	—	734
0.06	9	5.8	734
0.07	11	—	735
0.08	12	5.8	734
0.12	18	5.6	736
0.16	24	5.7	736

Note: [KCl] = 0.1 mol L^{-1}; [buffer] = 0.01 mol L^{-1}; [**2**] = 1.14×10^{-5} mol L^{-1}.

In Pluronic solutions, the aggregate peak undergoes a red shift as the Pluronic concentration is increased, probably reflecting the different geometry and size of the micelles. The pK_a values (Table 3) obtained were higher than those expected for a simple carboxylic acid, and probably reflect the local environment.

Increasing the P123 concentration ([P123]:[**2**]) lead to a decrease in pK_a; this effect was caused by a Pluronic micelle forcing molecules of **2** inside the micelle core (away from the micelle surface). Consequently, the porphyrin is exposed to a less hydrophilic environment (18). An abrupt change in pK_a was observed between 0.04% and 0.06% (6.4 to 5.8). This suggested two different micelle populations. Perhaps, one was a unimolecular micelle (0.04%) and the other one was a multimolecular micelle (in 0.06% or higher) (11, 12). These values are more appropriately called the apparent pK_a, because P123 micelles can induce local pH changes (18). Table 4 provides data for the effect of the concentration of **2** on its apparent pK_a.

The apparent pK_a increased as the concentration of **2** increased. This effect resulted from the limited capacity of P123 micelles (at 0.06%) to support high quantities of **2** inside the micelle core (drug loading). As the [P123]:[**2**] molar ratio decreased, more drug molecules were exposed to the micelle surface or bulk solution where they could be protonated and suffer aggregation.

Kinetic investigation of the aggregation process

Acidic solutions of **2** and P123 were prepared by buffer (phthalate) addition. Visible absorption vs. time showed a quasi-isosbestic point at approximately 702 nm that was not

© 2002 NRC Canada

Table 4. Apparent pK_a values of **2** at different concentrations.

[**2**] (10^{-5} mol L^{-1})	Molar ratio [P123]:[**2**]	Apparent pK_a
0.33	32	5.5
1.14	9	5.8
2.02	5	6.2

Note: [P123] concentration fixed at 0.06% (25°C); [KCl] = 0.1 mol L^{-1}; [buffer] = 0.01 mol L^{-1}.

Fig. 5. Kinetic behaviour of **2**–P123 solutions in acidic media ([**2**] = 1.14×10^{-5} mol L^{-1}, [P123] = 0.04%, [P123]:[**2**] = 6, [phthalate] = 0.01 mol L^{-1}, pH = 4, [KCl] = 0.1 mol L^{-1}, T = 25°C). The line represents the theoretical fitting.

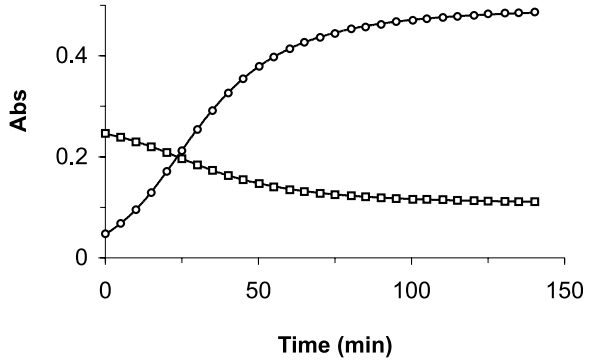

well-defined; the absence of a clear isosbestic point suggests a multiple-step reaction. Moreover, supposing dimeric aggregation, the kinetics data should obey a second-order rate equation (19), which is not shown in the present case. Figure 5 illustrates the monomer and aggregate absorption behavior with respect to time. As shown, there is a lag phase, which is preceded by what has been termed "a sigmoidal progress curve" indicating an autocatalytic-type reaction (20). The initial phase is a nucleation step, after which the nucleus promotes a catalytic process where more molecules are added, forming a polymeric aggregate. The initial nucleus could be a dimer of **2**, as is found in the aggregation process in homogeneous solutions (DMSO–water) (21). Figure 5 shows one example of the kinetics of the aggregation process for the drug in Pluronic solution at low pH. The kinetic data has been treated using an approach proposed by Micali et al. (20) and Pasternack et al. (22).

The basis of this kinetic treatment derives from chaos theory, which predicts that the rate constants are themselves time-dependent (20). The kinetic equation is shown in eq. [1]:

$$[1] \quad (abs - abs_i) \,/\, (abs_o - abs_i) = 1 \,/\, (1 + (m-1)\{k_o t + (n+1)^{-1} (k_c t)^{n+1}\})^{1/(m-1)}$$

where abs is the absorbance at time t, abs_o is the absorbance at $t = 0$, abs_i is the absorbance at infinite time, and m, n, k_o, and k_c are kinetic parameters.

The theoretical fit with experimental points (600 points) as a function of time was performed using the software Kaleidagraph (Synergy Software v 3.0.9), which resulted in an excellent correlation coefficient (>0.9999) for these absorption profiles at monomer and aggregate peaks.

Fig. 6. Absorption at monomer peak as a function of time ([**2**] = 1.4×10^{-3} mol L^{-1} (1 mg mL^{-1}), (25°C), pH = 7.4, [phosphate] = 0.01 mol L^{-1}). Light pathway cell length (0.01 cm). Sample 0 (●); sample 1 (■); samples 2–7 (▲).

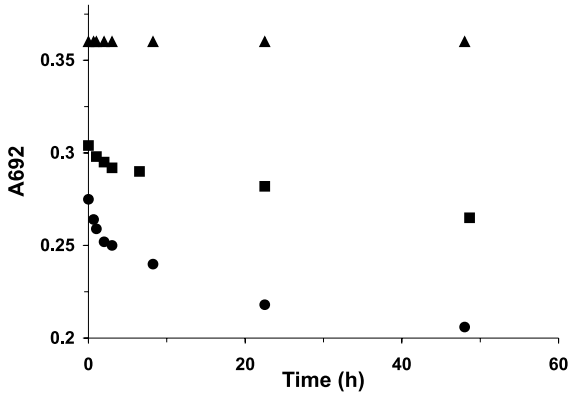

Micelle size determination

Laser light scattering experiments showed that a solution of **2** and 10% P123 (pH approximately 7.4) resulted in one population of micelles whose size ranged from 15 to 20 nm. After 1 day, these micelles maintained the same size, and the visible spectra confirmed the presence of the drug in monomeric form. For solutions with low concentrations of P123 (0.06%) and **2** (3.5×10^{-6} mol L^{-1}) at pH 7.4, the experiments showed two micelle populations with sizes approximately 20 nm and 100 nm, although with a high χ-square error ($\chi_r^2 = 5$). After 1 day, both micelle populations increased their micelle size (almost double) and the drug started to exhibit the aggregation band. The presence of drug aggregation probably promotes micelle destabilization, inducing an increase in total particle size. Similar micelle (or colloid) size increase was exhibited in a 0.2% P123 solution. Because of the high χ error these results are not accurate, but suggest that a low [P123] results in micelles that cannot adequately sustain monomeric species of the drug.

Drug loading and stability

Samples formulated at pH 7.4 and compositions described in Table 1 were used to investigated the concentrations of P123 that can support 1 mg mL^{-1} of drug (in monomeric form) and their stability, with respect to time, for prolonged use. Figure 6 shows the initial capacity of Pluronic solution that is able to solubilize **2** in monomer form, as well as their stability over time after rehydration with 1 mL of water.

Samples containing P123 at concentrations of 1.7 and 2.7% (samples 0 and 1) exhibited low capacity to load **2** in its monomeric form (time zero). Their spectra did not exhibit an aggregation peak; however, undissolved material remained in the flask. Taking [**2**] = 1.4×10^{-3} mol L^{-1}, ε = 27 000 M^{-1} cm^{-1}, and considering the light path of the cell (0.01 cm), the expected absorbance at 692 nm should be approximately 0.378, which is close to the value of 0.36 obtained experimentally for sample 2 (4.8%) and those at higher [P123].

After 48 h, samples 2 (4.8%) to 7 (20.0%) did not exhibit an aggregate peak, and the absorption at 692 nm did not change (Fig. 7). Samples 0 (1.7%) and 1 (2.7%) exhibited a

© 2002 NRC Canada

Fig. 7. Ratio of aggregate–monomer absorbances for [P123] solutions at 20 h after dilution (in pure water and in [phosphate] = 0.01 mol L^{-1}, pH = 7.4) ([**2**] = 2.8×10^{-5} mol L^{-1}, 25°C).

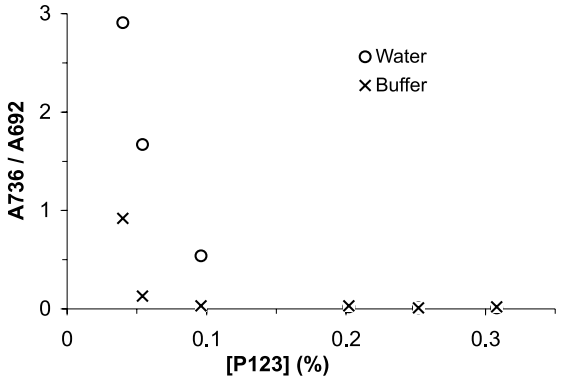

new band at 734–736 nm (not shown), which increased with time, while the monomer peak decreased. Thus, for drug loading and stability, samples formulated with P123 at concentrations below 4.8% are not useful for clinical use.

After 20 days (sample solutions were maintained at room temperature in the dark) the absorbance at 692 nm exhibited only a small decrease. The absorbance of sample 2 (4.8%) decreased 5.2%, and sample 4 (10.1%) decreased 4.3%. For samples 5 (12.6%) to 7 (20.0%), absorbance decreases were not observed. The pH of all solutions was 7.4, which means that despite the negative charge, **2** still tended to aggregate. It is important to note, however, that this tendency is much reduced when compared with low pH.

These results show that dilute buffered solutions (pH = 7.4) were more stable for all samples. This formulation process should, therefore, use buffer solutions at pH ≈ 7.4, rather than pure water. Previous buffer (from the cake) cannot adequately sustain the pH for formulations after dilution (1:50) in pure water. At 20 h, samples diluted in pure water exhibited aggregation at 0.20% (original 10.1%) of P123 (or higher), while for dilution made in the buffer, the solution at 0.10% (original 4.8%) of P123 was still stable.

Conclusion

Micelles of P123 in water can support **2** in its monomeric form. The monomer ⇄ aggregate equilibrium of the drug can provide a reasonable estimation of the pK_a for **2**, and permits cmc determinations for Pluronic. The apparent pK_a of **2** decreased as the molar ratio ([P123]:[**2**]) increased. Mixtures of **2** with low [P123] showed unstable micellar systems, leading to drug aggregation. Acidic solutions of the drug in Pluronic underwent aggregation via a self-catalytic process, where the rate constant, or "rate coefficient" (22), is time dependent, and can be analyzed by chaos theory. Prevention of the nucleation step can slow down the aggregation process. The best conditions for Pluronic micelles to sustain **2** as a monomeric species were high molar ratios and neutral pH. Samples with a Pluronic concentration of 4.8% (molar ratio = 6) or higher showed high drug loading and capacity to support the drug in monomeric form. After dilution (1:50) in buffer solution at pH 7.4, these samples still demonstrated high stability.

Acknowledgements

We express our gratitude to the Brazilian granting agency CNPq for the support of Noboru Hioka. This work was supported by the Natural Sciences and Engineering Research Council of Canada (NSERC).

References

1. E.D. Sternberg, D. Dolphin, and C. Brückner. Tetrahedron, **54**, 4151 (1998).
2. J.G. Levy. Trends Biotechnol. **13**, 14 (1995).
3. A.M. Richter, E. Waterfield, A.J. Jain, B. Allison, E.D. Sternberg, D. Dolphin, and J.G. Levy. Br. J. Cancer, **63**, 87 (1991).
4. A.M. Richter, E. Waterfield, A.K. Jain, E.D. Sternberg, and J.G. Levy. Photochem. Photobiol. **52**, 495 (1990).
5. E.D. Sternberg and D. Dolphin. Curr. Med. Chem. **3**, 239 (1996).
6. B.M. Aveline, T. Hasan, and R.W. Redmond. J. Photochem. Photobiol. B, **30**, 161 (1995).
7. B.M. Aveline, T. Hasan, and R.W. Redmond. Photochem. Photobiol. **59**, 328 (1994).
8. W.I. White. *In* The porphyrins. Vol. V. *Edited by* D. Dolphin. Academic Press, Inc., New York, U.S.A., 1990. Chap. 7. pp. 303–339.
9. N. Oku, N. Saito, Y. Namba, H. Tsukada, D. Dolphin, and S. Okada. Biol. Pharm. Bull. **20**, 670 (1997).
10. V.C. Colussi, D.K. Feyes, J.W. Mulvihill, Y. Li, M.E. Kenney, C.A. Elmets, N.L. Oleinick, and H. Mukhtar. Photochem. Photobiol. **69**, 236 (1999).
11. I.R. Schmolka. *In* Polymers for controlled drug delivery. *Edited by* P.J. Tarcha. CRC Press, Boca Raton, Florida, U.S.A. 1991. Chap. 10. pp. 189–208.
12. P. Alexandridis and T.A Hatton. Colloids Surf A, **96**, 1 (1995).
13. P. Alexandridis, J.F. Holyworth, and T.A. Hatton. Macromolecules, **27**, 2414 (1994).
14. I.R. Schmolka. J. Am. Oil Chem. Soc. **54**, 110 (1977).
15. E.D. Sternberg, D. Dolphin, A. Tovey, A.M. Richter, and J.G. Levy. U.S. Patent 5 880 145, 1999; *Chem. Abstr.* 130:223114.
16. N. Hioka. M.Sc. Thesis, University of Sao Paulo, Brazil, 1986.
17. P. Bahadur, K. Pandya, M. Almgreen, P. Li, and P. Stilbs. Colloid Polym. Sci. **271**, 657 (1993).
18. J.H. Fendler. Membrane mimetic chemistry: characterizations and applications of micelles, microemulsions, monolayers, bilayers, vesicles, host-guest systems, and polyions. John Wiley and Sons, New York, U.S.A. 1982.
19. K.J. Laidler. Chemical kinetics. Harper and Row Publishers, New York. 1987.
20. M. Micali, L.M. Scolaro, A. Romeo, and F. Mallamace. Physica A, **249**, 501 (1998).
21. D. Delmarre, N. Hioka, R. Boch, E. Sternberg, and D. Dolphin. Can. J. Chem. **79**, 1068 (2001).
22. R.F. Pasternack, E.J. Gibbs, P.J. Collings, J.C. dePaula, L.C. Turzo, and A. Terracina. J. Am. Chem. Soc. **120**, 5873 (1998).

© 2002 NRC Canada

One-pot sequential Pauson–Khand reaction – transfer hydrogenation

André Hätzelt and Sabine Laschat

Abstract: The Pauson–Khand reaction of norbornene (**1**) and phenylacetylene (**2**) and subsequent $RuCl_2(PPh_3)_3$-catalyzed transfer hydrogenation of the resulting enone (**3**) can be carried out in a one-pot sequence if the base is added after an induction period. The desired ketones (**4a**, **4b**) were obtained in good yield as a mixture of diastereomers (diastereomeric ratio (dr.) 58:42). The relative rates of both the Pauson–Khand reaction and the transfer hydrogenation are decreased by a factor of 2 in the sequence, as compared with the isolated reactions.

Key words: Pauson–Khand reaction, transfer hydrogenation.

Résumé : La réaction de Pauson–Khand du norbornène (**1**) et du phénylacétylène (**2**) et la réaction d'hydrogénation par transfert, catalysé par $RuCl_2(PPh_3)_3$, de l'énone **3** qui en résulte peuvent être effectuées par le biais d'une séquence unitope si la base est ajoutée après une période d'induction. Les cétones recherchées (**4a**, **4b**) sont obtenues avec un bon rendement sous la forme de diastéréomères (58:42). Comparées aux vitesses de réaction isolées, les vitesses relatives de chacune des réactions de Pauson–Khand et d'hydrogénation par transfert sont plus lentes par un facteur de deux.

Mots clés : réaction de Pauson–Khand, hydrogénation par transfert.

[Traduit par la Rédaction]

Introduction

Among the various stoichiometric and catalytic organometallic reactions two types have received increased interest recently. One is the heterobimetallic catalysis, in which two different metal centres cooperatively promote a certain reaction (1). The other type deals with metal-catalyzed tandem or domino reactions, in which one particular metal complex controls a sequence of two or more reactions (2, 3). In contrast, only a few examples are known where different metal complexes were employed for each step within a one-pot sequence. Takahashi reported a one-pot sequential asymmetric hydrogenation utilizing Rh(I) and Rh(III) complexes (4). A one-pot sequence of a Heck reaction and ring-closing metathesis involving Pd complexes and Grubbs catalyst, was discovered by Grigg (5). We anticipated that a combination of C-C coupling and hydrogenation might be synthetically useful. However, such a combination requires that the two different metal complexes employed for each step do not interfere with each other. To address this issue, we chose a sequence consisting of a Pauson–Khand reaction (6) of norbornene (**1**) and phenylacetylene (**2**) to the cyclopentenone (**3**) followed by catalytic transfer hydrogenation (7) as a model system to give the diastereomeric ketones (**4a**, **4b**) (Scheme 1). Although both reactions are well known (6, 7), a combination of these has not yet been studied. Our preliminary results towards this goal are reported below.

Results and discussion

Transfer hydrogenations employing $RuCl_2(PPh_3)_3$ as the catalyst precursor require the presence of a secondary alcohol and a base as the cocatalyst (8). We were worried that the Pauson–Khand reaction might not tolerate these reaction conditions, and thus we first investigated the influence of solvent and various additives on the $Co_2(CO)_8$-mediated thermal cocyclization of **1** and **2** to give **3**. The reactions were monitored by capillary GC. The results in Table 1 indicate that both toluene and *i*-PrOH gave high conversions to the desired enone (**3**) (Table 1, entries 1, 2). However, in *i*-PrOH small amounts of the transfer hydrogenation products **4a** and **4b** were formed as well (9).[2] The Pauson–Khand reaction also proceeded cleanly in *i*-PrOH in the presence of KOH (Table 1, entry 3). When PPh_3 was added, high conversion to **3** was again observed irrespective of the solvent (Table 1, entries 4, 5). Running the cocyclization in the presence of $RuCl_2(PPh_3)_3$ afforded only the enone (**3**) albeit with lower conversion (Table 1, entries 6, 7). However, treatment of **1** and **2** with $Co_2(CO)_8$ in refluxing *i*-PrOH in the

Received 15 March 2002. Published on the NRC Research Press Web site at http://canjchem.nrc.ca on 23 October 2002.

A. Hätzelt and S. Laschat.[1] Institut für Organische Chemie, Technische Universität Braunschweig, Hagenring 30, D-38106 Braunschweig, Germany.

[1]Corresponding author (e-mail: sabine.laschat@po.uni-stuttgart.de).

[2]Recently Krafft reported the conversion of enynes to bicyclic cyclopentanones in *i*-PrOH in the presence of $Co_4(CO)_{12}$. Deuterium labeling studies showed that this sequential Pauson–Khand reaction – 1,4-reduction involves $HCo(CO)_4$ as a catalytic species, which delivers the hydride from *i*-PrOH to the cyclopentenone.

 DOI: 10.1139/V02-172 © 2002 NRC Canada

Scheme 1.

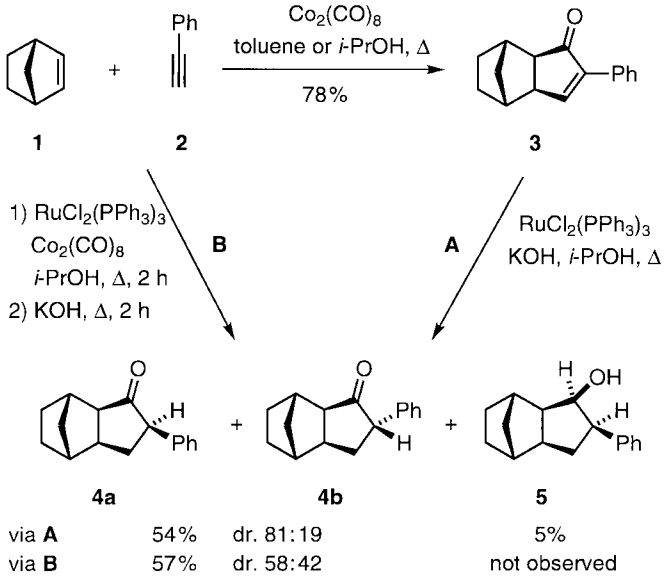

Fig. 1. Sequential one-pot Pauson–Khand reaction – transfer hydrogenation of norbornene **1** and phenylacetylene **2**. Reaction conditions: **1** (1.0 equiv), **2** (1.0 equiv), $Co_2(CO)_8$ (1.0 equiv), $RuCl_2(PPh_3)_3$ (0.1 equiv), *i*-PrOH, reflux, 2 h; then KOH (1.0 equiv). Conversion and product ratios of enone **3** and ketones **4a** and **4b** were determined by capillary GC.

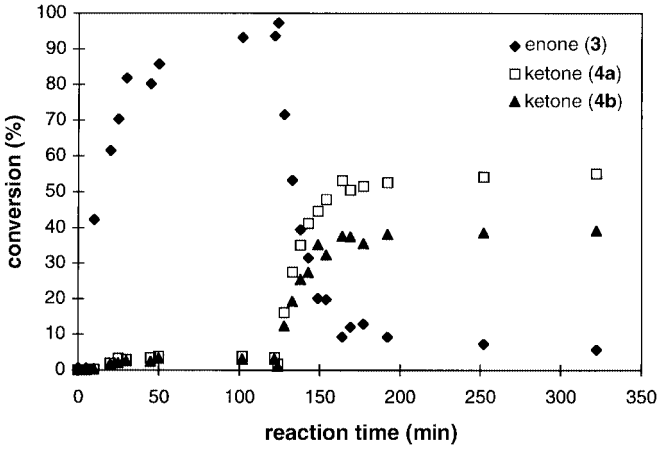

Table 1. Pauson–Khand reaction of norbornene **1** with phenylacetylene **2** under various conditions.[a,b]

					Product ratio (%)		
Entry	Solvent	Additive(s)	Equiv	Conversion (%)	**3**	**4a**	**4b**
(1)	Toluene	—	—	81	100	—	—
(2)	*i*-PrOH	—	—	98	96	2	2
(3)	*i*-PrOH	KOH	1.00	99	100	—	—
(4)	Toluene	PPh_3	0.20	91	100	—	—
(5)	*i*-PrOH	PPh_3	0.20	71	>99	—	<1
(6)	Toluene	$RuCl_2(PPh_3)_3$	0.10	47	100	—	—
(7)	*i*-PrOH	$RuCl_2(PPh_3)_3$	0.10	46	100	—	—
(8)	*i*-PrOH	$RuCl_2(PPh_3)_3$, KOH[c]	0.10, 1.00	46	100	—	—
(9)	*i*-PrOH	$RuCl_2(PPh_3)_3$, KOH[d]	0.10, 1.00	57	46	28	26
(10)	*i*-PrOH	$RuCl_2(PPh_3)_3$, KOH[e]	0.10, 1.00	93	7	54	39

[a]Reaction conditions: **1** (1.3 equiv), **2** (1.0 equiv), $Co_2(CO)_8$ (1.0 equiv), 4 h, reflux.
[b]Conversion and product ratios of enone **3** and ketones **4a** and **4b** were determined by capillary GC.
[c]KOH was added at the beginning.
[d]KOH was added after 30 min.
[e]KOH was added after 2 h.

presence of $RuCl_2(PPh_3)_3$ and KOH yielded exclusively enone **3** (entry 8). Surprisingly, the transfer hydrogenation was completely suppressed. In contrast, when isolated enone **3** was treated with 0.1 equiv of $RuCl_2(PPh_3)_3$ and 1.0 equiv of KOH in *i*-PrOH under reflux, the transfer hydrogenation was complete after 4 h, and the desired ketones (**4a**, **4b**) could be isolated after flash chromatography in 44% and 10% yield, respectively, together with 5% of the saturated alcohol **5** (Scheme 1).

According to results by Szabo and Bäckvall (8) in the transfer hydrogenations of ketones the active catalytic species ($RuH_2(PPh_3)_3$) is formed in situ during an induction period from $RuCl_2(PPh_3)_3$ via an alkoxide displacement – β-elimination sequence, giving $Ru(H)Cl(PPh_3)_3$, followed by a second alkoxide displacement – β-elimination sequence. Presumably, in our system the dihydride species or the chlorohydride complex interfere with the cobalt cluster. To avoid premature formation of $RuH_2(PPh_3)_3$ or $Ru(H)Cl(PPh_3)_3$, the base was added after a considerable induction period (30 min). As shown in entry 9 of Table 1, enone **3** and ketones **4a** and **4b** were obtained in a ratio of 46:28:26. In contrast to the above-mentioned case where the transfer hydrogenation was carried out in a separate step, no trace of the saturated alcohol (**5**) was observed in the sequential one-pot reaction. The amount of ketones **4a** and **4b** could be further increased when a prolonged induction period (2 h) was used (entry 10). Monitoring the consecutive reaction sequence by capillary GC (Fig. 1) revealed almost quantitative conversion to the enone (**3**) within 2 h, followed by clean transfer hydrogenation upon addition of the base, yielding **4a** and **4b** in a final diastereomeric ratio of 58:42. Again, no saturated alcohol (**5**) was found.

The inhibitory effect of $Co_2(CO)_8$ on the presumed Ru dihydride or Ru chlorohydride catalyst was further supported by the observation that the attempted transfer hydrogenation of enone **3** in the presence of $RuCl_2(PPh_3)_3$ (0.1 equiv),

© 2002 NRC Canada

KOH (1.0 equiv), and $Co_2(CO)_8$ (1.0 equiv) in *i*-PrOH did not gave any trace of the desired ketones (**4a**, **4b**). However, the enone (**3**) partially decomposed, and only 64% of **3** could be reisolated after 4 h.

According to qualitative kinetic experiments the reaction rates of both the Pauson–Khand reaction and transfer hydrogenation in the sequence are decreased by a factor of 2.3 and 1.7, respectively, as compared with the rates obtained for separately performed reactions.[3]

The results indicate that in our system the chlorohydride complex is probably the major active catalytic species. From seminal work by Sasson and co-workers (10) and Wilkinson and co-workers (11), it is known that $Ru(H)Cl(PPh_3)_3$ adds to C=C double bonds (in hydrogenations, isomerizations, and transfer hydrogenations) but is unreactive towards ketones (8, 12). In contrast, $RuH_2(PPh_3)_3$ readily converts ketones to the corresponding secondary alcohols (8). The dominating role of the chlorohydride would also explain the good results obtained when KOH was added after 2 h. In this case the conversion to the dihydride would be delayed and the chlorohydride would be present for a longer period of time. The decreased diastereoselectivity in the one-pot reaction may be due to conjugate hydride delivery to the enone (**3**) from the chlorohydride, giving the corresponding enolate, whose *Re* and *Si* faces are protonated by *i*-PrOH with equal probability. Alternatively, ketones **4a** and **4b** can undergo base-catalyzed enolization under the reaction conditions.

Experimental

General procedure for the thermal Pauson–Khand reaction

To a solution of $Co_2(CO)_8$ (680 mg, 2.00 mmol) in toluene or *i*-PrOH (20 mL) was added phenylacetylene (**2**) (200 mg, 2.00 mmol), and the resulting mixture was stirred for 1 h at room temperature. Norbornene (190 mg, 2.00 mmol) was then added, and the mixture was refluxed until TLC indicated complete conversion. The solvent was removed in vacuo and the residue was purified by flash chromatography on SiO_2 (hexanes – ethyl acetate 25:1) to give 350 mg (78%) of enone **3** as a colorless solid; mp 86°C. Spectroscopic and analytic data of **3** were in accordance with ref. 13.

General procedure for the transfer hydrogenation

To a solution of $RuCl_2(PPh_3)_3$ (40 mg, 0.042 mmol) in *i*-PrOH (30 mL) were added enone **3** (110 mg, 0.50 mmol) and KOH (28 mg, 0.50 mmol), and the mixture was refluxed for 4 h. After cooling to room temperature, the mixture was hydrolyzed with saturated (sat.) NH_4Cl solution (20 mL) and extracted with CH_2Cl_2 (3 × 20 mL). The combined organic layers were dried over $MgSO_4$ and purified by flash chromatography on SiO_2 (hexanes – ethyl acetate 50:1) to yield 50 mg (44%) of ketone **4a** as the first fraction, 10 mg (10%) of ketone **4b** as the second fraction, and 6 mg (5%) of alcohol **5** as the third fraction.

One-pot Pauson–Khand reaction – transfer hydrogenation

To a solution of $Co_2(CO)_8$ (0.86 g, 2.50 mmol) and $RuCl_2(PPh_3)_3$ (120 mg, 0.12 mmol) in *i*-PrOH (50 mL) were added phenylacetylene (**2**) (255 mg, 2.50 mmol) and then norbornene (**1**) (235 mg, 2.50 mmol), and the mixture was refluxed for 2 h. KOH (73 mg, 2.50 mmol) was then added, and heating was continued for 2 h. After cooling to room temperature, the mixture was hydrolyzed with sat. NH_4Cl solution (50 mL) and extracted with CH_2Cl_2 (3 × 50 mL). The combined organic layers were dried over $MgSO_4$, evaporated, and the crude product was purified by flash chromatography on SiO_2 (hexanes – ethyl acetate 50:1) to give 186 mg (33%) of **4a** and 136 mg (24%) of **4b**.

(1SR,2SR,4SR,6RS,7RS)-4-Phenyl-tricyclo[5.2.1.0^{2,6}]decan-3-one (4a)

Colorless solid; mp 83°C. IR (KBr) (cm^{-1}) ν: 1735. ^{1}H NMR (400 MHz, $CDCl_3$) δ: 7.35–7.29 (m, 2H), 7.26–7.21 (m, 1H), 7.13–7.09 (m, 2H), 3.48 (ddd, *J* = 13.8, 10.3, 1.5 Hz, 1H), 2.69 (s, 1H), 2.67–2.61 (m, *J* = 13.8 Hz, 1H), 2.35–2.30 (m, 1H), 2.28 (s, 1H), 2.25 (m, 1H), 1.61–1.55 (m, 2H), 1.54–1.49 (m, 1H), 1.25–1.15 (m, 2H), 1.15–1.10 (m, 2H). ^{13}C NMR (100 MHz, $CDCl_3$) δ: 217.9, 138.0, 128.5, 128.5, 126.9, 55.4, 54.9, 42.6, 40.5, 39.3, 34.7, 28.2, 28.0. GC–EI-MS (70 eV) *m*/*z* (%): 226 ([M]$^+$, 52), 198 (9), 180 (3), 129 (9), 120 (34), 115 (7), 104 (100), 91 (17), 77 (11). HR-MS calcd. for $C_{16}H_{18}O$: 226.1358; found: 226.1353.

(1SR,2SR,4RS,6RS,7RS)-4-Phenyl-tricyclo[5.2.1.0^{2,6}]decan-3-one (4b)

Colorless amorphous solid. IR (KBr) (cm^{-1}) ν: 1733. ^{1}H NMR (400 MHz, $CDCl_3$) δ: 7.33–7.29 (m, 2H), 7.25–7.19 (m, 3H), 3.42 (dd, *J* = 9.8, 3.9 Hz, 1H), 2.58 (s, 1H), 2.46–2.43 (m, 2H), 2.30–2.26 (m, 1H), 1.99–1.95 (m, 1H), 1.58–1.56 (m, 2H), 1.27–1.19 (m, 2H), 1.17–1.14 (m, 2H). ^{13}C NMR (100 MHz, $CDCl_3$) δ: 202.7, 139.7, 128.8, 127.3, 126.7, 55.6, 55.0, 43.4, 42.6, 40.2, 34.5, 33.7, 28.4, 28.2. GC–EI-MS (70 eV) *m*/*z* (%): 226 ([M]$^+$, 48), 198 (9), 180 (1), 141 (4), 129 (6), 115 (7), 104 (100), 91 (14), 77 (9). HR-MS calcd. for $C_{16}H_{18}O$: 226.1358; found: 226.1353.

(1SR,2SR,3SR,4SR,6RS,7RS)-4-Phenyl-tricyclo[5.2.1.0^{2,6}]decan-3-ol (5)

Colorless solid; mp 59°C. IR (KBr) (cm^{-1}) ν: 3484. ^{1}H NMR (400 MHz, $CDCl_3$) δ: 7.26–7.21 (m, 2H), 7.20–7.19 (m, 1H), 7.18–7.12 (m, 2H), 4.20 (dd, *J* = 5.2 Hz, 1H), 2.87 (ddd, *J* = 13.8, 9.8, 5.2 Hz, 1H), 2.25 (dd, *J* = 5.4 Hz, 1H), 2.03 (s, 1H), 1.96–1.93 (m, 2H), 1.91–1.86 (dd, *J* = 10.8, 5.4 Hz, 1H), 1.70–1.64 (m, 1H), 1.62–1.58 (m, 1H), 1.50–1.44 (m, 2H), 1.05–1.02 (m, 2H), 1.01–0.98 (m, 1H). ^{13}C NMR (100 MHz, $CDCl_3$) δ: 139.5, 128.6, 128.4, 126.5, 76.6, 52.2, 52.1, 48.6, 38.6, 36.7, 35.3, 32.5, 29.2, 29.0. EI-MS (70 eV) *m*/*z* (%): 228 ([M]$^+$, 100), 210 (53), 197 (17), 188 (12), 181 (20), 142 (26), 137 (22), 129 (22), 117 (22),

[3] The following qualitative rate dependence on the concentration of KOH was found for the transfer hydrogenation of **3** (conditions: 0.08 equiv of $RuCl_2(PPh_3)_3$, *i*-PrOH, reflux): k_{rel} = 1 (0.05 equiv), 1.81 (0.23 equiv), 2.59 (0.45 equiv), 3.52 (2.22 equiv), 3.53 (4.37 equiv of KOH).

© 2002 NRC Canada

109 (22), 104 (56), 91 (48), 77 (16). HR-MS calcd. for $C_{16}H_{20}O$: 228.1514; found: 228.1513.

The relative configurations of **4a**, **4b**, and **5** were established by 2D NMR experiments (COSY, CH correlation, and NOESY).

Conclusion

In conclusion, it has been demonstrated that a two-step sequence of cobalt-mediated cocyclization followed by a ruthenium-catalyzed transfer hydrogenation can be performed in one pot in the presence of both metal centres that do not interfere with each other, as long as the second reaction is triggered by delayed addition of base. However, to overcome limitations such as decreased diastereomeric ratio of the transfer hydrogenation step and decreased reaction rates other catalyst systems must be explored.

Acknowledgements

Generous financial support by the Deutsche Forschungsgemeinschaft (Gerhard-Hess-Prize for S.L.) and the Fonds der Chemischen Industrie is gratefully acknowledged. We would like to thank DEGUSSA AG for kind donation of chemicals. In addition we would like to thank the referees for valuable suggestions.

References

1. (*a*) G.J. Rowlands. Tetrahedron, **57**, 1865 (2001); (*b*) E.M. Vogl, H. Gröger, and M. Shibasaki. Angew. Chem. Int. Ed. **38**, 1570 (1999); (*c*) H. Steinhagen and G. Helmchen. Angew. Chem. Int. Ed. Engl. **35**, 2489 (1996).
2. (*a*) L.F. Tietze and U. Beifuss. Angew. Chem. Int. Ed. Engl. **32**, 131 (1993); (*b*) H.M.R. Hoffmann. Angew. Chem. Int. Ed. Engl. **31**, 1332 (1992).
3. Recent examples: (*a*) P. Eilbracht, C.L. Kranemann, and L. Bärfacker. Eur. J. Org. Chem. 1907 (1999); (*b*) T. Rische and P. Eilbracht. Tetrahedron, **54**, 8441 (1998); (*c*) G. Dyker and P. Grundt. Helv. Chim. Acta, **82**, 588 (1999); (*d*) D. Flubacher and G. Helmchen. Tetrahedron Lett. **40**, 3867 (1999); (*e*) S. Cacchi, G. Fabrizi, and F. Marinelli. Synlett, 401 (1999); (*f*) C.-H. Jun, C.-W. Huch, and S.-J. Na. Angew. Chem. Int. Ed. **37**, 145 (1998); (*g*) M. Thommen, L.A. Veretenov, R. Guidetti-Crept, and R. Keese. Helv. Chim. Acta, **79**, 461 (1996); (*h*) J. Schoepfer, C. Marquis, C. Pasquier, and R. Neier. Chem. Commun. 1001 (1994); (*i*) P.G. Andersson and J.E. Bäckvall. J. Am. Chem. Soc. **114**, 8696 (1992); (*j*) B.M. Trost and Y. Shi. J. Am. Chem. Soc. **113**, 701 (1991).
4. T. Doi, M. Kokuba, K. Yamamoto, and T. Takahashi. J. Org. Chem. **63**, 428 (1998).
5. (*a*) P. Evans, R. Grigg, M.I. Rasuzan, V. Sridharan, and M. York. Tetrahedron Lett. **40**, 3021 (1999); (*b*) R. Grigg, V. Sridharan, and M. York. Tetrahedron Lett. **39**, 4139 (1998).
6. Reviews: (*a*) K.M. Brummond and J.L. Kent. Tetrahedron, **56**, 1657 (2000); (*b*) Y.K. Chung. Coord. Chem. Rev. **188**, 297 (1999); (*c*) O. Geis and H.-G. Schmalz. Angew. Chem. Int. Ed. **37**, 911 (1998); (*d*) N. Jeong. *In* Transition metals for organic synthesis: Building blocks and fine chemicals. *Edited by* C. Bolm and M. Beller. Wiley-VCH, New York. 1998. p. 560; (*e*) N.E. Schore. *In* Comprehensive organometallic chemistry II: A review of the literature 1982-1994. Vol. 12. *Edited by* E.W. Abel, F.G.A. Stone, and G. Wilkinson. Pergamon Press, Oxford. 1995. p. 703; (*f*) N.E. Schore. Org. React. **40**, 1 (1991); (*g*) N.E. Schore. *In* Comprehensive organic synthesis: Selectivity, strategy, & efficiency in modern organic chemistry. Vol. 5. *Edited by* B.M. Trost. Pergamon Press, Oxford. 1991. p. 1037; (*h*) P.L. Pauson. Tetrahedron, **41**, 5855 (1985); (*i*) For a sequence of Pauson–Khand reaction and photochemical rearrangement see: I. Marchueta, S. Olivella, L. Sola, A. Moyano, M.A. Pericas, and A. Riera. Org. Lett. **3**, 3197 (2001).
7. Reviews: (*a*) S. Gladiali and G. Mestroni. *In* Transition metals for organic synthesis. Vol. 2. *Edited by* C. Bolm and M. Beller. Wiley-VCH, Weinheim. 1999. p. 97; (*b*) T. Naota, H. Takaya, and S.-I. Murahashi. Chem. Rev. **98**, 2599 (1998); (*c*) R. Noyori and S. Hashiguchi. Acc. Chem. Res. **30**, 97 (1997); (*d*) G. Zassinovich, G. Mestroni, and S. Gladiali. Chem. Rev. **92**, 1051 (1992); (*e*) J.-E. Bäckvall, R.L. Chowdhury, U. Karlsson, and G.-Z. Wang. *In* Perspective in coordination chemistry. *Edited by* A.F. Williams, C. Floriani, and A. E. Merbach. Verlag Helvetica Chimica Acta, Basel. 1992. p. 463; (*f*) R.A.W. Johnstone, A.H. Wilby, and I.D. Entwistle. Chem. Rev. **85**, 129 (1985); (*g*) U. Matteoli, P. Frediani, M. Bianchi, C. Botteghi, and S.J. Gladiali. J. Mol. Catal. **12**, 265 (1981).
8. A. Aranyos, G. Csjernyik, K.J. Szabo, and J.-E. Bäckvall. Chem. Commun. 351 (1999).
9. For details see: M.E. Krafft, L.V.R. Bonaga, J.A. Wright, and C. Hirosawa. J. Org. Chem. **67**, 1233 (2002).
10. (*a*) Y. Sasson and G.L. Rempel. Tetrahedron Lett. 4133 (1974); (*b*) Y. Sasson, P. Albin, and J. Blum. Tetrahedron Lett. 833 (1974); (*c*) Y. Sasson, M. Cohen, and J. Blum. Synthesis, 359 (1973); (*d*) Y. Sasson, J. Blum, and E. Dunkelblum. Tetrahedron Lett. 3199 (1973); (*e*) Y. Sasson and J. Blum. Tetrahedron Lett. 2167 (1971).
11. P.S. Hallman, D. Evans, J. A. Osborn, and G. Wilkinson. J. Chem. Soc. Chem. Commun. 305 (1967).
12. F.J. McQuillin, E.G. Parker, and G.R. Stephenson. Transition metal organometallics for organic synthesis. Cambridge University Press, Cambridge. 1991. p. 313.
13. (*a*) A.M. Hay, W.J. Kerr, G.G. Kirk, and D. Middlemiss. Organometallics, **14**, 4986 (1995); (*b*) P. Bladon, P.L. Pauson, H. Brunner, and H. Eder. J. Organomet. Chem. **355**, 449 (1988).

© 2002 NRC Canada

An ab initio investigation of scandium chloro complexes

Cory C. Pye and Christopher R. Corbeil

Abstract: A series of geometry, frequency, and energy calculations of chloroaquascandium(III) complexes were carried out at up to the MP2/6-31+G* level. A thorough examination of all species up to and including hexacoordinate species, and with up to six chlorides, was carried out. The structures of the complexes are compared with experimental data where available. The solution chemistry of scandium(III) in the presence of chloride is discussed.

Key words: scandium, aqua complexes, chloro complexes, ab initio.

Résumé : Opérant au niveau MP2/6-31+G* de la théorie, on a calculé une série de géométries, de fréquences et d'énergies de complexes chloroaquascandium(III). On a procédé à un examen approfondi de toutes les espèces allant jusqu'aux espèces hexacoordinées et celles comportant jusqu'à six ions chlorures. On a comparé les structures calculées des complexes avec les données expérimentales disponibles. On discute de la chimie en solution du scandium(III) en présence de chlorure.

Mots clés : scandium, complexes aqua, complexes chloro, ab initio.

[Traduit par la Rédaction]

Introduction

Scandium chloride plays an important role in the purification of scandium metal. For scandium, electrochemical deposition from aqueous or organic electrolytes is impossible or ineffective, and one must resort to fused-salt electrolysis. Careful control of the conditions can afford high-purity scandium from electrolysis (1–4). To avoid oxide formation, the scandium chloride should be as free of water as possible. This can be achieved by adding ammonium chloride, which forms the stable ammonium hexachloroscandate(III) (5–7). Other purification techniques include chemical vapor deposition (8).

Scandium has recently been shown to occur as a hexahydrate in aqueous perchlorate solution through a combination of theoretical ab initio and Raman spectroscopic techniques, contradicting earlier reports of a heptahydrate (9). In perchlorate solution, a single isotropic Raman band at 442 cm^{-1} is assigned to the Sc-O symmetric stretching vibration. In 2.55 M scandium chloride solution, this band, which moves to 436 cm^{-1}, has a shoulder at 420 cm^{-1} and a new polarized band at 306 cm^{-1} appears, which was previously interpreted as evidence against a hexaaqua complex. The band at 306 cm^{-1} can be diluted out, whereas the band at ca. 440 cm^{-1} remains, which suggests that there exists an equilibrium between hexaaquascandium(III) and some chloro complex of unknown stoichiometry. It is our aim in this paper to more precisely define this chloro complex through an analysis of our ab initio calculations and comparison with the experimental literature.

Received 10 June 2002. Published on the NRC Research Press Web site at http://canjchem.nrc.ca on 23 October 2002.

C.C. Pye[1] and C.R. Corbeil. Department of Chemistry, Saint Mary's University, Halifax, NS B3H 3C3, Canada.

[1]Corresponding author (e-mail cory.pye@stmarys.ca).

Method

Calculations were performed using Gaussian 98 (10), utilizing the 6-31G*(11) and 6-31+G*(12) basis sets. The MP2 calculations utilize the frozen core approximation. The geometries were optimized using a stepping stone approach, in which the geometries at the levels HF/STO-3G, HF/3-21G, HF/6-31G*, HF/6-31+G*, MP2/6-31G*, and MP2/6-31+G* were sequentially optimized. Default optimization specifications were normally used. After each level, where possible, a frequency calculation was performed at the same level and the resulting Hessian used in the following optimization. *Z*-Matrix coordinates constrained to the appropriate symmetry were used as required to speed up the optimizations. Since frequency calculations are done at each level, any problems with the *Z*-matrix coordinates would manifest themselves by giving imaginary frequencies corresponding to modes orthogonal to the spanned *Z*-matrix space. The Hessian was evaluated at the first geometry (opt = CalcFC) for the first level in a series to aid geometry convergence. For structures which proved not to be local minima at the HF/6-31G* level, the subsequent calculations were not performed.

Results and literature comparison

In our previous work with scandium, we used the 6-31G* basis set for water, with a different scandium basis set (9). Since the time that these calculations were done, a 6-31G* basis set for scandium has been published (11). We therefore repeat our calculations on the aquascandium species up to the hexahydrate with this new basis set. Ammonium

 DOI: 10.1139/V02-168 © 2002 NRC Canada

Fig. 1. Structures of aquascandium complexes.

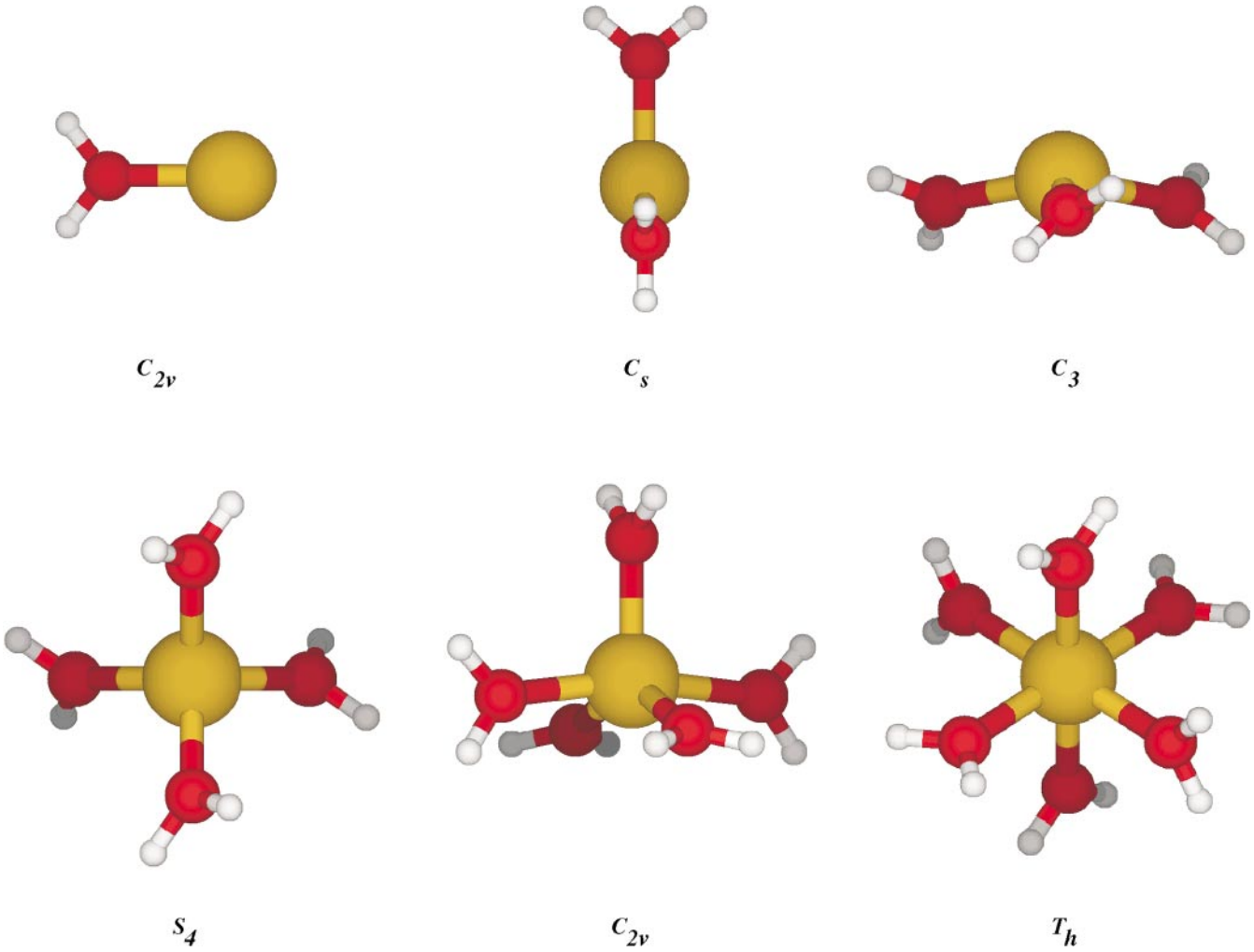

hexachloroscandate(III) exists, and thus it seems reasonable to restrict our attention up to and including hexacoordination.

Aquascandium complexes ($Sc(H_2O)_n^{3+}$)

Figure 1 gives the structures of the aquascandium clusters. Compared with results from our previous paper, the Sc—O distances are shorter by between 0.005 and 0.02 Å, with the biggest differences occuring for the smaller clusters (see supplementary data)[2]. The agreement with the experimental solution value for the Sc—O distance remains excellent (9). In Fig. 2, the total electronic binding energies are given as a function of the total coordination number. For the aqua complexes, the total binding energies are, for the most part, within 20 kJ mol^{-1} of our previous results with a smaller scandium basis set. For the symmetric stretching vibrational frequency, the frequencies are systematically within 10 cm^{-1} lower of the previous result and are given in Fig. 3. We emphasize again in this work that, because of the effect of the second hydration sphere on the vibrational frequencies, the vibrational modes are underestimated by about 50 cm^{-1}, and thus we expect that for the chloro complexes, a similar pattern will be observed.

Chloroaquascandium complexes ($ScCl(H_2O)_n^{2+}$)

The structures of the monochloroaquascandium complexes are given in Fig. 4. Initially, for a given stoichiometry, a structure with the highest reasonable symmetry was tried first, followed by desymmetrized structures. Initial point groups for the bare through to the pentahydrated structure are $C_{\infty v}$, C_{2v}, C_{2v}, C_{3v}, C_{4v}, and C_{2v}, respectively. For the monohydrate, imaginary modes suggested a desymmetrization to the C_s point group, for which there are two structures. Only one of these structures (no. 2) is a local minima. Here, all atoms are in the symmetry plane. At the HF/6-31G* level, the C_{2v} structure is 24.6 kJ mol^{-1} higher in energy than the C_s no. 2 structure, whereas the other structure C_s no. 1 is 8.1 kJ mol^{-1} higher.

For the dihydrate, two different C_{2v} structures are possible, but neither is a local minimum. Of these two, the structure in which all atoms are in the same plane (no. 1) is lower

[2] Supplementary material may be purchased from the Depository of Unpublished Data, Document Delivery, CISTI, National Research Council of Canada, Ottawa ON K1A 0S2, Canada (http://www.nrc.ca/cisti/irm/unpub_e.shtml for information on ordering electronically). The suppplementary crystallographic data can be obtained, free of charge, via www.ccdc.cam.uk/conts/retrieving.html (or from the Cambridge Crystallographic Data Centre, 12 Union Road, Cambridge, CB2 1EZ, U.K. (Fax: +44 1223 336033 or deposit@ccdc.cam.ac.uk).

© 2002 NRC Canada

Fig. 2. Electronic binding energies of scandium chloro complexes.

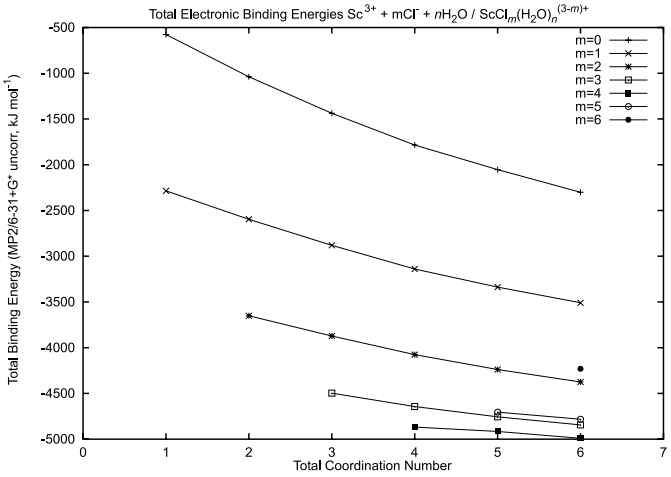

Fig. 3. Skeletal stretching frequencies of aquascandium complexes.

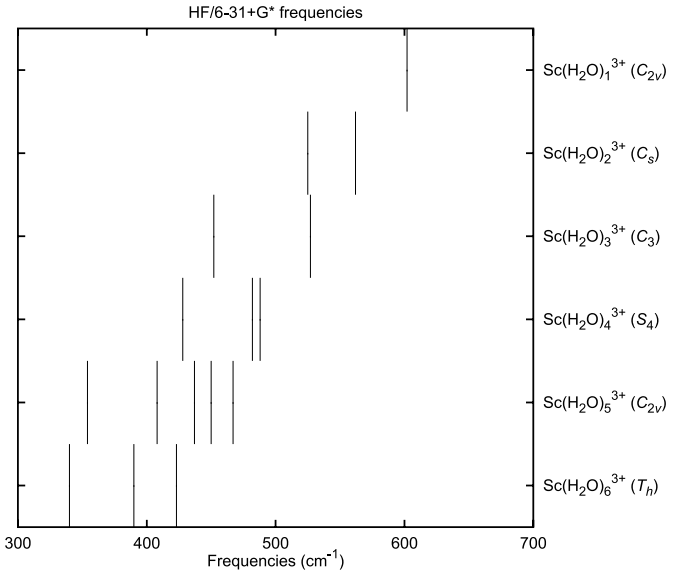

in energy, and so we retain this feature and desymmetrize to C_s, which is a local minimum and is only 0.14 kJ mol^{-1} lower in energy. This means that the potential energy surface is extremely flat in the out-of-plane deformation coordinate. The other C_{2v} structure (no. 2) is 15.6 kJ mol^{-1} higher in energy than the minimum, which is approximately twice as much as the difference between the two C_s structures in the monohydrate, and suggests that whatever factor is responsible for the difference is additive.

The trihydrate retained its symmetry. The C_{4v} tetrahydrate structure possessed an imaginary frequency of irreducible representation A_2. This suggested a desymmetrization to a C_4 point group, which was 9.3 kJ mol^{-1} lower, but also had an imaginary frequency. The final structure became C_{2v} and was an additional 2.9 kJ mol^{-1} more stable. The C_{2v} pentahydrate structure underwent a slight desymmetrization to C_2. Energetically there is very little difference, but the waters in the plane perpendicular to the Sc-Cl contact twist significantly out of that plane, which suggests a low twisting potential barrier.

The Sc—O and Sc—Cl distances of all monochloro complexes are given in the supplementary data.[2] The Sc—Cl distance increases with the addition of water, especially when the final water is added trans to the chlorine in the hexacoordinated species. All Sc—O distances lengthen considerably when a water is replaced by a chloride by between 0.01 to 0.07 Å, with typical values in the middle of this range. Although the Sc—O distance is moderately sensitive to the theoretical level (by 0.02 Å amongst HF/6-31G* to MP2/6-31+G*), the Sc—Cl distance is slightly more sensitive (0.04 Å) for the higher hydrates, with the correlated levels giving shorter distances. The longer distances upon chloride substitution should translate to smaller Sc-O vibrational frequencies, and the MP2 frequencies for the Sc-Cl vibration should be higher than those calculated at the Hartree–Fock level. These trends are verified, although the Sc-O decrease is much more pronounced.

In Fig. 5, the frequencies of the Sc-Cl and Sc-O stretching modes are plotted for the complexes. The Sc-Cl frequency is consistently the highest. For lithium chloride solutions, the effect of the environment as waters are added on the Li-Cl mode is to increase significantly the frequency, and thus we expect that the frequency will be even higher (13). This evidence, combined with the fact that dichloro complexes are energetically even more stable, makes it clear that the chloropentaaquascandium(III) complex is not responsible for the polarized mode at 306 cm^{-1}.

Dichloroaquascandium complexes ($ScCl_2(H_2O)_n^+$)

The structures of dichloroaquascandium complexes are given in Fig. 6. Initial point groups for the bare through to the dihydrated structure are $D_{\infty h}$, C_{2v}, and C_{2v}. For the trigonal bipyramidal pentacoordinate species, a D_{3h} trans and two C_s cis structures were tried, and for the octahedral hexacoordinate structures, a C_{2v} cis and D_{4h} trans structure were tried. The bare $ScCl_2^+$ distorted to form a C_{2v} structure, which was about 11 kJ mol^{-1} lower in energy at the HF/6-31G* level. Of the two C_{2v} structures tried for each of the monohydrate and dihydrate, structure no. 1 was preferred by 14 and 28 kJ mol^{-1}, respectively, at the same level. Of the two possible C_s structures for the cis trihydrate, neither was an energy minimum, and upon desymmetrization, underwent a pseudo-rotation to form the stable trans structure (D_{3h}). In the process, the structures gained 96 and 101 kJ mol^{-1}, respectively. Both the cis and the trans forms of the tetrahydrate are stable, although the cis structure desymmetrized to C_2 and is less stable than the trans by between 20–35 kJ mol^{-1}, depending on the level of theory.

The Sc—O and Sc—Cl distances of all dichloro complexes are given in the supplementary data.[2] The Sc—Cl distance is uniformly larger in the dichloro complex, regardless if we compare structures with the same number of waters (0.09 to 0.15 Å) or with the same coordination number (0.06 to

© 2002 NRC Canada

Fig. 4. Structures of aquamonochloroscandium complexes.

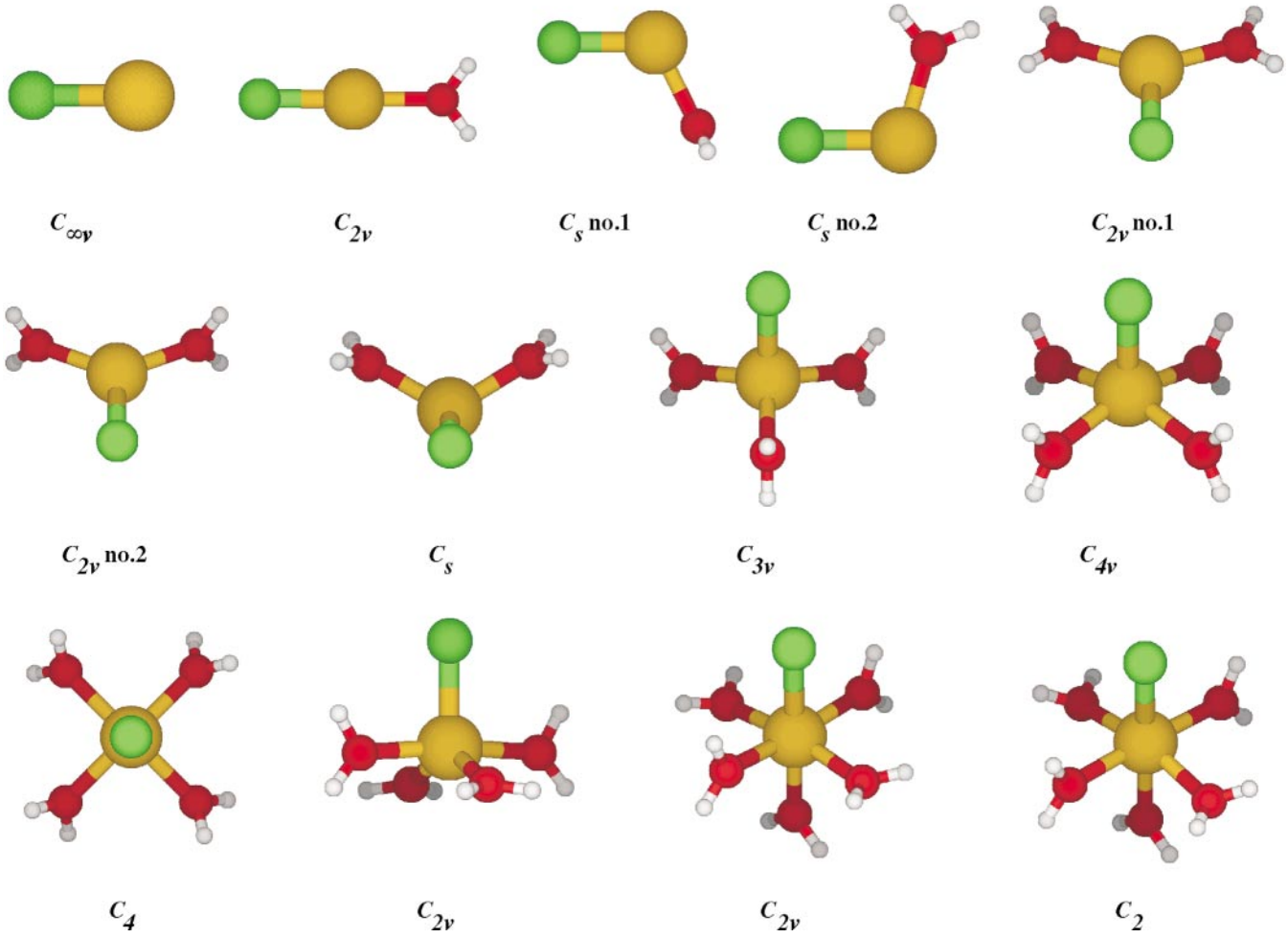

0.11 Å). The Sc—O distance is generally larger as well, but this effect is not as pronounced, and the difference tends to decrease as the number of waters increases. The longer distances upon chloride substitution should translate to smaller Sc-O and Sc-Cl vibrational frequencies.

We may compare the Sc—O and Sc—Cl distances found for $ScCl_2(H_2O)_4^+$ with the analog $ScCl_2(thf)_4^+$ from the experiment (14). The Sc—Cl distances are in the 2.405 to 2.408 Å range, whereas our calculations suggest a slightly shorter distance of 2.35 to 2.39 Å, depending on the level of theory. The theoretical distance of 2.21 Å is too long compared with the experimental Sc—O distance of 2.13 to 2.17 Å, although the effect of crystal packing forces and the different oxygen-bearing ligand must be considered as possible factors responsible for the deviation.

The experimental band at 306 cm^{-1} has been assigned to a Sc-Cl stretch in a chloro complex of scandium. The polarized nature of the band suggests that it would be a symmetric in-phase combination of both chlorides. Figure 7 gives the frequencies of the dichloro complexes. The only dichloro species fitting this description would be the *trans*-dichlorotetraaquascandium(III) species, which has a predicted Sc-Cl symmetric band at around 300 cm^{-1}. However, from known errors in metal–chloro stretching frequencies due to the neglect of the environmental effects, we know that

Fig. 5. Skeletal stretching frequencies of aquamonochloroscandium complexes.

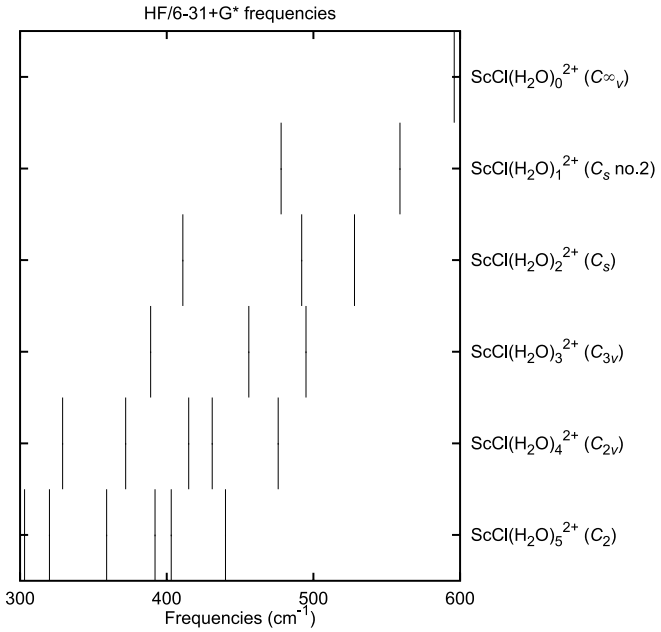

© 2002 NRC Canada

Fig. 6. Structures of aquadichloroscandium complexes.

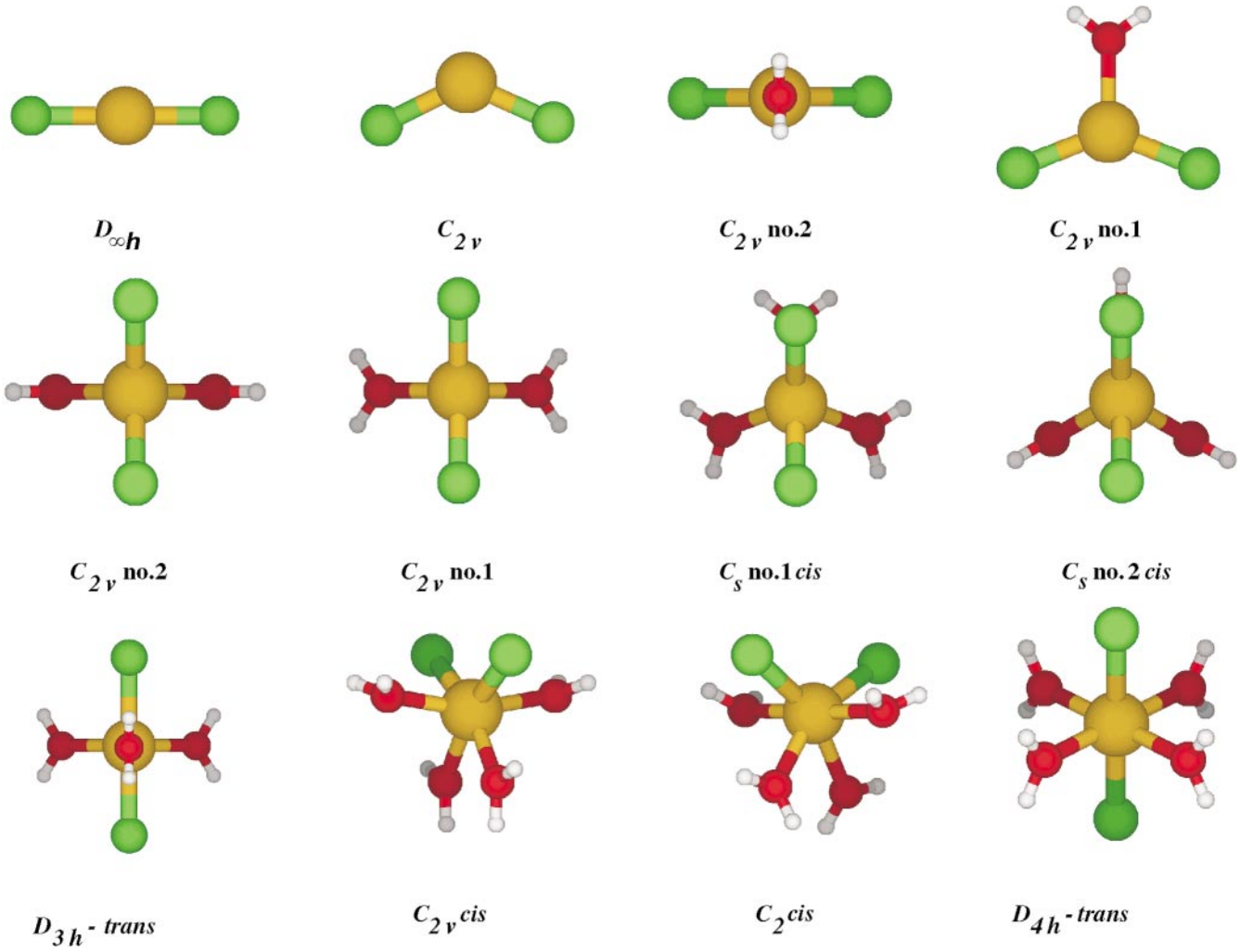

this is most likely underestimated. In addition, the shoulder observed experimentally at 420 cm^{-1} might correspond to the Sc-O stretching mode at 353 cm^{-1} predicted theoretically, especially considering that the experimental mode at 442 cm^{-1} is predicted theoretically at 390 cm^{-1}. This species thus remains a possibility.

Trichloroaquascandium complexes ($ScCl_3(H_2O)_n$)

The structures of trichloroaquascandium complexes are given in Fig. 8. Trichloroscandium(III) itself has D_{3h} symmetry. When a single water adds to $ScCl_3$, two possible C_s structures can be formed, depending on the orientation of the water. The second structure is preferred at the HF/6-31G* level by 0.6 kJ mol^{-1}, and has no imaginary frequencies. Clearly the potential is very flat with respect to water librations. A second water will give a trigonal bipyramidal structure and therefore gives rise to trans or cis possibilities. For the waters in a trans arrangement, either a C_s or a C_{2v} structure can be formed. Similar to the one-water case, the C_{2v} structure is a local minimum, whereas the C_s structure has an imaginary frequency and is higher in energy by 5.3 kJ mol^{-1}. A stable C_s cis structure was also found 14–22 kJ mol^{-1} higher in energy, depending on theory. For the octahedral trihydrate, both facial (fac) and meridianal

Fig. 7. Skeletal stretching frequencies of aquadichloroscandium complexes.

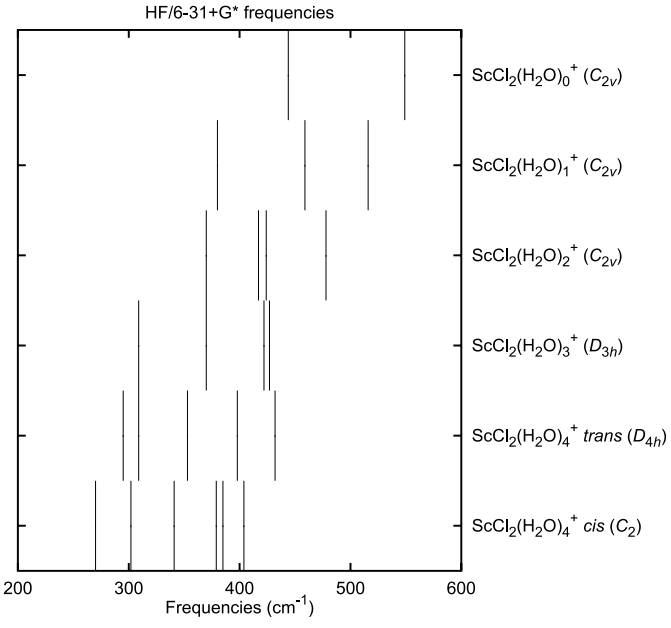

© 2002 NRC Canada

Fig. 8. Structures of aquatrichloroscandium complexes.

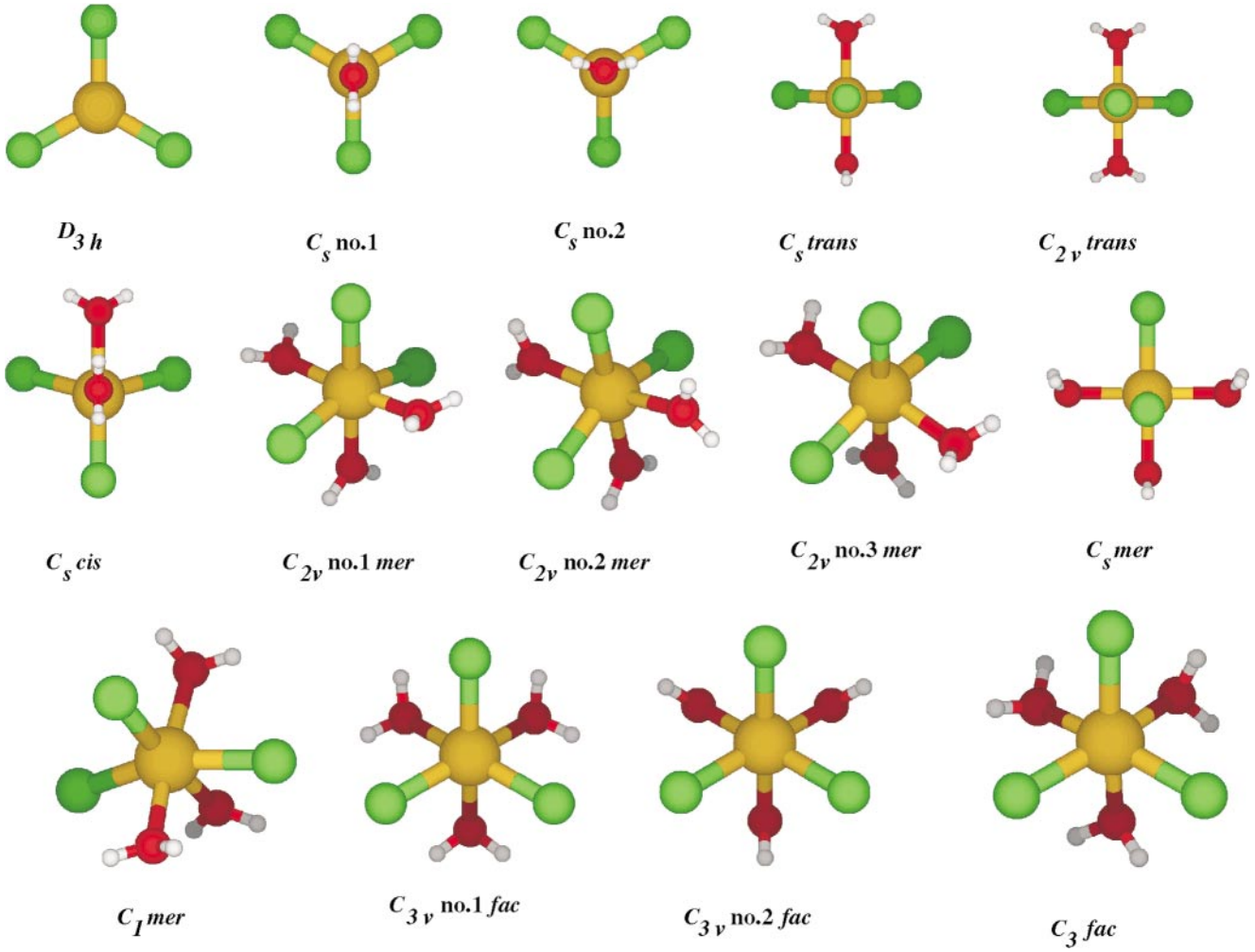

(mer) structures are possible. For the mer geometry, we tried three different C_{2v} structures. None of these structures were local minima, but the first one had the lowest energy overall, and were respectively 0.2, 25.5, and 29.8 kJ mol^{-1} higher than the best structure. The imaginary frequency suggested a desymmetrization to C_s. The structure obtained also has an imaginary frequency, so we removed symmetry, which gave a local minimum 0.2 kJ mol^{-1} lower. Of the fac structures, we started with two different C_{3v} structures, neither of which were minima, but both suggested a desymmetrization to C_3, which was a minima. The C_{3v} structures were 2.5 and 61.7 kJ mol^{-1} less stable than the C_3 structure. The fac structure was 9.0 kJ mol^{-1} less stable than the mer structure.

The Sc—O and Sc—Cl distances of all trichloro complexes are given in the supplementary data.[2] The Sc—Cl distance is uniformly larger in the trichloro complex, regardless if we compare structures with the same number of waters (0.06 to 0.09 Å) or with the same coordination number (0.02 to 0.05 Å). The Sc—O distance is generally larger as well, but this effect is not as pronounced.

We may compare these structures to some observed experimentally. From gas-phase electron diffraction measurements of $ScCl_3$, the bond length was determined to be 2.291 Å, and supported by BP86/TZP calculations (2.285 Å) (15). Our result of 2.289 Å at the MP2/6-31+G* level compares very

Fig. 9. Skeletal stretching frequencies of aquatrichloroscandium complexes.

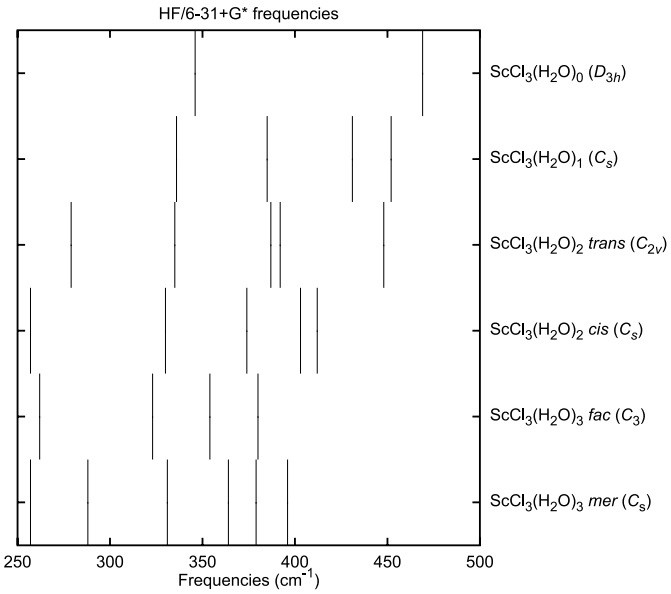

© 2002 NRC Canada

Fig. 10. Structures of aquatetrachloroscandium complexes.

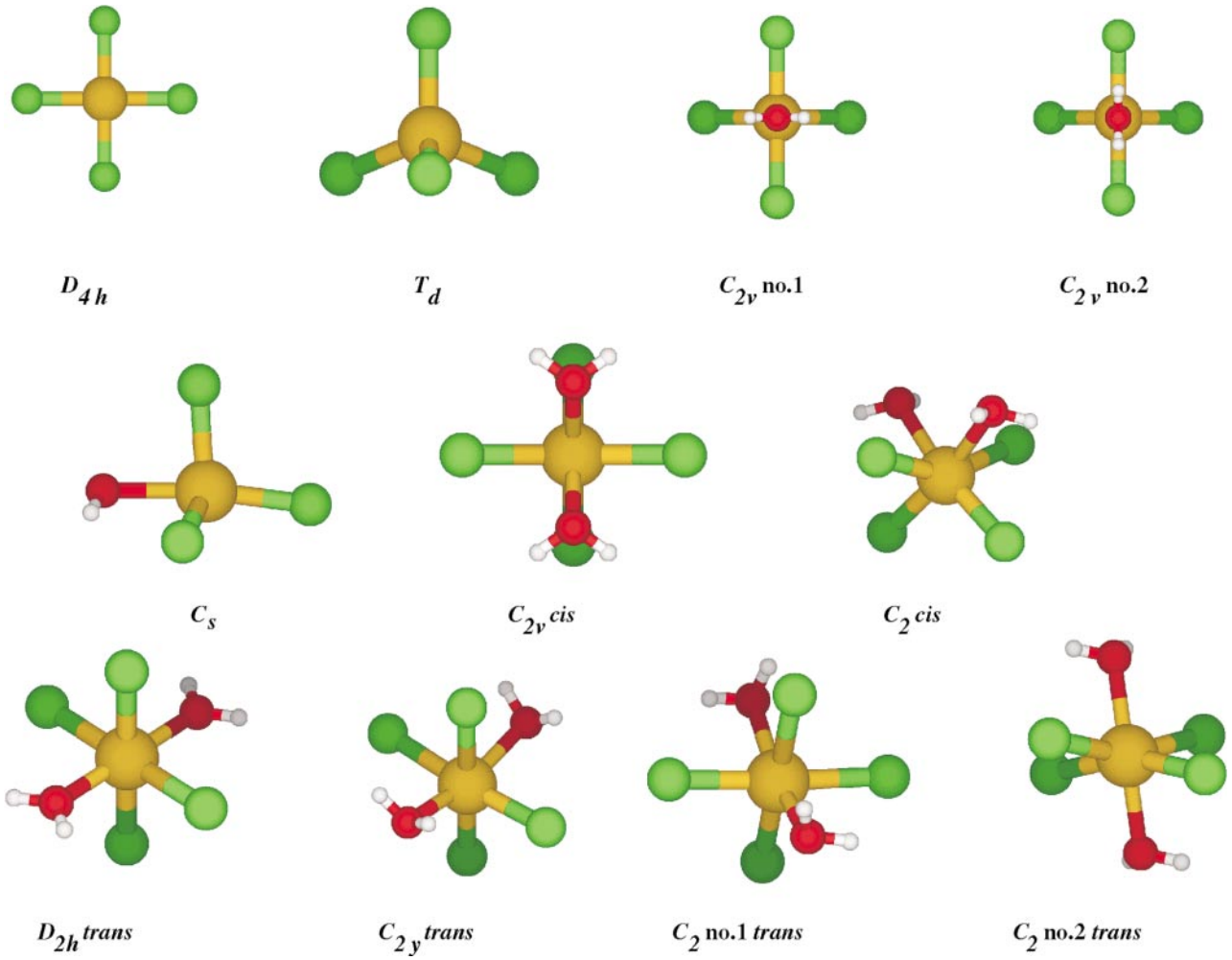

favorably with both the ED and DFT results. The X-ray structure of $ScCl_3$(diglyme) and $ScCl_3$(DME)(MeCN) indicate that the fac structure is obtained (16). Sc—Cl distances of 2.3686 to 2.4104 Å and Sc—O distances of 2.165 to 2.257 Å may be compared with the analogous Sc—Cl distances of 2.37 to 2.41 Å and Sc—O distances of 2.29 to 2.30 Å depending on the level of theory. The Sc—Cl distance is described well, whereas the Sc—O distance is overestimated. Ligand effects and crystal packing must be invoked to account for the difference. The X-ray structure of $ScCl_3(thf)_2(H_2O)$ has also been determined to have the mer geometry (17). The Sc—Cl X-ray distances range from 2.399 to 2.478 Å and the Sc—O distances range from 2.170 to 2.197 Å. In $ScCl_3(H_2O)_3$, the Sc—Cl distance varies from 2.413 to 2.419 Å, and the mean Sc—O distance is 2.122 Å (18). We may compare this to the analogous ranges 2.37 to 2.46 Å and 2.23 to 2.26 Å. Again, as was the case for the fac structure and for the dichloro structures, the Sc—O distance is overestimated. This would tend to underestimate the vibrational frequency of the Sc—O stretching vibration.

Figure 9 gives the frequencies of the trichloro complexes. Two trichloro species may be regarded as possible candidates based upon the frequency analysis. The *trans*-diaquatrichloroscandium(III) species has two polarized modes at 279 and 335 cm^{-1} which could correspond to modes

Fig. 11. Skeletal stretching frequencies of aquatetra, penta-, and hexachloroscandium complexes.

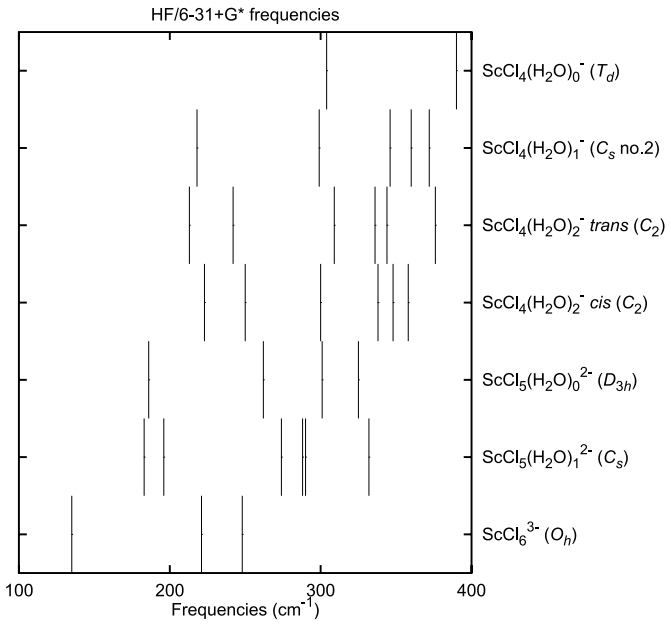

© 2002 NRC Canada

Fig. 12. Structures of aquapenta- and hexachloroscandium complexes.

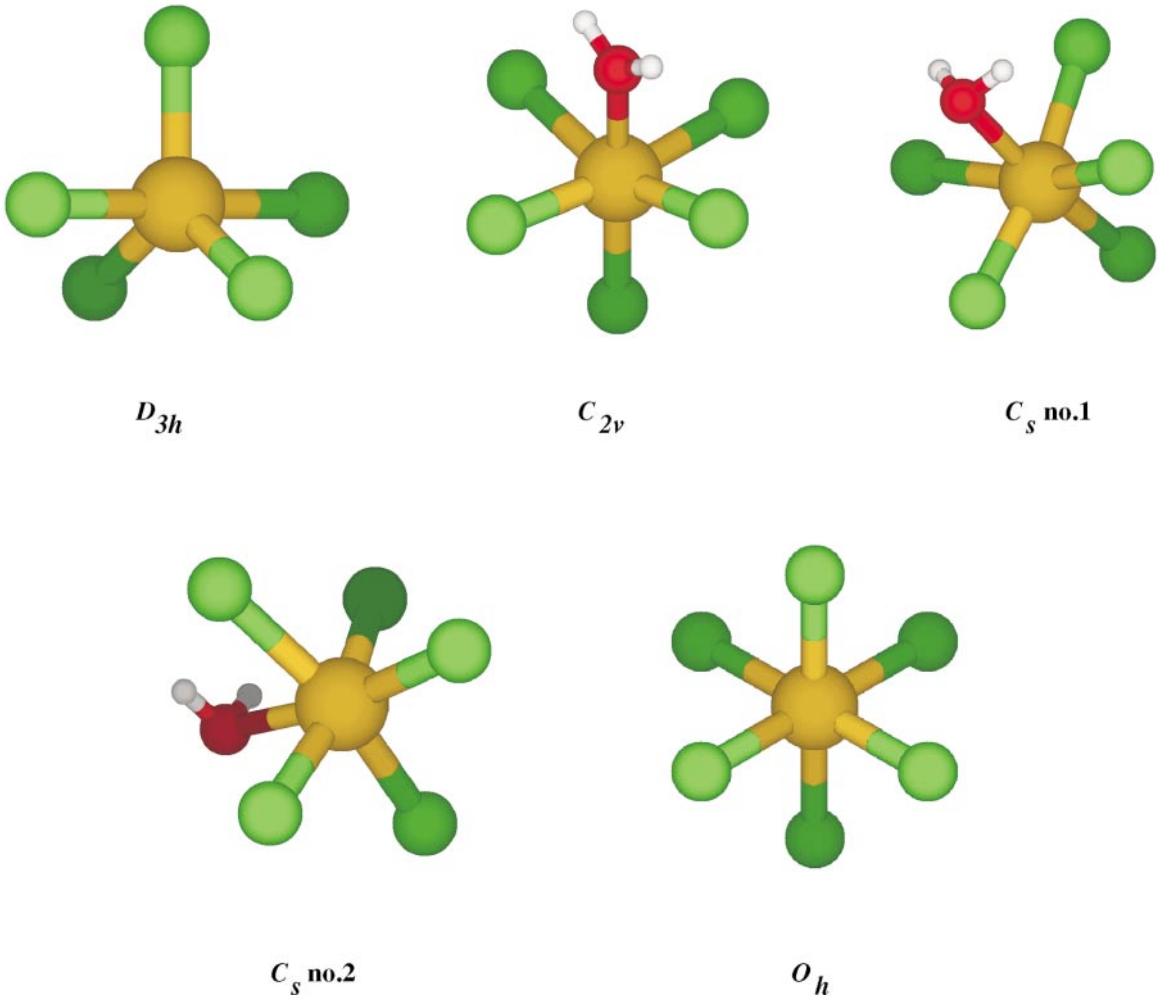

at 306 and 420 cm^{-1}. In addition, the *mer*-triaquatrichloroscandium(III) has polarized modes at 257, 288, and 330 cm^{-1} which are also in the right range and given the shortcomings of the theory discussed in the diaqua section, could also be a candidate.

Tetrachloroaquascandium complexes ($ScCl_4(H_2O)_n^-$)

The structures of tetrachloroaquascandium complexes are given in Fig. 10. Tetrachloroscandium(III) can potentially have D_{4h} symmetry, but this structure has imaginary frequencies and becomes T_d after optimization. If a single water is added in an equatorial position of the trigonal bipyramid, two possible C_{2v} structures can be generated, neither of which is an energy minimum and which undergo a pseudo-rotation to become a C_s structure with the water in an axial position. The two C_{2v} structures, at the HF/6-31G* level, are 18 and 66 kJ mol^{-1} less stable, respectively. Adding a second water can give either a trans or a cis configuration. A D_{2h} structure was initially tried for the trans, but the presence of imaginary frequencies suggested desymmetrization to a C_{2v} structure. The resulting structure also had imaginary frequencies, so we desymmetrized to a C_2 structure. This structure also had imaginary frequencies so we removed all constraints which gave us a different C_2 structure (no. 2) which was a local minimum. These structures were less stable than C_2 no. 2 at the HF/6-31G* level by 36.4, 9.9, and 6.5 kJ mol^{-1}, respectively. For the cis structure, we tried a C_{2v} structure initially, which had an imaginary frequency, so we desymmetrized to a C_2 structure which was a local minimum and was more stable by 0.05 kJ mol^{-1}, indicating than the water twisting has a flat potential. The cis structure was more stable than the trans structure at all levels investigated.

If we compare the tri- and tetrachloro species with the same number of waters, some trends are apparent. In the monoaqua species, the Sc—O distance lengthens by over 0.16 Å, whereas it is not so obvious for the diaqua. In addition, the Sc—O distances in the diaqua are actually shorter than the monoaqua. The same lengthening trend is apparent if we compare species with the same coordination number. The Sc—Cl distances are always longer.

The frequencies of the species with at least four chlorides are given in Fig. 11. None of the chloroscandium complexes are consistent with two polarized modes in the correct frequency ranges.

Penta- and hexachloroaquascandium complexes ($ScCl_5(H_2O)_{0\,-1}^{2-}$ and $ScCl_6^{3-}$)

The structures of the penta- and hexachloroaquascandium complexes are given in Fig. 12. The penta- and hexa-

© 2002 NRC Canada

chloroscandium(III) species belong to the D_{3h} and O_h point groups, respectively. For the pentachloroaquascandium(III) complex, we initially tried a C_{2v} structure, which has an imaginary frequency, as does our first attempt at desymmetrizing to a C_s. Our second C_s structure is a minimum. At the HF/6-31G* level, these structures are 27 and 5 kJ mol^{-1} higher in energy than C_s no. 2.

The Sc—O distance in the pentachloroaquascandium is very similar to that of the tetrachloroaqua, and longer than in the tetrachlorodiaqua. The Sc—Cl distances, however, continue to increase as more chlorides and waters are added. The Sc—Cl distances of 2.58 to 2.63 Å are larger than the experimentally observed values in $ScCl_3$ (2.515 to 2.528 Å) and $Ba_2Cl[ScCl_6]$ (2.42 to 2.52 Å) (18).

Discussion

We have identified some preliminary candidates for the chloroaquascandium complex that gives rise to a polarized mode at 306 cm^{-1} by a comparison of the vibrational frequencies predicted and measured in the Raman solution spectrum. Although systematic errors in the calculation were approximately taken into account (20–27 cm^{-1} for Sc-Cl stretch in $ScCl_4^-$, 50 cm^{-1} for Sc-O stretch in $Sc(H_2O)_6^{3+}$) we have no way of knowing whether these errors are the same in the mixed chloroaquascandium complexes. In the absence of definitive assignments of known structures, we make the assumption that they are. It is clear that on thermodynamic grounds, a penta or hexachloro species is unlikely to exist. The monochloro complexes also are not candidates. Some viable possibilities thus are *trans*-dichlorotetraaquascandium(III), *trans*-trichlorodiaquascandium(III), and *mer*-trichlorotriaquascandium(III). Although many modes are predicted, many would be very similar to that of bulk water and would probably be indistinguishable from it. It should be noted that the depolarization ratios of all of these are small, and the higher frequency band is incorrectly predicted to have a higher intensity compared to the experimental ones at 306 and 420 cm^{-1}. In some cases there is a significant difference between the Raman intensities at the 6-31G* and 6-31+G* level. It is known that the Raman intensities are not that sensitive to the type of theory employed (HF, MP2, DFT), but that the basis set is important. Addition of a diffuse function to heavy atoms reduces the average errors by about 30% (19). The difference may be due to the model employed, in much the same way that the frequencies are altered by the inclusion of a second hydration sphere. The predicted frequencies with intensities at the HF/6-31+G* level are given in Fig. 13, with the polarized skeletal stretching bands indicated by an arrow. It is difficult to differentiate which of these structures is most likely solely from a comparison of the theoretical and experimental Raman spectra and we must incorporate some other data. Adding waters to form a second hydration sphere may clarify the possibilities, but this is not straightforward and is computationally very intensive, and thus we bring in some additional literature data.

In anion exchange studies, scandium in the presence of 12 M (and to some extent 7 M) HCl exchanges, suggesting that an anionic form exists, which is formulated as $ScCl_4^-$ (20). This would be consistent with our calculations on thermodynamic grounds. A later ion-exchange study showed the presence of cationic species at low chloride concentrations (21). An early vibrational spectroscopic study (22) on scandium chloride solutions agrees with the frequencies, but not the depolarization ratios, measured in our earlier paper (13). Some 45-Sc NMR measurements on scandium chloride solutions were interpreted on the basis of a series of hexacoordinate scandium complexes of varying chloride content (23). A Raman band at 332 cm^{-1} in 12 M HCl suggested the presence of tetrachloroscandium, consistent with our ab initio data. It was proposed that between 0–4 M of added HCl, either hexaaqua or hydroxo species are present, between 6–8 M, mono and dichloro complexes are present, and between 10–12 M, the tetrachloro complex dominates. Additional data suggested that at 4 N and 7 N HCl, the monochloro and dichloro complexes were dominant, respectively (24). Complex formation with chloride seems to start taking place at a concentration of greater than 0.3 M, but it is also claimed that the same thing happens for perchlorate at 0.1 M (25). Ultrasonic absorption measurements indicate that chloro complexes are formed as well in a hexacoordinate species (26). The molal activity coefficients of chloride, nitrate, bromide, and perchlorate solutions of scandium were measured and interpreted based on heptacoordination (27).

It appears as though the experimental data are difficult to reconcile with each other. The assumption of linear change in the chemical shift of ^{45}Sc NMR upon increasing chloride substitution (24) has not yet been proven. The existence of a monochloroaqua species at 3 M concentration is unlikely, as this species would produce an intense Sc-Cl band at high frequency, predicted to be at least 440 cm^{-1}. It is possible that the Sc-Cl band overlaps with the Sc-O band in hexaaquascandium(III) and is not resolved. More detailed Raman concentration studies are warranted, especially in the low Cl:Sc region. Our data, taken together with the experimental literature, suggest that the experimentally observed polarized bands at 306 and 420 cm^{-1} are due to *trans*-dichlorotetraaquascandium(III).

An anonymous reviewer suggested that we carry out some geometry optimizations and frequency calculations on polar species using the Onsager model at the HF/6-31G* and HF/6-31+G* levels. As a consistency check, we also performed Onsager dipole calculations on some non-polar species as well. Standard keywords (Volume, SCRF = (Dipole,Solvent = Water)) were used. For the charged complexes, the monopole contribution to the solvation energy dominates. As expected, molecules lacking a dipole moment gave a zero dipolar energy and no geometry change. The effect on $ScCl(H_2O)_5^{2+}$ was to lengthen the Sc—Cl by 0.07 (0.08) Å and to decrease the Sc—O distances by 0.01 to 0.02 Å. There was little effect on the Sc-O vibrational modes (<5 cm^{-1}) but the Sc-Cl stretching mode decreased by 43 (48) cm^{-1}, consistent with the large change in Sc—Cl distance. However, the effect on the distances of *cis*-$ScCl_2(H_2O)_4^+$, and the $ScCl_3(H_2O)_3$ isomers, was much less pronounced, with the Sc—Cl and Sc—O distances changing by at most 0.03 Å and the vibrational frequencies usually decreasing by within 10 cm^{-1}. It is clear that the Onsager model as applied here is insufficient to account for the variations between calculated and experimental X-ray distances

© 2002 NRC Canada

Fig. 13. Frequencies and intensities of candidate structures.

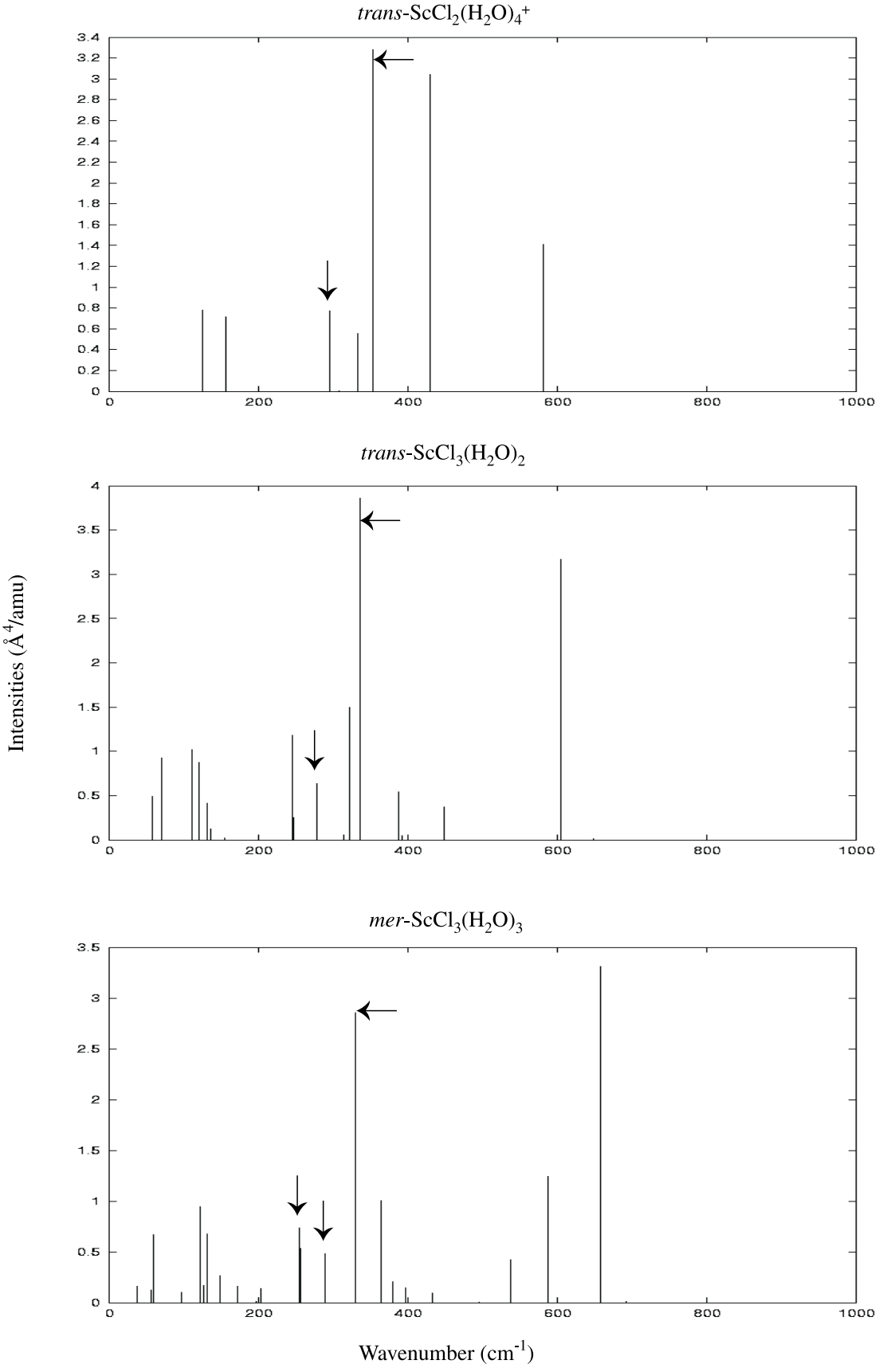

© 2002 NRC Canada

and frequencies. It is noteworthy that continuum model calculations with spherical cavities can sometimes give opposite changes in metal—oxygen bond lengths than molecularly shaped cavities or discrete models (28, 29). The solvation energy differences between isomers as predicted by the Onsager model (monopole + dipole) causes a reversal in the stability of the *cis-trans* dichlorotetraaqua (difference in solvation 90 kJ^{-1} mol) and *fac-mer* trichlorotriaqua (50 kJ mol^{-1}) complexes. Using the COSMO model of solvation at the gas-phase geometries does not cause a reversal in the stabilities. The trans isomer of $ScCl_2(H_2O)_4^+$ at the HF/6-31G* (HF/6-31+G*) level remains about 17 (23) kJ mol^{-1} more stable, although the cis isomer, as expected, is preferentially stabilized. Similarly, the meridianal isomer of $ScCl_3(H_2O)_3$ remains 6 (33) kJ mol^{-1} more stable than the facial isomer. It is clear that the calculation of solvation energies is very model-dependent, but a full account is beyond the scope of the paper. We prefer to use structural- and vibrational-based comparisons instead of energy criteria because lower levels of theory usually suffice for accurate descriptions of these.

Conclusions

Ab initio calculations on scandium aquachloro complexes are carried out. The agreement between the predicted and available X-ray structures is reasonable. The Sc—Cl distance is accurately predicted in the chloro complexes, whereas the Sc—O distance tends to be overestimated. Taking into account the systematic errors that this would likely cause on the Sc-O and Sc-Cl stretching frequencies, the experimental Raman spectrum of acidified 3.0 M scandium chloride solution is shown to be consistent with either a *trans*-dichlorotetraaqua, *trans*-trichlorodiaqua, or *mer*-trichlorotriaquascandium(III) complex. Assuming no band overlap, the monochloro, and the tetra- through hexachloro complexes can be ruled out at this concentration. The available experimental data, taken with our calculations, suggest that the dichloro species is most likely.

Acknowledgements

The authors thank the Department of Astronomy and Physics, Saint Mary's University (AP-SMU), for providing access to computing facilities, in particular, to cygnus, a 10-processor Sun server, purchased with assistance from the Canada Foundation for Innovation, Sun Microsystems, the Atlantic Canada Opportunities Agency, and SMU. CP also acknowledges the technical assistance of David Lane (AP-SMU). CP acknowledges the support of the Natural Sciences and Engineering Research Council of Canada (NSERC). CC acknowledges the support of the Department of Economic Development (Government of Nova Scotia), the Dean of Science and the Academic Vice President Development Funds (SMU), and the Cooperative Education Program (SMU - Work Term 1). CP would also like to thank his long-time friend and collaborator, Wolfram W. Rudolph, for his expert spectroscopic work and useful discussions.

References

1. F.V. Kovalev, V.S. Tyurin, and V.E. Kartsev. Russ. J. Non-Ferrous Met. **36**, 29 (1995).
2. S.V. Aleksandrovskii. Russ. J. Appl. Chem. **69**, 1441 (1996).
3. A. Kononov and E. Polyakov. J. Alloys. Compd. **239**, 103 (1996).
4. Y.P. Stangrit and V.P. Yurkinskii. Russ. J. Appl. Chem. **72**, 1371 (1999).
5. S.V. Aleksandrovskii. Russ. J. Appl. Chem. **70**, 1675 (1997).
6. A.F. Gutsol, V.Y. Kuznetsov, M.P. Ryskina, E.L. Tikhomirova, and V.T. Kalinnikov. Russ. J. Appl. Chem. **71**, 556 (1998).
7. A.F. Gutsol, and E.L. Tikhomirova. Russ. J. Appl. Chem. **71**, 1104 (1998).
8. J. Jiang, T. Ozaki, K. Machida, and G. Adachi. J. Alloys Compd. **264**, 157 (1998).
9. W.W. Rudolph and C.C. Pye. J. Phys. Chem. A, **104**, 1627 (2000).
10. Gaussian 98, Revision A.9. M.J. Frisch, G.W. Trucks, H.B. Schlegel, G.E. Scuseria, M.A. Robb, J.R. Cheeseman, V.G. Zakrzewski, J.A. Montgomery, Jr., R.E. Stratmann, J.C. Burant, S. Dapprich, J.M. Millam, A.D. Daniels, K.N. Kudin, M.C. Strain, O. Farkas, J. Tomasi, V. Barone, M. Cossi, R. Cammi, B. Mennucci, C. Pomelli, C. Adamo, S. Clifford, J. Ochterski, G.A. Petersson, P.Y. Ayala, Q. Cui, K. Morokuma, D.K. Malick, A.D. Rabuck, K. Raghavachari, J.B. Foresman, J. Cioslowski, J.V. Ortiz, A.G. Baboul, B.B. Stefanov, G. Liu, A. Liashenko, P. Piskorz, I. Komaromi, R. Gomperts, R.L. Martin, D.J. Fox, T. Keith, M.A. Al-Laham, C.Y. Peng, A. Nanayakkara, M. Challacombe, P.M.W. Gill, B. Johnson, W. Chen, M.W. Wong, J.L. Andres, C. Gonzalez, M. Head-Gordon, E.S. Replogle, and J.A. Pople. Gaussian, Inc., Pittsburgh. 1999.
11. C-F 6-31G: W.J. Hehre, R. Ditchfield, and J.A. Pople. J. Chem. Phys. **56**, 2257 (1972); H, C-F polarization functions: P.C. Hariharan and J.A. Pople. Theor. Chim. Acta (Berlin), **28**, 213 (1973); K-Zn: V.A. Rassolov, J.A. Pople, M.A. Ratner, and T.L. Windus. J. Chem. Phys. **109**, 1223 (1998).
12. H, Li-F diffuse: T. Clark, J. Chandrasekhar, G.W. Spitznagel, and P.v.R. Schleyer. J. Comput. Chem. **4**, 294 (1983).
13. C.C. Pye. Int. J. Quantum Chem. **76**, 62 (2000).
14. G.R. Willey, T.J. Woodman, and W. Errington. Transition Met. Chem. (Dordrecht, Neth.), **23**, 387 (1998).
15. A. Haaland, K.-G. Martinsen, D.J. Shorokhov, G.V. Girichev, and V.I. Sokolov. J. Chem. Soc. Dalton Trans. 2787 (1998).
16. V. Ripert, L.G. Hubert-Pfalzgraf, and J. Vaissermann. Polyhedron, **18**, 1845 (1999).
17. G.R. Willey, P.R. Meehan, and M.G.B. Drew. Polyhedron, **16**, 3485 (1997).
18. P.R. Meehan, D.R. Aris, and G.R. Willey. Coord. Chem. Rev. **181**, 121 (1999).
19. M.D. Halls and H.B. Schlegel. J. Chem. Phys. **111**, 8819 (1999).
20. K.A. Kraus, F. Nelson, and G.W. Smith. J. Phys. Chem. **58**, 11 (1954).
21. A.P. Samodelov. Sov. Radiochem. **6**, 548 (1964).
22. V.A. Sipachev and A.I. Grigorev. J. Struct. Chem. **10**, 710 (1969).
23. G.A. Melson, D.J. Olszanski, A.K. Rahimi. Spectrochim. Acta Part A, **33**, 301 (1977).
24. G.A. Kirakosyan, and V.P. Tarasov. Koord. Khim. **8**, 261 (1982).
25. V.P. Tarasov, G.A. Kirakosyan, S.V. Trots, Y.A. Buslaev, and V.T. Panyushkin. Koord. Khim. **9**, 205 (1983).
26. H.B. Silber and T. Mioduski. Inorg. Chem. **23**, 1577 (1984).
27. Y. Suzuki, R. Yoshino, H. Saitoh, K. Fukushi, and Y. Sonehara. J. Alloys Compd. **180**, 383 (1992).

© 2002 NRC Canada

28. J.M. Martinez, R.R. Pappalardo, E. Sanchez Marcos, B. Mennucci, and J. Tomasi. J. Phys. Chem. B, **106**, 1118 (2002).

29. W.W. Rudolph, R. Mason, and C.C. Pye. Phys. Chem. Chem. Phys. **2**, 5030 (2000).

© 2002 NRC Canada

Aspects of the hydrolysis of formamide: revisitation of the water reaction and determination of the solvent deuterium kinetic isotope effect in base

H. Slebocka-Tilk, F. Sauriol, Martine Monette, and R.S. Brown

Abstract: A study of the hydrolysis of formamide is reported with the aims of isolating the water reaction for hydrolysis from the acid and base hydrolysis terms and determining the solvent deuterium kinetic isotope effect (dkie) on base-catalyzed hydrolysis. Respective activation parameters ($\Delta H^{\ddagger}$ and $\Delta S^{\ddagger}$) of (17.0 ± 0.4) kcal mol^{-1} and (–18.8 ± 1.3) cal mol^{-1} K^{-1} for the acid reaction and (17.9 ± 0.2) kcal mol^{-1} and (–11.1 ± 0.5) cal mol^{-1} K^{-1} for the base reaction were determined from Eyring plots of the second-order rate constants over the range of 27–120°C. Kinetic studies at the minima of the pH/rate profiles in the pH range from 5.6 to 6.2 in MES buffers at 56°C, and in the pH range of 4.25–6.87 in acetate and phosphate buffers at 120°C are reported. At 56°C the available data fit the expression k_{obs}^{56} = 0.00303[H_3O^+] + 0.032[HO^-] + (3.6 ± 0.1) × 10^{-9}, while at 120°C the data fit k_{obs}^{120} = (0.15 ± 0.02)[H_3O^+] + (3.20 ± 0.24)[HO^-] + (1.09 ± 0.29) × 10^{-6}. Preliminary experimental estimates of E_a (ln A) of 22.5 kcal mol^{-1} (15.03) for the water rate constant (k_w) are calculated from an Arrhenius plot of the 56 and 120°C data giving an estimated k_w of 1.1 × 10^{-10} s^{-1} ($t_{1/2}$ = 199 years) at 25°C. Solvent dkie values of k_{OH}/k_{OD} = 1.15 and 0.77 ± 0.06 were determined at [OL^-] = 0.075 and 1.47 M, respectively. The inverse value is determined under conditions where the the first step of the reaction dominates and is analyzed in terms of a rate-limiting attack of OL^-.

Key words: formamide, activation parameters, water reaction, acid and base hydrolysis, solvent kinetic isotope effect.

Résumé : On a effectué une étude de l'hydrolyse du formamide dans le but d'isoler la réaction d'hydrolyse par l'eau des termes d'hydrolyses acide et basique et de déterminer l'effet isotopique cinétique du deutérium du solvant (eicd) sur l'hydrolyse catalysée par la base. En se basant sur les courbes de Eyring des constantes de vitesse du deuxième ordre entre 27 et 120°C, on a déterminé les paramètres d'activation respectifs ($\Delta H^{\ddagger}$ et $\Delta S^{\ddagger}$) de (17,0 ± 0,4) kcal mol^{-1} et (–18,8 ± 1,3) cal mol^{-1} K^{-1} pour la réaction acide et de (17,9 ± 0,2) kcal mol^{-1} et (–11,1 ± 0,5) cal mol^{-1} K^{-1} pour la réaction basique. On rapporte aussi les études cinétiques aux minima des profils pH/vitesse, à des pH allant de 5,6 à 6,2, dans des tampons de MES, à 56°C et à des pH allant de 4,25 à 6,87, dans des tampons d'acétate et de phosphate, à 120°C. À 56°C, les données peuvent être accommodées par l'expression k_{obs}^{56} = 0,00303[H_3O^+] + 0,032[HO^-] + (3,6 ± 0,1) × 10^{-9} alors que, à 120°C, les données peuvent être accommodées par l'expression k_{obs}^{120} = (0,15 ± 0,02)[H_3O^+] + (3,20 ± 0,24)[HO^-] + (1,09 ± 0,29) × 10^{-6}. Sur la base d'évaluations expérimentales préliminaires de E_a (ln A) de 22,5 kcal mol^{-1} (15,03) pour la constante de vitesse de l'eau (k_w) faites à l'aide d'une courbe d'Arrhenius des données de 56 à 120°C, on a évalué que, à 25°C, k_w = 1,1 × 10^{-10} s^{-1} ($t_{1/2}$ = 199 ans). Des valeurs de l'eicd du solvant de k_{OH}/k_{OD} = 1,15 et 0,77 ± 0,06 ont été déterminées pour des valeurs respectives de [OL^-] = 0,075 et 1,47 M. La valeur inverse a été déterminée pour des conditions dans lesquelles la première étape de la réaction est dominante et on l'a analysée en fonction d'une attaque cinétiquement limitante de OL^-.

Mots clés : formamide, paramètres d'activation, réaction de l'eau, hydrolyses acide et basique, effet isotopique cinétique du solvant.

[Traduit par la Rédaction]

Introduction

Due to the obvious relevance to biological processes, considerable attention has been devoted to understanding the mechanism of hydrolysis of amides under both acidic and basic conditions (1, 2). Far less is understood about the mechanism by which water alone promotes the hydrolysis of amides. Water reactions or their kinetic equivalent, HO^-

Received 2 April 2002. Published on the NRC Research Press Web site at http://canjchem.nrc.ca on 22 October 2002.

H. Slebocka-Tilk, F. Sauriol, M. Monette,[1] and R.S. Brown.[2] Department of Chemistry, Queen's University, Kingston, ON K7L 3N6, Canada.

[1]Present address: Bruker Canada, 555 Steeles Avenue East, Milton, ON L9T 1Y6, Canada.
[2]Corresponding author (rsbrown@chem.queensu.ca).

 DOI: 10.1139/V02-166 © 2002 NRC Canada

attack on the protonated amide, have been observed when the amide is activated in some way (3). Recently there has been interest in determining the water hydrolysis rate constants for peptides so that these values could be used as a background for comparison with enzyme-catalyzed rates (4). The latter water reactions are very much slower than those of activated amides so new, highly sensitive assay techniques using ^{14}C radioisotopic detection (4*a*) or post-hydrolytic conversion of products to fluorescent tracers (4*b*, 4*c*) were developed to follow reactions to a few percent completion at 25°C. Radzicka and Wolfenden (4*d*) determined activation parameters for water hydrolysis of some simple dipeptides by monitoring the hydrolyses in buffered media between pH 4.2 and 7.8 at several temperatures between 120 and 200°C, extrapolating the water rate constant to 25°C. In the latter studies, the $t_{1/2}$ for the water reactions at 25°C varied from 7 (4*a*) to 600 (4*d*) years.

Despite the above, information about the mechanism of the water reaction is sparse, particularly with respect to the partitioning of neutral tetrahedral addition intermediates. Earlier, we reported (5) ^{18}O=C exchange and solvent deuterium kinetic isotope (dkie) studies of the water reaction observed for trifluoromethyl-*p*-nitroacetanilide (**1**) (eq. [1]) an activated amide previously studied by Komiyama and Bender (3*d*).

[1] 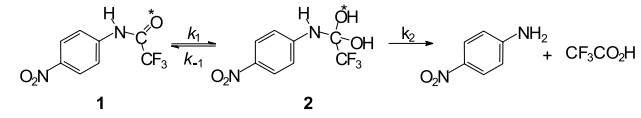

1 2

In that study we observed no ^{18}O=C exchange accompanying the hydrolysis in the water region, so we could not provide evidence that the reaction proceeded through a putative reversibly formed *gem*-diol intermediate (**2**). That intermediate, if formed, must break down to products faster than it reforms ^{18}O-exchanged starting material ($k_2 >> k_{-1}$) but how relevant those findings are to the water reaction of normal, and unactivated, amides remains to be established.

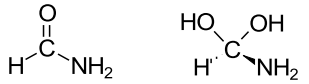

3 4

The water reaction of the simplest amide, formamide (**3**) has been investigated computationally to determine the overall reaction enthalpy for the neutral hydrolysis (6) and the free energy of activation for a hypothetical reaction involving one or more water molecules (7). The activation free energy for reaction with a single H_2O in the gas phase at 25°C is calculated to be ~55 kcal mol^{-1} (7*a*, 7*b*) but for the reaction in aqueous solvent involving three waters the value falls to ~48 kcal mol^{-1} (7*c*). The rate-limiting step for the three-water reaction is the formation of the tetrahedral addition product (**4**) with the great bulk of the free energy of activation (~33 kcal mol^{-1}) attributed to the entropy of restriction of freedom of the reaction partners in the transition state. More recently, Guthrie and Pitchko (8) introduced a valuable method termed the No Barrier Theory for calculating the activation free energies for hydration of carbonyl compounds, and computed a $\Delta G^{\ddagger}$ value of 31.9 kcal mol^{-1} for hydration of dimethyl formamide (DMF) via a three-water cyclic mechanism.

The high computed activation free energy for the water reaction of formamide and DMF can be compared to the activation parameters commonly found for the acid- and base-catalyzed hydrolysis of amides. Guthrie (9) reports that the free energies of activation for the acid hydrolysis of DMF and dimethyl acetamide at 25°C are 26.3 and 25.6 kcal mol^{-1}, respectively, while the corresponding base hydrolyses have values of 22.6 and 24.1 kcal mol^{-1}, respectively. Bolton and co-workers (10, 11) gave E_a ($\Delta S^{\ddagger}_{75}$) values of 18.8–21.5 kcal mol^{-1} (–17.4 to –22.0 cal K^{-1} mol^{-1}) for the acid hydrolysis of some primary amides and for *N*-methyl and *N*,*N*-dimethyl acetamide as well as $\Delta H^{\ddagger}$ and $\Delta S^{\ddagger}$ values of 11.7–17.4 kcal mol^{-1} (–29 to –39 cal K^{-1} mol^{-1}) for the base hydrolysis of a series of primary amides. Langlois and Broche (12) gave E_a ($\Delta S^{\ddagger}_{70}$) values of 18.4 kcal mol^{-1} (–24.7 cal K^{-1} mol^{-1}) for the acid hydrolysis of DMF, and 14.9 kcal mol^{-1} (–28.2 cal K^{-1} mol^{-1}) for its base hydrolysis. Although no experimental activation parameters for any of the reactions of **3** are available, it is striking that the computed barrier for its water reaction (7*c*), and that of DMF (8) is much larger than any experimental values for the acid- or base-catalyzed pathways of simple amides. An experimental search for the water reaction of some esters and simple amides like benzamide, butyramide, and acetamide was undertaken at high temperature in $NaHCO_3$–HOAc buffered media from pH 5–8 (13) but only the hydroxide process was claimed to be observed.

Our interest in amide water reactions was piqued by a report (14) stating that the pH/rate profile for hydrolysis of formamide between pH 1 and 9 at 80°C contains a slight plateau region at pH 6. The observed kinetics were fit to a general expression (k_{obs} = 0.0178[H^+] + 0.211[OH^-] + k_w) with the water reaction having a rate constant (k_w) of 8.4 × 10^{-8} s^{-1}, ($t_{1/2}$= 95 days). In the authors' words: "the k_w term is probably real, even though it is never large enough to contribute more than about 50% to the total reaction." Given the possibility that one might separate the water reaction from the H_3O^+ or HO^- reactions at some other temperature, we undertook a study of the hydrolysis of formamide at 56 and 120°C. Assessment of both the acid- and base-catalyzed hydrolyses at various temperatures was required to ascertain their importance in the neutral pH region where the water term is expected and so we obtained the activation parameters for both these processes. As part of the latter investigation we performed solvent deuterium kinetic isotope effect studies at 27°C in the base domain.

Experimental

Materials

MES buffer (morpholinoethanesulphonic acid) was reagent grade (Sigma). Acetic acid was distilled prior to use; NaH_2PO_4 and Na_2HPO_4 were used as supplied (Fisher). H_2O was made free from dissolved CO_2 and stored under Ar. D_2O (CDN Isotopes, 99.9 atom % D) was used as supplied as was formamide (99.5+%, A.C.S. reagent grade, Aldrich).

Kinetics

The rates of hydrolysis of formamide were determined by ^1H NMR analyses (Bruker DMX-Avance 500 spectrometer

© 2002 NRC Canada

Table 1. Second-order rate constants for formamide hydrolysis in base (I = 0.1 M KCl).[a]

T (K) (°C)	[OH^-] (M)	k_{HO^-} (M^{-1} s^{-1})
393 (120)	9.33×10^{-6} [b]	3.32
	3.98×10^{-6} [b]	3.76
353 (80)[c]		0.211
329 (56)	0.075	$(3.0 \pm 0.1) \times 10^{-2}$
	0.015	$(3.05 \pm 0.07) \times 10^{-2}$
319 (46)	0.075	$(1.37 \pm 0.08) \times 10^{-2}$
300 (27)	0.075	$(2.3 \pm 0.1) \times 10^{-3}$
	0.015	$(2.2 \pm 0.1) \times 10^{-3}$
	1.47	$(3.07 \pm 0.1) \times 10^{-3}$ [d]
	0.075 (D_2O)	$(1.98 \pm 0.01) \times 10^{-3}$
	1.47 (D_2O)	$(4.03 \pm 0.1) \times 10^{-3}$ [d]

[a]$\Delta H^{\ddagger}$ = 17.9 ± 0.2 kcal mol^{-1}; $\Delta S^{\ddagger}$ = –11.1 ± 0.5 cal K^{-1} mol^{-1}.
[b]Calculated from pH 6.87 and 6.55 buffer results in Table 4 assuming rates at those pH values are controlled by the HO^- process. See *Results* for calculation of [HO^-] at 120°C.
[c]Data from ref. (14).
[d]Ionic strength not controlled. Average of duplicate runs.

Table 2. Second-order rate constants for formamide hydrolysis in acid (I = 0.1 M KCl).[a]

T (K) (°C)	[H_3O^+] (M)	$k_{H_3O^+}$ (M^{-1} s^{-1})
393 (120)	5.6×10^{-5}	0.184[b]
353 (80)[c]		0.0178
329 (56)	0.1	$(3.3 \pm 0.1) \times 10^{-3}$
	0.01	$(3.1 \pm 0.1) \times 10^{-3}$
300 (27)	0.1	$(1.83 \pm 0.08) \times 10^{-4}$
	0.01	$(1.57 \pm 0.11) \times 10^{-4}$

[a]$\Delta H^{\ddagger}$ = 17.0 ± 0.4 kcal mol^{-1}; $\Delta S^{\ddagger}$ = –18.8 ± 1.3 cal K^{-1} mol^{-1}.
[b]Calculated from the pH 5.6 data in buffer given in Table 4.
[c]Data from ref. (14).

equipped with a broadband inverse probe). The ^1H NMR spectra in water were accumulated using a standard presaturation water suppression technique. Solutions of base (0.015 and 0.075 M, (I = 0.1 M (KCl)) in either H_2O or D_2O were prepared under CO_2-free conditions and stored under Ar. Base concentrations were determined by titration with standardized 0.1 N HCl, phenolphthalein indicator. Hydrolysis in acid was carried out in 0.01 M and 0.1 M HCl, I = 0.1 M (KCl). For reasons of solubility of the formamide, ionic strength was not kept constant for the kinetic experiments in MES buffer (pH 5.6, 5.9, 6.2; $[buffer]_t$ = 0.01, 0.02, and 0.04 M for each pH). Each NMR tube contained 0.5 mL of the acid, base, or buffer solution and 5×10^{-4} – 1×10^{-3} M of formamide along with 10 μL of D_2O as a lock. For slower reactions, sealed NMR tubes were thermostated at the desired temperature and removed at various times to collect the NMR spectra. For faster reactions, the NMR data were acquired continuously from the tube placed in the probe held at the desired temperature, and every 32 scans were summed separately (the time being recorded as the midpoint of the number of scans utilized). This process was repeated up to at least two hydrolysis half-times. For very slow reactions under buffered conditions (pH 5.6, 5.9, and 6.2), sealed NMR tubes with solutions of formamide in 0.5 mL of MES buffer were placed in a thermostated bath held at 56°C and the NMR spectra were collected at various time intervals over a period of 6 months (Tables 1–4).

Table 3. Pseudo-first-order rate constants for formamide hydrolysis in buffered media at 56°C.[a,b]

pH (Uncorrected) at ambient temperature	pH (Corrected) measured at 56 °C	k (s^{-1}) (Extrapolated to [buffer] = 0)
5.6	5.5	$(1.48 \pm 0.02) \times 10^{-8}$
5.9	5.8	$(9.85 \pm 0.16) \times 10^{-9}$
6.2	6.1	$(9.50 \pm 0.39) \times 10^{-9}$

[a]MES buffers, ionic strength not controlled.
[b]See Table 1S, *Supplementary material*[3] for original data.

Table 4. Pseudo-first order rate constants for hydrolysis of formamide in buffered media at 120°C.

pH (Measured at 25°C)	k (s^{-1})[a]
4.25[b]	1.035×10^{-5}
4.75[b]	3.75×10^{-6}
5.33[b]	2.8×10^{-6}
5.75[b]	3.8×10^{-6}
6.15[c]	5.9×10^{-6}
6.50[c]	1.5×10^{-5}
6.87[c]	3.1×10^{-5}

[a]Acetate buffer, ionic strength not controlled.
[b]Phosphate buffer, ionic strength not controlled.
[c]See Table 2S, *Supplementary material*[3] for original data.

The specific kinetic experiments for the 120°C conditions are as follows: a 10 mL solution of amide in acetate or phosphate buffer of known concentration and pH, measured at 25°C, buffered at various values between pH 6.15 and 6.87 for phosphate, and 4.25–5.75 for acetate, was divided into 10 portions, each being sealed in an ampoule. The ampoules were thermostated at 120°C (silicon oil, Hi-temp bath 160A, Fisher Scientific) for a maximum time corresponding approximately to one half-time of hydrolysis. Samples were withdrawn from the bath at various times and plunged into an ice bath. These were opened and, after the addition of 10 μL of D_2O to 0.5 mL of the sample solution, analyzed by NMR. The rate constants quoted in Tables 3 and 4 were obtained from the intercepts of the plots of the observed rate constant vs. [buffer]. All the individual rate constants were determined in duplicate (original data in Tables 1S and 2S).[3]

Solvent deuterium kinetic isotope experiments were undertaken in D_2O at [NaOD] = 0.075 and 1.47 M, respectively, at 27°C. For the latter concentration, two independent runs were undertaken, while a single run was performed at the former concentration.

Pseudo-first-order rate constants (k_{obs}) for formamide hydrolysis under the various conditions were obtained by observing the rate of increase of the intensity of the signal at δ 8.46 attributable to the O=C-*H* proton of the formic acid

[3]Supplementary material may be purchased from the Depository of Unpublished Data, Document Delivery, CISTI, National Research Council of Canada, Ottawa, ON K1A 0S2, Canada (http://www.nrc.ca/cisti/irm/unpub_e.shtml for information on ordering electronically).

© 2002 NRC Canada

formed (A) and the decrease of the intensity of the signal at δ 7.55 for that of formamide (B). The formamide signal at δ 7.55 appears as a doublet (J = 14.9 Hz) coupled to one of the NH protons while the two NH protons appear as two broad triplets coupled to ^{14}N. The one coupled to the formamide proton appears at δ 7.17 ($J_{N\text{-}H}$ ~ 60 Hz), while the other NH appear as a sharper triplet at δ 7.55 ($J_{N\text{-}H}$ ~ 62 Hz). Rate constants were evaluated from the slopes of the ln ($A/(A + B)$) vs. time plots with the errors in k_{obs} being determined as the standard deviation of the linear regression lines. Between 15 and 20 experimental points were used for each plot.

Activation parameters for the acid- and base-promoted hydrolyses were determined from plots of the log of the second-order rate constant ($k_{H_3O^+}$ or k_{HO^-}) vs. $1/T$ at four and five different temperatures including the reported data of Hine et. al (14) at 80°C with a total of seven and eight independent kinetic runs.

pH measurements of the reaction mixtures at ambient temperature and at 56°C were made with a Radiometer TTT2 unit and a Radiometer pHC4406 combined pH electrode. In the case of the reactions at 120°C, the pH was measured at ambient temperature before the reaction.

Results

Given in Tables 1 and 2 are the second-order rate constants for the HO^- and H_3O^+ catalyzed hydrolysis of formamide in water at various temperatures (including the 80°C data (14)). The 120°C acid and base values were derived under buffered conditions (Table 4, vide infra) at the lowest and highest pH values, where the respective reactions are first order in $[H_3O^+]$ and $[HO^-]$. Also included in Table 1 are the k_{OD^-} values at two $[OD^-]$ that give k_{OH}/k_{OD} values of 1.15 at $[OL^-]$ = 0.075 M, and 0.77 ± 0.06 at $[OL^-]$ = 1.47 M, T = 27°C.

Given in Table 3 are the rate constants determined under buffered conditions (MES, extrapolated to [buffer] = 0) at 56°C, while in Table 4 are the data at 120°C (acetate, phosphate extrapolated to [buffer] = 0). The original data in buffers used to construct these tables are given as Tables 1S and 2S, supplementary material.[3] The contribution of the acid plus base terms in the neutral pH region can be computed from the second-order rate constants provided in Tables 1 and 2. The hydroxide contribution at 5 < pH < 7 requires a correction of the $[HO^-]$ (13) attributable to the change in the K_w of water from $1 \times 10^{-13.997}$ at 25°C to $1 \times 10^{-13.11}$ at 56°C, and $1 \times 10^{-11.90}$ at 120°C (determined from the linear interpolation of the reported data (15) for K_w at 55 and 60°C, or the data at higher temperatures (16)).

Shown in Figs. 1 and 2 as dotted lines are the computed pH/rate profiles for hydrolysis only considering the H_3O^+ and HO^- terms at 56°C and 120°C, along with the experimental pseudo-first-order rate constants (■) in buffered conditions. The solid lines through the data in Figs. 1 and 2 come from NLLSQ fits of the 56 and 120°C data to the expression given in eq. [2], modeled for a process involving acid, base, and water terms. For the 56°C computation, values for the H_3O^+ and HO^- terms (Tables 1 and 2) were set as constants.

Fig. 1. Solid line: NLLSQ fit of the 56°C hydrolysis data in Table 3 to eq. [2] where $k_{H_3O^+}$ = 0.0032 M^{-1} s^{-1} and k_{OH} = 0.0303 M^{-1} s^{-1} are set constants and the autoprotolysis constant of water is pK_w = 13.11. Experimental data (■) for pseudo-first-order rate constants for hydrolysis from Table 3. Dotted line: computed pH/rate profile at 56°C for the hydrolysis of formamide assuming only the acid and base terms are operative.

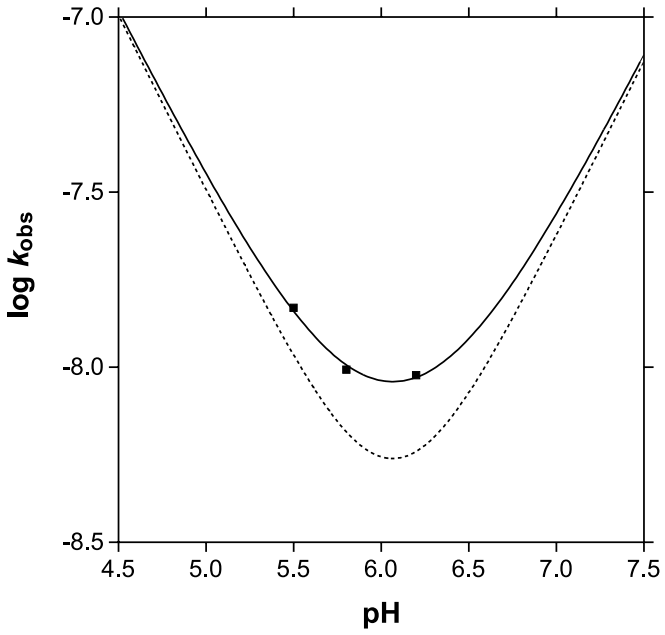

$$[2] \qquad k_{obs}{}^{t} = k_{H_3O^+}[H_3O^+] + k_{OH}[OH^-] + k_w$$

The best fit lines are: $k_{obs}^{56} = 0.00303[H_3O^+] + 0.032[HO^-] + (3.6 \pm 0.1) \times 10^{-9}$, and $k_{obs}^{120} = (0.15 \pm 0.02)[H_3O^+] + (3.20 \pm 0.24)[HO^-] + (1.09 \pm 0.29) \times 10^{-6}$.

Discussion

Water reaction?

Activation parameters ($\Delta H^{\ddagger}$ and $\Delta S^{\ddagger}$) of (17.0 ± 0.4) kcal mol^{-1} and (–18.8 ± 1.3) cal mol^{-1} K^{-1} for the H_3O^+ catalyzed reaction and (17.9 ± 0.2) kcal mol^{-1} and (–11.1 ± 0.5) cal mol^{-1} K^{-1} for the HO^- reaction were determined from standard Eyring plots of the second-order rate constants given in Tables 1 and 2. These experimental values for formamide compare favorably with those reported for other amides (9–12). On the other hand, the activation parameters for the OH^- catalyzed hydrolysis gave a $\Delta G_{25}^{\ddagger}$ of 21.2 kcal mol^{-1} which is about 25% lower than the recently reported computational value of 27.3 kcal mol^{-1} (17).

We envision that the acid, base, and water pathways must have different activation parameters so that one might isolate the water process by changing the reaction temperature. However it is not easily predicted whether one should move to higher or lower temperatures than the 80°C used by Hine et al. (14) because the literature gives little guidance concerning the activation parameters of the three processes in any given case. Computations can sometimes be of assistance but for formamide the calculated free energy of activation for the water reaction of 48 kcal mol^{-1} at 25°C (7*c*) seems too high relative to the experimental activation

© 2002 NRC Canada

Fig. 2. Solid line: unconstrained NLLSQ fit of the 120°C hydrolysis data in Table 4 to eq. [2] with the autoprotolysis constant of water being set at pK_w = 11.90. Experimental data (■) for pseudo-first-order rate constants for hydrolysis under buffered conditions from Table 4. Dotted line: computed pH/rate profile for the hydrolysis of formamide at 120°C assuming only the acid and base terms are operative.

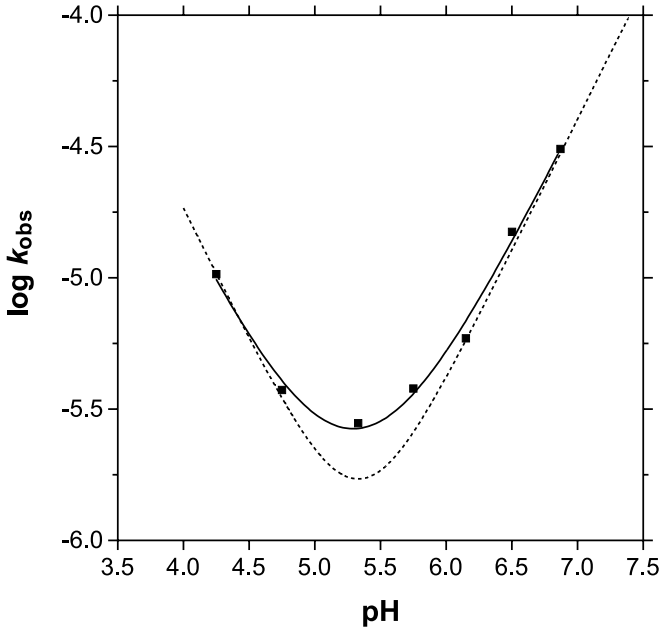

parameters we determined here for the acid and base processes for it to play any significant role at easily accessible temperatures. Guthrie and Pitchko's (8) recent computed value of $\Delta G^{\ddagger}_{25}$ = 31.9 kcal mol^{-1} for DMF hydrating via a three-water cyclic mechanism seems more reasonable as an upper limit for that amide, this value being some 5 to 6 kcal mol^{-1} larger than the acid and base values (9). Nevertheless, taken at face value the extant experimental rate data for formamide (14) suggest that the free energies for these processes must be similar if the water, acid, and base processes are competitive at 80°C. Esters, which are generally more reactive than their amide counterparts, might provide a starting point for comparison, but apparently the water reactions are exceedingly slow and little kinetic data are available. The water reaction for hydrolysis of methyl acetate has been estimated (18) to have a rate constant at 25°C of 3×10^{-10} s^{-1} corresponding to a half-time of 70 years, however, a plateau is not observed at intermediate pH in the hydrolysis of ethyl acetate (19). A more recent study involving six nonactivated esters at higher temperatures (13) concluded that only the hydroxide reaction is important down to pH values of about 5, except for *tert*-butyl acetate where a pH-independent reaction is said to occur. Kirby (20) has noted that activated esters such as alkyl and aryl haloacetates and substituted phenyl acetates do have water reactions with low activation enthalpies (7–14 kcal mol^{-1}) and large negative activation entropies (–40 to –50 cal K^{-1} mol^{-1}). This would be expected for highly ordered transition states in which charge buildup is avoided by several proton transfers accompanying the formation of a possible *gem*-diol intermediate. In our earlier study (5), we determined that the respective activation parameters of $\Delta H^{\ddagger}$ = 14.4 ± 0.6 and 11.7 ± 0.3 kcal mol^{-1} and $\Delta S^{\ddagger}$ = –36.1 ± 1.6 and –52.3 ± 1.3 cal K^{-1} mol^{-1} for the water-promoted hydrolysis of trifluoromethyl-*p*-nitroactetanilde and trifluoromethylacetanilide. Although the activation parameters were not determined for the acid and base processes, the above values are quite close to what was observed for the water reactions of activated esters.

How relevant these numbers might be to the hydrolysis of more normal, less-activated amides is unclear. As far as we know, the only other experimental activation parameters for water hydrolysis of amides were determined by Radzicka and Wolfenden (4*d*) who reported E_a values of 23–25 kcal mol^{-1} for the hydrolysis of three dipeptides, including glycyl-glycine, at pH 6.8 with temperatures between 120 and 200°C. The experimental $\Delta G^{\ddagger}_{25}$ = 31.71 kcal mol^{-1} for the hydrolysis of *N*-acetyl glycyl-glycine (4*d*) compares very well with the computed 31.9 kcal mol^{-1} value for DMF (8). These values can be compared with the reported (21) activation parameters for HCl- or NaOH-promoted hydrolysis for glycyl-glycine ($\Delta H^{\ddagger}$ ($\Delta S^{\ddagger}$), 20.3 kcal mol^{-1} (–24 cal K^{-1} mol^{-1}) and 16.9 kcal mol^{-1} (–26.8 cal K^{-1} mol^{-1}), respectively). Of course one must be mindful that acid, base, and neutral hydrolyses of dipeptides may involve different states of ionization of the substrates which may affect the various activation parameters in unpredictable ways.

Given the above, we set out to isolate the water reaction by obtaining the hydrolysis kinetics of formamide from initial rates at 56°C in the pH range of 5.6 to 6.2. The Table 3 data and Fig. 1 show a plateau at the pH minimum that we attribute to an observable water reaction having a computed k_{obs} value of (3.6 ± 0.1) × 10^{-9} s^{-1}, $t_{1/2}$ = 6.1 years! Concomitantly, we investigated the hydrolysis at 120°C in acetate and phosphate buffers. The enthalpies of ionization of these are small so that the dissociation constants do not vary much with temperature (15, 22). The kinetic data in Table 4, illustrated in Fig. 2, also plateau around the pH minimum. An unrestricted fit of these experimental buffer data to eq. [2] gives the values $k_{H_3O^+}$ = (0.15 ± 0.02) M^{-1} s^{-1}, k_{OH} = (3.20 ± 0.24) M^{-1} s^{-1}, and k_w = (1.09 ± 0.29) × 10^{-6} s^{-1}. For the latter term, $t_{1/2}$ = 7.3 days.

One can, through use of the best-fit rate constants above, determine that at the pH minima of 6.1 (56°C) and 5.3 (120°C), the water reaction contributes about 40% of the overall rate at either temperature. This, coupled with Hine's careful statements that the k_w term is never large enough to contribute more than about 50% to the total reaction at 80°C, is at first glance surprising. However, further analysis indicates this is a consequence of the similarity of the activation parameters for all three hydrolysis processes, and an interesting artifact of the drop in the autoprotolysis constant of water with increasing temperature which raises the [HO$^-$] and makes the base term more prominent at any given pH at high temperatures.

While it is now clear that there must be a water term in the hydrolysis of formamide, it is unfortunate that our best-fit water rate constants must have a 10–30% error which limits our ability to make conclusions and predictions. Nevertheless, since this is the only non-peptidic, nonactivated amide that has an experimentally demonstrated water reaction, we feel justified in putting forth a two-point experimental estimate of the Arrhenius parameters E_a (ln *A*) of 22.5 kcal

© 2002 NRC Canada

mol^{-1} (15.03) based on our 56 and 120°C data. Inclusion of Hine's 80°C k_w (14), which lies slightly above the two-point plot, does not change these values greatly. The estimated k_w at 25°C is thus 1.1×10^{-10} s^{-1} ($t_{1/2}$ = 199 years).[4]

Solvent deuterium kinetic isotope effect in base

The HO^- promoted hydrolysis of formamide has recently been investigated by Marlier et al. (23) through the application of heavy atom kinetic isotope effects. They point out that the experimental data concerning the ^{18}O content of the formate product arising from alkaline hydrolysis in a solvent enriched with $^{18}OH_2$ could be accommodated by either of two scenarios. With water as the attacking nucleophile, the ^{18}O solvent kinetic isotope effect ($^{18}k_{obs}$) would be 1.022 while with hydroxide as the attacking nucleophile, $^{18}k_{obs}$ would be 0.982. Based on the experimental precedence that almost all the known cases of heavy atom isotope effects for attacking nucleophiles are normal, they proposed that a water molecule solvating the hydroxide was the actual nucleophile (through a general base pathway) and not hydroxide itself. A general base mechanism was also proposed in their earlier report of the heavy atom isotope effects for the alkaline hydrolysis of methyl formate (24), and supported by a more recent analysis of a proton inventory study of the base-promoted hydrolysis of ethyl acetate (25). Given our expectation that the general base process is expected to exhibit a substantial primary solvent deuterium kinetic isotope effect (skie) due to a proton in flight, we undertook studies on the alkaline hydrolysis of formamide in D_2O. All previous solvent dkie studies of the base-catalyzed hydrolysis of amides such as benzamides, toluamides, and anilides (1*d*, 2) yield values of about 1.0 or slightly inverse which are consistent with a direct nucleophilic mechanism.

Analysis of the dkie requires consideration of the hydrolytic mechanism with respect to rate-limiting steps and partitioning of any anionic tetrahedral intermediates. Marlier et al. (23) and earlier, Kirsch (26), demonstrated that the rate law for alkaline hydrolysis of formamide contains both first- and second-order terms in hydroxide which is analyzed in terms of the mechanism presented in eq. [3] for which steady-state analysis gives the expression in eq. [4].

[3] 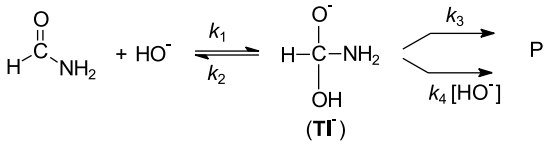

$$[4] \qquad k_{hyd} = \frac{k_1[HO^-](k_3 + k_4[HO^-])}{k_2 + k_3 + k_4[HO^-]}$$

Scheme 1.

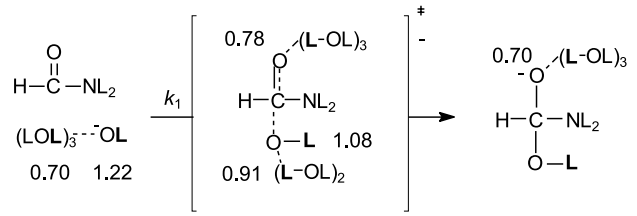

Scheme 2.

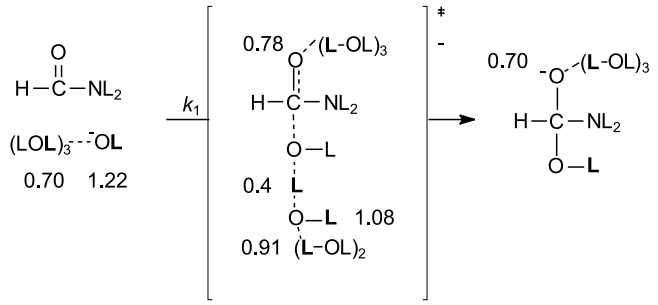

Graphical analysis (23, 26) of the partitioning of the tetrahedral intermediate (**TI**$^-$, eq. [3]) indicates that the k_3/k_2 ratio is 1.05, while the k_4/k_2 ratio is 2.15 M^{-1}. At low [HO^-] (<0.1 M), the second-order in [HO^-] pathway is relatively unimportant and **TI**$^-$ undergoes a substantial reversal, so k_{hyd} can be approximated as $k_1[HO^-]k_3/(k_2 + k_3)$. Analysis of the dkie at low [OH^-] is complicated since no step is entirely or substantially rate-limiting. On the other hand, at high [OH^-] the tetrahedral intermediate is driven forward via rapid capture by the second hydroxide so reversal becomes less important and attack becomes the rate-limiting step with k_{hyd} being approximated as $k_1[HO^-]$.[5] The skie data reported in Table 1 indicate that at [LO^-] = 0.075 M, where about 90% of the reaction proceeds by the first-order pathway (k_{OH}/k_{OD} = 1.15). At [LO^-] = 1.47 M, where about 75% of the reaction proceeds via the second-order pathway (k_{OH}/k_{OD} = 0.77 ± 0.06) which can thus be taken as the skie on k_1.

We analyze the latter data through the use of fractionation factors using the same general methodology we applied successfully to the base-promoted hydrolysis of some secondary and tertiary toluamides (27, 2*a*) and some esters (28). The solvent dkie can be predicted (29) as $k_{OD}/k_{OH} = \Pi\varphi^{TS}/\Pi\varphi^{GS}$, where $\Pi\varphi^{TS}$ and $\Pi\varphi^{GS}$ are the products of the various fractionation factors in the transition and ground states. Two possible cases that are considered are shown in Schemes 1 and 2 which involve, respectively, direct hydroxide attack and hydroxide acting as a general base for delivery of one of its solvating waters. In analyzing the dkie, we adopt Gold and Grist's (30) suggestion that HO^- has a fractionation factor of 1.22 while its three solvating waters each have fractionation factors of 0.7. During the direct attack of

[4] J.P. Guthrie (University of Western Ontario, private communication) informed us that the his No Barrier Theory calculations for the water reaction of dimethyl formamide (DMF, ($\Delta G^{\ddagger}_{25}$ 31.9 kcal mol^{-1})) lead to a computed water rate constant of 2.6×10^{-11} s^{-1}.

[5] This analysis is identical to that proposed by Marlier (ref. 23) and is substantially correct. However, at [HO^-] = 1.47 M the partitioning of the tetrahedral intermediate is ~4.1 in favour of product formation relative to reversal. Of that ratio, some 3.1 parts are attributed to the second-order pathway (k_4) and one part is attributed to the spontaneous pathway (k_3). Strictly speaking, while the dkie is substantially attributable to the attack step (k_1), there is a small additional component attributable to k_4 which should be inverse given OD^- in D_2O is a stronger base than is HO^- in H_2O.

© 2002 NRC Canada

hydroxide we assume in Scheme 1 that one of the solvating waters has been lost to liberate a lone pair required for attack on C=O, and that the developing O^- in **TI**$^-$ is associated with three solvating waters with fractionation factors similar to those of hydroxide. We assume that the transition state for attack (k_1) is late, being ~70% along the reaction coordinate to the tetrahedral species.

In the case of the general base mechanism given in Scheme 2, we assume that the fractionation factor for the proton in flight between the hydroxide and water is 0.4 (corresponding to a normal primary dkie of 2.5). All the assumed values are shown in bold type in Schemes 1 and 2: these give predicted solvent dkie's of ~1.0 for the direct attack of hydroxide and 2.2 for the general base mechanism.

The only substantial difference between the processes shown in Schemes 1 and 2 concerns the presence of the proton in flight which is solely responsible for the predicted normal dkie in the latter. Making the transition state in Scheme 1 later gives only a small increase in the predicted dkie because of the compensating effects of the loosening on waters solvating the attacking HO^-, and tightening of the waters solvating the developing O^- in **TI**$^-$. By converse, an earlier transition state for the direct attack of hydroxide, say 50% along the way to **TI**$^-$, gives a predicted dkie of 0.85, close to the experimentally observed value of 0.77 ± 0.06. That value seems to rule out the pathway given in Scheme 2, or any other pathway where there is much contribution from one or more protons in flight. In the limit of that mechanism, where the proton is nearly fully transferred from the attacking water to the general base HO^-, its associated fractionation factor would be close to unity leading to a drop in the predicted dkie toward the observed value. In the end this simply becomes a mechanism of direct hydroxide attack and cannot be distinguished from the process in Scheme 1.[6]

Conclusions

The main goals of the above study were to provide information about the water reaction of formamide, and provide the solvent dkie for the base reaction. Several important conclusions can be advanced.

We have determined the activation parameters for the H_3O^+ and HO^- promoted hydrolyses of formamide. The experimental $\Delta H^{\ddagger}$ and $\Delta S^{\ddagger}$ values are (17.0 ± 0.4) kcal mol^{-1} and (–18.8 ± 1.3) cal mol^{-1} K^{-1} for the H_3O^+ catalyzed reaction and (17.9 ± 0.2) kcal mol^{-1} and (–11.1 ± 0.5) cal mol^{-1} K^{-1} for the HO^- process. The values fit within the general range determined for acid- and base-catalyzed hydrolysis of other simple amides. However, the $\Delta H^{\ddagger}$ and $\Delta S^{\ddagger}$ values for the HO^- process give an experimental $\Delta G^{\ddagger}_{25}$ of 21.2 kcal mol^{-1} which is substantially lower than the recently computed value of 27.3 kcal mol^{-1} (17) which should prompt further efforts to refine the computational approaches.

We have determined k_w values of (1.09 ± 0.29) × 10^{-6} s^{-1} at 120°C and (3.6 ± 0.1) × 10^{-9} s^{-1} at 56°C, from which we estimated activation parameters of E_a = 22.5 kcal mol^{-1}, ln A = 15.03 from a two-point Arrhenius plot.

While it is apparent that a water reaction does exist at 56°C and at 120°C, in neither case does it contribute more than about 40% to the observed rate at the respective pH minima of 6.1 and 5.3. Hine et al. (14) also concluded that at 80°C, no more than 50% of the rate at the pH minimum can be attributed to the water reaction. Taken together, these studies indicate that it is improbable that conditions will be found where the water term for hydrolysis of formamide can be isolated (meaning contributing more than 95% at any given pH) from the corresponding acid and base reactions. This is an interesting consequence of two major factors: (1) the relative activation parameters of all three processes for this specific amide; and (2) the increase in the autoprotolysis constant of water as a function of temperature that increases the [HO^-] at any given pH, the net effect being to drive the pH minimum for the reaction to lower values at higher temperatures.

We have presented solvent deuterium kinetic isotope data for the base-catalyzed reaction at high [HO^-] where the kinetics are largely determined by the first step leading to the tetrahedral intermediate. The observed inverse value of k_{OH}/k_{OD} = 0.77 gives little evidence for a significant contribution of a proton in flight and strongly supports the mechanism involving the direct attack of hydroxide, similar to that believed operative for other amides, and at variance with a suggested water attack mediated by HO^-.

Acknowledgements

The authors gratefully acknowledge the financial support of the Natural Sciences and Engineering Research Council of Canada (NSERC) and Queen's University. In addition they acknowledge the generous donation of NMR time and expertise by Bruker Canada. In addition they are grateful for the helpful comments of the referees and for insightful personal communications from Professor J. P. Guthrie, University of Western Ontario.

References

1. (*a*) W.P. Jencks. *In* Catalysis in chemistry and enzymology. McGraw-Hill Inc., New York. 1969. pp. 523–527; (*b*) T.H. Lowry and K.S. Richardson. *In* Mechanism and theory in organic chemistry. 3rd. ed. Harper and Row Inc., New York. 1987. pp. 714–717; (*c*) C.J. O'Connor. Quart. Rev. Chem. Soc. **24**, 553 (1970); (*d*) M.L. Bender. Chem. Rev. **60**, 53 (1960); (*e*) N. Isaacs. *In* Physical organic chemistry. 2nd. ed. Longman Scientific and Technical and J. Wiley and Sons, New York. 1995. pp. 529–531; (*f*) J. March. *In* Advanced organic chemistry. 4th. ed. Wiley-Interscience, New York. 1992.
2. (*a*) R.S. Brown, A.J. Bennet, and H. Slebocka-Tilk. Acc. Chem. Res. **25**, 481 (1992); (*b*) A.J. Bennett and R.S. Brown. *In* Comprehensive biological catalysis: A mechanistic reference. Vol. 1. *Edited by* M. Sinnott. Academic Press, New York. 1997. pp 293–326; (*c*) R.S. Brown. *In* The amide link-

[6] This analysis differs from the one used by Mata-Segreda in assessing the mechanism for hydroxide attack on ethyl acetate (25). In that analysis the assumed transition structure involved $HO^-\cdots$H-(OH)$\cdots$C=O with no solvating waters and a proton in flight between the attacking water and the general base HO^-. A future publication from these laboratories will present our analysis of the proton inventory study of the base hydrolysis of formamide.

© 2002 NRC Canada

age: Selected structural aspects in chemistry, biochemistry, and materials science. *Edited by* A. Greenberg, C.M. Brenneman, and J.F. Liebman. Wiley-Interscience, New York. 1999. pp. 85–114.
3. (*a*) W.P. Jencks and J. Carriuolo. J. Biol. Chem. **234**, 1272 (1959); (*b*) T.H. Fife, R. Natarajan, and M.H. Werner. J. Org. Chem. **52**, 740 (1987); (*c*) T.H. Fife. Acc. Chem. Res. **26**, 325 (1993); (*d*) M. Komiyama and M.L. Bender. Bioorg. Chem. **7**, 133 (1978); Bioorg. Chem. **8**, 141 (1979); (*e*) A.M. Segretain, M. Beugelmans-Verrier, and M. Laloidiard. Bull. Soc. Chim. Fr. 3367 (1972); (*f*) V. Somayaji and R.S. Brown. J. Org. Chem. **51**, 2676 (1986); (*g*) G.M. Blackburn, C.J. Skaife, and I.T. Kay. J. Chem. Res. Synop. 294 (1980); (*h*) A. Cipiciani, P. Linda, and G. Savelli. J. Heterocycl. Chem. **15**, 1541 (1978); (*i*) A. Cipiciani, G. Savelli, and C.A. Bunton. J. Heterocycl. Chem. **21**, 975 (1984); (*j*) J.F. Patterson, W.P. Huskey, and J.L. Hogg. J. Org. Chem. **45**, 4675 (1980).
4. (*a*) D. Kahne and W.C. Still. J. Am. Chem. Soc. **110**, 7529 (1988); (*b*) R.A.R. Bryant and D.E. Hansen. J. Am. Chem. Soc. **118**, 5498 (1996); (*c*) R.M. Smith and D.E. Hansen. J. Am. Chem. Soc. **120**, 8910 (1998); (*d*) A. Radzicka and R. Wolfenden. J. Am. Chem. Soc. **118**, 6105 (1996).
5. H. Slebocka-Tilk, C. Rescorla, S. Shirin, A.J. Bennet, and R.S. Brown. J. Am. Chem. Soc. **119**, 10 969 (1997).
6. K.D. Dobbs and D.A. Dixon. J. Chem. Phys. **100**, 5712 (1996).
7. (*a*) T. Oie, G.H. Loew, S.K. Gurt, J.S. Binkley, and R.D. MacElroy. J. Am. Chem. Soc. **104**, 6169 (1982); (*b*) J.H. Jensen, K.K. Baldridge, and M.S. Gordon. J. Chem. Phys. **96**, 8340 (1992); (*c*) B. Kallies and R. Mitzner. J. Mol. Model. **4**, 183 (1998).
8. J.P. Guthrie and V. Pitchko. J. Am. Chem. Soc. **122**, 5520 (2000).
9. J.P. Guthrie. J. Am. Chem. Soc. **96**, 3608 (1974).
10. P.D. Bolton. Aust. J. Chem. **19**, 1013 (1966).
11. P.D. Bolton and G.L. Jackson. Aust. J. Chem. **24**, 969 (1971).
12. S. Langlois and A. Broche. Bull. Soc. Chim. Fr. 812 (1964).
13. B.A. Robinson and J. W. Tester. Int. J. Chem. Kinet. **22**, 431 (1990).
14. J. Hine, R.S.-M. King, R. Midden, and A. Sinha. J. Org. Chem. **46**, 3186 (1981).
15. R.C. Weast (*Editor*). CRC handbook of chemistry and physics. 58th ed. CRC Press, Cleveland. 1977/1978. D-152.
16. J.R. Fisher and H.L. Barnes. J. Phys. Chem. **76**, 90 (1972).
17. D. Bakowies and P.A. Kollman. J. Am. Chem. Soc. **121**, 5712 (1999).
18. J.P. Guthrie. J. Am. Chem. Soc. **95**, 6999 (1973).
19. H. Maskill. *In* The physical basis of organic chemistry. Oxford University Press, Oxford, U.K. 1985. pp. 350–355.
20. A.J. Kirby. *In* Comprehensive chemical kinetics. Vol 10. *Edited by* C.H. Bamford and C.F.H. Tipper. Elsevier, Amsterdam. 1972. pp. 57–207.
21. L. Lawrence and W.J. Moore. J. Am. Chem. Soc. **53**, 3973 (1951).
22. J.A. Dean (*Editor*). Lange's handbook of chemistry. 14th ed. McGraw Hill, Inc., New York. 1973. Table 8.9.
23. J.F. Marlier, N.C. Dopke, K.R. Johnstone, and T.J. Wirdzig. J. Am. Chem. Soc. **121**, 4356 (1999).
24. J.F. Marlier. J. Am. Chem. Soc. **115**, 5953 (1993).
25. J.F. Mata-Segreda. J. Am. Chem. Soc. **124**, 2259 (2002).
26. J.F. Kirsch. *In* Isotope effects on enzyme catalyzed reactions. *Edited by* W.W. Cleland, M.H. O'Leary, and D.B. Northrup. University Park Press, Baltimore. 1977. pp. 100–121.
27. (*a*) H. Slebocka-Tilk, A.J. Bennett, R.S. Brown, J.P. Guthrie, and A. Jodhan. J. Am. Chem. Soc. **112**, 8507 (1990); (*b*) H. Slebocka-Tilk, A.J. Bennett, H.J. Hogg, and R.S. Brown. J. Am. Chem. Soc. **113**, 1288 (1991); (*c*) R.S. Brown, A.J. Bennet, H. Slebocka-Tilk, and A. Jodhan. J. Am. Chem. Soc. **114**, 3092 (1992).
28. B.A. Kellogg and R.S. Brown. J. Org. Chem. **59**, 4652 (1994).
29. (*a*) R.L. Schowen. *In* Isotope effects on enzyme catalyzed reactions. *Edited by* W.W. Cleland, M.H. O'Leary, and D.B. Northrup. University Park Press, Baltimore. 1977; (*b*) R.L. Schowen. Prog. Phys. Org. Chem. **9**, 275 (1972); (*c*) K.B.J. Schowen. *In* Transition states of biochemical processes. *Edited by* R.D. Gandour and R.L. Schowen. Plenem Press, New York. 1978.
30. V. Gold and S. Grist. J. Chem. Soc. Perkin Trans. 2, 89 (1972).

© 2002 NRC Canada

Crystal chemistry of tetraradial species. Part 10. Tilting at windmills: conformations of the tetraphenyl species $ZPh_4^{0,\pm1}$ (Z = B, C, N)[1]

Osvald Knop, Kathryn N. Rankin, T. Stanley Cameron, and Russell J. Boyd

Abstract: The equilibrium geometries of the isoelectronic $ZPh_4^{0,\pm1}$ (Z = B, C, N) molecules have been optimized, in S_4 and D_{2d} symmetries, at the HF/6-31G(d,p) and B3LYP/6-31G(d,p) levels, with the phenyl rings constrained to be planar. The ground-state conformations of all three species are shown to be of S_4 symmetry, but the difference of the energies of the S_4 and the D_{2d} conformations is estimated to amount to only ~1 kcal mol^{-1}, with a barrier to concerted rotational reorientation of the phenyl rings of ~5.0 kcal mol^{-1} for BPh_4^-, ~6.4 kcal mol^{-1} for CPh_4, and ~7.9 kcal mol^{-1} for NPh_4^+. A redetermination of the crystal structure of CPh_4 from –60°C X-ray data agrees with the results of previous determinations at ambient temperature; the CPh_4 molecule in the crystal is slightly compressed along the S_4 axis relative to the free molecule, otherwise the geometries of the two are essentially the same. Correlations between the optimized geometric parameters of the $ZPh_4^{0,\pm1}$ molecules have been examined and analyzed in detail, as have the substitution-induced changes in the geometry of the phenyl ring. The results confirm and strengthen the conclusions from the statistical studies by Domenicano et al. on the geometry of benzene rings monosubstituted by atoms of elements from the first row of the Periodic system.

Key words: tetraphenylborate, tetraphenylmethane, tetraphenylammonium, ab initio molecular geometries.

Résumé : Opérant au niveau HF/6-31G(d,p) et B3LYP/6-31G(d,p) de la théorie et en contraignant les noyaux phényles à être plans, on a optimisé les géométries à l'équilibre des molécules isoélectroniques $ZPh_4^{0,\pm1}$ (Z = B, C, N) dans les symétries S_4 et D_{2d}. On démontre que les conformations des trois espèces à l'état fondamental sont de symétrie S_4; toutefois, on a évalué que la différence d'énergie entre les conformations S_4 et D_{2d} n'est que d'environ 1 kcal mol^{-1} alors que la barrière à la réorientation rotationnelle des noyaux phényles d'environ 5,0 kcal mol^{-1} pour le BPh_4^-, d'environ 6,4 kcal mol^{-1} pour le CPh_4 et d'environ 7,9 kcal mol^{-1} pour le NPh_4^+. Une redétermination de la structure cristalline du CPh_4 à partir de données de rayons X obtenues à –60°C est en accord avec les déterminations antérieures à la température ambiante; par rapport à la molécule libre, la molécule de CPh_4 dans le cristal est légèrement comprimée le long de l'axe S_4, mais autrement les géométries des deux sont essentiellement les mêmes. On a examiné les corrélations entre les paramètres géométriques optimisés des molécules de $ZPh_4^{0,\pm1}$ et on les a analysées en détail comme on l'a fait pour les changements dans la géométrie du noyau phényle induits par une substitution. Les résultats confirment et renforcent les conclusions obtenues par les études statistiques de Domenicano et ses collaborateurs sur les géométries des noyaux benzéniques monosubstitués par des atomes d'éléments de la première rangée du tableau périodique.

Mots clés : tétraphénylborate, tétraphénylméthane, tétraphénylammonium, géométries moléculaires ab initio.

[Traduit par la Rédaction]

Introduction

The tetraradial homotetraaryl $ZAr_4^{0,\pm1}$ have always held stereochemical and crystallographic fascination because of their windmill-like geometries and often high symmetries, and they have engendered a substantial literature dealing with various aspects of their properties (2–11).

Of the many $ZAr_4^{0,\pm1}$ species reported, the three simplest, the tetraphenyls $ZPh_4^{0,\pm1}$ (Z = B, C, N) are examined de novo in this paper. Apart from the present common denominator, viz. a comparison of their geometry and symmetry in the free state, they are of interest each for different reasons. The BPh_4^- anion is widely used in preparative chemistry as a bulky counter-anion for stabilizing cationic species that otherwise might be unstable. Its geometry and symmetry in the over 1800 crystal structures of tetraphenylborates known

Received 19 May 2002. Published on the NRC Research Press Web site at http://canjchem.nrc.ca on 25 October 2002.

Dedicated to Professor Dietrich Babel in his active retirement.

O. Knop,[2] K.N. Rankin,[3] T.S. Cameron, and R.J. Boyd. Department of Chemistry, Dalhousie University, Halifax NS B3H 4J3, Canada.

[1]For Part 9 see ref. 1.

[2]Corresponding author (e-mail: chemistry@dal.ca).
[3]Present address: Biotechnology Research Institute, National Research Council of Canada, 6100 Royalmount Avenue, Montreal, QC H4P 2R2, Canada.

 DOI: 10.1139/V02-171 © 2002 NRC Canada

show a remarkable variation,[4] the reasons for which have been pondered (13–15) without, however, leading to definite conclusions.

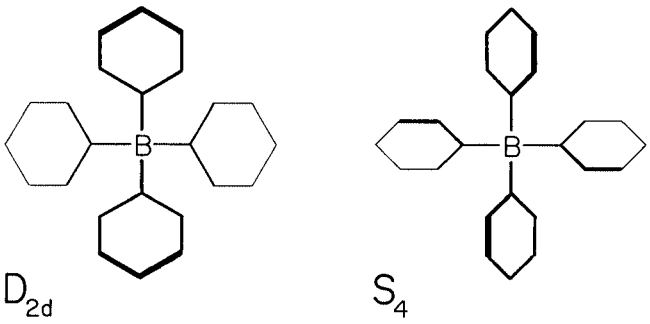

The neutral tetraphenylmethane molecule is of interest because of the uncertainty regarding its ground-state conformation. The conformation found in the crystal is undoubtedly of S_4 symmetry (TEPHME (16); TEPHME02, TEPHME03, TEPHME11 (17); ref. 18 and below),[5] as are the conformations of all the other Group IV crystalline ZPh_4 (Z = Si, Ge, Sn, Pb) species,[6] as well as of free $SiPh_4$ (4), and very likely of its homologs (8); the crystal structure of CPh_4 at room temperature was the subject of a deliberate interlaboratory comparison (17). The conformation of *free* CPh_4, however, has been concluded from semiempirical calculations (4) to be of symmetry D_{2d}. The availability of these combined data thus seemed to afford an opportunity for examining the effect of packing forces in a molecular crystal on the structure of a tetraradial hydrocarbon molecule of high symmetry.

The tetraphenylammonium cation NPh_4^+ is an elusive species. Reference 19 is the only reference to its existence uncovered in an up-to-date search of Chemical Abstracts. It describes the formation of $[N(C_6H_5)_3(C_6T_5)]^+X^-$ (X = BF_4, I) from triphenylamine and the free $C_6T_5^+$ cation generated by β-decay from pertritiated benzene. Unfortunately, the extremely small quantities of the radiochemically identified products, and their spontaneous dissociation by fragmentation of a phenyl group, precluded any investigation of the bulk stability and structural properties of the cation.

The principal aim of this investigation is to provide, from ab initio calculations, a reasonably reliable structure for free BPh_4^- to serve as a reference in our statistical analysis of this anion in crystalline tetraphenylborates (to follow), to resolve the ambiguity concerning the ground-state conformation of free CPh_4 and compare its geometry to that found in the crystal, and to see whether the results of the calculations for NPh_4^+ may uncover reasons for the reticence of the chemical literature on the subject of this cationic species. The calculations are supplemented by a redetermination of the crystal structure of CPh_4 from data collected at a moderately low temperature (–60°C).

Symbols and notation are explained at the end of the paper. The orientations of the molecules have been standardized by rotation about the $S_4 \equiv z$ so as to position the C_6 centroid in the *yz* axial plane, as shown in the schematic projection in Fig. 1. *Proximal* refers to carbons C5 and C6, *distal* refers to carbons C2 and C3 (z(C2) < z(C6), z(C3) < z(C5), d(Z···C6) < d(Z···C2)). All coordinates and interatomic distances are in Å.

Procedures

The ab initio geometry optimizations of BPh_4^-, CPh_4, and NPh_4^+ in S_4 and D_{2d} symmetries were performed at the RHF/6-31G(d,p) level using GAUSSIAN98 (20), with the initial parameter estimates derived from the CPh_4 geometry in the crystal, and with the C_6H_5 ring constrained to be planar, but not coplanar with Z. In the later stages of the investigation, improved geometry optimizations were realized using density functional theory (DFT), again with the ring-planarity constraint.

The DFT calculations were carried out using the GAUSSIAN98 suite of programs (20). All geometry optimizations were performed using the B3LYP functional and 6-31G(d,p) basis set. The B3LYP functional is composed of Becke's (21, 22) three-parameter hybrid exchange functional B3, as implemented in GAUSSIAN98 (23), and the correlation functional of Lee et al. (24). Harmonic vibrational frequencies and zero-point vibrational energy (ZPVE) corrections were calculated at the same level of theory.

Details of the crystal-structure determination of CPh_4 are given in Table 1. Atom coordinates, thermal parameters, and interatomic distances and bond angles have been deposited.[7] Atom C(7) of the deposited material corresponds to C0 ≡ Z of Table 6. To match the standardized optimized atom coordinates (in Å) of CPh_4 in Tables A and B,[8] the crystallographic fractional coordinates have been appropriately transformed, as have those of ref. 17 (*R* in Table 6).

[4] The part of this paper pertaining to BPh_4^- constitutes in fact a preliminary to a forthcoming statistical investigation of the variability of the anion geometry.

[5] The Cambridge Structural Database (12) reference codes of the individual crystal-structure determinations appear in capitals.

[6] TPENSI, TPENSI01, TPENSI02, TPENSI03, TPENSI04; TPENGE, TPENGE01, TPENGE02; TPHESN, TPHESN01, TPHESN02, TPHESN03; TPHEPB, TPHEPB01, TPHEPB03; refs. 8 and 18.

[7] CCDC contains the supplementary data for this paper. These data can be obtained, free of charge, via www.ccdc.cam.ac.uk/conts/retrieving.html (or from the Cambridge Crystallographic Data Centre, 12 Union Road, Cambridge, U.K.; fax +44 1223 336033; or deposit@ccdc.cam.ac.uk).

[8] Copies of material deposited may be purchased from the Depository of Unpublished Data, Document Delivery, CISTI, National Research Council of Canada, Ottawa, ON K1A 0S2, Canada (http://www.nrc.ca/cisti/irm/unpub_e.shtml for information on ordering electronically). The following tables have been deposited: A. Atomic coordinates and Mulliken net atom charges of BPh_4^-, CPh_4, and NPh_4^+ with geometries optimized in HF/6-31G(d,p). B. Atomic coordinates and Mulliken net atom charges of BPh_4^-, CPh_4, and NPh_4^+ with geometries optimized in B3LYP/6-31G(d,p). C. Intermolecular H···H contacts in CPh_4 at –60°C (data set *T*; out to 3Å). D. Linear correlations of ${S_4}^{00}$ parameters of $ZPh_4^{0,\pm1}$ (1st line, $r \times 1000$; 2nd line, $r^2 \times 1000$). E. Linear correlations of ${S_4}^0$ parameters of $ZPh_4^{0,\pm1}$ (1st line, $r \times 1000$; 2nd line, $r^2 \times 1000$). F. Regression equations $y = a_0 + a_1x$ for linear correlations between optimized parameters.

© 2002 NRC Canada

Results and discussion

Ground-state conformations of free BPh_4^-, CPh_4, and NPh_4^+

The results of the optimization of the equilibrium geometries of the three molecules in S_4 and D_{2d} symmetries are shown in Tables 2, 3, A, and B.[8] It was assumed: (*i*) that the minimum-energy conformation has one of these two symmetries; and (*ii*) that optimization at these levels is adequate to deliver geometries of these first-row species that will agree with the converging results of higher-level optimizations. The first assumption, unproven though almost certainly valid, was taken on trust, as it was not practical to examine the entire potential energy surface in general symmetry. The second assumption, however, can be tested against experiment, at least for CPh_4.

Optimizations in S_4 symmetry were started from a geometry with standard bond lengths and angles, a planar C_6H_5 ring, and valence angles C-Z-C = τ. They converged properly to an *E* minimum ($E(S_4^0)$ and $E(S_4^{00})$, respectively), corresponding to the geometries described in Tables 2, 3, A, and B.[8,9] Optimizations in D_{2d} symmetry, which were started with similar initial geometries, also converged to an *E* minimum ($E(D_{2d}^0)$ and $E(D_{2d}^{00})$, respectively), but their vibrational frequency analysis revealed that in every case there remained a single small imaginary frequency. This frequency ranged approximately (in the order Z = B, C, N) from –23 to –31 cm^{-1} for D_{2d}^0, and from –4 to –28 cm^{-1} for D_{2d}^{00}. Restarting the optimization from essentially the same initial geometry, but now under S_4 symmetry and with ϕ reduced from 90° by ~5°, returned the optimized geometry to that obtained in the D_{2d} optimization, with practically the same *E* but without removing the imaginary frequency. Examination of the computation results showed that it is the H and not the C atoms that undergo significant movement. The imaginary frequencies thus appear to arise from the inherent floppiness of the H atom in the D_{2d} conformation, in which the phenyl rings have C_s symmetry, and may reflect an incipient tendency of the molecule in this "averaging" conformation to assume a non-ambivalent conformation of S_4 symmetry, free from calculated imaginary frequencies (cf. S_4^ϕ below).

From the preceding it follows that the optimized energy of the D_{2d} conformation is a minimum. The differences $E_{min}(D_{2d}^0) - E_{min}(S_4^0)$ (Table 4) are quite small but, being all positive, they consistently favour the S_4 conformation as corresponding to the *global* (i.e., ground-state) minimum. The two minima are separated by a potential energy barrier to rotational reorientation of the phenyl rings about roughly the Z—C1 bond, with ϕ as the transition parameter; under S_4 symmetry the reorientations of the four phenyl rings along the $D_{2d} \rightarrow S_4$ transition path are concerted.

To obtain an estimate of the height of this barrier, an additional HF/6-31G(d,p) optimization (S_4^ϕ) was performed in S_4 symmetry for each Z, with ϕ fixed at ~68°, a value intermediate between those for the S_4 and D_{2d} minimum-energy conformations (cf. Tables 2 and A[8]). These optimizations converged properly, without imaginary frequencies. The $E(S_4^\phi)$ values were considerably above those for the S_4^0 and D_{2d}^0 minima, the difference $\Delta E(S_4^\phi) = E(S_4^\phi) - E(S_4^0)$ increasing from ~4.9 kcal mol^{-1} for BPh_4^- to ~6.0 kcal mol^{-1} for NPh_4^+ (Table 4). These $\Delta E(S_4^\phi)$ values thus provide lower-limit estimates of the three barrier heights.

Fig. 1. (*Left*) Numbering of the C atoms in a $ZPh_4^{0,\pm1}$ molecule. Standard orientation: Z at the origin, +*x* to the right of Z, +*y* up from Z in the page, +*z* up from the page. (*Right*) View of the shortest inter-ring H···H = *h* contact in the molecule. The horizontal line represents the intersection of the *xy* plane with the page; the +*z* axis is in the page, as indicated.

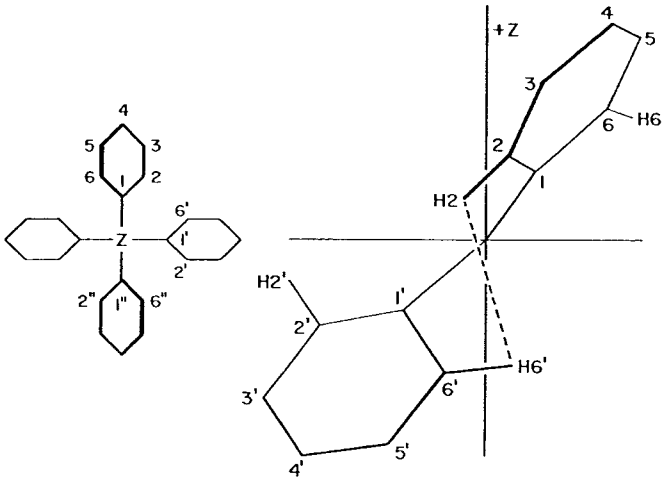

On the reasonable expectation that a comparison of the energies obtained for the isoelectronic BPh_4^-, CPh_4, and NPh_4^+ would reveal a trend, we carried out the analysis a step further. The curve representing the difference $\Delta E = E - E(S_4^0)$ as a function of ϕ is periodic, with $0° \le \phi \le 90°$ as the defining interval, but the portion of interest for the potential barrier to the $S_4 \leftrightarrow D_{2d}$ conversion extends only from ϕ ~ 45° to 90°. In this subinterval the function has, from the above, a minimum at ϕ ~ 50–58°, a minimum at ϕ = 90°, and a maximum between the two minima. Within these ϕ limits it should be possible to approximate $\Delta E(\phi)$ for each Z by a quartic polynomial $\sum_0^4 a_n \phi^n$ uniquely defined by the $\phi, \Delta E(\phi)$ pairs for S_4^0, S_4^ϕ, and D_{2d}^0 (Table 4), using the condition that, at the two minima, $(\Delta E)' = 0$. The height and the position of the barrier could then be estimated from the location of the maximum of the resulting polynomial. In addition, a cubic baseline could be constructed by a similar procedure.

The applicability of this approximation procedure was tested in two ways: (*i*) by using the approximation in an attempt to reproduce curve *a* of Fig. 3 of ref. 4 (strain energy E vs. torsional angle θ of the phenyl ring in CPh_4). This curve may be taken as representative of this type of energy vs. rotational displacement function; (*ii*) by equating $\Delta E(D_{2d}^0)$ for CPh_4 (Table 4) to zero, and again to twice its actual value, and repeating the above approximation procedure with the other $\phi, \Delta E(\phi)$ unchanged.

In (*i*) curve *a* is defined by 13 data points, with graphically interpolated positions of the two minima and of the maximum, the global minimum being at the smaller θ angle and the subsidiary minimum at θ = 90°. The coordinates of the data points were estimated from an electronic scan, and

[9] The optimized S_4 conformations of $ZPh_4^{0,\pm1}$ are typified by the CPh_4 molecule in the center of Fig. 3.

© 2002 NRC Canada

Table 1. Crystallographic data for tetraphenylmethane.

Empirical formula	$C_{25}H_{20}$
Formula weight	320.4
Colour, habit	Colourless needle
Crystal dimensions (mm)	0.12 × 0.17 × 0.38
Space group	$P\bar{4}2_1c$ (no. 114)
T	–60°C
Lattice parameters (Å)	a = 10.880(1)
	c = 7.2423(5)
Unit-cell volume (Å^3)	857.3(1)
Z	2
F(000) (e)	340
D_{calc} (g cm^{-3})	1.241
Radiation	Mo Kα (λ = 0.71070 Å)
Absorption coefficient (μ(Mo Kα)) (cm^{-1})	0.70
Diffractometer	RAXIS-II
Detector aperture (mm)	200 × 200
Data images	19 exposures @ 10.0 min.
Oscillation range	10.0°
Detector position (mm)	55.0°
Detector swing angle	30.0°
$2\theta_{max}$	67.9°
Reflections measured:	
total	6488
unique	905[a]
Collection ranges	$0 \le h \le 15$; $-15 \le k \le 15$; $-9 \le l \le 9$
Corrections	Lorentz-polarization, secondary extinction[b]
Structure solution	Direct methods
Refinement	Full-matrix least-squares on F
Function minimized	$\sum w(\|F_o\| - \|F_c\|)^2$
Least-squares weights	$1/\sigma^2(F_o) = 4F_o^2/\sigma^2(F_o^2)$
Anomalous dispersion	All non-hydrogen atoms
No. of observations [$I > 3.0\sigma(I)$]	556
No. of variables	78
Data/parameter ratio	7.13
Residuals R, R_w	0.043, 0.036
Goodness-of-fit	2.14
Maximum shift/error in final cycle	0.00
Max, min peak in final difference map (e Å^{-3})	0.11, –0.10

[a] R_{int} = 0.081 for 556 averaged Friedel mates.
[b] Secondary extinction coefficient, 6.1439 × 10^{-5}.

the curve was reconstituted by the above procedure from the positions of the minima (horizontal tangents) and a data point P chosen at or near the maximum and corresponding to the $\phi, \Delta E(\phi)$ point for S_4^{ϕ} in Fig. 2. The resulting θ_{max}, ΔE_{max} estimate was found to depend on the position of P; from the variation of the computed position of ΔE_{max}, it was estimated that the position of the interpolated maximum could be reproduced to within 5–10% of θ_{max} and ΔE_{max}. The *second* test produced changes of only ca ± 0.6° (i.e., ~1%) in the ϕ_{max}, and ca ± 0.2 kcal mol^{-1} (i.e., ~3%) in the ΔE_{max} estimates. A detailed examination of the results of the two tests showed that $\Delta E(\phi)$ is considerably robust with respect to the above approximation procedures. The procedure works best when the ΔE values at the two minima are similar, as is the case with $\Delta E(S_4^0)$ and $\Delta E(D_{2d}^0)$.

Estimates of the barrier heights above a horizontal ($\Delta E = 0$) and a cubic baseline (Fig. 2, inset) are listed in Table 4. They show a consistent increase from B to N, ranging from ~5.2 to ~8.1 kcal mol^{-1} for the horizontal and from ~4.7 to ~7.7 kcal mol^{-1} for the cubic baseline; the shifts of the position of ΔE_{max} are relatively small, from ~71° for B to ~74° for N. These low barrier values may explain the great variability of the BPh_4^- anion geometry with crystal environment.

As pointed out above, Mislow and co-workers (4) concluded, from their full-relaxation molecular mechanics calculations, that the ground-state conformation of free CPh_4 has the D_{2d} rather than S_4 symmetry, in contrast to all other observations on $ZPh_4^{0,\pm1}$ reported to date, with the exception of BPh_4^- in alkali and ammonium tetraphenylborates (10, 11). We do not know the reason for the disagreement with

© 2002 NRC Canada

Table 2. Geometries of BPh_4^-, CPh_4, and NPh_4^+ optimized in HF/6-31G(d,p).

	BPh_4^-			CPh_4			NPh_4^+		
Parameter	S_4^0	S_4^ϕ	D_{2d}^0	S_4^0	S_4^ϕ	D_{2d}^0	S_4^0	S_4^ϕ	D_{2d}^0
$-E$	945.25083	945.24296	945.24912	958.37903	958.37026	958.37734	974.71889	974.70944	974.71762
$\bar{x}$ (C)	0.0000	0.0000	0	0.0000	0.0000	0	0.0000	0.0000	0
$\bar{y}$ (C)	2.4611	2.2627	2.3561	2.3082	2.1384	2.2186	2.2302	2.0721	2.1525
$\bar{z}$ (C)	1.8997	2.1093	2.0201	1.8684	2.0398	1.9658	1.8610	2.0143	1.9427
$\bar{x}$ (H)	–0.0080	–0.0160	0	–0.0055	–0.0159	0	–0.0035	–0.0173	0
$\bar{y}$ (H)	2.8584	2.5953	2.7227	2.6867	2.4642	2.5719	2.6011	2.3842	2.4952
$\bar{z}$ (H)	2.2171	2.4941	2.3724	2.1949	2.4246	2.3233	2.1906	2.3993	2.3012
α	106.5	104.8	103.5	105.0	104.3	102.3	103.9	103.9	101.4
β	111.0	111.9	112.5	111.8	112.1	113.2	112.4	112.3	113.7
ϕ	50.2	67.5	90	54.8	67.5	90	57.2	67.6	90
Z—C1 (d_0)	1.673	1.670	1.670	1.557	1.554	1.555	1.524	1.520	1.522
C1—C2 (d_{12})	1.396	1.397	1.400	1.387	1.389	1.393	1.378	1.381	1.385
C2—C3 (d_{23})	1.391	1.390	1.387	1.392	1.391	1.385	1.393	1.391	1.385
C3—C4 (d_{34})	1.382	1.385	1.385	1.378	1.378	1.383	1.377	1.378	1.384
C4—C5 (d_{45})	1.388	1.388	1.385	1.389	1.388	1.383	1.390	1.389	1.384
C5—C6 (d_{56})	1.383	1.382	1.387	1.379	1.379	1.385	1.378	1.378	1.385
C6—C1 (d_{61})	1.405	1.405	1.400	1.400	1.400	1.393	1.392	1.393	1.385
C2—H2	1.075	1.076	1.076	1.071	1.073	1.073	1.068	1.070	1.071
C3—H3	1.079	1.079	1.079	1.076	1.076	1.076	1.074	1.074	1.074
C4—H4	1.078	1.078	1.079	1.076	1.076	1.076	1.074	1.074	1.074
C5—H5	1.079	1.079	1.079	1.076	1.076	1.076	1.074	1.074	1.074
C6—H6	1.077	1.078	1.076	1.075	1.075	1.073	1.073	1.073	1.071
Z-C1-C2 (ζ_2)	124.9	123.4	122.2	124.1	122.6	121.1	122.5	121.1	119.5
Z-C1-C6 (ζ_6)	119.9	120.2	122.2	118.5	119.0	121.1	117.0	117.4	119.5
C2-C1-C6 (δ_1)	115.2	114.8	115.2	117.3	116.7	117.3	120.4	119.7	120.5
C1-C2-C3 (δ_2)	122.6	122.9	122.7	121.6	121.6	121.4	119.2	119.7	119.5
C2-C3-C4 (δ_3)	120.5	120.5	120.4	120.3	120.6	120.5	120.8	120.7	120.6
C3-C4-C5 (δ_4)	118.6	118.5	118.5	118.9	118.9	118.9	119.4	119.4	119.4
C4-C5-C6 (δ_5)	120.2	120.3	120.4	120.7	120.3	120.5	120.3	120.4	120.6
C5-C6-C1 (δ_6)	122.9	123.1	122.7	121.2	121.9	121.4	120.0	120.1	119.5
Z···C2	2.724	2.705	2.691	2.602	2.583	2.568	2.545	2.528	2.512
Z···C6	2.667	2.669	2.691	2.543	2.546	2.568	2.488	2.490	2.512
Z···H2	2.914	2.892	2.855	2.830	2.807	2.765	2.794	2.774	2.728
Z···H6	2.802	2.820	2.855	2.707	2.728	2.765	2.669	2.689	2.728
C1···C1′	2.758	2.767	2.778	2.578	2.579	2.596	2.532	2.526	2.548
C2···C6′	3.341	3.378	3.248	3.127	3.182	3.073	3.030	3.089	2.990
H2···H6′ (h)	2.621	2.622	2.593	2.515	2.528	2.537	2.484	2.490	2.533

our ab initio results, but it might be noted that the results of ref. 4 were obtained with one of the earliest molecular-mechanics force fields.

HF and DFT results compared

Comparing the results of the two optimizations for individual parameters (e.g., bond lengths, bond angles) is, overall, less informative than assessing the agreement between the two *globally*, i.e., in terms of the difference between corresponding parameter values taken together. A suitable measure here is $\mu = \sum|\Delta|/n$, where Δ is the difference between the corresponding coordinates of a C or an H atom, the sum taken over all the C or H atoms, respectively (Table 5). Alternatively, one can compare the lengths of the differential displacement vectors $D = [(\Delta x)^2 + (\Delta y)^2 + (\Delta z)^2]^{1/2}$ between the two sets of atom coordinates, and the mean, $\overline{D}$ of these vectors.

Generally, μ(H) and $\overline{D}$(H) values are about twice those for the corresponding μ(C) and $\overline{D}$(C), respectively (Table 5). The smallest differences between the two optimizations are for D_{2d}^{00} and D_{2d}^0, 0.005–0.01 Å for μ(C) and 0.01–0.02 Å for $\overline{D}$(C); the individual values for Z from B to N are indistinguishable within their statistics, and they would also be well within the 3σ limits of conventional crystallographic determinations. The μ(C) and $\overline{D}$(C) differences for S_4^{00} and S_4^0, numerically, are larger than those for D_{2d}^{00} and D_{2d}^0, but their substantial standard deviations again render their significance, with respect to the effect of Z, uncertain. One may conclude that, on the present evidence and for our purposes, the HF and DFT treatments lead to results that are in reasonable

© 2002 NRC Canada

Table 3. Geometries of BPh_4^-, CPh_4, and NPh_4^+ optimized in B3LYP/6-31G(d,p).

	BPh_4^-		CPh_4		NPh_4^+	
Parameter	S_4^0	D_{2d}^0	S_4^0	D_{2d}^0	S_4^0	D_{2d}^0
$-E$	951.55508	951.55394	964.72333	964.72239	981.11432	981.11316
ZPE	0.36590	0.36584	0.37192	0.37176	0.37292	0.37263
$\bar{x}$ (C)	0.0000	0	0.0000	0	0.0000	0
$\bar{y}$ (C)	2.4831	2.3532	2.3302	2.2249	2.2620	2.1666
$\bar{z}$ (C)	1.8657	2.0161	1.8566	1.9709	1.8526	1.9531
$\bar{x}$ (H)	–0.0036	0	–0.0057	0	–0.0037	0
$\bar{y}$ (H)	2.8850	2.7228	2.6872	2.5795	2.6379	2.5103
$\bar{z}$ (H)	2.1811	2.3681	2.1792	2.3291	2.1775	2.3123
α	107.3	103.5	105.4	102.4	104.3	101.6
β	110.6	112.5	111.6	113.1	112.1	113.5
ϕ	48.2	90	53.2	90	55.5	90
Z—C1 (d_0)	1.660	1.656	1.558	1.555	1.536	1.533
C1—C2 (d_{12})	1.408	1.410	1.399	1.403	1.391	1.395
C2—C3 (d_{23})	1.399	1.397	1.399	1.395	1.400	1.395
C3—C4 (d_{34})	1.394	1.396	1.392	1.394	1.391	1.394
C4—C5 (d_{45})	1.397	1.396	1.397	1.394	1.391	1.394
C5—C6 (d_{56})	1.396	1.397	1.392	1.395	1.392	1.395
C6—C1 (d_{61})	1.413	1.410	1.408	1.403	1.399	1.395
C2—H2	1.086	1.087	1.083	1.084	1.080	1.082
C3—H3	1.089	1.089	1.086	1.086	1.085	1.085
C4—H4	1.088	1.088	1.086	1.086	1.085	1.085
C5—H5	1.089	1.089	1.086	1.086	1.085	1.085
C6—H6	1.088	1.087	1.085	1.084	1.085	1.082
Z-C1-C2 (ζ_2)	124.5	122.2	123.8	121.0	122.1	119.3
Z-C1-C6 (ζ_6)	120.3	122.2	118.6	121.0	117.1	119.3
C2-C1-C6 (δ_1)	115.2	115.3	117.5	117.6	120.8	120.8
C1-C2-C3 (δ_2)	122.7	122.7	121.1	121.3	119.0	119.2
C2-C3-C4 (δ_3)	120.4	120.3	120.6	120.4	120.8	120.6
C3-C4-C5 (δ_4)	118.7	118.7	119.0	119.0	119.5	119.5
C4-C5-C6 (δ_5)	120.1	120.3	120.2	120.4	120.4	120.6
C5-C6-C1 (δ_6)	122.9	122.7	121.5	121.3	119.5	120.6
Z···C2	2.718	2.687	2.610	2.575	2.562	2.528
Z···C6	2.667	2.687	2.552	2.575	2.505	2.528
Z···H2	2.905	2.853.	2.833	2.773	2.803	2.742
Z···H6	2.810	2.853	2.720	2.773	2.687	2.742
C1···C1′	2.729	2.754	2.577	2.594	2.549	2.564
C2···C6′	3.329	3.226	3.129	3.071	3.045	3.000
H2···H6′ (h)	2.628	2.566	2.506	2.534	2.482	2.536

overall agreement, without clear grounds for preferring one treatment to the other.

Tetraphenylmethane: ab initio vs. experiment

The three independent determinations of the crystal structure of CPh_4 from X-ray data obtained at 20°C and 26°C (17) agree closely among themselves.[10] The results of the present determination from –60°C X-ray data (set *T*, cf. Tables 1 and 6, Fig. 3, and material deposited[7]) are in excellent agreement with *R* (Table 5). Differences that might be attributed to the effect of temperature are, on the whole, well within 3σ of the *T* values: μ(C) for the coordinate differences between *T* and *R* is only 0.004(4) Å and $\overline{D}$(C) is only 0.009(6) Å, values eminently acceptable for careful conventional determinations from X-ray data. Within this accuracy, the experimental geometry of the CPh_4 molecule in the crystal can thus be regarded as established.

In the crystal, the CPh_4 molecule has a conformation of S_4 symmetry, so the comparison with the optimized ab initio molecular geometry has to be with S_4^{00} and S_4^0 and will involve essentially the carbon skeleton. Less reliance can be placed on the features involving the H atoms, in part because of the ring-planarity restriction in the ab initio calculations, and in part because of the residual uncertainties in the refined H atom location in experimental determinations. As seen in Table 6, the experimental ring geometry agrees well

[10]The parameters from the two 20°C data sets have been averaged here to give the *R* set, Table 6.

© 2002 NRC Canada

Table 4. Differences in the total electronic energy E and estimated heights of the barrier to rotational displacement of the phenyl ring in $ZPh_4^{0,\pm1}$.

	BPh_4^-		CPh_4		NPh_4^+	
	au	kcal mol^{-1}	au	kcal mol^{-1}	au	kcal mol^{-1}
$E(D_{2d}{}^0) - E(S_4{}^0)$	0.00171	1.07	0.00169	1.06	0.00137	0.86
$E(D_{2d}{}^{00}) - E(S_4{}^{00})$	0.00114	0.72	0.00094	0.60	0.00116	0.73
$E(S_4{}^{\phi}) - E(S_4{}^0)$	0.00787	4.9	0.00877	5.5	0.00955	6.0
Estimation of barrier height (Fig. 2)						
Relative to the horizontal baseline ($\Delta E = 0$)						
ΔE_{max}	0.00832	5.2	0.01063	6.7	0.01296	8.1
ϕ at ΔE_{max} (°)	71.0		73.0		73.9	
Relative to the cubic baseline[a]						
$(\Delta E_{max})_{cub}$	0.00741	4.7	0.00977	6.1	0.01225	7.7
ϕ at $(\Delta E_{max})_{cub}$ (°)	70.1		72.4		73.6	

[a] $\Delta E = \sum_0^3 b_n\phi^n$, $(\Delta E)' = 0$ at $S_4{}^0$ and $D_{2d}{}^0$.

with $S_4{}^{00}$ and $S_4{}^0$, especially when account is taken of the differences between the $S_4{}^{00}$ and $S_4{}^0$ parameters themselves. Moreover, the exocyclic ζ_2 and ζ_6 angles, defining the extent of nonalignment of the C1-C4 ring axis with the Z—C1 bond, are the same in the free molecule and in the crystal. The valence angles α and β, however, which between $S_4{}^{00}$ and $S_4{}^0$ average to 105.2(2)° and 111.7(1)°, respectively, and thus do not depend greatly on the model, are 1.5(2)° smaller and 1.0(2)° larger, respectively, than those in the crystal; the tilt angle ϕ, 49.0° in both T and R, averages to 54.0(8)° in the free molecule, a significant difference of ~5°, given that it is computed from the general positions of all six C atoms in the ring.

Closer examination of the atom coordinates shows that the largest differences between corresponding coordinates occur in the z coordinate. In terms of $\bar{z}$(C) and $\bar{z}$(H) (Table 6), the differences between the optimized $\bar{z}$(C) and $\bar{z}$(H) means and those in the crystal are 0.055 Å and 0.071 Å, respectively, compared with −0.030 Å and −0.006 Å, respectively, for the $\bar{y}$(C) and $\bar{y}$(H) means, all referred to the standard orientation. Relative to the free CPh_4 molecule, the molecule in the crystal is thus somewhat compressed along the $z \equiv S_4$ axis but otherwise almost unchanged. There are several short intermolecular H···H contacts in the structure (Fig. 3, Table C), but it is not obvious which H···H interactions in particular can be regarded as jointly instrumental in this compression. The shortest two of these contacts, 2.44(2) and 2.57(3) Å (between nearest H2 and H5, and H3 and H4 atoms, respectively, of adjacent molecules) are comparable to the H2···H6′ = h contact between the *ortho*-hydrogens within a molecule, 2.54(2) Å (Fig. 1, Table 6).

Ground-state geometry of BPh_4^-, CPh_4, and NPh_4^+

The salient parameters of the gross geometry of these ground-state conformations are the bond length Z—C1 = d_0, the valence angles α and β, the tilt angle ϕ, the angles ζ_2 and ζ_6, and the distance h between the *ortho*-hydrogens H2 and H6′ of neighboring phenyl rings. To these *exocyclic* parameters may be added $\bar{\varepsilon}$, the mean charge on the *ortho*-hydrogens. The C—C bond lengths d_{ij} and the C-C-C angles ζ_i will be referred to as the *endocyclic* parameters.

Fig. 2. Variation of $\Delta E = E - E(S_4{}^0)$ with the tilt angle ϕ in $ZPh_4^{0,\pm1}$ (constructed from the approximation explained in text). Inset: the $(\phi,\Delta E)$ curve for BPh_4^- fitted with a cubic baseline.

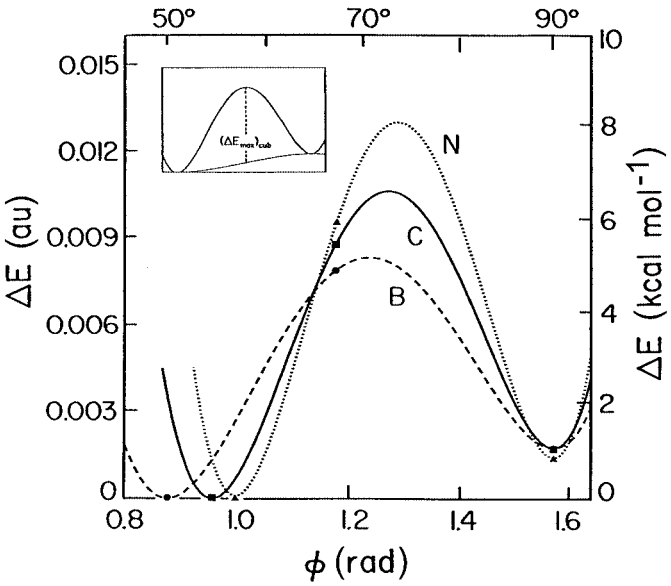

Before discussing the specifics of the variation of these parameters with Z we may note the following: $\alpha < \tau < \beta$ and $\zeta_2 < \zeta_6$; the sum $2\alpha + 4\beta$ of the six valence angles has a minimum of 6τ at $\alpha = \beta = \tau$. The approximate numerical ranges of the exocyclic parameters are 45° < ϕ < 60°, 1.52 Å < d_0 < 1.70 Å, 2.45 Å < h < 2.65 Å. The changes in δ_i are compensatory ($\sum\delta_i = 720°$, $\sum\Delta\delta_i = 0$), and there is also approximate local compensation between neighboring angles, e.g., δ_1 and δ_2. The sum $\sum d_{ij}$ of the six C—C bond lengths decreases by about 0.5% from B to N, indicating (together with d_0) an overall contraction of the molecular dimensions.

The geometric parameters and $\bar{\varepsilon}$ are all affected by a change of Z, but to a considerably unequal degree. The sensitivity of a parameter x to a variation of Z (i.e., the relative magnitude of the effect of Z variation) can be assessed from the range/mean ratio of x. This ratio is approximately equal

© 2002 NRC Canada

Table 5. Overall comparison of the differences between the calculated–calculated and calculated–experimental geometries of the $ZPh_4^{0,\pm1}$ molecules.[a]

$B - A$	μ(C)	μ(H)	$\overline{D}$(C)	$\overline{D}$(H)
BPh_4^-				
$S_4^{00} - S_4^0$	0.031 (25)	0.058 (33)	0.060 (34)	0.110 (34)
$D_{2d}^{00} - D_{2d}^0$	0.005 (4)	0.011 (7)	0.011 (4)	0.022 (5)
CPh_4				
$S_4^{00} - S_4^0$	0.018 (16)	0.035 (24)	0.037 (21)	0.069 (25)
$D_{2d}^{00} - D_{2d}^0$	0.006 (5)	0.013 (6)	0.012 (6)	0.024 (4)
$T - R$	0.004 (4)	0.027 (21)	0.009 (6)	0.052 (32)
$T - S_4^{00}$	0.044 (34)	0.093 (69)	0.084 (46)	0.196 (40)
$T - S_4^0$	0.061 (45)	0.127 (68)	0.115 (67)	0.241 (59)
$T - D_{2d}^{00}$	0.35 (24)	0.73 (33)	0.63 (40)	1.30 (51)
$T - D_{2d}^0$	0.35 (24)	0.73 (33)	0.63 (39)	1.29 (52)
NPh_4^+				
$S_4^{00} - S_4^0$	0.025 (19)	0.045 (27)	0.049 (24)	0.088 (25)
$D_{2d}^{00} - D_{2d}^0$	0.011 (6)	0.015 (9)	0.020 (6)	0.028 (9)

[a] $\mu = \Sigma|\Delta|/n$, Δ = difference between corresponding atom coordinates in *B* and *A*.
$D = [(\Delta x)^2 + (\Delta y)^2 + (\Delta z)^2]^{1/2}$, differential displacement of atom; $\overline{D}$ = mean of *D*. All values in Å.

to $2\sigma(x)/\bar{x}$ (Table 7). With the exception of d_{45}, the sequential order of the ratio is the same for S_4^{00} and S_4^0; the difference of the two means falls within a single joint $\overline{\sigma}$ of the means and in most cases well below it, except for $\overline{\varepsilon}$ (<1.5$\overline{\sigma}$), d_{45} (~2$\overline{\sigma}$), d_{56} and d_{34} (~3$\overline{\sigma}$), and d_{23} (~7$\overline{\sigma}$). The agreement of the parameter values between S_4^{00} and S_4^0 is thus very good (cf. also Table 5).

The values of the range/mean ratio extend from 72% to 0.1% for S_4^{00}, and from 37% to 0.1% for S_4^0. On the whole, the parameters that respond most to the change of Z are the exocyclic parameters $\overline{\varepsilon}$, ϕ, d_0, and h, with ratios >5. Of the endocyclic parameters, the internal angle δ_1 at the α-carbon is affected highly significantly and, to a lesser degree, so are the angles δ_2 and δ_6 at the *ortho*-carbons. The effect of Z on the other δ_i and d_{ij} is much smaller and, for the bottom six entries in Table 7, is established not without uncertainty.

The pairwise mutual dependence, $y = a_0 + a_1x$, of the angles, distances, and $\overline{\varepsilon}$ is summarized for S_4^{00} and S_4^0, in terms of the *linear* coefficients of determination (r^2), in Table 8 and in the connectivity graphs of Figs. 4–6.[11] There being only three *Z* in the set, the statistical validity of the bivariate linear correlation is of necessity limited. Where a plot of a parameter *y* vs. a parameter *x* shows a monotonic but clearly not linear trend, the r^2(linear) value will not be high and the functional dependence cannot be established, statistically, because of the insufficient *n*.[12] This would be true a fortiori for multivariate linear or other correlations that undoubtedly exist (cf. ref. 29). Still, examination of Table 8 and Figs. 4–6 shows that there are many highly significant linear correlations, and analysis of a selection from these permits a number of interesting conclusions.

There is generally a satisfactory agreement between the $r^2(S_4^{00})$ and $r^2(S_4^0)$ values in an *x*,*y* pair. The obvious discrepancies in Table 8 — the signs of $r(S_4^{00})$ and $r(S_4^0)$ in

Fig. 3. Projection of a portion of the crystal structure of CPh_4 down the $z \equiv S_4$ axis (origin at C0). The intermolecular H···H contacts out to 3 Å from ring A (cf. Table C) are indicated by broken lines.

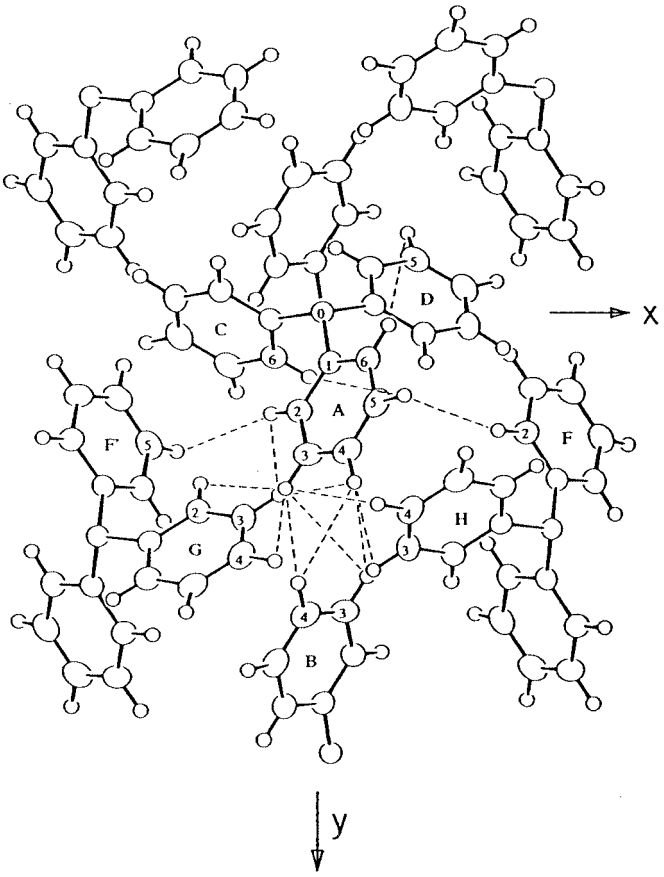

[11] Table 8 contains only those correlations for which $r^2 \geq 0.67$. A complete list of *r* and r^2 will be found in Tables D and E.
[12] Except for two-parameter model functions (power, exponential, logarithmic), but for these the regressions were found to yield r^2 and σ values not much different from those for the corresponding linear regression.

© 2002 NRC Canada

Table 6. Geometry of the tetraphenylmethane molecule: ab initio vs. experiment.

	Optimized geometry				In crystal	
Parameter	S_4^{00}	S_4^{0}	D_{2d}^{00}	D_{2d}^{0}	*R*	*T*
$\bar{x}$ (C)	0.0000	0.0000	0	0	0.0000	0.0000
$\bar{y}$ (C)	2.3302	2.3082	2.2249	2.2186	2.3460	2.3515
$\bar{z}$ (C)	1.8566	1.8684	1.9709	1.9658	1.8064	1.8097
$\bar{x}$ (H)	–0.0057	–0.0055	0	0	0.001	–0.002
$\bar{y}$ (H)	2.7175	2.6872	2.5795	2.5719	2.707	2.710
$\bar{z}$ (H)	2.1792	2.1949	2.3291	2.3233	2.107	2.125
α	105.4	105.0	102.4	102.3	106.7 (2)	106.7 (1)
β	111.6	111.8	113.1	113.2	110.9 (2)	110.4 (1)
ϕ	53.2	54.8	90	90	49.0	49.0
d_0	1.558	1.557	1.555	1.555	1.550[a]	1.551 (1)
d_{12}	1.399	1.387	1.403	1.393	1.389	1.397 (2)
d_{23}	1.399	1.392	1.395	1.385	1.391	1.394 (2)
d_{34}	1.392	1.378	1.394	1.383	1.377	1.382 (3)
d_{45}	1.397	1.389	1.394	1.383	1.378	1.392 (3)
d_{56}	1.392	1.379	1.395	1.385	1.382	1.389 (2)
d_{61}	1.408	1.400	1.403	1.393	1.401	1.397 (2)
C2—H2	1.083	1.071	1.084	1.073	1.00	0.98 (2)
C3—H3	1.086	1.076	1.086	1.076	0.97	1.02 (2)
C4—H4	1.086	1.076	1.086	1.076	0.98	1.02 (2)
C5—H5	1.086	1.076	1.086	1.076	0.99	1.04 (3)
C6—H6	1.085	1.075	1.084	1.073	1.00	0.98 (2)
ζ_2	123.8	124.1	121.0	121.1	123.7	123.8 (1)
ζ_6	118.6	118.5	121.0	121.1	118.8	118.8 (1)
δ_1	117.5	117.3	117.6	117.3	117.5	117.5 (1)
δ_2	121.1	121.6	121.3	121.4	120.9	121.2 (1)
δ_3	120.6	120.3	120.4	120.5	120.5	120.4 (1)
δ_4	119.0	118.9	119.0	118.9	119.4	119.3 (2)
δ_5	120.2	120.7	120.4	120.5	120.4	120.0 (2)
δ_6	121.5	121.2	121.3	121.4	121.2	121.6 (1)
C0···C2	2.610	2.602	2.575	2.568	2.593	2.601 (3)
C0···C6	2.552	2.543	2.575	2.568	2.540	2.538 (3)
C0···H2	2.833	2.830	2.773	2.765	2.79	2.78 (2)
C0···H6	2.720	2.707	2.773	2.765	2.66	2.65 (2)
C1···C1′	2.577	2.578	2.594	2.596	2.552	2.554 (3)
C2···C6′	3.129	3.127	3.071	3.073	3.124	3.128 (2)
H2···H6′ (*h*)	2.506	2.515	2.534	2.537	2.55	2.54 (2)
Planarity[b]	0	0	0	0	0.006	0.006

[a]1.553(3) Å when corrected for thermal motion (17).
[b]Mean deviation of a ring C atom from the best C_6 plane, in Å.

an *x*, *y* pair are not the same, or there is a gross difference in the magnitudes of the conjugate $r^2(S_4^{00})$ and $r^2(S_4^{0})$ — may have different origins: the trend in the *y*(*Z*) value is confused; the three values in a set are very small (numerical accuracy!); their range is too narrow; or a combination of these conditions may be present. The parameter triplets so affected are all endocyclic and have small range/mean ratios, typically <0.5 (Table 7). The statistical validity of the discrepant associations being questionable, they are ignored in the analysis below. Where strong, meaningful correlations exist, the $r^2(S_4^{00})$ and $r^2(S_4^{0})$ are both large and similar in value (Table 8), and the range/mean ratios of the correlated parameters are greater than ~0.5.

Regression equations for the strongest linear correlations ($r^2 \geq 0.95$) are listed in Table F. The signs of the correlation coefficients *r*(*x*,*y*), and the strength of the correlations as measured by $r^2(x,y)$, are presented synoptically in the connectivity graphs of Figs. 4–6.[13]

[13]To arrive at the sign of *r*(*x*,*y*) for a correlation between two parameters *x* and *y* that are not neighbours in the connectivity graph, a continuous path from *x* to *y* can be traced in the graph via intermediate legs. Obviously, for positive correlations this always leads to a positive *r*(*x*,*y*). In graphs for negative correlations, the sign changes at every step, so that *r*(*x*,*y*) will be positive for an even number of intermediate legs and negative for an odd number.

© 2002 NRC Canada

Fig. 4. Linear correlations between exocyclic, and between endocyclic parameters in $ZPh_4^{0,\pm1}$ (*i* stands for δ_i, *ij* stands for d_{ij}). Thick lines ($r^2 \geq 0.95$ for both $S_4{}^{00}$ and $S_4{}^0$), thin lines ($0.67 \leq r^2 < 0.95$ for either $S_4{}^{00}$ and $S_4{}^0$ or both). The tie lines imply correlations between nearest parameter neighbours only.

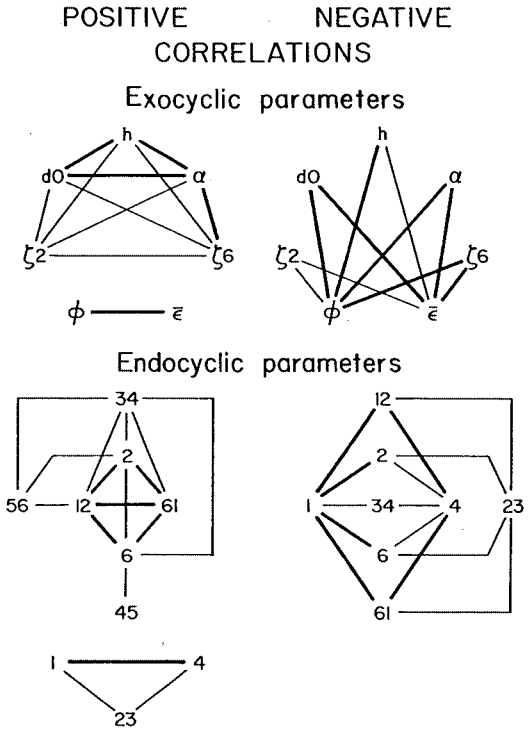

Exocyclic parameters (Fig. 4)

Since the underlying "chemical" variable Z is not specified numerically, to quantify the effect of its variation on the numerically expressed structural parameters one may select one of the latter as the primary parameter, through which Z correlates with the others. Such a parameter may be d_0, which governs the variation of the core geometry of the $ZPh_4^{0,\pm1}$, and which itself is electronically controlled by the Z—C(α) covalent bonding interaction, and is highly sensitive to the Z substitution (Table 7).

The Z—C1 bond length d_0 correlates strongly and positively with α and *h*. This is not unexpected. In the counterpart of the free $ZPh_4^{0,\pm1}$, the free $ZX_4^{0,\pm1}$ (X = H, halogen) molecules, the ligand is structureless, and the six X-Z-X angles are all equal to τ, regardless of the Z—X = d_0 bond length. In contrast, in the free $ZPh_4^{0,\pm1}$ the ligand is large and highly anisotropic, and its shape and steric interactions between neighboring ligands prevent the molecule from achieving T_d symmetry. Thus, under the S_4 symmetry of the ground-state conformation, the set of six C-Z-C angles is split into a subset of two angles ($\alpha < \tau$) and a set of four angles ($\beta > \tau$). While in $ZX_4^{0,\pm1}$ an increase in d_0 leaves the tetrahedral angle unchanged, in $ZPh_4^{0,\pm1}$ the factors causing α to be smaller than τ will weaken (the relative dimensions of the Ph group being essentially constant), and $\alpha \rightarrow \tau$ as $d_0 \rightarrow \infty$. The expected positive correlation of α with d_0 is observed, but the d_0,α variation is only approximately linear. The observed positive correlation of d_0 and *h* ($r^2 = 1.00$), the shortest distance between the *ortho*-hydrogens H2 and H6′ (Fig. 1), would be expected to arise for a similar reason.

Fig. 5. Linear correlations between mixed parameters in $ZPh_4^{0,\pm1}$ (see caption of Fig. 4).

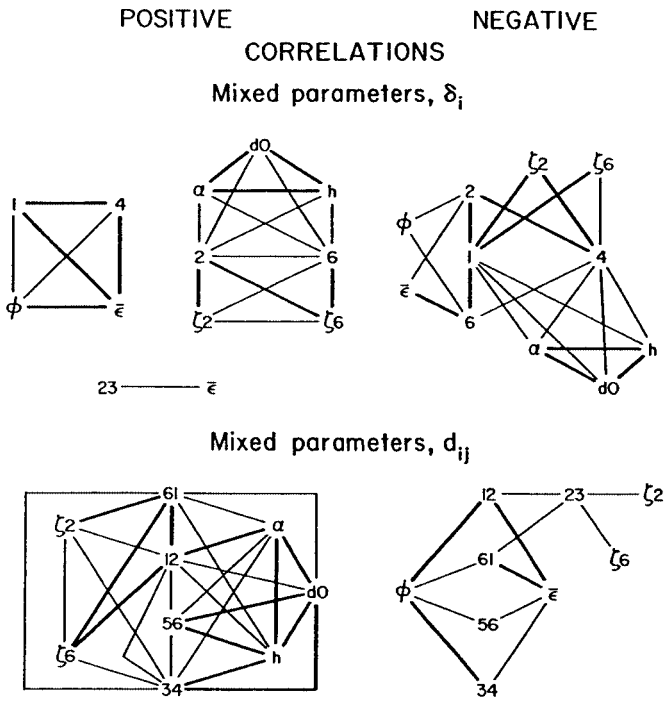

Fig. 6. Linear correlations between mixed parameters in $ZPh_4^{0,\pm1}$: effect of ring asymmetry (cf. caption of Fig. 4). Thick lines, $r^2 \geq 0.95$; thin lines, $0.9 \leq r^2 < 0.95$; broken lines, $0.67 \leq r^2 < 0.95$.

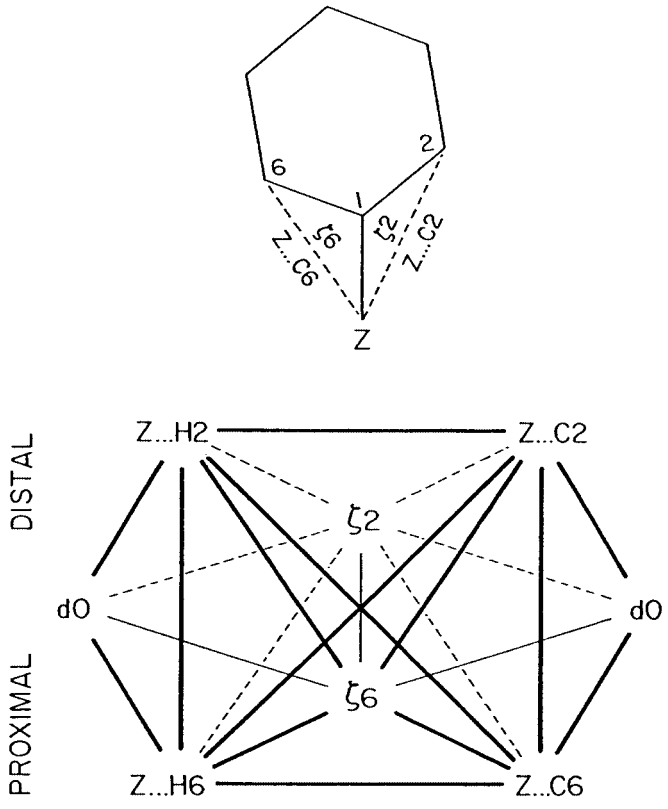

© 2002 NRC Canada

Table 7. Sensitivity of $ZPh_4^{0,\pm1}$ structure parameters to replacement of Z, expressed as the range/mean ratio (%)[a].

Parameter	S_4^{00}			S_4^{0}				
	Range	Mean	Ratio	Range	Mean	Ratio	Δ	$\bar{\sigma}$
ε (e)	0.070	0.098 (35)	72	0.061	0.163 (31)	37	–0.065	0.047
ϕ (deg)	7.3	52.3 (37)	14	7.0	54.1 (36)	13	–1.8	5.2
d_0 (Å)	0.124	1.585 (66)	7.8	0.149	1.585 (78)	9.4	0	0.102
h (Å)	0.146	2.539 (78)	5.8	0.137	2.540 (72)	5.4	–0.001	0.106
δ_1 (deg)	5.6	117.8 (28)	4.8	5.2	117.6 (26)	4.4	0.2	3.8
δ_2 (deg)	3.7	120.9 (19)	3.1	3.4	121.1 (17)	2.8	–0.2	2.5
α (deg)	3.0	105.7 (15)	2.8	2.6	105.1 (13)	2.5	0.6	1.8
δ_6 (deg)	3.4	121.3 (17)	2.8	2.9	121.4 (15)	2.4	–0.1	2.3
ζ_6 (deg)	3.2	118.7 (16)	2.7	2.9	118.5 (15)	2.5	0.2	2.2
ζ_2 (deg)	2.4	123.5 (12)	1.9	2.4	123.8 (12)	1.9	–0.3	1.7
d_{12} (Å)	0.017	1.399 (9)	1.2	0.018	1.387 (9)	1.3	0.012	0.013
d_{61} (Å)	0.014	1.407 (7)	1.0	0.013	1.399 (7)	0.9	0.008	0.010
δ_4 (deg)	0.8	119.1 (4)	0.7	0.8	119.0 (4)	0.7	0.1	0.6
d_{45} (Å)	0.006	1.395 (3)	0.4	0.002	1.389 (1)	0.1	0.006	0.003
δ_3 (deg)	0.4	120.6 (2)	0.3	0.5	120.5 (3)	0.4[b]	0.1	0.4
δ_5 (deg)	0.3	120.2 (2)	0.3	0.5	120.4 (3)	0.4[b]	–0.2	0.4
d_{56} (Å)	0.004	1.393 (2)	0.3	0.005	1.380 (3)	0.4	0.013	0.004
d_{34} (Å)	0.003	1.392 (2)	0.2	0.005	1.379 (3)	0.4	0.013	0.004
d_{23} (Å)	0.001	1.399 (0.6)	0.1	0.002	1.392 (1)	0.1	0.007	0.001

[a]Δ = mean(S_4^{00}) – mean(S_4^{0}); $\bar{\sigma}$ = joint σ of the means.
[b]Trend confused.

Fitting ϕ simultaneously to α and d_0 results in ϕ = 264.8 – 1.77α – 16.1d_0 (S_4^{00}, zero degrees of freedom), i.e., the negative contribution of α to ϕ is ca. seven times more important than the negative contribution from d_0.

Two of the exocyclic parameters, ϕ and $\bar{\varepsilon}$, are strongly positively correlated, but the correlations of both of them with the other five exocyclic parameters are negative, and most of them strong.

Endocyclic parameters (Fig. 4)

Collectively, the changes with Z, $\Delta\delta_i$, in the internal bond angles δ_i are subject to the condition $\sum\Delta\delta_i = 0$, which implies pair-wise correlations between all the δ_i. The strongest correlations are δ_1,δ_4 and δ_2,δ_6 (both positive), and δ_1,δ_2, δ_1,δ_6, δ_2,δ_4, and δ_6,δ_4 (all negative). The angle with the largest range (i.e., most responsive to Z, Table 7) is δ_1. The angle δ_4, with a range of only ~15% that for the δ_1 range, is covariant with δ_1 (δ_4 = 102.16 + 0.1435δ_1, r^2 = 0.998, for S_4^{00}, and δ_4 = 98.78 + 0.1722δ_1, r^2 = 0.999, for S_4^{0}); the two angles would be equal at ~119.3°, i.e., between C and N. The other strong positive correlation, δ_2,δ_6, arises from the contra-variant tendency of these two angles to compensate, unequally, for the change in the angle δ_1 they enclose (δ_6 = 9.966 + 0.921δ_1, r^2 = 0.999, for S_4^{00}; not indicated as strong in Fig. 4 because of the relatively low r^2 for S_4^{0}). The corresponding (δ_3,δ_5) also is positive and strong for S_4^{00} (δ_5 = 29.78 + 0.750δ_3, r^2 = 0.964), but again doubtful for S_4^{0}, and therefore not included in Fig. 4. The strong negative correlations δ_1,δ_2 and δ_1,δ_6 again are easily visualized because of compensation between neighboring angles.

Among the negative correlations between δ_i, evident for S_4^{00} but not for S_4^{0} (and therefore not included in Fig. 4), are δ_2,δ_3 (at the distal carbons C2 and C3) and the corresponding δ_6,δ_5 (at the proximal carbons C6 and C5). Both show clearly the difference between the proximal and the distal sides of the ring (δ_3 = 133.59 + 0.107δ_2, r^2 = 0.994, and δ_5 = 131.03 + 0.089δ_6, r^2 = 0.992).

The bond lengths d_{ij} show strong correlations among themselves (positive for d_{12},d_{61}) as well as with δ_i (positive for δ_2,d_{12}, δ_2,d_{61}, δ_6,d_{12}, δ_6,d_{61}; negative for δ_1,d_{12}, δ_1,d_{61}, δ_4,d_{12}, δ_4,d_{61}). It may be noted that, by virtue of their strong positive correlations, δ_1 and δ_4 correlate with other endocyclic parameters in the same fashion, though δ_4 somewhat less strongly. Thus δ_4 can replace δ_1 in the negative correlations δ_1,δ_2, δ_1,δ_6, δ_1,d_{12}, δ_1,d_{61}, and δ_1,d_{34}.

Mixed correlations (Fig. 5)

These are on the whole less predictable though more numerous. The strong negative correlations of δ_1 with ζ_2 and ζ_6 have their origin in the approximate coplanarity of the angles at C1 ($\delta_1 + \zeta_2 + \zeta_6$ ~ 360°). The angles δ_2 and ζ_2, and δ_6 and ζ_6 are covariant, as are d_{12} and ζ_2, and d_{61} and ζ_6, consistent with the quasi-isometric contraction of the molecular dimensions from B to N. The positive correlation between d_0 and δ_2, and between d_0 and δ_6, is the consequence of the successive negative correlations between d_0 and δ_1, and between δ_1 and δ_2 or δ_6.

To the correlations in Table 8 may be added those involving the exocyclic distances Z···C2, Z···C6, Z···H2, and Z···H6 (Table 9 and Fig. 6). With the exception of those involving $\bar{\varepsilon}$ they are all positive, again reflecting the contraction from B to N. As seen in the connectivity graph of Fig. 6, the distal parameters Z···C2 and Z···H2 (i.e., those on the H2···H6′ side of the ring) correlate much less strongly with ζ_2 than do the

© 2002 NRC Canada

Table 8. Coefficients of determination $r^2 \geq 0.67$ (× 100) of linear correlations in S_4^{00} (first line) and S_4^{0} (second line).[a]

	δ_2	δ_3	δ_4	δ_5	δ_6	d_{12}	d_{23}	d_{34}	d_{45}	d_{56}	d_{61}	ζ_2	ζ_6	α	ϕ	h	d_0	$\bar{\varepsilon}$
δ_1	100–	98.9	99.8	99.2	100–	98.1–	83	92–	83–	—	99.6–	98.2–	98.1–	94–	91	79–	80–	99.3
	98.5–	—	99.9	—	95.7–	98.8–	98.8	82–	98.8	82–	100–	99.4–	99.2–	96.1–	92	84–	83–	96.6
δ_2		99.4–	99.6–	98.7–	99.9	98.8	81–	93	81	68	99.3	97.5	98.7	95	92–	81	82	99.6–
		—	99.2–	—	89	95	95–	71	95–	71	99.0	99.8	95.5	90	84–	74	73	91–
δ_3			98.0	96.4	99.0–	99.9–	75	96.4–	75–	75–	97.4–	95–	99.9–	97.7–	95.6	87–	88–	100
			—	—	—	—	—	—	—	—	—	—	—	—	—	—	—	—
δ_4				99.8	99.8–	96.9–	86	89–	86–	—	100–	99.1–	96.8–	92–	88	76–	77–	98.4
				—	94–	98.0–	98.0	79–	98.0	79–	100–	99.8–	87–	95–	90	81–	81–	95.3
δ_5					99.2–	95.1–	89	86–	89–	—	99.9–	99.8–	95–	89–	85	72–	73–	97.1
					—	—	—	—	—	—	—	—	—	—	—	—	—	—
δ_6						98.2	83–	92	83	—	99.6	98.2	98.1	94	91–	79	80	99.3–
						99.0	99.0–	95	99.0	95	95	92	98.6	100	99.4–	95.8	95.6	99.9–
d_{12}							72–	97.6	72	78	96.2	92.9	100	98.6	96.9–	89	90	99.7–
							100–	89	100–	89	98.3	96.4	100	99.2	96.8–	91	91	99.4–
d_{23}								—	100–	—	88–	92–	72–	—	—	—	—	77
								89–	100	89–	98.3–	96.4–	100–	99.2–	96.8	91–	91–	99.4
d_{34}									—	89	88	83	97.6	99.9	100–	96.8	97.3	95.7–
									89–	100	80	75	88	94	97.7–	99.9	100	94–
d_{45}										—	88	92	72	—	—	—	—	77–
										89–	98.3–	96.4–	100–	99.2–	96.8	91–	91–	99.4
d_{56}											—	—	78	87	91–	97.7	97.2	73–
											80	75	88	94	97.7–	99.9	100	94–
d_{61}												99.5	96.1	91	87–	74	75	97.9–
												99.7	98.7	95.2	91–	82	82	95.7–
ζ_2													93	86	81–	68	69	95.3–
													97.1	92	87–	77	77	93–
ζ_6														98.6	97.0–	89	90	99.7–
														98.8	96.1–	90	89	99.1–
α															99.7–	95.4	95.9	97.1–
															99.2–	95.3	95.1	100–
ϕ																97.5–	97.9–	95
																98.4–	98.3–	98.9
h																	100	86–
																	100	95–
d_0																		87–
																		95–

[a] 99.4– etc., indicates that the correlation is negative. No entry indicates $r^2 < 0.67$; 100 stands for $r^2 \geq 0.999$ rounded up to 1.000.

© 2002 NRC Canada

proximal parameters Z···C6 and Z···H6 with ζ_6, the latter being unaffected by the interaction between the *ortho*-hydrogens, H2 and H6′.

As for the effects of the asymmetry of the Z···β-carbon distances (Z···C2 and Z···C6) on the skeletal geometry of the phenyl ring, these are small but not insignificant. The regression equations for the correlations δ_2,δ_6 ($\sigma = 0.1° \sim 3\%$ of range) and δ_3,δ_5 ($\sigma = 0.04° \sim 10\%$ of range) between the corresponding parameters in distal–proximal pairs in S_4^{00} (cf. preceding section) are evidence of the inequality arising from the lack of bilateral symmetry of the ring, i.e., the corresponding angles are consistently differentiated: $\delta_6/\delta_2 > 1$, $\delta_5/\delta_3 < 1$. The differences are even smaller for the d_{ij} bond lengths ($d_{61} = 0.262 + 0.818d_{12}$ for S_4^{00}, $r^2 = 0.962$, $\sigma = 0.0017$ Å $\sim 12\%$ of range, $d_{61}/d_{12} > 1$). These findings agree with the observations made on the statistical sample of ref. 26, where a similar conclusion was reached for the effects of the asymmetry in the Z···β-carbon distances in monosubstituted benzene derivatives (cf. below).

The mean atom change $\bar{\varepsilon}$ on the *ortho*-hydrogens H2 and H6 correlates highly with almost all the parameters (Tables 8 and 9). This, together with the large range/mean sensitivity ratio for Z substitution (Table 7), points to an important involvement of $\bar{\varepsilon}$ in the conformational behavior of the $ZPh_4^{0,\pm1}$ molecules.

Table 9. Coefficients of determination $r^2 \geq 0.67$ (×100) of linear correlations in S_4^{00} (first line) and S_4^0 (second line): effect of ring asymmetry.[a]

	Z···C6	Z···H2	Z···H6	ζ_2	ζ_6	d_0	$\bar{\varepsilon}$
Z···C2	100	99.9	99.8	81	99.4	98.1	95–
	100	100	99.9	85	95.0	98.9	98.3–
Z···C6		100	99.9	79	96.0	98.6	94–
		100	99.9	84	94	99.2	98–
Z···H2			99.9	80	96.2	98.5	94–
			100	84	94	99.3	97.7–
Z···H6				77	95.0	99.1	92–
				82	93	99.5	97.2–
ζ_2					93	69	95.3–
					97.1	77	93–
ζ_6						90	99.7–
						89	99.1–
d_0							87–
							95–

[a]See footnote of Table 8.

Substituent-induced changes in the phenyl ring geometry

The geometry optimization of the three species affords an opportunity for examining, in some detail, the effect of Z on the endocyclic bond lengths and angles. A pioneering systematic investigation of this kind was undertaken by Domenicano and co-workers (25–29). It was based on an analysis of a large variety of experimental results for substituted benzene derivatives. While our results for the above three species offer a much narrower range of substitution, and can be compared with those of Domenicano and coworkers (25, 26, 29) only for benzene monosubstituted by elements of the first row, they have the advantage of being internally closely consistent, and free from adventitious structural and experimental influences.

The geometry of the (planar) Ph ring in the ground-state conformations of the three isoelectronic $ZPh_4^{0,\pm1}$ varies with Z in general in conformity with the findings of Domenicano et al. Thus the angle δ_1 at the α-carbon (and the covariant angle δ_4 at the δ-carbon) is smallest, and the angles δ_2 and δ_6 flanking δ_1 are the largest, for the σ-electron-*releasing* B atom, whereas the opposite is true for the σ-electron-*withdrawing* N atom.[14] Concurrently, the increase in δ_1 from B to N is associated with a small (ca. 1%) but clearly discernible shortening of the C1—C2 and C1—C6 bonds enclosing δ_1.[15] The magnitude of the electronic effect of Z on the C-C-C angles diminishes with the increasing distance from Z: the *range* of δ_1 (5.2–5.6°) is almost seven times that for δ_4 (0.8°). The compensation for the variation in δ_1 takes place almost entirely in the δ_2 and δ_6 angles at the β-carbons, and depends only slightly on Z:

	B	C	N
$\delta_1 + \delta_2 + \delta_6$ (for S_4^{00})	360.8°	360.1°	359.3°
$\delta_1 + \delta_2 + \delta_6$ (for S_4^0)	360.7°	360.1°	359.6°

(the δ_2 and δ_6, and the δ_3 and δ_5 angles, equivalent under D_{2d} symmetry, are differentiated under S_4).[16] The δ_5 and δ_6 angles at the γ-carbons also are smallest in BPh_4^-, and their ranges are much smaller than for the other endocyclic angles.

A more detailed comparison can be made with the results of Domenicano et al.'s (29) statistical investigation of the effect of monosubstitution on the endocyclic parameters in benzene derivatives, in which the substituent atom attached to the ring is from the first row. The data set in that study comprised 149 entries extracted from high-precision structures. The benzene rings were treated as if of C_{2v} symmetry, and bivariate correlations were calculated for all combinations of the appropriately averaged δ_i and d_{ij}. Interestingly, the only one of the 21 non-self-correlations that had an $r^2 > 0.95$ was δ_1, $(\delta_2 + \delta_6)/2$, with $r^2 = 0.98$ and a regression equation $(\delta_2 + \delta_6)/2 = 190.62 - 0.591\delta_1$).[17] This compares with our $r^2 = 1.00$ for δ_1,δ_2 in S_4^{00} (0.985 in S_4^0), and with $r^2 = 1.00$ for δ_1,δ_6 in S_4^{00} (0.957 in S_4^0). The corresponding regression equations (Table F)[8] are very similar to eq. [35] of ref. 29, and have $\sigma = 0.07° \sim 2\%$ and $0.17° \sim 5\%$ of range for S_4^{00} and S_4^0, respectively.

The only other of the combinations with $r^2 > 0.5$ in ref. 29 was δ_4,$(d_{12} + d_{61})/2$, with $r^2 = 0.64$; this corresponds to $r^2 = 0.97$ (S_4^{00}) and 0.98 (S_4^0) for δ_4,d_{12}, and to $r^2 = 1.00$ for

[14]For a carbon atom as a substituent, δ_1 is smaller than the 120° angle in the free benzene molecule. The value suggested in ref. 25 is 117.5–118.0°, in agreement with $\delta_1 = 117.5°$ in CPh_4 (Table 6).
[15]Reasons for these trends are advanced, in terms of hybridization effects or, alternatively, the VSEPR model, in ref. 26.
[16]The angles δ_1, ζ_2, and ζ_6 at C1 add up to 360° for both S_4^{00} and S_4^0, even though the phenyl ring and the C0—C1 bond are not coplanar.
[17]Recast from $(\delta_2 + \delta_6)/2 - 120 = -0.301(15) - 0.591(7)(\delta_1 - 120)$.

© 2002 NRC Canada

Fig. 7. Correlations of the symmetry distortion coordinates D_4 and D_6 (see text) for $ZPh_4^{0,\pm1}$ (S_4^{00} (solid circles, thick solid line); S_4^0 (open circles, thin solid line)). The electronegativities χ of the -$ZPh_3^{0,\pm1}$ groups (solid squares) refer to the χ(Pauling) correlation baseline defined by the points for Li, C, O, and F; open squares, see footnote 19 in text).

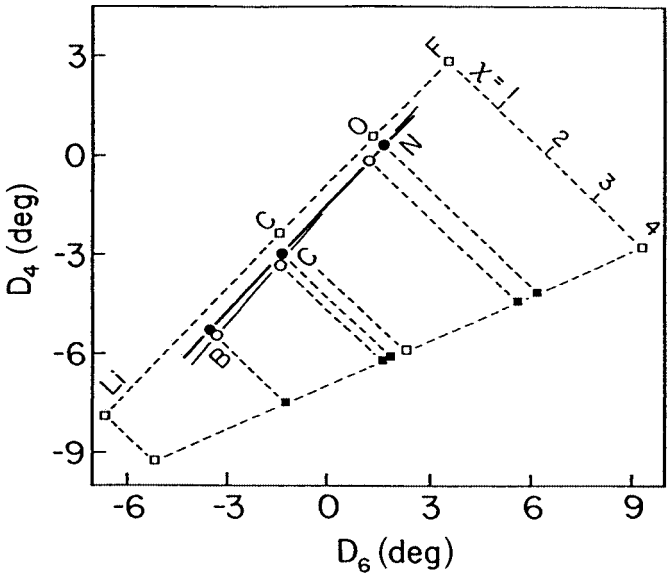

δ_4,d_{61} (both S_4^{00} and S_4^0). However, all the other correlations that for $ZPh_4^{0,\pm1}$ are highly significant have, in Table 3 of ref. 29, counterparts with r^2 values from ~0.3 to ~0.4, while for the remaining ones $r^2 \leq 0.1$. This seems to indicate that the statistical trends in ref. 29 parallel those for $ZPh_4^{0,\pm1}$ and, though obscured by the undiscriminating chemical variation in the underlying data set,[18] are in general agreement with our own observations.

The δ_1,$(d_{12} + d_{61})/2$ correlation in ref. 29 (expected to be high) was described as very poor ($r = -0.56$, $r^2 = 0.31$), the presumed reason stated being that the variance of $(d_{12} + d_{61})/2$ was due to thermal motion and inhomogeneity of the sample. The correlation improved significantly ($r = -0.83$, $r^2 = 0.69$) when instead of $(d_{12} + d_{61})/2$, the quantity a' (defined as the mean of the six C—C bond lengths subtracted from $(d_{12} + d_{61})/2$) was plotted against δ_1 (Fig. 5*a* of ref. 29). When we applied this averaging procedure to $ZPh_4^{0,\pm1}$, the resulting δ_1,a' correlation indeed was practically perfectly linear: $r^2 = 0.999$, $\sigma = 0.00014$ Å ~ 1.7% of the a' range for S_4^{00}, and $r^2 = 1.000$, $\sigma = 0.00006$ Å ~ 0.7% of the a' range for S_4^0. Since thermal motion and sample inhomogeneity are not factors in the ab initio set, the apparent improvement in this correlation over δ_1,d_{12} and δ_1,d_{61} (Table 8) is attributed to the averaging of the d_{12},d_{61}, d_{23},d_{56}, and d_{34},d_{45} values, and to the smoothing out of inaccuracies due to numerical rounding-off in the optimization.

Domenicano et al. (29) also investigated correlations between the symmetry distortion coordinates D_i, singling out those between D_3 and D_4, and between D_4 and D_6. They found that although D_3 and D_4 are of the same symmetry species, these two coordinates did not correlate, whereas D_4 and D_6, which are not of the same species, surprisingly correlated rather well. They also pointed out that "the angular variance of monosubstituted benzene rings can be completely represented by the latter two coordinates." Since the geometry of the phenyl rings in $ZPh_4^{0,\pm1}$, optimized under S_4, is not of C_{2v} symmetry (assumed in ref. 29), we examined the correlations with these coordinates appropriately modified:

$$D_3 = (2\sqrt{3})^{-1}(-d_{12} + 2d_{23} - d_{34} - d_{45} + 2d_{56} - d_{61})$$

$$D_4 = (2\sqrt{3})^{-1}(2\delta_1 - \delta_2 - \delta_3 + 2\delta_4 - \delta_5 - \delta_6)$$

$$D_6 = (2\sqrt{3})^{-1}(\delta_1 - \delta_2 + \delta_3 - \delta_4 + \delta_5 - \delta_6)$$

Unlike for the statistical sample, D_3 and D_4 for the three tetraphenyls *do* correlate: $D_3 = 0.00252 + 0.00181D_4$ for S_4^{00}, with $r^2 = 0.96$ as against $r^2 \sim 0.1$ for the statistical sample. The correlation between D_4 and D_6 was strongly confirmed: $D_4 = -1.512 + 1.079\ D_6$, $r^2 = 1.00$ for S_4^{00}; for S_4^0, $D_4 = -1.595 + 1.144D_6$, $r^2 = 0.999$. This compares with $D_4 = -0.99(7) + 1.20(4)D_6$, $r^2 = 0.81$ for the statistical sample, where most of the scatter seems to be due to chemical variation rather than to experimental error. In this correlation, low D_6,D_4 values correspond to substituents with low electronegativity, and high D_6,D_4 values to substituents with high electronegativity.

The good linearity of the D_6,D_4 plot in fact permits an estimate of the electronegativity of the $-ZPh_3^{0,\pm1}$ groups, viewed as substituents on the benzene ring, if one assumes that the electronegativity χ increases linearly, from Li to F, along the regression line. Using the D_6,D_4 points for $C_6H_5^-\cdots Li^+$, $C_6H_5CH_3$, C_6H_5OH, and C_6H_5F,[19] one obtains $D_4 = -0.899 + 1.005\ D_6$ ($r^2 = 1.00$), which is within 3σ of the corresponding line for the statistical sample, and quite close to the above regression line for the tetraphenyls. With Pauling's χ(Li) = 1.0 and χ(F) = 4.0, the values for χ(C) and χ(O) are 2.5 and 3.4, respectively; relative to this standard line, the χ for the tetraphenyls are then ~1.80, ~2.43, and ~3.55 for Z = B, C, and N, respectively (Fig. 7).

These three χ values for the tetraphenyls correlate well with δ_1 ($\delta_1 = 109.8 + 3.06\chi$, $r^2 = 0.997$, $\sigma = 0.22 \sim 4\%$ of range with δ_1 averaged over S_4^{00} and S_4^0). This compares with a corresponding correlation for a sample of benzene rings monosubstituted with elements of the *second* row (27) ($\delta_1 = 111.4 + 3.33\chi$), and confirms that in monosubstituted benzenes, in the absence of conjugation between the substituent and the ring, electronegativity of the substituent is by far the most important exocyclic factor affecting δ_1.

Transition-state geometry

The transition from the local-minimum D_{2d} conformation to the global-minimum S_4 conformation is a transition between two rotamers, characterized, essentially, by the tilt angle ϕ as the transition parameter. The tilt angle ϕ_b(Z) at the barrier (Table 4) and $\phi(S_4,Z)$ are related by $\phi(S_4^b, Z) = 50.1 + 0.417\phi(S_4^0,Z)$ ($r^2 = 0.999$) if the position of the barrier is estimated with $\Delta E = 0$ as the baseline, and by $\phi(S_4^b, Z) = 45.0 + 0.5\phi(S_4^0, Z)$ ($r^2 = 1.00$) with the cubic baseline of Fig. 2.

[18]Historical sampling is not necessarily a chemically representative sampling.
[19]Averaged from CALKOP, CALKUV, PHENLI, and SIMRUB for Li; TOLUEN for C; PHENOL03 for O; and C_6H_5F (30) for F.

© 2002 NRC Canada

Fig. 8. (*Top*) Positions of the C_6 and H_5 centroids of $ZPh_4^{0,\pm1}$, approximately in the *yz* axial plane. Note the large shifts in these positions on passing, via S_4^{ϕ} under S_4 symmetry, from the S_4^{0} to the D_{2d}^{0} conformation. Circles, S_4^{0} and D_{2d}^{0}; squares, S_4^{ϕ}; triangles up, S_4^{00} for CPh_4; triangles down, see text for *R* and *T*. (*Bottom*) Variation of the valence angle $\alpha(Z) - \alpha(N)$ (open squares) and the tilt angle $\phi(Z) - \phi(B)$ (full squares) with the positions of the C_6 and H_5 centroids in the S_4^{0} conformations (circles). Note the different $\bar{z}$ scales for the two centroids; $\alpha(Z) - \alpha(N)$ and $\phi(Z) - \phi(B)$ are on arbitrary relative scales.

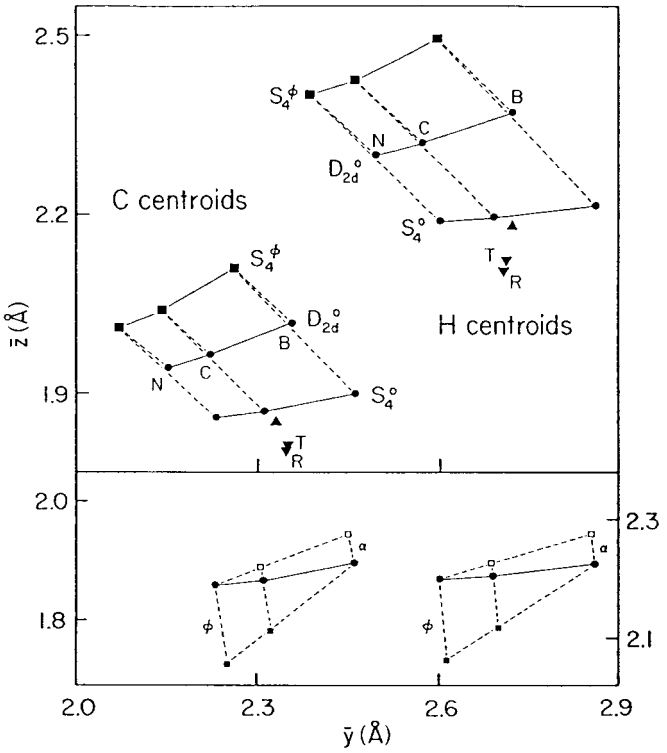

The valence angle $\alpha_b(Z)$ at the barrier is practically equal to the mean of $\alpha(S_4^{0},Z)$ and $\alpha(D_{2d}^{0},Z)$. For BPh_4^-, the value $\alpha_b(B) \sim 105°$ appears to coincide with the minimum in the bimodal distribution of experimental $\alpha(BPh_4^-)$ values in crystals (to be published). Apart from ϕ_b, however, the (interpolated) parameter values at the barrier are not dramatically different from those in the S_4 and D_{2d} conformations, and no particular geometric parameter can be singled out as privileged and distinctly associated with the conformation at the barrier. This is true even of the short H2···H6′ = *h* contact between the *ortho*-hydrogens, the repulsion between which has, traditionally, albeit vaguely, been regarded as responsible for the existence of the barrier. On the contrary, it appears that instead of any *single* factor, it is a combination of a number of geometric factors that produces the barrier to concerted reorientation of the rings under S_4 symmetry. This is illustrated by the shifts in the positions of the C_6 and H_5 centroids (Fig. 8). These shifts, for each Z, vary along the conformation pathway $D_{2d}^{0} \rightarrow S_4^{\phi} \rightarrow S_4^{0}$ in a manner that is analogous to going over the barrier in the $\phi,\Delta E$ plot of Fig. 2; the actual shifts at S_4^{b} would presumably be even larger than at S_4^{ϕ}. Since the positions of all six C atoms and all five H atoms are components of the centroids, the resulting means reflect the simultaneous involvement of all eleven independent atoms in the $ZPh_4^{0,\pm1}$ molecule (leaving aside the probably minor effects arising from the ring–planarity constraint in the model).

Figure 8 also shows the practically linear association of the centroid positions with α and φ.

Conclusions

The equilibrium molecular geometries of the isoelectronic BPh_4^-, CPh_4, and NPh_4^+ have been optimized, at the HF/6-31G(d,p) and B3LYP/6-31G(d,p) levels, in S_4 and D_{2d} symmetries, with the phenyl rings constrained to be planar. The ground-state conformations of all three $ZPh_4^{0,\pm1}$ species are found to be of S_4 symmetry, with the rings tilted (from Z = B to N) by an angle of $\phi \sim 48–57°$ relative to their positions ($\phi = 90°$) in the corresponding D_{2d} conformations. For CPh_4, this contradicts a conclusion from earlier, force-field calculations (4), according to which the ground-state conformation of the molecule has the D_{2d} symmetry, alone among its ZPh_4^0 congeners.

The energy of the D_{2d} conformation is only about 1 kcal mol^{-1} above that of the corresponding minimum-energy S_4 conformation. The height of the potential barrier to rotational reorientation of the ring under $S_4 \subset D_{2d}$ symmetry is estimated to range from ~5 kcal mol^{-1} for BPh_4^- to ~8 kcal mol^{-1} for NPh_4^+ (Table 4). The optimization results do not point to any clearly identifiable, distinguished geometric parameter that might be responsible for the existence of the barrier, except perhaps the short H···H distance *h* between the *ortho*-hydrogens of neighboring rings.

The crystal structure of CPh_4 has been redetermined from –60°C X-ray data, with the H atom positions reliably refined. It agrees well with the earlier determinations from room temperature data. The CPh_4 geometry in the crystal differs from the optimized geometry of CPh_4 only in that the molecule is slightly compressed along its S_4 axis.

All geometric parameters and the mean charge $\bar{\varepsilon}$ on the *ortho*-hydrogens are affected by change of Z, though to a widely unequal extent (Table 7). The $ZPh_4^{0,\pm1}$ molecule undergoes a quasi-isometric contraction of ~0.5% of the molecular dimensions from B to N. The C-Z-C valence angle ($\alpha < \tau$) decreases significantly from B to N, as does the Z—C bond length (d_0). The effects of the Z substitution are presented in terms of binary correlations between individual parameters, both numerically (Table 8) and in connectivity graphs (Figs. 4–6).

The ab initio calculations at the above levels show no obvious reason why the NPh_4^+ cation should be inherently unstable as an isolated molecule, at least in the absence of significant thermal energy.

The effect of Z on the geometry of the phenyl rings in $ZPh_4^{0,\pm1}$ has been examined in detail and compared with the results of statistical studies by Domenicano and co-workers (25–28). In this limited context, the internal consistency of the optimized parameters makes it possible to verify pertinent conclusions from these studies and significantly strengthen them. In particular, the small but not negligible effects of the lack of bilateral ring symmetry on the C—C bond lengths and endocyclic C-C-C bond angles have been assessed with some confidence.

© 2002 NRC Canada

Acknowledgements

We thank Drs. T.B. Grindley, D.C. Hamilton, K.N. Robertson, N.P. Schepp, and Jian Wang for their advice and assistance with the various aspects of this investigation. Financial support from the Natural Sciences and Engineering Research Council of Canada (NSERC) is acknowledged.

References

1. K.N. Robertson, P.K. Bakshi, S.D. Lantos, T.S. Cameron, and O. Knop. Can. J. Chem. **76**, 583 (1998).
2. N.A. Ahmed, A.I. Kitaigorodsky, and K.V. Mirskaya. Acta Crystallogr. Sect. B: Struct. Crystallogr. Cryst. Chem. **27**, 867 (1971).
3. A.I. Kitaigorodsky. Molecular crystals and molecules. Academic Press, New York and London. 1973. pp. 67–71.
4. M.G. Hutchings, J.D. Andose, and K. Mislow. J. Am. Chem. Soc. **97**, 4553 (1975).
5. M.G. Hutchings, J.D. Andose, and K. Mislow. J. Am. Chem. Soc. **97**, 4562 (1975).
6. J.G. Nourse and K. Mislow. J. Am. Chem. Soc. **97**, 4571 (1975).
7. U. Müller. Acta Crystallogr. Sect. B: Struct. Crystallogr. Cryst. Chem. **36**, 1075 (1980).
8. T.S. Cameron, O. Knop, B. Borecka, and W. Kwiatkowski. Abstract PD11. Book of abstracts. American Crystallographic Association, Annual Meeting, Albuquerque, New Mexico, May 23–28, 1993; cf. also A.W. Cordes, American Crystallographic Association Newsletter, no. 2, June 1993, p. 21.
9. O. Knop, T.S. Cameron, P.K. Bakshi, W. Kwiatkowski, S.C. Choi, and D. Adhikesavalu. Can. J. Chem. **71**, 1495 (1993).
10. M.A. Lloyd and C.P. Brock. Acta Crystallogr. Sect. B: Struct. Sci. **B53**, 773 (1997).
11. M.A. Lloyd and C.P. Brock. Acta Crystallogr. Sect. B: Struct. Sci. **B53**, 780 (1997).
12. F.H. Allen and O. Kennard. Chem. Design Automat. News, **8**, 1, 31 (1993). See also: CSD version 5.22, October 2001.
13. D.M. Duggan and D.N. Hendrickson. Inorg. Chem. **13**, 2056 (1974).
14. M. Di Vaira and A.B. Orlandini. J. Chem. Soc. Dalton Trans. 1707 (1972).
15. M. Di Vaira. Inorg. Chem. **14**, 1442 (1975).
16. H.T. Sumsion and D. McLachlan, Jr. Acta Crystallogr. **3**, 217 (1950).
17. A. Robbins, G.A. Jeffrey, J.P. Chesick, J. Donohue, F.A. Cotton, B.A. Frenz, and C.A. Murillo. Acta Crystallogr. Sect. B: Struct. Crystallogr. Cryst. Chem. **B31**, 2395 (1975).
18. B. Borecka. Ph.D. Thesis, Dalhousie University, Halifax, Nova Scotia, Canada, 1992.
19. N.E. Shchepina, V.D. Nefedov, M.A. Toropova, V.V. Avrorin, S.B. Lewis, and B. Mattson. Tetrahedron Lett. **41**, 5303 (2000).
20. M.J. Frisch, G.W. Trucks, H.B. Schlegel, G.E. Scuseria, M.A. Robb, J.R. Cheeseman, V.G. Zakrzewski, J.A. Montgomery, R.E. Stratmann, J.C. Burant, S. Dapprich, J.M. Millam, A.D. Daniels, K.N. Kudin, M.C. Strain, O. Farkas, J. Tomasi, V. Barone, M. Cossi, R. Cammi, B. Mennucci, C. Pomelli, C. Adamo, S. Clifford, J. Ochterski, G.A. Petersson, P.Y. Ayala, Q. Cui, K. Morokuma, D.K. Malick, A.D. Rabuck, K. Raghavachari, J.B. Foresman, J. Cioslowski, J.V. Ortiz, B.B. Stefanov, G. Liu, A. Liashenko, P. Piskorz, I. Komaromi, R. Gomperts, R.L. Martin, D.J. Fox, T. Keith, M.A. Al-Laham, C.Y. Peng, A. Nanayakkara, C. Gonzalez, M. Challacombe, P.M.W. Gill, B.G. Johnson, W. Chen, M.W. Wong, J. L. Andres, M. Head-Gordon, E.S. Replogle, J.A. Pople, GAUSSIAN98 [computer program]. Gaussian, Inc., Pittsburgh, Pennsylvania, U.S.A. 1998.
21. A.D. Becke. J. Chem. Phys. **98**, 1372 (1993).
22. A.D. Becke. J. Chem. Phys. **98**, 5648 (1993).
23. P.J. Stephens, F.J. Devlin, C.F. Chabalowski, and M.J. Frisch. J. Phys. Chem. **98**, 11 623 (1994).
24. C. Lee, W. Yang, and R.G. Parr. Phys. Rev. B: Condens. Matter Mater. Phys. **37**, 785 (1987).
25. A. Domenicano, P. Mazzeo, and A. Vaciago. Tetrahedron Lett. **13**, 1029 (1976).
26. A. Domenicano, A. Vaciago, and C.A. Coulson. Acta Crystallogr. Sect. B: Struct. Crystallogr. Cryst. Chem. **B31**, 221 (1975).
27. A. Domenicano, A. Vaciago, and C.A. Coulson. Acta Crystallogr. Sect. B: Struct. Crystallogr. Cryst. Chem. **B31**, 1630 (1975).
28. A. Domenicano and A. Vaciago. Acta Crystallogr. Sect. B: Struct. Crystallogr. Cryst. Chem. **B35**, 1382 (1979).
29. A. Domenicano, P. Murray-Rust, and A. Vaciago. Acta Crystallogr. Sect. B: Struct. Sci. **B39**, 457 (1983).
30. L. Nygaard, I. Bojesen, T. Pedersen, and J. Rastrup-Andersen. J. Mol. Struct. **2**, 209 (1968).

List of symbols

Z	the central atom, at (0, 0, 0)
X′	the symmetry equivalent of the X = C, H atom at (y, $-x$, $-z$)
X″	the symmetry equivalent of the X = C, H atom at ($-x$, $-y$, z)
x, y, z	Cartesian atom coordinates in Å
$\bar{x}$(C) etc.	Cartesian coordinates (Å) of the C_6 centroid of the phenyl ring
$\bar{x}$(H) etc.	Cartesian coordinates (Å) of the H_5 centroid of the phenyl ring
τ	The tetrahedral angle, 109.47°
α	The valence angle C1-Z-C1″ (bisected by the S_4 axis)
β	The valence angle C1-Z-C1′; $\tan^2(\beta/2) = 1 + 2/\tan^2(\alpha/2)$
ζ_2, ζ_6	The angles Z-C1-C2 and Z-C1-C6, respectively (cf. Fig. 6).
δ_i	Endocyclic C-C-C angles, cf. Tables 2 and 3
ϕ	The tilt angle = the angle formed by the axial yz plane with the plane of the phenyl ring, with the molecule in standard orientation specified by Z and the centroid of the C_6 ring in the yz plane, and the S_4 axis in z. It is the acute angle in the S_4 conformations and 90° in the D_{2d} conformation.
E	Total electronic energy (au)
ZPE	Zero-point energy (au)
ε	Net atom charge (Mulliken) (e)
$\bar{\varepsilon}$	[ε(H2) + ε(H6)]/2
S_4^0	Global minimum-energy conformation in S_4/HF/6-31G(d,p)
S_4^{00}	Global minimum-energy conformation in S_4/B3LYP/6-31G(d,p)
S_4^{ϕ}	Geometry optimized in S_4/HF/6-31G(d,p) with ϕ fixed at the stated value
D_{2d}^0	Global minimum-energy conformation in D_{2d}/HF/6–31G(d,p)
D_{2d}^{00}	Global minimum-energy conformation in D_{2d}/B3LYP/6–31G(d,p)
R	Mean of the two independent structure determinations from 20°C data, EaPa (TEPHME02) and Tex (TEPHME03), of ref. 17; CPh_4 in S_4 conformation
T	Structure determination from –60°C data, this work; CPh_4 in S_4 conformation

© 2002 NRC Canada

Radiolysis of liquid water: An attempt to reconcile Monte-Carlo calculations with new experimental hydrated electron yield data at early times

Yusa Muroya, Jintana Meesungnoen, Jean-Paul Jay-Gerin, Abdelali Filali-Mouhim, Thomas Goulet, Yosuke Katsumura, and Samlee Mankhetkorn

Abstract: A re-examination of our Monte-Carlo modeling of the radiolysis of liquid water by low linear-energy-transfer (LET ~ 0.3 keV μm^{-1}) radiation is undertaken herein in an attempt to reconcile the results of our simulation code with recently revised experimental hydrated electron (e^-_{aq}) yield data at early times. The thermalization distance of subexcitation electrons, the recombination cross section of the electrons with their water parent cations prior to thermalization, and the branching ratios of the different competing mechanisms in the dissociative decay of vibrationally excited states of water molecules were taken as adjustable parameters in our simulations. Using a global-fit procedure, we have been unable to find a set of values for those parameters to *simultaneously* reproduce (*i*) the revised e^-_{aq} yield of 4.0 ± 0.2 molecules per 100 eV at "time zero" (that is, a reduction of ~20% over the hitherto accepted value of 4.8 molecules per 100 eV), (*ii*) the newly measured e^-_{aq} decay kinetic profile from 100 ps to 10 ns, and (*iii*) the time-dependent yields of the other radiolytic species $H^•$, $^•OH$, H_2, and H_2O_2 (up to ~1 μs). The lowest possible limiting "time-zero" yield of e^-_{aq} that we could in fact obtain, while ensuring an acceptable agreement between *all* computed and experimental yields, was ~4.4 to 4.5 molecules per 100 eV. Under these conditions, the mean values of the electron thermalization distance and of the geminate electron–cation recombination probability, averaged over the subexcitation electron "entry spectrum," are found to be equal to ~139 Å and ~18%, respectively. These values are to be compared with those obtained in our previous simulations of liquid water radiolysis, namely ~88 Å and ~5.5%, respectively. Our average electron thermalization distance is also to be compared with the typical size (~64–80 Å) of the initial hydrated electron distributions estimated in current deterministic models of "spur" chemistry. Finally, our average probability for geminate electron–cation recombination agrees well with an estimated value of ~15% recently reported in the literature. In conclusion, this work shows that an adaptation of our calculations to a lower hydrated electron yield at early times is possible, but also suggests that the topic is not closed. Further measurements of the e^-_{aq} yields at very short times are needed.

Key words: liquid water, radiolysis, electron–cation geminate recombination, electron thermalization distance, hydrated electron (e^-_{aq}), e^-_{aq} decay kinetics, time-dependent molecular and radical yields, Monte-Carlo simulations.

Résumé : Nous avons réexaminé le code Monte-Carlo que nous avons développé précédemment pour simuler la radiolyse de l'eau liquide par des rayonnements à faible transfert d'énergie linéique (TEL ~ 0,3 keV μm^{-1}) afin de voir s'il est possible de réconcilier les résultats de notre code avec les données expérimentales récemment révisées du rendement en électrons hydratés (e^-_{aq}) à temps courts. Les paramètres ajustables utilisés dans nos simulations sont la distance de thermalisation des électrons de subexcitation, la section efficace de recombinaison des électrons avec leurs cations parents de l'eau avant thermalisation et les rapports de branchement des différents mécanismes intervenant lors de la dissociation des états excités vibrationnels des molécules d'eau. En utilisant une procédure d'ajustement global, nous n'avons pas réussi à trouver un jeu de valeurs de ces paramètres permettant de reproduire *simultanément* : (1) le rendement révisé en e^-_{aq} de 4,0 ± 0,2 molécules par 100 eV à « temps zéro » (c'est-à-dire, une réduction de ~20 % par rapport à la valeur acceptée jusqu'ici de 4,8 molécules par 100 eV), (2) le profil cinétique de déclin des e^-_{aq} nouvellement

Received 3 July 2002. Published on the NRC Research Press Web site at http://canjchem.nrc.ca on 28 October 2002.

Y. Muroya,[1], J.-P. Jay-Gerin,[2] A. Filali-Mouhim, and T. Goulet. Département de médecine nucléaire et de radiobiologie, Faculté de médecine, Université de Sherbrooke, Sherbrooke, QC J1H 5N4, Canada.
Y. Katsumura. Nuclear Engineering Research Laboratory, Graduate School of Engineering, University of Tokyo, 2–22 Shirakata-shirane, Tokai-mura, Naka-gun, Ibaraki 319-1188, Japan.
S. Mankhetkorn. Laboratory of Physical Chemistry, Molecular and Cellular Biology, Faculty of Science, Burapha University, Bangsaen, Chonburi 20131, Thailand.
J. Meesungnoen. Département de médecine nucléaire et de radiobiologie, Faculté de médecine, Université de Sherbrooke, Sherbrooke, QC J1H 5N4, Canada; and Laboratory of Physical Chemistry, Molecular and Cellular Biology, Faculty of Science, Burapha University, Bangsaen, Chonburi 20131, Thailand.

[1]Present address: Nuclear Engineering Research Laboratory, Graduate School of Engineering, University of Tokyo, 2–22 Shirakata-shirane, Tokai-mura, Naka-gun, Ibaraki 319-1188, Japan.
[2]Corresponding author (e-mail: jaygerin@courrier.usherb.ca).

 DOI: 10.1139/V02-173 © 2002 NRC Canada

mesuré entre 100 ps et 10 ns et (3) les rendements en fonction du temps des autres espèces radiolytiques H•, •OH, H_2 et H_2O_2 (jusqu'à ~1 μs). En fait, le rendement le plus faible possible en e^-_{aq} que nous avons réussi à obtenir à « temps zéro », tout en veillant à garder un accord acceptable entre *tous* les rendements expérimentaux et calculés, s'élève à ~4,4–4,5 molécules par 100 eV. Dans ces conditions, les valeurs de la distance de thermalisation des électrons et de la probabilité de recombinaison géminée électron–cation, moyennées en tenant compte du spectre énergétique des électrons de subexcitation, ont été trouvées respectivement égales à ~139 Å et ~18 %. Ces valeurs sont à comparer avec celles obtenues dans nos simulations antérieures de la radiolyse de l'eau liquide, à savoir, ~88 Å et ~5,5 %, respectivement. Notre valeur moyenne de la distance de thermalisation des électrons est aussi à comparer avec la taille typique (~64–80 Å) des distributions initiales d'électrons hydratés déduites des modèles déterministes actuels de la chimie des « grappes ». Enfin, notre probabilité moyenne de recombinaison géminée électron–cation s'accorde bien avec une valeur estimée de ~15 % rapportée récemment dans la littérature. En conclusion, ce travail montre qu'une adaptation de nos calculs à un rendement plus faible en électrons hydratés à temps courts est possible, mais suggère aussi que le sujet n'est pas clos. D'autres mesures des rendements en e^-_{aq} à temps courts s'avèrent nécessaires.

Mots clés : eau liquide, radiolyse, recombinaison géminée électron–cation, distance de thermalisation de l'électron, électron hydraté (e^-_{aq}), cinétique de déclin des e^-_{aq}, rendements radicalaires et moléculaires dépendants du temps, simulations Monte-Carlo.

Introduction

Besides its intrinsic scientific interest, the radiation chemistry of liquid water is of considerable importance because of its relevance to a number of practical applications in fields such as radiation biology, nuclear-reactor chemistry, nuclear technology relevant to the storage of radioactive waste materials, free radical chemistry, environment, etc. As a matter of fact, the radiolysis of water and aqueous solutions has been the subject of numerous experimental and theoretical investigations for almost a century (for reviews of its long history, see refs. 1 and 2). The most recent developments include the study of water radiolysis by high linear energy transfer[3] radiation (3) and at high temperatures and pressures under supercritical conditions (>374°C, >22.1 MPa or 218 atm) (4). On the theoretical side, the entire water radiolysis process can now be efficiently modeled using Monte-Carlo codes[4] simulating the interaction of a variety of ionizing radiations with aqueous media at various temperatures, pH, and LET (7–11).

Briefly, the radiolysis of pure deaerated liquid water by low-LET radiation (such as ^{60}Co γ-rays or high-energy electrons) principally leads to the formation of the radicals and molecular products e^-_{aq}, H•, •OH, H_2, H_2O_2, and H_3O^+ (for reviews, see refs. 2, 12, and 13). Under usual irradiation conditions, these species are generated nonhomogeneously in small, spatially isolated regions of dense ionization and excitation (commonly referred to as "spurs") along the track of the radiation. The so-called "primary" radical and molecular yields (or "escape" yields) $G_{e^-_{aq}}$, $G_{H\cdot}$, $G_{\cdot OH}$, G_{H_2}, and $G_{H_2O_2}$ represent the numbers of species of each kind produced per 100 eV of absorbed energy[5] that remain throughout the bulk of the solution after spur expansion. At room temperature, the time required before homogeneous chemistry takes over in the solution is ~1 μs. For ^{60}Co γ radiation (photon energies of 1.17 and 1.33 MeV) or fast electrons of the same energies, at neutral pH and 25°C (average LET ~ 0.3 keV μm^{-1}) (14), the standard values of the primary yields are (2, 12, 13, 15, 16):

$$G_{e^-_{aq}} = 2.65 G_{H\cdot} = 0.60 G_{H_2} = 0.45$$

$$G_{\cdot OH} = 2.80 G_{H_2O_2} = 0.68 G_{-H_2O} = 4.15$$

where G_{-H_2O} denotes, at this stage, the corresponding yield of decomposition of water.

Within the lifetime of spurs, the yields of the radicals and molecular species produced by the irradiation vary with time. One of the main goals in the study of the radiation chemistry of water is the determination of these yields and their time dependences. The hydrated electron (e^-_{aq}) is probably the most studied of the transient chemical species formed in the radiolysis of water. The yield of e^-_{aq} was previously measured at early times by several authors in picosecond pulse radiolysis experiments. Hunt and co-workers (17) first obtained 4.0 ± 0.3 at 30 ps. Jonah and co-workers (18) subsequently measured the decay of e^-_{aq} between 100 ps and 3 ns and reported 4.6 ± 0.2 at 100 ps, a value later renormalized by Pimblott et al. (19) to ~4.8 after a reanalysis of existing transient absorption measurements, scavenger yield data, and stochastic diffusion-kinetic simulations. Sumiyoshi and co-workers (20) also determined 4.8 ± 0.3 at 30 ps. Our Monte-Carlo simulation code of water radiolysis (7–11), like most others, was adjusted for the greatest part on the basis of the time dependence of the e^-_{aq} yield measured by Jonah and co-workers (18). However, the numbers for the early-time e^-_{aq} yield in refs. 18 and 19 were recently revised downward by Bartels et al. (21), who reinvestigated the radiolysis spur decay kinetics of e^-_{aq} from 100 ps to 10 ns using a new time-correlated absorption spectroscopy technique. These latter authors fitted the shape of their relative e^-_{aq} decay kinetics with a functional form containing four exponentials and a constant (G_{inf}). The value of

[3] LET, or "stopping power", defined as the energy transferred per unit length of the track ($-dE/dx$).

[4] A number of investigators have developed Monte-Carlo computer simulations for modeling the initial formation of radiolytic species along charged-particle tracks and their subsequent chemical behavior in liquid water. See for example refs. 5 and 6.

[5] Throughout this paper, radiation chemical yields (*G*-values) are given in the units of molecules per 100 eV. For conversion into SI units (mol J^{-1}): 1 molecule per 100 eV ≈ 1.0364×10^{-7} mol J^{-1}.

© 2002 NRC Canada

G_{inf} = 2.5 was selected to match the most reliable scavenger yield data for water (2.7) for a scavenging power[6] of 10^7 s^{-1}. Based on this normalization procedure, Bartels et al. (21) then "extrapolated" their fitting function to short times and found a "time-zero" e^-_{aq} yield of 4.0 ± 0.2, a value consistent with the earlier measurements of Hunt and co-workers (17). The result that the *G*-value of 4.8 at 100 ps could be too high has received some support from LaVerne (22), who recently reported: "An initial e^-_{aq} yield of about 4.2 per 100 eV absorbed can still be reconciled with the inverse Laplace transform of the scavenger data presented previously (ref. 19)". Similar support was also obtained from the deterministic "average" spur diffusion model calculations of Swiatla-Wojcik and Buxton (23), which showed that the experimental yields in water radiolysis with radiation of LET from 0.2 to 60 keV μm^{-1} could be reasonably matched with an initial e^-_{aq} yield value of 4.2. This significant reduction (~20%) in the yield of e^-_{aq} at short times (over the hitherto accepted value of 4.8) (19, 20) thus prompted us to reexamine the values of certain physical and physicochemical parameters that enter our Monte-Carlo simulation code (7–11) to see if this latter could be reconciled with Bartels et al's (21) new experimental findings.

Monte-Carlo simulations

A detailed description of our Monte-Carlo modeling of the radiolysis of liquid water has been given previously (7–11). Briefly, during the "physical stage", the energy deposition by the incident radiation (high-energy protons or heavier ions) and by all the secondary electrons that it has generated occurs through the slowing down of those particles via a variety of inelastic scattering processes, including ionization, electronic and (or) vibrational excitation of single water molecules, and excitation of plasmon-type collective modes. The species created during this first stage undergo fast reorganization in the "physicochemical stage" and produce the "initial" radical and molecular products of the radiolysis, distributed in a highly nonhomogeneous track structure. Secondary electrons slow down to subexcitation energies[7] and, following thermalization,[8] get trapped and eventually become hydrated.[9] All the events of those two stages are handled by our step-by-step simulation codes, called TRACPRO and TRACELE. To reproduce the effects of ^{60}Co γ-radiolysis or of fast electrons, we use short (~100 μm) segments of one hundred fifty 300-MeV proton tracks, over which the LET is essentially constant and equal to ~0.3 keV μm^{-1} at 25°C. Such an analysis thus gives the track segment yields at a well-defined LET. The complex initial spatial distribution of reactants, which is provided as an output of the program TRACELE, is then used directly as the starting point for the "stage of nonhomogeneous chemistry". This third and final stage, during which the radiolytic species diffuse and react with one another in spurs, is covered by our TRACIRT simulation code, using the "independent reaction times" (IRT) method (6, 9, 10, 28) to model the nonhomogeneous reaction kinetics.

To reproduce the newly measured e^-_{aq} decay time profile between 100 ps and 10 ns and the reported reduction of ~20% in the yield of e^-_{aq} at "time zero" (21), a reexamination of certain adjustable parameters that intervene in the physical and physicochemical stages of our Monte-Carlo code is in order. These parameters comprise (*i*) the thermalization distance (r_{th}) of subexcitation electrons, (*ii*) the recombination cross section (σ_{rec}) of the electrons with their water parent cations prior to thermalization, and (*iii*) the branching ratios used for the different competing mechanisms in the decay of directly excited electronic states of water molecules or of vibrationally excited water molecules formed by electron–cation geminate recombination (8). The values of these parameters are obtained here by using a global-fit procedure, which consists in *simultaneously* fitting our calculated time-dependent yields of e^-_{aq} and of the other species ($H^\bullet$, $^\bullet OH$, H_2, and H_2O_2) to the available experimental data.

Values of r_{th} are computed by our Monte-Carlo code MTHREC (29, 30), which simulates on an event-by-event basis the transport of subexcitation electrons in water from their initial energies until they become thermalized.[10] The elastic and inelastic electron scattering cross sections employed are based on those of Michaud and Sanche (32), obtained from slow (~1–18 eV) electron-impact experiments on thin amorphous solid water films condensed at 14 K. The thermalization distances are obtained by averaging r_{th} over a large number (200 000) of histories of random-walking electrons. In the calculations, r_{th} is mainly determined by the electron mean free path (that is, the average distance between two consecutive scatterings) given by $\lambda_m(E) = \alpha/[n\sigma_t(E)]$. Here *n* is the number of molecules per unit volume,

[6] Recall that the "scavenging power" is defined as the product of a solute (scavenger) concentration and its rate constant for the scavenging reaction (k_s[S]), with units of s^{-1}. The reciprocal of the scavenging power gives a measure of the time scale over which the scavenging is occurring. See for example ref. 14.

[7] Subexcitation electrons are those that have kinetic energies lower than the first electronic excitation threshold of the medium (~7.3 eV in liquid water). They lose energy relatively slowly, the dominant mode of energy loss being the excitation of molecular vibrations. See for example refs. 24 and 25.

[8] The thermalization process of a subexcitation electron occurs in competition with the recombination of the electron with its water parent cation (to give a vibrationally excited water molecule, which may dissociate to form: (*i*) $H^\bullet + {}^\bullet OH$, (*ii*) $2\,H^\bullet + O(^3P)$, or (*iii*) $H_2 + O(^1D)$, where $O(^3P)$ and $O(^1D)$ denote the atomic oxygen in its ^3P ground state and in its singlet ^1D state, respectively) and with its dissociative attachment to a water molecule (to produce $H_2O^{-\bullet}$, which decomposes by giving a hydride anion and subsequently H_2 and OH^- by rapid reaction of H^- with an adjacent water molecule) (8). Note that this latter process is resonant; that is, it occurs over a limited electron energy range (for amorphous solid water the onset for H^- formation is at 5.5 eV with a maximum yield at ~7.4 eV) (26).

[9] Let us recall here that the electron "trapping" and "hydration" times are ~110–300 and 240–620 fs, respectively, in pure liquid water at 25°C. See for example ref. 27.

[10] Note that because of the occurrence of high density of electron traps in a polar medium such as liquid water, the subexcitation electrons have a strong tendency to get trapped prior to thermalization. It is entirely possible that they could actually never become thermalized. See for example ref. 31.

© 2002 NRC Canada

$\sigma_t(E)$ is the sum of the total cross sections at the energy E of the various interaction processes involved, and α is an adjustable coefficient introduced to account for possible differences between solid- and liquid-phase cross sections (8, 30). All our simulations (7–11, 30) of liquid water radiolysis have hitherto been carried out with $\alpha = 0.52$, which amounts to an increase of the solid-phase electron scattering cross sections of Michaud and Sanche (32) by a factor of about 2 (8, 30).[11] Given this value of α, the corresponding mean electron thermalization distance and time, averaged over the energy spectrum of the subexcitation electrons (the so-called "entry spectrum") (25, 29), are found to be equal to ~88 Å and ~41 fs, respectively, at 25°C (30, 34).[12]

The recombination of a subexcitation electron with its geminate water cation before thermalization is complete is also modeled within our MTHREC random-flight simulation code. In the absence of experimental values for liquid water, the cross section σ_{rec} for these electron–cation recombination processes is taken from gas-phase data (29, 35). In our simulations, we consider the cation[13] to be surrounded by a perfectly absorbing sphere whose scavenging radius is $(\sigma_{rec}/\pi)^{1/2}$, with an electron-energy-dependent cross section given by $\sigma_{rec} = 3\beta/E^{1.86}$. Here σ_{rec} is expressed in Å^2, E is in eV, and β is an adjustable factor introduced in the calculations to take into account possible differences in σ_{rec} between the gas phase and liquid water. In all our previous simulations (7–11, 30, 34), we have adopted $\beta = 1$. Under these conditions ~5.5% of the subexcitation electrons are found to initially recombine with their water parent cations (with an average recombination time of ~3.3 fs)[14] instead of becoming thermalized and subsequently hydrated or instead of undergoing a dissociative attachment to a water molecule (8, 29).

The various channels through which the excited water molecules decay and the branching ratios associated with each of them remain largely unknown in the liquid phase (8, 23, 37). Tables 5 and 6 of ref. 8 show how the partitioning of the different competing decay channels was dealt with in our previous simulations. These are based mainly on gas phase data and include both directly excited electronic ($\tilde{A}(^1B_1)$ and $\tilde{B}(^1A_1)$) states of water molecules and vibrationally excited water molecules ($H_2O^*_{vib}$) formed by the recombination of a subexcitation electron with its parent cation (8). It appears from our previous studies that the branching ratios for the various decay channels of directly excited water molecules have little effect in the yield calculations. To keep at a minimum the number of adjustable parameters employed in the computations, those branching ratios are taken to be the same as those previously published (Table 5 of ref. 8). Thus, only the branching ratios for the

Fig. 1. Time dependences of the e^-_{aq} yields (in molecules per 100 eV) calculated from our Monte-Carlo simulations of the low-LET (~0.3 keV μm^{-1}) radiolysis of liquid water at 25°C over the time interval ~0.5 ps – 1 μs using the following sets of adjustable parameter values: (*i*) $\alpha = 0.975$, $\beta = 115$ (dashed curve), and (*ii*) $\alpha = 0.73$, $\beta = 24$, and the revised values of the branching ratios for the dissociative decay channels of $H_2O^*_{vib}$ given in Table 1 (dotted curve) (see text). For the sake of comparison, the corresponding e^-_{aq} yields computed using our previously published set of adjustable parameter values are also included in the figure (solid curve). The arrow indicates the extrapolated e^-_{aq} yield of 4.0 ± 0.2 at "time zero," as reported in ref. 21. Experiment: ref. 6 (▶), ref. 16 (▲), ref. 17 (□), ref. 20 (●), eq. [9] of ref. 21 (– - – - – -), ref. 38 (■), ref. 39 (▼), ref. 40 (◆), ref. 41 (▽), and ref. 42 (☆).

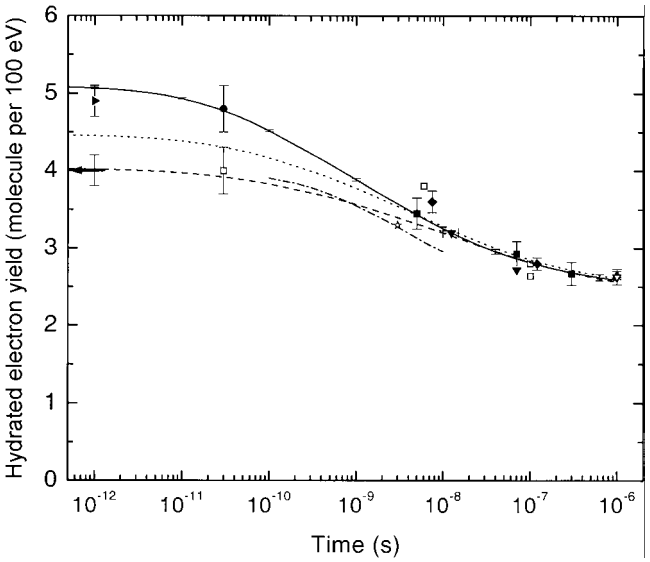

[11]Such an increase was required to reproduce the observed time dependence of the e^-_{aq} yield in room-temperature, low-LET liquid water radiolysis between 30 ps and ~1 μs. This increase in the electron scattering cross sections of Michaud and Sanche (32) may arise from the difference in the degree of structural disorder of the liquid phase in comparison to the solid phase. In fact, low-energy electrons in the subexcitation range are known to be very sensitive to such structural effects owing to their non-negligible delocalized character. Their scattering cross sections are generally found to increase rapidly when the degree of order diminishes. See for example ref. 33.

[12]Let us recall that for each subexcitation electron energy there exists a specific distribution of electron thermalization distances. Our calculated distribution of r_{th} values at 25°C, averaged over the ensemble of subexcitation electrons, is characterized by a "most probable" value of r_{th} (equal to ~6.5 Å) and by an "average" thermalization distance (~88 Å). This relatively large average thermalization distance comes from the presence of a long tail in the distribution, which indicates that a number of electrons travel large distances (up to ~450 Å) from subexcitation to thermal energies.

[13]Note that in the simulations the water cations H_2O^+ are allowed to undergo a random walk during their very short lifetime (~10 fs) by means of a sequence of electron transfers from neighboring water molecules to the H_2O^+ hole (8, 36).

[14]This average recombination time of ~3.3 fs (calculated from our simulations) shows that the recombination process mainly occurs on the water cation and that it is justified to ignore the reaction $H_2O^+ + H_2O \rightarrow H_3O^+ + {}^{\bullet}OH$ (which would change the nature of the cation and therefore affect the values of σ_{rec}) (8, 29). In other words, the "dry" subexcitation electron recombines quickly (that is, in the first steps of its random walk) on H_2O^+. If it does not recombine quickly, it will never recombine, and will thus become thermalized (~41 fs; unless, of course, it makes a dissociative attachment on a water molecule), trapped (~110–300 fs), and hydrated (~240–620 fs) (27). In fact, to test the validity of these results we included both types of electron recombination (on H_2O^+ and on H_3O^+) in our calculations; indeed, the recombination on H_3O^+ was found to be negligible.

© 2002 NRC Canada

Fig. 2. Time dependences of the yields of $H^{\bullet}$, $^{\bullet}OH$, H_2, and H_2O_2 (in molecules per 100 eV) calculated from our Monte-Carlo simulations of the low-LET (~0.3 keV μm^{-1}) radiolysis of liquid water at 25°C over the time interval ~0.5 ps – 1 μs using the same sets of adjustable parameter values as in Fig. 1, namely: (*i*) α = 0.975, β = 115 (dashed curves), and (*ii*) α = 0.73, β = 24, and the revised values of the branching ratios for the dissociative decay channels of $H_2O^*_{vib}$ given in Table 1 (dotted curves) (see text). For the sake of comparison, the corresponding yields of the various species computed using our previously published set of adjustable parameter values are also included in the figure (solid curves). Experiment: refs. 2, 12, 15, and 16 (▷), ref. 6 (▶), ref. 21 (▲), ref. 22 (●), refs. 22 and 43 (○), ref. 44 (□), ref. 45 (▼), ref. 46 (△), and ref. 47 (■).

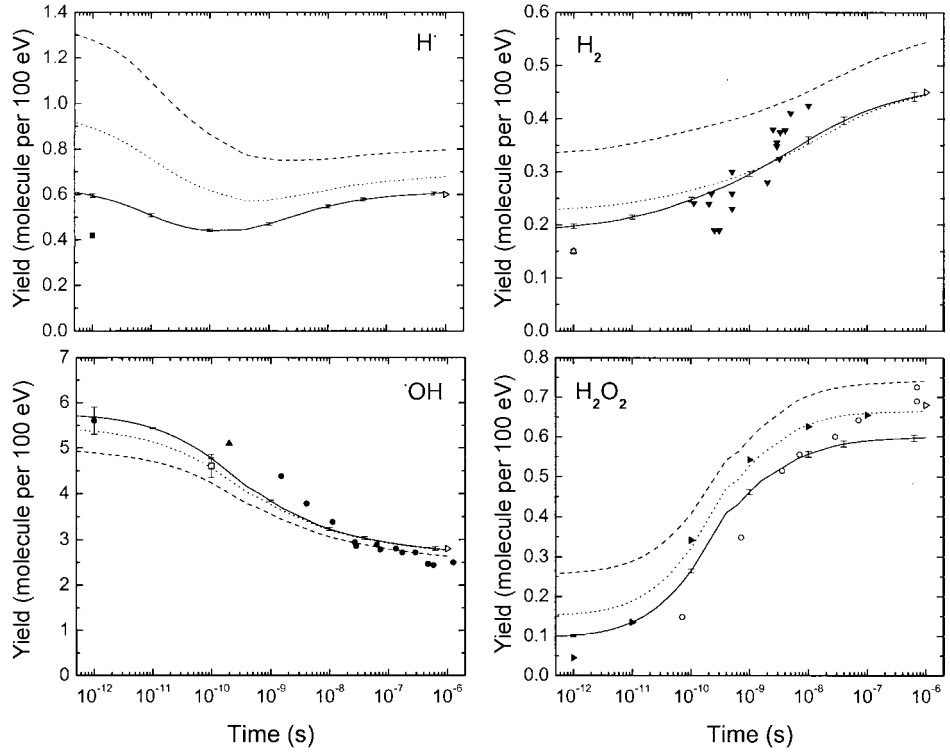

dissociative decay channels of $H_2O^*_{vib}$ (see Table 1) are treated here as fitting parameters.

Results and discussion

We have tried to readjust the above-mentioned parameters α and β to examine if our Monte-Carlo simulation results could be reconciled with Bartels et al's (21) new experimental findings; namely, the measured e^-_{aq} decay kinetics from 100 ps to 10 ns and the "extrapolated" e^-_{aq} yield of 4.0 ± 0.2 at "time zero." As a first step, the branching ratios for the dissociative deexcitations of $H_2O^*_{vib}$ were kept constant and equal to their previously employed values (Table 6 of ref. 8). We could, indeed, reproduce the ~20% decrease in the "time-zero" e^-_{aq} yield and also grossly the time dependence of the e^-_{aq} yield over the whole interval ~0.5 ps – 1 μs (Fig. 1), but at the expense of the yields of the other species ($H^{\bullet}$, $^{\bullet}OH$, H_2, and H_2O_2), which could not then be simultaneously and satisfactorily reproduced (Fig. 2). Moreover, closer examination of Fig. 1 clearly shows, in fact, that between 100 ps and 10 ns the shape of our computed time profile for the decay of e^-_{aq} is not in good accord with that measured by Bartels et al. (21). Such a fit was obtained with the values α = 0.975 and β = 115. Under these conditions, the mean electron thermalization distance calculated from our simulations is ~195 Å, a value that is relatively larger than the typical range (or "spur" radius) of ~64–80 Å used to describe the chemical evolution of the hydrated electrons in current deterministic models of "spur" chemistry.[15] In other respects, increasing the recombination cross section by a factor of 115 over the gas-phase value leads to an average ~25% recombination probability, which is also somewhat large in comparison with the probability for recombination of ~15% recently estimated by Bartels et al. (49) for the conduction-band secondary electrons in H_2O. Such an increase of the electron recombination cross section (from β = 1 to 115) was found to be necessary to decrease the initial e^-_{aq} yield from our previous value of ~5.1 to 4.0. The large increase in the thermalization distance then enabled us to reproduce the whole variation of the e^-_{aq} yield as a function of time down to the limiting yield ($G_{e^-_{aq}}$ = 2.65 at ~1 μs). As a second step, we tried to make various adjustments of the branching ratios associated with the dissociative deexcitations of $H_2O^*_{vib}$ to see if a better overall fit between computed yields and experiment could be achieved. The adjustments made had negligible effect on the calculated

[15]Our average thermalization distance should be compared with $< r > = 2\sqrt{2}\,\sigma/\sqrt{\pi}$, where σ is the characteristic radius of the three-dimensional Gaussian distribution describing the initial spatial distribution of e^-_{aq} in deterministic "average" spur models of liquid water radiolysis (29, 30). Most recent estimations of σ are 40–50 Å (6, 48).

© 2002 NRC Canada

Table 1. Branching ratios used in our simulations for the different competing mechanisms in the fate of vibrationally excited water molecules ($H_2O^*_{vib}$) formed by recombination of a subexcitation electron with its water parent cation (see footnote 9).

$H_2O^{+\bullet} + e^-$	→	$H_2O^*_{vib}$				
$H_2O^*_{vib}$	→	nondissociative deexcitation	35%	→	H_2O + release of thermal energy	
	→	dissociative deexcitation	65%	→	$H^\bullet + {}^\bullet OH$	79.8% (55%)
					$2H^\bullet + O(^3P)$	5.5% (24%)
					$H_2 + O(^1D)$	14.7% (21%)

Note: Previously employed values from ref. 8 are given in parenthesis.

time-dependent e^-_{aq} yield described above, while the time profiles of the calculated yields of $H^\bullet$, $^\bullet OH$, H_2, and H_2O_2 could be only slightly improved. Overall, the fits clearly remained largely unsatisfactory.

Having failed to satisfactorily reproduce Bartels et al's (21) new experimental data, we then applied our global-fit procedure in an attempt to find another set of values of the parameters α and β and also of the branching ratios for the dissociative decay channels of $H_2O^*_{vib}$ that would give: (*i*) the lowest possible e^-_{aq} yield at "time zero," (*ii*) a good reproduction of the time-dependent e^-_{aq} yield between ~0.5 ps and 1 μs, and in particular of the newly measured e^-_{aq} decay time profile between 100 ps and 10 ns, and (*iii*) a simultaneously acceptable overall agreement between our computed time-dependent yields for the other species, $H^\bullet$, $^\bullet OH$, H_2, and H_2O_2, and the existing experimental data. This could be achieved reasonably well with $\alpha = 0.73$ and $\beta = 24$. Here the corresponding limiting yield of e^-_{aq} at "time zero" is found to be ~4.4 to 4.5. As for the branching ratios for the dissociative deexcitations of $H_2O^*_{vib}$, their revised values are listed and compared with those previously employed (8) in Table 1. Under these conditions, the average electron thermalization distance and time calculated from our simulations are equal to ~139 Å and ~65 fs, respectively. Moreover, ~18% of the subexcitation electrons are found to initially recombine with their water parent cations (with an average recombination time of ~6.7 fs). This latter value is in good accord with the prompt electron–cation recombination (~15%) in water radiolysis reported recently by Bartels et al. (49). The various time-dependent yield results for e^-_{aq} and for the species $H^\bullet$, $^\bullet OH$, H_2, and H_2O_2 are shown in Figs. 1 and 2, respectively. As can be seen, there is a reasonable accord between our calculated yields and those measured experimentally (2, 6, 12, 15–17, 20–22, 38–47). Finally, to further test the validity of our results obtained with this new set of adjustable parameter values, we also performed various Monte-Carlo simulations under different experimental conditions (elevated temperatures, acidic pH, and high LET). The overall agreement between our computed yields and the available experimental data was satisfactory (data not shown).

Summary and conclusion

We have attempted to reconcile our Monte-Carlo calculations of the radiolysis of liquid water with the recently revised experimental e^-_{aq} yield data at early times of Bartels et al. (21). The electron thermalization distances, the geminate electron–cation recombination cross sections, and the branching ratios corresponding to the dissociative decay of vibrationally excited states of water molecules were taken as adjustable parameters in our simulations. Using a global-fit procedure, we have been unable to find a set of values for those parameters that could simultaneously reproduce the revised e^-_{aq} yield of 4.0 ± 0.2 at "time zero", the newly measured e^-_{aq} decay kinetic profile from 100 ps to 10 ns, and the time-dependent yields of the other radiolytic species ($H^\bullet$, $^\bullet OH$, H_2, and H_2O_2). The lowest possible limiting yield of e^-_{aq} at "time zero" that we could, in fact, obtain while ensuring an acceptable overall agreement between computed and experimental yields was ~4.4 to 4.5. Such a value turns out to be some compromise between the hitherto accepted value of 4.8 and that of 4.0 ± 0.2 "extrapolated" by Bartels et al. (21).

In conclusion, this work presents a possible adaptation of our calculations to a lower hydrated electron yield at early times, but it also suggests that the topic is not closed. To confirm Bartels et al.'s new experimental findings, as well as to clarify our understanding of the fast processes that occur in irradiated liquid water between the moment of energy deposition and ~1 μs later, further measurements of the e^-_{aq} yield values at very short times are needed.

Acknowledgments

We thank Professor Jay A. LaVerne (University of Notre Dame) for kindly sending us his data of refs. 22 and 43 on the $^\bullet OH$ and H_2O_2 yields as a function of time. The financial assistance of the Canadian Institutes of Health Research (Grant No. MT-14617) is gratefully acknowledged.

References

1. (*a*) A.O. Allen. The radiation chemistry of water and aqueous solutions. D. Van Nostrand Co., Princeton, New Jersey. 1961; (*b*) A.O. Allen. *In* Early developments in radiation chemistry. *Edited by* J. Kroh. The Royal Society of Chemistry, Cambridge. 1989. p. 1; (*c*) I.G. Draganić, and Z.D. Draganić. The radiation chemistry of water. Academic Press, New York. 1971; (*d*) I.G. Draganić. Radiochim. Acta, **70**/**71**, 317 (1995); (*e*) C.D. Jonah. Radiat. Res. **144**, 141 (1995); (*f*) J.D. Zimbrick. Radiat. Res. **158**, 127 (2002).
2. C. Ferradini and J.-P. Jay-Gerin. Can. J. Chem. **77**, 1542 (1999).
3. (*a*) A.J. Elliot, M.P. Chenier, D.C. Ouellette, and V.T. Koslowsky. J. Phys. Chem. **100**, 9014 (1996); (*b*) C. Ferradini and J.-P. Jay-Gerin. Radiat. Phys. Chem. **51**, 263 (1998); (*c*) J.A. LaVerne. Radiat. Res. **153**, 487 (2000); (*d*) N. Chitose, Y. Katsumura, M. Domae, Z. Cai, Y. Muroya, T. Murakami,

© 2002 NRC Canada

and J.A. LaVerne. J. Phys. Chem. A, **105**, 4902 (2001); (*e*) Y. Katsumura. Res. Chem. Intermed. **27**, 333 (2001).

4. (*a*) G. Wu, Y. Katsumura, Y. Muroya, X. Li, and Y. Terada. Chem. Phys. Lett. **325**, 531 (2000); (*b*) J. Cline, C.D. Jonah, D.M. Bartels, and K. Takahashi. *In* Proceedings of the first international symposium on supercritical water-cooled reactors, design and technology. *Edited by* Y. Katsumura. The University of Tokyo, Tokyo. 2000. p. 194; (*c*) G. Wu, Y. Katsumura, Y. Muroya, M. Lin, and T. Morioka. J. Phys. Chem. A, **105**, 4933 (2001); (*d*) K. Takahashi, D.M. Bartels, J.A. Cline, and C.D. Jonah. Chem. Phys. Lett. **357**, 358 (2002).
5. (*a*) J.E. Turner, J.L. Magee, H.A. Wright, A. Chatterjee, R.N. Hamm, and R.H. Ritchie. Radiat. Res. **96**, 437 (1983); (*b*) M. Zaider and D.J. Brenner. Radiat. Res. **100**, 245 (1984); (*c*) J.E. Turner, R.N. Hamm, H.A. Wright, R.H. Ritchie, J.L. Magee, A. Chatterjee, and W.E. Bolch. Radiat. Phys. Chem. **32**, 503 (1988); (*d*) N.J.B. Green, M.J. Pilling, S.M. Pimblott, and P. Clifford. J. Phys. Chem. **94**, 251 (1990); (*e*) M. Terrissol and A. Beaudré. Radiat. Prot. Dosim. **31**, 175 (1990); (*f*) I.G. Kaplan and V.Ya. Sukhonosov. Radiat. Res. **127**, 1 (1991); (*g*) A.V. Ponomarev, I.E. Makarov, and A.K. Pikaev. Khim. Vys. Énerg. **25**, 311 (1991). *English transl.*: High Energy Chem. **25**, 260 (1991); (*h*) S.M. Pimblott, M.J. Pilling, and N.J.B. Green. Radiat. Phys. Chem. **37**, 377 (1991); (*i*) M.A. Hill and F.A. Smith. Radiat. Phys. Chem. **43**, 265 (1994); (*j*) M.G. Stabin, R.N. Hamm, J.E. Turner, and W.E. Bolch. Radiat. Prot. Dosim. **52**, 255 (1994); (*k*) M.G. Stabin. Ph.D. Thesis, University of Tennessee, Knoxville, 1996; (*l*) H. Tomita, M. Kai, T. Kusama, and A. Ito. Radiat. Environ. Biophys. **36**, 105 (1997); (*m*) V. Michalik, M. Běgusová, and E.A. Bigildeev. Radiat. Res. **149**, 224 (1998); (*n*) V.V. Moiseenko, R.N. Hamm, A.J. Waker, and W.V. Prestwich. Int. J. Radiat. Biol. **74**, 533 (1998); (*o*) F. Ballarini, M. Biaggi, M. Merzagora, A. Ottolenghi, M. Dingfelder, W. Friedland, P. Jacob, and H.G. Paretzke. Radiat. Environ. Biophys. **39**, 179 (2000); (*p*) R. Watanabe and K. Saito. Radiat. Phys. Chem. **62**, 217 (2001).
6. S.M. Pimblott and J.A. LaVerne. J. Phys. Chem. A, **101**, 5828 (1997).
7. Y. Frongillo, M.-J. Fraser, V. Cobut, T. Goulet, J.-P. Jay-Gerin, and J.P. Patau. J. Chim. Phys. **93**, 93 (1996).
8. V. Cobut, Y. Frongillo, J.P. Patau, T. Goulet, M.-J. Fraser, and J.-P. Jay-Gerin. Radiat. Phys. Chem. **51**, 229 (1998).
9. Y. Frongillo, T. Goulet, M.-J. Fraser, V. Cobut, J.P. Patau, and J.-P. Jay-Gerin. Radiat. Phys. Chem. **51**, 245 (1998).
10. T. Goulet, M.-J. Fraser, Y. Frongillo, and J.-P. Jay-Gerin. Radiat. Phys. Chem. **51**, 85 (1998).
11. (*a*) M.-A. Hervé du Penhoat, T. Goulet, Y. Frongillo, M.-J. Fraser, Ph. Bernat, and J.-P. Jay-Gerin. J. Phys. Chem. A, **104**, 11 757 (2000); (*b*) M.-A. Hervé du Penhoat, J. Meesungnoen, T. Goulet, A. Filali-Mouhim, S. Mankhetkorn, and J.-P. Jay-Gerin. Chem. Phys. Lett. **341**, 135 (2001); (*c*) J. Meesungnoen, M. Benrahmoune, A. Filali-Mouhim, S. Mankhetkorn, and J.-P. Jay-Gerin. Radiat. Res. **155**, 269 (2001); (*d*) J. Meesungnoen, J.-P. Jay-Gerin, A. Filali-Mouhim, and S. Mankhetkorn. Chem. Phys. Lett. **335**, 458 (2001); Can. J. Chem. **80**, 68 (2002); Radiat. Res. (in press).
12. J.W.T. Spinks and R.J. Woods. An introduction to radiation chemistry. 3rd ed. Wiley, New York. 1990. p. 243.
13. (*a*) Y. Tabata, Y. Ito, and S. Tagawa (*Editors*). CRC Handbook of radiation chemistry. CRC Press, Boca Raton, Florida. 1991. p. 321; (*b*) A. Hummel. Radiation chemistry: The chemical effects of ionizing radiation and their applications. Interfaculty Reactor Institute-Delft University of Technology, Delft. 1995. p. 7.1.
14. D.R. McCracken, K.T. Tsang, and P.J. Laughton. Aspects of the physics and chemistry of water radiolysis by fast neutrons and fast electrons in nuclear reactors. Report AECL-11895. Atomic Energy of Canada Ltd., Chalk River, Ontario. 1998.
15. (*a*) C. Ferradini and J. Pucheault. Biologie de l'action des rayonnements ionisants. Masson, Paris. 1983. p. 25 ; (*b*) N.V. Klassen. J. Chim. Phys. **88**, 747 (1991); (*c*) H.A. Schwarz. J. Phys. Chem. **96**, 8937 (1992); (*d*) G.V. Buxton and Q.G. Mulazzani. *In* Electron transfer in chemistry. Vol. 1. *Edited by* V. Balzani and M.A.J. Rodgers. Wiley-VCH, Weinheim, Germany. 2001. p. 503.
16. A.J. Elliot, M.P. Chenier, and D.C. Ouellette. J. Chem. Soc. Faraday Trans. **89**, 1193 (1993).
17. (*a*) R.K. Wolff, M.J. Bronskill, J.E. Aldrich, and J.W. Hunt. J. Phys. Chem. **77**, 1350 (1973); (*b*) J.W. Hunt, R.K. Wolff, M.J. Bronskill, C.D. Jonah, E.J. Hart, and M.S. Matheson. J. Phys. Chem. **77**, 425 (1973); (*c*) J.W. Hunt, K.Y. Lam, and W.J. Chase. *In* Proceedings of the fifth international congress of radiation research, Seattle, Washington, July 14–20, 1974. *Edited by* O.F. Nygaard, H.I. Adler, and W.K. Sinclair. Academic, New York. 1975. p. 345; (*d*) R.K. Wolff, J.E. Aldrich, T.L. Penner, and J.W. Hunt. J. Phys. Chem. **79**, 210 (1975); (*e*) J.W. Hunt. Adv. Radiat. Chem. **5**, 185 (1976).
18. C.D. Jonah, M.S. Matheson, J.R. Miller, and E.J. Hart. J. Phys. Chem. **80**, 1267 (1976). See also C.D. Jonah, E.J. Hart, and M.S. Matheson. J. Phys. Chem. **77**, 1838 (1973); A.C. Chernovitz and C.D. Jonah. J. Phys. Chem. **92**, 5946 (1988).
19. S.M. Pimblott, J.A. LaVerne, D.M. Bartels, and C.D. Jonah. J. Phys. Chem. **100**, 9412 (1996).
20. (*a*) T. Sumiyoshi and M. Katayama. Chem. Lett. 1887 (1982); (*b*) T. Sumiyoshi, K. Tsugaru, T. Yamada, and M. Katayama. Bull. Chem. Soc. Jpn. **58**, 3073 (1985).
21. D.M. Bartels, A.R. Cook, M. Mudaliar, and C.D. Jonah. J. Phys. Chem. A, **104**, 1686 (2000).
22. J.A. LaVerne. Radiat. Res. **153**, 196 (2000).
23. D. Swiatla-Wojcik and G.V. Buxton. Res. Chem. Intermed. **27**, 875 (2001).
24. (*a*) R.L. Platzman. Radiat. Res. **1**, 558 (1954); **2**, 1 (1955); (*b*) J. Weiss. Nature (London), **174**, 78 (1954); J. Chim. Phys. **52**, 539 (1955); (*c*) M. Michaud, P. Cloutier, and L. Sanche. Phys. Rev. A: At. Mol. Opt. Phys. **44**, 5624 (1991).
25. A. Mozumder. Fundamentals of radiation chemistry. Academic, San Diego, California. 1999. p. 247.
26. P. Rowntree, L. Parenteau, and L. Sanche. J. Chem. Phys. **94**, 8570 (1991). See also V. Cobut, J.-P. Jay-Gerin, Y. Frongillo, and J.P. Patau. Radiat. Phys. Chem. **47**, 247 (1996).
27. (*a*) A. Migus, Y. Gauduel, J.L. Martin, and A. Antonetti. Phys. Rev. Lett. **58**, 1559 (1987); (*b*) F.H. Long, H. Lu, and K.B. Eisenthal. Phys. Rev. Lett. **64**, 1469 (1990); (*c*) X. Shi, F.H. Long, H. Lu, and K.B. Eisenthal. J. Phys. Chem. **100**, 11 903 (1996); (*d*) A. Reuther, A. Laubereau, and D.N. Nikogosyan. J. Phys. Chem. **100**, 16 794 (1996); (*e*) A. Bernas, C. Ferradini, and J.-P. Jay-Gerin. Can. J. Chem. **74**, 1 (1996) and refs. therein; (*f*) C. Pépin, T. Goulet, D. Houde, and J.-P. Jay-Gerin. J. Phys. Chem. A, **101**, 4351 (1997); (*g*) J.-P. Jay-Gerin. Can. J. Chem. **75**, 1310 (1997); (*h*) R. Laenen, T. Roth, and A. Laubereau. Phys. Rev. Lett. **85**, 50 (2000). See also A. Mozumder. Radiat. Phys. Chem. **32**, 287 (1988).
28. (*a*) P. Clifford, N.J.B. Green, and M.J. Pilling. J. Phys. Chem. **86**, 1318, 1322 (1982); (*b*) P. Clifford, N.J.B. Green, M.J. Oldfield, M.J. Pilling, and S.M. Pimblott. J. Chem. Soc. Faraday Trans. 1, **82**, 2673 (1986); (*c*) P. Clifford, N.J.B. Green, M.J. Pilling, and S.M. Pimblott. J. Phys. Chem. **91**,

© 2002 NRC Canada

4417 (1987). See also S.M. Pimblott and N.J.B. Green. Res. Chem. Kinet. **3**, 117 (1995).
29. (*a*) T. Goulet and J.-P. Jay-Gerin. J. Phys. Chem. **92**, 6871 (1988); Radiat. Res. **118**, 46 (1989); (*b*) T. Goulet, J.P. Patau, and J.-P. Jay-Gerin. Radiat. Prot. Dosim. **31**, 33 (1990); J. Phys. Chem. **94**, 7312 (1990).
30. T. Goulet, J.-P. Jay-Gerin, Y. Frongillo, V. Cobut, and M.-J. Fraser. J. Chim. Phys. **93**, 111 (1996).
31. (*a*) J.A. LaVerne and A. Mozumder. Radiat. Phys. Chem. **23**, 637 (1984); (*b*) C. Houée-Levin and J.-P. Jay-Gerin. J. Phys. Chem. **92**, 6454 (1988); (*c*) W.M. Bartczak and K. Pernal. Res. Chem. Intermed. **27**, 891 (2001).
32. M. Michaud and L. Sanche. Phys. Rev. A: At. Mol. Opt. Phys. **36**, 4672, 4684 (1987).
33. (*a*) G. Bader, G. Perluzzo, L.G. Caron, and L. Sanche. Phys. Rev. B: Cond. Mat. Mater. Phys. **26**, 6019 (1982); (*b*) N.J.B. Green, C.E. Bolton, and R.D. Spencer-Smith. Radiat. Environ. Biophys. **38**, 221 (1999); (*c*) Research needs and opportunities in radiation chemistry. Report DOE/SC-0003. U.S. Department of Energy, Germantown, Maryland. 1998; (*d*) N.J.B. Green and S.M. Pimblott. Res. Chem. Intermed. **27**, 529 (2001).
34. J. Meesungnoen, J.-P. Jay-Gerin, A. Filali-Mouhim, and S. Mankhetkorn. Can. J. Chem. **80**, 767 (2002).
35. P.M. Mul, J.Wm. McGowan, P. Defrance, and J.B.A. Mitchell. J. Phys. B.: At. Mol. Phys. **16**, 3099 (1983).
36. H. Ogura and W.H. Hamill. J. Phys. Chem. **77**, 2952 (1973). See also Dayashankar and M.A. Prasad. Radiat. Phys. Chem. **45**, 147 (1995).
37. D. Swiatla-Wojcik and G.V. Buxton. J. Phys. Chem. **99**, 11 464 (1995); Phys. Chem. Chem. Phys. **2**, 5113 (2000). See also G.V. Buxton. *In* Radiation chemistry: Present status and future trends. *Edited by* C.D. Jonah and B.S.M. Rao. Elsevier Science B.V., Amsterdam. 2001. p. 145.
38. H. Shiraishi, Y. Katsumura, D. Hiroishi, K. Ishigure, and M. Washio. J. Phys. Chem. **92**, 3011 (1988).
39. J.K. Thomas and R.V. Bensasson. J. Chem. Phys. **46**, 4147 (1967).
40. G.V. Buxton. Proc. R. Soc. London A, **328**, 9 (1972).
41. (*a*) E.M. Fielden and E.J. Hart. Radiat. Res. **32**, 564 (1967); (*b*) I.G. Draganić, M.T. Nenadović, and Z.D. Draganić. J. Phys. Chem. **73**, 2564 (1969).
42. J. Belloni, F. Billiau, J.A. Delaire, M.O. Delcourt, and J.L. Marignier. Radiat. Phys. Chem. **21**, 177 (1983).
43. B. Pastina and J.A. LaVerne. J. Phys. Chem. **103**, 1592 (1999).
44. J.-P. Jay-Gerin and C. Ferradini. Chem. Phys. Lett. **317**, 388 (2000).
45. Z.D. Draganić and I.G. Draganić. Int. J. Radiat. Phys. Chem. **7**, 381 (1975). Quoted in ref. 9.
46. H.A. Schwarz. J. Phys. Chem. **73**, 1928 (1969).
47. J.A. LaVerne and S.M. Pimblott. J. Phys. Chem. **95**, 3196 (1991).
48. J.A. LaVerne. Radiat. Res. **153**, 487 (2000).
49. D.M. Bartels, D. Gosztola, and C.D. Jonah. J. Phys. Chem. A, **105**, 8069 (2001).

© 2002 NRC Canada

L'échelle pK_{HB} de basicité de liaison hydrogène des amines tertiaires aliphatiques

Jérôme Graton, François Besseau, Michel Berthelot, Ewa D. Raczyńska et Christian Laurence

Résumé : Le pouvoir accepteur de liaison hydrogène (liaison H) de 40 amines tertiaires a été mesuré à partir de leurs constantes de complexation 1:1 avec le 4-fluorophénol dans CCl_4 à 25°C (échelle pK_{HB}) par spectrométrie infrarouge à transformée Fourier (IRTF), ainsi qu'au moyen du déplacement de fréquence $\Delta\nu$(OH) de la bande ν(OH) méthanol complexé par liaison H avec ces amines. La comparaison des échelles de basicité de liaison H thermodynamique pK_{HB} et spectroscopique $\Delta\nu$(OH) et de basicité de Brønsted pK_a met en évidence la grande sensibilité de l'échelle pK_{HB} aux effets stériques, et l'absence de corrélation entre les échelles pK_{HB} et pK_a. L'échelle pK_{HB} des amines tertiaires s'étend de 2,71 pour la quinuclidine à –0,34 pour la *N*,*N*-diisopropyl-3-pentylamine. Les principaux effets expliquant ces variations (17 kJ·mol^{-1} sur une échelle d'enthalpie libre) sont les effets inductifs électroattracteurs et les effets stériques (e.g., ouverture des angles CNC et difficulté plus grande de la fixation du groupe OH sur les paires libres de l'atome d'azote). Les spectres infrarouges (IR) montrent que le 4-fluorophénol, outre sa fixation sur l'azote amino, se fixe également sur l'azote nitrile des amino-nitriles $Me_2NCH_2C{\equiv}N$ et $Me_2NCH_2CH_2C{\equiv}N$, sur l'oxygène de la *N*-méthylmorpholine, et sur les sites π des tripropargylamine $(HC{\equiv}CCH_2)_3N$ et tribenzylamine $(PhCH_2)_3N$. Dans ce dernier cas, les effets inductifs des trois substituants benzyle et surtout l'exceptionnel encombrement stérique de l'azote réduisent quasiment à néant sa basicité de liaison H, de telle sorte que la tribenzylamine, base de Brønsted azotée, se comporte essentiellement comme une base π de liaison H. À partir de cet exemple, on insiste sur les différences importantes entre les échelles pK_{HB} et pK_a des bases organiques.

Mots clés : basicité, liaison hydrogène, amines tertiaires, échelle pK_{HB}.

Abstract: The hydrogen bond acceptor strength of 40 tertiary amines has been measured by Fourier transform – infrared (FTIR) spectrometry from their 1:1 complexation constant towards 4-fluorophenol in CCl_4 at 25°C (the pK_{HB} scale). Also measured was the frequency shift, $\Delta\nu$(OH), of the ν(OH) band of methanol hydrogen-bonded to these amines. The comparison of the thermodynamic hydrogen bond basicity scale, pK_{HB}, with the spectroscopic one, $\Delta\nu$(OH), and with the Brønsted pK_a scale, points to the great sensitivity of pK_{HB} to steric effects. The pK_{HB} scale of tertiary amines extends from 2.71 for quinuclidine to –0.34 for *N*,*N*-diisopropyl-3-pentylamine. The main factors governing this important variation (17 kJ·mol^{-1} on the Gibbs energy scale) are the electron-withdrawing inductive effect and various kinds of steric effects (e.g., opening of the CNC angles and hindrance to OH fixation on the nitrogen lone pair). Infrared (IR) spectra show the attachment of 4-fluorophenol to the nitrile nitrogen of $Me_2NCH_2C{\equiv}N$ and $Me_2NCH_2CH_2C{\equiv}N$, to the oxygen of *N*-methylmorpholine, and to the π electrons of $(HC{\equiv}CCH_2)_3N$ and $(PhCH_2)_3N$, in addition to the attachment to the amino nitrogen. In $(PhCH_2)_3N$, the electron-withdrawing effect of the three benzyl substituents and, mainly, the very important congestion of the nitrogen lone pair reduce the nitrogen hydrogen-bond basicity almost to nothing, so that tribenzylamine, a nitrogen Brønsted base, turns to a π base in hydrogen bonding. From this example, the large differences between the pK_{HB} and pK_a scales of organic bases are emphasized.

Key words: basicity, hydrogen bonding, tertiary amines, pK_{HB} scale.

Introduction

Nous construisons actuellement (1) une échelle thermodynamique du pouvoir accepteur de liaison hydrogène (liaison H) des molécules organiques. Cette échelle repose sur la constante de formation de liaison H entre ces bases organiques et un donneur de liaison H de référence, dans des conditions standard de solvant, de température et de stœchiométrie. Reprenant l'idée originale de Gurka et Taft (2), nous mesurons cette échelle, notée pK_{HB} et appelée

Reçu le 21 juin 2002. Publié sur le site Web des Presses scientifiques du CNRC à http://revcanchimie.cnrc.ca le 31 October 2002.

J. Graton, F. Besseau, M. Berthelot et C. Laurence[1]. Université de Nantes. Laboratoire de Spectrochimie. Faculté des Sciences et des Techniques, 2, rue de la Houssinière, B. P. 92208, 44322, Nantes CÉDEX 3, France.
E.D. Raczyńska. Department of Chemistry, Warsaw Agricultural University, 02776 Warsaw, Pologne.

[1]Auteur correspondant (courriel : Christian.Laurence@chimie.univ-nantes.fr).

 DOI: 10.1139/V02-176 © 2002 CNRC Canada

échelle de basicité de liaison H, à partir de la formation de complexes 1:1 du 4-fluorophénol dans CCl_4 à 25°C dans le tétrachlorure de carbone (équations [1]-[3]). Le choix

[1] $$B + 4\text{-}FC_6H_4OH \leftrightarrows 4\text{-}FC_6H_4OH\cdots B$$

[2] $$\frac{K_c}{dm^3 \cdot mol^{-1}} = \frac{[4 - FC_6H_4OH \cdots B]}{[B][4 - FC_6H_4OH]}$$

[3] $$pK_{HB} = \log_{10} K_c$$

de ces conditions permet de mesurer la constante d'équilibre K_c avec précision dans une large gamme de basicité s'étendant d'environ $pK_{HB} = -1$ pour les bases très faibles à $pK_{HB} = +4$ pour les bases fortes. Il suffit de déterminer la concentration du 4-fluorophénol à l'équilibre, soit par résonance magnétique nucléaire (RMN) du ^{19}F (2), soit par spectrométrie UV sur la transition $\pi \rightarrow \pi^*$ à 281 nm (3), soit par spectrométrie infrarouge (IR) sur la bande ν(OH) à 3614 cm^{-1} (4).

Ces techniques montrent que le 4-fluorophénol n'est pas suffisamment acide et que CCl_4 n'est pas un solvant suffisamment polaire pour permettre le transfert du proton, même avec les amines les plus basiques (5, 6). Dans ce travail l'équilibre de transfert de proton [4] peut donc être négligé.

[4] $$4\text{-}FC_6H_4OH + NR_3 \leftrightarrows 4\text{-}FC_6H_4O^{-}\cdots{}^{+}HNR_3$$

L'intérêt de construire l'échelle pK_{HB} est double. D'une part, l'échelle pK_{HB} permet une comparaison quantitative des énergies de Gibbs ($\Delta G° = -5{,}7\ pK_{HB}$, $\Delta G°$ en $kJ \cdot mol^{-1}$) de formation de liaison H, interaction moléculaire omniprésente en chimie (7) et en biologie (8). D'autre part, alors que la basicité protonique de Brønsted est quantitativement bien définie par les échelles pK_a en phase aqueuse (9), et *GB* en phase gazeuse (10), la mesure de la basicité de Lewis reste à effectuer (11). Certains auteurs (11–13) s'accordent à reconnaître qu'une description quantitative et générale de la basicité de Lewis doit reposer sur au moins deux paramètres, l'un électrostatique, l'autre covalent. Dans la mesure où la liaison H est une interaction principalement électrostatique (14), l'échelle pK_{HB} pourrait mesurer la partie électrostatique des interactions entre les acides et les bases de Lewis.

Nous avons déjà mesuré pK_{HB} pour un grand nombre de bases carbonées, halogénées, oxygénées, soufrées et azotées (1). Dans cette dernière famille, nous avons étudié les nitriles (15), les amidines (16) les pyridines (17), les amines primaires (18) et les amines secondaires (19). Ce travail concerne la mesure par spectrométrie infrarouge à transformée Fourier (IRTF), de l'échelle pK_{HB} des amines tertiaires.

De manière à couvrir un vaste domaine de basicité et à déterminer les principaux effets structuraux modifiant la basicité de liaison H des amines tertiaires, nous avons sélectionné 40 composés incluant 12 alkylamines avec des groupes alkyles de longueur et de ramification différentes, 17 amines hétérocycliques, 9 amines substituées par différents groupes électroattracteurs ($CH{=}CH_2$, Ph, $C{\equiv}CH$, Cl, $C{\equiv}N$) et deux diamines. Nous obtenons ainsi une échelle qui s'étend sur trois unités de p*K*, soit environ 17 $kJ \cdot mol^{-1}$, de la quinuclidine ($pK_{HB} = 2{,}71$) à *i*-$Pr_2NCH(Et)_2$ ($pK_{HB} = -0{,}34$). Au-delà, nous trouvons la tribenzylamine, $(PhCH_2)_3N$, qui est une base azotée de liaison H si faible qu'elle se comporte comme une base π.

L'utilisation de la spectrométrie IRTF comporte trois principaux avantages. D'abord, la grande précision photométrique des spectromètres IRTF permet de mesurer les concentrations des espèces de l'équilibre [1] avec une meilleure précision que la résonance magnétique nucléaire (RMN) du ^{19}F initialement utilisée (2). Un autre avantage de l'infrarouge est de pouvoir mesurer la fréquence OH du complexe de liaison H, qui est d'autant plus basse que la liaison H est forte. Le déplacement $\Delta\nu(OH) = \nu(OH, \text{libre}) - \nu(OH\cdots N)$ est considéré (20) comme une échelle spectroscopique de basicité de liaison H des amines qu'il est intéressant de comparer à l'échelle thermodynamique pK_{HB}. Enfin la spectrométrie IR permet de déterminer si les autres sites potentiellement accepteurs de liaison H dans les amines substituées, e.g., l'oxygène de la *N*-méthylmorpholine ou l'azote sp de $Me_2NCH_2CH_2C{\equiv}N$, contribuent à la constante K_c mesurée. Dans ce cas, elle permet de séparer, dans la constante totale K_c mesurée, la partie due à l'azote amino de celle due aux autres sites accepteurs de liaison H (vide infra).

Partie expérimentale

Produits

Toutes les amines étudiées sont des composés commerciaux, à l'exception de la 4-phénylquinuclidine fournie par R.W. Taft (Université de Californie, Irvine). Les 3-chloroquinuclidine (**15**), 3-chlorométhyl-*N*-méthylpipéridine (**19**), 4-chloro-*N*-méthyl-pipéridine (**20**), *N*,*N*-diméthyl-3-chloropropylamine (**27**) et 1-(2-chloroéthyl)-pyrrolidine (**29**) ont été extraites de leurs chlorhydrates par neutralisation avec un excès de soude. Les liquides sont distillés puis séchés sur tamis moléculaire 4 Å (1 Å = 0,1 nm) et (ou) par chromatographie sur alumine basique. Les amines solides, ainsi que le 4-fluorophénol, sont purifiés par sublimation puis séchés sur P_2O_5. Le tétrachlorure de carbone est distillé puis stocké sur une colonne de tamis moléculaire 4 Å avant d'être soutiré. Le méthanol de qualité spectroscopique est séché sur tamis moléculaire 3 Å. Les produits purifiés sont manipulés en boîte sèche pour préparer les solutions et remplir la cellule IR.

Spectres IR

Ils sont enregistrés sur des spectromètres Bruker IFS 48 ou Vector 22 avec une résolution de 1 cm^{-1}. La cellule en quartz possède un trajet optique de 1 cm. Elle est thermorégulée à 25,0 ± 0,2°C à l'aide d'un système thermoélectrique à effet Peltier.

Constantes K_c

Elles sont définies par l'équation [5] dans laquelle C_c, C_a et C_b sont respectivement les concentrations en $mol \cdot dm^{-3}$ à l'équilibre du complexe, du 4-fluorophénol et

[5] $$K_c = \frac{C_c}{C_a C_b} = \frac{C^{\circ}_a - C_a}{C_a(C^{\circ}_b - C^{\circ}_a + C_a)}$$

de l'amine; C°_a et C°_b sont les concentrations initiales, déterminées par pesées, sauf pour l'amine gazeuse Me_3N qui a été dosée dans CCl_4 par neutralisation avec une solution aqueuse d'acide chlorhydrique. C°_a est de l'ordre de 4 $mmol \cdot dm^{-3}$ pour éviter l'autoassociation du 4-fluorophenol.

© 2002 CNRC Canada

C_b^o est ajustée de manière à ce que 20 à 80 % de phénol soit complexé. Le rapport des concentrations C_b^o/C_a^o varie ainsi entre 2 et 5 pour la quinuclidine la plus basique, et entre 100 et 220 pour l'amine la moins basique. La concentration C_a en phénol non complexé est déterminée à partir de l'absorbance de la bande ν(OH) à 3614 cm^{-1} par la loi de Beer–Lambert (coefficient d'absorption molaire égal à 237 $dm^3 \cdot mol^{-1} \cdot cm^{-1}$ dans CCl_4 à 25°C). On vérifie que l'espèce formée est le complexe de stœchiométrie 1:1 à partir de la constance de K_c calculée à cinq concentrations différentes d'amine. En tout état de cause, les solutions très diluées en 4-fluorophénol, ainsi que l'excès d'amine permettent de rendre minimale la présence de complexes 1:2 tels que :

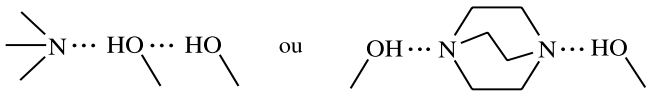

L'erreur maximale sur pK_{HB} est estimée à ±0,03.

Déplacements de fréquence Δν(OH)

Le déplacement de la fréquence d'élongation ν(OH) par formation d'une liaison hydrogène OH···N ne peut pas être facilement mesuré avec le 4-fluorophénol, car la bande ν(OH) du complexe de liaison H est perturbée par (*i*) les bandes ν(CH) du 4-fluorophénol et de l'amine qui ne peuvent être parfaitement soustraites car elles sont légèrement déplacées par complexation et (*ii*) des bandes de combinaison de ν(OH···) avec les fréquences d'élongation et de déformation de la liaison H (21). Nous avons donc remplacé le 4-fluorophénol par un donneur de liaison H moins fort, le méthanol. La bande ν(OH···) des complexes de ce dernier avec les amines se situe en effet avant les bandes ν(CH), et sa forme quasi gausso-lorentzienne permet de bien pointer son maximum. On définit alors Δν(OH) par la différence [6]. La précision sur Δν(OH) est estimée à ±3 cm^{-1}.

[6] $\Delta\nu(OH) = \nu(OH, \text{MeOH libre}) - \nu(OH\cdots, \text{MeOH complexé par liaison H})$

Calculs ab initio

Ils ont été effectués avec Gaussian 94 (22) sur un ordinateur personnel bi-processeur Pentium II 300 MHz. Les géométries des amines ont été optimisées au niveau HF/6–31G**. Pour les amines conformationnellement flexibles, nous n'avons pas exploré la totalité de l'espace conformationnel, mais nous sommes partis de plusieurs conformations initiales différentes et nous nous sommes appuyés sur des résultats conformationnels bien établis (23, 24). Les conformations trouvées les plus stables par calculs HF/6–31G** sont toujours en accord avec celles, expérimentales, des bases de données MOGADOC (25), pour la phase gazeuse ou structurale de Cambridge CSD (26), pour l'état solide.

Le potentiel électrostatique calculé autour de l'azote amino (pour la conformation la plus stable) est le potentiel électrostatique minimum sur la surface moléculaire définie, selon Bader et al. (27), par la surface d'isodensité électronique 0,001 e·$Bohr^{-3}$. Il est noté $V_{s,min}$ et donné généralement en $kcal \cdot mol^{-1}$ (1 cal = 4,184 J).

Fig. 1. Spectre IR dans la région (OH) d'une solution de méthanol (≈ 10^{-2} $mol \cdot dm^{-3}$) et de $Me_2NCH_2CH_2C{\equiv}N$ (en large excès) dans CCl_4 montrant (1) la bande ν(OH) du méthanol libre à 3644 cm^{-1}, (2) la bande ν(OH···N≡C) d'un premier complexe 1:1, déplacée de 80 cm^{-1}, et (3) la bande ν(OH···N) d'un second complexe 1:1, déplacée de 362 cm^{-1}.

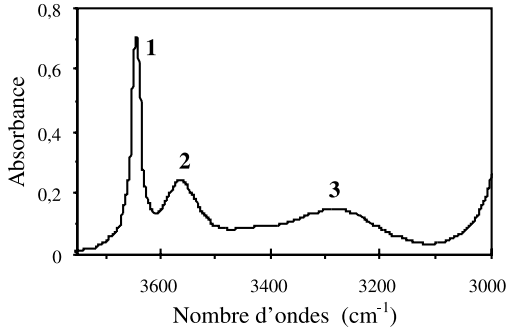

Résultats

L'échelle pK_{HB} de basicité de liaison H des amines tertiaires est donnée dans le tableau 1 conjointement avec (*i*) les valeurs Δν(OH) du déplacement de la fréquence ν(OH) du méthanol par complexation avec ces amines, (*ii*) les valeurs pK_a de ces amines, dans l'eau généralement à 298 K, et (*iii*) le potentiel électrostatique autour de la paire libre de l'azote amino.

Pour cinq amines, nous observons sur le spectre IR, entre la bande fine ν(OH) du 4-fluorophénol libre à 3614 cm^{-1} (ou celle à 3644 cm^{-1} du méthanol) et la bande large ν(OH···N) correspondant au complexe sur l'azote amino, une bande supplémentaire (fig. 1). Puisque ces cinq amines possèdent un (des) site(s) potentiel(s) accepteur(s) de liaison H supplémentaire, nous attribuons cette bande supplémentaire à un deuxième complexe de liaison H se formant soit sur l'oxygène éther de la *N*-méthylmorpholine (**26**), soit sur l'azote sp des aminonitriles (**33**) et (**37**), soit sur le nuage π acétylénique de la tripropargylamine (**36**), soit enfin sur le nuage π aromatique de la tribenzylamine (**40**). En effet, ces bandes supplémentaires sont bien aux positions attendues pour les complexes de liaison H avec des éthers (28), des nitriles (15), des bases π acétyléniques (29), ou aromatiques (29).

Puisque nous sommes toujours en excès d'amine, la formation d'un complexe de stœchiométrie 2:1 (2 phénols – 1 amine) est peu probable, et nous avons essentiellement en solution deux complexes 1:1, un complexe OH···N sur l'azote amino et un complexe OH···X sur le site accepteur de liaison H supplémentaire. Dans ce cas, la constante de complexation mesurée à partir de l'absorbance de la bande ν(OH) du 4-fluorophénol libre correspond à la formation de ces deux complexes, et il est facile de montrer qu'elle est la somme de deux constantes, K_c(N) et K_c(X), ou 3 K_c(X) pour la tripropargylamine (**36**) et la tribenzylamine (**40**). La constante propre à l'azote amino peut donc être calculée à partir de l'équation [7] s'il

[7] $K_c(\text{totale}) = K_c(N) + xK_c(X)$ (x = 1 ou 3)

est possible d'évaluer K_c(X). Nous l'avons fait à partir des déplacements de fréquence IR Δν(OH···X), en utilisant les corrélations entre pK_{HB} et Δν(OH) établies dans des travaux

© 2002 CNRC Canada

Tableau 1. Échelles de basicité de liaison hydrogène, pK_{HB} et $\Delta\nu$(OH) (cm^{-1}), et de Brønsted, pK_a, des amines tertiaires. Potentiel électrostatique minimum $V_{s,min}$ (kcal·mol^{-1}) autour de l'azote amino.

N°	Composé	Formule	pK_{HB}	$\Delta\nu$(OH)	pK_a	$-V_{s,min}$
1	Quinuclidine	[a]	2,71	444	11,29	40,72
2	4-Phénylquinuclidine	[a]	2,46	433	10,42	38,82
3	Tropane	[a]	2,39	446		36,00
4	Diazabicyclooctane	[a]	2,63 (2,33) [b]	417	8,82 (8,52) [b]	38,51
5	N-Méthylpyrrolidine	$CH_2CH_2CH_2CH_2NMe$	2,19	423	10,46	36,52
6	N,N-Diméthyléthylamine	$EtNMe_2$	2,17	418	10,16	37,51
7	N,N-Diméthylcyclohexylamine	c-$HexNMe_2$	2,15	433	10,72	35,19
8	Triméthylamine	Me_3N	2,13	409	9,80	36,60
9	N,N-Diméthylisopropylamine	i-$PrNMe_2$	2,11	425	10,47	35,48
10	N-Méthylpipéridine	$CH_2CH_2CH_2CH_2CH_2NMe$	2,11	421	10,08	35,27
11	N,N,N',N'-Tétraméthylhexane-1,6-diamine	$Me_2N(CH_2)_6NMe_2$	2,35 (2,05) [b]	415		37,15
12	N-Butylpyrrolidine	$CH_2CH_2CH_2CH_2NBu$	2,04	426	10,36	34,83
13	N,N,N',N'-Tétraméthyléthylènediamine	$Me_2N(CH_2)_2NMe_2$	2,32 (2,02) [b]	402	9,15 (8,85) [b]	36,33
14	Triéthylamine	Et_3N	1,98	429	10,72	33,71
15	3-Chloroquinuclidine	[a]	1,97	394	8,85	35,37
16	N,N-Diméthylallylamine	$H_2C{=}CHCH_2NMe_2$	1,92	399	8,64	35,81
17	N,N'-Diméthylpipérazine	$CH_2CH_2N(Me)CH_2CH_2NMe$	2,18 (1,88) [b]	402		34,52
18	N-Méthyltétrahydroisoquinoline	[a]	1,80	383		35,30
19	3-Chlorométhyl-N-méthylpipéridine	$CH_2CH(CH_2Cl)CH_2CH_2CH_2NMe$	1,74	401		32,01
20	4-Chloro-N-méthylpipéridine	$CH_2CH_2CHClCH_2CH_2NMe$	1,70	400		30,60
21	N,N-Diméthylpropargylamine	$HC{\equiv}CCH_2NMe_2$	1,60	367	7,45	33,22
22	N,N-Diméthylbenzylamine	$PhCH_2NMe_2$	1,59	387	8,91	29,07
23	1,3,5-Triméthylhexahydrotriazine	$CH_2N(Me)CH_2N(Me)CH_2NMe$	2,06 (1,58) [b]	356		36,17
24	Trioctylamine	n-Oct_3N	1,57			-
25	Tributylamine	n-Bu_3N	1,55	430	9,93	33,87
26	N-Méthylmorpholine	$CH_2CH_2OCH_2CH_2NMe$	1,66 (1,56) [c]	380	7,41	30,61
27	N,N-Diméthyl-3-chloropropylamine	$ClCH_2CH_2CH_2NMe_2$	1,54	397		30,91

© 2002 CNRC Canada

Tableau 1 (*suite et fin*).

N°	Composé	Formule	pK_{HB}	$\Delta\nu$(OH)	pK_a	- $V_{s,min}$
28	Tripropylamine	*n*-Pr_3N	1,47	427	10,66	33,57
29	1-(2-Chloroéthyl)pyrrolidine	$CH_2CH_2CH_2CH_2NCH_2CH_2Cl$	1,45	386		27,57
30	Triallylamine	$(H_2C{=}CHCH_2)_3N$	1,34	375	8,28	29,01
31	Hexaméthylènetétramine	[a]	1,93 (1,33) [b]	335	8,07 (7,47) [b]	34,42
32	1,2,2,6,6-Pentaméthylpipéridine	$Me_2CCH_2CH_2CH_2C(Me_2)NMe$	1,23	419	11,19	29,59
33	N,N-Diméthylaminopropionitrile	$N{\equiv}CCH_2CH_2NMe_2$	1,35 (1,15) [c]	362		23,67
34	N,N-Dicyclohexyléthylamine	*c*-Hex_2NEt	1,14	419		28,81
35	N,N-Diisopropyléthylamine	*i*-Pr_2NEt	1,05	414		27,91
36	Tripropargylamine	$(HC{\equiv}CCH_2)_3N$	0,87 (0,83) [c]		3,09	35,44
37	N,N-Diméthylaminoacétonitrile	$N{\equiv}CCH_2NMe_2$	1,02 (0,67) [c]	282		23,86
38	N,N-Diisopropylisobutylamine	*i*-Pr_2N-*i*-Bu	0,30	392		18,73
39	N,N-Diisopropyl-3-pentylamine	*i*-Pr_2NCHEt_2	-0,34			7,38
40	Tribenzylamine	$(PhCH_2)_3N$	0,10 (-1,5) [c]	33		19,4

[a]

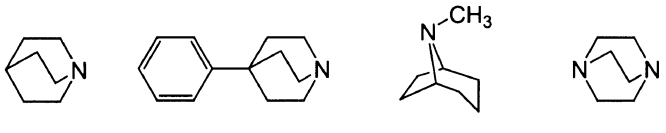

1 **2** **3** **4**

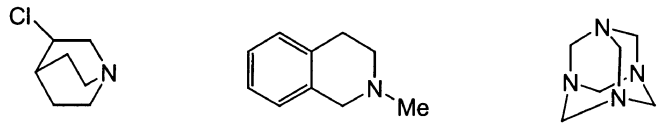

15 **18** **31**

[b]Valeur statistiquement corrigée (en parenthèses).
[c]Valeur corrigée (en parenthèses) de la contribution d'un (ou de plusieurs) autre(s) site(s) accepteur(s) de liaison hydrogène (voir tableau 2).

précédents pour les familles des éthers (28), des nitriles (15) et des bases π acétyléniques (29) et aromatiques (29). Le détail des calculs est donné dans le tableau 2. Pour la tribenzylamine, nous avons vérifié expérimentalement que la constante de complexation sur l'azote amino n'est pas complètement égale à zéro. Avec une solution très concentrée en tribenzylamine (0,5 mol·dm^{-3}) et en diminuant la température pour déplacer les équilibres vers la formation des complexes, nous voyons en effet apparaître (fig. 2) une très faible contribution attribuée à une bande ν(OH···N).

Pour les polyamines, la constante mesurée correspond à plusieurs complexes 1:1 sur les multiples atomes d'azote (un excès d'amine permet de minimiser la formation de complexes de stœchiométries supérieures). En supposant que les *n* atomes d'azote de ces polyamines ont la même basicité, la constante mesurée est égale à *n* fois la constante propre à un atome d'azote. Cette correction statistique (30) de la valeur pK_{HB} par –log *n* (*n* = 2 pour **4**, **11, 13, 17**; *n* = 3 pour **23**, et *n* = 4 pour **31**) doit être effectuée pour relier pK_{HB} aux propriétés moléculaires caractérisant la basicité par atome d'azote ($\Delta\nu$(OH) ou potentiel électrostatique, ou constantes de substituants).

Discussion

Comparaison des échelles de basicité pK_{HB}, pK_a et $\Delta\nu$(OH)

Il est aujourd'hui bien établi que les échelles pK_{HB} et pK_a présentent d'importantes différences (1). Certains auteurs ont cependant proposé des relations par familles entre

© 2002 CNRC Canada

Tableau 2. Évaluation de la constante de complexation sur l'azote amino, K_c(N), dans le cas des amines possédant un (d')autre(s) centre(s) X accepteur(s) de liaison H.

N°	Composé	X	K_c (totale)[a, b]	$\Delta\nu$(OH···X)[c]	K_c(X)[a, d]	K_c(N)[a, e]	% N[f]
26	N-Méthylmorpholine	O	45,6	271	9,2	36,4	80
33	N,N-Diméthylaminopropionitrile	C≡N	22,6	168	8,4	14,2	63
36	Tripropargylamine	3 C≡C	7,5	64	0,23	6,8	91
37	N,N-Diméthylaminoacétonitrile	C≡N	10,4	152	5,8	4,6	44
40	Tribenzylamine	3	1,26	58	0,41	≈0,03	≈2

[a] $dm^3\ mol^{-1}$.
[b] Valeur expérimentale.
[c] cm^{-1}. $\Delta\nu$(OH···X) = 3614 – ν(OH···X) est le déplacement de fréquence de la bande ν(OH) du 4-fluorophénol par complexation sur le(s) site(s) X.
[d] Calculée à partir des relations pK_{HB} versus $\Delta\nu$(OH···X) pour les familles des éthers (**26**), des nitriles (**33**, **37**), des bases π acétyléniques (**36**) et des bases π aromatiques (**40**).
[e] $K_c(N) = K_c$ (totale) – $x\ K_c(X)$, x = 1 (**26**, **33**, **37**) ou x = 3 (**36**, **40**).
[f] $\%N = 100\ K_c(N)/K_c$ (totale).

Fig. 2. Spectres IR dans la région ν(OH) d'une solution de 4-fluorophénol ($4{,}8 \times 10^{-3}$ mol·dm^{-3}) et de tribenzylamine (0,53 mol·dm^{-3}) dans CCl_4 à –5, 25 et 45°C montrant (1) la bande ν(OH) du 4-fluorophénol libre à 3614 cm^{-1}, (2) la bande ν(OH···π) d'un premier complexe 1:1, déplacée de 58 cm^{-1}, et (3) le début d'une bande très large ν(OH···N) d'un deuxième complexe 1:1 (une perte d'énergie vers 3100 cm^{-1} due aux absorptions ν(CH) de la tribenzylamine cache le reste de la bande).

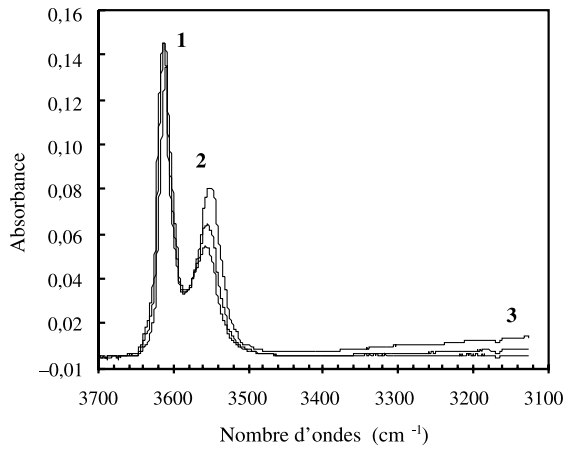

Fig. 3. Absence de corrélation entre les échelles pK_{HB} et pK_a des amines tertiaires. Les points des amines encombrées, e.g., **25**, **28** et **32**, ont des valeurs pK_{HB} trop faibles par rapport à la tendance générale.

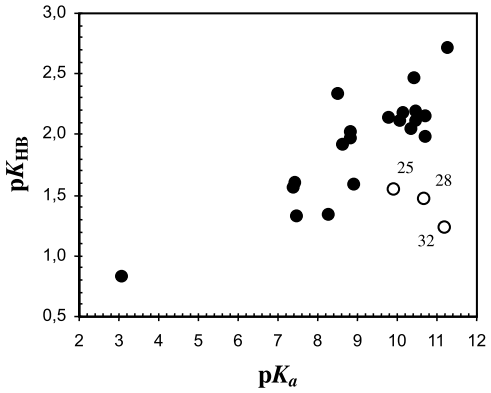

échelles de basicité de liaison H et l'échelle pK_a de protonation (31–34). Ces relations sont probablement fortuites ou n'ont qu'un domaine limité de validité, car pour la famille des amines primaires (18) il faut exclure les composés ayant une liaison hydrogène intramoléculaire, et pour celle des amines secondaires (19), pK_a n'explique que 74 % de la variance de pK_{HB}, ce que nous avons interprété (19) par une plus grande sensibilité de l'échelle pK_{HB} aux effets stériques que l'échelle pK_a. Les amines tertiaires donnent une corrélation encore plus mauvaise que les secondaires, puisque seulement 38 % de la variance de 23 valeurs pK_{HB} est expliquée par pK_a (fig. 3). La pentaméthylpipéridine (**32**), la tripropylamine (**28**) et la tributylamine (**25**) présentent à nouveau les déviations les plus importantes à la tendance générale (fig. 3). Elles montrent, puisque leur atome d'azote porte des substituants encombrants, que l'échelle pK_{HB} est plus sensible aux effets stériques que l'échelle pK_a.

La comparaison des échelles pK_{HB} et $\Delta\nu$(OH) met également en évidence la sensibilité de l'échelle pK_{HB} aux effets stériques. Dans des travaux précédents (17, 19, 28), nous avons montré que la diminution de basicité par effet stérique est plus importante pour pK_{HB} que pour $\Delta\nu$(OH). Ainsi les éthers ROR′ (28), les pyridines ortho-substituées 2-RC_5H_4N (17) et les amines secondaires RNHR′ (19), encombrées par des substituants R et R′ volumineux, ont-ils des valeurs pK_{HB} (très) faibles par rapport à leurs valeurs $\Delta\nu$(OH). Il en est de même pour les amines tertiaires. La figure 4 montre qu'il n'existe pas de relation générale entre

© 2002 CNRC Canada

Tableau 3. Constantes de polarisabilité, σ_α[a], inductive, σ_F[a], et stérique, υ[b], des substituants de l'azote des amines étudiées.

Substituant		σ_α[a]	σ_F[a]	υ[b]	Substituant	σ_F[a]
H[c]		0	0	0	$CH_2CH{=}CH_2$	0,03
Me	CH_3	–0,35	0	0,52	CH_2Ph	0,05
Et	CH_2CH_3	–0,49	0	0,56	$(CH_2)_3Cl$	0,06
n-Pr	$(CH_2)_2CH_3$	–0,54	0	0,68	$CH_2C{\equiv}CH$	0,12
n-Bu	$(CH_2)_3CH_3$	–0,57	0	0,68	NHMe	0,12
n-Oct	$(CH_2)_7CH_3$	–0,59	0	0,68	$(CH_2)_2Cl$	0,12
i-Pr	$CH(CH_3)_2$	–0,62	0	0,76	$(CH_2)_2C{\equiv}N$	0,16
c-Hex	c-C_6H_{11}	–0,61	0	0,87	CH_2Cl	0,23
i-Bu	$CH_2CH(CH_3)_2$		0	0,98	OH	0,30
3-Pent	$CH(CH_2CH_3)_2$		0	1,51	$CH_2C{\equiv}N$	0,31
	$(CH_2)_6NMe_2$		0		Cl	0,45
	$(CH_2)_2NMe_2$		0,03			

[a]Valeurs tirées de la référence 37.
[b]Valeurs tirées de la référence 46.
[c]Substituant de référence.

Fig. 4. Comparaison des échelles thermodynamique pK_{HB} et spectroscopique $\Delta\upsilon$(OH) de basicité de liaison H des amines tertiaires. Les amines (●) dont l'encombrement stérique est minimum dessinent une droite frontière au dessous de laquelle se placent les composés (○) dont l'encombrement stérique est plus ou moins important.

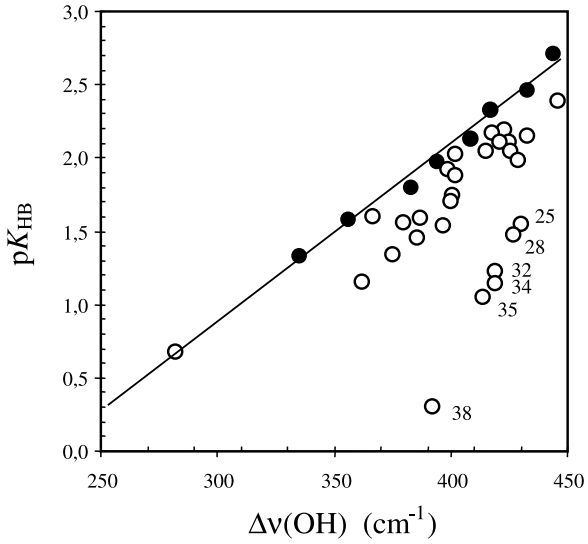

pK_{HB} et $\Delta\nu$(OH) (coefficient de corrélation r = 0,609 pour n = 36 points), principalement à cause des composés encombrés (e.g., **25**, **28**, **32**, **34**, **35** et **38**). Ainsi *c*-Hex_2NEt (**34**) a pratiquement la même valeur $\Delta\nu$(OH) (419 cm^{-1}) que $EtNMe_2$ (**6**) (418 cm^{-1}) mais une valeur pK_{HB} beaucoup plus faible (1,14 au lieu de 2,17). De même le passage de la 1-méthylpipéridine (**10**) à la 1,2,2,6,6-tétraméthylpipéridine (**32**) abaisse considérablement pK_{HB} (de 2,11 à 1,23) sans changer significativement $\Delta\nu$(OH) (421 cm^{-1} et 419 cm^{-1}). Il est cependant possible d'établir une corrélation limitée aux amines tertiaires les moins encombrées, en partant des amines bicycliques **1**, **2**, **4**, **15** et **31**, puisque la cyclisation tire vers l'arrière les trois chaînes alkyles, ce qui dégage au maximum la paire libre de l'azote. Ces composés, ainsi que deux amines monocycliques **18** et **23** et la triméthylamine (**8**) qui porte les trois groupes alkyles les moins volumineux dessinent une droite frontière (fig. 4, éq. [8]) au dessous de laquelle se placent les autres amines tertiaires. Celles-ci sont ainsi

[8] $pK_{HB} = 1{,}23\ [\Delta\nu(OH)/100] - 2{,}82$

$n = 8$; $r = 0{,}992$; écart type $s = 0{,}06$

désignées comme plus stériquement encombrées que les amines bicycliques. Ce sont effectivement les amines les plus encombrées **25**, **28**, **32**, **34**, **35** et **38** qui dévient le plus de la droite frontière (fig. 4).

Effets des substituants inductifs électroattracteurs

L'effet inductif et (ou) de champ (pour une discussion récente sur ces deux concepts d'effet électronique en série saturée, voir la référence 35) de substituants électroattracteurs diminue fortement la basicité de liaison H des amines tertiaires. Ainsi, l'effet inductif et (ou) de champ du chlore diminue pK_{HB} de 0,74 unité en passant de la quinuclidine (**1**), à la 3-chloroquinuclidine (**15**), et celui du groupe cyano diminue pK_{HB} de 1,46 unité de Me_3N (**8**) à $N{\equiv}CCH_2NMe_2$ (**37**). La constante de substituant σ_F (36) dont les valeurs (37) sont reportées dans le tableau 3 pourrait mesurer les variations de pK_{HB} dans les séries d'amines pour lesquelles les autres effets structuraux agissant sur la basicité de l'azote, essentiellement les effets stériques (38) et l'effet de polarisabilité (39) (il n'y a pas d'effet de résonance, car la paire libre de l'azote n'est conjuguée avec aucun système π dans les amines **1**–**40**), sont faibles et (ou) quasi constants. Cela semble être le cas dans la série des *N*,*N*-diméthylamines substituées $XNMe_2$ (éq. [9]), et mieux encore dans la série des amines hétérocycliques (éq. [10], fig. 5). Pour ces dernières, nous considérons la variation de pK_{HB}, ΔpK_{HB}, par

[9] $pK_{HB} = 2{,}02 - 4{,}57\ \sigma_F$

$n = 9$ (**8**, **11**, **13**, **16**, **21**, **22**, **27**, **33**, **37**);

$r = 0{,}956$; $s = 0{,}15$

© 2002 CNRC Canada

Tableau 4. Somme des angles CNC (°) autour de l'azote, ΣCNC, mesurée sur la géométrie HF/6–31G** des alkylamines tertiaires du tableau 1.

N°	Composé	ΣCNC	N°	Composé	ΣCNC
1	Quinuclidine	329,3	**14**	Triéthylamine	337,6
3	Tropane	340,3	**24**	Trioctylamine	338,3
5	*N*-Méthylpyrrolidine	334,0	**25**	Tributylamine	338,3
6	*N*,*N*-Diméthyléthylamine	341,8	**28**	Tripropylamine	338,3
7	*N*,*N*-Diméthylcyclohexylamine	341,8	**32**	1,2,2,6,6-Pentaméthylpipéridine	348,2
8	Triméthylamine	336,0	**34**	*N*,*N*-Dicyclohexyléthylamine	350,6
9	*N*,*N*-Diméthylisopropylamine	341,5	**35**	*N*,*N*-Diisopropyléthylamine	349,8
10	*N*-Méthylpipéridine	336,1	**38**	*N*,*N*-Diisopropylisobutylamine	348,4
12	*N*-Butylpyrrolidine	338,9	**39**	*N*,*N*-Diisopropyl-3-pentylamine	356,4

Fig. 5. Corrélation entre la constante de substituant inductive et (ou) de champ σ_F et la variation de pK_{HB} d'amines hétérocycliques par β-chloro, -oxo, et -aza substitution, et γ-chlorosubstitution.

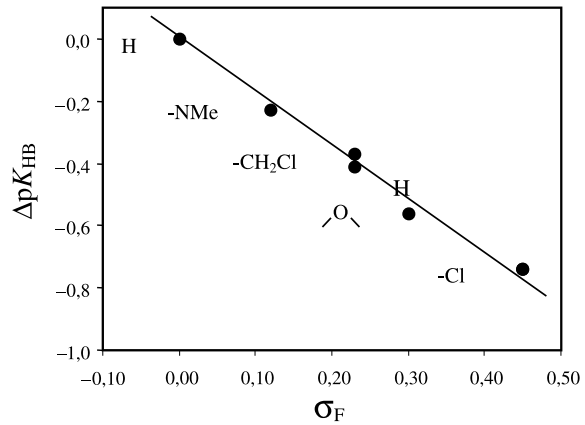

[10] $\Delta pK_{HB} = -0{,}02 - 1{,}63\ \sigma_F$

$n = 7$; $r = 0{,}995$; $s = 0{,}03$

(*i*) chloro-substitution en β de la fonction amine (**1**, **15** et **5**, **29**) (*ii*) chloro-substitution en γ, i.e., chlorométhyle-substitution en β (**10**, **19** et **10**, **20**), (*iii*) oxo-substitution en β (**10**, **26**) et (*iv*) aza-substitution en β (**10**, **17**). Dans la série $XNMe_2$, les constantes σ_F correspondent à une substitution directe de l'azote, tandis que pour les amines hétérocycliques, elles sont choisies pour une substitution en β; il est donc normal d'observer un plus faible coefficient de sensibilité aux effets mesurés par σ_F dans ce dernier cas. Le rapport des coefficients de régression des équations [9] et [10] correspond à un facteur d'atténuation de l'effet inductif de 1,67 par groupe méthylène qui est de l'ordre de grandeur de celui (1,95) trouvé pour les réactions de protonation en phase gazeuse (39).

Effets des substituants alkyles

Il est généralement établi que les groupes alkyles ont un effet inductif négligeable (36, 39, 40). Leur influence sur la basicité de liaison H des amines tertiaires est alors due principalement à leur effet de polarisabilité et à leurs effets stériques. Ces deux effets agissent en sens opposé sur pK_{HB}. L'effet de polarisabilité augmente la basicité de liaison H, probablement grâce à la contribution des forces de dispersion et de polarisation à l'énergie de liaison H (41). Cet effet est généralement mesuré par la constante de substituant σ_α de polarisabilité, définie par Hehre et al. (42) à partir de la variation, par substitution d'un modèle ad hoc (42, 43), du potentiel de polarisation calculé ab initio. La valeur absolue de σ_α augmente avec la longueur et la ramification du groupe alkyle (voir tableau 3).

Fig. 6. Corrélation entre $-V_{s,min}$, potentiel électrostatique autour de l'azote, et ΣCNC, somme des angles CNC, pour les alkylamines tertiaires.

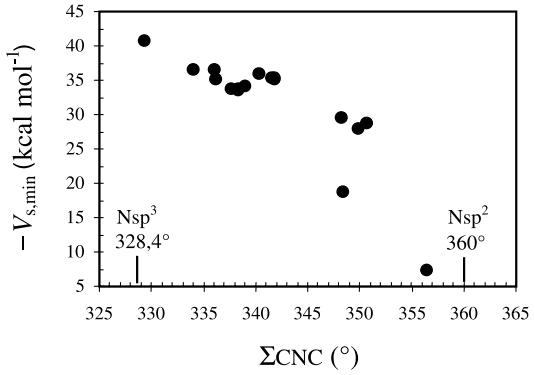

À l'inverse, l'effet stérique affaiblit la basicité de liaison H. Nous l'avons établi pour les éthers (28), les pyridines ortho-substituées (17), les amidines (16) et les amines secondaires (19). Plusieurs mécanismes peuvent être envisagés dans le cas de la complexation des amines tertiaires par le 4-fluorophénol. Le premier consiste en l'ouverture des angles CNC de l'amine par répulsion stérique entre les trois substituants alkyles de l'azote. Cette ouverture provoque une diminution du caractère p de la paire libre de l'azote et donc de sa basicité intrinsèque. Le tableau 4 rassemble les valeurs ΣCNC de la somme des trois angles CNC autour de l'azote. Ces valeurs montrent que l'azote passe d'un état tétragonal (ΣCNC = 328,4° pour un azote sp^3) pour la quinuclidine (**1**) à un état quasi trigonal (ΣCNC = 360° pour un azote sp^2) pour les amines les plus encombrées. Cela entraîne un potentiel électrostatique moins négatif autour de l'azote : $|V_{s,min}|$ diminue de 40,72 kcal·mol^{-1} pour la quinuclidine (**1**) à 7,38 kcal·mol^{-1} pour *i*-Pr_2NCHEt_2 (**39**). La figure 6 montre la relation significative (r = 0,85 pour 17 alkylamines) entre $V_{s,min}$ et ΣCNC. Il s'ensuit un affaiblissement de la liaison H (une interaction moléculaire principalement électrostatique (41)) par diminution de

© 2002 CNRC Canada

Fig. 7. Illustration de l'encombrement stérique de l'azote de *i*-Pr_2NCHEt_2 (**39**), comparativement à celui de la quinuclidine (**1**).

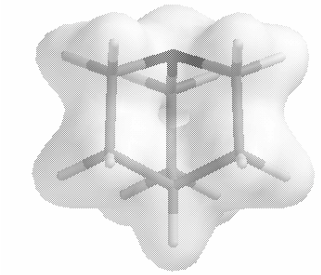

1

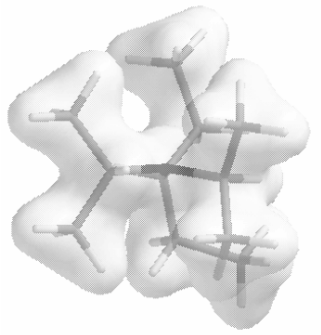

39

l'attraction électrostatique entre l'amine et le phénol. Le second mécanisme est dû à l'encombrement de la paire libre de l'azote. Celui-ci est évident pour *i*-Pr_2NCHEt_2 lorsque l'on compare son volume moléculaire à celui de la quinuclidine (fig. 7). Lorsqu'on approche une molécule de 4-fluorophénol dans l'axe de la paire libre de l'azote à une distance d(N···H) de 1,85 Å (valeur moyenne trouvée (44) dans la base structurale de Cambridge (26) pour 66 contacts de liaison H entre des phénols et des amines tertiaires), on constate un plus grand recouvrement des nuages électroniques du phénol et de l'amine pour les amines encombrées. Il s'ensuit une énergie de répulsion (le terme d'échange dans le calcul quantique de l'énergie (41)) plus importante qui diminue l'énergie de la liaison H. Le dernier mécanisme concerne l'augmentation de l'entropie de complexation. Nous avons trouvé (44) que celle-ci est de –55,8 $J \cdot K^{-1} \cdot mol^{-1}$ pour la complexation de la quinuclidine par le 4-fluorophénol, tandis que celle de l'amine encombrée *i*-Pr_2NEt s'élève à –74,0 $J \cdot K^{-1} \cdot mol^{-1}$ (valeur relative aux fractions molaires). Cette variation d'entropie de 18,2 $J \cdot K^{-1} \cdot mol^{-1}$ fait chuter pK_{HB} de 0,95 unité ($T\Delta S/5{,}709$) à 298 K.

De nombreux paramètres empiriques ont été proposés pour mesurer l'effet stérique des substituants, parmi lesquels les plus populaires sont les constantes de substituants E_s de Taft (45) et upsilon (υ) de Charton (46). Une équation multiparamétrique entre pK_{HB} et les constantes de

Fig. 8. Variation de pK_{HB} en fonction de la somme des constantes stériques υ des substituants alkyles de l'azote des amines tertiaires. Dans la série $AlkNMe_2$ (●), pK_{HB} reste quasiment constant entre 2,11 et 2,17 tandis qu'il chute jusqu'à –0,34 (**39**) quand les effets stériques augmentent.

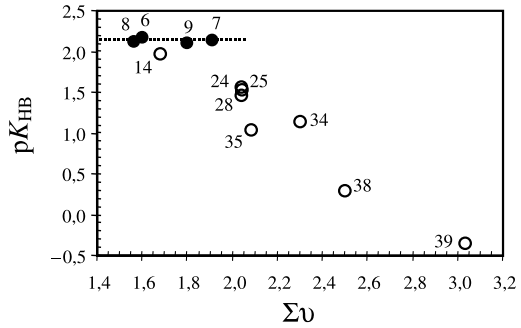

polarisabilité σ_α et stérique E_s (ou υ) est cependant impossible à établir pour les trialkylamines pour deux raisons principales. La première est due à la corrélation significative entre les constantes σ_α et υ (ou E_s) (r = 0,945 pour les neuf substituants alkyles du tableau 3), car toutes deux augmentent avec la taille (i.e., le nombre d'électrons) du groupe alkyle. La deuxième raison provient de la non-additivité des effets stériques qui imposent des équations complexes (47) pour faire intervenir les trois constantes stériques des substituants alkyles. Néanmoins, une analyse grossière de l'influence des substituants alkyles sur la basicité de liaison H des amines tertiaires est possible à partir du graphe pK_{HB} versus Συ (fig. 8). On peut voir que lorsque la somme des constantes stériques des trois substituants (i.e., le volume, le nombre d'électrons et la polarisabilité) augmente, pK_{HB} reste constant pour les faibles effets stériques, tandis qu'il chute spectaculairement quand les effets stériques augmentent. En d'autres termes l'effet de polarisabilité réussit à compenser les effets stériques quand ceux-ci sont faibles (série $AlkNMe_2$ **6**–**9**) mais quand les trois chaînes alkyles continuent à s'allonger et à se ramifier, les effets stériques prédominent largement.

La tribenzylamine

Nous avons montré que la tribenzylamine est principalement une base π de liaison H, puisque la basicité de liaison H de son azote est extraordinairement faible ($pK_{HB} \approx -1{,}5$). Au contraire, c'est une base de Brønsted azotée dont le pK de l'ion tribenzylammonium est de 4,1 dans le DMSO et de 6,4 dans le méthanol (48) (nous n'avons pas trouvé la valeur pK_a dans l'eau). La comparaison de ces valeurs avec celles de l'ion triéthylammonium (respectivement 9,0 et 10,9) dans les mêmes solvants (48) met en évidence l'effet inductif électroattracteur des trois groupes benzyle.

Cet effet inductif doit également diminuer la basicité de liaison H. À partir de l'équation [9] et en supposant additives les valeurs σ_F, nous estimons un pK_{HB} de 1,33. Cette valeur est très éloignée de celle (–1,5) estimée à partir de la valeur expérimentale après déduction de la contribution des trois sites π (voir tableau 2). Pour diminuer encore de 2,83 unités (16,2 $kJ \cdot mol^{-1}$) le pK_{HB}, nous ne pouvons invoquer que d'exceptionnels effets stériques des trois groupes

© 2002 CNRC Canada

Fig. 9. Structure cristalline de la tribenzylamine illustrant l'encombrement stérique de l'azote par les trois groupes benzyle.

40

benzyle. La structure cristalline de la tribenzylamine (49) montre que l'atome d'azote est particulièrement encombré : comme l'illustre la figure 9, les trois noyaux aromatiques encerclent l'atome d'azote et empêchent quasiment l'accès de la paire libre à un donneur de liaison H.

Notons qu'il n'y a pas d'augmentation des angles CNC autour de l'azote, leur somme étant (49) de 329,9°. Le faible potentiel électrostatique (–19,4 kcal·mol^{-1}) semble dû principalement aux effets inductifs des trois benzyles. En effet, la comparaison des $V_{s,min}$ de Me_3N et $PhCH_2NMe_2$ montre qu'un groupe benzyle diminue $V_{s,min}$ de 7,53 kcal·mol^{-1}, valeur comparable au tiers (5,73 kcal·mol^{-1}) de la différence entre $(PhCH_2)_3N$ et Me_3N.

Conclusions

1. Nous avons mesuré la basicité de liaison H de 40 amines tertiaires vis-à-vis du 4-fluorophénol, dans CCl_4 et à 298 K (échelle pK_{HB}).
2. Cette échelle s'étend sur 24 kJ·mol^{-1} d'énergie de Gibbs de la quinuclidine à la tribenzylamine.
3. Les effets structuraux modifiant la basicité de liaison H sont, par ordre croissant d'importance, l'effet de polarisabilité, l'effet inductif et les effets stériques.
4. Ces derniers réduisent pratiquement à zéro le pouvoir accepteur de liaison H de la tribenzylamine, qui devient de ce fait une base π de liaison H. La tribenzylamine rejoint ainsi la 2,6-di*tert*butylpyridine (50) comme deuxième exemple de base azotée à système(s) π qui se protonne sur l'azote mais accepte la liaison H sur ses électrons π.
5. Ces différences entre sites de liaison H et sites de protonation, ainsi que l'absence de corrélation générale entre les échelles pK_{HB} et pK_a pour les amines secondaires (19) et tertiaires (ce travail) montrent que l'usage de l'échelle pK_a pour prévoir la basicité de liaison H est risqué. C'est l'échelle pK_{HB} qui est l'échelle de choix pour étudier le comportement accepteur de liaison H des molécules organiques.

Bibliographie

1. C. Laurence et M. Berthelot. Perspect. Drug Discovery Des. **18**, 39 (2000).
2. D. Gurka et R.W. Taft. J. Am. Chem. Soc. **91**, 4794 (1969).
3. A. Chardin, M. Berthelot, C. Laurence et D.G. Morris. J. Phys. Org. Chem. **8**, 626 (1995).
4. E.M. Arnett, L. Joris, E. Mitchell, T.S.S.R. Murty, T.M. Gorrie et P.V.R. Schleyer. J. Am. Chem. Soc. **92,** 2365 (1970).
5. M. Szafran. J. Mol. Struct. **381**, 39 (1996).
6. G. Zundel. Adv. Chem. Phys. **111**, 1 (2000).
7. G.C. Pimentel et A.L. McClellan. The hydrogen bond. Freeman, San Francisco. 1960.
8. G.A. Jeffrey et W. Saenger. Hydrogen bonding in biological structures. Springer-Verlag, Berlin. 1991.
9. D.D. Perrin. Dissociation constants of organic bases in aqueous solution. Butterworth, London. 1965. Supplément. 1971.
10. E.P. Hunter et S.G. Lias. J. Phys. Chem. Ref. Data, **27**, 413 (1998).
11. W.B. Jensen. The Lewis acid–base concepts. Wiley, New York. 1980.
12. R.S. Drago et B.B. Wayland. J. Am. Chem. Soc. **87**, 3571 (1965).
13. P.C. Maria, J.F. Gal, J. de Franceschi et E. Fargin. J. Am. Chem. Soc. **109**, 487 (1987).
14. D. Hadzi. Theoretical treatments of hydrogen bonding. Wiley, New York. 1997.
15. M. Berthelot, M. Helbert, C. Laurence et J.Y. Le Questel. J. Phys. Org. Chem. **6**, 302 (1993).
16. E.D. Raczynska, C. Laurence et M. Berthelot. Can. J. Chem. **70**, 2203 (1992).
17. F. Besseau, M. Luçon, C. Laurence et M. Berthelot. J. Chem. Soc. Perkin Trans. 2, 101 (1998).
18. J. Graton, C. Laurence, M. Berthelot, J.-Y. Le Questel, F. Besseau et E.D. Raczynska. J. Chem. Soc. Perkin Trans. 2, 997 (1999).
19. J. Graton, M. Berthelot et C. Laurence. J. Chem. Soc. Perkin Trans. 2, 2130 (2001).
20. L. Joris et P.V.R. Schleyer. Tetrahedron, **24**, 5991 (1968).
21. C. Sandorfy. Topics in current chemistry. **120**, 41 (1984).
22. M.J. Frisch, G.W. Trucks, H.B. Schlegel, P.M.W. Gill, B.G. Johnson, M.A. Robb, J.R. Cheeseman, T. Keith, G.A. Petersson, J.A. Montgomery, K. Raghavachari, M.A. Al-Laham, V.G. Zakrzewski, J.V. Ortiz, J.B. Foresman, J. Ciolowski, B.B. Stefanov, A. Nanayakarra, M. Challacombe, C.Y. Peng, P.Y. Ayala, W. Chen, M.W. Wong, J.L. Andres, E.S. Repogle, R. Gomperts, R.L. Martin, D.J. Fox, J.S. Binkley, D.J. Defrees, J. Baker, J.P. Stewart, M. Head-Gordon, C. Gonzalez et J.A. Pople. GAUSSIAN 94 Rev. E.2. Gaussian Inc., Pittsburgh, Penna. 1995.
23. S. Profeta et N.J. Allinger. J. Am. Chem. Soc. **107**, 1907 (1985).
24. E.E. Eliel et S.H. Wilen. Stereochemistry of organic compounds. Wiley, New York. 1994.
25. J. Vogt, B. Mez-Stark, N. Vogt et W. Hutter. MOGADOC. J. Mol. Struct. **249**, 485 (1999).
26. F.H. Allen, J.E. Davies, J.J. Galloy, O. Johnson, O. Kennard, C.F. Macrae, E.M. Mitchell, G.F. Mitchell, J.M. Smith et D.G. Watson. J. Chem. Inf. Comput. Sci. **31**, 187 (1991).
27. R.F.W. Bader, M.T. Caroll, J.R. Cheeseman et C. Chang. J. Am. Chem. Soc. **109**, 7968 (1987).
28. M. Berthelot, F. Besseau et C. Laurence. Eur. J. Org. Chem. 925 (1998).

© 2002 CNRC Canada

29. F. Besseau, C. Laurence et M. Berthelot. Bull. Soc. Chim. Fr. **133**, 381 (1996).
30. J. Hine. Structural effects on equilibria in organic chemistry. Wiley, New York. 1975.
31. R.W. Taft, D. Gurka, L. Joris, P.V.R. Schleyer et W.J. Rakshys. J. Am. Chem. Soc. **91**, 4801 (1969).
32. M.H. Abraham, P.P. Duce, D.V. Prior, D.G Barratt, J.J. Morris et P.J. Taylor. J. Chem. Soc. Perkin Trans. 2, 1355 (1989).
33. M.H. Abraham, P.L. Grellier, D.V. Prior, J.J. Morris et P.J. Taylor. J. Chem. Soc. Perkin Trans. 2, 521 (1990).
34. M.J. Kamlet, J.F. Gal, P.C. Maria, and R.W. Taft. J. Chem. Soc. Perkin Trans. 2, 1583 (1985).
35. O. Exner. J. Phys. Org. Chem. **12**, 265 (1999).
36. S. Marriott et R.D. Topsom. J. Am. Chem. Soc. **106**, 7 (1984).
37. C. Hansch, A. Leo et R.W. Taft. Chem. Rev. **91**, 165 (1991).
38. R. Gallo. Prog. Phys. Org. Chem. **14**, 115 (1983).
39. R.W. Taft et R.D. Topsom. Prog. Phys. Org. Chem. **16**, 1 (1987).
40. (*a*) W. Adcock et T.C. Khor. J. Org. Chem. **43**, 1272 (1974); (*b*) F.G. Bordwell et H.E. Fried. Tetrahedron Lett. **13**, 1121 (1977).
41. S. Scheiner. Hydrogen bonding. A theoretical perspective. Oxford University Press, New York. 1997.
42. W.J. Hehre, C.F. Pau, A.D. Headley et R.W. Taft. J. Am. Chem. Soc. **108**, 1711 (1986).
43. P. Carsky, P. Naus et O. Exner. J. Phys. Org. Chem. **11**, 485 (1998).
44. J. Graton. Résultats non publiés.
45. R.W. Taft dans M.S. Newman. Steric effects in organic chemistry. Wiley, New York. 1956.
46. M. Charton. Topics in current chemistry. **114**, 57 (1983).
47. (*a*) J.A. MacPhee, A. Panaye et J.E. Dubois. J. Org. Chem. **45**, 1164 (1980); (*b*) M. Charton. J. Chem. Soc. Perkin Trans. 2, 97 (1983).
48. C.D. Ritchie. J. Am. Chem. Soc. **91**, 6749 (1969).
49. F. Iwasaki et H. Iwasaki. Acta Cryst. Sec. B, **28**, 3370 (1972).
50. A. Chardin, C. Laurence et M. Berthelot. J. Chem. Res. (S) 332 (1996).

© 2002 CNRC Canada

ERRATUM

Ref.: Can. J. Chem. **80**(8): x (2002).

NRC Research Press inadvertently omitted the name of Victor Snieckus, one of the editors of the special issue dedicated to the memory of Professor Ray Lemieux.

We apologize to Dr. Snieckus, the Editors of the *Canadian Journal of Chemistry*, and our readership for this error. The page should have been published as follows:

This special issue is dedicated to the memory of

Professor Ray Lemieux

who was Canada's most distinguished organic chemist. His contributions to synthesis, structure, and bonding in saccharide chemistry are truly legendary.

Associate Editors: Bert O. Fraser-Reid and Victor Snieckus

Ce numéro spécial est dédié à la mémoire du

Professeur Ray Lemieux

le plus éminent organicien du Canada. Ses contributions dans le domaine de la chimie des glucides, plus particulièrement leur synthèse, leur structure et leurs mécanismes de liaison, ont été véritablement exceptionnelles.

Directeurs scientifiques associés : Bert O. Fraser-Reid et Victor Snieckus

---

 DOI: 10.1139/V02-905 © 2002 NRC Canada

The addition of organometallic reagents to tetramesityldigermene

Kyle L. Fujdala, David W.K. Gracey, Erica F. Wong, and Kim M. Baines

Abstract: The thermolysis and photolysis of hexamesitylcyclotrigermane in the presence of ethylmagnesium bromide has been investigated. Under photochemical conditions, ethyldimesitylgermane, 1,2-diethyl-1,1,2-trimesityldigermane and ethyl-1,1,2,2-tetramesityldigermane were isolated and, under thermal conditions, 1,2,2-triethyl-1,1-dimesityldigermane and 2,2-diethyl-1,1,1-trimesityldigermane were isolated. The photolysis of hexamesitylcyclotrigermane in the presence of methyllithium has also been investigated. In both cases, the organometallic reagent adds to tetramesityldigermene and dimesitylgermylene formed by photochemical or thermal cleavage of the cyclotrigermane. In the case of the addition of the Grignard reagent, the resulting germyl Grignard reagent undergoes a facile ligand exchange reaction.

Key words: digermene, germylene, Grignard reagents, alkyllithium reagents, germylmagnesium compounds, germyllithium compounds.

Résumé : On a étudié la thermolyse et la photolyse de l'hexamésitylcyclotrigermane en présence de bromure d'éthylmagnésium. Dans les conditions photochimiques, on a isolé de l'éthyldimésitylgermane, du 1,2-diéthyl-1,1,2-trimésityldigermane et du éthyl-1,1,2,2-tétramésityldigermane alors, que dans des conditions thermiques, on a isolé du 1,2,2-triéthyl-1,1-dimésityldigermane et du 2,2-diéthyl-1,1,1-trimésityldigermane. On a aussi examiné la photolyse de l'hexamésitylcyclotrigermane en présence de méthyllithium. Dans les deux cas, le réactif organométallique s'additionne au tétraméthyldigermène et au dimésitylgermylène qui se forment par clivage photochimique ou thermique du cyclotrigermane. Dans le cas de l'addition du réactif de Grignard, le réactif germylmagnésien qui en résulte subit une réaction facile d'échange de ligands.

Mots clés : digermène, germylène, réactifs de Grignard, réactifs alkyllithium, composés germylmagnésium, composés germyllithium.

[Traduit par la Rédaction]

Introduction

The reactivity of digermenes has been of interest since stable and relatively stable derivatives of these compounds were first synthesized twenty years ago (1). Despite two decades of research in this area, the addition of organometallic reagents remains a relatively unexplored area of digermene chemistry. We have reported that the addition of methylmagnesium halide to $Mes_2Ge{=}GeMes_2$ (Mes = mesityl = 2,4,6-trimethylphenyl) gives (dimesitylmethylgermyl)dimesitylgermylmagnesium bromide in good yield (eq. [1]) (2).

[1] 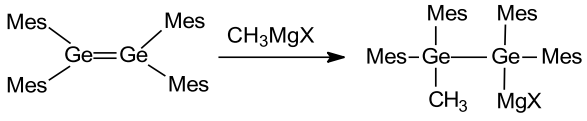

Received 5 February 2002. Published on the NRC Research Press Web site at http://canjchem.nrc.ca on 11 September 2002.

Dedicated to Professor Tristram Chivers in recognition of his contributions to the field of inorganic chemistry.

K.L. Fujdala, D.W.K. Gracey, E.F. Wong, and K.M. Baines.[1] Department of Chemistry, University of Western Ontario, London, ON N6A 5B7, Canada.

[1]Corresponding author (e-mail: kbaines2@uwo.ca).

Furthermore, we discovered that thermolysis of the resulting germyl Grignard reagent in the presence of excess MeMgX leads to a facile ligand exchange reaction in which the mesityl groups on the germanium bonded to the magnesium were exchanged for methyl groups (eq. [2]).

[2] 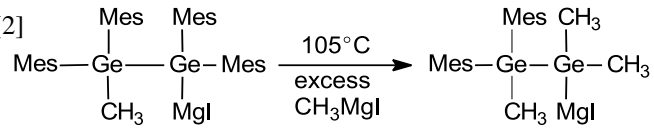

A mechanism involving the α-elimination of MesMgX followed by the addition of MeMgX to an intermediate germylene has been proposed to explain the observed ligand exchange (Scheme 1). Evidence in support of the proposed mechanism was provided by trapping the initially formed intermediate germylene with 2,3-dimethylbutadiene. We have also found that methylmagnesium halide adds regioselectively to germasilenes giving germyl Grignard reagents, which undergo an analogous methyl-for-mesityl exchange (2, 3). To investigate not only the generality of the Grignard addition to digermenes and the generality of the ligand exchange reaction, we now describe the addition of ethylmagnesium bromide to tetramesityldigermene generated either photochemically or thermally from hexamesitylcyclotrigermane. Furthermore, we also report on the addition of methyllithium to tetramesityldigermene and the thermal behaviour of the products obtained therefrom.

 DOI: 10.1139/V02-128 © 2002 NRC Canada

Scheme 1.

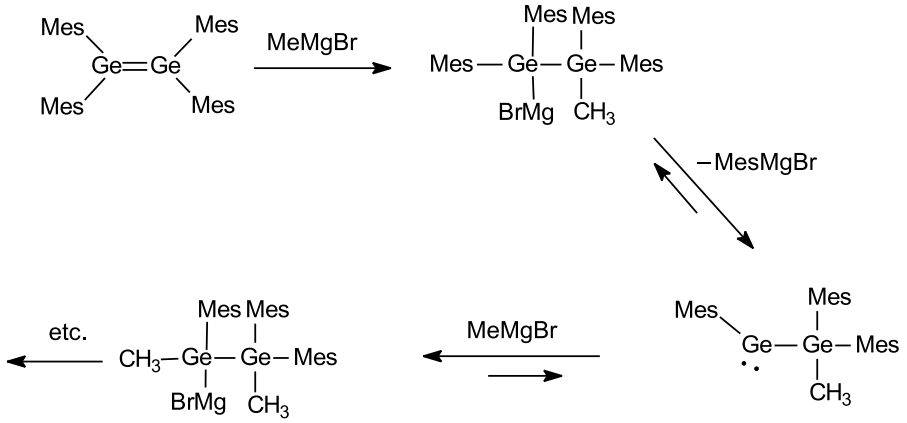

Results and discussion

The photolysis of hexamesitylcyclotrigermane (**1**) in toluene at –60°C in the presence of excess ethylmagnesium bromide, followed by hydrolysis using ammonium chloride, led to the isolation of three products: ethyldimesitylgermane (**2**), 1,2-diethyl-1,1,2-trimesityldigermane (**3**), and ethyl-1,1,2,2-tetramesityldigermane (**4**) in a 7.8:2.8:1 ratio (eq. [3]). All new compounds were characterized by ^{1}H, ^{13}C NMR, and IR spectroscopy and mass spectrometry, the details of which are given in the experimental section. In general, the greater shift dispersion of the ^{13}C NMR spectrum of a given compound was useful in determining the number of different mesityl or ethyl groups and the ^{1}H NMR spectrum gave the ratio of mesityl:ethyl:GeH groups. Finally, the high resolution mass spectrum was critical in determining the molecular formula of the compound.

The formation of compounds **2**–**4** can be understood on the basis of our previous mechanistic proposal. The photolysis of hexamesitylcyclotrigermane results in the formation of dimesitylgermylene and tetramesityldigermene (4). The formation of **2** is most easily accounted for by the quenching of ethyldimesitylgermylmagnesium bromide formed by the addition of ethylmagnesium bromide to dimesitylgermylene. Similarly, compound **4** is apparently derived from addition of the ethyl Grignard reagent to tetramesityldigermene to give the germyl Grignard reagent **5** followed by hydrolysis (Scheme 2). Compound **3** is believed to arise from **5** via an α-elimination of mesitylmagnesium bromide in the cold to give the germylgermylene **6**. Ethylmagnesium bromide could then add to **6**, giving **3** after hydrolysis (Scheme 2).

The reactivity observed in the addition of EtMgBr to $Mes_2Ge{=}GeMes_2$ parallels that for the addition of the methyl analog. However, unlike the methyl analog where a ligand exchange was observed only upon thermolysis of the germyl Grignard reagent at 105°C, the ethyl-for-mesityl exchange was observed at low temperature. Presumably, the more facile ligand exchange is the result of greater steric congestion in the germyl Grignard reagent, which is subsequently relieved upon elimination of mesitylmagnesium bromide. Ligand exchange in t-Bu_2MeSi-$GeMes_2MgX$ was also observed at lower temperatures compared to ligand exchange in Mes_2MeSi-$GeMes_2MgX$ (3).

Thermolysis of hexamesitylcyclotrigermane for extended periods of time gave two major products: 1,2,2-triethyl-1,1-dimesityldigermane (**8**) and 2,2-diethyl-1,1,1-trimesityldigermane (**9**) in a 1:1 to 2:1 ratio (eq. [4]). Compounds **8** and **9** were identified using standard spectroscopic techniques.

[3]

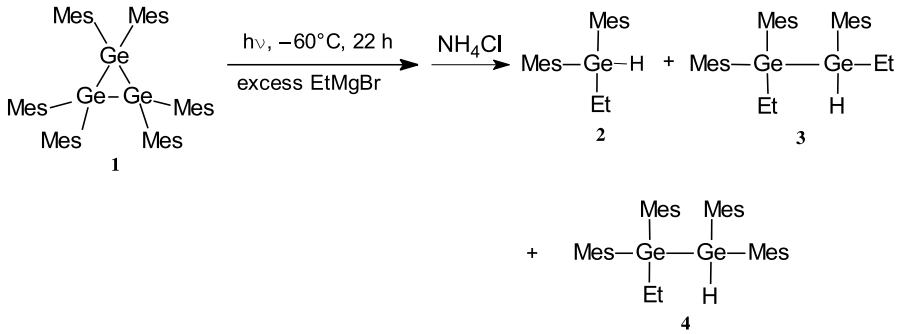

[4]

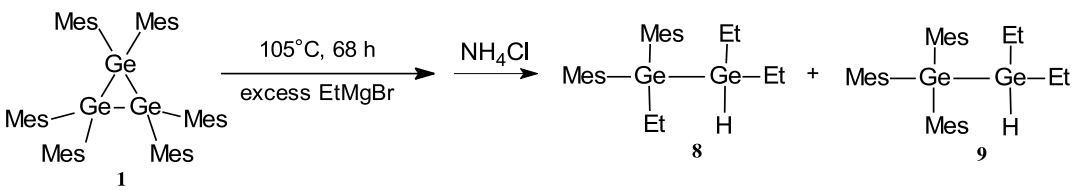

© 2002 NRC Canada

Scheme 2.

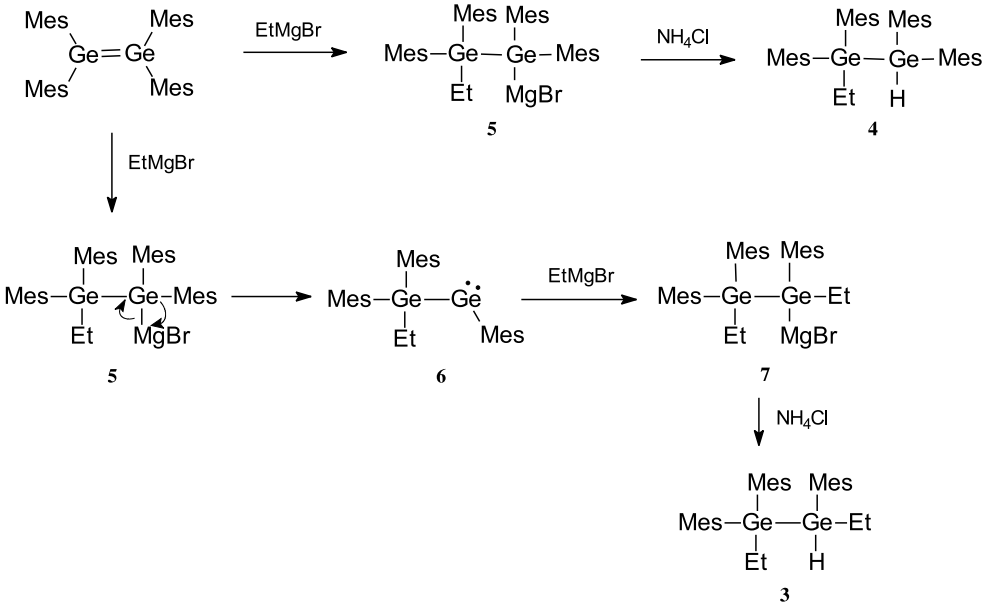

Scheme 3.

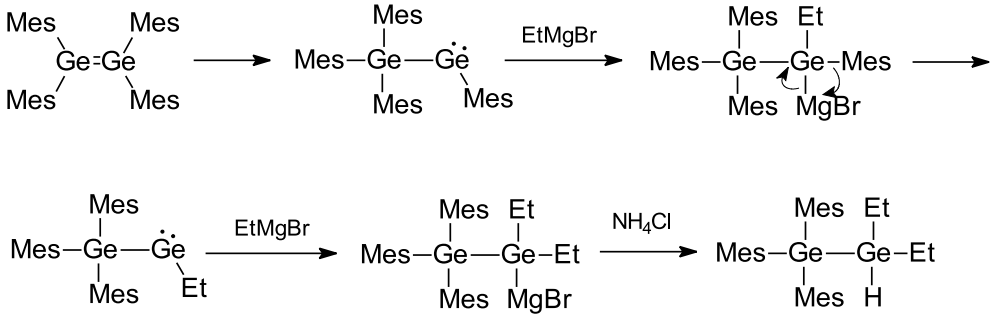

Formation of these two compounds can be easily explained based on our current mechanism. Compound **8** appears to be the result of an α-elimination of mesitylmagnesium bromide from germyl Grignard **7** to give ethyldimesitylgermylethylgermylene, followed by the addition of ethylmagnesium bromide to give **8** after hydrolysis. The formation of compound **9** is interesting since an analogous product was not observed in the addition of MeMgBr to the digermene. Tetramesityldigermene is known to undergo a facile mesityl migration to give trimesitylgermylmesitylgermylene (5). Addition of ethylmagnesium bromide to this germylene, followed by α-elimination of mesitylmagnesium bromide and the addition of a second equivalent of ethylmagnesium bromide, would result in the formation of germyl Grignard **10**, which upon quenching would give the observed product (Scheme 3). As in the analogous reaction with methylmagnesium halide, no apparent product derived from dimesitylgermylene was isolated. Presumably, ethylmagnesium bromide adds to Mes_2Ge: to give ethyldimesitylgermylmagnesium bromide; however, under the reaction conditions, complete ligand exchange occurs to give triethylgermane (after hydrolysis), which was not isolated. Thermolysis for shorter periods of time (2 h) gave a more complex reaction mixture. In addition to compounds **8** and **9**, compounds **2** and **3** were formed, providing evidence for the intermediate formation of ethyldimesitylgermylmagnesium bromide and the germyl Grignard **7**.

Again, there are both similarities and differences observed in comparison to the analogous thermolysis of hexamesitylcyclotrigermane with the methyl Grignard reagent. A facile ligand exchange was also observed in this system; however, the rate of addition of the bulkier ethyl group appears to compete with the 1,2-mesityl shift at 105°C.

Given the interesting reactivity of germyl Grignard reagents and the absence of any reported additions of alkyllithium reagents to Group 14 dimetallenes, we also investigated the addition of methyllithium to $Mes_2Ge{=}GeMes_2$ under similar conditions.

The photolysis of hexamesitylcyclotrigermane in the presence of methyllithium at –60°C followed by quenching the reaction mixture with a solution of ammonium chloride gave two products: methyl-1,1,2,2-tetramesityldigermane (2) (**11**)

© 2002 NRC Canada

[5] 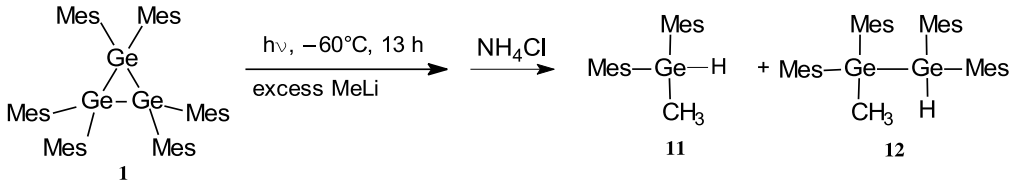

1 11 12

and dimesitylmethylgermane (6) (**12**) in modest isolated yields (eq. [5]). The compounds were identified by comparison of their spectroscopic data to that of authentic samples. Given that methyllithium does not react with the cyclotrigermane in the dark, it is reasonable to assume that methyllithium adds to both tetramesityldigermene and dimesitylgermylene (generated by photolysis of the cyclotrigermane) in the same manner as Grignard reagents. Thermolysis of hexamesitylcyclotrigermane in the presence of methyllithium gave only a complex reaction mixture, in contrast to the analogous reaction with methyl Grignard reagent.

In summary, the results described here for the addition of ethylmagnesium bromide to tetramesityldigermene and dimesitylgermylene parallel those previously observed for the addition of methylmagnesium bromide to digermenes and germasilenes. Hence, it has become increasingly apparent that the addition of Grignard reagents to both digermenes and germylenes and the ligand exchange of germyl Grignard reagents are all general reactions. Furthermore, alkyllithium reagents also appear to readily add to digermenes and germylenes, although thermolysis of the resulting mixture of germyllithium reagents does not lead to isolable species. We continue to explore the addition of a variety of organometallic reagents to digermenes and the chemistry of the resulting germyl metallic reagents.

Experimental

All experiments were carried out in flame-dried glassware under an inert argon atmosphere. Toluene, diethyl ether, and THF were freshly distilled from sodium/benzophenone. Ethylmagnesium bromide was prepared from commercially available ethyl bromide and magnesium (Lancaster Chemical Co.). The concentration of the Grignard reagent was determined by titration, prior to use. Chromatographic separations and purifications were carried out using a Chromatotron (Harrison Research) or on conventional silica gel preparative plates. Photolyses were carried out at 350 nm in a Rayonet photochemical reactor. The solution to be photolyzed was placed in a Schlenk tube and suspended in an immersion well filled with methanol at –60°C. The temperature of the methanol was maintained using a NESLAB ULT-80 low temperature bath circulator.

NMR spectra were recorded on a Varian Gemini 200, an XL-300, or a Varian Gemini 300 NMR spectrometer using benzene-d_6 as a solvent. IR spectra were recorded (cm^{-1}) as thin films on a PerkinElmer 2000 FT-IR spectrometer. A Finnegan MAT model 8200 mass spectrometer, with an ionizing voltage of 70 eV, was used to obtain electron impact mass spectra (recorded in mass-to-charge units (*m/z*) with ion identity and peak intensities relative to the base peak in parentheses).

Photolysis of hexamesitylcyclotrigermane in the presence of excess ethylmagnesium bromide

A solution of Ge_3Mes_6 (48 mg, 0.052 mmol) and freshly prepared ethylmagnesium bromide (1 mL, 1.5 mmol in Et_2O) in toluene (3 mL) was photolyzed (350 nm) for 22 h at –60°C. At the end of the photolysis, the solution was bright yellow-orange. The cold reaction mixture was quenched with aqueous ammonium chloride. The aqueous and organic phases were then separated. The aqueous phase was extracted with three portions of hexanes and the extracts were combined with the organic phase. The organic phase was dried over anhydrous magnesium sulfate and then filtered to remove the solid. Removal of the solvent in vacuo yielded a clear, colourless oil. ^{1}H NMR spectroscopic analysis of the reaction mixture showed three major products in a 7.8:1:2.8 ratio (**2**:**4**:**3**). The reaction mixture was separated by TLC using 8% CH_2Cl_2 in hexanes as the eluent to give ethyldimesitylgermane (**2**, 15.3 mg, 87%) and ethyl-1,1,2,2-tetramesityldigermane (**4**, 8.5 mg, 25%). Compound **3** was not isolated in pure form.

Ethyldimesitylgermane (2):

mp 76.5–78°C. IR (thin film) (cm^{-1}): 2045 (Ge-H). ^{1}H NMR (ppm) δ: 6.73 (s, 4H, Ar-H), 5.44 (t, J = 4.2 Hz, 1H, Ge-H), 2.35 (s, 12H, Mes *o*-CH_3), 2.11 (s, 6H, Mes *p*-CH_3), 1.34–1.45 (m, 2H, Et-CH_2), 1.12 (t, J = 7.7 Hz, 3H, Et-CH_3). ^{13}C NMR (ppm) δ: 143.46 (Mes-C), 138.12 (Mes-C), 134.25 (Mes-C), 129.08 (Mes-CH), 23.89 (Mes *o*-CH_3), 21.02 (Mes *p*-CH_3), 11.58 (CH_2), 11.26 (CH_3). MS *m/z*: 342 ([M]$^+$, 10), 313 ([$HGeMes_2$], 100), 222 ([GeEtMes], 34), 191 ([GeMes], 42), 119 ([Mes], 18), 105 (25). HR-MS calcd. for $C_{20}H_{28}{}^{74}Ge$: 342.1403; found: 342.1393.

Ethyl-1,1,2,2-tetramesityldigermane (4):

IR (thin film) (cm^{-1}): 2032 (Ge-H). ^{1}H NMR (ppm) δ: 6.72 (s, 4H, Ar-H), 6.70 (s, 4H, Ar-H), 5.92 (s, 1H, Ge-H), 2.36 (s, 12H, Mes *o*-CH_3), 2.21 (s, 12H, Mes *o*-CH_3), 2.10 (s, 6H, Mes *p*-CH_3), 2.09 (s, 6H, Mes *p*-CH_3), 1.92 (q, J = 7.8 Hz, 2H, Et-CH_2), 1.1 (t, J = 7.8 Hz, 3H, Et-CH_3). ^{13}C NMR (ppm) δ: 143.80, 143.73, 137.83, 137.48, 137.45, 136.58 (all C), 129.44 (Mes-CH), 128.96 (Mes-CH), 24.90, 24.85, 21.00, 20.91 (all CH_3), 15.20 (CH_2), 11.06 (CH_3). CI-MS *m/z* (isobutane): 651 ([M – H]$^+$, 5), 533 ([M – Mes]$^+$, 13), 431 ([$GeMes_3$], 17), 341 ([$GeMes_2Et$], 100), 311 ([$GeMes_2$ – H], 22), 223 ([GeEtMesH], 18), 191 ([GeMes], 10), 121 ([MesH + H], 88). HR-MS calcd. for $C_{38}H_{50}{}^{72}Ge^{74}Ge$-H: 651.2267; found: 651.2276.

Thermolysis of hexamesitylcyclotrigermane in the presence of excess ethylmagnesium bromide

A solution of Ge_3Mes_6 (50.3 mg, 0.055 mmol) and freshly prepared ethylmagnesium bromide (1 mL, 1.65 mmol in Et_2O) in toluene (4 mL) was heated for 68 h at 105°C. After a few minutes of heating, the clear and colourless solution

© 2002 NRC Canada

became light yellow and some solid precipitated from solution. At the end of the thermolysis, the solution was cloudy grey in colour with a white solid precipitate. Following the thermolysis, the reaction mixture was quenched with aqueous ammonium chloride. The aqueous and organic phases were then separated. The aqueous phase was extracted with three portions of hexanes and the extracts were combined with the organic phase. The organic phase was dried over anhydrous magnesium sulfate and then filtered to remove the solid. Removal of the solvent in vacuo yielded a clear, colourless oil. ^{1}H NMR spectroscopic analysis of the reaction mixture showed two major products (**8** and **9**) in a 1:1 or 2:1 ratio. The product mixture was separated by TLC using 10% CH_2Cl_2 in hexanes as the eluent to give 2,2-diethyl-1,1,1-trimesityldigermane (**9**, 1.1 mg, 3.8%) and 1,2,2-triethyl-1,1-dimesityldigermane (**8**, 4.8 mg, 18.5%).[2]

1,2,2-Triethyl-1,1-dimesityldigermane (8):

Oily solid. IR (thin film) (cm^{-1}): 1996 (Ge-H). ^{1}H NMR (ppm) δ: 6.72 (s, 4H, Mes-H), 4.28 (m, 1H, Ge-H), 2.35 (s, 12H, Mes *o*-CH_3), 2.11 (s, 6H, Mes *p*-CH_3), 1.65 (q, J = 7.8 Hz, 2H, Et-CH_2), 0.95–1.15 (m, 13H, 2 Et + Et-CH_3). ^{13}C NMR (ppm) δ: 142.80, 137.64, 137.57, 129.26 (CH), 24.89 (CH_3), 20.94 (CH_3), 14.86 (CH_2), 11.98 (CH_3), 11.03 (CH_3), 5.76 (CH_2). MS *m/z*: 472 ([M]$^+$, 2), 443 ([M – Et]$^+$, 4), 415 ([M – 2Et + H]$^+$, 2), 385 ([M – 3Et]$^+$, 1), 341 ([$GeMes_2Et$], 100), 313 ([$GeMes_2$ + H], 20), 221 ([GeEtMes – H], 6), 193 ([GeMes], 36), 119 ([Mes], 14). HR-MS calcd. for $C_{24}H_{43}{}^{72}Ge^{74}Ge$: 472.1406; found: 472.1390.

2,2-Diethyl-1,1,1-trimesityldigermane (9):

mp 176–180°C. IR (thin film) (cm^{-1}): 1982 (Ge-H). ^{1}H NMR (ppm) δ: 6.75 (s, 6H, Mes-H), 4.18 (tt, J = 1.0 Hz, J = 5.0 Hz, 1H, Ge-H), 2.27 (s, 18H, Mes *o*-CH_3), 2.11 (s, 9H, Mes *p*-CH_3), 1.21 (pseudo t, 6H, Et-CH_3), 0.8–1.1 (m, 4H, Et-CH_2). ^{13}C NMR (ppm) δ: 143.82, 138.86, 137.85, 129.57, 24.92, 20.95, 13.42, 8.14 (CH_2). MS *m/z*: 561 ([M – H]$^+$, 17), 533 ([M – Et]$^+$, 4), 443 ([M – Mes]$^+$, 47), 431 ([$GeMes_3$], 100), 311 ([$GeMes_2$ – H], 7), 191 ([GeMes], 12), 119 ([Mes], 10). HR-MS calcd. for $C_{31}H_{43}{}^{72}Ge^{74}Ge$ ([M – H]): 561.1797; found: 561.1807.

The experiment was repeated (49 mg Ge_3Mes_6, 1 mL of EtMgBr in Et_2O, toluene (1.5 mmol, 3 mL), 105°C), except the reaction mixture was heated for 2 h only. Under these conditions the following products were obtained: Mes_3Ge-$GeHEt_2$ (**9**), Mes_2GeEtH (**2**), Mes_2EtGe-$GeEt_2H$ (**8**), and a fourth product tentatively identified as Mes_2EtGe-GeHEtMes (**3**) in a 3.3:2.9:1:1.2 ratio. The products were separated by TLC using 6% CH_2Cl_2 in hexanes as the eluent. Compound **3** was obtained as a mixture with Mes_3Ge-$GeHEt_2$.

1,2-Diethyl-1,1,2-trimesityldigermane (3):

^{1}H NMR (ppm) δ: 6.74 (s), 6.70 (s, 2H, Mes-H), 5.21 (dd, J = 3 Hz, J = 6 Hz, 1H, Ge-H), 2.31 (s, 6H, Mes CH_3), 2.20 (s, 6H, Mes CH_3), 2.18 (s, 6H, Mes CH_3), 2.12 (s, 6H, Mes CH_3), 2.11 (s, 3H, Mes CH_3), 1–1.8 (m, Et). ^{13}C NMR (ppm) δ: 144.20, 142.99, 138.50, 137.65, 137.60, 133.33, 129.25 (CH), 129.17 (CH), 128.81 (CH), 25.05 (CH_3), 24.91 (CH_3), 24.88 (CH_3), 20.94 (CH_3), 14.69 (CH_2), 12.62 (CH_3), 11.00 (CH_3), 9.87 (CH_2). MS *m/z*: 562 ([M]$^+$).

Photolysis of hexamesitylcyclotrigermane in the presence of methyllithium

Methyllithium (1.0 mL of a 1.4 M solution in diethyl ether, 1.4 mmol) was added to a Schlenk tube containing a clear, pale yellow solution of Ge_3Mes_6 (53 mg, 0.057 mmol) dissolved in toluene (4 mL). The Schlenk tube was then sealed and placed in an immersion well, cooled to –60°C, and then irradiated for 13 h. After photolysis, the clear, deep yellow solution was warmed to room temperature and was quenched with aqueous ammonium chloride. The aqueous and organic phases were then separated. The aqueous phase was extracted with four portions of hexanes and the extracts were combined with the organic phase. The organic phase was washed three times with water and then dried over anhydrous magnesium sulfate. After filtration to remove the solid, removal of the solvent in vacuo yielded a pale yellow solid. The product mixture was separated by preparative TLC using hexanes–dichloromethane (99:1) as the eluent to give 1,1,2,2-tetramesitylmethyldigermane (2) (**12**, 16 mg, 44%) and dimesitylmethylgermane (6) (**11**, 7 mg, 38%), which were identified by comparison of their ^{1}H NMR spectra with authentic samples.

Attempted reaction of hexamesitylcyclotrigermane with methyllithium in the dark

Methyllithium (1.0 mL of a 1.4 M solution in diethyl ether, 1.4 mmol) was added to a Schlenk tube containing a clear, pale yellow solution of Ge_3Mes_6 (50 mg, 0.054 mmol) dissolved in toluene (4 mL). The Schlenk tube was covered in aluminum foil and left undisturbed for 14 h at room temperature (rt). No change in the colour of the solution was observed. Saturated aqueous ammonium chloride was then added to the solution. The aqueous and organic phases were then separated. The aqueous phase was extracted with four portions of hexanes and the extracts were combined with the organic phase. The organic phase was washed three times with water and then dried over anhydrous magnesium sulfate. After filtration to remove the solid, removal of the solvent in vacuo yielded a pale yellow solid. The solid was identified as hexamesitylcyclotrigermane (41.6 mg, 83%) by ^{1}H NMR spectroscopy.

Thermolysis of hexamesitylcyclotrigermane in the presence of methyllithium

Methyllithium (1.0 mL of a 1.4 M solution in diethyl ether, 1.4 mmol) was added to a Schlenk tube containing a clear, pale yellow solution of Ge_3Mes_6 (50 mg, 0.054 mmol) dissolved in toluene (4 mL). The Schlenk tube was then placed in an oil bath at 100°C for 14 h. The orange-brown solution was allowed to cool to rt. The colour of the solution changed to pale yellow upon quenching with saturated ammonium chloride; a gas was evolved. The aqueous and organic phases were then separated. The aqueous phase was extracted with four portions of hexanes and the extracts were combined with the organic phase. The organic phase was washed three times with water and then dried over anhydrous magnesium sulfate. After filtration to remove the solid, removal of the solvent in vacuo yielded a yellow oil. Analysis

[2] Due to the small quantities of samples, it was impossible to obtain enough material for elemental analysis.

© 2002 NRC Canada

of the oil by ^{1}H NMR spectroscopy revealed a complex mixture of products, which could not be separated or identified.

Acknowledgements

The financial support of the Natural Sciences and Engineering Research Council of Canada (NSERC) is gratefully acknowledged.

References

1. For recent reviews on digermene chemistry see: (*a*) J. Escudié and H. Ranaivonjatovo. Adv. Organomet. Chem. **44**, 113 (1999); (*b*) K.M. Baines and W.G. Stibbs. Adv. Organomet. Chem. **39**, 275 (1996); (*c*) J. Escudié, C. Couret, H. Ranaivonjatovo, and J. Satgé. Coord. Chem. Rev. **130**, 427 (1994); (*d*) T. Tsumuraya, S.A. Batcheller, and S.A. Masamune. Angew. Chem. Int. Ed. Engl. **30**, 902 (1991); (*e*) J. Barrau, J. Escudié, and J. Satgé. Chem. Rev. **90**, 283 (1990).
2. C.E. Dixon, M.R. Netherton, and K.M. Baines. J. Am. Chem. Soc. **120**, 10 365 (1998).
3. M.S. Samuel, K.M. Baines, and D.W. Hughes. Can. J. Chem. **78**, 1474 (2000).
4. (*a*) T. Tsumuraya, S. Sato, and W. Ando. Organometallics, **7**, 2015 (1988); (*b*) N.P. Toltl, W.J. Leigh, G.M. Kollegger, W.G. Stibbs, and K.M. Baines. Organometallics, **15**, 3732 (1996).
5. K.M. Baines, J.A. Cooke, and J.J. Vittal. J. Chem. Soc. Chem. Commun. 1484 (1992).
6. A. Castel, P. Rivière, J. Satgé, and H.Y. Ko. Organometallics, **9**, 205 (1990).

© 2002 NRC Canada

Organophosphazenes. 25. The synthesis and electrochemistry of the dicobalt hexacarbonyl complexes of phenylethynylcyclophosphazenes[1]

Maneesh Bahadur, Christopher W. Allen, William E. Geiger, and Adam Bridges

Abstract: The syntheses of the dicobalt hexacarbonyl complexes, $N_3P_3F_{6-n}(C{\equiv}CPhCo_2(CO)_6)_n$ (n = 1 (**3**), n = 2 (**4**)), is reported. The introduction of the organometallic fragment allows for simplification of the NMR spectra and separation of the isomers of the disubstituted (**4**) derivatives. Electrochemical studies show that **3** undergoes a reversible one-electron reduction. At 233 K, the geminal isomer of **4** undergoes two separate reversible one-electron reductions. The ESR spectra of the radical anions of **3** and **4** have been obtained and show the absence of delocalization of unpaired spin density from the organometallic cluster to the phosphazene.

Key words: cyclophosphazenes, cobalt–alkyne clusters, electrochemistry, ESR.

Résumé : On a réalisé la synthèse de complexes de dicobalt hexacarbonyle, $N_3P_3F_{6-n}(C{\equiv}CPhCo_2(CO)_6)_n$ (n = 1 (**3**), n = 2 (**4**)). L'introduction du fragment organométallique simplifie les spectres RMN et la séparation des isomères des dérivés disubstitués (**4**). Des études électrochimiques montrent que le composé **3** subit une réduction réversible à un électron. À 233 K, l'isomère géminé du composé **4** subit deux réactions séparées de réductions réversibles à un électron. Les spectres RPE des anions radicaux des composés **3** et **4** ont été mesurés et ils mettent en évidence l'absence de délocalisation de la densité de spin non pairée de l'agrégat organométallique vers le phosphazène.

Mots clés : cyclophosphazène, agrégats cobalt–alcyne, électrochimie, RPE.

[Traduit par la Rédaction]

Introduction

The reactions of main group organometallic reagents with halocyclophosphazenes has lead to the formation of a broad array of organophosphazene derivatives (1, 2). Within this class of compounds, the aryl derivatives have attracted the most attention (1, 3–5). The ethenyl derivatives have been widely exploited as monomers in olefin addition polymerization reactions leading to carbon chain polymers with cyclophosphazene substituents (6–8). By way of contrast, significantly less interest has been shown in the corresponding ethynyl derivatives, in which a direct phosphorus — ethynyl carbon bond exists. The first examples of this class of compounds, $N_3P_3F_{6-n}$ $(C{\equiv}CPh)_n$ (n = 1,2), and the dicobalt hexacarbonyl derivative of $N_3P_3F_5C{\equiv}CPh$ were reported by Chivers (9). Utilization of the reactions of lithioethynyl reagents with $N_3P_3F_6$ also provides trimethylsilylethynyl (10), alkylethynyl (11), and mixed aryl-phenylethynyl derivatives (12). Indirect routes involve catalyzed rearrangements of propargyl derivatives (13) and byproducts in the reaction of lithiopropene with $N_3P_3F_6$ (14). The electronic structure of these materials has been probed by UV–photoelectron spectroscopy (15). In this paper, we present the results of a study of the synthesis and redox processes of the dicobalt hexacarbonyl derivatives of phenylethynylfluorocyclotriphosphazenes. These investigations provide additional insights into the nature of the interactions between unsaturated organic substituents and the cyclophosphazene ring. A preliminary report of certain aspects of this work has appeared (16).

Received 26 January 2002. Published on the NRC Research Press Web site at http://canjchem.nrc.ca on 23 September 2002.

This paper is dedicated to Professor Tris Chivers who has continually demonstrated the ability to produce outstanding chemistry while retaining the highest standards of collegiality and personal integrity.

M. Bahadur, C.W. Allen,[2] W.E. Geiger, and A. Bridges. The Department of Chemistry, University of Vermont, Burlington, VT 05405–0125, U.S.A.

[1]Part 24. C.W. Allen and S.D. Worley. Inorg. Chem. **38**, 5187 (2000).

[2]Corresponding author (email: cwallen@zoo.uvm.edu)

Experimental

Materials

Hexachlorocyclotriphosphazene ($N_3P_3Cl_6$) was converted to $N_3P_3F_6$ (17), which in turn was converted to $N_3P_3F_5(C{\equiv}CPh)$ (**1**), $N_3P_3F_4(C{\equiv}CPh)_2$ (**2**) (9, 10), and $P_3N_3F_5C_6H_4CMe{=}CH_2$ (5) by previously reported procedures. Butyllithium (2.5 M in hexane) and phenylacetylene were obtained from Aldrich Co. Dicobalt octacarbonyl (Johnson Matthey) was sublimed and used immediately. All manipulations were performed under nitrogen. All solvents were distilled from the appropriate drying agents prior to use, and further purification of the solvents for electrochemical and ESR experiments was achieved by three freeze–pump–thaw cycles followed by vacuum distillation.

 DOI: 10.1139/V02-138 © 2002 NRC Canada

Measurements

Infrared spectra were recorded on a PerkinElmer 1430 spectrophotometer. Mass spectrometry was carried out on a Finnigan 4610 spectrometer operating at 70 eV. NMR spectra were recorded on a Bruker WM250 spectrometer operating at: 250.1 MHz (^{1}H); 62.9 MHz (^{13}C); 235.35 MHz (^{19}F); 101.2 MHz (^{31}P) and using $CDCl_3$ for a lock compound. Tetramethylsilane (TMS) (^{1}H and ^{13}C) was used as an internal reference, while 85% H_3PO_4 (^{31}P) and $CFCl_3$ (^{19}F) were used as external references. Chemical shifts upfield from the reference are negative. Broad band ^{1}H decoupling was used for the ^{13}C, ^{19}F, and ^{31}P spectra. ESR measurements were performed on a modified Varian E-3 spectrometer with external diphenylpicrylhydrazide (DPPH) as a standard. Elemental analyses were performed by Robertson Laboratory, Inc. Electrochemical measurements were carried out using a Princeton Applied Research Model 173 potentiostat with a Hewlett-Packard 7004B *x-y* recorder as described in the literature (18). Solutions for cyclic voltammetry (CV) contained 0.5 mM of the metal complex and also contained 0.1 M Bu_4NPF_6 as the supporting electrolyte in THF. Potentials are reported vs. Ag/AgCl. Low-temperature CV solutions contained 0.1 M $Bu_4NCF_3SO_3$ as the supporting electrolyte. Low temperature was achieved by immersing the voltammetry cell in a dry ice – acetone slush bath. For rotating platinum electrode (RPE) measurements, a Sargent synchronous rotor (1800 rpm) was employed.

Syntheses of (dicobalt hexacarbonyl phenylethynyl) pentafluorocyclotriphosphazene ($N_3P_3F_5C{\equiv}CPhCo_2(CO)_6$) (3)

This preparation is a modification of a previously reported procedure (9). (β-Phenylethynyl)pentafluorocyclotriphosphazene ($N_3P_3F_5C{\equiv}CPh$, **1**) (0.74 g, 2.25 mmol), and dicobalt octacarbonyl (0.78 g, 2.25 mmol), were allowed to react in hexane (40 mL) in a nitrogen filled flask connected to a gas bubbler system. The reaction mixture was stirred at room temperature. The reaction was monitored by IR spectroscopy and found to be complete within 30 min. After the solvent was removed, the material was chromatographed on silica gel with hexane and methylene chloride (90:10 v/v) as the eluent. The product eluted as a red band. The red compound was isolated and crystallized from hexane as red microcrystalline material. MW: calcd. 616; found 617 (CI-MS). ^{13}C NMR δ: 99.5 ([*C*≡$CC_6H_5{\cdot}Co_2(CO)_6]_2$), 136.5 ([C≡*C*$C_6H_5Co_2(CO)_6]_2$), 130.0, 129.0, 128.8, (C_6H_5), 197.3 ($Co_2(CO)_6$). ^{19}F NMR δ: 57.4 (d, J_{PF} = 974 Hz, ≡PF[C≡$CC_6H_5Co_2(CO)_6$]), 72.9 (d, J_{PF} = 919 Hz, PF_2[cis]), 72.2 (d, J_{PF} = 946 Hz, ≡PF_2[trans]). ^{31}P NMR δ: 9.4 (t, J_{PF} = 929 Hz, ≡PF_2), 38.0 (d of t, J_{PF} = 975 Hz, $^2J_{PP}$ = 68.8 Hz, ≡PF[C≡$C_6H_5Co_2(CO)_6$]).

Synthesis of bis(dicobalt hexacarbonylphenylethynyl)-tetrafluorocyclotriphosphazene (2,2-$N_3P_3F_4(C{\equiv}CPhCo_2(CO)_6)_2$) (4)

Bis(phenylethynyl)tetrafluorocyclotriphosphazene ($N_3P_3F_4$[C≡CPh]$_2$) (0.7 g, 2.25 mmol), and dicobalt octacarbonyl (1.55 g, 4.5 mmol), were allowed to react in hexane (60 mL) in a nitrogen filled flask connected to a gas bubbler system. The reaction mixture was stirred at room temperature for 30 min and monitored by IR. After the solvent was removed, the material was chromatographed on silica gel with hexane and methylene chloride (90:10) as the eluent. Two red fractions were isolated, which were shown to be the geminal isomer and the cis–trans non-geminal mixture. The pure geminal isomer was obtained as dark red crystals from hexane solution at –20°C (0.89 g, 40% yield). The melting point of the geminal isomer was found to be greater than 225°C. Attempts to crystallize or sublime either of the non-geminal isomers were unsuccessful, nor could the isomers be separated. A yield of 0.14 g (15%) was obtained. Anal. calcd. for $C_{28}H_{10}F_4N_3P_3O_{12}Co_2$: C 34.12, H 1.01, MW 985; found: (geminal) C 34.21, H 0.92. Molecular ion M^+ was not observed in either EI- or CI-MS.

Geminal

IR (KBr pellet) (cm^{-1}): 2098, 2077, 2067, 2044, 2031, 2026, 2008 ($\nu_{terminal\ CO}$), 1562 ($\nu_{c\equiv c}$), 1476, 1439, 1242 ($\nu_{as\ PNP}$), 1184, 926, 915 (sh) ($\nu_{as\ PF}$), 811 (($\nu_{sym\ PF}$); hexane solution), 2018, 2032 (sh), 2040, 2071, 2097 ($\nu_{terminal\ CO}$). ^{13}C NMR δ: 99.5 (≡P[*C*≡C $C_6H_5Co_2(CO)_6]_2$), 136.5 (≡P[C≡*C*-$C_6H_5Co_2(CO)_6]_2$), 130.0, 129.0, 128.8 (C_6H_5), 197.3 ($Co_2(CO)_6$). ^{19}F NMR δ: 72.9 (d, J_{FP} = 889 Hz, ≡PF_2). ^{31}P NMR δ: 8.2 (t, J_{PF} = 892 Hz, ≡PF_2), 32.5 (t, $^2J_{PP}$ = 50.1 Hz, ≡P[C≡$CC_6H_5Co_2(CO)_6]_2$). MS (molecular ion ([M^+]) not observed), *m/e* (%): 901 ([M – 3CO]$^+$, 10), 845 ([M – 5CO]$^+$, 1.7), 817 ([M – 6CO]$^+$, 6.6), 789 ([M – 7CO]$^+$, 20.8), 761 ([M – 8CO]$^+$, 26), 733 ([M – 9CO]$^+$, 6), 705 ([M – 10CO]$^+$, 15), 677 ([M – 11CO]$^+$, 8), 649 ([M – 12CO]$^+$, 100).

Cis non-geminal

^{19}F NMR δ: 68.4 (d, J_{FP} = 912 Hz, ≡PF_2[trans]), 73.2 (d, J_{FP} = 912 Hz, ≡PF_2[cis]), 46.5 (d, J_{FP} = 962 Hz, ≡PF(C≡$CC_6H_5Co_2(CO)_6$]). ^{31}P NMR δ: 6.2 (t of t, J_{PF} = 997 Hz, $^2J_{PP}$ = 78 Hz, ≡PF_2), 36.1 (d of d, J_{PF} = 979 Hz, $^2J_{PP}$ = 70 Hz, ≡PF[C≡$CC_6H_5Co_2(CO)_6$]). MS, cis-trans mixture (molecular ion ([M^+]) not observed), *m/e* (%): 901 ([M – 3CO]$^+$, 10), 845 ([M – 5CO]$^+$, 1.7), 817 ([M – 6CO]$^+$, 6.6), 789 ([M – 7CO]$^+$, 20.8), 761 ([M – 8CO]$^+$, 26), 733 ([M – 9CO]$^+$, 6), 705 ([M – 10CO]$^+$, 15), 677 ([M – 11CO]$^+$, 8), 649 ([M – 12CO]$^+$, 100).

Trans non-geminal

^{19}F NMR δ: 72.3 (complex d, J_{FP} = 888 Hz, ≡PF_2), 52.8 (complex d, J_{FP} = 937 Hz, ≡PF[C≡$CC_6H_5Co_2(CO)_6$]). ^{31}P NMR δ: 6.2 (t, J_{PF} = 997 Hz, ≡PF_2), 34.8 (d of d, J_{PF} = 944 Hz, $^2J_{PP}$ = 70 Hz, ≡PF[C≡$CC_6H_5Co_2(CO)_6$]).

Attempted reaction of the lithium salt of hexacarbonyl(phenylethyne)dicobalt

The reaction of $LiC{\equiv}CPhCo_2(CO)_6$, generated from lithium diisopropylamide and $HC{\equiv}CPhCo_2(CO)_6$, with an equimolar quantity of $N_3P_3F_5C_6H_4CMe{=}CH_2$ in hexane, resulted in a dark green solution, from which a green solid was isolated. The absence of detectable ^{31}P NMR resonances indicated that the phosphazene derivative was not formed.

Chemical reduction of 3 and 4

The reduction was carried out on a vacuum line with 0.75 mmol of **3**, or the geminal isomer of **4**, and 0.18 mg (0.75 mmol) of cobaltocene, in an ESR tube. The ESR tube

© 2002 NRC Canada

was connected to the vacuum line and evacuated. Approximately 0.5 mL of 2:1 tetrahydrofuran–dichloromethane (v/v) was introduced by vacuum transfer, and subsequently the ESR tube was sealed off. After thawing the sample, the reaction was carried out at –65°C (in a dry ice – acetone slush bath) for less than 5 min, and then the sample was frozen in liquid nitrogen. The ESR spectra were then immediately recorded at liquid nitrogen temperature.

Results and discussion

The reaction of dicobalt octacarbonyl with **1** (9) and **2** lead cleanly to the respective dicobalt hexacarbonyl – alkyne cluster derivatives.

[1] $N_3P_3F_5C{\equiv}CPh + Co_2(CO)_8$ (**1**) $\rightarrow N_3P_3F_5(C{\equiv}CPhCo_2(CO)_6)$ (**3**)

[2] $N_3P_3F_4(C{\equiv}CPh)_2 + Co_2(CO)_8$ (**2**) $\rightarrow N_3P_3F_4(C{\equiv}CPhCo_2(CO)_6)_2$ (**4**)

An alternative route to the synthesis of dicobalt hexacarbonyl – alkyne complexes, via the reactions of $LiC{\equiv}CPhCo_2(CO)_6$ (19), was also attempted. All attempts to isolate cyclophosphazene derivatives failed. The major product was a green solid, which is believed to be an alkyne coupling product. A similar product was observed in the reactions of $LiC{\equiv}CSiMe_3Co_2(CO)_6$ with electrophiles, and was shown to be a dimer, $Co_2(CO)_6Me_3SiC{\equiv}C\text{-}C{\equiv}CSiMe_3Co_2(CO)_6$ (19).

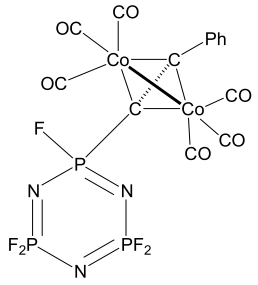

3

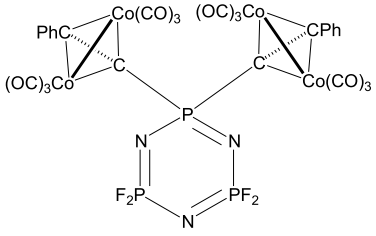

4

Previous NMR studies have shown that **2** consists of a mixture of inseparable isomers, with the geminal (2,2-) species being in large excess over the non-geminal (2,4-) components (10). The addition of the dicobalt hexacarbonyl fragment allowed for the chromatographic separation of the geminal (**4g**) and non-geminal isomers (**4ng**). The cis and trans isomers of 2,4-[(α-methylethenyl)phenylethynyl]tetrafluorocyclotriphosphazene have also been separated as their dicobalt hexacarbonyl complexes (12). These studies show the applicability of metal complex formation to the often intractable problem of separation of cyclophosphazene regio- and stereoisomers. The addition of the dicobalt hexacarbonyl fragment to the alkyne also had a significant effect on the ^{31}P NMR spectra. A comparison of the NMR spectra of **1** (10) to **3** showed that the alkynylphosphorus center ^{31}P resonance undergoes a 32 ppm downfield shift while the $\equiv PF_2$ centers only change by about 2 ppm. This leads to a considerable simplification in the spectrum in **3**, since in **1** the two phosphorus shifts are only separated by 2 ppm. The intra-ring phosphorus–phosphorus coupling constant ($^2J_{PP}$) decreased by 32 Hz. Similar changes were observed in a comparison of the geminal isomer of **2** to **4g**, wherein the corresponding bis(alkynyl)phosphorus resonance underwent a 66 ppm downfield shift and $^2J_{PP}$ decreased by 41 ppm. The NMR spectra of the **4ng** isomers were also sufficiently simplified so that the principle parameters could be measured and reported. The factors controlling the chemical shifts in cyclophosphazenes are complex and not well understood (20). In the present case, a change of the exocyclic bond angle at the phosphorus center or an introduction of a significant paramagnetic term to the shift tensor from the transition metal component are both viable proposals. The $^2J_{PP}$ values in cyclophosphazenes are controlled by the electronegativities of the phosphorus substituents (20). The carbon atoms of the phosphazene substituent change, from approximate *sp* hydridization in **1** and **2**, to a lower *s* character in the organometallic derivatives, and hence the orbital electronegativity decreases, leading to the observed decrease in $^2J_{PP}$.

The IR spectra for complexes **3** (9) and **4g** showed five CO bands between 2000 and 2110 cm^{-1}. The IR spectrum for **3** (9) showed a PN stretching band at 1269 cm^{-1}, while the PN stretching band for **4g** appeared at 1242 cm^{-1}. The PN stretching frequency showed a steady decrease in going from $P_3N_3F_6$, to **3**, to **4g**, which reflects an increased electron donation to the phosphazene ring by the [C≡C-$C_6H_5Co_2(CO)_6$] substituent, in comparison to the fluorine atom (21). The change in the $\upsilon_{C\equiv C}$ absorbance from **2** (2139 cm^{-1}) to **4** (1562 cm^{-1}) indicates a significant reduction in bond order, and hence in orbital electronegativity. The mass spectrum of **3** showed the parent ion and the peaks associated with the sequential loss of the six carbonyl groups. By way of contrast, in both **4g** and **4ng**, the $[M - 3CO]^+$ fragment is the highest mass peak, followed by the $[M - 5CO]^+$ ion. The base peak was the $[M - 12CO]^+$ ion.

The electrochemistry of alkyne – dicobalt hexacarbonyl clusters ($Co_2(CO)_6(\mu\text{-}RC_2R)$ (R = CF_3, Bu, Ph)) has been examined in some detail (22–24). This background provides a frame of reference for understanding the electrochemical behavior of **3** and **4**. The cyclic voltammogram (CV) of **3** showed a reversible reduction at $E^\circ = -0.64$ V (298 K). The anodic to cathodic (i_a/i_c) current ratios were unity over a scan rate range of 40–400 mV s^{-1}. Comparison of CV peak separations (ΔE_p), and $i_p/\upsilon^{1/2}$ with those of ferrocene, under the same experimental conditions,[3] established the process as diffusion-controlled, leading to the formation of $\mathbf{3}^-$. A second irreversible reduction was observed at –1.67 V. If one scans beyond the second reduction, the reverse scan reveals an anodic peak at −0.98 V, presumably due to a decomposition product of $\mathbf{3}^{2-}$. Low temperature CV studies did not show any change in the behavior of **3**, except for shifts in the E° values (E° (**3**) = –0.55 V at 233 K) and smaller diffusion

[3] The variable scan rate data for **3** and **4**, Tables D1 and D2, can be found in the supplementary material. Supplementary data may be purchased from the Depository of Unpublished Data, Document Delivery, CISTI, National Research Council Canada, Ottawa, ON K1A 0S2, Canada (http://www.nrc.ca/cisti/irm/unpub_e.shtml for information on ordering electronically).

© 2002 NRC Canada

Fig. 1. Cyclic voltammogram of **4g** at 233 K.

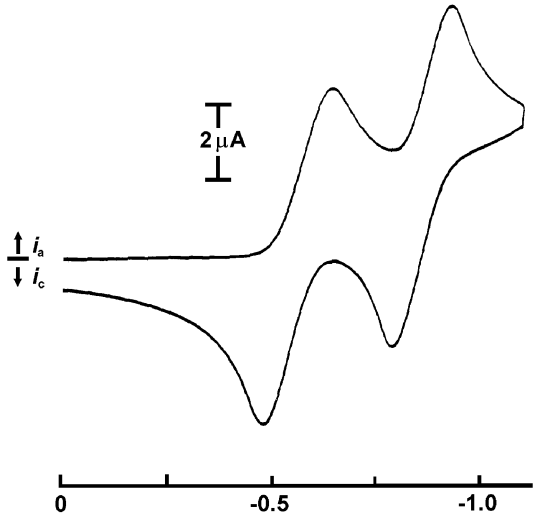

Fig. 2. Frozen solution ESR spectrum of the radical anion of **3**.

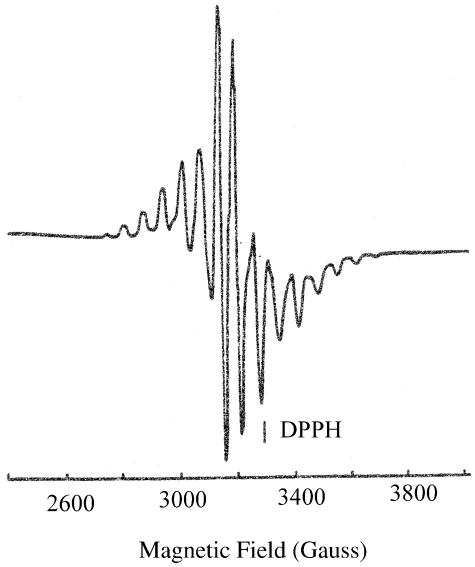

currents.[3] The room temperature CV for **4g** showed two closely spaced reduction waves in the potential range where only one was observed for **3**. The first process ($E°$ = −0.69 V) is reversible whereas the second (E = –1.08 V) is irreversible. The second process gives a follow-up product with an irreversible oxidation peak at 0.20 V, which was assigned to $Co(CO)_4^{-/0}$ (25). Other features in the potential range of 1.0 to –2.0 V are equivalent to those observed for **3**. There are, however, differences in the stabilities and formal potentials for formation of $\mathbf{3}^-$ and $\mathbf{4g}^-$**.** For **4g**, the i_a/i_c ratio increased from 0.66 at 40 mV s^{-1} to 0.96 at 400 mV s^{-1}. This indicates that the $\mathbf{4g}^{0/1-}$ redox process is only chemically reversible at the higher scan rates. Assuming that the decomposition of $\mathbf{4g}^-$ is a first-order process, a half-life of approximately 6 s can be calculated. The dianion, $\mathbf{4g}^{2-}$, has an even smaller half-life. The decomposition step of $\mathbf{4g}^{2-}$ can be avoided by a reduction in temperature. At 233 K, the CV of **4g** showed two reversible reduction steps, at −0.61 V and −0.94 V, for the $\mathbf{4g}^{0/-}$ and $\mathbf{4g}^{-/2-}$ steps, respectively (Fig. 1). Scans of the waves with a rotating platinum electrode established that they are both one-electron processes. Traditional diagnostic criteria (26) were used to demonstrate diffusion control through CV scans (Supplementary material, Tables D.1, D.2).[3] Within the limits of experimental error, the $i_p/\upsilon^{1/2}$ ratios for **3** or **4g** are the same (0.65 vs. 0.61) over the scan rate of 0.1 to 0.4 V s^{-1}. Thus, the following reactions (eq. [3]) govern the reductive behavior of the species under investigation. Previous investigations (22–24) have established that the lifetime of the radical anion derived from

[3] $\mathbf{3} + e^- \rightleftarrows \mathbf{3}^-$; $E°$ = –0.55 V

$\mathbf{4g} + e^- \rightleftarrows \mathbf{4g}^-$; $E°$ = –0.61 V

$\mathbf{4g}^- + e^- \rightleftarrows \mathbf{4g}^{2-}$; $E°$ = –0.94 V

dicobalt hexacarbonyl – alkyne clusters decreases as the electronegativity of the alkyne substituents decrease. For example, the room temperature lifetime of $[(CF_3)_2C_2Co_2(CO)_6]^-$ is greater than 1 h, whereas that of $[Ph_2C_2Co(CO)_6]^-$ is 17 ms (27). In **3** and **4g**, the effect of the strongly electron-withdrawing phosphazene (15) and the electron-donating phenyl group are counterbalanced to produce radicals of intermediate stability. The first reduction of **4g** takes place at a more negative potential compared with **3**, and the radical anion $\mathbf{3}^-$ is more stable than $\mathbf{4g}^-$. Both of these observations are a reflection of the decrease in the group electronegativity of the phosphazene substituent as a result of the replacement of a fluorine atom with the more electron donating alkyne – cobalt carbonyl cluster on going from **3** to **4g**.

The moderate stability of the radical anions allows for their characterization by ESR spectroscopy in frozen solutions. Chemical reduction was accomplished using cobaltocene (Cp_2Co) as the reductant. The ESR spectra of both $\mathbf{3}^-$ and $\mathbf{4g}^-$ showed 15 lines from hyperfine coupling to the two equivalent cobalt (I = 7/2) nuclei (Fig. 2). Hyperfine coupling to phosphorus was not observed. A first-order analysis yielded values of $\mathbf{g}_1$ = 2.04 and $\mathbf{a}_1$ = 67.8 G. These values are higher than those obtained from similar complexes that were interpreted in terms of anisotropic g and cobalt hyperfine tensors (27). The absence of phosphorus hyperfine coupling indicates that the unpaired electron is localized on the organometallic fragment and not delocalized to the phosphazene. The ultraviolet photoelectron spectra of alkynyl phosphazenes have also been interpreted as showing absence of π donation of the alkyne to the phosphazene (15). Thus, alkynylphosphazenes and their organometallic complexes are similar to alkenyl (15, 28) and arylphosphophosphazenes (5, 28, 29) in that the carbon–carbon π electron density is localized on the organic exocyclic substituent.

Acknowledgements

The support of this work by the National Science Foundation (NSF CHE 0092702) and the Vermont NSF EPSCoR program is gratefully acknowledged.

References

1. C.W. Allen. Chem. Rev. **91**, 119 (1991).
2. H.R. Allcock, J.L. Desorcie, and G.H. Riding. Polyhedron, **6**, 119 (1987).

© 2002 NRC Canada

3. C.W. Allen and T. Moeller. Inorg. Chem. **7**, 2183 (1968).
4. T. Chivers and N.L. Paddock. Inorg. Chem. **11**, 848 (1972).
5. J.C. Shaw and C.W. Allen. Inorg. Chem. **21**, 4632 (1986).
6. C.W. Allen. Trends Polym. Sci. **2**, 342 (1994).
7. C.W. Allen. MGCN Main Group Chem. News, **6**, 6 (1998).
8. J.C. van de Grampel and G. Bosscher. MGCN Main Group Chem. News, **6**, 10 (1998).
9. T. Chivers. Inorg. Nucl. Chem. Lett. **7**, 827 (1971).
10. C.W. Allen, J.L. Desorcie, and K. Ramachandran. J. Chem. Soc. Dalton Trans. 2843 (1984).
11. C.W. Allen and M. Bahadur. Phosphorus Sulfur Silicon, **73**, 203 (1993).
12. C.W. Allen and M. Bahadur. J. Inorg. Organomet. Polym. **8**, 23 (1998).
13. H.R. Allcock, P.J. Harris, and R.A. Nissan. J. Am. Chem. Soc. **103**, 2256 (1983).
14. J.G. Dupont and C.W. Allen. Inorg. Chem. **17**, 3093 (1978).
15. C.W. Allen and S.D. Worley. Inorg. Chem., **38**, 5187 (1999).
16. C.W. Allen, P. Malik, A. Bridges, J. Desorcie, and B. Pellon. Phosphorus Sulfur Silicon Relat. Elem. **49–50**, 433 (1990).
17. T. Moeller, K. John, and F. Tsang. Chem. Ind. (London), 347 (1961).
18. J. Moraczewski and W.E. Geiger. Organometallics, **1**, 1385 (1982).
19. P. Magnus and B. Becker. J. Chem. Soc. Chem. Commun. 640 (1985).
20. C.W. Allen. Applications of ^{31}P NMR spectroscopy in cyclophosphazene chemistry. *In* Phosphorus-31 NMR spectral properties in compound characterization and structural analysis. *Edited by* L.D. Quin and J.G. Verkade. VCH, New York. 1994. Chap. 9. pp. 103–113.
21. C.W. Allen. Cyclophosphazenes and heterocyclophosphazenes. *In* The chemistry of inorganic homo- and heterocycles. Vol. 2. *Edited by* I. Haiduc and D.B. Sowerby. Academic Press, London. 1987. pp. 501–616.
22. R.S. Dickson, B.M. Peake, P.H. Reiger, B.H. Robinson, and J. Simpson. J. Organomet. Chem. **172**, C63 (1979).
23. M. Arewoda, B.H. Robinson, J. Simpson, P.H. Reiger, and S.J. Visco. J. Am. Chem. Soc. **104**, 5633 (1982).
24. M. Arewgoda, B.H. Robinson, and J. Simpson. J. Am. Chem. Soc. **105**, 1893 (1983).
25. A.A. Vlcek. Collect. Czech. Chem. Commun. **24**, 1748 (1959).
26. A.J. Bard and L.R. Faulkner. Electrochemical methods: fundamentals and applications. Wiley, New York. 1980.
27. B.M. Peake, P.H. Reiger, B.H. Robinson, and J. Simpson. J. Am. Chem. Soc. **102**, 156 (1980).
28. M. Calichman, D. Hernandez-Rubio, and C.W. Allen. Phosphorus Sulfur Silicon Relat. Elem. **177**, 1 (2002).
29. C.W. Allen and J. Green. Inorg. Chem. **19**, 1719 (1980).

© 2002 NRC Canada

The coordination chemistry of *o,o′-i*-$Pr_2C_6H_3$-bis(imino)acenaphthene to group 13 trihalides

Hilary A. Jenkins, Carla L. Dumaresque, Dragoslav Vidovic, and Jason A. C. Clyburne

Abstract: The preparation of several complexes of the diimine ligand *o,o′-i*-$Pr_2C_6H_3$-bis(imino)acenaphthene (Ar-BIAN (**1**)) with group 13 trihalides (EX_3, E = B, Al, Ga; X = Cl, Br) is reported. Four compounds with the general formula [(Ar-BIAN)(EX_2)][EX_4] (**2**) have been prepared and isolated. Two complexes have been crystallographically characterized: [(Ar-BIAN)(BCl_2)][BCl_4] (orthorhombic, $P2_12_12_1$, a = 10.408(3) Å, b = 14.376(4) Å, c = 30.908(8) Å, Z = 4) and [(Ar-BIAN)($GaCl_2$)][$GaCl_4$] (monoclinic, $P2_1/m$, a = 9.0822(7) Å, b = 15.390(1) Å, c = 15.458(1) Å, β = 92.519(2)°, Z = 2). Attempts to prepare diazametaloles via reduction of the [(Ar-BIAN)(EX_2)][EX_4] compounds using sodium or potassium have thus far been unsuccessful.

Key words: boron, aluminium, gallium, complex, crystal structure, heterocycle.

Résumé : On a préparé plusieurs complexes du ligand diimide *o,o′-i*-$Pr_2C_6H_3$-bis(imino)acénaphtène (Ar-BIAN (**1**)) avec des halogénures d'éléments du groupe 13 (EX_3, E = B, Al, Ga; X = Cl, Br). On a spécifiquement préparé et isolé quatre composés de formule générale [(Ar-BIAN)(EX_2)][EX_4] (**2**). On a caractérisé deux de ces complexes par diffraction des rayons X, le [(Ar-BIAN)(BCl_2)][BCl_4] (orthorhombique, $P2_12_12_1$, a = 10,408(3), b = 14,376(4) et c = 30,908(8) Å, Z = 4) et le [(Ar-BIAN)($GaCl_2$)][$GaCl_4$] (monoclinique, $P2_1/m$, a = 9,0822(7), b = 15,390(1) et c = 15,458(1) Å, β = 92,519(2)°, Z = 4). On n'a pas réussi à préparer des diazamétaloles par le biais d'une réduction des composés [(Ar-BIAN)(EX_2)][EX_4] à l'aide du sodium ou du potassium.

Mots clés : bore, aluminium, gallium, complexes, structure cristalline, hétérocycle.

[Traduit par la Rédaction]

Introduction

Hydroborations are an important class of reaction in synthetic organic chemistry because the B—H bond readily adds across a wide variety of unsaturated fragments, including C=O and C=N bonds (1). Recently, reactions involving chloroboration (B-Cl addition) have been identified (2). To our knowledge, these reactions have not been extended to heavier group 13 elements, although enhanced reactivity would be anticipated for Al—Cl and Ga—Cl bonds as compared with the B—Cl bonds.

Our interest in group 13 element chemistry (3) led us to look at the synthesis of suitable heterocyclic systems as precursors to compounds that may engage in reactions analogous to hydroboration and haloboration. The ideal candidates for such reactions would be heterocyclic compounds, with donor substituents bound to the group 13 metal site; these donors would stabilize a tricoordinate metal centre via delocalization. The presence of a bulky substituent would facilitate synthesis and enhance the thermal stability of the complex. Currently there is great interest in unusual main group element heterocycles, including B (4, 5), Al (6), and Ga (7, 8) derivatives.

It became apparent to us that the bulky diimine ligand **1** (9) would be ideal for our studies since it is both a good donor and extremely bulky.

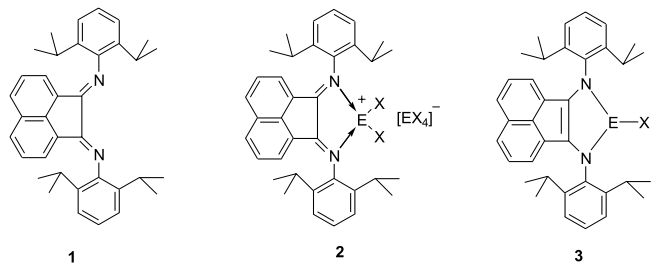

1 **2** **3**

E = B, Al, Ga; X = Cl, Br

Diimines are bidentate ligands consisting of two nitrogen atoms bridged by at least two carbon atoms, and having two C=N double bonds (10). The bis(arylimino)acenaphthene

Received 21 January 2002. Published on the NRC Research Press Web site at http://canjchem.nrc.ca on 23 September 2002.

This paper is dedicated to Professor Tristram Chivers for his many contributions to main group chemistry.

H.A. Jenkins.[1] Department of Chemistry, Saint Mary's University, Halifax, NS B3H 3C3, Canada.
C.L. Dumaresque, D. Vidovic, and J.A.C. Clyburne.[2] Department of Chemistry, 8888 University Drive, Simon Fraser University, Burnaby, BC V5A 1S6, Canada.

[1]Corresponding author (crystallography) (e-mail: hilary.jenkins@stmarys.ca).
[2]Corresponding author (e-mail: clyburne@sfu.ca).

 DOI: 10.1139/V02-084 © 2002 NRC Canada

diimine ligand (**1**) is different from other diimine ligands as it has both better σ-donating and π-accepting properties than nonrigid diimines (9). Therefore, **1** could serve as an ideal starting material for the preparation of stable heterocyclic metal-containing ions (metal = boron, aluminium, and gallium) (**2**), which would serve as precursors to the requisite heterocycles (**3**). The nitrogen atoms are locked into a rigid *s-cis* conformation due to the presence of the naphthalene backbone, thus allowing for better metal coordination. Brookhart and co-workers (11) have recently reported Ni(II) and Pd(II) complexes of **1** that catalyze the polymerization of ethylene. These catalysts have activities similar to those of the early transition metal catalysts; however, they produce polymers with different structures and properties. Despite extensive use in transition metal chemistry ligand design, **1** has not been used in main group chemistry.

Herein we report our synthetic and structural studies on a series of bulky diazametalolium (**2**) complexes. A series of reactions involving **1** with EX_3 (E = B, Al, Ga; X = Cl, Br) has been examined, and the reaction products have been isolated and characterized. The products have the general formula $[(Ar\text{-}BIAN)(EX_2)][EX_4]$ (**3**). Attempts to prepare molecules such as **3** via reduction of **2** have thus far been unsuccessful.

Experimental methods

An MBraun UL-99–245 dry box and standard Schlenk techniques on a double manifold vacuum line were used in the manipulation of air- and moisture-sensitive compounds. Anhydrous solvents were used as received from Aldrich Chemical Company. NMR spectra were recorded on a Bruker AMX 400 MHz spectrometer in 5-mm quartz tubes. ^1H chemical shifts were reported in parts per million (ppm) downfield from tetramethylsilane (TMS) and were calibrated to the residual signal of the solvent. Infrared spectra were obtained using a Bomem MB spectrometer with the % transmittance reported in cm^{-1}. Melting points were measured using a Mel-Temp apparatus and are uncorrected. Ligand **1** was prepared using the published procedure (9). Note that ^{13}C NMR spectra were not obtained due to decomposition and low solubility of the ionic compounds.

Synthesis of [(Ar-BIAN)(BCl_2)][BCl_4]

Ar-BIAN (1.20 g, 2.5 mmol in 10 mL CH_2Cl_2) was added to a solution of 25 mL CH_2Cl_2 and 5 mL (5.0 mmol) of 1 M BCl_3 in hexanes, resulting in the formation of a dark red solution. The volume of solvent was reduced to ca. 25% of the original volume, and then the solution was cooled to –30°C. Small red crystals were obtained and the supernatant was removed via cannula under an atmosphere of argon. Yield: 1.05 g (1.47 mmol, 59%), decomposition temperature ≈ 140°C. IR (Nujol mull) (cm^{-1}): 1643, 1600, 1569, 1418, 1366, 1318, 1260, 854, 835, 802, 774, 691, 658, 634, 546. ^1H NMR (CD_2Cl_2) δ (ppm): 1.14 (broad, 12H), 1.42 (d, J_{HH} = 6 Hz, 12H), 3.01 (m, 4H), 6.9 (d, 7 Hz), 7.6 (m, 2H), 8.28 (d, J_{HH} = 8 Hz, 2H), 7.3–7.8 (6H aryl). Anal. calcd. for $C_{36}H_{40}B_2Cl_6N_2$: C 58.82, H 5.48, N 3.81; found: C 59.16, H 5.60, N 3.64.

Synthesis of [(Ar-BIAN)(BBr_2)][BBr_4]

Ar-BIAN (1.20 g, 2.5 mmol in 10 mL of CH_2Cl_2) was added to a solution of 25 mL of CH_2Cl_2 and 5 mL (5.0 mmol) of 1 M BBr_3 in CH_2Cl_2 to produce a dark red solution. The volume of solvent was reduced to ca. 25% of the original volume, and then the solution was cooled to –30°C. Solvent was removed under an argon atmosphere and dark red crystals were isolated in the dry box. Yield: 1.35 g (1.38 mmol, 55%), decomposition temperature ≈ 185°C. IR (Nujol mull) (cm^{-1}): 1635, 1597, 1570, 1319, 834, 733, 615, 588, 541. ^1H NMR (CD_2Cl_2, poor solubility) δ (ppm): 1.0 (d, J_{HH} = 6Hz, 12H), 1.45 (d, J_{HH} = 6 Hz, 12H), 3.3 (broad, 4H), aromatic region broad and not resolved. Anal. calcd. for $C_{36}H_{40}B_2Br_6N_2$: C 43.16, H 4.02, N 2.80; found: C 42.80, H 3.92, N 2.65.

Synthesis of [(Ar-BIAN)($AlCl_2$)][$AlCl_4$]

Aluminium trichloride (1.0 g, 7.50 mmol) was added to an oven-dried Schlenk flask containing 40 mL of CH_2Cl_2. Ar-BIAN (1.80 g, 3.75 mmol) in 5 mL of CH_2Cl_2 was added, and the solution turned dark red. Half of the solvent was removed under vacuum, and the reaction was cooled to –30°C in the freezer. A microcrystalline powder was obtained, and this material was washed with CH_2Cl_2. Yield: 0.95 g (1.27 mmol, 34%), decomposition temperature ≈ 185°C. IR (Nujol mull) (cm^{-1}): 1626, 1617, 1569, 1418, 1366, 1318, 1221, 854, 835, 802, 774, 490, 460. ^1H NMR (CD_2Cl_2) δ (ppm): 1.14 (d, J_{HH} = 6Hz, 12H), 1.30 (d, J_{HH} = 6 Hz, 12H), 3.0 (m, 4H), 7.2 (d, J_{HH} = 7 Hz, 4H), 7.3–7.8 (6 H aryl), 7.70 (m, 2H), 8.50 (d, J_{HH} = 8 Hz, 2H). Anal. calcd. for $C_{36}H_{40}Al_2Cl_6N_2$: C 56.34, H 5.25, N 3.65; found: C 56.20, H 5.11, N 3.59.

Synthesis of [(Ar-BIAN)($GaCl_2$)][$GaCl_4$]

Gallium trichloride (1.00 g, 5.68 mmol) in 15 mL of CH_2Cl_2 was added to an oven-dried Schlenk flask. Ar-BIAN (1.37 g, 2.84 mmol in 5 mL of CH_2Cl_2) was added to this colourless solution, which turned dark red. Another 5 mL of CH_2Cl_2 was added, and this solution was then cooled to –30°C. Flat red crystals were obtained and isolated after removal of the supernatant, via cannula, under an atmosphere of argon. Yield: 1.75 g (2.10 mmol, 74%), decomposition temperature ≈ 140°C. IR (Nujol mull) (cm^{-1}): 1621, 1596, 1572, 1488, 1420, 1366, 1300, 1270, 1055, 803, 777, 734, 584, 545. ^1H NMR (CD_2Cl_2) δ (ppm): 1.02 (broad, s, 12H), 1.45 (d, J_{HH} = 6 Hz, 12H), 3.1 (m, 4H), 6.90 (d, J_{HH} = 7 Hz, 2H), 7.3–7.8 (6 H aryl), 7.64 (m, 2H) 8.42 (d, J_{HH} = 8 Hz, 2H). Anal. calcd. for $C_{36}H_{40}Ga_2Cl_6N_2$: C 50.70, H 4.73, N 3.28; found C 50.54, H 4.63, N 3.15.

Attempts to reduce the compounds above in THF (1 to 2 mmol scale) with sodium or potassium were made, but unfortunately in our hands no pure compounds could be isolated from the reaction mixtures. The only compound identified (by NMR and melting point) was Ar-BIAN. Likewise, attempts were made to exchange the $[EX_4]$ anions with the weakly coordinating anion $[B(C_6F_5)_4]$ by treating **3** with $Li[B(C_6F_5)_4]$ in CH_2Cl_2 solution. In general, these attempts were unsuccessful, resulting in the formation of dark coloured solutions, from which the only pure compound isolated was Ar-BIAN.

© 2002 NRC Canada

Table 1. Crystal data and structure refinement for [(Ar-BIAN)BCl_2][BCl_4]·1.25 CH_2Cl_2 and [(Ar-BIAN)$GaCl_2$][$GaCl_4$].

Compound	[(Ar-BIAN)BCl_2][BCl_4]·1.25 CH_2Cl_2	[(Ar-BIAN)$GaCl_2$][$GaCl_4$]
Empirical formula	$C_{37.26}H_{42.50}B_2Cl_{8.5}N_2$	$C_{37}H_{40}Cl_8Ga_2N_2$
Formula weight (g ml^{-1})	841.18	935.75
Temperature (K)	223(2)	223(2)
Crystal system	Orthorhombic	Monoclinic
Space group	$P2_12_12_1$	$P2_1/m$
a (Å)	10.408(3)	9.0822(7)
b (Å)	14.376(4)	15.390(1)
c (Å)	30.908(8)	15.458(1)
α (°)	90	90
β (°)	90	92.519(2)
γ (°)	90	90
Volume ($Å^3$)	4625(2)	2158.5(3)(2)
Z	4	2
Density (calculated) mg m^{-3}	1.239	1.440
Absorption coefficient (μ) (mm^{-1})	0.572	1.771
F(000)	1780	948
Crystal size (mm^3)	0.20 × 0.20 × 0.20	0.20 × 0.20 × 0.30
θ range for data collection (°)	1.32–25.00	1.87–25.00
Index ranges	$9 \le h \le 12$	$-10 \le h \le 8$
	$-16 \le k \le 17$	$-18 \le k \le 18$
	$-29 \le l \le 36$	$-17 \le l \le 18$
Reflections collected	24 923	10 799
Independent reflections	8146	3907 (R_{int} = 0.0608)
Absorption correction	none	none
Max and min transmission	0.745 and −0.392	0.447 and −0.597
Refinement method	Full-matrix least-squares on F^2	Full-matrix least-squares on F^2
Data/restraints/parameters	8137/3/516	3907/0/251
Goodness-of-fit on F^2	1.162	1.018
Final R indices [$I > 2\sigma(I)$]	R_1 = 0.1152, wR_2 = 0.2798	R_1 = 0.0534, wR_2 = 0.1094
R indices (all data)	R_1 = 0.2117, wR_2 = 0.3222	R_1 = 0.1092, wR_2 = 0.1290
Extinction coefficient	0.018(4)	0.0014(5)

Crystallographic studies

A single crystal of either [(Ar-BIAN)BCl_2][BCl_4]·1.25[CH_2Cl_2] or [(Ar-BIAN)$GaCl_2$][$GaCl_4$] was mounted on a glass fibre and centred on a Seimens 1K SMART/CCD diffractometer. Data were collected at –50°C using Mo (Kα) radiation. Lorentz and polarization corrections were applied, and data were also corrected for absorption using redundant data and the SADABS program. Direct methods and Fourier techniques were used to solve the crystal structures. Refinement was conducted using full-matrix least-squares calculations and SHELX-TL PC V 5.03. All non-hydrogen atoms were refined with anisotropic displacement parameters. The hydrogen atoms were included in calculated positions and were refined using a riding model. In the final stages of the refinement of [(Ar-BIAN)BCl_2][BCl_4]·1.25[CH_2Cl_2], R_1 = 0.1152, wR_2 = 0.2798, and the largest peak was 0.745 e $Å^{-3}$ and was associated with one of the methylene chloride solvent molecules. In the final stages of refinement of [(Ar-BIAN)$GaCl_2$][$GaCl_4$]· [CH_2Cl_2], R_1 = 0.0534, wR_2 = 0.1094, and the largest residual peak was 0.447 e $Å^{-3}$ and was associated with the residual methylene chloride solvent. Full crystallographic details can be found in Table 1.

Results and discussion

The Ar-BIAN ligand **1** was treated with a variety of group 13 compounds to prepare Lewis base coordination complexes. Lewis acids studied included BCl_3, BBr_3, $AlCl_3$, and $GaCl_3$. Of these reactions, solid materials were successfully isolated from BCl_3, BBr_3, $AlCl_3$, and $GaCl_3$. In general, treatment of **1** with 2 equiv of EX_3 in CH_2Cl_2 solution, followed by reduction of the solvent volume, resulted in the formation of a solid, bright red material. These compounds were characterized by ^1H NMR and IR spectroscopy. Poor solubility of these ionic compounds made NMR studies difficult, and it was discovered that the compounds decompose in CD_2Cl_2 solution (12). Fortunately, X-ray-quality crystals were obtained from the mother liquors of [(Ar-BIAN)BCl_2][BCl_4] and [(Ar-BIAN)$GaCl_2$][$GaCl_4$].

IR spectroscopic studies were performed on the [(Ar-BIAN)(EX_2)][EX_4] series of compounds. The stretching frequencies observed between 1660 and 1610 cm^{-1} have been tentatively assigned to the ν(C=N) stretches. The assignments for the [(Ar-BIAN)(EX_2)][EX_4] complexes are as follows (cm^{-1}): free ligand (1660 or 1640); E = B, X = Cl (1646); E = B, X = Br (1636); E = Al, X = Cl (1627);

© 2002 NRC Canada

Fig. 1. ORTEP view of cation $[(Ar\text{-}BIAN)BCl_2]^+$ showing the labelling scheme. Thermal ellipsoids are shown at 50% probability level; hydrogen atoms have been removed for clarity.

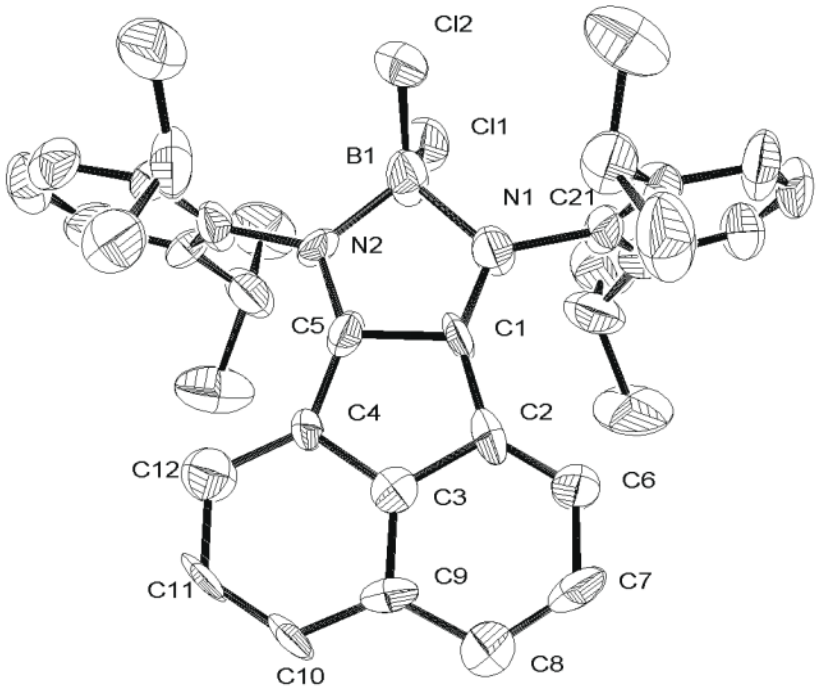

E = Ga, X = Cl (1621). The C=N stretching frequency in the free ligand cannot be assigned unambiguously because of the presence of C—C stretching frequencies from the naphthalene backbone in this region (9). The absorptions for the C=N stretches in the complexes have been assigned because of the fact that these peaks were discernible as being quite strong and broad, consistent with a C=N stretch. More importantly, the position of this absorption shifts upon complex formation, and is dependent on the Lewis acid used in the complexation reaction.

The absorptions for the E—X bonds are also informative. The IR spectrum for $[(Ar\text{-}BIAN)EX_2][EX_4]$ reveals two different E—X stretches from the two types of E—X bonds present (i.e., one from the cation and one from the anion). These two stretching bands are present at 691(s-br) and 658(s-br) cm^{-1} (E = B, X = Cl), 588(s) and 541(s) cm^{-1} (E = B, X = Br), and 490(s) and 460(m) cm^{-1} (E = Al, X = Cl). The stretching bands have been assigned based on known E—X stretching regions and intensities (13). The stretches for Ga—Cl bonds were not observed in the IR spectrum of the $[(Ar\text{-}BIAN)GaCl_2][GaCl_4]$ complex, as Ga—Cl bonds absorb below 450 cm^{-1}.

Crystallographic studies on $[(Ar\text{-}BAIN)BCl_2][BCl_4]$ and $[(Ar\text{-}BAIN)GaCl_2][GaCl_4]$

$[(Ar\text{-}BIAN)BCl_2][BCl_4]\cdot 1.25[CH_2Cl_2]$ crystallizes in the uniquely determined orthorhombic space group $P2_12_12_1$, with four molecules in the unit cell. Crystals of this compound were not well-formed, and resulted in overall *R* values that are somewhat high. The X-ray analysis does show that $[(Ar\text{-}BIAN)BCl_2][BCl_4]$ exists in the solid state as discrete anions and cations, with no unusual interactions between the ions or the solvent.

The anion ($[BCl_4]^-$) is a distorted tetrahedron, with bond angles between 100(1)° and 118(1)°, and B—Cl bond lengths ranging from 1.74(3) to 1.95(3) Å. There are no unusual structural features associated with this anion. The closest interactions between ions are between Cl4 and C21 (3.77 Å), and B2 and the centre of the ring formed by C2–C9 (4.25 Å). The primary coordination sphere of the boron centre in the $[(Ar\text{-}BIAN)BCl_2]^+$ cation features two N→B dative bonds from the Ar-BIAN ligand (1.57(2) and 1.54(2) Å). Two B—Cl bonds complete the $[(Ar\text{-}BIAN)BCl_2]^+$ coordination sphere. The B—Cl bond lengths in the cationic fragment, 1.78(2) and 1.89(1) Å, are about the same as those of the anionic fragment. For comparison, the B—Cl bond length in BCl_3 is 1.74 Å.[3] An ORTEP view of the cation $[(Ar\text{-}BIAN)BCl_2]^+$ is shown in Fig. 1, and important bond lengths and angles are presented in Table 2.

$[(Ar\text{-}BIAN)GaCl_2][GaCl_4]$ crystallizes in the monoclinic space group $P2_1/m$, with two molecules in the unit cell. The X-ray analysis of this complex also revealed that it exists in the solid state as discrete anions and cations. The $[GaCl_4]^-$ anion is tetrahedral, with Ga—Cl bond angles between 106.54(9)° and 111.26(6)°, and bond lengths between 2.159(2) and 2.175(1) Å. There are no unusual structural features associated with this anion.

The primary coordination sphere of the cationic $[(Ar\text{-}BIAN)GaCl_2]^+$ fragment features two N→Ga dative bonds from the Ar-BIAN ligand (1.985(3) Å). This Ga—N bond

[3] Recently the reaction of a bulky 1,4-diazabutadiene with BCl_3 was reported, and the isolated compound was characterised as a 2,4,5-trichloro-1,3,2-diazaborolidine, which is a covalent alternative to the ionic diazaborolium salt. See reference 12. It is possible that a similar rearrangement occurs in the $[(Ar\text{-}BIAN)(EX_2)][EX_4]$ compounds reported here.

© 2002 NRC Canada

Table 2. Comparison of $[(Ar\text{-}BIAN)GaCl_2][GaCl_4]$, $[(Ar\text{-}BIAN)BCl_2][BCl_4]$, and $[(DAB)GaCl_2][GaCl_4]$.

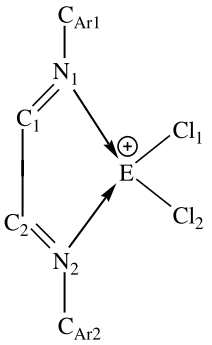

General structure for comparison of bond lengths and angles in Ar-BIAN and DAB complexes

Parameter	$[(Ar\text{-}BIAN)BCl_2]^+$	$[(Ar\text{-}BIAN)GaCl_2]^+$	$[(DAB)GaCl_2]^+$
N—E	1.57(2), 1.54(2)	1.985(3)	1.979(5), 1.982(6)
E—Cl	1.78(2), 1.89(1)	2.106(2), 2.124(3)	2.105(2), 2.104(2)
N-E-N	99.6(9)	85.1(2)	84.4(2)
N-E-Cl	115(1), 115(1), 108(1), 110.7(9)	114.1(1), 111.9(1)	Not reported
Cl-E-Cl	108.5(7)	115.9(1)	118.2(1)

Fig. 2. ORTEP view of cation $[(Ar\text{-}BIAN)GaCl_2]^+$ showing the labelling scheme. Thermal ellipsoids are shown at 50% probability level; hydrogen atoms have been removed for clarity.

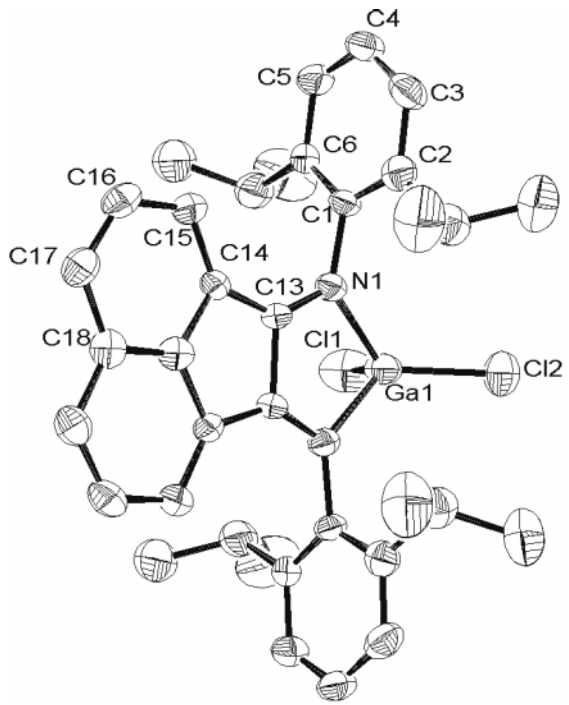

distance is somewhat unusual because in most acyclic trialkylamine adducts, the Ga—N bond distances are much longer, being somewhere between 2.1 and 2.2 Å (14). This is, however, not so surprising because N is sp^2 hybridized and therefore has a shorter covalent radius than an sp^3 hybridized nitrogen centre. The coordination sphere around the cationic gallium centre in $[(Ar\text{-}BIAN)GaCl_2]^+$ is completed by two Ga—Cl bonds of 2.106(2) and 2.124(3) Å. Important bond lengths and angles are reported in Table 2. An ORTEP view of $[(Ar\text{-}BIAN)GaCl_2]^+$ is presented in Fig. 2. As shown in Table 2, the metrical parameters observed for $[(Ar\text{-}BIAN)GaCl_2][GaCl_4]$ are similar to those reported for $[DABGaCl_2][GaCl_4]$ (DAB = *t*-BuN=C(H)-C(H) = N*t*Bu) (14).

There are no unusual long-range interactions between ions, and the closest interactions are the Cl5—C18 distance at 3.582 Å, and the Cl4 — centre of C13-C13A distance of 3.528 Å, and Ga2—C19 at 4.808 Å.

Attempts to prepare $[(Ar\text{-}BIAN)ECl_2][B(C_6F_6)_4]$ via ion-exchange reactions were unsuccessful. It was hoped that the strong electron donating ability of **1** would facilitate formation of $[(Ar\text{-}BIAN)ECl]^{++}$, via ion-exchange and halide abstraction from $[(Ar\text{-}BIAN)ECl_2]^+$, but this was not realised. We are currently working on the preparation of amido-substituted derivatives to facilitate the formation of $[(Ar\text{-}BIAN)ENR_2]^{++}$, recognising the isoelectronic relationship with, for example, the carbocation $[CR_3]^+$. Finally, attempts to reduce $[(Ar\text{-}BIAN)(EX_2)][EX_4]$ using Na or K to generate compounds such as **3** have thus far been unsuccessful.

Conclusions

Several new main group complexes were prepared based upon the *o*,*o*′-*i*-$Pr_2C_6H_3$-bis(imino)acenaphthene ligand. The Ar-BIAN ligand is easily prepared and is a robust ligand for supporting highly Lewis acidic main group element sites. Unfortunately, attempted reduction of $[(Ar\text{-}BIAN)(EX_2)][EX_4]$ to produce heterocycles such as **3** were unsuccessful.

Acknowledgements

The authors would like to thank the Natural Sciences and Engineering Research Council of Canada (NSERC) and Simon Fraser University for financial support.

© 2002 NRC Canada

References

1. For a review see: K. Burgess and M.J. Ohlmeyer. Chem. Rev. **91**, 1179 (1991).
2. For a review see: A. Suzuki. Rev. Heteroat. Chem. **17**, 271 (1997).
3. D. Abeysekera, K.N. Robertson, T.S. Cameron, and J.A.C. Clyburne. Organometallics, **20**, 5532 (2001).
4. L. Weber, M. Schnieder, and P. Lönnecke. J. Chem. Soc. Dalton Trans. 3459 (2001).
5. L. Weber, E. Dobbert, R. Boese, M.T. Kirchner, and D. Bläser. Eur. J. Inorg. Chem. 1145 (1998).
6. D.S. Brown, A. Decken, C.A. Schnee, and A.H. Cowley. Inorg. Chem. **34**, 6415 (1995).
7. D.S. Brown, A. Decken, and A.H. Cowley. J. Am. Chem. Soc. **117**, 5421 (1995).
8. E.S. Schmidt, A. Jockisch, and H Schmidbaur. J. Am. Chem. Soc. **121**, 9758 (1999).
9. R. van Asselt, C.J. Elsevier, W.J.J. Smeets, A.L. Spek, and R. Benedix. Recl. Trav. Chim. Pays–Bas, **113**, 88 (1994).
10. G. van Koten and K. Vrieze. Adv. Inorg. Chem. **21**, 151 (1982).
11. S.A. Svejda and M. Brookhart. Organometallics, **18**, 65 (1999); D.P. Gates, S.A. Svejda, E. Oñate, C.M. Killian, L.K. Johnson, P.S. White, and M. Brookhart. Macromolecules, **33**, 2320 (2000); L.K. Johnson, C.M. Killian, and M Brookhart. J. Am. Chem. Soc. **117**, 6414 (1995); S.A. Svejda, L.K. Johnson, and M. Brookhart. J. Am. Chem. Soc. **121**, 10 634 (1999); C.M. Killian, L.K. Johnson, and M. Brookhart. Organometallics, **16**, 2005 (1997); S. Mecking, L.K. Johnson, L. Wang, and M. Brookhart. J. Am. Chem. Soc. **120**, 888 (1998); S.D. Ittel and L.K. Johnson. Chem. Rev. **100**, 1169 (2000).
12. F.S. Mair, R. Manning, R.G. Pritchard, and J.E. Warren. Chem. Commun. 1136 (2001).
13. K. Nakamoto. Infrared spectra of inorganic and coordination compounds. 2nd ed. John Wiley and Sons, Inc., New York. 1970.
14. J.A.C. Clyburne, R.D. Culp, S. Kamepalli, A.H. Cowley, and A. Decken. Inorg. Chem. **35**, 6651 (1996).

© 2002 NRC Canada

Sequential dehydrochloride coupling of trichlorophosphine with 2,6-di-isopropylaniline: aminophosphine precursors to phosphetidines

Neil Burford, T. Stanley Cameron, Korey D. Conroy, Bobby Ellis, Charles L.B. Macdonald, Robyn Ovans, Andrew D. Phillips, Paul J. Ragogna, and Denise Walsh

Abstract: Various stoichiometric combinations of PCl_3 with $DippNH_2$ (Dipp = 2,6-di-isopropylphenyl) have been examined using ^{31}P NMR spectroscopy. The dehydrochloride coupling reaction is mediated by the moderate steric bulk of the Dipp substituent. Isolation procedures and characterization data are reported for the aminodichlorophosphine (**1**), the aminotetrachlorodiphosphine (**4**), and the dichlorophosphetidine (**7**). The observations offer new appreciation of dehydrochloride coupling products of halophosphines with primary amines.

Key words: phosphorus, nitrogen, phosphazanes, phosphetidines, iminophosphine.

Résumé : Faisant appel à la spectroscopie RMN du ^{31}P, on a étudié diverses combinaisons stoechiométriques de PCl_3 avec de la $DippNH_2$ ($DippNH_2$ = 2,6-di-isopropylphényle). La réaction de couplage avec déshydrochloruration est favorisée par l'empêchement stérique modéré du substituant Dipp. On rapporte les méthodes d'isolement et les données de caractérisation de l'aminodichlorophosphine (**1**), de l'aminotétrachlorodiphosphine (**4**), et de la dichlorophosphétidine (**7**). Les faits observés offrent une nouvelle appréciation sur la nature des produits de couplage avec déshydrochloruration d'halophosphines avec des amines primaires.

Mots clés : phosphore, azote, phosphazanes, phosphétidines, iminophosphine.

[Traduit par la Rédaction]

Introduction

The established structural diversity of nitrogen-phosphorus compounds is a manifestation of the strong and versatile N—P bond. A variety of N—P coupling reactions have been employed, but elimination of hydrogen chloride is prototypical and is responsible for the formation of mono-, bis-, and tris-aminophosphines from appropriate stoichiometric combinations of PCl_3 and a secondary amine (1). In comparison, reactions of PCl_3 with primary amines offer a more diverse array of structural options because of the possibility of P-N-P linkages, as illustrated in Fig. 1. In spite of ring strain, the four-membered, dimeric phosphetidine (phosphazane) frameworks **7** and **9** (2–7) are routinely isolated for conventional derivatives (R = Me, Et, Ph) (8). Less common are reports of the sequential (intermediate) metathesis products **1** (8), **2** (8), **3** (5), **4** (5), and **5** (9), and examples of the higher order chain **6** have not been reported (10–14).

Primary amines bearing 'bulky' substituents are predictably restricted from multi-dehydrochloride coupling reactions. In the case of R = 2,4,6-tri-tert-butylphenyl (Mes*), intramolecular hydrogen chloride elimination occurs to produce the iminophosphine Mes*N=PCl (15). We now show how both phosphetidine formation and intramolecular elimination are impeded by the presence of the 2,6-di-isopropylphenyl (Dipp) substituent, which provides intermediate steric influence on the thermodynamic and kinetic factors governing the coupling reaction. ^{31}P NMR spectroscopic studies of a series of stoichiometric combinations of PCl_3 and $DippNH_2$ reveal many of the sequential dehydrochloride coupling products, and assignments of ^{31}P chemical shifts have been confirmed for isolated samples of **1**, **4**, **7**, and **9** (3).

Received 26 February 2002. Published on the NRC Research Press Web site at http://canjchem.nrc.ca on 7 October 2002.

This article is dedicated to Professor Tristram Chivers in recognition of his outstanding contributions to the chemistry community in Canada.

N. Burford,[1] T.S. Cameron, K.D. Conroy, B. Ellis, C.L.B. Macdonald,[2] R. Ovans, A.D. Phillips, P.J. Ragogna, and D. Walsh. Department of Chemistry, Dalhousie University, Halifax, NS B3H 4J3, Canada.

[1]Corresponding author (e-mail: Neil.Burford@dal.ca).
[2]Present address: Department of Chemistry and Biochemistry, University of Windsor, 401 Sunset Avenue, Windsor, ON N9B 3P4, Canada.

Experimental procedures (16)

General

Diethylether was obtained from ACP Chemicals Inc. and hexane from Anachemia. All other chemicals and reagents were obtained from Aldrich Chemical Company. All solvents were degassed and stored in evacuated bulbs. Solids were handled in a nitrogen-filled glove-box. Sample

 DOI: 10.1139/V02-161 © 2002 NRC Canada

Fig. 1 Potential products of sequential dehydrochloride metathesis from PCl_3 and RNH_2. Solid arrows represent addition of amine with loss of HCl, dashed arrows represent addition of phosphine with loss of HCl, and wavy arrows represent cyclisation with HCl elimination. ^{31}P NMR chemical shift assignments (ppm) are given in parentheses for *R* = Dipp, and in square brackets for *R* = Ph.

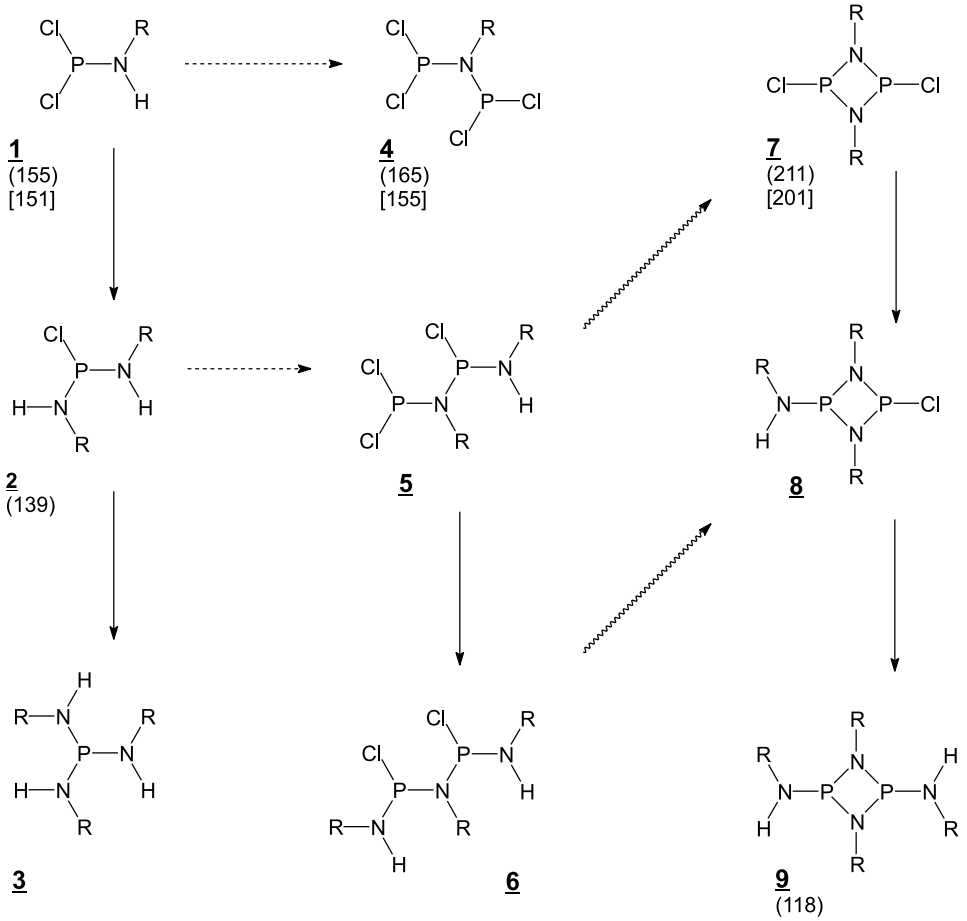

handling and reactions were performed under oxygen and moisture-free conditions. 2,6-Di-isopropylaniline ($DippNH_2$) was used as received. Dichloromethane was dried at reflux over CaH_2, P_4O_{10}, and CaH_2; hexane, toluene, and benzene were dried over potassium; and diethylether was dried over sodium/benzophenone. Deuterated solvents were dried over CaH_2. PCl_3 was distilled under vacuum.

IR spectra were recorded as Nujol mulls on CsI plates using a Nicolet 510 FT-IR spectrometer, and are presented as wavenumber (cm^{-1}) maxima, with ranked intensities for each absorption given in parentheses. The most intense peak is given a ranking of 1. Melting point samples were placed in 1.0 mm (O.D.) Pyrex capillaries, sealed under nitrogen, and measured using an Electrothermal® melting point apparatus. Solution and variable-temperature (VT) NMR spectra were recorded on a Bruker AC-250 NMR spectrometer. Solution NMR samples were flame-sealed in 5 mm Pyrex tubes. NMR spectra were referenced to the solvent and chemical shifts are reported in ppm relative to an external standard (TMS for ^1H and ^{13}C, 85% H_3PO_4 for ^{31}P).

^{31}P NMR spectra of reactions between PCl_3 and RNH_2 (*R* = Dipp or Ph)

Table 1 summarizes ^{31}P NMR spectra obtained for reaction mixtures, prepared at 0°C by the addition of $DippNH_2$ in toluene to PCl_3 in toluene at approximately 1 M concentration. The mixtures were stirred overnight with warming to room temperature and were filtered. Spectra of similar reaction mixtures involving $PhNH_2$ revealed many products. At equimolar stoichiometry, the prominent peaks were assigned to **1** (*R* = Ph, 151 ppm) and **7** (*R* = Ph, 201 ppm), with substantial unreacted PCl_3 (220 ppm). The aminodiphosphine **4** (*R* = Ph, 155 ppm) (12) was observed as a minor component. It was not possible to make other unequivocal assignments for reaction mixtures containing excess $PhNH_2$.

Isolation procedures and characterization data

DippN(H)PCl$_2$ (1)

$DippNH_2$ (4.0 mL, 21 mmol) in benzene (15 mL) was added via cannula to a stirred solution of PCl_3 (1.9 mL, 21 mmol) in benzene (15 mL) at 0°C. The resultant slurry was stirred overnight and the white precipitate was filtered through a fine glass filter. Benzene was slowly removed from the pale yellow solution to give colourless rod-shaped crystals. Yield 2.23 g (43%); mp 58–61°C. IR (Nujol mull) (cm^{-1}): 3314 (17), 2959 (2), 2923 (1), 2852 (3), 1583 (19), 1519 (13), 1462 (4), 1383 (11), 1364 (12), 1329 (14), 1252 (8), 1182 (6), 1100 (7), 1043 (9), 931 (10), 885 (15), 797 (5), 749 (18), 512 (16). ^1H NMR: 1.08 (d, $^3J_{HH}$ = 12 Hz),

© 2002 NRC Canada

Table 1. Summary of ^{31}P NMR spectroscopic data for reaction mixtures of PCl_3 $DippNH_2$ at seven different stoichiometric combinations.

						148		161							
δ ^{31}P (ppm)		155	221	139	140	182	8	195	224	242	118	133	136	211	165
Assignments		**1**	PCl_3	(**2**)	(**3**)	(**8**)		(**5**)	(**6**)		**9**			**7**	**4**
Reaction stoichiometry PCl_3:$DippNH_2$	2:1	100	80												
	1:1	100	20												
	1:2	100		15											
	1:3	10		100	30	10	10	5	1	1		5	5		
	1:4	10		100	10	5	5	2				2	2		
	1:5			100	40	60		5	5	5	5		5	1	
	1:6			100	30	90	70	10	10	10	10		1	5	

Note: Chemical shifts are listed in order of peak intensity. Approximate peak intensities in each spectrum are given relative to the most intense peak (100%). Assignments are confirmed for **1**, **4**, **7**, and **9** (3) by characterization of isolated samples. Parentheses indicating assignments for **2**, **3**, **5**, **6**, and **8** are tentative and other minor signals are not assigned.

3.25 (sept, $^3J_{HH}$ = 12 Hz), 4.53 (s), 6.93–6.96 (m). ^{31}P NMR: 155. Anal. calcd. for $DippN(H)PCl_2$: C 51.81, H 6.52, N 5.03; found: C 51.36, H 6.79, N 5.08.

DippN(PCl$_2$)$_2$ (4)

PCl_3 (20 mL) and NEt_3 (40 mL) were distilled onto a frozen solution of $DippNH_2$ (5.0 g, 28 mmol) in hexane (30 mL). A yellow solution and a white precipitate formed on warming to room temperature. After stirring for 7 days, the solution was filtered and the solvent removed in vacuo. The resulting solid was sublimed onto a water cooled finger, under static vacuum with warming to 80°C, to give tan crystals of **4**. Yield 5.3 g (14 mmol, 50%); mp 69–71°C. IR (Nujol mull) (cm^{-1}): 1584 (20), 1433 (9), 1362 (8), 1322 (15), 1309 (18), 1158 (7), 1104 (12), 1095 (13), 1050 (17), 1040 (19), 903 (6), 883 (1), 799 (6), 718 (16), 515 (4), 490 (3), 481 (2), 451 (10), 437 (11), 417 (14). ^1H NMR: 1.19 (d, $^3J_{HH}$ = 7 Hz), 3.12 (sept, $^3J_{HH}$ = 7 Hz), 7.26 (m). ^{31}P NMR: 165 (reaction mixture), 165 and 211 (assigned to **7**). Anal. calcd.: C 38.03, H 4.52, N 3.70; found: C 38.08, H 4.52, N 3.75.

[DippNPCl]$_2$ (7)

$DippNH_2$ (10 mL, 53 mmol) in toluene (20 mL) was added via cannula to a three-chamber reaction vessel containing a stirring solution of PCl_3 (2.3 mL, 26 mmol) in toluene (15 mL) at 0°C. The solution was warmed to room temperature and a white precipitate formed. After stirring overnight, the mixture was degassed and filtered through a fine glass frit. Toluene was removed under vacuum and the resulting oil was dissolved in hexane (20 mL) to promote precipitation. The mixture was filtered and NEt_3 (3.7 mL, 26 mmol) was added, with the immediate production of a yellow solution and white precipitate. The mixture was filtered again and the solvent was slowly removed to give large white crystals, which were washed with fresh hexane. Yield 1.4 g (3.0 mmol, 23%); mp 208–215°C. IR (Nujol mull) (cm^{-1}): 1444 (4), 1363 (8), 1320 (11), 1276 (15), 1260 (14), 1249 (10), 1198 (5), 1180 (16), 1104 (9), 1056 (19), 1039 (17), 935 (13), 923 (7), 907 (2), 801 (1), 537 (12), 529 (18), 496 (5), 421 (3), 379 (20). ^1H NMR: 1.31 (d, $^3J_{HH}$ = 10 Hz), 3.04 (sept, $^3J_{HH}$ = 8 Hz), 7.2–7.4 (m). ^{31}P NMR: 211. Anal. calcd.: C 59.63, H 7.09, N 5.80; found: C 59.54, H 7.20, N 5.76.

X-ray crystallography

Crystals of **1**, **4**, and **7** were selected and mounted in Pyrex capillaries in the dry box. Data were corrected for Lorentz and polarization effects, and absorption. Structures were solved by direct methods and expanded using Fourier techniques. For compound **4**, only the chlorine atoms, the phosphorus atoms, and C(11) and C(12) were refined anisotropically. The standard reflections decreased by 25% during data collection, and a linear correction factor was applied. For compound **7**, only the chlorine atoms, phosphorus atoms, and C(9)-C(12) and C(19)-C(24) were refined anisotropically. Extinction corrections were not applied for compounds **4** and **7**. Hydrogen atoms were allowed to ride on the heavy atoms to which they are bonded, with C-H distances of 0.95 Å and fixed isotropic temperature factors. Calculations were performed using the teXsan crystallographic package (17). A summary of the crystallographic data is given in Table 2.[3]

Results and discussion

Reaction mixtures of PCl_3 and $DippNH_2$ with different stoichiometric combinations have been examined using ^{31}P NMR spectroscopy. Contrary to the reports describing isolation of phosphetidine (**7**) for many RNH_2 derivatives (R = alkyl and aryl) (4, 18), a number of products were observed for $DippNH_2$, with **7** as a minor component even at high excess of amine. Table 1 lists the ^{31}P chemical shifts observed for each stoichiometric combination, according to the relative peak intensity with respect to the most intense peak (100%). Chemical shift assignments for compounds **1**, **7**, and **9** (3) have been confirmed by characterization of isolated materials. In contrast to reactions involving amines

[3] Supplementary data may be purchased from the Depository of Unpublished Data, Document Delivery, CISTI, National Research Council Canada, Ottawa, ON K1A 0S2, Canada (http://www.nrc.ca/cisti/irm/unpub_e.shtml for information on ordering electronically). CCDC 191247–191249 contain the supplementary data for this paper. These data can be obtained, free of charge, via www.ccdc.cam.ac.uk/conts/retrieving.html (or from the Cambridge Crystallographic Data Centre, 12 Union Road, Cambridge, U.K.; fax +44 1223 336033; or deposit@ccdc.cam.ac.uk).

© 2002 NRC Canada

Table 2. Crystal data for compounds **1**, **4**, and **7**.

	$Dipp(H)NPCl_2$	$DippN(PCl_2)_2$	$[DippNPCl]_2$
Compound label	**1**	**4**	**7**
Empirical formula	$C_{12}H_{18}Cl_2NP$	$C_{12}H_{17}Cl_4NP_2$	$C_{24}H_{34}P_2N_2Cl_2$
Formula weight	278.16	379.03	483.40
Crystal system	Monoclinic	Monoclinic	Monoclinic
Space group	$P2_1/n$	$P2_1/c$	$P2_1/c$
a (Å)	23.80(1)	14.34(1)	9.814(9)
b (Å)	5.531(2)	9.455(4)	17.579(8)
c (Å)	23.82(6)	26.478(9)	16.002(5)
β (°)	109.21(3)	103.70(5)	103.37(4)
V (Å^3), Z	2962(2), 8	3487(3), 8	2686(3), 4
D_{calc} (mg m^{-3})	1.248	1.444	1.195
λ (Å)	0.71069	0.71069	0.71069
μ (cm^{-1}), F(000)	5.22, 1168	8.48, 1552	3.74, 1024
Crystal size (mm^3)	0.08 × 0.28 × 0.60	0.20 × 0.40 × 0.50	0.15 × 0.20 × 0.60
Diffractometer	Rigaku AFC5R	Rigaku AFC5R	Rigaku AFC5R
Scan type	ω–2θ	ω–2θ	ω–2θ
Temperature (K)	296(1)	296(1)	296(1)
Absorption correction	1.0–0.68	ψ-scan	ψ-scan
Transmission factors	0.6791–1.0000	0.6263–1.0000	0.9030–0.9977
Data collected	3777	5767	4616
Unique data	3233	5479	4316
Observed data [$I > 3\sigma(I)$]	1104	889	841
R_{int}, $2\theta_{max}$ (°)	0.063, 46.1	0.031, 50.1	0.053, 50.1
Refined parameters	200	223	192
Refinement on	F	F	F
$R(F)$, $wR(F)$, $S(F)$[a]	0.068, 0.073, 2.27	0.074, 0.084, 1.86	0.068, 0.083, 2.05
Final Δρ map (e Å^{-3})	0.33, –0.30	0.44, –0.51	0.34, –0.33

[a] $R(F) = \sum(||F_o| - |F_c||)/\sum|F_o|$; $wR(F) = [\sum w(|F_o| - |F_c|)^2/\sum w(F_o)^2]^{1/2}$; $S(F) = [\sum w(|F_o| - |F_c|)^2/(n - p)]^{1/2}$; n = number of data; p = number of refined parameters.

with small substituents (R = Me, Et, Bu) (18), the aminodiphosphine **4** (R = Dipp, 165 ppm) was not observed, even at a two-fold excess of PCl_3. Instead, compound **4** has been isolated from reactions in the presence of NEt_3 (see below).

Referring to Table 1, PCl_3 is observed as an excess component in the equimolar reaction with $DippNH_2$, and the prominent peak (155 ppm) is assigned to monoaminophosphine (**1**). The prominent peak (139 ppm) at a three-fold excess of $DippNH_2$ is assigned to the diaminophosphine (**2**), and is the prominent component at all reactions involving higher excesses of $DippNH_2$. Evidence for P-N-P linkages is only observed above a two-fold excess of $DippNH_2$, with two sets of doublets (148, 182 ppm; 161, 195 ppm; $^2J_{PP}$ = 45 Hz) exhibiting typical two-bond coupling constants. Although high-order tetraphosphorus assemblies are possible, these doublets are speculatively assigned to the nonsymmetric systems **5** and **8**, which are the likely precursors to **9** (3). Previous reports confirm that derivatives of **5** can been isolated (9). They are, however, prone to rapid cyclisation to give the phosphetidine framework (13), and on this basis the more prominent doublet signals are assigned to **8**.

^{31}P NMR spectra of reaction mixtures containing equimolar amounts of PCl_3 and $PhNH_2$ show **1** and **7** (R = Ph) as well as unreacted PCl_3, consistent with the established facile isolation of the phosphetidine **7** (8), but the spectra are more complicated in the presence of excess $PhNH_2$. In this context, the relative impedance of dehydrochloride PCl_3–$DippNH_2$ coupling is interpreted in terms of the steric imposition of the Dipp substituent restricting intermolecular interactions and influencing the nucleophilicity of the amine.

The absence of aminodiphosphine (**4**) in all reaction mixtures of PCl_3 with $DippNH_2$, and the prominence of the mono- (**1**) and diaminophosphine (**2**) (R = Dipp), indicates that the nucleophilicity of the nitrogen centre in **1** is insufficient to interact with a second PCl_3, so that attack at the phosphorus centre in **1** by $DippNH_2$ is relatively favoured. In this context, it is reasonable to assign the peak at 140 ppm to the trisaminophosphine (**3**) (R = Dipp), and to conclude that the formation of **5** is preferred over **4**, which facilitates the formation of **7** and renders **4** redundant in the reaction pathway.

High yield formation of compound **4** from PCl_3 and $DippNH_2$ in the presence of NEt_3 indicates that the nucleophilicity of the nitrogen center in **1** is enhanced by the presence of triethylamine, presumably due to partial or full deprotonation. ^{31}P NMR spectra of reaction mixtures containing NEt_3 show **4** and **7** as the only products, emphasizing the special stability of the phosphetidine (**7**).

Assignments of peaks in the ^{31}P NMR spectra to compounds **1**, **4**, **7**, and **9** (3) (R = Dipp) have been confirmed by isolation and structural characterization, as illustrated in Fig. 2. Some of the structural features of these compounds

© 2002 NRC Canada

Fig. 2 Views of the solid state structures of **1**, **4**, **7**, and **9** (3) for *R* = Dipp.

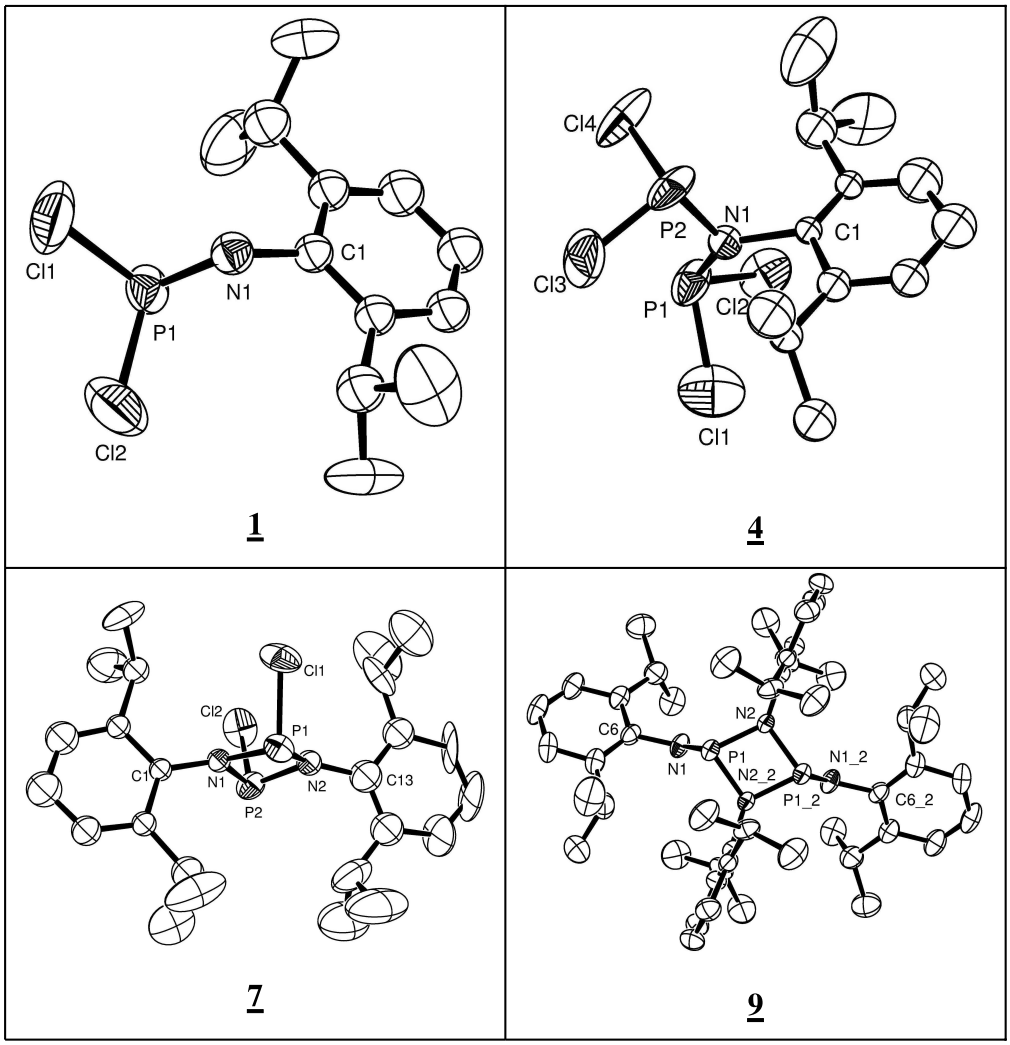

Table 3. Comparison of selected bond lengths (Å) and angles (°) for **1**, **4**, **7**, and **9** (3) for *R* = Dipp.

	$R(H)NPCl_2$[a]	$RN(PCl_2)_2$ [ii]	$[RNPCl]_2$	$[RNPN(H)R]_2$[4]
Compound label (*R* = Dipp)	**1**	4	7	9
P(1/2)—N(1/2)	1.64(1), 1.63(1)	1.59(3), 1.69(2), 1.76(2), 1.68(2)	1.71(1), 1.69(1), 1.73(1), 1.69(2)	1.727(3), 1.739(3)
P(1)—Cl(1/2); P(2)—Cl(3/4)	2.033(7), 2.062(7); 2.010(8), 2.024(8)	2.11(2), 2.03(2); 2.05(2), 2.02(2) 2.06(2), 2.01(2); 2.06(2), 2.07(1)	P(1)—Cl(1): 2.071(8); P(2)—Cl(2): 2.085(8)	—
N(1/2)-P(1/2)-N(1/2)	—	—	81.3(7), 80.5(7)	80.01(15)
P(1)-N(1/2)-P(2)	—	122(2), 122(1)	98.6(7), 97.9(8)	97.54(14)
N(1)-P(1)-Cl(1/2); N(1)-P(2)-Cl(3/4)	99.5(5), 105.0(5); 95.9(4), 102.2(6)	102(1), 104(1), 106(1), 103(1), 102(1), 99(1), 102(1), 101(1)	N(1/2)-P(1)-Cl(1): 103.2(6), 105.8(6) N(1/2)-P(2)-Cl(2): 103.2(6), 106.1(6)	—
Σ@N(1/2)	—	359, 360	355.6, 354.9	348

[a]Two molecules in the asymmetric unit.

(Table 3) are worthy of comment. The aminodiphosphine (**4**) (*R* = Dipp) adopts a C_s conformation (*endo*,*exo*), contrasting the C_{2v} conformation (*exo*,*exo*) reported for the phenyl derivative of **4** (*R* = Ph) (12) and pentaphenylaminodiphosphine (5). Nevertheless, the structural trends indicate that larger substituents, such as Dipp, impose the (*endo*,*exo*) conformation (12). The typical planar environment at nitrogen bound to phosphorus is observed for all Dipp-N-P compounds described in this report, as demonstrated by the sum (approximately 360°) of the bond angles at nitrogen. The resulting $P(N)_2P$ plane in the phosphetidine (**7**) clearly demonstrates a *cis* conformation for the chlorine substituents,

© 2002 NRC Canada

consistent with the phenyl derivative (7), and the aryl substituents are perpendicular to the NP_2 plane.

Conclusions

Reactions of $DippNH_2$ with PCl_3 have been comprehensively evaluated by ^{31}P NMR spectroscopy. The observations confirm the intermediacy of aminophosphines in phosphetidine formation and offer insight to the mechanisms of P-N-P linkage assembly.

Acknowledgements

We thank the Natural Sciences and Engineering Research Council of Canada (NSERC), the Killam Foundation (NB), and the Canada Research Chairs Program (NB) for funding, the Atlantic Region Magnetic Resonance Center for the use of instrumentation, and Dr. Katherine N. Robertson for assistance with the crystallographic studies.

References

1. R.B. King. Inorganc chemistry of main group elements. VCH, New York. 1994.
2. R. Keat. Top. Curr. Chem. **102**, 89 (1982).
3. N. Burford, T.S. Cameron, K.-C. Lam, D.J. LeBlanc, C.L.B. Macdonald, A.D. Phillips, A.L. Rheingold, L. Stark, and D. Walsh. Can. J. Chem. **79**, 342 (2001).
4. L. Stahl. Coord. Chem. Rev. **210**, 203 (2000).
5. A. Tarassoli, R.C. Haltiwanger, and A.D. Norman. Inorg. Chem. **21**, 2684 (1982).
6. N.D. Reddy, A.J. Elias, and A. Vij. J. Chem. Soc. Dalton Trans. 2167 (1997).
7. H.-J. Chen, R.C. Haltiwanger, T.G. Hill, M.L. Thompson, D.E. Coons, and A.D. Norman. Inorg. Chem. **24**, 4725 (1985).
8. R.A. Shaw. Phosphorus Sulfur Silicon Relat. Elem. **4**, 101 (1978).
9. O.J. Scherer and G. Schnabl. Angew. Chem. Int. Ed. Engl. **15**, 772 (1976).
10. R. Jefferson, J.F. Nixon, T.M. Painter, R. Keat, and L. Stobbs. J. Chem. Soc. Dalton Trans. 1414 (1973).
11. R. Keat, L. Manojlovic-Muir, K.W. Muir, and D.S. Rycroft. J. Chem. Soc. Dalton Trans. 2192 (1981).
12. H.-J. Chen, J.M. Barendt, R.C. Haltiwanger, T.G. Hill, and A.D. Norman. Phosphorus Sulfur Silicon Relat. Elem. **26**, 155 (1986).
13. G. Bulloch and R. Keat. J. Chem. Soc. Dalton Trans. 2010 (1974).
14. A.R. Davies, A.T. Dronsfield, R.N. Haszeldine, and D.R. Taylor. J. Chem. Soc. Perkin. Trans. 1: 379 (1973).
15. E. Niecke and D. Gudat. Angew. Chem. Int. Ed. Engl. **30**, 217 (1991).
16. N. Burford, J. Mueller, and T.M. Parks. J. Chem. Educ. **71**, 807 (1994).
17. Molecular Structure Corporation. 2000. teXsan for Windows [computer program]. Version 1. Molecular Structure Corporation, The Woodlands, Texas.
18. M.S. Balakrishna, V.S. Reddy, S.S. Krishnamurthy, J.F. Nixon, and J.C.T.R. Burckett St. Laurent. Coord. Chem. Rev. **129**, 1 (1994).

© 2002 NRC Canada

Sulfimidation of thio-ether crown systems: the X-ray crystal structure of the $\{[9\text{-ane}]S_2S(NH_2)\}^+$, $\{[9\text{-ane}]SS(NH_2)S(NH_2)\}^{2+}$, and $\{[9\text{-ane}]S(NH_2)S_2(\mu\text{-}N)\}^{2+}$ cations

Mark R. J. Elsegood, Liam M. Gilby, Kathryn E. Holmes, and Paul F. Kelly

Abstract: Treatment of the thio-ether crown [9-ane]S_3 (**1**) with 1 equiv of *O*-mesitylsulfonylhydroxylamine (MSH) yields the water-soluble protonated sulfimide $\{[9\text{-ane}]S_2S(NH_2)\}^+$ (**2**). Two equiv of MSH leads to the formation of $\{[9\text{-ane}]SS(NH_2)S(NH_2)\}^{2+}$ (**3**), while excess MSH generates the $\{[9\text{-ane}]S(NH_2)S_2(\mu\text{-N})\}^{2+}$ cation (**4**) (**2**–**4** form as salts of the $[Me_3C_6H_2SO_3]^-$ anion); the X-ray crystal structure of **2** and **3** confirms that one and two of the ring sulfurs, respectively, have been converted to terminal protonated sulfimides, while that of **4** reveals the presence of both terminal and bridging nitrogens.

Key words: sulfur-nitrides, macrocycles, sulfimides, amination.

Résumé : Le traitement du thioéther couronne [9-ane]S_3 (**1**) avec un équivalent de *O*-mésitylsulfonylhydroxylamine (MSH) fournit le sulfimide protoné soluble dans l'eau $\{[9\text{-ane}]S_2S(NH_2)\}^+$ (**2**). Deux équivalents de MSH conduisent à la formation du $\{[9\text{-ane}]SS(NH_2)S(NH_2)\}^{2+}$ (**3**) alors qu'un excès de MSH génère le cation $\{[9\text{-ane}]S(NH_2)S_2(\mu\text{-N})\}^{2+}$ (**4**) (les cations **2**–**4** ont été isolés sous la forme de sels avec l'anion $[Me_3C_6H_2SO_3]^-$). Les structures des composés **2**, **3** et **4** ont été déterminées par diffraction des rayons X; les deux premières confirment que respectivement un et deux des cycles contenant du soufre ont été transformés en sulfimides terminales protonées alors que la structure de la dernière révèle la présence d'atomes d'azote agissant comme ponts alors que d'autres sont en positions terminales.

Mots clés : soufre-nitrures, macrocycles, sulfimides, amination.

[Traduit par la Rédaction]

Introduction and discussion

We have recently reported on the reactivity of *S*,*S*′-diphenylsulfimide, (Ph_2SNH) towards a number of metal centres (1) and have subsequently extended such reactions to novel sulfimides prepared from disulfide starting materials (2). Although the reagent used to effect such reactions, *O*-mesitylsulfonylhydroxylamine (MSH), has long been known to react in this way with monosulfides (3), the concept of reacting with systems bearing two sulfide units does not appear to have been investigated before. This technique has the advantage of generating products with great potential to act as multidentate ligands, either because of the presence of a combination of N-donating sulfimide and S-donating sulfide units, or two sulfimides. Thus we have prepared 1,2-(PhS{NH})(PhS)C_6H_4 and 1,4-(PhS{NH})$_2C_6H_4$, which have the potential to act as a bidentate S,N donor, and as a bridging ligand, respectively.

In this study we have extended such reactions to a different class of starting material – the cyclic crown system [9-ane]S_3 (**1**). The latter is a classic example of a cyclic thioether, much studied for their ability to coordinate to metal centres through a number of the sulfur atoms (4). Many variations upon such systems have been prepared, in which the nature of the carbon backbone has been changed, or in which the sulfur(s) have been oxidized to SO units (5). The latter are isoelectronic with sulfimides (SNH (or SNR)), but do not share the potential versatility of the latter. Not only is the sulfimide nitrogen a very effective donor to metal centres, but it may also be derivatized by introduction of pertinent R groups, which could allow significant modification of the coordination properties. On the latter front we have already shown that effective coordination of sulfimide units is not simply limited to the "free" sulfimides by isolating complexes of $Ph_2SNCH_2CH_2CN$ (6).

Reaction of MSH with **1** in an equimolar ratio results in the formation of a salt of the protonated sulfimide (**2**) (Scheme 1). This precipitates from dichloromethane solutions as a white solid and may be recrystallized by diffusion of ether vapour into a methanolic solution. Compound **2** may be characterized by spectroscopy and X-ray crystallography. The diffraction study confirms the presence of the

Received 12 December 2001. Published on the NRC Research Press Web site at http://canjchem.nrc.ca on 7 October 2002.

Dedicated to Professor Tris Chivers for his contributions to Canadian chemistry.

M.R.J. Elsegood, L.M. Gilby, K.E. Holmes, and P.F. Kelly.[1] Department of Chemistry, Loughborough University, Loughborough, Leicestershire LE11 3TU, U.K.

[1]Corresponding author (P.F.Kelly@lboro.ac.uk).

 DOI: 10.1139/V02-051 © 2002 NRC Canada

Scheme 1. The products of the reaction of **1** with varying equivalents of MSH.

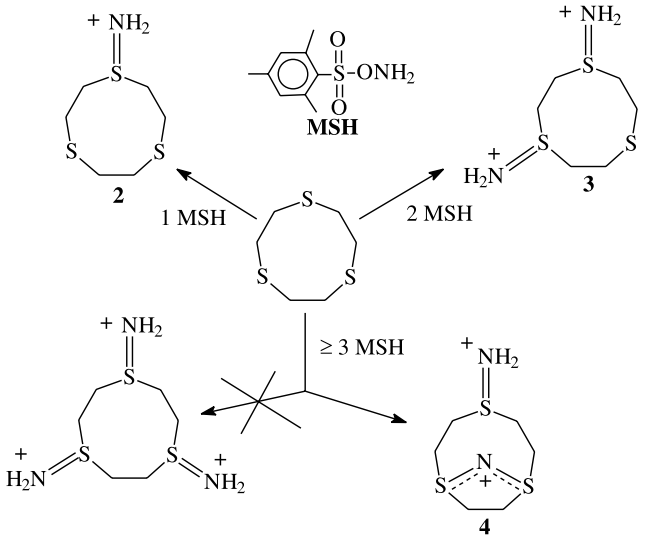

$\{[9ane]S_2S(NH_2)\}^+$ cation in the salt $\{[9ane]S_2S(NH_2)\}[Me_3C_6H_2SO_3]$ (Fig. 1). As Fig. 1 shows, the cation **2** retains a cyclic structure, within which one of the sulfur atoms has the $[NH_2]^+$ group of the sulfimide unit attached (S—N bond distance = 1.6417(14) Å). The non-sulfimide sulfur atoms arrange themselves in an "up, down" manner relative to the sulfur atom that has reacted. The anion exhibits the expected structure, with significant H-bonding interactions between the N—H bonds of the cation and two of the oxygen atoms of the anion. Thus O(2) and O(3) have close, but asymmetric, contacts to H(1B) (2.25(2) Å to O(2) and 2.42(2) Å to O(3)), while O(2) from an adjacent anion interacts with the other N—H bond (H(1A)···O(2′) = 2.01(2) Å). Of the three oxygen atoms bound to the sulfur of the anion, therefore, O(1) has no close interactions, O(3) has one, and O(2), two. The net effect of this is to produce an overall array structure as shown. Only three lines are seen in the ^{13}C spectrum of the cation; this indicates that the solid state structure is not retained in solution (had it been, then all six carbons would appear unique). The ^1H spectrum, however, consists of six 8-line multiplets, indicating that while S(2) and S(3) may be undergoing fast inversion, the sulfimide sulfur is not (previous work has shown that optically active sulfimides racemize at around 80°C, for example) (7). Significantly, **[2]**$[Me_3C_6H_2SO_3]$ readily dissolves in water; if, after one hour, the water is removed in vacuo and the residue crystallized, IR spectroscopy and microanalysis suggest that there is no decomposition in aqueous solution, at least on a short timescale.

Spectroscopy and X-ray crystallography have shown that 2 equiv of MSH react with **1** to give $\{[9\text{-ane}]SS(NH_2)S(NH_2)\}^{2+}$ (**3**), in which two of the sulfur atoms of the crown have reacted to give terminal sulfimides (Scheme 1). The S—N distances of 1.6457(17) and 1.6450(15) Å are comparable with those in **2**. Again, the cyclic structure of the macrocycle is retained, yet the conformation of the ring is somewhat different, being less "twisted" than in **2**, and forming a "boat"-type structure (Fig. 2). ^1H NMR spectroscopy suggests that the solid-state

Fig. 1. The X-ray crystal structure of the cation in **[2]** $[Me_3C_6H_2SO_3]$ and its hydrogen bonding links to the oxygen atoms of adjacent anions (N.B. the overall stoichiometry has only one anion per cation). Selected bond distances (Å) and angles (°): N(1)—S(1) 1.6417(14), S(1)—C(1) 1.8090(14), C(1)—C(2) 1.5198(19), C(2)—S(2) 1.8114(15), S(2)—C(3) 1.8225(16), C(3)—C(4) 1.522(2), C(4)—S(3) 1.8157(16), S(3)—C(5) 1.8258(17), C(5)—C(6) 1.529(2), C(6)—S(1) 1.8120(16). N(1)-S(1)-C(1) 101.85(7), S(1)-C(1)-C(2) 108.58(10), C(1)-C(2)-S(2) 113.57(10), C(2)-S(2)-C(3) 103.09(7), S(2)-C(3)-C(4) 114.24(11), C(3)-C(4)-S(3) 116.43(11), C(4)-S(3)-C(5) 104.47(8), S(3)-C(5)-C(6) 114.72(11), C(5)-C(6)-S(1) 113.61(11), C(6)-S(1)-C(1) 104.61(7), C(6)-S(1)-N(1) 107.84(7).

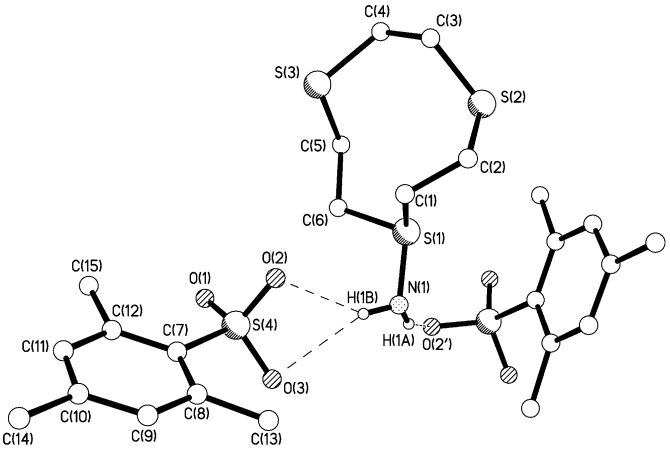

structure is not retained in solution. The crystal structure determination reveals that the sulfimide nitrogen atoms are orientated such as to be divergent from the ring, with an angle of approximately 55° between them. The NH_2 units are involved in extensive H-bonding between the two $[Me_3C_6H_2SO_3]^-$ anions and two molecules of MeOH in the structure.

The analogous triply substituted species, however, is not isolated when 3 equiv (or an excess) of MSH are used. In this case **4** forms (Fig. 3), in which one terminal sulfimide and one nitrogen-bridging sulfimide unit are found. The latter N-sulfoniosulfimidium unit is well known but has always been reported in reactions between discrete units (such as the reaction of Ph_2SNBr with organo-sulfides) rather than the intramolecular rearrangement that presumably generates **4** (7). The mechanism for its formation is unclear, but the fact that the aforementioned *bis*-sulfimide forms from the reaction of 2 equiv of MSH indicates that there is no inherent instability for two adjacent sulfimide units. If we assume that $\{[9\text{-ane}]S(NH_2)S(NH_2)S(NH_2)\}^{3+}$ does initially form, it may simply be that the high charge–small size combination makes this unstable with respect to conversion to **4**, possibly by loss of $[NH_4]^+$. Indeed, prior to crystallization, crude **4** shows an IR stretch at 3182 cm^{-1}, which is indicative of the ammonium cation (we have noted the same band in $[NH_4][Me_3C_6H_2SO_3]$). Within the structure of **4**, the nitrogen bridge results in the formation of an NSCCS heterocycle, within which the atoms are effectively planar (max deviation from mean plane: ca 0.2 Å at the nitrogen). Although this motif is not uncommon, a search of the Cambridge Structural

© 2002 NRC Canada

Fig. 2. The X-ray crystal structure of the cation in [**3**][$Me_3C_6H_2SO_3]_2$. Selected bond distances (Å) and angles (°): S(1)—N(1) 1.6357(17), S(2)—N(2) 1.6450(15), S(1)—C(1) 1.8166(17), C(1)—C(2) 1.526(2), S(2)—C(2) 1.8202(17), S(2)—C(3) 1.8283(17), C(3)—C(4) 1.525(2), S(3)—C(4) 1.8141(18), S(3)—C(5) 1.8089(18), C(5)—C(6) 1.520(2), S(1)—C(6) 1.8094(17). N(1)-S(1)-C(6) 98.24(9), N(1)-S(1)-C(1) 108.02(9), C(6)-S(1)-C(1) 106.79(8), N(2)-S(2)-C(2) 98.08(8), N(2)-S(2)-C(3) 106.79(8), C(2)-S(2)-C(3) 104.02(8), C(5)-S(3)-C(4)103.22(8), C(2)-C(1)-S(1) 118.21(12), C(6)-C(5)-S(3) 117.53(12), C(5)-C(6)-S(1) 114.25(12).

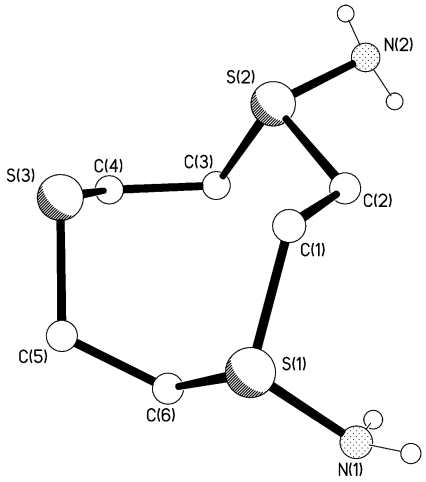

Database (8) revealed only one other example in which the ring is fused to another ring via S—C bonds (9). The latter species is a 1,4-dithia-7-azanorbornylium cation formed by the addition of the $[S_2N]^+$ cation to ethene. As a consequence of the formation of the NCSSC ring, the remainder of the atoms in the macrocycle are forced to adopt a "chair"-type conformation. The terminal sulfimide nitrogen atom is orientated perpendicular to the approximate "plane" made by the macrocycle.

The isolation of **2**, **3**, and **4** is significant for a number of reasons. In the case of **2** and **3** it represents an easy, one-pot, post-ring-closure derivatization of the crown that should allow further introduction of pertinent groups (including pendant arms potentially coordinating in their own right) via reaction at the nitrogen (7). This would, of course, greatly enhance the coordination chemistry of the crown systems, as would the fact that, unlike the parent crown, **2** is water soluble. Work to exploit both aspects of the chemistry of **2** is underway. In the case of **4**, the unique post-ring-closure formation of the transannular nitrogen bridge generates an unusual fused ring arrangement, and may well prove applicable to other systems. In this light, investigations into the reactivity of larger ring systems towards MSH are underway.

Experimental

MSH was prepared by the literature method (10) and [9-ane]S_3 was used as received from Aldrich. All reactions were performed under nitrogen using dichloromethane dried over calcium hydride and diethylether over sodium. Elemental analyses (PerkinElmer 2400 CHN Analyser) were performed by the Loughborough University service within the department of chemistry. NMR spectra were recorded in $CDCl_3$ on a Bruker AC250. IR spectra were recorded on a PerkinElmer PE2000 IR spectrometer as KBr discs (4000–400 cm^{-1}) and FAB-MS in 3-nitrobenzyl alcohol (positive-ion mode) on a JEOL JMS SX-102 mass spectrometer.

Fig. 3. The X-ray crystal structure of the cation in [**4**][$Me_3C_6H_2SO_3]_2$. Selected bond distances (Å) and angles (°): S(1)—N(1) 1.612(4), S(2)—N(2) 1.627(3), N(2)—S(3) 1.639(4), S(1)—C(1) 1.793(4), C(1)—C(2) 1.508(6), C(2)—S(2) 1.821(4), S(2)—C(3) 1.814(4), C(3)—C(4) 1.526(6), C(4)—S(3) 1.825(5), S(3)—C(5) 1.825(5), C(5)—C(6) 1.518(6), C(6)—S(1) 1.805(4). C(6)-S(1)-C(1) 106.2(2), C(6)-S(1)-N(1) 107.7(2), C(1)-S(1)-N(1) 104.3(2), C(2)-S(2)-N(2) 110.14(18), C(3)-S(2)-N(2) 101.33(19), C(3)-S(2)-C(2) 99.10(19), C(5)-S(3)-N(2) 109.44(19), C(4)-S(3)-N(2) 101.69(19), C(5)-S(3)-C(4) 102.8(2), S(3)-N(2)-S(2) 112.0(2).

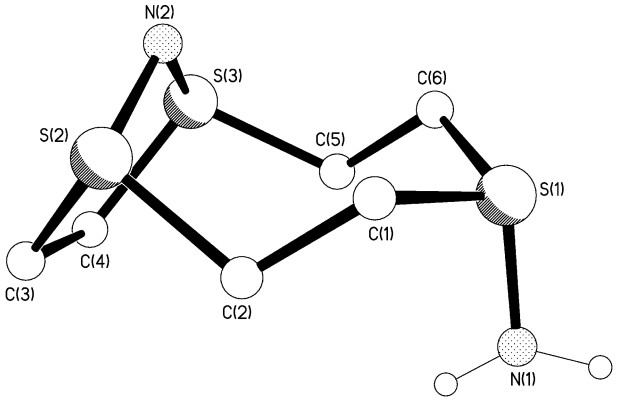

[2][$Me_3C_6H_2SO_3$]

A solution of MSH (0.60 g, 2.8 mmol) in CH_2Cl_2 (10 ml) was added dropwise to a solution of [9-ane]S_3 (0.50 g, 2.8 mmol) in an equal volume of the same solvent. A precipitate appeared within a short time; after stirring overnight, the resulting precipitate was filtered, washed with CH_2Cl_2, and dried in vacuo, yielding [**2**][$Me_3C_6H_2SO_3$] as a white solid. Slow diffusion of ether vapour into a methanol solution yielded crystals suitable for X-ray crystallography.

Yield 0.70 g (63%); mp 105°C (decomposition (dec)). IR (cm^{-1}) 3462 (w), 3403 (w), 3183 (s, (ν N-H)), 2980 (s), 1605 (s), 1567 (s), 1446 (s), 1407 (s), 1379 (m), 1186 (s), 1085 (s), 1012 (s), 944 (m), 892 (s), 849 (s (ν N-S)), 730 (m), 681 (s), 582 (s), 548 (s), 425 (m). ^{1}H NMR (CD_3OD) δ: 6.90 (2H, s, CH), 4.45 (2H, m, CH_2), 3.80 (2H, m, CH_2), 3.35 (2H, m, CH_2), 3.20 (2H, m, CH_2), 3.05 (2H, m, CH_2), 2.85 (2H, m, CH_2), 2.65 (6H, s, CH_3), 2.26 (3H, s, CH_3). ^{13}C NMR (CD_3OD) δ: 141.3, 140.7, 138.7, 132.3, 53.5, 36.9, 29.5, 23.8, 21.3. FAB-MS *m/e*: 196 ($[M]^+$). Anal. calc. for $C_{15}H_{25}NS_4O_3$ (%): C 45.6, H 6.3, N 3.5; found: C 45.3, H 6.7, N 3.9.

[3][$Me_3C_6H_2SO_3]_2$

A solution of MSH (10) (1.2 g, 5.6 mmol) in CH_2Cl_2 (10 ml) was added dropwise to a solution of [9-ane]S_3 (0.50 g, 2.8 mmol) in an equal volume of the same solvent. A precipitate appeared within a short time; after stirring overnight, the resulting precipitate was filtered, washed with CH_2Cl_2, and dried in vacuo yielding [**3**][$Me_3C_6H_2SO_3]_2$ as a white

© 2002 NRC Canada

Table 1. Experimental data for the X-ray diffraction studies of compounds prepared in this work.

Crystal	[**2**][$Me_3C_6H_2SO_3$]	[**3**][$Me_3C_6H_2SO_3$]$_2$	[**4**][$Me_3C_6H_2SO_3$]$_2$
Empirical formula	$C_{15}H_{25}NO_3S_4$	$C_{24}H_{38}N_2O_6S_5{\cdot}2CH_3OH$	$C_{24}H_{36}N_2O_6S_5$
Formula weight	395.60	674.95	608.85
Crystal system	Monoclinic	Monoclinic	Orthorhombic
Space group	$P2_1/c$	$P2_1/n$	$P2_12_12_1$
Crystal size (mm)	0.84 × 0.16 × 0.07	0.50 × 0.18 × 0.08	0.49 × 0.06 × 0.04
Crystal colour and shape	Colourless lath	Colourless needle	Colourless needle
a (Å)	7.6828(4)	8.2772	8.5583
b (Å)	24.8629(12)	31.1424	20.1517
c (Å)	9.6580(4)	12.7651	32.575
β (°)	93.253(2)	93.465	
V (Å^3)	1841.87(15)	3284.5	5614.4
Z	4	4	8
$D_{calcd.}$ (g cm^{-3})	1.427	1.365	1.441
Absorption coefficient (μ) (mm^{-1})	0.528	0.400	0.455
F(000)	840	1440	2576
θ range for data collection (°)	1.64 to 28.89	1.73 to 28.99	1.61 to 27.50
Data completeness to θ = 26°	99.9%	99.8%	98.8%
Reflections collected	15861	28838	48042
Independent reflections	4398	7922	12398
Reflections with $F^2 > 2\sigma(F^2)$	3909	6625	9697
R_{int}	0.0234	0.0211	0.0592
Parameters	217	415	691
Weighting parameters (a, b)[a]	0.0399, 0.7948	0.0334, 2.3043	0.0581, 3.1765
Goodness-of-fit on F^2	1.047	1.052	1.069
R^b, $wR2^c$	0.0288, 0.0794	0.0351, 0.0870	0.0522, 0.1273
Largest residuals (e Å^{-3})	0.361, –0.271	0.448, –0.277	0.770, –0.415

[a] $w^{-1} = \sigma(F_o^2) + (aP)^2 + bP$, where $P = (F_o^2 + 2F_c^2)/3$.
[b] $R = \sum||F_o| - |F_c||/\sum|F_o|$.
[c] $wR2 = \{\sum[w(F_o^2 - F_c^2)^2/\sum[w(F_o^2)^2]\}^{1/2}$.

solid. Slow diffusion of ether vapour into a methanol solution yielded crystals suitable for X-ray crystallography.

Yield 1.11g (59%) after recrystallization; mp 100ºC (dec). IR (cm^{-1}): 3461 (w), 3187 (s (ν N-H)), 2973 (s), 1603 (s), 1567 (m), 1434 (m), 1411 (m), 1165 (s), 1087 (s), 1013 (s), 936 (m), 888 (w), 848 (m (ν N-S)) 815 (w), 751 (m), 681 (s), 579 (s), 547 (s), 527 (m). ^{1}H NMR (CD_3OD) δ: 6.90 (4H, s, CH), 4.36 (2H, m, CH_2), 4.22 (2H, m, CH_2), 3.88 (2H, m, CH_2), 3.65 (2H, m, CH_2), 3.26 (2H, m, CH_2), 3.01 (2H, m, CH_2), 2.65 (12H, s, CH_3), 2.26 (6H, s, CH_3). ^{13}C NMR (CD_3OD) δ: 140.8, 140.3, 138.2, 131.8, 51.7, 39.1, 27.4, 23.3, 20.8. FAB-MS *m/e*: 211 ([M – H]$^+$). Anal calc. for $C_{24}H_{38}N_2S_5O_6{\cdot}2CH_3OH$ (%): C 46.4, H 6.8, N 4.2; found: C 46.2, H 6.4, N 4.2.

[4][$Me_3C_6H_2SO_3$]$_2$

A solution of MSH (1.20 g, 5.6 mmol) in CH_2Cl_2 (10 ml) was added dropwise to a solution of [9-ane]S_3 (0.25 g, 1.4 mmol) in an equal volume of the same solvent. A precipitate appeared within a short time; after stirring overnight, the resulting precipitate was filtered, washed with CH_2Cl_2, and dried in vacuo yielding [**4**][$Me_3C_6H_2SO_3$]$_2$ as a white solid.

Slow diffusion of ether vapour into a methanol solution yielded crystals suitable for X-ray crystallography.

Yield 0.51g (60%); mp 132°C (dec). IR (cm^{-1}): 3442 (w), 3154 (m, br (ν N-H)), 2947 (s), 1604 (m), 1566 (m), 1444 (m), 1405 (m), 1226 (s), 1183 (s), 1161 (s), 1082 (s), 1011 (s), 892 (s), 851 (m (ν N-S)), 731 (m), 678 (s), 581 (s), 549 (m), 528 (m), 426 (m). ^{1}H NMR (CD_3OD) δ: 6.78 (4H, s, CH), 4.45 (2H, m, CH_2), 3.90–4.20 (10H, m, CH_2), 2.53 (12H, s, CH_3), 2.14 (6H, s, CH_3). ^{13}C NMR (CD_3OD) δ: 141.3, 140.8, 138.6, 132.2, 50.3, 44.0, 42.7, 23.7, 21.2. FAB-MS *m/e*: 210 ([M]$^+$). Anal. calc. for $C_{24}H_{36}N_2S_5O_6$ (%): C 47.4, H 5.9, N 4.6; found C 47.2, H 5.9, N 4.5.

X-ray crystallography for [2][$Me_3C_6H_2SO_3$], [3][$Me_3C_6H_2SO_3$]$_2$, and [4][$Me_3C_6H_2SO_3$]$_2$

Intensity data were collected using a Bruker AXS SMART 1000 CCD area detector diffractometer equipped with graphite monochromated Mo Kα radiation (λ = 0.71073) at 150 K. Narrow frames were collected (0.3° in ω) and an empirical absorption correction applied based on redundant and symmetry equivalent data. The structures were solved by direct methods and refined by full-matrix least squares on F^2. H atoms were refined with a riding model with H-atom U_{iso} values tied to those of the carrier atoms and set to 1.2 times U_{eq} (1.5 for methyl-H), except N*H*, where coordinates were freely refined. In compound [**3**][$Me_3C_6H_2SO_3$]$_2$, atoms S(1) and N(1) are disordered over 2 sets of positions, with occupancies of 94.0(2) and 6.0(2)%. This disorder was modelled with the aid of restraints on geometry and displacement parameters. Hydrogen atoms were not included on the minor disorder component. Compound

© 2002 NRC Canada

[**4**][$Me_3C_6H_2SO_3$]$_2$ comprises two cations and four anions in the asymmetric unit. Programs used were Bruker SMART (11(*a*)), SAINT (11(*a*)), SHELXTL (11(*b*)), and local programs. Details of the data collection and structure refinements are shown in Table 1.[2]

References

1. P.F. Kelly and A.M.Z. Slawin. Eur. J. Inorg. Chem. 263 (2001), and refs. therein.
2. M.R.J. Elsegood, K.E. Holmes, P.F. Kelly, J.Parr, and J.M. Stonehouse. New J. Chem. **26**, 202 (2002).
3. For example, see: A.D.M. Curtis, R. McCague, C.A. Ramsden, and M.R. Raza. Chem. Commun. 189 (1999).
4. For example, see: A.J. Blake and M. Schroder. Adv. Inorg. Chem. **1**, 35 (1990); G.H. Robinson. Coord. Chem. Rev. **112**, 227 (1992).
5. A.J. Blake, M. Schroder, and M.J. Sullivan. Acta. Crystallogr. Sect. C: Cryst. Struct. **C47**, 2717 (1991).
6. P.F. Kelly, K.G. Parker, M.A. Rodiel, and A.M.Z. Slawin. J. Organomet. Chem. **623**, 120 (2001).
7. S. Oae and N. Furukawa. *In* Sulfilimines and related derivatives. ACS, Washington, DC. 1983.
8. F.H. Allen and O. Kennard. Chem. Des. Autom. News, **8**, 31 (1993).
9. N. Burford, J.P. Johnson, J. Passmore, M.J. Schriver, and P.S. White. J. Chem. Soc. Chem. Commun. 966 (1986); W.V.F. Brooks, S. Brownridge, J. Passmore, M.J. Schriver, and X.P. Sun, J. Chem. Soc. Dalton Trans. 1997 (1996).
10. Y. Tamura, J. Minamikawa, K. Sumoto, S. Fujii, and M. Ikeda, J. Org. Chem. **38**, 1239 (1973).
11. (*a*) Bruker AXS Inc. 1994. SMART and SAINT software for CCD diffractometers [computer program]. Bruker AXS Inc., Madison, WI; (*b*) G.M. Sheldrick. SHELXTL user manual. Version 5. Bruker AXS Inc., Madison, WI, 1994.

[2] Crystallographic data for the structures reported in this paper have been deposited with the Cambridge Crystallographic Data Centre (CCDC 172384 (**2**), 172385 (**3**), and 172386 (**4**)). These data can be obtained, free of charge, via www.ccdc.cam.ac.uk/conts/retrieving.html (or from the Cambridge Crystallographic Data Centre, 12 Union Road, Cambridge, U.K.; fax +44 1223 336033; or deposit@ccdc.cam.ac.uk).

© 2002 NRC Canada

New hybrid inorganic-organic polymers containing cyclophosphazenes as pendant groups: Cyclophosphazene ligands containing hydrazone linkages and their conversion to polymers

Vadapalli Chandrasekhar, Venkatasubbaiah Krishnan, Arunachalampillai Athimoolam, and Gurusamy Thangavelu Senthil Andavan

Abstract: The reaction of the cyclotriphosphazene $N_3P_3Cl_5$[O-C_6H_4-*p*-C_6H_4-*p*-CH=CH_2] (**2**) with 10 equiv of *N*-methylhydrazine proceeds in a regio-specific manner to afford the multi-functional hydrazide N_3P_3[N(Me)NH_2]$_5$[O-C_6H_4-*p*-C_6H_4-*p*-CH=CH_2] (**3**). Condensation of **3** with *o*-hydroxy benzaldehyde or pyridine-2-carboxaldehyde affords the corresponding hydrazones N_3P_3[N(Me)N=CH-C_6H_4-*o*-OH]$_5$[O-C_6H_4-*p*-C_6H_4-*p*-CH=CH_2] (**4**) and N_3P_3[N(Me)N=CH-C_6H_4N]$_5$[O-C_6H_4-*p*-C_6H_4-*p*-CH=CH_2] (**5**), respectively. These hydrazones can be homopolymerized to afford polymers **6** and **7** containing multi-site coordinating cyclophosphazenes as pendant groups.

Key words: cyclophosphazene, hydrazone, pendant polymers, hybrid polymers, polymeric ligands.

Résumé : La réaction du cyclotriphosphazène $N_3P_3Cl_5$[O-C_6H_4-*p*-C_6H_4-*p*-CH=CH_2] (**2**) avec dix équivalents de *N*-méthylhydrazine se produit d'une façon régiospécifique et conduit à la formation de l'hydrazide multifonctionnel N_3P_3[N(Me)NH_2]$_5$[O-C_6H_4-*p*-C_6H_4-*p*-CH=CH_2] (**3**). Les condensations du composé **3** avec l'*o*-hydroxybenzaldéhyde ou la pyridine-2-carboxaldéhyde fournissent respectivement les hydrazones correspondantes N_3P_3[N(Me)N=CH-C_6H_4-*o*-OH]$_5$[O-C_6H_4-*p*-C_6H_4-*p*-CH=CH_2] (**4**) et N_3P_3[N(Me)N=CH-C_6H_4N]$_5$[O-C_6H_4-*p*-C_6H_4-*p*-CH=CH_2] (**5**). Ces hydrazones peuvent être soumises à des homopolymérisations qui conduisent aux polymères **6** et **7** portant cyclophosphazènes à plusieurs sites de coordination comme groupes pendants.

Mots clés : cyclophosphazène, hydrazone, polymères pendants, polymères hybrides, ligands polymériques.

[Traduit par la Rédaction]

Introduction

Among the inorganic polymers, polyphosphazenes ([N=PR_2]$_n$) occupy a prominent place (1). These constitute the largest family of inorganic polymers with over 800 representative examples. A remarkable feature of polyphosphazenes is that the property and function of each polymer can be readily fine tuned by varying the nature of the "R" group on the phosphorus atom. Thus, polymers with diametrically opposite properties such as water solubility or hydrophobicity, or with varied applications such as bio-inert materials or polymer electrolytes, are readily assembled by choosing an appropriate substituent on the phosphorus atom (1). Another versatility of polyphosphazenes is that unlike organic polymers, the structural diversity can be introduced by a macromolecular nucleophilic substitution reaction involving the reactive P—Cl bonds of polydichlorophosphazene ([N=PCl_2]$_n$) (2, 3). The latter itself is prepared from a ring opening polymerization of $N_3P_3Cl_6$, or by a condensation reaction involving either Cl_3P=$NSiMe_3$ (4) or Cl_3P=NP(O)Cl_2 (5, 6).

Another class of closely related polymers is those that contain a cyclophosphazene unit as a pendant group (7–15). In contrast to polyphosphazenes, which contain an inorganic backbone and (mostly) organic substituents, the pendant polymers contain an organic backbone and *intact* cyclophosphazene groups as the substituents. Although these polymers have received much less attention than polyphosphazenes, in principle these systems also possess a similar potential in terms of easy tunability of polymer property and function. The pendant polymers are obtained by polymerizing cyclophosphazenes containing vinyl groups (Scheme 1).

Pioneering studies by Allen and co-workers (7–11) have revealed that the presence of an appropriate spacer group "Z" and (or) the presence of electron releasing substituents on the olefinic moiety facilitate the homopolymerization of the monomer by minimizing the σ-electron withdrawing effect of the cyclophosphazene group (11). The utility of this approach for the preparation of useful polymers has been demonstrated by Inoue and co-workers (13–15). They have found that polymers containing etheroxy-substituted cyclophosphazenes readily form complexes with lithium

Received 23 February 2002. Published on the NRC Research Press Web site at http://canjchem.nrc.ca on 11 October 2002.

Dedicated to Professor Tristram Chivers for his contributions to Canadian chemistry.

V. Chandrasekhar,[1] V. Krishnan, A. Athimoolam, and G.T.S. Andavan. Department of Chemistry, Indian Institute of Technology, Kanpur – 208 016, India.

[1]Corresponding author (e-mail: vc@iitk.ac.in).

 DOI: 10.1139/V02-099 © 2002 NRC Canada

Scheme 1.

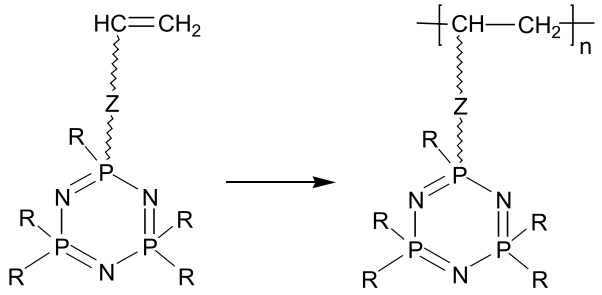

salts, which function as novel polymer electrolytes for lithium ion transport. We have been intrigued by the possibility of extending this approach to prepare new types of polymeric ligands that can bind to transition metal ions. Such ligands would also be of contemporary interest, in view of the importance of polymeric materials in organic synthesis, in the form of solid-phase inert supports or in the form of reagents and catalysts (16–21). Herein, we describe the synthesis and utility of a multi-functional cyclophosphazene monomer ($N_3P_3[N(Me)NH_2]_5[O\text{-}C_6H_4\text{-}p\text{-}C_6H_4\text{-}p\text{-}CH{=}CH_2]$) towards building new polymeric ligand systems.

Experimental section

General

Solvents and other general reagents used in this work were purified according to standard procedures. 4-Hydroxy-4′-vinylbiphenyl was prepared according to the reported procedure (13). 4-Hydroxy biphenyl (SD Fine Chemicals, India), *o*-hydroxybenzaldehyde (Fluka, Switzerland), and pyridine-2-carboxaldehyde (Fluka, Switzerland) were used as received. Hexachlorocyclotriphosphazene (Nippon Soda, Japan) was recrystallized from *n*-hexane before use. $N_3P_3Cl_5(O\text{-}C_6H_4\text{-}p\text{-}C_6H_4\text{-}p\text{-}CH{=}CH_2)$ was prepared according to the literature procedure (13, 22).

Instrumentation

^1H and ^{31}P NMR spectra were recorded on a JEOL-JNM LAMBDA 400 model spectrometer operating at 400.0 and 161.7 MHz, respectively. The chemical shifts are reported with respect to internal tetramethylsilane (^1H) and external 85% H_3PO_4 (^{31}P). FAB-MS were recorded on a JEOL SX 102/DA 6000 mass spectrometer using xenon (6 kV, 10 mA) as the FAB gas. TGA were recorded on a PerkinElmer Pyris 6 TGA model in a nitrogen atmosphere at a heating rate of 20°C min^{-1}. DSC were recorded on a PerkinElmer Pyris 6 DSC model in a nitrogen atmosphere at a heating rate of 10°C min^{-1}. Dilute solution viscosity studies were done on a Schott-Gerate viscometer using an Ubbelohde viscometer with a capillary pore size of 0.645 mm.

Preparation of $N_3P_3[N(Me)NH_2]_5[O\text{-}C_6H_4\text{-}p\text{-}C_6H_4\text{-}p\text{-}CH{=}CH_2]$ (3)

N-Methylhydrazine (2.03 g, 44.00 mmol) was dissolved in chloroform (40 mL) and to this was added a solution of **2** (2.03 g, 4.00 mmol) in chloroform. The reaction mixture was stirred at room temperature for 24 h. The *N*-methylhydrazine hydrochloride that formed was filtered and the solvent was evaporated in vacuo to afford **3**. It was purified, first by adding *n*-hexane to a solution of **3** in chloroform, and secondly by recrystallization from a mixture of chloroform and *n*-hexane (1:1). Yield: 1.82 g (81.9%); mp 62°C. ^1H NMR ($CDCl_3$) δ: 7.47–7.22 (m, 8H, aromatic), 6.75 (dd, 1H, J = 17.6 and 10.8 Hz, *H*RC=CH_2), 5.78 (d, 1H, J = 17.5 Hz, *trans*-HRC=C*H*H), 5.27 (d, 1H, J = 10.8 Hz, *cis*-HRC=CH*H*), 3.20 (broad, 10H, -NH_2), 3.06, 2.85, and 2.68 (d, 15H, J = 11.5, 11.0, and 10.8 Hz, -N(*Me*)). ^{31}P NMR ($CDCl_3$) δ: 29.4 (d, *P*(N(Me)NH_2)$_2$), 22.4 (t, $^2J_{P\text{-}N\text{-}P}$ = 40.4 Hz, *P*(OR)N(Me)NH_2). FAB-MS *m/z*: 555 ($[M]^+$). Anal. calcd. for $C_{19}H_{36}N_{13}OP_3$ (555.49): C 41.1, H 6.5, N 32.8; found: C 40.9, H 6.8, N 32.5.

Preparation of $N_3P_3[N(Me)N{=}CH\text{-}C_6H_4\text{-}o\text{-}OH]_5[O\text{-}C_6H_4\text{-}p\text{-}C_6H_4\text{-}p\text{-}CH{=}CH_2]$ (4)

To a solution of **3** (1.11 g, 2.00 mmol) in ethanol (50 mL) was added a solution of *o*-hydroxybenzaldehyde (1.46 g, 12.00 mmol) in ethanol (50 mL). The reaction mixture was heated under reflux for 17 h. It was then allowed to cool to room temperature and the solvent removed from it in vacuo to obtain **4**. Compound **4** was dissolved in acetonitrile (10 mL) and an excess of *n*-hexane was added to it, to allow re-precipitation. Yield: 1.39 g (64.5%); mp 117°C. ^1H NMR ($CDCl_3$) δ: 11.28, 11.09, and 11.03 (s, 5H, -O*H*), 7.64–7.51, 7.35–7.18, 7.13–6.99, and 6.82–6.75 (m, 28H, aromatic, N=CH), 6.72 (dd, 1H, J = 17.5 and 10.5 Hz, *H*RC=CH_2); 5.78 (d, 1H, J = 17.5 Hz, *trans*-HRC=C*H*H), 5.27 (d, 1H, J = 10.5 Hz, *cis*-HRC=CH*H*), 3.22, 3.14, and 2.99 (d, 15H, J = 8.8, 8.8, and 8.5 Hz, N(*Me*)). ^{31}P NMR ($CDCl_3$) δ: 16.4 (d, *P*(N(Me)N=CH-C_6H_4-*o*-OH)$_2$), 14.0 (t, $^2J_{P\text{-}N\text{-}P}$ = 58.2 Hz, *P*(OR)N(Me)N=CH-C_6H_4-*o*-OH). FAB-MS *m/z*: 1076 ($[M]^+$). Anal. calcd. for $C_{54}H_{56}N_{13}O_6P_3$ (1076.02): C 60.3, H 5.2, N 16.9; found: C 60.6, H 5.0, N 16.5.

Preparation of $N_3P_3[N(Me)N{=}CH\text{-}C_6H_4N]_5[O\text{-}C_6H_4\text{-}p\text{-}C_6H_4\text{-}p\text{-}CH{=}CH_2]$ (5)

To a solution of **3** (1.11 g, 2.00 mmol) in ethanol (50 mL) was added a solution of pyridine-2-carboxaldehyde (1.28 g, 12.00 mmol) in ethanol (50 mL). The reaction mixture was heated under reflux for 17 h. After allowing the reaction mixture to cool to room temperature, solvent was removed from it under vacuum to obtain **5**. Compound **5** was re-precipitated using acetonitrile as the polar solvent and *n*-hexane as the non-polar solvent. Yield: 1.34 g (66.9%); mp. 99°C. ^1H NMR ($CDCl_3$) δ: 8.53–7.09 (m, 33H, aromatic and N=C*H*), 6.74 (dd, 1H, J = 17.7 and 11.0 Hz, *H*RC=CH_2), 5.78 (d, 1H, J = 17.8 Hz, *trans*-HRC=C*H*H), and 5.27 (d, 1H, J = 11.0 Hz, *cis*-HRC=C*H*H), 3.38, 3.28, and 3.14 (d, 15H, J = 8.3, 8.3, and 8.3 Hz, N(*Me*)). ^{31}P NMR ($CDCl_3$) δ: 18.1 (d, *P*(N(Me)N=CH-C_6H_4N)$_2$), 13.7 (t, $^2J_{P\text{-}N\text{-}P}$ = 56.6 Hz, *P*(OR)N(Me)N=CH-C_6H_4N). FAB-MS *m/z*: 1001 ($[M]^+$). Anal. calcd. for $C_{49}H_{51}N_{18}OP_3$ (1000.97): C 58.8, H 5.1, N 25.2; found: C 58.5, H 5.7, N 25.5.

Preparation of (6)

Compound **4** (0.79 g, 7.4×10^{-1} mmol) was dissolved in 1,2-dichloroethane (10 mL) along with AIBN (2% by weight). The contents were purged with oxygen-free nitrogen for 30 min, and the reaction mixture was then

© 2002 NRC Canada

Scheme 2.

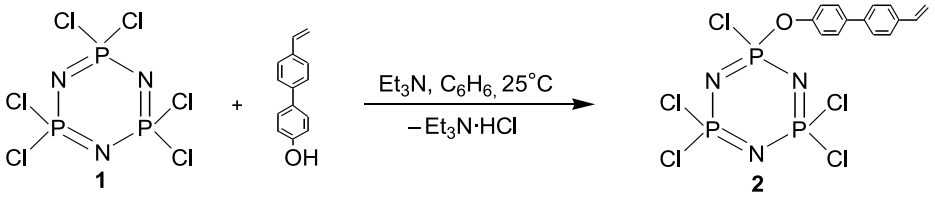

Scheme 3.

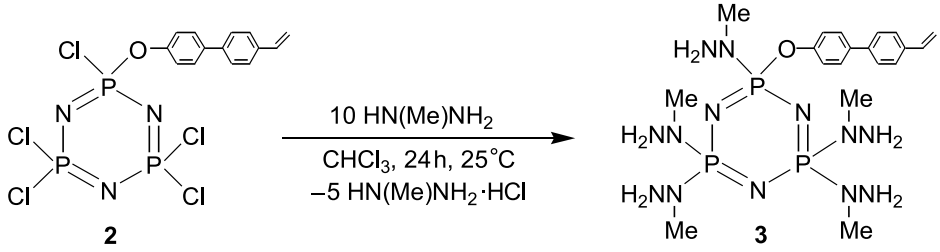

Scheme 4.

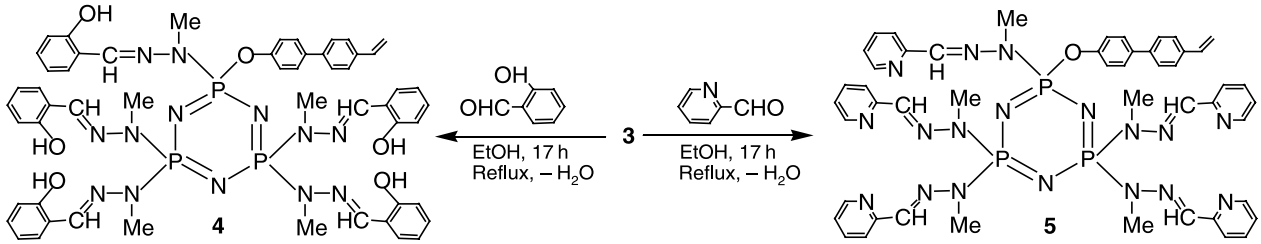

heated at 80°C for 24 h. It was then allowed to come to room temperature and poured into an excess of *n*-hexane to afford **6** as a powder. This was further purified by repeated re-precipitations (dichloromethane as the solvent and *n*-hexane as the non-solvent). Pure **6** was obtained as a white solid. It was dried in vacuum (10^{-3} torr (1 torr = 133.322 kPa)) at 40°C for 6 h. Yield: 0.48 g (60.7%). ^{1}H NMR ($CDCl_3$) δ: 11.27, 11.10, and 11.03 (s, 5H, O*H*), 7.10 (m(broad), 28H, aromatic and N=C*H*), 3.10 (m(broad), 15H, N(*Me*)), 1.25 (m, 3H, C*H*-CH_2). ^{31}P NMR ($CDCl_3$) δ: 16.4 (d, *P*(N(Me)N=CH-C_6H_4-*o*-OH)$_2$), 13.9 (t, $^2J_{P\text{-}N\text{-}P}$ = 58.3 Hz, *P*(OR)N(Me)N=CH-C_6H_4-*o*-OH). Intrinsic viscosity: 1.29 cm^3 g^{-1} (benzene), indicating a molecular weight of approximately 15 000 (22).

Preparation of (7)

The polymerization of **5** into **7** was carried out by using a similar procedure as those outlined above. The quantities used in this preparation are: **5** (0.74 g, 7.4 × 10^{-1} mmol). Yield: 0.40 g (54%). ^{1}H NMR ($CDCl_3$) δ: 8.48–7.10 (m(broad), 33H, aromatic and N=C*H*), 3.2 (m(broad), 15H, N(*Me*)), 1.26 (m, 3H, C*H*-CH_2). ^{31}P NMR ($CDCl_3$) δ: 18.06 (d, *P*(N(Me)N=CH-C_6H_4N)$_2$), 13.7 (t, $^2J_{P\text{-}N\text{-}P}$ = 54.9 Hz, P(OR)N(Me)N=CH-C_6H_4N). Intrinsic viscosity: 1.35 cm^3 g^{-1} (benzene), indicating a molecular weight of approximately 15 000 (22).

Results and discussion

Synthesis and spectroscopy of the cyclophosphazene derivatives 3 to 5

The cyclophosphazene $N_3P_3Cl_5$[O-C_6H_4-*p*-C_6H_4-*p*-CH=CH_2] (**2**) has been shown previously by Inoue and co-workers (13 to 15) and by us (22) to be an excellent monomer in terms of its ease of preparation, hydrolytic stability, and ready polymerizability. It is readily prepared by the reaction of $N_3P_3Cl_6$ (**1**) with 4-hydroxy-4′-vinyl biphenyl in the presence of triethylamine as the hydrogen chloride scavenger (Scheme 2).

The presence of five reactive P—Cl bonds allows **2** to be used as a precursor for further reactions with nucleophiles. Accordingly the reaction of **2** with 10 equiv of *N*-methylhydrazine results in the complete substitution of the chlorine atoms, affording N_3P_3[N(Me)NH_2]$_5$[O-C_6H_4-*p*-C_6H_4-*p*-CH=CH_2] (**3**). in an excellent yield (Scheme 3). This reaction is regio-specific; the *N*-methyl end of the difunctional reagent is found to exclusively attach to the phosphorus atom. Such behavior has also been noted earlier in the reactions of *N*-methylhydrazine with acyclic phosphorus(V) halides, such as P(O)Cl_3 or PhP(O)Cl_2 (23–26). The most important feature of the reaction of **2** with *N*-methylhydrazine is that the product (**3**) still contains five reactive groups in the form of peripheral -NH_2 units. Also, the polymerizable vinyl group remains intact in the conversion of **2** to **3**.

© 2002 NRC Canada

The condensation of **3** with 5 equiv of *o*-hydroxybenzaldehyde proceeds in boiling ethanol to afford the hydrazone **4**. Similarly condensation of **3** with pyridine-2-carboxaldehyde affords the hydrazone **5** (Scheme 4). Both of these cyclophosphazene derivatives contain a multi-site coordination environment in the form of the imino nitrogens, the cyclophosphazene ring nitrogen atoms, and the phenoxy oxygen (or the pyridyl nitrogen). The FAB-MS of **3**, **4**, and **5** show prominent parent ion peaks at 555, 1076, and 1001 respectively. The ^{1}H NMR spectrum of **3** shows the presence of the terminal -NH_2 groups as indicated by the appearance of a broad resonance at 3.2 ppm. This signal disappears upon the conversion of **3** into the hydrazones **4** and **5**. Interestingly, in the case of **4**, three hydroxy signals are seen as sharp singlets at 11.21, 11.01, and 10.95 ppm, respectively. The C*H*=N protons of **4** resonate at 7.55, 7.50, and 7.35 ppm. The vinyl protons appear as an AMX multiplet for all the three compounds **3**, **4**, and **5**. A representative ^{1}H NMR spectrum for compound **4** is given in Fig. 1. The presence (absence) of second order virtual coupling effects are helpful in the assignment of individual N-CH_3 chemical shifts. As can be seen from Fig. 2, in each of the compounds **3**, **4**, and **5**, three types of N-CH_3 resonances are expected. The most downfield N-CH_3 resonance is readily assigned to =P(OR)[N(CH_3)N=CHR′], because of the chemical shift, as well as the absence of virtual coupling effects. The other two

Fig. 1. ^{1}H NMR spectrum of compound **4**.

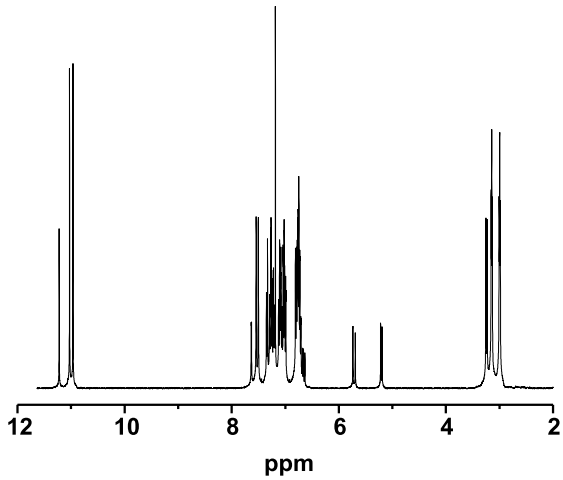

N-CH_3 resonances (Types B and C) show pronounced virtual coupling; these resonances are seen as virtual triplets with an intense central line. B and C themselves can be distinguished from each other. Thus the more shielded signal (C) is assigned as arising from the substituent flanked by the aryloxy group. Such effects have been well demonstrated in other situations among cyclophosphazenes (27).

Fig. 2. Virtual coupling effects in the N-Me region of the ^{1}H NMR of **4**.

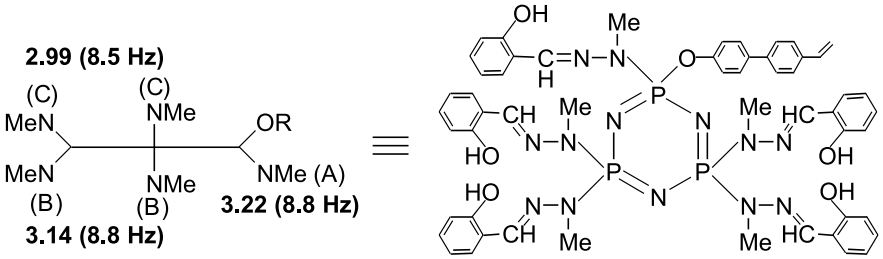

© 2002 NRC Canada

Scheme 5.

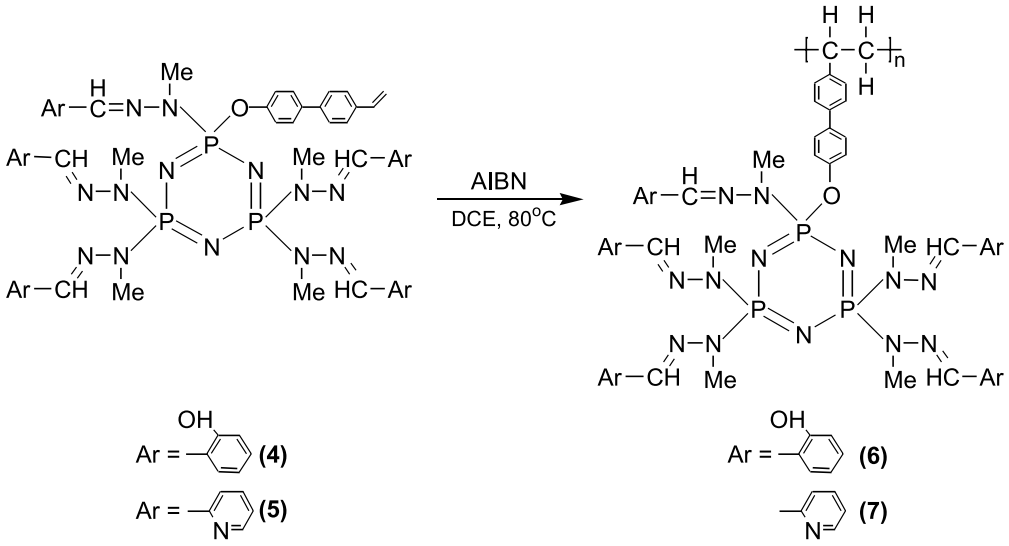

Table 1. ^{31}P NMR data for compounds **2**–**7**.

Compound	δ P(OR)(R) ν_A	δ P(R_2) ν_X	$^2J_{P\text{-}N\text{-}P}$ Hz
2	12.3	22.5	58.2
3	22.4	29.4	40.4
4	14.0	16.4	58.2
5	13.7	18.1	56.6
6	13.9	16.4	58.3
7	13.7	18.1	54.9

The ^{31}P NMR spectra of **3**, **4**, and **5** are of the AX_2 type. The chemical shift and coupling constant data for compounds **2**–**7** are summarized in Table 1. An interesting observation is that the conversion of the hydrazide **3** to the hydrazones **4** and **5** is accompanied by an upfield shift of the signals, along with a concomitant increase in the $^2J_{P\text{-}N\text{-}P}$ values.

Homopolymerization of 4 and 5

The compounds **4** and **5** can be readily homopolymerized in dichloroethane by using AIBN as the initiator to afford polymers **6** and **7** (Scheme 5). These polymers are obtained in their pure form by several re-precipitations, by dissolving in dichloroethane and using *n*-hexane as a non-polar solvent. The final dried products are air-stable powders soluble in a variety of organic solvents such as dichloromethane, tetrahydrofuran, etc. Dilute solution viscosity studies on **6** and **7** reveal that they have intrinsic viscosities of 1.29 and 1.35 $cm^3\ g^{-1}$, respectively, as measured in benzene. This suggests that these polymers have an MW of approximately 15 000 (22).

^{1}H NMR spectra of **6** and **7** show the complete disappearance of the AMX multiplet due to the vinyl protons and a broadening of other signals. The ^{31}P NMR spectra of **6** and **7** are of the AX_2 type, and the signal positions are unchanged vis-à-vis **4** and **5**. This strongly suggests that the cyclophosphazene moiety remains intact and does not suffer any degradation during the polymerization reaction.

Thermogravimetric analysis of the polymers **6** and **7** reveal that these are fairly robust polymers. Both of these polymers have similar degradation profiles. An initial decomposition leads to a char yield of approximately 68.5% at 400°C for **6** and 61.6% for **7**. Four further gradual decompositions occur. Even at 800°C, however, the char yields are fairly high (49.6% (**6**) and 45.9% (**7**)). Differential scanning calorimetric studies reveal that polymers **6** and **7** have high glass transition temperatures (T_g) viz., 139.4 and 119.6°C, respectively.

Conclusion

In conclusion, we have prepared new cyclophosphazene ligands containing hydrazone linkages and have successfully converted them into soluble and thermally stable polymeric systems, retaining the ligand framework as pendant groups. The metalation studies of these ligands are being pursued.

Acknowledgments

We are thankful to The Council of Scientific and Industrial Research India (CSIR) for funding, including CSIR senior research fellowships to VK, AM, and GTS.

References

1. J.E. Mark, H.R. Allcock, and R. West. Inorganic polymers. Prentice Hall, New Jersey. 1992.
2. H.R. Allcock. Acc. Chem. Res. **12**, 351 (1979).
3. H.R. Allcock. Chem. Eng. News, 22, (1985).
4. C.H. Honeyman, I. Manners, C.T. Morrissey, and H.R. Allcock. J. Am. Chem. Soc. **117**, 7035 (1995).
5. G. D'Halluin, R. De Jaeger, J.P. Chambrette, and P. Potin. Macromolecules, **25**, 1254 (1992).
6. R.D. Jaeger and P. Potin. Phosphorous Sulfur Silicon Relat. Elem. **76**, 223 (1993).
7. C.W. Allen and R.P. Bright. Macromolecules, **19**, 571 (1986).
8. C.W. Allen. Stud. Inorg. Chem. **14**, 171 (1992).
9. C.W. Allen. Trends. Polym. Sci. **2**, 342 (1994).
10. C.W. Allen. MGCN Main Group Chem News, **6**, 6 (1998).
11. C.W. Allen, E.D. Brown, and S.D. Worley. Inorg. Chem. **39**, 810 (2000).

© 2002 NRC Canada

12. H.R. Allcock, W.R. Laredo, E.C. Kellam III, and R.V. Morford. Macromolecules, **34**, 787 (2001).
13. K. Inoue, M. Takagi, M. Nakano, H. Nakamura, and T. Tanigaki. Makromol. Chem. Rapid Commun. **9**, 345 (1988).
14. K. Inoue, M. Nakano, M. Takagi, and T. Tanigaki. Macromolecules, **22**, 1530 (1989).
15. K. Inoue, M. Nakano, M. Takagi, and T. Tanigaki. J. Am. Chem. Soc. **113**, 7609 (1991).
16. G.W. Kabalka and R.M. Pagni. Tetrahedron, **53**, 7999 (1997).
17. S.J. Shuttleworth, S.M. Allin, and P.K. Sharma. Synthesis, 1217 (1997).
18. S. Kobayashi and S. Nagayama. J. Am. Chem. Soc. **120**, 2985 (1998).
19. R.B. Merrifield. Angew. Chem. Int. Ed. Engl. **24**, 799 (1985).
20. S. Itsuno, K. Watanabe, T. Koizumu, and K. Ito. React. Polym. **24**, 219 (1995).
21. F. Minutolo and J.A. Katzenellenbogen. Angew. Chem. Int. Ed. Engl. **38**, 1617 (1999).
22. I.I. Selvaraj and V. Chandrasekhar. Polymer, **38**, 3617 (1997).
23. J.P. Majoral, R. Kraemer, J. Navech, and F. Mathis. Tetrahedron, **32**, 2633 (1976).
24. A.M. Caminade and J.P. Majoral. Chem. Rev. **94**, 1183 (1994).
25. A.M. Caminade and J.P. Majoral. Synlett, 1019 (1996).
26. K.V. Katti, V.S. Reddy, and P.R. Singh. Chem. Soc. Rev. **24**, 97 (1995).
27. S.S. Krishnamurthy and M. Woods. Ann. Rep. NMR Spectrosc. **19**, 175 (1987).

© 2002 NRC Canada

Formation and decomposition of the Sb(III)/Li cage [{Sb(P-*t*-Bu)$_3$}$_2$Li$_6$·6THF]

Alan Bashall, Felipe García, Gavin T. Lawson, Mary McPartlin, Alexander Rothenberger, Anthony D. Woods, and Dominic S. Wright

Abstract: The heterometallic Sb(III)/Li cage complex [{Sb(P-*t*-Bu)$_3$}$_2$Li$_6$·6THF] (**1**) is obtained by the low-temperature (<0°C) reaction of Sb(NMe$_2$)$_3$ with *t*-BuPHLi (1:3 equiv) in THF. Thermolysis of this reaction solution leads to the formation of the bicyclic distibane [(*t*-BuP)$_3$Sb]$_2$ (**2**). ^{31}P NMR spectroscopic studies reveal that this process involves initial formation of [(*t*-BuP)$_3$Sb]$^-$ and [*t*-Bu(H)PP-*t*-Bu]$^-$ anions. Complexes **1** and **2** have been characterized in the solid state by X-ray diffraction studies.

Key words: antimony, lithium, cage.

Résumé : La réaction dans le THF, à basse température (<0°C), du Sb(NMe$_2$)$_3$ avec du *t*-BuPHLi (1:3 équivalents) conduit à la formation du complexe hétérométallique en cage du Sb(III)/Li, le [{Sb(P-*t*-Bu)$_3$}$_2$Li$_6$·6THF] (**1**). La thermolyse de cette solution réactionnelle conduit à la formation du distibane bicyclique [(*t*-BuP)$_3$Sb]$_2$ (**2**). Des études par spectroscopie RMN du ^{31}P révèlent que ce processus implique une formation initiale d'anions [(*t*-BuP)$_3$Sb]$^-$ et [(*t*-Bu(H)PP-*t*-Bu]$^-$. Les complexes **1** et **2** ont été caractérisés à l'état solide par des études de diffraction des rayons X.

Mots clés : antimoine, lithium, cage.

[Traduit par la Rédaction]

Introduction

In the past decade there has been considerable interest in the coordination chemistry of *p* block imido anions (1, 2). Our principal focus in this area has been the applications of dimethylamido group 15 reagents (E(NMe$_2$)$_3$ (E = As-Bi)) in the synthesis of various group 15 imido anion frameworks (2). For example, the 1:3 stoichiometric reactions of E(NMe$_2$)$_3$ with primary amido lithium complexes (RNHLi) give general access to cage complexes of the type [{E(NR)$_3$}$_2$Li$_6$], containing [E(NR)$_3$]$^{3-}$ trianions (Scheme 1(*a*)) (3). The research groups of Stalke (1(*a*)) and Chivers (1(*b*)) have explored cage compounds containing the valence-isoelectronic group 16 dianions [E(NR)$_3$]$^{2-}$ (E = S, Se, Te) which can be obtained by the 1:2 reactions of RNHLi with [E(NR)$_2$] (Scheme 1(*b*)).

Group 15 and 16 imido anions of this type are normally chemically robust, and can be transferred *intact* to a range of main group and transition metals (2). In contrast, however, we have found that phosphinidine counterparts, such as [Sb(PR)$_3$]$^{3-}$, are considerably less thermodynamically stable (4). The phosphinidine cage [{Sb(PCy)$_3$}$_2$Li$_6$·6NHMe$_2$] (Cy = cyclohexyl) can only be obtained from the reaction of Sb(NMe$_2$)$_3$ with CyPHLi at temperatures below ca. 0°C (4(*a*)). At ca. 30–40°C this complex decomposes to form the Zintl compound [Sb$_7$Li$_3$·6Me$_2$NH], containing the Sb$_7^{3-}$ anion (4(*b*)). Comparatively little is known about the mechanism of "cage-to-alloy" reactions of this type (5). Likely key intermediates in this process are heterocyclic [(RP)$_n$Sb]$^-$ anions, from which elimination of cyclic phosphanes ((RP)$_n$) appears to be a fundamental step (6). The generally greater thermodynamic stability of the analogous [(RP)$_n$As]$^-$ anions has allowed the investigation of the reactivity and coordination chemistry of these species in their own right (7). However, their thermolability depends markedly on the organic group (R), and only when the organic substituent is aliphatic (e.g., R = *t*-Bu, Cy, 1-adamantyl) has it been possible to isolate [(RP)$_n$As]$^-$ anions at room temperature (*n* = 3 or 4) (6). In contrast, when an aromatic substituent is present rapid formation of the As$_7^{3-}$ ion occurs under these conditions (6(*b*)). The results of attempts to prepare [(RAs)$_n$As]$^-$ anions illustrate an even greater tendency for the formation of Zintl compounds. Significantly, only the bicylic diarsane [(*t*-BuAs)$_3$As]$_2$ could be isolated from the reaction of As(NMe$_2$)$_3$ with the aliphatic arsenide *t*-BuAsHLi at room temperature (6(*b*)), suggesting that oxidative coupling of the intermediate heterocyclic anions is a fundamental step in metal—metal bond formation.

We present here a study of the synthesis of the Sb(III) cage [{Sb(P-*t*-Bu)$_3$}$_2$Li$_6$·thf] (**1**) and its thermal decomposition.

Received 3 April 2002. Published on the NRC Research Press Web site at http://canjchem.nrc.ca on 11 October 2002.

Dedicated to Professor Tristram Chivers.

A. Bashall and M. McPartlin. School of Chemistry, University of North London, London N7 8DB, U.K.
F. García, G.T. Lawson, A. Rothenberger, A.D. Woods, and D.S. Wright.[1] Chemistry Department, Cambridge University, Lensfield Road, Cambridge CB2 1EW, U.K.

[1]Corresponding author (e-mail: dsw1000@cus.cam.ac.uk).

 DOI: 10.1139/V02-154 © 2002 NRC Canada

Scheme 1.

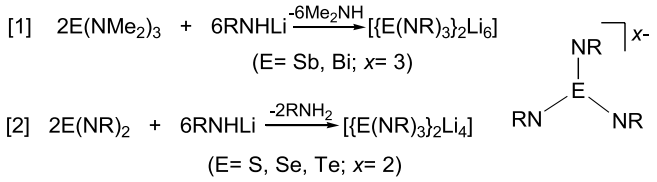

Surprisingly, the product in this case is not the anticipated Sb_7^{3-} anion but the new bicyclic distibane $[(t\text{-BuP})_3Sb]_2$ (**2**). The formation of **2** from **1**, both of which have been fully characterized in the solution and solid states, provides strong support for our hypothesis concerning the fate of $[(RP)_nSb]^-$ anions within a single, well-defined reaction system.

Results and discussion

Prior to the studies reported in this paper, the only group 15 phosphinidine cage to have been reported was $[\{Sb(PCy)_3\}_2Li_6{\cdot}6NHMe_2]$ (4(*a*)). The initial aims of the present study were to further explore the synthesis and structures of related cages containing $[Sb(PR)_3]^{3-}$ trianions and to examine the potential influence of the organic substituents (R) on their mode of decomposition. The low-temperature (<0°C) reaction of [*t*-BuPHLi] with $Sb(NMe_2)_3$ (3:1 equiv, respectively) in THF gives an orange-red solution from which the new phosphinidine cage $[\{Sb(P\text{-}t\text{-}Bu)_3\}_2Li_6{\cdot}6THF]$ (**1**) can be obtained as yellow crystals at –20°C, in 43% yield (Scheme 2). Although X-ray crystallography later showed that there are three uncoordinated THF molecules present in the lattice (in addition to the six-coordinated ligands of the cage), placing the complex under vacuum during isolation completely removes this lattice-bound solvent.

Like the previously reported complex $[\{Sb(PCy)_3\}_2Li_6{\cdot}6NHMe_2]$ (4(*a*)), crystalline **1** rapidly decomposes to a black solid even at room temperature under argon. For this reason it was necessary to use freshly prepared samples of the complex in all analytical and spectroscopic studies. These studies provided an initial indication of the empirical formula of the complex, and revealed that the Li^+ cations of the core of **1** are solvated by THF ligands rather than Me_2NH. Significantly, the room-temperature ^7Li NMR spectrum of the complex is that of a poorly resolved binomial septet ($^1J_{P\text{-}Li}$ ca. 12 Hz), which can be interpreted as arising from the coupling of the Li^+ cations to six equivalent ^{31}P centres of two $[Sb(P\text{-}t\text{-}Bu)_3]^{3-}$ trianions. This behaviour is identical to that of the previously reported complex $[\{Sb(PCy)_3\}_2Li_6{\cdot}6NHMe_2]$ ($^1J_{P\text{-}Li}$ ca. 14 Hz) (4(*a*)) and indicates that a similar fluxional "carousel" process is involved for **1** (in which the six Li^+ cations migrate around the equator of the cage). Unfortunately, the broadness of the resonance in the room-temperature ^{31}P NMR spectrum ($W_{1/2}$ ca. 60 Hz) made it impossible to discern any ^{31}P–^7Li coupling. The significant differences between the ^7Li and ^{31}P chemical shifts for **1** (δ 1.7 and δ –96.2 (in THF), respectively) compared to those observed for $[\{Sb(PCy)_3\}_2Li_6{\cdot}6NHMe_2]$ (δ 5.6 and δ –123.5 (in toluene), respectively) (4(*a*)) suggest that the electronic environments of both nuclei are highly sensitive to the nature of the Lewis base solvation of the Li^+ cations and the organic substituents present. In particular, the ^{31}P chemical shift indicates that the there is a lower development of negative charge on the P centres of **1** than is present in $[\{Sb(PCy)_3\}_2Li_6{\cdot}6NHMe_2]$.

Scheme 2.

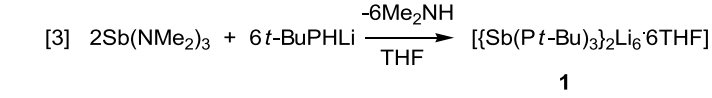

Despite the careful handling of **1** during NMR spectroscopic studies, some thermal decomposition was nonetheless apparent in the room-temperature ^1H, ^{31}P, and ^7Li spectra. The decomposition process was followed by obtaining the ^{31}P NMR spectrum of the reaction solution (in THF) after prolonged storage at room temperature. After approximately 1 week, significant decomposition is apparent, with the deposition of a black solid (assumed to be Sb metal) and with the solution becoming redder in colour. The room temperature ^{31}P NMR spectrum of the reaction mixture shows that a significant amount of **1** remains (Fig. 1 (top) shows the fully coupled spectrum). The major product of this decomposition process is observed as an AX_2 system (t. δ 15.8, d. δ –125.7; $^1J_{PP}$ = 197.1 ± 1.1 Hz) (species **A** in Fig. 1). The chemical shifts and coupling constants of this species can be compared to those observed for the structurally characterized complexes $[(t\text{-BuP})_3AsLi{\cdot}TMEDA{\cdot}THF]$ (t., δ 7.9, d. δ –74.5; $^1J_{PP}$ = 176 Hz) and $[(t\text{-BuP})_3AsLi{\cdot}2DABCO{\cdot}THF]$ (DABCO = $N\{CH_2CH_2\}_3N$) (t., δ 5.0, d. δ –73.4; $^1J_{PP}$ = 178 Hz), containing the $[(t\text{-BuP})As]^-$ anion (6(*b*)). This species can be tentatively assigned to $[(t\text{-BuP})_3SbLi{\cdot}x THF]$, in which there is a significantly greater development of negative charge on the Sb-bonded P centres of the $[(t\text{-BuP})_3Sb]^-$ anion than occurs in the As counterparts (as is expected on the basis of the greater electronegativity of As). A minor product is also observed, which is characterized by an AMX system in the fully coupled ^{31}P NMR spectrum (dd. δ –16.2, d. δ –70.4; $^1J_{PH}$ = 205 ± 7 Hz, $^1J_{PP}$ = 291 ± 1 Hz) (species **B** in Fig. 1). On the basis of the similar appearance of the ^{31}P NMR spectrum to that of [*t*-Bu(H)PP(*t*-Bu)K·PMDETA] (PMDETA = $(Me_2NCH_2CH_2)_2NMe$) (dd. δ –8.9, d. δ –57.4; $^1J_{PH}$ = 201.4 Hz, $^1J_{PP}$ = 321.5 Hz) (8), this species is most likely to be [*t*-Bu(H)PP(*t*-Bu)Li·*x*THF]. The ^7Li spectrum of this solution (see Fig. 1, bottom) shows two major resonances, a binomial septet (δ 1.7) and a broad singlet (δ –0.4). The former corresponds to *intact* **1** and the latter (presumably) to $[(t\text{-BuP})_3SbLi{\cdot}x THF]$; a third ^7Li resonance corresponding to [*t*-Bu(H)PP(*t*-Bu)Li.·*x*THF] was not be observed, presumably owing to the minor amount of this species present.

The bicyclic distibane $[(t\text{-BuP})_3Sb]_2$ (**2**) was obtained initially by storage of the reaction solution from which **1** was obtained at room temperature for ca. 3 weeks. The complex can be obtained more reliably by bringing a solution of **1** (prepared in situ in the manner described above) to reflux briefly (ca. 10 min), followed by storage of the resulting solution for ca. 7 days at room temperature; **2** being obtained as large yellow crystals in 69% yield. The complex was characterized by mass spectroscopy (*m*/*z* $[MH]^+$ = 773), elemental analysis, and ^1H and ^{31}P NMR spectroscopy. There are only minor changes in the coupling constants and chemical

© 2002 NRC Canada

Fig. 1. In situ ^{31}P NMR spectrum of the reaction solution from which **1** is obtained (+25°C), after storage at room temperature for ca. 1 week (top); the ^{7}Li NMR spectrum of the same solution (bottom).

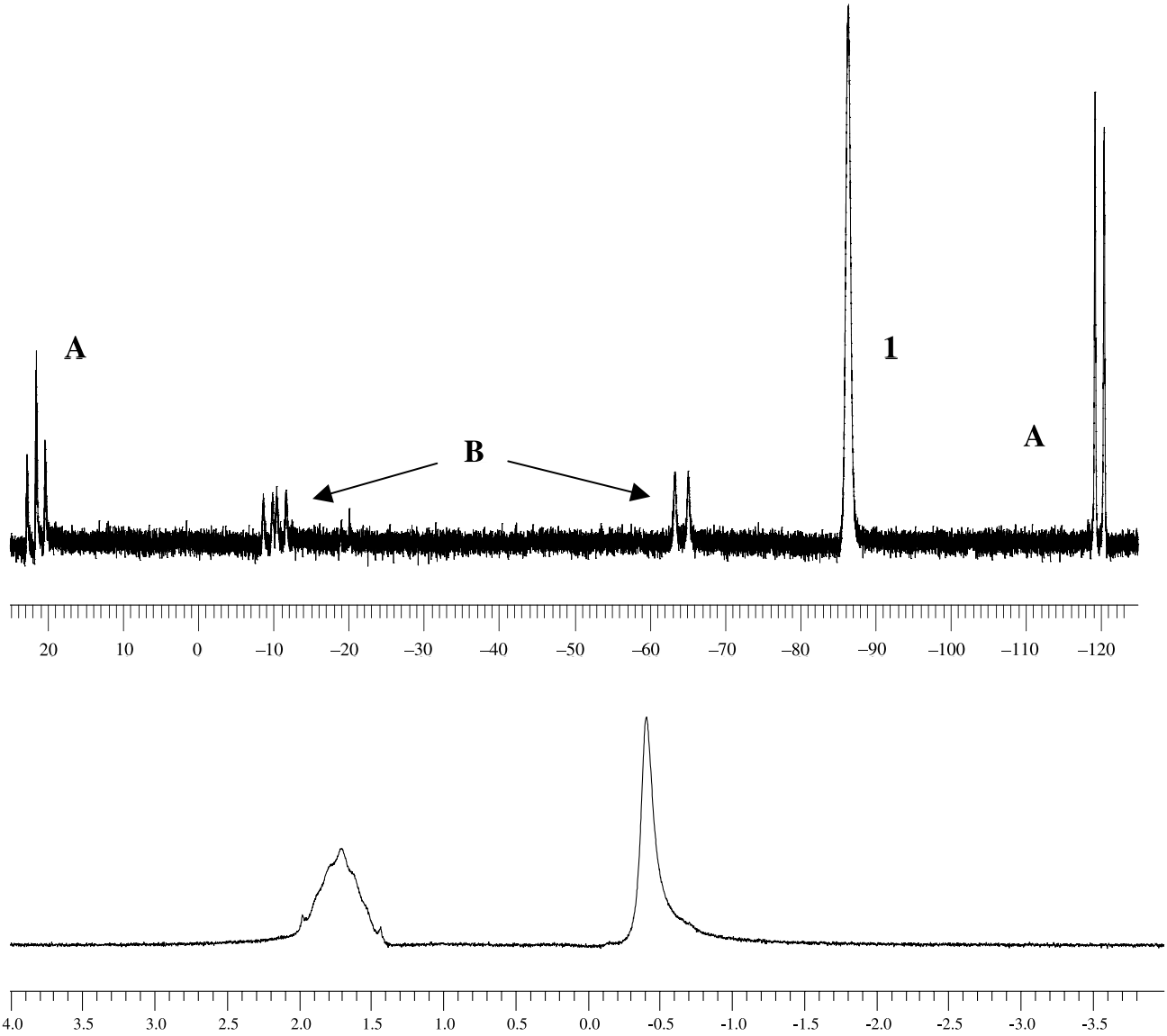

shifts observed in the ^{31}P NMR spectra of **2** in benzene (t., δ –11.9, d. δ –87.4; $^{1}J_{PP}$ = 173.2 Hz) and THF (t., δ –13.5, d. δ –89.2; $^{1}J_{PP}$ = 173.3 Hz). It should be noted that these parameters are significantly different to those assigned to the [(*t*-BuP)$_3$Sb]$^-$ anion, noted above. Pertinent to the ultimate formation of **2**, we have observed previously that the reaction of [(*t*-BuP)$_3$AsLi·2DABCO·THF] with [Au(PPh$_3$)Cl] or NH_4PF_6 gives the closely related diarsane [(*t*-BuP)$_3$As]$_2$ (9, 10). Thus, it appears that **2** arises from the coupling of [(*t*-BuP)Sb]$^-$ anions (observed in solution), either via one-electron oxidation or via protonation then loss of H_2 (Scheme 3).

The low-temperature X-ray structures of **1** and **2** were obtained. Details of the data collections and refinements for both are listed in Table 1. Tables 2 and 3 give selected bond lengths and angles for **1** and **2**, respectively.

The X-ray structure of **1** shows it to consist of heterobimetallic cage molecules containing a 14-membered $Sb_2P_6Li_6$ core (Fig. 2). In addition, there are three uncoordinated THF molecules in the lattice per molecule of **1**. The structure is similar to that of the previously characterized complex [{Sb(PCy)$_3$}$_2$Li$_6$·6NHMe$_2$] (4(*a*)). However, whereas the six Li^+ cations of the latter were solvated by Me_2NH ligands, in **1** all the Li^+ cations are coordinated by THF. The Sb—P bond lengths (mean 2.506 Å) and P-Sb-P bond angles (101.16(8)°) found in the [Sb(P-*t*-Bu)$_3$]$^{2-}$ anion units of **1** are similar to those observed for the [Sb(PCy)$_3$]$^{3-}$ trianions of [{Sb(PCy)$_3$}$_2$Li$_6$·6NHMe$_2$] (Sb—P range 2.516(5)–2.519(6) Å, P-Sb-P range 100.3(2)–103.4(2)°). The Sb—P bonds found in **1** are also similar to those observed in [SbP(2,4,6-Me$_3$C$_6$H$_2$)]$_2$ (2.561(2)–2.583(1) Å) (11) and [(CyP)$_4$SbNa·TMEDA·Me$_2$NH]$_2$ (2.489(3)–2.541(3) Å) (6(*a*)). Also similar to [{Sb(PCy)$_3$}$_2$Li$_6$·6NHMe$_2$] is the pattern of P—Li bond lengths, which are on average longer for the P—Li bonds connecting the two [Sb(P-*t*-Bu)$_3$]$^{3-}$ trianions in **1** (P(1)—Li(1) 2.640(18) Å) compared to those

© 2002 NRC Canada

Table 1. Details of the data collections and refinements of [{Sb(P-*t*-Bu)$_3$}$_2$Li$_6$·6THF]·3THF (**1**·3THF) and [(*t*-BuP)$_3$Sb]$_2$ (**2**) (λ = 0.71073 Å).

Compound	**1**·3THF	2
Formula	$C_{60}H_{126}Li_6O_9P_6Sb_2$	$C_{12}H_{27}P_3Sb$
FW	1462.57	386.00
Crystal system	Cubic	Triclinic
Space group	*Pa*–3	*P*–1
ρ_{calc} (mg m^{-3})	1.274	1.470
Z	4	2
U (Å^3)	8004(3)	872.3(2)
μ (Mo Kα) (mm^{-1})	0.838	0.882
T (K)	223(2)	213(2)
Unit cell dimensions		
a (Å)	20.00(3)	9.0414(12)
b (Å)	—	—
c (Å)	—	12.1400(19)
α (°)	—	97.757(13)
β (°)	—	103/310(10)
γ (°)	—	112.070(10)
Independent reflect. (R_{int})	1856 (0.090)	2330 (0.028)
R indices ($(I > 2\sigma(I))$)	R_1 = 0.048, wR_2 = 0.110	R_1 = 0.049, wR_2 = 0.145
R indices (all data)	R_1 = 0.112, wR_2 = 0.160	R_1 = 0.051, wR_2 = 0.148

Scheme 3.

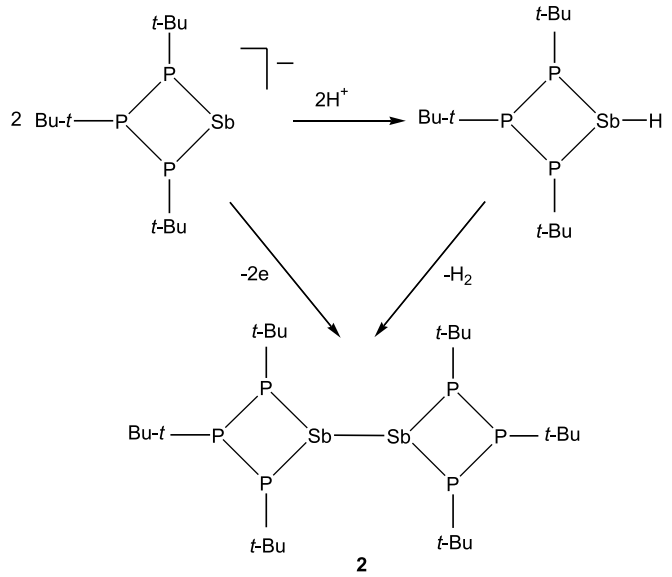

found within the [Sb(P-*t*-Bu)$_3$Li$_3$] subunits of the complex (2.598(18)–2.605(18) Å) (cf. 2.62(3) Å for the bonds connecting the two [Sb(PCy)$_3$]$^{3-}$ trianions and 2.56(3)–2.62(3) Å within the [Sb(PCy)$_3$Li$_3$] units of [{Sb(PCy)$_3$}$_2$Li$_6$·6NHMe$_2$] (6(*a*)). These P—Li bonds are typical of those observed in the structures of Li phosphide complexes (12), e.g., with a mean of 2.61 Å in [CyPHLi·THF]$_\infty$ (13). One intriguing feature of [{Sb(PCy)$_3$}$_2$Li$_6$·6NHMe$_2$] was the solvation of all six of the Li$^+$ cations of the core by Me$_2$NH ligands, despite the fact that the complex was prepared in THF as the solvent (6(*a*)). The reasons for the absence of THF solvation in [{Sb(PCy)$_3$}$_2$Li$_6$·6NHMe$_2$] may well be steric in origin. It is noticeable in this regard that the average distance defining

Table 2. Selected bond lengths and angles for [{Sb(P-*t*-Bu)$_3$}$_2$Li$_6$·6THF]·3THF (**1**·3THF).

Bond lengths (Å)	
Sb(1)—P(1)	2.507(2)
P(1)—Li(1)	2.643(10)
P(1)—Li(1D)	2.604(10)
P(1)—Li(1E)	2.603(10)
Li(1)—O(1)	1.937(11)
Bond angles (°)	
P(1)-Sb(1)-P(1A)	101.16(5)
P(1D)-Li(1)-P(1E)	96.1(3)
P(1)-Li(1)-P(1D,1E)	Mean 103.5
O(1)-Li(1)-P(1D)	128.1(5)
O(1)-Li(1)-P(1E)	116.8(5)
O(1)-Li(1)-P(1)	106.2(4)

Table 3. Selected bond lengths and angles for [(*t*-BuP)$_3$Sb]$_2$ (**2**).

Bond lengths (Å)	
Sb(1)—P(1)	2.5363(15)
Sb(1)—P(2)	2.5303(15)
P(1)—P(3)	2.214(2)
P(2)—P(3)	2.214(2)
Sb(1)—Sb(1A)	2.7922(7)
Bond angles (°)	
P(1)-Sb(1)-P(2)	78.95(5)
P(2)-Sb(1)-Sb(1A)	91.03(4)
P(1)-Sb(1)-Sb(1A)	92.53(4)
P(3)-P(1)-Sb(1)	87.53(6)
P(3)-P(2)-Sb(1)	87.67(6)
P(1)-P(3)-P(2)	93.31(7)

© 2002 NRC Canada

Fig. 2. Structure of cage molecules of $[\{Sb(Pt\text{-}Bu)_3\}_2Li_6{\cdot}6THF]$ (**1**). H-atoms have been omitted for clarity.

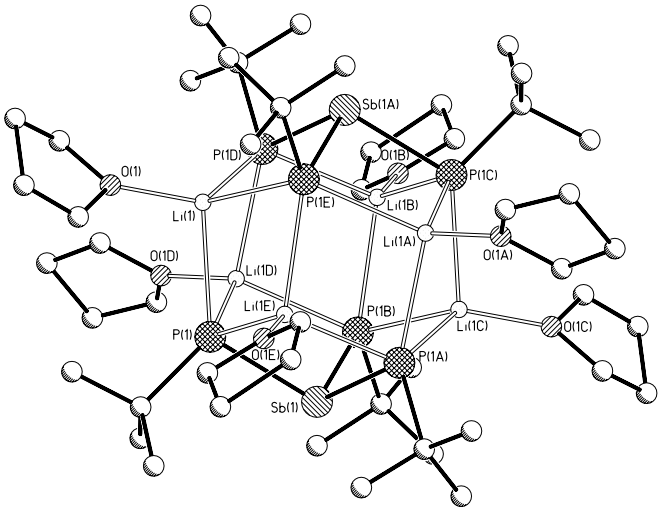

the space for complexation of the Li^+ cations in $[\{Sb(PCy)_3\}_2Li_6{\cdot}6NHMe_2]$ (7.64 Å) is significantly greater than that in **1** (7.26 Å).

The X-ray structure of **2** shows that molecules of the complex have a centrosymmetric arrangement in the solid state, consisting of two $[(t\text{-}BuP)_3Sb]$ rings joined by an Sb—Sb bond (Fig. 3). The *t*-Bu groups of each ring unit adopt an all-*trans* arrangement with respect to each other, as is also the case in the As(III) analogue $[(t\text{-}BuP)_3As]_2$ (obtained by the coupling reaction of $t\text{-}BuPCl_2$ and $AsCl_3$ with Mg metal) (10). The latter is the most closely related compound to **2**. The Sb—Sb bond length in **2** (2.7922(7) Å) is similar to those found in other compounds containing Sb—Sb single bonds (14). The Sb—P bond lengths (mean 2.53 Å) are within the range of values found previously in the few Sb(III) phosphinidine compounds, e.g., $[SbP(2,4,6\text{-}Me_3C_6H_2)]_2$ (range 2.561(2)–2.583(1) Å) (11), $[\{Sb(PCy)_3\}_2Li_6{\cdot}6NHMe_2]$ (range 2.516(5)–2.519(6) Å) (6(*a*)) and in **1** (mean 2.506 Å). The P—P bonds within the $[(t\text{-}BuP)_3Sb]$ rings of **2** (2.214(2) Å) are as expected for single P—P bonds (ca. 2.21 Å[15]). The P-P-Sb (mean 87.6°), P-P-P (93.31(7)°), and P-Sb-P (78.92(5)°) bond angles within the $[(t\text{-}BuP)_3Sb]$ rings of **2** are well below the expected values for sp^3 hybridization at the P and Sb centres, as are the exocyclic P-Sb-Sb angles (mean 91.8°). The geometry at Sb can be rationalized in terms of this centre using essentially *p* orbitals to form the σ bonds, with the lone pairs on each metal centre having essentially *s*-character. Although intermolecular Sb···Sb interactions can often be observed in distibanes (Sb···Sb ca. 3.5–4.5 Å (14)), there are no such "closed-shell" interactions in the crystal lattice of **2**.

Experimental section

General experimental

The starting materials $Sb(NMe_2)_3$, $t\text{-}BuPH_2$, and compound **1** are air- and moisture-sensitive. They were handled on a vacuum line using standard inert-atmosphere techniques and under dry and oxygen-free argon. Although **2** was also handled in a similar way, it is considerably less air-sensitive and will survive brief air exposure without decomposition. $Sb(NMe_2)_3$ was prepared in the manner described in the literature (16). $t\text{-}BuPH_2$ was prepared by the reduction of $t\text{-}BuPCl_2$ with $LiAlH_4$ in Et_2O, in the manner described by us previously (6(*b*)). Toluene and THF were dried by distillation over sodium–benzophenone under N_2 prior to the reactions. The products were isolated and characterized with the aid of a N_2-filled glove box fitted with a Belle Technology O_2 and H_2O internal recirculation system. Elemental analyses were performed by first sealing the samples under argon in air-tight aluminium boats (1 to 2 mg) and C, H, and N content was analysed using an Exeter Analytical CE-440 elemental analyser. ^1H, ^{31}P and ^7Li NMR spectra were recorded on a Bruker AM 400 MHz spectrometer in dry deuterated THF and (or) benzene. ^1H NMR spectra were referenced to the internal solvent resonances. ^{31}P NMR spectra were referenced to an external standard of 80% H_3PO_4–D_2O and ^7Li spectra were referenced to a saturated solution of LiCl–D_2O. For the in situ studies of the decomposition reaction of **1**, a sealed D_6-acetone-filled capillary was used to obtain a lock.

Fig. 3. Structure of the distibane $[(t\text{-}BuP)_3Sb]_2$ (**2**). H-atoms have been omitted for clarity.

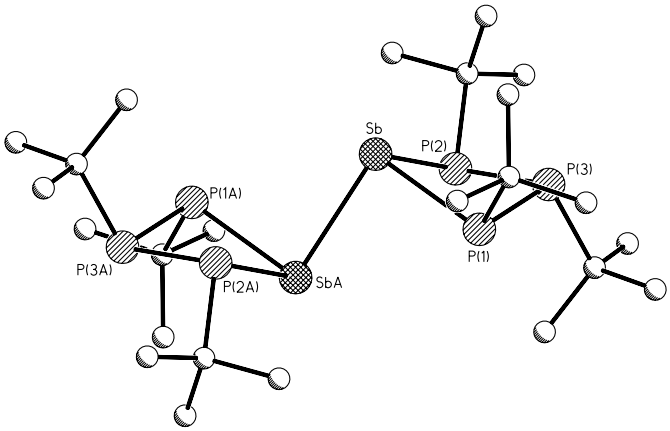

Synthesis of 1

A solution of $t\text{-}BuPH_2$ (1.1 mL, 9.0 mmol) in THF was reacted with *n*-BuLi (5.9 mL, 1.6 mol dm^{-3} in hexanes, 9.0 mmol) at 0°C. To the stirred solution of [*t*-BuPHLi] was added a solution of $Sb(NMe_2)_3$ (1.5 mL, 2.0 mol dm^{-3} in toluene, 3.0 mmol). The reaction mixture was allowed to warm gradually to 0°C, at which stage an orange-red solution was formed. Storage of the solution at –20°C (12 h) gave yellow crystals of **1**, suitable for X-ray diffraction studies. Elemental analysis and ^1H NMR spectroscopy shows that the three THF molecules in the lattice of **1**·3THF are removed by placing the crystalline complex under vacuum (1×10^{-1} atm (1 atm = 101.325 kPa), ca. 15 min). The following data refer to the dry, amorphous material obtained. Yield: 0.80 g (43%, based on Sb). ^1H NMR (D_6-benzene, +25°C, 400.16 MHz) δ: 3.6 (m., 12H, O–CH_2, THF), 1.7 (m., 12H, O-CH_2CH_2-, THF), 0.9 (m., 27H, *t*-BuP). ^{31}P NMR (D_8-THF, +25°C, 161.975 MHz) δ: –92.2 (s.). ^7Li NMR (D_8-THF, +25°C, 100.61 MHz) δ: 1.7 (s.) (minor resonance at –0.4 (s.)). Elemental anal. calcd. for **1**: C 46.9, H 8.3, P 13.9; found: C 46.3, H 8.2, P 14.9.

© 2002 NRC Canada

Synthesis of 2

The orange-red solution obtained from the reaction of $Sb(NMe_2)_3$ with [*t*-BuPHLi] (above) was allowed to warm to room temperature, at which stage a dark red solution was obtained (with some formation of Sb metal). The mixture was brought briefly to reflux (10 min) and the solution stored at room temperature (7(*d*)). Large, light-yellow crystals of **2** were formed (together with a black solid, presumed to be Sb metal). Crystals were suitable for X-ray diffraction studies. Yield: 0.80 g (69% based on Sb). Decomp. 220°C to black solid. MS (+ve ion *m/z* (%): 773 (60) ($[MH]^+$). ^{1}H NMR (D_6-benzene, +25°C, 400.16 MHz) δ: 1.38 (d., $^3J_{PH}$ = 11 Hz, 36H, *t-Bu*P-Sb), 1.35 (d., $^3J_{PH}$ = 7 Hz, 18H, P-P(*t-Bu*)P). ^{31}P NMR (D_6-benzene, +25°C, 161.975 MHz) δ: –11.9 (t., 2P, P-*P*(*t*-Bu)-P), –87.4 (d., 4P, *t*-Bu*P*-Sb) ($^1J_{PP}$ = 173.2 Hz) (s.) (t., –13.5, d. –89.2; $^1J_{PP}$ = 173.3 Hz in D_8-THF]. Elemental anal. calcd. for **2**: C 37.2, H 6.9, P 23.5.: found: C 37.3, H 7.1, P 24.1.

X-ray crystallographic studies of 1 and 2

Crystals of **1** and **2** were mounted directly from solution under argon using an inert oil (17) which protected them from atmospheric oxygen and moisture. X-ray intensity data for both complexes were collected using a Siemens *P*4 four-circle diffractometer. Details of the data collections and structural refinements are given in Table 1. Three carbon atoms of the unique, Li-bonded THF ligand in **1** are disordered equally over two sites, corresponding to two arrangements of the THF ligands being present in the crystal. Regions of ill-defined electron density in the voids of **1** were interpreted as severely disordered THF lattice molecules. Hydrogen atoms were placed in calculated positions in both structures (apart from those of the solute molecules in **1**). The structures were solved by direct methods and refined by full-matrix least-squares on F^2 (18).[2]

Conclusions and closing remarks

The study of the thermal decomposition of **1** into the bicyclic distibane **2** reported here provides further support for some of the overall conclusions which we had made previously, based on structural evidence from several different As(III) and Sb(III) systems (as outlined in the introduction to this paper) (5). However, this is the first *individual* reaction system in which we have been able to identify the key metal—metal bond forming process from a well-characterized cage precursor. The reasons why the decomposition of **1** stops at **2** (rather than proceeding to a Zintl compound, as was the case for $[\{Sb(PCy)_3\}_2Li_6{\cdot}6NHMe_2]$ (6(*a*)) are uncertain. However, the absence of Me_2NH solvation of the Li^+ cations of **1** provides some circumstantial evidence for the importance of Me_2NH in the decomposition process (5). In addition, the organic substituents may also have a subtle influence on the final product(s) of decomposition.

There still remain some fundamental features of the formation of Zintl ions that are unknown. In particular, the precise mechanism by which cages such as **1** are converted into heterocyclic anions of the type $[(RP)_nSb]^-$ is uncertain, as are the further steps involved in the formation of Sb_7^{3-} anions from bicyclic intermediates like **2**. Further studies (particularly of the reactivity of species like **2**) will focus on these issues.

Acknowledgements

We gratefully acknowledge the EPSRC (G.T.L., A.R., M.McP., D.S.W), St. Catharine's College (A.D.W.), Churchill and Fitzwilliam Colleges (A.D.H.), the Cambridge European Trust (F.G., A.R.), and Gottlieb Daimler- and Karl Benz-Stiftung (A.R.) for financial support.

References

1. For examples see: (*a*) R. Fleischer, S. Freitag, F. Pauer, and D. Stalke. Angew. Chem. **108**, 208 (1996); Angew. Chem. Int. Ed. Engl. **35**, 204 (1996); (*b*) T. Chivers, X. Gao, M. Parvez, and G. Schatte. Inorg. Chem., **35**, 4094 (1996), and refs. therein.
2. (*a*) M.A. Beswick and D. S. Wright. Coord. Chem. Rev. **176**, 373 (1998); (*b*) M.A. Beswick, M.E.G. Mosquera, and D.S. Wright. J. Chem. Soc. Dalton Trans. 2437 (1998), and refs. therein.
3. M.A. Beswick, N. Choi, C.N. Harmer, A.D. Hopkins, M.A. Paver, M. McPartlin, P.R. Raithby, A. Steiner, M. Tombul, and D.S. Wright. Inorg. Chem. **37**, 2177 (1998).
4. (*a*) M.A. Beswick, J.M. Goodman, C.N. Harmer, A.D. Hopkins, M.A. Paver, P.R. Raithby, A.E.H. Wheatley, and D.S. Wright. J. Chem. Soc. Chem. Commun. 1897 (1997); (*b*) M.A. Beswick, C.N. Harmer, A.D. Hopkins, M. McPartlin, and D.S. Wright. Science (London), **281**, 1500 (1998).
5. A.D. Hopkins, J.A. Wood, and D.S. Wright. Coord. Chem. Rev. **216**, 155 (2001).
6. (*a*) M.A. Beswick, N. Choi, A.D. Hopkins, M.E.G. Mosquera, M. McPartlin, P.R. Raithby, A. Rothenberger, D. Stalke, A.E.H. Wheatley, and D.S. Wright. J. Chem. Soc. Chem. Commun. 2485 (1998); (*b*) A. Bashall, M.A. Beswick, N. Choi, A.D. Hopkins, S.J. Kidd, Y.G. Lawson, M.E.G. Mosquera, M. McPartlin, P.R. Raithby, A.E.H. Wheatley, J.A. Wood, and D.S. Wright. J. Chem. Soc. Dalton Trans. 479 (2000).
7. A. Bashall, A.D. Hopkins, M.J. Mays, M. McPartlin, J.A. Wood, A.D. Woods, and D.S. Wright. Chem. Soc. Dalton Trans. 1825 (2000); A.R. Armstrong, N. Feeder, A.D. Hopkins, M.J. Mays, D. Moncrieff, J.A. Wood, A.D. Woods, and D.S. Wright. J. Chem. Soc. Chem. Commun. 2483 (2000).
8. M.A. Beswick, A.D. Hopkins, L.C. Kerr, M.E.G. Mosquera, P.R. Raithby, D. Stalke, A. Steiner, and D.S. Wright. J. Chem. Soc. Chem. Commun. 1527 (1998).
9. J.A. Wood. Ph.D. Thesis, Cambridge University, Cambridge, U.K., 2000.

[2] CCDC 191100 and 191101 contains the supplementary crystallographic data for this paper. These data can be obtained, free of charge, via www.ccdc.ac.cam.uk/conts/retrieving.html (or from the Cambridge Crystallographic Data Centre, 12 Union Road, Cambridge CB2 1EZ, U.K. (fax: +44 1223 336033 or deposit@ccdc.cam.ac.uk). Supplementary material may be purchased from the Depository of Unpublished Data Document Delivery, CISTI, National Research Council of Canada, Ottawa, ON K1A OS2, Canada (http://www.nrc.ca/cisti/irm/unpub_e.shtml for information on ordering electronically).

© 2002 NRC Canada

10. The X-ray structure of this species was reported previously, see: M. Baudler, Y. Aktalay, T. Heinlein, and K.-F. Tebbe. Z. Naturforsch. B: Anorg. Chem. Org. Chem. **37B**, 299 (1982).
11. P. Jutzi, U. Meyer, S. Opiela, M.M. Olmstead, and P.P. Power. Organometallics, **9**, 1459 (1991).
12. M.A. Beswick and D.S. Wright. Comprehensive organometallic chemistry II, alkali metals. Vol. 1. *Edited by* E.W. Abel. F.G.A. Stone, and G. Wilkinson. C. E. Housecroft (*Volume editor*). Pergamon, Oxford, U.K. p. 1 (1996), and refs. therein.
13. E. Hey-Hawkins and S. Kurz. Phosphorus Sulfur and Silicon, **90**, 218 (1994).
14. For examples see: G. Becker, H. Freudenblum, and C. Witthauer. Z. Anorg. Allg. Chem. **492**, 37 (1982); A.J. Ashe, III, E.G. Ludwig, Jr., J. Oleksyszyn, and J.C. Huffman, Organometallics, **3**, 337 (1984); H.J. Breunig, R. Rösler, and E. Lork, Organometallics, **17**, 5594 (1998); O. Mundt, G. Becker, H.-J. Wesley, H.J. Breunig and H. Kischkel, Z. Anorg. Allg. Chem. **486**, 70 (1982).
15. R.A. Jones, M.H. Seeberger, and B.R. Whittlesey. J. Am. Chem. Soc. **107**, 6424 (1985), and refs. therein.
16. A. Kiennemann, G. Levy, F. Schué, and C. Taniélian. J. Organomet. Chem. **35**, 143 (1972).
17. T. Kottke and D. Stalke. J. Appl. Crystallogr. **26**, 615 (1993).
18. SHELXTL PC version 5.03. Siemens Analytical Instruments, Madison, Wisconsin. 1994.

© 2002 NRC Canada

Studies on electrochemical and coordination behaviour of phosphiniminocyclotrithiazenes

U. Swarnalatha, A. Sivaramakrishna, C.S. Venkatachalam, M.N. Sudheendra Rao, Tomonori Inoue, Tadaharu Ueda, and Masashi Hojo

Abstract: Electrochemical (polarographic, cyclic voltammetric, and coulometric) and coordination behaviour of several symmetrically and unsymmetrically substituted phosphiniminocyclotrithiazenes have been studied. Polarograms of $R_3PN\text{-}S_3N_3$ (R = C_6H_5, *p*-ClC_6H_4, *p*-$H_3CC_6H_4$, and (OC_4H_8N)), $Ph_2(OC_4H_8N)PN\text{-}S_3N_3$, and $Ph(OC_4H_8N)_2PN\text{-}S_3N_3$ give two cathodic waves. Cyclic voltammograms of $Ph_3PN\text{-}S_3N_3$ (**1**) and $(OC_4H_8N)_3PN\text{-}S_3N_3$ (**2**) reveal nearly the same oxidation peak potential but different reduction potentials. Controlled potential electrolysis of **1** and **2** at +0.6 V indicates exocyclic cleavage and ring degradation. Cathodic reduction behaviour of $Ph_3PN\text{-}S_3N_3$ suggests the possibility for the formation of 1,5-$(Ph_3PN)_2S_4N_4$ under electrochemical conditions. Reaction of nickel chloride hexahydrate with heterocycle **1** in 1:2 molar ratio in acetonitrile affords the complex, $[Ni(S_2N_2H)_2]$ (**A**) (90% yield) and $[Ph_3PNH_2]Cl$ salt as products. Analogous reactions with other ligands of this type (two symmetrical (sym.) and three unsymmetrical (unsym.)) except **2** also give **A,** while ligand **2** reacts with anhyd $NiCl_2$ in an equimolar ratio to afford a dark green, square-planar complex ($(OC_4H_8N)_3PN\text{-}S_3N{\cdot}NiCl_2$ (**B**)) whose ESCA results assist in providing its coordination details. The study reveals a high tendency of these heterocycles to different types of ring cleavage.

Key words: phosphiniminocyclotrithiazenes, polarography and cyclic voltammetry, substituent effect, nickel complexes, ESCA.

Résumé : On a étudié le comportement électrochimique (polarographique, voltampérométrie cyclique et coulométrique) et de coordination de plusieurs phosphiniminocyclotrithiazènes substitués de façon symétrique et asymétrique. Les polarogrammes des $R_3PN\text{-}S_3N_3$ (R = C_6H_5, *p*-ClC_6H_4, *p*-$H_3CC_6H_4$, OC_4H_8N) $Ph_2(OC_4H_8N)PN\text{-}S_3N_3$ et $Ph(OC_4H_8N)_2PN\text{-}S_3N_3$ présentent deux vagues cathodiques. Les voltampérogrammes cycliques du $Ph_3PN\text{-}S_3N_3$ (**1**) et $(OC_4H_8N)_3PN\text{-}S_3N_3$ (**2**) présentent des potentiels d'oxydation maxima qui sont pratiquement les mêmes, mais les potentiels de réduction sont différents. Une électrolyse du composé **1** à potentiel contrôlé, à 0,6 V, indique la présence de clivage exocyclique et de dégradation de cycle. Le comportement du $Ph_3PN\text{-}S_3N_3$ lors de la réduction cathodique suggère la possibilité de formation du 1,5-$(Ph_3PN)_2S_4N_4$ dans les conditions électrochimiques. La réaction du chlorure de nickel hexahydraté avec l'hétérocycle **1**, dans un rapport molaire de 2:1 dans l'acétonitrile, conduit à la formation du complexe $[Ni(S_2N_2H)_2]$ (**A**) (rendement de 90 %) et du $[Ph_3PNH_2]Cl$. Des réactions analogues (excepté celles avec le produit **2**) avec d'autres ligands de ce type (deux symétriques et trois non symétriques) conduisent aussi au produit à **A**. Le composé **2** réagit avec le $NiCl_2$ anhydre, dans un rapport moléculaire de 1:1, pour fournir un complexe plan carré, vert, $(OC_4H_8N)_3PN\text{-}S_3N{\cdot}NiCl_2$ (**B**) dont les résultats de spectroscopie d'électrons pour analyse chimique (« ESCA ») fournissent des détails relatifs à sa coordination. Cette étude révèle la grande tendance de ces hétérocycles à donner lieu à des types différents de clivage de cycle.

Mots clés : phosphiniminocyclotrithiazènes, polarographie, voltampérométrie cyclique, effet de substituant, complexes de nickel, ESCA.

[Traduit par la Rédaction]

Introduction

A variety of inorganic ring systems (1–2) have been the subject of both coordination and electrochemical studies in the last couple of decades. Electrochemical studies have helped in providing insight of chemical reactions and served also as a preparative method for both known and new compounds (3–9). Likewise, coordination studies have lead to

Received 14 February 2002. Published on the NRC Research Press Web site at http://canjchem.nrc.ca on 18 October 2002.

Dedicated to Professor Tristram Chivers for his contributions to Canadian chemistry.

U. Swarnalatha, A. Sivaramakrishna, C.S. Venkatachalam, and M.N.S. Rao.[1,2] Department of Chemistry, Indian Institute of Technology Madras, Chennai-600 036, India.
T. Inoue, T. Ueda, and M. Hojo.[3] Department of Chemistry, Faculty of Science, Kochi University, Akebono-cho, Kochi 780-8520, Japan.

[1]Corresponding author (e-mail: mns_rao@yahoo.com).
[2]Present address: Department of Chemistry, Faculty of Science, Kochi University, Akebono-cho, Kochi 780-8520, Japan.
[3]Corresponding author (e-mail: mhojo@cc.kochi-u.ac.jp).

 DOI: 10.1139/V02-140 © 2002 NRC Canada

realizing many interesting results and novel complexes of transition metals (10–14).

Phosphiniminocyclotrithiazenes, $R_3PN\text{-}S_3N_3$ are a class of electron-rich inorganic heterocycles (15, 16) having a phosphinimino moiety as the exocyclic substituent and have served as stable derivatives of monosubstituted cyclotrithiazenes ($\text{-}S_3N_3$) (17–18). $Ph_3PN\text{-}S_3N_3$, the first example in this class (8 π system) to be reported in 1961 was subsequently obtained in an improved yield from a detailed reinvestigation study by Chivers and co-workers (19). Some of its reactivity aspects have also been demonstrated (20–22). Oakley and co-workers (20) have shown the usefulness of the redox potential data in rationalizing its electronic absorption and some reactivity features. In an extension of this work, we have prepared a variety of $R_3PN\text{-}S_3N_3$ heterocycles and studied their structural and reactivity aspects and have obtained many interesting results (23–26). In addition to the noticeable structural differences (27, 28), we have observed substituent-dependent pyrolytic behaviour of these heterocycles (29). We believe that the presence of a relatively bulky phosphinimino moiety as an exocyclic part of the S_3N_3 ring skeleton and the possibility of substituent variation on phosphorus render them as interesting examples for further studies. Sometime ago, we observed the tendency of these heterocyclic systems to nucleophilic attack by ammonia, amines (30), and phosphines (31, 32) and recently to oxidative cleavage by mild oxidants such as iodine (33).[4] The results suggested the preferential cleavage of the trithiazene ring skeleton over that of exocyclic substituent. These observations prompted us to undertake this study to probe the coordination and electrochemical behaviour of $R_3PN\text{-}S_3N_3$ ring systems for the first time. In this paper, we report polarographic, cyclic voltammetric, and bulk electrolysis studies as well as coordination behaviour with nickel chloride of many examples of symmetrically and unsymmetrically substituted phosphiniminocyclotrithiazenes.

Experimental

All handling and manipulation of air-sensitive compounds were done in a nitrogen or argon atmosphere. Solvents were purified using standard procedures (34). $NiCl_2{\cdot}6H_2O$, $NiSO_4{\cdot}7H_2O$, and NiI_2 (s.d. Fine Chemicals), and Ph_3P (Fluka) were used as received. Anhydrous $NiCl_2$ was prepared by the literature method (35). S_4N_4 (caution: explosion sensitive!) (36), $(OC_4H_8N)_3P$ (37), and different $R_3PN\text{-}S_3N_3$ derivatives employed in this study were synthesized by the reported methods (19, 23, 26, 37). Various spectral and analytical facilities used for characterization have been published elsewhere (26). Magnetic measurements were done in a vibrating sample magnetometer (EG & G PARC VSM-155) with 2 mg of the sample. Conductivity measurements were done using a conductometer (Toshniwal CL01/02A) with a glass electrode (cell constant: 1.2708 cm^{-1}) on 1 mM solution of the sample in CH_3CN. ESCA measurements were made using a VG ESCA LAB MK II X-ray photoelectron spectrometer.

Direct-current polarograms were measured on a dropping mercury electrode (DME) using a Yanagimoto polarograph (P-1000) and a Graphtec X-Y recorder (WX-4410-L0). Cyclic voltammograms were recorded at 25 ± 0.1°C with a microcomputer-controlled system at a scan rate of 100 mV s^{-1}. Glassy carbon electrode (Tokai Carbon GC-30S), freshly polished with a 0.1 μm diamond slurry was used as the working electrode and a platinum wire served as the counter electrode. $Ag/AgNO_3$ (0.01 mol dm^{-3} in MeCN) was the reference electrode. Coulometric experiments were performed on a GC fiber electrode using a potentiostat (Hokuto Denko HA-151). Dichloromethane (Wako GR grade) was used as the solvent. The electrolysis was followed by ^{31}P NMR spectroscopy using a JEOL JNM-LA400 instrument and (or) electronic spectroscopy using a double-beam spectrophotometer (Hitachi U-2000).

(*a*) Reaction of $Ph_3PN\text{-}S_3N_3$ (1) with $NiCl_2{\cdot}6H_2O$ in CH_3CN (2:1)

To a stirred slurry of $NiCl_2{\cdot}6H_2O$ (0.40 g, 1.67 mmol) in acetonitrile (25 mL), the red heterocyclic ligand **1** (1.39 g, 3.36 mmol) was added in batches over a 15 min interval at room temperature. The colour of the solution changed gradually to dark purple. After 20 h, it was filtered to isolate an off-white precipitate (0.26 g) and a dark purple filtrate. The CH_3CN extract of the precipitate (4 × 3 mL) when cooled gave a small amount of $[Ph_3PNH_2]Cl$ (40 mg), mp 228 to 229°C (lit. (38) value mp 230–232°C). Its IR and ^{31}P NMR chemical shift agreed well with an authentic sample (38). The acetonitrile insoluble residue (0.20 g) was metal free (chemical test for Ni was negative) and found to be water soluble.

The purple filtrate upon cooling for 36 h in the refrigerator gave $[Ph_3PNH_2]Cl$ (0.86 g). The residual mother liquor was concentrated and cooled in the deep freezer for a day to isolate purple crystals of $[Ni(S_2N_2H)_2]$ (**A**) (0.37 g, 90%), mp 155 to 156°C (lit. (39) value mp 156–158°C). Its nickel content, IR, and UV–Vis spectral data (552 nm (2.1×10^3); 399 nm (4.7×10^3); 305 nm (11.4×10^3)) agreed well with the literature data (39).

(*b*) Reaction of $Ph_3PN\text{-}S_3N_3$ (1) with $NiCl_2$ in CH_3CN (2:1)

Anhydrous nickel chloride (0.10 g, 0.77 mmol) was added in small amounts over a 15 min interval to a stirred slurry of ligand **1** (0.64 g, 1.55 mmol) in CH_3CN (25 mL) at room temperature. The observations were same as in reaction (*a*). After 16 h, it was worked up as in reaction (*a*) to isolate an off-white crystalline material ($[Ph_3PNH_2]Cl$ (0.23 g)) followed by the purple crystals of $[Ni(S_2N_2H)_2]$ (80 mg, 42%). An yellowish white insoluble residue (0.13 g) was also obtained from the precipitate part of the reaction.

(*c*) Reaction of anhyd $NiCl_2$ with Ph_3P and S_4N_4 in CH_3CN

To a stirred solution of Ph_3P (1.44 g, 5.50 mmol) in CH_3CN (25 mL) at room temperature, S_4N_4 (0.50 g, 2.72 mmol) was added as a solid in small amounts over a 20 min interval. When the reaction mixture had turned dark red in colour (ca. 2 h), anhyd $NiCl_2$ (0.18 g, 1.39 mmol) was added in aliquots over a 15 min interval and stirred for 20 h. The reaction mixture was filtered to obtain a dark purple

[4] A. Sivaramakrishna, B. Varghese, and M.N.S. Rao. Unpublished results.

© 2002 NRC Canada

Table 1. Reactions of $R_3PN\text{-}S_3N_3$ heterocycles with nickel salts.[a]

	Nickel salt		$R_3PNS_3N_3$ ligands			Product isolated[b]		
	(g)	(mmol)	(g)	(mmol)	Mol ratio		(g)	(%)
$NiCl_2$	0.30	2.31	(**1**) 0.96	2.32	1:1	**A**	0.15	27
						C	0.50	34
$NiCl_2{\cdot}6H_2O$	0.25	1.05	(**1**) 0.44	1.06	1:1	**A**	0.11	43
						C	0.27	41
$NiCl_2{\cdot}6H_2O$	0.25	1.05	(**1**) 0.88	2.13	1:2[c]	**A**	0.14	54
						C	0.43	65
NiI_2	0.22	0.70	(**1**) 0.30	0.72	1:1	**A**	0.06	35
						D	0.22	39
$NiSO_4{\cdot}7H_2O$	0.20	0.71	(**1**) 0.60	1.45	1:2	**A**	0.15	86
						E[d]	0.36	77
$NiCl_2$	0.21	1.62	(**5**) 0.71	1.63	1:1	**A**	0.12	30
						F	0.31	29
$NiCl_2$	0.25	1.93	(**6**) 0.93	1.94	1:1	**A**	0.20	42
						G[d]	0.20	27
$NiCl_2$	0.18	1.39	(**7**) 0.59	1.39	1:1	**A**[e]	0.15	44
							—	
$NiCl_2$	0.15	1.16	(**8**) 0.50	1.16	1:1	**A**[e]	0.12	42
							—	
$NiCl_2$	0.20	1.54	(**9**) 0.66	1.54	1:1	**A**[e]	0.12	32
							—	

Note: **A** = $Ni(S_2N_2H)_2$; **C** = $[Ph_3PNH_2]Cl$; **D** = $[Ph_3PNH_2]I$; (40); **E** = $[Ph_3PNH_2]_2SO_4$; **F** = $[(C_5H_{10}N)_3PNH_2]Cl$ (mp 147–150°C); ^{31}P NMR: singlet at 36.0 ppm, gave satisfactory CHN analysis; **G** = $[(H_3C\text{-}NC_4H_8N)_3PNH_2]Cl$.

[a]All reactions were done in CH_3CN at room temperature for ca. 18 h by adding the ligand to a stirred slurry of the nickel salt.

[b]In all the reactions, an off-white insoluble residue was obtained in varying amounts. The ionic nature of this water soluble residue was revealed by its broad IR absorptions in the ν_{NH} and ν_{SO} regions at 3345 and 1095 cm^{-1}, respectively. It is possibly an ammonium salt of the S_xO_y anion.

[c]This reaction was done by the addition of five drops of water.

[d]Impure samples, ^{31}P NMR spectra showed strong singlets at 35.1 (E) and 35.6 ppm (G).

[e]Not isolated, ^{31}P NMR spectrum showed a strong singlet at 41.1, 40.6, and 42.0 ppm for the purple coloured reaction mixtures of **7**, **8**, and **9**, respectively.

filtrate and a pale yellow precipitate which when worked up as in reaction (*a*) gave $[Ph_3PNH_2]Cl$ (0.10 g) and a residue (0.11 g). The oily mass left after removal of the solvent from the purple filtrate was chromatographed over a silica gel column using benzene (caution: carcinogen!!) followed by benzene–dichloromethane (1:1) eluants to isolate Ph_3PS (0.40 g), $[Ph_3PNH_2]Cl$ (0.38 g), and $[Ni(S_2N_2H)_2]$ (0.20 g, 61%).

(*d*) Reaction of $(OC_4H_8N)_3PN\text{-}S_3N_3$ (2) with anhyd $NiCl_2$ in CH_3CN (1:1)

To a stirred slurry of anhyd $NiCl_2$ (0.15 g, 1.16 mmol) in acetonitrile (25 mL), was added the red ligand **2** (0.53 g, 1.20 mmol) as a solid in small amounts over a 15 min interval at room temperature. The colour of the solution gradually changed to purple along with the formation of a green precipitate. After 20 h, the green precipitate (0.32 g) was separated by a filtration and extracted with CH_3CN (8 × 3 mL). This extract, on cooling in the refrigerator for 10 h, gave a lustrous dark-green solid (0.22 g, 46%) which was identified as $(OC_4H_8N)_3PNS_3N{\cdot}NiCl_2$ (**B**), mp 184–186°C. IR (Nujol, cm^{-1}): 1443 (m), 1344 (m), 1293 (w), 1251 (m), 1152 (s), 1126 (s), 1104 (vs), 1018 (s), 1014 (m), 960 (vs), 880 (w), 835 (w), 700 (vs), 662 (w), and 595 (w). UV–vis (nm, L mol^{-1} cm^{-1}): 580 (9.1×10^3), 420 (4.1×10^3), 300 (1.9×10^3). ^1H NMR δ (ppm): 3.12 (m, 12H) and 3.60 (m, 12H). ^{31}P NMR δ (ppm): 33.7 (s,1P). XPE (B.E. in eV): 141.0 (P_{2p}), 170.5 (S_{2p}), 205.0 (Cl_{2p}), 292.5 (C_{1s}), 405.5 (N_{1s}), 536.5 (O_{1s}), 858.5 (Ni_{2p}). Elemental anal. calcd. for $C_{12}H_{24}N_5O_3PS_3NiCl_2$ (%): C 26.54, H 4.46, N 12.90, Cl 13.08, Ni 10.83; found: C 26.49, H 4.41, N 12.51, Cl 12.93, Ni 10.73 (leaving behind a white insoluble residue (60 mg)). A further quantity of **B** (0.12 g, 25%) was obtained when the concentrated purple filtrate was cooled in the freezer for a day.

(*e*) Reaction of $(OC_4H_8N)_3PN\text{-}S_3N_3$ (2) with $NiCl_2{\cdot}6H_2O$ in CH_3CN (1:1)

Nickel chloride hexahydrate (0.20 g, 0.84 mmol) stirred in CH_3CN (25 mL) at room temperature was added the ligand **2** (0.37 g, 0.84 mmol) in small amounts over a 15 min interval. The reaction mixture, which turned gradually to dark purple along with the formation of a green precipitate, was filtered after 18 h. The acetonitrile extract (3 × 10 mL) of the precipitate when cooled in the freezer for a day yielded a lustrous dark-green solid **B** (0.13 g, 38%). The purple filtrate was concentrated and cooled in the freezer to obtain a further quantity of **B** (50 mg, 14%).

(*f*) Reaction of anhyd $NiCl_2$ with $(OC_4H_8N)_3P$ and S_4N_4 in CH_3CN (1:1)

To a stirred solution of $(OC_4H_8N)_3P$ (1.05 g, 3.63 mmol) in CH_3CN (25 mL), S_4N_4 (0.33 g, 1.79 mmol) was added at room temperature over a 20 min interval. When the reaction mixture became dark red (ca. 2 h), anhyd $NiCl_2$ (0.23 g, 1.77 mmol) was added in aliquots over a 15 min interval and stirred for 15 h. The reaction mixture was then filtered to get

© 2002 NRC Canada

Table 2. The cathodic half-wave potentials ($E_{1/2}$) and the ^{31}P NMR chemical shifts of $R_3PN\text{-}S_3N_3$ heterocycles and 1,5-$(Ph_3PN)_2S_4N_4$.

Compound	$E_{1/2}$ (V) vs. Ag/Ag^+		^{31}P NMR chemical shift
$Ph_3PNS_3N_3$	–1.59	–1.97	24.8
$(4\text{-}ClC_6H_4)_3PNS_3N_3$	–1.54	–1.90	23.4
$(4\text{-}MeC_6H_4)_3PNS_3N_3$	–1.58	–1.94	23.1
$Ph_2(OC_4H_8N)PNS_3N_3$	–1.57	–1.94	31.2
$Ph(OC_4H_8N)_2PNS_3N_3$	–0.88	–1.58	30.9
$(OC_4H_8N)_3PNS_3N_3$	–1.62	–2.07	23.1
1,5-$[Ph_3PN]_2S_4N_4$	–1.56	–1.99	18.1 and 23.6

Fig. 1. Phosphiniminocyclotrithiazenes ((R)(R′)(R″)PN-S_3N_3) considered in this study.

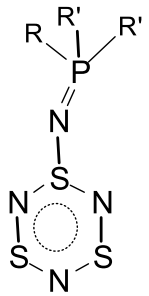

R	R'	R"
C_6H_5	C_6H_5	C_6H_5 (**1**)
OC_4H_8N	OC_4H_8N	OC_4H_8N (**2**)
p-ClC_6H_4	p-ClC_6H_4	*p*-ClC_6H_4 (**3**)
p-$H_3CC_6H_4$	p-$H_3CC_6H_4$	*p*-$H_3CC_6H_4$ (**4**)
$C_5H_{10}N$	$C_5H_{10}N$	$C_5H_{10}N$ (**5**)
$CH_3NC_4H_8N$	$CH_3NC_4H_8N$	$CH_3NC_4H_8N$ (**6**)
C_6H_5	C_6H_5	OC_4H_8N (**7**)
C_6H_5	OC_4H_8N	OC_4H_8N (**8**)
C_6H_5	$C_5H_{10}N$	$C_5H_{10}N$ (**9**)

a green precipitate and dark purple filtrate. The CH_3CN extract (6 × 5 mL) of the precipitate when cooled in the freezer for a day gave the lustrous dark-green solid **B** (0.23 g, 31%). A further quantity of **B** (0.12 g, 17%) was recovered from the purple filtrate from which a slightly impure $(OC_4H_8N)_3PS$ (0.38 g) was also isolated in two subsequent crops.

All other reactions performed in this study are summarized in Table 1.

Results and discussion

The reported reactions of phosphiniminocyclotrithiazenes include: (*i*) adduct formation (20, 37); (*ii*) thermolysis (21, 23); (*iii*) substituent exchange (22); (*iv*) ring conversions (23); and (*v*) chemical and hydrolytic degradation (41). We have now studied the first electrochemical and coordination behaviour of several such heterocyclic systems carrying different substituents on phosphorus (Fig. 1) and the results are described here.

Electrochemical behaviour

A polarographic investigation was carried out on $R_3PN\text{-}S_3N_3$ (R = phenyl (**1**), morpholino (**2**), p-chlorophenyl (**3**), and *p*-tolyl (**4**)) (symmetrically substituted) and $Ph_2(OC_4H_8N)PN\text{-}S_3N_3$ (**7**) and $Ph(OC_4H_8N)_2PN\text{-}S_3N_3$ (**8**) (unsymmetrically substituted) to evaluate substituent effects on redox potentials, if any, in this class of heterocycles. All of them were found to give two cathodic waves (Fig. 2) with significantly differing $E_{1/2}$ values. A comparison (Table 2) reveals that among the symmetrical ones, $E_{1/2}$ for first and second waves vary over a 80 to 170 mV range, respectively.

Fig. 2. The polarograms of: (*a*) 0.5 mmol dm^{-3} $Ph_3PN\text{-}S_3N_3$, and (*b*) 0.5 mmol dm^{-3} 1,5-$(Ph_3PN)_2S_4N_4$ in dichloromethane containing 0.1 mol dm^{-3} *n*-Bu_4NClO_4.

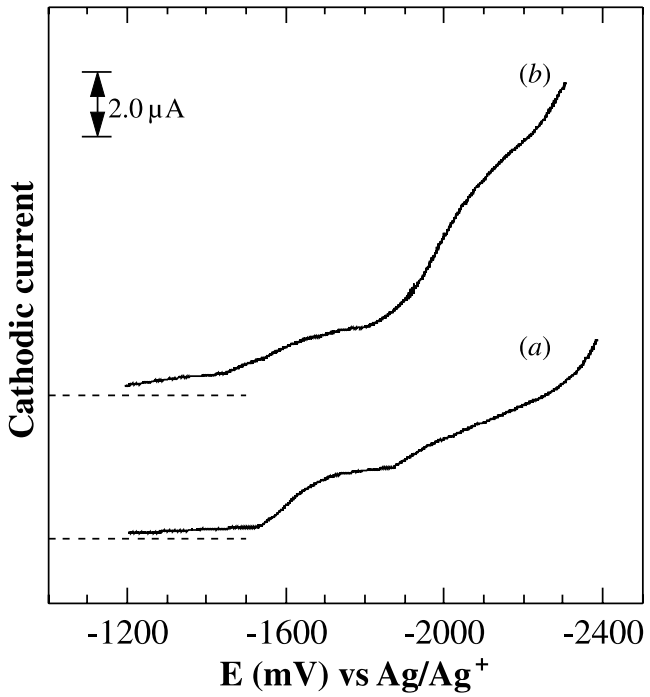

The *p*-chlorophenyl derivative had the lowest value while the morpholino derivative had the greatest. Unsymmetrical ones showed very different $E_{1/2}$ values to each other. Also, no smooth trend in the $E_{1/2}$ values was observed in the series $(C_6H_5)_x(OC_4H_8N)_{3-x}PN\text{-}S_3N_3$ (x = 0, 1, 2, 3). Similar irregularities have been observed in ^{31}P NMR chemical shifts of several unsymmetrically substituted tri-coordinate phosphorus(III) and tetra-coordinate phosphorus(V) compounds containing amino substituents (42), which seem to suggest that the unsymmetrical environment around phosphorus has a more pronounced effect than the additive effects of the substituents attached (Table 2).

An interesting observation made in this study is that the polarographic reduction of **1** at –1.6 V produced a reduction wave at ca. –2.0 V that corresponded with the reduction wave of 1,5-$(Ph_3PN)_2S_4N_4$ (–1.99 V) thereby suggesting the possibility of the conversion of **1** to 1,5-$(Ph_3PN)_2S_4N_4$ under electrochemical reduction. Such a ring conversion occurring under the influence of a nucleophile has been previously observed (23, 30, 32). Conceivably, the dimerization of "$Ph_3PN\text{-}S_2N_2$" arising from the cleavage of $Ph_3PN\text{-}S_3N_3$ leads to the formation of this eight-membered heterocycle (eqs. [1] and [2]).

$$[1]\quad Ph_3PN\text{-}S_3N_3 + e^- \rightarrow Ph_3PN\text{-}S_3N_3^{-\bullet} \rightarrow Ph_3PN\text{-}S_2N_2 + NS^{\bullet}$$

$$[2]\quad 2Ph_3PN\text{-}S_2N_2 \rightarrow 1,5\text{-}(Ph_3PN)_2S_4N_4$$

The fragment $NS^{\bullet}$ possibly gets converted to S_4N_4. Chivers and Hojo (4) have observed a similar dimerization of "$Ph_2CNSNSO$" under electrochemical reduction. The polarograms of $R_3PNS_3N_3$ in acetonitrile containing

© 2002 NRC Canada

Fig. 3. The cyclic voltammograms of: (*a*) 0.5 mmol dm^{-3} $Ph_3PN\text{-}S_3N_3$, and (*b*) 0.5 mmol dm^{-3} $(OC_4H_8N)_3PN\text{-}S_3N_3$ in dichloromethane containing 0.1 mol dm^{-3} $n\text{-}Bu_4NClO_4$.

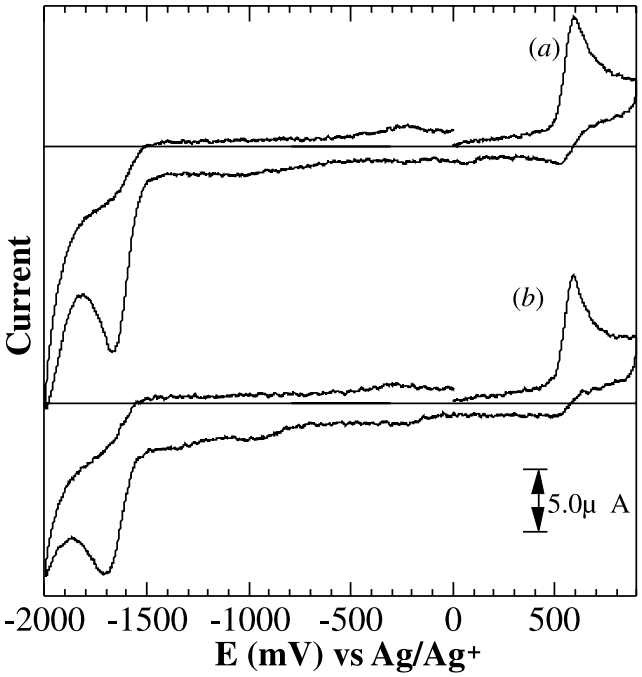

0.1 mol dm^{-3} Et_4NClO_4 were rather complicated; e.g., $Ph_3PNS_3N_3$ gave successively five cathodic waves at –1.25, –1.59, –1.98, –2.47, and –2.73 V vs. Ag/0.01 mol dm^{-3} $AgNO_3$–MeCN. The second and the third waves correspond to the two waves observed in dichloromethane.

Figure 3 shows the cyclic voltammograms on the GC electrode of **1** and **2**. Both gave a sharp anodic peak nearly at the same potential (+0.6 V) but their cathodic peak potentials are found to be different. Other examples considered in the study also gave a similar anodic peak in the range +0.60 to +0.65 V. In an earlier study, Swarnalatha (33) observed the anodic peak potential values ($E_{a,p}$ vs. SCE) for **5**, $Ph[(C_6H_{11})_2N](C_5H_{10}N)PN\text{-}S_3N_3$, and $Ph[(C_6H_{11})_2N](Me_2N)\text{-}PN\text{-}S_3N_3$ in acetonitrile at 0.51, 0.56, and 0.61 V, respectively.

Controlled potential electrolysis of $Ph_3PNS_3N_3$ and $(OC_4H_8N)_3PNS_3N_3$ were carried out on a GC fiber electrode at +0.60 V. The initial red colour of the solution disappeared within a few minutes and the ^{31}P NMR spectra recorded for the solutions after electrolysis gave only one signal at 37.5 and 34.6 ppm, respectively, which may be due to the formation of the corresponding phosphinimines. The absence of characteristic UV–Vis absorptions of the heterocycle (15, 16) after electrolysis suggests the disruption of the S_3N_3 ring skeleton during electrolysis.

Coordination behaviour

A detailed study of the reactions of nickel chloride with $Ph_3PN\text{-}S_3N_3$ (**1**) was first carried out and only selected reactions were done in other cases which include **2**, **5**, and **6** (symmetrical variety) and **7**, **8**, and **9** (unsymmetrical variety). Ligand **1** reacts with nickel chloride at room temperature to afford the previously known nickel complex

Fig. 4. Complexes of nickel obtained in this study.

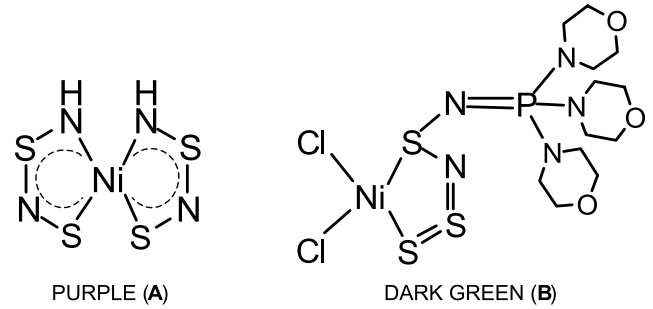

($[Ni(S_2N_2H)_2]$ (**A**)) (43) and the phosphiniminium salt ($[Ph_3PNH_2]Cl$ (**C**)) (38) as major products. Both the products were isolated in ca. 90% yield when the ligand (**1**) to hydrated $NiCl_2$ ratio was 2:1 which suggests that the reaction conceivably proceeds as in the eq. [3].

$$[3]\quad 2Ph_3PN\text{-}S_3N_3 + [Ni(H_2O)_6]Cl_2 \rightarrow [Ni(S_2N_2H)_2] + 2[Ph_3PNH_2]Cl + \cdots$$

The coordinated water molecules of nickel chloride are found to participate in the reaction but those performed with deliberate addition of water or with anhyd $NiCl_2$ afforded relatively low yields of **A** and **C** implying that: (*i*) H_2O only in small amounts is necessary for the reaction; and (*ii*) $NiCl_2$ and (or) CH_3CN employed in the study are presumably slightly wet. Depending on the conditions, varying yields of **A** and **C** were isolated from several of these reactions. This reaction, which occurs for different anions of nickel (Cl^-, I^-, SO_4^{2-}) was also favoured when the precursor reaction (that of S_4N_4 and Ph_3P) was performed in the presence of $NiCl_2$ (*Experimental*).

The purple complex **A** has attracted in the past, several studies. Scheme 1 shows the different reaction routes from which **A** has been isolated previously. It is noteworthy that methanol is used in all the methods which is presumably the source of protons. A notable feature of the present work is that **A** is isolated in near quantitative yield and by a simple work-up procedure without involving chromatography. Interestingly, ligands **5**–**9** also afforded the same complex (**A**) but its recovery from the reaction mixtures posed considerable difficulty. The corresponding phosphiniminium chloride by-product was either isolated in small amounts or identified by ^{31}P NMR spectroscopy.

Contrary to the ligands **1** and **5**–**9**, $(OC_4H_8N)_3PN\text{-}S_3N_3$ (**2**) reacts in an equimolar ratio with $NiCl_2$ (in both hydrated and anhydrous forms) under similar conditions to afford a dark green lustrous complex (**B**) in moderate to good yield (Fig. 4). The use of anhydrous salt and dry solvent were found to be more favourable for the formation of **B**, which could also be isolated from the analogous reaction of $(OC_4H_8N)_3P$ with S_4N_4 in presence of $NiCl_2$ in ca. 50% yield. Neither **A** nor the corresponding phosphiniminium chloride ($[(OC_4H_8N)_3PNH_2]Cl$) was isolated from any of the reactions tried. Though reasons for this unique behaviour are not clear, the differences in the stabilities of the (amino) phosphinimines and their possible derivatives may well be a contributing factor for this difference.

The complex **B** is air stable and less soluble in CH_3CN, CH_2Cl_2 and THF compared to **A**. Its solution though appears

© 2002 NRC Canada

Scheme 1. Reported methods for the preparation of the $Ni(S_2N_2H)_2$ complex.

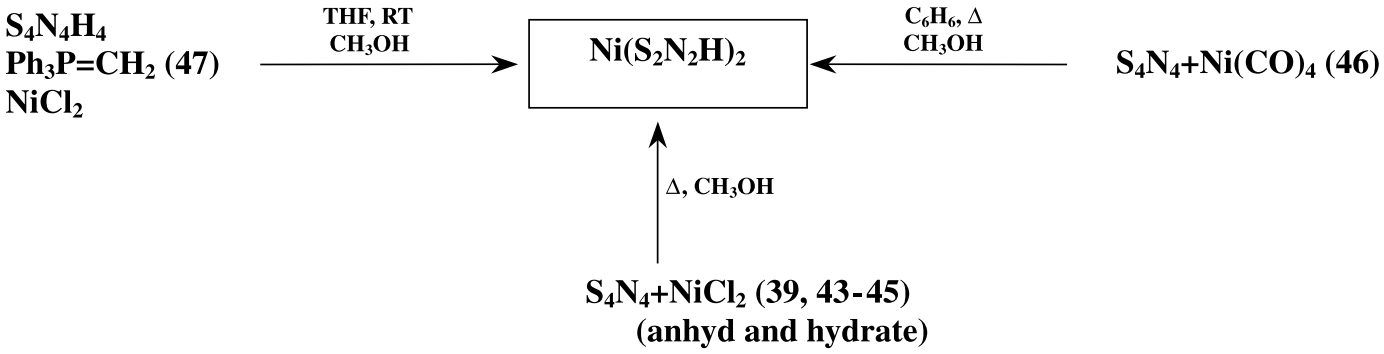

Fig. 5. Sulfur region of the XPE spectrum of complex **B** showing deconvolution and curve fitting (the dotted line represents the experimental curve).

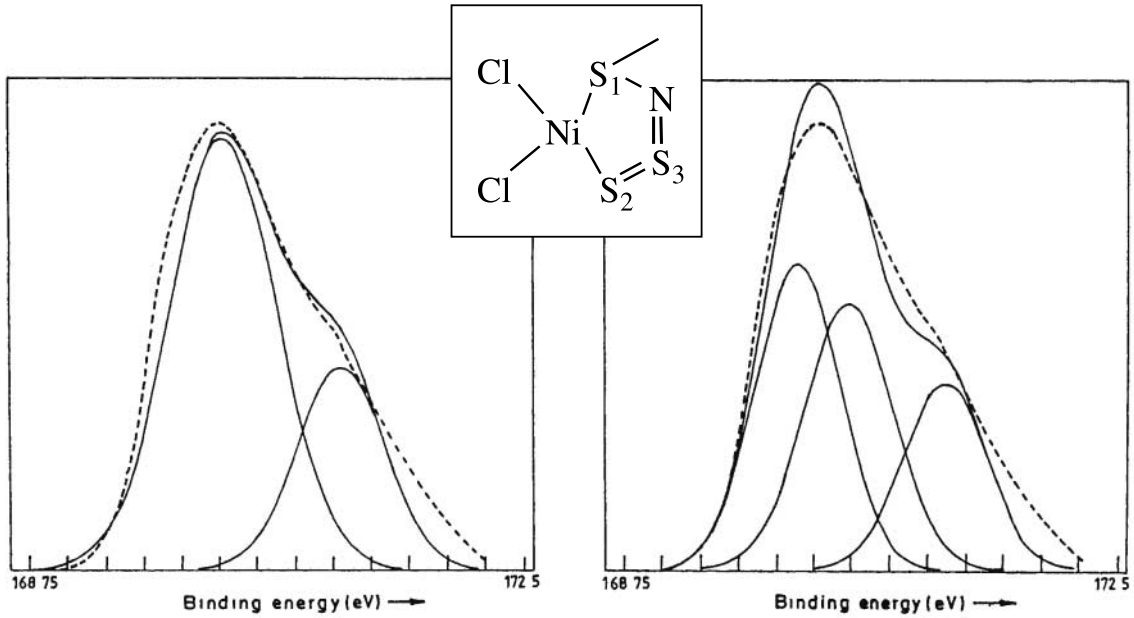

purple, affords upon cooling shining dark green microcrystalline solid which is very different to **A**. On the basis of its elemental analysis, diamagnetic nature (μ_B = 0.13), negligible electrical conductivity (λ = 0.0021 ohm^{-1} cm^2), ^1H and ^{31}P NMR data and the fact that its IR spectrum resembles that of $(OC_4H_8N)_3PN\text{-}S_3N$ (31), we propose its structure as shown in Fig. 4. Complex **B** is a tetracoordinate, neutral, square-planar complex that has $(OC_4H_8N)_3PN\text{-}S_3N$ as the new ligand. Though many metal complexes of the bidentate ligand S_3N^- have been reported in the literature (45, 48–50), to the best of our knowledge this is the first time that a neutral S_3N ligand and its bidentate mode of ligation are observed. Unfortunately, all the efforts to obtain single crystals of **B** proved futile. However, its X-ray photoelectron spectral results (ESCA) were found to be in accordance with the structure proposed. The spectrum reveals the presence of all the constituent elements (*Experimental*) as well as the divalent and low-spin nature of nickel (51). The broad and unsymmetrical nature of the peak observed in the sulfur region (ca. 170 eV) was suggestive of the nonequivalent nature of sulfur atoms present in the ligand. This peak, upon repetitive deconvolution steps, gave features supportive of three kinds of sulfurs (Fig. 5) as in the structure proposed. In contrast, the nitrogen peak was found to be symmetrical and unresolved (FWHM = 2.52 V). A similar symmetrical and unresolved nitrogen peak was observed by Bossa et al. (52) for the nitrogens of $[Ni(S_2N_2H)_2]$.

Conclusion

New and interesting results as well as substituent-dependent behaviour were observed in the electrochemical and coordination studies of several phosphinimino cyclotrithiazenes (symmetrical and unsymmetrical ones). The synthetic advantage of the use of such heterocycles has been demonstrated. $Ph_3PN\text{-}S_3N_3$ serves as a source of the "$S_2N_2H^-$" ligand and affords $[Ni(S_2N_2H)_2]$ in near quantitative yield while $(OC_4H_8N)_3PN\text{-}S_3N_3$ offers a new and neutral S-N ligand. Its complex with nickel chloride was isolated and characterized. More coordination studies especially of the neutral ligand, $R_3PN\text{-}S_3N$ with different metal substrates merit consideration. Such studies are underway.

© 2002 NRC Canada

Acknowledgement

Financial support by IITM, Chennai (to U.S.), and the Department of Science and Technology, New Delhi (to A.S.) are gratefully acknowledged. The Regional Sophisticated Instrumentation Centre, IITM is thanked for providing various instrumentation facilities. MNSR thanks the Japan Society for Promotion of Science (JSPS) for an invitation fellowship. MH thanks the Faculty of Science, Kochi University for financial help. Thanks are also due to Professor S. Subramanian and Dr. T. Pradeep of IITM for helpful discussions in analyzing ESCA results.

References

1. I. Haiduc and D.B. Sowerby. The inorganic homo- and heterocyclic chemistry. Vols. 1 and 2. Academic Press, London. 1987.
2. R.T. Oakley. Cyclic and heterocyclic thiazenes. *In* Progress in inorganic chemistry. Vol. 36. John Wiley Interscience, New York. 1988. p. 300.
3. M. Hojo. Bull. Chem. Soc. Jpn. **53**, 2856 (1980).
4. T. Chivers and M. Hojo. Inorg. Chem. **23**, 4088 (1984).
5. T. Chivers and M. Hojo. Inorg. Chem. **23**, 2738 (1984).
6. T. Chivers and M. Hojo. Inorg. Chem. **23**, 1526 (1984).
7. N. Burford, T. Chivers, M. Hojo, W.G. Laidlaw, J.F. Richardson, and M. Trsic. Inorg. Chem. **24**, 709 (1985).
8. A.W. Cordes, M. Hojo, H. Koenig, M.C. Noble, R.T. Oakley, and W.T. Pennington. Inorg. Chem. **25**, 1137 (1986).
9. R.T. Boere and K.H. Moock. J. Am. Chem. Soc. **117**, 4775 (1995).
10. T. Chivers and F. Edelmann. Polyhedron, **5**, 1661 (1986).
11. P.F. Kelly and J.D. Woollins. Polyhedron, **5**, 607 (1986).
12. H.W. Roesky. Synlett. 651 (1990).
13. P.F. Kelly, A.M.Z. Slawin, D.J. Williams, and J.D. Woollins. Chem. Soc. Rev. **21**, 245 (1992).
14. S.S. Krishnamurthy, V.S. Reddy, A. Chandrasekaran, and M. Nethaji. Phosphorus, Sulfur Silicon Relat. Elem. **64**, 99 (1992).
15. T. Chivers. Acc. Chem. Res. **17**, 166 (1984).
16. T. Chivers. Chem. Rev. **85**, 341 (1985).
17. T. Chivers and M.N.S. Rao. Can. J. Chem. **61**, 1957 (1983).
18. T. Chivers, R.T. Oakley, A.W. Coats, and W.T. Pennington. J. Chem. Soc. Chem. Commun. 1214 (1981).
19. J. Bojes, T.Chivers, A.W. Coats, G. MacLean, and R.T. Oakley. Inorg. Chem. **20**, 16 (1981).
20. S.W. Liblong, R.T. Oakley, A.W. Cordes, and M.C. Noble. Can. J. Chem. **61**, 2062 (1983).
21. T. Chivers, A.W. Cordes, R.T. Oakley, and P.N. Swepston. Inorg. Chem. **20**, 2376 (1981).
22. I. Ruppert, V. Bastian, and R. Appel. Chem. Ber. **107**, 3426 (1974).
23. M.N.S. Rao. Curr. Sci. **78**, 479 (2000).
24. C.J. Thomas and M.N.S. Rao. J. Chem. Soc. Dalton Trans. 1445 (1988).
25. T. Mohan, C.J. Thomas, M.N.S. Rao, G. Aravamudan, A. Meetsma, and J.C. van de Grampel. Heteroat. Chem. **5**, 19 (1994).
26. T. Mohan and M.N.S. Rao. Heteroat. Chem. **8**, 225 (1997).
27. J. Srinivas, G. Srinivasamurthy, C.J. Thomas, and M.N.S. Rao. J. Chem. Crystallogr. **26**, 403 (1996).
28. G. Janarthanan, J. Srinivas, G. Srinivasamurthy, and M.N.S. Rao. Polyhedron, **16**, 1089 (1997).
29. U. Swarnalatha, M.N.S. Rao, and M.R. Udupa. Thermochim. Acta, **297**, 139 (1997).
30. A.J. Elias and M.N.S. Rao. Phosphorus Sulfur Relat. Elem. **37**, 179 (1988).
31. A.J. Elias. Ph.D. Thesis, Indian Institute of Technology, Madras, India, 1988.
32. C.J. Thomas and M.N.S. Rao. Indian J. Chem. Sect. A: Inorg. Phys. Theor. Anal. **29A**, 450 (1990).
33. U. Swarnalatha. Ph.D. Thesis, Indian Institute of Technology, Madras, India, 1997.
34. D.D. Perrin, W.L.F. Armarego, and D.R. Perrin. Purification of laboratory chemicals. 2nd ed. Pergamon Press, Oxford. 1980.
35. D.F. Shriver and M.A. Drezdzon. The manipulation of air sensitive compounds. 2nd ed. Wiley Interscience Publications, New York. 1986.
36. V.M. Blanco and W.L. Jolly. Inorg. Synth. **29**, 98 (1967).
37. A.J. Elias, M.N.S. Rao, and B. Varghese. Polyhedron, **9**, 1433 (1990).
38. M.B. Hursthouse, N.P.C. Walker, C.P. Warren, and J.D. Woollins. J. Chem. Soc. Dalton Trans. 1043 (1985).
39. D.T. Haworth, J.D. Brown, and Y. Chen. Inorg. Synth. **18**, 124 (1978).
40. R. Appel and A. Hauss. Z. Anorg. Allg. Chem. **311**, 290 (1961).
41. C.J. Thomas and M.N.S. Rao. Z. Anorg. Allg. Chem. **615**, 149 (1992).
42. T. Mohan. Ph.D. Thesis, Indian Institute of Technology, Madras, India, 1990.
43. T.S. Piper. J. Am. Chem. Soc. **80**, 30 (1958).
44. K.F. Mayer and J. Weiss. Acta. Crystallogr. Sect. B: Struct. Crystallogr. Cryst. Chem. **34B**, 1999 (1978).
45. J.D. Woollins, R. Grinter, M.K. Johnson, and A.J. Thomas. J. Chem. Soc. Dalton Trans. 1914 (1980).
46. K.W. Daum. M. Goehring, and J. Weiss. Z. Anorg. Chem. **278**, 260 (1955).
47. T. Chivers, F. Edelmann, U. Behrens, and R. Drews. Inorg. Chim. Acta, **116**, 145 (1986).
48. A. Heberhold, L. Haumaier, and U. Schubert. Inorg. Chim. Acta, **49**, 21 (1981).
49. U. Thewalt. Z. Naturforsch. B: Anorg. Chem. Org. Chem. **37B**, 276 (1982).
50. J.M. Jolliffe, P.F. Kelly, and J.D. Woollins. J. Chem. Soc. Dalton Trans. 2179 (1989).
51. L.J. Matienzo, L.I. Yin, S.O. Grim, and E. Swartz. Inorg. Chem. **12**, 2762 (1973).
52. M. Bossa, C. Furlani, G. Mattogne, and E. Paparazzo. Inorg. Chim. Acta, **27**, 2117 (1978).

© 2002 NRC Canada

A theoretical study of the ^{77}Se NMR and vibrational spectroscopic properties of Se_nS_{8-n} ring molecules

J. Komulainen, R.S. Laitinen, and R.J. Suontamo

Abstract: The structures and spectroscopic properties of Se_nS_{8-n} ring molecules have been studied by the use of ab initio molecular orbital techniques and density functional techniques involving Stuttgart relativistic large core effective core potential approximation with double zeta basis sets for valence orbitals augmented by two polarization functions for both sulfur and selenium. Full geometry optimizations have been carried out for all 30 isomers at the Hartree–Fock level of theory. The optimized geometries and the calculated fundamental vibrations and Raman intensities of the Se_nS_{8-n} molecules agree closely with experimental information where available. The nuclear magnetic shielding tensor calculations have been carried out by the Gauge-independent atomic orbital method at the DFT level using Becke's three-parameter hybrid functional with Perdew/Wang 91 correlation. The isotropic shielding tensors correlate well with the observed chemical shift data. The calculated chemical shifts provide a definite assignment of the observed ^{77}Se NMR spectroscopic data and can be used in the prediction of the chemical shifts of unknown Se_nS_{8-n} ring molecules.

Key words: selenium sulfides, ab initio, DFT, effective core potentials, geometry optimization, energetics, fundamental vibrations, ^{77}Se chemical shifts.

Résumé : On a étudié les structures et les propriétés spectroscopiques de molécules cycliques de formule Se_nS_{8-n} en faisant appel à des techniques d'orbitales moléculaires ab initio et à des techniques de densité fonctionnelle impliquant l'approximation relativiste élevée de Stuttgart du potentiel effectif de coeur avec des ensembles doubles de bases zêta pour les orbitales de valence augmentées de deux fonctions de polarisation pour le soufre ainsi que le sélénium. On a réalisé des optimisations complètes de la géométrie pour chacun des trente isomères au niveau Hartree–Fock de la théorie. Les géométries optimisées ainsi que les vibrations fondamentales calculées et les intensités Raman des molécules de Se_nS_{8-n} sont en très bon accord avec les informations expérimentales disponibles. On a effectué des calculs de tenseur de blindage magnétique nucléaire en faisant appel à la méthode de l'orbitale moléculaire indépendante de Gauge, au niveau DFT, et à l'aide de trois paramètres fonctionnels hybrides avec corrélation de Perdew/Wang 91. Les tenseurs de blindage isotrope donnent une bonne corrélation avec les données de déplacements chimiques observés. Les déplacements chimiques observés fournissent une attribution définitive des données de spectroscopie RMN du ^{77}Se observées et peuvent être utilisés pour prédire les déplacements chimiques de molécules cycliques Se_nS_{8-n} inconnues.

Mots clés : sulfures de sélénium, ab initio, DFT, potentiels effectifs de coeur, optimisation de la géométrie, énergétiques, vibrations fondamentales, déplacements chimiques du ^{77}Se.

[Traduit par la Rédaction]

Introduction

It is well established that heteronuclear Se_nS_{8-n} ring molecules are formed in molten mixtures of sulfur and selenium or can be produced by a variety of synthetic routes (for a review see ref. 1). In most cases complicated molecular mixtures are formed, the characterization of which has turned out to be problematic. Because all crystal structures are disordered (2–11), X-ray crystallography has only demonstrated that the selenium sulfide phases contain crown-shaped ring molecules like S_8 (12–16) and Se_8 (17–20), but it has not been possible to identify individual molecular species or determine accurate bond parameters. Vibrational analysis has been used to assign the Raman spectra of 1,2,3-Se_3S_5 (8), 1,2,5,6-Se_4S_4 (9), and Se_7S (11) that are stoichiometrically pure or nearly so. While in more complicated mixtures it has not been possible to assign the Raman peaks to individual molecules, the force-field calculations have indicated the presence of Se—Se, Se—S, and S—S bonds in all sulfur-selenium mixtures even when the selenium content is low (21–24).

^{77}Se NMR spectroscopy is a powerful technique used to characterize selenium sulfide mixtures of complicated molecular composition (25–34). The assignment of the

Received 27 February 2002. Published on the NRC Research Press Web site at http://canjchem.nrc.ca on 25 October 2002.

Dedicated to Professor Tris Chivers for his contributions to Canadian chemistry.

J. Komulainen and R.S. Laitinen.[1] Department of Chemistry, P.O. Box 3000, 90014 University of Oulu, Finland.
R.J. Suontamo. Department of Chemistry, University of Jyväskylä, P.O. Box 35, 40350 Jyväskylä, Finland.

[1]Corresponding author (e-mail: risto.laitinen@oulu.fi).

 DOI: 10.1139/V02-153 © 2002 NRC Canada

Table 1. The abbreviated notation for the 30 Se_nS_{8-n} molecules.

S_8	SeS_7	1,2-Se_2S_6	1,2,3-Se_3S_5	1,2,3,4-Se_4S_4	1,2,3,4,5-Se_5S_3	1,2,3,4,5,6-Se_6S_2	Se_7S	Se_8
A_0	A_1	A_2	A_3	A_4	A_5	A_6	A_7	A_8
		1,3-Se_2S_6	1,2,4-Se_3S_5	1,2,3,5-Se_4S_4	1,2,3,4,6-Se_5S_3	1,2,3,4,5,7-Se_6S_2		
		B_2	B_3	B_4	**B_5**	B_6		
		1,4-Se_2S_6	1,2,5-Se_3S_5	1,2,3,6-Se_4S_4	1,2,3,5,6-Se_5S_3	1,2,3,4,6,7-Se_6S_2		
		C_2	C_3	C_4	C_5	C_6		
		1,5-Se_2S_6	1,3,5-Se_3S_5	1,2,4,5-Se_4S_4	1,2,3,5,7-Se_5S_3	1,2,3,5,6,7-Se_6S_2		
		D_2	D_3	D_4	D_5	D_6		
			1,4,6-Se_3S_5	1,2,4,6-Se_4S_4	1,2,4,6,7-Se_5S_3			
			E_3	E_4	E_5			
				1,2,4,7-Se_4S_4				
				F_4				
				1,2,5,6-Se_4S_4				
				G_4				
				1,3,5,7-Se_4S_4				
				H_4				

^{77}Se NMR chemical shifts and the identification of individual Se_nS_{8-n} molecules have been based on the coupling information from the spectra of ^{77}Se-enriched samples (enrichment 92%) and the comparison of the enriched spectra with those from the natural-abundance samples where coupling information is only seen by the appearance of small satellites because of the low abundance of the ^{77}Se isotope. However, there remain several resonances in the ^{77}Se NMR spectra of the selenium sulfide phases, the assignment of which is only tentative (26).

While there are numerous MO calculations for S_8 at different levels of theory, the computational information for Se_8 is much sparser (see refs. 1, 35, and 36, and references therein). Theoretical studies of heterocyclic Se_nS_{8-n} mainly comprise the use of semi-empirical calculations in an attempt to assign the photoelectron spectrum of a binary selenium sulfide phase obtained from the equimolar melt (37), as well as the density functional calculations on geometries and the relative stabilities of the isomers of Se_2S_6 and Se_6S_2 (38). Recently we have explored the geometries and energetics of the whole series of thirty 8-membered selenium sulfide ring molecules by use of ab initio techniques involving split valence MIDI-4* basis sets for sulfur and selenium (39).

The goal of the present study is to gain theoretical support for the assignment of the ^{77}Se chemical shifts of the Se_nS_{8-n} ring molecules by MO techniques and to provide a definitive assignment for all the resonances observed by ^{77}Se NMR spectroscopy. Several theoretical calculations of ^{77}Se shielding constants and chemical shifts have been reported (see for instance refs. 40–42). It has been shown that accurate chemical shift calculations require large basis sets augmented by polarization functions with the effects of electron correlation taken into account. These kinds of calculations are very time consuming in the case of Se_nS_{8-n} molecules. Schreckenbach and Ziegler (43) have, however, demonstrated that the relative magnitudes of the ^{77}Se shielding tensors and chemical shifts can be calculated reliably using density functional theory and the frozen-core approximation. Se_nS_{8-n} ring molecules form a uniform homologous series (39), and the pseudopotential approach might well be suitable for extracting a definite interpretation of the ^{77}Se NMR spectrum of this complicated molecular system.

Calculations

The ab initio MO calculations of the 30 Se_nS_{8-n} ring molecules (see Table 1) have been carried out using the Stuttgart relativistic large core effective core potential approximation (RLC ECP) (44–46) by augmenting the double-zeta quality basis sets of the valence orbitals by two polarization functions (47). Full geometry optimizations and fundamental vibrations have been carried out at the RHF level of theory using gradient techniques. The fundamental vibrations and the zero point energies (ZPE) of the molecules were scaled by 0.8929 to eliminate systematic errors (48). The relative energies of the molecules were explored by calculating the total energies of the molecules at the DFT level of theory involving Becke's three-parameter hybrid functionals with the Perdew/Wang 91 correlation (B3PW91) (49–55) and using the HF-optimized geometries. The nuclear magnetic shielding tensor calculations were carried out using the Gauge-independent atomic orbital method (GIAO) (56–59) at the B3PW91 level of theory. All calculations were carried out with the GAUSSIAN 98 series of programs (60).

Results and discussion

Optimized geometries of Se_nS_{8-n}

The optimized bond lengths, bond angles, and dihedral angles of all 30 Se_nS_{8-n} molecules are presented in Table 2. The calculated S—S bond lengths range from 2.052 to 2.056 Å, the Se—S bond lengths show a range of 2.196–2.203 Å, and the Se—Se bonds vary between 2.332 and 2.338 Å. These values represent single bond lengths and are in excellent agreement with the experimental bond lengths in S_8 (12–16) and Se_8 (17–20). There is no experimental information of the bond lengths in heterocyclic Se_nS_{8-n} molecules. The calculated values, however, can be compared with the experimental Se—S bond lengths of 2.153(4)–2.181(3) Å observed in the $[(O_3S)SeS(SO_3)]^{2-}$ anion (61, 62).

The calculated bond angles of sulfur range from 107.33 to 108.03° and those of selenium from 104.91 to 105.85°. The torsional angles of all bonds in every molecule lie within a narrow range of 96.0 to 104.1°. Both the bond angles and

© 2002 NRC Canada

Table 2. The optimized geometries of the Se_nS_{8-n} molecules.[a]

Molecule	Parameter	A_n[b]	B_n[b]	C_n[b]	D_n[b]	E_n[b]	F_n[b]	G_n[b]	H_n[b]
S_8[c]	$r_{S—S}$ (Å)	2.053							
	$\alpha_{E\text{-}S\text{-}E}$ (°)	107.33							
	τ (°)	99.5							
SeS_7	$r_{S—S}$ (Å)	2.052–2.055							
	$r_{Se—S}$ (Å)	2.198							
	$\alpha_{E\text{-}S\text{-}E}$ (°)	107.35–107.57							
	$\alpha_{E\text{-}Se\text{-}E}$ (°)	104.91							
	τ (°)	98.0–101.9							
Se_2S_6	$r_{S—S}$ (Å)	2.053–2.056	2.054–2.055	2.052–2.055	2.053				
	$r_{Se—S}$ (Å)	2.200	2.197–2.198	2.197–2.199	2.199				
	$r_{Se—Se}$ (Å)	2.332							
	$\alpha_{E\text{-}S\text{-}E}$ (°)	107.38–107.72	107.44–107.80	107.38–107.55	107.66–107.61				
	$\alpha_{E\text{-}Se\text{-}E}$ (°)	104.95	104.95	105.20	105.18				
	τ (°)	96.4–104.0	97.7–101.9	98.3–101.7	99.6–100.4				
Se_3S_5	$r_{S—S}$ (Å)	2.054–2.055	2.052–2.056	2.052–2.054	2.054	2.056			
	$r_{Se—S}$ (Å)	2.199	2.197–2.201	2.198–2.201	2.197–2.199	2.196–2.199			
	$r_{Se—Se}$ (Å)	2.334	2.331	2.333					
	$\alpha_{E\text{-}S\text{-}E}$ (°)	107.61–107.92	107.46–107.77	107.38–107.76	107.44–107.79	107.54–107.63			
	$\alpha_{E\text{-}Se\text{-}E}$ (°)	105.00–105.01	105.00–105.25	105.22–105.45	104.94–105.15	105.21–105.49			
	τ (°)	96.3–104.0	96.9–103.9	98.8–102.6	98.1–101.9	98.6–101.6			
Se_4S_4	$r_{S—S}$ (Å)	2.053–2.055	2.053–2.055	2.054	2.052	2.054	2.057	2.052	
	$r_{Se—S}$ (Å)	2.200	2.198–2.200	2.198–2.199	2.199–2.203	2.196–2.200	2.197–2.201	2.200	2.198
	$r_{Se—Se}$ (Å)	2.333–2.336	2.333–2.335	2.335	2.332	2.333	2.331	2.335	
	$\alpha_{E\text{-}S\text{-}E}$ (°)	107.73–107.88	107.65–107.96	107.57–107.75	107.46–107.72	107.51–107.84	107.62–107.71	107.58	107.90
	$\alpha_{E\text{-}Se\text{-}E}$ (°)	105.06–105.30	105.02–105.46	105.27–105.31	105.30–105.48	105.22–105.54	105.26–105.50	105.50	105.18
	τ (°)	96.0–104.1	96.6–103.8	98.6–102.6	97.9–102.7	98.4–102.4	97.3–103.8	99.8–101.0	100.5
Se_5S_3	$r_{S—S}$ (Å)	2.053	2.055	2.053					
	$r_{Se—S}$ (Å)	2.201	2.198–2.200	2.198–2.201	2.196–2.200	2.197–2.202			
	$r_{Se—Se}$ (Å)	2.334–2.335	2.332–2.337	2.334–2.337	2.334	2.332			
	$\alpha_{E\text{-}S\text{-}E}$ (°)	107.83–107.92	107.68–107.91	107.65–107.76	107.86–108.03	107.58–107.79			
	$\alpha_{E\text{-}Se\text{-}E}$ (°)	105.11–105.51	105.27–105.68	105.29–105.74	105.24–105.63	105.46–105.54			
	τ (°)	96.4–103.8	97.1–103.8	98.4–102.6	99.1–102.6	99.5–102.3			
Se_6S_2	$r_{S—S}$ (Å)	2.054							
	$r_{Se—S}$ (Å)	2.200	2.198–2.201	2.199–2.201	2.199				
	$r_{Se—Se}$ (Å)	2.334–2.336	2.333–2.336	2.333–2.338	2.335				
	$\alpha_{E\text{-}S\text{-}E}$ (°)	107.85	107.99	107.76	107.82				
	$\alpha_{E\text{-}Se\text{-}E}$ (°)	105.37–105.75	105.34–105.63	105.51–105.74	105.48–105.85				
	τ (°)	97.0–103.8	98.9–102.7	99.3–102.5	100.6–101.1				
Se_7S	$r_{Se—S}$ (Å)	2.200							
	$r_{Se—Se}$ (Å)	2.224–2.337							
	$\alpha_{E\text{-}S\text{-}E}$ (°)	107.93							
	$\alpha_{E\text{-}Se\text{-}E}$ (°)	105.57–105.84							
	τ (°)	99.2–102.6							
Se_8[d]	$r_{Se—Se}$ (Å)	2.336							
	$\alpha_{E\text{-}Se\text{-}E}$ (°)	105.84							
	τ (°)	101.2							

[a]The basis sets consist of the Stuttgart relativistic large core effective core potential approximation (RLC ECP) (44–46) with the double zeta quality basis sets for valence shell orbitals augmented by two polarization functions.
[b]The subscrift *n* denotes the number of selenium atoms in the molecule.
[c]Experimental bond parameters of S_8: $r_{S—S}$ = 2.023–2.060 Å, α_S = 105.8–109.0°, τ = 96.4–101.3° (12–16).
[d]Experimental bond parameters of Se_8: $r_{Se—Se}$ = 2.334–2.340 Å, α_S = 105.7–105.8°, τ = 101.0–101.4° (17–19).

the torsional angles also agree with the experimental values from S_8 (12–16) and Se_8 (17–20).

While our previous HF/MIDI-4* calculations slightly overestimate the chalcogen–chalcogen bond lengths (39), they are generally consistent with the present calculations for the Se_nS_{8-n} molecules.

Vibrational spectra of Se_nS_{8-n}

The calculated frequencies are all real, indicating that each molecule lies at a local energy minimum. The Raman spectra of S_8 (63), SeS_7 (23), 1,2,3-Se_3S_5 (8), 1,2,5,6-Se_4S_4 (9), Se_7S (11), and Se_8 (64) have been reported and can be compared with the calculated fundamental vibrations (see Table 3).

© 2002 NRC Canada

Table 3. Calculated fundamental vibrations ($\tilde{\nu}_{HF}$) and the Raman spectra ($\tilde{\nu}_{R}$) of S_8, SeS_7, 1,2,3-Se_3S_5, 1,2,5,6-Se_4S_4, Se_7S, and Se_8.[a]

S_8 (D_{4d})			SeS_7 (C_s)			1,2,3-Se_3S_5 (C_s)			1,2,5,6-Se_4S_4 (D_2)			Se_7S (C_s)				Se_8 (D_{4d})		
$\tilde{\nu}_{HF}$[a] (cm^{-1})	I_{HF}[b] (%)	$\tilde{\nu}_{R}$[c] (cm^{-1})	$\tilde{\nu}_{HF}$[a] (cm^{-1})	I_{HF}[b] (%)	$\tilde{\nu}_{R}$[d] (cm^{-1})	$\tilde{\nu}_{HF}$[a] (cm^{-1})	I_{HF}[b] (%)	$\tilde{\nu}_{R}$[e] (cm^{-1})	$\tilde{\nu}_{HF}$[a] (cm^{-1})	I_{HF}[a] (%)	$\tilde{\nu}_{R}$[f] (cm^{-1})	$\tilde{\nu}_{HF}$[a] (cm^{-1})	I_{HF}[b] (%)	$\tilde{\nu}_{R}$[g] (cm^{-1})	I_{R}[g] (%)	$\tilde{\nu}_{HF}$[a] (cm^{-1})	I_{HF}[b] (%)	$\tilde{\nu}_{R}$[h] (cm^{-1})
$64e_2$	4	82.5 *w*	54*a*′	6	73	45*a*″	8		41*a*	4		31*a*″	5	28	35	31e_2	3	37*m*
153e_2	16	153 *s*	62*a*″	6	80	50*a*′	8	69*m*	43b_1	5		35*a*′	5			75e_2	13	75*m*
191e_1	—		130*a*′	19	137	100*a*′	24	106*s*	101*a*	18	99*m*	79*a*″	19	76	10	93e_1	—	—
214a_1	44	218.5*vs*	139*a*″	25	127	108*a*″	29	114*s*	102b_1	14	109*s*	80*a*′	21	89	23	105a_1	32	112*vs*
242e_3	3	245.5*vw*	163*a*′	12	152	134*a*′	24	137*m*	120b_2	1	125*w*	97*a*″	1	96	9	117e_3	2	120*sh*
253b_2	—		183*a*″	1	180.5	154*a*′	23	154*m*	133b_3	4	137*w*	100*a*′	18	110	37	121b_2	—	—
463e_1	—		198*a*′	34	198	159*a*″	1	179*w*	156b_3	0	—	119*a*″	4			252a_1	100	253*vs*
465a_1	100	473*vs*	212*a*′	34	215	193*a*′	77	198*vs*	159*a*	61	168*vs*	119*a*′	29	125	36	253e_1	—	—
477b_1	—		238*a*″	3	243	212*a*″	9	217*w*	192b_1	7	188*w*	121*a*′	7			263e_2	4	259*w*
481e_3	18		245*a*′	1	243	236*a*′	3	252*m*	206b_2	1		161*a*′	10	161	8	264b_1	—	
481e_2	3		365*a*″	17	348	260*a*′	58	263*vs*	260b_2	13		253*a*′	100	257	100	265e_3	21	268*vw*
			377*a*′	60	383	264*a*″	24	—	264*a*	30	260*s*	254*a*″	1					
			463*a*′	100	441	369*a*″	11		367b_2	7		261*a*′	27					
			464*a*″	2	423	372*a*′	100	361*s*	367*a*	100	353*vs*	263*a*″	4					
			475*a*′	17	467	461*a*′	99	465*s*	369b_2	20	368*sh*	265*a*″	21					
			478*a*″	10	465	471*a*″	3		373b_1	7		265*a*′	34					
			481*a*″	9	471	478*a*″	22		474b_3	18	458*w*	351*a*′	50	351	18			
			481*a*′	25	471	480*a*′	25		476*a*	10		383*a*″	sh	364	sh			

[a]The calculated wavenumbers have been multiplied by 0.8929 to eliminate systematic errors (48).
[b]Calculated Raman intensities.
[c]Ref. 63.
[d]Ref. 23.
[e]Ref. 8.
[f]Ref. 9.
[g]Ref. 11.
[h]Ref. 64.

© 2002 NRC Canada

Fig. 1. (*a*) Observed Raman spectrum of 1,2,3-Se_3S_5.[8] (Adapted with permission by VCH-Wiley). (*b*) Calculated HF/RLC ECP frequencies and Raman intensities of 1,2,3-Se_3S_5. (*c*) Observed Raman spectrum of 1,2,5,6-Se_4S_4.[9] (Adapted with permission by American Chemical Society). (*d*) Calculated HF/RLC ECP frequencies and Raman intensities of 1,2,5,6-Se_4S_4.

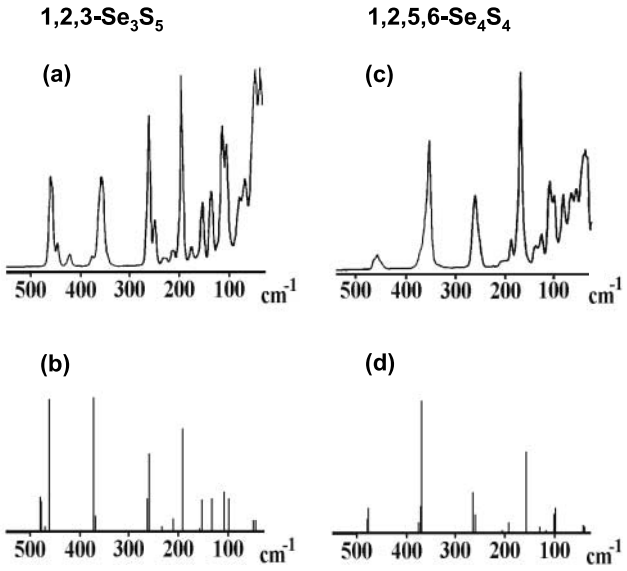

It has been shown in Fig. 1 for 1,2,3-Se_3S_5 and 1,2,5,6-Se_4S_4 that there is a good agreement not only between the observed and HF/RLC ECP calculated frequencies but also between the observed and calculated Raman intensities. The spectral assignments obtained by the present calculations are also consistent with those based previously on the normal coordinate treatment (8, 22, 23). The calculated HF/RLC ECP fundamental vibrations can therefore form a basis for the assignment and identification of unknown eight-membered selenium sulfide ring molecules.

Energetics

The total energies of all Se_nS_{8-n} molecules are presented in Table 4. The total binding energies have been discussed at the B3PW91 level and are shown in Fig. 2. All molecules are stable with respect to free atoms. It can also be seen from Fig. 2 that the binding energy and therefore the stability of the species decrease with increasing selenium content. Qualitatively the predicted stabilities are consistent with those calculated previously at the MP2/MIDI-4* level of theory (39).

Compositions Se_2S_6, Se_3S_5, Se_4S_4, Se_5S_3, and Se_6S_2 lead to the possibility of isomerism. The relative stabilities of the different isomers can be calculated from B3PW91 total energies given in Table 4 and have been shown in Fig. 3. The zero-point energy and entropy contributions to relative energies are negligible. It can be seen that 1,2-Se_2S_6 (**A_2**), 1,2,3-Se_3S_5 (**A_3**), 1,2,3,4-Se_4S_4 (**A_4**), 1,2,3,4,5-Se_5S_3 (**A_5**), and 1,2,3,4,5,6-Se_6S_2 (**A_6**) are the most stable isomers within the given composition. They contain all selenium atoms and all sulfur atoms adjacent to each other, thereby maximizing the number of homonuclear bonds in the molecule and minimizing the number of heteronuclear Se—S bonds. This is in qualitative agreement with both the density functional

Table 4. Total energies and zero-point energies of Se_nS_{8-n} molecules.

Molecule		E(HF) (au)	E(B3PW91) (au)	ZPE [a] (au)
S_8	$\mathbf{A_0}$	–79.958348	–81.839302	0.012662
SeS_7	$\mathbf{A_1}$	–79.119371	–81.006366	0.011865
Se_2S_6	$\mathbf{A_2}$	–78.282136	–80.175108	0.011109
	$\mathbf{B_2}$	–78.280498	–80.173531	0.011062
	$\mathbf{C_2}$	–78.280480	–80.173614	0.011067
	$\mathbf{D_2}$	–78.280549	–80.173731	0.011075
Se_3S_5	$\mathbf{A_3}$	–77.445038	–79.343824	0.010356
	$\mathbf{B_3}$	–77.443394	–79.342323	0.010315
	$\mathbf{C_3}$	–77.443400	–79.342474	0.010322
	$\mathbf{D_3}$	–77.441784	–79.340798	0.010272
	$\mathbf{E_3}$	–77.441680	–79.340753	0.010270
Se_4S_4	$\mathbf{A_4}$	–76.608090	–78.512680	0.009607
	$\mathbf{B_4}$	–76.606443	–78.511226	0.009567
	$\mathbf{C_4}$	–76.606369	–78.511229	0.009568
	$\mathbf{D_4}$	–76.606434	–78.511272	0.009572
	$\mathbf{E_4}$	–76.604746	–78.509602	0.009524
	$\mathbf{F_4}$	–76.604704	–78.509574	0.009519
	$\mathbf{G_4}$	–76.606393	–78.511336	0.009577
	$\mathbf{H_4}$	–76.603172	–78.508162	0.009478
Se_5S_3	$\mathbf{A_5}$	–75.771274	–77.681708	0.008864
	$\mathbf{B_5}$	–75.769539	–77.680090	0.008817
	$\mathbf{C_5}$	–75.769537	–77.680193	0.008825
	$\mathbf{D_5}$	–75.767930	–77.678524	0.008777
	$\mathbf{E_5}$	–75.767868	–77.678509	0.008775
Se_6S_2	$\mathbf{A_6}$	–74.934491	–76.850675	0.008120
	$\mathbf{B_6}$	–74.932838	–76.849094	0.008073
	$\mathbf{C_6}$	–74.932786	–76.849078	0.008077
	$\mathbf{D_6}$	–74.932805	–76.849087	0.008080
Se_7S	$\mathbf{A_7}$	–74.097856	–76.019703	0.007377
Se_8	$\mathbf{A_8}$	–73.263009	–75.190447	0.006681

[a]The zero-point energies have been calculated at the HF level of theory and have been multiplied by 0.8929 to eliminate systematic errors (48).

Fig. 2. Total B3PW91 binding energies of 30 Se_nS_{8-n} ring molecules (in kJ mol^{-1}).

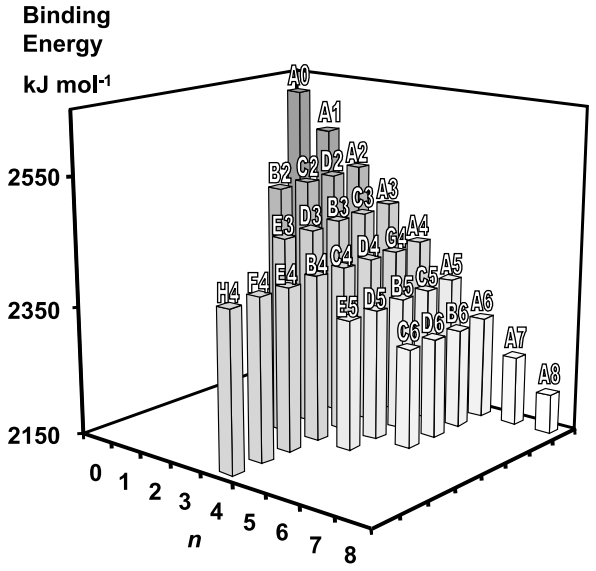

© 2002 NRC Canada

Fig. 3. Relative energies (in kJ mol^{-1}) of the different isomers of Se_2S_6, Se_3S_5, Se_4S_4, Se_5S_3, and Se_6S_2.

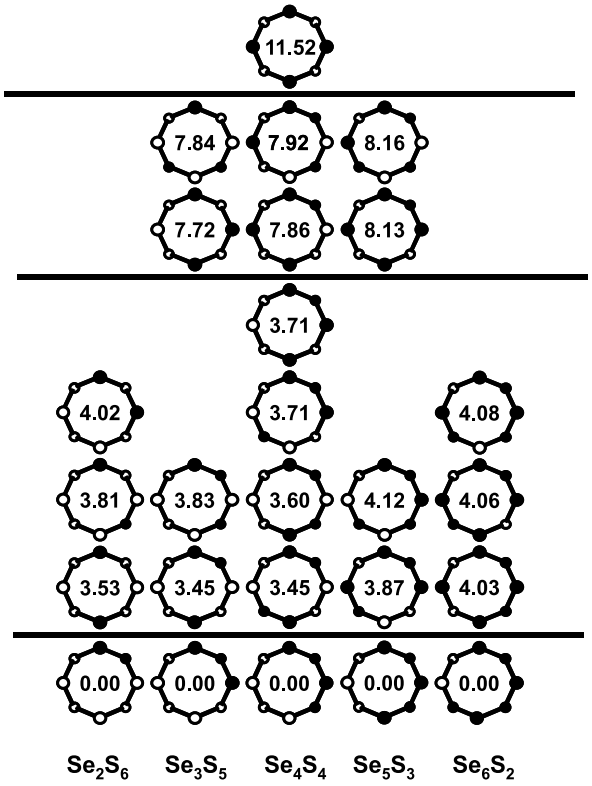

Fig. 4. The correlation of the calculated isotropic shielding tensors with the observed chemical shifts of Se_nS_{8-n} molecules for which the NMR spectroscopic information is unambiguous. The data points marked with ■ have been taken from ref. 26 and have been used in the least-squares fit. Those marked with ○ have been taken from refs. 9, 11, and 30, but they have not been used in the least-squares fit. The ^{77}Se chemical shifts are reported relative to neat Me_2Se ($\delta(Me_2Se) = \delta(SeO_2) + 1302.6$) (67).

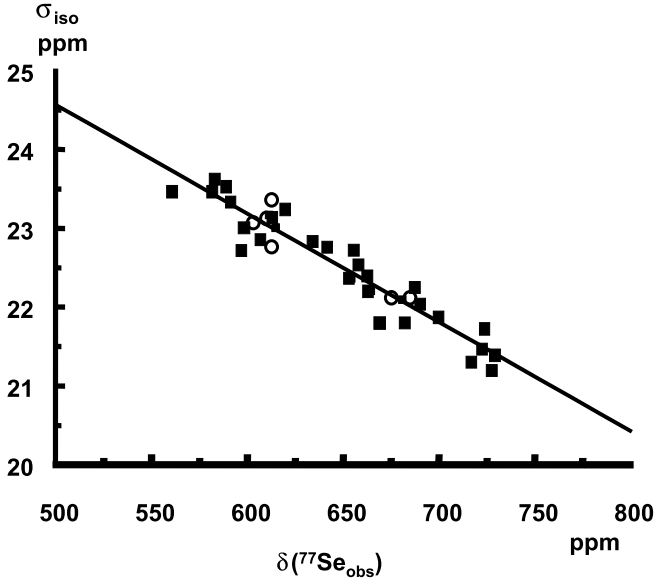

calculations on the energetics of Se_2S_6 and Se_6S_2 isomers (38) and our previous ab initio calculations on all Se_nS_{8-n} molecules (39). The highest relative stability of $\mathbf{A_2}$–$\mathbf{A_6}$ is also consistent with the Raman spectroscopic (21–24) and ^{77}Se NMR spectroscopic (26) observations that the most abundant species in the mixtures of eight-membered selenium sulfides have all selenium atoms and all sulfur atoms adjacent to each other.

The most stable isomers of Se_2S_6, Se_3S_5, Se_4S_4, Se_5S_3, and Se_6S_2 ($\mathbf{A_2}$–$\mathbf{A_6}$) each contain two heteronuclear Se—S bonds. It can be seen from Fig. 3 that the next most stable isomers (1,3-, 1,4-, and 1,5-isomers of Se_2S_6; 1,2,4- and 1,2,5-isomers of Se_3S_5; 1,2,3,5-, 1,2,3,6-, 1,2,4,5-, and 1,2,5,6-isomers of Se_4S_4; 1,2,3,4,6- and 1,2,3,5,6-isomers of Se_5S_3; 1,2,3,4,5,7-, 1,2,3,4,6,7-, and 1,2,3,5,6,7-isomers of Se_6S_2) each contain four Se—S bonds. They span a narrow energy range approximately 3.8(2) kJ mol^{-1} above the most stable isomer of the same chemical composition. An increment of ca. 4 kJ mol^{-1} is found in the energies of the isomers containing six Se—S bonds in the molecule (1,3,5- and 1,4,6-isomers of Se_3S_5; 1,2,4,6- and 1,2,4,7-isomers of Se_4S_4; 1,2,3,5,7- and 1,2,4,5,7-isomers of Se_5S_3). These isomers lie approximately 7.9(2) kJ mol^{-1} above the most stable isomers. The 1,3,5,7-Se_4S_4 isomer ($\mathbf{H_4}$), which contains eight Se—S bonds and lies 11.5 kJ mol^{-1} above the isomer $\mathbf{A_4}$, follows the same trend. These calculations indicate that the transformation of one Se—Se and one S—S bond into two Se—S bonds is an endothermic process with an energy difference of ca. 3.8 kJ mol^{-1}. It is in agreement with the earlier calculations (38, 39, 65) and is also consistent with the enthalpy of mixing of an equimolar sulfur–selenium melt of 1.3 kJ mol^{-1} (66) and with the reaction enthalpy of 5(3) kJ mol^{-1} (67), when 1 mol of $S_2(g)$ and $Se_2(g)$ is transformed into 2 mol of SeS(g). The maximum number of homonuclear bonds in the selenium sulfide rings can be rationalized by virtually identical electronegativities of sulfur and selenium, since the ionic contribution to heteronuclear bonding may be insufficient to compensate the orbital mismatch in size between sulfur and selenium.[2]

^{77}Se chemical shifts of Se_nS_{8-n}

The NMR shielding tensors of all selenium atoms in every Se_nS_{8-n} ring molecule have been calculated at the B3PW91 level using HF optimized geometries. While the present method does not provide for the absolute values of the shielding tensors, their relative values can be used to assign and predict the chemical shifts of Se_nS_{8-n} molecules that are a homologous series, the members of which have very similar molecular and electronic structures as well as chemical properties. The correlation between the calculated isotropic shielding tensors and the observed chemical shifts of the Se_nS_{8-n} molecules for which the chemical shift data are unambiguous (see ref. 26) is excellent, as shown in Fig. 4. The least-squares refinement of the calculated isotropic shielding tensors with the observed chemical shifts leads to the following relationship:

$$[1] \qquad \sigma_{iso} = -0.0138(8)\delta_{obs}(^{77}Se) + 31.5(5)$$

where σ_{iso} is the calculated B3PW91 isotropic shielding tensor and $\delta_{obs}(^{77}Se)$ is the observed chemical shift. The correlation

[2] We are grateful for the referee for his helpful comments regarding this point.

© 2002 NRC Canada

Table 5. Observed and calculated ^{77}Se chemical shifts of selected Se_nS_{8-n} ring molecules for which NMR spectroscopic information is unambiguous.

Molecule	Se atom position[a]	$\delta_{calc.}$ (ppm)[b]	$\delta_{obs.}$ (ppm)[c]	Molecule	Se atom position[a]	$\delta_{calc.}$ (ppm)[b]	$\delta_{obs.}$ (ppm)[c]
1,2,3-Se_3S_5 (**A_3**)[d]	1,3	661	654	1,2,4,5-Se_4S_4 (**D_4**)[d]	1,5	637	655
	2	551	561		2,4	680	681
1,2,4-Se_3S_5 (**B_3**)[d]	1	661	653	1,2,5,6-Se_4S_4 (**G_4**)[e]	1,2,5,6	637	656
	2	673	663	1,2,3,4,5-Se_5S_3 (**A_5**)[d]	1,5	650	658
	4	741	727		2,4	595	598
1,2,5-Se_3S_5 (**C_3**)[d]	1	601	620		3	617	591
	2	659	663	1,2,3,4,5,6-Se_6S_2 (**A_6**)[f]	1,6	684	695
	5	705	724		2,5	575	585
					3,4	628	608
				1,2,3,5,6,7-Se_6S_2 (**D_6**)[g]	1,3,5,7	687	669
1,2,3,4-Se_4S_4 (**A_4**)[d]	1,4	672	664		2,6	593	615
	2,3	586	582	Se_7S (**A_7**)[g]	1,7	699	682
1,2,3,5-Se_4S_4 (**B_4**)[d]	1	634	642		2,6	608	611
	2	582	589		3,5	606	597
	3	700	669		4	637	613
	5	723	722	Se_8 (**A_8**)[d]		617	615

[a]The numbering of the atoms starts from one selenium atom and proceeds around the ring molecule in such a fashion as to provide the lowest locants for all selenium atoms.
[b]The calculated chemical shifts have been obtained by the least-squares fit of the observed chemical shifts to the calculated isotropic shielding tensors. See Fig. 4 and eq. [1].
[c]The chemical shifts are reported relative to neat Me_2Se ($\delta(Me_2Se) = \delta(SeO_2) + 1302.6$) (67).
[d]For observed chemical shifts see ref. 26.
[e]For observed chemical shifts see ref. 9.
[f]For observed chemical shifts see ref. 30.
[g]For observed chemical shifts see ref. 11.

Fig. 5. The designation of the atomic positions relative to the active ^{77}Se nucleus.

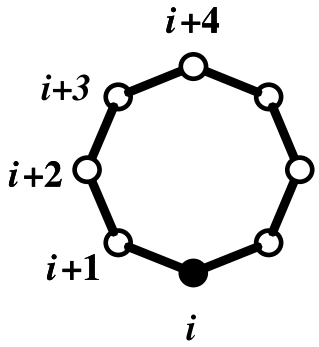

coefficient of the least-squares fit is –0.952. The comparison of the calculated and observed chemical shifts is presented in Table 5.

While the coupling information observed in the ^{77}Se-enriched samples (enrichment 92%) could be used in the assignment of most resonances observed in the CS_2 solution of the quenched molten mixtures of sulfur and selenium to individual Se_nS_{8-n} molecules, several resonances appear as singlets even in the enriched samples, implying chemical and magnetic equivalence (26). The tentative assignment of these singlets was based on the resonances of the species that could be isolated, on the qualitative consideration of the trends in the chemical shifts, and on the relative intensities of the signals as a function of the selenium content in different samples (25, 26). In some cases alternative assignments were considered possible (26).

Table 6. Assignment of the singlets.

Molecule	Se atom position[a]	$\delta_{calc.}$ (ppm)[b]	δ_{trnd} (ppm)[c]	$\delta_{obs.}$ (ppm)[d,e]
SeS_7 (**A_1**)	1	696	699	699
1,2-Se_2S_6 (**A_2**)	1,2	629	632	634
1,3-Se_2S_6 (**B_2**)	1,3	717	713	717
1,4-Se_2S_6 (**C_2**)	1,4	729	719	729
1,5-Se_2S_6 (**D_2**)	1,5	669	693	687

[a]The numbering of the atoms starts from one selenium atom and proceeds around the ring molecule in such a fashion as to provide the lowest locants for all selenium atoms.
[b]The calculated chemical shifts have been obtained by the least-squares fit of the observed chemical shifts to the calculated isotropic shielding tensors. See Fig. 4 and eq. [1].
[c]The δ_{trnd} values have been calculated by using eq. [2] by considering the relative orientations of selenium and sulfur atoms in the molecules.
[d]The chemical shifts are reported relative to neat Me_2Se ($\delta(Me_2Se) = \delta(SeO_2) + 1302.6$) (67). [e]For observed chemical shifts see ref. 26.

A quantitative relationship between the chemical shifts ($\delta_{trnd}(^{77}Se)$) and the relative locations of the sulfur and selenium atoms in the eight-membered ring molecules has recently been derived (33):

$$[2] \qquad \delta_{trnd}(^{77}Se) = -66.6n_1 + 14.2n_2 + 19.7n_3 + 6.0n_4 + 699.0$$

where n_1 is the number of selenium atoms adjacent to the active selenium nucleus (i) and n_2, n_3, and n_4 are the number of selenium atoms in the i+2, i+3, and i+4 positions, respectively (see Fig. 5). The tentative assignment of most singlets

© 2002 NRC Canada

Table 7. Predicted ^{77}Se chemical shifts for currently unknown Se_nS_{8-n} ring molecules.

Molecule	Se atom position[a]	$\delta_{calc.}$ (ppm)[b]	Molecule	Se atom position[a]	$\delta_{calc.}$ (ppm)[b]
1,3,5-Se_3S_5 (**D_3**)	1,5	708.9	1,2,3,5,6-Se_5S_3 (**C_5**)	1	707.4
	3	767.5		2	559.0
1,4,6-Se_4S_4 (**E_3**)	1	756.4		3	667.6
	4,6	760.0		5	672.6
1,2,3,6-Se_4S_4 (**C_4**)	1,3	688.9		6	660.2
	2	523.1	1,2,3,5,7-Se_5S_3 (**D_5**)	1,3	674.7
	6	739.0		2	614.6
1,2,4,6-Se_4S_4 (**E_4**)	1	691.5		5,7	754.0
	2	646.3	1,2,4,5,7-Se_5S_3 (**E_5**)	1,5	680.0
	4	771.8		2,4	710.5
	6	740.4		7	780.9
1,2,4,7-Se_4S_4 (**F_4**)	1,2	701.0	1,2,3,4,5,7-Se_6S_2 (**B_6**)	1,5	688.2
	4,7	769.8		2,4	627.1
1,3,5,7-Se_4S_4 (**H_4**)	1,3,5,7	743.2		3	592.9
1,2,3,4,6-Se_5S_3 (**B_5**)	1	701.5		7	766.6
	2	560.1	1,2,3,4,6,7-Se_6S_2 (**C_6**)	1,4	716.3
	3	616.3		2,3	593.6
	4	708.2		6,7	692.7
	6	755.2			

[a]The numbering of the atoms starts from one selenium atom and proceeds around the ring molecule in such a fashion as to provide the lowest locants for all selenium atoms.

[b]The calculated chemical shifts have been obtained by the least-squares fit of the observed chemical shifts to the calculated isotropic shielding tensors. See Fig. 4 and eq. [2].

(26) could be confirmed, but a revision in the assignment of the resonances to Se_2S_6 had to be made (33). Verna and Rauchfuss (32) also proposed a similar modification in the assignment of resonances to the Se_2S_6 isomers. It can be seen from Table 6 that our present B3PW91 calculations unambiguously verify the revised assignments.

The present calculations can also be used to predict chemical shift data for species the formation of which has not yet been observed. The predicted values are shown in Table 7.

Conclusions

Eight-membered selenium sulfide ring molecules Se_nS_{8-n} form a uniform homologous series with similar molecular and electronic structures. In this contribution we have demonstrated that Hartree–Fock calculations employing Stuttgart relativistic large core effective core potentials with double zeta quality basis sets for valence orbitals augmented by two polarization functions for both sulfur and selenium can efficiently be used in reliable geometry predictions of the molecules. The calculated fundamental vibrations and Raman intensities agree closely with experimental information where available and can be used in the identification of hitherto unknown molecular species, provided that they can be prepared stoichiometrically pure or nearly pure.

The energetics of the Se_nS_{8-n} molecules have been calculated at the B3PW91 level using HF-optimized structures. All molecules are stable with respect to free atoms, but the stability of the molecules decreases with increasing selenium content. It has also been shown that in the case of the existence of several isomers the most stable isomer contains all sulfur and all selenium atoms adjacent to each other, thereby maximizing the number of homonuclear bonds and minimizing the number of heteronuclear bonds. The stability of the isomers of a same molecular composition decreases with increasing number of Se—S bonds.

The GIAO calculations at the B3PW91 level using HF-optimized geometries provided isotropic shielding tensors that correlated well with the observed chemical shift data. The calculated values provided the unambiguous definite assignment of the observed ^{77}Se NMR spectroscopic data and can be used in the prediction of the chemical shifts of unknown Se_nS_{8-n} ring molecules.

Acknowledgements

Financial support from the Academy of Finland and Ministry of Education of Finland (Chemistry Graduate School of Inorganic Materials) is gratefully acknowledged.

References

1. R.S. Laitinen, P. Pekonen, and R.J. Suontamo. Coord. Chem. Rev. **130**, 1 (1994).
2. T. Kawada, T. Matsunoto, H. Burzlaff, and E. Hellner. Acta Crystallogr. **A28**, S61 (1972).
3. J. Weiss. Z. Anorg. Allg. Chem. **435**, 113 (1977).
4. C. Calvo, R.J. Gillespie, J.E. Vekris, and N.N. Ng. Acta Crystallogr. **B34**, 911 (1978).
5. R. Laitinen, L. Niinistö, and R. Steudel. Acta Chem. Scand. **A33**, 737 (1979).
7. R.A. Boudereau and H.M. Haendler. J. Solid State Chem. **36**, 289 (1981).
8. R. Laitinen, N. Rautenberg, J. Steidel, and R. Steudel. Z. Anorg. Allg. Chem. **486**, 116 (1982).
9. D.M. Giolando, M. Papavassiliou, J. Pickardt, T.B. Rauchfuss, and R. Steudel. Inorg. Chem. **27**, 2596 (1988).

© 2002 NRC Canada

10. L.L. Hawes. Nature (London), **198**, 1267 (1963).
11. R. Steudel, M. Papavassiliou, and F. Baumgart. Z. Naturforsch. **46b**, 1674 (1991).
12. Y. Watanabe. Acta Crystallogr. **B30**, 1396 (1974).
13. L.K. Templeton, D.H. Templeton, and A. Zalkin, Inorg. Chem. **15**, 1999 (1976).
14. P. Coppens, Y.W. Yang, R.H. Blessing, W.F. Cooper, and F.K. Larsen. J. Am. Chem. Soc. **99**, 760 (1977).
15. L.M. Goldsmith and C.E. Strouse. J. Am. Chem. Soc. **99**, 7580 (1977).
16. S.J. Rettig and J. Trotter. Acta Crystallogr. **C43**, 2260 (1987).
17. P. Cherin and P. Unger. Acta Crystallogr. **B28**, 313 (1972).
18. R.E. Marsh, L. Pauling, and J.D. McCullough. Acta Crystallogr. **16**, 71 (1953).
19. O. Foss, and J.V. Janickis. J. Chem. Soc., Dalton Trans. 624 (1980).
20. A. Maaninen, J. Konu, R.S. Laitinen, T. Chivers, G. Schatte, J. Pietikäinen, and M. Ahlgren. Inorg. Chem. **40**, 3539 (2001).
21. H.H. Eysel and S. Sunder. Inorg. Chem. **18**, 2626 (1979).
22. R. Laitinen and R. Steudel. J. Mol Struct. **68**, 19 (1980).
23. H.H. Eysel. J. Mol. Struct. **78**, 203 (1982).
24. R. Frey and H.H. Eysel. Z. Anorg. Allg. Chem. **489**, 173 (1982).
25. R.S. Laitinen and T.A. Pakkanen. J. Chem. Soc., Chem. Commun. 1381 (1986).
26. R.S. Laitinen and T.A. Pakkanen. Inorg. Chem. **26**, 2598 (1987).
27. R.S. Laitinen, P. Pekonen, Y. Hiltunen, and T.A. Pakkanen. Acta Chem. Scand. **43**, 436 (1989).
28. R. Steudel, D. Jensen, and F. Baumgart. Polyhedron, **9**, 1199 (1990).
29. R. Steudel, B. Plinke, D. Jensen, and F. Baumart. Polyhedron, **10**, 1037 (1991).
30. P. Pekonen, Y. Hiltunen, R.S. Laitinen, and T.A. Pakkanen. Inorg. Chem. **30**, 3679 (1991).
31. T. Chivers, R.S. Laitinen, and K.J. Schmidt. Can. J. Chem. **70**, 719 (1992).
32. A.K. Verma and T.B. Rauchfuss. Inorg. Chem. **34**, 6199 (1995).
33. P. Pekonen, J. Taavitsainen, and R.S. Laitinen. Acta Chem. Scand. **52**, 1188 (1998).
34. A. Maaninen, T. Chivers, M. Parvez, J. Pietikäinen, and R.S. Laitinen. Inorg. Chem. **38**, 4093 (1999).
35. J. Cioslowski, A. Szarecka, and D. Moncrieff. J. Phys. Chem. A, **105**, 501 (2001).
36. J.-L.M. Abboung, M. Essefar, M. Herreros, O. Mó, M.T. Molina, R. Notario, and M. Yáñez. J. Phys. Chem. A, **102**, 7996 (1998).
37. A. Datta. J. Mol. Struct. **92**, 93 (1983).
38. R.O. Jones and D. Hohl. J. Am. Chem. Soc. **112**, 2590 (1990).
39. J. Taavitsainen, H. Lange, and R.S. Laitinen. THEOCHEM, **453**, 197 (1998).
40. M. Bühl, J. Gauss, and J.F. Stanton. Chem. Phys. Lett. **241**, 248 (1995), and refs. therein.
41. G. Schreckenbach, Y. Ruiz-Morales, and T. Ziegler. J. Chem. Phys. **104**, 8605 (1996), and refs. therein.
42. W. Nakanishi and S. Hayashi. J. Phys. Chem. A, **103**, 6074 (1999), and refs. therein.
43. G. Schreckenbach and T. Ziegler. Int. J. Quantum Chem. **60**, 753 (1996).
44. M. Bühl, W. Thiel, U. Fleischer, and W. Kutzelnigg. J. Phys. Chem. **99**, 4000 (1995).
45. W. Kuechle, M. Dolg, H. Stoll, and H. Preuß. Mol. Phys. **74**, 1245 (1991).
46. A. Bergner, M. Dolg, W. Küchle, H. Stoll, and H. Preuß. Mol. Phys. **80**, 1431 (1993).
47. S. Huzinaga (*Editor*). Gaussian basis sets for molecular calculations. Physical Science Data 16, Elsevier, Amsterdam. 1984.
48. J.A. Pople, H.B. Schlegel, R. Krishnan, J.S. Binkley, M.J. Frisch, R.A. Whiteside, R.F. Hout, and W.J. Hehre. Int. J. Quantum Chem. Symp. **15**, 269 (1981).
49. A.D. Becke. J. Chem. Phys. **98**, 5648 (1993).
50. K. Burke, J.P. Perdew, and Y. Wang. *In* Electronic density functional theory: Recent progress and new directions. *Edited by* J.F. Dobson, G. Vignale, and M.P. Das. Plenum, New York. 1998.
51. J.P. Perdew. *In* Electronic structure of solids '91. *Edited by* P. Ziesche and H. Eschrig. Akademie Verlag, Berlin. 1991.
52. J.P. Perdew and Y. Wang. Phys. Rev. **B45**, 13 244 (1992).
53. J.P. Perdew, J.A. Chevary, S.H. Vosko, K.A. Jackson, M.R. Pederson, D.J. Singh, and C. Fiolhais. Phys. Rev. **B46**, 6671 (1992).
54. J.P. Perdew, J.A. Chevary, S.H. Vosko, K.A. Jackson, M.R. Pederson, D.J. Singh, and C. Fiolhais. Phys. Rev. **B48**, 4978 (1993).
55. J.P. Perdew, K. Burke, and Y. Wang. Phys. Rev. **B54**, 16 533 (1996).
56. K. Wolinski, J.F. Hilton, and P. Pulay. J. Am. Chem. Soc. **112**, 8251 (1990).
57. K. Wolinski and A.J. Sadlej. Mol. Phys. **41**, 1419 (1980).
58. R. Ditchfield. Mol. Phys. **27**, 789 (1974).
59. R. McWeeny. Phys. Rev. **126**, 1028 (1962).
60. M.J. Frisch, G.W. Trucks, H.B. Schlegel, G.E. Scuseria, M.A. Robb, J.R. Cheeseman, V.G. Zakrzewski, J.A. Montgomery, R.E. Stratmann, J.C. Burant, S. Dapprich, J.M. Millam, A.D. Daniels, K.N. Kudin, M.C. Strain, O. Farkas, J. Tomasi, V. Barone, M. Cossi, R. Cammi, B. Mennucci, C. Pomelli, C. Adamo, S. Clifford, J. Ochterski, G.A. Petersson, P.Y. Ayala, Q. Cui, K. Morokuma, D.K. Malick, A.D. Rabuck, K. Raghavachari, J.B. Foresman, J. Cioslowski, J.V. Ortiz, B.B. Stefanov, G. Liu, A. Liashenko, P. Piskorz, I. Komaromi, R. Gomperts, R.L. Martin, D.J. Fox, T. Keith, M.A. Al-Laham, C.Y. Peng, A. Nanayakkara, C. Gonzalez, M. Challacombe, P.M.W. Gill, B.G. Johnson, W. Chen, M.W. Wong, J.L. Andres, M. Head-Gordon, E.S. Replogle, and J.A. Pople. GAUSSIAN 98, Revision A.7. Gaussian, Inc., Pittsburgh, Pa. 1998.
61. K. Marøy. Acta Chem. Scand. **26**, 45 (1972).
62. K. Bøyum and K. Marøy. Acta Chem. Scand. **25**, 2569 (1971).
63. R. Steudel and H.-J. Mäusle. Z. Naturforsch. **28b**, 951 (1978).
64. R. Steudel. Z. Naturforsch. **30**, 1481 (1975).
65. T. Maekawa, T. Yokokawa, and K. Niwa. Bull. Chem. Soc. Jpn. **46**, 761 (1973).
66. J. Drowart and S. Smoes. J. Chem. Soc., Faraday Trans. 2, 1755 (1977).
67. R.C. Burns, M.J. Collins, R.J. Gillespie, and G.J. Schrobilgen. Inorg. Chem. **25**, 4465 (1986).

© 2002 NRC Canada

Pentafluorophenyl and phenyl substituted azidoborates

Wolfgang Fraenk, Thomas M. Klapötke, Burkhard Krumm, Heinrich Nöth, Max Suter, Martin Vogt, and Marcus Warchhold

Abstract: The azidoborates $[(C_6F_5)_{4-n}B(N_3)_n]^-$ (n = 1–3) (**1**–**3**) were synthesized by reacting the corresponding borane with $[R]N_3$ (R = Me_4N, Ph_4P). To study the influence of the electron withdrawing C_6F_5-substituent on the boron atom, $[Me_4N][(C_6H_5)_3BN_3]$ (**4**) was also prepared. All compounds were fully characterized by IR, Raman, and multinuclear NMR spectroscopy in addition to characterization by single crystal diffraction analyses.

Key words: azidoborate, pentafluorophenyl, multinuclear NMR spectroscopy, X-ray crystallography.

Résumé : Les borates d'azide $[(C_6F_5)_{4-n}B(N_3)_n]^-$ (n = 1–3) (**1**–**3**) ont été synthétisé à l'aide de la réaction du borane correspondant avec les azides $[R]N_3$ (R = Me_4N, Ph_4P). Afin d'étudier l'influence de l'électron accepteur du substituant C_6F_5 sur l'atome du bore $[Me_4N][(C_6H_5)_3BN_3]$ (**4**) a été aussi préparé. Tous les produits ont été complètement caractérisé à l'aide de la spectroscopie multinucléaire RMN, IR, Raman, et de la diffraction des rayons X.

Mots clés : azidoborate, pentafluorophenyle, spectroscopie multinucleaire RMN, diffraction des rayons X.

Introduction

The preparation, chemistry, and thermal decomposition of boron azides R_2BN_3, diazides $RB(N_3)_2$, and their pyridine adducts R_2BN_3·py, $RB(N_3)_2$·py (R = organic substituent) is well established (1, 2). However, it is surprising that only a few examples of azido borates $R_{4-n}B(N_3)_n^-$ (n = 1–3, R = organic substituent) are known.

The first reported azidoborate was the $B(N_3)_4^-$ anion in the form of its lithium and sodium salts (3). It was obtained either by reacting $LiBH_4$ with an excess of HN_3 or by the reaction of $B(N_3)_3$ prepared in situ with NaN_3. Recently, we re-examined the highly energetic $B(N_3)_4^-$ anion and demonstrated that the tetraazidoborate anion can be synthesized in an alternative route by the reaction of $tmpB(N_3)_2$ (tmp = 2,2,6,6-tetramethylpiperidino) with 2 equiv of HN_3 (4). To our knowledge, $BCl_3N_3^-$ is the only well-investigated azido borate besides $B(N_3)_4^-$ (5). $[Me_4N][BCl_3N_3]$ was prepared by reacting $[Me_4N]N_3$ with BCl_3. To suppress competitive reactions (ligand exchange of $BCl_3N_3^-$ into $(BCl_2N_3)_3$ and BCl_4^-), it is absolutely necessary to avoid any excess of BCl_3. Apparently the $BF_3N_3^-$ anion shows a similar tendency to competing reactions, and therefore $BF_3N_3^-$ and $BF_2(N_3)_2^-$ were detected only by their ^{19}F NMR resonances (6).

We recently reported the irreversible dimerization of $(C_6F_5)_2BN_3$ (7), the reversible trimerization of $C_6F_5B(N_3)_2$ (8), as well as of *o*-difluorophenyl- and *o*-fluorophenyl substituted boron azides and diazides (9). Now we present the preparation and characterization of several pentafluorophenyl substituted azidoborates $[(C_6F_5)_{4-n}B(N_3)_n]^-$ (n = 1–3) (**1**–**3**). To investigate the electron withdrawing effect of C_6F_5 substituents on boron and the attached azide, we also prepared the $[(C_6H_5)_3BN_3]^-$ anion (**4**). The azidoborates were obtained in high yields by the reaction of $[R]N_3$ (R = Me_4N, Ph_4P) with the corresponding borane $(C_6F_5)_{3-n}B(N_3)_n$ (n = 0–2) or $(C_6H_5)_3B$, respectively. In addition to spectroscopic characterization (multinuclear NMR, IR, and Raman), the structures of all compounds have been confirmed by single crystal X-ray diffraction.

Received 31 July 2001. Published on the NRC Research Press Web site at http://canjchem.nrc.ca on 29 October 2002.

Dedicated to Professor Tristram Chivers.

W. Fraenk, T.M. Klapötke,[1] B. Krumm, H. Nöth, M. Suter, M. Vogt, and M. Warchhold. Department of Chemistry, University of Munich, Butenandtstr. 5–13(D), D-81377 Munich, Germany.

[1]Corresponding author (e-mail: tmk@cup.uni-muenchen.de).

Results and discussion

As already mentioned, azidoborates are, in principle, accessible by two different methods. They can be prepared by the reaction of hydridoborates $[R_{4-n}BH_n]^-$ (n = 1–4; R = organic substituent) with HN_3 or by the reaction of boranes R_3B (R = organic substituent, halogen, azide, etc.) with ionic azides $[R]N_3$ (R = Na, K, Me_4N, etc.).

Because the first method requires a rather complicated synthesis of substituted hydridoborates, we decided to prepare the azidoborates **1**–**4** by the 1:1 reaction of $(C_6F_5)_{4-n}B(N_3)_n$ (n = 1–3) or Ph_3B with $[Me_4N]N_3$ (**1**, **4**) and $[Ph_4P]N_3$ (**2**, **3**) (eq. [1], [2]).

[1] $$(C_6F_5)_{4-n}B(N_3)_n + [R]N_3 \xrightarrow[CH_2Cl_2]{25°C} [R][(C_6F_5)_{4-n}B(N_3)_n]$$

(R = $[Me_4N]$, $[Ph_4P]$; n = 1–3 (**1**–**3**))

[2] $$(C_6H_5)_3B + [Me_4N]N_3 \xrightarrow[CH_2Cl_2]{25°C} [Me_4N][(C_6H_5)_3BN_3]$$

(**4**)

 DOI: 10.1139/V02-031 © 2002 NRC Canada

Fig 1. IR and Raman spectrum of $[Ph_4P][(C_6F_5)_2B(N_3)_2]$ (**2**).

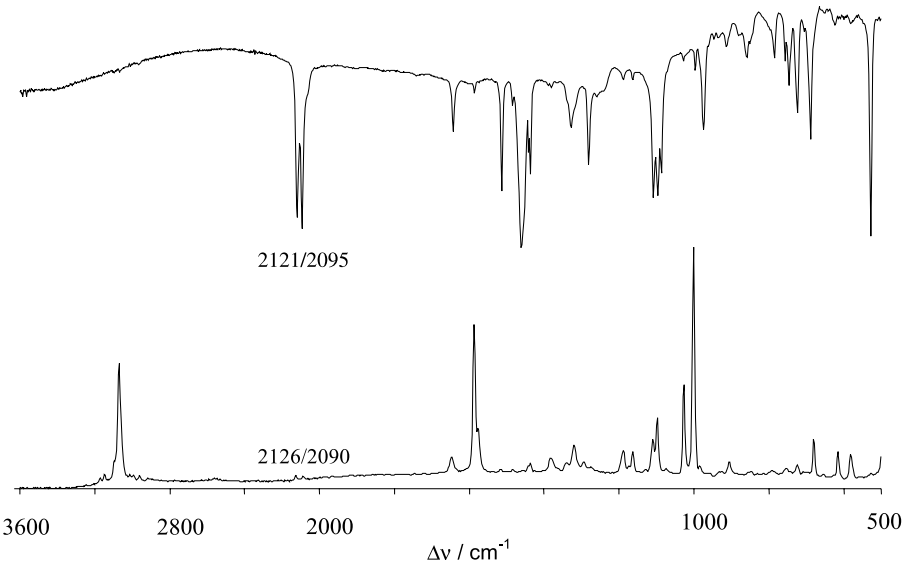

The boron azides $(C_6F_5)_2BN_3$ and $C_6F_5B(N_3)_2$ were prepared by the reaction of the corresponding boron chloride with Me_3SiN_3 and were reacted with $[R]N_3$ (R = Me_4N, Ph_4P). The tetraphenylphosphonium cation was selected for **2** and **3** to guarantee solubility in common organic solvents.

All salts were obtained as colorless, non-explosive solids that decompose only slowly in air with the exception of the triazidoborate **3**. This observation is in agreement with the properties observed for $Ph_{3-n}B(N_3)_n$·py (n = 1–3) (1). In contrast to Ph_2BN_3·py and $PhB(N_3)_2$·py, the azide rich $B(N_3)_3$·py is highly sensitive towards moisture. Whereas **1**–**3** are readily soluble in CH_2Cl_2 and $CHCl_3$, **4** is soluble only in more polar solvents such as CH_3CN and DMSO.

Spectra

All azidoborates discussed here show the characteristic antisymmetric stretching vibration of the azide group ($\upsilon_{asym}N_3$) in the typical region for covalent boron azides, which is around 2120 cm^{-1} in the vibrational spectra. The IR spectra are dominated by a very strong absorption of $\upsilon_{asym}N_3$, whereas the Raman spectra show $\upsilon_{asym}N_3$ as a peak of very weak intensity. As in most other boron azides, $\upsilon_{sym}N_3$ cannot be definitely assigned. Figure 1 depicts the IR and Raman spectra of **2** as a representative example.

Azidoborates (**1**–**4**) can be well characterized by multinuclear NMR spectroscopy because all nuclei (^{11}B, ^{19}F, ^{14}N, ^{13}C, ^{1}H) are NMR active. The ^{11}B NMR resonances of **1**–**4** are shifted to a higher field, as expected, in comparison with the corresponding borane and are observed in the region of tetra-coordinated boron (δ = –9 to –1) (10). The largest high-field shifts are observed for **1** and **4** (Δ 67 and 69 ppm). The ^{11}B NMR nucleus of **4** (δ = –1.0) is deshielded compared with **1** (δ = –9.0). This can be explained by the increased shielding effect of the pentafluorophenyl groups. A high-field shift relative to the corresponding borane is also observed in the ^{19}F NMR spectra for the resonances of the *o*-fluorine atoms in **1**–**3**, which is generally found for adducts of pentafluorophenyl substituted boranes (8, 11–13). The ^{14}N NMR spectra show three well-resolved resonances for the nitrogen atoms of the covalently bound azide groups in the expected area (14). To determine one exact chemical shift, the ^{15}N NMR spectrum of **3** was additionally recorded over a longer period. The resonances were found at δ = –140.1 (N_β), –207.8 (N_γ), and –311.0 (N_α), which are in excellent agreement with the corresponding ^{14}N NMR data. The ^{13}C NMR spectra all show, in addition to the signals for the *o*-, *m*-, and *p*-carbon atoms of the C_6F_5 and C_6H_5 substituents, the B-C resonances as broad signals in the region of δ = 121–117. Characteristic data of the reported pentafluorophenyl substituted boron azides and triphenylazidoborate **4** are summarized in Table 1.

Crystal structures

In addition to characterization by multinuclear NMR and vibrational spectroscopy, the molecular structures of the azidoborates have been determined by single crystal X-ray crystallography. The crystallographic data for **1**–**4** are summarized in Table 3.

In all structures, the boron atom is surrounded by four substituents in a slightly distorted tetrahedral fashion, as is expected (Figs. 2–6).

The azidoborate anions and the $[Me_4N]$ and $[Ph_4P]$ cations are spatially separated and therefore no interactions exist. For **1**–**3** the B—N_α bond lengths range from 1.584(4) to 1.545(7) Å and are slightly longer than the corresponding distances found for the $B(N_3)_4^-$ anion (4). The azide unit is slightly bent (176.5(3)–174.6(4)°), as is typical for covalent azides, and the B-N-N angle is on an average 120°. The N_α—N_β bond lengths (1.220(5)–1.193(5) Å) are longer than the N_β—N_γ bond lengths (1.140(4)–1.132(4) Å), which show considerable N—N triple bond character. Selected bond lengths and angles of structurally characterized C_6F_5-substituted boron azides are summarized in Table 2.

The packing diagram of **3** (Fig. 5) allows for the rationalization of its high kinetic stability. Although **3** has three covalently bound azide groups, it is insensitive to electrostatic discharge, friction, and impact, in contrast to the explosive $[C_6F_5B(N_3)_2]_3$. This can be explained by the fact that the large and bulky $[Ph_4P]$ cations separate the $C_6F_5B(N_3)_3$ an-

© 2002 NRC Canada

Table 1. Selected spectroscopic data of pentafluorophenyl substituted boron azides and $[Me_4N][(C_6H_5)_3BN_3]$ (**4**).

	δ ^{11}B	δ ^{19}F (*o*-F)	δ ^{14}N (N_β, N_γ, N_α)	$\upsilon_{asym}N_3$ (cm^{-1}) IR; Raman	mp. (°C)	Reference
$(C_6H_5)_3BN_3^-$ (**4**)[a]	–1.0	—	–135, –230, –300	2084; 2084	195–200	This work
$(C_6F_5)_3BN_3^-$ (**1**)[a]	–9.0	–135.3	–139, –217, –305	2113; 2118	179–180	This work
$[(C_6F_5)_2BN_3]_2$[b]	43.9	–131.4	–144, –160, –322	2202; 2208	76–80	7
$(C_6F_5)_2BN_3$·py	–0.5	–134.1	–144, –204, –308[c(i)]	2137; 2138	80–82	7
$(C_6F_5)_2B(N_3)_2^-$ (**2**)[d]	–3.0	–136.0	–140, –210, –310	2121, 2095; 2126, 2090	113–115	This work
$[C_6F_5B(N_3)_2]_3$[b,e]	34.6	–131.7	–149, –168, –277	2200, 2180, 2142; 2206, 2169, 2135	35–37	8
$C_6F_5B(N_3)_2$·py[c]	1.4	–135.4	–143, –201, –316[c(ii)]	2146, 2130; 2146, 2130	88–90	8
$C_6F_5B(N_3)_3^-$ (**3**)[d]	–1.0	–135.8	–140, –208, –310[f]	2132, 2109; 2143, 2131, 2115	98–101	This work

[a] $[Me_4N]$ salt; additional ^{14}N NMR resonance for $[Me_4N]$: δ: –338 (**1**, **4**).
[b] In solution monomer.
[c] Additional ^{14}N NMR resonance for N-py: (*i*) δ: –159; (*ii*) δ: –201.
[d] $[Ph_4P]$ salt.
[e] Raman (40°C): 2170, 2156 ($\upsilon_{asym}N_3$).
[f] ^{15}N NMR: δ: –140.1, –207.8, –311.0.

Table 2. Selected bond lengths (Å) and angles (°) of structurally characterized pentafluorophenyl substituted boron azides and $[Me_4N][(C_6H_5)_3BN_3]$ (**4**) (average values except for **1** and **4**).

	B—N	N_α—N_β	N_β—N_γ	N-N-N	B-N-N	Reference
$(C_6H_5)_3BN_3^-$ (**4**)[a]	1.601(2)	1.197(2)	1.141(2)	176.3(2)	122.6(1)	This work
$(C_6F_5)_3BN_3^-$ (**1**)[a]	1.584(4)	1.206(4)	1.137(4)	176.2(3)	122.4(3)	This work
$[(C_6F_5)_2BN_3]_2$	1.60	1.24	1.11	178	130	7
$(C_6F_5)_2B(N_3)_2^-$ (**2**)[b]	1.57	1.21	1.14	176	119	This work
$[C_6F_5B(N_3)_2]_3$[c]	1.50; 1.60	1.23; 1.27	1.13; 1.11	175; 179	121; 116	8
$C_6F_5B(N_3)_2$·py[d]	1.54	1.21	1.13	174	121	8
$C_6F_5B(N_3)_3^-$ (**3**)[b]	1.55	1.21	1.13	175	121	This work

[a] $[Me_4N]$ salt.
[b] $[Ph_4P]$ salt.
[c] Terminal; bridging azide groups.
[d] B—N_{py} 1.612(3) Å.

Fig 2. Molecular structure of the $[(C_6F_5)_3BN_3]$ anion of **1** with thermal ellipsoids drawn at the 25% probability level. The $[Me_4N]$ cation is omitted for clarity. Selected bond lengths (Å) and angles (°): B(1)—N(1) 1.584(4), N(1)—N(2) 1.206(4), N(2)—N(3) 1.137(4), B(1)—C(1) 1.641(4), B(1)—C(7) 1.646(4); N(1)-N(2)-N(3) 176.2(3), B(1)-N(1)-N(2) 122.4(3), (N1)-B(1)-C(1) 108.4(2), N(1)-B(1)-C(7) 102.6(2), N(1)-B(1)-C(13) 108.9(2).

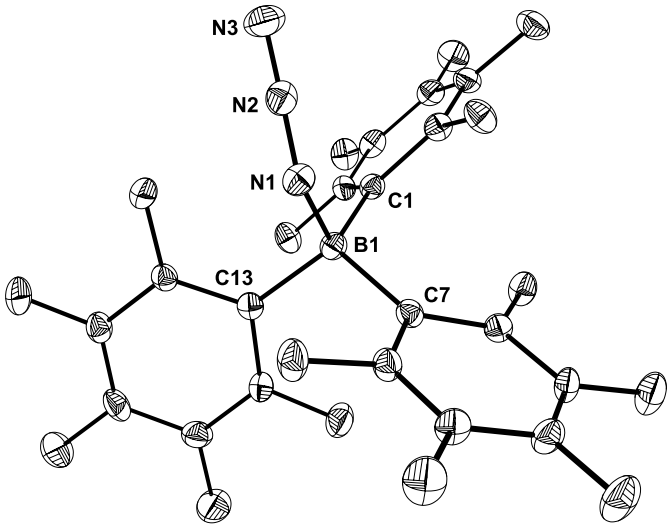

Fig 3. Molecular structure of the $[(C_6F_5)_2B(N_3)_2]$ anion of **2** with thermal ellipsoids drawn at the 25% probability level. The $[Ph_4P]$ cation is omitted for clarity. Selected bond lengths (Å) and angles (°): B(1)—N(1) 1.562(4), B(1)—N(4) 1.574(4), N(1)—N(2) 1.214(4), N(2)—N(3) 1.140(4), B(1)—C(1) 1.627(4), B(1)—C(7) 1.633(5); N(1)-N(2)-N(3) 176.5(3), B(1)-N(1)-N(2) 117.3(2), B(1)-N(4)-N(5) 120.6(3), N(1)-B(1)-N(4) 107.6(3), N(1)-B(1)-C(1) 105.3(2), C(1)-B(1)-C(7) 113.4(3).

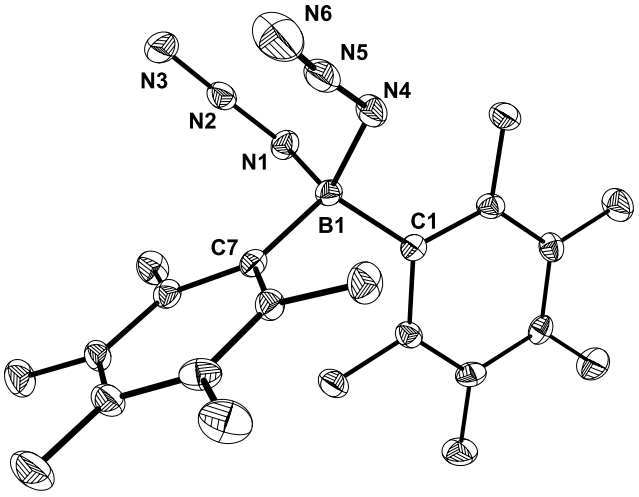

© 2002 NRC Canada

Table 3. Crystal data and structural refinements for **1**–**4**.

	1	**2**	**3**	**4**
Empirical formula	$C_{22}H_{12}BF_{15}N_4$	$C_{36}H_{20}BF_{10}N_6P$	$C_{30}H_{20}BF_5N_9P$	$C_{22}H_{27}BN_4$
Formula mass	628.17	768.36	643.33	358.29
Temperature (K)	188(2)	193(2)	200(2)	193(2)
Crystal size (mm)	0.50 × 0.20 × 0.20	0.20 × 0.20 × 0.20	0.25 × 0.08 × 0.04	0.30 × 0.20 × 0.10
Crystal system	Orthorhombic	Orthorhombic	Monoclinic	Monoclinic
Space group	$Pna2_1$	$Pna2_1$	$P2_1/c$	$I2/a$ [a]
a (Å)	16.307(1)	13.941(2)	7.5398(1)	15.752(5)
b (Å)	15.937(1)	31.081(5)	24.5964(4)	10.993(3)
c (Å)	9.4060(9)	7.748(1)	16.0799(3)[b]	23.012(8)[c]
V (Å^3)	2444.4(4)	3357.4(8)	2936.61(8)	3975(2)
Z	4	4	4	8
$D_{calcd.}$ (g cm^{-3})	1.707	1.520	1.455	1.198
Absorption coefficient (μ) (mm^{-1})	0.183	0.176	0.165	0.071
F(000)	1248	1552	1312	1536
θ range (°)	1.79–29.12	1.31–29.18	1.53–19.80	1.77–29.13
Index range	$-19 \le h \le 19$	$-17 \le h \le 16$	$-7 \le h \le 7$	$-20 \le h \le 19$
	$-21 \le k \le 19$	$-40 \le k \le 40$	$-23 \le k \le 23$	$-14 \le k \le 9$
	$-11 \le l \le 11$	$-10 \le l \le 10$	$-15 \le l \le 15$	$-28 \le l \le 29$
Reflections collected	13668	18972	35094	11417
Independent reflections	3752 (R_{int} = 0.0325)	6992 (R_{int} = 0.0568)	2664 (R_{int} = 0.1116)	3803 (R_{int} = 0.0395)
Observed reflections	3752	4554	2120	2397
Max and min transm.	0.9562 and 0.7615	0.9703 and 0.7104	0.9930 and 0.9719	0.9486 and 0.6117
Data/restraints/parameters	4937/1/404	6992/1/487	2664/0/415	3803/0/248
Goodness-of-fit on F^2	1.047	0.960	1.179	1.021
R_1, wR_2	0.0422, 0.0953	0.0469, 0.0791	0.0385, 0.0897	0.0480, 0.1151
	[$I > 4\sigma(I)$]	[$I > 4\sigma(I)$]	[$I > 2\sigma(I)$]	[$I > 4\sigma(I)$]
R_1, wR_2 (all data)	0.0652, 0.1057	0.0918, 0.0906	0.0612, 0.1179	0.0894, 0.1308
Largest diff. peak and hole (e Å^{-3})	0.404 and –0.269	0.207 and –0.213	0.317 and –0.411	0.168 and –0.184
Flack parameter	0.5(6)[d]	0.01(11)		

[a]The alternative cell choice *I*2/*a* was preferred, since it resulted in a smaller β-angle than *C*2/*c*.
[b]β = 100.0154(7).
[c]β = 94.139(5).
[d]Best value.

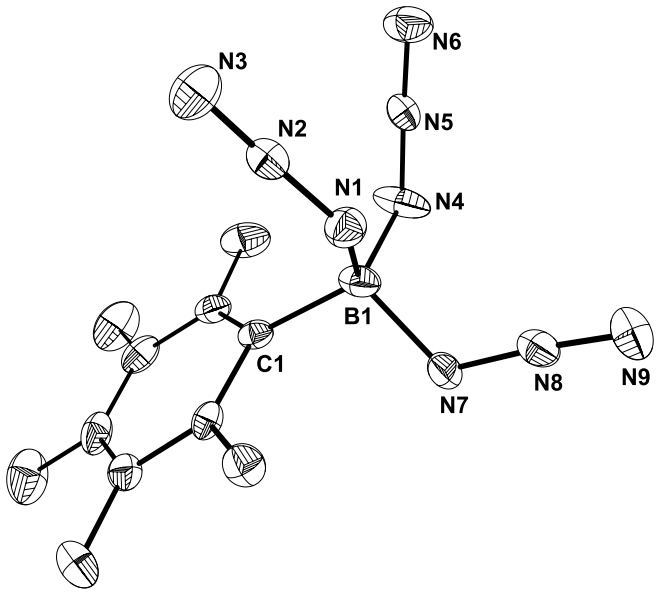

Fig 4. Molecular structure of the $[C_6F_5B(N_3)_3]$ anion of **3** with thermal ellipsoids drawn at the 25% probability level. The $[Ph_4P]$ cation is omitted for clarity. Selected bond lengths (Å) and angles (°): B(1)—N(1) 1.552(6), B(1)—N(4) 1.550(7), B(1)—N(7) 1.545(7), N(1)—N(2) 1.208(5), N(2)—N(3) 1.132(5), B(1)—C(1) 1.619(7); N(1)-N(2)-N(3) 174.6(4), B(1)-N(1)-N(2) 121.0(4), N(1)-B(1)-N(4) 109.9(4), N(1)-B(1)-N(7) 107.2(4), N(4)-B(1)-N(7) 106.6(4), N(1)-B(1)-C(1) 112.5(4), N(7)-B(1)-C(1) 107.0(4).

ions in the solid state and stop propagation of decomposition.

This observation has also been made for several binary azido-element anions such as $[Sn(N_3)_6]^{2-}$, $[Pb(N_3)_6]^{2-}$, $[As(N_3)_6]^-$, $[I(N_3)_2]^-$, and $[Au(N_3)_4]^-$ anions, which are kinetically stable as $[Ph_4P]$ and $[Ph_4As]$ salts despite possessing relatively high nitrogen contents (15–19).

Meanwhile, the results of a determination of the crystal structure of $[B(N_3)_4]^-$ as a tetraphenylphosphonium salt are also in agreement with the above species (20).

To investigate the difference between the C_6F_5- and the C_6H_5-substituents, the crystal structure of $[Me_4N][(C_6H_5)_3BN_3]$ (**4**) was determined (Fig. 6). The B(1)—N(1) distance is

© 2002 NRC Canada

Fig 5. View of the unit cell of **3** showing the separation of anion and cation.

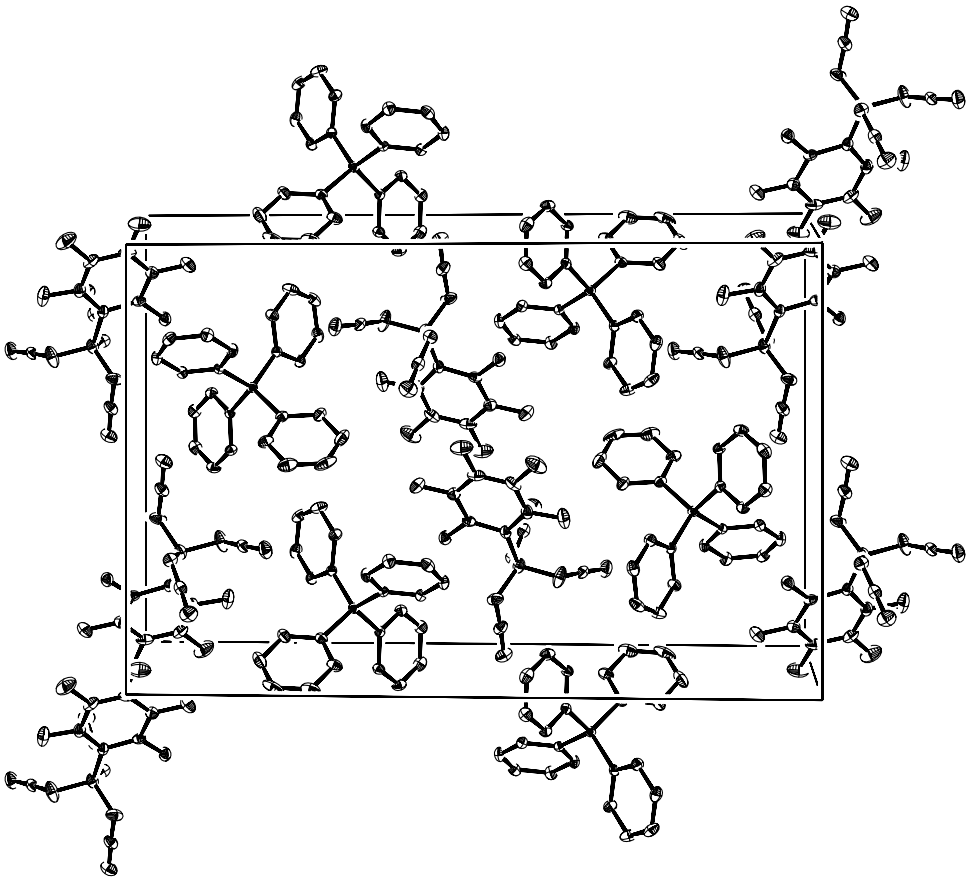

Fig 6. Molecular structure of the $[(C_6H_5)_3BN_3]$ anion of **4** with thermal ellipsoids drawn at the 25% probability level. The $[Me_4N]$ cation and hydrogen atoms are omitted for clarity. Selected bond lengths (Å) and angles (°): B(1)—N(1) 1.601(2), N(1)—N(2) 1.197(2), N(2)—N(3) 1.141(2), B(1)—C(1) 1.614(3), B(1)—C(7) 1.623(3); N(1)-N(2)-N(3) 176.3(2), B(1)-N(1)-N(2) 122.6(1), N(1)-B(1)-C(1) 104.9(1), N(1)-B(1)-C(7) 107.6(1), N(1)-B(1)-C(13) 109.0(1).

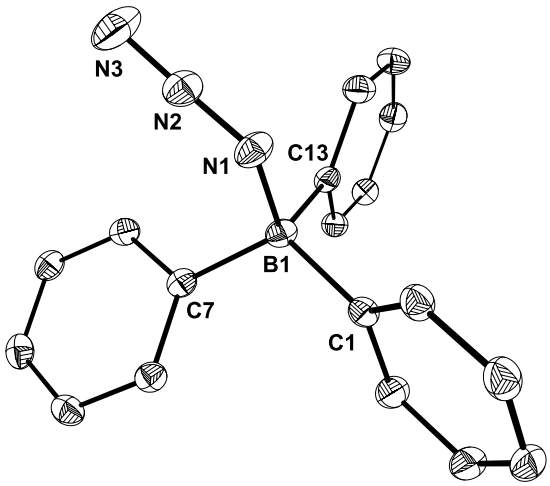

1.601(2) Å, slightly longer than the corresponding distance in **1** (1.584(4) Å). This can be explained by the fact that the electron withdrawing C_6F_5 substituents create a more Lewis acidic boron center than the C_6H_5 substituents, and therefore cause a shortening of the B—N_α bond length. In contrast, the N_α—N_β (1.197(2) and 1.206(4) Å) and N_β—N_γ (1.141(2) and 1.137(4) Å) bond lengths and the N-N-N (176.3(2) and 176.2(3)°) angles are almost identical.

Experimental

General

All manipulations of air- and moisture-sensitive materials were performed under an inert atmosphere of dry nitrogen using standard Schlenk techniques. Solvents were dried and degassed by standard methods prior to use. Raman spectra were recorded on a PerkinElmer 2000 NIR FT-Raman spectrometer fitted with a Nd-YAG laser (1064 nm) and infrared spectra on a PerkinElmer Spectrum One FT-IR spectrometer, as neat solids between KBr plates. The elemental analyses were performed with a C, H, N-Analysator Elementar Vario EL. NMR spectra were recorded on a JEOL Eclipse 400 instrument. Chemical shifts are recorded with respect to $(CH_3)_4Si$ (^1H, ^{13}C), $BF_3{\cdot}OEt_2$ (^{11}B), $CFCl_3$ (^{19}F), CH_3NO_2 (^{14}N), and H_3PO_4 (^{31}P). For the determination of the melting points, samples were heated in capillaries in a Büchi B540 instrument. C_6F_5H, C_6F_5Br, $[Me_4N]F$, $[Ph_4P]Br$, $AgNO_3$, Me_2SnCl_2, BCl_3 (1.0 M in hexane), Ph_3B, Me_3SiN_3, *n*-BuLi (2.5 M in hexane) were used as received (Aldrich, Fluka, FluoroChem). $[Me_4N]N_3$ (21), $[Ph_4P]N_3$ (22), $(C_6F_5)_2SnMe_2$

© 2002 NRC Canada

and $(C_6F_5)_2BCl$ (23), $C_6F_5BCl_2$ (11), and $(C_6F_5)_3B$ (12) were prepared as described in the literature.

X-ray crystallography

Data for **1**, **2**, and **4** were collected on a Siemens P4 instrument equipped with an area detector in the hemisphere mode, the data for **3** on a KappaCCD by using Mo Kα radiation. Data reduction was performed with the program SAINT. The structures were solved by direct methods (SHELXS-97 (24)) and data were refined by means of the full-matrix least squares on F^2 procedures using SHELXS-97 (Table 3).[2]

Preparations

Caution: Covalent azides are potentially explosive, AgN_3 is explosive; appropriate safety precautions are strongly advised.

$[Me_4N][(C_6F_5)_3BN_3]$ (1)

$[Me_4N]N_3$ (0.12 g (1.0 mmol)) was added to a stirred solution of 0.51 g (1.0 mmol) $(C_6F_5)_3B$ in 5 mL CH_2Cl_2 at ambient temperature. After stirring for 1 h the solvent was removed by vacuum evaporation. The remaining solid was purified by recrystallization from CH_2Cl_2 yielding **1** as colorless crystals. Yield: 0.50 g (80%); mp 179–180°C (decomp.).

IR (KBr pellet) (cm^{-1}): 3021 (vw), 3012 (vw), 2113 (vs, $\upsilon_{asym}N_3$), 1642 (s), 1513 (vs), 1486 (m), 1445 (vs), 1457 (vs), 1268 (s), 1090 (vs), 968 (vs), 945 (s), 859 (s), 799 (m), 769 (m), 740 (m), 687 (m), 666 (m), 615 (m), 572 (w), 476 (w). Raman (250 mW) (cm^{-1}): 3046 (2), 2988 (4), 2962 (2), 2929 (2), 2118 (1, $\upsilon_{asym}N_3$), 1646 (6), 1453 (5), 1383 (3), 1338 (3), 1113 (2), 949 (3), 862 (3), 803 (3), 772 (3), 752 (5), 705 (2), 583 (8), 493 (9), 478 (7), 448 (10), 425 (4), 403 (6), 391 (9), 353 (4), 310 (3), 287 (3), 250 (4), 217 (4), 148 (5). ^1H NMR (CD_2Cl_2) δ: 3.16 (s, CH_3). ^{13}C NMR (CD_2Cl_2) δ: 148.2 (m, C-2, $^1J_{CF}$ = 250.5 Hz), 139.1 (m, C-4, $^1J_{CF}$ = 249.4 Hz), 136.9 (m, C-3, $^1J_{CF}$ = 250.6 Hz), 121 (br, CB), 56.5 (t, Me_4N, $^1J_{C14N}$ = 4.0 Hz). ^{11}B NMR (CD_2Cl_2) δ: –9.0 (s). ^{19}F NMR (CD_2Cl_2) δ: –135.3 (m, *o*-F, 2F), –161.6 (t, *p*-F, 1F, $^3J_{FF}$ = 20.4 Hz), –166.7 (m, *m*-F, 2F). ^{14}N NMR (CD_2Cl_2, $\Delta\upsilon_{1/2}$/Hz) δ: –139 (120, N_β), –217 (250, N_γ), –305 (460, N_α), –338 (Me_4N). Anal calcd. for $C_{22}H_{12}BF_{15}N_4$ (628.15): C 42.1, H 1.9, N 8.9; found: C 41.1, H 2.0, N 8.1.

$[Ph_4P][(C_6F_5)_2B(N_3)_2]$ (2)

To a stirred solution of 0.38 g (1.0 mmol) $(C_6F_5)_2BCl$ in 10 mL CH_2Cl_2, 0.15 mL Me_3SiN_3 (1.1 mmol) and 0.38 g (1.0 mmol) $[Ph_4P]N_3$ were added at –78°C. After stirring at ambient temperature for 1.5 h all volatiles were removed in vacuo leaving a colorless oil. The oil was purified by recrystallization from a mixture of CH_2Cl_2 and *n*-hexane (~1:20). Colorless crystals were isolated and dried in vacuo. Yield: 0.65 g (85%); mp 113–115°C.

IR (KBr pellet) (cm^{-1}): 3068 (vw), 2121 and 2095 (vs, $\upsilon_{asym}N_3$), 1644 (m), 1586 (m), 1514 (s), 1461 (vs), 1442 (s), 1437 (m), 1379 (vw), 1329 (m), 1282 (s), 1258 (w), 1189 (vw), 1161 (vw), 1110 (vs), 1095 (vs), 1087 (vs), 1026 (w), 999 (w), 975 (s), 910 (w), 872 (vw), 858 (w), 846 (m), 784 (w), 753 (w), 724 (m), 688 (s), 624 (vw), 579 (vw), 528 (vs). Raman (150 mW) (cm^{-1}): 3147 (1), 3071 (5), 2126 and 2090 (1, $\upsilon_{asym}N_3$), 1646 (1), 1587 (7), 1436 (1), 1383 (1), 1320 (2), 1189 (2), 1163 (2), 1110 (2), 1098 (3), 1027 (4), 1001 (10), 905 (1), 724 (1), 680 (2), 616 (2), 581 (1), 494 (3), 447 (3), 395 (3), 351 (1), 293 (2), 246 (5), 198 (3), 167 (2), 117 (8). ^{13}C NMR (CD_2Cl_2) δ: 148.2 (dm, C-2, $^1J_{CF}$ = 250.2 Hz), 139.5 (dm, C-4, $^1J_{CF}$ = 251.7 Hz), 137.2 (dm, C-3, $^1J_{CF}$ = 253.3 Hz), 135.8 (dm, C-4, 1C, $^4J_{CP}$ = 3.1 Hz), 134.5 (d, C-3, $^3J_{CP}$ = 10.3 Hz), 130.9 (d, C-2, $^2J_{CP}$ = 12.6 Hz), 119 (br, CB), 118.0 (d, C-1, $^1J_{CP}$ = 89.0 Hz). $^{13}C\{^{19}F\}$ NMR (CD_2Cl_2) δ: 148.2 (s, C-2), 139.5 (s, C-4), 137.2 (s, C-3), 135.8 (dm, C-4, $^1J_{CH}$ = 127.8 Hz), 134.5 (dm, C-3, $^1J_{CH}$ = 128.0 Hz), 130.9 (dm, C-2, $^1J_{CH}$ = 160.0 Hz), 119 (br, CB), 118.0 (dm, C-1, $^1J_{CP}$ = 89.2 Hz). ^{11}B NMR (CD_2Cl_2) δ: –3.0 (s). ^{19}F NMR (CD_2Cl_2) δ: –136.0 (m, *o*-F, 2F), –160.9 (t, *p*-F, 1F, $^3J_{FF}$ = 20.4 Hz), –165.9 (m, *m*-F, 2F). ^{14}N NMR (CD_2Cl_2, $\Delta\upsilon_{1/2}$/Hz) δ: –140 (80, N_β), –210 (120, N_γ), –310 (500, N_α). ^{31}P NMR (CD_2Cl_2) δ: 25.0. Anal calcd. for $C_{36}H_{20}BF_{10}N_6P$ (768.36): C 56.2, H 2.6, N 10.9; found: C 55.9, H 2.7, N 10.7.

$[Ph_4P][C_6F_5B(N_3)_3]$ (3)

$[Ph_4P][C_6F_5B(N_3)_3]$ (**3**) was prepared from 0.25 g (1.0 mmol) $C_6F_5BCl_2$, 0.33 mL Me_3SiN_3 (2.6 mmol), and 0.38 g (1.0 mmol) $[Ph_4P]N_3$, following the method described for **2**. Yield: 0.52 g (80%); mp 98–101°C.

IR (KBr) (cm^{-1}): 3068 (m), 2132 and 2109 (vs, $\upsilon_{asym}N_3$), 1645 (m), 1587 (m), 1516 (s), 1483 (m), 1461 (vs), 1437 (s), 1385 (m), 1308 (s), 1281 (m), 1187 (m), 1108 (vs), 1097 (vs), 1026 (m), 996 (m), 975 (s), 885 (m), 854 (m), 753 (m), 723 (s), 688 (s), 632 (w), 606 (w), 590 (w), 527 (vs), 481 (w), 463 (w), 449 (w). Raman (150 mW) (cm^{-1}): 3069 (5), 2143, 2131, and 2115 (1, $\upsilon_{asym}N_3$), 1646 (1), 1588 (7), 1484 (1), 1437 (1), 1380 (1), 1332 (1), 1187 (2), 1165 (2), 1110 (2), 1099 (3), 1026 (4), 1001 (10), 946 (1), 750 (1), 724 (1), 680 (2), 616 (1), 581 (1), 494 (2), 464 (1), 447 (2), 429 (2), 395 (2), 351 (1), 292 (2), 250 (4), 232 (2). ^1H NMR (CD_2Cl_2) δ: 7.90 (m, *p*-H, 1H), 7.76 (m, *o*-H, 2H), 7.65 (m, *m*-H, 2H). ^{13}C NMR (CD_2Cl_2) δ: 148.0 (dm, C-2, $^1J_{CF}$ = 250.8 Hz), 139.5 (dm, C-4, $^1J_{CF}$ = 252.3 Hz), 137.0 (dm, C-3, $^1J_{CF}$ = 250.0 Hz), 135.6 (d, C-4, $^4J_{CP}$ = 3.1 Hz), 134.5 (d, C-3, $^3J_{CP}$ = 9.9 Hz), 130.6 (d, C-2, $^2J_{CP}$ = 12.2 Hz), 117.6 (d, $^1J_{CP}$ = 88.7 Hz), 117 (br, CB). ^{11}B NMR (CD_2Cl_2) δ: –1.0 (s). ^{19}F NMR (CD_2Cl_2) δ: –135.8 (m, *o*-F, 2F), –159.7 (t, *p*-F, 1F, $^3J_{FF}$ = 20.4 Hz), –165.3 (m, *m*-F, 2F). ^{14}N NMR (CD_2Cl_2, $\Delta\upsilon_{1/2}$/Hz) δ: –140 (50, N_β), –208 (90, N_γ), –310 (600, N_α). ^{15}N NMR (CD_2Cl_2) δ: –140.1 (N_β), –207.8 (N_γ), –311.0 (N_α). ^{31}P NMR (CD_2Cl_2) δ: 23.9. Anal. calcd.

[2] Supplementary data may be purchased from the Depository of Unpublished Data, Document Delivery, CISTI, National Research Council Canada, Ottawa, ON K1A 0S2, Canada (http://www.nrc.ca/cisti/irm/unpub_e.shtml for information on ordering electronically). CCDC 166892–166895 contain the supplementary data for this paper (excluding structure factors). These data can be obtained, free of charge, via www.ccdc.cam.ac.uk/conts/retrieving.html (or from the Cambridge Crystallographic Data Centre, 12 Union Road, Cambridge, U.K.; fax +44 1223 336033; or deposit@ccdc.cam.ac.uk).

© 2002 NRC Canada

for $C_{30}H_{20}BF_5N_9P$ (643.33): C 56.0, H 3.1, N 19.6; found: C 54.7, H 3.1, N 18.1.

[Me$_4$N][(C$_6$H$_5$)$_3$BN$_3$] (4)

4 was prepared from 0.24 g (1.0 mmol) Ph_3B and 0.12 g (1.0 mmol) $[Me_4N]N_3$ following the method described for **1**. Colorless crystals were obtained by recrystallization from CH_3CN. Yield: 0.31 g (85%); mp 195–200°C (decomp.).

IR (KBr) (cm^{-1}): 3061 (m), 3020 (m), 2084 (vs, $\upsilon_{asym}N_3$), 1480 (m), 1427 (w), 1314 (m), 1162 (m), 944 (m), 866 (m), 813 (m), 761 (m), 742 (m), 713 (m), 645 (m), 619 (m), 605 (m). Raman (250 mW) (cm^{-1}): 3045 (6), 3025 (3), 2973 (2), 2916 (1), 2084 (1, $\upsilon_{asym}N_3$), 1586 (4), 1563 (2), 1446 (1), 1316 (2), 1184 (1), 1120 (1), 1031 (3), 999 (10), 945 (1), 750 (1), 687 (1), 621 (1), 378 (1), 267 (3), 258 (3), 180 (2), 119 (9). ^{1}H NMR (CD_3CN) δ: 7.30 (dm, *o*-H, 2H), 7.13 (tm, *m*-H, 2H), 7.01 (tm, *p*-H, 1H), 2.94 (s, CH_3, 12H). ^{13}C NMR (CD_3CN) δ: 133.8 (s, C-2), 126.6 (s, C-4), 123.9 (s, C-3), 118 (br, CB), 55.4 (t, CH_3, $^1J_{C14N}$ = 4.2 Hz). ^{11}B NMR (CD_3CN) δ: –1.0 (s). ^{14}N NMR (DMSO-D_6, $\Delta\upsilon_{1/2}$/Hz) δ: –135 (130, N_β), –230 (210, N_γ), –300 (600, N_α), –338 (Me_4N). Anal. calcd. for $C_{22}H_{27}BN_4$ (358.30): C 73.8, H 7.6, N 15.6; found: C 72.0, H 7.8, N 15.6.

Conclusion

The first organo-substituted azidoborates $[(C_6F_5)_{4-n}B(N_3)_n]^-$ (n = 1–3) (**1**–**3**) and $[(C_6H_5)_3BN_3]^-$ (**4**) were isolated in high yields in a one-pot synthesis and structurally characterized, by reacting the corresponding boranes with $[R]N_3$ (R = Me_4N, Ph_4P). In contrast to $BCl_3N_3^-$ and $BF_3N_3^-$, **1**–**4** showed no substituent exchange reaction. A comparison of the crystal structures of $[(C_6F_5)_3BN_3]^-$ (**1**) and $[(C_6H_5)_3BN_3]^-$ (**4**) showed that the electronegative C_6F_5-substituent causes a (slight) shortening of the B—N_α bond length. The spatial separation of the anion and the rather bulky tetraphenylphosphonium cation explains the stability of **3**.

Acknowledgments

Financial support of this work by the University of Munich and the Fonds der Chemischen Industrie is gratefully acknowledged.

References

1. P.I. Paetzold. Fortschr. Chem. Forsch. **8**, 437 (1967).
2. P.I. Paetzold. Adv. Inorg. Chem. **31**, 123 (1987) and refs. therein.
3. E. Wiberg and H. Michaud. Z. Naturforsch. **96**, 497 (1954); **96**, 499 (1954).
4. W. Fraenk, T. Habereder, A. Hammerl, T.M. Klapötke, B. Krumm, P. Mayer, H. Nöth, and M. Warchhold. Inorg. Chem. **40**, 1334 (2001).
5. L. Chow and F. Schmock, U. Müller. Z. Naturforsch. **33b**, 1472 (1978).
6. S. Brownstein and G. Latremouille. Can. J. Chem. **56**, 2764 (1978).
7. W. Fraenk, T.M. Klapötke, B. Krumm, and P. Mayer. J. Chem. Soc. Chem. Commun. 667 (2000).
8. W. Fraenk, T.M. Klapötke, B. Krumm, H. Nöth, M. Suter, and M. Warchhold. J. Chem. Soc. Dalton Trans. 4635 (2000).
9. W. Fraenk, T.M. Klapötke, B. Krumm, P. Mayer, H. Nöth, H. Piotrowski, and M. Suter. J. Fluorine Chem. **112**, 73 (2001).
10. H. Nöth and B. Wrackmeyer. *In* Nuclear magnetic resonance, spectroscopy of boron compounds. Vol. 14. Springer Verlag, Berlin. 1978.
11. R.D. Chambers and T. Chivers. J. Chem. Soc. 3933 (1965).
12. H. Jacobsen, H. Berke, S. Döring, G. Kehr, G. Erker, R. Fröhlich, and O. Meyer. Organometallics, **18**, 1724 (1999).
13. W. Fraenk. Ph.D. thesis. Ludwig-Maximilians-Universität, München, Germany, 2001.
14. M. Witanowski, L. Stefaniak, and G. Webb. Annu. Rep. NMR Spectrosc. **18**, 486 (1986).
15. D. Fenske, H.D. Doerner, and K. Dehnicke. Z. Naturforsch. B, **38**, 1301 (1983).
16. K. Polborn, E. Leidl, and W. Beck. Z. Naturforsch. B, **43**, 1206 (1988).
17. T.M. Klapötke, H. Nöth, T. Schütt, and M. Warchhold. Angew. Chem. **112**, 2197 (2000); Angew. Chem. Int. Ed. Engl. **39**, 2108 (2000).
18. U. Müller, R. Dübgen, and K. Dehnicke. Z. Anorg. Allg. Chem. **463**, 7 (1980).
19. (*a*) W. Beck and H. Nöth. Chem. Ber. **117**, 419 (1984); (*b*) W. Beck, T.M. Klapötke, P. Klüfers, and C.M. Rienäcker, Z. Anorg. Allg. Chem. **627**, 1669 (2001).
20. W. Fraenk, T.M. Klapötke, H. Nöth, and M. Suter. Z. Naturforsch. **57b**, 621 (2002)
21. K.O. Christe, W.W. Wilson, R. Bau, and S.W. Bunte. J. Am. Chem. Soc. **114**, 3411 (1992).
22. B. Neumüller, F. Schmock, and K. Dehnicke. Z. Anorg. Allg. Chem. **625**, 1243 (1999).
23. D.J. Parks, W.E. Piers, and G.P. Yap. Organometallics, **17**, 5492 (1998).
24. G.M. Sheldrick. 1997. SHELXS-97-2 [computer program]. University of Göttingen, Germany.

© 2002 NRC Canada

Self-assembly using stannylplatinum(IV) halide complexes as ligands for organotin halides

Michael C. Janzen, Michael C. Jennings, and Richard J. Puddephatt

Abstract: The possibility of forming extended structures by self-association using transition metal halides as donors to organotin acceptors has been investigated. The stannylplatinum(IV) complex $[PtClMe_2(SnMe_2Cl)(bu_2bpy)]$ forms a 1:1 adduct $[PtClMe_2(SnMe_2Cl)(bu_2bpy)]\cdot Me_2SnCl_2$ with Me_2SnCl_2 in which the organoplatinum complex acts as a donor to the organotin halide. Similarly, $[PtClMe_2(SnMeCl_2)(bu_2bpy)]$ forms adducts $[PtClMe_2(SnMeCl_2)(bu_2bpy)]\cdot MeSnCl_3$ or $[PtClMe_2(SnMeCl_2)(bu_2bpy)]\cdot Me_2SnCl_2$, and $[\{PtClMe_2(bu_2bpy)\}_2(\mu\text{-}SnCl_2)]$ forms $[\{PtClMe_2(bu_2bpy)\}_2(\mu\text{-}SnCl_2)]\cdot Me_2SnCl_2$. Structure determinations on selected compounds show that the donor is the Pt-Cl group and the acceptor tin centre is 5-coordinate. In the similar bromo complex $[PtBrMe_2(SnMeBr_2)(bu_2bpy)]\cdot Me_2SnBr_2$ both the Pt-Br and PtSn-Br groups coordinate to the Me_2SnBr_2 acceptor with short (3.14 or 3.29 Å) and long (3.99 or 4.05 Å) contacts, respectively, so that the acceptor tin centre adopts distorted octahedral stereochemistry in the solid state and a folded polymeric structure is formed. Reaction of $[\{PtClMe_2(bu_2bpy)\}_2(\mu\text{-}SnCl_2)]$ with AgO_3SCF_3 yields the complex $[\{PtClMe_2(bu_2bpy)\}(\mu\text{-}SnCl_2)\{PtMe_2(bu_2bpy)O_3SCF_3\}]$, which is fluxional in solution.

Key words: platinum, tin, self-assembly, coordination chemistry, organometallics.

Résumé : On a étudié la possibilité de former des structures étendues par autoassociation en utilisant des halogénures de métaux de transition comme donneurs à des composés organostanniques agissant comme accepteurs. Le complexe stannylplatine(IV) $[PtClMe_2(SnMe_2Cl)(bu_2bpy)]$ et le Me_2SnCl_2 forment un adduit 1:1 $[PtClMe_2(SnMe_2Cl)(bu_2bpy)]\cdot Me_2SnCl_2$ dans le complexe organoplatine agit comme donneur pour l'halogénure d'organoétain. De la même manière, $[PtClMe_2(SnMeCl_2)(bu_2bpy)]$ forme les adduits $[PtClMe_2(SnMeCl_2)(bu_2bpy)]\cdot MeSnCl_3$ ou $[PtClMe_2(SnMeCl_2)(bu_2bpy)]\cdot Me_2SnCl_2$ alors que $[\{PtClMe_2(bu_2bpy)\}_2(\mu\text{-}SnCl_2)]$ forme $[\{PtClMe_2(bu_2bpy)\}_2(\mu\text{-}SnCl_2)]\cdot Me_2SnCl_2$. Des déterminations de structure effectuées sur des composés choisis montrent que le donneur est le groupe Pt-Cl et que le centre étain accepteur est pentacoordiné. Dans le complexe bromé semblable $[PtBrMe_2(SnMeBr_2)(bu_2bpy)]\cdot Me_2SnBr_2$ les deux groupes Pt-Br et PtSn-Br se coordonnent à l'accepteur Me_2SnBr_2 avec des contacts respectivement courts (3,14 ou 3,29 Å) et longs (3,99 ou 4,05 Å) qui font que le centre étain accepteur adopte une stéréochimie octaédrique déformée à l'état solide et qu'il y a formation d'une structure polymérique repliée. La réaction du $[\{PtClMe_2(bu_2bpy)\}_2(\mu\text{-}SnCl_2)]$ avec le AgO_3SCF_3 conduit à la formation du complexe $[\{PtClMe_2(bu_2bpy)\}_2(\mu\text{-}SnCl_2)\{PtMe_2(bu_2bpy)O_3SCF_3\}]$ qui, en solution, est en état de fluxion.

Mots clés : platine, étain, autoassemblage, chimie de coordination, organométalliques.

[Traduit par la Rédaction]

Introduction

The oxidative addition of the tin–halogen bond in organotin(IV) halides to transition-metal complexes is well established and provides an easy synthesis of stannylplatinum(IV) halides (1–7). For example, the oxidative addition of Me_3SnI to $[PtMe_2(bu_2bpy)]$ (**1**) (bu_2bpy = 4,4′-di-*tert*-butyl-2,2′-bipyridine) gives $[PtIMe_2(Me_3Sn)(bu_2bpy)]$ (1), which forms a complex $[PtIMe_2(SnMe_3)(bu_2bpy)]\cdot Me_3SnI$ by coordination of the Pt-I donor to the Me_3SnI acceptor, as shown in Scheme 1 (8). It was argued that the Pt-I group *trans* to Me_3Sn is polarized $Pt^{\delta+}\text{-}I^{\delta-}$, and as a result the iodide is a strong enough donor to form a complex with the weak acceptor Me_3SnI (9, 10). The platinum complex thus acts as a ligand for Me_3SnI through the Pt-I group.

Trimethyltin iodide is a tetrahedral monomer in the solid state, but many other organotin halides undergo self-association in the solid state (9–11). For example, Me_2SnCl_2 self-associates to form one-dimensional chains (Sn—Cl = 2.40(4) Å, Sn···Cl = 3.54(5) Å), and $MeSnCl_3$ also undergoes association by weak bridging through two of the three chlorine atoms (Sn—Cl = 2.283(2) Å, 2.318(1) Å; Sn···Cl = 3.714(2) Å) as illustrated in Chart 1 below (12, 13). The dimethyltin dihalides can also form adducts with one or two halide ions in which the tin centres adopt distorted trigonal bipyramidal or octahedral stereochemistry, respectively (Chart 1); they are stronger acceptors than the trimethyltin halides (14).

Based on the structures shown in Scheme 1 and Chart 1, it was considered possible that association between stannyl-

Received 20 January 2002. Published on the NRC Research Press Web site at http://canjchem.nrc.ca on 30 October 2002.

Dedicated to Professor Tris Chivers for his contributions to Canadian chemistry.

M.C. Janzen, M.C. Jennings, and R.J. Puddephatt.[1] Department of Chemistry, The University of Western Ontario, London, ON N6A 5B7, Canada.

[1]Corresponding author (e-mail: pudd@uwo.ca).

 DOI: 10.1139/V02-093 © 2002 NRC Canada

Scheme 1. S = solvent.

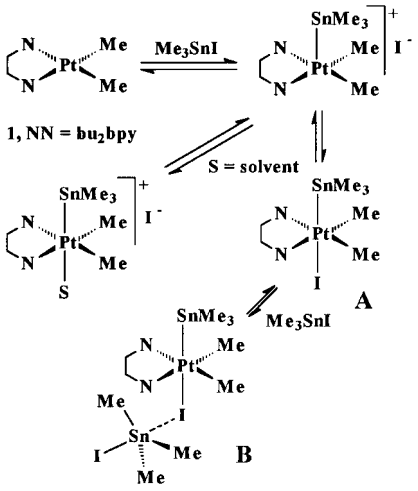

platinum(IV) complexes and excess Me_2SnX_2 (X= Cl, Br) or $MeSnCl_3$ could lead to new forms of supramolecular association through Pt-X···Sn and (or) PtSnX···Sn secondary bonding, and this paper reports the results of a systematic study of such systems.

Chart 1

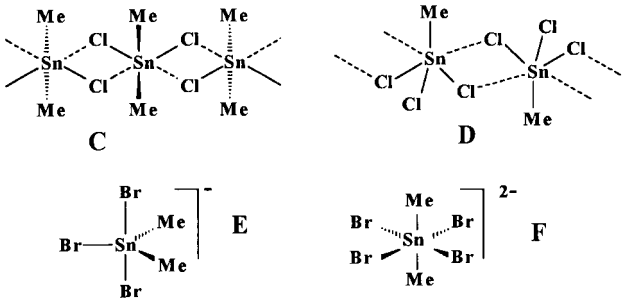

Results and discussion

Synthesis of the complexes

The reaction of complex **1** with Me_2SnX_2 gave the corresponding products of *trans* oxidative addition $[PtXMe_2(SnMe_2X)(bu_2bpy)]$ (**2a**: X = Cl, **2b**: X = Br), and crystallization in the presence of excess Me_2SnX_2 allowed isolation of the corresponding complexes $[PtXMe_2(SnMe_2X)(bu_2bpy)]\cdot Me_2SnX_2$ (**3a**: X = Cl, 3b:, X = Br) (Scheme 2). Similarly, reaction of **1** with $MeSnCl_3$ gave $[PtClMe_2(SnMeCl_2)(bu_2bpy)]$ (**4**), which could be crystallized with either $MeSnCl_3$ or Me_2SnCl_2 to give the complexes $[PtClMe_2(SnMeCl_2)(bu_2bpy)]\cdot MeSnCl_3$ (**5**) or $[PtClMe_2(SnMeCl_2)(bu_2bpy)]\cdot Me_2SnCl_2$ (**6**), respectively (Scheme 3). It was not possible to crystallize **2a** with $MeSnCl_3$, since a reaction occurred to give **4** with displacement of Me_2SnCl_2 from platinum.

In a similar way, crystallization of the μ-stannylene complex $[(\mu\text{-}SnCl_2)\{PtClMe_2(bu_2bpy)\}_2]$ (**7**) (2) with excess Me_2SnCl_2 yielded air-stable, colorless crystals of the complex $[(\mu\text{-}SnCl_2)\{PtClMe_2(bu_2bpy)\}_2]\cdot Me_2SnCl_2$ (**8**), as shown in Scheme 4. Although complex **7** contains two Pt-Cl groups that could act as ligands, it was not possible to crystallize a potential 1:2 complex $[(\mu\text{-}SnCl_2)\{PtClMe_2(bu_2bpy)\}_2]\cdot 2Me_2SnCl_2$.

Scheme 2. NN = bu_2bpy.

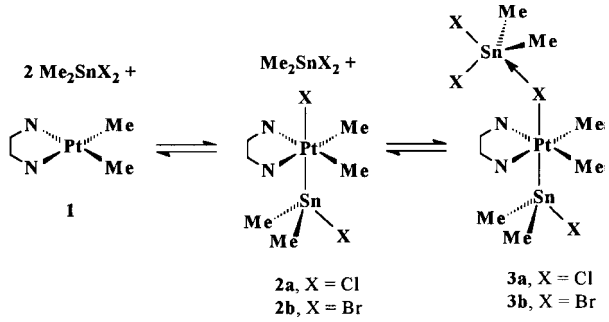

Scheme 3. NN = bu_2bpy.

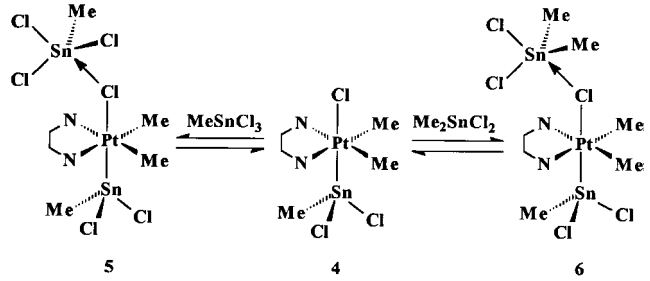

Scheme 4. NN = bu_2bpy.

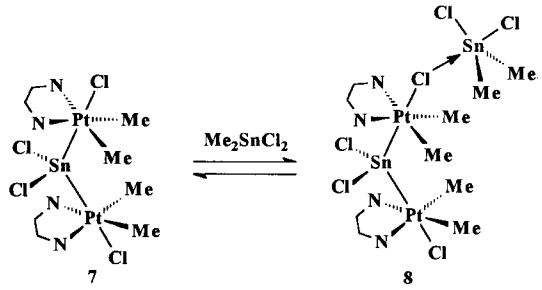

In each case the adduct formation was reversible and the complexes existed in solution mainly in dissociated form at room temperature. For example, the ^1H NMR spectrum of **3a** at room temperature contained peaks assigned to the complex **2a** and free Me_2SnCl_2 (δ(MeSn) = 1.14, ^2J(SnMe) = 69 Hx) only, indicating effectively complete dissociation in solution. However, at lower temperatures there is an increase in the magnitude of the coupling constant ^2J(SnMe) for the Me_2SnCl_2 resonance (75 Hz at –2°C, 80 Hz at –67°C) indicating reversible coordination to the Me_2SnCl_2 that is more favorable at lower temperatures (8). At no temperature were separate signals for free and complexed Me_2SnCl_2 observed, indicating that exchange between free and complexed forms was rapid and making it difficult to determine the association constant. The adducts clearly must be characterized in the solid state by X-ray structure determinations, since the easy exchange, involving reversible addition of Me_2SnCl_2, makes solution characterization difficult.

One extreme formulation of the adducts is as complexes of 16-electron platinum(IV) complexes (15) with $[SnMe_xX_{5-x}]^-$ anions, and we have attempted to isolate further examples of

© 2002 NRC Canada

Scheme 5. NN = bu_2bpy.

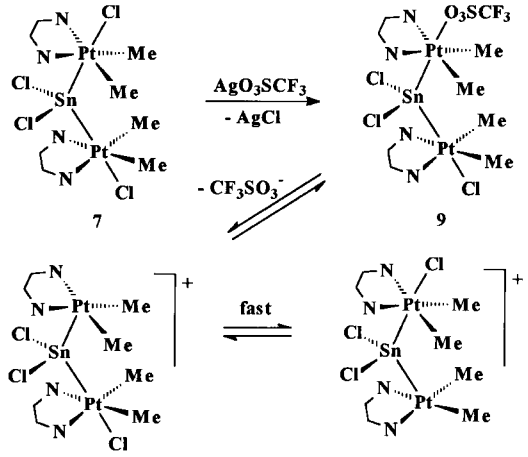

the 16-electron complexes. In one case, a pure compound was isolated, but it could not be crystallized for structural characterization. Thus reaction of **7** with 1 equiv of silver triflate gave the corresponding triflate derivative [(μ-$SnCl_2$){$PtClMe_2(bu_2bpy)$}{$Pt(O_3SCF_3)Me_2(bu_2bpy)$}] (**9**) (Scheme 5). The ^{1}H NMR spectrum of **9** at room temperature contained only three aromatic bu_2bpy peaks, one *tert*-butyl peak, and one Pt-Me resonance. All peaks were broad, indicating fluxionality such that the two platinum centres become effectively equivalent through chloride for triflate exchange. At –80°C the ^{1}H NMR spectrum is very complex, indicating the presence of several complexes in equilibrium. In the solid state, the structure could be as shown in Scheme 5 but it could also be polymeric with intermolecular PtCl···Pt coordination and free triflate ions. The exchange in solution indicates very easy dissociation of triflate is possible, with subsequent chloride exchange giving effective twofold symmetry.

Structural chemistry

Complexes **5**, **6**, and **8** exist in the solid state as 1:1 complexes, as shown in Figs. 1–3, and relevant bond parameters are listed in Table 1. In each case, the chloride atom of the Pt-Cl group acts as a donor to the acceptor $MeSnCl_3$ in **5** or Me_2SnCl_2 in **6** or **8**, so that the organotin chloride has distorted trigonal bipyramidal stereochemistry. These structures therefore complement that found previously for a trimethyltin halide acceptor in [$PtIMe_2(Me_3Sn)(bu_2bpy)$]·Me_3SnI (Scheme 1) (8). The Pt—Sn bond lengths appear not to be greatly affected by adduct formation. For example, the Pt—Sn distances in complex **8** (2.5561(6) and 2.5479(6) Å) are similar to those in the parent complex **7** (2.5451(5) and 2.5386(6) Å),[2] and the distances in complexes **5** (2.5055(5) Å) and **6** (2.5011(6) Å) are similar to that in [$PtClMe_2(SnCl_2Ph)(bu_2bpy)$] (2.5186(6) Å) (2). They also fall in the range reported for other Pt—Sn bonded compounds (2.34–2.80 Å) (7).

Fig. 1. A view of the structure of complex **5**.

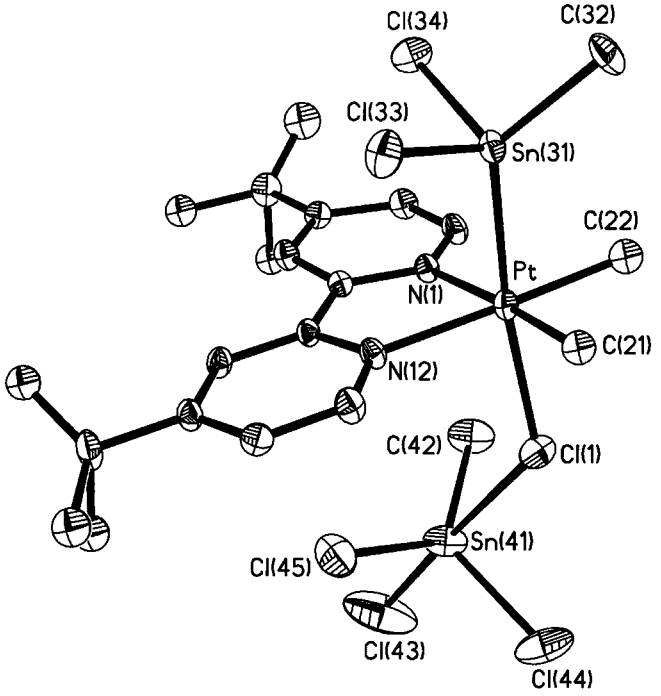

Fig. 2. A view of the structure of complex **6**.

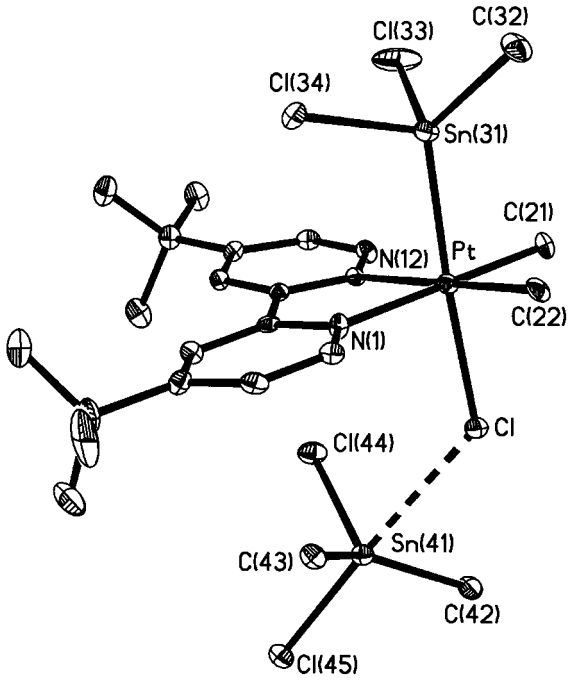

The main point of interest is the nature of the bridging chloride in the adducts. There are two extreme formulations possible, namely as 18-electron platinum complexes with weak Pt-X···Sn bonding or as weak complexes between a

[2] Supplementary data (tables of X-ray data for the complexes) may be purchased from the Depository of Unpublished Data, Document Delivery, CISTI, National Research Council Canada, Ottawa, ON K1A 0S2, Canada (http://www.nrc.ca/cisti/irm/unpub_e.shtml for information on ordering electronically). CCDC 185200–185203 inclusive contain the supplementary data for this paper. These data can be obtained, free of charge, via www.ccdc.cam.ac.uk/conts/retrieving.html (or from the Cambridge Crystallographic Data Centre, 12 Union Road, Cambridge, U.K.; fax +44 1223 336033; or deposit@ccdc.cam.ac.uk).

© 2002 NRC Canada

Fig. 3. A view of the structure of complex **8**.

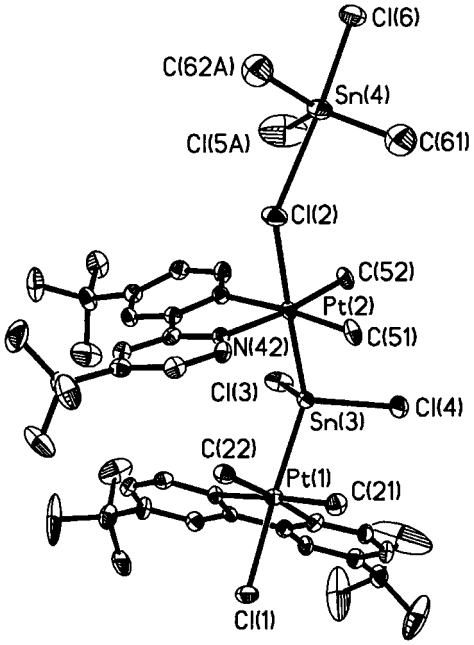

16-electron platinum(IV) cation and the anionic tin halide complex $[Me_2SnCl_3]^-$ or $[MeSnCl_4]^-$. The first true 16-electron platinum(IV) complexes have been isolated recently (15). This issue is most readily addressed for complex **8**, since it contains Pt-Cl groups involved and not involved in coordination to tin, and axial Sn-Cl groups involved and not involved in coordination to platinum. The differences in bond lengths are *d*[Pt(2)Cl(2)] – *d*[Pt(1)Cl(1)] = 2.524(2) – 2.466(2) = 0.058 Å and *d*[Sn(4)Cl(2)] – *d*[Sn(4)Cl(6)] = 2.870(3) – 2.457(3) = 0.413 Å. It is clear that the formulation as 18-electron platinum complexes with weak Pt-X···Sn bonding is the correct one, based on this structural criterion, and it is also consistent with the solution properties discussed above. The Pt-Cl···Sn angles for the complexes fall in the narrow range 129–132° (Table 1).

The stereochemistry of the Cl···$SnMeCl_3$ unit of complex **5** is distorted trigonal bipyramidal with axial Cl.Sn-Cl and equatorial $SnMeCl_2$ groups. The equatorial substituents are displaced towards Cl(1) and away from Cl(43), as indicated by the angles Cl(1)Sn(41)C(42), Cl(1)Sn(41)Cl(44), Cl(1)Sn(41)Cl(45) = 83.3(3), 81.7(1), 84.8(1)° and Cl(43)Sn(41)C(42), Cl(43)Sn(41)Cl(44), Cl(43)Sn(41)Cl(45) = 97.1(3), 95.9(2), 97.0(2)°, respectively. The Sn—Cl bond distances follow the series bridging Sn—Cl (2.813(2) Å) >> axial Sn—Cl (2.365(3) Å) > equatorial Sn—Cl (2.319(3) Å, 2.311(3) Å). The Sn—Cl bond lengths in free $MeSnCl_3$ (2.283(2), 2.318(1) Å) are similar to the Sn—-Cl(equatorial) distances in **5**. The intermolecular Sn···ClSn bond distance in $MeSnCl_3$ (Chart 1, **D** (13)) is 3.714(2) Å and is significantly longer than the bridging Sn···Cl-Pt distance of 2.813(2) Å in complex **5**. There are no short intermolecular SnCl···Sn contacts involving the chloride ligands in the $PtSnMeCl_2$ and $MeSnCl_3$ groups in complex **5**. It is clear therefore that the Pt-Cl group is a stronger donor than the $SnMeCl_2$ group.

The Cl···$SnMe_2Cl_2$ units in complexes **6** and **8** have similar distorted trigonal bipyramidal stereochemistries at tin, with axial Cl···Sn-Cl and equatorial $SnMe_2Cl$ groups. The equatorial substituents are also displaced away from the terminal axial chloride and toward the more weakly bonding bridging chloride. For example, in **6** the angles Cl(45)Sn(41)C(42), Cl(45)Sn(41)C(43), and Cl(45)Sn(41)Cl(44) (99.4(2), 97.7(2), and 96.6(1)°, respectively) are all greater than 90°. The C-Sn-C angles for Me_2SnCl_2 in **6** (133.9(3)°) and **8** (126(1)°) are larger than the ideal angle of 120°, and the Cl···Sn-Cl bond angle (**6**, 177° (**6**), **8**, 175.90(9)° (**8**)) is close to linear in each complex. The order of the Sn—Cl bond lengths again follows the series: bridging chloride (3.04(1) Å (**6**), 2.870(3) Å (**8**)) >> axial chloride (2.457(3) Å (**6**), 2.428(2) Å (8)) > equatorial chloride (2.342(2) (**6**), 2.313(7) Å (**8**)). For comparison, the Sn—Cl distance in Me_2SnCl_2 is 2.40(4) Å and the intermolecular Sn···Cl distance is 3.54(5) Å (11). There are no short intermolecular SnCl···Sn contacts in complexes **6** and **8**, whereas such interactions in Me_2SnCl_2 give rise to the infinite chain structure **C** (Chart 1).

The structure of complex **3b** is of particular interest, and is shown in Fig. 4. Selected bond parameters are in Table 2. There are two independent molecules of $[PtBrMe_2(SnMe_2Br)(bu_2bpy)]$ and of Me_2SnBr_2 in the unit cell. The independent platinum complexes differ primarily

Table 1. Selected bond distances (Å) and angles (°) for complexes **5**, **6**, and **8**.

Complex	**5**	**6**	**8**·pentane
Pt—X	2.510(2)	2.480(2)	2.524(2)
			2.466(2)
Pt—Sn	2.5011(6)	2.5055(5)	2.5561(6)
			2.5479(6)
Sn—X	2.366(2)	2.359(2)	2.386(2)
	2.357(2)	2.352(2)	2.384(2)
Sn—C	2.111(7)	2.099(6)	
Sn—X	2.365(3)	2.428(2)	2.457(3)
	2.319(3)	2.342(2)	2.313(7)
	2.311(3)		
Sn—C	2.098(9)	2.109(6)	2.14(2)
		2.096(5)	2.14(1)
Sn···X	2.813(2)	3.04	2.870(3)
Pt-X··*Sn*	132	130	129.0(1)
C-Sn-X	105.3(3)	105.6(2)	
	103.1(3)	103.7(2)	
X-Sn-X	102.35(8)	100.60(9)	97.1(1)
C-*Sn*-C		133.9(3)	126(1)
C-*Sn*-X_e	125.9(3)	111.3(2)	122.1(5)
	123.4(4)	108.8(2)	110.5(8)
C-*Sn*-X_a	97.1(3)	99.4(2)	95.2(4)
		97.7(2)	90(1)
X-*Sn*-X_e	106.6(1)		
X-*Sn*-X_a	97.1(2)	96.61(6)	95.5(4)
X··*Sn*-C	83.3(3)	83	87.2(4)
		78	86(1)
X··*Sn*-X_a	177.3(2)	177	175.90(9)
X··*Sn*-X_e	84.83(9)	86	86.0(4)
	81.7(1)		

Note: Italicized *Sn* refers to the coordinated organotin compound, e = equatorial, a = axial.

© 2002 NRC Canada

by rotation about the Pt—Sn bond, and the independent Me_2SnBr_2 molecules differ mostly by rotation about the bridging PtBr···Sn bond, as shown in Fig. 4*a*. There is a clear PtBr···Sn secondary bond to each molecule of Me_2SnBr_2 with distances Br(1)···Sn(60) and Br(2)···Sn(70) of 3.14 and 3.29 Å. There are also longer contacts between the bromide atoms of the $PtSnMe_2Br$ groups and the Me_2SnBr_2 groups. These distances Br(26)···Sn(70) and Br(56)···Sn(60) are 3.99 and 4.05 Å, which is marginally longer than the sum of the van der Waals radii of Br and Sn of 3.95 Å (16). The orientation of the SnBr···Sn groups is such that the bromide is directed towards the tin atom and essentially bisects the C-Sn-C angle of the Me_2SnBr_2 acceptor molecule. This orientation, observed in both independent units, suggests that there is an attraction involved but it must be a very weak one. To place these distances in perspective, the covalent bond distances are Sn(23)—Br(26) = 2.533(1) and Sn(53)—Br(56) = 2.557(1) Å for the $PtSnMe_2Br$ groups and for the Me_2SnBr_2 molecules, pseudo-axial Sn(60)—Br(63) = 2.558(1), Sn(70)—Br(74) = 2.587(1) Å and pseudo-equatorial Sn(60)—Br(64) = 2.492(1), Sn(70)—Br(73) = 2.499(1) Å. The differences between primary and secondary Sn—Br distances is then approximately 0.64 Å for the pseudo-axial bonds and 1.52 Å for the pseudo-equatorial bonds, again emphasizing that the PtBr···Sn secondary bonds are strong relative to the PtSnBr···Sn interactions. In the solid state structure of Et_2SnBr_2, the difference between primary and secondary Sn—Br distances is 1.27 Å, about midway between the values for the stronger and weaker secondary interactions in **3b**.

Another criterion for the strength of the secondary bonding is based on the stereochemistry at tin in the Me_2SnBr_2 acceptor molecules. In trigonal bipyramidal $[SnMe_2Br_3]^-$ the C-Sn-C angle is 133.2(8)°, whereas in octahedral $[SnMe_2Br_4]^{2-}$ the angle is 180° (14). In **3b**, the C-Sn-C angles are 131.9(3)° and 137.4(4)° for the two independent Me_2SnBr_2 acceptor molecules, very similar to the angle in the trigonal bipyramidal model compound. The analogous angle in the Me_2SnCl_2 complex (**6**) is 133.9(3)°, again very similar to the average C-Sn-C angle in **3b**. These data also indicate that the secondary SnBr···Sn bonding must be very weak, since the stereochemistry at the acceptor molecule is not significantly affected by it. If both types of secondary bonds are included, the solid state structure can be considered as a folded polymer, as illustrated in Fig. 4*b*.

Overall, it is clear that the secondary bonds formed by dimethyltin dihalide or methyltin trihalide acceptors can lead to supramolecular association and even to polymer formation in the solid state. At present, though, it is not easy to predict or control the degree of association. The secondary X···Sn bonds are weak coordinate bonds, and they appear to have similar energies to hydrogen bonds, aryl–aryl secondary bonds, or aurophilic attractions that have been used more extensively in supramolecular chemistry for assembling complex organometallic structures (11, 17). There is therefore a clear potential for further expansion of this field of research.

Experimental

NMR spectra were recorded by using Varian Mercury 400 or Inova 600 MHz spectrometers. Chemical shifts are reported in ppm with respect to TMS (^{1}H) reference. Unless otherwise specified, all quoted couplings to tin are for the ^{119}Sn isotope only. $[PtMe_2(bu_2bpy)]$ (18) and $[(PtClMe_2bu_2bpy)_2(\mu\text{-}SnCl_2)]$ (2) were prepared according to the literature procedures.

Fig. 4. Views of the structure of complex **3b**: (*a*) the two independent units $[PtBrMe_2(SnMe_2Br)(bu_2bpy)]\cdot Me_2SnBr_2$; (*b*) part of the folded polymeric structure formed by secondary Br···Sn bonding. Only the inner atoms of the bu_2bpy ligands are shown for clarity.

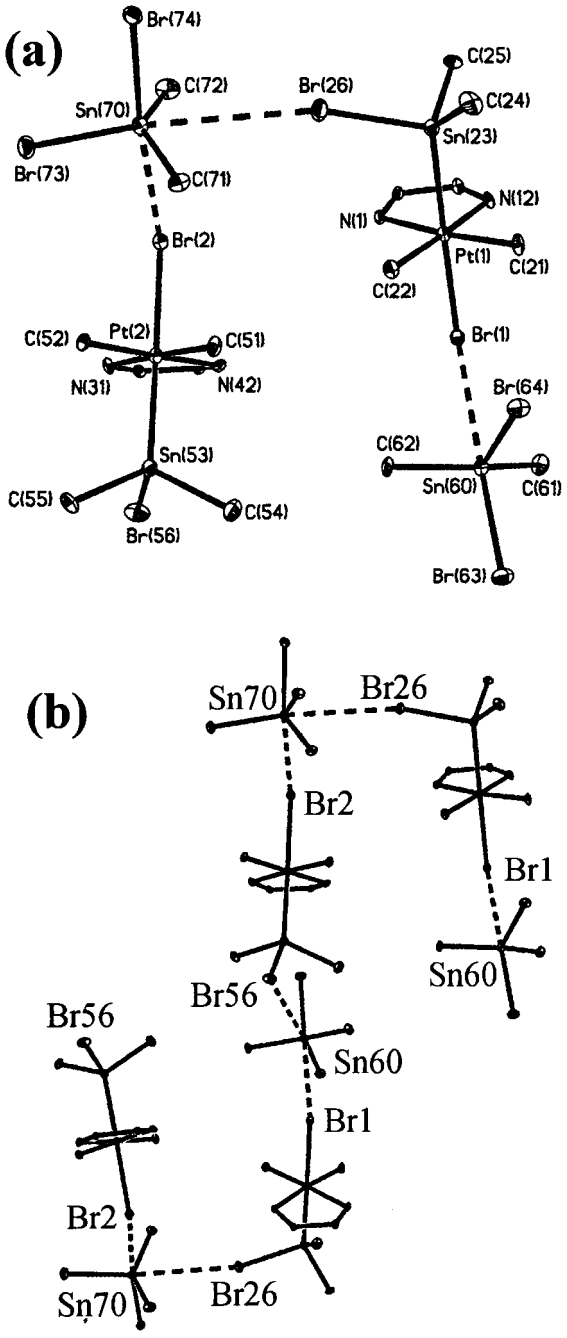

$[PtClMe_2(SnMe_2Cl)(bu_2bpy)]\cdot Me_2SnCl_2$ (3a)

An NMR tube was charged with **1** (40 mg, 0.081 mmol), Me_2SnCl_2 (178 mg, 0.810 mmol), and CH_2Cl_2 (0.5 mL). After 5 min, pentane was slowly layered on top of the solution

© 2002 NRC Canada

Table 2. Selected bond distances (Å) and angles (°) for complex **3b**.

Pt(1)—Br(1)	2.675(1)	Pt(2)—Br(2)	2.706(1)
Pt(1)—Sn(23)	2.5332(7)	Pt(2)—Sn(53)	2.5465(7)
Sn(23)—Br(26)	2.533(1)	Sn(53)—Br(56)	2.557(1)
Sn(23)—C(24)	2.148(8)	Sn(53)—C(54)	2.135(8)
Sn(23)—C(25)	2.146(8)	Sn(53)—C(55)	2.130(7)
Sn(60)—Br(63)	2.558(1)	Sn(70)—Br(73)	2.499(1)
Sn(60)—Br(64)	2.492(1)	Sn(70)—Br(74)	2.587(1)
Sn(60)—C(61)	2.117(8)	Sn(70)—C(71)	2.115(8)
Sn(60)—C(62)	2.119(7)	Sn(70)—C(72)	2.105(9)
Sn(60)···Br(1)	3.29	Sn(70)···Br(2)	3.14
Br(56)···Sn(60)	4.05	Br(26)···Sn(70)	3.99
C(24)-Sn(23)-C(25)	111.8(4)	C(54)-Sn(53)-C(55)	113.9(4)
C(24)-Sn(23)-Br(26)	103.3(3)	C(54)-Sn(53)-Br(56)	100.6(3)
C(25)-Sn(23)-Br(26)	101.5(2)	C(55)-Sn(53)-Br(56)	102.9(2)
C(61)-Sn(60)-C(62)	131.9(3)	C(71)-Sn(70)-C(72)	137.4(4)
C(61)-Sn(60)-Br(63)	100.6(3)	C(71)-Sn(70)-Br(73)	107.6(2)
C(61)-Sn(60)-Br(64)	113.7(3)	C(71)-Sn(70)-Br(74)	98.4(3)
C(62)-Sn(60)-Br(63)	99.8(2)	C(72)-Sn(70)-Br(73)	110.3(3)
C(62)-Sn(60)-Br(64)	106.6(3)	C(72)-Sn(70)-Br(74)	95.4(3)
Br(63)-Sn(60)-Br(64)	96.60(4)	Br(73)-Sn(70)-Br(74)	97.27(4)
Br(1)···Sn(60)-Br(63)	178	Br(2)···Sn(70)-Br(73)	88
Br(1)···Sn(60)-Br(64)	85	Br(2)···Sn(70)-Br(74)	173
Br(56)···Sn(60)-Br(63)	84	Br(26)···Sn(70)-Br(73)	174
Br(56)···Sn(60)-Br(64)	177	Br(26)···Sn(70)-Br(74)	89
Sn(60)···Br(1)-Pt(1)	127	Sn(70)···Br(2)-Pt(2)	126
Sn(60)···Br(56)-Sn(53)	150	Sn(70)···Br(26)-Sn(23)	166

and the sample stored at –5°C. After several days colorless crystals suitable for X-ray crystallographic studies were formed. Yield 72%. ^{1}H NMR ($CDCl_3$) δ: 8.76 (d, 2H, $^3J_{H6H5}$ = 6 Hz, $^3J_{PtH6}$ = 16 Hz, H-6, 8.11 (d, 2H, $^4J_{H3H5}$ = 1.5 Hz, H-3), 7.60 (dd, 2H, $^3J_{H5H6}$ = 6 Hz, $^4J_{H5H3}$ = 1.5 Hz, H-5), 1.43 (s, 18H, *t*-bu), 1.32 (s, 6H, $^2J_{PtMe}$ = 55 Hz, Pt-Me), 1.18 (s, 6H, $^2J_{SnH}$ = 68.5 Hz, free Me_2SnCl_2), 0.38 (br s, 6H, $^2J_{SnH}$ = 50 Hz, Sn-Me). Anal. calcd. for $C_{24}H_{42}Cl_4N_2PtSn_2$ (%): C 30.90, H 4.54, N 3.00; found: C 30.77, H 4.46, N 2.94.

[PtBrMe$_2$(SnMe$_2$Br)(bu$_2$bpy)]·Me$_2$SnBr$_2$ (3b)

This was prepared similarly but using Me_2SnBr_2 in place of Me_2SnCl_2. Yield 74%. ^{1}H NMR ($CDCl_3$) δ: 8.78 (d, 2H, $^3J_{H6H5}$ = 4.5 Hz, $^3J_{PtH6}$ = 16 Hz, H-6), 8.11 (d, 2H, $^4J_{H3H5}$ = 1 Hz, H-3), 7.60 (dd, 2H, $^3J_{H5H6}$ = 4.5 Hz, $^4J_{H5H3}$ = 1 Hz, H-5), 1.43 (s, 18H, *t*-bu), 1.42 (s, 6H, $^2J_{PtMe}$ = 56 Hz, Pt-Me), 1.34 (s, 6H, $^2J_{SnH}$ = 65 Hz, free Me_2SnBr_2), 0.46 (br s, 6H, $^2J_{SnH}$ = 49 Hz, Sn-Me). Anal. calcd. for $C_{24}H_{42}Br_4N_2PtSn_2$ (%): C 25.95, H 3.81, N 2.62: found: C 26.05, H 3.89, N 2.63.

[PtClMe$_2$(SnMeCl$_2$)(bu$_2$bpy)]·MeSnCl$_3$ (5)

This was prepared similarly from **1** (40 mg, 0.081 mmol), $MeSnCl_3$ (195 mg, 0.810 mmol), and CH_2Cl_2 (0.5 mL). Yield 68%. ^{1}H NMR ($CDCl_3$) δ: 8.74 (d, 2H, $^3J_{H6H5}$ = 6 Hz, $^3J_{PtH6}$ = 15 Hz, H-6), 8.43 (d, 2H, $^4J_{H3H5}$ = 2 Hz, H-3), 7.72 (dd, 2H, $^3J_{H5H6}$ = 6 Hz, $^4J_{H5H3}$ = 2 Hz, H-5), 1.67 (s, 6H, $^2J_{SnH}$ = 99 Hz, free $MeSnCl_3$), 1.48 (s, 18H, *t*-bu), 1.45 (s, 6H, $^2J_{PtMe}$ = 56 Hz, Pt-Me), 1.03 (s, 3H, $^2J_{SnH}$ = 52 Hz, Sn-Me). Anal. calcd. for $C_{22}H_{36}Cl_6N_2PtSn_2$ (%): C 27.14, H 3.73, N 2.88; found: C 27.07, H 3.65, N 2.77.

[PtClMe$_2$(SnMeCl$_2$)(bu$_2$bpy)]·Me$_2$SnCl$_2$ (6)

This was prepared similarly from **1** (40 mg, 0.081 mmol), $MeSnCl_3$ (20 mg, 0.081 mmol), and CH_2Cl_2 (0.5 mL) followed by addition of Me_2SnCl_2 (89 mg, 0.405 mmol). Yield 77%. ^{1}H NMR ($CDCl_3$) δ: 8.74 (d, 2H, $^3J_{H6H5}$ = 6 Hz, $^3J_{PtH6}$ = 15 Hz, H-6), 8.43 (d, 2H, $^4J_{H3H5}$ = 2 Hz, H-3), 7.72 (dd, 2H, $^3J_{H5H6}$ = 6 Hz, $^4J_{H5H3}$ = 2 Hz, H-5), 1.48 (s, 18H, *t*-bu), 1.45 (s, 6H, $^2J_{PtMe}$ = 56 Hz, Pt-Me), 1.18 (s, 6H, $^2J_{SnH}$ = 68 Hz, free Me_2SnCl_2), 1.03 (s, 3H, $^2J_{SnH}$ = 52 Hz, Sn-Me). Anal. calcd. for $C_{23}H_{39}Cl_5N_2Pt$ (%): C 28.98, H 4.12, N 2.94; found: C 28.90, H 4.06, N 2.88.

[(PtClMe$_2$bu$_2$bpy)$_2$(μ-SnCl$_2$)]·Me$_2$SnCl$_2$ (8)

This was prepared similarly from complex **9** (45 mg, 0.035 mmol), Me_2SnCl_2 (38 mg, 0.175 mmol), and CH_2Cl_2 (0.5 mL). Yield 83%. ^{1}H NMR ($CDCl_3$) δ: 8.69 (d, 2H, $^3J_{H6H5}$ = 6 Hz, $^3J_{PtH}{}^6$ = 16 Hz, H-6), 8.07 (d, 2H, $^4J_{H3H5}$ = 1 Hz, H-3), 7.55 (dd, 2H, $^3J_{H5H6}$ = 6 Hz, $^4J_{H5H3}$ = 1 Hz, H-5), 1.40 (s, 36H, *t*-bu), 1.36 (br s, 12H, $^2J_{PtMe}$ = 59 Hz, Pt-Me), 1.18 (s, 6H, $^2J_{SnH}$ = 68 Hz, free Me_2SnCl_2). Anal. calcd. for $C_{43}H_{66}Cl_6N_4Pt_2Sn_2$.pentane (%): C 36.67, H 5.11, N 3.64; found: C 36.75, H 5.18, N 3.70.

(PtClMe$_2$bu$_2$bpy)(μ-SnCl$_2$)(PtMe$_2$bu$_2$bpy)(CF$_3$SO$_3$) (9)

To a solution of **9** (100 mg, 0.078 mmol) in CH_2Cl_2 (10 mL) was added AgO_3SCF_3 (20 mg, 0.078 mmol), and the mixture was stirred for 30 min in the dark. The solution was filtered through dry celite to remove AgCl. Pentane (40 mL) was added to the filtrate to precipitate the product, which was isolated by filtration, washed with pentane, and dried in vacuo. Yield 88%. ^{1}H NMR ($CDCl_3$) δ: 8.55 (br d,

© 2002 NRC Canada

Table 3. Crystal data and experimental details.

Complex	**5**	**3b**	**6**	**8**·pentane
Empirical formula	$C_{22}H_{36}Cl_6N_2PtSn_2$	$C_{24}H_{42}Br_4N_2PtSn_2$	$C_{23}H_{39}C_{l5}N_2PtSn_2$	$C_{47}H_{78}C_{l6}N_4Pt_2Sn_2$
Formula weight	973.7	1110.71	953.28	1539.39
T (°C)	25(2)	–123(2)	–123(2)	21(2)
λ (Å)	0.71073	0.71073	0.71073	0.71073
Space group	$P2_1/c$	$P2_1/c$	$P2_1/c$	$P2_1/n$
a (Å)	12.1321(2)	23.8100(7)	12.5953(5)	18.7589(4)
b (/Å)	25.9092(5)	13.4608(3)	24.6511(6)	13.5089(3)
c (Å)	12.0843(2)	22.0228(6)	11.9861(5)	22.7772(5)
β (°)	118.490(1)	106.169(1)	118.111(2)	92.835(1)
V (Å^3)	3338.5(1)	6779.1(3)	3282.5(2)	5765.0(2)
Z	4	8	4	4
$D_{calcd.}$ (g cm^{-1})	1.937	2.177	1.929	1.774
Absorption coefficient μ (mm)	6.159	10.309	6.183	6.006
F(000)	1848	4144	1816	2984
R [$I > 2\sigma(I)$][a]				
R_1	0.0510	0.0471	0.0397	0.0576
wR_2	0.1444	0.0898	0.0634	0.1422

[a] $R_1 = \Sigma(||F_o|-|F_c||)/\Sigma|F_o|$; $wR_2 = [\Sigma w(F_o^2 - F_c^2)^2/\Sigma wF_o^2]^{1/2}$.

2H, $^3J_{H6H5}$ = 6 Hz, H-6), 8.07 (br s, 2H, H-3), 7.59 (d, 2H, $^3J_{H5H6}$ = 6 Hz, H-5), 1.38 (s, 36H, *t*-bu), 1.07 (br s, 12H, Pt-Me). Anal. calcd. for $C_{41}H_{60}Cl_3F_3N_4O_3Pt_2SSn$ (%): C 36.18, H 4.44, N 4.12; found: C 36.10, H 4.38, N 4.02.

X-ray structure determinations

Crystals were mounted on glass fibers. Data were collected by using a Nonius Kappa-CCD diffractometer with COLLECT (Nonius, 1998) software. Crystal cell refinement and data reduction were carried out using the Nonius DENZO package. The data were scaled using SCALEPACK (Nonius, 1998), and no other absorption corrections were applied. The SHEXTL 5.1 (G.M. Sheldrick, Madison, Wisc.) program was used to solve the structures by direct methods, followed by refinement by successive difference Fouriers. For complex **5** the *tert*-butyl groups were modeled as two half-occupancy isotropic groups. For **8** there was disorder at the $SnMe_2Cl_2$ acceptor, and atoms Cl(5) and C(62) were disordered across their two positions. This disorder was modeled as 50% of each atom type with the Sn—Cl (2.39 Å) and Sn—C (2.13 Å) distances being fixed. Crystal and refinement data are listed in Table 3.

Acknowledgments

We thank the Natural Sciences and Engineering Research Council of Canada (NSERC) for financial support. RJP thanks the government of Canada for a Canada Research Chair.

References

1. C.J. Levy and R. J. Puddephatt. J. Am. Chem. Soc. **119**, 10 127 (1999).
2. M.C. Janzen, M. C. Jennings, and R.J. Puddephatt. Organometallics, **20**, 4100 (2001).
3. (*a*) I.C.M. Wehman-Ooyevaar, D.M. Grove, P. de Vaal, A. Dedieu, and G. van Koten. Inorg. Chem. **31**, 5484 (1992); (*b*) I.C.M. Wehman-Ooyevaar, D.M. Grove, P. van der Sluis, A.L. Spek, and G. van Koten. J. Chem. Soc. Chem. Commun. 1367 (1990); (*c*) I.C.M. Wehman-Ooyevaar, D.M. Grove, H. Kooijman, P. van der Sluis, A.L. Spek, and G. van Koten. J. Am. Chem. Soc. **114**, 9916 (1992).
4. V.G. Albano, C. Castellari, V. De Felice, A. Panunzi, and F. Ruffo. J. Organomet. Chem. **425**, 177 (1992).
5. (*a*) G. Butler, C. Eaborn, and A. Pidcock. J. Organomet. Chem. **181**, 47 (1979); (*b*) G. Butler, C. Eaborn, and A. Pidcock. J. Organomet. Chem. **185**, 367 (1980).
6. J. Kuyper. Inorg. Chem. **17**, 77 (1978).
7. M.S. Holt, W.L. Wilson, and J.H. Nelson. Chem. Rev. **89**, 11 (1989).
8. (*a*) C.J. Levy, J.J. Vittal, and R.J. Puddephatt. Organometallics, **15**, 2108 (1996); (*b*) C.J. Levy, J.J. Vittal, and R.J. Puddephatt. Organometallics, **15**, 35 (1996).
9. H. Preut and F. Huber. Acta Crystallogr. **B35**, 744 (1979).
10. (*a*) A.G. Davies. *In* Organotin chemistry. VCH, New York. 1997; (*b*) P.J. Smith (*Editor*). Chemistry of tin. Blackie Academic and Professional, New York. 1998.
11. I. Haiduc and F.T. Edelmann. Supramolecular organometallic chemistry. Wiley-VCH, New York. 1999.
12. (*a*) A.G. Davies, H.J. Milledge, D.C. Puxley, and P.J. Smith. J. Chem. Soc. A, 2862 (1970); (*b*) N.W. Alcock and J.F. Sawyer. J. Chem. Soc. Dalton Trans. 1090 (1977).
13. H.R. Hoveyda, C. Orvig, and S.J. Rettig. Acta Crystallogr. C, **50**, 1904 (1994).
14. D. Tudela, M. Diaz, D.A. Alvaro, J. Ignacio, L. Seijo, and V.K. Belsky. Organometallics, **20**, 654 (2001).
15. (*a*) U. Fekl, W. Kaminsky, and K.I. Goldberg. J. Am. Chem. Soc. **123**, 6423 (2001); (*b*) S. Reinartz, P.S. White, M. Brookhart, and J.L. Templeton. J. Am. Chem. Soc. **123**, 6425 (2001).
16. A. Bondi. J. Phys. Chem. **68**, 441 (1964).
17. (*a*) C.S.A. Fraser, M. C. Jennings, and R.J. Puddephatt. J. Chem. Soc. Chem. Commun. 1310 (2001); (*b*) C.P. McArdle, M. C. Jennings, J.J. Vittal, and R.J. Puddephatt. Chem. Eur. J. **7**, 3572 (2001).
18. (*a*) G.S. Hill, M.J. Irwin, C.J. Levy, L.M. Rendina, and R.J. Puddephatt. Inorg. Synth. **32**, 149 (1998); (*b*) J.D. Scott and R.J. Puddephatt. Organometallics, **2**, 1643 (1983).

© 2002 NRC Canada

Syntheses and structures of bis(imido)organophosphine dianions

Kevin S. Jack, John C. Jeffery, Angela P. Leedham, Jason M. Lynam, Michael Niedzwiecki, and Christopher A. Russell

Abstract: A bis(imido)phosphine dianion, $[R'P(NR)_2]^{2-}$ (R′ = *n*-Bu, R = N-N=CPh_2) is produced from the reaction of PCl_3 with benzophenone hydrazone (1:3 equiv) in THF–NEt_3, followed by metallation of the reaction mixture with 3 equiv *n*-BuLi. A more straightforward synthesis of a comparable dianion (with R′ = Ph, R = N-N=CPh_2) is the reaction of $PhPCl_2$ with benzophenone hydrazone (1:2 equiv) in THF–NEt_3, followed by metallation of the reaction mixture with 2 equiv *n*-BuLi.

Key words: phosphorus, lithium, imido, complexes, X-ray.

Résumé : Un dianion bis(imido)phosphines, $[R'P(NR_2)_2]^{2-}$ (R′ = *n*-Bu, R = N-N=CPh_2) est obtenu par une réaction du PCl_3 avec l'hydrazone de la benzophénone (1:3 équivalents), dans un mélange de THF–NEt_3, suivie d'une métallation du mélange réactionnel à l'aide de trois équivalents de *n*-BuLi. La synthèse d'un anion comparable (avec R′ = Ph, R = N-N=CPh_2) peut être réalisée plus facilement par réaction du $PhPCl_2$ avec l'hydrazone de la benzophénone (1:2 équivalents), dans le THF–NEt_3, suivie d'une métallation du mélange réactionnel à l'aide de deux équivalents de *n*-BuLi.

Mots clés : phosphore, lithium, imido, complexes, rayons X.

[Traduit par la Rédaction]

Introduction

Our recent studies have focussed upon the preparation of a family of ligands that are imido main group anions. Besides our own contributions to this rapidly developing area of main group chemistry, other distinguished scientists (such as Bailey, Chivers, Stalke, and Wright) have been instrumental in developing routes towards, and investigating the properties of, similar imido *p*-block anions; this area has recently been the subject of two review articles (1, 2). Many of the compounds that have been prepared are imido analogues of classical *p*-block oxoanions and several have the potential to act as ambidentate ligands. Four main synthetic strategies have been employed in the preparation of such anions.

Firstly, mixed metallation using alkyllithium and *p*-block dimethylamido reagents (notably $Sn(NMe_2)_2$, $As(NMe_2)_3$, $Sb(NMe_2)_3$, and $Bi(NMe_2)_3$) has been used extensively by Wright and co-workers (3) in the preparation of both imido and the related phosphinidene (RP^{2-}) anions of heavy group 14 and 15 elements.

Secondly, nucleophilic addition of lithium salts of primary amines to group 16 imines has been employed in the groups of Chivers and co-workers (2) and Stalke and co-workers (4) to generate imido analogues of group 16 oxoanions.

Thirdly, reaction of dilithium salts of primary amines with *p*-block element halides has been used by Chivers and co-workers (5) to prepare the imido analogue of the silicate tetraanion.

Fourthly, our own preferred method involves amination of a *p*-block element halide followed by metallation using an alkyllithium base to make an imido anion (1). As part of these investigations, we reported the preparation of the imido analogue of the phosphite dianion, $[HP(NR)_3]^{2-}$ (R = 2-methoxyphenyl) as a dilithium salt from the reaction of PCl_3 with 3 equiv of 2-methoxyaniline in THF–NEt_3, followed by metallation with *n*-BuLi (2 equiv) (6). We postulated that the product arose from a proton shift from an amide (N(H)R) group to the phosphorus center upon metallation of the proposed $E(N(H)R)_3$ intermediate. Our studies into related reactions using hydrazones in place of primary amines has inadvertently introduced to us a new direction that leads to this current report.

Results and discussion

Reaction of PCl_3 with benzophenone hydrazone (1:3 equiv) in THF–NEt_3, followed by metallation of the reaction mixture with 3 equiv *n*-BuLi produces $[Li_2$-*n*-$BuP(NR)_2]_2{\cdot}4THF$ (**1**), as shown in Scheme 1. Attempts to prepare and isolate the tris(amino)phosphine, $P(Ph_2C{=}N\text{-}N(H))_3$, and then investigate comparable metallation reactions have proved unsuccessful. Presumably, complex **1** results from one of two pathways: either amination in the first step is incomplete giving $ClP(N(H)R)_2$ (reaction of this with

Received 7 March 2002. Published on the NRC Research Press Web site at http://canjchem.nrc.ca on 01 November 2002.

Dedicated to Professor Tris Chivers in recognition of his many scholarly contributions to main group chemistry.

K.S. Jack, J.C. Jeffery, A.P. Leedham, J.M. Lynam, M. Niedzwiecki, and C.A. Russell.[1] School of Chemistry, University of Bristol, Cantock's Close, Bristol BS8 1TS, U.K.

[1]Corresponding author (e-mail: Chris.Russell@bristol.ac.uk).

 DOI: 10.1139/V02-144 © 2002 NRC Canada

Fig. 1. The crystal structure of **1**. Hydrogen atoms have been omitted for clarity.

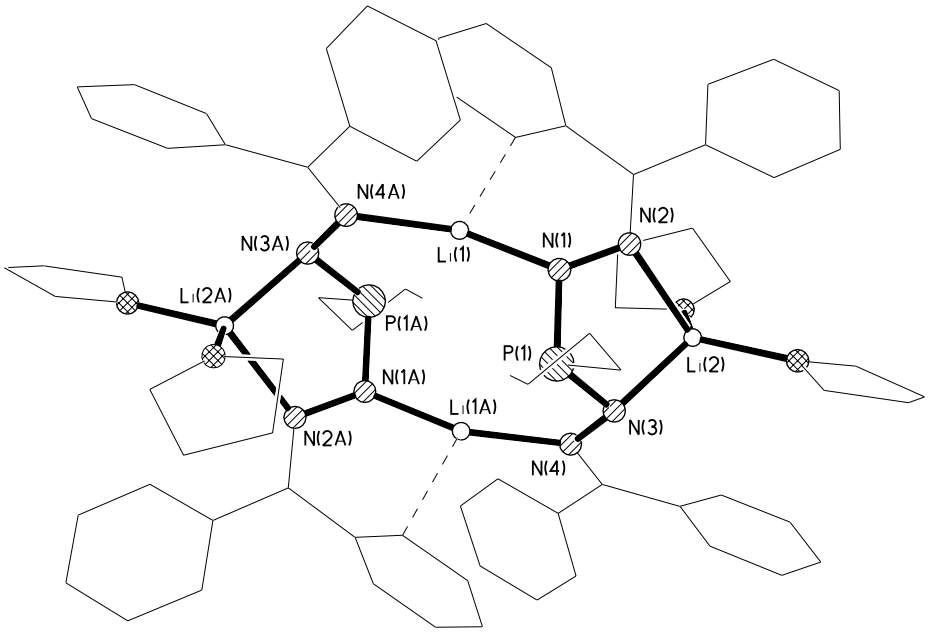

Scheme 1.

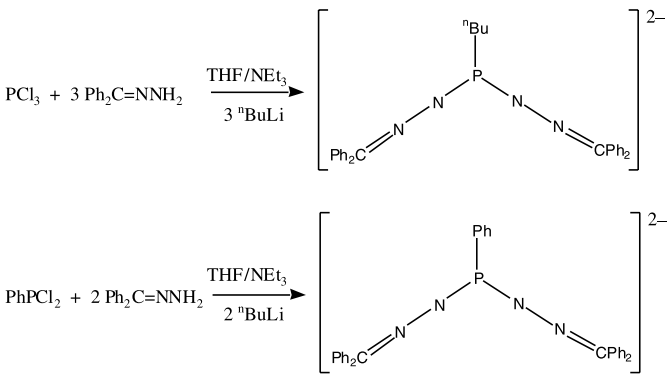

n-BuLi would be expected to deprotonate the amido protons and to eliminate LiCl to produce **1**), or alternatively, the *n*-BuLi may act as both a nucleophile and a base and may substitute an amide group of a fully aminated intermediate, $P(Ph_2C{=}N\text{-}N(H))_3$, which accompanied by metallation of the remaining amide protons would produce **1**.

We then devised a more logical and controlled synthetic route to comparable bis(imido)phosphine dianions (Scheme 1). This was achieved by the straightforward reaction of $PhPCl_2$ with benzophenone hydrazone (1:2 equiv) in THF–NEt_3, followed by metallation of the reaction mixture with 2 equiv *n*-BuLi, giving $[Li_2PhP(NR)_2]_2{\cdot}6THF$ (**2**) in good yield.

Complexes **1** and **2** are closely related to the bis(amido)organophosphine dianions recently reported by Nöth and co-workers (7). They prepared the complexes $[Li_2R'(P(NR)_2)]_n{\cdot}L_x$ ((**3**): R′ = *n*-Bu, R = *t*-Bu, L = OEt_2, *n* = 2, *x* = 2; (**4**): R′ = Ph, R = *t*-Bu, *n* = 2; (**5**): R′ = R = Ph, L = OEt_2, *n* = 2, *x* = 4; (**6**): R′ = Me, R = *i*-Pr, *n* = 4) as lithium salts by reaction of the bis(amino)organophosphine with *n*-butyllithium. Complexes **4**–**6** were synthesized by metallation of the parent bis(amino)organophosphine, whereas complex **3** was prepared by the substitution of the mesityl group of $mesP(N(H)t\text{-}Bu)_2$ by the butyl moiety.

Complexes **1** and **2** were initially characterised using ^1H, ^{31}P, and ^7Li NMR spectroscopy, IR spectroscopy, and elemental analyses. The lack of an N-H stretch in the IR spectra of **1** and **2** showed that all the N-bound protons of the hydrazone had been removed in each case. The ^{31}P NMR spectrum revealed singlet resonances at δ = 64.5 for **1** and 61.4 for **2**. More intriguingly, the ^7Li spectra for **2** showed one resonance if carried out in a polar solvent (δ = 2.1 in D_5-pyridine) but two resonances if carried out in a non-polar solvent (δ = 0.3 and –0.3 in D_8-toluene). This was taken to imply that either the compound is ion-separated in a polar solvent but ion-contacted in a non-polar solvent, or the degree of oligomerisation was variable in different solvents. To confirm these assignments and to explore further features of these molecules we undertook low-temperature single crystal X-ray diffraction studies. The crystal structures of **1** and **2** are illustrated in Figs. 1 and 2, and key bond lengths and angles are given in Tables 1 and 2, respectively.

Complexes **1** and **2** crystallize in essentially isostructural forms as centrosymmetric dimers, although complex **2** contains an additional molecule of lattice THF per monomer unit. Each dimeric molecule contains two bis(imido)organophosphine dianion units that are linked by two "bridging" lithium cations. An additional lithium cation is bound to each dianion unit in a "terminal" mode and plays no obvious role in holding the dimeric units together in the solid state. The phosphorus atoms of the bis(imido)organophosphine dianions are bound in distorted pyramidal geometries to a single organic moiety (*n*-Bu for **1**, Ph for **2**) and approximately equally to two benzophenone hydrazone units (P—N = 1.7038(18) and 1.7129(19) Å for **1**; 1.6883(13) and 1.7069(14) Å for **2**).

The "bridging" lithium cations exhibit the relatively rare two-coordinate bent geometry (N-Li-N = 153.0(2)° for **1;** N-Li-N = 152.70(17)° for **2**), coordinating asymmetrically to

© 2002 NRC Canada

Fig. 2. The crystal structure of **2**. Hydrogen atoms and lattice THF molecules have been omitted for clarity.

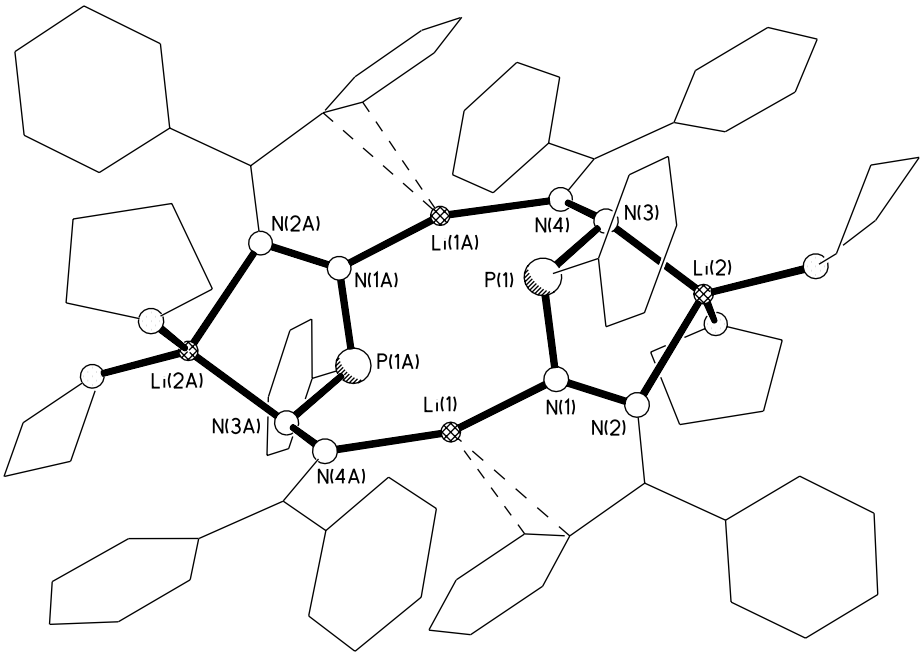

Table 1. Key bond lengths (Å) and angles (°) for **1**.

Bond lengths (Å)			
P(1)—N(1)	1.7038(18)	P(1)—C(71)	1.847(3)
P(1)—N(3)	1.7129(19)	N(1)—Li(1)	1.935(4)
N(1)—N(2)	1.371(2)	N(3)—N(4)	1.374(3)
N(2)—Li(2)	2.204(4)	Li(1)—N(4A)	2.053(4)
N(3)—Li(2)	2.013(4)	Li(1)—C(11)	2.707(4)
Li(1)—C(16)	2.497(5)		
Bond angles (°)			
N(1)-P(1)-N(3)	108.28(9)	N(1)-P(1)-C(71)	102.95(11)
N(3)-P(1)-C(71)	97.75(11)	N(1)-Li(1)-N(4A)	153.0(2)
N(1)-Li(1)-C(16)	90.02(15)	N(4A)-Li(1)-C(16)	115.14(19)
O(61)-Li(2)-O(51)	111.08(18)	O(61)-Li(2)-N(3)	116.7(2)
O(51)-Li(2)-N(3)	114.42(19)	O(61)-Li(2)-N(2)	122.8(2)
O(51)-Li(2)-N(2)	99.30(17)	N(3)-Li(2)-N(2)	90.30(15)

Table 2. Key bond lengths (Å) and angles (°) for **2**.

Bond lengths (Å)			
P(1)—N(1)	1.6883(13)	P(1)—N(3)	1.7069(14)
P(1)—C(51)	1.8341(16)	N(1)—N(2)	1.3844(18)
N(1)—Li(1)	1.937(3)	N(2)—Li(2)	2.226(3)
C(26)—Li(1)	2.575(3)	N(3)—N(4)	1.3817(17)
N(3)—Li(2)	2.011(3)	N(4)—Li(1A)	2.079(3)
Bond angles (°)			
N(1)-P(1)-N(3)	109.87(7)	N(1)-P(1)-C(51)	104.12(7)
N(3)-P(1)-C(51)	98.87(7)	N(1)-Li(1)-N(4A)	152.70(17)
N(1)-Li(1)-C(26)	88.56(12)	N(4A)-Li(1)-C(26)	118.00(13)
N(1)-Li(1)-C(21)	69.33(10)	N(4A)-Li(1)-C(21)	130.68(14)
C(26)-Li(1)-C(21)	31.29(7)	O(71)-Li(2)-O(61)	107.30(14)
O(71)-Li(2)-N(3)	112.49(15)	O(61)-Li(2)-N(3)	122.25(15)
O(71)-Li(2)-N(2)	100.04(13)	O(61)-Li(2)-N(2)	119.77(15)
N(3)-Li(2)-N(2)	92.63(12)		

the two bis(imido)organophosphine dianion units (Li—N = 1.935(4) and 2.079(3) Å in **1**; 1.937(3) and 2.053(4) Å in **2**). The asymmetry can be rationalized, as one of the nitrogen centers formally possesses a negative charge (and hence forms relatively short bonds with a strong ionic contribution) whereas the other nitrogen atom is formally saturated and hence forms a longer donor bond. There are long-range contacts in complex **1** between this lithium center and the *ortho*-carbon of one of the phenyl rings. In complex **2**, this lithium center has an η^2- contact with two of the carbon atoms of a phenyl ring. In both **1** and **2**, the formally two-coordinate lithium atom also forms long-range contacts with one of the phosphorus centers (Li···P = 2.625(4) Å in **1**; 2.598(3) Å in **2**). The "terminal" lithium atoms are bound to two nitrogen atoms (Li—N = 2.013(4) and 2.204(4) Å for **1**; 2.011(3) and 2.226(3) Å for **2**) from the same bis(imido)-organophosphine dianions and additionally bind two molecules of THF to complete a distorted tetrahedral coordination environment.

To probe the unusual lithium coordination geometries further we undertook a solid state ^{7}Li-MAS NMR study of **1** and **2**. This showed that both **1** and **2** give two lithium resonances (δ = –0.80 and 0.37 for **1**; δ = –0.84 and 0.71 for **2**) consistent with the two lithium environments observed in their solid-state structures. We have tentatively assigned the lower field resonance in each spectrum to be from the two-coordinate lithium center on the basis that proton dipolar decoupling of the ^{7}Li NMR spectrum of **2** results in a small narrowing of this peak. Moreover, the significantly larger quadrupolar coupling constant for the low-field resonance (from the manifold of side bands at low-spinning speeds) suggests that it is associated with the site of largest N-Li-N bond angles (8), i.e., the two-coordinate Li site. This may be

© 2002 NRC Canada

an indication of direct interaction with the protons on the phenyl rings that were alluded to in the solid-state structure. However, owing to the line width, overlap of the two resonances, and the small magnitude of the coupling, this purported interaction could not be assigned definitively.

Complexes **1** and **2** are structurally similar in the solid state to complexes **3** and **4**, which also form ion-contacted dimers with two bridging two-coordinate lithium centers and two "terminal" lithium centers. The chemically similar complexes **5** and **6** adopt a quite different structural arrangement to **1**–**4**. Complex **5** is a dimer where all the lithium centers bind the two bis(imido)organophosphine dianions together and are further solvated by diethylether molecules. Complex **6** forms a tetrameric unit where the lithium and nitrogen atoms form an intricate network. The precise factors that determine the structural make-up of the products are unclear at this moment.

The ligating ability of bis(imido)organophosphines has already been demonstrated by Nöth and co-workers (7). We are currently investigating the coordination chemistry of complexes **1** and **2** to a range of main group and transition metal centers.

Experimental

All reagents and products were handled on a vacuum line (in an efficient fume cupboard) under dry and oxygen-free argon or dinitrogen using standard inert atmosphere techniques (9). Toluene, THF, and hexane were dried over alumina, while a supported copper catalyst was used to remove trace oxygen from hydrocarbons prior to the reactions (10). The products were isolated and characterized with the aid of an argon-filled Saffron Beta glove box. ^{1}H, ^{31}P, and ^{7}Li NMR spectra were recorded on a Jeol Lambda 300 MHz Multinuclear FT spectrometer in dry deuterated pyridine or toluene (using the solvent resonances as the internal reference standard for ^{1}H spectra and an external standard of 85% H_3PO_4 and saturated aqueous LiBr as the references for ^{31}P and ^{7}Li, respectively). Solid-state ^{7}Li spectra were collected on a Bruker Avance 400 spectrometer operating at a resonant frequency of 155.52 MHz, using a standard Bruker 4 mm CPMAS probe and sample spinning of 5–15 kHz. All spectra were obtained using a single pulse and acquire sequence with ^{1}H decoupling (ca. 55 kHz) applied during the acquisition of the ^{7}Li FID. The ^{7}Li excitation pulse length was set at 1 μs (π/4 pulse) and 32 K imaginary points of data were collected with a total sweep width of 1 MHz, giving a total data acquisition time of 16 ms. Chemical shifts are reported with respect to the ^{7}Li resonance of a LiBr solution (0 ppm). Infrared spectra were recorded as Nujol mulls using NaCl plates and were run on a PerkinElmer Spectrum One FTIR spectrophotometer. Elemental analyses were performed by first sealing the samples under argon in air-tight aluminium boats (1–2 mg) and C, H, and N content was analysed using a PerkinElmer 240 Elemental Analyser.

Synthesis of 1

To a stirred solution of benzophenone hydrazone (1.47 g, 7.5 mmol) in 30 mL THF and NEt_3 (2 mL,), was added PCl_3 (0.22 mL, 2.5 mmol) dropwise. This solution was stirred for 1 h at room temperature before being filtered (porosity 3 sinter with Celite) and metallated with 3 equiv of *n*-BuLi (3.8 mL, 1.6 M solution in hexanes, 6 mmol). The resulting dark yellowy-orange solution was left for 72 h at 5°C and yielded pale yellow blocks of **1**.

Yield: 0.53 g (33%); mp 198–202°C. IR (cm^{-1}): no N-H bands. ^{1}H NMR (300 MHz, [D$_5$]-pyridine) δ: 7.8–6.9 (collection of overlapping m, 20H, $(C_6H_5)_2$C=N-N-), 3.6–3.7 (m, 12H, THF), 2.29 (m, 2H, -CH_2CH$_2$CH$_2$CH$_3$), 1.92 (m, 2H, -CH$_2$CH_2CH$_2$CH$_3$), 1.62 (m, 12H, THF), 1.49 (m, 2H, -CH$_2$CH$_2$CH_2CH$_3$), 0.82 (t, 3H, -CH$_2$CH$_2$CH$_2$CH_3). ^{31}P NMR (121.55 MHz, [D$_5$]-pyridine) δ: 64.5(s). ^{7}Li NMR (116.57 MHz, [D$_5$]-pyridine) δ: 2.1 (s). ^{7}Li NMR (116.57 MHz, [D$_8$]-toluene) δ: 1.0(s), –0.1(s). Anal. calcd. (%): C 71.9, H 7.1, N 8.8; found: C 72.7, H 7.3, N 8.6.

Synthesis of 2

Dichlorophenylphosphine (0.27 mL, 2 mmol) was reacted with 2 equiv of benzophenone hydrazone (0.79 g, 4 mmol) in THF (15 mL) and NEt_3 (3 mL). The resulting yellow solution was stirred for 3 h at room temperature before being filtered (porosity 3 sinter with Celite) and metallated with 2 equiv of *n*-BuLi (2.5 mL, 1.6 M solution in hexanes, 4 mmol). The solvent was removed in vacuo and the solid was redissolved in THF (3 mL), which was layered with hexane (6 mL). Golden yellow blocks of **2** were produced by storage of this mixture for 16 h at 20°C.

Yield: 1.18 g (81%); mp: no melting or decomposition up to 250°C. IR (cm^{-1}): no N-H bands. ^{1}H NMR (300 MHz, [D$_5$]-pyridine) δ: 7.6–6.7 (collection of overlapping m, 30H, $(C_6H_5)_2$C=N-N- and PC_6H_5), 3.5 (m, 24H, THF), 1.5 (m, 24H, THF). ^{31}P NMR (121.55 MHz, [D$_5$]-pyridine) δ: 61.4. ^{7}Li NMR (116.57 MHz, [D$_5$]-pyridine) δ: –0.6 (s). ^{7}Li NMR

Table 3.

Crystal	**1**	**2**
Chemical formula	$C_{76}H_{90}Li_4N_8O_4P_2$	$C_{88}H_{98}Li_4N_8O_6P_2$
MW	1269.26	1453.44
Crystal habit	Yellow cubic blocks	Yellow cubic blocks
Crystal size (mm)	0.5 × 0.5 × 0.5	0.6 × 0.5 × 0.5
Crystal system	Monoclinic	Monoclinic
Space group	*P*2(1)/*c*	*P*2(1)/*n*
a (Å)	11.177(2)	11.9299(15)
b (Å)	15.091(3)	21.950(5)
c (Å)	21.477(4)	15.936(3)
α (°)	90	90
β (°)	97.292(4)	104.058(17)
γ (°)	90	90
Volume (Å^3)	3593.3(13)	4047.9(12)
Z	2	2
μ (Mo Kα) (mm^{-1})	0.114	0.111
$D_{calcd.}$ (mg m^{-3})	1.173	1.192
T (K)	216(2)	173(2)
Reflections collected	36028	25838
Independent reflections	8261	9279
R_1 [I > 2σ(I)]	0.0571	0.0470
wR_2 (all data)	0.1835	0.1420

Note: Weighting scheme: $w^{-1} = 2(F_o^2) + (aP)^2 + (bP)$, where $P = (\max(F_o^2, 0) + 2F_c^2)/3$ and (**1**) $a = 0.1080$, $b = 0$; (**2**) $a = 0.0840$, $b = 0$.

© 2002 NRC Canada

(116.57 MHz, [D_8]-toluene) δ: 0.3(s), –0.3(s). Anal calcd. (%): C 72.7, H 6.2, N 7.7; found: C 72.2, H 6.0, N 7.6.

X-ray crystallography

Data were collected on a Siemens SMART CCD area-detector diffractometer with Mo Kα radiation (λ = 0.71073 Å) (11) using a crystal mounted on a glass fibre in a rapidly cooled perfluoropolyether (12). Intensities were integrated from several series of exposures, each exposure covering 0.3° in ω. Details of the data collection, refinement and crystal data are listed in Table 3.[2] The structures were solved by direct methods and refined by least squares on F^2 values for all reflections (13). Absorption corrections were applied, based on multiple and symmetry equivalent measurements (14). All hydrogen atoms were constrained to ideal geometries and refined with fixed isotropic displacement parameters.

Acknowledgements

We gratefully acknowledge The Royal Society (University Research Fellowship for C.A.R.), the University of Bristol (Scholarship for A.P.L.), and the Ramsey Memorial Trust (J.M.L.) for financial support. One of the authors (J.C.J.) thanks the EPSRC for supporting diffractometer facilities.

References

1. G.M. Aspinall, M.C. Copsey, A.P. Leedham, C.A. Russell. Coord. Chem. Rev. **227**, 217 (2002).
2. J.K. Brask and T. Chivers. Angew. Chem. Int. Ed. Engl. **40**, 3960 (2001).
3. M.A. Beswick and D.S. Wright. Coord. Chem. Rev. **176**, 373 (1998).
4. R. Fleischer and D. Stalke. Coord. Chem. Rev. **176**, 431 (1998).
5. J.K. Brask, T. Chivers, and M. Parvez. Inorg. Chem. **39**, 2508 (2000).
6. L.T. Burke, E. Hevia-Freire, R. Holland, J.C. Jeffery, A.P. Leedham, C.A. Russell, A. Steiner, and A. Zagorski. Chem. Commun. 1769 (2000).
7. B. Eichhorn, H. Nöth, and T. Seifert. Eur. J. Inorg. Chem. 2355 (1999).
8. M. Hartung, H. Günther, J.-P. Amoureaux, and C. Fernandéz. Magn. Reson. Chem. **36**, S61 (1998).
9. D.F. Shriver and M.A. Drezdzon. The manipulation of air-sensitive compounds. 2nd ed. Wiley, New York. 1986.
10. A.B. Pangborn, M.A. Giardello, R.H. Grubbs, R.K. Rosen, and F.J. Timmers. Organometallics, **15**, 1518 (1996).
11. Bruker Analytical X-ray Intruments Inc. 1998. SMART diffractometer control software [computer program]. Bruker Analytical X-ray Instruments Inc., Madison, WI.
12. T. Kottke and D. Stalke. J. Appl. Crystallogr. **26**, 615 (1993).
13. G.M. Sheldrick. 1998. SHELXTL [computer program]. Version 5.1. Bruker Analytical X-ray Instruments Inc., Madison, WI.
14. G. M. Sheldrick. 1996. SADABS [computer program]. University of Göttingen, Germany.

[2] Supplementary data may be purchased from the Depository of Unpublished Data, Document Delivery, CISTI, National Research Council Canada, Ottawa, ON K1A 0S2, Canada (http://www.nrc.ca/cisti/irm/unpub_e.shtml for information on ordering electronically). CCDC 179106 and 179107 contain the supplementary data for this paper. These data can be obtained, free of charge, via www.ccdc.cam.ac.uk/conts/retrieving.html (or from the Cambridge Crystallographic Data Centre, 12 Union Road, Cambridge, U.K.; fax +44 1223 336033; or deposit@ccdc.cam.ac.uk).

© 2002 NRC Canada

Boron halide chelate compounds and their activity towards the demethylation of trimethylphosphate

Timothy S. Keizer, Lauren J. De Pue, Sean Parkin, and David A. Atwood

Abstract: Salen(*t*-Bu)H_2 (*N*,*N*′-ethylenebis(3,5-di-*tert*-butyl(2-hydroxy)benzylidenimine) and its derivatives were used to prepare boron compounds having the formula L$(BCl_2)_2$ (L = salen(*t*-Bu) (**1**), salpen(*t*-Bu) (**2**), salben(*t*-Bu) (**3**), salpten(*t*-Bu) (**4**), salhen(*t*-Bu) (**5**)). These are formed from the reaction of the corresponding L$[B(OMe)_2]_2$ with BCl_3. In addition to being a new type of boron compound, they are also potential two-point Lewis acids. Indeed, they demonstrate Lewis acidic behavior in the dealkylation of trimethylphosphate. All of the compounds were characterized by mp, elemental analysis, ^{1}H and ^{11}B NMR, IR, MS, and in the case of **2** by X-ray crystallography.

Key words: boron, salen, dealkylation.

Résumé : On a utilisé le salen(*t*-Bu)H_2 (*N*,*N*′-éthylènebis(3,5-di-*tert*-butyl(2-hydroxy)benzylidènimide) et ses dérivés pour préparer des composés du bore de formules L$(BCl_2)_2$ (L = salen(*t*-Bu) (**1**), salpen(*t*-Bu) (**2**), salben(*t*-Bu) (**3**), salpten(*t*-Bu) (**4**) et salhen(*t*-Bu) (**5**) qui se forment par réaction du L$[B(OMe)_2]_2$ avec du BCl_3. En plus de correspondre à un nouveau type de composé du bore, ces produits sont potentiellement des acides de Lewis en deux points. Ils démontrent effectivement un comportement d'acide de Lewis dans la désalkylation du phosphate de triméthyle. Tous les composés ont été caractérisés par leurs points de fusion, une analyse élémentaire, par RMN du ^{1}H et du ^{11}B, par infrarouge et spectrométrie de masse et, dans le cas du produit **2**, par diffraction des rayons X.

Mots clés : bore, salen, désalkylation.

[Traduit par la Rédaction]

Introduction

Over the years, the dianionic Salen ligands (salen(*t*-Bu) = *N*,*N*′-ethylenebis(3,5-di-*tert*-butyl(2-oxo)benzylidenimine)) (Fig. 1) have been used in many applications (1, 2). The versatility of the ligand allows for the isolation of both monometallic and bimetallic derivatives usually involving the group 13 elements. For example, many compounds have been reported for aluminum (3–5), gallium (5, 6), and indium (7, 8). However, boron compounds of this type have been studied less extensively (9–11). Examples of Salen (L) boron compounds include alkoxide (L$[B(OR)_2]_2$, *R* = Me, Et) (9), siloxide (L$[B(OSiOPh_3)_2]_2$ (10), fluoride (L$[BF_2]_2$) (12), and acetate (L$[B(OAc)_2]_2$) (11) derivatives. Although these compounds are interesting from a fundamental standpoint, they are limited in usefulness because of their lack of reactivity or Lewis acid potential. In this paper we report the high-yield syntheses of new Salen-supported boron chloride derivatives, L$[BCl_2]_2$ (**1**–**5**). Preliminary work indicates that these chloride compounds will undergo salt elimination reactions, allowing for further derivatization of the boron atoms and thereby increasing their potential utility (13).

For instance, boron compounds could be useful as two-point Lewis acids. Many biological systems use a bis-metal complex to promote the binding and hydrolysis of phosphate esters (14). In recent years, synthetic derivatives containing *d*-block metals such as cobalt (15, 16), zinc (17–20), and copper (21, 22) have been used as catalysts for this reaction. A potentially important development in this area is the recent demonstration that boron bromide compounds such as salpen(*t*-Bu)$[BBr_2]_2$ can catalytically dealkylate a wide variety of phosphate esters (23). Herein, the boron chloride compounds L$[BCl_2]_2$ (**1**–**5**) will be synthesized, characterized, and examined as dealkylation agents for trimethylphosphate.

Received 5 January 2002. Published on the NRC Research Press Web site at http://canjchem.nrc.ca on 31 October 2002.

Dedicated to Professor Tris Chivers for his contributions to Canadian chemistry.

T.S. Keizer, L.J. De Pue, S. Parkin, and D.A. Atwood.[1] Department of Chemistry, University of Kentucky, Lexington, KY 40506–0055, U.S.A.

[1]Corresponding author (e-mail: datwood@pop.uky.edu).

Results and discussion

Synthesis and characterization of 1–5

The boron chlorides (**1**–**5**) were prepared in nearly quantitative yield by combining the corresponding salen(*t*-Bu)$[B(OMe)_2]_2$ reagent with BCl_3 (Scheme 1). The resulting compounds have two four-coordinate boron atoms held in a bidentate manner by the Salen ligand. Each boron atom is bound by two chlorides, a nitrogen, and an oxygen from the Salen ligand. This reaction is unique and unusual in that all of the methoxide groups are replaced with chloride groups. It is known that boron trichloride mixed with trimethylborate (eq. [1]) undergoes a ligand redistribution to form $BCl(OMe)_2$ and BCl_2(Ome) (24). Thus, the reaction described in Scheme 1 is expected to produce compounds with various combinations of chlorides and methoxides on the boron

 DOI: 10.1139/V02-050 © 2002 NRC Canada

Fig. 1. Nomenclature of the Salen ligand precursors used herein.

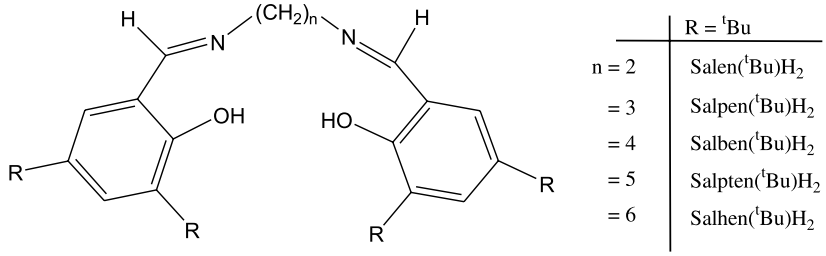

	R = ^{t}Bu
n = 2	Salen(^{t}Bu)H_2
= 3	Salpen(^{t}Bu)H_2
= 4	Salben(^{t}Bu)H_2
= 5	Salpten(^{t}Bu)H_2
= 6	Salhen(^{t}Bu)H_2

[1] $BCl_3 + B(OMe)_3 \rightleftharpoons BCl_2OMe + BCl(OMe)_2$

Scheme 1.

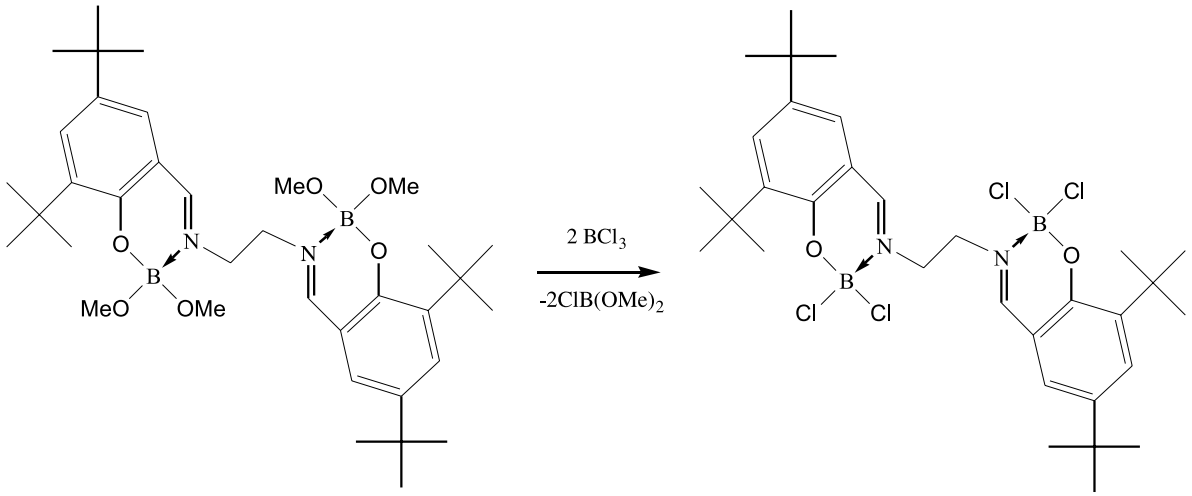

atoms. However, only the desired products $L[BCl_2]_2$ (**1**–**5**) were formed. The presence of the chelate apparently stabilizes the dihalide derivative relative to the other possibilities.

The ^{1}H NMR data for **1**–**5** contain two singlets for the *t*-Bu-Ph groups in the range δ: 1.22–1.45 ppm. There are multiple CH_2 peaks corresponding to the backbone protons from the ligand ranging from δ: 1.55–4.62 ppm depending on ligand type. There is one imine singlet for each compound in the range δ: 8.19–8.52 ppm. These values decrease with increasing backbone length. Thus, the most shielded shift (8.2 ppm) is associated with **4** and **5** and the less shielded shift at 8.5 ppm is associated with **1**. This might indicate a slight increase in nitrogen basicity for electron releasing "carbon rich" ligands and a moderate decrease in basicity for the "carbon poor" **1**, with a comparatively lower inductive effect. The ^{13}C NMR data also supports this trend. The chemical shift for the C=N group for **1**–**5** (166.7–163.4 ppm) decreases with the increase in the backbone length. The effect is more distinct between **1** (166.7 ppm) and **2** (164.9 ppm) than between **4** (163.7 ppm) and **5** (163.4 ppm). Thus, the inductive effect on the C=N is further evident when the backbone is increased from two carbons to three carbons rather than five carbons to six carbons. The ^{11}B NMR shows broad single peaks ranging from δ: 5.99–6.39 ppm with $w_{1/2}$ ranging from 28.2–56.7 Hz, which are in the region for tetrahedral boron (25). The IR data shows strong B-Cl stretches between 697–743 cm^{-1}. In the mass spectrum, the compounds show the parent ion with the isotope pattern appropriate for four chlorines and two borons. The most abundant peak for the compounds is the parent ion minus chlorine with the correct isotope pattern for three chlorines and two borons.

The structure of **2** (Fig. 2) was determined by X-ray crystallography. The geometry around the two boron atoms is slightly distorted from a tetrahedral geometry. Other Salen boron derivatives also show this distortion (9). The bite angles of the ligand on the boron atoms (N-B-O) are 110.1(4)° and 111.8(4)° (Table 1). These are slightly larger than other Salen-supported boron systems such as $salenN_3H[B(OMe)_2]_2$, which has an angle of 105.9(3)° (10). This deviation is in keeping with an increased *sp* hybridization in the N,O bonds and more obtuse angles with these atoms for **2** resulting from an increase in *p* character for the B—Cl bonds by comparison to B—OMe bonds (26). The (N-B-O) angles are significantly larger than the (N-Al-O) angle in salben(*t*-Bu)$[AlMeCl]_2$ (96.0(4)°) and the (N-Ga-O) angle in salphen(*t*-Bu)$[Ga(Et)_2]_2$ (92.5(2)°) (5). Thus, the angle decreases as the atoms increase in size, and displaces further "out" of the chelate. The B—Cl bond lengths are 1.849(5) Å, 1.855(5) Å, 1.841(5) Å, and 1.907(5) Å. These are comparable to a similar Schiff base compound, dichloro-[2-(1-imino-2,2,2-trichloroethyl)-4-methoxyphenoxido-O,N]boron, which

© 2002 NRC Canada

Fig. 2. Crystal structure of salpen(*t*-Bu)[BCl_2]$_2$ (**2**).

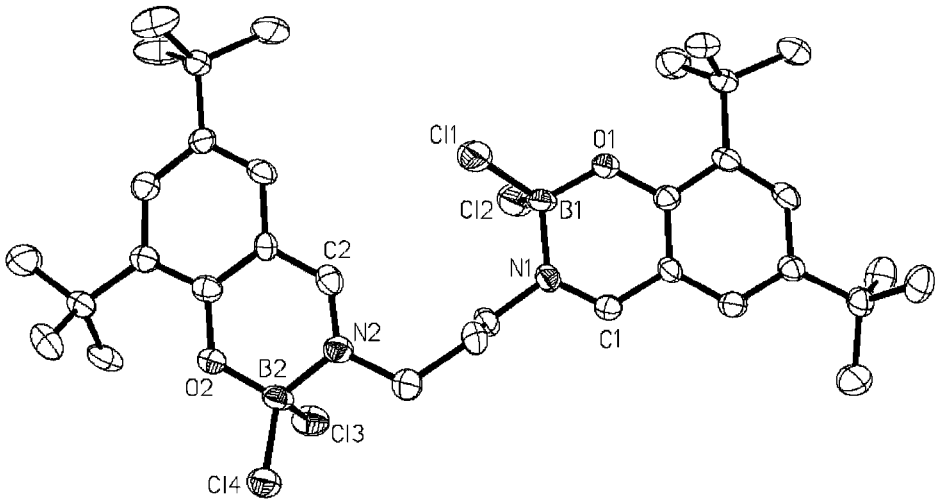

Fig. 3. Bimetallic (*a*) and monometallic (*b* and *c*) metal compounds with Salen ligands.

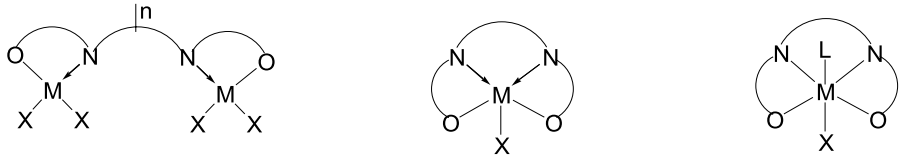

(*a*) (*b*) (*c*)

Table 1. Selected bond lengths (Å) and angles (°) for compound **2**.

Bond lengths	(Å)	Bond angles	(°)
B(1)—O(1)	1.422(5)	O(1)-B(1)-N(1)	110.1(4)
B(1)—N(1)	1.561(5)	O(1)-B(1)-Cl(1)	108.2(3)
B(1)—Cl(1)	1.849(5)	N(1)-B(1)-Cl(1)	109.7(3)
B(1)—Cl(2)	1.855(5)	O(1)-B(1)-Cl(2)	111.7(3)
C(1)—N(1)	1.295(4)	N(1)-B(1)-Cl(2)	106.5(3)
B(2)—O(2)	1.418(5)	Cl(1)-B(1)-Cl(2)	110.6(3)
B(2)—N(4)	1.548(5)	O(2)-B(2)-N(2)	111.8(4)
B(2)—Cl(3)	1.907(5)	O(2)-B(2)-Cl(4)	109.1(3)
B(2)—Cl(4)	1.841(5)	N(2)-B(2)-Cl(4)	111.0(3)
C(2)—N(2)	1.294(4)	O(2)-B(2)-Cl(3)	110.5(3)
		N(2)-B(2)-Cl(3)	104.9(3)
		Cl(4)-B(2)-Cl(3)	109.4(2)

has B—Cl bonds lengths of 1.855(7) Å and 1.841(7) Å (27). A noticeable trend in the length of the N→B dative bond occurs with the exchange of the substituents on the boron atom (28). The N→B lengths for **2** are 1.561(5) Å and 1.548(5) Å. These are shorter than the N→B bond length of salen[$B(OMe)_2$]$_2$ (1.615(2) Å) (9). An inverse relationship exists between the lengths of the C=N and N→B bonds. Where the N→B bond shortens the C=N bond lengthens. The C=N bond for 2 is 1.295(4) Å which is longer than that of the borate C=N bond (1.288(2) Å). The C=N and N→B bond lengths of **2** compare closely to those in the boron bromine derivative salben(*t*-Bu)[BBr_2]$_2$ (1.295(4) Å and 1.539(5) Å, respectively) (23).

Table 2. Percent dealkylation of trimethylphosphate.

L[BCl_2]$_2$	% Conversion[a] 30 min	% Conversion[a] 24 h
1	14	45
2	20	32
3	11	53
4	42	62
5	7	47

[a]Yields were calculated from the amount of MeCl produced to the amount of trimethylphosphate remaining in the ^{1}H NMR.

One unique aspect of these compounds (Fig. 3(*a*)) is that there are no corresponding transition metal derivatives. Rather, transition metals adopt fully chelated five-coordinate and more often six-coordinate complexes with the Salen ligands (Figs. 3(*b*) and 3(*c*)) (1). These ligands are very versatile in the fact that the "backbone" of the ligand may be altered. For instance, the length of the backbone may be increased to the point that binding to a single metal is ineffectual. Thus, the existence of **1**–**5** may indicate the possibility of isolating transition metals of the form L[MX_2]$_2$.

Demethylation of trimethylphosphate with compounds 1–5

It is known that boron trichloride will demethylate aryl ethers (29). Nevertheless, it has been found that BCl_3 alone is ineffective towards the demethylation of trimethylphosphate. Compounds (**1**–**5**), however, are capable of demethylating trimethylphosphate (Table 2). When compounds **1**–**5**

© 2002 NRC Canada

Table 3. Crystal structure data.

	Salpen(*t*-Bu)$[BCl_2]_2$ (**2**)
Color, shape	Pale yellow, plate
Chemical formula	$C_{33}H_{48}B_2Cl_4N_2O_2\cdot(1/2)C_7H_8$
Formula weight	714.22
Temperature (K)	145(1)
Crystal system	Triclinic
Space group	*P*-1
a (Å)	9.086(3)
b (Å)	14.604(4)
c (Å)	14.947(4)
α (°)	84.29(2)
β (°)	81.62(2)
γ (°)	89.24(2)
Volume (Å^3)	1952.4(10)
Z	2
$D_{calcd.}$ (mg m^{-3})	1.215
Absorption coefficient (mm^{-1})	0.336
Crystal size (mm)	0.12 × 0.10 × 0.04
Diffractometer, scan	Nonius CCD
θ range for data collection (°)	1.38–22.50
Reflections measured	10 240
Independent reflections	5122 (R_{int} = 0.0984)
Data/restraints/parameters	5122/414/424
Goodness of fit on F^2	1.046
Final *R* indices [I > 2σ(I)]	R_1 = 0.0700, wR_2 = 0.1006
R indices (all data)	R_1 = 0.1409, wR_2 = 0.1172

are added to a stoichiometric amount of trimethylphosphate, methyl chloride is produced. However, these species are less reactive than the boron bromide analogue, salpen(*t*-Bu)$[BBr_2]_2$ (23). For example, compound **2** demethylates 20% of the trimethylphosphate within 30 min whereas salpen(*t*-Bu)$[BBr_2]_2$ demethylates 89% of the trimethylphosphate within 30 min. This heightened activity may be explained by the fact that the B—Cl bond is less labile than the B—Br bond. In demonstration of this, it has been found that THF does not displace the chloride from **2** as readily as in the boron bromide compound, which forms an in situ cation (23). By analogy then, trimethylphosphate does not displace the chloride as well as bromide resulting in a decrease in dealkylation efficiency of the boron chloride compared with the boron bromide chelate. The bromide derivative can be made catalytic for the dealkylation of a wide range of phosphate esters, including trimethylphosphate, by the addition of BBr_3 (23). In this process it was not necessary to have two connected sites. This was confirmed by using a monometallic boron compound under the same conditions.

Experimental

General remarks

All glassware was rigorously cleaned and dried in an oven at 130°C for 24 h prior to use. They were assembled hot and cooled under nitrogen. All air-sensitive manipulations were conducted using standard bench top inert-atmosphere techniques in conjunction with an inert-atmosphere glove box. The ligand precursors (30) salen(*t*-Bu)H_2, salpen(*t*-Bu)H_2, salben(*t*-Bu)H_2, salpten(*t*-Bu)H_2, and salhen(*t*-Bu)H_2 were synthesized according to the literature procedure. Salen(*t*-Bu)$[B(OMe)_2]_2$, salpen(*t*-Bu)$[B(OMe)_2]_2$, salben(*t*-Bu)$[B(OMe)_2]_2$, salpten(*t*-Bu)$[B(OMe)_2]_2$, and salhen(*t*-Bu)$[B(OMe)_2]_2$ were prepared as reported previously (9). NMR data (^{1}H, ^{11}B) were obtained on JEOL-GSX-400 and 200 MHz instruments. Chemical shifts are reported relative to $SiMe_4$ for ^{1}H and ^{13}C and relative to $BF_3\cdot Et_2O$ in $CDCl_3$ for ^{11}B and are in ppm. Infrared data were recorded as KBr pellets on a Matheson Instruments 2020 Galaxy Series Spectrometer and are reported in cm^{-1}. EI (positive) (direct probe) spectra were acquired on a Kratos Concept IH at 70 eV. Elemental analyses were obtained on Vario EL III Elementar. X-ray data for **2** were obtained on a Nonius CCD unit employing Mo Kα radiation.[2] The structures were refined using the Siemens software package SHELXTL 4.0. All of the non-hydrogen atoms were refined anisotropically. The hydrogen atoms were put into calculated positions. Absorption corrections were not employed. Further details of the structure analyses are given in Table 3.

Salen(*t*-Bu)$[BCl_2]_2$ (1)

To a stirring solution of salen(*t*-Bu)$[B(OMe)_2]_2$ (2.5 g, 3.93 mmol) in toluene (75 mL) was added 1M BCl_3 in heptane (7.8 mL, 7.80 mmol). The reaction mixture was stirred for 24 h. The solution was concentrated to 5 mL, filtered, and dried. Yield: 2.41g (94%); mp 314–320°C (decomposition temperature (dec.)). IR (KBr pellet) (cm^{-1}): 2962 (s), 2905 (m), 2862 (w), 1627 (s), 1622 (m), 1573 (m), 1456 (m), 1427 (w), 1359 (w), 1310 (w), 1258 (m), 1210 (w), 1138 (w), 1026 (s), 995 (w), 917 (m), 869 (m), 769 (w), 470 (m), 706 (vs). ^{1}H NMR ($CDCl_3$) δ: 1.22 (s, 18H, C(C*H*$_3$)$_3$), 1.45 (s, 18H, C(C*H*$_3$)$_3$), 4.62 (br s, 4H, NC*H*$_2$), 7.10 (d, 2H, C$_6$*H*$_2$), 7.73 (d, 2H, C$_6$*H*$_2$), 8.52 (s, 2H, N=C*H*) ^{13}C NMR ($CDCl_3$) δ: 29.3 (C(*C*H$_3$)$_3$), 31.1 (C(*C*H$_3$)$_3$), 34.4 (N*C*H$_2$), 35.1 (N*C*H$_2$), 54.5 (*C*(CH$_3$)$_3$), 115.6 (Ph), 126.2 (Ph), 135.7 (Ph), 139.7 (Ph), 144.2 (Ph), 154.7 (Ph), 166.7 (N=*C*H). ^{11}B NMR ($CDCl_3$) δ: 6.21 ($w_{1/2}$ = 43.9 Hz). MS (%): 654 ([M]$^+$, 5), 617 ([M – Cl], 100), 582 ([M – 2Cl], 15), 547 ([M – 3Cl], 55). Anal. calcd. for $B_2C_{32}H_{46}N_2O_2Cl_4$: C 58.87, H 7.11, N 4.29; found: C 58.52, H 7.18, N 4.20.

Salpen(*t*-Bu)$[BCl_2]_2$ (2)

To a stirring solution of salpen(*t*-Bu)$[B(OMe)_2]_2$ (1.0 g, 1.54 mmol) in toluene (50 mL) was added 1M BCl_3 in heptane (3.1 mL, 3.10 mmol). The reaction mixture was stirred for 24 h. The solvent was removed and washed with 5 mL of hexanes. Filtration and vacuum drying afforded salpen(*t*-Bu)$[BCl_2]_2$. Yield: 0.85g (83%); mp 234°C. IR (KBr pellet) (cm^{-1}): 2963 (s), 2862 (w), 1631 (s), 1569 (m), 1557 (m), 1454 (m), 1429 (w), 1394 (w), 1364 (m), 1346

[2] Supplementary data may be purchased from the Depository of Unpublished Data, Document Delivery, CISTI, National Research Council Canada, Ottawa, ON K1A 0S2, Canada (http://www.nrc.ca/cisti/irm/unpub_e.shtml for information on ordering electronically). CCDC 174675 contain the supplementary data for this paper. These data can be obtained, free of charge, via www.ccdc.cam.ac.uk/conts/retrieving.html (or from the Cambridge Crystallographic Data Centre, 12 Union Road, Cambridge, U.K.; fax +44 1223 336033; or deposit@ccdc.cam.ac.uk).

© 2002 NRC Canada

(w), 1259 (m), 1223 (m), 1190 (w), 1115 (m), 1018 (s), 981 (w), 915 (w), 876 (m), 769 (m), 697 (s), 642 (m). ^{1}H NMR ($CDCl_3$) δ: 1.29 (s, 18H, C(CH_3)$_3$), 1.43 (s, 18H, C(CH_3)$_3$), 2.75 (m, 2H, CH_2), 4.09 (m, 4H, NCH_2), 7.12 (d, 2H, C$_6H_2$), 7.73 (d, 2H, C$_6H_2$), 8.38 (s, 2H, N=C*H*). ^{13}C NMR ($CDCl_3$) δ: 29.6 (C(*C*H$_3$)$_3$), 30.0 (*C*H$_2$), 31.4 (C(*C*H$_3$)$_3$), 34.6 (N*C*H$_2$), 35.3 (N*C*H$_2$), 54.8 (*C*(CH$_3$)$_3$), 115.7 (Ph), 126.2 (Ph), 135.4 (Ph), 139.8 (Ph), 144.2 (Ph), 154.7 (Ph), 164.9 (N=*C*H). ^{11}B NMR ($CDCl_3$) δ: 6.05 ($w_{1/2}$ = 46.7 Hz). MS (%): 668 ([M]$^+$, 2), 631 ([M – Cl], 100). Anal. calcd. for $B_2C_{33}H_{48}N_2O_2Cl_4$: C 59.44, H 7.26, N 4.20; found: C 60.08, H 7.82, N 3.96.

Salben(*t*-Bu)[BCl_2]$_2$ (3)

To a stirring solution of salben(*t*-Bu)[B(OMe)$_2$]$_2$ (0.5 g, 0.75 mmol) in toluene (50 mL) was added 1M BCl_3 in heptane (1.5 mL, 1.50 mmol). The reaction mixture was stirred for 24 h. The solution was concentrated to 5 mL, filtered, and dried. Yield: 0.41g (81%); mp 316–318°C (dec.). IR (KBr pellet) (cm^{-1}): 2949 (s), 2893 (w), 2862 (w), 1631 (s), 1574 (m), 1470 (w), 1405 (w), 1361 (w), 1254 (m), 1219 (m), 1204 (w), 1095 (w), 1018 (m), 1008 (m), 872 (s), 771 (m), 743 (m), 705 (m), 641 (w). ^{1}H NMR ($CDCl_3$) δ: 1.22 (s, 18H, C(CH_3)$_3$), 1.41 (s, 18H, C(CH_3)$_3$), 2.17 (m, 4H, CH_2), 4.03 (m, 4H, NCH_2), 7.20 (d, 2H, C$_6H_2$), 7.70 (d, 2H, C$_6H_2$), 8.21 (s, 2H, N=C*H*). ^{13}C NMR ($CDCl_3$) δ: 26.7 (*C*H$_2$), 29.6 (C(*C*H$_3$)$_3$), 31.1 (C(*C*H$_3$)$_3$), 34.2 (N*C*H$_2$), 35.0 (N*C*H$_2$), 52.5 (*C*(CH$_3$)$_3$), 125.3 (Ph), 125.9 (Ph), 128.2 (Ph), 129.0 (Ph), 137.8 (Ph), 154.5 (Ph), 164.2 (N=*C*H). ^{11}B NMR ($CDCl_3$) δ: 5.99 ($w_{1/2}$ = 49.5 Hz). MS (%): 681 ([M]$^+$, 2), 645 ([M – Cl], 100), 610 ([M – 2Cl], 20). Anal. calcd. for $B_2C_{34}H_{50}N_2O_2Cl_4$: C 59.98, H 7.41, N 4.12; found: C 61.35, H 7.36, N 4.01.

Salpten(*t*-Bu)[BCl_2]$_2$ (4)

To a stirring solution of salpten(*t*-Bu)[B(OMe)$_2$]$_2$ (0.68 g, 1.00 mmol) in toluene (50 mL) was added 1M BCl_3 in heptane (2.0 mL, 2.0 mmol). The reaction mixture was stirred for 24 h. The solution was concentrated to 5 mL, filtered, and dried. Yield: 0.64g (98%); mp 261–262°C (dec.). IR (KBr pellet) (cm^{-1}): 2961 (s), 2869 (w), 1630 (s), 1575 (m), 1474 (m), 1437 (m), 1395 (w), 1363 (m), 1251 (m), 1217 (w), 1190 (w), 1135 (w), 1078 (m), 1025 (m), 914 (m), 8749 (m), 771 (m), 731 (s), 644 (w). ^{1}H NMR ($CDCl_3$) δ: 1.28 (s, 18H, C(CH_3)$_3$), 1.45 (s, 18H, C(CH_3)$_3$), 1.59 (m, 2H, CH$_2$), 2.19 (m, 4H, CH_2), 3.98 (m, 4H, NCH_2), 7.19 (d, 2H, C$_6H_2$), 7.69 (d, 2H, C$_6H_2$), 8.19 (s, 2H, N=C*H*). ^{13}C NMR ($CDCl_3$) δ: 23.4 (*C*H$_2$), 29.2 (C(*C*H$_3$)$_3$), 29.5 (*C*H$_2$), 31.2 (C(*C*H$_3$)$_3$), 34.3 (N*C*H$_2$), 35.0 (N*C*H$_2$), 54.2 (*C*(CH$_3$)$_3$), 115.3 (Ph), 125.8 (Ph), 134.7 (Ph), 139.5 (Ph), 143.7 (Ph), 154.2 (Ph), 163.7 (N=*C*H). ^{11}B NMR ($CDCl_3$) δ: 5.90 ($w_{1/2}$ = 37.6 Hz). MS (%): 696 ([M]$^+$, 5), 659 ([M – Cl], 100), 624 ([M – 2Cl], 20). Anal. calcd. for $B_2C_{35}H_{52}N_2O_2Cl_4$: C 60.49, H 7.55, N 4.03; found: C 60.48, H 8.56, N 3.82.

Salhen(*t*-Bu)[BCl_2]$_2$ (5)

To a stirring solution of salhen(*t*-Bu)[B(OMe)$_2$]$_2$ (1.0 g, 1.46 mmol) in toluene (50 mL) was added 1M BCl_3 in heptane (2.9 mL, 2.92 mmol). The reaction mixture was stirred for 24 h. The solution was concentrated to 5 mL, filtered, and dried. Yield: 0.91g (91%); mp 302–304°C (dec.). IR (KBr pellet) (cm^{-1}): 2952 (s), 2904 (w), 2862 (w), 1632 (s), 1573 (m), 1458 (m), 1433 (w), 1359 (w), 1295 (w), 1254 (m), 1215 (w), 1079 (w), 1010 (m), 974 (w), 847 (m), 771 (m), 712 (s), 641 (w). ^{1}H NMR ($CDCl_3$) δ: 1.27 (s, 18H, C(CH_3)$_3$), 1.43 (s, 18H, C(CH_3)$_3$), 1.55 (m, 4H, CH_2), 2.02 (m, 4H, CH_2), 3.91 (m, 4H, NCH_2), 7.18 (d, 2H, C$_6H_2$), 7.68 (d, 2H, C$_6H_2$), 8.19 (s, 2H, N=C*H*). ^{13}C NMR ($CDCl_3$) δ: 25.7 (*C*H$_2$), 29.5 (C(*C*H$_3$)$_3$), 31.1 (C(*C*H$_3$)$_3$), 34.3 (N*C*H$_2$), 35.0 (N*C*H$_2$), 54.4 (*C*(CH$_3$)$_3$), 125.2 (Ph), 125.6 (Ph), 128.1 (Ph), 129.0 (Ph), 134.6 (Ph), 154.6 (Ph), 163.4 (N=*C*H). ^{11}B NMR ($CDCl_3$) δ: 6.39 ($w_{1/2}$ = 28.2 Hz). MS (%): 673 ([M – Cl], 100), 658 ([M – Cl – Me], 10), 638 ([M – 2Cl], 50). Anal. calcd. for $B_2C_{36}H_{54}N_2O_2Cl_4$: C 60.99, H 7.68, N 3.95; found: C 61.40, H 8.04, N 3.66.

Dealkylation of the trimethylphosphate

In an NMR tube, trimethylphosphate was added to an equimolar solution of the compound (**1**–**5**) in $CDCl_3$ and held at room temperature for 30 min and 24 h. The reaction was monitored by ^{1}H NMR (Table 2).

Addition of a Lewis base

In an NMR tube, 5 equiv of THF were added to a solution of **2** in $CDCl_3$. ^{11}B NMR ($CDCl_3$) δ: 6.04 ($w_{1/2}$ = 52.6 Hz).

Conclusion

A range of chelated boron compounds have been synthesized and fully characterized. They demonstrate that further derivatization of boron alkoxide compounds with Salen are possible and that some are active in the dealkylation of trimethylphosphate. It has been demonstrated that **1**–**5** are inefficient dealkylating compounds by comparison to the bromide analogues (23). Future work in this area entails increasing the activity of the boron chloride compounds and broadening their use as Lewis acid activators.

Acknowledgements

This work was supported by the National Science Foundation NSF-CAREER award (CHE 9816155). L.J.D. was supported by the National Science Foundation Research Experiences for Undergraduates (NSF-REU) program (CHE -0097668) in the summer of 2001. NMR instruments used in this research were obtained with funds from the Chemical Research Instrumentation Fund (CRIF) program of the National Science Foundation (CHE 997841) and from the Research Challenge Trust Fund of the University of Kentucky.

References

1. M.J. Harvey and D.A. Atwood. Chem. Rev. **101**, 37 (2001).
2. L. Canali and D.C. Sherrington. Chem. Soc. Rev. **28**, 85 (1999).
3. S.J. Dzugan and V.L. Goedken. Inorg. Chem. **25**, 2858 (1986).
4. W.-H. Leung, E.Y.Y. Chan, E.K.F. Chow, I.D. Williams, and S.-M. Peng. J. Chem. Soc. Dalton Trans. 1229 (1996).
5. M.A. Van Aelstyn, T.S. Keizer, D.L. Klopotek, S. Liu, M. Munoz-Hernandez, P. Wei, and D.A. Atwood. Organometallics, **19**, 1796 (2000).
6. M.S. Hill and D.A. Atwood. Eur. J. Inorg. Chem. 67 (1998).
7. D.A. Atwood, J.A. Jegier, and D. Rutherford. Bull. Chem. Soc. Jpn. **70**, 2093 (1997).

© 2002 NRC Canada

8. M.S. Hill and D.A. Atwood. Main Group Chem. **2**, 191 (1998).
9. P. Wei and D.A. Atwood. Inorg. Chem. **37**, 4934 (1998).
10. P. Wei, D.A. Atwood, and T.S. Keizer. Inorg. Chem. **38**, 3914 (1999).
11. B.N. Ghose. Synth. React. Inorg. Met.-Org. Chem. **16**, 1383 (1986).
12. D. Agustin, G. Rima, H. Gornitzka, and J. Barrau. J. Organomet. Chem. **592**, 1 (1999).
13. M. Sanchez, T.S. Keizer, S. Parkin, H. Hopfl, and D.A Atwood. J. Organomet. Chem. **654**, 36 (2002).
14. P. Hendry and A.M. Sargeson. Prog. Inorg. Chem. **38**, 201 (1990).
15. D.R. Jones, L.F. Lindoy, and A.M. Sargeson. J. Am. Chem. Soc. **106**, 7807 (1984).
16. D.H. Vance and A.W. Czarnik. J. Am. Chem. Soc. **115**, 12 165 (1993).
17. N.V. Kaminskaia, C. He, and S.J. Lippard. Inorg. Chem. **39**, 3365 (2000).
18. M. Yamami, H. Furutachi, T. Yokoyama, and H. Okawa. Inorg. Chem. **37**, 6832 (1998).
19. W.H. Chapman and R. Breslow. J. Am. Chem. Soc. **117**, 5462 (1995).
20. P. Molenveld, S. Kapsabelis, J.F.J. Engbersen, and D.N. Reinhoudt. J. Am. Chem. Soc. **119**, 2948 (1997).
21. K.P. McCue and J.R. Morrow. Inorg. Chem. **38**, 6136 (1999).
22. P. Scrimin, G. Ghirlanda, P. Tecilla, and R. A. Moss. Langmuir, **12**, 6235 (1996).
23. T.S. Keizer, L.J. Depue, S. Parkin, and D.A. Atwood. J. Am. Chem. Soc. **124**, 1864 (2002).
24. E. Wiberg and W.Z. Sutterlin. Anorg. Allg. Chem. **222**, 92 (1935).
25. R.G. Kidd. *In* NMR of newly accessible nuclei. Vol. 2. Academic Press. 1983.
26. H.A. Bent. J. Chem. Educ. **37**, 616 (1960).
27. F. Bigi, R. Maggi, G. Sartori, G. Casnati, and G. Bocelli. Gazz. Chim. Ital. **122**, 283 (1992).
28. H. Hopfl. J. Organomet. Chem. **581**, 129 (1999).
29. B.C. Ranu and S. Bhar. Org. Prep. Proced. Int. **28**, 371 (1996).
30. L. Deng and E.N. Jacobsen. J. Org. Chem. **57**, 4320 (1992).

© 2002 NRC Canada

Synthesis, characterization, and structures of zircona- and boracyclosiloxanes with ferrocenyl substituents

Karena Thieme, Sara C. Bourke, Juan Zheng, Mark J. MacLachlan, Fojan Zamanian, Alan J. Lough, and Ian Manners

Abstract: The novel zirconatetraferrocenylcyclotrisiloxane $Cp_2Zr(OSiFc_2)_2O$ (**6**), dizirconatetraferrocenylcyclotetrasiloxane $[Cp_2Zr(OSiFc_2)O]_2$ (**7**), boratetraferrocenylcyclotrisiloxane $(C_6H_5)B(OSiFc_2)_2O$ (**8**), and diboratetraferrocenylcyclotetrasiloxane $[(C_6H_5)B(OSiFc_2)O]_2$ (**9**) with ferrocenyl (Fc = $Fe(\eta\text{-}C_5H_4)(\eta\text{-}C_5H_5)$) substituents at silicon have been prepared from the reactions of $Cp_2Zr(NMe_2)_2$ and $PhBCl_2$ with diferrocenylsilanediol $Fc_2Si(OH)_2$ (**3**) and tetraferrocenyldisiloxanediol $[Fc_2SiOH]_2O$ (**5**). The compounds were characterized by mass spectrometry, elemental analysis, UV–vis, IR, Raman, and multinuclear NMR spectroscopy, as well as single crystal X-ray diffraction. Thermogravimetric analysis and differential scanning calorimetry investigation of **6**–**9** showed that the cycles decompose before they can undergo any thermal ring-opening polymerization. In addition, no polymerization was detected in the presence of either $KOSiMe_3$ or HOTf. The bulky ferrocenyl substituents on the Si atoms are likely to be at least partially responsible for the inability of these heterocycles to undergo ring-opening polymerization.

Key words: heterocyclosiloxanes, ferrocenyl.

Résumé : Les réactions de $Cp_2Zr(NMe_2)_2$ et $PhBCl_2$ avec le diferrocénylsilandiol, $Fc_2Si(OH)_2$ (**3**) et le tétraferrocényldisiloxanediol, $[Fc_2SiOH]_2O$ (**5**), permettent de préparer les nouveaux composés zirconatétraferrocénylcyclotrisiloxane, $Cp_2Zr(OSiFc_2)_2O$ (**6**); dizirconatétraferrocénylcyclotétrasiloxane, $[Cp_2Zr(OSiFc_2)O]_2$ (**7**); boratétraferrocénylcyclotrisiloxane, $(C_6H_5)B(OSiFc_2)_2O$ (**8**) et diboratétraferrocénylcyclotétrasiloxane, $[(C_6H_5)B(OSiFc_2)O]_2$ (**9**) portant des substituants ferrocényles (Fc = $Fe(\eta\text{-}C_5H_4)(\eta\text{-}C_5H_5)$ au niveau du silicium. Les composés ont été caractérisés par spectrométrie de masse, analyse élémentaire, spectres UV–vis, IR, Raman et RMN multinoyaux ainsi que par diffraction des rayons X par des cristaux uniques. Une étude des composés **6**–**9** par analyse thermogravimétrique et par analyse calorimétrique différentielle permet de montrer que les cycles se décomposent avant de pouvoir subir la moindre polymérisation par ouverture de cycle. De plus, on n'a observé aucune polymérisation en présence de $KOSiMe_3$ ou de HOTf. Il est probable que l'empêchement stérique dû aux substituants ferrocényles attachés aux atomes de silicium est partiellement responsable pour le fait que ces hétérocycles soient incapables de subir une réaction de polymérisation par ouverture de cycle.

Mots clés : hétérocyclosiloxanes, ferrocényle.

[Traduit par la Rédaction]

Introduction

Inorganic rings continue to attract attention with respect to their novel structures and bonding (1), as potential catalysts (2), as ligands for transition metals (3), and as polymer precursors via ring-opening polymerization (ROP) processes (4). Cyclic siloxanes are well known as ROP monomers for the preparation of polysiloxanes (silicones) (5). In contrast, the polymerization behavior of cycloheterosiloxanes, analogous species in which atoms of heteroelements are incorporated into the ring structure, is much less explored (6). We have previously reported detailed studies of cyclic borasiloxanes (7, 8) and siloxane-bridged [3]-, [5]-, and [7]ferrocenophanes (9), which were found to undergo ring–ring redistribution reactions rather than ROP under the conditions studied. Recently an interesting reversible conversion

Received 19 February 2002. Published on the NRC Research Press Web site at http://canjchem.nrc.ca on 4 November 2002.

Dedicated to Professor Tristram Chivers in recognition of his outstanding contributions both to chemistry and to the scientific community.

K. Thieme, S.C. Bourke, J. Zheng, M.J. MacLachlan,[1] F. Zamanian, A.J. Lough, and I. Manners.[2] Department of Chemistry, University of Toronto, 80 St. George Street, Toronto, ON M5S 3H6, Canada.

[1]Present address: Department of Chemistry, The University of British Columbia, 2036 Main Mall, Vancouver, BC V6T 1Z1, Canada.

[2]Corresponding author (e-mail: imanners@chem.utoronto.ca).

 DOI: 10.1139/V02-129 © 2002 NRC Canada

Scheme 1.

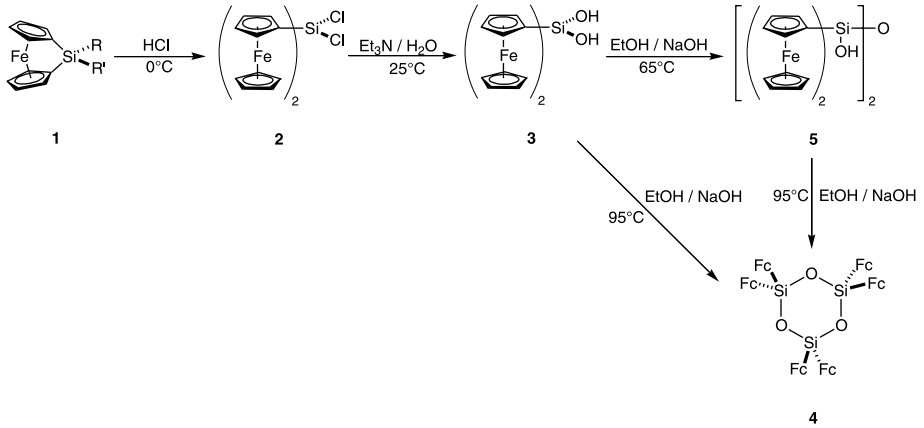

between a cyclotristannoxane (in solution) and a polystannoxane (in the solid state) has been demonstrated by Jurkschat and co-workers (10).

Our group has recently developed a facile route to dichlorodiferrocenylsilane (**2**) from the addition of 2 equiv. of HCl to the spirocyclic [1]ferrocenophane **1** (11, 12). Controlled hydrolysis of **2** affords diferrocenylsilanediol (**3**), which can then be condensed to give hexaferrocenylcyclotrisiloxane (**4**) (13). An intermediate in the condensation, tetraferrocenyldisiloxanediol (**5**), was isolated and found to possess an interesting hydrogen-bonded double-chain structure (14). We identified silanediol **3** and disiloxanediol **5** as convenient precursors to heterocyclosiloxanes with ferrocenyl substituents. In this paper we report on the synthesis, characterization, and ROP behavior of some ferrocenyl-substituted zircona- and borasiloxanes as part of our continuing studies on the ROP of inorganic heterocycles (15).

Results and discussion

Metallasiloxanes have attracted considerable interest because of their possible applications in many areas of chemistry and materials science. For example, these species have been studied as models for a variety of silica-based heterogeneous catalyst systems. A number of transition metals have been incorporated into heterosiloxanes, and the field has been recently reviewed (6).

As a consequence of the important role of Zr-based olefin polymerization catalysts, the incorporation of this metal into heterosiloxane rings is of significant interest. Moreover, zirconaheterocyclosiloxanes may be attractive as precursors to refractory $Zr_xSi_yO_z$ ceramics. However, to date, relatively few studies of such species have been reported. Roesky et al. (16) prepared an 8-membered $Zr_2O_4Si_2$ ring through reaction of a silanetriol with zirconocene dichloride. Under mass spectral conditions, this compound dimerized to form the cubic zirconasiloxane $[RSiO_3ZrCp]_4$. Hursthouse and coworkers (17), on the other hand, isolated a dianionic tris-chelate metallasiloxane $[NEt_2H_2]_2[(Ph_4Si_2O_3)_3Zr]$ from the reaction of diphenylsilanediol with tetrakis(diethylamino)zirconium. The structure of this compound revealed a central zirconium coordinated by six oxygen atoms in a distorted octahedral geometry. Finally, reaction of tetraphenyldisiloxanediol with

Scheme 2.

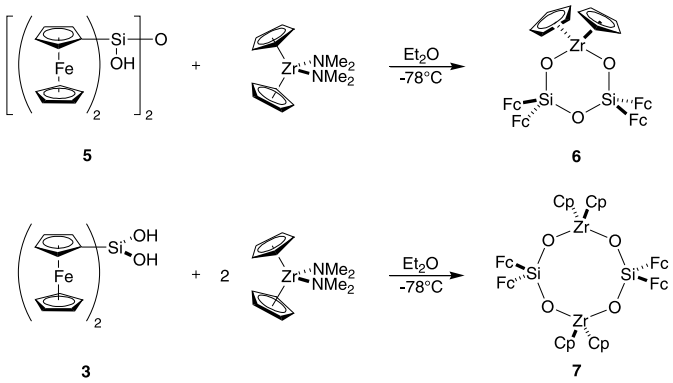

$Zr(CH_2SiMe_3)_4$ gave a siloxane with a 6-membered ZrO_3Si_2 ring that could be fired into a refractory coating (18).

Boracyclosiloxanes are also an interesting class of heterocycles to study. Wannagat and Eisele (19) reported the synthesis of the first example, the 6-membered ring $PhB(OSiMe_2)_2O$, via the [3 + 3] condensation reaction of 1,3-dichlorotetramethyldisiloxane with phenylboric acid in the presence of triethylamine. Further attempts to synthesize 6-membered rings often resulted in less strained 8- or higher-membered ring systems. Our previous studies of cyclic borasiloxanes with phenyl substituents on B and Si have shown that they do not ring-open to form linear polymer but instead undergo ring–ring interconversions (7). Similar systems have also been investigated resulting in 8-membered rings with different substituents, e.g., *tert*-butyl groups (20). The reaction of BI_3 with a trisilanol afforded an unusual dimeric boron-containing siloxane, with two trigonal-planar boron atoms bridging two silsesquioxane moieties (21).

Synthesis and characterization of zirconatetraferrocenylcyclosiloxanes 6 and 7

As ferrocene is sensitive to oxidation by acids, we selected bis(dialkylamino)zirconocene (rather than a zirconocene dihalide) to explore the use of **3** and **5** for the preparation of zirconasiloxanes. Dropwise addition of bis(dimethylamino)zirconocene to **5** in diethyl ether at –78°C afforded, after work-up, the zirconatetraferrocenylcyclosiloxane **6** in 95% yield (Scheme 2). Similarly, reaction of bis(dimethyl-

© 2002 NRC Canada

Fig. 1. IR spectra of (*a*) zirconacyclotrisiloxane **6** and (*b*) dizirconacyclotetrasiloxane **7** in a Nujol mull between 1600 and 500 cm^{-1}. Peaks marked with * are due to Nujol.

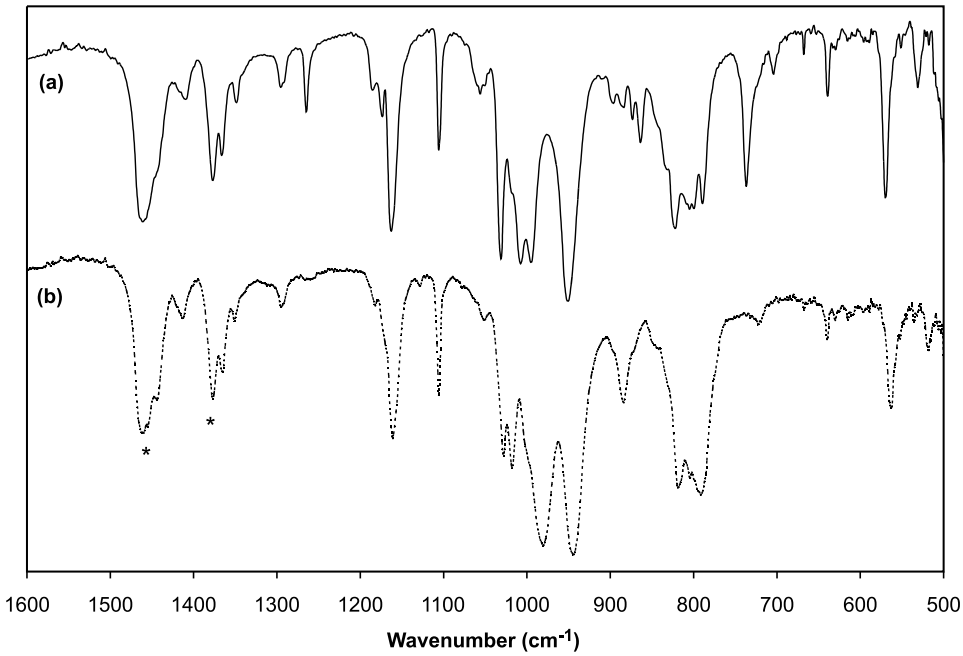

Scheme 3.

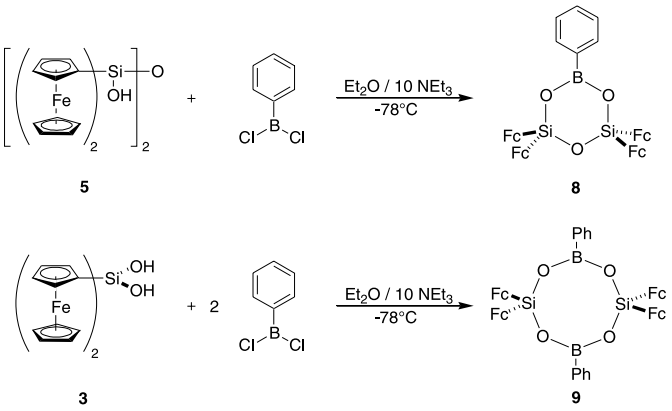

amino)zirconocene with **3** in diethyl ether at –78°C gave the dizirconatetraferrocenylcyclotetrasiloxane **7** in 95% yield. Both **6** and **7** were found to be orange, air-stable crystalline solids that decomposed only after a few days in solution in air.

Compounds **6** and **7** were both characterized by ^{1}H, ^{13}C, and ^{29}Si NMR, mass spectrometry, and IR, Raman, and UV–vis spectroscopy. The ^{1}H and ^{13}C NMR spectra of both compounds were consistent with the proposed structures. The ^{1}H NMR spectrum of **6** showed four signals attributed to Fe–Cp protons, whereas **7** showed only three such signals. This results from the higher symmetry of **7** with respect to **6**. Because of this effect, different coupling patterns are observed in the two compounds and smaller coupling constants are observed for the Cp ligands attached to Si in **6** (J = 0.9–1.2 Hz) than **7** (J = 1.5 Hz). Zirconasiloxanes **6** and **7** showed single ^{29}Si NMR resonances at –33.0 and –35.7 ppm (in C_6D_6), respectively. These are slightly upfield of the signals observed for **5** (–25.6 ppm in $CDCl_3$) and **3** (–25.1 ppm in DMSO-d_6). Both compounds **6** and **7** showed the molecular ions in their respective mass spectra and have UV–vis absorptions between 452 and 458 nm, typical of unstrained ferrocene derivatives bound to silicon (e.g., **5** has λ_{max} = 449 nm).

Synthesis and characterization of boratetraferrocenylcyclosiloxanes 8 and 9

Borasiloxanes containing a 6-membered ring were targeted, as such species would be expected to be significantly strained and likely to undergo ROP. Dropwise addition of phenylborondichloride, $PhBCl_2$, to a solution of siloxanediol **5** and triethylamine (as HCl acceptor) in ether at –78°C afforded the boracyclotrisiloxane **8** in 85% yield (Scheme 3). By an analogous procedure, the 8-membered heterocycle **9** was prepared in a low (ca. 25%) yield from silanediol **3**.

The new compounds were characterized by ^{1}H, ^{13}C, ^{29}Si, and ^{11}B NMR, mass spectrometry, IR, Raman, and UV–vis spectroscopy. The difference in the proton resonances of the boracyclosiloxanes was similar to that for the zirconacyclosiloxanes. That is, the increased symmetry from **8** to **9** simplified the Cp spectral region and changed the coupling constants of the protons on the Cp ligand attached to Si. In contrast to the zirconacyclosiloxanes, these rings showed rather different ^{29}Si NMR chemical shifts. While the chemical shift for **9** (–31.8 ppm in $CDCl_3$) was comparable to that observed for **7**, the value for **8** (–20.0 ppm in C_6D_6) was shifted downfield with respect to that of **6**. In comparison, the ^{29}Si NMR signal for the analog of **8** with phenyl substituents on each Si is observed at –16.5 ppm (in $CDCl_3$). The 6-membered ring **8** showed a broad signal in the ^{11}B NMR spectrum (30.5 ppm) in the region expected for a boron atom bonded to two oxygen atoms while the signal for **9** was slightly upfield (28.1 ppm) in the same region. Both **8** and **9** showed the molecular ion as the most intense peak in the mass spectrum and UV–vis absorptions characteristic of unstrained ferrocene moieties at λ_{max} = 450 nm.

© 2002 NRC Canada

Table 1. IR and Raman frequencies (cm^{-1}) for the vibrational modes of **6** and **7.**

Assignment[a]	**6** (IR)[b]	**6** (Raman)[c]	**7** (IR)[b]	**7** (Raman)[c]
ν C-H	3087(s)	3116(s)	3088(s)	3110(s)
		3097(m)		
			1460(s)	
ν C-C (sym)				1447(w)
ν C-C (sym)	1409(w)	1418(w)	1413(w)	1417(w)
		1387(w)		1382(w)
ν C-C	1366(m)	1371(w)	1365(m)	1366(w)
ν C-C	1348(w)		1350(w)	
	1173(m)	1193(w)		1185(w)
δ $C-H_{ip}$	1163(s)	1168(m)	1161(s)	1162(m)
		1133(m)		1131(s)
Asym. ring breathing	1106(m)	1113(s)	1106(m)	1109(s)
δ $C-H_{oop}$	1065(w)	1067(m)		1062(m)
δ $C-H_{ip}$	1031(s)	1040(w)	1028(s)	1032(w)
ν Si-O (asym)	1008(s)		1018(s)	
			980(s)	
ν Zr-O-Si	950(s)		944(s)	
Ring distortion	884(w)	894(w)	884(m)	891(w)
δ $C-H_{oop}$	822(m)		819(s)	
δ $C-H_{oop}$	805(m)			
δ $C-H_{oop}$	737(m)	711(w)		
π C-C	639(m)		630(m)	
δ $C-H_{oop}$	570(m)		563(m)	
Ring tilt		409(w)		412(w)
Ring tilt		397(w)		
ν Fe-Cp (sym)		336(s)		331(s)
				309(m)
		282(w)		252(s)

[a]Legend: ν = stretch, δ = bend, ip = in-plane, oop = out-of-plane, w = weak, m = medium, s = strong.
[b]Nujol mull.
[c]Crystalline sample.

Vibrational spectra of the zircona- and boratetraferrocenylcyclosiloxanes 6–9

Heterocyclosiloxanes **6–9** were investigated by IR and Raman spectroscopies. Both IR and Raman confirmed the presence of ferrocenyl moieties in the structures. Hexaferrocenylcyclotrisiloxane **4** was used as a model compound to assign the peaks attributed to ferrocenyl substituents. Table 1 lists the peaks observed in the IR (Nujol mull) and Raman spectra for the zirconacyclosiloxanes **6** and **7**. The IR spectra of **6** and **7**, which are very similar, are shown between 1600 and 500 cm^{-1} in Fig. 1. An Si-O stretching mode was observed in the IR spectrum at 1008 cm^{-1} in **6** and 1018 cm^{-1} in **7**. In addition, modes attributed to Zr-O-Si absorptions were observed in the IR spectra at 950 cm^{-1} in **6** and 980 and 944 cm^{-1} in **7**. For comparison, Hrncir (18) identified the Zr-O-Si mode at 962 cm^{-1} in a zirconatetraphenylcyclotrisiloxane. In general, Si-O modes occur between 900 and 1100 cm^{-1} and are highly dependent on the substituents on the silicon and the atoms attached to the silicon and oxygen. The symmetric Si-O stretch expected between 450 and 630 cm^{-1} could not be identified.

Peaks observed in the IR and Raman spectra of boracyclosiloxanes **8** and **9** are listed in Table 2. Vibrations attributed to Si-O stretching were observed near 980 cm^{-1} in the IR spectra of both compounds. Resonances observed near 1380 cm^{-1} in **8** and **9** were attributed to the B-O stretching mode. They could only be observed in the Raman spectra and in the IR of the 8-membered ring, which was measured in CCl_4 solution. A larger number of peaks observed in **8** and **9** that were not present in **4**, **6**, or **7** can be assigned to C-C or C-H stretching of the phenyl ring attached to the boron atom.

Single crystal X-ray diffraction studies of 6–9

To examine the conformations of the heterosiloxane rings with very bulky ferrocenyl substituents all four novel rings **6–9** were investigated by single-crystal X-ray diffraction. All four compounds were crystallized from dichloromethane or chloroform. For both systems the 6-membered ring was found to crystallize much more readily than the 8-membered ring. Crystals of the 8-membered rings (**7** and **9**) suitable for X-ray diffraction were obtained by slow evaporation of the solvent in an inert atmosphere glovebox. Data collection and refinement parameters for the cyclic heterosiloxane systems are summarized in Table 3. Selected bond lengths and angles of **6–9** are given in Tables 4–7, respectively.

Compound **6** crystallizes in the monoclinic space group $P2_1/n$ with $Z = 8$. The asymmetric unit contains two

© 2002 NRC Canada

Table 2. IR and Raman frequencies (cm^{-1}) for the vibrational modes of **8** and **9**.

Assignment[a]	**8** (IR)[b]	**8** (Raman)[c]	**9** (IR)[d]	**9** (Raman)[c]
ν C-H	3093(s)	3109(s)		3106(s)
ν C-H	3075(s)	3087(s)		3090(s)
ν C-C (sym)	1599(s)	1602(m)		1602(m)
	1460(s)		1465(s)	
	1437(s)		1437(m)	
	1421(m)		1419(m)	
ν C-C (sym)	1410(w)	1413(w)		1413(w)
ν B-O		1385(w)	1381(m)	1386(w)
ν C-C	1366(m)	1370(w)		1370(w)
ν C-C	1344(m)	1355(w)	1350(m)	
	1327(s)			1326(w)
	1301(s)	1302(w)		
ν C-C	1263(s)		1253(w)	
	1179(m)	1182(m)		1184(w)
δ $C-H_{ip}$	1170(s)	1172(m)	1150(m)	1172(m)
Asym.ring breathing	1104(s)	1108(s)	1106(m)	1110(s)
	1070(w)		1073(m)	
δ $C-H_{oop}$	1057(w)	1062(m)		1064(m)
δ $C-H_{ip}$	1033(s)	1037(m)		1044(m)
δ $C-H_{ip}$	1001(m)	1003(m)	1003(w)	1002(m)
ν Si-O (asym)	982(s)		978(w)	
		904(w)		908(w)
Ring distortion	858(m)			
δ $C-H_{oop}$	820(s)			
δ $C-H_{oop}$	760(m)		773(w)	
	703(s)			
	682(m)	684(w)		
	654(s)		669(s)	658(w)
π C-C	628(w)		631(s)	622(w)
δ C-C	564(m)			
Cp-Fe-Cp deform	550(m)			
Ring tilt		397(m)		400(m)
ν Fe-Cp (sym)		330(m)		327(m)
		320(s)		321(s)
		300(m)		
				230(w)

[a]Legend: ν = stretch, δ = bend, ip = in-plane, oop = out-of-plane, w = weak, m = medium, s = strong.
[b]Nujol mull.
[c]Crystalline sample
[d]CCl_4 solution.

independent molecules, A and B, which are shown in Fig. 2. The $ZrSi_2O_3$ rings observed in **6** appear in boat and twist–boat conformations; the sums of the interior bond angles, 717.15(27)° and 716.40(25)°, are close to the sum of 720° expected for a planar ring. The Fe atoms of the ferrocenyl groups attached to the same silicon centre are separated by 5.34–5.53 Å. Ferrocenyl substituents on adjacent silicon atoms have Fe centers separated by 6.64–7.13 Å for the *cis*-adjacent ferrocenyl groups and 6.74–9.58 Å for the *trans*-adjacent ferrocenyl group. These values, which are quite similar to the values observed in hexaferrocenylcyclotrisiloxane (**4**), should lead to significant metal–metal interactions and be observable by cyclic voltammetry. Steric crowding in the molecule is probably responsible for the slight ring tilts (0.6°–4.2°) observed in the ferrocenyl units. However, the values for the C—C bond length and the Fe–Cp and Fe–(η-C_5H_4)distances (1.640(3)–1.658(3) Å) are similar to those found in ferrocene.

Compound **7** crystallizes in the triclinic space group *P*-1 with $Z = 2$. Figure 3 shows two representations of the structure of **7**. The bond lengths observed in **7**, as given in Table 5, are similar to those observed in the 6-membered ring. Unlike the 6-membered ring **6**, which is essentially planar, the $Zr_2Si_2O_4$ ring in **7** adopts a twist–boat conformation in which the mean deviation from planarity is 0.29 Å. Fe atoms of ferrocene groups attached to the same silicon atom are separated by distances (5.48 and 5.56 Å) comparable to those in the 6-membered ring. However, the distance between the Fe atoms in the ferrocenyl groups on the opposite silicon atoms is much larger because of the larger ring size.

© 2002 NRC Canada

Table 3. Crystal data for compounds **6**–**9**.

	6·CH_2Cl_2	**7**·2$CHCl_3$	**8**·2CH_2Cl_2	**9**
Empirical formula	$C_{51}H_{48}Cl_2Fe_4O_3Si_2Zr$	$C_{62}H_{58}Cl_6Fe_4O_4Si_2Zr_2$	$C_{48}H_{45}BCl_4Fe_4O_3Si_2$	$C_{52}H_{46}B_2Fe_4O_4Si_2$
FW	1150.59	1541.80	1098.00	1036.09
Colour/habit	Orange-yellow/needle	Yellow/needle	Orange/needle	Orange/needle
T (K)	100(1)	150(1)	100(1)	100(1)
Wavelength (Å)	0.71073	0.71073	0.71073	0.71073
Crystal system	Monoclinic	Triclinic	Monoclinic	Triclinic
Space group	$P2_1/n$	P-1	$C2/c$	P-1
a (Å)	11.988(2)	12.2043(3)	19.4733(5)	10.1976(3)
b (Å)	20.226(4)	15.3707(3)	13.2413(5)	11.3083(3)
c (Å)	37.609(8)	16.8440(3)	17.9316(6)	11.4036(3)
α (°)	90	77.227(1)	90	114.443(1)
β (°)	96.51(3)	82.602(1)	99.653(2)	100.785(1)
γ (°)	90	77.113(1)	90	103.692(1)
Volume (Å^3)	9060(3)	2993.42(11)	4558.2(3)	1101.08(5)
Z	8	2	4	1
$D_{calcd.}$ (g cm^{-3})	1.687	1.711	1.606	1.563
Abs. coeff. (mm^{-1})	1.688	1.635	1.577	1.394
F(000)	4672	1552	2248	532
Crystal size (mm)	0.30 × 0.26 × 0.22	0.30 × 0.15 × 0.12	0.20 × 0.18 × 0.18	0.30 × 0.20 × 0.20
θ range collected (°)	4.08 to 26.38	4.08 to 26.38	4.08 to 26.37	4.11 to 26.36
Limiting indices	$0 \le h \le 14$	$0 \le h \le 15$	$0 \le h \le 24$	$0 \le h \le 12$
	$0 \le k \le 25$	$-18 \le k \le 19$	$0 \le k \le 16$	$-14 \le k \le 13$
	$-46 \le l \le 46$	$-20 \le l \le 21$	$-22 \le l \le 22$	$-14 \le l \le 13$
Reflections collected	60 890	33 511	15 610	14 197
Independent reflections	18 338 (R_{int} = 0.064)	12 172 (R_{int} = 0.047)	4650 (R_{int} = 0.055)	4469 (R_{int} = 0.037)
Data / restraints / parameters	18 338 / 0 / 1135	12 172 / 0 / 721	4650 / 5 / 302	4469 / 0 / 289
Goodness of fit on F^2	1.078	1.092	1.036	1.043
Final R indices [$I > 2\sigma(I)$]	R_1 = 0.0340	R_1 = 0.0336	R_1 = 0.0380	R_1 = 0.0277
	wR_2 = 0.0762	wR_2 = 0.0812	wR_2 = 0.0873	wR_2 = 0.0674
R indices (all data)	R_1 = 0.0512	R_1 = 0.0461	R_1 = 0.0581	R_1 = 0.0339
	wR_2 = 0.0808	wR_2 = 0.0855	wR_2 = 0.0952	wR_2 = 0.0711
Largest diff. peak/hole (e Å^{-3})	1.430/–1.061	1.185/–0.929	0.739/–0.812	0.411/–0.369

The *trans* ferrocenyl groups on opposing Si atoms are separated by 10.28 and 10.31 Å. Folding of the heterosiloxane ring leads to Fe–Fe distances for the *cis* ferrocenyl groups that are very different (7.77 and 10.63 Å). The cyclopentadienyl rings of the two closer ferrocenyl groups are tilted by 2.5° and 4.2°, whereas the other two ferrocenyl groups have ring tilts between 0.9° and 1.3°. With values between 1.647(3) and 1.653(3) Å, the Fe–Cp and Fe(η-C_5H_4) distances are in the range of ferrocene.

The 6-membered boraferrocenylcyclosiloxane **8** shows the highest crystallographic symmetry of the rings studied. As with the zirconaferrocenylsiloxane **6** it crystallizes in a monoclinic space group, $C2/c$, but **8** lies on a two-fold axis, and so only half of the molecule is in the asymmetric unit. Figure 4 shows two views of the borasiloxane **8**. The BSi_2O_3 ring is in a slight twist conformation with an interior angle sum of 716.91(54)° and a mean deviation from planarity of 0.066 Å. The Si–O distances in the ring system are similar to **6**, but the B—O bond lengths of **8** are much shorter than the Zr—O bond lengths of **6**. Moreover, the O-Si-O angles in **8** are smaller than in **6**. The ring tilts of the ferrocenyl groups are 1.3° and 3.3°. Ferrocenyl groups attached to the same Si are separated by 5.52 Å, whereas Fe–Fe distances for ferrocenes on adjacent Si atoms are 6.79, 7.46, and 9.09 Å.

Only the 8-membered borasiloxane ring **9** crystallized without solvent molecules in the lattice. This species crystallized in the triclinic space group P-1 with Z = 1, therefore the molecule has crystallographic inversion symmetry. The molecular structure of **9** is illustrated in Fig. 5. The B-O-Si angles are 137.37(13)° and 166.73(14)°, much larger than observed in **8** where the B-O-Si angles are 128.3(2)°. The $B_2Si_2O_4$ ring is in a chair-like conformation. The atoms in the ring are displaced by an average of 0.054 Å from planarity. Significantly, two of the ferrocenyl groups in this structure are almost parallel to the ring plane and are sitting right above it. This observation is in contrast to the other ferrocenylsiloxane rings **4** and **6**–**8** that we have investigated where the ferrocenes are arranged in a "pinwheel" above and below the ring. The distance between the Fe atoms of the two ferrocenyl substituents arranged over and beneath the ring is 8.21 Å, smaller than the distance between the Fe atoms of the remaining two opposite ferrocenyl groups (10.59 Å). The Fe–Fe distances between the *cis*-opposite ferrocenyl groups are equal (7.32 Å) as a consequence of the center of inversion. Compared with the corresponding 6-membered ring **8**, the Fe atoms of the ferrocenyl groups on the same silicon atom in **9** are separated by longer distances (6.01 Å). The ferrocenyl moieties show small ring tilts (1.2° and 1.3°).

© 2002 NRC Canada

Table 4. Selected bond distances (Å) and angles (°) for **6.**

Bond distances (Å)			
Si(1A)—O(1A)	1.638(2)	Si(1B)—O(1B)	1.645(2)
Si(1A)—O(2A)	1.623(2)	Si(1B)—O(2B)	1.620(2)
Si(1A)—C(11A)	1.850(3)	Si(1B)—C(11B)	1.853(3)
Si(1A)—C(21A)	1.849(3)	Si(1B)—C(21B)	1.861(3)
Si(2A)—O(1A)	1.644(2)	Si(2B)—O(1B)	1.642(2)
Si(2A)—O(3A)	1.621(2)	Si(2B)—O(3B)	1.622(2)
Si(2A)—C(31A)	1.861(3)	Si(2B)—C(31B)	1.861(3)
Si(2A)—C(41A)	1.852(3)	Si(2B)—C(41B)	1.851(3)
Zr(1A)—O(2A)	2.008(2)	Zr(1B)—O(2B)	1.993(2)
Zr(1A)—O(3A)	1.999(2)	Zr(1B)—O(3B)	2.001(2)
Zr(1A)—Cp(1A)	2.250(5)	Zr(1B)—Cp(1A)	2.238(5)
Zr(1A)—Cp(2A)	2.244(2)	Zr(1B)—Cp(2A)	2.249(8)
Bond angles (°)			
Si(1A)-O(1A)-Si(2A)	137.17(12)	Si(1B)-O(1B)-Si(2B)	136.39(12)
Si(1A)-O(2A)-Zr(1A)	135.47(12)	Si(1B)-O(2B)-Zr(1B)	136.15(11)
Si(2A)-O(3A)-Zr(1A)	135.87(12)	Si(2B)-O(3B)-Zr(1B)	135.17(11)
O(1A)-Si(1A)-O(2A)	107.79(10)	O(1B)-Si(1B)-O(2B)	107.26(10)
O(1A)-Si(2A)-O(3A)	108.33(11)	O(1B)-Si(2B)-O(3B)	108.23(10)
O(2A)-Zr(1A)-O(3A)	92.52(8)	O(2B)-Zr(1B)-O(3B)	92.13(8)
O(1A)-Si(1A)-C(11A)	107.71(12)	O(1B)-Si(1B)-C(11B)	106.46(12)
O(1A)-Si(1A)-C(21A)	106.82(11)	O(1B)-Si(1B)-C(21B)	110.28(11)
O(1A)-Si(2A)-C(31A)	107.79(11)	O(1B)-Si(2B)-C(31B)	105.51(11)
O(1A)-Si(2A)-C(41A)	106.71(11)	O(1B)-Si(2B)-C(41B)	109.95(12)
O(2A)-Si(1A)-C(11A)	110.74(11)	O(2B)-Si(1B)-C(11B)	110.56(11)
O(2A)-Si(1A)-C(21A)	112.09(11)	O(2B)-Si(1B)-C(21B)	109.99(11)
O(3A)-Si(2A)-C(31A)	111.57(11)	O(3B)-Si(2B)-C(31B)	112.84(11)
O(3A)-Si(2A)-C(41A)	110.62(11)	O(3B)-Si(2B)-C(41B)	107.50(11)
C(11A)-Si(1A)-C(21A)	111.46(13)	C(11B)-Si(1B)-C(21B)	112.13(13)
C(31A)-Si(2A)-C(41A)	111.60(13)	C(31B)-Si(2B)-C(41B)	112.72(13)
Cp(1A)-Zr(1A)-Cp(2A)	127.7(2)	Cp(1B)-Zr(1B)-Cp(2B)	128.0(2)

Fig. 2. (*a*) Molecular structure of the two molecules of **6** found in the asymmetric unit. (*b*) Side-on view of the same molecules of **6**. The structures are shown with thermal ellipsoids at the 30% probability level.

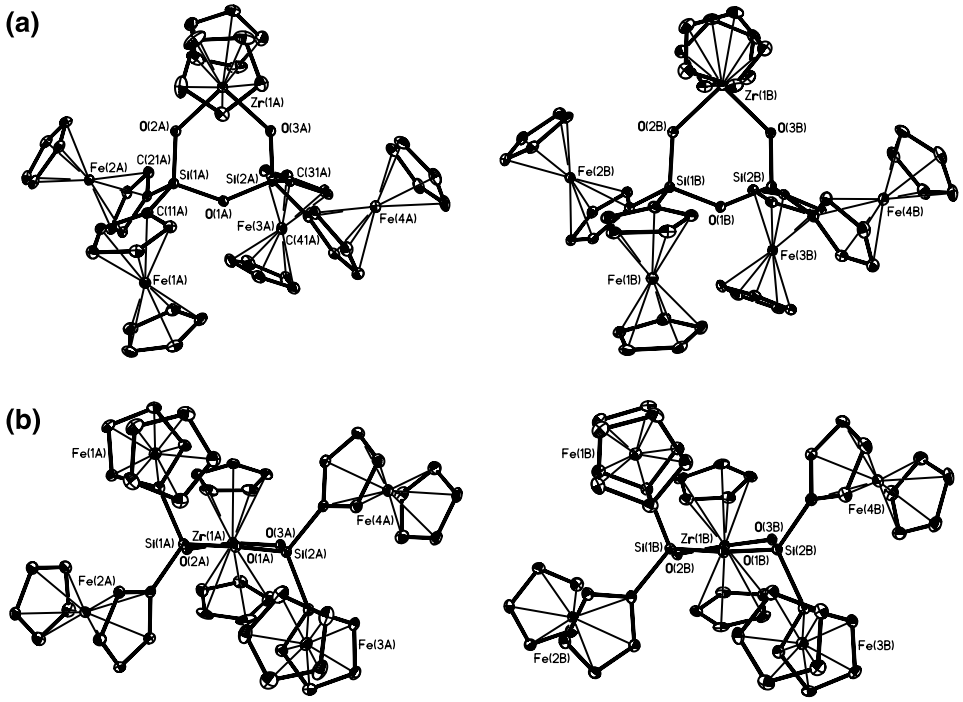

© 2002 NRC Canada

Fig. 3. (*a*) Molecular structure of **7**. (*b*) Side-on view of **7**. The structures are shown with thermal ellipsoids at the 30% probability level.

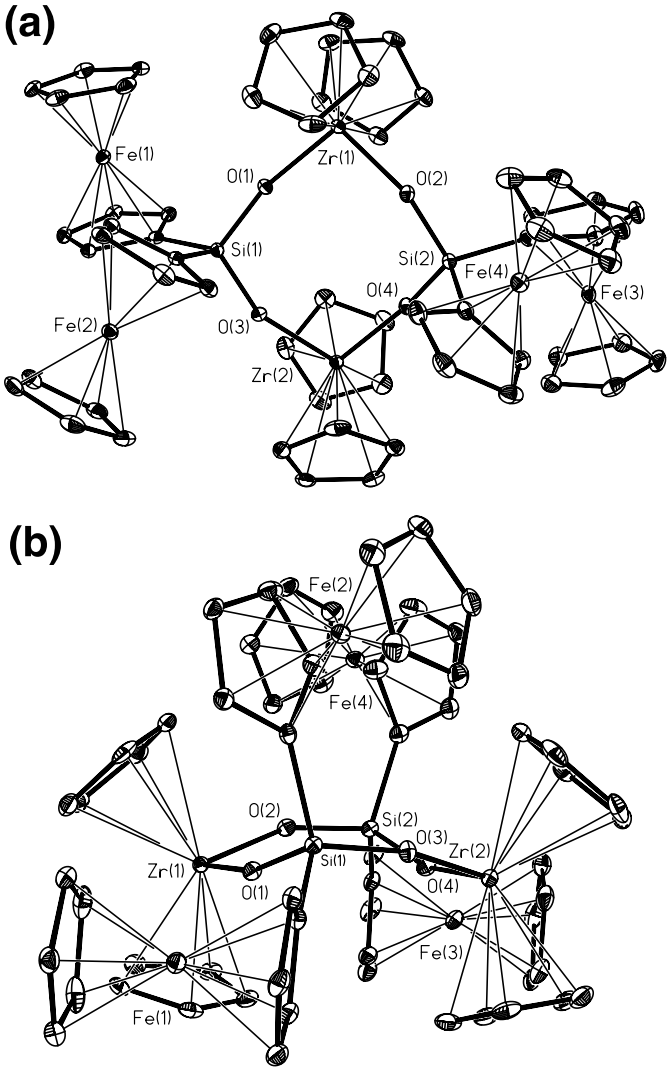

Ring-opening polymerization behaviour of the heterosiloxanes 6–9

Many inorganic rings, including many cyclosiloxanes, undergo thermal ROP. To explore the possibility for thermal ROP of the zirconaferrocenylcyclosiloxanes **6** and **7**, the thermal behaviour of these species was examined. The thermogravimetric analyses (TGA) of both **6** and **7** showed onsets of decomposition at ~170°C. Past this temperature **6** shows a multistep decomposition that ends at ~600°C and gives a ceramic yield of about 30%. In the case of **7** there is a rapid one-step decomposition that ends at ~300°C and gives an ultimate ceramic yield of approximately 35%. Differential scanning calorimetry (DSC) of **6** and **7** up to 150°C showed no melt transitions or exothermic events that could be attributed to ROP processes. Subsequent ^{1}H NMR analyses of the DSC samples showed the presence of only **6** and **7**, respectively, and confirmed that thermal ROP was not taking place prior to decomposition.

The thermal behaviour of the boraferrocenylcyclosiloxanes **8** and **9** was also investigated by TGA and DSC.

Table 5. Selected bond distances (Å) and angles (°) for **7**.

Bond distances (Å)			
Si(1)—O(1)	1.618(2)	Zr(1)—O(1)	1.982(2)
Si(1)—O(3)	1.613(2)	Zr(1)—O(2)	1.981(2)
Si(1)—C(21)	1.863(3)	Zr(1)—Cp(1)	2.252(3)
Si(1)—C(31)	1.853(3)	Zr(1)—Cp(2)	2.251(3)
Si(2)—O(2)	1.617(2)	Zr(2)—O(3)	1.986(2)
Si(2)—O(4)	1.625(2)	Zr(2)—O(4)	1.974(2)
Si(2)—C(41)	1.861(3)	Zr(2)—Cp(3)	2.252(3)
Si(2)—C(51)	1.859(3)	Zr(2)—Cp(4)	2.547(3)
Bond angles (°)			
Si(1)-O(1)-Zr(1)	158.41(12)	O(2)-Si(2)-C(41)	109.30(12)
Si(1)-O(3)-Zr(2)	155.72(12)	O(2)-Si(2)-C(51)	108.36(12)
Si(2)-O(2)-Zr(1)	153.19(12)	O(3)-Si(1)-C(21)	109.57(11)
Si(2)-O(4)-Zr(2)	157.38(11)	O(3)-Si(1)-C(31)	110.11(11)
O(1)-Si(1)-O(3)	109.92(10)	O(4)-Si(2)-C(41)	109.25(11)
O(2)-Si(2)-O(4)	109.43(10)	O(4)-Si(2)-C(51)	108.91(12)
O(1)-Zr(1)-O(2)	99.73(8)	C(21)-Si(1)-C(31)	111.00(12)
O(3)-Zr(2)-O(4)	100.06(8)	C(41)-Si(2)-C(51)	111.56(13)
O(1)-Si(1)-C(21)	109.45(11)	Cp(1)-Zr(1)-Cp(2)	128.0(1)
O(1)-Si(1)-C(31)	106.74(11)	Cp(3)-Zr(2)-Cp(4)	127.7(1)

Table 6. Selected bond distances (Å) and angles (°) for **8.**

Bond distances (Å)			
Si(1)—O(1)	1.655(2)	Si(1)—C(11)	1.835(3)
Si(1)—O(2)	1.641(1)	B(1)—O(1)	1.374(3)
Si(1)—C(1)	1.832(3)	B(1)—C(31)	1.554(6)
Bond angles (°)			
Si(1)-O(1)-B(1)	128.5(2)	O(1)-Si(1)-C(1)	106.95(12)
Si(1)-O(2)-Si(1)#1	128.49(16)	O(1)-Si(1)-C(11)	108.25(11)
O(1)-Si(1)-O(2)	105.26(11)	O(2)-Si(1)-C(1)	109.54(10)
O(1)-B(1)-O(1)#1	121.2(4)	O(2)-Si(1)-C(11)	111.14(11)
O(1)-B(1)-C(21)	119.42(18)	C(11)-Si(1)-C(21)	115.14(13)

Table 7. Selected bond distances (Å) and angles (deg) for **9**.

Bond distances (Å)			
Si(1)—O(1)	1.626(1)	B(1)—O(1)	1.354(2)
Si(1)—O(2)	1.636(1)	B(1)—O(2)#1	1.366(3)
Si(1)—C(11)	1.839(2)	B(1)—C(1)	1.566(3)
Si(1)—C(21)	1.839(2)	B(1)#1—O(2)	1.366(3)
Bond angles (°)			
Si(1)-O(1)-B(1)	166.73(14)	O(2)-Si(1)-C(11)	110.03(8)
Si(1)-O(2)-B(1)#1	137.37(13)	O(2)-Si(1)-C(21)	108.72(8)
O(1)-Si(1)-O(2)	111.22(7)	O(1)-B(1)-C(1)	118.63(18)
O(1)-B(1)-O(2)#1	122.10(17)	O(2)#1-B(1)-C(1)	119.27(17)
O(1)-Si(1)-C(11)	107.72(8)	C(11)-Si(1)-C(21)	111.41(9)
O(1)-Si(1)-C(21)	107.73(8)		

The 6-membered ring **8** showed a decomposition between ~275 and 540°C, with an ultimate ceramic yield of 77%. The 8-membered ring **9** showed decomposition between ~230 and 450°C and had an ultimate ceramic yield of ~18%. The DSC scans of **8** and **9** (up to 200°C) showed no melt transitions or exotherms that could be attributed to ROP. As

© 2002 NRC Canada

Fig. 4. (*a*) Molecular structure of **8**. (*b*) Side-on view of **8**. The structures are shown with thermal ellipsoids at the 30% probability level.

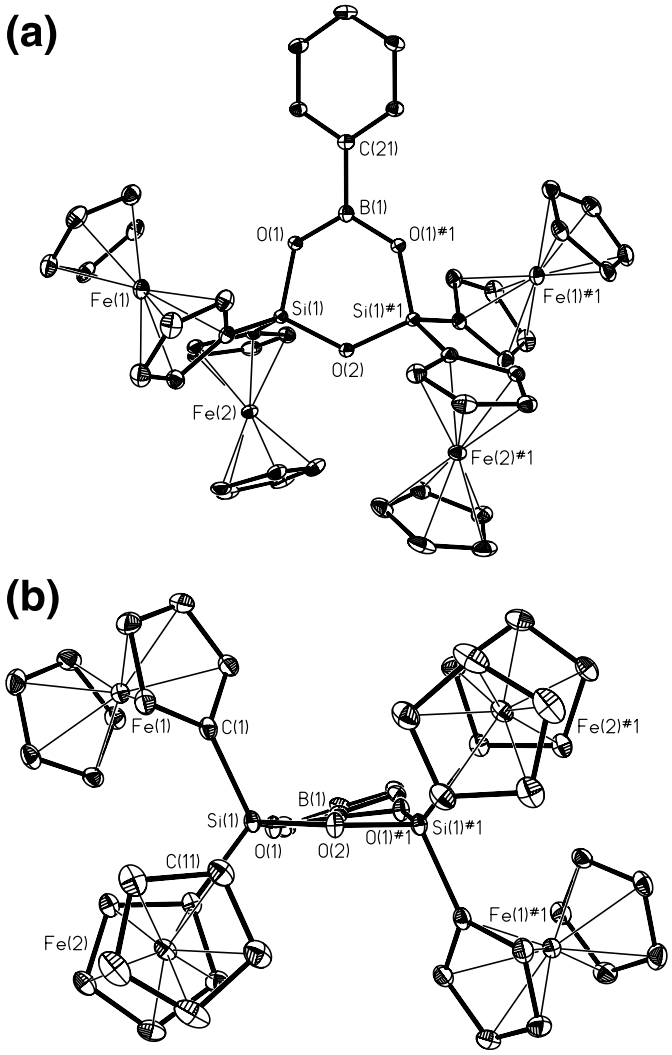

Fig. 5. (*a*) Molecular structure of **9**. (*b*) Side-on view of **9**. The structures are shown with thermal ellipsoids at the 30% probability level.

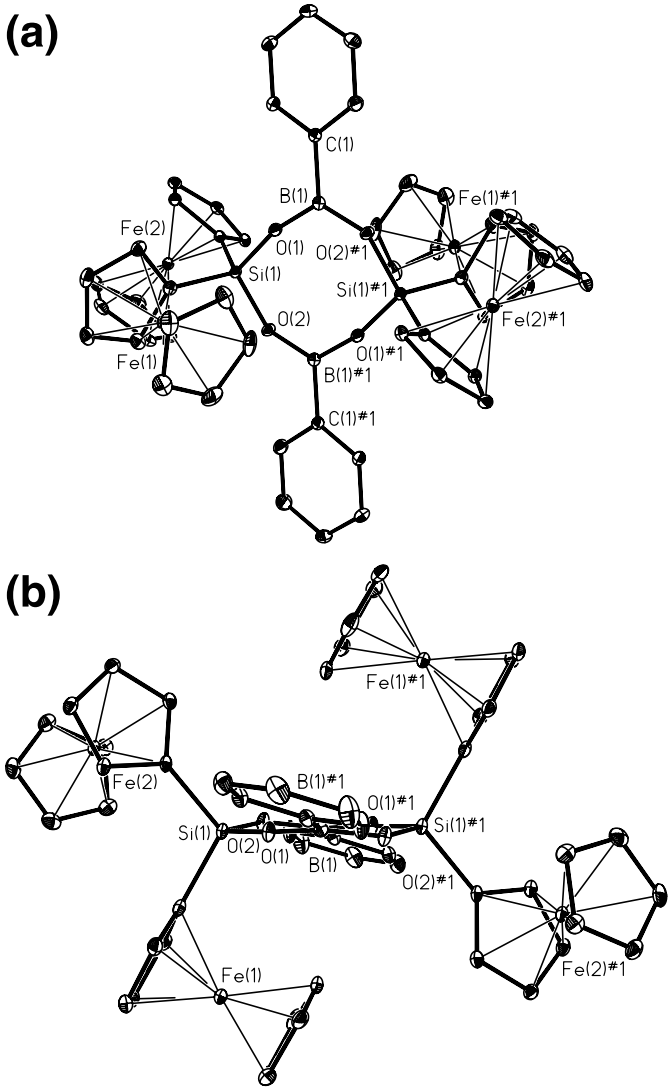

in the cases of the zirconium-containing rings, the ^{1}H NMR of the samples of **8** and **9** after DSC showed only the original rings and confirmed the lack of thermal ROP for these systems.

Attempts to induce anionic and cationic ROP of the rings were also made, but in no case was there evidence for the formation of ring-opened polymer or oligomers upon treatment with 10 mol% anionic ($KOSiMe_3$) or cationic (HOTf) initiator. In the case of the 8-membered boraferrocenylcyclosiloxane ring **9** there is ^{1}H NMR evidence for ring–ring redistributions in the presence of $KOSiMe_3$, as seen by the appearance of resonances due to both **8** and another unidentified product. Under these conditions ring rearrangement reactions are likely favoured over ROP, as previously observed for other boracyclosiloxane systems (7). It is well known that the presence of large substituents on monomers hinder ROP, and it is possible that the large ferrocenyl substituents on the silicon atoms of **6**–**9** significantly disfavour the formation of extended chain polyheterosiloxanes.

Experimental

General

$PhBCl_2$, $KOSiMe_3$, and HOTf were purchased from Aldrich and used as received. Triethylamine (Aldrich) was dried over sodium, distilled, and stored over molecular sieves prior to use. $Cp_2Zr(NMe_2)_2$ (22), $Fc_2Si(OH)_2$ (**3**) (13), and $[Fc_2SiOH]_2O$ (**5**) (13) were prepared according to literature methods.

All reactions and manipulations were carried out under an atmosphere of prepurified nitrogen using either an inert-atmosphere glovebox or Schlenk techniques, unless otherwise noted. Solvents were dried by standard methods, distilled, and stored under nitrogen. The 400 MHz ^{1}H NMR and 100 MHz ^{13}C NMR spectra were recorded on a Varian Unity 400 spectrometer. ^{1}H NMR spectra were referenced to residual protons in C_6D_6 at 7.15 ppm or $CDCl_3$ at 7.24 ppm, and ^{13}C NMR spectra were referenced to the C_6D_6 signal at 128.0 ppm or the $CDCl_3$ signal at 77.0 ppm. The 79.5 MHz

© 2002 NRC Canada

^{29}Si NMR spectra were recorded on a Varian Unity 400 spectrometer using a proton-decoupled pulse sequence and were referenced externally to $SiMe_4$ (TMS). The 160 MHz ^{11}B NMR spectra were recorded on a Varian Unity 500 spectrometer and were visualized by cutting off the broad glass peak from the FID. The spectra were referenced externally to $BF_3{\cdot}Et_2O$. UV–vis spectra were obtained in CH_2Cl_2 on a Perkin-Elmer Lambda 900 UV/VIS-near IR spectrometer using a 1-cm quartz cuvette. IR spectra were obtained as Nujol mulls or CCl_4 solutions with a Perkin-Elmer Protagon 500 FT-IR spectrometer. FT-Raman spectra were collected on a Bomem MB-157 FT spectrometer with a Spectra Physics diode pumped Nd:YLF laser (1064 nm, 350 kHz repetition rate). The instrument was configured in 180° backscattering mode using sealed glass capillary tubes to hold the neat samples. Electron impact (EI) and fast atom bombardment (FAB) mass spectra were obtained with a VG 70-250S mass spectrometer. Elemental analyses were performed by Quantitative Technologies Inc., Whitehouse, N.J. Thermogravimetric analysis was performed on a TA Instruments TGA Q500 instrument at 10°C min^{-1}, from 25°C to 900°C, under an atmosphere of prepurified nitrogen. Differential scanning calorimetry was performed on a TA Instruments DSC 2920 instrument calibrated at a heating rate of 10°C min^{-1} using a traceable indium reference standard with a melting point of 156.6°C and a heat of fusion of 28.71 J g^{-1}. Melting points were obtained with a Fisher-Johns melting point apparatus and are uncorrected.

Synthesis of $Cp_2Zr(OSiFc_2)_2O$ (6)

A solution of 0.200 g (0.236 mmol) of tetraferrocenyldisiloxanediol (**5**) dissolved in 150 mL diethyl ether was cooled to –78°C. A cooled solution of 72 mg (0.23 mmol) bis(dimethylamino)zirconocene in 20 mL ether was added dropwise to the stirred reaction mixture. The reaction solution was stirred for several hours while it warmed to room temperature and was then filtered through a frit. The solvent was removed from the yellow filtrate to give the crude product. Recrystallization from dichloromethane afforded 0.235 g (0.221 mmol, 95%) of **6** as an orange-yellow powder. ^{1}H NMR (400 MHz, C_6D_6) δ: 6.20 (s, 10H, Zr-Cp), 4.88 (qt, $^3J_{HH}$ = 0.88 Hz, 4H, C_5H_4), 4.80 (qt, $^3J_{HH}$ = 1.10 Hz, 4H, C_5H_4), 4.39 (qt, $^3J_{HH}$ = 1.18 Hz, 8H, C_5H_4), 4.23 (s, 20H, Fe-Cp) ppm. ^{13}C NMR (100 MHz, C_6D_6) δ: 114.03 (Zr-Cp), 74.74 (C_5H_4), 74.24 (C_5H_4), 71.49 (C_5H_4), 71.29 (C_5H_4), 69.44 (Fe-Cp), 69.21 (*ipso*-C_5H_4) ppm. ^{29}Si NMR (79.5 MHz, C_6D_6) δ: –33.0 ppm. UV–vis (CH_2Cl_2): λ (ε) 452 (408) nm (L mol^{-1} cm^{-1}). MS (EI, 70 eV): m/z (%) 1064 (M^+, 100), 627 (M^+-2FcH-Cp, 46), 186 (FcH^+, 68), 121 ($CpFe^+$, 39). mp: dec. >120°C. Anal. calcd.: C 53.24, H 4.20; found: C 52.38, H 4.11.

Synthesis of $[Cp_2Zr(OSiFc_2)O]_2$ (7)

A solution of 0.100 g (0.323 mmol) bis(dimethylamino)zirconocene in 30 mL diethyl ether was dropped into a stirred solution of 0.14 g (0.323 mmol) diferrocenylsilanediol (**3**) in ether at –78°C. A white precipitate formed while the mixture was warmed to room temperature over 6 h. The solvent was removed under vacuum, leaving a yellow residue. The product was dissolved in a minimum of dichloromethane, filtered, and recrystallized at –20°C. After the yellow powder was collected, it was dissolved in chloroform. Slow evaporation of the solvent gave yellow X-ray quality crystals of **7**. The overall yield was 95% (0.200 g, 0.153 mmol). ^{1}H NMR (400 MHz, C_6D_6) δ: 6.22 (s, 20H, Zr-Cp), 4.77 (t, $^3J_{HH}$ = 1.60 Hz, 8H, C_5H_4), 4.41 (t, $^3J_{HH}$ = 1.65 Hz, 8H, C_5H_4), 4.32 (s, 20H, Fe-Cp) ppm. ^{13}C NMR (100 MHz, C_6D_6) δ: 113.50 (Zr-Cp), 74.45 (C_5H_4), 72.82 (*ipso*-C_5H_4), 71.19 (C_5H_4), 69.32 (Fe-Cp) ppm. ^{29}Si NMR (79.5 MHz, C_6D_6) δ: –35.7 ppm. UV–vis (CH_2Cl_2): λ (ε) 458 (551) nm (L mol^{-1} cm^{-1}). MS (EI, 70 eV): m/z (%) 1302 (M^+, 15), 1051 (M^+-O_2ZrCp_2+H_2, 5), 865 (M^+-O_2ZrCp_2-FcH+H_2, 19), 799 (M^+-O_2ZrCp_2-FcH-Cp+H^+, 6), 733 (M^+-O_2ZrCp_2-FcH-2Cp, 4), 679 (M^+-O_2ZrCp_2-2FcH+H_2, 8), 186 (FcH^+, 100), 121 ($CpFe^+$, 40). mp: dec. >200°C. Anal. calcd.: C 55.30, H 4.33; found: C 54.62, H 4.21.

Synthesis of $(C_6H_5)B(OSiFc_2)_2O$ (8)

Tetraferrocenyldisiloxanediol (**5**) (0.106 g, 0.125 mmol) was dissolved in 150 mL of diethyl ether and cooled to –78°C. Ten equivalents (100 μL, 1.25 mmol) of triethylamine were then added to the solution. A solution of 20 mg (0.125 mmol) $PhBCl_2$ in 7 mL of diethyl ether was then added dropwise. The reaction mixture was stirred for an additional 2 h at –78°C and was then warmed to room temperature overnight. The mixture was filtered under nitrogen and the slightly yellow precipitate was washed with THF. Solvent removal under vacuum afforded a crude yellow solid that was dried under vacuum to remove excess triethylamine. The residue was then dissolved in dichloromethane and recrystallized at –55°C. Dark orange crystals that shattered under vacuum because of loss of solvent from the structure, were obtained. Compound **8** was isolated in an 85% (0.099 g, 0.106 mmol) yield. ^{1}H NMR (400 MHz, C_6D_6) δ: 8.36 (m, 2H, Ph), 7.30 (m, 3H, Ph), 4.68 (m, 4H, C_5H_4), 4.58 (m, 4H, C_5H_4), 4.30 (m, 4H, C_5H_4), 4.28 (m, 4H, C_5H_4), 4.22 (s, 20H, Cp) ppm. ^{11}B NMR (160 MHz, C_6D_6) δ: 30.5 ppm. ^{13}C NMR (100 MHz, C_6D_6) δ: 135.90 (Ph), 131.89 (B-Ph), 74.42 (C_5H_4), 74.20 (C_5H_4), 72.09 (C_5H_4), 71.95 (C_5H_4), 69.41 (Fe-Cp), 65.81 (*ipso*-C_5H_4) ppm. ^{29}Si NMR (79.5 MHz, C_6D_6) δ: –20.0 ppm. UV–vis (CH_2Cl_2): λ (ε) 450 (465) nm (L mol^{-1} cm^{-1}). MS (EI, 70 eV): m/z (%) 932 (M^+, 100), 746 (M^+-FcH, 9), 681 (M^+-FcH-Cp, 27), 577 (M^+-FcH-Cp-OBPh, 19), 466 (M^{++}, 11), 186 (FcH^+, 68), 121 ($CpFe^+$, 39). mp 249°C. Anal. calcd.: C 59.28, H 4.43, N 0.00; found: C 58.70, H 4.46, N 0.09.

Synthesis of $[(C_6H_5)B(OSiFc_2)O]_2$ (9)

A solution of 39.7 mg (0.249 mmol) $PhBCl_2$ in 10 mL diethylether was added dropwise to a stirred mixture of 0.108 g (0.249 mmol) diferrocenylsilanediol (**3**) and 0.348 mL (2.49 mmol) triethylamine in 150 mL ether at –78°C. A white precipitate, $[HNEt_3]Cl$, formed after 15 min, but to achieve complete conversion the mixture was stirred for another 8 h while it warmed to room temperature. Filtration through a glass frit, followed by washing with THF until the washings ran clear, gave a yellow solution that was evaporated to dryness to remove solvent and excess triethylamine. The yellow powder was then recrystallized from dichloromethane at –40°C to finally give ca. 30 mg (0.029 mmol, 23%) light orange crystals of **9**. ^{1}H NMR (400 MHz, $CDCl_3$) δ: 8.18 (d, $^3J_{HH}$ = 7.8 Hz, 4H, Ph), 7.53 (m, 6H, Ph), 4.42

© 2002 NRC Canada

(t, $^3J_{HH}$ = 1.65 Hz, 8H, C_5H_4), 4.37 (t, $^3J_{HH}$ = 1.65 Hz, 8H, C_5H_4), 4.03 (s, 20H, Cp) ppm; ^{11}B NMR (160 MHz, $CDCl_3$) δ: 28.1 ppm; ^{13}C NMR (100.5 MHz, $CDCl_3$) δ: 135.05 (Ph), 131.56 (B-Ph), 127.93 (Ph), 73.44 (C_5H_4), 71.16 (C_5H_4), 68.58 (Cp), 66.81 (*ipso*-C_5H_4) ppm; ^{29}Si NMR (79.5 MHz, $CDCl_3$) δ: –31.8 ppm. UV–vis (CH_2Cl_2): λ 449 nm. MS (EI, 70 eV): m/z (%) 1036 (M^+, 100), 932 (M^+-OBPh, 7), 850 (M^+-FcH, 5), 785 (M^+-FcH-Cp, 4), 746 (M^+-FcH-OBPh, 7), 681 (M^+-FcH-Cp-OBPh, 35), 577 (M^+-FcH-Cp-2OBPh, 20), 518 (M^{++}, 16), 186 (FcH^+, 17). mp 232–5°C.

Thermogravimetric analysis of 6–9

For **6**: 5.6160 mg; multistage decomp. (% char yield): 170–195°C (83%); 195–250°C (52%); 250–295°C (46%); 295–600°C (30%); ceramic yield (900°C): 30%. For **7**: 5.3350 mg; one-stage decomp. (% char yield): 170–300°C (35%); ceramic yield (900°C): 35%. For **8**: 6.9610 mg; two-stage decomp. (% char yield): 275–400°C (80%), 400–540°C (78%); ceramic yield (900°C): 77%. For **9**: 5.7710 mg; two-stage decomp. (% char yield): 230–300°C (95%), 300–450°C (30%); ceramic yield (900°C): 18%.

Differential scanning calorimetry of 6–9

For **6**: 10.1 mg; 10–150°C. For **7**: 7.9 mg; 10–150°C. For **8**: 7.8 mg; 10–200°C. For **9**: 7.8 mg; 10–200°C. No thermal events consistent with melt transitions or ROP exotherms were observed for **6–9**.

Attempted anionic polymerizations of 6–9

The procedure for each sample is analogous and follows the sample procedure detailed. $Cp_2Zr(OSiFc_2)_2O$ (**6**) (11 mg, 9 μmol) was dissolved in 8 mL THF. The solution was initiated with 132 μL $KOSiMe_3$ (1 mg mL^{-1} in THF; 0.9 μmol). After the reaction mixture stirred for ca. 1d solvent was removed under vacuum to leave a yellow residue. The residue was redissolved in C_6D_6 and characterized using ^{1}H NMR. Only resonances for **6** and $KOSiMe_3$ were observed. For **7**: 22 mg, 16 mmol, 15 mL THF, 216 μL of 1 mg mL^{-1} $KOSiMe_3$ in THF. Only resonances for **7** and $KOSiMe_3$ were observed. For **8**: 20 mg, 22 mmol, 15 mL THF, 275 μL of 1 mg mL^{-1} $KOSiMe_3$ in THF. Only resonances for **8** and $KOSiMe_3$ were observed. For **9**: 15 mg, 15 mmol, 12 mL THF, 185 μL of 1 mg mL^{-1} $KOSiMe_3$ in THF. Resonances for **9**, the ring-contraction product **8**, and an unidentified nonpolymeric species were observed.

Attempted cationic polymerizations of 6–9

The procedure for each sample is analogous and follows the sample procedure detailed. $Cp_2Zr(OSiFc_2)_2O$ (**6**) (12 mg, 10 μmol) was dissolved in 8 mL CH_2Cl_2. The solution was initiated with 99 μL HOTf (1 μL mL^{-1} in CH_2Cl_2; 1.0 μmol). After the reaction mixture stirred for ca. 1 d, solvent was removed under vacuum to leave a yellow residue. The residue was redissolved in C_6D_6 and characterized using ^{1}H NMR. The presence of **6** and free ferrocene, due to Si–Fc cleavage (~5%), was detected. For **7**: 26 mg, 17 mmol, 15 mL CH_2Cl_2, 177 μL of 1 μL mL^{-1} HOTf in CH_2Cl_2. Only the presence of **7** was detected. For **8**: 21 mg, 22 mmol, 15 mL CH_2Cl_2, 199 μL of 1 μL mL^{-1} HOTf in CH_2Cl_2. The presence of **8** and free ferrocene, due to Si–Fc cleavage (~90%), were detected. For **9**: 17 mg, 16 mmol, 12 mL CH_2Cl_2, 145 μL of 1 μL mL^{-1} HOTf in CH_2Cl_2. **9** was no longer identifiable in the sample but a large ferrocene resonance is indicative of almost complete cleavage of this substituent from the ring. No resonances due to polymer or oligomer were observed for any of the trials.

Crystallographic structural determination

Selected crystal, data collection, and refinement parameters for **6–9** are given in Table 3. Selected intermolecular bond lengths and angles for **6–9** are given in Tables 4–7, respectively.[3] Single-crystal X-ray diffraction data were collected at low temperature under nitrogen with a Nonius Kappa-CCD diffractometer using graphite monochromated MoK_α radiation (λ = 0.710 73 Å). The data were integrated and scaled using the Denzo-SMN package (23). The SHELXTL/PC package was used to solve and refine the structures (24). Refinement was by full-matrix least-squares on F^2 using all data (negative intensities included). Refinement was optimized with hydrogen atoms in calculated positions. The weighting schemes were $w = 1/[\sigma^2(F_o^2) + (0.0328P)^2 + 4.0372P]$ for **6**, $w = 1/[\sigma^2(F_o^2) + (0.0321P)^2 + 1.8184P]$ for **7**, $w = 1/[\sigma^2(F_o^2) + (0.0443P)^2 + 5.6603P]$ for **8**, and $w = 1/[\sigma^2(F_o^2) + (0.0252P)^2 + 0.9821P]$ for **9**, where $P = (F_o^2 + 2F_c^2)/3$.

Summary

Our results show that diferrocenylsilanediol (**3**) and tetraferrocenyldisiloxanediol (**5**) are useful precursors to novel heterocyclosiloxanes with redox-active ferrocenyl substituents on the Si atoms. Zirconatetraferrocenylcyclosiloxanes **6** and **7** and boratetraferrocenylcyclosiloxanes **8** and **9** have been synthesized and characterized. The inorganic heterosiloxanes were also investigated by single crystal X-ray diffraction. Attempts to induce ROP of the cyclics have been unsuccessful to date. Future work will involve expansion of the range of inorganic elements incorporated into cyclosiloxane frameworks with an emphasis on the use of small substituents that would be expected to favour ROP processes.

Acknowledgments

K.T. thanks the Deutscher Akademischer Auslandsdienst (DAAD) for a research fellowship. S.C.B. thanks the Ontario Government for Postgraduate Scholarships (1998–2002). M.J.M. thanks the Natural Sciences and Engineering Research Council of Canada (NSERC) for Postgraduate Scholarships (1995–1999). I.M. thanks NSERC for an E.W.R. Steacie Fellowship (1997–1999) and the University of Toronto for a McLean Fellowship (1997–2003), the Ontario Government for a PREA Award (1999–2004), and the Canadian Government for a Canada Research Chair. We thank Dr. Timothy J. Peckham for kindly donating

[3] CCDC 179871 (**6**·CH_2Cl_2), 179872 (**7**·2$CHCl_3$), 179873 (**8**·2CH_2Cl_2) and 179874 (**9**) contain the supplementary crystallographic data for this paper. These data can be obtained, free of charge, via www.ccdc.cam.ac.uk/conts/retrieving.html (or from the Cambridge Crystallographic Data Centre, 12 Union Road, Cambridge CB2 1EZ, U.K.; Fax: 44–1223–336033 or e-mail: deposit@ccdc.cam.ac.uk)

© 2002 NRC Canada

bis(dimethylamino)zirconocene and K. Nicole Power-Billard, Alison Cheng, and Sébastien Fournier for performing DSC and TGA analyses.

References

1. See, for example (*a*) T. Kato, H. Gornitzka, A. Baceiredo, W.W. Schoeller, and G. Bertrand. Science (Washington, D.C.), **289**, 754 (2000); (*b*) N.J. Hardman, P.P. Power, J.D. Gorden, C.L.B. Macdonald, and A.H. Cowley. Chem. Commun. 1866 (2001); (*c*) N.J. Hardman, C. Cui, H.W. Roesky, W.H. Fink, and P.P. Power. Angew. Chem. Int. Ed. **40**, 2172 (2001); (*d*) P.D. Boyle, S. Parsons, J. Passmore, and D.J. Wood. Chem. Commun. 199 (1993); (*e*) N. Burford, C.L.B. Macdonald, T.M. Parks, G. Wu, B. Borecka, W. Kwiatkowski, and T.S. Cameron. Can. J. Chem. **74**, 2209 (1996); (*f*) S.B. Clendenning, P.B. Hitchcock, J.F. Nixon, and L. Nyulászi. Chem. Commun. 1305 (2000); (*g*) T. Chivers, X. Gao, and M. Parvez. J. Am. Chem. Soc. **117**, 2359 (1995); (*h*) D.P. Gates, A.R. McWilliams, R. Ziembinski, L.M. Liable-Sands, I.A. Guzei, G.P.A. Yap, A.L. Rheingold, and I. Manners. Chem. Eur. J. **4**, 1489 (1998).
2. (*a*) C.E. Radzewich, M.P. Coles, and R.F. Jordan. J. Am. Chem. Soc. **120**, 9384 (1998); (*b*) A.V. Korolev, E. Ihara, I.A. Guzei, V.G. Young, Jr., and R.F. Jordan. J. Am. Chem. Soc. **123**, 8291 (2001).
3. (*a*) P. Binger, S. Stutzmann, J. Stannek, B. Gabor, and R. Mynott. Eur. J. Inorg. Chem. 83 (1999); (*b*) M.D. Francis, D.E. Hibbs, P.B. Hitchcock, M.B. Hursthouse, C. Jones, T. Mackewitz, J.F. Nixon, L. Nyulaszi, M. Regitz, and N. Sakarya. J. Organomet. Chem. **580**, 156 (1999); (*c*) T. Chivers, X. Gao, and M. Parvez. Inorg. Chem. **34**, 1681 (1995); (*d*) A.J. Ashe, III, X. Fang, X. Fang, and J.W. Kampf. Organometallics, **20**, 5413 (2001); (*e*) S.-Y. Liu, M.M.-C. Lo, and G.C. Fu. Angew. Chem. Int. Ed. **41**, 174 (2002).
4. (*a*) I. Manners. Angew. Chem. Int. Ed. Engl. **35**, 1602 (1996); (*b*) P. Nguyen, P. Gómez-Elipe, and I. Manners. Chem Rev. **99**, 1515 (1999).
5. (*a*) J.C. Saam. *In* Silicon based polymer science: A comprehensive resource. *Edited by* J.M. Ziegler and F.W.G. Fearon. Advances in Chemistry Series **224.** American Chemical Society, Washington, DC. 1990. pp. 71–90; (*b*) S.J. Clarson and J.A. Semlyen (*Editors*). Siloxane polymers. Prentice-Hall, Englewood Cliffs, N.J. 1993.
6. (*a*) R. Murugavel, A. Voigt, M.G. Walawalkar, and H.W. Roesky. Chem. Rev. **96**, 2205 (1996); (*b*) L. King and A.C. Sullivan. Coord. Chem. Rev. **189**, 19 (1999); (*c*) V. Lorenz, A. Fischer, S. Giessmann, J.W. Gilje, Y. Gun'ko, K. Jacob, and F.T. Edelmann. Coord. Chem. Rev. **206–207**, 321 (2000).
7. (*a*) D.A. Foucher, A.J. Lough, and I. Manners. J. Organomet. Chem. **414**, C1 (1991); (*b*) D.A. Foucher, A.J. Lough, and I. Manners. Inorg. Chem. **31**, 3034 (1992).
8. For other work on these systems see: B.J. Brisdon, M.F. Mahon, K.C. Molloy, and P.J. Schofield. J. Organomet. Chem. **436**, 11 (1992).
9. C. Angelakos, D.B. Zamble, D.A. Foucher, A.J. Lough, and I. Manners. Inorg. Chem. **33**, 1709 (1994).
10. (*a*) J. Beckmann and K. Jurkschat. Coord. Chem. Rev. **215**, 267 (2001); (*b*) J. Beckmann, K. Jurkschat, U. Kaltenbrunner, N. Pieper, and M. Schurmann. Organometallics, **18**, 1586 (1999).
11. M.J. MacLachlan, A.J. Lough, W.E. Geiger, and I. Manners. Organometallics, **17**, 1873 (1998).
12. M.J. MacLachlan, M. Ginzburg, J. Zheng, O. Knöll, A.J. Lough, and I. Manners. New J. Chem. **22**, 1409 (1998).
13. M.J. MacLachlan, J. Zheng, A.J. Lough, I. Manners, C. Mordas, R. LeSuer, W.E. Geiger, L.M. Liable-Sands, and A.L. Rheingold. Organometallics, **18**, 1337 (1999).
14. For recent studies of other ferrocenyl siloxanediols and related species see: E.A. Reyes-García, F. Cervantes-Lee, and K.H. Pannell. Organometallics, **20**, 4734 (2001).
15. (*a*) M. Liang and I. Manners. J. Am. Chem. Soc. **113**, 4044 (1991); (*b*) D.P. Gates and I. Manners. J. Chem. Soc., Dalton Trans. 2525 (1997).
16. A. Voigt, R. Murugavel, H.W. Roesky, and H.-G. Schmidt. J. Mol. Struct. **436–437**, 49 (1997).
17. M.A. Hossain and M.B. Hursthouse. Inorg. Chim. Acta, **44**, L259 (1980).
18. D.C. Hrncir. Mater. Res. Soc. Symp. Proc. **121**, 127 (1988).
19. U. Wannagat and G. Eisele. Z. Naturforsch. **33b**, 475 (1978).
20. A. Mazzah, A. Haoudi-Mazzah, M. Noltemeyer, and H.W. Roesky. Z. Anorg. Allg. Chem. **604**, 93 (1991).
21. F.J. Feher, T.A. Budzichowski, and J.W. Ziller. Inorg. Chem. **31**, 5100 (1992).
22. G. Chandra and M.F. Lappert. J. Chem. Soc. A, 1940 (1968).
23. Z. Otwinowski and W. Minor. Methods Enzymol. **276**, 307 (1997).
24. G.M. Sheldrick. SHELXTL\PC v5.1. Bruker Analytical X-Ray Systems. Madison, Wisc., U.S.A. 1997.

© 2002 NRC Canada

The synthesis of [{*n*-$Bu_2Sn(S_2N_2)$}$_2$] and its use in the preparation of organometallic iridium sulfur nitrogen complexes

Stephen M. Aucott, Alexandra M.Z. Slawin, and J. Derek Woollins

Abstract: The addition of [*n*-Bu_2SnCl_2] to a solution of $[S_4N_3][Cl]$ in liquid ammonia gave after extraction of the dry reaction mixture the new tin disulfur dinitrido compound [{*n*-$Bu_2Sn(S_2N_2)$}$_2$] (**1**). Reaction of [{*n*-$Bu_2Sn(S_2N_2)$}$_2$] (**1**) with the pentamethylcyclopentadienyl (Cp*) iridium derivatives [{$IrCl(\mu\text{-}Cl)(\eta^5\text{-}C_5Me_5)$}$_2$] or [($\eta^5$-$C_5Me_5$)$IrCl_2(PPh_3)$] gave different products, which were dependent on the reactant ratios. A 1:1 reaction between **1** and [{$IrCl(\mu\text{-}Cl)(\eta^5\text{-}C_5Me_5)$}$_2$] gave only [($\eta^5$-$C_5Me_5$)$Ir(S_2N_2)$] (**2**) in moderate yield; the same product in higher yield was obtained from a 2:1 reaction between **1** and [(η^5-C_5Me_5)$IrCl_2(PPh_3)$]. Reaction of **1** and [(η^5-C_5Me_5)$_2IrCl_2(PPh_3)$] (1:1 molar ratio) in the presence of $NH_4[PF_6]$ gave the unusual bimetallic species [(η^5-C_5Me_5)$IrCl(PPh_3)(S_2N_2)Ir(\eta^5\text{-}C_5Me_5)][PF_6]$ (**3**). The X-ray crystal structures of **1**, **2**, and **3** are reported.

Key words: liquid ammonia, tin sulfur–nitrogen reagent, metathesis, sulfur–nitrogen metallacycle, iridium complexes.

Résumé : L'addition du [*n*-Bu_2SnCl_2] à une solution de $[S_4N_3][Cl]$, dans de l'ammoniac liquide, suivie d'une extraction conduit à la formation d'un mélange réactionnel sec du nouveau composé dinitrido disoufre étain [{*n*-$Bu_2Sn(S_2N_2)$}$_2$] (**1**). La réaction du composé [{*n*-$Bu_2Sn(S_2N_2)$}$_2$] (**1**) avec les dérivés pentaméthylcyclopentadiényl (Cp*) iridium [{$IrCl(\mu\text{-}Cl)(\eta^5\text{-}C_5Me_5)$}$_2$] ou [($\eta^5$-$C_5Me_5$)$IrCl_2(PPh_3)$] conduit à des produits différents suivant les rapports de réactifs. Une réaction 1:1 entre **1** et [{$IrCl(\mu\text{-}Cl)(\eta^5\text{-}C_5Me_5)$}$_2$] ne conduit qu'au produit [(η^5-C_5Me_5)$Ir(S_2N_2)$] (**2**) avec un rendement moyen; on obtient le même produit, avec un rendement un peu plus élevé par réaction 2:1 entre **1** et [(η^5-C_5Me_5)$IrCl_2(PPh_3)$]. La réaction du composé **1** avec [(η^5-C_5Me_5)$_2IrCl_2(PPh_3)$] (rapport molaire 1:1) en présence de $NH_4[PF_6]$ conduit à la formation de l'espèce bimétallique inhabituelle [(η^5-C_5Me_5)$IrCl(PPh_3)(S_2N_2)Ir(\eta^5\text{-}C_5Me_5)][PF_6]$ (**3**). On a déterminé les structures cristallines des composés **1**, **2** et **3** par diffraction des rayons X.

Mots clés : ammoniac liquide, réactif azote–soufre étain, métathèse, métallacycle soufre–étain, complexes de l'iridium.

[Traduit par la Rédaction]

Introduction

Silyl and tin reagents have proven useful sources of sulfur–nitrogen fragments in the synthesis of heterocycles (1, 2). In many examples the driving force of these reactions is the formation of M—X (M = Si or Sn; X = Br, Cl, or F) bonds. Thus, for example, bis(trimethylsilyl)sulfur diimide $(Me_3Si)_2N_2S$ reacts with $S_4N_4Cl_2$ and *o*-$C_6H_4(SCl)_2$, providing an $[N_2S]^{2-}$ fragment, to give S_5N_6 (3) and *o*-$C_6H_4(SN)_2S$ (4), respectively. Similarly [{$Me_2Sn(S_2N_2)$}$_2$] (5) supplies an $[S_2N_2]^{2-}$ fragment and gives the five-membered ring compounds $C(O)S_2N_2$ (6) and $S(O)S_2N_2$ (7) with carbonyl fluoride (COF_2) and thionyl fluoride (SOF_2), respectively. Metal sulfur nitrides (see references 8 and 9 for reviews) have been prepared analogously from Group 14 sulfur–nitrogen reagents and metal halides. Examples include formation of the eight-membered ring compound $(MeAsNSN)_2$ (10) by reaction of $(Me_3Si)_2N_2S$ with $MeAsCl_2$ and complexes of the type $[M(S_2N_2H)(PR_3)_2][X]$ (X = Me_2SnCl_3, PF_6, or BF_4) (11) by treating *cis*-$[MCl_2(PR_3)_2]$ (M = Pt or Pd) with [{$Me_2Sn(S_2N_2)$}$_2$] via the elimination of Me_3SiCl and Me_2SnCl_2, respectively. Group 9 metal complexes containing the $[S_2N_2]^{2-}$ ligand are uncommon (especially when compared with those of Group 10 and in particular those of platinum) examples being [(η^5-C_5H_5)$Co(S_2N_2)$] (12–14), [(η^5-C_5Me_5)$Co(S_2N_2)$] (13–14), and $[Ir(dppe)_2(S_2N_2)][BPh_4]$ (15) (dppe = *cis*-1,2-bis(diphenylphosphino)ethane) prepared by the action of S_4N_4 on [(η^5-C_5H_5)$Co(CO)_2$] or [(η^5-C_5H_5)Co(cod)], [(η^5-C_5Me_5)$Co(CO)_2$], and $[Ir(dppe)_2(CO)][BPh_4]$, respectively. We report here the synthesis of two new organometallic thiazene complexes of iridium [(η^5-C_5Me_5)$Ir(S_2N_2)$] (**2**) and [(η^5-C_5Me_5)$IrCl(PPh_3)$-$(S_2N_2)Ir(\eta^5\text{-}C_5Me_5)][PF_6]$ (**3**) prepared by metathesis using [{*n*-$Bu_2Sn(S_2N_2)$}$_2$] (**1**), a new example of a dialkyl–SnS_2N_2 dimer, of which only two other examples are known, the aforementioned methyl derivative [{$Me_2Sn(S_2N_2)$}$_2$] (5) and the *tert*-butyl analogue [{*t*-$Bu_2Sn(S_2N_2)$}$_2$] (16, 17).

Received 2 February 2002. Published on the NRC Research Press Web site at http://canjchem.nrc.ca on 12 November 2002.

Dedicated to Professor Tris Chivers in recognition of his unique contribution to main group chemistry.

S.M. Aucott, A.M.Z. Slawin, and J.D. Woollins.[1] School of Chemistry, University of St Andrews, Fife, Scotland KY16 9ST.

[1]Corresponding author (e-mail: jdw3@st-and.ac.uk).

 DOI: 10.1139/V02-085 © 2002 NRC Canada

Experimental

General

Unless otherwise stated, manipulations were performed under an oxygen-free nitrogen or argon atmosphere using pre-dried solvents and standard Schlenk techniques. The ammonia used was obtained from BOC Ltd and dried by passage through a column of NaOH. The reagents $[S_4N_3][Cl]$ (18) and $[\{IrCl(\mu\text{-}Cl)(\eta^5\text{-}C_5Me_5)\}_2]$ (19) were both prepared according to literature procedures, the latter from $IrCl_3{\cdot}3H_2O$ and pentamethylcyclopentadiene (both Strem). $[(\eta^5\text{-}C_5Me_5)IrCl_2(PPh_3)]$ was prepared by treating a CH_2Cl_2 solution of $[\{IrCl(\mu\text{-}Cl)(\eta^5\text{-}C_5Me_5)\}_2]$ with 2 equiv of PPh_3 (Aldrich) followed by precipitation of the product by the addition of diethyl ether. $[n\text{-}Bu_2SnCl_2]$, $NH_4[PF_6]$, and $Ag[PF_6]$ were purchased from Aldrich and used as received.

IR spectra were recorded as KBr pellets in the range 4000–220 cm^{-1} on a PerkinElmer system 2000 Fourier transform spectrometer. ^1H NMR spectra (250 MHz) were obtained using a Bruker AC250 FT spectrometer with δ referenced to external $SiMe_4$, ^{31}P NMR spectra (109.4 MHz or 101.3 MHz) either on a JEOL GSX270 or a Bruker AC250 FT spectrometer with δ referenced to external H_3PO_4, and ^{119}Sn NMR spectra (100.7 MHz) on a JEOL GSX270 spectrometer with δ referenced to external $SnMe_4$. Microanalyses were performed by the University of St Andrews Chemistry Department Service.

Preparations

$[\{n\text{-}Bu_2Sn(S_2N_2)\}_2]$ (1)

Ammonia (~200 cm^3) was condensed into a pre-cooled (–78°C, cardice–acetone) Schlenk flask. $[S_4N_3][Cl]$ (9.22 g, 44.82 mmol) was added to the ammonia in small portions over a 5 min period. The resulting dark red reaction mixture was stirred at –78°C for an additional 30 min. $[n\text{-}Bu_2SnCl_2]$ (27.24 g, 89.64 mmol) was then added to this mixture in small portions again over 5 min. Once the addition was complete the reaction vessel was topped with a bubbler and stirred at –78°C for 2.5 h then the cooling bath was removed and the reaction gradually warmed to room temperature. Once the ammonia had evaporated the reaction residue was dried in vacuo for ca. 1 h before being placed in a Sohxlet thimble. The residue was extracted with (40–60°C) petroleum ether (250 cm^3) until the extracts were nearly colourless (approximately 4–5 h). The resulting deep orange–red solution was placed in a freezer (–20°C) overnight and the deposited bright yellow crystals were collected by filtration under an atmosphere of nitrogen or argon and washed with cold (<0°C) hexanes (2 × 100 cm^3) and dried in vacuo. Yield: 20.98 g, 72%. IR (KBr pellet) (cm^{-1}): 2956 (m), 2918 (m), 2871 (m), 2853 (m), 1063 (s), 1033 (vs), 899 (vs), 769 (m), 697 (s), 668 (w), 622 (s), 443 (m), 385 (m). ^1H NMR (C_6D_6) δ: 1.55–0.78 (m, 36 H, *n*-Bu). ^{119}Sn (C_6D_6) δ: 37.8 (br s). EI–CI-MS *m/z* (%): 267 (*n*-$BuSnS_2N_2$, 20), 210 (SnS_2N_2, 13), 177 (*n*-BuSn, 17), 166 (SnSN, 11), 120 (Sn, 9), 64 sulfur–nitrogen(S_2, 100), 60 (NSN, 70), and 46 (SN, 35). Anal. calcd. for $C_{16}H_{36}N_4S_4Sn_2$ (%): C 29.45, H 5.56, N 8.59, S 19.62; found: C 29.21, H 5.29, N 8.50, S 19.73.

$[(\eta^5\text{-}C_5Me_5)Ir(S_2N_2)]$ (2)

Method A.

To an orange solution of $[\{IrCl(\mu\text{-}Cl)(\eta^5\text{-}C_5Me_5)\}_2]$ (197 mg, 0.247 mmol) in dichloromethane (20 cm^3) was added $[\{n\text{-}Bu_2Sn(S_2N_2)\}_2]$ (**1**) (161 mg, 0.248 mmol) in one portion. Over the course of 25 min the reaction mixture darkened to a deep red colour and stirring was continued for a total of 8 h. The reaction mixture was evaporated to dryness under reduced pressure and then taken up in toluene (25 cm^3). The slightly cloudy dark orange solution was then added to a column of silica (20 × 2 cm) and first eluted with toluene (200 cm^3), which was discarded, and then with acetone; the orange band that moved with the solvent front was collected and taken to dryness. The residue was dissolved in the min amount of warm (60–70°C) toluene and stored at 4°C overnight. The resulting well-formed dark orange–red crystals were collected by suction filtration and dried in vacuo. Yield: 107 mg, 53%.

Method B.

$[(\eta^5\text{-}C_5Me_5)IrCl_2(PPh_3)]$ (245 mg, 0.371 mmol) and $[\{n\text{-}Bu_2Sn(S_2N_2)\}_2]$ (**1**) (242 mg, 0.372 mmol) were stirred together in dichloromethane (20 cm^3) for 8 h. The product isolation procedure is exactly as described above (Method A). Yield: 131 mg, 84%. IR (KBr pellet) (cm^{-1}): 2984 (w), 2962 (w), 2921 (w), 2854 (w), 1490 (w), 1458 (s), 1427 (w), 1376 (s), 1158 (w), 1079 (w), 1027 (vs), 957 (s), 701 (vs), 697 (w), 636 (s), 612 (w), 590 (w), 502 (s), 453 (m), 397 (s), 383 (w). ^1H NMR (C_6D_6) δ: 1.65 (s, 15 H, C_5Me_5). FAB^+-MS *m/z*: 420 ($[M]^+$). Anal. calcd. for $C_{10}H_{15}IrN_2S_2$ (%): C 28.57, H 3.60, N 6.67, S 15.22; found: C 28.58, H 3.35, N 6.31, S 15.17.

$[(\eta^5\text{-}C_5Me_5)IrCl(PPh_3)(S_2N_2)Ir(\eta^5\text{-}C_5Me_5)][PF_6]$ (3)

Method A.

To a dichloromethane (20 cm^3) solution of $[(\eta^5\text{-}C_5Me_5)IrCl_2(PPh_3)]$ (237 mg, 0.359 mmol) were added as solids $[\{n\text{-}Bu_2Sn(S_2N_2)\}_2]$ (**1**) (117 mg, 0.180 mmol) and $NH_4[PF_6]$ (45 mg, 0.360 mmol); the resulting red–brown reaction mixture was stirred for 18 h at room temperature before filtration through Celite; the Celite was washed with a further 10 cm^3 of dichloromethane. The filtrate and the washings were evaporated to ca. 15 cm^3 and allowed to slowly decrease in volume over 2 weeks giving a small crop of orange–brown crystals, which were manually separated from the reaction residue, washed with diethyl ether, and dried in vacuo. Yield: 79 mg, 37%. Single crystals suitable for X-ray analysis were grown by diffusion of diethyl ether into a dilute dichloromethane solution of **3**.

Method B.

To a dichloromethane (20 cm^3) solution of $[(\eta^5\text{-}C_5Me_5)IrCl_2(PPh_3)]$ (105 mg, 0.159 mmol) was added as a solid $Ag[PF_6]$ (40 mg, 0.158 mmol), and the reaction mixture was stirred in the dark for 2 h. To this reaction mixture was added solid $[(\eta^5\text{-}C_5Me_5)Ir(S_2N_2)]$ (**2**) (67 mg, 0.160 mmol) in one portion and a further 10 cm^3 of dichloromethane. The mixture was stirred for an additional 2 h at room temperature in the dark and then filtered through Celite to remove the precipitated AgCl. The filtrate was then evaporated to ca. 5–6 cm^3 under reduced pressure. Precipitation was induced

© 2002 NRC Canada

Table 1. Crystallographic data for compounds **1**–**3**.

Crystal	**1**	**2**	**4**
Empirical formula	$C_{16}H_{36}N_4S_4Sn_2$	$C_{10}H_{15}IrN_2S_2$	$C_{38}H_{45}ClF_6Ir_2N_2P_2S_2{\cdot}2H_2O$
Crystal colour, habit	Yellow, plate	Orange, prism	Yellow, plate
Crystal system	Triclinic	Monoclinic	Monoclinic
Space group	*P*-1	$P2_1/n$	$P2_1/n$
a (Å)	9.2230(7)	7.8051(4)	12.0603(17)
b (Å)	14.4851(12)	13.3519(6)	14.879(2)
c (Å)	16.0210(13)	12.9863(6)	25.281(4)
α (°)	84.692(2)	90	90
β (°)	75.640(2)	102.2640(10)	91.202(3)
γ (°)	88.436(3)	90	90
V (Å^3)	2064.6(3)	1322.46(11)	4553.5(11)
Z	3	4	4
Molecular weight	650.11	419.56	1225.70
$D_{calcd.}$ (mg m^{-3})	1.57	2.11	1.79
Absorption correction (μ) (mm^{-1})	2.13	10.38	6.12
F(000)	972	792	2376
Measured reflections	12839	5550	25195
Observed independent reflections	5855	1871	6470
Final R_1, $wR_2[I > 2\sigma(I)]$	0.0609, 0.1629	0.0238, 0.0535	0.0849, 0.1710
Largest diff. peak hole (e Å^{-3})	0.693, –1.091	0.720, –0.855	0.2219, 0.2296

by the slow addition of diethyl ether (90 cm^3) to the stirred filtrate to give bright orange micro-crystals, which were collected by suction filtration, washed with diethyl ether (10 cm^3), and dried in vacuo. Yield: 0.151 mg (80%). IR (KBr pellet) (cm^{-1}): 3080 (w), 3061 (w), 3027 (w), 2990 (w), 2970 (w), 2920 (w), 1484 (w), 1453 (w), 1437 (s), 1386 (w), 1097 (m), 1024 (m), 973 (m), 876 (m), 841 (vs), 781 (w), 756 (m), 746 (s), 738 (m), 701 (s), 558 (s), 530 (s), 513 (m), 494 (m), 453 (w), 440 (w), 414 (w), 398 (w), 257 (w), 248 (w). ^{1}H NMR (CD_2Cl_2) δ: 7.67–6.85 (m, 15 H, aromatics), 2.08 (s, 15 H, C_5Me_5), 1.31 (d, 15 H, $^4J_{^{31}P-^1H}$ = 3 Hz, C_5Me_5). ^{31}P NMR (CD_2Cl_2) δ: 9.7 (PPh_3), –143.9 (*sept*, $[PF_6]^{-1}$, $^1J_{^{31}P-^{19}F}$ = 709 Hz). FAB$^+$-MS *m*/*z*: 1045 ([M-(PF_6)]$^+$), 625 ([Cp*IrCl(PPh_3)]$^+$), 420 ([Cp*Ir(S_2N_2)]$^+$), 363 ([Cp*IrCl]$^+$). Anal. calcd. for $C_{38}H_{45}ClF_6Ir_2N_2P_2S_2$ (%): C 38.31, H 3.81, N 2.35, S 5.37; found: C 37.97, H 3.62, N 2.28, S 4.99.

The crystals used in the X-ray analysis of **3** were obtained via Method A. Further characterization was performed using material synthesized by Method B.

X-Ray crystallography

Table 1 lists details of data collections and refinements for **1**, **2**, and **3**. Data were collected at room temperature using Mo Kα radiation with a SMART system. Intensities were corrected for Lorentz polarization and for absorption. The structures were solved by the heavy atom method or by direct methods. The positions of the hydrogen atoms were idealized. High thermal motion in the *n*-butyl groups of compound **1** meant that the carbon atoms were refined isotropically subject to distance constraints. Refinements were by full-matrix least squares based on F^2 using SHELXTL (20).[2]

Results and discussion

The addition of [*n*-Bu_2SnCl_2] to a reaction mixture of [S_4N_3][Cl] in liquid ammonia gives, after extraction of the dry reaction residue with 40–60°C petroleum ether, the di-*n*-butyltin disulfur dinitrido compound [{*n*-$Bu_2Sn(S_2N_2)$}$_2$] (**1**) in 72% yield (eq. [1]). This reaction represents a more convenient route to this class of compound and uses a commercial source of tin and a stable readily prepared source of sulfur and nitrogen. By comparison the two previously reported examples of this type of compound employ tris(timethylstannyl)amine [$(Me_3Sn)_3N$] and S_4N_4 (eq. [2]) and the tin starting material **4** and elemental sulfur (eq. [3]) in their syntheses, which give [{$Me_2Sn(S_2N_2)$}$_2$] and [{*t*-$Bu_2Sn(S_2N_2)$}$_2$] + compound **5**, respectively. Compound **1** is a moderately air- and moisture-sensitive yellow crystalline

[1]

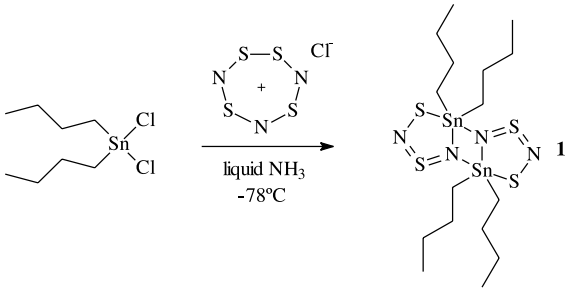

[2] Supplementary data may be purchased from the Depository of Unpublished Data, Document Delivery, CISTI, National Research Council Canada, Ottawa, ON K1A 0S2, Canada (http://www.nrc.ca/cisti/irm/unpub_e.shtml for information on ordering electronically). CCDC 178367–178369 contain the supplementary data (excluding structure factors) for this paper. These data can be obtained, free of charge, via www.ccdc.cam.ac.uk/conts/retrieving.html (or from the Cambridge Crystallographic Data Centre, 12 Union Road, Cambridge, U.K.; fax +44 1223 336033; or deposit@ccdc.cam.ac.uk).

© 2002 NRC Canada

Table 2. Selected bond lengths (Å) and bond angles (°) for [{*n*-$Bu_2Sn(S_2N_2)$}$_2$] (**1**) (listing the three independent *n*-$Bu_2Sn(S_2N_2)$ units that make up the unit cell) and [{*t*-$Bu_2Sn(S_2N_2)$}$_2$] for comparison.

[{*n*-$Bu_2Sn(S_2N_2)$}$_2$] (**1**)						[{*t*-$Bu_2Sn(S_2N_2)$}$_2$]	
n-$Bu_2Sn(S_2N_2)$ (1)		*n*-$Bu_2Sn(S_2N_2)$ (2)		n-$Bu_2Sn(S_2N_2)$ (3)			
Bond lengths (Å)							
Sn(1)—C(1)	2.1497(7)	Sn(2)—C(9)	2.1499(7)	Sn(3)—C(17)	2.1499(8)	Sn(1)—C(1)	2.22(1)
Sn(1)—C(5)	2.1501(7)	Sn(2)—C(13)	2.1498(7)	Sn(3)—C(21)	2.1501(6)	Sn(1)—C(5)	2.20(1)
Sn(1)—N(1)	2.0995(5)	Sn(2)—N(3)	2.144(2)	Sn(3)—N(5)	2.133(5)	Sn(1)—N(1)	2.15(1)
N(1)—S(1)	1.528(6)	N(3)—S(3)	1.553(6)	N(5)—S(5)	1.526(5)	N(1)—S(1)	1.54(1)
S(1)—N(2)	1.571(6)	S(3)—N(4)	1.571(6)	S(5)—N(6)	1.552(7)	S(1)—N(2)	1.56(1)
N(2)—S(2)	1.621(6)	N(4)—S(4)	1.681(7)	N(6)—S(6)	1.666(7)	N(2)—S(2)	1.66(1)
S(2)—Sn(1)	2.594(2)	S(4)—Sn(2)	2.598(2)	S(6)—Sn(3)	2.591(2)	S(2)—Sn(1)	2.62(7)
Sn(1)—N(3)	2.322(5)	Sn(2)—N(1)	2.382(5)	Sn(3)—N(5A)	2.349(5)	Sn(1)—N(3)	2.33(1)
Bond angles (°)							
N(1)-Sn(1)-C(1)	115.4(2)	N(3)-Sn(2)-C(9)	116.4(2)	N(5)-Sn(3)-C(17)	116.3(2)	N(1)-Sn(1)-C(1)	118.7(5)
N(1)-Sn(1)-C(5)	121.3(2)	N(3)-Sn(2)-C(13)	113.7(2)	N(5)-Sn(3)-C(21)	112.8(2)	N(1)-Sn(1)-C(5)	117.7(5)
C(1)-Sn(1)-C(5)	120.77(3)	C(9)-Sn(2)-C(13)	128.06(3)	C(17)-Sn(3)-C(21)	128.55(6)	C(1)-Sn(1)-C(5)	123.4(5)
N(1)-Sn(1)-N(3)	72.9(2)	N(3)-Sn(2)-N(1)	70.9(2)	N(5)-Sn(3)-N(5A)	72.5(2)	N(1)-Sn(1)-N(3)	72.7(5)
N(1)-Sn(1)-S(2)	79.81(15)	N(3)-Sn(2)-S(4)	80.9(2)	N(5)-Sn(3)-S(6)	79.9(1)	N(1)-Sn(1)-S(2)	80.2(3)
C(1)-Sn(1)-S(2)	100.92(7)	C(9)-Sn(2)-S(4)	100.95(7)	C(17)-Sn(3)-S(6)	99.4(1)	C(1)-Sn(1)-S(2)	96.1(4)
C(5)-Sn(1)-S(2)	104.21(7)	C(13)-Sn(2)-S(4)	99.32(7)	C(21)-Sn(3)-S(6)	103.4(1)	C(5)-Sn(1)-S(2)	96.2(4)
S(1)-N(1)-Sn(1)	123.1(3)	S(3)-N(3)-Sn(2)	120.5(3)	S(5)-N(5)-Sn(3)	122.0(3)	S(1)-N(1)-Sn(1)	120.8(6)
Sn(1)-N(1)-Sn(2)	107.7(2)	Sn(2)-N(3)-Sn(1)	108.3(2)	Sn(3)-N(5)-Sn(3A)	107.5(2)	Sn(1)-N(1)-Sn(2)	107.2(4)
N(1)-S(1)-N(2)	113.9(3)	N(3)-S(3)-N(4)	116.7(3)	N(5)-S(5)-N(6)	116.0(3)	N(1)-S(1)-N(2)	116.9(7)
S(1)-N(2)-S(2)	121.4(4)	S(3)-N(4)-S(4)	119.5(4)	S(5)-N(6)-S(6)	120.0(4)	S(1)-N(2)-S(2)	120.2(9)
N(2)-S(2)-Sn(1)	101.8(2)	N(4)-S(4)-Sn(2)	102.0(2)	N(6)-S(6)-Sn(3)	102.1(2)	N(2)-S(2)-Sn(1)	101.8(5)

[2]

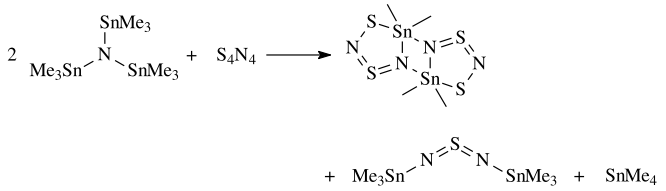

[3]

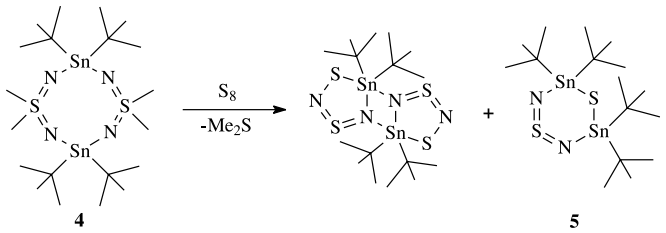

solid that is extremely soluble in most common organic solvents including pentane and hexane. The ^{1}H NMR (C_6D_6) is uninformative and is very similar to that of its precursor [*n*-Bu_2SnCl_2] with no evident ^{1}H-^{117}Sn or ^{1}H-^{119}Sn couplings. The ^{119}Sn NMR (C_6D_6) consists of a broad singlet at 37.8 ppm while the corresponding value of *n*-Bu_2SnCl_2 is 124.7 ppm. The IR spectrum shows absorptions that are comparable to those reported for [{$Me_2Sn(S_2N_2)$}$_2$] (5). The EI–CI mass spectrum of **1** failed to show the molecular ion of either the dimer or monomer, however it did show *m*/*z* 267, which corresponds to [*n*-$BuSnS_2N_2$]$^+$ along with other tin-containing fragments (see Experimental); in addition elemental analysis was within specified limits. The slow passage of nitrogen for 24 h over a diethyl ether solution of **1** led to small but well-formed crystals that were suitable for X-ray analysis. The crystal structure of **1** (Fig. 1) and selected bond lengths and angles together with those of [{*t*-$Bu_2Sn(S_2N_2)$}$_2$] for comparison are given (Table 2). The X-ray structural determination of [{*n*-$Bu_2Sn(S_2N_2)$}$_2$] (**1**) identified the SnS_2N_2 unit as a 1,3,2,4,5-dithiadiazastannole

Fig. 1. Crystal structure of [{*n*-$Bu_2Sn(S_2N_2)$}$_2$] (**1**) showing the 1.5 independent molecules.

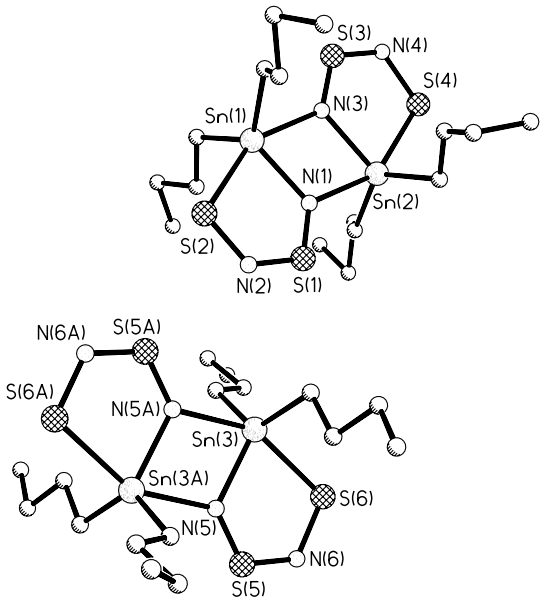

© 2002 NRC Canada

Scheme 1. (*i*) [{IrCl(μ-Cl)(η^5-C_5Me_5)}$_2$]; (*ii*) [(η^5-C_5Me_5)IrCl_2(PPh_3)]; (*iii*) [(η^5-C_5Me_5)IrCl_2(PPh_3)], $NH_4[PF_6]$; (*iv*) [(η^5-C_5Me_5)IrCl_2(PPh_3)], Ag[PF_6], [(η^5-C_5Me_5)Ir(S_2N_2)].

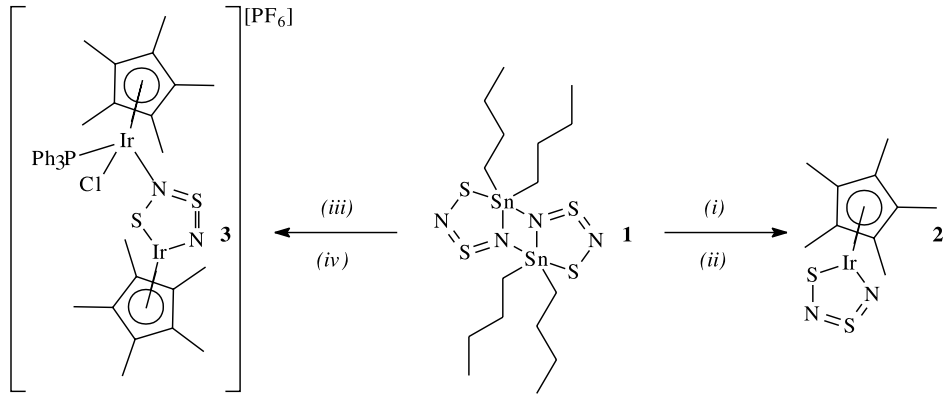

ring and highlighted the dimeric nature of the molecule. The unit cell of [{*n*-$Bu_2Sn(S_2N_2)$}$_2$] (**1**) contains 1.5 independent molecules consisting of three distinct *n*-$Bu_2Sn(S_2N_2)$ monomer units that have similar bond lengths and angles. The geometry about the tin atoms is distorted trigonal bipyramidal, the *n*-butyl groups and the tin-bound nitrogen atoms of the SnS_2N_2 rings in the equatorial positions with the tin-bound sulfur atoms of each SnS_2N_2 unit and the bridging nitrogen atoms occupying the axial sites. The three bond angles in the trigonal plane are all close to 120°, but the axial substituents occupy far from linear positions with average S-Sn-N = 152.3°. The ring Sn—N and Sn—S distances are close to those found in [{*t*-$Bu_2Sn(S_2N_2)$}$_2$] (17) and [{$Me_2Sn(S_2N_2)$}$_2$] (21) as is the pattern of average S—N bond lengths within the SnS_2N_2 ring, i.e., short (1.536 Å), medium (1.566 Å), and long (1.656 Å), a pattern also observed in other MS_2N_2 rings, for example [$(H_3N)Pb(S_2N_2)$] (22). The four-membered Sn_2N_2 rings are parallelograms, formed by the *n*-$Bu_2Sn(S_2N_2)$ dimer pairs and have average internal angles of N-Sn-N = 72.08° and Sn-N-Sn = 107.83°. The [$Sn(S_2N_2)$]$_2$ unit of the dimer consisting of two different *n*-$Bu_2Sn(S_2N_2)$ molecules is essentially planar with a mean deviation from the least squares plane of 0.06 Å and a maximum deviation of only 0.10 Å above the plane for Sn(1). The second pictured dimer made up of two repeat *n*-$Bu_2Sn(S_2N_2)$ units is closer to planarity with a mean deviation of 0.01 Å and a maximum deviation above the plane of 0.03 Å for N(5).

A previous attempt to obtain monocyclopentadienyl IrS_2N_2 complexes via oxidative addition to [(η^5-C_5H_5)Ir$(CO)_2$] with S_4N_4, a method that works well for the cobalt analogues [(η^5-C_5H_5)Co$(CO)_2$] and [(η^5-C_5Me_5)Co$(CO)_2$], gave only an insoluble black precipitate (14). An alternative synthetic method involving the treatment of [{IrCl(μ-Cl)(η^5-C_5Me_5)}$_2$] with [{*n*-$Bu_2Sn(S_2N_2)$}$_2$] (**1**) in dichloromethane proceeds via the elimination of [*n*-Bu_2SnCl_2] (^{119}Sn NMR evidence) and gives after chromatography on silica (eluting first with toluene and then with acetone) [(η^5-C_5Me_5)Ir(S_2N_2)] (**2**) in 53% yield (Scheme 1). Alternatively compound **2** can be prepared in higher yield (84%) by the reaction of 1 equiv of **1** and [(η^5-C_5Me_5)IrCl_2(PPh_3)], which proceeds via the elimination of PPh_3 (which undergoes further reaction with 0.5 equiv of **1** to give P(S)Ph_3 (^{31}P NMR evidence) and [*n*-Bu_2SnCl_2] (^{119}Sn NMR evidence); also shown by ^{119}Sn NMR were a number of other ^{119}Sn signals, presumably the by-products of the reaction between **1** and PPh_3, which we were unable to identify (Scheme 1). The air- and moisture-tolerant orange–red crystalline product is highly soluble in chlorinated solvents, benzene, and toluene and is slightly soluble in diethyl ether but is much less so in petroleum ether, hexane, and alcohols. The ^{1}H NMR (CD_2Cl_2) data shows the 15 Cp* (Cp* = pentamethylcyclopentadienyl) methyl group protons as a sharp singlet at δ 1.65 compared with 1.51 and a doublet at 1.32 $^4J_{^{31}P-^1H}$ = 2 Hz (both CD_2Cl_2) for [{IrCl(μ-Cl)(η^5-C_5Me_5)}$_2$] and [(η^5-C_5Me_5)IrCl_2(PPh_3)], respectively. The vibrational spectrum of complex **2** (KBr pellet) shows the expected bands due to the $[S_2N_2]^{2-}$ ligand at 1027 (vs) ν(NS), 701 (vs) ν(NS), 636 (s) ν(NS), 453 (m) ν(IrN), 397 (m) δ(NS), and 383 (w) cm^{-1} ν(IrS). Microanalytical data were in excellent agreement with the proposed formulation and the positive-ion FAB$^+$ mass spectra showed the molecular ion of **2** at *m*/*z* 420 ([M]$^+$). Large well-formed orange–red crystals, which were of X-ray quality were obtained by crystallization from hot (60–70°C) toluene. The X-ray structure of [(η^5-C_5Me_5)Ir(S_2N_2)] (**2**) is shown in Fig. 2 with bond distances and angles in Table 3 (along with those of [Ir(dppe)$_2$(S_2N_2)][BPh_4] (15) for comparison) and reveals that the IrS_2N_2 cycle is essentially planar, the largest deviation from the mean plane being only

Fig. 2. Crystal structure of [(η^5-C_5Me_5)Ir(S_2N_2)] (**2**).

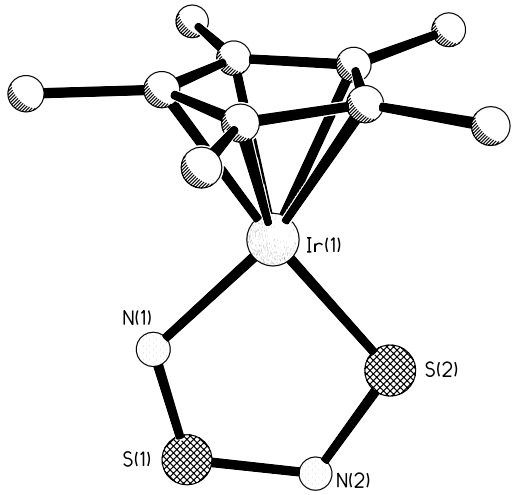

© 2002 NRC Canada

Table 3. Selected bond lengths (Å) and bond angles (°) for [(η^5-C_5Me_5)Ir(S_2N_2)] (**2**), [(η^5-C_5Me_5)IrCl(PPh_3)(S_2N_2)Ir(η^5-C_5Me_5)][PF_6]·2H_2O (**3**), and [Ir(dppe)$_2$(S_2N_2)][BPh_4].

[(η^5-C_5Me_5)Ir(S_2N_2)] (**1**)		(**3**)		[Ir(dppe)$_2$(S_2N_2)][BPh_4]	
Bond lengths (Å)					
Ir(1)—N(1)	1.962(6)	Ir(1)—N(1)	1.961(10)	Ir(1)—N(1)	2.289(12)
N(1)—S(1)	1.509(7)	N(1)—S(1)	1.558(10)	N(1)—S(1)	1.38(2)
S(1)—N(2)	1.563(9)	S(1)—N(2)	1.531(9)	S(1)—N(2)	1.75(2)
N(2)—S(2)	1.632(8)	N(2)—S(2)	1.685(9)	N(2)—S(2)	1.40(2)
S(2)—Ir(2)	2.175(2)	S(2)—Ir(2)	2.179(3)	S(2)—Ir(2)	2.379(9)
Ir(1)—C(1)	2.172(6)	Ir(1)—C(31)	2.120(12)		
Ir(1)—C(2)	2.192(6)	Ir(1)—C(32)	2.183(10)		
Ir(1)—C(3)	2.178(6)	Ir(1)—C(33)	2.120(11)		
Ir(1)—C(4)	2.194(6)	Ir(1)—C(34)	2.179(12)		
Ir(1)—C(5)	2.191(6)	Ir(1)—C(35)	2.158(10)		
		Ir(2)—Cl(1)	2.421(3)		
		Ir(2)—P(1)	2.336(3)		
		Ir(2)—N(2)	2.178(8)		
Bond angles (°)					
Ir(1)-N(1)-S(1)	120.2(4)	Ir(1)-N(1)-S(1)	120.6(5)	Ir(1)-N(1)-S(1)	111.1(8)
N(1)-S(1)-N(2)	112.4(3)	N(1)-S(1)-N(2)	110.0(5)	N(1)-S(1)-N(2)	119.7(9)
S(1)-N(2)-S(2)	114.0(4)	S(1)-N(2)-S(2)	117.4(5)	S(1)-N(2)-S(2)	117.4(10)
N(2)-S(2)-Ir(1)	108.3(3)	N(2)-S(2)-Ir(1)	105.5(3)	N(2)-S(2)-Ir(1)	109.0(8)
S(2)-Ir(1)-N(1)	85.1(2)	S(2)-Ir(1)-N(1)	86.5(3)	S(2)-Ir(1)-N(1)	82.5(4)
		P(1)-Ir(2)-Cl(1)	90.39(10)		
		P(1)-Ir(2)-N(2)	90.6(2)		
		N(2)-Ir(2)-Cl(1)	86.4(2)		
		Ir(2)-N(2)-S(1)	125.1(5)		
		Ir(2)-N(2)-S(2)	117.1(5)		

0.007 Å with an S_2N_2 "bite angle" of 85.1(2)°. The bond lengths within the S_2N_2 unit of **1**, i.e., short (1.509(7) Å), medium (1.563(9) Å), and long (1.632(8) Å) seem to be in good agreement with those noted in previous studies (23–24) on monomeric PtS_2N_2 species, and in particular are consistent with the values reported for the only other crystallographically characterized monocyclopentadienyl MS_2N_2 complex [(η^5-C_5H_5)Co(S_2N_2)] (12), i.e., short (1.548(3) Å), medium (1.579(4) Å), and long (1.650(4) Å).

The reaction of [(η^5-C_5Me_5)IrCl_2(PPh_3)] with 0.5 equiv of **1** in the presence of $NH_4[PF_6]$ leads to the unusual bimetallic complex [(η^5-C_5Me_5)IrCl(PPh_3)(S_2N_2)Ir(η^5-C_5Me_5)][PF_6]·2H_2O (**3**) in low yield (37%) and poor purity (Scheme 1). A more rational approach, which gives this material in much higher yield (80%) and of more satisfactory purity involves the abstraction of a chloride ligand from [(η^5-C_5Me_5)IrCl_2(PPh_3)] with Ag[PF_6] followed by treatment of the resulting coordinatively unsaturated species with pre-formed [(η^5-C_5Me_5)Ir(S_2N_2)] (**2**). The resulting bright orange microcrystalline product is soluble in alcohols, THF, and chlorinated solvents, sparingly soluble in benzene and toluene, and insoluble in diethyl ether and hexane. The ^{1}H and ^{31}P NMR data (C_6D_6) of the dry crude reaction mixture suggests that this reaction proceeds cleanly to give only [(η^5-C_5Me_5)IrCl(PPh_3)(S_2N_2)Ir(η^5-C_5Me_5)][PF_6] (**3**), as only two Cp* environments are evident (Scheme 1). The first, bound to the iridium centre bearing the PPh_3 ligand, is a doublet at δ 1.31 $^4J_{^{31}P-^1H}$ = 2 Hz; the singlet at δ 2.08 we have assigned to the Cp* ligand of the (S_2N_2)Ir(η^5-C_5Me_5)] moiety. The ^{31}P NMR (CD_2Cl_2) data of **3** shows two phosphorus environments, a singlet at δ 9.7 ppm (cf. δ 2.4 (CD_2Cl_2) for [(η^5-C_5Me_5)IrCl_2(PPh_3)]) assigned to the PPh_3 ligand and the anticipated septet centred at –143.9 ppm due to the [PF_6]$^-$ counter-ion. The IR spectra of **3** (KBr pellet) displays characteristic absorption at 1024 (m) ν(NS), 701 (s) ν(NS), 636 (s) ν(NS), and 398 (w) cm^{-1} δ(NS) of the [S_2N_2]$^{2-}$ ligand (8, 23, 24, 25) and also a very strong band at 841 cm^{-1}, which is characteristic of the [PF_6]$^-$ anion. Microanalytical data were in good agreement with the proposed structure and the positive-ion FAB$^+$ mass spectra showed [M-(PF_6)]$^+$ at *m*/*z* 1045 along with several other identifiable fragments. Crystals suitable for X-ray crystallography were grown over 4 days by layering a dichloromethane solution of **3** with diethyl ether. Figure 3 shows a perspective view of the complex cation of **3** (water molecules and the [PF_6]$^-$ counter ion are not shown for the sake of clarity) and selected bond distances and angles are given in Table 3. The coordination geometry around Ir(1) closely resembles that in the mononuclear complex **2** (mean deviation from IrS_2N_2 plane = 0.008 Å) and it is evident that coordination to Ir(2) by the non-metal bound nitrogen N(2) causes only minimal changes in the bond lengths and bond angles of the IrS_2N_2 cycle. The geometry about Ir(2) is unremarkable; the P(1)-Ir(2)-Cl(1), P(1)-Ir(2)-N(2), and N(2)-Ir(2)-Cl(1) bond angles all being close to 90°. The iridium atom of the (η^5-C_5Me_5)IrCl(PPh_3) group Ir(2) lies 0.28 Å below the Ir(1)S_2N_2 plane and the Ir(2)-N(2) bond length 2.178(8) Å and the Ir(2)-N(2)-S(1) and Ir(2)-N(2)-S(2) bond angles

© 2002 NRC Canada

Fig. 3. Crystal structure of $[(\eta^5\text{-}C_5Me_5)IrCl(PPh_3)(S_2N_2)Ir(\eta^5\text{-}C_5Me_5)][PF_6]\cdot 2H_2O$ (**3**) (the water molecules and the $[PF_6]^-$ counter ion have been omitted for clarity).

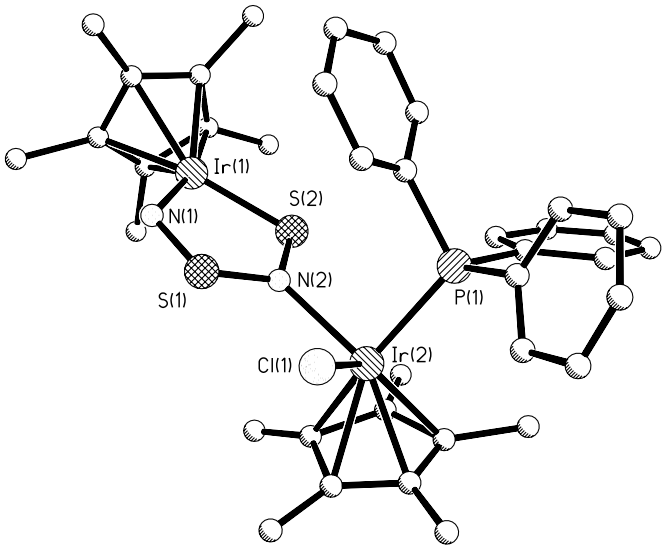

117.1(5) and 125.1(5)° are in excellent agreement with those of the only other known example of a similar binuclear dithiadiaza complex — $[Ir(dppe)_2(S_2N_2)\{W(CO)_5\}][BPh_4]$ (15) [W—N(2) = 2.22(2) Å, W-N(2)-S(1) and W-N(2)-S(2) = 117.6(10) and 126.6(11)°, respectively.

Conclusion

The synthesis of $[\{n\text{-}Bu_2Sn(S_2N_2)\}_2]$ (**1**) from $[n\text{-}Bu_2SnCl_2]$ and $[S_4N_3][Cl]$ in liquid ammonia represents a convenient high-yield preparation of a potentially synthetically useful reagent. This usefulness is highlighted by its use in the preparation of $[(\eta^5\text{-}C_5Me_5)Ir(S_2N_2)]$ (**2**) only the third known monocyclopentadienyl MS_2N_2 complex and the first iridium example of this type of compound in good yield. This synthetic procedure involving the metathesis of metal halides with $[\{n\text{-}Bu_2Sn(S_2N_2)\}_2]$ (**1**) is currently being applied to the preparation of other monocyclopentadienyl MS_2N_2 complexes. We have also shown that novel binuclear species can be readily prepared from $[(\eta^5\text{-}C_5Me_5)Ir(S_2N_2)]$ (**2**) by simple halide abstraction reactions, which we are also studying in more detail.

References

1. A.Y. Makarov, I.Y. Bagryanakaya, Y.V. Gatilov, T.V. Mikhalina, M.M. Shakirov, L.N. Shchegoleva, and A.V. Zibarev. Heteroatom Chem. **12(7)**, 563 (2001).
2. A.Y. Makarov, M.A. Shakirov, K.V. Shuvaev, I.Y. Bagryanakaya, Y.V. Gatilov, and A.V. Zibarev. Chem. Commun. 1774, (2001).
3. W.S. Sheldrick, M.N.R. Sudheendra, and H.W. Roesky. Inorg. Chem. **19**, 538 (1980).
4. J.L. Morris, C.W. Rees, and D.J. Rigg. J. Chem. Soc. Chem. Commun. **7**, 396 (1985).
5. H.W. Roesky and H. Weizer. Angew. Chem. Int. Ed. Engl. **12**, 674 (1973).
6. H.W. Roesky and M. Witt. Inorg. Synth. **25**, 49 (1989).
7. H.W. Roesky. Z. Naturforsch. **31B**, 680 (1976).
8. P.F. Kelly and J.D. Woollins. Polyhedron, **5**, 607 (1985).
9. P.F. Kelly, A.M.Z. Slawin, D.J. Williams, and J.D. Woollins. Chem. Soc. Rev. 245 sulfur–nitrogen(1992).
10. O.J. Scherer and R. Wies. Angew. Chem. Int. Ed. Engl. **11**, 529 (1972).
11. R. Jones, C.P. Warrens, D.J. Williams, and J.D. Woollins. J. Chem. Soc. Dalton Trans. 907 (1987).
12. F. Edelmann. J. Organomet. Chem. **228**, C47 (1982).
13. G. Granozzi, M. Casarin, F. Edelmann, T.A. Albright, and E.D. Jemmis. Organometallics, **6**, 2223 (1987).
14. R.T. Boeré, B.Klassen, and K.H. Moock. J. Organomet. Chem. **467**, 127 (1994).
15. C.A. Ghilardi, S. Midollini, S. Moneti, and A. Orlandini. J. Organomet. Chem. **312**, 383 (1986).
16. D. Hänssgen, H. Salz, S. Rheindorf, and C. Schrage. J. Organomet. Chem. **443**, 61 (1993).
17. D. Hänssgen, M. Jansen, W. Assenmacher, and H. Salz. J. Organomet. Chem. **445**, 61 (1993).
18. W.L. Jolly and K.D. Maguire. Inorg. Synth. **9**, 103 (1967).
19. C. White, A.Yates, and P.M. Maitliss. Inorg. Synth. **29**, 228 (1992).
20. G.M. Sheldrick. 1999. SHELXTL [computer program]. Bruker AXS, Madison, WI.
21. H.W. Roesky. Adv. Inorg. Chem. Radiochem. **22**, 245 (1979).
22. H. Martan and J.Weiss. Z. Anorg. Allg. Chem. **514**, 107 (1984).
23. P.A. Bates, M.B.Hursthouse, P.F. Kelly, and J.D. Woollins. J. Chem. Soc. Dalton Trans. 2367 (1986).
24. P.F. Kelly, A.M.Z. Slawin, D.J. Williams, and J.D. Woollins. Polyhedron, **7**, 1925 (1988).
25. D.B. Powell and J.D. Woollins. Spectrochim. Acta, **A36**, 447 (1980).

© 2002 NRC Canada

Characterization of indirect ^{31}P-^{31}P spin-spin coupling and phosphorus chemical shift tensors in pentaphenylphosphinophosphonium tetrachlorogallate, $[Ph_3P\text{-}PPh_2][GaCl_4]$

Myrlene Gee, Roderick E. Wasylishen, Paul J. Ragogna, Neil Burford, and Robert McDonald

Abstract: Phosphorus chemical shift and ^{31}P,^{31}P spin-spin coupling tensors have been characterized for pentaphenylphosphinophosphonium tetrachlorogallate, $[Ph_3P\text{-}PPh_2][GaCl_4]$, using solid-state ^{31}P NMR spectroscopy. Spectra obtained with magic-angle spinning yield the isotropic value of the indirect spin-spin coupling, $|^1J(^{31}P,^{31}P)_{iso}|$, 323 ± 2 Hz, while 2D spin-echo and rotational resonance experiments provide the effective dipolar coupling constant, R_{eff}, 1.70 ± 0.02 kHz, and demonstrate that J_{iso} is negative. Within experimental error, the effective dipolar coupling constant and J_{iso} are unchanged at –120°C. The anisotropy in $^1\mathbf{J}(^{31}P,^{31}P)$, ΔJ, has been estimated by comparison of R_{eff} and the value of the dipolar coupling constant, R_{DD}, calculated from the P—P bond length as determined by X-ray diffraction. It is concluded that $|\Delta J|$ is small, with an upper limit of 300 Hz. Calculations of $^1\mathbf{J}(^{31}P,^{31}P)$ for model systems $H_3P\text{-}PH_2^+$ and $(CH_3)_3P\text{-}P(CH_3)_2^+$ using density functional theory as well as multiconfigurational self-consistent field theory ($H_3P\text{-}PH_2^+$) support this conclusion. The experimental spin-spin coupling parameters were used to analyze the ^{31}P NMR spectrum of a stationary powder sample and provide information about the phosphorus chemical shift tensors. The principal components of the phosphorus chemical shift tensor for the phosphorus nucleus bonded to three phenyl groups are δ_{11} = 36 ppm, δ_{22} = 23 ppm, and δ_{33} = –14 ppm with an experimental error of ±2 ppm for each component. The components are oriented such that δ_{33} is approximately perpendicular to the P—P bond while δ_{11} forms an angle of 31° with the P—P bond. For the phosphorus nucleus bonded to two phenyl groups, the principal components of the phosphorus chemical shift tensor are δ_{11} = 23 ppm, δ_{22} = –8 ppm, and δ_{33} = –68 ppm with experimental errors of ±2 ppm. In this case, δ_{33} is also approximately perpendicular to the P—P bond; however, δ_{22} is close to the P—P bond for this phosphorus nucleus, forming an angle of 13°. The dihedral angle between the δ_{33} components of the two phosphorus chemical shift tensors is 25°. Results from ab initio calculations are in good agreement with experiment and suggest orientations of the phosphorus chemical shift tensors in the molecular frame of reference.

Key words: Nuclear magnetic resonance spectroscopy, phosphorus chemical shift tensors, ^{31}P-^{31}P *J*-coupling tensors, density functional theory, multiconfigurational self-consistent field theory, phosphinophosphonium salts.

Résumé : Faisant appel à la spectroscopie RMN du ^{31}P, on a caractérisé les déplacements chimiques du phosphore et les tenseurs du couplage spin-spin ^{31}P,^{31}P du tétrachlorogallate de pentaphénylphosphinophosphonium, $[Ph_3P\text{-}PPh_2][GaCl_4]$. Les spectres déterminés en faisant appel à technique de rotation à l'angle magique permettent de tirer la valeur isotrope du couplage spin-spin indirect, $|^1J(^{31}P,^{31}P)_{iso}|$, 323 ± 2 Hz, alors que des expériences bidimensionnelles d'écho de spin et de résonance rotationnelle fournissent la constante de couplage dipolaire effective, R_{eff}, 1,70 ± 0,02 kHz et mettent en évidence que la valeur de J_{iso} est négative. Aux incertitudes près, la constante de couplage dipolaire effective et J_{iso} ne changent pas à –120°C. On a évalué l'anisotropie dans $^1\mathbf{J}(^{31}P,^{31}P)$, ΔJ, en comparant la valeur de R_{eff} et la valeur de la constante de couplage dipolaire, R_{DD}, calculée à partir de la longueur de la liaison P—P telle que déterminée par une étude de diffraction des rayons-X. On peut en conclure que la valeur $|\Delta J|$ est faible et que sa limite supérieure est de 300 Hz. Ces conclusions sont supportées par des calculs des valeurs $^1\mathbf{J}(^{31}P,^{31}P)$ pour les systèmes modèles $H_3P\text{-}PH_2^+$ et $(CH_3)_3P\text{-}P(CH_3)_2^+$ qui ont été effectués à l'aide de la théorie de la densité fonctionnelle et, dans le cas de $H_3P\text{-}PH_2^+$, à l'aide de la théorie de champ autocohérent multiconfigurationnel. On a

Received 5 April 2002. Published on the NRC Research Press Web site at http://canjchem.nrc.ca on 18 November 2002.

Dedicated to Professor Tristram Chivers for his contributions to Canadian chemistry.

M. Gee.[1] Department of Chemistry, University of Alberta, Edmonton, AB T6G 2G2, Canada, and Department of Chemistry, Dalhousie University, Halifax, NS B3H 4J3, Canada.
R.E. Wasylishen[2] **and R. McDonald.** Department of Chemistry, University of Alberta, Edmonton, AB T6G 2G2, Canada.
P.J. Ragogna and N. Burford. Department of Chemistry, Dalhousie University, Halifax, NS B3H 4J3, Canada.

[1]Present address: Department of Biomedical Engineering, University of Alberta, Edmonton, AB T6G 2V2, Canada.
[2]Corresponding author (e-mail: Roderick.Wasylishen@ualberta.ca).

 DOI: 10.1139/V02-178 © 2002 NRC Canada

utilisé les paramètres de couplage spin-spin observés expérimentalement pour analyser le spectre RMN du ^{31}P d'un échantillon de poudre stationnaire et d'en tirer des informations relatives aux tenseurs du déplacement chimique du phosphore. Les principaux composants du tenseur du déplacement chimique de noyaux phosphore liés à trois groupes phényles sont δ_{11} = 36 ppm, δ_{22} = 23 ppm et δ_{33} = –14 ppm avec une erreur expérimentale de ±2 ppm pour chacun des composants. Les composants sont orientés d'une façon telle que δ_{33} est approximativement perpendiculaire à la liaison P—P alors que δ_{11} forme un angle de 31° avec la liaison P—P. Pour les noyaux de phosphore liés à deux groupes phényles, les principaux composants du tenseur du déplacement chimique du phosphore sont δ_{11} = 23 ppm, δ_{22} = –8 ppm et δ_{33} = –68 ppm avec une erreur expérimentale de ±2 ppm pour chacun des composants. Dans ce cas, δ_{33} est approximativement perpendiculaire à la liaison P—P; toutefois, δ_{22} est près de la liaison P—P parce que ce noyau de phosphore forme un angle de 13°. L'angle dièdre entre les composants δ_{33} des tenseurs des déplacements chimiques de ces deux noyaux de phosphore est de 25°. Les résultats de calculs ab initio sont en bon accord avec les données expérimentales et ils donnent une idée sur les orientations des tenseurs des déplacements chimiques du phosphore dans le cadre de référence moléculaire.

Mots clés : spectroscopie de résonance magnétique nucléaire, tenseurs du déplacement chimique du phosphore, tenseurs de couplages J ^{31}P-^{31}P, théorie de la densité fonctionnelle, théorie du champ autocohérent multiconfigurationnel, sels de phosphinophosphonium.

Introduction

The preparation and structural characterization of the first pentaphenylphosphinophosphonium salts was recently reported (1). In the solid state, the two different phosphorus nuclei are easily resolved using cross polarization (CP) magic-angle spinning (MAS) NMR spectroscopy. Initially, the observation of a large value for $|^1J(^{31}P,^{31}P)_{iso}|$, 323 Hz, was critical in identifying the presence of a P—P bond in this compound. As part of our continuing efforts to better understand phosphorus chemical shifts and indirect spin-spin couplings, the phosphorus chemical shift tensors as well as the one-bond P-P indirect spin-spin coupling tensor, $^1\mathbf{J}(^{31}P,^{31}P)$, have been characterized in the present work for pentaphenylphosphinophosphonium tetrachlorogallate, $[Ph_3P\text{-}PPh_2][GaCl_4]$, Fig. 1(*a*), using the dipolar-chemical shift method (2–11). X-ray diffraction data (1) for $[Ph_3P\text{-}PPh_2][GaCl_4]$ provide valuable structural information required for the determination of the anisotropy of $^1\mathbf{J}(^{31}P,^{31}P)$, ΔJ, from the observed spin-spin coupling data.

In addition to experimental characterization of NMR parameters, theoretical calculations offer a valuable tool for exploring trends in spin-spin coupling and chemical shift tensors (12–18). Theoretical methods have been applied to the calculation of *J*-coupling for a number of systems, for example the calculation of *J*-coupling across hydrogen bonds (19–22). In particular, density functional theory (DFT) (23–30) and multiconfigurational self-consistent field (MCSCF) (12, 31–36) theory provide estimates of $^1\mathbf{J}(^{31}P,^{31}P)$ for comparison with experimental results. The application of DFT methods to the calculation of *J*-coupling tensors has been successful in a number of cases (24–30, 37, 38). Here we apply DFT calculations on $H_3P\text{-}PH_2^+$ (Fig. 1(*b*)) and $(CH_3)_3P\text{-}P(CH_3)_2^+$ to serve as models for $Ph_3P\text{-}PPh_2^+$. While ab initio approaches such as MCSCF are more rigorous, they are limited to small molecules with relatively light nuclei. For this reason, MCSCF calculations have been performed on only the smaller of the two model systems, $H_3P\text{-}PH_2^+$. The experimental results for the phosphorus chemical shift tensors are complemented by ab initio calculations, which aid in fixing the chemical shift tensor orientation with respect to the molecular frame of reference (39–47).

Fig. 1. Schematic representation of (*a*) $[Ph_3P\text{-}PPh_2][GaCl_4]$, indicating the labelling convention for the two phosphorus nuclei and (*b*) $H_3P\text{-}PH_2^+$ with a Newman projection illustrating the definition of ϕ, which is the angle between the plane containing the P(1)—H(1) bond and the bisector of the H-P(2)-H angle.

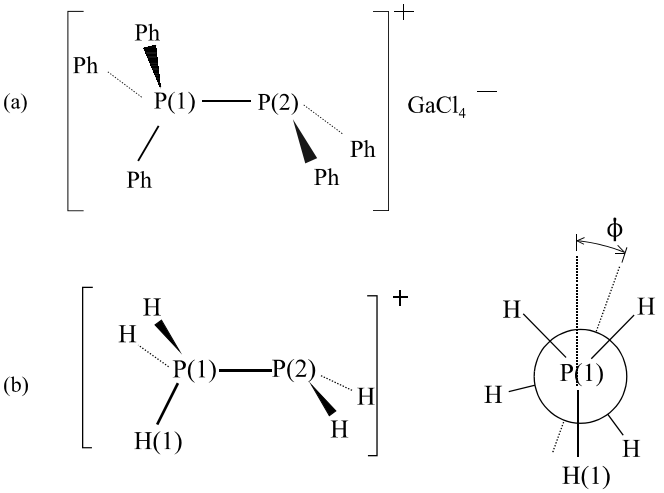

Background theory

The conventions used to describe chemical shift and *J*-coupling tensors will be given in this section. The theory behind the dipolar – chemical shift method has been discussed extensively in the literature (2–7) and will not be presented in detail here.

For a solid powder sample containing an isolated spin-1/2 nucleus, the solid-state NMR spectrum yields the principal components of the chemical shift tensor, denoted by δ_{11}, δ_{22}, and δ_{33}, such that $\delta_{11} \geq \delta_{22} \geq \delta_{33}$; δ_{33} corresponds to the direction of greatest shielding. Three derived parameters may also be used to describe the principal components: the isotropic chemical shift, $\delta_{iso} = (\delta_{11} + \delta_{22} + \delta_{33})/3$, the span, Ω =

© 2002 NRC Canada

$\delta_{11} - \delta_{33}$, and the skew, $\kappa = 3\ (\delta_{22} - \delta_{iso})\ /\ \Omega$ (48). The latter two parameters describe, respectively, the breadth and shape of the observed powder pattern. The chemical shift, δ, and nuclear magnetic shielding, σ, are related as follows:

$$[1] \qquad \delta = \frac{\sigma_{ref} - \sigma}{1 - \sigma_{ref}} \approx \sigma_{ref} - \sigma$$

where σ_{ref} is the nuclear magnetic shielding constant for the reference compound. In the case of phosphorus, σ_{ref} is 328.35×10^{-6} for 85% H_3PO_4(aq) (49); hence it may be neglected in the denominator. The magnetic shielding is the more fundamental parameter as it describes the shielding in the compound of interest with respect to the bare nucleus.

The indirect spin-spin or *J*-coupling tensor, **J**, is described by three principal components, J_{11}, J_{22}, and J_{33}, such that $|J_{33} - J_{iso}| \geq |J_{11} - J_{iso}| \geq |J_{22} - J_{iso}|$. The isotropic *J*-coupling constant is $J_{iso} = (J_{11} + J_{22} + J_{33})/3$, while the anisotropy is $\Delta J = J_{33} - (J_{11} + J_{22})/2$, and the asymmetry, η, is $(J_{22} - J_{11})/(J_{33} - J_{iso})$ (50–52). According to Ramsey's theory (12, 13, 52–55), the observed **J** is a sum of contributions from three mechanisms. The spin-orbit (SO) mechanism involves the coupling between the nuclear spin and the orbital angular momentum of the electrons and is usually divided into diamagnetic (DSO) and paramagnetic (PSO) parts. The spin-dipolar (SD) mechanism involves the dipolar interaction between the nuclear and electron magnetic moments. Finally, the Fermi contact (FC) mechanism describes the interaction between a nucleus and electrons that have a finite probability of being at the nucleus of interest. Of all the mechanisms, only the FC is completely isotropic; hence it contributes to J_{iso} but not to ΔJ. There is also a cross term between the FC and SD mechanisms that contributes to ΔJ but not to J_{iso}. Observation of a sizable ΔJ indicates that this cross term and (or) mechanisms other than FC are significant (56–61). Although the FC is often assumed to make the largest contribution to J_{iso}, this is not always true (62 and refs. therein).

For samples containing isolated ^{31}P-^{31}P spin pairs, the standard MAS experiment yields δ_{iso} for each phosphorus site and $^1J(^{31}P,^{31}P)_{iso}$. If a stationary powder sample of such a spin pair is examined, the three principal components of each chemical shift tensor may be obtained as well as some information regarding the orientation of these tensors with respect to the effective dipolar coupling tensor. The unique axis of the direct dipolar coupling tensor is usually coincident with the internuclear vector, **r**; hence, some information regarding the chemical shift tensor orientation with respect to the molecular framework is available from the NMR spectra of powder samples. The orientation of the chemical shift tensor components with respect to **r** may be described by the Euler angles α, β, and γ (63, 64). This method of obtaining orientation information from the NMR spectra of powdered samples is termed the dipolar – chemical shift method (2–7). Unfortunately, since the dipolar tensor is axially symmetric, the orientation of the chemical shift tensors cannot be completely fixed in the molecular frame of reference (vide infra) (2–7) by experiment.

The actual dipolar coupling constant that is measured in any NMR experiment is an effective coupling constant, R_{eff}, with contributions from the direct dipolar coupling constant, R_{DD}, and ΔJ:

$$[2] \qquad R_{eff} = R_{DD} - \frac{\Delta J}{3}$$

R_{DD} is given by:

$$[3] \qquad R_{DD} = \frac{\mu_0}{4\pi}\left(\frac{\hbar}{2\pi}\right)\gamma_I\gamma_S\left\langle r_{IS}^{-3}\right\rangle$$

where $\langle r_{IS}^{-3}\rangle$ is the motional average of the inverse cube of the internuclear distance between the two spins, *I* and *S*. This relationship between R_{DD} and the distance between the two spins is important for structural investigations via solid-state NMR. For systems where R_{eff} is significantly different from R_{DD}, ΔJ may be determined unambiguously. When ΔJ is small, its contribution to R_{eff} may be masked by motional averaging. In such cases, precise characterization of ΔJ is very difficult. Conversely, quantitative determination of internuclear distances by measurement of R_{eff} requires that ΔJ and motional averaging be accounted for in some manner.

For systems containing effectively isolated homonuclear spin pairs, such as $Ph_3P\text{-}PPh_2^+$, analysis of the NMR spectra is facilitated by an independent measurement of R_{eff} using a 2D spin-echo experiment (45, 47, 65–68), which separates the chemical shift and spin-spin coupling interactions. The value of R_{eff} may be determined independently using rotational resonance (RR) experiments (43, 69–71) if the difference between the isotropic chemical shifts of the coupled nuclei is comparable to achievable MAS rates. Rotational resonance is achieved when the following condition is fulfilled:

$$[4] \qquad n\nu_{rot} = \nu_{iso}(I) - \nu_{iso}(S); \qquad n = 1,2,3,\ldots$$

where ν_{rot} is the MAS rate and ν_{iso} is the isotropic chemical shift in frequency units. The dipolar coupling interaction is "re-introduced" under these conditions; thus, R_{eff} may be obtained (43, 71).

Experimental and computational details

Sample preparation

A sample of $[Ph_3P\text{-}PPh_2][GaCl_4]$ was prepared as described in ref. 1. All samples were packed in an inert atmosphere as this compound is air sensitive.

NMR spectra

Phosphorus-31 NMR spectra were acquired for stationary or MAS samples of powdered crystalline $[Ph_3P\text{-}PPh_2][GaCl_4]$ at applied magnetic fields of 4.7 T (Chemagnetics CMX 200 spectrometer) and 9.4 T (Bruker AMX 400 spectrometer). The spectrometer frequencies for ^{31}P are 81.023 MHz and 161.978 MHz, respectively, for the applied fields mentioned above. The standard CP experiment with high-power proton decoupling was used in both cases. For experiments at 4.7 T, the sample was packed into a 4 mm zirconium oxide rotor. A proton $\pi/2$ pulse of 3.0 μs, contact time of 5.0 ms, and recycle delays of between 5 and 8 s were used. Spectra for MAS samples were also acquired on the 4.7 T system at several temperatures, ranging from ambient temperature to –120°C

© 2002 NRC Canada

using heated–cooled N_2 gas. Experiments at 9.4 T were performed on a sample packed into a 2.5 mm zirconium oxide rotor. Parameters similar to those for experiments at 4.7 T were used. All ^{31}P NMR spectra are referenced to the primary standard, 85% H_3PO_4(aq), by setting the isotropic peak in the ^{31}P CPMAS NMR spectrum of solid $NH_4H_2PO_4$ to +0.81 ppm (72). Gaussian line broadening of between 20 and 40 Hz for the spectra of MAS samples and between 100 and 200 Hz for spectra of stationary samples was applied. The 2D spin-echo experiment (65–67) was performed at 4.7 T using parameters identical to the 1D experiments. For each of 64 t_1 increments, 224 transients were acquired. The phase cycling of Rance and Byrd was used for this experiment (73).

Phosphorus-31 NMR spectra of stationary samples were simulated using WSOLIDS (74), a program developed in this laboratory that incorporates the POWDER routine of Alderman et al. (75). NMR spectra of MAS samples were calculated using NMRLAB (76), which uses the Monte Carlo method to sample crystal orientations for powder averaging. In our calculations, 10 000 crystallite orientations were used. The $F1$ projection of the 2D spectrum was calculated using SpinEcho (77), a program developed in this laboratory.

X-ray data collection at 20°C and –120°C

Although ambient temperature (23°C) X-ray diffraction data for $[Ph_3P\text{-}PPh_2][GaCl_4]$ have been previously reported (1); X-ray diffraction experiments have been repeated at 20°C and –120°C to remove instrument dependent variability. Results are summarized in Table 1. Agreement of the structures determined in ref. 1 and here is excellent.

Computational details

Density functional calculations were carried out using the Amsterdam density functional (ADF) package (78) in conjunction with the CPL module for calculating J-coupling (26, 27, 30, 79). The Vosko, Wilk, and Nusair (VWN) local density approximation (80) with the Becke88 (81) and Perdew86 (82) nonlocal gradient corrections were used for the exchange-correlation potential. Basis V, which is part of the standard ADF package, was used on all atoms. This triple-zeta basis set is composed of Slater-type orbitals and includes two polarization functions. Multiconfigurational self-consistent field calculations with complete active space self-consistent field (CASSCF) wavefunctions (31, 83–85) for **J** were performed using DALTON, an ab initio electronic structure program (86), installed on an IBM RS/6000 workstation. The cc-pVTZ basis set (87) was used on all atoms. For CASSCF wavefunctions, inactive and active molecular orbital combinations must be chosen. This selection was made based on MP2 natural molecular orbital occupation numbers and energies (88, 89). The inactive and active spaces are designated by *m*/*n*, indicating that there are *m* inactive orbitals and *n* active orbitals in the CASSCF space. The structure used for $H_3P\text{-}PH_2^+$ was optimized at the restricted Hartree-Fock (RHF) level using Gaussian 98 (90) with the 6–311++G(3df,3pd) basis set on all atoms. Calculations were also performed for different conformations, as described by the angle ϕ, which is the dihedral angle between the plane containing the P(1)—P(2) bond and also bisecting the H-P(2)-H bond angle and the plane containing the P(1)—P(2) and P(1)—H(1) bonds (see Fig. 1(*b*)). With the exception of ϕ, the structure is the same for each conformation. The structure used for $(CH_3)_3P\text{-}P(CH_3)_2^+$ is derived from the structure for $[Ph_3P\text{-}PPh_2][GaCl_4]$ obtained from X-ray diffraction data (1). The phenyl groups in $[Ph_3P\text{-}PPh_2][GaCl_4]$ are replaced by CH_3 groups with C—H bond lengths of 1.09 Å and all bond angles involving hydrogen set at 109.5°.

Calculations of phosphorus nuclear magnetic shielding tensors for $[Ph_3P\text{-}PPh_2][GaCl_4]$ were carried out at the RHF level using locally dense basis sets (91, 92); the 6–311++G(3df,3pd) basis set was used on the phosphorus and adjacent carbon atoms while the 6–31G basis set was used for the remaining atoms. The structure is taken from an X-ray diffraction study (1) with the exception of the C—H bond lengths, which were fixed at 1.08 Å. All calculations were performed with Gaussian 98 (90) using an IBM RS/6000 workstation. To facilitate comparison with experimental results, the calculated phosphorus nuclear magnetic shielding tensors were converted to chemical shift tensors using the relationship, $\delta_i = \sigma_{ref} - \sigma_i$. The absolute shielding scale for phosphorus is based on a shielding of 328.35 ± 0.63 ppm for the phosphorus nucleus of the reference, 85% H_3PO_4(aq) (49).

Results and discussion

Phosphorus-31 NMR spectra of $[Ph_3P\text{-}PPh_2][GaCl_4]$

The ^{31}P CPMAS NMR spectra for a crystalline powder sample of $[Ph_3P\text{-}PPh_2][GaCl_4]$ obtained at 4.7 T and 9.4 T are shown in Figs. 2 and 3, respectively. From the MAS spectra, the isotropic chemical shifts for each phosphorus nucleus and the magnitude of $^1J(^{31}P,^{31}P)_{iso}$ may be obtained (see Table 2, Fig. 2(*a*), and Fig. 3(*a*)). The assignment of the least shielded phosphorus site, δ_{iso} = 15.4 ppm, to P(1) is made on the basis of ab initio calculations of phosphorus nuclear magnetic shielding in $[Ph_3P\text{-}PPh_2][GaCl_4]$ (see Table 3). Known trends in phosphorus shielding — phosphines are in general more shielded than phosphonium centres (93–98) — support this assignment of phosphorus sites. The very small impurity peak at $\delta \approx 1$ ppm in Fig. 3 is attributed to a decomposition product. This is not observed in the spectra at 4.7 T (Fig. 2), probably owing to differences in the effectiveness of the rotors at excluding air from their contents.

To obtain information concerning the relative sign of J_{iso} and R_{eff} as well as the magnitude of R_{eff}, a 2D spin-echo experiment was carried out. The $F1$ projection is shown in Fig. 4 along with simulations using opposite signs (Fig. 4(*a*)) and the same signs (Fig. 4(*b*)) for $^1J(^{31}P,^{31}P)_{iso}$ and R_{eff}. From these simulations, $^1J(^{31}P,^{31}P)_{iso} = -323 \pm 2$ Hz and $R_{eff} = 1.70 \pm 0.05$ kHz. It should be noted that the $F1$ projection may be simulated using a positive J_{iso}; however, an unreasonably small value for R_{eff}, 1.10 kHz, must be used. Also, rotational resonance experiments at both 4.7 T and 9.4 T (see Figs. 2(*c*) and 3(*b–c*) confirm that R_{eff} = 1.70 kHz. In fact, the simulations shown in Figs. 2(*c*) and 3(*b–c*) lead to an error in R_{eff} of ±0.02 kHz. Hence, the combined analysis of the 2D spin-echo and RR spectra yields a value of 1.70 ± 0.02 kHz for R_{eff}.

Analysis of ^{31}P NMR spectra acquired at –70°C and –120°C at RR and off RR indicate that R_{eff} and J_{iso} are

© 2002 NRC Canada

Table 1. Crystallographic experimental details.

Crystal Data	(*a*) –120°C	(*b*) 20°C
Formula	$C_{30}H_{25}Cl_4GaP_2$	$C_{30}H_{25}Cl_4GaP_2$
Formula weight	658.96	658.96
Crystal colour, habit	Colourless block	Colourless block
Crystallization solvent	CH_2Cl_2	CH_2Cl_2
Crystal dimensions (mm)	0.67 × 0.48 × 0.30	0.67 × 0.48 × 0.30
Crystal system	Monoclinic	Monoclinic
Space group	*C*2/*c* (No. 15)	*C*2/*c* (No. 15)
Unit cell parameters		
a (Å)	24.6344 (16)[a]	24.6754 (17)[b]
b (Å)	9.6866 (6)	9.8174 (7)
c (Å)	25.4693 (16)	25.7182 (18)
Index ranges	$-28 \le h \le 30$	$-28 \le h \le 30$
	$-12 \le k \le 11$	$-12 \le k \le 12$
	$-31 \le l \le 31$	$-32 \le l \le 31$
β (deg)	102.8970 (12)	103.0762 (13)
V (Å^3)	5924.3 (6)	6068.6 (7)
*Z**	8	8
D_{calcd} (g cm^{-3})	1.478	1.442
μ (mm^{-1})	1.417	1.383
Data Collection		
Diffractometer*	Bruker PLATFORM/SMART 1000 CCD[c]	
Radiation (λ (Å))*	Graphite-monochromated Mo Kα (0.71073)	
Scan type*	ω scans (0.2°) (25 s exposures)	
Temperature (°C)	–120	20
Data collection 2θ limit (°)	52.74	52.76
Total data collected	17092	17368
Independent reflections	5987 (R_{int} = 0.0227)	6162 (R_{int} = 0.0224)
Observed reflections [$F_o^2 \ge 2\sigma(F_o^2)$]	5310	4948
Structure Solution and Refinement		
Structure solution method*	Direct methods (*SIR92*[d])	
Refinement method*	Full-matrix least-squares on F^2 (*SHELXL–93*[e])	
Absorption correction method*	Empirical (*SADABS*)	
Range of transmission factors	0.6759–0.4503	0.6817–0.4576
Data/restraints/parameters	5987/0/334	6162/0/334
Goodness-of-fit (*S*) [$F_o^2 \ge -3\sigma(F_o^2)$][f]	1.037	1.026
R_1 [$F_o^2 \ge 2\sigma(F_o^2)$][g]	0.0297	0.0404
wR_2 [$F_o^2 \ge -3\sigma(F_o^2)$][h]	0.0759	0.1092
Largest diff. peak and hole (e Å^{-3})	0.639 and –0.399	0.665 and –0.544

Note: Parameters common to both data collections are indicated with an asterisk (*).

[a]Obtained from least-squares refinement of 6453 reflections with 6.52° < 2θ < 52.73°.

[b]Obtained from least-squares refinement of 4307 reflections with 5.76° < 2θ < 51.82°.

[c]Programs for diffractometer operation, data collection, data reduction and absorption correction were those supplied by Bruker.

[d]See ref. (109). The room-temperature structure of this compound has been previously reported; see ref (1).

[e]See ref. (110).

[f]$S = [\Sigma w(F_o^2 - F_c^2)^2/(n-p)]^{1/2}$ (n = number of data; p = number of parameters varied; $w = [\sigma^2(F_o^2) + (a_0P)^2 + a_1P]^{-1}$ where $P = [\max(F_o^2,0) + 2F_c^2]/3$; for the –120°C dataset, a_0 = 0.0399, a_1 = 5.6777; for the 20°C dataset, a_0 = 0.0532, a_1 = 6.9078).

[g]$R_1 = \Sigma||F_o| - |F_c||/\Sigma|F_o|$.

[h]$wR_2 = [\Sigma w(F_o^2 - F_c^2)^2/\Sigma w(F_o^4)]^{1/2}$.

independent of temperature within the error limits of our experiment. The larger error in R_{eff} obtained at lower temperatures, 1.70 ± 0.05 kHz, was necessary to account for the poorer quality of the spectra (not shown).

Using the data from the analysis of the ^{31}P NMR spectra of MAS samples and the spin-spin coupling data from the 2D spin-echo and RR spectra, the ^{31}P NMR spectra shown in Fig. 5, which are obtained at two applied magnetic fields for a stationary sample, may be analyzed. The simulations are shown in Fig. 5 and the principal components of the two phosphorus chemical shift tensors as well as spin-spin coupling parameters that give the best overall fit to all the experimental spectra are given in Table 2. Also, the MAS line shapes, especially for slower spinning (Figs. 2(*b*–*c*) and 3(*b*–*c*)), are sensitive to most of the parameters and are well reproduced using the data in Table 2. Further discussion of

© 2002 NRC Canada

Table 2. Experimental phosphorus chemical shift tensor principal components and spin-spin coupling parameters for [Ph_3P-PPh_2][$GaCl_4$].

Parameter	P(1)		P(2)
Solution [a]			
δ_{iso} (ppm)	15.4		–10.6
$^1J(^{31}P,^{31}P)$ (Hz)		±340 [b]	
Solid state			
δ_{iso} (ppm) [c]	15.4		–17.8
δ_{11} (ppm) [d]	36		23
δ_{22} (ppm)	23		–8
δ_{33} (ppm)	–14		–68
Ω (ppm)	50		91
κ	0.48		0.32
$^1J(^{31}P,^{31}P)_{iso}$ (Hz)		–323 ± 2	
$\lvert\Delta J\rvert$ (Hz)		<300	
R_{eff} (kHz)		1.70 ± 0.02	

[a]Reference 1. The solvent is CH_2Cl_2.
[b]Observed in the reaction mixture solution. See reference 1.
[c]Experimental error on δ_{iso} is ±0.1 ppm, obtained from spectra of MAS samples. These data were also reported in reference 1.
[d]Experimental error on the principal components is ±2 ppm, obtained from spectra of stationary samples.

the chemical shift tensors is presented together with theoretical calculations below.

Anisotropy in $^1J(^{31}P,^{31}P)$ for [Ph_3P-PPh_2][$GaCl_4$]

The P—P bond length in [Ph_3P-PPh_2][$GaCl_4$] is 2.220(6) Å (1), for which R_{DD} is calculated to be 1.80 ± 0.04 kHz from eq. [3]. Using this value and the measured R_{eff}, eq. [2] yields ΔJ = 300 Hz if one assumes that R_{DD} and R_{eff} have the same sign. If the signs are opposite, then ΔJ = 10.5 kHz; given that the magnitude of $^1J(^{31}P,^{31}P)_{iso}$ is 323 Hz, it is highly unlikely that ΔJ has this latter value. In fact, on the basis of theoretical calculations (vide infra) the latter value can be discarded. The value of 300 Hz for ΔJ is an upper limit, since part of the difference between R_{DD} and R_{eff} may arise from motional averaging. Bond lengths from X-ray diffraction and NMR data differ since different mean values are determined by the two experiments (99, 100), i.e., NMR measures $\langle r^{-3}\rangle^{-1/3}$, not $\langle r\rangle$. X-ray diffraction data tend to give values that are shorter than r_{eq} (100). Furthermore, any motion of the P—P bond axis will also reduce R_{eff} and lead to an apparent enhanced value of ΔJ. Variable temperature experiments were undertaken to investigate the significance of motion in the determination of R_{eff}. Our results indicate that R_{eff} is unchanged at lower temperatures, suggesting that either any motion is not sufficiently removed or that most of the difference between R_{eff} and R_{DD} is due to ΔJ. Data from X-ray diffraction experiments at low temperature may provide some insight. Perspective ORTEP views of [Ph_2P-PPh_3][$GaCl_4$] are shown in Fig. 6 for 20°C and –120°C. The method of Hirshfeld (101) as implemented in the *PLATON* program system (102) was used to calculate values for the P(1)—P(2) bond lengths that are corrected for librational effects, as manifested in the values of the anisotropic displacement parameters. For the ambient temperature dataset, a value of 2.2281 Å is obtained, compared with the value obtained without librational correction, 2.2242(9) Å. For the data collected at –120°C, the corrected bond length is 2.2238 Å, compared with the uncorrected value, 2.2222(7) Å. The difference between the R_{DD} values calculated using the corrected P—P bond lengths for the two temperatures is 10 Hz, which is within the experimental error in R_{eff} measured at both ambient temperature and at –120°C. In general, this motion is difficult to quantify, hence ΔJ is reported as an upper limit and additional NMR and X-ray experiments, particularly at lower temperature (e.g., liquid helium temperatures), may be necessary to evaluate what portion of the difference between R_{eff} and R_{DD} is due to averaging of R_{DD} by motion as opposed to ΔJ.

The anisotropy in **J** may be estimated from DFT or ab initio methods such as MCSCF. To minimize calculation time, particularly for the MCSCF calculations, a model system, H_3P-PH_2^+, is used for Ph_3P-PPh_2^+. In addition, a more realistic model system, $(CH_3)_3P$-$P(CH_3)_2^+$, is used for a DFT

Fig. 2. Experimental and calculated ^{31}P CP NMR spectra of MAS samples of [Ph_3P-PPh_2][$GaCl_4$], acquired at 4.7 T. The spinning rates are (*a*) 5.02 kHz (256 transients), (*b*) 2.17 kHz (128 transients), and (*c*) 2.70 kHz (256 transients). The centreband for each phosphorus nucleus is indicated. Note that spinning at 2.70 kHz corresponds to the $n \approx 1$ RR condition at 4.7 T.

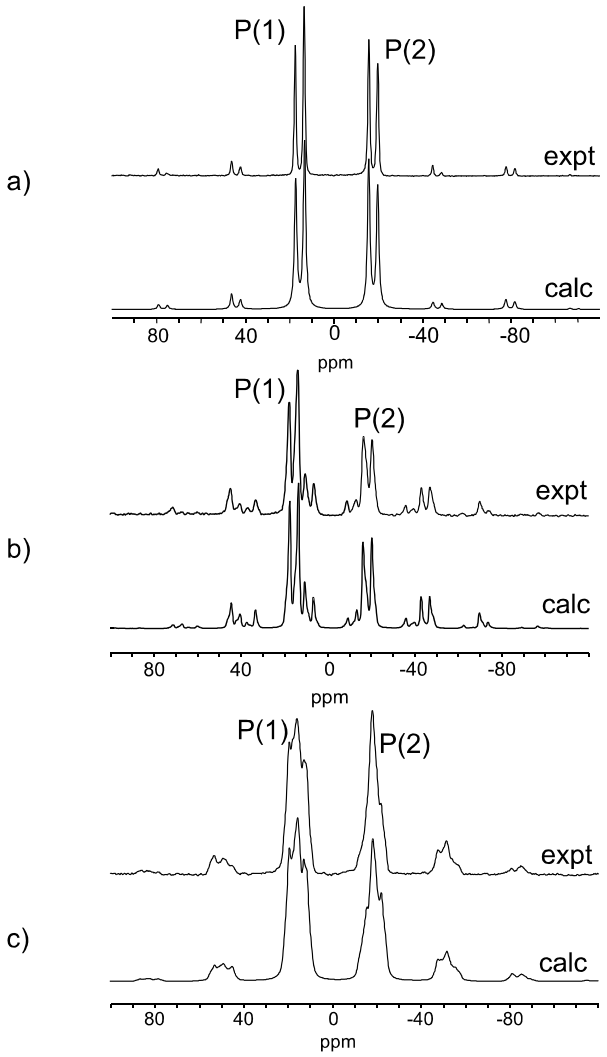

© 2002 NRC Canada

Table 3. Experimental and calculated[a] phosphorus chemical shift tensor principal components (ppm), isotropic chemical shift (ppm), Ω (ppm), and κ for $[Ph_3P\text{-}PPh_2][GaCl_4]$ (Structure 1) and $Ph_3P\text{-}PPh_2^+$ (Structure 2).

	δ_{11}	δ_{22}	δ_{33}	δ_{iso}	Ω	κ
P(1)						
Experimental						
Solid	36	23	–14	15.4	50	0.48
Solution				15.4		
RHF (Structure 1)	23	6	–37	–2.4	60	0.44
RHF (Structure 2)	24	6	–36	–1.9	60	0.41
P(2)						
Experimental						
Solid	23	–8	–68	–17.8	91	0.32
Solution				–10.6		
RHF (Structure 1)	28	–17	–105	–31.2	133	0.32
RHF (Structure 2)	25	–21	–109	–35.0	134	0.31
Difference between δ_{iso} of P(1) and P(2)						
Experimental (solid)				33.2		
RHF (Structure 1)				28.8		
RHF (Structure 2)				33.1		

[a]Calculations performed at the RHF level using the 6–311++G(3df,3pd) basis set on all phosphorus and directly bonded carbon atoms and the 6–31G basis set on the remaining atoms.

calculation for the purpose of determining the limitations of the smaller model, $H_3P\text{-}PH_2^+$. The results from both computational approaches and for both model systems are given in Table 4. The conformational dependence of the P-P *J*-coupling, as described by ϕ (Fig. 1(*b*)), is considered for the smaller model system, $H_3P\text{-}PH_2^+$. It is evident from Table 4 that **J** is virtually independent of ϕ for $H_3P\text{-}PH_2^+$. This result is expected, since rotation of the PH_3 group about the P—P bond does not result in a significant change in the overall structure. This has also been observed in semi-empirical calculations of $^1J(^{15}N,^{13}C)_{iso}$ in CH_3NH_2 when the NH_2 group is rotated about the C—N bond (103). The average $^1J(^{31}P,^{31}P)_{iso}$ and ΔJ values over all conformations are approximately –341 and 361 Hz, respectively from DFT and –193 and 131 Hz, respectively from MCSCF. These averages are obtained by weighting the results according to the calculated Boltzmann distribution. For $(CH_3)_3P\text{-}P(CH_3)_2^+$, DFT predicts a significantly larger magnitude for J_{iso} relative to J_{iso} for $H_3P\text{-}PH_2^+$, due primarily to a larger FC contribution. The anisotropy in **J** is predicted to be 300 Hz, which is the same order of magnitude as the values of ΔJ for $H_3P\text{-}PH_2^+$.

Both the DFT and MCSCF calculations predict that J_{iso} and ΔJ are approximately equal in magnitude. This is in agreement with the experimental observations for $[Ph_3P\text{-}PPh_2][GaCl_4]$ and also with the literature (47, 104). There is a significant difference between the DFT and MCSCF results. Modification of the active–inactive space for the MCSCF calculations changes the calculated value of J_{iso} by about 9%, which does not account for the difference between the MCSCF and DFT data. Examination of the contributions from the various coupling mechanisms to J_{iso} (Table 4) reveals that the significant difference between the results for the two methods for J_{iso} lies in the FC contribution. Both methods predict that the FC mechanism dominates the value of J_{iso}. The DFT approach appears to be more successful in general when compared with the experimental results.

The DFT calculations presented in the literature have provided results for J_{iso} that are in good agreement with experiment for a number of systems. For example, Malkin et al. (28) calculated isotropic *J*-coupling constants involving ^1H, ^{13}C, $^{14/15}N$, ^{17}O, and ^{19}F in a number of small molecules as well as some larger organic molecules. Further work by Malkina et al. (29) identified some problems for systems containing formal lone pairs; however, the qualitative agreement is good. The use of Slater-type rather than Gaussian-type basis sets in conjunction with DFT has also been successful (30). This approach has been further developed to include relativistic corrections, giving very good results for coupling involving heavier nuclei (25–27, 105). Given the past performance of DFT for the calculation of *J*-coupling, the results presented here for $H_3P\text{-}PH_2^+$ and $(CH_3)_3P\text{-}P(CH_3)_2^+$ may be considered to be qualitatively reliable.

Comparison of experimental and calculated phosphorus chemical shift tensors

The experimental and calculated values of δ_{11}, δ_{22}, δ_{33}, δ_{iso}, Ω, and κ for the two phosphorus environments in $[Ph_3P\text{-}PPh_2][GaCl_4]$ are presented in Table 3. Calculations were performed on structure 1, which consists of $Ph_3P\text{-}PPh_2^+$ and the closest $GaCl_4^-$ ion, and structure 2, which consists of the isolated $Ph_3P\text{-}PPh_2^+$ ion. As is evident from comparison of the spans and skews for structure 1, the line shapes predicted by the ab initio calculations are in good agreement with the experimental results.

The difference in the isotropic phosphorus chemical shifts is reproduced reasonably well by ab initio calculations (Table 3). However, the calculated isotropic chemical shifts are significantly smaller than those from experiment; for P(1) in structure 1, the calculations predict a value for δ_{iso}, which is too shielded by 18 ppm and for P(2), δ_{iso} is predicted to be 13 ppm more shielded compared with experiment. This difference between experimental and calculated results may be attributed to deficiencies in the ab initio

© 2002 NRC Canada

Fig. 3. Experimental and calculated ^{31}P CP NMR spectra of MAS samples of $[Ph_3P\text{-}PPh_2][GaCl_4]$, acquired at 9.4 T. The spinning rates are (*a*) 7.03 kHz, (*b*) 2.65 kHz, and (*c*) 5.36 kHz. In each case, 512 transients were acquired. The centreband for each phosphorus nucleus is indicated. A signal attributed to a decomposition product is indicated by an asterisk. Note that spinning at 5.36 kHz corresponds to the $n \approx 1$ RR condition at 9.4 T.

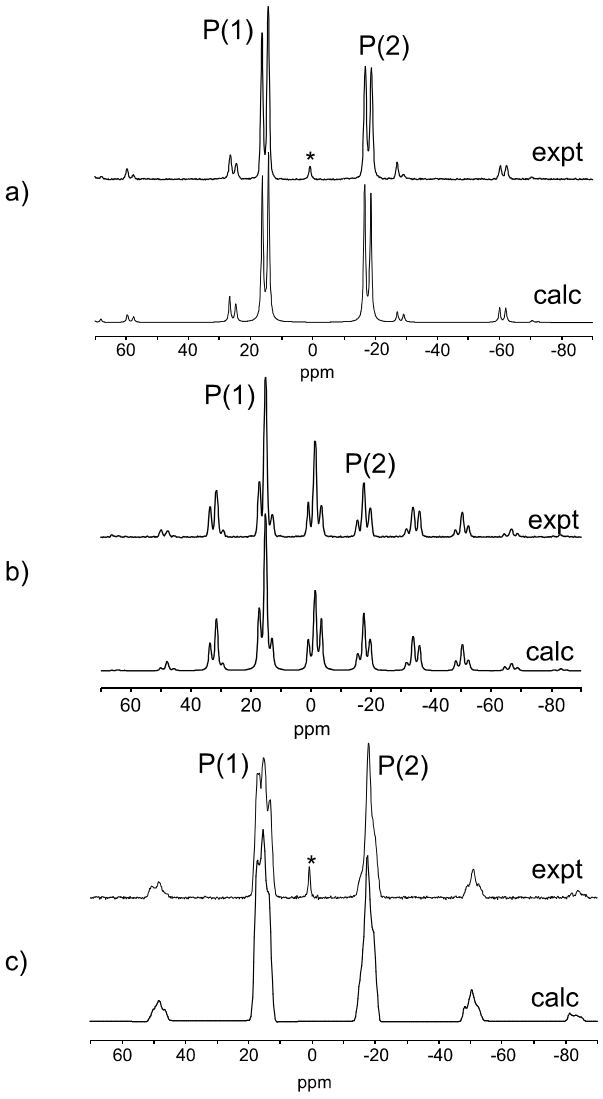

approach and (or) to intermolecular effects that are not properly accounted for in the calculations. For $[Ph_3P\text{-}PPh_2][GaCl_4]$, the difference between the phosphorus chemical shifts in solution (methylene chloride solvent) and the solid state is an indication of the significance of specific intermolecular effects such as ion pairing. The difference is greatest for P(2), which is more shielded by 7.2 ppm in the solid compared with solution. The presence of $GaCl_4^-$ ions may contribute to the difference between the experimental and calculated results. The closest contact between the $Ph_3P\text{-}PPh_2^+$ ion and the $GaCl_4^-$ ion occurs between P(2) and a chlorine atom, at a distance of 6.061 Å (1). Calculations for structure 1, which consists of $Ph_3P\text{-}PPh_2^+$ and the nearest $GaCl_4^-$, and structure 2, which consists of an isolated $Ph_3P\text{-}PPh_2^+$ ion, indicate that P(2) is most affected; each component is deshielded by about 4 ppm owing to the

Fig. 4. Experimental and calculated *F*1 projections of the 2D spin-echo ^{31}P NMR spectrum of $[Ph_3P\text{-}PPh_2][GaCl_4]$ acquired at 4.7 T. The peak marked by an asterisk is an experimental artifact. Simulations are shown with R_{eff} = 1.70 kHz and (*a*) $^1J(^{31}P,^{31}P)_{iso}$ = –323 Hz and (*b*) $^1J(^{31}P,^{31}P)_{iso}$ = +323 Hz.

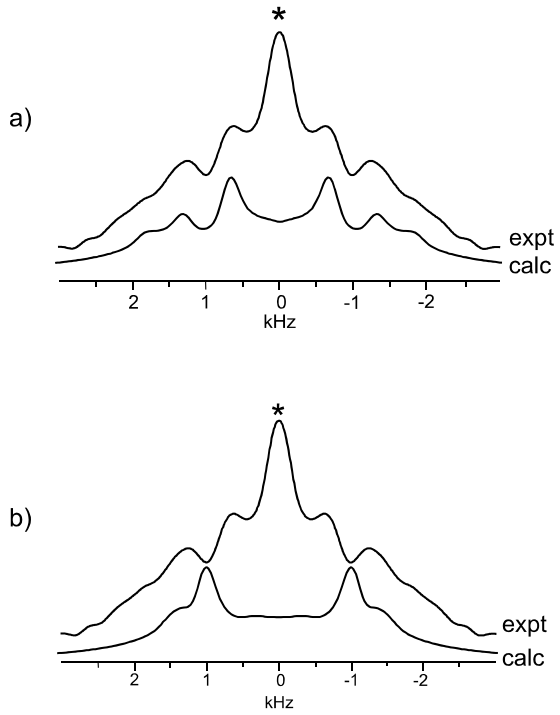

Fig. 5. Experimental and calculated ^{31}P CP NMR spectra of stationary powder samples of $[Ph_3P\text{-}PPh_2][GaCl_4]$ at applied magnetic fields of (*a*) 4.7 T (5000 transients, 200 Hz gaussian line broadening), and (*b*) 9.4 T (3774 transients, 100 Hz gaussian line broadening).

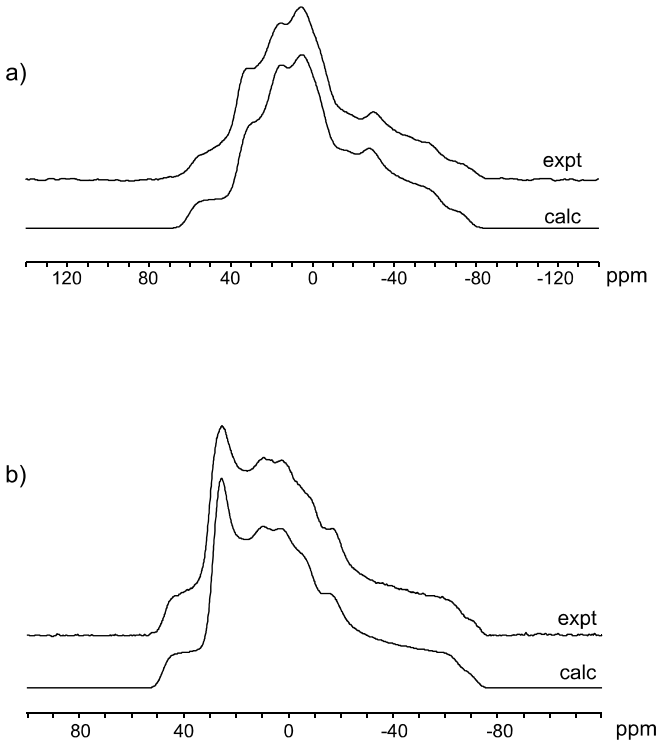

© 2002 NRC Canada

Table 4. Calculated values of $^1J(^{31}P,^{31}P)_{iso}$ and ΔJ for $H_3P\text{-}PH_2^+$ and $(CH_3)_3P\text{-}P(CH_3)_2^+$. Also given are the contributions from the diamagnetic and paramagnetic spin-orbit (DSO and PSO), spin-dipolar (SD), and Fermi contact (FC) mechanisms to J_{iso}.

			Contributions to $^1J(^{31}P,^{31}P)_{iso}$ (Hz) [a]		
ϕ (°)[b]	$^1J(^{31}P,^{31}P)_{iso}$ (Hz)	$\lvert\Delta J(^{31}P,^{31}P)\rvert$ (Hz)	PSO	SD	FC
Experimental[c]	–323 ± 2 (solid) ±340 (solution)	300			
$H_3P\text{-}PH_2^+$: MCSCF results[d]					
0	–195	107	–7	4	–193
30	–198	120	–11	3	–189
60	–200	126	–15	2	–187
90	–189	118	–11	3	–181
120	–177	108	–7	3	–173
150	–188	128	–13	3	–176
180	–195	137	–18	2	–180
average[e]	–193	131	–16	2	–180
$H_3P\text{-}PH_2^+$:DFT results[f]					
0	–344	339	–11	27	–360
30	–351	346	–15	26	–361
60	–355	354	–19	26	–361
90	–342	350	–14	25	–353
120	–330	349	–11	26	–345
150	–334	359	–17	25	–342
180	–340	366	–22	24	–342
average[e]	–341	361	–20	25	–346
$(CH_3)_3P\text{-}P(CH_3)_2^+$: DFT results					
	–427	300	–28	18	–417

[a]The calculated DSO contribution for both MCSCF and DFT is 0.1 Hz for all values of ϕ for $H_3P\text{-}PH_2^+$; the DSO contribution is 0.3 Hz for $(CH_3)_3P\text{-}P(CH_3)_2^+$.
[b]See Fig. 1(*b*) for the definition of ϕ for $H_3P\text{-}PH_2^+$.
[c]For $[Ph_3P\text{-}PPh_2][GaCl_4]$. Solid-state data from this work. Solution data from reference 1.
[d]Calculations performed at the MCSCF level with the cc-pVTZ basis set using an inactive/active space of 10/8.
[e]Averages are obtained by weighting according to the Boltzmann distribution.
[f]DFT results (using VWN local density approximation and Becke88 (81) + Perdew86 (82) nonlocal gradient corrections) with basis set V.

presence of the anion. However, consideration of one anion is clearly not sufficient to reproduce the experimental trend. The line shapes, as described by Ω and κ, are not significantly different for structures 1 and 2.

As was noted in the background section, some chemical shift tensor orientation information is available from simulation of the experimental spectra obtained from powdered crystalline samples containing spin pairs. To describe the orientation of the chemical shift tensors, we employ the angles α, β, and γ (63, 64). The angle β is the angle between δ_{33} and **r**, while γ indicates if δ_{11} or δ_{22} is closest to **r**. The difference between the α angles for the two chemical shift tensors, $\Delta\alpha$, is the dihedral angle between the δ_{33} components. For P(1), it is concluded that δ_{33} forms an angle, β, of 99° ± 2° with respect to the P—P bond. This is equally well described by the supplement angle, 81°. For P(2), the corresponding angle is smaller, 78° ± 2°. The orientation of the δ_{33} components is illustrated in Fig. 7(*a*). The best simulations of the experimental spectra are obtained using a dihedral angle between the δ_{33} components, $\Delta\alpha$, of 25° ± 2°. The value of γ for P(1) is 2° ± 5° and 78° ± 2° for P(2), indicating that the orientations of δ_{11} and δ_{22} with respect to the P—P bond are quite different for the two phosphorus chemical shift tensors.

The orientations of the phosphorus chemical shift tensors in the molecular frame of reference may be predicted by ab initio calculations. The orientation of the P(1) and P(2) chemical shift tensors for structure 1 shown in Fig. 7(*b*) was obtained at the RHF level of theory. For P(1), δ_{33} forms an angle of 92° with respect to the P—P bond. This is in good agreement with the experimental result. The other two components are oriented as follows: δ_{11} forms an angle of 31° with respect to the P—P bond while δ_{22} is situated at an angle of 60° from the P—P bond; hence δ_{11} is closest to the P—P bond for P(1). The δ_{33} component for P(2) forms an angle of 80° with respect to the P—P bond, in excellent agreement with the experimentally observed value of this parameter. For this phosphorus environment, δ_{22} is closest to the P—P bond, forming an angle of 13°, while δ_{11} is situated at an angle of 81° from the P—P bond. This calculated result (δ_{11} is closest to the P—P bond for P(1) while δ_{22} is closest for P(2)) is in agreement with the experimental observation that the values of γ are very different for the two phosphorus chemical shift tensors. Finally, the experimental and calculated orientations may be compared by examining the relative orientation of the phosphorus chemical shift tensors, via $\Delta\alpha$. The calculated dihedral angle between the δ_{33} components, $\Delta\alpha$, is 23°, in excellent agreement with the

© 2002 NRC Canada

Fig. 6. Perspective ORTEP views of the $[Ph_2P–PPh_3]^+$ ion and the associated $[GaCl_4]^-$ ion at (*a*) –120°C and (*b*) 20°C. Non-hydrogen atoms are represented by Gaussian ellipsoids at the 50% probability level. Hydrogen atoms are not shown. The ions are shown in their relative crystallographic positions; no unusually close contacts (i.e., nearer than summed van der Waals radii) exist between these ions (or those generated by crystallographic symmetry). The atom P1 in this figure corresponds to P(2) in Fig. 1(*a*) and elsewhere in this manuscript; similarly, P2 in this figure corresponds to P(1) in Fig. 1(*a*) and elsewhere in this manuscript.

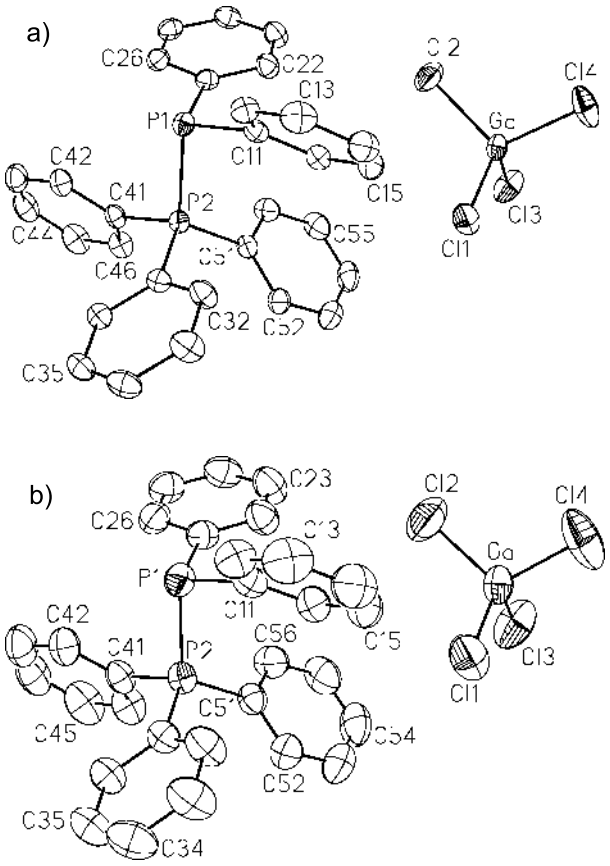

Fig. 7. Experimental (*a*) and calculated (*b*) orientation of the phosphorus chemical shift tensors for P(1) and P(2) in $[Ph_3P-PPh_2][GaCl_4]$. For P(1) in (*b*), the tensor is shown such that δ_{33} is in the plane of the page while δ_{22} is slightly in front of the plane and δ_{11} is behind the plane. For P(2) in (*b*), δ_{11} is perpendicular to the plane of the page and the other two components are in the plane. The $GaCl_4^-$ ion and hydrogen atoms have been omitted for clarity.

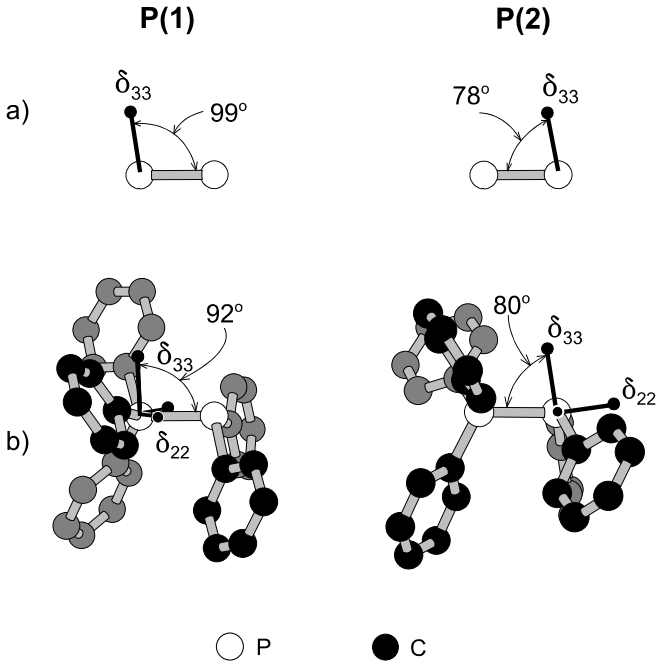

experimental value of 25°. The good agreement between the calculated orientation and the orientation information available from the experimental data suggests that the calculated phosphorus shift tensor orientations in the molecular axis system illustrated in Fig. 7(*b*) are reliable.

The phosphorus magnetic shielding tensors for P(1) and P(2) may be compared with phosphorus chemical shift tensors in related compounds. The observed span of the phosphorus chemical shift tensor for P(2) is larger than typical values for phosphines (106). The phosphorus NMR parameters obtained for a similar compound, $Mo(CO)_5(Ph_2P-PPh_2)$ (98), are comparable to the results presented here for $[Ph_3P-PPh_2][GaCl_4]$. It is also interesting to note that, although P(1) has a formal positive charge, the chemical shift is hardly affected compared with P(2), whereas for carbocations, the carbon site with the formal positive charge is highly deshielded (107). Also, the phosphorus environment for P(1) may be compared with a series of phosphine-X adducts (X = BH_3, CH_2, NH, and O). In these compounds, the phosphorus chemical shift tensor is oriented such that δ_{33} is along the P—X bond (108), which is quite different from P(1) in $[Ph_3P-PPh_2][GaCl_4]$. For example, in Ph_3P-BH_3, δ_{33} is oriented at an angle of 6.5° with respect to the P—B bond, while in $[Ph_3P-PPh_2][GaCl_4]$, δ_{33} is at 81° from the P—P bond. For P(2), the phosphorus chemical shift tensor orientation could be compared with the orientation in Ph_2P-PPh_2 (65); however, in that case, it was assumed that δ_{33} is along the direction of the formal lone pairs.

Conclusions

The indirect spin-spin coupling tensor, $^1\mathbf{J}(^{31}P,^{31}P)$, and the phosphorus chemical shift tensors for $[Ph_3P-PPh_2][GaCl_4]$ have been characterized by combining the dipolar-chemical shift NMR method with calculations from first principles and DFT. By using the P—P bond length from an X-ray diffraction study (1) and the effective dipolar coupling constant presented in this work, it is concluded that $|\Delta J|$ for $^1\mathbf{J}(^{31}P,^{31}P)$ has an upper limit of 300 Hz. This conclusion is supported by DFT and MCSCF calculations of $^1\mathbf{J}(^{31}P,^{31}P)$ for model compounds, $H_3P-PH_2^+$ and $(CH_3)_3P-P(CH_3)_2^+$. As well, the properties of $^1\mathbf{J}(^{31}P,^{31}P)$ for these model compounds have been investigated using these theoretical approaches.

The phosphorus chemical shift tensors obtained experimentally for $[Ph_3P-PPh_2][GaCl_4]$ are compared with the results from ab initio molecular orbital calculations. Good agreement is obtained between the experimental and calculated principal components of the chemical shift tensor. In

© 2002 NRC Canada

addition, the orientation of the two phosphorus chemical shift tensors in the molecular frame of reference is suggested by the theoretical calculations.

Acknowledgments

The Wasylishen group at the University of Alberta and the Burford group at Dalhousie University are acknowledged for their interest in this work. In particular, Dr. Edgar Ocando-Mavarez is acknowledged for his contribution to the early stages of this project as well as Dr. Guy Bernard for his assistance with the VT experiments. We are grateful to Dr. Jochen Autschbach and Prof. Tom Ziegler at the University of Calgary for providing the code to perform DFT calculations of **J**. R.E.W. acknowledges the financial support of the Natural Sciences and Engineering Research Council of Canada (NSERC) and the University of Alberta. R.E.W. is a Canada Research Chair in physical chemistry. M.G. thanks NSERC, the Izaak Walton Killam Memorial Trust, and the Walter C. Sumner Foundation for postgraduate scholarships at Dalhousie University. Spectra at 9.4 T were acquired at the Atlantic Region Magnetic Resonance Centre (Dalhousie University), which is also supported by NSERC.

References

1. N. Burford, T.S. Cameron, P.J. Ragogna, E. Ocando-Mavarez, M. Gee, R. McDonald, and R.E. Wasylishen. J. Am. Chem. Soc. **123**, 7947 (2001).
2. D.L. VanderHart and H.S. Gutowsky. J. Chem. Phys. **49**, 261 (1968).
3. H. van Willigen, R.G. Griffin, and R.A. Haberkorn. J. Chem. Phys. **67**, 5855 (1977).
4. M. Linder, A. Höhener, and R.R. Ernst. J. Chem. Phys. **73**, 4959 (1980).
5. K.W. Zilm and D.M. Grant. J. Am. Chem. Soc. **103**, 2913 (1981).
6. W.P. Power and R.E. Wasylishen. Ann. Rep. NMR Spectrosc. **23**, 1 (1991).
7. R.E. Wasylishen, R.D. Curtis, K. Eichele, M.D. Lumsden, G.H. Penner, W.P. Power, and G. Wu. *In* Nuclear magnetic shieldings and molecular structure. *Edited by* J.A. Tossell. Kluwer Academic Publishers, Dordrecht. 1993. p. 297.
8. R.D. Curtis, J.W. Hilborn, G. Wu, M.D. Lumsden, R.E. Wasylishen, and J.A. Pincock. J. Phys. Chem. **97**, 1856 (1993).
9. M.D. Lumsden, G. Wu, R.E. Wasylishen, and R.D. Curtis. J. Am. Chem. Soc. **115**, 2825 (1993).
10. K. Eichele and R.E. Wasylishen. J. Magn. Reson. A, **106**, 46 (1994).
11. G. Wu and R.E. Wasylishen. Solid State Nucl. Magn. Reson. **4**, 47 (1995).
12. T. Helgaker, M. Jaszuński, and K. Ruud. Chem. Rev. **99**, 293 (1999).
13. H. Fukui. Prog. Nucl. Magn. Reson. Spectrosc. **35**, 267 (1999).
14. D.B. Chesnut. Ann. Rep. NMR Spectrosc. **29**, 71 (1994).
15. A.C. de Dios. Prog. Nucl. Magn. Reson. Spectrosc. **29**, 229 (1996).
16. H. Fukui. Prog. Nucl. Magn. Reson. Spectrosc. **31**, 317 (1997).
17. U. Fleischer, C. van Wüllen, and W. Kutzelnigg. *In* Encyclopedia of computational chemistry. *Edited by* P. von R. Schleyer. John Wiley and Sons, Chichester. 1998. p. 1927.
18. C.J. Jameson. *In* Modeling NMR chemical shifts: Gaining insights into structure and environment. *Edited by* J.C. Facelli and A.C. de Dios. American Chemical Society, Washington, DC. 1999. p. 1.
19. C. Scheurer and R. Brüschweiler. J. Am. Chem. Soc. **121**, 8661 (1999).
20. H. Benedict, I.G. Shenderovich, O.L. Malkina, V.G. Malkin, G.S. Denisov, N.S. Golubev, and H.-H. Limbach. J. Am. Chem. Soc. **122**, 1979 (2000).
21. S.A. Perera and R.J. Bartlett. J. Am. Chem. Soc. **122**, 1231 (2000).
22. D.L. Bryce and R.E. Wasylishen. J. Biomol. NMR, **19**, 371 (2001).
23. V.G. Malkin, O.L. Malkina, L.A. Eriksson, and D.R. Salahub. *In* Modern density functional theory: A tool for chemistry. *Edited by* J.M. Seminario and P. Politzer. Elsevier Science B. V., Amsterdam. 1995. p. 273.
24. V. Sychrovský, J. Gräfenstein, and D. Cremer. J. Chem. Phys. **113**, 3530 (2000).
25. J. Khandogin and T. Ziegler. J. Phys. Chem. A, **104**, 113 (2000).
26. J. Autschbach and T. Ziegler. J. Chem. Phys. **113**, 936 (2000).
27. J. Autschbach and T. Ziegler. J. Chem. Phys. **113**, 9410 (2000).
28. V.G. Malkin, O.L. Malkina, and D.R. Salahub. Chem. Phys. Lett. **221**, 91 (1994).
29. O.L. Malkina, D.R. Salahub, and V.G. Malkin. J. Chem. Phys. **105**, 8793 (1996).
30. R.M. Dickson and T. Ziegler. J. Phys. Chem. **100**, 5286 (1996).
31. O. Vahtras, H. Ågren, P. Jørgensen, H.J. Aa. Jensen, S.B. Padkjær, and T. Helgaker. J. Chem. Phys. **96**, 6120 (1992).
32. J. Kaski, P. Lantto, J. Vaara, and J. Jokisaari. J. Am. Chem. Soc. **120**, 3993 (1998).
33. J. Kaski, P. Lantto, T.T. Rantala, J. Schroderus, J. Vaara, and J. Jokisaari. J. Phys. Chem. A, **103**, 9669 (1999).
34. J. Vaara, J. Kaski, and J. Jokisaari. J. Phys. Chem. A, **103**, 5675 (1999).
35. D.L. Bryce and R.E. Wasylishen. J. Am. Chem. Soc. **122**, 11 236 (2000).
36. D.L. Bryce and R.E. Wasylishen. J. Mol. Struct. **602–603**, 463 (2002).
37. D.L. Bryce and R.E. Wasylishen. Inorg. Chem. **41**, 3091 (2002).
38. D.L. Bryce, R.E. Wasylishen, J. Autschbach, and T. Ziegler. J. Am. Chem. Soc. **124**, 4894 (2002).
39. R.W. Schurko, R.E. Wasylishen, and H. Foerster. J. Phys. Chem. A, **102**, 9750 (1998).
40. G.M. Bernard, G. Wu, and R.E. Wasylishen. J. Phys. Chem. A, **102**, 3184 (1998).
41. D.L. Bryce and R.E. Wasylishen. J. Phys. Chem. A, **103**, 7364 (1999).
42. G.M. Bernard, G. Wu, M.D. Lumsden, R.E. Wasylishen, N. Maigrot, C. Charrier, and F. Mathey. J. Phys. Chem. A, **103**, 1029 (1999).
43. D.L. Bryce and R.E. Wasylishen. J. Phys. Chem. A, **104**, 7700 (2000).
44. R.W. Schurko and R.E. Wasylishen. J. Phys. Chem. A, **104**, 3410 (2000).
45. M. Gee, R.E. Wasylishen, K. Eichele, G. Wu, T.S. Cameron, F. Mathey, and F. Laporte. Can. J. Chem. **78**, 118 (2000).
46. G.M. Bernard, R.E. Wasylishen, and A.D. Phillips. J. Phys. Chem. A, **104**, 8131 (2000).
47. M. Gee, R.E. Wasylishen, K. Eichele, and J.F. Britten. J. Phys. Chem. A, **104**, 4598 (2000).
48. J. Mason. Solid State Nucl. Magn. Reson. **2**, 285 (1993).

© 2002 NRC Canada

49. C.J. Jameson, A. de Dios, and A.K. Jameson. Chem. Phys. Lett. **167**, 575 (1990).
50. A.D. Buckingham and I. Love. J. Magn. Reson. **2**, 338 (1970).
51. H.W. Spiess. NMR Basic Princ. Prog. **15**, 55 (1978).
52. R.E. Wasylishen. *In* Encyclopedia of nuclear magnetic resonance. *Edited by* D.M. Grant and R.K. Harris. Wiley Inc., Chichester, U.K. 1996. p. 1685.
53. N.F. Ramsey. Phys. Rev. **91**, 303 (1953).
54. N.F. Ramsey. Molecular beams. Oxford University Press, London. 1956.
55. C.J. Jameson and J. Mason. *In* Multinuclear NMR. *Edited by* J. Mason. Plenum Press, New York. 1987. p. 3.
56. W.P. Power, M.D. Lumsden, and R.E. Wasylishen. J. Am. Chem. Soc. **113**, 8257 (1991).
57. W.P. Power and R.E. Wasylishen. Inorg. Chem. **31**, 2176 (1992).
58. R.E. Wasylishen, K.C. Wright, K. Eichele, and T.S. Cameron. Inorg. Chem. **33**, 407 (1994).
59. M.D. Lumsden, K. Eichele, R.E. Wasylishen, T.S. Cameron, and J.F. Britten. J. Am. Chem. Soc. **116**, 11 129 (1994).
60. M.D. Lumsden, R.E. Wasylishen, and J.F. Britten. J. Phys. Chem. **99**, 16 602 (1995).
61. J. Lounila and J. Jokisaari. Prog. Nucl. Magn. Reson. Spectrosc. **15**, 249 (1982).
62. D.L. Bryce and R.E. Wasylishen. J. Am. Chem. Soc. **122**, 3197 (2000).
63. M. Mehring. Principles of high resolution NMR in solids. Springer-Verlag, Berlin. 1983. p. 292.
64. K. Schmidt-Rohr and H.W. Spiess. Multidimensional solid-state NMR and polymers. Academic Press, London. 1994. p. 444.
65. T. Nakai and C.A. McDowell. J. Am. Chem. Soc. **116**, 6373 (1994).
66. K.W. Zilm, G.G. Webb, A.H. Cowley, M. Pakulski, and A. Orendt. J. Am. Chem. Soc. **110**, 2032 (1988).
67. T. Nakai and C.A. McDowell. Chem. Phys. Lett. **217**, 234 (1994).
68. K. Eichele, R.E. Wasylishen, R.W. Schurko, N. Burford, and W.A. Whitla. Can. J. Chem. **74**, 2372 (1996).
69. E.R. Andrew, A. Bradbury, R.G. Eades, and V.T. Wynn. Phys. Lett. **4**, 99 (1963).
70. D.P. Raleigh, M.H. Levitt, and R.G. Griffin. Chem. Phys. Lett. **146**, 71 (1988).
71. D.L. Bryce and R.E. Wasylishen. *In* Encyclopedia of spectroscopy and spectrometry. *Edited by* J.C. Lindon, G.E. Tranter, and J.L. Holmes. Academic Press, San Diego. 2000. p. 2136.
72. D.L. Bryce, G.M. Bernard, M. Gee, M.D. Lumsden, K. Eichele, and R.E. Wasylishen. Can. J. Anal. Sci. Spect. **46**, 46 (2001).
73. M. Rance and R.A. Byrd. J. Magn. Reson. **52**, 221 (1983).
74. K. Eichele and R.E. Wasylishen. 2000. WSOLIDS [computer program]. Version 2.0.18. Edmonton, AB, Canada.
75. D.W. Alderman, M.S. Solum, and D.M. Grant. J. Chem. Phys. **84**, 3717 (1986).
76. B. Sun and R.G. Griffin. unpublished results.
77. K. Eichele and R.E. Wasylishen. SpinEcho, version 1.2.5, 2000.
78. Vrije University. ADF2000.02 Theoretical chemistry [online]. Vrije University, Amsterdam. Available from http://www.scm.com [cited 4 April, 2002]; *see also* E.J. Baerends, D.E. Ellis, and P. Ros. Chem. Phys. **2**, 41 (1973); L. Versluis and T. Ziegler. J. Chem. Phys. **88**, 322 (1988); G. te Velde and E.J. Baerends. J. Comput. Phys. **99**, 84 (1992); C. Fonseca Guerra, J.G. Snijders, G. te Velde, and E.J. Baerends. Theor. Chem. Acc. **99**, 391 (1998).
79. J. Khandogin and T. Ziegler. Spectrochim. Acta, **A55**, 607 (1999).
80. S.H. Vosko, L. Wilk, and M. Nusair. Can. J. Phys. **58**, 1200 (1980).
81. A.D. Becke. Phys. Rev. A, **38**, 3098 (1988).
82. J.P. Perdew. Phys. Rev. B, **33**, 8822 (1986); **34**, 7406(E) (1986).
83. B.O. Roos, P.R. Taylor, and P.E.M. Siegbahn. Chem. Phys. **48**, 157 (1980).
84. P.E.M. Siegbahn, J. Almlöf, A. Heiberg, and B.O. Roos. J. Chem. Phys. **74**, 2384 (1981).
85. B.O. Roos. Adv. Chem. Phys. **69**, 399 (1987).
86. T. Helgaker, H.J.Å. Jensen, P. Jørgensen, J. Olsen, K. Ruud, H. Ågren, T. Andersen, K.L. Bak, V. Bakken, O. Christiansen, P. Dahle, E.K. Dalskov, T. Enevoldsen, B. Fernandez, H. Heiberg, H. Hettema, D. Jonsson, S. Kirpekar, R. Kobayashi, H. Koch, K.V. Mikkelsen, P. Norman, M.J. Packer, T. Saue, P.R. Taylor, and O. Vahtras. 1997. DALTON: an ab initio electronic structure program [computer program]. Release 1.0. Oslo, Norway.
87. T.H. Dunning, Jr. J. Chem. Phys. **90**, 1007 (1989).
88. H. Jørgen, Aa. Jensen, P. Jørgensen, H. Ågren, and J. Olsen. J. Chem. Phys. **88**, 3834 (1988).
89. J. Guilleme and J. San Fabián. J. Chem. Phys. **109**, 8168 (1998).
90. M.J. Frisch, G.W. Trucks, H.B. Schlegel, G.E. Scuseria, M.A. Robb, J.R. Cheeseman, V.G. Zakrzewski, J.A. Montgomery, Jr., R.E. Stratmann, J.C. Burant, S. Dapprich, J.M. Millam, A.D. Daniels, K.N. Kudin, M.C. Strain, O. Farkas, J. Tomasi, V. Barone, M. Cossi, R. Cammi, B. Mennucci, C. Pomelli, C. Adamo, S. Clifford, J. Ochterski, G.A. Petersson, P.Y. Ayala, Q. Cui, K. Morokuma, D.K. Malick, A.D. Rabuck, K. Raghavachari, J.B. Foresman, J. Cioslowski, J.V. Ortiz, B.B. Stefanov, G. Liu, A. Liashenko, P. Piskorz, I. Komaromi, R. Gomperts, R.L. Martin, D.J. Fox, T. Keith, M.A. Al-Laham, C.Y. Peng, A. Nanayakkara, C. Gonzalez, M. Challacombe, P. Gill, B. Johnson, W. Chen, M.W. Wong, J.L. Andres, C. Gonzalez, M. Head-Gordon, E.S. Replogle, and J.A. Pople. 1998. Gaussian 98 [computer program]. Revision A.4. Gaussian, Inc., Pittsburgh PA.
91. D.B. Chesnut and K.D. Moore. J. Comp. Chem. **10**, 648 (1989).
92. D.B. Chesnut, B.E. Rusiloski, K.D. Moore, and D.A. Egolf. J. Comp. Chem. **14**, 1364 (1993).
93. K.R. Dixon. *In* Multinuclear NMR. *Edited by* J. Mason. Plenum Press, New York. 1987. p. 369.
94. G.A. Olah and C.W. McFarland. J. Org. Chem. **34**, 1832 (1969).
95. B.E. Mann. J. Chem. Soc. Perkin Trans. **2**, 30 (1972).
96. S.O. Grim, E.F. Davidoff, and T.J. Marks. Z. Naturforsch. **26b**, 184 (1971).
97. G.P. Schiemenz. Phosphorus, **3**, 125 (1973).
98. K. Eichele, G.C. Ossenkamp, R.E. Wasylishen, and T.S. Cameron. Inorg. Chem. **38**, 639 (1999).
99. P. Diehl and C.L. Khetrapal. NMR: Basic Princ. Prog. **1**, 3 (1969).
100. Y. Ishii, T. Terao, and S. Hayashi. J. Chem. Phys. **107**, 2760 (1997).
101. F.L. Hirshfeld. Acta Crystallogr. **A32**, 239 (1976).
102. A.L. Spek. Acta Crystallogr. **A46**, C34 (1990). *PLATON* – a multipurpose crystallographic tool [computer program]. Utrecht University, Utrecht, The Netherlands.
103. J.M. Schulman, J. Ruggio, and T.J. Venanzi. J. Am. Chem. Soc. **99**, 2045 (1977).
104. K. Eichele, G. Wu, R.E. Wasylishen, and J.F. Britten. J. Phys. Chem. **99**, 1030 (1995).

© 2002 NRC Canada

105. T. Enevoldsen, L. Visscher, T. Saue, H.J. Aa. Jensen, and J. Oddershede. J. Chem. Phys. **112**, 3493 (2000).
106. G.H. Penner and R.E. Wasylishen. Can. J. Chem. **67**, 1909 (1989).
107. W. Kutzelnigg, U. Fleischer, and M. Schindler. NMR, Basic Princ. Prog. **23**, 163 (1990).
108. W.P. Power. J. Am. Chem. Soc. **117**, 1800 (1995).
109. A. Altomare, G. Cascarano, G. Giacovazzo, A. Guagliardi, M.C. Burla, G. Polidori, and M. Camalli. J. Appl. Cryst. **27**, 435 (1994).
110. G.M. Sheldrick. 1993. SHELXL-93: Program for crystal structure determination [computer program]. University of Göttingen, Germany.

© 2002 NRC Canada

Synthesis and characterization of a spirocyclic phosphaverdazyl radical – cyclophosphazene hybrid: Evidence for spin transfer from a verdazyl radical to a phosphazene ring

Tosha M. Barclay, Robin G. Hicks, Andrew S. Ichimura, and Greg W. Patenaude

Abstract: The synthesis and characterization of a new 6-phosphaverdazyl radical incorporated into a spirocyclic framework containing a cyclotriphosphazene ring is described. Reaction of 1,1,3,3-bis[*spiro*-2′,2″-dioxy-1′,1″-biphenyl]-5,5-bis(1-methylhydrazido)-1,3,5,2,4,6-cyclotriphosphazene (**7**) with trimethylorthobenzoate yielded 6-[2,2,4,4-bis(2,2′-dioxy-1,1′-biphenyl)-2,4,6,1,3,5-cyclotriphosphazen-6-yl]-1,2,5,6-tetrahydro-1,5-dimethyl-3-phenyl-1,2,4,5,6-tetrazaphosphorine (**8**), which was characterized spectroscopically and by X-ray diffraction. Oxidation of **8** yielded 6-[2,2,4,4-bis(2,2′-dioxy-1,1′-biphenyl)-2,4,6,1,3,5-cyclotriphosphazen-6-yl]-1,5-dimethyl-3-phenyl-6-phosphaverdazyl (**5**), which was characterized by EPR and ENDOR spectroscopy. Analysis of both spectra indicate that spin density from the phosphaverdazyl ring induces spin polarization into the phosphazene ring, as evidenced by hyperfine coupling to all three phosphorus nuclei.

Key words: heterocycle, phosphorus–nitrogen compounds, phosphazenes, stable radicals, verdazyls.

Résumé : On décrit la synthèse et la caractérisation d'un nouveau radical 6-phosphoverdazyle incorporé dans un squelette spirocyclique contenant un noyau cyclotriphosphazène. La réaction du 1,1,3,3-bis[spiro-2′,2″-dioxy-1′,1″-biphényl]-5,5-bis(1-méthylhydrazido)-1,3,5,2,4,6-cyclotriphosphazène (**7**) avec l'orthobenzoate de triméthyle conduit à la formation de la 6-[2,2,4,4-bis(2,2′-dioxy-1,1′-biphényl)-2,4,6,1,3,5-cyclotriphosphazén-6-yl]-1,2,5,6-tétrahydro-1,5-diméthyl-3-phényl-1,2,4,5,6-tétrazaphosphorine (**8**) que l'on a caractérisé de façon spectroscopique et par diffraction des rayons X. L'oxydation du composé **8** fournit le 6-[2,2,4,4-bis(2,2′-dioxy-1,1′-biphényl)-2,4,6,1,3,5-cyclotriphosphazén-6-yl]-1,5-diméthyl-3-phényl-6-phosphavervazyle (**5**) que l'on a caractérisé par RPE et par spectroscopie ENDOR. L'analyse des deux spectres, sur la base du couplage hyperfin avec les trois noyaux de phosphore, indique que la densité de spin provenant du noyau phosphaverdazyle induit une polarisation de spin dans le noyau phosphazène.

Mots clés : hétérocycle, composés phosphore–azote, phosphazènes, radicaux stables, verdazyles.

[Traduit par la Rédaction]

Introduction

Stable radicals have a long history (1, 2) and new examples of isolable molecules with unpaired electrons continue to fascinate chemists (3–5). There are also a number of useful applications of stable radicals, including their role in spin labeling (6), or their acting as building blocks for electronically conducting (7, 8) or magnetic (9, 10) materials, and catalysts for living radical polymer synthesis (11–13). For all these applications, a thorough understanding of the electronic structures of stable radicals is critical. Furthermore, purposeful designs and study of new stable radicals could lead to better components for the aforementioned applications.

We have been investigating the chemical and physical properties of verdazyl radicals (**1**) for quite some time (14–17). As part of our efforts to probe structure–property relationships in these systems we have prepared verdazyl analogues in which one of the skeletal carbon atoms has been replaced by a phosphorus atom — so-called "phosphaverdazyl" radicals (**2**; X or Y = P) (18). One derivative (compound **3**) exhibited unusually large EPR hyperfine coupling to the exocyclic nitrogen atom. Computational studies suggested that a novel spiroconjugative overlap

Received 23 February 2002. Published on the NRC Research Press Web site at http://cjchem.nrc.ca on 25 November 2002.

Warmly dedicated to Professor Tris Chivers, a true leader in main group chemistry research and in the Canadian chemistry community.

Tosha M. Barclay. Department of Chemistry, North Harris College, 2700 N.W. Thorne Drive, Houston, TX 77073, U.S.A.
R.G. Hicks,[1] and G.W. Patenaude. Department of Chemistry, University of Victoria, PO Box 3065, Victoria, B.C. V8W 3V6.
A.S. Ichimura. Department of Chemistry & Biochemistry, San Francisco State University, 1600 Holloway Avenue, San Francisco, CA 94132–4163, U.S.A.

[1]Corresponding author (e-mail: rhicks@uvic.ca).

 DOI: 10.1139/V02-090 © 2002 NRC Canada

(depicted schematically in **4**) (19, 20) between the *p*-orbital of the exocyclic N and the verdazyl π system provided a through-space mode of spin propagation in phosphaverdazyl radicals (21). Connecting another ring to a phosphaverdazyl in a spirocyclic manner could lead to enhancement of spin leakage via spiroconjugation and provide a new mechanism for spin propagation (as an alternative to the more conventional π conjugation in delocalized radicals). These possibilities motivated the design and synthesis of compound **5** in which the phosphaverdazyl group is connected in a spirocyclic manner to a phosphazene ring. In this paper we describe the synthesis and characterization of an example of radical **5** and present spectroscopic evidence for spin transfer from the verdazyl to the phosphazene ring.

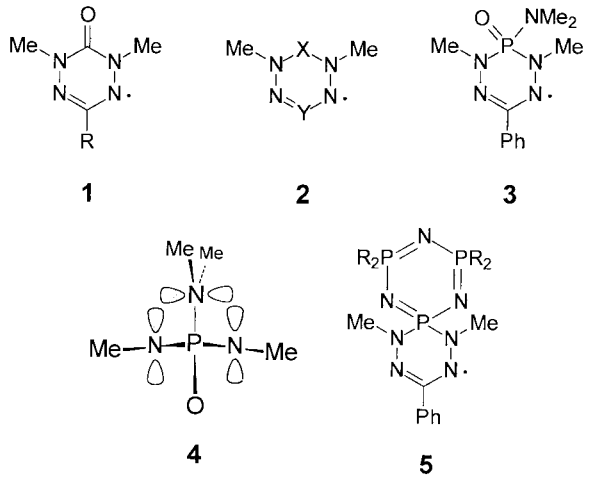

Results

The radical was prepared as shown in Scheme 1. Treatment of hexachlorocyclotriphosphazene with 2 equiv of 2,2′-biphenol according to literature procedures gave substituted dichlorophosphazene **6** (22). This intermediate was reacted with excess methylhydrazine to produce bis(hydrazide) **7**, which was subsequently condensed with trimethylorthobenzoate to give the spirocyclic phosphatetrazine **8**. Oxidation of **8** with benzoquinone gave the phosphaverdazyl radical **5** as a red-brown solid. Although **5** is very persistent, it gradually decomposes in solution or the solid state, predominantly back to the tetrazine **8**. Solutions of **5** can be quantitatively reduced back to **8** with ascorbic acid, confirming the identity of the radical (in conjunction with spectroscopic evidence, see below).

Single crystals of tetrazine **8** suitable for X-ray diffraction studies were grown from diethyl ether. Figure 1 displays the molecular structure of the tetrazine (which crystallizes with 1 equiv of ether in the lattice); a summary of pertinent bond lengths and angles is given in Table 1. The phosphazene ring is planar within experimental error and the P—N bond lengths within this ring range from 1.56 to 1.59 Å, values that can be regarded as typical for cyclotriphosphazene rings (23). The phosphatetrazine ring is puckered at the NPN portion and the two N-methyl groups are in quite different stereochemical environments. The methyl group on N7, which is adjacent to the C1—N6 double bond, is essentially coplanar with that bond. The other N-methyl group attached

Scheme 1. Reagents: (*i*) $MeNHNH_2$ (4 equiv); (*ii*) $PhC(OMe)_3$; (*iii*) 1,4-benzoquinone; (*iv*) ascorbic acid.

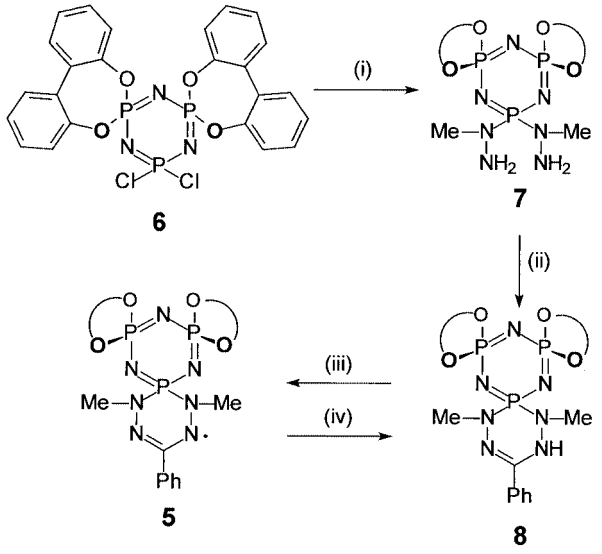

Fig. 1. ORTEP drawing of **8** (30% probability ellipsoids). Hydrogen atoms other than those attached to N1 have been omitted for clarity.

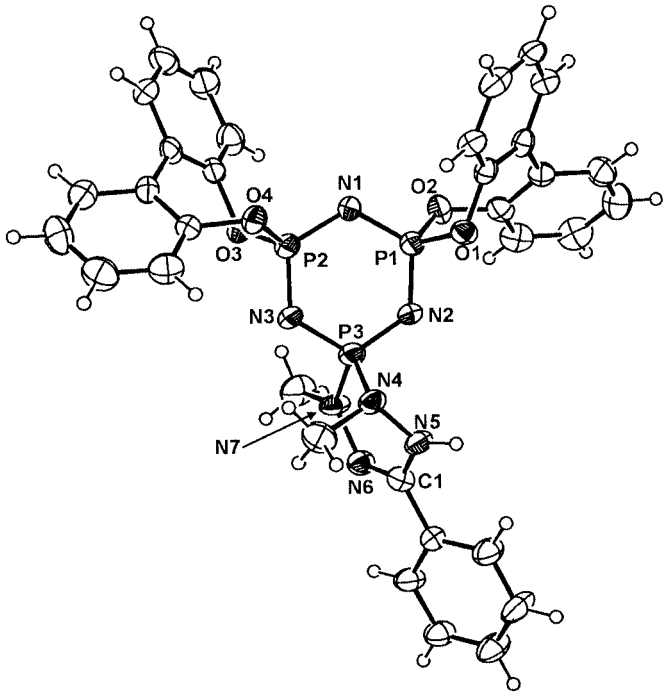

to N4, however, is oriented nearly perpendicular to the N6-C1-N5 plane. This conformation is maintained in solution, as evidenced by the difference in chemical shifts (δ = 3.30 vs. 2.90 ppm) and in particular the difference in coupling constants to the P3 nucleus (J_{HP} = 8.82 vs. 11.04 Hz) in the ^{1}H NMR spectrum.

The EPR spectrum of **5** (g = 2.0043), Fig. 2, consists of (at least) 14 broad featureless lines that could not be further resolved despite considerable efforts to improve the spectral resolution. However, the isotropic hyperfine splitting evident in the EPR spectrum was resolved into unique pairs of

© 2002 NRC Canada

Table 1. Selected bond lengths (Å) and angles (°) for **8**.

Bond Length (Å)	
P(1)—N(2)	1.573(4)
P(1)—N(1)	1.584(4)
P(1)—O(1)	1.587(4)
P(1)—O(2)	1.590(4)
P(2)—N(3)	1.561(4)
P(2)—N(1)	1.574(4)
P(2)—O(4)	1.577(4)
P(2)—O(3)	1.589(4)
P(3)—N(3)	1.588(4)
P(3)—N(2)	1.597(4)
P(3)—N(7)	1.648(5)
P(3)—N(4)	1.679(4)
N(4)—N(5)	1.422(5)
N(5)—C(1)	1.386(7)
N(6)—C(1)	1.286(7)
N(6)—N(7)	1.407(5)
Bond Angle (°)	
N(2)-P(1)-N(1)	118.9(2)
N(3)-P(2)-N(1)	118.7(2)
N(3)-P(3)-N(2)	115.9(2)
P(2)-N(1)-P(1)	120.1(3)
P(1)-N(2)-P(3)	120.9(3)
P(2)-N(3)-P(3)	123.0(3)
N(5)-N(4)-P(3)	106.1(3)
C(1)-N(5)-N(4)	117.2(4)
C(1)-N(6)-N(7)	118.0(5)
N(6)-N(7)-P(3)	123.6(4)

frequencies by the application of double resonance techniques. The Electron nuclear double resonance (ENDOR) spectrum of **5** is shown in Fig. 3. The hyperfine splitting is small enough so that the first order perturbation theory applies and two conditions must be considered to interpret the ENDOR spectrum. When the hyperfine splitting (a_N) is less than the larmor frequency (ν_N), a pair of resonances is observed that are centered at the larmor frequency and separated by the hyperfine splitting. When $a_N > \nu_N$, the two resonances are separated by twice the larmor frequency ($2\nu_N$) and centered at half the hyperfine splitting ($a_N/2$) (24). The application of these rules permits the unambiguous assignment of all observable and overlapping resonances in the spectrum. The final deconvolution of the ENDOR spectrum is also shown in Fig. 3 in which the seven pairs of resonances that correspond to ^{1}H, ^{31}P, and ^{14}N are clearly indicated. The hyperfine values obtained from this spectrum are $a(P_1)$ = 7.29 G, $a(2P_2)$ = 1.06 G, $a(2N_1)$ = 6.45 G, $a(2N_2)$ = 5.18 G, $a(6CH_3)$ = 4.24 G, $a(3H_{Ar})$ = 0.40 G, and $a(2H_{Ar})$ = 0.20 G. Based on our previous work on 6-phosphaverdazyls (18, 21), we assign the larger of the $a(^{31}P)$ values to the spirocyclic phosphorus atom and the smaller to the other two P atoms of the phosphazene ring. The ^{14}N hyperfine values of 6.45 and 5.18 G are assigned to the verdazyl di- and tri-coordinate nitrogens, respectively, and the largest of the proton hyperfine values corresponds to the six N-methyl protons; these three sets of couplings are fairly typical of verdazyl and phosphaverdazyl radicals. The small

Fig. 2. EPR spectra of **5** in toluene solution at 273 K (top, experimental solution; bottom, simulated solution). The sweep width of the experimental spectrum is 100 G. The arrow indicates the static field used for the acquisition of the ENDOR spectrum. The small asymmetric doublet in the center of the EPR spectrum is due to an unknown impurity.

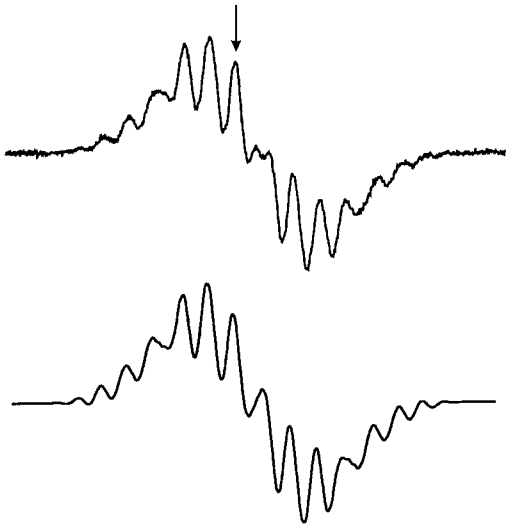

Fig. 3. ENDOR spectrum of **5** with peak assignments indicated.

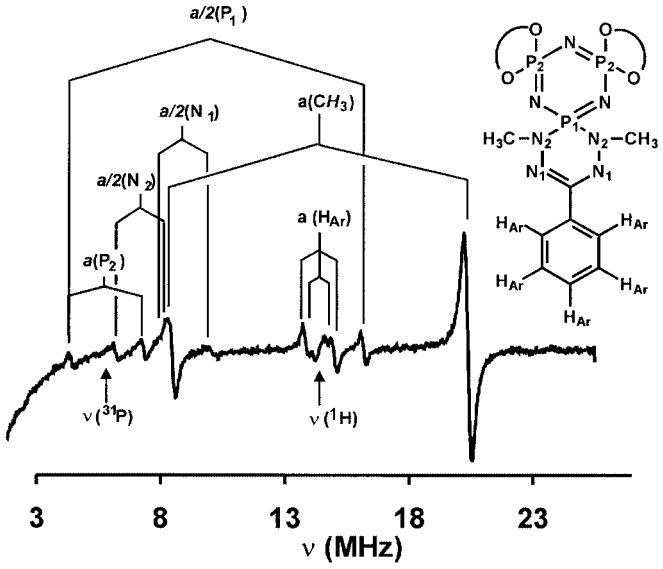

proton hyperfine couplings are assigned to the aromatic substituent of the verdazyl ring; these values are consistent with aromatic groups on related verdazyl radicals (25, 26). Hyperfine coupling to the nitrogen atoms of the phosphazene ring was not observed in the ENDOR spectrum. However, it proved possible to extract an approximate value for the pair of equivalent phosphazene nitrogen atoms through simulation of the EPR spectrum. The hyperfine splitting values to the other nuclei determined from the ENDOR spectrum constants, a value of 0.65 ± 0.15 G for the pair of phosphazene nitrogen atoms, and the appropriate number of equivalent nuclei were used in a first order perturbation treatment to simulate the EPR spectrum. The con-

© 2002 NRC Canada

volution employed a Gaussian lineshape and linewidth of 0.90 G. The simulated spectrum, Fig. 2, closely matches the experimental one and demonstrates that the hyperfine splitting constants were assigned correctly. The uncertainty in the phosphazene ^{14}N hyperfine splittings comes from the relatively large linewidth needed to reproduce the intensity distribution of the solution spectrum. Such small hyperfine coupling to nitrogen, < 0.65 G, may be undetectable by ENDOR at X-band because of quadrupole broadening from the ^{14}N (I = 1) nucleus.

Discussion

Rings, chains, and polymers built from catenated phosphazene units $(R_2P{=}N)_n$ are among the best known nonmetal inorganic systems (27, 28). Their fundamental chemistry, structure, and bonding has attracted a great deal of attention, and the general robustness of the PN backbone has led to a variety of technological applications based on phosphazene high polymers (29). However, despite their formally conjugated electronic structures, they exhibit poor delocalization compared with conjugated organic systems. As such, phosphazenes are generally colorless and are poor electrical conductors in their native ("undoped") state, and charge carriers in them can be introduced (by oxidation or reduction) only with great difficulty (30, 31). The concept of introducing spin into a PN backbone has also received little attention. Two other cyclophosphazenes with radicals as substituents, compounds **9** (32) and **10** (33), have been reported. In both these systems, EPR evidence suggested that the radicals induced spin polarization in the phosphazene ring. Hyperfine coupling to the phosphorus nucleus ($a(^{31}P)$ = 5.25 G for **9**, 1.275 G for **10**) closest to the radical centers was inferred based on spectral simulations for each, although it should be noted that the assignments for **10** were tentative owing to the complexity of the EPR spectrum. In the present work on radical **5**, the spectroscopic evidence shows that there is substantial spin polarization through the spirocyclic phosphorus ($a(^{31}P)$ = 7.29 G) that extends to the remote ^{31}P ($a(^{31}P)$ = 1.06 G) and ^{14}N atoms of the phosphazene ring.

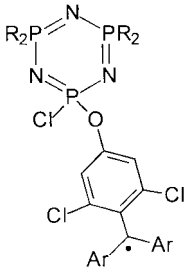

9

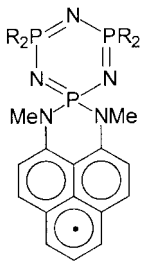

10

It is instructive to compare the results for **5** to related phosphaverdazyls. Our EPR and computational studies on **3** and other derivatives establish a correlation between the hyperfine coupling to the phosphorus atom and the overall ring geometry (21). Briefly, when the P atom has strong π-donor substituents (as is the case for **3**) a planar phosphaverdazyl ring **11** is favoured, and the phosphorus hyperfine coupling in this radical is very small (<< 1 G). Other phosphaverdazyl radicals lacking in π-donor groups tend to favour a half-chair geometry (**12**) and have substantial $a(^{31}P)$'s (e.g., when X = Ph and Y = O, $a(^{31}P)$ = 5.2 G (18)). The relatively large hyperfine value for the analogous phosphorus atom in **5** suggests that the phosphaverdazyl ring of this radical is also bent.

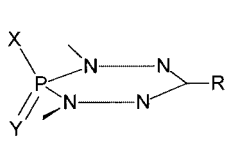

11

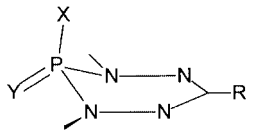

12

Spiroconjugation as a means of spin propagation in radicals is rare but has been noted previously on other radical systems (8, 34–36). The design of phosphaverdazyl radical **5** was meant to enhance the spiroconjugative interactions seen in **3** (depicted schematically in **4**). The spectroscopic data suggest that the amount of spin density on the phosphazene nitrogen atoms of **5** is, at best, much smaller than was found on the exocyclic nitrogen atom in **3**. This may be evidence that, for the phosphaverdazyl systems, the relative orientation of the interacting orbitals is a necessary but not sufficient condition for spiroconjugation. The natures of the nitrogen atoms of **3** and **5** potentially engaged in spiroconjugation with the verdazyl SOMO are in fact quite different: In the former, the tricoordinate nitrogen atom possesses a doubly occupied *p*-orbital (i.e., a lone pair) that can adopt the appropriate orientation for spiroconjugative overlap with the verdazyl SOMO. In the latter, the phosphazene nitrogen atoms are dicoordinate and the lone pair is constrained to point directly towards the verdazyl ring (**13**). This lone pair orbital is therefore orthogonal to the verdazyl π-SOMO. There is, of course, a nitrogen atom *p*-orbital forming part of the phosphazene π framework that is oriented ideally for spiroconjugation, but our spectroscopic data seem to suggest that the effect is not realized. However, the observation of some spin density on the remote phosphorus atoms suggests that some other mechanism — likely through-bond — is responsible for spin leakage within the phosphazene ring.

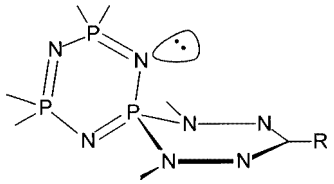

13

Experimental

General

All reactions and manipulations were carried out under an argon atmosphere using standard Schlenk or glove box techniques. Solvents were dried and distilled under argon prior to use (CH_2Cl_2, CaH_2, THF, Na/benzophenone). All reagents were purchased from Aldrich and used as received. Mass spectra were recorded on a Kratos Concept IH MS system. IR Spectra were recorded as Nujol mulls or KBr presses on

© 2002 NRC Canada

a PerkinElmer Spectrum One Spectrometer. NMR spectra were recorded on a Bruker AMX360 spectrometer. Elemental analyses were carried out by Canadian Microanalytical Services Ltd. (Vancouver, B.C.).

Synthesis of 1,1,3,3-bis[*spiro*-2′,2″-dioxy-1′,1″-biphenyl]-5,5-bis(1-methylhydrazido)-1,3,5,2,4,6-cyclotriphosphazene (7)

A solution of **6** (22) (1.045 g, 1.81 mmol) in 35 mL CH_2Cl_2 was added dropwise to a solution of $MeNHNH_2$ (0.44 mL, 8.3 mmol) in 30 mL CH_2Cl_2 at 0°C. A white precipitate formed during the addition. The reaction mixture was stirred for 12 h. The solution was filtered in vacuo and the filtrate concentrated to a white solid. The crude solid was chromatographed on silica gel (3:1, $CHCl_3$–CH_3CN) to give **7**. Yield: 1.045 g (97%); mp 245–246°C. IR (KBr) (cm^{-1}): 3327 (w), 3259 (w), 3185 (w), 2786 (w), 1609 (m), 1568 (w), 1500 (s), 1476 (s), 1438 (s), 1264 (s), 1230 (s), 1197 (s), 1173 (s), 1093 (s), 1037 (m), 1016 (m), 982 (m), 959 (s), 945 (s), 919 (s), 866 (s), 812 (m), 783 (s), 754 (s), 735 (s), 719 (s), 685 (m), 624 (s), 609 (s), 588 (w), 569 (w), 533 (s), 523 (m), 497 (m), 477 (m). ^{1}H NMR (CD_2Cl_2) δ: 7.6–7.3 (m, 16H), 3.61 (br s, 4H), 2.94 ppm (d, 6H, J = 11.0 Hz). ^{13}C NMR (CD_2Cl_2) δ: 148.7 (t, J = 3.4 Hz), 130.1, 130.0, 129.3, 126.3, 122.1, 40.2 ppm (d, J = 7.91 Hz). ^{31}P NMR ($CDCl_3$) δ: 31.3–30.5 (m), 29.0–28.5 ppm (m). CI-MS (methane) *m/z* (%): 594 ([M + 1], 100), 622 ([M + 29], 21). Anal. calcd. for $C_{26}H_{26}N_7O_4P_3$: C 52.62, H 4.42, N 16.52, P 15.66; found: C 52.71, H 4.44, N 16.48, P 16.57.

Synthesis of 6-[2,2,4,4-bis(2,2′-dioxy-1,1′-biphenyl)-2,4,6,1,3,5-cyclotriphosphazen-6-yl]-1,2,5,6-tetrahydro-1,5-dimethyl-3-phenyl-1,2,4,5,6-tetrazaphosphorine (8)

A solution of **7** (410 mg, 0.691 mmol), trimethylorthobenzoate (0.24 mL, 1.40 mmol), and ~10 drops acetic acid in 110 mL MeOH was gently refluxed for 5 days during which a white precipitate formed. The solution was cooled in an ice bath and the solution was gravity filtered to yield crude **8**. The product was purified by chromatography on silica gel (benzene) to give the product as a clear oil, which on crystallization from ether gave light pink rectangular rod-like crystals. Yield: 273 mg (58%); mp 251–253°C. IR (KBr) (cm^{-1}): 3333 (w), 1501 (w), 1476 (w), 1438 (w), 1264 (m), 1228 (s), 1192 (sh), 1168 (s), 1117 (w), 1093 (s), 1044 (w), 1014 (w), 962 (m), 946 (w), 926 (w), 908 (m), 874 (m), 818 (w), 785 (w), 754 (w), 741 (w), 719 (w), 711 (w), 693 (w), 624 (w), 610 (m), 584 (w), 534 (w), 521 (w), 476 (w). ^{1}H NMR ($CDCl_3$) δ: 7.7–7.3 (m, 21H), 6.17 (d, 1H, J = 5.88 Hz), 3.30 (d, 3H, J = 8.82 Hz), 2.90 ppm (d, 3H, J = 11.04 Hz). ^{13}C NMR ($CDCl_3$) δ: 148.3 (t, J = 4.52 Hz), 141.0 (d, J = 15.8 Hz), 132.5, 129.7, 129.6, 129.5, 128.9 (d, J = 7.91 Hz), 128.4, 126.5, 125.9, 121.8 (d, J = 12.4 Hz), 38.9 (d, J = 4.52 Hz), 36.6 ppm (d, J = 7.91 Hz). ^{31}P NMR ($CDCl_3$) δ: 28.5 (d, J = 67.88 Hz), 10.72 ppm (t, J = 68.33 Hz). EI-MS *m/z* (%): 680 ([M + 1]). Anal. calcd. for $C_{33}H_{28}N_7O_4P_3$: C 58.33, H 4.15, N 14.43, P 13.67; found: C 58.13, H 4.07, N 14.27, P 13.83.

Table 2. Crystal data collection and refinement parameters.

Empirical formula	$P_3O_5N_7C_{37}H_{38}$
Formula weight	753.65
Crystal dimensions (mm)	0.31 × 0.36 × 0.38
Crystal system	Triclinic
Space group	$P\bar{1}$
a (Å)	11.806(2)
b (Å)	12.037(2)
c (Å)	14.155(3)
α (°)	100.027(4)
β (°)	91.935(5)
γ (°)	110.325(4)
V (Å^3)	1848.1(7)
$D_{calcd.}$ (g cm^{-3})	1.35
Absorption coefficient (μ) (mm^{-1})	0.21
R_1, wR_2[a,b]	0.064, 0.131

[a] $R_1 = (\Sigma||F_o| - |F_c||)/\Sigma|F_o|$ for reflections with $F > 2\sigma(F)$.
[b] $wR_2 = [\Sigma[w(F_o^2 - F_c^2)^2]/\Sigma[w(F_o^2)^2]]^{0.5}$ for all reflections.

Synthesis of 6-[2,2,4,4-bis(2,2′-dioxy-1,1′-biphenyl)-2,4,6,1,3,5-cyclotriphosphazen-6-yl]-1,5-dimethyl-3-phenyl-6-phosphaverdazyl (5)

Benzoquinone (~8 mg) was added to a solution of **8** (99 mg, 0.146 mmol) in 5 mL THF. The solution turned an intense cherry red. The solution was concentrated in vacuo to give a red oil. The crude product was chromatographed on alumina (CH_2Cl_2) to give **8** as a red oil. UV–vis (THF): λ_{max} = 540 nm. ($t(1/2)$ = 2.1 days at 1.5 × 10^{-3} mol L^{-1}). The solid radical also decomposed over a period of several days, predominantly to the tetraazaphosphorine **8**. Freshly prepared solutions of **5** could be quantitatively (as monitored by ^{1}H NMR) reduced back to **8** using ascorbic acid as a reducing agent.

X-ray measurements on 8

Relevant crystallographic information is presented in Table 2. Colorless blocks were mounted on a glass fibre with silicone grease. Data were collected on a Smart 1000 diffractometer (Mo Kα, graphite monochromated radiation (λ = 0.71073 Å). Data were collected for $4 < 2\theta < 50°$. A total of 13 920 reflections were measured, of which 6474 were independent and 2261 were used in the refinement of 470 parameters ($I > 2.0\sigma(I)$). An empirical absorption correction (SADABS) was applied. The structure was solved by direct methods (SHELXS-97: G.M. Sheldrick. SHELXS user manual. Madison, WI. (1997)), and the hydrogen atoms were placed at idealized positions and refined according to the riding model. The structure was refined according to the full-matrix least squares method on F^2 (SHELXL-97: G.M. Sheldrick. SHELXS user manual. Madison, WI. (1997)). Complete crystallographic data for **9** has been deposited in Supporting Information.[2]

[2] Supplementary data may be purchased from the Depository of Unpublished Data, Document Delivery, CISTI, National Research Council Canada, Ottawa, ON K1A 0S2, Canada (http://www.nrc.ca/cisti/irm/unpub_e.shtml for information on ordering electronically). CCDC 185011 contain the supplementary data for this paper. These data can be obtained, free of charge, via www.ccdc.cam.ac.uk/conts/retrieving.html (or from the Cambridge Crystallographic Data Centre, 12 Union Road, Cambridge, U.K.; fax +44 1223 336033; or deposit@ccdc.cam.ac.uk).

© 2002 NRC Canada

EPR and ENDOR spectroscopy

A solution of **5** suitable for ENDOR measurements was prepared by dissolving 0.0735 mmol of **8** in 10 mL toluene under a nitrogen atmosphere. Then, 0.037 mmol of *p*-benzoquinone was added and the solution was stirred for 1.5 h at room temperature. An additional 40 mL of toluene was added to the flask so that the final concentration of the radical was ~1.5 mM. An aliquot of the solution was placed in a suprasil quartz EPR tube, degassed three times, and sealed off under vacuum. Spectra of solution EPR and ENDOR were recorded at 273 K on a Bruker ESP300E spectrometer equipped with a DICE ENDOR accessory. The temperature was controlled with an Oxford Instruments 900E liquid helium cryostat. The EPR spectrum was obtained using a modulation amplitude of 0.2 G, power setting of 0.1 mW, and a modulation frequency of 100 kHz. For the ENDOR spectrum, the power was set at 32 mW, the modulation amplitude was 141 kHz, modulation frequency was 12.5 kHz, and the static field is indicated by the arrow in Fig. 3.

Conclusion

In conclusion, the spirocyclic fusion of a phosphaverdazyl radical to a phosphazene has been shown to be an effective means of introducing spin into the PN backbone. This raises some intriguing questions pertaining to the possibility of phosphazene rings or linear chains being effective mediators of spin-spin *communication* in di- or polyradicals. Virtually all exchange-coupled diradicals involve systems in which linear π conjugation provides the predominant pathway for spin exchange; alternative effective pathways are essentially unknown. Efforts to prepare phosphazene-bridged verdazyl di- and tri-radicals are now underway and results will be reported in due course.

Acknowledgments

We thank the Natural Sciences and Engineering Research Council of Canada (NSERC) and the University of Victoria for financial support for this research.

References

1. M. Gomberg. J. Am. Chem. Soc. **22**, 757 (1901).
2. A.R. Forrester, J.M. Hay, and R.H. Thomson. *In* Organic chemistry of stable free radicals. Academic Press, London. 1968.
3. N. Jux, K. Holczer, and Y. Rubin. Angew. Chem. Int. Ed. **35**, 1986 (1996).
4. T. Peymann, C.B. Knobler, and M.F. Hawthorne. Chem. Commun. 2039 (1999).
5. Y. Apeloig, D. Bravo-Zhivotovskii, M. Bendikov, D. Danovich, M. Botoshansky, T. Vakul'skaya, M. Voronkov, R. Samoilova, M. Zdravkova, V. Igonin, V. Shklover, and Y. Struchov. J. Am. Chem. Soc. **121**, 8118 (1999).
6. L.J. Berliner. *In* Spin labelling: Theory and applications. Vol. 2. Academic Press, New York. 1979.
7. R.T. Oakley. Can. J. Chem. **71**, 1775 (1993).
8. X. Chi, M.E. Itkis, B.O. Patrick, T.M. Barclay, R.W. Reed, R.T. Oakley, A.W. Cordes, and R.C. Haddon. J. Am. Chem. Soc. **121**, 10 395 (1999).
9. P.M. Lahti (*Editor*). Magnetic properties of organic materials. Marcel Dekker, Inc., New York. 1999.
10. K. Itoh and M. Kinoshita (*Editors*). Molecular magnetism: New materials. Kodansha, Tokyo, 2000.
11. M.K. Georges, R.P.N. Veregin, P.M. Kazmeier, and G.K. Hamer. Macromolecules, **26**, 2987 (1993).
12. C.J. Hawker, A.W. Bosman, and E. Harth. Chem. Rev. (Washington, D.C.), **101**, 3661 (2001).
13. H. Fischer. Chem. Rev. **101**, 3581 (2001).
14. C.L. Barr, P.A. Chase, R.G. Hicks, M.T. Lemaire, and C.L. Stevens. J. Org. Chem. **64**, 8893 (1999).
15. R.G. Hicks, M.T. Lemaire, L.K. Thompson, and T.M. Barclay. J. Am. Chem. Soc. **122**, 8077 (2000).
16. T.M. Barclay, R.G. Hicks, M.T. Lemaire, and L.K. Thompson. Chem. Commun. 2141 (2000).
17. R.G. Hicks, M.T. Lemaire, L. Ohrstrom, J.F. Richardson, L.K. Thompson, and Z. Xu. J. Am. Chem. Soc. **123**, 7154 (2001).
18. R.G. Hicks and R. Hooper. Inorg. Chem. **38**, 284 (1999).
19. H.E. Simmons and T. Fukunaga. J. Am. Chem. Soc. **89**, 5208 (1967).
20. H. Durr and R. Gleiter. Angew. Chem. Int. Ed. **17**, 559 (1978).
21. R.G. Hicks, L. Ohrstrom, and G.W. Patenaude. Inorg. Chem. **40**, 1865 (2001).
22. A.G. Carriedo, L. Fernandez-Catuxo, F.J. Garcia-Alonso, P. Gomez-Elipe, and P.A. Gonzalez. Macromolecules, **29**, 5320 (1996).
23. N.N. Greenwood and A. Earnshaw. Chemistry of the elements. 2nd ed. Butterworth-Heineman, Oxford. 2001.
24. H. Kurreck, B. Kirste, and W. Lubitz. Electron nuclear double resonance spectroscopy of radicals in solution. VCH, New York. 1988.
25. F.A. Neugebauer, H. Brunner, and K.H. Hausser. Tetrahedron, **27**, 3623 (1971).
26. F.A. Neugebauer, H. Fischer, and C. Krieger. J. Chem. Soc. Perkin Trans. 2, 535 (1993).
27. H.R. Allcock. Chem. Rev. (Washington, D.C.), **72**, 315 (1972).
28. C.W. Allen. Chem. Rev. (Washington, D.C.), **91**, 119 (1991).
29. I. Manners. Angew. Chem. Int. Ed. **35**, 1602 (1996).
30. H.R. Allcock and W.J. Birdsall. J. Am. Chem. Soc. **91**, 7541 (1969).
31. H.R. Allcock and W.J. Birdsall. Inorg. Chem. **10**, 2495 (1971).
32. G.A. Carriedo, F.J. Garcia-Alonso, P. Gomez-Elipe, E. Brillas, and L. Julia. Org. Lett. **3**, 1625 (2001).
33. R.C. Haddon, S.L. Mayo, S.V. Chichester, and J.H. Marshall. J. Am. Chem. Soc. **107**, 7585 (1985).
34. R.C. Haddon, S.V. Chichseter, and J.H. Marshall. Tetrahedron, **42**, 6293 (1986).
35. X. Chi, M.E. Itkis, K. Kirschbaum, A.A. Pinkerton, R.T. Oakley, A.W. Cordes, and R.C. Haddon. J. Am. Chem. Soc. **123**, 4041 (2001).
36. N.L. Frank, R. Clerac, J.P. Sutter, N. Daro, O. Kahn, C. Coulon, M.T. Green, S. Golhen, and L. Ouahab. J. Am. Chem. Soc. **122**, 2053 (2000).

© 2002 NRC Canada

Structural studies of dithiatetrazocines: X-ray crystal structures of the symmetric dithiatetrazocines *p*-$XC_6H_4CN_4S_2CC_6H_4X$ [X = NO_2, Br] and the first unsymmetric dithiatetrazocine, *p*-$BrC_6H_4CN_4S_2CC_6H_4NO_2$

Andrew D. Bond, Delia A. Haynes, and Jeremy M. Rawson

Abstract: Oxidation of equimolar amounts of [*p*-BrC_6H_4CNSSN]Cl and [*p*-$O_2NC_6H_4CNSSN$]Cl with elemental O_2 in the presence of Ph_3Sb in MeCN yields a mixture of the symmetric dithiatetrazocines, $O_2NC_6H_4CN_4S_2CC_6H_4NO_2$ (**1**) and $BrC_6H_4CN_4S_2CC_6H_4Br$ (**2**) as well as the unsymmetrically substituted derivative $BrC_6H_4CN_4S_2CC_6H_4NO_2$ (**3**). The structures of compounds **1**–**3** are determined by X-ray diffraction: **1** crystallizes in the monoclinic space group $P2_1/c$ (a = 8.6397(4), b = 5.8359(4), c = 14.9767(11) Å, β = 92.088(4)°) with half a molecule in the asymmetric unit; **2** crystallizes in the triclinic space group $P\bar{1}$ (a = 6.5330(5), b = 8.2084(6), c = 14.7264(9) Å, α = 84.483(4)°, β = 77.112(4)°, γ = 87.879(3)°); **3** was found to crystallize in two forms: recrystallization from CH_2Cl_2 at room temperature yielded a solvent-free, triclinic phase, space group $P\bar{1}$ (a = 6.5060(9), b = 7.0739(9), c = 9.1164(8) Å, α = 81.860(3)°, β = 83.406(5)°, γ = 66.589(5)°), whereas cooling a solution to –5°C yielded a solvated form, **3**·CH_2Cl_2, which crystallizes in the monoclinic space group $P2_1/m$ (a = 6.179(1), b = 10.960(2), c = 13.884(3) Å, β = 92.69(3)°). The NO_2···Br intermolecular interactions observed in the unsolvated structure of **3** are disrupted in the solvate structure; the CH_2Cl_2 molecule in the latter is aligned such that its molecular dipole interacts with both nitro and bromo groups, retaining a molecular chain motif. The structures are discussed in relation to their semi-empirically calculated molecular electrostatic potentials and calculations of intermolecular interactions using van der Waals forces combined with an electrostatic point charge model.

Key words: dithiatetrazocine, crystal structure, crystal engineering, molecular electrostatic potential.

Résumé : L'oxydation de quantités équimolaires de [*p*-BrC_6H_4CNSSN]Cl et de [*p*-$O_2NC_6H_4CNSSN$]Cl avec de l'oxygène élémentaire, en présence de Ph_3Sb, dans du MeCN, conduit à un mélange de dithiatétrazocines symétriques, $O_2NC_6H_4CN_4S_2CC_6H_4NO_2$ (**1**) et $BrC_6H_4CN_4S_2CC_6H_4Br$ (**2**), aux côtés du dérivé substitué de façon non symétrique, $BrC_6H_4CN_4S_2CC_6H_4NO_2$ (**3**). On a déterminé les structures des composés **1**–**3** par diffraction des rayons X: le composé **1** cristallise dans le groupe d'espace monoclinique $P2_1/c$ (a = 8,6397(4), b = 5,8359(4) et c = 14,9767(11) Å, β = 92,088(4)°), avec une demi-molécule dans la maille asymétrique; **2** cristallise dans le groupe d'espace triclinique $P\bar{1}$ (a = 6,5330(5), b = 8,2084(6) et c = 14,7264(9) Å, α = 84,483(4)°, β = 77,112(4)° et γ = 87,879(3)°); on a trouvé que **3** cristallise sous deux formes, la recristallisation dans le CH_2Cl_2, à température ambiante, conduit à des cristaux ne contenant pas de solvant, de phase triclinique et de groupe d'espace $P\bar{1}$ (a = 6,5060(9), b = 7,0739(9) et c = 9,1164(8) Å, α = 81,860(3)°, β = 83,406(5)° et γ = 66,589(5)°) alors que le refroidissement de la solution à –5°C livre une forme solvatée, **3**·CH_2Cl_2 qui cristallise dans le groupe d'espace monoclinique $P2_1/m$ (a = 6,179(1), b = 10,960(2) et c = 13,884(3) Å, β = 92,69(3)°). Les interactions intermoléculaires NO_2···Br observées dans la structure non solvatée de **3** sont interrompues dans la structure solvatée; la molécule de CH_2Cl_2 de cette dernière est alignée d'une façon telle que son dipôle moléculaire interagit à la fois avec le groupe nitro et le bromo tout en maintenant un motif de chaîne moléculaire. On discute des structures en fonction de leurs potentiels électrostatiques moléculaires calculés de façon semi-empirique et de calculs d'interactions intermoléculaires à l'aide de forces de van der Waals combinées à un modèle de charge ponctuelle électrostatique.

Mots clés : dithiatétrazocine, structure cristalline, génie cristallin, potentiel électrostatique moléculaire.

[Traduit par la Rédaction]

Received 3 April 2002. Published on the NRC Research Press Web site at http://canjchem.nrc.ca on 22 November 2002.

Dedicated to Prof. T. Chivers in recognition of his continued interest, support, and encouragement.

A.D. Bond, D.A. Haynes, and J.M. Rawson.[1] Department of Chemistry, The University of Cambridge, Lensfield Road, Cambridge, CB2 1EW, U.K.

[1]Corresponding author (e-mail: jmr31@cam.ac.uk).

 DOI: 10.1139/V02-159 © 2002 NRC Canada

Introduction

We have been interested in the application of crystal engineering (1) in the design of sulfur–nitrogen radicals with unusual magnetic properties (2), including long range order (3) and structural bistability (4). A particular interest has been dithiadiazolyl radicals bearing perfluorinated substituents, and we have recently extended our studies to the design of simple fluorinated organics (5), as non-linear optical (NLO) materials, which will produce a second harmonic generation (SHG) response (6). A key component of the latter group of materials is the presence of a conjugated organic system with polarizable π-electrons. In addition, the material has to be macroscopically polar in order to show non-linear optical activity, and it is often the control of the crystal structure in all three dimensions to generate a macroscopically polar structure that proves problematic (7). In the current paper we report our initial studies on the synthesis of unsymmetrically substituted dithiatetrazocines (DTTA), bearing donor and acceptor groups, and report the first crystal structure of an unsymmetrically substituted dithiatetrazocine (**3**). We have found that it can be crystallized from CH_2Cl_2 in both solvated and desolvated forms dependent upon recrystallization conditions. The structures of **3** are compared with the symmetric derivatives, **1** and **2**.

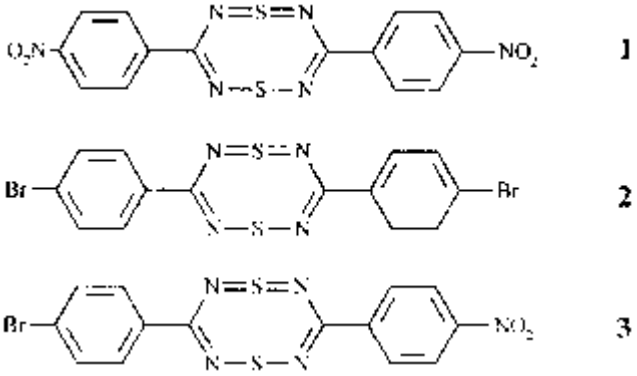

Dithiatetrazocines were first prepared in 1981 by Woodward and coworkers (8) and exhibit an unusual structural dichotomy. A series of crystallographic studies have revealed two different geometries possible for the dithiatetrazocine ring, either a planar 10π aromatic structure (8, 9) with a nonbonding transannular S···S contact (**A**) or a folded structure (8, 10) with a long S—S bond (**B**).

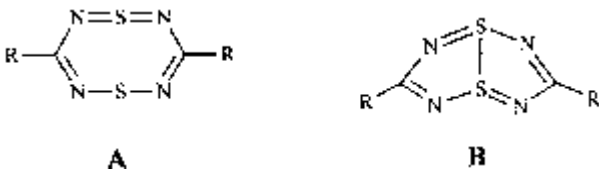

A series of theoretical studies have been undertaken (11). Gleiter et al. suggested (12) that the planar, cyclic system is favoured by aromatic substituents, whereas heterocyclic rings bearing π-donor substituents induce a folding of the heterocyclic ring. The π-donor groups give rise to a lowering of the HOMO-LUMO gap in the planar geometry and the molecule then becomes susceptible to a pseudo Jahn-Teller distortion, generating a folded geometry.

Table 1. Optimized geometric parameters for **1**, determined using semi-empirical methods.

Parameter	**1**	AM1	PM3	PM5	MNDO
C—N (Å)	1.327–1.333	1.333	1.339	1.330	1.338
N—S (Å)	1.559–1.563	1.473	1.434	1.525	1.580
N-C-N (°)	128.8	123.0	129.4	126.5	128.2
C-N-S (°)	141.6–143.1	147.8	145.3	145.0	144.6

Initial studies indicated that the dithiatetrazocine ring is thermally very stable (8). Electrochemical studies (9) indicate that the planar dithiatetrazocines are quite resistant to oxidation and, for example, attempted oxidation (at S) using MCPBA or N_2O_4 proved unsuccessful (8, 13). This is, perhaps, surprising, given the isolation of both the S^{IV} and S^{VI} derivatives i.e., SR and S(O)R by other synthetic methods (14). By contrast, the folded dithiatetrazocines are significantly easier to oxidize (9) and chlorination of $(Me_2N)_2C_2N_4S_2$ with elemental Cl_2 leads to the unusual salt, $[(Me_2N)_2C_2N_4S_2Cl][Cl_3]$ (15). Reactivity studies on the heterocyclic ring N have focused on its basicity. It has been found to be a very poor base, showing no basic properties towards the strong acid $HClO_4$ (8). The ring also showed little reactivity towards nucleophiles, although hydrolysis by OH^- could be achieved to liberate the amidine (8). Subsequent work by Chivers et al. (16) has shown that the N atom can act as a very weak donor towards Pt, although it is liberated from the metal by other donor ligands such as THF. Electrochemical studies indicate a 1 e^- reduction to an 11π radical. Chemical studies indicate no reaction at the heterocyclic ring N with hydrazine, although reduction to the amidine could be achieved using Pd/C (13). Given the thermal stability of this ring system and its comparatively air-stable nature compared to many thiazyl rings, unsymmetrically substituted DTTAs seemed potentially novel and stable precursors for NLO-active materials.

Experimental section

The salts $[p\text{-}BrC_6H_4CNSSN]Cl$ and $[p\text{-}O_2NC_6H_4CNSSN]Cl$ were prepared according to the literature method (17). Ph_3Sb (Aldrich) was sublimed prior to use. All solvents were dried and freshly distilled under argon prior to use. Oxygen (BOC) was dried by passing through a P_4O_{10} column.

^1H NMR data were collected on a Bruker DPX 400 MHz NMR spectrometer. Mass spectra and accurate mass spectra were recorded on a Kratos Concept instrument in EI mode.

Semi-empirical molecular orbital calculations were made using MOPAC implemented through Quantum Cache 5.0 (Fujitsu Co.) running on a 1.8 GHz Pentium computer. Geometry optimization using PM3 proved to give marginally improved structural compatibility with the observed structures than MNDO, INDO, AM1, or PM5. In all cases geometry optimization led to planar DTTA rings, which exhibited substantial twist angles to the aryl substituents. Selected geometry-optimized structural parameters are given in Table 1. The PM3 method was utilized to determine subsequent molecular electrostatic potential maps and point charges for further calculations, since these produced the smallest twist

© 2002 NRC Canada

Table 2. Crystal data for **1–3** and **3**·CH_2Cl_2.

	1	**2**	**3**	**3**·CH_2Cl_2
Empirical formula	$C_{14}H_8N_6O_4S_2$	$C_{14}H_8Br_2N_4S_2$	$C_{14}H_8BrN_5O_2S_2$	$C_{15}H_{10}BrCl_2N_5O_2S_2$
Molecular weight	388.38	456.18	422.28	507.21
Crystal system	Monoclinic	Triclinic	Triclinic	Monoclinic
Space group	$P2_1/c$	$P\bar{1}$	$P\bar{1}$	$P2_1/m$
a (Å)	8.6397(4)	6.5330(5)	6.5060(9)	6.179(1)
b (Å)	5.8359(4)	8.2084(6)	7.0739(9)	10.960(2)
c (Å)	14.9767(11)	14.7264(9)	9.1164(8)	13.884(3)
α (°)	90	86.483(4)	81.860(3)	90
β (°)	92.088(4)	77.112(4)	83.406(5)	92.69(3)
γ (°)	90	87.879(3)	66.589(5)	90
V (Å^3)	754.63(8)	768.15(9)	380.35(8)	939.2(3)
Z	2	2	1	2
$D_{calcd.}$ (g cm^{-3})	1.709	1.972	1.844	1.794
T (K)	180	180	180	180
λ (Å)	0.7107	0.7107	0.7107	0.7107
$2\theta_{max}$	27.5	27.3	25.01	24.92
Total data	6060	7378	3480	4757
Unique data	1728	3392	1338	1715
R_{int}	0.0638	0.0679	0.0355	0.1161
R_1 [$F^2>2\sigma(F^2)$]	0.0432	0.0437	0.0781	0.1052
wR_2 (all data)	0.1053	0.1137	0.1875	0.2758
Goodness-of-fit on F^2	1.04	1.02	1.30	1.05
Largest diff. peak and hole (e Å^{-3})	–0.331 and 0.330	–0.854 and 0.693	–0.805 and 0.625	–0.512 and 0.524

angle between aryl and DTTA rings during geometry optimization. Molecular electrostatic isopotential maps for **1–3** were determined using PM3 constrained to the crystal-structure geometry. Intermolecular interactions utilized in-house software (J.M. Rawson, 2001), including an atom-atom point charge model (using theoretically calculated point charges) and an atom-atom dispersion term for the van der Waals interactions. Full details are published elsewhere (18).

Preparation of 1–3

A solution of Ph_3Sb (0.68 g) in CH_3CN (10 ml) was added in small aliquots to a yellow suspension of equimolar quantities of [*p*-$BrC_6H_4CN_2S_2$]Cl (0.250 g, 0.846 mmol) and [*p*-$NO_2C_6H_4CN_2S_2$]Cl (0.220 g, 0.841 mmol) in CH_3CN (15 ml) under an oxygen atmosphere. The resulting purple solution was stirred at 60–75°C for 6 h under an atmosphere of oxygen. The resulting yellow product was adsorbed onto silica and separated by column chromatography (silica column, CH_2Cl_2 eluant). Pure samples of the dithiatetrazocines **1**, **2**, and **3** were isolated sequentially and identified by their ^{1}H NMR and mass spectroscopic data. The volume of each fraction was reduced and crystals of **1–3** suitable for X-ray diffraction formed by slow evaporation at room temperature. A further set of crystals of **3**·CH_2Cl_2 were also recovered from a solution stored at –5°C. Typical yields: **1** (24 mg, 14%), **2** (8 mg, 4%), **3** (10 mg, 3%), based on amount of [*p*-$O_2NC_6H_4CNSSN$]Cl and [*p*-BrC_6H_4CNSSN]Cl available.

Analytical data for 1

^{1}H NMR ($CDCl_3$) δ: 8.75 (d, 9.1 Hz), 8.41 (d, 9.1 Hz) (lit. (9) value 8.42 (d, 8.8 Hz), 8.07 (d,8.8 Hz) in d^6-DMSO). EI+-MS *m/z*: 388.0 ([$M^+ = C_{14}H_8N_6S_2O_4$]).

Analytical data for 2

^{1}H NMR ($CDCl_3$) δ: 8.41 (d, 8.8 Hz), 7.67 (d, 8.8 Hz). EI+-MS *m/z* (%): 457.9 ([$M^+ = {}^{81}Br^{81}BrC_{14}H_8N_4S_2$], 24.5), 455.9 ([$M^+ = {}^{81}Br^{79}BrC_{14}H_8N_4S_2$], 50.0), 453.9 ([$M^+ = {}^{79}Br^{79}BrC_{14}H_8N_4S_2$], 25.5). Calculated accurate mass data are, respectively: 457.85188, 455.85380, 453.85571.

Analytical data for 3

^{1}H NMR ($CDCl_3$) δ: 8.73 (d, 8.9 Hz), 8.43 (d, 8.6 Hz), 8.40 (d, 8.9 Hz), 7.69 (d, 8.6 Hz). EI+-MS *m/z* (%): 420.9 ([$M^+ = {}^{81}BrC_{14}H_8N_5S_2O_2$], 50), 422.9 ([$M^+ = {}^{79}BrC_{14}H_8N_5S_2O_2$], 50).

Crystal structure determination

Single crystal X-ray diffraction analyses were performed using a Nonius Kappa CCD diffractometer equipped with an Oxford Cryosystems cryostream device. Crystals were mounted on the end of glass fibres using perfluoropolyether oil and data were collected at 180(2) K. Data were processed using the HKL package (19), and unit cell parameters were refined against all data.

Details of the crystal data and refinement are given in Table 2. Selected intramolecular bond lengths and angles are compiled in Table 3.[2]

[2] Supplementary data may be purchased from the Depository of Unpublished Data, Document Delivery, CISTI, National Research Council Canada, Ottawa, ON K1A 0S2, Canada (http://www.nrc.ca/cisti/irm/unpub_e.shtml for information on ordering electronically). CCDC 179766–179769 contain the supplementary data for this paper. These data can be obtained, free of charge, via www.ccdc.cam.ac.uk/conts/retrieving.html (or from the Cambridge Crystallographic Data Centre, 12 Union Road, Cambridge, U.K.; fax +44 1223 336033; or deposit@ccdc.cam.ac.uk).

© 2002 NRC Canada

Table 3. Intramolecular dimensions in **1**–**3** and related planar DTTA derivatives (from references 8 and 9).

Compound	C—N (Å)	N—S (Å)	S···S (Å)	N-C-N (°)	C-N-S (°)	N-S-N (°)
1	1.333(2)	1.5628(18)	3.806(1)	128.8(2)	141.60(16)	126.47(9)
	1.327(2)	1.5593(18)			143.09(16)	
2	1.323(5)	1.569(3)	3.796(2)	129.9(4)	140.9(3)	127.0(2)
	1.326(6)	1.558(4)	3.788(2)	128.6(4)	142.1(4)	127.2(2)
	1.329(6)	1.560(4)			142.1(3)	
	1.338(5)	1.555(4)			142.0(4)	
3	1.339(10)	1.561(7)	3.815(4)	129.5(7)	140.6(6)	126.5(4)
	1.322(10)	1.568(6)			143.5(6)	
3·CH_2Cl_2	1.323(9)	1.566(8)	3.789(6)	129.7(13)	141.3(9)	127.1(5)
	1.327(10)	1.566(8)		128.5(12)	142.4(8)	
$Ph_2C_2N_4S_2$	1.319	1.569	3.79	129.2	140.9	127.0
	1.327	1.559			142.9	
$(CF_3C_6H_4)_2C_2N_4S_2$	1.322(3)	1.563(2)	3.788	129.2(2)	142.4(2)	126.8(1)
	1.323(3)	1.561(2)			141.6(2)	
$(MeOC_6H_4)_2C_2NH_4S_2$	1.330(3)	1.559(2)	3.781	128.5(2)	142.2(2)	127.2(1)
	1.328(3)	1.564(2)			142.2(2)	
t-$Bu_2C_2N_4S_2$	1.323(3)	1.567(2)	3.784	128.6(2)	142.2(2)	127.20(12)
	1.328(3)	1.570(2)			142.0(2)	
$(C_4H_3S)_2C_2N_4S_2$	1.324(4)	1.557(3)	3.803	130.1(3)	141.8(2)	126.60(16)
	1.329(4)	1.554(3)			141.5(3)	

Results

Preparation and crystal growth

Unsymmetrically substituted DTTAs were first reported by Rees and co-workers in 1989 (13), by condensation of a mixture of benzamidine and dimethylguanidine with SCl_2. They recovered a mixture of symmetrically substituted products (14.5%) and unsymmetrically substituted products (3%) in a non-statistical ratio. Subsequent studies by Boeré et al. (9) showed that unsymmetric dithiatetrazocines can be prepared by reaction of a dithiadiazolylium chloride salt with the silylated amidine in the minimum volume of refluxing MeCN. This scrambling reaction led to a statistical distribution of products (i.e., 50% unsymmetric product).

In our current studies, we utilized an alternative preparative route to DTTA rings, also developed by Boeré et al. (9). The two dithiadiazolylium salts, [*p*-BrC_6H_4CNSSN]Cl and [*p*-$O_2NC_6H_4CNSSN$]Cl, were prepared according to the literature method (17). Oxidation of equimolar quantities of these two salts with dry O_2 according to the literature method yielded a mixture of the symmetric dithiatetrazocines, **1** and **2**, as well as the unsymmetric derivative, **3**. Given the persistently low yields of this reaction, the relative recovered yields (ca. 14:4:3 for **1**:**2**:**3**) are perhaps not too significant, but likely indicate that a non-statistical mixture is present. We have not attempted alternative routes to these unsymmetrically substituted analogues, but it should be noted that purification by column chromatography proved facile. The three compounds were readily characterized by their ^{1}H NMR spectra and mass spectra. Both **2** and **3** provided signature isotope distribution patterns for their molecular ions caused by the two bromine isotopes (^{79}Br and ^{81}Br have equal natural abundances). The ^{1}H NMR chemical shifts and coupling constants for the aromatic ^{1}H nuclei in **3** can be tentatively assigned by direct comparison with the symmetrically substituted derivatives, **1** and **2**, and are in agreement with previous data (9).

The three dithiatetrazocines, **1**, **2**, and **3**, were separated by column chromatography and recrystallized from dichloromethane, yielding single crystals suitable for X-ray diffraction studies. Two sets of crystals of **3** were grown, one set from CH_2Cl_2 solution stored at room temperature, the other from a CH_2Cl_2 solution cooled to –5°C.

Crystal and molecular structure of 1

Compound **1** crystallizes in the monoclinic spacegroup $P2_1/c$, with half a molecule of **1** in the asymmetric unit. The intramolecular bond lengths and angles in the heterocyclic ring are similar to those previously reported and also to the other DTTA structures reported herein (Table 3). The whole molecule is close to planarity; the DTTA ring exhibits a mean deviation of 0.001 Å from planarity and the aromatic substituents are twisted by just 0.6° with respect to the DTTA ring plane.

There are no intermolecular contacts substantially less than the sum of the van der Waals radii. The closest of the intermolecular contacts is an S···O contact (3.292(2)Å) between the DTTA ring and the nitro-substituent on the aromatic ring of an adjacent molecule. These contacts are slightly beyond the sum of the van der Waals radii (20) close to the ring plane (3.14 Å), but shorter than the sum of the van der Waals radii perpendicular to the plane (3.57 Å). Two pairs of these contacts link molecules together into a one-dimensional chain (Fig. 1). There are also N···O contacts between nitro groups; these comprise N(3)···O(1b) at 3.221(2) Å and N(3)···O(2b) at 3.582(3) Å and are also greater than the sum of the van der Waals radii (20) (3.14 Å). These interactions generate a herring-bone motif (Fig. 2).

Crystal and molecular structure of 2

Heterocycle **2** crystallizes in the triclinic space group $P\bar{1}$, with the asymmetric unit consisting of two half molecules of **2**. The intramolecular bond lengths are comparable with those of **1** (above, and see Table 3) and there is no significant

© 2002 NRC Canada

Fig. 1. Packing of **1** illustrating the intermolecular S···O contacts close to the molecular plane.

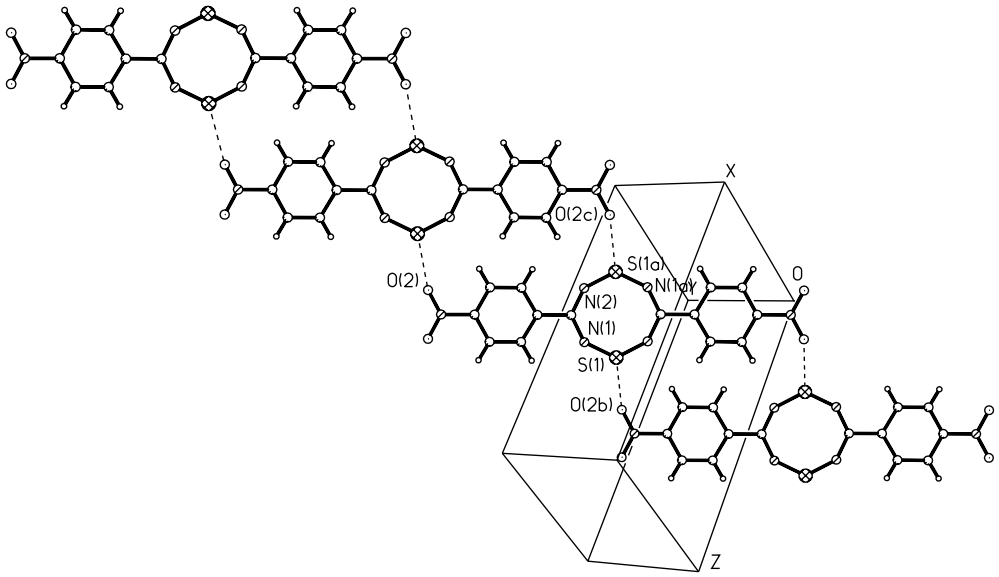

difference in molecular geometry between the two crystallographically unique molecules. In both cases the DTTA ring is essentially flat (mean deviation within 0.006 Å). In one of the unique molecules in the asymmetric unit, the phenylene and heterocyclic rings are essentially co-parallel (angle between mean planes is 1.5°), although the second crystallographically unique molecule is slightly more twisted with the corresponding twist angle being 8.8°.

There are no particularly close intermolecular contacts. One of the two crystallographically independent molecules forms pairs of S···Br contacts at 3.885(1) Å, close to the molecular plane linking crystallographically related molecules into chains (Fig. 3*a*). These contacts are beyond the sum of the van der Waals radii (3.14–3.87 Å). The second of the two crystallographically independent molecules also forms chains linked via pairs of S···N contacts (S(21)···N(22b) at 3.596(4) Å) also around, or beyond, the sum of the van der Waals radii (3.2–3.63 Å) (Fig. 3*b*). These two sets of chains are linked via Br···Br contacts at 3.526(1) Å, which are also close to the sum of the van der Waals contacts, i.e., 3.08 – 3.68 Å. This leads to a set of interlocking sheets of molecules.

Crystal and molecular structure of 3

Attempts to crystallize the unsymmetric DTTA derivative **3** from CH_2Cl_2 yielded two sets of needle-like crystals; a solvate **3**·CH_2Cl_2 and an unsolvated form **3**.

Structure of 3

Dithiatetrazocine **3** crystallizes in the triclinic space group $P\bar{1}$, with half a molecule in the asymmetric unit and a consequent 50:50 disorder of the Br and NO_2 groups. The heterocyclic geometry is similar to those observed for **1** and **2**, although there is a slight increase in the intramolecular S···S contact. The heterocyclic ring, like **1** and **2**, is essentially planar (mean deviation 0.007 Å). The twist angle (15.1°) between aryl and DTTA rings is more marked than any of the other structures reported here. Nevertheless, the three rings in **3** remain close to co-planarity.

Fig. 2. Packing of **1** emphasizing the herring-bone motif and intermolecular nitro···nitro interactions.

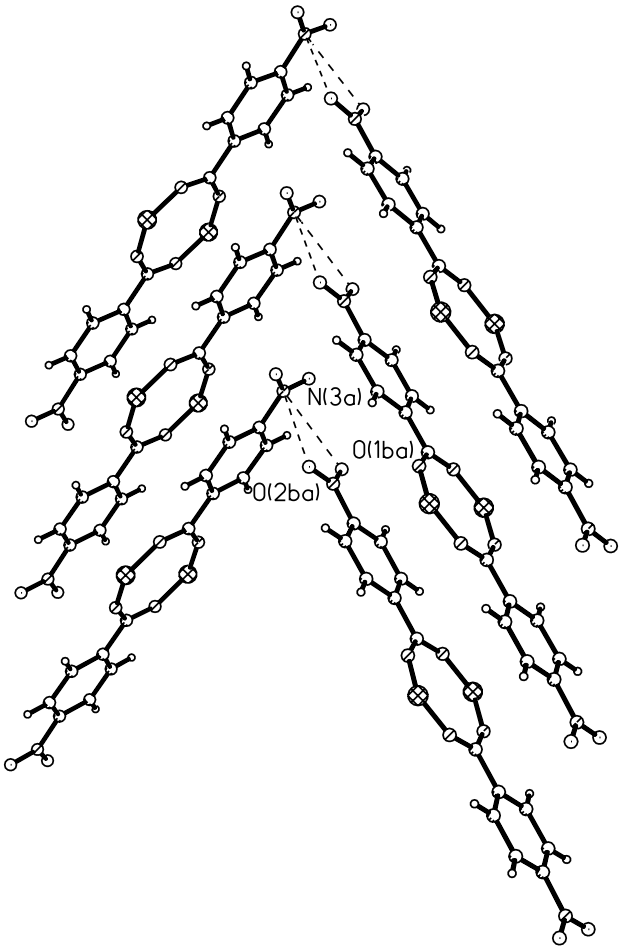

The disorder in the substituent positions complicates discussion of some aspects of the crystal structure. However, the disorder does not affect the S···N contacts (S(11)···N(12c)

© 2002 NRC Canada

Fig. 3. Views of the packing of the two crystallographically unique molecules of **2** illustrating the intermolecular contacts to S close to the ring plane. These comprise (*a*) S···Br contacts and (*b*) S···N contacts.

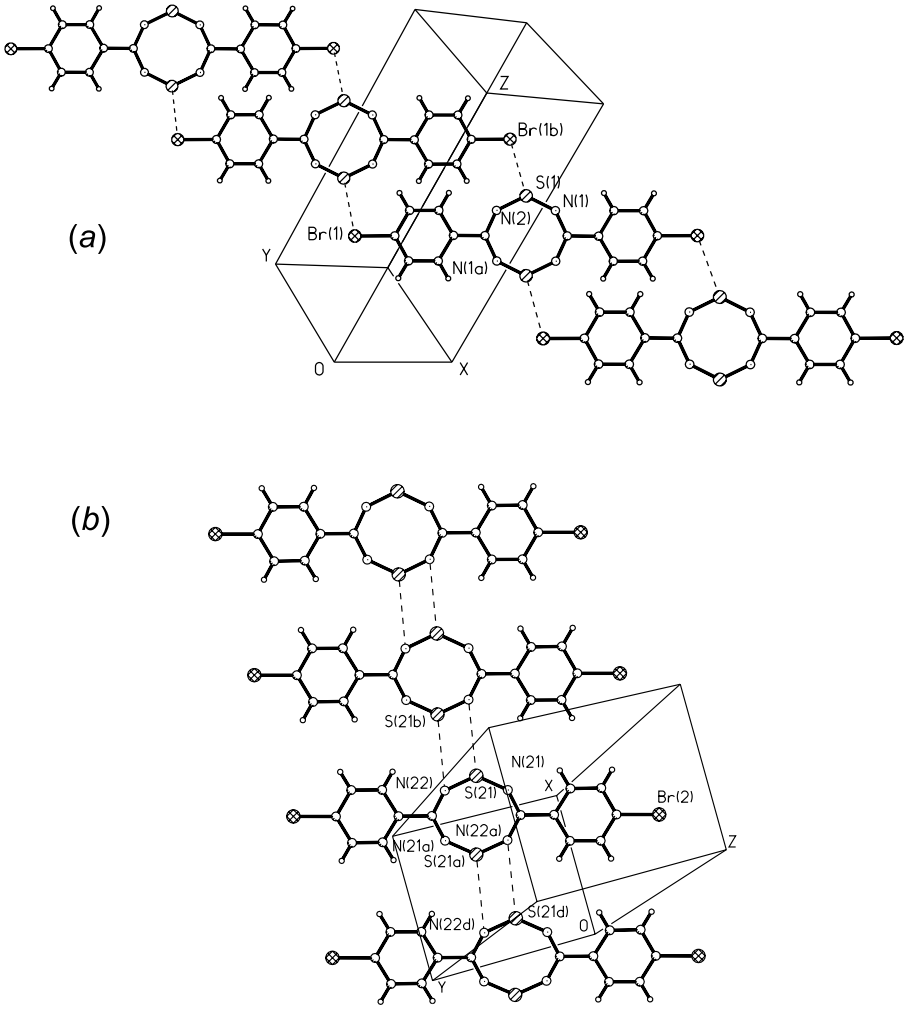

Fig. 4. View of the structure of **3** (with the 50:50 disorder of the Br and NO_2 substituents removed for clarity).

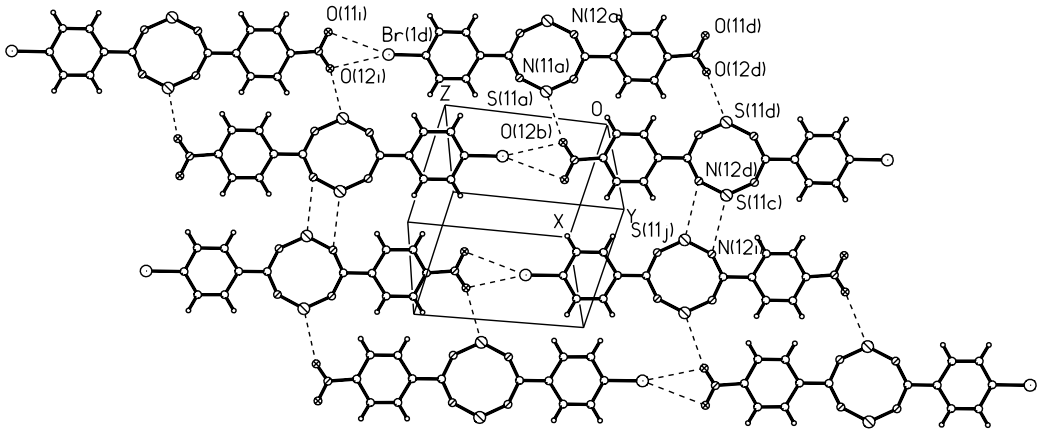

at 3.663(7) Å, cf. sum of the van der Waals radii at 3.20–3.63 Å) between DTTA rings, which link molecules along the crystallographic *a*-axis (Fig. 4). These contacts are similar in nature to those observed in **2** (Fig. 3). In addition a second in-plane contact is observed between the nitro–bromo substituent and the DTTA sulfur atom (Fig. 4). These are similar to the corresponding in-plane NO_2···S and Br···S interactions observed in **1** and **2**, respectively. The disorder in the nitro–bromo substituents inhibits a detailed discussion of the geometry of this contact. Nevertheless, the supramolecular NO_2···Br interaction appears present in the structure of **3**, and links molecules together along the crystallographic *c*-axis.

© 2002 NRC Canada

Fig. 5. View of the structure of **3**·CH_2Cl_2 (illustrating only the major components of the positional disorder of nitro and bromo substituents and CH_2Cl_2 solvate molecule).

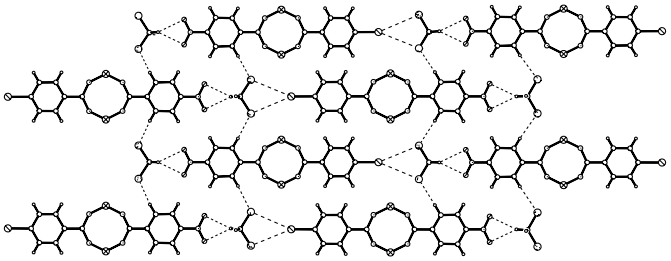

Structure of 3·CH_2Cl_2

The structures of **1**, **2**, and the unsolvated form of **3** (above), as well as many other DTTA derivatives contain half-molecules in the asymmetric unit related through an inversion centre. In the case of **3**·CH_2Cl_2, the asymmetric unit comprises half a molecule of **3** and half a molecule of CH_2Cl_2, which are located on a mirror plane passing through the two Br–NO_2 functional groups. In the case of **3**·CH_2Cl_2 the Br–NO_2 functional groups exhibit positional disorder in an approximately 3:1 ratio. The terminal group disorder does not affect the DTTA ring geometry, which is comparable with other aryl derivatives described above (Table 3). The DTTA ring is planar within (0.01 Å) and approximately coplanar with the aryl ring (twist angle 0.4°).

A comparison of the structures of **3** and **3**·CH_2Cl_2 immediately reveals a disruption of the chain-like motif present in unsolvated **3**. The CH_2Cl_2 molecule is sited on the mirror plane and is also orientationally disordered over two sites in an approximately 1:1 ratio. The CH_2Cl_2 is located between molecules of **3** along the chain-forming direction. The disorder in both CH_2Cl_2 and Br–NO_2 groups complicates discussion of the intermolecular interactions between these two groups, although it is tempting to envisage the molecular dipole of the CH_2Cl_2 molecule aligning with the molecular dipole of **3**. Lateral interactions between molecular chains comprise S···Br (and S···O_2N) interactions (Fig. 5). The S···Br contact, present in the major component of the disorder, is 4.243(3) Å, somewhat longer than the corresponding S···Br contacts in **2**.

Discussion

The molecular structures of the aryl-substituted DTTA molecules, described herein, are similar to those reported for other derivatives described in earlier reports (8–10). Their planar 10π aromatic structures are consistent with previous studies, which indicate that folded structures are stabilized only when there is the possibility of π-donation into the thiazyl ring.

Our recent structural studies in dithiadiazolyl radical chemistry has successfully utilized molecular electrostatic potential (MEP) maps, coupled with a point charge model, to analyse the observation of polymorphism in the rigid dithiadiazolyl radicals, ClCNSSN and HCNSSN (18). To attempt to rationalize the structures of **1**–**3**, we have employed similar techniques. The focus of these current studies has been to examine whether structure-directing groups can be utilized to manipulate the solid state structures of DTTAs. In the current paper we examine the structures of these DTTAs, using the same methodology.

Molecular electrostatic potential maps

Calculations of the molecular electrostatic potential maps were carried out using semi-empirical methods. We found that of the methods employed (MNDO, AM1, PM3, and PM5), several gave similar geometries for the DTTA ring (Table 1) close to that observed experimentally for **2**. Whilst the twist angle between DTTA and aryl substituent is susceptible to crystal-packing effects, all semi-empirical methods gave substantial deviations from coplanarity. We chose the PM3 method, since this provided the smallest deviations from planarity and therefore best agreement with the observed structure. The molecular electrostatic potential maps (MEPs) determined using other methodologies did not differ substantially, although some variations in partial point charges were found.

The molecular electrostatic potential is the energy of a unit of positive charge ("a proton") as it interacts with a molecule, i.e., its interaction with the unperturbed molecular charge distribution, caused by the electrons and positive nuclei. The isopotential map represents a contour linking points with the same interaction energy. The value of the plot may be positive if the MEP at that point is repulsive, or negative if the sum of the electrostatic interactions is attractive (21). The isopotential maps for **1**–**3** are shown in Fig. 6 with dark grey regions representing a negative, attractive potential towards a positive charge, and light grey regions corresponding to positive, repulsive interactions. We feel that the electrostatic approach to analyse the bonding in thiazyl rings is particularly appropriate because of the strong polarity of the thiazyl bonds. Since electrostatic interactions exhibit an r^{-1} dependency, whereas van der Waals forces are a function of r^{-6}, then contacts beyond the sum of the van der Waals contacts may exhibit a substantial ionic contribution to the lattice energy. Current semi-empirical calculations on the DTTA heterocycle indicate substantial bond polarity within the heterocyclic ring as well as substantial partial charges on the nitro functional group. Conversely the Br atom is electrostatically near neutral. Given the sparsity of contacts less than the sum of the van der Waals radii in **1**–**3**, the electrostatic contribution is likely to be significant.

An examination of the in-plane packing motifs of **1**, **2**, and **3** (i.e., close to the molecular plane) reveals a recurring theme of intermolecular contacts to S. In **1**, the S···O contacts are 3.292(2) Å (Fig. 1) and geometrically similar interactions also occur in **3** and **3**·CH_2Cl_2 (Figs 4 and 5). Intermolecular S···Br contacts are observed in **2** and **3**. In **2**, the S···Br contact is 3.885(1) Å. In **3** and **3**·CH_2Cl_2 the corresponding values are somewhat longer (around 3.997(3) Å and 4.243(3) Å respectively). In addition, intermolecular S···N contacts close to the ring plane are observed in **2** and **3**. The intermolecular S···N contact between symmetry-related DTTA rings in the second crystallographically unique molecule of **2** is 3.596(4) Å. These are also observed in the structure of unsolvated **3**, at 3.663(7) Å.

A comparison of the observed structures with their molecular electrostatic potential maps clearly reveals the matching of electropositive (light grey) and electronegative (dark grey)

© 2002 NRC Canada

Fig. 6. Molecular electrostatic potential maps for (*a*) **1**, (*b*) **2**, and (*c*) **3** calculated using semi-empirical methods (MOPAC/PM3 employed through Quantum Cache (v. 5.0, Fujitsu Co.)). MEP determined at 0.04 au.

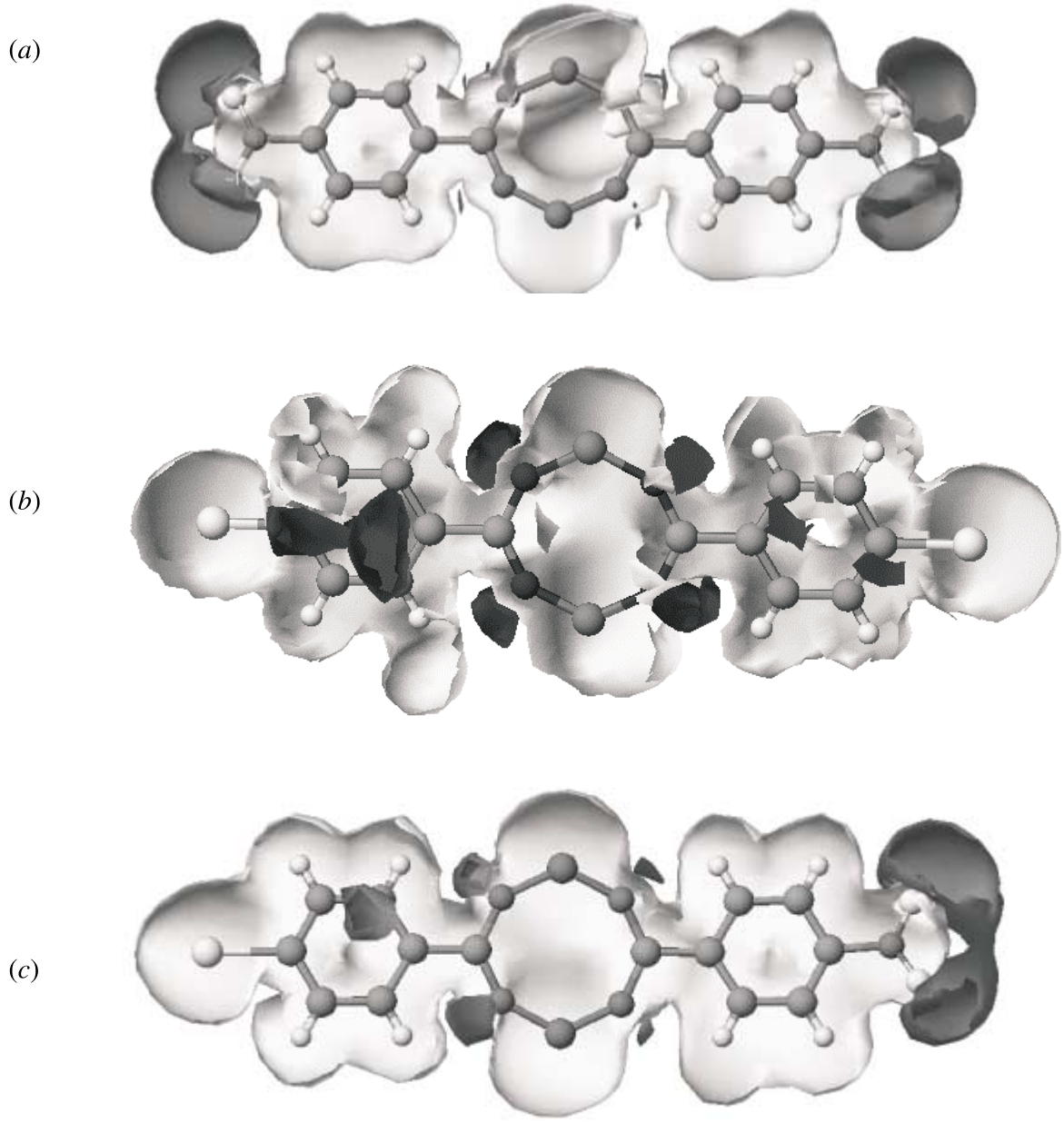

regions of the molecule in **1** and **3**, i.e., favouring S···O and S···N contacts. In contrast, the S···Br contact would appear to have little electrostatic contribution, and is likely to be predominantly induced-dipole – induced-dipole (van der Waals) forces, associated with the softer Br and S atoms. The greater partial charge on the DTTA ring N in **2** (cf. **1**) also promotes intermolecular S···N contacts between the DTTA rings. The observation of two sets of crystallographically distinct supramolecular chains of molecules, one linked via four S···Br contacts per molecule, and the other linked through four S···N contacts per molecule in **2**, is indicative of both sets of interactions having similar stabilities. Only in the case of **3** is a head-to-tail alignment of molecules anticipated (via NO_2···Br contacts), and indeed observed. In **1** and **2**, electrostatic N···O and van der Waals Br···Br contacts orient molecules approximately orthogonal to each other.

To examine the nature and relative stabilities of these interactions further, we utilized a point charge model to refine the packing geometry for a pair of interacting DTTA molecules. To simplify the problem, the molecular geometries were forced to be planar, and energy minimization was carried out with both molecules lying in the same plane, with their molecular long-axes parallel. It may be argued that the additional packing forces present in the solid state structure, coupled with the planarity restriction are likely to lead to some deviations between observed and calculated geometries. Nevertheless, our previous studies and the current investigations have generally found gratifying agreement

© 2002 NRC Canada

Fig. 7. Energy minima (kJ mol^{-1}) for parallel arrangements of **1**, **2**, and **3**, calculated using van der Waals interactions with a point charge model (Point charges were utilized from semi-empirical MNDO/PM3 calculations).

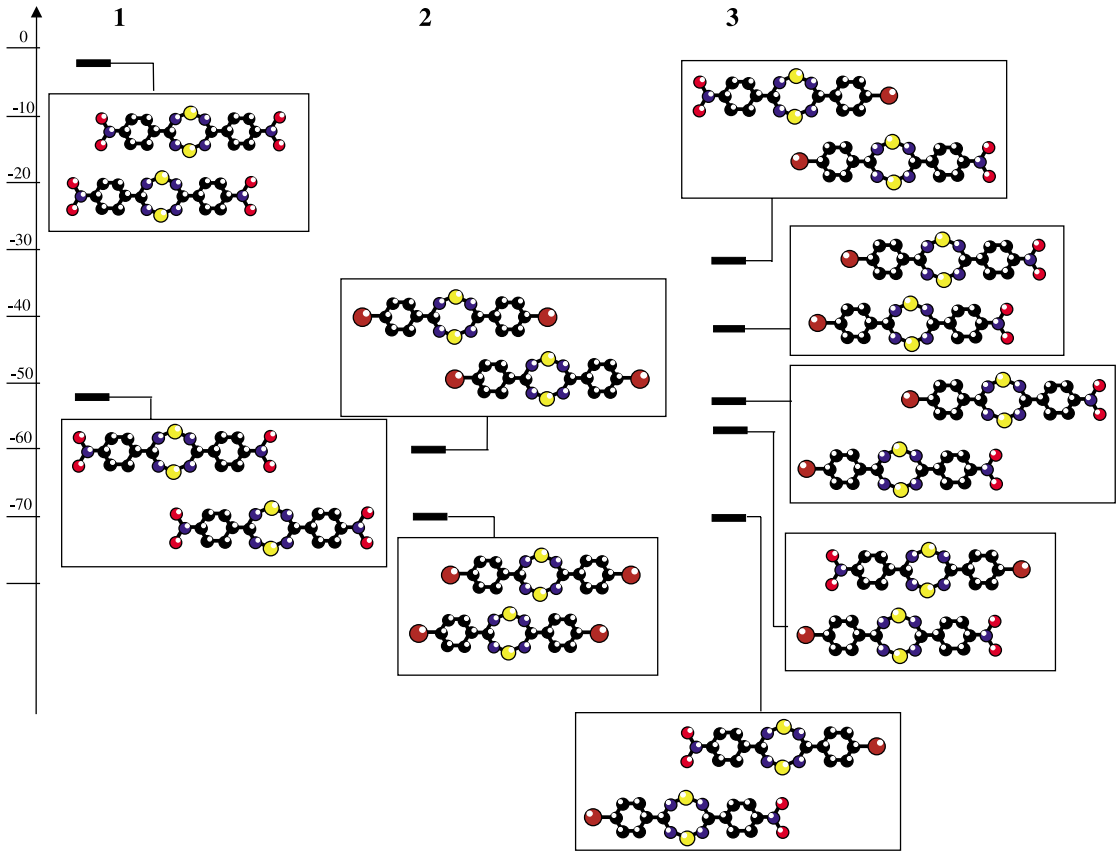

between observed and calculated molecular predisposition. Figure 7 shows the energy minima for the parallel arrangements of **1**–**3**.

In the case of **1**, the intermolecular S···N contacts between DTTA rings is clearly disfavoured in comparison to the S···O interactions. Whilst the optimized geometry gives some discrepancy with that observed (cf. calculated and experimental S···O contacts at 3.014 and 3.292(2) Å), the gross geometry of this energy minimum is clearly consistent with the crystal data.

In the case of **2**, the geometries associated with the intermolecular S···N and S···Br contacts were calculated to be much closer in energy and are consistent with the observation of both packing motifs in the structure of **2**. The calculated point charge on Br is essentially zero, and so the S···Br contact is predominantly van der Waals in nature, whereas the S···N interaction is electrostatically favoured. The detailed geometries of these interactions also show some discrepancy with the observed data (cf. calculated and observed S···N contacts of 3.184 and 3.596(4) Å and S···Br contacts of 3.990 and 3.885(1) Å). Despite these deviations, these geometries are in broad agreement with the observed structure and, we feel, remarkable given the simplicity of the model employed.

Calculations on **3** reveal similar energies for the two co-parallel modes of attachment via heterocyclic S···N contacts. Both of the parallel and anti-parallel modes with molecules linked via S···O contacts are calculated to be more stable with the anti-parallel arrangement preferred.

Origin of the disorder in 3

The observed structural disorder in **3** could arise from several possibilities. These have been discussed at length in the discussion of the biphenyl derivative, *p*-$IC_6H_4C_6H_4NO_2$ (22), which also exhibits similar structural disorder. Inclusion of small amounts of the symmetric derivatives **1** or **2** could result in inversion of the direction of chain polarity, giving rise to structural disorder. However, we discount this since the different components were separated by column chromatography and no evidence for contamination was observed by ^1H NMR or mass spectrometry. Alternatively the structure could be subject to random disorder within the chain. The calculated attachment energy for the NO_2···Br contact is ca. –7 kJ mol^{-1}, whereas both the NO_2···O_2N interaction and Br···Br interactions are calculated to be unfavourable by ca. +1 and +7 kJ mol^{-1}, respectively. Whilst this does not preclude random positional disorder, the nitro···bromo contact is the only one calculated to be favourable. It is notable that the energetically disfavoured in-plane NO_2···O_2N interactions and Br···Br interactions are not observed in either **1** or **2** and other packing motifs are adopted to avoid this unfavourable interaction. A third possibility is that the chains are macroscopically polar, but there is disorder in the arrangement of parallel chains. Calculations of the energy minima for

© 2002 NRC Canada

Fig. 8. Possible origins of the disorder in **3** arising from (*a*) doping with impurity (**1**), (*b*) random positional disorder, and (*c*) orientational disorder of parallel chains.

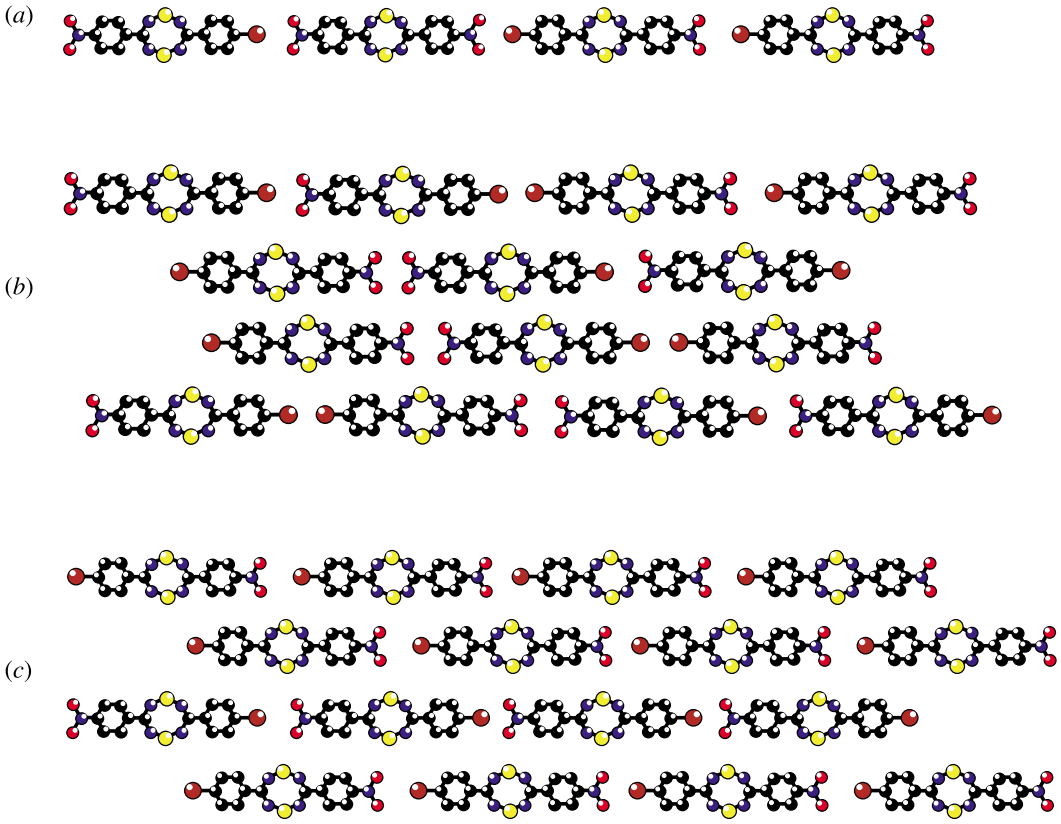

co-parallel and anti-parallel alignment of molecules on neighbouring chains (determined above) indicate that the small energy difference between these minima may give rise to the observed disorder. In light of the arguments presented here, we favour this latter possibility. These three possibilities are represented in Fig. 8.

Further studies are underway to investigate whether the disorder generates macroscopically polar regions of co-parallel alignment, which would give rise to an SHG response, or whether microscopic (random positional) disorder is present.

Summary and conclusion

Three new dithiatetrazocines have been characterized by X-ray crystallography, including the first structural study on a DTTA to possess unsymmetric substituents. Calculations indicate that the solid-state structures of these compounds are dictated by a combination of electrostatic and van der Waals interactions. In the structures of **1**–**3**, both electrostatic $S^{\delta+}\cdots N^{\delta-}$ and $S^{\delta+}\cdots O^{\delta-}$ contacts are identified as contributing to the packing, whereas van der Waals S···Br contacts compete with $S^{\delta+}\cdots N^{\delta-}$ interactions in **2**. The substantial orientational disorder in **3** may arise from either random disorder in the lattice at a molecular level, or through structural disorder at the macroscopic level. The structural analysis of these derivatives indicates that a model, combining electrostatic and van der Waals forces, may prove useful in predicting the structures of DTTA rings. We are currently pursuing the development of this model in the design of macroscopically polar materials.

Acknowledgments

We would like to thank the Engineering and Physical Sciences Research Council (EPSRC) for post-doctoral support (A.D.B.), the Cambridge Commonwealth Trust, and the Cecil Renaud Trust for their continuing financial support (D.A.H.).

References

1. G.R. Desiraju. Crystal engineering. Elsevier Press, Amsterdam. 1989.
2. J.M. Rawson, R.J. Less, J.N.B. Smith, F. Palacio, and G. Antorrena. Mol. Cryst. Liq. Cryst. **334**, 275 (1999).
3. A.J. Banister, N. Bricklebank, I. Lavender, J.M. Rawson, C.I. Gregory, B.K. Tanner, W. Clegg, M.R.J. Elsegood, and F. Palacio. Angew. Chem. Int. Ed. Engl. **35**, 2533 (1996); F. Palacio, G. Antorrena, M. Castro, R. Burriel, J.M. Rawson, J.N.B. Smith, N. Bricklebank, J. Novoa, and C. Ritter. Phys. Rev. Lett. **79**, 2336 (1997); F.L. Pratt, A.E. Goeta, F. Palacio, J.M. Rawson, and J.N.B. Smith. Physica B, **289**, 119 (2000); M. Mito, T. Kawae, K. Takeda, S. Takagi, Y. Matsushita, H. Deguchi, J.M. Rawson, and F. Palacio, Polyhedron, **20**, 1509 (2001).
4. G.D. McManus, J.M. Rawson, N. Feeder, J. van Duijn, E.J.L. McInnes, J.J. Novoa, R. Burriel, F. Palacio, and P. Oliete. J. Mater. Chem. **11**, 1992 (2001).

© 2002 NRC Canada

5. A.D. Bond, J.Griffiths, J.M. Rawson, and J. Hulliger. Chem. Commun. 2488 (2001).
6. J.D. Wright. Molecular crystals. 2nd ed. Cambridge University Press, Cambridge. 1995.
7. N.J. Long. Angew. Chem. Int. Ed. Engl. **34**, 21 (1995).
8. I. Ernest, W. Holick, G. Rihs, D. Schomburg, G. Shoham, D. Wenkert, and R.B. Woodward. J. Amer. Chem. Soc. **103**, 1540 (1981).
9. R.T. Boeré, K.H. Moock, S. Derrick, W. Hoogerdijk, K. Preuss, J. Yip, and M. Parvez. Can. J. Chem. **71**, 473 (1993); M. Parvez. Acta. Crystallogr. Sect. C, **51**, 2116 (1995); T.M. Barclay, A.W. Cordes, R.T. Oakley, and K.E. Preuss. Acta. Crystallogr. Sect. C, **52**, 3250 (1996).
10. D.M. Ho and R.A. Pascal, Jr. Acta. Crystallogr. Sect. C, **50**, 108 (1994); S. Dell, D.M. Ho, and R.A. Pascal, Jr. Inorg. Chem. **35**, 2866 (1996).
11. R.T. Oakley. Can. J. Chem. **62**, 2763 (1984); S. Millefiori. Inorg. Chim. Acta, **L55**, 90 (1984); J.P. Boutique, J. Riga, J.J. Verbist, J. Delhalle, J.G. Fripiat, R.C. Haddon, and M.L. Kaplan. J. Amer. Chem. Soc. **106**, 312 (1984).
12. R. Gleiter, R. Bartetzko, and D. Cremer. J. Amer. Chem. Soc. **106**, 3437 (1984).
13. M. Amin and C.W. Rees. J. Chem. Soc. Perkin I, 2495 (1989).
14. T. Chivers, M. Gibson, M. Parvez, and I. Vargas-Baca. Inorg. Chem. **39**, 1697 (2000).
15. R.T. Boeré, A.W. Cordes, S.L. Craig, R.T. Oakley, and R.W. Reed. J. Amer. Chem. Soc. **109**, 868, (1987).
16. T. Chivers and W. Hilts. J. Amer. Chem. Soc. **31**, 5272 (1992); T. Chivers, K.S. Dhathathreyan, and T. Ziegler. J. Chem. Soc. Chem. Commun. 87 (1989).
17. C.M. Aherne, A.J. Banister, I.B. Gorrell, M.I. Hansford, Z.V. Hauptman, A.W. Luke, and J.M. Rawson. J. Chem. Soc. Dalton Trans. 967 (1993).
18. A.D. Bond, D.A. Haynes, C.M. Pask, and J.M. Rawson. J. Chem. Soc. Dalton Trans., **8**, 2522 (2002).
19. Z. Otwinski and W. Minor. *In* Methods in enzymology. Part A: Macromolecular chemistry. Vol. 276, *Edited by* C.W. Carter and R.M. Sweet. Academic Press, London.
20. S.C. Nyburg and C.H. Faerman. Acta Crystallogr. Sect. B, **41**, 274 (1985).
21. Quantum Cache, version 5.0, on-line manual, Fujitsu Co. 2001.
22. J.A.R.P. Sarma, F.H. Allen, V.J. Hoy, J.A.K. Howard, R. Thaimattam, K. Biradha, and G. Desiraju. J. Chem. Soc. Chem. Commun. 101 (1997); N. Masciocchi, M. Bergamo, and A. Sironi. J. Chem. Soc. Chem. Commun. 1347 (1998).

© 2002 NRC Canada

Structural interrelationships between the bis(pentamethylcyclopentadienyl)arsenic(III) and antimony(III) cations and their precursor chlorides

Robert J. Wiacek, Jamie N. Jones, Charles L.B. Macdonald, and Alan H. Cowley

Abstract: The chloropnictines $(\eta\text{-}C_5Me_5)_2AsCl$ (**1**), $(\eta\text{-}C_5Me_5)_2SbCl$ (**2**), and $(\eta\text{-}C_5Me_5)_2BiCl$ (**3**) have been prepared by treatment of the appropriate element trichloride with LiC_5Me_5. X-ray crystallographic assays establish that in the case of **1**, both C_5Me_5 rings are attached to As in an $\eta^1(\sigma)$ fashion. In **2** and **3**, the C_5Me_5 rings are π delocalized and feature tri- and pentahapto ring binding, respectively, to the group 15 element. Conversion of **1** and **2** to the salts $[As(\eta\text{-}C_5Me_5)_2][AlCl_4]$ (**4**) and $[Sb(\eta\text{-}C_5Me_5)_2][AlCl_4]$ (**5**) was effected by reaction with the stoichiometric quantity of Al_2Cl_6. The X-ray crystal structure of **4** is surprisingly complex and features four independent ion pairs in the asymmetric unit with a variety of hapticities for the π-bonded C_5Me_5 rings. The structure of the stibocenium cation of **5** involves bis(η^4) attachment of the π-bonded C_5Me_5 rings.

Key words: main group metallocenes, arsocenium cations, stibocenium cations, group 15 pentamethylcyclopentadienyl chlorides.

Résumé : On a préparé les chloropnictines $(\eta\text{-}C_5Me_5)_2AsCl$ (**1**), $(\eta\text{-}C_5Me_5)_2SbCl$ (**2**) et $(\eta\text{-}C_5Me_5)_2BiCl$ (**3**) par traitement d'un trichlorure de l'élément approprié avec du LiC_5Me_5. Des essais à l'aide de la diffraction des rayons X ont permis d'établir que, dans le cas du composé **1**, les deux noyaux C_5Me_5 sont attachés au As d'une façon $\eta^1(\sigma)$. Dans les composés **2** et **3**, les noyaux C_5Me_5 comportent une délocalisation π et des liaisons de cycles tri- et pentahapto respectivement à l'élément du groupe 15. La conversion des composés **1** et **2** en sels $[As(\eta\text{-}C_5Me_5)_2][AlCl_4]$ (**4**) et $[Sb(\eta\text{-}C_5Me_5)_2][AlCl_4]$ (**5**) a été réalisée par réaction avec une quantité stoechiométrique de Al_2Cl_6. De façon surprenant, la structure obtenue par diffraction des rayons X par le composé **4** est complexe et implique quatre paires d'ions indépendantes dans une maille asymétrique d'hapticités variables pour les noyaux C_5Me_5 à liaisons π. La structure du cation stibocénium du composé **5** comporte une fixation bis(η^4) des noyaux C_5Me_5 à liaisons π.

Mots clés : métallocènes du groupe principal; cations arsocénium; cations stibocénium; chlorures de pentaméthylcyclopentadiényles du groupe 15.

[Traduit par la Rédaction]

Introduction

Our interest in group 15 metallocenium cations was prompted originally by collaborative structural work on the isoelectronic neutral metallocenes $Sn(\eta^5\text{-}C_5H_5)_2$ and $Pb(\eta^5\text{-}C_5Me_5)_2$ (1). In 1981, we presented spectroscopic evidence (2) for the formation of $[As(\eta^5\text{-}C_5H_5)(\eta^5\text{-}C_5Me_5)][AlCl_4]$, and the bis-pentahapto nature of this arsocenium cation was supported by semiempirical MO calculations (2, 3) on the prototypical phosphocenium cation $[P(C_5H_5)_2]^+$. Two years later, Jutzi et al. (4) isolated and structurally characterized the $[BF_4]^-$ salt of $[As(C_5Me_5)_2]^+$ and showed that the C_5Me_5 ligands are attached in an η^2 and η^3 fashion. Interestingly, nonempirical MO calculations on $[P(C_5H_5)_2]^+$ revealed that of four relatively stable structures, the one of lowest energy features η^1 and η^2 attachment of the two C_5H_5 rings (5). Thus far, no example of a structurally characterized phosphocenium ion has been reported. However, X-ray crystal structures have become available for the heavier congeneric stibocenium and bismocenium salts $[Sb(C_5Me_5)_2][AlI_4]$ (6), $[Sb(C_5H_2(t\text{-}Bu)_3)_2][AlCl_4]$ (6), and $[Bi(C_5H_2(t\text{-}Bu)_3)_2][AlCl_4]$ (7).

In view of the closeness in energy of several structures for the model phosphocenium cation noted above, it was anticipated that the geometries and ring hapticities of pnictocenium cations could be sensitive to the nature of the counteranion. Accordingly, we decided to attempt the synthesis and X-ray crystallographic characterization of the series $[M(\eta\text{-}C_5Me_5)_2][AlCl_4]$ (M = As, Sb, Bi). A further objective of the study was to assess the structural changes that take place as each metallocenium cation is generated by

Received 12 February 2002. Published on the NRC Research Press Web site at http://canjchem.nrc.ca on 22 November 2002.

Dedicated to Professor Tristram Chivers in recognition of his pioneering work in main group chemistry.

R.J. Wiacek, J.N. Jones, C.L.B. Macdonald,[1] and A.H. Cowley.[2] Department of Chemistry and Biochemistry, University of Texas at Austin, Austin, TX 78712, U.S.A.

[1]Present address: Department of Chemistry and Biochemistry, 401 Sunset Ave., University of Windsor, Windsor, ON N9B 3P4, Canada.

[2]Corresponding author (e-mail: Cowley@mail.utexas.edu).

 DOI: 10.1139/V02-075 © 2002 NRC Canada

Table 1. Crystallographic data for **1**–**5**.

	1	**2**	**3**	**4**	**5**
Chemical formula	$C_{20}H_{30}AsCl$	$C_{20}H_{30}SbCl$	$C_{20}H_{30}BiCl$	$C_{20}H_{30}AsAlCl_4$	$C_{20}H_{30}SbAlCl_4$
Formula weight	380.81	427.64	514.87	514.14	561.01
Crystal size (mm)	0.2 × 0.2 × 0.2	0.2 × 0.2 × 0.2	0.2 × 0.2 × 0.2	0.2 × 0.2 × 0.2	0.2 × 0.2 × 0.2
Crystal system	Triclinic	Triclinic	Triclinic	Triclinic	Orthorhombic
Space group	*P*-1	*P*-1	*P*-1	*P*-1	*Pcmn*
T (°C)	–120	–120	–120	–120	–120
λ (Å)	0.71069	0.71073	0.71073	0.71069	0.71069
a (Å)	7.427(5)	8.5857(17)	8.6040(2)	17.0338(4)	8.655(5)
b (Å)	8.714(5)	10.029(2)	10.0137(3)	17.0960(3)	16.095(5)
c (Å)	16.987(5)	13.412(3)	13.4551(4)	18.8251(4)	17.826(5)
α (°)	78.448(5)	74.92(3)	74.2930(10)	66.5597(9)	90.000(5)
β (°)	87.456(5)	71.33(3)	71.7530(10)	82.9387(9)	90.000(5)
γ (°)	66.041(5)	64.66(3)	65.1040(10)	86.5066(9)	90.000(5)
V (Å^3)	983.5(9)	978.5(3)	985.59(5)	4991.06(18)	2483.2(18)
Z	2	2	2	8	8
D_{calcd} (g cm^{-3})	1.286	1.451	1.854	1.368	1.501
F(000)	400	436	534	2112	1128
μ (cm^{-1})	18.60	15.42	92.14	18.29	15.80
$2\theta_{max}$ (°)	30.51	30.51	27.48	26.37	27.48
GoF	1.047	1.044	1.071	1.017	1.070
R_1	0.0569	0.0518	0.0830	0.0761	0.0327
wR_2	0.0830	0.0975	0.2094	0.1328	0.0709

Note: $R_1 = (|F_o - F_c|/\sum|F_o|[I > 3\sigma(I)]$; $wR_2 = [\sum w(F_o^2 - F_c^2)^2/\sum wF_o^4]^{0.5}$ (all data).

chloride anion abstraction from the respective chloropnictine.

Experimental

General procedures

All solvents (diethyl ether, THF, pentane) were distilled over sodium benzophenone ketyl or CaH_2 (dichloromethane) and degassed prior to usage. Solid reactants were handled in a VAC Vacuum Atmospheres or M-Braun argon-filled drybox. All reactions were performed under a dry, oxygen-free argon atmosphere or under vacuum using standard Schlenk or drybox techniques. All glassware was oven-dried before usage.

The group 15 trichlorides and pentamethylcyclopentadiene were purchased from a commercial source and used without further purification. CD_2Cl_2 was obtained in sealed vials from a commercial source and used without further purification and $Li(C_5Me_5)$ was prepared via the reaction of C_5Me_5H with *n*-BuLi in THF solution.

Physical measurements

High-resolution mass spectra were measured on a VG Analytical ZAB-VE sector instrument. Solution-phase NMR spectra were recorded at 295 K on a GE QE-300 instrument (^{1}H, 300 MHz; ^{13}C, 75 MHz; ^{27}Al, 78.21 MHz) or a Varian Inovo-500 spectrometer (^{1}H, 500 MHz; ^{13}C, 125 MHz; ^{27}Al, 130 MHz). All NMR samples were flame-sealed or run immediately following removal from the drybox. ^{1}H and ^{13}C NMR spectra are reported relative to tetramethylsilane (0.00 ppm) and are referenced to solvent. ^{27}Al chemical shifts are reported relative to $[Al(D_2O)_6]^{3+}$ (0.00 ppm). All ^{13}C spectra were obtained under conditions of broadband proton decoupling. Melting points were obtained in sealed capillaries under argon (1 atm (101.325 kPa)) on a Fisher-Johns apparatus and are uncorrected.

X-ray crystallography

Suitable single crystals were covered with a perfluorinated polyether oil and the X-ray data were collected on a Nonius Kappa CCD diffractometer at 153 K. All structures were solved by direct methods and refined by full-matrix least squares on F^2 using the Siemens SHELX PLUS 5.0 (PC) software package (8). All nonhydrogen atoms were corrected for anisotropic thermal motion, and hydrogen atoms, which were included at calculated positions (C—H 0.96 Å), were refined using a riding model and a general isotropic thermal parameter. A correction was applied for Lorentz polarization for each structure. The total number of reflections, collection ranges, and final *R* values are listed in Table 1.[3]

Preparation of $(\eta\text{-}C_5Me_5)_2AsCl$ (1)

$Li(C_5Me_5)$ (0.814 g, 5.726 mmol) was added neat to a solution of $AsCl_3$ (0.532 g, 2.935 mmol) in THF (50 mL) at 0°C. The reaction mixture, which became yellow–orange immediately, was stirred overnight with gradual warming to

[3] Supplementary data may be purchased from the Depository of Unpublished Data, Document Delivery, CISTI, National Research Council Canada, Ottawa, ON K1A 0S2, Canada (http://www.nrc.ca/cisti/irm/unpub_e.shtml for information on ordering electronically). CCDC 182877–182881 contain the supplementary data for this paper. These data can be obtained, free of charge, via www.ccdc.cam.ac.uk/conts/retrieving.html (or from the Cambridge Crystallographic Data Centre, 12 Union Road, Cambridge, U.K.; fax +44 1223 336033; or deposit@ccdc.cam.ac.uk).

© 2002 NRC Canada

Fig. 1. Molecular structure of $(\eta\text{-}C_5Me_5)_2AsCl$ (**1**) showing the atom numbering scheme.

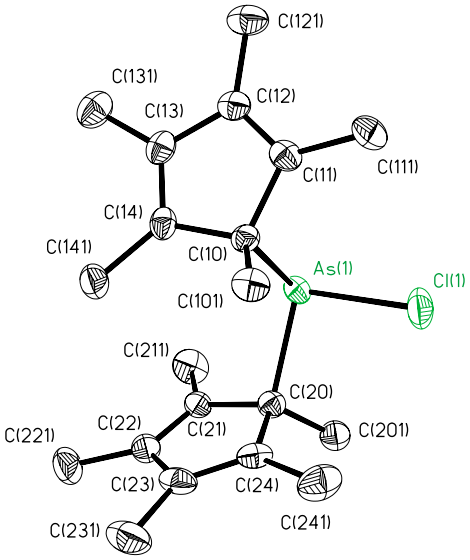

room temperature. After removing the solvent in vacuo, the product was extracted with pentane (100 mL), filtered through Celite®, and the filtrate concentrated to a volume of 20 mL. The resulting yellow solution was cooled to –20°C to afford a crop of yellow crystals, 0.913 g, 83.3% yield; mp 62–65°C. HR-MS (Cl^+, CH_4): calcd. for $C_{20}H_{29}AsCl$ $(M\text{-}H)^+$, 379.1173; found, 379.1167. ^1H NMR (CD_2Cl_2) δ: 1.69 (s, 30 H, C_5Me_5). ^{13}C NMR (CD_2Cl_2) δ: 124.48 (s, C_5Me_5), 13.02 (s, $C_5\mathit{Me}_5$).

Preparation of $(\eta\text{-}C_5Me_5)_2SbCl$ (2)

$Li(C_5Me_5)$ (1.071 g, 7.533 mmol) was added neat to a solution of $SbCl_3$ (0.862 g, 3.779 mmol) in THF (50 mL) at 0°C. The reaction mixture, which became red–orange immediately, was stirred overnight, with gradual warming to room temperature. After removing the solvent in vacuo, the product was extracted with pentane (100 mL), filtered through Celite®, and the filtrate concentrated to a volume of 20 mL. The resulting dark red solution was cooled to –20°C to afford a crop of purple crystals, 1.413 g, 87.4% yield; mp 100–103°C. HR-MS (Cl^+, CH_4): calcd. for $C_{20}H_{29}SbCl$ $(M\text{-}H)^+$, 425.0996; found, 425.1030. ^1H NMR (CD_2Cl_2) δ: 2.04 (s, 30 H, C_5Me_5). ^{13}C NMR (CD_2Cl_2) δ: 124.04 (s, C_5Me_5), 11.15 (s, $C_5\mathit{Me}_5$).

Preparation of $(\eta\text{-}C_5Me_5)_2BiCl$ (3)

$Li(C_5Me_5)$ (0.570 g, 4.009 mmol) was added neat to a solution of $BiCl_3$ (0.6430 g, 2.039 mmol) in Et_2O (50 mL) at –76°C. The reaction mixture, which became purple immediately, was stirred for 4 h. After the addition of pentane (50 mL), the mixture was filtered through Celite® and the filtrate concentrated to a volume of 20 mL. The resulting purple solution was cooled to –20°C to afford a crop of purple crystals, 0.205 g, 19.5% yield; mp 55–60°C. HR-MS (Cl^+, CH_4): calcd. for $C_{20}H_{29}BiCl$ $(M\text{-}H)^+$, 514.1840; found, 514.1819. ^1H NMR (CD_2Cl_2) δ: 2.58 (s, 30 H, C_5Me_5). ^{13}C NMR (CD_2Cl_2) δ: 123.35 (s, C_5Me_5), 10.03 (s, $C_5\mathit{Me}_5$).

Table 2. Selected bond distances and angles for $(\eta\text{-}C_5Me_5)_2AsCl$ (**1**).

Bond distance (Å)			
As(1)—Cl(1)	2.2395(13)	C(13)—C(14)	1.354(4)
As(1)—C(10)	2.038(3)	C(14)—C(10)	1.508(4)
As(1)—C(20)	2.045(3)	C(20)—C(21)	1.509(4)
C(10)—C(11)	1.508(4)	C(21)—C(22)	1.344(4)
C(11)—C(12)	1.355(4)	C(22)—C(23)	1.465(5)
C(12)—C(13)	1.454(4)	C(23)—C(24)	1.349(5)
		C(24)—C(20)	1.506(4)
Bond angle (°)			
C(10)-As(1)-Cl(1)	98.62(9)	As(1)-C(10)-C(101)	117.3(2)
C(20)-As(1)-Cl(1)	95.51(9)	As(1)-C(20)-C(201)	105.9(2)
C(10)-As(1)-C(20)	112.16(12)		

Preparation of $[As(\eta\text{-}C_5Me_5)_2][AlCl_4]$ (4)

A suspension of Al_2Cl_6 (0.104 g, 0.390 mmol) in CH_2Cl_2 (20 mL) was added to a stirred solution of $(\eta\text{-}C_5Me_5)_2AsCl$ (0.257 g, 0.675 mmol) in CH_2Cl_2 (20 mL) at room temperature. After stirring overnight, the resulting brown solution was filtered through Celite® and layered with an equal volume of pentane to afford red–brown crystals, 0.207 g, 51.7% yield; 156–160°C. HR-MS (Cl^+, CH_4): calcd. for $C_{20}H_{30}As$, 345.1563; found, 345.1565. ^1H NMR (CD_2Cl_2) δ: 2.13 (s, 30 H, C_5Me_5). ^{13}C NMR (CD_2Cl_2) δ: 130.80 (s, C_5Me_5), 10.62 (s, $C_5\mathit{Me}_5$). ^{27}Al NMR (CD_2Cl_2) δ: 116.3 (s, $[AlCl_4]^-$).

Preparation of $[Sb(\eta\text{-}C_5Me_5)_2][AlCl_4]$ (5)

A suspension of Al_2Cl_6 (0.264 g, 0.990 mmol) in CH_2Cl_2 (20 mL) was added to a stirred solution of $(\eta\text{-}C_5Me_5)_2SbCl$ (0.812 g, 2.777 mmol) in CH_2Cl_2 (20 mL) at room temperature. After stirring overnight, the resulting red solution was filtered through Celite® and layered with an equal volume of pentane to afford orange–red crystals, 0.704 g, 45.2% yield; 182–184°C. HR-MS (Cl^+, CH_4): calcd. for $C_{20}H_{30}Sb$, 391.1386; found, 391.1402. ^1H NMR (CD_2Cl_2) δ: 2.20 (s, 30 H, C_5Me_5). ^{13}C NMR (CD_2Cl_2) δ: 127.86 (s, C_5Me_5), 10.53 (s, $C_5\mathit{Me}_5$). ^{27}Al NMR (CD_2Cl_2) δ: 99.7 (s, $[AlCl_4]^-$).

Results and discussion

Of the chloropnictines $(\eta\text{-}C_5Me_5)_2ECl$ (E = P, As, Sb, Bi), only the phosphorus compound has been reported previously (9). We have prepared the heavier analogues by the salt elimination reactions of the element trichlorides with two equivalents of LiC_5Me_5:

$$[1] \qquad ECl_3 + 2LiC_5Me_5 \xrightarrow[-2LiCl]{} (\eta\text{-}C_5Me_5)_2ECl$$

(E = As (**1**), Sb (**2**), Bi (**3**))

The yields of **1** and **2** were excellent (~85%); however, that of **3** was considerably less (~20%) due to light sensitivity and facile thermal decomposition at ambient temperature. Satisfactory HRMS data were obtained for **1**–**3**; however, the ^1H and $^{13}C\{^1H\}$ NMR data were not particularly informative, showing complete equivalence of the methyl groups and ring carbon atoms. Given the strong probability of fluxional C_5Me_5 behavior in solution (10), X-ray crystal structure determinations for **1**–**3** became desirable. Each compound crystallizes in the triclinic space group *P*-1, and there are no unusually short intermolecular contacts.

© 2002 NRC Canada

Fig. 2. Molecular structure of $(\eta\text{-}C_5Me_5)_2SbCl$ (**2**) showing the atom numbering scheme.

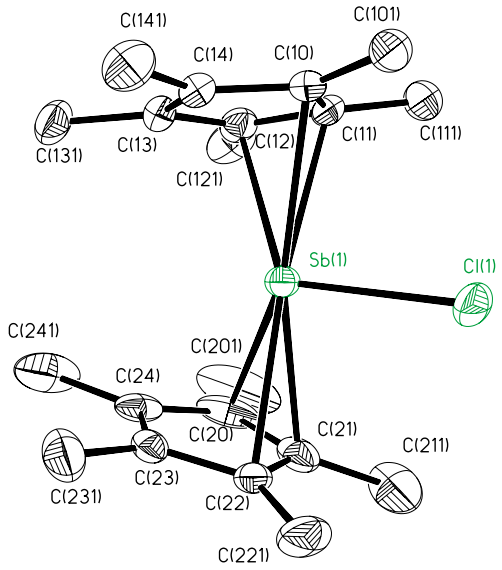

Fig. 3. Molecular structure of $(\eta\text{-}C_5Me_5)_2BiCl$ (**3**) showing the atom numbering scheme.

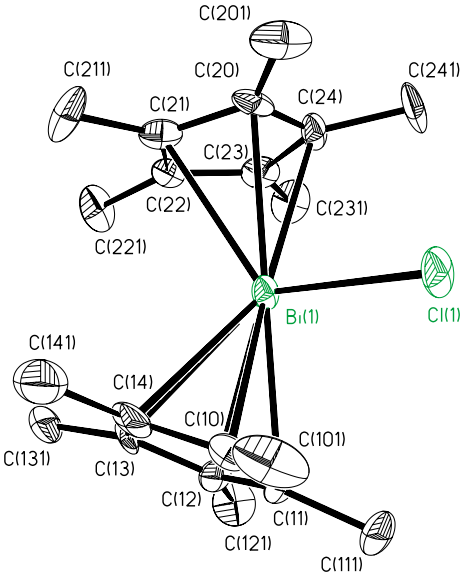

Table 3. Selected bond distances and angles for $(\eta\text{-}C_5Me_5)_2SbCl$ (**2**).

Bond distance (Å)			
Sb(1)—Cl(1)	2.5733(15)	C(12)—C(13)	1.409(6)
Sb(1)—C(10)	2.630(4)	C(13)—C(14)	1.427(7)
Sb(1)—C(11)	2.507(4)	C(14)—C(10)	1.418(6)
Sb(1)—C(12)	2.671(4)	C(20)—C(21)	1.419(8)
Sb(1)—C(20)	2.633(5)	C(21)—C(22)	1.408(7)
Sb(1)—C(21)	2.527(4)	C(22)—C(23)	1.411(6)
Sb(1)—C(22)	2.625(4)	C(23)—C(24)	1.394(7)
C(10)—C(11)	1.428(7)	C(24)—C(20)	1.419(8)
C(11)—C(12)	1.429(7)		
Bond angle (°)			
C(10)-Sb(1)-Cl(1)	84.87(11)	C(20)-Sb(1)-Cl(1)	113.43(15)
C(11)-Sb(1)-Cl(1)	87.64(12)	C(21)-Sb(1)-Cl(1)	85.06(14)
C(12)-Sb(1)-Cl(1)	118.24(11)	C(22)-Sb(1)-Cl(1)	85.57(11)

Table 4. Selected bond distances and angles for $(\eta\text{-}C_5Me_5)_2BiCl$ (**3**).

Bond distance (Å)			
Bi(1)—Cl(1)	2.707(3)	C(10)—C(11)	1.434(19)
Bi(1)—C(10)	2.625(12)	C(11)—C(12)	1.426(16)
Bi(1)—C(11)	2.709(12)	C(12)—C(13)	1.430(19)
Bi(1)—C(12)	2.798(12)	C(13)—C(14)	1.43(2)
Bi(1)—C(13)	2.831(12)	C(14)—C(10)	1.42(2)
Bi(1)—C(14)	2.704(12)	C(20)—C(21)	1.43(2)
Bi(1)—C(20)	2.638(12)	C(21)—C(22)	1.398(17)
Bi(1)—C(21)	2.719(13)	C(22)—C(23)	1.44(2)
Bi(1)—C(22)	2.880(13)	C(23)—C(24)	1.423(18)
Bi(1)—C(23)	2.838(12)	C(24)—C(20)	1.43(2)
Bi(1)—C(24)	2.677(12)		
Bond angle (°)			
C(10)-Bi(1)-Cl(1)	85.4(3)	C(20)-Bi(1)-Cl(1)	87.9(3)
C(11)-Bi(1)-Cl(1)	87.8(3)	C(23)-Bi(1)-Cl(1)	112.0(3)
C(12)-Bi(1)-Cl(1)	116.3(3)	C(24)-Bi(1)-Cl(1)	85.3(3)

Molecules of chloroarsine **1** possess a ring-canted structure of C_1 symmetry (Fig. 1). Moreover, the noneclipsed arrangement of the C_5Me_5 rings is strikingly different from the essentially eclipsed ring-parallel conformation of the analogous chlorophosphine $(\eta\text{-}C_5Me_5)_2PCl$ (**9**). However, like the latter compound, the C_5Me_5 rings of **1** are attached to the pyramidal group 15 center in an η^1 fashion and the double bonding within these rings is localized (Table 2). The fact that the sum of bond angles at arsenic for **1** (306.3(1)°) is less than that for the phosphorus analogue (314.8(1)°) (**9**) is consistent with periodic trends.

The chlorostibine **2** adopts a "bent-sandwich" structure (Fig. 2) and the C—C bond distances within the essentially planar rings, which range from 1.394(7) to 1.429(7) Å, are indicative of delocalized bonding (Table 3). The fact that for each ring, three Sb—C distances are ~0.2 Å longer (average 2.599(5) Å) than the other two (average 2.814(5) Å) implies that both of the C_5Me_5 rings are attached to antimony in an η^3 fashion. The ring centroid – Sb – ring centroid angle is 140.7(9)° and the interring angle is 28.5°.

Akin to **2**, chlorobismuthine **3** adopts a bent-sandwich arrangement of virtually planar, π-delocalized C_5Me_5 groups with an average intraring C—C bond distance of 1.43(2) Å (Fig. 3). The trend toward multihapto bonding is even more marked in the case of **3**, presumably due to the increased metallic character and more spatially extensive valence orbitals of this heavy group 15 element. Although the Bi—C distances range from 2.625(12) to 2.880(13) Å in both rings (Table 4), the C_5Me_5 rings are best regarded as η^5 bonded. The interring and ring centroid – Bi – ring centroid angles are 29.2 and 141.9(2)°, respectively.

The arsenocenium (**4**) and stibocenium (**5**) tetrachloroaluminates were prepared in moderate yields (~50%) by chloride anion abstraction from the precursor chlorides **1** and **2**, respectively:

[2] $(\eta\text{-}C_5Me_5)_2ECl + 1/2Al_2Cl_6 \rightarrow [E(\eta\text{-}C_5Me_5)_2][AlCl_4]$ (E = As (**4**), Sb (**5**))

© 2002 NRC Canada

Table 5. Selected bond distances and angles for the four independent cations of $[As(\eta\text{-}C_5Me_5)_2][AlCl_4]$ (**4**).

Cation 1		Cation 2		Cation 3		Cation 4	
Bond distance (Å)							
As(1)—C(10)	2.451(8)	As(2)—C(20)	2.441(8)	As(3)—C(31)	2.230(8)	As(4)—C(40)	2.466(8)
As(1)—C(11)	2.268(8)	As(2)—C(21)	2.312(7)	As(3)—C(32)	2.360(8)	As(4)—C(41)	2.268(8)
As(1)—C(12)	2.333(8)	As(2)—C(22)	2.367(8)	As(3)—C(35)	2.397(8)	As(4)—C(42)	2.357(8)
As(1)—C(15)	2.413(8)	As(2)—C(25)	2.426(8)	As(3)—C(36)	2.267(8)	As(4)—C(45)	2.418(8)
As(1)—C(16)	2.281(8)	As(2)—C(26)	2.293(8)	As(3)—C(37)	2.278(8)	As(4)—C(46)	2.305(8)
As(1)—C(17)	2.334(8)	As(2)—C(27)	2.316(8)			As(4)—C(47)	2.313(8)
						As(4)—C(48)	2.467(8)
Bond angle (°)							
C(11)-As(1)-C(16)	113.3(3)	C(21)-As(2)-C(26)	118.0(3)	C(31)-As(3)-C(36)	113.4(3)	C(41)-As(4)-C(46)	116.8(3)
C(15)-As(1)-C(17)	118.7(3)	C(25)-As(2)-C(27)	122.5(3)	C(35)-As(3)-C(37)	118.7(3)	C(45)-As(4)-C(47)	120.1(3)
Ring centroid – As – ring centroid and interring angle (°)							
173.9(9), 24.2		173.6(13), 19.5		175.8(5), 28.3		175.5(9), 20.3	

Fig. 4. Molecular structure of $[As(\eta\text{-}C_5Me_5)_2][AlCl_4]$ (**4**) showing the four independent cations and anions.

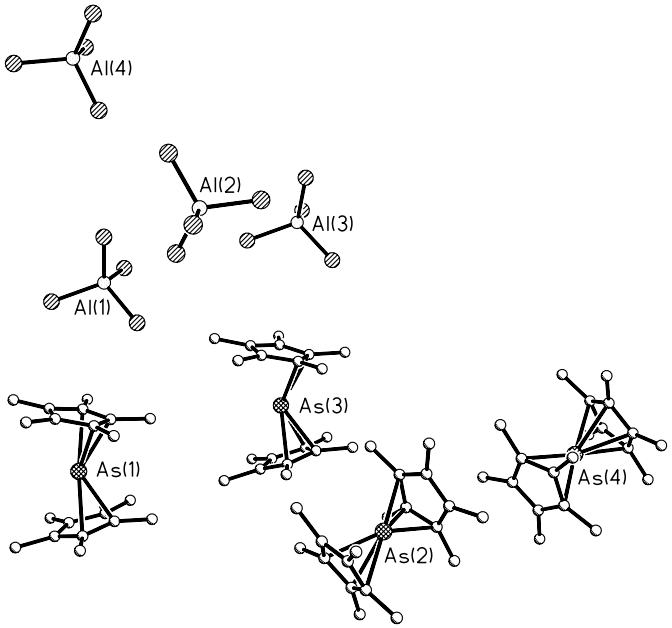

In the case of the corresponding reaction of $(\eta\text{-}C_5Me_5)_2BiCl$ (**3**) with Al_2Cl_6, the resulting bismuthocenium tetrachloraluminate was too unstable to isolate. The fact that a hexakis (*tert*-butyl)bismocenium tetrachloroaluminate salt has been isolated (7) (and structurally authenticated) is consistent with the relative sizes and kinetic stabilization capabilities of the C_5Me_5 and 1,2,4-*t*-$Bu_3C_6H_2$ ligands. For both **4** and **5**, the presence of the tetrachloroaluminate anion in solution was evidenced by a characteristically sharp ^{27}Al resonance in the approximate range δ: 100–120 (11). However, as with the precursor chlorides, ^1H and $^{13}C\{^1H\}$ NMR data were not particularly informative because of the possibility of rapid structural interconversions. More definitive information regarding the solid-state structures of **4** and **5** was forthcoming from X-ray crystallography. The solid state of **4** is unexpectedly complex in that the asymmetric unit contains four different cations that are distinguished primarily on the basis of ring hapticity. As shown in Fig. 4, cations 1

Fig. 5. Molecular structure of arsocenium cation number 1 of $[As(\eta\text{-}C_5Me_5)_2][AlCl_4]$ (**4**).

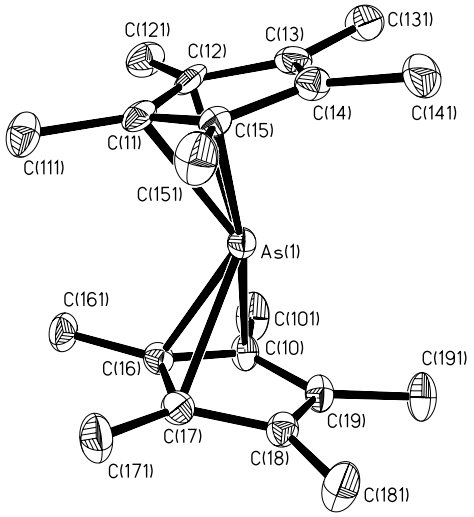

Fig. 6. Molecular structure of $[Sb(\eta\text{-}C_5Me_5)_2][AlCl_4]$ (**5**) showing the atom numbering scheme.

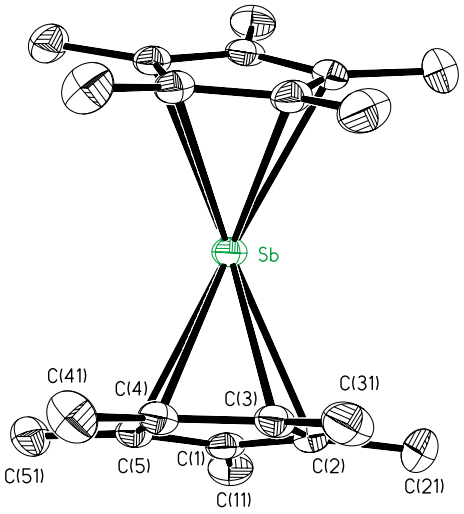

© 2002 NRC Canada

Table 6. Selected bond distances and angles for [Sb(η-$C_5Me_5)_2$][$AlCl_4$] (**5**).

Bond distance (Å)			
Sb—C(2)	2.613(2)	C(4)—C(5)	1.428(4)
Sb—C(3)	2.484(2)	C(5)—C(1)	1.416(4)
Sb—C(4)	2.510(3)	Al—Cl(1)	2.1265(11)
Sb—C(5)	2.653(2)	Al—Cl(2)	2.1430(18)
C(1)—C(2)	1.421(4)	Al—Cl(3)	2.1405(17)
C(2)—C(3)	1.436(4)		
C(3)—C(4)	1.431(4)		
Bond angle (°)			
C(3)-Sb-C(3′)	1.506(12)	Cl-Al-Cl(2)	1.944(2)
C(4)-Sb-C(4′)	106.95(13)	Cl(1)-Al-Cl(3)	109.49(5)
C(5)-Sb-C(5′)	129.96(11)	Cl(2)-Al-Cl(3)	107.73(6)

and 2 both feature η^3/η^3 attachment of the C_5Me_5 rings, while for cations 3 and 4, the hapticities are η^2/η^3 and η^3/η^4, respectively. For each molecule, the C_5Me_5 ligands are planar within experimental error and arranged in a staggered fashion (Fig. 5). A summary of pertinent metrical parameters for the four cations appears in Table 5. These results contrast interestingly with those reported for [As(η-$C_5Me_5)_2$][BF_4], the cation of which exhibits η^2 and η^3 binding of the C_5Me_5 moieties to arsenic (4). Clearly, the change of counteranion has a marked influence on the crystal structure of the resulting salt. Moreover, the present findings are consistent with MO calculations (5) on the model cation $[P(C_5H_5)_2]^+$, which revealed that four selected structures with different phosphorus-ring bonding modes lie within an energy range (25 kcal·mol^{-1}) that is commensurate with the sensitivity of such systems to crystal packing forces.

The stibocenium cation of **5** adopts a bent-sandwich structure of C_{2v} symmetry (Fig. 6). The eclipsed C_5Me_5 rings are planar within experimental error and the interring angle is 32.8° (Table 6). Since the Sb···C(1) distance (2.728(3) Å) is larger than the other four, which range from 2.484(2) to 2.653(2) Å and average 2.565(3) Å, the hapticity is considered to be bis-η^4 and the ring centroid – Sb – ring centroid angle is 161.1(2)°. Not unexpectedly, the structure of **5** is similar to that of [Sb(η-$C_5Me_5)_2$][AlI_4] (6). Here, however, the hapticity appears to be bis-η^3 and there is an interaction between antimony and one of the iodide ligands of the counteranion. Finally, the bulky nature of the 1,2,4-*t*-$Bu_3C_5H_2$ substituent is evidenced by the fact that these rings are essentially parallel in [Sb(1,2,4-*t*-$Bu_3C_5H_2)_2$][$AlCl_4$] (6).

Acknowledgments

The authors are grateful to the Robert A. Welch Foundation and the National Science Foundation for financial support.

References

1. J.L. Atwood, W.E. Hunter, A.H. Cowley, R.A. Jones, and C.A. Stewart. J. Chem. Soc. Chem. Commun. 925 (1981).
2. S.G. Baxter, A.H. Cowley, and S.K. Mehrotra. J. Am. Chem. Soc. **103**, 5572 (1981).
3. *Also see* S.G. Baxter, A.H. Cowley, J.G. Lasch, M. Lattman, W.P. Sharum, and C.A. Stewart. J. Am. Chem. Soc. **104**, 4064 (1982).
4. P. Jutzi, T. Wipperman, C. Krüger, and H.-J. Kraus. Angew. Chem. Int. Ed. Engl. **22**, 250 (1983).
5. T.J. Lee, H.F. Schaefer, III, and E.A. Magnusson. J. Am. Chem. Soc. **107**, 7239 (1985).
6. H. Sitzmann, Y. Ehleiter, G. Wolmershäuser, A. Ecker, C. Üffing, and H. Schnöckel. J. Organomet. Chem. **527**, 209 (1997).
7. H. Sitzmann and G. Wolmershäuser. Z. Naturforsch. **52b**, 398 (1997).
8. G.M. Sheldrick. SHELX PC [computer program]. Version 5.0. Siemens Analytical X-ray Instruments, Inc. 1994.
9. R. Pietschnig. J. Ebels, M. Nieger, N. Zoche, M. Jansen, and E. Niecke. Bull. Soc. Chim. Fr. **134**, 1039 (1997).
10. P. Jutzi and N. Burford. Chem. Rev. **99**, 969 (1999) and references therein.
11. J.W. Akitt. Annu. Rep. NMR Spectrosc. **5**, 465 (1972).

© 2002 NRC Canada

Synthesis and characterization of the binuclear diamido titanium chalcogenides $[(Ar)NCH_2CH_2CH_2N(Ar)]_2Ti(\mu\text{-}E)_2$ (E = Se, Te)

Tianle Zhang, Warren E. Piers, and Masood Parvez

Abstract: Reaction of McConville's chelating amido titanium complex $[(Ar)NCH_2CH_2CH_2N(Ar)]Ti(CH_3)_2$ (Ar = 2,6-*i*-$Pr_2C_6H_3$) with either elemental Se or the tellurium atom source Te=PBu_3 resulted in the formation of *bis*-μ-chalcogenido dimers $[(Ar)NCH_2CH_2CH_2N(Ar)]_2Ti(\mu\text{-}E)_2$ (E = Se, **2**; Te, **3**) with concommitant loss of EMe_2. The dimers **2** and **3** were characterized spectroscopically and via X-ray crystallography. The two compounds are isostructural in the solid state. The tellurido dimer **3** may also be synthesized by reduction of the diamido dichloride $[(Ar)NCH_2CH_2CH_2N(Ar)]_2TiCl_2$ with Na–Hg amalgam followed by treatment with Te=PBu_3. This dimer is unreactive toward further Te=PBu_3 or stannanes such as $HSnBu_3$. Unlike decamethyltitanocene derivatives, the diamido complex is not an effective catalyst precursor for the heterohydrodecoupling of Te=PBu_3 and $HSnBu_3$.

Key words: diamido titanium complexes, selenides, tellurides.

Résumé : La réaction de McConville qui permet de chélater le complexe amido titane $[(Ar)NCH_2CH_2CH_2N(Ar)]Ti(CH_3)_2$ (Ar = 2,6-*i*-$Pr_2C_6H_3$) avec du sélénium élémentaire ou avec la source de tellure Te=PBu_3 conduit à la formation de dimères *bis*-μ-chalcogénido $[(Ar)NCH_2CH_2CH_2N(Ar)]Ti(\mu\text{-}E)_2$ (E = Se, **2**; Te, **3**), avec la perte concomitante de EMe_2. Les dimères **2** et **3** ont été caractérisés par spectroscopie et par diffraction des rayons X. À l'état solide, les deux composés sont isostructuraux. Le dimère tellurido (**3**) peut aussi être synthétisé par réduction du dichlorure de diamido, $[(Ar)NCH_2CH_2CH_2N(Ar)]TiCl_2$, avec de l'amalgame de sodium (Na–Hg), suivie par un traitement avec du Te=PBu_3. Ce dimère n'est pas réactif vis-à-vis le Te=PBu_3 ou les stannanes tels que $HSnBu_3$. Contrairement à ce qui est observé avec les dérivés du décaméthyltitanocène, le complexe diamido n'est pas un précurseur efficace du catalyseur pour l'hétérohydrodécouplage de Te=PBu_3 et $HSnBu_3$.

Mots clés : complexes amido titane, séléniures, telluriures.

[Traduit par la Rédaction]

Introduction

Decamethyltitanocene complexes have been found to mediate the heterodehydrocoupling of "Te" and $HSnBu_3$ to yield the distannyl telluride $[Bu_3Sn]_2(\mu\text{-}Te)$ (1). The reaction is highly selective for this product, but turnover numbers are relatively low. Mechanistic studies have shown that catalyst precursors in various oxidation states can provide entry into the catalytic cycle. Furthermore, these studies suggest that σ-bond metathesis reactions between Ti-X (X = alkyl or tellurium) and Sn-H moieties, insertion of "Te" into Ti—X bonds, and loss of $Te(SnR_3)_2$ from stannyltellurolates $Ti(TeSnR_3)_n$ are all potential primary reactions in the overall catalytic reaction.

The initial studies were carried out using titanocene(III) derivatives incorporating the bulky and electron donating C_5Me_5 (Cp*) ligand (2). In terms of catalyst modification, only a small range of changes in the nature of the Cp donor were possible, since a significant amount of steric bulk had to be maintained in order for the reaction to turnover (3). Thus, to find a catalyst that would offer improved performance for this reaction, we turned to non-Cp organotitanium complexes as potential catalyst candidates. One such family are the chelating diamido Ti(IV) complexes introduced by McConville and Scollard as living olefin polymerization catalysts (4), whose chemistry in other arenas has been explored only to a limited extent. While catalyst precursors incorporating this ligand do not catalyze the heterodehydrocoupling reaction, new Ti(IV) selenido and tellurido complexes are observed.

Received 8 January 2002. Published on the NRC Research Press Web site at http://canjchem.nrc.ca on 21 November 2002.

Dedicated to Professor Tris Chivers, deeply appreciated friend, colleague, mentor, scholar and gentleman.

T. Zhang, W.E. Piers,[1] and M. Parvez. Department of Chemistry, 2500 University Drive N. W., University of Calgary, Calgary, AB T2N 1N4, Canada.

[1]Corresponding author (e-mail: wpiers@ucalgary.ca).

Results and discussion

McConville's dichloride complex $[(Ar)NCH_2CH_2CH_2N(Ar)]TiCl_2$ (Ar = 2,6-*i*-$Pr_2C_6H_3$) was prepared and converted to the corresponding dimethyl derivative **1** according to the literature procedure (4). Reaction of an excess of elemental selenium led to the slow uptake of the selenium while the reaction mixture changed in colour from yellow to red. On the other hand, reaction with 2 equiv of Te=PBu_3 (which serves as a soluble source of Te atoms (5)) gave a similar colour change

 DOI: 10.1139/V02-052 © 2002 NRC Canada

Fig. 1. ORTEP diagram of **2**. Selected bond distances (Å): Se(1)—Ti(1) 2.4009(19), Se(1)—Ti(1*) 2.488(2), Ti(1)—N(1) 1.896(5), N(1)—C(2) 1.481(8), N(1)—C(3) 1.436(9), C(2)—C(1) 1.519(9). Selected bond angles (°): Ti(1)-Se(1)-Ti(1*) 84.45(7), Se(1)-Ti(1)-Se(1*) 95.55(7), N(1)-Ti(1)-N(1*) 103.0(3), N(1)-Ti(1)-Se(1) 117.25(17), N(1)-Ti(1)-Se(1*) 112.05(17), Ti(1)-N(1)-C(2) 117.8(4), Ti(1)-N(1)-C(3) 131.4(4), C(2)-N(1)-C(3) 110.7(5).

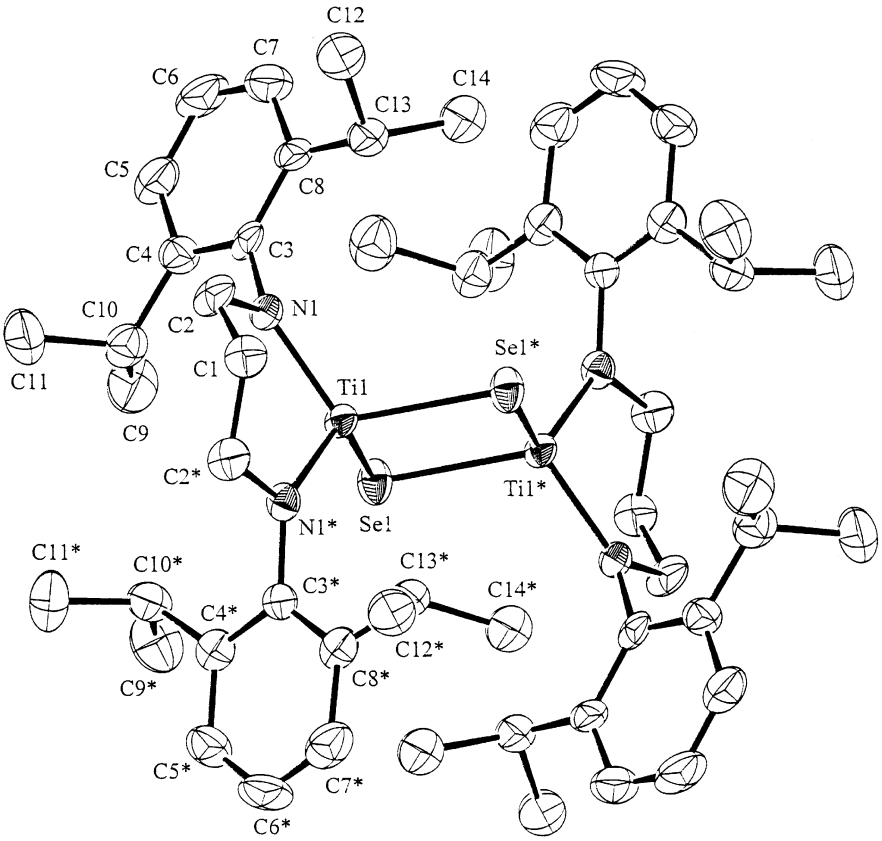

instantaneously (Scheme 1). From these dark red solutions, red precipitates were observed to form over time. Analysis of these solids revealed them to be the dimeric μ-chalcogenides $[(Ar)NCH_2CH_2CH_2N(Ar)]_2Ti(\mu\text{-}E)_2$ (E = Se, **2**; Te, **3**).

Proton NMR spectroscopy showed only amide ligand resonances, and resonances for the bridging chalcogenides could not be found in the ^{77}Se or ^{125}Te NMR spectra. Elemental analysis, however, supported the assignment, as did the results of X-ray diffaction analysis of single crystals of **2** and **3**. Figures 1 and 2 show the molecular structure of selenide **2** and telluride **3**, respectively, along with selected metrical parameters; further details on these structures can be found in the Supplementary Information.[2] The dimers are isostructural, containing two tetrahedral titanium centers edge-joined by the chalcogen atoms. The chelating amido ligands adopt a boat-like conformation, and although the dimers possess an inversion center, the two Ti—E bonds are as a result slightly different in length, making the Ti_2E_2 core slightly distorted from regularity. The equatorial Ti—E bonds (Ti—E(1)) are both shorter than the axial bonds

Scheme 1.

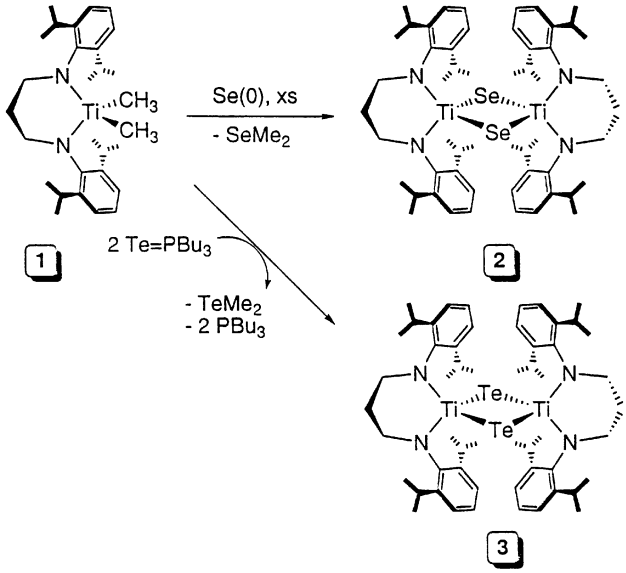

[2] Supplementary data may be purchased from the Depository of Unpublished Data, Document Delivery, CISTI, National Research Council Canada, Ottawa, ON K1A 0S2, Canada (http://www.nrc.ca/cisti/irm/unpub_e.shtml for information on ordering electronically). CCDC 175665 and 175666 contain the supplementary data for this paper. These data can be obtained, free of charge, via www.ccdc.cam.ac.uk/conts/retrieving.html (or from the Cambridge Crystallographic Data Centre, 12 Union Road, Cambridge, U.K.; fax +44 1223 336033; or deposit@ccdc.cam.ac.uk).

© 2002 NRC Canada

Fig. 2. ORTEP diagram of **3**. Selected bond distances (Å): Te(1)—Ti(1) 2.6169(14), Te(1)—Ti(1*) 2.6892(12), Ti(1)—N(1) 1.880(3), N(1)-C(2) 1.480(4), N(1)—C(3) 1.441(5), C(2)—C(1) 1.511(5). Selected bond angles (°): Ti(1)-Te(1)-Ti(1*) 81.82(3), Te(1)-Ti(1)-Te(1*) 98.18(3), N(1)-Ti(1)-N(1*) 102.84(19), N(1)-Ti(1)-Te(1) 117.55(10), N(1)-Ti(1)-Te(1*) 110.37(10), Ti(1)-N(1)-C(2) 118.0(3), Ti(1)-N(1)-C(3) 130.5(2), C(2)-N(1)-C(3) 111.5(3).

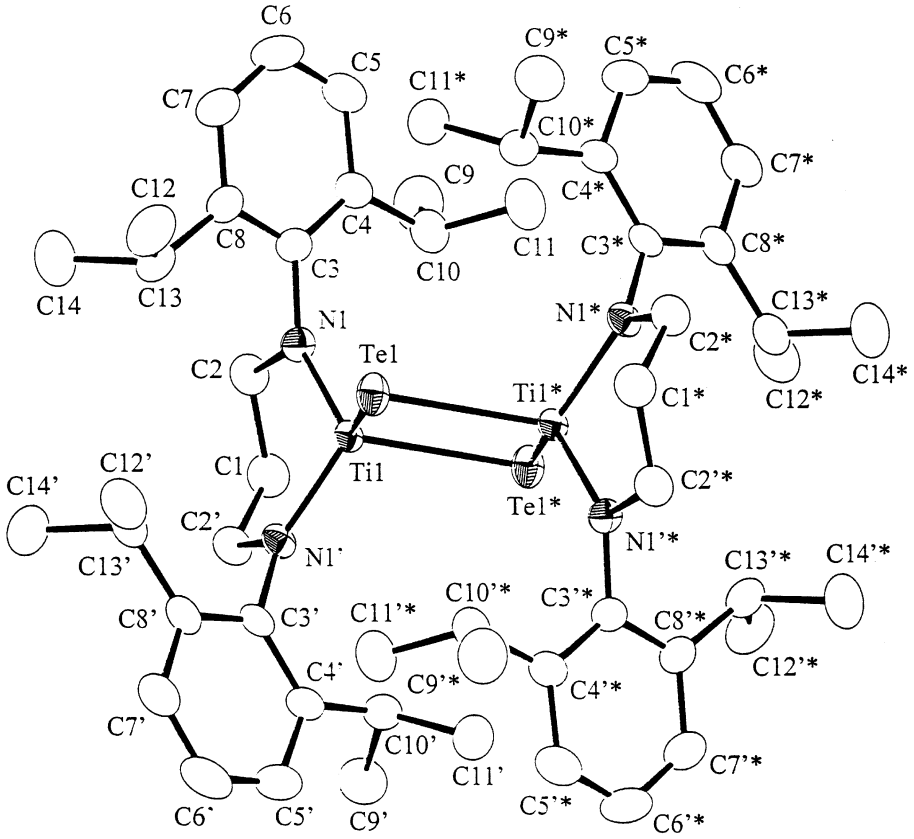

(Ti—E(1*)). The Ti—Se bonds of **2** are about 0.210 Å shorter than the Ti—Te bonds of **3** as expected on the basis of the differing atomic radii of the two chalcogens (6). Aside from other slight differences in the bond angles associated with the Ti_2E_2 cores, the molecules are very similar in structure.[2]

Insertion of chalcogen atoms into the M—C bonds of d° alkyl derivatives is facile (7) and thus a plausible route to these dimers likely begins with insertion of chalcogen into the Ti—C bonds to form methyl chalcogenolates. Previous work from our laboratories (7*a*, 7*b*, 8) and others (9) show that such derivatives are prone to loss of ER_2 to form chalcogenides; in this instance, loss of EMe_2 occurs. Both $SeMe_2$ and $TeMe_2$ were detected by ^1H and ^{77}Se or ^{125}Te NMR spectroscopy by comparison with authentic samples. We have also shown previously that loss of TeR_2 from some scandium *bis*-tellurolates is a bimolecular process (7*a*, *b*), so two distinct pathways to dimers **2** and **3** may be envisioned (Scheme 2). For E = Se, where the insertion reactions are much slower owing to the heterogeneity of the reaction, path "a" may be operative, while for E = Te, insertion is rapid and likely path "b" dominates. However, in situ NMR experiments have not been performed to pursue these issues. In any event, unimolecular loss of EMe_2 from putative *bis*-chalcogenolates $[(Ar)NCH_2CH_2CH_2N(Ar)]Ti(EMe)_2$ to form a terminal chalcogenide that dimerizes is unlikely, given our previous studies and the inherent instability of the Ti=E bonds of the heavier chalcogens (8).

Compound **3** was tested for activity as a catalyst precursor for the heterodehydrocoupling reaction between "Te" and $HSnBu_3$ and was found to be completely inactive. The production of $[Bu_3Sn]_2(\mu\text{-Te})$ occurs slowly in the absence of catalyst; addition of 10% of **3** did not result in noticeable rate acceleration, nor were any spectral changes in **3** observed. Indeed, separate experiments showed that **3** was unreactive toward both $HSnBu_3$ and $Te{=}PBu_3$ at room temperature. This contrasts sharply with the chemistry observed for the decamethyltitanocenes and suggests that the doubly telluride bridged **3** is not susceptable to dissociation and is also kinetically quite stable. A similar lack of reactivity toward further $Te{=}PBu_3$ and other small molecules was observed for the related β-diketiminato supported ditelluride dimer of scandium, $[(Ar)NC(Me)CHC(Me)N(Ar)]_2Sc(\mu\text{-Te})_2$ (Ar = 2,6-*i*-$Pr_2C_6H_3$) (7*b*).

In the titanocene chemistry, lower valent derivatives were also found to be catalyst precursors for the heterodehydrocoupling reaction (1). For example, the Ti(III)–Ti(III) dimer $[Cp^*_2Ti]_2(\mu\text{-Te})$ can be prepared from $Cp^*_2Ti(II)$ precursors and 0.5 equiv of $Te{=}PBu_3$ (10) and is catalytically competent. We thus attempted to prepare a similar diamido Ti(III)–Ti(III) dimer by reducing the diamido dichloride complex with Na–Hg amalgam to a suitable

© 2002 NRC Canada

Table 1. Summary of data collection and structure refinement details for **2** and **3**.

	2	**3**
Empirical formula	$C_{27}H_{37}N_2SeTi{\cdot}C_6H_{14}$	$C_{27}H_{40}N_2TeTi{\cdot}C_6H_{14}$
Formula weight	605.64	654.28
Temperature (K)	170(2)	170(2)
Crystal size (mm^{-1})	0.48×0.45×0.40	0.55×0.45×0.38
λ (Å)	0.71069	0.71069
Crystal system	Monoclinic	Monoclinic
Space group	$C2_1/m$	$C2/m$
a (Å)	19.319(6)	19.234(4)
b (Å)	17.366(5)	17.260(3)
c (Å)	12.482(4)	12.295(4)
β (Å)	129.31(2)	129.18(1)
V ($Å^3$)	3240.1(17)	3164.0(13)
Z	4	4
$D_{calcd.}$ (mg m^{-1})	1.242	1.374
μ (mm^{-1})	1.41	1.20
F(000)	1288	1360
Max/min transmission	0.602/0.551	0.659/0.559
θ range (°)	2.5–25.0	2.5–25.0
Reflections	3067	3005
Unique reflections	2973	2898
No. of variables	169	172
Restraints	0	0
R_1	0.059	0.035
wR_2	0.165	0.091
GoF	1.02	1.12
Residual density (e $Å^{-3}$)	–0.47 and –1.00	–0.79 and –0.96

Scheme 2.

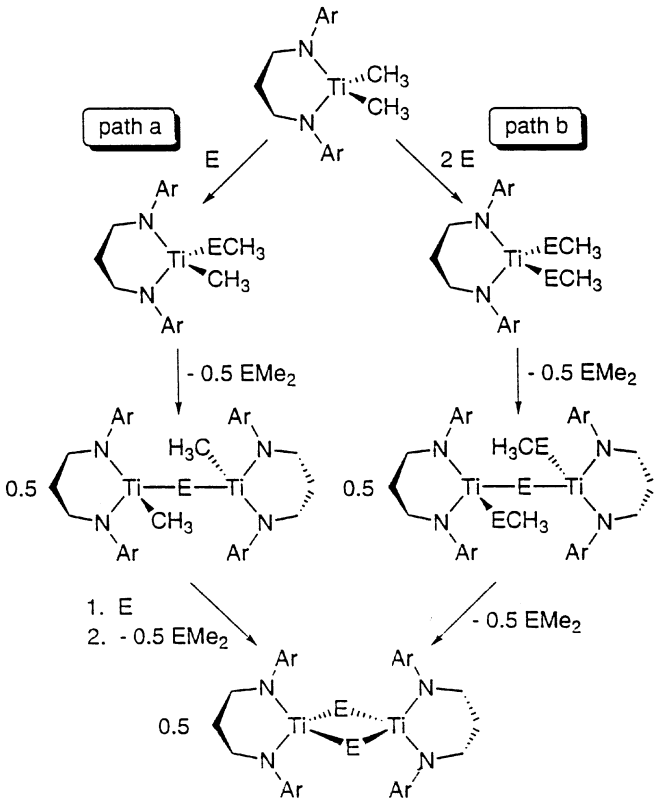

[(Ar)$NCH_2CH_2CH_2N$(Ar)]Ti(II) precursor. Although we could not isolate any of these compounds, in situ reduction of [(Ar)$NCH_2CH_2CH_2N$(Ar)]$TiCl_2$ in the presence of excess PMe_3 led to green-brown solutions that exhibited behavior consistent with reduced titanium amido complexes (11). Treatment of these solutions with varying amounts of $Te{=}PBu_3$ gave reaction mixtures from which we could isolate only Ti(IV)–Ti(IV) dimer **3** in as much as 32% yield (eq. [1]).

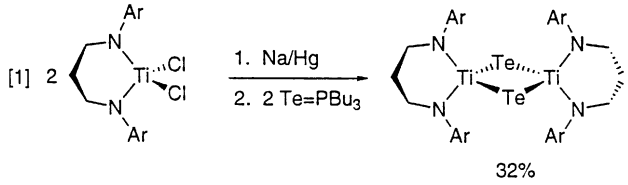

Experimental section

^1H, ^{77}Se, and ^{125}Te NMR experiments were performed on Bruker AC-200 or WH-400 MHz spectrometers and were recorded in C_6D_6, unless otherwise noted. Data are reported in ppm relative to solvent signals for ^1H spectra; for ^{77}Se and ^{125}Te spectra, the data are referenced relative to external EMe_2 (0.0 ppm). Chemicals were purchased from Aldrich-Sigma and used as received or purified according to standard procedures. Solvents were purified using the Grubbs–Dow purification system (12).

© 2002 NRC Canada

Synthesis of $[(Ar)NCH_2CH_2CH_2N(Ar)]_2Ti(\mu\text{-}Se)_2$, 2

Dimethyl complex **1** (0.100 g, 0.212 mmol) and elemental Se powder (0.040 g, 0.506 mmol) were loaded into a 25 mL round-bottomed flask and toluene (10 mL) was added. The mixture was stirred at room temperature for 2–3 days. The solvent was removed in vacuo and the resulting dark red solid taken up in dichloromethane (6 mL) and filtered to remove the excess selenium. The volume of the filtrate was reduced to ≈1 mL and hexanes were layered onto the solution. The resulting red precipitate was collected by filtration, washed with hexanes, and dried. Yield 0.038 g, 34%. ^{1}H NMR (CD_2Cl_2): 7.20 (m, 6H, Ar*H*), 3.65 (br m, 4H, NCH_2), 3.20 (sp, 4H, $CHMe_2$), 2.10 (m, 2H, NCH_2CH_2), 1.10 (d, 24H, $CHMe_2$). Anal. calcd. for $C_{27}H_{40}N_2SeTi$: C 62.42, H 7.72, N 5.39; found: C 62.25, H 7.88, N 4.89.

Synthesis of $[(Ar)NCH_2CH_2CH_2N(Ar)]_2Ti(\mu\text{-}Te)_2$, 3

Dimethyl complex **1** (0.100 g, 0.212 mmol) was dissolved in benzene (5 mL). A solution of $Te{=}PBu_3$ (0.140 g, 0.430 mmol) in benzene (3 mL) was added dropwise to the solution of **1** with stirring. The resulting solution was stirred for 24 h until a precipitate was observed, and concentrated to about 1–2 mL. Hexanes were added to precipitate the product. The product was collected by filtration and dried in vacuo. Yield: 0.068 g, 57%. ^{1}H NMR (CD_2Cl_2): 7.30 (m, 6H, Ar*H*), 3.61 (br m, 4H, NCH_2), 3.30 (sp, 4H, $CHMe_2$), 1.83 (m, 2H, NCH_2CH_2), 1.10 (d, 24H, $CHMe_2$). Anal. calcd. for $C_{27}H_{40}N_2TeTi$: C 57.06, H 7.10, N 4.93; found: C 57.10, H 7.32, N 4.53.

Alternative method

Dichloride $[(Ar)NCH_2CH_2CH_2N(Ar)]TiCl_2$ (0.800 g, 1.564 mmol) was added to a suspension of Na–Hg (0.430 g, 18.7 mmol Na, 40 g Hg) in benzene (30 mL) in the presence of excess PMe_3 (0.51 mL, 5.368 mmol). This mixture was stirred for 2 days and filtered. The resulting green-brown filtrate was transferred to a flask containing $Te{=}PBu_3$ (0.610 g, 1.85 mmol) and stirred for 4 h at which time a precipitate was observed. The solvent was reduced in volume and hexanes were added and the resulting suspension was filtered. Yield: 0.285 g, 32%.

X-ray crystallography

Suitable crystals were coated with Paratone-8277 oil (Exxon) and mounted on a glass fiber. All measurements were made on a Rigaku AFC6S diffractometer with Mo Kα radiation monochromatized with a Zr-filter. The data were collected at a temperature of 170(2) using the ω–2θ scan technique to a maximum 2θ value of 50.0; crystal data have been provided in Table 1. For **2**, of the 3067 reflections that were collected, 2973 were unique (R_{int} = 0.050), while for **3**, of the 3005 reflections that were collected, 2898 were unique (R_{int} = 0.021). The intensities of three representative reflections were measured after every 200 reflections. Over the course of data collection, the standards did not decrease. An empirical absorption correction (13) based on azimuthal scans of several reflections was applied, which resulted in transmission factors ranging from 0.551 to 0.602 for **2** and 0.559 to 0.659 for **3**. The data were corrected for Lorentz and polarization effects. The structures were solved by direct methods (14) and expanded using Fourier techniques (15). The non-hydrogen atoms of the complex were refined anisotropically. The structures of both **2** and **3** contain two partially occupied molecules of hexane solvates that were disordered. The carbon atoms of the solvates were refined with isotropic displacement parameters. Hydrogen atoms were included at geometrically idealized positions and were not refined; H's of the solvates were ignored. The final cycle of full-matrix least-squares refinement using F^2 was completed with the aid of SHELXL97 (16). The maximum and minimum peaks on the final difference Fourier map were in close proximity of the solvent molecules. All calculations for data reduction were performed using the teXsan (17) crystallographic software package of Molecular Structure Corporation.

Conclusion

In summary, diamido supported titanium complexes are not effective catalysts for the heterodehydrocoupling of Te and $HSnBu_3$, mainly owing to the dominance of the unreactive *bis*-μ-telluride complex **3** and the unavailability of lower valent complexes. The most effective means of preparing chalcogenides **2** and **3** is via the well-known elimination of ER_2 from chalcogenolato derivatives, which again is facile in these diamido titanium species.

Acknowledgments

Funding for this work was provided by the Petroleum Research Fund (#33436-AC3) as administered by the American Chemical Society.

References

1. J.M. Fischer, W.E. Piers, S.D. Pearce-Batchilder, and M.J. Zaworotko. J. Am. Chem. Soc. **118**, 283 (1996).
2. (*a*) J.W. Pattiasina, H.J. Heeres, F. van Bolhuis, A. Meetsma, and J.H. Teuben. Organometallics, **6**, 1004 (1987); (*b*) G.A. Luinstra, L.C. ten Cate, J.W. Pattiasina, H.J. Heeres, A. Meetsma, and J.H. Teuben. Organometallics, **10**, 3227 (1991); (*c*) G.A. Luinstra and J H. Teuben. J. Am. Chem. Soc. **114**, 3361 (1992).
3. C.D. MacKinnon and W.E. Piers. Unpublished results.
4. J.D. Scollard, D.H. McConville, J.J. Vittal, and N.C. Payne. J. Mol. Catal. A: Chem. **128**, 201 (1998).
5. R.A. Zingaro, B.H. Steeves, and K.J. Irgolic. J. Organomet. Chem. **4**, 320 (1965).
6. W.A. Howard and G. Parkin. J. Am. Chem. Soc. **116**, 606 (1994).
7. (*a*) W.E. Piers, D.J. Parks, L.R. MacGillivray, and M.J. Zaworotko. Organometallics, **13**, 4547 (1994); (*b*) L.K. Knight, W.E. Piers, and R. McDonald. Chem. Eur. J. **6**, 4322 (2000); (*c*) Z.K. Sweeney, J.L. Polse, R.G. Bergman, and R.A. Andersen. Organometallics, **18**, 5502 (1999); (*d*) G. Tainturier, M. Fahim, G. Trouve-Bellan, and B. Gautheron. J. Organomet. Chem. **376**, 321 (1989).
8. J.M. Fischer, W.E. Piers, T. Ziegler, L.R. MacGillivray, and M.J. Zaworotko. Chem. Eur. J. **2**, 1221 (1996).
9. J. Arnold. Prog. Inorg. Chem. **43**, 353 (1995).
10. J.M. Fischer, W.E. Piers, L.R. MacGillivray, and M.J. Zaworotko. Inorg. Chem. **34**, 2499 (1995).
11. (*a*) L. Scoles, R. Minhas, R. Duchateau, J. Jubb, and S. Gambarotta. Organometallics, **13**, 4978 (1994); (*b*) L.B. Kool,

© 2002 NRC Canada

M.D. Rausch, H.G. Alt, M. heberhold, U. Thewalt, and B. Wolf. Angew. Chem. Int. Ed. **24**, 394 (1985).
12. A.B. Pangborn, M.A. Giardello, R.H. Grubbs, R.K. Rosen, and F.J. Timmers. Organometallics, **15**, 1518 (1996).
13. A.C.T. North, D.C. Phillips, and F.S. Mathews. Acta Cryst. **A24**, 351 (1968).
14. A. Altomare, M. Cascarano, C. Giacovazzo, and A. Guagliardi. 1993. SIR92 [computer program]. J. Appl. Cryst. **26**, 343 (1993).
15. P.T. Beurskens, G. Admiraal, G. Beurskens, W.P. Bosman, R. de Gelder, R. Israel, and J.M.M. Smits. 1994. DIRDIF94 [computer program]. The DIRDIF-94 program system, Technical Report of the Crystallography Laboratory, University of Nijmegen, The Netherlands.
16. G.M. Sheldrick. 1997. SHELXL97 [computer program]. University of Gottingen, Germany.
17. Molecular Structure Corporation. 1985 and 1992. teXsan: Crystal structure analysis package [computer program]. Molecular Structure Corporation.

© 2002 NRC Canada

Supramolecular self-assembly through tellurium···halogen secondary bonds: A hexagonal grid of Te_2Cl_2 and Te_6Cl_6 rings in the solid state structure of 1,1,3-trichloro-2,4,5,6-tetrahydro-1*H*-1λ^4-benzo[b]tellurophene

Julio Zukerman-Schpector, Ionel Haiduc, Robinson L. Camillo, João V. Comasseto, Rodrigo Luiz Oliveira R. Cunha, and Alvim Jorge

Abstract: 1,1,3-Trichloro-2,4,5,6-tetrahydro-1*H*-1λ^4-benzo[b]tellurophene (a = 8.807(1), b = 14.495(2), c = 9.263(1) Å, β = 110.18(1)°; $P2_1/a$, Z= 4, $R[F^2 > 2\sigma(F^2)]$ = 0.0383), prepared by reacting 1-ethynyl-1-cyclohexanol with tellurium tetrachloride, displays a hexagonal grid structure made of four-membered Te_2Cl_2 and 12-membered Te_6Cl_6 rings formed by self-assembly of Cl-Te-Cl rods through Te···Cl secondary bonds into a supramolecular 2D network. The comparison with structurally related compounds reveals that 2D layers can also be formed by similar self-assembly of eight-membered Te_4I_4 rings alone or in a combination of four-membered Te_2I_2 with eight-membered Te_4I_4 rings.

Key words: diorganotellurium(IV), supramolecular 2D assembly, self-assembly, secondary bonding.

Résumé : Le 1,1,3-trichloro-2,4,5,6-tétrahydro-1*H*-1λ^4-benzo[b]tellurophène (a = 8,807(1), b = 14,495(2) et c = 9,263(1) Å, β = 110,18(1)°; $P2_1/a$; Z = 4; $R[F^2>2\sigma(F^2)]$ = 0,0383), préparé par réaction du 1-éthynylcyclohexan-1-ol avec du tétrachlorure de tellure se présente sous la forme d'une structure en grille hexagonale formée de cycles à quatre chaînons de Te_2Cl_2 et à douze chaînons de Te_6Cl_6 qui résultent d'autoassemblages de tiges Cl-Te-Cl dans des liaisons secondaires Te···Cl formant un réseau supramoléculaire bidimensionnel. Une comparaison de cette structure avec celles de composés apparentés révèle que les couches bidimensionnelles peuvent aussi se former par un autoassemblage semblable de cycles à huit chaînons de Te_4I_4 seuls ou en combinaison de cycles à quatre chaînons de Te_2I_2 avec des cycles à huit chaînons de Te_4I_4.

Mots clés : diorganotellure(IV), assemblage supramoléculaire bidimensionnel, autoassemblage, liaison secondaire.

[Traduit par la Rédaction]

Introduction

The molecules of diorganotellurium(IV) dihalides, R_2TeX_2, display a ψ-trigonal bipyramidal geometry with the halogen atoms in axial positions and equatorial Te—C bonds. It is generally assumed, mainly on the basis of the well-known VSEPR theory (1), that a lone pair occupies a third equatorial site. However, these compounds are seldom monomolecular in the solid state, and they tend to form additional Te···X secondary bonds, leading to supramolecular self-assembly and self-organization (2). The secondary bond concept has been introduced by N.W. Alcock (3) to describe interactions between molecules that result in interatomic distances longer than covalent bonds and shorter than the sum of van der Waals radii. Secondary bonds (sometimes called "soft-soft interactions") (4) are typical for heavier p-block elements and they play an important role as bonding motifs in supramolecular organometallic chemistry (5).

Diorganotellurium(IV) dihalides display a broad variety of supramolecular structures in the solid state. Isolated, non-interconnected molecules are rare and occur only when the organic groups are very bulky (e.g., in $(1\text{-naphthyl})_2TeCl_2$)

Received 10 January 2002. Published on the NRC Research Press Web site at http://canjchem.nrc.ca on 22 November 2002.

Dedicated to Tris Chivers with appreciation for his significant contributions to inorganic rings, tellurium chemistry, and many other areas.

J. Zukerman-Schpector[1] and R.L. Camillo. Departamento de Química, Universidade Federal de São Carlos, Caixa Postal 676, 13565–905 São Carlos, SP-Brazil.
I. Haiduc.[2] Facultatea de Chimie, Universitatea Babes-Bolyai, RO-3400 Cluj-Napoca, România.
J. Zukerman-Schpector, J.V. Comasseto, R.L.O.R. Cunha, and A. Jorge. Instituto de Quimica, Universidade de São Paulo, São Paulo, Brazil.

[1]Corresponding author (crystallography) (e-mail: julio@power.ufscar.br).
[2]Corresponding author (self-assembly) (e-mail: ihaiduc@chem.ubbcluj.ro)

 DOI: 10.1139/V02-136 © 2002 NRC Canada

Scheme 1.

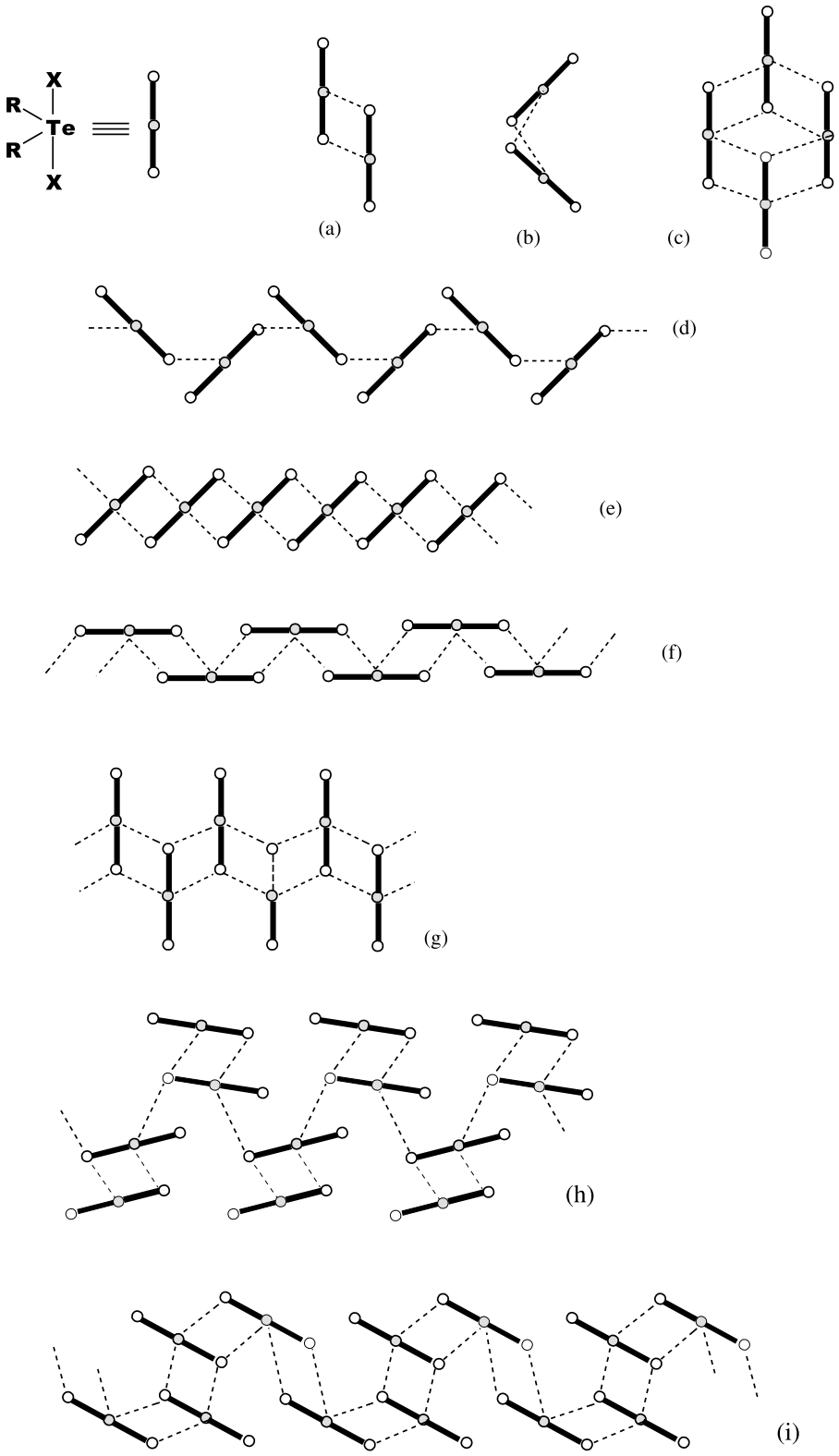

(6). The most common are dimeric and tetrameric supermolecules (7) (i.e., well-defined discrete oligomolecular species that result from the intermolecular association of a few components) and monodimensional chain-like arrays (8) (i.e., polymolecular entities that result from the spontaneous association of a large, undefined number of components) (9). These are illustrated in Scheme 1 where only the self-assembly of X-Te-X (X = halogen) rods is shown, with the

© 2002 NRC Canada

Scheme 2.

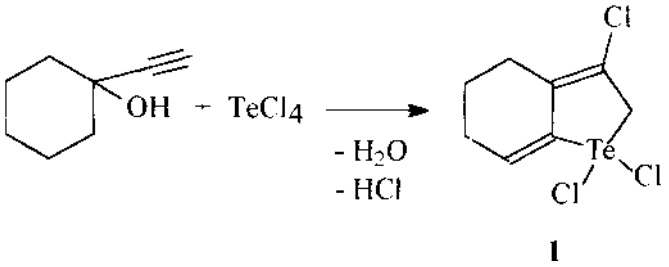

1

Scheme 3.

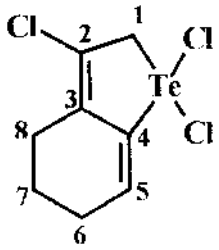

organic groups omitted for clarity. A tendency of X-Te-X rods to form dimers, which can further self-organize into various types of chains, is obvious in structures (f)–(i).

The supramolecular self-organization of diorganotellurium dihalides is accompanied by an increase in the coordination number of tellurium and severe alteration of the coordination geometry (10). Thus, the generally assumed ψ-trigonal bipyramidal geometry frequently becomes octahedral and the actual coordination number of tellurium is increased to six, by considering the secondary bonds.

The self-assembly modes shown in Scheme 1 illustrate an amazing structural diversity of diorganotellurium(IV) halides, which are sometimes ignored in crystal structure determinations, and are limited only to the description of the molecular structure. It can be anticipated that the work of the laddering principle (11) may reveal new types of such supramolecular self-organization.

Bidimensional layers and tridimensional networks are rare (vide infra). Intricate 3D networks occur in α-Me_2TeI_2 (12), Ph_2TeBr_2 (13), and Ph_2TeI_2(14).

We report here a novel mode of self-assembly for diorganotellurium(IV) dihalides, namely a 2D layered system based upon Te···Cl secondary interactions in rhomboidal Te_2Cl_2 and hexagonal Te_6Cl_6 cyclic units, which is observed in the crystal structure of 1,1,3-trichloro-2,4,5,6-tetrahydro-1*H*-1λ^4-benzo[b]tellurophene.

Experimental

Preparation of 1,1,3-trichloro-2,4,5,6-tetrahydro-1*H*-1λ^4-benzo[b]tellurophene (1)

The title compound was prepared by a cyclization reaction between 1-ethynyl-1-cyclohexanol and $TeCl_4$, in benzene, at room temperature, in ca. 12% yield (Scheme 2).

To a suspension of tellurium tetrachloride (2.69 g, 10 mmol) in dry and degassed benzene (50 mL) 1-ethynyl-1-cyclohexanol (1.36 g, 11 mmol) was added, and the mixture was stirred at room temperature for 12 h. Then the mixture was concentrated, and the solid residue was recrystallized from dichloromethane. Yield: 1.23 g (12%), yellow crystals, mp 223.6–224.7°C (uncorrected).

^{1}H and ^{13}C NMR spectra were recorded on a Bruker DRX-500 spectrometer and referenced to $(CD_3)_2SO$ (2.5 ppm for hydrogen spectra and 39.52 ppm for carbon-13 spectra). The ^{125}Te NMR spectrum was also recorded on a Bruker DRX-500 spectrometer and referenced to a diphenylditelluride solution (1 M in $CDCl_3$) as an external standard (419.536 ppm). The infrared spectrum was recorded on a PerkinElmer 1600 spectrophotometer. An uncorrected melting point was obtained on a Büchi Melting Point B-545. The elemental analysis was performed at the Microanalytical Laboratory of the Chemistry Institute, University of São Paulo. The solvents used were previously dried and distilled according to the usual methods (15), and they were degassed before use. Tellurium tetrachloride was prepared from elemental tellurium (230 mesh) and chlorine gas (16), and 1-ethynyl-1-cyclohexanol was purchased from Aldrich and used without further purification.

The individual resonances are assigned according to Scheme 3:

IR (KBr pellet) (cm^{-1}) 3040, 2922, 2866, 1615, 1595, 1493, 1423, 1380, 1171, 1085, 915, 837, 815, 662, 552. ^{1}H NMR (500.13 MHz, DMSO) δ: 6.03–6.01 (m, 1H, CH), 3.08 (s, 2H, CH_2TeCl_2), 1.64–1.62 (m, 2H, CH_2), 1.54–1.51 (m, 2H, CH_2), 0.83–0.78 (m, 2H, $CH_2CH_2CH_2$). ^{13}C NMR (125.77 MHz, DMSO) δ: 140.4 ($^1J_{^{13}C\text{-}^{125}Te}$ = 227.3 Hz, C_4), 137.2 ($^2J_{^{13}C\text{-}^{125}Te}$ = 42.9 Hz, C_5), 136.7 (C_2), 128.7 (C_3), 54.1 ($^1J_{^{13}C\text{-}^{125}Te}$ = 184.5 Hz, C_1), 27.2 (C_6), 25.9 (C_8), 19.8 (C_7). ^{125}Te NMR (157.79 MHz, DMSO) δ: 900.22. Anal. calcd. for $C_8H_9Cl_3Te$: C 28.33, H 2.68; found: C 28.24, H 2.66.

The well-resolved signals in the ^{13}C and ^{125}Te spectra shows that the compound is monomeric in solution.

Crystal structure determination

Data were collected on a CAD-4 Mach 3 Enraf Nonius diffractometer, in the $\omega/2\theta$ scan mode with ω scan width = 0.80 + 0.35 tan θ, using graphite monochromated Mo Kα radiation. Data were corrected for Lorentz, polarization, and absorption effects. The structure was solved by the standard heavy-atom Patterson method, followed by normal difference Fourier techniques. H-atoms were located on stereochemical grounds and refined with fixed geometry, each riding on a carrier atom with an isotropic displacement parameter amounting to 1.2 times the value of the equivalent isotropic displacement parameter of the atom to which they were attached. A summary of crystallographic parameters is presented in Table 1 (17).[3]

[3] Supplementary data may be purchased from the Depository of Unpublished Data, Document Delivery, CISTI, National Research Council Canada, Ottawa, ON K1A 0S2, Canada (http://www.nrc.ca/cisti/irm/unpub_e.shtml for information on ordering electronically). CCDC 185695 contains the supplementary data for this paper. These data can be obtained, free of charge, via www.ccdc.cam.ac.uk/conts/retrieving.html (or from the Cambridge Crystallographic Data Centre, 12 Union Road, Cambridge, U.K.; fax +44 1223 336033; or deposit@ccdc.cam.ac.uk).

© 2002 NRC Canada

Table 1. Crystal data and structure refinement for **1**.

Crystal	**1**
Empirical formula	C_8 H_9 Cl_3Te
Molecular weight	339.10
Appearance	Yellow block
Crystal dimensions (mm)	0.25 × 0.10 × 0.08
Crystal system	Monoclinic
Space group	$P2_1/a$
a (Å)	8.807(1)
b (Å)	14.495(2)
c (Å)	9.263(1)
β (°)	110.18(1)
V (Å^3)	1109.9(2)
Z	4
$D_{calcd.}$ (Mg m^{-3})	2.029
T (K)	293
μ (mm^{-1})	3.349
Radiation	Mo Kα
λ (Å)	0.71073
Range measured	$0 \le h \le 10$ $1 \le k \le 17$ $-10 \le l \le 10$
Reflections collected	2074
Independent reflections	1938
θ_{max} (°)	25
Data collection	Enraf-Noius CAD-4 Mach 3; ω-20 scans; 3 standard reflections every 1200 s
R_{int}	0.0466
Intensity decay (%)	0.3
Absorption corrections (T_{min}, T_{max})	0.488, 0.776
Refinement	Refinement on F^2; H atoms riding
Final R indices [$F^2 > 2\sigma(F^2)$]	R_1 = 0.0383 wR_2 = 0.0996
R indices (all data)	0.1213
Largest diff. peak and hole (e Å^{-3})	0.703 and –0.914
Number of parameters	109
$(\Delta/\sigma)_{max}$	0.000

Note: See reference 17 for programs used.

Results and discussion

X-ray diffraction quality crystals were obtained by recrystallization from hexane–dichloromethane by slow evaporation and were structurally investigated. The crystallographic data are listed in Table 1. The molecular structure of **1** is shown in Fig. 1 with the atom numbering scheme. The molecular parameters (bond lengths and bond angles) are summarized in Table 2. The molecule shows little deviation from planarity, which occurs in the partially unsaturated six-membered ring. The two Te—Cl bonds are basically colinear (Cl(1)-Te-Cl(2) 174.5(8)°) and the Cl-Te-Cl rod is perpendicular to the plane of the heterocycle (Cl(1)-Te-C(1) 87.5(2)°, Cl(1)-Te-C(8) 87.6(3)°, Cl(2)-Te-C(1) 90.0(2)°, and Cl(2)-Te-C(8) 87.2(3)°). The C(1)-Te-C(8) angle in the five-membered ring (83.2(3)°) shows the severe distortion from the regular trigonal bipyramidal geometry imposed by the inclusion of the tellurium atom in a five-membered ring. In fact, with the two additional secondary Te···Cl bonds, and with the bond angles observed, the coordination polyhedron of tellurium is more appropriately described as an octahedron with minor distortions only. The Te—Cl bond lengths (Te—Cl(1) = 2.519(3) and Te—Cl(2) = 2.510(3) Å) are in a range normally found for covalent tellurium—chlorine bonds, and are slightly elongated because of their

Fig. 1. ZORTEP diagram of the molecular structure of **1**. Thermal elipsoids at 30% probability level.

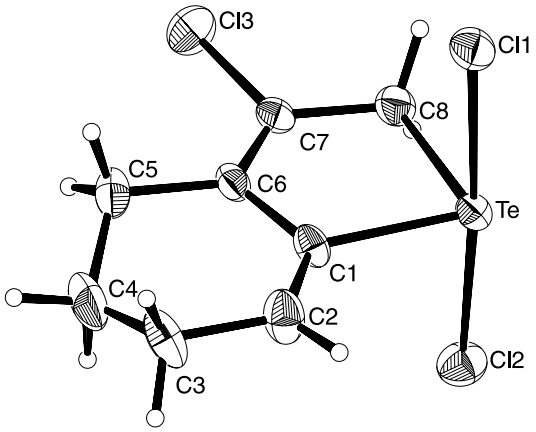

© 2002 NRC Canada

Table 2. Selected bond lengths (Å) and bond angles (°) in **1**.

Bond lengths (Å)			
Te—C(1)	2.087(8)		
Te—C(8)	2.110(8)		
Te—Cl(1)	2.519(3)		
Te—Cl(2)	2.510(3)		
Te···Cl(1a)[a]	3.474(3)		
Te···Cl(2a)[b]	3.340(3)		
Bond angles (°)			
C(1)-Te-C(8)	83.2(3)	C(1)-Te···Cl(1a)	87.5(2)
C(1)-Te-Cl(1)	87.9(2)	C(1)-Te···Cl(2a)	161.2(2)
C(8)-Te-Cl(1)	87.6(3)	C(8)-Te···Cl(1a)	169.0(2)
C(1)-Te-Cl(2)	90.0(2)	C(8)-Te···Cl(2a)	80.3(2)
C(8)-Te-Cl(2)	87.2(3)	Cl(1a)···Te···Cl(2a)	107.89(6)
Cl(1)-Te-Cl(2)	174.55(8)		

[a]2–x, –y, –z.
[b]0.5 + x, 0.5–y, z.

Fig. 2. The structure of the 2D supramolecular layer.

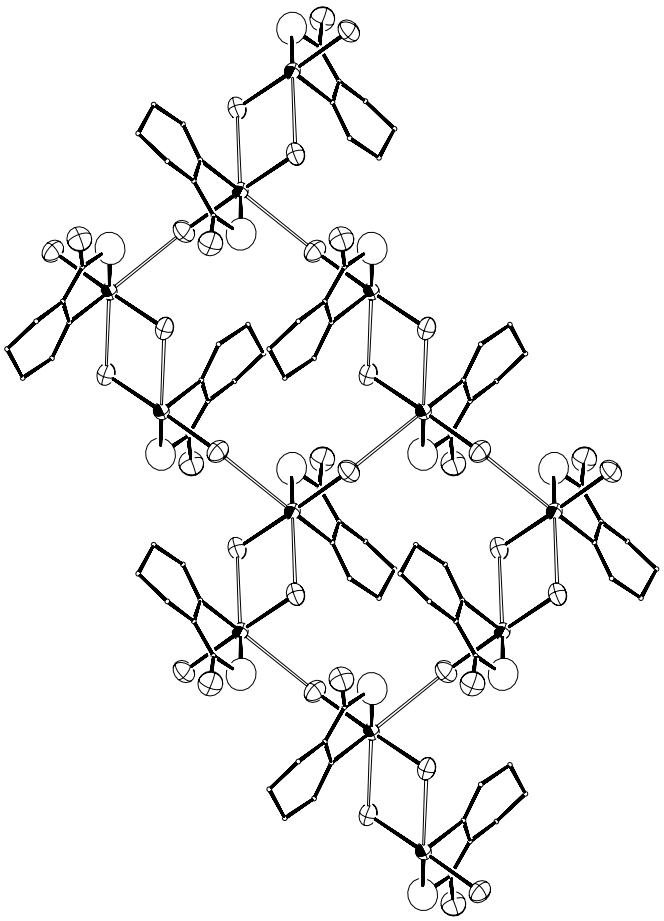

involvement in secondary bonds (see Table 3 (18) for some comparisons).

The molecules of **1** are associated into dimeric units through tellurium—chlorine secondary bonds. The dimeric units are formed with the participation of Cl(1) atoms, and the lengths of the Te···Cl(1a) secondary bonds are both 3.474(3) Å. In this pair, the Te_2Cl_2 rhomboid ring is basically planar and the organic parts of the molecules are located on opposite sides of the Te_2Cl_2 plane (*trans*-configuration). The second chlorine, Cl(2) connects the dimers through Te(1)-Cl(2)···Te(1a) bridges into a 2D corrugated sheet [Te···Cl(2) = 3.340(3) Å] with the organic rings alternating on the two sides of the layers, which are oriented parallel to the xy plane in the crystal. The layers are then stacked on top of each other along the z axis. It will be noted that the inter-dimeric Te···Cl(2) secondary bonds are shorter, and therefore stronger, than the Te···Cl(1) intradimeric bonds.

Fig. 3. The tellurium-chlorine skeleton of the layers. (*a*) View of the two stacked layers illustrating their relative sliding; (*b*) Side view illustrating the corrugated nature of the 2D layer.

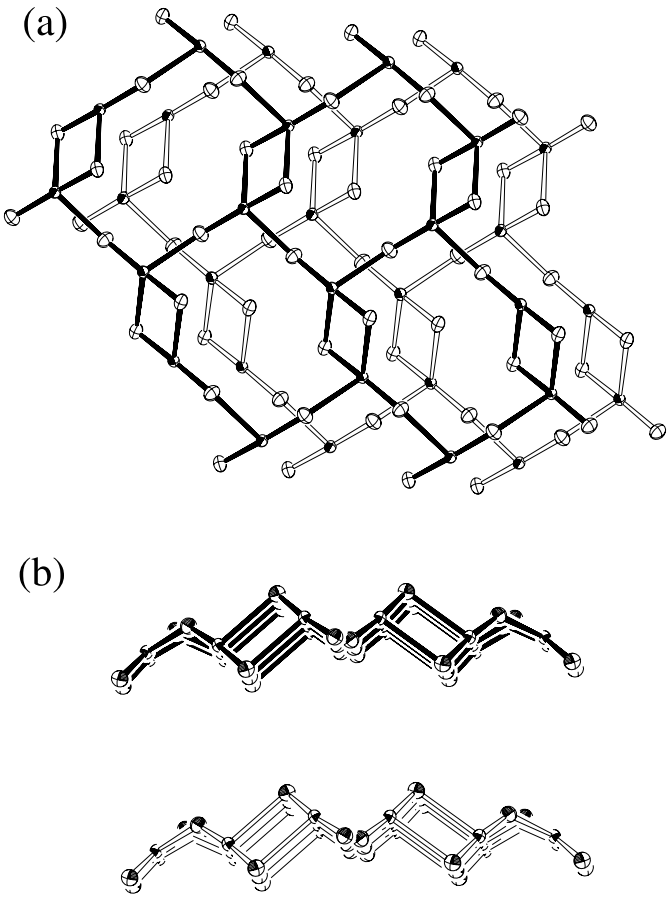

A fragment of the 2D layer is shown in Fig. 2. Full lines represent normal covalent bonds and open lines indicate Te···Cl secondary interactions. The Te_2Cl_2 rings are associated with 12-membered Te_6Cl_6 rings and are incorporated into the hexagons, the latter thus defining the structure type. For more clarity, Fig. 3*a* is presented, in which the organic part of the molecules was omitted, leaving only the tellurium-chlorine backbone. In this figure two stacked layers are shown: one with all bonds as full lines, the other, located below, with open lines (again all bonds). The figure illustrates a sliding of the layers relative to each other, along the direction of the x-axis only. The corrugated structure of the layer is obvious in Fig. 3*b*, representing a side view along the x-axis. The apparently empty space is occupied by the organic part of the molecules, which determine a separation between two parallel layers A and B, measured by the

© 2002 NRC Canada

Table 3. Comparison of the Te—Cl bond lengths and Cl-Te-Cl bond angles in some diorganotellurium dichlorides.

Compound		Te—Cl (Å)	Te···Cl (Å)	Cl-Te-Cl (°)	Reference
Me_2TeCl_2		2.488(1)	3.412(1)	172.44(1)	18(*a*)
		2.541(1)	3.478(1)		
Ph_2TeCl_2		2.529(3)	3.677(3)	175.54(7)	18(*b*)
		2.482(2)			
$(C_6F_5)_2TeCl_2$		2.485(1)	3.589(1)	175.33(4)	18(*c*)
		2.478(1)	3.478(1)		
Ph(*p*-Br-C_6H_4)$TeCl_2$	Te(1)	2.530(2)	3.723(2)	176.0(1)	18(*d*)
		2.496(2)	3.500(2)		
	Te(2)	2.437(3)	3.413(3)	176.6(1)	
		2.590(2)	3.592(3)		
(*p*-$MeOC_6H_4$)$_2TeCl_2$	Te(1)	2.518(1)	3.501(1)	177.9(1)	18(*e*)
		2.514(2)	3.559(2)		
	Te(2)	2.474(1)	3.446(1)	178.8(1)	
		2.569(1)	3.675(1)		
(*p*-$PhOC_6H_4$)$_2TeCl_2$		2.506(1)	3.741(1)	177.2(1)	18(*f*)
		2.510(1)			
O(C_6H_4)$_2TeCl_2$	Te(1)	2.576(3)	3.502(3)	176.8(1)	18(*g*)
		2.478(3)	3.368(3)		
	Te(2)	2.501(3)	3.398(3)	176.8(1)	
		2.563(3)	3.504(3)		
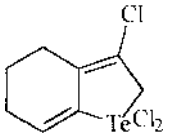		2.519(3)	3.474(3)	174.55(8)	This work
		2.510(3)	3.340(3)		

Te(A)···Te(B) distance of 9.26 Å. The intermolecular forces within the layers, due to Te···Cl secondary interactions, are stronger than the interlayer van der Waals forces and play a structure determining role. This can be correlated with the lamellar aspect of the crystals of compound (**1**).

The 2D layer structure found in this work prompted us to analyze the crystal packings and self-assembly modes of some other diorganotellurium(IV) dihalides that were reported as layered or 3D structures in the solid state. Thus, we found that an interesting comparison can be made with the structures of two polymorphs of a structurally related compound, α- and β-diiodobenzotelluracyclopentane (**2**) (Scheme 4). The results are illustrated in Scheme 5. Structure (a) is that of compound **1**, reported here.

A redrawing of the structure of α-diiodobenzotelluracyclopentane (19) from deposited data (CSD code DIPTEB10) reveals the presence of 2D layers made of four-membered Te_2I_2 rings combined with eight-membered Te_4I_4 rings in a corrugated layer (structure (b) in Scheme 5). It should be noted that in this image only the Te and I atoms effectively participating in the formation of the supramolecular array through Te···I(1) secondary bonds are shown; the I(2) atoms were omitted to simplify the picture. They are outside the plane of the paper.

Scheme 4.

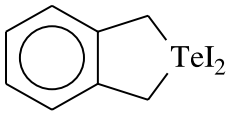

2

The β-polymorph of diiodobenzotelluracyclopentane (20) (CSD code DIPTEB02) is a supramolecular isomer and contains layers made of eight-membered Te_4I_4 rings only (structure (c) in Scheme 5). Since this is a view from the top it is somewhat misleading, as it suggests planarity. The corrugated nature of the layer is better illustrated by another view, shown in structure (d) (Scheme 5), which shows a reciprocal position and the interconnection of the I-Te-I rods related to that in the tetrameric supermolecules cited above.

The hexagonal grid structure, based upon the Te···Cl secondary interactions reported here, is reminiscent of the,

© 2002 NRC Canada

Scheme 5.

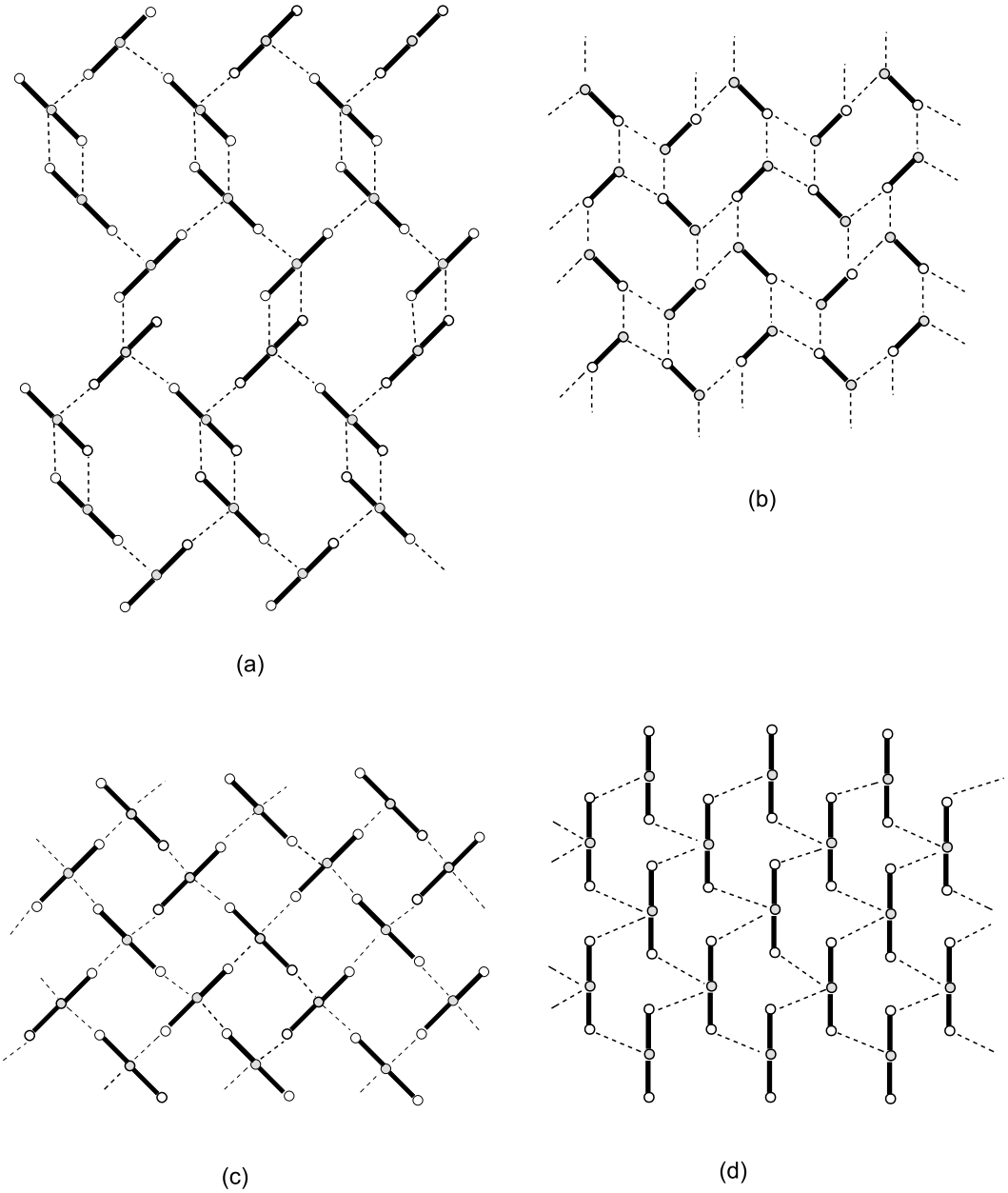

albeit different, hexagonal grid structure ("graphite-like") of $[O(SnMe_3)_3]Cl$, which is based upon Sn···Cl secondary bonds (21). Supramolecular hexagonal grids formed through hydrogen bonds can also be mentioned, e.g., in the structures of some cobalt-cupferrone-ethanol complexes (22) or the $Ni(HBim)_3$ anion (HBim = biimidazole) (23). This suggests that various types of intermolecular forces can lead to similar supramolecular architectures, and the subject deserves further attention.

Conclusions and outlook

We found in the title compound a hexagonal grid structure made of four-membered Te_2Cl_2 and twelve-membered Te_6Cl_6 rings formed through the self-assembly of Cl-Te-Cl rods through Te···Cl secondary bonds into a supramolecular 2D network. The comparison with a structurally related compound reveals that 2D layers can also be formed by similar self-assembly of four-membered Te_2I_2 with eight-membered Te_4I_4 rings (in α-diiodobenzotelluracyclopentane) or only of eight-membered Te_4I_4 rings (in β-diiodobenzotelluracyclopentane).

It is obvious from the data discussed here and illustrated in Schemes 1 and 5 that the mode of self-assembly of diorganotellurium(IV) halides is very sensitive to the size and shape of the organic part of the molecules (alkyl groups, aryl groups, heterocyclic moieties) and the nature of the halogen atoms. Therefore, it is worth exploring a range as broad as possible of such compounds by synthesizing new derivatives with different steric requirements of the R_2Te

© 2002 NRC Canada

fragments and with all four halogens, followed by their structural characterization and crystal packing analysis with the aid of modern X-ray diffraction techniques.

Acknowledgements

We gratefully acknowledge the assistance of Fundação de Amparo à Pesquisa do Estado de São Paulo, São Paulo, Brazil, which supported financially the work presented here, a Visiting Professorship of IH and a scholarship to RLC. We thank Prof. M. Martinez-Ripoll for making possible the use of the Cambridge Structural Database.

References

1. R.J. Gillespie and I. Hargittai. The VSEPR model of molecular geometry. Allyn and Bacon, New York. 1991.
2. I. Haiduc and J. Zukerman-Schpector. Phosphurus, Sulfur, Silicon, **171**, 171 (2001).
3. N.W. Alcock. Advan. Inorg. Chem. Radiochem. **15**, 1 (1972); N.W. Alcock. Bonding and structure. Structural principles in inorganic and organic chemistry. Ellis Horwood, New York, London. 1993.
4. P. Pyykkö. Chem. Rev. **97**, 597 (1997).
5. I. Haiduc and F.T. Edelmann. Supramolecular organometallic chemistry. Wiley-VCH, Weinheim. 1999.
6. J. Farran, A. Alvarez-Lorena, J.F. Piniella, G. Germain, and L. Torres-Castellano. Z. Kristallogr. **210**, 65 (1995).
7. Examples are (Scheme 1):- dimers, type (a) $(C_6F_5)_2TeF_2$: J. Aramini, R.J. Batchelor, C.H.W Jones, F.W.B. Einstein, and R.D. Sharma. Can. J. Chem. **65**, 2643 (1987); type (b) $(p\text{-}PhOC_6H_4)_2TeCl_2$: M. De Matheus, L. Torres, J.F. Piniella, J.L. Brianso, and C. Miravitles. Acta Crystallogr. Ser. C, **47C**, 703 (1991); - tetramers, type (c) $(p\text{-}MeOC_6H_4)_2TeCl_2$: R.K. Chadha and J.E. Drake. Acta Crystallogr. Ser. C, **40C**, 1349 (1984); $(p\text{-}BrC_6H_4)PhTeCl_2$: R.J. Chadha, J.E. Drake, and M.A. Khan. Acta Crystallogr. Ser. C, **39C**, 45 (1983); $O(C_6H_4)_2TeCl_2$: J.D. Korp, I. Bernal, J.C. Turley, and G.E. Martin. Inorg. Chem. **19**, 2556 (1980).
8. Examples are (Scheme 1): type (d) Ph_2TeCl_2: N.W. Alcock and W.D. Harrison. J. Chem. Soc. Dalton Trans. 251 (1982); type (e) $(C_6F_5)_2TeCl_2$: D.Naumann, L. Ehmanns, K.F. Tebbe, and W. Crump. Z. Anorg. Allg. Chem. **619**, 1269 (1993); $(p\text{-}ClC_6H_4)_2TeCl_2$: G.Y. Chao and J.D. McCullough. Acta Crystallogr. Ser. C, **C15**, 887 (1962); type (f) Ph_2TeF_2: F.J. Berry and A.J. Edwards. J. Chem. Soc. Dalton Trans. **1980**, 2306; $(C_6H_4)_2TeI_2$: J.D. McCullough. Inorg. Chem. **14**, 1142 (1975); $O(C_6H_4)_2TeI_2$: J.D. McCullough. Inorg. Chem. **12**, 2669 (1973); type (g) Me_2TeCl_2: R.F. Ziolo and J.M. Troup, J. Am. Chem. Soc. **105**, 229 (1983); type (h) Me_2TeBr_2: P.C. Srivastava, A. Sinha, S. Bajpai, H.G. Schmidt, and M. Noltemeyer. J. Organomet. Chem. **575**, 261 (1999); J.E. Drake, L.N. Khasrou, A.G. Mislankar, and R. Ratnani, Inorg. Chem. **38**, 3994 (1999) (redrawn from deposited data, CSD code COQNOL); type (i) $(CH_2)_4TeI_2$: R. Montoya, R.A. Toscano, S. Hernandez-Ortega, and R. Cea-Olivares. J. Organomet. Chem. **623**, 74 (2001) (redrawn from deposited data, CSD code QIXZAY).
9. J.-M. Lehn. Angew. Chem. Int. Ed. Engl. **27**, 89 (1988); J.-M. Lehn. Supramolecular chemistry. Concepts and perspectives. VCH Weinheim, Germany, 1995.
10. J. Zukerman-Schpector and I. Haiduc. Phosphorus, Sulfur, Silicon, **171**, 73 (2001).
11. A. Downard and T. Chivers. Eur. J. Inorg. Chem. 2193 (2001).
12. L.Y.Y. Chan and F.W.B. Einstein. J. Chem. Soc.,\ Dalton Trans. 316 (1972).
13. G.D. Christofferson and J.D. McCullough. Acta Crystallogr. Ser. C, **C11**, 249 (1958).
14. N.W. Alcock and W.D. Harrison. J.Chem. Soc. Dalton Trans. 869 (1984).
15. D.D. Perrin and W.L.F. Amarego. Purification of laboratory chemicals. 2nd ed. Pergamon, London. 1980.
16. N. Petragnani. *In* Best synthetic methods. *Edited by* A.R. Katritzky, O. Meth-Cohn, and C.W. Rees. Academic Press, London. 1994. p. 3.
17. G.M. Sheldrick. 1990. SHELXS-86 [computer program]. University of Göttingen, Germany; G.M. Sheldrick. 1997. SHELXL-97 [computer program]. University of Göttingen, Germany; L. Zsolnay. 1995. ZORTEP [computer program]. University of Heidelberg, Germany; M. Nardelli. 1995. PARST-95 [computer program]. J. Appl. Cryst. **28**, 659 (1995).
18. (*a*) R.F. Ziolo and J.M. Troup. J. Am. Chem. Soc. **105**, 229 (1983); (*b*) N.W. Alcock and W.D. Harrison. J. Chem. Soc. Dalton Trans. 251 (1982); (*c*) D. Naumann, L. Ehmanns, K.F. Tebbe, and W. Crump. Z. Anorg. Allg. Chem. **619**, 1269 (1993); (*d*) R.J. Chadha, J.E. Drake, and M.A. Khan. Acta Crystallogr. **C39**, 45 (1983); (*e*) R.J. Chadha and J.E. Drake. Acta Crystallogr. **C40**, 1349 (1984); (*f*) M. De Matheus, L. Torres, J.F. Piniella, J.L. Brianso, and C. Miravitles. Acta Crystallogr. **C47**, 703 (1991); (*g*) J.D. Korp, I. Bernal, J.C. Turley, and G.E, Martin. Inorg. Chem. **19**, 2556 (1980).
19. C. Knobler and R.F. Ziolo. J. Organomet. Chem. **178**, 423 (1979).
20. J.D. McCullough, C. Knobler, and R.F. Ziolo. Inorg. Chem. **24**, 1814 (1985).
21. B. Rake, P. Müller, H.W. Roesky, and I. Uson. Angew. Chem. Int. Ed. Engl. **38**, 2050 (1999).
22. A. Deák, A. Kálmán, L. Párkányi, and I. Haiduc. Acta Crystallogr. Sec. B, **57B**, 303 (2001).
23. M. Tadokor, K. Isobe, H. Uekusa, Y. Ohashi, J. Toyoda, K. Tashiro, and K. Nakasuji. Angew. Chem. Int. Ed. Engl. **38**, 95 (1999).

© 2002 NRC Canada

The synthesis and reactivity of a mixed nitrosyl–phosphinidene cluster of ruthenium: Formation of nitride and nitrene clusters

Ludmila Scoles, Brian T. Sterenberg, Konstantin A. Udachin, and Arthur J. Carty

Abstract: Reaction of the aminophosphinidene complex $[Ru_5(CO)_{15}(\mu_4\text{-PN-}i\text{-}Pr_2)]$ (**1**) with $[PPN][NO_2]$ (PPN = $Ph_3P{=}N{=}PPh_3$) led to the mixed nitrosyl–phosphinidene cluster complex $[PPN][Ru_5(CO)_{13}(\mu_2\text{-NO})(\mu_4\text{-PN-}i\text{-}Pr_2)]$ (**2**). Reaction of **2** with $HBF_4{\cdot}Et_2O$ led to a mixture of the nitrido–phosphido cluster $[Ru_5(CO)_{13}(\mu_5\text{-N})\{\mu_2\text{-P(F)N-}i\text{-}Pr_2\}]$ (**3**) and the nitrene–phosphinidene cluster $[Ru_5(CO)_{10}(\mu\text{-CO})_2(\mu_3\text{-CO})(\mu_4\text{-NH})(\mu_3\text{-PN-}i\text{-}Pr_2)]$ (**4**). If the BF_4^- counterion is avoided through use of trifluoromethanesulfonic acid, **4** is the only isolated product. Reaction of **2** with methyltrifluoromethanesulfonate leads to the nitrido–phosphido cluster $[Ru_5(CO)_{13}(\mu_5\text{-N})\{\mu_2\text{-P(OMe)N-}i\text{-}Pr_2\}]$ (**5**), which is structurally analogous to **3**.

Key words: ruthenium, cluster, nitrosyl, nitrene, phosphinidene, phosphido.

Résumé : La réaction du complexe aminophosphinidène $[Ru_5(CO)_{15}(\mu_4\text{-PN-}i\text{-}Pr_2)]$ (**1**) avec du $[PPN][NO_2]$ (PPN = $Ph_3P{=}N{=}PPh_3$) conduit à la formation d'un agrégat complexe nitrosyle–phosphinidène $[PPN][Ru_5(CO)_{13}(\mu_2\text{-NO})(\mu_4\text{-PN-}i\text{-}Pr_2]$ (**2**). La réaction du composé **2** avec du $HBF_4{\cdot}Et_2O$ conduit à un mélange d'agrégat nitrido–phosphido $[Ru_5(CO)_{13}(\mu_5\text{-N})\{\mu_2\text{-P(F)N-}i\text{-}Pr_2\}]$ (**3**) et d'agrégat nitrène–phosphinidène $[Ru_5(CO)_{10}(\mu\text{-CO})_2(\mu_3\text{-CO})(\mu_4\text{-NH})(\mu_3\text{-PN-}i\text{-}Pr_2)]$ (**4**). Si l'on évite la présence du contre-ion BF_4^- en utilisant de l'acide trifluorométhanesulfonique, le produit **4** est le seul à être isolé. La réaction du produit **2** avec du trifluorométhanesulfonate de méthyle conduit à la formation de l'agrégat nitrido–phosphido $[Ru_5(CO)_{13}(\mu_5\text{-N})\{\mu_2\text{-P(OMe)N-}i\text{-}Pr_2\}]$ (**5**) qui est analogue d'un point de vue structural au composé **3**.

Mots clés : ruthénium, agrégat, nitrosyle, nitrène, phosphinidène, phosphido.

[Traduit par la Rédaction]

Introduction

Phosphinidenes (PR) are important and versatile ligands in organometallic chemistry (1). The phosphinidene fragment is isolobal with carbene (CR_2) and there are interesting relationships between the well–established nucleophilic (Schrock type) and electrophilic (Fischer type) carbene complexes and their only recently discovered and highly reactive phosphinidene counterparts (2). The PR group is also, however, a powerful polynucleating ligand in metal cluster chemistry that enhances structural integrity and stability through μ_3- and μ_4-face-capping co-ordination (3). Yet another interesting family of phosphinidene complexes consists of a dimetal fragment bridged by a μ_2–PR ligand. The three membered $\overline{\text{M–M'–P}}$ ring in such molecules is unsaturated and bonding in the ring is partially delocalized owing to the availability of an empty pπ-orbital on the phosphinidene phosphorus atom, resulting in a planar geometry at phosphorus (4).

Over the past several years, we have developed an extensive chemistry based on the transformation of functionalized phosphinidenes on metal clusters (5) including the design of a versatile route to phosphorus monoxide (PO) complexes via the acid-catalysed hydrolysis of P—N bonds in co-ordinated aminophosphinidenes (6–8). Phosphorus monoxide is the heavier congener of NO, and the availability of a range of PO clusters has allowed us to gain some insights, via DFT calculations, into the bonding and electronic structure in these PO clusters for comparison with nitrosyl bonding (9). In pursuing the PO–NO analogy, we were struck by the broader need for a comparison of structure, bonding, and reactivity between pairs of related isolobal phosphorus and nitrogen ligands (phosphinidene (PR), nitrene (NR), phosphide (P), nitride (N)), preferably within the same cluster molecule. There are to our knowledge no examples of PO–NO, PR–NR, or P–N complexes or indeed of clusters bearing any combinations of these in the literature.

In this paper, we report on the formation of the nitrosyl–phosphinidene cluster $[PPN][Ru_5(CO)_{13}(\mu_2\text{-NO})(\mu_4\text{-PN-}i\text{-}Pr_2)]$ (**2**), and its transformation into nitrene–phosphinidene

Received 6 February 2002. Published on the NRC Research Press Web site at http://canjchem.nrc.ca on 25 November 2002.

Dedicated to Professor Tris Chivers for his contributions to Canadian chemistry.

L. Scoles, B.T. Sterenberg, K.A. Udachin, and A.J. Carty.[1] Steacie Institute for Molecular Sciences, National Research Council Canada, 100 Sussex Drive, Ottawa, ON K1A 0R6, Canada and the Ottawa-Carleton Chemistry Research Institute, Department of Chemistry, University of Ottawa, Ottawa, ON K1N 6N5, Canada.

[1]Corresponding author (e-mail: arthur.carty@nrc.ca)

 DOI: 10.1139/V02-100 © 2002 NRC Canada

Scheme 1.

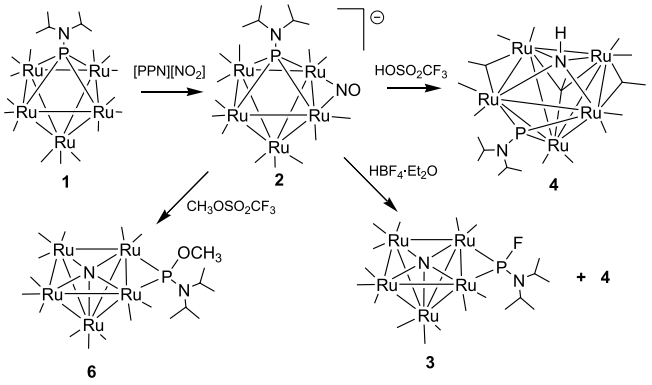

and nitride–phosphido clusters via reactions with electrophiles. Portions of this work have been communicated (10).

Formation of a nitrosyl–phosphinidene cluster

After attempts to form nitrosyl–phosphinidene clusters using NO gas or nitrosonium tetrafluoroborate failed owing to cluster decomposition, we turned to the milder reagent $[PPN][NO_2]$ that is effective in the formation of anionic nitrosyl clusters (11, 12). Reactions with the nitrite anion occur via oxidation of a carbonyl ligand and CO_2 elimination. Thus, treatment of the aminophosphinidene complex $[Ru_5(CO)_{15}(\mu_4\text{-PN-}i\text{-Pr}_2)]$ (**1**) with $[PPN][NO_2]$ led to the anionic nitrosyl–phosphinidene cluster $[PPN][Ru_5(CO)_{13}(\mu_2\text{-NO})(\mu_4\text{-PN-}i\text{-Pr}_2)]$ (**2**) in good yield (see Scheme 1).

Compound **2** has been structurally characterized. An ORTEP diagram of the cluster anion is shown in Fig. 1 and selected distances and angles are given in Table 1. The five ruthenium atoms are arranged in a square-based pyramid. The aminophosphinidene ligand caps the square face of the pyramid while the nitrosyl ligand bridges one edge of the square base. The nitrosyl bridged Ru—Ru bond distance (2.7077(4) Å) is significantly shorter than the other Ru—Ru distances in the square base (2.8493(4) – 2.8986(4) Å). Distances to the apical Ru(5) atom range from 2.8345(4) to 2.8583(4) Å. Thirteen carbonyl ligands are terminally bound to the cluster, two to each of the nitrosyl–bound ruthenium atoms and three to each of the other three ruthenium centres. The Ru—N bond lengths to the nitrosyl ligand (Ru(3)—N(9) 1.984(3) Å; Ru(4)—N(9) 2.016(3) Å) indicate a slight asymmetry in the Ru–N–Ru bridge.

The infrared spectrum of **2** shows a weak band at 1543 cm^{-1}, consistent with the stretching frequency of a doubly bridging nitrosyl ligand (13). The ^{31}P NMR spectrum shows a singlet at δ 550.7 for the phosphinidene ligand, a downfield shift of more than 60 ppm compared to the starting cluster **1**.

The formation of **2** involves a loss of two carbonyl ligands and co-ordination of NO in a doubly bridging co-ordination mode as a 3-electron donor, resulting in a overall 74-electron count, consistent with a *nido* M_5 structure or a *closo* M_5P framework if the μ_4-PN-*i*-Pr_2 fragment is considered part of the cluster framework. The octahedral metal–phosphinidene core does not change significantly in the reaction. Compound **2** is the first mixed phosphinidene–nitrosyl cluster.

Table 1. Selected bond distances (Å) and angles (°) for $[PPN][Ru_5(CO)_{13}(\mu\text{-NO})(\mu_4\text{-PN-}i\text{-Pr}_2)]$ (**2**).

Bond distances (Å)			
Ru(1)—Ru(2)	2.8493(4)	Ru(1)—P(1)	2.3469(8)
Ru(1)—Ru(4)	2.8986(4)	Ru(2)—P(1)	2.3576(8)
Ru(1)—Ru(5)	2.8583(4)	Ru(3)—P(1)	2.4277(8)
Ru(2)—Ru(3)	2.8890(4)	Ru(4)—P(1)	2.4071(8)
Ru(2)—Ru(5)	2.8489(4)	P(1)—N(15)	1.684(3)
Ru(3)—Ru(4)	2.7077(4)	Ru(3)—N(9)	1.984(3)
Ru(3)—Ru(5)	2.8214(4)	Ru(4)—N(9)	2.016(3)
Ru(4)—Ru(5)	2.8345(4)	O(9)—N(9)	1.192(4)
Bond angles (°)			
O(9)-N(9)-Ru(3)	139.2(3)	Ru(3)-N(9)-Ru(4)	85.19(12)
O(9)-N(9)-Ru(4)	135.6(3)		

Fig. 1. Molecular structure (ORTEP) of the anion of $[PPN][Ru_5(CO)_{13}(\mu\text{-NO})(\mu_4\text{-PN-}i\text{-Pr}_2)]$ (**2**). Hydrogen atoms have been omitted. Thermal ellipsoids are shown at the 50% probability level.

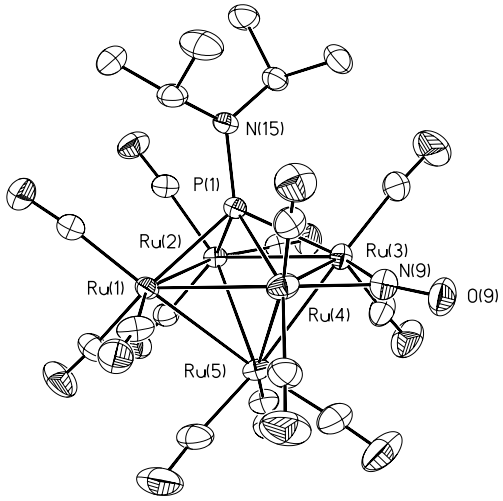

Protonation of the nitrosyl cluster

In our previous work, we described the acid-catalysed hydrolysis of aminophosphinidenes to form PO clusters. Compound **2** is thus a potential precursor to a PO–NO complex. However, nitrosyl complexes are also known to be reactive towards acid. The reactivity of the aminophosphinidene–nitrosyl cluster towards protonation was therefore examined. Reaction of **2** with $HBF_4{\cdot}Et_2O$ led to two new cluster complexes that were separated by thin layer chromatography.

The first compound isolated from the reaction was the nitrido–phosphido cluster $[Ru_5(CO)_{13}(\mu_5\text{-N})\{\mu_2\text{-P(F)N-}i\text{-Pr}_2\}]$ (**3**). The ORTEP diagram of **3** is shown in Fig. 2 and selected bond distances and angles are shown in Table 2. The molecule consists of a square-based pyramidal arrangement of five ruthenium atoms around the μ_5-nitride ligand. The molecule lies upon a mirror plane with the position of the nitride nitrogen atom N(1) and apical ruthenium atom Ru(3)

© 2002 NRC Canada

Fig. 2. Structure of $[Ru_5(CO)_{13}(\mu_5\text{-N})(\mu_2\text{-P(F)N-}i\text{-Pr}_2)]$ (**3**). Thermal ellipsoids are shown at the 50% level. Hydrogen atoms have been eliminated.

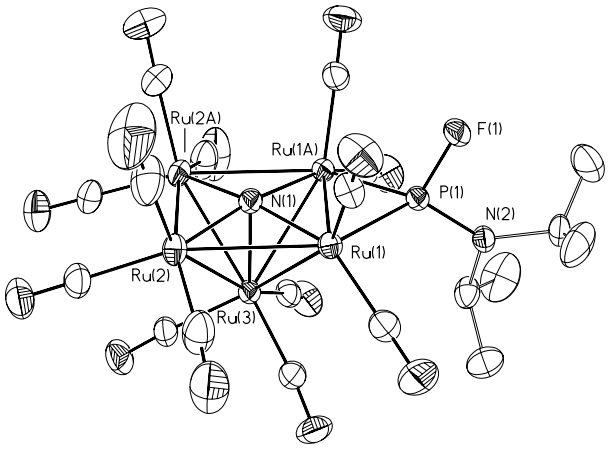

lying in the plane. The other ruthenium atoms are thus symmetry pairs. Metal—metal distances are 2.8261(4), 2.8687(3), and 2.8447(4) Å between basal ruthenium atoms and 2.8349(3) and 2.7424(3) Å to the apical ruthenium atom. Distances from N(1) to the basal ruthenium atoms are 2.036(2) and 2.010(2) Å, while the distance to the apical ruthenium atom is slightly longer (2.086(3) Å). The nitride atom lies above the plane formed by the basal ruthenium atoms by 0.160(3) Å. The fluoroaminophosphido ligand bridges two of the basal ruthenium atoms, with the phosphorus, nitrogen, and fluorine atoms of the ligand lying on the crystallographic mirror plane. The fluorine substituent is directed towards the basal ruthenium atoms while the amino group is directed towards the apical ruthenium atom Ru(3). The two isopropyl groups are disordered over two symmetry-related positions. The P(1)—Ru(1) distance is 2.2547(7), and the P—F and P—N distances are 1.579(2) and 1.635(3), respectively. The 13 carbonyl ligands are all terminally coordinated, two to each of the phosphorus bound ruthenium atoms and three to the other ruthenium atoms. The nitride ligand contributes five electrons and the phosphido ligand donates three resulting in a cluster electron count of 74. To our knowledge, **3** is the first compound containing a fluoroaminophosphido ligand, although analogous chloro- and bromoaminophosphido ligands have been reported (14).

The structural parameters involving the nitrido ligand and the metal core of **3** are very similar to those of the known anionic nitrido cluster $[Ru_5(CO)_{13}(\mu\text{-CO})(\mu_5\text{-N})]^-$ (15). In fact, the clusters are nearly isostructural, with one doubly bridging carbonyl ligand in $[Ru_5(CO)_{13}(\mu\text{-CO})(\mu_5\text{-N})]^-$ being replaced by the doubly bridging phosphido ligand in **3**. The arrangement of all other ligands in the two is the same, and the electron counts of the two clusters are the same.

The phosphorus NMR spectrum of **3** shows a doublet at δ 391 with a ^1J(PF) of 1087 Hz. The spectrum also reveals the presence of a second, minor isomer with a chemical shift of δ 387 and ^1J(PF) = 1110 Hz. This isomer comprises approximately 10% of the sample and is attributed to the geometric isomer in which the fluorine and amino substituent on the phosphido ligand are interchanged (see Scheme 2). The ratio of the two isomers does not change with temperature and there is no evidence of exchange, suggesting that there is no equilibrium between them. The X-ray crystal structure contains only the major isomer.

Table 2. Selected bond distances (Å) and angles (°) for $[Ru_5(CO)_{13}(\mu_5\text{-N})(\mu_2\text{-P(F)N-}i\text{-Pr}_2)]$ (**3**) and $[Ru_5(CO)_{13}(\mu_5\text{-N})(\mu_2\text{-P(OMe)N-}i\text{-Pr}_2)]$ (**6**).

	3	**6**
Bond distances (Å)		
Ru(1)—Ru(1′)	2.8261(4)	2.8013(13)
Ru(1)—Ru(2)	2.8687(3)	2.8703(10)
Ru(1)—Ru(3)	2.8349(3)	2.8472(10)
Ru(2)—Ru(2′)	2.8447(4)	2.8493(13)
Ru(2)—Ru(3)	2.7424(3)	2.7342(10)
Ru(1)—N(1)	2.036(2)	2.027(7)
Ru(2)—N(1)	2.010(2)	2.010(7)
Ru(3)—N(1)	2.086(3)	2.068(10)
Ru(1)—P(1)	2.2547(7)	2.302(2)
P(1)—N(2)	1.635(3)	1.630(10)
P(1)—F(1)	1.579(2)	
P(1)—O(8)		1.578(8)
Bond angles (°)		
F(1)-P(1)-N(2)	99.44(13)	
O(8)-P(1)-N(2)		97.3(5)
F(1)-P(1)-Ru(1)	113.43(7)	
O(8)-P(1)-Ru(1)		120.3(3)
N(2)-P(1)-Ru(1)	126.57(7)	123.0(3)
Ru(1′)-P(1)-Ru(1)	77.61(3)	74.96(9)
Ru(2)-N(1)-Ru(2′)	90.07(12)	90.3(4)
Ru(2)-N(1)-Ru(1′)	170.83(17)	172.1(6)
Ru(2)-N(1)-Ru(1)	90.298(16)	90.63(5)
Ru(1′)-N(1)-Ru(1)	87.89(12)	87.4(4)
Ru(2)-N(1)-Ru(3)	84.04(10)	84.2(3)
Ru(1)-N(1)-Ru(3)	86.89(10)	88.1(4)

Scheme 2.

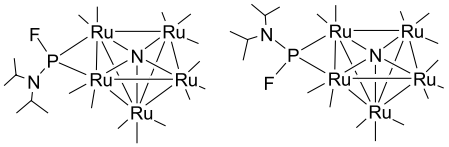

3a (major) **3b** (minor)

The second compound isolated is the nitrene–phosphinidene cluster $[Ru_5(CO)_{10}(\mu\text{-CO})_2(\mu_3\text{-CO})(\mu_4\text{-NH})(\mu_3\text{-PN-}i\text{-Pr}_2)]$ (**4**). An ORTEP diagram of **4** is shown in Fig. 3 and distances and angles are given in Table 3. The cluster consists of five ruthenium atoms arranged in a square-based pyramid. The square face is capped by the NH ligand. The Ru—N distances range from 2.136 to 2.158 Å, comparable to those observed in the very few other known μ_4-NH clusters (16, 17). The hydrogen atom of the nitrene ligand was readily located in the Fourier map and its position and thermal parameters were refined. One of the triangular faces of the metal core is bridged by the phosphinidene ligand. The Ru—P distances of 2.2607(5)–2.2839(5) Å are typical for μ_3-phosphinidene ligands (6, 18). The P—N distance of 1.6295(16) is slightly shorter than a typical P—N

© 2002 NRC Canada

Fig. 3. Structure of $[Ru_5(CO)_{10}(\mu\text{-}CO)_2(\mu_3\text{-}CO)(\mu_3\text{-}PN\text{-}i\text{-}Pr_2)(\mu_4\text{-}NH)]$ (**4**). Thermal ellipsoids are shown at the 50% level. Hydrogen atoms have been eliminated from the isopropyl groups.

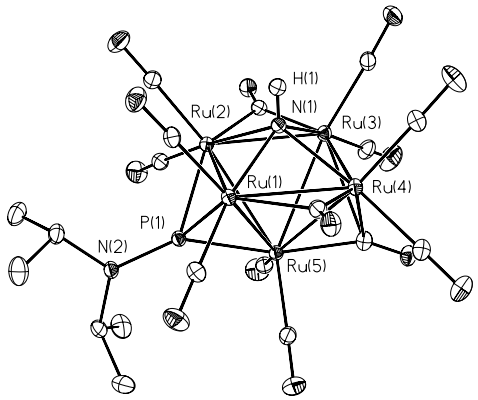

single bond and is consistent with the P—N distance in related μ_3-aminophosphinidene ligands (6, 18). The cluster contains 13 carbonyl ligands. One forms a triply bridging interaction at the triangular face opposite to the μ_3-phosphinidene ligand, while two carbonyls doubly bridge at the Ru(2)–Ru(3) and Ru(1)–Ru(4) edges of the square base, adjacent to the uncapped trigonal faces. The remaining carbonyl ligands are terminal, two on each metal. The metal—metal distances of the μ_2-carbonyl-bridged edges are short (2.6929(2) and 2.6978(2) Å). The other distances within the square base are 2.8335(3) and 2.7894(3) Å, while those to the apical ruthenium atom range from 2.8721(2) to 2.9324(2) Å. The nitrene and phosphinidene ligands each contribute 4 electrons, resulting in a cluster electron count of 74, consistent with a *nido* M_5 or *closo* M_5N structure.

The resonance for the hydrogen atom of the nitrene ligand in **4** appears in the ^{1}H NMR spectrum at δ 3.22 as a 1:1:1 triplet with $^1J(^{14}NH)$ = 50 Hz. These values compare well with reported μ_4-NH ligands. The sharpness of the peak, which allows resolution of the coupling, results from the symmetric environment of the quadrupolar nitrogen atom. The phosphorus chemical shift of δ 495.8 is in the expected range for triply bridging phosphinidene ligands and is shifted upfield from that of the μ_4-phosphinidene in **2** by 55 ppm.

The formation of nitrene (NH) ligands via protonation of a nitrosyl ligand was initially observed in the transformation of $\{(\eta^5\text{-}C_5H_4Me)Mn(NO)\}_3(\mu_3\text{-}NO)$ into $[\{(\eta^5\text{-}C_5H_4Me)Mn(NO)\}_3(\mu_3\text{-}NH)]^+$ (19). The present example is of interest because it is the first example of the transformation of a μ_2-NO ligand to a μ_4-NH ligand. Quadruply bridging NH ligands are relatively rare but have previously been produced by protonation of nitrides (17), or via thermolysis or hydrogenation of $NOCH_3$ ligands (16). Also of note in the reaction is the apparent preference for a quadruply bridging nitrene ligand, requiring that the μ_4-phosphinidene ligand of the starting cluster move into a μ_3-coordination mode. This is somewhat surprising given the greater tendency of phosphorus than nitrogen to support hypervalency.

The source of the nitrene hydrogen in **4** was investigated by reaction of **2** with triflic acid-*d*. Deuteration of the nitrene ligand in the resulting product was confirmed by ^{2}H NMR spectroscopy, which showed a broad singlet at δ 3.22 for the ND ligand. Further evidence for the reaction pathway in the conversion of **2** to **4** was provided by the mass spectrometric detection of CO_2 in the gas above the reaction mixture, suggesting that CO acts as a reducing agent in the transformation. Since the number of carbonyl ligands in **2**, **3**, and **4** is the same, cluster decomposition must provide an additional source of CO for co-ordination, consistent with the moderate yields observed.

Table 3. Selected bond distances (Å) and angles (°) for $[Ru_5(CO)_{10}(\mu\text{-}CO)_2(\mu_3\text{-}CO)(\mu_3\text{-}PN\text{-}i\text{-}Pr_2)(\mu_4\text{-}NH)]$ (**4**).

Bond distances (Å)			
Ru(1)—Ru(2)	2.8335(3)	Ru(1)—N(1)	2.1511(16)
Ru(1)—Ru(4)	2.6929(2)	Ru(2)—N(1)	2.1582(16)
Ru(1)—Ru(5)	2.9068(2)	Ru(3)—N(1)	2.1355(16)
Ru(2)—Ru(3)	2.6978(2)	Ru(4)—N(1)	2.1529(16)
Ru(2)—Ru(5)	2.8721(2)	Ru(1)—P(1)	2.2839(5)
Ru(3)—Ru(4)	2.7894(3)	Ru(2)—P(1)	2.2826(5)
Ru(3)—Ru(5)	2.9324(2)	Ru(5)—P(1)	2.2607(5)
Ru(4)—Ru(5)	2.9096(2)	P(1)—N(2)	1.6295(16)
Bond angles (°)			
Ru(1)-N(1)-Ru(2)	82.22(5)	Ru(3)-N(1)-Ru(4)	81.15(6)
Ru(1)-N(1)-Ru(4)	77.47(5)	Ru(3)-N(1)-Ru(2)	77.85(5)
Ru(3)-N(1)-Ru(1)	130.80(8)	Ru(4)-N(1)-Ru(2)	129.01(8)

Protonation of the nitrosyl cluster in the presence of excess water results in the formation of the same products with similar yields. In no case was hydrolysis of the aminophosphinidene ligand observed. Clearly, the nitrosyl ligand is the most reactive site in compound **2** towards protonation. The formation of **3** can be avoided by using trifluoromethanesulfonic acid to protonate **2**, leading to **4** as the sole isolated product. However, the yield of **4** in the triflic acid reaction is not significantly better than in the reaction with tetrafluoroboric acid. Reducing the reaction temperature also appears to suppress the formation of **3** in favour of **4**.

The fluorine–substituted phosphido ligand in **3** results from fluoride abstraction from the BF_4^- counterion. We have previously observed such reactivity with BF_4^- in the formation of fluorophosphinidene ligands (7, 20) and difluorophosphido ligands (21). To confirm that BF_4^- is simply acting as a fluoride source, the reaction of **2** with triflic acid was carried out in the presence of excess Bu_4NF. This reaction led to compounds **3** and **4** in roughly the same yields as the reaction with tetrafluoroboric acid.

Characterization of intermediates in the formation of **3** and **4** was attempted by monitoring the protonation reaction at low temperature. The nitrosyl cluster **2** was thus treated with triflic acid at –80°C. Below –40°C, one major species is observed that is tentatively assigned as the hydroxyimido complex $[Ru_5(CO)_{13}(\mu\text{-}NOH)(\mu_4\text{-}PN\text{-}i\text{-}Pr_2)]$ (**5**), which results from protonation of the nitrosyl oxygen. Its ^{31}P chemical shift of δ 558 clearly indicates that the μ_4-phosphinidene ligand is retained. Peaks for the amine isopropyl groups are apparent in the ^{1}H NMR but no peak for the NOH hydrogen was observed. The failure to observe a peak for the NOH ligand could indicate that the proton is rapidly exchanging with acid in solution. Above –40°C, several new species, including compound **4** are formed, but the mixture is too

© 2002 NRC Canada

Scheme 3.

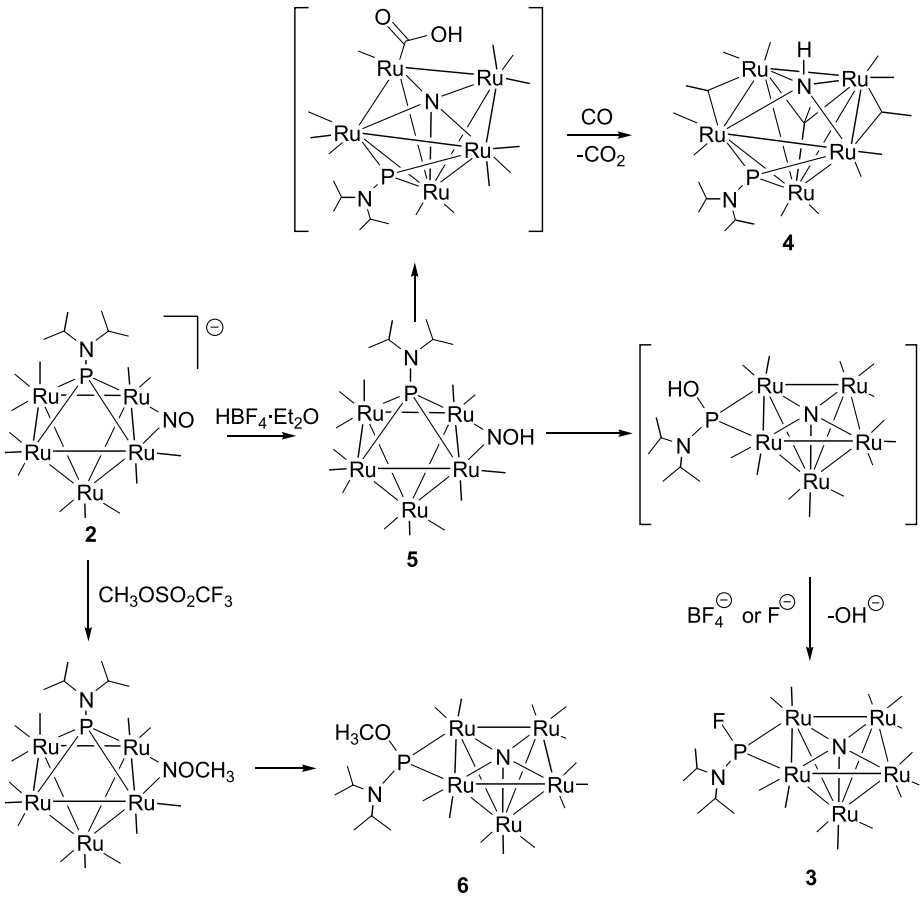

complex to characterize any of the compounds. At higher temperature, compound **4** becomes the predominant species.

Nitrosyl methylation

To expand the chemistry, as well as to help elucidate the mechanism of the protonation reactions, the phosphinidene–nitrosyl cluster was reacted with methyltrifluoromethanesulfonate. One product was isolated from the reaction in moderate yield and identified as the phosphido–nitride cluster $[Ru_5(CO)_{13}(\mu_5\text{-}N)\{\mu_2\text{-}P(OMe)N\text{-}i\text{-}Pr_2\}]$ (**6**). The ORTEP diagram of **6** is shown in Fig. 4 and selected distances and angles are given in Table 2. Compound **6** is structurally analogous to the fluoroaminophosphido cluster **3** except that the fluoro group on the phosphinidene ligand is replaced by an alkoxy group. A comparison of parameters involving the phosphido ligands in the two structures reveals shorter metal—phosphorus distances and a slightly longer phosphido-bridged metal—metal distance in the fluorophosphido complex **3**. The differences reflect the greater π-acceptor ability of the fluorophosphido ligand over the alkoxyphosphido ligand. The other structural parameters of the two clusters are very similar (see Table 2).

The ^{31}P NMR spectrum of **6** shows a singlet at δ 378, close to that observed for the analogous cluster **3**. As for **3**, a minor isomer at δ 376 (13%) is observed and is again attributed to the isomer in which the amino and alkoxy substituents on phosphorus are interchanged. The methoxy group appears in the ^1H NMR spectrum at δ 3.65 (major isomer) or δ 3.47 (minor isomer) with a $^2J(PH)$ of 15 (major) or 18 (minor) Hz.

Fig. 4. Structure of $[Ru_5(CO)_{13}(\mu_5\text{-}N)(\mu_2\text{-}P(OMe)N\text{-}i\text{-}Pr_2)]$ (**6**). Thermal ellipsoids are shown at the 50% level. Hydrogen atoms have been eliminated.

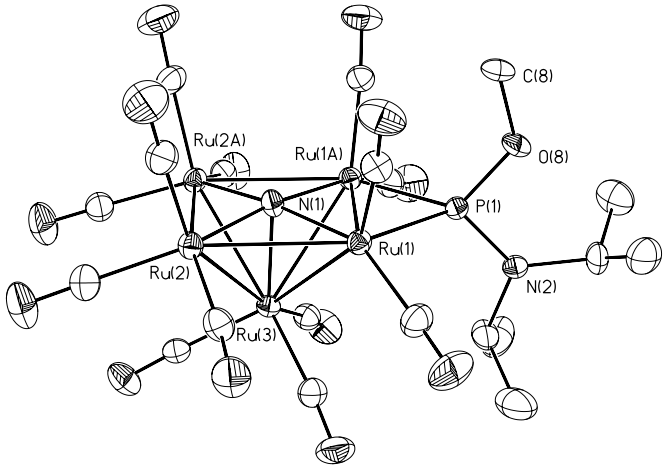

The formation of cluster **6** results from initial methylation at the nitrosyl oxygen to form an $NOCH_3$ ligand. Migration of the alkoxy group from nitrogen to the phosphorus atom of

© 2002 NRC Canada

the phosphinidene ligand leads to the phosphido group and the nitride ligand as shown in Scheme 3. Attempts to observe the methoxyimido intermediate were unsuccessful as elevated temperatures were required to induce reactivity with methyl triflate, and at these temperatures, the reaction proceeds rapidly to the final product. In the reaction, the phosphorus ligand moves from μ_4-coordination to μ_2-coordination, allowing the nitride to occupy the square face of the square-based pyramid. In this reaction, the rearrangement is expected because the three-electron donor phosphido ligand generally prefers a doubly bridging co-ordination mode, while the five-electron donor nitride ligand requires a higher co-ordination number.

Mechanism

A proposed mechanism for the formation of compounds **3** and **4** is shown in Scheme 3. The initial site of electrophilic attack by H^+ is at the oxygen of the nitrosyl ligand forming the hydroxyimido intermediate **5**. This is based on (*i*) characterization of **5** at low temperature, (*ii*) the reactivity with methyl triflate in which the electrophile remains attached to the oxygen in the final product, and (*iii*) literature precedence for electrophilic attack at the oxygen of cluster-bound nitrosyl ligands (22).

Two pathways are available for the decomposition of the hydroxyimido intermediate. The first leads to the nitrene complex **4**, via CO reduction of the NOH ligand and CO_2 loss (detected by GC-MS). This reduction may occur via hydroxide migration to a carbonyl ligand, forming an intermediate nitride–acyl complex, although a concerted mechanism is not ruled out. Formation of the nitride–acyl intermediate requires cluster rearrangement to allow a μ_5 co-ordination mode for the nitride ligand, forcing the phosphinidene ligand into a μ_3 co-ordination mode. A nitride intermediate in the formation of **4** may explain the preference for μ_4-nitrene co-ordination over μ_4-phosphinidene co-ordination in the final product. Carbon dioxide loss and proton migration to the nitride ligand then lead to the final product.

The second pathway for hydroxide migration is to the phosphorus atom of the phosphinidene ligand to form an intermediate hydroxyaminophosphido complex. This migration directly parallels the methoxy migration that leads to the methoxy-amino phosphido complex **6**, and the similar isomer distributions in **3** and **6** suggests a similar mechanism for their formation. In the presence of BF_4^- or fluoride, the hydroxy group is displaced by fluoride leading to **3**. In the absence of fluoride, the hydroxyphosphinidene complex apparently decomposes. Although a mechanism in which fluoride substitution occurs at the nitrogen of the hydroxyphosphinidene cluster **5** leading to a fluoroimido complex can be envisioned, the insensitivity of the yield of **4** to the presence of BF_4^- or F^- suggests that fluoride substitution takes place after differentiation between the two pathways.

Experimental

Unless specified, all procedures were carried out under a nitrogen atmosphere. Solvents were dried and distilled before use. The reagents $HOSO_2CF_3$, $HBF_4{\cdot}Et_2O$, and $CH_3OSO_2CF_3$ were purchased from Aldrich and used as received. The compounds $[Ru_5(CO)_{15}(\mu_4\text{-PN-}i\text{-Pr}_2)]$ (20) and $[PPN][NO_2]$ (11) were prepared according to published procedures. The TLC separations were performed in air using silica gel plates (60 Å F254 5–15 μm). Elemental analyses were carried out by Guelph Chemical Laboratories.

Preparation of compounds

[PPN][Ru$_5$(CO)$_{13}$(μ-NO)(μ$_4$-PN-i-Pr$_2$)] (2)

The cluster $[Ru_5(CO)_{15}(\mu_4\text{-PN-}i\text{-Pr}_2)]$ (78 mg, 0.074 mmol) and $[PPN][NO_2]$ (45 mg, 0.077 mmol) were dissolved in 10 mL of THF resulting in a colour change from dark green to dark red. The solution was stirred for 2 h, the solvent was removed in vacuo, and the residue was extracted with diethyl ether (10 mL) and filtered. Purple crystals were grown from diethyl ether at –30°C. Yield: 54 mg, 47%. IR (CH_2Cl_2 soln) (cm^{-1}) (ν*C*O): 2053 (m), 2005 (vs), 1987 (s), 1949 (vw), 1925 (sh) ν(NO): 1543 (w). ^{1}H NMR ($CDCl_3$) δ: 7.5 (m, Ph), 3.85 (sept, C*H*, ^1J(HH) = 7.0 Hz), 1.15 (d, CH_3, ^1J(HH) = 7.0 Hz). ^{31}P NMR ($CDCl_3$) δ: 550.7 (s, *P*N-*i*-Pr$_2$), 21.7 (s, PPN). FAB-MS (*m*/*z*): 1031 ($[M]^-$), 1003–947 ($[M - nCO]^-$ (*n* = 1–3)). Anal. calcd. for $C_{55}H_{44}O_{14}P_3N_3Ru_5$: C 42.10, H 2.83, N 2.68; found: C 42.17, H 3.02, N 2.22.

Reaction of [PPN][Ru$_5$(CO)$_{13}$(μ-NO)(μ$_4$-PN-i-Pr$_2$)] (2) with HBF$_4$·Et$_2$O

To a solution of $[PPN][Ru_5(CO)_{13}(\mu\text{-NO})(\mu_4\text{-PN-}i\text{-Pr}_2)]$ (**2**) (60 mg, 0.049 mmol) in CH_2Cl_2 (20 mL) was added an excess of $HBF_4{\cdot}Et_2O$ (10 μL, 0.159 mmol) resulting in a colour change from dark red to orange. Then solvent was removed in vacuo, and the resulting residue was purified via thin layer chromatography using hexane–CH_2Cl_2 50:50. Two orange bands were isolated that were characterized as $[Ru_5(CO)_{13}(\mu_5\text{-N})(\mu_2\text{-P(F)N-}i\text{-Pr}_2)]$ (**3**, 9 mg, 23%, two isomers 90:10) and $[Ru_5(CO)_{10}(\mu\text{-CO})_2(\mu_3\text{-CO})(\mu_4\text{-NH})(\mu_3\text{-PN-}i\text{-Pr}_2)]$ (**4**, 12 mg, 31%). Crystals of **3** and **4** were grown from CH_2Cl_2–hexane at –30°C.

Data for 3

IR (CH_2Cl_2 soln) (cm^{-1}) (ν CO): 2083 (m), 2044 (vs), 2023 (vs), 2005 (vw), 1994 (vw). ^{1}H NMR δ: 3.63 (**3a**, sept, ^3J(HH) = 6.7 Hz, CH), 3.87 (**3b**, sept, ^3J(HH) = 6.8 Hz, CH), 1.5 (**3b**, d, ^3J(HH) = 6.8 Hz, CH_3), 1.58 (**3a**, d, ^3J(HH) = 6.7 Hz, CH_3). ^{31}P NMR δ: 391 (**3a**, d, ^1J(PF) = 1087 Hz), 387.1 (**3b**, d, ^1J(PF) = 1110 Hz). ^{19}F NMR δ: 65.9 (**3a**, d, ^1J(PF) = 1087) 61.4 (**3b**, d, ^1J(PF) = 1110 Hz). FAB-MS (*m*/*z*): 1033 ($[M]^+$), 1033–835 ($[M - nCO]^+$ (*n* = 1–7)). Anal. calcd. for $C_{19}H_{14}O_{13}PFN_2Ru_5$: C 22.06, H 1.37, N 2.71; found: C 21.66, H 1.18, N 2.71.

Data for 4

IR (CH_2Cl_2 soln) (cm^{-1}): (ν NH) 3319 s, (ν CO) 2076 (w), 2033 (vs), 1995 (m), 1855 (br). ^{2}H NMR δ: 3.22 (b). ^{1}H NMR δ: 4.76 (sept, ^3J(HH) = 6.8 Hz, CH), 3.22 (1:1:1 triplet, $^1J(^{14}NH)$ = 50 Hz), 1.71 (d, ^3J(HH) = 6.8 Hz, CH_3). ^{31}P NMR δ: 495.8. FAB-MS (*m*/*z*): 1016 ($[M]^+$), 988–820 ($[M - nCO]^+$ (*n* = 1–7)). Anal. calcd. for $C_{19}H_{15}O_{13}PN_2Ru_5$: C 22.47, H 1.49, N 2.76; found: C 22.14, H 1.31, N 2.79.

© 2002 NRC Canada

Table 4. Crystallographic data for compounds **2**, **3**, **4**, and **6**.

	2	**3**	**4**	**6**
Formula	$C_{55}H_{44}N_3O_{14}P_3Ru_5$	$C_{19}H_{14}FN_2O_{13}PRu_5$	$C_{20}H_{17}Cl_2N_2O_{13}PRu_5$	$C_{20}H_{17}N_2O_{14}PRu_5$
Formula weight	1569.19	1033.64	1100.58	1045.68
Crystal system	Triclinic	Orthorhombic	Monoclinic	Monoclinic
Space group	$P\bar{1}$	$Pmn2_1$	$P2_1/c$	$P2_1/m$
Lattice parameters				
a (Å)	11.0845(7)	15.4524(9)	13.4582(7)	9.413(1)
b (Å)	16.463(1)	8.1778(5)	12.9073(7)	14.430(2)
c (Å)	16.763(1)	11.6829(7)	19.465(1)	11.992(2)
α (°)	101.743(1)			
β (°)	102.556(1)		109.780(1)	109.425(2)
γ (°)	97.369(1)			
V (Å^3)	2875.2(3)	1476.3(1)	3181.8(3)	1536.2(4)
Z	2	2	4	2
$D_{calcd.}$ (mg m^{-3})	1.813	2.325	2.298	2.261
μ (Mo Kα) (mm^{-1})	1.433	2.621	2.598	2.519
$2\theta_{max}$ (°)	57.44	57.40	57.42	57.46
Reflections measured	34264	16897	37058	14129
Unique reflections	14739	3945	8224	4077
Variables	721	224	402	208
Residuals: R, R_w	0.0351, 0.0811	0.0155, 0.0370	0.0182, 0.0416	0.0496, 0.1693
Largest peak in final difference map (e Å^{-3})	6.227	0.521	0.595	3.297

[Ru$_5$(CO)$_{10}$(μ-CO)$_2$(μ$_3$-CO)(μ$_4$-NH)(μ$_3$-PN-i-Pr$_2$)] (4)

To a solution of [PPN][Ru$_5$(CO)$_{13}$(μ-NO)(μ$_4$-PN-*i*-Pr$_2$)] (**2**) (112 mg, 0.072 mmol) in 10 mL of CH_2Cl_2 was added $HOSO_2CF_3$ (10 μL, 17 mg, 0.113 mmol) resulting in an immediate colour change to dark orange. The solution was stirred for 20 min. Separation by thin layer chromatography (50:50 CH_2Cl_2–hexane) resulted in the isolation of one major dark orange product which was shown to be [Ru$_5$(CO)$_{10}$(μ-CO)$_2$(μ$_3$-CO)(μ$_4$-NH)(μ$_3$-PN-*i*-Pr$_2$)] (**4**, 25 mg, 34%). If the reaction is carried out in a closed system, CO_2 can be detected in the headspace by GC–MS analysis.

	m/z	Abundance	%
Sample	28 (N_2/CO)	582144	96
	32 (O_2)	63952	1
	44 (CO_2)	157952	3
Air blank	28 (N_2)	2504704	80
	32 (O_2)	635392	20
	44 (CO_2)	3717	0.1

[Ru$_5$(CO)$_{13}$(μ-NOH)(μ$_4$-PN-i-Pr$_2$)] (5)

A sample of [PPN][Ru$_5$(CO)$_{13}$(μ-NO)(μ$_4$-PN-*i*-Pr$_2$)] (**2**) (30 mg, 0.019 mmol) in 0.5 mL of CD_2Cl_2 in an NMR tube was cooled to –80°C. Triflic acid (1.7 μL, 2.9 mg, 0.019 mmol) was added and the sample was introduced into the NMR spectrometer at –60°C. One major species was observed at –60°C and attributed to [Ru$_5$(CO)$_{13}$(μ-NOH)(μ$_4$-PN-*i*-Pr$_2$)] (**5**). Above –40°C, compound **4** is formed along with several minor products.

Data for 5

^{1}H NMR δ: 3.8 (bm), 1.1 (d, CH_3, ^1J(HH) = 5.8 Hz). ^{31}P NMR δ: 558 (s, *P*N-*i*-Pr$_2$).

[Ru$_5$(CO)$_{13}$(μ$_5$-N)(μ$_2$-P(OMe)N-i-Pr$_2$)] (6)

To a solution of [PPN][Ru$_5$(CO)$_{13}$(μ$_2$-NO)(μ$_4$-PN-*i*-Pr$_2$)] (**2**) (52 mg, 0.033 mmol) in CH_2Cl_2 (20 mL) was added an excess $CF_3SO_3CH_3$ (10 μL, 0.088 mmol). The reaction mixture was heated under reflux for 16 h resulting in a colour change from red to dark orange. The solvent was removed in vacuo. Thin layer chromatography (hexane–CH_2Cl_2 75:25) resulted in the isolation of one orange band. Crystals of [Ru$_5$(CO)$_{13}$(μ$_5$-N)(μ$_2$-P(OMe)N-*i*-Pr$_2$)] (**6**) were grown from CH_2Cl_2–hexane at –30°C. Yield: 10 mg, 29%. IR (CH_2Cl_2) (cm^{-1}) (ν CO): 2079 (m), 2041 (s), 2030 (s), 2020 (vs), 1997 (w), 1986 (w). ^{1}H NMR ($CDCl_3$) δ: 3.57 (sept, ^3J(HH) = 6.2 Hz, CH, **6a**), 3.70 (sept, ^3J(HH) = 6.8 Hz, CH, **6b**), 3.67 (d, ^2J(HH) = 15.2 Hz, OCH_3, **6a**), 3.46 (d, ^2J(HH) = 14.2 Hz, OCH_3, **6b**), 1.45 (d, ^3J(HH) = 6.7 Hz, CH_3, **6a**), 1.53 (d, ^3J(HH) = 6.6 Hz, CH_3, **6b**). ^{31}P NMR ($CDCl_3$) δ: 378 (s, **6a**), 376 (s, **6b**). Anal. calcd. for $C_{20}H_{17}O_{14}PN_2Ru_5$: C 22.97, H 1.64, N 2.68; found: C 22.48, H 1.78, N 2.66.

X-ray crystallography

Crystals of compounds **2**, **3**, **4**, and **6** were mounted on glass fibres. Intensity data were collected on a Siemens SMART CCD diffractometer with the use of graphite-monochromated Mo Kα radiation at 173 K. Unit cells were determined from randomly selected reflections obtained using the SMART CCD automatic search, centre, index, and least-squares routines. Integration was carried out using SAINT and empirical absorption corrections were applied using SADABS. Structure solution was carried out using the SHELXTL 5.1 suite of programs. Initial solutions were obtained by direct methods and refined by successive least-squares cycles. Full matrix least-squares refinements minimized the function $\Sigma_{hkl}w(|F_o|- |F_c|)^2$ where $w = 1/\sigma(F_o)^2$,

© 2002 NRC Canada

$\sigma(F_o) = \sigma(F_o^2)/2F_o$, and $\sigma(F_o^2) = [\sigma(I_{raw})^2 + (0.02I_{net})^2]^{1/2}/Lp$. Crystal data and collection parameters are listed in Table 4.[2]

Conclusions

We have synthesized the first example of a mixed nitrosyl–phosphinidene cluster. Reaction of the nitrosyl–phosphinidene complex with acid leads to nitrogen—oxygen bond cleavage and nitrene or nitride complexes. Amino-phosphinidene hydrolysis is not observed although the phosphinidene is transformed into a phosphido group in one case. Our results suggest that the μ-NO ligand is the most nucleophilic site in these Ru_5 systems, while the μ_4-PN-*i*-Pr_2 group is susceptible to nucleophilic attack at phosphorus. The conversion of NO to nitrene and nitride provides insight into the reduction of nitrosyl ligands on cluster frameworks and the clusters provide an opportunity to compare the properties of related phosphorus and nitrogen ligands. We are currently exploring the generation of μ_n-NO ligands on preformed PO clusters and the comparative chemistry of the four NO–PO–PR–NR combinations.

Acknowledgements

We are grateful to the Natural Sciences and Engineering Research Council of Canada (NSERC) and the National Research Council of Canada (NRC) for financial support of this work.

References

1. C.E. Housecroft. *In* Inorganometallic chemistry. T.P. Fehlner (*Ed.*) Plenum Press, New York. 1992. pp 115–130; K.B. Dillon, F. Mathey, and J.F. Nixon. *In* Phosphorus: The carbon copy. John Wiley & Sons, Ltd., Chichester. 1998. Chap. 3.
2. A.H. Cowley. Acc. Chem. Res. **30**, 445 (1997); B.T. Sterenberg, K.A. Udachin, and A.J. Carty. Organometallics, **20**, 2657 (2001).
3. G. Huttner and K. Knoll. Angew. Chem. Int. Ed. Engl. **26**, 743 (1987).
4. A.M. Arif, A.H. Cowley, N.C. Norman, A.G. Orpen, and M. Pakulski. Organometallics, **7**, 309 (1988).
5. W. Wang, J.F. Corrigan, G.D. Enright, N.J. Taylor, and A.J. Carty. Organometallics, **17**, 427 (1998); W. Wang, G.D. Enright, and A.J. Carty. J. Am. Chem. Soc. **119**, 12 370 (1997); W. Wang, G.D. Enright, J. Driediger, and A. J. Carty. J. Organomet. Chem. **541**, 461 (1997).
6. J.F. Corrigan, S. Doherty, N.J. Taylor, and A.J. Carty. J. Am. Chem. Soc. **116**, 9799 (1994); W. Wang, J.F. Corrigan, S. Doherty, G.D. Enright, N.J. Taylor, and A.J. Carty. Organometallics, **15**, 2770 (1996).
7. W. Wang and A.J. Carty. New J. Chem. **21**, 773 (1997); J.H. Yamamoto, K.A. Udachin, G.D. Enright, and A.J. Carty. Chem. Commun. 2259 (1998).
8. L. Scoles, J.H. Yamamoto, L. Brissieux, B.T. Sterenberg, K.A. Udachin, and A.J. Carty. Inorg. Chem. **40**, 6731 (2001).
9. A. Bérces, O. Koentjoro, B.T. Sterenberg, J.H. Yamamoto, J. Tse, and A.J. Carty. Organometallics, **19**, 4336 (2000).
10. L. Scoles, B.T. Sterenberg, K.A. Udachin, and A.J. Carty. Chem. Commun. 320, (2002).
11. R.E. Stevens, T.J. Yanta, and W.L. Gladfelter. J. Am. Chem. Soc. **103**, 4981 (1981).
12. R.E. Stevens and W.L. Gladfelter. Inorg. Chem. **22**, 2034 (1983).
13. G.B. Richter-Addo and P. Legzdins. *In* Metal nitrosyls. Oxford University Press, New York. 1992. pp 61–68.
14. V. Kumar, D.W. Lee, M.G. Newton, and R.B. King. J. Organomet. Chem. **512**, 1 (1996); B.T. Sterenberg and A.J. Carty. J. Organomet. Chem. **617–618**, 696 (2001); A.H. Cowley, D.M. Giolando, C.M. Nunn, M. Pakulski, D. Westmoreland, and N.C. Norman. J. Chem. Soc. Dalton Trans. 2127 (1988).
15. M.L. Blohm and W.L. Gladfelter. Organometallics, **4**, 45 (1985).
16. E.N.-M. Ho and W.-T. Wong. J. Chem. Soc. Dalton Trans. 4215 (1998); K.K.H. Lee and W.T. Wong. J. Chem. Soc. Dalton Trans. 1707 (1996); E.N.-M. Ho and W.T. Wong. J. Chem. Soc. Dalton Trans. 513 (1998); K.K.H. Lee and W.T. Wong. J. Organomet. Chem. **503**, C43 (1995).
17. M.L. Blohm and W.L. Gladfelter. Organometallics, **5**, 1049 (1986).
18. J.H. Yamamoto, G.D. Enright, and A.J. Carty. J. Organomet. Chem. **577**, 126 (1999).
19. P. Legzdins, C.R. Nurse, and S.J. Rettig. J. Am. Chem. Soc. **105**, 3727 (1983).
20. J.H. Yamamoto, L. Scoles, K.A. Udachin, G.D. Enright, and A.J. Carty. J. Organomet. Chem. **600**, 84 (2000).
21. S. Kahlal, W. Wang, L. Scoles, K.A. Udachin, J.-Y. Saillard, and A. J. Carty. Organometallics, **20**, 4469 (2001).
22. W.L. Gladfelter. Adv. Organomet. Chem. **24**, 41 (1985).

[2] Supplementary data may be purchased from the Depository of Unpublished Data, Document Delivery, CISTI, National Research Council Canada, Ottawa, ON K1A 0S2, Canada (http://www.nrc.ca/cisti/irm/unpub_e.shtml for information on ordering electronically). CCDC 176891, 176892, 183959, and 183960 contain the supplementary data for this paper. These data can be obtained, free of charge, via www.ccdc.cam.ac.uk/conts/retrieving.html (or from the Cambridge Crystallographic Data Centre, 12 Union Road, Cambridge, U.K.; fax +44 1223 336033; or deposit@ccdc.cam.ac.uk).

© 2002 NRC Canada

$SiCl_4$–ethanol as a trimerization agent for organometallics: convenient syntheses of the symmetrically substituted arenes 1,3,5-$C_6H_3R_3$ where R = $(C_5H_4)Mn(CO)_3$ and $(C_5H_4)Fe(C_5H_5)$

Hari K. Gupta, Nada Reginato, Francis O. Ogini, Stacey Brydges, and Michael J. McGlinchey

Abstract: Trimerization of acetylferrocene and of (acetylcyclopentadienyl)tricarbonyl-manganese proceeds efficiently in the presence of ethanol and tetrachlorosilane. The resulting 1,3,5-trisubstituted benzenes have been characterized by X-ray crystallography and compared with the structure of (1,3,5-triphenylbenzene)tris(tricarbonylchromium). The efficacy of EtOH–$SiCl_4$ as a combined reagent for the trimerization of polycyclic ketones is also discussed. Finally, the synthesis and structure of $[CpMn(CO)_2]_2(\mu\text{-}C{=}CHPr)$, derived from the reaction of cymantrene with butyllithium and phenylacetyl chloride at room temperature, is described.

Key words: ketone, condensation, cyclization, organometallics, arenes.

Résume : La trimérisation de l'acétylferrocène et du (acétylcyclopentadiényl)tricarbonylmanganèse se produit de façon efficace en présence d'éthanol et de tétrachlorosilane. Les benzènes 1,3,5-trisubstitués qui en résultent ont été caractérisés par diffraction des rayons X et on a comparé leurs structures avec celle du (1,3,5-triphénylbenzène)tris(tricarbonylchrome). On discute aussi de l'efficacité du EtOH–$SiCl_4$ comme réactif combiné pour la trimérisation de cétones polycycliques. Enfin, on décrit la synthèse et la structure du $[CpMn(CO)_2]_2(\mu\text{-}C{=}CHPr)$ dérivé de la réaction du cymantrène avec le butyllithium et la chlorure de phénylacétyle à la température ambiante.

Mots clés : cétone, condensation, cyclisation, organométalliques, arènes.

[Traduit par la Rédaction]

Introduction

The use of polycyclic aromatic hydrocarbons as building blocks for discrete nanostructures, such as fullerene (C_{60}) derivatives and extended two- and three-dimensional arrays, is contingent upon the advancement of novel design schemes and facile synthetic approaches (1, 2). In turn, these motifs are rooted in the fact that structure and internal motion are governed by symmetry, sterics, and strain. Diversely functionalized tri- and hexasubstituted (triannulated) benzenes may be widely exploited in these regards, allowing one to amalgamate the topological concepts advanced by Katz (3) and Stang and co-workers (4) with the assembly principles first introduced by Chapman (5). The versatility of these synthons is further enhanced by their general access via cyclotrimerization methods. For example, our recent studies on metal complexes of trindane, **1** (6–8), prepared by the successive dehydration–cyclotrimerization of cyclopentanone, were aided by an efficient route to the $C_{15}H_{18}$ ligand. Whereas early syntheses required concentrated sulfuric acid (9), hydrochloric acid, or sodium ethoxide (10), milder approaches, such as the use of ethanol–tetrachlorosilane, are gaining in popularity (11).

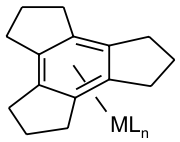

1

ML_n = $Cr(CO)_3$, $Mn(CO)_3^+$, $(C_5H_5)Fe^+$, $RuCl_2[P(OMe)_3]$, $Mn(CO)_2Br$, *etc.*

Both disilane (12) and transition metal homo- and heterogeneous catalysts (13) have been employed for the oligomerization of symmetrical and unsymmetrical alkynes. In the latter instances, cyclotrimerization generally gives rise to isomeric mixtures, as demonstrated by the conversion of phenylacetylene to 1,2,4- and 1,3,5-substituted benzenes, **2** and **3**, respectively, at elevated temperatures in the presence of Si_2Cl_6 (12*a*). In contrast, acid-catalyzed condensation of ketones of the type $R(CO)CH_2R'$ produces only the threefold symmetric arenes, as exemplified by truxene, **4**, or the triazulenyl system, **5** (14, 15). In this report, we describe the use of EtOH–$SiCl_4$ as a convenient reagent for the trimerization of select acetyl–organometallic complexes and

Received 18 February 2002. Published on the NRC Research Press Web site at http://canjchem.nrc.ca on 25 November 2002.

Dedicated to Professor Tristram Chivers in recognition of his services to inorganic chemistry in Canada.

H.K. Gupta, N. Reginato, F.O. Ogini, S. Brydges, and M.J. McGlinchey.[1] Department of Chemistry, McMaster University, Hamilton, ON L8S 4M1, Canada.

[1]Corresponding author (e-mail: mcglinc@mcmaster.ca).

 DOI: 10.1139/V02-152 © 2002 NRC Canada

Scheme 1. Typical trimerizations involving either (*a*) an alkyne or (*b* and *c*) a ketone to generate 1,3,5-tri- and hexasubstituted benzenes.

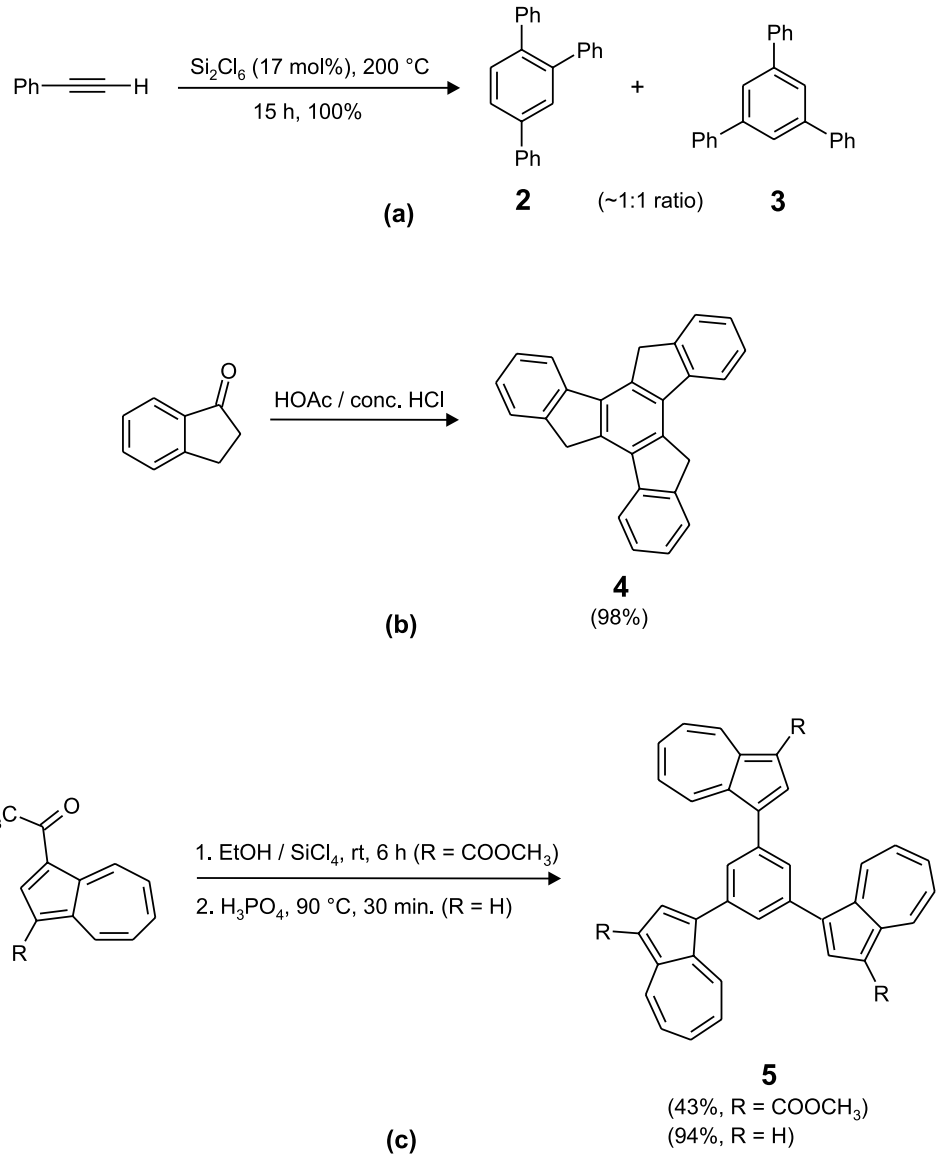

polycyclic ketones to yield the corresponding 1,3,5-trisubstituted arenes and polyphenylene frameworks, respectively (Scheme 1).

Results and discussion

Syntheses and structures of 1,3,5-$C_6H_3R_3$ where R = $(C_6H_5)Cr(CO)_3$, $(C_5H_4)Mn(CO)_3$, and $(C_5H_4)Fe(C_5H_5)$

Systematic modification of the periphery of C_6R_6 arrays by the introduction of new pendant groups is expected to have static and dynamic stereochemical consequences. In 1987, Katz (3) proposed that 1,3,5-trialkyl-2,4,6-triarylbenzenes could be exploited as rigidly oriented and convergent tridentate metal-binding units. More recently, Stang and co-workers (4) have introduced a supramolecular assembly approach to polycyclic nanostructures from combinations of linear and angular building units capable of metal chelation. Among the latter, 1,3,5-trisubstituted benzenes with both flexible and rigid backbones have been extensively employed. In combining these design principles with our long-standing interest in sterically congested organometallic systems, we eventually hope to construct extended covalent networks from such trimetallic precursors.

Several years ago, we reported the synthesis and single crystal X-ray diffraction analysis of (1,3,5-triphenylbenzene)tris(tricarbonylchromium), **6**, prepared in rather low yield by treatment of the polyaryl ligand with a large excess of $Cr(CO)_6$ (Scheme 2*a*). After initial multiple fractional crystallizations, separation of the trimetallic product from the two monochromium isomers and from the bis-$Cr(CO)_3$ adduct was finally achieved by reverse-phase low-pressure liquid chromatography (16). The solid-state structure of **6** revealed a "two-up, one-down" arrangement of the organometallic moieties. In solution, however, the variable-temperature NMR spectra showed no evidence for slowed rotation of the metal-ligated rings, unlike the case of (hexaphenylbenzene)chromium tricarbonyl, for which the

© 2002 NRC Canada

Scheme 2. (*a*) Multiple $Cr(CO)_3$ complexation of 1,3,5-triphenylbenzene and (*b*) EtOH–$SiCl_4$-promoted generation of the organometallic derivatives **9** and **10**.

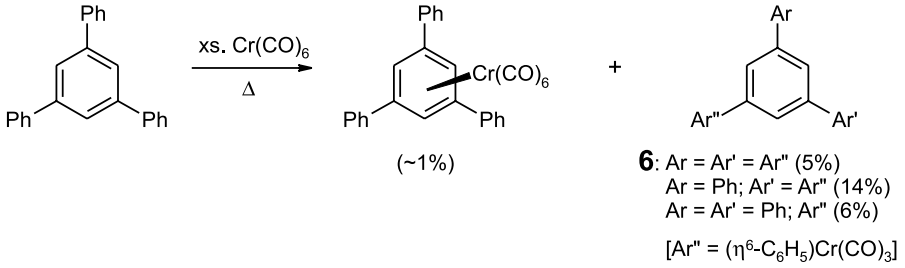

(a)

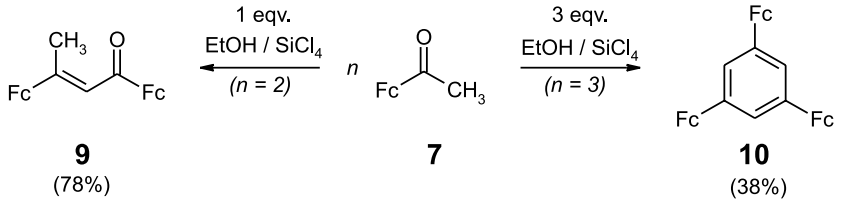

(b)

barrier to rotation of the peripheral $(C_6H_5)Cr(CO)_3$ group was found to be 12.2 kcal mol^{-1} (17).

The preparation of arenes bearing (cyclopentadienyl)ML_n moieties in the 1,3,5 positions cannot parallel the synthetic methodologies exploited for **6**, since the corresponding free polycyclic ligands are not readily available. However, we find that acetylcyclopentadienyl complexes, in particular acetylferrocene, **7**, and (acetylcyclopentadienyl)tricarbonylmanganese, **8**, can be readily trimerized upon treatment with EtOH–$SiCl_4$. In the former case, reaction of acetylferrocene with one equivalent of this reagent at room temperature furnishes (78%) the diferrocenyl complex, **9**, arising from the elimination of a single water molecule. Use of a threefold excess of EtOH–$SiCl_4$ leads directly to 1,3,5-triferrocenylbenzene, **10**, in reasonable yield (40%). The dimer **9** had been described previously by Sasaki and Pittman (18) as the major product (no yield cited) of the reaction of **7** with triethyl orthoformate and dry HCl, and was later isolated by Erasmus et al. (19) as an unexpected by-product (20%) during an attempted preparation of the β-diketone $FcCOCH_2COFc$. A variety of synthetic routes to **10** (20, 21) and its unsymmetrical (1,2,4)-isomer **11** (20, 21*b*, 22, 23) have also been detailed in the literature, although discrepancies regarding reaction conditions and isolable yields exist. The transformation of ethynylferrocene to **10** requires the use of $TaCl_5$ or catalytic amounts of acids, whereas treatment with dicobalt octacarbonyl or the application of thermal and free-radical polymerization methods results in the latter benzene derivative. The current procedure extends the facile process disclosed by Elmorsy and co-workers (11) to organometallic systems, demonstrating a direct, convenient (mild conditions), and rational (stoichiometrically controlled) route to both dimeric and trimeric condensation products (Scheme 2*b*), whose spectroscopic characterizations were previously incomplete.

Fig. 1. Perspective view of the molecular structure of 1,3,5-C_6H_3-[(η^5-C_5H_4)$Mn(CO)_3$]$_3$, **13**.

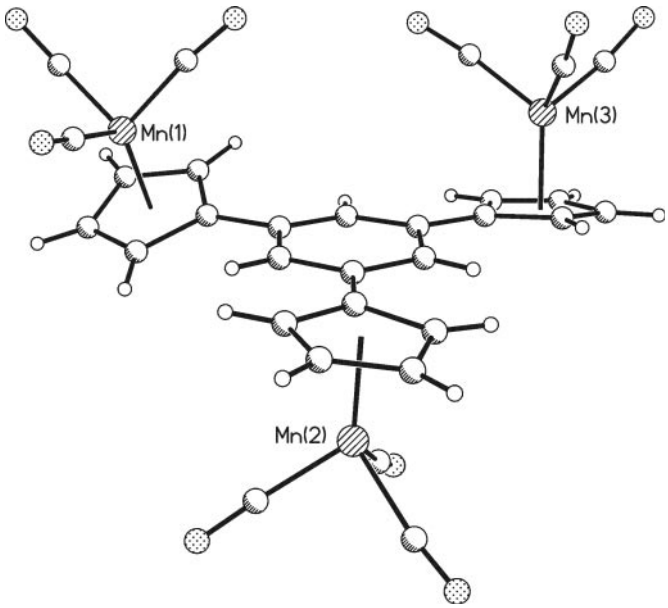

Similarly, (acetylcyclopentadienyl)tricarbonylmanganese, **8**, reacts at room temperature with EtOH–$SiCl_4$ to yield the dimanganese complex **12** (analogous to **9**) and 1,3,5-tris(cyclopentadienytricarbonylmanganese)benzene, **13**, the X-ray crystal structure of which is shown in Fig. 1. In the solid state, the organometallic substituents in the chromium, manganese, and iron trimers **6**, **13**, and **10**, respectively, are each oriented in the now familiar "two-up, one-down" arrangement with dihedral angles between the central and peripheral rings of 152° (up), 67° (up), and 37° (down) for chromium, 24° (up), 11° (up), and 175° (down) for manganese,

© 2002 NRC Canada

Scheme 3. Proposed mechanism for the triple condensation of ketones.

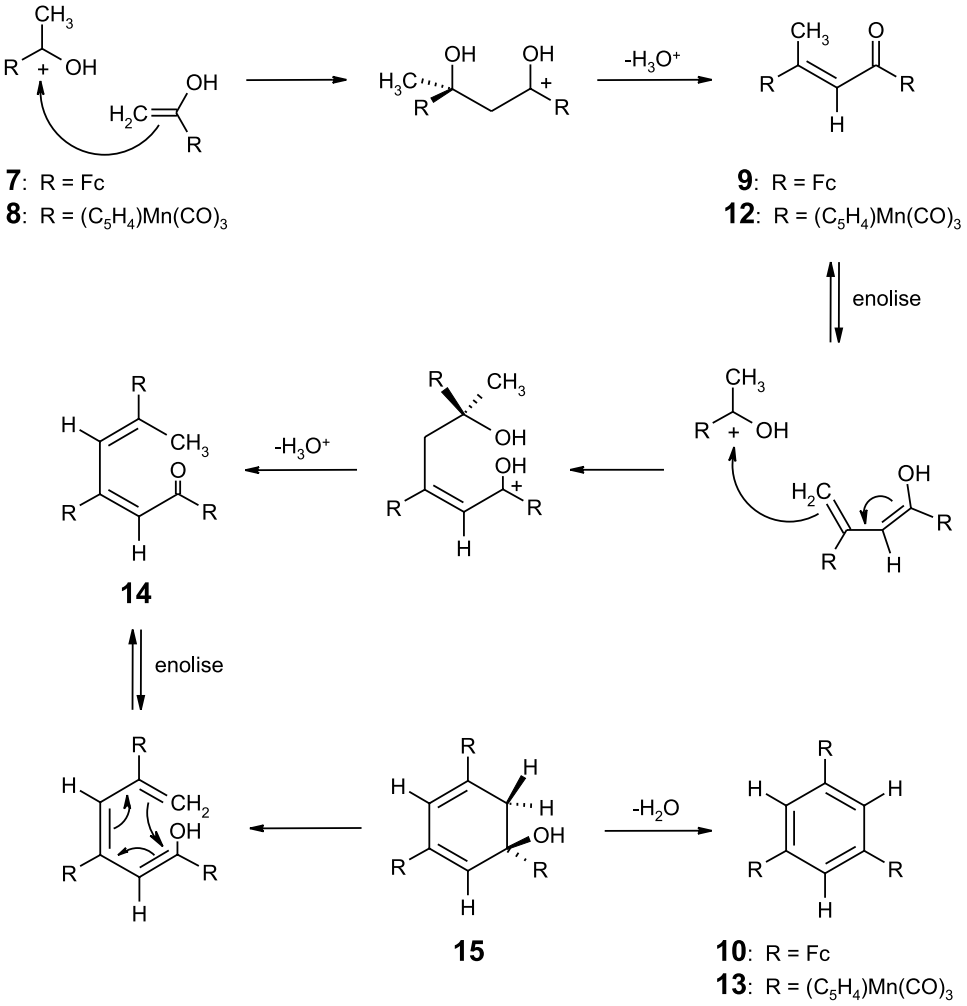

and 153° (up), 14° (up), and 173° (down) for iron. However, the simplicity of the ^{1}H and ^{13}C NMR spectra indicates that, as in the case of **6**, rotation of the $(C_6H_5)Mn(CO)_3$ or $(C_5H_4)FeCp$ substituents is fast on the NMR time scale (298–183 K). To enforce the necessary stereochemistry (i.e., mutually syn orientation) and simultaneously enhance the barrier to aryl—aryl bond rotation in these trimeric units, further derivatization of the benzene framework may be required (vide infra). Very recent X-ray crystal structure determinations of triferrocenylboroxine and -borazine demonstrate that a convergent arrangement of metal-bearing fragments is indeed possible (24).

It has been suggested (18) that these trimerizations proceed via initial formation of a metal-stabilized carbocation, which then reacts with another molecule of the appropriate acetyl complex *in its enol form*. The dimetallic products, typified by **9** and **12**, may then combine, via their enol tautomers, with a third molecule of the protonated acetyl complex to produce the trimetallic arene precursor **14**. Subsequent electrocyclic ring closure can generate the arene hydrate **15** and ultimately the desired 1,3,5-trisubstituted benzene, as depicted in Scheme 3. Although the proposed intermediates are depicted as simple enols, it is likely that they are really silyl enol ethers of presently unknown composition. Moreover, while species of the form $Cl_xSi(OEt)_{4-x}$ most likely serve as a template for the condensation reactions, clarifying the precise nature of the silicon reagent(s) would require extensive mechanistic studies.

A crucial factor contributing to the ease of these reactions is presumably the enhanced stability of the intermediate carbocations, for which the electron deficiency at the α-carbon is alleviated through overlap of the "vacant *p* orbital" with a filled *d* orbital on the relatively electron-rich metal. NMR spectroscopic, X-ray crystallographic, and computational data of similar organometallic complexes, which could also be viewed as (fulvene)ML_n^+ derivatives, have revealed that the α-carbon bends (by ~25–40°) toward the metal so as to enhance this orbital interaction; the net result is to stabilize the HOMO, destabilize the LUMO, and augment the HOMO–LUMO gap (25).

Attempted trimerisations of polycyclic ketones

As part of the continuing worldwide effort to synthesize curved fragments of fullerenes (Buckybowls) (5), several research groups have based their approaches on threefold symmetric polycyclic precursors such as truxenetrione, **16** (14, 26), and the C_{45} molecule, **17** (27), which are derived from the ketone precursors 1,3-indandione and trindanone, respectively (Scheme 4). Whereas the structure of **16** has been unequivocally established, the existence of **17**, an

© 2002 NRC Canada

Scheme 4. Acid-catalyzed condensations of (*a*) 1,3-indanone and (*b*) truxenone.

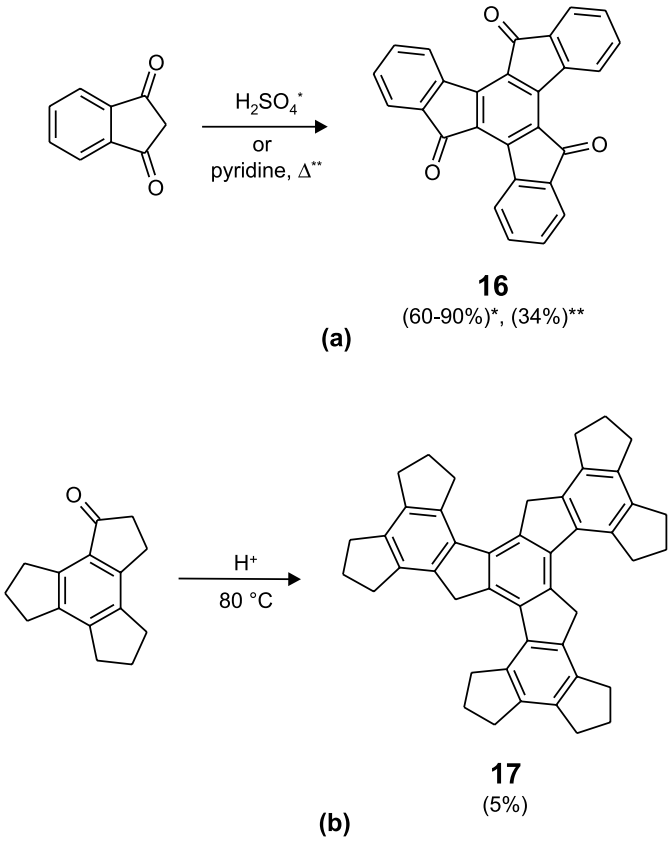

insoluble material, is tentatively based on infrared spectroscopic and mass spectrometric data (27).

In a preliminary investigation of related "tectons" (28), we chose to attempt the trimerization of the tetracyclic ketone **18** with the goal of generating successively the octacyclic and tridecacyclic systems **19** and **20**, respectively (Scheme 5). Treatment of 1,3-dihydro-2H-cyclopenta[*l*]phenanthren-2-one, **18** (29), with either EtOH–$SiCl_4$ or concentrated sulfuric acid yielded two major products. The former, a light yellow crystalline solid, was identified as **19**, but a crystallographic disorder prevented satisfactory refinement of the structure. Figure 2 shows the atom connectivity for **19** and reveals that the structure is decidedly nonplanar because of steric interactions between a peripheral aryl ring in the ketonic half of the molecule and the five-membered ring in the other half. The twist angle between the two five-membered rings linked by the central double bond is approximately 37°. However, the quality of the data is such that we cannot claim accurate bond lengths and angles. The second isolated product, a purple, relatively insoluble solid, yields inconclusive mass spectrometric data and resists all attempts at crystallization. Microanalytical data indicate an empirical formula of approximately $(C_{17}H_{12}O_2)_x$, but at this time, we prefer not to speculate as to its identity. The inability to unambiguously verify products by use of contemporary methods of chemical analysis is an all too common impediment in the preparation of such extended polycyclic hydrocarbons. Enhanced solubility may be achieved by suitable functionalization of the arene periphery, as demonstrated by Plater (28) for related 1,3,5-triarylbenzene fullerene precursors containing more flexible, albeit weaker, aryl–aryl linkages. Regardless, this experiment concurs with earlier evidence (11) that the triple condensation of ketones to yield benzenoids or triarylbenzenes can be inhibited by the steric demands of the substrate.

Fig. 2. Molecular structure of **19** depicting only the atom connectivity.

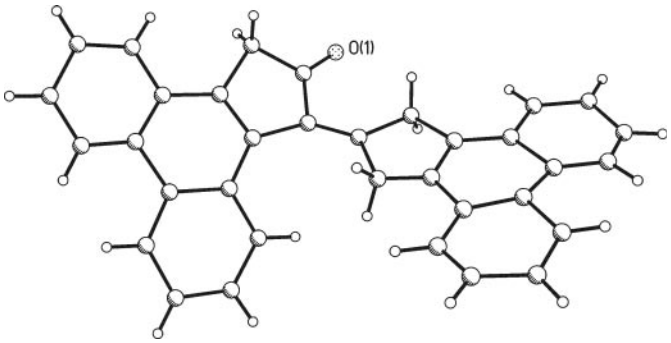

Reaction of $(C_5H_5)Mn(CO)_3$ with *n*-butyllithium at room temperature

As an extension of our investigations of the ethanol–tetrachlorosilane-induced self-condensation of aryl methyl ketones, we identified the more sterically hindered, hexasubstituted scaffold 1,3,5-tris[(cyclopentadienyl)tricarbonylmanganese]-2,4,6-triphenylbenzene, **22**, as a viable synthetic target (Scheme 6). The successful cyclotrimerization of (phenacetylcyclopentadienyl)tricarbonylmanganese, **21**, would not only yield a topologically attractive organometallic propeller, but it would advance further the scope of this preparative technique.

Acetylation of cyclopentadienyltricarbonylmanganese is known to proceed either via Friedel–Crafts reaction with acetyl chloride – aluminum trichloride (30) or by lithiation of $(C_5H_5)Mn(CO)_3$ at –78°C, prior to treatment with CH_3COCl (31). However, it is also well established that, at higher temperatures, aryl-lithium reagents can attack carbonyl ligands (32), and this is the basis of Fischer's route to carbene complexes.

When $(C_5H_5)Mn(CO)_3$ was treated with *n*-butyllithium at –78°C, allowed to warm to 0°C, and subsequently reacted with phenacetyl chloride (as opposed to acetyl chloride), the purplish red crystalline product afforded a mass spectrum consistent with the formula $(C_5H_5)_2Mn_2(CO)_4(C_5H_8)$. The ^1H and ^{13}C NMR spectra alerted us to the presence of a propyl unit, a vinylic moiety, and two nonequivalent (cyclopentadienyl)manganese(dicarbonyl) fragments, suggesting the bridged vinylidene structure **23**. This assignment was confirmed by X-ray crystallography; the resulting structure is depicted in Fig. 3 and compares favorably with those of previously reported $[(C_5H_5)Mn(CO)_2]_2(\mu\text{-}C{=}CHR)$ systems where R is H, Ph, CHO, or $CH(OCH_2CH_2CH_2O)$ (33). Ultimately, repeated attempts to generate the hexaarylated derivative **22**, even under a variety of conditions, were unsuccessful, presumably because of steric restrictions.

© 2002 NRC Canada

Scheme 5. Attempted trimerization of 1,3-dihydro-2H-cyclopenta[*l*]phenanthren-2-one, **18**.

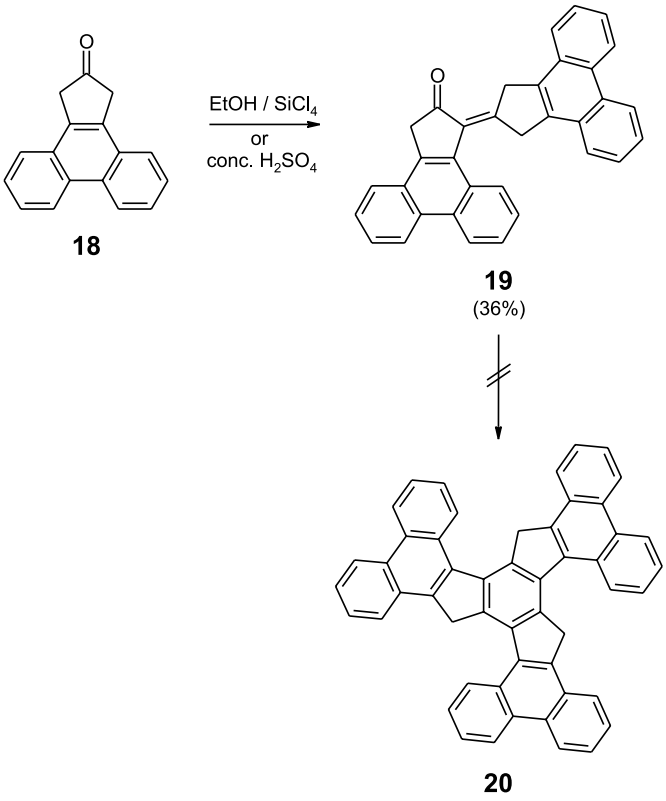

The proposed mechanism for the formation of **23** is shown in Scheme 7 and is suggested to proceed via nucleophilic attack on a carbonyl ligand by the *n*-butyl anion, formation of the organometallic ester **24**, proton abstraction by excess base, and elimination of phenylacetate to produce the vinylidene complex **25**. Vinylidene systems, $RCH{=}C{=}ML_n$, are normally generated either via rearrangement of a coordinated terminal alkyne complex or by the electrophilic protonation or alkylation of the α-carbon atom of an alkynylmetal complex (34). It has already been shown that such monometallic systems react with $(C_5H_5)Mn(CO)_3$ to yield bridged vinylidene species (33). This route to such systems is reminiscent of Hughes' report of the synthesis of $[(C_5H_5)Mn(CO)_2]_2(\mu\text{-}C{=}CH_2)$ by treatment of $(C_5H_5)Mn(CO)_3$ successively with methyllithium, triflic anhydride, and Proton-Sponge (35).

Experimental

All reactions involving organometallic reagents were performed under an atmosphere of dry nitrogen utilizing conventional benchtop and glovebag techniques. Solvents were dried and distilled according to standard procedures (36). Acetyl ferrocene, cymantrene, and phenacetyl chloride were purchased from either Aldrich Chemical Co., Inc. (Milwaukee, Wisconsin) or Strem Chemicals Inc. (Newburyport, MA.) and used as received. Silica gel (particle size 20–45 μm) was employed for flash column chromatography. ^{1}H and ^{13}C NMR spectra were acquired on Bruker AC 300 or AC 200 spectrometers and were referenced to the residual proton or ^{13}C solvent signal, respectively. Direct

Fig. 3. Molecular structure of **23** (30% thermal ellipsoids) depicting the atom numbering scheme.

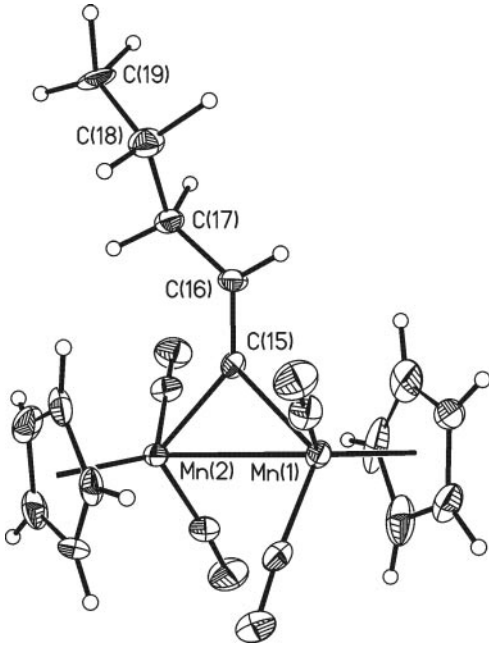

electron impact (DEI) and direct chemical ionization (DCI) mass spectra were obtained by use of a Finnigan 4500 spectrometer. Infrared spectra were recorded on a Bio-Rad FTS-40 spectrometer. Melting points (uncorrected) were recorded on a Thomas–Hoover melting point apparatus.

Preparation of 1,3-diferrocenyl-2-buten-1-one (9)

To a solution of acetylferrocene (835 mg, 3.66 mmol) dissolved in dry ethanol (25 mL) was slowly added tetrachlorosilane (0.9 mL). The resulting mixture, which was observed to change from a transparent orange to a dark murky purple, was subsequently stirred at room temperature overnight. After quenching with water (10 mL), extracting with dichloromethane (3 × 30 mL), and drying over $CaCl_2$, the residue was chromatographed with 70:30 ethyl acetate – hexanes. The first fraction to elute was 1,3-diferrocenyl-2-buten-1-one, **9** (625 mg, 1.43 mmol, 78%); mp 119–121°C (lit. (37) value mp 118–120°C). IR (KBr) (cm^{-1}): 1633 ($\nu_{C=O}$), 1584 ($\nu_{C=C}$). ^{1}H NMR (200 MHz, CD_2Cl_2) δ: 6.75 (s, 1H), 4.81 (m, 2H), 4.64 (m, 2H), 4.51 (m, 2H), 4.45 (m, 2H), 4.24 (s, 5H), 4.20 (s, 5H), 2.55 (s, 3H). ^{13}C NMR (50 MHz, CD_2Cl_2) δ: 194.8 (C=O), 153.8 (C_5H_5), 119.7 (=*C*H), 86.4 (=*C*-CH_3), 83.6 (Cp C), 72.5, 71.1, 70.4, 70.3 (Cp *C*H's), 69.9, 67.6 (C_5H_5's), 18.9 (=C-*C*H_3). LR-MS (DEI) *m*/*z* (%): 438 ([M$^+$], 100), 373 ([M – C_5H_5]$^+$, 21), 121 ([C_5H_5Fe]$^+$, 57). LR-MS (DCI) *m*/*z* (%): 439 ([M + H]$^+$, 100).

Preparation of 1,3,5-triferrocenylbenzene (10)

To a solution of acetylferrocene (2.00 g, 8.77 mmol) dissolved in dry ethanol (25 mL) was slowly added tetrachlorosilane (4 mL). Upon addition of this reagent, the mixture was observed to change from a transparent orange to a dark murky purple and was stirred at room temperature overnight. After quenching with water (15 mL), extraction with dichloromethane (3 × 30 mL), and drying over $CaCl_2$, the residue was chromatographed with 50:50 dichloromethane–

© 2002 NRC Canada

Scheme 6. Anticipated EtOH/$SiCl_4$-induced triple condensation of (phenacetylcyclopentadienyl)tricarbonylmanganese, **21**.

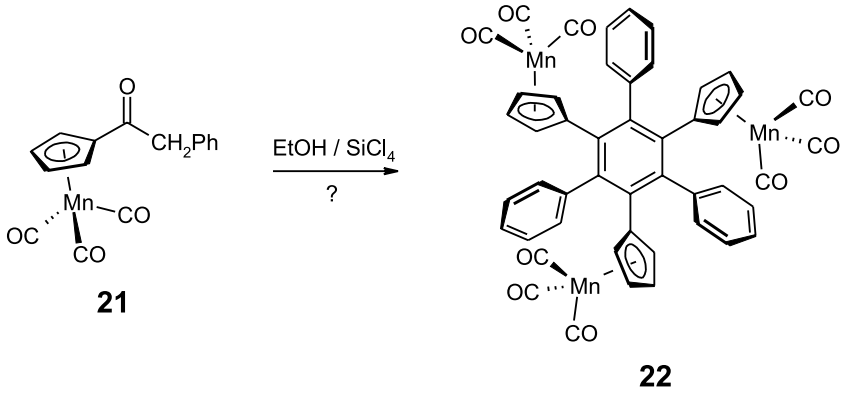

Scheme 7. Proposed mechanism for the generation of the bridged vinylidene complex, **23**.

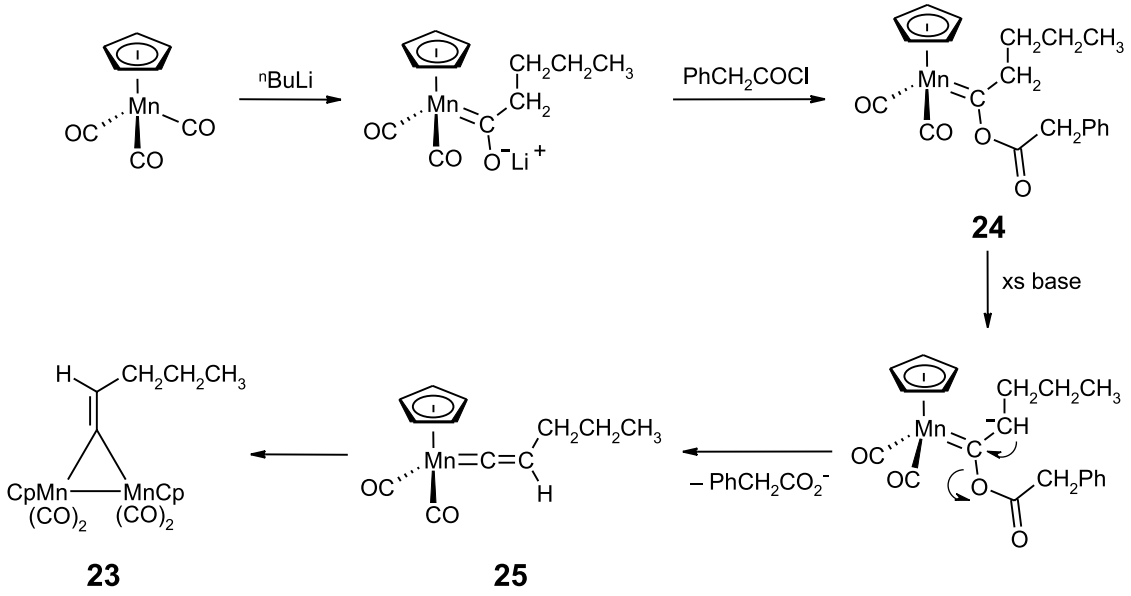

hexanes. The second fraction to elute was 1,3,5-triferrocenylbenzene, **10** (700 mg, 1.11 mmol, 38%); mp 261–263°C (lit. (21) value mp 265–266°C). ^{1}H NMR (200 MHz, CD_2Cl_2) δ: 7.45 (s, 3H), 4.78 (m, 6H), 4.39 (m, 6H), 4.12 (s, 15H). ^{13}C NMR (50 MHz, CD_2Cl_2) δ: 139.7 (Ar C's), 122.2 (Ar CH's), 86.0 (Cp C's), 70.2, 69.5 (*C*H's in C_5H_4's), 67.1 (C_5H_5's). LR-MS (DEI) *m/z* (%): 630 ([M]$^+$, 100), 315 (23), 149 (16), 121 ([C_5H_5Fe]$^+$, 18). LR-MS (DCI) *m/z* (%): 631 ([M + H]$^+$, 100).

Preparation of 1,3-dicymantrenyl-2-buten-1-one (12) and 1,3,5-tricymantrenylbenzene (13)

Following the dissolution of (acetylcyclopentadienyl)tricarbonylmanganese (30) (835 mg, 3.39 mmol) in ethanol (20 mL) and the addition of tetrachlorosilane (0.8 mL), the resulting mixture was stirred at room temperature overnight. After addition of water (10 mL), extraction with dichloromethane, and drying over $CaCl_2$, the residue was flash chromatographed with 50:50 CH_2Cl_2–MeOH. The first fraction to elute was 1,3,5-tricymantrenylbenzene, **13** (396 mg, 0.58 mmol, 51%), obtainable as yellow crystals (from dichloromethane–hexane); mp 198°C. IR (CH_2Cl_2) (cm^{-1}): 2024, 1940 (ν_{CO}). ^{1}H NMR (200 MHz, $CDCl_3$) δ: 7.24 (s, 3H), 5.22 (m, 6H), 4.82 (m, 6H). ^{13}C NMR (50 MHz, $CDCl_3$) δ: 224.4 (Mn-CO's), 134.3 (Ar C's), 123.7 (Ar CH's), 101.4 (Cp C), 82.4, 81.9 (Cp CH's). LR-MS (DEI) *m/z* (%): 684 ([M]$^+$, 14), 600 ([M – 3CO]$^+$, 21), 516 ([M – 6CO]$^+$, 10), 432 ([M – 9CO]$^+$, 20), 377 ([M – Mn – 9CO]$^+$, 43), 322 ([M – 2Mn – 9CO]$^+$, 47), 267 ([M – 3Mn – 9CO]$^+$, 85), 265 (100). Anal. calcd. for $C_{30}H_{15}Mn_3O_9$: C 52.63, H 2.19%; found: C 52.31, H 2.44%.

The second fraction to elute was 1,3-dicymantrenyl-2-buten-1-one, **12** (96 mg, 0.20 mmol, 12%), as a yellow oil. IR (CH_2Cl_2) (cm^{-1}): 2032, 1939 (ν_{CO}). ^{1}H NMR (200 MHz, $CDCl_3$) δ: 6.51 (s, 1H, =CH), 5.44 (m, 2H), 5.18 (m, 2H), 4.83 (m, 4H) (Cp H's), 2.33 (s, 3H, CH_3). LR-MS (DEI) *m/z* (%): 474 ([M]$^+$, 6), 390 ([M – 3CO]$^+$, 29), 336 (13), 306 ([M – 6CO]$^+$, 100), 252 (76), 120 ([C_5H_5Mn]$^+$, 54), 55 ([Mn]$^+$, 100).

Reaction of ketone 18 with tetrachlorosilane and ethanol

To a solution of 1,3-dihydro-2H-cyclopenta[*l*]phenanthren-2-one, **18** (28) (276 mg, 1.19 mmol), dissolved in

© 2002 NRC Canada

ethanol (10 mL) was added tetrachlorosilane (0.5 mL) and the mixture stirred at room temperature overnight. After addition of water (10 mL), extraction with dichloromethane, and drying over $CaCl_2$, the residue was flash chromatographed with 50:50 CH_2Cl_2–MeOH to yield an unidentified purple compound (130 mg) and a pale yellow material, **19** (95 mg, 0.21 mmol, 36%). Repeated chromatographic separations finally yielded crystals of moderate quality that were subsequently identified by an X-ray diffraction experiment.

Reaction of cymantrene with butyllithium and phenacetyl chloride

Cymantrene (1.02 g, 5.0 mmol) was treated with *n*-butyllithium (3.75 mL of a 1.6 M solution) at –78°C and allowed to warm to 0°C over a period of several hours. Phenacetyl chloride (0.9 mL) was added and the solution stirred overnight before being quenched with water, extracted with dichloromethane, and chromatographed over silica gel to give purple–red crystals of **23** (462 mg, 1.1 mmol, 44%). IR (CH_2Cl_2) (cm^{-1}): 2024 (w), 1977 (m), 1939 (s), 1913 (s) (ν_{CO}). ^1H NMR (200 MHz, $CDCl_3$) δ: 7.63 (s, 1H, =CH), 5.33 (s, 5H), 5.30 (s, 5H), 3.22 (m, 2H), 2.26 (m, 2H), 1.72 (t, 3H). ^{13}C NMR (50 MHz, $CDCl_3$) δ: 145.1 (C=*C*H), 88.7, 87.9 (Cp *C*H's), 40.3 (*C*H_2), 24.3 (*C*H_2), 14.3 (*C*H_3). LR-MS (DEI) *m*/*z* (%): 420 ($[M]^+$, 5), 364 ($[M - 2CO]^+$, 8), 308 ($[M - 4CO]^+$, 27), 240 ($[C_{10}H_{10}Mn_2]^+$, 42), 185 ($[C_{10}H_{10}Mn]^+$, 85), 120 ($[C_5H_5Mn]^+$, 100), 55 ($[Mn]^+$, 52). Anal. calcd. for $C_{19}H_{18}Mn_2O_4$: C 54.29, H 4.29%; found: C 54.62, H 4.51%.

X-ray crystal structure determinations of 13, 19, and 23

X-ray crystallographic data[2] were collected from single crystal samples of **13** (0.22 × 0.14 × 0.04 mm^3), **19** (0.24 × 0.22 × 0.05 mm^3), and **23** (0.25 × 0.15 × 0.10 mm^3) mounted on glass fibers. Data were collected using a P4 Bruker diffractometer equipped with a Bruker SMART 1K charge coupled device (CCD) area detector using the program SMART (38) and a rotating anode using graphite-monochromated Mo Kα radiation (λ = 0.71073 Å). The crystal-to-detector distance was 4.987 cm for all samples and the data collection was carried out in 512 × 512 pixel mode utilizing 2 × 2 pixel binning. The initial unit cell parameters were determined by a least-squares fit of the angular settings of the strong reflections collected by a 12 scan in 40 frames over three different sections of reciprocal space (120 frames in total). A hemisphere of data was collected with high redundancy to better than 0.8 Å resolution for **23** (at 195 K), whereas only 1.00 Å resolution was obtainable for **13** and **19** (at 299 and 293 K, respectively). Data reduction was carried out using the program SAINT (39), which applied Lorentz and polarization corrections to the three-dimensionally integrated diffraction spots. The program SADABS (40) was utilized for the scaling of diffraction data, the application of a decay correction, and an empirical absorption correction based on redundant reflections. Structures **13** and **23** were solved by use of the direct-methods procedure in the Bruker SHELXTL program library (41) followed by full-matrix least-squares refinement on F^2 with anisotropic thermal parameters for all nonhydrogen atoms in **23** and only Mn1, Mn2, and Mn3 in **13**. All hydrogen atoms in **13** and **19** and only H1, H6, H7, H8, H9, H10A, and H16A in **23** were added as fixed contributors at calculated positions with isotropic thermal parameters (based on the carbon atom to which they were bonded), whereas the remaining hydrogen atoms in **23** were determined from the least-squares map. Partial decomposition of the crystal sample resulted in poor data quality and hence incomplete refinement of structure **19**.[3]

Conclusion

To conclude, it has been demonstrated that the ethanol–tetrachlorosilane-mediated trimerization of acetyl-organometallics is a convenient and directed route to 1,3,5-trisubstituted arenes. Future reports will detail the preparation of mixed compounds bearing both organic (alkyl, aryl) and organometallic addenda by treatment of dimetallic condensation products, such as **9** or **12**, with a variety of methyl ketones. It is anticipated that the functional versatility of these angular building units will render them ideally suitable to the construction of macro- and supramolecular structures of various sizes and shapes using covalent and noncovalent linkages.

Acknowledgements

Financial support from the Natural Sciences and Engineering Research Council of Canada (NSERC) is gratefully acknowledged. Mass spectra were obtained courtesy of Dr. Kirk Green of the McMaster Regional Centre for Mass Spectrometry. S.B. thanks the Government of Ontario and NSERC for graduate fellowships.

References

1. A. Hirsch (*Editor*). Fullerenes and related structures. Vol. 199. Springer, Berlin. 1999.
2. For a review of polyphenylene nanostructures, see A.J. Berresheim, M. Muller, and K. Mullen. Chem. Rev. **99**, 1747 (1999); for a recent example, see R.A. Pascal, Jr., L. Barnett, X. Qiao, and D.M. Ho. J. Org. Chem. **65**, 7711 (2000).
3. H.E. Katz. J. Org. Chem. **52**, 3932 (1987).
4. (*a*) F.M. Tabellion, S.R. Seidel, A.M. Arif, and P.J. Stang. J. Am. Chem. Soc. **123**, 7740 (2001); (*b*) S. Leininger, B. Olenyuk, and P.J. Stang. Chem. Rev. **100**, 853 (2000); (*c*) P.J. Stang. Chem. Eur. J. **4**, 19 (1998); (*d*) P.J. Stang and B. Olenyuk. Acc. Chem. Res. **30**, 502 (1997); for a related and

[2] Supplementary data may be purchased from the Depository of Unpublished Data, Document Delivery, CISTI, National Research Council Canada, Ottawa, ON K1A 0S2, Canada (http://www.nrc.ca/cisti/irm/unpub_e.shtml for information on ordering electronically). CCDC 190666 (**13**) and 190665 (**23**) contain the supplementary data for this paper. These data can be obtained, free of charge, via www.ccdc.cam.ac.uk/conts/retrieving.html (or from the Cambridge Crystallographic Data Centre, 12 Union Road, Cambridge, U.K.; fax +44 1223 336033; or deposit@ccdc.cam.ac.uk).

[3] Unit cell parameters for **19** (red prism): $P\bar{1}$ (triclinic), a = 8.0060 Å, b = 9.5390 Å, c = 15.3082 Å, α = 78.527°, β = 79.512°, γ = 70.750°, V = 1073.06 $Å^3$, Z = 2.

© 2002 NRC Canada

interesting application of this approach, see (*e*) K.V. Kilway and J.S. Siegel. Tetrahedron, **57**, 3615 (2001).
5. *From O.L. Chapman's Lab*: (*a*) R.H. Jacobson. Searching for the soccer ball: an unsuccessful synthesis of corannulene. Ph.D. thesis, University of California at Los Angeles. 1986; (*b*) Y. Xiong. Part B. Syntheses of [1.1.1]paracyclophane and other strained aromatic compounds, in search for the soccer ball C_{60}. Ph.D. thesis, University of California at Los Angeles. 1987; (*c*) D. Loguercio, Jr. Studies toward a convergent synthesis of C_{60}. Ph.D. thesis, University of California at Los Angeles. 1988; (*d*) D. Shen. Approaches to soccerene (I_h–C_{60}) and other carbon spheres. Ph.D. thesis, University of California at Los Angeles. 1990; *as a further example*: (*e*) L.T. Scott, M.M. Boorum, B.J. McMahon, S. Hagen, J. Mack, J. Blank, H. Wegner, and A. de Meijere. Science (Washington, D.C.), **295**, 1500 (2002).
6. H.K. Gupta, P.E. Lock, and M.J. McGlinchey. Organometallics, **16**, 3628 (1997).
7. H.K. Gupta, P.E. Lock, D.W. Hughes, and M.J. McGlinchey. Organometallics, **16**, 4355 (1997).
8. N. Reginato and M.J. McGlinchey. Organometallics, **20**, 4147 (2001).
9. F. Petru and V. Galik. Chem. Listy, **51**, 2371 (1957).
10. (*a*) R. Meyer. Chem. Ber. **89**, 1443 (1956); (*b*) O. Wallach. Chem. Ber. **30**, 1094 (1897).
11. (*a*) S.S. Elmorsy, A. Pelter, and K. Smith. Tetrahedron Lett. **32**, 4175 (1991); (*b*) S.S. Elmorsy, A. Pelter, K. Smith, and M.B. Hursthouse. Tetrahedron Lett. **33**, 821 (1992); (*c*) S.S. Elmorsy, A.G.M. Khalil, M.M. Girges, and T.A. Salama. J. Chem. Res. (S), 232 (1997); J. Chem. Res. (M), 1537 (1997); (*d*) M.J. Plater. J. Chem. Soc. Perkin Trans. **1**, 2897 (1997); (*e*) S. Kotha, K. Chakraborty, and E. Brahmachary. Synlett, 1621 (1999).
12. (*a*) J. Yang and J.G. Verkade. J. Am. Chem. Soc. **120**, 6834 (1998); (*b*) J. Yang and J.G. Verkade. Organometallics, **19**, 893 (2000).
13. For example, see K.P.C. Vollhardt. Acc. Chem. Res. **10**, 1 (1977).
14. E.V. Dehmlow and T. Kelle. Synth. Commun. **27**, 2021 (1997).
15. K. Sato, S. Yamashiro, K. Imafuku, S. Ito, N. Morita, and K. Fujimori. J. Chem. Res. (S), 334 (2000).
16. B. Mailvaganam, B.E. McCarry, B.G. Sayer, R.E. Perrier, R. Faggiani, and M.J. McGlinchey. J. Organomet. Chem. **335**, 213 (1987).
17. B. Mailvaganam, B.G. Sayer, and M.J. McGlinchey. J. Organomet. Chem. **395**, 177 (1990).
18. Y. Sasaki and C.U. Pittman, Jr. J. Org. Chem. **38**, 3723 (1973).
19. J.J.C. Erasmus, G.J. Lamprecht, J.C. Swarts, A. Roodt, and A. Oskarsson. Acta Crystallogr. Sect. C. Cryst. Struct. Commun. **52**, 3000 (1996).
20. Use of $TaCl_5$: P. Štěpnička, I. Císařová, J. Sedláček, J. Vohlídal, and M. Polášek. Collect. Czech. Chem. Commun. **62**, 1577 (1997).
21. Acid-catalysed: (*a*) K. Schlögl and H. Soukup. Tetrahedron Lett. **13**, 1181 (1967); (*b*) K. Schlögl and H. Soukup. Monatsh. Chem. **99**, 927 (1968).
22. $Co_2(CO)_8$-catalyzed: M. Rosenblum, N.M. Brawn, and B.J. King. Tetrahedron Lett. 4421 (1967).
23. Free-radical polymerization: C. Simionescu, T. Lixandru, J. Mazilu, and L. Tataru. Makromol. Chem. **147**, 69 (1971).
24. J.W. Bats, K. Ma, and M. Wagner. Acta Crystallogr. Sect. C. Cryst. Struct. Commun. **58**, m129 (2002).
25. (*a*) M.J. McGlinchey, L. Girard, and R. Ruffolo. Coord. Chem. Rev. **143**, 331 (1995); (*b*) S. Barlow, A. Cowley, J.C. Green, T.J. Brunker, and T. Hascall. Organometallics, **20**, 5351 (2001), and refs. therein.
26. K. Jacob, M. Sigalov, J.Y. Becker, A. Ellern, and V. Khodorkovsky. Eur. J. Org. Chem. 2047 (2000).
27. C. Fabré and A. Rassat. C.R. Acad. Sci. Paris Ser. II, **308**, 1223 (1989).
28. M.J. Plater. J. Chem. Soc. Perkin Trans. **1**, 2897 (1997).
29. (*a*) A.C. Cope, L. Field, D.W.H. MacDowell, and M.E. Wright. J. Am. Chem. Soc. **78**, 2547 (1956); (*b*) B. Eliasson, M.H. Nouri-Sorkjabi, L. Trogen, I. Sethson, U. Edlund, A. Sygula, and M. Rabinovitz. J. Org. Chem. **54**, 171 (1989); (*c*) S.S. Rigby, H.K. Gupta, N.H. Werstiuk, A.D. Bain, and M.J. McGlinchey. Inorg. Chim. Acta, **251**, 355 (1996).
30. F.A. Cotton and J.R. Leto. Chem. Ind. 1368 (1958).
31. M.E. Wright and V.W. Day. J. Organometal. Chem. **329**, 43 (1987).
32. E.O. Fischer and A. Maasböl. Chem. Ber. **100**, 2445 (1967).
33. (*a*) K. Folting, J.C. Huffman, L.N. Lewis, and K.G. Caulton. Inorg. Chem. **18**, 3483 (1979); (*b*) A.N. Nesmeyanov, G.G. Aleksandrov, A.B. Antonova, K.N. Anisimov, N.E. Kolobova, and Yu.T. Struchkov. J. Organomet. Chem. **110**, C36 (1976); (*c*) A.B. Antonova, N.E. Kolobova, P.V. Petrovsky, B.V. Lokshin, and N.S. Obezyuk. J. Organomet. Chem. **137**, 55 (1977); (*d*) C. Löwe, H-U. Hund, and H. Berke. J. Organomet. Chem. **378**, 211 (1989).
34. For example, see (*a*) H. Werner, P. Bachmann, and M. Martin. Can. J. Chem. **79**, 519 (2001); (*b*) C. Bruneau and P.H. Dixneuf. Acc. Chem. Res. **32**, 311 (1999), and refs. therein; (*c*) K.G. Frank. Synthesis and physical studies of transition metal vinylidene, alkyne, and ethynediyl complexes. Ph.D. thesis, University of Kentucky, Lexington, Ky. 1990; (*d*) M.I. Bruce and A.G. Swincer. Adv. Organomet. Chem. **22**, 59 (1983).
35. B.E. Boland-Lussier, M.R. Churchill, R.P. Hughes, and A.L. Rheingold. Organometallics, **1**, 628 (1982).
36. D.D. Perrin, W.L.F. Armarego, and D.R. Perrin. Purification of laboratory chemicals. Pergamon Press, New York. 1980.
37. P.L. Pauson and W.E. Watts. J. Chem. Soc. 3880 (1962).
38. Bruker AXS Inc. 1996. SMART [computer program]. Version 4.05. Bruker AXS Inc., Madison, WI 53711, U.S.A.
39. Bruker AXS Inc. 1996. SAINT [computer program]. Version 4.05. Bruker AXS Inc., Madison, WI 53711, U.S.A. 1996.
40. G.M. Sheldrick. SADABS. University of Gottingen, Gottingen, Germany. 1996.
41. G.M. Sheldrick. 1994. SHELXTL [computer program]. Version 5.03. Bruker AXS Inc., Madison, WI 53711, U.S.A. 1994.

© 2002 NRC Canada

Synthesis of a PennPhos–ruthenium(II) complex: The first crystal structure of a PennPhos–metal complex

Okwado M. Akotsi, Robert McDonald, and Steven H. Bergens

Abstract: The chiral bis(phosphine) ligand *P,P′*-1,2-phenylenebis[(1*R*,2*S*,4*R*,5*S*)-2,5-dimethyl-7-phosphabicyclo-[2.2.1]heptane], [(*R*,*S*,*R*,*S*)-Me-PennPhos] (**1**) reacts with *trans*-$RuCl_2(NBD)Py_2$ (NBD = norbornadiene, Py = pyridine) (**2**) in CH_2Cl_2 at 45°C to form two diastereomers of the triply chloride bridged cation $[\{(\mathbf{1})RuPy\}_2(\mu\text{-}Cl)_3)][Cl^-]$ (**3**) in the ratio 1:3. The isomers were studied by NMR spectroscopy and separated by crystallization from CD_2Cl_2–hexanes mixture. The major diastereomer is one of the *anti*-diastereomers and contains face-sharing bioctahedral diruthenium (Ru(II, II)) molecules with a Ru—Ru distance of 3.289 Å. This diastereomer crystallizes in the monoclinic space group *C*2 (No. 5) with the cell dimensions *a*(Å) = 28.102(2), *b*(Å) = 20.5344(15), *c*(Å) = 12.7692(10), β(°) = 95.7411(16), *V*(Å^3) = 7331.6(9), and *Z* = 4. The Me-PennPhos ligand adopts an unexpected bent, non-*C*2 symmetric conformation upon coordination to ruthenium.

Key words: PennPhos crystal structure, diruthenium complexes, triply bridged complexes, bisphosphine ruthenium complexes.

Résumé : Le ligand chiral bis(phosphine), *P,P′*-1,2-phénylènebis[(1*R*,2*S*,4*R*,5*S*)-2,5-diméthyl-7-phosphabicyclo-[2.2.1]heptane], [(*R,S,R,S*)-Me-PennPhos] (**1**) réagit avec le *trans*-$RuCl_2(NBD)Py_2$ (NBD = norbornadiène; Py = pyridine) (**2**), dans le CH_2Cl_2, à 45°C, pour former deux diastéréomères du cation triplement ponté par des ions chlorures $[\{(\mathbf{1})RuPy\}_2(\mu\text{-}Cl)_3)][Cl^-]$ (**3**) dans un rapport de 1:3. Les isomères ont été étudiés par spectroscopie RMN et séparés par cristallisation à partir de mélanges CD_2Cl_2–hexane. Le diastéréomère principal est l'un des diastéréomères *anti*- et comporte des molécules de diruthénium (Ru(II, II)) bioctaédriques qui se partagent les faces avec une distance Ru—Ru de 3,289 Å. Ce diastéréomère cristallise dans le groupe d'espace monoclinique *C*2 (No. 5), avec *a* = 28,102(2), *b* = 20,5344(15) et *c* = 12,7692(10) Å, β = 95,7411(16)°, *V* = 7331,6(9) Å^3 et *Z* = 4. Lors de sa coordination au ruthénium, le ligand Me-PennPhos adopte une conformation symétrique non *C*2 avec une courbure inattendue.

Mots clés : structure cristalline PennPhos, complexes de diruthénium, complexes triplement pontés, complexes du ruthénium avec une bisphosphine.

[Traduit par la Rédaction]

Introduction

Complexes of ruthenium(II) and chiral bis(phosphines) are the most successful catalyst systems for the enantioselective hydrogenation of prochiral olefins and ketones (1, 2). We recently reported a versatile procedure to synthesize ruthenium–bis(phosphine) catalyst precursors that compliment the existing procedures in the literature (3). We showed that most common chiral bis(phosphine) ligands react with the complex *trans*-$RuCl_2(NBD)Py_2$ (NBD = norbornadiene, Py = pyridine) (**2**) to generate in high yields the crystalline complexes *trans*-$RuCl_2(P\text{-}P^*)Py_2$ (P-P* is the corresponding chiral bis(phosphine)). Examples of *trans*-$RuCl_2(P\text{-}P)Py_2$ and similar compounds have been reported previously by the James group (4). We found that these complexes are active enantioselective hydrogenation catalysts for keto esters and for noncarboxylic olefins in presence of small amounts of HBF_4(aq) (3). Further, reaction of these complexes with 1,2-diphenylethylenediamine (N-N*, either enantiomer) forms in good yields (3) the corresponding compounds developed by Noyori and co-workers (1, 2), *trans*-$RuCl_2(P\text{-}P^*)(N\text{-}N^*)$, which are well-known, extremely active, and selective enantioselective hydrogenation catalysts for simple ketones.

Zhang and co-workers (5) recently reported a rhodium catalyst system containing their ligand *P,P′*-1,2-phenylenebis[{(1*R*,2*S*,4*R*,5*S*)-2,5-dimethyl}-7-phosphabicyclo-[2.2.1]heptane] ([(*R*,*S*,*R*,*S*)-Me-PennPhos] (**1**)) that has achieved the highest enantioselectivities for the hydrogenation

Received 16 February 2002. Published on the NRC Research Press Web site at http://canjchem.nrc.ca on 25 November 2002.

Dedicated to Professor Tris Chivers for his contributions to Canadian chemistry.

O.M. Akotsi, R. McDonald,[1] and S.H. Bergens.[2] Department of Chemistry, University of Alberta, Edmonton, AB T6G 2G2, Canada.

[1]Corresponding author (X-ray crystallography) (e-mail: Bob.McDonald@ualberta.ca)
[2]Corresponding author (e-mail: steve.bergens@ualberta.ca).

 DOI: 10.1139/V02-151 © 2002 NRC Canada

of simple dialkyl ketones. We now report that **1** reacts with the ruthenium precursor **2**, not to form the monomeric dichlorides obtained with most common chiral bisphosphine ligands but rather to form cationic triply chloride bridged dimers. Further, the ligand unexpectedly adopts a bent, non-*C*2 symmetric geometry upon coordination to ruthenium. This is the first reported crystal structure of a PennPhos–metal complex.

Materials and methods

Instrumentation

All ^{1}H and ^{31}P NMR spectra were measured on a Bruker AM-400 spectrometer operating at 400.13 and 161.97 MHz, respectively, or on a Bruker AM-200 spectrometer operating at 200.13 and 80.02 MHz, respectively. ^{1}H NMR chemical shifts are reported in parts per million (δ) relative to tetramethylsilane using solvent as an internal reference. ^{31}P NMR chemical shifts are reported in parts per million (δ) relative to an 85% H_3PO_4 external reference.

Reagents and solvents

The solvents and reagents, *n*-hexanes (K, Ph_2CO), methylene chloride-d_2 (CaH_2), and pyridine (CaH_2) were distilled from drying agents under argon. The argon gas was passed through a bed of Drierite drying agent. Compound **2** was prepared by a published procedure (3).

General methods

Unless stated otherwise, all manipulations were carried out in oven-dried glassware using standard air-sensitive techniques.

[{Ru(Me-PennPhos)Py}$_2$(μ-Cl)$_3$][Cl$^-$] (3)

17.0 mg (0.0474 mmol) of **1** and 20.03 mg (0.0474 mmol) of **2** were weighed in air and charged into an NMR tube. The tube was sealed with a rubber septum and the contents flushed with dinitrogen gas. Zero point five mL of dry degassed methylene chloride-d_2 was added to the tube by cannula and the tube shaken to dissolve the solids. The septum was further wrapped with paraffin film to attach it firmly onto the tube. NMR spectroscopy showed that the reaction was ~70% complete after 20 h at room temperature. The reaction was complete in less than 16 h when carried out at 45°C. The original orange–brown solution of the starting materials gradually turns yellow during this period.

Separation of diastereomers

An NMR tube containing the CD_2Cl_2 reaction mixture was cooled to –78°C (with dry-ice – acetone) and layered with hexanes that were added slowly and dropwise to ensure that the drops flowing down the walls of the tube were cooled before coming into contact with the reaction mixture. The tube was then carefully removed from the cold bath and stored for 5 days at 8°C. The major diastereomer of *anti*-**3** formed as yellow crystals suitable for X-ray analysis. The other isomer of **3** remained in solution. The crystals were recovered by filtration using a cannula with filter paper. NMR spectroscopy showed that the crystals contained only the major *anti*-diastereomer **3**.

NMR data for 3

Isolated major anti-isomer

^{1}H NMR (400 MHz, CD_2Cl_2) δ: 8.25 (m, 4H, Ar), 7.26 (m, 6H, Ar), 6.63 (m, 8H, Ar), 2.98 (d, 2H, $^2J_{PH}$ = 10 Hz, PC*H*), 2.85–2.75 (br m, 4H, PC*H*), 2.52 (d, 2H, $^2J_{PH}$ = 10 Hz, PC*H*), 2.43–1.66 (br m, 12H), 1.51 (d, 6H, $^3J_{HH}$ = 9 Hz, CH_3), 1.46 (d, 6H, $^3J_{HH}$ = 9 Hz, CH_3), 0.76 (d, 6H, $^3J_{HH}$ = 7 Hz, CH_3), and 0.62 (d, 6H, $^3J_{HH}$ = 7 Hz, CH_3). ^{31}P NMR (162 MHz, CD_2Cl_2) δ: 82.8 (d, $^2J_{pp}$ = 32 Hz) and 68.7 (d, $^2J_{pp}$ = 32 Hz).

Minor isomer [3]

^{1}H NMR (400 MHz, CD_2Cl_2) δ: 8.46 (m, 4H, Ar), 7.71–7.35 (br m, 6H, Ar), 7.05 (m, 8H, Ar), 2.75–2.68 (m, 4H, PC*H*), 2.43 (d, 2H, $^2J_{PH}$ = 18 Hz, PC*H*), 2.33–2.15 (br m, 12H), 1.15 (d, 6H, $^3J_{HH}$ = 7 Hz, CH_3), 1.02 (d, 6H, $^3J_{HH}$ = 7 Hz, CH_3), 0.67 (d, 6H, $^3J_{HH}$ = 7 Hz, CH_3), and 0.57 (d, 6H, $^3J_{HH}$ = 7 Hz, CH_3). ^{31}P NMR (162 MHz, CD_2Cl_2) δ: 87.9 (d, $^2J_{pp}$ = 32 Hz) and 62.7 (d, $^2J_{pp}$ = 32 Hz).

X-ray crystallographic studies

Yellow crystals of the major diastereomer of *anti*-**3**·3CD_2Cl_2 were obtained from slow diffusion of hexanes into CD_2Cl_2 as described above. Data were collected on a Bruker P4/RA/SMART 1000 CCD diffractometer[4] using Mo Kα radiation at –80°C. Unit cell parameters were obtained from a least-squares refinement of the setting angles of 5574 reflections from the data collection. The monoclinic diffraction symmetry and systematic absences indicated the space group to be *C*2 (No. 5). The data were corrected for absorption through use of the SADABS (6) procedure. See Table 1 for a summary of crystal data and X-ray data collection information.[5] The structure of the compound was solved using the DIRDIF-96 program system (7), and refinement was completed using the program SHELXL-93 (8). Hydrogen atoms were assigned positions based on the geometries of their attached carbon atoms and were given thermal parameters 20% greater than those of the attached carbons.

Distance restraints were employed to impose an idealized geometry upon one of the solvent CH_2Cl_2 molecules: *d*(Cl(6S)–C(4S)) = *d*(Cl(6S)–C(4S)) = 1.80 Å, *d*(Cl(6S)···Cl(7S)) = 2.95 Å. The final model for the compound refined to values of $R_1(F)$ = 0.0639 (for 8806 data with $F_o \geq 2\sigma(F_o^2)$) and $wR_2(F^2)$ = 0.1993 (for all 12 330 independent data).

[3] NMR data for **3** (minor isomer) were assigned from the spectra of the mixture of the two isomers.

[4] Programs for diffractometer operation, data collection, data reduction, and absorption correction were those supplied by Bruker.

[5] Supplementary data may be purchased from the Depository of Unpublished Data, Document Delivery, CISTI, National Research Council Canada, Ottawa, ON K1A 0S2, Canada (http://www.nrc.ca/cisti/irm/unpub_e.shtml for information on ordering electronically). CCDC 183902 contain the supplementary data for this paper. These data can be obtained, free of charge, via www.ccdc.cam.ac.uk/conts/retrieving.html (or from the Cambridge Crystallographic Data Centre, 12 Union Road, Cambridge, U.K.; fax +44 1223 336033; or deposit@ccdc.cam.ac.uk).

© 2002 NRC Canada

Table 1. Crystallographic experimental details.

Crystal data	
Formula	$C_{57}H_{80}Cl_{10}N_2P_4Ru_2$
Formula weight	1473.75
Crystal dimensions (mm)	0.34 × 0.17 × 0.07
Crystal system	Monoclinic
Space group	*C*2 (No. 5)
Unit cell parameters	
a (Å)	28.102 (2)
b (Å)	20.5344 (15)
c (Å)	12.7692 (10)
β (°)	95.7411 (16)
V (Å^3)	7331.6 (9)
Z	4
$D_{calcd.}$ (g cm^{-3})	1.335
μ (mm^{-1})	0.897
Data collection and refinement conditions	
Diffractometer	Bruker P4/RA/SMART 1000 CCD
Radiation (λ (Å))	Graphite-monochromated Mo Kα (0.71073)
Temperature (°C)	–80
Scan type	φ rotations (0.3°)/ω scans (0.3°) (30-s exposures)
Data collection 2θ limit (°)	51.50
Total data collected	21 122 (–34 ≤ *h* ≤ 33, –24 ≤ *k* ≤ 25, –15 ≤ *l* ≤ 15)
Independent reflections	12 330
Number of observations	8806 [$F_o^2 \geq 2\sigma(F_o^2)$]
Structure solution method	Direct methods/fragment search (DIRDIF-96)
Refinement method	Full-matrix least-squares on F^2 (SHELXL–93)
Absorption correction method	SADABS
Range of transmission factors	0.8620–0.5954
Data/restraints/parameters	12 330 [$F_o^2 \geq -3\sigma(F_o^2)$]/3/663
Flack absolute structure parameter	0.0 (3)
Goodness-of-fit (*S*)	1.005 [$F_o^2 \geq -3\sigma(F_o^2)$]
Final *R* indices	
R_1 [$F_o^2 \geq 2\sigma(F_o^2)$]	0.0639
wR_2 [$F_o^2 \geq -3\sigma(F_o^2)$]	0.1993
Largest difference peak and hole (e Å^{-3})	1.200 and –0.924

Results and discussion

(*R*,*S*,*R*,*S*)-Me-PennPhos (**1**) reacts cleanly with **2** to generate two diastereomers of the triply chloride bridged cationic dimer **3**, as illustrated in Scheme 1. Related monocationic dimers containing nitrile ligands and mono- or bidentate phosphine ligands have been reported by James and coworkers (4*b*, 9). At room temperature, this reaction proceeds to give two diastereomers of **3** in the ratio ~2:3. The ratio of diastereomers formed is dependent on the reaction temperature. If the reaction is carried out at 45°C, the minor diastereomer formed at room temperature is then formed as the major diastereomer in the ratio ~3:1. The major diastereomer formed at 45°C was identified as one of the *anti*-diastereomers by X-ray diffraction vide infra. If made at room temperature, the ratio of diastereomers (~2:3) converts to the limiting ratio (~3:1) upon heating the reaction mixture at 45°C overnight. These observations suggest that the major diastereomer formed at room temperature is a kinetic product that is thermodynamically less stable than the other formed diastereomer. Further, it appears that the diastereomers interconvert slowly at 45°C. Similar interconversions

Scheme 1. Reaction of **1** and **2**.

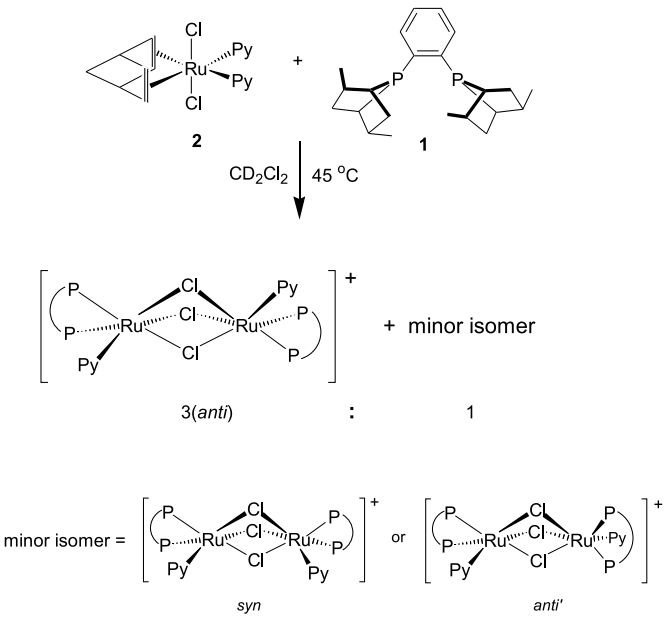

© 2002 NRC Canada

Fig. 1. Perspective view (ORTEP) of the major diastereomer of the cation *anti*-**3** (20%) thermal ellipsoids showing the atom-labeling scheme. Hydrogen atoms have been omitted for clarity. The Cl^- counter ion is also not shown.

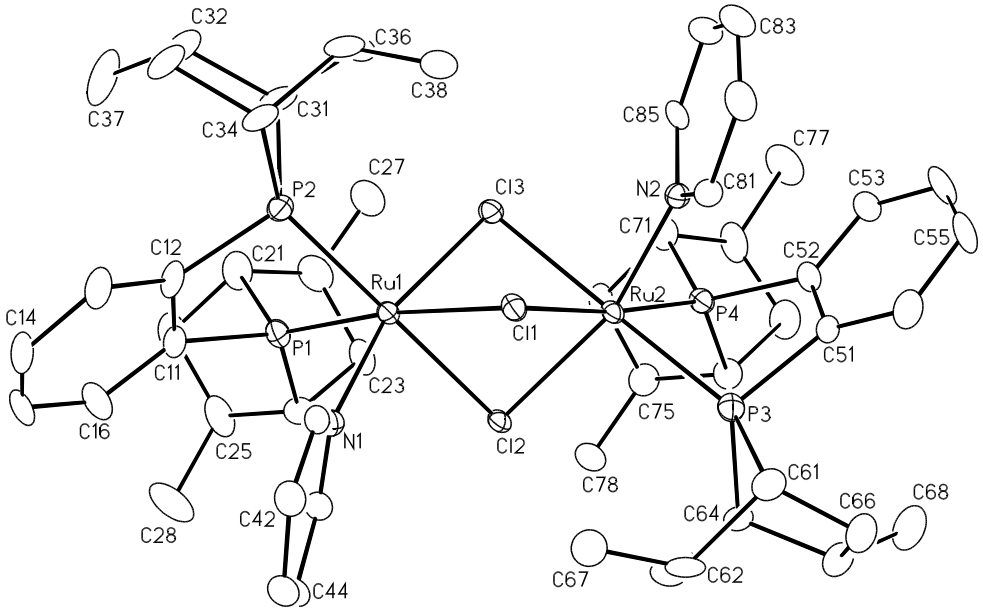

Fig. 2. Spatial distribution within the unit cell of the major *anti*-diastereomer of **3**.

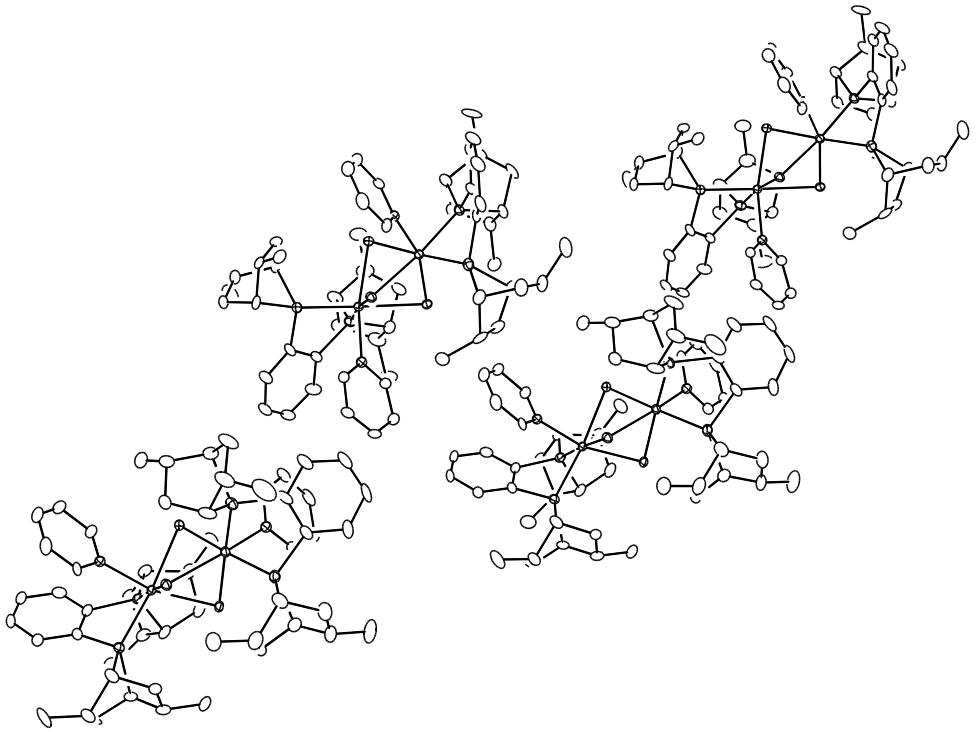

have been observed, for example, with ruthenium bis(phosphine) complexes such as $RuCl_2(dppb)(L)_2$ (dppb = 1,4-bis(diphenylphosphino)butane, L = NH_3, py, 4-NH_2Py, 4-CNPy, 4-MePy, PhPy) (4*b*, 4*c*, 10).

The ^{31}P spectrum of the minor diastereomer of **3** formed at 45°C exhibits an AB pattern with two doublets at $\delta = 87.9$ and $\delta = 62.7$. The major *anti*-diastereomer shows a similar pattern but with peaks at $\delta = 82.8$ and $\delta = 68.7$. There are three possible diastereomers of **3**, two with *anti* relative orientations of the Py rings and one with a *syn* relative orientation.

Scheme 1 shows the *syn*- and the two *anti*-diastereomers. A similar situation was observed by James and co-workers (4*b*, 10) for other Ru(II) triply chloride bridged dimers. As all three diastereomers of **3** have twofold rotation axes, NMR spectroscopy could not be used to distinguish between them.

© 2002 NRC Canada

Table 2. Selected interatomic distances.

	Bond length (Å)
Ru1—P1	2.28(2)
Ru1—P2	2.26(2)
Ru1—Cl1	2.456(19)
Ru1—Cl2	2.515(18)
Ru1—Cl3	2.439(18)
Ru1—N1	2.09(6)
Ru2—Cl1	2.462(18)
Ru2—Cl2	2.435(17)
Ru2—Cl3	2.50(2)
Ru2—P3	2.26(2)
Ru2—P4	2.286(18)
Ru2—N2	2.09(6)
P1—C11	1.85(8)
P1—C21	1.91(9)
P1—C24	1.85(9)
P2—C12	1.83(9)
P2—C31	1.88(8)
P2—C34	1.88(8)
P3—C51	1.85(8)
P3—C61	1.86(9)
P3—C64	1.85(8)
P4—C52	1.82(8)
P4—C71	1.89(8)
P4—C74	1.87(7)
N1—C41	1.32(10)
N1—C45	1.33(10)
N2—C81	1.33(11)
N2—C85	1.37(10)
C11—C12	1.41(13)
C11—C16	1.43(12)
C12—C13	1.40(10)
C13—C14	1.37(14)
C14—C15	1.35(15)
C15—C16	1.40(14)
C21—C22	1.56(14)
C21—C26	1.55(14)
C22—C23	1.58(14)
C22—C27	1.49(15)
C23—C24	1.51(12)

Table 3. Selected interatomic angles.

	Bond angles (°)
Cl1-Ru1-Cl2	79.9(6)
Cl1-Ru1-Cl3	81.9(6)
Cl1-Ru1-P1	173.4(8)
Cl1-Ru1-P2	102.9(7)
Cl1-Ru1-N1	84.4(17)
Cl2-Ru1-Cl3	79.0(6)
Cl2-Ru1-P1	97.8(7)
Cl2-Ru1-P2	176.7(7)
Cl2-Ru1-N1	89.3(17)
Cl3-Ru1-P1	103.8(7
Cl3-Ru1-P2	99.6(7)
Cl3-Ru1-N1	163.4(17)
P1-Ru1-P2	79.5(8)
P1-Ru1-N1	89.4(17)
P2-Ru1-N1	92.6(17)
Cl1-Ru2-Cl2	81.4(6)
Cl1-Ru2-Cl3	80.7(6)
Cl1-Ru2-P3	102.9(7)
Cl1-Ru2-P4	173.3(7)
Cl1-Ru2-N2	83.1(16)
Cl2-Ru2-Cl3	79.5(6)
Cl2-Ru2-P3	100.3(7)
Cl2-Ru2-P4	105.0(7)
Cl2-Ru2-N2	161.6(17)
Cl3-Ru2-P3	176.4(7)
Cl3-Ru2-P4	98.2(7)
Cl3-Ru2-N2	88.2(17)
P3-Ru2-P4	78.3(7)
P3-Ru2-N2	92.8(17)
P4-Ru2-N2	90.3(17)
Ru1-Cl1-Ru2	83.9(6)
Ru1-Cl2-Ru2	83.3(5)
Ru1-Cl3-Ru2	83.6(6)
Ru1-P1-C11	100(3)
Ru1-P1-C21	136(3)
Ru1-P1-C24	119(3)
C11-P1-C21	102(4)
C11-P1-C24	122(4)
C21-P1-C24	80(5)
Ru1-P2-C12	101(3)
Ru1-P2-C31	116(3)
Ru1-P2-C34	138(3)

The dimeric structure of **3** and the identity of the major diastereomer formed at 45°C were confirmed by X-ray crystal studies. Yellow crystals of major *anti*-**3** were obtained upon crystallization by layering hexanes onto a CH_2Cl_2 solution of **3**. Dissolution at low temperature in CD_2Cl_2 and NMR spectroscopy confirmed that these crystals are of the major diastereomer formed at 45°C. The compound crystallizes with three molecules of CD_2Cl_2 per molecule of complex. The structure formed is a distorted octahedral configuration in which the Ru center is surrounded in the equatorial plane by two P atoms and two Cl atoms. The apical positions are occupied by Cl on one side and Py on the other as shown in Fig. 1. There are four molecules of **3** per unit cell arranged as shown in Fig. 2.

The structure of **3** is a triply bridged diruthenium(II, II) face-sharing bioctahedral. Similar X-ray structures for Ru(II, II) dinuclear species have been reported with bis(phosphine) (4*d*, 10) or monophosphine (11) ligands coordinated to the metal center. The Ru—Ru internuclear distance obtained for this compound was 3.289 Å, a distance much longer than a typical Ru—Ru single bond (2.632–3.034 Å) (12). The Ru—Ru distance in this compound is, however, within the range expected for diruthenium complexes with triply bridging Cl atoms. Some examples and their respective Ru—Ru distances are as follows: $[H_2NEt_2][Ru_2Cl_5((R)$-*p*-MeO-BINAP$)_2]$, 3.3 Å (13); $[(\eta^2\text{-}H_2)(dppb)Ru(\mu\text{-}Cl)_3RuCl(dppb)]$, 3.278 Å (4*d*); $[Ru_2Cl_3(PBu_3)_6][BPh_4]$, 3.39 Å (11). The Ru—Cl and Ru—N distances fall within the expected ranges for such Ru(II) complexes (4*a*, 4*c*, 4*e*, 14, 15). Table 2 lists the interatomic distances within major *anti*-**3**.

© 2002 NRC Canada

Table 3 lists some selected interatomic angles for major *anti*-**3**. Of interest is the marked contraction of the Cl-Ru-Cl angle (average 80.9°) from the expected 90° for a regular octahedral. This contraction has been explained by Cotton and Torralba (11) to result from repulsive forces between the two d^6 Ru(II) centers in the molecule with consequent increase in Ru—Ru internuclear distance. The increased Ru—Ru internuclear distances result in contraction of the Cl-Ru-Cl bond angles and expansion of the Ru-Cl-Ru angles. The average value for angles obtained in this compound, 80.9° for Cl-Ru-Cl and 83.6° for Ru-Cl-Ru, fall within the expected respective ranges (77.2–80.9 and 82.9–87.9°) for this type of complex (4*d*, 10, 11, 13).

Unexpectedly, the PennPhos P–aryl–P plane was tilted relative to the P–Ru–P plane. This tilt removes the *C*2 dissymmetry of the ligand. While it is not known whether this tilting is typical of PennPhos compounds, we note that Zhang and co-workers (5) observed that the ^{31}P NMR spectrum of [Rh(**1**)(COD)]$^+$ contained two sets of signals for the phosphorus centers, showing that they were inequivalent. A possible explanation put forward by Zhang and co-workers (5*a*) was that the phosphabicyclo[2.2.1]heptane groups are too bulky to allow the PennPhos to adopt a planar, *C*2-symmetric geometry. The results obtained in the present work appear to confirm this explanation.

Conclusions

The work presented in this paper further illustrates the versatility of compound **2** as a starting material for synthesis of various Ru–bis(phosphine) complexes. The reported crystal structure is the first of a metal complex containing the PennPhos ligand. The formation of dimers upon reaction of **2** with PennPhos rather than the monomeric species formed with most common chiral bis(phosphine) ligands (3) illustrates how the structure of the chiral bis(phosphine) ligand can have unexpected consequences on the structures of their metal complexes. In this case, two methyl groups of PennPhos (in this case, C38 and C27 as well as C67 and C78 of major *anti*-**3**) project into the spatial domain occupied by other ligands on the ruthenium center (5). We propose that it is this projection that favors formation of the cationic dimers **3** rather than the corresponding monomeric bis(pyridine) complex *trans*-$RuCl_2$(PennPhos)Py_2. Inspection of molecular models and the solid-state structure of major *anti*-**3** shows that the methyl groups (e.g., C67 and C38) in *trans*-$RuCl_2$(PennPhos)Py_2 would protrude into the spatial domain occupied by the Py ligands (3, 4*c*). No such steric congestion is present in major *anti*-**3**. Further, since we have shown previously (3) that reaction of (*R*,*R*)-Me-DUPHOS ((–)-1,2-bis((2*R*,5*R*)-2,5-dimethylphospholano)benzene) with **2** generates the monomeric complex *trans*-$RuCl_2$((*R*,*R*)-Me-DUPHOS)Py_2, the present results indicate that it is more the steric requirements and less the electronic requirements of PennPhos that govern formation of the cationic dimers **3**.

Acknowledgements

We thank the Natural Sciences and Engineering Research Council of Canada (NSERC) and the University of Alberta for financial support. We would also like to sincerely thank Prof. Xumu Zhang of the Department of Chemistry, Pennsylvania State University, for his generous donation of the Me-PennPhos used in this work.

References

1. Recent reviews: (*a*) R. Noyori and H. Takaya. Acc. Chem. Res. **23**, 345 (1990); (*b*) H. Brunner and W. Zettlemeier. Handbook of enantioselective catalysis. VCH, Weinheim. 1993; (*c*) R. Noyori. Asymmetric catalysis in organic synthesis. John Wiley & Sons, Inc., New York. 1994. p. 16; (*d*) J.P. Genêt. *In* Advances in asymmetric synthesis. *Edited by* G.R. Stephenson. Chapman and Hall, London, U.K. 1996. p. 60; (*e*) J.P. Genêt. *In* Reductions in organic synthesis. A.C.S. Symp. Ser. **641**, 31 (1996); (*f*) D.J. Ager and S.A. Laneman. Tetrahedron Asymmetry, **8**, 3327 (1997); (*g*) V. Ratovelomanana-Vidal and J.P. Genêt. J. Organomet. Chem. **567**, 163 (1998); (*h*) V. Fehring and R. Selke. Angew. Chem. Int. Ed. **37**, 1827 (1998); (*i*) E.N. Jacobsen, A. Pfalz, and H. Yamamoto (*Editors*). Comprehensive asymmetric catalysis I–III. Springer, New York. 1999; (*j*) T. Ohkuma, M. Kitamura, and R. Noyori. *In* Catalytic asymmetric synthesis. 2nd ed. *Edited by* I. Ojima. Wiley-VCH, New York. 2000. Chap. 1.
2. (*a*) R. Noyori and T. Ohkuma. Angew. Chem. Int. Ed. Eng. **40**, 40 (2001); (*b*) K. Abdur-Rashid, A.J. Lough, and R.H. Morris. Organometallics, **19**, 2655 (2000); (*c*) K. Abdur-Rashid, A.J. Lough, M. Faatz, and R.H. Morris. J. Am. Chem. Soc. **123**, 7473 (2001).
3. O.M. Akotsi, K. Metera, R.D. Reid, R. McDonald, and S.H. Bergens. Chirality, **12**, 514 (2000).
4. The James group has prepared Ru(BINAP)Py_2Cl_2 (personal communication). Also see (*a*) A.A. Batista, E.A. Plato, S.L. Queiroz, O.R. Nascimento, B.R. James, and S.J. Rettig. Inorg. Chim. Acta, **230**, 111 (1995); (*b*) D.E. Fogg and B.R. James. Inorg. Chem. **36**, 1961 (1997); (*c*) S.L. Queiroz, A.A. Batista, G. Oliva, M.T. do P. Gambardella, R.H.A. Santos, K.S. MacFarlane, S.J. Rettig, and B.R. James. Inorg. Chim. Acta, **267**, 209 (1998); (*d*) K.S. McFarlane, I.S. Thornburn, P.W. Cyr, D.E.K.-Y. Chau, S.J. Rettig, and B.R. James. Inorg. Chim. Acta, **270**, 130 (1998); (*e*) P.W. Cyr, B.O. Patrick, and B.R. James. Chem. Commun. 1570 (2001) and refs. cited therein.
5. (*a*) Q. Jiang, Y. Jiang, D. Xiao, P. Cao, and X. Zhang. Angew. Chem. Int. Ed. **37**, 1100 (1998); (*b*) Q. Jiang, Y. Jiang, Z. Zhang, G. Zhu, Q. Jiang, D. Xiao, and X. Zhang. J. Org. Chem. **64**, 1174 (1999).
6. G.M. Sheldrick. 1996. SADABS, a program for absorption correction of Siemens Area Detector Data [computer program]. University of Gottingen, Gottingen, Germany.
7. P.T. Beurskens, G. Beurskens, W.P. Bosman, R. de Gelder, G.S. Garcia, R.O. Gould, R. Israel, and J.M. Smits. 1996. The DIRDIF-96 program system [computer program]. Crystallography Laboratory, University of Nijimegen, Netherlands.
8. G.M. Sheldrick. 1993. SHELXL-93 [computer program]. University of Gottingen, Gottingen, Germany.
9. I.S. Thornburn, S.J. Rettig, and B.R. James. J. Organomet. Chem. **296**, 103 (1985).
10. A.M. Joshi, I.S. Thorburn, S.J. Rettig, and B.R. James. Inorg. Chim. Acta, **198–200**, 283 (1992).
11. F.A. Cotton and R.C. Torralba. Inorg. Chem. **30**, 2196 (1991).
12. For examples of Ru—Ru single bond distances, see (*a*) R. Mason and K.M. Thomas. J. Organomet. Chem. **40**, C67 (1972); (*b*) B.M. Mattson, J.R. Heinman, and L.H. Pignolet. Inorg. Chem. **15**, 564 (1976); (*c*) M.B. Hursthouse, R.A. Jones, K.M. Abdul Malik, and G. Wilkinson. J. Am. Chem. Soc. **101**, 4128 (1979); (*d*) C. Hampton, W.R. Cullen, and B.R. James. J. Am.

© 2002 NRC Canada

Chem. Soc. **110**, 6918 (1988); (*e*) S. Kuwata, M. Andou, K. Hashizume, Y. Mizobe, and M. Hidai. Organometallics, **17**, 3429 (1998); (*f*) J.A. Cabeza, I. del Rio, F. Grepioni, M. Moreno, V. Riera, and M. Suarez. Organometallics, **20**, 4190 (2001) and refs. cited therein; (*g*) R. Okamura, K. Tada, K. Matsubara, M. Oshima, and H. Suzuki. Organometallics, **20**, 4772 (2001).

13. T. Ohta, Y. Tonomura, K. Nozaki, H. Takaya, and K. Mashima. Organometallics, **15**, 1521 (1996).
14. C.R.S.M. Hampton, I.R. Butler, W.R. Cullen, B.R. James, J-P. Charland, and J. Simpson. Inorg. Chem. **31**, 5509 (1992).
15. A.G. Orpen, L. Brammer, F.H. Allen, O. Kennard, D.G.Watson, and R. Taylor. J. Chem. Soc. Dalton Trans. **S1** (1989).

© 2002 NRC Canada

Palladium and platinum complexes of L-PhePhos: Acetyl-*p*-(diphenylphosphino)-L-phenylalanine methyl ester — a chiral ligand for transition metal complexation

Vineeth Iyengar, Patrycja V. Galka, Andreas Pletsch, and Heinz-Bernhard Kraatz

Abstract: The crystal structure of the new phenylalanine-based phosphino amino acid L-PhePhos and its reactivity to form the Pd and Pt complexes (L-PhePhos)$PdCl_2$ and (L-PhePhos)$PtCl_2$ is reported. A new platinum hydride was quantitatively formed in the reaction of (L-PhePhos)$PtCl_2$ with $NaBH_4$.

Key words: phosphine, amino acid, hydride, platinum, palladium, structure.

Résumé : On a déterminé la structure cristalline d'un nouvel acide phosphino-aminé à base de phénylalanine, L-PhePhos, on a déterminé sa réactivité à former des complexes de Pd et de Pt, (L-PhePhos)$PdCl_2$ et (L-PhePhos)$PtCl_2$. Un nouvel hydrure du platine se forme quantitativement par réaction du (L-PhePhos)$PtCl_2$ avec le $NaBH_4$.

Mots clés : phosphine, acide aminé, hydrure, platine, palladium, structure.

[Traduit par la Rédaction]

Introduction

Phosphines have proven extremely versatile ligands for a wide range of transition metal catalyzed transformations (1, 2). Chiral phosphines such as the bidentate DIOP, DUPHOS, and others coordinated to late transition metals have allowed asymmetric transformations with high product yield and high enantiomeric excess (3). Despite the success, even commercial success, of many of these chiral phosphine ligands as part of a catalyst, the potential for discovering ligands that result in a more active and more selective catalyst is continuing to fuel interest in the design of novel P-based ligands. In particular, effective and stable chiral ligands that do not require expensive chiral precursors or a laborious multistep reaction are desirable.

In this regard, phosphine-based amino acids offer an exciting opportunity to synthesize both enantiomers of a particular phosphine ligand. Inexpensive optically pure amino acids have been converted to chiral phosphino ligands and have been employed in the laboratory in numerous asymmetric catalytic systems. Chiral phosphine, aminophosphine, and phosphinito ligands based on hydroxyproline (4) have been used for the hydrocarbonylation and hydrogenation of olefins. Recently, Gilbertson reported examples of helical peptides carrying phosphino amino acid donors and described their catalytic behaviour (5).

We recently reported the facile synthesis of enantiomerically pure L-PhePhos, a chiral triphenylphosphine analogue (Scheme 1) (6), by a Pd-catalyzed P–C cross-coupling reaction of L-*p*-iodophenylalanine with Ph_2PH. As part of our ongoing research aimed at exploring the use of P-modified peptides as chiral ligands for transition metal coordination and catalysis, we now report the crystal structure of this new phosphine ligand and our first results of its Pt and Pd coordination chemistry.

Received 2 February 2002. Published on the NRC Research Press Web site at http://canjchem.nrc.ca on 26 November 2002.

Dedicated to Professor Tris Chivers for his contributions to Canadian chemistry.

V. Iyengar, P.V. Galka, A. Pletsch, and H.-B. Kraatz.[1] Department of Chemistry, 110 Science Place, University of Saskatchewan, Saskatoon, SK S7N 5C9, Canada.

[1]Corresponding author (e-mail: kraatz@skyway.usask.ca).

Results and discussion

Structure of L-PhePhos

We recently reported the preparation of enantiopure and reasonably airstable L-PhePhos (**1**), a new phosphine amino acid ligand, which has a PPh_2 group attached to the phenyl ring of phenylalanine. The ORTEP plot of compound **1** is shown in Fig. 1(*a*). The P atom in compound **1** exhibits trigonal pyramidal coordination, with both phenyl substituents and the phenyl ring of L-Phe adopting a propeller-like arrangement about the P atom, similar to that in triphenylphosphine (7). Bond distances and angles in L-PhePhos also compare well with those reported by Dunne and Orpen for PPh_3 (7). The average P—C bond length is 1.818 Å (1 Å = 0.1 nm), falling slightly short of the 1.831 Å reported for PPh_3. The C-P-C angle separating the two PPh_2 rings is 103.5°. In the solid state, individual molecules of **1** orient themselves in alternating "up–down–up–down" positions, which aligns their amino acid termini and allows strong N–H···O=CH bonding between adjacent molecules. This results in the formation of linear H-bonded chains, in which the H-bonding distance d(N···O) was found to be 2.867(2) Å

 DOI: 10.1139/V02-143 © 2002 NRC Canada

Fig. 1. (*a*) ORTEP diagram of L-PhePhos (**1**) at the 30% probability level. Hydrogen atoms have been omitted for clarity. Selected bond distances: P(1A)—C(21A) = 1.838(11) Å, P(1A)—C(31A) = 1.809(5) Å, P(1A)—C(14) = 1.872(4) Å, C(31A)-P(1A)-C(21A) = 104.7°, C(31A)-P(1A)-C(14) = 101.00(19)°, C(21A)-P(1A)-C(14) = 101.0(4)°. (*b*) Hydrogen-bonding interaction of L-PhePhos molecules d(N···O) = 2.867(2) Å.

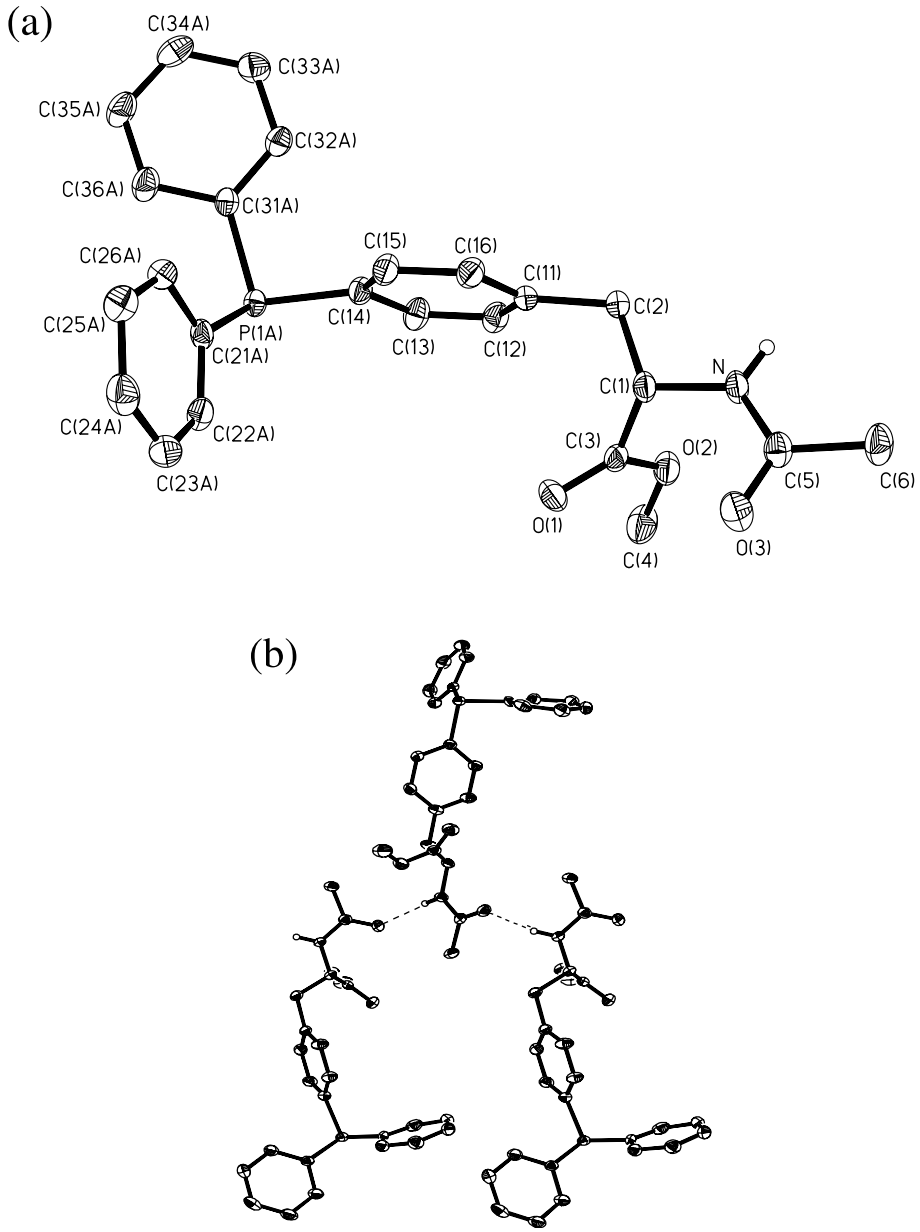

Scheme 1. Synthesis of L-PhePhos (**1**) by Pd-catalyzed P–C cross-coupling (6).

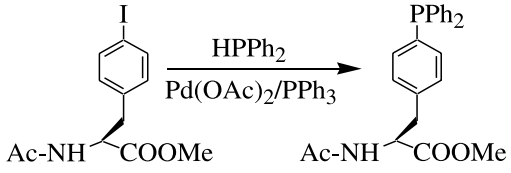

(Fig. 1*b*). The H-bonded region is flanked on either side by aromatic phosphine residues of the Ph_3P portion of adjacent amino acids. The aromatic groups of individual one-dimensional chains are pointing towards each other (Fig. 2). The H-bonded chains are stacked 14.5 Å apart, separated by the aromatic phosphine residues. There is no H bonding between adjacent H-bonded planes.

^{1}H NMR resonances of protons involved in H bonding, such as the amide NH in compound **1**, experience upfield shifts as H-bonding strength decreases. Variable temperature (VT) ^{1}H NMR is the tool of choice for evaluating H bonding in solution and has been used before to evaluate the interaction between peptides (8). At high temperatures, H bonding between molecules generally decreases, resulting in a shift closer to the "unperturbed" non-H-bonded signal. To evaluate H bonding in solution, a VT NMR study in $CDCl_3$, a nonpolar solvent widely used to evaluate weak H-bonding interactions, was carried out over a temperature range of

© 2002 NRC Canada

Table 1. Selected ^{1}H and ^{31}P NMR data for L-PhePhos (**1**), *cis*-(L-PhePhos)$_2$PtCl$_2$ (**2**), *cis*-(L-PhePhos)$_2$PdCl$_2$ (**3**), and *trans*-(L-PhePhos)$_2$Pt(H)Cl (**4**).

	^{1}H NMR (δ, ppm)			
Compound	NH	α-CH	β-CH$_2$	^{31}P NMR (δ, ppm)
L-PhePhos (**1**)	5.91	4.88	3.10	–5.8 (s)
cis-(L-PhePhos)$_2$PtCl$_2$ (**2**)	5.98	4.88	3.12	23.4 (s)
cis-(L-PhePhos)$_2$PdCl$_2$ (**3**)	6.14	4.86	3.10	14.5 (J_{P-Pt} = 3665 Hz)
trans-(L-PhePhos)$_2$Pt(H)Cl (**4**)	6.50	4.72	3.00	28.4 (J_{P-Pt} = 2700 Hz)

Fig. 2. Interaction between adjacent H-bonded 1-dimensional chains of compound **1** forming a layered structure with a separation of 14.5 Å between adjacent H-bonded layers.

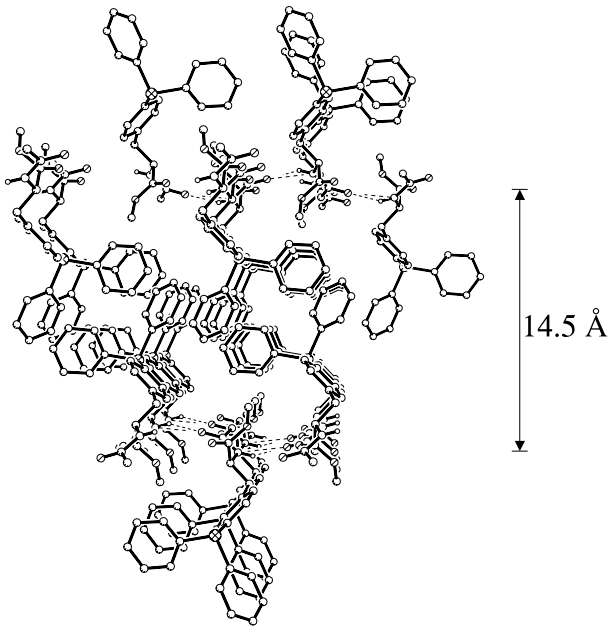

35 K (293–320 K). $CDCl_3$ was chosen as solvent. Absolute NMR shifts larger than 4–5 ppb K^{-1} suggest the presence of H bonding (8). Interestingly, the NH signal of **1** exhibits only a small highfield shift with increasing temperature. The observed temperature dependence is low (–2.8 ppb K^{-1}) and provides no evidence for H bonding in solution.

Metal complexes of L-PhePhos

Scheme 2 illustrates the synthetic routes used to prepare Pd(II) and Pt(II) complexes from stoichiometric amounts of (COD)MCl_2 or (PhCN)$_2MCl_2$ (M = Pt, Pd) in the presence of L-PhePhos. The COD and PhCN ligands are both readily replaced by the phosphine, and identical products were obtained from each route. The ^{31}P NMR spectrum of uncoordinated L-PhePhos in $CDCl_3$ shows a single resonance at δ –5.8 (δ –4.6 for PPh_3) (9). Upon coordination to Pt to give *cis*-(L-PhePhos)$_2$PtCl$_2$ (**2**), this signal is shifted downfield to δ 14.5, with a ^{31}P–^{195}Pt coupling of 3665 Hz, characteristic for *cis*-phosphine coordination (9). The Pd analogue *cis*-(L-PhePhos)$_2$PdCl$_2$ (**3**) exhibits a singlet at δ 23.4. The ^{1}H NMR spectra of compounds **2** and **3** show single resonances for the amide NHs, shifted from δ 5.91 in the uncomplexed L-PhePhos to δ 6.14 and δ 5.98 for complexed L-PhePhos in compounds **2** and **3**, respectively (Table 1). The splitting of

Scheme 2. Coordination chemistry of L-PhePhos. (*i*) CH_2Cl_2, L-PhePhos; (*ii*) $NaBH_4$, MeOH.

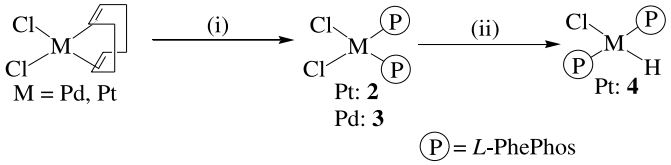

Scheme 3. Attempted prepatation of [(L-PhePhos)$_3$PtCl][BF_4] in the presence of Ag^+ and L-PhePhos.

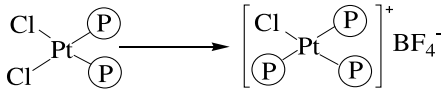

the two diastereotopic β-CH_2 proton signals increases upon coordination, which is compatible with a decrease in the mobility of the side-chain. We have observed similar effects in the related serine phosphinito complex (L-SerOPhos)$_2$PtCl$_2$ in which the two diphenylphosphine serine ligands are strongly H bonded (10). Hydrogen bonding, in addition to the steric bulk of the PPh_2 group, is thought of being responsible for this increase. Both complexes are stable in air. We carried out VT NMR experiments on a 4.5 mM solution of compound **2**. Temperature-dependent upfield shifts of the amide resonance of compound **2** from δ 6.092 at 293 K to δ 5.975 at 320 K confirms very weak intramolecular H bonding (–4.4 ppb K^{-1}).

In the presence of one equivalent of $AgBF_4$ and an additional equivalent of L-PhePhos, halide abstraction takes place, as is evident from the precipitation of AgCl from CH_2Cl_2 solution (Scheme 3).

After filtration, the solution exhibits a broad ^{31}P resonance at δ 23.2 ($J_{31P-195Pt}$ = 2425 Hz, $\upsilon_{1/2}$ = 100 Hz) in addition to the resonance of unreacted starting material (δ 14.5). Addition of a second equivalent of $AgBF_4$ results in the decomposition of the complex. These reactions are currently under further investigation.

The reaction of compound **2** with $NaBH_4$ in MeOH solution under basic conditions results in the quantitative formation of the corresponding hydrido complex, *trans*-(L-PhePhos)$_2$PtHCl (**4**). Figure 3 shows the ^{31}P{^{1}H} NMR spectra of the Pt complexes **2** and **4**. Upon borohydride reduction, the ^{31}P signal shifts upfield from δ 14.5 to δ 28.4. At the same time, J_{P-Pt} decreases to a value of 2700 Hz, indicative of a *trans*-coordination of the two phosphine ligands. The ^{1}H NMR spectrum of **4** exhibits a hydride signal as a triplet at δ –15.5 (J_{HP} = 27 Hz and J_{HPt} = 1170 Hz), which unequivocally established the coordination about the Pt cen-

© 2002 NRC Canada

Fig. 3. ^{31}P NMR spectra of (A) L-PhePhos, (B) *cis*-(PhePhos)$_2$PtCl$_2$, and (C) *trans*-(L-PhePhos)$_2$Pt(H)Cl.

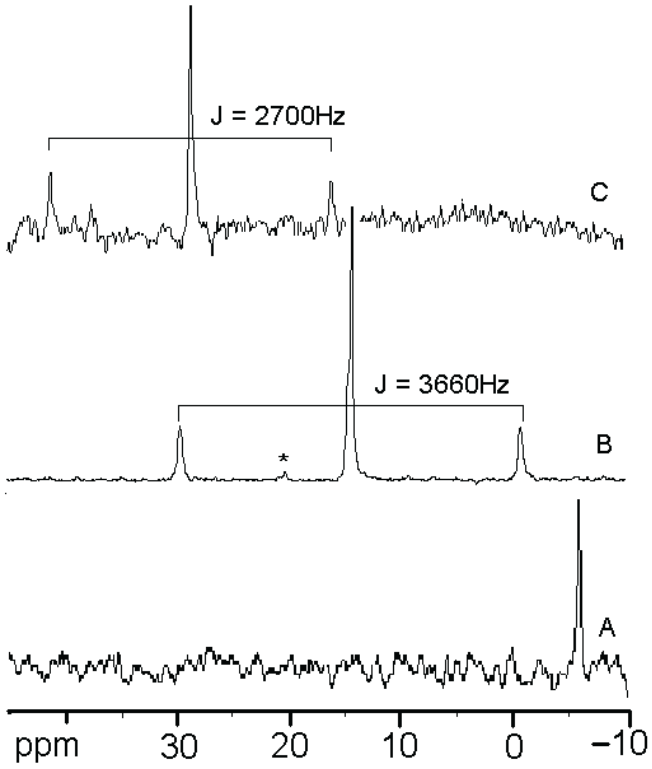

tre as *trans* (Fig. 4). The chemical shift and the coupling constants of compound **4** compare well with other platinum hydride complexes reported in the literature (11). The related reaction of the Pd complex **3** with $NaBH_4$ under identical conditions does not result in any isolable palladium

Experimental

General methods

All manipulations involving air- and-moisture sensitive materials were carried out under an argon or nitrogen atmosphere using a conventional Schlenk line. CH_2Cl_2 (CaH_2), $CHCl_3$ (CaH_2), and benzene (Na, benzophenone) were dried using the appropriate drying agents and distilled under nitrogen prior to use. Diethylamine was refluxed over NaOH, distilled, and stored over 4-Å molecular sieves. ^1H, ^{13}C, and ^{31}P NMR spectra were recorded at 300.135, 75.478, and 121.496 MHz, respectively, on a Bruker AMX 300 NMR spectrometer. All chemical shifts (δ) are reported in parts per million and coupling constants (*J*) in hertz. $CDCl_3$ (Aldrich) was stored over molecular sieves (4 Å). ^1H NMR shifts are referenced to the nondeutero impurity in $CDCl_3$ (δ = 7.24 ppm) or in MeCN-d_3 and are reported relative to tetramethylsilane (δ = 0 ppm). Assignments in the ^1H and $^{13}C\{^1H\}$ NMR were made using J modulation and by ^1H–^1H COSY. All measurements were carried out at 293 K unless otherwise specified. Mass spectrometry was carried out on a VG Analytical 70/20 VSE chromatograph. Elemental analyses were obtained in-house on a Perkin-Elmer 2400 CHN elemental analyzer.

Fig. 4. Hydride region of the ^1H NMR spectrum of *trans*-(L-PhePhos)$_2$Pt(H)Cl (**4**) showing a triplet at δ –15.5 (J_{HP} = 27 Hz, J_{HPt} = 1170 Hz).

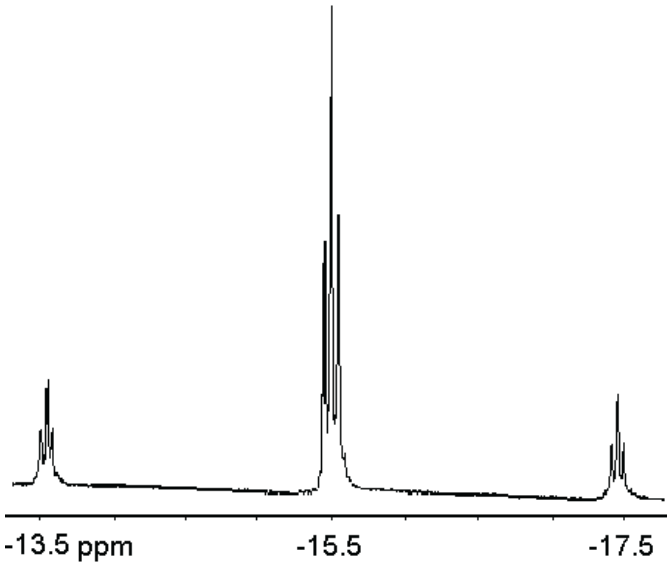

Preparation of *cis*-[*N*-Ac-Phe(PPh$_2$)-OMe]$_2$PtCl$_2$ (*cis*-(L-PhePhos)$_2$PtCl$_2$) (2)

To a stirring solution of (COD)PtCl$_2$ (50 mg, 0.14 mmol) in THF (5 mL), a solution of *N*-acetyl-L-(4-diphenylphosphine)phenylalanine methyl ester (113 mg, 0.28 mmol) in THF (5 mL) was added. The mixture was stirred at room temperature overnight and the solvent removed in vacuo and then washed with hexanes (5 mL), leaving an off-white solid. Using (PhCN)$_2$PtCl$_2$ as a starting material resulted in the formation of the identical product.

^1H NMR ($CDCl_3$) δ: 7.01–7.51 (14H, m, Ph), 6.14 (1H, d, *J* = 8 Hz, NH), 4.86 (1H, apparent dd, J^1 = 6 Hz, J^2 = 7 Hz, α-CH), 3.67 (3H, s, OMe), 3.10 (2H, apparent dd, J^1 = 6 Hz, J^2 = 9 Hz, β-CH_2), 1.96 (3H, s, MeC(O)). ^{13}C NMR ($CDCl_3$) δ: 172.0 (C=O), 170.0 (C=O ester), 135.4–128.1 (aromatic), 53.3, 52.7, 38.0, 23.4. ^{31}P NMR ($CDCl_3$) δ: 14.5 (s, $J_{P–Pt}$ = 3660 Hz).

Preparation of *cis*-[*N*-Ac-Phe(PPh$_2$)-OMe]$_2$PdCl$_2$ (*cis*-(L-PhePhos)$_2$PdCl$_2$) (3)

The procedure is identical for that of the Pt analogue. ^1H NMR ($CDCl_3$) δ: 7.72–7.37 (12H, m, Ph), 7.14 (2H, d, *J* = 7.8 Hz, Phe aromatics), 5.98 (1H, d, *J* = 8 Hz, NH), 4.88 (1H, apparent dd, J^1 = 6 Hz, J^2 = 8 Hz, α-CH), 3.66 (3H, s, OMe), 3.12 (2H, apparent dd, J^1 = 3 Hz, J^2 = 6 Hz, β-CH_2), 1.96 (3H, s, MeC(O)). ^{31}P NMR ($CDCl_3$) δ: 23.4 (s). Anal. calcd. for $C_{48}H_{48}Cl_2N_2O_6P_2Pd$: C 58.34, H 4.90, N 2.83; found: C 58.50, H 4.75, N 2.86.

Preparation of *trans*-[*N*-Ac-Phe(PPh$_2$)-OMe]$_2$PtHCl (*trans*-(L-PhePhos)$_2$PtHCl) (4)

125 mg of *cis*-(L-PhePhos)$_2$PtCl$_2$ (0.116 mmol, 1 equiv) was added to 5 mL of methanol and the resulting mixture was dissolved by 1.5 mL of diethylamine. Five milligrams of Na[BH_4] was slowly stirred into the solution and stirring continued for approximately 5 min until the evolution of

© 2002 NRC Canada

Table 2. Crystal data and structure refinement for L-PhePhos (**1**).

Empirical formula	$C_{24}H_{24}NO_3P$
Formula weight	405.41
Temperature (K)	193(2)
Wavelength (Å)	0.71073
Crystal system	Orthorhombic
Space group	$P2_12_12_1$
Unit cell dimensions	
a = 8.5187(7)	α = 90°
b = 9.1273(7)	β = 90°
c = 27.947(2)	γ = 90°
Volume (Å^3)	2172.9(3)
Z	4
$D_{calcd.}$ (mg m^{-3})	1.239
Absorption coefficient (mm^{-1})	0.151
F(000)	856
Crystal dimensions (mm)	0.60 × 0.36 × 0.11
Range for data collection	2.35–26.40°
Limiting indices	$-10 < h < 10$, $-11 < k < 11$, $-34 < l < 34$
Reflections collected	13 032
Independent reflections	4455 (R_{int} = 0.0388)
Completeness (%)	99.8
Max and min transmission	0.9836 and 0.9151
Refinement method	Full-matrix least squares on F^2
Data/restraints/parameters	4455/0/380
Goodness-of-fit on F^2	1.065
Final R indices [$I > 2\sigma(I)$]	R_1 = 0.0390, wR_2 = 0.0890
R indices (all data)	R_1 = 0.0466, wR_2 = 0.0922
Absolute structure parameter	0.16 (9)
Largest diff. peak and hole (e Å^3)	0.254 and –0.128

Note: $R_1 = \Sigma||F_o| - |F_c||/\Sigma|F_o|$; $wR_2 = [\Sigma w(F_o^2 - F_c^2)^2/\Sigma w(F_o^4)]^{1/2}$; $w = [\sigma^2(F_o^2) + (0.0879P)^2 + 0.0229P]^{-1}$ where $P = ([\max(F_o^2, 0) + 2F_c^2]/3)$.

pale white gas had ceased. The resulting clear yellow solution was reduced to a greyish brown solid under vacuum. 15 mL of benzene was used to dissolve the material, and any residual solids were removed by filtration. The benzene filtrate was then dried under vacuum giving a white residue. 15 mL of toluene was added and the solution was filtered twice and then vacuumed to dryness. ^{1}H NMR ($CDCl_3$) δ: 7.60–6.90 (14H, m, aromatics), 6.50 (1H, d, NH), 4.88 (1H, apparent dd, J^1 = 6 Hz, J^2 = 14 Hz, α-CH), 3.63 (3H, s, OMe), 3.00 (2H, apparent dd, J^1 = 3 Hz, J^2 = 8 Hz, β-CH_2), 2.05 (3H, s, MeC(O)), –15.50 (1H, t, J_{HP} = 28 Hz, J_{HPt} = 1172 Hz).

X-ray crystallography

Suitable crystals of L-PhePhos (**1**) were obtained by layering a $CHCl_3$ solution of **1** with hexanes. Colourless needles suitable for X-ray crystallography were deposited after 2 days. A single crystal of approximate dimentions 0.60 × 0.36 × 0.11 mm was mounted onto a glass fibre. Data for **1** were measured using a Bruker P4 SMART diffractometer equipped with a rotating anode and a 1000 CCD using Mo Kα radiation (graphite monochromated).[2] The structure was solved using direct methods (12). All non-H atoms were refined anisotropically using full-matrix least squares on F^2 (13). The position of the Ph_2P group was disordered over two positions and was modelled satisfactorily with a 1:1 occupancy for the two positions. The position of the H atoms was found in the difference Fourier map and refined isotropically. The final R value for **1** was R = 0.0390 for 3938 reflection with $I > 2\sigma(I)$ (4455 total reflections). Crystallographic details are summarized in Table 2.

Summary

The P atom in the new phenylalanine-based phosphino amino acid L-PhePhos readily coordinates to Pd(II) and Pt(II) to form the new square-planar complexes *cis*-(L-PhePhos)$_2$PdCl$_2$ and *cis*-(L-PhePhos)$_2$PtCl$_2$. The metal complexes are air stable and exhibit spectroscopic parameters typical of *cis*-coordination of the phosphine ligands to the metal centre. VT NMR gives some indications of intramolecular H bonding between the two amide NH of the L-PhePhos ligands. The rection of (L-PhePhos)PtCl$_2$ with $NaBH_4$ results in the formation of a new platinum hydride (L-PhePhos)PtHCl. We continue to explore the coordination chemistry of L-PhePhos and the chemistry of its Pt and Pd complexes, in particular with reference to their potential application in homogeneous catalysis.

Acknowledgements

We thank the Natural Sciences and Engineering Research Council of Canada (NSERC) for financial support in the form of an operating grant to H.B.K. H.B.K. is a recipient of the PetroCanada Young Innovator Award. A.P. wishes to express his gratitude to the student exchange program between the Universität Marburg, Germany, and the University of Saskatchewan. We thank Mr. Ken Thoms for the elemental analyses.

References

1. I. Ojima (*Editor*). Catalytic asymmetric synthesis. VCH, New York. 1993.
2. R. Noyori. Asymmetric catalysis in organic synthesis. Wiley, New York. 1994.
3. I. Omea. Application of organometallic compounds. Wiley, New York. 1999.
4. (*a*) S. Naili, J.-F. Carpentier, F. Agbossou, A. Mortreux, G. Nowogrocki, and J.-P. Wignacourt. Organometallics, **14**, 401 (1995); (*b*) S. Naili, I. Suisse, A. Mortreux, F. Agbossou-Niedercorn, and G. Nowogrocki. J. Organomet. Chem. **628**, 114 (2001); (*c*) K. Everaere, A. Mortreux, M. Bulliard, J. Brussee, A. van der Gen, G. Nowogrocki, and J.-F. Carpentier. Eur. J. Org. Chem. **2**, 274 (2001); (*d*) V. Blandin, J.-F. Carpentier, and A. Mortreux. New J. Chem. **24**, 309 (2000).

[2] Supplementary data may be purchased from the Depository of Unpublished Data, Document Delivery, CISTI, National Research Council Canada, Ottawa, ON K1A 0S2, Canada (http://www.nrc.ca/cisti/irm/unpub_e.shtml for information on ordering electronically). CCDC 178034 contains the supplementary data for this paper. These data can be obtained, free of charge, via www.ccdc.cam.ac.uk/conts/retrieving.html (or from the Cambridge Crystallographic Data Centre, 12 Union Road, Cambridge, U.K.; fax +44 1223 336033; or deposit@ccdc.cam.ac.uk).

© 2002 NRC Canada

5. (*a*) S.R. Gilbertson and R.V. Pawlick. Angew. Chem. Int. Ed. Engl. **35**, 902 (1996); (*b*) S.R. Gilbertson and X. Wang. J. Org. Chem. **61**, 434 (1996).
6. H.-B. Kraatz and A. Pletsch. Tetrahedron: Asymmetry, **11**, 1617 (2000).
7. B.J. Dunne and A.G. Orpen. Acta Crystallogr. **C47**, 345 (1991).
8. (*a*) P. Saweczko, G.D. Enright, and H.-B. Kraatz. Inorg. Chem. **40**, 4409 (2001); (*b*) E.S. Stevens, N. Sugawara, G.M. Bonora, and C. Toniolo. J. Am. Chem. Soc. **102**, 7048 (1980).
9. J.G. Verkade and J.A. Mosbo. *In* ^{31}P NMR in stereochemical analysis. VCH, New York. 1987. p. 439.
10. P.V. Galka and H.-B. Kraatz. *In* Catalysis of organic reactions. *Edited by* M.E. Ford. Marcel Dekker, New York. 2001. pp. 589–594.
11. (*a*) T.G. Attig and H.C. Clark. Can. J. Chem. **53**, 3466 (1975); (*b*) C. Wieser, D. Matt, L. Toupet, H. Bourgeois, and J.-P. Kintzinger. J. Chem. Soc. Dalton Trans. 4041 (1996); (*c*) S.S. Stahl, J.A. Labinger, and J.E. Bercaw. Inorg. Chem. **37**, 2422 (1998); (*d*) S.P. Millar, M. Jang, R.J. Lachine, and R. Eisenberg. Inorg. Chim. Acta, **270**, 363 (1998); (*e*) N.A. Jasim and R.N. Perutz. J. Am. Chem. Soc. **122**, 8685 (2000).
12. G.M. Sheldrick. Acta Crystallogr. **A46**, 467 (1990).
13. G.M. Sheldrick. 1993. SHELXL-93 [computer program]. University of Göttingen, Germany.

© 2002 NRC Canada

The neutral diradical 5,5′-bis(1,3,2,4-dithiadiazolyl) [SNSNC-CNSNS], the first main group radical to exhibit a dramatic increase in paramagnetism on mechanical grinding

Guillermo Antorrena, Scott Brownridge, T. Stanley Cameron, Fernando Palacio, Simon Parsons, Jack Passmore, Laurence K. Thompson, and Fitri Zarlaida

Abstract: Reduction of $[(CNSNS)_2][AsF_6]_2$ with triphenylantimony and tetrabutylammonium chloride produced the diradical 5,5′-bis(1,3,2,4-dithiadiazolyl) [SNSNC-CNSNS] in high yield as a black solid with widely ranging magnetic susceptibilities (e.g., 0.6 to 2.6 μ_B), which on oxidation with AsF_5 regenerated $[(CNSNS)_2][AsF_6]_2$. The identity of [SNSNC-CNSNS] was established from EPR, vibrational, and mass spectra. Ab initio molecular orbital [MPW1PW91/6-311G(2df)] calculations show the lowest energy structure to consist of two coplanar rings separated by a C—C single bond (1.444 Å), reflected in the comparison of the vibrational spectra of the diradical with that of $[(CNSNS)_2][AsF_6]_2$ and the calculated spectra. Confidence in the calculated [MPW1PW91/6-311G(2df)] structure of the diradical is supported by the excellent agreement between the calculated and X-ray single crystal structure geometries of $[CNSSN]_2$ and $[(CNSNS)_2]^{2+}$ in $[(CNSNS)_2][AsF_6]_2$. The molecular orbitals indicate the diradical is essentially disjoint, confirmed by a very small (0.07 kJ mol^{-1}) GVB-PP(TC-SCF)/6-311G* calculated singlet–triplet energy gap. Accordingly, the EPR spectrum of the diradical (in tetrahydrofuran, 293 K) shows a simple 3-line pattern (g = 2.0043, $a(^{14}N)$ = 1.11 mT) with no observable exchange coupling between the two radical centers. Mechanical grinding of the diradical results in a large increase in paramagnetism (e.g., from 1.03 to 2.55 μ_B) that is unprecedented in main group chemistry. The X-ray diffraction data of the ground and unground powder are consistent with a second order phase change on grinding. Attempts to obtain crystals of the diradical by sublimation led instead to numerous decomposition and rearrangement products, including 4-cyano-1,2,3,5-dithiadiazolyl [NC-CNSSN], monoclinic space group $C2/c$, a = 9.46(2) Å, b = 7.625(5) Å, c = 13.17(2) Å, β = 107.94(4)°, Z = 8. The structure consists of axially symmetric, cofacial, *cis* dimers linked to form strands through two sets of $C{\equiv}N^{\delta-}\cdots S^{\delta+}$ contacts. More efficient and larger scale preparations of [SNS][AsF_6] and $[(CNSNS)_2][AsF_6]_2$ are reported.

Key words: 5,5′-bis(1,3,2,4-dithiadiazolyl), diradical, paramagnetism, mechanical grinding, second order phase change, 4-cyano-1,2,3,5-dithiadiazolyl.

Résumé : La réduction du $[(CNSNS)_2][AsF_6]_2$ à l'aide du triphénylantimoine et du chlorure de tétrabutylammonium fournit le biradical 5,5-bis(1,3,2,4-dithiadiazolyl) [SNSNC-CNSNS], avec un rendement élevé et sous la forme d'un solide noir de susceptibilités magnétiques très variables (par exemple, de 0,6 à 2,6 μ_B) qui, par oxydation à l'aide de AsF_5 régénère le $[(CNSNS)_2][AsF_6]_2$. L'identité du [SNSNC-CNSNS] a été établie par RPE et ses spectres vibrationnels et de masse. Des calculs d'orbitales moléculaires ab initio [MPW1PW91/6-311G(2df)] montrent que la structure de plus faible énergie est formée de deux cycles coplanaires séparés par une seule liaison C—C (1,444 Å) qui se reflète dans la comparaison du spectre de vibration du biradical avec celui du $[(CNSNS)_2][AsF_6]_2$ et du spectre calculé. La confiance dans la structure calculée [MPW1PW91/6-311G(2df)] du biradical est supportée par l'excellent

Received 2 February 2002. Published on the NRC Research Press Web site at http://canjchem.nrc.ca on 27 November 2002.

Dedicated to Dr. Tristram Chivers for his outstanding contributions to Canadian chemistry and for his friendship over the years.

G. Antorrena and F. Palacio.[1] Instituto de Ciencia de Materiales de Aragón, CSIC-Universidad de Zaragoza, 50009 Zaragoza, Spain
S. Brownridge, J. Passmore,[2] **and F. Zarlaida.** Department of Chemistry, University of New Brunswick, Fredericton, NB E3B 6E2, Canada.
T.S. Cameron.[3] Department of Chemistry, Dalhousie University, Halifax, NS B3H 4J3, Canada.
S. Parsons. Department of Chemistry, The University of Edinburgh, King's Buildings, West Mains Road, Edinburgh EH9 3JJ, Scotland.
L.K. Thompson.[4] Department of Chemistry, Memorial University of Newfoundland, St. John's, NF A1B 3X7, Canada.

[1]Corresponding author for variable field and ac magnetization studies (e-mail: palacio@posta.unizar.es).
[2]Corresponding author (e-mail passmore@unb.ca).
[3]Corresponding author for powder diffraction (e-mail: cameron@is.dal.ca).
[4]Corresponding author for variable temperature magnetic measurements (e-mail: lthomp@mun.ca).

 DOI: 10.1139/V02-149 © 2002 NRC Canada

accord entre les géométries calculées et observées pour $[\overline{CNSSN}]_2$ et $[(\overline{CNSNS})_2]^{2+}$ par diffraction des rayons X d'un cristal unique de $[(\overline{CNSNS})_2][AsF_6]_2$. Les orbitales moléculaires indiquent que le biradical est essentiellement incohérent, ce qui est confirmé par la très faible valeur (0,07 kJ mol^{-1}) de la bande d'énergie triplet–singulet calculée, GVB-PP (TC-SCF)/6-311G*. En conséquence, le spectre RPE du biradical (dans le tétrahydrofurane, à 293 K) présente un diagramme simple de trois raies (g = 2,0043, $a(^{14}N)$ = 1,11 mT) sans couplage d'échange observable entre les deux centres radicalaires. Un broyage mécanique du biradical augmente considérablement son paramagnétisme (par exemple, de 1,03 à 2,55 μ_B), ce qui est sans précédent dans la chimie du groupe principal. Les données de diffraction des rayons X sur les poudres broyées et non broyées sont en accord le fait que le broyage s'accompagne d'un changement de phase du deuxième ordre. Des essais en vue d'obtenir des cristaux du biradical par sublimation ont plutôt conduit à de nombreux produits de décomposition et de réarrangement, y compris du 4-cyano-1,2,3,5-dithiadiazolyle [NC-$\overline{CNSSN}$], groupe d'espace monoclinique, $C2/c$, a = 9,46(2), b = 7,625(5) et c = 13,17(2) Å, β = 107,94(4)° et Z = 8. La structure est formée de dimères *cis*, cofaciaux et de symétrie axiale reliés pour former des brins par le biais de deux ensembles de contacts $C{\equiv}N^{\delta-}\cdots S^{\delta+}$. On rapporte aussi des préparations plus efficaces et à plus grandes échelles de $[SNS][AsF_6]$ et $[(\overline{CNSNS})_2][AsF_6]_2$.

Mots clés : 5,5′-bis(1,3,2,4-dithiadiazolyle), biradical, paramagnétisme, broyage mécanique, changement de phase du deuxième ordre, 4-cyano-1,2,3,5-dithiadiazolyle.

[Traduit par la Rédaction]

Introduction

The synthesis of the soluble $[SNS][AsF_6]$ in high yield on a large scale (1) made possible the extensive quantitative symmetry-allowed cycloaddition chemistry of $[SNS]^+$ (1*b*, *c*). Reactions with a wide variety of alkynes and nitriles gave the respective 1,3,2-dithiazolylium and 1,3,2,4-dithiadiazolylium cations (1*c*), and on reduction the corresponding 7π radicals **1** and **2** (see Fig. 1) (2). Simple derivatives of **1** were not generally isolated as pure materials. Exceptions include 4,5-bis(trifluoromethyl)-1,3,2-dithiazol-2-yl, **1** ($R = CF_3$), a thermally stable but photochemically unstable blue gas over a green paramagnetic liquid at room temperature, which freezes to a diamagnetic solid (2, 3), and **1** (R = CN) prepared by Wolmerhäuser et al. by a different route (4). Some derivatives of the [R-$\overline{CNSNS}$] class of radicals (**2**) have been isolated and characterized (e.g., $R = CH_3$ (5*a*), CF_3 (5*b*), Ph (5*c*), *p*-$O_2NC_6H_4$ (5*c*), 4,4′-$\overline{SNSNCC_6H_4}$-C_6H_4 (5*d*)), as well as [*t*-Bu-$\overline{CNSNS}$] (5*d*, *e*), a paramagnetic liquid that undergoes a concerted photochemical symmetry-allowed rearrangement in solution to a thermodynamically more stable isomer [*t*-Bu-$\overline{CNSSN}$], also a paramagnetic liquid (5*d*, *e*). However, rearrangement of simple derivatives of **2** to the isomeric **3** is the norm and can occur in solution in the dark, although more slowly; and the solid [*p*-C_6H_4-$(\overline{CNSNS})_2$] (6) rearranges on heating. Simple derivatives of the radicals **1**, **2**, and **3** are generally diamagnetic in the solid state with electrons pairing up via weak π*-π* bonding. Banister et al. (7*a*) prepared the α-phase of [*p*-NCC_6F_4-$\overline{CNSSN}$], the first dithiadiazolyl radical that was paramagnetic in the solid state, and Banister et al. (7*a*) and Rawson and co-workers (7*b*, *c*) the β-phase, which surprisingly exhibited weak ferromagnetism below 36 K. Oakley and co-workers (8) showed that the solid state structure of [1,2,5,-thiadiazolo[3,4,*b*]-1,3,2-dithiazolo[3,4,*b*]pyrazin-2-yl] (**4**) undergoes a lateral shift from a paramagnetic slipped π-stack arrangement at 293 K to arrays of dimers at ca. 150 K. The related **5**, first prepared by Wolmerhäuser and Johann (9), undergoes a transition between a purple high-temperature paramagnetic phase consisting of a uniform 1-dimensional slipped π-stack

Fig. 1. Structure legend.

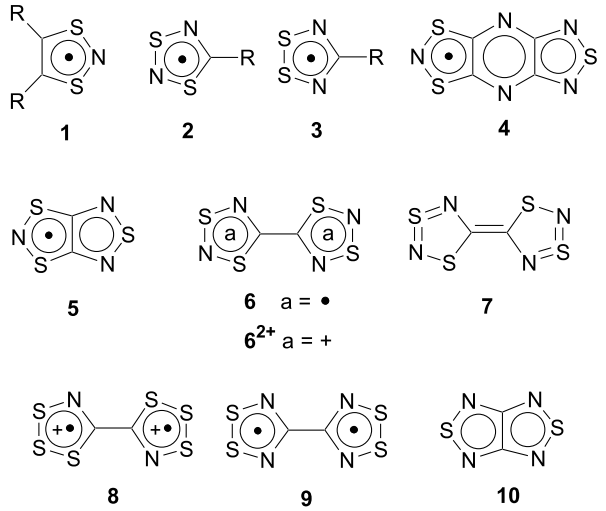

arrangement to a green diamagnetic low-temperature phase with strong dimerization along the stacking direction (10).

The general lability of the simple derivatives of monoradicals of **2** would imply that the preparation of stable diradicals containing a pair of **2** would be problematic. If prepared and isolated, however, it was anticipated that they might well have unusual physical properties based on the behaviour of related compounds (see above). The simplest example of such a diradical is **6**, containing two monoradicals joined by a single C—C bond. However, **6** could adopt the classical Lewis structure (**7**). On the other hand the isolobal **8**, which is a diradical containing a single C—C bond, has been prepared and characterized (11) and has an almost degenerate singlet and triplet ground state. In addition, the isomeric **9** has been prepared by Oakley and co-workers and is also a diradical containing a single C—C bond (12). In the solid state **9** is diamagnetic, forming dimers through π*-π* bonding.

$[(\overline{CNSNS})_2][AsF_6]_2$, containing $\mathbf{6}^{2+}$, the precursor to **6**, had been prepared by the quantitative 2:1 cycloaddition of

© 2002 NRC Canada

$[SNS][AsF_6]$ with dicyanogen (13). There are eight possible derivatives formally obtainable from $\mathbf{6}^{2+}$ by reduction, isomerization, and reoxidation (13*b*). $(CNSNS)_2$ (**6**) represents one of those possibilities formally given by the double reduction of $\mathbf{6}^{2+}$ in $\mathbf{6}\cdot[AsF_6]_2$. The compound **6** is the first example of a non-aryl diradical containing two units of **2**. We present evidence that **6** is a diradical and does not have the classical structure (**7**). In addition we show that **6** is, as far as we are aware, the first example of a main group radical that undergoes a dramatic increase in paramagnetism on mechanical grinding; however, similar cases are well documented for compounds that contain transition metal elements (14, 15). Compounds **6**, **4**, **5**, and **9** are all radicals and members of a class of neutral ternary carbon–sulfur–nitrogen compounds. A great variety of $C_xN_yS_z$ compounds can be envisaged, and the 21 examples whose X-ray structures have been determined and included in the Cambridge database (December 2001, (16)) are included in the Supplemental Material.[5] Compound **6** is one of a small class of main group non-sterically hindered diradicals that are paramagnetic in the solid state, in addition to dioxygen (17). The initial preparation and proposal of a structure for **6** was noted in 1991 (13*a*). Below we present evidence to show that the proposed structure of **6** is correct, although a single crystal X-ray crystal structure has yet to be obtained.

Experimental

General aspects

General techniques and apparatus are described in ref. 18. Unless stated otherwise, all reactions were carried out in a carefully dried one piece apparatus consisting of two Pyrex bulbs (V = 50 cm^3) linked by a glass tube (o.d. 10 mm) incorporating a sintered glass frit (medium porosity). Both bulbs were fitted with 5 mm Pyrex glass valves with PTFE pistons (J. Young, London, U.K.). All glassware was carefully dried prior to use. Light was excluded from reactions by wrapping the reaction vessel in Al foil. Moisture-sensitive materials and all solid products were manipulated in a Vacuum Atmospheres Dri-Lab using dry nitrogen and equipped with a Dri-Train (HE-493) and an internal circulating drying unit containing 1 kg of 3 Å molecular sieves. Sulfur dioxide (Matheson) was vacuum distilled onto and stored over CaH_2. Arsenic pentafluoride (Ozark-Mahoning), cyanogen (Matheson), triphenylantimony (Fluka), and tetrabutylammonium chloride (Eastman Kodak, Lancaster Synthesis) were used as received. Dithionitronium hexafluoroarsenate $[SNS][AsF_6]$ (1) and $\mathbf{6}\cdot[AsF_6]_2$ (13) were prepared as previously described but using modifications that led to increased efficiency at a larger scale ($[SNS][AsF_6]$: 25 g, 85% recovered yield based on S_4N_4; $\mathbf{6}\cdot[AsF_6]_2$: 12.5 g, 96.5% yield based on $[SNS][AsF_6]$); details are described in the Supplemental Material.[5] Elemental analyses were carried out by Beller Mikroanalytisches Laboratorium, Göttingen, Germany. Mass spectra (27 eV, EI) were measured on a Kratos MS50TC spectrometer by the direct inlet method. Density measurements were carried out in a 10 mL pycnometer as described in ref. 19, using acetone in which **6** is insoluble and with which it does not react.

X-ray powder photography

Samples for X-ray powder photography were loaded into 0.5 mm or 0.3 mm glass capillary tubes sealed under nitrogen atmosphere; diffraction photographs were obtained using a Rapide powder diffractometer with nickel filtered Cu Kα radiation with 3 h exposures and calibrated with a Corundum spectrum. The unit cell was extracted with the use of the indexing routines in Jade (20).

Infrared and FT-Raman spectroscopy

Infrared spectra of Nujol and fluorolube mulls of prepared compounds between CsI plates were recorded on a PerkinElmer model 683 grating spectrometer in the range of 4200 to 200 cm^{-1} or on a Bruker IFS66 FT-IR spectrometer in the range 4000 to 400 cm^{-1}. FT-Raman spectra were obtained from neat samples, sealed under nitrogen atmosphere in 5 mm NMR tubes (Wilmad), using an FT-IR spectrometer (Bruker IFS66) equipped with an FT-Raman accessory (Bruker FRA106) incorporating a Nd-YAG laser (emission wavelength: 1064 nm; maximum laser power: 300 mW). Details of data collection have been described previously (21).

EPR spectroscopy

Solution EPR spectra were recorded using a locally modified version of a Varian E-4 spectrometer fitted with an external Bruker B-ST 100/700 temperature control unit. Samples were prepared in a reaction vessel (described above) but incorporating a quartz tube (o.d. 4 mm, i.d. 2 mm), and one thick-walled 10 mL round bottom flask containing the sample (ca. 2 mg), solvent, and a Teflon-coated magnetic stir bar. After the mixture was stirred for 1 h, a portion of the very pale grey solution was poured through the frit into the quartz tube. If an EPR spectrum was not recorded within ca. 1 h of sample preparation, black powder was observed to settle out in the bottom of the tube; the quartz tube was immersed in a sonic bath for 10 min to redisperse **6** into the solvent.

Magnetic measurements

Preliminary magnetic susceptibilities were determined by the Gouy method using a Newport 1.5 in. (1 in. = 0.0254 m) electromagnet in conjunction with a Stanton Instruments Model MC5 microbalance with a sensitivity of 0.02 mg. Variable-temperature magnetic measurements (Memorial University) were made on a fully automated Oxford Instruments superconducting Faraday susceptometer equipped with a Sartorius 4432 microbalance (main solenoid field 1.5 T, gradient field 10 T m^{-1}). Samples were loaded into the sealed sample holder on a Vacuum Atmospheres Dri-Lab.

[5] Supplementary data may be purchased from the Depository of Unpublished Data, Document Delivery, CISTI, National Research Council Canada, Ottawa, ON K1A 0S2, Canada (http://www.nrc.ca/cisti/irm/unpub_e.shtml for information on ordering electronically). CCDC 191701 contains the supplementary data for this paper. These data can be obtained, free of charge, via www.ccdc.cam.ac.uk/conts/retrieving.html (or from the Cambridge Crystallographic Data Centre, 12 Union Road, Cambridge, U.K.; fax +44 1223 336033; or deposit@ccdc.cam.ac.uk).

© 2002 NRC Canada

Table 1. Preparation of **6**.

Reaction	**6**·$[AsF_6]_2$ (g, mmol)	$[NBu_4][Cl]$ (g, mmol)	$SbPh_3$ (g, mmol)	SO_2 (g)	Recovered yield of **6**[a] (g, mmol, %)	Light[b]	Gouy (μ_B)	Purification method[c]	Sublimation products
1	1.975, 3.37	1.940, 6.98	1.237, 3.50	15.93	0.613, 2.941, 87	y	1.21	Static	$C_2N_4S_3$(?)
2	2.002, 3.42	1.916, 6.89	1.217, 3.45	15.69	0.647, 3.107, 91	y	0.99	Static, ΔT	NSNCCNSN (**10**)[d]
3	2.090, 3.57	2.107, 7.58	1.368, 3.87	21.89	0.607, 2.914, 82 (5.453 g byprod)	n	0.71	Static, ΔT	S_4N_4, [NC-CNSSN]
4	1.998, 3.41	1.997, 7.18	1.285, 3.64	13.53	0.662, 3.178, 93	n	1.32	Dynamic, ΔT	S_8

[a]Recovered yield is based on **6**·$[AsF_6]_2$ and assumes complete removal of byproducts. Byprod = recovered weight of reaction byproducts ($SbPh_3Cl_2$ + $[NBu_4][AsF_6]$). Reactions were generally allowed to stir overnight before work up.

[b]Indicates whether the reaction was carried out in the presence (y) or absence (n) of direct, bright incandescent light. The reaction products were protected from direct light exposure by wrapping the reaction vessel with Al foil and by working up the reaction in dim light.

[c]SO_2 indicates prolonged washing and grinding of the product with a 50°C oil bath, as described in the experimental section. Static and dynamic refer to vacuum sublimation, ΔT indicates a temperature gradient was used in heating the reaction tube. See main text for details.

[d]Reference 28.

Variable temperature and variable field magnetic measurements (Spain) were carried out on a Quantum Design MPMS5S SQUID (superconducting quantum interference device) magnetometer equipped with an ac susceptibility attachment, using powdered samples of **6**, which were stored in a drybox in an Ar atmosphere and loaded into the sample holder under Ar atmosphere using a plastic bag.

Samples of **6** were ground, inside a Vacuum Atmospheres Dri-Lab, with a clean and dry agate mortar and pestle, previously cleaned with nitric acid. Samples were handled with glass or Teflon spatulas to minimize contamination with metals. A similar set of grinding experiments and subsequent magnetic measurements were carried out on NaCl and showed that no contaminants had been introduced in the Dri-Lab.

Fig. 2. (*a*) EPR of **6** in THF at 193 K. (*b*) EPR of **6** in THF at 293 K, showing partial rearrangement from -(CNSNS) to -(CNSSN) due to non-rigorously dried glassware.

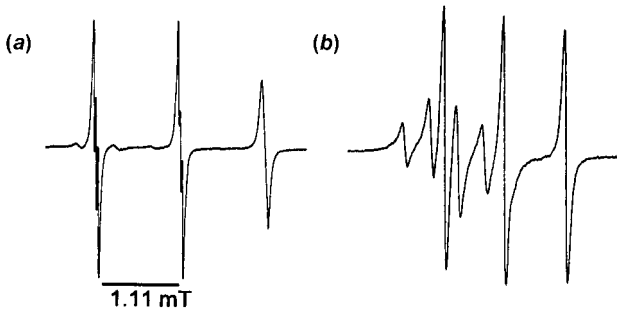

Preparation of 6

$[SNS][AsF_6]$ was reacted with $(CN)_2$ in SO_2 at 50°C for 5 days to produce **6**·$[AsF_6]_2$ in quantitative yield (13), the purity of which was checked by vibrational spectra of the crystalline product. In a typical reaction, SO_2 (7.036 g) was condensed onto **6**·$[AsF_6]_2$ (1.560 g, 2.66 mmol), $[NBu_4][Cl]$ (1.493 g, 5.37 mmol), and $SbPh_3$ (0.959 g, 2.68 mmol) at –196°C. A black precipitate was immediately observable on melting of the solid SO_2, indicating a rapid reduction to black insoluble **6** (eq. [1]).

$$[1] \quad \mathbf{6}\cdot[AsF_6]_2 + SbPh_3 + 2[NBu_4][Cl] \xrightarrow[SO_2]{} \mathbf{6} + SbPh_3Cl_2 + 2[NBu_4][AsF_6]$$

The reaction was stirred overnight, and the mixture was filtered. The solvent was condensed back into the first bulb; the mixture was stirred for 30 min and refiltered. This procedure was repeated until the colour of the solution had lightened from orange-yellow to a pale yellow. Further separation of the yellow-orange soluble $[NBu_4][AsF_6]$ and $SbPh_3Cl_2$ was accomplished by placing **6** on a sintered glass frit incorporated into a condenser with a pressure-equalizing side-arm joined to a Pyrex bulb (V = 50 cm^3) and closed with a J. Young valve (see Fig. 1 in ref. 22). The soluble products were extracted for up to 3 weeks by refluxing with SO_2 at 50°C, with removal of the SO_2 every few days to break up any large particles with a glass rod. This increased the purity of **6**, as judged by FT-Raman, with an 85% recovered yield (0.466 g, 2.236 mmol) of **6** and reaction byproducts. More extensive washing and grinding did not increase purity and did not afford completely pure material (FT-Raman). Numerous preparations were carried out under varying conditions to establish the reproducibility and quantitative yield of this reduction (Table 1, additional reaction data given in the Supplemental Material) and to reproduce the initial results, which showed the material was paramagnetic, including the exclusion of light to determine if **6** undergoes photochemical rearrangement or decomposition. A large excess of reducing agents was not used owing to the difficulty in separating them and the associated byproducts from **6**. Reaction vessels were rigorously dried otherwise partial rearrangement of the rings to -CNSSN occurred (EPR: Fig. 2*b*); however, if present partially rearranged material could be removed by washing with SO_2 followed by CH_2Cl_2.

Attempts to prepare **6** in acetonitrile, in which **6**·$[AsF_6]_2$ is soluble, using purified $[NBu_4][Cl]$ did not lead to purer **6** (IR and Raman spectra, elemental analysis) (23).

IR and FT-Raman spectral data for **6**·$[AsF_6]_2$ and **6** are listed in Table 2. FT-Raman spectra are shown in Fig. 3; the FT-Raman spectra of **6** from 50–3000 cm^{-1} and the IR spectra of **6** and **6**·$[AsF_6]_2$ are given in the Supplemental

© 2002 NRC Canada

Table 2. Vibrational spectral data for **6**·$[AsF_6]_2$ and **6**.

6·$[AsF_6]_2$				**6** Diradical triplet			
Observed IR	Observed Raman[b]	Calculated (scale 0.97)	Assignment[a]	Observed IR	Observed Raman	Calculated (scale 0.91)	Assignment[a]
	1586 (1)		[c]		1585 (1)		[c]
1536 (*w*) [e]	1520 (5)		[c]				
	1491 (100)	**1492** (0, 100)	ν_s(CN) (ν(CC))		1494 (4)		[c]
	1475 (4)	1446	^{13}C isotope		1474 (14)		[c]
					1444 (100)	**1437** (0, 100)	ν_s(CN) (ν(CC))
1430 (*w*) [e]	1461 (4)	1434	^{13}C (^{15}N) isotope	***1408*** (*w*) [e]	**1418** (4)	**1427** (23, 0)	ν_{as}(CN)
1393 (s)		**1426** (44, 0)	ν_{as}(CN)		1345 (3)	1374	^{13}C (^{15}N) isotope
1375 (*sh*) [e]							
	1217 (sh)						
	1208 (9)	**1199** (0, 12)	ν(CC) (ν_s(CS))	**1203** (mw)	**1239** (1)	**1143** (0, 4)	ν(CC) (ν_s(CS))
979 (s)		**1001** (100, 0)	ν_{as}(S(3)N(2)) + ν_{as}((S(1)N(2))		1009 (1)		
	955 (14)	978 (0, 7)	ν_{as}(S(3)N(2)) + ν_{ss}((S(1)N(2))		952 (1)		
	905 (7)	896 (0, 3)	ν_s(S(3)N(4))	846 (m)	853 (2)	791 (0, 3)	ν_s(S(3)N(2)) + ν_s(S(1)N(2))
861 (s)		847 (19, 0)	ν_{as}(S(3)N(4))	**820** (m)	**839** (4)	**785** (10, 0)	ν_{as}(S(3)N(2)) + ν_{as}(S(1)N(2))
829 (m)		**826** (76, 0)	ν_{as}(CS) (ν_{as}(S(3)N(2)))		**811** (26)	**773** (0, 16)	ν_s(S(3)N(4))
	794 (62)	**801** (0, 11)	ν_s(S(3)N(2)) + ν_s(S(1)N(2))	**799** (vs)		**750** (100, 0)	ν_{as}(CS) (ν_{as}(S(3)N(2)))
751 (s,br)	**742** (1)	**744** (27, 0)	ν_{as}(S(3)N(4))	**726** (s)		**685** (75, 0)	ν_{as}(S(3)N(4))
	719 (1)				719 (3)	664 (0, 0.4)	δ_s(SNS)
	689 (sh)			707 (ms)		648 (15, 0)	δ_{as}(SNS) ($\nu_3([AsF_6]^-$)[d]
698 (vs)	683 (34)	677 (0, 0.3)	δ_{as}(NCS) Out of plane ($\nu_3([AsF_6]^-$))		655 (6)	610 (0, 0.3)	δ_s(CSN) + δ_s(SNS)
	657 (2)	671 (0, 1)	ν_s(CS) + δ_s(CNS)			598 (0, 0.1)	δ_{as}(NCS) Out of plane
664 (s)		654 (54, 0)	ν_{as}(CS) + δ_{as}(CNS)	626 (m)	535 (7)	580 (11, 0)	ν_{as}(CS) (δ_{as}(CSN))
	593 (32)	587 (0, 4)	δ_s(SNS)		505 (4)	501 (0, 1)	δ_s(NSN)
	575 (1)						
590 (m)	567 (2)		$\nu_2([AsF_6]^-$)				
578 (m)		569 (37, 0)	δ_{as}(SNS)			490 (5, 0)	δ_{as}(NSN) (δ_{as}(SNS))
553 (ms)		562 (11, 0)	δ_s(NCS) Out of plane	504 (w)		483 (7, 0)	δ_s(NCS) Out of plane
	476 (8)	456 (0, 0.1)	δ_{as}(SNS) Out of plane		348 (1)	316 (0, 0.4)	δ_s(CCN)
437 (s)	441 (1)	440 (48, 0)	δ_s(SNS) Out of plane			278 (0, 0.1)	δ(CNS) Out of plane
395 (s)			$\nu_5([AsF_6]^-$)				
	379 (1)	340 (0, 1)	δ_s(CCN)		263 (1)	229 (0, 0.1)	Ring breathe
	369 (14)		$\nu_4([AsF_6]^-$)				
	347 (14)						
	293 (8)	281 (0, 0.3)	Ring out of plane deformation		200 (1)	186 (13, 0)	δ_s(SNS) Out of plane
	261 (6)	246 (0, 1)	Ring breathe		157 (1)	169 (0, 0.1)	δ_{as}(SNS) Out of plane
	252 (sh)						
	219 (6)						
	157 (5)	111 (0.3, 0)	Out of plane ring folding		130 (1)	92 (0.5, 0)	Ring folding
	113 (11)	94 (3, 0)	δ_{as}(CCS)		115 (1)	88 (2, 0)	δ_{as}(CCN)
		45 (0.3, 0)	Out of plane ring twist			51 (0.1, 0)	Ring twist out of plane

Note: FT-Raman spectra are shown in Fig. 3. Calculated (MPW1PW91/6-311G(2df)) frequencies are scaled as listed. Relative intensities in parentheses, listed as (IR, Raman) for calculated intensities.

[a]Assignments based on visualization of calculated vibrations using HYPERCHEM (37*e*). When two modes are listed, parentheses around the second mode indicate that the first mode is the predominant vibrational mode; a "+" indicates the two modes are of equal importance. See Fig. 6 for atom labelling scheme.

[b]Relative intensities measured as area under the peak.

[c]Unassigned, but are a consistent feature in the spectra of **6**, **6**·$[AsF_6]_2$, and both the solid state and solution spectra of salts of **8** (11*c*).

[d]In addition to peaks assigned to $[AsF_6]^-$, unlisted weak peaks at 1953, 2078, 2156, 2219, 2717, and 2780, and a strong peak at 2876 cm^{-1} are assigned to reduction byproducts.

[e]IR peaks in italics are from a fluorolube mull, all others from a Nujol mull.

© 2002 NRC Canada

Table 3. Comparison of EPR data for -$\overline{\text{CNSNS}}$ and -$\overline{\text{CNSSN}}$ ring containing compounds.

Species	g_{iso}	$a(^{14}N)$ (mT)[a]	$a(^{14}N)$ calcd. (mT)[e]	Reference
6	2.0043[b]	1.11, 0.04	1.02	This work
$\mathbf{6}^{+\bullet}$	2.0069[b]	1.1		13*b*
($\overline{\text{NSSNC}}$-$\overline{\text{CNSNS}}$)$^{+\bullet}$	2.0129[c,d]	0.47		23
9	2.011[d]	0.5	0.52	12
[Ph-$\overline{\text{CNSNS}}$]	2.0068[b]	1.1		24
[Ph-$\overline{\text{CNSSN}}$]	2.011[d]	0.51		24
[$CF_3$$\overline{\text{CNSNS}}$]	2.0057[b]	1.11		5
[$CF_3$$\overline{\text{CNSSN}}$]	2.0106[d]	0.5		5
[*t*-Bu-$\overline{\text{CNSNS}}$]	2.0048[b]	1.09, 0.05		5
[*t*-Bu-$\overline{\text{CNSSN}}$]	2.0106[d]	0.51		25
[I-$\overline{\text{CNSNS}}$]	2.0048[b]	1.12, 0.06		5
[I-$\overline{\text{CNSSN}}$]	2.0106[d]	0.5		5

[a]The first value refers to S*N*S, second number refers to C*N*S. Hyperfine coupling to C*N*S is very small for -$\overline{\text{CNSNS}}$ rings and is not always observable, even at high dilution (5). Hyperfine coupling to C*N*S (0.04 mT) observed only for **6** at 193 K, not at room temperature.
[b]1:1:1 triplet.
[c]As the $[SbF_6]^-$ salt.
[d]1:2:3:2:1 pentet.
[e]MPW1PW91/6-311G(2df).

Fig. 3. FT-Raman spectra of $\mathbf{6}^{2+}$ (top: 18 mW, resolution 4 cm^{-1}, 1024 scans, T = 140 K) and **6** (bottom: 60 mW, resolution 4 cm^{-1}, 6000 scans, T = 140 K).

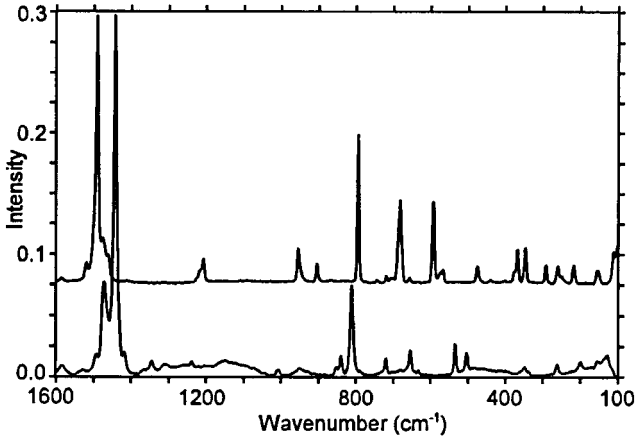

Material. EI-MS data listed below are for **6** (27 eV, I > 5%); data for I > 1% may be found in Supplemental Material.

EI-MS *m/z* (%): 212 ([$C_2N_4{}^{34}S_2{}^{32}S_2$], 6), 210 ([$C_2N_4{}^{34}S^{32}S_3$], 14), 208 ([M]$^+$, 100), 162 ([M – NS]$^+$, 5), 130 ([M – NS_2]$^+$, 36), 80 ([$^{34}SN^{32}S$]$^+$, 8), 78 ([S_2N]$^+$, 71), 64 ([S_2]$^+$, 7). Anal. calcd. for 95% **6** with impurities reasonably assigned as 5% [NBu_4][AsF_6] and $SbPh_3Cl_2$ in a 2:1 ratio (calcd. for pure **6**): C 15.16 (11.53), H 0.60, N 24.37 (26.90), S 55.40 (61.57), Cl 0.84, F 1.32, Sb 1.44, As 0.87; found: C 10.63, H 0.66, N 24.17, S 55.69, Cl < 0.2, F 3.20, Sb 1.16, As 0.77.

The mass spectrum of **6** did not change after up to 3 weeks washing with SO_2 or after storage at –20°C for two years. The EPR spectrum of **6** in THF at room temperature is given in Table 3; no resonance at half field corresponding to the $\Delta m_s = \pm 2$ transition was observed at either room or low temperature, suggesting **6** is not a triplet. Similar spectra were also obtained in SO_2 and CH_2Cl_2 (23).

Compound **6** changes from a black fluffy powder to black graphite-like shiny plates on mechanical grinding, with an apparent large change in volume. The density of **6** (0.035 g of **6** in 8.061 g acetone) was measured to be 1.7 ± 0.1 g cm^{-3} after 1 h of mechanical grinding. A measurement 1.4 g cm^{-3} was obtained for an unground sample of **6**. However, we surmise that this fluffy powder contained empty spaces within the bulk, leading to an erroneously low measured density.

Reoxidation of 6 (26)

Reoxidation of **6** (0.018 g, 0.09 mmol) with AsF_5 (0.130 g, 0.76 mmol) in SO_2 (0.887 g) in the presence of a trace (1 mg) of Br_2 in a 5 mm NMR tube gave a dark brown solution and a very small amount of colourless solid after 10 min at room temperature.

^{13}C NMR δ: 187 (lit (13*b*) value ^{13}C NMR δ: 187 for **6**·[AsF_6]$_2$).

In a larger scale reaction SO_2 (5.686 g), AsF_5 (0.521 g, 3.07 mmol), and Br_2 (6 mg) were condensed onto **6** (0.200 g, 0.96 mmol). The brown mixture was stirred at room temperature for 3 days, filtered, and the reaction volatiles (SO_2, AsF_5 (trace), AsF_3, and SiF_4 (very minor trace)) removed, leaving a black solid (0.550 g, 98% yield) consisting mainly of **6**·[AsF_6]$_2$ with some [$\overline{\text{NSSNC}}$-$\overline{\text{CNSNS}}$][AsF_6]$_2$ and [$\overline{\text{NSSNC}}$-$\overline{\text{CNSNS}}$][AsF_6] (IR: see Table 1 in ref. 13*b*). The IR spectrum also showed bands at 3200 (br), 1723 (w), 1704 (w), 1295 (m), 1076 (w), and 637 (sh) cm^{-1}, which possibly arose from the reaction of AsF_5 with the impurities in **6**. The very low intensity of the band at 1028 cm^{-1} due to SiF_4 in the reaction volatiles precludes hydrolysis as a source of these bands.

Attempts to purify and grow crystals of 6

Various solvents were investigated in an attempt to grow crystals and (or) separate the reaction byproducts from **6**. Compound **6** proved insoluble in $CFCl_3$, CH_3CN, CH_2Cl_2, SO_2, CS_2, AsF_3, benzene, toluene, acetone, and DMSO, as shown by the absence of any black material colouring the solvent after stirring for 24 h and the absence of black material after filtering off the solvent. Although EPR spectra

© 2002 NRC Canada

were obtained in THF (and in SO_2 and CH_2Cl_2) after vigorous stirring or placing the sample in a sonic bath, a black precipitate was observed at the bottom of the sample tube on standing within 1 h, implying **6** is only very sparingly soluble in these solvents.

Sublimation was carried out under static vacuum (10^{-3} mmHg (1 mmHg = 133.322 Pa)) at 90°C in a 14 × 300 mm sealed glass tube (reaction 1 in Table 1), which gave a few black block-like crystals, shown to be [NC-$\overline{\text{CNSSN}}$] by X-ray analysis (see below), and a very few extremely brittle colourless needle-like crystals. Attempts to mount the colourless needle-like crystals were frustrated by their brittleness. EI-MS data for the the colourless crystals (27 eV, I > 5%) is listed below.

EI-MS *m*/*z* (%): 178 ($[C_2N_4{}^{34}S^{32}S_2]^+$, 15), 177 (6), 176 ($[C_2N_4S_3]^+$, 100), 130 ($[C_2N_3S_3]^+$, 32), 104 ($[C_2N_3S_2]^+$, 11), 90 ($[CNS_2]^+$, 5), 78 ($[S_2N]^+$, 19), 46 ($[SN]^+$, 35).

The peak at 176 and the intensity of the ^{34}S-isotopomer peak at 178 suggest $C_2N_4S_3$ as a possible molecular formula. The lack of an abundant ion at 124 ($[S_3N_2]^+$) and the intense $[M - SN]^+$ fragment discounted the structure NC-CNSNSNS, a derivative of the 1,3,5,2,4,6-trithiatriazepine ring system, which has been studied extensively by Rees and co-workers (27).

Another attempt at static vacuum (10^{-3} mmHg) sublimation in a sealed tube with the temperature slowly increased from 30 to 110°C over 5 days (reaction 2 in Table 1) resulted in a few very small black crystals and numerous colourless needle-like crystals after 3 weeks. Crystals were not successfully mounted because of their small size and brittleness. The mass spectrum data of the colourless needles are listed below (27 eV, I > 5%; I > 1% in the Supplemental Material) and were nearly identical to those reported for NSNCCNSN (**10**) (28).

EI-MS *m*/*z* (%): 146 ($[C_2N_4{}^{34}S^{32}S]^+$, 9), 144 ($[C_2N_4S_2]^+$, 100), 78 (S_2N^+, 26), 72 ($[CN_2S]^+$, 31).

Sublimation under static vacuum (10^{-3} mmHg) in a sealed tube with a temperature gradient of 25–80°C for 2 weeks (reaction 3 in Table 1) produced a few large rhombohedral yellow crystals (S_4N_4: FT-Raman spectra (29), see Supplemental Material) and black amorphous material. The mass spectrum of the black material (listed below for 27 eV, I > 5%; I > 1% in the Supplemental Material) and FT-Raman spectrum (strong peak at 2250 cm^{-1} (ν(CN)) and 129 cm^{-1} (indicative of dimer S···S interactions (12), spectrum shown in the Supplemental Material) were consistent with data for [NC-$\overline{\text{CNSSN}}$].

EI-MS *m*/*z* (%): 132 ($[C_2N_3{}^{34}S^{32}S]^+$, 10), 130 ($[C_2N_3S_2]^+$, 61), 84 ($[C_2N_2S]^+$, 23), 80 ($[{}^{34}S^{32}SN]^+$, 11), 78 ($[S_2N]^+$, 100), 72 ($[CN_2S]^+$, 16), 64 ($[S_2]^+$, 38), 58 ($[CNS]^+$, 18).

Sublimation at 50–100°C under dynamic vacuum (10^{-5} mmHg), in a 14 × 400 mm tube capped with a J. Young valve for 2 weeks (reaction 4 in Table 1) was most successful at producing pure **6**, as evidenced by the mass spectrum (data listed below for 27 eV, I > 5%; I > 1% in the Supplemental Material). However, the quantity of sublimed material was extremely small. Sublimation under dynamic vacuum (10^{-3} mmHg, 40–80°C) yielded numerous green-yellow crystals, identified as S_8 (FT-Raman).

Table 4. Crystal data and refinement details for [NC-$\overline{\text{CNSSN}}$].

Chemical formula	$C_2N_3S_2$
Crystal size (mm)	0.05 × 0.25 × 0.30
Crystal colour, habit	Black, plate
Space group	*C*2/*c*
a (Å)	9.46 (2)
b (Å)	7.625 (5)
c (Å)	13.17 (2)
β (°)	107.94 (4)
V (Å^3)	903.9 (20)
Z	8
Formula weight (g mol^{-1})	130.16
F(000)	520
T (K)	296
$D_{calcd.}$ (g cm^{-3})	1.91
μ (Mo Kα) (mm^{-1})	1.014
Scan mode	ω–2θ
2θmax (°)	46
Measured reflections	728
Unique reflections	634
Observed reflections	270
R_1 [$I > 2\sigma(I)$][a]	0.069
wR_2[b]	0.074

[a] $R_1 = \Sigma||F_o| - |F_c||/\Sigma|F_o|$.
[b] $wR_2 = (\Sigma\omega(|F_o| - |F_c|^2/\Sigma\omega F_o^2]^{1/2}$.

EI-MS *m*/*z* (%): 210 ($[C_2N_4{}^{34}S^{32}S_3]^+$, 5), 208 ($[C_2N_4S_4]^+$, 29), 130 ($[C_2N_3S_2]^+$, 39), 78 ($[S_2N]^+$, 100).

Characterization and crystal structure of [NC-$\overline{\text{CNSSN}}$]

Several black block-like crystals (from reaction 1 in Table 1) were loaded into rigorously dried glass capillaries and, though of poor quality, were shown to be [NC-$\overline{\text{CNSSN}}$] by single crystal X-ray crystallography. An empirical absorption correction based on azimuthal scans of several reflections was applied, which resulted in transmission factors ranging from 0.82 to 1.00. The data were corrected for Lorentz and polarization effects. A correction for secondary extinction was applied (coefficient = 1.45351×10^{-6}). The structure was solved by direct methods (30) and expanded using Fourier techniques (31); all atoms were refined anisotropically. The full cycle of full-matrix least-squares refinement[6] on F was based on 270 observed reflections [$I > 2.00\,\sigma(I)$] and 65 parameters and converged (largest parameter shift was 0.01 times its esd) with R_1 = 0.069 and wR_2 = 0.074. Neutral atom scattering factors were taken from Cromer and Waber (32). Anomalous dispersion effects were included in $F_{calcd.}$ (33); the values of $\Delta f'$ and $\Delta f''$ were those of Creagh and McAuley (34). The values for the mass attenuation coefficients are those of Creagh and Hubbell (35). All calculations were performed using the teXsan (36) crystallographic software package of Molecular Structure Corporation. Crystal data are summarized in Table 4; full details are given in the Supplemental Material.

Ab initio calculations

Full geometry optimizations and vibrational frequency calculations for **6** (diradical triplet and "quinoidal" closed-

[6] Least-squares function minimized: $\Sigma w(|F_o| - |F_c|)^2$ where w = 1.

© 2002 NRC Canada

shell singlet), $\mathbf{6}^{2+}$, $[(\overline{CNSNS})_2]^{+\bullet}$ ($\mathbf{6}^{+\bullet}$), **9**, and [NC-$\overline{CNSSN}$] were carried out using the GAUSSIAN 98W suite of programs (37*a*) with the 6-311G(2df) basis set and the recently implemented MPW1PW91 HF/DFT hybrid functional (37*b*), which has proved successful in reproducing geometries, vibrational spectra, and energies of heavy-atom containing species (e.g., S_8^{2+} (38) and S_4^{2+} (39)) where other recent high-level calculations (40) did not. The starting geometry for **6**, $\mathbf{6}^{+\bullet}$, and $\mathbf{6}^{2+}$ was the average of the two crystallographically unique cations in the X-ray single crystal structure of $\mathbf{6}\cdot[AsF_6]_2$ (13). Calculated molecular orbitals were visualized with CHEM3D Ultra (37*d*). Calculated vibrational frequencies were animated using HYPERCHEM (37*e*), and assigned by these visualisations. All calculated structures were stationary points (i.e., no imaginary frequencies).

Geometry optimizations on the diradical singlet and triplet states of **6** were also performed at the 6-311G(*d*) level using the GAMESS suite of programs (37*c*) by Goddard and Mawhinney (41); the diradical singlet was calculated by the GVB-PP (TC-SCF) method using the ROHF triplet MOs (41). This method was chosen since electron correlation is required for an accurate energy difference calculation of these two states (42), and the MPW1PW91 method is inadequate for this task. Results are given in the Supplemental Material.

The effects of rotation about the C—C bond for **6** (diradical triplet and "quinoidal" closed-shell singlet **7**), $\mathbf{6}^{2+}$, $\mathbf{6}^{+\bullet}$, and **9** were examined via a series of MPW1PW91/6-31G(*d*) geometry optimizations in which the S-C-C-S dihedral angle (N(1)-C-C-N(1′) for **9**) was held constant in 15° steps from 0° (*cis*) to 180° (*trans*). Vibrational frequencies were not determined in this study.

Results and discussion

Preparation of 6

Double reduction of $\mathbf{6}\cdot[AsF_6]_2$ with $[NBu_4][Cl]$ and $SbPh_3$ gives **6** as an insoluble black powder (eq. [1]). This reaction is almost quantitative (Table 1), as is the preparation of the trisulfide analog $[(\overline{CNSSS})_2][AsF_6]_2$ ($\mathbf{8}\cdot[AsF_6]_2$) from $(CN)_2$ and a mixture of $[S_4][AsF_6]_2$ and (or) $[S_8][AsF_6]_2$ (11), in contrast to the 15% overall yield in the preparation of **9** (12). However, crystals suitable for X-ray structure determination were obtained for the latter two compounds but to date crystals of **6** have been elusive. This is due in part to the insolubility of **6** in numerous solvents. In contrast to the success with **9** (12), numerous attempts at sublimation to obtain crystals and (or) pure **6** resulted only in traces of **6** (mass spectra) and various decomposition products, depending on the sublimation conditions (see Table 1). This suggests that the sublimation and decomposition temperatures for **6** are very similar.

The first Gouy measurement on a sample of **6**, prepared as described above, gave a value of 2.92 μ_B (26) (2.83 μ_B is expected for two strongly coupled unpaired electrons ($s = 1$) and 2.45 μ_B if they are weakly coupled or non-interacting (43)); the second preparation of **6** gave a value of 0.62 μ_B (reaction 2). This drastic difference in magnetic moments led to a search for a correlation between reaction conditions and magnetic moment. Changes in reaction conditions included reaction temperature, reaction time, and method of mixing reagents, some of which are listed in Table 1, and more are given in the Supplemental Material. No obvious correlation was found, but magnetic moments from before and after extensive washing imply that the values are intrinsic to the sample and not the reaction byproducts: complete removal of impurities should lead to an increase in the magnetic moment. There was no obvious benefit to excluding light from the reactions, since there was no evidence that solid **6** rearranged photochemically (EPR, IR, FT-Raman, MS) when purposely exposed to light.

Structure elucidation

In the absence of an X-ray single crystal structure, extensive spectroscopic and computational characterization was carried out to determine the structure of **6**.

Mass spectra

The mass spectra fragmentation pattern of **6** contains a strong parent ion peak with a fragmentation pattern that is in complete agreement with the assigned structure. There are significant differences in the mass spectra of **6** and **9**, in particular the S_2^+ (mass = 64) peak is the most intense peak for **9** but only 8% (70 eV, 7% at 27 eV) for **6**; and a peak at mass = 144 $[M - S_2]^+$ is absent for **6**. These differences imply the rings of **6** do not contain S-S units and therefore **6** does not undergo rearrangement to [NSNSC-CNSSN] or **9** upon reduction.

EPR

The EPR spectrum of **6** in THF at room temperature consists of a triplet of triplets with $g = 2.0043$, $a(^{14}N(2)) = 1.11$ mT and $a(^{14}N(4)) = 0.04$ mT (Fig. 2*a*, Table 3). The differences in line width and intensity of the lines is due to spin-rotation interactions in solution (44). The EPR spectrum of **9** in $CHCl_3$ (Table 3) consists of a pentet ($g = 2.011$, $a(^{14}N) = 0.50$ mT) (12), suggesting there is little or no exchange interaction between the two radical centers for either **9** or **6** (45). For **9**, the onset of exchange coupling between the two rings is observed at 303 K (12*b*), and greater interaction is found in the 1,3- and 1,4-phenylene-bridged bis(1,2,3,5-dithiadiazolyl) species (46, 47), facilitated by the phenyl rings (12*b*), e.g., 5-*tert*-butyl-1,3-bis-(1,2,3,5-dithiadiazolyl)benzene at 240 K shows a simple 5-line pattern with a more complex pattern due to intramolecular exchange observed at room temperature (46).

The absence of a pentet and the similarity of the g and $a(^{14}N)$ values to -$\overline{CNSNS}$ rings rather than -$\overline{CNSSN}$ rings (Table 3) and the good agreement between the calculated and observed $a(^{14}N)$ values indicate the two rings of **6** remain as -$\overline{CNSNS}$ on reduction rather than rearranging to -$\overline{CNSSN}$. The in situ reoxidation of **6** to $\mathbf{6}\cdot[AsF_6]_2$ with AsF_5 in SO_2 showed only $\mathbf{6}^{2+}$ in the ^{13}C NMR and **6** as the main product in a larger scale reaction. The absence of signals attributable to $\mathbf{6}^{+\bullet}$ or $[\overline{NSSNC}\text{-}\overline{CNSNS}]^{+\bullet}$ in the EPR spectrum of **6** (Table 3) suggests the reduction goes to completion.

Theoretical studies

Theoretical calculations were carried out to aid in the assignment of the vibrational spectra (see below) and to use the comparison of the calculated and X-ray structures of $\mathbf{6}^{2+}$

© 2002 NRC Canada

Table 5. Calculated [UMPW1PW91/6-311G(2df)] geometries for **6**, $\mathbf{6}^{+\bullet}$, $\mathbf{6}^{2+}$, and **7**.

Parameter	$\mathbf{6}^{2+}$ Observed[a]	$\mathbf{6}^{2+}$ Calcd.	**6** Diradical triplet, calcd.	**7** Closed shell singlet, calcd.	$\mathbf{6}^{+\bullet}$ Calcd.
Energy (a.u.)		–1887.33888443	–1888.01520749	–1887.99103823	–1887.75889916
ΔE (kJ mol^{-1})		1775	0	63	673
Bond distances (Å)					
C(5)—C(5′)	1.454 (15)	1.465 ((1.06))	1.444[b,c] ((1.08))	1.358 ((1.43))	1.409 ((1.20))
C(5)—S(1)	1.718 (8)	1.747 ((1.19))	1.766 ((1.07))	1.822 ((0.96))	1.777 ((1.06))
S(1)—N(2)	1.593 (8)	1.588 ((1.36))	1.651 ((1.10))	1.678 ((1.04))	1.630 ((1.17))
N(2)—S(3)	1.600 (8)	1.582 ((1.39))	1.642 ((1.11))	1.563 ((1.37))	1.580 ((1.34))
S(3)—N(4)	1.615 (7)	1.613 ((1.21))	1.645 ((1.09))	1.562 ((1.34))	1.585 ((1.28))
C(5)—N(4)	1.298 (10)	1.298 ((1.57))	1.282 ((1.63))	1.355 ((1.26))	1.320 ((1.42))
Bond angles (°)					
C(5′)-C(5)-S(1)	122.4 (6)	123	120.9	123.7	123.3
C(5′)-C(5)-N(4)	121.2 (7)	121.9	122.4	123.6	122.5
S(1)-C(5)-N(4)	116.5 (6)	115.1	116.7	112.6	114.2
C(5)-S(1)-N(2)	96.1 (4)	95.1	96.1	95	95.2
S(1)-N(2)-S(3)	113.4 (4)	115.1	111.4	111.6	113.1
N(2)-S(3)-N(4)	102.2 (4)	101.4	102.7	107.7	104.3
C(5)-N(4)-S(3)	112.0 (6)	113.2	113	113.1	113.2
S(1)-C(5)-C(5′)-S(1′)	0	0	0	0	0

Note: Bond distances in Å, bond angles in degrees (°), estimated standard deviations (esd) in parentheses, calculated Wiberg bond orders in double parentheses. See Fig. 6 for atom labelling scheme.

[a]Average of the two crystallographically unique dications in the single crystal X-ray structure of $\mathbf{6}\cdot[AsF_6]_2$ (13).

[b]Slightly shorter than the "standard" sp^2-sp^2 C—C single bond length (lit. (57*a*) value *d*(C—C) 1.46 Å and lit. (48*b*) value *d*(C—C) 1.516 Å). For comparison, the H_5C_6-C_6H_5 C—C bond length in biphenyl is 1.493 (3) Å (49*b*).

[c]The bond lengths for the diradical singlet and triplet **6** calculated using the GVB-PP (TC-SCF) method were identical to within 0.001 Å (41). Details given in the Supplemental Material.

Table 6. Calculated [UMPW1PW91/6-311G(2df)] and observed geometries for **9**.

Parameter	Observed[a]	Calculated[b]
Bond distances (Å)		
C(5)—C(5′)	1.488 (7) ((0.97))	1.487 ((0.96))
C(5)—N(1), C(5)—N(4)	1.331 (7) ((1.41))	1.323 ((1.41))
N(1)—S(2), S(3)—N(4)	1.630 (5) ((1.16))	1.621 ((1.16))
S(2)—S(3)	2.088 (2) ((0.94))	2.118 ((0.92))
Bond angles (°)		
C(5′)-C(5)-N(1)	119.5 (b)	118.3
C(5′)-C(5)-N(4)	117.5 (b)	118.3
N(1)-C(5)-N(4)	123.1 (5)	123.4
C(5)-N(1)-S(2), C(5)-N(4)-S(3)	114.1 (4)	114.5
N(1)-S(2)-S(3), S(2)-S(3)-N(4)	94.4 (2)	93.8
N(3)-C(1)-C(2)-N(7)	0	10.5

Note: Bond distances in Å, bond angles in degrees (°), estimated standard deviations (esd) in parentheses, calculated Wiberg bond orders in double parentheses. See Fig. 6 for atom labelling scheme.

[a]Reference 12. Wiberg bond orders calculated in GAUSSIAN 98 using the observed geometry.

[b]Stationary point geometry, energy = –1888.05080103 a.u. Calculated planar geometry optimized as a first order saddle point, energy = –1888.05079384 a.u. (i.e., ΔE = 0.02 kJ mol^{-1}).

and **9** as a gauge of the quality of the calculated structure of **6**. Tables 5 and 6 show the excellent agreement between the calculated and X-ray crystal structures for both $\mathbf{6}^{2+}$ (in $\mathbf{6}\cdot[AsF_6]_2$ (13)) and **9** (12), respectively, with only the S—S and C—S bond lengths and the S-N-S bond angle slightly outside 3 × (esd) of the experimental data.

Fig. 4. π molecular orbitals 51–54 and MPW1PW91/6-311G(2df) orbital energies (eV) for the $(CNSNS)_2$ series of molecules.

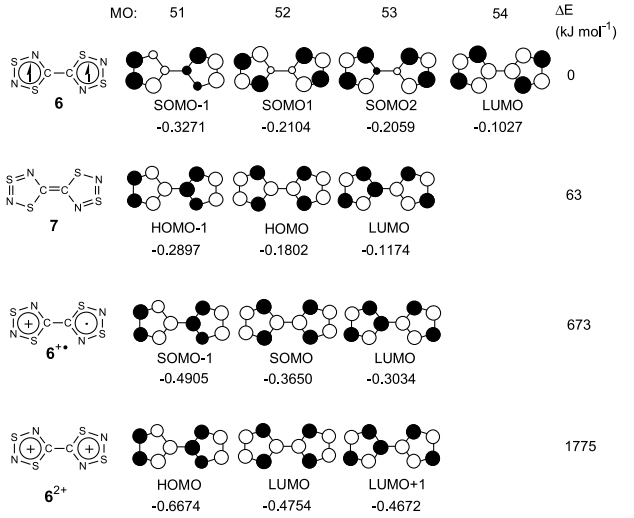

The two rings of **6** were calculated to be coplanar and separated by an sp^2-sp^2 C—C single bond (see Table 5) similar to **9** (12) and the dication in $\mathbf{6}\cdot[AsF_6]_2$ (13). The differences in bond lengths between **6** and $\mathbf{6}^{2+}$ largely reflect the nature of SOMO1 and SOMO2 (see Fig. 4) and the low coefficients on the carbon atoms of **6** (C_5 SOMO1: –0.037, SOMO2: 0.037). Thus the antibonding contributions of the S—N bonds in SOMO1 and SOMO2 with large S (S_1 SOMO1: 0.092, SOMO2: 0.092) and N (N_4 SOMO1: –0.133, SOMO2: –0.133) coefficients lead to S—N bond lengths

© 2002 NRC Canada

Fig. 5. Calculated [MPW1MPW91/6-311g(2df)] energetics of rotation about the C—C bond for **6** (▼), $\mathbf{6}^{2+}$ (●), $\mathbf{6}^{+\bullet}$ (■), and **9** (▲).

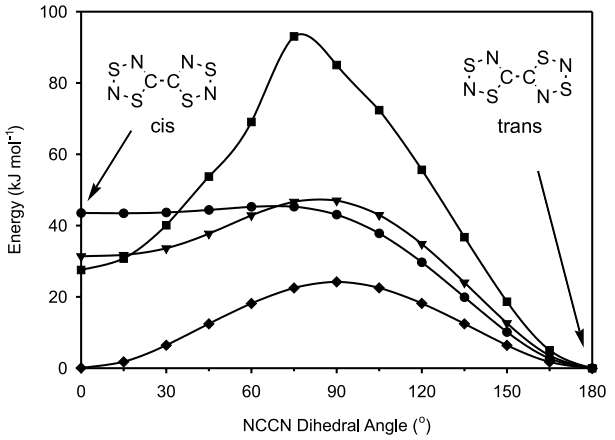

longer in **6** than in $\mathbf{6}^{2+}$. In contrast the C—C and C—N bond lengths in **6** (1.444, 1.282 Å) and $\mathbf{6}^{2+}$ (1.465, 1.298 Å) are rather similar, as directly observed in the vibrational spectra (Table 2), the slight differences being accounted for by inclusion of the differences in the HOMO of $\mathbf{6}^{2+}$ and the corresponding SOMO1 of **6** and the higher carbon and nitrogen coefficients in the HOMO of $\mathbf{6}^{2+}$ (C_5 0.183, N_4 0.127) and the SOMO1 of **6** (C_5 0.115, N_4 0.107). We note that the occupancies of the lower energy orbitals of **6** and $\mathbf{6}^{2+}$ are very similar.

Double occupation of SOMO1 results in a strengthening of the C—C bond, as observed for the calculated closed-shell "quinoidal" singlet **7** (1.358 Å), for which the HOMO is also C—C bonding. The HOMO of **7** is C—N antibonding, resulting in a longer (1.355 Å) C—N bond than that calculated for **6** (1.282 Å).

The SOMO1 is occupied (C coefficient: 0.104, see Fig. 4) in the monocation-monoradical $\mathbf{6}^{+\bullet}$, and the C—C distance is therefore intermediate (1.409 Å) to that of the diradical triplet and closed-shell singlet states. Similarly the C—N bond length (1.320 Å) falls between that of **6** and **7**, since the SOMO is C—N antibonding, as is the HOMO of **7**, but only singly occupied.

Rotation about the C—C bond (Fig. 5) confirmed that, in the gas phase, the *trans*-coplanar arrangements of the rings in both **6** and $\mathbf{6}^{2+}$ are the lowest energy conformations. This is in contrast to the previously published ROHF/6-311G* calculations carried out for the diradical triplet **9**, for which the confirmation with the two rings canted at 43.5° was 2.5 kJ mol^{-1} lower in energy than the observed coplanar arrangement in the solid state (12). Our recalculation of **9** at the MPW1PW91/6-311G(2df) level resulted in a lowest energy conformation with the rings twisted 10.5° out of plane, only 0.02 kJ mol^{-1} lower than the coplanar form (Table 6). These differences in ring orientation between the [$(\overline{CNSNS})_2$] series of compounds and **9** is attributed to the $S^{\delta+}\cdots N^{\delta-}$ attractions for **6**, $\mathbf{6}^{2+}$, and **8** vs. the $N^{\delta-}\cdots N^{\delta-}$ repulsions in **9** (see Fig. 6). Similarly, the larger positive charge on the sulfur atoms in $\mathbf{6}^{2+}$ compared with **6** (see Fig. 6) could account for the higher energy of the *cis* orientation in Fig. 5 for $\mathbf{6}^{2+}$ (33.8 kJ mol^{-1}) vs. **6** (27.1 kJ mol^{-1}). The relatively high energy of the twisted geometries of $\mathbf{6}^{+\bullet}$ compared with the other species indicates that the non-planarity prevents electron (and charge) delocalization throughout the

Fig. 6. Atom numbering scheme and calculated (NBO) charges for the $(\overline{CNSNS})_2$ series of molecules, $(\overline{CNSSN})_2$ and [NC-$\overline{CNSSN}$].

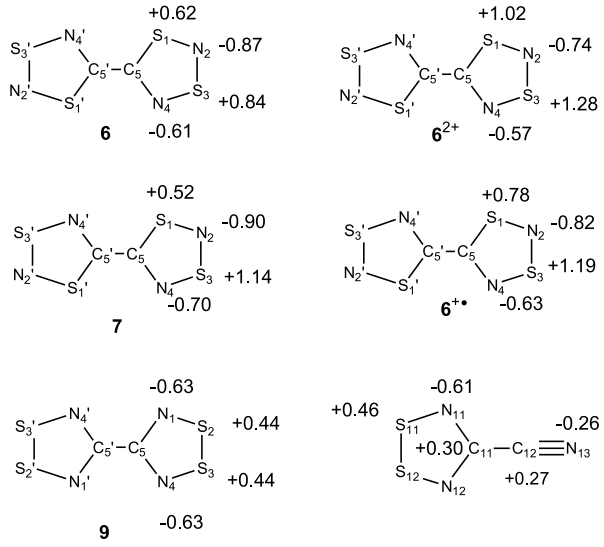

Scheme 1.

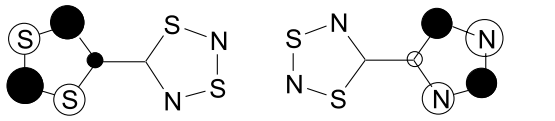

two rings of $\mathbf{6}^{+\bullet}$. The EPR results for $\mathbf{6}^{+\bullet}$ (Table 3) contradict this, however, since the simple 3-line pattern implies that the electron is localized in one ring of $\mathbf{6}^{+\bullet}$. These differences are possibly due to solvent effects and the inability of the gas phase calculations at this level to correctly model $\mathbf{6}^{+\bullet}$.

The calculated molecular orbitals indicate **6** is in essentially a disjoint diradical state, since the two singly occupied molecular orbitals (SOMOs) of **6** (Fig. 4) consist of linear combinations of the localized orbitals **11a** and **11b** (Scheme 1) (12*b*, 42, 50, 51) even though there is no node at carbon (Fig. 4) to restrict "spin leakage" (47) as there is for **9** (12*b*). The diradical singlet for **9** was calculated (HF/6-311G*) to be lower than the diradical triplet by 2.1 kJ mol^{-1} (12), and recent calculations on tetramethyleneethane determined the diradical triplet to be 4.2–6.3 kJ mol^{-1} lower in energy than the diradical singlet (51). The diradical triplet **6** was calculated (GVB-PP(TC-SCF)/6-311G*) to be lower than the diradical singlet state by 0.07 kJ mol^{-1}, and the calculated bond lengths (see Supplemental Material) were identical to within 0.001 Å (41). Our EPR and magnetic data (see below) are consistent with the expected small exchange interactions between the two unpaired electrons, and the triplet and open shell singlet states of **6** should be essentially degenerate, in agreement with our calculations.

The "quinoidal" closed shell singlet **7**, calculated to be 63 kJ mol^{-1} higher in energy than **6**, is ruled out as a possible product of the double reduction of $\mathbf{6}\cdot[AsF_6]_2$, since **7** would be distinguished by a markedly different vibrational spectra, as expected from the noticeably different bonding (e.g., ν(CC) expected at 1554 cm^{-1} for a bond length of 1.358 Å, see above and Table 5 (calculated spectra listed in

© 2002 NRC Canada

the Supplemental Material)), and since no EPR spectra would be observed experimentally.

Vibrational spectra

For the *trans*-coplanar centrosymmetric (C_{2h} symmetry) **6** and $\mathbf{6}^{2+}$, the 24 expected vibrational modes (12 IR, 12 Raman active) are mutually exclusive owing to the center of inversion present in these species. This is evident in the observed vibrational spectra of **6** (Table 2, FT-Raman shown in Fig. 3, IR in the Supplemental Material), but the high-quality FT-Raman spectrum of $\mathbf{6}\cdot[AsF_6]_2$ shows a few forbidden bands as well (e.g., 751, 437 cm^{-1}). The calculated and observed vibrational frequencies of **6** and $\mathbf{6}^{2+}$ are in excellent agreement with each other (see the values for the more intense vibrations in bold in Table 2) and add significant support to our structural proposal for **6**. For example, the peaks at 1444 and 1239 cm^{-1} in the FT-Raman spectrum of **6** are consistent with C—C single bond stretching heavily mixed with the respective symmetric C–N and C–S stretching modes (see Table 2) and are shifted appropriately from those at 1491 and 1208 cm^{-1} for $\mathbf{6}^{2+}$, considering the differences in C—C and C—N bond lengths between **6** (1.444 and 1.282 Å, respectively) and $\mathbf{6}^{2+}$ (1.454 (15) and 1.298 (10) Å, respectively). These also compare well with those observed (1513, 1230 cm^{-1}) for $\mathbf{8}\cdot[AsF_6]_2$ (d(C—C) = 1.462 (5) Å, d(C—N) = 1.284 (3) Å (11)) and **9** (d(C—C) = 1.488 (7), d(C—N) = 1.331 (7) Å; IR: 1264 (m) cm^{-1}, although peaks due to Nujol at 1460 and 1376 cm^{-1} obscured other expected C—N stretching modes for **9** (12*b*)). Other IR peaks reported for **9** (1244 (s), 1090 (br), 1012 (m), 820 (w), 804 (s), 793 (s), 784 (s), 559 (m), 507 (m), 495 (m), 421 (m) cm^{-1} (12*b*)) were not observed in the vibrational spectra of **6**, supporting the proposal garnered from the MS data (see above) that **6** contains no S—S bonds.

The observed FT-Raman and IR spectra of **6** also indicated the presence of small amounts of the reduction by-products (e.g., $[AsF_6]^-$ (IR: 707 cm^{-1}), C-H (FT-Raman: 2876 cm^{-1})) in agreement with elemental analysis. FT-Raman and IR spectra are given in the Supplemental Material. A lack of change in the vibrational spectra on grinding suggests there is no significant change in geometry to a lower symmetry, e.g., rotomer. This is not definitive, however, since an investigation of the vibrational spectra of the solid (dihedral angle = 0°) and gas phase (42°) of biphenyl yielded negligible differences in the observed spectra (49).

X-ray powder photography

X-ray powder diffraction on samples of **6** was carried out to obtain structural information and observe any possible phase changes in **6** on mechanical grinding. Details are shown in the Supplemental Material. The powder diffraction pattern of **6** did not contain lines attributable to the soluble reaction byproducts (eq. 1: $[NBu_4][AsF_6]$, $SbPh_3Cl_2$), S_4N_4, S_8, or obvious possible products, as well as neutral ternary carbon–sulfur–nitrogen compounds whose X-ray structures have been determined and included in the Cambridge Structural Database (16) as of December 2001 (see Supplemental Material).

A reasonable indexing of the trace and a unit cell were obtained for 54 of 55 reflections from a sample ground for 12 h, and 19 of 20 for an unground sample. The one reflection (d = 2.747 Å) that was omitted was much sharper than the others and probably comes from some other (unidentified) material. However, this reflection is strong, and the results of the indexing should be treated with caution.

Results from an unground sample of **6**: possible space group *Pnma*, a = 10.310 Å, b = 8.210 Å, c = 4.749 Å, V = 401.98 $Å^3$, Z = 4. The probable space group for a sample of **6** ground 12 h is $Pna2_1$, a = 4.817 Å, b = 10.321 Å, c = 8.090 Å, V = 402.2 $Å^3$, Z = 4, and a density of 1.718 g cm^{-3}.

There were subtle, but definite, differences between unground powder samples and those ground for 12 h. The main features stayed the same on grinding, but there were definite changes on grinding. In particular, a shoulder on one of the strong peaks (2θ = 28°) disappeared on grinding, whereas small but definite features elsewhere increased in intensity (see Supplemental Material). These differences coincided with a switch in indexing from centrosymmetric (*Pnma*) to the equivalent non-centrosymmetric ($Pna2_1$) space group. These changes are indicative of a grinding-induced second order phase change consistent with the absence of any significant change in cell volume (52). The sample thus becomes ordered slightly differently on grinding, but with the molecular constituents remaining the same and with very few differences between the phases.

The density of the sample of **6** ground 12 h (1.718 g cm^{-3}) and the density of the unground sample (1.719 g cm^{-3}) are not significantly different and are in the general range of similar planar non-hydrogen atom systems: 1.63 g cm^{-3} for $[CF_3\overline{CSNS}\overline{C}CF_3]^{\bullet}$ (paramagnetic liquid, 22°C; 1.97 g cm^{-3} for the diamagnetic solid) (2), 1.91 g cm^{-3} for diamagnetic [NC-$\overline{C}$NSS$\overline{N}$], 2.26 g cm^{-3} for diamagnetic **9** (12*b*); the low temperature (150 K) less paramagnetic phase of 1,2,5,-thiadiazolo[3,4,*b*]-1,3,2-dithiazolo[3,4,*b*]pyrazin-2-yl (TDP-DTA (**4**)) was ca. 2% higher in density (2.13 g cm^{-3}) than the high temperature (293 K) more paramagnetic phase (2.08 g cm^{-3}) (8). The densities were not reported for the two phases of 1,3,5-trithia-2,4,6-triazapentalenyl (**5**) (10). These are in good agreement with the density of **6** obtained via pycnometer (1.7 g cm^{-3} after 1 h grinding). The density of **6** is significantly lower than that of **9**, implying that the distance between molecules of **6** is greater than that in **9** (intradimer S···S 3.131(2), 3.025(2) Å, interdimer 3.711(2), 3.811(2) Å (12*b*)).

Magnetic measurements: increase in paramagnetism on mechanical grinding

Preliminary room temperature Gouy measurements performed on samples of **6** varied from 2.8 μ_B to as low as 0.6 μ_B. There was no apparent correlation to changes that were made to the procedure for the double reduction of $\mathbf{6}\cdot[AsF_6]_2$ (see Table 1). However, on mechanical grinding with an agate mortar and pestle under a dry nitrogen atmosphere (in a Vacuum Atmospheres Dri-Lab drybox), samples of **6** changed from a black fluffy powder to black graphite-like shiny plates, with a large increase in magnetic moment and no observable changes in the FT-Raman, IR, and mass spectra.

Variable temperature magnetic measurements (4–300 K) were carried out on unground samples and on samples from the same batch ground for periods up to 12 h. The room temperature effective magnetic moments, μ_{eff}, increased on

© 2002 NRC Canada

Fig. 7. Change in effective magnetic moment of **6** on mechanical grinding: (▲) 0 min, (●) 15 min, (▼) 60 min, (■) 720 min grinding time.

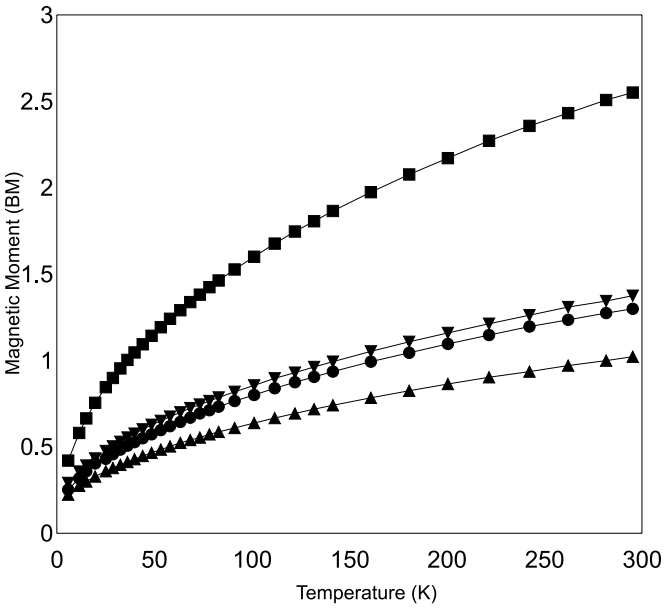

Fig. 8. Magnetization curve of **6**: (□) unground sample, (●) unground paramagnetic sample, (○) sample ground 720 min.

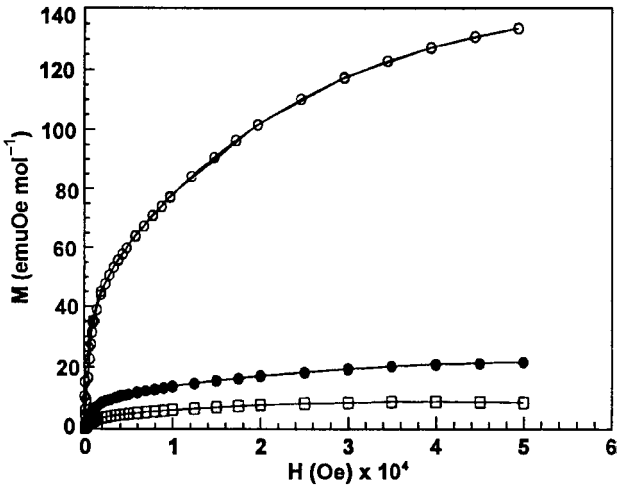

grinding from 1.03 μ_B (unground) to 1.3 μ_B (15 min), 1.38 μ_B (1 h), and 2.55 μ_B (12 h). The effective magnetic moment data as a function of temperature are shown in Fig. 7. The data for **6** clearly show an increase in paramagnetism on grinding. The general decrease in μ_{eff} as the temperature decreases is indicative of the presence of exchange coupling, and it is reasonable to assume that it is antiferromagnetic in nature. None of the magnetic data sets could be fitted successfully to the Bleaney-Bowers equation (53) for a simple S = 1/2 dimer model, suggesting that intramolecular exchange between the unpaired electrons in each of the rings of **6** is unlikely. Given the propensity of systems of this sort to form associated chain-like structures, a simple 1-dimensional chain structure involving associated diradical subunits with interchain interaction corrections was

Fig. 9. Variable temperature AC susceptibility of **6**: (□) unground diamagnetic sample (0.98 μ_B), (●) unground paramagnetic sample (1.39 μ_B), (○) sample ground 720 min (3.02 μ_B at 300 K).

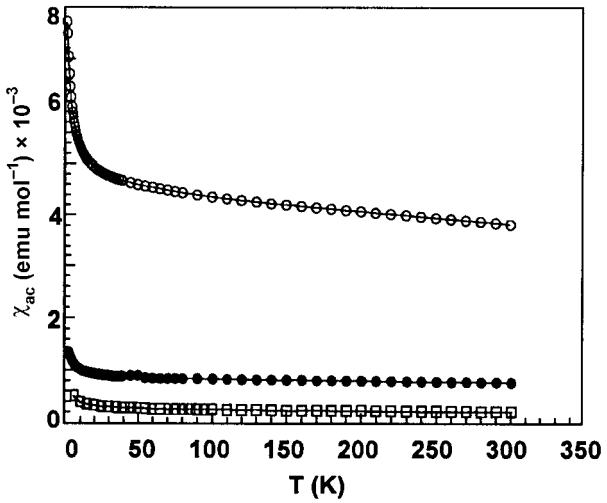

considered as a possible model. However, none of the data sets could be fitted successfully to a Heisenberg 1-dimensional chain model of this sort. Approximate fits were obtained at low temperatures (<150 K, data given in the Supplemental Material), but this was not considered to be rigorous. Notwithstanding the failure to rigorously fit the data, the analysis implies the absence of an intramolecular exchange within subunits of **6**, which is in agreement with the theoretical calculations (calculated $a(^{14}N)$ values, see Table 3) and EPR spectra (e.g., observing only a 1:1:1 triplet), which show that **6** behaves as a disjoint diradical (45, 50).

The change in magnetic behaviour of **6** on mechanical grinding is unique in main group chemistry, although dramatic increases in paramagnetism on grinding are well documented in transition metal chemistry (e.g., refs. 14, 15). Low-temperature (2 K) magnetization vs. field studies (Fig. 8) and variable temperature ac susceptibility measurements (Fig. 9) show that samples of **6** did not display any ferromagnetic character, but exhibited increased magnetization as a function of grinding time, in agreement with variable temperature DC susceptibility studies.

It is reasonable to assume that there must be some association between the disjoint diradical subunits and that it varies in magnitude as a function of grinding. The increase in paramagnetism on grinding suggests that the associations may be disrupted or at least changed by these mechanical forces to induce the second order phase change observed by the X-ray powder diffraction results. We propose that the putative chains form as a result of electrostatic attractions, e.g., between N(2) (–0.87) and S(3) (+0.84) on one molecule with an adjacent S(3)′ and N(2)′ on another, and that these are the strongest intermolecular forces present, as is the case for the tetrameric 4,5-bis(trifluoromethyl)-1,3,2-dithiazol-2-yl $[CF_3\overline{CSNSC}CF_3]^{\bullet}$ in the solid phase (4). The phase change leads to disruption of the π*-π* interactions in the diamagnetic phase, leading to decreased antiferromagnetic coupling, perhaps similar to that observed for **5** (10) (Fig. 10*a*) where a crystallographic phase change on warming decreases

© 2002 NRC Canada

Fig. 10. High- and low-temperature phases of **5**(*a*) and **4**(*b*). Reproduced with permission from: (*a*) W. Fujita et al., Science, **286**, 261 (1999), copyright 1999 American Association for the Advancement of Science; (*b*) T.M. Barclay et al., J. Am. Chem. Soc. **120**, 352 (1998), copyright 1998 American Chemical Society.

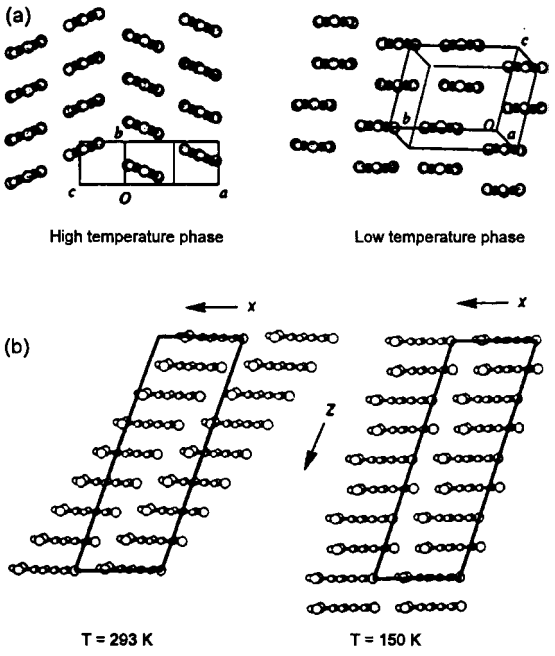

the effect of dimerization along the 1-dimensional stacks, shifting from a stacked dimers phase at low temperature to a phase of evenly spaced slipped π-stacks at high temperature (10). Alternatively, the phase change in **6** may be similar to that observed for TDP-DTA (**4**), shown in Fig. 10*b* (8), where ribbons of TDP-DTA are in slipped π-stacks at room temperature but shift laterally into arrays of dimers at low temperature (8). In contrast to **5**, dimerization of **4** at low temperature does not lead to complete quenching of paramagnetism (8).

We await single crystals of **6** to confirm the associated structural arrangement, which will hopefully allow a fuller understanding of the unique magnetic properties of this diradical species. Thus far suitable crystals have not been produced.

Purity of 6

Despite many attempts to purify **6** we were successful only in preparing **6** in ca. 95% purity by weight, with the impurities reasonably assigned as $[NBu_4][AsF_6]$ and $SbPh_3Cl_2$ in a 2:1 ratio (IR, Raman, elemental analysis). Nevertheless all but one of the major lines in the X-ray powder photographs (see the Supplemental Material) were assigned to **6**, and the calculated density was in good agreement with that determined experimentally. The majority of the bands in the IR and Raman spectra are attributable to **6**, and the features of the EPR and mass spectra were essentially exclusively due to **6**. All these properties were found from samples from all syntheses. The ca. 5% by weight probable impurities are diamagnetic and do not affect the magnetic measurements. It is likely that the impurities are occluded in fragments of the insoluble **6**, severely

Fig. 11. Proposed decomposition pathway for **6**: (*a*) characterized by FT-Raman spectroscopy; (*b*) proposed from EPR spectroscopy in wet glassware; (*c*) X-ray crystal structure; (*d*) proposed from MS; (*e*) characterized by MS (28).

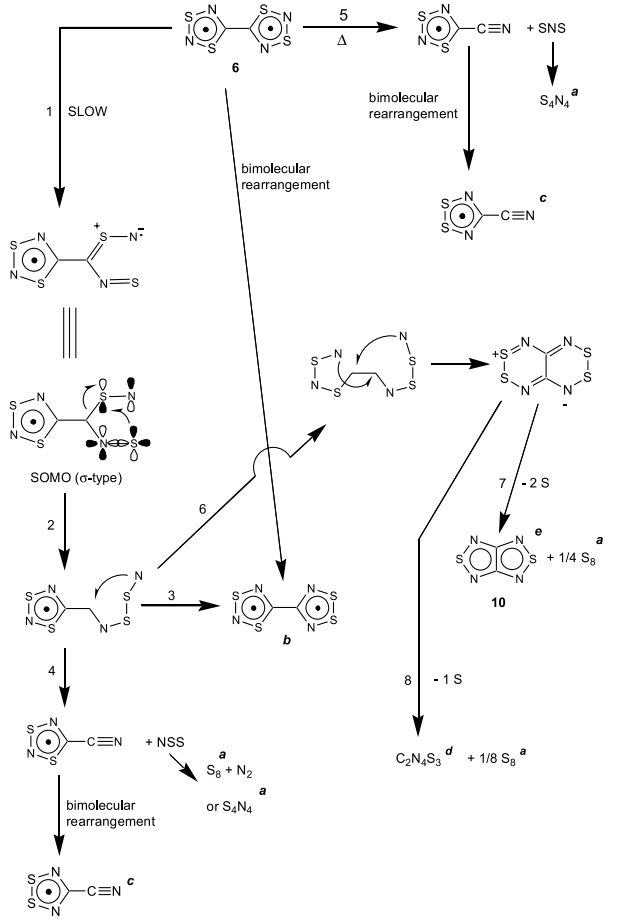

hindering and (or) preventing their removal by repeated grinding and extraction with solvent.

Thermal rearrangement of 6

Explanation of the wide variety of products obtained from attempted crystal growth of **6** by vacuum sublimation may come from work on the ring opening of [H-CNSNS] by Grein (54), together with the known solid state bimolecular rearrangement of 1,3,2,4-dithiadiazolyl rings to 1,2,3,5-isomers (5*d*, 5*e*, 6), the favoured rearrangement process. Figure 11 shows some possible decomposition pathways of **6** in addition to the bimolecular rearrangement. The ring opening of [H-CNSNS] was calculated (HF/3-21G*) to be endothermic by 121 kJ mol^{-1}, i.e., slow but accessible (54), especially on heating. The -NSSN fragment could then close (step 2) to form [NSSNC-CNSNS] (step 3) or lose SSN to form [NC-CNSNS] (step 4). Alternatively [NSSNC-CNSNS] could arise from the bimolecular rearrangement of **6**. [NC-CNSNS] could also be produced directly from **6** (step 5) via the thermal symmetry-allowed loss of SNS•. This loss of SNS• from [Ph-CNSNS] was shown to occur via photolysis (55). [NC-CNSNS] readily rearranges to the more stable isomer [NC-CNSSN] (6), and S_4N_4 could be formed from decomposition of SNS•.

© 2002 NRC Canada

Fig. 12. [NC-CNSSN] packing. Intermolecular contacts: S(12)···N(13) = 3.01 (2) Å, S(11)···N(13) = 3.03(2) Å, S(11)···S(12) = 3.074 (9) Å.

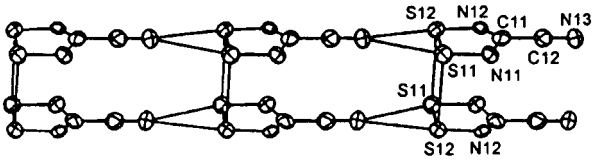

Fig. 13. ORTEP of [NC-CNSSN]. Ellipsoids are 50% probability.

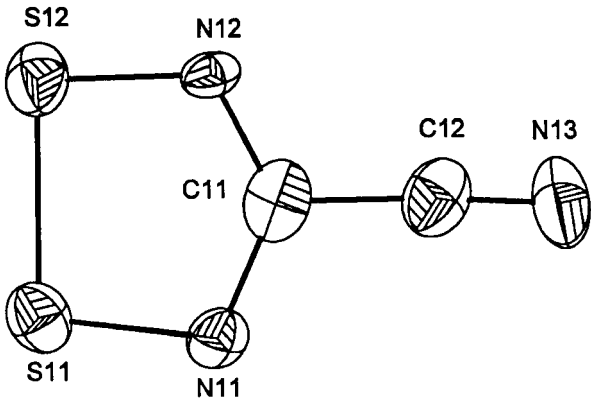

Additionally, a second intramolecular ring opening (step 6) could lead to two fused ring compounds with loss of sulfur: the known **10** (28) from step 7; and $C_2N_4S_3$ (step 8) from observed mass spectra data (see above), which has not been observed hitherto.

Structure of [NC-CNSSN]

Although not well resolved (R_1 = 0.069), the structure of [NC-CNSSN] clearly consists of axially symmetric, cofacial, *cis* dimers of planar [NC-CNSSN] units bound by two long (3.092 (5) Å) S···S π*-π* contacts (55). The dimers are linked to form strands (Fig. 12) via two sets of $N13^{\delta-}$—$S11^{\delta+}$ (2.97 (1) Å) and $N13^{\delta-}$—$S12^{\delta+}$ (2.98 (1) Å) contacts (sum of S and N van der Waals radii: 3.35 Å) per dimer unit; see Fig. 13 for atom-labelling scheme. There are no significant contacts between neighbouring strands, which run in the opposite direction. The average bond lengths within the -CNSSN heterocycles are typical for derivatives of this ring system (56) and compare well with the calculated structure (Table 7). The inter-dimer interaction is due to an in-plane electrostatic interaction between the lone pair on N13 (charge: –0.61 from natural bond order (NBO) analysis) and the positively charged sulfur atoms (+0.46) in a neighbouring dimer (see Fig. 12), similar to that found in cyano-substituted 5-phenyl-2,3,1,4-dithiadiazolium radicals (57). The EPR spectrum of a crystal of [NC-CNSSN] under Freon-11 consists of a broad, featureless band at g = 2.015 (typically g lies between 2.010 and 2.013 for -CNSSN rings, see Table 3) and presumably arises from monomers trapped in the crystal (as for **4**).

Conclusions

Although neither completely pure material nor the single crystal X-ray structure of **6** have been obtained, the identity and the *trans*-planar structure of **6** is supported by EPR and mass spectra, the similarity of the measured density with that calculated from the X-ray powder diffraction data, the re-formation of **6**$(AsF_6)_2$ on oxidation of **6** by AsF_5, the correlation between the calculated and observed vibrational spectra of **6** and $\mathbf{6}^{2+}$, as well as a computational study [MPW1PW91/6-311G(2df)] of **6** and its rotational isomers. Compound **6**, like the isomer **9** and the dication $\mathbf{6}^{2+}$, has a C—C bond order ca. 1 and behaves as a disjoint diradical, even though there is no formal node in the in-plane π SOMOs. Compound **6** does not adopt the classical Lewis structure **7**, which corresponds to a low-lying excited state of **6**.

The structure of **6** can be written as **12a** (Scheme 2), containing two C—N π bonds (1230 kJ mol^{-1}) and one S—N π bond (one half π bond per ring) (335 kJ mol^{-1}). The quinoidal structure **12b** contains one C—C π bond (602 kJ mol^{-1}) and two S—N π bonds (670 kJ mol^{-1}). The difference is 293 kJ mol^{-1} in favour of **12a**, plus energy required to form the polar S^+—N^- bond in **12b**, which is unfavourable.

The synthesis of **6** by reduction of **6**·[$(AsF_6)_2$] led to samples of **6** with room temperature Gouy measurements that

Table 7. Calculated [UMPW1PW91/6-311G(2df)] and experimental geometries for [NC-CNSSN].

Parameter	Observed	Calculated[a]
Bond distances (Å)		
S(11)—S(12)	2.099 (8)	2.117 ((0.93))
S(11)—N(11)	1.65 (2)	1.624 ((1.16))
S(12)—N(12)	1.59 (2)	1.624 ((1.16))
N(11)—C(11)	1.25 (3)	1.324 ((1.40))
N(12)—C(11)	1.37 (3)	1.324 ((1.40))
C(11)—C(12)	1.50 (3)	1.436 ((1.03))
C(12)—N(13)	1.09 (2)	1.147 ((2.88))
Bond angles (°)		
S(12)-S(11)-N(11)	91.9 (8)	94
S(11)-S(12)-N(12)	96.1 (7)	94
S(11)-N(11)-C(11)	114.8 (16)	113.9
S(12)-N(12)-C(11)	111.3 (14)	113.8
N(11)-C(11)-N(12)	125.5 (15)	124.4
N(11)-C(11)-C(12)	119.3 (24)	117.8
N(12)-C(11)-C(12)	114.5 (25)	117.8
N(13)-C(12)-C(11)	177.6 (31)	180
S(12)-N(12)-C(11)-N(11)	[b]	0.02[b]
S(11)-N(11)-C(11)-C(12)	[b]	0.02[b]

Note: Bond distances in Å, bond angles in degrees (°), estimated standard deviations (esd) in parentheses, and calculated Wiberg bond orders in double parentheses. See Fig. 13 for atom labelling scheme.

[a]Stationary point geometry, energy = –1036.85231585 a.u.

[b]Essentially planar, with an observed mean deviation from planarity of 0.0176 Å, χ^2 = 7.0 for the five ring atoms.

Scheme 2.

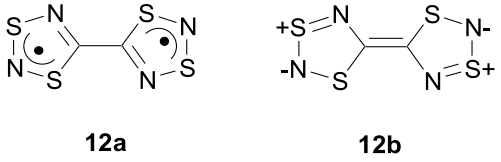

© 2002 NRC Canada

varied between 0.6 to 2.8 μ_B. Variable temperature magnetic measurements show that the material exhibits antiferromagnetic behaviour, undergoing a large increase in magnetic moment on mechanical grinding. The presence of reduction byproducts in the samples of **6** has been taken into account in the form of simple diamagnetic impurities, and the presence of ferromagnetic impurities has been ruled out by variable temperature ac susceptibility measurements. This change in magnetic behaviour of **6** on mechanical grinding is unique in main group chemistry, although well documented for transition metal compounds (e.g., refs. 14, 15). The grinding likely provides the energy needed to overcome the activation energy barrier of the transition from the diamagnetic to the more thermodynamically stable paramagnetic phase. The powder diffraction data for the diamagnetic unground and the paramagnetic ground material are consistent with a second order phase transition between the two phases; i.e., there are only small structural differences between phases with no change in the structure of **6**, as shown by the identical vibrational spectra before and after grinding.

The lability of **6** is illustrated by the variety of dissociation and rearrangement products (e.g., S_8, S_4N_4, [NC-$\overline{\text{CNSSN}}$], $C_2N_4S_2$, and the hitherto unknown $C_2N_4S_3$) obtained on attempted sublimation of **6** to obtain single crystals, the search for which continues.

Compound **6** is the first example of a diradical containing two -$\overline{\text{CNSN}}$S radical groups that is not connected to, or fused to, a phenyl ring (e.g., [*p*-$C_6H_4(\overline{\text{CNSN}}\text{S})_2$] (6)). Compound **6**, like the isomeric **9** (12) and the isolobal **8** (11), is a disjoint diradical. However, unlike **9**, **6** exists in one phase, in which both electrons pair neither by intra- or intermolecular interactions, i.e., as a paramagnetic solid. Compound **6** is one of a small class of non-sterically hindered diradicals that are paramagnetic in the solid state. Other examples include O_2 (17) and **8** (11).

Acknowledgments

We thank Dr. F. Grein for helpful discussions on theoretical aspects and for the ring opening calculations of [H-$\overline{\text{CNSN}}$S], Drs. J. D. Goddard and R. Mawhinney for GVB-PP(TC-SCF)/6-311G* calculations of the diradical singlet and triplet states of **6**, Dr. W.V.F. Brooks for assistance with the interpretation of vibrational spectra, Dr. L. Calhoun for ^{13}C NMR spectra, Dr. D. Wood for the observation that **8**·$[AsF_6]_2$ increases paramagnetism on grinding, Dr. M.A. White for discussions on thermodynamics, Mr. D. Drummond (MS), Mr. R. MacGregor (EPR) and Mr. D. Mitrovic (synthesis and grinding samples of **6** for up to 12 h in the drybox) for technical assistance, and the Natural Sciences and Engineering Research Council Canada (NSERC) for operating grants (T.S.C., J.P., L.K.T.) and a graduate fellowship (S.B.), as well as the Indonesian Government scholarship administered by the World University and Service of Canada (F.Z.). The work in Spain has been supported by CICYT grant MAT2000-1388-C03-03.

References

1. (*a*) E.G. Awere and J. Passmore. J. Chem. Soc. Dalton Trans. 1343 (1992); (*b*) R. Faggiani, R.J. Gillespie, C.J.L. Lock, and J.D. Tyrer. Inorg. Chem. **17**, 2975 (1978); (*c*) S. Parsons and J. Passmore. Acc. Chem. Res. **27**, 101 (1994) and refs. therein.
2. (*a*) W.V.F. Brooks, N. Burford, J. Passmore, M.J. Schriver, and L.H. Sutcliffe. J. Chem. Soc. Chem. Commun. 66 (1987); (*b*) S. Brownridge, R.C. Haddon, H. Oberhammer, S. Parsons, J. Passmore, M.J. Schriver, L.H. Sutcliffe, and N.P.C. Westwood. J. Chem. Soc. Dalton Trans. 3365 (2000).
3. H. Du, R.C. Haddon, I. Krossing, J. Passmore, J.M. Rawson, and M.J. Schriver. J. Chem. Soc. Chem. Comm. 1836 (2002).
4. G. Wolmerhäuser and G. Kraft. Chem. Ber. **123**, 881 (1990).
5. (*a*) G.K. MacLean, J. Passmore, M.N.S. Rao, M.J. Schriver, P.S. White, D. Bethell, R.S. Pilkington, and L.H. Sutcliffe. J. Chem. Soc. Dalton Trans. 1405 (1985); (*b*) N. Burford, J. Passmore, and M.J. Schriver. J. Chem. Soc. Chem. Commun. 140 (1986); (*c*) J. Passmore, X. Sun, and S. Parsons. Can. J. Chem. **70**, 3342 (1991); (*d*) W.V.F. Brooks, N. Burford, J. Passmore, M.J. Schriver, and L.H. Sutcliffe. J. Chem. Soc. Chem. Commun. 69 (1987); (*e*) J. Passmore and X. Sun. Inorg. Chem. **35**, 1313 (1996).
6. C. Aherne, A.J. Banister, A.W. Luke, J.M. Rawson, and R.J. Whitehead. J. Chem. Soc. Dalton Trans. 1277 (1992).
7. (*a*) A.J. Banister, N. Bricklebank, W. Clegg, M.R.J. Elsewood, C.I. Gregory, I. Lavender, J.M. Rawson, and B.K. Tanner. J. Chem. Soc. Chem. Commun. 679 (1995); (*b*) A.J. Banister, N. Bricklebank, I. Lavender, J.M. Rawson, C.I. Gregory, B.K. Tanner, W. Clegg, M.J. Elsewood, and F. Palacio. Angew. Chem. Int. Ed. Engl. **6**, 679 (1995); (*c*) F. Palacio, G. Antorrena, M. Castro, R. Burriel, J.M. Rawson, J.B.S. Smith, N. Bricklebank, J. Novoa, and C. Ritter. Phys. Rev. Lett. **79**, 2336 (1997).
8. T.M. Barclay, A.W. Cordes, N.A. George, R.C. Haddon, M.E. Itkis, M.S. Mashuta, R.T. Oakley, G.W. Patenaude, R.W. Reed, J.F. Richardson, and H. Zhang. J. Am. Chem. Soc. **120**, 352 (1998).
9. G. Wolmerhäuser and R. Johann. Angew. Chem. Int. Ed. Engl. **28**, 920 (1989).
10. (*a*) W. Fujita and K. Awaga. Science, **286**, 261 (1999); (*b*) G.D. McManus, J.M. Rawson, N. Feeder, J. van Duijin, E.J.L. McInnes, J. Novoa, R. Burriel, F. Palacio, and P. Oliete. J. Mat. Chem. **11**, 1992 (2001).
11. (*a*) P.D. Boyle, S. Parsons, J. Passmore, and D.J. Wood. J. Chem. Soc. Chem. Commun. 199 (1993); (*b*) G.D. Enright, J.R. Morton, J. Passmore, K.F. Preston, R.C. Thompson, and D.J. Wood. J. Chem. Soc. Chem. Commun. 967 (1996); (*c*) A. Berces, G. D. Enright, G. E. McLaurin, J.R. Morton, K.F. Preston, J. Passmore, and D.J. Wood. Mag. Res. Chem. **37**, 353 (1999); (*d*) A. Berces, P.D. Boyle, T.S. Cameron, G.D. Enright, G.E. McLaurin, J.R. Morton, J. Passmore, K.F. Preston, R.C. Thompson, and D.J. Wood, manuscript in preparation.
12. (*a*) C.D. Bryan, A.W. Cordes, R.C. Haddon, R.G. Hicks, R.T. Oakley, T.T.M. Palstra, and A. S. Perel. J. Chem. Soc. Chem. Commun. 1447 (1994); (*b*) C.D. Bryan, A.W. Cordes, J.D. Goddard, R.C. Haddon, R.G. Hicks, C.D. MacKinnon, R.C. Mawhinney, R.T. Oakley, T.T.M. Palstra, and A.S. Perel. J. Am. Chem. Soc. **118**, 330 (1996) and refs. therein.
13. (*a*) S. Parsons, J. Passmore, M.J. Schriver, and P.S. White. J. Chem. Soc. Chem. Commun. 369 (1991); (*b*) S. Parsons, J. Passmore, P.S. White. J. Chem. Soc. Dalton Trans. 1499 (1993).
14. P. Gütlich, A. Hauser, and H. Spiering. Angew. Chem. Int. Ed. Engl. **33**, 2024 (1994) and refs. therein.
15. B. Chevalier, J.-L. Bobet, M. Nakhl, and J. Etourneau. J. Alloys Compd. **320**, 33 (2001).
16. Cambridge Crystallographic Data Centre. 2001. Cambridge structural database [online]. Cambridge Crystallographic Data

© 2002 NRC Canada

Centre, U.K. Available from www.ccdc.cam.ac.uk [cited 20 December 2001].
17. E. Müller, A. Rieker, K. Scheffler, and A. Moosmayer. Angew. Chem. Int. Ed. Engl. **5**, 6 (1966).
18. (*a*) M.P. Murchie, J. Passmore. Inorg. Synth. **24**, 76 (1986); (*b*) M.P. Murchie, R. Kapoor, J. Passmore, G. Schatte, and T. Way. Inorg. Synth. **31**, 102 (1997).
19. W.L. Jolly. The synthesis and characterization of inorganic compounds. Waveland Press, Illinois. 1991. p. 287.
20. Material Data Inc. 1991–1999. Jade 5 [computer program]. Material Data Inc., Livermore, CA, U.S.A.
21. S. Brownridge, T.S. Cameron, J. Passmore, G. Schatte, and T.C. Way. J. Chem. Soc. Dalton Trans. 2553 (1996).
22. R.W.H. Small, A.J. Banister, and Z.V. Hauptman. J. Chem. Soc. Dalton Trans. 1377 (1984).
23. F. Zarlaida. M.Sc. thesis, University of New Brunswick, NB, Canada, 2001.
24. J. Passmore, X. Sun, and S. Parsons. Can. J. Chem. **70**, 2972 (1992).
25. Y.-L. Chung, S.A. Fairhurst, D.G. Gillies, and L.H. Sutcliffe. Magn. Reson. Chem. **30**, 666 (1992).
26. S. Parsons. Ph.D. thesis, University of New Brunswick, NB, Canada, 1994.
27. (*a*) S.T.A.K. Daley and C.W. Rees. J. Chem. Soc. Perkin Trans I. 203 (1987); (*b*) J.L. Morris, C.W. Rees. J. Chem. Soc. Perkin Trans I. 211 (1987); 217 (1987).
28. A.P. Komin, R.W. Street, and M. Carmack. J. Org. Chem. **40**, 2749 (1975).
29. T. Chivers. Chem. Rev. **85**, 341 (1985) and refs. therein.
30. A. Altomare, M. Cascarano, C. Giacovazzo, and A. Guagliardi. J. Appl. Cryst. **26**, 343 (1993).
31. P.T. Beurskens, G. Admiraal, G. Beurskens, W.P. Bosman, R. de Gelder, R. Israel, and J.M.M. Smits. 1994. The DIRDIF-94 program system, technical report of the crystallography laboratory [computer program]. University of Nijmegen, The Netherlands.
32. D.T. Cromer and J.T. Waber. International tables for X-ray crystallography. Vol. IV. The Kynoch Press, Birmingham, England. 1974. Table 2.2 A.
33. J.A. Ibers and W.C. Hamilton. Acta Crystallogr. **17**, 781 (1964).
34. D.C. Creagh and W.J. McAuley. *In* International tables for crystallography. Vol. C. *Edited by* A.J.C. Wilson. Kluwer Academic Publishers, Boston. 1992. Table 4.2.6.8, pp. 219–222.
35. D.C. Creagh and J.H. Hubbell. *In* International tables for crystallography. Vol. C. *Edited by* A.J.C. Wilson. Kluwer Academic Publishers, Boston. 1992. Table 4.2.4.3, pp. 200–206.
36. Molecular Structure Corporation. 1997–1998. teXsan for Windows: Crystal structure analysis package [computer program]. Version 1.05. Molecular Structure Corporation. The Woodlands, TX, U.S.A.
37. (*a*) M.J. Frisch, G.W. Trucks, H.B. Schlegel, G.E. Scuseria, M.A. Robb, J.R. Cheeseman, V.G. Zakrzewski, J.A. Montgomery, Jr., R.E. Stratmann, J.C. Burant, S. Dapprich, J.M. Millam, A.D. Daniels, K.N. Kudin, M.C. Strain, O. Farkas, J. Tomasi, V. Barone, M. Cossi, R. Cammi, B. Mennucci, C. Pomelli, C. Adamo, S. Clifford, J. Ochterski, G.A. Petersson, P.Y. Ayala, Q. Cui, K. Morokuma, D.K. Malick, A.D. Rabuck, K. Raghavachari, J.B. Foresman, J. Cioslowski, J.V. Ortiz, B.B. Stefanov, G. Liu, A. Liashenko, P. Piskorz, I. Komaromi, R. Gomperts, R.L. Martin, D.J. Fox, T. Keith, M.A. Al-Laham, C.Y. Peng, A. Nanayakkara, C. Gonzalez, M. Challacombe, P.M.W. Gill, B. Johnson, W. Chen, M.W. Wong, J.L. Andres, C. Gonzalez, M. Head-Gordon, E.S. Replogle, and J.A. Pople. 1998. GAUSSIAN 98 [computer program]. Revision A.3. Gaussian, Inc., Pittsburgh PA; (*b*) C. Adamo, V. Barone. Chem. Phys. Lett. **274**, 242 (1997); C. Adamo, V. Barone. J. Chem. Phys. **108**, 664 (1998); (*c*) M. Schmidt, K.K. Baldridge, J.A. Boatz, S.T. Elbert, M.S. Gordon, J.J. Jensen, S. Keski, N. Matsunaga, K.A. Nguyen, S. Su, T.L. Windus, M. Dupuis, and J.A. Montgomery. J. Comput. Chem. **14**, 1347 (1993); (*d*) CambridgeSoft Corporation. 1998. CHEM3D Ultra [computer program]. CambridgeSoft Corporation, Cambridge, MA; (*e*) Hypercube, Inc. 1993. HYPERCHEM 3.0 [computer program]. Hypercube, Inc., Gainsville, FL.
38. T.S. Cameron, R.J. Deeth, I. Dionne, H. Du, H.D.B. Jenkins, I. Krossing, J. Passmore, and H.K. Roobottom. Inorg. Chem. **39**, 5614 (2000).
39. I. Krossing and J. Passmore. Inorg. Chem. **38**, 5203 (1999).
40. J. Cioslowski and X. Gao. Int. J. Quantum Chem. **65**, 609 (1997).
41. J.D. Goddard and R. Mawhinney. Personal communication.
42. W.T. Borden. *In* Diradicals. *Edited by* W.T. Borden. J. Wiley and Sons, New York, NY. 1982. Chap. 1.
43. L.N. Mulay. Magnetic susceptibility. Interscience, New York, NY. 1963.
44. (*a*) J.E. Wertz and J.R. Bolton. Electron spin resonance; elementary theory and applications. McGraw Hill, New York, NY. 1972; (*b*) R. Wilson and D. Kivelson. J. Chem. Phys. **44**, 154 (1966).
45. S.H. Glarum and J.H. Marshall. J. Chem. Phys. **47**, 1374 (1967).
46. R.A. Beekman, R.T. Boeré, K.H. Moock, and M. Parvez. Can. J. Chem. **76**, 85 (1998).
47. A.W. Cordes, R.C. Haddon, R.T. Oakley, L.F. Schneemeyer, J.V. Waszczak, K.M. Young, and N.M. Zimmerman. J. Am. Chem. Soc. **113**, 582 (1991).
48. (*a*) H.A. Bent. Chem. Rev. **61**, 275 (1961); (*b*) R. McWeeney. Coulson's valence. 3rd ed. Oxford University Press, Oxford, U.K. 1979.
49. (*a*) H. Bock, S. Nick, C. Näther, and W. Bensch. Chem. Eur. J. **1**, 557 (1995); (*b*) G.-P. Charbonneau, Y. Delugeard. Acta Crystallogr. Sect. B. **33**, 1586 (1977).
50. L. Salem. Electrons in chemical reactions: first principles. John Wiley and Sons, New York, NY. 1982.
51. P. Nachtigall and K.D. Jordan. J. Am. Chem. Soc. **115**, 270 (1993).
52. M.A. White. Properties of materials. Oxford University Press, New York, NY. 1999. pp. 116–118.
53. B. Bleaney and K.D. Bowers. Proc. R. Soc. London, **A214**, 451 (1952).
54. F. Grein. Personal communication.
55. S. Parsons, J. Passmore, X. Sun, and M. Regitz. Can. J. Chem. **73**, 1312 (1995).
56. A.W. Cordes, J.D. Goddard, R.T. Oakley, and N.P.C. Westwood. J. Am. Chem. Soc. **11**1 6147 (1989).
57. (*a*) R. Gleiter. Angew. Chem. Int. Ed. Engl. **20**, 444 (1981); (*b*) A. Vegas, A. Perez-Salazar, A.J. Banister, and R. Hey. J. Chem. Soc. Dalton Trans. 1812 (1980).

© 2002 NRC Canada

Condensed versus open channel structures in cysteic acid coordination frameworks containing d^{10}-d^{10} dimers

Patrick J. Riley, Jennifer L. Reid, Adrien P. Côté, and George K.H. Shimizu

Abstract: Single crystal X-ray structures have been obtained for $[Ag(\text{L-cysteic acid})]_\infty$ (**1**) and $[Ag(\text{L-cysteic acid})(H_2O)]_\infty$ (**2**) These compounds represent the first two structurally characterized complexes of cysteic acid. Network **1** is shown to adopt an infinite two-dimensional structure, describable as one-dimensional ribbons cross-linked into layers. The basic building block is a doubly carboxylate-bridged silver(I) dimer. Compound **1** crystallizes in the monoclinic space group $P2_1$ (a = 5.5066(3) Å, b = 7.5761(4) Å, c = 16.644(1) Å, β = 94.335(1)°). Compound **2**, while differing chemically from **1** by only one water molecule, forms a three-dimensional structure built upon the same core dimer unit as that observed in **1**. In **2**, these units assemble in a different manner via the weak interactions and form a channel structure in which the guest water molecules are included. Compound **2** crystallizes in the monoclinic space group $P2_1$ (a = 8.120(2) Å, b = 9.805(2) Å, c = 9.204(2) Å, β = 98.45(3)°).

Key words: silver, carboxylates, sulfonates, coordination polymer.

Résumé : Faisant appel à la diffraction des rayons X par des cristaux uniques, on a déterminé les structures cristallines de $[Ag(\text{acide L-cystéique})]_\infty$ (**1**) et $[Ag(\text{acide L-cystéique})(H_2O)]_\infty$ (**2**). Ces composés correspondent aux deux premiers complexes de l'acide cystéique à être caractérisés. On a démontré que le réseau de la molécule **1** adopte une structure bidimensionnelle infinie qui peut être décrite par des rubans unidimensionnels reliés entre eux pour former des couches. L'unité de base est un dimère d'argent(I) doublement ponté par le carboxylate. Le composé **1** cristallise dans le groupe d'espace monoclinique, $P2_1$, avec a = 5,5066(3), b = 7,5761(4) et c = 16,644(1) Å, β = 94,335(1)°. Le composé, même s'il ne diffère chimiquement du composé **1** que par une molécule d'eau, forme une structure tridimensionnelle construite sur la même unité dimère de base observée dans la molécule **1**. Dans le composé **2**, celles-ci s'assemblent d'une manière différente par le biais de faibles interactions et forment une structure à canal dans lequel des molécules d'eau invitées sont incluses. Le composé **2** cristallise dans le groupe d'espace monoclinique $P2_1$, avec a = 8,120(2), b = 9,805(2) et c = 9,204(2) Å, β = 98,45(3)°.

Mots clés : argent, carboxylates, sulfonates, polymère de coordination.

[Traduit par la Rédaction]

Introduction

We have been interested in studying the soft coordination networks that result when the interactions between silver(I) and the sulfonate group (RSO_3^-) are employed as the "glue" for the framework (1–4). The sulfonate group, while generally not regarded as a particularly good ligand, can form very stable coordinative interactions when incorporated into an extended structure (5–7). This results from cooperative bonding effects, discussed more typically for hydrogen-bonded solids (8). With silver(I), there appears to be a particularly good hard–soft acid–base match with the sulfonate group as, even from aqueous solution, silver complexes with homoleptic sulfonate coordination are obtainable. In terms of using these interactions to build extended structures, they offer an interesting flexibility not attainable with, for example, metal oxide frameworks (3, 4). The sulfonate group can adopt many different coordination modes, from monodentate to μ^6 (1, 2, 9). Factoring in the roughly spherical shape of the $-SO_3$ moiety, we have employed the analogy of the sulfonate group with a ball of Velcro to describe its coordinative diversity (3).

The present work concerns two coordination frameworks incorporating silver(I) and L-cysteic acid as a ligand. Cysteic acid was chosen as a ligand owing to the presence of three distinct ligating functionalities (10) although, as the structures will show, it readily forms a zwitterionic species negating the Lewis basicity of the amino group. The two structures, 1 and 2, differ chemically only by a single water molecule; however, the structural changes between them are much more significant. The structures contain a mix of strong- and weak-coordination bonding coupled with hydrogen bonding (11). In each structure, the basic building unit, a doubly carboxylate-bridged silver(I) dimer, is the same as

Received 13 February 2002. Published on the NRC Research Press Web site at http://canjchem.nrc.ca on 27 November 2002.

Dedicated to Professor Tris Chivers for his contributions to Canadian chemistry.

P.J. Riley, J.L. Reid, A.P. Côté, and G.K.H. Shimizu.[1]
Department of Chemistry, University of Calgary, 2500 University Drive N.W., Calgary, AB T2N 1N4, Canada.

[1]Corresponding author (e-mail: gshimizu@ucalgary.ca).

 DOI: 10.1139/V02-148 © 2002 NRC Canada

would be expected, since it is sustained by stronger bonds. The one-dimensional assembly of these units is also the same in the two structures. The difference between structures, when water is included or excluded from the system, is in how the one-dimensional columns arrange via weak interactions. For the anhydrous form, **1**, a two-dimensional structure is obtained with extensive interlayer hydrogen bonding. For the hydrated form, **2**, the result is a three-dimensional framework with channels filled with guest water molecules. This compound is fully interconnected by coordinative interactions, albeit weak ones. Compounds **1** and **2** represent the first structurally characterized complexes of cysteic acid.

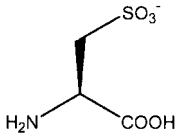

L-Cysteic acid

Experimental

Silver carbonate, silver nitrate, and L-cysteic acid monohydrate were obtained from Aldrich Chemical Company and used as received. Powder X-ray diffraction data were collected in a capillary mounted on a Nonius Kappa CCD diffractometer using Mo Kα radiation (λ = 0.71073 Å) and visualized using Powderize software. Thermogravimetric analyses were performed on a Netzsch STA449C Simultaneous Thermal analyzer at a scan rate of 5°C min^{-1} under an N_2 flow.

Preparation of X-ray-quality single crystals of 1

A solution of L-cysteic acid monohydrate (0.050 g, 0.267 mmol) in water was added to a solution of Ag_2CO_3 (0.074 g, 0.267 mmol) in water and stirred for 22 h. A portion of this solution (1.5 mL) was filtered into a 15 × 45 mm glass vial, which was placed into a larger 20 mL glass scintillation vial containing EtOH (2 mL), as a diffusion solvent. The larger vial was capped and the filtrate was allowed to stand at room temperature for 1 month. Solvent diffusion yielded colourless single crystals suitable for X-ray data collection. Yield: 0.108 g (0.197 mmol), 73.8%. IR (KBr) (cm^{-1}): 2361.5 (m), 2324.1 (m), 1624.2 (s), 1465.6 (s), 1390.0 (vs), 1320.9 (s), 1236.9 (s), 1171.6 (m), 1134.3 (s), 1031.6 (vs), 966.3 (m), 900.9 (s), 831.0 (s), 742.3 (s), 583.6 (vs), 518.3 (s). Elemental anal. calcd. for **1**: C 13.01, H 2.55, N 5.06; found: C 12.81, H 2.32, N 4.67.

Preparation of X-ray-quality single crystals of 2

A solution of L-cysteic acid monohydrate (0.050 g, 0.267 mmol) in water was added to a solution of $AgNO_3$ (0.046 g, 0.267 mmol) in water and stirred for 26 h. A portion of this solution (1.5 mL) was filtered into a 15 × 45 mm glass vial, which was placed into a larger 20 mL glass scintillation vial containing EtOH (2 mL), as a diffusion solvent. The larger vial was capped and the filtrate was allowed to stand at room temperature for 6 weeks. Solvent diffusion yielded colourless single crystals suitable for X-ray data collection. Yield: 0.105 g (0.184 mmol), 68.7%. IR (KBr) (cm^{-1}): 3459.2 (br), 3180.6 (br), 2361.1 (m), 2333.8 (m), 1612.7 (s), 1470.7 (s), 1394.2 (vs), 1323.2 (s), 1230.4 (s), 1181.2 (m), 1132.0 (s), 1033.7 (vs), 897.1 (s), 820.6 (s), 744.2 (s), 667.7 (s), 580.3 (vs), 514.7 (s). Elemental anal. calcd. for **1**: C 12.60, H 2.82, N 4.90; found: C 12.74, H 2.21, N 4.77.

X-ray data collection and structure determination

Crystals were selected under an optical microscope, coated in oil, and frozen onto a glass fiber. The data for **1** was collected on a Siemens SMART CCD diffractometer at the Steacie Institute of the National Research Council Canada. The data for **2** was collected on a Nonius Kappa CCD diffractometer. Both structures were collected at 173 K using Mo Kα radiation (λ = 0.71073 Å). Both structures were also solved by direct methods and refined by full-matrix least squares, based on F^2, using SHELXTL (12). The structures were refined and hydrogen atoms generated as riding spheres to their parent atoms with the exception of the hydrogen atoms of O11 in compound **2**, in which they were located. The Flack parameters were 0.0065 ± 0.0263 for compound **1** and –0.049 ± 0.023 for compound **2**. A summary of the crystallographic data is given in Table 1. Selected bond distances and angles are shown in Tables 2–5.[2]

Results and discussion

Crystallographic data for **1** and **2** are presented in Tables 1–5.

Structure of Compound 1

The structure of $[Ag(OOCCH(CH_2SO_3)NH_3)]_\infty$ (**1**) is composed of carboxylate-bridged dimers, which are linked by metal sulfonate interactions to form one-dimensional ribbons. These ribbons are further cross-linked by additional metal sulfonate interactions and hydrogen bonding to yield layers. In this structure, L-cysteic acid exists as a zwitterion with the carboxyl and sulfonate groups deprotonated and the ammonium group positively charged. Based upon metal–ligand bonding, this structure is two-dimensional. There is further extensive hydrogen bonding between lamellae to give a three-dimensional architecture considering these weaker interactions.

The core unit of structure **1** is the silver dimer structure; its ORTEP diagram is shown in Fig. 1. The asymmetric unit consists of two types of Ag center and two different molecules of cysteic acid. Two carboxylate groups from two cysteic acid ligands bridge each silver dimer unit (Ag1—O4 = 2.229(3), Ag1—O10 = 2.184(3), Ag2—O5 = 2.225(3), Ag2—O9 = 2.267(3) Å). The carboxylate ligation supports

[2] Supplementary data may be purchased from the Depository of Unpublished Data, Document Delivery, CISTI, National Research Council Canada, Ottawa, ON K1A 0S2, Canada (http://www.nrc.ca/cisti/irm/unpub_e.shtml for information on ordering electronically). CCDC 179391 (**1**) and CCDC 179390 (**2**) contain the supplementary data for this paper. These data can be obtained, free of charge, via www.ccdc.cam.ac.uk/conts/retrieving.html (or from the Cambridge Crystallographic Data Centre, 12 Union Road, Cambridge, U.K.; fax +44 1223 336033; or deposit@ccdc.cam.ac.uk).

© 2002 NRC Canada

Table 1. Crystallographic data for **1** and **2**.

Formula	$C_6H_{12}Ag_2N_2O_{10}S_2$ (**1**)	$C_6H_{12}Ag_2N_2O_{11}S_2$ (**2**)
Formula weight	552.04	570.05
Crystal system	Monoclinic	Monoclinic
Space group	$P2_1$	$P2_1$
a (Å)	5.5066(3)	8.119(2)
b (Å)	7.5761(4)	9.805(2)
c (Å)	16.644(1)	9.204(2)
β (°)	94.335(1)	98.45(3)
V (Å^3)	692.39(7)	724.8(2)
Z (molecules per unit cell)	2	2
$D_{calcd.}$ (g cm^{-3})	1.324	1.306
μ (mm^{-1})	1.592	1.501
Crystal dimensions (mm^3)	0.10 × 0.10 × 0.20	0.07 × 0.20 × 0.30
Radiation (λ) (Å)	0.71073	0.71073
$2\theta_{max}$	57.4	55.0
Unique reflections [$I > 2.0\sigma(I)$]	3584	2959
Total measured reflections	8295	3147
R_f (significant reflections)	0.0221	0.0238
R_w (significant reflections)	0.0545	0.0489
Goodness of fit	1.050	1.061
Largest diff. peak and hole (e Å^{-3})	0.830 and –0.527	0.467 and –0.612

$R_f = (\sum(F_o - F_c) / \sum(F_o)$, $R_w = (\sum\omega(F_o - F_c)^2 / \sum\omega(F_o)^2)^{0.5}$

Table 2. Selected bond distances for **1**.

Bond	Length (Å)	Bond	Length (Å)
Ag1—O4	2.229(3)	Ag2—O5	2.225(3)
Ag1—O10	2.184(3)	Ag2—O3	2.403(3)
Ag1—O6	2.760(3)	Ag2—O3	2.402(3)
Ag1—O3	2.803(3)	Ag2—O6	2.605(3)
Ag1···Ag2	2.8011(3)	Ag2—O9	2.267(3)
S1—O1	1.460(3)	S2—O6	1.444(3)
S1—O2	1.467(2)	S2—O7	1.454(3)
S1—O3	1.456(3)	S2—O8	1.475(2)
O4—C3	1.249(4)	O9—C6	1.245(4)
O5—C3	1.260(5)	O10—C6	1.256(5)

Table 3. Selected bond distances for **2**.

Bond	Length (Å)	Bond	Length (Å)
Ag1—O10	2.265(3)	Ag1—O4	2.293(3)
Ag1—O7	2.563(5)	Ag1—Ag2	2.8562(7)
Ag1—O6	2.616(5)	Ag2—O5	2.211(3)
Ag1—O7	2.563(3)	Ag2—O9	2.226(3)
Ag1—O8	2.811(6)	Ag—O2	2.610(5)
Ag2—O3	2.630(7)		
S1—O1	1.459(3)	S2—O6	1.466(3)
S1—O2	1.460(3)	S2—O7	1.457(3)
S1—O3	1.471(3)	S2—O8	1.458(3)
O4—C3	1.250(5)	O5—C3	1.265(5)
O9—C6	1.255(5)	O10—C6	1.255(9)

an Ag1···Ag2 interaction of 2.8011(3) Å, to be discussed in more detail later. The carboxylate–silver dimer is not planar, as illustrated by the torsion angles about the four C–O bonds (C3–O4 = 23.2(5)°, C3–O5 = 0.8(5)°, C6–O9 = –7.6(5)°, C6–O10 = –4.5(5)°). The geometry about Ag1 is six-coordinate and can be described as a basal plane, composed of two *trans*-carboxylate oxygen atoms, one sulfonate interaction (Ag1—O6 = 2.760(3) Å), and the silver–silver contact. Two other sulfonate oxygen atoms complete the coordination sphere. One of these is directed in an axial orientation and forms the linkage to the next dimer unit along the *b*-axis (Ag1—O3 = 2.803(3) Å) to form ribbons, as visible in Fig. 1. The final sulfonate interaction is to O8, from the same SO_3 group as O6 (Ag1—O8 = 2.672(2) Å). This chelating sulfonate group bridges to an adjacent dimer unit, along the *a*-axis to crosslink the ribbons into layers, shown in Fig. 2. Overall, the geometry is a distorted octahedron. Ag2 is a five-coordinate center with very slightly distorted square pyramidal geometry but has very similar features as those of Ag1. The basal plane is again composed of two

Table 4. Selected bond angles for **1**.

Bond	Angle (°)	Bond	Angle (°)
O10-Ag1-O4	162.8(1)	O10-Ag1-Ag2	83.60(8)
O4-Ag1-Ag2	79.96(8)	O5-Ag2-O9	155.3(1)
O5-Ag2-O3	102.8(1)	O9-Ag2-O3	92.0(1)
O5-Ag2-Ag1	83.74(7)	O9-Ag2-Ag1	81.64(7)
O3-Ag2-Ag1	173.46(7)	O6-S2-O7	113.9(2)
O3-S1-O1	112.8(2)	O3-S1-O2	112.8(2)
O1-S1-O2	112.3(2)	O3-S1-C1	105.5(2)
O1-S1-C1	105.6(2)	O2-S1-C1	107.1(2)
O6-S2-O8	111.5(2)	O7-S2-O8	111.6(2)
O6-S2-C4	107.6(2)	O7-S2-C4	106.4(2)
O8-S2-C4	105.2(1)	C6-O10-Ag1	123.2(3)
S1-O3-Ag2	112.9(2)	C3-O4-Ag1	121.8(3)
C6-O9-Ag2	121.6(3)	C3-O5-Ag2	118.8(2)
O4-C3-O5	128.6(4)	O4-C3-C2	115.2(3)
O5-C3-C2	116.2(3)	O9-C6-O10	128.3(4)
O9-C6-C5	116.9(3)	O10-C6-C5	114.7(3)

© 2002 NRC Canada

Table 5. Selected bond angles for **2**.

Bond	Angle (°)	Bond	Angle (°)
O10-Ag1-O4	153.5(2)	O10-Ag1-O7	96.3(1)
O4-Ag1-O7	107.4(2)	O10-Ag1-Ag2	75.65(9)
O4-Ag1-Ag2	78.38(7)	O7-Ag1-Ag2	163.10(7)
O5-Ag2-O9	158.5(1)	O5-Ag2-Ag1	80.49(8)
O9-Ag2-Ag1	87.75(9)	O1-S1-O2	112.4(2)
O1-S1-O3	112.3(2)	O2-S1-O3	112.3(2)
O1-S1-C1	106.4(2)	O2-S1-C1	106.6(2)
O3-S1-C1	106.0(2)	O8-S2-O7	111.9(2)
O8-S2-O6	111.8(2)	O7-S2-O6	114.3(2)
O7-S2-C4	105.7(2)	O8-S2-C4	107.1(2)
O6-S2-C4	105.7(2)	C3-O4-Ag1	116.2(3)
C3-O5-Ag2	120.6(3)	C6-O9-Ag2	115.8(4)
C6-O10-Ag1	126.4(4)	S2-O7-Ag1	100.7(2)
O4-C3-O5	127.6(4)	O4-C3-C2	117.1(4)
O5-C3-C2	115.2(5)	O9-C6-O10	127.9(5)
O9-C6-C5	115.5(5)	O10-C6-C5	116.6(5)

Fig. 1. ORTEP diagram of **1**, showing the Ag dimer motif and its extension to one-dimensional ribbons. Hydrogen atoms have been omitted for clarity. Thermal ellipsoids of 50% probability are represented.

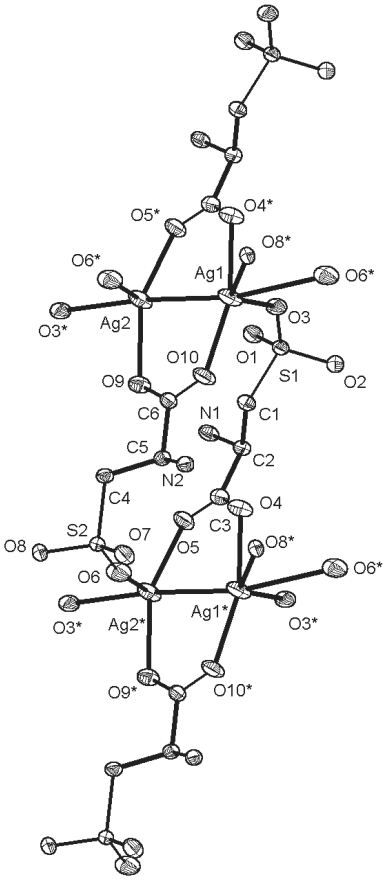

trans carboxylate interactions, the silver–silver interaction and a sulfonate oxygen atom (Ag2—O3 = 2.402(3) Å) that propagates the structure along the *a*-axis. The lone axial site is occupied by a sulfonate oxygen atom (Ag2—O6 = 2.605(3) Å) that serves to link the structure along the *b*-axis.

Fig. 2. View down the *c*-axis of **1**, showing the linking of ribbons into layers. One ribbon unit, extending along the *b*-axis, is depicted with thick bonds. Hydrogen atoms are shown as points for clarity.

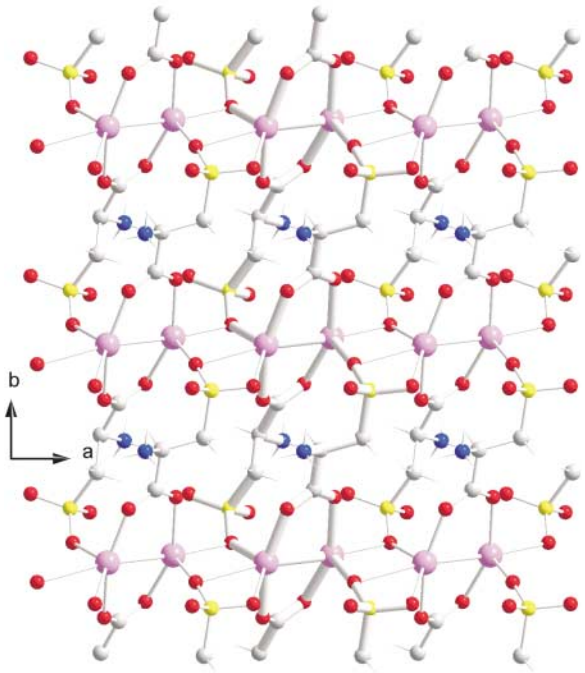

The inter-dimer silver···silver distances along the *a*-axis are 3.450(1) Å, longer than the sum of the van der Waals radii (3.42 Å). The layer formation, primarily sustained by the silver coordination of the bridging sulfonate groups, is augmented by charge-assisted ammonium–sulfonate hydrogen bonds (N1—O2 = 2.967(4), N2—O8 = 2.872(4) Å). Thus, by a combination of weak interactions, parallel ribbons, as depicted in Fig. 1, are assembled into layers, shown in Fig. 2. A single ribbon is rendered with thick bonds.

The layers are mutually interacting by a myriad of further ammonium–sulfonate hydrogen bonding. Figure 3 shows a cross section of the layers with the $-NH_3$ and $-SO_3$ groups directed into the interlayer region. Each ammonium group forms hydrogen bonds to two sulfonate oxygen atoms from the adjacent layer (N1—O1 = 2.854(4), N1—O2 = 2.910(4), N2—O7 = 2.823(4), N2—O8 = 2.844(4) Å). Each interlayer is lined exclusively with ammonium groups centered on N1 and sulfonate groups centered on S1, or ammonium groups centered on N2 and sulfonate groups centered on S2. The shortest interlayer Ag···Ag distance is between Ag1 centers at 7.942(2) Å.

Structure of compound 2

As with **1**, the core building unit of compound **2**, $\{[Ag(OOCCH(CH_2SO_3)NH_3)]H_2O\}_\infty$, is the silver(I) dimer bridged by two carboxylate groups. Also as in **1**, these dimeric units assemble via silver sulfonate interactions to form one-dimensional ribbons, and the cysteic acid ligand exists with a protonated ammonium group and deprotonated sulfonate and carboxyl groups. The ribbon motif is depicted in the ORTEP diagram shown in Fig. 4. In contrast to **1**, the silver sulfonate interactions extend into three dimensions

© 2002 NRC Canada

Fig. 3. View down the *a*-axis of **1**, showing four layers as depicted in Fig. 2. Note the interlayer region lined with ammonium groups and sulfonate groups for hydrogen bonding.

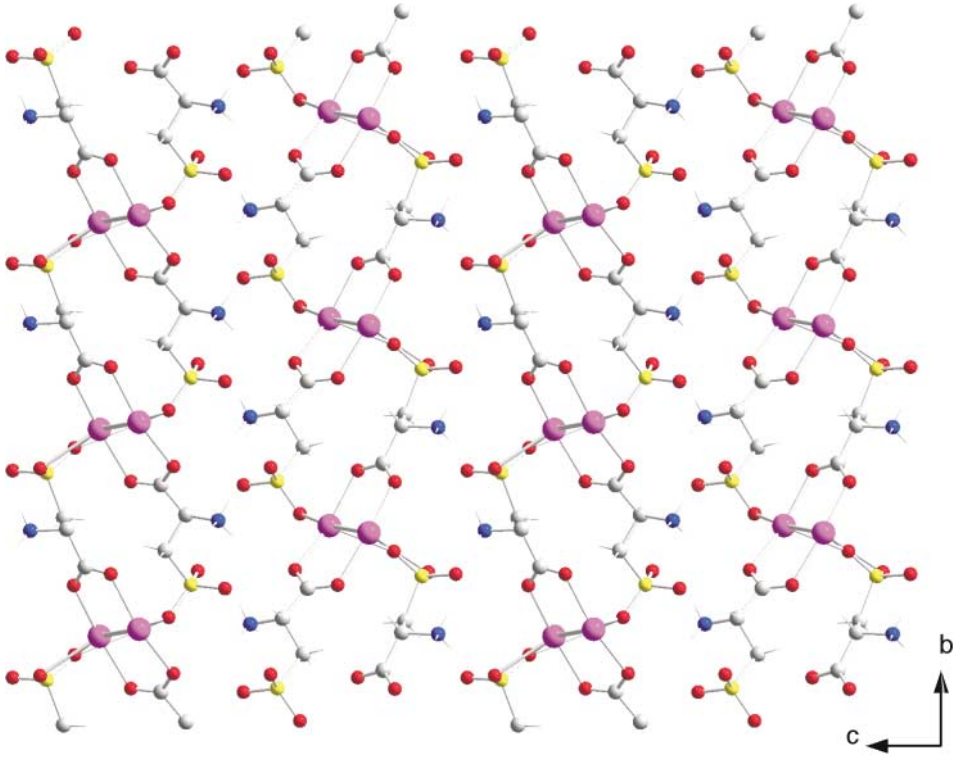

rather than layers. Augmented by hydrogen bonding, **2** forms a structure with channels in one dimension, in which are located guest water molecules.

For **2**, the core building unit is again the carboxylate-bridged silver(I) dimer. The two silver centers are distinct. Including the contact to the adjacent silver center, Ag1 has a six-coordinate geometry with a coordination sphere composed of two carboxylate oxygen atoms (Ag1—O4 = 2.295(5), Ag1—O10 = 2.269(5) Å), three sulfonate oxygen atoms (Ag1—O6 = 2.616(7), Ag1—O7 = 2.56(3), Ag1—O8 = 2.81(1) Å), and the silver contact (Ag1···Ag2 = 2.8567(9) Å). The geometry is best described as a square pyramid but where one basal site is bifurcated between two sulfonate oxygen atoms from the same SO_3 group. The coordination to this sulfonate group serves as part of the linking motif to form ribbons in the direction of the *c*-axis. The carboxylate oxygen atoms occupy *trans* sites in the equatorial plane, and a sulfonate oxygen atom, O6, which serves to link the ribbons in the direction of the *a*-axis, occupies the axial site. Ag2 has a five-coordinate, slightly distorted trigonal bipyramidal geometry. The axial sites are occupied by the two carboxylate oxygen atoms (Ag2—O5 = 2.212(5), Ag2—O9 = 2.224(5) Å). Two of the equatorial positions are filled by two sulfonate oxygen atoms from two different SO_3 groups (Ag2—O2 = 2.61(2), Ag2—O3 = 2.63(2) Å) and the remaining site is the previously mentioned Ag–Ag contact. The bond to O3 is involved in forming the ribbon motif along the direction of the *c*-axis. The carboxylate-bridged Ag dimeric unit is, as in **1**, quite distorted from a planar arrangement as indicated by the torsion angles about each of the four C—O bonds (C3—O4 = 31.7(9), C3—O5 = 4.7(9), C6—O9 = –11.5(1), C6—O10 = 31.8(1)°).

In **1**, the one-dimensional ribbons of silver dimers are linked in a parallel fashion to form layers. In **2**, the same ribbons are arranged to form a three-dimensional assembly. Essentially, each second ribbon undergoes a "turnstile-like" rotation along its primary axis to create space for the guest water molecules. The mutual orientation of adjacent ribbons is shown in Fig. 5. A view perpendicular to the ribbons, as shown in Fig. 6, reveals that the ribbons adopt a herringbone motif. Each ribbon is coordinated to four adjacent ribbons through the Ag1—O6 and Ag2—O2 interactions mentioned above. As in **1**, the silver sulfonate interactions are augmented by hydrogen bonding between ammonium and sulfonate groups (N1—O4 = 3.009(9), N2—O3 = 2.87(1) Å). The reorientation from the layered to the herringbone motif results in the generation of pockets that can accommodate the guest water molecules. These pockets align into channels as shown in Fig. 7.

Metal–metal interactions

One of the notable structural features of the building block for the coordination polymers, **1** and **2**, is the dimeric silver(I) unit (13). There is currently much interest in metal d^{10}-d^{10} interactions, whether they involve copper(I), silver(I), or gold(I) (14). They are of interest at many levels, ranging from a fundamental bonding perspective to their application in the generation of luminescent supramolecular networks. To focus on silver(I) systems, the question that frequently arises is whether a particular compound with a short Ag···Ag contact displays true "argentophilicity" or whether the metal centers are simply at a distance enforced by the remaining ligation (15). An excellent illustration of these interactions was reported by Chivers et al. (16). The Chivers group

© 2002 NRC Canada

Fig. 4. ORTEP diagram of **2**, showing, once again, the Ag dimer motif and its extension to one-dimensional ribbons. Note the additional water molecules (O11). Hydrogen atoms have been omitted for clarity. Thermal ellipsoids of 50% probability are represented.

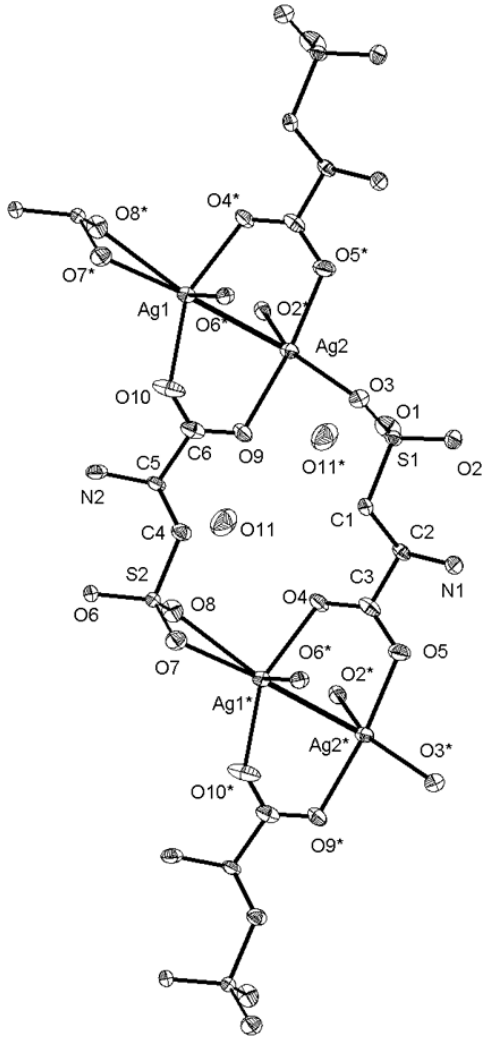

reported a silver(I) complex of a tellurium diimide ligand with two Ag centers positioned 2.888(2) Å apart. This is a value significantly shorter than the sum of the van der Waals radii for silver, a value of 3.42 Å. In comparison, compounds **1** and **2** contain Ag···Ag distances of 2.8011(3) and 2.8567(9) Å, respectively. The principal difference between these cases is that in the Chivers complex, the two silver centers are displaced towards one another relative to their ideal positions in the absence of any Ag···Ag interaction. This results in a bowing of the 180° bond angle at silver to a mean value of 163.3(5)°. In **1** and **2**, the mean O-Ag-O angles made with the carboxylate oxygen atoms are 159.1(1)° and 155.7(1)°, respectively. However, in these compounds, the silver(I) centers are not displaced towards one another and this bowing at the silver centers is actually away from one another. That said, for the silver centers to align in a linear fashion with the carboxylate oxygen atoms would require an Ag···Ag distance of roughly 2.25 Å, an extremely small value. Thus, the bowing of the metal centers away from each other in this case does also not preclude a possible interaction. This compound is one of numerous examples where the Ag···Ag interaction is not easily distinguishable from the effects of further ligation.

Powder X-ray diffraction (PXRD), thermogravimetric analyses (TGA), and structural interconversion of 1 and 2

PXRD and TGA analyses revealed that structure **1** converts to **2** on hydration. PXRD analyses of bulk samples of both **1** and **2** matched that of the simulation from a single crystal determination, indicating that the single crystal structure was in fact representative of the bulk phase. For **1**, all powders obtained rapidly converted to **2** before a powder analysis was possible. This was also the case with ground single crystalline material. Dehydration of these samples yielded a similar situation where during the powder preparation and analysis, the samples rehydrated. Thermal gravimetric analysis of the anhydrous compound **1** revealed a stable structure below 245°C but at 245°C the sample decomposed. For the hydrate compound **2**, a stable mass was observed below 177°C but at 177°C loss of the included water molecule was observed (3.16% calcd., 3.10% obsd). This compound was then stable up to 245°C at which point decomposition was observed. From the similarities in the thermal behavior, it may be inferred that upon dehydration, **2** converts back to **1**, although we have not been able to show that without variable temperature PXRD.

Chemically, the only difference between the structures of **1** and **2** is the inclusion of one molecule of water per asymmetric unit in **2**. Structurally, however, there are significant changes between the two complexes. This is quite an interesting observation given that the core building unit in the two structures is the same. The difference is in how these units assemble through weak interactions. In these cases, the weak interactions are a combination of silver sulfonate interactions and hydrogen bonding between ammonium and sulfonate groups. The stronger coordinate covalent bonds in the system, the Ag–carboxylate interactions, sustain a dimeric motif observed in both structures (13). Also, in both structures the dimers are linked into ribbons by coordination of silver to a sulfonate group from a neighboring dimer. In **1**, further silver sulfonate interactions serve to link the ribbons into perfect layers that interact via hydrogen bonding. Inclusion of water in **2** disrupts these interribbon contacts via H-bonding and shifts the ribbons into a herringbone motif.

A somewhat perplexing aspect of compounds **1** and **2** is that both structures are obtained from aqueous solutions but only **2** incorporates water. This is made even more puzzling by the fact that the two structures are seemingly interconvertible. The only difference in the preparations of the compounds is that **1** is formed from the carbonate salt of silver(I), whereas **2** results from the nitrate salt. Therefore, it is apparent that the nature of the anion is significant even though it is not incorporated into the final structure. For carbonate, it would have been lost as CO_2. This type of "structure-directing role" of a component in a reaction is not unprecedented and, in fact, likely to occur more frequently than is recognized. Tian et al. (17) have recently reported a porous cobalt imidazolate structure that has a

© 2002 NRC Canada

Fig. 5. View of **2**, showing a two-dimensional assembly of ribbons, as depicted in Fig. 4. The ribbons assemble in an equivalent manner perpendicular to the image to form a three-dimensional structure.

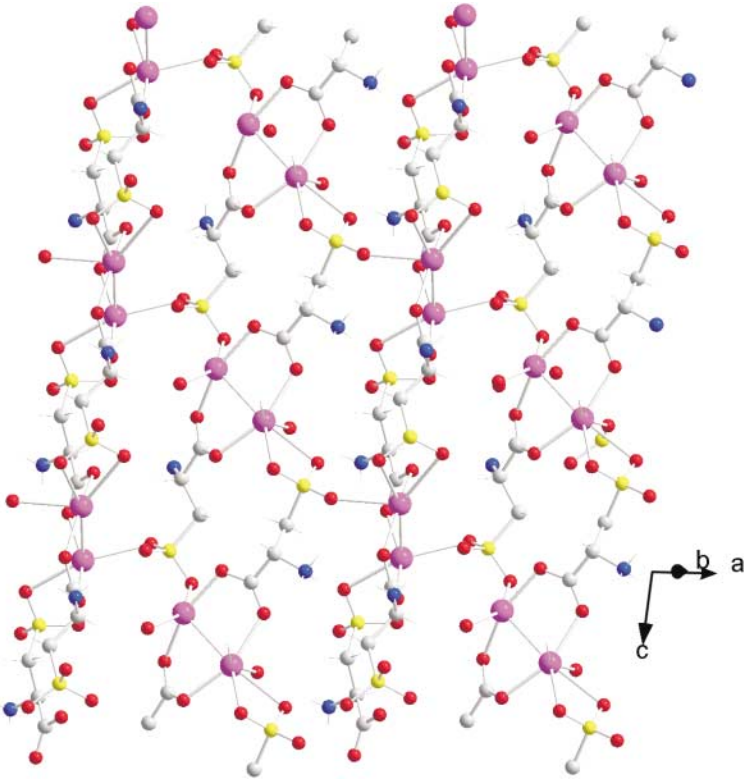

Fig. 6. View of **2**, down the *c*-axis (i.e., down the ribbons) showing the "herringbone" assembly of the one-dimensional structures into three dimensions. Large spheres represent included water molecules. Thick bonds depict a single ribbon as shown in Fig. 4.

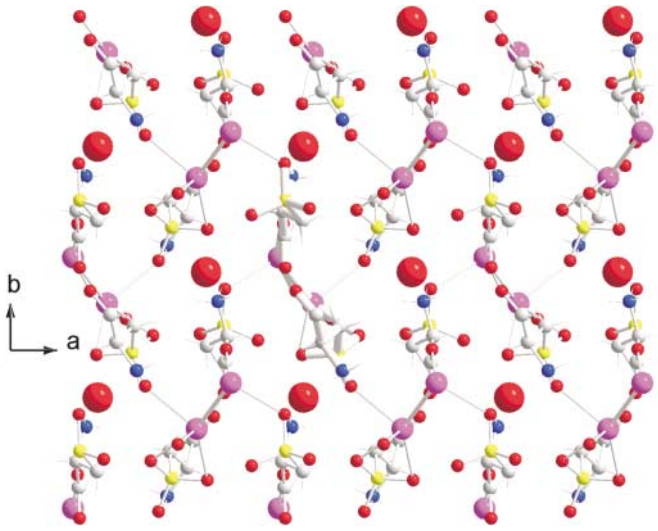

Fig. 7. View of **2**, down the *a*-axis, showing the channels, which permeate the structure, filled with guest water molecules, again represented as large spheres. Thick bonds depict a single ribbon as shown in Fig. 4.

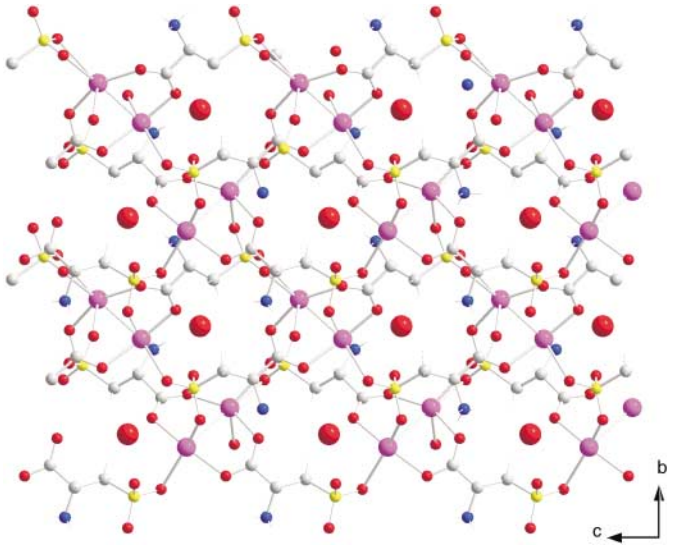

critical dependence on the presence of piperazine to form, even though piperazine itself is not incorporated as part of the final structure.

The structural flexibility exhibited by this system is exactly the reason for our examining frameworks linked by silver sulfonate interactions. Employed cooperatively, we have shown that these weaker interactions can sustain robust architectures yet, at the same time, offer a degree of flexibility typically not associated with extended inorganic frameworks (3, 4). With L-cysteic acid, there also exists the potential for the generation of porous coordination frameworks for enantioselective guest uptake.

© 2002 NRC Canada

References

1. G.K.H. Shimizu, G.D. Enright, C.I. Ratcliffe, G.S. Rego, J.L. Reid, and J.A. Ripmeester. Chem. Mater. **10**, 3282 (1998).
2. G.K.H. Shimizu, G.D. Enright, C.I. Ratcliffe, K.F. Preston, J.L. Reid, and J.A. Ripmeester. Chem. Commun. 1485 (1999).
3. S.K. Mäkinen, N.J. Melcer, M. Parvez, and G.K.H. Shimizu. Chem. Eur. J. **7**, 5176 (2001).
4. A.P. Côté, M.J. Ferguson, K.A. Khan, G.D. Enright, A.D. Kulynych, S.A. Dalrymple, and G.K.H. Shimizu. Inorg. Chem. **41**, 287 (2002).
5. J.W. Cai, C.H. Cheng. X.L. Feng, C.Z. Liao, and X.M. Chen. J. Chem. Soc. Dalton Trans. 2370 (2001); J.W. Cai, C.H. Chen, C.Z. Liao, J.H. Yao, X.P. Hu, and X.M. Chen. J. Chem. Soc. Dalton Trans. 1137 (2001).
6. A.L. Arduini, M. Garnett, R.C. Thompson, and T.C.T. Wong. Can. J. Chem. **53**, 3812 (1975); J.S. Haynes, J.R. Sams, and R.C. Thompson. Can. J. Chem. **59**, 669 (1981).
7. A.P. Côté and G.K.H. Shimizu. Chem. Commun. 251 (2001).
8. B.M. Moulton and M.J. Zaworotko. Chem. Rev. **101**, 1629 (2001).
9. G.A. Lawrance. Chem. Rev. **86**, 17 (1986); G.L. Ning, M. Munakata, L.P. Wu, M. Maekawa, Y. Suenaga, T. Kuroda-Sowa, and K. Sugimoto. Inorg. Chem. **38**, 5668 (1998); M. Munakata, L.P. Wu, T. Kuroda-Sowa, M. Maekawa, Y. Suenaga, K. Sugimoto, and I. Ino. J. Chem. Soc. Dalton Trans. 373 (1999); P.J.J.A. Timmermans and A. Mackor. J. Organomet. Chem. **276**, 287 (1984); G.L. Ning, L.P. Wu, K. Sugimoto, M. Munakata, T. Kuroda-Sowa, and M. Maekawa. J. Chem. Soc. Dalton Trans. 2529 (1999); I. Ino, L.P. Wu, M. Munakata, T. Kuroda-Sowa, M. Maekawa, Y. Suenaga, and R. Sakai. Inorg. Chem. **39**, 5430 (2000).
10. There are no structurally characterized complexes of L-cysteic acid; for L-cysteic acid itself, see: H. Konishi, T. Ashida, and M. Kakudo. Bull. Chem. Soc. Jpn. **41**, 2305 (1968); L-cysteic acid hydrate: W.A. Hendrickson and J. Karle. Acta Crystallogr. B, **27**, 427 (1971).
11. For reviews on hydrogen-bonded metal complexes, see: A.D. Burrows, C.W. Chan, M.M. Chowdhry, J.E. McGrady, and D.M.P. Mingos. Chem. Soc. Rev. **24**, 329 (1995); A. Beatty. Cryst. Eng. Comm. **51**, 1 (2001).
12. Bruker AXS Inc. 1997. SHELXTL [computer program]. Madison, Wisconsin.
13. Ag trifluoroacetate: R.G. Griffin, J.D. Ellett, M. Mehring, J.G. Bullitt, and J.S. Waugh. J. Chem. Phys. **57**, 2157 (1972); Ag benzoate: B.T. Usubaliev, E.M. Movsumov, I.R. Amiraslonov, A.I. Akhmedov, A.A. Musaev, and K.S. Mamedov. Zh. Strukt. Khim. **22**, 98 (1981); Ag β-alanine nitrate: M.E. Kamwaya, E. Papavinasam, S.G. Teoh, and R.K. Rajaram. Acta Crystallogr. C, **40**, 1318 (1984); Ag (3-trimethylammoniopropionate) perchlorate: X.-M. Chen and T.C.W. Mak. J. Chem. Soc. Dalton Trans. 3253 (1991); Ag hexamethylenetetramine acetate: M.-L. Tong, S.-L. Zheng, and X.-M. Chen. Chem. Commun. 561 (1999); Ag trifluoracetate *p*-diiodobenzene: J. Powell, M.J. Horvath, A. Lough, A. Phillips, and J. Brunet. J. Chem. Soc. Dalton Trans. 637 (1998); Ag chloroacetate: M. Eppel and H. Kirschnick. Chem. Ber. **130**, 291 (1997); Ag glutarate: A. Michaelides, S. Skoulika, V. Kiritisis, and A. Aubry. Chem. Commun. 1415 (1995); Ag (N-carboxymethyl) dimethylammonioacetate: P.R. Wei, D.D. Wu, and T.C.W. Mak, Inorg. Chim. Acta, **249**, 169 (1996).
14. H. Schmidbaur. Gold Bull. **33**, 3 (2000); K.M. Merz, Jr. and R. Hoffmann. Inorg. Chem. **27**, 2120 (1988); F.A. Cotton, X. Feng, M. Matusz, and R. Poli. J. Am. Chem. Soc. **110**, 7077 (1988); C.P. McArdle, M.J. Irwin, M.C. Jennings, J.J. Vittal, and R.J. Puddephatt. Chem. Eur. J. **8**, 723 (2002); D.B. Leznoff, B.Y. Xue, R.J. Batchelor, F.W.B. Einstein, and B.O. Patrick, Inorg. Chem. **40**, 6026 (2001); M.C. Brandys and R.J. Puddephatt. Chem. Commun. 1280 (2001); E.J. Fernandez, J.M. Lopez-de-Luzuriaga, M. Monge, and M.A. Rodriguez. Inorg. Chem. **37**, 6002 (1998); C.M. Che, Z. Mao, V.M. Miskowski, M.C. Tse, C.K. Chan, K.K. Cheung, D.L. Phillips, and K.H. Leung, Angew. Chem. Int. Ed. **39**, 4084 (2000); K. Singh, J.R. Long, and P. Stavropoulos. J. Am. Chem. Soc. **119**, 2942 (1997); H.L. Hermann, G. Boche, and P. Schwerdtfeger. Chem. Eur. J. **7**, 5333 (2001); M.M. Olmstead, F.L. Jiang, S. Attar, and A.L. Balch. J. Am. Chem. Soc. **123**, 3260 (2001).
15. C.-M. Che, M.-C. Tse, M.C.W. Chan, K.-K. Cheung, D.L. Phillips, and K.-H. Leung. J. Am. Chem. Soc. **122**, 2464 (2000); M.A. Omary, T.R. Webb, Z. Assefa, G.E. Shankle, and H.H. Patterson. Inorg. Chem. **37**, 1380 (1998); M.A. Rawashdeh-Omary, M.A. Omary, and H.H. Patterson. J. Am. Chem. Soc. **122**, 10 371 (2000); Q.-M. Wang and T.C.W. Mak. J. Am. Chem. Soc. **122**, 7608 (2000); Q.-M. Wang and T.C.W. Mak. J. Am. Chem. Soc. **123**, 1501 (2001); Q.-M. Wang and T.C.W. Mak. Angew. Chem. Int. Ed. **40**, 1130 (2001).
16. T. Chivers, M. Parvez, and G. Schatte. Angew. Chem. Int. Ed. **38**, 2217 (1999); T. Chivers, M. Parvez, and G. Schatte. Inorg. Chem. **38**, 5171 (1999).
17. Y.Q. Tian, C.X. Cai, Y. Ji, X.Z. You, S.M. Peng, and G.H. Lee. Angew. Chem. Int. Ed. **41**, 1384 (2001).

© 2002 NRC Canada

Triply bridged dicopper-bis(trimethylsilyl-chalcogenolates): Synthesis and characterization of the series of helical complexes [$(Me_3SiE\text{-}Cu)_2(\mu\text{-}Ph_2PC{\equiv}CPPh_2\text{-}\kappa^2P)_3$] (E = S, Se, Te)

Andrew I. Wallbank and John F. Corrigan

Abstract: The copper-chalcogenolates [$(Me_3SiE\text{-}Cu)_2(\mu\text{-}Ph_2PC{\equiv}CPPh_2\text{-}\kappa^2P)_3$] (**1**, E = S; **2**, E = Se; **3**, E = Te) have been prepared in good yield from [$(OAcCu)_2(\mu\text{-}Ph_2PC{\equiv}CPPh_2\text{-}\kappa^2P)_3$] and $E(SiMe_3)_2$ at low temperatures. Complexes **1**–**3** contain two pendant -$ESiMe_3$ moieties bonded to copper(I) centres, which are also bridged by three didentate ligands to form helical structures. Complexes **1**–**3** have been characterized by single crystal crystallographic and spectroscopic methods.

Key words: copper, chalcogen, helical, trimethylsilyl groups, phosphinoacetylene.

Résumé : On a préparé les complexes de cuivre-chalcogénates [$(Me_3SiE\text{-}Cu)_2(\mu\text{-}Ph_2PC{\equiv}CPPh_2\text{-}\kappa^2P)_3$] (**1**, E = S; **2**, E = Se; **3**, E = Te) avec de bons rendements à partir de [$(OAcCu)_2(\mu\text{-}Ph_2PC{\equiv}CPPh_2\text{-}\kappa^2P)_3$] et de $E(SiMe_3)_2$ et en opérant à basses températures. Les complexes **1**–**3** comportent deux portions -$ESiMe_3$ pendantes liées à des centres de cuivre(I) qui sont aussi pontés par trois ligands didentates pour former des structures hélicoïdales. On a caractérisé les complexes **1**–**3** par diffraction des rayons X par des cristaux uniques ainsi que par des méthodes spectroscopiques.

Mots clés : cuivre, chalcogène, hélicoïdale, groupes triméthylsilyles, phosphinoacétylène.

[Traduit par la Rédaction]

Introduction

There are now several reports detailing the synthesis of silylated chalcogen complexes of the type $E(R)SiMe_3$, $E(Ar)SiMe_3$, and $E(SiMe_3)_2$ (E = S, Se, Te; R = Me, *n*-Bu, *t*-Bu; Ar = Ph, mes, etc.) (1). In addition to their utility in organic synthesis, Ar–$R(E)SiMe_3$ reagents are well known to react with main group and transition metal salts to yield well-defined polynuclear (cluster) complexes (eqs. [1] and [2]), and these represent a powerful method for metal—chalcogen bond formation (2). These reactions are driven by the formation of the soluble silane Me_3SiX (X = Cl, Br, OAc, etc.) and metal—chalcogen bonds. In such cases, the flexible coordination geometries and bonding ability of the generated chalcogenide (E^{2-}) and chalcogenolate ($E(R)^-$ and $E(Ar)^-$) ligands have resulted in a variety of binary crystalline nanoclusters being synthesized using this strategy (3). Despite the propensity for chalcogenolate ligands to adopt bridging coordination modes, it has been demonstrated that terminal coordination can be promoted by using large substituents (e.g., -$Si(SiMe_3)_3$) (4) about the chalcogen centre, and terminal coordination can be ensured by restricting the number of vacant coordination sites about the metal centres. In this general vein, we are pursuing the synthesis of conjugated bis(trimethylchalcogenide) complexes Me_3SiE-M-spacer-M-$ESiMe_3$ (5), which may potentially be used to "link" metal centres and cluster molecules. Herein, we describe the synthesis and the structural and spectroscopic characterization of [$(Me_3SiE\text{-}Cu)_2(\mu\text{-}Ph_2PC{\equiv}CPPh_2\text{-}\kappa^2P)_3$] (**1**, E = S; **2**, E = Se; **3**, E = Te).

[1] $$x[L_nMX_m + m\ E(R)SiMe_3] \rightarrow [L_nM\text{-}ER]_x + xm\ XSiMe_3$$

[2] $$x[L_nMX_m + m/2\ E(SiMe_3)_2] \rightarrow [L_nME_{m/2}]_x + xm\ XSiMe_3$$

Received 25 July 2001. Published on the NRC Research Press Web site at http://canjchem.nrc.ca on 27 November 2002.

Dedicated to Professor Tris Chivers for his contributions to Canadian chemistry.

A.I. Wallbank and J.F. Corrigan.[1] Department of Chemistry, The University of Western Ontario, London, ON N6A 5B7, Canada.

[1]Corresponding author (e-mail: corrigan@uwo.ca).

Experimental

General

All manipulations were carried out under an inert atmosphere using standard Schlenk and glovebox techniques. Bis(diphenylphosphino)acetylene (dppa) (6), bis(trimethylsilyl)sulfide (7), bis(trimethylsilyl)selenide (8), bis(trimethylsilyl)telluride (9), and copper(I) acetate (10) were prepared according to literature procedures. All solvents were dried over sodium/benzophenone. NMR spectra were recorded on either an INOVA 600 MHz or INOVA 400 MHz spectrometer at –30°C in C_7D_8. ^1H spectra were obtained at either 599.672 (**2** and **3**) or 399.766 MHz (**1**) and chemical

 DOI: 10.1139/V02-032 © 2002 NRC Canada

shifts are reported in ppm and referenced to internal solvent. ^{31}P chemical shifts are reported in ppm and referenced to external 85% H_3PO_4. ^{77}Se chemical shifts are indirectly referenced to Me_2Se at 0 ppm using $Se(Ph)SiMe_3$ (+82.0 ppm) using an excitation pulse of 2.667 μs at 54 dB with a recycle delay of 3.5 s. Raman spectra were recorded on solid samples on a Bruker RFS 100/S spectrometer equipped with a Nd^{3+}:YAG laser operating at 1064.1 nm and an N_2(l)-cooled Ge detector. The laser power was 80 mW for **1** and **2** and 15 mW for **3** (resolution = 2 cm^{-1}). Chemical analyses were performed by Chemisar Laboratories, Guelph, Ont.

Preparation of [$Me_3SiSCu(\mu$-$Ph_2PC{\equiv}CPPh_2)_3CuSSiMe_3$] 1

Dppa (0.82 g, 2.1 mmol) was added to a stirred suspension of copper(I) acetate (0.17 g, 1.4 mmol) in THF (20 mL). A clear yellow solution resulted after 5 min. The solution was cooled to –55°C and bis(trimethylsilyl)sulfide (0.29 mL, 1.4 mmol) was added dropwise via pipette. The solution was warmed slowly to 5°C. The resultant clear yellow solution was cooled to –40°C and layered with cold hexanes (20 mL). The solution was maintained at –25°C and clear colourless crystals formed after 2 days. At –35°C, the solution was decanted off and the crystals washed with cold pentane (2 × 10 mL) and cold diethylether (2 × 10 mL). The off-white solid was dried in vacuo (0.71 g, 67% yield). mp 114–115°C (decomposes). ^{1}H NMR (–30°C, C_7D_8, ppm) δ: 7.96 (br s, 24H), 6.78 (mult, 36H), 0.55 (s, 18H). ^{13}C NMR (–30°C, C_7D_8, ppm) δ: 7.83 (-Si(CH_3)$_3$). ^{31}P NMR (–30°C, C_7D_8, ppm) δ: –34.1 (br s, $w_{1/2}$ = 38 Hz). ^{29}Si NMR (–30°C, C_7D_8, ppm) δ: 8.3. Anal. calcd. for $C_{84}H_{78}Cu_2P_6S_2Si_2$ (%): C 66.34, H 5.17; found: C 66.23, H 5.43.

Preparation of [$Me_3SiSeCu(\mu$-$Ph_2PC{\equiv}CPPh_2)_3CuSeSiMe_3$] 2

Dppa (0.87 g, 2.2 mmol) was added to a stirred suspension of copper(I) acetate (0.18 g, 1.4 mmol) in THF (20 mL) to yield a clear yellow solution after 5 min. The solution was cooled to –55°C and bis(trimethylsilyl)selenide (0.32 mL, 1.5 mmol) was added dropwise via pipette. The solution was warmed slowly to –5°C. The resultant clear yellow solution was cooled to –30°C and layered with cold hexanes (30 mL). The solution was maintained at –25°C and clear colourless crystals formed after 2 days. At –35°C, the solution was decanted off and the crystals washed with cold pentane (2 × 10 mL) and cold diethylether (2 × 10 mL). The off-white solid was dried in vacuo (0.82 g, 69% yield). mp 112–113°C (decomposes). ^{1}H NMR (–30°C, C_7D_8, ppm) δ: 7.96 (br s, 24H), 6.78 (mult, 24H), 0.64 (s, 18H). ^{13}C NMR (–30°C, C_7D_8, ppm) δ: 7.99 (-Si(CH_3)$_3$). ^{31}P NMR (–30°C, C_7D_8, ppm) δ: –34.8 (br s, $w_{1/2}$ = 75 Hz). ^{29}Si NMR (–30°C, C_7D_8, ppm) δ: 3.9. Anal. calcd. for $C_{84}H_{78}P_6Se_2Si_2Cu_2$ (%): C 62.49, H 4.87; found: C 62.10, H 4.74.

Preparation of [$Me_3SiTeCu(\mu$-$Ph_2PC{\equiv}CPPh_2)_3CuTeSiMe_3$] 3

CuOAc (0.133 g, 1.08 mmol) was combined with dppa (0.64 g, 1.62 mmol) and dissolved with THF (30 mL) at room temperature. After 5 min, a pale yellow solution had formed and stirring was continued for 30 min to ensure complete complex formation. The solution was cooled to –78°C and $Te(SiMe_3)_2$ (0.24 mL, 1.12 mmol) was added dropwise via pipette. A bright yellow solution formed immediately upon addition. The stirred solution was warmed slowly. At –50°C the solution became orange and at –20°C became pale brown. The solution was maintained between –15 and –20°C for 20 min. The pale brown solution was cooled to –40°C and cold pentane (–60°C, 30 mL) was added and the solution was stirred to ensure complete mixing. The stir bar was removed and the flask was maintained at –25°C. Yellow crystals of **3** formed after a few hours. Further cooling to –70°C was used to induce further crystallization. The mother liquor was decanted off and the crystals were washed with cold diethyl ether (–60°C, 2 × 10 mL). The resultant yellow-brown solid was dried in vacuo, 0.25 g (24% yield). mp 96–97°C (decomposes). ^{1}H NMR (–30°C, C_7D_8, ppm) δ: 7.95 (br s, 24H), 6.77 (mult, 36H), 0.78 (s, 18H). ^{13}C NMR (–30°C, C_7D_8, ppm) δ: 8.46 (-Si(CH_3)$_3$). ^{31}P NMR (–30°C, C_7D_8, ppm) δ: –26.8 (br s, $W_{1/2}$ = 161 Hz). ^{29}Si NMR (–30°C, C_7D_8, ppm) δ: –19.5. Anal. calcd. for $C_{84}H_{78}P_6Te_2Si_2Cu_2$ (%): C 58.9, H 4.57; found: C 58.2, H 4.59.

X-ray analyses

Crystals were mounted immersed in cooled mineral oil and placed in a cold stream of N_2 during data collection. A single crystal suitable for X-ray analysis was mounted on a glass fibre. X-ray structural analyses were carried out on STOE IPDS equipped with an imaging plate area detector and a rotating anode (**3**) and Enraf-Nonius KappaCCD single crystal X-ray diffractometers (**1**–**2**) at 200 K (**2**–**3**) or 150 K (**1**). Crystals of **1**, **2**, and **3** all desolvate once removed from their mother liquors, as evidenced by crazing of the crystal faces; this process occurred especially quickly (seconds) for complex **1**. Data were corrected for Lorentz and polarization effects. The SHELXTL (G. M. Sheldrick, Madison, WI) program package was used to solve (direct methods, Cu, E (S, Se, Te) and P) and refine the structures. The weighting scheme employed was of the form $w = 1/[\sigma^2(F_o^2) + (a{\cdot}P)^2 + b{\cdot}P]$ (a, b = refined variables, $P = 1/3\max(F_o^2, 0) + 2/3\ F_c^2$). All non-hydrogen atoms, with the exception of disordered carbon centers, were refined with anisotropic thermal parameters. Hydrogen atoms were included as riding on their respective carbon atoms. The structures solved and refined without complications, with the following exceptions: In **1**, molecule 2 exhibits two-site disorder at both S and Si centres, along with the respective methyl groups, as well as four phenyl rings (C82–C132, C472–C522, C542–C592, C732–C782). These rings were refined as rigid groups (SHELX AFIX command). These atoms refined satisfactorily with 50% occupancies, as did a hexane solvent molecule of crystallization (C1H–C6H). In **2** both Se atoms, one Si site, the methyl carbons on the $SiMe_3$ groups (C79–C84), and ten phenyl rings (C3–C7, C15–C20, C21–C26, C34–C39, C41–C46, C47–C52, C54–C59, C60–C65, C67–C72, C73–C78) exhibited a two-site disorder that refined satisfactorily with 50% occupancies. Tetrahydrofuran molecules of solvation were also disordered over two positions and were refined with 50:50 occupancies. In **3**, two of the phenyl rings (C21–C26; C73–C78) and the methyl substituents about Si2 exhibited two-site disorder and were refined satisfactorily with 60:40 occupancy. The solvent molecule O3S–C12S was refined with 50% site occupancy. A summary of the X-ray determinations is given in Table 1.

© 2002 NRC Canada

Table 1. A summary of the X-ray data for **1**–**3**.

	1	**2**	**3**
Empirical formula	$C_{84}H_{78}Cu_2P_6S_2Si_2{\cdot}3(OC_4H_8){\cdot}0.25(C_6H_{14})$	$C_{84}H_{78}Cu_2P_6Se_2Si_2{\cdot}2(OC_4H_8)$	$C_{84}H_{78}Cu_2P_6Te_2Si_2{\cdot}2.5(OC_4H_8)$
Wavelength		0.71073 Å	
T (K)	150(2)	200(2)	200(2)
Radiation type		Mo Kα_1	
Monochromator		Graphite	
Space group	$P\bar{1}$ (Z = 4)	$P2_1/n$ (Z = 4)	$P2_1/c$ (Z = 4)
a (Å)	19.5152(3)	15.5978(2)	28.816(6)
b (Å)	20.6327(4)	31.5158(7)	12.721(3)
c (Å)	25.4778(4)	17.5976(4)	26.747(5)
α (°)	105.6570(9)	90	90
β (°)	96.9101(11)	90.5171(11)	108.89(3)
γ (°)	90.3412(11)	90	90
μ (mm^{-1})	0.645	1.519	1.250
Diffractometer	Enraf Nonius KappaCCD	Enraf Nonius KappaCCD	STOE IPDS
F(000)	3690	3624	3848
θ range (°)	2.55 to 27.48	2.59 to 30.04	1.77 to 24.24
Index ranges	$-24 \le h \le 25$	$0 \le h \le 21$	$-32 \le h \le 33$
	$-20 \le k \le 26$	$0 \le k \le 44$	$-14 \le k \le 14$
	$-33 \le l \le 31$	$-24 \le l \le 24$	$-22 \le l \le 30$
Reflections collected	96 136	58 331	35 364
Independent reflections	44 273 [R_{int} = 0.057]	24 191 [R_{int} = 0.060]	13 801 [R_{int} = 0.059]
R indices [$(I) > 2\sigma(I)$]	R_1 = 0.0891	R_1 = 0.0600	R_1 = 0.0540
	wR_2 = 0.2435	wR_2 = 0.1273	wR_2 = 0.1548
R indices (all data)	R_1 = 0.1356	R_1 = 0.0981	R_1 = 0.0638
	wR_2 = 0.2659	wR_2 = 0.1458	wR_2 = 0.1644
Refinement method	Full-matrix-blocked least-squares on F^2	Full-matrix least-squares on F^2	
Refinement software		SHELXTL	

Note: $R_1 = \Sigma||F_o| - |F_c||/\Sigma|F_o|\cdot\ wR_2 = \{\Sigma[w(F_o^2 - F_c^2)^2/\Sigma[wF_o^2]^2\}^{1/2}$

Results and discussion

Our on-going interests in the synthesis of bis(trimethylsilyl)chalcogen reagents with a conjugated spacer, prompted us to focus our attention on dinuclear metal complexes bridged by didentate ligands $P(Ph_2)C{\equiv}CPPh_2$ (11). Carty and Efraty (11*r*) first reported the synthesis and spectroscopic characterization of X-Cu(μ-dppa)$_3$Cu-X coordination complexes (**I**), providing evidence for d(π)-d(π) Cu—P interactions, with concomitant reduction in C(pπ)—P(dπ) interactions within the P-C≡C-P linkages (11*q*). We reported recently (12) that the P_3Cu–X tetrahedral coordination geometry about the copper centres, as is observed in the coordination complexes **I**, is suitable for the preparation of tris(trialkylphoshpine)copper(I)trimethylsilylchalcogenolates **II** (eq. [3]). Quintessential to the successful synthesis of the terminal silylchalcogenolate complexes is the sequestering of all additional coordination sites about copper, lest the chalcogenolate ligand adopt a preferred bridging coordination mode (13).

[3] $$CuOAc + 4PR_3 + E(SiMe_3)_2 \rightarrow (R_3P)_3Cu\text{-}ESiMe_3 + AcOSiMe_3 + PR_3$$

II

R = Et, Pr; E = S, Se, Te

In a similar vein, the three didentate ligands in **I** provide the required coordination geometry about two copper centres to force terminal coordination of the formed -E-SiMe$_3$ ligands in **1**–**3**. Thus, when solutions of AcO-Cu(μ-dppa)$_3$Cu-OAc are treated at low temperatures (–55°C) with 2 equiv of S(SiMe$_3$)$_2$, colourless, X-ray quality crystals of **1** form after several days after layering with hexanes and crystallizing at –25°C (Scheme 1). ^{1}H NMR spectroscopic characterization of **1** confirmed the displacement of the -OAc groups from copper and suggested the formation of a Cu–SSiMe$_3$ linkage with, in addition to signals assigned readily to the phenyl rings of the dppa ligands, a high field signal of appropriate integration (δ = 0.55(s) ppm) is observed. A single crystal X-ray analysis provided full structural details and confirmed the formulation of **1**·(THF)$_3$(C$_6$H$_{14}$)$_{0.25}$ as [(Me$_3$SiS-Cu)$_2$(μ-Ph$_2$PC≡CPPh$_2$-κ^2*P*)$_3$]. The molecular structure of **1** is illustrated in Fig. 1 and a selection of bond lengths and angles is

Scheme 1.

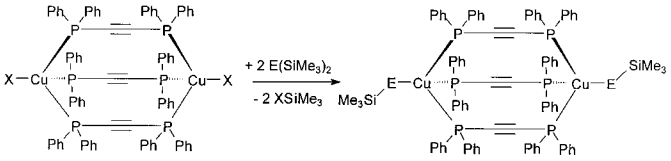

I **1**, E = S; **2**, E = Se; **3**, E = Te

© 2002 NRC Canada

Fig. 1. A perspective view of the molecular structure of $[(Me_3SiS\text{-}Cu)_2(\mu\text{-}Ph_2PC{\equiv}CPPh_2\text{-}\kappa^2P)_3]$ **1** (molecule 1). Thermal ellipsoids are drawn at the 40% probability level and H atoms have been omitted for clarity.

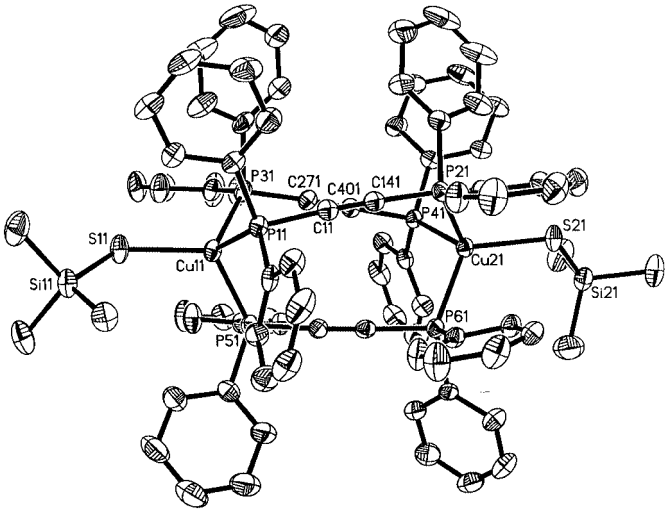

Fig. 2. A perspective view of the molecular structure of $[(Me_3SiSe\text{-}Cu)_2(\mu\text{-}Ph_2PC{\equiv}CPPh_2\text{-}\kappa^2P)_3]$ **2**. Thermal ellipsoids are drawn at the 40% probability level and H atoms have been omitted for clarity.

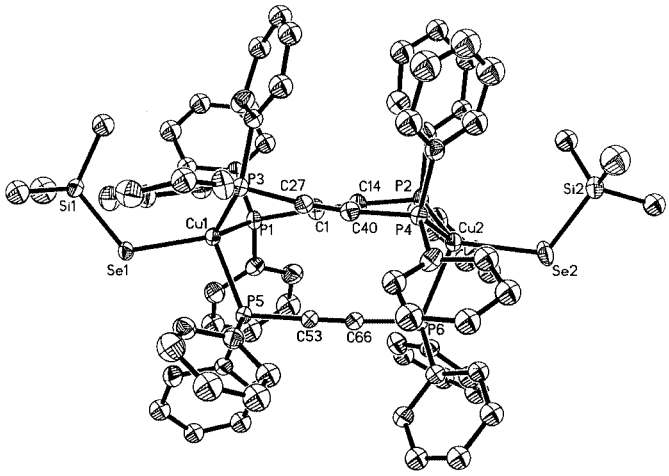

listed in Table 2. Complex **1** crystallizes with two identical yet crystallographically independent molecules in the asymmetric unit, and structural parameters in the text refer to molecule 1. Although stable indefinitely under N_2 atmosphere in the solid state, **1** hydrolyses rapidly in ambient atmosphere and solutions (THF) of **1** need be kept below 5°C to avoid the formation of insoluble unidentified materials.

The molecule consists of two pseudo-tetrahedral copper centres, each bonded to one sulfur and three phosphorus atoms. The two Cu centres are spanned by three dppa ligands, with a Cu···Cu distance of 6.496(1) Å. Of particular interest are the two trimethylsilylthiolate ligands that are bonded terminally (Cu11—S11 = 2.289(2); Cu21—S21 = 2.285(2) Å) to the two copper metals in this dimetallic complex. A similar coordination mode was observed in the related monomeric complexes $(R_3P)_3Cu\text{-}SSiMe_3$ (12). These pendant -$SiMe_3$ moieties represent potential reactive sites for additional sulfur—metal bond formation (12*b*) and complex **1** represents a rare example of a bis(trimethylsilyl)chalcogenolate where two reactive -$ESiMe_3$ moieties are separated by a conjugated spacer group (5,14). The dihedral angle between the two Cu-S-Si is 113.1°, the two S-$SiMe_3$ groups adopting a staggered orientation in the solid state. In solution there is one ^{31}P NMR chemical shift observed at –34.1 ppm; this peak noticeably broadened ($\Delta\nu_{1/2}$ = 38 Hz) owing to quadrupolar coupling to the copper centres (15). An examination of the six Cu—P bonding distances in **1** reveals a pattern of two shorter and one longer Cu—P bonds at each of the copper centres (Cu11—P11 = 2.271(1); Cu11—P31 = 2.336(2); Cu11—P51 = 2.286(2); Cu21—P21 = 2.378(2); Cu21—P41 = 2.286(1); Cu21—P61 = 2.307(2) Å), as was observed for the complexes $(R_3P)_3Cu\text{-}ESiMe_3$ (12). The longest Cu—P contact is that associated with the phosphorus centre *trans* to the S-Si vector (dihedral angle between Si11-S11-Cu11 and S11-Cu11-P31 = 164.1°; between Si21-S21-Cu21 and S21-Cu21-P21 = 177.9°). In addition, the angles P-Cu11-S11 and P-Cu21-S21 are smallest for P31 and P21, respectively (Table 2). These two structural parameters about the Cu centres may suggest steric repulsion between these phosphorus and sulfur centres, as the steric interactions between the -$SiMe_3$ moieties and neighbouring phenyl rings may force a close S11—P31 and S21—P21 contact, which is alleviated by a lengthening of the two Cu—P bonds. The P-C≡C angles are clustered about linear values (177.5(5)–172.4(5)°), the most significant deviations associated with the angles P(61)-C(661)-C(531) and P(51)-C(531)-C(661). As has been observed in other $[M_2(\mu\text{-}Ph_2PC{\equiv}CPPh_2\text{-}\kappa^2P)_3]$ complexes, (11*s*, 11*u*) there is a helical twist about the Cu11—Cu21 vector of approximately 29°, taking the average of the three torsion angles P-Cu11-Cu21-P for the three dppa ligands. Complex **1** crystallizes in the centrosymmetric space group $P\bar{1}$, with both achiral enantiomers present in the unit cell. The resulting magnetic inequivalence of the phenyl rings in the solid state does not manifest itself in solution NMR studies as one type of phenyl ring is observed in the ^1H spectrum, suggesting either fast interconversion of the two enantiomers on the NMR timescale even at low temperatures (–30°C), or that the complex loses its helical structure in solution all together (11s).

The synthesis of the selenium analogue $[(Me_3SiSe\text{-}Cu)_2(\mu\text{-}Ph_2PC{\equiv}CPPh_2\text{-}\kappa^2P)_3]$ **2** from AcO-Cu(μ-dppa)$_3$Cu-OAc and $Se(SiMe_3)_2$ is achieved readily as described for **1**, with virtually identical yields (69% for **2**; 67% for **1**). The ^1H NMR spectrum for **2** also confirmed the presence of -$SiMe_3$ (δ = 0.64 ppm), and the absence of signals assignable to -OAc ligands. X-ray quality crystals of **2**·$(THF)_2$ (space group $P2_1/n$) were grown at –25°C and the molecular structure of **2** is illustrated in Fig. 2, with selected bond lengths and angles listed in Table 2. As for **1**, the structure of **2** consists of two Cu centres bridged by three dppa ligands, each copper also bonded to a trimethylsilylchalcogenolate group (Se) and adopting tetrahedral coordination. A high degree of site disorder was observed in **2**, as all 12

© 2002 NRC Canada

Table 2. Selected bond lengths (Å) and angles (°).

1 (Molecule 1)		(Molecule 2)		**2**		**3**	
Bond lengths (Å)							
Cu(11)—S(11)	2.289(2)	Cu(12)—S(12)	2.288(4)	Cu(1)—Se(1)	2.374(1)	Cu(1)—Te(1)	2.570(1)
Cu(21)—S(21)	2.285(2)	Cu(22)—S(22)	2.356(4)	Cu(2)—Se(2)	2.381(4)	Cu(2)—Te(2)	2.593(1)
Cu(11)—P(11)	2.271(1)	Cu(12)—P(12)	2.328(2)	Cu(1)—P(1)	2.284(1)	Cu(1)—P(1)	2.278(1)
Cu(11)—P(31)	2.336(2)	Cu(12)—P(32)	2.270(2)	Cu(1)—P(3)	2.277(1)	Cu(1)—P(3)	2.295(1)
Cu(11)—P(51)	2.286(2)	Cu(12)—P(52)	2.300(2)	Cu(1)—P(5)	2.305(1)	Cu(1)—P(5)	2.308(1)
Cu(21)—P(21)	2.338(2)	Cu(22)—P(22)	2.266(2)	Cu(2)—P(2)	2.299(1)	Cu(2)—P(2)	2.313(2)
Cu(21)—P(41)	2.286(1)	Cu(22)—P(42)	2.332(2)	Cu(2)—P(4)	2.282(1)	Cu(2)—P(4)	2.312(1)
Cu(21)—P(61)	2.307(2)	Cu(22)—P(62)	2.290(2)	Cu(2)—P(6)	2.315(1)	Cu(2)—P(6)	2.273(1)
S(11)—Si(11)	2.101(2)	S(12A)—Si(12)	2.181(6)	Se(1)—Si(1)	2.21(2)	Te(1)—Si(1)	2.472(2)
S(21)—Si(21)	2.102(2)	S(22A)—Si(22)	2.118(7)	Se(2)—Si(2)	2.187(4)	Te(2)—Si(2)	2.451(2)
P(11)—C(11)	1.759(6)	P(12)—C(12)	1.752(6)	P(1)—C(1)	1.763(4)	P(1)—C(1)	1.771(5)
P(21)—C(141)	1.756(6)	P(22)—C(142)	1.770(6)	P(2)—C(14)	1.774(4)	P(2)—C(14)	1.767(5)
P(31)—C(271)	1.766(5)	P(32)—C(272)	1.776(6)	P(3)—C(27)	1.764(4)	P(3)—C(27)	1.757(5)
P(41)—C(401)	1.774(6)	P(42)—C(402)	1.759(6)	P(4)—C(40)	1.767(4)	P(4)—C(40)	1.760(5)
P(51)—C(531)	1.755(5)	P(52)—C(532)	1.769(6)	P(5)—C(53)	1.768(4)	P(5)—C(53)	1.762(6)
P(61)—C(661)	1.768(6)	P(62)—C(662)	1.760(4)	P(6)—C(66)	1.760(4)	P(6)—C(66)	1.767(5)
C(11)—C(141)	1.212(8)	C(12)—C(142)	1.205(8)	C(1)—C(14)	1.196(5)	C(1)—C(14)	1.195(7)
C(271)—C(401)	1.200(7)	C(272)—C(402)	1.190(8)	C(27)—C(40)	1.201(5)	C(27)—C(40)	1.203(7)
C(531)—C(661)	1.205(7)	C(532)—C(662)	1.200(7)	C(53)—C(66)	1.197(5)	C(53)—C(66)	1.194(7)
Bond angles (°)							
Cu(11)-S(11)-Si(11)	122.00(8)	Cu(12)-S(12A)-Si(12)	119.2(2)	Cu(1)-Se(1)-Si(1)	119.4(5)	Cu(1)-Te(1)-Si(1)	113.46(5)
Cu(21)-S(21)-Si(21)	115.64(8)	Cu(22)-S(22A)-Si(22)	118.0(3)	Cu(2)-Se(2)-Si(2)	117.75(16)	Cu(2)-Te(2)-Si(2)	118.83(6)
P(11)-Cu(11)-S(11)	119.48(6)	P(12)-Cu(12)-S(12)	109.03(13)	P(1)-Cu(1)-Se(1)	114.5(3)	P(1)-Cu(1)-Te(1)	119.49(5)
P(21)-Cu(21)-S(21)	105.78(6)	P(22)-Cu(22)-S(22)	122.53(13)	P(2)-Cu(2)-Se(2)	114.24(13)	P(2)-Cu(2)-Te(2)	106.18(4)
P(31)-Cu(11)-S(11)	107.92(6)	P(32)-Cu(12)-S(12)	122.72(11)	P(3)-Cu(1)-Se(1)	119.7(3)	P(3)-Cu(1)-Te(1)	110.80(4)
P(41)-Cu(21)-S(21)	117.76(6)	P(42)-Cu(22)-S(22)	107.88(14)	P(4)-Cu(2)-Se(2)	117.72(11)	P(4)-Cu(2)-Te(2)	112.08(4)
P(51)-Cu(11)-S(11)	114.73(6)	P(52)-Cu(12)-S(12)	107.50(10)	P(5)-Cu(1)-Se(1)	103.1(3)	P(5)-Cu(1)-Te(1)	110.38(4)
P(61)-Cu(21)-S(21)	116.72(6)	P(62)-Cu(22)-S(22)	109.39(15)	P(6)-Cu(2)-Se(2)	105.03(9)	P(6)-Cu(2)-Te(2)	119.78(4)
P(11)-Cu(11)-P(31)	103.78(6)	P(12)-Cu(12)-P(32)	103.88(6)	P(1)-Cu(1)-P(3)	111.77(4)	P(1)-Cu(1)-P(3)	110.62(5)
P(11)-Cu(11)-P(51)	109.56(5)	P(12)-Cu(12)-P(52)	100.27(6)	P(1)-Cu(1)-P(5)	102.24(4)	P(1)-Cu(1)-P(5)	101.46(4)
P(31)-Cu(11)-P(51)	98.61(6)	P(32)-Cu(12)-P(52)	111.07(6)	P(3)-Cu(1)-P(5)	102.58(4)	P(3)-Cu(1)-P(5)	102.36(5)
P(21)-Cu(21)-P(41)	102.49(5)	P(22)-Cu(22)-P(42)	103.77(6)	P(2)-Cu(2)-P(4)	110.83(4)	P(2)-Cu(2)-P(4)	101.59(5)
P(21)-Cu(21)-P(61)	99.92(5)	P(22)-Cu(22)-P(62)	110.74(6)	P(2)-Cu(2)-P(6)	102.52(4)	P(2)-Cu(2)-P(6)	107.11(5)
P(41)-Cu(21)-P(61)	111.18(5)	P(42)-Cu(22)-P(62)	99.92(6)	P(4)-Cu(2)-P(6)	104.69(4)	P(2)-Cu(2)-P(6)	108.40(5)
C(11)-C(141)-P(21)	177.5(5)	C(12)-C(142)-P(22)	176.7(5)	C(1)-C(14)-P(2)	177.4(4)	C(1)-C(14)-P(2)	177.6(5)
C(141)-C(11)-P(11)	175.6(5)	C(142)-C(12)-P(12)	175.9(5)	C(14)-C(1)-P(1)	174.0(3)	C(14)-C(1)-P(1)	177.4(4)
C(271)-C(401)-P(41)	176.4(5)	C(272)-C(402)-P(42)	177.7(6)	C(27)-C(40)-P(4)	173.2(3)	C(27)-C(40)-P(4)	173.6(5)
C(401)-C(271)-P(31)	177.5(5)	C(402)-C(272)-P(32)	175.9(5)	C(40)-C(27)-P(3)	171.1(3)	C(40)-C(27)-P(3)	174.7(5)
C(531)-C(661)-P(61)	172.4(5)	C(532)-C(662)-P(62)	173.4(5)	C(53)-C(66)-P(6)	174.4(3)	C(53)-C(66)-P(6)	177.8(4)
C(661)-C(531)-P(51)	173.4(5)	C(662)-C(532)-P(52)	173.0(5)	C(66)-C(53)-P(5)	177.7(3)	C(66)-C(53)-P(5)	177.4(4)

phenyl rings of the phosphine ligands and both -$SeSiMe_3$ moieties were refined using a two-site (50:50) model (see supplementary material).[2] The helical twist (as defined for **1**) in **2** is 20°, and unlike for **1**, in which the two trimethylsilyl groups adopt a staggered conformation (angle = 113.1°), the two -$SiMe_3$ moieties in **2** are best described as being eclipsed (dihedral angle Cu1-Se1-Si1 and Cu2-Se2-Si1 = 11.3°). The solution ^{77}Se NMR spectrum for **2** displays a single resonance at δ = –573.2 (q, $^2J_{PSe}$ = 27 Hz) ppm, and this chemical shift value lies between those reported for $(THF)_2LiSeSi(SiMe_3)_3$ (16) (–825 ppm) and $Se(SiMe_3)_2$, (–334 ppm) (17) and is very close to those reported for the complexes $(R_3P)_3Cu\text{-}SeSiMe_3$ (–570.4 and –565.8 ppm for R = Et and Pr, respectively) (12). As for **1**, only one set of phenyl resonances is observed in the ^{1}H NMR spectrum of **2** (Table 3).

[2] Supplementary data may be purchased from the Depository of Unpublished Data, Document Delivery, CISTI, National Research Council Canada, Ottawa, ON K1A 0S2, Canada (http://www.nrc.ca/cisti/irm/unpub_e.shtml for information on ordering electronically). CCDC 167249–167251 contain the supplementary data for this paper. These data can be obtained, free of charge, via www.ccdc.cam.ac.uk/conts/retrieving.html (or from the Cambridge Crystallographic Data Centre, 12 Union Road, Cambridge, U.K.; fax +44 1223 336033; or deposit@ccdc.cam.ac.uk).

© 2002 NRC Canada

Table 3. Summary of NMR data (δ, ppm) for **1**–**3** at –30°C in C_7D_8.

	$^1H^a$	$^{13}C^a$	^{31}P	^{77}Se
1	0.55	7.83	–34.1	—
2	0.64	7.99	–34.8	–573.2 (J_{PSe} = 27 Hz)
3	0.74	8.46	–26.5	—

[a]Tabulated chemical shift values are those of the -CH_3 groups only.

Fig. 3. A perspective view of the molecular structure of [$(Me_3SiTe\text{-}Cu)_2(\mu\text{-}Ph_2PC{\equiv}CPPh_2\text{-}\kappa^2P)_3$] **3**. Thermal ellipsoids are drawn at the 40% probability level and H atoms have been omitted for clarity.

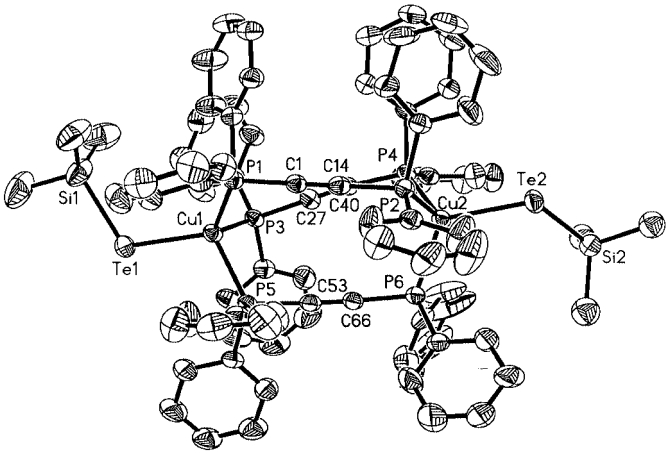

The tellurium analogue [$(Me_3SiTe\text{-}Cu)_2(\mu\text{-}Ph_2PC{\equiv}CPPh_2\text{-}\kappa^2P)_3$] **3** can also be prepared from [$(OAcCu)_2(\mu\text{-}Ph_2PC{\equiv}CPPh_2\text{-}\kappa^2P)_3$] and $Te(SiMe_3)_2$ although the yields are much poorer (25%) than for **1** or **2**. Extremely air- and moisture-sensitive crystals of **3**·$(THF)_{2.5}$ form from concentrated THF–pentane solutions, allowing for crystallographic analysis (Figs. 3 and 4, Tables 1 and 2). The tetrahedral coordination geometries about the two Cu centres in **3** are, expectedly, similar to those observed in the lighter congeners. The helical twist (as defined for **1** and **2**) of the three dppa ligands in **3** is 24°, and the two -$SiMe_3$ groups are staggered (angle = 139.1°, Fig. 4). Unfortunately, the relative instability of **3** in solution has thus far prohibited us from observing a signal in the ^{125}Te NMR spectrum.

The copper—chalcogen bonding distances in **1**–**3** follow the expected trend: Cu—S (2.285(2)–2.356(2) Å) < Cu—Se (2.374(1)–2.381(4) Å) < Cu—Te (2.570(1)–2.593(1) Å). Noteworthy however is that these Cu—E bonding distances are significantly shorter than those reported for complexes **II** (e.g., $(Et_3P)_3Cu\text{-}ESiMe_3$: E = S: 2.4022(5); E = Se: 2.5124(6); E = Te: 2.7126(4) Å)(13). The Cu···Cu distances in this series are longest for **3** (6.454(1) Å) and shortest for **2** (6.442(1) Å).

Spectroscopic characterization

Raman spectra for **1**–**3** each display strong $\nu_{C\equiv C}$, and the position of this peak varies little from **1** (S, 2122 cm^{-1}) to **2** (Se, 2117 cm^{-1}) to **3** (Te, 2116 cm^{-1}). Indeed, the positions of these peaks are similar to those reported for related [$(X\text{-}Cu)_2(\mu\text{-}Ph_2PC{\equiv}CPPh_2\text{-}\kappa^2P)_3$] complexes, and they are markedly (~20 cm^{-1}) shifted to higher energy relative to the free ligand (11*q*). This has been attributed by Carty and Efraty (11*r*) to the decrease in the extent of C(pπ)–P(dπ) interaction in the ligand upon coordination to a metal centre.

Fig. 4. A view of the molecular structure of [$(Me_3SiTe\text{-}Cu)_2(\mu\text{-}Ph_2PC{\equiv}CPPh_2\text{-}\kappa^2P)_3$] **3**, viewed along the Cu···Cu vector and illustrating the helical twist associated with the molecule (H atoms omitted).

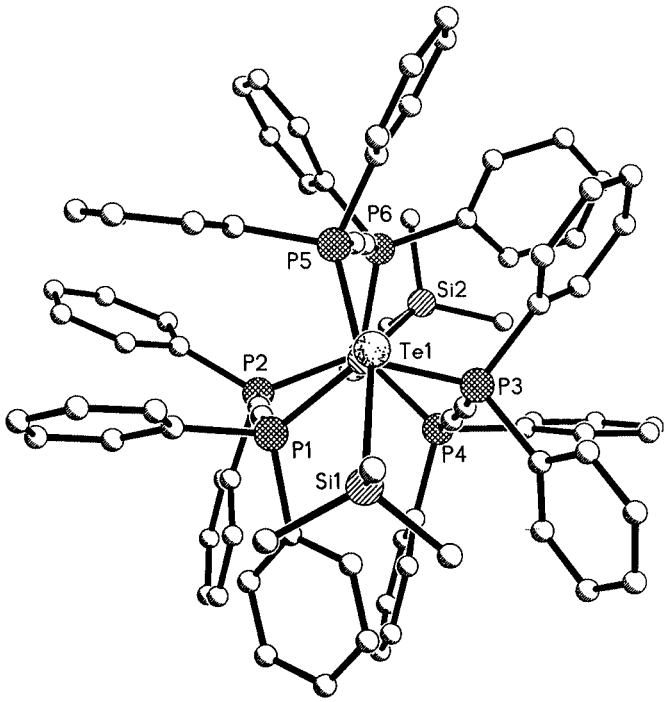

Solution NMR spectra for all three complexes were obtained at low temperatures as **1**–**3** decompose rapidly at room temperature in solvent. In the series **1** → **2** → **3**, the ^{1}H resonances of the trimethylsilyl moieties display a stepwise downfield shift (δ = 0.55 (**1**), 0.64 (**2**), 0.78 ppm (**3**)) from S → Se → Te, as has been observed for $E(SiMe_3)_2$ (1*o*, 18) and $(R_3P)_3Cu\text{-}ESiMe_3$ (13*a*) The ^{1}H NMR spectra for **1**–**3** all exhibit one set of phenyl resonances, despite the inequivalence of the aromatic rings in the solid state, as has been described for related $[Ag_2(\mu\text{-dppa-}\kappa^2P)_3]^{2+}$ complexes (11*s*). Thus, complexes **1**–**3** either interconvert between enantiomers rapidly on the NMR timescale (at –30°C), or their helical structure is lost in solution (11*s*). This helical twist is not observed for related bis(diphenylphosphinobutadiynyl) complex [$(PhSe\text{-}Cu)_2(\mu\text{-}Ph_2PC{\equiv}C\text{-}C{\equiv}CPPh_2\text{-}\kappa^2P)_3$] (11*v*).

Conclusions

We have demonstrated that a series of dinuclear tris(phosphine)copper(I) (trimethylsilyl)chalcogenolates (E = S, Se, Te) with terminally bonded -$ESiMe_3$ groups can be prepared from the reaction of 2 equiv of $E(SiMe_3)_2$ and [$(X\text{-}Cu)_2(\mu\text{-}Ph_2PC{\equiv}CPPh_2\text{-}\kappa^2P)_3$] (X = Cl, OAc). The series **1**–**3** represents a rare example of structurally related trimethylsilylchalcogenolate metal complexes and the two pendant -$ESiMe_3$ functionalities are potential sites for metal—chalcogen bond formation. The orientation of three dppa

© 2002 NRC Canada

ligands in these complexes results in triple-strand helicate structures. Although unstable in solution, these complexes are stable indefinitely in the solid state under inert atmosphere at low temperatures.

Acknowledgments

We thank the Natural Sciences and Engineering Research Council of Canada (NSERC) for financial support and The University of Western Ontario's Academic Development Fund (ADF) program and the Canada Foundation for Innovation for equipment funding. We also thank Dr. M. Jennings (UWO) for collecting X-ray diffraction data for complexes **1** and **2** and Professor Y. Huang for assistance in obtaining the Raman data. A.I.W. thanks the Government of Ontario for an Ontario Graduate Scholarship in Science and Technology (OGSST) scholarship.

References

1. (*a*) J.F. Corrigan, S. Balter, and D. Fenske. J. Chem. Soc. Dalton Trans. 729 (1996); (*b*) I. Ojima, M. Nihonyanagi, and Y. Nagai. J. Organometal. Chem. **50**, C26, (1973); (*c*) I. Mori, P. A. Bartlett, and C. H. Heathcock. J. Org. Chem. **55**, 5966 (1990); (*d*) P. Jutzi, W. Steiner, E. Koenig, G. Huttner, A Frank, and U. Schubert. Chem. Ber. **111**, 606 (1978); (*e*) I. Kuwajima and T. Abe. Bull. Chem. Soc. Jpn. **51**, 2183 (1978); (*f*) E. Nakamura, K. Hashimoto, and I. Kuwajima. Bull. Chem. Soc. Jpn. **54**, 805 (1981); *(g)* U. Herzog and G. Roewer. Main Group Met. Chem. **22**, 579 (1999); (*h*) M. Schmidt, E. Kiewert, H. Lux, and C. Sametschek. Phosphorus Sulfur, **26**, 163 (1986); (*i*) J.E. Drake and R.T. Hemmings. J. Chem. Soc. Dalton Trans. 1730 (1976); (*j*) M.R. Detty. Tetrahedron Lett. 5087 (1978); (*k*) N. Miyoshi, H. Ishii, K. Kondo, S. Murai, and N. Sonoda. Synthesis, 300 (1979); (*l*) H. Abe, A. Yamasaki, and T. Harayama. Chem. Pharm. Bull. **46**, 1311 (1998); (*m*) N. Zhu and D. Fenske. J. Chem. Soc. Dalton Trans. 1067 (1999); (*n*) U. Herzog. J. Prakt. Chem. **342**, 379 (2000); (*o*) J.E. Drake and R.T. Hemmings. Inorg. Chem. **19**, 1879 (1980); (*p*) D. Fenske and N. Zhu. J. Cluster Sci. **11**, 135 (2000); (*q*) R.S. Glass. J. Organometal. Chem. **61**, 83 (1973).
2. (*a*) M.W. DeGroot and J.F. Corrigan. J. Chem. Soc. Dalton Trans. 1235 (2000); (*b*) D. Fenske and M. Bettenhausen. Angew. Chem. Int. Ed. Engl. **37**, 1291 (1998); (*c*) J.F. Corrigan and D. Fenske. Chem. Commun. 943 (1996); (*d*) J.F. Corrigan and D. Fenske. Angew. Chem. Int. Ed. Engl. **36**, 1981 (1997); (*e*) M. Bettenhausen and D. Fenske. Z. Anorg. Allg. Chem. **624**, 1245 (1998); (*f*) J.F. Corrigan, D. Fenske, and W.P. Power. Angew. Chem. Int. Ed. Engl. **36**, 1176 (1997); (*g*) Y.-W. Jun, C.-S. Choi, and J. Cheon. Chem. Commun. 101 (2001); (*h*) H. Matsuzaka, T. Ogino, M. Nishio, M. Hidai, Y. Nishibayashi, and S. Uemura. J. Chem. Soc. Chem. Commun. 223 (1994); (*i*) S. M. Stuczynski, J.G. Brennan, and M.L. Steigerwald. Inorg. Chem. **28**, 4431 (1989); (*j*) A.R. Strzelecki, C.L. Likar, B.A. Helsel, T. Utz, M.C. Lin, and P. Bianconi. Inorg. Chem. **33**, 5188 (1994); (*k*) N. Ueyama, T. Sugawara, K. Sasaki, A. Nakamura, S. Yamashita, Y. Wakatsuki, H. Yamazaki, and N. Yasuoka. Inorg. Chem. **27**, 741 (1988); (*l*) D. Fenske, J. Meyer, and K. Merzweiler. Z. Naturforsch. B, **42**, 1207 (1987); (*m*) P.M. Boorman, J.M. Ball, K.J. Moynihan, V.D. Patel, and J.F. Richardson. Can. J. Chem. **61**, 2809 (1983); (*n*) G.G. Hoffmann. Chem. Ber. **116**, 3858 (1983); (*o*) H. Schumann, G. Cielusek, and J. Pickardt, Angew. Chem. **92**, 60 (1980); (*p*) C. Eaborn, K.J. Odell, and A. Pidcock. J. Organomet. Chem. **170**, 105 (1979); (*q*) E.W. Abel and C.R. Jenkins. J. Organometal. Chem. **14**, 285 (1968); (*r*) H. Schumann, G. Cielusek, S. Jurgis, E. Hahn, J. Pickardt, J. Blum, Y. Sasson, and A. Zoran. Chem. Ber. **117**, 2825 (1984); (*s*) P.M. Boorman, T. Chivers, K.N. Mahadev, and B.D. O'Dell. Inorg. Chim. Acta, **19**, L35 (1976); (*t*) H.-O. Stephan and G. Henkel. Angew. Chem. Int. Ed. Engl. **33**, 2322 (1994); (*u*) S. Schulz, M. Andruh, T. Pape, T. Heinze, H.W. Roesky, L. Haeming, A. Kuhn, and R. Herbst-Irmer. Organometallics, **13**, 4004 (1994); (*v*) D. Fenske, T. Langetepe, M.M. Kappes, O. Hampe, and P. Weis. Angew. Chem. Int. Ed. **39**, 1857 (2000). (*w*) U. App and K. Merzweiler. Z. Anorg. Allg. Chem. **623**, 478 (1997); (*x*) S. Schulz, E.G. Gillan, J.L. Ross, L.M. Rogers, R.D. Rogers, and A.R. Barron. Organometallics, **15**, 4880 (1996); (*y*) S. Uriel, K. Boubekeur, P. Batail, J. Orduna, and E. Canadell. Inorg. Chem. **34**, 5307 (1995); (*z*) A. Venturelli and T.B. Rauchfuss. J. Am. Chem. Soc. **116**, 4824 (1994); (*aa*) T.A. Bright, R.A. Jones, S.U. Koschmieder, and C.M. Nunn. Inorg. Chem. **27**, 3819 (1988); (*bb*) J. Darkwa, J.R. Lockemeyer, P.D.W. Boyd, T.B. Rauchfuss, and A.L. Rheingold. J. Am. Chem. Soc. **110**, 141 (1988); (*cc*) J. Sola, Y. Do, J.M. Berg, and R.H. Holm. J. Am. Chem. Soc. **105**, 7784 (1983). (*dd*) Y. Do, E.D. Simhon, and R.H. Holm. Inorg. Chem. **22**, 3809 (1983).
3. (*a*) S. Behrens, M. Bettenhausen, A.C. Deveson, A. Eichhöfer, D. Fenske, A. Lohde, and U. Woggon. Angew. Chem. Int. Ed. Engl. **35**, 2215 (1996); (*b*) A. Eichhöfer, D. Fenske, H. Pfistner, and M. Wunder. Z. Anorg. Allg. Chem. **624**, 1909 (1998); (*c*) J.F. Corrigan and D. Fenske. Chem. Commun. 1837 (1997); (*d*) D. Fenske, N. Zhu, and T. Langetepe. Angew. Chem. Int. Ed. Engl. **37**, 2640 (1998); (*e*) M. Bettenhausen and D. Fenske. Z. Anorg. Allg. Chem. **624**, 1245 (1998); (*f*) S. Dehnen and D. Fenske. Chem. Eur. J. **2**, 1407 (1996); (*g*) H. Krautscheid, D. Fenske, G. Baum, and M. Semmelmann Angew. Chem. Int. Ed. Engl. **32**, 1303 (1993).
4. (*a*) A.L. Seligson and J. Arnold. J. Am. Chem. Soc. **115**, 8214 (1993); (*b*) P.J. Bonasia, D.E. Gindelberger, and J. Arnold. Inorg. Chem. **32**, 5126 (1993); (*c*) C.P. Gerlach and J. Arnold. Inorg. Chem. **37**, 2393 (1998); (*d*). C.P. Gerlach, V. Christou, and J. Arnold. Inorg. Chem. **35**, 2758 (1996); (*e*) S.P. Wuller, A.L. Seligson, G.P. Mitchell, and J. Arnold. Inorg. Chem. **34**, 4854 (1995); (*f*) D.R. Cary, G.E. Ball, and J. Arnold. J. Am. Chem. Soc. **117**, 3492 (1995); (*g*) A.L. Seligson and J. Arnold. J. Am. Chem. Soc. **115**, 8214 (1993); (*h*) D.E. Gindelberger and J. Arnold. Inorg. Chem. **32**, 5813 (1993); (*i*) P.J. Bonasia and J. Arnold. Inorg. Chem. **31**, 2508 (1992).
5. A.I. Wallbank and J.F. Corrigan. Chem. Commun. 377 (2001).
6. D.R.M. Walton and F. Waugh. J. Organomet. Chem. **37**, 45 (1972).
7. X. Bu, Q. Meng, X. You, and S. Sun. Synthesis, 306 (1989).
8. V.M. Schmidt and H. Ruf. Z. Anorg. Allg. Chem. **321**, 270 (1963).
9. J.E. Drake, B.M. Glavincevski, R.T. Hemmings, and H.E. Henderson. Inorg. Synth. **20**, 171 (1980).
10. D.A. Edwards and R. Richards. J. Chem. Soc. Dalton Trans. 246 (1973).
11. (*a*) S. Singhal, V.K. Jain, and R.J. Butcher. J. Coord. Chem. **46**, 355 (1999); (*b*) D. Xu, H.J. Murfee, W.E. van der Veer, and B. Hong. J. Organomet. Chem. **596**, 53 (2000); (*c*) W. Oberhauser, C. Bachmann, T. Stampfl, and P. Brueggeller. Inorg. Chim. Acta, **256**, 223 (1997); (*d*) R.S. Dickson, T. de Simone, R.J. Parker, and G.D. Fallon. Organometallics, **16**, 1531 (1997); (*e*) P.K. Baker and E.M. Armstrong.

© 2002 NRC Canada

Polyhedron, **9**, 801 (1990); (*f*) H.C. Clark, G. Ferguson, P.N. Kapoor, and M. Parvez. Inorg. Chem. **24**, 3924 (1985). (*g*) H.C. Clark, P.N. Kapoor, and I.J. McMahon. J. Organomet. Chem. **265**, 107 (1984); (*h*) C.M. Bolinger and T.B. Rauchfuss. Inorg. Chem. **21**, 3947 (1982); (*i*) H.C. Bechthold and D. Rehder. J. Organomet. Chem. **172**, 331 (1979); (*j*) H.C. Clark and L.E. Manzer. J. Organometal. Chem. **59**, 411 (1973); (*k*) R.H. Holm and G.R. Eaton. Inorg. Chem. **10**, 805 (1971); (*l*) K.S. Wheelock, J.H. Nelson, and H.B. Jonassen. Inorg. Chim. Acta, **4**, 399 (1970); (*m*) A.J. Carty and A. Efraty. Can. J. Chem. **47**, 2573 (1969); (*n*) A.J. Carty, A. Efraty, and T.W. Ng. Can. J. Chem. **47**, 1429 (1969); (*o*) A.J. Carty and A. Efraty. Inorg. Chem. **8**, 543 (1969); (*p*) A.J. Carty and A. Efraty. Chem. Commun. 1559 (1968); (*q*) A.J. Carty and A. Efraty. Inorg. Nucl. Chem. Lett. **4**, 427 (1968); (*r*) A.J. Carty and A. Efraty. Can. J. Chem. **46**, 1598 (1968); (*s*) S.L. James, E. Lozano, and M. Nieuwenhuyzen. Chem. Commun. 617 (2000); (*t*) G. Hogarth and T. Norman. J. Chem. Soc. Dalton Trans. 1077 (1996); (*u*) G. Hogarth and T. Norman. Polyhedron, **15**, 2859 (1996); (*v*) M. Semmelmann, D. Fenske, and J.F. Corrigan. J. Chem. Soc. Dalton Trans. 2541 (1998).

12. (*a*) D.T.T. Tran and J.F. Corrigan. Organometallics, **19**, 5202 (2000); (*b*) D.T.T. Tran, N.J. Taylor, and J.F. Corrigan. Angew. Chem. Intl. Ed. Engl. **39**, 935 (2000).
13. (*a*) J. Arnold. Prog. Inorg. Chem. **43**, 353 (1995); (*b*) H.J. Gysling. Coord. Chem. Rev. **42**, 133 (1982); (*c*) M.D. Janssen, D.M. Grove, and G. van Koten. Prog. Inorg. Chem. **46**, 97 (1997); (*d*) J.R. Dilworth and J. Hu. Adv. Inorg. Chem. **40**, 411 (1993).
14. S.L. Stoll, S.G. Bott, and A.R. Barron. J. Chem. Soc. Dalton Trans. 1315 (1997).
15. R.K. Harris. Nuclear magnetic resonance spectroscopy: a physicochemical view. Longman Scientific & Technical, New York. 1986. p. 90.
16. P.J. Bonasia, V. Christou, and J. Arnold. J. Am. Chem. Soc. **115**, 6777 (1993).
17. M. Semmelmann. Doctoral dissertation. Universität Karlsruhe, Germany (1997).
18. (*a*) I. Mathieu-Pelta and S.A. Evans. J. Org. Chem. **57**, 3409 (1992); (*b*) M.R. Detty. J. Org. Chem. **44**, 4528 (1979); (*c*) J.E. Drake and R.T. Hemmings. Inorg. Chem. **19**, 1879 (1980).

© 2002 NRC Canada

Bisphosphine ligands containing two *o*-*N*,*N*-dimethylanilinyl substituents at each phosphorus atom

Nathan D. Jones, Patric Meessen, Martin B. Smith, Udo Losehand, Steven J. Rettig, Brian O. Patrick, and Brian R. James

Abstract: The synthesis and complete characterization of the family of tetra(amine)bisphosphine ligands (*o*-$NMe_2C_6H_4)_2P$-(X)-P(*o*-$NMe_2C_6H_4)_2$, where X = CH_2 (dmapm), $(CH_2)_2$ (dmape), and $CH(CH_2)_3CH$ (dmapcp), are described. Crystal structure data are compared with known, analogous bisphosphines containing *o*-pyridyl or phenyl substituents in place of the *o*-dimethylanilinyl groups. Several short, intramolecular C-H···N distances in the anilinyl derivatives may represent the presence of weak hydrogen bonds.

Key words: phosphine, amine, polydentate, hydrogen-bonding to N atoms.

Résumé : On décrit la synthèse et la caractérisation complète d'une famille de ligands tétra(amine)bisphosphine, (*o*-$NMe_2C_6H_4)_2P$-(X)-P(*o*-$NMe_2C_6H_4)_2$, dans lesquels X = CH_2 (dmapm), $(CH_2)_2$ (dmape) et $CH(CH_2)_3CH$ (dmapcp). On a comparé leurs structures cristallines à celles de bisphosphines connues, analogues, contenant des substituants *o*-pyridyle ou phényle à la place des groupes *o*-diméthylanilinyles. Plusieurs distances intramoléculaires C-H···N dans les dérivés anilinyles sont courtes et elles peuvent être le reflet de la présence de faibles liaisons hydrogènes.

Mots clés : phosphine, amine, polydentate, liaison hydrogène avec des atomes d'azote.

[Traduit par la Rédaction]

Introduction

The introduction of an amine moiety into a *mono*phosphine compound for use as a P-N ligand has a long history and dates from the 1940s; early examples include the 2-pyridylphosphines made by Mann and co-workers (1) and *o*-diphenylphosphino-*N*,*N*-dimethyl-aniline [$Ph_2P(o\text{-}C_6H_4NMe_2)$] reported by Venanzi and co-workers (2); we have used the latter extensively in some recent Ru chemistry (3). This aminophosphine is just one example of a wide range of bidentate, chelating P-N ligands (4). The incorporation of an amine functionality into a *bis*(phosphine) ligand is more recent and dates from about 25 years or so, an early example being that of Achiwa who incorporated two PPh_2 moieties into proline derivatives (5). The amino-bisphosphine systems, which have been reviewed (6), have been developed mainly with the aim of surmounting the severe problem in homogeneous catalysis of separating the catalyst from the reaction products. Approaches to solving this problem, including representative literature references, have been: (*i*) to "heterogenize" the homogeneous catalyst by incorporating it into an insoluble polymer via attachment through the N atom (5, 7–9); (*ii*) to solubilize the catalyst in water (in which the reactants and products are only slightly miscible) by quaternization of the N atom via protonation or alkylation (10–16); (*iii*) to water solubilize the catalyst via incorporation of a sulfonate group within an elaborated N-containing functionality (17); and (*iv*) to extract the catalyst post-reaction with aqueous acid in which the product does not dissolve (18, 19).

Our group here has reported extensively on the use of mono- and bis-phosphine ligands containing the *o*-pyridyl moiety, with the goal of developing platinum metal complexes rendered water soluble by protonation of the pyridyl N atom (20); examples include the compound $py_2P(CH_2)_2Ppy_2$ and the related $py_2P(C_5H_8)Ppy_2$, where py = *o*-pyridyl and C_5H_8 is a cyclopentane moiety bridging the two P atoms (cf. Fig. 1). We have now extended this theme by replacing the *o*-pyridyl group by the *o*-dimethylanilinyl group and report here on the synthesis of the new ligands dmapm (1,1-bis(di(*o*-*N*,*N*-dimethylanilinyl)phosphino)methane), dmape (1,2-bis(di(*o*-*N*,*N*-dimethylanilinyl)phosphino)ethane), and dmapcp (*rac*-

Received 6 March 2002. Published on the NRC Research Press Web site at http://canjchem.nrc.ca on 28 November 2002.

Dedicated to Tris Chivers, a close friend, fellow cricketer, squash player, and chemistry colleague for 35 years (at least for BRJ!).

N.D. Jones, P. Meessen,[1] M.B. Smith,[2] U. Losehand, S.J. Rettig,[3] B.O. Patrick, and B.R. James.[4] Department of Chemistry, The University of British Columbia, Vancouver, BC V6T 1Z1, Canada.

[1]Present address: BASF AG, D-67056 Ludwigshafen, Germany.
[2]Present address: Department of Chemistry, Loughborough University, Leicestershire, LE11 3TU, U.K.
[3]Deceased 27 October 1998.
[4]Corresponding author (e-mail: brj@chem.ubc.ca).

 DOI: 10.1139/V02-127 © 2002 NRC Canada

Fig. 1. Tetra(*o*-*N*,*N*-dimethylanilinyl)bisphosphines.

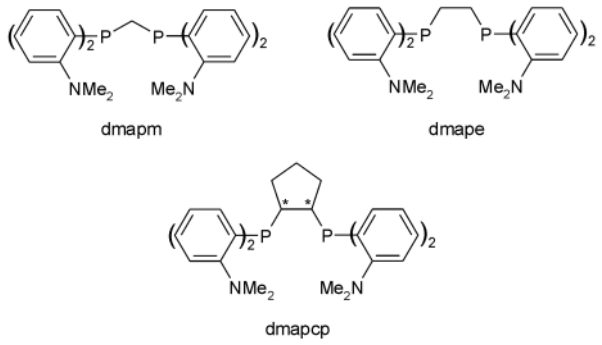

1,2-bis(di(*o*-*N*,*N*-dimethylanilinyl)phosphino)cyclopentane), illustrated in Fig. 1. Tóth and co-workers (11–15) have made related ligands, but bearing *para*-$C_6H_4(NMe_2)$ substituents, including chiral derivatives for catalytic asymmetric hydrogenation in water, once the N atoms have been quaternized; with these systems, simultaneous coordination to the same metal centre by both the P and N atoms of the same ligand is not possible, and there are no reports of bridging by these *para*-substituted ligands. Our new *ortho*-substituted ligands make the N atoms available for coordination to the same metal as the P atoms, as well as for providing convenient μ(P-N) environments; the extensive coordination chemistry of these ligands, particularly within Ru, Pd, and Pt systems, and their applications in catalysis (6, 21) will be published elsewhere. One benefit of excluding coordination chemistry from this article is that the findings presented amount to a contribution in main group chemistry, Tris Chivers's forte!

Experimental

General

Unless otherwise noted, synthetic procedures were performed using standard Schlenk techniques under a dry Ar or N_2 atmosphere. The precursors 1,1-bis(dichlorophosphino)methane and 1,2-bis(dichlorophosphino)ethane were purchased from commercial sources and stored in an N_2-filled glovebox, while 1,2-bis(dichlorophosphino)cyclopentane was made according to a literature procedure (22) and stored in a Schlenk tube under Ar. *N*,*N*-Dimethyl-*o*-bromoaniline was made by reaction of *o*-bromoaniline and dimethylsulfate according to a literature procedure (23); all other reagents were purchased from commercial sources and used as supplied. Solvents were dried and distilled under N_2 prior to use.

NMR spectra were recorded on a Bruker AV300 spectrometer (300.13 MHz for ^{1}H, 75.46 MHz for ^{13}C, 40.56 MHz for ^{15}N, 121.49 MHz for ^{31}P) at 300 K in $CDCl_3$. Residual solvent proton (^{1}H, δ 7.24 relative to external $SiMe_4$), solvent carbon (^{13}C, δ 77.0 relative to external $SiMe_4$), external $MeNO_3$ (^{15}N), or external $P(OMe)_3$ (^{31}P, δ 141.00 relative to 85% aq H_3PO_4), were used as references (*s* = singlet, *d* = doublet, *t* = triplet, *p* = pseudo). Downfield shifts were taken as positive. All *J*-values are given in Hz. Mass spectral and elemental analyses were conducted in the UBC Chemistry Department (B.C., Canada) by G. Eigendorf using a Kratos Concept II HQ mass spectrometer and by P. Borda using a Carlo Erba 1108 analyzer, respectively.

1,1-Bis(di(*o*-*N*,*N*-dimethylanilinyl)phosphino)methane, dmapm

To a solution of *n*-BuLi in hexanes (1.6 M, 16.5 mL, 26.4 mmol), cooled to –40°C on a dry ice – CH_3CN bath, was added *o*-bromo-*N*,*N*-dimethylaniline (5.05 g, 25.2 mmol) in Et_2O (20 mL) via cannula over 20 min. The yellow solution was stirred for 15 min and a white precipitate formed. The slurry was allowed to warm to room temperature (r.t.) and stirring was continued for 1 h. After the solution was cooled again to –40°C, 1,1-bis(dichlorophosphino)methane (1.33 g, 6.09 mmol) in Et_2O (15 mL) was added over 5 min. The resulting orange slurry was stirred for 15 min and then allowed to warm to r.t. Stirring was continued for 1 h and then HCl (~1 M, 50 mL) was added. The organic layer was removed and KOH (~2 M) was added dropwise to the aqueous layer to neutrality. The aqueous fraction was extracted with CH_2Cl_2 (3 × 20 mL) and the combined extracts were dried over $MgSO_4$. After removal of the solvent in vacuo, EtOH (15 mL) was added. The slurry was refluxed for 0.5 h, cooled to r.t., and the mixture filtered to give a white powder that was washed with cold EtOH (3 × 5 mL) and dried in vacuo. Yield: 1.84 g (54%). ^{1}H NMR δ: 2.23 (t, 2H, CH_2, $^2J_{HP}$ = 4.2), 2.68 (s, 24H, NCH_3), 7.02 (pt, 2H, Ar), 7.11 (pd, 4H, Ar), 7.25 (pt, 4H, Ar), 7.40 (pd, 4H, Ar). ^{13}C{^{1}H} NMR δ: 28.0 (t, *C*H_2, $^1J_{CP}$ = 26.2), 45.3 (s, N*C*H_3), 119.7 (s, *C*H), 124.2 (s, *C*H), 128.6 (s, *C*H), 132.3 (s, *C*H), 139.2 (s, *C*N), 157.1 (m, *C*P). ^{15}N NMR δ: –343.7 (s, *N*Me_2). ^{31}P{^{1}H} NMR δ: –36.0 (s). CI-MS *m*/*z*: 557 ([M–H]$^+$). Anal. calcd. for $C_{33}H_{42}N_4P_2$: C 71.2, H 7.6, N 10.1; found: C 71.0, H 7.8, N 9.9. Crystals of dmapm suitable for X-ray diffraction were grown from an acetone solution layered with hexanes.

1,2-Bis(di(*o*-*N*,*N*-dimethylanilinyl)phosphino)ethane, dmape

The synthesis of this compound follows that of dmapm. Thus, reaction of *n*-BuLi (1.6 M, 17.4 mL, 27.8 mmol), *o*-bromo-*N*,*N*-dimethylaniline (5.56 g, 27.8 mmol), and 1,2-bis(dichlorophosphino)ethane (1.61 g, 6.94 mmol) gave 2.44 g (61%) of a white powder. ^{1}H NMR δ: 1.91 (pt, 4H, CH_2, $^2J_{HP}$ = 4.1), 2.62 (s, 24H, NCH_3), 6.94 (m, 8H, Ar), 7.09 (m, 4H, Ar), 7.22 (m, 4H, Ar). ^{13}C{^{1}H} NMR δ: 24.3 (s, *C*H_2), 45.2 (s, N*C*H_3), 119.8 (s, *C*H), 124.1 (s, *C*H), 128.8 (s, *C*H), 132.3 (s, *C*H), 136.9 (pt, *C*N, *J* = 9.5), 157.7 (pt, *C*P, *J* = 6.6). ^{15}N NMR δ: –343.8 (s, *N*Me_2). ^{31}P{^{1}H} NMR δ: –28.9 (s). CI-MS *m*/*z*: 571 ([M – H]$^+$). Anal. calcd. for $C_{34}H_{44}N_4P_2$: C 71.6, H 7.8, N 9.8; found: C 71.0, H 7.6, N 9.5. Crystals of dmape suitable for X-ray diffraction were grown from a CH_2Cl_2 solution layered with EtOH.

Rac-1,2-bis(di(*o*-*N*,*N*-dimethylanilinyl)phosphino)cyclopentane, dmapcp

The synthesis of this compound corresponds to that of dmapm. Thus, reaction of *n*-BuLi in hexanes (1.6 M, 23.0 mL, 36.8 mmol), *o*-bromo-*N*,*N*-dimethylaniline (6.83 g, 34.1 mmol), and 1,2-bis(dichlorophosphino)cyclopentane (2.33 g, 8.57 mmol) at –40°C gave 2.72 g (52%) of a white powder. ^{1}H NMR δ: 1.51 (m, 2H, $C_{(4)}H_2$), 1.70 (m, 2H, $C_{(3/5)}H$H), 2.23 (m, 3H, $C_{(3/5)}H$H, C*H*), 2.55 (s, 12H, NCH_3), 2.60 (s, 12H, NCH_3, obscures C*H* protons), 6.49 (m, 2H, Ar), 6.71 (m, 2H, Ar), 6.96–7.28 (m, 12H, Ar). The ^{13}C{^{1}H} NMR spectrum shows a complicated pattern of signals due to coupling to phosphorus. Chemical shifts are presented

© 2002 NRC Canada

Fig. 2. Molecular structure of dmapcp (50% ellipsoids); H2 and H3b are labelled because they are discussed in the text.

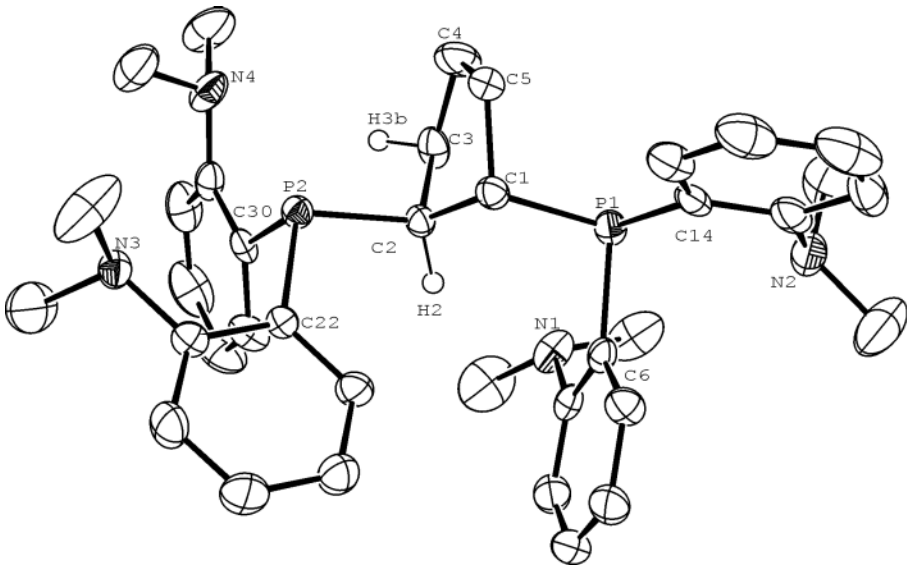

and the number of lines in each signal are given in parentheses following the peak frequencies. $^{13}C\{^1H\}$ NMR δ: 24.6 (1, $C_{(4)}H_2$), 29.9 (3, $C_{(3/5)}H_2$), 40.4 (3, $C_{(1/2)}H$), 45.0 (2, NCH_3), 119.9 (2, *C*H), 124.1 (2, *C*H), 128.5 (1, *C*H), 133.1 (2, *C*H), 137.9 (9, *C*N), 157.8 (7, *C*P). ^{15}N NMR δ: –338.8 (s, NMe_2). $^{31}P\{^1H\}$ NMR δ: –25.6 (s). CI-MS *m/z* 611 ($[M–H]^+$). Anal. calcd. for $C_{37}H_{48}N_4P_2$: C 72.8, H 8.0, N 9.2; found: C 72.9, H 8.1, N 9.1. Crystals of dmapcp suitable for X-ray diffraction were grown from a CH_2Cl_2 solution layered with EtOH. The labelling of the C atoms in the NMR corresponds to that shown in the crystal structure (Fig. 2).

X-ray crystallography of dmapm, dmape, and dmapcp

Suitable crystals were selected, mounted on a glass fibre using Paratone-N oil, and the unit frozen to –100°C. All measurements were made on a Rigaku/ADSC CCD area detector with graphite monochromated Mo Kα radiation. Selected crystallographic data appear in Table 1.[5] In each case the data were processed and corrected for Lorentz and polarization effects and absorption (24). Neutral atom scattering factors for all non-hydrogen atoms were taken from the *International Tables for X-ray Crystallography* (25, 26). All structures were solved by direct methods (27) and expanded using Fourier techniques (28). All non-hydrogen atoms were refined anisotropically. Hydrogen atoms were not refined, but were included in calculated positions (with C—H = 0.98 Å) that were updated as the refinement progressed.

Results and discussion

Synthesis

The compounds dmapm, dmape, and dmapcp were prepared in a low-temperature, two-step, one-pot procedure in which *N*,*N*-dimethyl-2-lithioaniline is first generated by reaction of *n*-BuLi with *N*,*N*-dimethyl-2-bromoaniline, and then this is exposed to 0.25 mol equiv of the appropriate tetra(chloro)bisphosphine; Scheme 1 summarizes the method for dmapm. The compounds were isolated from the reaction mixture by extraction with dilute aq HCl and purified after neutralization by recrystallization from boiling EtOH. The syntheses are analogous to those used for syntheses of the related (pyridyl) mono- and bis(phosphine) ligands (20, 29–31). Of note, owing to the activating nature of the NMe_2 groups, the lithium exchange in step one of the synthesis proceeds with higher yields than for the deactivated pyridyl halides in the corresponding tetra(pyridyl)bisphosphine analogues (>50 vs. ~30%) (20). The new ligands are white, microcrystalline powders that are indefinitely air- and moisture-stable in the solid state and for prolonged periods in metal-free solution. They are freely soluble in chlorinated solvents and in dilute aq HCl, partially soluble in alcohols and Et_2O, and insoluble in hexanes.

Scheme 1.

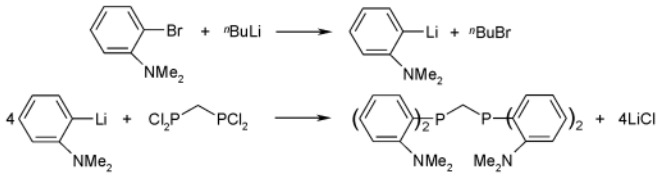

The precursor 1,2-bis(dichlorophosphino)cyclopentane was made by reaction of cyclopentene, white phosphorus, and PCl_3 (22). This procedure results almost exclusively in the *trans* product and, because of this, dmapcp is produced as a racemic mixture of *R*,*R*- and *S*,*S*-enantiomers, as with

[5] Supplementary data (full crystal data and details on data collection and refinement have been deposited, along with tables of atomic coordinates, anisotropic thermal parameters, all bond lengths and angles, and torsion angles) may be purchased from the Depository of Unpublished Data, Document Delivery, CISTI, National Research Council Canada, Ottawa, ON K1A 0S2, Canada (http://www.nrc.ca/cisti/irm/unpub_e.shtml for information on ordering electronically). CCDC 185016–185018 contain the supplementary data for this paper. These data can be obtained, free of charge, via www.ccdc.cam.ac.uk/conts/retrieving.html (or from the Cambridge Crystallographic Data Centre, 12 Union Road, Cambridge, U.K.; fax +44 1223 336033; or deposit@ccdc.cam.ac.uk).

© 2002 NRC Canada

Table 1. Crystallographic data for dmapm, dmape, and dmapcp.

	dmapm	dmape	dmapcp
Formula	$C_{33}H_{42}N_4P_2$	$C_{34}H_{44}N_4P_2$	$C_{37}H_{48}N_4P_2$
Formula weight	556.67	570.70	610.73
Crystal system	Monoclinic	Triclinic	Orthorhombic
Space group	*Cc*(#9)	$P\bar{1}$(#2)	$P2_12_12_1$(#19)
a (Å)	12.076(2)	8.1849(4)	11.975(1)
b (Å)	19.674(2)	15.500(1)	14.9163(2)
c (Å)	14.341(3)	19.882(2)	19.8124(5)
α (°)	90	73.501(4)	90
β (°)	114.142(8)	81.052(1)	90
γ (°)	90	79.9046(9)	90
V (Å^3)	3109.1(8)	2364.9(3)	3539.2(3)
Z	4	3	4
$D_{calcd.}$ (g cm^{-3})	1.189	1.202	1.146
μ (Mo Kα) (mm^{-1})	0.168	0.167	0.153
T (°C)	–100	–100	–93
Total data collected	14209	21881	9864
Independent reflections	5977	10698	9864
R_1 (on F^2, all data)	0.073	0.077	0.0942
wR_2 (on F^2, all data)	0.097	0.083	0.0705

the 1,2-bis(diphenylphosphino)cyclopentane analogue, dppcp (22); the chirality designators refer to the absolute configurations of the methine C atoms 1 and 2 in the backbone of the ligand (Figs. 1 and 2).

Characterization

The dmapm, dmape, and dmapcp compounds have been fully identified by means of NMR spectroscopy of all the nuclei present (^{1}H, ^{13}C, ^{31}P, and ^{15}N), mass spectrometry, elemental analysis, and molecular structure determination by low-temperature X-ray diffraction.

The compounds show the expected chemical shifts in their ^{1}H NMR signals, but the multiplicity of the backbone protons needs comment. Whereas the CH_2 in dmapm gives the expected triplet due to H–P coupling ($^2J_{HP}$ = 4.2 Hz), the protons in dmape appear as a pseudo triplet, resulting from the overlapping of the expected doublet of doublets, as in the *o*-pyridyl analogue, dpype (30). In the case of the racemic dmapcp, only multiplets were observed for the cyclopentyl protons, and these are assigned by comparison with data for the *o*-pyridyl analogue, dpypcp (20); the assignments of the ^{13}C{^{1}H} signals are tentative and are also based on well-established data for dpypcp (20). The ^{31}P{^{1}H} NMR spectra show singlets at δ –36.0 (dmapm), –28.9 (dmape), and –25.6 (dmapcp); the values for the last two are about 20 ppm to higher fields than those of the *o*-pyridyl analogues (20, 30). The ^{15}N NMR signals for the NMe_2-type ligands appear in the δ –340 region.

It is constructive to consider structural features of dmapm, dmape, and dmapcp along with those of their phenyl analogues: bis(diphenylphosphino)methane, dppm (32), 1,2-bis(diphenylphosphino)ethane, dppe (33), and dppcp (see above) (22), and those we have determined for the pyridyl analogues dpype (20) and dpypcp (20, 34), respectively. As far as we are aware, the pyridyl analogue of dmapm has not been reported. The molecular structures of the three new compounds are, not surprisingly, very similar to those of their phenyl and pyridyl analogues.

Table 2. Selected bond lengths (Å) and angles (°) for dppm and dmapm with estimated standard deviations in parentheses.

	dppm[a]	dmapm
Bond lengths (Å)		
P1—C17	1.846(5)	1.854(3)
P2—C17	1.868(5)	1.844(3)
P1—C9	1.828(5)	1.835(2)
P1—C1	1.842(5)	1.856(2)
P2—C18	1.839(6)	1.843(3)
P2—C26	1.842(5)	1.843(3)
P1···P2	2.97(1)	3.099(3)
Bond angles (°)		
Σ<P1, Σ<P2[b]	306.3(6), 303.7(6)	301.5(3), 303.4(3)
P1-C17-P2	106.2(3)	113.9(1)
C1-P1-C17	101.7(2)	95.9(1)
C17-P2-C26	103.2(2)	98.9(1)

[a]Data taken from ref. 32.
[b]Sum of angles at P1 and P2.

Table 2 lists some geometrical parameters for dmapm and dppm, and Fig. 3 shows the molecular structure of dmapm, which shows minor differences to that of dppm. The increased steric bulk of the NMe_2 substituents in dmapm leads to a different rotation of the arene moieties that induces two sub van der Waals contacts between N and H atoms in adjacent *N*,*N*-dimethylanilinyl moieties on each side of the molecule (N1···H23 = 2.65 Å and N4···H14 = 2.50 Å vs. the van der Waals contact of 2.75 Å (35)); the corresponding C···N bond lengths are 3.61 and 3.45 Å (larger than the 3.30 Å value for the sum of the radii), and the corresponding N···C-H angles are about 147 and 163°. These interactions may represent weak C-H···N hydrogen bonds, which do exist (35). This steric hindrance forces the molecule to "stretch", which leads to a 7° wider P-C-P angle (113.9°) and a longer P···P distance (3.099 Å) with respect to dppm. Also, the corresponding C-P-C angles are compressed in comparison to

© 2002 NRC Canada

Table 3. Selected bond lengths (Å) and angles (°) for dppe, dpype, and dmape with estimated standard deviations in parentheses.

	dppe[a]	dpype[b]	dmape(C_S)		dmape(C_1)
Bond lengths (Å)					
P3—C35	1.829(3)	1.842(3)	1.849(2)	P1—C1	1.858(2)
P3—C44	1.825(7)	1.845(3)	1.837(2)	P1—C3	1.847(2)
P3—C36	1.819(3)	1.849(3)	1.844(2)	P1—C11	1.846(2)
C35—C35*	1.521(7)	1.527(6)	1.538(4)	C1—C2	1.526(3)
P3···P3*	4.436(13)	4.453(9)	4.481(6)	P1···P2	4.508(6)
Bond angles (°)					
Σ<P1, Σ<P2[c]	304.2(12)	301.6(9)	300.0(5)	Σ<P1, Σ<P2	301.7(2), 301.3(2)
P1-C35-C35*	110.9(4)	110.4(3)	110.7(2)	P1-C1-C2	110.9(1)
				P2-C2-C1	113.7(1)
P-C-C-P	0.0	0.0	0.0	P-C-C-P	7.0

[a]Data taken from ref. 33; weighted mean of two independent measurements.
[b]Data taken from ref. 20.
[c]Sum of angles at P1 and P2.

Fig. 3. Molecular structure of dmapm (50% ellipsoids); H14 is labelled because it is discussed in the text.

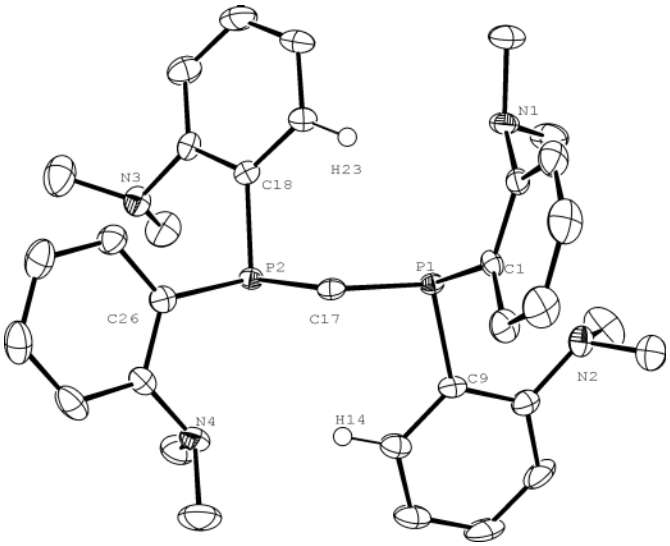

those of dppm (C1-P1-C17 (95.9°) and C17-P2-C26 (98.9°) vs. 101.7° and 103.2°), which leads to slightly more "pyramidal" P atoms as defined by the sum of the angles at P1 and P2 (av 302.5 vs. av 304.9°). The P—C bond lengths within the two molecules are essentially the same.

The asymmetric unit cell of dmape contains 1.5 crystallographically independent molecules, 1 being in a general position and 1 lying on a centre of symmetry. The main difference (see Fig. 4) is that in the C_S molecule one of the phosphine groups is twisted 180° with respect to the other, whereas in the dissymmetric molecule both phosphine moieties are facing the same side, the *N*,*N*-dimethylanilinyl substituents taking gauche positions with respect to each other. The corresponding bond lengths and angles within each molecule differ only marginally (Table 3). While the centrosymmetric molecule exhibits a planar backbone with a P-C-C-P torsion angle constrained by symmetry to be –180°, the C_S molecule is slightly puckered with a corresponding torsion angle of 173°. The C_S molecule exhibits geometry very similar to that of the also centrosymmetrical analogues dppe and dpype. The pyramidal geometry at the P atom is not affected by the different aromatic substituents, but the average P—$C_{(aromatic)}$ bond lengths are longer in dmape (av 1.844 Å) and dpype (av 1.847 Å) than in dppe (av 1.822 Å), presumably reflecting electronic differences between the *ipso* carbons in the anilinyl and pyridyl moieties compared with those in the phenyl groups (the same difference is seen on comparing data for dmapm and dppm, see Table 2). The C_S molecule shows a short N6···H42 contact (2.53 Å) with C—N = 3.49 Å and an N···H-C angle of 165°, again indicative of a weak H-bonding interaction.

In the case of dmapcp, the backbone is puckered owing to the steric demand of the cyclopentyl ring (P-C-C-P, 168°) (Fig. 2). The four *N*,*N*-dimethylanilinyl moieties lead to steric crowding, inducing sub van der Waals contacts (and possible H-bonding) between two of the N atoms and the closest H atoms of the cyclopentyl backbone (N4···H3b (2.67 Å), C—N (3.49 Å), N···H–C (140.7°); and N1···H2 (2.53 Å), C—N (3.33 Å), N···H–C (136.4°)). These contacts might explain the relatively long P—$C_{(aliphatic)}$ bonds (1.882 and 1.879 Å) and the increased P—P distance (4.505 Å) compared with data for dppcp and dpypcp (Table 4). Accordingly, the P—$C_{(aromatic)}$ bonds of the strained *N*,*N*-dimethylanilinyl moieties are also slightly elongated compared with those of the non-interacting *N*,*N*-dimethylanilinyl groups: P1—C6 (1.852) vs. P1—C14 (1.837 Å) and P2—C30 (1.847) vs. P2—C22 (1.831 Å). The P—$C_{(aliphatic)}$ bonds are about 0.04 Å longer than the P—$C_{(aromatic)}$ bonds.

The unit cell of the dmapcp crystal chosen for the analysis shows that only the *S*,*S* enantiomer is present (chiral space group $P2_12_12_1$), implying a spontaneous resolution has taken place; other crystals must contain only *R*,*R* enantiomers, but no attempt was made to separate these by the Pasteur method of inspection. The analogous dppcp and dpypcp systems crystallize with both enantiomers in the unit cell. Apart from the slight distortions mentioned above, the *S*,*S* enantiomers of the three compounds exhibit a very similar overall molecular geometry (Table 4).

Coordination chemistry

As alluded to in the Introduction, the new ligands have revealed diverse coordination chemistry (6, 21). Established bonding modes include: (*i*) *P*,*P*-, *P*,*N*-, and *P*,*P*,*N*-coordination within d^8 square planar systems, including interconversions

© 2002 NRC Canada

Fig. 4. Structures of the dissymmetric (C_1) and symmetric (C_S) molecules of dmape (50% ellipsoids); H42 is labelled because it is discussed in the text.

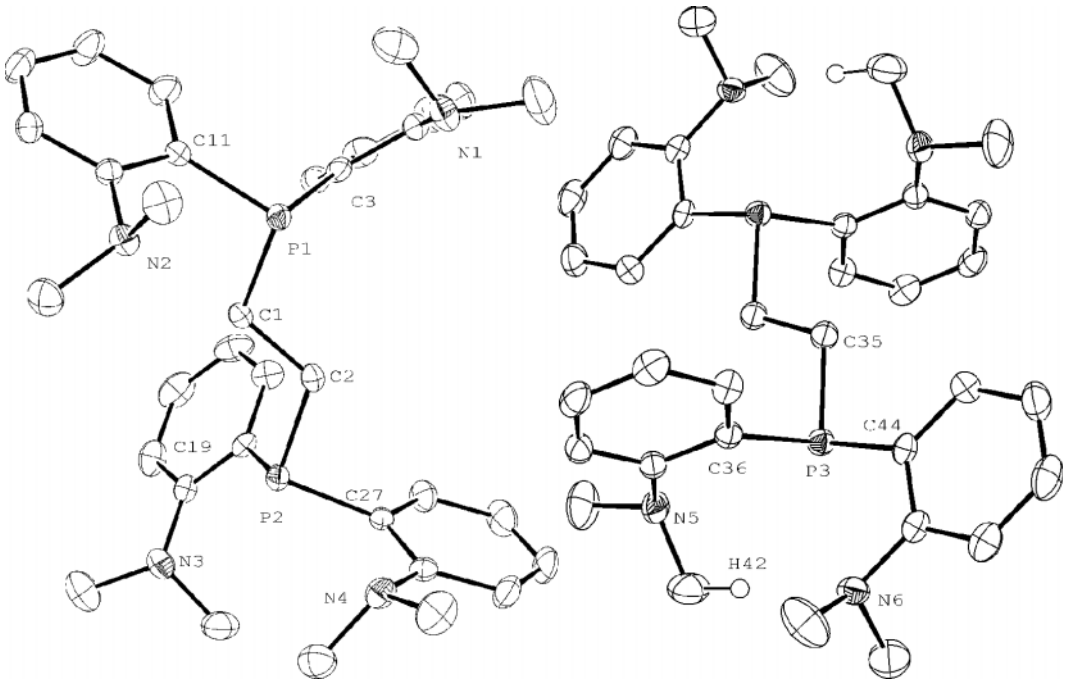

Table 4. Selected bond lengths (Å) and angles (°) for dpcp, dpypcp, and dmapcp with estimated standard deviations in parentheses.

	dppcp[a]	dpypcp[b]	dmapcp
Bond lengths (Å)			
P1—C1	1.866(2)	1.862(2)	1.882(3)
P1—C6	1.836(2)	1.850(2)	1.852(3)
P1—C14	1.833(2)	1.847(2)	1.837(3)
P2—C2	1.857(2)	1.863(2)	1.879(3)
P2—C22	1.833(2)	1.834(2)	1.831(3)
P2—C30	1.831(2)	1.854(2)	1.847(3)
C1—C2	1.546(2)	1.546(3)	1.537(3)
P1···P2	4.448(6)	4.457(7)	4.505(9)
Bond angles (°)			
Σ<P1, Σ<P2[c]	306.4(3), 304.6(3)	304.2(3), 303.8(3)	302.4(3), 299.1(3)
P1-C1-C2	109.2(1)	109.0(1)	108.5(1)
P2-C2-C1	109.8(1)	109.9(1)	111.3(1)
P-C-C-P	161.7	–164.3	168.2

[a]Data taken from ref. 22.
[b]Data taken from ref. 34.
[c]Sum of angles at P1 and P2.

between types sometimes involving loss of initially coordinated ancillary halides; (*ii*) *P*,*P*,*N*,*N*-coordination with the dmapm ligand that bridges metal–metal bonded systems of formally d^8 centres; and (*iii*) *P*,*P*,*N*,*N*- and *P*,*P*,*N*,*N*,*N*,*N*-coordination modes within Ru^{II}-d^6 octahedral systems. These findings will be reported in future publications.

Acknowledgments

We thank the Natural Sciences and Engineering Research Council of Canada (NSERC) for financial support, the Royal Society for a fellowship for M.B.S., and the Deutsche Forschungsgemeinschaft for a fellowship for U.L.

References

1. W.C. Davies and F.G. Mann. J. Chem. Soc. 276 (1944).
2. H.P. Fritz, I.R. Gordon, K.E. Schwarzhans, and L.M. Venanzi. J. Chem. Soc. 5210 (1965).
3. C.B. Pamplin, E.S.F. Ma, N. Safari, S.J. Rettig, and B.R. James. J. Am. Chem. Soc. **123**, 8596 (2001), and refs. therein.
4. D.C. Mudalige. Ph.D. Thesis, The University of British Columbia, Vancouver, B.C. 1994. Chap. 1.
5. K. Achiwa. Chem. Lett. 905 (1978).
6. N.D. Jones. Ph.D. Thesis, The University of British Columbia, Vancouver, B.C. 2001. Chap. 2.
7. G.L. Baker, S.J. Fritschel, J.R. Stille, and J. K. Stille. J. Org. Chem. **46**, 2954 (1981).

© 2002 NRC Canada

8. T. Malmström and C. Andersson. Chem. Commun. 1135 (1996).
9. R. ter Halle, B. Colasson, E. Schulz, M. Spagnol, and M. Lemaire. Terahedron Lett. **41**, 643 (2000).
10. U. Nagel and E. Kinzel. Chem. Ber. **119**, 1731 (1986).
11. I. Tóth and B.E. Hanson. Tetrahedron: Asymmetry, **1**, 913 (1990).
12. I. Tóth and B.E. Hanson. Tetrahedron: Asymmetry, **1**, 895 (1990).
13. I. Tóth, B.E. Hanson, and M.E. Davis. J. Organomet. Chem. **396**, 363 (1990).
14. I. Tóth, B.E. Hanson, and M.E. Davis. Catalysis Letters, **5**, 183 (1990).
15. I. Tóth, B.E. Hanson, and M. E Davis. J. Organomet. Chem. **109**, 397 (1990).
16. T. Lamouille, C. Saluzzo, R. ter Halle, F.L. Guyada, and M. Lemaire. Tetrahedron Lett. **42**, 663 (2001).
17 R.G. Nuzzo, D. Feitler, and G.M. Whitesides. J. Am. Chem. Soc. **101**, 3683 (1979).
18. A. Buhling, J.W. Elgersma, S. Nkrumah, P.C.J. Kamer, and P.W.N.M. van Leeuwen. J. Chem. Soc. 2143 (1996).
19 A. Buhling, P.C.J. Kamer, P.W.M.N. van Leeuwen, J.W. Elgersma, K. Goubitz, and J. Fraanje. Organometallics, **16**, 3027 (1997).
20. N.D. Jones, K.S. MacFarlane, M.B. Smith, R.P. Schutte, S.J. Rettig, and B.R. James. Inorg. Chem. **38**, 3956 (1999), and refs. therein.
21. N.D. Jones, U. Losehand, and B.R. James. To be published.
22. D.L. Allen, V.C. Gibson, M.L.H. Green, J.F. Skinner, J. Bashkin, and P.D. Grebenik. J. Chem. Soc. Chem. Commun. 895 (1983).
23. H. Gilman, and I. Banner. J. Am. Chem. Soc. **62**, 344 (1940).
24. Molecular Structure Corp. 1995. teXsan Crystal Structure Analysis Package [computer program]. Molecular Structure Corp., The Woodlands, Tex., U.S.A.
25. International tables for X-ray crystallography. Vol. IV. Kynoch Press, Birmingham, U.K. (present distributer Kluwer Academic, Boston, Mass.). 1974. pp 99–102.
26. International tables for X-ray crystallography. Vol. C. Kluwer Academic, Boston, Mass., U.S.A. 1992. pp 200–206.
27. A. Altomare, M.C. Burla, G. Cammali, M. Cascarano, C. Giacovazzo, A. Guagliardi, A.G.G. Moliterni, G. Polidori, and A. Spagna. 1999. SIR97: A new tool for crystal structure determination and refinement [computer program].
28. Beurskens, P.T. Admiraal, G., Beurskens, G., Bosman, W. P., de Gelder, R. Israel, and R. Smits, J.M.M. 1994. DIRDIF94: The DIRDIF-94 program system [computer program]. Technical report of the crystallography laboratory, University of Nijmegen, The Netherlands.
29. K. Kurter, D. Ribola, R.A. Jones, D.J. Cole Hamilton, and G. Wilkinson. J. Chem. Soc. Dalton Trans. 55 (1980).
30. I.R. Baird, M.B. Smith, and B.R. James. Inorg. Chim. Acta, **235**, 291 (1995).
31. S.J. Berners-Price, R.J. Bowen, P. Gallettis, P.C. Healy, and M.K. McKeage. Coord. Chem. Rev. **185–186**, 823 (1999).
32. H. Schmidbaur, G. Reber, A. Schier, F.E. Wagner, and G. Müller. Inorg. Chim. Acta,. **147**, 143 (1988).
33. G. Pelizzi and G. Pelizzi. Acta Crystallogr. Sect. B, **35**, 1785 (1979).
34. M.D. Le Page. Ph.D. Thesis, The University of British Columbia, Vancouver, B.C. 2000.
35. R. Taylor and O. Kennard. J. Am. Chem. Soc. **104**, 5063 (1982).

© 2002 NRC Canada

2,6-Diisopropylphenylphosphane: A new, bulky primary phosphane and its mono- and disilylated $Si(CH_3)_3$ and $Si(CH_3)_2$-*t*-Bu derivatives — A synthetic, crystallographic, and dynamic NMR investigation[1]

René T. Boeré and Jason D. Masuda

Abstract: The bulky primary phosphane 2,6-diisopropylphenylphosphane, $DipPH_2$, has been prepared from 1-bromo-2,6-diisopropylbenzene via the reaction of the Grignard reagent with PCl_3. The resulting mixed phosphonous dihalides $DipP(Cl,Br)_2$ are reduced with $LiAlH_4$ to yield the title compound in reasonable yield and on a synthetically useful scale. $DipPH_2$ is also used to prepare the monosilylated derivatives $DipPHSi(CH_3)_3$ and $DipPH\{Si(CH_3)_2$-*t*-Bu$\}$ as well as the disilylated compounds $DipP\{Si(CH_3)_3\}_2$ and $DipP\{Si(CH_3)_2$-*t*-Bu$\}_2$. All products have been fully characterized by IR, mass, and NMR spectroscopy. The crystal structure of $DipPH\{Si(CH_3)_2$-*t*-Bu$\}$ was determined from single-crystal diffraction data: $C_{18}H_{33}PSi$, $P2_1/c$, $Z = 4$, $a = 8.5768(10)$, $b = 28.104(3)$, $c = 8.1102(4)$ Å, $\beta = 93.341(3)°$ ($R = 0.0518$). Changes in the NMR spectrum of $DipPH\{Si(CH_3)_2$-*t*-Bu$\}$ were observed over the temperature range 178–380 K. Barrier heights were determined from the peak separation at low temperature and the coalescence points: $\Delta G^{\ddagger} \approx 40$ kJ mol^{-1} for C(aryl)—P bond rotation and ≈ 72 kJ mol^{-1} for pyramidal inversion at phosphorus.

Key words: crystal structure, 2,6-diisopropylphenyl, bulky substituents, steric congestion, dynamic NMR, primary phosphane, silyl phosphane.

Résumé : On a préparé le phosphane primaire encombré 2,6-diisopropylphénylphosphane, $DipPH_2$, à partir du 1-bromo-2,6-diisopropylbenzène, par le biais d'une réaction de Grignard avec le PCl_3. On a réduit les dihalogénures phosphoneux mixtes qui en résultent, $DipP(Cl,Br)_2$, à l'aide de $LiAlH_4$ pour obtenir le composé mentionné dans le titre avec un rendement raisonnable et à une échelle utile d'un point de vue synthétique. On a aussi utilisé le $DipPH_2$ pour préparer les dérivés monosilylés $DipPHSi(CH_3)_3$ et $DipPH\{Si(CH_3)_2$-*t*-Bu$\}$ ainsi que les produits disilylés $DipP\{Si(CH_3)_3\}_2$ et $DipP\{Si(CH_3)_2$-*t*-Bu$\}_2$. On a caractérisé tous les produits par spectroscopie IR, de masse et RMN. On a déterminé la structure cristalline du $DipPH\{Si(CH_3)_2$-*t*-Bu$\}$ par diffraction des rayons X par un cristal unique; les données pour $C_{18}H_{33}PSi$, $P2_1/c$, $Z = 4$, $a = 8{,}5768(10)$, $b = 28{,}104(3)$ et $c = 8{,}1102(4)$ Å, $\beta = 93{,}341(3)°$ ($R = 0{,}0518$). En faisant varier la température de 178 à 310 K, on a observer des changements dans le spectre RMN du $DipPH\{Si(CH_3)_2$-*t*-Bu$\}$. Les hauteurs de barrières ont été déterminées sur la base de la séparation des pics à basse température et des points de coalescence: $\Delta G^{\ddagger} \approx 40$ kJ mol^{-1} pour la rotation autour de la liaison C(aryle)—P et ≈ 72 kJ mol^{-1} pour l'inversion pyramidale au niveau du phosphore.

Mots clés : structure cristalline, 2,6-diisopropylphényle, substituants volumineux, congestion stérique, RMN dynamique, phosphane primaire, phosphane silylé.

[Traduit par la Rédaction]

Introduction

The chemistry of primary phosphanes has received much attention in recent years, and their utility in both main group chemistry (1–8) and coordination chemistry (9–18) is under active investigation. Aryl phosphanes bearing bulky substituents in the *ortho* positions have been particularly popular, as they have considerably greater stability and more

Received 14 February 2002. Published on the NRC Research Press Web site at http://canjchem.nrc.ca on 29 November 2002.

This work is dedicated to Professor Tristram Chivers in grateful acknowledgment for his constant support and sound collegial advice. Tris has served his Department, University, and Canadian chemistry impeccably and enthusiastically. His efforts have helped put main group chemistry in the forefront of Canadian science.

R.T. Boeré[2] and J.D. Masuda. Department of Chemistry and Biochemistry, University of Lethbridge, Lethbridge, AB T1K 3M4, Canada.

[1]Presented in part at the 84th Canadian Chemical Conference and Exhibition, Montreal, QC, 26–30 May 2001.
[2]Corresponding author (e-mail: boere@uleth.ca).

 DOI: 10.1139/V02-150 © 2002 NRC Canada

Scheme 1.

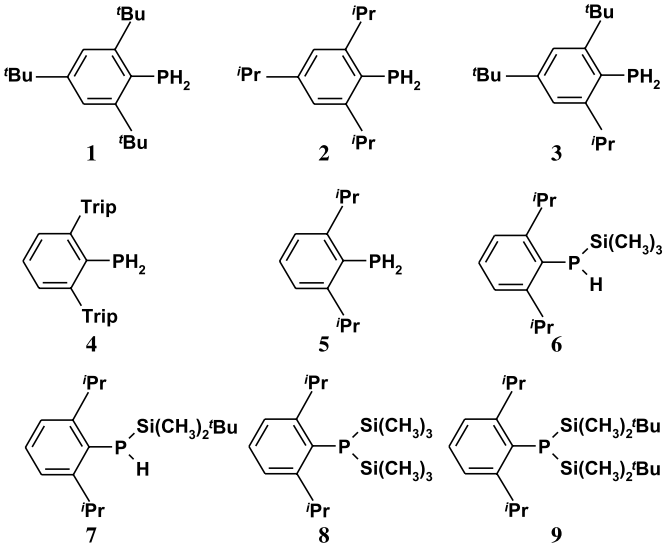

controlled reactions (3, 4, 17). The risk associated with the high toxicity of primary phosphanes such as $PhPH_2$ is also mitigated by the bulky substituents, if by nothing more than lowering the volatility of the compounds. The most commonly used bulky primary phosphane (Scheme 1) has undoubtedly been 2,4,6-tri-*tert*-butylphosphane, Mes*PH_2 (**1**) (19). The closely related 2,4,6-triisopropylphenylphosphane, TripPH_2 (**2**) is known, and its chemistry has received some attention (20). A laborious, multi-step, small-scale synthesis of 2,4-di-*tert*-butyl-6-isopropylphenylphosphane, DtbiPH_2 (**3**) has recently been reported (3). The terphenyl compound 2,6-(2,4,6-triisopropylphenyl)-phenylphosphane, TterphPH_2 (**4**) has been prepared and its crystal structure determined (4).

We have been exploiting for some time the 2,6-diisopropylphenyl (Dip) group as a bulky substituent on nitrogen, in particular for the preparation of *N*,*N′*-disubstituted amidines (21, 22) and *N*,*N′*,*N″*-trisubstituted guanidines (23). We are currently in the process of preparing directly analogous phosphorus-containing compounds via primary phosphanes (24) and we were therefore surprised to find that DipPH_2 (**5**) has not been reported heretofore in the literature and indeed there are no reports of the Dip group attached to phosphorus in any compound. At the cost of being slightly less sterically shielding, the use of *ortho* diisopropyl groups imparts to bulky substituents the advantage over *tert*-butyl of providing a wealth of stereochemical information from the ^{1}H NMR signals of the diastereotopic isopropyl groups. The 2,4,6-triisopropylphenyl (Trip) substituent has such groups, but has the disadvantage that the sterically unnecessary *para* isopropyl substituent tends to obscure the often complex and always interesting ^{1}H NMR signals of the sterically essential *ortho* isopropyl substituents. For example, in **2** the chemical shifts of the *ortho* and *para* *i*-Pr CH_3 groups are 1.23 and 1.24 ppm (20). In our experience, the *meta* and the *para* hydrogen atoms on the aromatic backbone of Dip groups tend to be well resolved and can be useful spectroscopic probes in a region of the spectrum removed from the crowded aliphatic regions. There is considerable merit in the use of the Dip substituent, and in this paper we report a practical large-scale synthesis of **5**.

Scheme 2.

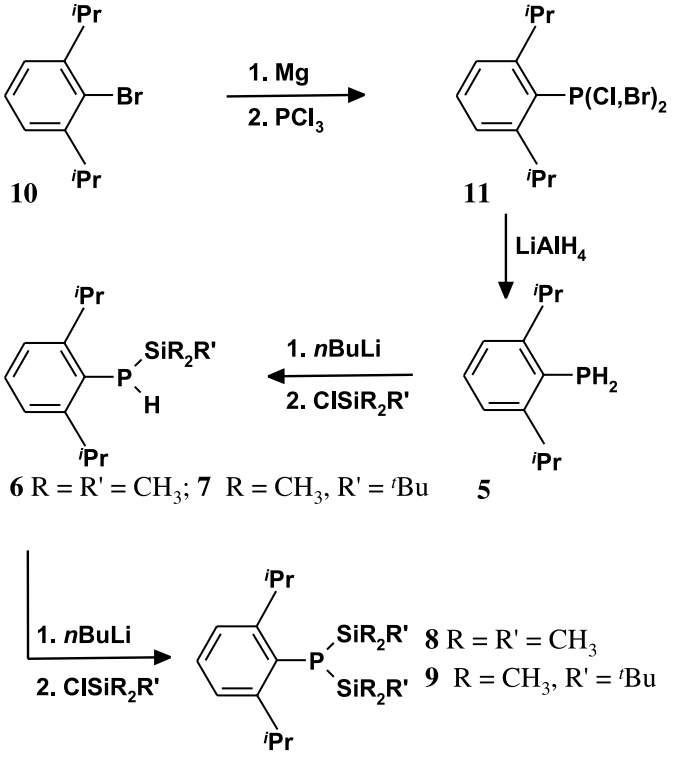

Many applications of primary phosphanes either require, or are enhanced by, replacement of one or both hydrides with silyl groups (6, 25–27). We have therefore prepared the silyl compounds Dip$PHSi(CH_3)_3$ (**6**), Dip$PH\{Si(CH_3)_2$-*t*-Bu$\}$ (**7**), Dip$P\{Si(CH_3)_3\}_2$ (**8**), and Dip$P\{Si(CH_3)_2$-*t*-Bu$\}_2$ (**9**). Although the $Si(CH_3)_3$ compounds could be prepared quite easily in sufficient purity to be of synthetic utility, it was difficult to obtain analytically pure samples of these low-melting compounds. The $Si(CH_3)_2$-*t*-Bu derivatives, on the other hand, are easily purified, crystalline solids and have been fully characterized. The strong asymmetry induced by the bulky substituent in **7** induces a dynamic process observable by NMR spectroscopy, and the results of investigations in $C_6D_5CD_3$ are reported over the temperature range 178–380 K. These solution state changes are correlated to the structure found in the solid state by a single-crystal X-ray diffraction study.

Results and discussion

Synthesis and characterization

Our synthetic route (Scheme 2) starts from DipBr (**10**) for which a large-scale synthesis has been worked out starting from the commercially available aniline (28). The Grignard reagent prepared from **10** is added to a cold solution of PCl_3 in THF. This reaction leads consistently to mixtures of all three possible halides, which co-distil as identified by their ^{31}P chemical shifts (Table 1), i.e., DipPCl_2 (**11a**), DipPClBr (**11b**), and DipPBr_2 (**11c**). Typical product distributions of the three are 1.6:2.4:1.0, which by mass balance means that virtually all of the bromide contained in the Grignard reagent ends up on phosphorus, remarkable testimony to the higher nucleophilicity of bromide versus chloride. Mixed

© 2002 NRC Canada

Table 1. ^{31}P NMR data for phosphonous dihalides, phosphanes, and silylated phosphanes[a].

No.	Compound	δ (^{31}P)	$^{1}J_{PH}$, Hz	Conditions	Reference
11a	$DipPCl_2$	+164.5	—	$CDCl_3$, RT	This work
11b	DipPClBr	+159.2	—	$CDCl_3$, RT	This work
11c	$DipPBr_2$	+151.9	—	$CDCl_3$, RT	This work
12	$DtbiPCl_2$	+164.5	—	$CDCl_3$, RT	(3)
13	$Mes*PCl_2$	+153.8	—	$CDCl_3$, RT	(3)
14	CH_3PCl_2	+191[b]	—	Not specified	(29)
15	CH_3PClBr	+190[b]	—	Not specified	(29)
16	CH_3PBr_2	+184[b]	—	Not specified	(29)
17	$PhPH_2$	–122[b]	207	Not specified	(29)
1	$Mes*PH_2$	–128.9	211	$CDCl_3$, RT	(30)
4	$TterphPH_2$	–139.8	208	$CDCl_3$, RT	(4)
3	$DtbiPH_2$	–143.9	207	$CDCl_3$, RT	(3)
18	$MesPH_2$	–153.0	204	Not specified	(17)
5	$DipPH_2$	–156.4	208	$CDCl_3$, RT	This work
2	$TripPH_2$	–158.2	203	$CDCl_3$, RT	(20)
19	$Mes*PHSi(CH_3)_3$	–130.1	212	THF	(30)
20	$Mes*PH\{Si(CH_3)_2$-*t*-Bu$\}$	–136.2	210	$CDCl_3$, RT	(30)
6	$DipPHSi(CH_3)_3$	–163.8	211	$CDCl_3$, RT	This work
21	$TripPHSiPh_3$	–169	211	C_6D_6, RT	(27)
7	$DipPH\{Si(CH_3)_2$-*t*-Bu$\}$	–175.6	212	$CDCl_3$, RT	This work
22	$PhP\{Si(CH_3)_3\}_2$	–132.8	—	Not specified	(31)
23	$Mes*P\{Si(CH_3)_3\}_2$	–142.7	—	C_6D_6, RT	(26)
8	$DipP\{Si(CH_3)_3\}_2$	–167.1	—	$CDCl_3$, RT	This work
24	$TripP\{Si(CH_3)_3\}_2$	–169.3	—	$CDCl_3$, RT	(20)
9	$DipP\{Si(CH_3)_2$-*t*-Bu$\}_2$	–193.3	—	$CDCl_3$, RT	This work

[a]Referenced to external 85% H_3PO_4; positive chemical shifts to low field (IUPAC recommendation).
[b]Sign of chemical shift adjusted to the IUPAC convention.

phosphorus halides have been observed previously, for example, in the Grignard preparation of $Mes_2P(Cl,Br)$, where Mes = 2,4,6-trimethylphenyl (32). Reduction of mixtures of **11a–c** with $LiAlH_4$ in THF yielded the phosphane **5**, as a clear, colourless liquid. It has very little odour and is quite easy to handle if stored below room temperature and under nitrogen.

Compound **5** has been fully characterized by ^{1}H, ^{31}P, and ^{13}C NMR spectroscopy, as well as by mass spectrometry and IR spectroscopy. The P–H stretch (recorded as a liquid smear) has a frequency of 2306 cm^{-1}, comparable to 2302 cm^{-1} in CH_2Cl_2 solution reported for $MesPH_2$ (**18**) (17). The ^{31}P NMR spectrum displays the expected 1:2:1 triplet with $^{1}J_{PH}$ = 208 Hz at δ –156.4. As the ^{31}P NMR spectral data for primary phosphanes with bulky substituents and their silyl derivatives are extremely scattered in the literature, we have collected values for as many derivatives as we could locate and compiled them in Table 1. A survey of these data shows that bulky primary phosphanes differ quite widely in ^{31}P chemical shift but that the $^{1}J_{PH}$ values are remarkably consistent and hence diagnostic. The ^{1}H NMR spectrum measured in $CDCl_3$ (Table 2) contains the typical aromatic and aliphatic signals of the Dip group, with the additional aspect that the isopropyl methine septet appears to be split further into doublets with 3.0 Hz coupling to phosphorus. Whether this is four-bond dipolar or through space coupling is yet to be determined. The expected doublet for the PH signal is observed. In addition, almost all the ^{13}C signals are doublets owing to coupling to the single phosphorus nucleus.

After repeated handling of a container of **5**, a new signal was detected in the ^{31}P NMR spectrum at δ –14.6, consisting of a 1:2:1 triplet with $^{1}J_{PH}$ = 477 Hz. We attribute this signal to the phosphane oxide, $DipP(O)H_2$, formed by aerobic oxidation of the phosphane, and base our assignment on the close correspondence of its NMR parameters to those of $Mes*P(O)H_2$: triplet, $^{1}J_{PH}$ = 490.7 Hz at δ –10.0 (33). Saturation of the NMR sample with dry O_2 caused the intensity of this signal to increase, consistent with our hypothesis. We have not attempted to isolate bulk phosphane oxide.

The general procedure for the preparation of the silylated compounds (Scheme 2) was to cleave P—H bonds with *n*-BuLi, then quench the resulting phosphide anions with $R_2R'SiCl$. However, either these reactions do not go to completion, or the base also cleaves P—Si bonds, so that the cleaving and quenching sequences had to be repeated more than once per step. The success of this procedure was greatly assisted by the use of ^{31}P NMR spectroscopy. Aliquots taken directly from the reaction mixture were used to assess the progress of each reaction, and in this way, we were able to prepare phosphanes **6–9** in acceptable yields. Use of the larger *t*-$BuMe_2Si$ group yielded analytically pure samples of **7** and **9**, whereas **6** and **8** always contained some minor impurities. The monosilylated phosphane **7** was

© 2002 NRC Canada

Table 2. Solution NMR data for **5**–**7** and related compounds[a].

Nuclei	Feature	**5**	**6**	**7**[b]	**8**	**9**[c]	**27**[d]	**21**[e]
$CH_3^{(A,D)}$	δ (^{1}H)	1.25	1.21	1.21	1.18	1.21	1.2	0.98
	$^3J_{HH}$ (Hz)	6.7	6.7	6.9	6.9	6.7	6.8	[f]
$CH_3^{(B,C)}$	δ (^{1}H)	= (A,D)	1.26	1.26	= (A,D)	= (A,D)	= (A,D)	1.09
	$^3J_{HH}$ (Hz)		6.7	6.7				[f]
$CH^{(1,2)}$	δ (^{1}H)	3.36	3.41	3.43	4.06	4.29	3.8	3.52
	$^3J_{HH}$ (Hz)	6.8	6.7	6.8	6.6	6.7	6.8	[f]
	$^4J_{PH}$ (Hz)	3.0	3.8	4.0			4.8	[f]
PH	δ (^{1}H)	3.84	3.46	3.51			5.6 [g]	4.44
	$^1J_{PH}$ (Hz)	207.2	210.7	211.0			216.6 [g]	211
$SiCH_3^{(E)}$	δ (^{1}H)		0.18	0.06	0.22	0.18		
	$^3J_{PH}$ (Hz)		4.3	5.3	6.1	4.3		
$SiCH_3^{(F)}$	δ (^{1}H)		= (E)	0.02	= (E)	= (E)		
	$^3J_{PH}$ (Hz)			0.9				
Si-*t*-Bu	δ (^{1}H)			1.01		0.91		
	$^3J_{PH}$ (Hz)			2.4		0.8		
H–C_4	δ (^{1}H)	7.35–7.25	7.35–7.19	7.26–7.17	7.35–7.23	7.28–7.21		
H–C_3	δ (^{1}H)	7.22–7.10	7.17–7.08	7.12–7.08	7.20–7.07	7.12–7.08		
$CH_3^{(A,D)}$	δ (^{13}C)	23.84	23.97	24.00	25.32	25.67	24.9	[f]
$CH_3^{(B,C)}$	δ (^{13}C)		24.18	24.16				[f]
$CH^{(1,2)}$	δ (^{13}C)	33.15	33.50	33.53	33.98	33.96	32.7	[f]
	$^3J_{PC}$ (Hz)	11.7	13.7	13.7	16.1	16.1	14.4	[f]
$SiCH_3^{(E)}$	δ (^{13}C)		0.67	–4.20	2.55	–1.54		
	$^2J_{CH}$ (Hz)		10.3	15.6	17.0	7.8		
$SiCH_3^{(F)}$	δ (^{13}C)			–2.93		= (C)		
C_{ipso}	δ (^{13}C)	126.04	129.21	129.04	128.29	130.44	130.4	[f]
	$^1J_{PC}$ (Hz)	13.7	20.5	21.5	14.2	9.3	15.7	[f]
C_{ortho}	δ (^{13}C)	152.08	152.03	152.47	156.44	156.57	153.0	[f]
	$^2J_{PC}$ (Hz)	9.8	9.3	9.3	10.7	11.2	11.1	[f]
C_{meta}	δ (^{13}C)	122.91	122.94	122.97	123.43	128.92	121.6	[f]
	$^3J_{PC}$ (Hz)	2.4	3.4	3.4	5.4	5.4	3.4	[f]
C_{para}	δ (^{13}C)	128.53	127.44	127.52	128.55	128.59	149.7	[f]
	$^4J_{PC}$ (Hz)				2.0	1.95		[f]
P	δ (^{31}P)	–156.4	–163.8	–175.6	–167.1	–192.9	–113.2	–169
	$^1J_{HP}$ (Hz)	207.5	210.6	212.1			214.1	211

[a]Measured in $CDCl_3$ at room temperature unless otherwise noted; label scheme:

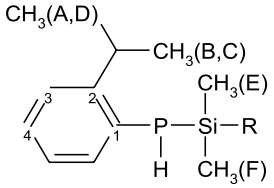

[b]*t*-Bu signals: ^{1}H NMR: 1.01 (d, $^4J_{PH}$ = 2.4 Hz, 9H). ^{13}C NMR: 27.02 (d, $^4J_{P,C}$ = 2.9 Hz, C(CH_3)$_3$), 18.70 (d, $^2J_{PC}$ = 9.8 Hz, C(CH$_3$)$_3$).
[c]*t*-Bu signals: ^{1}H NMR: 25.67 (s, C(CH_3)$_3$). ^{13}C NMR: 27.79 (d, $^4J_{PC}$ = 3.9 Hz, C(CH_3)$_3$), 20.18 (d, $^2J_{PC}$ = 20.5 Hz, C(CH$_3$)$_3$).
[d]Reference (35), measured in C_6D_6 solution at room temperature.
[e]Reference (27), measured in C_6D_6 solution at room temperature.
[f]No data provided for this parameter.
[g]Data taken from the closely related TripPHPh, **25**.

sufficiently stable to allow the investigation of its dynamic behaviour in solution by VT NMR, and this compound yielded crystals suitable for an X-ray diffraction study.

The P–H stretch of **7** (recorded as a KBr pellet) has a frequency of 2330 cm^{-1}, thus considerably higher in energy than the 2301 cm^{-1} value for **5**. ^{1}H, ^{13}C, and ^{31}P data are compiled in Tables 1 and 2. We again note the large variation in phosphorus chemical shift and the consistency of the $^1J_{PH}$ values, which are found between 203 and 212 Hz for all the trivalent P–H compounds listed in Table 1.

Structure of 7 in the solid state

The crystal structure of DipPH{Si(CH$_3$)$_2$-*t*-Bu} (**7**) was determined by X-ray diffraction at –80°C. Crystal data and structure solutions for **7** are given in Table 3, and its selected inter-atomic distances and angles in Table 4. The compound

© 2002 NRC Canada

Table 3. Crystal data for **7**.

Formula	$C_{18}H_{33}PSi$
Molecular weight	308.50
Colour, habit	Colourless, block
Dimensions (mm)	0.14 × 0.19 × 0.20
Crystal system	Monoclinic
Space Group	$P2_1/c$
a (Å)	8.5768(10)
b (Å)	28.104(3)
c (Å)	8.1102(4)
β (°)	93.341(3)
V (Å^3)	1951.6(4)
Z	4
$D_{calcd.}$ (g cm^{-3})	1.050
T (K)	193(2)
Absorption coefficient (μ) (mm^{-1})	0.194
Radiation	Mo Kα (λ=0.71073)
Crystal growth method	Sublimation
Data collection	Bruker CCD area detector; Φ and Ω scans
θ range for data collection (°)	2.38–26.41
Collection ranges	$-10 \le h \le 10$; $-29 \le k \le 35$; $-8 \le l \le 10$
Reflections collect	11 570
Independent reflections	4009 (R_{int} = 0.0618)
Absorption correction	None
Refinement	Refinement on F^2 (all data); H atoms constrained, except H(1)
Number of parameters refined	194
Final R indices [$F^2>2\sigma(F^2)$]	R_1 = 0.0518, wR_2 = 0.1114
R indices (all data)	R_1 = 0.0918, wR_2 = 0.1308
Largest diff. peak and hole (e Å^{-3})	0.338 and –0.196

Table 4. Selected bond lengths (Å) and angles (°) for **7**.

Bond lengths (Å)			
P(1)—C(1)	1.854(2)	P(1)—Si(1)	2.2681(9)
P(1)—H(1)	1.31(4)	Si(1)—C(13)	1.861(3)
Si(1)—C(14)	1.864(3)	Si(1)—C(15)	1.894(3)
C(1)—C(2)	1.415(3)	C(1)—C(9)	1.410(3)
C(2)—C(6)	1.396(3)	C(6)—C(7)	1.375(4)
C(7)—C(8)	1.374(3)	C(8)-—C(9)	1.396(3)
C(2)—C(3)	1.521(3)	C(9)—C(10)	1.521(3)
C(3)—C(4)	1.523(4)	C(3)—C(5)	1.524(3)
C(10)—C(11)	1.5331(4)	C(10)—C(12)	1.527(4)
Bond angles (°)			
C(1)-P(1)-Si(1)	104.03(7)	C(1)-P(1)-H(1)	105(2)
Si(1)-P(1)-H(1)	93(2)	C(2)-C(1)-P(1)	118.49(17)
C(1)-C(2)-C(3)	123.4(2)	C(9)-C(1)-P(1)	121.30(18)
C(2)-C(3)-C(5)	112.6(2)	C(2)-C(3)-C(4)	111.54(2)
C(9)-C(10)-C(11)	113.3(2)	C(1)-C(9)-C(10)	123.1(2)
P(1)-Si(1)-C(13)	111.97(9)	C(9)-C(10)-C(12)	110.98(2)
P(1)-Si(1)-C(15)	106.42(8)	P(1)-Si(1)-C(14)	111.20(9)

Fig. 1. An ORTEP diagram (25% probability) of the structure of **7** as found in the solid state by single-crystal X-ray crystallography. The atom numbering scheme is indicated. Hydrogen atoms are indicated by spheres of minimum radii for the sake of clarity.

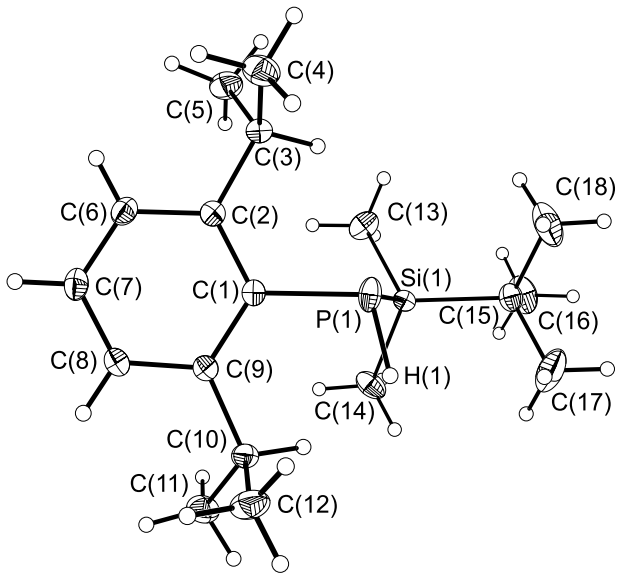

crystallizes as discrete molecules. The shortest intermolecular contacts are between H12C and H16A (2.357 Å) and H4B and H16C (2.385 Å), fractionally less than the sum of the van der Waals' radii of two H atoms. A drawing of the molecular structure and the atom-numbering scheme is presented in Fig. 1. The essential co-planarity of C(7), C(1), P(1), Si(1), C(15), and C(16) is noticeable. The RMS deviation of these atoms from a least-squares plane is 0.05 Å, with Si(1) deviating most. This molecular plane is almost exactly orthogonal to that of the aryl ring (86.38(7)° dihedral angle), with the result that the $Si(CH_3)_2$-*t*-Bu group is

© 2002 NRC Canada

Fig. 2. Calculated geometries with full optimization at the B3LYP/6–31G(*d*) level of theory for: (*a*) **5**; (*b*) **6**; (*c*) **7**; (*d*) **8**; (*e*) **9**. In each representation, the atom labelled $C_{(2)}$ is the aryl ring carbon located above the carbon $C_{(1)}$ *ipso* to phosphorus, while $C_{(9)}$ is on the lower side. See footnote (*a*) of Table 5.

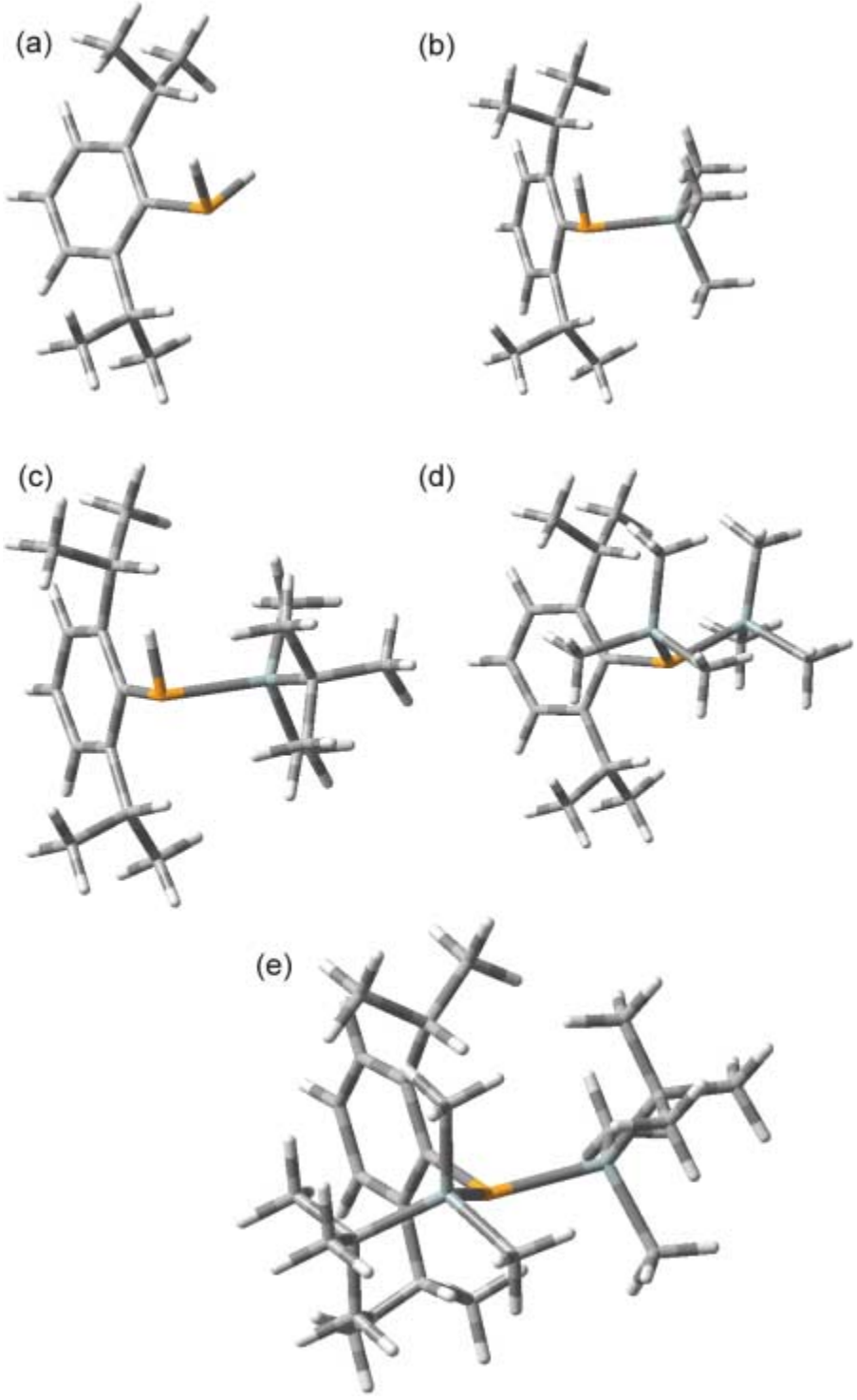

located entirely to one side of the aryl ring. Along the *t*-Bu–Si–P–aryl vector, the structure has adopted a staggered conformation about each bond. The two *ortho* isopropyl groups are oriented in the "Vee-back" conformation that we have observed in all solid-state structures determined for Dip groups (21–23, 34). However, these groups are significantly tilted such that C(5) and C(11) avoid contact with the $Si(CH_3)_2$-*t*-Bu group. In the $N\{Si(CH_3)_3\}_2$ substituted Dip group found in the structure of $Cl_3SeC_6H_2$-*i*-$Pr_2N\{Si(CH_3)_3\}_2$, where the symmetrical disilylamino group is co-planar with the aryl ring, such a tilt is not observed (34). Another noticeable feature of the structure is the large

© 2002 NRC Canada

Table 5. Calculated geometry at B3LYP/6–31G(d) level with full optimization of **5–9**.[a]

	5	**6**	**7**	**8**[b]	**9**
Distance (Å)					
$C_{(1)}$—P	1.871	1.874	1.874	1.881	1.881
$H_{(1)}$,$Si_{(1)}$—P	1.424	1.424	1.416	2.276	2.276
$H_{(2)}$,$Si_{(2)}$—P	1.425	2.298	2.307	2.276	2.296
Angle (°)					
$C_{(1)}$-P-$H_{(1)}$,$Si_{(1)}$	98.9	99.9	99.8	111.2	117.3
$C_{(1)}$-P-$H_{(2)}$,$Si_{(2)}$	99.0	105.1	103.9	111.3	111.2
$H_{(1)}$,$Si_{(1)}$-P-$H_{(2)}$,$Si_{(2)}$	93.3	95.3	96.3	113.7	117.6
$\sum$(<P)	291.7	300.3	300.3	336.2	346.1
$C_{(2)}$-$C_{(1)}$-P	122.8	124.1	124.1	125.3	125.5
$C_{(9)}$-$C_{(1)}$-P	117.4	116.3	116.3	115.9	115.9

[a]Full geometry optimization and stationary point verification, unless otherwise indicated. Label scheme:

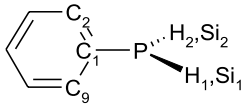

[b]Frequency calculation to verify stationary point fails.

deviations of the phosphorus (0.318(4) Å) and the *ipso* carbon C(1) (0.038(3) Å) atoms from the mean aryl plane defined by the remaining five carbon atoms. Such a deviation for the phosphorus atom has been observed previously in other "secondary" and "tertiary" phosphane structures with bulky *ortho* groups: in **23**, 0.85 Å (25), in Mes*P{OCH_2}$_2$, 0.82 Å (25), and in TripPHPh (**25**), 0.48 Å (35). However, both the structures with *ortho* isopropyl groups have the P atom displaced on the side opposite to that of the "R" substituent, while the Mes*PR_2 structures have the phosphorus pushed out on the same side of the ring as the "axial" substituent.

The sum of angles around phosphorus is only 301.5(26)°, indicative of a highly pyramidal structure at phosphorus. This is commonly observed for secondary phosphanes with bulky Trip or Mes* substituents (**25**, 304° (35); Mes*$PHSiPh_3$ (**26**), 303.9° (27)), values that are statistically indistinguishable from our results.

Calculated (gas phase) structures of 5–9

The structures of **5–9** have been calculated at the B3LYP/6–31G(d) level. Illustrations of the calculated structures are provided in Fig. 2, and some of the core geometric parameters are presented in Table 5. We started our analysis by comparing the calculated structure of **7** with that determined from the crystal structure. There is a remarkable agreement between the two, right down to the conformations adopted by the aryl isopropyl and the triorganosilyl groups. These results serve to confirm that the structure obtained in the solid state is relatively unaffected by intermolecular forces. The calculated bond lengths are 1–2% longer than the measured values, typical for the DFT methodology that we employed. However, the calculated sum of angles at phosphorus was within experimental error of the measured value.

The structures of the symmetrically substituted phosphanes **5**, **8**, and **9** are quite similar, having one substituent at each side of the aryl ring. This is unlike the results from crystallography for Mes*PX_2 derivatives, such as Mes*P{OCH_2}$_2$ or **23** (25), where both substituents are found on the same side of a (distorted) aryl ring. The pyramidal geometry at phosphorus causes a slight distortion of the bond angles, such that the angle $C_{(2)}$–$C_{(1)}$–P (the upper side for each picture in Fig. 2) is in each case somewhat larger than the angle $C_{(9)}$–$C_{(1)}$–P. The unsymmetrically substituted **6** and **7** have significantly twisted isopropyl substituents to minimize steric interactions, whereas the symmetrically substituted compounds have the isopropyl groups symmetrically disposed to the aryl rings and in the "Vee-back" conformation.

Finally, we note the great similarity in the sum of angles at phosphorus calculated for **5–7**, and the agreement of calculated and measured values for **7** (within experimental error). In contrast, when two silyl groups are attached as in **8** and **9**, the sum of angles is greatly increased (by 36–46°). We note that the calculated values of 336.2 and 346.1° are significantly greater than the average measured for Mes_3P (329.0°) from two independent molecules in the unit cell of a single crystal X-ray structure (36). However, these values are comparable to that obtained in a crystal structure for **23**, 343.2° (25)

Solution structures by NMR

The pertinent NMR data for all five phosphanes as determined in $CDCl_3$ solution have been compiled in Table 2. Data from two previously reported compounds, $TripPHCH_3$ (**27**) (35) and $TripPHSiPh_3$ (**21**) (27) have also been included to substantiate the assignment and interpretation of our results. The former is of course a secondary phosphane and hence has a ^{31}P chemical shift that is not comparable to that of ours. However, there is remarkable agreement between the NMR data for **27** and the more symmetrical of our phosphanes $DipPR_2$ (R = H, Si{CH_3}$_3$, and Si{CH_3}$_2$-*t*-Bu). This applies to the ^1H and ^{13}C parameters of the *ortho* isopropyl groups and the ^{13}C parameters of the aromatic rings, for which all the carbon nuclei except the *para* atom C_4 are doublets from coupling to phosphorus. We have also found that the silyl methyl and even the methyl hydrogen atoms of the *t*-Bu groups in **6–9** show evidence of coupling to the phosphorus nucleus.

The unsymmetrically substituted phosphanes **6** and **7** have room temperature (RT) ^1H NMR spectra in which there are two isopropyl methyl environments, but only a single CH environment. Similar effects are reported in the literature for the *ortho* isopropyl groups of **21** (27). Additionally, **7** also displays two distinct silyl methyl resonances, which have different degrees of coupling to ^{31}P, i.e., 5.3 and ~1 Hz.

VT NMR study

A variable temperature NMR study of **7** was conducted in $C_6D_5CD_3$ solution. Compound **7** is superior to **6** for this purpose, not only in being a pure crystalline material but also in possessing a pair of diastereotopic methyl groups on silicon which are direct probes for the chirality induced by the asymmetric phosphorus atom in the absence of fast pyramidal inversion. The basic spectral features of the dynamic NMR sample, which was made up in $C_6D_5CD_3$, are very similar to the RT spectrum in deuterochloroform as reported

© 2002 NRC Canada

Scheme 3.

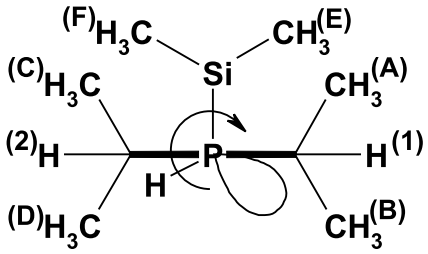

in Table 2. In Scheme 3, the molecule is viewed end-on to highlight the symmetry relationships relevant to solution dynamics (the *t*-Bu group is located in front of the Si atom, and is omitted for clarity). Figure 3 presents several traces selected from the series of spectra that illustrate the key spectral changes; full VT data have been deposited.[3]

At 380 K, the dynamic processes are in the high temperature limit. Here there is only one kind of isopropyl ($CH^{(1,2)}$ equivalent), one isopropyl methyl ($CH_3^{(A–D)}$ equivalent), and one silyl methyl group ($CH_3^{(E,F)}$ equivalent). This is achieved by a combination of rapid rotation about single bonds and rapid inversion at phosphorus. We note that the $CH_3^{(E,F)}$ signal is a phosphorus-coupled doublet with a coupling constant of ~3 Hz.

On cooling, coalescence of the $CH_3^{(A,B,C,D)}$ as well as the $CH_3^{(E,F)}$ signals occurs, and the coalesced signals become sharp at lower temperature, e.g., as in the 263 K spectrum. Here $CH_3^{(F)}$ appears as a singlet (the splitting of ~1 Hz observed in $CDCl_3$ is not resolved in the more viscous $C_6D_5CD_3$), while $CH_3^{(E)}$ is a doublet with coupling to phosphorus of ~5 Hz. The isopropyl methyl signals break into two distinct sets, labelled $CH_3^{(A,D)}$ and $CH_3^{(B,C)}$, while the $CH^{(1,2)}$ signals remain identical, as in the 380 K spectrum. These changes are consistent with slowed pyramidal inversion at the chiral phosphorus atom. Thus $CH_3^{(E)}$ and $CH_3^{(F)}$ as well as the $CH_3^{(A,D)}$ and $CH_3^{(B,C)}$ pairs become diastereotopic with respect to the chiral phosphorus atom.

Rapid rotation about single bonds has the effect of mapping $CH^{(1)}$ on $CH^{(2)}$, $CH_3^{(A)}$ on $CH_3^{(D)}$, and $CH_3^{(B)}$ on $CH_3^{(C)}$ (Scheme 3), averaging their chemical shifts in the intermediate temperature regime. Below 263 K, this rotational averaging slows down, with coalescence of the methine signals occurring at 213 K. Partial coalescence of the methyl signals is also observed at this temperature. By 178 K we had not reached the low temperature limit of this additional dynamic process, and further cooling of our solution led only to general line broadening. However, at 178 K the methine signals split up into two distinct, though broadened, signals labelled $CH^{(1)}$ and $CH^{(2)}$ (Fig. 3). We attribute this inequivalence to slowed rotation about single bonds. Other workers refer to this as slow rotation about the $C_{(aryl)}$—P bond (27), though several bond rotations are likely coupled in a molecule as sterically congested as **7**.

Using the classical expression of Gutowsky and Holm (37) with Eyring absolute rate theory (38), we can estimate the barrier heights as $\Delta G^{\ddagger}$ ~ 40 kJ mol^{-1} for rotation about single bonds and $\Delta G^{\ddagger}$ ~ 72 kJ mol^{-1} for pyramidal inversion at phosphorus. These numbers are in remarkable agreement

Fig. 3. NMR spectra of **7** at various temperatures as recorded in $C_6D_5CD_3$. Spectra were monitored at 10° intervals over the range 178 to 380 K, and in the intervening spectra to those displayed here, smooth transitions between the peaks were observed. Only the aliphatic region of each spectrum is displayed, including the silyl, the isopropyl, and the PH signals. The residual $C_6D_5CHD_2$ peak (X) is cut short in the low-temperature spectra. Similarly, the *t*-Bu peak is cut short for the middle traces.

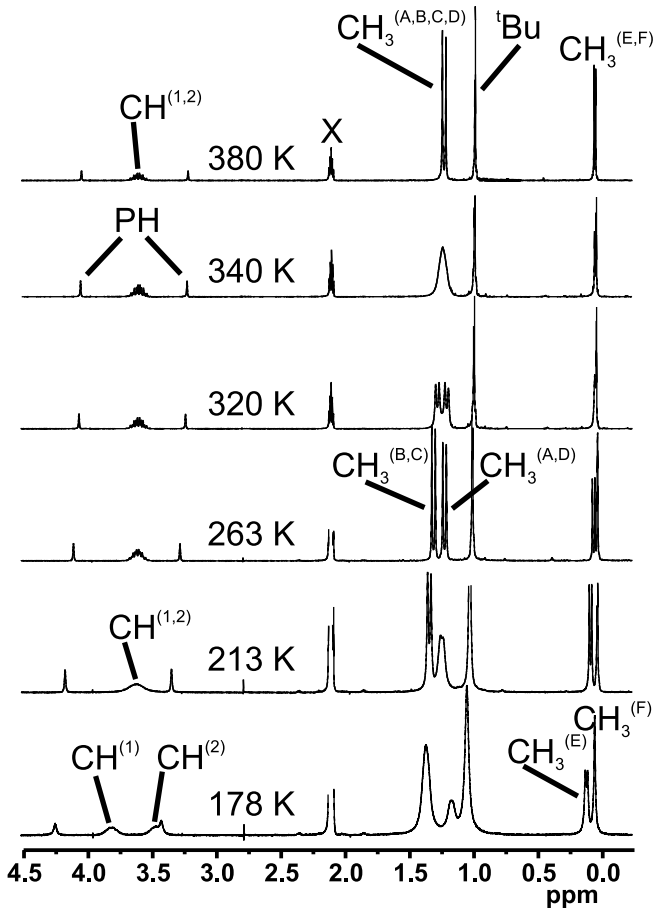

with values previously reported in a dynamic study of $TripPHSiPh_3$ (**21**): 39 kJ mol^{-1} for rotation and 71 kJ mol^{-1} for inversion (27). The assignments of the processes in **21** were made by comparison to literature data on phosphorus inversion barriers. The presence of diastereotopic groups $CH_3^{(E,F)}$ on silicon in **7** provides internal corroboration that this is the correct assignment.

Experimental

Starting materials and general procedures

All experimental procedures were performed under a nitrogen atmosphere using modified Schlenk techniques. 2,6-Diisopropylaniline (Aldrich) was distilled from KOH and stored under nitrogen prior to use. PCl_3, $SiMe_3Cl$, $SiMe_2$-*t*-BuCl (Aldrich), and HBr (Merck) were commercial products and used as received. Tetrahydrofuran was dried and distilled under a nitrogen atmosphere from sodium/benzophenone.

[3] Table S1 presents the full VT NMR Data for **7** at ~10 K intervals from 178 to 380 K.

© 2002 NRC Canada

Hexanes and pentane were dried and distilled under a nitrogen atmosphere from $LiAlH_4$. ^1H, ^{13}C, and ^{31}P NMR spectra were recorded on a Bruker AC250/Tecmag Macspect spectrometer operating at 250.13, 101.26, and 62.90 MHz, respectively. The ^1H and ^{13}C chemical shifts of $CDCl_3$ solutions were referenced to TMS and of $C_6D_5CD_3$ solutions to the residual CHD_2 pentet at δ 2.09, while ^{31}P was referenced to external 85% H_3PO_4. Infrared spectra were recorded on Bomem MB-100 or Nicolet Avatar 360 spectrometers as KBr pressed pellets (solids) or as neat liquid smears. Mass spectra were undertaken in the Department of Chemistry, University of Alberta, and elemental analyses were done by MHW Laboratories, Phoenix, Ariz. 1-Bromo-2,6-diisopropylbenzene was prepared from 2,6-diisopropylaniline by the literature method (28).

Preparation of 2,6-diisporopylphenylphosphonus mixed halide, 11

A solution of Grignard reagent was prepared from 60.0 g (247 mmol) of **10** and 6.0 g of activated magnesium turnings in 1150 mL of THF, and transferred via cannula to a solution of 67.0 g (488 mmol) PCl_3 in 200 mL THF held at –15°C. The mixture was allowed to warm to room temperature with stirring (12 h) and then heated to reflux for 2 h. Evaporation of solvent, extraction with 500 mL ether, filtering, and distillation (106–111°C, 0.5 mbar) produced 14.2 g of viscous, colourless oil. Careful integration of the ^{31}P NMR spectrum ($CDCl_3$) showed this to be the mixed phosphonous dihalides $DipPCl_2$ (**11a**) (δ 164.5, 4.5 g), DipPClBr (**11b**) (δ 159.2, 6.9 g), and $DipPBr_2$ (**11c**) (δ 151.9, 2.8 g); total molar yield 38.1%. ^1H NMR ($CDCl_3$) δ: 7.44–7.21 (m, 3H), 4.14–4.11(three sept, each with J_{HH} = 6.8 Hz, 2H), 1.34–1.29 (three d, each with J_{HH} = 6.8 Hz, 6H). ^{13}C NMR δ: 154 (d, $^2J_{PC}$ = 23 Hz), 133.49–133.41 (three d, $^3J_{PC}$ ~1 Hz), 124.97, 124.91 (two s), 31.25, (d, $^3J_{PC}$ = 27.8 Hz), 31.08, (d, $^3J_{PC}$ = 27.8 Hz), 30.89, (d, $^3J_{PC}$ = 27.3 Hz), 24.91–24.81 (three doublets, not resolved). MS (70eV) (calculated on ^{81}Br and ^{35}Cl) *m/z* (%): 354 ($[DipPBr_2]^+$, 5.5), 308 ($[DipPBrCl]^+$, 26.5), 273 ($[DipPBr]^+$, 9.8), 262 ($[DipPCl_2]^+$, 44.9), 227 ($[DipPCl]^+$, 100).

Preparation of 2,6-diisopropylphenylphosphane, 5

A solution of 10.0 g (32.7 mmol) of **11** in 150 mL anhydrous ether was transferred via cannula to a vigorously stirred suspension of 2.78 g (73.2 mmol) $LiAlH_4$ in 150 mL anhydrous ether held at –5°C. After warming to room temperature and heating to reflux for 22 h, the mixture was cooled to 0°C and treated with 53 mL of saturated aqueous NH_4Cl. The organic layer was decanted and the solids washed with 3 × 100 mL degassed ether. The combined ethereal solutions were dried, filtered, and evaporated to a milky oil. Distillation (73–85°C, 0.5 mbar) produced **5** as a clear oil (4.76 g, 24.6 mmol, 75.3% yield). IR (neat) (cm^{-1}): 3056 (w), 2961 (vs), 2868 (m), 2627 (s), 2306 (m), 1572 (w), 1461 (s), 1423 (w), 1383 (m), 1362 (m), 1247 (w), 1181 (w), 1162 (w), 1106 (w), 1086 (m), 1054 (m), 1037 (w), 923 (w), 831 (m), 792 (s), 720 (s), 499 (w). NMR, see Table 2. MS (70eV) *m/z* (%): 194.12306 ($[M]^+$, 100), 193 ($[DipPH]^+$, 44), 179 ($[C_{11}H_{16}P]^+$, 30), 161 ($[C_{12}H_{17}]^+$, 54), 152 ($[C_9H_{13}P]^+$, 44), 151 ($[C_9H_{12}P]^+$, 26), 137 ($[C_8H_{10}P]^+$, 25), 110 ($[C_6H_7P]^+$, 52), 91 ($[C_7H_7]^+$, 26). Anal. calcd. for $C_{12}H_{19}P$ (%): C 74.20, H 9.86; found: C 74.43, H 9.74.

Preparation of DipPHSi$(CH_3)_3$, 6

A solution of 28.4 mL of 1.6 M *n*-BuLi was added slowly by syringe to a vigorously stirred solution of 8.412 g (43.3 mmol) **5** in 80 mL THF held at 0°C. The now red solution was warmed to RT and stirred for 20 min, then cooled again to 0°C, whereupon 5.77 mL (45.5 mmol, 5% excess) $ClSi(CH_3)_3$ was added via syringe, followed by warming to RT and heating to reflux for 2 h. Removal of the volatile components, extraction with 100 mL hexanes, filtering, evaporation, and distillation (110–115°C, 0.5 mbar) of the residue produced 7.39 g of clear oil (29.6 mmol, 64%). NMR, see Table 2. MS (70eV) *m/z* (%): 266.16084 ($[M]^+$, 64), 193 ($[DipPH]^+$, 57), 149 ($[C_9H_{10}P]$, 14), 73 ($[SiMe_3]^+$, 100). Analytically pure material was not obtained, and all samples tended to be contaminated with very small amounts of either **5** or **8**.

Preparation of DipPH{Si$(CH_3)_2$-*t*-Bu}, 7

A solution of 4.00 g (20.6 mmol) **5** in 40 mL THF cooled to 0°C was treated with 13.5 mL (21.6 mmol, 5% excess) of 1.6 M *n*-BuLi. After warming the now yellow solution to RT for 30 min and cooling back to 0°C, 3.10 g (20.6 mmol) $ClSi(CH_3)_2$-*t*-Bu was added by syringe. After warming to RT and then refluxing for 1 h, the solution was shown by ^{31}P NMR to have 70% conversion to **7**. A further 4.5 mL of *n*-BuLi followed by 1.05 g (3.6 mmol) was used in a repeat of the above procedure. NMR indicated complete conversion at this stage. The solids remaining after evaporation of the solvent were extracted with 20 mL hexanes, filtered, evaporated, and the residue sublimed under static vacuum onto a water-cooled cold finger, yielding 3.60 g of colourless crystalline **7** (11.7 mmol, 57% yield, mp 45–51°C). X-ray quality crystals were grown by sublimation under dynamic vacuum in a three-zone tube furnace. IR (KBr pellet) (cm^{-1}): 3050(w), 2958(vs), 2925(vs), 2856(s), 2330(m), 1567(w), 1463(s), 1417(w), 1381(w), 1362(s), 1246(m), 1176(w), 1050(w), 1006(w), 938(w), 839(s), 821(s), 804(vs), 773(w), 737(vs), 680(w), 601(w), 578(w), 444(w), 430(w). NMR, see Table 2. MS (70 eV) *m/z* (%): 308.20866 ($[M]^+$, 53), 251 ($[DipP(Si(CH_3)_2]^+$, 11), 193 ($[DipPH]^+$, 15), 115 ($[(CH_3)_3CSi(CH_3)_2]^+$, 13.7), 73 ($[Si(CH_3)_3]^+$, 100). Anal. calcd. for $C_{18}H_{33}PSi$ (%): C 70.08, H 10.78; found: C 69.84, H 10.62.

Preparation of DipP{Si$(CH_3)_3$}$_2$, 8

A stirred solution prepared from 2.00 g (10.3 mmol) **5** and 20 mL THF held at 0°C was treated with 6.76 mL (10.8 mmol, 5% excess) of 1.6 M *n*-BuLi. After 20 min, the stirred orange solution was treated with 1.37 mL (10.8 mmol) $ClSi(CH_3)_3$, yielding a colourless solution with a white precipitate. ^{31}P NMR indicated that conversion to **7** was incomplete; a further 5.07 mL (8.11 mmol) of *n*-BuLi and 1.03 mL (8.11 mmol) $ClSi(CH_3)_3$ were added following the same procedure as before. ^{31}P NMR analysis indicated 75% **8** and 25% **7**. Again 5.07 mL (8.11 mmol) of *n*-BuLi and 1.03 mL (8.11 mmol) $ClSi(CH_3)_3$ were added following the same procedure and NMR analysis showed complete conversion to **8**. Evaporation of solvent, extraction with 100 mL hexanes, filtration, evaporation, and distillation of the residue (120–130°C, 0.5 mbar) gave 2.20 g of **8**, which cooled to a pasty white solid (6.5 mmol, 63% yield). IR (neat) (cm^{-1}): 3050 (m), 2957 (vs), 2867 (s), 1935 (w), 1861

© 2002 NRC Canada

(w), 1695 (w), 1651 (w), 1633 (w), 1589 (w), 1569 (m), 1557 (w), 1463 (s), 1381 (m), 1361 (m), 1304 (m), 1246 (s), 1177 (m), 1048 (m), 992 (m), 835 (s), 801 (m), 748 (m), 684 (m), 625 (m), 509 (w), 402 (w). NMR, see Table 2. MS (70eV) *m/z* (%): 338.20229 ([M]$^+$, 49), 266 ([DipPHSi(CH$_3$)$_2$]$^+$, 15), 193 ([DipPH]$^+$, 16), 147 ([C$_{11}$H$_{15}$]$^+$, 13.7), 73 ([Si(CH$_3$)$_3$]$^+$, 100). An analytically pure sample was not obtained.

Preparation of DipP{Si(CH$_3$)$_2$-*t*-Bu}$_2$, 9

A solution of 2.00 g (10.3 mmol) **5** in 20 mL THF held at 0°C was treated with 6.43 mL (10.29 mmol) of 1.6 M *n*-BuLi. After warming to RT, the yellow solution was cooled again and treated with 1.55 g (10.29 mmol) ClSi(CH$_3$)$_2$-*t*-Bu. The faint yellow solution was allowed to warm to room temperature over 30 min. Cooling again in an ice bath and treating with another 6.43 mL of 1.6 M *n*-BuLi gave an orange solution. Again 1.55 g ClSi{CH$_3$)$_2$-*t*-Bu} was added after warming the reaction mixture to room temperature and cooling to 0°C. The faint yellow solution was then heated to reflux for 12 h and ^{31}P NMR analysis showed complete conversion to **9**. Evaporation of solvent, extraction into 30 mL pentane, filtering, and evaporation yielded a white solid, which was purified by sublimation under dynamic vacuum onto a water-cooled cold finger to give 2.934 g of a white crystalline **9** (7.7 mmol, 75% yield, mp 57–62°C). IR (KBr pellet) (cm^{-1}): 3047 (w), 2958 (vs), 2929 (vs), 2894 (s), 2857 (s), 2569 (w), 1471 (m), 1460 (m), 1403 (w), 1388 (m), 1380 (m), 1360 (m), 1251 (s), 1245 (s), 1177 (w), 1048 (w), 1024 (w), 1005 (w), 834 (vs), 820 (s), 794 (vs), 760 (s), 742 (m), 681 (w), 670 (m), 660 (w), 575 (w), 470 (w), 408 (w). NMR, see Table 2. MS (70 eV) *m/z* (%): 422.29533 ([M]$^+$, 30), 251 ([M – *t*-Bu]$^+$, 11), 73 ([Si(CH$_3$)$_3$], 100). Anal. calcd. for C$_{24}$H$_{47}$PSi$_2$ (%): C 68.18, H 11.21; found: C 67.99, H 10.94.

X-ray diffraction analysis of DipPH{Si(CH$_3$)$_2$-*t*-Bu}, 7

The crystal structure of **7** was determined using a Bruker instrument fitted with a SMART 1000 area detector. Experimental details are summarized in Table 3. The structure was solved by direct methods using SHELXS-97 (39) and refined by full-matrix least-squares on F^2 against all reflections using SHELXL-97 (40). Neutral atom scattering factors are from *International Tables for X-ray Crystallography*, Vol. C. The weighting scheme used was $w = 1/[\sigma^2(c) + (0.0705P)^2]$, where $P = (F_o^2 + 2F_c^2)/3$. The non-hydrogen atoms were refined anisotropically, and the H atoms on C were refined using a riding model (C—H = 0.95 Å). The H atom attached to P was refined freely. Additional crystallographic details have been deposited.[4]

Electronic structure calculations

The structures of the full geometries of **5–9** were optimized by DFT methods, using the B3LYP hybrid function and the 6–31G(d) basis set, as implemented in the Gaussian98 suite of programs (41) running on AMD K7 computers under Windows 2000 or on four processor Compaq Alpha ES40 or ES45 workstations. Full frequency calculations were performed on all models, and stationary states were confirmed by the absence of imaginary frequencies. In the case of **8** the frequency calculation was unsuccessful, but the strong agreement with the structures of other members of the series provides confidence in the calculated structure.

Conclusions

A new bulky phosphane and two mono- as well as two disilyl derivatives were prepared by routes that provide these materials in synthetically useful quantities. The silyl compounds as well as the phosphane itself are expected to be useful synthons for both main group and transition metal chemistry. We have identified a further example of dynamic effects in compounds of the general class ArPHSiR$_3$ where both the aryl group and silicon bear sterically congested substituents. Studies on the utility of **5–9** as synthons are ongoing in our laboratory.

Acknowledgments

We thank the Natural Sciences and Engineering Research Council of Canada (NSERC) and the University of Lethbridge for financial support (R.T.B.). We thank Dr. Bob Macdonald, Department of Chemistry, University of Alberta, for the collection of the intensity data for the X-ray diffraction study, and Meg O'Shea for performing the DFT calculations. Access to the Multimedia Advanced Computation Infrastructure (MACI) Alpha cluster at the University of Calgary is gratefully acknowledged. We thank Dr. Paul Hazendonk for helpful discussions, and anonymous referees for useful suggestions.

References

1. R.A. Berrigan, D.K. Russell, W. Henderson, M.T. Leach, B.K. Nicholson, G. Woodward, and C. Harris. New J. Chem. **25**, 322 (2001).
2. C. Frenzel, F. Somoza, S. Blaurock, and E. Hey-Hawkins. J. Chem. Soc. Dalton Trans. 3115 (2001).
3. K. Toyota, Y. Matsushita, N. Shinohara, and M. Yoshifuji. Heteroat. Chem. **12**, 418 (2001).
4. B. Twamley, C-S. Hwang, N.J. Hardman, and P.P. Power. J. Organomet. Chem. **609**, 152 (2000).
5. H. Dorn, R.A. Singh, J.A. Massey, J.M. Nelson, C.A. Jaska, A.J. Lough, and I. Manners. J. Am. Chem. Soc. **122**, 6669 (2000).
6. M. Driess, S. Kuntz, C. Monse, and K. Merz. Chem. Eur. J. **6**, 4343 (2000).
7. G.W. Rabe, H. Heise, L.M. Liable-Sands, I.A. Guzei, and A.L. Rheingold. J. Chem. Soc. Dalton Trans. 1863 (2000).
8. G.W. Rabe, S. Kheradmandan, and G.P.A. Yap. Inorg. Chem. **37**, 6541 (1998).

[4] Supplementary data (Tables S1–S7) may be purchased from the Depository of Unpublished Data, Document Delivery, CISTI, National Research Council Canada, Ottawa, ON K1A 0S2, Canada (http://www.nrc.ca/cisti/irm/unpub_e.shtml for information on ordering electronically). CCDC 186019 contain the supplementary data for this paper. These data can be obtained, free of charge, via www.ccdc.cam.ac.uk/conts/retrieving.html (or from the Cambridge Crystallographic Data Centre, 12 Union Road, Cambridge, U.K.; fax +44 1223 336033; or deposit@ccdc.cam.ac.uk).

© 2002 NRC Canada

9. N.J. Goodwin, W. Henderson, B.K. Nicholson, J. Fawcett, and D.R. Russell. J. Chem. Soc. Dalton Trans. 1785 (1999).
10. S.J.A. Pope and G. Reid. J. Chem. Soc. Dalton Trans. 1615 (1999).
11. J.T. Scheper, K.C. Jayaratne, L.M. Liable-Sands, G.P.A. Yap, A.L. Rheingold, and C.H. Winter. Inorg. Chem. **38**, 4354 (1999).
12. T. Campbell, A.M. Gibson, R. Hart, S.D. Orchard, S.J.A. Pope, and G. Reid. J. Organomet. Chem. **592**, 296 (1999).
13. D.J. Darensbourg, J.D. Draper, B.J. Frost, and J.H. Reibenspies. Inorg. Chem. **38**, 4705 (1999).
14. W. Malisch, K. Thirase, F.J. Rehmann, J. Reising, and N. Gunzelmann. Eur. J. Inorg. Chem. 1589 (1998).
15. G.A.A. Hadi, K. Fromm, S. Blaurock, S. Jelonek, and E. Hey-Hawkins. Polyhedron, **16**, 721 (1997).
16. R. Felsberg, S. Blaurock, S. Jelonek, T. Gelbrich, R. Kirmse, A. Voigt, and E. Hey-Hawkins. Chem. Ber. **130**, 807 (1997).
17. I.V. Kourkine, S.V. Maslennikov, R. Ditchfield, D.S. Glueck, G.P.A. Yap, L.M. Liable-Sands, and A.L. Rheingold. Inorg. Chem. **35**, 6708 (1996).
18. J. Ho, T.L. Breen, A. Ozarowski, and D.W. Stephan. Inorg. Chem. **33**, 865 (1994).
19. A.H. Cowley, N.C. Norman, and M. Pakulski. Inorg. Synth. **27**, 235 (1990).
20. Y. v.d. Winkel, H.M.M. Bastiaans, and F. Bickelhaupt. J. Organomet. Chem. **405**, 183 (1991).
21. R.T. Boeré, V. Klassen, and G. Wolmershäuser. J. Chem. Soc. Dalton Trans. 4147 (1998).
22. R.T. Boeré, V. Klassen, and G. Wolmershäuser. Can. J. Chem. **78**, 583 (2000).
23. R.E. Boeré, R.T. Boeré, J. Masuda, and G. Wolmershäuser. Can. J. Chem. **78**, 1613 (2000).
24. R.T. Boeré and J.D. Masuda. Abstract #902. 84th Canadian Chemical Conference and Exhibition, Montreal, May 26–30, 2001.
25. A.H. Cowley, M. Pakulski, and N.C. Norman. Polyhedron, **6**, 915 (1987).
26. M. Yoshifuji, K. Shimura, and K. Toyota. Bull. Chem. Soc. Jpn, **67**, 1980 (1994).
27. M.A. Petrie and P.P. Power. J. Chem. Soc. Dalton Trans. 1737 (1993).
28. R.R. Shrock, M. Wesolek, A.H. Liu, K.C. Wallance, and J.C. Dewan. Inorg. Chem. **27**, 2050 (1988).
29. V. Mark, C.H. Dungan, M.M. Crutchfield, and J.R. Van Wazer. Top. Phosphorus Chem. **5**, 227 (1967).
30. M. Yoshifuji, K. Toyota, K. Shibayama, and N. Inamoto. Chem. Lett. 1653 (1983).
31. R. Appel and K. Geisler. J. Organomet. Chem. **112**, 61 (1976).
32. J.B. Lambert and J-H. So. J. Org. Chem. **56**, 5960 (1991).
33. M. Yoshifuji, K. Shibayama, K. Toyota, and N. Inamoto. Tetrahedron Lett. **24**, 4227 (1983).
34. A. Maaninen, R.T. Boeré, T. Chivers, and M. Parvez. Z. Naturforsch. B Chem Sci. **54**, 1170 (1999).
35. D.J. Brauer, F. Bitterer, F. Dörrenbach, G. Heßler, O. Stelzer, C. Krüger, and F. Lutz. Z. Naturforsch. B Chem Sci. **51**, 1183 (1996).
36. J.F. Blount, C.A. Marynoff, and K. Mislow. Tettrahedron Lett. 913 (1975).
37. H.S. Gutowsky and C.H. Holm. J. Chem. Phys. **25**, 1228 (1956).
38. J. Sandström. Dynamic NMR spectroscopy. Academic Press, London. 1982.
39. G. Sheldrick. 1997. SHELXS-97 [computer program]. University of Göttingen, Göttingen, Germany.
40. G. Sheldrick. 1997. SHELXL-97 [computer program]. University of Göttingen, Göttingen, Germany.
41. M.J. Frisch, G.W. Trucks, H.B. Schlegel, G.E. Scuseria, M.A. Robb, J.R. Cheeseman, V.G. Zakrzewski, J.A. Montgomery, Jr., R.E. Stratmann, J.C. Burant, S. Dapprich, J.M. Millam, A.D. Daniels, K.N. Kudin, M.C. Strain, O. Farkas, J. Tomasi, V. Barone, M. Cossi, R. Cammi, B. Mennucci, C. Pomelli, C. Adamo, S. Clifford, J. Ochterski, G.A. Petersson, P.Y. Ayala, Q. Cui, K. Morokuma, D.K. Malick, A.D. Rabuck, K. Raghavachari, J.B. Foresman, J. Cioslowski, J.V. Ortiz, A.G. Baboul, B.B. Stefanov, G. Liu, A. Liashenko, P. Piskorz, I. Komaromi, R. Gomperts, R.L. Martin, D.J. Fox, T. Keith, M.A. Al-Laham, C.Y. Peng, A. Nanayakkara, M. Challacombe, P.M.W. Gill, B. Johnson, W. Chen, M.W. Wong, J.L. Andres, C. Gonzalez, M. Head-Gordon, E. S. Replogle, and J.A. Pople. 1998. Gaussian 98 [computer program]. Revision A.9. Gaussian, Inc., Pittsburgh, Pa.

© 2002 NRC Canada

Synthesis and characterization of titanium complexes containing phosphinimido and tropidinyl ligands: Crystal structure of (trop)(*t*-$Bu_3PN)TiCl_2$

Steve J. Brown, Xiaoliang Gao, Matthew G. Kowalchuk, Rupert E.v.H. Spence, Douglas W. Stephan, and John Swabey

Abstract: A new class of titanium complexes containing a tropidinyl (trop) ligand and a phosphinimido (R_3P=N-) or a ketimide ligand (R_2C=N-) were synthesized and characterized. The combination of the cyclopentadienyl equivalent tropidinyl and phosphinimido ligands enables the formation of a group of novel non-metallocene catalysts for olefin polymerization. The crystal structure of (trop)(*t*-$Bu_3PN)TiCl_2$ was determined by single crystal X-ray crystallography. Polymerization of ethylene with this complex was studied in a high-temperature solution process.

Key words: tropidinyl, phosphinimido, ketimide, catalyst, polymerization.

Résumé : On a synthétisé et caractérisé une nouvelle classe de complexes du titane contenant un ligand tropidinyle (trop) et un phosphinimido (R_3P=N-) ou un ligand cétimide (R_2C=N-). La combinaison des ligands phosphinimido et tropidinyle, équivalent du cyclopentadiényle, rend possible la formation d'un groupe de nouveaux catalyseurs non métallocènes pour la polymérisation des oléfines. On a déterminé la structure cristalline du (trop)(*t*-$Bu_3PN)TiCl_2$ par diffraction des rayons X par un cristal unique. On a étudié la polymérisation de l'éthylène à l'aide de ce catalyseur, dans un procédé en solution et à haute température.

Mots clés : tropidinyle, phosphinimido, cétimide, catalyseur, polymérisation.

[Traduit par la Rédaction]

Introduction

Metallocene catalysts ($CpCp'MX_2$, M = Ti, Zr, Hf; with or without a bridge between the Cps) (1–8) and Constrained geometry catalysts ($CpSiR_2NR'TiX_2$) (9–13) have been the subject of intense studies for olefin polymerization in both academia and industrial organizations in the past two decades. Compared to the traditional Ziegler–Natta catalysts, these catalysts have well-defined structures, which makes it possible to control the properties of polymer products through the modification of catalyst structures.

In the past few years, ligands that are considered cyclopentadienyl equivalent in terms of both electronic and steric structures have been synthesized and used to form a variety of single site catalysts for olefin polymerization. For example, the core structure of zirconium complexes with boratabenzene ligands (14–17) is very similar to that of Cp_2ZrCl_2. The activity of the boratabenzene complexes for olefin polymerization was reported to be similar to that of Cp_2ZrCl_2 under the same conditions. Catalysts of the types $(R_3PN)CpTiX_2$ (18–20), $(R_3PN)_2TiX_2$ (21–22), and $(R_3PN)(L')TiX_2$ (23) (where L′ is a heteroatomic ligand) were found to be highly active towards olefin polymerization. The properties of the polymeric products made with these phosphinimido catalysts are similar or superior to those made with conventional metallocene catalysts. Other catalysts or metal complexes with ligands isoelectronic–isolobal with the cyclopentadienyl ligands including the *o*-dicarbollide anions (24), η^3–"nacnac" anions (25), and the $(4\sigma + 2\pi)$ amidinate (26) ligands have also been extensively studied.

A tropidinyl ligand consists of an η^3 4π-electron allylic moiety and a 2σ-electron neutral nitrogen donor. The ligand is considered to be equivalent to a cyclopentadienyl ligand, and $Cp(trop)ZrCl_2$ and $(trop)_2ZrCl_2$ (27–28) were synthesized and were tested for ethylene polymerization. $Cp(trop)ZrCl_2$ exhibited high activity towards ethylene polymerization. $(Trop)_2ZrCl_2$ was only moderately active.

As an extension of our studies of group 4 metal catalysts containing a phosphinimido ligand and a heteroatomic ligand, the synthesis, structures, and polymerization studies of $(trop)(R_3PN)TiCl_2$ were performed, where trop is the N-methyl tropidinyl ligand. Also a titanium complex

Received 2 February 2002. Published on the NRC Research Press Web site at http://canjchem.nrc.ca on 29 November 2002.

Dedicated to Professor Tris Chivers for his contributions to Canadian chemistry.

S.J. Brown, X. Gao,[1] M.G. Kowalchuk, R.E.vH. Spence, and J. Swabey. NOVA Research & Technology Corporation, 2928 16 Street N.E., Calgary, AB T2E 7K7, Canada.
D.W. Stephan. School of Physical Sciences, Chemistry and Biochemistry, University of Windsor, Windsor, ON N9B 3P4, Canada.

[1]Corresponding author (e-mail: gaox@novachem.com).

 DOI: 10.1139/V02-170 © 2002 NRC Canada

Fig. 1. ORTEP drawings of **2**, 30% thermal ellipsoids are shown. Hydrogen atoms have been omitted for clarity.

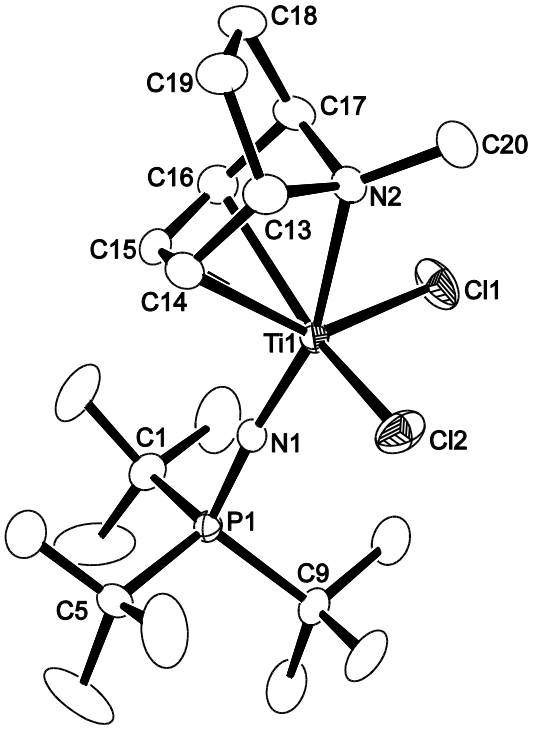

(trop)(R_2CN)$TiCl_2$ containing a ketimide ligand (29, 30) and the tropidinyl ligand was synthesized and characterized.

Results and discussion

Synthesis

Tropidine was prepared from dehydration of tropine (31). The 1-trimethyl tin derivative was prepared from the lithium salt of tropidine and trimethyl tin chloride (27). Tropidinyl titanium trichloride, (trop)$TiCl_3$, **1**, was conveniently prepared by the reaction of the 1-trimethyl tin tropidine with $TiCl_4$. The elimination of Me_3Sn-Cl from the reaction of $TiCl_4$ and 1-trimethyltin-tropidine to produce **1** is similar to the syntheses of (Indenyl)$TiCl_3$ (36) and (C_5Me_5)$TiCl_3$ (37) by the elimination of Me_3Si-Cl from $TiCl_4$ and 1-(trimethysilyl)indene and trimethylsilylpentamethylcyclopentadiene, respectively. The reactions again suggest the thermodynamic stability of (trop)$TiCl_3$, **1**, and the equivalence of tropidinyl and the cyclopentadienyl ligands. (Trop)$TiCl_3$, **1**, is an excellent starting material for the preparation of titanium complexes containing the tropidinyl ligand. Thus the reaction of **1** with *t*-Bu_3P=NLi and *i*-Pr_3P=NLi gave (*t*-Bu_3P=N)(trop)$TiCl_2$, **2**, and (*i*-Pr_3P=N)(trop)$TiCl_2$, **3**, respectively. The reaction of **1** with *t*-Bu_2C=NLi resulted in the formation of (*t*-Bu_2C=N)(trop)$TiCl_2$, **4**. Unlike the reactions of $CpTiCl_3$ with anionic ligands, which are usually fast and could be completed within a few minutes even at temperatures below 0°C, the reactions of **1** with the nitrogen-containing anionic ligands are very slow at room temperature. Therefore, heating was found to be necessary to drive the reactions to completion. Scheme 1 summaries the synthesis of the ligand and metal complexes.

Table 1. Crystallographic parameters for **2**.[a]

Formula	$C_{20}H_{39}Cl_2N_2PTi$
Formula weight	457.30
Space group	*Pbca*
Crystal system	Orthorhombic
a (Å)	15.435(3)
b (Å)	12.006(3)
c (Å)	26.633(5)
V (Å^3)	4935.2(19)
Z	8
$D_{calcd.}$ (g cm^{-1})	1.231
Absorption coefficient (μ) (mm^{-1})	0.373
Data collected	23 697
Data [$F_o^2 > 3\sigma(F_o^2)$]	4344
Goodness-of-fit	1.041
No. of variables	235
R, R_w (%)	5.65, 15.74

[a]All data collected at 24°C with Mo Kα radiation (λ = 0.71069 Å), $R = \Sigma||F_o| - |F_c||/ \Sigma|F_o|$, $R_w = [\Sigma[\omega(F_o^2 - F_c^2)^2]/ \Sigma(\omega F_o^2)^2]]^{0.5}$.

Structure

Purple crystals of **2** were grown from a mixture of toluene and heptane. The solid-state structure was determined by X-ray crystallography. The ORTEP diagram of this complex is shown in Fig. 1. Crystal data and selected bond lengths and angles are provided in Tables 1 and 2, respectively. The solid state structure of the molecule shows that the tropidinyl ligand binds to the titanium via a dative bond through the nitrogen atom and an η^3 π bond through the anionic allyl moiety. The tropidinyl ligand is oriented symmetrically with respect to the two Cl ligands. The N—methyl bond in the tropidinyl ligand bisects the Cl-Ti-Cl plane and points to the same direction as the vector from the central titanium to the middle of the Cl ligands (i.e., points to the front of the molecule), which was also seen in the solid structure of Cp(trop)$ZrCl_2$ (28). The average Ti—C bond distance for the allyl moiety in the tropidinyl ligand is 2.37 Å, which is similar to the average Ti—C distance (2.38 Å) found in titanocene dichloride (32, 33). The *t*-Bu_3P=N ligand binds to the titanium center via the nitrogen atom and the geometry of the P-N-Ti moiety is almost linear, as seen from the P-N-Ti angle of 174.50(18)°. This near linear geometry was previously seen in Cp(*t*-Bu_3P=N)$TiCl_2$ (20), Cp(Ph_3P=N)$TiCl_2$ (34), and (*t*-Bu_3P=N)$_2TiCl_2$ (22). The Cl-Ti-Cl angles are 100(1)° in Cp_2TiCl_2 (32, 33), 103.41(12)° in Cp(*t*-Bu_3P=N)$TiCl_2$ (20), and 106.93(7)° in (*t*-Bu_3P=N)$_2TiCl_2$ (22). The Cl-Ti-Cl angle in the complexes increases from Cp, (*t*-Bu_3P=N) to the tropidinyl ligand.

Ethylene polymerization

The dimethylated derivative of **2**, prepared by treatment of **2** with 2 molar equiv of MeMgBr was tested in high-temperature solution polymerization. It showed moderate activity when activated with [Ph_3C][(C_6F_5)$_4$]. The ethylene polymerization rate was 60 L mmol^{-1} min^{-1} at 160°C. For comparative purposes Cp_2ZrMe_2 under the same polymerization conditions has a polymerization rate of 750 L mmol^{-1} min^{-1}.

© 2002 NRC Canada

Scheme 1.

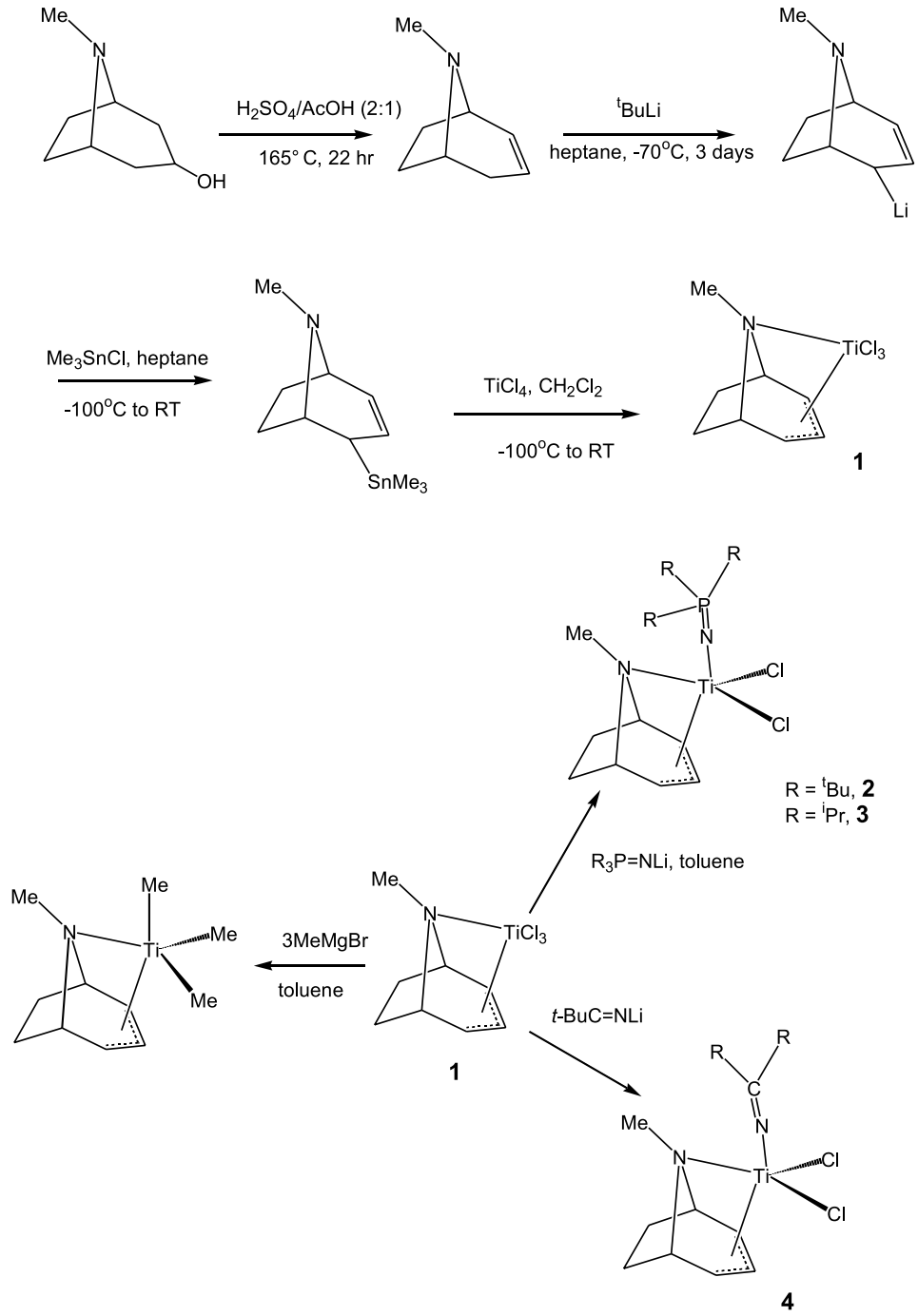

Polymer molecular weight was exceptionally high for both ethylene and ethylene – 1-octene polymerization with a molecular weight of 199 000 g mol^{-1} being produced in co-polymerization at 160°C and a low-ethylene conversion of 68%. The molecular weight distribution (MWD = (weight average)/(number average molecular weight)) for ethylene polymerization was 2.2 indicating single site performance. However, in co-polymerization of ethylene and 1-octene, the MWD for this catalyst was 9.2, indicating non single site catalyst performance with the activation method employed.

Experimental

All preparations, reactions, and manipulations were carried out under a purified nitrogen atmosphere, using both Schlenk techniques and glove boxes. All commercially available chemicals were purchased from Aldrich. Solvents were anhydrous grades, which were first dried through use of a deoxygen catalyst and activated molecular sieve beds and then stored over activated molecular sieves in either Kontes flasks or plastics bottles in glove boxes. R_3P=N-$SiMe_3$

© 2002 NRC Canada

Table 2. Selected bond lengths (Å) and angles (°) for **2**.

Bond lengths (Å)					
Ti(1)—N(1)	1.783(3)	Ti(1)—N(2)	2.255(3)	Ti(1)—Cl(1)	2.3342(12)
Ti(1)—Cl(2)	2.3426(12)	Ti(1)—C(15)	2.354(4)	Ti(1)—C(16)	2.377(4)
Ti(1)—C(14)	2.394(4)	P(1)—N(1)	1.596(3)	C(14)—C(15)	1.375(6)
C(15)—C(16)	1.374(6)	C(16)—C(17)	1.514(6)		
Bond angles (°)					
N(1)-Ti(1)-N(2)	163.27(11)		N(1)-Ti(1)-Cl(1)	102.73(9)	
N(2)-Ti(1)-Cl(1)	87.22(8)		N(1)-Ti(1)-Cl(2)	102.39(10)	
N(2)-Ti(1)-Cl(2)	86.90(8)		Cl(1)-Ti(1)-Cl(2)	108.07(6)	
N(1)-Ti(1)-C(14)	105.61(13)		N(2)-Ti(1)-C(14)	60.20(12)	
Cl(1)-Ti(1)-C(14)	142.87(10)		Cl(2)-Ti(1)-C(14)	88.77(11)	
C(15)-Ti(1)-C(14)	33.65(14)		C(16)-Ti(1)-C(14)	59.57(14)	
N(1)-Ti(1)-C(15)	91.40(13)		N(2)-Ti(1)-C(15)	71.87(13)	
Cl(1)-Ti(1)-C(15)	123.46(11)		Cl(2)-Ti(1)-C(15)	121.91(11)	
N(1)-Ti(1)-C(16)	105.42(13)		N(2)-Ti(1)-C(16)	60.61(12)	
Cl(1)-Ti(1)-C(16)	90.10(11)		Cl(2)-Ti(1)-C(16)	142.30(11)	
C(15)-Ti(1)-C(16)	33.76(14)		P(1)-N(1)-Ti(1)	174.50(18)	
C(17)-N(2)-C(20)	113.9(3)		C(17)-N(2)-C(13)	101.0(3)	
C(20)-N(2)-C(13)	114.6(3)				

(*R* = *t*-Bu, *i*-Pr) were prepared by reacting the neat phosphines with an excess amount of Me_3SiN_3 at 95°C until no more nitrogen evolution. R_3P=N-H (*R* = *t*-Bu, *i*-Pr) were prepared by reacting R_3P=N-$SiMe_3$ (*R* = *t*-Bu, *i*-Pr) with a catalytic amount of NaOMe in dry methanol followed by removing volatiles and extraction with heptane. NMR spectra were recorded on a Bruker 300 MHz NMR machine. Elemental analyses were obtained from Canadian Microanalytical Services Ltd., Delta, B.C. V4G 1G7. GC–MS analyses were performed at NOVA Chemicals Research and Technology Center, Calgary, AB, T2E 7K7.

Preparation of tropidine

To tropine (25.0 g, 177 mmol) and glacial acetic acid (12 g, 11.5 mL) cooled to 0°C and combined in a 200 mL Schlenk flask was added concentrated H_2SO_4 (46 g, 25 mL) causing fuming. The reaction vessel was fitted with a condenser, and under a slight flow of N_2 the reaction mixture was refluxed for 22 h at 165°C. A 300 mL volume of deionized distilled water was added with stirring and pH adjusted to 13–14 by addition of 50 g (1.25 mol) of NaOH in ~170 mL water. The product was extracted into ether and the organic phase dried over $MgSO_4$. Solids were removed by filtration and the solvent removed in vacuo. The liquid was distilled under ambient pressure at 165–170°C. The distillate was diluted in pentane and the solution was passed through a column of neutral alumina (Brockman Activity I) to remove a small amount of residual starting material. The product was a clear colorless liquid with 99.8% purity as determined by GC–MS ($[M]^+$: 123). The yield was 10.71 g (49.1%).

Preparation of 1-trimethyltintropidine

To a solution of tropidine (10.707 g, 86.9 mmol) in heptane (~300 mL) at –70°C was added *tert*-butyllithium (51.1 mL, 86.9 mmol, 1.7 M in pentane). The reaction mixture assumed a greenish tinge, and within 15–20 min of addition completion a fluffy precipitate was observed in the clear yellow solution. The mixture was maintained at –70°C for 3 days with occasional stirring, at which time the mixture was a combination of an orange supernatant and a yellowish solid.

To the slurry of lithium tropidinide in heptane at –100°C was added trimethyltin chloride (17.3 g, 86.9 mmol) in heptane dropwise over 15–20 min. The color of the reaction mixture gradually became lighter and white solid was observed to have formed. After complete addition, the mixture was warmed to room temperature and stirred for an additional 2.5 h. A 100 mL volume of deionized distilled water was added and the mixture stirred under N_2 overnight. The organic compounds were extracted into heptane–pentane, rinsed vigorously with a solution of brine, and dried over $MgSO_4$. Solids were removed by filtration and the dark liquid passed through a column of neutral alumina (Brockman Activity I), affording a clear liquid with a yellow tinge. The liquid was distilled to give a clear colorless viscous oil with 99.2% purity as determined by GC–MS ($[M]^+$: 286). The yield was 13.65 g (54.9%). ^{1}H NMR (C_7D_8) δ: 5.52 (m, 2H), 3.12 (m, 1H), 3.03 (m, 1H), 2.43 (s, 4H), 2.04 (m, 2H), 1.81 (m, 1H), 1.46 (m, 1H), 0.08 (s, 9H, Sn*Me*$_3$ (further split by 8.7 and 7.7% of ^{119}Sn and ^{117}Sn, respectively), *J* = 25.7 Hz).

Preparation of (tropidinyl)titanium trichloride, 1

To titanium (IV) chloride (0.379 g, 2 mmol) in dichloromethane (15 mL) at –78°C was added dropwise trimethyltin tropidine (0.572 g, 2 mmol) in dichloromethane (20 mL), initiating a dark blue coloration in the reaction mixture. The reaction was warmed to room temperature and stirred overnight under N_2. The solvent was removed under vacuum; the blue solid was slurried in pentane and isolated by filtration. The final product was dried in vacuo and determined to be 99% pure by ^{1}H NMR. The yield was 0.502 g (90.8%). ^{1}H NMR (C_7D_8) δ: 5.14 (t, 1H, *J* = 7.61 Hz), 4.84 (dd, 2H, J_1 = 7.21 Hz, J_2 = 5.01 Hz), 3.10 (br s, 2H), 1.95 (s, 3H, N*Me*), 1.20 (m, 4H, CH_2). Anal. calcd. for $C_8H_{12}Cl_3NTi$: C 34.76, H 4.38, N 5.07; found: C 34.06, H 4.54, N 4.95.

© 2002 NRC Canada

Preparation of (tropidinyl)titanium trimethyl

To a stirred solution of **1** (1 mmol, 0.276 g) in toluene (30 mL) cooled at –70°C was added MeMgBr (4.5 mmol, 3 M in diethyl ether, 1.5 mL). The deep blue solution was allowed to warm to room temperature and was stirred at room temperature for 2 h. The orange slurry was pumped to dryness and the solid was extracted with pentane. The pentane solution was filtered to remove MgClBr and the excess of MeMgBr. The filtrate was pumped to dryness to give pure (trop)(*t*-Bu_3PN)$TiMe_3$ in 47% yield. ^{1}H NMR (C_7D_8) δ: 4.79 (t, 1H, J = 7.50 Hz), 4.69 (dd, 2H, J_1 = 7.20 Hz, J_2 = 5.0 Hz), 2.72 (br s, 2H), 1.91 (m, 2H), 1.62 (m, 2H), 1.50(s, 9H, TiMe3), 1.43 (3H, N*Me*).

(Tropidinyl)(tri-*tert*-butylphosphinimido)titanium dichloride, 2

To (tropidinyl)titanium trichloride (0.502 g, 1.816 mmol) in toluene (15 mL) at –78°C was added a slurry of lithium tri-*tert*-butylphosphinimide (*t*-Bu_3PNLi) (0.405 g, 1.816 mmol) in toluene (25 mL). No apparent reaction was observed. The reaction mixture was heated to 60°C for ~1 h, resulting in a purple colored solution. The solution was filtered to remove LiCl and the product was crystallized after heptane was added to the toluene solution. The yield was 0.669 g (80.6%). ^{1}H NMR (C_7D_8) δ: 5.48 (t, 1H, J = 7.41 Hz), 4.63 (dd, 2H, J_1 = 7.51 Hz, J_2 = 4.61 Hz), 3.61 (br s, 2H), 2.41 (s, 3H), 1.80 (m, 4H, CH_2), 1.22 (d, 27H, N=P-*t*-Bu_3, J = 13.22 Hz). Anal. calcd. for $C_{20}H_{39}Cl_2N_2PTi$: C 52.53, H 8.59, N 6.13; found: C 52.30, H 8.35, N 6.04.

(Tropidinyl)(tri-*tert*-butylphosphinimido)titanium dimethyl

To a stirred solution of **2** (0.325 g, 0.71 mmol) in toluene (~30 mL) cooled at –70°C was added slowly a solution of MeMgBr in dietyl ether (3 M, 0.71 mL, 2.13 mmol, excess). The mixture was left to warm to room temperature and was stirred for 2 h. The dark purple color turned orange. The orange solution was pumped to dryness and the solid was extracted with pentane. After filtration, the pentane filtrate was pumped to dryness and an orange crystalline solid was obtained in 87% (0.26 g) yield. ^{1}H NMR (C_7D_8) δ: 4.73 (t, 1H, J = 7.3 Hz), 4.34 (dd, 2H, J_1 = 7.45 Hz, J_2 = 4.60 Hz), 3.45 (br s, 2H), 2.25 (s, 3H), 2.0 (m, 4H, CH_2), 1.26 (d, 27H, N=P-*t*-Bu_3, J = 12.7 Hz), 0.74 (s, 6H).

(Tropidinyl)(tri-*iso*-propylphosphinimido)titanium dichloride, 3

To (tropidinyl)titanium trichloride (0.442 g, 1.6 mmol) in toluene (20 mL) at –78°C was added a solution of lithium tri-*iso*-propylphosphinimide (*i*-Pr_3PNLi) (0.290 g, 1.6 mmol) in toluene (10 mL). The reaction mixture assumed a dark purple coloration. After warming to room temperature, the solution was stirred an additional 1 h and was filtered. The product, a crystalline purple solid, was crystallized from toluene–pentane with a yield of 0.519 g (72.0%). ^{1}H NMR (C_7D_8) δ: 5.56 (m, 1H), 4.67 (m, 2H), 3.58 (br s, 2H), 2.38 (s, NM*e*), 1.79 (m, 7H, CH_2 and CH(CH_3)$_2$), 0.99 (dd, 18H, J_1 = 15.32 Hz, J_2 = 7.31 Hz). Anal. calcd. for $C_{17}H_{33}Cl_2N_2PTi$: C 49.17, H 8.01, N 6.74; found: C 48.80, H 8.33, N 6.43.

(Tropidinyl)(di-*tert*-butylketimido)titanium dichloride, 4

To (tropidinyl)titanium trichloride (0.449 g, 1.62 mmol) in toluene (15 mL) at –100°C was added a slurry of lithium di-*tert*-butylketimide (*t*-Bu_2C=NLi) (0.239 g, 1.62 mmol) in toluene. No apparent reaction was observed. The mixture was stirred at room temperature for 1 h and then at 55°C for 0.5 h. The solution was filtered and heptane was added to the filtrate. The product, a blue-black solid, was crystallized with a yield of 0.22 g (35.6%). ^{1}H NMR (C_7D_8) δ: 5.35 (t, 1H, J = 7.61 Hz), 4.45 (dd, 2H, J_1 = 7.51 Hz, J_2 = 4.91 Hz), 3.47 (br s, 2H), 2.43 (s, 3H, N*Me*), 1.62 (m, 4H, CH_2), 1.19 (s, 18H). Anal. calcd. for $C_{17}H_{30}Cl_2N_2Ti$: C 53.56, H 7.93, N 7.34; found: C 53.10, H 7.66, N 7.68.

X-ray data collection and reduction

X-ray quality crystals were obtained directly from the preparation as described above. The crystals were manipulated and mounted in capillaries in a glove box, thus maintaining a dry, O_2-free environment for each crystal. Diffraction experiments were performed on a Siemens SMART System CCD diffractometer collecting a hemisphere of data in 1329 frames with 10 s exposure times. Crystal data are summarized in Table 1. The observed extinctions were consistent with the space groups in each case. The data sets were collected ($4.5° < 2\theta < 45–50.0°$). A measure of decay was obtained by re-collecting the first 50 frames of each data set. The intensities of the reflections within these frames showed no statistically significant change over the duration of the data collections. The data were processed using the SAINT and XPREP processing package. An empirical absorption correction based on redundant data was applied to each data set. Subsequent solution and refinement was performed using the SHELXTL solution package operating on a PC. The reflections with $F_o^2 > 3\sigma F_o^2$ were used in the refinements.

Structure solution and refinement

Non-hydrogen atomic scattering factors were taken from the literature tabulations (35). The heavy atom positions were determined using direct methods employing either the SHELXTL or the direct methods routines. The remaining non-hydrogen atoms were located from successive difference Fourier map calculations. The refinements were carried out by using full-matrix least-squares techniques on F, minimizing the function $\omega(|F_o|-|F_c|)^2$ where the weight ω is defined as $4F_o^2/2\sigma(F_o^2)$, and F_o and F_c are the observed and calculated structure factor amplitudes. In the final cycles of each refinement all non-hydrogen atoms were assigned anisotropic temperature factors. Carbon-bound hydrogen atom positions were calculated and allowed to ride on the carbon to which they are bonded assuming a C—H bond length of 0.95 Å. Hydrogen atom temperature factors were fixed at 1.10 times the isotropic temperature factor of the carbon atom to which they are bonded. The hydrogen atom contributions were calculated, but not refined. The final values of refinement parameters are given in Table 1. The locations of the largest peaks in the final difference Fourier map calculation as well as the magnitude of the residual electron densities in each case were of no chemical significance. Positional parameters, hydrogen atom parameters, thermal

© 2002 NRC Canada

parameters, and bond distances and angles have been deposited as supplementary material.[2]

Solution polymerization

All the polymerization experiments described below were conducted on a continuous solution polymerization reactor. The process is continuous in all feed streams (solvent, monomers, and catalyst) and in the removal of product. All feed streams were purified prior to the reactor by contact with various absorption media to remove catalyst poisons such as water, oxygen, and polar materials, as is known to those skilled in the art. All components were stored and manipulated under an atmosphere of purified nitrogen.

All the examples discussed below were from experiments conducted in a reactor of 71.5 mL internal volume. In each experiment the volumetric feed to the reactor was kept constant and as a consequence so was the reactor residence time.

The catalyst solutions were pumped to the reactor independently and there was no pre-contact between the activator and the catalyst. Because of the low solubility of the catalysts, activators, and MAO in cyclohexane, solutions were prepared in purified xylene. The catalyst was activated in situ (in the polymerization reactor) at the reaction temperature in the presence of the monomers. The polymerizations were carried out in cyclohexane at a pressure of 1500 psi (1 psi = 6894.757 Pa). Ethylene was supplied to the reactor by a calibrated thermal mass flow meter and was dissolved in the reaction solvent prior to the polymerization reactor. If a co-monomer (for example 1-octene) was used, it was also premixed with the ethylene before entering the polymerization reactor. Under these conditions the ethylene conversion is a dependent variable controlled by the catalyst concentration, reaction temperature, catalyst activity, etc.

The internal reactor temperature is monitored by a thermocouple in the polymerization medium and can be controlled at the required set point to ±0.5°C. Downstream of the reactor the pressure was reduced from the reaction pressure (1500 psi (1 psi = 6894.757 Pa)) to atmospheric. The solid polymer was then recovered as a slurry in the condensed solvent and was dried by evaporation before analysis.

The ethylene conversion was determined by a dedicated on-line gas chromatograph by referencing to propane, which was used as an internal standard. The average polymerization rate constant was calculated based on the reactor hold-up time, the catalyst concentration in the reactor, and the ethylene conversion and is expressed in L $mmol^{-1}$ min^{-1}.

Average polymerization rate (kp) = $(Q \times (100 - Q)^{-1}) \times [M]^{-1} \times (HUT)^{-1}$, where Q is the percent ethylene conversion, [M] is the catalyst (metal) concentration in the reactor expressed in mM, and HUT is the reactor hold-up time in minutes.

The polymers were characterized by high-temperature GPC in trichlorobenzene using a Waters Instrument.

Conclusions

The elimination of trimethyltin chloride from the reaction of $TiCl_4$ and 1-trimethyltin-tropidine is an excellent synthetic route to tropidinyl titanium trichloride **1**. The facial synthesis of **1** has made it possible for the synthesis of titanium complexes containing a tropidinyl ligand and other nitrogen bearing ligands. The structure of complex (*t*-$Bu_3P{=}N)(trop)TiCl_2$, **2**, suggests that the core structures of $(trop)(R_3PN)TiCl_2$ are similar to those of (L)(L′)TiCl2 where L and L′ are cyclopentadienyl and phosphinimide ligands, respectively. Polymerization studies of the dimethyl derivative of **2** in a high-temperature solution process indicated that the catalyst had low activity compared to that of Cp_2ZrMe_2.

Acknowledgments

We thank Dr. John McMeeking for the useful discussions and NOVA Chemicals Corporation for permission to publish. Financial support from NOVA Chemicals Corporation and the Natural Sciences and Engineering Research Council of Canada (NSERC) is gratefully acknowledged.

References

1. Exxon Chemical Patents Inc. Jr. Welborn and C. Howard. U.S. Patent 4 808 561, February 28, 1988.
2. Z. Wu, R.F. Jordan, and J.L. Petersen. J. Am. Chem. Soc. **117**, 5867 (1995).
3. M.K. Leclerc and H.H. Brintzinger. J. Am. Chem. Soc. **118**, 9024 (1996).
4. X. Yang, C.L. Stern, and T.J. Marks. J. Am. Chem. Soc. **116**, 10 015 (1994).
5. X. Yang, C.L. Stern, and T.J. Marks. J. Am. Chem. Soc. **113**, 3623 (1991).
6. M.K. Leclerc and H.H.G. Brintzinger. J. Am. Chem. Soc. **117**, 1651 (1995).
7. H. van der Heijden, B. Hessen, and A.G. Orpen. J. Am. Chem. Soc. **120**, 1112 (1998).
8. C.J. Hatlan, S.G. Bott, and A.R. Barron. J. Am. Chem. Soc. **117**, 6455 (1995).
9. Dow Chemicals. D.R. Neithamer and J.C. Stevens. U.S. Patent 5 350 723, September 27, 1994.
10. J.C. Stevens. Insite catalysts structure/activity relationships for olefin polymerization. Vol. 89. *Edited by* K. Soga and M. Terano. Elsevier, Amsterdam. 1994. pp. 277–284.
11. P.J. Shapiro, E. Bunel, W.P. Schaefer, and J.E. Bercaw. Organometallics, **9**, 867 (1990).
12. P.J. Shapiro, W.D. Cotter, W.P. Schaefer, J.A. Labinger, and J.E. Bercaw. J. Am. Chem. Soc. **116**, 4623 (1994).
13. D.D. Devore, F.J. Timmers, D.L. Hasha, R.K. Rosen, T.J. Marks, P.A. Deck, and C.L. Stern. Organometallics, **14**, 3132 (1995).
14. G.C. Bazan, G. Rodriguez, A.J. Ashe, S. Al-Ahmad, and C. Muller. J. Am. Chem. Soc. **118**, 2291 (1996).

[2] Supplementary data may be purchased from the Depository of Unpublished Data, Document Delivery, CISTI, National Research Council Canada, Ottawa, ON K1A 0S2, Canada (http://www.nrc.ca/cisti/irm/unpub_e.shtml for information on ordering electronically). CCDC 192463 contain the supplementary data for this paper. These data can be obtained, free of charge, via www.ccdc.cam.ac.uk/conts/retrieving.html (or from the Cambridge Crystallographic Data Centre, 12 Union Road, Cambridge, U.K.; fax +44 1223 336033; or deposit@ccdc.cam.ac.uk).

© 2002 NRC Canada

15. Occidental Chemicals Corporation. R. Krishnamurti and S. Nagy. U.S. Patent 5 554 775, September 10, 1996.
16. G.E. Herberich, U. Englert, and A. Schmitz. Organometallics, **16**, 3751 (1997).
17. A.J. Ashe, III, X. Fang, and J.W. Kampf. Organometallics, **18**, 1363 (1999).
18. Nova Chemicals. D.W. Stephan, J.C. Stewart, and D.G. Harrison. U.S. Patent 5 965 677, October 12, 1999.
19. Nova Chemicals. D.W. Stephan, J.C. Stewart, S.J. Brown, J.W. Swabey, and Q. Wang. U.S. Patent 6 063 879, May 16, 2000.
20. D.W. Stephan. unpublished results.
21. Nova Chemicals. S.J. Brown, X. Gao, D.G. Harrison, I. McKay, L. Koch, Q. Wang, W. Xu, R.E.v.H. Spence, and D. Stephan. U.S. Patent 6 239 238 B1, May 29, 2001.
22. D. Stephan, F. Guerin, R.E.v.H. Spence, L. Koch, X. Gao, S.J. Brown, J.W. Swabey, Q. Wang, W. Xu, P. Zoricak, and D. Harrison. Organometallics, **18**, 2046 (1999).
23. Nova Chemicals. S.J. Brown, X. Gao, Q. Wang, P. Zoricak, R.E.v.H. Spence, and W. Xu. U.S. Patent 6 147 172, November 14, 2000.
24. (*a*) A. Grassi, G. Maffei, S. Milione, and R.F. Jordan. Macromol. Chem. and Phys. **202**, 1239 (2001); (*b*) X. Bei, V.G. Young, Jr., and R.F. Jordan. Organometallics, **20**, 355 (2001); (*c*) S. Saccheo, G. Gioia, A. Grassi, D.E. Bowen, and R.F. Jordan. J. Mol. Catal. A: Chem. **128**, 111 (1998); (*d*) M. Yoshida and R.F. Jordan. Organometallics, **16**, 4508 (1997); (*e*) D.J. Crowther, D.C. Swenson, and R.F. Jordan. J. Am. Chem. Soc. **117**, 10 403 (1995); (*f*) D.E. Bowen, R.F. Jordan, and R.D. Rogers. Organometallics, **14**, 3630 (1995); (*g*) C. Kreuder, R.F. Jordan, and H. Zhang. Organometallics, **14**, 2993 (1995); (*h*) R. Uhrhammer, Y-X. Su, D.C. Swenson, and J.F. Jordan. Inorg. Chem. **33**, 4398 (1994); (*i*) R.F. Jordan, and D.J. Crowther. U.S. Patent 5 214 173, 25 May, 1993; (*j*) R. Uhrhammer, D.J. Crowther, J.D. Olson, D.C. Swenson, and R.F. Jordan. Organometallics, **11**, 3098 (1992); (*k*) D.J. Crowther, N.C. Baenziger, and R.F. Jordan. J. Am. Chem. Soc. **113**, 1455 (1991).
25. (*a*) P.G. Hayes, W.E. Piers, and R. McDonald. J. Am. Chem. Soc. **124**, 2132 (2002); (*b*) W-K. Kim, M.J. Fevola, L.M. Liable-Sands, A.L. Rheingold, and K.H. Theopold. Organometallics, **17**, 4541 (1998); (*c*) L.A. MacAdams, W-K. Kim, L.M. Liable-Sands, I.A. Guzei, A.L. Rheingold, and K.H. Theopold. Organometallics, **21**, 952 (2002); (*d*) K.H. Theopold, W-K. Kim, J.M. Power, J.M. Mora, and A.P. Masino. WO 01–12 637, 22 February, 2001; (*e*) K.H. Theopold, L.A. MacAdams, C. Puttnual, G.P. Buffone, and A.L. Rheingold. Polym. Mater. Sci. and Eng. **86**, 310 (2002).
26. (*a*) C-T. Chen, L.H. Rees, A.R. Cowley, and M.L.H. Green. J. Chem. Soc. Dalton Trans. **11**, 1761 (2001); (*b*) M.S. Eisen and M. Kapon. J. Chem. Soc. Dalton Trans. **23**, 3507 (1994); (*c*) S.R. Foley, C. Bensimon, and D.S. Richeson. J. Am. Chem. Soc. **119**, 10 359 (1997); (*d*) K.C. Jayaratne, R.J. Keaton, D.A. Henningsen, and L.R. Sita. J. Am. Chem. Soc. **122**, 10 490 (2000); (*e*) K.C. Jayaratne and L.R. Sita. J. Am. Chem. Soc. **122**, 958 (2000); (*f*) R.J. Keaton, K.C. Jayaratne, J.C. Fettinger, and L.R. Sita. J. Am. Chem. Soc. **122**, 12 909 (2000); (*g*) L.A. Koterwas, J.C. Fettinger, and L.R. Sita. Organometallics, **18**, 4183 (1999); (*h*) A. Littke, N. Sleiman, C. Bensimon, D.S. Richeson, G.P.A. Yap, and S.J. Brown. Organometallics, **17**, 446 (1998); (*i*) L.R. Sita and J.R. Babcock. Organometallics, **17**, 5228 (1998).
27. G.G. Lavoie and R.G. Bergman. Angew. Chem. Int. Ed. Engl. **36**, 2450 (1997).
28. S.J. Skoog, C. Mateo, G.G. Lavoie, F.J. Hollander, and R.G. Bergman. Organometallics, **19**, 1406 (2000).
29. Nova Chemicals. J. McMeeking, X. Gao, R.E.v.H. Spence, S.J.Brown, and D. Jeremic. U.S. Patent 6 114 481, September 5, 2000.
30. Dutch Polymer Institute. W.P. Kretschmer, A. Meetsma, J.H. Teuben, and P.H.M. Budzelaar. High active thermal stable Ti-based olefin polymerization catalysts with monohapto guanidinate ancillary ligands. Presented at the International Symposium on Olefin Mathesis XIV, MIT, Massechussetts, U.S.A. August 5–9, 2001.
31. A. Ladenburg. Justus Liebigs Ann. Chem. **217**, 118 (1888).
32. I.A. Ronova and N.V. Alekseev. Dokl. Akad Nauk SSSR, **174**, 614 (1967).
33. N.V. Alekseev and I.A. Ronova. Zh. Strukt. Khim. **7**, 103 (1966).
34. I.A. Latham and G.J. Leigh. J. Chem. Soc. Dalton Trans. 377 (1986).
35. D.T. Cromer and J.B. Mann. Acta Crystallogr. A. **A24**, 390 (1968).
36. T.E. Ready, R.O. Day, J.C.W. Chien, and M.D. Raush. Macromolecules, **26**, 5822 (1993).
37. G.H. Llinas, M. Mena, F. Palacios, P. Royo, and R. Serrrano. J. Organomet. Chem. **340**, 37 (1988).

© 2002 NRC Canada

Linear and nonlinear optical responses of a dye anchored to gold nanoparticles dispersed in liquid and polymeric matrixes

Ignacio Vargas-Baca, Andrew P. Brown, Mark P. Andrews, Tigran Galstian, Yuejun Li, Hojatollah Vali, and Mark G. Kuzyk

Abstract: The compound [4-$CH_3C_6H_4$-SS-CH_2CH_2-N(CH_3)$C_6H_4C(C_6H_4N(CH_3)_2)$-4)$_2$]Cl (**1a**) consists of the triarylmethyl chromophore of crystal violet appended to an organic disulfide, to entail direct attachment of this dye to gold surfaces. Addition of **1a** to colloidal dispersions of the metal produced a stable dispersion in methanol–water mixtures. Transmission electron microscopy of Freeze-Fracture sections shadowed with carbon and platinum confirmed that the dispersion remains unaggregated. Local-field effects and coupling to the surface plasmon of gold magnified the interaction of the chromophore with optical fields. A large oscillator strength in the visible spectrum (*f* ca. 35) and a first hyperpolarizability (β ca. 10^{-26} esu, hyper-Rayleigh scattering) were observed as the colloid adsorbed dye molecules. A Hill-type analysis indicated that the adsorption process is cooperative. This combination of organic chromophore and nanoparticle was adapted for incorporation into PMMA-based composite films whose electrooptic coefficient (r_{113} = 2.20 pm V^{-1}) is larger than the sum of the individual contributions of dye and metallic particles.

Key words: chromophores, colloids, gold, local-field effects, nonlinear optical materials.

Résumé : Le composé [4-$CH_3C_6H_4$-SS-CH_2CH_2-N(CH_3)$C_6H_4C(C_6H_4N(CH_3)_2)$-4)$_2$]Cl (**1a**) comprend le chromophore triarylméthyle du cristal violet fixé sur un disulfure organique qui permet d'attacher directement ce colorant sur des surfaces d'or. L'addition du composé **1a** à des dispersions colloïdales du métal conduit à la formation d'une dispersion stable dans des mélanges méthanol–eau. La microscopie électronique de transmission de sections Freeze-Fracture ombragées par du carbone et du platine permet de confirmer que la dispersion dans un état qui n'est pas agrégé. Les effets de champs locaux et le couplage de l'or à la surface plasmonique amplifient l'interaction du chromophore avec les champs optiques. Avec l'absorption de molécules de colorant par le colloïde, on a observé une grande force oscillatoire dans le spectre visible (*f* d'environ 35) ainsi qu'une première hyperpolarisabilité (β environ 10^{-26} esu, diffusion hyper-Rayleigh). Cette combinaison de chromophore organique et de nanoparticule est adaptée à une incorporation dans des films composites à base de PMMA dont le coefficient électrooptique (r_{113} = 2,20 ppm V^{-1}) est supérieur à la somme des contributions individuelles du colorant et des particules métalliques.

Mots clés : chromophores, colloïdes, or, effets de champs locaux, matériaux optiques non linéaires.

[Traduit par la Rédaction]

Introduction

It is predicted that a third of current electronic technologies for data transmission and processing will eventually be replaced by their faster photonic counterparts. The development of practical electrooptic and photorefractive applications depends on the availability of materials with large nonlinear optical (NLO) responses. Crystals of $LiNbO_3$, KH_2PO_4, and BaB_2O_4 are used to change the wavelength of laser light through parametric processes. Such materials are expensive and cumbersome to tailor into the waveguide configurations that are compatible with optical fibre systems. Because of their processability, polymers and glasses with NLO properties are a convenient alternative to inorganic crystals. Conjugated polymers such as polydiacetylenes have inherent third-order NLO activity but most systems consist of a transparent host-matrix uniformly doped with a NLO-active species. Two kinds of such NLO dopants can be dis-

Received 31 January 2002. Published on the NRC Research Press Web site at http://canjchem.nrc.ca on 29 November 2002.

Dedicated to Professor Tris Chivers for his contributions to Canadian chemistry.

I. Vargas-Baca,[1] A.P. Brown,[2] M.P. Andrews,[3] Y. Li, and H. Vali. Department of Chemistry, McGill University, 801 Sherbrooke St. W., Montréal, QC H3A 2K6, Canada.
T. Galstian. Department of Physics, Laval University, Québec, QC G1K 7P4, Canada.
M.G. Kuzyk. Department of Physics, Washington State University, Pullman, WA 99164-2814, U.S.A.

[1]Present address: Department of Chemistry, McMaster University, 1280 Main Street West, Hamilton, ON, Canada.
[2]Present address: Corning Incorporated, Corning, NY 14831, U.S.A.
[3]Corresponding author (e-mail: andrews@chemistry.mcgill.ca).

 DOI: 10.1139/V02-147 © 2002 NRC Canada

tinguished: organic chromophores and nanoparticles of semiconductors or metals.

Second- (1, 2) and third-order NLO activity (3) can be induced with organic dyes. The nonlinear response of the composite is in principle proportional to the amount of chromophore present. However, large loadings have an unfavourable effect on mechanical properties, may decrease transparency, and lead to attenuation by dipolar coupling as the inter-chromophore distance decreases. It is therefore desirable to prepare chromophores with the largest hyperpolarizabilities possible. Systematic research during the past two decades has identified features such as a high degree of bond alternation that give organic molecules large hyperpolarizabilities (4). Furthermore, the NLO response of organic species can be augmented up to an order of magnitude when they are organized in orientationally correlated assemblies (5) and chiral supramolecular architectures (6). A remarkable achievement in this field was the preparation of a chromophore that conferred a polymer a high electrooptic coefficient of about 20 pm V^{-1}. This, in turn, led to the fabrication of a 0.1 THz electrooptic modulator operating with a drive voltage of less than 1.0 V (7).

A completely different class of NLO dopants includes small particles of gold, silver, or metal chalcogenides. Because of their inherent symmetry, dispersions of such particles have been considered only as third-order NLO materials (8, 9). A two-wave-mixing device capable of operating as an all-optical switch or gate has been demonstrated (10). The recent discovery of second-order NLO activity for liquid colloidal dispersions of gold (11, 12) opened the possibility of their use in electrooptic devices.

The optical response of metallic colloids arises from the ease with which electromagnetic fields excite electrons at the surface of the particles. Photo-excitation induces charge density oscillations, in particular a collective movement of electrons. This surface plasmon is partially responsible for the intense absorptions at 500–550 and 400 nm, which are characteristic of wine-red gold and yellow-brown silver hydrosols, respectively. It is well known that electronic excitation leads to an electric field redistribution near the metal surface, especially an enhancement in small step sites or protrusions (13, 14) as well as in tiny particles and their aggregates (15, 16). Molecules in the vicinity of such surfaces experience an intense electric field and an increase in their cross-sections for optical interactions. This antenna effect is thought to play an important role in surface enhanced Raman spectroscopy (17). Numerous theoretical calculations have predicted large enhancement factors for luminescence and light absorption of molecules on the surface of small metallic particles (18–20), with further enhancement of absorptivity for systems in which molecular electronic transitions and the plasmon resonance overlap.

Previous studies of the enhancement of linear optical responses in dye–metal composites have been carried out, depositing dyes on metal island films through sublimation, solvent evaporation, spin coating, or adsorption from liquid solutions (21–26). Those systems indeed exhibited stronger linear optical responses as compared to metal-free controls. Alternatively, dyes have been combined with colloidal dispersions and activated quartz slides have been dipped in the mixtures (27). On such heterogeneous surfaces it is not possible to unambiguously distinguish true local field enhancement from changes of composition due to preferential adsorption of dye on the metal. Thus quantitative conclusions must be drawn cautiously.

We are specifically interested in theoretical predictions of local field enhancements of the nonlinear response of chromophores (28–30). Experimentally, it has been reported that dispersions of gold clusters in polydiacetylenes induce an enhancement of the third-order susceptibility ($\chi^{(3)}$) by two orders of magnitude in comparison to the polymer alone (31, 32). In addition, strong hyper-Rayleigh scattering (HRS) has been observed for silver colloids in the presence of *para*-nitroaniline (33). Important factors such as particle aggregation, the actual distance of the chromophore to the surface, coupling of electronic excitations, and the particle shape have not been carefully considered.

In this report, we present the synthesis of an NLO active chromophore modified with a disulphide group **1a** (See below) to anchor the molecule to the surface of colloidal gold particles. We observed increases of the linear and nonlinear optical responses as the molecules are adsorbed onto the metal surface and produce stable dispersions of dye-coated metal colloids. We also prepared polymer films doped with these dye–gold particles and observed an enhanced electrooptic coefficient.

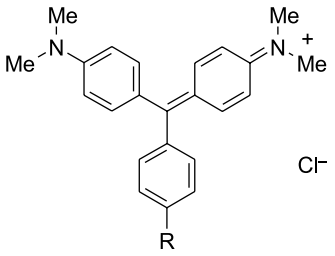

1

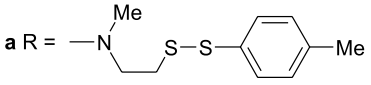

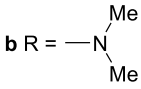

Experimental

Materials and methods

The manipulation of moisture sensitive materials was carried out under an atmosphere of dry nitrogen using Schlenk and dry box techniques. Organic solvents used for synthesis were purified by distillation over the appropriate drying agent. Most chemicals were obtained from Aldrich and used as received. The disulfide substituted aniline 4-$CH_3C_6H_4$-SS-CH_2CH_2-N(CH_3)-C_6H_5 (**2**) was prepared stepwise; treating N-methyl aniline with ethylene sulfide to obtain $C_6H_5N(CH_3)$-CH_2CH_2-SH and reacting the corresponding lithium salt with 4-$CH_3C_6H_4$-SCl. HPLC grade methanol and Milli-Q™ water were used for the preparation of

© 2002 NRC Canada

Fig. 1. Mach-Zender Interferometric system for the measurement of electrooptic coefficients. P, polarizing beamsplitter; B, beamsplitter; C, chopper; S, test sample; R, reference sample; G, glass slide; L, microscope objective; D, silicon photodiode detector; H, pinhole; LA, lock-in amplifier; EA, electronic amplifier.

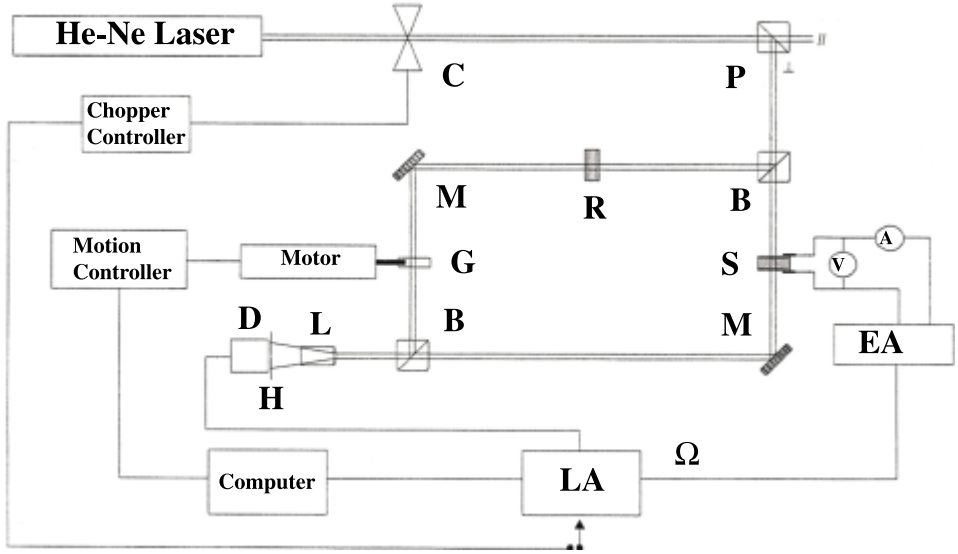

colloids. Soda-lime glass slides 1 mm-thick with a 200 Å layer of indium-tin oxide (ITO) were obtained from Delta Technologies and cleaned with acetone and aqueous NaOH.

Instrumentation

All NMR spectra were acquired in a Varian XL200 instrument. IR spectra were recorded in a Brucker IFS-48 FT spectrometer. Raman spectra were collected on a home-built instrument described elsewhere (34); the 514.5 nm line of an Ar^+ laser was used to excite scattering with less than 30 mW of power to minimize sample degradation. Mass spectra were obtained on a KratosMS25RFA spectrometer, FAB was performed with a Xe source (7 kV, 0.4 mA) and an NBA matrix. A diode-array HP-8452A spectrophotometer was adapted with optical-fiber bundles to measure UV–Vis spectra in a custom-built thermostated cell holder with magnetic stirring. Transmission electron microscopy studies were conducted on a Jeol JEM2000FX instrument operating at 80.0 kV. Freeze fracture samples were prepared in a Reichert-Jung KF80 Universal Cryofixation Unit and shadowed in a BALZERS BAF300 Freeze-Etch Unit

Hyper-Rayleigh scattering measurements were performed with a custom-built instrument. A Q-switched Continuum Surelite II Nd:YAG laser provided the fundamental wavelength of 1064 nm in 5 ns pulses with a 10-Hz repetition rate. The laser output, 300–400 mJ per pulse, was reduced to approximately 2 mJ and controlled with the combination of a half-wave retarder, a polarizing cube, and a visible filter as attenuator. This pump beam was focussed onto the sample and the second harmonic signal collected on a photomultiplier with the appropriate sets of lenses. A broad-band infrared filter and an interferential filter were used to prevent all wavelengths but 532 nm from reaching the detector connected to an oscilloscope.

Thin film samples were prepared with a Headway photoresist spin-coater; their thickness was measured using a Dektak 3030ST surface profilometer. Transparent gold electrodes were produced in an Edwards Auto 306 metal-atom evaporator.

The second-order NLO properties of film samples were determined by measuring the Electrooptic coefficient r_{113} in a custom-built set up. The experimental apparatus is shown in Fig. 1. The central element is a Mach-Zehnder interferometer operating with a randomly polarized He-Ne laser (632.8 nm, 8 mW) as the optical source. The input beam was polarized using a 50/50 polarizing beam-splitter and separated into the sample and reference arms using a second beam-splitter. For background measurements, the beam was modulated with a chopper operating 1000 Hz. The test and reference samples had identical structure, which improved the fringe visibility of the interferometer by balancing the light intensity of the arms. The reference arm also contained a glass slide that was rotated by a precision step motor with a controller interfaced to a microcomputer. This slide provided a variable path-length difference (and therefore a phase shift) between the two arms of the interferometer. The beams were recombined and a microscope objective (2O ×) was used to expand the output light beam onto a silicon photodiode detector. The fringe visibility was improved further with the help of a pinhole (d = 400 μm). The detector was connected to a lock-in amplifier, which also provided an internal reference (Ω = 1000 Hz) and oscillation for measurements of the modulated sample. The applied voltage (V_{rms}) was controlled further using an electronic amplifier. Oscillations due to air drafts were minimized by enclosing the optical set-up in a plastic encasing and vibrations were damped using an optical table with pneumatic isolation.

Synthesis of 1a

By adaptation of a technique for the preparation of crystal violet, thionyl chloride (0.55 mL, 6.9 mmol) was carefully added to Micheler's ketone (1.84 g, 6.9 mmol) in 20 mL of toluene at 100°C. After 10 min a brown glassy phase separated from the solvent. Compound **2** (2.61 g, 9.0 mmol) was added with the help of 5 mL of toluene. The mixture was

© 2002 NRC Canada

cooled after 40 min and 1 mL of triethyl amine was added slowly with vigorous stirring. After 16 h the solvent was decanted and the residue was reprecipitated from ethanol-toluene, washed with warm hexane, and dried under vacuum. The crude product was purified by chromatography with a toluene–ethanol gradient of increasing polarity on a cellulose column. The product was obtained as a dark-purple microcrystalline solid with metallic lustre. Yield 11% (0.43 g, 0.7 mmol). UV–Vis (MeOH, MeOH 20%): λ_{max} (ε), 558 (94 000, 70 500), 590 nm (10 400, 68 400 mol^{-1} dm^3 cm^{-1}). FT-IR (KBr) (cm^{-1}): 422, 524, 562, 665, 722, 743, 758, 800, 828, 913, 942, 1063, 1133, 1173, 1227, 1295, 1335, 1363, 1445, 1478, 1522, 1583 (ν). Resonance Raman (MeOH 20%, 2.9×10^{-5} M, 514 nm) (cm^{-1}): 1618, 1586, 1538, 1381, 1306, 1180, 920, 809, 434. ^{1}H NMR (200 MHz, $CDCl_3$) δ: 7.6–6.5 (m, 16H), 4.0–3.5 (m, 19), 2.4–2.1 (broad, 3H). FAB-MS (NBA) *m*/*z* (%): 540 ([M^+], 20), 416 ([$M^+ - HSC_4H_4CH_3$], 10).

Preparation of colloids

Gold dispersions stable in aqueous methanol were prepared by reduction of $HAuCl_4$ in glassware that had been carefully cleaned with aqua regia and rinsed with Milli-Q™ water. All solutions were prepared in methanol 20% (w/v) and filtered through a 0.2 µm PTFE membrane immediately before mixing. In a typical preparation $NaBH_4$ (6.6 mg, 0.17 mmol) was dissolved in 10 mL and added dropwise to $HAuCl_4 \cdot 3H_2O$ (11.0 mg, 2.8×10^{-2} mmol) in 40 g of solvent mixture with vigorous stirring. After 1 h, 10 mL of a 0.4% (w/v) solution of H_2O_2 were added slowly to remove any excess of $NaBH_4$. The next day the sol was diluted to complete 100 mL. Colloids prepared this way were stable for weeks. Each batch was characterized by UV–Vis spectroscopy and TEM.

For adsorption studies, the UV–Vis spectra and (or) hyper-Rayleigh scattering intensity were measured as the gold sol was titrated in a cuvette with small additions of a dilute solution of **1a** under vigorous stirring with delay period of 10 s after each addition for equilibration.

Transmission electron microscopy

Colloid samples for routine particle-size measurements were prepared by solvent evaporation on carbon-coated copper grids (300 mesh). To examine the morphology of a colloid, a drop of the liquid sample was frozen at –142°C (liquid propane). The sample was then cut and etched at –102°C under high vacuum, and a replica was made by shadowing with platinum and carbon (200 V, 100 mA each). The replica was deposited on a plain-copper grid (300 mesh) with distilled water.

Preparation of dye–colloid dispersions in polymer films

A conductive strip was patterned on an ITO slide by acid etching. Films of about 10 µm thickness were cast from a solution of PMMA in *iso*-propanol/toluene (39% w/v) that also contained dodecylamine-coated gold particles (0.22% metal/polymer by weight) (35) and (or) **1a** (0.05 molar ratio to gold). The films were allowed to age in order to remove residual solvents and a thin layer of gold was deposited to serve as a transparent electrode.

Results and discussion

We designed an experiment in which colloidal metallic particles were to be mixed with a NLO dye in solution while their linear (absorbance) and nonlinear (second harmonic scattering) optical responses could be monitored. Guided by published theoretical predictions, we focussed on those factors that would maximize local field effects, namely minimal separation between the chromophore and metal surface and overlap of electronic excitations of dye and metal particle.

The chromophore of crystal violet (**1b**), the tris(*para*-dialkylaminophenyl)methyl cation, was chosen for this study, since it displays (*a*) extensive overlap of its visible absorption (λ_{max} = 590 nm) with the plasma resonance of colloidal gold, (*b*) a large octupolar hyperpolarizability (36), and (*c*) an emission in hyper-Rayleigh scattering that is well separated from multi-photon fluorescence when irradiated at 1064 nm (37).

In recent years, there has been considerable development of self-assembly processes at interfaces. A number of protocols for efficient adsorption of molecules on gold surfaces have been successfully extended to the derivatisation of gold nanocrystals, especially with organosulfur compounds: thiols, disulfides, and sulfides (38–40). We decided to use a disulfide group to directly anchor the chromophore to the surface of gold colloidal particles, using a short chain to maximize interaction with the particle.

It is known that metal colloids in water adsorb many organic molecules, including dyes. However, in some cases it is uncertain whether the molecules are truly in contact with the surface of the particle or sit on top of other adsorbates. The anionic 4,5-benzoindotricarbocyanine builds a multilayered structure onto gold hydrosols stabilized with poly(vinyl alcohol). This is accompanied by a bathocromic shift from 778 to 895 nm but no enhancement of absorbance (41). Silver colloids with adsorbed malachite green (**1c**) require inorganic salts as stabilizing agents. The ions may be a mayor component of the surface structure, since the number and intensity of bands in the visible and Raman spectra are strongly influenced by the salts (42, 43).

Synthesis and properties of 1a

Common methods for the preparation of triarylmethyl dyes involve oxidation steps that are incompatible with some sulfur functional groups. Coupling of the disulfide-containing aniline **2** with Micheler's ketone, activated with thionyl chloride, avoided harsh conditions, but the overall yield was low and repeated chromatographic elutions were necessary to remove impurities. The product was identified by the peak of its cation in the FAB mass spectrum. The ^{1}H NMR spectrum displayed a complex broadened pattern due to dynamic exchange of the conformers defined by different orientations of the disulfide bond. Variable temperature studies confirmed the fluxional nature of the structure but failed to simplify completely the spectrum up to 90°C in DMSO-d_6. The same phenomenon was observed in the disulfide substituted aniline **2**. The purity of the product was assessed by chromatography and UV–Vis spectroscopy. Figure 2 compares its spectrum to that of a commercial sample of crystal violet (95%+ pure). In pure methanol their spectra are virtually identical, with maxima at 590 nm and shoulders

© 2002 NRC Canada

Fig. 2. UV–Vis spectra: (*a*) **1a** in MeOH; (*b*) **1b** in MeOH; (*c*) **1a** in MeOH 20% (w/v).

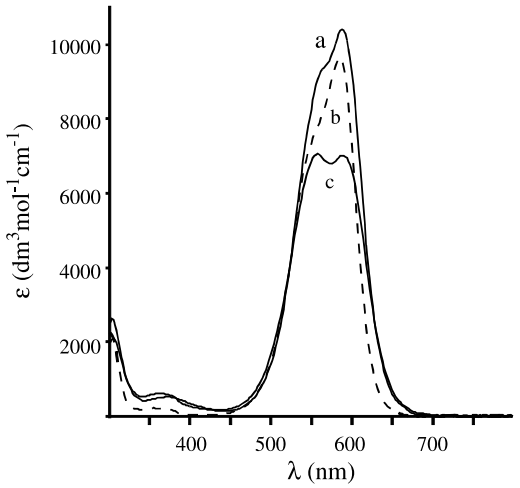

at 558 nm due to the formation of aggregates. On the basis of the calculated molar absorptivities **1a** was considered pure and used without further treatment. Different from **1b**, **1a** is sparingly soluble in water and solubilization is facilitated by addition of alcohol. In methanol 20% (w/v) the total absorptivity is smaller and the aggregate's band is well resolved. For all adsorption studies, the equilibrium of self-association was neglected, since the two maxima followed the Beer-Lambert law within the range of concentrations employed.

Adsorption of 1a onto gold colloids

Gold colloids prepared in methanol 20% were titrated with **1a** while their visible absorption spectra were monitored. The result of a typical titration is shown in Fig. 3. Upon addition of the dye an intense band appears at long wavelengths; its position depends on the diameter of the particles (λ_{max} = 740 nm for d = 13 ± 5 nm and 676 nm for d = 6 ± 2 nm). The absorbance kept increasing after each addition until a certain amount of dye, characteristic for each size of colloid, was reached. As well, the height of this peak depended linearly on the total concentration of gold for a single size of particle. This behaviour suggests that the new band is due to the dye molecules adsorbed on the surface of the colloidal particles and that the surface is eventually saturated. In the case of 13 nm particles and based on the amount of dye adsorbed by the colloid, the oscillator strength (*f*) was estimated to be close to 35 for this band.

However, the changes observed in the visible spectrum also resemble those due to particle aggregation; thus appropriate control experiments were performed. We noted that addition of NaCl, *p*-tolyldisulfide, and even **1b** as flocculating agents to the 13 ± 5 nm colloid each produced a distinctive maximum always at 704 nm, as shown in Fig. 4. More important, those aggregated colloids were extremely unstable and precipitated within seconds; colloids treated with **1a** did not require any stabilizer and were stable for days provided that all glassware was scrupulously clean, all solutions were filtered to exclude nucleation points, and evaporation was prevented. As the visible spectra alone are not evidence against aggregation, the morphology of colloids treated with **1a** was examined by transmission electron microscopy. Freeze-fracture sections of the same samples used for absorbance measurements were shadowed with carbon and platinum. The micrograph in Fig. 5 displays well-separated metal nanoparticles following a radial distribution of mass with a coefficient practically equal to 2.0; thus the particles are evenly spread in two dimensions. This is in striking contrast with the well-known properties of flocculated metal colloids, whose aggregation proceeds through a mechanism of collisions between clusters and results in highly branched structures with radial distribution coefficients of about 1.75. Because of the non-integer value of this "Hausdorf dimension", such aggregates are usually considered to be "fractal" (44). On the basis of the stability of the **1a**–gold dispersions and the radial distributions in the

Fig. 3. UV–Vis spectra in MeOH 20% (w/v): (*a*) **1a** 19.3 × 10^{-6} mol dm^{-3}; (*b*) gold colloid (d = 6 ± 2 nm, C_{Au} = 2.1 × 10^{-4} mol dm^{-3}, v_0 = 3.045 mL); (*c*) to (*l*) evolution after addition of **1a** (1.2 × 10^{-4} mol dm^{-3}) in 0.025 mL increments. Inset: dependence on the absorbance at 680 nm on the concentration of added **1a**.

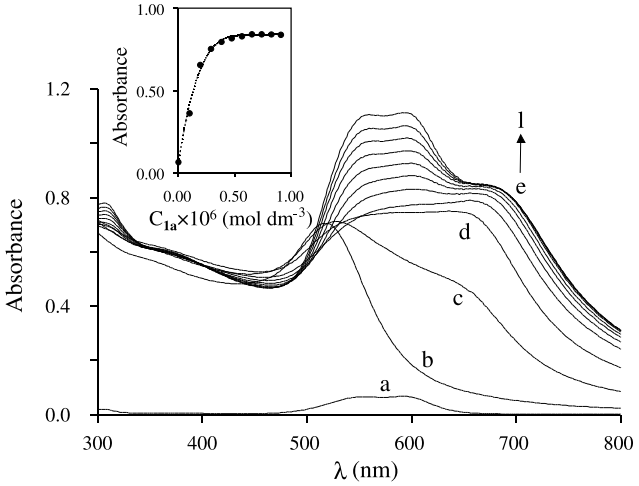

Fig. 4. Visible spectra of control experiments in MeOH 20% (w/v): (*a*) gold colloid, d = 13 ± 5 nm, λ_{max} = 526 nm, C_{Au} = 2.8 mol dm^{-3}, v_0 = 3.0 mL. (*b*) a + 0.25 mL saturated NaCl, t = 10 s, λ_{max} = 704 nm; (*c*) flocculated b at t = 500 s; (*d*) a + 0.15 mL (4-$CH_3C_6H_4S)_2$ 2.0 × 10^{-4} mol dm^{-3}, t = 30 s, λ_{max} = 704 nm; (*e*) a + 0.10 mL **1b** 2.1 × 10^{-4} mol dm^{-3}, t = 30 s, λ_{max}= 706 nm. (*f*) a + 0.25 mL **1a** 2.9 × 10^{-4} mol dm^{-3}, t = 30 min, λ_{max} = 740 nm.

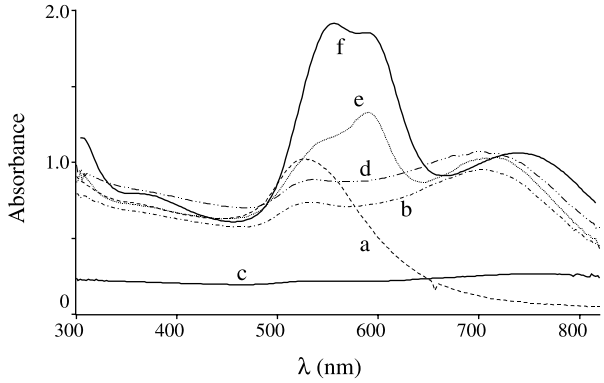

© 2002 NRC Canada

Fig. 5. Transmission electron micrograph and radial particle distribution of a freeze-fracture section from a gold colloid treated with **1a**.

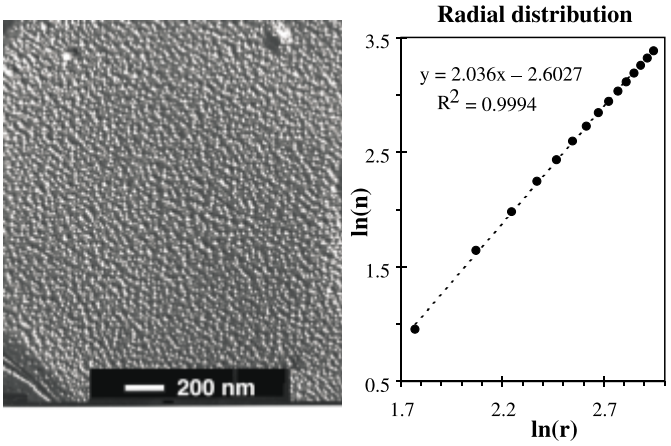

Fig. 6. Hill plot for the colorimetric titration of gold colloid (d = 6 ± 2 nm, $C_{Au} = 2.1 \times 10^{-4}$ mol dm^{-3}) with **1a** from absorbance measurements at 680 nm.

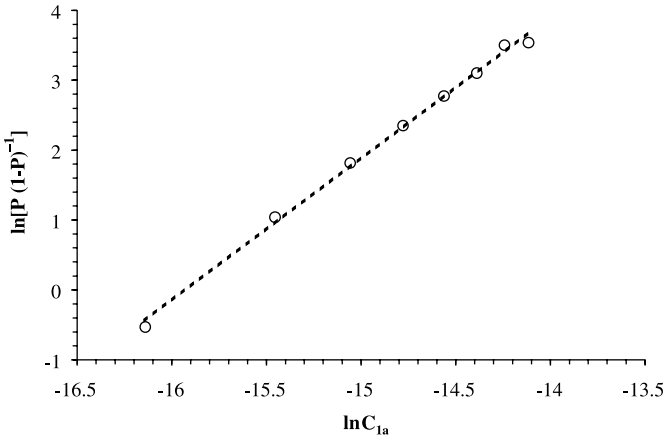

electron micrographs we concluded that colloidal particles treated with **1a** remain in dispersion.

After ruling out aggregation as the cause of the changes in the visible spectra, the absorbance data were used to examine in detail the process of dye adsorption onto the colloid. The inset of Fig. 3 shows the dependence of absorbance, at the maximum of the new band, on the concentration of added dye; it resembles a Langmuir isotherm. However, the corresponding Scatchard plots (45) were highly nonlinear. Figure 6 shows the linear fit that is obtained with eq. [1], which is Hill's model for cooperative adsorption. P is the fraction of occupied binding sites, $C_{\mathbf{1a}}$ the concentration of dye added to the dispersion, K the equilibrium constant, and n_H the Hill coefficient. For several samples of different particle size the correlation coefficients were about 0.99, and n_H values larger than 1.0 (see Table 1). This is consistent with the cooperative character of the process. Similar behaviour is known for the assembly of rotaxanes on functionalised gold nanocrystals (46). Analysis of Hill plots obtained by colorimetric titration of three separate batches of colloid afforded consistent values for the adsorption equilibrium constant, which was temperature insensitive within the experimental error between 15 and 55°C.

$$[1] \qquad \ln\left(\frac{P}{1-P}\right) = n_H \ln C_{1a} + n_H \ln K$$

Raman spectroscopy was used to investigate the orientation of the chromophore with respect to the metallic surface. In solution, the spectrum of the dye was acquired under resonance conditions. Only those modes involving the chromophore were preferentially enhanced for scattering, thus the spectrum of **1a** was virtually identical to that of **1b** (47, 48) without any vibrations from the pendant disulfide branch. Upon adsorption on the gold colloid, a surface-enhanced spectrum with a larger signal-to-noise ratio was obtained, but it did not reveal any new features. Similar spectra were expected because resonance is the dominant effect in surface enhanced Raman spectroscopy of tryphenylmethane dyes (49). A perpendicular orientation of the chromophore with respect to the surface would entail a reduction of symmetry, but none of the anticipated band splittings were observed.

Table 1. Hill analyses for the adsorption of **1a** on colloidal gold at room temperature.

Particle size (nm)	Method	n_H	ln K
6 ± 2	Absorbance, 680 nm	2.0 ± 0.1	15.9 ± 0.1
13 ± 5	Absorbance, 800 nm	1.3 ± 0.5	14 ± 0.1
7 ± 2	Absorbance, 800 nm	2.6 ± 0.1	14 ± 1
7 ± 2	HRS, 532 nm	2.8 ± 0.3	13 ± 2

Therefore a parallel orientation is suggested. This arrangement of the chromophore on the surface provides the minimum distance possible to the metal surface, which is ideal for the enhancement of nonlinear optical properties.

HRS measurements

To evaluate its nonlinear optical response, one of the colloids used in the absorbance study (d = 7 ± 2 nm) was excited with the fundamental wavelength of 1064 nm and the scattered light was measured at the frequency of the second harmonic 532 nm. In this technique, the intensity of the signal ($S_{2\omega}$) depends on the square of the pump power (I_0) as modeled by eq. [2] (50). This includes a correction for absorbance (Abs); the constant G is characteristic of the experimental set-up and was evaluated with a standard of *para*-nitroaniline in methanol. The term B^2 contains the sum of the orientational average of β^2 of each component multiplied by its number density N. The initial colloidal dispersions of gold in MeOH 20% produced second harmonic light on their own. Based on the accepted values of hyperpolarizabilities for water and methanol, we found $\beta_{Au} = (2.1 \pm 0.5) \times 10^{-27}$ esu per gold atom, in agreement with a previous report (11, 12).

$$[2] \qquad S_{2\omega} = GB^2 I_0^2 10^{-\mathrm{Abs}}, \quad B^2 = \sum N_i \left\langle B_i^2 \right\rangle$$

Addition of **1a** to the colloid produced unusually strong HRS signals, which deviated from the linear dependence on the square of the pump intensity. As seen in Fig. 7, this was especially true for the samples with larger amounts of dye and may be due to the activation of nonlinear processes of higher order such as three-photon fluorescence and third

© 2002 NRC Canada

Fig. 7. Dependence of the HRS intensity, $S_{2\omega}$, on the fundamental intensity, 1064 nm, of a gold colloid (d = 7 ± 2 nm, C_{Au} = 2.0 × 10^{-4} mol dm^{-3}) upon addition of increasing amounts of **1a**. Inset: Magnification of the response at low pump intensity.

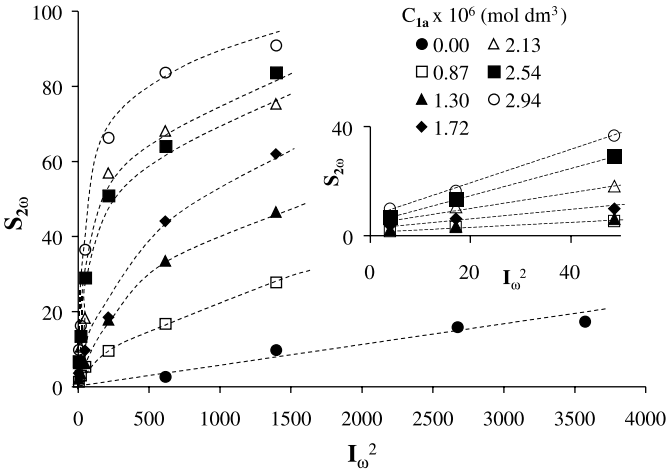

harmonic generation. The magnitude of B^2 was extracted from the initial slopes and used to construct a Hill plot that was consistent with the one obtained from absorbance measurements (Table 1). After subtraction of the contribution from gold and evaluation of the amount of **1a** that saturates the surface of the particles, a value of β ca. 10^{-26} esu was estimated for the chromophore. This is at least one order of magnitude larger than the reported values for the parent dye, **1b**. Since the dye-coated particles absorb strongly at the wavelength of the second harmonic, the apparent increase of hyperpolarizability could be due to resonant enhancement. This interpretation should be approached cautiously. The direct electronic interaction between metal and chromophore cannot be ruled out at this point; the new band in the visible absorption spectrum may arise from a dye–gold charge transfer, in which case the coated metallic particle should be regarded as a new "molecular" entity with its own oscillator strength and hyperpolarizability. Furthermore, the optical properties that were observed are the collective response of a set of colloidal particles with a variety of sizes and shapes; it is known that contributions from only a few "hot particles" may dominate local field effects (51). Measurements under aggregation conditions were not possible because of the instability of such samples.

Electrooptic coefficients of polymer films

To take advantage of the intense NLO activity of the gold–**1a** combination, the dispersion must be incorporated into a suitable matrix. The dye **1a** is very soluble in polar organic solvents, whereas gold colloids are not. Long-chain alkyl amines readily adsorb on gold nanoparticles and render them dispersible in toluene. Such amine coatings are only kinetically stable and can be readily replaced by stronger adsorbates with sulfur functional groups, including **1a**. Concentrated PMMA solutions in toluene–isopropanol mixtures were used to prepare thin films on glass slides. Samples were prepared with and without dodecylamine-coated colloids and (or) **1a** in appropriate proportions. The films were placed between transparent electrodes of ITO and gold

Fig. 8. Electrooptic-experiment interferometer fringe profiles for the measurement of films containing (*a*) gold–amine dispersions, (*b*) **1a**, (*c*) gold–**1a** dispersion.

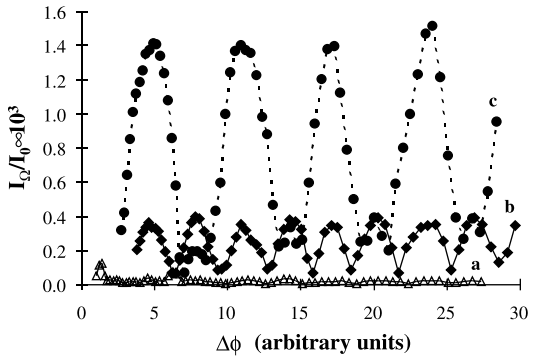

and were subject to a transversal modulated voltage. This caused a variation of refractive index due to the nonlinear susceptibilities of the material (Pockel's effect). With a Mach-Zender interferometer the phase retardation of a laser beam propagating parallel to the electric field was measured. Measurements were carried out with a variable phase on the reference arm of the interferometer to determine the amplitude of intensity at the modulating frequency. The electrooptic coefficient r_{113} was defined by eq. [3] (52), where λ is the wavelength of the probe laser beam, n the refractive index of the material, V_{rms} the root-mean-square modulating potential, I_Ω and I_0 the intensity out of the interferometer modulated and unmodulated, respectively.

$$[3] \qquad r_{113} = \frac{\lambda}{\pi n^3 V_{rms}} \frac{I_\Omega}{2\sqrt{2I_0}}$$

The fringe profiles from which the EO coefficients were extracted are displayed in Fig. 8. The combined gold–**1a** sample had an EO coefficient (r_{113} = 2.20 pm V^{-1}) larger than those of the films containing only **1a** (0.80 pm V^{-1}) or amine-coated gold particles (0.36 pm V^{-1}) in the same concentrations. The observed coefficient is even larger than the sum of the individual contributions. Current efforts are directed towards maximizing the activity of such composites. Despite the intense harmonic light scattered by dye-coated colloids in liquid dispersion, the observed nonlinear processes are inherently incoherent because of the random distribution of particles. The activity of the polymeric films may be a consequence of anisotropy induced by spin-casting. It can be conceived that more efficient composites will be accessible by tailoring the morphology of the metal dispersion into two- or three-dimensional arrays (53–57).

Conclusions

We have derivatized a triarylmethyl dye by appending a short hydrocarbon arm with a disulfide group to anchor the chromophore to the surface of nanoscopic gold particles. The colloids treated with this dye were stable. Adsorption of the derivatized molecule proceeded by a cooperative process that was followed by monitoring the linear and nonlinear optical responses. TEM demonstrated that aggregation is not a factor in these observations.

© 2002 NRC Canada

Similarly, an enhanced electrooptic coefficient was observed for polymer films that contained both the dye and gold particles. The observed enhancement of optical properties offers opportunities to implement methodologies for chemical analysis and sensors. There is considerable interest in composites containing metal nanoparticles for chemical analysis (58), sensing (59), and nanoscale electronics (60). Local field enhancement of the NLO response of a chromophore will be advantageous for the construction of devices with combined functionality. For example, metallic particles can be grafted on waveguides for an evanescent wave to probe spectroscopically species and chemical processes at the surface (34).

Supplemental material available

Hill plot obtained from HRS measurements.[4]

Acknowledgements

This work was supported by the Collaborative Research Program of the Natural Sciences and Engineering Research Council of Canada (NSERC). We thank Ms. K. Saravanamuttu for her assistance in acquiring the Raman spectra.

References

1. T.J. Marks and M.A. Ratner. Angew. Chem., Int. Ed. Engl. **34**, 155 (1995).
2. S.R. Marder, B. Kippelen, A.K.Y. Jen, and N. Peyghammbarian. Nature (London), **388**, 845 (1997).
3. R.R. Tykwinski, U. Gubler, R.E. Martin, F. Diederich, C. Bosshard, and P. Guenter. J. Phys. Chem. B, **102**, 4451 (1998).
4. T. Verbiest, S. Houbrechts, M. Kauranen, K. Clays, and A. Persoons. J. Mater. Chem. **7**, 2175 (1997).
5. E. Kelderman, G.J.T. Heesink, L. Derhaeg, T. Verbiest, P.T.A. Klaase, W. Verboom, J.F.J. Engbersen, N.F. Van Hulst, and K. Clays. Adv. Mater. (Weinheim, Fed. Repub. Ger.). **5**, 925 (1993).
6. M. Albota, D. Beljonne, J.-L. Bredas, J.E. Ehrlich, J.-Y. Fu, A.A. Heikal, S.E. Hess, T. Kogej, M.D. Levin, S.R. Marder, D. Mccord-Maughon, J.W. Perry, H. Rockel, M. Rumi, G. Subramaniam, W.W. Webb, X.-L. Wu, and C. Xu. Science (Washington, D.C.), **281**, 1653 (1998).
7. Y. Shi, C. Zhang, H. Zhang, J.H. Bechtel, L.R. Dalton, B.H. Robinson, and W.H. Steier. Science (London), **288**, 119 (2000).
8. L.L. Beecroft and C.K. Ober. Chem. Mater. **9**, 1302 (1997).
9. N.N. Lepeshkin, W. Kim, V.P. Safonov, J.G. Zhu, R.L. Armstrong, C.W. White, R.A. Zuhr, and V.M. Shalaev. J. Nonlinear Opt. Phys. Mater. **8**, 191 (1999).
10. E. Giorgetti, G. Margheri, L. Palchetti, S. Sottini, and M. Mennig. Appl. Phys. B: Lasers Opt. **B67**, 587 (1998).
11. F.W. Vance, B.I. Lemon, and J.T. Hupp. J. Phys. Chem. B, **102**, 10091 (1998).
12. P. Galletto, P.F. Brevet, H.H. Girault, R. Antoine, and M. Broyer. Chem. Commun. (Cambridge), 581 (1999).
13. Y. Suchorski, W.A. Schmidt, and J.H. Block. Appl. Surf. Sci. **76–77**, 101 (1994).
14. Y. Suchorski, W.A. Schmidt, J.H. Block, and H.J. Kreuzer. Vacuum, **45**, 259 (1994).
15. V.M. Shalaev, V.A. Markel, E.Y. Poliakov, R.L. Armstrong, V.P. Safonov, and A.K. Sarychev. J. Nonlinear Opt. Phys. Mater. **7**, 131 (1998).
16. V.M. Shalaev, V.P. Safonov, E.Y. Poliakov, V.A. Markel, and A.K. Sarychev. ACS Symp. Ser. **679**, 88 (1997).
17. A. Campion and P. Kambhampati. Chem. Soc. Rev. **27**, 241 (1998).
18. M. Kerker. J. Colloid Interface Sci. **105**, 297 (1985).
19. C.F. Eagen. Appl. Opt. **20**, 3035 (1981).
20. H.G. Craighead and A.M. Glass. Opt. Lett. **6**, 248 (1981).
21. A.M. Glass, A. Wokaun, J.P. Heritage, J.G. Bergman, P.F. Liao, and D.H. Olson. Phys. Rev. B, Cond. Matter, **24**, 4906 (1981).
22. S. Garoff, D.A. Weitz, T.J. Gramila, and C.D. Hanson. Opt. Lett. **6**, 245 (1981).
23. D.A. Weitz and S. Garoff. Proc. Int. Conf. Lasers, 55 (1982).
24. O. Stenzel, S. Wilbrandt, A. Stendal, U. Beckers, K. Voigtsberger, and C. Von Borczyskowski. J. Phys. D: Appl. Phys. **28**, 2154 (1995).
25. O. Stenzel, A. Stendal, K. Voigtsberger, and C. Von Borczyskowski. Sol. Energy Mater. Sol. Cells, **37**, 337 (1995).
26. M. Ihara, K. Tanaka, K. Sakaki, I. Honma, and K. Yamada. J. Phys. Chem. B, **101**, 5153 (1997).
27. N. Kometani, M. Tsubonishi, T. Fujita, K. Asami, and Y. Yonezawa, Langmuir. **17**, 578 (2001).
28. A.E. Neeves and M.H. Birnboim. J. Opt. Soc. Am. B: Opt. Phys. **6**, 787 (1989).
29. A.E. Neeves and M.H. Birnboim. Opt. Lett. **13**, 1087 (1988).
30. P. Ye and Y.R. Shen. Phys. Rev. B: Condens. Matter. **28**, 4288 (1983).
31. A.W. Olsen and Z.H. Kafafi. Mater. Res. Soc. Symp. Proc. **206**, 175 (1991).
32. A.W. Olsen and Z.H. Kafafi. J. Am. Chem. Soc. **113**, 7758 (1991).
33. K. Clays, E. Hendrickx, M. Triest, and A. Persoons. J. Mol. Liq. **67**, 133 (1995).
34. J. Baldwin, N. Schuehler, I. S. Butler, and M. P. Andrews. Langmuir. **12**, 6389 (1996).
35. D.V. Leff, L. Brandt, and J.R. Heath. Langmuir. **12**, 4723 (1996).
36. J. Zyss, V. Thai Chau, C. Dhenaut, and I. Ledoux. Chem. Phys. **177**, 281 (1993).
37. T.W. Chui and K.Y. Wong. J. Chem. Phys. **109**, 1391 (1998).
38. M. Brust, M. Walker, D. Bethell, D.J. Schiffrin, and R. Whyman. J. Chem. Soc., Chem. Commun. 801 (1994).
39. L.A. Porter, Jr., D. Ji, S.L. Westcott, M. Graupe, R.S. Czernuszewicz, N.J. Halas, and T.R. Lee. Langmuir. **14**, 7378 (1998).
40. X.-M. Li, M.R. De Jong, K. Inoue, S. Shinkai, J. Huskens, and D.N. Reinhoudt. J. Mater. Chem. **11**, 1919 (2001).
41. P.C. Lee, and D. Meisel, J. Phys. Chem. **86**, 3391 (1982).
42. U. Nickel, P. Halbig, H. Gliemann, and S. Schneider. Ber. Bunsen-Ges. **101**, 41 (1997).
43. E.J. Liang, X.L. Ye, and W. Kiefer. J. Phys. Chem. A, **101**, 7330 (1997).
44. D.A. Weitz, M.Y. Lin, and C.J. Sandroff. Surf. Sci. **158**, 147 (1985).
45. A.J. Gibb. *In* Medicinal Chemistry. *Edited by* C.R. Ganellin and S.M. Roberts. Academic Press, London. 1994. pp. 37–60.
46. D. Fitzmaurice, S.N. Rao, J.A. Preece, J.F. Stoddart, S. Wenger, and N. Zaccheroni. Angew. Chem., Int. Ed. **38**, 1147 (1999).

[4] Supplementary data may be purchased from the Depository of Unpublished Data, Document Delivery, CISTI, National Research Council Canada, Ottawa, ON K1A 0S2, Canada (http://www.nrc.ca/cisti/irm/unpub_e.shtml for information on ordering electronically).

© 2002 NRC Canada

47. S. Schneider, G. Brehm, and P. Freunscht. Phys. Status Solidi B, **189**, 37 (1995).
48. I. Persaud and W.E.L. Grossman. J. Raman Spectrosc. **24**, 107 (1993).
49. A. Kudelski and J. Bukowska. Chem. Phys. Lett. **253**, 246 (1996).
50. E. Hendrickx, K. Clays, and A. Persoons. Acc. Chem. Res. **31**, 675 (1998).
51. S. Nie and S.R. Emory, Science (Washington, D.C.). **275**, 1102 (1997).
52. K.D. Singer, M.G. Kuzyk, W.R. Holland, J.E. Sohn, S.J. Lalama, R.B. Comizzoli, H.E. Katz, and M.L. Schilling. Appl. Phys. Lett. **53**, 1800 (1988).
53. C.J. Kiely, J. Fink, M. Brust, D. Bethell, and D.J. Schiffrin. Nature (London), **396**, 444 (1998).
54. J. Fink, C.J. Kiely, D. Bethell, and D.J. Schiffrin. Chem. Mater. **10**, 922 (1998).
55. G. Schmid, S. Peschel, and T. Sawitowski. Z. Anorg. Allg. Chem. **623**, 719 (1997).
56. H. Fan, Y. Zhou, and G.P. Lopez, Adv. Mater. (Weinheim, Ger.), **9**, 728 (1997).
57. R. Blonder and L. Sheeney. Chem. Commun. (Cambridge), 1393 (1998).
58. C.R. Martin and D.T. Mitchell. Anal. Chem. **70**, 322A (1998).
59. S. Bharathi. Anal. Commun. **35**, 29 (1998).
60. R.P. Andres, J.D. Bielefeld, J.I. Henderson, D.B. Janes, V.R. Kolagunta, C.P. Kubiak, W.J. Mahoney, and R.G. Osifchin. Science (Washington, D.C.), **273,** 1690 (1996).

© 2002 NRC Canada

This special issue is dedicated to

Professor Tristram Chivers

to honour his outstanding contributions to the chemistry of the main group elements.

Associate Editors: Neil Burford and Chris Orvig

Ce numéro spécial rend hommage au

Professeur Tristram Chivers

et à ses précieuses contributions à la chimie des éléments des groupes principaux.

Directeurs scientifiques associés : Neil Burford et Chris Orvig

© 2002 NRC Canada

Professor Tristram Chivers

© 2002 NRC Canada

Professor Tristram Chivers, FCIC

This Special Issue of The Canadian Journal of Chemistry honours the outstanding achievements of Professor Tristram Chivers as a scientist, an educator, and an administrator. This collection of papers by his colleagues, friends, and former research students demonstrates Tris' broad influence. He is recognised as a pioneer for Main Group Chemistry, but his passion for science is obvious in all aspects of his career. He has an outstanding reputation as both a lecturer and research mentor and has set new standards for the role of science representative, executive, and ambassador for the chemical community in Canada.

Tristram Chivers was born in Bath, England on 22 August, 1940. He received his B.Sc. (first class honours in Chemistry, 1961), Ph.D. (1964), and D.Sc. (1981) degrees from the University of Durham (U.K.). His Ph.D. thesis with R.D. Chambers involved studies of pentafluorophenylboron compounds, which are now important Lewis acids in the olefin polymerization industry. Following a post-doctoral position (1964–1965) in organometallic electrochemistry with R.E. Dessy at the University of Cincinnati he returned to the U.K. for a two year appointment as a Tutorial Fellow at the University of Sussex. Upon emigration to Canada in 1967, he spent two years at U.B.C. as a Teaching Post-doctoral Fellow with N.L. Paddock, where he developed an interest in inorganic ring systems that later became the foundation of his independent research program. He joined the Department of Chemistry at the University of Calgary in 1969 as Assistant Professor and was promoted to Professor in 1978. He served as Head of the Department from 1977 to 1982.

Tris Chivers and his group have made many seminal contributions to the chemistry of chalcogen compounds. An important early finding was to identify the blue species formed by sulfur in reducing media as the trisulfur radical anion (S_3^-), subsequently shown by R.J.H. Clark to be the blue chromophore in the mineral lapis lazuli. This finding was followed by the discovery of novel acyclic sulfur–nitrogen anions, $SSNSS^-$ and $SNSS^-$, the cyclic $S_3N_3^-$ anion (a 10 π-electron system) and the bicyclic $S_4N_5^+$ cation. The insightful recognition of the isoelectronic relationship between a PR_2 group and an S^+ unit led to the characterization of hybrid PN–SN systems, e.g., $R_2PN_3S_2$ (an 8 π-electron system) and $R_4P_2N_4S_2$ (with a transannular S···S π*-π* interaction). Several of the ring and cage compounds discovered in the Chivers group are now textbook examples and the 1998 edition of "Chemistry of the elements" by N. Greenwood and A. Earnshaw devotes twelve pages to sulfur–nitrogen chemistry that originates from his laboratory. Tris' research is characterized by a creative and imaginative approach to the design and synthesis of unusual compounds. In addition, application of a wide variety of spectroscopic, crystallographic, and electrochemical techniques has led to an understanding of the relationship between the molecular structures and the properties and reactivity of π-electron-rich compounds.

Tris Chivers and his group have also made major contributions to selenium and tellurium chemistry. In collaboration with Risto Laitinen (University of Oulu, Finland) novel acyclic and cyclic selenium imides, e.g., $Se_3(NR)_3$

Professeur Tristram Chivers, MICC

Le présent numéro spécial de La Revue canadienne de chimie rend hommage aux remarquables talents de scientifique, d'enseignant et d'administrateur du professeur Tristram Chivers. Cet assemblage d'articles signés par ses collègues, amis et anciens protégés témoigne de la vaste influence de celui que nous surnommons « Tris ». Si son travail de défrichement de la chimie des éléments des groupes principaux est particulièrement mémorable, sa riche carrière est loin de se limiter à cette seule contribution. Tristram jouit d'une brillante réputation de conférencier et de maître de recherche et, par son exemple, a à jamais resserré les attentes à l'endroit des représentants, directeurs et ambassadeurs de la collectivité des chimistes du Canada.

Tristram Chivers est né à Bath, en Angleterre, le 22 août 1940. Il a reçu un B. Sc. (chimie, mention très honorable, 1961), un Ph.D. (1964) et un D.Sc. (1981) de la University of Durham, au R.-U. Son mémoire de Ph. D., sous la direction de R.D. Chambers, portait sur les composés pentafluorophénylborique, acides de Lewis aujourd'hui largement utilisés dans l'industrie de la polymérisation de l'oléfine. Après un stage postdoctoral dans le secteur de l'électrochimie des composés organométalliques aux côtés de R.E. Dessy à la University of Cincinnati (1964–1965), Tris a regagné sa patrie pour assumer une charge de cours à la University of Sussex. Après avoir émigré au Canada en 1967, il a passé deux ans à la University of British Columbia, à titre de boursier en enseignement postdoctoral auprès de N.L. Paddock. Cette affectation a éveillé chez lui un intérêt pour les systèmes à anneaux inorganiques, futures fondations de son propre programme de recherche indépendant. Il a joint le département de chimie de la University of Calgary en 1969 à titre de professeur adjoint et y a été promu professeur en 1978. Il a assumé la direction du Département de 1977 à 1982.

Tris Chivers et son groupe ont résolument contribué au secteur de la chimie des composés chalcogénés. Un de leurs premiers résultats marquants a été l'identification de l'espèce chimique bleutée formée par le souffre en milieu réducteur : l'anion du radical trisulfure (S_3^-). R.J.H. Clark a subséquemment démontré qu'il s'agissait du chromophore bleu du lapis lazuli. Les travaux de Tris et de son équipe ont donné lieu à la découverte des anions acycliques soufre-azote, $SSNSS^-$ et $SNSS^-$, de l'anion cyclique $S_3N_3^-$ (système à 10 électrons π) et du cation bicyclique $S_4N_5^+$. La judicieuse reconnaissance de la relation isoélectronique entre un groupe PR_2 et une unité S^+ a tracé la voie à la caractérisation des systèmes hybrides, p. ex. $R_2PN_3S_2$ (système à 8 électrons π) et $R_4P_2N_4S_2$ (avec une interaction transannulaire S···S π*-π*). Nombre de composés anneau et cage découverts par le groupe de Chivers font l'objet de manuels de cours. À preuve, N. Greenwood et A. Earnshaw, dans l'édition de 1998 de Chemistry of the elements, consacrent douze pages à la chimie soufre-hydrogène, enfantée par le laboratoire de Tris. Les recherches de Tris se distinguent par une démarche inspirée et originale à l'élaboration et à la synthèse de composés singuliers. De plus, le vaste recours de son laboratoire à la spectroscopie, à la cristallographie et à l'électrochimie a permis de jeter la lumière sur la relation entre les structures moléculaires et les propriétés et la réactivité des composés riches en électrons π.

© 2002 NRC Canada

and $Se_3(NR)_2$, have been characterized. In tellurium chemistry the discovery of the first tellurium(IV) diimides and the polyimido anion $[Te(N\text{-}t\text{-}Bu)_3]^{2-}$, isoelectronic with tellurite $[TeO_3]^{2-}$ represent important landmarks. The creative exploitation of the isoelectronic relationship between imido (NR) and oxo (O) ligands has enabled the Chivers group to open new areas in both inorganic cluster chemistry and coordination chemistry involving polyimido analogues of common oxo-anions with p-block element centres. Significant contributions to this developing field from the Chivers lab include the homoleptic polyimido anions $[C(NR)_3]^{2-}$, $[Si(NR)_4]^{4-}$, $[P(NR)_4]^{3-}$, and $[Se(NR)_4]^{2-}$. These studies have been extended to heteroleptic systems involving both imido and oxo (or thio) moieties attached to the central p-block element, and these anions are attracting interest as novel ligands for catalytic systems. In addition, their metal derivatives form extended structures (coordination polymers or porous materials) in which the mode of aggregation can be controlled by changing the size of the NR group.

Tris Chivers and his group have co-authored more than 300 refereed publications (including reviews and book chapters). Tris has received many awards, most notably the Alcan Lecture Award of the CSC in 1987, the Royal Society of Chemistry Award (U.K.) for Main Group Element Chemistry in 1993, and the E.W.R. Steacie Award of the CSC in 2001. He was elected a Fellow of the Royal Society of Canada in 1991. At the University of Calgary he has been honoured with one of the first Awards of Excellence for Research from the Faculty of Science (1990) and was the first recipient of the University President's Circle Award (2000) in the Faculties of Science and Engineering for achievement in research and creative activity. He has also received Teaching Excellence Awards from the Students' Union (1993 and 1998) and from the Graduate Students' Association (1997) of the University of Calgary.

For more than three decades, Tris has made major contributions to Chemistry in Canada. He was the Senior Editor for the Canadian Journal of Chemistry (1993–1998) and was previously the Inorganic Chemistry Editor (1988–1993). He served on NSERC Chemistry Grant Selection Committees on two occasions (1979–1981 and 1990) and chaired the Committee in 1981. In addition, he performed as group chair for both chemistry GSCs (1996–1999). He was the Chair of the CIC Inorganic Division (1982–1984), Treasurer of the CSC (1990–1992), and President of the CSC (2000–2001). He has also served on a number of international editorial boards, most notably for the Encyclopedia of Inorganic Chemistry. He was Chair of the highly successful 7th International Symposium on Inorganic Ring Systems (IRIS) in Banff 1994. This extensive list of administrative achievements were made possible by Tris' outstanding organizational skills, pleasant manner, boundless energy, and a positive philosophy to achieve the best possible outcome.

Tris Chivers is a strong believer in a balanced approach to work and play. At the University of Durham his activities included contract bridge at which he represented the University team-of-four and became a club master. He also played cricket for Durham City, the B.C. provincial team, and he was selected to represent Canada in the annual test match

Tris Chivers et son groupe ont aussi enrichi les connaissances de la chimie du sélénium et du tellure. Ainsi, en collaboration avec Risto Laitinen (Université de Oulu, en Finlande), ils ont caractérisé des imides de sélénium cycliques et acycliques nouveau genre, notamment $Se_3(NR)_3$ et $Se_3(NR)_2$. Dans l'histoire de la chimie du tellure, la découverte des premières diimides de tellure(IV) et de l'anion polyimide $[Te(N\text{-}t\text{-}Bu)_3]^{2-}$, isoélectronique avec la tellurite $[TeO_3]^{2-}$, constitue un point tournant. L'exploitation innovatrice de la relation entre les ligands imido (NR) et oxo (O) a ouvert de nouveaux horizons en chimie des amas inorganiques ainsi qu'en chimie de coordination des analogues polyimides d'oxoanions communs ayant en leur centre des éléments du bloc-p. De ces premiers efforts du laboratoire de Chivers sont nés les anions polyimides homoleptiques $[C(NR)_3]^{2-}$, $[Si(NR)_4]^{4-}$, $[P(NR)_4]^{3-}$ et $[Se(NR)_4]^{2-}$. Ces études ont été prolongées aux systèmes hétéroleptiques faisant intervenir des groupes imido et oxo (ou thio) liés à un élément du bloc-p central. Ces anions sont actuellement étudiés en raison de leur potentiel en tant que ligands de systèmes catalytiques. De plus, ces dérivés métalliques forment des structures allongées (matériaux poreux ou polymères de coordination) dont le mode d'agrégation peut être contrôlé en modifiant la dimension du groupe NR.

Tris Chivers et son groupe ont cosigné plus de 300 articles dans des publications avérées (y compris des synthèses et des chapitres de livre). Tris a récolté les prix, notamment le Prix de conférence Alcan de la SCC (1987), le prix de la Royal Society of Chemistry (R.-U.) de chimie des éléments des groupes principaux (1993) et le Prix E.W.R. Steacie de la SCC (2001). Il a été reçu membre de la Société royale du Canada en 1991. À la University of Calgary, ses contributions ont été saluées par l'un des premiers prix d'excellence en recherche attribués par la faculté des sciences (1990). Tris a également été le premier lauréat du University President's Circle Award (2000) des facultés des sciences et du génie, prix qui souligne les réalisations et la pensée créative en recherche. Enfin, il peut s'enorgueillir de prix d'excellence en enseignement, adjugés par l'union des étudiants de la University of Calgary en 1993 et 1998 ainsi que par l'association des étudiants diplômés de la University of Calgary en 1997.

Depuis plus de trente ans, Tris est une éminente figure de la chimie au Canada. Il a été directeur scientifique principal de la Revue canadienne de chimie (1993–1998) après avoir été directeur scientifique de Inorganic Chemistry Editor (1988–1993). Il a été membre du Comité de sélection des subventions en chimie du CRSNG à deux reprises (1979–1981 et 1990) et a présidé le Comité en 1981. Il a aussi présidé les deux CSS de chimie (1996–1999). Il a été président de la division de chimie organique de l'ICC (1982–1984), trésorier de la SCC (1990–1992) et président de la SCC (2000–2001). Il a été membre d'innombrables comités éditoriaux internationaux, y compris celui de la Encyclopedia of Inorganic Chemistry. Il a été président du 7th International Symposium on Inorganic Ring Systems (IRIS), qui a eu lieu à Banff en 1994 et qui a obtenu un immense succès. Tris doit un tel bilan à son impeccable sens de l'organisation, à son juste doigté, à son indéfectible énergie et à sa constante visée sur l'excellence.

Tris Chivers a toujours prêché par l'exemple l'équilibre entre le travail et le loisir. Amateur de bridge, il a fait partie de

© 2002 NRC Canada

against U.S.A. in 1969. As a choral singer he has been a member of the tenor section of the Calgary Philharmonic Chorus for almost twenty years. Squash has been (and continues to be) an important influence in his life. He met his wife Sue at a squash club while at the University of Sussex. He credits Sue's support and encouragement for much of his success. Sue and Tris have two children. Peter is an Assistant Professor in the Department of Biochemistry and Molecular Biophysics in the School of Medicine at Washington University and Sally is an SSHRC post-doctoral Fellow in English – Disability Studies at the University of Illinois in Chicago.

Neil Burford

l'Équipe de 4 de la University of Durham et en a été le master. Adroit joueur de cricket, il a été appelé à représenter Durham et l'équipe provinciale de la C.-B. dans ce sport. Il a également porté les couleurs du Canada lors du match préliminaire de cricket au É.-U. de 1969. Choriste d'expérience, il chante la partition de ténor auprès du Calgary Philharmonic Chorus depuis près de vingt ans. Et on ne saurait oublier de mentionner son amour du squash, sport qui a occupé et continue d'occuper une place importante dans sa vie. De fait, c'est au club de squash de la University of Sussex qu'il a rencontré celle qui allait devenir son épouse, Sue. Tris se plaît à dire qu'il doit à Sue la majeure partie de ses réalisations. Le couple a deux enfants. Leur fils, Peter, est professeur adjoint au département de biochimie et de biophysique moléculaire de la faculté de médecine de la Washington University. Leur fille, Sally, est détentrice d'une bourse postdoctorale de perfectionnement du CRSHC et oeuvre au département de littérature anglaise et d'études sur le handicap de la University of Illinois, à Chicago.

Neil Burford

© 2002 NRC Canada

AWARD LECTURE / CONFÉRÉNCE D'HONNEUR

Local modes[1]

Bryan R. Henry and Henrik G. Kjaergaard

Abstract: The historical background for the development of the local mode approach is reviewed, including the critical role of the radiation field. The harmonically coupled anharmonic oscillator model is described. Local modes have been used in the interpretation of XH stretching overtone spectra. These spectra can be used as sensitive probes of molecular properties such as bond length and molecular conformation. Examples of these spectral features are discussed. An intensity theory has been developed that permits the accurate calculation of relative and absolute overtone intensities. In molecules with low barriers to methyl rotation, torsional states contribute to the XH stretching band profile. A successful theoretical approach is presented that accounts for these effects and provides insight into the vibrational dynamics. The application of calculated local mode overtone spectra to atmospheric chemistry is discussed.

Key words: local mode, overtone, vibrational intensity.

Résumé : On passe en revue l'historique des origines de l'approche du mode local, y compris le rôle critique du champ de radiation. On décrit le modèle de l'oscillateur anharmonique à couplage harmonique. On a utilisé les modes locaux dans l'interprétation des spectres d'harmonique d'élongation XH. On peut utiliser ces spectres comme sondes sensibles de propriétés moléculaires telles que la longueur de liaison et la conformation moléculaire. On discute d'exemples de telles caractéristiques spectrales. On a mis au point une théorie d'intensité qui permet de faire un calcul précis des intensités relatives et absolues des harmoniques. Dans les molécules avec de faibles barrières à la rotation des méthyles, les états de torsion contribuent au profit de la bande d'élongation XH. On présente une approche théorique qui permet de tenir compte avec succès de ces effets et qui donne un aperçu des dynamiques vibrationnelles. On discute de l'application à la chimie de l'atmosphère des spectres d'harmoniques calculés sur la base du mode local.

Mots clés : mode local, harmonique, intensité vibrationnelle.

[Traduit par la Rédaction]

Introduction and historical perspective

The local mode model was developed in the 1970s to describe highly excited vibrational states of molecules. It has been used to describe XH stretching overtone spectra where X is some heavier atom like C, N, or O. However, the genesis of the model dates back to the 1960s and the work of Siebrand and his collaborators on radiationless transitions in aromatic hydrocarbons (1–3). The most studied radiationless transition in those days was intersystem crossing from $T_1 \rightarrow S_0$ in aromatic hydrocarbons. This radiationless transition converts the electronic triplet-state energy into vibrational energy of the ground electronic state. The resultant highly excited ground vibrational states that accept the electronic energy involve carbon–hydrogen stretching vibrations. Existing theory worked very well in explaining relative rates for these transitions from one molecule to another, but there was a problem with the calculation of the absolute magnitude of these rates. We believed the problem was with the description of the highly vibrationally excited states.

Why should there be a problem? When a small amount of vibrational energy is placed in a molecule, the bonds behave like springs or harmonic oscillators. This behavior is the basis of the traditional normal mode model of molecular vibrations. For example, the normal modes of water consist of a symmetric and an antisymmetric stretch and a bending mode. What happens when more and more vibrational energy is added to the molecule? Eventually the molecule will dissociate, but it is unlikely to do so along one of the normal mode stretching coordinates. Such a process would require the simultaneous breaking of two O—H bonds. It is much more likely that the molecule will seek a low energy pathway for dissociation and break a single O—H bond. In other words it will dissociate along a local coordinate. The higher the vibrational energy is, the less harmonic the vibration. The vibration becomes anharmonic, and not surprisingly, we were able to show that in terms of a normal mode basis most of this anharmonicity is nondiagonal (4). In other words, the

Received 4 September 2002. Published on the NRC Research Press Web site at http://canjchem.nrc.ca on 19 December 2002.

B.R. Henry.[2] Department of Chemistry and Biochemistry, University of Guelph, Guelph, ON N1G 2W1, Canada.
H.G. Kjaergaard. Department of Chemistry, University of Otago, P.O. Box 56, Dunedin, New Zealand.

[1]2001 Montreal Award Lecture. Presented by BRH in Montréal, May 2001.

[2]Corresponding author (e-mail: chmhenry@uoguelph.ca).

 DOI: 10.1139/V02-188 © 2002 NRC Canada

effect of anharmonicity is to mix the symmetric and antisymmetric stretching modes. The sum of these two is a local mode. So, as the vibrational energy increases and anharmonicity becomes more important, we expect the vibrational pattern to become more localized.

Henry and Siebrand used these localization ideas to try to understand XH-stretching overtone spectra (4). The overtone spectrum of benzene had been measured in the liquid phase all the way out to $\Delta v_{CH} = 8$ (8 quanta in CH stretching) by Ellis in 1929 (5). On the basis of the assumption that the six local CH stretching modes were weakly coupled, Henry and Siebrand (4) used a transformation from local to normal coordinates and derived values for CH stretching anharmonicity constants expressed in the normal mode basis. Thus they could calculate the energies of all of the components of the overtone bands expressed in terms of normal modes. For benzene at $\Delta v_{CH} = 6$ there are 462 such components of which 150 are allowed. These are the 75 doubly degenerate E_{1u} states.

In attempting to generalize this work to other molecules (6), we found that there was little evidence for the involvement of all of the symmetry-allowed normal mode components. In the early 1970s, Hayward and Henry came to the conclusion that the radiation field was selectively exciting only the most anharmonic of the normal mode components (7). This would be a state where all the vibrational energy was effectively localized in one X—H bond (X = C, N, O, etc.). We called such a state a pure local mode state and postulated that it was absorption to these states that accounted for the overtone spectra. It happens that some of these ideas had been published in 1936 in Germany by Mecke and Ziegler (8). However this work seemed to have been largely unknown and after the war appeared to have been totally ignored.

There was some difficulty in getting the initial local mode work published. Referees consistently wanted a description in terms of the conventional normal mode approach to molecular vibrations. After the work appeared in 1975 (7), Albrecht and his collaborators used thermal lensing spectroscopy to look at liquid phase overtone spectra of benzene and other aromatic molecules (9). In referring to the overtone spectrum of benzene, they noted that the local mode model is "an excellent zeroth order description" of the spectroscopically allowed states in the overtone spectrum of benzene. Around the same time, papers by Gelbart and his collaborators (10, 11) confirmed the theoretical basis for a local mode description, and the local mode approach was firmly established.

Thus, in summary, XH stretching overtone spectra can be understood in terms of a local mode model in which the local oscillators are considered to be anharmonic but only weakly coupled. The radiation field selectively excites a state whose components have all of the vibrational energy localized in one of a set of equivalent X—H bonds. Thus in benzene at $\Delta v_{CH} = 6$ the only state that absorbs light is

$$[1] \quad \Psi = N [c_1 \mid 600000 \rangle + c_2 \mid 060000 \rangle + c_3 \mid 006000 \rangle + c_4 \mid 000600 \rangle + c_5 \mid 000060 \rangle + c_6 \mid 000006 \rangle]$$

Fig. 1. Local mode coupling scheme (kinetic energy coupling only) for a two oscillator system in the $v = 5$ vibrational manifold (see text) (from ref. 31).

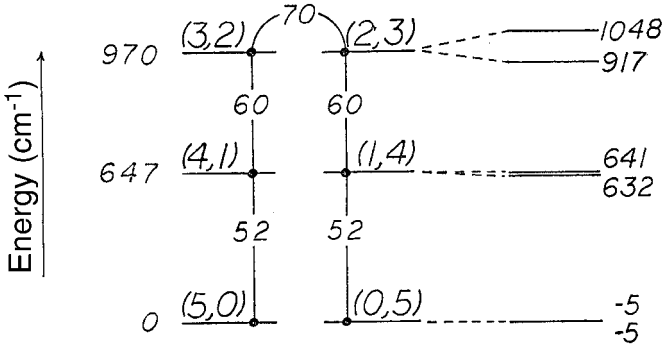

where the components can be described as products of one-dimensional vibrational wave functions.

$$[2] \quad \mid 600000 \rangle = \mid 6 \rangle \mid 0 \rangle \mid 0 \rangle \mid 0 \rangle \mid 0 \rangle \mid 0 \rangle$$

The individual basis functions $\mid v \rangle$ are anharmonic and, for example, could be taken to be Morse oscillator wave functions. Such a description predicts only a single transition at $\Delta v_{CH} = 6$, in agreement with experiment.

The local mode model is now generally accepted and has been applied in a number of areas (12–15). Because of the localization of energy for spectrally active states in a single chemical bond, XH-stretching overtone spectra are very sensitive to bond properties and have been used to study subtle effects in molecular structure and molecular conformation (9, 13, 16–18). The spectra along with the local mode model have been used to investigate intermolecular forces and nonbonded intramolecular interactions (19–23). The gas phase spectra have also been used in studies of intramolecular vibrational energy redistribution (IVR) (24–30).

The harmonically coupled anharmonic oscillator model

Let us return to the water molecule and assume that the potentials associated with each of the O—H bonds are Morse potentials. We will also assume that the only coupling between the OH oscillators occurs through the kinetic energy. Thus the Hamiltonian takes the form

$$[3] \quad H = T(p_1, p_2) + V(r_1) + V(r_2)$$

where the kinetic energy term is given by

$$[4] \quad T(p_1, p_2) = -\hbar^2\{(\mu_O + \mu_H)[(\partial^2/\partial r_1^2 + \partial^2/\partial r_2^2)] + \mu_O \cos\theta\,(\partial^2/\partial r_1 \partial r_2)\}$$

and the μs are reciprocal atomic masses.

Watson et al. used this Hamiltonian for calculations of the OH stretching overtone spectrum of water (31). Zero order states were taken as simple products of Morse oscillator wavefunctions. Thus the state $\mid 5,0 \rangle$ corresponds to five quanta in one O—H bond and none in the other. Figure 1 shows the interactions between these zero order states in the $v = 5$ vibrational manifold. It turns out that interaction is only large if a given one of the two Morse oscillators differs in excitation by a single quantum. In other words, although

© 2002 NRC Canada

the oscillators are anharmonic, their off-diagonal coupling is well approximated by the rules that govern coupling of harmonic oscillators.

The energy levels in Fig. 1 are shown relative to $|\ 5,0\ \rangle$ and $|\ 0,5\ \rangle$, which occur at 16 886 cm^{-1} (31). The relative zero order energies of the states are given, as well as the significant couplings. On the right are the final energies of the eigenstates after complete diagonalization. Note that the coupling between $|\ 5,0\ \rangle$ and $|\ 0,5\ \rangle$ occurs only indirectly. As v increases the coupling between $|\ v,0\ \rangle$ and $|\ 0,v\ \rangle$ will become more indirect and the two lowest energy final eigenstates will tend toward degeneracy. The two final eigenfunctions are very well approximated by the in-phase and out-of-phase combinations of $|\ v,0\ \rangle$ and $|\ 0,v\ \rangle$. Moreover, early intensity calculations predicted that transitions from the vibrational ground state should have intensity increasingly concentrated in these two lowest states as v increases (9, 31, 32). Thus, as v increases and the splitting between the two lowest eigenstates becomes very small, the spectra become simple and appear as if only a single state is excited.

In 1981, the harmonically coupled anharmonic oscillator (HCAO) model was developed independently by Mortensen et al. (33) and by Child and Lawton (34). The HCAO model was developed to analyze XH stretching overtone spectra in the same spirit as the detailed Morse oscillator calculations for water (31) but with a simpler approach. It is based on the following simple Hamiltonian, which is shown here for two oscillators with local mode frequency ϖ and local mode anharmonicity ϖx.

$$[5]\qquad (H - E_O)/hc = (v_1 + v_2)\varpi - (v_1^2 + v_2^2 + v_1 + v_2)\varpi\, x - (\gamma - \varphi)\varpi\,(a_1^+\, a_2 + a_1\, a_2^+)$$

γ and φ characterize the off-diagonal kinetic and potential energy coupling, respectively.

The a are the familiar step-up and step-down operators, and in the model, coupling is restricted to the harmonic limit. Thus, states are allowed to couple only within a given vibrational manifold, i.e., a given total v, and where oscillator population differs by ±1. All of the parameters of the model, ω, ωx, γ, and φ, are obtained either directly from the spectra or from ab initio calculations. The model works extremely well in accounting for the observed energies of overtone peaks in XH stretching overtone spectra. The model has been generalized to more than two equivalent oscillators and to sets of nonequivalent oscillators (35–37). For the purposes of calculating peak energies, no identification of the wave functions is needed. However, if the component wave functions are taken to be products of one-dimensional Morse oscillators, the HCAO model can be used to generate eigenstate wave functions. Such wave functions have been used successfully along with ab initio calculations of dipole moment functions (simply expanded in local coordinates) to determine overtone intensities (36–45).

Overtone spectra as a sensitive probe of X—H bond lengths

One of the primary reasons for the interest and activity in the local mode field in the last 25 years is that overtone spectra have become accessible in the vapor phase for relatively high values of Δv. XH stretching overtone spectra are already dominated by local modes at around $\Delta v = 3$. However, the spectral resolution of subtle properties such as differences in X—H bond length increases the higher is the overtone. These high energy overtones are extremely weak transitions and are not observable with conventional light absorption techniques. However, a number of laser-based techniques have been developed and successfully applied. One of the most popular of these techniques is intracavity laser photoacoustic spectroscopy (ICL-PAS). This technique has been reviewed in detail elsewhere (46, 47), and here we simply provide a very brief outline. A 20 W Ar ion laser pumps a broad band dye or titanium sapphire laser, and the photoacoustic cell is placed inside the dye or titanium sapphire laser cavity. The molecule absorbs light in an overtone transition, and subsequently the light energy is converted into heat. Since the cell is closed, the pressure of the vapor increases. The pump laser is modulated by a chopper and gives rise to pressure fluctuations that are detected as sound waves by a hearing aid microphone. This very sensitive absorption technique has permitted us to observe vapor phase overtone transitions as high in energy as $\Delta v_{CH} = 9$ (38, 48).

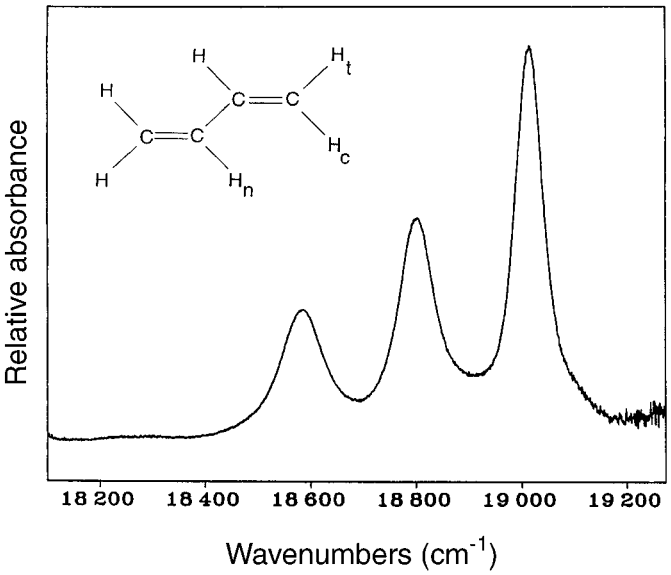

Fig. 2. The gas phase ICL-PAS spectrum of 1,3-butadiene in the $\Delta v_{CH} = 7$ region. The ab initio calculated bond lengths are: C—H_t = 1.0748 Å, C—H_c = 1.0766 Å, and C—H_n = 1.0782 Å (45).

A bond property that is of great interest to chemists is the length. Bond length reflects electronic structure, and we can calculate bond lengths with ab initio electronic structure programs, such as Gaussian (49). For larger molecules these programs calculate bond length differences that are much too small to be verified by standard experimental methods. Do these differences have any physical meaning? Overtone spectra interpreted with the local mode model allow us to resolve small changes in bond length of the order of a thousandth of an Ångstrom (mÅ). Figure 2 shows the spectrum of gas phase 1,3-butadiene at $\Delta v_{CH} = 7$ (45). Even though the bonds are predicted to differ by only milliÅngstroms, they are clearly resolved in the overtone spectrum. The shortest bond, C—H_t, corresponds to absorption at the highest energy.

© 2002 NRC Canada

Fig. 3. The vapor phase ICL-PAS spectrum of naphthalene in the $\Delta v_{CH} = 5$ region.

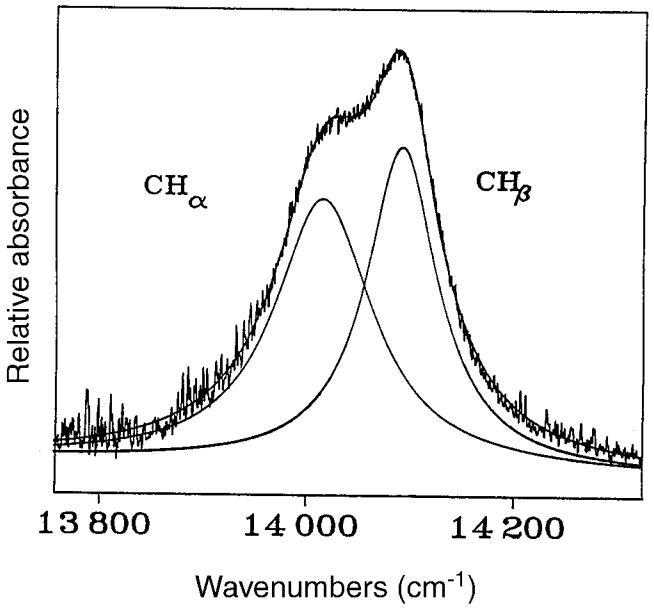

Fig. 4. The vapor phase ICL-PAS spectrum of cyclohexane in the $\Delta v_{CH} = 6$ region.

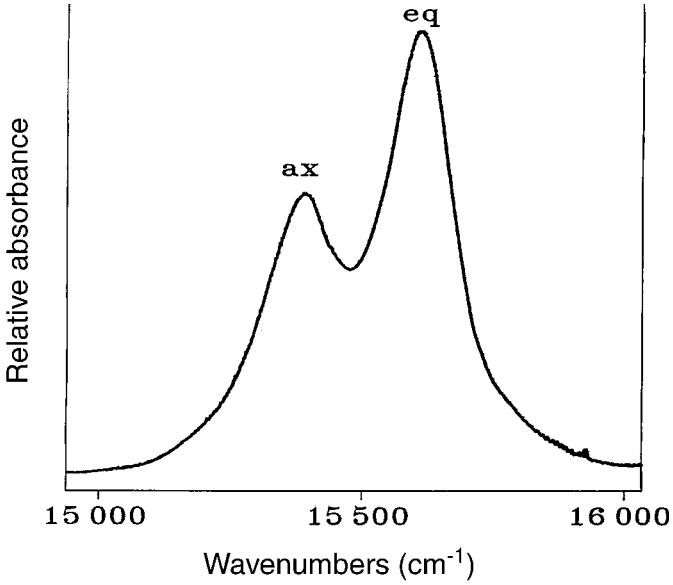

In addition, there are three kinds of bonds and there are two bonds of each type, but these three peaks are of very different intensity. We have developed a theory to calculate overtone intensity that uses ab initio methods to obtain the dipole moment surface of the molecule and the HCAO model to obtain the wave functions (36, 37, 43, 45). These calculations help us to assign the spectra and can successfully account for the intensity differences.

The vapor phase spectrum of naphthalene at $\Delta v_{CH} = 5$ is shown in Fig. 3 (50, 51). Naphthalene represents a more demanding example because the low vapor pressure gives a much lower sample concentration than for 1,3-butadiene, so it is much more difficult to measure the spectrum. Moreover, the predicted bond length difference between the two bond types is smaller, only 0.6 mÅ. This band at $\Delta v_{CH} = 5$ can be decomposed into two Lorentzian components, the high-energy peak for the shorter β-C—H bonds and the low energy peak for the longer α-C—H bonds. We assign these peaks on the basis of the correlation between overtone frequency and bond length — higher frequency corresponds to shorter bond length — and on the basis of our intensity calculations. The assignment can be checked by measuring the spectrum of the molecule where all of the β-Hs have been replaced with deuterium. In the spectrum of naphthalene-β-d_4, the higher energy component disappears (51).

As molecules execute internal motion, the environment of the chemical bonds changes. Because of the short vibrational timescale, overtone absorption spectroscopy can by used to distinguish between these conformationally nonequivalent X—H bonds. For example, as the molecule cyclohexane flips back and forth between equivalent chair conformations, the axial and equatorial bonds are interchanged. Ab initio theory predicts the bond length difference to be 2 mÅ. Figure 4 shows the vapor phase overtone spectrum of cyclohexane at $\Delta v_{CH} = 6$ (43). Peaks due to the axial and equatorial C—H bonds are clearly resolved.

In propane, dimethylether, and acetone, the methyl groups do not rotate freely because of a significant barrier to internal methyl rotation. As a result, there are two types of methyl C—H bonds: one in the plane of the molecular backbone and two out-of-plane C—H bonds that straddle the backbone. Ab initio theory predicts a difference in bond length between the shorter in-plane and the longer out-of-plane bonds of 0.8, 5.2, and 7.6 mÅ for propane, acetone, and dimethylether, respectively (37). Figure 5 shows the vapor phase overtone spectrum at $\Delta v_{CH} = 7$. The spectral splittings scale with the predicted bond length differences.

Catechol is one of the lowest pressure samples for which we have recorded vapor phase overtone spectra (52). The two OH groups form a weak internal hydrogen bond, which elongates the O—H bond of the hydrogen donor by about 2 mÅ. This small change in bond length is clearly visible in the overtone spectrum even in the $\Delta v_{OH} = 3$ region (52), despite the low rotational barrier along the coordinate that breaks the hydrogen bond.

Effects of internal methyl rotation on overtone spectra

If the barrier to methyl rotation is small, the effect on XH stretching overtone spectra is dramatically different than in molecules like propane and acetone. It is no longer possible to associate individual methyl C—H bonds with a specific conformation. However, the methyl C—H bond length still changes as the methyl group rotates. This means that the rotation of the methyl group is coupled to the stretching of the methyl C—H bonds and methyl torsion would be expected to contribute to CH stretching overtone methyl band profiles (23, 26, 53–64).

We were able to account for these effects in detail for the molecule 2,6-difluorotoluene with a model that treated the methyl group as a rigid rotor and the methyl CH oscillators within the HCAO model (57). We introduced terms in the Hamiltonian that accounted for the interaction between

© 2002 NRC Canada

stretching and torsion. In effect the bond length change with methyl rotation implies a dependence of the local mode frequency and the local mode anharmonicity on the methyl torsional angle. We also incorporated our theory for calculating overtone intensities but modified it to introduce rotational angle dependence in the dipole moment operator.

With this approach we were able to simulate successfully the methyl band profiles in the local mode regions of Δv_{CH} = 3 to 6. The parameters that were needed for the model were obtained either from ab initio calculations or directly from the spectra. As a result of the coupling between torsion and stretching, both in the Hamiltonian and through the dipole moment function, a very large number of transitions are predicted to carry intensity and contribute to the overall spectral profile (57).

For toluene, the barrier to methyl group rotation about the benzene ring is essentially zero. Even so the methyl C—H bond length changes by about 3 mÅ as it rotates, and thus we expect torsional involvement in the overtone spectra. We have measured these spectra in the regions of Δv_{CH} = 3 to 6 for toluene and for the toluene-αd_1 and toluene-αd_2 isomers (60–62). Not surprisingly, the methyl regions of the spectra are very different for the three molecules toluene-d_0, toluene-αd_1, and toluene-αd_2.

We used a theoretical approach similar to the one for 2,6-difluorotoluene to analyze the toluene results. The theory could account for the spectral shapes, the change in spectral shapes from toluene-d_0 to -αd_1 to -αd_2, and the change in spectral shape from one overtone to another (62). Figure 6 shows the spectra and our calculated profiles for Δv_{CH} = 4 and 5 for toluene-d_0 and toluene–αd_1, respectively (62).

We can do these calculations in two ways. In the first, the adiabatic approach, we simplify the problem by separating the fast methyl CH stretching motion from the slower motion of methyl rotation. Alternatively, we could combine the two motions and perform the calculation in a basis that includes both the CH stretching and methyl rotation. If we compare these two calculations we get a very interesting result that serves to distinguish between three time scales (62). The fastest time scale involves CH stretching, while methyl rotation is slower. The third time scale is the time it takes all of the CH stretching vibrational energy to transfer from one methyl C—H bond to another. That latter time scale gets longer the higher the vibrational quantum number v, i.e., the more vibrational energy transferred. Recall that the coupling of $|\, v,0\,\rangle$ and $|\, 0,v\,\rangle$ becomes weaker with higher v. When the time for this transfer is slower than the time for coupling of torsion and stretching, the latter dominates. Essentially the CH oscillators do not have time to interact before they are fully mixed with methyl torsional motion. From a CH stretching point of view they become fully localized vibrational modes.

Application of calculated overtone spectra

Earlier calculations of overtone intensities focused on the determination of relative intensities within a given overtone region. As we have noted, these types of intensity calculations are extremely helpful in the assignment of spectra (36, 37, 43, 45). A comparison with exact variational calculations for the water molecule showed that the simple HCAO local mode model provided a vibrational description that was adequate but that improvements in the ab initio dipole moment surfaces were required to achieve accurate absolute overtone intensities (65). Systematic tests of the requirements of the ab initio theory have followed (66–69) to the point where accurate absolute intensities can now be calculated (67, 69, 70–72). All these HCAO calculations rely on local mode parameters that have been derived from observed fundamental and overtone XH stretching transitions. Recently we have developed an approach based on the HCAO local mode model and ab initio calculations that allows overtone spectra of species that have not been measured in the laboratory to be calculated (73, 74). In this method the local mode parameters are determined from ab initio calculations with scaling parameters obtained from known spectra of similar compounds (74).

We have applied these techniques to neutral and charged polycyclic aromatic hydrocarbons (75) and to the water dimer complex (74). The results for the water dimer complex were in excellent agreement with the very few available experimental results. These calculated overtone spectra, combined with estimates of the atmospheric abundance of water dimer, have allowed the atmospheric impact of water

Fig. 5. The vapor phase ICL-PAS spectrum of propane (top trace), acetone (middle trace), and dimethylether (bottom trace) in the Δv_{CH} = 7 region. The lowest energy band in the propane spectrum is due to the methylene group.

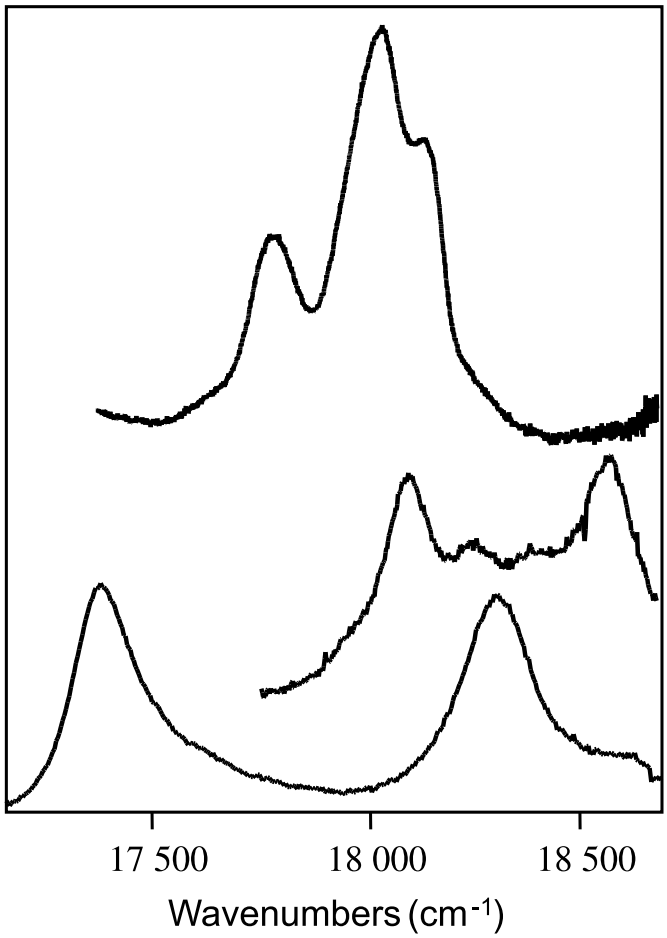

© 2002 NRC Canada

Fig. 6. The vapor phase ICL-PAS spectrum of toluene-d_0 (left side) and toluene-αd_1 (right side) in Δv_{CH} = 4 (top panels) and 5 (bottom panels). In each panel the experimental spectrum is shown as the bottom trace and the simulated spectrum as the top trace.

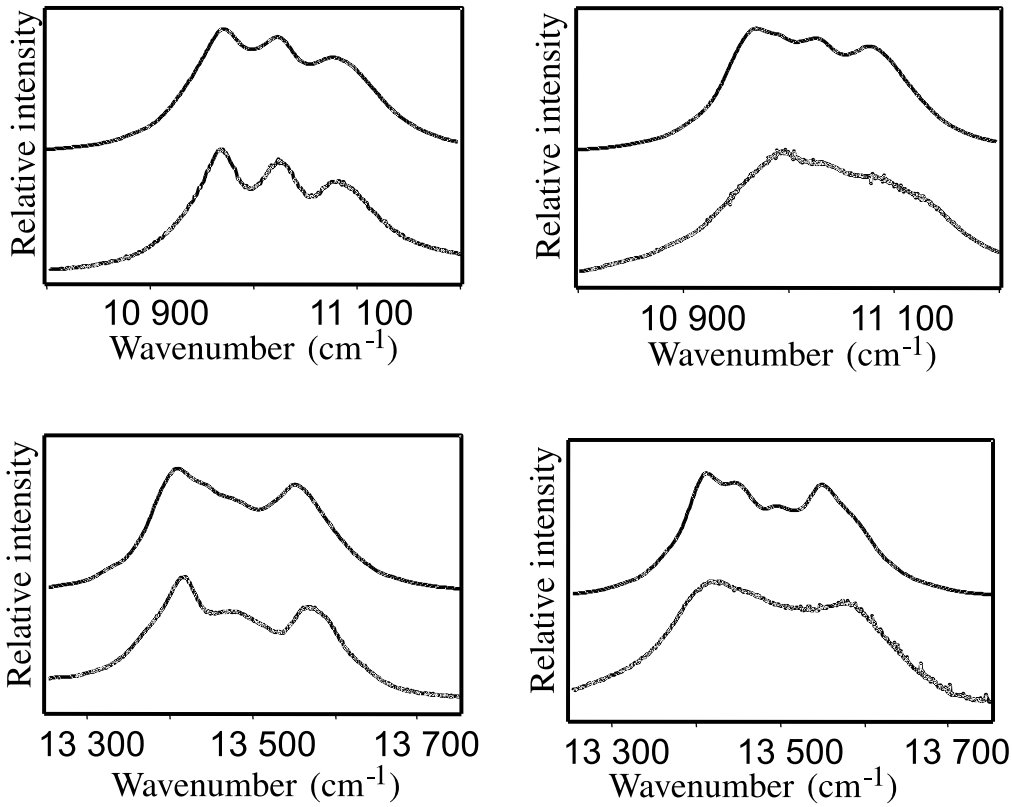

dimer on the absorption of solar radiation to be estimated by radiative transfer calculations (76). Subsequently, we have calculated overtone spectra of a series of mono-hydrated complexes (77, 78) and are currently investigating their impact on absorption of solar radiation (79).

Absorption of solar radiation in OH stretching vibrational overtones in atmospheric trace species can lead to formation of OH radicals. This has been suggested to be an important source of OH radicals at dawn and dusk when the available UV radiation is low (70, 71, 80). Again the local mode model provides a suitable description of the OH stretching vibrations. It then becomes possible to calculate these transitions for various species and to allow their atmospheric impact to be assessed.

Conclusion

An historical perspective has been presented for the development of the local mode model. For XH stretching, anharmonicity appears predominately in off-diagonal terms in a normal mode basis but in diagonal terms in a local mode basis. Thus for vibrations corresponding to XH stretching overtones, the vibrational energy becomes increasingly nondiagonal in a normal mode basis relative to a local mode basis, as the vibrational energy increases. One of the most important elements in the local mode model is the recognition that the radiation field selectively excites states whose components have all of the vibrational energy localized in a single one of a set of equivalent oscillators. Although local modes are anharmonic, the coupling of XH oscillators is well approximated by a harmonic coupling regime, and this characteristic is used in the HCAO model. The HCAO model allows straightforward calculations of state energies for XH stretching overtones and provides simple wave functions that are useful in calculations of overtone intensities. Because of their localized character, XH stretching overtone spectra can be used as sensitive probes of molecular properties such as bond length and molecular conformation. Examples are presented that show the resolution of spectral features for bond length differences less than 1 mÅ. Methyl torsion has a dramatic effect on XH stretching overtone spectra in molecules with a low barrier to internal methyl rotation. A successful theoretical approach is outlined to account for these effects and to provide insight into vibrational dynamics. We have developed an approach based on the HCAO local mode model, ab initio dipole moment functions, and ab initio local mode parameters that can calculate overtone spectra of species for which laboratory spectra have not yet been measured. These calculated spectra facilitate studies of the atmospheric impact of these species.

Acknowledgment

Funding for this research has been provided by the Natural Science and Engineering Research Council of Canada (NSERC), the Marsden Fund administrated by the Royal Society of New Zealand, and the University of Otago.

© 2002 NRC Canada

References

1. W. Siebrand. J. Chem. Phys. **46**, 440 (1967).
2. W. Siebrand. J. Chem. Phys. **47**, 2411 (1967).
3. W. Siebrand and D.F. Williams. J. Chem. Phys. **49**, 1860 (1968).
4. B.R. Henry and W. Siebrand. J. Chem. Phys. **49**, 5369 (1968).
5. J.W. Ellis. Trans. Faraday Soc. **25**, 888 (1929).
6. R.J. Hayward and B.R. Henry. J. Mol. Spectrosc. **50**, 58 (1974).
7. R.J. Hayward and B.R. Henry. J. Mol. Spectrosc. **57**, 221 (1975).
8. R. Mecke and R. Ziegler. Z. Phys. **101**, 405 (1936).
9. R.L. Swofford, M.E. Long, and A.C. Albrecht. J. Chem. Phys. **65**, 179 (1976).
10. M.L. Elert, P.R. Stannard, and W.M. Gelbart. J. Chem. Phys. **67**, 5395 (1977).
11. W.M. Gelbart, P.R. Stannard, and M.L. Elert. Int. J. Quantum Chem. **14**, 703 (1978).
12. B.R. Henry. *In* Vibrational spectra and structure. Vol. 10. *Edited by* J.R. Durig. Elsevier Scientific, Amsterdam. 1981. p. 269.
13. B.R. Henry. Acc. Chem. Res. **20**, 429 (1987).
14. M.L. Sage and J. Jortner. Adv. Chem. Phys. **47**, 293 (1981).
15. L. Halonen. Adv. Chem. Phys. **104**, 41 (1998).
16. B.R. Henry and M.A. Mohammadi. Chem. Phys. **55**, 385 (1981).
17. B.R. Henry, K.M. Gough, and M.G. Sowa. Int. Rev. Phys. Chem. **5**, 133 (1986).
18. B.R. Henry and D.J. Swanton. J. Mol. Struct. **202**, 193 (1989).
19. B.R. Henry and R.J.D. Miller. Chem. Phys. Lett. **60**, 81 (1978).
20. W.R.A. Greenlay and B.R. Henry. Chem. Phys. Lett. **53**, 325 (1978).
21. M.A. Mohammadi and B.R. Henry. Proc. Natl. Acad. Sci. U.S.A. **78**, 686 (1981).
22. B.R. Henry, M.A. Mohammadi, and J.A. Thomson. J. Chem. Phys. **75**, 3165 (1981).
23. M.W.P. Petryk and B.R. Henry. J. Phys. Chem. A, **106**, 8599 (2002).
24. A.W. Tarr and B.R. Henry. J. Chem. Phys. **84**, 1355 (1986).
25. J.W. Perry and A.H. Zewail. J. Phys. Chem. **86**, 5197 (1982).
26. K.V. Reddy, D.F. Heller, and M.J. Berry. J. Chem. Phys. **76**, 2814 (1982).
27. A.W. Tarr and B.R. Henry. Chem. Phys. Lett. **112**, 295 (1984).
28. P.R. Stannard and W.M. Gelbart. J. Phys. Chem. **85**, 3592 (1981).
29. M.L. Sage and J. Jortner. Chem. Phys. Lett. **62**, 451 (1979).
30. E.L. Sibert III, W.P. Reinhardt, and J.T. Hynes. J. Chem. Phys. **81**, 1115 (1984).
31. I.A. Watson, B.R. Henry, and I.G. Ross. Spectrochim. Acta A, **37**, 857 (1981).
32. R. Wallace. Chem. Phys. **11**, 189 (1975).
33. O.S. Mortensen, B.R. Henry, and M.A. Mohammadi. J. Chem. Phys. **75**, 4800 (1981).
34. M.S. Child and R.T. Lawton. Faraday Discuss. Chem. Soc. **71**, 273 (1981).
35. B.R. Henry, A.W. Tarr, O.S. Mortensen, W.F. Murphy, and D.A.C. Compton. J. Chem. Phys. **79**, 2583 (1983).
36. H.G. Kjaergaard, H. Yu, B.J. Schattka, B.R. Henry, and A.W. Tarr. J. Chem. Phys. **93**, 6239 (1990).
37. H.G. Kjaergaard, B.R. Henry, and A.W. Tarr. J. Chem. Phys. **94**, 5844 (1991).
38. D.M. Turnbull, H.G. Kjaergaard, and B.R. Henry. Chem. Phys. **195**, 129 (1995).
39. O.S. Mortensen, M.K. Ahmed, B.R. Henry, and A.W. Tarr. J. Chem. Phys. **82**, 3903 (1985).
40. L.A. Findsen, H.L. Fang, R.L. Swofford, and R.R. Birge. J. Chem. Phys. **84**, 16 (1986).
41. A.W. Tarr, D.J. Swanton, and B.R. Henry. J. Chem. Phys. **85**, 3463 (1986).
42. A.W. Tarr and F. Zerbetto. Chem. Phys. Lett. **154**, 273 (1989).
43. H.G. Kjaergaard and B.R. Henry. J. Chem. Phys. **96**, 4841 (1992).
44. B.I. Niefer, H.G. Kjaergaard, and B.R. Henry. J. Chem. Phys. **99**, 5682 (1993).
45. H.G. Kjaergaard, D.M. Turnbull, and B.R. Henry. J. Chem. Phys. **99**, 9438 (1993).
46. B.R. Henry and M.G. Sowa. Prog. Anal. Spectrosc. **12**, 349 (1989).
47. B.R. Henry, H.G. Kjaergaard, B. Neifer, B.J. Schattka, and D.M. Turnbull. Can. J. Appl. Spec. **38**, 42 (1993).
48. M.W.P. Petryk and B.R. Henry. Can. J. Chem. **79**, 279 (2001).
49. M.J. Frisch, G.W. Trucks, H.B. Schlegel, G.E. Scuseria, M.A. Robb, J.R. Cheeseman, V.G. Zakrzewski, J.A. Montgomery, Jr, R.E. Stratmann, J.C. Burant, S. Dapprich, J.M. Millam, A.D. Daniels, K.N. Kudin, M.C. Strain, O. Farkas, J. Tomasi, V. Barone, M. Cossi, R. Cammi, B. Mennucci, C. Pomelli, C. Adamo, S. Clifford, J. Ochterski, G.A. Petersson, P.Y. Ayala, Q. Cui, K. Morokuma, D.K. Malick, A.D. Rabuck, K. Raghavachari, J.B. Foresman, J. Cioslowski, J.V. Ortiz, B.B. Stefanov, G. Liu, A. Liashenko, P. Piskorz, I. Komaromi, R. Gomperts, R.L. Martin, D.J. Fox, T. Keith, M.A. Al-Laham, C.Y. Peng, A. Nanayakkara, C. Gonzalez, M. Challacombe, P.M.W. Gill, B. Johnson, W. Chen, M.W. Wong, J.L. Andres, C. Gonzalez, M. Head-Gordon, E.S. Replogle, and J.A. Pople. 1998. Gaussian 98 [computer program]. Revision A.5. Gaussian, Inc., Pittsburgh, PA, U.S.A.
50. H.G. Kjaergaard and B.R. Henry. J. Phys. Chem. **99**, 899 (1995).
51. H.G. Kjaergaard and B.R. Henry. J. Phys. Chem. **100**, 4749 (1996).
52. H.G. Kjaergaard, D.L. Howard, D.P. Schofield, T.W. Robinson, S. Ishiuchi, and M. Fujii. J. Phys. Chem. A. **106**, 258 (2002).
53. K.M. Gough and B.R. Henry. J. Phys. Chem. **88**, 1298 (1984).
54. D. Cavagnat, L. Lespade, and C. Lapouge. J. Chem. Phys. **103**, 10 502 (1995).
55. C. Lapouge and D. Cavagnat. J. Phys. Chem. A, **102**, 8393 (1998).
56. D. Cavagnat and L. Lespade. J. Chem. Phys. **106**, 7946 (1997).
57. C. Zhu, H.G. Kjaergaard, and B.R. Henry. J. Chem. Phys. **107**, 691 (1997).
58. R.J. Proos and B.R. Henry. J. Phys. Chem. A, **103**, 8762 (1999).
59. D. Cavagnat and J.Lascombe. J. Chem. Phys. **76**, 4336 (1982).
60. H.G. Kjaergaard, D.M. Turnbull, and B.R. Henry. J. Phys. Chem. A, **102**, 6095 (1998).
61. H.G. Kjaergaard, D.M. Turnbull, and B.R. Henry. J. Phys. Chem. A, **101**, 2589 (1997).
62. H.G. Kjaergaard, Z. Rong, A.J. McAlees, D.L. Howard, and B.R. Henry. J. Phys. Chem. A, **104**, 6398 (2000).
63. Z. Rong, H.G. Kjaergaard, and B.R. Henry. J. Phys. Chem. A, **106**, 4368 (2002).
64. Z. Rong and H.G. Kjaergaard. J. Phys. Chem. A, **106**, 6242 (2002).
65. H.G. Kjaergaard, B.R. Henry, H. Wei, S. Lefebvre, T. Carrington Jr., O.S. Mortensen, and M.L. Sage. J. Chem. Phys. **100**, 6228 (1994).
66. H.G. Kjaergaard and B.R. Henry. Mol. Phys. **83**, 1099 (1994).

© 2002 NRC Canada

67. H.G. Kjaergaard, C.D. Daub, and B.R. Henry. Mol. Phys. **90**, 201 (1997).
68. C.D. Daub, B.R. Henry, M.L. Sage, and H.G. Kjaergaard. Can. J. Chem. **77**, 1775 (1999).
69. H.G. Kjaergaard, K.J. Bezar, and K.A. Brooking. Mol. Phys. **96**, 1125 (1999).
70. D.J. Donaldson, J.J. Orlando, S. Amann, G.S. Tyndall, R.J. Proos, B.R. Henry, and V. Vaida. J. Phys. Chem. A, **102**, 5171 (1998).
71. L. Fono, D.J. Donaldson, R.J. Proos, and B.R. Henry. Chem. Phys. Lett. **311**, 131 (1999).
72. P. Hintze, H.G. Kjaergaard, V.Vaida, and J.B. Burkeholder. J. Phys. Chem. A, in press.
73. M.G. Sowa, B.R. Henry, and Y. Mizugai. J. Phys. Chem. **97**, 809 (1991).
74. G.R. Low and H.G. Kjaergaard. J. Chem. Phys. **110**, 9104 (1999).
75. H.G. Kjaergaard, T.W. Robinson, and K.A. Brooking. J. Phys. Chem. A, **104**, 11 297 (2000).
76. V. Vaida, J.S. Daniel, H.G. Kjaergaard, L.M. Gross, and A.F. Tuck. Q. J. R. Meteorol. Soc. **127**, 1627 (2001)
77. H.G. Kjaergaard. J. Phys. Chem. A, **106**, 2979 (2002).
78. H.G. Kjaergaard, G.R. Low, T.W. Robinson, and D.L. Howard. J. Phys. Chem. A, **106**, 8955 (2002).
79. H.G. Kjaergaard, T.W. Robinson, D.L. Howard, J.E. Headerick, J.S. Daniel, and V. Vaida. Unpublished.
80. D.J. Donaldson, G.J. Frost, K.H. Rosenlof, A.F. Tuck, and V. Vaida. Geophys. Res. Lett. **24**, 2651 (1997).

© 2002 NRC Canada

Antibody-catalyzed formation of a 14-membered ring lactone

Michael D. Pungente, Larry Weiler, and Hermann J. Ziltener

Abstract: Monoclonal antibody (MAb) F123, raised against a macrocyclic phosphonate transition-state analogue, catalyzed an intramolecular transesterification of the corresponding hydroxy ester to give a 14-membered ring lactone. The MAb reaction displayed enzyme-like Michaelis–Menten kinetics with a K_m of 255 μM and a k_{cat} of 0.01 min^{-1} based on *p*-nitrophenol release and calculated on an active-site basis. Substrate specificity and competitive inhibition by a transition state analogue (K_i = 3 μM) demonstrated that the catalytic activity was associated with binding in the antibody-combining site. The lactone product was isolated from a large-scale catalytic experiment through ether extraction and identified by gas chromatography – mass spectroscopy.

Key words: macrocyclization, lactones, catalytic antibodies.

Résumé : L'anticorps monoclonal (AcM) F123, élevé contre un analogue d'état de transition phosphonate macrocyclique, catalyse une réaction de transestérification intramoléculaire de l'ester hydroxylé correspondant pour conduire à la formation d'un cycle lactonique à quatorze chaînons. La réaction de l'AcM présente une cinétique de Michaelis–Menten semblable à celle observée avec les enzymes avec un K_m de 255 μM et un k_{cat} de 0,01 min^{-1} basé sur l'élimination du *p*-nitrophénol et calculé sur une base de site actif. La spécificité du substrat et l'inhibition compétitive par un analogue de l'état de transition (K_i = 3 μM) démontrent que l'activité catalytique est associée à la fixation dans un site de combinaison d'anticorps. La lactone produite lors d'une expérience catalytique à grande échelle a été isolée par extraction à l'éther et on l'a identifiée par spectrométrie de masse liée à un chromatographe en phase gazeuse.

Mots clés : macrocyclisation, lactones, anticorps catalytiques.

[Traduit par la Rédaction]

Introduction

The macrolide antibiotics contain a ring moiety, in many cases represented by a 14-membered lactone. The syntheses of these large-ring compounds pose a challenge for chemists, particularly in controlling the ring-forming step. Attempts to use enzymes in aqueous and organic solvents to catalyze medium to large ring lactonizations have met with limited success, particularly with secondary alcohols (1). Antibodies raised against transition state analogues have offered an alternative class of catalysts for complex reactions, many of which have been highlighted in review articles (2). Indeed, in 1987 Napper et al. (3) reported that an antibody raised against a transition state analogue for an intramolecular six-membered ring cyclization acted as a catalyst for the appropriate substrate to give a δ-lactone. To our knowledge, no antibody-catalyzed macrocyclization has been reported to date. To this end, we extended this antibody methodology to the formation of the 14-membered ring lactone **1**. We therefore synthesized the 14-membered ring transition state analogue **2**, which we subsequently conjugated to a carrier protein for the production of monoclonal antibodies.[4]

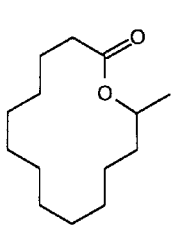

1

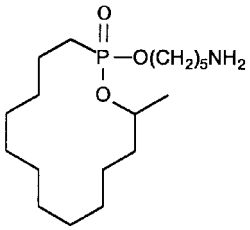

2

Received 28 June 2002. Published on the NRC Research Press Web site at http://canjchem.nrc.ca on 3 December 2002.

M. Pungente[1,2] and L. Weiler.[3] Department of Chemistry, The University of British Columbia, Vancouver, BC V6T 1Z1, Canada. **H. Ziltener.** The Biomedical Research Centre and Department of Pathology and Laboratory Medicine, The University of British Columbia, Vancouver, BC V6T 1Z1, Canada.

[1]Present address: Department of Chemistry, Lakehead University, 955 Oliver Road, Thunder Bay, ON P7B 5E1, Canada.
[2]Corresponding author (e-mail: mike.pungente@lakeheadu.ca).
[3]Deceased 28 April, 1999.
[4]Supplementary data (Methods) may be purchased from the Depository of Unpublished Data, Document Delivery, CISTI, National Research Council Canada, Ottawa, ON K1A 0S2, Canada (http://www.nrc.ca/cisti/irm/unpub_e.shtml for information on ordering electronically).

 DOI: 10.1139/V02-185 © 2002 NRC Canada

Scheme 1. (*a*) *n*-BuLi, THF, –78°C, $HO(CH_2)_5NHCbz$ (**4**), 59%. (*b*) H_2, 10% Pd/C, EtOH, 85%.

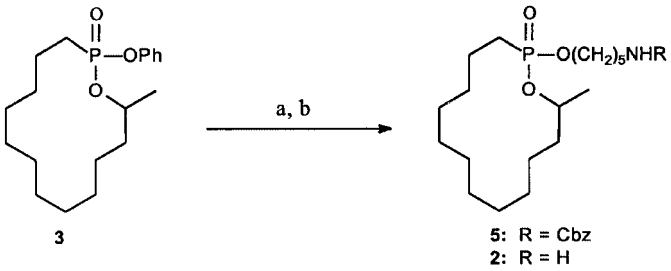

Results and discussion

The synthesis of hapten **2** (Scheme 1) was achieved by substitution of the phenyl moiety of the S*R* diastereomer of phosphonate **3** (4) with the anion of alcohol **4** to give **5** in a 59% yield.

Hydrogenolysis of **5** in ethanol with hydrogen and 10% Pd/C afforded amine **2** in 85% yield.

Amine **2** was coupled to carboxyl residues of the carrier protein keyhole limpet hemocyanin (KLH) using the water soluble coupling reagent 1-(3-dimethylaminopropyl)-3-ethylcarbodiimide hydrochloride (EDC), emulsified in Freund's complete adjuvant and used to immunized Balb/c mice. After three subsequent booster injections with KLH·**2** in Freund's incomplete adjuvant, spleens of mice were harvested and MAbs were produced using standard hybridoma methodology (5). Three MAbs (F123, F125, and F150) were selected in an immunoassay based on their selective binding to **2** coupled to bovine serum albumin (BSA). MAbs were purified by sheep anti-mouse affinity chromatography and dialyzed against PBS buffer, pH 7.4. Antibody concentration was determined by measuring optical density at 280 nm (where 1.2 absorbance units correspond to 1 mg mL^{-1} antibody in solution (6)) and using 190 kDa for the molecular weight of IgM monomer.

The three MAbs that showed selective binding to **2** were tested for catalytic activity against substrate **6** while monitoring the release of *p*-nitrophenolate. Of these, only F123 (an IgM monoclonal antibody as determined by isotyping) showed significant activity and was selected for further study. The F123-catalyzed reaction with **6** was shown to obey Michaelis–Menten kinetics with a K_m of 255 μM, and a k_{cat} of 0.01 min^{-1} (based on *p*-nitrophenol release and calculated on an active site basis). The observed rates were corrected for the background hydrolysis in buffer.

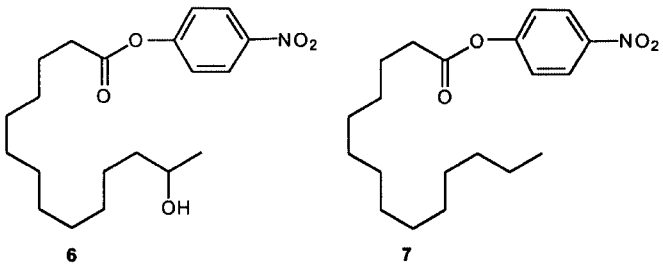

To illustrate that the activity of antibody F123 with **6** is not due to an esterolytic contaminant of the serum, an affinity purified control MAb raised against an unrelated hapten was run in parallel with F123. The control MAb showed no activity with substrate **6**. It should be noted that while this evidence is supportive, it is by no means definitive. In addition, substrate **7**, which lacks the secondary hydroxyl necessary for lactonization, was tested as a substrate for F123 and showed little or no *p*-nitrophenolate release compared with **6** (Fig. 1). This provided strong evidence that the catalytic MAb was not simply behaving as an esterase by hydrolyzing the *p*-nitrophenyl ester moiety. An alternate reason as to why **7** is not processed by F123 could simply be lack of recognition by the antibody. However, these two control experiments together provide substantial evidence that it is indeed the antibody that is carrying out the catalysis.

Fig. 1. Comparison of antibody F123 activity with hydroxy ester substrate **6** (○); with ester **7** (●). In each case, antibody was 0.46 μM; substrates were 100 μM; carried out in PBS buffer (pH 7.4) containing 10% DMSO and 0.5% Triton X-100; total reaction volume was 225 μL.

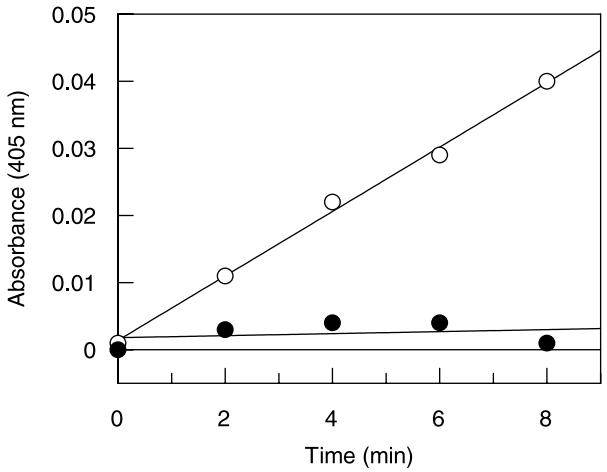

The 4-nitrophenyl phosphonate derivative **8** was synthesized by base hydrolysis of phenyl phosphonate **3** using refluxing 3 N NaOH–THF, producing the corresponding

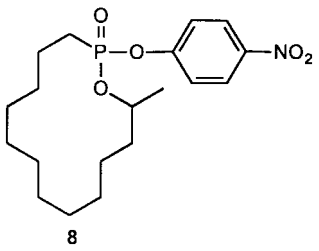

phosphonic acid derivative in a 73% yield. Conversion of the phosphonic acid derivative to the acid chloride with oxalyl chloride, followed by coupling of this phosphoryl chloride intermediate with *p*-nitrophenol, gave a 1.2:1 ratio of diastereomers of **8** in 69% yield.

Owing to a lack of compound **2**, compound **8** was chosen for inhibition studies as we felt it would sufficiently mimic the putative transition state for the cyclization of substrate **6** to give lactone **1**. Inhibition assays with **8** (using a 1:1 mixture of diastereomers) were performed by varying the concentration of **8** at fixed levels of substrate **6** and MAb F123

© 2002 NRC Canada

Fig. 2. Inhibition of the F123-catalyzed macrolactonization of substrate **6** by a mixture of 4-nitrophenyl phosphonate diastereomers of compound **8**. The reactions were performed in PBS buffer (pH 7.4) containing 10% DMSO and 0.5% Triton X-100. The concentrations of compound **8** were: (●) 0 μM; (○) 2 μM; and (▼) 5 μM.

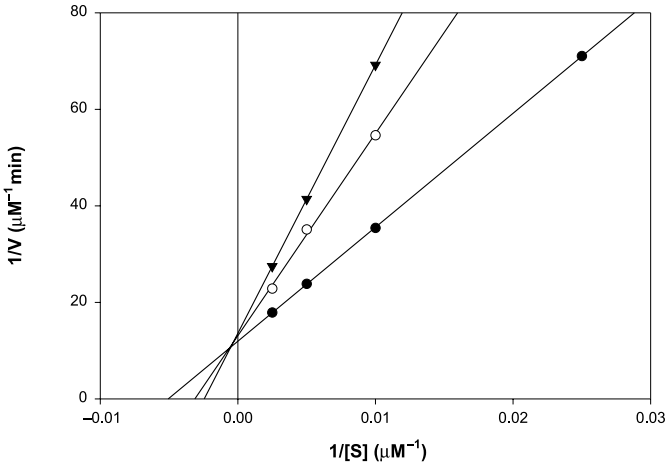

(Fig. 2). Unfortunately, accurate determination of K_i was precluded by the insensitivity of the assay employed. Concentrations of antibody in the same range as the apparent K_i value ultimately determined were needed to get measurable reaction rates. As a consequence the K_i value determined (K_i = 3 μM) can be regarded only as a rough estimate of the true K_i value. However, this result does clearly indicate that binding is tight and is fully consistent with the catalytic activity measured arising from the active site.

Lactone **1** was isolated from pooled catalytic experiments through ether extractions. Unambiguous identification of the lactone was carried out by comparison with authentic **1** (7) by GC, GC–MS, and HR-MS. No lactone was detected in the absence of antibody catalyst.

In summary, we have shown that monoclonal antibody F123, an IgM antibody, has catalyzed macrocyclic lactone ring formation. We feel this preliminary work opens the door for further potential methodology studies toward macrocycle synthesis.

Acknowledgements

We are grateful for financial support from the Natural Sciences and Engineering Research Council of Canada (NSERC) and the Protein Engineering Centres of Excellence: Canada. We also thank Professor Stephen G. Withers of the Department of Chemistry (UBC) for his very helpful suggestions and discussions, as well as Helen Merkens and Michael Williams of The Biomedical Research Centre for their expert technical assistance in antibody production, characterization, and purification, and finally Dr. G. Eigendorf of the Department of Chemistry at UBC for performing the GC–MS and HR-MS analyses.

References

1. (*a*) K. Mori and H. Tomioka. Liebigs Ann. Chem. 1001 (1992); (*b*) M. Lobell and M.P. Schneider. Tet. Asym. **4**, 1027 (1993).
2. (*a*) J.D.Stevenson and N.R. Thomas. Nat. Prod. Rep. **17**, 535 (2000); (*b*) G.A. Nevinsky, D.V. Semenov, and V.N. Buneva. Biochemistry (Mosc), **65**, 1233 (2000); (*c*) C. Rader and B. List. Chem. Eur. J. **6**, 2091 (2000); (*d*) P. Wentworth and K.D. Janda. Curr. Opin. Chem. Biol. **2**, 138 (1998); (*e*) M.M. Mader and P.A. Bartlett. Chem. Rev. **97**, 1281 (1997); (*f*) N.R. Thomas. Nat. Prod. Rep. **13**, 479 (1996); (*g*) S. Paul. Mol. Biotechnol. **5**, 197 (1996); (*h*) A.J. Kirby. Acta. Chem. Scand. **50**, 203 (1996); (*i*) E.M. Driggers and P.G. Schultz. Adv. Protein Chem. **49**, 261 (1996); (*j*) J.R. Jacobsen and P.G. Schultz. Curr. Opin. Struct. Biol. **5**, 818 (1995); (*k*) R.A. Lerner and K.D. Janda. EXS, **73**, 121 (1995); (*l*) D.S. Tawfik, Z. Eshhar, and B.S. Green. Mol. Biotechnol. **1**, 87 (1994); (*m*) H.J. Suzuki. Biochem. **115**, 623 (1994).
3. A.D. Napper, S.J. Benkovic, A. Tramontano, and R.A. Lerner. Science (Washington, D.C.), **237**, 1041 (1987).
4. M.D. Pungente and L. Weiler. Org. Lett. **3**, 643 (2001).
5. J.W. Goding. Monoclonal antibodies: Principles and practices. Academic, New York. 1983. pp. 234–255.
6. E. Harlow and D. Lane. Antibodies: A laboratory manual. Cold Spring Harbor Laboratory, Cold Spring Harbor. 1988. pp. 673.
7. D.S. Clyne, and L. Weiler. Tetrahedron, **55**, 13 659 (1999).

© 2002 NRC Canada

Magnetic properties of some Fe–S six-membered ring compounds

Ping Liu, Jia Cheng Liu, Jian Wang, Jian Kai Cheng, Wen Jie Li, and Xin Huang

Abstract: The Fe_3S_3 cluster is an important component located in the active centres of some iron–sulfur proteins. The magnetic properties of three Fe_3S_3 compounds have been studied for the first time by fitting the temperature-dependent magnetic susceptibilities. The calculated *g* factors and *J* couplings reproduce the magnetic behavior of such compounds very well. There is an antiferromagnetic spin interaction between pairs of magnetic centers in the Fe_3S_3 cluster compounds. The magnetic exchange of Fe-S-Fe model magnetic molecules is discussed.

Key words: Fe_3S_3 compounds, magnetic, antiferromagnetic.

Résumé : L'agrégat Fe_3S_3 est une composante importante de centres actifs des protéines fer–soufre. On a étudié les propriétés magnétiques de trois composés Fe_3S_3 basée sur les susceptibilités magnétiques qui varient avec la température. Les facteurs *g* et les constantes de couplage *J* calculées permettent de très bien reproduire le comportement magnétique de tels composés. Il existe une interaction de spin antiferromagnétique entre les paires de centres magnétiques des composés agrégats Fe_3S_3. On discute de l'échange magnétique de molécules magnétiques modèles de Fe-S-Fe.

Mots clés : composés Fe_3S_3, magnétique, antiferromagnétique.

[Traduit par la Rédaction]

Introduction

Iron–sulfur proteins (including enzymes) exist in most life forms. They are redox proteins and their active centers are the Fe–S clusters in various forms. For example, the Fe–S clusters discovered in nitrogenase are Fe_2S_2, Fe_4S_4, Fe_3S_4, and Fe_8S_7 (1, 2). The Fe_6S_6 clusters have been found in the Fe-hydrogenase (3), and their structures have been determined by X-ray diffraction (1, 2) and spectra (3), respectively. Their schematic structures are shown in Fig. 1. According to structural characteristics of these Fe–S clusters and other Fe–S clusters, they can be divided into two groups; one contains at least one Fe_2S_2 unit, such as Fe_2S_2, Fe_4S_4, or Fe_8S_7; the other contains an Fe_3S_3 unit, such as Fe_3S_4 or Fe_6S_6. Two Fe_2S_2 can re-form an Fe_4S_4, and two Fe_4S_4 can form an Fe_8S_7; one Fe_3S_3 and an S atom can form an Fe_3S_4, and two Fe_3S_3 can form an Fe_6S_6. The Fe_2S_2 unit has been much studied, but the study of the Fe_3S_3 unit is quite rare.

M_3S_3 clusters (M = Fe, Cu, Pd, B, etc.) containing a six-membered ring are very interesting compounds. The six-membered M_3S_3 ring is analogous to benzene in organic compounds, in which electron delocalization is responsible for the molecular aromaticity. The M_3N_3 cluster B_3O_3 (where M = B and N = O) is the anion group of a nonlinear optic material and shows particular properties (4, 5). During the 1990s the study of the magnetic property of transition metal cluster compounds and biological magnetic materials increased dramatically because it overlapped and advanced studies on inorganic and organic magnetic molecules. The study of transition metal cluster compounds (including complex compounds) is a new field of magnetism research that has begun to attract wide attention (6, 7). We hope to infer the magnetic properties of metal active centers of iron–sulfur proteins through a study of the magnetic susceptibility of Fe_3S_3 ring compounds, thus paving the way for the discovery of new advanced biological functional materials.

We have synthesized some Fe_3S_3 ring compounds and determined their crystal structures and molecular structures (8–13). The molecular formulas of compounds **1–3** are as follows:

[1] α-$(Et_4N)_3(Fe_3(PhS)_3Cl_3Br_3)$

[2] $(Et_4N)_3(Fe_3(p\text{-}CH_3PhS)_3Cl_3Br_3)$

[3] $(Et_4N)_3(Fe_3(p\text{-}CH_3PhS)_3Cl_6)$

A perspective view and the conformation of the anion in compound **1** (10) are shown in Fig. 2.

Experimental section

Preparation

Compounds **1–3** have been synthesized in a one-step reaction (10–12). The water and oxygen were removed from the solvents, and the reaction was carried out in an N_2 atmosphere. Molar equivalents of $FeCl_2$, *p*-PhSNa, Et_4NX (X = Cl or Br), and appropriate acetonitrile were added to a

Received 7 April 2002. Published on the NRC Web site at http://canjchem.nrc.ca on 6 December 2002.

P. Liu,[1] J.C. Liu, J. Wang, J.K. Cheng, and X. Huang. Fujian Institute of Research on the Structure of Matter, Chinese Academy of Sciences, Fuzhou 350002, China.
W.J. Li. Department of Radio Engineering, Fuzhou University, Fuzhou 350002, China.

[1]Corresponding author (e-mail: pliu@ms.fjirsm.ac.cn).

 DOI: 10.1139/V02-184 © 2002 NRC Canada

Fig. 1. Schematic structures of Fe_2S_2, Fe_4S_4, Fe_3S_4, Fe_8S_7, and Fe_6S_6.

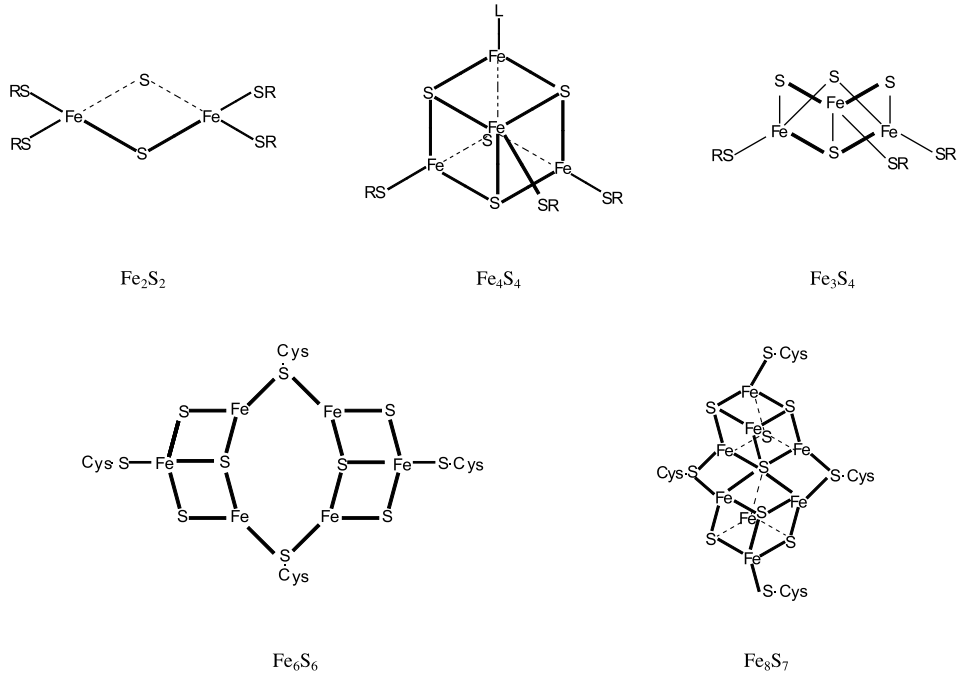

Fig. 2. Perspective view and the conformation of the Fe_3S_3 anion in compound **1**.

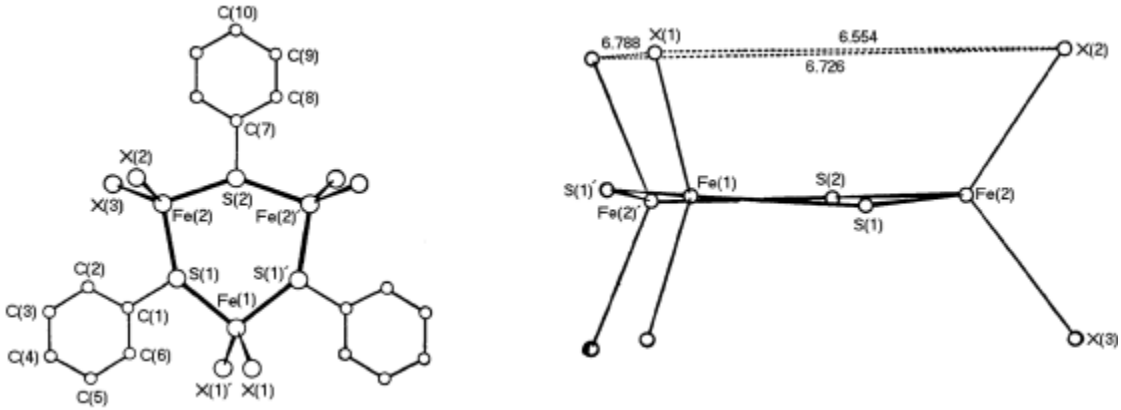

round-bottomed flask, and under magnetic stirring the colour of the reaction solution changed to yellow-green gradually. After the reaction, the reaction mixture was filtered, the filtrate concentrated, and yellow-green crystals were obtained.

Reaction formula:

$$3FeCl_2 + 3R\text{-}PhSNa + 3Et_4NX \longrightarrow (Et_4N)_3(Fe_3(R\text{-}PhS)_3X_3Cl_3)$$

(Compound **1**: R = H, X = Br; compound **2**: R = p-CH_3, X = Br; compound **3**: R = p-CH_3, X = Cl.)

Magnetic measurements

Variable-temperature magnetic susceptibilities in the temperature range 5–300 K were measured on a CF-1 superconducting extracting sample magnetometer at a magnetic field of 5.0 T with the powdered samples kept in capsules filled with N_2 for weighing. The temperature was raised gradually from 5 to 300 K. Data were recorded at an applied field gradient $H(dH/dx) = 1.4 \times 10^7$ Oe·Oe·cm^{-1}. The contribution of diamagnetic susceptibilities of compounds was accounted for.

Result and discussion

Magnetic properties

The model of Fe-Fe magnetic exchange of Fe_3S_3 six-membered ring compounds was assumed to be as an equilateral triangle with three Fe corners.

The temperature dependence of the molar magnetic susceptibility for clusters **1**–**3** are depicted in Figs. 3–5, respectively, in the form of the product $\chi_M T$ vs. absolute

© 2002 NRC Canada

Fig. 3. Plots of the temperature dependences of $\chi_M T$ and χ_M for compound **1**. The solid lines represent the best calculated curves.

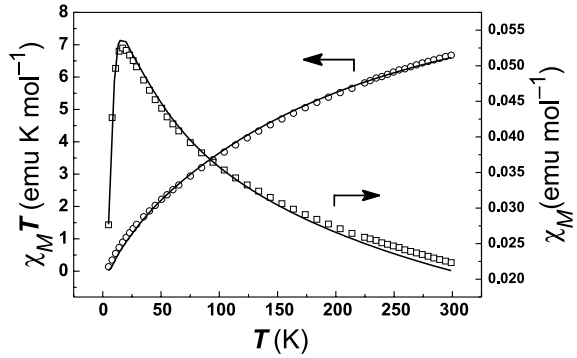

temperature T. The inserts show the thermal dependence of the magnetic susceptibility, where χ_M is the corrected molar magnetic susceptibility per $Fe(II)_3$ cluster unit.

For compound **1**, at room temperature, the value of the $\chi_M T$ product (6.68 emu·K·mol^{-1}) is smaller than the expected high-temperature limit for the three Fe(II) (g = 2.05) unit ($\chi_M T$ = 9.45 emu·K·mol^{-1}). As the temperature decreases, $\chi_M T$ decreases continuously to 0.14 emu·K·mol^{-1} at 5 K, suggesting the presence of an antiferromagnetic exchange interaction. The geometrical model of the Fe_3S_3 six-membered ring compounds based on its structure was assumed to be as an equilateral triangle with three Fe corners. In theory (14) there are 4 nonpair orbitals in the 3d orbit of Fe(II), and it must have high spin S = 2. So the spin-spin coupling Hamiltonian formula using the isotropic Heisenberg model can be written as

$$[4] \qquad \hat{H} = -2\,J\,(S_1 \cdot S_2 + S_1 \cdot S_3 + S_2 \cdot S_3)$$

($S_1 = S_2 = S_3 = 2$ and $J = J_{12} = J_{13} = J_{23}$). Applying the Van Vleck equation (15) gives the following molar susceptibility expression for the equilateral triangle Fe_3 system of **1**:

$$[5] \qquad \chi_M = \frac{2Ng^2\beta^2}{kT} \times \frac{3x^{40} + 25x^{36} + 56x^{30} + 90x^{22} + 110x^{12} + 91}{x^{42} + 9x^{40} + 25x^{36} + 28x^{30} + 27x^{22} + 22x^{12} + 13}$$

in which $x = \exp(-J/kT)$; the other symbols have their usual meanings.

The best fit for both $\chi_M T$ and χ_M for compound **1** leads to the parameters J = –11.09 cm^{-1}, g = 2.11, and $R = 6.67 \times 10^{-4}$ ($R = \Sigma((\chi_M T)_{obsd} - (\chi_M T)_{calcd})^2/\Sigma(\chi_M T)_{obsd}^2$). The result is quite satisfactory. There is no obvious minimum point near the fitting values and convergence in the fitting process is very quick, showing that the result is reliable. The negative J value also illustrates that compound **1** is paramagnetic with an antiferromagnetic coupling of spin.

The Fe_3S_3 ring compound possesses a typical M-S-M structure (M = Fe). The magnetic exchange among Fe atoms is through super-exchange. The distribution of electrons in the sulfur atom and two neighbouring iron atoms could be a merge of the "normal" iron state Fe^{2+}-S^{2-}-Fe^{2+} and the excited state Fe^{1+}-S^{1-}-Fe^{2+}, Fe^{2+}-S^{1-}-Fe^{1+}. When S^{1-} loses a 2p electron, the exchange integral J_{pd} between this sulfur ion and another iron ion will influence the relative direction of the d orbitals in two iron ions. We can say that the super exchange between two iron atoms is realized through a sulfur atom. Based on the fact that compounds containing an M-O-M system have a stronger exchange effect, we note that in Fe_3S_3 the Fe—S distance is short (2.3Å) and the Fe-S-Fe angles are 138° and 141° (between 90° and 180°), which can produce a stronger exchange effect.

Fig. 4. Plots of the temperature dependences of $\chi_M T$ and χ_M for compound **2**. The solid lines represent the best calculated curves.

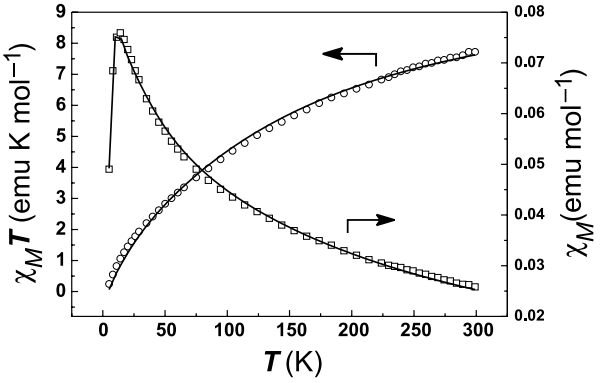

Fig. 5. Plots of the temperature dependences of $\chi_M T$ and χ_M for compound **3**. The solid lines represent the best calculated curves.

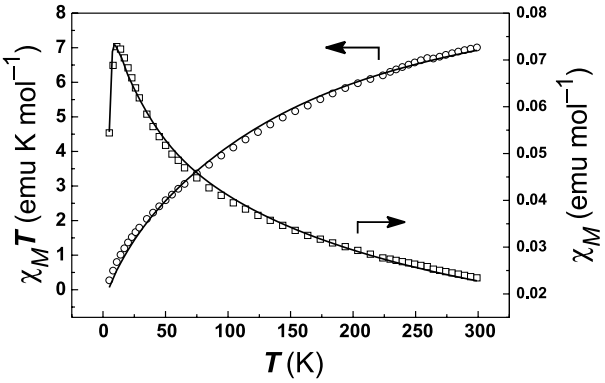

The experimental fitting curves of the temperature dependence of the molar susceptibilities (the product $\chi_M T$ and χ_M) of compounds **2** and **3** are shown in Figs. 4 and 5, respectively.

The curves of $\chi_M T$ and χ_M of compounds **2** and **3** are similar to those of compound **1**. The experimental curves are very flat, and the theoretical curves are fitted satisfactorily. According to the model in Fig. 4, for compound **2**, J = –8.76 cm^{-1} and g = 2.17, which together indicated a paramagnetic compound with antiferromagnetic coupling of spin. For compound **3**, J = –8.57 cm^{-1} and g = 2.06; both belong to paramagnetic compounds with antiferromagnetic coupling of spin.

The J values of compounds **1**–**3** decrease steadily in that order, and the g values are over 2.05. From the molecular structures, the main difference is that there are different *para*-substituted groups in the thiophenol and different halogen coordination in Fe.

© 2002 NRC Canada

Acknowledgments

We acknowledge financial support from the National Natural Science Foundation of China and the Natural Science Foundation of Fujian Province.

References

1. C.D. Stout. J. Biol. Chem. **268**, 25 920 (1993).
2. (*a*). J.A. Christner, E. Münck, T.A. Kent, P.A. Janick, J.C. Salerno, and L.M. Siegel. J. Am. Chem. Soc. **106**, 6786 (1984); (*b*) B.R. Crane, L.M. Siegel, and E.D. Getzoff. Science (Washington, D.C.), **270**, 59 (1995).
3. J. Kim and D.C. Rees. Biochemistry, **33**, 393 (1994).
4. C.T. Chen, Y.C. Wu, and R.K. Li. Chinese Phys. Lett. **2**, 389, (1985).
5. D. Eimerl, L. Davis, and S. Velsko. J. Appl. Phys. **62**, 1968 (1987).
6. O. Kahn, Y. Pei, K. Nakatani, and J. Yves. Mol. Cryst. Liq. Cryst. **176**, 481 (1989).
7. T.J. Marks. Angew. Chem. 102, **8**, 886 (1990).
8. P. Liu, L.R. Huang, L.L.Wang, B.S. Kang, and J.X. Lu. Chinese J. Struct. Chem. **2**, 135 (1984).
9. L.R. Huang, P.Liu, and L.L.Wang. Chinese J. Struct. Chem. **1**, 72 (1985).
10. P. Liu, L.R. Huang, L.L. Wang, B.S. Kang, and J.X. Lu. Acta. Chim. Sin. (Chin. Ed.), **46**, 972 (1988).
11. P. Liu, L.R. Huang, L.L. Wang, Y. Yang, and J.X. Lu. Chinese J. Inorg. Chem. **2**, 1 (1988).
12. P. Liu, J. Wang, and Y. Zheng. Chinese J. Struct. Chem. **2**, 132 (2000).
13. P. Liu, J. Wang, Z. Chen, and Q. Peng. Chinese J. Struct. Chem. **5**, 352 (2000).
14. A. Bencini, S. Midollini, and C. Zanchini. Inorg. Chem. **31**, 2132 (1992).
15. J.H. Van Vleck. Electric and magnetic susceptibilities. Oxford University Press, London. 1992.

© 2002 NRC Canada

Synthesis and structural characterization of binuclear titanium(IV) and tantalum(V) cyclopentadienyl complexes containing bridging phosphinate ligands

Hendrik Dorn, Emira Vejzovic, Alan J. Lough, and Ian Manners

Abstract: The reaction of $Ph_2P(O)(OSiMe_3)$ with $[(\eta^5\text{-}C_5H_5)TiCl_3]$ or $[(\eta^5\text{-}C_5Me_5)TaCl_4]$ in dichloromethane yields the complexes $[\{(\eta^5\text{-}C_5H_5)TiCl_2(\mu\text{-}Ph_2PO_2)\}_2]$ (**1**) or $[\{(\eta^5\text{-}C_5Me_5)TaCl_3(\mu\text{-}Ph_2PO_2)\}_2]$ (**2**), respectively. Structural analysis of **1** and **2** by single-crystal X-ray diffraction revealed the presence of eight-membered metallacycles consisting of bridging–bidentate diphenylphosphinate groups between two metal centers.

Key words: inorganic rings, phosphinate complexes, tantalum, titanium.

Résumé : La réaction du $Ph_2P(O)(OSiMe_3)$ avec le $[(\eta^5\text{-}C_5H_5)TiCl_3]$ et le $[(\eta^5\text{-}C_5Me_5)TaCl_4]$ dans le dichlorométhane conduisent à la formation de $[\{(\eta^5\text{-}C_5H_5)TiCl_2(\mu\text{-}Ph_2PO_2)\}_2]$ (**1**) ou de $[\{(\eta^5\text{-}C_5Me_5)TaCl_3(\mu\text{-}Ph_2PO_2)\}_2]$ (**2**) respectivement. On a déterminé les structures des composés **1** et **2** par diffraction des rayons X; elles révèlent la présence de métallacycles à huit chaînons résultant de l'interaction de groupes diphénylphosphinates bidentates, capables de former des ponts, avec deux centres métalliques adjacents.

Mots clés : cycles inorganiques, complexes de phosphinates, tantale, titane.

[Traduit par la Rédaction]

Introduction

Metal–phosphinate complexes have been extensively investigated because of their interesting structural and chemical properties. Diphenylphosphinate, $[Ph_2PO_2]^-$, is widely used in inorganic coordination chemistry and usually acts as a bridging–bidentate ligand in bi- or polynuclear molecular structures. For example, binuclear complexes are known involving main group metals such as aluminum (1, 2), gallium (3, 4), and indium (3), and involving transition metals such as titanium (5), zirconium (6), vanadium (7, 8), rhenium (9), iron (10), ruthenium (11), rhodium (12), palladium (13), and platinum (13). Polynuclear diphenylphosphinate structures have been prepared incorporating tin (14–18), lead (19), titanium (20), manganese (21), cobalt (21, 22), and copper (23); however, these solid state coordination polymers are often found to dissociate or rearrange in solution.

As part of our interest in inorganic rings and polymers (24–26) we report here the preparation of the binuclear cyclopentadienyl transition metal complexes $[\{(\eta^5\text{-}C_5H_5)TiCl_2(\mu\text{-}Ph_2PO_2)\}_2]$ (**1**) and $[\{(\eta^5\text{-}C_5Me_5)TaCl_3(\mu\text{-}Ph_2PO_2)\}_2]$ (**2**) as well as their spectroscopic and X-ray structural characterization.

Received 16 July 2002. Published on the NRC Research Press Web site at http://canjchem.nrc.ca on 12 December 2002.

H. Dorn,[1] E. Vejzovic, A.J. Lough, and I. Manners.[2] Department of Chemistry, University of Toronto, 80 St. George Street, Toronto, ON M5S 3H6, Canada.

[1]Present address: The Centre of Forensic Sciences, 25 Grosvenor Street, Toronto, ON M7A 2G8, Canada.
[2]Corresponding author (email: imanners@chem.utoronto.ca).

Results and discussion

Synthesis and characterization

The reaction between $[(\eta^5\text{-}C_5H_5)TiCl_3]$ or $[(\eta^5\text{-}C_5Me_5)TaCl_4]$ and an equimolar amount of $Ph_2P(O)(OSiMe_3)$ in dichloromethane at room temperature readily gave the binuclear complexes $[\{(\eta^5\text{-}C_5H_5)TiCl_2(\mu\text{-}Ph_2PO_2)\}_2]$ (**1**) and $[\{(\eta^5\text{-}C_5Me_5)TaCl_3(\mu\text{-}Ph_2PO_2)\}_2]$ (**2**), respectively. Compound **1** was isolated in a 78% yield as orange crystals, while compound **2** was obtained in a 60% yield as dark yellow crystals. Both compounds were found to be air and moisture sensitive.

$$2\,[(\eta^5\text{-}C_5R_5)MCl_x] + 2\,Ph_2P(O)(OSiMe_3) \xrightarrow[-2\,SiMe_3Cl]{CH_2Cl_2,\ 25^\circ C} [\{(\eta^5\text{-}C_5R_5)MCl_{x-1}(\mu\text{-}Ph_2PO_2)\}_2]$$

1: M = Ti, R = H, x = 3
2: M = Ta, R = Me, x = 4

The ^{31}P NMR spectra of **1** and **2** in $CDCl_3$ showed singlets at δ 34.5 and 32.0 ppm, respectively, which is consistent with ^{31}P NMR spectroscopic data of other binuclear, bridging–bidentate transition metal phosphinates such as $[\{(\eta^5\text{-}C_5Me_5)TiF(\mu\text{-}F)(\mu\text{-}Ph_2PO_2)\}_2]$ (δ 35.1 and 32.9 ppm) (5) or $[\{PtCl(\mu\text{-}Ph_2PO_2)(PBu_3)\}_2]$ (δ 37.2 ppm) (13). For comparison, the starting material $Ph_2P(O)(OSiMe_3)$ displayed an upfield ^{31}P NMR resonance at δ 23.4 ppm. The ^1H NMR spectra of **1** and **2** exhibited the anticipated

 DOI: 10.1139/V02-186 © 2002 NRC Canada

Fig. 1. Molecular structure of [{(η^5-C_5H_5)$TiCl_2$(μ-Ph_2PO_2)}$_2$] (**1**), showing the shape of the $Ti_2P_2O_4$ ring with the boat–boat conformation. Only the ipso carbon atoms of the phenyl rings are shown. Solvent molecules and hydrogen atoms have been omitted.

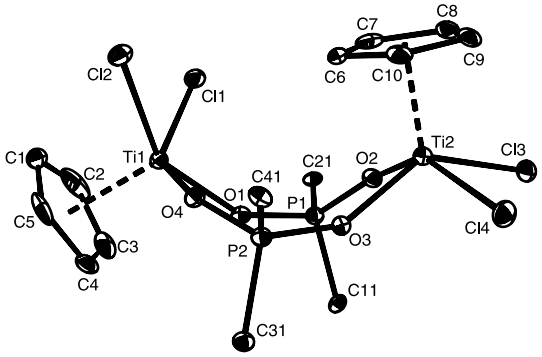

Fig. 2. Molecular structure of [{(η^5-C_5Me_5)$TaCl_3$(μ-Ph_2PO_2)}$_2$] (**2**), showing the shape of the $Ta_2P_2O_4$ ring with the boat–chair conformation. Only the ipso carbon atoms of the phenyl rings are shown. Solvent molecules and hydrogen atoms have been omitted.

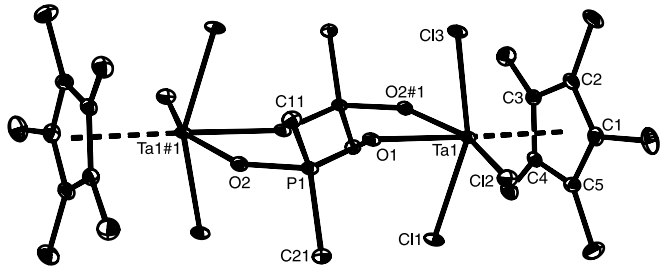

signals in the phenyl region as well as singlets at δ 7.01 (C_5H_5, **1**) and 2.19 ppm (C_5Me_5, **2**), respectively, in the required ratio of integration. The NMR spectra of **1** and **2** suggest a symmetric structure in solution; however, it is unclear whether these complexes are in fact dimeric or perhaps monomeric. The IR spectra of crystalline **1** and **2** were obtained as Nujol mulls between KBr plates and showed several strong νPO_2 absorption bands in the region of 1200–1000 cm^{-1}, which is diagnostic of a bidentate coordination mode of the phosphinate groups (14). The EI mass spectra of **1** and **2** were quite complex and showed many fragments of low intensity; however, peaks corresponding to molecular ions (or their monomeric forms) were not observed, even at lower ionization energies of ~20 eV. Elemental analysis for C and H afforded data consistent with the suggested formulas. The low value for carbon found in compound **2** is most likely due to the presence of dichloromethane in the crystal lattice, which could not be entirely removed under vacuum. A calculation to fit the observed value for carbon (39.2%) gave the approximate formula **2**·1.3CH_2Cl_2.

Detailed structural analysis

The molecular structures of **1**·2$CHCl_3$ and **2**·2CH_2Cl_2 were determined by single-crystal X-ray diffraction and are shown as SHELXTL drawings in Figs. 1 and 2, respectively. X-ray data were collected under the conditions summarized in Table 1. While molecule **1** has no crystallographically imposed symmetry, molecule **2** has a crystallographic inversion center, which relates the halves of the dimer (symmetry code #1: 1–*x*, 1–*y*, 1–*z*).

Both compounds exist as binuclear transition metal complexes with two bridging–bidentate phosphinate groups to form eight-membered $M_2P_2O_4$-rings. In **1**, the eight-membered ring adopts a boat–boat conformation (Fig. 1), while in **2** a boat–chair conformation is observed (Fig. 2). Some important structural features of **1** and **2** are compared in Table 2.

The titanium atoms in **1** possess a 14-electron configuration (if the phosphinate oxygen atoms are considered as two-electron donors) and have a "four-legged piano-stool" geometry with η^5-bound cyclopentadienyl rings. The cyclopentadienyl rings occupy one equatorial (Ti1) and one axial ring position (Ti2), thus reducing the steric interactions between the ligands. The Ti—C_5H_5(centroid) and Ti—Cl distances in **1** (Table 2) are similar to those reported for [(η^5-C_5H_5)$TiCl_3$] (27). Furthermore, all Ti—O and P—O distances as well as O-P-O angles are effectively equivalent (Table 2). This equivalence suggests electron delocalization throughout the bridging diphenylphosphinate groups. The distances are slightly shorter than those reported for the other structurally characterized titanium diphenylphosphinates (5, 20). Analysis of the Ti-O-P bond angles (Table 2) shows an average value of 148.43°, which is significantly larger than the idealized 120° angle expected for a two-electron donating oxygen atom, thus perhaps indicating some Ti—O multiple bond character. Both the O-Ti-O bond angles in **1** (O1-Ti1-O4 82.72(10)°, O2-Ti2-O3 81.58(10)°) are smaller than those in the other binuclear titanium diphenylphosphinate [{(η^5-C_5Me_5)TiF(μ-F)(μ-Ph_2PO_2)}$_2$] (O-Ti-O 155.13(10)°); however, this is a consequence of the different titanium coordination geometry in the latter complex (5).

To our knowledge, compound **2** (Fig. 2) represents the first example of a structurally characterized tantalum phosphinate complex. Both tantalum centers have 16-electron configurations and can be described as having distorted octahedral geometries if the η^5-C_5Me_5 ligands are considered to occupy single coordination sites. The angular distortions from the ideal octahedra are probably due to the steric bulk of the C_5Me_5 ring. Hence, the O-Ta-O angle of 78.48(9)° is compressed relative to the ideal value of 90°. The Ta—C_5Me_5(centroid) distance of 2.435(4) Å and the three Ta—Cl distances ranging from 2.3141(8) to 2.4001(7) Å are normal. It is notable that the Ta—O distances in **2** are quite different. The Ta—O bond *trans* to the C_5Me_5 ring (Ta1—O1 2.329(2) Å) is significantly longer than the other Ta—O distance (Ta1—O2#1 1.978(2) Å), and this feature may be construed as evidence for a strong *trans* influence of the C_5Me_5 substituent. Also, the Ta1—Cl2 bond length of 2.4001(7) Å is longer than the other two Ta—Cl distances (Ta1—Cl1 2.3141(8), Ta1—Cl3 2.3482(8) Å), reflecting a weak *trans* influence of the oxygen atom O2#1. Moreover, the P—O distances show an interesting variation: the P1—O1 bond length (1.648(3) Å) is abnormally long, while the P1—O2 bond length (1.533(2) Å) is within the expected range and comparable to the P—O distances observed in compound **1** (Table 2). This asymmetric bonding arrangement is further reflected by the differing Ta-O-P angles (P1-O1-Ta1 159.43(12), P1-O2-Ta1#1 150.79(16)°) and may also

© 2002 NRC Canada

Table 1. Crystallographic data and structure refinement.

	1·2CHCl$_3$	**2**·2CH$_2$Cl$_2$
Chemical formula	$C_{36}H_{32}Cl_{10}O_4P_2Ti_2$	$C_{46}H_{54}Cl_{10}O_4P_2Ta_2$
Formula weight	1040.86	1449.23
Colour, form	Orange, blocks	Dark yellow, blocks
Crystal dimensions (mm)	0.20 × 0.10 × 0.05	0.25 × 0.23 × 0.20
Temperature (K)	100(1)	150(1)
Crystal system	Monoclinic	Triclinic
Space group	$P2_1/c$	$P\bar{1}$
a (Å)	19.2307(10)	10.6512(3)
b (Å)	10.5717(5)	11.9040(2)
c (Å)	22.0932(12)	11.9983(4)
α (°)	90	73.943(2)
β (°)	109.065(3)	76.9270(10)
γ (°)	90	69.3590(10)
Volume (Å^3)	4245.2(4)	1354.01(6)
Z	4	1
Density (g cm^{-3})	1.629	1.777
Absorption coefficient (mm^{-1})	1.120	4.630
F(000)	2096	708
θ range (°)	2.58 to 26.04	2.85 to 27.00
Index ranges	$0 = h = 23$	$0 = h = 13$
	$0 = k = 12$	$-13 = k = 15$
	$-27 = l = 25$	$-14 = l = 15$
Reflections collected	31249	13261
Independent reflections	8225	5510
GoF on F^2	1.012	1.029
$R_1{}^a$ ($I > 2\sigma(I)$)	0.0538	0.0253
$wR_2{}^b$ (all data)	0.1157	0.0554
Largest diff. peak and hole (e Å^{-3})	0.571 and –0.425	1.291 and –1.401

$^a R_1 = \Sigma||F_o| - |F_c||/\Sigma|F_o|$

$^b wR_2 = \{\Sigma[w(F_o^2 - F_c^2)^2]/\Sigma[w(F_o^2)^2]\}^{1/2}$.

indicate some Ta—O multiple bond character between Ta1 and O2#1. However, the O-P-O angle of 116.42(12)° is typical for bridging diphenylphosphinate ligands (cf. average O-P-O angle in **1**: 115.63°).

Experimental section

General Information

All reactions were performed under an atmosphere of dry nitrogen. [(η^5-C$_5$Me$_5$)TaCl$_4$] (Strem) and Ph$_2$P(O)(OH) (Aldrich) were purchased and used as received. [(η^5-C$_5$H$_5$)TiCl$_3$] (28) and Ph$_2$P(O)(OSiMe$_3$) (29) were prepared following literature procedures. NMR spectra were recorded on a Varian Gemini or Mercury 300 MHz spectrometer. Chemical shifts are referenced to solvent peaks (^{1}H) or external 85% H$_3$PO$_4$ (^{31}P). Infrared spectra were recorded on a Nicolet Magna 550 FT-IR instrument as Nujol mulls between KBr plates. Mass spectra were obtained with a VG 70-250S mass spectrometer operating in electron impact (EI) mode at 70 eV. Elemental analyses were performed by Quantitative Technologies, Inc., Whitehouse, NJ.

X-ray structural characterization

Crystal data and details of the data collection are provided in Table 1. Diffraction data were collected on a Nonius Kappa-CCD using graphite-monochromated Mo Kα radiation (λ = 0.71073 Å). A combination of 1° ϕ and ω (with κ offsets) scans were used to collect sufficient data. The structures were solved and refined with the SHELXTL-PC V5.1 software package (30). The data frames were integrated and scaled using the Denzo-SMN package (31). Refinement was by full-matrix least-squares analysis on F^2 using all data (negative intensities included). Molecular structures are presented with ellipsoids at a 30% probability level. In all structures hydrogens bonded to carbon atoms were included in calculated positions and treated as riding atoms.[3]

[{(η^5-C$_5$H$_5$)TiCl$_2$(μ-Ph$_2$PO$_2$)}$_2$] (1)

[(η^5-C$_5$H$_5$)TiCl$_3$] (2.50 g, 11.4 mmol) was dissolved in dichloromethane (60 mL) and a solution of Ph$_2$P(O)(OSiMe$_3$)

[3] Supplementary data may be purchased from the Depository of Unpublished Data, Document Delivery, CISTI, National Research Council Canada, Ottawa, ON K1A 0S2, Canada (http://www.nrc.ca/cisti/irm/unpub_e.shtml for information on ordering electronically). CCDC 186950 (**1**) and CCDC 186951 (**2**) contain the supplementary data for this paper. These data can be obtained, free of charge, via www.ccdc.cam.ac.uk/conts/retrieving.html (or from the Cambridge Crystallographic Data Centre, 12 Union Road, Cambridge, U.K.; fax +44 1223 336033; or deposit@ccdc.cam.ac.uk).

© 2002 NRC Canada

Table 2. Selected bond lengths (Å) and angles (°) for **1** and **2** with ESDs in parentheses.

1		**2**	
Bond lengths (Å)			
Ti1—Cl1	2.3244(11)	Ta1—Cl1	2.3141(8)
Ti1—Cl2	2.3689(11)	Ta1—Cl2	2.4001(7)
Ti2—Cl3	2.3326(12)	Ta1—Cl3	2.3482(8)
Ti2—Cl4	2.3796(12)		
Ti1—O1	1.975(2)	Ta1—O1	2.329(2)
Ti1—O4	1.978(2)	Ta1—O2#1	1.978(2)
Ti2—O2	1.985(2)		
Ti2—O3	1.986(2)		
Ti1—X1A[a]	2.026(4)	Ta1—X1A[a]	2.435(4)
Ti2—X1B[b]	2.038(4)		
P1—O1	1.526(3)	P1—O1	1.648(3)
P1—O2	1.519(3)	P1—O2	1.533(2)
P2—O3	1.520(3)		
P2—O4	1.526(3)		
Bond angles (°)			
P1-O1-Ti1	148.98(15)	P1-O1-Ta1	159.43(12)
P1-O2-Ti2	147.51(16)	P1-O2-Ta1#1	150.79(16)
P2-O3-Ti2	148.75(15)		
P2-O4-Ti1	148.48(15)		
O1-Ti1-O4	82.72(10)	O2#1-Ta1-O1	78.48(9)
O2-Ti2-O3	81.58(10)		
O2-P1-O1	115.70(14)	O2-P1-O1	116.42(12)
O3-P2-O4	115.55(14)		

[a]X1A is the centroid of the C1···C5 ring
[b]X1B is the centroid of the C6···C10 ring.

(3.31 g, 11.4 mmol) in dichloromethane (20 mL) was added at room temperature. After stirring for 16 h the solution was filtered, concentrated under vacuum, and set aside for crystallization. Orange crystals of **1** grew at room temperature over a period of 1 week. Isolated yield 3.56 g (78%). Crystals suitable for an X-ray diffraction study were obtained after storing a solution of **1** in $CHCl_3$ for 1 week at room temperature. IR (Nujol, KBr) (cm^{-1}): 1593 (w), 1146 (s), 1128 (s), 1055 (m), 1037 (m), 1023 (s), 994 (m), 830 (m), 757 (w), 693 (m). ^{1}H NMR (300 MHz, $CDCl_3$) δ: 7.84–7.65 (m, Ph, 4H), 7.42–7.32 (m, Ph, 2H), 7.32–7.15 (m, Ph, 4H), 7.01 (s, C_5H_5, 5H). ^{31}P NMR (121 MHz, $CDCl_3$) δ: 34.5 (s). EI-MS (70 eV) *m/z* (%): 248 ([(η^5-C_5H_5)$_2$TiCl$_2$], 47), 183 ([(η^5-C_5H_5)TiCl$_2$], 100), 148 ([(η^5-C_5H_5)TiCl], 57). Anal. calcd. for $C_{34}H_{30}Cl_4O_4P_2Ti_2$: C 50.9, H 3.77; found: C 50.1, H 3.67.

[{(η^5-C_5Me_5)TaCl$_3$(μ-Ph_2PO_2)}$_2$] (2)

[(η^5-C_5Me_5)TaCl$_4$] (1.00 g, 2.18 mmol) was suspended in dichloromethane (50 mL) and a solution of $Ph_2P(O)(OSiMe_3)$ (0.63 g, 2.18 mmol) in dichloromethane (20 mL) was added. After stirring for 16 h at room temperature the clear, yellow-orange solution was filtered and concentrated under vacuum. Dark yellow crystals of **2** grew over a period of 2 to 3 days at room temperature and were of suitable quality for X-ray diffraction. Isolated yield 0.83 g (60%). IR (Nujol, KBr) (cm^{-1}): 1596 (w), 1269 (m), 1152 (s), 1127 (s), 1113 (s), 1037 (m), 1017 (s), 991 (s), 754 (w), 697 (m). ^{1}H NMR (300 MHz, $CDCl_3$) δ: 8.09–8.01 (m, Ph, 4H), 7.51–7.45 (m, Ph, 2H), 7.40–7.34 (m, Ph, 4H), 2.19 (s, C_5Me_5, 15H). ^{31}P NMR (121 MHz, $CDCl_3$) δ: 32.0 (s). EI-MS (70 eV) *m/z* (%): 503 ([TaCl$_3$(Ph_2PO_2)], 100), 201 ([Ph_2PO], 95), 135 ([C_5Me_5], 41), 77 ([Ph], 53). Anal. calcd. for $C_{44}H_{50}Cl_6O_4P_2Ta_2$: C 41.3, H 3.94; found: C 39.2, H 3.75.

Summary

The reaction of $Ph_2P(O)(OSiMe_3)$ with [(η^5-C_5H_5)TiCl$_3$] and [(η^5-C_5Me_5)TaCl$_4$] is a convenient and selective route for the preparation of the binuclear transition metal phosphinate complexes **1** and **2**. NMR spectroscopic data obtained for **1** and **2** indicated the existence of highly symmetric structures in solution, while solid state characterization by single-crystal X-ray analysis revealed the presence of eight-membered metallacycles incorporating bridging–bidentate diphenylphosphinate groups. Both compounds and, in particular, mononuclear analogs may be suitable catalysts for the polymerization of olefins and experiments in this direction are of interest.

Acknowledgments

This research was supported by the Environmental Science and Technology Alliance Canada (ESTAC) and the Natural Sciences and Engineering Research Council of Canada (NSERC). H.D. wishes to acknowledge Mr. Eric Rivard for useful discussions.

References

1. S.A. Sangokoya, W.T. Pennington, G.H. Robinson, and D.C. Hrncir. J. Organomet. Chem. **385**, 23 (1990).
2. J.M. Corker, D.J. Browning, and M. Webster. Acta Cryst. **C52**, 583 (1996).
3. F.E. Hahn, B. Schneider, and F.-W. Reier. Z. Naturforsch. **45b**, 134 (1990).
4. D.J. Browning, J.M. Corker, and M. Webster. Acta Cryst. **C52**, 882 (1996).
5. S.A.A. Shah, H. Dorn, J. Gindl, M. Noltemeyer, H.-G. Schmidt, and H.W. Roesky. J. Organomet. Chem. **550**, 1 (1998).
6. D. Chakraborty, V. Chandrasekhar, M. Bhattacharjee, R. Krätzner, H.W. Roesky, M. Noltemeyer, and H.-G. Schmidt. Inorg. Chem. **39**, 23 (2000).
7. N.S. Dean, L.M. Mokry, M.R. Bond, C.J. O'Connor, and C.J. Carrano. Inorg. Chem. **35**, 2818 (1996).
8. N.S. Dean, M.R. Bond, C.J. O'Connor, and C.J. Carrano. Inorg. Chem. **35**, 7643 (1996).
9. H.-H. Oetjen, E. Lindner, and J. Strähle. Chem. Ber. **111**, 2067 (1978).
10. P.N. Turowski, W.H. Armstrong, M.E. Roth, and S.J. Lippard. J. Am. Chem. Soc. **112**, 681 (1990).
11. C.M. Barnes, D.S. Bohle, and S.K. Madsen. Inorg. Chem. **33**, 6411 (1994).
12. D. Carmona, M.P. Lamata, M. Esteban, F.J. Lahoz, L.A. Oro, M.C. Apreda, C. Foces-Foces, and F.H. Cano. J. Chem. Soc. Dalton Trans. 159 (1994).
13. V.K. Jain and R.J. Butcher. Polyhedron, **17**, 1317 (1998).
14. A.-F. Shihada and F. Weller. Z. Naturforsch. **51b**, 1111 (1996).
15. R.O. Day, J.M. Holmes, V. Chandrasekhar, and R.R. Holmes. J. Am. Chem. Soc. **109**, 940 (1987).
16. K.C. Kumara Swamy, C.G. Schmid, R.O. Day, and R.R. Holmes. J. Am. Chem. Soc. **110**, 7067 (1988).

© 2002 NRC Canada

17. K.C. Kumara Swamy, R.O. Day, and R.R. Holmes. J. Am. Chem. Soc. **110**, 7543 (1988).
18. K.C. Kumara Swamy, R.O. Day, and R.R. Holmes. Inorg. Chem. **31**, 4184 (1992).
19. P. Colamarino, P.L. Orioli, W.D. Benzinger, and H.D. Gillman. Inorg. Chem. **15**, 800 (1976).
20. G. Guerrero, M. Mehring, P.H. Mutin, F. Dahan, and A. Vioux. J. Chem. Soc. Dalton Trans. 1537 (1999).
21. J.-L. Du, S.J. Rettig, R.C. Thompson, and J. Trotter. Can. J. Chem. **69**, 277 (1991).
22. S.-J. Liu, R.J. Staples, and J.P. Fackler, Jr. Polyhedron, **11**, 2427 (1992).
23. A. Bino and L. Sissman. Inorg. Chim. Acta, **128**, L21 (1987).
24. M. Liang and I. Manners. J. Am. Chem. Soc. **113**, 4044 (1991).
25. (*a*) D.A. Foucher, B.-Z. Tang, and I. Manners. J. Am. Chem. Soc. **114**, 6246 (1992); (*b*) D.A. Foucher, A.J. Lough, and I. Manners. Inorg. Chem. **31**, 3034 (1992).
26. D.P. Gates, L.M. Liable-Sands, G.P.A. Yap, A.L. Rheingold, and I. Manners. J. Am. Chem. Soc. **119**, 1125 (1997).
27. L.M. Engelhardt, R.I. Papasergio, C.L. Raston, and A.H. White. Organometallics **3**, 18 (1984).
28. T.E. Patten and B.M. Novak. J. Am. Chem. Soc. **118**, 1906 (1996).
29. L. Wozniak, M. Cypryk, and J. Chojnowski. Tetrahedron, **45**, 4403 (1989).
30. G.M. Sheldrick. 1997. SHELXTL-PC [computer program]. Version 5.1. Bruker Analytical X-ray Systems Inc., Madison, WI, U.S.A.
31. Z. Otwinowski and W. Minor. Methods. Enzymol. **276**, 307 (1997).

© 2002 NRC Canada

pH-controlled location and metalation of an amphiphilic porphyrin in sodium dodecyl sulfate micelle

Lin Guo and Ying-qiu Liang

Abstract: 5,10,15-Tri(4-hydroxyphenyl)-20-(4-hexadecyloxyphenyl)porphyrin (**P**) was solubilized in sodium dodecyl sulfate (SDS) micelle solutions. Taking advantage of the protonation and deprotonation properties of the amphiphilic porphyrin allowed the study of the pH-controlled transfer process of **P** in SDS micelle by means of UV–vis and fluorescence spectra. In neutral SDS micelle, **P** may be protonated and located at the outer surface of the micelle. In mildly basic conditions the hydrophilic ability of **P** decreases and the porphyrin moiety may transfer to the inner layer of SDS micelle. In strong basic conditions the porphyrin may transfer back to the outer aqueous surface of the micelle. The kinetic study of the porphyrin complexed with Cu(II) shows that the metalation rate of **P** could be controlled by changing the pH.

Key words: porphyrin, location, metalation, sodium dodecyl sulfate, micelle.

Résumé : On a solubilité la 5,10,15-tri(4-hydroxyphényl)-20-(4-hexadécyloxyphényl)porphyrine (**P**) dans des solutions de micelle de dodécylsulfate de sodium (« SDS »). Faisant appel à la spectroscopie UV–vis et à celle de fluorescente et prenant avantage des propriétés de protonation et de déprotonation de la porphyrine amphiphile, on a pu étudier le processus de transfert de **P** à la micelle de « SDS » sous un contrôle du pH. Dans une micelle de « SDS » neutre, **P** peut être protonée et se trouve à la surface externe de la micelle. Dans des conditions basiques, l'habilité hydrophile de **P** diminue et la portion porphyrine peut être transférée vers la couche interne de la micelle de « SDS ». Dans des conditions fortement basiques, la porphyrine peut être éjectée vers la surface extérieure de la micelle. L'étude cinétique de la porphyrine dans laquelle on a incorporé du Cu(II) montre que la vitesse métalatique de **P** peut être contrôlée par un changement de pH.

Mots clés : porphyrine, situation, métalation, dodécylsulfate de sodium, micelle.

[Traduit par la Rédaction]

Introduction

Biochemical processes occurring in biomembranes are in many cases enabled by the cooperative action of functional molecules (or parts of molecules) in special positions of the matrix membrane. An important example is the porphyrin functional unit, located in the photosynthetic reaction center, which plays an important role in biological processes such as light energy conversion, oxygen transport, and catalysis (1–5). Therefore, special incorporation of porphyrin molecule guests in biomimic membranes and their functions have been of great interest. Porphyrins anchored to lipid bilayers have successfully been applied to the reversible binding of dioxygen in aqueous solutions (6). Incorporation of porphyrins in micelles dramatically influences the aggregation mode and location of these molecules and alters their metalation rate (7–8). It has been suggested that hydrophobic porphyrins can penetrate the lipid regions of membranes and be distributed into the protein-rich membrane domain (9), while highly polar species are supposed to partition mainly in the aqueous compartments (10). The interaction of water-soluble synthetic porphyrins with ionic micelles has been studied intensively (8, 11–12). In the presence of ionic surfactants below their critical micelle concentration (CMC), both tetra-(4-sulfonatophenyl) porphyrin ($TPPS_4$) (13–15) and some meso-tetraaryl-substituted picket fence porphyrins (16) were shown to form aggregates. Above CMC, micelles usually solubilize the aggregates of porphyrin derivatives into monomers (11–13, 17–18).

So far, however, there are still few reports about controlling amphiphilic porphyrin transfer processes in micelle. Although some efforts have been made to study porphyrin aggregation and location in micelle surfactant solutions as well as in aqueous solutions, most of these have concentrated on water-soluble porphyrinic molecules (11–13). Moreover, metalation in microheterogeneous media has been less investigated, although it is a biological phenomenon (19–20). In this work, an attempt is made to gain more insight into the nature of amphiphilic porphyrin interactions with biological structures using the simplest model for membranes and proteinic reaction centers: aqueous ionic micelles. An amphiphilic porphyrin (**P**, shown in Fig. 1) with

Received 24 April 2002. Published on the NRC Research Press Web site at http://canjchem.nrc.ca on 12 December 2002.

L. Guo and Y. Liang[1]. Institute of Mesocopic Solid State Chemistry and National Key Laboratory of Coordination Chemistry, Nanjing University, Nanjing 210093, P.R. China.

[1] Corresponding author (e-mail: yqliang@nju.edu.cn.

 DOI: 10.1139/V02-180 © 2002 NRC Canada

Fig. 1. Structure of amphiphilic porphyrin (**P**).

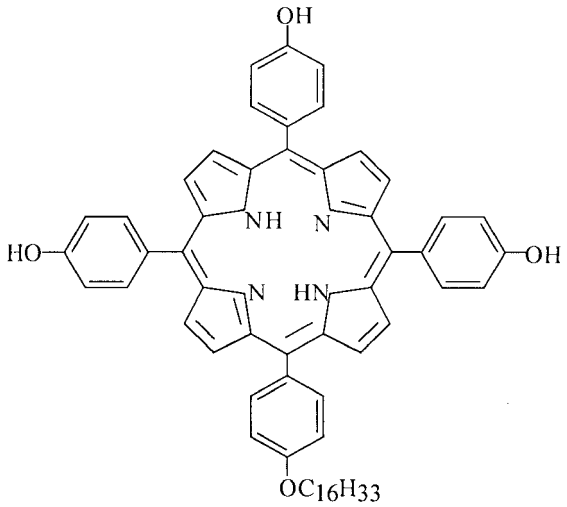

one hexadecyl chain was solubilized in micelle sodium dodecyl sulfate (SDS) solutions. The co-existence of the big hydrophobic porphyrin moiety and the long hydrophobic chain in the same molecule suggests that such a molecule can be solubilized in organic solvents as well as in the nonpolar region of micelles. Furthermore, this kind of amphiphilic porphyrin shows an interesting property: the hydrophilic ability of **P** could be changed with a variation in pH (21). Based on this property, the metalation process of **P** in SDS micelle with the use of a pH-controlled environment will be discussed below.

Experimental

Tetra(4-hydroxyphenyl)porphyrin (THPP) was prepared first (22) and was then hexadecylated by 1-bromohexadecane in an ethanol solution of potassium hydroxide. The products were then separated and purified 4 times by thin-layer chromatography over silica gel C with a solvent mixture of chloroform and with ethanol as the eluant. 5,10,15-Tri(4-hydroxyphenyl)-20-(4-hexadecyloxyphenyl) porphyrin (**P**) was obtained and characterized by elemental analysis, MS, IR, and H NMR spectroscopy (23–24). SDS was the analytical reagent and was recrystallized twice from 90% ethanol. Water was doubly distilled after passing through an ion-exchange resin column. All the organic solvents were analytical-grade pure and used without further purification.

SDS micelle, aqueous, and organic solutions of porphyrin were prepared by injection of a specific amount of a 2.5×10^{-3} mol dm^{-3} dioxane solution of porphyrins into the different solvents to obtained 25 mL solutions. The volume ratio of dioxane and water or other mixture solvents was greater than 1000, so the effects of traces of dioxane on the solution polarity could be neglected. After 20 min of sonication, the UV–vis and fluorescence spectra of the solutions were recorded on a Shimudu UV-3100 spectrophotometer and a PerkinElmer LS50B fluorescence spectrophotometer, respectively, using a 1 cm quartz cell. Excitation wavelength (λ_{ex}) was 423 nm. The pH of the solution was measured by a Leici (Shanghai) pH-250 pH meter, and the pH was controlled by addition of 1.5 mol dm^{-3} NaOH and 1:4 HCl aqueous solutions. The kinetic processes of the porphyrin complexed with Cu(II) were carried out, at room temperature, by adding a specific amount of 0.1 mol dm^{-3} $CuSO_4$ aqueous solution to the pH-variable porphyrin – SDS micelle solutions and then recording the UV–vis spectra of the mixtures at different reaction times.

Fig. 2. UV–vis spectra of **P** in different solutions: (*a*) **P** in methanol; (*b*) acid titration of **P** in SDS micelle solutions. [SDS] = 3.1×10^{-2} mol dm^{-3}; [**P**] = 2.1×10^{-6} mol dm^{-3}.

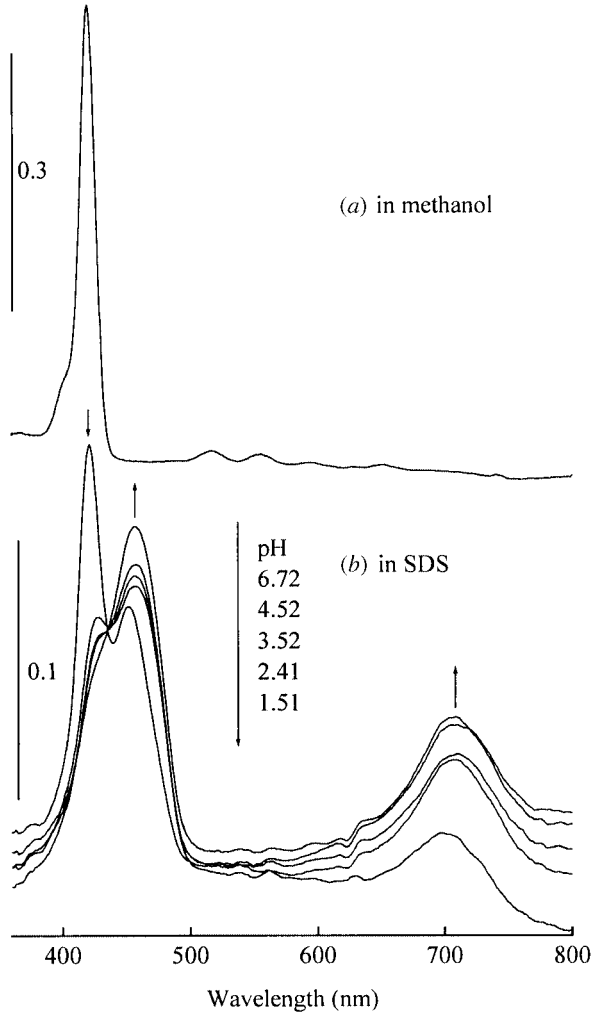

Results and discussion

Protonization of P in neutral SDS micelle

Figure 2 shows the UV–vis spectra of the acid titration of **P** in SDS micelle solutions. It can be seen that under neutral conditions (pH 6.72) (Fig. 2*b*), **P** shows two split Soret bands at 423 and 455 nm, and four Q bands appear at 519, 562, 602, and 707 nm, respectively. These spectral characteristics are different from those of porphyrin monomer in organic solvent, which include a strong and a narrow Soret band at 419 nm and four Q bands at 518, 556, 595, and 649 nm, respectively (Fig. 2*a*). When pH was decreased to 1.51, The Soret band at 423 nm decreased and eventually disappeared, while the Soret band of **P** at 455 nm increased proportionately. Furthermore, the number of Q bands was observed to change from four to two when the bulk pH

© 2002 NRC Canada

Table 1. The UV–vis spectra data of **P** in different solutions.[a]

Solutions	pH	Soret bands (nm)			Q bands (nm)			
		B(1)	B(2)	$W_{1/2}$	Q_1	Q_2	Q_3	Q_4
SDS aqueous solutions	6.90	423	455		519	562	602	707
	1.51		456	30	555			706
	9.60	423		23	525	562	593	665
	10.18	423		21	525	562	593	663
	12.06	424		26	523	562	595	659
Pure aqueous solutions	2.65	425	457		520	565	602	709
	8.10	428		52	425	566	595	655
Methanol	—	419		13	518	556	595	649
1:1 THF–HCl	strong acid		454	25	550			701

[a][**P**] = 2.1×10^{-6} mol dm^{-3}; [SDS] = 3.1×10^{-2} mol dm^{-3}.

approached 1.51 (Table 1), indicating that **P** has a higher molecular symmetry (D_{4h}) — similar to protonated porphyrin — under this condition (13, 25). The overall absorption characteristics of **P** in pH 1.51 SDS solutions are similar to those of protonated **P** in strong aqueous acid solutions (see Table 1), indicating that **P** may be protonated under this condition. The four Q bands and spilt Soret bands of **P** under neutral SDS conditions indicate that part of **P** was protonated, and the two split Soret bands at 423 and 455 nm may be due to the porphyrin monomer and the protonated porphyrin, respectively.

It should be pointed out that the protonation of porphyrin could take place only under acidic conditions. However, it was found that part of **P** could be protonated in neutral SDS micelle solutions, indicating that SDS micelles could be providing an acid surface microenvironment to **P**, although the bulk pH was not acidic. This function is attributed to the surface-potential effect on the intrinsic pH values near the surface of micelles. The relationship between surface-potential and surface-effective concentration of H^+ (α_H) of micelles is shown by the following equation (26):

$$[1] \qquad \alpha_H{}^i = \alpha_H{}^w \, e^{-F\Psi/RT}$$

where $\alpha_H{}^i$ and $\alpha_H{}^w$ are the effective concentration of H^+ ion in micelle surface and bulk aqueous phases, respectively, F is the Faraday constant, Ψ is the surface potential of the micelle, T is the temperature in Kelvins, and R is the Boltzman constant. Previously, studies have found that the anion surfactant SDS micelle exhibits a negative surface potential ($\Psi < 0$), and the surface potential of the SDS micelle is about –140 mV in the dilute micelle SDS solutions without added electrolyte (27–29); so, according to eq. [1], $\alpha_H{}^i > \alpha_H{}^w$. Drummond et al. (27) studied the acid–base equilibria of azine derivatives and found that the intrinsic pH value decreased 2.4 units at the surface of the SDS micelle compared with the bulk pH value (27). Therefore, it can be understood that a low pH value should exist at the surface layer of SDS micelles — similar to an aqueous acid solution — when the apparent bulk pH approaches 6.72. These phenomena also indicate that **P** may be complexed with SDS micelles rather than just dissolved in the bulk aqueous phase.

Surfactant–dye interaction and dye–dye aggregation are fairly common for oppositely charged dye–detergent pairs and are possible for neutral dyes as well (16, 30). To prevent hydrophobic dyes from undergoing dye–dye aggregation, a high concentration ratio between the surfactant molecules and the solubilized dyes is usually selected to increase the possibility of obtaining only one dye per micelle (26). In this paper, a high concentration ratio of [SDS]:[**P**] was used to decrease any disturbance due to porphyrin aggregation; the bulk pH was the only parameter that was changed. The pH-controlled transfer process of the porphyrin moiety in SDS micelles is discussed below.

pH-controlled transfer process of P in SDS micelle

UV–vis spectra

Figure 3 shows the UV–vis spectra of the base titration of **P** in SDS micelle solutions. It can be seen from this figure that as pH increases from 6.72 to 10.18, the Soret band of the porphyrin monomer at 423 nm obviously narrows and increases, while the band at 455 nm decreases and finally disappears. The four Q bands of **P** shift to 523, 562, 595, and 659 nm, respectively. These spectral characteristics are similar to those of **P** in organic solvent, where it exists as monomers (Table 1). This indicates that with increasing pH the protonated porphyrin may be deprotonized to form a neutral porphyrin in SDS micelle solution. As the bulk pH further increases from 10.18 to 12.06, the Soret band of **P** shows some broadening and decreasing.

It is well known that absorption Soret bands of porphyrins are often sensitive to the nature of local environments in micelle and aggregation forms and to solvent microenvironments (31–32). From the analysis of the spectral parameters such as peak position, intensity, and full-widths at half-height of the Soret band **P** in different solvent environments and in the micelle SDS solutions we can draw further conclusions as to what is happening concerning the site solubilization of **P** in SDS micelles in this pH titration process. It is clear from the data in Table 1 and Fig. 3 that the absorption spectra characteristics of **P** in micelle SDS solutions under neutral conditions are very similar to those of protonated **P** in aqueous acid solutions rather than those of **P** in organic solvent. The protonation of **P** in the neutral SDS micelle solution indicates that **P** may be incorporated into the SDS micelle rather than just dissolved in the bulk aqueous phase. Hence, it can be suggested that the porphyrin moiety of **P** should be located on the outer surface of an SDS micelle within a strong polar microenvironment — similar to aqueous acid solutions — as shown in Fig. 4*a*. Such a solubilization location is thermodynamically stable for the

© 2002 NRC Canada

Fig. 3. UV–vis spectra of **P** in different pH SDS micelle aqueous solutions. [SDS] = 3.1×10^{-2} mol dm^{-3}; [**P**] = 2.1×10^{-6} mol dm^{-3}.

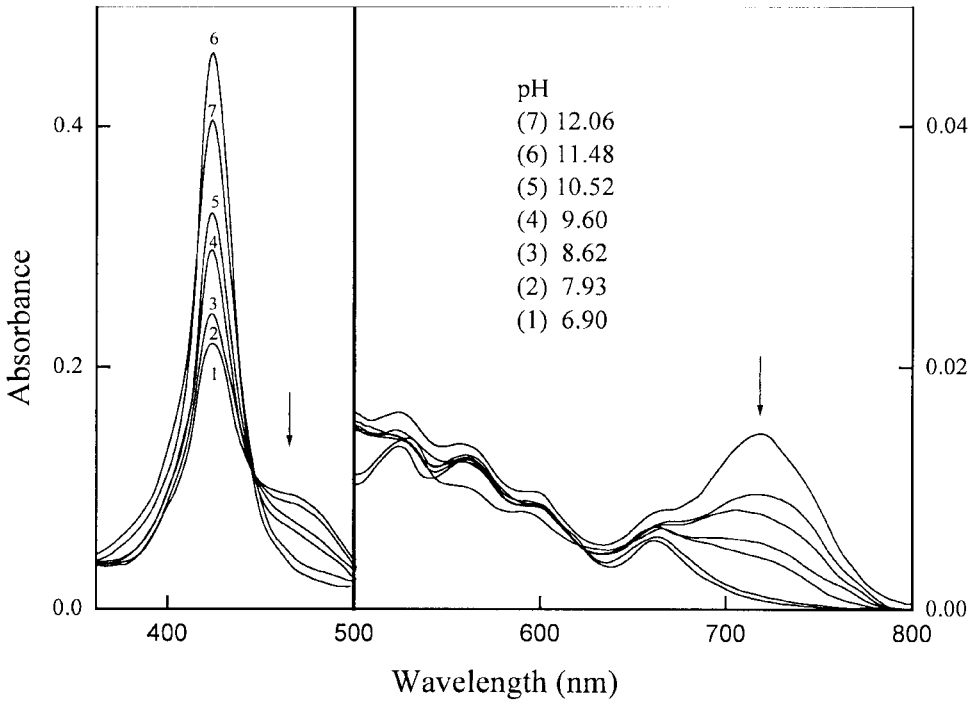

Fig. 4. Scheme of the transfer process of **P** in SDS micelles with increasing bulk pH.

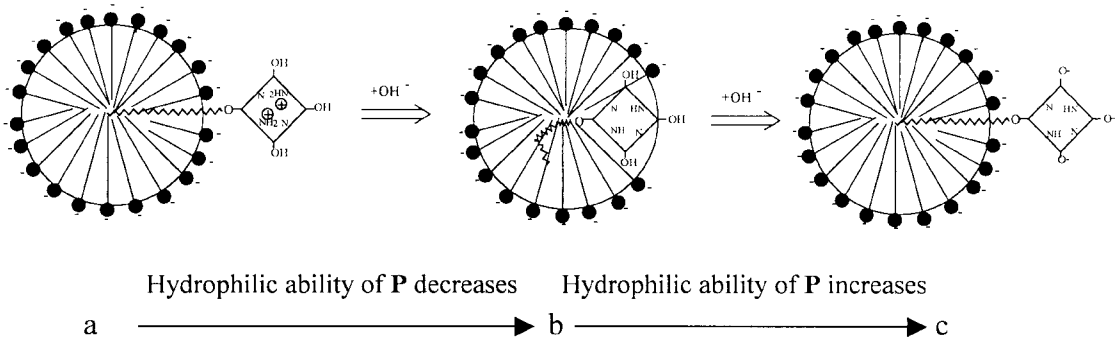

hydrophilic protonated porphyrin moiety and hydrophenyl groups even though there is one hydrophobic hexadecyl chain. However, by increasing the pH, the protonated porphyrin $H_2\mathbf{P}^{2+}$ can be deprotonized to form the neutral porphyrin **P**, and thus reduce the hydrophilic ability of **P**. Consequently, the hydrophenyl groups of **P** can also be deprotonated to form $\mathbf{P}^{1-}$, $\mathbf{P}^{2-}$, and $\mathbf{P}^{3-}$ ions and the hydrophilic ability of **P** increased proportionately. Therefore, the hydrophilic ability of **P** can be adjusted by controlling the pH values. This is the force for the porphyrin macrocycle transferring in or out of the micelles. In fact, when pH is increased up to 10.18, the overall absorption characteristics of **P** are quite similar to those of **P** in organic solvent (Table 1 and Fig. 3). These results infer that **P** may transfer to a weak polar microenvironment in the inner layer of the SDS micelle (Fig. 4*b*). However, when pH is further increased up to 12.06, the decrease of the Soret band intensity as well as the increase of full-widths at half-height of the Soret band suggest that the porphyrin moiety may transfer from the inner layer of the micelle back to the surface layer of the micelle (Fig. 4*c*) for a relatively low value of the Soret band intensity. An increased full-widths at half-height of the Soret band are also observed for **P** in diluted aqueous solutions (33). Figure 4 shows the scheme of this transfer process.

Fluorescence spectra

It is well known that in aqueous media that the microenvironment of many organic or amphiphilic molecules that interact with other macromolecules, micelles, membranes, or adsorption sites is a mixture of hydrocarbon-like and aqueous environments. Generally, the inner core of the spherical micelle has shown low polarity, and the effective dielectric constants of the stern layer are approximately 36–46 (34); the outer surface of the micelle, as well as nearby bulk aqueous phase, exhibit strong polarity. Therefore, the further from the hydrophobic center of the micelle, the greater polarity exhibited by the microenvironment. Hence, the polarity-dependent spectral characteristics are likely to be useful indicators of the nature of microenvironments of molecules in many situations including

© 2002 NRC Canada

Fig. 5. (*a*) Fluorescence emission spectra of **P** in different solutions: λex = 423 nm; (1) dioxane; (2) 2-propanol; (3) 50% methanol–H_2O; (4) 20% 2-propanol–H_2O; (5) H_2O; (*b*) plot of intensity ratios of 610 nm and 660 nm of **P** against the dielectric constants of different solvents. The solvents and their dielectric constants used in this experiment are, from left to right: dioxane (2.3), chloroform (4.8), tetrahydrofuran (7.6), 2-propanol (18.3), 95% ethanol (26.1), methanol (32.6), 70% MeOH–H_2O (45.0), 50% MeOH–H_2O (54.9), 20% 2-propanol–H_2O (64.1), H_2O (78.5).

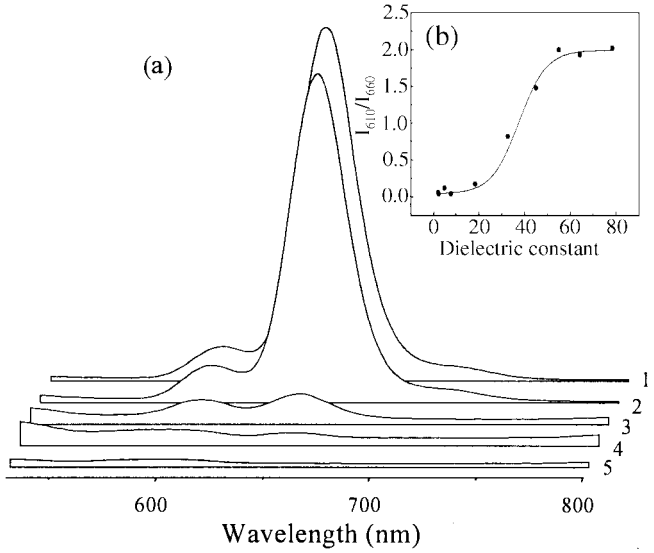

solubilization in micelle systems, and the effect of solvents on the fluorescence spectra of porphyrinic molecules has been studied extensively (35–36). Figure 5 shows the emission fluorescence spectra of **P** in different solvents. It can be seen from this figure that the fluorescence emission intensity of **P** is sensitive to the solvent polarity. In low-polar solvents such as methanol and dioxane, **P** exhibits a strong emission band at 660 nm and a relatively weak shoulder band at approximately 610 nm. When the polarity of solvents increases, the fluorescence intensity of **P** decreases rapidly, whereas the fluorescence maximum of **P** at 660 nm is not shifted. In pure aqueous solution **P** shows no obvious emission band within the experimental region. However, the fluorescence emission band at 610 nm is not changed as rapidly as that of the 660 nm band, and it even increases by comparison. Based on this behavior, the polar microenvironment of **P** in different solvents could be represented by the fluorescence intensity ratio of 610 and 660 nm, R (I_{610}/I_{660}). Figure 5*b* shows the plot of the R value of **P** against the dielectric constants of different solvents. It can be seen from this plot that with the increasing dielectric constant of the solvent, the intensity ratio of porphyrin increases proportionately. This may be due to the tendency, in the increase of solvent polarity, to favor face-to-face association of porphyrins, which tends to diminish fluorescence quantum yield.

Figure 6 shows the fluorescence emission spectra of **P** in SDS micelle solutions with different bulk pH. It is clear from this figure that in bulk pH 7.08 solution, **P** has a very low quantum yield of fluorescence, similar to that of **P** in high polar aqueous solutions. With increasing pH, the overall fluorescence intensity increases proportionately, and at pH 10.18 a strong emission band appears at 660 nm and a

Fig. 6. Plot of dielectric constants against the pH values of SDS micelle solutions of **P**.

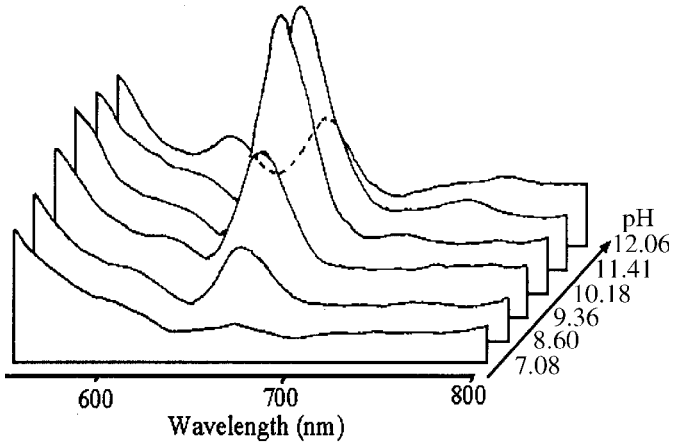

Fig. 7. Fluorescence emission spectra of **P** in different pH SDS micelle aqueous solutions: λ_{ex} = 423 nm; [**P**] = 2.1 × 10^{-6} mol dm^{-3}; [SDS] = 3.1 × 10^{-2} mol dm^{-3}.

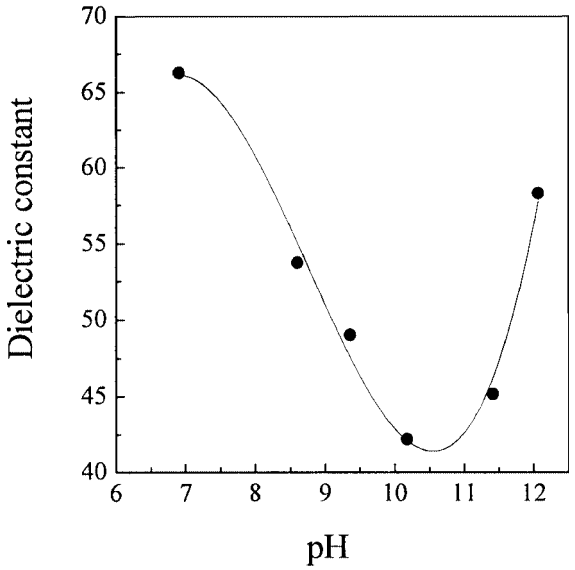

shoulder band at 610 nm. The overall fluorescence spectral characteristics are similar to those of **P** in organic solvent. When the pH value further increases up to 12.06, the fluorescence band of **P** at 660 nm exhibits some decrease. However, the fluorescence emission band at 610 nm does not change as rapidly as that of the 660 nm band. In this paper a high surfactant concentration – porphyrin ratio was used to decrease any disturbance caused by porphyrin aggregation. Consequently, the variation of the fluorescence parameters of porphyrin with bulk pH will now be primarily due to the change in the local microenvironment polarity of **P** in SDS micelle. Based on the R of **P** in different pH values, the corresponding microenvironment polarity of **P** in SDS micelle may be obtained through the information provided by Fig. 5*b*. Figure 7 shows the plot of pH against the corresponding microenvironment dielectric constants of **P** in SDS micelle. It is clear from this plot that the bulk pH is a con-

© 2002 NRC Canada

Fig. 8. UV–Vis spectra of **P** complexed with Cu(II) at different reaction times in a pH 6.90 SDS micelle aqueous solution. [**P**] = 2.1×10^{-6} mol dm^{-3}; [Cu^{2+}] = 2.5×10^{-4} mol dm^{-3}; [SDS] = 3.1×10^{-2} mol dm^{-3}.

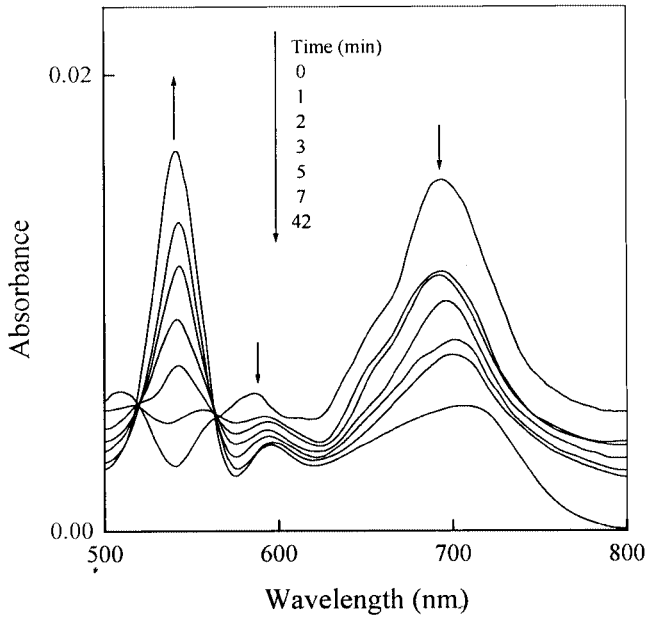

trolling factor in the transfer process of the solubilizing location of **P** in SDS micelle. Under neutral conditions, **P** may be located in the outer surface of the SDS micelle, which has a strong polar microenvironment with microenvironment dielectric constant (ε) around 66. With the pH of the solution increasing up to 10.18, the porphyrin moiety transfers to the inner layer of the SDS micelle, where there is a relatively weak polar microenvironment (ε ≈ 41). With pH further increased from 10.18 to 12.06, the porphyrin moiety transfers from the inner layer of the SDS micelle back to the outer layer of the SDS micelle (ε ≈ 58). These results correspond to the same results obtained by the UV–vis spectra study (Fig. 4).

pH-controlled metalation rate of P in SDS micelle

It is apparent from the above results that changes in the bulk pH value leads to changes in the hydrophilic ability of the porphyrin and eventually to control of the solubilized location of porphyrin in SDS micelle. By taking advantage of this property, the metalation of porphyrin in SDS micelle could also be controlled by changing the pH, which could be predicted by the kinetics of the porphyrin complexing with Cu(II).

Figure 8 shows the regional UV–vis spectra of **P** complexed with Cu(II) at different reaction times in a pH 6.90 solution of SDS micelle. It can be seen from this figure that the four Q bands of **P** decrease and finally disappear with increasing reaction times, while a new band that increases gradually appears at 542 nm. Furthermore, two isosbestic points appear at 530 and 553 nm. This implies that the solubilized location and polar microenvironment of **P** in SDS micelle are not changed during metalation in neutral SDS solution.

Table 2. The pseudo-first-order reaction rate constant (k_{obs}) of porphyrin complexed with Cu(II) in different bulk pH SDS micelle solutions.[a]

Porphyrin	Micelle	[Cu^{2+}] (mol dm^{-3})	pH	k_{obs} (min^{-1})
P	SDS	2.5×10^{-4}	6.90	1.4×10^{-1}
P	SDS	2.5×10^{-4}	7.71	9.4×10^{-2}
P	SDS	2.5×10^{-4}	8.50	6.9×10^{-2}
P				
P	SDS	6.5×10^{-4}	9.55	4.3×10^{-2}
P	SDS	3.3×10^{-4}	9.55	4.2×10^{-2}
P	SDS	1.6×10^{-4}	9.55	4.2×10^{-2}
P	SDS	0.7×10^{-4}	9.58	3.9×10^{-2}

[a][**P**] = 2.1×10^{-6} mol dm^{-3}; [SDS] = 3.1×10^{-2} mol dm^{-3}.

As the reaction was performed with a great excess of Cu(II), the reaction could be regarded as pseudo-first-order reaction (37). To verify that the pseudo-first-order condition is met in mild basic micelle solution, the apparent metalation rate constants k_{obs}, dependent on a concentration of Cu(II) approximately 10^{-4} mol dm^{-3}, were obtained and listed in Table 2. It is clear from this table that for the pH 9.55 SDS micelle solutions, k_{obs} shows no obvious change when the concentration of Cu(II) is increased from 1.6×10^{-4} to 6.5×10^{-4} mol dm^{-3}. This indicates that, as opposed to aqueous solutions, the precipitation of copper hydroxides in microheterogeneous SDS micelle solutions is so slow that the pseudo-first-order condition is met under mild basic (pH 6.90–9.55) conditions. The pseudo-first-order reaction rate constants of the porphyrins complexed with Cu(II) in SDS micelle solutions with differing pH values (k_Ψ) are listed in Table 1. It can be seen from this table that as the pH increased from 6.90 to 9.58 the metalation rate constants of **P** decreased proportionately.

There are several factors that influence the metalation rate of **P** in SDS micelle when the other experimental conditions are not changed. One of these is the pH of the solutions. Some previous work has suggested that deprotonation is an important process in the complexation of Cu(II) with porphyrin (39). Hence, an increase of pH will eventually lead to an increase of the metalation rate of **P**. However, when the pH of the solution is too high and the concentration of OH^- is too great, the concentration of Cu(II) in solution will decrease and the reaction rate will finally decrease. Another is the solubilizing location of **P** in SDS micelle. It is well accepted that Cu(II) is involved in bonding to porphyrin nitrogen atoms and then promotes a plane structure (39); at the same time the Cu(II) ion is difficult to diffuse into the inner nonpolar core of the micelle (20, 40). Hence, the solubilized location of the porphyrin in SDS micelle influences the metalation rate of porphyrin intensely. If a porphyrin moiety is located at the outer surface of the micelle, the probability of that porphyrin moiety meeting a Cu(II) ion becomes greater, so the metalation rate of porphyrin is greater. When the porphyrin moiety stays at the inner layer of the micelle, although the porphyrin could still form a complex with Cu(II), the metalation rate is relative low.

In this paper, the metalation rates of **P** were measured only in the mildly basic region (pH 6.90–9.58), and the pseudo-first-order condition can be met within this pH

© 2002 NRC Canada

region. Therefore, the variation in the metalation rate of **P** is due mainly to the change of the solubilizing location of **P** in SDS micelles. In the case of neutral SDS solution, the porphyrin moiety stays at the outer layer of the micelle; hence, the matalatic rate is relatively high. As the pH of the solution increases, the porphyrin moiety transfers to the inner layer of the micelle, and the probability of the porphyrin meeting Cu(II) ions becomes lower; hence, the metalation rate of porphyrin decreases proportionately.

Conclusion

By analyzing the UV–vis and fluorescence spectra of the synthesized amphiphilic porphyrin **P** in different solvent environments and the relationship between the solubilizing location of the porphyrin in SDS micelle and the microenvironment polarity, it has been shown that, as the pH is changed, a transfer process exists for the porphyrin moiety of **P** in SDS micelle. In neutral SDS micelle solutions, **P** may be protonated and located at the outer surface of micelle. In mildly basic conditions, the hydrophilic ability of **P** decreases and the porphyrin moiety may transfer to the inner layer of the SDS micelle. In strongly basic conditions the hydrophenyl groups of **P** would be deprotonated; consequently, porphyrin may transfer back to the outer aqueous surface of the SDS micelle. The kinetic study of **P** complexed with Cu(II) shows that the metalation rate could be controlled by changing the pH.

Acknowledgments

This work was financially supported by the Natural Science Foundation of China (grant number 20 073 019).

References

1. T. Miyasaka, T. Watanabe, A. Fujishima, and K. Honda. J. Am. Chem. Soc. **100**, 6657 (1978).
2. T. Miyasaka, T. Watanabe, A. Fujishima, and K. Honda. Nature (London), **277**, 638 (1979).
3. C.M. Drain, S. Gentemann, J.A. Roberts, N.Y. Helson, C.J. Medforth, S.L. Jia, M.C. Simpson, K.M. Smith, J. Fajer, J.A. Shelnutt, and D. Holten. J. Am. Chem. Soc. **120**, 3781 (1998).
4. G. Steinberg-Yfrach, P.A. Liddell, S.-C. Hung, A.L. Moore, D. Gust, and T.A. Moore. Nature (London), **385**, 239 (1997).
5. K. Kano, T. Migake, K. Uomoto, T. Sato, T. Ogawa, and S. Hashimoto. Chem. Lett. **144**, 1867 (1983).
6. E. Tsuchida and H. Nishide. Top. Curr. Chem. **132**, 63 (1986).
7. S.C.M. Gandini, V.E. Yushmanov, I.E. Borissevitch, and M. Tabak. Langmuir, **15**, 6233 (1999).
8. D.C. Barber and D.G. Whiten. J. Am. Chem. Soc. **109**, 6842 (1987).
9. F. Ricchelli, S. Gobbo, G. Jori, G. Moreno, F. Vinzens, and C. Salet. Photochem. Photobiol. **58**, 53 (1993).
10. F. Ricchelli and G. Jori. Photochem. Photobiol. **44**, 151 (1986).
11. K.M. Kadish, G.B. Maiya, C. Araullo, and R. Guilard. Inorg. Chem. **28**, 2725 (1989).
12. K.M. Kadish, G.B. Maiya, and C. Araullo. J. Phys. Chem. **95**, 427 (1991).
13. N.C. Maiti, S. Mazumdar, and N. Periasamy. J. Phys. Chem. B, **102**, 1528 (1998).
14. T. Tominaga, S. Endoh, and H. Ishimaru. Bull. Chem. Soc. Jpn. **64**, 942 (1991).
15. R.H. Schmehl and D.G. Whitten. J. Phys. Chem. **85**, 3473 (1981).
16. D.C. Barber, R.A. Freitag-Beeston, and D.G. Whitten. J. Phys. Chem. **95**, 4074 (1991).
17. S. Mazumdar, O.K. Medhi, and S. Mitra. Inorg. Chem. **27**, 2541 (1988).
18. J. Simplicio. Biochemistry, **11**, 2525 (1972).
19. D.K. Lavallee. Coord. Chem. Rev. **61**, 55 (1985).
20. V.H. Rao and V. Krishhan. Inorg. Chem. **24**, 3538 (1985).
21. Y.H. Zhang, L. Guo, Q.S. Li, and Y.Q. Wang. Chem. J. Chin. Univer. **18**, 1703 (1997).
22. R.G. Little. J. Heterocyl. Chem. **18**, 129 (1981).
23. Y.C. Tian, Y.Q. Wang, T. Huang, and Y.Q. Liang. Bull. Inst. Chem. Rev. Kyoto Univ. **71**, 86 (1993).
24. Y.Q. Wang. Ph.D. Thesis, Jilin University, Changchun, China. 1993.
25. M. Gouterman. J. Molecular Spectroscopy **6**, 138 (1961).
26. G.S. Hartley and J.W. Roe. Trans. Faraday. Soc. **60**, 101 (1940).
27. C.J. Drummond, F. Grieser, and T.W. Healy. J. Chem. Soc. Faraday Trans. 1, **85**, 551 (1989).
28. M.S. Feromherz and P. Fromherz. J. Phys. Chem. **81**, 1755 (1977).
29. G.V. Hartland, F. Grieser, and L.R. White. J. Chem. Soc. Faraday Trans. 1, **83**, 5911 (1987).
30. P. Mukerjee and K.J. Mysels. J. Am. Chem. Soc. **77**, 2937 (1955).
31. M. Vermathen, E.A. Louie, A.B. Chodosh, C. Sandra Reid, and U. Simonis. Langmuir, **16**, 210 (2000).
32. A.P.H.J. Schenning, D.H.W. Hubert, M.C. Feiters, and R.J.M. Notle. Langmuir, **12**, 1572 (1996).
33. Y.H. Zhang, L. Guo, Q.S. Li, and Y.Q. Wang. J. Beijing Inst. Technol. **19**, 239 (1999).
34. J.H. Fendler. Membrane mimetic chemistry. John Wiley & Sons, New York. 1982. Chap 2.
35. Z. Pan, M. Xu, and J. Li. J. WuHan Univers. Nature Sci. Ed. **4**, 51 (1993).
36. A.P. Savitski, E.V. Vorobyova, I.V. Berezin, and N.N. Ugarova. J. Colloid Interface Sci. **84**, 175 (1981).
37. J.S. Jin. Theory of liquid state chemical reaction kinetic. Shanghai Tech. Press, Shanghai, China. 1984. p. 13.
38. Y. Inada, Y. Sugimoto, Y. Nakano, and Y.S. Funahashi. Inorg. Chem. **37**, 5519 (1998).
39. J.E. Falk. Porphyrins and metal porphyrins. Elsevier Press, New York. 1975.
40. G.M. Williams, R.F.X. Willams, and A.J. Lewis. Inorg. Nucl. Chem. **41**, 441 (1979).

© 2002 NRC Canada

Ryanoids and related compounds — Chemoselective electrocatalytic hydrogenation of alkyl α-pyrrole carboxylates: Selective hydrogenation of ryanodine

Luc Ruest, Hugues Ménard, Vincent Moreau, and François Laplante

Abstract: A study of the electrocatalytic hydrogenation (ECH) process of pyrrole and different alkyl pyrrole-2-carboxylates is presented. Once hydrogenated, the alkyl pyrrole-2-carboxylate becomes an ester of proline, an important natural amino acid. The process is chemoselective to the pyrrole ring. Ryanodine is a natural ryanoid known to be biologically active. The tetrahydroryanodine derivative thus obtained may now represent a molecule of high biological interest. The hydrogenation of ryanodine is possible with electrocatalytic and catalytic processes. In both cases the reaction is not diastereoselective.

Key words: electrocatalytic hydrogenation, proline esters, ryanodine, tetrahydroryanodine.

Résumé : Une étude sur l'hydrogénation électrocatalytique (HEC) du pyrrole et de quelques esters de l'acide pyrrole-2-carboxylique est présentée. Une fois hydrogéné, le pyrrole-2-carboxylate d'alkyle devient un ester de la proline, un acide aminé naturel important. Le procédé est chimiosélectif au cycle pyrrole. La ryanodine est un ryanoïde connu pour son activité biologique. Le dérivé tétrahydroryanodine ainsi obtenu peut maintenant présenter un grand intérêt biologique. L'hydrogénation de la ryanodine est possible par le procédé électrocatalytique et catalytique. Dans les deux cas, la réaction n'est pas diastéréosélective.

Mots clés: hydrogénation électrocatalytique, esters de proline, ryanodine, tétrahydroryanodine.

Introduction

Ryanodine (Fig. 1) is a natural ryanoid extracted from the plant *Ryania speciosa*. This molecule is known to be a potent modulator of the sarcoplasmic reticulum calcium release channel (1). The interesting functional group of ryanodine in the present study is the aromatic pyrrole ring attached to the main polycyclic structure (ryanodol) by an ester function. Once hydrogenated, this heterocycle becomes an ester of proline, a natural amino acid. This tetrahydroryanodine derivative may now represent a molecule of high biological interest. Theoretically, removal of the pyrrole moiety and then esterification of the free hydroxyl group in position 3 with proline could lead to the desired compound, but in fact it has been shown that specific esterification at this endo hydroxyl group is not possible (1*c* and references therein).

We began the present study with simple molecules like pyrrole (**1**), pyrrole-2-carboxylic acid (**3A**), and its methyl (**3B**), ethyl (**3C**), and isopropyl (**3D**) esters (Fig. 1). All these molecules have a pyrrole ring and, except for pyrrole and pyrrole-2-carboxylic acid, an ester group, as seen in ryanodine. With these simple molecules we determined the best conditions (electrocatalyst and electrolyte) for the electrocatalytic hydrogenation (ECH) process of ryanodine.

The ECH process is achieved at room temperature and atmospheric pressure, unlike most of the classical catalytic hydrogenation methods. The classical process often requires a high pressure of hydrogen to reduce an aromatic pyrrole ring (2, 3). Recently, a pressure of 20 bar (1 bar = 10^5 Pa) was used to hydrogenate a compound with a pyrrole ring (4). Previous works in our laboratory used the ECH of phenol, cyclohexanone, and 2-cyclohexen-1-one to develop new electrocatalysts (5–7). The ECH of alkyl pyrrole-2-carboxylate molecules proceeds in acidic medium to prevent the poisoning of the catalyst by pyrrole or its derivatives (8, 9)

The ECH mechanism can be explained by the equations presented in Fig. 2. The electrocatalysts used in an ECH are constituted of a metallic part (M) and an adsorbent part (A). In the first step there is an electroadsorption of hydrogen atoms on the metallic part resulting from the reduction of water (eq. [1]). The alkyl pyrrole-2-carboxylate compound is adsorbed by the adsorbent of the electrocatalyst (eq. [2]). The hydrogenation is possible when the site of adsorption of the molecule is near to the electroadsorbed hydrogen (eq. [3]); this site is called the "triple point" (5). After saturation of the ring, the hydrogenated molecule is liberated by

Received June 26 2002. Published on the NRC Research Press Web site at http://canjchem.nrc.ca on 12 December 2002.

L. Ruest,[1] H. Ménard, V. Moreau, and F. Laplante. Centre de Recherche en Électrochimie et Électrocatalyse, Département de Chimie, Université de Sherbrooke, Sherbrooke, QC J1K 2R1, Canada.

[1]Corresponding author (e-mail: Luc.Ruest@USherbrooke.ca).

 DOI: 10.1139/V02-182 © 2002 NRC Canada

Fig. 1. Simple alkyl pyrrole-2-carboxylates and their hydrogenated products, ryanodine and anhydroryanodine.

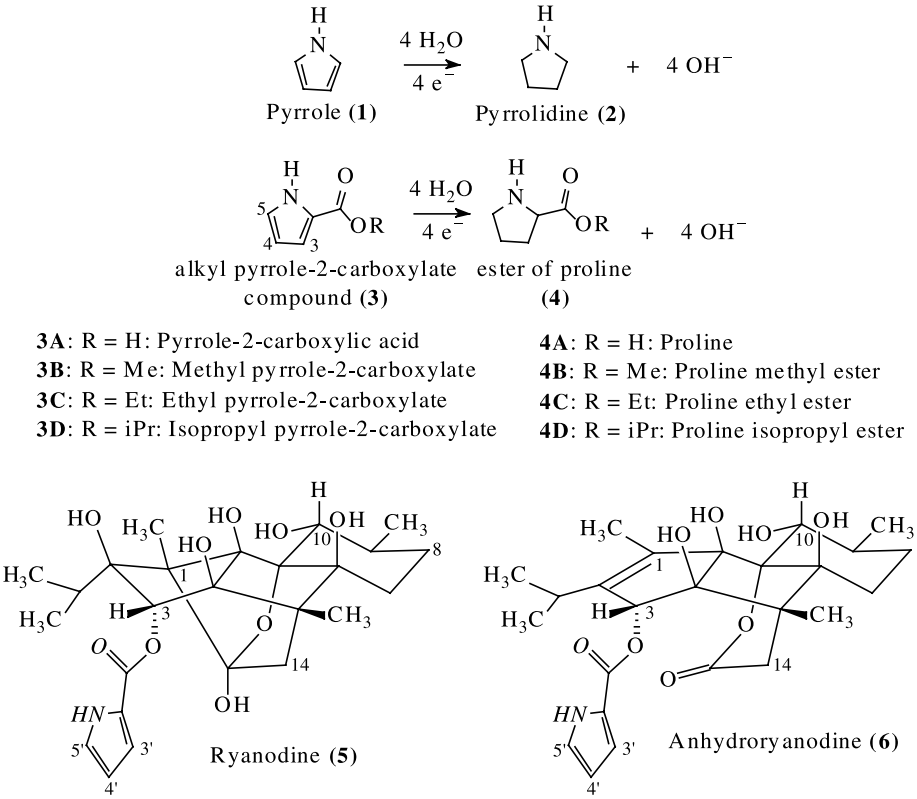

Fig. 2. The electrocatalytic hydrogenation (ECH) mechanism of alkyl pyrrole-2-carboxylate compound.

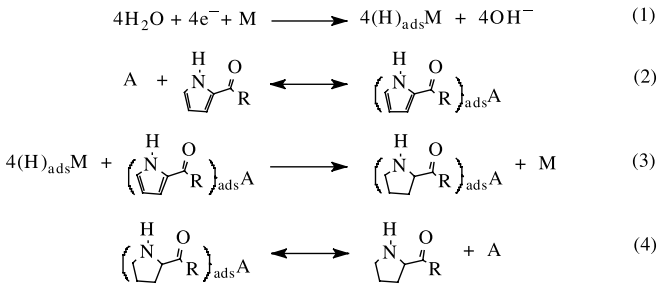

the adsorbent (eq. [4]). These equations represent the global hydrogenation process of the alkyl pyrrole-2-carboxylate compounds.

Experimental section

Melting points were recorded on a Melter Toledo FP62 hot stage apparatus and are uncorrected. Mass spectra (MS) and peak matching (HR-MS) data were determined at 70 eV on a VG Micromass ZAB-1F spectrometer. The ^{1}H (300 MHz) NMR spectra were recorded on a Bruker AC-300 instrument with CD_2HOD as internal standard centered at 3.30. The usual standard abbreviations have been used to indicate the multiplicity of the proton signals. Column chromatography (flash) was performed with Merck silica gel (200–400 mesh). All the electrocatalysts (5% Pd/Al_2O_3, 5% Pt/Al_2O_3, 5% Rh/Al_2O_3, and 5% Rh/C) were purchased from Sigma-Aldrich. The solvents used for chromatography were HPLC grade. The electrolyte solutions were made with deionized water.

Starting materials

Pyrrole-2-carboxylic acid and pyrrole were purchased from Sigma-Aldrich. Commercial pyrrole was distilled before use. Compounds **3B**, **3C**, and **3D** were synthesized by the following procedure: a solution of *N*,*N*′-dicyclohexylcarbodiimide (4 g, 19 mmol) in distilled CH_2Cl_2 (10 mL) was transferred (cannula) to a solution of pyrrole-2-carboxylic acid (1.9 g, 17 mmol) dissolved in 25 mL of the corresponding alcohol used as solvent (methanol for **3B**, ethanol for **3C**, and isopropanol for **3D**). After the addition of 100 mg of 4-dimethylaminopyridine, the mixture was stirred for 12 h at ambient temperature and under an inert atmosphere. The mixture was filtered on silica gel (40% EtOAc – 60% hexane) before purification by flash chromatography to give esters **3B**, **3C**, and **3D** in 90% yield.

Methyl pyrrole-2-carboxylate (3B)

White crystalline solid; mp 71°C (lit. (10) value mp 72–73°C). ^{1}H NMR (CD_3OD) (ppm): 6.95 (m, 1H, HC5), 6.84 (m, 1H, HC3), 6.18 (m, 1H, HC4), 3.80 (s, 3H, O-CH_3). MS *m*/*e*: 125 ($[M]^+$). HR-MS calcd. for $C_6H_7NO_2$: 125.0477; found: 125.0474.

Ethyl pyrrole-2-carboxylate (3C)

Beige solid; mp 38°C (lit. (11) value mp 40–42°C). ^{1}H NMR (CD_3OD) (ppm): 6.94 (m, 1H, HC5), 6.84 (m, 1H, HC3), 6.17 (m, 1H, HC4), 4.27 (q, 7.1 Hz, 2H, O-CH_2-CH_3), 1.33

© 2002 NRC Canada

(t, 7.1 Hz, 3H, O-CH_2-CH_3). MS *m/e*: 139 ($[M]^+$). HR-MS calcd. for $C_7H_9NO_2$: 139.0633; found: 139.0627.

Isopropyl pyrrole-2-carboxylate (3D)

White solid; mp 41°C. ^{1}H NMR (CD_3OD) (ppm): 6.93 (m, 1H, HC5), 6.82 (m, 1H, HC3), 6.16 (m, 1H, HC4), 5.12 (h, 6.3 Hz, 1H, O-CH-$(CH_3)_2$), 1.31 (d, 6.3 Hz, 6H, O-CH-$(CH_3)_2$). MS *m/e*: 153 ($[M]^+$). HR-MS calcd. for $C_8H_{11}NO_2$: 153.0790; found: 153.0793.

Ryanodine used in the study was purified by a known procedure (1).

Hydrogenated products

All the products obtained by ECH were characterized by ^{1}H NMR and a comparison with authentic samples was done. Pyrrolidine, proline, and proline methyl ester hydrochloride (**4B**) were purchased from Sigma-Aldrich.

Proline ethyl ester hydrochloride (4C)

This material was prepared by a very slow addition of $SOCl_2$ (300 µL, 3.6 mmol) to a solution of proline (244 mg, 2.1 mmol) in ethanol (6 mL) following a known method (12). The mixture was kept at 0°C during the addition. After 5 h, the solvent was evaporated to leave a pure product, an amorphous beige solid (mp 55°C) (99%). ^{1}H NMR (CD_3OD) (ppm): 4.42 (m, 1H, HC2), 4.30 (q, 7.1 Hz, 2H, O-CH_2-CH_3), 3.38 (m, 2H, H_2C5), 2.42 (m, 1H, H_AC3), 2.12 (m, 3H, H_BC3, H_2C4), 1.32 (t, 3H, O-CH_2-CH_3). MS *m/e*: 143 ($[M]^+$). HR-MS calcd. for $C_7H_{13}NO_2$: 143.0946; found: 143.0950.

Proline isopropyl ester hydrochloride (4D)

Synthesis of proline isopropyl ester hydrochloride (4D) was prepared by the previous procedure using isopropanol (99%). The product obtained was a yellowish oil. ^{1}H NMR (CD_3OD) (ppm): 5.12 (h, 6.2 Hz, 1H, O-CH-$(CH_3)_2$), 4.35 (m, 1H, HC2), 3.35 (m, 2H, H_2C5), 2.40 (m, 1H, H_AC3), 2.05 (m, 3H, H_BC3, H_2C4), 1.30 and 1.31 (two d, 6.3 Hz, 6H, O-CH-$(CH_3)_2$). MS *m/e*: 157 ($[M]^+$). HR-MS calcd. for $C_8H_{15}NO_2$: 157.1103; found: 157.1098.

Electrolysis

The electrolysis was carried out in a two-compartment jacketed glass H-cell having a Nafion-324 (E.I. Dupont de Nemours & Co.) membrane as separator. The cell temperature was fixed at 21°C during the ECH by a circulating thermostated bath (VWR 1160A). The working electrode was a reticulous vitreous carbon (RVC) foam (25 × 20 × 6 mm, 80 pores per inch (ppi; 1 inch = 25.4 mm), Electrosynthesis Co.). The electrode was mounted by inserting a glass rod (o.d. 5–6 mm, i.d. 3.5 mm) in the horizontal axis of the piece of RVC. The excess RVC was then removed and a copper wire was inserted into the RVC to be further cemented with silver epoxy (Epoxy Technology). Finally, the electrical contact zone on the RVC matrix was fixed to the glass rod with epoxy to isolate the electrical contact from the electroactive part of the electrode (5).

Both compartments were filled with the 0.1 M NaCl solution whose pH was adjusted to 1.2 with concentrated HCl. The ECH process occurred in the cathodic compartment (filled with 24 mL of the electrolyte) containing the working electrode and the electrocatalyst (200 mg). A platinum counter electrode was used in the anodic compartment. Mechanical stirring was applied during the ECH. When another electrolyte was used, the anodic compartment was filled with 2 M NaOH (5). A constant current of 5 mA was applied during the electrolysis. After passing 50 C of electricity to condition the working electrode, a solution of 0.6 M of starting material in methanol (1.0 mL) was added to the cathodic compartment.

The electrical charge passed through the system was noted in Faraday equivalents. A Faraday equivalent is the minimal amount of electrical charge needed to hydrogenate all the starting material in the cell. The equivalent charge can be calculated by the multiplication of the quantity of starting material by the number of electrons required to complete the reaction and by the Faraday constant (96 485 C per mole of electrons). Thus, 1 Faraday equivalent for 0.6 mmol of a simple alkyl pyrrole-2-carboxylate compound is 232 C, and 1 Faraday equivalent for 0.08 mmol ryanodine is 32 C.

Analysis

The hydrogenation process was tracked by monitoring the consumption of the starting material according to the Faraday equivalent. Aliquots of 500 µL were collected in the cathodic compartment during the ECH and analysed by HPLC (ZORBAX Eclipse XDB-C8 column (4.6 mm (i.d.) × 150 mm)) with an isocratic elution (40% acetonitrile – 60% water). Before the HPLC analysis, the aliquots were filtered on a 0.2 µm syringe filter. The HPLC system was an Agilent 1100 Series. A diode array detector performed the data acquisition. The wavelength was set to 265 nm for **3A**, **3B**, **3C**, and ryanodine; 280 nm for **3D**; and 207 nm for pyrrole.

Recovery of the hydrogenated products

The recovery of the hydrogenated simple alkyl pyrrole-2-carboxylate molecules, except pyrrolidine, was achieved by first evaporating water from the solution on a rotatory evaporator after filtration to remove the electrocatalyst. The product was then recovered by trituration with distilled chloroform. For pyrrolidine, the solution was saturated with K_3PO_4 to adjust the pH to 12. Pyrrolidine was extracted with ether (15 mL). The combined organic phases were dried (Na_2SO_4) and analysed by GC (HP-5890 with DB-1 column (30 m × 0.25 mm (i.d.), J&W Scientific)).

The product obtained after the hydrogenation of ryanodine was recovered with a C-18 SPE cartridge. The pH of the solution was adjusted to 8 for the elution. Distilled methanol was used to recover the product from the cartridge.

Results and discussion

Influence of the electrocatalyst

Figure 3 shows the evolution of the ECH process of **3B** (in 0.1 M NaCl at pH = 1.2 as the electrolyte (saline solution)) with the use of different electrocatalysts. The best results were obtained with the 5% Rh/Al_2O_3 electrocatalyst. The other electrocatalysts (5% Pd/Al_2O_3 and 5% Pt/Al_2O_3) allowed for only a 35% reduction of the starting material for the same Faraday equivalent. These results are consistent with the literature (2–4, 8, 9) where rhodium is the metal that is most effective in the hydrogenation of a pyrrole ring

© 2002 NRC Canada

Fig. 3. The influence of the electrocatalyst on the ECH of methyl pyrrole-2-carboxylate (**3B**) in saline solution.

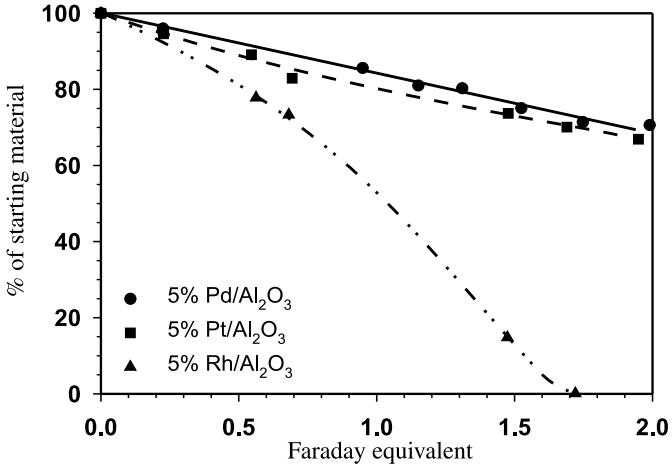

Fig. 4. The ECH process of the simple alkyl pyrrole-2-carboxylate molecules with 5% Rh/Al_2O_3 electrocatalyst and saline solution.

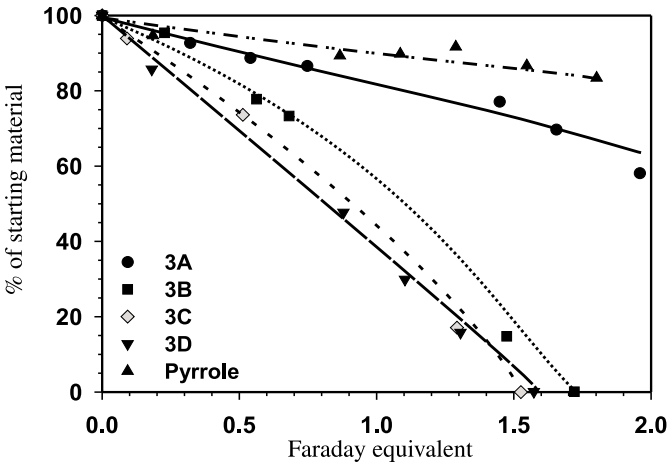

Table 1. The ECH process of ethyl pyrrole-2-carboxylate (**3C**) with 5% Rh/Al_2O_3 electrocatalyst and different electrolytes.

Electrolyte	Faraday equivalent	% of **3C**[a]
Methanol solution	1.5	69
Saline solution	1.5	0
Borate solution	1.5	0
Phosphate solution	1.5	0

[a]Percentage of ethyl pyrrole-2-carboxylate (**3C**) remaining at the indicated Faraday equivalent.

Table 2. The ECH process of pyrrole and pyrrole-2-carboxylic acid (**3A**) according the electrolyte (saline or phosphate solution) with 5% Rh/Al_2O_3 electrocatalyst.

Starting material	Electrolyte	Faraday equivalent	% of SM[a]
Pyrrole	Saline solution	2.7	81
Pyrrole	Phosphate solution	1.3	0
3A	Saline solution	2.0	58
3A	Phosphate solution	1.4	0

[a]Percentage of starting material (SM) remaining at the indicated Faraday equivalent.

compound in classical catalytic hydrogenation. The stability of the metal in the electrolyte is critical: rhodium and platinum electrocatalysts are resistant to acidic conditions but palladium was observed to dissolve in these conditions. The rhodium electrocatalyst was used for the remainder of the experiment.

Influence of the electrolyte

Several types of electrolyte were tested: phosphate solution (1 M KH_2PO_4 – 1 M NaOH; pH = 7.0), borate solution (0.1 M NaCl – 0.05 M boric acid; pH = 2.5), aqueous methanol solution (0.1 M NaCl in 5% H_2O – MeOH), and saline solution (0.1 M NaCl; pH = 1.2).

A limiting factor in the choice of the electrolyte is its pH. A high pH results in hydrolysis of the ester group of the starting material, giving the pyrrole-2-carboxylic acid and the alcohol residue (ryanodol for ryanodine). At low pH (pH < 0), ryanodine loses water through an important cleavage of the diterpenic skeleton leading to the anhydro series (anhydroryanodine (**6**)) (1).

An ECH of **3C** was performed with each electrolyte, using 5% Rh/Al_2O_3 as the electrocatalyst. The results are shown in Table 1. Aqueous methanol solution was shown to be a relatively poor electrolyte for the reaction. These results suggest a modification in quality of adsorption of the pyrrole ring onto the electrocatalyst (eq. [2]) due to the different solvents used.

The results for the other electrolytes were approximately similar. The difference between them is the stability of the hydrogenated product and its recovery. The hydrogenated products are not stable in the phosphate solution: hydrolysis is rapid, leading to proline, not to ester. The recovery of the hydrogenated product with this electrolyte is also quite difficult owing to the presence of the phosphate salts. All the alkyl pyrrole-2-carboxylate molecules used in this study are stable in this electrolyte. We did not use boric acid (borate solution) in the case of ryanodine owing to the formation of a complex between boric acid and the numerous hydroxyl groups of the molecule (1*c*).

The best electrolyte was the saline solution, and we obtained the best recovery of hydrogenated products with this electrolyte. The ECH process of pyrrole and pyrrole-2-carboxylic acid were more effective with the phosphate solution than with the saline solution (Table 2). These results suggest that the adsorption of the molecule on the electrocatalyst is influenced by the nature and the pH of the electrolyte.

ECH process of the simple alkyl pyrrole-2-carboxylate molecules

Figure 4 shows the ECH of the different alkyl pyrrole-2-carboxylate molecules under the same conditions (5% Rh/Al_2O_3 and saline solution). We can see that the rate of hydrogenation of pyrrole and pyrrole-2-carboxylic acid is very different from that of the other molecules, as mentioned before. The complete ECH of **3B**, **3C**, and **3D** was achieved using from 1.5 to 1.7 Faraday equivalents. Thus, we can

© 2002 NRC Canada

Fig. 5. The ECH process of ryanodine with two different electrocatalysts (5% Rh/Al_2O_3 and 5% Rh/C) in saline solution.

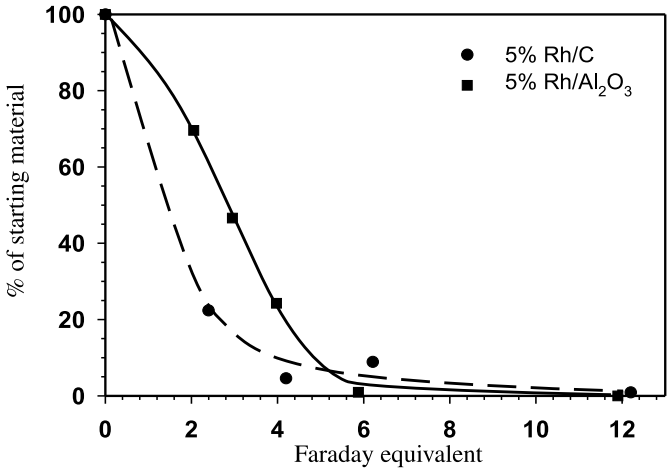

suppose that the differences between these molecules are not large enough to have a significant influence on the ECH process.

Even if the hydrogenation was shown to be complete, we did not succeed in recovering all of the hydrogenated product. With the techniques used, in the best case, we were able to recover only 59% of the hydrogenated product of **3C** (proline ethyl ester (**4C**)). We recovered 75% of the hydrogenated product of **3B** (proline methyl ester (**4B**)) and 87% of the hydrogenated product of **3D** (proline isopropyl ester (**4D**)). The recovery of the hydrogenated pyrrole-2-carboxylic acid (proline) was difficult owing to the phosphate salts (ECH with phosphate electrolyte). We recovered, in the best case, only 28% of proline. The yield of recovery of pyrrolidine is quite difficult to determine owing to its great volatility. The purity of recovered pyrrolidine was evaluated by GC to be 95%. The SPE technique cannot be used to recover the hydrogenated product of the simple alkyl pyrrole-2-carboxylate molecules.

ECH process of ryanodine

The results of the ECH of ryanodine are presented in Fig. 5. The ECH was attempted with two electrocatalysts, 5% Rh/Al_2O_3 and 5% Rh/C (activated charcoal). With ryanodine more Faraday equivalents are needed to hydrogenate the totality of the starting material owing to the greater dilution (3.2 mM of ryanodine vs. 24 mM for a simple alkyl pyrrole-2-carboxylate molecule). The ECH process with 5% Rh/C electrocatalyst seems to be faster than with 5% Rh/Al_2O_3, but there is stronger adsorption of the hydrogenated product. With 5% Rh/C, we recovered only 7% of the hydrogenated ryanodine vs. 73% with 5% Rh/Al_2O_3 electrocatalyst.

Tetrahydroryanodine (**7**) (hydrogenated ryanodine) (Fig. 6) can be identified by ^1H NMR spectroscopy. The proton supporting the proline moiety (HC(3)) appears at a different position for each diastereomers (D or L). The ^1H NMR spectrum of hydrogenated ryanodine shows an equal amount of the two diastereomers. This reveals the equal accessibility of both sides of the pyrrole ring. These epimers are invisible

Fig. 6. Electrocatalytic hydrogenation of ryanodine.

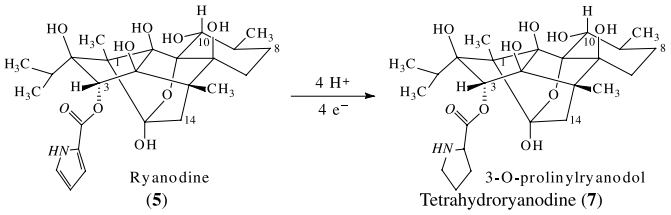

under UV and are very close in polarity; we did not attempt to separate them.

Tetrahydroryanodine (3-O-prolinylryanodol) (7)

White solid. ^1H NMR (CD_3OD) (ppm): 5.55 and 5.58 (2 × s, 1H, HC3), 3.77 (d, 1H, 10.2 Hz, HC10), 3.73 (m, 1H, HC2′), 3.06 (m, 1H, H_AC5'), 2.86 (m, 1H, H_BC5'), 2.33 (m, 1H, H_AC14), 2.25–2.00 (m, 3H, HC3′, HC13 and $H_{ax}C7$), 2.00–1.70 (m, 5H, HC3′, H_2C4', HC9 and H_BC14), 1.59–1.49 (m, 2H, $H_{eq}C7$ and $H_{ax}C8$), 1.36 (s, 3H, CH_3(C1)), 1.30–1.25 (m, 1H, $H_{eq}C8$), 1.10 (d, 3H, CH_3(C18)), 1.02 (d, 3H, CH_3(C9)), 0.98 (d, 3H, CH_3(C5)), 0.75 (2d, 3H, CH_3(C19)). MS *m/e*: 498 ($[MH]^+$). HR-MS calcd. for $C_{25}H_{40}NO_9$: 498.2703; found: 498.2706.

Catalytic hydrogenation of ryanodine

To our knowledge, the pyrrole ring of ryanodine has never been reduced by a classical catalytic hydrogenation. In our experiments, palladium and platinum catalysts over different supports were not effective in reducing the aromatic ring at atmospheric pressure. The electrocatalytic hydrogenation gave us excellent results. The classical catalytic hydrogenation with 5% Rh/Al_2O_3 in methanol allowed for only 33% hydrogenation of ryanodine after 4 days. When the saline solution (0.1 M NaCl; pH = 1.2) and the same catalyst were used in classical hydrogenation, the reaction was completed after 6 to 12 h. These results can be explained by the difference of adsorption of ryanodine onto the catalyst according to the solvent used. The quantity of solvent, catalyst, and starting material were the same as for the ECH process. All the classical catalytic hydrogenation experiments of this study were done at atmospheric pressure.

Conclusion

The hydrogenation of an alkyl pyrrole-2-carboxylate compound is possible using an electrocatalytic hydrogenation (ECH) process. We have shown that the hydrogenation reaction is specific to the pyrrole ring of alkyl pyrrole-2-carboxylate and does not modify the ester function of the molecule. The ECH of **3B**, **3C**, and **3D** was found to be most effective with rhodium electrocatalyst (5% Rh/Al_2O_3) in saline solution (0.1 M NaCl at pH = 1.2). Pyrrole and pyrrole-2-carboxylic acid ECH gave better results in phosphate solution (1 M KH_2PO_4 – 1 M NaOH; pH = 7.0). All the simple alkyl pyrrole-2-carboxylate compounds were totally hydrogenated after the passage of 1.7 Faraday equivalents of electrical charge.

© 2002 NRC Canada

The ECH process can be used to hydrogenate a complex molecule like ryanodine. Once again, the hydrogenation was complete but there was no diastereoselection in the formation of the reduced compound because of easy access of hydrogen to both sides of the pyrrole ring. The hydrogenation of ryanodine proves that the ECH process can be used efficiently in the selective modification of complex molecules. The biological activity of the new tetrahydroryanodines is currently under study by W. Welch, University of Nevada at Reno, Nevada.

Acknowledgments

We are grateful to Professor W. Welch, Department of Biochemistry, University of Nevada, Reno, who allowed us to do this work with subcontracts of research funded by the National Science Foundation (NSF). We also thank Professor Alan J. Williams, Department of Cardiac Medicine, Imperial College School of Medicine at the National Heart and Lung Institute (NHLI), London, U.K., for a research contract from the British Heart Foundation. The study was also financially supported by the Natural Sciences and Engineering Research Council of Canada (NSERC) and the Fonds FCAR du Québec. We wish to thank Dr. N. Pothier and Mr. G. Boulay, Département de Chimie, Université de Sherbrooke, for their technical assistance (NMR spectroscopy and MS).

References

1. (*a*) K. Wiesner. Adv. Org. Chem. **8**, 295 (1972; (*b*). L. Ruest and M. Dodier. Can. J. Chem. **74**, 2424 (1996); (*c*) J.L Sutko, J.A. Airey, W. Welch, and L. Ruest. Pharm. Rev. **49**, 53 (1997); (*d*) L. Ruest, C. Berthelette, M. Dodier, L. Dubé, and D. St-Martin. Can. J. Chem. **77**, 12 (1999).
2. R.L. Augustine. Catalytic hydrogenation. Marcel Dekker Inc., New York. 1965. Chap 3.
3. G.W. Gribble, B.M. Trost, and I. Flemming. Comprehensive organic synthesis. Vol. 8. Pergamon Press, Oxford, U.K. 1991. Chap 3.7.2.
4. V. Háda, A. Tungler, and L. Szepesy. Appl. Catal. A. **210**, 165 (2001).
5. F. Laplante, L. Brossard, and H. Ménard. Submitted for publication.
6. P. Dubé, L. Brossard, and H. Ménard. Can. J. Chem. **80**, 345 (2002).
7. P. Dabo, B. Mahdavi, H. Ménard, and J. Lessard. Electrochim. Acta, **42**, 1457 (1997).
8. P.N. Rylander. Catalytic hydrogenation over platinum metals. Academic Press, New York. 1967. Chap 22.
9. M Freifelder. J. Org. Chem. **26**, 1835 (1961).
10. (*a*) B. Oddo. Mem. Accad. Lincei **14**, 510 (1923); (*b*) P. Hodge and R.W. Rickards. J. Chem. Soc. 2543 (1963).
11. D.M. Bailey, R.E. Johnson, and N.F. Albertson. Org. Synth. **51**, 100 (1971).
12. S. Guttmann. Helv. Chim. Acta, **44**, 721 (1961).

© 2002 NRC Canada

Fast, efficient syntheses of linear poly(dipyrromethene)s

Qingqi Chen and David Dolphin

Abstract: The synthesis of three octapyrrolic, **8**–**10**, and four dodecapyrrolic, **15**–**18**, oligomers is reported. They are linear poly(dipyrromethene)s and potential ligands as building blocks for supramolecular architectures through self-assembly. Octapyrrolic oligomers **8**–**10** were prepared in 90–95% yields by condensation of 2 equiv of a tripyrrolic compound **4** with 1 equiv of diformyldipyrrolic compounds **5**–**7**. A similar procedure, involving the condensation of 2 equiv of a pentapyrrolic starting material **13** with 1 equiv of **5**–**7** or **14**, was found to give rise to the corresponding dodecameric systems **15**–**18** in 41–56% yields.

Key words: poly(dipyrromethene), linear polypyrroles, dipyrromethane, dipyrromethene.

Résumé : On rapporte la synthèse de trois oligomères octapyrroliques (**8**–**10**) et de quatre dodécapyrroliques (**15**–**18**). Il s'agit de poly(dipyrrométhènes) linéaires et des ligands potentiels comme blocs pouvant servir à la construction d'architectures supramoléculaires par le biais d'autoassemblages. Les oligomères octapyrroliques **8**–**10** ont été préparés avec des rendements allant de 90 à 95% par le biais de condensations de deux équivalents d'un composé tripyrrolique (**4**) avec un équivalent de composés diformylpyrroliques (**5**–**7**). Une procédure semblable impliquant la condensation de deux équivalents d'un produit de départ pentapyrrolique (**13**) avec un équivalent de composés **5**–**7** ou **14** conduit à la formation des systèmes dodécamères correspondant (**15**–**18**) avec des rendements allant de 41 à 56%.

Mots clés : poly(dipyrrométhène), polypyrroles linéaires, dipyrrométhane, dipyrrométhène.

[Traduit par la Rédaction]

Introduction

Dipyrromethenes (**I**) are yellow colored and fully conjugated flat compounds containing 10-π-electrons and can be precursors of chlorins; expanded, contracted, and isomeric porphyrins (1); bilirubins (2); biliverdin (2); and many other bile pigments (3). They have been extensively used in the synthesis of porphyrins (1) and linear polypyrroles (4). Owing to their stable monoanionic nature, dipyrromethenes have been found to be useful ligands for a variety of metal ions (5). In addition, bile pigments containing dipyrromethene moieties linked by a methylene group such as biladienes-*ac* (**II**) are useful ligands for the formation of well-defined architectures through self-assembly (6). A salient feature of dipyrromethene superstructures is that counterions are not required, since the dipyrromethene unit is a monoanionic ligand and the complex will be neutral when chelated with divalent metal ions. This is in contrast to bipyridine ligands, the standard building blocks for supramolecular assemblies used by Lehn and co-workers (7, 8).

The use of dipyrromethenes as novel ligands to build double helical supramolecules was originally proposed by one of us in 1965 (9), when it was suggested that a 2:2 bis(dipyrromethene) ligand – Co^{II} complex exists in a helical conformation. Since then several crystal structures of 2:2 biladiene-*ac* ligand – M^{II} complexes have been reported where the 2:2 complex existed as a helix (10). Our group re-examined these reactions (6) and explored the use of a 2,2-spacer between dipyrromethene units (such as **III**) and the 3,3′- positions (such as **IV**) and hexapyrins (**V**) (Scheme 1).

Like biladienes-*ac* (**II**), bis(dipyrromethenes) (**III**) and hexapyrrins (**V**) reacted with Zn^{II} to form a double stranded helical complex (5), while the complex of the 3,3′-bidipyrromethene **IV** ($n = 0$) with Zn^{II} showed triangular geometry with the ligand linking the three metal centers in an overlapping progressive fashion. For each ligand one dipyrromethene binding domain lies above the averaged plane of the molecule, while the other dipyrromethene lies below this plane (Scheme 2).

To extend our work, we were interested in linear polydipyrromethenes, which include 2,2′-linked (**A**), 3,3′-linked (**B**), 3,3′- sulfur bridged (**C**), and 2,2- directly linked intermediates (**D**). In this paper we will report on the synthesis and characterization of novel ligands that contain multiple dipyrromethene units.

Received 15 April 2002. Published on the NRC Research Press Web site at http://canjchem.nrc.ca on 17 December 2002.

Q. Chen[1] and D. Dolphin.[2] Department of Chemistry, The University of British Columbia, 2036 Main Mall, Vancouver, BC V6T 1Z1, Canada.

[1]Present address: Synapse Technologies Inc., 6660 NW Marine Drive, Vancouver, BC V6T 1Z4, Canada.
[2]Corresponding author (e-mail: ddolphin@qltinc.com).

 DOI: 10.1139/V02-179 © 2002 NRC Canada

Scheme 1.

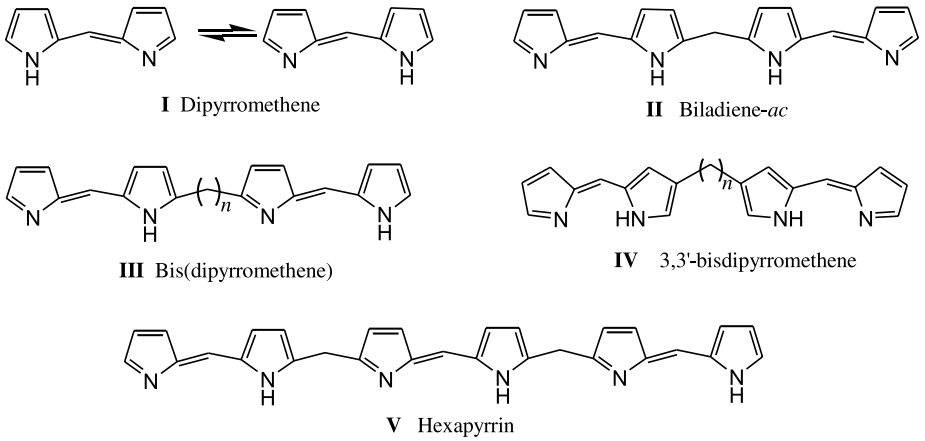

Scheme 2.

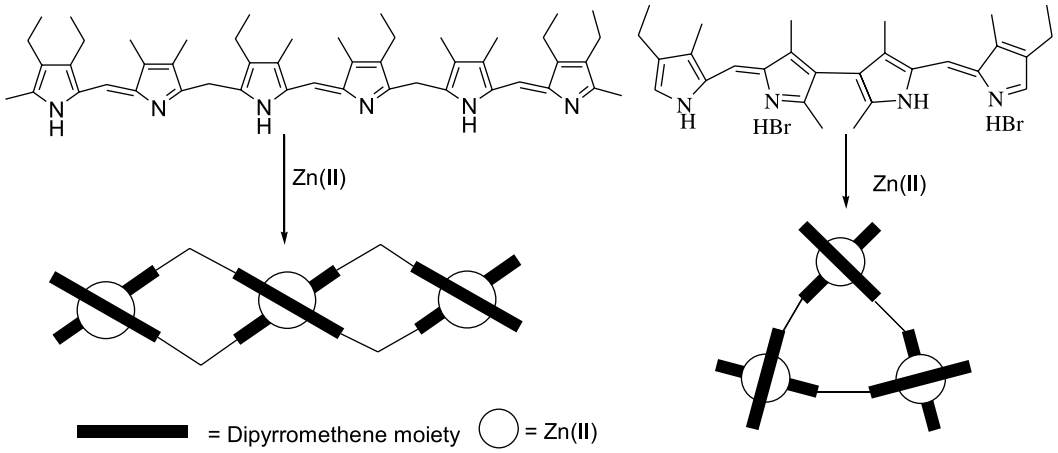

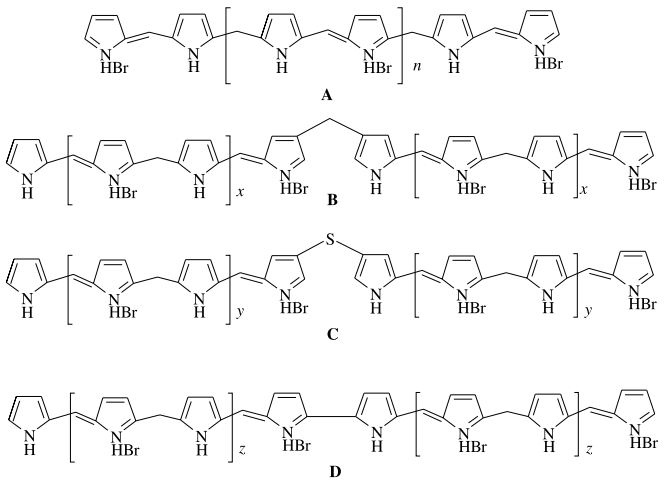

Linear polypyrroles such as hexanornonapyrrin (11*a*), decahydrohexapyrrin (11*b*–11*d*), and pentapyrrole (11*e*) have been recently reported and characterized. However, synthetic methods for linear oligopyrroles containing more than three dipyrromethene units are not currently available.

The key precursor required for the synthesis of **8**–**9** was tripyrrole **4**. It was synthesized from the known 5-acetoxymethylpyrrole (**1**) via two steps, as shown in Scheme 3. Briefly, the procedure involved first treatment of **1** with pyrrole at reflux in a mixture of *p*-toluenesulfonic acid and dichloromethane or at 40°C in acetic acid, followed by purification of the reaction mixture by direct crystallization from dichloromethane–hexane. The asymmetric dipyrromethane **2** was obtained in 66% yield. Acid-catalyzed coupling of this intermediate with 3,4,5-trimethyl-5-formylpyrrole (**3**) then afforded the requisite hydrobromide salt of tripyrrole **4** in an 86% yield after crystallization.

Once **4** was in hand, the synthesis of the target compounds **8**–**10** proved straightforward. After simple precipitating using anhydrous ether, the acid-catalyzed condensation of 2 equiv of **4** and 1 equiv of **5**–**7** in methanol–dichloromethane was found to give the desired linear octapyrrins **8**–**10** as their corresponding tetrahydrobromide salts, in excellent yields. (detailed in Scheme 3).

Our synthetic procedure for dodecapyrrins **15**–**18** is outlined in Schemes 4 and 5. For this purpose, the key precursor **13** was required; this was prepared from 5-acetoxymethylpyrrole **1a** via two steps. The procedure involved first treating **1** with the 5-unsubstituted 2-formylpyrrole (**11**) at 50°C in acetic acid or at room temperature in a mixture of dichloromethane and *p*-toluenesulfonic acid. Crystallization from dichloromethane–hexane gave the asymmetric dipyrro-

© 2002 NRC Canada

Scheme 3.

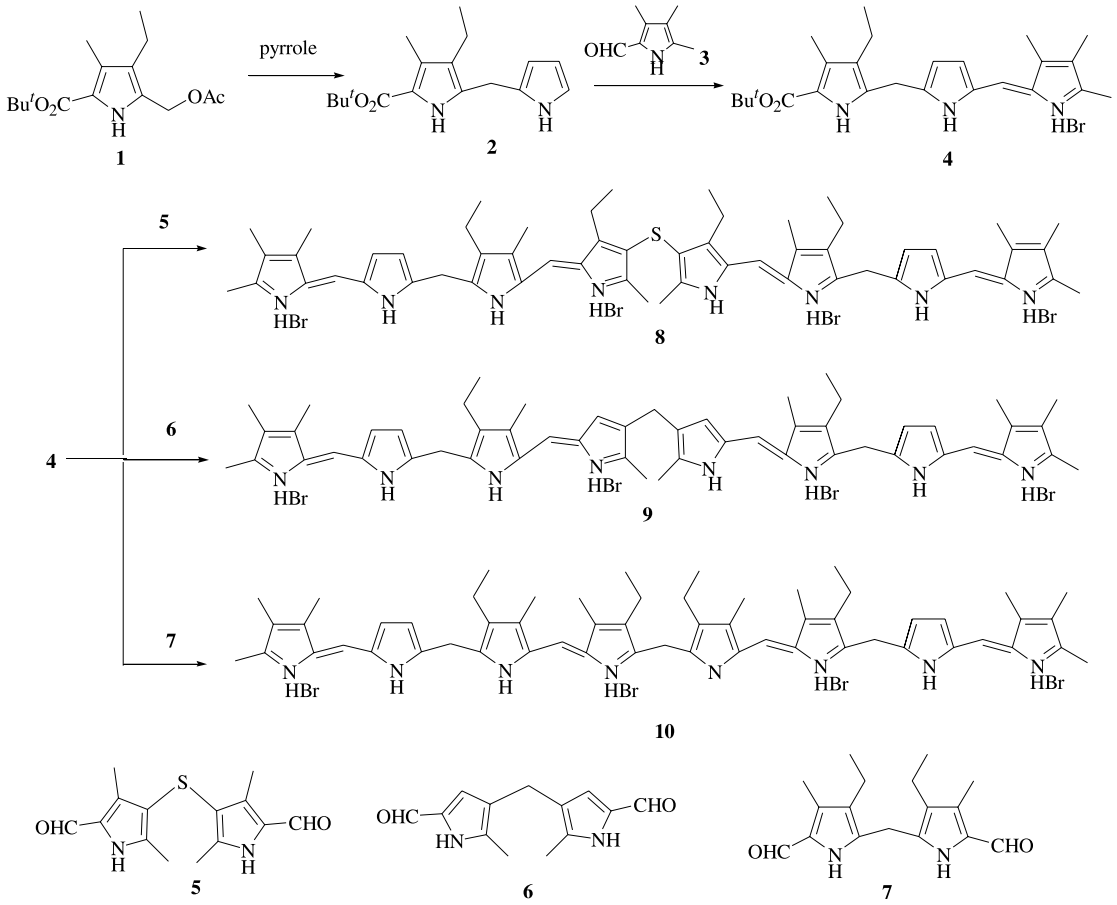

Scheme 4.

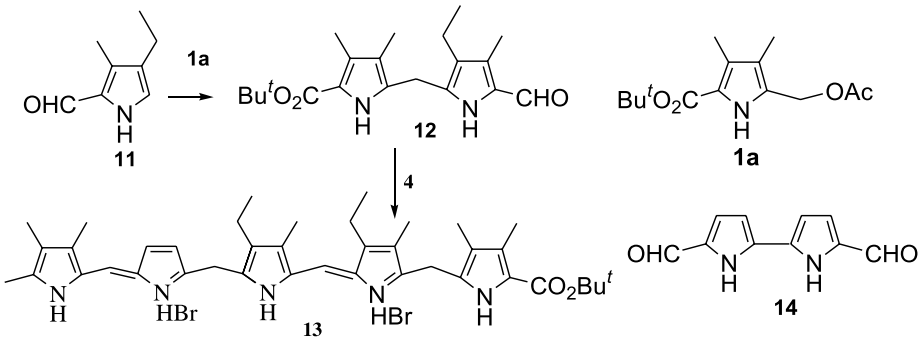

methane **12** in 72% yield. Condensation of **12** with tripyrrole acid, generated in situ by treating **4** with trifluoroacetic acid at room temperature for 20 min, afforded the desired intermediate as the dihydrobromide salt **13** in 93% yield after precipitating with anhydrous ether. Acid-catalyzed condensation between **14** and 2 equiv of **13** with 1 equiv of **5**–**7** gave, in good yields, the desired dodecapyrrins **15**–**18** as their corresponding hexahydrobromide salts.

Experimental section

5-Acetoxymethyl-4-ethyl-3-methyl-2-*tert*-butoxycarbonylpyrrole (**1**) (12), 5-acetoxymethyl-3,4-dimethyl-2-*tert*-butoxycarbonylpyrrole (**1a**) (12), 3,4,5-trimethyl-2-formyl-pyrrole (**3**) (13), bis(2,4-dimethyl-5-formyl-pyrrole-3-yl) sulfide (**5**) (14), 5-methyl-2-benzoxycarbonylpyrrole (15), 5,5′-diformyl-4,4′-dimethyl-3,3′-diethyl-dipyrromethane **7** (14), 3-methyl-4-ethyl-2-formylpyrrole (**11**) (16), and 5,5′-diformylbipyrrole (**14**) (15) were synthesized according to the previously reported procedures.

5,5′-Bisethoxycarbony-2,2′-dimethyl-3,3′-dipyrromethane

Paraformaldehyde (1.40 g, 47 mmol, 2.0 mol equiv) was suspended in ethanol (300 mL) containing hydrochloric acid (33%, 5 mL). The mixture was stirred with heating until all

© 2002 NRC Canada

Scheme 5.

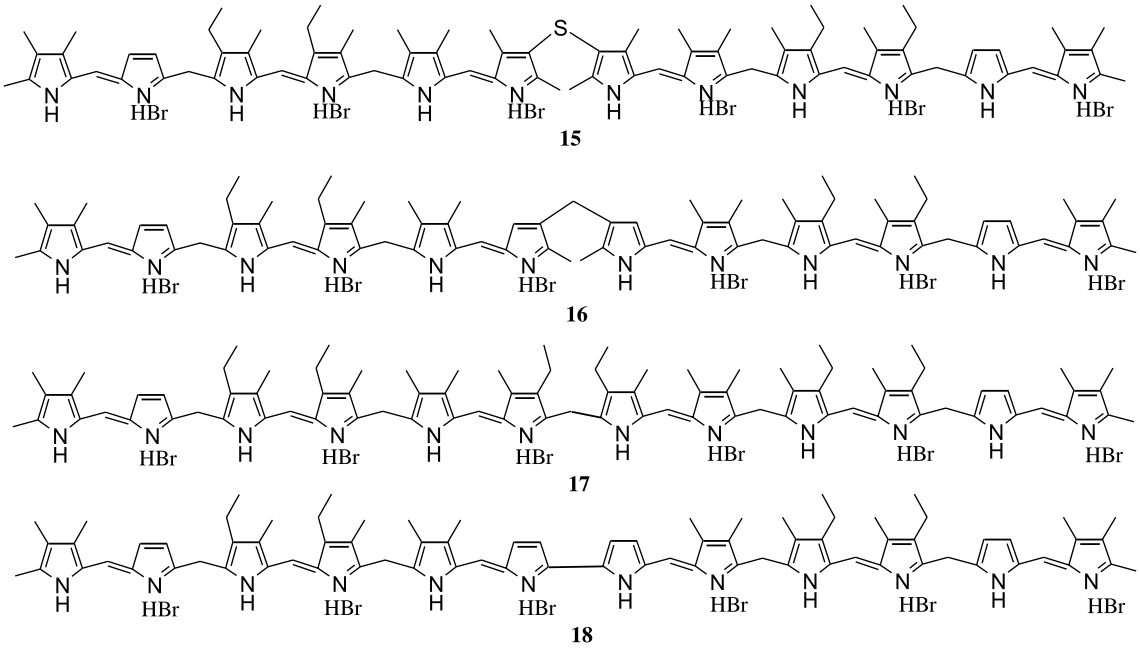

the solid dissolved. After cooling to room temperature, 2-benzoxycarbonyl-5-methylpyrrole (20 g, 46.8 mmol) was added. The mixture was allowed to stir at 40°C for 3 h. After removal of solvent, the residue was crystallized from methanol. The product was obtained as white crystals (11.32 g, 55%); mp 222–224°C. ^{1}H NMR (200 MHz, $CDCl_3$) (ppm) δ: 2.20 (s, 6H, 2 CH_3), 3.20 (s, 2H, CH_2), 5.20 (s, 4H, 2OCH_2), 6.60 (s, 2H, 2 pyrrolyl-H), 7.40 (m, 10H, 2 phenyl), 9.20 (s, 2H, 2NH). ^{13}C NMR (50 MHz, $CDCl_3$) (ppm) δ: 11.57 (CH_3), 19.51 (s, CH_2), 65.55 (OCH_2), 113.13, 116.74, 119.38, 121.71, 128.12, 128.53, 130.76, 136.43, 162.55 (COO). LSIMS *m/e*: 443 ([M^+ + 1]). Anal. calcd. for $C_{27}H_{26}N_2O_4$: C 73.29, H 5.92, N 6.33; found: C 73.02, H 5.90, N 5.98.

1,2-Bis(5-carboxy-2,4-dimethyl-pyrrole-3-yl)methane

1,2-Bis(5-benzoxycarbonyl-2-methylpyrrole-3-yl)methane (20 g, 63 mmol) was dissolved in tetrahydrofuran (400 mL). Palladium on carbon (10%, 1.0 g) and triethylamine (1 mL) were added to this solution. The mixture was stirred for 20 h under hydrogen at atmospheric pressure and room temperature. The catalyst was removed by filtration. After removal of solvent, the residue was dried under vacuum. The product was obtained as a white powder (16 g, 98%), which was used directly for the next step without further purification. An analytical sample was purified by twice repeating the following procedure: the crude product (100 mg) was dissolved in aqueous saturated sodium bicarbonate (5 mL); the mixture was then filtrated to remove any insoluble materials and carefully adjusted to pH 4 with glacial acetic acid. The white precipitate was collected by suction filtration; mp 220°C (decomposition temperature (dec.)). ^{1}H NMR (200 MHz, DMSO-d_6) (ppm) δ: 2.10 (s, 6H, 3 CH_3), 3.30 (s, 2H, CH_2), 6.40 (s, 2H, 2 pyrr-H), 11.02 (s, 2H, 2 COOH), 11.85 (s, 2H, 2 NH). ^{13}C NMR (50 MHz, DMSO-d_6) (ppm) δ: 9.30 (CH_3), 19.20 (CH_2), 119.90, 127.55, 131.44, 137.55, 161.33 (COO). Anal. calcd. for $C_{13}H_{14}N_2O_4$: C 59.54, H 5.38, N 10.68; found: C 59.33, H 5.28, N 10.39.

5-*tert*-Butoxycarbonyl-4-methyl-3-methoxycarbonylmethyl-2,2′-dipyrromethane (2)

Method A

A 500 mL three-necked, round-bottomed flask equipped with magnetic stirrer bar and a nitrogen inlet was charged with 5-acetoxymethyl-4-ethyl-3-methyl-2-*tert*-butoxycarbonylpyrrole (**1**, 10.0 g, 35.5 mmol) and acetic acid (250 mL). After 20 min of stirring under nitrogen, pyrrole (2.86 g, 42.7 mmol, 1.2 mol equiv) and *p*-toluenesulfonic acid monohydrate (330 mg) were added. The reaction mixture was stirred at 40°C overnight. The solvent was removed under vacuum. The residue was taken into dichloromethane (500 mL) and washed successively by water (2 × 100 mL), aqueous saturated sodium bicarbonate (2 × 100 mL), and saturated brine (100 ml). After drying over anhydrous sodium sulfate and removing solvent under vacuum, the residue was crystallized from dichloromethane–hexane to give the product (3.33 g, 32%).

Method B

A 500 mL three-necked, round-bottomed flask equipped with a magnetic stirrer, nitrogen inlet, and reflux condenser was charged with 5-acetoxymethyl-4-ethyl-3-methyl-2-*tert*-butoxycarbonylpyrrole (**1**, 18.6 g, 66 mmol), pyrrole (4.6 mL, 66 mmol, 1.0 mol equiv), and dichloromethane (200 mL). The mixture was stirred at room temperature for 30 min while nitrogen was bubbled through the solution. *p*-Toluenesulfonic acid monohydrate (250 mg) was then added in one portion. The solution immediately turned yellow-red. The mixture was stirred under reflux for 30 min. TLC then showed the reaction was complete (CH_2Cl_2, 5-acetoxymethylpyrrole R_f = 0.4, product R_f = 0.5, and pyrrole R_f = 0.9). The product dipyrromethane turned yellow-red, pyrrole

© 2002 NRC Canada

turned to brown-black, and the starting 5-acetoxymethyl-pyrrole remained unchanged upon contacting the TLC plate over bromine vapor. After cooling to room temperature, triethylamine (1 mL) in methanol (5 mL) was added to neutralize the acid. Solvent was completely removed under vacuum (first rotovapor, then high vacuum). The yellow semi-solid was mixed with aqueous methanol (90%, 30 mL) and ultrasonicated to aid solidification. The crude material was immediately collected by suction filtration to yield the expected product (11.6 g, 61%), which was pure enough for subsequent use, as judged by ^{1}H NMR. Note that this compound is not very stable and should be stored in the dark and at low temperature. mp 120–122°C. ^{1}H NMR (200 MHz, $CDCl_3$) (ppm) δ: 1.05 (t, J = 7.32 Hz, 3H, CH_3), 1.50 (s, 9H, 3 CH_3), 2.20 (s, 3H, CH_3), 2.30 (q, J = 7.32 Hz, 2H, CH_2), 3.80 (s, 2H, CH_2), 5.80 (s, 1H, pyrrole-H), 6.05 (s, 1H, pyrrole-H), 6.60 (s, 1H, pyrrole-H), 7.60 (s, 1H, NH), 8.60 (s, 1H, NH). ^{13}C NMR (50 MHz, $CDCl_3$) (ppm) δ: 10.23 (CH_3), 14.55 (CH_3), 24.44 (CH_2), 28.33 (CH_2), 29.35 (CH_3), 86.88 ($OCMe_3$), 113.44, 114.55, 116.77, 123.55, 124.56, 125.44, 127.44, 128.33, 161.20 (COO). EI-MS (150 °C) *m/z* (%): 288 ([M^+], 52), 232 (40), 165 (100), 147 (25). Anal. calcd. for $C_{17}H_{24}N_2O_2$: C 70.80, H 8.39, N 9.71; found: C 70.60, H 8.61, N 8.53.

1-*tert*-Butoxycarbonyl-2-methyl-3-ethyl-12,13,14-trimethyl-4,5-dihydro-tripyrrin hydrogen bromide salt (4)

A 250 mL round-bottomed flask equipped with magnetic stirrer bar was charged with 2-*tert*-butoxycarbonyl-3-methyl-4-methoxycarbonylmethyl-dipyrromethane (**2**) (1.0 g, 3.47 mmol), 3,4,5-trimethyl-2-formyl-pyrrole (**3**) (0.48 g, 3.47 mmol, 1.0 mol equiv), dichloromethane (50 mL), and methanol (20 mL). Hydrogen bromide (48% in glacial acetic acid, 3 mL) was added with stirring. The red mixture was allowed to stir for 2 h at room temperature. Anhydrous ether (50 mL) was added and the suspension was allowed to stir for another 30 min. The red solid was collected by suction filtration and washed with anhydrous ether. The crude product was suspended in methanol (50 mL) containing 5 drops of hydrogen bromide (45% in glacial acid) and stirred for 30 min. The solid was collected by filtration (1.46 g, 86%). An analytical sample was obtained as follows: crude product was dissolved in a minimum amount of dichloromethane, and methanol (~1 mL) containing a drop of hydrogen bromide (45% in glacial acid) was added, followed by anhydrous ether to precipitate the product. The red solid was collected by suction filtration; mp 220 (dec.). UV–Vis (CH_2Cl_2) (nm): $\lambda_{max}(\varepsilon)$ = 483 (80 400). ^{1}H NMR (200 MHz, $CDCl_3$) (ppm) δ: 1.05 (t, J = 7.35 Hz, 3H, CH_3), 1.55 (s, 9H, $3CH_3$), 2.00 (s, 3H, CH_3), 2.20 (s, 6H, 2 CH_3), 2.40 (q, J = 7.35 Hz, 2H, CH_2), 2.60 (s, 3H, CH_3), 4.25 (s, 2H, CH_2), 6.30 (s, 1H, pyrrole-H), 7.00 (s, 1H, -CH=), 7.05 (s, 1H, pyrrole-H), 10.05 (s, 1H, NH), 13.10 (s, 1H, NH), 13.20 (s, 1H, NH). ^{13}C NMR (50 MHz, $CDCl_3$) (ppm) δ: 8.89 (CH_3), 10.29 (CH_3), 13.55 (CH_3), 15.55 (CH_3), 17.28 (CH_3), 24.77 (CH_2), 28.71 (CH_3), 30.05 (CH2), 80.20 ($OCMe_3$), 114.93, 119.57, 123.57, 124.13, 125.83, 126.11, 126.39, 127.33, 128.28, 133.13, 144.65, 152.49, 159.68 (C=N), 160.91 (COO). FAB-MS *m/e*: 408 ([M^+ + 1]), 334. Anal. calcd. for $C_{25}H_{33}N_3O_2$·HBr: C 61.47, H 7.02, N 8.60, Br 16.31; found: C 61.58, H 7.10, N 8.32, Br 16.25.

5,5′-Diformyl-2,2′-dimethyl-3,3′-dipyrromethane (6)

5,5′-Dicarboxy-2,2′-dimethyl-3,3′-dipyrromethane (3.0 g, 11 mmol) was suspended in trifluoroacetic acid (15 mL). The mixture was stirred at 40°C until all the solid had dissolved. The mixture was then cooled to –5°C using an ice–salt bath. Trimethyl orthoformate (4.5 mL) was added dropwise over 5 min and the mixture was allowed to stir another 10 min before being poured into a solution of 10% ammonia (100 mL), which was pre-cooled to 0°C. The yellow-brown precipitated was collected by filtration and washed with water. After drying under vacuum and crystallizing from dichloromethane–hexane, the title compound was obtained (2.1 g, 80%); mp 210–212°C. ^{1}H NMR (200 MHz, $CDCl_3$) (ppm) δ: 1.90 (s, 6H, 2 CH_3), 3.30 (s, 2H, CH_2), 6.35 (s, 2H, 2 pyrr-H), 9.40 (s, 2H, 2 CHO), 10.50 (s, 2H, 2NH). ^{13}C NMR (50 MHz, $CDCl_3$) (ppm) δ: 9.50 (CH_3), 19.50 (CH_3), 121.44, 126.78, 130.45, 136.55, 177.55 (CHO). LSIMS *m/e*: 231 ([M^+ + 1]). Anal. calcd. for $C_{13}H_{14}N_2O_2$: C 67.81, H 6.13, N 12.17; found: C 67.51, H 5.90, N 11.89.

General procedure for 8–10

Tripyrrole (**4**, 100 mg, 0.20 mmol) was suspended in trifluoroacetic acid (5 mL), and stirred at room temperature until all solid had dissolved. To this brown-red mixture **5**, **6**, or **7** (0.10 mmol, 0.5 mol equiv) was added under continuous stirring. After 10 min, a mixture of dichloromethane (20 mL), methanol (20 mL), and hydrogen bromide (48% in acetic acid) was added. The red mixture was stirred at room temperature and anhydrous ether (100 mL) was added. The suspension was then allowed to stir for another 30 min. The red solid was collected by suction filtration and washed with anhydrous ether. The crude product was suspended in methanol (50 mL) containing 5 drops of hydrogen bromide (45% in glacial acid) and stirred at room temperature for 30 min. The solid was collected by filtration to afford the expected product. An analytic sample was obtained by repeating the following procedure three times: The crude product (~20 mg) was dissolved in a minimum amount of trifluoroacetic acid. To this red mixture, dichloromethane (1 mL) and methanol (1 mL) containing a drop of HBr (48% in acetic acid) were added, followed by anhydrous ether to precipitate the product. The red solid was collected by suction filtration.

Octapyrrin tetrahydrobromide salt (8)

Yield 95%, mp 300°C (dec.). UV–Vis (CH_2Cl_2) (nm): $\lambda_{max}(\varepsilon)$ = 544 (110 600), 505 (97 700), 444 (81 000). ^{1}H NMR ($CDCl_3$/TFA-*d*, 9:1 (v/v), 200 MHz) (ppm) δ: 1.05 (t, J = 7.35 Hz, 6H, $2CH_3$), 2.00 (s, 6H, $2CH_3$), 2.15 (s, 6H, $2CH_3$), 2.20 (s, 6H, $2CH_3$), 2.30 (s, 6H, $2CH_3$), 2.50 (q, J = 7.35 Hz, 4H, CH_2), 2.60 (s, 6H, $2CH_3$), 2.70 (s, 6H, $2CH_3$), 4.50 (s, 4H, $2CH_2$), 6.40 (s, 2H, 2CH), 7.20 (s, 2H, 2CH), 7.26 (m, 4H, 4 pyrrole-H), 11.80–12.05 (m, 8H, 8NH). ^{1}H NMR ($CDCl_3$/TFA-*d*, 9:1 (v/v), 400 MHz) (ppm) δ: 1.05 (t, J = 7.6 Hz, 6H, 2 CH_3), 2.05 (s, 6H, $2CH_3$), 2.25 (s, 6H, $2CH_3$), 2.29 (s, 6H, $2CH_3$), 2.36 (s, 6H, $2CH_3$), 2.53 (q, J = 7.6 Hz, 4H, $2CH_2$), 2.64 (s, 6H, $2CH_3$), 2.66 (s, 6H, $2CH_3$), 4.52 (s, 4H, 2 CH_2), 6.42 (s, 2H, 2 -CH=), 7.24 (m, 4H, 4 pyrrolyl-H), 12.10–12.40 (m, 8H, 8 NH). ^{13}C NMR ($CDCl_3$/TFA-*d*, 9:1 (v/v), 100 MHz) (ppm) δ: 8.78 (CH_3),

© 2002 NRC Canada

10.14 (CH_3), 10.27 (CH_3), 11.25 (CH_3), 13.33 (CH_3), 13.49 (CH_3), 14.15 (CH_3), 17.11 (CH_2), 25.42 (CH_2), 115.48, 119.22, 121.55, 124.14, 126.36, 126.51, 127.67, 127.84, 128.17, 129.74, 132.12, 145.06, 145.94, 147.44, 148.08, 151.48, 156.69 (C=N), 162.46 (C=N). FAB-MS *m/z*: 1017 ([M^+ + 1 + 2HBr]), 937 ([M^+ + 2 + HBr]), 855 ([M^+ + 1]). HR-MS (LSIMS, matrix: thioglycerol) for $C_{54}H_{63}N_8S$ calcd.: 855.48964; found: 855.48906. Anal. calcd. for $C_{54}H_{62}N_8S{\cdot}4HBr$: C 55.02, H 5.64, N 9.51; found: C 55.33, H 5.86, N 9.38.

Octapyrrin tetrahydrobromide salt (9)

Yield 93%; mp 320°C (dec.). ^{1}H NMR ($CDCl_3$/TFA-*d*, 9:1 (v/v), 200 MHz) (ppm) δ: 1.05 (t, *J* = 7.35 Hz, 6H, $2CH_3$), 2.00 (s, 6H, $2CH_3$), 2.18 (s, 6H, $2CH_3$), 2.20 (s, 6H, $2CH_3$), 2.45 (q, *J* = 7.35 Hz, 4H, CH_2), 2.55 (s, 6H, $2CH_3$), 2.60 (s, 6H, $2CH_3$), 3.70 (s, 4H, $2CH_2$), 4.00 (s, 4H, $2CH_2$), 6.45 (s, 2H, 2CH), 7.05 (s, 2H, 2CH), 7.10–7.20 (m, 4H, 4 pyrrole-H), 7.80 (s, 2H, 2 pyrrole-H), 11.80–12.05 (m, 8H, 8NH). ^{1}H NMR ($CDCl_3$/TFA-*d*, 9:1 (v/v), 300 MHz) (ppm) δ: 1.10 (t, *J* = 7.5 Hz, 6H, $2CH_3CH_2$), 2.00 (s, 6H, 2 CH_3), 2.25 (s, 6H, 2 CH_3), 2.28 (s, 6H, 2 CH_3), 2.50 (q, *J* = 7.5 Hz, 4H, $2CH_3CH_2$), 2.60 (s, 6H, 2 CH_3), 2.70 (s, 6H, 2 CH_3), 3.60 (s, 2 H, -CH_2-Bridge-), 4.40 (s, 4H, 2 CH_2 -Bridge-), 6.50 (s, 2H, 2 pyrrolyl-H), 7.00–7.30 (m, 8H, 4 -CH=, 4 pyrrolyl-H), 11.80–12.30 (m, 8H, 8 NH). ^{13}C NMR ($CDCl_3$/TFA-*d*, 9:1 (v/v), 75 MHz) (ppm) δ: 8.60 (CH_3), 9.86 (CH_3), 10.14 (CH_3), 12.83 (CH_3), 13.37 (CH_3), 14.10 (CH_3), 17.08 (CH_2), 21.75 (CH_2), 25.18(CH_2), 115.48, 124.12, 124.86, 126.60, 127.63, 127.85, 128.01, 129.73, 131.77, 132.49, 134.90, 144.69, 145.71, 147.68, 149.36, 150.01, 154.90 (C=N), 162.98 (C=N). FAB-MS *m/z*: 809 ([M^+ + 1]). HR-MS (LSIMS: matrix: thioglycerol) for $C_{53}H_{61}N_8$ calcd.: 809.50192, found: 809.50203. UV–Vis (CH_2Cl_2) (nm): $\lambda_{max}(\varepsilon)$ = 538 (111 400), 504 (81 800), 444 (108 400). Anal. calcd. for $C_{53}H_{60}N_8{\cdot}4HBr{\cdot}0.5H_2O$: C 54.97, H 5.62, N 9.68; found: C 55.16, H 5.83, N 9.36.

Octapyrrin tetrahydrobromide salts (10)

Yield 91%; mp 310°C (dec.). UV–Vis (CH_2Cl_2) (nm): $\lambda_{max}(\varepsilon)$ = 555 (71 200), 499 (107 900), 445 (88 300), 380 (27 300). ^{1}H NMR ($CDCl_3$/TFA-*d*, 9:1 (v/v), 200 MHz) (ppm) δ: 1.05 (t, *J* = 7.35 Hz, 6H, $2CH_3$), 2.05 (s, 6H, $2CH_3$), 2.20 (s, 6H, $2CH_3$), 2.30 (s, 6H, $2CH_3$), 2.35 (s, 6H, $2CH_3$), 2.45 (q, *J* = 7.35 Hz, 4H, CH_2), 3.60 (s, 6H, $2CH_3$), 4.50 (s, 4H, $2CH_2$), 4.80 (s, 2H, CH_2), 7.20 (m, 8H, 4 pyrrole-H, 4 -CH=), 11.80–12.00 (m, 8H, 8 NH). ^{1}H NMR ($CDCl_3$/TFA-*d*, 9:1 (v/v), 300 MHz) (ppm) δ: 0.95 (m, 12H, 4 CH_3CH_2), 2.05 (s, 6H, 2 CH_3), 2.25 (s, 6H, 2 CH_3), 2.33 (s, 6H, 2 CH_3), 2.40 (s, 6H, 2 CH_3), 2.45 (m, 8 H, 4 CH_3CH_2), 4.50 (s, 4H, 2 -CH_2-bridge), 4.70 (s, 2H, -CH_2-bridge), 7.22 (s, 2H, 2 pyrrolyl-H), 7.35 (s, 2H, 2 pyrrolyl-H), 7.45 (s, 4H, 4 –CH=), 11.80–12.00 (m, 8H, 8 NH). ^{13}C NMR ($CDCl_3$/TFA-*d*, 9:1 (v/v), 75 MHz) (ppm) δ: 8.60 (CH_3), 9.97 (CH_3), 9.99 (CH_3), 10.13 (CH_3), 13.44 (CH_3), 13.83 (CH_3), 13.97 (CH_3), 17.07 (CH_2), 17.33 (CH_2), 24.88 (-CH_2-bridge), 25.78 (CH_2-bridge), 119.96, 121.99, 124.45, 124.92, 127.74, 127.80, 128.05, 128.24, 129.87, 131.31, 144.78, 145.20, 145.33, 147.45, 148.46, 148. 88, 150.84 (C=N), 162.36 (C=N). FAB-MS *m/z*: 865 ([M^+ + 1]), 665, 439. HR-MS (LSIMS, matrix: thioglycerol) for $C_{57}H_{69}N_8$ calcd.: 865.56452; found: 865.56457. Anal. calcd. for $C_{57}H_{68}N_8{\cdot}4HBr$: C 57.59, H 6.10, N 9.43; found: C 57.43, H 6.31, N 9.21.

5-*tert*-Butoxycarbonyl-3,4-dimethyl-5′-formyl-4′-ethyl-3′-methyl-2,2′-dipyrromethane (12)

Method A

A 250 mL three-necked, round-bottomed flask equipped with a magnetic stirrer bar and a nitrogen inlet was charged with 5-acetoxymethyl-3,4-dimethyl-2-*tert*-butoxycarbonylpyrrole (3.44 g, 12.5 mmol) and acetic acid (100 mL). Nitrogen was bubbled through the solution with stirring, and after 20 min 2-formyl-3-ethyl-4-methylpyrrole (1.71 g, 12.5 mmol, 1.0 mol equiv) was added. The reaction mixture was stirred at 50°C overnight. The solvent was removed under vacuum (rotovapor). The residue was taken up in dichloromethane (200 mL) and washed successively with water (2 × 100 mL), aqueous saturated sodium bicarbonate (2 × 100 mL), and saturated brine (100 ml). After drying over anhydrous sodium sulfate and removing solvent (rotovapor), the solid was crystallized from dichloromethane–hexane, yielding 0.85 g (20%).

Method B

A 250 mL three-necked, round-bottomed flask equipped with a magnetic stirrer, nitrogen inlet, and a reflux condenser was charged with 5-acetoxymethyl-3,4-dimethyl-2-*tert*-butoxycarbonylpyrrole (1.94 g, 7.30 mmol), 4-methyl-3-ethyl-2-formylpyrrole (1.0 g, 7.30 mmol, 1.0 mol equiv), and dichloromethane (150 mL). The mixture was stirred at room temperature for 30 min while nitrogen was bubbled through the solution. *p*-Toluenesulfonic acid monohydrate (150 mg) was then added in one portion. The solution turned yellow-red immediately. The mixture was stirred under reflux for 30 min. TLC showed the reaction was complete (CH_2Cl_2, 5-acetoxymethylpyrrole R_f = 0.4, product R_f = 0.5, and pyrrole R_f = 0.9). The product dipyrromethane turned red, the pyrrole turned brown-black, and the starting 5-actoxymethylpyrrole remained unchanged upon contacting the TLC plate over bromine vapor. After cooling to room temperature, triethylamine (1 mL) in methanol (5 mL) was added to neutralize the acid. Solvent was completely removed under vacuum (first rotovapor, then high vacuum). The yellow semi-solid was mixed with aqueous methanol (90%, 30 mL) and ultrasonicated to aid solidification. The suspension was kept at 0°C for 4 h. The solid was collected by suction filtration to yield the product (1.80 g, 72%), mp 189–191°C. ^{1}H NMR (200 MHz, $CDCl_3$) (ppm) δ: 1.02 (t, *J* = 7.32 Hz, 3H, CH_3), 1.45 (s, 9H, 3 CH_3), 1.70 (s, 3H, CH_3), 1.75 (s, 3H, CH_3), 1.95 (s, 3H, CH_3), 2.50 (q, *J* = 7.32 Hz, 2H, CH_2), 3.80 (s, 2H, CH_2), 9.25 (s, 1H, CHO), 9.85 (s, 1H, NH), 10.80 (s, 1H, NH). ^{13}C NMR (50 MHz, $CDCl_3$) (ppm) δ: 8.85 (CH_3), 9.00 (CH_3), 10.67 (CH_3), 16.49 (CH_3), 17.35 (CH_2), 28.58 ($OC(CH_3)_3$), 80.18($OCMe_3$), 116.88, 117.35, 119.33, 126.22, 127.55, 127.99, 137.40, 140.53, 161.35 (COO), 176.49 (CHO). EI-MS *m/e* (%): 402 (2), 344 ([M]$^+$, 80), 288 (90), 271 (20), 259 (20), 244 (30), 149 (100). Anal calcd. for $C_{20}H_{28}N_2O_3$: C 69.74, H 8.19, N 8.13; found: C 69.26, H 8.27, N 7.94.

© 2002 NRC Canada

Pentapyrrole (13)

Starting tripyrrole (**4**) (300 mg, 0.61 mmol) was suspended in trifluoroacetic acid (10 mL) and stirred at room temperature for 10 min until all the solid had dissolved. A solution of 5-*tert*-butoxycarbonyl-3,4-dimethyl-5′-formyl-4-ethyl-3-methyl-2,2′-dipyrromethane (**12**) (211 mg, 0.61 mmol, 1.0 mol equiv) in dichloromethane (20 mL) was added to the brown-red solution under continuous stirring. After 10 min, a mixture of methanol (20 mL) and hydrogen bromide (2 mL, 48% in acetic acid) was added. The red mixture was allowed to stir for 3 h at room temperature. Anhydrous ether (100 mL) was then added and the suspension was stirred for another 30 min. The red solid was collected by suction filtration and washed with anhydrous ether to afford the product (450 mg, 93%); mp 252°C (dec.). UV–Vis (CH_2Cl_2) (nm): $\lambda_{max}(\varepsilon)$ = 525 (71 800), 447 (62 800). ^{1}H NMR ($CDCl_3$, 200 MHz) (ppm) δ: 0.95 (t, *J* = 7.35 Hz, 3H, CH_3), 1.00 (t, *J* = 7.35 Hz, 3H, CH_3), 1.50 (s, 9H, 3 CH_3), 1.80 (s, 6H, 2 CH_3), 2.20 (m, 9H, 3 CH_3), 2.40 (s, 6H, 2 CH_3), 2.60 (q, *J* = 7.32 Hz, 2H, -CH_2-), 3.40 (q, *J* = 7.32 Hz, 2H, -CH_2-), 4.20 (s, 2H, -CH_2-), 4.80 (s, 2H, -CH_2-), 6.80 (s, 2H, 2 –CH=), 6.90 (s, 2H, 2 pyrrole-H), 7.20 (m, 2H, 2 pyrrole-H), 10.40 (s, 1H, NH), 13.20 (s, 2H, 2 NH), 13.40 (s, 2H, 2 NH). FAB-MS *m*/*z*: 634 ([M^+ + 1]), 425, 199. HR-MS (LSIMS, matrix: thioglycerol) for $C_{40}H_{52}N_5O_2$, calcd.: 634.41210; found: 634.41180. Anal calcd. for $C_{40}H_{51}N_5O_2{\cdot}2HBr{\cdot}H_2O$: C 59.04, H 6.84, N 8.61, Br 19.64; found: C 58.89, H 6.64, N 8.66, Br 19.30.

General procedure for 15–18

The pentapyrrole (**13**, 100 mg, 0.125 mmol) was suspended in trifluoroacetic acid (5 mL) and stirred at room temperature for 10 min until all the solid had dissolved. To this brown-red solution was added a solution of **5**, **6**, **7**, or **14** (0.0625 mmol, 0.5 mol equiv) in dichloromethane (20 mL) under continuous stirring. After 10 min, a mixture of methanol (20 mL) and hydrogen bromide (2 mL, 48% in acetic acid) was added. The red mixture was stirred for 3 h at room temperature. Anhydrous ether (100 mL) was added and the suspension was allowed to stir for another 30 min. The red solid was collected by suction filtration and washed by anhydrous ether containing a few drops of HBr (48% in acetic acid) to afford the expected product. An analytic sample was obtained by repeating the following procedure three times: the crude product (~20 mg) was dissolved in dichloromethane (1 mL), and methanol (1 mL) containing a few drops of HBr (48% in acetic acid) was added, followed by the addition of anhydrous ether to precipitate the product. The red solid was collected by suction filtration.

Dodecapyrrin hexahydrogen bromide salt (15)

Yield 41%, mp 300°C (dec.). UV–Vis (CH_2Cl_2) (nm): $\lambda_{max}(\varepsilon)$ = 565 (211 100), 543 (209 100), 494 (142 700), 448 (142 700), 376 (47 900). ^{1}H NMR ($CDCl_3$/TFA-*d*, 9:1 (v/v), 200 MHz) (ppm) δ: 0.90 (br s, 6H, 2CH_3), 1.40 (br s, 6H, 2CH_3), 1.80 (s, 12H, 4 CH_3), 2.00 (s, 12H, 4 CH_3), 2.40 (m, 26H, 6 CH_3, 4 CH_2), 2.60 (m, 12H, 4 CH_3), 5.00 (s, 4H, 2 CH_2), 5.10 (s, 4H, 2 CH_2), 7.20 (m, 10H, 4 pyrrole-H, 6 -CH=), 13.20–13.40 (m, 12H, 12 NH). FAB-MS (matrix: 3-NBA) *m*/*z*: 1308 ([M^+ + 2]). HR-MS (LSIMS, thioglycerol) for $C_{84}H_{99}N_{12}S$ calcd.: 1307.78364; found: 1307.78342. Anal calcd. for $C_{84}H_{98}N_{12}S{\cdot}6HBr$: C 56.25, H 5.80, N 9.37; found: C 56.87, H 6.07, N 9.00.

Dodecapyrrin hexahydrobromide salt (16)

Yield 45%, mp 280°C (dec.). ^{1}H NMR ($CDCl_3$/TFA-*d*, 9:1 (v/v), 200 MHz) (ppm) δ: 0.95 (t, *J* = 7.6 Hz, 6H, 2CH_3), 1.05 (t, *J* = 7.6 Hz, 6H, 2CH_3), 1.60 (s, 6H, 2 CH_3), 1.90 (s, 6H, 2 CH_3), 2.20 (m, 26H, 6 CH_3, 4 CH_2), 2.60 (m, 18H, 6 CH_3), 3.40 (s, 2H, -CH_2-bridge), 4.9–5.10 (m, 4H, 2 -CH_2-bridge), 7.30 (m, 12H, 6 pyrrole-H, 6 -CH=), 13.20–13.40 (m, 12H, 12 NH). LSIMS (matrix: thioglycerol) *m*/*z*: 1262 ([M^+ + 2]), 1064. HR-MS (LSIMS, thioglycerol) for $C_{83}H_{97}N_{12}$ calcd.: 1261.78809; found: 1261.79638. UV–Vis (CH_2Cl_2) (nm): $\lambda_{max}(\varepsilon)$ = 554 (258 000), 486 (242 000), 442 (173 700), 369 (57 000). Anal. calcd. for $C_{87}H_{106}N_{12}{\cdot}6HBr{\cdot}H_2O$: C 56.46, H 5.90, N 9.52; found: C 56.32, H 6.09, N 9.11.

Dodecapyrrin hexahydrobromide salt (17)

Yield 56%, mp 288°C (dec.). UV–Vis (CH_2Cl_2) (nm): $\lambda_{max}(\varepsilon)$ = 569 (70 800), 539 (72 500), 498 (63 700), 450 (53 800), 377 (32 000). ^{1}H NMR ($CDCl_3$/TFA-*d*, 9:1 (v/v), 200 MHz) (ppm) δ: 0.85 (t, *J* = 7.35 Hz, 6H, 2CH_3), 1.05 (t, *J* = 7.35 Hz, 6H, 2CH_3), 1.20 (t, *J* = 7.35 Hz, 6H, 2CH_3), 2.00 (m, 18H, 6 CH_3), 2.30 (m, 26H, 6 CH_3, 4 CH_2), 2.60 (m, 10H, 2 CH_3, 2 CH_2), 4.50–4.80 (m, 10H, 5 CH_2), 7.30 (m, 10H, 4 pyrrole-H, 6 -CH=), 12.00–12.40 (m, 12H, 12 NH). FAB-MS (matrix: 3-NBA) *m*/*z*: 1558 ([M^+ + 3HBr]), 1399 ([M^+ + HBr]), 1318 ([M^+ + 2]), 1119, 878, 651, 465. HR-MS (LSIMS, thioglycerol) for $C_{87}H_{106}N_{12}$ calcd.: 1318.86634; found: 1318.86809. Anal calcd. for $C_{87}H_{106}N_{12}{\cdot}6HBr$: C 57.59, H 6.15, N 9.32, Br 26.60; found: C 57.61, H 6.00, N 9.07, Br 26.30.

Dodecapyrrin hexahydrobromide salt (18)

Yield 47%, mp 320°C (dec.). UV–Vis (CH_2Cl_2) (nm): $\lambda_{max}(\varepsilon)$ = 585 (88 900), 515 (137 000), 475 (113 000), 446 (114 300). ^{1}H NMR ($CDCl_3$/TFA-*d*, 9:1 (v/v), 200 MHz) (ppm) δ: 0.95 (t, *J* = 7.6 Hz, 6H, 2CH_3), 1.20 (t, *J* = 7.6 Hz, 6H, 2 CH_3), 2.00 (s, 6H, 2 CH_3), 2.05 (s, 6H, 2 CH_3), 2.10 (s, 6H, 2 CH_3), 2.20 (s, 6H, 2 CH_3), 2.30 (s, 6H, 2 CH_3), 2.36 (s, 6H, 2 CH_3), 2.40 (q, *J* = 7.6 Hz, 2H, CH_2), 2.50 (s, 6H, 2 CH_3), 2.60 (q, *J* = 7.6 Hz, 2H, CH_2), 4.60 (s, 2H, CH_2), 4.70 (s, 2H, CH_2), 7.20 (m, 14H, 8 pyrrole-H, 6 -CH=), 12.00–12.40 (m, 12H, 12 NH). LSIMS (matrix: thioglycerol) *m*/*z*: 1219 ([M^+ + 1]). HR-MS (LSIMS, thioglycerol) for $C_{80}H_{90}N_{12}$ calcd.: 1218.74114; found: 1218.74182. Anal calcd. for $C_{80}H_{90}N_{12}{\cdot}6HBr{\cdot}2H_2O$: C 55.17, H 5.75, N 9.65; found: C 55.19, H 5.86, N 9.16.

Conclusion

In summary, we have developed a fast, highly efficient synthetic methodology that appears to be of versatile utility in terms of allowing for the construction of linear polypyrromethenes. The resulting compounds are stable and exist as the corresponding hydrobromide salts. Self-assembly of those novel ligands with transition metal ions is currently being studied.

© 2002 NRC Canada

Acknowledgment

This work was supported by Natural Sciences and Engineering Council of Canada (NSERC).

References

1. (*a*) D. Dolphin (*Editor*). The porphyrins. Vol. 2B. Academic Press, London. 1978; (*b*) A. Jasat and D. Dolphin. Chem. Rev. **97**, 2267 (1997); (*c*) E.D. Sternberg, D. Dolphin, and C. Bruckner. Tetrahedron, **54**, 4151 (1998); (*d*) T.P. Wijesekera, and D. Dolphin. *In* Metalloporphyrins in catalytic oxidations. *Edited by* R.A. Sheldon. Marcel Dekker Inc., New York. 1994. pp. 193–239; (*e*) J.L. Sessler and S.J. Weghorn. Expanded, contracted, & isomeric porphyrins. Pergamon Press, Oxford, U.K. 1997; (*f*) H. Falk and Q. Chen. Monatsh. Chem. **127**, 69 (1996).
2. (*a*) H. Falk. The chemistry of linear oligopyrroles and bile pigments. Springer-Verlag, New York and Wien. 1989; (*b*) A.F. McDonagh. Bile pigments: Bilatrienes and 5,15-biladienes. *In* The porphyrins. Vol. VI. *Edited by* D. Dolphin. Academic Press, New York. 1979. pp. 293; (*c*) A. Gossauer and J. Engel. Linear polypyrrolic compound. *In* The porphyrins. Vol. 2. *Edited by* D. Dolphin. Academic Press, New York. 1979. p. 197.
3. (*a*) Q. Chen, M.T. Huggins, D.A. Lightner, W. Norona, and A.F. McDonagh. J. Am. Chem. Soc. **121**, 9253 (1999); (*b*) Q. Chen and D.A. Lightner. J. Org. Chem. **63**, 2665 (1998); (*c*) Q. Chen, B. Chen, and X. Li. Synth. Commun. **30**, 383 (2000); (*d*) Q. Chen, X. Li, and B. Chen. Synth. Commun. **28**, 3359 (1998).
4. (*a*) Y. Zhang, A. Thompson, S.J. Rettig, and D. Dolphin. J. Am. Chem. Soc. **120**, 13 537 (1998); (*b*) A. Thompson, S.J. Rettig, and D. Dolphin. J. Chem. Soc. Chem. Comm. 631 (1999); (*c*) A. Thompson and D. Dolphin. Org. Lett. **2**, 1315 (2000); (*d*) A. Thompson and D. Dolphin. J. Org. Chem. **65**, 78 870 (2000).
5. (*a*) C. Bruckner, Y. Zhang, S.J. Rettig, and D. Dolphin. Inorg. Chim. Acta, **263**, 279 (1997); (*b*) E.C. Taylor and R.A. Jones (*Editors*). Pyrroles. John Wiley & Sons, New York. 1990; (*c*) A. Jauma, J.A. Farrera, and J.M. Ribo. Monatsh. Chem. **127**, 927 (1996); (*d*) E.T. Clarke, P.J. Squattrito, P.R. Rudole, R.R. Motekaitis, A.E. Matrell, and A. Clearfield. Inorg. Chim. Acta. **166**, 221 (1989); (*e*) D. Eichinger and H. Falk. Monatsh. Chem. **118**, 91 (1987).
6. (*a*) G. Struckmeier, U. Thewalt, and J.-H. Fuhrhop. J. Am. Chem. Soc. **98**, 278 (1976); (*b*) W.S. Sheldrick and J. Engel. J. Chem. Soc. Chem. Commun. 5 (1980).
7. (*a*). K. Wärnmark, P.N.W. Baxter, and J.-M. Lehn. J. Chem. Soc. Chem. Commun. 993 (1998); (*b*) I. Weissbuch, P.N.W. Baxter, S. Cohen, H. Cohen, K. Kjaer, P.B. Howes, J. Als-Nielsen, G.S. Hanan, U.S. Schubert, J.-M. Lehn, L. Leiserowitz, and M. Lahav. J. Am. Chem. Soc. **120**, 4850 (1998); (*c*). A.M. Garcia, F.J. Romero-Salguero, D.M. Bassani, J.-M. Lehn, G. Baum, and D. Fenske. Chem. Eur. J. **5**, 1803 (1999).
8. (*a*) J.-M. Lehn and A. Rigault. Angew. Chem. Int. Ed. Engl. **27**, 1095 (1988); (*b*) P.N.W. Baxter, G.S. Hanan, and J.-M. Lehn. J. Chem. Soc. Chem. Commun. 2019 (1996); A.M. Garcia, D.M. Bassani, J.-M. Lehn, G. Baum, and D. Fenske. Chem. Eur. J. **5**, 1234 (1999); (*c*) D.P. Funeriu, J.-M. Lehn, G. Baum, and D. Fenske. Chem. Eur. J. **3**, 99 (1997).
9. (*a*) D.H. Dolphin, Ph.D. Thesis. The University of Nottingham, Nottingham, U.K. 1965; (*b*) D. Dolphin, R.L.N. Harris, J.L. Huppatz, A.W. Johnson, I.T. Kay, and J. Leng. J. Chem. Soc. C, 98 (1966); (*c*) D. Dolphin, R.L.N. Harris, J.L. Huppatz, A.W. Johnson, and I.T. Kay. J. Chem. Soc. C, 30 (1966).
10. (*a*) G. Struckmeier, U. Thewalt, J.H. Fuhrhop. J. Am. Chem. Soc. **98**, 278 (1976); (*b*) W.S. Sheldrick and J. Engle. J. Chem. Soc. Chem. Commun. 5 (1980).
11. (*a*) P. Morosini, M. Scherer, S. Meyer, L. Vynch, S.J. Lessler. J. Org. Chem. **62**, 8848 (1997); (*b*) M.J. Kogan. J. Hereocycl. Chem. **35**, 907 (1998); (*c*) K.M. Valasinas and B. Frydman. Tetrahedron Lett. **37**, 763 (1996); (*d*). G.B. Maravin, A.Y. Tauber, and A.F. Mironov. Synlett, 355 (1993); (*e*) K. Okada, H. Takakura, K. Nomura, and K. Saburi. Tetrahedron Lett. **41**, 2915 (2000).
12. K.M. Smith and R.K. Pandey. J. Heterocycl. Chem. **20**, 1383 (1983).
13. J.B. Paine III, R.B. Woodward, and D. Dolphin. J. Org. Chem. **41**, 2826 (1976).
14. K.M. Smith, E.M. Fujinari, R.K. Pandey, and H.D. Tabba. J. Org. Chem. **51**, 4667 (1986).
15. Y.S. Byun and D.A. Lightner. J. Heterocycl. Chem. **28**, 1683 (1991).
16. J.B. Paine III and D. Dolphin. J. Org. Chem. **53**, 2787 (1988).

© 2002 NRC Canada

Kinetics and mechanism of the oxidation of disaccharides by Cr^{VI}

Viviana Roldán, Juan Carlos González, Mabel Santoro, Silvia García, Nieves Casado, Silvina Olivera, Juan Carlos Boggio, Juan Manuel Salas-Peregrin, Sandra Signorella, and Luis F. Sala

Abstract: The oxidation of D-lactose, D-maltose, D-melibiose, and D-cellobiose by Cr^{VI} yields the corresponding aldobionic acid and Cr^{3+} as final products when an excess of reducing disaccharide over Cr^{VI} is used. The rate law for the Cr^{VI} oxidation reaction is expressed by $-d[Cr^{VI}]/dt = k_H$ [disaccharide][Cr^{VI}], where the second-order kinetic constant, k_H, depends on [H^+]. The relative reactivity of the disaccharides with Cr^{VI} is expressed as follows: Mel > Lac > Cel > Mal, at 33°C. In acid medium, intermediate Cr^V forms and reacts with the substrate faster than Cr^{VI}. The EPR spectra show that five- and six-coordinate oxo-Cr^V intermediates are formed, with the disaccharide acting as bidentate ligand. Five-coordinate oxo-Cr^V species are present at any [H^+], whereas six-coordinate ones are observed only at pH < 2, where they rapidly decompose to the redox products. In the pH 3–7 range, where hexa-coordinate oxo-Cr^V species are not observed, Cr^V complexes are stable enough to remain in solution from several days to several months.

Key words: chromium, saccharides, kinetics, EPR.

Résumé : Lorsqu'on utilise un excès de du disaccharide réducteur par rapport au Cr(VI), l'oxydation du D-lactose, du D-maltose, du D-melibiose et du D-cellobiose par le Cr(VI) conduit à la formation de l'acide aldobionique correspondant et de Cr^{3+} comme produits finaux. La constante de vitesse de la réaction pour la réaction d'oxydation par le Cr(VI) peut être exprimée par l'équation $-d[Cr(VI)]/dt = k_H$ [disaccharide] [Cr(VI)], dans laquelle la constante cinétique du deuxième ordre, k_H, dépend de [H^+]; à 33°C, les réactivités relatives des disaccharides vis-à-vis du Cr(VI) sont les suivantes: Mel > Lac > Cel > Mal. En milieu acide, il se forme du Cr(V) comme intermédiaire qui réagit avec le substrat plus rapidement que le Cr(VI). Les spectres de RPE montrent qu'il se forme des intermédiaires penta- et hexacoordinés d'oxo-Cr(V) dans lesquels le disaccharide agit comme ligand bidentate. Les espèces pentacoordinées oxo-Cr(V) sont présentes à toutes les [H^+] alors qu'on n'observe les espèces hexacoordinées qu'à des pH < 2 et que dans ces conditions elles se décomposent rapidement en produits d'oxydoréduction. À des pH allant de 3 à 7 où on n'observe pas de formation des espèces hexacoordinées d'oxo-Cr(V), les complexes de Cr(V) sont suffisamment stables pour être observés en solution pour des périodes allant de plusieurs jours à plusieurs mois.

Mots clés : chrome, disaccharides, cinétique, RPE.

[Traduit par la Rédaction]

Introduction

Compounds of Cr^{VI} represent a potential environmental hazard because of their mammalian carcinogenicity and toxicity (1, 2), and they are known to bioaccumulate in flora and fauna, creating ecological problems (3–5). The observation of Cr^V and Cr^{IV} intermediates in the selective oxidation of organic substrates by Cr^{VI} and their implication in the mechanism of Cr-induced cancers (1, 6–7) has generated a considerable amount of interest in their chemistry and biochemistry (8–10).

The major coordination sites involved in Cr binding are hydroxo, alcoholato, carboxylato, and thiolato donor groups (2, 11–12). Five-membered, *O*-donor, chelate ligands, such as 1,2-diols and 2-hydroxy acids, are effective as non-enzymatic reductants (at low pH values) and chelates for high oxidation states of Cr (13–19). Carbohydrates constitute 5–20% (average 10%) of soil organic matter, and they

Received 7 June 2002. Published on the NRC Research Press Web site at http://canjchem.nrc.ca on 20 December 2002.

V. Roldán. Departamento de Ciencias Básicas, Facultad de Ciencias Veterinarias, UNL, R.P. Kreder 735, Esperanza, Argentina.
J.C. González, M. Santoro, S. Garcia, S. Olivera, S. Signorella,[1] and L.F. Sala.[2] Departamento de Química, Facultad de Ciencias Bioquímicas y Farmacéuticas, UNR, Suipacha 531, 2000 Rosario, Argentina.
N. Casado. Instituto de Desarrollo Tecnológico para la Industria Química, Güemes 3450, 3000 Santa Fe, Argentina.
J.C. Boggio. Departamento de Farmacología y Toxicología, Facultad de Ciencias Veterinarias, UNL, R.P. Kreder 735, Esperanza, Argentina.
J.M. Salas-Peregrin. Departamento de Química Inorgánica, Facultad de Ciencias, Universidad de Granada, Fuentenueva s/n, 18071 Granada, España.

[1]Corresponding author (e-mail: signorel@infovia.com.ar).
[2]Corresponding author (e-mail: inquibir@satlink.com).

 DOI: 10.1139/V02-187 © 2002 NRC Canada

constitute more than 50% of dry matter in plants (20). For this reason, it is interesting to examine the ability of saccharides and their derivatives to reduce or stabilize high oxidation states of Cr, to understand their potential roles in the biochemistry of Cr.

We are studying the possible fate of Cr^{VI} and Cr^{V} in biological systems by examining reactions of Cr^{VI} with low-molecular-weight molecules (21–37). Our studies on the reduction of Cr^{VI} and the intermediate Cr^{V} by aldoses (21–26), deoxyaldoses (27–28), sugar acids (31, 32, 35), and methyl glycosides (29–30) showed that the relative redox reactivities of these saccharides toward chromate are based on the relative rates of the oxidation vs. complexation processes. In view of some preliminary results obtained on the milk–Cr^{VI} system suggesting the formation of long lived lactose–Cr^{V} species generated by direct reaction of Cr^{VI} with lactose (5), we decided to evaluate the kinetics of the reaction of Cr^{VI} with four disaccharides: D-lactose (Lac), D-maltose (Mal), D-cellobiose (Cel), and D-melibiose (Mel), to determine the influence of the glycoside moiety attached to the C^6 or C^4 of glucose (glc) on the chelating and (or) redox reactivity of the saccharide with high oxidation states of chromium.

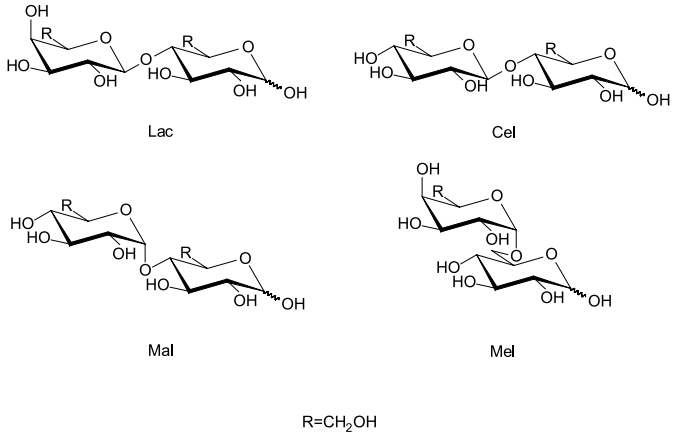

Lac, the most important representative of the β-galactosides, is found in the milk of all mammals up to a concentration of approximately 5% and in some plants in low concentrations. Mal is a product of enzymatic hydrolysis of starch; Mel is a constituent of the trisaccharide raffinose; and Cel is the basic repeating unit of cellulose and lichetin (38). In this work, we study the Cr^{VI} oxidation of these four disaccharides and provide information on the mechanism of oxidation as well as on the structure and stability of the Cr^{V} species formed as redox intermediates.

Experimental

Materials

D-Lactose monohydrate (Anedra, RA-ACS grade), D-maltose monohydrate (Sigma grade, 99%, less than 1.0% of maltotriose and less than 0.3% of D-glucose), D-melibiose

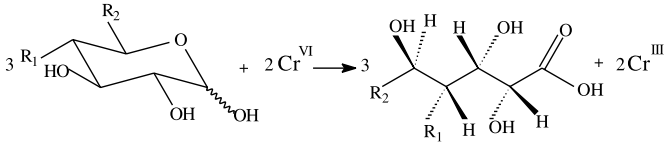

$R_1 = C_6H_{11}O_6$ (Lac, Cel, Mal)
CH_2OH (Mel)

$R_2 = CH_2OH$ (Lac, Cel, Mal)
$C_6H_{11}O_6$ (Mel)

(Sigma grade), D-cellobiose (Pfanshtiehl 99.9%), potassium dichromate (Cicarelli c.a.), potassium chromate (Aldrich grade), glutathione (Sigma grade), acrylonitrile (Aldrich grade), perchloric acid 70% (Merck P.A.), phosphoric acid (Anedra P.A.), and sulfuric acid (Merck P.A.) were used without further purification. Water was purified by deionisation, followed by double distillation from a potassium permanganate solution.

In experiments performed at constant ionic strength (I = 1.0 M) and in different hydrogen ion concentrations, mixtures of sodium perchlorate solutions and perchloric acid solutions were used. Sodium perchlorate solutions were prepared from sodium hydroxide and perchloric acid solutions. The concentration of stock solutions of perchloric acid was determined by titration using standard analytical methods.

The stability of the organic substrate under conditions used in the kinetic studies was tested by paper chromatography and HPLC at given hydrogen ion concentrations.

Caution: Cr^{VI} compounds are human carcinogens, and Cr^{V} complexes are mutagenic and potential carcinogens (39). Contact with skin and inhalation must be avoided. Acrylonitrile is a carcinogen and must be handled in a well-ventilated fume hood (40).

Spectrophotometric measurements

Kinetic measurements were performed by monitoring absorbance changes using a Jasco V-530 spectrophotometer with a fully thermostated cell compartment (±0.2°C). The reactions were followed under pseudo-first-order conditions, using an excess of disaccharide over Cr^{VI}. Reactant solutions were previously thermostated and transferred into a 1-cm pathlength cell immediately after mixing. Experiments were performed at 33°C unless otherwise stated.

The disappearance of Cr^{VI} was followed at 350 nm until at least 80% of the Cr^{VI} was consumed. In the kinetic measurements, the concentration of Cr^{VI} was kept constant at 8.0×10^{-4} M and the disaccharide concentration was varied from 0.08 to 0.36 M. Mixtures of sodium perchlorate and perchloric acid were used to maintain a constant ionic strength (I) of 1.0 M.

The observed pseudo-first-order rate constants (k_{obs}), determined from the slopes of plots of $\ln(A_{350} - A_8)$ vs. time, were averages of at least three determinations and were within ±5% of each other. The first-order dependence of the rate upon $[Cr^{VI}]$ was verified by calculating the k_{obs} values at various $[Cr^{VI}]_0$ ($4.0 \times 10^{-4} - 8.0 \times 10^{-4}$ M) at constant

© 2002 NRC Canada

Table 1. Observed pseudo-first-order rate constants (k_{obs})[a] for different concentrations of disaccharide in 0.2 M $HClO_4$.

	10^5 k_{obs} (s^{-1}) for							
	Lac		Mal		Cel		Mel	
[disaccharide] (M)	λ_{350}[b]	λ_{570}[c]	λ_{350}[b]	λ_{570}[c]	λ_{350}[b]	λ_{570}[c]	λ_{350}[b]	λ_{570}[c]
0.02	—	—	1.30(3)	1.28(3)	1.35(4)	—	—	—
0.04	—	—	2.42(5)	2.36(7)	3.34(1)	—	—	—
0.06	—	—	3.09(1)	2.98(7)	4.6(1)	—	—	—
0.08	7.35(9)	7.03(7)	4.35(1)	4.42(4)	6.36(6)	6.77(6)	10.2(5)	—
0.12	—	—	—	—	8.10(3)	8.5(2)	—	—
0.125	—	—	6.16(3)	6.07(5)	—	—	—	—
0.16	14.0(1)	13.9(6)	—	—	12.2(3)	12.1(2)	19.8(1)	19.0(1)
0.20	16.5(1)	16.0(3)	—	—	15.4(2)	—	25.0(2)	25.0(5)
0.24	19.2(1)	19.4(2)	—	—	17.0(3)	—	28.0(9)	28.6(6)
0.28	24.2(2)	22.8(1)	13.9(5)	—	20.7(5)	—	—	—
0.32	28.6(2)	27.0(3)	—	—	—	—	38.5(6)	38.8(2)
0.36	31.4(1)	31.6(6)	—	—	—	—	—	—
10^4 k_H (M^{-1} s^{-1})	8.6(1)	5.2(1)	7.4(1)	12.1(2)				

Note: T = 33°C; I = 1 M.
[a]Mean values from multiple determinations.
[b]$[Cr^{VI}]_0 = 8 \times 10^{-4}$ M.
[c]$[Cr^{VI}]_0 = 8 \times 10^{-3}$ M.

temperature, initial disaccharide concentration, acidity, and ionic strength.

The formation of Cr^{III} was monitored at 570 nm ($[Cr^{VI}]_o = 8.0 \times 10^{-3}$ M) in the presence of excess disaccharide (0.08 to 0.36 M) in 0.20 M $HClO_4$. Under these conditions, the first-order dependence of the rate upon $[Cr^{VI}]$ was verified and k_{obs} were obtained following the Cr^{III} growth at 570 nm. Initial reaction rates were obtained by fitting the time-dependent data for the absorbance at 570 nm to a polynomial expression (41) and calculating the slope of the tangent at time zero (r_i). First-order rate constants were calculated from these initial rates using the equation $-r_i/(A_o - A_f)$, with average values of the initial rate and calculated estimates of $(A_o - A_f)$. The results at 570 nm are in total agreement with those obtained at 350 nm (Table 1). At the end of the reaction, the two *d-d* bands ascribed to Cr^{III} were observed at λ_{max} = 410 nm (ε = 18 M^{-1} cm^{-1}) and λ_{max} = 570 nm (ε = 15 M^{-1} cm^{-1}). Both visible and UV spectral maxima and intensities are in close agreement with those observed for the $[Cr(H_2O)_6]^{3+}$ ion. These bands are attributable to the octahedral $^4A_{2g} \rightarrow {}^4T_{1g}$ and $^4A_{2g} \rightarrow {}^4T_{2g}$ transitions in O_h symmetry, and are distinctive of the free Cr^{III} aqua complex (42). However, in experiments performed at 20°C the reaction of Cr^{VI} with Lac (33:1 ratio, $[Cr^{VI}] = 12.7 \times 10^{-3}$ M) in 0.2 M $HClO_4$ affords two *d-d* bands at λ_{max} = 409 nm (ε = 26.8 M^{-1} cm^{-1}) and 574 nm (ε = 21.9 $M^{-1}cm^{-1}$) with higher absorbance than expected for $[Cr(OH_2)_6]^{3+}$. These two bands agree closely with those of the acid solutions of the Cr^{III} – aldobionic acid complex, which was independently prepared. The intensity of these *d-d* bands slowly decreases with time toward the two bands with the molar absorption coefficients corresponding to the $[Cr(H_2O)_6]^{3+}$ ion. This behaviour has been observed previously, i.e., when a Cr^{III} complex forms as the final redox product and then hydrolyses to the Cr^{3+} ion (29, 31, 43, 44). The hydrolysis of the Cr^{III} – aldobionic acid complex in 0.2 M $HClO_4$ precludes its separation, and consequently, its structural characterization. At pH > 2, where these kind of complexes are stable enough toward hydrolysis to be characterized (44, 45), the redox reaction between Cr^{VI} and the disaccharide is extremely slow at the temperature used in this work and does not reach completion, even after 1 year. The reaction of chromate with saccharides is completed in shorter periods only when the reaction is allowed to proceed under reflux (44, 45).

Chromate esters were investigated by UV–vis spectrophotometry in the 350–400 nm region in which these esters show characteristic absorption bands. Reactions were performed at pH 4.7, where the redox reaction is slow enough to enable the observation of the ester formation. The instruments were zeroed to both the reference and sample beams passing through matched cuvettes, both containing Cr^{VI} in H_2O at pH 4.7. The solution in the sample cell was replaced with the reaction solution containing 8×10^{-4} M Cr^{VI} and 0.12–0.32 M Lac at pH = 4.7, I = 1.0 M, and T = 33°C. Spectra obtained within 30 min after mixing revealed a distinctive absorption band at 377 nm.

The formation of Cr^{II} was examined by periodic scanning of solutions containing 0.21 M Lac and 0.016–0.09 mM Cr^{VI} in 0.1–0.2 M $HClO_4$ in the presence of dioxygen. Under aerobic conditions if Cr^{II} forms it rapidly converts to CrO_2^{2+}, which has characteristic absorption bands at 290 and 245 nm (33, 46) and can be detected at low $[Cr^{VI}]$. No new bands were detected at these wavelengths in the reaction of Cr^{VI} with Lac. The presence of Cr^{II} was also examined by carrying out experiments with Cr^{VI} and Lac in the presence of $[Co(NH_3)_5Cl]^{2+}$ (a Cr^{II} trapping agent) under anaerobic conditions (8, 47). A solution containing 0.3 M Lac, 4 mM Cr^{VI}, and 4 mM $[Co(NH_3)_5Cl]^{2+}$ in 0.2 M $HClO_4$, I = 1 M and T = 33°C, was left to react, and the Co^{II} content was analyzed after 10-fold dilution with concentrated HCl, centrifuging, and measuring the absorbance at 692 nm (the wavelength expected for the absorption band of $CoCl_4^{2-}$) in the supernatant. No Co^{II} was detected spectrophotometrically. These results suggest that the formation of Cr^{II} in the reaction of Cr^{VI} with Lac can be ruled out.

© 2002 NRC Canada

Product analysis

HPLC was employed to detect the reaction products under the conditions used in the kinetic measurements (excess disaccharide over Cr^{VI}). The chromatograms were obtained on a KNK-500A chromatograph provided with a 7125 HPLC pump. The effluent was monitored with refractive index (ERC-7522, ERMA INC) and UV (115 UV Gilson) detectors. The $[H^+]$ of the standard and the reaction mixture samples was adjusted to 0.1 or 0.2 M by addition of $HClO_4$, and then the samples were filtered through a 0.2 μm membrane prior to injection into the chromatographic system.

Standard solutions of the disaccharides and aldobionic acids were prepared individually in 0.10 M $HClO_4$ and chromatographed separately to determine the retention time of each sample. D-Maltobionic acid, D-cellobionic acid, and D-melibionic acid, used as standards, were synthesized according to the literature methods (48). The stability of the disaccharides and their respective acids was controlled by HPLC. Chromatograms registered after incubation of the standard samples in 0.2 M $HClO_4$ (the highest $[H^+]$ used in the kinetic measurements) at 34°C over 48 h were identical to those of freshly prepared samples.

Experimental conditions and retention times for the disaccharides and oxidation products are given as supplementary material.[3]

EPR measurements

The EPR spectra were obtained on a Bruker ESP 300 E spectrometer. The microwave frequency was generated with a Bruker 04 ER (9–10 GHz) and measured with a Racal-Dana frequency meter. The magnetic field was measured with a Bruker NMR-probe gaussmeter. All of the EPR experiments were carried out at 20°C. Reactions were carried out by direct reaction of $K_2Cr_2O_7$ with 16- to 33-times excess disaccharide at a given pH or by addition of Na_2CrO_4 (8.3 mM) + glutathione (8.3 mM) to solutions of disaccharide (83 mM) at pH 5.0 and 20 ± 1°C.

EPR spectra were simulated using the program PEST WinSIM (49) with 100% Lorentzian lineshapes. The spectral parameters for each Cr^V species were consistent within all simulations, with maximum deviations between g_{iso} values being ±0.0001 units. In the simulations, values for ^1H a_{iso} were included only where the ^1H a_{iso} value was greater than the LW (line width) of the Cr^V species, since the signal is not significantly affected where the ^1H a_{iso} value is ≤LW.

Polymerization test

The presence of free radicals in the reactions of all of the disaccharides with Cr^{VI} was tested by the acrylonitrile polymerization test. In a typical experiment, acrylonitrile in 0.2 M $HClO_4$ (0.5 mL) at 33°C was added to a solution of 2.66×10^{-3} M $K_2Cr_2O_7$ and 0.04 M disaccharide in 0.2 M $HClO_4$ (2.0 mL). After a few minutes a white precipitate appeared. Control experiments (without $K_2Cr_2O_7$ or reductant present) did not show the formation of a precipitate. Possible reactions of Cr^V and Cr^{IV} with acrylonitrile were tested with $Na[Cr^VO(ehba)_2]$ (50) and $[Cr^{IV}O(ehba)_2]$ (ehba = 2-ethyl-2-hydroxybutanoic acid); the latter was generated in solution according to the literature method (51). No precipitation occurred on mixing the Cr^V or Cr^{IV} complexes with acrylonitrile under the same conditions as those used in the Cr^{VI} + disaccharide reactions.

Fig. 1. Effect of [disaccharide] on k_{obs} at 33°C and 0.20 M $HClO_4$. Inset: Effect of acidity on k_H, for Lac.

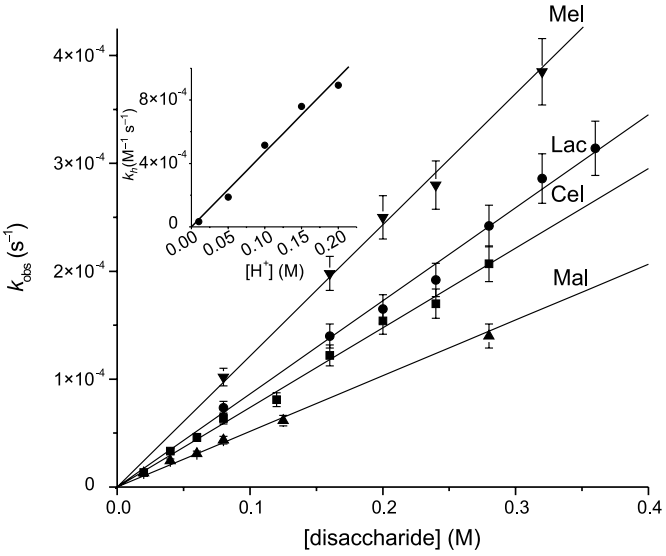

Results

Cr^{VI} oxidation of disaccharides

Over the whole range of perchloric acid concentrations used in the kinetic measurements, UV–vis studies showed that the reaction of each of the studied disaccharides with Cr^{VI} resulted in an absorbance band at 350 nm and a shoulder at 420–500 nm, characteristic of Cr^{VI} in acidic medium. At 350 nm a monotonic decrease in absorbance was observed and it could be described by a single exponential decay. Table 1 summarizes the values of the pseudo-first-order rate constants (k_{obs}), calculated from the slopes of the $\ln(A_{350} - A_8)$ vs. time data, for various concentrations of Lac, Mal, Cel, and Mel, in 0.20 M $HClO_4$. In every case, plots of k_{obs} vs. [disaccharide] show a first-order dependence on [disaccharide] (Fig. 1), and the values of the second-order rate constants (k_H) were determined from the slopes of the straight lines (Table 1, bottom). Consequently, at constant $[HClO_4]$, the rate law is expressed as:

$$[1] \qquad -d[Cr^{VI}]/dt = k_{obs}\,[Cr^{VI}]_T = k_H\,[\text{disaccharide}]\,[Cr^{VI}]$$

where $[Cr^{VI}]_T$ refers to the total Cr^{VI} concentration. For Lac, k_H shows first-order dependence with $[HClO_4]$ (inset of Fig. 1), which may be expressed as $k_H = k\,[H^+]$, with $k = 0.0047(1)$ M^{-2} s^{-1}.

As expected on the basis of the rate law, $-d(\ln[Cr^{VI}])/dt = k_{obs}$, where $k_{obs} = f([\text{saccharide}][H^+])$; k_{obs} was essentially constant with increasing $[Cr^{VI}]_0$.

[3] Supplementary data may be purchased from the Depository of Unpublished Data, Document Delivery, CISTI, National Research Council Canada, Ottawa, ON K1A 0S2, Canada (http://www.nrc.ca/cisti/irm/unpub_e.shtml for information on ordering electronically).

© 2002 NRC Canada

Fig. 2. Time evolution of the UV–vis spectrum of a mixture of Lac (0.32 M) and Cr^{VI} (8×10^{-3} M). [$HClO_4$] = 0.20 M; T = 33°C, I = 1.0 M over a period of ca. 250 min.

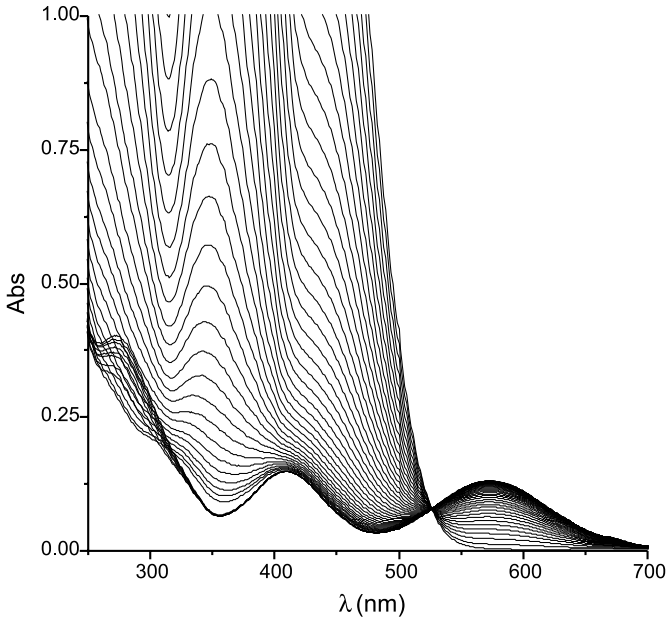

Fig. 3. UV–vis difference spectra of Cr^{VI}–Lac solutions at pH 4.7, showing the increasing band at 377 nm with increasing [Lac]: (*a*) 0.12, (*b*) 0.20, and (*c*) 0.32 M. [Cr^{VI}] = 8×10^{-4} M, T = 33°C, I = 1 M. Spectra taken after 2 min.

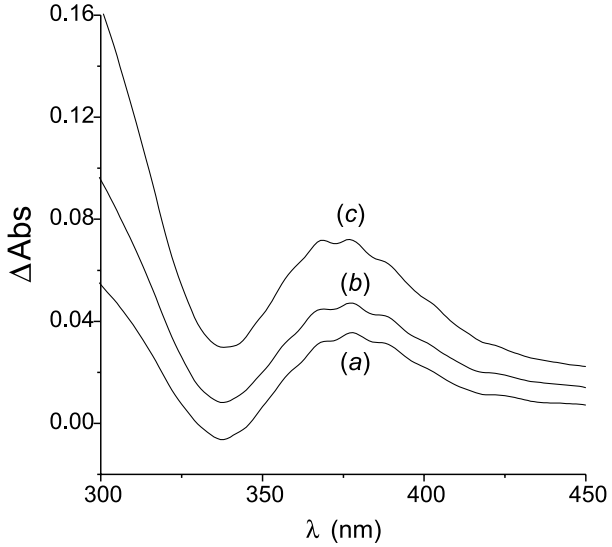

We followed the formation of Cr^{III} at 570 nm for various [disaccharide] in 0.20 M $HClO_4$ to determine the rate of Cr^{III} formation relative to that of Cr^{VI} consumption. The pseudo-first-order rate constants obtained at this wavelength (Table 1) are coincident with those obtained from the Cr^{VI} decay at 350 nm, with the same dependence on [disaccharide]. This means that Cr^{III} forms as fast as Cr^{VI} is consumed; this is consistent with the observation of an isosbestic point at 525 nm (Fig. 2). This result was independently confirmed by following the redox reaction by EPR spectroscopy. The rate

Fig. 4. X-band EPR spectra of mixtures of (*a*) Cr^{VI}–Lac = 1:33, [H^+] = 0.20 M, t = 6 min, modulated amplitude (mod. ampl.) = 4 G; (*b*) Cr^{VI}–Lac = 1:19, pH = 5.0, t = 24 h, mod. ampl. = 0.4 G. I = 1.0 M, T = 20°C, frequency ≈ 9.7 GHz.

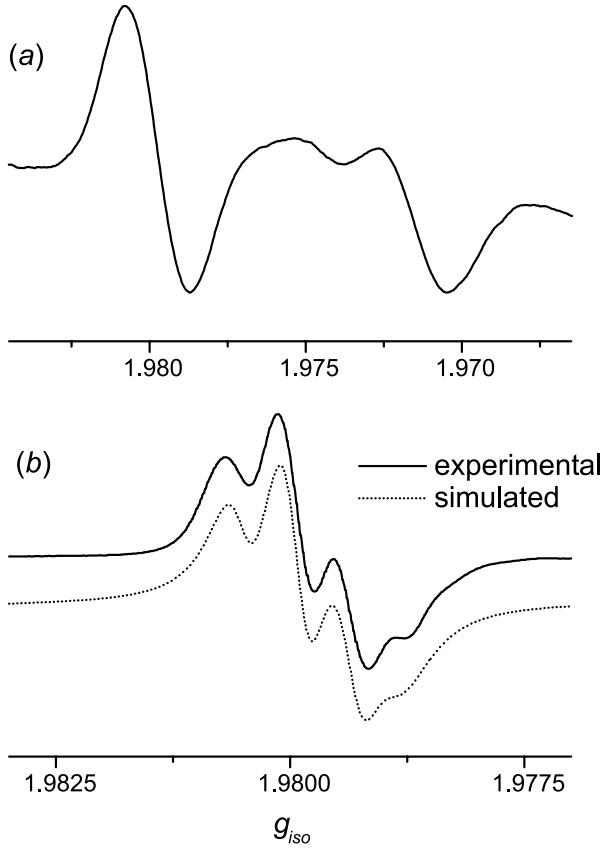

constant of the reduction of Cr^{VI} by the saccharide (k_6) was found to be much lower than that of the reduction of Cr^V (k_5). The fact that $k_5 >> k_6$ implies that the slow redox step involves the reduction of Cr^{VI}.

Detection of the intermediate Cr^{VI} ester

Differential UV–vis spectra of mixtures of Cr^{VI} and Lac exhibited an absorption band with λ_{max} = 377 nm (Fig. 3) consistent with that ascribed to Cr^{VI} oxy-esters (52, 53). At pH 4.7, the redox reactions of the studied disaccharides proceed very slowly with negligible reduction of Cr^{VI} within the first hour. Thus, at this pH the ester formation step can be distinguished clearly from the electron transfer reaction. Spectra obtained within 2 min after mixing revealed a distinctive absorption band at 377 nm. Continued scanning for 30 min showed no further change in the spectra. Varying the excess concentration of disaccharide at pH = 4.7 showed that the absorbance at 377 nm increased with increasing concentration of disaccharide (Fig. 3), probably as a result of a shift toward the ester in the esterification equilibrium.

Intermediacy of Cr^V

Using EPR spectroscopy, we have detected the formation of intermediate Cr^V species in the reaction of the disaccharides with Cr^{VI}. The EPR spectra of mixtures of Lac and Cr^{VI} in 0.2 M $HClO_4$ show the formation of several intermediate Cr^V species (Fig. 4*a*). At this [H^+], the EPR spec-

© 2002 NRC Canada

Fig. 5. Experimental and simulated X-band EPR spectra of mixtures of (*a*) Cr^{VI}–Mal = 1:19; (*b*) Cr^{VI}–Cel = 1:16; (*c*) Cr^{VI}–Mel = 1:19. [Cr^{VI}] = 0.015 M, I = 1.0 M, pH 5.0, t = 24 h, T = 20°C, frequency ≈ 9.7 GHz, mod. ampl. = 0.4 G.

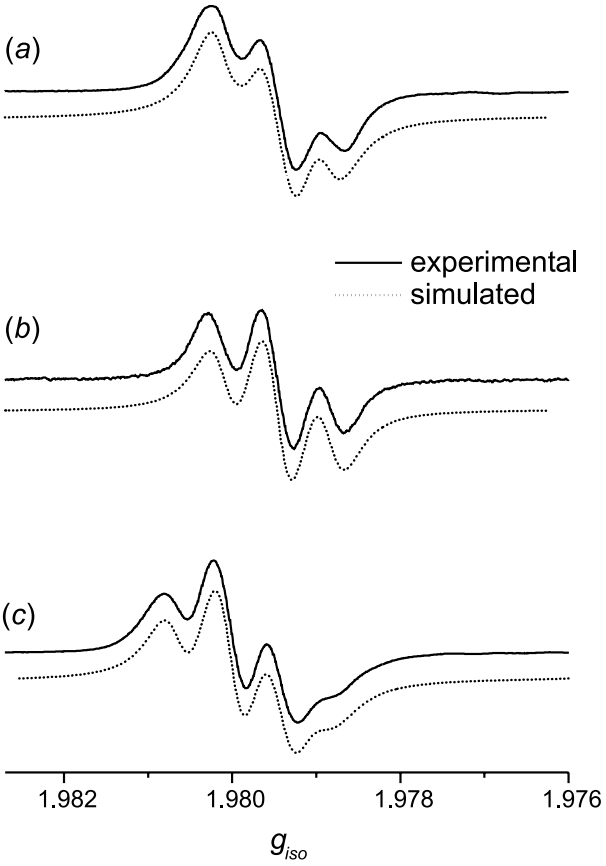

tra consist of one signal at g_{iso} = 1.9797, which persists at higher pH, and two additional signals at g_{iso} = 1.9743 and 1.9715. At this [H^+], the EPR signals are not resolved because of the high modulation amplitude required to observe the Cr^V species. The signals at lower g_{iso} are not observed at pH > 2, where the electron transfer reaction becomes extremely slow; by contrast, the Cr^V species with g_{iso} = 1.9797 remains stable in solution for a long time.

At the [H^+] used in the kinetics measurements, the Cr^V EPR signal intensities grow and decay rapidly. For the reduction of Cr^{VI} by Lac ([H^+] = 0.2 M, [Lac] = 0.424 M, $[Cr^{VI}]_0$ = 0.0127 M, T = 20°C), the Cr^V EPR signal grows and decays within 3 h, while the total conversion of Cr^{VI} into Cr^{III} requires 20 h. Under these conditions, changes in the EPR signal intensity give values for the rate constant of the disappearance of Cr^{VI} (k_6), which is ~50-times higher than the corresponding rate constant for the disappearance of Cr^V (k_5). The k_6 values obtained from EPR data agree with the k_{obs} values calculated spectrophotometrically at 570 nm under the same conditions. Thus, the fact that $k_5 > k_6$ means that changes in absorbance at 350 nm reflect changes in Cr^{VI} concentration.

We have also performed the reaction of the disaccharides and Cr^{VI} at a lower [H^+] than was used in the kinetic measurements to obtain information on the structure of Cr^V species formed as intermediates in the reduction of Cr^{VI} to Cr^{III}.

Table 2. EPR spectral parameters for Cr^V intermediates in the reactions.[a]

Cr^V species	g_{iso}	a_{iso} (10^4 cm^{-1}) (N)
$[Cr(O)(cis\text{-}O,O\text{-Lac})_2]^-$	1.98	0.93 (2)
	1.9794	0.85 (2)
$[Cr(O)(O^1,O^2\text{-lactobionato})(H_2O)_3]^+$	1.9743	ND
$[Cr(O)(cis\text{-}O,O\text{-Lac})(H_2O)_3]^+$	1.9715	ND
$[Cr(O)(O^1,O^2\text{-Mal})_2]^-$	1.9795	0.76 (2)
	1.9794	0.92 (2)
$[Cr(O)(O^1,O^2\text{-Cel})_2]^-$	1.9793	0.97 (2)
$[Cr(O)(cis\text{-}O,O\text{-Mel})_2]^-$	1.9802	0.88 (2)
	1.9798	0.98 (2)

[a] N: number of equivalent protons. ND: not determined.

In the pH 3–7 range and with a Lac–Cr^{VI} ratio of 19:1, the EPR spectrum, taken 24 h after mixing, is composed (signals were deconvoluted by fitting the spectra to Lorentzian derivatives) of two triplets at g_{iso1} = 1.9800 and g_{iso2} = 1.9794 in an ~1:1 proportion. Each of these triplets shows four weak ^{53}Cr (9.55% abundance, I = 3/2) hyperfine peaks at 16.5(3) × 10^{-4} cm^{-1} spacing (Fig. 4*b*, Table 2).

In the pH 5–7 range, the EPR spectrum of a 19:1 Mal–Cr^{VI} reaction mixture affords two triplets at g_{iso1} = 1.9795 and g_{iso2} = 1.9794 in a 1:1 ratio (Fig. 5*a*). In the same pH range, a 16:1 Cel–Cr^{VI} reaction mixture yields one triplet at g_{iso} = 1.9793 (Fig. 5*b*, Table 2).

Mel behaves similarly to Lac. The best fit of the EPR spectrum of a 19:1 Mel–Cr^{VI} mixture in the pH 3–7 range taken 24 h after mixing affords two triplets at g_{iso1} = 1.9802 and g_{iso2} = 1.9798 (Fig. 5*c*, Table 2). These two signals are present in a 1:1 ratio independent of pH.

The ultimate fate of the chromium in these reactions is a Cr^{III} species, and a typical broad Cr^{III} EPR signal, centred at g ~ 1.98, is always observed at later times.

At room temperature and pH 5.0, the reaction of chromate with glutathione (1:1 ratio) in the presence of a 10-times excess disaccharide over Cr^{VI} affords Cr^V EPR spectra identical to those obtained by direct reaction of the disaccharide with Cr^{VI}.

Discussion

Cr^{VI} oxidation of disaccharides

For the ranges of substrate and acid concentrations used in the kinetics measurements, the oxidation of the disaccharides by Cr^{VI} is a complex reaction, yielding $[Cr(H_2O)_6]^{3+}$ and the aldobionic acid as the final redox products. We propose a mechanism that takes into account: (*a*) the kinetic results; (*b*) the polymerization of acrylonitrile added to the reaction mixture; (*c*) the detection of an intermediate Cr^{VI} ester; (*d*) the detection of intermediate of oxochromate(V) species by EPR; and (*e*) the formation of the aldobionic acid as the only organic reaction product.

At the [H^+] and [Cr^{VI}] used in the kinetics studies, Cr^{VI} may exist as $HCrO_4^-$ (54), and this species is proposed as the reactive form of Cr^{VI}, in agreement with the first-order dependence of the reaction rate on [Cr^{VI}]. The chromic oxidation of alcohols and glycols are preceded by the formation of a chromate ester (52, 53). The observation of the

© 2002 NRC Canada

Scheme 1. Cr^{VI}–Mel: $R_1 = O^5$-glc, R_2 = H; Cr^{VI}–Lac: R_1 = H, $R_2 = O^4$-glc. Cr^{VI}–Lac(Mal, Cel): R_3 = glycoside, R_4 = H; Cr^{VI}–Mel: R_3 = H, R_4 = glycoside. Cr^{VI}–Lac: R_5 = OH, R_6 = H; Cr^{VI}–Cel: R_5 = H, R_6 = OH. AldA = aldobionic acid; w = water.

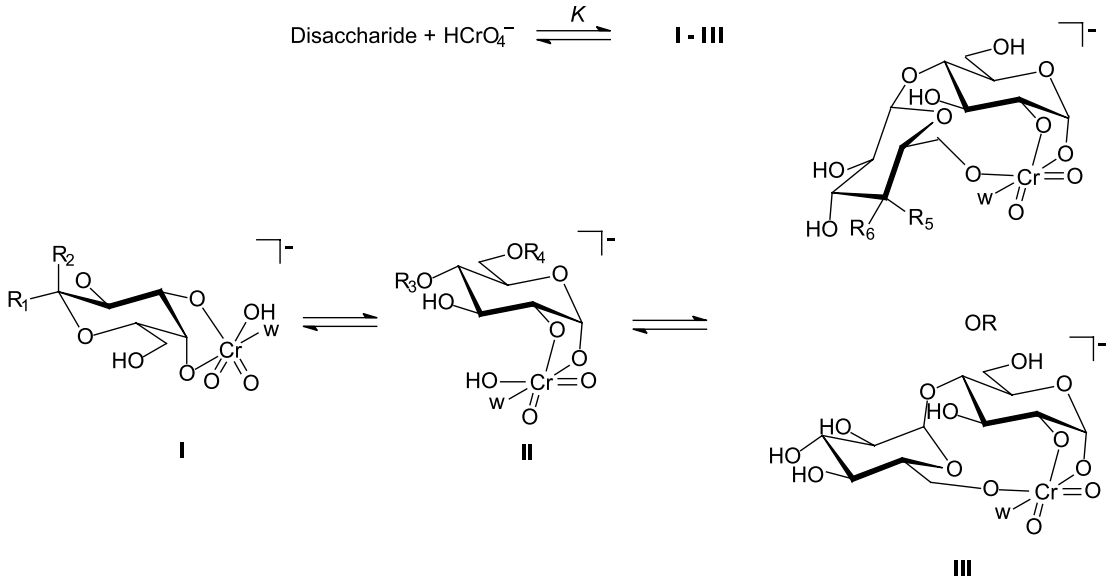

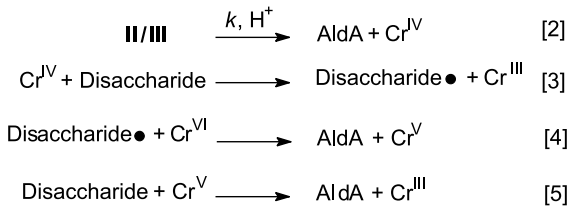

absorbance band, characteristic of chromate oxy-esters, at approximately 377 nm (a few minutes after mixing the disaccharides and Cr^{VI} under conditions where the redox reaction is extremely slow) reveals that such an intermediate Cr^{VI} complex is rapidly formed prior to the redox steps. Thus, the first step of the mechanism proposed in Scheme 1 is the formation of the disaccharide–Cr^{VI} mono-chelate. The disaccharide acts as a bidentate ligand bound to Cr^{VI} via any pair of properly disposed hydroxyl groups. While there is no direct evidence for bidentate chelation of the sugar to Cr^{VI}, it is likely that this is the case, especially since Cr^{VI} chelates have been observed by NMR spectroscopy in the oxidations of another bidentate oxygen donor (18). The chelates proposed in Scheme 1 are those with the ligand bound to Cr^{VI} at the *cis*-$O^{3'}$,$O^{4'}$-diolato (**I**) and *cis*-O^1,O^2-diolato (**II**) moieties of Lac and Mel and the *cis*-O^1,O^2-diolato (**II**) moiety of Mal and Cel. These are proposed on the basis that α-glc forms the Cr^{VI}–glc chelate faster than the β-D-anomer — a fact attributed to the *cis*-1,2-diolato moiety present only in the α-anomer — (21) and the observation of the marked preference of the CrO^{3+} ion for binding to *cis*- rather than *trans*-diol groups of cyclic diols (21, 22, 29, 55). For Mal, Lac, and Cel, **II** is proposed to be in equilibrium with Cr^{VI}–O^1,O^2,$O^{6'}$-disaccharide chelates (**III**). Molecular models show that Lac, Mal, and Cel can afford Cr^{VI}–chelates with the disaccharide bound to Cr^{VI} at O^1,O^2,$O^{6'}$ and with retention of the $^4C_1$ chair conformation of the glycoside moiety. Taking into account that in the redox reaction only the anomeric hydroxyl group is oxidized, it seems reasonable to hypothesize that the complexes with the primary hydroxyl group bound to Cr^{VI} (**II**, **III**) should be the precursors of the slow redox steps.

The slow redox step in the mechanism might take place by either a one-electron or a two-electron transfer (56). The slow step proposed in Scheme 1 involves the intramolecular transfer of two electrons to yield Cr^{IV} and the aldobionic acid (eq. [2]). This is based on the mechanism reported for aldoses, which are also selectively oxidized by Cr^{VI} at the hemiacetalic group with an initial two-electron transfer slow step (21–28). After the slow redox step, Cr^{IV} is predicted to react with excess saccharide to yield Cr^{III} and a disaccharide radical in a fast step (eq. [3]). The latter is supported by the observed polymerization of acrylonitrile when it is added to the reaction mixture. The rapid reaction of the disaccharide radical with Cr^{VI} affords Cr^{V} (eq. [4]), which can further oxidize the disaccharide to yield Cr^{III} and the aldobionic acid as the final oxidation product (eq. [5]).

The k_H in the rate law corresponds to $kK[H^+]$ in this mechanism. This means that the relative reactivity of the disaccharides may be interpreted by taking into account both the rate of formation of the Cr^{VI} ester and its redox rate. Our experimental data show that the disaccharide–Cr^{VI} chelate formation is much faster than the redox steps. For certain aldoses the rate constant for the formation of the aldose–Cr^{VI} chelate (K) in 0.75 M $HClO_4$ has been determined and was found to be 500- to 2000-times higher than the redox

© 2002 NRC Canada

constant (k). Thus, the redox rate should depend, essentially, on the energy barrier the Cr^{VI} chelate has to overcome to attain the five-membered cyclic transition state for the intramolecular H transfer (22). The kinetics data show that the relative reactivity of the disaccharides toward Cr^{VI} is Mel > Lac > Cel > Mal. If we compare the reactivity of these saccharides with glc, which is oxidized by Cr^{VI} with a rate constant of $k_H = 9.9 \times 10^{-4}$ M^{-1} s^{-1} in 0.2 M $HClO_4$ at 33°C (22), we can observe that substitution of the O^4H group of glc by the glycoside moiety results in the retardation of the redox rate, while substitution of the primary O^6H accelerates the redox reaction. The retardation of the redox reaction observed for Mal, Cel, and Lac is probably related to the formation of the Cr^{VI}–O^1,O^2,$O^{6'}$-disaccharide chelates (III). The probability for Mel to act as a tridentate ligand is very low because of the less favourable spatial orientation of the galactoside moiety; therefore, it shows the highest reactivity in the series.

Cr^V intermediates

The most common means of characterizing Cr^V complexes in solution is EPR spectroscopy. The EPR spectral parameters, g_{iso} and A_{iso}, together with the proton superhyperfine (shf) coupling, are useful in determining the binding modes of sugars to the Cr^V center (1, 22, 24, 26, 27, 57, 58). An empirical relationship between the nature and number of donor groups and the EPR spectral parameters of Cr^V complexes has been established (1, 57). Five-coordinate Cr^V species show higher g_{iso} and lower ^{53}Cr A_{iso} values than the corresponding six-coordinate species (57, 59, 60). Thus, the assignment of the structures of new oxo-Cr^V species in solution was made according to the isotropic EPR parameters (g_{iso} and A_{iso} values) and the superhyperfine (shf) pattern of the signal (1, 59).

The EPR spectrum of a Cr^V-diolato species of six-membered ring *cis*-diols yields a doublet, since only one proton is in the plane of the unpaired electron density of the Cr^V ion, while the EPR spectrum of a Cr^V-diolato species of six-membered ring *trans*-diols (with no protons lying in the ligand plane) yields a singlet (55). Consequently, the EPR spectral multiplicity of the bis-chelate Cr^V-diolato$_2$ species formed between Cr^V and pyranosic *cis*- and *trans*-diols will exhibit a triplet and a singlet, respectively, which arise from the orientation of the ring protons of the coordinated diol groups with respect to the basal plane of the complex (1, 55, 57). Based on this, the isotropic EPR parameters g_{iso} and A_{iso} were used to deduce the coordination number and nature of the donor groups of the Cr^V species formed, either for the reaction of Cr^{VI} with the disaccharides or for the reaction of Cr^{VI} with glutathione in the presence of excess disaccharide, according to a described empirical method (1, 57, 59, 60).

The *cis*-diolato moieties of the disaccharides under study are potential binding sites to give five-membered Cr^V species. The five-membered Cr^V chelates are the most thermodynamically favoured, and CrO^{3+} shows a marked preference for binding to *cis*- rather than *trans*-diol groups of cyclic diols (21, 22, 29, 55). Based on this, the EPR spectral features of disaccharide–Cr^V mixtures were interpreted in terms of Cr^V-diolato species involving binding mainly through the *cis*-O^1,O^2-diolato of Mal and Cel and the *cis*-O^1,O^2-diolato and *cis*-$O^{3'}$,$O^{4'}$-diolato of Lac and Mel. The contribution to the EPR signals from other species, involving *trans*-diolato moieties, should be small.

Lactose–Cr^V

The reaction of Cr^{VI} with a 20-times excess of Lac in the pH 3–7 range affords an EPR spectrum dominated by a single detectable signal at $g_{iso} = 1.9797$ with the four weak ^{53}Cr (9.55% abundance, $I = 3/2$) hyperfine peaks at 16.5×10^{-4} cm^{-1} spacing; the product remains in solution from several days to several months. When the modulation amplitude is lowered to 0.4 G, the EPR signal resolves into two triplets at $g_{iso1} = 1.9800$ and $g_{iso2} = 1.9794$ ($A_{iso} = 16.5(3) \times 10^{-4}$ cm^{-1}, ~50:50 g_{iso1}–g_{iso2} ratio) (Fig. 4*b*, Table 2). The g_{iso} and A_{iso} values are consistent with those calculated for five-coordinate oxochromate(V) complexes with four alcoholato donors ($g_{calc} = 1.9800$, $A_{calc} = 16.5 \times 10^{-4}$ cm^{-1}) (1, 57). The shf pattern indicates that the EPR signal is a composite of two oxo-Cr^V-*cis*-diolato$_2$ species with two (one from each chelate ring) carbinolic protons coupled to the Cr^V electronic spin. The two components can be attributed to linkage isomers of the $[Cr(O)(cis\text{-}O,O\text{-Lac})_2]^-$ (61). Even when three different linkage isomers $[Cr(O)(cis\text{-}O^{3'},O^{4'}\text{-Lac})_2]^-$, $[Cr(O)(cis\text{-}O^1,O^2\text{-Lac})_2]^-$, and $[Cr(O)(cis\text{-}O^1,O^2\text{-Lac})(cis\text{-}O^{3'},O^{4'}\text{-Lac})]^-$ (**IV**–**VI** in Fig. 6) are possible, only two species are required to simulate the EPR signal. It seems reasonable to assume that the angles between the carbinolic protons and the Cr^V–ligand plane in two of the linkage isomers of $[Cr(O)(cis\text{-}O,O\text{-Lac})_2]^-$ are very similar, as we cannot distinguish between them.

A more complex EPR spectral pattern is observed in a 0.2 M $HClO_4$ solution. At this $[H^+]$ and a 33:1 ligand–Cr^{VI} ratio, two additional signals at $g_{iso3} = 1.9743$ and $g_{iso4} = 1.9715$ appear, together with the signal at $g_{iso} = 1.9797$ (Fig. 4*a*, Table 2). The shf pattern of these two new signals was not resolved, but the signal at $g_{iso} = 1.9715$ suggests the presence of six-coordinate oxo-Cr^V species, possibly $[Cr(O)(cis\text{-}O,O\text{-Lac})(H_2O)_3]^+$ (**VII**). The calculated g_{iso} value for a six-coordinate oxo-Cr^V species with two alcoholato donors and three water molecules ($g_{clc} = 1.9724$) is in reasonable agreement with the observed g_{iso4} value. The positive charge of this species is also consistent with its appearance at high $[H^+]$. The signal at $g_{iso3} = 1.9743$ may be tentatively attributed to another positively charged six-coordinate oxo-Cr^V mono-chelate $[Cr(O)(O^1,O^2\text{-lactobionato})(H_2O)_3]^+$ (**VIII**, $g_{clc} = 1.9735$), with Cr^V bound to the 2-hydroxyacid moiety of the oxidized product and to three water molecules. Coordination to the oxidized ligand is consistent with the fact that Cr^{VI} is a stronger oxidant in more acidic medium. The six-coordinate oxo-Cr^V mono-chelate **VII** is possibly responsible for the higher rates observed for the Cr^V–disaccharide redox reactions at pH < 2. At higher pH, where Cr^V mono-chelates are not observed, Cr^V complexes are stable enough to remain in solution from several days to several months.

Maltose–Cr^V

For the reaction of Cr^{VI} with Mal, in the pH 5–7 range and with a 19:1 ligand–metal ratio, the EPR spectra (Fig. 5*a*, Table 2) consist of two triplets at $g_{iso1} = 1.9795$ and $g_{iso2} = 1.9794$. The g_{iso} values and the shf pattern indicate these signals may be attributed to two geometric isomers (typical

© 2002 NRC Canada

Fig. 6. Structures of Cr^V complexes with disaccharide ligands. R_1 = CH_2OH, R_5 = $C_{10}O_9H_{19}$, w = water. Cr^V–Lac: R_2 = O^4-glc; Cr^V–Mel_2: R_2 = O^6-glc; Cr^V–Lac_2 (Cr^V–Mal_2, Cr^V–Cel_2): R_3 = glycoside, R_4 = H; Cr^V–Mel_2: R_3 = H, R_4 = glycoside.

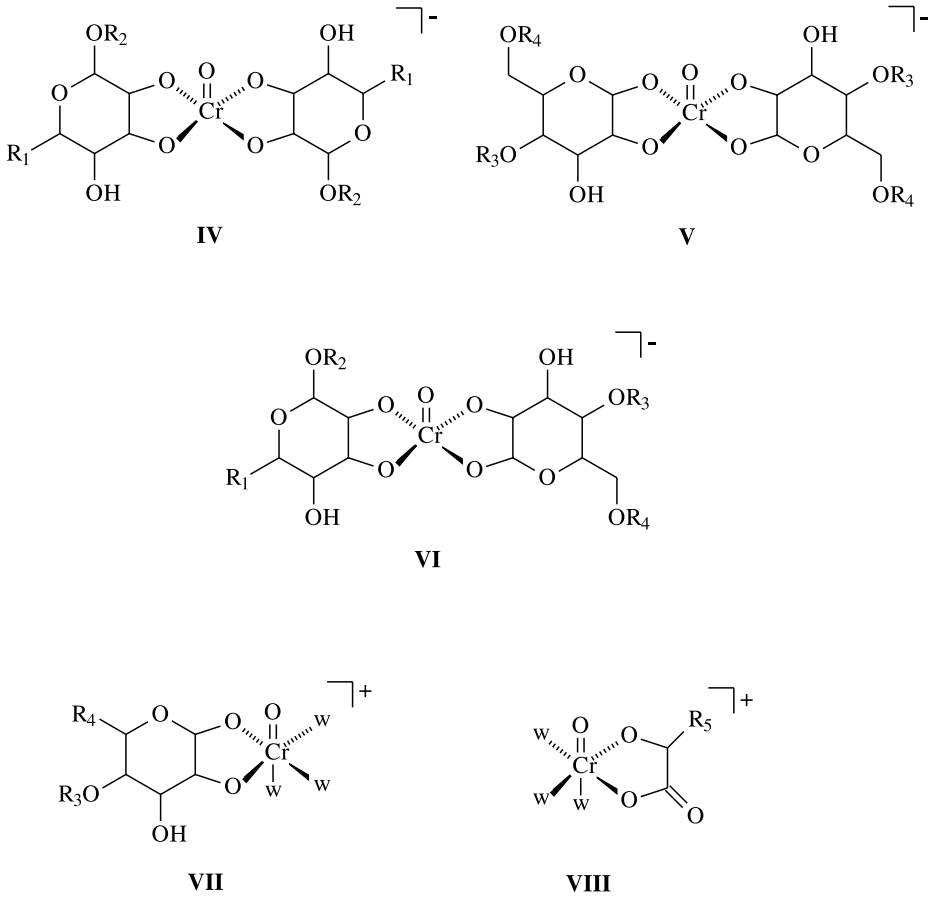

Δg_{iso} for geometric isomers are $1 \times 10^{-4} - 2 \times 10^{-4}$) (27, 30) of the five-coordinate oxo-Cr^V complex $[Cr(O)(O^1,O^2\text{-Mal})_2]^-$ (**V**), with Mal bound to Cr^V via the 1,2-*cis* diolato moiety.

Cellobiose–Cr^V

Intermediate Cel–Cr^V species formed in the reaction of Cr^{VI} with Cel, in the pH 5–7 range and with a 14:1 ligand–metal ratio, yield EPR spectra (Fig. 5*b*, Table 2) consisting of one triplet at g_{iso1} = 1.9793. The g_{iso} value corresponds to that calculated for a five-coordinate oxochromate(V) complex with four alcoholato donors, and the shf pattern indicates this signal may be assigned to the $[Cr(O)(O^1,O^2\text{-Cel})_2]^-$ chelate (**V**), with Cel bound to Cr^V via the 1,2-*cis* diolato moiety.

Melibiose–Cr^V

In the reaction of Cr^{VI} with Mel at a pH 3–7 range and a 19:1 ligand–metal ratio, the EPR spectra of the intermediate Cr^V species show two triplets at g_{iso1} = 1.9802 and g_{iso2} = 1.9798 (~50:50 g_{iso1}–g_{iso2} ratio). The g_{iso} values and the shf pattern reveal that these signals correspond to different linkage isomers of the five-coordinate oxo-Cr^V complex $[Cr(O)(O,O\text{-Mel})_2]^-$. As in the case of Lac, the three linkage isomers $[Cr(O)(O^{3'},O^{4'}\text{-Mel})_2]^-$ (**IV**), $[Cr(O)(O^1,O^2\text{-Mel})_2]^-$ (**V**), and $[Cr(O)(O^{3'},O^{4'}\text{-Mel})(O^1,O^2\text{-Mel})]^-$ (**VI**) are possible, but only two Cr^V species are required to simulate the EPR signal, probably for the same reasons as for the Lac–Cr^V system.

EPR spectra identical to those shown in Figs. 4*b* and 5*a*–5*c* are obtained when Cr^V is generated by the reaction of Cr^{VI} with glutathione (1:1 ratio) at pH = 5.0 and stabilized by the presence of a 10-times excess of disaccharide over Cr^{VI}. This result indicates that Cr^V species formed at this pH effectively correspond to chelates formed with the disaccharide and not with the oxidized product (aldobionic acid).

Conclusions

Disaccharides form stable high-valent chromium chelates at pH > 2, while at higher $[H^+]$ their oxidation by Cr^{VI} and (or) Cr^V is favoured. The oxidation occurs selectively at the hemiacetalyc C^1OH group, with first-order kinetics for both $[Cr^{VI}]$ and [disaccharide]. The relative ability of the studied disaccharides to reduce Cr^{VI} — Mel > Lac > Cel > Mal — can be attributed to the increasing stability of the intermediate disaccharide–Cr^{VI} chelates formed with Mel through Mal. The redox and complexation chemistry observed for the disaccharide–Cr^{VI} systems parallels that of aldoses. The glycoside moiety can retard the redox rate of the aglycone when additional binding to Cr^{VI} by the glycoside moiety is possible. In the case of Mal, this effect reduces k_H to one half of the value obtained for glc.

© 2002 NRC Canada

At pH 3–7, redox reactions between Cr^V and disaccharides are extremely slow, since once the bis-chelates are formed they are long-lived. A different reactivity pattern is observed at high [H^+], where intramolecular electron-transfer processes take place and mono-chelates are observed. The observation of six-coordinate $[Cr^VO(O,O\text{-disaccharide})(OH_2)_3]^+$ at only high [H^+], together with the selectivity of the redox reaction, suggest that the six-coordinate Cr^V mono-chelate **VII** could be the precursor of the intramolecular electron-transfer reaction step in the redox reactions.

Acknowledgments

We thank the National Research Council of Argentina (CONICET), the Third World Academy of Sciences (TWAS), the National University of Rosario (UNR), ANTORCHAS Foundation, and the International Foundation for Sciences (IFS) for financial support.

References

1. C.B. Klein. *In* Toxicology of metals. *Edited by* L.W. Chang. CRC-Lewis Publishers, New York. 1996. pp. 205–220.
2. R. Codd, C.T. Dillon, A. Levina, and P.A. Lay. Coord. Chem. Rev. **216/217**, 537 (2001).
3. S.A. Katz and H. Salem. The biological and environmental chemistry of chromium. VCH Publishers, New York. 1994.
4. G.H. Smith and Q.L. Lloyd. Chem. Br. 139 (1986).
5. D.M.L. Goodgame and A.M. Joy. Inorg. Chim. Acta, **135**, L5 (1987).
6. X. Shi, A. Chiu, C.T. Chen, B. Halliwell, V. Castranova, and V. Vallyathan. J. Toxicol. Environ. Health Part B: 87 (1999).
7. M. Costa. Crit. Rev. Toxicol. **27**, 431 (1997).
8. E.S. Gould. Coord. Chem. Rev. **135/136**, 651 (1994).
9. D.K. Geiger. Coord. Chem. Rev. **164**, 261 (1997).
10. A. Levina, P.A. Lay, and N.E. Dixon. Inorg. Chem. **39**, 385 (2000).
11. B. Gyurcsik and L. Nagy. Coord. Chem. Rev. **203**, 81 (2000).
12. M. Ciéslak-Golonka. Polyhedron, **15**, 3667 (1996).
13. M. Krumpolc, B.G. de Boer, and J. Rocek. J. Am. Chem. Soc. **100**, 145 (1978).
14. S.L. Brauer and K.E. Wetterhahn. J. Am. Chem. Soc. **113**, 3001 (1991).
15. D.M.L. Goodgame, P.B. Hayman, and D.E. Hathaway. Polyhedron, **1**, 497 (1982).
16. D.M.L. Goodgame and A.M. Joy. J. Inorg. Biochem. **26**, 219 (1986).
17. R. Codd, P.A. Lay, and A. Levina. Inorg. Chem. **36**, 5440 (1997).
18. R.P. Farrell, P.A. Lay, A. Levina, I.A. Maxwell, R. Bramley, S. Brumby, and J. Ji. Inorg. Chem. **37**, 3159 (1998).
19. R. Codd, A. Levina, L. Zhang, T.W. Hambley, and P.A. Lay. Inorg. Chem. **39**, 990 (2000).
20. N. Mehta, P. Dubach, and H. Deuel. Adv. Carbohydr. Chem. Biochem. **16**, 335 (1958).
21. S. Signorella, R. Lafarga, V. Daier, and L.F. Sala. Carbohydr. Res. **324**, 127 (2000).
22. S. Signorella, V. Daier, S. García, R. Cargnello, J.C. González, M. Rizzotto, and L.F. Sala. Carbohydr. Res. **316**, 14 (1999).
23. S. Signorella, S. García, and L.F. Sala. J. Chem. Educ. **76**, 405 (1999).
24. V. Daier, S. Signorella, M. Rizzotto, M.I. Frascaroli, C. Palopoli, C. Brondino, J.M. Salas-Peregrin, and L.F. Sala. Can. J. Chem. **77**, 57 (1999).
25. M. Rizzotto, M.I. Frascaroli, S. Signorella, and L.F. Sala. Polyhedron, **15**, 1517 (1996).
26. L.F. Sala, S. Signorella, M. Rizzotto, M.I. Frascaroli, and F. Gandolfo. Can. J. Chem. **70**, 2046 (1992).
27. S. Signorella, M. Rizzotto, V. Daier, M.I. Frascaroli, C. Palopoli, D. Martino, A. Bousseksou, and L.F. Sala. J. Chem. Soc. Dalton Trans. 1607 (1996).
28. M. Rizzotto, S. Signorella, M.I. Frascaroli, V. Daier, and L.F. Sala. J. Carbohydr. Chem. **14**, 45 (1995).
29. S. Signorella, M.I. Frascaroli, S. García, M. Santoro, J.C. González, C. Palopoli, N. Casado, and L.F. Sala. J. Chem. Soc. Dalton Trans. 1617 (2000).
30. M. Rizzotto, A. Levina, M. Santoro, S. García, M.I. Frascaroli, S. Signorella, L.F. Sala, and P.A. Lay. J. Chem. Soc. Dalton Trans. 3206 (2002).
31. S. Signorella, M. Santoro, C. Palopoli, C. Brondino, J.M. Salas-Peregrin, M. Quirós, and L.F. Sala. Polyhedron, **17**, 2739 (1998).
32. S. Signorella, S. García, and L. F. Sala. Polyhedron, **16**, 701 (1997).
33. C. Palopoli, S. Signorella, and L.F. Sala. New J. Chem. **21**, 343 (1997).
34. L.F. Sala, C. Palopoli, and S. Signorella. Polyhedron, **14**, 1725 (1995).
35. S.R. Signorella, M.I. Santoro, M.N. Mulero, and L.F. Sala. Can. J. Chem. **72**, 398 (1994).
36. S. Signorella, S. García, and L.F. Sala. Polyhedron, **11**, 1391 (1992).
37. V.P. Roldán, V.A. Daier, B. Goodman, M. Santoro, J.C. González, N. Calisto, S. Signorella, and L.F. Sala. Helv. Chim. Acta, **83**, 3211 (2000).
38. W. Pigman. The carbohydrates: Chemistry, biochemistry, physiology. Academic Press Inc. Publishers, New York. 1957. pp. 490, 495, 498–501, 788, 795.
39. International Agency for Research on Cancer (IARC). IARC Monogr. Eval. Carcinog. Risk Chem. Hum. Suppl. **7**, 165 (1987).
40. R. Feldam. *In* Occupational and environmental neurotoxicology. Lippincott-Raven Publishers, Philadelphia. 1999. pp. 337–338.
41. W. Chandler, E. Lee, and D. Lee. J. Chem. Ed. **64**, 878 (1987).
42. A.B.P. Lever. *In* Inorganic electronic spectroscopy. 2nd ed. Elsevier, Amsterdam. 1984. pp. 419.
43. S. Signorella, M. Santoro, A. Frutos, G. Escandar, J.M. Salas Peregrin, V. Moreno, M. González Sierra, and L.F. Sala. J. Inorg. Biochem. **73**, 93 (1999).
44. C.P. Rao and S.P. Kaiwar. Carbohydr. Res. **244**, 15 (1993).
45. S.P. Kaiwar, M.S. Srinivasa Raghavan, and C.P. Rao. J. Chem. Soc. Dalton Trans. 1569 (1995).
46. S. Scott, A. Bakac, and J. Espenson. J. Am. Chem. Soc. **114**, 4205 (1992).
47. O.A. Babich and E.S. Gould. Inorg. Chem. **40**, 5708 (2001).
48. R.L. Wistler and M.L. Wolfrom. (*Editors*). *In* Methods in carbohydrates chemistry. Vol. II. Academic Press, New York. 1963. pp. 13–14.
49. National Institute of Environmental Health Sciences. 1995. WinSIM EPR calculations for MS-Windows [computer program]. Version 0.96. National Institute of Environmental Health Sciences.
50. M. Krumpolc and J. Rocek. Inorg. Synth. **20**, 63 (1980).
51. M.C. Ghosh and E.S. Gould. Inorg. Chem. **30**, 491 (1991).

© 2002 NRC Canada

52. J.K. Beattie and G.P. Haight. *In* Inorganic reaction mechanisms. Part II. *Edited by* J.O. Edwards. Wiley, New York. 1972.
53. M. Mitewa and P. Bontchev. Coord. Chem. Rev. **61**, 241 (1985).
54. N.E. Brasch, D.A. Buckingham, A.B. Evans, and C.R. Clark. J. Am. Chem. Soc. **118**, 7969 (1996).
55. R. Codd and P.A. Lay. J. Am. Chem. Soc. **121**, 7864 (1999).
56. G. Haight, G. Jwisich, M. Kelso, and P. Merril. Inorg. Chem. **24**, 2740 (1985).
57. G. Barr-David, M. Charara, R. Codd, R.P. Farrell, J.A. Irwin, P.A. Lay, R. Bramley, S. Brumby, J. Ji, and G.R. Hanson. J. Chem. Soc. Faraday Trans. **91**, 1207 (1995).
58. M. Branca, A. Dessí, H. Kozlowski, G. Micera, and J. Swiatek. J. Inorg. Biochem. **39**, 217 (1990).
59. R. Bramley, J.Y. Ji, R.J. Judd, and P.A. Lay. Inorg. Chem. **29**, 3089 (1990).
60. R.P. Farrell, R.J. Judd, P.A. Lay, R. Bramley, and J.Y. Ji. Inorg. Chem. **28**, 3401 (1989).
61. R. Brambley, J.Y. Li, and P.A. Lay. Inorg. Chem. **30**, 1557 (1991).

© 2002 NRC Canada

Synthesis, characterization, and X-ray crystal structures of Co(II) and La(III) complexes of a pyridine containing self-assembling system and solution studies of the Co(II) complex

A. Moghimi, M. Ranjbar, H. Aghabozorg, F. Jalali, M. Shamsipur, and Kaj K. Chadha

Abstract: The complexes $[pyda.H]_2[Co(pydc)_2]\cdot H_2O$ (**I**) and $[pyda\cdot H]_2[La_2(pydc)_4(H_2O)_4]\cdot 2H_2O$ (**II**) were prepared from the complexation of a novel pyridine containing self-assembling system $\mathbf{LH_2}$, $([pyda\cdot H_2]^{2+}[pydc]^{2-})$ (pyda = 2,6-pyridinediamine and pydc·H_2 = 2,6-pyridinedicarboxylic acid), with cobalt(II) and lanthanum(III) salts in 82% and 74% yields, respectively. The characterizations were performed using elemental analysis, ESI mass spectroscopy as well as ^1H and ^{13}C solution NMR spectroscopy, and X-ray crystallography. The crystal systems **I** and **II** are monoclinic and triclinic with space groups $P2_1/n$ and $P\bar{1}$, respectively. Coordination number around each Co atom is six with distorted octahedral geometry, while coordination number around each La atom is nine with highly distorted tricapped trigonal prism geometry. The paramagnetic Co(II) and diamagnetic La(III) complexes show ^1H NMR resonances of both anionic $[pydc]^{2-}$ and cationic counter ion $[pyda\cdot H]^+$ in DMSO-d_6. The complexation reactions of the complex **I** in aqueous solution were investigated by potentiometric pH titrations and the equilibrium constants for all major complexes formed are described. The results are presented in the form of distribution diagrams revealing the concentrations of individual complex species as a function of pH. The results revealed that at a pH range 4.0–4.5 the major complex species is $[(pyda\cdot H)]_2[Co(pydc)_2]$.

Key words: self-assembly, X-ray crystal structure, Co(II) complex, La(III) complex, 2,6- pyridinedicarboxylic acid, 2,6-pyridinediamine, hydrogen bonding.

Résumé : On a préparé les complexes $[pyda\cdot H]_2(Co(pydc)_2]\cdot H_2O$ (**I**) et $[pyda\cdot H]_2(La_2(pydc)_4(H_2O)_4]\cdot 2H_2O$ (**II**) par complexation d'une nouvelle pyridine comportant un système d'autoassemblage, $\mathbf{LH_2}$, $([pyda\cdot H_2)^{2+}[pydc]^{2-})$ (pyda = pyridine-2,6-diamine et pydc·H_2 = pyridine-2,6-dicarboxylique) avec des sels de cobalt(II) et de lanthane(III), avec des rendements respectifs de 82% et de 74%. On a caractérisé ces complexes par analyse élémentaire, spectrométrie de masse « ESI », par spectroscopie RMN du ^1H et du ^{13}C en solution ainsi que par diffraction des rayons X. Les systèmes cristallins des composés **I** et **II** sont respectivement monoclinique et triclinique avec des groupes d'espace $P2_1/n$ et $P\bar{1}$. Le nombre de coordination autour de chaque atome de cobalt est de six, avec une géométrie octaédrique déformée, alors que le nombre de coordination autour de chaque atome de lanthane est de neuf, avec une géométrie à prisme trigonal fortement déformée. En solution dans le DMSO-d_6, les complexes paramagnétique du Co(II) et diamagnétique du La(III) présentent des résonances RMN du ^1H tant pour la partie anionique $[pydc]^{2-}$ que pour le contre-ion cationique $[pyda\cdot H]^+$. Faisant appel à des titrages potentiométriques, pH, on a étudié les réactions de complexation du complexe **I** en solution aqueuse et on décrit les constantes d'équilibre de tous les complexes principaux qui se forment. Les résultats sont présentés sous la forme de diagrammes de distribution qui mettent en évidence les concentrations des espèces de chaque complexe individuel en fonction du pH. Les résultats démontrent que dans la plage de pH allant de 4,0 à 4,5, l'espèce complexée le plus important est le $[(pyda\cdot H)]_2[Co(pydc)_2]$.

Mots clés : autoassemblage, structure cristalline par diffraction des rayons X, complexe du Co(II), complexe du La(III), acide pyridine-2,6-dicarboxylique, pyridine-2,6-diamine, liaison hydrogène.

[Traduit par la Rédaction]

Received 5 January 2002. Published on the NRC Research Press Web site at http://canjchem.nrc.ca on 20 December 2002.

A. Moghimi.[1] Department of Chemistry, University of Imam Hossein, Tehran, Iran.
M. Ranjbar and H. Aghabozorg. Department of Chemistry, Teacher Training University, Tehran, Iran.
F. Jalali and M. Shamsipur. Department of Chemistry, University of Razi, Kermanshah, Iran.
K.K. Chadha. Department of Chemistry, The Scripps Research Institute, La Jolla, CA 92037, U.S.A.

[1]Corresponding author(e-mail: samoghimi@yahoo.com).

 DOI: 10.1139/V02-183 © 2002 NRC Canada

Scheme 1. Synthesis method of ([pyda·H]$_2$[Co(pydc)$_2$]·H$_2$O and [pyda·H]$_2$[La$_2$(pydc)$_4$(H$_2$O)$_4$]·2H$_2$O complexes.

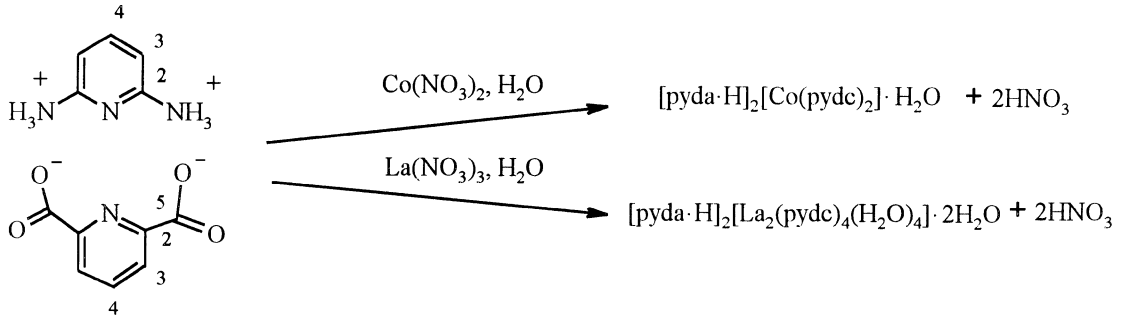

[pyda.H$_2$][pydc]

Introduction

Much effort has been made in recent years for the preparation and characterization of self-assembling systems (1). The generation of a self-assembling system that could function in polar solvents such as DMSO and H$_2$O has been a difficult task in this field. This is because of the competitive solvation of donor and acceptor sites by the polar solvents (2). In connection with such stable self-assembling systems in polar solvents, we succeeded in making the water-soluble system, [pyda·H$_2$]$^{2+}$[pydc]$^{2-}$ **LH$_2$**, containing doubly protonated 2,6-pyridinediamine, [pyda·H$_2$]$^{2+}$, and doubly deprotonated 2,6-pyridinedicarboxylic acid, [pydc]$^{2-}$, units (Scheme 1) (3). Recently, Schmuck reported a highly stable self-association of 5-(guanidinocarbonyl)-1H-pyrrole-2-carboxylate in DMSO (4). One of, or a combination of, intermolecular binding forces such as ion pairing, hydrogen bonding, hydrophobic or hydrophilic, host guest, π stacking, and donor–acceptor interactions could stabilize these systems in solution or in solid phase. Zafar et al. have recently tried to control the molecular self-assembly by designing a component containing both carboxylic acid and amino pyridine groups within the same framework (5).

A review of the literature showed that the rigid flat chelates [pydc·H$_2$] and [pyda] can individually form complexes with bivalent and trivalent transition metals (6–14). The La(III) complexes (6) involving [pydc]$^{2-}$ or [pydc·H]$^-$ ligands, [Ag(pydc)(pydc·H$_2$)]·H$_2$O (7), Ni(pydc·H)$_2$]·3H$_2$O (8), [Zn(pydc·H)$_2$]·2H$_2$O (9), [Fe$_2$(pydc)$_2$(OH$_2$)$_6$]·2[pydc·H$_2$] (10), NH$_4$[VO$_2$(pydc)] (11), and [Pd(pydc)(PBu$_3$)]$_2$ (12) are some examples in this regards. Although the solution studies, performed by Platas-Iglesias et al. (13), show that stable triple helical nine-coordinated La(III) complexes are formed from [pydc.H2] derivatives, to the best of our knowledge, no X-ray crystal structure data have yet been reported for the La(III) complex of dipicolinic acid.

Moreover, in a recent publication (15), some coordination complexes that self assemble in two-dimensional supramolecular networks or layers in the solid phase have been reported. These complexes contain bis(imidazolium 2,6-pyridinedicarboxylate) as a ligand. Accordingly, we became interested in investigating the influence of the counter ion [pyda·H$_2$]$^{2+}$ in the complexation process and succeeded in reporting {[BiCl(H$_2$O)(pydc)]$_2$}$_n$ (16), [pyda·H][Zn(pydc)(pydc·H]·3H$_2$O (17), and [pyda·H][Cr(pydc)$_2$]·pydc·H$_2$·0.5H$_2$O (18) complexes from **LH$_2$**. We have found out that a suitable

Fig. 1. ^{1}H NMR spectra of **LH$_2$**, [pyda·H]$_2$[Co(pydc)$_2$]·H$_2$O, and [pyda·H]$_2$[La$_2$(pydc)$_4$(H$_2$O)$_4$]·2H$_2$O complexes in DMSO-d6.

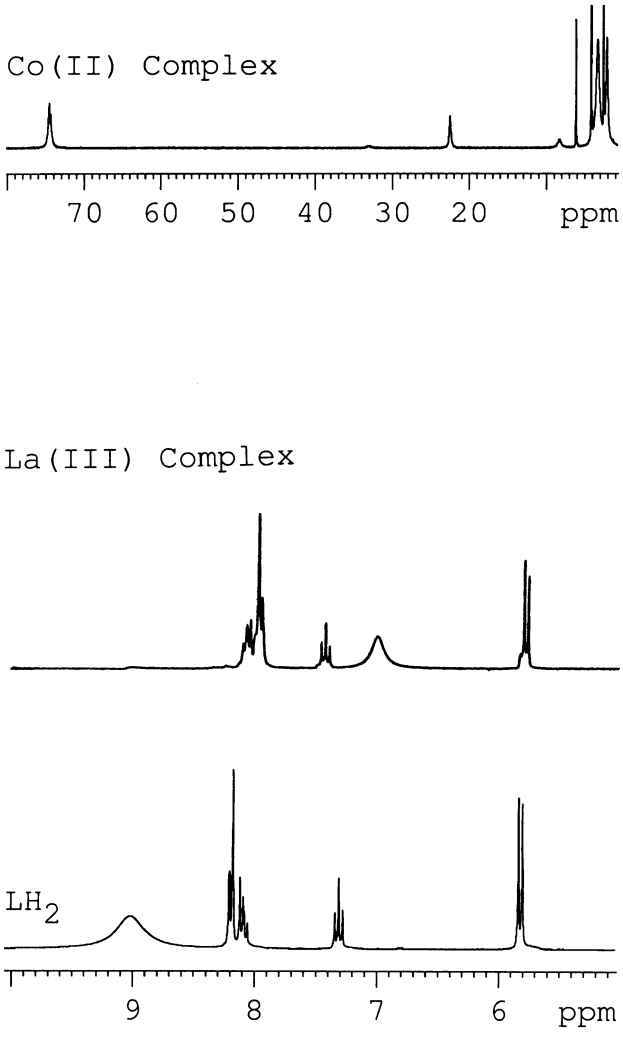

Lewis acid like [pyda] can play an important role in the preparation of anionic M[pydc]$^{n-}$, metal complexes. It also participates in the construction of extensive H-bonding networks within the lattice. In this paper we report the results of the complexation of **LH$_2$** with Co(II) and La(III), characterization of the resulting complexes, and their X-ray crystal structures and NMR data.

© 2002 NRC Canada

Table 1. Comparison between solution ^{13}C NMR data[a] of $\mathbf{LH_2}$ and La(III) complex.

Compound	C3 (cation)	C3 (anion)	C4 (cation)	C4 (anion)	C2 (cation)	C2 (anion)	C5 (anion)
$\mathbf{LH_2}$[b]	94.8	126.4	143.5	138.3	150.9	153.9	167.9
La(III) complex	95.1	124.7	144.4	139.4	152.3	152.8	169.3

[a]DMSO-d_6 signal at 39.6 ppm.
[b]Data from ref. 3.

Table 2. Crystal data and structure refinement for Co(II) and La(III) complexes.

Empirical formula	C_{24} H_{24} CoN_8 O_9	$C_{38}H_{40}La_2N_{10}O_{22}$
Formula weight	627.44	1266.62
Temperature (K)	296 (2)	110(2)
Wavelength (Å)	0.71073	0.71073
Crystal system, space group	Monoclinic, $P2_1/n$	Triclinic, $P\bar{1}$
Unit cell dimensions (Å)	a = 8.4080 (8)	a = 9.7435(17)
	b = 13.2982 (12)	b = 10.5288(19)
	c = 23.034 (2)	c = 10.7589(19)
α, β, γ (°)	β (°) = 95.502(2)	83.902(4), 88.114(4), 92.350(12)
Volume (Å^3)	2563.6(4)	1087.5(3)
Z, calculated density (g cm^{-3})	4, 1.626	1, 1.934
Absorption coefficient (mm^{-1})	0.741	2.039
F(000)	1292	628
Crystal size (mm)	0.33 × 0.25 × 0.20	0.33 × 0.28 × 0.11
θ range for data collection (°)	1.78 to 28.26	1.90 to 30.10
Limiting indices	$-7 \le h \le 11$, $-17 \le k \le 17$, $-25 \le l \le 29$	$-13 \le h \le 13$, $-14 \le k, \le 14$, $-14 \le l \le 15$
Reflections collected, unique	16116, 6025 [R_{int} = 0.0531]	12984, 6280[R_{int} = 0.0448]
Goodness-of-fit on F^2	0.894	0.871
Final R indices ($I >> 2s(I)$)	R_1 = 0.0482, wR_2 = 0.0957	R_1 = 0.0442, wR_2 = 0.0992
R indices (all data)	R_1 = 0.0935, wR_2 = 0.1096	R_1 = 0.0560, wR_2 = 0.0945
Largest diff. peak and hole (e Å^{-3})	0.451 and –0.410	1.919 and –1.532

Results and discussion

Synthesis and characterization of Co(II) and La(III) complexes of $\mathbf{LH_2}$

The reaction between $Co(NO_3)_2$ and $La(NO_3)_3$ with $\mathbf{LH_2}$ in water leads to the formation of crystalline products (Scheme 1) in 82% and 74% yields, respectively. These complexes displayed distinct mp and elemental analysis consistent with the formula $C_{24}H_{24}CoN_8O_9$ and $C_{38}H_{40}La_2N_{10}O_{22}$, respectively. The presence of $[pyda{\cdot}H]^+$ and $(M + H)^+$ ions in both complexes were confirmed from the expected fragments observed in ESI-MS spectra. This method was selected because of its proper response to the starting ionic ligand $\mathbf{LH_2}$ (3).

The ^1H NMR spectra of the complexes as well as the $\mathbf{LH_2}$ ligand are shown in Fig. 1, and the corresponding ^{13}C NMR data are presented in Table 1. As seen from Fig. 1, the $[pydc]^{2-}$ protons in the paramagnetic Co(II) complex were shifted downfield to 22.5 and 75.0 ppm whereas the resonances of $[pyda{\cdot}H]^+$ were not much disturbed. The upfield shift for NH_3^+ protons can be attributed to the functional group transformation, $-NH_3^+$ to $-NH_2$, upon complexation. From the integration of two characteristic sets of ^1H resonances of both complexes, the $[pydc]^{2-}$:$[pyda{\cdot}H]^+$ mole ratio was found to be 2. A comparison between the NMR data (Fig. 1 and Table 1) indicates that, contrary to the Co(II) complex, the $\mathbf{LH_2}$ resonances are not much shifted upon complexation with La(III).

As a result of complex formation, the strong IR absorptions of $\mathbf{LH_2}$ at 1700 and 1340 cm^{-1} indicative of carboxylate groups are replaced by very strong and broad bands centered at 1660 and 1380 cm^{-1} for the Co(II) complex and at 1600 cm^{-1} and 1420 cm^{-1} for the La(III) complex. The shifts in the position and shape of these bands suggest that both carboxylate groups of $[pydc]^{2-}$ are coordinated to the metal atoms. The two bands at 645 and 420 cm^{-1} that are ascribed to the C—H out of plane bending of the pyridine ring of $[pyda{\cdot}H_2]$ are split and shifted to the higher frequencies due to the pyridine coordination (19). The band at 1580 cm^{-1}, related to the NH of the free ligand, is also shifted to a lower frequency (i.e., 1560 cm^{-1}). This shift may be due to the decreased positive charge in the $[pyda{\cdot}H]^+$ counter ion in comparison with $[pyda{\cdot}H_2]^{2+}$. The new bands in the 360–440 cm^{-1} region result from the new metal–ligand, M—N and M—O, bond formation (20).

X-ray crystallographic structure for Co(II) and La(III) complexes

The numbering schemes and ORTEP diagrams of the Co(II) and La(III) complexes are presented in Fig. 2. A summary of crystallographic data, selected bond lengths and angles for Co(II) and La(III) complexes, and H-bonding data are given in Tables 2 and 3.

An important feature of the crystal structures is the existence of ionic complexes consisting of $[M(pydc)_2]^{n-}$ and $[pyda{\cdot}H]^+$ units (M = Co and La). The cobalt atom is in the

© 2002 NRC Canada

Fig. 2. ORTEP diagrams and numbering schemes of (*a*) [pyda·H]$_2$[Co(pydc)$_2$]·H$_2$O and (*b*) [pyda·H]$_2$[La$_2$(pydc)$_4$(H$_2$O)$_4$]·2H$_2$O complexes.

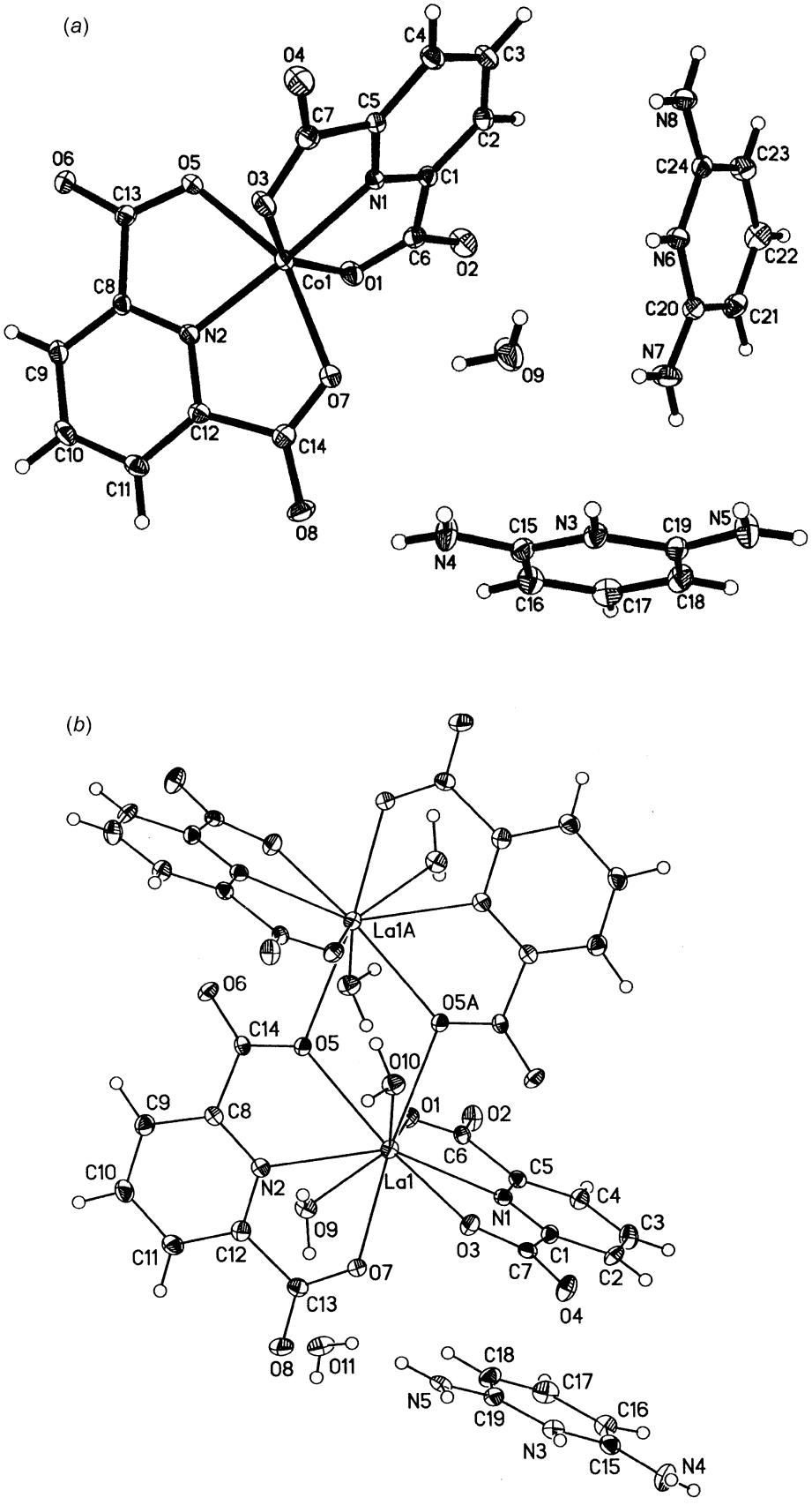

© 2002 NRC Canada

Table 3. Selected bond lengths (Å) and angles (°) for Co(II) and La(III) complexes.

Bond lengths (Å)			
Co (1)—N (1)	2.010 (2)	Co (1)—N (2)	2.018 (2)
Co (1)—O (7)	2.144 (2)	Co (1)—O (5)	2.148 (2)
Co (1)—O (3)	2.2078 (19)	Co (1)—O (1)	2.219 (2)
Bond angles (°)			
N (1)-Co (1)-N (2)	176.49 (10)	N (1)-Co (1)-O (7)	107.14 (9)
N (2)-Co (1)-O (7)	76.34 (8)	N (1)-Co (1)-O (5)	100.13 (8)
N (2)-Co (1)-O (5)	76.39 (8)	O (7)-Co (1)-O (5)	152.73 (8)
N (1)-Co (1)-O (3)	75.89 (8)	N (2)-Co (1)-O (3)	104.37 (8)
O (7)-Co (1)-O (3)	96.43 (8)	O (5)-Co (1)-O (3)	90.33 (8)
N (1)-Co (1)-O (1)	76.22 (8)	N (2)-Co (1)-O (1)	103.65 (8)
O (7)-Co (1)-O (1)	89.04 (8)	O (5)-Co (1)-O (1)	97.32 (8)
O (3)-Co (1)-O (1)	151.96 (7)		
Bond lengths (Å)			
La(1)—O(3)	2.468(3)	La(1)—O(9)	2.545(3)
La(1)—O(7)	2.550(3)	La(1)—O(1)	2.554(3)
La(1)—O(5)	2.560(3)	La(1)—O(5)#1	2.603(2)
La(1)—N(1)	2.623(3)	La(1)—O(10)	2.665(3)
La(1)—N(2)	2.702(3)	O(1)-La(1)-O(5)#1	70.12(8)
Bond angles (°)			
O(3)-La(1)-O(9)	77.00(9)	O(5)-La(1)-O(5)#1	60.95(10)
O(3)-La(1)-O(7)	79.17(8)	O(3)-La(1)-N(1)	62.23(9)
O(9)-La(1)-O(7)	71.79(10)	O(9)-La(1)-N(1)	130.11(10)
O(3)-La(1)-O(1)	123.94(9)	O(7)-La(1)-N(1)	73.14(9)
O(9)-La(1)-O(1)	144.57(9)	O(1)-La(1)-N(1)	61.73(9)
O(7)-La(1)-O(1)	83.70(9)	O(5)-La(1)-N(1)	138.69(9)
O(3)-La(1)-O(5)	152.46(9)	O(5)#1-La(1)-N(1)	89.88(9)
O(9)-La(1)-O(5)	90.09(9)	O(3)-La(1)-O(10)	78.11(9)
O(7)-La(1)-O(5)	120.17(8)	O(9)-La(1)-O(10)	69.72(10)
O(1)-La(1)-O(5)	80.13(8)	O(7)-La(1)-O(10)	138.82(10)
O(3)-La(1)-O(5)#1	111.33(9)	O(1)-La(1)-O(10)	137.35(9)
O(9)-La(1)-O(5)#1	133.29(9)	O(5)-La(1)-O(10)	74.59(9)
O(7)-La(1)-O(5)#1	153.41(9)	N(1)-La(1)-O(10)	123.23(10)
O(5)#1-La(1)-O(10)	67.67(9)	O(9)-La(1)-N(2)	69.76(10)
O(3)-La(1)-N(2)	133.65(9)	O(1) -La(1)-N(2)	75.95(9)
O(7)-La(1)-N(2)	60.55(9)	O(5)#1-La(1)-N(2)	114.93(9)
O(5)-La(1)-N(2)	59.68(9)	O(10)-La(1)-N(2)	117.19(9)
N(1)-La(1)-N(2)	119.56(10)		

Note: # 1: *–x*, *–y*, *–z*.

center of a distorted octahedral arrangement consisting of six donor atoms of two tridentate ligands of $[pydc]^{2-}$. The two O3-Co-O1 and O7-Co-O5 angles indicate that the four carboxylate groups of the two dianions are oriented in a flattened tetrahedral arrangement around the Co(II) atom. The two dianionic $[pydc]^{2-}$ units are almost perpendicular to each other. The molecular structure of the La(III) complex, $[pyda.H]_2[La_2(pydc)_4[(H_2O)_4]\cdot 2H_2O$, consists of two metal fragments linked *via* the central four-membered La_2O_2 ring. The binuclear self-assembled La(III) complex is built up from two equivalent nine-coordinated lanthanum complex ions. Each of the two La atoms has a highly distorted tricapped trigonal prism geometry and is surrounded by seven oxygen and two nitrogen donor atoms (Fig. 2).

It is worthy to note that, although we started the complexation with $[pyda\cdot H_2]^{2+}[pydc]^{2-}$ ligand, the monocationic $[pyda\cdot H]^+$ counter ion exists in both complexes. The protonated site of the cationic counter ion in both complexes is the pyridine nitrogen. Interestingly, the two protonation sites in **LH_2** are the two -NH_2 nitrogens (3).

The mean of the Co—N and Co—O bond distances (i.e., 2.014 and 2.179 Å, respectively) are different from the corresponding values reported for bis (imidazolium) - 2,6-pyridinedicarboxylate Co(II) complex. For instance, the Co—N1, Co—O2, and Co—O3 distances in the imidazolium complex are 2.157, 2.223, and 2.219 Å, respectively. With respect to the axial N-Co-N angle involving the nitrogen atoms on the two pyridyl ligands, a small deviation (i.e., 3.51°) from linearity is observed. This bond angle is close to the values reported for N-Cu-N than N-Co-N angles in imidazolium carboxylate complexes. The data presented specify that these key bond distances and angles are affected by the nature of the cationic counter ion.

The average La—O (carboxylate) distance, 2.538 Å, in the La(III) complex is comparable with the similar average distance, 2.52 Å, in the $[La_2(C_4H_4O_5)_3(H_2O)_3.5H_2O]_n$ complex

© 2002 NRC Canada

Fig. 3. The hydrogen bonding representation in the $[pyda{\cdot}H]_2[La_2(pydc)_4(H_2O)_4]{\cdot}2H_2O$ complex.

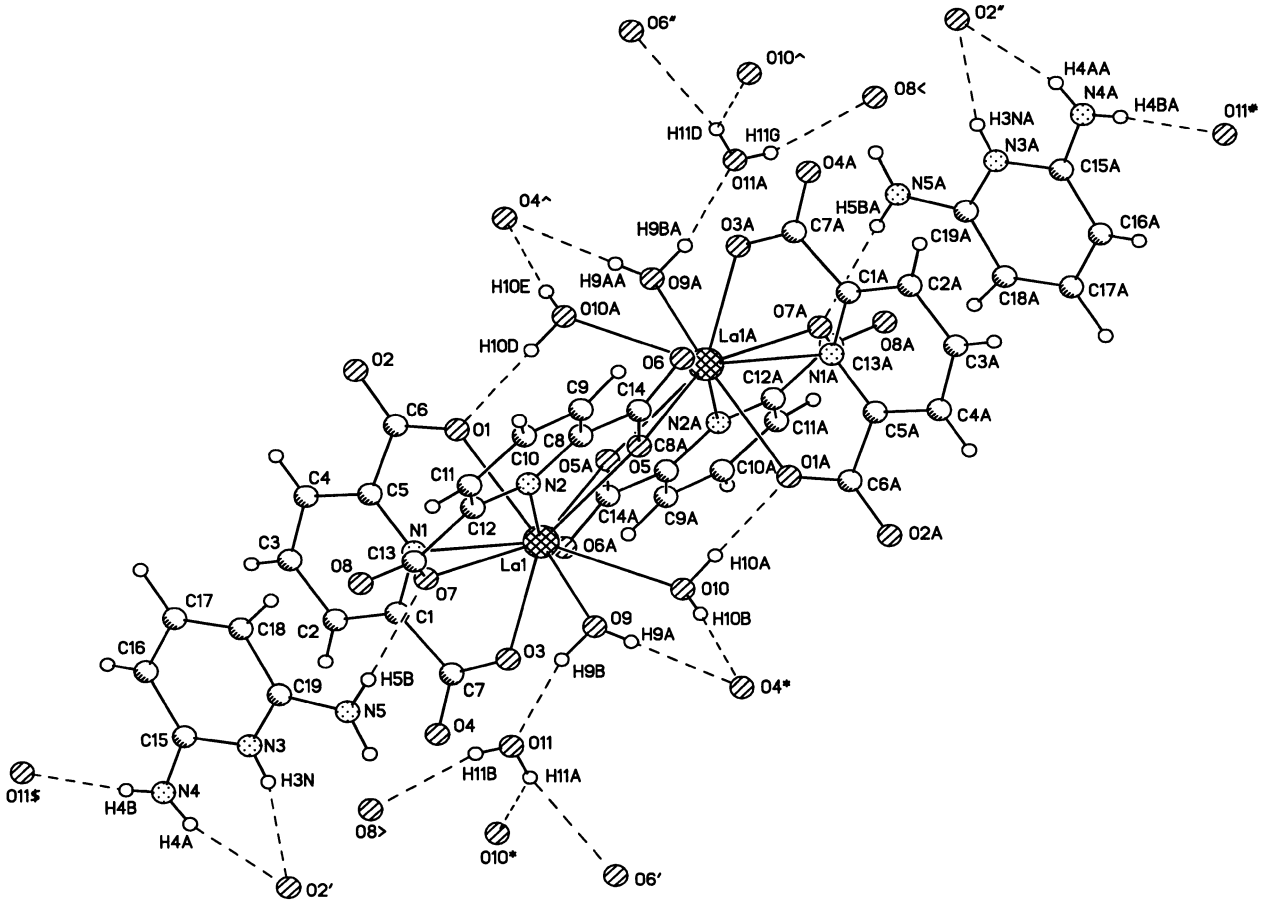

(21), whereas it is larger (2.545Å) in the lanthanum oxalate complexes (22, 23). Also, the average donor–acceptor La—O (water) bond lengths in the present La(III) complex and $[La_2(C_4H_4O_5)_3(H_2O)_3.5H_2O]_n$ are 2.605 and 2.556 Å, respectively (21, 24). The average La—O distances in [La Br_2(diglyme)$_2$][$LaBr_2$(diglyme)] (25), (η^5: η^1: η^1-$C_5H_3(CH_2CH_2NMe_2)_2$-1,3) LaI_2(THF) (26) and $[La_2(C_3H_2O)_3(H_2O)_4].H_2O$ (27) have been reported as 2.58, 2.59, and 2.62 Å, respectively.

As seen in Fig. 3, there are extensive intermolecular H-bondings between coordinated and uncoordinated water molecules, $[pyda{\cdot}H]^+$ and $[pydc]^{2-}$ units in La(III) complex. The D—H and H….A distances and DHA angles in these two complexes indicate that the number of H-bondings in the Co(II) complex is less than those in La(III) complex. The counter ions $[pyda{\cdot}H]^+$ have important role in facilitating the formation of extensive H-bondings in both complexes, particularly in the La(III) complex. Therefore, both ion pairing and H-bonding factors are involved in the construction of the final extended layers that connect to each other to provide self -assembling complexes. As a result, the lattice energy in each case is expected to be large.

By considering some of the $\mathbf{LH_2}$ complexes already reported by this research group (16–18), the two cases under discussion, and the examples provided from the literature (11, 15), one may conclude that in the presence of an amine the ionic metal complex of $[pydc]^{2-}$ should be formed. However, it has to be noticed that this is not necessarily true for all complexes (16).

Solution studies for Co(II) complexes

The equilibrium potentiometric pH titration profiles of $\mathbf{LH_2}$ in (*a*) absence and (*b*) presence of Co^{2+} ion in a 1:2 (Co^{2+}:$\mathbf{LH_2}$) ratio are shown in Fig. 4. The protonation constants ($K_n^H = [H_nL]/[H_{(n-1)}L][H]^n$) were calculated by fitting the potentiometric pH data to the program BEST (28). The abbreviations L, LH, LH_3 and L_2H_2 in Figs 4 and 5 denote to the $\{[pyda][pydc]\}^{2-}$, $\{[pyda{\cdot}H][pydc]\}^-$, $\{[pyda{\cdot}H_2][pydc{\cdot}H]\}^+$, and $\{[pyda{\cdot}H]_2[pydc]_2\}^{2-}$ species, respectively. The results are listed in Table 4, and the species distribution in the absence of metal ion is shown in Fig. 5. As is obvious from Fig. 5, the self-assembling system cannot exist at all at pH>8 and pH<1; at the high pH limits, the partners exist as a neutral amine $[pyda]^{\cdot}$ and a dicarboxylate anion $[pydc]^{2-}$, whereas at the low pH limits, they exist as a diprotonated amine $[pyda{\cdot}H_2]^{2+}$ and a neutral dicarboxylic acid $[pydc{\cdot}H_2]^{\cdot}$. However, maximum amount of the self-assembling system ($[pyda{\cdot}H_2]^{2+}[pydc]^{2-}$), ($\mathbf{LH_2}$) exists (at an about 90% level) at a pH range of about 4.0–4.5, in solution. It is interesting to note that, although both [pyda] and $[pydc{\cdot}H_2]$ exist in three-protonated forms, the pH metric data of their 1:1 mixture cannot be fitted to a six-protonation model. This is obviously in support of the formation of the ion-association compound, in solution.

As is seen from Fig. 4, the potentiometric titration curve of $\mathbf{LH_2}$ system is depressed considerably in the presence of Co^{2+} ion at the metal-to-ligand mole ratio of 1:2. The extent of depression obviously depends both on the stoichiometries

© 2002 NRC Canada

Fig. 4. Potentiometric pH titration curves of $\mathbf{LH_2}$ in the (*a*) absence and (*b*) presence of Co^{2+} ion. Conditions: $[\mathbf{LH_2}] = 1.0 \times 10^{-3}$ M; $[Co^{2+}] = 5.0 \times 10^{-4}$ M; $[H^+] = 0.01$ M; "a" is the molar ratio of $[OH]^-/[LH_2]$, negative values being that of $[OH]^-/[H^+]_{excess}$.

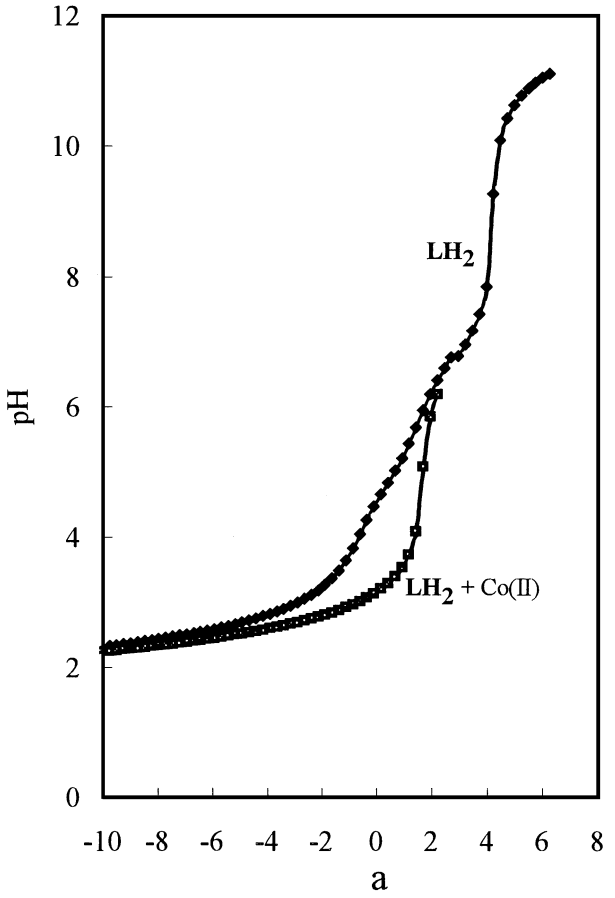

of the resulting complexes and the ability of metal ion to bind to the ligand components. The cumulative stability constants, β_{pqr}, are defined by eq. [1] (charges are omitted for simplicity).

$$[1] \qquad pM + qL + rH \overset{\beta_{pqr}}{\rightleftharpoons} M_pL_qH_r$$

$$\beta_{pqr} = \frac{[M_pL_qH_r]}{[M]^p[L]^q[H]^r}$$

where M is the metal ion, L is the ligand $\mathbf{LH_2}$, H is the proton, and p, q, and r are the respective stoichiometric coefficients. Since the ligand and complex activity coefficients are unknown, the β_{pqr} values are defined in terms of concentrations. The errors are minimized by use of a high constant ionic strength (0.1 M) and low ligand concentration (1.0×10^{-3} M).

The potentiometric pH titration curve of $\mathbf{LH_2}$ in the presence of Co^{2+} ion was fitted to the program BEST, in order to calculate the cumulative stability constants of likely complexed species in solution. The results are included in Table 4, and the species distribution diagram of $\mathbf{LH_2}$ in the presence of Co^{2+} ion is shown in Fig. 6. From Fig. 6, it is obvious that negligible amounts of deprotonated CoL and CoL_2 complexes are formed in solution, over the entire pH

Fig. 5. Distribution curves for L^{2-}, LH^-, $\mathbf{LH_2}$, LH_3^+, and LH_4^{2+} in the self-assembling system in the absence of Co^{2+}.

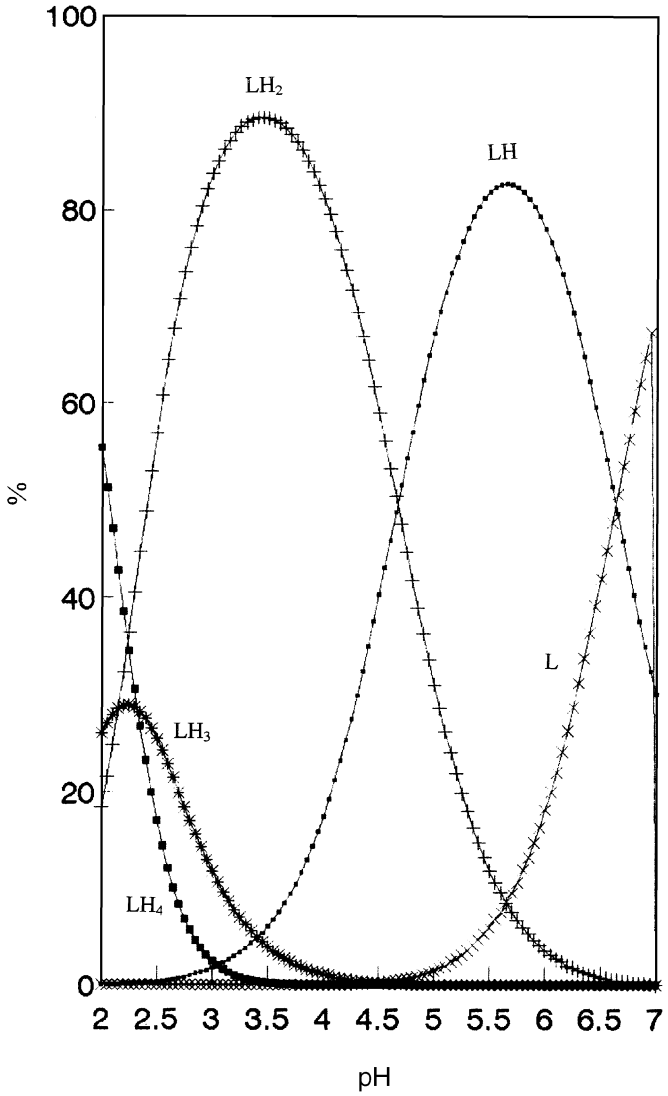

range of 2.0 to 7.0, while the monoprotonated forms of these species (i.e., CoLH and CoL_2H) show an extent of about 21% (at pH 2.5) and 46% (at pH 7.0), respectively. On the other hand, a CoL_2H_2 complex (i.e., $[(pyda{\cdot}H)]_2[Co(pydc)_2]$) is formed to an extent of about 41% at a pH range of about 4.0–4.5 and decreases in concentration at higher and lower pH values in the expense of increased amount of CoL_2H and CoLH, respectively. Thus, the solution studies strongly support the predominance of the formation of a CoL_2H_2 complexed species with a stoichiometry similar to that of the isolated crystalline complex.

Experimental

Materials

2,6-Pyridinediamine (98%) was purchased from Aldrich and 2,6-pyridinedicarboxylic acid (98%), triethylamine (99%), and tetrahydrofuran (99.7%) were purchased from Merck. Potassium hydroxide, potassium nitrate, potassium hydrogen phthalate, cobalt(II) nitrate hexahydrate 99%, and

© 2002 NRC Canada

Table 4. Logarithm of cumulative stability constants of H^+ and Co^{2+} complexes with $\mathbf{LH_2}$ at 25°C and ionic strength of 0.1 M.

Cation	Stoichiometry			Log β[a]
	P	q	r	
H^+	0	1	1	6.63
	0	1	2	11.30
	0	1	3	13.45
	0	1	4	15.77
Co^{2+}	1	1	0	3.24
	1	1	1	12.10
	1	2	0	8.66
	1	2	1	18.45
	1	2	2	24.07

[a]Uncertainties in the cumulative stability constants estimated as ±0.5 of the last significant digit.

lanthanum(III) nitrate hexahydrate were of analytical grade from Merck. Doubly distilled deionized water was used throughout. The synthesis of $\mathbf{LH_2}$ was performed using a previously reported procedure (3).

Instruments

IR spectra were recorded on a Perkin-Elmer 343 and 1720X spectrophotometer using KBr discs. Melting points were determined with a Buchi 520 and were not corrected. ^{1}H NMR and ^{13}C NMR spectra were obtained on a Bruker 250 (250 and 62.5 MHz, respectively) spectrometer. Chemical shifts are reported on the δ scale relative to TMS. Mass spectra were recorded with a MS80RFA spectrometer. Elemental analyses were performed with a Perkin-Elmer 240 apparatus. A Pre-Unicam Spa Philips atomic absorption was used to determine the percentage of Co(II) and La(III) in the complexes. A Jeneway ion analyzer 3045 was applied for quantitative analysis of the NO_3^- anion. All pH measurements were carried out with a model 632 digital pH meter equipped with a combined glass–calomel electrode.

Synthesis of $[pyda{\cdot}H]_2[Co(pydc)_2]{\cdot}H_2O$ complex

To a solution of $Co(NO_3)_2.6H_2O$ (0.26g, 0.9 mmol) in water (20 mL) was added a solution of $\mathbf{LH_2}$ (0.5g, 1.8 mmol) in water (100 mL) and the resulting light brown solution stirred for 15 min. After three weeks, light brown crystals were isolated. The crystals were collected, washed with fresh distilled water, and dried. The pure light brown block shaped crystalline Co(II) complex (0.47g) was prepared in 82.2% yield. mp 285–88°C. IR (KBr) (cm^{-1}): 3520 (s), 3360 (s), 3280 (s), 3160 (s), 1660 (s), 1560 (s), 1480 (w), 1420 (m), 1380 (m), 1320 (m), 1280 (m), 1180 (w), 1130 (w), 1078 (m), 960 (m), 905 (m), 820 (w), 760 (m), 720 (m), 680 (m), 670 (m), 560 (m), 520 (w), 480 (w), 440 (w), 400 (w), 360 (w), 300 (w). ^{1}H NMR (DMSO-d_6) (ppm) δ: H 4.40 (d, 4H, ^3J = 8 Hz, H3,5, pyda·H), 6.31 (t, 2H, ^3J = 8Hz, H4, pyda·H), 22.5 (H4, pydc), 75.0 (H3,5, pydc). ESI-MS *m/e* (%): 609.9 ([M – H_2O + H^+], 0.68), 432.2 (1.3), 406.1 (0.3), 333.9 (1.5), 144.9 (14.3), 109.8 ([pyda·H^+], 100). Anal. calcd. for $C_{24}H_{24}CoN_8O_9$ (%): C 45.90, H 3.82, N 17.85, Co 9.39; found: C 46.27, H 3.64, N 17.87, Co 9.20.

Fig. 6. Distribution curves for CoL, CoLH, CoL_2, CoL_2H, CoL_2H_2, and Co^{2+} in the 1:2 Co^{2+} : $\mathbf{LH_2}$ system.

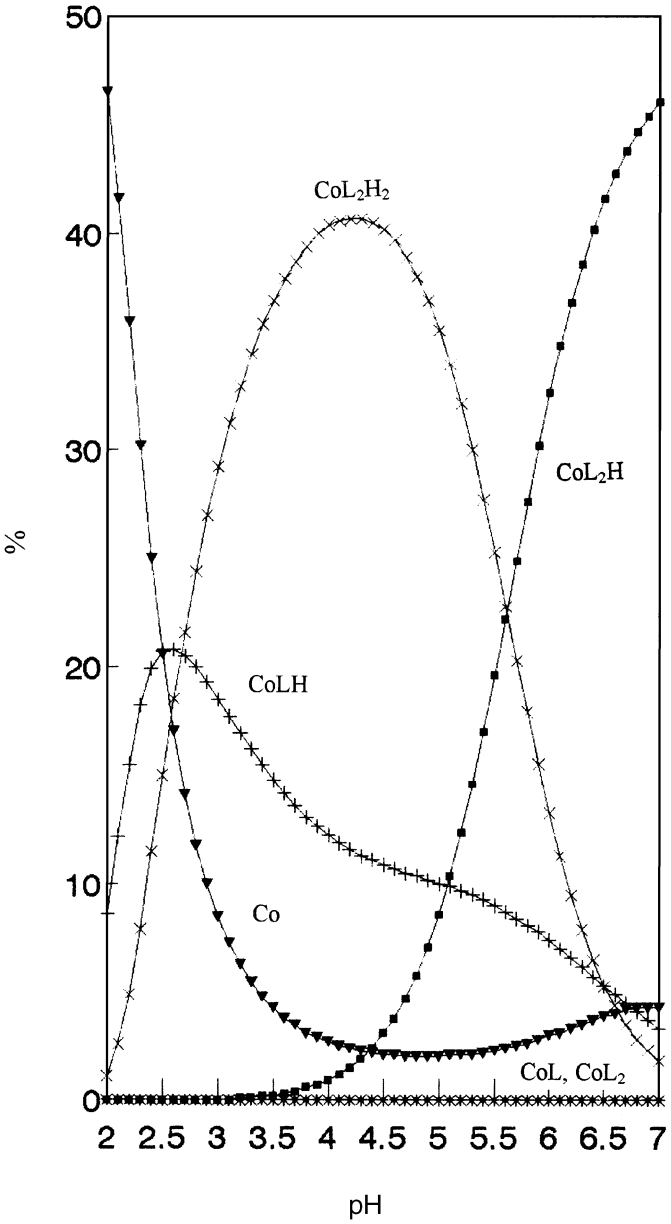

Synthesis of $[pyda{\cdot}H]_2[La_2(pydc)_4(H_2O)_4]{\cdot}2H_2O$ complex

The procedure applied for Co(II) complex was followed. The pure light yellow block shaped crystals of La(III) complex (0.85g) were obtained in 74% yield, decomposed at 250°C. IR (KBr) (cm^{-1}): 3520 (m), 3320 (s), 3000 (sh), 2920 (sh), 2800 (sh), 1680 (s), 1580 (s), 1560 (s), 1420 (s), 1360 (s), 1300 (m), 1260 (m), 1180 (m), 1160 (m), 1140 (w), 1080 (m), 1000 (m), 980 (w), 920 (m), 860 (w), 820 (w), 760 (m), 720 (m), 680 (m), 660 (w), 580 (w), 520 (w), 480 (w), 440 (w), 400 (w), 320 (w). ^{1}H NMR (DMSO-d_6) (ppm) δ: H 5.90 (d, 2H, H3,5 pyda·H), 7.04 (br, s, 4H, NH_2), 7.45 (t, 1H, H4, pyda·H), 7.15 (m, 4H, pydc), 8.06 (m, 2H, pydc). ^{13}C NMR (DMSO-d_6) (ppm) δ: C 95.1 (C3′), 124.4 (C3), 139.4 (C4), 144.4 (C4′), 152.3 (C2′), 152.8 (C2), 169.3

© 2002 NRC Canada

(C5). Anal. calcd. for $C_{38}H_{40}La_2N_{10}O_{22}$ (%): C 36.00, H 3.15, N 11.05, La 21.93; found: C 35.81, H 3.19, N 10.99, La 22.00.

Determination of X-ray crystal structure

X-ray crystallographic data were obtained on a Bruker SMART diffractometer equipped with a molybdenum sealed tube and a graphite monochromator at 296 (2) K for the complex **I** and 110 (2) K for the complex **II**. The final cell parameters were determined using the SAINT$^+$ software. It was not found necessary to apply decay or absorption corrections to the data. The data were reduced to give the number of unique reflections.

The structure was solved by automatic direct methods using SHELXTL-PC. The structure was refined by full-matrix least-squares analysis on F^2 with SHELXL. The non-hydrogen atoms were refined anisotropically and all the hydrogen atoms were located from subsequent difference Fourier maps and refined with individual temperature factors to a final R value of 0.0482 for the complex **I** and 0.0442 for the complex **II**.

pH metric titrations

The base used for potentiometric pH titrations was carbonate free potassium hydroxide, which was standardized against primary standard oven-dried potassium hydrogen phthalate. A CO_2-free atmosphere for the base was ensured throughout. The potentiometric apparatus used consisted of a 50 mL glass jacketed cell, a constant temperature bath (MLW thermostat, 25.0 ± 0.1°C), a combined glass electrode, and a 10 mL capacity Metrohm piston burette, for which the tip was sealed in the cap of the titration cell with a clamp and O-rings. Atmospheric CO_2 was excluded from the titration cell with a purging steam of purified nitrogen gas. The electrodes were calibrated in the thermostated cell with standard acid–base to read pH directly (pH = –log $[H^+]$). The value of $K_w = [H^+][OH^-]$ used in the calculations was $10^{-13.78}$ (28). In all experiments, a 1.0×10^{-3} M solution of the ligand was used. The ionic strength was adjusted to 0.1 M with KNO_3. Before an experimental point (pH) was measured, sufficient time allowed for establishment of equilibrium.

Ligand protonation constants and its metal complexes' protonation, stability, and hydrolysis constants were calculated using the program BEST methods described by Martell and Motekaitis (29).

Conclusions

We have demonstrated that the complexation reaction between a novel pyridine containing self-assembling system ligand $\mathbf{LH_2}$ with $Co(NO_3)_2$ and $La(NO_3)_3$ in water leads to the formation of anionic complexes involving $[pyda{\cdot}H]^+$ counter ion. The 2,6-pyridinediamine can serve as a proton acceptor source and the protonated position in the cationic counter ion is the pyridine nitrogen atom while the two protons in the ligand $\mathbf{LH_2}$ are located at the two -NH_2 nitrogen positions. The intermolecular forces existing between anionic and cationic units in the Co(II) and the La(III) complexes consist of both H-bonding and ion-pairing. The solution ^{1}H NMR spectra of the resulting paramagnetic Co(II) and diamagnetic La(III) complexes show the resonances of both cationic and anionic ions $[pyda{\cdot}H]^+$ and $[pydc]^{2-}$ in DMSO-d_6. The results of the potentiometric pH titrations in aqueous solutions also revealed the predominance of the $[pyda{\cdot}H]_2[Co(pydc)_2]$ complex at a pH range 4.0–4.5. The equilibrium constants for all major complexes formed in aqueous solutions are reported. We are now expanding our research to investigate complexes synthesized from Hg, Pd, Pt, Cd, Pb, Tl, V, Sb, Sn, and Zr cations.

Acknowledgments

Teacher Training University and University of Razi financially supported this work. We are grateful to Prof. M. Reza Ghadiri's research group at Scripps Research Institute for X-ray crystallographic data for Co(II) complex. We are also grateful to Dr. G.U. Grintseleu-Knyazev from General and Technical Chemistry Division of Academy of Science of Russia for X-ray crystallographic data for La(III) complex.

References

1. J.A. Zerkowski, C.T. Seto, and G.M. Whitesides. J. Am. Chem. Soc. **114**, 5473 (1992); C.T. Seto and G.M. Whitesides. J. Am. Chem. Soc. **115**, 1330 (1993); C.T. Seto and G.M. Whitesides. J. Am. Chem. Soc. **112**, 6409 (1990); Z.-T. Li, P.C. Stein, J. Becher, D. Jensen, P. Mork, and N. Svenstrup. Chem. Eur. J. **2**, 624 (1996); C.T. Seto, J.P. Mathias, and G.M. Whitesides. J. Am. Chem. Soc. **115**, 1321 (1993); C.T. Seto and G.M. Whitesides. J. Am. Chem. Soc. **113**, 712 (1991); C.T. Seto and G.M. Whitesides. J. Am. Chem. Soc. **115**, 905 (1993); J.A. Zerkowski, C.T. Seto, D.A. Wierda, and G.M. Whitesides. J. Am. Chem. Soc. **112**, 9025 (1990); J. Jr Rebek. Angew. Chem. Int. Ed. Engl. **29**, 245 (1990); J.-M. Lehn. Angew. Chem. Int. Ed. Engl. **27**, 89 (1988); P. Tecilla, R.P. Dixon, G. Slobodkin, D.S. Alavi, D.H. Waldeck, and A. D. Hamilton. J. Am. Chem. Soc. **112**, 9408 (1990); S.-K. Chang and A.D. Hamilton. J. Am. Chem. Soc. **110**, 1318 (1988); S.C. Zimmerman, C. M. Vanzyl, and A.D. Hamilton. J. Am. Chem. Soc. **111**, 1373 (1989); A.J. Doig and D.H. Williams. J. Am. Chem. Soc. **114**, 338 (1992); B. Linton and A.D. Hamilton. Chem. Rev. **97**, 1669 (1997); J.-M. Lehn and A. Rigault. Angew. Chem. Int. Ed. Engl. **27**, 1095 (1988); A. Pfeil and J.-M. Lehn. J. Chem. Soc., Chem. Commun. 838 (1992); E.C. Constable. Chem. Ind. 56 (1994); J.-C. Chambron, C.O. Dietrich-Buchecker, and J.-P. Sauvage. Top. Curr. Chem. **165**, 131 (1993); J.-C. Chambron, C.O. Dietrich-Buchecker, and J.-P. Sauvage. New J. Chem. **16**, 931 (1992); F.C.- Tellado, S.J. Geib, S. Goswami, and A.D. Hamilton. J. Am. Chem. Soc. **113**, 9265 (1991); J. Yang, S.J. Geib, and A.D. Hamilton. J. Am. Chem. Soc. **115**, 5314 (1998); B. Konig, O. Moller, and P. Bubenitschek. J. Org. Chem. **60**, 4291 (1995); Q. Lin, S.J.Geib, and A.D. Hamilton. J. Chem. Soc. Perkin Trans. 2, 2109 (1998).
2. M.M. Conn and J. Jr Rebek. Chem. Rev. **97**, 1647 (1997); M.O. Adeboya, R.L. Edwards, T. Lasse, D.J. Maitland, L. Shields, and A.J.S. Whalley. J. Chem. Soc. Perkin Trans. 1, 1419 (1996).
3. A. Moghimi, M. Rangbar, H. Aghabozorg, F. Jalali, M. Shamsipur, G.P.A. Rap, and H. Rahbarnoohi. J. Mol. Struct. **605**, 133 (2002).
4. C. Schmuck. Eur. J. Org. Chem. 2397 (1999).
5. A. Zafar, S.J. Geib, Y. Hamuro, A.J. Carr, and A.D. Hamilton. Tetrahedron, **56**, 8419 (2000).

© 2002 NRC Canada

6. D.L. Hoof, D.G. Tisky, and R.A. Walton. J. Chem. Soc. Dalton Trans. 200 (1973); M.X. An, S.L. Fang, and N.J. Zhang. J. Mol. Sci. **4**, 103 (1986); B.M. Alsaadi, F.J.C. Rossitti, and R.J.P. Williams. J. Chem. Soc. Dalton Trans. 598 (1980).
7. M.G.B. Drew, R.W. Matthews, and R.A. Walton. J. Chem. Soc. A, 1405 (1970).
8. M. Biagini, C. Villa, C. Guastini, and M. Nardelli. Gazz. Chim. Italy. **102**, 1026 (1972).
9. G.D. Ascenzo, A. Marino, M. Sabbatini, and T. Bica. Thermochim. Acta. **25**, 325 (1978).
10. P. Lainé, A. Gourdon, J.-P.Launay, and J.-P. Tuchagues. Inorg. Chem. **34**, 5150 (1995).
11. D.C. Crans, L. Yang, T. Jakusch, and T. Kiss. Inorg. Chem. **39**, 4409 (2000).
12. P. Espinet, J.A. Miguel, S.G.-Granada, and D. Miguel. Inorg. Chem. **35**, 2287 (1996).
13. C. Platas-Iglesias, C. Piguet, N. Andre, and Jean-Claude G. Bünzli. J. Chem. Soc. Dalton Trans. 3084 (2001); G. Muller, B. Schmidt, J. Jiricek, G. Hopfgartner, J.P. Riehl, Jean-Claude G. Bünzli, and C. Piguet. J. Chem. Soc. Dalton Trans. 2655 (2001).
14. D.P. Murtha and R.A. Walton. Inorg. Chem. **12**, 368 (1973); M.G.B. Drew, G.W.A. Fowles, R.W. Matthews, and R.A. Walton. J. Am. Chem. Soc. **91**, 7769 (1969); D.P. Murtha and R.A. Walton. Inorg. Chem. **12**, 1278 (1973); R.W. Matthews, A.D. Hamer, D.L. Hoof, D.G. Tisley, and R.A. Walton. J. Chem. Soc. Dalton Trans. 1035 (1973); D. Schwarzenbach. Helv. Chim. Acta, **55**(8), 299 (1972); P.E. Hoggard and H.H. Schmidtke. Inorg. Chem. **12**, 1986 (1973); X.Y. Zhou and N.M. Kostic. Inorg. Chem. **27**, 4402 (1988); J.G.H. du Preez and B.J.A.M. van Brecht. J. Chem. Soc. Dalton Trans. 253 (1989); P.P. Quaglieri, H. Loiseleur, and G. Thomas. Acta Crystallogr. Sect. B, **28**, 2583 (1972); H.G. Ang, W.L. Kwick, G.R. Hanson, J.A. Crowther, M. McPartlin, and N. Choi. J. Chem. Soc. Dalton Trans. 3193 (1991). H. Gaw, W.R. Robinson, and R.A. Walton. Inorg. Nucl. Chem. Lett. **7**, 695 (1971); J. Albertsson. Acta Chem. Scand. **24(4)**, 1213 (1970); U. Casellato, R. Graziani, R.P. Bonomo, and A.J. DiBilio. J. Chem. Soc. Dalton Trans. 23 (1991); G. Chessa, G. Marangoni, B. Pitteri, V. Bertolassi, G. Gilli, and V. Ferreti. Inorg. Chim. Acta, 201 (1991); C. Madhumita, C. Saktiprosad, and A.N. Kumar. Polyhedron, **16**, 2917 (1997); W. Brzyska and W. Ozga. Pol. J. Chem. **71**, 436 (1997); M.A. Sorkis and H.A. Tagim. J. Pharm. Sci. 1977, 66, 1515; A. Vassilian, A.B. Bikhazi, and H.A. Tagim. J. Inorg. Nucl. Chem. **41**, 775 (1979); P. Lainé, A. Gourdon, and J.-P.Launay. Inorg. Chem. **34**, 5129 (1995); P. Lainé, A. Gourdon, and J.-P. Launay. Inorg. Chem. **34**, 5138 (1995); P. Lainé, A. Gourdon, and J.-P.Launay. Inorg. Chem. **34**, 5156 (1995); T. Zevaco, M. Postel, and N. Benali-Cherif. Main Group Met. Chem. **15**, 217 (1992).
15. J.C. MacDonald, P.C. Dorrestein, M.M. Pilley, M.M. Foote, J.L. Lundburg, R.W. Henning, A.J. Schultz, and J.L. Manson. J. Am. Chem. Soc. **122**, 11692 (2000).
16. M. Ranjbar, H. Aghabozorg, A. Moghimi, and A. Yanovsky. Anal. Sci. **17**, 1469 (2001).
17. M. Ranjbar, A. Moghimi, H. Aghabozorg, and G.P.A. Yap. Anal. Sci. **18**, 219 (2002).
18. M. Ranjbar, H. Aghabozorg, A. Moghimi, and A. Yanovsky. Z. Kristallogr. NCS **216**, 626 (2001).
19. D.M. Adams. "Metal-ligand and related vibrations", Edward Arnold, Londen. 1967.
20. K. Nakamoto. "Infrared and Raman spectra of inorganic and coordination compounds, Part B, Applications in coordination, organometallic, and bioinorganic chemistry", 5th ed., New York. 1997.
21. R. Baggio, M.T. Garland, M. Perec, and D. Vega. Inorg. Chem. **35**, 2396 (1996).
22. S.H. Huang, G.D. Zhou, and T.C.W. Mak. J. Crystallogr. Spectrosc. Res. **21**, 127 (1991).
23. A. Michaelides, S. Skoulika, and A. Aubry. Matter. Res. Bull. **23**, 579 (1988).
24. A.G. Orpen, L. Brammer, F.H. Allen, O. Kennard, D.G. Watson, and R. Taylor. J. Chem. Soc. Dalton Trans. S1–S83 (1989).
25. G.B. Deacon, T. Feng, P.C. Junk, G. Meyer, N.M. Scott, B.W. Skelton, and A.H. White. Aust. J. Chem. **53**, 853 (2000).
26. I.L. Fedushkin, S. Dechert, and H. Schumann. Organometallics, **19**, 4066 (2000).
27. B. Benmerab, A.G. Laidoudi, G. Bernardinelli, and F. Balegroune. Acta Crystallogr. C, **56**, 321 (2000).
28. G. Schwarzenbach and H. Flaschlea. Complexometric titrations. Methuen, London. 1969.
29. A.E. Martell and R.J. Motekaitis. Determination and use of stability constants. 2nd ed., VCH, New York. 1992.

© 2002 NRC Canada

Novel terpenoids from the Sea Hare *Aplysia punctata*

John A. Findlay and Guoqiang Li

Abstract: The structures of 23 compounds isolated from the sea hare *Aplysia punctata* have been determined by spectroscopic means. These include four new diterpenes (**1**–**4**): **1**, neoparguerol dione, is a tricyclic diterpene featuring a novel octane-1,5-dione A ring; **2** is deacetylparguerol; **3**, punctatene acetate, shares the same [2:2:1] bicyclic system as dactylomelol from *A. dactylomela*; and **4**, punctatol, has the same skeleton as laurencianol of algal origin. Diastereomeric sesquiterpenes **5** and **6** are similar to some compounds of algal origin, as is **7**, perforatol, which shares the same carbon framework as perforatone from *Laurentia perforata*. In addition we have isolated 16 known compounds comprising 12 sesquiterpenes: perforenone, laurene, α-bromocuparane, α-isobromocuparane, laurinterol, debromoallolaurinterol, laurenisol, isofiliformin, obtusenol, β-snyderol, a dibromochamigrane, a friedosnyderane, two diterpenes: isoconncindiol and parguerol, and two C-15 acetogenins: laurenyne and laurencenyne. These known compounds have been reported previously either from other *Aplysia* species or from *Laurencia* species.

Key words: *Aplysia punctata*, terpenoids, Sea Hare constituents.

Résumé : Faisant appel à des méthodes spectroscopiques, on a déterminé les structures des 23 composés isolés du lièvre de mer, *Aplysia punctata*. Ils comprennent quatre nouveaux diterpènes (**1**–**4**): **1**, la néoparguéroldione, est un diterpène tricyclique comportant un nouveau cycle A formé d'une octane-1,5-dione; **2**, est le désacétylparguérol; **3**, l'acétate de punctatène comporte le même système bicyclo[2.2.1] que le dactylomélol extrait d'*A. dactylomela* et **4**, le puntatol, comporte le même squelette que le laurencianol tiré d'algues. Les sesquiterpènes diastéréomères **5** et **6** sont semblables à quelques composés tirés d'algues et il en est de même pour le composé **7** qui comporte le même squelette carboné que la perforatone isolée de *Laurentia perforata*. On a isolé de plus 16 composés connus, dont 12 sesquiterpènes: perforénone, laurène, α-bromocuparane, α-isobromocuparane, laurintérol, débromoallolaurintérol, laurénisol, isofiliformine; obtusénol, β-snyderol, un dibromochamigrane, un friedosnyderane, deux terpènes (l'isoconncindiol et le parguérol) et deux acétogénines en C-15 (la laurényne et la laurencényne). Ces composés connus avaient été isolés antérieurement d'autres espèces d'*Aplysia* ou d'espèces de *Laurencia*.

Mots clés : *Aplysia punctata*, terpénoïdes, constituants du lièvre de mer.

[Traduit par la Rédaction]

Introduction

The sea hare *Aplysia punctata* is widely distributed from the Atlantic coasts of Greenland, Norway, and the Baltic to the Mediterranean and the Canary Islands (1); its toxic properties have been known since ancient times, and it was reported (2) that the secretion of *A. punctata* was capable of producing urticaria, severe inflammation, and alopecia. Previous chemical studies on this species led to the isolation of uroporphyrin (3), epidioxysterols (4), and seven monocyclic polyhalogenated monoterpenes (5), the latter originating from the red alga *Plocamium collineum*. In addition, data exists concerning the ecological relationship between sea hares (Opistobranch molluscs) and their diet of red algae, mostly of the *Laurencia* and *Plocamium* genera (6). Evidence suggests that many of the terpenoid compounds found in *Aplysia* species (sp.) are of algal origin, and that the animals are capable of modifying some of the terpenoid compounds via metabolic transformations. Thus, the toxic and predator deterrent factors in sea hares may well be due, in large part, to their ability to accumulate and modify compounds of dietary origin.

In our studies, the animals (*Aplysia punctata*, 150 g, wet wt), collected from the northwest coast of Sardinia, Italy, were chopped and extracted with ethanol (95%). The crude extract was subjected to solvent partitioning and repeated chromatographic separation, and 23 compounds were isolated; their structures have been deduced from spectral data. Among these compounds only one, 5-epidioxycholest-6-ene, has been reported from *A. punctata* before (4). The remainder, isolated from this animal for the first time, include four new diterpenes **1**–**4**, three new sesquiterpenes **5**–**7** (see Scheme 1), as well as 16 known compounds comprising 12 sesquiterpenes: perforenone (7), laurene (8), α-bromocuparane, α-isobromocuparane (9), laurinterol (10), debromoallolaurinterol (11), laurenisol (12), isofiliformin (13), obtusenol (14), β-snyderol (15), a dibromochamigrane (16), a friedosnyderane (17), the two diterpenes isoconcinndiol (18)

Received 13 May 2002. Published on the NRC Research Press Web site at http://canjchem.nrc.ca on 20 December 2002.

J.A. Findlay[1] and G. Li. Department of Chemistry, University of New Brunswick, Fredericton, NS E3B 6E2, Canada.

[1]Corresponding author (e-mail: findlay@unb.ca).

 DOI: 10.1139/V02-189 © 2002 NRC Canada

Scheme 1.

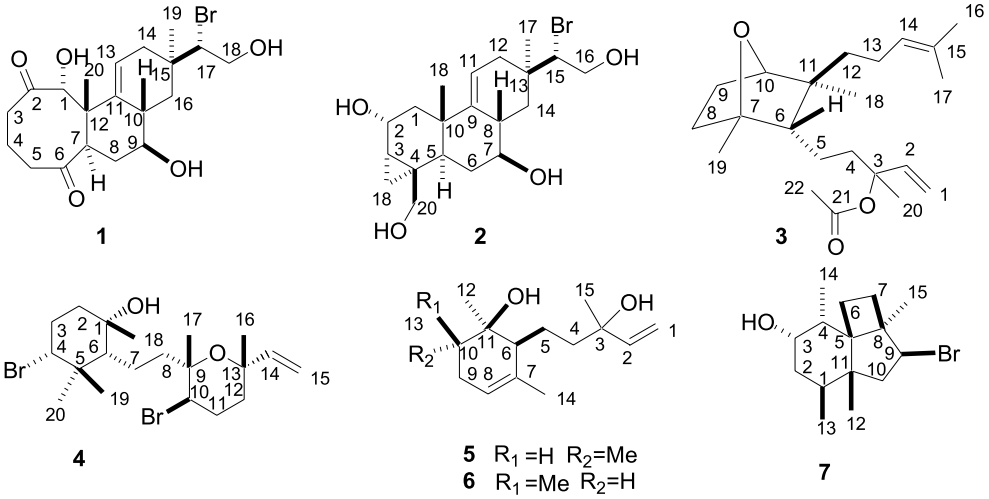

and parguerol (19), and two C-15 acetogenins: laurenyne (20) and laurencenyne (21). These were identified by comparison of spectroscopic and optical rotation data with values in the literature. These known compounds have been previously reported either from other *Aplysia* species or from *Laurencia* species.

Compound **1** was isolated as an optically active semisolid. The ^{13}C NMR and DEPT spectra (Table 1) show a total of twenty carbons, which comprise two methyls, seven methylenes, six methines, and five quaternary carbons. In addition to the two carbonyls and two double bond carbons, four downfield signals correspond to three oxygen-bearing carbons and one bromide methine carbon in view of their proton and carbon chemical shifts. The molecular formula, $C_{20}H_{29}BrO_5$, deduced from these data is supported by EI-MS (found m/z = 412/410 ([$M^+ - H_2O$]) and 411/409 ([$M^+ - H - H_2O$]) and implies the presence of three rings. The proton coupling systems revealed from the ^1H-^1H COSY spectrum show several distinct patterns consistent with structural features in **1**, namely, coupled protons assigned to H-3/H-4/H-5, H-7/H-8/H-9/H-10/H-16, H-13/H-14, and H-17/H-18. Analysis of HMBC data allows the incorporation of these coupling systems into structure **1**. Thus, the features of the C ring are indicated by HMBC correlations Me-19 to C-14, C-15, C-16, and C-17 and the correlations from H-13 to C-10, C-12, and C-15. Ring B is supported by the correlations from Me-20 to C-11, C-12, and C-7. Finally, the correlations of H-5 to C-3, C-4, C-6, and C-7, and of H-1 to C-2, C-7, C-11, C-12, and C-20, and of H-3 to C-2, C-4, and C-5 affirm the novel cyclooctadione A ring system. The bromine is assigned to C-17 on the basis of chemical shifts and is consistent with biogenetically related compounds in the literature such as parguerol and isoparguerol (19).

The stereochemical features of compound **1** were deduced from NOE experiments. The strong NOE enhancements between H_3-20 and H-10 imply these groups are axial. The α configuration of the hydroxyl at C-1 follows from the NOE enhancements between H-1 and H-13 and between H-1 and H_3-20. The β orientation of the hydroxyl group at C-9 is assigned on the basis of the observed NOE between H-9 and H-7. The large J value for H-9 (~11.2 Hz) also indicates that this methine proton is axial. Finally, the Me-19 must possess an α orientation in view of the NOE enhancements between Me-19, H-14 α, and H-16 α. The large NOE enhancements between H-17 and H-10 imply that rotation around the C15—C17 bond is severely restricted, and this allows determination of the orientation of bromine and the relative configuration at C-17. The two possible configurations for bromine at C-17, together with possible side chain conformations based on stereochemical considerations and NOE results, are shown in partial structures A and B (Fig. 1). The NOE enhancements at H-16 β when protons at C-18 were saturated suggested that these methylene protons are close to C-16. This result is consistent only with case A. The lack of significant NOE enhancements between H-18 and H-14 further supports the configuration and conformation in A. Thus, it is possible to assign the relative stereochemistry as shown.

Fig. 1. Configuration of C-17 in neoparguerolidione (**1**).

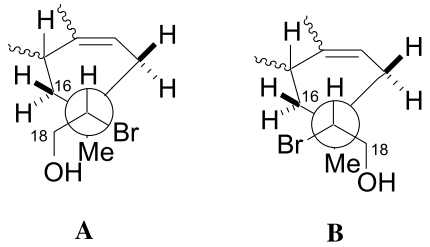

A global conformational search using MacroModel 4.5 software, MM2 force field (22), and the proposed structure **1** gives a total of 15 conformations in which the energy differs within 3 kcal mol^{-1}. The results indicate a flexible eight-membered ring, with maximum mobility at the C-4 methylene. The rotations of the OH group at C-18 along the C—O bond (energy barrier ~ 2.9 kcal mol^{-1}) and side chain along the C-15—C-17 bond (energy barrier ~ 13.3 kcal mol^{-1}) are restricted owing to steric hindrance. The interatomic distances for the most stable conformation are consistent with NOE data, and in particular, indicate a distance of 2.0 Å between H-16 β and a proton at H-18.

Diterpene **1** possesses a new carbocyclic skeleton, which is a modification of the known pimarane framework. Its

© 2002 NRC Canada

Table 1. NMR data (400 MHz, $CDCl_3$) for neoparguerolidione (**1**).

Carbon	δ	Proton (*J* (Hz))	COSY	HMBC	NOE enhanced signals (%)[a]
1	81.1 (d)	4.30 (s)		C-2, C-7, C-11, C-12, C-20	5.49 (15.0), 1.15 (2.5)
2	213.0 (s)				
3	42.4 (t)	3.18 (m)	2.88, 2.21, 1.90	C-2, C-4, C-5	2.21 (16.2)
		2.21 (m)	3.18, 2.88, 1.90		3.18 (18.7)
4	20.5 (t)	2.88 (m)	3.18, 2.58, 2.32, 2.21, 1.90	C-2, C-3, C-5	1.90 (20.1), 3.46 (8.1)
		1.90 (m)	3.18, 2.88, 2.58, 2.32, 2.21		2.88 (11.3)
5	44.8 (t)	2.58 (brd, 17.6)	2.88, 2.30, 1.90	C-3, C-4, C-6, C-7	2.88 (–1.2), 2.21 (2.1), 2.32 (6.3), 3.46 (1.9)
		2.32 (dd, 17.6, 3.2)	2.88, 2.58, 1.90		2.58 (11.6)
6	212.6 (s)				
7	44.6 (d)	3.46 (dd, 10.4, 3.2)	1.91, 1.72		2.88 (5.6), 2.58 (2.9), 1.72 (1.1), 3.18 (3.6)
8	34.0 (t)	1.91 (ddd, 12.8, 11.2, 10.4)	3.46, 3.18, 1.72	C-6, C-7, C-9, C-12	1.72 (5.1), 1.15 (2.1)
		1.72 (ddd, 12.8, 4.0, 3.2)	3.46, 3.18, 1.91	C-6, C-7, C-9, C-12	1.91 (-8.5), 3.46 (2.1)
9	73.6 (t)	3.18 (ddd, 11.2, 11.2, 4.0)	2.22, 1.91, 1.72	C-7, C-8, C-16	3.46 (1.2), 1.72 (1.5), 1.41 (3.4),
10	39.1 (d)	2.22 (ddd, 11.2, 11.2, 2.8)	3.18, 2.32, 1.41		2.32 (2.0), 5.490 (1.6), 4.18 (6.9)
11	140.9 (s)				
12	47.5 (s)				
13	119.7 (d)	5.49 (ddd, 6.0, 2.0, 1.6)	2.52, 1.94	C-10, C-12, C-14, C-15	4.30 (20.0), 2.52 (5.7), 1.94 (1.4)
14	38.9 (t)	2.52 (m)	5.49, 1.94	C-19	4.30 (1.3), 5.49 (4.4), 1.94 (10.9)
		1.94 (m)	5.49, 2.52		5.49 (4.0), 2.52 (17.8), 1.09 (3.2)
15	35.1 (s)				
16	36.9 (t)	2.32 (dd, 13.6, 2.8)	2.22, 1.41	C-14, C-15, C-19	1.41 (12.6), 1.09 (1.1)
		1.41 (dd, 13.6, 11.2)	2.32, 2.22	C-9, C-14, C-15, C-17, C-19	3.18 (4.3), 1.94 (2.5), 2.32 (13.0), 1.09 (3.0)
17	68.0 (d)	4.18 (dd, 9.0, 3.1)	3.92, 3.84	C-14, C-15, C-18, C-19	2.22 (4.3), 2.52 (1.3), 3.92 (1.3)
18	64.0 (t)	3.92 (dd, 12.4, 3.1)	4.18, 3.84	C-15, C-17	2.22 (1.3), 2.32 (1.7), 4.18 (2.2), 1.09 (1.2)
		3.84 (dd, 12.4, 9.0)	4.18, 3.92	C-17	2.32 (1.2), 1.09 (2.3)
19	24.8 (q)	1.09 (s)		C-14, C-15, C-16, C-17	2.52 (1.5), 1.41 (1.2), 3.84 (1.2)
20	19.0 (q)	1.15 (s)		C-1, 7, C-11, C-12	4.3 (2.2), 1.91 (1.1), 2.22 (2.0)

[a]Observed NOE signals when the proton on column 3 is irradiated.

structure is closely related to isoparguerol and parguerol, cytotoxins isolated from the sea hare *Aplysia dactylomela* by Schmitz et al. (19). A possible biogenetic pathway for the formation of **1** from isoparguerol is outlined in Fig. 2. In view of the structural relationship of **1** to isoparguerol we suggest this new carbon skeleton be designated neoparguerane and diterpene **1**, neoparguerolidione.

From the same fraction that contained neoparguerolidione (**1**), two other polar metabolites were isolated, one of which proved to be the known cytotoxic parguerol, while the other was shown to be deacetylparguerol **2**, previously reported only as a hydrolysis product of parguerol (19). Chemical shift assignments are shown in Table 2. The structure and stereochemistry of **2** were established primarily by 1D and 2D NMR experiments. Of special interest are the NOE correlations that support the previously unassigned stereochemistry of the Br at C-17 as shown. Thus, **1** and **2** possess

Fig. 2. Proposed biogenesis of neoparguerolidione (**1**) from isoparguerol.

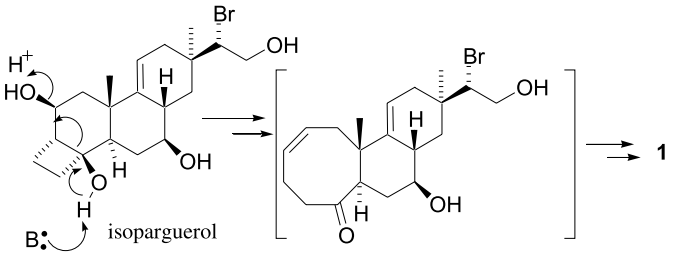

the same relative stereochemistry in their B, C, and D rings and side chain. Both proved to be unstable, particularly in chloroform, perhaps due to the bromohydrin feature and unfortunately precluded obtaining HR-EI-MS data.

© 2002 NRC Canada

Table 2. NMR data (400 MHz, CD_3OD) for deacetylparguerol (**2**).

Carbon	δ	Proton (*J* (Hz))	COSY	HMBC	NOE enhanced signals (%)[a]
1	41.7 (t)	1.85 (dd, 15.2, 4.0)	4.30, 1.23	C-2, C-3, C-5, C-9, C-10, C-18	1.23 (21.9), 4.30 (4.9), 5.38 (14.1), 1.12 (3.7)
		1.23 (dd, 15.2, 5.2)	4.30, 1.85	C-2, C-3, C-5, C-9, C-10, C-18	1.85 (13.5), 1.02 (7.6), 5.38 (3.1)
2	66.8 (d)	4.30 (dm, 5.2, 4.0, <2.0)	1.85, 1.23, 1.02	C-2, C-3, C-4, C-10, C-19	1.23 (4.5), 1.85 (1.7), 3 (4.9), –0.01 (1.6)
3	24.9 (d)	1.02 (ddd, 10.6, 6.2, <2.0)	4.30, 0.83, –0.01	C-1, C-2, C-4, C-5, C-19, C-20	4.30 (2.2), 0.83 (1.1), 3.43 (2.1)
4	24.8 (s)				
5	47.8 (d)	1.19 (dd, 9.6, 3.8)	2.35, 1.86	C-1, C-3, C-4, C-6, C-7, C-9, C-10, C-18, C-19, C-20	2.35 (3.4), 3.05 (2.9), –0.01 (2.7),
6	34.2 (t)	2.35 (ddd, 12.4, 4.6, 3.8)	3.05, 1.86, 1.19	C-4, C-5, C-7, C-8, C-10	1.19 (4.0), 1.86 (20.5), 3.05 (5.9), 3.43 (3.0)
		1.86 (ddd, 12.4, 9.6, 9.6)	3.05, 2.35, 1.19	C-4, C-5, C-7, C-8, C-10	2.35 (23.0), 1.12 (3.7), 3.43 (2.7)
7	78.1 (d)	3.05 (ddd, 10.8, 9.6, 4.6)	2.35, 2.28, 1.86	C-8, C-14	2.35 (4.0), 1.19 (7.0), 1.32 (4.3)
8	39.4 (d)	2.28 (m)	3.05, 2.30, 1.32	C-7, C-9, C-13, C-14	1.86 (1.8), 4.22 (6.5), 4.01 (4.1), 1.12 (4.1)
9	145.7 (s)				
10	38.0 (s)				
11	117.9 (d)	5.38 (dm, 6.0, ~2.0)	2.46, 1.78	C-8, C-10, C-12, C-13	1.23 (3.5), 1.85 (8.1), 1.78 (2.4), 2.46 (4.5)
12	40.3 (t)	2.46 (ddm, 17.6, 6.0, 2.4)	5.38, 1.78	C-13, C-14, C-15, C-17	5.38 (6.4), 1.78 (21.2), 4.22 (3.9), 1.03 (1.1)
		1.78 (ddd, 17.6, 3.2, 2.0)	5.38, 2.46	C-9, C-11, C-13, C-14, C-15, C-17	5.38 (3.2), 2.46 (17.8), 1.03 (2.4)
13	36.3 (s)				
14	39.5 (t)	2.30 (m, 15.2)	2.28, 1.32	C-7, C-8, C-9, C-12, C-13, C-15, C-17	1.32 (10.6), 4.22 (4.0), 4.01 (4.1)
		1.32 (m, 15.2, 12.4)	2.30, 2.28	C-7, C-8, C-9, C-12, C-13, C-15, C-17	3.05 (6.3), 1.78 (2.4), 2.30 (16.0), 1.03 (2.1)
15	68.0 (d)	4.22 (dd, 9.4, 2.8)	4.01, 3.76	C-12, C-13, C-16, C-17	2.28 (6.6), 2.46 (1.3), 4.01 (2.6), 3.76 (0.5)
16	65.0 (t)	4.01 (dd, 12.6, 2.8)	4.22, 3.76	C-13, C-15	2.30 (8.4), 4.22 (4.0), 3.76 (25.9)
		3.76 (12.6, 9.4)	4.22, 4.01	C-13	4.22 (2.7), 4.01 (19.3), 1.03 (3.6)
17	24.8 (q)	1.03 (s)		C-12, C-13, C-14, C-15	1.78 (3.0), 1.32 (2.4), 3.76 (2.7)
18	21.2 (q)	1.12 (s)		C-1, C-5, C-9, C-10	1.85 (3.6), 2.28 (2.9), 5.38 (0.4), 3.43 (0.4)
19	18.9 (t)	0.83 (dd, 10.6, 4.8),	1.02, –0.01	C-2, C-3, C-5, C-20	1.02 (4.8), –0.01 (20.6), 3.43 (2.8)
		–0.01 (dd, 6.2, 4.8)	1.02, 0.83	C-2, C-3, C-5, C-20	4.30 (4.7), 1.02 (3.9), 1.19 (15.5), 0.83 (28.7)
20	68.7 (t)	3.43 (2H, s)		C-3, C-4, C-5, C-19	1.02 (6.1), 2.35 (2.0), 1.86 (1.7), 0.83 (2.3)

[a]Observed NOE signals when the proton on column 2 is irradiated.

Diterpene **3** was isolated as an optically active oily substance whose composition $C_{22}H_{36}O_3$ was revealed by HR-EI-MS. The strong absorption peaks in the IR spectrum at 1739 and 1240 cm^{-1} indicate the presence of an ester group, and the weak absorption at 1640 cm^{-1} is consistent with the presence of vinyl groups. The ^{13}C NMR and DEPT spectra show a total of 22 carbon signals, which consist of six methyls, seven methylenes, four methines, and five quaternary carbons. Eight downfield carbons are assigned to a carbonyl group, four double bond carbons, and three oxygen-bearing carbons and thus, diterpene **3** has two rings.

Analysis of ^1H NMR, ^1H-^1H COSY, HMBC, and HMQC spectra affords the chemical shift assignments compiled in Table 3. An examination of ^1H NMR and ^1H-^1H COSY spectra reveals several coupled spin systems: an ABX system assigned to the mono-substituted olefin protons at C-1/C-2, and three sequences of $-CH_2CH_2CH-$ assigned to protons at C-4/C-5/C-6, C-8/C-9/C-10, and C-12/C-13/C-14. The bicyclic system was established by the HMBC correlations from H-10 to C-6, C-7, C-8, and C-11. The side chains were located via the correlation of H_3-20 to C-2, C-3, and C-4 and from H_3-18 to C-6, C-10, and C-11. The location of the acetate moiety is confirmed by the C-3 chemical shift. For the oxygen-bridged bicyclic ring system in diterpene **3**, the H-10 proton and H_3-19 must be on the same face of the bicyclo [2.2.1] ring system, allowing for the assignment of

© 2002 NRC Canada

Table 3. NMR data (400 MHz, $CDCl_3$) for punctatene acetate (**3**).

Carbon	δ	Proton (*J* (Hz))	COSY	HMBC	NOE enhanced signals (%)[a]
1	113.3 (t)	5.13 (dd, 17.6, 0.4)	5.93, 5.11	C-2, C-3	5.93 (11.6)
		5.11 (dd, 11.2, 0.4)	5.93, 5.13		
2	141.7 (d)	5.93 (dd, 17.6, 11.2)	5.13, 5.11	C-3, C-11, C-12, C-20	5.13 (5.2), 1.51 (0.2)
3	82.9 (s)				
4	39.7 (t)	1.76 (m, 2H)	1.26–1.11	C-2, C-3, C-5	
5	20.8 (t)	1.26 (m)	1.76, 1.14–1.11	C-4, C-6, C-7, C-11	
		1.14 (m)			
6	56.1 (d)	1.11 (m)	1.76, 1.26	C-7, C-8, C-11	
7	87.6 (s)				
8	29.1 (t)	1.62 (m)	1.75, 1.17	C-6, C-7,	
		1.17 (m)	1.75, 1.62		1.62 (14.0), 1.36 (3.7)
9	26.7 (t)	1.75 (m)	3.94, 1.61–1.62, 1.17	C-10	3.94 (3.0), 1.61 (6.1), 0.82 (3.5)
		1.61 (m)	3.94, 1.75, 1.17		3.94 (2.3), 1.75 (4.0), 1.17 (5.3)
10	83.7 (d)	3.94 (d, 4.8)	1.75, 1.61	C-6, C-7, C-8, C-11	1.75 (0.8), 1.61 (2.3), 1.43 (1.5), 1.88 (3.4)
11	45.1 (s)				
12	44.2 (t)	1.43 (ddd, 13.2, 8.0)	1.88, 1.30	C-6, C-10, C-14, C-18	
		1.30 (ddd, 8.4, 8.0)			
			1.88, 1.43		
13	23.1 (t)	1.88 (brdt, 2H, 8.4, 8.0)	5.07, 1.43, 1.30	C-11, C-14, C-15	5.07 (6.1), 3.94 (5.2), 1.58 (4.6), 1.43 (3.4), 1.30 (3.9), 1.11 (3.6), 0.82 (3.1)
14	124.8 (d)	5.07 (brt, 8.0, 1.6)	1.88	C-12, C-13, C-16, C-17	1.88 (4.3), 1.65 (6.7)
15	131.1 (s)				
16	17.6 (q))	1.58 (s))		C-14, C-15, C-17	
17	25.7 (q)	1.65 (s)		C-14, C-15, C-17	5.07 (4.9)
18	16.8 (q)	0.82 (s)		C-6, C-10, C-11, C-12	1.26 (6.3), 1.75 (6.7), 3.94 (2.6), 1.88 (4.3)
19	21.6 (q)	1.36 (s)		C-6, C-7, C-8	1.62 (1.6), 1.17 (6.5)
20	23.5 (q)	1.51 (s)		C-2, C-3, C-4	5.13 (3.9), 5.93 (2.5), 1.76 (2.6), 1.26 (2.3)
21	169.9 (s)				
22	22.2 (q)	1.99 (s)		C-21	

[a]Observed NOE signals when the proton on column 3 is irradiated.

Hα-8, Hβ-8, Hα-9, and Hβ-9 by NOE. The strong NOE enhancement at H_3-18 when H-9 α was irradiated indicates an α methyl group. The absence of NOE observed at H-6 when irradiating H_3-18 is consistent with H-6 having a β conformation.

Diterpene **3** shares the same relative configuration of the bicyclic system as dactylomelol, a related diterpene reported from *Aplysia dactylomela* whose strucure, including absolute stereochemistry, was established by X-ray analysis (23). Dactylomelol differs from **3** by featuring bromine at C-14 and chlorine at C-15 instead of a double bond and a hydroxyl at C-3. We designate **3** punctatene acetate; it is the second example of the novel dactylomelol skeleton in compounds isolated from sea hares, and no similar metabolites have been isolated from algae thus far.

The ^{13}C NMR and DEPT spectra of dibromoditerpene **4** reveal a total of 20 carbon signals comprising five methyls, seven methylenes, four methines, and four quaternary carbons. Seven downfield signals correspond to a double bond, three oxygen-bearing quaternary carbons, and two bromine-bearing methine carbons. The molecular formula, $C_{20}H_{34}Br_2O_2$, is supported by the HR-EI-MS derived ion [M^+ – 2HBr] (*m*/*z* = 304.2414; calcd. 304.24023) and a low-energy EI-MS (27 eV) in which the isotopic pattern of the ions (*m*/*z* = 453, 451, 449, [M^+-CH_3]) indicates the presence of two bromine atoms. Examination of ^1H NMR, ^{13}C NMR, DEPT, HMQC, and HMBC spectra allowed the assignment of proton and carbon chemical shifts, which are summarized in Table 4. Two kinds of coupled spin systems are evident from the ^1H-^1H COSY spectrum. An ABX system involving proton signals at δ 5.80, 5.12, and 4.92 indicates a mono-substituted olefin group while three other separate systems, typical of two adjacent methylene groups further coupled with one methine proton, are assigned to the protons H_2-2/H_2-3/H-4, H-6/H_2-7/H_2-8, and H-10/H_2-11/H_2-12.

Analysis of HMBC correlations allows incorporation of the structural units into a bicyclic diterpene skeleton. Thus, the HMBC correlations from Me-18 to C-1, C-2, and C-6, and the correlations from geminal dimethyl protons Me-19 and Me-20 to C-4, C-5, and C-6 allow the elaboration of

© 2002 NRC Canada

Table 4. NMR data (400 MHz, $CDCl_3$) for epilaurencianol chlorohydrin (**4**).

Carbon	δ	Proton (*J* (Hz))	COSY	HMBC	NOE enhanced signals (%)[a]
1	72.7 (s)				
2	41.9 (t)	1.67 (m)	2.39, 2.02, 1.53	C-1, C-4, C-6, C-18	
		1.53 (m)	2.39, 2.02, 1.67		
3	30.5 (t)	2.39 (m)	3.99, 2.02, 1.67, 1.53	C-2, C-4	1.67 (2.0), 2.02 (20.0), 1.13 (5.3)
		2.02 (m)	3.99, 2.39, 1.66, 1.53	C-2, C-4	3.99 (4.2), 2.39 (19.3)
4	68.3 (d)	3.99 (dd, 12.8, 3.6)	3.99, 2.39, 2.02	C-2, C-5, C-6, C-19, C-20	1.53 (2.5), 2.02 (3.9), 1.08 (3.0), 0.88 (5.4)
5	41.0 (s)				
6	54.4 (d)	0.88 (m)	1.63, 1.56	C-19, C-20	3.99 (7.0), 1.85 (1.5), 1.63 (2.2), 1.17 (1.2), 1.08 (1.5)
7	20.5 (t)	1.63 (m)	1.85, 1.56, 0.88		
		1.56 (m)	1.85, 0.88	C-1, C-6	
8	45.7 (t)	1.85 (m)	1.63, 1.63	C-7, C-9, C-10	1.63 (12.9), 1.43 (2.4), 1.17 (2.3), 0.88 (5.8)
		1.63 (m)	1.85, 1.56		
9	76.0 (s)				
10	55.9 (d)	4.08 (dd, 10.8, 4.4)	2.31, 2.14	C-8, C-9, C-11, C-12, C-17	2.31 (0.4), 2.14 ((3.7), 1.74 (1.6), 1.56 (3.2)
11	27.9 (t)	2.31 (m)	4.08, 2.14, 1.74	C-9, C-10, C-12	4.08 (0.4), 2.31 (13.7), 1.74 (1.8), 1.43 (1.2), 1.32 (2.5)
		2.14 (m)	4.08, 2.31, 1.74	C-9, C-10, C-12	4.08 (4.6), 2.31 (16.8), 1.74 (1.7)
12	36.3 (t)	1.74 (t, 2H, 5.2)	2.31, 2.14	C-10, C-11, C-14	5.80 (3.4), 5.12 (1.9), 4.08 (3.3), 2.31 (1.2), 2.14 (2.0), 1.32 (1.9)
13	74.0 (s)				
14	146.7 (d)	5.80 (ddd, 17.2, 10.8, 2.0)	5.12, 4.92	C-13, C-16	4.92 (3.6), 1.32 (1.5)
15	110.2 (t)	5.12 (dd, 17.2, 1.6)	5.80, 4.92	C-13, C-14	4.92 (14.8)
		4.92 (dd, 10.8, 1.6)	5.80, 5.12	C-13	5.80 (4.2), 5.12 (15.7)
16	26.8 (q)	1.32 (s)		C-12, C-13, C-14	5.80 (2.3), 5.12 (0.8), 4.92 (1.6), 1.74 (1.7), 1.43 (1.0)
17	23.8 (q)	1.43 (s)		C-8, C-9, C-10	2.31 (3.8), 1.32 (1.8)
18	30.3 (q)	1.17 (s)		C-1, C-6, C-9	1.53 (3.0), 0.88 (1.1)
19	29.6 (q)	1.08 (s)		C-4, C-5, C-6, C-20	3.99 (3.5), 0.88 (1.8), 1.56 (1.5)
20	17.6 (q)	1.13 (s)		C-4, C-5, C-6, C-19	2.39 (1.9), 1.56 (1.0)

[a]Observed NOE signals when the proton on column 3 is irradiated.

Fig. 3. Significant NOE correlations in 4.

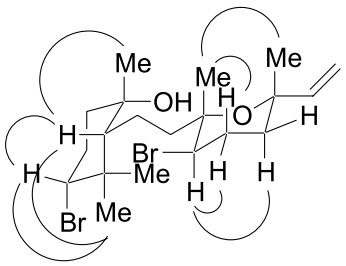

ring A. Furthermore, the HMBC correlations from Me-17 to C-8, C-9, and C-10, and the correlations from Me-16 to C-12, C-13, and C-14 are consistent with the ring B features.

The NOE enhancement data allowed distinction of the structure and stereochemistry of **4** from alternatives. Thus, the NOE enhancements between Me-18 and H-6 is indicative of a *cis* relationship. The equatorial bromine at C-4 follows from the large coupling constant (J = 12.8 Hz) between H-4 and the axial proton at C-3 and is supported by large NOE enhancements between H-4 and H-6. The lack of NOE between Me-17/Me-18 and H-10/Me-17 mitigates against alternative structures featuring an ether bridge from C-1 to C-9 and hydroxyl at C-13. The conformation and relative stereochemistry consistent with NOE data are illustrated in Fig. 3. Compound **4** has the same skeleton as laurencianol, an antibacterial diterpene previously isolated from the alga *Laurencia obtusa*, whose structure was determined by an X-ray diffraction study (24). Laurencianol differs from **4** by featuring a saturated side chain with a hydroxyl at C-14 and chlorine at C-15 and the reverse configuration at C-1. We designate **4** punctatol.

Two diastereoisomers, sesquiterpene alcohols **5** and **6**, were isolated from a polar fraction. Their structures were deduced on the basis of spectral data analysis. Alcohols **5** and **6** possess the same carbon skeleton as several sesquiterpenes such as dactyloxenes, dactylenol, and dactylenol acetate (25), which are quite common in *Aplysia* and *Laurencia* species.

Compound **5** was isolated as an optically active, oily substance whose IR spectrum indicates the presence of hydroxyl (3406 cm^{-1}) and alkenic (1658 and 1649 cm^{-1}) functionalities. The ^{13}C NMR and DEPT spectra indicate a

© 2002 NRC Canada

Table 5. NMR data (400 MHz, $CDCl_3$) for sesquiterpene **5**.

Carbon	δ	Proton (*J* (Hz))	COSY	HMBC	NOE enhanced signals (%)[a]	NOESY correlations
1	112.0 (t)	5.20 (dd, 17.2, 1.2)	5.88, 5.07	C-2, C-3	5.07 (14.5), 1.63 (1.7), 1.26 (1.6)	5.88, 5.07, 1.26
		5.07 (dd, 10.8, 1.2)	5.88, 5.20	C-3	5.20 (12.6), 5.88 (2.5)	5.88, 5.20, 1.26
2	144.9 (d)	5.88 (dd, 17.2, 10.8)	5.20, 5.07	C-3, C-4, C-15	5.07 (1.7), 1.26 (1.1)	5.20, 5.02, 1.63, 1.26
3	73.3 (s)					
4	42.1 (t)	1.63 (m)	1.49, 1.41	C-2, C-3, C-5, C-6, C-15		5.88, 1.49, 1.41, 1.26
		1.62 (m)	1.49, 1.41	C-2, C-3, C-5, C-6, C-15		5.88, 1.49, 1.41, 1.26
5	26.0 (t)	1.49 (m)	1.78, 1.6, 1.41	C-3, C-4, C-6, C-7, C-11		1.78, 1.63, 1.62, 1.41, 1.26
		1.41 (m)	1.78, 1.6, 1.49	C-3, C-4, C-6, C-7, C-11		1.63, 1.62, 1.49
6	52.8 (d)	1.78 (t, 4.8)	1.49, 1.41	C-4, C-5, C-7, C-8, C-10, C-11, C-12, C-14	1.41 (1.1) , 5.38 (2.2), 1.18 (2.6), 0.89 (2.1), 1.68 (1.6)	1.62, 1.18
7	135.7 (s)					
8	121.2 (d)	5.38 (m)	2.06, 1.72–1.68	C-6, C-9, C-10, C-14	2.06 (1.6), 1.68 (5.6)	2.06, 1.72, 1.68
9	31.4 (t)	2.06 (dm)	5.38, 1.72, 1.69	C-7, C-8, C-10, C-11	5.38 (4.2), 1.72 (10.0), 1.69 (11.0), 0.89 (2.3)	5.38, 1.72, 1.69
		1.72 (m)	5.38, 2.06			2.06, 1.18, 0.89
10	32.1 (d)	1.69 (m)	2.06, 0.89	C-6, C-8, C-9, C-11, C-3	2.06 (6.7), 1.18 (1.0), 0.89 (2.4)	2.06, 1.18, 0.89
11	73.6 (s)					
12	23.7 (q)	1.18 (s)		C-6, C-10, C-11	1.78 (1.4), 0.89 (1.3), 1.69 (0.6)	1.78, 1.72, 0.89
13	14.7 (q)	0.89 (d, 9.6)	1.69	C-9, C-10, C-11	1.72 (1.0), 1.69 (2.0), 1.18 (1.0)	2.06, 1.72, 1.69, 1.18
14	23.2 (q)	1.68 (d, 2.0)	5.38	C-6, C-7, C-8	1.79 (1.1), 5.38 (5.2)	5.38, 1.78, 1.49
15	27.8 (q)	1.26 (s)		C-2, C-3, C-4	5.20 (0.9), 5.88 (1.3)	5.88, 5.20, 5.02, 1.63, 1.62, 1.49, 1.41

[a]Observed NOE signals when the proton on column 3 is irradiated.

total of 15 carbon signals comprising four methyls, four methylenes, four methines, and three quaternary carbons. Six downfield carbons are assigned to two double bonds and two oxygen-bearing quaternary carbons in view of their carbon chemical shifts (Table 5). The molecular formula, $C_{15}H_{26}O_2$, is assigned on the basis of spectral data and supported by a mass spectrum (found *m*/*z* = 221 and 220, corresponding to $[M^+ - OH]$ and $[M^+ - H_2O]$, respectively).

The ^1H-^1H COSY spectrum displays three types of coupled spin systems: an ABX system corresponds to H-1/H-2 of the vinyl group, while a system, due to two adjacent methylenes further coupled with a methine proton, is assigned to protons H-4/H-5/H-6. The remaining sequence involves a methyl doublet, one methylene, and two methines corresponding to H-8/H-9/H-10/Me-13. Assembly of these sequences and the remaining structural units follows from HMBC correlations. Thus, the cyclohexenol ring system devolves from the HMBC correlations from Me-14 C-6, C-7, and C-8, and the Me-12 protons to C-10, C-11, and C-6. The side chain is established from the HMBC correlations of Me-15 protons to C-2, C-3, and C-4.

The relative configuration in the cyclohexenol ring is resolved by NOE experiments. Thus, the NOE enhancements at H_3-13 (2.1%) and H_3-12 (2.6%) when H-6 was irradiated suggest the *cis* relationships of these groups. This relative stereochemistry is further supported by correlations between H-6, H_3-12, and H_3-13 in the NOESY spectrum. The relative configuration at C-3 remains unknown.

Sesquiterpene **6** was isolated as an optically active, oily substance whose IR spectrum is nearly identical to that of sesquiterpene **5** indicating the presence of hydroxyl (3416 cm^{-1}) and alkenic (1658 cm^{-1}) functional groups. Its ^{13}C NMR and DEPT spectra are similar to those of sesquiterpene **5** indicating a total of 15 carbon signals comprising four methyls, four methylenes, four methines, and three quaternary carbons. Six downfield carbons are assigned to two double bonds and two oxygen-bearing quaternary carbons in view of their carbon chemical shifts (Table 6). The molecular formula, $C_{15}H_{26}O_2$, is assigned on the basis of spectral data and supported by ions corresponding to $[M^+ - H]$, $[M^+ - OH]$, and $[M^+ - H_2O]$ in EI-MS.

The ^1H–^1H COSY spectrum displays the same three spin systems noted in **5**. The connection of these partial structures and the remaining structural units is completed via analysis of HMBC correlations. The relative stereochemistry of sesquiterpene **6** was revealed by NOE experiments and NOESY correlations. Thus, the NOE enhancement at H-6 (1.9%) when Me-12 was irradiated indicates a *cis* relationship.

The ^{13}C NMR and DEPT spectra (Table 7) of sesquiterpene **7** indicate a total of 15 carbons corresponding to four methyls, four methylenes, four methines, and three

© 2002 NRC Canada

Table 6. NMR data (400 MHz, $CDCl_3$) for sesquiterpene **6**.

Carbon	δ	Proton (*J* (Hz))	COSY	HMBC	NOE enhanced signals (%)[a]	NOESY correlations
1	111.5 (t)	5.20 (dd, 17.2, 1.2)	5.90, 5.02	C-2, C-3	5.02 (12.3), 5.90 (0.7), 1.25 (0.9)	5.90, 5.02, 1.25
		5.02 (dd, 10.4, 1.2)	5.90, 5.02	C-3	5.20 (11.1), 5.90 (2.3)	5.90, 5.20, 1.25
2	145.5 (d)	5.90 (dd, 17.2, 10.4)	5.20, 5.02	C-3, C-15	5.02 (2.3), 1.72 (1.2), 1.25 (1.0)	5.20, 5.02, 1.72, 1.25
3	73.4 (s)					
4	42.7 (t)	1.74 (m, 2H)		C-2, C-3, C-6, C-15	5.90 (1.8), 1.25 (1.3)	1.72, 1.39, 1.78
5	24.4 (t)	1.72 (m)	1.39	C-3, C-4, C-6, C-7, C-11	1.39 (2.8), 1.25 (2.6)	1.78, 1.74, 1.72
		1.39 (m)	1.74, 1.72			1.72
6	52.2 (d)	1.78 (m)	1.72, 1.39	C-4, C-5, C-7, C-8, C-10, C-11, C-12, C-14	1.05 (3.3)	1.86, 1.72, 1.67, 1.39, 1.05
7	137.4 (s)					
8	119.7 (d)	5.16 (m)	2.11, 1.58, 1.67	C-6, C-9, C-10, C-14	1.67 (7.3), 2.11 (3.3)	2.11, 1.67, 1.58
9	33.5 (t)	2.11 (dm, 17.2)	5.16, 1.86, 1.58		5.16 (3.7), 1.58 (4.5), 1.86 (2.0), 0.91 (1.9)	5.16, 1.58, 0.91
		1.58 (m, 17.2)	5.16, 2.11, 1.86	C-7, C-8, C-10, C-11, C-13		2.11, 1.86, 1.05
10	32.8 (d)	1.86 (m, 6.4)	2.11, 1.58, 0.91	C-6, C-9, C-11, C-12, C-13	1.58 (4.0), 2.11 (2.5), 1.05 (1.9), 0.91 (4.3)	1.78, 1.58, 1.05, 0.91
11	74.8 (s)					
12	22.2 (q)	1.05 (s)		C-6, C-10, C-11	1.78 (1.9), 1.58 (0.6), 0.91 (0.3)	1.86, 1.78, 1.72, 1.58
13	14.4 (q)	0.91 (d, 6.4)	1.86	C-9, C-10, C-11	1.58 (2.0), 2.11 (1.3), 1.86 (2.4), 1.05 (0.6)	2.11, 1.86
14	23.0 (q)	1.67 (d, 1.6)	5.16	C-6, C-7, C-8	5.16 (8.9),	5.16, 1.78, 1.72
15	27.5 (q)	1.25 (s)		C-2, C-3, C-4	5.20 (0.5), 5.02 (0.2), 5.90 (1.0), 1.72 (0.3)	5.90, 1.74

[a]Observed NOE signals when the proton on column 3 is irradiated.

quaternary carbons. Two downfield carbons are indicative of a secondary alcohol and a bromine methine in view of their chemical shifts. The molecular formula $C_{15}H_{25}BrO$ is supported by HR-EI-MS ions $[M^+ - H_2O]$ and $[M^+ - Br]$ (*m/z* = 284.0967, 282.0982, and 221.1896; calcd. for $C_{15}H_{23}{}^{81}Br$, $C_{15}H_{23}{}^{79}Br$, and $C_{15}H_{25}O$: 284.0968, 282.0983, and 221.1905, respectively). The molecular ion was not observed even when using lower electron impact energy (27 eV).

The ^1H-^1H COSY spectrum displays three coupled spin systems consistent with proton sequences H_3-13/H-1/H_2-2/H-3/H-4/H_3-14, H_2-6/H_2-7, and H-9/H_2-10. The assembly of the tricyclic system of **7** is readily achieved by analysis of HMBC correlations. Thus, the cyclohexanol ring is supported by the HMBC correlations from the methine proton H-4 to C-5, C-6, and C-11, and from H_3-12 protons to carbons C-1, C-5, C-10, and C-11. The remaining two rings are established by HMBC correlations from H_3-15 to C-5, C-7, C-8, and C-9.

The relative stereochemistry of **7** is resolved by NOE experiments. Thus, the *cis* cyclohexanol–cyclopentane ring junction is deduced from the large NOE enhancements between H-1 and H-9 and dictates the configuration at C-1, C-5, C-9, and C-11. The *cis* fusion of the cyclobutane–cyclopentane rings is supported by the NOE between H_3-15 and H-9 and between H_3-12 and protons H_2-6 and H_2-7. The α configuration of the H_3-14 is assigned based on the NOE enhancements between H_3-12 and H-4. The hydroxyl group at C-3 is in an α configuration, in view of the NOE between H-3 and H-4.

Sesquiterpene **7** possesses the same skeleton as perforatone, a sesquiterpene previously isolated by Gonzalez et al. (26) from *Laurencia perforata*, whose structure and relative stereochemistry were assigned based on ^1H chemical shift, coupling constant data, and chemical modifications. However, these authors did not offer any evidence for their proposed stereochemistry at C-5, C-8, and C-9, which is opposite to that observed in **7**. We propose the name perforatol for **7**. The absolute configurations of compounds **1**–**7** are unknown.

Experimental section

General

Melting points were determined on a Kolfler hot stage apparatus and are uncorrected. Optical rotations were measured on a PerkinElmer 241 polarimeter. IR spectra were recorded on a Bruker IFS-25 spectrometer using 32 scans at a resolution of 2 cm^{-1}. Mass spectra were taken using a Kratos MS-50 spectrometer and UV spectra were recorded on a Hewlett-Packard 8452A diode array spectrophotometer.

© 2002 NRC Canada

Table 7. NMR data (400 MHz, $CDCl_3$) for perforatol (**7**).

Carbon	δ	Proton (*J* (Hz))	COSY	HMBC	NOE enhanced signals (%)[a]
1	27.9 (d)	1.69 (m)	1.50, 0.82	C-2, C-11, C-12, C-13	4.31 (7.8), 0.82 (3.0)
2	37.3 (t)	1.50 (m, 2H)	3.74, 1.69	C-1, C-3, C-4, C-11	3.74 (8.0), 0.68 (5.5)
3	70.2 (d)	3.74 (ddd, 2.8, 2.8, 3.2)	1.59, 1.50	C-1, C-5	1.59 (4.9), 1.50 (5.4), 1.29 (2.7)
4	39.0 (d)	1.59 (m)	3.74, 1.29	C-5, C-6, C-8, C-11, C-14	3.74 (3.4), 1.29 (5.0)
5	56.2 (s)				
6	22.9 (t)	1.78 (m)	2.13, 1.56, 1.50	C-4, C-5, C-7, C-8	2.04 (3.4), 0.82 (3.1), 0.68 (3.4)
		1.56 (m)	2.13, 1.78, 1.50	C-4, C-5, C-7, C-8	1.78 (6.9)
7	26.8 (t)	2.13 (m)	1.78, 1.56, 1.50	C-5, C-6. C-8. C-9	1.50 (8.4)
		1.50 (m)	2.13, 1.78, 1.56	C-5, C-6. C-8. C-9	2.13 (12.9), 1.78 (8.8)
8	50.3 (s)				
9	64.2 (d)	4.31 (ddd, 12.7, 6.8, 0.9)	4.31, 2.29, 2.04	C-7, 8, 10	2.29 (3.5), 2.04 (0.4), 1.69 (10.1), 1.30 (2.0)
10	44.5 (t)	2.29 (dd, 12.9, 6.8;)	4.31, 2.04	C-1, C-5, C-8, C-9, C-11	2.04 (13.3), 4.31 (2.4), 0.82 (3.0)
		2.04 (dd, 12.9, 12.7)	4.31, 2.29	C-1, C-5, C-8, C-9	4.31 (1.1), 2.29 (14.6), 1.78 (3.4), 0.68 (1.6)
11	46.9 (s)				
12	11.9 (q)	0.68 (s)		C-1, C-10, C-11, C-5	0.82 (1.2), 2.29 (0.7), 2.04 (1.5), 1.78 (2.1), 1.50 (1.2), 1.59 (1.8), 1.50 (1.2)
13	16.6 (q)	0.82 (d, 6.8)	1.69	C-1, C-2, C-11	0.68 (1.0), 2.29 (2.2), 1.69 (1.8)
14	13.5 (q)	1.29 (d)	1.59		3.74 (2.3)
15	26.2 (q)	1.30 (s)		C-5, C-7, C-8, C-9	4.31 (2.7)

[a]Observed NOE signals when the proton on column 3 is irradiated.

NMR spectra were recorded at room temperature in $CDCl_3$ (unless otherwise specified) on a Varian Unity 400 spectrometer operating at 399.944 MHz for ^1H and 100.575 MHz for ^{13}C. Signal positions were reported on the δ scale in parts per million (ppm) downfield from tetramethylsilane (TMS) as internal standard or reference using the solvent residue peaks. All 2D NMR were recorded (non-spinning) at 25°C using standard Varian software (Version 4.3). Analytical and preparative thin layer chromatography (ptlc) were performed on precoated plates (Kieselgel 60F254, Baker Si500F, and Baker Si-C18F). Substances were made visible on chromatographic plates by viewing under UV light (254 nm), or spraying with phosphomolybdic acid reagent. Vacuum liquid chromatography was carried out on Kieselgel 60G type of silica gel.

Animal material

The animals, *Aplysia punctata* (wet weight 150 g), were collected at Porto San Paolo (Olbia), Sardinia, Italy in April 1993. A voucher specimen was identified and stored by Dr. David G. Reid of the Department of Zoology at The Natural History Museum, London, U.K. under register no. BM(NH) 1994038

Isolation

The sea hares were cut into small pieces and extracted with 95% ethanol (3 × 300 mL). Ethanol was striped off under vacuum at 40°C. The residue was treated with water (250 mL) and re-extracted with methylene chloride (3 × 200 mL) and ethyl acetate (3 × 200 mL). Solvents were evaporated under vacuum below 40°C. The combined methylene chloride and ethyl acetate crude extract (4.4 g) was chromatographed on a short silica gel column (230–400 mesh, 86 g, 7.0 × 6.5 cm) and eluted with hexane containing 10%, 25%, and 50–100% ethyl acetate yielding 4 fractions A, B, C, and D. Fraction A (0.41 g) was rechromatographed on a short column (Kiesegel 60 G, 2.0 × 3.5 cm) and eluted with hexane (60 mL), $CHCl_3$ (80 mL), and EtOAc (30 mL) giving fractions A1 (0.18 g), A2 (0.12 g), and A3 (0.10 g). Fraction A2 and A3 were combined with fraction B for further purification. Fraction A1 was further purified by repeated ptlc and yielded laurencenyne (6.8 mg) (Baker Si-C_{18} F, 0.2 mm, acetone, R_f = 0.63), laurene (16.6 mg) (Baker Si500 F, 0.5 mm, hexane, R_f = 0.49), α-isobromocuparene (4.0 mg) (Baker Si500F, 0.5 mm, hexane, R_f = 0.44), and a mixture of α-bromocuparene and bromolaurene (~1:1) (6 mg) (Baker Si500 F, 0.5 mm, hexane, R_f = 0.56). Fraction B (2.4 g) was purified on a silica gel column (230–400 mesh, 35 g, 4.0 × 4.5 cm) and eluted with an increasing gradient of EtOAc (0 ~ 100%) in hexane, producing 36 fractions (~90 mL each). A combination of fractions 3 to approximately 5 was further purified using silica gel column and ptlc on Kieselgel $60F_{254}$ plates (0.5 mm) giving debromoallolaurinterol (~0.57 g) (hexane–EtOAc = 20:1, R_f = 0.36), laurenisol (~ 0.31 g) (hexane–$CHCl_3$ = 3:1, R_f = 0.32), and laurenyne (4.6 mg) (hexane–$CHCl_3$ = 1:1, R_f = 0.49). Combined fractions 16–19 were further purified by repeated ptlc on Kieselgel 60F254 plates (0.5 mm) giving laurinterol (6.9 mg) (hexane–$CHCl_3$ = 3:1, R_f = 0.55), the dibromo chamigrane derivative (59.0 mg) (hexane–EtOAc = 20:1, R_f = 0.18), and perforenone (9.3 mg) (hexane–EtOAc = 20:1, R_f = 0.07). Fraction C (0.98 g) was separated on a silica gel column (Kieselgel 230–400 mesh, 22 g) using a solvent system of hexane containing increasing portions of EtOAc (0 ~ 100%) yielding 20 fractions (~40 mL each). A combination of fractions 4 to approximately 7 was further

© 2002 NRC Canada

purified via ptlc on Kieselgel $60F_{254}$ plates (0.5 mm) producing the friedosnyderane, 2,3,6-trimethyl-1-(3′-hydroxy-3′-methyl-5′-pentenyl)benzene (3.5 mg) (C_6H_6–CH_2Cl_2 = 3:1, R_f = 0.05), obtusenol (4.2 mg) (CH_2Cl_2, R_f = 0.44), punctatene acetate **3** (4.9 mg) (hexane–EtOAc = 9:1, R_f = 0.38), perforatol **7** (2.8 mg) (C_6H_6–$CHCl_3$ = 3:2, R_f = 0.32), β-snyderol (2.0 mg) (0.25 mm plate, hexane–$CHCl_3$ = 1:1, R_f = 0.12), and punctatol **4** (0.5 mg) (0.25 mm plate, hexane–$CHCl_3$ = 1:1, R_f = 0.08). From the combination of fractions 8 to approximately 19, 5-epidioxycholest-6-ene (3.3 mg) was isolated via ptlc on a Baker Si500 F (0.5 mm) plate using a solvent mixture of hexane–EtOAc = 3:1 (R_f = 0.21). Fraction D (1.5 g) was further separated on a short column (Kieselgel 60G) using solvents $CHCl_3$, $CHCl_3$–MeOH (4:1), and $CHCl_3$–MeOH (3:2), giving three fractions D1 (23 mg), D2 (1.0 g), and D3 (0.31 g). The fraction D3 was partitioned between ether and methanol–water (1:1). Evaporation of the ether phase gave a fraction D3*a* and concentration of the methanol solution resulted in fraction D3*b*. Fraction D2 (1.0 g) was chromatographed on a short column followed by ptlc on Baker Si-C_{18}F (0.25 mm) plate giving isoconcinndiol (13.7 mg) (acetone–H_2O = 4:1, R_f = 0.36) and two diastereoisomers : sesquiterpene **5** (7.8 mg) (MeOH/H_2O = 4:1, R_f = 0.41) and sesquiterpene **6** (4.4 mg) (MeOH/H_2O = 4:1, R_f = 0.28). Fraction D3b (0.25 g) was further purified on a short column (Kieselgel 60G, 2.7 × 3.3 cm, $CHCl_3$ – 0 to 20% MeOH gradient) and yielded 7 subfractions: D3*b*1 through D3*b*7. D3*b*2 (0.14 g), which underwent further purification via ptlc on Kieselgel $60F_{254}$ plates (0.5 mm) using a solvent of hexane–acetone (7:3), afforded neopargueroldione **1** (4.3 mg) (R_f = 0.05). D3*b*3 (0.09 g) was further purified via ptlc on Kieselgel 60 F254 (0.5 mm) using hexane–acetone (7:3) to yield parguerol (3.8 mg) (R_f = 0.03). Fraction D3*b*4 (0.09 g) was purified via ptlc on Baker Si-C_{18}F (0.25 mm) plates using acetone–H_2O (3:2) to give deacetylparguerol **2** (7.9 mg) (R_f = 0.55).

Neopargueroldione 1

Viscous semi-solid, $[\alpha]_D$ = +2.5° (acetone, *c* = 0.0020). NMR data see Table 1. IR (film) (cm^{-1}): 3309, 1696, 732. EI-MS *m/z* (%): 412 ([M^+ – H_2O], 3.6), 411 ([M^+ – H – H_2O], 7.4), 410 ([M^+ – H_2O], 3.2), 409 ([M^+ – H – H_2O], 7.0), 394 (6.1), 393 (3.4), 391 (3.3), 375 (3.3), 373 (3.0), 367 (9.5), 330 (13.0), 312 (28.6), 311 (39.5), 310 (11.4), 294 (9.1), 292 (7.0), 284 (14.0), 266 (14.2), 264 (16.0), 236 (17.8), 213 (26.8), 185 (100), 184 (86.8).

Deacetylparguerol 2

Semi-solid, $[\alpha]_D$ = –18.4° (CH_3OH, *c* = 0.0049). NMR data see Table 2. IR (film) (cm^{-1}): 3355, 2955, 1653, 1457, 1379, 1056, 1018, 668. EI-MS *m/z* (%): 398 (2.8), 396 (3.0), 380 (11.7), 278 (16.3), 363 (21.1), 362 (23.3), 361 (16.3), 360 (19.2), 349 (20.8), 347 (18.2), 346 (16.2), 345 (18.4), 327 (11.8), 299 (18.6), 298 (14.1), 281 (27.6), 273 (24.5), 272 (29.3), 2.57 (10.2), 256 (22.7), 255 (32.6), 254 (40.0), 237 (36.3).

Punctatene acetate 3

An oil, $[\alpha]_D$ = –14.5° ($CHCl_3$, *c* = 0.0024). NMR data see Table 3. IR (film) (cm^{-1}): 2970, 1730, 1454, 1370, 1240, 1002. HR-EI-MS *m/z*: 348.26025 ([M^+]) (calcd. for $C_{22}H_{36}O_3$: 348.26644). EI-MS *m/z* (%): 348 ([M^+], 2.0), 347 (7.8), 305 (1.7), 289 (5.4), 288 (10.3), 287 (18.0), 269 (10.2), 231 (12.9), 219 (18.4), 218 (15.7), 217 (11.1), 205 (52.6), 187 (44.7), 161 (53.1), 147 (92.8), 109 (100), 81 (81.4).

Punctatol 4

Solid, mp = 101–103°C, $[\alpha]_D$ = + 40° ($CHCl_3$, *c* = 0.00015). NMR data see Table 4. IR (film) (cm^{-1}): 3350, 2952, 1456, 1374, 1177, 1072. HR-EI-MS *m/z*: 304.2414 ([M^+ – 2HBr]) (calcd. for $C_{20}H_{32}O_2$: 304.24023). EI-MS *m/z* (27eV) (%): 453 ([M^+ – CH_3], 2.1), 451 (3.9), 450 (1.3), 449(2.5), 436 (1.2), 435 (3.3), 434 (1.5), 433 (5.3), 431 (2.7), 388 (1.6), 387 (5.3), 386 (4.6), 385 (5.1), 384 (6.9), 369 (14.7), 367 (14.4), 275 (18.4), 273 (20.3), 219 (96.1), 217 (100), 193 (79.8), 175 (30.6), 151 (29.9), 135 (62.1), 119 (38.1), 95 (52.3), 81 (56.3).

Sesquiterpene 5

An oil, $[\alpha]_D$ = +31.1° ($CHCl_3$, *c* = 0.0023). NMR data see Table 5. IR (film) (cm^{-1}): 3406, 2973, 1658, 1649, 1452, 1372, 1118, 1077, 919. EI-MS *m/z* (%): 221 ([M^+ – OH], 1.8), 220 ([M^+ – H_2O], 6.0), 205 (3.7), 203 (1.7), 202 (4.9), 187 (5.8), 177 (6.0), 177 (6.0), 152 (36.8), 148 (15.6), 139 (5.4), 137 (16.2), 135 (42.3), 133 (45.1), 121 (61.2), 109 (75.2), 81 (100), 71 (66.8).

Sesquiterpene 6

An oil, $[\alpha]_D$ = +10.4° ($CHCl_3$, *c* = 0.0012). NMR data see Table 6. IR (film) (cm^{-1}): 3416, 2973, 1658, 1452, 1379, 1118, 1043, 921. EI-MS *m/z* (%): 237 ([M^+ – H], 3.4), 221 ([M^+ – OH], 6.0), 220 ([M^+ – H_2O], 2.3), 219 (10.5), 205 (7.0), 203 (5.8), 191 (17.8), 181 (23.0), 175 (14.6), 137 (37.1), 123 (60.4), 121 (56.2), 109 (56.2), 99 (15.7), 95 (70.5), 81 (64.1), 71 (100).

Perforatol 7

Semi-solid, $[\alpha]_D$ = +14.8° ($CHCl_3$, *c* = 0.0016). NMR data see Table 7. IR (film) (cm^{-1}): 3340, 2965, 1462, 1453, 1057, 769. HR-EI-MS *m/z*: 284.0967 ([M^+ – H_2O]) (calcd. for $C_{15}H_{23}Br_{81}$: 284.09676), 282.0982 ([M^+ – H_2O]) (calcd. for $C_{15}H_{23}Br_{79}$: 282.09830), 221.1896 ([M^+ – Br]) (calcd. for $C_{15}H_{25}O$: 221.19054). EI-MS *m/z* (27eV) (%): 284 (1.6), 282 (1.6), 221 (14.9), 203 (56.2), 175 (22.7), 147 (27.9), 133 (31.0), 121 (36.3), 119 (42.4), 109 (100).

Acknowledgments

Thanks are due to the Natural Science and Engineering Research Council of Canada (NSERC) for financial support; to David G. Reid, Department of Zoology, The Natural History Museum, London, England and Dr. Flegra Bentivengna, Stazione Zoologica, Villa Comunale, Napoli, Italy for identification of specimens; to Ghislain Deslongchamps for the MM2 global conformational searches; and to Ing. Luciano Porilli, Porto San Paolo, Sardinia, Italy for facilitating the collection of the sea hares.

© 2002 NRC Canada

References

1. N.B. Eales. Revision of the world species of *Aplysia* (Gastropoda, Opistobranchia). Bull. Br. Mus. (Nat. Hist.) Zool. **5**, 292 (1960).
2. B.W. Halstead. Poisonous and venomous marine animals of the world. Vol. 1. U.S. Government Printing Office, Washington D.C. 1965. p. 709.
3. G.Y. Kennedy and H. Vevers. J. Mar. Biol. Assoc. U. K. **33**, 663 (1954).
4. C. Jimänez, E. Quinoa, L. Castedo, and R. Riguera. J. Nat. Prod. **49**, 905 (1986).
5. E. Quinoa, L. Castedo, and R. Riguera. Comp. Biochem. Physiol. B: Comp. Biochem. **92B**, 99 (1989).
6. D.J. Faulkner. Nat. Products Rep. **3**, 1–33 (1986).
7. A.G. Gonzalez, J. Darias, and J.D. Martin. Tetrahedron Lett. **38**, 3375 (1977).
8. R. Kaslauskas, P.T. Murphy, R.J.Quinn, and R.J.Wells. Aust. J. Chem. **29**, 2533 (1976).
9. T. Susuki, M. Susuki, and E. Kurosawa. Tetrahedron Lett. **35**, 3057 (1975).
10. T. Irie, M. Susuki, E. Kurosawa, and T. Masamune. Tetrahedron, **26**, 3271 (1970).
11. S.J.Wratten, T. Nishiguchi, and R.W. Skeean. J. Org. Chem. **42**, 3343 (1977).
12. T. Irie, A. Fukuzawa, M. Izawa, and E. Kurosawa. Tetrahedron Lett. **17**, 1343 (1969).
13. M. Susuki and E. Kurosawa. Bull. Chem. Soc. Jpn. **52**, 3349 (1979).
14. S. Imre, S. Islemyela, A. Ozytuk, and R.H. Thomson. Phytochemistry, **20**, 833 (1981).
15. B.M. Howard and W. Fenical. Tetrahedron Lett. **41**, 4, (1976).
16. A.G. Gonzalez, J.D. Martin, M. Norte, R. Perez, and V. Weyler. Tetrahedron Lett. **24**, 847 (1983).
17. M.L. Rodriguez, J.D. Martin, and D. Estrada. Acta Cryst. **C45**, 306 (1989).
18. B.M. Howard and W. Fenical. Phytochemistry, **19**, 2774 (1980).
19. F.J. Schmitz, D.P. Michaud, and J. Schmidt. J. Am. Chem. Soc. **104**, 6415 (1982).
20. C.P. Falshaw, T.J. King, S. Imre, S. Islimyeli, and R.H. Thomson. Tetrahedron Lett. **21**, 4951 (1980).
21. H. Kigoshi, Y. Shizuri, H. Niwa, and K. Yamada. Tetrahedron Lett. **22**, 4729 (1981).
22. F. Mohamadi, N.G. Richards, W.C. Guida, R. Liscamp, M. Lipton, C. Caufield, G. Chang, T. Hendrickson, and W.C. Still. J. Comput. Chem. **11**, 440 (1991).
23. D.N. Estrada, J.L. Ravelo, C. Ruiz-Perez, J.D. Martin, and X. Solans. Tetrahedron Lett. **30**, 6219 (1989).
24. S. Caccamese, R. Toscano, S. Cerrini, and E. Gavuzzo. Tetrahedron Lett. **23**, 3415 (1982). 25. F.J. Schmitz, F.J. McDonald, and D.J. Vanderah. J. Org. Chem. **43**, 4220 (1978).
26. A.G. Gonzalez, J.M. Aguiar, J.D. Martin, and M. Norte. Tetrahedron Lett. **29**, 2499 (1975).

© 2002 NRC Canada

Lamellar polysilicate nanocomposite materials: Intercalation of polyethylene glycols into protonated magadiite

Marie-Josée Binette and Christian Detellier

Abstract: This paper reports the direct intercalation of organic polymers into the interlamellar spaces of the layered polysilicate magadiite. Poly(ethylene glycols) (PEG 3400 and PEG 1000) were intercalated into acidified magadiite (*H*-magadiite) by displacing a dipolar aprotic solvent (e.g., dimethylsulfoxide (DMSO)) from the *H*-magadiite – DMSO intercalate. This was done directly from the polymer melt at 155°C. The polysilicid acid (*H*-magadiite) was obtained by HCl titration of the sodic form of magadiite obtained by hydrothermal synthesis. Dipolar aprotic solvents (dimethylsulfoxide, *N*-methylformamide, and hexamethylphosphorictriamide) were intercalated in the interlamellar spaces of *H*-magadiite. PEG 3400 and PEG 1000 were then intercalated by dispersing the *H*-magadiite intercalates in a large excess of the polymers heated above their fusion temperature, without any solvent. The resulting polymer intercalated *H*-magadiite nanocomposites were isolated and purified and were shown by chemical analysis to have chemical formulae of $H_2Si_{14}O_{29}(\text{-}OCH_2CH_2\text{-})_{3.1}$ and $H_2Si_{14}O_{29}(\text{-}OCH_2CH_2\text{-})_{2.9}$, respectively, in agreement with a structure in which one unit cell of magadiite corresponds to three oxyethylene units. The dipolar aprotic solvents have been completely removed from the interlamellar spaces. ^{13}C NMR dipolar diphasing techniques show that the polymer chains in the interlamellar spaces of *H*-magadiite are more constrained than in the bulk polymer. ^{29}Si NMR spectra show that the structure of magadiite is unchanged by the two processes of intercalation. The polymer intercalates are characterized by interlamellar spacings of 4.6 and 4.4 Å, as determined by XRD. These values correspond to a flattened arrangement of the polymer chains in the interlamellar spaces. This is also in agreement with DSC data, which demonstrate that the polymer chains are no longer in the aggregation state characteristic of the bulk polymer.

Key words: lamellar polysilicates, polyethylene glycols, nanocomposite materials, polymer intercalation, magadiite.

Résumé : Ce travail décrit l'intercalation directe de polymères organiques dans l'entrecouche du polysilicate lamellaire magadiite. Deux polyéthylène glycols (PEG 3400 et PEG 1000) ont été intercalés dans la magadiite acidifiée (*H*-magadiite) par déplacement d'un solvant aprotique dipolaire (le diméthylsulfoxyde, DMSO) de l'intercalat *H*-magadiite–DMSO. Ceci a été fait directement à partir du polymère fondu à une température de 155 °C. L'acide polysilicique, *H*-magadiite, a été obtenue en titrant avec HCl la forme sodique de la magadiite obtenue par synthèse hydrothermale. Les solvants aprotiques dipolaires (DMSO, *N*-méthylformamide et hexaméthylphosphoramide) ont été intercalés dans l'espace interlamellaire de *H*-magadiite. PEG 3400 et PEG 1000 ont par la suite été intercalés en dispersant les intercalats *H*-magadiite dans un important excès de polymères chauffés au-delà de leur température de fusion, sans l'utilisation de solvant. Les nanocomposites *H*-magadiite intercalés de polymères ayant été obtenus ont, selon l'analyse chimique, les formules chimiques suivantes $H_2Si_{14}O_{29}(\text{-}OCH_2CH_2\text{-})_{3.1}$ et $H_2Si_{14}O_{29}(\text{-}OCH_2CH_2\text{-})_{2.9,}$ respectivement. Ces formules sont en accord avec une structure dans laquelle un unité cellulaire de la magadiite correspond à trois unités oxyéthylènes. Les solvants aprotiques dipolaires ont été complètement expulsés de l'espace interlamellaire. La résonance magnétique nucléaire en déphasage dipolaire du ^{13}C montre que les chaînes de polymère dans l'espace interlamellaire de *H*-magadiite sont moins mobiles qu'à l'état pur. La RMN du ^{29}Si montre que la structure de la magadiite demeure inchangée suite aux deux processus d'intercalation. Les intercalats de polymère sont caractérisés par un espace interlamellaire de 4,6 et 4,4 Å, comme démontré par la diffraction des rayons X. Ces valeurs correspondent à un arrangement en monocouche aplatie du polymère dans les espaces interlamellaires. Ceci est en accord avec les résultats de l'analyse par calorimétrie différentielle à balayage, qui démontre que les chaînes de polymère ne sont plus dans leur état caractéristique du polymère pur.

Mots clés : polysilicates lamellaires, glycols de polyethylène, matériaux nanocomposites, intercalation de polymères, magadiite.

Received 15 January 2002. Published on the NRC Research Press Web site at http://canjchem.nrc.ca on 23 December 2002.

M.-J. Binette and C. Detellier.[1] Ottawa-Carleton Chemistry Institute, Department of Chemistry, University of Ottawa, Ottawa, ON K1N 6N5, Canada.

[1]Corresponding author (e-mail: dete@science.uottawa.ca).

 DOI: 10.1139/V02-181 © 2002 NRC Canada

Introduction

Nanocomposite materials are a relatively new class of materials, which are formed when organic and inorganic phases are mixed on a nanometer length scale. In particular, the study of polymer-based nanocomposites has recently attracted considerable attention mainly because this new class of materials represents an alternative to conventionally filled polymers (1). Such nanocomposites have been proven to lead to new and improved properties, compared to that of the pure parent polymer, such as reduced gas permeability (1*y*), increased modulus (1*b*), enhanced ionic conductivity (1*j*), increased solvent and heat resistance as well as decreased flammability (1*d*).

In general, polymers can be intercalated into an inorganic lamellar material by two different approaches: incorporation of a monomer followed by its "in situ" polymerization or by direct insertion of the polymer from solution or from the melt. It has been shown that polymer melt intercalation is the most promising approach to fabricate polymer-based nanocomposites (1*q*, 1*z*). Using this method, several groups studied the intercalation of polyethylene oxide (1*a*, 1*f*, 1*j*, 1*l*, 1*bb*) and polystyrene (1*c*, 1*o*, 1*q*, 1*u*) into lamellar inorganic materials. Several papers describe efforts to incorporate polymers into aluminosilicates, such as smectites, montmorillonite, and hectorite in particular (1*b–d*, 1*f*, 1*i*, 1*l*, 1*n–s*, 1*u*, 1*v*, 1*x*, 1*aa*, 1*bb*), or kaolinite (1*a*), which are used as the inorganic layered phase. Since layered aluminosilicates are rather organophobic, to facilitate the transport of the polymer chains into their interlamellar spaces, it is essential to first modify the silicate. Therefore, in most of the reported inclusions of polymers into aluminosilicate compounds, the interlamellar cations were exchanged with long-chain alkyl ammonium ions prior to polymer insertion (1*c–i*, 2).

In comparison, little work has been done on the preparation of nanocomposite materials derived from polymers and layered polysilicate. The family of crystalline alkali metal polysilicates includes kanemite, makatite, octosilicate, magadiite, and kenyaite. Their structures consist of one or more SiO_4 tetrahedra. Their layers contain terminal oxygen ions that are neutralized by sodium and (or) protons. All are naturally occuring minerals (3) that can also be prepared in the laboratory by hydrothermal synthesis (4). The layered compounds and their silicic acid derivatives are known to be host materials for intercalation and ion exchange (5). They can be used as alternative inorganic components for the formation of nanostructured hybrid-composites. Sugahara et al. (1*g*) prepared a magadiite–polyacrylonitrile intercalation compound and Wang and co-workers reported exfoliation of magadiite in an elastomeric epoxy polymer (1*e*, 1*h*). In both cases, the interlamellar sodium ions of magadiite were first exchanged with long-chain alkyl ammonium ions before the polymers were inserted.

Generally, two types of hybrid structures can be obtained: intercalated, in which one polymer chain is incorporated between the silicate layers; and delaminated, in which the silicate layers are dispersed individually in the organic matrix.

In this work, we report the synthesis of intercalated nanocomposites derived from the silicic acid, *H*-magadiite, and polyethylene glycol. The preparation is done by using the polymer melt intercalation approach. The resulting material has well-ordered multilayers in which inorganic and polymer layers alternate.

Experimental section

Na-magadiite

Na-magadiite was synthesized by the reaction of SiO_2 and NaOH under hydrothermal conditions according to a previously described method (4*b*, 6). SiO_2 (0.537 mol) was added to 80 mL of a solution of 1.25 M NaOH. The reaction mixture was stirred for 1 h and was then heated at autogenous pressure in a stainless steel-lined autoclave to 180°C for 20 h. The Na-magadiite was recovered by filtration, washed with water, and air-dried.

H-magadiite

Titration of Na-magadiite was performed according to the procedure of Lagaly et al. (5*b*). A suspension of 9.6 g of Na-magadiite per 100 mL water was stirred for 1 h. The suspension was then titrated with 0.1 N HCl to a final pH of 2.0. The mixture was stirred for an additional 24 h. The *H*-magadiite reaction product was separated by filtration and air-dried.

Intercalation

H-magadiite (0.5 g), dried at 100°C for 24 h, was dispersed in 20 mL of a polar organic substance (*N*-methyl formamide (NMF), dimethylsulfoxyde (DMSO), or hexamethylphosphorictriamide (HMPA)). For NMF and DMSO, the mixtures were stirred for 24 h at room temperature. In the case of HMPA, a temperature of 50°C was used. The resulting compounds are referred to as H-mag–NMF, H-mag–DMSO, and H-mag–HMPA.

Nanocomposite

The intercalation compound (most reactions were done with H-mag–DMSO) was separated from the organic liquid by centrifugation and was used without removing the adherent liquid for the incorporation of the polymer. Thus, 10 g of PEG 3400 (from Aldrich) was heated to 155°C. To this viscous melt, 2.0 g of *H*-mag–DMSO was added. After 7 days, the reaction was stopped by cooling. The product was worked up by washing and centrifuging in methanol to remove excess polyethylene glycol followed by air-drying and then drying in an oven at 110°C. Polyethylene glycol 1000 (Aldrich) was also used, under the same reaction conditions. These samples are referred to as H-mag–PEG3400 and H-mag–PEG1000.

Physical mixture

A physical mixture of *H*-magadiite and PEG 3400 was prepared by adding 0.9 g of *H*-magadiite to 0.09 g of PEG 3400 dissolved in 30 mL of hot chloroform. The suspension was stirred until total evaporation of chloroform occurred. This sample is referred to as H-mag–PEG3400.

Instrumentation

X-ray diffraction powder patterns were obtained on a Philips PW 3710 diffractometer using a generator voltage of 45 kV and a generator current of 40 mA. Samples were prepared on a circular silicon disk by dispersing 15 mg of

© 2002 NRC Canada

Fig. 1. (*a*) Solid-state ^{29}Si MAS NMR spectra with high-power decoupling and pulse delay of 1400 s for Na-magadiite; (*b*) graph showing the variation of the Q^4/Q^3 ratio as a function of the pulse delay used for the solid-state ^{29}Si MAS NMR analysis with high-power decoupling of Na-magadiite.

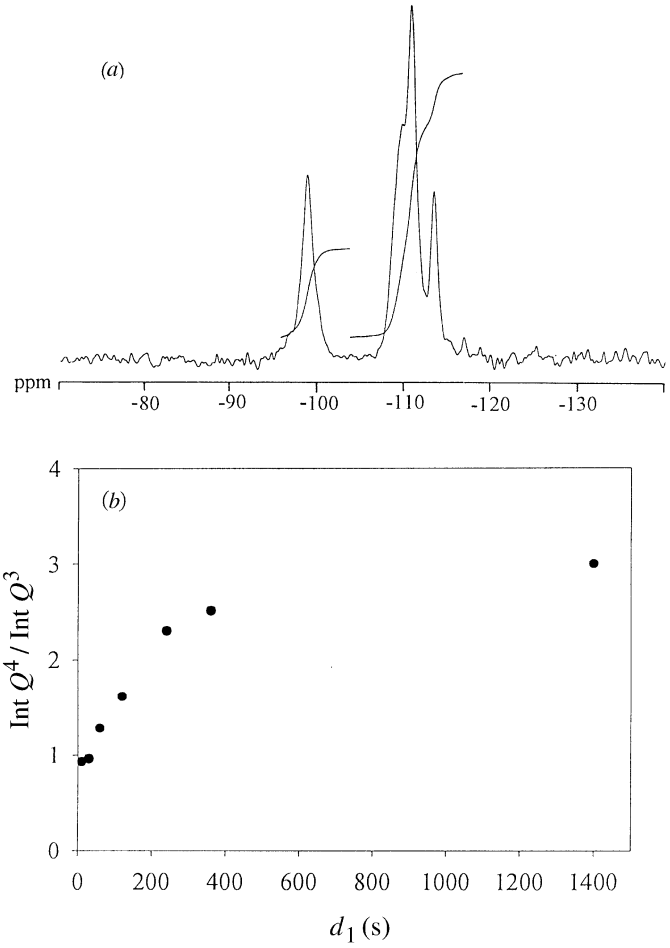

sample with 1 mL of water, followed by sonication for 10 s, and drying on the silicon disk. All DSC (differential scanning calorimetry) analyses were obtained on a thermal analysis controller TAC7/DX from Perkin Elmer. Samples (4–10 mg) were sealed in an aluminum pan and heated at 40°C min^{-1}. All NMR experiments were done on a Bruker ASX-200 spectrometer using a spinning rate of 4 kHz. ^{29}Si MAS NMR with high power decoupling used a pulse of 4 μs and a delay of 240 s, unless otherwise specified. The spectra were referenced to tetramethylsilane. ^{13}C CP-MAS and DD-MAS experiments were performed using a contact time of 0.2 ms and were referenced to hexamethylbenzene.

Results and discussion

Sodium magadiite was obtained by a hydrothermal synthesis following a published method (6), in which a mixture of silica, sodium hydroxide and water, in a molar ratio of 5:1:44, were heated at autogeneous pressure in a stainless steel-lined autoclave to 180°C for 20 h. This procedure avoids possible contamination by Teflon of the resulting product, which can occur when a Teflon-lined reactor is used (6).

Scheme 1. Structural model for magadiite.

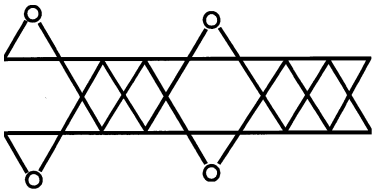

The material obtained was characterized by FT IR, XRD, TGA, and ^{29}Si solid-state NMR. All data were in perfect agreement with previously published observations (7), showing that the material obtained was sodium magadiite. Of particular interest for the characterization is the ratio of the Q^4 ($Si(OSi)_4$) and Q^3 ($HOSi(OSi)_3$) peaks which are observed at –112 and –99 ppm, respectively, on the ^{29}Si NMR spectra. A series of spectra was obtained using various pulse delays. The longest delay used was 1400 s, corresponding to a value of $5T_1$ for the Q^4 resonance (8). The integrations give a ratio of 3.0. Figure 1*a* shows the ^{29}Si NMR spectrum obtained under those conditions. Figure 1*b* gives the variation of the Q^4/Q^3 ratio as a function of the delay. It appears that the spectrum of Fig. 1*a*, which gives a Q^4/Q^3 ratio of 3.0, is quantitatively reliable. This result is in agreement with the model previously proposed by different groups for the structure of magadiite (9) (Scheme 1). Combining the results from the thermogravimetric and elemental analysis gives the following chemical formula: $Na_{1.8}Si_{14}O_{30.2}\cdot 6.9H_2O$, which is in agreement with previously reported values (3*e*, 5*a*, 10).

The corresponding polysilicic acid (*H*-magadiite) was obtained by a titration of Na-magadiite by diluted HCl until a pH of 2 was obtained and maintained (11). The material obtained shows less crystallinity than Na-magadiite (Fig. 2); a basal spacing of 11.2 Å was observed corresponding to a collapse of the layers, resulting from a strong H-bond network between the silanol groups. The high-power decoupling ^{29}Si MAS NMR spectra, under high-decoupling conditions, shows that the characteristic Q^4/Q^3 of Na-magadiite is maintained. Under CP-MAS conditions, the Q^3 signal, observed at –101 ppm is strongly enhanced, in agreement with the protonation of the Q^3 sites. The thermogravimetric analysis shows a total weight loss of 5.5%, corresponding to the loss of physisorbed water below 100°C and of condensation of hydroxyl groups in the range 100–500°C.

To succeed in the intercalation of polymeric species in the interlamellar spacing of *H*-magadiite, it was first necessary to intercalate small polar organic molecules (POM) to break the network of H-bonds between the silanol groups (Scheme 2). Three different intercalates were prepared from DMSO, NMF, and HMPA. The corresponding X-ray diffraction patterns are given in Fig. 3 and show basal spacings of 15.6, 15.9, and 21.8 Å, respectively. These values are in good agreement with literature data for the DMSO (11) and the NMF intercalates (11, 12) and are in agreement with an arrangement where the HMPA molecule lies with its PO bond parallel to the interlamellar surfaces (according to the CPK model, HMPA in this orientation would occupy a minimum of 8.7 Å in the interlamellar region). ^{13}C CP-MAS NMR

© 2002 NRC Canada

Fig. 2. X-ray diffraction pattern (2–50°, 2θ) of *H*-magadiite.

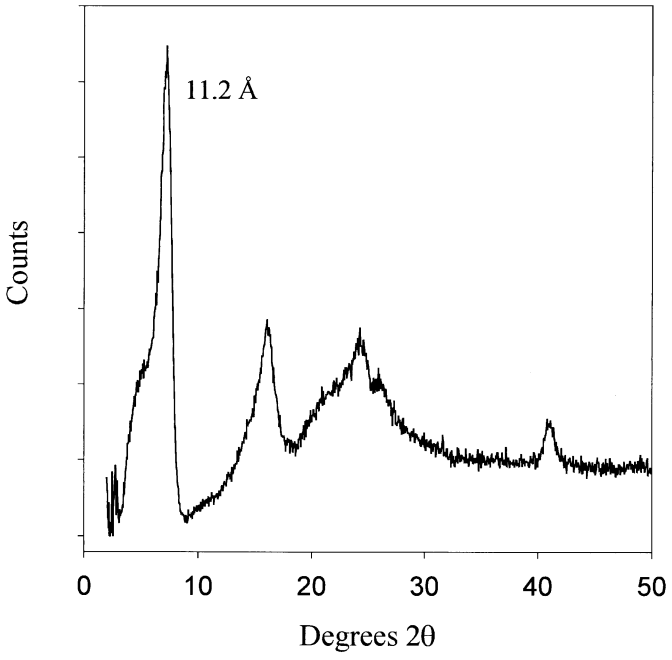

Scheme 2. Schematic representation of the different steps involved in the preparation of nanocomposites from *H*-magadiite.

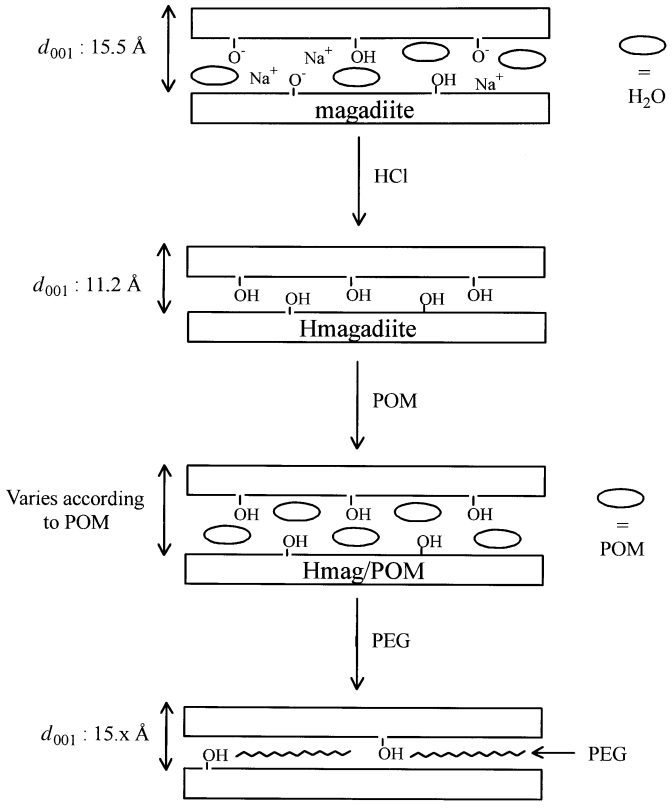

analyses of the three intercalates show signals at 38.5 ppm (*H*-magadiite–DMSO), 25.6 and 164.1 ppm (*H*-magadiite–NMF), and 36.9 ppm (*H*-magadiite–HMPA). HPD ^{29}Si NMR analysis confirmed that this intercalation process did not modify the characteristic Q^4/Q^3 ratio of the magadiite structure.

Fig. 3. X-ray diffraction patterns (2–50°, 2θ) of: (*a*) H-mag–HMPA; (*b*) H-mag–DMSO; (*c*) H-mag–NMF.

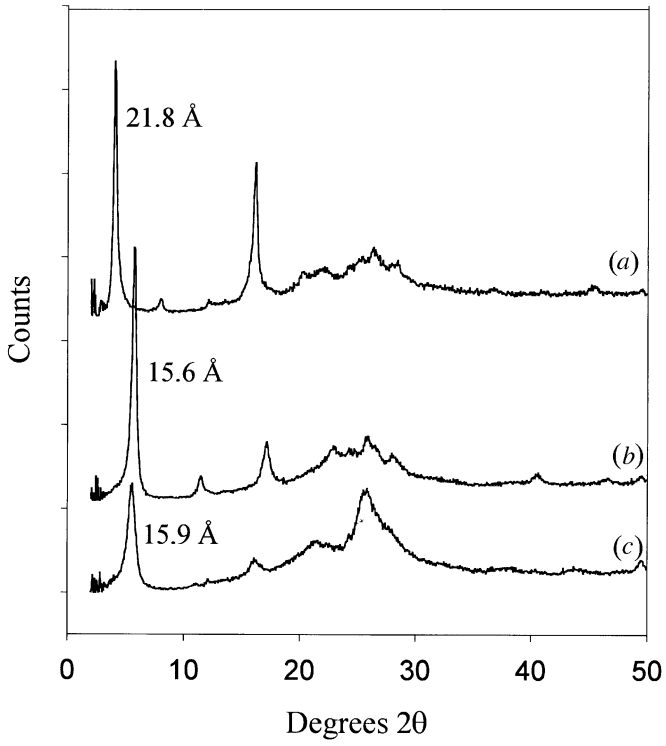

Two polyethylene glycols of molecular weight 1000 and 3400 (PEG 1000 and PEG 3400) were intercalated following a procedure previously described in the case of other lamellar minerals such as montmorillonite (1*q*) and kaolinite (1*a*). The POM-intercalated magadiites were vigorously dispersed in a large excess of the polymers heated above their fusion temperatures, without any solvent. Characterization of the resulting materials was done by XRD, FT IR, ^{13}C and ^{29}Si NMR, DSC, and elemental analysis. These data were systematically compared to those from control samples, consisting of physical mixtures of *H*-magadiite and PEG 1000 and 3400. Most of the intercalation experiments were carried out on the *H*-magadiite–DMSO intercalate.

The resulting polymer-intercalated *H*-magadiite materials (H-mag–PEG1000 and H-mag–PEG3400) were analyzed for their carbon and hydrogen contents. The analysis was done at high temperature (above 1000°C) to insure the total combustion of the organic materials. Percentages of carbon were 7.4 and 7.1, respectively, for H-mag–PEG1000 and H-mag–PEG3400 and the percentages of hydrogen were respectively, 1.6 and 1.7. From these results the chemical formulae of the two compounds were calculated, giving $H_2Si_{14}O_{29}(\text{-}OCH_2CH_2\text{-})_{3.1}$ and $H_2Si_{14}O_{29}(\text{-}OCH_2CH_2\text{-})_{2.9}$, respectively, in agreement with a structure in which one unit cell of magadiite corresponds to three oxyethylene units. The accepted value of the unit cell surface area is 52.8 Å^2 (5*b*). Knowing that the projected surface area of an oxyethylene unit is 14 Å^2, as determined from CPK models, one can estimate a maximum ratio of 3.8 oxyethylene units per magadiite unit cell. This is in agreement with our

© 2002 NRC Canada

Fig. 4. Solid-state ^{13}C CP–MAS NMR spectra for H-mag–PEG3400: (*a*) no dipolar dephasing; with dipolar dephasing: (*b*) τ = 10 μs; (*c*) τ = 30 μs; (*d*) τ = 50 μs; (*e*) τ = 70 μs.

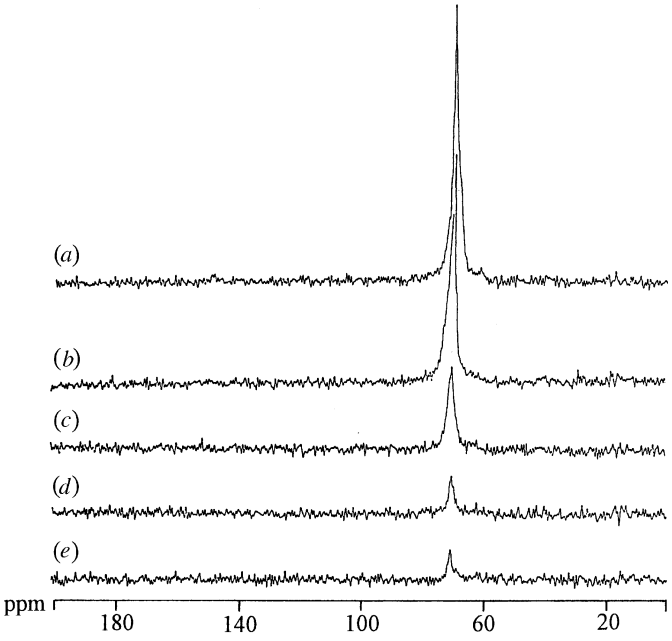

experimental values of 3.1 and 2.9, indicating that the interlamellar region is not fully saturated with oxyethylene units.

Spectroscopic experimental evidence shows that the DMSO molecules have been completely removed from the interlamellar spaces of magadiite after the intercalation of the polymer; ^{13}C CP-MAS no longer shows the expected band at 38.5 ppm and the FT IR spectra do not show the characteristic bands at 1438, 1417, 1405, and 1318 cm^{-1}. The ^{13}C CP-MAS spectrum gives only one peak at 69.9 ppm in both cases, associated with the ethylene units of the PEG chains. This value is close to that observed at 72.2 ppm for the bulk polymer. The shift to high field could be due to an increase in the number of gauche conformations in the chain when the polymer is intercalated (1*f*). In any case, the observed chemical shift precludes the decomposition of the polymeric chains, since the presence of ethylene glycol units intercalated in magadiite would give a chemical shift at 65 ppm (13). Moreover, this is confirmed by the complete absence of any carbonyl band in the IR spectra of H-mag–PEG1000 and H-mag–PEG3400, which would indicate a decomposition of the polymer into smaller oligomeric chains.

The dipolar dephasing technique is a semiquantitative technique that can assess the mobility of organic groups (1*a,* 17). The ratio of I_{DD}/I_o is a measure of the dynamic state of the molecular group. I_{DD} and I_o are, respectively, the peak intensities of the ^{13}C resonance obtained with and without dipolar dephasing conditions. The signal decay for carbon strongly coupled to protons is described by eq. [1] (14).

$$[1] \qquad I_{DD} = I_0 e^{-\tau^2/(2T_2^2)}$$

where τ is the dipolar dephasing delay time and T_2 is a relaxation time constant. The ratio I_{DD}/I_0 decreases with an increase of the rigidity of the molecular group. The

Fig. 5. Plot of ln (I_{DD}/I_O) vs. the square of the dipolar dephasing time (τ^2) for the ^{13}C DD-MAS spectra acquired for H-mag–PEG3400.

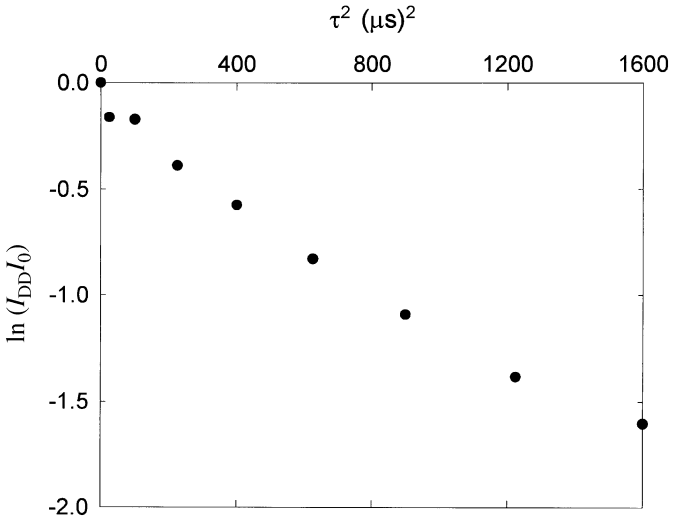

dipolar dephasing time was varied from 0 to 70 μs for both H-mag–PEG3400 and H-mag–PEG1000 (Fig. 4). The results were analyzed on the basis of eq. [1] (Fig. 5). In both cases, a 29% decrease of T_2, the time constant reflecting the mobility of the CH_2 groups, was observed when the polymer was intercalated compared to a simple physical mixture of the *H*-magadiite and the polymer. For both systems, T_2 varied from 28 μs for the physical mixture to 20 μs for the intercalated polymer. These results show that the polymer chains in the interlamellar spaces of *H*-magadiite are more constrained than in the bulk polymer. The T_2 data are comparable to those observed for other constrained systems such as kaolinite–PEG 3400 (15 μs) (1*a*) and diols intercalated in magadiite for which T_2 values ranged from 14–20 μs (15).

The ^{29}Si MAS NMR spectra with high power decoupling are shown in Fig. 6 for *H*-magadiite, H-mag–DMSO, H-mag–PEG1000, and H-mag–PEG3400. The Q^4/Q^3 ratio is constant throughout the intercalation process indicating that the structure of magadiite is unchanged.

Figure 7 shows the X-ray diffraction patterns of H-mag–PEG 1000 and H-mag–PEG 3400. The intercalates are characterized by basal spacings of 15.8 and 15.6 Å, respectively. This corresponds to interlamellar spacings of 4.6 and 4.4 Å since the polysilicate layer is 11.2 Å thick. As mentioned above, from the IR and ^{13}C NMR results, all the DMSO molecules have been expelled from the interlamellar spaces of magadiite during the polymer intercalation process. Consequently, the species responsible for the swelling of magadiite are exclusively the polymeric chains. Similar spacings have been reported for systems in which ethylene glycol or oxyethylene units have been intercalated: ethylene glycol in *H*-magadiite (3.0 Å) (15), ethylene glycol in vermiculite (3.7 Å) (16), polyethylene glycol in lamellar α-zirconium phosphate (2.8 Å), (17) polyethylene glycol in kaolinite (3.7–4.1 Å) (1*a*), and polyethylene oxide in V_2O_5 (4.5 Å) (18). It has to be noted that the X-ray diffraction patterns obtained on the physical mixture of *H*-magadiite and PEG do not show the d_{001} reflection characteristic of an intercalated nanocomposite species.

© 2002 NRC Canada

Fig. 6. Solid-state ^{29}Si MAS NMR spectra with high-power decoupling for: (*a*) *H*-magadiite; (*b*) H-mag–DMSO; (*c*) H-mag–PEG1000; (*d*) H-mag–PEG3400.

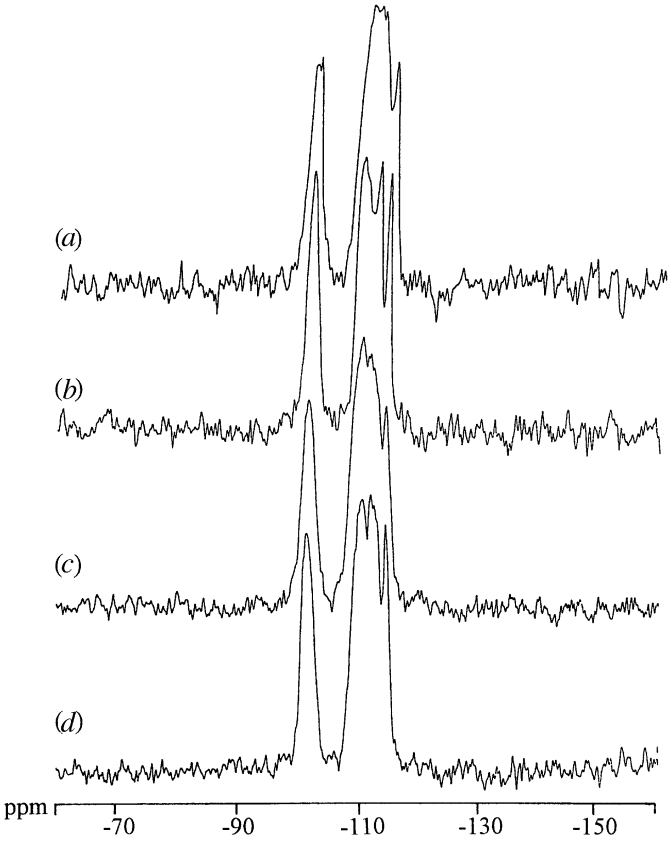

Fig. 7. X-ray diffraction pattern (2–50°, 2θ) of: (*a*) H-mag–PEG1000; (*b*) H-mag–PEG3400.

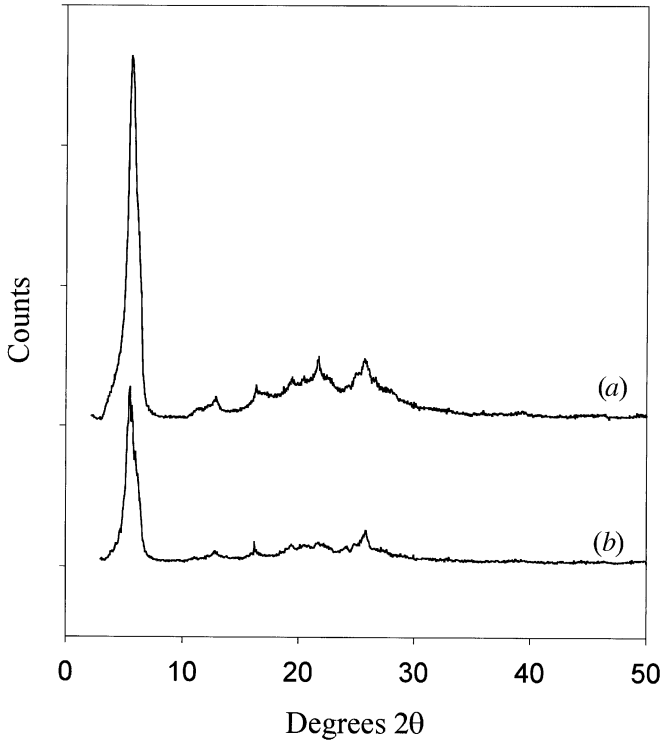

Fig. 8. DSC curves for: (*a*) PEG 3400; (*b*) H-mag–PEG3400 (physical mixture); (*c*) H-mag–PEG3400; (*d*) *H*-magadiite.

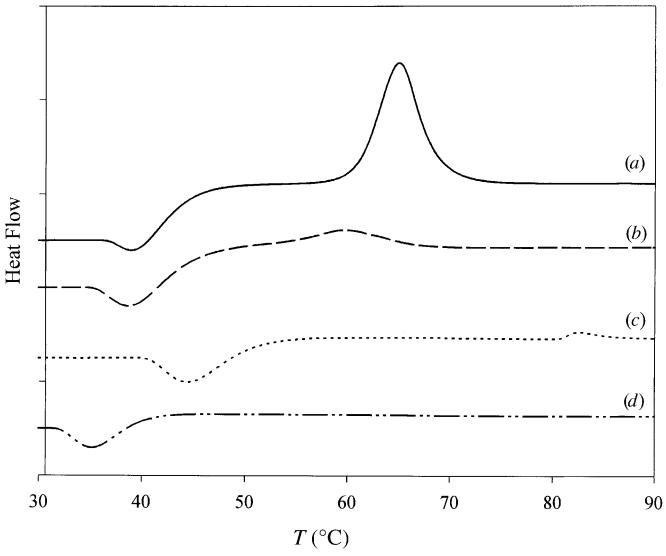

The nanocomposites were also characterized by DSC. The two polymers give endothermic peaks at 59°C (PEG 1000) and 67°C (PEG 3400) corresponding to their melting points. Figure 8 gives the DSC curves for *H*-magadiite, PEG 3400, their physical mixture, and the intercalated nanocomposite. In each case, a starting transient peak is obtained below 50°C. While the endothermic peak corresponding to the polymer melting can still be observed in the case of the physical mixture (as expected, at a lower temperature than for the pure polymer), it is completely absent in the case of the intercalated nanocomposite. This observation is similar to those reported previously in the cases of polyoxyethylene intercalated in montmorillonite (19) and of PEG3400 in kaolinite (1*a*). This is a crucial observation, demonstrating that the polymeric chains are not in an aggregation state characteristic of the bulk polymer. This is consistent with a model in which the polymeric chains interact strongly with the interlamellar surface of magadiite and have lost their bulk properties. Similar results were obtained for H-mag–PEG1000.

This work demonstrates that nanocomposite materials can be prepared from polyethylene glycols and polysilicates. The resulting materials are layered, with alternating organic and inorganic polymeric layers. The inorganic layers have kept the structural characteristics of the parent polysilicate (magadiite) and the organic polymeric monolayers are constrained in a flattened arrangement, resulting from their strong interactions with the interlamellar silicate surfaces of magadiite.

Acknowledgments

The Natural Sciences and Engineering Research Council of Canada (NSERC) is gratefully acknowledged for a research grant (CD). We thank Dr. Glenn Facey (University of Ottawa) for recording the NMR spectra.

© 2002 NRC Canada

References

1. (*a*) J.J. Tunney and C. Detellier. Chem. Mater. **8**, 927 (1996); (*b*) P.B. Messersmith and E.P. Giannelis. Chem. Mater. **6**, 1719 (1994); (*c*) R.A. Vaia, K.D. Jandt, E.J. Kramer, and E.P. Giannelis. Chem. Mater. **8**, 2628 (1996); (*d*) E.P. Giannelis. Appl. Organomet. Chem. **12**, 675 (1998); (*e*) Z. Wang, T. Lan, and T.J. Pinnavaia. Chem. Mater. **8**, 2200 (1996); (*f*) S.D. Burnside and E.P. Giannelis. Chem. Mater. **7**, 1597 (1995); (*g*) Y. Sugahara, M. Sugimoto, T. Yanagisawa, Y. Nomizu, K. Kuroda, and C. Kato. J. Ceram. Soc. Jpn. Int. Ed. **95**, 109 (1998); (*h*) Z. Wang and T.J. Pinnavaia. Chem. Mater. **10**, 1820 (1998); (*i*) A.G. Stepanov, M.V. Luzgin, V.N. Romannikov, V.N. Sidelnikov, and K.I. Zamaraev. J. Catal. **164**, 411 (1996); (*j*) D. Guillaume, S. Gautier, I. Despujol, F. Alario, and P. Beccat. Catal. Lett. **43**, 213 (1997); (*k*) B. Pawelec, J.L.G. Fierro, J.F. Cambra, P.L. Arias, J.A. Legarreta, G. Vorbeck, J.W. Dehaan, V.H.J. Debeer, and R.A. Vansanten. Zeolites, **18**, 250 (1997); (*l*) E. Ruiz-Hitzky and P. Aranda. An. Quim. Int. Ed. **93**, 197 (1997); (*m*) B.M. Novak. Adv. Mater. **5**, 422 (1993); (*n*) T.J. Pinnavaia, T. Lan, Z. Wang, H. Shi, and P.D. Kaviratna. Nanocomposites: ACS Symp. Series **622**, 250 (1996); (*o*) H.M. Kao and C.P. Grey, J. Am. Chem. Soc. **119**, 627 (1997); (*p*) E.P. Giannelis. Adv. Mater. **8**, 29 (1996); (*q*) R.A. Vaia, H. Ishii, and E.P. Giannelis. Chem. Mater. **5**, 1694 (1993); (*r*) C. Sellmer, V. Schmatloch, and N. Kruse. Catal. Lett. **35**, 165 (1995); (*s*) A. Usuki, M. Kato, A. Okada, and T. Kurauchi. J. Appl. Polym. Sci. **63**, 137 (1997); (*t*) V. Bosacek, H. Ernst, D. Freude, and T. Mildner. Zeolites, **18**, 196 (1997); (*u*) M. Sikka, L.N. Cerini, S.S. Ghosh, and K.I. Winey. J. Polym. Sci. Part B: Polym. Phys. **34**, 1443 (1996); (*v*) T. Lan, P.D. Kaviratna, and T.J. Pinnavaia. Chem. Mater. **7**, 2144 (1995); (*w*) M.S. Wang and T.J. Pinnavaia. Chem. Mater. **6**, 468 (1994); (*x*) A. Philippou and M.W. Anderson. J. Catal. **167**, 266 (1997); (*y*) M. Ogawa, M. Inagaki, N. Kodama, K. Kuroda, and C. Kato. J. Phys. Chem. **97**, 3819, (1993); (*z*) P. Aranda and E. Ruiz-Hitzky. Chem. Mater. **4**, 1395 (1992); (*aa*) D.J. Harris, T.J. Bonagamba, and K. Schmidt-Rohr. Macromolecules, **32**, 6718 (1999); (*bb*) S. Wong, S. Vasudevan, R.A. Vaia, E.P. Giannelis, and D.B. Zax. J. Am. Chem. Soc. **117**, 7568 (1995).
2. K. Isoda and K. Kuroda. Chem. Mater. **12**, 1702 (2000).
3. (*a*) H.P. Eugster. Science (Washington, D.C.), **157**, 1177 (1967); (*b*) B.F. Jones, S.L. Rettig, and H.P. Eugster. Science (Washington, D.C.), **158**, 1310 (1967); (*c*) T.P. Rooney, B.F. Jones, and J.T. Neal. Am. Mineral. **54**, 1034 (1969); (*d*) R.C. Surdam, H.P. Eugster, and R.H. Mariner. Geol. Soc. Am. Bull. **83**, 2261 (1972); (*e*) J.L. McAtee, Jr., R. House, and H.P. Eugster. Am. Mineral. **53**, 2061 (1968); (*f*) R.A. Sheppard and A.J. Gude. Am. Mineral. **55**, 358 (1970); (*g*) J. Zdenek and G.F. Maglione. Bull. Soc. Fr. Mineral. Cristallogr. **95**, 371 (1972).
4. (*a*) L. McCulloch. J. Am. Chem. Soc. **74**, 2453 (1952); (*b*) R.A. Fletcher and D.M. Bibby. Clays Clay Miner. **35**, 318 (1987); (*c*) K. Beneke and G. Lagaly. Am. Mineral. **68**, 818 (1983); (*d*) R. Sprung, M.E. Davis, J.S. Kauffman, and C. Dybowsky. Ind. Eng. Chem. Res. **29**, 213 (1990); (*e*) A.F. Janzen and X.B. Ou. J. Fluorine Chem. **71**, 207 (1995).
5. (*a*) G. Lagaly, K. Beneke, and A. Weiss. Am. Mineral. **60**, 642 (1975); (*b*) G. Lagaly, K. Beneke, and A. Weiss. Am. Mineral. **60**, 650 (1975).
6. M.-J. Binette and C. Detellier. Clays Clay Miner. **46**, 478 (1998).
7. (*a*) P.F. Mcmillan and R.J. Kirkpatrick. Am. Mineral. **77,** 898 (1992); (*b*) M. Hirano, H. Kudo, and T. Morimoto. Bull. Chem. Soc. Jpn. **65**, 1744 (1992); (*c*) S. Liu, L. Gelmini, S.J. Rettig, R.C. Thompson, and C. Orvig. J. Am. Chem. Soc. **114**, 6081 (1992); (*d*) D. Mustafi, J. Telser, and M.W. Makinen. J. Am. Chem. Soc. **114**, 6219 (1992); (*e*) D. Avnir, D. Farin, and P. Pfeifer. New J. Chem. **16**, 439 (1992).
8. S. Okuno and G.E. Matsubayashi. J. Chem. Soc. Dalton Trans. 2441 (1992).
9. (*a*) M. Borja and P.K. Dutta. J. Phys. Chem. **96**, 5434 (1992); (*b*) C.D. Benham. Nature (London), **359**, 103 (1992).
10. (*a*) J.M. Garces, S.C. Rocke, C.E. Crowder, and D.L. Hasha. Clays Clay Miner. **36**, 409 (1988); (*b*) J.S. Dailey and T.J. Pinnavaia. Chem. Mater. **4**, 855 (1992); (*c*) C. Eypert-Blaison, E. Sauzéat, M. Pelletier, L.J. Michot, F. Villiéras, and B. Humbert. Chem. Mater. **13**, 1480 (2001).
11. K. Stumpfnothof, N. Weiden, and G. Muller. Z. Kristallogr. **200**, 265 (1992).
12. L.C. Klein, C. Yu, R. Woodman, and R. Pavlik. Catal. Today, **14**, 165 (1992).
13. T.C. Chang, S.Y. Ho, and K.J. Chao. J. Chin. Chem. Soc. (Taipei), **39**, 209 (1992).
14. L.B. Alemany, D.M. Grant, T.D. Alger, and R.J. Pugmire. J. Am. Chem. Soc. **105**, 6697 (1983).
15. L. Mercier, G.A. Facey, and C. Detellier. J. Chem. Soc. Chem. Comm. 2111 (1994).
16. W.F. Bradley, E.J. Weiss, and R.A. Rowland. Clays Clay Miner. **10**, 117 (1963).
17. (*a*) J.P. Lemmon and M.M. Lerner. Chem. Mater. **6**, 207 (1994); (*b*) C.Y. Ortiz-Avila and A. Clearfield. Inorg. Chem. **24**, 1773 (1985).
18. Y.J. Liu, D.C. DeGroot, J.L. Schindler, C.R. Kannewurf, and M.G. Kanatzidis. Chem. Mater. **3**, 992 (1991).
19. P. Aranda and E. Ruiz-Hitzky. Acta Polym. **45**, 59 (1994).

© 2002 NRC Canada

ERRATUM

Erratum: The core oligosaccharide component from *Mannheimia* (*Pasteurella*) *haemolytica* serotype A1 lipopolysaccharide contains L-*glycero*-D-*manno*- and D-*glycero*-D-*manno*-heptoses: Analysis of the structure and conformation by high-resolution NMR spectroscopy

Jean-Robert Brisson, Ellen Crawford, Dušan Uhrín, Nam Huan Khieu, Malcolm B. Perry, Wayne B. Severn, and James C. Richards

Ref.: Can. J. Chem. 80(8): 949–963 (2002).

Text in two subsections of the Experimental section was inadvertently omitted in the printed version of this article. The correct text, from the heading "D-*glycero*-L-*manno*-heptose" on page 959 to the paragraph above the heading "Electrospray mass spectrometry" on page 961 should read

D-*glycero*-L-*manno*-Heptose

The heptose was prepared by the condensation of D-galactose with nitromethane in alkaline methanol (76). The crystalline 1-deoxy-1-nitro-D-*glycero*-L-*manno*-heptitol obtained from the aqueous solution of the deionized products (mp 158°C, 21% yield) was converted to its sodium salt. On treatment with dilute sulphuric acid (35°C), followed by deionization with Rexyn 101(H^+) and Amberlite A4(OH^-) ion-exchange resins, the solution was lyophilized to give the heptose as a syrup (80% yield). The product was fractionated by cellulose column chromatography using butan-1-ol–water (1:10 v/v) as the eluant. Fractions containing the heptose were concentrated to dryness under reduced pressure. The D-*glycero*-L-*manno*-heptose having $[\alpha]_D$ –14° (*c* 0.2, water) was pure by paper chromatography and its reduced ($NaBH_4$) and acetylated product on GLC gave a single peak corresponding in retention time with that of authentic hepta-*O*-acetyl-D-*glycero*-L-*manno*-heptitol, establishing its purity.

D-*glycero*-D-*manno*-Heptose

The heptose was prepared from D-altrose via its condensation with nitromethane to yield 1-deoxy-1-nitro-D-*glycero*-D-*manno*-heptitol (mp 109°C, $[\alpha]_D$ –7.0° (*c* 1.1, EtOH), 27% yield)) whose aqueous sodium salt solution on slow dropwise addition to stirred 20% (v/v) sulfuric acid maintained at 0°C was converted to D-*glycero*-D-*manno*-heptose (77). The reaction mixture was neutralized with sat. $Ba(OH)_2$ solution, filtered, passed through Rexyn 101(H^+) and Duolite A4(OH^-) ion-exchange resins to remove residual ionic material, and was concentrated to a syrup (92% yield). The heptose product, as indicated by paper chromatography, was contaminated with altrose and unchanged 1-deoxy-1-nitro-D-*glycero*-D-*manno*-heptitol (ca. 2 to 3%). The product was purified by cellulose column chromatography using butan-1-ol–water (1:10 v/v) as the mobile phase. The D-*glycero*-D-*manno*-mannose had $[\alpha]_D$ +22° (*c* 2, MeOH). A reduced ($NaBH_4$) and acetylated sample on GLC gave a single peak corresponding to authentic hepta-*O*-acetyl-D-*glycero*-D-*manno*-D-heptitol indicating the identity and purity of the synthesized heptose.

NRC Research Press apologizes for this error.

Received 5 November 2002. Published on the NRC Research Press Web site at http://canjchem.nrc.ca on 23 December 2002.

J.-R. Brisson, E. Crawford, N.H. Khieu, M.B. Perry, and J.C. Richards.[1] Institute for Biological Sciences, National Research Council, Ottawa, ON K1A 0R6, Canada.
W.B. Severn. Agricultural Research, Department of Diseases, PO Box 40063, Ward Street, Upper Hutt, New Zealand.
D. Uhrín. University of Edinburgh, Department of Chemistry, West Mains Road, Edinburgh EH9 3JJ, U.K.

[1]Corresponding author (e-mail: jim.richards@nrc.ca).

 DOI: 10.1139/V02-197 © 2002 NRC Canada

ERRATUM

Erratum: Radiolysis of liquid water: An attempt to reconcile Monte-Carlo calculations with new experimental hydrated electron yield data at early times

Yusa Muroya, Jintana Meesungnoen, Jean-Paul Jay-Gerin, Abdelali Filali-Mouhim, Thomas Goulet, Yosuke Katsumura, and Samlee Mankhetkorn

Ref: Can. J. Chem. **80**(10): 1367–1374 (2002).

NRC Research Press inadvertently published the incorrect footnote number in the caption of Table 1. The caption for Table 1 should read as follows:

Table 1. Branching ratios used in our simulations for the different competing mechanisms in the fate of vibrationally excited water molecules ($H_2O^*_{vib}$) formed by recombination of a subexcitation electron with its water parent cation (see footnote 8).

In addition, references 1(*c*), 1(*d*), 41(*b*), and 45 were incorrectly published in the printed form. These references should read

1. (*c*) I.G. Draganić and Z.D. Draganić. The radiation chemistry of water. Academic Press, New York. 1971; (*d*) I.G. Draganić. Radiochim. Acta, **70/71**, 317 (1995).

41. (*b*) I.G. Draganić, M.T. Nenadović, and Z.D. Draganić. J. Phys. Chem. **73**, 2564 (1969).

45. Z.D. Draganić and I.G. Draganić. Int. J. Radiat. Phys. Chem. **7**, 381 (1975).

Received 29 October 2002. Published on the NRC Research Press Web site at http://canjchem.nrc.ca on 29 October 2002.

Y. Muroya,[1] J.-P. Jay-Gerin,[2] A. Filali-Mouhim, and T. Goulet. Département de médecine nucléaire et de radiobiologie, Faculté de médecine, Université de Sherbrooke, Sherbrooke, QC J1H 5N4, Canada.
Y. Katsumura. Nuclear Engineering Research Laboratory, Graduate School of Engineering, University of Tokyo, 2–22 Shirakata-shirane, Tokai-mura, Naka-gun, Ibaraki 319–1188, Japan.
S. Mankhetkorn. Laboratory of Physical Chemistry, Molecular and Cellular Biology, Faculty of Science, Burapha University, Bangsaen, Chonburi 20131, Thailand.
J. Meesungnoen. Département de médecine nucléaire et de radiobiologie, Faculté de médecine, Université de Sherbrooke, Sherbrooke, QC J1H 5N4, Canada; and Laboratory of Physical Chemistry, Molecular and Cellular Biology, Faculty of Science, Burapha University, Bangsaen, Chonburi 20131, Thailand.

[1]Present address: Nuclear Engineering Research Laboratory, Graduate School of Engineering, University of Tokyo, 2–22 Shirakata-shirane, Tokai-mura, Naka-gun, Ibaraki 319–1188, Japan.
[2]Corresponding author (e-mail: jaygerin@courrier.usherb.ca).

 DOI: 10.1139/V02-198 © 2002 NRC Canada

Canadian Journal of Chemistry

Author Index
Volume 80, 2002

Revue canadienne de chimie

Index des auteurs
Volume 80, 2002

Aghabozorg, H., 1687
Ahmad, N., 1096
Ahmad, S., 1279
Akotsi, O.M., 1555
Alas, S.J., 801
Al-Awadi, N.A., 499
Alcalde, M., 743
Alex, S., 350
Al-Juwaiser, I.A., 499
Al-Kamali, A.S., 1293
Allen, C.C.R., 589
Allen, C.W., 1393
Amat-Guerri, F., 62
Amirnasr, M., 1196
Andavan, G.T.S., 1415
Andraos, J., 141
André, S., 1096
Andrews, M.P., 1625
Angulo, J., 917
Anthonsen, T., 577
Antorrena, G., 1568
Appleton, J., 1141
Arancibia, E.L., 462
Arévalo, E.A., 76
Armstrong, G.D., 871
Athimoolam, A., 1415
Atwood, D.A., 1463
Aubke, F., 1265
Aucott, S.M., 1481
Audette, G.F., 1010
Auzanneau, F.-I., 1088
Aycard, J.P., 455
Azad, M., 148
Baer, A.J., 496
Bahadur, M., 1393
Baines, K.M., 1387
Baker, J., 708
Bakker, M., 622
Baldoni, H.A., 832
Ball, R.G., 646
Ballesteros, A., 743
Barclay, T., 1285
Barclay, T.M., 1501
Barta, N., 646
Basak, P., 943
Bashall, A., 1421
Bazzi, L., 106
Bélanger-Gariépy, F., 813
Beltrán, H.I., 801
Bendiak, B., 1032
Benrahmoune, M., 333
Berg, D.J., 1285
Bergens, S.H., 1555
Berglund, P., 529
Berthelot, M., 1375
Bertolotti, S., 62
Besseau, F., 1375
Best, W.M., 857
Bhadury, P.S., 504
Bhardwaj, N., 141
Bhardwaj, R.K., 467
Bhaskar, A.S.B., 504
Bhattacharya, A.K., 973
Bickley, J.F., 546
Binette, M.-J., 1708
Biswas, S., 1204
Blumenstein, M., 894
Bodenbinder, M., 1265
Boeré, R.T., 1607
Boggio, J.C., 1676
Bonal, C., 163
Bond, A.D., 1507
Bottomley, F., 55
Bourke, S.C., 1469
Boyd, D.R., 589
Boyd, R., 646
Boyd, R.J., 1351
Brask, J.K., 821
Brenna, E., 714
Breuer, M., 692
Brewer, C.F., 1096
Bridges, A., 1393
Bridson, J.N., 155
Brion, C.E., 222
Brisson, J.-R., 904, 949, 1055, 1715
Bröchler, R., 1265
Brossard, L., 345
Brown, A.P., 1625
Brown, F.M., 633
Brown, G.R., 89
Brown, R.S., 183, 1343
Brownridge, S., 1568
Brunet, E., 169
Brydges, S., 1546
Buchanan, G.W., 148
Bühler, H., 671
Bui, V.P., 708
Bunce, N.J., 200
Bundle, D.R., 904, 1112, 1131, 1141
Burford, N., 1404, 1488
Butler, I.S., 813
Cameron, T.S., 1351, 1404, 1568
Camillo, R.L., 1530
Campbell, J.S., 646
Carballo, E., 370
Cargnoni, F., 235
Carrea, G., 551, 559
Carrière, J.-F., 653
Carroll, J.G., 589
Carty, A.J., 1538
Casado, N., 1676
Castellan, A., 1223
Cerdeiriña, C.A., 370
Chadha, K.K., 1687
Chandrasekhar, V., 1415
Chang, H.-m., 761
Chansarkar, N., 1321
Chantigny, Y.A., 875
Chapados, C., 113
Chartrain, M., 646
Chass, G.A., 845
Chen, G., 613
Chen, G., 894
Chen, H., 601
Chen, Q., 1668
Cheng, J.K., 1646,
Chiang, Y., 82
Chilov, G.G., 699
Chinapoo, S.M., 937
Chivers, T., 821
Chong, D.P., 222
Chowdhary, R.K., 1321
Clyburne, J.A.C., 1398
Cobos, J.C., 292
Cole, J.G., 46
Comasseto, J.V., 1530
Conroy, K.D., 1404
Cooper, G., 222
Corbeil, C.R., 1331
Corley, E.G., 646
Corrigan, J.F., 1592
Côté, A.P., 496, 1584
Cowley, A.H., 1518
Craig, A.G., 1022

© 2002 NRC Canada

Cravero, R.M., 774
Crawford, E., 949, 1715
Csizmadia, I.G., 832, 845
Cunha, R.L.O.R., 1530
Dalton, H., 589
Daneault, S., 113
Dangi, R.S., 504
Davidson, G.J.E., 496
Davis, B.G., 555
Decken, A., 31, 55
de Dios, A., 1302
Delamere, C., 94
de la Puente, M.L., 1302
Delbaere, L.T.J., 1010
Delmarre, D., 1321
Deperasińska, I., 1242
De Pue, L.J., 1463
Deretey, E., 832
de Ruiz Holgado, M.E.F., 462
DeSantis, G., 643
De Sève, H., 483
Deslongchamps, P., 875
Detellier, C., 163, 1708
DiCosimo, R., 608
Diedrichs, N., 686
Dodier, M., 483
Dolphin, D., 1321, 1668
Domanska, U., 476
Dorn, H., 1650
Dory, Y.L., 875
Dubé, P., 345
Ducret, A., 653
Duffy, S.J., 1217
Dumaresque, C.L., 1398
Dyker, C.A., 55
Easteal, A.J., 789
Edwards, J.P., 31
Effenberger, F., 671
Eichler, E., 1112
Eipper, A., 626
El-Alali, A., 1293
El-Dusouqui, O.M.E., 499
El Issami, S., 106
Ellis, B., 1404
Elsegood, M.R.J., 1410
England, D.B., 992
Enriz, R.D., 832
Espinosa, J.F., 1302
Estrada, M., 845
Faber, K., 362
Fan, H.-N., 900
Fang, C.-L., 728
Fang, T.T., 1032
Farfán, N., 801
Farkas, O., 832
Fedorchuk, C., 821
Feher, M., 1088
Feicht, A., 796
Fernández, H., 1232
Fernandez, J., 462
Ferretti, F.H., 845
Fessner, W.-D., 739
Filali-Mouhim, A., 68, 333, 767, 1367, 1716
Findlay, J.F., 1697
Fraenk, W., 1444
Franck, R.W., 894
Fraser-Reid, B., 1075
Friedrich, T., 692
Fuganti, C., 714
Fujdala, K.L., 1387
Fülöp, F., 565
Furneaux, R.H., 964
Gabbaï, F.P., 1308
Gabius, H.-J., 1096
Gadosy, T.A., 302
Galezowski, W., 1259
Galka, P.V., 1562
Galley, W.C., 89
Galstian, T., 1625
Gan, Z., 908
Gao, Z., 440
García, F., 1421
García, N.A., 62
García, S., 1676
Garcia de la Fuente, I., 292
García-Losada, P., 169
Garegg, P.J., 1105
Gbewonyo, K., 646
Geatti, P., 779
Gedey, S., 565
Gedrath, I., 686
Gee, M., 1488
Geiger, W.E., 1393
Geller, J.M., 813
Gendron, R.A.L., 1285
Ghavami, A., 937
Gibbs, K.D., Jr., 999
Gibson, D.T., 589
Gilby, L.M., 1410
Gilson, D.F.R., 813
Giumanini, A.G., 779
Glew, D.N., 418
Glister, J.F., 447
Głowiak, T., 1242
Gomez, A., 1075
Gomez de Segura, A., 743
Gonzalez, J.A., 292, 476
González, J.C., 1676
González-Salgado, D., 370
Goulet, T., 1367, 1716
Gracey, D.W.K., 1387
Graton, J., 1375
Graves, C.R., 1217
Graziano, G., 388, 401
Green, D.F., 281
Grelier, S., 1223
Griffin, A.M., 885
Guo, L., 1655
Gupta, H.K., 1546
Hägele, G., 1265
Haggi, E., 62
Haiduc, I., 1530
Hamer, G.K., 1162
Hamilton, J.T.G., 589
Hammouti, B., 106
Hanan, G.S., 496
Hanessian, S., 885
Hansen, J., 708
Harrison, P.H.M., 517, 601
Harrod, J.F., 489
Hasegawa, Y., 613
Hätzelt, A., 1327
Hauer, B., 546, 692
Haynes, D.A., 1507
He, W., 263
Hedin, E.M.K., 529
Henrissat, B., 1162
Henry, B.R., 1635
Hicks, R.G., 1501
Hillebrand, M., 455
Hilvert, D., 657
Hioka, N., 1321
Hirahara, M., 207, 510
Hojo, M., 1428
Holland, H.L., 633, 640
Holmes, K.E., 1410
Hu, C.Y., 222
Hu, E., 646
Huang, X.-F., 1051
Huang, X., 1646
Hudlicky, T., 708
Hudson, R.H.E., 1217
Hult, K., 529
Ibrahim, M.S., 1313
Ichimura, A.S., 1501
Ihasz, N., 640
Ikemoto, N., 646
Ingham, A.M., 155
Inoue, T., 1428
Ionescu, A., 455
Ireland, R.J., 1217
Isab, A.A., 1279
Israëli, Y., 163
Ito, Y., 1174
Iwaki, H., 613
Iyengar, V., 1562
Jack, K.S., 1458

© 2002 NRC Canada

Jacobsen, E.E., 577
Jaiswal, D.K., 504
Jakeman, D.L. 866
Jakins, C., 94
Jalali, F., 1687
Jameel, H., 761
James, B.R., 1600
James, M.N.G., 1064
Janzen, M.C., 41, 1451
Jarczewski, A., 1259
Jay-Gerin, J.-P., 68, 333, 767, 1367, 1716
Jeffery, J.C., 1458
Jenkins, H.A., 281, 1398
Jenkins, S.I., 517
Jennings, H.J., 1055
Jennings, M.C., 41, 1451
Jensen, M.T., 937
Jiang, F., 281
Jiang, X., 263
Jnoff, E., 885
Johnston, B.D., 937
Jones, D.N.M., 1032
Jones, J.N, 1518
Jones, N.D.,1600
Jorge, A., 1530
Juanes, O., 169
Juárez Ruiz, J.M., 739
Kabir, S.M.H., 413
Kadla, J.F., 761
Kalovidouris, S.A., 983
Kaltner, H., 1096
Kam, K., 517
Kamath, V.P., 540
Kamerling, J.P., 76
Kaminski, A., 1217
Kanerva, L.T., 565
Katsumura, Y., 1367, 1716
Kayser, M.M., 613, 796
Keizer, T.S., 1463
Kelly, P.F., 1410
Kenne, L., 1022
Kerr, M.A., 992
Kertit, S., 106
Khieu, N.H., 949, 1055, 1715
Kiburz, B.M., 999
Kinastowski, S., 192
Kindahl, L., 1022
King, A.S., 1217
Kipkemboi, P.K., 789
Kjaergaard, H.G., 1635
Klapötke, T.M., 1444
Klempier, N., 724
Kluger, R., 217
Knop, O., 1351
Kobler, C., 671
Koerner, T.B., 183
Komba, S., 1174
Komulainen, J., 1435
Konradsson, P., 1105
Kraatz, H.-B., 1562
Kratochvil, B., 440
Krelaus, R., 686
Křen, V., 724
Kresge, A.J., 82
Krishnan, V., 1415
Krumm, B., 1444
Kucsman, A., 832
Kühn-Velten, J., 1265
Kurzeck, J., 973
Kuwabara, I., 1096
Kuzma, M., 724
Kuzyk, M.G., 1625
Labadie, G.R., 774
Lahmann, M., 889, 1105
Laitinen, R.S., 1435
Laplante, F., 1662
Larsen, R.D., 646
Laschat, S., 1327
Lau, K.S., 845
Lau, P.C.K., 613
Laurence, C., 1375
Lawson, G.T., 1421
Lázár, L., 565
Lebuis, A.-M., 489
Lee, J., 1252
Lee, K.-S., 582
Lee, Y.C., 900
Leedham, A.P., 1458
Lefeber, D.J., 76
Lessard, C., 483
Lewandowska, E., 192
Lewars, E., 94
Leznoff, C.C., 141
Li, G., 1697
Li, H., 540
Li, W., 646
Li, W.J., 1646
Li, Y., 1625
Liang, Y.-q., 1655
Liljeblad, A., 565
Lin, R., 753
Ling, C.-C., 1131, 1141
Liu, F.-T., 1096
Liu, J., 643
Liu, J.C., 1646
Liu, M.-Z., 900
Liu, P., 1646
Liu, X., 263
Liu, Y.C., 540
Loncke, P.G., 302
Lopez, J.C., 1075
Lortie, R., 653
Losehand, U., 1600
Lough, A.J., 1469, 1650
Lounsbery, B.J., 640
Lowary, T.L., 943, 1112
Lozada, D., 633
Lu, J., 263
Lu, X., 228
Lundquist, J.J., 999
Lynam, J.M., 1458
Ma, P., 608
Macdonald, C.L.B., 1404, 1518
Macdonald, J.M., 857
Mach, M., 1075
MacLachlan, M.J., 1469
Maddess, M.D., 937
Mahiuddin, S., 175
Mahmoudkhani, A.H., 1196
Malone, J.F., 589
Mang, H., 362
Mankhetkorn, S., 68, 767, 1367, 1716
Manners, I., 1469, 1650
Mantas, A., 845
Marchessault, R.H., 1162
Mark, B.L., 1064
Martín, M.T., 743
Martínková, L., 724
Martín-Lomas, M., 917
Massue, J., 546
Masuda, J.D., 1607
Matty, L., 646
Maughan, M.A.T., 555
Max, J.-J., 113
Mayer, P.M., 25
Mayer, S.F., 362
Mayne, B., 633
McAuley, A., 155
McBeth, D., 692
McClelland, R.A., 269
McDonald, R., 1488, 1555
McDonald, R.S., 517
McGlinchey, M.J., 1546
McNulty, K.C., 608
McPartlin, M., 1421
Meegalla, S.K., 728
Meessen, P., 1600
Meesungnoen, J., 68, 767, 1367, 1716
Ménard, H., 345, 1662
Meng, Q., 82
Merkley, N., 1187
Mihovilovic, M.D., 796
Miller, R.J.D., 1
Miskoski, S., 62
Modyanova, L.V., 589
Moghimi, A., 1687
Monette, M., 1343

© 2002 NRC Canada

Mongrain, P., 483
Monnier, M., 455
Moreau, V., 1662
Morel, J.-P., 163
Morel-Desrosiers, N., 163
Moressi, M.B., 1232
Morin, F.G., 813
Moulik, S.P., 1204
Mukherjee, D.C., 1204
Mukherjee, K., 1204
Mulvey, G., 871
Murgolo, N.J., 1166
Muroya, Y., 1367, 1716
Mylerová, V., 724
Nagabhushan, T.L., 1166
Nakamura, N., 207, 510
Neil, M.A., 55
Nguyen, D., 608
Nguyen, M., 708
Niedzwiecki, M., 1458
Nieto, P.M., 917
Niikura, K., 1051
Nikolcheva, L.G., 1217
Norberg, T., 1022, 1096
Norman, D.W., 31
Nöth, H., 1444
Nourmamode, A., 1223
Ogini, F.O., 1546
Ojeda, R., 917
Olivera, S., 1676
Olson, D.J.H., 1010
Oniciu, L., 315
Oscarson, S., 889, 1096, 1105
Otter, A., 540
Ottolina, G., 559
Ovans, R., 1404
Ovesná, M., 724
Pakulski, Z., 964
Pal, A., 467
Palacio, F., 1568
Palcic, M.M., 540
Parales, R.E., 589
Pardo, J.M., 370
Parkin, S., 1463
Parsons, S., 1568
Parvez, M., 245, 413, 1524
Passmore, J., 1568
Patenaude, G.W., 1501
Patkar, S.A., 529
Patrick, B.O., 1600
Paz Andrade, M.I., 462
Pedroni, P., 692
Pena, P.C.A., 546
Perczel, A., 832
Perry, M.B., 949, 1715
Perzanowski, H.P., 1279
Peslherbe, G.H., 302
Pesti, J.A., 608
Phillips, A.D., 1404
Phillips, R.S., 680
Piatesi, A., 657
Piers, W.E., 1524
Piétri, N., 455
Pinto, B.M., 937
Pletsch, A., 1562
Plou, F.J., 743
Pol, E., 779
Pomeroy, R.K., 281
Pon, R.A., 1055
Poon, C., 25
Popescu, I.C., 315
Prasad, A.V.K., 904
Preiml, M., 724
Puddephatt, R.J., 41, 1451
Pugh, D.J., 626
Pungente, M.D., 1643
Puszko, A., 1242
Pye, C.C., 447, 1331
Quail, J.W., 1010
Raczyńska, E.D., 1375
Radhakrishnan, K.V., 1075
Rafter, D.J., 871
Ragogna, P.J., 1404, 1488
Rahimizadeh, M., 517
Ranjbar, M., 1687
Rankin, K.N., 1351
Rankin, M.A., 1210
Rao, M.K., 504
Rao, M.N.S., 1428
Rawson, J.M., 1507
Raza, S.K., 504
Reetz, M.T., 626
Reginato, N., 1546
Reichert, P., 1166
Reid, J.L., 1584
Reider, P.J., 646
Rettig, S.J., 1600
Reymond, J.-L., 665
Richards, J.C., 949, 1715
Richter-Addo, G.B., 1252
Riley, P.J., 1584
Rivera-Sagredo, A., 1302
Roberts, S.M., 546
Rochon, F.D., 379, 796
Rodrigo, R., 728
Rodriguez, A.M., 832
Rodríguez-Ubis, J.-C., 169
Roldán, V., 1676
Rolke, J., 222
Romaní, L., 370
Ronzani, S., 714
Roos, J., 671
Rosazza, J.P.N., 582
Ross, A.R.S., 1010
Rothenberger, A., 1421
Roy, R. 908
Ruest, L., 483, 1662
Ruffin, B., 1223
Rüger, W., 973
Russell, C.A., 1458
Saf, R., 362
Sala, L.F., 1676
Salas-Peregrin, J.M., 1676
Salghi, R., 106
Sanchez, C., 269
Sánchez, V., 133
Sandström, C., 1022
Santillan, R., 801
Santoro, M., 1676
Sauer, E., 269
Sauriol, F., 1343
Sauro, V.A., 250
Scavini, M., 235
Schatte, G., 821
Scheck, M., 571
Schlueter, U., 1075
Schmidt, J.M., 1088
Schmidt, R.R., 973
Schrader, W., 626
Schulte, M. 1308
Scoles, L., 1538
Secundo, F., 551
Serra, S., 714
Severn, W.B., 949, 1715
Shamsipur, M., 1687
Sharma, M., 504
Sharma, N.D., 589
Shehatta, I.S., 1313
Sheldon, R.A., 622
Sherren, A.C., 1210
Shi, Z., 222
Shimizu, G.K.H., 1584
Shu, R., 489
Sidler, D.R., 646
Sierra, M.G., 774
Sigmund, A.E., 608
Signorella, S., 1676
Silverman, C.E., 608
Sivaramakrishna, A., 1428
Skelton, B.W., 857
Skidmore, J., 546
Slawin, A.M.Z., 1481
Slebocka-Tilk, H., 1343
Smith, M.B., 1600
Sorensen, T.S., 245, 413
Sosa, C.P., 832
Sourial, E., 1088
Stanczyk-Dunaj, M., 1259

© 2002 NRC Canada

Steinreiber, A., 362
Stephan, D.W., 125
Sterenberg, B.T., 1538
Sternberg, E., 1321
Stick, R.V., 857
Stock, N.L., 200
Stoddart, J.F., 983
Stolz, F., 973
Storr, A., 133
Streiff, M.B., 540
Sultan, M.R., 1313
Sun, F., 245, 413
Suontamo, R.J., 1435
Suter, M., 1444
Švedas, V.K., 699
Svendsen, A., 529
Svenson, D., 761
Svensson, B., 937
Swarnalatha, U., 1428
Szemik-Hojniak, A., 1242
Szerminski, W.R., 633
Tanaka, K., 510
Tanaka, Y., 496
Taylor, M.G., 1162
Taylor, N., 728
Taylor, N.J., 496
Tessier, C., 379
Thieme, K., 1469
Thompson, L.K., 1568
Thompson, R.C., 133
Tilbrook, D.M.G., 857
Toone, E.J., 999
Toró, A., 875
Tovar, C.A., 370
Trani, M., 653
Tsuchihashi, K., 207, 510
Tsuzuki, H., 207
Turdean, G., 315
Turnbull, W.B., 983
Twamley, B., 1252
Tyler, P.C., 964
Udachin, K.A., 1538
Ueda, T., 1428
Uhrín, D., 904, 949, 1715
Uriel, C., 1075
Vafazadeh, R., 1196
Vali, H.., 1625
Vank, J.C., 832
van Rantwijk, F., 622
van Vliet, A.J., 633
Vargas-Baca, I., 1625
Vaughan, K., 447
Vejzovic, E., 1650
Venkatachalam, C.S., 1428
Verardo, G., 779
Veronese, F.M., 551
Vidovic, D., 1398
Vind, J., 529
Vliegenthart, J.F.G., 76
Vogels, C.M., 31, 1217
Vogt, M., 1444
Vukovic, S., 269
Wagner, B.D., 1210
Wahab, A., 175
Wahler, D., 665
Waldmann, H., 571
Wallbank, A.I., 1592
Walsh, D., 1404
Walter, M.R., 1166
Wan, P., 46
Wang, J., 753
Wang, J., 1646
Wang, L., 728
Wang, S., 613
Warchhold, M., 1444
Warkentin, J., 228, 1187
Wasylishen, R.E., 1488
Watanabe, M., 496
Watson, B., 413
Weiler, L., 1643
Westcott, S.A., 31, 1217
Westermann, B., 686
Whitcombe, T.W., 155
White. A.H. 857
Wiacek, R.J., 1518
Williams, C.K., 89
Withers, S.G., 866
Wnuk, S.F., 192
Wolfe, S., 222
Wong, C.-H., 643, 1051
Wong, E.F., 1387
Woo, T.K., 992
Wood, S.D., 555
Woods, A.D., 1421
Woollins, J.D.,1481
Workentin, M.S., 250
Wosnick, J.H., 813
Wright, D.S., 1421
Wu, J.K., 999
Xie, Y., 263
Xu, C., 155
Xu, C., 155
Yamato, T., 207, 510
Yang, G., 894
Yang, Q.-L., 1055
Yang, Y., 796
Yap, G.P.A., 148, 281
Yu, H.N., 1131
Zamanian, F., 1469
Zamarbide, G., 845
Zamora, M.A., 832
Zarlaida, F., 1568
Zhang, P., 1141
Zhang, T., 1524
Zhang, Z., 1051
Zhao, Y., 753
Zheng, J., 1469
Zheng, Y., 222
Zhu, L., 263
Zhuo, K., 753
Ziltener, H.J., 1643
Zine, E., 106
Zón, M.A., 1232
Zukerman-Schpector, J., 1530

© 2002 NRC Canada

Canadian Journal of Chemistry

Contents
Volume 80, 2002

Revue canadienne de chimie

Sommaire
Volume 80, 2002

January / janvier

ARTICLES

R.J. Dwayne Miller 2000 John C. Polanyi Award Lecture Mother Nature and the molecular Big Bang

Clement Poon and Paul M. Mayer Electron-spin conservation and methyl-substitution effects on bonds in closed- and open-shell systems — A G3 ab initio study of small boron-containing molecules and radicals **25**

David W. Norman, Janet P. Edwards, Christopher M. Vogels, Andreas Decken, and Stephen A. Westcott Synthesis and reactivity of novel Schiff bases containing boronate esters **31**

Michael C. Janzen, Michael C. Jennings, and Richard J. Puddephatt Cationic thiolate and selenolate complexes of platinum(IV) **41**

John G. Cole and Peter Wan Mechanistic studies of photohydration of *m*-hydroxy-1,1-diaryl alkenes **46**

Andreas Decken, Melanie A. Neil, C. Adam Dyker, and Frank Bottomley Iron complexes of the dibenzophospholyl ligand: a synthetic and crystallographic study **55**

E. Haggi, S. Bertolotti, S. Miskoski, F. Amat-Guerri, and N.A. García Environmental photodegradation of pyrimidine fungicides — Kinetics of the visible-light-promoted interactions between riboflavin and 2-amino-4-hydroxy-6-methylpyrimidine **62**

Jintana Meesungnoen, Jean-Paul Jay-Gerin, Abdelali Filali-Mouhim, and Samlee Mankhetkorn Monte-Carlo calculation of the primary yields of H_2O_2 in the $^{1}H^{+}$, $^{2}H^{+}$, $^{4}He^{2+}$, $^{7}Li^{3+}$, and $^{12}C^{6+}$ radiolysis of liquid water at 25 and 300°C **68**

Dirk J. Lefeber, Eneko Aldaba Arévalo, Johannis P. Kamerling, and Johannes F.G. Vliegenthart Synthesis of a hexasaccharide fragment of the capsular polysaccharide of *Streptococcus pneumoniae* type 3 **76**

Y. Chiang, A.J. Kresge, and Q. Meng Kinetics and mechanism of hydrolysis of 3-diazobenzo-furan-2-one and its hydrolysis product (3-hydroxybenzo-furan-2-one) **82**

Celia K. Williams, William C. Galley, and G. Ronald Brown The endothermic nature of the binding of anionic bile salts to a cationic adsorbent **89**

C. Delamere, C. Jakins, and E. Lewars On the generation of oxirene and dimethyloxirene by retro-Diels–Alder reactions, and reactions of dimethyl-oxirene: a computational study **94**

L. Bazzi, R. Salghi, E. Zine, S. El Issami, S. Kertit et B. Hammouti Inhibition de la corrosion de l'alliage d'aluminium 6063 au moyen de composés inorganiques dans une solution de chlorure de sodium à 3 % **106**

Jean-Joseph Max, S. Daneault, and Camille Chapados 1-Propanol hydrate by IR spectroscopy **113**

Additions and corrections: Revised contents / Ajouts et corrections : Table des matières révisée

Instructions to Authors / Recommendations aux auteurs **I-1**

Notes for authors of papers presenting the results of X-ray crystal structure analyses / Recommandations aux auteurs d'articles décrivant la détermination de structures par diffraction des rayons X **I-5**

February / février

ARTICLES

Douglas W. Stephan 2001 Alcan Award Lecture From academic research to industrial applications and back again **125**

© 2002 NRC Canada

Victor Sánchez, Alan Storr, and Robert C. Thompson Magnetic and structural studies on 1,3-diazolate complexes of cobalt(II) — The characterization of three new cobalt(II) molecule-based magnets **133**

Namrta Bhardwaj, John Andraos, and Clifford C. Leznoff The syntheses and NMR studies of hexadeca- and octaneopentoxyphthalocyanines **141**

G.W. Buchanan, M. Azad, and G.P.A. Yap The first observed complex of 11-crown-3 ether. X-ray crystal structure and NMR study of (benzo-11-crown-3)$_2$·LiNCS **148**

Alison M. Ingham, Chao Xu, T.W. Whitcombe, Chengtian Xu, J.N. Bridson, and Alexander McAuley Substitution reactions at the Ni(III) cation in macro-bicyclic complexes — Reaction of metal ion complexes prepared from ligands L^1 (17-oxa-1,4,8,11-tetraaza-bicyclo[6.5.6]nonadecane) and L^2 (17-oxa-1,4,8,11-tetraazabicyclo[10.5.2]nonadecane) with chloride ion **155**

Yaël Israëli, Christine Bonal, Christian Detellier, Jean-Pierre Morel, and Nicole Morel-Desrosiers Complexation of the La(III) cation by *p*-sulfonato-calix[4]arene — A ^{139}La NMR study **163**

Ernesto Brunet, Pablo García-Losada, Juan-Carlos Rodríguez-Ubis, and Olga Juanes Synthesis of new fluorophores derived from monoazacrown ethers and coumarin nucleus **169**

Abdul Wahab and Sekh Mahiuddin Isentropic compressibility and viscosity of aqueous and methanolic lithium chloride solutions **175**

Terry B. Koerner and R.S. Brown The hydrolysis of an activated ester by a tris(4,5-di-*n*-propyl-2-imidazolyl)phosphine–Zn^{2+} complex in neutral micellar medium as a model for carbonic anhydrase **183**

Elzbieta Lewandowska, Stefan Kinastowski, and Stanislaw F. Wnuk Studies on the rearrangement of *ortho*-nitro-benzylidenemalonates and their analogues to 2-aminobenzoate derivatives **192**

Naomi L. Stock and Nigel J. Bunce Electrocatalytic dechlorination of atrazine **200**

Takehiko Yamato, Koji Tsuchihashi, Noriko Nakamura, Mai Hirahara, and Hirohisa Tsuzuki Medium-sized cyclophanes, part 59:[1] Nitration of [3.3]- and [3.3.3]metacyclophanes — Through-space electronic interactions between two or three benzene rings **207**

Author Index / Index des auteurs **AI-1**

March / mars

ARTICLES

Ronald Kluger 2001 Lemieux Award Lecture: Organic chemistry and hemoglobin: Benefits from controlled alteration **217**

Saul Wolfe, Zheng Shi, C.E. Brion, James Rolke, Yenyou Zheng, Glyn Cooper, Delano P. Chong, and C.Y. Hu Electron momentum spectroscopy of the frontier electrons of DABCO does not support an sp^3 hybrid lone-pair description **222**

Xiaosong Lu and John Warkentin *Ortho* substituent effects on transfer of aryl groups from oxygen to carbon in adducts from diaryloxycarbenes and DMAD **228**

Fausto Cargnoni and Marco Scavini Direct-space analysis of the electronic structure of the $YBa_2Cu_3O_6$ and $YBa_2Cu_3O_7$ crystals **235**

Masood Parvez, Ted S. Sorensen, and Fang Sun Conformational analysis of the bicyclo[4.4.1]undecan-11-one ring system **245**

Vittorio A. Sauro and Mark S. Workentin The redox properties of ferrocenyl-substituted aryl azines **250**

Xuchuan Jiang, Yi Xie, Jun Lu, Liying Zhu, Wei He, and Xianming Liu Low temperature interface-mineralizing route to hollow CuS, CdS, and NiS spheres **263**

Robert A. McClelland, Cristina Sanchez, Effiette Sauer, and Sinisa Vukovic Reaction of the tamoxifen cation and the bis-(4-methoxyphenyl)methyl cation in aqueous solutions containing 2′-deoxyguanosine **269**

Faming Jiang, Hilary A. Jenkins, David F. Green, Glenn P.A. Yap, and Roland K. Pomeroy A novel metal-chain extension reaction: synthesis of $(X)[Os(CO)_3(CN\text{-}t\text{-}Bu)]_nMn(CO)_5$ (X = Cl, Br, I; n = 1, 2, 3) **281**

Jose Carlos Cobos, Isaias Garcia de la Fuente, and Juan Antonio Gonzalez Molar excess enthalpies for some systems containing the OH and (or) O groups in the same or in different molecules **292**

© 2002 NRC Canada

Paul G. Loncke, Timothy A. Gadosy, and Gilles H. Peslherbe A theoretical study of the mechanism of 1,2-migrations in methoxysiloxycarbene **302**

Graziella Turdean, Ionel Catalin Popescu et Liviu Oniciu Biocapteurs ampérométriques à cholinestérases pour la détermination des pesticides organophosphorés **315**

Author Index / Index des auteurs **AI-1**

April / avril

ARTICLES

Abdelali Filali-Mouhim, Mustapha Benrahmoune, and Jean-Paul Jay-Gerin Effect of protein binding on charge transfer in DNA: A simple model based on the superexchange mechanism **333**

Patrick Dubé, Louis Brossard et Hugues Ménard Hydrogénation électrocatalytique sur des catalyseurs composites de nickel et hydroxyde d'aluminium en cellule dynamique **345**

Serge Alex Utilisation de vecteurs tournants pour l'optimisation de la formulation de mélanges de solvants **350**

Sandra F. Mayer, Harald Mang, Andreas Steinreiber, Robert Saf, and Kurt Faber Asymmetric total synthesis of (+)-*exo*-brevicomin based on enantioconvergent biocatalytic hydrolysis of an alkene-functionalized 2,3-disubstituted epoxide **362**

José M. Pardo, Diego González-Salgado, Clara A. Tovar, Claudio A. Cerdeiriña, Enrique Carballo, and Luís Romaní Comparative study of the thermodynamic behaviour of the binary mixtures dimethyl carbonate + (benzene, *n*-heptane, cyclohexane, or toluene) **370**

Fernande D. Rochon and Christian Tessier Multinuclear magnetic resonance studies of the aqueous products of the complexes *cis*- and *trans*-$Pt(Ypy)_2(NO_3)_2$ where Ypy = pyridine derivative **379**

Giuseppe Graziano Size and temperature dependence of hydrocarbon solubility in concentrated aqueous solutions of urea and guanidine hydrochloride **388**

Giuseppe Graziano Size dependence of the solubility of nonpolar compounds in different solvents **401**

Masood Parvez, S.M. Humayan Kabir, Ted S. Sorensen, Fang Sun, and Brian Watson Assigning structures to diastereomeric aliphatic α,α'-dibromo ketones **413**

David N. Glew Aqueous nonelectrolyte solutions. Part XVIII. Equilibrium pressures of two methane hydrates with water. Formulae and dissociation thermo-dynamic functions for the structures I and II methane hydrates **418**

Zhi Gao and Byron Kratochvil Sampling variance as a function of single-increment size for estimation of bitumen in an oil-sand core **440**

Author Index / Index des auteurs **AI-1**

May / mai

ARTICLES

Cory C. Pye, Keith Vaughan, and Julie F. Glister An ab initio study of conformations and sigmatropic shifts in triazene and its mono-, di-, and trimethyl derivatives **447**

A. Ionescu, N. Piétri, M. Hillebrand, M. Monnier, and J.P. Aycard Experimental and theoretical study of the photochemical and thermal decomposition of maleic and dichloromaleic anhydrides **455**

M.E.F. de Ruiz Holgado, J. Fernandez, M.I. Paz Andrade, and E.L. Arancibia Excess molar enthalpies of mixtures of methyl derivatives of polyethylene glycol with 1-alkanol at 298.15 K and 101.3 kPa **462**

Amalendu Pal and Rakesh Kumar Bhardwaj Excess molar volumes and viscosities of binary mixtures of some polyethers with propylamine at 298.15 K **467**

Urszula Domanska and Juan Antonio Gonzalez Thermodynamics of mixtures containing a very strongly polar compound. Part II. Solid–liquid equilibria for sulfolane + nitrile systems and characterization of the sulfolane–nitrile and sulfolane–1-alkyne interactions in terms of DISQUAC **476**

Luc Ruest, Marco Dodier, Hélène De Sève, Christian Lessard, and Pascal Mongrain Ryanoids and related compounds — Isolation and characterization of 11 new minor ryanoids from the plant *Ryania Speciosa* Vahl **483**

© 2002 NRC Canada

Ronghua Shu, John F. Harrod, and Anne-Marie Lebuis Catalytic reduction of benzoate esters and lactones in the presence of $PhMeSiH_2$ and a titanocene-based catalyst **489**

Greg J.E. Davidson, Andrew J. Baer, Adrien P. Côté, Nicholas J. Taylor, Garry S. Hanan, Yasutaka Tanaka, and Masashi Watanabe Solution and solid-state characterization of a dicopper receptor for large substrates **496**

Ibtehal A. Al-Juwaiser, Nouria A. Al-Awadi, and Osman M.E. El-Dusouqui Gas-phase pyrolysis of thiopheneacetic acids, thienylethanols, and related compounds — protophilicity of ring π-electrons and relative acidities of hydrogen-bond donors of hydroxyl groups **499**

Mula Kameswara Rao, Pinaki S. Bhadury, Mamta Sharma, Rajinder S. Dangi, Appanabhotla S.B. Bhaskar, Syed K. Raza, and Devendra K. Jaiswal A facile methodology for the synthesis and detection of N7-guanine adduct of sulfur mustard as a biomarker **504**

Takehiko Yamato, Koji Tsuchihashi, Noriko Nakamura, Mai Hirahara, and Kan Tanaka Medium-size cyclophanes. Part 60: Synthesis and conformational studies of 9-substituted [3.3]metacyclophane-2,11-diones and conversion to the corresponding [3.3]metacyclophanes **510**

Mohammad Rahimizadeh, Karen Kam, Stephen I. Jenkins, Robert S. McDonald, and Paul H.M. Harrison Kinetics of glycoluril template-directed Claisen condensations and mechanistic implications **517**

Author Index / Index des auteurs **AI-1**

June / juin

This issue is dedicated to Professor J. Bryan Jones
Ce tirage est dédié au Professeur J. Bryan Jones

Dedication / Dédicace **iii**

Biography / Biographie **v**

ARTICLES

Eva M.K. Hedin, Shamkant A. Patkar, Jesper Vind, Allan Svendsen, Karl Hult, and Per Berglund Selective reduction and chemical modification of oxidized lipase cysteine mutants **529**

Yeuk Chuen Liu, Hong Li, Albin Otter, Vivekanand P. Kamath, Markus B. Streiff, and Monica M. Palcic Chemo-enzymatic synthesis of trimeric sialyl Lewis^x pentadecasaccharide **540**

Bernhard Hauer, Jamie F. Bickley, Julien Massue, Paula C. A. Pena, Stanley M. Roberts, and John Skidmore Biomimetic reactions in organic synthesis: Semi-pinacol rearrangements of some spirocyclic epoxyalcohols derived from Juliá–Colonna asymmetric epoxidations **546**

Francesco Secundo, Giacomo Carrea, and Francesco Maria Veronese Discriminating between dispersion and lyoprotection effects in biocatalysis in organic media **551**

Benjamin G. Davis, Steven D. Wood, and Michael A.T. Maughan Towards an unprotected self-activating glycosyl donor system: Bromobutyl glycosides **555**

Gianluca Ottolina and Giacomo Carrea Rationalization of enzyme enantioselectivity by active-site cubic-space models **559**

Szilvia Gedey, Arto Liljeblad, László Lázár, Ferenc Fülöp, and Liisa T. Kanerva Structural effects on chemo- and enantio-selectivity of *Candida antarctica* lipase B — Resolution of β-amino esters **565**

Michael Scheck and Herbert Waldmann Chemo-enzymatic synthesis of the C_{15}–C_{23} unit of Leptomycin B **571**

Elisabeth Egholm Jacobsen and Thorleif Anthonsen Water content influences the selectivity of CALB-catalyzed kinetic resolution of phenoxymethyl-substituted secondary alcohols **577**

Kyung-Seon Lee and John P.N. Rosazza Biocatalytic oxidation of 4-vinylphenol by *Nocardia* **582**

Derek R. Boyd, Narain D. Sharma, Ludmila V. Modyanova, Jonathan G. Carroll, John F. Malone, Christopher C.R. Allen, John T.G. Hamilton, David T. Gibson, Rebecca E. Parales, and Howard Dalton Dioxygenase-catalyzed *cis*-dihydroxylation of pyridine-ring systems **589**

Hao Chen and Paul H.M. Harrison Biomimetic decarboxylative condensation between malonate and acetate units attached to a glycoluril template **601**

© 2002 NRC Canada

Amy E. Sigmund, Kenneth C. McNulty, Dzuy Nguyen, Charlotte E. Silverman, Philip Ma, Jaan A. Pesti, and Robert DiCosimo Enantioselective enzymatic aminolysis of a racemic 2-isoxazolylacetate alkyl ester **608**

Shaozhao Wang, Gang Chen, Margaret M. Kayser, Hiroaki Iwaki, Peter C.K. Lau, and Yoshie Hasegawa Baeyer-Villiger oxidations catalyzed by engineered microorganisms: Enantioselective synthesis of δ-valerolactones with functionalized chains **613**

Martin Bakker, Fred van Rantwijk, and Roger A. Sheldon Metal substitution in thermolysin: Catalytic properties of tungstate thermolysin in sulfoxidation with H_2O_2 **622**

Wolfgang Schrader, Andreas Eipper, D. Jonathan Pugh, and Manfred T. Reetz Second-generation MS-based high-throughput screening system for enantioselective catalysts and biocatalysts **626**

Herbert L. Holland, Frances M. Brown, Damian Lozada, Benjamin Mayne, W. Rick Szerminski, and Aaron J. van Vliet Chloroperoxidase-catalyzed oxidation of methionine derivatives **633**

Herbert L. Holland, Nancy Ihasz, and Brendan J. Lounsbery Formation of single diastereomers of β-hydroxy-sulfoxides by biotransformation of β-ketosulfides using *Helminthosporium* species NRRL 4671 **640**

Junjie Liu, Grace DeSantis, and Chi-Huey Wong Structure-based rationalization of aldolase-catalyzed asymmetric synthesis **643**

Daniel R. Sidler, Nancy Barta, Wenjie Li, Essa Hu, Louis Matty, Nori Ikemoto, Jeffrey S. Campbell, Michel Chartrain, Kozo Gbewonyo, Russell Boyd, Edward G. Corley, Richard G. Ball, Robert D. Larsen, and Paul J. Reider Efficient synthesis of the optically active dihydropyrimidinone of a potent α_{1A}-selective adrenoceptor antagonist **646**

Amélie Ducret, Jean-François Carrière, Michael Trani, and Robert Lortie Enzymatic synthesis of octyl glucoside catalyzed by almond β-glucosidase in organic media **653**

Andrea Piatesi and Donald Hilvert Optimized production of the Diels–Alderase antibody 1E9 as a chimeric Fab **657**

Denis Wahler and Jean-Louis Reymond Methylamine adenine dinucleotide (MAD): A co-factor to turn alcohol dehydrogenases into aldolases **665**

Franz Effenberger, Jürgen Roos, Christoph Kobler, and Holger Bühler Hydroxynitrile lyase-catalyzed addition of HCN to 4-substituted cyclohexanones: stereoselective preparation of tetronic acids **671**

Robert S. Phillips Tailoring the substrate specificity of secondary alcohol dehydrogenase **680**

Nicole Diedrichs, Ralf Krelaus, Ina Gedrath, and Bernhard Westermann Kinetic resolution of oxime esters with lipases — synthesis of enantiomerically enriched building blocks with quaternary carbon centers and formal total synthesis of perhydro histrionicotoxin **686**

Paola Pedroni, Thomas Friedrich, Michael Breuer, Dani McBeth, and Bernhard Hauer Novel esterase activity of dihydrolipoamide acetyltransferase AcoC of *Pseudomonas putida* identified by mutation of the *acoR* regulator **692**

Ghermes G. Chilov and Vytas K. Švedas Enzymatic hydrolysis of β-lactam antibiotics at low pH in a two-phase "aqueous solution – water-immiscible organic solvent" system **699**

Vu P. Bui, Minh Nguyen, Jeff Hansen, John Baker, and Tomas Hudlicky Enzymatic oxidation of cyclopropylbenzene: structures of new metabolites and possible mechanistic implications **708**

Elisabetta Brenna, Claudio Fuganti, Sabrina Ronzani, and Stefano Serra Bio-catalyzed preparation of the optically enriched stereoisomers of 4-methyl-2-phenyl-tetrahydro-2*H*-pyran (Doremox®) **714**

Ludmila Martínková, Norbert Klempier, Margit Preiml, Mária Ovesná, Marek Kuzma, Veronika Mylerová, and Vladimír Křen Selective biotransformation of substituted alicyclic nitriles by *Rhodococcus equi* A4 **724**

Lan Wang, Sanath K. Meegalla, Cheng-Lin Fang, Nicholas Taylor, and Russell Rodrigo Exploratory synthetic investigations related to 12a-deoxypillaromycinone **728**

Wolf-Dieter Fessner and Juan Manuel Juárez Ruiz Regiospecific synthesis of lactose analog Gal-(β 1,4)-Xyl by transgalactosylation **739**

Francisco J. Plou, M. Teresa Martín, Aránzazu Gomez de Segura, Miguel Alcalde, and Antonio Ballesteros Glucosyltransferases acting on starch or sucrose for the synthesis of oligosaccharides **743**

Author Index / Index des auteurs **AI-1**

© 2002 NRC Canada

July / juillet

ARTICLES

Jianji Wang, Yang Zhao, Kelei Zhuo, and Ruisen Lin A partial-molar volume study of electrolytes in propylene carbonate-based lithium battery electrolyte solutions at 298.15 K **753**

Doug Svenson, John F. Kadla, Hou-min Chang, and Hasan Jameel Effect of pH on the mechanism of $OClO^{\bullet}$ oxidation of aromatic compounds **761**

Jintana Meesungnoen, Jean-Paul Jay-Gerin, Abdelali Filali-Mouhim, and Samlee Mankhetkorn On the temperature dependence of the primary yield and the product $G\varepsilon_{max}$ of hydrated electrons in the low-LET radiolysis of liquid water **767**

Raquel M. Cravero, Guillermo R. Labadie, and Manuel González Sierra The determination of the stereochemistry of epoxides located at the 5,6-positions of decalinic systems: An empirical method based on ^{13}C NMR chemical shifts **774**

Giancarlo Verardo, Paola Geatti, Elena Pol, and Angelo G. Giumanini Sodium borohydride: A versatile reagent in the reductive *N*-monoalkylation of α-amino acids and α-amino methyl esters **779**

Pius K. Kipkemboi and Allan J. Easteal Vibrational spectroscopic studies of aqueous solutions of *tert*-butyl alcohol and *tert*-butylamine **789**

Margaret M. Kayser, Yan Yang, Marko D. Mihovilovic, Anton Feicht, and Fernande D. Rochon Baker's yeast-catalyzed synthesis of optically pure 4-*tert*-butyl-3-hydroxy β-lactam *cis*-(3*R*,4*S*) and *trans*-(3*R*,4*R*) diastereomers **796**

Hiram I. Beltrán, S. Jesús Alas, Rosa Santillan, and Norberto Farfán Fixed stereochemical control in the synthesis of new mono- and disubstituted 2-phenyl-6-aza-1,3-dioxa-2-borabenzocyclononenes **801**

J. Geller, J.H. Wosnick, I.S. Butler, D.F.R. Gilson, F.G. Morin, and F. Bélanger-Gariépy X-ray diffraction, Raman spectroscopic, and solid-state NMR studies of the group 14 metal–(tetracarbonyl)cobalt complexes $Ph_3MCo(CO)_4$ (M = Si, Sn, Pb) **813**

Tristram Chivers, Chantall Fedorchuk, Gabriele Schatte, and Justin K. Brask Syntheses and X-ray structures of boraamidinate complexes of lithium, phosphorus, and tellurium **821**

M.A. Zamora, H.A. Baldoni, A.M. Rodriguez, R.D. Enriz, C.P. Sosa, A. Perczel, A. Kucsman, O. Farkas, E. Deretey, J.C. Vank, and I.G. Csizmadia Peptide model XXVIII: An exploratory ab initio and density functional study on the side-chain–backbone interaction in *N*-acetyl-L-cysteine-*N*-methylamide and *N*-formyl-L-cysteinamide in their γ_L-backbone conformations **832**

Ken S. Lau, Athena Mantas, Gregory A. Chass, Fernando H. Ferretti, Mario Estrada, Graziela Zamarbide, and Imre G. Csizmadia Ab initio and DFT conformational analysis of selected flavones: 5,7-dihydroxyflavone (chrysin) and 7,8-dihydroxyflavone **845**

Author Index / Index des auteurs **AI-1**

August / août

This issue is dedicated to Professor Raymond U. Lemieux
Ce tirage est dédié au Professeur Raymond U. Lemieux

Dedication / Dédicace **x**

Biography / Biographie **xii**

ARTICLES

Wayne M. Best, James M. Macdonald, Brian W. Skelton, Robert V. Stick, D. Matthew G. Tilbrook, and Allan H. White The synthesis of a carbohydrate-like dihydrooxazine and tetrahydrooxazine as putative inhibitors of glycoside hydrolases: A direct synthesis of isofagomine **857**

David L. Jakeman and Stephen G. Withers On expanding the repertoire of glycosynthases: Mutant β-galactosidases forming β-(1,6)-linkages **866**

George Mulvey, David J. Rafter, and Glen D. Armstrong Potential for using antibiotics combined with a Shiga toxin-absorbing agent for treating 0157:H7 *Escherichia coli* infections **871**

© 2002 NRC Canada

Yves A. Chantigny, Yves L. Dory, András Toró, and Pierre Deslongchamps Use of the transannular Diels–Alder (TADA) reaction to probe biological receptors: Rational design and synthesis of tricyclic TADA adducts capable of rigidly holding pharmacophore parts **875**

Stephen Hanessian, Eric Jnoff, and Andrew M. Griffin Penicillamine as a ligand in the catalytic asymmetric reduction of ketones **885**

Martina Lahmann and Stefan Oscarson Investigation of the reactivity difference between thioglycoside donors with variant aglycon parts **889**

Guangwu Chen, Richard W. Franck, Guangli Yang, and Michael Blumenstein Anomeric effects of sulfones **894**

Hong-Ni Fan, Mei-Zheng Liu, and Yuan C. Lee Large-scale preparation of α-D-(1→4)-oligogalacturonic acids from pectic acid **900**

Dušan Uhrín, A.V. Krishna Prasad, Jean-Robert Brisson, and David R. Bundle Carbohydrate–antibody interactions by NMR for a ^{13}C-labelled disaccharide ligand **904**

Zhonghong Gan and René Roy Sialoside clusters as potential ligands for siglecs (sialoadhesins) **908**

Rafael Ojeda, Jesús Angulo, Pedro M. Nieto, and Manuel Martín-Lomas The activation of fibroblast growth factors by heparin: Synthesis and structural study of rationally modified heparin-like oligosaccharides **917**

Ahmad Ghavami, Blair D. Johnston, Matthew D. Maddess, Sarah M. Chinapoo, Morten T. Jensen, Birte Svensson, and B. Mario Pinto Synthesis of 1,4-anhydro-D-xylitol heteroanalogues of the naturally occurring glycosidase inhibitor salacinol and their evaluation as glycosidase inhibitors **937**

Prakriti Basak and Todd L. Lowary Synthesis of conjugates of L-fucose and *ortho*-carborane as potential agents for boron neutron capture therapy **943**

Jean-Robert Brisson, Ellen Crawford, Dušan Uhrín, Nam Huan Khieu, Malcolm B. Perry, Wayne B. Severn, and James C. Richards The core oligosaccharide component from *Mannheimia (Pasteurella) haemolytica* serotype A1 lipopolysaccharide contains L-*glycero*-D-*manno*- and D-*glycero*-D-*manno*-heptoses: Analysis of the structure and conformation by high-resolution NMR spectroscopy. **949**

Richard H. Furneaux, Zbigniew Pakulski, and Peter C. Tyler New mannotriosides and trimannosides as potential ligands for mannose-specific binding proteins **964**

Asish K. Bhattacharya, Florian Stolz, Jürgen Kurzeck, Wolfgang Rüger, and Richard R. Schmidt Synthesis and in vitro evaluation of substituted aryl- and hetarylmethyl phosphonate and phosphate — UMP derivatives as potential glucosyltransferase inhibitors **973**

Stacey A. Kalovidouris, W. Bruce Turnbull, and J. Fraser Stoddart Glycodendrimers based on cellobiosyl-derived monomers **983**

Dylan B. England, Tom K. Woo, and Michael A. Kerr The reactions of 3-alkylindoles with cyclopropanes: An unusual rearrangement leading to 2,3-disubstitution **992**

Joseph J. Lundquist, Brendan M. Kiburz, Jeffrey K. Wu, Kenneth D. Gibbs, Jr., and Eric J. Toone Towards high affinity carbohydrate-binding proteins: Directed evolution of murine galectin-3 **999**

Gerald F. Audette, Douglas J.H. Olson, Andrew R.S. Ross, J. Wilson Quail, and Louis T.J. Delbaere Examination of the structural basis for O(H) blood group specificity by *Ulex europaeus* Lectin I **1010**

Lill Kindahl, Corine Sandström, A. Grey Craig, Thomas Norberg, and Lennart Kenne ^{1}H NMR studies on the solution conformation of contulakin-G and analogues **1022**

Brad Bendiak, Tammy T. Fang, and David N.M. Jones An effective strategy for structural elucidation of oligosaccharides through NMR spectroscopy combined with peracetylation using doubly ^{13}C-labeled acetyl groups **1032**

Zhiyuan Zhang, Kenichi Niikura, Xue-Fei Huang, and Chi-Huey Wong A strategy for the one-pot synthesis of sialylated oligosaccharides **1051**

Robert A. Pon, Nam Huan Khieu, Qing-Ling Yang, Jean-Robert Brisson, and Harold J. Jennings Serological and conformational properties of *E. coli* K92 capsular polysaccharide and its *N*-propionylated derivative both illustrate that induced antibody does not recognize extended epitopes of polysialic acid: Implications for a comprehensive conjugate vaccine against groups B and C *N. meningitidis* **1055**

Brian L. Mark and Michael N.G. James Anchimeric assistance in hexosaminidases **1064**

Bert Fraser-Reid, J. Cristobal Lopez, K.V. Radhakrishnan, Mateusz Mach, Urs Schlueter, Ana Gomez, and Clara Uriel Reciprocal donor acceptor selectivity (RDAS): A new concept for "matching" donors with acceptors **1075**

© 2002 NRC Canada

France-Isabelle Auzanneau, Elizabeth Sourial, Jonathan M. Schmidt, and Miklos Feher Stochastic conformational search on the Lewis X (Le^x) trisaccharide and three Le^x analogues **1088**

Nisar Ahmad, Hans-J. Gabius, Herbert Kaltner, Sabine André, Ichiro Kuwabara, Fu-Tong Liu, Stefan Oscarson, Thomas Norberg, and C. Fred Brewer Thermodynamic binding studies of cell surface carbohydrate epitopes to galectins-1, -3, and -7: Evidence for differential binding specificities **1096**

Martina Lahmann, Per J. Garegg, Peter Konradsson, and Stefan Oscarson Synthesis of a polyphosphorylated GPI-anchor core structure **1105**

T.L. Lowary, E. Eichler, and D.R. Bundle Oligosaccharide recognition by antibodies: Synthesis and evaluation of talose oligosaccharide analogues **1112**

Henry N. Yu, Chang-Chun Ling, and David R. Bundle Synthesis of three *Salmonella* epitopes for biosensor studies of carbohydrate–antibody interactions **1131**

Ping Zhang, Judith Appleton, Chang-Chun Ling, and David R. Bundle Synthesis of disaccharide congeners of the *Trichinella spiralis* glycan and binding site mapping of two monoclonal antibodies **1141**

B. Henrissat, G.K. Hamer, M.G. Taylor, and R.H. Marchessault Characterization of some mesogenic alkyl 1-thioglycosides **1162**

Tattanahalli L. Nagabhushan, Paul Reichert, Mark R. Walter, and Nicholas J. Murgolo Type I interferon structures: Possible scaffolds for the interferon-alpha receptor complex **1166**

Shiro Komba and Yukishige Ito Novel substrates for efficient enzymatic transglycosylation by *Bacillus circulans* **1174**

Author Index / Index des auteurs **AI-1**

September / septembre

ARTICLES

Nadine Merkley and John Warkentin Thermolysis of a spiro-fused oxadiazoline: The carbonyl ylide–cyclic carbene–diradical sequence **1187**

Mehdi Amirnasr, Rasoul Vafazadeh, and Amir H. Mahmoudkhani Synthesis, structure, and electrochemistry of cobalt(III) complexes with bis(benzoylacetone)ethylenediimine Schiff base **1196**

Sudeshna Biswas, Kallol Mukherjee, Dulal Chandra Mukherjee, and Satya Priya Moulik Thermal oscillations in the bromate – oxalic acid – $MnSO_4$ – H_2SO_4 – acetone system: A calorimetric study **1204**

Brian D. Wagner, Adam C. Sherren, and Matthew A. Rankin Cyclodextrin-, UV-, and high pH-induced fluorescence enhancement of the pesticide azinphos-methyl: Applications to its trace analysis **1210**

Arienne S. King, Liliya G. Nikolcheva, Christopher R. Graves, Anna Kaminski, Christopher M. Vogels, Robert H.E. Hudson, Robert J. Ireland, Stephen J. Duffy, and Stephen A. Westcott Synthesis and reactivity of palladium and platinum diimine complexes containing boronate esters **1217**

Brigitte Ruffin, Stéphane Grelier, Aziz Nourmamode, and Alain Castellan Attempt to approach the role of phenolic phenylpropenol structures in the photoyellowing of softwood mechanical pulps **1223**

Marcela Beatriz Moressi, María Alicia Zón, and Héctor Fernández Electrochemical oxidation of 6-propionyl-2-(*N*,*N*-dimethylamino)naphthalene (prodan) in acetonitrile on Pt electrodes: Reversible dimerization of prodan radical cations **1232**

A. Szemik-Hojniak, T. Głowiak, I. Deperasińska, and A. Puszko Crystal structure and spectral considerations of 5-methyl-2-nitraminopyridine *N*-oxide **1242**

Jonghyuk Lee, Brendan Twamley, and George B. Richter-Addo Synthesis and solid-state molecular structures of bis- and mono-nitrosobenzene complexes of ruthenium porphyrins **1252**

M. Stanczyk-Dunaj, W. Galezowski, and A. Jarczewski Potentiometric study of equilibrium acidities of some carbon acids in acetonitrile **1259**

Jobst Kühn-Velten, Matthias Bodenbinder, Raimund Bröchler, Gerhard Hägele, and Friedhelm Aubke A ^{19}F nuclear magnetic resonance study of the conjugate Brønsted–Lewis superacid HSO_3F–SbF_5. Part II. **1265**

Author Index / Index des auteurs **AI-1**

© 2002 NRC Canada

October / octobre

ARTICLES

Saeed Ahmad, Anvarhusein A. Isab, and Herman P. Perzanowski Ligand scrambling reactions of cyano(thione)gold(I) complexes and determination of their equilibrium constants **1279**

Roland A.L. Gendron, David J. Berg, and Tosha Barclay Alkoxide-functionalized cyclopentadienyl complexes of yttrium containing a two-carbon tether **1285**

Abdullah El-Alali and Ahmed S. Al-Kamali Reactions of 1,3-dipolar aldazines and ketazines with the dipolarophile dimethyl acetylenedicarboxylate **1293**

Alfonso de Dios, Maria Luz de la Puente, Alfonso Rivera-Sagredo, and Juan Felix Espinosa Structural and conformational studies of 5-(1*H*-pyrrol-2-ylmethylene)-substituted imidazolidine-2,4-diones and thiazolidine-2,4-diones **1302**

Marcus Schulte and François P. Gabbaï Synthesis of heteronuclear bifunctional Lewis acids by transmetalation of 1,8-bis(trimethylstannyl)naphthalene with BCl_3 **1308**

I.S. Shehatta, M.S. Ibrahim, and M.R. Sultan The antimicrobial nalidixic acid as a probe for molecular recognition of α- and β-cyclodextrins **1313**

N. Hioka, R.K. Chowdhary, N. Chansarkar, D. Delmarre, E. Sternberg, and D. Dolphin Studies of a benzoporphyrin derivative with Pluronics **1321**

André Hätzelt and Sabine Laschat One-pot sequential Pauson–Khand reaction – transfer hydrogenation **1327**

Cory C. Pye and Christopher R. Corbeil An ab initio investigation of scandium chloro complexes **1331**

H. Slebocka-Tilk, F. Sauriol, Martine Monette, and R.S. Brown Aspects of the hydrolysis of formamide: revisitation of the water reaction and determination of the solvent deuterium kinetic isotope effect in base **1343**

Osvald Knop, Kathryn N. Rankin, T. Stanley Cameron, and Russell J. Boyd Crystal chemistry of tetraradial species. Part 10. Tilting at windmills: conformations of the tetraphenyl species $ZPh_4^{0,\pm1}$ (Z = B, C, N) **1351**

Yusa Muroya, Jintana Meesungnoen, Jean-Paul Jay-Gerin, Abdelali Filali-Mouhim, Thomas Goulet, Yosuke Katsumura, and Samlee Mankhetkorn Radiolysis of liquid water: An attempt to reconcile Monte-Carlo calculations with new experimental hydrated electron yield data at early times **1367**

Jérôme Graton, François Besseau, Michel Berthelot, Ewa D. Raczyńska et Christian Laurence L'échelle pK_{HB} de basicité de liaison hydrogène des amines tertiaires aliphatiques **1375**

ERRATUM **1386**

Author Index / Index des auteurs **AI-1**

November / novembre

This issue is dedicated to Professor Tristram Chivers
Ce tirage est dédié au Professeur Tristram Chivers

Dedication / Dédicace **x**

Biography / Biographie **xii**

ARTICLES

Kyle L. Fujdala, David W.K. Gracey, Erica F. Wong, and Kim M. Baines The addition of organometallic reagents to tetramesityldigermene **1387**

Maneesh Bahadur, Christopher W. Allen, William E. Geiger, and Adam Bridges Organophosphazenes. 25. The synthesis and electrochemistry of the dicobalt hexacarbonyl complexes of phenylethynylcyclophosphazenes **1393**

Hilary A. Jenkins, Carla L. Dumaresque, Dragoslav Vidovic, and Jason A.C. Clyburne The coordination chemistry of *o*,*o*′-*i*-$Pr_2C_6H_3$-bis(imino)acenaphthene to group 13 trihalides **1398**

Neil Burford, T. Stanley Cameron, Korey D. Conroy, Bobby Ellis, Charles L.B. Macdonald, Robyn Ovans, Andrew D. Phillips, Paul J. Ragogna, and Denise Walsh Sequential dehydrochloride coupling of trichlorophosphine with 2,6-di-isopropylaniline: aminophosphine precursors to phosphetidines **1404**

© 2002 NRC Canada

Mark R.J. Elsegood, Liam M. Gilby, Kathryn E. Holmes, and Paul F. Kelly Sulfimidation of thio-ether crown systems: the X-ray crystal structure of the $\{[9\text{-ane}]S_2S(NH_2)\}^+$, $\{[9\text{-ane}]SS(NH_2)S(NH_2)\}^{2+}$, and $\{[9\text{-ane}]S(NH_2)S_2(\mu\text{-}N)\}^{2+}$ cations **1410**

Vadapalli Chandrasekhar, Venkatasubbaiah Krishnan, Arunachalampillai Athimoolam, and Gurusamy Thangavelu Senthil Andavan New hybrid inorganic-organic polymers containing cyclophosphazenes as pendant groups: Cyclophosphazene ligands containing hydrazone linkages and their conversion to polymers **1415**

Alan Bashall, Felipe García, Gavin T. Lawson, Mary McPartlin, Alexander Rothenberger, Anthony D. Woods, and Dominic S. Wright Formation and decomposition of the Sb(III)/Li cage $[\{Sb(P\text{-}t\text{-}Bu)_3\}_2Li_6\cdot 6THF]$ **1421**

U. Swarnalatha, A. Sivaramakrishna, C.S. Venkatachalam, M.N. Sudheendra Rao, Tomonori Inoue, Tadaharu Ueda, and Masashi Hojo Studies on electrochemical and coordination behaviour of phosphiniminocyclotrithiazenes **1428**

J. Komulainen, R.S. Laitinen, and R.J. Suontamo A theoretical study of the ^{77}Se NMR and vibrational spectroscopic properties of Se_nS_{8-n} ring molecules **1435**

Wolfgang Fraenk, Thomas M. Klapötke, Burkhard Krumm, Heinrich Nöth, Max Suter, Martin Vogt, and Marcus Warchhold Pentafluorophenyl and phenyl substituted azidoborates **1444**

Michael C. Janzen, Michael C. Jennings, and Richard J. Puddephatt Self-assembly using stannylplatinum(IV) halide complexes as ligands for organotin halides **1451**

Kevin S. Jack, John C. Jeffery, Angela P. Leedham, Jason M. Lynam, Michael Niedzwiecki, and Christopher A. Russell Syntheses and structures of bis(imido)organophosphine dianions **1458**

Timothy S. Keizer, Lauren J. De Pue, Sean Parkin, and David A. Atwood Boron halide chelate compounds and their activity towards the demethylation of trimethylphosphate **1463**

Karena Thieme, Sara C. Bourke, Juan Zheng, Mark J. MacLachlan, Fojan Zamanian, Alan J. Lough, and Ian Manners Synthesis, characterization, and structures of zircona- and boracyclosiloxanes with ferrocenyl substituents **1469**

Stephen M. Aucott, Alexandra M.Z. Slawin, and J. Derek Woollins The synthesis of $[\{n\text{-}Bu_2Sn(S_2N_2)\}_2]$ and its use in the preparation of organometallic iridium sulfur nitrogen complexes **1481**

Myrlene Gee, Roderick E. Wasylishen, Paul J. Ragogna, Neil Burford, and Robert McDonald Characterization of indirect $^{31}P\text{-}^{31}P$ spin-spin coupling and phosphorus chemical shift tensors in pentaphenylphosphinophosphonium tetrachlorogallate, $[Ph_3P\text{-}PPh_2][GaCl_4]$ **1488**

Tosha M. Barclay, Robin G. Hicks, Andrew S. Ichimura, and Greg W. Patenaude Synthesis and characterization of a spirocyclic phosphaverdazyl radical – cyclophosphazene hybrid: Evidence for spin transfer from a verdazyl radical to a phosphazene ring **1501**

Andrew D. Bond, Delia A. Haynes, and Jeremy M. Rawson Structural studies of dithiatetrazocines: X-ray crystal structures of the symmetric dithiatetrazocines $p\text{-}XC_6H_4CN_4S_2CC_6H_4X$ [X = NO_2, Br] and the first unsymmetric dithiatetrazocine, $p\text{-}BrC_6H_4CN_4S_2CC_6H_4NO_2$ **1507**

Robert J. Wiacek, Jamie N. Jones, Charles L.B. Macdonald, and Alan H. Cowley Structural interrelationships between the bis(pentamethylcyclopentadienyl)arsenic(III) and antimony(III) cations and their precursor chlorides **1518**

Tianle Zhang, Warren E. Piers, and Masood Parvez Synthesis and characterization of the binuclear diamido titanium chalcogenides $[(Ar)NCH_2CH_2CH_2N(Ar)]_2Ti(\mu\text{-}E)_2$ (E = Se, Te) **1524**

Julio Zukerman-Schpector, Ionel Haiduc, Robinson L. Camillo, João V. Comasseto, Rodrigo Luiz Oliveira R. Cunha, and Alvim Jorge Supramolecular self-assembly through tellurium···halogen secondary bonds: A hexagonal grid of Te_2Cl_2 and Te_6Cl_6 rings in the solid state structure of 1,1,3-trichloro-2,4,5,6-tetrahydro-1*H*-$1\lambda^4$-benzo[b]tellurophene **1530**

Ludmila Scoles, Brian T. Sterenberg, Konstantin A. Udachin, and Arthur J. Carty The synthesis and reactivity of a mixed nitrosyl–phosphinidene cluster of ruthenium: Formation of nitride and nitrene clusters **1538**

Hari K. Gupta, Nada Reginato, Francis O. Ogini, Stacey Brydges, and Michael J. McGlinchey $SiCl_4$–ethanol as a trimerization agent for organometallics: convenient syntheses of the symmetrically substituted arenes 1,3,5-$C_6H_3R_3$ where R = $(C_5H_4)Mn(CO)_3$ and $(C_5H_4)Fe(C_5H_5)$ **1546**

Okwado M. Akotsi, Robert McDonald, and Steven H. Bergens Synthesis of a PennPhos–ruthenium(II) complex: The first crystal structure of a PennPhos–metal complex **1555**

© 2002 NRC Canada

Vineeth Iyengar, Patrycja V. Galka, Andreas Pletsch, and Heinz-Bernhard Kraatz Palladium and platinum complexes of L-PhePhos: Acetyl-*p*-(diphenylphosphino)-L-phenylalanine methyl ester — a chiral ligand for transition metal complexation **1562**

Guillermo Antorrena, Scott Brownridge, T. Stanley Cameron, Fernando Palacio, Simon Parsons, Jack Passmore, Laurence K. Thompson, and Fitri Zarlaida The neutral diradical 5,5′-bis(1,3,2,4-dithiadiazolyl) [SNSNC-CNSNS], the first main group radical to exhibit a dramatic increase in paramagnetism on mechanical grinding **1568**

Patrick J. Riley, Jennifer L. Reid, Adrien P. Côté, and George K.H. Shimizu Condensed versus open channel structures in cysteic acid coordination frameworks containing d^{10}-d^{10} dimers **1584**

Andrew I. Wallbank and John F. Corrigan Triply bridged dicopper-bis(trimethylsilylchalcogenolates): Synthesis and characterization of the series of helical complexes $[(Me_3SiE\text{-}Cu)_2(\mu\text{-}Ph_2PC{\equiv}CPPh_2\text{-}\kappa^2P)_3]$ (E = S, Se, Te) **1592**

Nathan D. Jones, Patric Meessen, Martin B. Smith, Udo Losehand, Steven J. Rettig, Brian O. Patrick, and Brian R. James Bisphosphine ligands containing two *o*-*N*,*N*-dimethylanilinyl substituents at each phosphorus atom **1600**

René T. Boeré and Jason D. Masuda 2,6-Diisopropylphenylphosphane: A new, bulky primary phosphane and its mono- and disilylated $Si(CH_3)_3$ and $Si(CH_3)_2$-*t*-Bu derivatives — A synthetic, crystallographic, and dynamic NMR investigation **1607**

Steve J. Brown, Xiaoliang Gao, Matthew G. Kowalchuk, Rupert E.v.H. Spence, Douglas W. Stephan, and John Swabey Synthesis and characterization of titanium complexes containing phosphinimido and tropidinyl ligands: Crystal structure of (trop)(*t*-Bu_3PN)$TiCl_2$ **1618**

Ignacio Vargas-Baca, Andrew P. Brown, Mark P. Andrews, Tigran Galstian, Yuejun Li, Hojatollah Vali, and Mark G. Kuzyk Linear and nonlinear optical responses of a dye anchored to gold nanoparticles dispersed in liquid and polymeric matrixes **1625**

Author Index / Index des auteurs **AI-1**

December / décembre

AWARD LECTURE / CONFÉRÉNCE D'HONNEUR

Bryan R. Henry and Henrik G. Kjaergaard Local modes **1635**

ARTICLES

Michael D. Pungente, Larry Weiler, and Hermann J. Ziltener Antibody-catalyzed formation of a 14-membered ring lactone **1643**

Ping Liu, Jia Cheng Liu, Jian Wang, Jian Kai Cheng, Wen Jie Li, and Xin Huang Magnetic properties of some Fe–S six-membered ring compounds **1646**

Hendrik Dorn, Emira Vejzovic, Alan J. Lough, and Ian Manners Synthesis and structural characterization of binuclear titanium(IV) and tantalum(V) cyclopentadienyl complexes containing bridging phosphinate ligands **1650**

Lin Guo and Ying-qiu Liang pH-controlled location and metalation of an amphiphilic porphyrin in sodium dodecyl sulfate micelle **1655**

Luc Ruest, Hugues Ménard, Vincent Moreau, and François Laplante Ryanoids and related compounds — Chemoselective electrocatalytic hydrogenation of alkyl **α**-pyrrole carboxylates: Selective hydrogenation of ryanodine **1662**

Qingqi Chen and David Dolphin Fast, efficient syntheses of linear poly(dipyrromethene)s **1668**

Viviana Roldán, Juan Carlos González, Mabel Santoro, Silvia García, Nieves Casado, Silvina Olivera, Juan Carlos Boggio, Juan Manuel Salas-Peregrin, Sandra Signorella, and Luis F. Sala Kinetics and mechanism of the oxidation of disaccharides by Cr^{VI} **1676**

A. Moghimi, M. Ranjbar, H. Aghabozorg, F. Jalali, M. Shamsipur, and Kaj K. Chadha Synthesis, characterization, and X-ray crystal structures of Co(II) and La(III) complexes of a pyridine containing self-assembling system and solution studies of the Co(II) complex **1687**

John A. Findlay and Guoqiang Li Novel terpenoids from the Sea Hare *Aplysia punctata* **1697**

Marie-Josée Binette and Christian Detellier Lamellar polysilicate nanocomposite materials: Intercalation of polyethylene glycols into protonated magadiite **1708**

© 2002 NRC Canada

ERRATA

Jean-Robert Brisson, Ellen Crawford, Dušan Uhrín, Nam Huan Khieu, Malcolm B. Perry, Wayne B. Severn, and James C. Richards Erratum: The core oligosaccharide component from *Mannheimia* (*Pasteurella*) *haemolytica* serotype A1 lipopolysaccharide contains L-*glycero*-D-*manno*- and D-*glycero*-D-*manno*-heptoses: Analysis of the structure and conformation by high-resolution NMR spectroscopy **1715**

Yusa Muroya, Jintana Meesungnoen, Jean-Paul Jay-Gerin, Abdelali Filali-Mouhim, Thomas Goulet, Yosuke Katsumura, and Samlee Mankhetkorn Erratum: Radiolysis of liquid water: An attempt to reconcile Monte-Carlo calculations with new experimental hydrated electron yield data at early times **1716**

Note of appreciation / Note de reconnaissance **iii**

Author Index / Index des auteurs **AI-1**

Contents for volume 80 / Sommaire pour volume 80 **C-1**

© 2002 NRC Canada

NOTE OF APPRECIATION / NOTE DE RECONNAISSANCE

The quality of the papers in this journal depends a great deal on the efforts of those who agree to act as critical readers of manuscripts. The editors gratefully acknowledge the following, who helped us between November 1, 2001 and October 31, 2002:

Abbatt, J.
Abramovitch, R.A.
Acree, W.E.
Adlercreutz, P.
Ahnen, D.J.
Almeida, R.M.
Appendino, G.
Argyropoulos, D.S.
Armstrong, D.A.
Armstrong, J.D.
Arnold, J.
Asano, Y.
Ashbaugh, H.S.
Aspinall, G.O.
Auclair, K.
Auger, M.
Auzanneau, F.-I.
Azerad, R.
Backvall, J.-E.
Bain, A.D.
Baines, K.M.
Baker, M.D.
Balch, A.L.
Baldridge, K.
Balfour, W.J.
Bandrauk, A.D.
Banks, J.
Baranski, A.S.
Bardwell, J.
Barra, M.
Barrero, A.F.
Barrett, A.G.M.
Barriault, L.
Bartels, D.M.
Barthel, J.
Bartlett, R.J.
Bayly, S.
Bazan, G.
Beauchamp, A.
Beaulieu, P.
Bell, T.W.
Bennet, A.J.
Benson, G.C.
Beratan, D.
Bercaw, J.
Bergens, S.H.
Berry, D.H.
Bertie, J.E.
Bertrand, G.
Birch, B.
Bird, P.H.
Birss, V.L.
Bizzotto, D.
Blandamer, M.J.
Blazejowski, J.
Bock, C.W.
Boeré, R.T.
Boger, D.
Bohme, D.K.
Bohne, C.
Bols, M.
Bomont, J.-M.
Boons, G.-J.
Borkovec, M.
Borve, K.J.
Bosnich, B.
Boyd, M.K.
Boyd, D.R.
Branchaud, B.
Brechbiel, M.W.
Brewer, C.F.
Brisard, G.M.
Brisson, J.-R.
Brock, C.P.
Brookhart, M.
Brown, R.S.
Bruce, M.
Bruice, T.C.
Brunton, J.L.
Bryce, D.
Buchanan, G.W.
Buchwald, S.L.
Buist, P.H.
Buncel, E.
Bundle, D.R.
Burford, N.
Burgess, J.
Butcher, R.
Calhoun, L.A.
Cameron, T.S.
Carlson, R.
Carr, R.W.
Carrano, C.
Carrea, G.
Casanova, C.
Cavell, R.
Cavic, B.
Charette, A.B.
Charlton, J.L.
Chartrain, M.
Chatt, A.
Chen, D.Z.
Chenevert, R.
Chin, S.
Chivers, T.
Chow, A.
Cimolai, N.
Claridge, T.D.W.
Clark, W.M.
Clearfield, A.
Clive, D.
Clyburne, J.A.C.
Collins, S.
Colonna, S.
Corey, J.Y.
Costas, S.
Costes, J.P.
Cowie, M.
Cowley, A.H.
Cox, S.
Cramb, D.T.
Crans, D.C.
Cremer, D.
Crich, D.
Crout, D.H.G.
Crozier, D.
Cruickshank, F.R.
Crutchley, R.J.
Csizmadia, I.G.
Cullen, W.R.
Cullen, J.M.
D'Amboise, M.
Dahn, J.
Damha, M.J.
Danishefsky, S.
Dannenberg, J.J.
Davies, G.
Dean, P.A.W.
Delbaere, L.T.J.
Deslongchamps, P.
Detellier, C.
Di Bella, S.
Dines, T.J.
Dolphin, D.
Donaldson, D.J.
Donard, O.F.X.
Dondoni, A.
Dougherty, R.C.
Doyle, M.P.
Driguez, H.
Du Preez, J.G.H.
Dubouch, M.-P.
Durocher, G.
Durr, H.
Dwek, X.
Edelmann, F.T.
Eisenberg, A.
Ellis, D.
Elson, C.
Ernst, B.
Escudie, J.
Etzler, M.E.
Eumura, S.
Evans, C.H.
Fabian, W.M.F.

La qualité des articles publié dans notre revue dépend beaucoup de ceux qui acceptent de faire une lecture critique des manuscripts. Les directeurs scientifique expriment leur reconnaissance aux personne suivantes qui nous ont aidé, du 1er novembre 2001 au 31 octobre 2002 :

© 2000 NRC Canada

Fallis, A.G.
Farrar, D.
Fedkiw, P.S.
Fehlner, T.P.
Fernandez-Lafuente, R.
Fernández, J.
Ferrier, R.
Fessner, W.-D.
Fetzner, S.
Field, R.A.
Fink, M.
Finke, R.
Finlay, J.
Fischer, R.D.
Fliszar , S.
Ford, P.C.
Franssen, M.C.R.
Fraser-Reid, B.
Fryzuk, M.D.
Fuchs, P.L.
Fujita, M.
Fukamiya, N.
Xfurstoss, N.
Fyfe, C.A.
Fyles, T.M.
Gabbai, F.P.
Galembeck, S.E.
Galley, W.C.
Gambarotta, S.
Gates, D.
Gauld, J.
Geiger, W.E.
Gerlt, J.A.
Getoff, N.
Giannelis, E.P.
Giasson, S.
Gibson, D.T.
Gielen, M.
Gilchrist, T.
Gladfelter, W.L.
Goff, H.
Gogan, N.J.
Goh, C.
Goldberg, K.
Goodgame, D.
Gossage, R.A.
Gotor, V.
Gould, E.S.
Gray, G.
Gray, H.B.
Gribble, G.W.
Griengl, H.
Griffith, W.P.
Grindley, T.B.
Grossert, J.S.
Guthrie, J.P.
Guy, R.D.
Haddon, B.
Hager, L.P.
Haines, R.I.
Haley, M.M.
Hall, M.B.
Halling, P.
Hanessian, S.
Hansen, E.
HR Hardy, H.R.
Harrington, D.A.
Harris, K.
Harrison, P.H.M.
Harrison, L.J.
Harrod, J.F.
Harvey, P.D.
Hauer, B.
Haushalter, R.C.
Hedwig, G.R.
Hicks, R.G.
Hill, R.
Hindsgaul, O.
Holland, H.L.
Holloway, C.E.
Holm, R.H.
Holmes, R.R.
Holst, O.
Hu, L.J.
Huang, Y.
Hudlicky, T.
Hult, K.
Hultin, P.
Hummel, A.
Ikushima, Y.
Imperiali, B.
Jackeman, D.L.
Jaeger, K.-E.
James, B.R.
Janda, K.D.
Jarrell, H.C.
Jenks, W.S.
Johnson, C.R.
Jolicoeur, C.
Jones, J.B.
Jones, C.
Jordan, R.B.
Jordan, R.
Jouille, M.
Joule, J.
Just, G.
Jutzi, P.
Kadish, K.M.
Kahne, D.
Kammerling, J.
Kanatzidis, M.
Kanerva, L.T.
Katritzky, A.R.
Katti, K.V.
Katz, M.
Kayser, M.M.
Kelly, T.R.
Kenne, L.
Kennedy, K.
Kiener, A.
Kihlberg, J.
King, J.F.
Kinghorn, A.D.
Kingston, D.G.I.
Kirby, A.J.
Kiss, T.
Klassen, N.V.
Kliegel, W.
Kluger, R.H.
Koch, S.A.
Koga, Y.
Kotovych, G.
Koudoumas, E .
Kovak, P.
Kraatz, H.-B.
Kragl, U.
Kren, V.
Kresge, A.J.
Krossing, I.
Krull, U.J.
Kulkarni, V.M.
Kumacheva, E.
Kutney, J.
Kwak, J.C.T.
Lacelle, S.
Lalonde, J.
Lash, T.
Lautens, M.
Lay, P.A.
Le Questel, J.-Y.
Le Van Mao, R.
Leach, G.
Lebel, H.
Lee, D.G.
Lee, Y.C.
Legzdins, P.
Leigh, W.J.
Lemieux, R.P.
Leszczynski, J.
Lever, A.B.P.
Lewars, E.
Ley, S.V.
Leznoff, C.C.
Leznoff, D.B.
Lindhorst, T.K.
Lippert, B.
Lipscomb, W.N.
Lipshutz, B.
Lipson, R.
Loeb, S.J.
Long, E.C.
Loppnow, G.R.
Lortie, R.
Lowary, T.L.
Lown, W.J.
Lubell, W.D.
Lucy, C.
Mabury, S.A.
MacEwan, K.
MacLachlan, M.J.
Macartney, D.H.
Macdonald, P.M.
Macdonald, C.L.B.
Macedo, E.
Mak, C.H.
Malkin, V.G.
Mamer, O.A.
Manderville, R.E.
Manners, I.
Mansfield, S.
Mar, A.
Marangoni, D.G.
Marat, K.
Marder, T.B.
Margerum, D.W.
Marongiu, B.
Marsan, B.
Martin, R.R.

© 2000 NRC Canada

Martin, N.
Marzilli, L.G.
Mather, A.
Matile, S.
Matta, K.
Maurer, G.
McAuley, A.
McDonald, R.S.
McGlinchey, M.J.
McHale, J.L.
McKinnon, D.
Menard, H.
Menzinger, M.
Mihichuk, L.M.
Miller, J.M.
Miller, R.J.D.
Miller, S.J.
Mitchell, R.H.
Mitchell, H.
Moody, C.
Moore, J.
Morgon, N.H.
Morris, R.H.
Moulik, S.P.
Muchall, H.
Munakata, M.
Nagabhushan, T.L.
Narbaitz, R.
Natansohn, A.
Nazar, L.F.
Nickon, A.
Nilsson, K.
Norman, N.C.
Noszticzius, Z.
Novak, B.
Nowogrocki, G.
Noyori, R.
O'Brien, P.
O'Neil, J.
Oakley, R.T.
Ohta, O.
Ohta, T.
Oldham, K.B.
Olsson, U.
Onuchic, J.N.
Onyszchuk, M.
Oscarson, S.
Otter, A.
Otvos, L.
Pacey, P.D.
Paine, R.T.
Pal, A.
Palcic, M.M.
Pando, C.
Passmore, J.
Pasternack, R.F.
Pavia, A.A.
Pawliszyn, J.B.
Payne, N.C.
Peiris, S.M.
Perrin, C.L.
Peslherbe, G.H.
Peters, T.
Peterson, E.
Petrov, A.S.
Piers, W.E.
Piers, E.
Pietro, W.J.
Pincock, J.A.
Pingarrón, J.M.
Pinnavaia, T.J.
Pinto, B.M.
Planalp, R.P.
Poirier, R.A.
Pomeroy, P.K.
Porter, N.A.
Power, W.P.
Pozsgay, V.
Prausnitz, J.M.
Prud'homme, R.E.
Pulley, S.R.
Pye, C.C.
Quail, J.W.
Ragauskas, A.J.
Rainwater, J.C.
Ramek, M.
Rao, M.N.S.
Rard, J.A.
Ratner, M.A.
Rauchfuss, T.B.
Rauk, A.
Rawson, J.
Reardon, J.F.
Reber, C.
Rees, W.S.
Rehspringer, J.-L.
Reimer, K.J.
Reinsborough, V.C.
Reynolds, W.F.
Rich, J.O.
Richards, J.C.
Richeson, D.S.
Riva, S.
Roberge, P.R.
Roberts, S.M.
Rochon, F.D.
Rodgers, K.
Rodrigo, R.
Roduner, E.
Roesky, H.
Rogers, R.D.
Romani, L.
Rosazza, J.P.N.
Roscoe, J.M.
Rosenberg, L.
Rothstein, S.M.
Rotzinger, F.P.
Roundhill, D.M.
Roy, R.
Rozzell, D.
Ruckenstein, E.
Sadler, P.J.
Sadus, R.J.
Sage, M.L.
Saito, I.
Salva, J.
Satha, H.
Saunders, W.H.
Savidge, R.
Sayari, A.
Scarrow, R.
Schafer, L.
Scheffer, J.R.
Schmidt, R.R.
Schmidt, M.
Schrobilgen, G.
Schurko, R.
Scott, A.I.
Sessler, J.
Sharon, N.
Shaw, C.F.
Shen, Y.-C.
Sheridan, R.
Sherman, J.C.
Sherman, P.M.
Sherr, D.
Sherry, A.D.
Shibuya , T.-I.
Shieh, W.-C.
Shimizu, G.H.K.
Siddiqui, A.
Siebbeles, L.D.A.
Siebert, W.
Sloan, J.J.
Sloan, E.D.
Smith, K.M.
Snyder, J.K.
Spatola, A.
St-Amant, A.
Stahl, L.
Stalke, D.
Steer, R.P.
Stephan, D.W.
Sterner, O.
Stewart, J.
Stobart, S.
Storr, A.
Stradiotto, M.
Stryker, J.
Stynes, D.V.
Sun, H.
Swaddle, T.W.
Swanson, P.
Swofford, R.L.
Szarek, W.A.
Tajmir-Riahi, H.A.
Takats, J.
Tanner, M.E.
Tavitian, B.
Taylor, S.D.
Tee, O.S.
Templeton, J.L.
Testa, B.
Thatcher, G.R.J.
Therien, M.J.
Thiem, J.
Thompson, R.C.
Thompson, L.K.
Thompson, M.
Thummel, R.
Tidwell, T.T.
Tietze, L.F.
Tilley, T.D.
Togni, A.
Toone, E.
Townsend , L.B.
Trebble, M.A.
Tremaine, P.R.

© 2000 NRC Canada

Trexler, D.T.
Trost, B.
Turner, N.J.
Tykwinski, R.
Uemura, D.
Urieta, J.S.
Urquhart, S.
Valderrama, J.O.
Valenta, Z.
Vallet-Regi, M.
van Koten, G.
vanLoon, G.W.
Vederas, J.C.
Velasco, D.
Villemure, G.
Vogtle, F.
Waghorne, W.E.
Wagner, B.D.
Waldmann, H.
Wan, P.
Wan, J.F.K.
Wang, S.
Wang, Z.-X.
Wang, Y.A.
Wania, F.
Warriner, S.
Wasylishen, R.E.
Wayland, B.B.
Weidenbruch, M.
Welsh, W.J.
Wentrup, C.
Werstiuk, N.H.
West, R.
West, F.G.
West, F.
Westaway, K.C.
Westcott, S.A.
White, M.A.
White, R.
Whitehead, M.A.
Wiberg, K.B.
Williams, B.
Willick, G.
Wilson, P.D.
Winnik, M.A.
Winpenny, R.
Wisian-Nielson, P.
Withers, S.G.
Wolf, M.
Wolfe, S.
Wong, C.-H.
Wong, R.M.W.
Wood, R.H.
Woods, R.J.
Woollins, J.D.
Workentin, M.S.
Worsfold, P.J.
Wright, J.S.
Wright, D.S.
Wuest, J.D.
Yaghi, O.M.
Ye, Z.-G.
Yuasa, H.
Zamir, L.O.
Zargarian, D.
Zhan, B.-Z.
Zhang, X.
Zheng, Z.
Zhu, J.X.X.
Ziegler, T.
Zimmerman, H.E.

© 2000 NRC Canada